

# COMPREHENSIVE CORROSION



ELSEVIER  
CORROSION  
ELSEVIER



## 1.01 Chemical Thermodynamics

**R. A. Cottis**

Corrosion and Protection Centre, School of Materials, University of Manchester, P.O. Box 88, Sackville Street, Manchester, M60 1QD, UK

**L. L. Shreir<sup>†</sup> and G. T. Burstein**

Department of Materials Science and Metallurgy, University of Cambridge, Pembroke Street, Cambridge CB2 3QZ, UK

This article is a revision of the Third Edition article 20.2 by L. L. Shreir and G. T. Burstein, volume 2, pp 20:57–20:75, © 2010 Elsevier B.V.

1.01.1	Scope	1
1.01.2	Some Definitions	2
1.01.2.1	First Law of Thermodynamics	2
1.01.2.2	Second Law of Thermodynamics	3
1.01.2.3	Entropy	4
1.01.2.4	Gibbs Free Energy or Free Enthalpy	5
1.01.2.5	The Chemical Potential	5
1.01.2.6	Activity	6
1.01.2.7	Gibbs–Duhem Equation	6
1.01.3	Spontaneity of a Reaction	7
1.01.3.1	Reversible Cells	7
1.01.4	Chemical Potentials and Equilibrium	8
1.01.4.1	Sign Convention for Equilibrium emfs and Potentials	12

### Symbols

**a** Activity (strictly dimensionless – see section 1.01.2.6)  
**c** Concentration ( $\text{mol kg}^{-1}$  or  $\text{mol m}^{-3}$  or  $\text{mol dm}^{-3}$ )  
**c°** Concentration in standard state ( $\text{mol kg}^{-1}$  or  $\text{mol m}^{-3}$  or  $\text{mol dm}^{-3}$ )  
**C<sub>p</sub>** Molar heat capacity at constant pressure ( $\text{J mol}^{-1} \text{K}^{-1}$ )  
**E** Equilibrium potential (V)  
**E°** Standard equilibrium potential (V)  
**F** Faraday constant ( $96\,485 \text{ C mol}^{-1}$ )  
**G** Gibbs free energy or free enthalpy (J)  
**G°** Standard Gibbs free energy or free enthalpy (J)  
**H** Enthalpy (J)  
**I** Ionic strength ( $\text{mol kg}^{-1}$  or  $\text{mol m}^{-3}$  or  $\text{mol dm}^{-3}$ )  
**K** Equilibrium constant  
**n** Number of moles  
**P** Pressure (Pa, atm)  
**p°** Standard pressure (usually 1 atm)  
**Q** Activity quotient  
**q** Heat (J)

**R** The gas constant ( $8.314 \text{ J K}^{-1} \text{ mol}^{-1}$ )  
**S** Entropy (J)  
**T** Temperature (K)  
**U** Internal energy (J)  
**V** Volume ( $\text{m}^3$ )  
**w** Work (J)  
**z** Number of electrons or equivalent positive charge  
**γ** Activity coefficient  
**μ** Chemical potential ( $\text{J mol}^{-1}$ )  
**μ°** Standard chemical potential ( $\text{J mol}^{-1}$ )  
**v** Number of ions or molecules

### 1.01.1 Scope

Thermodynamics is concerned with the relationship between heat energy and work and is based on two general laws, the first and second laws of thermodynamics, both of which deal with the interconversion of different forms of energy. The third law states that at the absolute zero of temperature, the entropy of a perfect crystal is zero, and thus provides a method for determining absolute entropies.

<sup>†</sup>Deceased

The following features of the thermodynamic approach to chemical reactions should be noted:

1. It does not involve time as a variable, and does not provide information on rates.
2. It does not normally involve a knowledge of the detailed structure of the system or of the detailed mechanism of the reaction.
3. The second law is true only statistically and does not apply to individual particles or to a small number of particles, that is, thermodynamics is concerned with bulk properties of systems. Thus, thermodynamics has many limitations, but it is particularly valuable in defining the nature and structure of phases when *equilibrium* (a state that does not vary with time) has been attained; thermodynamics provides no information on the *rate* at which the reaction proceeds to equilibrium, which belongs to the realm of *chemical kinetics*.

### 1.01.2 Some Definitions

A *system* is any part of external reality that can be subjected to thermodynamic treatment; the material with which the system is in contact forms the *surroundings*, for example, an electrochemical cell could be the system and the external atmosphere the surroundings.

A *homogeneous* system is one in which the properties are uniform or vary uniformly throughout the system, whereas a *heterogeneous* system is one consisting of two or more homogeneous systems. Pure copper and a pure solution of  $\text{CuSO}_4$  are both homogeneous systems, but copper immersed in a solution of  $\text{CuSO}_4$  is a heterogeneous system characterized by an interface. The state of a system is described by its properties, which may be *intensive* or *extensive*; intensive properties are independent of quantity, for example, temperature, pressure, electrical potential, activation energy, etc., whereas extensive properties depend upon the amount of the material, for example, mass, volume, internal energy, enthalpy, entropy, free energy, chemical potential, etc.

The state of a system containing a constant amount of material depends on a few variables, for example, pressure  $p$ , volume  $V$ , and temperature  $T$ . For a given mass of pure substance, the volume can be expressed solely as a function of pressure and temperature

$$V = f(p, T) \quad [1]$$

If pressure changes from  $p$  to  $p + dp$  and temperature from  $T$  to  $T + dT$ , then the change in  $V$  is given by

$$dV = \left(\frac{\partial V}{\partial p}\right)_T dp + \left(\frac{\partial V}{\partial T}\right)_p dT \quad [2]$$

where  $(\partial V/\partial p)_T$  is the rate of change of volume with pressure at constant temperature, and  $(\partial V/\partial T)_p$  is the rate of change of volume with temperature at constant pressure. They are referred to as *partial derivatives*; the subscripts  $T$  and  $p$  denoting the variables that are maintained constant.

A *reversible* system is one that is so perfectly balanced that only infinitesimal change in an external conditions is required to reverse the direction of the process; for reversibility, the change must either be infinitesimally small or, if large, it must be carried out at an infinitely slow rate. Although these concepts are hypothetical, it is possible to approximate to reversibility by balancing the electromotive force (emf) of a reversible cell with the emf of a potentiometer circuit so that only a minute change ( $<10^{-6}$  V) in the emf produced by the latter will result in a reversal of the direction of the cell reaction. An ideal reversible cell must consist of two reversible electrodes, which are so completely nonpolarizable that their potentials are unaffected by charge transfer even at high rates. This too is a hypothetical concept, but a number of electrodes will approximate to reversibility, provided the rate of charge transfer is small, and cells composed of these electrodes may be treated thermodynamically.

#### 1.01.2.1 First Law of Thermodynamics

The first law is essentially a statement of the experimental fact that during a chemical reaction in an isolated system, *energy is conserved*, although it may be converted from one form to another.

If a system changes from state  $A$  to state  $B$  and if  $\Delta U$  is the change in the internal energy of the system, then it follows from the first law that the surroundings must gain or lose an equivalent amount of energy. A convention of signs is necessary to take into account the direction of heat transfer  $q$  and work performed  $w$ :  $q$  is taken as positive if heat is transferred to the system from the surroundings and negative if the transfer is in the reverse direction; in many textbooks,  $w$  is taken as positive if work is done by the system on the surroundings and negative if it is done on the system by the surroundings, but it is preferable to allow the sign of  $w$  to develop from the

mathematics. Thus, since energy must be conserved

$$\Delta U = q - w \quad [3]$$

where  $\Delta U$  is the change in the internal energy of the system,  $q$  is the heat transferred between the system and the surroundings, and  $w$  is the work done. Equation [3] may be regarded as an algebraic expression of the conservation of energy, and it should be noted that  $\Delta U$  is the difference in the internal energy of the system between its initial and final stages and that the absolute value of  $U$  is not known.

If a change from state  $A$  to state  $B$  occurs in a system at constant pressure (isobaric) so that only  $pV$  work is done, then  $w = p \Delta V$  and

$$\Delta U = q_p - p(V_B - V_A) \quad [4]$$

which can be written in the form

$$\begin{aligned} q_p &= U_B - U_A + p(V_B - V_A) \\ &= (U_B + pV_B) - (U_A + pV_A) \end{aligned} \quad [5]$$

Thus, it is convenient to define another function

$$H = U + pV \quad [6]$$

where  $H$  is the *enthalpy* or *heat content* of the system, so that

$$q_p = H_B - H_A = \Delta H \quad [7]$$

where  $q_p$  is the heat exchanged between the system and the surroundings at constant pressure, and  $\Delta H$ , like  $\Delta U$ , depends only upon the initial and final states of the system.

### 1.01.2.2 Second Law of Thermodynamics

The first law implies that energy is interconvertible and that when one form of energy disappears another form of energy must appear in its place. However, it provides no information on (a) the transformations of energy that are possible and (b) the extent to which one form of energy can be converted into another. Some energy transformations are possible and occur spontaneously, while transformations in the reverse direction are nonspontaneous and can be made to proceed only by supplying energy from an external source. Thus, heat will flow spontaneously from a source at a higher temperature to one at a lower temperature, but it cannot pass spontaneously in the reverse direction. The heat energy flowing spontaneously can be converted by means of suitable machinery to work energy, but it is evident from the

Carnot cycle (see below) that there is a theoretical limit to the extent of this interconversion.

Oxidation of hydrogen to water ( $\text{H}_2 + \frac{1}{2}\text{O}_2 \rightarrow \text{H}_2\text{O}$ ) is thermodynamically spontaneous, and the energy released as a result of the chemical reaction appears as heat energy, but the decomposition of water into its elements is a non-spontaneous process and can be achieved only by supplying energy from an external source, for example, a source of emf that decomposes the water electrolytically. Furthermore, although the heat energy produced by the spontaneous reaction could be converted into electrical energy; the electrical energy thus obtained would not be sufficient to restore the original state of chemical energy of the system, that is, to regenerate 1 mol of  $\text{H}_2$  and  $\frac{1}{2}$  mol of  $\text{O}_2$ .

The second law, which can be stated in a number of different ways, expresses the fact that heat can only be transformed into work when it flows from a higher to a lower temperature. Clausius stated the second law as follows: "It is impossible for a self-acting machine, unaided by an external agency, to convey heat from a lower to a higher temperature."

In principle, all spontaneous processes may be harnessed and made to do work, but owing to the wastage of a proportion of the energy as heat energy there is a theoretical limit to the amount of useful work that can be obtained, and this can never be exceeded in practice. A high-efficiency power station converting chemical energy (solid or liquid fuel) into electrical energy achieves only 30–40% efficiency.

The maximum theoretical work  $w_{\max}$  obtainable from a system was derived by Carnot who considered the transformation of heat energy into work when a perfect gas in a cylinder with a piston was taken through a reversible cycle (the Carnot cycle), in which the system was almost at equilibrium during each step of the cycle. It was shown that

$$w_{\max} = q_2 \left( \frac{T_2 - T_1}{T_2} \right) \quad [8]$$

where  $q_2$  is the heat absorbed from a reservoir at the higher temperature  $T_2$  (K), and  $T_1$  is the temperature of a second heat reservoir at a temperature lower than  $T_2$  which receives the heat that has not been converted into work. Equation [8] is applicable to any reversible system that undergoes a cyclic process in which the original and final states of the system and the surroundings are the same. Under these circumstances, all that has changed permanently is that a quantity of heat  $q_2$  at  $T_2$  has been transformed into

work  $w_{\max}$  together with a quantity of heat  $q_1 = q_2 - w_{\max}$  that is returned to the reservoir at the lower temperature  $T_1$ . It can be shown that the efficiencies of all reversible cyclic processes are the same provided  $T_1$  and  $T_2$  are the same, that is

$$\begin{aligned}\text{Thermodynamic efficiency} &= \frac{w_{\max}}{q_2} = \frac{q_2 - q_1}{q_2} \\ &= \frac{T_2 - T_1}{T_2}\end{aligned}\quad [9]$$

It is evident from eqn [9] that (a) the efficiency increases as  $(T_2 - T_1)/T_2$  increases and (b) the efficiency is zero when  $T_1 = T_2$  so that no heat can be converted into work.

### 1.01.2.3 Entropy

The concept of entropy  $S$  is implicit in the second law, and it may be regarded as a thermodynamic property of a system that is associated with its capacity for spontaneous change. As the system undergoes spontaneous change, the entropy increases and the capacity for further spontaneous change decreases. Rearranging the  $q$  and  $T$  terms in eqn [9] and applying the convention of signs

$$\frac{q_1}{T_1} - \frac{q_2}{T_2} = 0 \quad [10]$$

and generalizing for any reversible cyclic change that proceeds isothermally at a temperature  $T$

$$\sum \frac{q_{\text{rev}}}{T} = 0 \quad [11]$$

where  $\sum q_{\text{rev}}$  is the sum of the heat absorbed or evolved reversibly. The function  $q_{\text{rev}}/T$  is a measure of the change in entropy  $\Delta S$ , and this change for an isothermal process is defined as

$$\Delta S = \frac{q_{\text{rev}}}{T} \quad [12]$$

and for an infinitesimal reversible process

$$dS = \frac{\delta q}{T} \quad [13]$$

If the process is nonisothermal but finite

$$\Delta S = S_2 - S_1 = \int_{S_1}^{S_2} \frac{\delta q}{T} \quad [14]$$

It must be emphasized that the heat  $q_{\text{rev}}$ , which appears in the definition of entropy (eqn [12]), is always that which is absorbed (or evolved) when the

process is conducted reversibly. If the process is conducted irreversibly and the heat absorbed is  $q$ , then  $q$  will be less than  $q_{\text{rev}}$  and  $q/T$  will be less than the entropy change  $\Delta S$  eqn [12]. It follows that if an irreversible process takes place between the temperatures  $T_2$  and  $T_1$  and has the same heat intake  $q$  at the higher temperature  $T_2$  as the corresponding reversible process, then the efficiency of the former must be less than that of the latter, that is

$$\left( \frac{q_1}{T_1} - \frac{q_2}{T_2} \right)_{\text{irrev.}} > \left( \frac{q_1}{T_1} - \frac{q_2}{T_2} \right)_{\text{rev.}} \quad [15]$$

Thus, from eqns. [11] and [15] it follows that for an irreversible cycle

$$\sum \frac{q}{T} > 0 \quad [15a]$$

and that more positive  $\sum(q/T)$  is the more irreversible is the cycle. In the Carnot cycle, each stage is carried out reversibly and the entropy change is zero, and it can be shown that any complete cycle can be reduced to the sum of a large number of infinitesimal Carnot cycles so that the entropy change for any complete reversible cycle must always be zero. Thus, for any reversible process, the sum of all entropy changes for all the participating systems is given by

$$\sum dS = 0 \quad [16]$$

which provides a criterion for equilibrium.

On the other hand, in any irreversible process, although the system may gain (or lose) entropy and the surroundings lose (or gain) entropy, the system plus surrounding will always gain in entropy eqn [16]. Thus, for a real process proceeding spontaneously at a finite rate

$$\sum dS > 0 \quad [17]$$

For example, if a hot body (the system) is in contact with the surroundings at an infinitesimally lower temperature, then there will be an isothermal and reversible transfer of heat at  $T_2$ , and the loss in entropy of the hot body will be  $\Delta S_b = -q_{\text{rev}}/T_2$ , the gain in entropy of the surroundings will be  $\Delta S_s = +q_{\text{rev}}/T_2$ , and  $\Delta S_b + \Delta S_s = 0$ . On the other hand, if the surroundings are at a lower temperature  $T_1$  than the body, then the transfer of heat will be irreversible and spontaneous, and the entropy changes will be  $\Delta S_b = -q_{\text{rev}}/T_2$  and  $\Delta S_s = +q_{\text{rev}}/T_1$ . Since  $T_2 > T_1$ , the total change in entropy will be greater than zero, and the greater the difference between  $T_2$  and  $T_1$  the greater will be the gain in the total entropy of the

system as a whole, that is, the more spontaneous or irreversible is the transfer of heat.

When a substance is heated at constant pressure without change of phase through a temperature rise  $dT$ , the heat absorbed is  $C_p dT$ , where  $C_p$  is the molar heat capacity at constant pressure, and the entropy increase is

$$\int_{S_1}^{S_2} dS = \int_{T_1}^{T_2} \frac{C_p}{T} = \int_{T_1}^{T_2} C_p d \ln T \quad [18]$$

Thus, the entropy increase when the substance is heated from  $T_1$  to  $T_2$  is

$$\Delta S = \int_{T_1}^{T_2} C_p d \ln T = 2.303 \int_{T_1}^{T_2} C_p d \log T \quad [19]$$

$\Delta S$  may be evaluated by determining the heat capacity  $C_p$  at various temperatures between  $T_2$  and  $T_1$ , and plotting the values against  $\log T$ ; the area enclosed by the curve multiplied by 2.303 gives the entropy increase. When there is a change of phase such as the evaporation of a liquid to saturated vapor, melting of a solid to a liquid, or transition from one crystalline form to another, the process is isothermal and reversible, and

$$\Delta S = \frac{q}{T} \quad [20]$$

where  $q$  is the heat associated with the phase change at  $T$ .

For example, in the case of the reversible isothermal transformation of ice to water at the melting point (273 K), the heat gained by the ice will be the latent heat of fusion ( $\Delta H_f = 6006 \text{ J mol}^{-1}$ ) and a corresponding quantity of heat will be lost by the surrounding, and

$$\Delta S_{\text{system}} = \Delta S_{\text{ice}} + \Delta S_{\text{surr}} = \frac{6.006}{273} - \frac{6.006}{273} = 0$$

#### 1.01.2.4 Gibbs Free Energy or Free Enthalpy

Gibbs free energy  $G$  provides a means of defining equilibrium or of the tendency of a reaction to proceed in a given direction. It is similar to the other thermodynamic functions described above in which the change in free energy  $\Delta G$  is determined solely by the initial and final states of the system. The maximum work, or maximum available energy, defined in terms of the Gibbs free energy  $G$ , also called the *free enthalpy*, is

$$G = H - TS \quad [21]$$

or, for a finite change

$$\Delta G = \Delta H - T\Delta S \quad [22]$$

It can be shown that for a system in which the total mass, or the concentrations of the components, remains constant

$$\left(\frac{\partial G}{\partial P}\right)_{T, n_i \dots} = V \quad [23]$$

and

$$\left(\frac{\partial G}{\partial T}\right)_{p, n_i \dots} = -S \quad [24]$$

Combining eqns [21] and [24]

$$G - H = T \left(\frac{\partial G}{\partial T}\right)_{p, n_i \dots} \quad [25]$$

which is the important Gibbs–Helmholtz equation. Since in thermodynamics we are concerned mainly with changes in free energy and enthalpy, eqn [25] can be written as

$$\Delta G - \Delta H = T \left(\frac{\partial \Delta G}{\partial T}\right)_{p, n_i \dots} \quad [26]$$

*Units:* Free energy is an *extensive* quantity, but the *standard* free energy for 1 mol  $\Delta G_{298\text{K}}^\circ$  (in units of  $\text{J mol}^{-1}$ ) defined above is an *intensive* quantity.

#### 1.01.2.5 The Chemical Potential

The energy of a system can be changed by means of thermal energy or work energy, but a further possibility is to add or subtract moles of various substances to or from the system. The free energy of a pure substance depends upon its chemical nature, its quantity ( $\Delta G$  is an extensive property), its state (solid, liquid, or gas), and temperature and pressure. Gibbs called the partial molar free heat content (free energy) of the  $i$ th component of a system its *chemical potential*

$$\mu_i = \left(\frac{\partial G}{\partial n_i}\right)_{T, p, n_j} \quad [27]$$

that is, the change in free enthalpy of the system when 1 mol of component  $i$  is added to the system, the  $T, p$  and concentration of all other substances ( $n_j$ ) being maintained constant. The partial molar free energy of a pure compound is synonymous with the *standard chemical potential*  $\mu_i^\circ$ , which is the free enthalpy change when 1 mol of the substance is

formed from its elements under isothermal isobaric conditions. In order to evaluate the chemical potentials of compounds, and of ions in solution, it is necessary to define the following standard states:

1. The standard chemical potentials of the elements in the form that they are normally stable at the temperature and pressure under consideration are given an arbitrary value zero

$$\mu^\circ(\text{element}) = 0 \quad [28]$$

2. In the case of ions in solution and of gases, the chemical potential will depend upon concentration and pressure, respectively. An arbitrary value of zero at a specified concentration is given for ions in solution, the standard chemical potential of the hydrogen ion, at the temperature and pressure under consideration

$$\mu_{\text{H}^+}^\circ = 0, \text{ when } a_{\text{H}^+} = 1 \quad [29]$$

where  $a_{\text{H}^+}$  is the activity of the hydrogen ion.

### 1.01.2.6 Activity

The chemical potential of the hydrogen ion, or of any other ion, will vary with activity

$$\mu_i = \mu_i^\circ + RT \ln a_i \quad [30]$$

where the activity  $a_i$  is a thermodynamic quantity that is related to the concentration of the ion and takes into account the fact that a solute in solution does not behave ideally at finite concentrations; only at infinite dilution, will  $a_i$  be equal to  $c_i$  numerically, where  $c_i$  is the concentration ( $\text{mol kg}^{-1}$ ,  $\text{mol m}^{-3}$ , or  $\text{mol dm}^{-3}$ ).

Substituting for  $R = 8.314 \text{ J K}^{-1} \text{ mol}^{-1}$  and  $T = 298 \text{ K}$ , and using the identity  $\ln x = 2.303 \log x$ , eqn [30] can be expressed as

$$\mu_i = \mu_i^\circ + 5710 \log a_i \quad [31]$$

A similar equation is applicable to a gas, but the pressure of the gas  $p_g$  (or more strictly its fugacity) replaces the activity of the ion

$$\mu_g = \mu_g^\circ + 5710 \log (p_g/p^\circ) \quad [32]$$

where  $p^\circ$  refers to a standard pressure of 1 atm or  $101325 \times 10^5 \text{ Pa}$ . For a nondissociating solute (e.g., urea)

$$a = \gamma c/c^\circ \quad [33]$$

where  $\gamma$  is the activity coefficient ( $\gamma \rightarrow 1$  as  $c \rightarrow 0$ ) and  $c^\circ$  is the concentration in the standard state.

For a 1:1 electrolyte (NaCl), a similar procedure may be adopted, but in this case not only do the constituent ions ( $\text{Na}^+$  and  $\text{Cl}^-$ ) become more ideal in behavior as the concentration decreases, but also the electrolyte becomes more completely dissociated into ions. It is not possible to determine individual ionic activity coefficient since anions and cations cannot be studied in the absence of one another. Thus, for a 1:1 electrolyte eqn [30] is written as

$$\mu = \mu^\circ + 2RT \ln a_{\pm} = \mu^\circ + 2RT \ln (\gamma_{\pm} c/c^\circ) \quad [34]$$

where  $a_{\pm}$  is the mean ionic activity,  $\gamma_{\pm}$  is the mean activity coefficient, and  $\gamma_{\pm} \rightarrow 1$  when  $c \rightarrow 0$ . More complex relationships are required for unsymmetrical electrolytes, such as  $\text{Na}_2\text{SO}_4$ ,  $\text{La}_2(\text{SO}_4)_3$ ,  $\text{TiCl}_4$ , etc.

At sufficiently low ionic strengths, the activity coefficient of each electrolyte in a mixture is given by the Debye–Hückel limiting law

$$\log \gamma_{\pm} = - |z_+ z_-| A \sqrt{I} \quad [35]$$

where  $I$  the *ionic strength* is defined as

$$I = \frac{1}{2} \sum c_i z_i^2 \quad [36]$$

and  $z_+$  and  $z_-$  are the valencies of the cation and anion (NaCl is a 1:1 electrolyte,  $\text{Na}_2\text{SO}_4$  a 2:1 electrolyte,  $\text{La}_2(\text{SO}_4)_3$  a 2:3 electrolyte, etc.), and  $A$  is a constant which is  $0.51 \text{ mol}^{-1/2} \text{ kg}^{1/2}$  for water at  $25^\circ \text{C}$  ( $c_i$  is in  $\text{mol kg}^{-1}$ ).

*Units:* It should be noted that in the SI the activity of a solute is defined with reference to a standard state, that is, an ideal solution of molality  $1 \text{ mol kg}^{-1}$ . Thus, the *relative activity* of a metal ion in solution is given by

$$a_{M^{z+}} = \frac{m_{M^{z+}}}{m^\circ} \gamma_{M^{z+}} \quad [37]$$

where  $m^\circ = 1 \text{ mol kg}^{-1}$ ,  $m_{M^{z+}}$  is in  $\text{mol kg}^{-1}$ , and  $\gamma_{M^{z+}}$  is dimensionless. It follows that the relative activity is dimensionless, although units, such as  $\text{mol kg}^{-1}$ , g ion per litre, etc., are still being used (see below).

### 1.01.2.7 Gibbs–Duhem Equation

The Gibbs free energy change of a system will depend not only on temperature and pressure, but also on the chemical potentials of the species involved, and this statement may be expressed in the form of the partial differential

$$dG + \left( \frac{\partial G}{\partial T} \right)_{p, m_1, m_2, \dots} dT + \left( \frac{\partial G}{\partial p} \right)_{T, m_1, m_2, \dots} dp + \mu_1 dm_1 + \mu_2 dm_2 \quad [38]$$

and combining with eqns [23] and [24]

$$dG = -S dT + V dp + \sum \mu_i dn_i \quad [39]$$

For a process carried out under isothermal and isobaric conditions

$$(dG)_{T,p} = \sum \mu_i dn_i \quad [40]$$

and integration of this equation for a system of given chemical composition gives

$$G_{T,p,n} = \sum n_i \mu_i \quad [41]$$

General differentiation of this equation gives

$$dG_{T,p} = \sum (n_i d\mu_i + \mu_i dn_i) \quad [42]$$

Since at equilibrium  $(dG)_{T,p,n} = \text{zero}$ , it follows from eqn [40] that

$$\sum n_i d\mu_i = 0 \quad [43]$$

which is referred to as the Gibbs–Duhem equation.

For a binary solution of say A and B

$$n_A d\mu_A = -n_B d\mu_B \quad [44]$$

Since

$$\mu_i = \mu_i^\circ + RT \ln a_i \quad [45]$$

$$d\mu_i = RT d \ln a_i \quad [46]$$

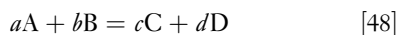
Hence

$$n_A d \ln a_A = -n_B d \ln a_B \quad [47]$$

The Gibbs–Duhem equation is extremely important in solution chemistry, and it can be seen from eqn [47] that it provides a means of determining the activity of one component in a binary solution provided the activity of the other is known.

### 1.01.3 Spontaneity of a Reaction

An isothermal reaction can proceed spontaneously only if the total Gibbs free energy of the system decreases; that is, the free energy of the reactants must be greater than the free energy of the products. For a reaction



$$\Delta G = \sum \mu_{\text{products}} - \sum \mu_{\text{reactants}} \quad [49]$$

where  $\Delta G$  is the change in free enthalpy. It follows that if  $\Delta G < 0$ , then the reaction will tend to proceed spontaneously in the direction shown; if  $\Delta G > 0$ , then the reaction will tend to proceed spontaneously in the reverse direction, and if  $\Delta G = 0$ , then the system will be

at equilibrium and will not have any tendency to proceed in either direction.

Thus, for a spontaneous reaction

$$\Delta G = (c\mu_C + d\mu_D) - (a\mu_A + b\mu_B) < 0 \quad [50]$$

and if all the substances are in their standard states

$$\Delta G = (c\mu_C^\circ + d\mu_D^\circ) - (a\mu_A^\circ + b\mu_B^\circ) < 0 \quad [51]$$

#### 1.01.3.1 Reversible Cells

By definition

$$\Delta G = -zFE \quad [52]$$

where  $E$  (the reversible emf) is the intensity factor in the energy term and  $zF$  (the total charge per mole of ions involved in the reaction) is the capacity factor. If the activities of the reactants and products are fixed,  $E$  will be a constant, and if  $a_A = a_B = a_C = a_D = 1$  is taken as the standard state, then

$$\Delta G^\circ = -zFE^\circ \quad [53]$$

where  $\Delta G^\circ$  is the standard free enthalpy change and  $E^\circ$  is the standard emf which is a constant for a given equilibrium at constant  $T$ .

Substituting  $-zFE$  for  $\Delta G$  eqn [53] in eqn [26] gives

$$\Delta H = -zFE + zFT \left( \frac{\partial E}{\partial T} \right)_p \quad [54]$$

which provides an accurate method of evaluating  $\Delta H$  and  $\Delta S$  in eqn [54] from the emf of a reversible cell and the coefficient of the change of emf with temperature at constant  $p$ , since

$$-T \left( \frac{\partial(\Delta G)}{\partial T} \right)_p = zFT \left( \frac{\partial E}{\partial T} \right)_p = T\Delta S \quad [55]$$

From eqn [49]

$$\Delta G^\circ = \sum v_i \mu_i^\circ \quad [56]$$

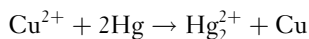
where  $v_i$  is the number of each of the ions or molecules involved in the equilibrium; combining eqns [53] and [54]

$$E^\circ = \frac{\sum v_i \mu_i^\circ}{zF} = -\frac{\sum v_i \mu_i^\circ}{96\,500z} \quad [57]$$

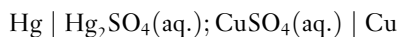
Equations [53] and [57] emphasize the essentially thermodynamic nature of the standard equilibrium emf of a cell or the standard equilibrium potential



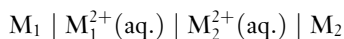
of a half-reaction  $E^\circ$ , which may be evaluated directly from the emf measurements of a reversible cell or indirectly from  $\Delta G^\circ$ , which must in turn be evaluated from the enthalpy of the reaction and the entropies of the species involved (see eqn [22]). Thus, for the equilibrium  $\text{Cu}^{2+} + 2\text{e} \rightleftharpoons \text{Cu}$  the standard electrode potential  $E^\circ_{\text{Cu}^{2+}/\text{Cu}}$ , and hence  $\mu^\circ_{\text{Cu}^{2+}}$ , can be determined by an emf method by harnessing the reaction



which can be represented by a cell without a liquid junction (or liquid junction potential)

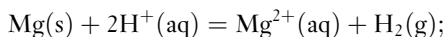


in which ‘|’ represents the phase boundaries. When a cell has a liquid junction, the latter is represented by | as in the cell



Although in certain cells the liquid junction can be eliminated by appropriate choice of electrolyte solution, this is not always possible. However, the liquid junction potential can be minimized by the use of a salt bridge (a saturated solution of KCl of about 4.2 M) and the liquid junction potential is then only 1–2 mV; this elimination of the liquid junction potential is indicated by ||.

The standard electrode potential of  $M^{z+}/M$  can be evaluated accurately and conveniently provided it forms a reversible electrode and can be coupled with a reference electrode to form a reversible cell. However, a number of  $M^{z+}/M$  systems do not conform to this criterion, and calorimetric methods must be used to evaluate  $\Delta H^\circ$  and  $\Delta S^\circ$ , and hence  $\Delta G^\circ$  from which  $E^\circ$  can be calculated. Thus, in the case of the  $\text{Mg}^{2+}(\text{aq.})/\text{Mg}$  equilibrium, the enthalpy change during the dissolution of the metal in dilute acid at 25 °C is determined from the reaction



$$\Delta H^\circ = -461\,200 \text{ J mol}^{-1}$$

and the standard entropy change  $\Delta S^\circ$  is evaluated from the standard partial molar entropies of the reactants and products

$$\begin{aligned} \Delta S^\circ &= S^\circ(\text{Mg}^{2+}) + S^\circ(\text{H}_2) - S^\circ(\text{Mg}) \\ &\quad + 2S^\circ(\text{H}^+) \\ &= -43.3 \text{ J K}^{-1} \text{ mol}^{-1} \end{aligned}$$

$$\text{Since } \Delta G^\circ = \Delta H^\circ - TS^\circ$$

$$\begin{aligned} \Delta G^\circ &= -461\,200 - (298 \times 43.3) \\ &= -448\,300 \text{ J mol}^{-1} \text{ at } 298 \text{ K} \end{aligned}$$

$$E^\circ_{\text{reaction}} = \frac{-\Delta G^\circ}{zF} = \frac{-448\,300}{2 \times 96\,500} = -2.3 \text{ V}$$

$$\text{and since } a_{\text{H}^+} = p_{\text{H}_2} = 1, E^\circ_{\text{Mg}^{2+}/\text{Mg}} = -2.3 \text{ V.}$$

### 1.01.4 Chemical Potentials and Equilibrium

The relationship between the change in free energy  $\Delta G$  and the equilibrium constant  $K$  is given by the van't Hoff isotherm

$$\Delta G = -RT \ln K + RT \ln Q \quad [58]$$

and from eqn [48]

$$K = \frac{a_{\text{C}}^c a_{\text{D}}^d}{a_{\text{A}}^a a_{\text{B}}^b} \quad [59]$$

where  $a$  denotes the equilibrium activity of the component and  $Q$  is the activity quotient. Note that the activities of the products are in the numerator and activities of reactants in the denominator.

Equation [58] shows that  $\Delta G$  is dependent on  $K$  and on any arbitrary activity of reactants and products that may be introduced into the equation. When the reactants and products are in their standard states

$$a_{\text{A}} = a_{\text{B}} = a_{\text{C}} = a_{\text{D}} = 1 \text{ and } \ln Q = 0 \quad [60]$$

Hence, from eqn [53]

$$\Delta G = \Delta G^\circ = -RT \ln K = -zFE^\circ \quad [61]$$

∴

$$\Delta G^\circ = -RT \ln K = -zFE^\circ \quad [62]$$

and

$$E^\circ = \frac{RT}{zF} \ln K = \frac{0.0591}{z} \log K \quad [63]$$

since at 25 °C, the term  $2.303RT/F = 2.303 \times 8.314 \times 298/96\,500 = 0.0591 \text{ V}$ . Combining eqns [52] and [58]

$$E = \frac{RT}{zF} \ln K - \frac{RT}{zF} \ln Q \quad [64]$$

and from eqn [63]

$$\begin{aligned} E &= E^\circ - \frac{0.0591}{z} \log Q \\ &= E^\circ - \frac{0.0591}{z} \log \frac{a_{\text{C}}^c a_{\text{D}}^d}{a_{\text{A}}^a a_{\text{B}}^b} \end{aligned} \quad [65]$$

which shows how the equilibrium potential  $E$  is



dependent on the standard electrode potential  $E^\circ$ , a constant for a given equilibrium, and the activities of reactants and products. Equation [65] is termed the *Nernst* equation and is applicable only when the system is reversible. Since

$$\Delta G^\circ = \sum v_i \mu_i^\circ = -RT \ln K \quad [66]$$

$$\log K = -\frac{\sum v_i \mu_i^\circ}{5710} \text{ at } 25^\circ\text{C} \quad [67]$$

Thus, the equilibrium constant  $K$  can be evaluated from standard electrode potential  $E^\circ$  or from the standard chemical potentials  $\mu^\circ$ .

The importance of the Gibbs free energy and the chemical potential is very great in chemical thermodynamics. Any thermodynamic discussion of chemical equilibria involves the properties of these quantities. It is therefore worthwhile considering the derivation of eqn [58] in some detail since it forms a prime link between the thermodynamics of a reaction ( $\Delta G$  and  $\Delta G^\circ$ ) and its chemistry.

From the defining equations of  $H$  (eqn [6]) and  $G$  (eqn [21]), differentiation gives

$$dH = dU + p dV + V dp \quad [68]$$

and

$$dG = dH - T dS - S dT \quad [69]$$

In addition, application of the first and second laws (eqns [3] and [13]) gives

$$dU = T dS - p dV \quad [70]$$

Combination of these gives

$$dG = V dp - S dT \quad [71]$$

This equation is particularly important because by carrying out a process isothermally ( $dT = 0$ ) the change in the value of  $G$  can be related to the volume and pressure change alone; both of these quantities are controllable and measurable. Thus, for isothermal processes

$$dG = V dp \quad [72]$$

It remains only to integrate this expression. To do this, we apply initially the equation for  $n$  moles of an ideal gas

$$V = \frac{nRT}{p} \quad [73]$$

so that

$$dG = nRT \int \frac{1}{p} dp \quad [74]$$

Integration of this requires a limit to be defined. The limit is taken simply as follows. We define a standard pressure  $p^\circ$  at which the Gibbs free energy has a standard value  $G^\circ$ . We have thereby defined a standard state for this component of the system: a standard temperature too is implicit in this since the above equations are treated for constant temperature.

Integration of eqn [74] now gives

$$G = G^\circ + nRT \ln \frac{p}{p^\circ} \quad [75]$$

If only one mole of the gas is considered, the quantity  $G$  is called the chemical potential,  $\mu$ , or the partial molar free energy. In this case,  $n = 1$ ; and eqn [75] becomes

$$\mu = \mu^\circ + RT \ln \frac{p}{p^\circ} \quad [76]$$

Note that the standard state has simply to be defined; there is no *a priori* reason why it should have any particular value, save for the fact that it might as well be a convenient value. A pressure of 1 atm is commonly adopted. We can thus abbreviate the equation to

$$\mu = \mu^\circ + RT \ln p \quad [77]$$

provided the pressure of the gas,  $p$ , is expressed in atmospheres if the standard pressure has a numerical value of 1 atm. But note that the term inside the logarithm is actually dimensionless because of the *implicit*  $p^\circ$ .

If the gas is not ideal, so that the ideal gas equation cannot be used, we replace the pressure  $p$  in eqns [76] and [77] by the fugacity,  $f$ , such that the ideal gas equation still holds if the pressure  $p$  is replaced by the fugacity, an effective pressure, when the real pressure is  $p$ . This form is most convenient because of the numerous ways in which nonideality can be expressed and we note that the fugacity is related to, but not necessarily proportional to, the pressure. We can express the fugacity as a function of the pressure by introducing the fugacity coefficient,  $\gamma_p$ , as  $f = \gamma_p p$ , which then replaces  $p$  in eqn [77] for the nonideal case. The value of  $\gamma_p$  tends to unity as the gas behaves more ideally, which means that the pressure decreases.

Consider now, a simple gas phase (with ideal gases) reaction



For each component, we may write eqn [77]. The free energy change,  $\Delta G$  for the reaction, is then given by

$$\begin{aligned}\Delta G &= \mu_C - \mu_B - \mu_A \\ &= \mu_C^\circ - \mu_B^\circ - \mu_A^\circ + RT \ln \frac{p_C}{p_C^\circ} - RT \ln \frac{p_B}{p_B^\circ} \\ &\quad - RT \ln \frac{p_A}{p_A^\circ} \quad [79] \\ &= \Delta G^\circ + RT \ln \frac{(p_C/p_C^\circ)}{(p_B/p_B^\circ)(p_A/p_A^\circ)}\end{aligned}$$

Again, we define the standard state for a gas as 1 atm, that is,  $p_A^\circ = p_B^\circ = p_C^\circ = 1 \text{ atm}$  so that the eqn [79] becomes

$$\Delta G = \Delta G^\circ + RT \ln \frac{p_C}{p_B p_A} \quad [80]$$

Now, since  $\Delta G$  is the driving force for the reaction to proceed, equilibrium is represented by the condition that  $\Delta G = 0$ . Thus, the value of  $\Delta G^\circ$  is given as

$$\begin{aligned}\Delta G^\circ &= -RT \ln \frac{(p_C^\varepsilon/p_C^\circ)}{(p_B^\varepsilon/p_B^\circ)(p_A^\varepsilon/p_A^\circ)} \\ &= -RT \ln \frac{p_C^\varepsilon}{p_B^\varepsilon p_A^\varepsilon}\end{aligned} \quad [81]$$

where the superscript  $\varepsilon$  refers to the pressure of the particular component *when the reaction is at equilibrium*. It will be recognized that the term inside the logarithm in eqn [81] is the equilibrium constant for the reaction. This relationship (together with eqn [80]) is extremely important because it links the thermodynamics with the chemistry. We have derived the fact that  $\Delta G^\circ$  is simply another way of expressing the equilibrium constant for the reaction. It is important once again to bear in mind that the term inside the logarithm is actually dimensionless: each pressure is the ratio of the pressure to the standard pressure (expressed in the same units). Thus, the equilibrium constant is also strictly a dimensionless quantity. Although units are often quoted for the equilibrium constant  $K$  for the reaction (they would be  $\text{atm}^{-1}$  in the above example), units are of course inconsistent with the exponentiation of eqn [81], for which

$$K = \frac{p_C^\varepsilon}{p_B^\varepsilon p_A^\varepsilon} = \exp - \frac{\Delta G^\circ}{RT} \quad [82]$$

and the exponential term is always dimensionless. Citing of units for  $K$  (sometimes called  $K_p$  since it is

a ratio of pressures as defined above) is really a method of telling one's audience what the standard states really are. Thus, we could, for example, consider 1 Pa of pressure as the standard state instead of 1 atm. It would equally be possible to use the concentration of the gas, since the ideal gas equation contains the term  $n/V$  which is the concentration (in, say,  $\text{mol dm}^{-3}$ ), for which the standard state could be  $1 \text{ mol dm}^{-3}$ . This does not of course change the reaction, but it does change the numerical value of  $K$  and correspondingly the numerical value of  $\Delta G^\circ$ . It is not common to do this in gas phase chemistry – the usual standard state for gas is 1 atm. However, it is important to understand the principle of it, particularly in corrosion and electrochemistry, since electrochemical systems incorporate not only gases but also solids and solutions, the latter comprising solutes and a solvent. We can now express

$$\Delta G = -RT \ln K + RT \ln \frac{p_C}{p_A p_B} \quad [83]$$

Note that the term inside the second logarithm is *not* the equilibrium, unless the reaction is in equilibrium (for which  $\Delta G = 0$ ). These pressures are the actual pressures used for the reaction, and the equation essentially describes the fact that the driving force for the reaction (as written) is represented by the excess pressure quotient of the reaction over and above the equilibrium.

All the above deal with gases and gas phase processes. We can now turn to nongaseous components of the system. There are many ways of expressing this. Probably, the simplest is to consider an ideal solution of a solute in a solvent. If the solution is ideal, the vapor pressure of the solute is proportional to its concentration, that is,  $p = kc$ , where  $c$  is the concentration and  $k$  is the proportionality constant. Similarly,  $p^\circ = kc^\circ$  which expresses the fact that the standard pressure is related to a standard concentration. Thus, for a particular component we have from eqn [76]

$$\mu = \mu^\circ + RT \ln \frac{c}{c^\circ} \quad [84]$$

This formulation now entirely eliminates the need for a pressure and replaces it by the concentration and a standard concentration. As defined above, the standard concentration is that concentration which gives rise to the standard pressure  $p^\circ$ . However, we have defined the original standard pressure arbitrarily as 1 atm. We can equally and validly redefine the

standard concentration of the solute as  $1 \text{ mol dm}^{-3}$  of solution (unit molar or 1 M), or  $1 \text{ mol kg}^{-1}$  of solvent (unit molal or 1 m). This, in essence, redefines the standard pressure, but that is of little consequence, since in corrosion and electrochemistry, we are usually concerned with concentrations in solution (as an electrolyte in water, for example) and with concentrations of metal in an alloy. Moreover, because the value of  $k$  may be different for different components of the system, from the point of view of the gas pressures, we may be assigning different standard states for different gases. But that does not matter either, since we are free to define the standard states in any way we choose, and we are now interested in solution components and not gases. Thus, for example, unit concentration of hydrochloric acid (say 1 m) is a far more convenient standard state than that concentration which would equilibrate with a vapor pressure of 1 atm. However, there is an added complication, already met with gases, that many solutions are not ideal. So far, the derivation has still been in terms of ideal solutions because we assumed that the pressure is proportional to the concentration; hence, the constant  $k$  is used above. Handling of this is analogous to the nonideal gas. We define a new term, the activity  $a$ , of the component which replaces the concentration in eqn [84]. Thus

$$a = \gamma \frac{c}{c^\circ} \quad [85]$$

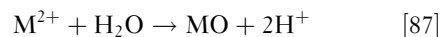
and thence for a nonideal component

$$\mu = \mu^\circ + RT \ln \frac{\gamma c}{c^\circ} \quad [86]$$

where  $c$  and  $c^\circ$  are the concentration and standard concentration, respectively, expressed as molalities, and  $\gamma$  is the activity coefficient. We are here defining the standard concentration as 1 mole of solute per kilogram of solvent. This simply means that we are fixing the value of the chemical potential of the component as  $\mu^\circ$  when the concentration is the standard value. Note that the activity and the activity coefficient are dimensionless and a defined standard state is implied.

But that is not all. For dilute solutions, the solvent concentration is high ( $55 \text{ mol kg}^{-1}$ ) for pure water and does not vary significantly unless the solute is fairly concentrated. It is therefore a common practice and is fully justified to use unit mole fraction as the standard state for the solvent. The standard state of a close up pure solid in an electrochemical reaction is similarly treated as unit mole fraction (sometimes referred to as the pure component); this includes metals, solid oxides, etc.

Exactly analogous, then, to the gas phase reaction above, the value of  $\Delta G$  and  $\Delta G^\circ$  can be formulated. Thus, for the following reaction, for example



$\Delta G$  is given by

$$\Delta G = \Delta G^\circ + RT \ln \frac{(\gamma_{\text{MO}} c_{\text{MO}} / c_{\text{MO}}^\circ)(\gamma_{\text{H}} c_{\text{H}} / c_{\text{H}}^\circ)^2}{(\gamma_{\text{M}} c_{\text{M}} / c_{\text{M}}^\circ)(\gamma_{\text{w}} c_{\text{w}} / c_{\text{w}}^\circ)} \quad [88]$$

where the subscripts MO, H, M, and w refer to the MO,  $\text{H}^+$ ,  $\text{M}^{2+}$ , and  $\text{H}_2\text{O}$  components, respectively.  $\Delta G^\circ$  is derived from the equilibrium activities as in eqn [81], but by using the appropriate concentration terms instead of pressure terms. Note that the equilibrium constant and the activity quotient in the above equation are again strictly dimensionless. Although dimensions are often quoted for  $K$  (sometimes called  $K_c$ ) as described above (for reaction [82] this would be  $\text{mol kg}^{-1}$  or  $\text{mol dm}^{-3}$ ), these are simply an expression of the standard states involved. Now, the standard state of the solid component (MO) and the solvent ( $\text{H}_2\text{O}$ ) are defined by convention as the pure components (unit mole fraction). If the solution is dilute,  $c_{\text{w}} \approx c_{\text{w}}^\circ$  and  $\gamma_{\text{w}} = 1$ . Thus the components of the equation above involving MO and  $\text{H}_2\text{O}$  are both unity. In addition, if we define the standard states of the dissolved ions as 1 M, then the relationship becomes the more familiar

$$\Delta G = \Delta G^\circ + RT \ln \frac{\gamma_{\text{H}}^2 c_{\text{H}}^2}{\gamma_{\text{M}} c_{\text{M}}} \quad [89]$$

Note that if the water in the reaction is not of unit mole fraction (or nearly so), then its activity would have to be incorporated into eqn [89]. This could, for example, be as in a mixed water/methanol solution. The water concentration would then be expressed as unit mole fraction, and for accuracy, its activity coefficient relative to pure water (the standard state) would need to be known. The same is true if one of the reactants is a metal (whose standard state is the pure metal of unit mole fraction), but the reactant is in alloy form. In summary, it is common in electrochemical reactions to adopt the following standard states: for solid components and for the solvent, the standard state is unit mole fraction; for dissolved components (such as ions), the standard state is 1 mol solute per kilogram of solvent, or 1 mol solute per cubic decimeter of solution, and for gas phase components, the standard state is 1 atm pressure.

### 1.01.4.1 Sign Convention for Equilibrium emfs and Potentials

For ions in solution, the standard reference state is the hydrogen ion whose standard chemical potential at  $a_{\text{H}^+} = 1$  is given an arbitrary value of zero. Similarly, for pure hydrogen at  $p_{\text{H}_2} = 1$  atm,  $\mu_{\text{H}_2}^\circ = 0$ . Thus, for the  $\text{H}^+/\frac{1}{2}\text{H}_2$  equilibrium (eqn [57]),

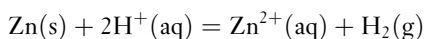
$$E^\circ = -\frac{\sum v_i \mu_i}{zF} = 0.00 \text{ V} \quad [90]$$

and the standard hydrogen electrode (SHE) is taken as the reference electrode for all other equilibria.

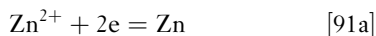
For a cell, the equilibrium must be written in the direction in which it proceeds spontaneously, and under these circumstances

$$\Delta G < 0 \text{ and } E > 0$$

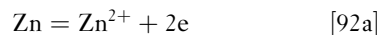
that is, the emf of the cell will be positive. Thus, for the equilibrium between Zn and  $\text{H}^+$ , the reaction is written as



and if  $a_{\text{H}^+} = a_{\text{Zn}^{2+}} = a_{\text{H}_2} = 1$ ,  $E = E^\circ = +0.76 \text{ V}$ . However, in the case of a half-reaction, it is quite arbitrary as to whether the equilibrium is written as a reduction (electrons on the LHS) or as an oxidation (electrons on the RHS)



or



since both are correct. Substituting in the Nernst equation eqn [65] for eqn [91a]

$$E = E^\circ - 0.030 \log \frac{1}{a_{\text{Zn}^{2+}}} = E^\circ + 0.030 \log a_{\text{Zn}^{2+}} \quad [91\text{b}]$$

and for eqn [92a]

$$E = E^\circ - 0.030 \log a_{\text{Zn}^{2+}} \quad [92\text{b}]$$

Thus, if the magnitudes of  $E$  are to be the same the signs of  $E^\circ$  must be different, that is,  $E^\circ = -0.76 \text{ V}$  for eqn [91b] and  $E^\circ = +0.76 \text{ V}$  for eqn [92b]. If this convention is adopted, the respective electrode potentials become

$$E = -0.76 + 0.030 \log a_{\text{Zn}^{2+}} \quad [91\text{c}]$$

$$E = +0.76 - 0.030 \log a_{\text{Zn}^{2+}} \quad [92\text{c}]$$

and for any given activity of  $\text{Zn}^{2+}$ , the  $E$ s will be the same in magnitude but opposite in sign.

It is now internationally accepted (Stockholm Convention) that the half-reaction must be written with the electrons on the RHS:



## 1.02 Electrochemistry

**C. Lefrou and R. P. Nogueira**

Grenoble – INP – Grenoble Institute of Technology, UMR 5631 and 5266 of CNRS “LEPMI” and “SIMAP”, Grenoble, France

**F. Huet and H. Takenouti**

Laboratoire Interfaces et Systèmes Electrochimiques, Université Pierre et Marie Curie – Paris 6, CNRS, UPR15-LISE, Paris, France

© 2010 Elsevier B.V. All rights reserved.

<b>1.02.1</b>	<b>Introduction</b>	14
<b>1.02.2</b>	<b>Current, Potential, and Interfaces</b>	15
1.02.2.1	Electronic and Electrolytic Materials: The Two Sides of an Electrified Interface	15
1.02.2.2	Electrochemical Reactions	16
1.02.2.3	Electrochemical Reactions and Corrosion: Some Preliminary Remarks	18
1.02.2.4	Basic Description of Metal–Electrolyte Interfaces	19
1.02.2.4.1	Elementary steps and intermediate interfacial species	19
1.02.2.4.2	The electrical double layer	20
1.02.2.4.3	Current and mass transport mechanisms	21
1.02.2.4.4	Potential and concentration profiles across the interface	22
<b>1.02.3</b>	<b>Electrochemical Equilibrium</b>	24
1.02.3.1	Definition and Introductory Remarks	24
1.02.3.2	Electrochemical Equilibrium as a Dynamic State: the Exchange Current Density	24
1.02.3.3	Formal Expression of $E_{\text{eq}}$ : the Nernst Law for the $M^{z+}/M$ Couple	25
1.02.3.4	Some More Complex Applications of the Nernst Law	27
1.02.3.5	Applications of the Nernst Law to Pourbaix ( $E$ –pH) Diagrams	28
1.02.3.5.1	Purely potential-dependent equilibrium	28
1.02.3.5.2	Purely pH-dependent equilibrium	29
1.02.3.5.3	pH and potential-dependent equilibrium	29
1.02.3.6	Pourbaix Diagram of Gold, Iron, and Aluminum	30
<b>1.02.4</b>	<b>Electrochemical Kinetics in the Case of a Single Forward–Backward Reaction</b>	32
1.02.4.1	Qualitative Approach	32
1.02.4.2	Quantitative Approach	33
1.02.4.2.1	Activation-controlled systems: Butler–Volmer equation	33
1.02.4.2.2	Mass-transport limited systems: Fick’s law and limiting current density	38
1.02.4.2.3	General case: Mixed controlled systems	39
<b>1.02.5</b>	<b>Corrosion: Far from Equilibrium Zero Net Current Systems</b>	41
1.02.5.1	Qualitative Description of the Free Corrosion Scenario	41
1.02.5.2	Electrochemical Kinetics Around the Corrosion Potential	43
<b>1.02.6</b>	<b>The Electrochemical Cell</b>	45
1.02.6.1	Design of the Electrochemical Cell	45
1.02.6.1.1	The working electrode	46
1.02.6.1.2	The counter-electrode	46
1.02.6.1.3	The reference electrode	46
1.02.6.2	Potential Control and Current Control	49
<b>References</b>		50

### Abbreviations

**CE** Counter electrode

**DC** Direct current

**IUPAC** International union of pure and applied chemistry

**NHE** Normal hydrogen electrode

**OCP** Open-circuit potential

**OHP** Outer Helmholtz plane  
**OPA** Operational amplifier  
**RE** Reference electrode  
**SHE** Standard hydrogen electrode  
**WE** Working electrode  
**ZRA** Zero-resistance ammeter

## Symbols

**a** Activity of a species  
<sub>a</sub> Related to the anodic reaction  
<sub>act</sub> Related to activation control  
**A<sub>1</sub>** Constant in eqn [36] (V)  
**b** Tafel coefficient (V<sup>-1</sup>)  
**C** Concentration of a species (mol m<sup>-3</sup>)  
<sub>c</sub> Related to the cathodic reaction  
**d** Distance between two electrodes (m)  
**D** Diffusion coefficient (m<sup>2</sup> s<sup>-1</sup>)  
**e** Charge on the electron =  $-1.602 \times 10^{-19}$  C  
**E** Electrical potential (V)  
**E<sub>corr</sub>** Corrosion potential (V)  
**E<sub>eq</sub>** Equilibrium potential (V)  
**F** Faraday constant = 96 486 C mol<sup>-1</sup>  
**g** Constant in eqn [32]  
**G** Chemical Gibbs free energy (J mol<sup>-1</sup>)  
 **$\bar{G}$**  Electrochemical Gibbs free energy (J mol<sup>-1</sup>)  
**G<sub>I</sub>** Gain of a current amplifier  
**G<sub>V</sub>** Gain of a voltage amplifier  
<sub>int</sub> Related to the interface  
**I** Current (A)  
**I<sub>0</sub>** Exchange current (A)  
**I<sub>corr</sub>** Corrosion current (A)  
**I<sub>set</sub>** Set current (A)  
**j** Current density (A m<sup>-2</sup>)  
**j<sub>0</sub>** Exchange current density (A m<sup>-2</sup>)  
**j<sub>corr</sub>** Corrosion current density (A m<sup>-2</sup>)  
**k** Reaction rate constant (m s<sup>-1</sup>)  
**K** Constant in eqns [31] and [32] (mol l<sup>-1</sup>)  
<sub>lim</sub> Related to diffusion limitation  
<sub>mix</sub> Related to mixed control  
<sub>mt</sub> Related to mass transport control  
**M** Molar mass (kg mol<sup>-1</sup>)  
**n** Number of moles (mol)  
**N** Avogadro's number =  $6.022 \times 10^{23}$   
**q** Electrical charge (C)  
**r** Disk electrode radius (m)  
<sub>ref</sub> Related to the reference electrode  
**R** Gas constant = 8.31 J mol<sup>-1</sup> K<sup>-1</sup>  
**R<sub>control</sub>** Current-control resistance (Ω)  
**R<sub>ct</sub>** Charge-transfer resistance (Ω)  
**R<sub>e</sub>** Electrolyte resistance (Ω)  
**R<sub>m</sub>** Current-measuring resistance (Ω)

**R<sub>p</sub>** Polarization resistance (Ω)  
**S** Electrode surface area (m<sup>2</sup>)  
**t** Time (s)  
**T** Temperature (K)  
**V<sub>set</sub>** Set potential (V)  
**y** Axial distance to a disk electrode (m)  
**z** Number of electrons exchanged in a reaction  
<sub>∞</sub> Related to the bulk of the electrolyte  
**[X]** Concentration of species X (mol l<sup>-1</sup>)  
<sup>0</sup> Related to the standard state  
 $\alpha$  Charge-transfer coefficient  
 $\beta$  Tafel slope (V per current decade)  
 $\delta$  Thickness of the diffusion layer (m)  
 $\Delta X$  Difference in X values (X unit)  
 $\Delta_r G$   $\bar{G}$  variation for reaction *r* (J mol<sup>-1</sup>)  
 $\epsilon$  Thickness loss (m)  
 $\phi$  Flux of species (mol m<sup>-2</sup> s<sup>-1</sup>)  
 $\Phi$  Electrical potential (V)  
 $\gamma$  Electrolyte conductivity (Ω<sup>-1</sup> m<sup>-1</sup>)  
 $\eta$  Overpotential (V)  
 $\nu$  Kinematic viscosity (m<sup>2</sup> s<sup>-1</sup>)  
 $\pi$  Polarization (V)  
 $\theta$  Coverage ratio of adsorbed species  
 $\rho$  Density (kg m<sup>-3</sup>)  
 $\omega$  Electrode angular rotation rate (rad s<sup>-1</sup>)

## 1.02.1 Introduction

The starting point of a chapter devoted to the introduction of basic aspects of electrochemistry that are absolutely vital for understanding corrosion processes can take advantage of the meaning of corrosion itself. In fact, corrosion processes encompass reactive phenomena of metal oxidation, hence yielding a progressive and more or less fast chemical deterioration of the material exposed to an aggressive environment by oxide formation or free dissolution in the form of dissolved cations. This implicates the existence of oxidation–reduction reactions, hereafter referred to as redox reactions, in which the role of the metallic surface and its interactions with the surrounding medium are particularly crucial. The basic concepts issuing from electrochemistry (roughly speaking, the branch of chemical sciences devoted to the study and investigation of reactive systems involving electrical charge transfer) are well adapted and necessary for a convenient description. These basic concepts will be helpful for the subsequent understanding of complex corrosion phenomena. The main goal of this chapter is, therefore, to provide an overview of basic electrochemical concepts, with a special focus



on electrochemical reaction near the equilibrium potential. Then, these concepts will be extended to those directly related to corrosion processes. For the sake of readability for nonexpert readers in electrochemistry, simplified representations of reactive interactions, actually much more complex, will be introduced in some cases. This is a conscious option taken by the authors to provide a self-sustained text conveying the main concepts and tools to understand the physicochemical processes associated with corrosion phenomena.

## 1.02.2 Current, Potential, and Interfaces

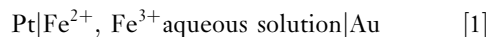
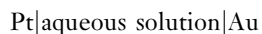
### 1.02.2.1 Electronic and Electrolytic Materials: The Two Sides of an Electrified Interface

Electrochemistry is a science, as well as an industrial domain, based on physicochemical phenomena taking place whenever electrical and chemical energy exchanges intervene in a reactive scheme. In this sense, most of the time electrochemistry investigates systems in which electrical currents flow, as in the case of electrochemical generators or batteries present in numerous everyday applications such as cars, mobile telephones, and so on. From this point of view, the archetypical corrosion process, that is a metallic piece freely exposed to a given aggressive environment is, to some extent, a bit marginal in the sense that the overall current flow observed from the outside of the system is zero; the system spontaneously evolves and is said to be at rest or at open-circuit. This is clearly the actual practical corrosion scenario, unless, an external source is applied as in the case of corrosion characterization or measurements and in some corrosion protection techniques such as cathodic or anodic protection. In spite of this feature, the concepts and tools involved in general electrochemistry remain valid and constitute the cornerstone of corrosion description and understanding.

It is possible to find redox reactions in a single phase, as in a bulk solution. Nevertheless, when talking about electrochemistry and more particularly corrosion, only heterogeneous systems are concerned, which means that the reactive system is composed of two or more distinct phases. As an example, let us consider a classical electrochemical system implying electrical energy exchanges such as a battery connected either to an electrical load (the battery hence discharges) or to an external electrical energy source (the battery hence charges). This is usually achieved by a multiphase ‘sandwich’ of at least three

different materials with two different metals at the battery terminals. Since they involve electrical energy exchange, the electrochemical systems only employ conductive materials. Electrical conductivity exists as soon as the materials have mobile charges. Without going through an exhaustive survey, these key materials can be classified into three main categories according to the nature of the charge carriers: electronic conductors like metals or semiconductors, ionic conductors (or electrolytes), and finally mixed conductors (such as some conducting polymers) when the two types of electrical conduction coexist. To illustrate corrosion phenomena in the following, the text will concentrate only on metals, which are electronic conductors undergoing corrosion, and on electrolytes, which can be aqueous or organic solutions, molten salts, ionic solids, polymers, or even gases.

Besides the electrical conductivity of these materials, the specificity of the electrochemical systems comes from the way they are assembled. Regions in which the different materials (the metal and the electrolyte, for instance) are in contact and in which the electrical continuity between the electronic and ionic conduction is ensured are generally called interfaces. (The term ‘interphase’ would probably be more appropriate for bringing up the idea that this is not a single surface in a purely mathematical point of view, but a small physical volume usually a layer of some nanometers as roughly described hereafter in [Section 1.02.2.4.2](#)) The simplest electrochemical assembly is thus composed of two metals having an interface with the same electrolyte. This kind of system is referred to as a galvanic chain, where each interface is schematically represented by a vertical stroke as in the following examples:



In the first example, where no corrosion process is expected at least in normal experimental conditions (concentration, temperature, etc.), both interfaces are said to be impermeable and nonreactive. In the second example, where the electrolyte is composed of an aqueous solution containing  $\text{Fe}^{2+}$  and  $\text{Fe}^{3+}$  cations, one of the most reactive couples and one often employed in analytical electrochemistry, the interfaces would still be impermeable but could then be reactive – even if corrosion of platinum and gold is considered as being negligible – since, under certain conditions,  $\text{Fe}^{2+}$  oxidation at one interface and  $\text{Fe}^{3+}$  reduction at the other should be observed. The term impermeable implies that the mobile species (the charge

carriers) at each side of the interfaces are different. Free electrons are mobile and can hence ensure the current flow across the metallic phases but are not present in the electrolyte phase, in which ions are mobile and ensure the electrical charge transport between the two metallic phases. In some more complex situations, such as certain corroding systems where a more or less ionically conductive oxide may partially or totally cover the metallic surface, hence creating an intermediate layer between the metal and the electrolyte, an interface between two ionic conductors is established and referred to as an ionic junction.

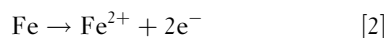
In contrast to that double interface configuration, from a macroscopic point of view, most corrosion processes take place at a single interface. This is the case, for instance, of the simplest corrosion situation: a piece of metal immersed in an electrolyte. It is obviously not possible for a net electrical current to flow in or out of this closed system. As discussed in more depth later in this chapter, this does not mean that no electrochemical reaction is taking place at the interface. It is also important to notice that this macroscopic single interface can be considered either as uniform, as for the corrosion of an almost homogeneous metallic surface (uniform or generalized corrosion) or nonuniform, as for the corrosion of a markedly heterogeneous metallic surface where inclusions or precipitates are preferentially corroded rather than the metallic matrix (an example of localized corrosion). It is then easy to understand that in the latter case two interfaces are actually concerned (metal|electrolyte|inclusion) in a microscopic approach, even if there is a single macroscopic interface.

### 1.02.2.2 Electrochemical Reactions

As indicated above, a common example of an electrochemical system is that of an impermeable interface between a metal and a solution containing ions where the species (charge carriers) ensuring the current flow at each side of the interface cannot traverse it. Indeed, on the one hand electrons are 'free' in the metallic lattice but trapped in the liquid phase by different cationic configurations and, on the other hand, ions can move in a liquid but are macroscopically frozen in the metallic phase by the lattice arrangement. This means that there is no straightforward continuity of the charge transport across the interface. Consequently, a steady-state current flow, for example, from the electrolyte to the metal requires the transformation at the interface of the ionic flow in the electrolyte into an electronic flow in the metal. This is done by

heterogeneous chemical reactions taking place at the interface, which allow electrons to be released by mobile species in the electrolyte and incorporated into the electron 'gas' in the metallic phase (anodic reaction) or, conversely, allow electrons leaving the electronic gas at the metal side to be trapped by an electrolyte species (cathodic reaction). (Remember that one of the most important characteristics of metals is that the valence electrons are free in a state that can be likened to a gas.) These heterogeneous (since they concern both the electrolyte and metallic phases) interfacial reactions entail the loss or the gain of electrons through a charge-transfer process (either oxidation or reduction). A single oxidation or reduction reaction is known as a half-cell reaction (since another reaction of the opposite type is needed to complete the full current path and create an electrochemical cell).

Whenever the current flow is straightforwardly related to one or several heterogeneous reactions, one refers to Faradaic current or, more generally, Faradaic processes because these phenomena can be described by a quantitative law called Faraday's law. The current flow across the interface can also be related to other types of electrochemical processes, namely capacitive processes, which correspond mostly to transient phenomena and will briefly be discussed in [Section 1.02.2.4.2](#). Of much concern in corrosion processes, Faraday's law mathematically expresses the relationship between the electrical charge transferred during a heterogeneous reaction and the amount of mass transformed at the same time. This is the Lavoisier principle of conservation of mass extended to electrons. As shown in the following example, Faraday's law is the very origin of the relationship (extremely important in corrosion engineering) between the corrosion current (experimentally measured or estimated) and the corrosion rate (in terms of mass or thickness loss), in the case of uniform corrosion. Let us consider the case of a uniformly corroding iron plate. For a divalent corrosion reaction



the corrosion current density (the current density is the corrosion current normalized by the geometrical surface area and is a simple and intuitive way of comparing corrosion rates independently of the size of the metallic surface considered) corresponding to the consumption of a certain quantity of Fe moles per unit time and per unit surface can be expressed by Faraday's law, as

$$\frac{1}{S} \frac{\Delta n}{\Delta t} = \frac{j}{2F} \quad [3]$$

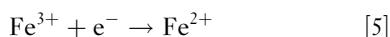


where  $\Delta n/\Delta t$  is the number of moles of iron consumed per unit time,  $S$  is the corroding surface area,  $j$  is the corrosion current density, and  $F$  is the Faraday constant. This constant represents the electrical charge of one mole of electrons, that is,  $F = -Ne$ , where  $N$  is Avogadro's number and  $e$  the charge on the electron ( $F = -6.022 \times 10^{23} \times -1.602 \times 10^{-19} = 96\,486 \text{ C mol}^{-1}$ ). For engineering applications, the expression of the corrosion rate in terms of thickness loss per year, for instance, is more useful:

$$\frac{\Delta \varepsilon}{\Delta t} = \frac{j}{2F} \frac{M}{\rho} \quad [4]$$

where  $M$  is the molar mass of the corroding compound and  $\rho$  is its density. In the case of iron corrosion ( $M = 55.84 \text{ g mol}^{-1}$  and  $\rho = 7.85 \text{ g cm}^{-3}$ ), a uniform corrosion current density of  $5 \mu\text{A cm}^{-2}$ , corresponds to a thickness loss of  $58 \mu\text{m year}^{-1}$ . A convenient rule of thumb is that for most metals  $1 \text{ A m}^{-2}$  corresponds to a penetration rate of approximately  $1 \text{ mm year}^{-1}$ .

Let us come back to the more general description of the processes related to a current flow. One of the simplest examples in electrochemistry concerns the interface between a platinum electrode and an electrolyte containing  $\text{Fe}^{3+}$  and  $\text{Fe}^{2+}$  ions. If an external power source imposes an electron flux from the metal towards the interface, a heterogeneous chemical reaction takes place at the interface. In this example, the transformation of ferric ions into ferrous ions takes place according to the reaction:



This reaction indicates that a certain amount of  $\text{Fe}^{3+}$  cations, proportional to the current, is transformed into  $\text{Fe}^{2+}$  ions, capturing the electrons coming from the metal and ensuring the continuity of current flow. This interface, on which a reduction reaction occurs, is called a cathode. In the case of a current flow in the opposite direction, electrons are produced by the redox reaction. Thus, the interface is the site of an oxidation reaction and is called an anode. **Figure 1** schematically illustrates this phenomenon for reaction [5]. The arrows represent the direction in which each reacting species moves (more rigorously, they indicate the direction of the corresponding mass flow vector).

It can be seen in **Figure 1** that, even in this very simple example, the current flow entails at least three important phenomena: electron transport inside the metal, ionic transport in the electrolyte, and the heterogeneous redox reaction, that is, charge-transfer reaction.

In classical electrochemical situations, the system comprises two interfaces and the existence of a steady-state current flow implies that one of the interfaces behaves as a cathode whilst the other plays the role of an anode; that is, one of them consumes the electrons produced by the other. Two typical scenarios are depicted in **Figures 2 and 3**. They illustrate, for instance, what happens in a mobile telephone when it is being used (its battery is discharging, **Figure 2**), or being recharged, **Figure 3**).

**Figure 2** presents the situation in which there is a spontaneous flow of electrons produced by an interfacial oxidation reaction at the anode. These electrons go through a resistor to be consumed at the

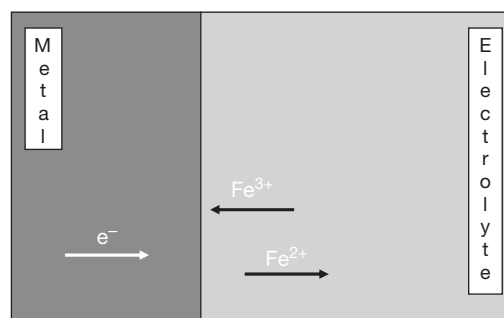


**Figure 1** Schematic representation of an impermeable metal-electrolyte interface at which a reduction reaction takes place; the interface acts as a cathode.

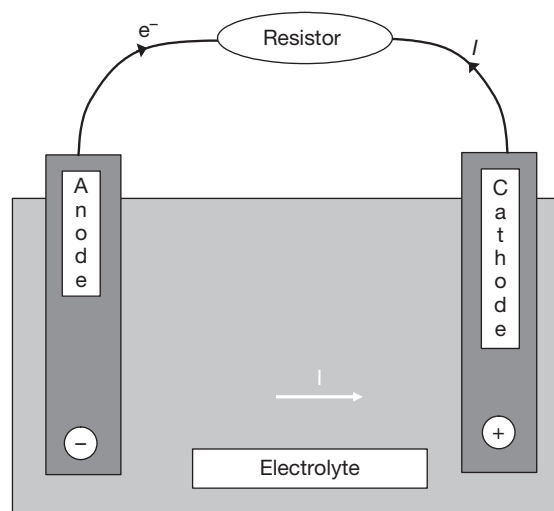


**Figure 2** Electrochemical battery during discharge: electrons are delivered to the external circuit by oxidation at the anode ( $\text{Red} \rightarrow \text{Ox} + n\text{e}^-$ ) and are consumed by reduction at the cathode ( $\text{Ox} + n\text{e}^- \rightarrow \text{Red}$ ).

cathode by a reduction reaction. In that case, the chemical energy of the reactants is converted to electrical energy, which is then converted into thermal energy by the Joule effect in the resistor. For mobile telephones, the energy delivered by the electrochemical system is converted into light, sound, radio waves, etc. As soon as the discharge process leads to a chemical transformation, the recharge process requires the reverse reaction to occur. While the discharge reaction in [Figure 2](#) takes place spontaneously, the recharge reaction can only occur if an external power source is connected to the system, as illustrated in [Figure 3](#). It is exactly like in mechanics when a ball that will spontaneously roll down a slope needs an external force to go up the slope. The electrode that was spontaneously a cathode is forced to work as an anode and the electron flow is reversed. It is worth noticing that the current and electron flows are identified by arrows in opposite directions, as illustrated in [Figures 2 and 3](#), since by convention the current flow direction is given by the positive charge carriers.

In another international convention (IUPAC), largely accepted but not always respected, it is considered that the anodic and cathodic currents are positive and negative, respectively. As a consequence, when anodic and cathodic processes occur on the same electrode, as in corrosion processes, the current is then positive when it flows from the anodic areas to the electrolyte and negative when it flows from the electrolyte to the cathodic areas.

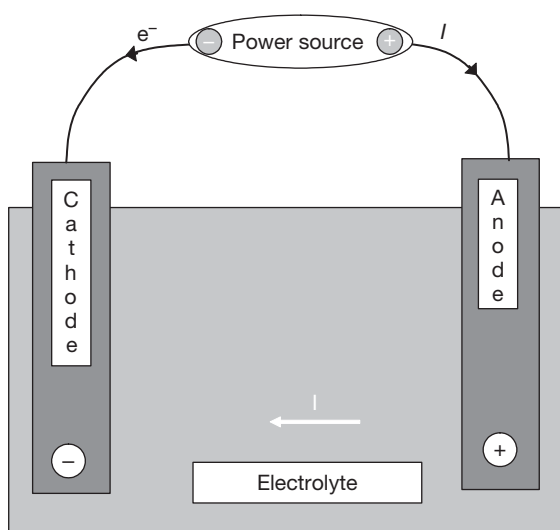


**Figure 3** Electrochemical battery in charge: electrons are consumed by reduction at the cathode ( $\text{Ox} + n\text{e}^- \rightarrow \text{Red}$ ) and produced by oxidation at the anode ( $\text{Red} \rightarrow \text{Ox} + n\text{e}^-$ ).

### 1.02.2.3 Electrochemical Reactions and Corrosion: Some Preliminary Remarks

In most corrosion processes, a single macroscopic interface is concerned. However, a system at rest, which is the most common corrosion situation, is a particular case of an electrochemical system under discharge analogous to that in [Figure 2](#) in the sense that the oxidation and reduction reactions are spontaneous. In contrast with [Figure 2](#), no external circuit allowing the current to flow is available and the overall current flow is null since both the anodic and cathodic reactions take place at the same metallic surface. This idea can be easily handled by considering the example of galvanic coupling depicted in [Figure 4](#), in which two different metals (iron and zinc) assembled together to form a single piece are exposed to an electrolyte rich in dissolved oxygen. In this situation, the zinc is an anode and hence corrodes whilst the iron tends to be protected since it plays the role of a cathode on which oxygen is reduced. It is important to notice that the fact that iron is a cathode does not mean that iron will necessarily be deposited on the metallic surface according to the reverse of reaction [2]. It means that the iron surface is the preferential site for cathodic (i.e., reduction) reactions. The exact nature of these reactions depends on the electrolyte and other important characteristics of the electrochemical systems that will be better discussed in [Section 1.02.2.4.1](#). For the sake of clarity, the cathodic reaction is

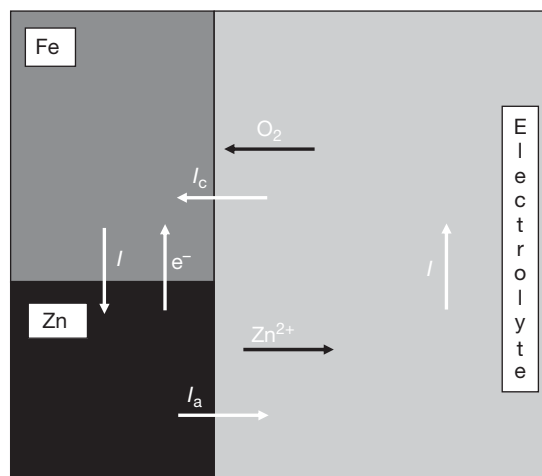


**Figure 4** Null net current balance in a freely corroding system: galvanic coupling between iron and zinc in contact with an electrolyte rich in dissolved oxygen.

represented in **Figure 4** by oxygen reduction, one of the most important reactions in corrosion processes.

Many similar situations with anodic and cathodic areas on the same electrode are encountered in corrosion, as when a metallic surface is not perfectly homogeneous, which is often the case. For instance, there are regions that are preferentially anodic, such as grain boundaries, intermetallic inclusions, zinc-rich phases in brasses, and so on. The existence of cathodic and anodic areas along the same surface can also be the result of inhomogeneous electrolytes, such as those in contact with partially submersed structures. Indeed, dissolved oxygen is easily available near the air–liquid interface, inducing a preferentially cathodic behavior of the metallic surface. For a completely uniform metallic surface immersed in a perfectly homogeneous electrolyte, the idea of a zero net current balance related to simultaneous anodic and cathodic reactions still holds, even if no preferential anodic or cathodic locations appear at the interface. Indeed, each surface site dynamically and randomly switch between anodic and cathodic behavior so that the overall net current is permanently zero and general corrosion occurs.

Thus, for the bimetallic surface in **Figure 4** as well as for any system left at rest, the anodic,  $I_a$ , and cathodic,  $I_c$ , currents must perfectly and permanently balance out each other, so that no overall current flows to or from this closed system, so that:

$$I_{Zn} = I_a = -I_c = -I_{Fe} > 0 \quad [6]$$

(The equality represented in eqn [6] is only true for the average behavior; short-term differences can be accommodated by charging or discharging of the double-layer capacitance, and this leads to the phenomenon of electrochemical noise.) It is important to note that in this equation, the anodic and cathodic currents are identical in absolute values. Also, this equation holds for currents,  $I_a$  and  $I_c$ , and not for current densities,  $j_a$  and  $j_c$ , defined as follows:

$$I_a = j_a S_a = -j_c S_c = -I_c \quad [7]$$

where  $S_a$  and  $S_c$  are the surface of the anodic (zinc) and cathodic (iron) areas, respectively. Thus

$$j_a = |j_c| \frac{S_c}{S_a} \quad [8]$$

or

$$|j_c| = j_a \frac{S_a}{S_c} \quad [9]$$

If the surface areas of iron and zinc in **Figure 4**, and more generally the surfaces of preferential anodic or

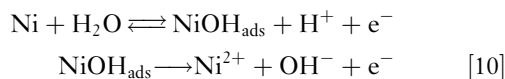
cathodic zones in any given electrode are different, eqn [8] clearly points out that the system may have very high partial current densities because of the surface ratio. This is extremely important in corrosion applications. As an example, let us go back to the iron–zinc example and consider the possibility of using zinc rivets to assemble large iron plates. Equation [8] immediately shows that the zinc rivets in contact with an electrolyte such as rain water corrode very rapidly because of the very high anodic (corrosion) current density related to the huge cathodic (iron)/anodic (zinc) surface ratio.

### 1.02.2.4 Basic Description of Metal–Electrolyte Interfaces

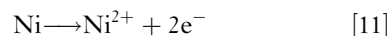
#### 1.02.2.4.1 Elementary steps and intermediate interfacial species

The simplified and common aspects of electrochemical reactions taking place at metal–electrolyte interfaces considered up to now deserve a better although still simple description. The first important aspect is that the overall charge-transfer reactions involved in corrosion processes are often the consequence of complex interfacial phenomena that can be described by a more or less intricate reaction mechanism comprising several intermediate elementary steps. The reactive species implied in this mechanism are not only the ensemble of reactants and products of the overall reaction such as electrons, the metal itself, ions or dissolved gas as in the previous examples, but also other species produced as reaction intermediates.

Intermediate species can be very important in the kinetics of heterogeneous phenomena. In corrosion, these species are surface adsorbates that physico-chemically adhere to the metallic surface, such as water itself, neutral species or anionic species. Let us consider two examples of complex mechanisms concerning corrosion processes. The first is the mechanism of nickel corrosion (to a first approximation, this is also the mechanism of iron dissolution) proposed in the literature<sup>1,2</sup>:



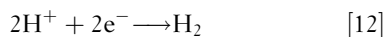
The simple algebraic addition of both elementary (single electron) reactions gives the global reaction [11]:



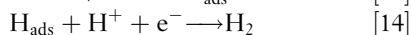
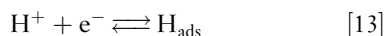
(or reaction [2] in the case of iron). This multielectronic reaction is the overall and simplified chemical representation of a more complex process. It is also

important to notice that the intermediate adsorbed species (identified by the subscript 'ads') plays an important role in the kinetics of the overall reaction. If the first ( $\text{NiOH}_{\text{ads}}$  adsorption) or the second ( $\text{NiOH}_{\text{ads}}$  desorption giving  $\text{Ni}^{2+}$ ) elementary step is hindered, the overall Ni dissolution is slower since Ni dissolution occurs through two consecutive steps.

Adsorbates can also be produced by cathodic reactions, an important example coming from the proton reduction on metallic surfaces, roughly represented as



but actually composed of two (or more) intermediate elementary steps, as those of the so-called Volmer–Heyrovski route<sup>3</sup>:



It is easily seen that the addition of the Volmer (reaction [13]) and Heyrovski (reaction [14]) elementary steps gives the global representation of reaction [12]. (An alternative to the Heyrovski reaction, known as the Tafel reaction, involves the direct combination of two adsorbed hydrogen atoms to form a hydrogen molecule – this dominates at low overpotentials.) Adsorbates can also play a critical role in the overall kinetics of corrosion since they constitute some of the elementary building blocks of corrosion mechanisms.<sup>4</sup> It is interesting to note that, under certain conditions, the adsorption site can be considered as temporarily blocked by the  $\text{H}_{\text{ads}}$  adsorbate from the point of view of corrosion,<sup>5,6</sup> which means that it is not able to dissolve as long as this site is occupied by  $\text{H}_{\text{ads}}$ . This is obviously not an evidence of an effective protective role of  $\text{H}_{\text{ads}}$  against corrosion, otherwise acidic solutions would not be aggressive, which is evidently far from true. It is worth recalling that the hydrogen evolution reaction in acidic media is rather fast, so that  $\text{H}_{\text{ads}}$  is transformed into  $\text{H}_2$  at a significant rate. In addition, the active dissolution rate, for instance of iron, is also fast. Even if only 1% of the surface area is devoted to this process, the corrosion current density is far from zero. This brief discussion illustrates the complexity of corrosion kinetics. In other situations, the protective role of adsorbates as blocking agents is extremely important and is fully employed in the development of inhibitors for corrosion protection.<sup>7,8</sup> Very often, in the presence of organic inhibitors, the cathodic reaction rate is slowed down markedly, whereas inorganic substances, so-called anodic inhibitors, are more effective at reducing the metal dissolution rate. Since the corrosion

takes place at a zero overall current, the decrease in the rates of either of these processes (anodic or cathodic) slows down the net corrosion rate.

Reactions [10]–[14] are simple mechanisms involving single-adsorbate reactions. Other important reactions, such as iron dissolution<sup>9–14</sup> or oxygen reduction,<sup>15,16</sup> can involve several adsorbates, the identification of which is often a difficult task. Besides these complex features of redox reactions with the presence or the absence of intermediate species, the current flow across the interface is also dependent on the transport of reactive species in the electrolyte. Hence, a complete or at least better description of the kinetics of the metal–electrolyte interface must encompass the behavior of these charge carriers in the interfacial region.

#### 1.02.2.4.2 The electrical double layer

In a first approach, this description can be made simpler by considering a metal–electrolyte interface at which no redox reaction takes place so that no Faradaic current flows across it. This interface is thus impermeable and nonreactive like the first one in scheme [1] and the only observable phenomenon is the accumulation of species at both sides of the interface. When these species are electrically charged, important electrical constraints appear. Indeed, since both metallic and electrolytic phases are conductive, the attractive and repulsive electrical forces exerted on the charge carriers imposes electroneutrality (that means a net charge equal to zero) of any significant volume of metal and electrolyte. (Strictly there can be a net positive or negative charge at a point. This is described by the Poisson equation, which states that the local charge density  $= -\epsilon\epsilon_0 \text{d}^2\varphi/\text{d}x^2$ , where  $\varphi$  is the local potential,  $\epsilon$  the dielectric constant and  $\epsilon_0$  the permittivity of free space. However,  $\epsilon\epsilon_0$  is so small that the net charge is negligible except in exceptional circumstances (such as at the metal–solution interface).) Significant deviations from electroneutrality can only exist at very short distances, as in a water molecule composed of two  $\text{H}^+$  and one  $\text{O}^{2-}$ . Nevertheless, due to the intrinsic differences in the conducting mechanism in each phase (electronic conduction in the metal and ionic conduction in the electrolyte), a local deviation from electroneutrality occurs at the interface. For example, as schematically represented by a solid line in Figure 5, an excess of electrons at the metallic side can permanently exist provided that positive charges (for instance, an excess of cations) are in excess at the other side.

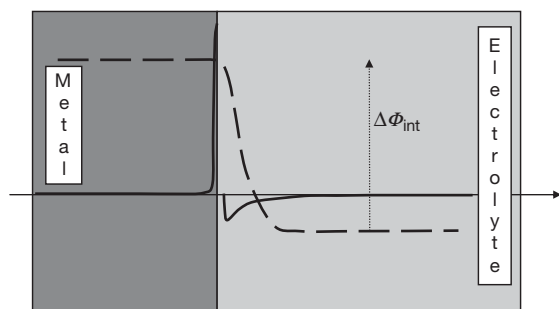


**Figure 5** Schematic representation of the electrical charge density (solid line) and of the induced potential  $\phi$  (dashed line) at both sides of the interface.

Even in these conditions of local charge separation, the overall electroneutrality must be respected, which means that these face-to-face opposite charges in excess at the interface must be perfectly balanced out. These spatial and electrical configurations are essentially the same as those of an electrical capacitor composed of two parallel plates electrically charged with opposite signs. However, this electrochemical capacitor typically has a distance between the plates of only a few nanometres. The charge distribution across the interface entails a potential shift  $\Delta\phi_{\text{int}}$  across the interface, as illustrated by the dashed line in [Figure 5](#). In steady-state conditions, the electroneutrality being respected, no current flows across the electrochemical capacitor. Nevertheless, any potential or current perturbation of the system may induce a local rearrangement of the charge distribution at each side of the interface, which leads to a transient flow of ‘capacitive current.’ As a consequence, the measured current in an electrochemical experiment generally includes the effects of this capacitive process, in addition to the Faradaic response.

As shown schematically in [Figure 5](#), the distribution of the excess charge at each side of the interface is asymmetric. It is sharply confined in a virtually zero volume at the metallic side, but spread out over a nonnegligible distance at the other side. This electrolyte zone, in which the electroneutrality is not respected, is called double layer<sup>17,18</sup> as it is frequently divided into a first layer, close to the metallic surface, called the ‘compact layer’ and a second, called the ‘diffuse layer,’ as represented in [Figure 6](#).<sup>19</sup>

In order to better understand how the double layer is configured, let us remember that ions in an electrolyte are solvated (roughly speaking, for an aqueous electrolyte, they are wrapped by water molecules). As shown in [Figure 6](#), the distance between

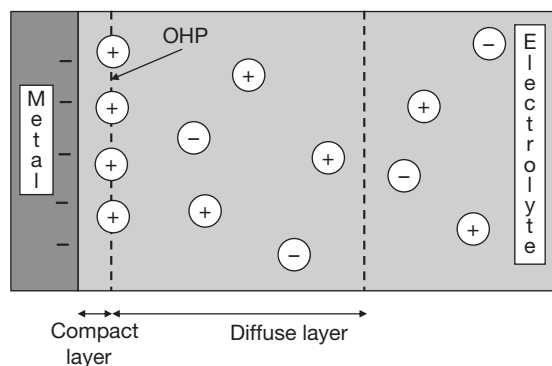


**Figure 6** Simplified scheme of the electrolyte double layer: compact and diffuse layers with solvated cations and anions in the electrolyte.

the closest centers of the ions and the metallic surface defines the so-called outer Helmholtz plane (OHP),<sup>18</sup> which is the boundary of the compact layer (thickness of about 1 nm). Under certain conditions, ions can show specific adsorption behavior at the interface (called electrosorption) so that they can penetrate into the compact layer. As a consequence, they establish a new lower minimal approach distance of the closest adsorbed ion centers that defines the inner Helmholtz plane (IHP), which logically modifies the potential profiles in this region.

Beyond the Helmholtz plane, the double layer spreads into the diffuse layer. The thickness of this layer depends on the ionic composition of the electrolyte. It is about 1  $\mu\text{m}$  in pure water, whereas it may vary in an electrolytic medium from several tens to a fraction of nm depending on the salt concentration. For instance, the typical thickness of a diffuse layer varies from 6 to 20 nm when the concentration of the ionic species in the electrolyte decreases from 0.01 to 0.001  $\text{mol l}^{-1}$ . Thus, in the presence of a supporting electrolyte (auxiliary electrolyte constituted of non-reactive ions at high concentration to increase the electrolyte conductivity) the diffuse layer becomes much thinner.

#### 1.02.2.4.3 Current and mass transport mechanisms

As mentioned in the preceding sections, electrochemical kinetics encompasses not only interfacial reactions but also the transport of mobile species inside the conductive phases to and from the interface. Without going into mathematical details, the current in a given infinitesimal volume is the resultant of macroscopic movements of all the charged species in this



volume. A complete discussion on mass transport and its influence on electrochemical processes can be found elsewhere.<sup>20–22</sup> In this chapter, it is sufficient to consider that the mass transport phenomena can be macroscopically described with three types of driving force, roughly portrayed as follows:

- *Migration* is the movement of charged species under the effect of an electrical field (which is an electrical potential gradient). It may be neglected for the electroactive species in the presence of a supporting electrolyte.
- *Diffusion* is a process analogous to that of migration in which species are transported under the effect of a concentration gradient towards the regions of low concentration, which tends to homogenize the solution.
- *Convection* is the relative movement of a fluid medium, liquid or gaseous, which takes place even for macroscopically stationary electrolytes. This is the case of natural convection caused by mechanical vibrations or by density gradients, such as those induced by local differences in temperature between the wall of a reservoir and the bulk solution, by gas evolution or by the release of dense ions into solution. Convection can also be forced by mechanical stirring or, very often in electrochemistry, by using rotating disk electrodes or impinging jet cells.

In electrochemistry, under certain experimental conditions (see examples below), diffusion phenomena are negligible compared to migration and convection at a distance sufficiently far from the interface. Hence, the region in which diffusion cannot be neglected, compared to other mass transport mechanisms, is defined as the diffusion layer. This zone close to the interface plays a crucial role in the kinetics of electrochemical phenomena. It can spontaneously appear because of the interfacial depletion or abundance of reactants induced by the (electro) chemical reactions, since only the species present at the interface are able to react. Depending on the kinetics of the reactions, the interfacial concentrations can be markedly different from those in the bulk solution (the region where the concentration is homogeneous) and are a key parameter for the description of electrochemical and hence corrosion phenomena.

In the absence of convection, the current flow or simply the natural evolution of a metal–electrolyte interface at rest, as in corrosion processes, induces the formation of a diffusion layer that grows continuously with time. The changes in the electrolyte

concentration generated by chemical perturbations at the interface, move progressively towards the bulk solution as the diffusion front progresses. However, convection often occurs in practice, both natural convection and especially forced convection, as in water distribution networks, pipelines, and many industrial systems. An accurate and quantitative analysis of convection phenomena is covered in another section of this book but the general result of Nernst's model illustrated in [Figure 7](#) can be retained. This model predicts that in spite of the presence of convection, there is a region close to the interface (called Nernst layer) in which the convective forces vanish since the electrolyte velocity at the interface is actually zero. This is the consequence of the existence of viscoelastic forces at the interface that prevent the liquid phase from sliding along the solid phase and lead to a continuous decrease of the convection effects from the bulk to the interface. The model approximates this monotonic evolution by assuming a discontinuity between the bulk and the Nernst layer. Mass transport is controlled by diffusion and migration inside this layer and the reactants exhibit concentration gradients, while outside this layer the electrolyte is stirred by convection and, therefore, the reactant concentrations are considered to be homogeneous. The thickness of the Nernst layer, also called diffusion layer, depends on the stirring conditions. Typical thicknesses are 10 and 300  $\mu\text{m}$  for forced and natural convection, respectively.

#### 1.02.2.4.4 Potential and concentration profiles across the interface

The spatial variations of the reactant concentrations and of the electrical potential in the region close to

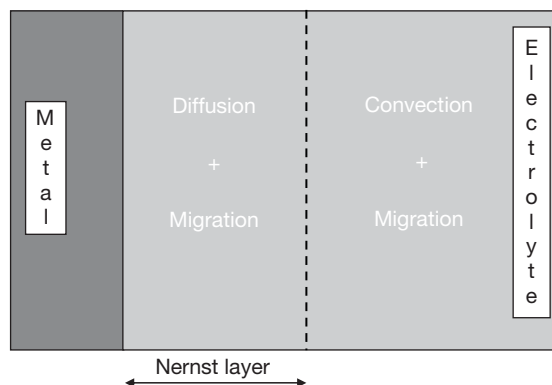


**Figure 7** Simplified schematic representation of the metal–electrolyte interface for the Nernst mass-transport model.

the interface, play an important role in the accurate modeling of the kinetics of electrochemical phenomena and hence of the corrosion processes. First of all, it is important to point out the differences in the thickness of the double layer (typically a few nanometres) and that of the diffusion layer (typically a few tens of micrometres). **Figure 8** presents the schematic concentration and potential profiles across the double and diffusion layers. In most cases, the diffusion layer is actually the most pertinent scale for a convenient analytical approach, so that it is sufficient to define the electrical potential and the reactant concentrations at the boundary of the double layer.

Indeed, the double layer being so thin at this scale, the interfacial concentration  $C_{\text{int}}$  of a reactant, that is, the concentration at the Helmholtz plane (see the zoom in **Figure 8**), which is the key parameter concerning the kinetics of the mass transport and redox reactions, may be considered as constant in the double layer. In the same way, even if the potential varies strongly in the double layer, it is sufficient to consider the driving force of the redox reactions as being controlled by the interfacial potential difference  $\Delta\Phi_{\text{int}}$ , that is, the potential difference across the double layer. In the diffusion layer and in the electrolyte bulk, the potential will vary according to

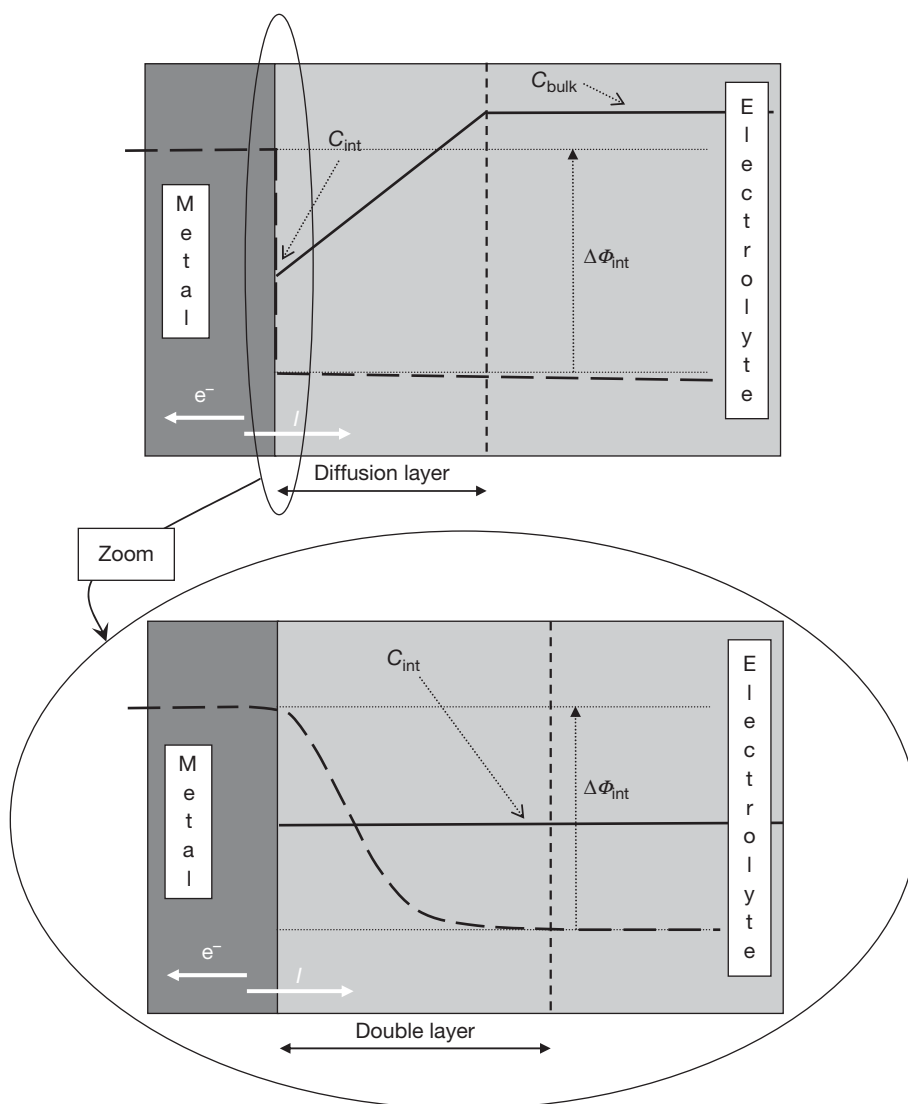


**Figure 8** Schematic representation of the metal–electrolyte interface: concentration (solid line) and potential (dashed line) profiles.

the solution conductivity and current density, as in [Figure 8](#) (ohmic drop effect, see more details in [Section 1.02.6.1.2](#)).

### 1.02.3 Electrochemical Equilibrium

#### 1.02.3.1 Definition and Introductory Remarks

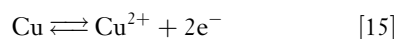
Electrochemical equilibrium is one of the major concepts that needs to be correctly handled to really understand corrosion processes. A proper definition should take into account the fact that the equilibrium of an electrochemical system involves the equilibrium of all materials and all interfaces. In a true equilibrium, no macroscopic gradient of any physical variable (temperature, pressure, concentration, etc.) exists in the bulk of any phase and there is no net macroscopic flux across any interface. Thus, in the framework of the present work, the electrochemical equilibrium will be frequently related to an interface state in which no overall current flows to or from the interface.

Before going further with the analysis of electrochemical equilibrium, two critical remarks must be kept in mind. Firstly, some systems can show a very slow evolution constituting a quasisteady behavior that is not a true equilibrium. As seen below, passive stainless steels can be considered as nonevolving systems under certain conditions, but they are actually far from being at thermodynamic equilibrium. The knowledge of electrochemical equilibrium characteristics is, however, still indispensable for the comprehension and the macroscopic global description of the quasisteady state of such systems and most corrosion processes. Another major point is that the equilibrium state necessarily means a net zero current, but the converse is far from being true. As already pointed out in [Section 1.02.2.3](#), for any corroding system freely evolving in any aggressive media, the net current flowing to or from the interface is also zero, but the system will not be in a state of true equilibrium.

#### 1.02.3.2 Electrochemical Equilibrium as a Dynamic State: the Exchange Current Density

Let us consider a static body in equilibrium. No net macroscopic movement is expected (the body does not move provided the ensemble of variables remains constant), but each constituent particle spins,

vibrates, or even moves due to thermal agitation. A static object is hence an intrinsically dynamic system at the molecular level and this is not inconsistent with its macroscopic motionless state. The same holds for an electrochemical system: reaching and observing the electrochemical equilibrium absolutely does not indicate that, besides the thermal agitation, the interface is frozen without any charge transfer going on with time. For example, a copper bar immersed in a weak acid solution (no dissolved oxygen present and copper oxides are not stable) containing a certain amount of copper  $\text{Cu}^{2+}$  cations undergoes the forward–backward redox reaction at equilibrium:



In any given time interval the same number  $n$  of moles of  $\text{Cu}^{2+}$  and  $2n$  of electrons is produced by metal dissolution (corresponding to an anodic current  $I_a$ ) and concomitantly consumed by metal deposition on the metallic surface (corresponding to a cathodic current  $I_c$ ). Dissolution and deposition are the forward and backward elementary steps of the same overall reaction [\[15\]](#) and take place with the same rate, thus yielding  $I_a + I_c = 0$  or  $|I_a| = |I_c| = I_0$ ,  $I_0$  being called the exchange current. Provided that the ensemble of physicochemical parameters (temperature, pressure, etc.) is kept constant, the dynamic zero current balance between the forward and backward reactions implies that the system does not evolve with time: the  $\text{Cu}^{2+}$  concentration, as well as the mass of metallic copper, remains unchanged *ad aeternum* or, at least, as long as the equilibrium holds (as seen later, the equilibrium can be broken as a consequence of the polarization of the system under the action of a parallel reaction, such as oxygen reduction that leads to copper corrosion: the system then evolves in nonequilibrium conditions as for every corrosion process). It can then be concluded that the exchange current is an important attribute of the dynamics of the system. Indeed, the constant  $\text{Cu}^{2+}$  (or  $\text{M}^{z+}$  for a more general  $\text{M}^{z+}/\text{M}$  couple) concentration, characteristic of the electrochemical equilibrium, may result from very different interfacial behaviors. High values of  $I_0$  (for instance,  $10^{-1} \text{ A cm}^{-2}$  for aqueous systems at room temperature) indicate that the system is very active with many reactive interactions per unit time in each direction (anodic and cathodic), whilst low  $I_0$  values (typically  $10^{-5} \text{ A cm}^{-2}$  for aqueous systems at room temperature) indicate slow systems. This is a key concept in reaction kinetics as discussed later in this chapter.



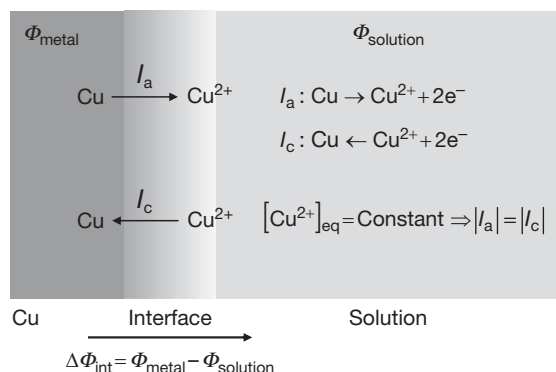


**Figure 9** Schematic representation of the potential difference and current exchanges across the metal–electrolyte interface for a  $\text{Cu}^{2+}/\text{Cu}$  equilibrium.

The asymmetric distribution of electrical charges at both sides of the interface, as depicted in **Figure 9** (charged cations at one side, electrons in metallic sites at the other), entails a well-defined potential difference,  $\Delta\Phi_{\text{int}} = \Phi_{\text{metal}} - \Phi_{\text{solution}}$ . The  $\Delta\Phi_{\text{int}}$  value thus depends on the thermodynamic characteristics of each phase – in particular their composition – and is related to the equilibrium potential,  $E_{\text{eq}}$ , as will be formalized in the next section.

### 1.02.3.3 Formal Expression of $E_{\text{eq}}$ : the Nernst Law for the $\text{M}^{z+}/\text{M}$ Couple

Classical thermochemistry deals with the transformation of a given species at constant temperature and pressure leading to the concept of Gibbs free energy. In the case of charged species intervening in electrochemistry, an electrochemical Gibbs free energy  $\bar{G}$  can then be defined. As for any electrical charge  $q$ , a part of this electrochemical energy is electric and is related to the work,  $q\Phi$ , supplied for moving this particle inside an electrical field associated with the potential  $\Phi$ . For one mole of the  $\text{M}^{z+}$  cation, the electrical contribution to the total electrochemical energy  $\bar{G}$  can be written as

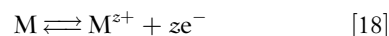
$$q\Phi = z|e|N\Phi = zF\Phi \quad [16]$$

Hence, the electrochemical free energy of  $\text{M}^{z+}$  usually expressed as the addition of a chemical term,  $G$ , to the electrical term,  $zF\Phi$ :

$$\bar{G} = G + zF\Phi \quad [17]$$

For any reactive system, it can be demonstrated that the thermochemical equilibrium is related to the

absence of change in the reaction free energy, in this case, electrochemical,  $\Delta_r\bar{G} = 0$ , where the subscript  $r$  stands for any possible reaction. The electrochemical reaction free energy decomposition in chemical and electric terms as in **eqn [17]**, entails the important conclusion that the equilibrium of a redox reaction involving  $z$  electrons sets up an interfacial potential difference  $\Delta\Phi_{\text{int}}$  expressed as a function of the chemical reaction free energy. It can be demonstrated that, for reaction **[18]**<sup>23</sup>:



one has

$$\Delta_r\bar{G} = 0 \Rightarrow \Delta\Phi = \frac{\Delta_r G}{zF} \quad [19]$$

The change in the chemical free energy can be mathematically expressed as<sup>24,25</sup>

$$\Delta_r G = \Delta_r G^0 + RT \ln \frac{a_{\text{M}^{z+}}}{a_{\text{metal}}} = \Delta_r G^0 + RT \ln [\text{M}^{z+}] \quad [20]$$

where the superscript indicates that all reactants are in a standard state, and  $R$  is the gas constant ( $8.31 \text{ J mol}^{-1} \text{ K}^{-1}$ ). The symbol  $a$  denotes the species activity, which is equal to 1 in the standard state and is considered as unity in the right-hand side of **eqn [20]** for the metal. Besides, as an approximation that is sufficient for dilute solutions, it is assumed that the cation activity is equal to its concentration (represented by square brackets) in moles per liter.<sup>26</sup> According to **eqn [19]**, the potential difference  $\Delta\Phi_{\text{int}}$  associated with reaction **[18]** can be expressed as

$$\Delta\Phi_{\text{int}} = \Delta\Phi_{\text{int}}^0 + \frac{RT}{zF} \ln [\text{M}^{z+}] \quad [21]$$

**Equation [21]** is however experimentally useless, since the  $\Delta\Phi_{\text{int}}$  values are not directly measurable. Indeed, even if the metallic phase can be connected to one of the terminals of a voltmeter with a conducting wire, the other terminal of the voltmeter must be connected to a probe dipped in the aqueous phase. The potential difference,  $\Delta\Phi_{\text{probe}}$ , between the probe (necessarily conductive to allow potential measurements) and the aqueous phase must be taken into account in addition to the potential difference,  $\Delta\Phi_{\text{M}^{z+}/\text{M}}$ , of the metal–solution interface in the presence of the  $\text{M}^{z+}/\text{M}$  couple under investigation. A voltage  $\Delta\Phi_{\text{M}^{z+}/\text{M}} - \Delta\Phi_{\text{probe}}$  is then actually measured. To be able to give a value to the  $\Delta\Phi_{\text{M}^{z+}/\text{M}}$  term, the solution is to work with a reference system to which all electrochemical potentials are referred.

The reference system chosen is the standard hydrogen electrode (SHE) related to the  $\text{H}^+/\text{H}_2$  equilibrium, in which the reactants are in the standard state. By convention, a 0 V value is attributed to  $\Delta\Phi_{\text{probe}}$  in this case at all temperatures. The SHE is difficult to realize experimentally, since it requires that the acid solution has a hydrogen ion activity of 1 (which requires a molarity greater than 1, of about  $1.19 \text{ mol l}^{-1}$  for HCl), and a hydrogen activity of 1 (which requires a partial pressure of hydrogen of 1 bar plus an allowance for the vapor pressure of the solution). A very similar electrode (with a very similar potential) is obtained by bubbling pure hydrogen gas at the surface of a Pt electrode in a normal (molar) acidic solution, which constitutes the so-called normal hydrogen electrode (NHE). **Figure 10** illustrates the experimental assembly of a NHE and the complete apparatus for the measurement of the  $\text{Ag}^+/\text{Ag}$  potential.

It is clear that the experimental set-up depicted in **Figure 10** is impractical for daily experiments. This is why several other very stable redox couples are used for reference electrodes as presented in **Section 1.02.6**. In every potential measurement, the potential determined includes both the desired metallic couple and the reference one. In such conditions, the usual notation introduces the electrode potential  $E$  as

$$E = \Delta\Phi_{\text{M}^{z+}/\text{M}} - \Delta\Phi_{\text{ref}} \quad [22]$$

This means that the potential value read on the voltmeter in **Figure 10** is not the actual potential value of the metallic couple, it is the potential difference between two redox couples.

Finally, adding  $-\Delta\Phi_{\text{ref}}$  at both sides of eqn [21] leads to the usual form of the Nernst equation

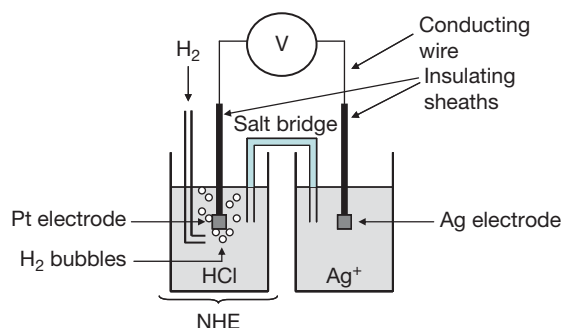


**Figure 10** Experimental set-up for measuring the  $\text{Ag}^+/\text{Ag}$  potential difference,  $\Delta\Phi_{\text{Ag}^+/\text{Ag}}$ , versus a normal hydrogen electrode.

applied to corrosion studies (where  $[\text{M}^{z+}]$  is given in  $\text{mol l}^{-1}$ ) giving the equilibrium potential,  $E_{\text{eq}}$ , of the redox reaction [18]:

$$E_{\text{eq}} = E^0 + \frac{RT}{zF} \ln [\text{M}^{z+}] \quad [23]$$

or, in the more convenient decimal logarithmic scale ( $RT \ln(10)/F = 0.059 \text{ V}$  at  $25^\circ \text{C}$ ):

$$E_{\text{eq}} = E^0 + \frac{0.059}{z} \log [\text{M}^{z+}] \quad [24]$$

It is worth noting that the charge transfer process physically takes place at the metal–electrolyte interface. This means that  $[\text{M}^{z+}]$  in the Nernst equation corresponds to the interfacial concentration of  $\text{M}^{z+}$ . Since there is no concentration gradient in solution at the electrochemical equilibrium,  $[\text{M}^{z+}]$  is also the  $\text{M}^{z+}$  concentration in the solution bulk. However, in nonequilibrium conditions, necessarily the case when corrosion occurs, the interfacial concentration,  $C_{\text{int}}$ , is generally different from the bulk concentration,  $C_{\infty}$ , and the electrode potential is no longer related to  $C_{\text{int}}$  or  $C_{\infty}$  in a simple way. Nevertheless, for some redox couples, termed Nernstian, which are almost always fast and reversible in a kinetic sense, a local near-equilibrium can be considered at the interface so that the electrode potential obeys a Nernst-like equation:

$$E(I \neq 0) = E^0 + \frac{0.059}{z} \log C_{\text{int}} \neq E_{\text{eq}} \quad [25]$$

The Nernst equation is an extremely rich tool for a first approach of the analysis and comprehension of corrosion processes, as shown below. Let us first note that  $E^0$ , the equilibrium potential for the couple  $\text{M}^{z+}/\text{M}$  in the well-defined standard state, is a thermodynamic constant that can be easily found in tables and reference books.<sup>27</sup> **Table 1** gives some important examples in the context of corrosion.

**Table 1** Standard electrochemical equilibrium potential values of redox couples

Couple	$E^0 (V_{\text{SHE}})$
$\text{Au}^{3+}/\text{Au}$	1.43
$\text{Ag}^+/\text{Ag}$	0.79
$\text{Cu}^{2+}/\text{Cu}$	0.34
$\text{H}^+/\text{H}_2$	0
$\text{Ni}^{2+}/\text{Ni}$	−0.26
$\text{Fe}^{2+}/\text{Fe}$	−0.44
$\text{Zn}^{2+}/\text{Zn}$	−0.76
$\text{Al}^{3+}/\text{Al}$	−1.33

A first glance at [Table 1](#) shows that noble metals such as gold and silver for which corrosion is not expected, have high positive values (hence called noble potentials), whilst those which are promptly recognized as corroding metals (Fe, Zn) have low (less noble)  $E^0$  values. It then clearly appears that  $E^0$  gives relevant information on the tendency of each metal to corrode. An apparent contradiction appears in the case of Al, which nonexpert common experience would describe as corrosion resistant. In reality, from a thermodynamic point of view, aluminum is actually extremely reactive and easily transformed into  $\text{Al}^{3+}$ . However, this reaction leads to the formation of a very homogeneous and corrosion-resistant film on the metallic surface, in a self-protective process called passivation, largely discussed elsewhere in this book. For the purpose of this chapter, it is important to retain this false paradox as the consequence of the fact that the Nernst equation is the result of a thermodynamic treatment concerning only the first formation of  $\text{Al}^{3+}$  and not the solid protective oxide formation, though thermodynamically predicted, as shown in the next section.

It is also easy to see from the Nernst [eqn \[23\]](#), that changes in cation concentration yield changes in the equilibrium potential. The equilibrium potential of any metal in contact with a solution containing the corresponding cation can be easily calculated for a given cation concentration. As an example, the equilibrium potential of Zn with  $[\text{Zn}^{2+}] = 10^{-2} \text{ mol l}^{-1}$  is  $E_{\text{eq}} = -0.76 + 0.0295 \times (-2) = -0.82 \text{ V}_{\text{SHE}}$  according to [eqn \[24\]](#) and [Table 1](#). If the potential is shifted, for instance, to  $-0.7 \text{ V}_{\text{SHE}}$ , the Nernst equation predicts that Zn is no longer at equilibrium with  $[\text{Zn}^{2+}] = 10^{-2} \text{ mol l}^{-1}$ , but with  $[\text{Zn}^{2+}] = 10^2 \text{ mol l}^{-1}$ , that is a 10 000-fold increase in concentration. This means that Zn will corrode, liberating  $\text{Zn}^{2+}$  cations to the solution until the cation concentration predicted by the Nernst equation is reached and a new equilibrium is established. It is then clear that during a certain time needed for electrolyte homogenization at this new  $\text{Zn}^{2+}$  concentration, a positive (anodic) current appears: the system is transiently out of equilibrium. Alternatively, if the new potential value is lower than that of the initial equilibrium, it is easy to deduce that a certain amount of cations have to be reduced and deposited on the metallic Zn surface to diminish the cation concentration in solution. The value of the potential shift from the equilibrium potential

$$\eta = E - E_{\text{eq}} \quad [26]$$

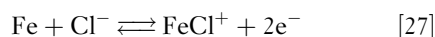
is independent of the reference employed and is called overpotential. The above discussion can be summarized as follows:

$$E > E_{\text{eq}}, \eta > 0 \quad \text{possibility of metal dissolution (i.e., corrosion)}$$

$$E < E_{\text{eq}}, \eta < 0 \quad \text{possibility of electrodeposition}$$

#### 1.02.3.4 Some More Complex Applications of the Nernst Law

Up to now, only the archetypical corrosion redox couple  $\text{M}^{z+}/\text{M}$  has been dealt with. Nevertheless, it is important to consider the more general approach of the Nernst law used for other redox couples. Some important examples concerning acid–base properties will be treated in [Section 1.02.3.5](#). As a first example, let us consider here a solution containing complexing ions, for instance, an aqueous electrolyte with a high concentration of chloride ions ( $\text{Cl}^-$ ) in contact with an iron plate, thus undergoing corrosion. In that case, the equilibrium potential of the complex couple  $\text{FeCl}^+/\text{Fe}$ :



can be written according to the Nernst law:

$$E_{\text{eq}} = E^0 + \frac{0.059}{2} \log \frac{[\text{FeCl}^+]}{[\text{Cl}^-]} \quad [28]$$

Another application of the Nernst law concerns reactions with adsorbed species. As explained in the preceding sections, even if the balance of reactive phenomena could be written according to the overall  $\text{M}^{z+}/\text{M}$  redox reaction, intermediate species are frequently adsorbed on the metallic surface and play an important role in corrosion processes. Without going through the mathematical details of the exhaustive theoretical treatment of the interface, a very brief thermodynamic description of the simplest adsorption models can be presented. In the case of ideal systems, those in which no interaction between adsorbates occurs, the activity of an adsorbed species is given by its fractional covering ratio  $\theta$ , defined as the ratio between the number of adsorbed species and the maximal number of adsorbed species when the surface is completely covered. In the previous example of Ni (or Fe) corrosion illustrated by reaction [\[10\]](#), the Nernst equation can be derived from the reaction explicitly indicating the free metallic sites available for adsorption:



Since there is a single adsorbed species, the number of free sites is proportional to  $1 - \theta$  so that the Nernst law takes the following form (remember that  $\text{pH} = -\log [\text{H}^+]$ ):

$$E_{\text{eq}} = E^0 - 0.059\text{pH} + 0.059 \log \frac{\theta}{1 - \theta} \quad [30]$$

Equation [30] is the mathematical representation of the so-called Langmuir isotherm, often represented as

$$\frac{\theta}{1 - \theta} = \frac{K}{[\text{H}^+]} \quad [31]$$

where  $K$  is a potential-dependent thermodynamic constant.

In contrast with the assumption of the Langmuir-type isotherm, it is often necessary to take into account the possibility of interaction – attraction, repulsion – between adsorbates, mainly for high covering rates  $\theta$ . This is achieved by introducing activity coefficients in the Nernst law (eqn [31]). The most usual model dealing with these nonideal electrochemical systems is the Frumkin isotherm that gathers the nonideal attributes in the form of an exponential function of the covering rate:

$$\frac{\theta}{1 - \theta} \exp(g\theta) = \frac{K}{[\text{H}^+]} \quad [32]$$

where  $g$  is a constant.  $g > 0$  and  $g < 0$  correspond, respectively, to repulsive and attractive interactions between the adsorbates. With  $g = 0$ , no interaction is expected and the Langmuir isotherm is retrieved.

### 1.02.3.5 Applications of the Nernst Law to Pourbaix ( $E$ -pH) Diagrams

An important application of the Nernst law for corrosion applications is the potential–pH diagram, also known as the Pourbaix diagram in honor of Marcel Pourbaix's exhaustive work devoted to the calculation, interpretation, and diffusion of those diagrams.<sup>28</sup> The importance and high usefulness of Pourbaix diagrams come from the fact that corrosion is not simply a matter of redox reactions like the basic reaction [2], but very frequently involves species with acid–base properties, such as water itself (remember that most corrosion phenomena are in fact related to aqueous corrosion). Also important for its wide applicability, is the very wide range of in-service conditions of metals that may be susceptible to corrosion. Indeed, corrosion occurs in widely differing environments in terms of both pH (from acidic environments to alkali industry, or very basic mortars and cements)

and potential (highly oxidizing atmospheres, rich in oxygen or nitrates, or reducing atmospheres as in deaerated closed water circuits).

In this section, the main principles of Pourbaix diagrams and rough guidelines for their calculation are introduced. With the help of three typical and important cases (gold, iron, and aluminum), the large amount of information contained in those diagrams is shown. Their key objective is, for a given metal–electrolyte system at known constant temperature and pressure, the establishment of domains of thermodynamic stability or predominance of any potential species for the entire range of pH and electrode potential. As a result, for practical purposes, the whole inventory of service-life conditions of an interface can be represented. It then allows the global thermodynamic predictions of the behavior of a given metal–electrolyte system (corrosion, immunity, oxide formation, etc.) to be accessed readily.

While more complex diagrams, including the formation of complexes in corrosive media, can of course be established, only pure metal–water systems will be considered in this chapter. The starting point of Pourbaix diagram is based on the fact that there are three types of electrochemical equilibrium for a metal–water system, those depending only on the electrochemical potential, those depending only on the pH, and those depending on both potential and pH. The general guidelines of the diagram construction are given below for a simple example of a metal  $M$  that can dissolve into cations  $M^{z+}$  or form a solid oxide  $M_2O_x$ .

#### 1.02.3.5.1 Purely potential-dependent equilibrium

This is the case of the simple redox reaction [18] between the pure metal and its cation for which the equilibrium is described by the Nernst equation [24], as discussed above. For a given  $M^{z+}$  concentration (different Pourbaix diagrams have to be drawn if this value is changed),  $E_{\text{eq}}$  is independent of pH and is represented in an  $E/\text{pH}$  diagram as a horizontal line, as shown in Figure 11(a). Hence, regardless of the electrolyte pH, the metal  $M$  is in thermodynamic equilibrium with its cation at the given  $M^{z+}$  concentration only on this line. For  $E < E_{\text{eq}}$ ,  $M^{z+}$  cations reduce to metal, while for  $E > E_{\text{eq}}$  the metal undergoes dissolution to form cations in solution. This indicates that, for this kind of equilibrium and a given  $M^{z+}$  concentration, the thermodynamic domain of metallic stability is the whole region below the horizontal line, whilst the domain of cation predominance is the upper

region. It is important to appreciate that the position of the line is dependent on the  $M^{z+}$  concentration considered: a modification in the concentration would therefore change the stability or predominance domain of the  $M^{z+}$  species.

### 1.02.3.5.2 Purely pH-dependent equilibrium

When dissolved cations precipitate in the form of solid compounds in which the metal keeps the same oxidation number as the cation, for instance, for the  $M^{z+}/M_2O_z$  equilibrium, the corresponding forward and backward reactions:



convey no charge transfer. Hence, no redox reaction is present (each reactant keeps its valence on both sides of the reaction) and the equilibrium is independent of the potential, but it is a function of the pH because of the protons on the right-hand side of the equation. The corresponding line of the Pourbaix diagram can be determined with the help of the classical chemical equilibrium theory by introducing the equilibrium constant  $K$  of reaction [33]<sup>29</sup>:

$$K = \frac{[H^+]^{2z}}{[M^{z+}]^2} \Rightarrow \log K = 2z \log[H^+] - 2\log[M^{z+}]$$

$$pK = -\log K \Rightarrow \log[M^{z+}] = \frac{pK}{2} - zpH \quad [34]$$

It can be seen from reaction [33] that for low pH values (high proton concentration), the reaction equilibrium is shifted to the left side, the oxide combining with protons and producing cations. Low pH values hence entail high dissolved cation concentration. As a consequence, for a fixed  $M^{z+}$  concentration, the  $M^{z+}/M_2O_z$  equilibrium is characterized by a vertical line in the  $E/pH$  diagram ( $pH = \text{constant}$ , line 2 in Figure 11(b)), the left side being the predominance domain of the cations and the right side the oxide stability region. As shown in Figure 11(b), lines 1 and 2 must in reality be mutually truncated at their intersection to take into account the existence of the metal oxide. One should then look for the equilibrium between  $M$  and  $M_2O_z$ , the third kind of equilibrium, which is dependent on the pH and on the potential simultaneously, to complete the Pourbaix diagram.

### 1.02.3.5.3 pH and potential-dependent equilibrium

As indicated above, the oxidized  $M$  species takes the form of a solid oxide  $M_2O_z$  for high pH values ( $M^{z+}$  can actually exist but its concentration is low). It is then intuitively more appropriate to consider the

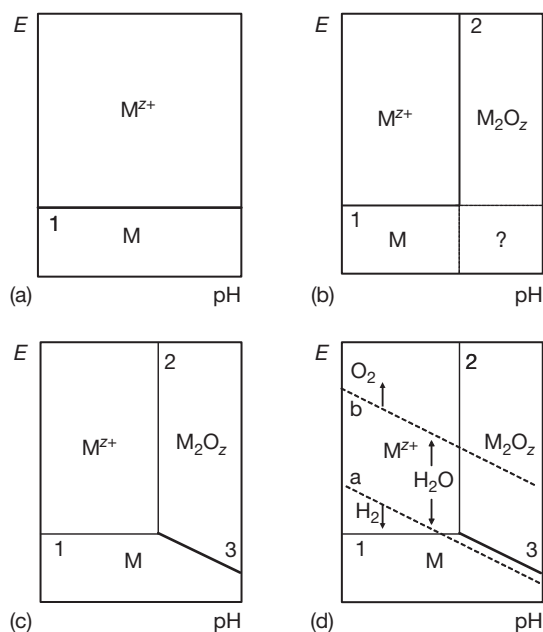
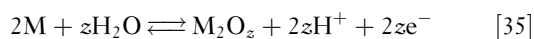


**Figure 11** Building-up a generic Pourbaix diagram: (a) the metal/cation equilibrium, line 1; (b) the cation–metal oxide equilibrium, line 2; (c) the metal–metal oxide equilibrium, line 3; (d) the complete schematic Pourbaix diagram, including the water stability domain, lines a and b.

$M_2O_z/M$  equilibrium. It is also clear that reaction requires a source of oxygen, which leads to the very important observation concerning corrosion that oxygen comes mainly from the dissociation of water molecules and not from the atmosphere, contrary to an extremely widespread idea. The overall reaction is then



for which the equilibrium potential can be written

$$E_{eq} = A_1 - 0.059 \text{ pH} \quad [36]$$

where  $A_1$  is a constant. The equilibrium, described by a linear relationship between the pH and the potential is represented by the straight line 3 of slope  $-0.059 \text{ V pH}^{-1}$  in Figure 11(c). This line, which separates  $M$  and  $M_2O_z$ , must start at the intersection of lines 1 and 2 and must be plotted towards lower potentials and more alkaline pH according to the negative slope of line 3. Indeed, in the other direction the line would be in the  $M^{z+}$  domain where neither  $M$  nor  $M_2O_z$  can exist at a steady state.

Figure 11(c) depicts the stability domains of the three species considered. Since this is a metal–water system, the diagram must also incorporate the water stability domain, according to the equilibria  $H_2O/H_2$



and  $\text{O}_2/\text{H}_2\text{O}$ , characterized at 25 °C by the following equations:

$$E_{\text{eq}} = 0.00 - 0.059\text{pH} \text{ for } \text{H}_2\text{O}/\text{H}_2$$

$$E_{\text{eq}} = 1.23 - 0.059\text{pH} \text{ for } \text{O}_2/\text{H}_2\text{O} \quad [37]$$

The limits of the water stability domain are thus represented by two parallel lines, identified in **Figure 11(d)** as **a** (for the  $\text{H}_2\text{O}/\text{H}_2$  equilibrium) and **b** (for the  $\text{O}_2/\text{H}_2\text{O}$  one), indicating that water is thermodynamically stable between these two lines: below line **a** hydrogen evolves and above line **b**, oxygen evolves, as depicted in **Figure 11(d)**, which is the final form of the schematic Pourbaix diagram for the M– $\text{H}_2\text{O}$  system involving the three species, M,  $\text{M}^{z+}$ , and  $\text{M}_2\text{O}_z$ .

**Figure 11(d)** respects the usual graphic notation used for the sake of readability of the diagrams. Dashed lines indicate an equilibrium between two dissolved species (not illustrated in this simple example), such as two cations ( $\text{Fe}^{3+}/\text{Fe}^{2+}$ , for instance). Thin solid lines indicate an equilibrium between a dissolved and a solid species (lines 1 and 2), and thick solid lines indicate an equilibrium between two solid species (line 3).

Even if schematic, **Figure 11(d)** illustrates a common feature of metal–water Pourbaix diagrams, that is, metal immunity at more negative potential values, film-free metal dissolution at more positive potentials in acids and oxide formation in the neutral and alkaline pH ranges (though many metals will also corrode as oxy-anions in alkali). (The terms ‘more positive’ and ‘more negative’ are used here in place of ‘higher’, ‘lower’ and similar terms when referring to electrochemical potentials to avoid any possible confusion. Because metal potentials are often negative, there is an unfortunate tendency (particularly in the field of cathodic protection, where potentials are always negative) to say, for example, that  $-1.2\text{ V}$  is ‘higher’ than  $-1\text{ V}$  (and in some cases even to omit the negative sign).)

### 1.02.3.6 Pourbaix Diagram of Gold, Iron, and Aluminum

Let us now analyze some typical examples of Pourbaix diagrams to illustrate their usefulness. (For the sake of clarity, these are simplified diagrams that consider only some of the possible dissolved or solid species. The reader is invited to refer to the Pourbaix’s Atlas of electrochemical equilibrium for more detailed pictures.<sup>28</sup>) **Figure 12** shows the Au– $\text{H}_2\text{O}$  diagram at 25 °C and 1 atm. The first remarkable feature is that gold has a wide immunity domain occupying a large extent of the  $E/\text{pH}$  space. The existence

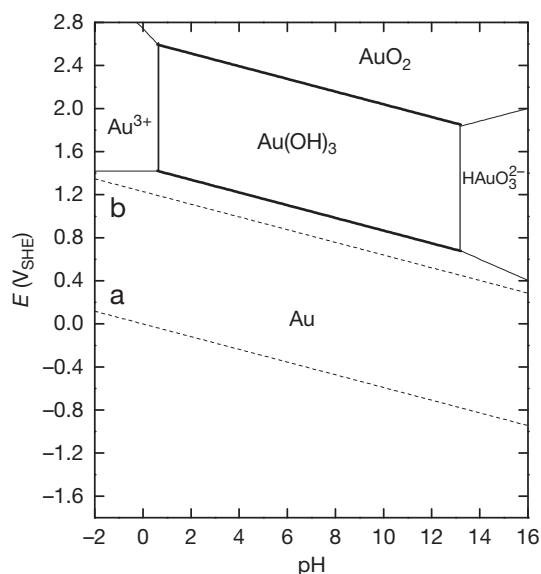


**Figure 12** Simplified Pourbaix diagram for the Au– $\text{H}_2\text{O}$  system at 25 °C. Concentration of dissolved species taken as  $[X] = 10^{-6}\text{ mol l}^{-1}$ .

of  $\text{Au}^{3+}$ ,  $\text{Au}(\text{OH})_3$ ,  $\text{AuO}_2$ , and  $\text{H[AuO}_2]^{2-}$  stability domains indicate, at first glance, that gold can undergo corrosion at very oxidizing conditions (very high potential values). A deeper look, however, shows that the gold immunity domain comprises and overhangs that of water. This means that gold is always thermodynamically stable whenever stable water is present, which obviously includes all natural environments on earth and gives a sound idea of the conditions to be achieved for gold corrosion. This is also why gold is always found in its metallic form and not in mineral compounds, unlike most of the metals.

In the case of iron, certainly the most common constructional metal, the Pourbaix diagram at 25 °C and 1 atm pressure (**Figure 13**) shows a very different behavior that explains why corrosion has always been a matter of much concern. In contrast with gold, the existence of metallic iron is thermodynamically impossible in the whole water stability domain: corrosion is hence a spontaneous process bringing iron back to its stable form in nature. Thus, iron is found in different mineral forms such as hematite ( $\text{Fe}_2\text{O}_3$ ) and magnetite ( $\text{Fe}_3\text{O}_4$ ) and the industrial transformation into metallic iron requires huge amounts of energy (supplied by the oxidation of carbon inside furnaces during the production of iron and steel) to break the oxygen–iron bonds. This spontaneous reverse route (iron towards oxide) is clearly demonstrated by the fact that the Pourbaix diagram in

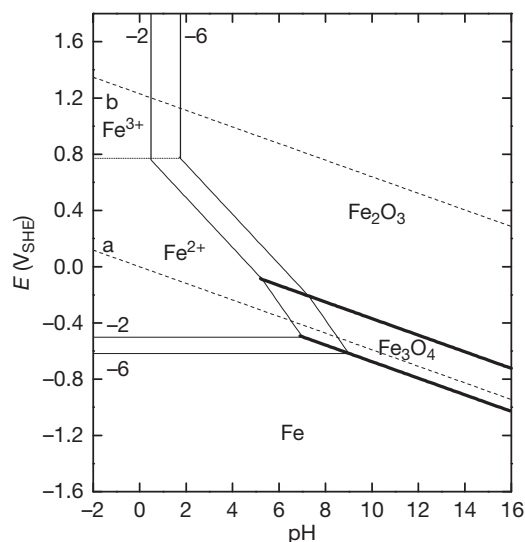


**Figure 13** Simplified Pourbaix diagram for the Fe-H<sub>2</sub>O system at 25 °C. Concentration of dissolved species taken as  $[X] = 10^{-2}$  or  $10^{-6} \text{ mol l}^{-1}$ .

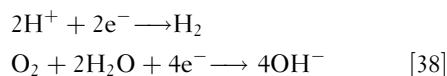
**Figure 13** predicts iron transformation into magnetite (less oxidized species) at more negative potentials or hematite at more positive potentials.

**Figure 13** also shows a large active dissolution region (the predominance domain of the ferrous cation  $\text{Fe}^{2+}$ , followed by that of the ferric cation  $\text{Fe}^{3+}$  for potential values more positive than  $E = 0.77 \text{ V}_{\text{SHE}}$ ), often referred to as the corrosion triangle, lying in the neutral-acid pH range, illustrating and justifying the high sensitivity of iron to corrosion in acidic environments.

As mentioned in **Section 1.02.3.5.1**, the stability domain of the species depends on the concentration of the dissolved species considered to be at equilibrium with the solid compounds. The concentrations used in building the diagram in **Figure 13** ( $10^{-2}$  and  $10^{-6} \text{ mol l}^{-1}$ ), for example, for the  $\text{Fe}^{2+}/\text{Fe}$  equilibrium, indicate the range of concentrations expected when iron corrosion is taking place. In other words, beyond these values, the stable species is no longer metallic iron, but the ferrous cation, thus leading to corrosion. The line separating the metallic iron and ferrous cation domains move up when the concentration threshold for corrosion is increased from  $10^{-6}$  to  $10^{-2} \text{ mol l}^{-1}$ , leaving a larger iron stability domain below it.

As already discussed, overall corrosion processes at free potential are the result of coupled anodic and cathodic reactions taking place simultaneously on the metallic surface. The most common cathodic reactions occurring during iron dissolution (reaction [2])

are the hydrogen evolution (in acidic media) and the reduction of dissolved oxygen (in neutral or alkaline electrolytes in contact with air),



Note that both cathodic reactions yield an alkalization of the interface, the first by direct consumption of  $\text{H}^+$  and the second by production of  $\text{OH}^-$ . As a consequence, the system can locally shift from a given point inside the  $\text{Fe}^{2+}$  domain to, for instance, the hematite domain, which gives a precipitate in the form of what is generically called rust. Only ferrous species can exist at the interface, as ferric ions are stable only at much more positive potentials than normal corrosion potentials. However, in aerated solutions the ferrous ions can be oxidized in solution to ferric by dissolved oxygen, and the ferric ions can then precipitate, usually as an oxyhydroxide ( $\alpha$ ,  $\beta$ ,  $\gamma$ , or  $\delta$ - $\text{FeOOH}$ ) which are, roughly speaking, the different hydrated forms of hematite ( $\text{Fe}_2\text{O}_3 \cdot \text{H}_2\text{O} = 2 \times \text{FeOOH}$ ). (The hematite is the thermodynamically stable species, the other forms are metastable but their transformation is so slow that they can be identified in corrosion products or even in minerals.) Note that the precipitation cannot occur at the metal surface because the ferric species are not stable there, so the corrosion product is necessarily porous and nonprotective.

The last illustrative example concerns aluminum, the Pourbaix diagram of which in **Figure 14** shows a wide oxide domain and an extremely narrow immunity one, well below the domain of water stability. Aluminum is thus a particularly reactive metal, as already deduced from the very negative standard equilibrium potential (**Table 1**). It is important to note that its high corrosion resistance does not come from a marked immunity and stability, as for gold or other noble metals, but from the formation of a homogeneous and impermeable oxide layer in a very large domain of potential and pH, as shown in **Figure 14**. This very adherent oxide layer protects the metal from further corrosion. This process, called passivation, is also at the origin of the high corrosion resistance of several metals and alloys such as titanium and stainless steels. In the latter case, passivation of chromium, one of the main alloying elements in those steels, provides the corrosion protection.

The difference between the corrosion resistance of iron and aluminum in practical life illustrates an important aspect that must be taken into account when using Pourbaix diagrams. In fact, both diagrams

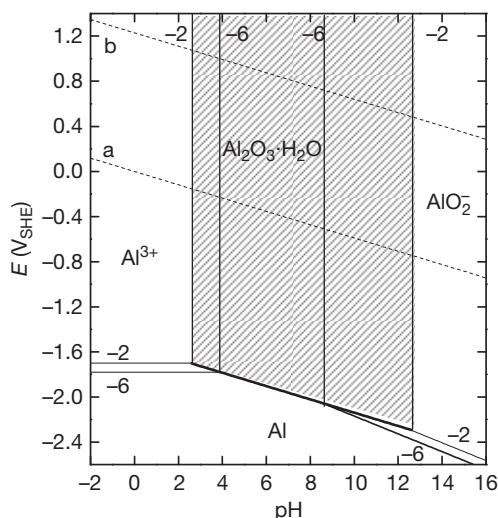


**Figure 14** Simplified Pourbaix diagram for the Al-H<sub>2</sub>O system at 25 °C. Concentration of dissolved species taken as  $[X] = 10^{-2}$  or  $10^{-6} \text{ mol l}^{-1}$ . The hatched region identifies the large passivation domain of aluminum.

predict the existence of oxide stability domains, but, in contrast with aluminum, iron is not protected by these oxides, which are usually nonadherent, friable, and easily hydrated as mentioned before. Some exceptions are nonetheless of great technological importance. In specific conditions, such as highly alkaline environments, a thin and highly protective oxide is formed on steel, which explains, for instance, the very low corrosion rate (at least initially) of reinforcing bars of low carbon steel embedded in concrete.

It is important to stress that Pourbaix diagrams are based on thermodynamic equilibria. The exchange current density is outside the scope of this approach, which gives no indication about electrode kinetics. Furthermore, corrosion is not an equilibrium process, and the anodic and cathodic reactions are completely different in nature, as explained above. In spite of these restrictions, Pourbaix diagrams constitute a very useful tool to predict if the metal is protected by immunity or passivity when the solution pH and the open-circuit potential are known.

## 1.02.4 Electrochemical Kinetics in the Case of a Single Forward-Backward Reaction

### 1.02.4.1 Qualitative Approach

Up to now in this chapter, only reactions at equilibrium, for which zero overall current characterizes the electrochemical system, have been discussed. Even

when an overpotential  $\eta$  was imposed to the interface (see [Section 1.02.3.3](#) with the  $\text{Zn}^{2+}/\text{Zn}$  couple as illustration), the discussion concerned the description of the new equilibrium state with a new zero overall current towards which the system was going.

Let us now consider that a constant overpotential  $\eta$  is applied to the interface by means of an external device so that the system is kept out of equilibrium. This idea can be easily handled with the same example of Zn in contact with a solution of  $\text{Zn}^{2+}$  concentration  $C_\infty = 10^{-2} \text{ mol l}^{-1}$  ( $E_{\text{eq}} = -0.82 \text{ V}_{\text{SHE}}$ ). If this redox couple is supposed to be Nernstian (cf. [Section 1.02.3.3](#)), the overpotential at the interface is linked to the interfacial concentration,  $C_{\text{int}}$ , as (see eqns [24] and [25]):

$$\begin{aligned} \eta(I \neq 0) &= E(I \neq 0) - E_{\text{eq}} \\ &= E^0 + \frac{0.059}{2} \log C_{\text{int}} - \left( E^0 + \frac{0.059}{2} \log C_\infty \right) \\ &= \frac{0.059}{2} \log \frac{C_{\text{int}}}{C_\infty} \quad [39] \end{aligned}$$

When an overvoltage  $\eta$  of 0.12 V ( $E = -0.7 \text{ V}_{\text{SHE}}$ ), for instance, is applied to the interface, [eqn \[39\]](#) points out that Zn must corrode to supply  $\text{Zn}^{2+}$  cations in such amount that the interfacial concentration is 10 000 times higher than the bulk concentration. This new equilibrium will be reached after a very long time for typical volumes of electrolyte. In the transient period, a nonzero current balance ( $I > 0$  corresponding to a net oxidation) is established and, since the interfacial concentration is high, the diffusion flux of the cations is directed from the metal to the electrolyte. In the other direction,  $\eta < 0$  entails metallic deposition ( $I < 0$  corresponding to a net reduction) so that the interfacial concentration is lower than the bulk concentration. The cation flux towards the interface can last a long time since the electrolyte reservoir is hardly changed.

In this system, the potentiostatic out-of-equilibrium conditions involve a transient behavior. In particular, the absolute value of the current decreases as a result of the thickening of the diffusion layer. Forced convection is very often used to control the interfacial concentration of the cations. As explained in [Section 1.02.2.4.3](#), convection allows the thickness of the diffusion layer to be fixed and the bulk concentration to be maintained constant, provided that large volumes of electrolyte are used. In that case, the transient behavior is considerably accelerated and a steady state, different from that at equilibrium, is rapidly achieved. (In practice, a steady



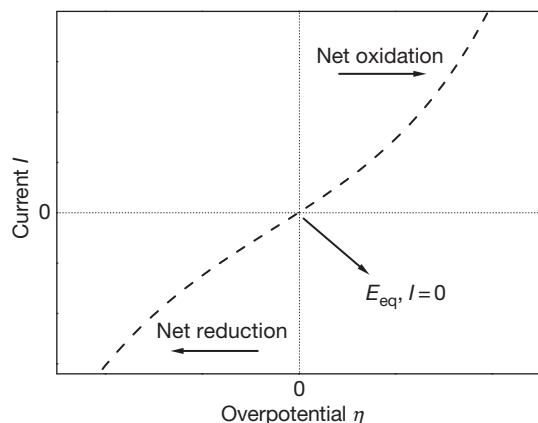


**Figure 15** Schematic drawing of the current-overpotential curve involving the cathodic (net reduction) and the anodic (net oxidation) domains.

state is impossible to obtain but the evolution of the system is so slow that it can be considered in a steady state during the experiment.) The value of the net steady-state current, at each potential or overpotential then provides important information about the kinetics of the electrochemical reaction. The ensemble of  $(E, I)$  or  $(\eta, I)$  couples is often plotted in the form of a current-potential or current-overpotential curve, as illustrated in **Figure 15**. This curve is called a polarization curve and its slope near the equilibrium depends very often on the exchange current density of the redox reaction kinetics, as shown in **Section 1.02.4.2**.

Since the product  $\eta I$  is always positive, as illustrated in the Zn dissolution example given above, the current-potential curve increases monotonically around the equilibrium: the higher the overpotential, the higher the net current (both in absolute values). It is important to notice that nonmonotonic curves also exist, mainly in the corrosion domain, as in the case of stainless steels or passivating metals. Such a feature is, however, closely linked to systems in far-from-equilibrium conditions.

The property that the polarization curve in **Figure 15** is monotonically increasing requires two conditions: first, the metal is always available at the interface so that, whatever the overpotential in the anodic part, the metal can keep supplying cations. Second, in the cathodic region, the cations must be available to ensure the increase in  $|I|$  with increasing  $|\eta|$ . However, beyond a certain overpotential negative value, the amount of cations arriving at the interface per unit time is limited by mass transport. The consequence is that the current reaches a diffusion limiting plateau, as illustrated in **Figure 16**. For all

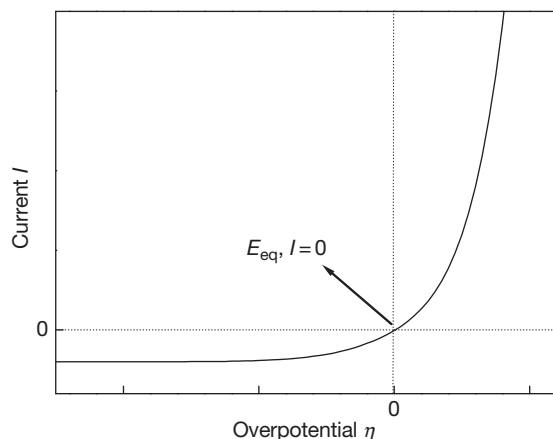
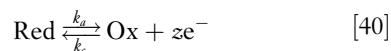


**Figure 16** Schematic representation of a current-overpotential curve with a mass-transport controlled plateau in the cathodic domain.

electrode potentials in this region, the corresponding cation concentration at the interface is essentially zero, as discussed in the following sections.

#### 1.02.4.2 Quantitative Approach

The qualitative description of **Figure 16** shows that the actual current flow is the final result of combined kinetic phenomena, charge transfer of the redox reaction and mass transport of the cations. The following sections discuss in a more detailed and quantitative way the two limiting cases obtained when the kinetics are controlled by a single phenomenon and finally describe the general case of mixed control. Let us first restate, however, that the following development is only valid for a single forward-backward redox reaction with two reacting species present at the interface, as in the case of the elementary redox reaction:



such as, for example, the widely employed redox couple  $\text{Fe}^{3+}/\text{Fe}^{2+}$  taking place at an inert Pt electrode. The current-potential relationships are described below for steady-state conditions and the electrolyte is assumed to be ideal: the activities of the species are equal to their corresponding concentrations, expressed in  $\text{mol l}^{-1}$ .

##### 1.02.4.2.1 Activation-controlled systems: Butler-Volmer equation

In the activation limited case, the interfacial kinetics are the controlling factor. The influence of mass transport in the electrolyte, in particular diffusion, is negligible because it is much faster than the charge-transfer

process. Therefore, the concentrations are identical at the interface and in the electrolyte bulk:

$$[\text{Ox}]_{\text{int}} \approx [\text{Ox}]_{\infty} \text{ and } [\text{Red}]_{\text{int}} \approx [\text{Red}]_{\infty} \quad [41]$$

Any chemical reaction evolves according to an intrinsic speed called reaction rate. Obviously, this is also valid in the case of electrochemical reactions. As already mentioned, the zero overall current, characterizes the electrochemical equilibrium, at which the forward and backward reaction currents are equal, irrespective of the exchange current density.

The knowledge of the mechanism of the overall reaction allows the rate law of each elementary step to be derived (see [Section 1.02.2.4.1](#)). In the case considered here, the stoichiometry being very simple for the forward and backward heterogeneous reactions, their rate laws can be easily written in terms of the cathodic and anodic fluxes,  $\phi_{\text{cathodic}}$  and  $\phi_{\text{anodic}}$ , expressed in moles produced or consumed per unit time and unit surface ( $\text{mol cm}^{-2} \text{ s}^{-1}$ ):

$$\phi_{\text{cathodic}} = k_{\text{c}}[\text{Ox}]_{\text{int}} \approx k_{\text{c}}[\text{Ox}]_{\infty} \quad [42]$$

$$\phi_{\text{anodic}} = k_{\text{a}}[\text{Red}]_{\text{int}} \approx k_{\text{a}}[\text{Red}]_{\infty} \quad [43]$$

where both rate constants  $k$  are expressed in  $\text{m s}^{-1}$ , or more usually in  $\text{cm s}^{-1}$ . (From a rigorous point of view, [eqn \[42\]](#) should also involve the electron concentration at the interface. Nevertheless, since electrons are fully available in a metallic surface, their concentration is considered as being constant and is implicitly incorporated in the constant  $k_{\text{c}}$ .) (It should be noted that a rate constant does not necessarily have units of meters per second, in particular when the order of the reaction is not 1 or when  $k$  depends on the concentration of adsorbates in moles per square centimeters.) Each electrochemical reaction rate depends on the potential, according to the Arrhenius-type [eqns \[45\] and \[46\]](#) presented below.<sup>4</sup> In the standard state, which is a particular case of electrochemical equilibrium, as explained before, the fluxes of the anodic and cathodic reactions are identical with the same concentrations of the redox species so that the reaction rates are also identical and denoted  $k^0$ :

$$k_{\text{c}} = k_{\text{a}} = k^0 \quad [44]$$

The following expressions of electrochemical rate constants are derived:

$$k_{\text{a}} = k^0 \exp\left(\frac{\alpha z F}{RT}(E - E^0)\right) \quad [45]$$

$$k_{\text{c}} = k^0 \exp\left(-\frac{(1 - \alpha) z F}{RT}(E - E^0)\right) \quad [46]$$

(Hereafter the usual mathematical treatment that admits global multielectron reactions ( $z > 1$ ) is preferred. It must, however, be kept in mind that, as mentioned in [Section 1.02.2.3](#), a rigorous analysis of the reaction mechanisms encompasses the existence of intermediate single electron steps with  $z = 1$ .) The  $\alpha$  parameter in the exponentials, which is called charge-transfer coefficient ( $0 \leq \alpha \leq 1$ ), indicates how the electrical energy related to a potential shift from the standard state,  $zF(E - E^0)$  is shared between the anodic and cathodic reactions, as illustrated below in this section.

The overall current density related to this electrochemical reaction can be written as the algebraic sum of the anodic and cathodic currents:

$$\begin{aligned} j &= j_{\text{a}} + j_{\text{c}} = zF(k_{\text{a}}[\text{Red}]_{\infty} - k_{\text{c}}[\text{Ox}]_{\infty}) \\ &= zFk^0 \left[ [\text{Red}]_{\infty} \exp\left(\frac{\alpha z F}{RT}(E - E^0)\right) \right. \\ &\quad \left. - [\text{Ox}]_{\infty} \exp\left(-\frac{(1 - \alpha) z F}{RT}(E - E^0)\right) \right] \quad [47] \end{aligned}$$

It must be noticed that this equation remains valid even if there is only one species in the solution. For example, if there is no Ox species introduced in the electrolyte, the cathodic terms in [eqn \[47\]](#) vanish and the expression of the current density is reduced to the anodic branch. As a consequence, there is no equilibrium or zero-current polarization point simply because there is no cathodic reaction counterpart: the steady-state current density tends to zero only at very high negative overpotentials. Steady-states in which only one species is present are very particular. Indeed, the development of the oxidation reaction itself produces Ox species that progressively accumulate at the interface and can in turn be reduced, hence creating a redox process.

Let us now come back to the previous example in which both Ox and Red species are initially present in the electrolyte. Instead of working with the potential difference relative to the standard state,  $E - E^0$ , as in [eqn \[47\]](#), it is more interesting to refer to the equilibrium potential and deal straightforwardly with the overpotential  $\eta = E - E_{\text{eq}}$  to write:

$$\begin{aligned} \frac{zF}{RT}(E - E^0) &= \frac{zF}{RT}(E - E_{\text{eq}}) + \frac{zF}{RT}(E_{\text{eq}} - E^0) \\ &= \frac{zF}{RT}\eta + \frac{zF}{RT}(E_{\text{eq}} - E^0) \quad [48] \end{aligned}$$

According to the Nernst equation (similar to eqn [23]),  $E_{\text{eq}}$  can be written as

$$E_{\text{eq}} = E^0 + \frac{RT}{zF} \times \ln \frac{[\text{Ox}]_{\infty}}{[\text{Red}]_{\infty}} \quad [49]$$

so that

$$\frac{zF}{RT} (E - E^0) = \frac{zF}{RT} \eta + \ln \frac{[\text{Ox}]_{\infty}}{[\text{Red}]_{\infty}} \quad [50]$$

By combining eqns [48] and [50], the current density can be expressed as:

$$\begin{aligned} j &= zFk^0 \left( [\text{Red}]_{\infty} \frac{[\text{Ox}]_{\infty}^{\alpha}}{[\text{Red}]_{\infty}^{\alpha}} \exp\left(\frac{\alpha zF}{RT} \eta\right) \right. \\ &\quad \left. - [\text{Ox}]_{\infty} \frac{[\text{Ox}]_{\infty}^{-1+\alpha}}{[\text{Red}]_{\infty}^{-1+\alpha}} \exp\left(-\frac{(1-\alpha)zF}{RT} \eta\right) \right) \\ &= zFk^0 [\text{Ox}]_{\infty}^{\alpha} [\text{Red}]_{\infty}^{1-\alpha} \left( \exp\left(\frac{\alpha zF}{RT} \eta\right) \right. \\ &\quad \left. - \exp\left(-\frac{(1-\alpha)zF}{RT} \eta\right) \right) \end{aligned} \quad [51]$$

and finally, the so-called Butler–Volmer equation is derived:

$$j = j_0 \left( \exp\left(\frac{\alpha zF}{RT} \eta\right) - \exp\left(-\frac{(1-\alpha)zF}{RT} \eta\right) \right) \quad [52]$$

where the exchange current density  $j_0$  is

$$j_0 = zFk^0 [\text{Ox}]_{\infty}^{\alpha} [\text{Red}]_{\infty}^{1-\alpha} \quad [53]$$

As discussed above, at the equilibrium ( $\eta=0$ ), the current density is equal to 0 so that  $j_a = |j_c| = j_0$ . In eqn [53], the idea of exchange current density expressed as a function of two kinetic parameters,  $k^0$  and  $\alpha$ , of the redox system investigated is retrieved.

The two terms in the right-hand side of eqn [52] stand for the purely anodic and cathodic branches of the current–overpotential curve, respectively:

$$j_a = j_0 \exp\left(\frac{\alpha zF}{RT} \eta\right) \quad [54]$$

$$j_c = -j_0 \exp\left(-\frac{(1-\alpha)zF}{RT} \eta\right) \quad [55]$$

Figure 17 presents the anodic and cathodic branches (eqns [54] and [55]) and the sum of both currents at each potential related to the overall Butler–Volmer equation [52], which fully describes the kinetic behavior of an electrochemical interface in the case of pure activation control.

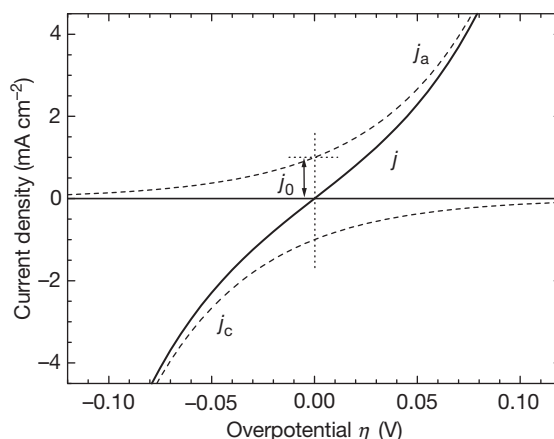


**Figure 17** Current–overpotential curve of a purely charge-transfer controlled system illustrating  $j_a$  and  $j_c$  (eqns [54] and [55]) in the upper and lower halves, respectively (dashed lines) and the overall Butler–Volmer equation [52] (solid line):  $\alpha = 0.5$ ,  $z = 1$  and  $j_0 = 1 \text{ mA cm}^{-2}$ .

As already pointed out, the upper curve in Figure 17 is obtained when only Red species are present in the solution (eqn [54]). In the same way, the lower curve is obtained when only Ox species are present in the solution (eqn [55]). The Butler–Volmer curve, obtained when the two species are present in the electrolyte, appears then as the addition of the two curves at each overpotential. Any current value depicted in the curve is the net result of a dynamic balance between the anodic and cathodic reactions, giving for example a zero current at equilibrium. In other words, except for very high overpotentials (see Section 1.02.4.2.2), the cathodic (anodic) reaction, although markedly slowed down, is still taking place on the metallic surface even at positive (negative) overpotentials, which is an important feature of corrosion processes, as seen hereafter.

The Butler–Volmer equation illustrates an important difference between purely chemical reactions and electrochemical reactions. In the first case, for given concentrations of reactants and hydrodynamic conditions, the only way of modifying the reaction rate is to change the electrolyte temperature. In the case of electrochemical reactions, however, besides the temperature (explicitly present in the argument of the exponentials but also implicitly present in the  $k^0$  value), the electrode potential also strongly affects the reaction rate and, therefore, the resultant current. As an example, for a single electron reaction with  $\alpha = 0.5$  and  $T = 25^\circ \text{C}$  (298 K), a simple calculation from the Butler–Volmer equation indicates that an

overpotential of only 0.5 V entails a  $\exp(\alpha F\eta/RT) = 17\,000$ -fold increase of the anodic reaction, while the cathodic one is depressed by the same magnitude.

This example can be used to better discuss the physical meaning of the charge transfer coefficient as the kinetic parameter. This coefficient conveys information on how the electric energy supplied to the electrochemical system is shared between the anodic and cathodic reactions. The value  $\alpha = 0.5$  indicates that both reactions are boosted or hindered by the same factor. The arguments of both exponentials are identical (in absolute values) for any overpotential  $\eta$  so that the curves are symmetric in **Figure 17**, but this is no longer the case in **Figure 18** with  $\alpha = 0.8$ : the anodic branch increases more steeply than the cathodic one. This slight bias relative to a symmetric behavior obtained for  $\alpha = 0.5$  illustrates the fact that the response of the forward and backward reactions to a same electric energy shift ( $|zF\eta|$ ) is different from the mutual mirrored kinetic behavior, depending on the  $\alpha$  value.

It is also worth stressing that the final value of the current density at any overpotential is directly dependent on the exchange current density, as illustrated in **Figure 19**.

When  $j_0$  is large, the redox couple is said to be fast and can be considered as reversible, at least for applied overpotentials not too large. High  $j_0$  values mean that both cathodic and anodic components strongly contribute to the final net  $j$  value and small applied overpotentials are enough to produce a significant current in either direction. However, since high current values mean a high flux of reactants at the interface, the mass-transport kinetics are no

longer negligible and the Butler–Volmer equation no longer valid (see **Sections 1.02.4.2.1** and **1.02.4.2.2**). On the contrary, for small  $j_0$ , that is, for slow redox couples, high overpotentials are needed to get a significant net current, as shown in **Figure 19**. The system is then said to be irreversible, not in the thermodynamic sense, but to express that it is prone to be polarized in one of the parts of the current–overpotential curve where only one of the forward and backward reactions completely governs the overall reaction. In that case, once a given species has been oxidized (reduced), the overvoltage is too large for it to be reduced (oxidized) back, so that the species has much more chances to move away from the interface than to react at the interface.

The following paragraphs deal with two approximations of the Butler–Volmer equation depending on the overpotential value. They are valid for slow redox couples and allow the kinetic parameters  $k^0$  and/or  $\alpha$  to be determined.

#### Small overpotential limit of the Butler–Volmer equation

As highlighted in **Figure 20**, in the region close to the equilibrium potential (typically  $|\eta| < 10$  mV), the current–potential curve can be considered as linear. Indeed, by using the Taylor expansion at the first order (small  $\eta$ ) of the exponentials ( $\exp(x) = \sum_{k=0}^{\infty} (x^k/k!) \approx 1 + x$ ) in the Butler–Volmer equation, the current density is shown to be proportional to the overvoltage:

$$j = j_0 \frac{zF}{RT} \eta \quad [56]$$

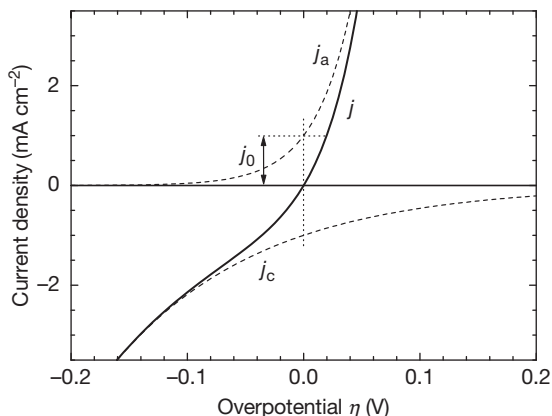


**Figure 18** Current–overpotential curve as in **Figure 17** but with a biased charge-transfer coefficient  $\alpha = 0.8$ ,  $z = 1$ , and  $j_0 = 1 \text{ mA cm}^{-2}$ .

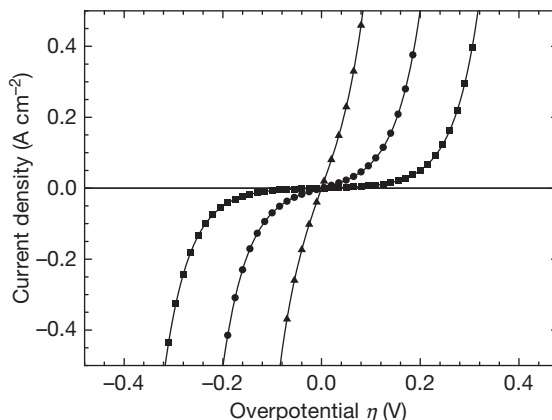


**Figure 19** Effect of the exchange current density on the shape of the current–overpotential curves for  $\alpha = 0.5$ ,  $z = 1$ , and  $j_0 = 1 \text{ mA cm}^{-2}$  (■),  $10 \text{ mA cm}^{-2}$  (●),  $100 \text{ mA cm}^{-2}$  (▲).

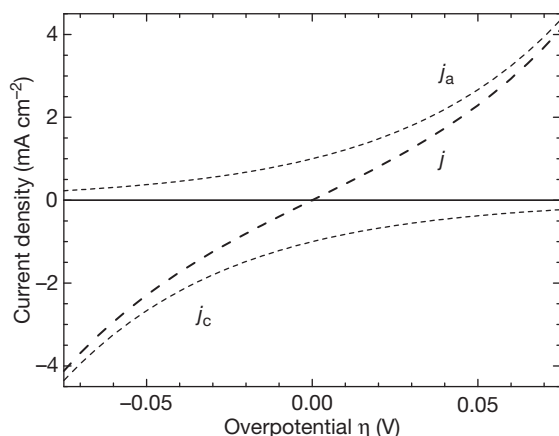


**Figure 20** Small-overpotential limiting case: the linear behavior of the Butler–Volmer equation close to the equilibrium potential ( $\alpha = 0.5$ ,  $z = 1$ , and  $j_0 = 1 \text{ mA cm}^{-2}$ ).

Equation [56] does not give any information about the charge-transfer coefficient  $\alpha$  since it depends only on the exchange current density  $j_0$ . However, the determination of  $j_0$ , through the slope of the linearized Butler–Volmer equation around the equilibrium, is an important kinetic attribute, since it is easily related to  $k^0$  with eqn [53]. It is also important to mention that the slope of the linearized Butler–Volmer equation [56] around the equilibrium can be rewritten with the easily experimentally measurable ‘polarization resistance’ ( $R_p = \partial\eta/\partial I$ ) at the equilibrium ( $I = 0$ ), and expressed in ohms. In the particular case presented here, this resistance is equal to the charge-transfer resistance,  $R_{ct}$ , also defined as  $\partial\eta/\partial I$  at  $I = 0$ , but under conditions where only activation polarization contributes to  $\eta$  (i.e.,  $R_p$  includes the effects of mass transport and solution resistance, but  $R_{ct}$  does not):

$$jS = \frac{1}{R_p} \eta \Rightarrow R_p = R_{ct} = \frac{RT}{zFSj_0} \quad [57]$$

In practice, the  $SR_p$  value in  $\Omega \text{ cm}^2$  is more commonly used (and usually also termed  $R_p$ , but with units of  $\Omega \text{ cm}^2$ ) because it does not depend on the surface area of the electrode.

### Large overpotential limit of the Butler–Volmer equation

When a large overpotential is applied to the interface, one of the exponential terms (for instance, the cathodic one for large positive  $\eta$ ) of the Butler–Volmer equation [52] vanishes and the corresponding reaction (cathodic in this case) can be neglected.

Consequently, the following equations, similar to eqns [54] and [55], can be readily derived:

$$j \approx j_a = j_0 \exp\left(\frac{\alpha z F}{RT} \eta\right) \quad [58]$$

for positive large overpotential

$$j \approx j_c = -j_0 \exp\left(-\frac{(1-\alpha)zF}{RT} \eta\right)$$

for negative large overpotential [59]

The system is said to be in the irreversible domain where one of the reactions is substantially hindered and can be neglected. In that case, the global current–overpotential curve tends asymptotically to the purely anodic curve or the purely cathodic curve in Figures 17 and 18. This happens when the ratio  $|j_c/j_a| = \exp(-zF\eta/RT)$  for  $\eta > 0$  or its reciprocal  $|j_a/j_c| = \exp(zF\eta/RT)$  for  $\eta < 0$  become small. It must be realized that these ratios are lower than 5% as soon as  $|\eta|$  is greater than about  $80 \text{ mV}/z$  and lower than 1% as soon as  $|\eta|$  is greater than about  $120 \text{ mV}/z$ .

It is more convenient to express eqns [58] and [59] in a semilogarithmic scale (the  $\ln 10 = 2.3$  factor stands for the conversion of the natural logarithm into the more easily handled decimal logarithm), as in the following relationships, often called Tafel laws:

$$\log j \approx \log j_a = \log j_0 + \frac{\alpha z F}{2.3 RT} \eta \quad [60]$$

for  $\eta > \frac{0.08}{z} (j_a \gg |j_c|)$

$$\log(-j) \approx \log(-j_c) = \log j_0 - \frac{(1-\alpha)zF}{2.3 RT} \eta \quad [61]$$

for  $\eta < -\frac{0.08}{z} (|j_c| \gg j_a)$

The terms  $\alpha z F / 2.3 RT$  and  $(1-\alpha)zF / 2.3 RT$  are known as the anodic and cathodic Tafel coefficients,  $\beta_a$  and  $\beta_c$  respectively.

Thus, in the irreversible domains (high  $\eta$ ) the Butler–Volmer equation is represented by two straight lines in a semilogarithmic scale, as depicted in Figure 21 (same data as in Figure 18) showing a  $\log |j|$  vs.  $\eta$  plot generally called a Tafel plot. In this case, the system is therefore said to exhibit Tafel behavior. The Tafel plot is then a powerful tool to derive kinetic parameters: the equilibrium potential and the exchange current density are obtained at the intersection of the extrapolations of the Tafel lines at  $\eta = 0$ , while the charge-transfer coefficient  $\alpha$  is derived from the slope of the cathodic or anodic lines (see Figure 21). It is important to keep in mind that up to now the cathodic and anodic



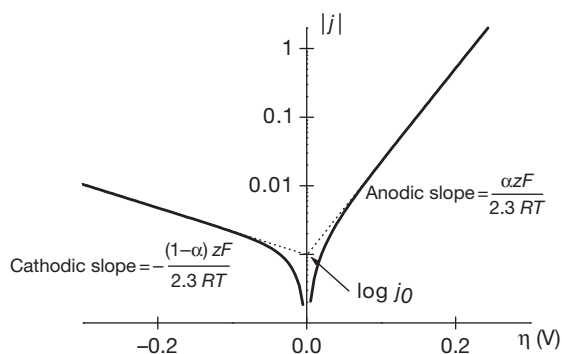


**Figure 21** High-overpotential limiting case: the Tafel behavior of the Butler–Volmer equation over a wide potential domain ( $z = 1$ ,  $j_0 = 1 \text{ mA cm}^{-2}$ , and  $\alpha = 0.8$ ).

reactions are the forward and backward reactions of the same redox process and, therefore, they have the same kinetic parameters (charge-transfer coefficient  $\alpha$  and standard rate constant  $k^0$ ). The slopes of the two straight lines are then mutually linked according to

$$|(\text{Anodic slope}) - (\text{Cathodic slope})| = \frac{zF}{2.3RT} \quad [62]$$

Thus, the slope of a given branch automatically determines the slope of the other one.

In **Figure 21**, the steep increase of the anodic current for positive potentials, due to a high value  $\alpha = 0.8$ , is then necessarily coupled with a slower evolution of the cathodic current (in absolute value) with respect to the potential.

Another crucial aspect that deserves to be mentioned again is that Tafel behavior assumes the absence of mass transport effects (see the next section). This assumption is valid for systems requiring high overpotentials to reach significant current values, as for slow redox couples characterized by a small exchange current density. Indeed, as already discussed, mass transport has no influence on the current in that case. In contrast, for fast redox processes, that is, for redox couples with a high exchange current density, the consumption of the reacting species at the interface is faster than the supply of species by mass transport and the system no longer exhibits Tafel behavior. As a consequence, the Tafel laws (eqns [60] and [61]) cannot be experimentally observed for fast redox processes, which leads to the idea that Tafel behavior is an indication of slow kinetics. It must also be emphasized that the determination of the kinetic parameters from the linear part of the current–overpotential curves, as described in **Figure 21**, is not as simple as it may appear. Indeed, if an unambiguous linear behavior is not

present, the graphic determination of  $j_0$  and  $\alpha$  can be seriously biased. Hence, it is widely accepted that a system can be considered as exhibiting Tafel behavior and, therefore, the kinetic parameters can be graphically estimated, only if the linear behavior extends over at least one decade of current.

#### 1.02.4.2.2 Mass-transport limited systems: Fick's law and limiting current density

As already mentioned, mass transport plays a dominant role in the overall kinetics of the electrochemical system in some important situations. This section is then devoted to systems for which the kinetics of the redox reaction is so fast that it is completely controlled by mass transport. Only Nernstian systems, already discussed in **Section 1.02.3.3**, for which the potential and the interfacial concentrations are directly related, are now considered. This is particularly the case of fast redox systems that are reversible in a large range of overpotentials.

The qualitative description of the kinetics of the redox couple  $\text{Zn}^{2+}/\text{Zn}$ , illustrated in **Figure 16** and discussed in **Section 1.02.2.4.4**, allowed the idea of concentration profile across the interface related to a current flow to be introduced. This issue is now treated in a more quantitative way with special attention to interfaces in steady-state conditions. Let us first remember that, according to Nernst's model (see **Section 1.02.2.4.3**), convection controls the thickness,  $\delta$ , of the diffusion layer at the interface, and allows the bulk concentration to be kept constant not only by electrolyte homogenization but also because the bulk is voluminous. In these conditions, the concentration profiles of the reactive species across the diffusion layer are assumed to be linear.

As an example, in the anodic branch ( $\eta > 0$ ) of the  $\text{Zn}^{2+}/\text{Zn}$  couple, metallic Zn is transformed into  $\text{Zn}^{2+}$  cations. Therefore, the interfacial concentration of  $\text{Zn}^{2+}$ ,  $C_{\text{int}}$ , is higher than that in the electrolyte bulk,  $C_{\infty}$ , so that the concentration profile decreases, as depicted in **Figure 22**.  $\text{Zn}^{2+}$  cations in excess at the interface diffuse towards the bulk electrolyte.

Since the concentration profile is assumed to be linear inside the diffusion layer, Faraday's and Fick's laws<sup>30,31</sup> yield the following relationship between the current density and the concentration gradient for any  $\text{M}^{z+}/\text{M}$  couple:

$$j = -zDF \frac{C_{\infty} - C_{\text{int}}}{\delta} \quad [63]$$

where  $D$  is the diffusion coefficient of the cation, often

expressed in  $\text{cm}^2 \text{s}^{-1}$  (about  $10^{-5}$  to  $10^{-6} \text{cm}^2 \text{s}^{-1}$  in aqueous solutions). (Fick's first law states that a diffusive flux is proportional to the diffusion coefficient  $D$  of the diffusing species in a given electrolyte and to the concentration gradient across the diffusion layer,<sup>31</sup> that is  $j = -D(\partial C(x)/\partial x)$ .)

In the cathodic branch ( $\eta < 0$ ), the concentration increases with the distance from the electrode because of the depletion of cations at the interface, as represented in **Figure 23**. The reduction reaction that entails metallic Zn deposition on the surface, now depends on the supply of cations diffusing from the bulk towards the interface, so that eqn [63] remains valid. However, in contrast to the anodic branch where the metallic Zn can be regarded as an infinite reservoir, a limiting

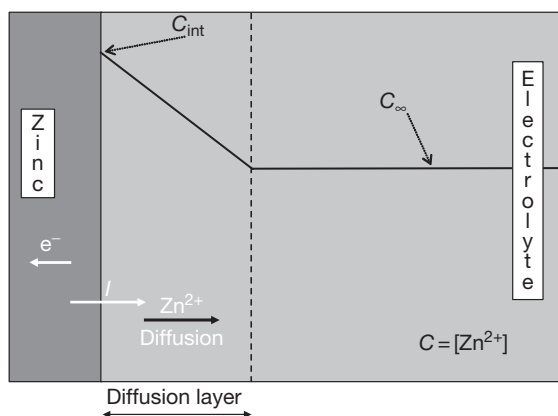


**Figure 22**  $\text{Zn}^{2+}$  concentration profile across the Nernst diffusion layer for an anodic reaction according to Nernst's model.

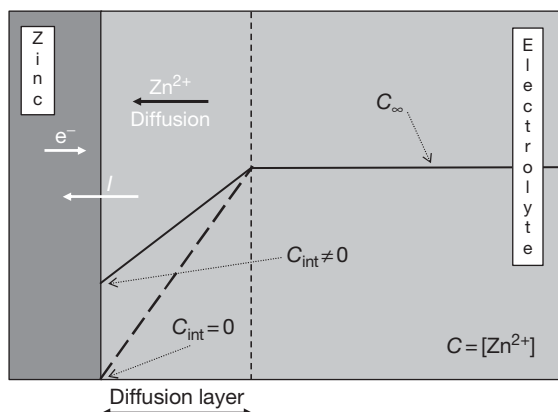


**Figure 23**  $\text{Zn}^{2+}$  steady-state concentration profile across the diffusion layer for a cathodic reaction. Dashed line: limiting case with  $C_{\text{int}} = 0$ , corresponding to the diffusion limited current plateau in **Figure 16**.

situation is reached when the interfacial concentration becomes equal to zero. In that case, the charge-transfer activation process (redox kinetics) is so fast, relative to mass transport, that any cation reaching the interface is immediately reduced. At large negative overpotentials, this leads to the appearance of a plateau defining a limiting current in the current–potential curve, as illustrated in **Figure 16**. Introducing zero interfacial concentration in eqn [63] yields:

$$j_{\text{lim,c}} = -zDF \frac{C_{\infty}}{\delta} \quad [64]$$

The effective value of the limiting current depends on the hydrodynamics (roughly speaking, the stirring conditions) of the system, which directly defines the thickness of the diffusion layer  $\delta$ . Just to give an idea, for a  $10^{-6} \text{cm}^2 \text{s}^{-1}$  diffusion coefficient,  $0.1 \text{mol l}^{-1}$  concentration,  $10 \mu\text{m}$  thick diffusion layer, and  $z = 1$ , the limiting current density is about  $10 \text{mA cm}^{-2}$  in absolute value, according to eqn [64]. Another example concerns the rotating disk electrode, for which the Levich equation predicts the limiting current density, taking into account both the diffusion rate across the diffusion layer and the complex solution flow pattern<sup>32</sup>:

$$j_{\text{lim,c}} = -0.620zFD^{2/3}\omega^{1/2}\nu^{-1/6}C_{\infty} \quad [65]$$

where  $\omega$  is the angular rotation rate of the electrode (in  $\text{rad s}^{-1}$ ) and  $\nu$  is the kinematic viscosity of the solution (about  $10^{-2} \text{cm}^2 \text{s}^{-1}$  in common aqueous solutions). For the parameter values given above and a rotation rate of  $1000 \text{rpm}$  ( $104.7 \text{rad s}^{-1}$ ), the current density is about  $-13 \text{mA cm}^{-2}$ .

In addition to the quantitative expression of the limiting current given by eqn [64], the mathematical expression for the whole current–potential curve can be derived by combining eqns [39], [63], and [64]. For example, the current–potential curve of a fast redox couple  $\text{M}^{z+}/\text{M}$ , schematically represented in **Figure 16**, has the following form:

$$\eta = \frac{RT}{zF} \ln \frac{j_{\text{lim,c}} - j}{j_{\text{lim,c}}} \quad [66]$$

#### 1.02.4.2.3 General case: Mixed controlled systems

In the general case of an electrochemical system, interfacial charge-transfer and mass transport simultaneously intervene in the kinetics of the reactions at the interface. The mathematical expression of the current is similar to that used in the current–



potential equation [47] with interfacial concentrations instead of bulk concentrations. As an example, for the model corrosion reaction [18] in which mass transport is assumed to intervene for the cation  $M^{z+}$  only when

$$\begin{aligned} j &= j_a + j_c = zF(k_a - k_c[M^{z+}]_{\text{int}}) \\ &= zFk^0 \left[ \exp\left(\frac{\alpha zF}{RT}(E - E^0)\right) - [M^{z+}]_{\text{int}} \exp\left(-\frac{(1-\alpha)zF}{RT}(E - E^0)\right) \right] \end{aligned} \quad [67]$$

where  $k_a$  is now expressed in  $\text{mol m}^{-2} \text{s}^{-1}$  while  $k_c$  is still expressed in  $\text{m s}^{-1}$ . With reasoning similar to that used in eqns [48]–[51], the following relationship, similar to the usual Butler–Volmer equation, can be derived:

$$j = j_0 \left[ \exp\left(\frac{\alpha zF}{RT}\eta\right) - \frac{[M^{z+}]_{\text{int}}}{[M^{z+}]_{\infty}} \exp\left(-\frac{(1-\alpha)zF}{RT}\eta\right) \right] \quad [68]$$

where  $j_0$  is now given by:

$$j_0 = zFk^0[M^{z+}]_{\infty}^{\alpha} \quad [69]$$

The interfacial concentration of  $M^{z+}$  can be evaluated with the Fick's first law (eqn [63]), which gives the following expression of the current–potential curve:

$$j = j_{\text{act}} \frac{1}{1 + j_0 \frac{\delta}{zFD[M^{z+}]_{\infty}} \exp\left(-\frac{(1-\alpha)zF}{RT}\eta\right)} \quad [70]$$

where  $j_{\text{act}}$  stands for the ‘activation current density’ for which the concentration of the cations at the interface is equal to that in the solution bulk ( $j_{\text{act}} = j$  in eqn [52]). Equation [70] reduces to the diffusion-limited current density in the cathodic region, already given by eqn [64] with  $C_{\infty} = [M^{z+}]_{\infty}$ , when  $\eta$  tends to  $-\infty$ .

Figure 24 compares the current–potential curves of a purely-activated system and a mixed controlled system with the same kinetic parameters (eqns [52] and [70]). It can be seen that at any potential the current (in absolute value) is always smaller under mixed control. Another general expression for any redox reaction may be derived from eqn [70]:

$$\frac{1}{j} = \frac{1}{j_{\text{act}}} + \frac{1}{j_{\text{mt}}} \quad [71]$$

where the mass-transport current density,  $j_{\text{mt}}$ ,

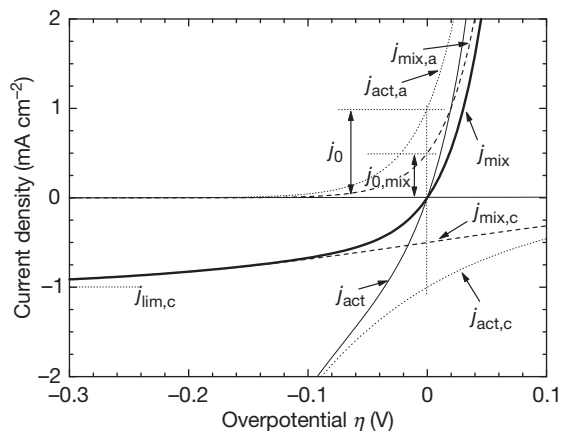


**Figure 24** Comparison of the current–overpotential curves for pure activation (thin solid line and dotted lines for the anodic and cathodic currents) and mixed (activation and mass transport: thick solid line and dashed lines for the anodic and cathodic currents) kinetics with a cathodic limiting diffusion current ( $z = 1$ ,  $j_0 = 1 \text{ mA cm}^{-2}$ ,  $\alpha = 0.8$ ,  $j_{\text{lim},c} = -1 \text{ mA cm}^{-2}$ ).

corresponds to the current density for a very fast redox reaction ( $j_0 \rightarrow \infty$  in eqn [70]), that is, for a reaction under complete mass transport control. This simple expression highlights the cornerstone of the idea of interface control. If  $j_{\text{act}}$  is much larger than  $j_{\text{mt}}$ , eqn [71] predicts that the mixed current is very close to  $j_{\text{mt}}$ . From a physical point of view the kinetic behavior can be seen as a series connection of two steps: the slowest step determines the overall reaction rate. If the activation kinetics is fast, then the mass-transport process is the limiting step. Conversely, if the activation kinetics is slow, the diffusion process does not hinder the overall reaction rate.

An important consequence of the mixed control depicted in Figure 24 is that the exchange current density,  $j_{0,\text{mix}}$ , is smaller than the kinetic exchange current density  $j_0$  derived from the  $k^0$  and  $\alpha$  parameters. The expression of  $j_{0,\text{mix}}$  can be obtained from eqn [70] with  $\eta = 0$ . In the same way, the polarization resistance (reciprocal of the slope of the current–potential curve in the vicinity of  $E_{\text{eq}}$ , see eqn [57]) depends on mass transport.<sup>33</sup> Its expression, derived from the linear approximation of the polarization curve at small overpotentials, is:

$$R_p = \frac{1}{S} \left( \frac{\partial \eta}{\partial j} \right)_{j=0} = \frac{RT}{zFS} \left( \frac{1}{j_0} - \frac{1}{j_{\text{lim},c}} \right) \quad [72]$$

This illustrates the fact that the overall polarization

resistance is always higher under mixed control than under activation control (for the same  $j_0$  and  $\alpha$ ).

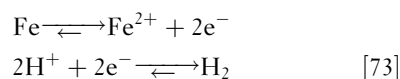
## 1.02.5 Corrosion: Far from Equilibrium Zero Net Current Systems

### 1.02.5.1 Qualitative Description of the Free Corrosion Scenario

Everybody knows or easily guesses the consequence of abandoning a metallic piece in an aggressive medium without specific protection, for instance, iron in seawater: the metal will be annihilated by corrosion. Regardless of the rate of the process, which depends on many factors such as the nature of the metal and of the electrolyte, temperature, pressure, and so on, this primary experimental evidence leads to an important conclusion: any corrosion process evolves under long-term out-of-equilibrium conditions. In spite of being permanently in non-equilibrium conditions, the system is, in some senses, at rest in the free corrosion scenario. In other words, no net current flux is crossing the metal–electrolyte interface.

As an obvious consequence, if the metal is being consumed by corrosion processes, oxidation reactions inevitably take place at its surface although the net current flow is zero. Therefore, at every instant the amount of current generated by these oxidation reactions (for instance, reaction [2]) must be balanced by cathodic counterparts. This implies that anodic and cathodic reactions must be occurring simultaneously. In contrast with the previous sections, this scenario cannot involve a single redox couple with a simple forward–backward reaction, otherwise the zero net current would correspond to an equilibrium condition in which the iron dissolution and deposition would perfectly balance out and no corrosion would occur. Corrosion phenomena, therefore, involve at least two different redox couples, one (or more) supplying the anodic current and the other one (or more) supplying the cathodic current and ensuring the zero current balance. This kind of self-regulated coupled system yields the two fundamental parameters of corrosion processes, the corrosion current,  $I_{\text{corr}}$  and the corrosion potential,  $E_{\text{corr}}$  also called rest potential or open-circuit potential (OCP). (The term coupled here refers to the fact that the anodic and cathodic reactions must deliver the same average current (in absolute value) to maintain a zero current balance, and not to coupled kinetic parameters  $k^0$  and  $\alpha$  as

in the case of a single forward–backward reaction (with  $\alpha$  and  $1-\alpha$ , respectively), as discussed before.) As described below, both  $E_{\text{corr}}$  and  $I_{\text{corr}}$  are time-evolving variables that define the intrinsic thermodynamic and kinetic characteristics of each redox couple taking part in the global reaction. This is why the corrosion potential is often referred to as a mixed potential. A simple qualitative description of a coupled system can be proposed with the example of the free corrosion of iron in acidic media: the zero net current balance is then a result of the following coupled equations:



The two individual equilibrium potentials,  $E_{\text{eq,Fe}^{2+}/\text{Fe}}$  and  $E_{\text{eq,H}^+/\text{H}_2}$ , can be defined for reactions [73] if the four species are present at the metal–electrolyte interface. Their exact values depend on the experimental conditions, as described by the Nernst law (see Section 1.02.3). The fact that each couple behaves in a stationary way allows the steady state of the corrosion system to be defined from their individual polarization curves (see Section 1.02.4) and its corrosion rate to be calculated. Since iron is oxidized when corroding, its polarization point must be somewhere along the anodic branch of the  $\text{Fe}^{2+}/\text{Fe}$   $\eta$ - $I$  curve, the shape of which is a function of the thermodynamic and kinetic attributes of the couple, as illustrated in Figure 25. The behavior of the second couple is quite evident, since it must ensure the zero overall current by consuming the electrons supplied by the anodic reaction.  $\text{H}^+$  is then reduced and the polarization point of the couple is located on the cathodic branch of the  $\text{H}^+/\text{H}_2$   $\eta$ - $I$  curve. The corrosion process is then iron dissolution with hydrogen evolution according to reactions [73]. The exact situation is graphically determined by the potential for which  $|I_c| = I_a$ , as shown in Figure 25.

Since, very often corrosion processes can be considered as activation-controlled systems (at least for low current values), another useful representation for free corrosion conditions is the so-called Evans diagram, which gives the potential evolution against the logarithm of the current absolute value, as depicted in Figure 26, strictly Evans originally plotted  $E$  against  $|I|$ , i.e., using linear rather than log scales. However, the name is now widely used for diagrams plotting  $E$  against  $\log |I|$ .

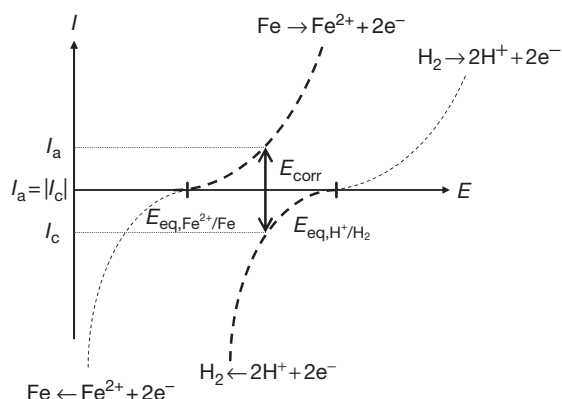


**Figure 25** Schematic representation of the polarization curves of the two redox couples around their respective equilibrium potential allowing the corrosion potential  $E_{\text{corr}}$ , at which  $|I_c| = I_a$ , to be determined. Note that the ordinates are plotted in terms of net currents and not current densities, since the equality between the anodic and cathodic counterparts concerns the electron flux (see Section 1.02.2.3).

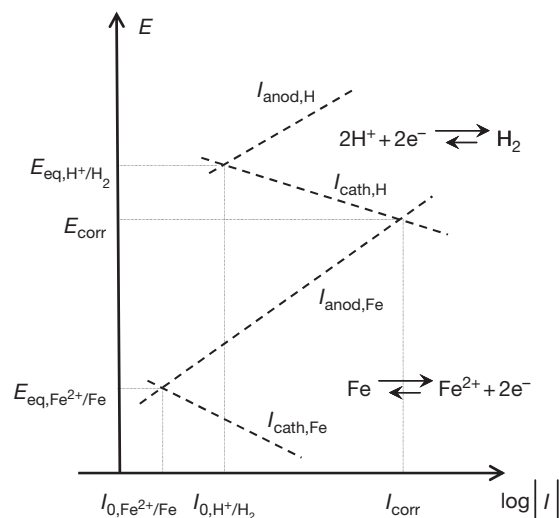


**Figure 26** The Evans diagram: a simplified representation of the mixed potential and the mutually balancing cathodic and anodic electron fluxes that determine the corrosion potential and exchange current values. The figure is arbitrarily asymmetric with  $E_{\text{corr}} - E_{\text{eq, Fe}^{2+}/\text{Fe}} > |E_{\text{corr}} - E_{\text{eq, H}^+/\text{H}_2}|$ . The values of the exchange currents are also arbitrary.

The main advantage of the Evans diagram is to clearly illustrate the fact that when two different redox couples coexist, the electrode potential always takes a single value, the corrosion potential, which is easily determined by the intersection of two branches. The exact  $E_{\text{corr}}$  value (as well as the corrosion current value) depends on the kinetic and thermodynamic characteristics of both couples that are

out of equilibrium and follow the behavior predicted by their own polarization curves, as shown in Figure 25. In spite of this complex behavior,  $E_{\text{corr}}$  naturally lies between the two individual equilibrium potentials. The two (or more) reactions do not usually take place with the same overpotential  $\eta_{\text{Fe}^{2+}/\text{Fe}} = E_{\text{corr}} - E_{\text{eq, Fe}^{2+}/\text{Fe}}$  and  $|\eta_{\text{H}^+/\text{H}_2}| = |E_{\text{corr}} - E_{\text{eq, H}^+/\text{H}_2}|$  (even if the equality  $\eta_{\text{Fe}^{2+}/\text{Fe}} = |\eta_{\text{H}^+/\text{H}_2}|$  is of course not forbidden), since what they must ensure is an identical electron flux, identified to the corrosion current,  $I_{\text{corr}}$ , as depicted in Figure 26. Both redox couples are displaced from their respective equilibrium potential, which means that the  $\text{Fe}^{2+}/\text{Fe}$  couple shifts the proton reaction in the cathodic direction while the  $\text{H}^+/\text{H}_2$  couple shifts the iron reaction in the anodic direction.

This idea of mixed potential is extremely important as it indicates that the reaction with the lower equilibrium potential will be anodic and that with the higher equilibrium potential will be cathodic. It then defines in principle which metal will corrode in a given situation of galvanic corrosion. (This is only necessarily true when both metals are corroding in an active state; in practical situations (which often involve one or both of the metals being passive) the standard equilibrium potentials are not reliable indicators of the behavior of galvanic couples.) Let us take the example of iron and copper in the presence of an acidic electrolyte, that is, in the presence of the  $\text{H}^+/\text{H}_2$  couple, but in the absence of dissolved oxygen. The respective standard equilibrium potentials are  $-0.44$ ,  $0.34$ ,  $0$  V<sub>SHE</sub> for iron, copper, and hydrogen, respectively. It clearly appears that iron and copper behave differently in contact with an acidic solution. The iron will corrode, driven by the proton reduction with concomitant  $\text{H}_2$  evolution, whilst the copper will remain intact since its potential is higher than that of the  $\text{H}^+/\text{H}_2$  couple. The importance of specifying the absence of oxygen in this example is due to the high potential of the  $\text{O}_2/\text{H}_2\text{O}$  couple ( $1.23$  V<sub>SHE</sub>) that can induce the corrosion of copper as well as that of iron.

As already mentioned, it is assumed in reactions [73] that the species produced by the forward reactions are available at the interface, in particular, the  $\text{Fe}^{2+}$  cations are not all trapped in indissoluble corrosion products. Reactions [73] were intentionally represented with forward and backward arrows of different size instead of purely anodic and cathodic reactions [2] and [12]. This is of high importance because, depending on the overpotential of each reaction relative to the actual corrosion potential,

the reverse reaction (iron deposition or anodic hydrogen oxidation) can also take place on the metallic surface even though its rate will be less than the anodic and cathodic counterparts (iron dissolution and proton reduction, respectively). When the mixed potential  $E_{\text{corr}}$  entails an overpotential, high enough to bring the reaction inside the irreversible domain, the reverse reaction can be neglected, as discussed in [Section 1.02.3.2](#). This is often the case in corrosion processes and this constitutes the basis of the simplified kinetic treatment applied to corrosion studies, which is developed in the next section.

### 1.02.5.2 Electrochemical Kinetics Around the Corrosion Potential

In spite of the enormous physical difference between the equilibrium and the corrosion potentials, both potentials concern systems that are released at rest and thus show a permanent zero-net current balance. In [Section 1.02.4](#), the kinetic behavior was investigated when imposing a potential shift with respect to the equilibrium potential. It is interesting now to consider the kinetic consequences of imposing a potential shift with respect to the corrosion potential. This raises a strongly intuitive analogy between the kinetic behaviors around  $E_{\text{eq}}$  and  $E_{\text{corr}}$  that is fully verified experimentally. The first aspect in this analogy is that, as seen in [Section 1.02.4.2.2](#), beyond a certain deviation from equilibrium, generally about a  $\pm 100$  mV overpotential, the system can be considered to be in the irreversible Tafel domain. Considering the Pourbaix diagrams, or simply a standard equilibrium potential table, it can be seen that the differences between the equilibrium potentials of most of the typical redox couples inducing metallic corrosion are much larger than this value of  $\pm 100$  mV (e.g.,  $1.23 - (-0.62) = 1.85$  V for  $\text{Fe}-\text{O}_2$ , and  $0.62$  V for  $\text{Fe}-\text{H}^+$  according to [Figure 13](#) for  $[\text{Fe}^{2+}] = 10^{-6} \text{ mol l}^{-1}$  and  $\text{pH} = 0$ , just to mention the most common corrosion couples involving iron). This indicates that most of the common corrosion processes take place in the irreversible domain. In such conditions, and provided that the mass transport effects are negligible, the Butler–Volmer equation related to each reaction is reduced to a single anodic or cathodic branch so that the polarization curve of the overall coupled system is defined as follows:

$$j = j_{0,a} \exp\left(\frac{\alpha_a z_a F}{RT} \eta_a\right) - j_{0,c} \exp\left(-\frac{(1 - \alpha_c) z_c F}{RT} \eta_c\right) \quad [74]$$

where the subscripts a and c stand for anodic and cathodic respectively and where  $\eta_a = E - E_{\text{eq},a}$  and  $\eta_c = E - E_{\text{eq},c}$ . [Equation \[74\]](#) is implicitly derived for conditions where both processes are completely independent and in a steady state. This means, for example, that the sharing of the surface area in anodic and cathodic zones does not change with the potential, and is constant during the experiment.

Let us now define the polarization  $\pi = E - E_{\text{corr}}$ , analogous to the overpotential  $\eta$  when dealing with equilibrium systems. Assuming, as discussed above, that both couples are sufficiently far from equilibrium to be in the irreversible domain, the current–potential curve of the overall system is composed of a single anodic branch (corresponding to one of the oxidation process of the redox couples) and a single cathodic branch (corresponding to the reduction process of the other redox couple). The current–potential relationship can hence be described by the following equation, which is derived from [eqn \[74\]](#) and is very similar to the Butler–Volmer equation<sup>34</sup>:

$$j = j_{\text{corr}} \left( \exp\left(\frac{\alpha_a z_a F}{RT} \pi\right) - \exp\left(-\frac{(1 - \alpha_c) z_c F}{RT} \pi\right) \right) \quad [75]$$

with

$$\begin{aligned} j_{\text{corr}} &= j_{0,a} \exp\left(\frac{\alpha_a z_a F}{RT} \eta_{a,\text{corr}}\right) \\ &= j_{0,c} \exp\left(-\frac{(1 - \alpha_c) z_c F}{RT} \eta_{c,\text{corr}}\right) \end{aligned} \quad [76]$$

The parameters  $\alpha_a$  and  $\alpha_c$  are no longer mutually related as for a single transfer coefficient ( $\alpha_a \neq \alpha_c$ ), and [eqn \[75\]](#) is often represented in a simpler way:

$$j = j_{\text{corr}} (\exp(b_a \pi) - \exp(b_c \pi)) \quad [77]$$

where  $b_a$  ( $b_a > 0$ ) and  $b_c$  ( $b_c < 0$ ) are the anodic and cathodic Tafel coefficients, respectively, expressed in  $\text{V}^{-1}$ . It is easily seen that for potentials sufficiently far from  $E_{\text{corr}}$  and in the absence of mass-transport effects, the anodic or cathodic branches yield a linear behavior in a semilogarithmic scale, as depicted in [Figure 27](#).

The experimental Tafel slopes,  $\beta_a$  and  $\beta_c$ , expressed in volt per current decade, can be determined from [Figure 27](#) with the following equations:

$$\beta_a = \frac{2.303}{b_a} \quad \text{and} \quad \beta_c = \frac{2.303}{b_c} \quad [78]$$

The corrosion current density can also be estimated by extrapolation of the Tafel lines at the corrosion

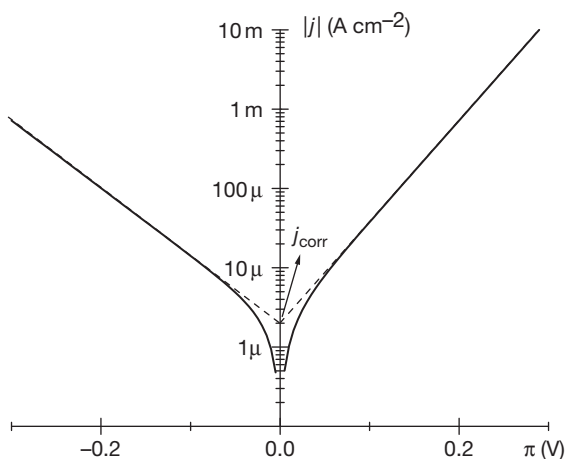


**Figure 27** Kinetic behavior within a large potential domain: Tafel (linear) region and estimation of the corrosion current density. Arbitrary values of  $j_{\text{corr}} = 2 \mu\text{A cm}^{-2}$ ,  $\alpha_a = 0.75$ ,  $\alpha_c = 0.5$ ,  $z_a = z_c = 1$ .

potential ( $\pi = 0$ ), similar to the estimation of the exchange current density for a redox couple (Figure 21). It is worth emphasizing that both characteristics correspond to far-from-equilibrium conditions, each branch following its intrinsic kinetic behavior independently of the other.

From a practical point of view, the accurate determination of the corrosion current, a sort of Holy Grail for corrosion engineers, deserves two important remarks. The first, extremely relevant and often disregarded, is that the polarization curve should show a large and unambiguous region of Tafel behavior; the linear domain should encompass at least one decade of current to allow the graphical determination of the corrosion current to be carried out. Despite that, several commercial corrosion analysis programs allow manual Tafel fits from small truncated straight lines or even when there is no linear behavior at all. Figure 28 illustrates this issue in the case of a non-linear anodic curve measured during corrosion of Zn in a highly aerated carbonate solution at 60 °C after several hours of immersion (for illustration, the cathodic branch is ignored for the moment). The magnitude of the possible error in  $j_{\text{corr}}$  due to the arbitrary choice of two linear fits (represented by straight lines 1 and 2), corresponds to a factor of about 3 between the values of  $j_{\text{corr},1}$  and  $j_{\text{corr},2}$ .

The second remark is more positive: since  $j_{\text{corr}}$  is determined at the corrosion potential, the existence of a single Tafel region (anodic or cathodic) is sufficient. This is particularly useful when the anodic branch, for example, does not present a well defined

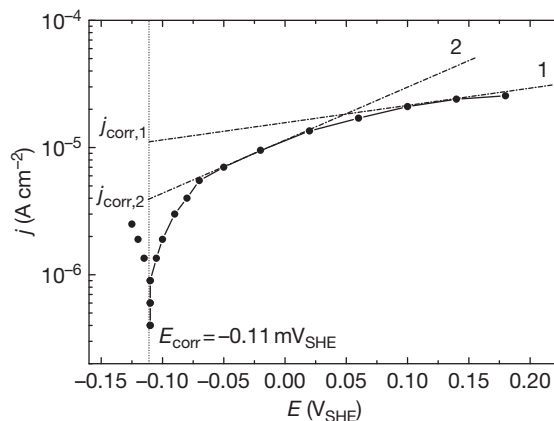


**Figure 28** Anodic polarization curve of Zn in a  $0.01 \text{ mol l}^{-1}$   $\text{NaHCO}_3$  solution under  $\text{O}_2$  bubbling at 60 °C, pH = 8.1: misestimation of the corrosion current density from a nonlinear or small-range Tafel behavior.

Tafel line as in Figure 28. If the cathodic branch exhibits a Tafel domain, which is often the case for hydrogen evolution but rare for oxygen reduction, the corrosion current can be determined by extrapolating the cathodic linear branch up to the corrosion potential. (A common error in applying Tafel extrapolation is to extrapolate the Tafel line for hydrogen evolution, even though the dominant cathodic reaction is oxygen reduction.) This is really useful, as the anodic and cathodic branches are independent without any expected symmetry or even equivalent shape. Let us come back to the previous figure but in its complete form, showing the anodic and cathodic branches (Figure 29). Even if the anodic reaction does not present a marked linear  $\log(j_{\text{corr}}) - E$  characteristic, as seen before, the corrosion current density can be correctly estimated by means of the unambiguous and wide Tafel behavior of the cathodic branch.

In the example presented in Figures 28 and 29, the  $j_{\text{corr}}$  values badly estimated with the anodic branch are higher than the actual  $j_{\text{corr}}$  value. This overestimation is certainly less harmful than an underestimation, but the reverse situation cannot be simply excluded. Indeed, due to the logarithmic scale, this loose approach to the Tafel laws can yield significant errors, the impact of which in the nuclear domain, for instance, is easy to imagine and hard to mitigate.

It is worth noting, however, that it is possible to evaluate the corrosion current density with the Stern–Geary relationship in a narrow potential domain. In addition, the four unknown variables,



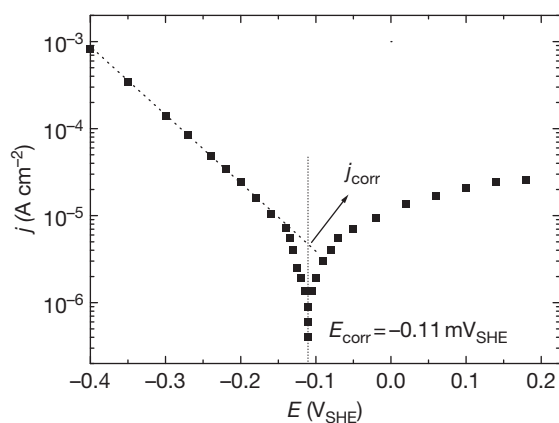


**Figure 29** Complete polarization curve obtained in the same conditions as in [Figure 28](#): good estimation of the corrosion current density by means of a single wide Tafel region.

$j_{\text{corr}}$ ,  $E_{\text{corr}}$ ,  $\alpha_a$ , and  $\alpha_c$  can be evaluated with a parameter regression calculation, provided that the potential domain is sufficiently large (about  $\pm 50$  mV from  $E_{\text{corr}}$ ) to give a nonlinear current–potential curve (four unknowns can then be determined instead of two for a linear curve) and, at the same time, sufficiently narrow in order that the system behavior obeys [eqn \[75\]](#).

One reason that the anodic branch exhibits a poorly defined Tafel domain is the dissolution mechanism itself. The metal is dissolving with multiple elementary steps, and the rate-limiting reaction step may change with the potential, as illustrated by the extensive work of Keddad *et al.* On the other hand, at the corrosion potential of iron in sulfuric acid, the coverage of the electrode surface by hydrogen atoms is close to unity,<sup>9</sup> and, as can be conceived readily, the surface area available for iron dissolution increases with increasing potential. This is another reason explaining the narrow linear domain of Tafel behavior of the anodic process. In contrast, the surface area at which hydrogen evolution is taking place does not change significantly so the polarization curve exhibits Tafel behavior in the cathodic domain.

It is worth mentioning that when mass-transport phenomena influence the electrochemical response, leading to a non-Tafel behavior of the two couples, the determination of the corrosion current cannot be achieved as straightforwardly as for Tafel behavior. Indeed, for a redox couple under mixed control at equilibrium ([Section 1.02.4.2.3](#)), it can be shown that the corrosion current is lower when mass transport is controlling the kinetics of the corrosion system. As a

consequence, the polarization resistance, which is an important parameter for the assessment of corrosion current in field applications, is higher in that case.

## 1.02.6 The Electrochemical Cell

This section is devoted to a brief description of an electrochemical cell and of the basic instrumentation used for controlling the electrode potential (potentiostat) or the current flowing across the electrode (galvanostat). Numerous techniques, electrochemical or *in situ* spectroscopic, may be used for studying electrode reactions at equilibrium or out-of-equilibrium, such as potentiometry, amperometry, voltammetry, electrochemical impedance, electrochemical noise, scanning electrochemical microscopy, atomic force microscopy, Raman spectroscopy, etc. These techniques will not be described in this section, the reader may consult other chapters in this book, or Marcus and Mansfeld,<sup>35</sup> Greef *et al.*,<sup>36</sup> Bard and Faulkner<sup>37</sup> for more information.

### 1.02.6.1 Design of the Electrochemical Cell

Although the electrochemical phenomena occur on a single electrode in most corrosion processes, as described in [Section 1.02.2](#), the understanding and quantitative analysis of these phenomena are usually performed with the help of three electrodes in contact with the same electrolyte, to measure and/or control the electrode potential and current precisely, as described briefly in the following.

Basically, the electrochemical cell comprises three electrodes immersed in an electrolyte, the working electrode (WE), which is the electrode under study, the counter-electrode (CE), the role of which is to ensure the current flow across the cell, and the reference electrode (RE) versus which the potential of the WE is measured. The electrodes may be located in single-compartment containers or in containers with two compartments separated by a membrane or a sintered glass, for example, to prevent the species produced at the counter electrode from reaching the working electrode.

Depending on the system under investigation, the reaction kinetics may be studied in stagnant solutions or in forced convection conditions. Mass-transport control in the cell may be realized by agitating the solution with gas or a stirrer, by rotating the electrode (a disk or a cylinder), or by flowing the solution in front of the WE (immersed jet cell or channel flow). Whenever feasible, controlling mass transport effectively



allows a better control and definition of the flow conditions. This helps to ensure steady state conditions, improve reproducibility, and make quantitative analysis easier with the help of the Fick and Levich equations.

#### **1.02.6.1.1 The working electrode**

The design, size, and materials of the WEs are diverse. Very often, especially in corrosion, the WE is a metallic disk or square, the lateral surface of which is embedded in an epoxy resin or covered with an electrical insulator. Care must be taken for mounting the WE since crevice effects between the sample and the insulator are possible. A thin layer of cataphoretic paint may be deposited on the lateral surface of the sample before mounting in the insulator to avoid this. The size of the WE may be very large in industrial applications but in most laboratory investigations, the surface area is of the order of  $1\text{ cm}^2$ . To obtain a reproducible surface state, the WE is usually polished before the experiment with abrasive paper, alumina, or diamond paste, rinsed and placed in an ultrasonic bath to remove the polishing particles. In most cases, the WE is fully immersed in the electrolyte but in marine corrosion applications, the sample may pass through the air–electrolyte interface, which provokes water-line attack due to enhanced oxygen availability (see [Section 1.02.2.3](#)).

#### **1.02.6.1.2 The counter-electrode**

The CE is often a cylindrical grid of large surface area compared to the WE for several reasons. First, this minimizes the polarization of the CE (because of the low current density on a large electrode) and, therefore, the overall voltage required from the power source. Second, the current lines between the WE and the CE spread inside a larger electrolyte volume with a large CE, so that the electrolyte resistance is located near the WE, as shown below, which gives a lower influence of the RE position on the measured potential. When possible, the CE is positioned far from the WE so that the cylindrical shape ensures that the CE is an equipotential surface. (The ready availability of numerical modeling tools that can determine the current distribution now makes it possible to improve the design of electrochemical cells for specified situations.) Inert electrodes, metallic grids (often in platinum or titanium) or carbon sheets may be used. When a single compartment is used, the reactions taking place on the CE have to be considered with great care since they may cause changes in the concentration of the reactants in

solution. In practice, the reaction occurring on the CE is that of presenting the lower CE overvoltage. In corrosion studies, they usually consist in the oxidation or reduction of a component of the electrolytic solution, such as hydrogen evolution when the WE is polarized anodically and oxygen evolution when it is polarized cathodically (or chlorine evolution in chloride solutions). Another oxidation reaction may take place when using a noninert CE, such as stainless steel (special care must be taken in that case to avoid contamination of the working electrolyte). As mentioned above, the CE must be located in a specific compartment separated with an ion-exchange membrane or a sintered glass when using a stainless steel CE or when the reaction product, such as dissolved oxygen, may alter the behavior of the WE.

#### **1.02.6.1.3 The reference electrode**

A RE is used to control and/or measure the electrode potential in almost all electrochemical investigations. However, in early work, before the common use of RE, the potential was sometimes measured with respect to a CE of large surface area. This is also the case at times for experiments performed with microelectrodes. This section is aimed at discussing the main principles of the RE and its positioning in the electrochemical cell.

#### **The main reference electrodes**

As explained in [Section 1.02.3.3](#), the electrode potentials in the electrochemical systems are referred to a standard system called SHE, which, strictly speaking, cannot be realized, and the derived experimental RE, the NHE, is not easy to handle. A number of practical REs were, therefore, developed and are now commonly used.<sup>18</sup> There are two basic classes of practical RE, sometimes called secondary REs since they are calibrated against the primary reference of SHE:

- REs of the first kind consist of a metal in equilibrium with a controlled concentration of its salt. An example of this type is copper metal in a solution of copper sulfate. Then the copper ion concentration controls the potential as defined by the Nernst equation.
- REs of the second kind consist of a metal in contact with a sparingly soluble salt of the metal; this is placed in a solution with a controlled concentration of a soluble salt with the same anion. An example of this type is silver in contact with silver chloride in a solution of potassium chloride. In this case the chloride concentration in solution

controls the silver ion concentration by way of the solubility product of silver chloride, and the silver ion concentration controls the potential as defined by the Nernst equation.

Commercially-available REs include:

- Hg|Hg<sub>2</sub>Cl<sub>2</sub> (calomel) in a saturated KCl solution, named SCE for saturated calomel electrode. This system is a very common commercial product (though tending to lose favor because of toxicity issues and a ban on the transportation of products containing mercury by air): a platinum wire is dipped into a mercury pool (Figure 30), which is in contact with a paste of mercury and Hg<sub>2</sub>Cl<sub>2</sub>, itself in contact with a saturated KCl solution ( $\sim 4 \text{ mol l}^{-1}$  at room temperature).
- Hg|Hg<sub>2</sub>SO<sub>4</sub> in a saturated K<sub>2</sub>SO<sub>4</sub> solution. This system may be used for general purposes where the absence of chloride ions in the electrolyte is crucial.
- Hg|HgO in a KOH solution of fixed concentration, for alkaline electrolytes.
- Ag|AgCl in a KCl or NaCl solution of fixed concentration. This RE is quite easy to prepare: for instance, an Ag wire can be dipped into a concentrated KCl solution and anodically electrolyzed or it can be dipped a few minutes in a concentrated FeCl<sub>3</sub> aqueous solution in which it is spontaneously oxidized. The resulting wire is covered with an AgCl deposit and may be used in any solution of fixed chloride concentration. It is very commonly used in marine applications when the Ag|AgCl wire can be directly used in the seawater without a specific electrolyte compartment, in contrast with the above REs.
- Cu in a saturated CuSO<sub>4</sub> solution – this is the only widely used RE of the first kind. This electrode is commonly used in the field, for instance, to evaluate the efficiency of cathodic protection of buried carbon steel pipelines. It consists of a copper rod dipped in a saturated CuSO<sub>4</sub> solution, as shown in Figure 31.

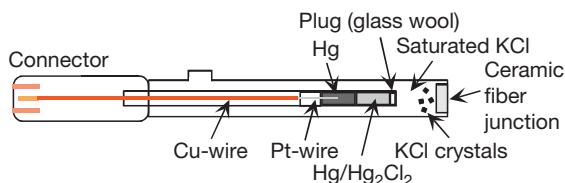


**Figure 30** Scheme of the saturated calomel reference electrode.

A generic consequence of the Nernst equation for the reversible redox couple involved in these REs, is that in order to obtain a RE showing a constant potential with time, the electrolyte inside the RE must contain a salt at fixed concentration. One of the advantages of using a saturated salt solution (as in the first two examples) is that the presence of the solid salt maintains a fixed ionic concentration, given by the solubility of the salt, even if small perturbations may lead to a slight consumption of this ion. However, the saturation concentration is temperature sensitive and this kind of RE has a rather high temperature coefficient (e.g.,  $\sim 0.65 \text{ mV } ^\circ\text{C}^{-1}$  for the SCE compared to  $0.06 \text{ mV } ^\circ\text{C}^{-1}$  for the calomel RE in  $0.1 \text{ mol l}^{-1} \text{ KCl}$ ).

To avoid contaminating the working solution with the salt used in the RE, a salt bridge filled with the working solution is often used, thereby increasing the distance that ions leaking out of the RE have to diffuse. Additionally, the use of the Hg|Hg<sub>2</sub>SO<sub>4</sub> RE filled with saturated K<sub>2</sub>SO<sub>4</sub> in sulfate media, or the use of the Hg|HgO RE filled with KOH in strongly alkaline media, may minimize solution contamination. Except for the Ag|AgCl RE that can be directly dipped in seawater, the use of these solid REs always introduces one or more liquid–liquid interfaces (e.g., in the porous material used to separate the RE solution from the studied solution) in the potential measurement chain. This will inevitably produce liquid junction potentials that introduce some errors in the measurement and/or control of the WE interface potential. The liquid junction potentials may reach a few tens of millivolts in specific conditions. However, when the solution in the RE is highly concentrated with a cation and an anion of similar ionic molar conductivity as, for example, in saturated KCl solution, the junction potential can be neglected.<sup>38</sup> In most corrosion applications, the error introduced by the junction potentials is usually of no consequence since the electrode potential does not have to be measured with an accuracy better than 1 mV.

Table 2 indicates the measured potential of the REs presented above.

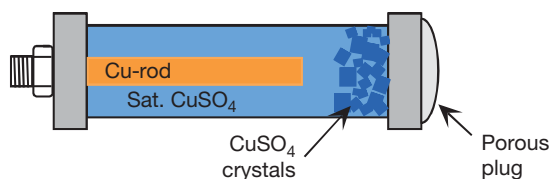


**Figure 31** Scheme of the Cu|saturated CuSO<sub>4</sub> reference electrode.

### Position of the reference electrode

For a simple electrochemical cell, consisting of two planar electrodes of the same size and positioned face to face, similar to a conductivity measurement cell, the potential gradient between the two electrodes is essentially uniform and the solution resistance  $R_e$  can then be calculated as follows:

$$R_e = \frac{1}{\gamma} \frac{d}{S} \quad [79]$$

where  $\gamma$ ,  $d$ , and  $S$  are the conductivity of the electrolyte, the distance between the two electrodes, and their surface area, respectively.

For more general cell geometries, the potential is no longer uniform in the electrolyte. **Figure 32** illustrates the potential and current distributions around a disk electrode when no polarization occurs at the WE and CE and in a cell with an ideal geometry, that is, the counter electrode of hemispherical shape is located at an infinite distance, the disk electrode (radius  $r$ ) is mounted in an infinite insulating plane, and the electrolyte between the disk and the CE is homogeneous.<sup>42</sup> In these conditions, the equipotential surfaces, which can be calculated by solving the Laplace equation in elliptic coordinates, are ellipsoids. The potential and current distribution with no polarization at the WE and CE electrodes is called primary.

Provided the diffusion layers at the WE and CE are two very thin parts of the electrolyte volume, which is often the case with forced convection, and assuming that the polarization of the electrode can be neglected (this may not be true because of the non-uniform current density), the homogeneous part of the electrolyte contributes almost the whole electrolyte resistance and the corresponding potential distribution in the electrolyte is close to that given by **Figure 32**. The electrolyte resistance can then be calculated from the potential distribution<sup>42</sup>:

$$R_e = \frac{1}{\gamma} \frac{1}{4r} \quad [80]$$

**Table 2** Potential of the main reference electrodes used in corrosion<sup>39–41</sup>

Electrode	Couple	Potential ( $V_{SHE}$ )
NHE	Pt H <sub>2</sub>  1 M HCl	+0
SCE	Hg Hg <sub>2</sub> Cl <sub>2</sub>  sat. KCl	+0.24
Mercurous sulfate	Hg Hg <sub>2</sub> SO <sub>4</sub>  sat. K <sub>2</sub> SO <sub>4</sub>	+0.64
Silver chloride	Ag AgCl 3 M NaCl	+0.21
Silver chloride	Ag AgCl 0.1 M NaCl	+0.29
Mercuric oxide	Hg HgO 20% KOH	+0.10
Copper sulfate	Cu sat. CuSO <sub>4</sub>	+0.32

**Figure 33** shows that the normalized potential  $\Phi^0/\Phi_{\text{int}}$  along the disk symmetry axis decreases almost linearly with the distance  $y$  from the electrode when  $y$  is smaller than the electrode radius. This potential profile justifies the use of a Luggin–Haber probe (the tip of the RE is a capillary usually filled with the studied solution and positioned close to the WE) to reduce

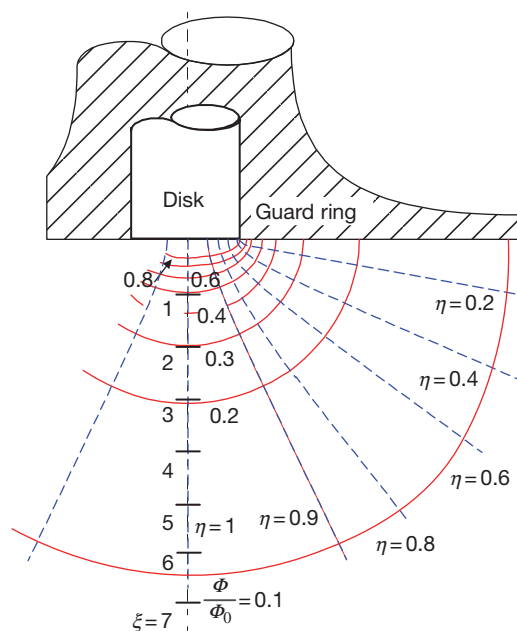


**Figure 32** Primary potential (dotted lines) and current (dashed lines) distributions around a disk electrode for an ideal geometry cell. Adapted from Newman, J. J. *Electrochem. Soc.* **1966**, 113, 501–502.

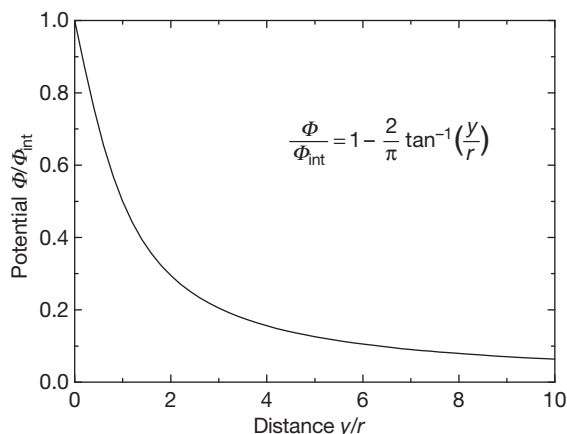


**Figure 33** Potential profile along the symmetry axis of the disk electrode.

the distance between the WE and RE as much as possible and, therefore, decrease the corresponding ohmic drop,  $R_e I$ .<sup>31</sup> However, it is important to remark that the presence of the capillary close to the electrode surface induces a screening effect that may disturb the electrode potential markedly. In practice, it is then not essential to use a Luggin–Haber probe in conductive solutions since the electrolyte resistivity is low, especially in corrosion applications where the current is low as well. Because the majority of the solution resistance is concentrated close to the electrode (note in **Figure 32** that 80% of the resistance occurs within  $3r$

of the disc) and because the potential drop decreases as  $1/r$  (the current is proportional to  $r^2$ , whereas the resistance is proportional to  $1/r$ ), an alternative approach to the minimization of solution resistance effects is to use a very small electrode (a microelectrode), in which case the RE is situated remotely from the WE.

### 1.02.6.2 Potential Control and Current Control

In most recent commercial potentiostats and galvanostats, the potential or current control is performed

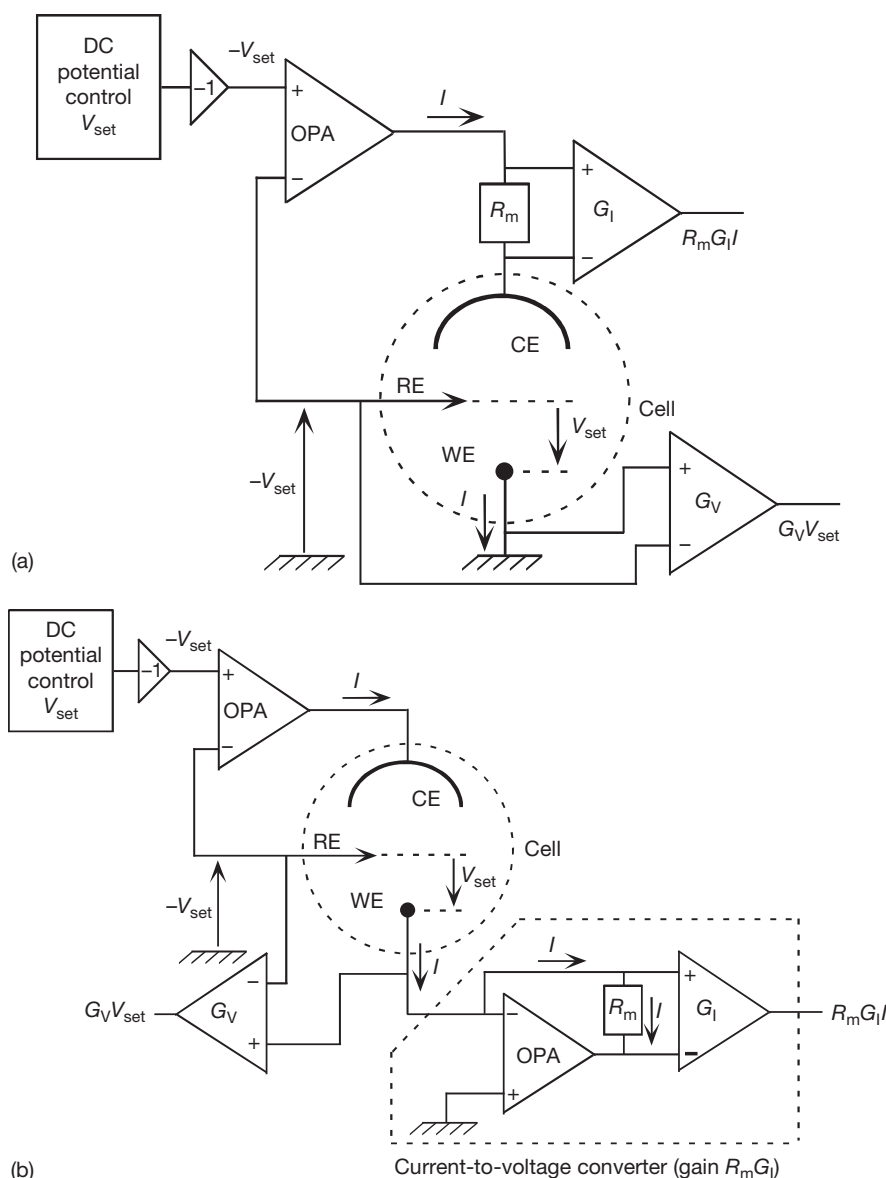


**Figure 34** Schematic circuit of a potentiostat: the current is measured in the CE branch with a differential amplifier of gain  $G_I$  (a) or in the WE branch with a current-to-voltage converter of gain  $R_m G_I$  (b).

by using one or several operational amplifiers (OPA) according to the electrical schemes described below. For simplicity, only ideal OPA will be considered here, which means that no current can flow in the positive and negative inputs of the OPA and that both inputs have the same potential at any time (assuming that negative feedback is used to keep the OPA in the linear region of its behavior). Deviations from this ideal case, including nonzero input currents, limited frequency bandwidth, etc., and their consequences on the potential or current control, have been investigated thoroughly elsewhere.<sup>43,44</sup>

**Figure 34** shows the experimental set-up used for controlling the electrochemical potential of a WE connected to the ground. Usually, this ground is floating, the chassis being connected to the earth ground for safety reasons. The voltage  $V_{\text{set}}$  (with respect to the ground) set by the user on the direct current (DC) potential control is first inverted with an amplifier of gain  $-1$  (this is provided only in order to give the controlled potential the same sign as  $V_{\text{set}}$ , and it may be omitted in some designs). The voltage  $-V_{\text{set}}$  on the positive input of the OPA is then imposed by the OPA on its negative input so that the potential difference between the RE and the WE is  $-V_{\text{set}}$  as well and, therefore, the potential of the WE with respect to the RE is actually equal to  $V_{\text{set}}$ . In **Figure 34(a)**, the current  $I$ , which necessarily flows to the WE since no current can enter the negative input of the OPA through the RE, is measured from the voltage drop  $R_m I$  across the resistor  $R_m$  in the CE branch. This voltage is amplified with a differential amplifier of high input impedance and gain  $G_I$  so that the gain in  $V/A$  of the current measurement is  $R_m G_I$ . In some equipment, the actual potential of the WE is measured with another differential amplifier of high input impedance (of gain  $G_V$  in **Figure 34**).

The current flowing to the WE can also be measured in the WE branch by using a current-to-voltage converter, also called zero-resistance ammeter (ZRA), of gain  $R_m G_I$ , as shown in **Figure 34(b)**. In that case, the WE is held at a virtual ground (the same potential as ground, but not connected directly to ground) via the OPA of the ZRA. This arrangement has the advantage of measuring the current actually flowing across the WE. As a consequence, in specific applications involving several WEs, it is possible to associate a ZRA with each WE to measure the current flowing into it, all WEs being at the same potential (virtual ground).

**Figure 35** shows a simple way for imposing a constant current  $I_{\text{set}}$  with a potentiostat. A resistor

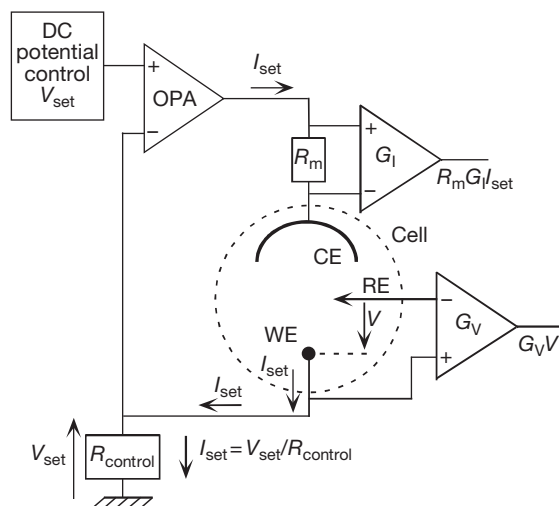


**Figure 35** Schematic circuit of a simple galvanostat.

$R_{\text{control}}$  is positioned between the WE and the ground and a voltage  $V_{\text{set}} = R_{\text{control}} I_{\text{set}}$  (with respect to the ground) is applied at the positive input of the OPA. In these conditions, the voltage at the negative input of the OPA is equal to  $V_{\text{set}}$  as well, so that a current  $I_{\text{set}} = V_{\text{set}} / R_{\text{control}}$  crosses the resistor. Since no current can flow at the negative input of the OPA, this current  $I_{\text{set}}$  actually flows through the WE. Note that the WE is no longer grounded, which may be a drawback in some applications. To work correctly with a grounded WE, the potentiostat power supply must be isolated from ground or a galvanostat with a more complex electrical circuit must be used.

## References

1. Itagaki, M.; Nakasawa, H.; Watanabe, K.; Noda, K. *Corros. Sci.* **1997**, *39*, 901–911.
2. Muñoz, A. G.; Vel, M. E.; Salvarezza, R. C. *Langmuir* **2005**, *21*, 9238–9245.
3. O'M. Bockris, J.; Khan, U. M. *Surface Electrochemistry: A Molecular Level Approach*; Plenum Press: New York, 1993; Chapter 3, pp 310–318.
4. Huet, F.; Nogueira, R. P.; Normand, B.; Takenouti, H. In *ASM Handbook Corrosion: Fundamentals, Testing and Protection* Cramer, S.D., Covino, B.S., Jr., Eds.; ASM International: Materials Park, OH, 2003; Vol. 13A, pp 52–60.
5. Plonski, I. H. *Int. J. Hydrogen Energy* **1996**, *21*, 837–851.
6. Epelboin, I.; Morel, Ph.; Takenouti, H. *J. Electrochem. Soc.* **1971**, *118*, 1282–1287.
7. Sastri, V. S. *Corrosion Inhibitors: Principles and Applications*; Wiley: West Sussex, 1998.
8. Kaesche, H. *Corrosion of Metals: Physicochemical Principles and Current Problems*; Springer: Berlin, 2003; Chapter 7, pp 144–158.

9. Keddam, M.; Mattos, O. R.; Takenouti, H. *J. Electrochem. Soc.* **1981**, *128*, 257–265, 266–274.
10. Heusler, K. E. *Z. Elektrochem.* **1958**, *62*, 582–587.
11. O'M Bockris, J.; Drazic, D.; Despic, A. R. *Electrochim. Acta* **1961**, *4*, 325–361.
12. Kelly, E. J. *J. Electrochem. Soc.* **1965**, *112*, 124–131.
13. Hilbert, F.; Miyoshi, Y.; Eichkorn, G.; Lorenz, W. J. *J. Electrochem. Soc.* **1971**, *118*, 1919–1926, 1927–1935.
14. Epelboin, I.; Keddam, M. *J. Electrochem. Soc.* **1970**, *117*, 1052–1056.
15. Greef, R.; Peat, R.; Peter, L. M.; Pletcher, D.; Robinson, J. In *Electrochemistry: Southampton Electrochemistry Group*; Ellis Horwood: West Sussex, 1985; Chapter 4, pp 139–143.
16. O'M. Bockris, J.; Khan, U. M. *Surface Electrochemistry: A molecular Level Approach*, Plenum Press: New York, 1993; Chapter 3, pp 319–348.
17. Crow, D. R. *Principles and Applications of Electrochemistry*, 4th ed.; Blackie Academic and Professional: Glasgow, 1994; Chapter 5, pp 68–71.
18. Bard, A. J.; Faulkner, L. R. *Electrochemical Methods: Fundamentals and Applications*, 2nd ed.; Wiley & Sons: Hoboken, 2001; Chapter 1, pp 12–14.
19. Stern, O. *Z. Elektrochem.* **1924**, *30*, 508–516.
20. Bagotsky, V. S. *Fundamentals of Electrochemistry*, 2nd ed.; Wiley & Sons: Hoboken, 2006; Chapter 4, pp 51–68.
21. Atkins, P. W. *Physical Chemistry*, 4th ed.; Oxford University Press: Oxford, 1990; Chapter 25, pp 763–769.
22. Fisher, A. C. *Electrode Dynamics*, 4th ed.; Oxford University Press: Oxford 1996; Chapter 2, pp 13–25.
23. Bard, A. J.; Faulkner, L. R. *Electrochemical Methods: Fundamentals and Applications*, 2nd ed.; John Wiley and Sons: Hoboken, 2001; Chapter 2, pp 60–62.
24. Oldham, K. B.; Myland, J. C. *Fundamentals of Electrochemical Science*; Academic Press: San Diego, 1994; Chapter 4, pp 117–120.
25. Bagotsky, V. S. *Fundamentals of Electrochemistry*, 2nd ed.; Wiley & Sons: Hoboken, 2006; Chapter 3, pp 39–45.
26. Compton, R. G.; Sanders, G. H. W. *Electrode Potentials*; Oxford University Press: Oxford, 1996; Chapter 1, pp 12–13.
27. *Handbook of Chemistry and Physics*, 78th ed.; Chemical Rubber Publishing Company: Boca Raton, 1997; 8-20–8-30.
28. Pourbaix, M. *Atlas of Electrochemical Equilibrium in Aqueous Solutions*; NACE: Houston, 1974.
29. Atkins, P. W. *Physical Chemistry*, 4th ed.; Oxford University Press: Oxford, 1990; Chapter 9, pp 225–237.
30. Landolt, D. In *Corrosion Mechanisms in Theory and Practice*; Marcus, P., Oudar, J., Eds.; Marcel Dekker: New York, 1995; pp 13–16.
31. Greef, R.; Peat, R.; Peter, L. M.; Pletcher, D.; Robinson, J. In *Electrochemistry: Southampton Electrochemistry Group*; Ellis Horwood: West Sussex, 1985; Chapter 1, pp 26–32.
32. Bard, A. J.; Faulkner, L. R. *Electrochemical Methods: Fundamentals and Applications*, Wiley & Sons: Hoboken, 2001; Chapter 9, p 339.
33. Scully, J. R. *Electrochemical Methods in Corrosion Science and Engineering*; Marcel Dekker: New York, 2002; Chapter 4, pp 125–150.
34. Stern, M.; Geary, A. L. *J. Electrochem. Soc.* **1957**, *104*, 56–63.
35. Marcus, P.; Mansfeld, F. *Analytical Methods in Corrosion Science and Engineering*; Taylor & Francis/CRC: Boca Raton, FL, 2006; Vol. 22: Corrosion Technology.
36. Greef, R.; Peat, R.; Peter, L. M.; Pletcher, D.; Robinson, J. In *Electrochemistry: Southampton Electrochemistry Group*; Ellis Horwood: West Sussex, 1985.
37. Bard, A. J.; Faulkner, L. R. *Electrochemical Methods: Fundamentals and Applications*, 2nd ed.; Wiley & Sons: Hoboken 2001.
38. Bard, A. J.; Faulkner, L. R. *Electrochemical Methods: Fundamentals and Applications*, 2nd ed.; Wiley & Sons: Hoboken, 2001; Chapter 2, pp 69–74.
39. Bard, A. J.; Faulkner, L. R. *Electrochemical Methods: Fundamentals and Applications*, 2nd ed.; Wiley & Sons: Hoboken, 2001; Appendix C, pp 808–810.
40. Bernard, M.; Busnot, F. *Usuel de chimie générale et minérale*; Dunod – Bordas: Paris, 1984; Chapter 3, p 205.
41. <http://www.consultrsr.com/resources/ref/refpotls.htm>.
42. Newman, J. *J. Electrochem. Soc.* **1966**, *113*, 501–502.
43. Schiller, C.-A. In *Analytical Methods in Corrosion Science and Engineering*; Marcus, P., Mansfeld, F., Eds.; Taylor & Francis/CRC Press: Boca Raton, FL, 2006; Vol. 22: Corrosion Technology, pp. 361–434.
44. Gabrielli, C. Identification of electrochemical processes by frequency response analysis Solartron, Farnborough: England, 1980; Technical Report no. 4/83; <http://www.solartronanalytical.com/downloads/technotes/technote04.pdf>.



## 1.04 Mechanical Properties and Fracture of Materials

**A. H. Sherry**

University of Manchester, Manchester, UK

**T. J. Marrow**

School of Materials, University of Manchester, Manchester, UK

© 2010 Elsevier B.V. All rights reserved.

<b>1.04.1</b>	<b>Mechanical Properties</b>	78
1.04.1.1	Elastic Properties	78
1.04.1.2	Elastic–Plastic Properties	80
<b>1.04.2</b>	<b>Fracture Properties</b>	81
1.04.2.1	The Elastic Stress Intensity Factor	81
1.04.2.2	The $J$ -Integral	84
1.04.2.3	Fracture Toughness	85
<b>1.04.3</b>	<b>Application of Fracture Mechanics to SCC</b>	86
<b>References</b>		88

### Abbreviations

**BS** British Standard

**EN** Euro Norm

**ASTM** ASTM International

**HRR** Hutchinson, Rice and Rosegren

**SCC** Stress Corrosion Cracking

**UTS** Ultimate Tensile Stress (also Ultimate Tensile Strength)

### Symbols

**$a$**  Crack length

**$A$**  Cross-sectional area

**$A_0$**  Initial cross-sectional area

**$B$**  Thickness

**$d\epsilon$**  Increment of true strain

**$dL$**  Change in gauge length under an applied load  $P$

**$ds$**  Increment of length along contour used to derive the  $J$ -integral

**$D$**  Diameter

**$E$**  Young's modulus

**$E'$**  Young's modulus  $E$  under plane stress and  $E/(1-\nu^2)$  under plane strain

**$F_Q$**  Load at fracture in a fracture mechanics test

**$G_0$ – $G_5$**  Geometry coefficients

**$I_n$**  Integration parameter

**$J$**   $J$ -integral

**$J_c$**  Fracture toughness under elastic–plastic conditions

**$K_I$**  Mode I stress intensity factor

**$K_{Ic}$**  Mode I fracture toughness under linear-elastic conditions

**$K_{ISCC}$**  Threshold stress intensity factor for stress corrosion cracking

**$L_0$**  Initial gauge length

**$L$**  Gauge length

**$n$**  Ramberg–Osgood work hardening exponent

**$P$**  Pressure

**$P$**  Load

**$R$**  Polar coordinate centered on the crack tip

**$R_i$**  Inner radius of cylinder

**$R_o$**  Outer radius of cylinder

**$r_p$**  Radius of crack-tip plastic zone

**$T$**  Wall thickness of cylinder

**$T_i$**  Components of traction vector

**$U$**  Strain energy

**$U_e$**  Elastic strain energy

**$u_i$**  Components of displacement vector

**$U_p$**  Plastic strain energy

**$W$**  Strain energy

**$W$**  Width

**$Y$**  Geometry parameter

**$\Gamma$**  Anticlockwise contour around crack-tip used to calculate  $J$ -integral

**$\alpha$**  Material parameter in Ramberg–Osgood equation

**$\epsilon$**  True strain

**$\epsilon_0$**  Reference strain in Ramberg–Osgood equation

**$\epsilon_e$**  Engineering strain

**$\epsilon_{el}$**  True elastic strain

**$\epsilon_{pl}$**  True plastic strain

$\eta_p$	Nondimensional function of crack length
$\nu$	Poisson's ratio
$\theta$	Angular polar coordinate, centered on the crack tip
$\sigma$	True stress
$\sigma_0$	Reference stress in Ramberg–Osgood equation
$\sigma_{0.2}$	Proof stress at 0.2% plastic true strain
$\sigma_e$	Engineering stress
$\sigma_{SCC}$	Threshold stress for stress corrosion cracking
$\sigma_{xx}$	Stress in x-direction
$\sigma_y$	Yield stress
$\sigma_{yy}$	Stress in y-direction
$\sigma_{zz}$	Stress in z-direction
$\tilde{\sigma}_{ij}(n, \theta)$	Dimensionless function of $r$ and $\theta$
$\tau_{xy}$	Shear stress (in the x–y plane)

### 1.04.1 Mechanical Properties

The mechanical properties of materials are conveniently measured and described with respect to the standard uniaxial tensile testing of round-bar or flat-plate specimens. Standard testing procedures, such as BS EN 10002–1:2001 and ASTM E8-04,<sup>1,2</sup> provide guidance on the measurement and interpretation of tensile load-versus-displacement (i.e., gauge length extension) data to obtain stress-versus-strain curves. Typical curves are illustrated in **Figures 1(a) and 1(b)** for a high-strength aluminum alloy and a ferritic pressure vessel steel respectively. The key regions of the stress-versus-strain curve are indicated in **Figure 2** and described in **Sections 1.04.2.1 and 1.04.2.2**. In order to interpret these, it is important to first provide a definition of stress and strain.

Consider the round tensile bar specimen illustrated in **Figure 3**, which has an initial gauge length  $L_0$ , a diameter  $D$  and is under an applied load  $P$ . The engineering stress within the specimen  $\sigma_e$  is defined by the applied load normalized by the *initial* cross-sectional area of the specimen,  $A_0$ , that is

$$\sigma_e = \frac{P}{A_0} \quad [1]$$

For a round bar tensile specimen,  $A_0$  is equal to  $\pi D^2/4$ , where  $D$  is the initial diameter of the bar. For a specimen of rectangular cross-section,  $A_0$  is equal to  $WB$ , where  $W$  is the initial specimen width and  $B$ , the initial thickness. **Equation [1]** shows that the engineering stress is directly proportional to the load applied to the specimen. The same load applied to a

specimen of smaller diameter will result in a higher applied stress.

The true stress applied to the specimen  $\sigma$  is defined as

$$\sigma = \frac{P}{A} \quad [2]$$

where  $A$  is the *actual* cross-sectional area of the specimen under the load  $P$ . The true stress applied to the specimen is not directly proportional to the applied load, since the cross-sectional area of the specimen reduces progressively under an increasing tensile load. This is because the total volume of the specimen remains practically unchanged as the specimen deforms. **Equation [1]** therefore becomes an increasingly inaccurate measure of the true stress with increasing extension.

Engineering strain  $\epsilon_e$  at a given applied load is defined by the increase in the gauge length of the specimen,  $dL$ , normalized by the *initial* gauge length of the specimen,  $L_0$ , that is

$$\epsilon_e = \frac{dL}{L_0} \quad [3]$$

Since the gauge length increases under load, the true strain  $\epsilon$  at a given instant in the test is more accurately defined as

$$\epsilon = \int_{L_0}^L \frac{dL}{L} = \ln(1 + \epsilon_e) \quad [4]$$

where  $L$  is the *actual* gauge length of the specimen at the load of interest.

The true stress can be related to the engineering stress and strain through the following relation, which assumes constant volume<sup>3</sup>:

$$\sigma = \sigma_e(1 + \epsilon_e) \quad [5]$$

#### 1.04.1.1 Elastic Properties

The stress-versus-strain curves illustrated in **Figures 1(a) and 1(b)** exhibit a number of distinct regions. The first of these is characterized by a relationship between the applied stress and strain that is linear for most materials. Within this region, the strain accumulated under an applied tensile stress is fully recoverable upon unloading, that is, the material is ‘elastic’ and its shape is not permanently changed by the applied stress. The stress–strain relationship in this elastic (linear) region is defined by Hooke’s law in which Young’s modulus  $E$  given by

$$E = \frac{\sigma}{\epsilon} \quad [6]$$

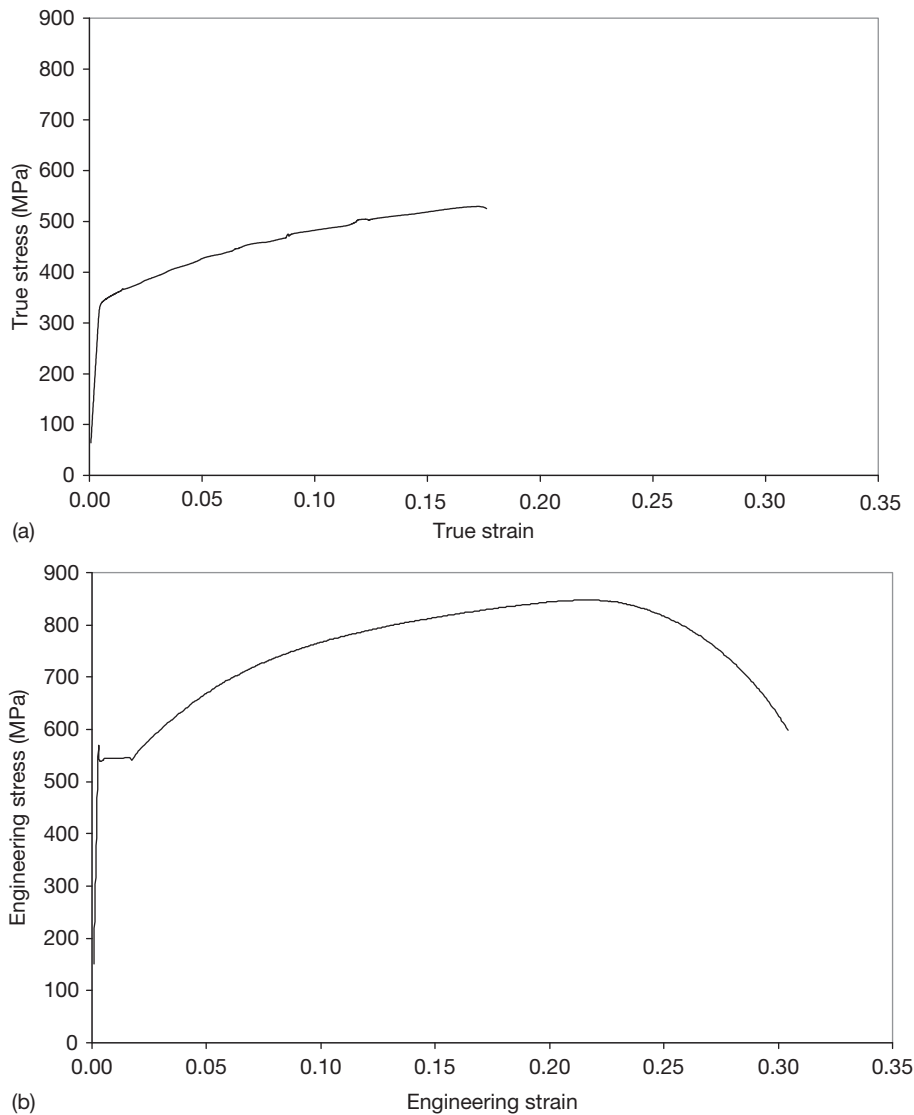


**Figure 1** Typical stress–strain curves for (a) high strength aluminum alloy 2024-T351 tested at room temperature and (b) Euro-material – a quenched and tempered ferritic pressure vessel steel DIN 22Ni–MoCr37 (similar to steel type ASTM A508 Cl.3) tested at  $-90^{\circ}\text{C}$ . (a) Adapted from Heerens, J.; Hellmann, D. *Eng. Fract. Mech.* **2002**, 69, 421–449 and (b) Adapted from Bernauer, G.; Brocks, W. *Fat. Fract. Eng. Mater. Struct.* **2002**, 25, 363–384.

Engineering stress and strain are normally sufficiently accurate to define Young's modulus for most materials with a reasonable degree of accuracy for engineering calculations. Within the linear elastic regime, eqn [6] can be used for loading in either tension or compression.

It is worth noting that the Young's modulus of many engineering materials is extremely high. For example, mild steel has a Young's modulus of  $\sim 210$  GPa at room temperature. Consequently, any small inaccuracies in the measurement of displacement in this region will

result in significant errors in the derived value of  $E$ . For this reason, other approaches have been developed for the accurate determination of Young's modulus. These include the measurement of the natural frequency of a vibrating loaded bar by spectroscopic techniques or derivation from the velocity of sound in the material.<sup>3</sup>

Although not measurable from the data shown in Figures 1(a) and 1(b), Poisson's ratio  $\nu$  is an important materials parameter, since it defines the ratio of the tensile strain accumulated in the loading direction to the compressive (or negative) strain accumulated in

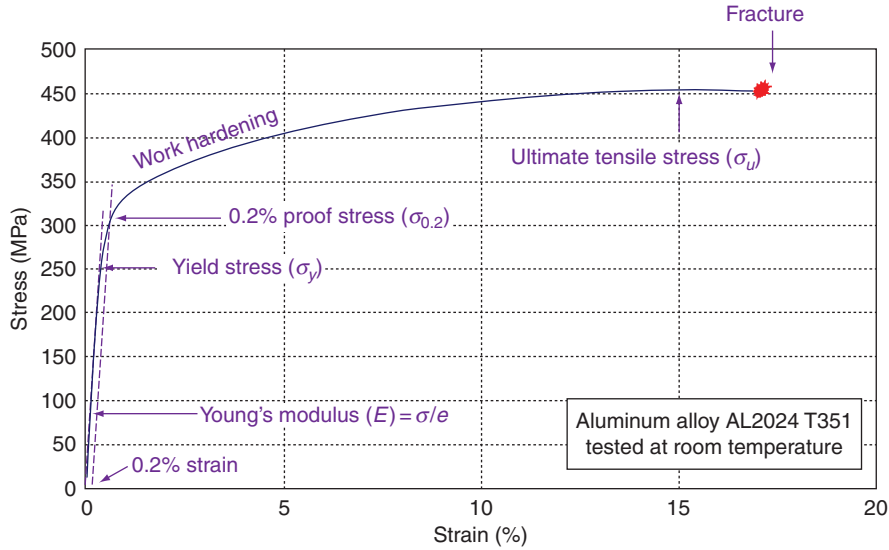


**Figure 2** Key regions of a typical engineering stress–strain curve.

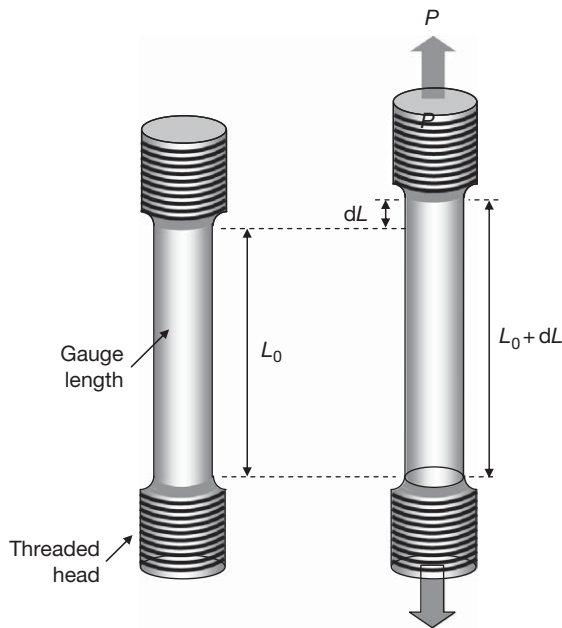


**Figure 3** Schematic illustration of a round tensile specimen under an applied load  $P$ .

the perpendicular directions. Poisson's ratio is defined in the elastic regime and is given by

$$v = -\frac{\text{transverse strain}}{\text{axial strain}} \quad [7]$$

For many engineering materials,  $v$  is close to 0.3 in the elastic regime. Poisson's ratio can be obtained by measurement of the cross-section dimensions of the

specimen during testing, but accurate measurement requires other methods, similar to those used for Young's modulus.

The strain energy density or work per unit volume,  $U$ , that is expended by deforming a material is defined by the area under the true stress–true strain curve, that is,

$$U = \int_0^{\epsilon} \sigma \, d\epsilon \quad [8]$$

Under linear elastic conditions, the elastic strain energy  $U_e$  is defined by

$$U_e = \frac{\sigma^2}{2E'} \quad [9]$$

where elastic theory shows that  $E' = E$  under plane stress conditions and  $E/(1-\nu^2)$  under plane strain conditions. (Plane stress is defined as the condition where the out-of-plane stress is zero or negligible, i.e., in thin sheets or on the material surface. Plane strain is defined here as the condition where the out-of-plane strain is zero or negligible compared to the in-plane strains, i.e. in thick sections.)

#### 1.04.1.2 Elastic–Plastic Properties

As the applied stress is increased in the tensile test, there comes a point where the resulting displacement can no longer be taken up by the elastic deformation of the material, and the material 'yields' plastically. Yielding, which occurs in metals by the movement of

crystallographic imperfections called ‘dislocations,’ is characterized by an increase in strain over and above that predicted by Young’s modulus. The total strain of the specimen is thus a combination of elastic and plastic strain, that is,

$$\varepsilon = \varepsilon_{el} + \varepsilon_{pl} \quad [10]$$

where  $\varepsilon$  is the total true strain,  $\varepsilon_{el}$  is the elastic strain defined by  $\sigma/E$ , and  $\varepsilon_{pl}$  is the plastic strain.

The applied stress at the limit of proportionality is defined as the yield stress  $\sigma_y$  and is a characteristic property of the material. Loading the specimen up to a stress higher than the yield stress and subsequently unloading will result in the permanent deformation of the specimen equal to  $\varepsilon_{pl}$ . Thus, in contrast to elastic strain, plastic strain is not recovered.

The limit of proportionality is often difficult to discern accurately, and therefore, the yield stress is commonly defined by a proof stress. This is typically the 0.2% proof stress,  $\sigma_{0.2}$ , which is defined using a construction-line of gradient  $E$  drawn from an initial strain of 0.2%. The point at which this construction-line intersects the stress–strain curve is defined as  $\sigma_{0.2}$ . This is shown in **Figure 2**. This is also done in the case of materials, particularly ferritic steels that show a yield point (e.g., **Figure 1(b)**).

At applied stresses above the yield stress, the resistance to yielding increases, because the material work hardens as plastic deformation is accumulated. This is also known as cold work or strain hardening and is a consequence of an increase in the number of dislocations and their interactions with each other. The gradient of the stress–strain curve reduces in the work hardening region. This region may be characterized by a power-law relationship between stress and strain. In this way, eqn [10] may be formulated in terms of true stress and true strain to provide a full description of the stress–strain properties of materials.<sup>4</sup> For many materials, a suitable expression is

$$\frac{\varepsilon}{\varepsilon_0} = \left( \frac{\sigma}{\sigma_0} \right) + \alpha \left( \frac{\sigma}{\sigma_0} \right)^n \quad [11]$$

where  $\alpha$  is a material parameter, often close to unity,  $\sigma_0$  is a reference stress usually taken as the yield or 0.2% proof stress,  $\varepsilon_0$  is the reference strain ( $=\sigma_0/E$ ), and  $n$  is the Ramberg–Osgood work hardening exponent. This work hardening exponent is typically between 5 and 10 for ferritic steels. Equation [11] is known as the Ramberg–Osgood equation, and is illustrated in **Figure 4** with normalized stress-versus-strain curves plotted for  $\alpha = 1$  and  $3 \leq n \leq \infty$ .

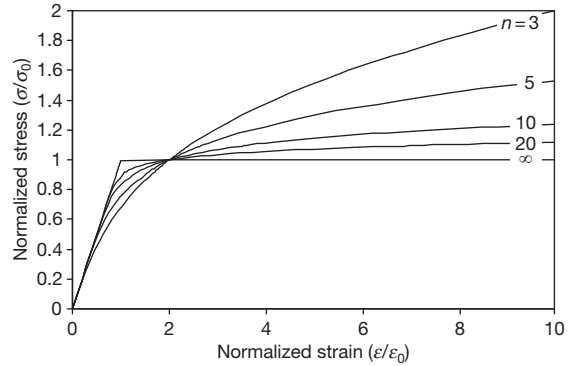


**Figure 4** Normalized stress–strain curves plotted using the Ramberg–Osgood equation.

In ductile metals, at a critical strain, the tensile specimen begins to ‘neck.’ Up to this point, the plastic deformation occurs uniformly and stably throughout the gauge length as the rate of increase in stress due to the geometric reduction in cross-section is balanced by the rate of increase in yield stress due to work hardening. At the onset of necking, the plasticity becomes unstable and is concentrated within a localized region of the gauge length, when the geometric and work hardening factors become unbalanced. This is shown in **Figure 5(a)**. This critical strain for necking occurs at the maximum load, and thus corresponds to the maximum in the engineering stress, which is termed the ultimate tensile stress (UTS)  $\sigma_u$  (**Figure 2**). It can be shown by Considère’s construction that, for a material following the Ramberg–Osgood equation, necking begins at a strain  $\varepsilon = 1/n$ .<sup>5</sup>

For ductile materials, fracture follows necking and normally shows a characteristic ‘cup-and-cone’ fracture. Ductile void growth and coalescence occurs within the neck of the specimen, and then extends by shear fracture, leading to the characteristic appearance of ‘ductile dimples’ from this ‘microvoid coalescence’ process, **Figures 5(b) and 5(c)**.

## 1.04.2 Fracture Properties

### 1.04.2.1 The Elastic Stress Intensity Factor

The linear elastic stress intensity factor,  $K_I$ , is a parameter that quantifies the conditions of stress local to the tip of an infinitely sharp crack in an elastic material. It has the units of  $\text{MPa m}^{-1/2}$ . The subscript ‘I’ denotes that the stress intensity factor relates to Mode I loading, in which the applied loading is perpendicular to the plane of the crack, **Figure 6**. Whilst there are other modes of loading including in-plane and out-of-plane

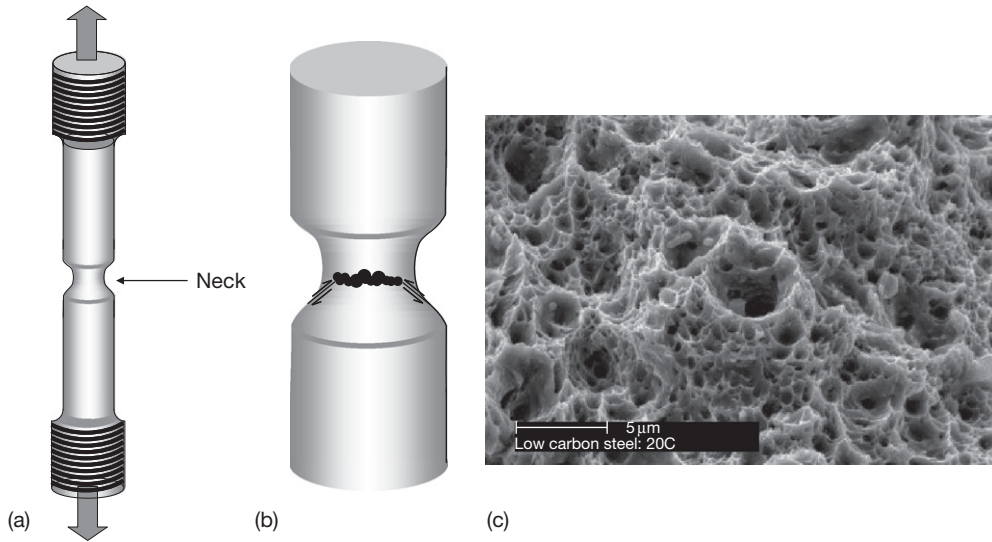


**Figure 5** Schematic illustration of: (a) neck formed in tensile specimen tested beyond UTS, (b) development of cup-and-cone fracture, and (c) Scanning electron micrograph of ductile microvoid coalescence in low carbon steel.

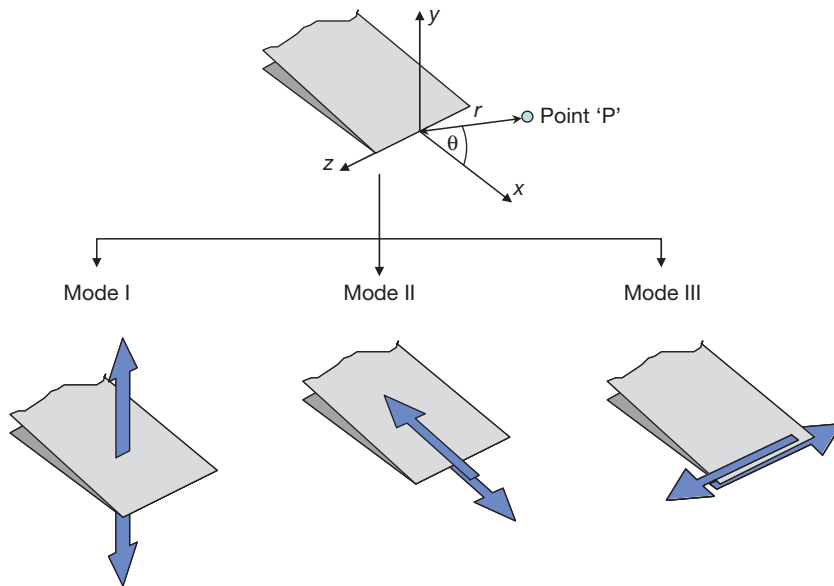


**Figure 6** Definition of coordinate system and three modes of loading on a crack: Mode I opening, Mode II in-plane shear, Mode III out-of-plane shear.

shear and combinations thereof, Mode I loading is normally considered the most severe and discussion within this section is restricted to this mode.

The equations that relate  $K_I$  to the stress at a point 'P' in the vicinity of a sharp crack-tip in an elastic material (Figure 6) are given by series expressions known as the Westergaard functions. The first and dominant term in the series expansion are given below for plane strain conditions:

$$\begin{aligned}\sigma_{xx} &= \frac{K_I}{(2\pi r)^{1/2}} \cos\left(\frac{\theta}{2}\right) \left[ 1 - \sin\left(\frac{\theta}{2}\right) \sin\left(\frac{3\theta}{2}\right) \right] \\ \sigma_{yy} &= \frac{K_I}{(2\pi r)^{1/2}} \cos\left(\frac{\theta}{2}\right) \left[ 1 + \sin\left(\frac{\theta}{2}\right) \sin\left(\frac{3\theta}{2}\right) \right] \\ \sigma_{zz} &= \nu(\sigma_{xx} - \sigma_{yy}) \\ \tau_{xy} &= \frac{K_I}{(2\pi r)^{1/2}} \sin\left(\frac{\theta}{2}\right) \cos\left(\frac{\theta}{2}\right) \cos\left(\frac{3\theta}{2}\right)\end{aligned}\quad [12]$$



Within eqn [12], the subscripts indicate the Cartesian coordinate system that defines the plane of the crack and the loading direction,  $r$  and  $\theta$  are polar coordinates of the point of interest (Figure 6), and  $\nu$  is Poisson's ratio. Figure 7 illustrates the distribution of opening stress  $\sigma_{yy}$  directly ahead of a crack in an elastic material under Mode I loading, that is, increasing  $r$  with  $\theta = 0^\circ$ . The stresses are proportional to  $K_I$  and hence the magnitude of the stress field within elastic material in the vicinity of a sharp crack under Mode I loading may thus be deduced from a knowledge of  $K_I$ .

A similar set of Westergaard functions relates the local strain in elastic material in the vicinity of a crack tip to  $K_I$ . Thus, as was the case for local stress, the magnitude of the strain field within elastic material in the vicinity of a sharp crack under Mode I loading may also be deduced from knowledge of  $K_I$ . The stress intensity factor is therefore a direct measure of the elastic strain energy in a stressed material that contains a crack.

Since failure by fracture is controlled by critical combinations of stress and strain in material close to the crack tip, the stress intensity factor,  $K_I$ , provides a means for quantifying the 'crack driving force' acting on a crack-like flaw in a stressed component – *albeit* strictly only within the elastic regime. The higher the value of  $K_I$ , the higher the crack driving force. In terms of thermodynamics, crack growth requires sufficient elastic strain energy to balance the energy needed to create the surfaces of the crack. This includes the work associated with the deformation and fracture mechanisms of the material. A critical stress intensity factor, which is sufficient for crack propagation, can therefore be determined.

The magnitude of  $K_I$  acting on a given crack-like flaw is dependent upon three factors: (1) the

magnitude of the applied stress, (2) the size of the flaw, and (3) the geometry of the component. The general form of the equation that relates the applied stress  $\sigma$  and the flaw size  $a$  to  $K_I$  is as follows:

$$K_I = \sigma Y \sqrt{\pi a} \quad [13]$$

where  $Y$  is a geometry parameter. Values for  $Y$  for common component geometries are tabulated in standards such as, <sup>6</sup> and are typically of the order of unity. As shown by eqn [13], the magnitude of  $K_I$  is directly proportional to the applied stress acting on the component. Thus, increasing the stress applied to a cracked component by a factor of two will double the magnitude of  $K_I$ . The stress intensity factor  $K_I$  is also dependent on the square root of the crack depth  $a$ .  $Y$  is also dependent on crack length in some geometries, but the effect is generally less strong. Consequently, under a fixed applied stress, the magnitude of  $K_I$  increases as the crack depth increases. Hence, for a crack extending gradually by a mechanism such as SCC, in which the rate of crack growth can increase with  $K_I$ , there can be an acceleration of crack growth.

An example of equations defining the stress,  $\sigma$ , and the geometry parameter,  $Y$ , is given in Figure 8 for an axially cracked pipe under internal pressure, in which the crack (e.g., a stress corrosion crack) is on the inner surface<sup>7</sup>:

$$\sigma = \frac{pR_o^2}{(R_o^2 - R_i^2)}$$

$$Y = 2G_0 - 2G_1 \left( \frac{a}{R_i} \right) + 3G_2 \left( \frac{a}{R_i} \right)^2 - 4G_3 \left( \frac{a}{R_i} \right)^3 + 5G_5 \left( \frac{a}{R_i} \right)^4 \quad [14]$$

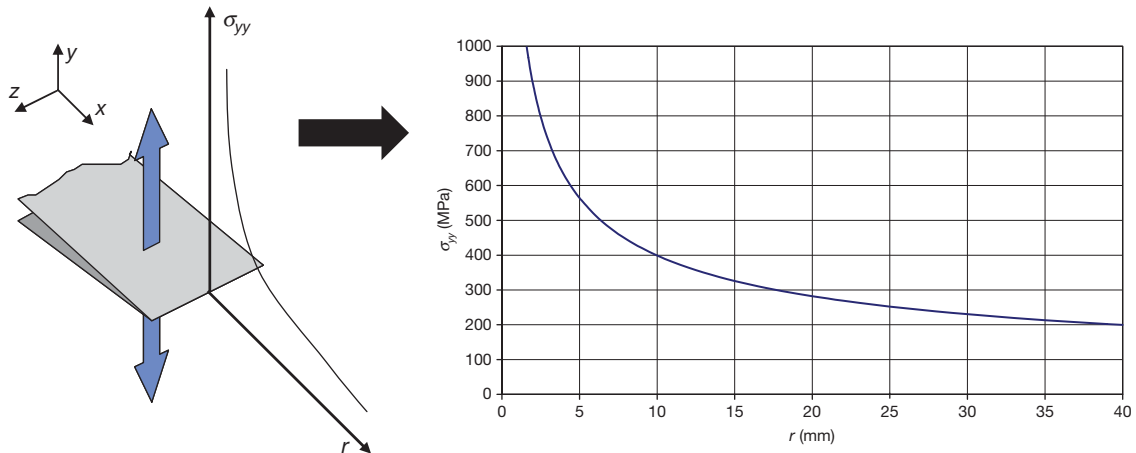


Figure 7 Elastic opening stress field ahead of a crack in an elastic material under Mode I loading with  $K_I = 100 \text{ MPa m}^{-1/2}$ .

where  $\sigma$  is the circumferential stress acting on the plane of the crack due to the internal pressure,  $a$  is the crack depth,  $R_i$  is the internal radius of the cylinder, and  $R_o$  is the outside radius of the cylinder. The coefficients  $G_0$ – $G_5$  are tabulated in API 579.<sup>7</sup> Equation [14] is valid within the following geometric limits:  $0 \leq a/t \leq 0.8$  and  $2 \leq R_i/t \leq 1000$  where  $t$  is the wall thickness of the pipe,  $t = (R_o - R_i)$ .

The stress intensity factor is a valid parameter to characterize fracture properties of materials under linear-elastic conditions. However, simple inspection of eqn [12] and Figure 7 shows that in a metal the stresses close to the crack tip will readily exceed the yield stress. Plastic deformation therefore occurs at the crack tip, in a region called the plastic zone, and the assumption of elastic conditions would strictly not be valid. However, when the plastic zone size at the tip of the crack-like flaw is small compared with the dimensions of the component, the deformation of the component may be regarded as elastic and the stress intensity factor can be valid also. Under plane strain conditions the radius of the plastic zone,  $r_p$ , may be calculated according to the following expression<sup>8</sup>:

$$r_p = \frac{1}{6\pi} \left( \frac{K_I}{\sigma_y} \right)^2 \quad [15]$$

Fracture toughness testing standards (see Section 1.04.3) specify that for  $K_I$  to be a valid, the crack-tip parameter  $r_p$  must be less than  $\sim 1/50$ th of the characteristic dimensions of the specimen, that is

$$a, B, (W - a) \geq 2.5 \left( \frac{K_I}{\sigma_y} \right)^2 \quad [16]$$

where  $B$  is the specimen thickness,  $W$  is the specimen width, and  $(W - a)$  is the uncracked ligament associated with the fracture mechanics test specimen geometry, see Figure 9. Where this condition is not satisfied for any of these three measures of specimen dimension, a nonlinear parameter is required to account for the plastic deformation and to thereby characterize the crack-driving force. The  $\mathcal{J}$ -integral provides this parameter and is briefly described in the following section.

#### 1.04.2.2 The $J$ -Integral

For a material that follows the Ramberg–Osgood stress–strain law, eqn [11], the crack-tip deformation fields may be characterized by the Hutchinson,<sup>9</sup> Rice, and Rosegren (HRR) fields<sup>10</sup> in a manner similar to that of the Westergaard functions given previously as eqn [12]. The HRR field equation for the crack-tip stress field is defined as follows:

$$\sigma_{ij} = \sigma_0 \left( \frac{E\mathcal{J}}{\alpha\sigma_0^2 I_n r} \right)^{1/n+1} \tilde{\sigma}_{ij}(n, \theta) \quad [17]$$

where  $I_n$  is an integration parameter dependent on the work hardening exponent,  $n$ ,  $\tilde{\sigma}_{ij}(n, \theta)$  is a dimensionless function of  $n$  and  $\theta$ , and  $\mathcal{J}$  is the so-called  $\mathcal{J}$ -integral; a contour integral following an

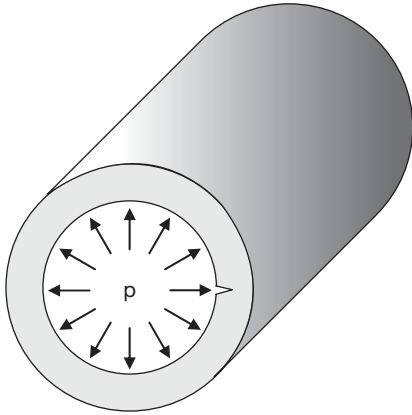


Figure 8 Schematic illustration of axially-cracked pipe.

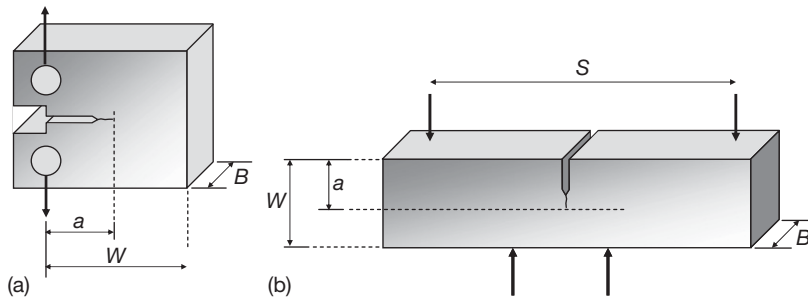
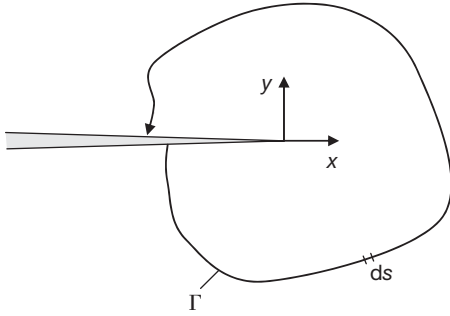


Figure 9 Schematic illustration of fracture mechanics test specimens (a) compact-tension specimen and (b) four-point bend specimen. Note arrows indicate direction of loading.



**Figure 10** Anticlockwise contour around crack tip used to define the  $J$ -integral, eqn [18].

anticlockwise path around the tip of a crack, Figure 10, which defined as follows:

$$\mathcal{J} = \int_{\Gamma} \left( w \, dy - T_i \frac{\partial u_i}{\partial x} \, ds \right) \quad [18]$$

where  $w$  is the strain energy density,  $T_i$  are components of the traction vector,  $u_i$  are the components of the displacement vector, and  $ds$  is an increment of length along the contour  $\Gamma$ .<sup>8</sup>

The  $\mathcal{J}$ -integral is widely used to define the crack-tip stress and strain fields for materials in the elastic-plastic regime, that is, in circumstances where eqn [16] does not hold. Under small-scale yielding conditions (i.e., in the elastic regime where the plastic zone size is small compared with the component and the assumption of elastic deformation implicit in eqn [16] is adequate),  $\mathcal{J}$  is related to  $K_I$  via eqn [19]<sup>8</sup>

$$K_I^2 = E' \mathcal{J} \quad [19]$$

### 1.04.2.3 Fracture Toughness

The fracture toughness of a material is a measure of its capacity to resist failure by the onset of crack extension. It can therefore be used to determine whether a crack in a component will grow by fracture processes under certain conditions of loading. Under linear elastic conditions, the critical stress intensity factor  $K_I$  measured at the onset of fracture is used to define the fracture toughness of materials and is given the subscript 'c,' that is,  $K_{Ic}$ . The unit of  $K_{Ic}$  is  $\text{MPa m}^{-1/2}$ . Under conditions of more widespread plasticity, the elastic-plastic  $\mathcal{J}$ -integral is widely used to define the critical crack-tip conditions and hence the fracture toughness in the elastic-plastic regime,  $\mathcal{J}_c$ . The unit of  $\mathcal{J}_c$  is  $\text{kJ m}^{-2}$ .

Fracture toughness properties of materials are conveniently measured using standard specimens

containing cracks such as compact-tension (CT) specimens or Single Edge-Notched Bend (SENB) specimens, Figure 9. Standard sized specimens tend to be used, with  $B$  between 12.5 and 50 mm. Much larger and smaller specimens are possible, however.

Standard testing procedures provide guidance on the derivation of fracture toughness properties from tests performed on fracture mechanics specimens. These standards describe stringent test conditions to ensure that valid measurements of  $K_{Ic}$  or  $\mathcal{J}_c$  are obtained. For example:

- BS7448: 'Fracture Mechanics Toughness Tests.' Part 1:1991, 'Method for determination of  $K_{Ic}$ , Critical CTOD, and Critical  $\mathcal{J}$  values of metallic material.' British Standards Institute, London.
- ASTM E399-90, 'Standard Test Method for Plane Strain Fracture Toughness of Metallic Materials,' American Society for Testing and Materials, Philadelphia, 1990.

Within these procedures, the fracture toughness of the material is determined from the measured load versus displacement behavior of the specimen, tested at the temperature of interest. The displacement is measured as the crack mouth opening displacement (CMOD) along the load line, which is the line between the points of loading. Loading is generally applied in a quasi-static manner (i.e., slow displacement rates of the order of mm/min) so that dynamic loading effects do not influence the test results. Dynamic effects arise because the mechanism of yielding (i.e., movement of dislocations) is strain rate sensitive. This can cause the yield stress to rise and fracture toughness to be lowered by high strain rates, particularly in ferritic steels.

Under *linear elastic conditions*, the fracture toughness is derived from expressions that relate the applied load at fracture to the stress intensity factor. For a CT specimen, the expression is as follows<sup>11</sup>:

$$K_{Ic} = \frac{F_Q}{BW^{1/2}} Y \sqrt{\pi a} \quad [20]$$

where  $F_Q$  is the load at fracture,  $B$  is the specimen thickness,  $W$  is the specimen width, and  $a$  is the crack length (Figure 11). The geometry term  $Y$  is a function of the crack length-to-specimen width ratio,  $a/W$ . Linear elastic conditions can be obtained in standard sized specimens in high-strength materials such as age-hardened aluminum alloys, or structural ferritic steels tested at low temperatures.

Under *elastic-plastic conditions*, the fracture toughness is derived from expressions that depend on the

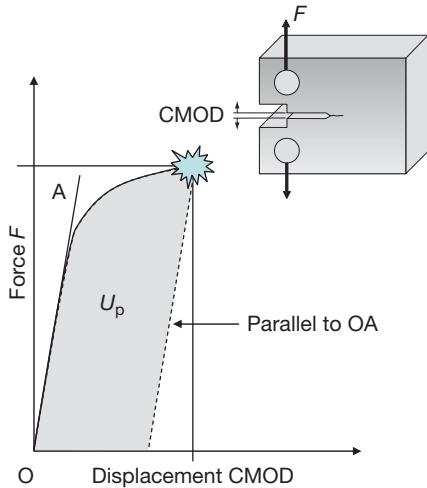


**Figure 11** Schematic illustration of load  $F$  versus crack mouth opening displacement (CMOD) trace and definition of area under curve  $U$ .

applied load at fracture, but which also account for the additional work done by deformation in the crack tip plastic zone. For a CT specimen, the expression for  $\mathcal{J}$  is as follows<sup>11</sup>

$$\mathcal{J} = \left[ \frac{F}{BW^{1/2}} Y \sqrt{\pi a} \right]^2 \frac{(1-\nu)}{E} + \frac{\eta_p U_p}{B(W-a)} \quad [21]$$

where  $\nu$  is Poisson's ratio,  $E$  is Young's modulus,  $a$  is the current crack length, and  $U_p$  is the plastic strain energy. This is defined by the plastic area under the measured load-versus-displacement curve, which is the shaded region in **Figure 11**. The parameter  $\eta_p$  is a function of crack length.

The crack length,  $a$ , at which  $\mathcal{J}$  is measured can be larger than the initial crack length  $a_0$ , since stable crack extension  $\Delta a$  can occur during test, for example, by ductile tearing. To obtain the initiation fracture toughness,  $\mathcal{J}_c$ , it is necessary to plot the variation of  $\mathcal{J}$  as a function of  $\Delta a$ , either using data obtained from a number of interrupted tests, or using a single specimen tested using the unloading compliance technique.<sup>8</sup> A power-law curve is fitted to the valid data and the initiation toughness defined by the intersection of a 0.2 mm offset line and the  $\mathcal{J}$  versus  $\Delta a$  power-law curve (known as the  $\mathcal{J}$  R-curve) as illustrated in **Figure 12**.

Elastic-plastic conditions are typically obtained in standard sized specimens in tough materials, such as structural ferritic steels at ambient or elevated temperatures, or austenitic stainless steels. The measured fracture toughness,  $\mathcal{J}_c$ , can be used to calculate the fracture toughness,  $K_{Ic}$ , using eqn [19], in order to predict the

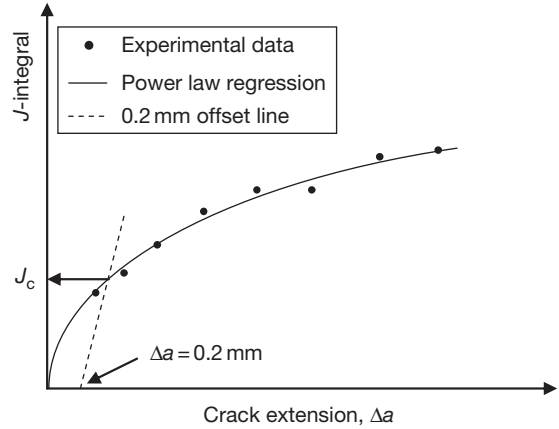


**Figure 12** Schematic illustration of definition of  $J_c$  from a  $J$  R-curve.

behavior of structural components that are much larger than the standard test specimen and in which linear elastic conditions would apply.

In most materials, the fracture toughness is not strongly affected by temperature. However, the fracture toughness of ferritic steels is sensitive to temperature. This is due to an effect of their body-centered cubic crystal structure on the mechanism of yielding. For example, the fracture toughness of ferritic pressure vessel steels at low temperatures can be as low as  $20 \text{ MPa m}^{-1/2}$ . This is the brittle fracture regime. In the ductile fracture regime, observed at higher temperatures, the fracture toughness of ferritic steel at the onset of ductile tearing is typically of the order of  $200 \text{ MPa m}^{-1/2}$ . The 'brittle-ductile transition temperature' describes fracture behavior between these two regimes and can be strongly sensitive to the microstructure of the steel. Neutron irradiation also affects the yield behavior and toughness of ferritic steels. The fracture toughness test is therefore a very important tool to predict the effect of temperature and other factors such as neutron irradiation, on the structural integrity of ferritic steel components containing crack-like flaws.

### 1.04.3 Application of Fracture Mechanics to SCC

Under a static loading condition, the growth of stress corrosion cracks is often characterized using a fracture mechanics-based approach to define the crack growth rate as a function of the stress intensity factor  $K_I$ . This approach assumes that the crack length relative to the length scale of both the material microstructure and

component is sufficient such that the crack driving force can be defined by  $K_I$ . Linear elastic conditions therefore apply, and such cracks may be described as 'long cracks.' Under such circumstances the required condition for crack growth by SCC is

$$K_I \geq K_{ISCC} \quad [22]$$

where  $K_{ISCC}$  defines the threshold stress intensity factor for sustained crack growth.

For  $K_I \geq K_{ISCC}$ , an initiated crack will continue to propagate, whereas for  $K_I < K_{ISCC}$ , an initiated crack will arrest. (Strictly, the condition for arrest is that crack propagation is not measurable. It may therefore be necessary to assume that crack growth may occur at a rate below the resolution of the measurements.) The stresses in a component can change during the lifetime, sometimes as a consequence of crack growth, and this approach can be used to determine whether a growing stress corrosion crack will arrest.

Cracks initiated at stress concentrating features (e.g., corrosion pits) can be too short to be characterized by  $K_I$ , due to either their length relative to the microstructure scale or the development of elastic-plastic deformation at the stresses needed to achieve  $K_I$  values approaching  $K_{ISCC}$ . A threshold stress  $\sigma_{SCC}$  may then be used to define the conditions required to propagate such cracks. Under these circumstances, the required condition for 'short crack' growth by SCC is

$$\sigma \geq \sigma_{SCC} \quad [23]$$

where  $\sigma$  is the applied tensile stress. For a component where  $\sigma \geq \sigma_{SCC}$ , an initiated short crack will continue to propagate, whereas for  $\sigma < \sigma_{SCC}$ , an initiated short crack will arrest. The critical stress,  $\sigma_{SCC}$ , is measured experimentally by observation of the behavior of cracks nucleated in statically stressed specimens.

This transition between short and long SCC cracks, and  $\sigma$ - or  $K_I$ -controlled crack growth may be considered using a two-parameter approach to SCC. This is illustrated schematically in Figure 13. The solid line defines the conditions above which SCC will be sustained (the unacceptable region). Below this line, any crack that has formed will arrest (the acceptable region). It can be seen that incorrectly applying long crack  $K_I$ -controlled behavior to short cracks can be nonconservative, that is, shallow cracks may propagate even when  $K_I < K_{ISCC}$ .

The prediction of component lifetime requires data for the effect of the crack-driving force on the crack growth rate. As shown by Figure 13, depending on the crack length, the driving force for SCC crack growth

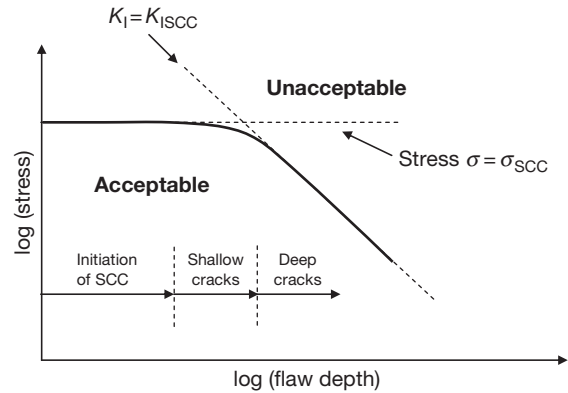


**Figure 13** Schematic illustration of the two-parameter approach to stress corrosion cracking.

may either be too low and SCC does not occur (long cracks) or may be stress-controlled (short cracks). For short cracks, the crack growth rate tends to increase with stress. For long cracks, as the applied  $K_I$  increases above  $K_{ISCC}$ , the crack growth rate rises rapidly to a plateau, Figure 14(a). It is important to note that the magnitude of both  $K_{ISCC}$  and the crack growth rate plateau are both material and environment dependent. For example, Figure 14(b), reproduced from Reference 12, shows the influence of copper content on long SCC crack growth rates for Al–Cu–Mg alloys. Reference 13 provides guidance regarding the generation of  $K_{ISCC}$  data using precracked laboratory specimens loaded under fixed load or fixed displacement conditions.

In practice, most crack-like flaws in components in which SCC is of concern are found using NDE techniques. Cracks nucleating from weld defects are typical of this. Such cracks are often of a size that can be treated using the principles of fracture mechanics, and the  $K_I$  parameter is appropriate. However, there may be some circumstances when a stress-based approach is required – particularly when the crack initiates at a surface from pitting and significant crack growth occurs under stress-control. Under these circumstances, it is important to take full account of the stress-controlled extent of crack extension.

There are a number of further important issues that should be considered in the measurement and application of  $K_{ISCC}$  data. These include:

- $K_{ISCC}$  will depend on the environment, material condition, and loading configuration used. For example, the loading configuration may affect the transport of chemical species to the crack tip. The conditions used to generate the data should

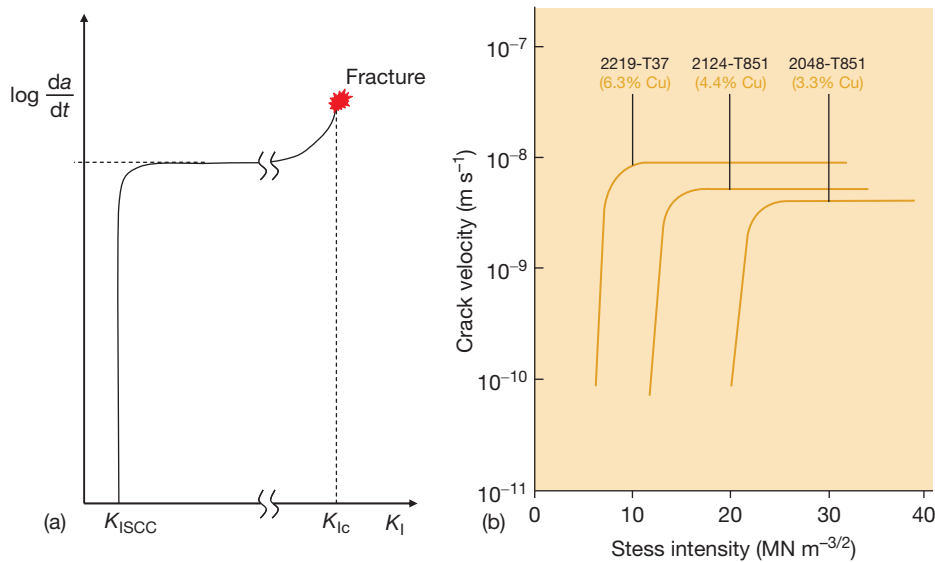


**Figure 14** (a) Schematic illustration of SCC crack growth rate as a function of applied  $K_I$ , (b) SCC data for Al-Cu-Mg alloys of varying copper content. Reproduced from Cottis, R. A. *Guides to good practice in corrosion control: stress corrosion cracking*, NPL Report, 2000.

therefore reflect as closely as possible the service conditions of interest.

- The timescales used to generate  $K_{ISCC}$  are often shorter than typical timescales for components. For example, components in power generation may require lifetimes in excess of 40 years. As stress corrosion involves time-dependent chemical reactions, rate effects should be considered.
- While  $K_{ISCC}$  testing is conventionally carried out under static loading, service loading often includes periodic unloads and reloads (e.g., due to start-up and shutdown), in which the loading rates can be quite slow or very fast relative to the  $K_{ISCC}$  test. Under such circumstances,  $K_{ISCC}$  may be affected.

## References

1. BS EN 10002-1:2001, Tensile testing of metallic materials. Method of test at ambient temperature; British Standards Institution, 2001.
2. ASTM E8-04, Standard Test Methods for Tension Testing of Metallic Materials American Society for Testing and Materials (ASTM) International, 2004.
3. Ashby, M. F.; Jones, D. R. H. *Engineering Materials: An Introduction to their Properties and Applications*; Pergamon Press: New York, 1980.
4. Patel, S. A.; Venkatraman, B.; Bentson, J. J. *Franklin Inst.* **1963**, 275, 98–106.
5. Weil, N. A. *J. Franklin Inst.* **1958**, 265, 97–116.
6. Murakami, Y. *Stress Intensity Factors Handbook*; Pergamon Press: New York, 1987; Vol. 1 and Vol. 2; 1992; Vol. 3.
7. API 579, Fitness for Service; American Petroleum Institute Recommended Practice, 2000.
8. Anderson, T. L. *Fracture Mechanics: Fundamentals and Applications*, 2nd ed.; CRC Press: New York, 1995.
9. Hutchinson, J. W. *J. Mech. Phys. Solids*, **1968**, pp 13–31, Vol. 16.
10. Rice, J. R.; Rosengren, G. F. *J. Mech. Phys. Solids* **1968**, 16, 1–12.
11. BS7448, *Fracture Mechanics Toughness Tests. Part 1, Method for Determination of  $K_{Ic}$ , Critical CTOD and Critical  $J$  Values of Metallic Material*; British Standards Institute: London, 1991.
12. Cottis, R. A. *Guides to good practice in corrosion control: SCC*, NPL Report 2000.
13. ISO 7539-6:2003, Corrosion of metals and alloys – stress corrosion testing – part 6: preparation of pre-cracked specimens for tests under constant load or constant displacement, International Standards Organisation, 2003.



## 1.05 Basic Concepts of Corrosion

L. L. Shreir<sup>†</sup>

This article is a revision of the Third Edition article 1.1 by L. L. Shreir, volume 1, pp 1:3–1:15, © 2010 Elsevier B.V.

1.05.1	Introduction	89
1.05.2	Definitions of Corrosion	90
1.05.3	Methods of Approach to Corrosion Phenomena	91
1.05.3.1	Corrosion as a Chemical Reaction at a Metal–Environment Interface	92
1.05.3.2	Environment	92
1.05.3.3	Metal	93
1.05.4	Types of Corrosion	93
1.05.5	Principles of Corrosion	96
1.05.5.1	Terminology	96
Appendix A – Classification of Corrosion Processes		96
Existing Classifications		96
‘Dry’ Corrosion		97
‘Wet’ Corrosion		98
Corrosion in Organic Solvents		98
Suggested Classification and Nomenclature		99
References		100

### 1.05.1 Introduction

Modern technology has at its disposal a wide range of constructional materials – metals and alloys, plastics, rubber, ceramics, composites, wood, etc., and the selection of an appropriate material for a given application is the important responsibility of the design engineer. No general rule governs the choice of a particular material for a specific purpose, and a logical decision involves a consideration of the relevant properties, ease of fabrication, availability, relative costs, etc. of a variety of materials; often, the ultimate decision is determined by economics rather than by properties, and ideally, the material selected should be the cheapest possible that has adequate properties to fulfill the specific function.

Where metals are involved, mechanical, physical, and *chemical* properties must be considered, and in this connection, it should be observed that while mechanical and physical properties can be expressed in terms of constants, the chemical properties of a given metal are dependent entirely on the precise environmental conditions prevailing during service. The relative importance of mechanical, physical, and chemical properties depends, in any given case, on the application of the metal. For example, for railway lines, elasticity, tensile

strength, hardness, and abrasion resistance are of major importance, whereas electrical conductivity is of primary significance in electrical transmission. In the case of heat-exchanger tubes, good thermal conductivity is necessary, but this may be outweighed in certain environments by chemical properties in relation to the aggressiveness of the two fluids involved – thus, although the thermal conductivity of copper is superior to that of aluminum brass or the cupronickels, the alloys are preferred when high-velocity seawater is used as the coolant, as copper has very poor chemical properties under these conditions.

While a metal or alloy may be selected largely on the basis of its mechanical or physical properties, the fact remains that there are very few applications where the effect of the interaction of a metal with its environment can be completely ignored, although the importance of this interaction is of varying significance according to circumstances; for example, the slow uniform wastage of a steel structure of massive cross-section (such as railway lines or sleepers) is of far less importance than the rapid perforation of a buried steel pipe or the sudden failure of a vital stressed steel component in sodium hydroxide solution.

The effect of the metal–environment interaction on the environment itself is often more important than the actual deterioration of the metal. For instance, lead pipes cannot be used for conveying plumbo-solvent

<sup>†</sup>Deceased.

waters, since a lead level of  $>0.1$  ppm is toxic; similarly, galvanized steel may not be used for certain foodstuffs owing to the toxicity of zinc salts. In many chemical processes, the selection of a particular metal may be determined by the need to avoid the contamination of the environment with traces of metallic impurities that would affect the color or taste of products or catalyze undesirable reactions; therefore, copper and copper alloys cannot be used in soap manufacture, since traces of copper ions result in the coloration and rancidification of the soap. In these circumstances, it is essential to use unreactive and relatively expensive metals, even though the environment would not result in the rapid deterioration of cheaper metals such as mild steel. A further possibility is that the contamination of the environment by metal ions due to the corrosion of one metal can result in an enhanced corrosion of another when the two are in contact with the same environment. Thus, the slow uniform corrosion of copper by a cuprosolvent domestic water may not be particularly deleterious to copper plumbing, but it can result in the rapid pitting and consequent perforation of galvanized steel and aluminum that subsequently comes into contact with the copper-containing water.

Finally, it is necessary to point out that for a number of applications, metals are selected in preference to other materials because of their visual appearance, and for this reason, it is essential that brightness and reflectivity are retained during exposure to the atmosphere; stainless steel is now widely used for architectural purposes, and for outdoor exposure, the surface must remain bright and rust-free without periodic cleaning. On the other hand, the slow-weathering steels, which react with the constituents of the atmosphere to form an adherent uniform coating of rust, are now being used for cladding buildings, in spite of the fact that a rusty surface is usually regarded as aesthetically unpleasant.

The interaction of a metal or alloy (or a nonmetallic material) with its environment is clearly of vital importance in the performance of materials of construction, and the fact that the present work is largely confined to a detailed consideration of such interactions could create the impression that this was the sole factor of importance in material selection. This, of course, is not the case, although it is probably true that this factor is most neglected by the design engineer.

### 1.05.2 Definitions of Corrosion

In the case of nonmetallic materials, the term *corrosion* invariably refers to their deterioration from chemical causes, but a similar concept is not necessarily

applicable to metals. Many authorities<sup>1</sup> consider that the term *metallic corrosion* embraces all interactions of a metal or alloy (solid or liquid) with its environment irrespective of whether this is deliberate and beneficial or adventitious and deleterious. Thus, this definition of corrosion, which, for convenience, is referred to as the *transformation* definition, includes, for example, the deliberate anodic dissolution of zinc in cathodic protection and electroplating as well as the spontaneous gradual wastage of zinc roofing sheet, resulting from atmospheric exposure.

On the other hand, *corrosion* has been defined<sup>2</sup> as 'the undesirable deterioration' of a metal or alloy, that is, an interaction of the metal with its environment that adversely affects those properties of the metal that are to be preserved. This definition – which is referred to as the *deterioration* definition – is also applicable to nonmetallic materials such as glass, concrete, etc. and embodies the concept that corrosion is always deleterious. However, the restriction of the definition to undesirable chemical reactions of a metal results in anomalies that become apparent from a consideration of the following examples.

Steel, when exposed to an industrial atmosphere, reacts to form the reaction product rust of approximate composition  $\text{Fe}_2\text{O}_3 \cdot \text{H}_2\text{O}$ , which, being loosely adherent, does not form a protective barrier that isolates the metal from the environment; the reaction thus proceeds at an approximately linear rate until the metal is completely consumed. Copper, on the other hand, forms an adherent green patina corresponding approximately to bronchantite,  $\text{CuSO}_4 \cdot 3\text{Cu}(\text{OH})_2$ , which is protective and isolates the metal from the atmosphere. Copper roofs installed 200 years ago are still performing satisfactorily, and it is apparent that the formation of bronchantite is not deleterious to the function of copper as a roofing material – indeed, in this particular application, it is considered to enhance the appearance of the roof, although a similar patina formed on copper water pipes would be aesthetically objectionable.

The rapid dissolution of a vessel constructed of titanium in hot 40%  $\text{H}_2\text{SO}_4$ , with the formation of  $\text{Ti}^{4+}$  aquo cations, conforms to both definitions of corrosion, but if the potential of the metal is raised (anodic protection), a thin adherent protective film of anatase,  $\text{TiO}_2$ , is formed, which isolates the metal from the acid so that the rate of corrosion is enormously decreased. The formation of this very thin oxide film on titanium, like that of the relatively thick bronchantite film on copper, clearly conforms to the *transformation* definition of corrosion, but not with the *deterioration* definition, since in these examples, the rate and extent of the reaction are not significantly

detrimental to the metal concerned. Again, magnesium, zinc, or aluminum is deliberately sacrificed when these metals are used for the cathodic protection of steel structures, but as these metals are clearly not required to be maintained as such, their consumption in this particular application cannot, according to the *deterioration*, be regarded as corrosion. Furthermore, corrosion reactions are used to advantage in technological processes such as pickling, etching, chemical, and electrochemical polishing and machining, etc.

The examples already discussed lead to the conclusion that any reaction of a metal with its environment must be regarded as a corrosion process irrespective of the extent of the reaction or of the rates of the initial and subsequent stages of the reaction. It is not illogical, therefore, to regard *passivity*, in which the reaction product forms a very thin protective film that controls rate of the reaction at an acceptable level, as a limiting case of a corrosion reaction. Thus, both the rapid dissolution of *active* titanium in 40%  $\text{H}_2\text{SO}_4$  and the slow dissolution of *passive* titanium in that acid must be regarded as corrosion processes, even though the latter is not detrimental to the metal during the anticipated life of the vessel.

It follows that in deciding whether the corrosion reaction is detrimental to a metal in a given application, the precise form of attack on the metal (general, intergranular, etc.), the nature of the reaction products (protective or nonprotective), the velocity and extent of the reaction, and the location of the corrosion reaction must all be taken into account. In addition, due consideration must be given to the effect of the corrosion reaction on the environment itself. Thus, corrosion reactions are not always detrimental, and our ability to use highly reactive metals such as aluminum, titanium, etc. in aggressive environments is due to a limited initial corrosion reaction, which results in the formation of a rate-controlling corrosion product. Expressions such as 'preventing corrosion,' 'combating corrosion,' or even 'fighting corrosion' are misleading; with the majority of metals, corrosion cannot be avoided and 'corrosion control' rather than 'prevention' is the desired goal. The implication of 'control' in this context is that (1) neither the form nor the extent, nor the rate of the corrosion reaction must be detrimental to the metal used as a constructional material for a specific purpose and (2) for certain applications, the corrosion reaction must not result in the contamination of the environment. Corrosion control must involve a consideration of materials, availability, fabrication, protective methods, and economics in relation to the specific function of the metal and its anticipated life. At one extreme, corrosion control in certain environments may be effected by the use of thick sections of mild steel without any protective

system, at the other, the environmental conditions prevailing may necessitate the use of platinum.

The scope of the term 'corrosion' is continually being extended, and Fontana and Staehle have stated<sup>3</sup> that '*corrosion*' includes the reaction of metals, glasses, ionic solids, polymeric solids, and composites with environments that embrace liquid metals, gases, non-aqueous electrolytes, and other nonaqueous solutions.

Vermilyea, who has defined corrosion as a process in which atoms or molecules are removed one at a time, considers that the evaporation of a metal into vacuum should come within the scope of the term, since atomically it is similar to other corrosion processes.<sup>4</sup>

Evans<sup>5</sup> considers that corrosion may be regarded as a branch of chemical thermodynamics or kinetics, as the outcome of electron affinities of metals and non-metals, as short-circuited electrochemical cells, or as the demolition of the crystal structure of a metal.

These considerations lead to the conclusion that there is probably a need for two definitions of corrosion that depend upon the approach adopted:

1. Definition of corrosion in the context of Corrosion Science: the reaction of a solid with its environment.
2. Definition of corrosion in the context of Corrosion Engineering: the reaction of an engineering constructional metal (material) with its environment with a consequent deterioration in properties of the metal (material).

### 1.05.3 Methods of Approach to Corrosion Phenomena

The effective use of metals as materials of construction must be based on an understanding of their physical, mechanical, and chemical properties. The last, as pointed out earlier, cannot be divorced from the environmental conditions prevailing. Any fundamental approach to the phenomena of corrosion must therefore involve a consideration of the structural features of the metal, the nature of the environment, and the reactions that occur at the metal–environment interface. The more important factors involved may be summarized as follows:

1. *Metal* – composition, detailed atomic structure, microscopic and macroscopic heterogeneities, stress (tensile, compressive, cyclic), etc.
2. *Environment* – chemical nature, concentrations of reactive species and deleterious impurities, pressure, temperature, velocity, impingement, etc.
3. *Metal–environment interface* – kinetics of metal oxidation and dissolution, kinetics of the reduction

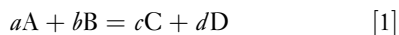
of species in solution, nature and location of corrosion products, film growth and film dissolution, etc.

From these considerations, it is evident that the detailed mechanism of metallic corrosion is highly complex and that an understanding of the various phenomena involves many branches of the pure and applied sciences, for example, metal physics, physical metallurgy, the various branches of chemistry, bacteriology, etc., although the emphasis may vary with the particular system under consideration. Thus, in stress-corrosion cracking, emphasis may be placed on the detailed metallurgical structure in relation to crack propagation resulting from the conjoint action of corrosion at localized areas and mechanical tearing, while in underground corrosion, the emphasis may be on the mechanism of bacterial action in relation to the kinetics of the overall corrosion reaction.

Although the mechanism of corrosion is highly complex, the actual control of the majority of corrosion reactions can be effected by the application of relatively simple concepts. Indeed, the Committee on Corrosion and Protection<sup>6</sup> concluded that 'better dissemination of existing knowledge' was the most important single factor that would be instrumental in decreasing the enormous cost of corrosion in the United Kingdom.

### 1.05.3.1 Corrosion as a Chemical Reaction at a Metal–Environment Interface

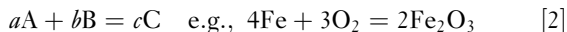
As the first approach to the principles which govern the behavior of metals in specific environments, it is preferable, for simplicity, to disregard the detailed structure of the metal and to consider corrosion as a heterogeneous chemical reaction that occurs at a metal–nonmetal interface and that involves the metal itself as one of the reactants (cf. catalysis). Corrosion can be expressed, therefore, by the simple chemical reaction:



where A is the metal and B the nonmetal reactant (or reactants), and C and D, the products of the reaction. The nonmetallic reactants are often referred to as *the environment*, although it should be observed that in a complex environment, the major constituents may play a very subsidiary role in the reaction. Hence, in the 'atmospheric' corrosion of steel, although nitrogen constitutes ~75% of the atmosphere, its effect, compared with that of moisture, oxygen, sulfur dioxide, solid particles, etc., can be disregarded (in the high temperature reaction of titanium with the atmosphere, on the other hand, nitrogen is a significant factor).

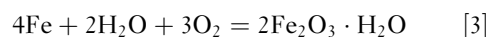
One of the reaction products (say, C) will be an oxidized form of the metal, and D will be a reduced

form of the nonmetal – C is usually referred to as the *corrosion product*, although the term could apply equally to D. In its simplest form, reaction [1] becomes



where the reaction product can be regarded either as an oxidized form of the metal or as the reduced form of the nonmetal. Reactions of this type, which do not involve water or aqueous solutions, are referred to as 'dry' corrosion reactions.

The corresponding reaction in aqueous solution is referred to as a 'wet' corrosion reaction, and the overall reaction (which actually occurs by a series of intermediate steps) can be expressed as



Thus, in all corrosion reactions, one (or more) of the reaction products will be an oxidized form of the metal, aquo cations (e.g.,  $\text{Fe}^{2+}(\text{aq.})$ ,  $\text{Fe}^{3+}(\text{aq.})$ ), aquo anions (e.g.,  $\text{HFeO}_2^-(\text{aq.})$ ,  $\text{FeO}_4^{2-}(\text{aq.})$ ), or solid compounds (e.g.,  $\text{Fe}(\text{OH})_2$ ,  $\text{Fe}_3\text{O}_4$ ,  $\text{Fe}_3\text{O}_4 \cdot \text{H}_2\text{O}$ ,  $\text{Fe}_2\text{O}_3 \cdot \text{H}_2\text{O}$ ), while the other reaction product (or products) will be the reduced form of the nonmetal. Corrosion may be regarded, therefore, as a *heterogeneous redox reaction at a metal–nonmetal interface in which the metal is oxidized and the nonmetal is reduced*. In the interaction of a metal with a specific nonmetal (or nonmetals) under specific environmental conditions, the chemical nature of the nonmetal, the chemical and physical properties of the reaction products, and the environmental conditions (temperature, pressure, velocity, viscosity, etc.) are clearly important in determining the form, extent, and rate of the reaction.

### 1.05.3.2 Environment

Some examples of the behavior of normally reactive and nonreactive metals in simple chemical solutions are considered here to illustrate the fact that corrosion is dependent on the nature of the environment; the thermodynamics of the systems and the kinetic factors involved are considered in subsequent chapters.

Gold is stable in most strong reducing acids, whereas iron corrodes rapidly, yet finely divided gold can be quickly dissolved in oxygenated cyanide solutions that may be contained in steel tanks. A mixture of caustic soda and sodium nitrate can be fused in an iron or nickel crucible, whereas this melt would have a disastrous effect on a platinum crucible.

Copper is relatively resistant to dilute sulfuric acid, but corrodes if oxygen or oxidizing agents are present in the acid, whereas austenitic stainless steels are stable in this acid only if oxygen or other

oxidizing agents are present. Iron corrodes rapidly in oxygenated water, but extremely slowly if all oxygen is removed; if, however, oxygen is brought rapidly and simultaneously to all parts of the metal surface, the rate will become very low, owing to the formation of a protective oxide film. Lead dissolves rapidly in nitric acid, more slowly in hydrochloric acid, and very slowly in sulfuric acid. These examples show that the corrosion behavior of a metal cannot be divorced from the specific environmental conditions prevailing, which determine the rate, extent (after a given period of time), and form of the corrosion process.

### 1.05.3.3 Metal

Heterogeneities associated with a metal have been classified in [Table 1](#) as atomic (see [Figure 1](#)), microscopic (visible under an optical microscope), and macroscopic, and their effects are considered in various sections of the present work. It is relevant to observe, however, that the detailed mechanism of all aspects of corrosion, for example, the passage of a metallic cation from the lattice to the solution, specific effects of ions and species in solution in accelerating or inhibiting corrosion or causing stress-corrosion cracking, etc. must involve a consideration of the detailed atomic structure of the metal or alloy.

The corrosion behavior of different constituents of an alloy is well known, since the etching techniques used in metallography are essentially corrosion processes that take advantage of the different corrosion rates of phases as a means of identification, for example, the grain boundaries are usually etched more rapidly than the rest of the grain owing to the greater reactivity of the disarrayed metal.

Macroscopic heterogeneities, for example, crevices, discontinuities in surface films, bimetallic contacts, etc.

have a pronounced effect on the location and the kinetics of the corrosion reaction and are considered in various sections throughout this work. Practical environments are shown schematically in [Figure 2](#), which also serves to emphasize the relationship between the detailed structure of the metal, the environment, and external factors such as stress, fatigue, velocity, impingement, etc.

## 1.05.4 Types of Corrosion

Corrosion can affect the metal in a variety of ways, which depend on its nature and the precise environmental conditions prevailing, and a broad classification of the various forms of corrosion, in which five major types have been identified, is presented in [Table 2](#). Thus, an 18Cr–8Ni stainless steel corrodes uniformly during polishing, active dissolution, or passivation, but locally during intergranular attack, crevice corrosion, or pitting; in certain circumstances, selective attack along an ‘active path’ in conjunction with a tensile stress may lead to a transgranular fracture. Types of corrosion are dealt with in more detail in Appendix A.

Ideally, the metal selected, or the protective system applied to the metal, should be such that no corrosion occurs at all, but this is seldom technologically or economically feasible. It is necessary, therefore, to tolerate a rate and a form of corrosion that will not be significantly detrimental to the properties of the metal during its anticipated life. Thus, provided the corrosion rate is known, the slow uniform corrosion of a metal can often be allowed for in the design of the structure; for example, in the case of a metal that shows an active–passive transition, the rate of corrosion in the passive region is usually acceptable, whereas the rate in the active region is not. It follows that certain forms of

**Table 1** Heterogeneities in metal

1. *Atomic* (as classified by Ehrlich and Turnbull,<sup>7</sup> see [Figure 1](#)).
  - a. Sites within a given surface layer (‘normal’ sites); these vary according to the particular crystal plane ([Figure 3](#)).
  - b. Sites at edges of partially complete layers.
  - c. Point defects in the surface layer: vacancies (molecules missing in surface layer), kink sites (molecules missing at edge of layer), molecules adsorbed on top of complete layer.
  - d. Disordered molecules at point of emergence of dislocations (screw or edge) in metal surface.
2. *Microscopic*
  - a. Grain boundaries – usually, but not invariably, more reactive than grain interior.
  - b. Phases – metallic (single metals, solid solutions, intermetallic compounds), nonmetallic, metal compounds, impurities, etc. – heterogeneities due to thermal or mechanical causes.
3. *Macroscopic*
  - a. Grain boundaries.
  - b. Discontinuities on metal surface – cut edges, scratches, discontinuities in oxide films (or other chemical films) or in applied metallic or nonmetallic coatings.
  - c. Bimetallic couples of dissimilar metals.
  - d. Geometrical factors – general design, crevices, contact with nonmetallic materials, etc.



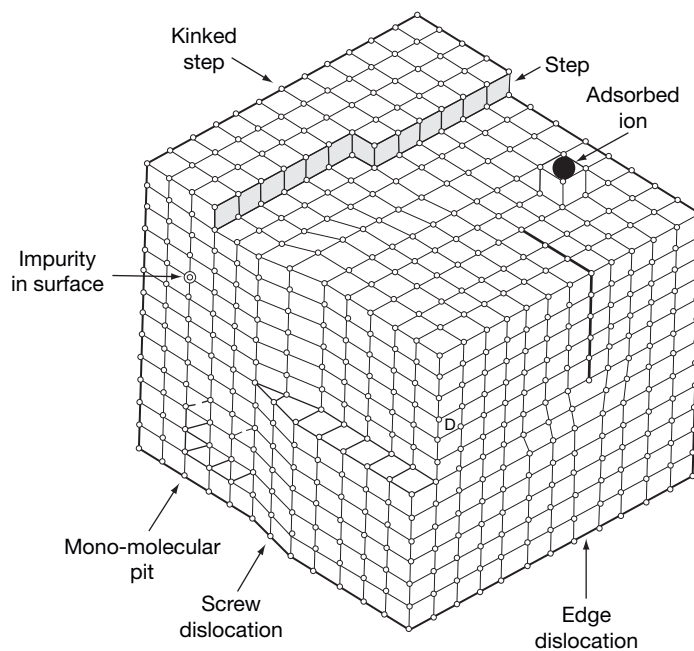


**Figure 1** Surface imperfections in a crystal. Reproduced from Ehrlich, G.; Turnbull, D. *Physical Metallurgy of Stress Corrosion Fracture*; Interscience: New York and London, 1959; p 47, with permission from Interscience.

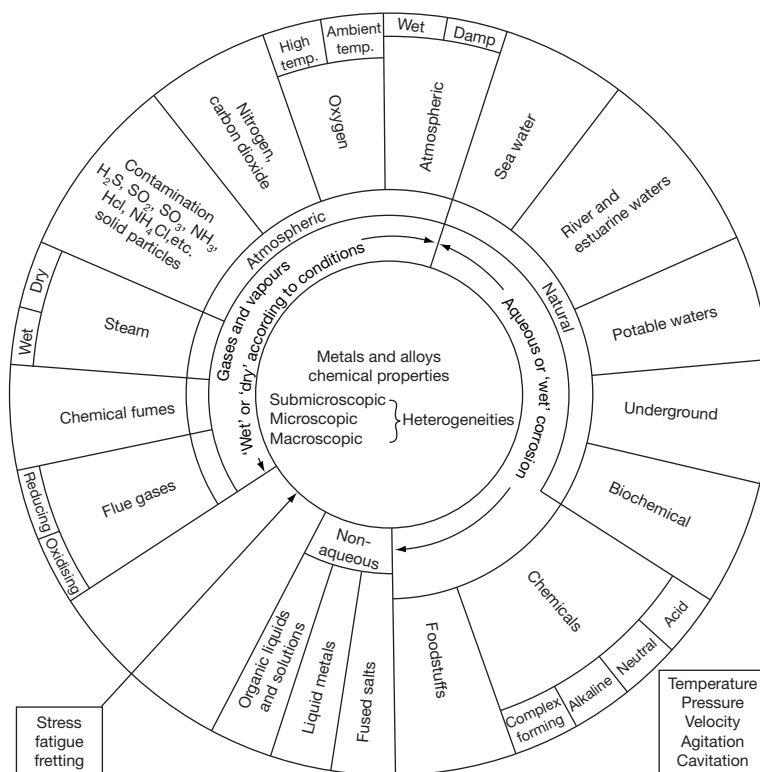


**Figure 2** Environments in corrosion.



corrosion can be tolerated and that corrosion control is possible, provided that the rate and the form of the corrosion reaction are predictable and can be allowed for in the design of the structure.

Pitting is regarded as one of the most insidious forms of corrosion, since it often leads to perforation and to a consequent corrosion failure. In other cases, pitting may result in a loss of appearance, which is of major importance when the metal concerned is used for decorative architectural purposes. However, aluminum saucepans that have been in service for some

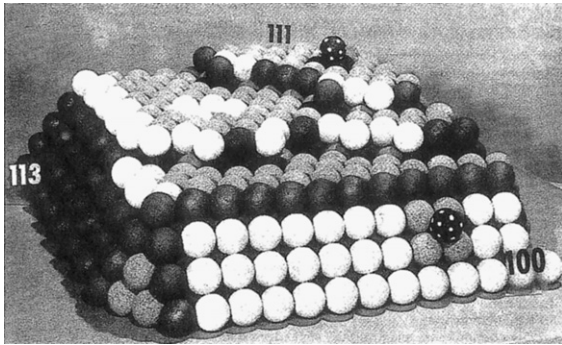


**Figure 3** Hard-sphere model of face-centered cubic (fcc) lattice showing various types of sites. Numbers denote Miller indices of atom places and the different shadings correspond to differences in the number of nearest neighbors. Reproduced from Ehrlich, G.; Turnbull, D. *Physical Metallurgy of Stress Corrosion Fracture*; Interscience: New York and London, 1959; p 47, with permission from Interscience.

time are invariably pitted, although the pits seldom penetrate the metal, that is, the saucepan remains functional and the pitted appearance is of no significance in that particular application.

These considerations lead to the conclusion that the relationship between corrosion and the deterioration of properties of a metal is highly complex and involves a consideration of a variety of factors such as the rate and the form of corrosion and the specific function of the metal concerned; certain forms of corrosion such as uniform attack can be tolerated, whereas others such as pitting and stress corrosion cracking that ultimately lead to complete loss of function cannot be.

The implications of the terms *predictable* and *unpredictable* used in the context of corrosion require further consideration, since they are clearly dependent on the knowledge and expertise of the engineer, designer, or corrosion designer who takes the decision on the metal or alloy to be used, or the procedure to be adopted, to control corrosion in a specific environmental situation. On this basis, a corrosion failure (i.e., failure of the function of the metal due to corrosion within a period that is significantly less than the anticipated life of the structure) may be the result of one or more of the following possibilities:

1. *Predictable.* (1) The knowledge and technology are available, but have not been utilized by the designer; this category includes a wide variety of

**Table 2** Types of corrosion

Type	Characteristic	Examples
1. Uniform (or almost uniform)	All areas of the metal corrode at the same (or similar) rate	Oxidation and tarnishing; active dissolution in acids; anodic oxidation and passivity; chemical and electrochemical polishing; atmospheric and immersed corrosion in certain cases
2. Localized	Certain areas of the metal surface corrode at higher rates than others due to 'heterogeneities' in the metal, the environment or in the geometry of the structure as a whole. Attack can range from being slightly localized to pitting	Crevice corrosion; filiform corrosion; deposit attack; bimetallic corrosion; intergranular corrosion; weld decay
3. Pitting	Highly localized attack at specific areas resulting in small pits that penetrate into the metal and may lead to perforation	Pitting of passive metals such as the stainless steels, aluminum alloys, etc., in the presence of specific ions, for example, $\text{Cl}^-$ ions
4. Selective dissolution	One component of an alloy (usually the most active) is selectively removed from an alloy	Dezincification; dealuminification; graphitization
5. Conjoint action of corrosion and a mechanical factor	Localized attack or fracture due to the synergistic action of a mechanical factor and corrosion	Erosion – corrosion, fretting corrosion, impingement attack, cavitation damage; stress corrosion cracking, hydrogen cracking, corrosion fatigue

design features such as a wrong choice of materials, introduction of crevices and bimetallic contacts, etc., and is the most common cause of corrosion failures. (2) The knowledge and technology are available, but have not been applied for economic reasons; for example, inadequate pretreatment of steel prior to painting and the use of unprotected mild steel for silencers and exhaust systems of cars.

2. *Unpredictable.* (1) The design has been based on specific environmental conditions, which have subsequently changed during the operation of the process; in this connection, it should be noted that small changes in the chemical nature of the environment, temperature, pressure, and velocity may lead to significant changes in the corrosion rate and form: the catastrophic oxidation and the failure of steel bolts in nuclear reactors in the United Kingdom, resulting from an increase in the temperature of the carbon dioxide, is an example of an unpredictable failure due to a change in environmental conditions. (2) The knowledge of and the experience with the metal, alloy, or the environment are insufficient to predict with certainty that failure will not occur; examples could be quoted of new alloys that have been subjected to an extensive series of carefully planned corrosion tests, but have failed in service.

Professor M. Fontana<sup>8</sup> has made the statement that “Virtually all premature corrosion failures these days occur for reasons which were already well known and these failures can be prevented.” It is apparent from this statement and from the conclusions reached by the Committee on Corrosion and Protection that category 1 is responsible for the majority of incidents of corrosion failure that could have been avoided if those responsible were better informed on the hazards of corrosion and on the methods that should have been used to control it.

### 1.05.5 Principles of Corrosion

It has been stated that metallic corrosion is an art rather than a science and that, at present, the available knowledge is insufficient to predict with any certainty how a particular metal or alloy will behave in a specific environment.<sup>4</sup> It should be appreciated that the decision to use a particular metal or alloy in preference to others in a given environment or to employ a particular protective system is based usually on previous experience and empirical testing rather than on the application of scientific knowledge – the technology of corrosion is, without doubt, in advance of corrosion

science, and many of the phenomena of corrosion are not fully understood. Thus, the phenomenon of passivity, which was first observed by Faraday in 1836, is still a subject of controversy; the specific effect of certain anions in causing stress-corrosion cracking of certain alloy systems is not fully understood; and the dezincification of brasses can be prevented by additions of arsenic (or other elements such as antimony or phosphorus), but no adequate theory has been submitted to explain the action of these elements. (Editor’s note: Arguably this phenomenon is now somewhat better understood, see **Chapter 2.05, Dealloying**.)

An understanding of the basic principles of the science of metallic corrosion is clearly vital for corrosion control, and as the knowledge of the subject advances, the application of scientific principle rather than an empirical approach may be used for such purposes as the selection of corrosion inhibitors, the formulation of corrosion-resisting alloys, etc.

#### 1.05.5.1 Terminology

The classification given in **Table 2** is based on the various forms that corrosion may take, but the terminology used in describing corrosion phenomena often places emphasis on the environment or the cause of attack rather than on the form of attack. Thus, the broad classification of corrosion reactions into ‘wet’ or ‘dry’ is now generally accepted, and the nature of the process is often made more specific by the use of an adjective that indicates the type or the environment, for example, concentration-cell corrosion, crevice corrosion, bimetallic corrosion and atmospheric corrosion, high temperature corrosion, seawater corrosion, etc. Alternatively, the phenomenon is described in terms of the corrosion product itself – tarnishing, rusting, and green rot. The terminology used in corrosion is given in **Table 3** and is considered in more detail in Appendix A.

## Appendix A – Classification of Corrosion Processes

### Existing Classifications

A logical and scientific classification of corrosion processes, although desirable, is by no means simple owing to the enormous variety of corrosive environments and the diversity of corrosion reactions, but the broad classification of corrosion reactions into ‘wet’ or ‘dry’ is now generally accepted, and the terms are in common use. The term ‘wet’ includes all reactions

**Table 3** Terminology in corrosion

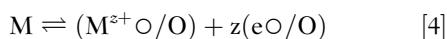
Type of attack	Environmental	Cause of attack	Mechanical factors	Corrosion product
General (uniform)	Wet <sup>a</sup>	Concentration cell	Stress	Rusting
Localized	Dry	Bimetallic cell	Fretting	Tarnishing
Pitting (or intense)	Atmospheric	Active-passive cell	Fatigue	Scaling
Intergranular	Immersed	Stray current (electrolysis)	Cavitation	Green rot
Transgranular	Underground	Hydrogen evolution	Erosion	Tin pest
Selective	Seawater	Oxygen absorption	Impingement	
Parting	Chemical	Impingement		
Catastrophic	Fused-salt	Hydrogen embrittlement		
Layer	Flue-gas	Caustic embrittlement		
Filiform	Biochemical			
	Bacterial			
	High temperature			
	Liquid-metal			

<sup>a</sup>See Appendix to this section.

in which an aqueous solution is involved in the reaction mechanism; implicit in the term 'dry' is the absence of water or an aqueous solution.

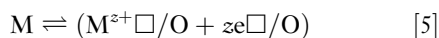
These terms are evidently ambiguous; for example, it is not always clear whether 'wet' is confined to aqueous solutions – the 'wetting' of solids by mercury indicates that liquid-metal corrosion should be classified as 'wet'. Even if the term is restricted to aqueous solutions, the difficulty arises that the mechanism of the growth of magnetite scale during the reaction of the interior of a boiler drum with dilute caustic soda at high temperatures and pressures is best interpreted in terms of a 'dry' corrosion process. Similar considerations apply to the reactions of aluminum and zirconium with high temperature water.

Considering oxidation as a typical 'dry' reaction, it follows, as shown in **Figure A1(a)**, that at the *interfaces*



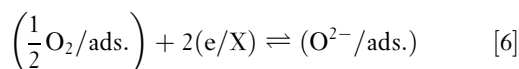
where  $M^{z+}\bigcirc$  is an interstitial metal ion,  $e\bigcirc$  an interstitial electron, and  $/O$  indicates the metal–oxide interface.

If the metal dissolves to enter a vacant site, then



where  $M^{z+}\square$  represents a cation vacancy and  $e\square$  a positive hole.

At the gas–oxide interface, the  $O_2$  gas ionizes



where  $/X$  indicates the gas–oxide interface.

By definition, these *interfaces* can be considered as anodes and cathodes respectively.

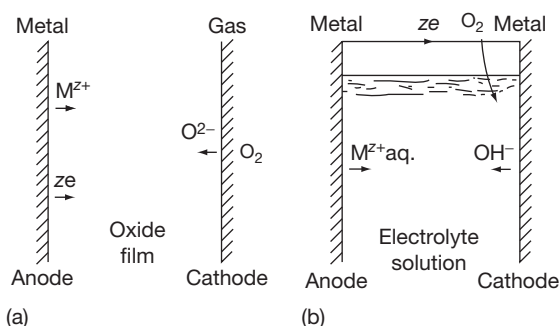
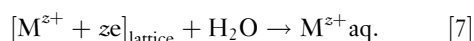
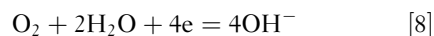


**Figure A1** Anodes and cathodes in corrosion processes: (a) 'dry' corrosion and (b) 'wet' corrosion.

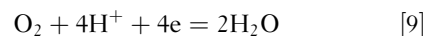
The corresponding 'wet' corrosion half-reactions (**Figure A1(b)**) are



and



or



### 'Dry' Corrosion

These are generally metal–gas or metal–vapor reactions involving nonmetals such as oxygen, halogens, hydrogen sulfide, sulfur vapor, etc., and oxidation, scaling, and tarnishing are the more important forms. A characteristic of these reactions is that the initial oxidation of the metal, the reduction of the nonmetal, and the formation of the compound occur at one and the same place at the metal–nonmetal interface. Should the compound be volatile or

discontinuous, further interaction at the interface (or through a thin film of constant thickness) is possible, and in most cases, the reaction rate tends to remain constant with time (linear law). If the film is continuous, it will present a barrier to the reactants, and further interaction will necessitate the passage of the reactants through the film by (a) diffusion of the nonmetal or (b) diffusion and migration of ions of the reactants. The detailed mechanisms of these reactions are considered in subsequent chapters, but it is appropriate to observe that the formation of a continuous film of reactant product at a metal–nonmetal interface results in a growth rate that, when the film becomes sufficiently thick to be rate determining, decreases as the film thickens, that is, parabolic, logarithmic, asymptotic, cubic, etc.

### 'Wet' Corrosion

In 'wet' corrosion, the oxidation of the metal and the reduction of a species in solution (electron acceptor or oxidizing agent) occur at different areas on the metal surface with consequent electron transfer through the metal from the anode (metal oxidized) to the cathode (electron acceptor reduced); the thermodynamically stable phases formed at the metal–solution interface may be solid compounds or hydrated ions (cations or anions), which may be transported away from the interface by processes such as migration, diffusion, and convection (natural or forced). Under these circumstances, the reactants will not be separated by a barrier, and the rate law will tend to be linear. Subsequent reaction with the solution may result in the formation of a stable

solid phase, but as this will form away from the interface, it will not be protective – the thermodynamically stable oxide can affect the kinetics of the reaction only if it forms a film or precipitates on the metal surface.

Further points that distinguish 'wet' from 'dry' corrosion are

1. In 'wet' corrosion, the metal ions are hydrated – the hydration energy of most metal ions is very high and thus facilitates ionization.
2. In 'wet' corrosion, the ionization of oxygen to hydroxyl must involve the hydronium ion or water.
3. In 'dry' corrosion, the direct ionization of oxygen occurs.

### Corrosion in Organic Solvents

Corrosion reactions in aggressive organic solvents are becoming a more common occurrence owing to the developments in the chemical and petrochemical industries, and these reactions can lead to the deterioration of the metal and to undesirable changes in the solvent. This aspect of corrosion has recently been the subject of an extensive review by Heitz,<sup>9</sup> who has considered the mechanisms of the reactions, the similarities between corrosion in organic solvents and in aqueous solutions, the methods of study, and the occurrence of the phenomenon in industrial processes.

Figure A2 shows the weight loss against time curve for nickel in various solvents containing 0.05 wt%  $\text{H}_2\text{SO}_4$  at various temperatures, and illustrates the unpredictable nature of corrosion in organic solvents. Thus, the corrosion rates in ethanol are far

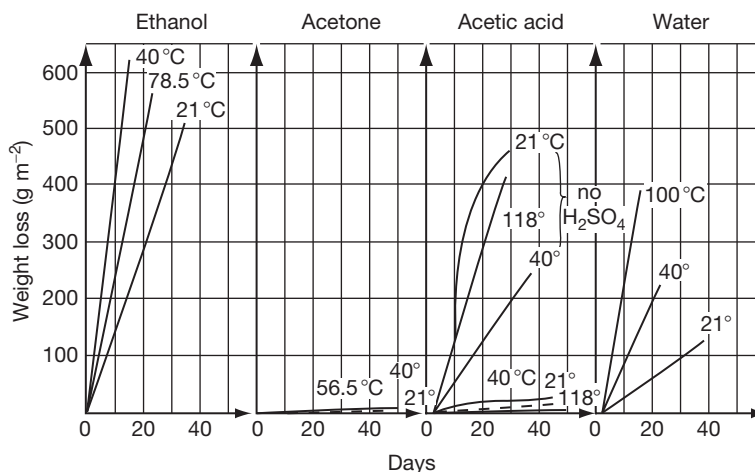


**Figure A2** Corrosion of nickel in different solvents containing 0.05 wt.%  $\text{H}_2\text{SO}_4$  at various temperatures. Reproduced from Heitz, E. In *Advances in Corrosion Science and Technology*; Fontana, M. G., Staehle, R. W., Eds.; Plenum Press, 1974; Vol. 4, p 149, with permission from Plenum Press.

greater than those in the aqueous acid, whereas in acetone, the rate is practically zero; even more surprising is the fact that in acetic acid, the addition of 0.05%  $\text{H}_2\text{SO}_4$  actually decreases the corrosion rate.

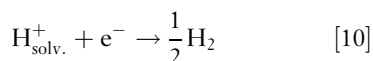
Heitz classifies corrosion reactions in organic solvents into

1. Electrochemical reactions, which follow a similar mechanism to those in aqueous solution.
2. Chemical reactions, which involve direct charge transfer between the metal atom in the lattice of the metal and the oxidizing species.

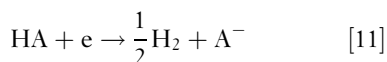
In the case of electrochemical reactions, the partial anodic reaction results in the formation of a solvated metal cation  $\text{M}_{\text{solv.}}^{z+}$ , a charged or uncharged metal complex  $\text{MX}^-$ , or a solid compound  $\text{MX}_z$ , where X is a halogen ion, organic acid anion, etc.

The cathodic partial reactions are as follows:

- (a) Reduction of a solvated proton to  $\text{H}_2$  gas

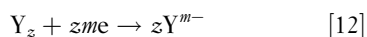


- (b) Reduction of acidic hydrogen of a proton donor



where  $\text{A}^-$  is a carboxylic acid anion, alcoholate ion, etc.

- (c) Reduction of an oxidizing gas Y

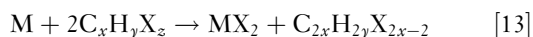


where Y can be  $\text{O}_2$ ,  $\text{Cl}_2$ ,  $\text{F}_2$ ,  $\text{Br}_2$ ,  $\text{O}_3$ ,  $\text{N}_2\text{O}_4$ , etc.

- (d) Reduction of oxidizing ions such as  $\text{Fe}^{3+}$ ,  $\text{Cu}^{2+}$ ,  $\text{MnO}_4^-$ ,  $\text{ClO}_3^-$ , etc.

It is evident from these equations that in many systems, the reaction of a metal with an organic solvent follows a mechanism that is similar to the electrochemical mechanism of corrosion in aqueous solution.

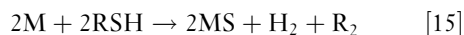
Nonelectrochemical processes may be represented by the general equation



where X is a halogen and M is a divalent metal, for example, the Grignard reaction



A further type of chemical process, which is analogous to high temperature corrosion, is the reaction of metals with organic sulfur compounds, which follow the equation



Heitz quotes a number of case studies of corrosion of metals in organic solvents and concludes that the phenomenology indicates no specific differences from that experienced in aqueous corrosion. Thus, general corrosion, pitting, crevice corrosion, intergranular corrosion, erosion–corrosion cracking, hydrogen embrittlement, etc. can all occur in organic solvents. The methods of control also follow those used for corrosion in aqueous solutions, although there are certain differences. Thus, cathodic and anodic protection are seriously limited by the resistivity of the solvent, and paint coatings deteriorate rapidly in contact with the solvent.

## Suggested Classification and Nomenclature

On a basis of the preceding discussion, the classification and nomenclature outlined in Table A1 are suggested as a possible alternative to the accepted classification of corrosion reactions into ‘wet’ and ‘dry.’

It is considered that the main types of corrosion reactions can be classified as follows:

1. Film-free chemical interaction in which there is direct chemical reaction of a metal with its environment. The metal remains film-free, and there is no transport of charge.
2. Electrochemical reactions that involve transfer of charge across an interface. These electrochemical reactions can be further subdivided into:
  - a. Inseparable anode–cathode type (insep. A/C). The anodes and cathodes cannot be distinguished by experimental methods, although their presence is postulated by theory, that is, the *uniform* dissolution of metals in acid, alkaline, or neutral aqueous solutions, in nonaqueous solution, or in fused salts. (Dr. Pryor considers that in certain cases of uniform dissolution of metals in acids (e.g., A1 in hydrochloric or sulfuric acid) or alkalis a thin film of oxide is present on the metal surface – the film is not rate-determining but its presence would indicate that reactions of this type should be classified under 2(c)).
  - b. Separable anode–cathode type (sep. A/C). Certain areas of the metal can be distinguished experimentally as predominantly anodic or cathodic, although the distances of separation of these areas may be as small as fractions of a millimeter. In these reactions, there will be a macroscopic flow of charge through the metal.

**Table A1** Classification of spontaneous corrosion reactions**1. Film-free Chemical Interaction**

- (a) Metal/gas–oxide or compound volatile (e.g., reaction of molybdenum with oxygen, reaction of iron or aluminum with chlorine).
- (b) Metal/liquid
  - Reactions of solid metals with liquid metals (e.g., dissolution of aluminum in mercury)
  - Dissolution of metal in their fused halides (e.g., lead in lead chloride).
  - Dissolution of metals in nonaqueous solutions (e.g., reaction of aluminum with carbon tetrachloride).

**2. Electrochemical**

- (a) *Inseparable anode/cathode type (insep. A/C)*
  - Reactions with aqueous solutions. Uniform dissolution or corrosion of metals in acid, alkaline, or neutral solutions (e.g., dissolution of zinc in hydrochloric acid or in caustic soda solution; general corrosion of zinc in water or during atmospheric exposure). Reactions with nonaqueous solution (e.g., dissolution of copper in a solution of ammonium acetate and bromine in alcohol). Reactions with fused salts.
- (b) *Separable anode/cathode type (sep. A/C)*
  - All reactions of metals in aqueous or nonaqueous solutions or in fused salts where one area of the metal surface is predominantly anodic and the other is predominantly cathodic so that the sites are physically identifiable.
- (c) *Interfacial anode/cathode type in which the metal surface is filmed*
  - i. Metal/gas and metal/vapor reactions
    - All reactions in which charge is transported through a film of reaction product on the metal surface – the film may or may not be rate determining (e.g., parabolic, logarithmic, asymptotic, etc., or linear growth laws, respectively).
  - ii. Metal/solution reactions
    - All reactions involving the uniform formation and growth of a film of reaction product (e.g., reaction of metals with high temperature water, reaction of copper with sulfur dissolved in carbon disulfide).

- c. Interfacial anode–cathode type (interfacial A/C). One entire interface will be the anode and the other will be the cathode. Thus, as shown in **Figure A1(a)**, the metal–metal oxide interface might be regarded as the anode and the metal–oxygen interface as the cathode.

It is apparent that, in general, 2(a) and 2(b) include corrosion reactions that are normally classified as ‘wet,’ while 2(c) includes those that are normally classified as ‘dry.’

The terminology suggested can be illustrated by reference to the corrosion behavior of iron:

1. Reaction of iron with oxygen at room temperature or with oxygen or water at high temperatures – interfacial A/C type.
2. Reaction of iron with oxygenated water or with reducing acids – inseparable A/C type.
3. Reaction of iron containing a discontinuous magnetite scale with oxygenated water, crevice corrosion, water-line attack, ‘long-line’ corrosion of buried iron pipes, etc. – separable A/C type.

Although it is realized that this classification and terminology has certain limitations, it represents a preliminary attempt to provide a more rational classification of corrosion processes than that based on ‘wet’ and ‘dry.’

**Acknowledgements**

Grateful thanks are due to Dr W.B. Jepson, Dr M. Pryor, and Mr J.N. Wanklyn for the helpful discussions during the preparation of this Appendix.

**References**

1. Hoar, T. P. *J. Appl. Chem.* **1961**, *11*, 121; Vernon, W. H. J. *The Conservation of Natural Resources*; Institution of Civil Engineers: London, 1957; Vol. 105; Potter, E. C. *Electrochemistry*; Cleaver-Hume: London, 1956; 231.
2. Uhlig, H. H. Ed. *The Corrosion Handbook*; Wiley: New York/Chapman and Hall: London, 1948; Uhlig, H. H. *Corrosion and Corrosion Control*; Wiley: New York, 1971; Fontana, M. G.; Greene, N. D. *Corrosion Engineering*; McGraw-Hill, 1967.
3. Fontana, M. G.; Staehle, R. W. *Advances in Corrosion Science and Technology*; Plenum Press: New York, 1990.
4. Vermilyea, D. A. In *Proceedings of the 1st International Congress on Metallic Corrosion*, London, 1961; Butterworths: London, 1962; p 62.
5. Evans, U. R. *The Corrosion and Oxidation of Metals*; Arnold: London, 1960; 12.
6. Report of the Committee on Corrosion and Protection, Department of Trade and Industry, HMSO, 1971.
7. Ehrlich, G.; Turnbull, D. *Physical Metallurgy of Stress Corrosion Fracture*; Interscience: New York and London, 1959; 47.
8. Fontana, M. G. *Corrosion* **1971**, *27*, 129.
9. Heitz, E. In *Advances in Corrosion Science and Technology*; Fontana, M. G., Staehle, R. W., Eds.; Plenum Press: New York, 1974; Vol. 4, 149.



## 1.03 Outline of Structural Metallurgy Relevant to Corrosion

**R. P. M. Procter**

Corrosion and Protection Centre, School of Materials, University of Manchester, Manchester M60 1QD, UK

This article is a revision of the Third Edition article 20.4 by R. P. M. Procter, volume 2, pp 20:94–20:130, © 2010 Elsevier B.V.

<b>1.03.1</b>	<b>Structure of Pure Metals</b>	53
1.03.1.1	Point Defects in Crystals	54
1.03.1.2	Stacking Faults and Twins	55
1.03.1.3	Line Defects	56
1.03.1.4	Movement and Interaction of Dislocations	57
1.03.1.5	Polycrystalline Metals: Grains and Grain Boundaries	58
1.03.1.6	Annealing: Recovery and Recrystallization	60
1.03.1.7	Macroscopic Defects in Metals	60
1.03.1.8	Structure of Metal Surfaces and Surface Defects	60
<b>1.03.2</b>	<b>Structure of Alloys</b>	61
1.03.2.1	Components and Phases	62
1.03.2.2	Solid Solutions	62
1.03.2.3	Segregation at Dislocations and Grain Boundaries	63
1.03.2.4	Limited and Complete Solid Solubility	63
1.03.2.5	Intermediate Phases and Intermetallic Compounds	63
<b>1.03.3</b>	<b>Equilibrium Phase Diagrams</b>	63
1.03.3.1	Binary Isomorphous Phase Diagrams	64
1.03.3.2	Coring	65
1.03.3.3	Eutectic Phase Diagrams	65
1.03.3.4	More Complex Binary Phase Diagrams	66
<b>1.03.4</b>	<b>The Fe–Fe<sub>3</sub>C Phase Diagram</b>	66
1.03.4.1	Decomposition of Austenite	66
1.03.4.2	Formation of Pearlite	69
1.03.4.3	Formation of Bainite	70
1.03.4.4	Formation of Martensite	70
1.03.4.5	Isothermal Transformation Diagrams	71
1.03.4.6	Transformation of Hypo-Eutectoid Steels	71
1.03.4.7	Tempering of Martensite	72
1.03.4.8	Spheroidized Structures in Steels	73
<b>1.03.5</b>	<b>Strengthening Mechanisms in Metals</b>	73
1.03.5.1	Precipitation Hardening	74
1.03.5.2	Complex Alloy Systems	75
1.03.5.3	Inclusions in Metals	76
<b>References</b>		76

### Glossary

**Binary** A mixture of two elements (referring to phase diagrams).

**Hyper-eutectic** With more solute than the eutectic composition.

**Hyper-eutectoid** With more solute than the eutectoid composition.

**Hypo-eutectic** With more solute than the eutectic composition.

**Hypo-eutectoid** With more solute than the eutectoid composition.

**Intergranular** Between the grains (i.e., at the grain boundary).

**Intragranular** Within the grains (i.e., in the bulk of the grain).

**Pro-eutectoid** Formed at above the eutectoid temperature.

**Quaternary** A mixture of four elements (referring to phase diagrams).

**Ternary** A mixture of three elements (referring to phase diagrams).

**Widmanstätten** A lamellar microstructure first observed in iron meteorites, now used generally to describe a well defined lamellar microstructure.

**$\alpha$ -ferrite** The low temperature b.c.c. allotrope of iron.

**$\delta$ -ferrite** The high temperature b.c.c. allotrope of iron.

## Abbreviations

**b.c.c.** body centered cubic

**c.p.h.** close packed hexagonal (sometimes also known as hexagonal close packed, h.c.p.)

**f.c.c.** face centered cubic

The corrosion of a metal invariably involves some kind of interaction between the metal and its environment, and in many cases, the corrosion (location, form, and rate) is significantly affected or even caused by some structural feature of the metal. It is essential, therefore, for the corrosion engineer to have some appreciation of the structure of metals; an elementary survey is provided in this chapter, which is reproduced from the 3rd edition.

The structure of pure metals is discussed in this chapter and this is followed by a description of the structure of alloys. In general, structural features are discussed in order of increasing size, that is, starting with atomic features and continuing through microscopic features to macroscopic features.

### 1.03.1 Structure of Pure Metals

A crystal may be defined as an orderly three-dimensional array of atoms, and all metals are aggregates of more or less imperfect crystals. In considering the structure of metals, therefore, it is convenient to start with the arrangement of atoms in a perfect metal crystal and then to proceed to the imperfections that are always present in the crystal structure.

Although there are many different crystal structures, some of which are rather complicated, most common metals fortunately have one of the three relatively simple structures: face-centered cubic (f.c.c.), close-packed hexagonal (c.p.h.), and body-centered

cubic (b.c.c.). The unit cell (i.e., the smallest group of atoms possessing the symmetry of the crystal and which, when repeated in all directions, develops the crystal lattice) of each of these metallurgically common and important crystal structures is illustrated in [Figure 1](#); the crystal structure of each of the more important metals is given in [Table 1](#). It is clear from this table that the crystal structures of some metals change with temperature, that is, these metals are polymorphic, and this phenomenon is of very great practical significance, particularly in the case of iron, as will become apparent later.

The atoms in a metal crystal can often be satisfactorily regarded as hard spheres of about  $10^{-10}$  m radius. A sheet of such hard balls can be most densely and closely packed together in the configuration shown in [Figure 2\(a\)](#); such sheets or layers of atoms are therefore known as close-packed planes. Similarly, the directions arrowed in [Figure 2\(a\)](#) are referred to as close-packed directions. Close-packed hexagonal and face-centered cubic crystal structures can be built up by stacking close-packed planes on top of each other in the correct sequence. Consider a sheet of eight close-packed atoms, designated by the full circles *a* in [Figure 2\(b\)](#); as shown, a second layer of four close-packed atoms, designated by the dotted circles *b*, may be laid on top of the first plane. Each of the *b* atoms 'sits' in one of the natural 'valleys' which occur between any three contiguous *a* atoms. There are now two such low-energy valleys in the plane of *b* atoms, one of which is immediately above an *a* atom and one of which is not ([Figure 2\(b\)](#)). An atom placed in the former results in an *aba* stacking of three close-packed planes, while an atom placed in the latter would result in *abc* stacking. Stacking *abababab*, etc., develops the c.p.h. crystal structure while stacking *abcbabcb*, etc., develops the f.c.c. crystal structure. The b.c.c. crystal structure cannot be built up by stacking close-packed planes on top of each other.

In the f.c.c. and c.p.h. crystal structures, each atom has 12 nearest neighbors and is therefore said to have a coordination number of 12. In the non-close-packed b.c.c. structure, on the other hand, the coordination number is only 8. In the f.c.c. structure, the four octahedral  $\{111\}$  planes are close packed and so are the  $\langle 110 \rangle$  directions. (An account of the use of Miller indices to describe crystal planes and lattice directions is beyond the scope of this article; a very adequate treatment of this topic is, however, given in Reed-Hill)<sup>1</sup> In the c.p.h. structure, on the other hand, there is only one close-packed plane, the (0001) basal plane; the  $\langle 11\bar{2}0 \rangle$  directions are close

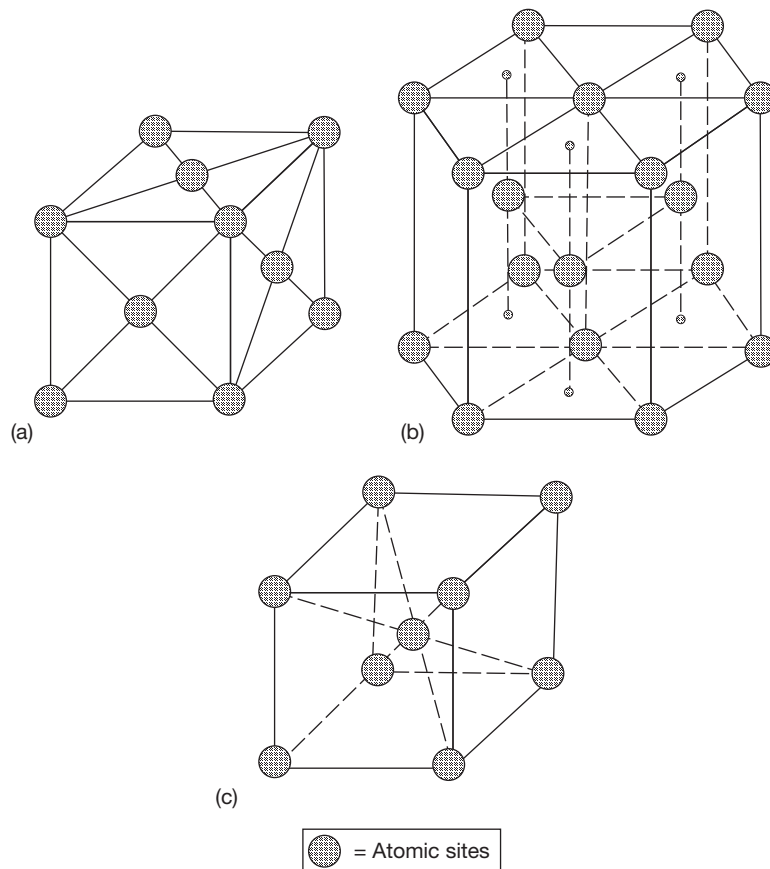


**Figure 1** Unit cells of (a) the face-centered cubic (f.c.c.), (b) the close-packed hexagonal (c.p.h.), and (c) the body-centered cubic (b.c.c.) crystal structures.

packed. The different number of close-packed planes in f.c.c. and c.p.h. crystals results in the very different plastic deformation characteristics of metals with the two structures. In the b.c.c. structure, the  $\langle 111 \rangle$  directions are close packed, but there are no truly close-packed planes of the type shown in [Figure 2\(a\)](#); the planes of closest packing, however, are  $\{110\}$ .

In any crystal structure, the close-packed or closest-packed planes are the lowest energy planes. On all other planes, the density of atoms is lower, and the interatomic distance and the energy of the plane are greater. Contrary to intuitive expectations, the diameter of the largest holes or interstices between atoms in the close-packed f.c.c. structure is considerably greater than the diameter of the largest interstices between atoms in the non-close-packed b.c.c. structure.

### 1.03.1.1 Point Defects in Crystals

The smallest imperfections in metal crystals are point defects, in particular, vacant lattice sites (vacancies)

and interstitial atoms. As illustrated in [Figure 3\(a\)](#), a vacancy occurs where an atom is missing from the crystal structure while an interstitial occurs when an extra atom is inserted in an interstitial site (an interstice). Vacancies and interstitials are equilibrium defects because even though vacancies (and interstitials) increase the internal energy of a crystal, they also increase the entropy, and therefore, the free energy of a perfect crystal is reduced by the presence of a number of point defects. The equilibrium vacancy concentration increases exponentially with temperature and typically, in copper at room temperature, one site in  $10^{14-15}$  may be vacant, while at 1300 K, one site in  $10^{3-4}$  might be vacant (equivalent to  $10^{17-18}$  vacancies per cubic millimeter). The internal energy associated with an interstitial is much greater than that associated with a vacancy; the concentration of interstitial atoms at any temperature is correspondingly very much lower than that of vacant atomic sites. Radiation damage, however, introduces many interstitials. Often, a vacancy and an interstitial are associated as a pair.

The practical importance of vacancies is that they are mobile and, at elevated temperatures, can move relatively easily through the crystal lattice.

**Table 1** Crystal structure of the more important metals

<i>Metal</i>	<i>Temperature (K)</i>	<i>Crystal structure</i>
Alkali metals	Ambient to m.p.	b.c.c.
Aluminum	Below m.p.	f.c.c.
Beryllium	Below m.p.	c.p.h.
Cadmium	Below m.p.	c.p.h.
Chromium	Below m.p.	b.c.c.
Cobalt	Below 690	c.p.h.
	690 to m.p.	f.c.c.
Copper	Below m.p.	f.c.c.
Gold	Below m.p.	f.c.c.
Iron	Below 1180	b.c.c.
	1180–1665	f.c.c.
	1665 to m.p.	b.c.c.
Lead	Below m.p.	f.c.c.
Magnesium	Below m.p.	c.p.h.
Manganese	Below m.p.	Four complex structures
Molybdenum	Below m.p.	b.c.c.
Nickel	Below m.p.	f.c.c.
Platinum	Below m.p.	f.c.c.
Silver	Below m.p.	f.c.c.
Tin	Below m.p.	Two complex structures
Titanium	Below 1155	c.p.h.
	1155 to m.p.	b.c.c.
Tungsten	Below m.p.	b.c.c.
Vanadium	Below m.p.	b.c.c.
Zinc	Below m.p.	c.p.h.
Zirconium	Below 1135	c.p.h.
	1135 to m.p.	b.c.c.

As illustrated in [Figure 3\(b\)](#), this is accompanied by movement of an atom in the opposite direction; indeed, the existence of vacancies was originally postulated to explain solid-state diffusion in metals. In order to ‘jump’ into a vacancy, an adjacent atom must overcome an energy barrier. The energy required for this is supplied by thermal vibrations. Thus, the diffusion rate in metals increases exponentially with temperature, not only because the vacancy concentration increases with temperature, but also because there is more thermal energy available to overcome the activation energy required for each ‘jump’ in the diffusion process.

### 1.03.1.2 Stacking Faults and Twins

In certain close-packed metals and alloys there are errors in the sequence of stacking of the close-packed planes. Thus, for example, the sequence of planes in a c.p.h. metal might be ... *ababab* ... , in which the region in italics is termed a ‘stacking fault’ and represents a small volume of f.c.c. material in the c.p.h. structure. Stacking faults have an energy that is higher than that of the perfect crystal structure; however, the value of the stacking-fault energy varies very widely between different metals and alloys. Stacking faults are readily visible in thin-foil transmission electron micrographs, as illustrated in [Figure 4](#) (top).

Twins are a somewhat similar form of defect. In certain metals, adjacent areas of crystal bear a mirror-image orientation relationship to each other across the twin boundary, as illustrated schematically in [Figure 5](#). The twin boundaries, like stacking faults,

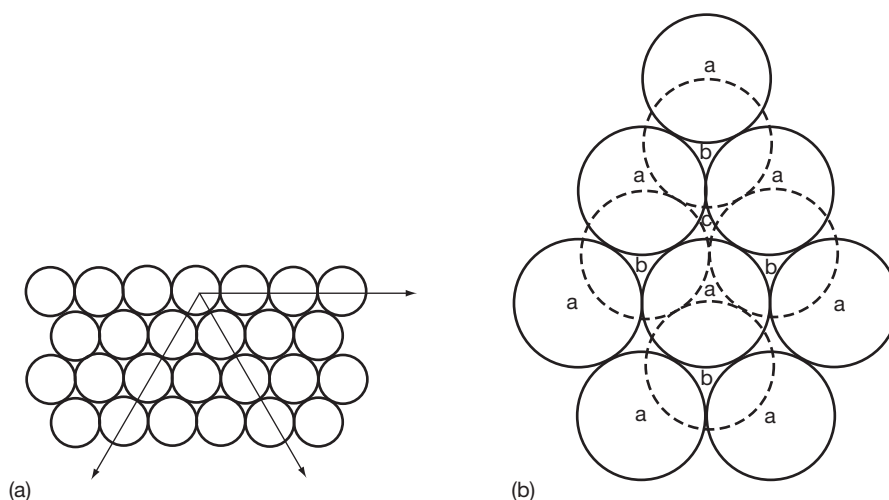


**Figure 2** (a) Single close-packed sheet of atoms, with the close-packed directions arrowed and (b) stacking of three close-packed planes of atoms, showing *aba* and *abc* positions.

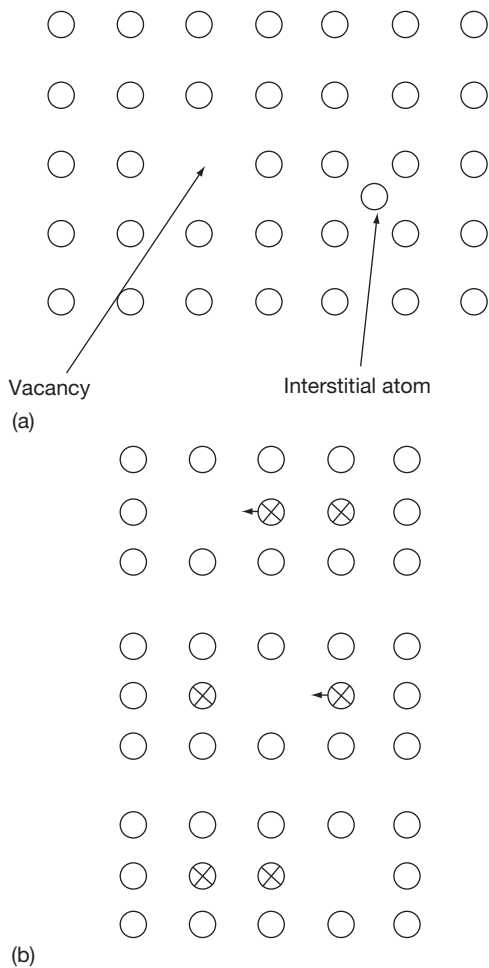


**Figure 3** (a) Schematic illustration of two types of point defect and (b) three stages in diffusion by the motion of a vacancy through a crystal.

have a somewhat higher energy than the surrounding perfect crystal structure. Twins arise during the annealing of cold-worked f.c.c. material, during the room-temperature deformation of c.p.h. materials and during the low-temperature (or shock) deformation of b.c.c. materials. Twins are often readily apparent on metallographic sections at relatively low magnifications, as shown in [Figure 4](#) (bottom).

### 1.03.1.3 Line Defects

Point defects, stacking faults, and twins are crystalline imperfections that basically involve misalignment of single atoms or of a single plane of atoms. Line defects, or dislocations, are somewhat larger-scale imperfections involving misalignment along a line of atoms.

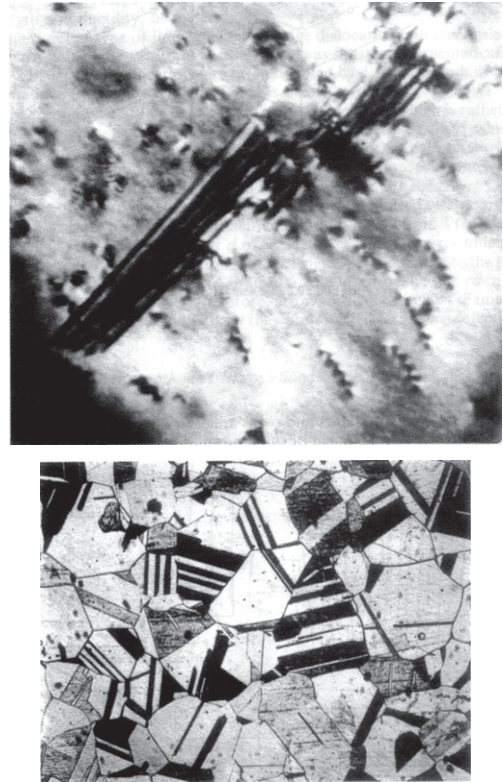


**Figure 4** (top) Transmission electronmicrograph showing a stacking fault and isolation dislocations in a stainless steel ( $\times 70\,000$ , courtesy I. Brough) and (bottom) light micrograph showing an equiaxed grain structure and twins in an annealed 70/30 brass ( $\times 200$ , courtesy of M. Islam).

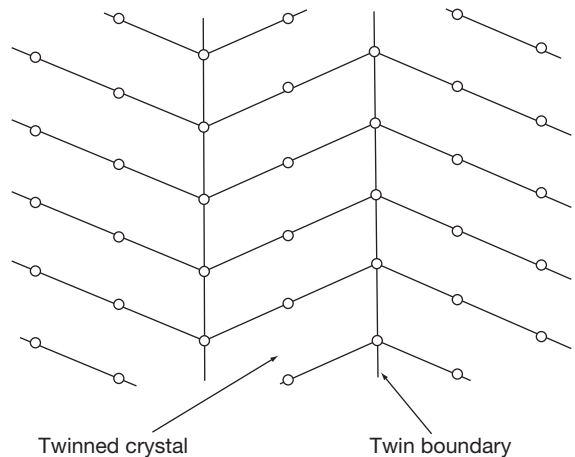


**Figure 5** Twinned crystal.

Dislocations are extremely important defects, in that the dislocation density and dislocation interactions control the mechanical properties to a very large extent, in particular, the strength and ductility of metals.

The simplest type of line defect is the edge dislocation, which consists of an extra-half plane of atoms in the crystal, as illustrated schematically in **Figure 6(a)**; edge dislocations are often denoted by  $\perp$  if the extra-half plane  $ab$  is above the plane  $sp$  or by  $\top$  if it is below.

The second type of line defect is the screw dislocation, which is somewhat less easy to visualize. Consider, however, a block of material, half of which is sheared one interatomic distance with respect to the other half, as shown in **Figure 6(b)**. The line  $cd$  then constitutes a screw dislocation; the arrangement of atoms around a screw dislocation is shown in **Figure 6(c)**.

To a good approximation, only atoms within the dotted circles in **Figures 6(a) and 6(b)** are displaced from their equilibrium position; in a real three-dimensional crystal, the diameter  $d$  of these circles would be very much less than the length  $l$  of the dislocation, that is, the length, perpendicular to the page, of the extra-half plane of atoms  $ab$  in **Figure 6(a)**, or of the line  $cd$  in **Figure 6(b)**. Strictly therefore, dislocations are cylindrical defects of diameter  $d$  and length  $l$ ; however, since  $l \gg d$ , they are referred to as line defects.

#### 1.03.1.4 Movement and Interaction of Dislocations

As with vacancies, the importance of dislocations derives from the fact that they are readily mobile, in this case under the influence of applied stresses.

**Figures 7(a)–7(c)** illustrate the slip or glide of an edge dislocation through a crystal under the influence of a shear stress. The atom  $a$  in **Figure 7(a)** moves, under the influence of the applied stress, to position  $a'$  in **Figure 7(b)**, and the extra-half plane of atoms shifts one atomic distance to the left, from plane  $y$  to  $x$ . As this process continues, the dislocation moves right through the crystal, the final result, shown in **Figure 7(c)**, being that the crystal is sheared or slipped by one interatomic distance across the slip plane  $sp$ . Each step in the movement of the dislocation (i.e., from **Figures 7(a) and 7(b)**) clearly requires only a slight rearrangement of the atoms around the bottom of the extra-half plane, and is therefore a low-energy process; dislocations are, therefore, readily mobile under low applied stresses. However, producing the slip, shown in **Figure 7(c)**, from a perfect dislocation-free crystal would be a very high-energy process requiring very high stresses. The difference between these two modes of slip is that in the latter, all the bonds on the slip plane are broken at the same time, while in the former, they are broken one at a time. The existence of dislocations was in fact postulated, long before they were observed, to account for the observation that the yield stress of metals is very much lower than that predicted by theoretical calculations. It is important to note that the crystal structure, after passage of a dislocation, is perfect and in no way misaligned. From **Figure 8**, it is clear that the dislocation line is merely

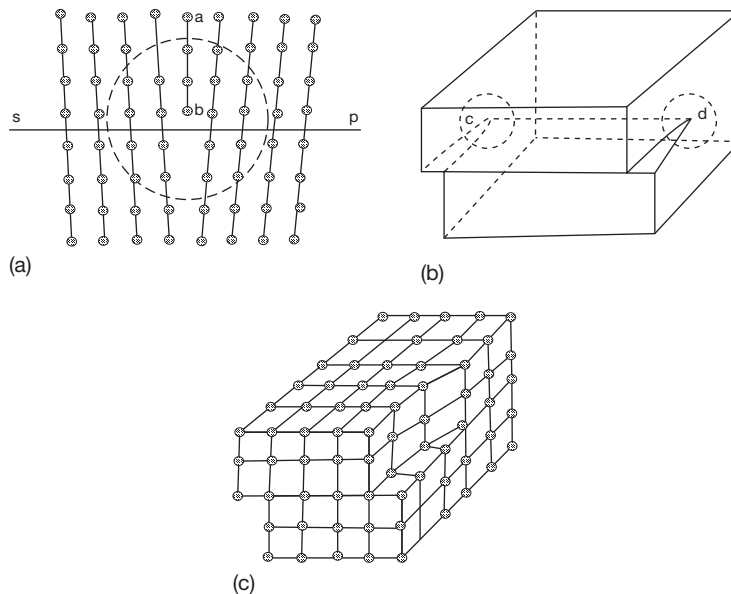


**Figure 6** (a) Atomic arrangement around an edge dislocation, (b) shear required in a homogeneous solid to produce a screw dislocation, and (c) atomic arrangement around a screw dislocation.



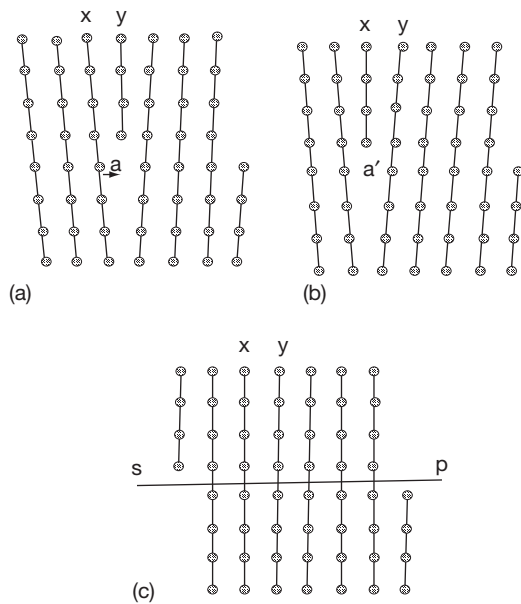


**Figure 7** Three stages in plastic deformation by the motion of an edge dislocation through a crystal.

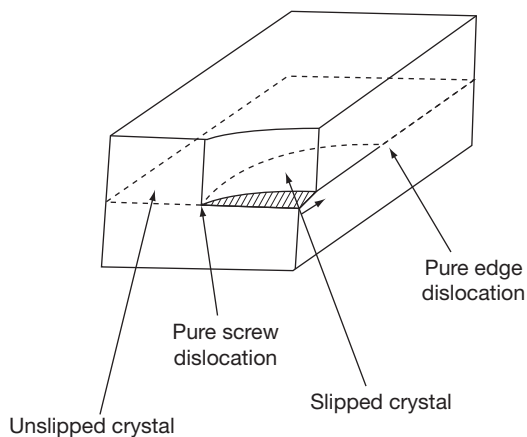


**Figure 8** Schematic illustration of a mixed dislocation as the boundary between slipped and unslipped crystal. The arrow shows the Burgers vector.

the boundary between slipped and unslipped crystal. The magnitude and direction of the slip is given by what is known as the Burgers vector; in a screw dislocation, the Burgers vector is parallel to the line of the dislocation, while in an edge dislocation, it is perpendicular to it. In real crystals, dislocation lines are not straight, but are usually bowed or curved. As illustrated schematically in [Figure 8](#), such dislocations are mixed, being part screw and part edge. Slip occurs on the plane containing both the Burgers

vector and the line of the dislocation. In practice, it is observed that metals slip most easily on close-packed planes and in close-packed directions, that is,  $\{111\}$  and  $\langle 110 \rangle$  in f.c.c. metals and usually  $\{0001\}$  and  $\langle 11\bar{2}0 \rangle$  in c.p.h. metals. Since f.c.c. crystals have four close-packed  $\{111\}$  planes, they are generally much more ductile than c.p.h. crystals, which have only one  $\{0001\}$  close-packed plane. In b.c.c. metals, slip occurs in  $\langle 111 \rangle$  directions on a variety of planes. The movement of dislocations by other mechanisms, in particular by cross-slip and climb, is beyond the scope of this section.

All real metals contain dislocations; even a well-annealed metal would typically contain  $10^{4-6}$  dislocations per square millimeter, while a heavily cold-worked metal could contain up to  $10^{10} \text{ mm}^{-2}$ . At first sight, this is an anomaly; dislocations were postulated to account for the low yield strength of metals, and whereas an annealed material with a low dislocation density is weak, a cold-worked metal with a high dislocation density is strong. The answer lies in the fact that when the dislocation density is low, the dislocations are generally too far apart to interact with each other very often and are more free to move under the influence of a low applied stress. On the other hand, when the dislocation density is high, the dislocations do interact, and they become tangled up with each other; dislocation motion is then difficult and the material is therefore strong. The interaction of dislocations with each other and with other structural features in metals is a very complex field; it is also, however, extremely important, as it greatly affects the strength of the metals.

The atomic bonds in a cylinder of material around dislocations are elastically stretched; dislocations, like other crystalline defects are, therefore, high-energy regions.

Dislocations are readily visible in thin-film transmission electron micrographs, as shown in [Figures 4](#) (top) and [9](#) (top). The slip step ([Figure 7\(c\)](#)) produced by the passage of a single dislocation is not readily apparent. However, for a variety of reasons, a large number of dislocations often move on the same slip plane or on bands of closely adjacent slip planes; this results in slip steps that are very easily seen in the light microscope, as shown by the slip lines in [Figure 9](#) (bottom).

### 1.03.1.5 Polycrystalline Metals: Grains and Grain Boundaries

So far, we have regarded metals as single crystals; in fact, most metals, in practice, are polycrystalline and

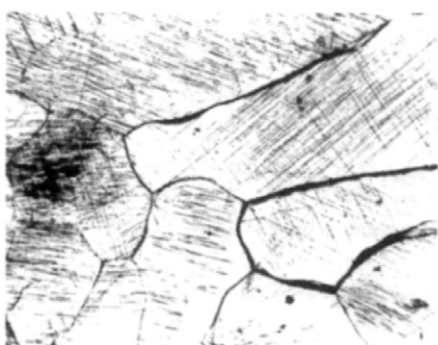
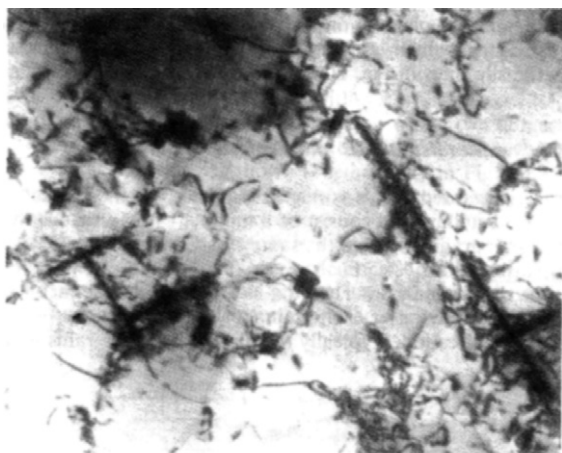


**Figure 9** (top) Transmission electronmicrograph showing dislocation tangles associated with precipitates in an Al-Cu-Mg-Si alloy ( $\times 24\,000$ , courtesy S. Blain) and (bottom) light micrograph showing slip lines in pure lead ( $\times 100$ ).

consist of a number of crystals or grains. In a pure metal, each grain has the same crystal structure and contains vacancies, dislocations, etc., but the crystallographic orientation of each grain is different; in other words, in a polycrystalline metal, the [111] crystallographic direction of each grain points in a different spatial direction. Typically, the diameter of the grains in a coarse-grained material might be about 0.5 mm, while that in a fine-grained metal might be about 0.005 mm. However, in certain electrodeposits, the grain size is too fine to be resolved with the light microscope, while at the other extreme, jet-engine turbine blades about 150 mm long, of nickel-base superalloy, may sometimes be single crystals. The grain size of metals may be controlled by heat treatment. All the grains may be of more or less the same size and shape as in the equiaxed grain structure shown in [Figure 4](#) (bottom). Alternatively, if the metal has been heavily cold-worked, for example by rolling or extrusion, the grains may be



**Figure 10** Light micrograph showing the highly elongated grain structure of a commercial wrought high-strength precipitation-hardening Al-Zn-Mg-Cu alloy ( $\times 40$ , section perpendicular to the long transverse direction).

deformed and elongated in the work direction, giving the highly directional, elongated, grain structure shown in [Figure 10](#). Although the crystallographic orientation of all the grains in a polycrystalline metal is usually different and random, occasionally the orientation of most of the grains in a piece of metal is similar. Such preferred orientation can arise in a number of ways; it is important to note, however, that metals with elongated, columnar grain structures ([Figure 10](#)) do not necessarily have preferred orientation.

However perfect the crystal structure within a grain, there will inevitably be crystallographic mismatch and imperfection where two adjacent grains meet, that is, at grain boundaries; this region of mismatch is, however, only a few atomic diameters wide, as shown schematically in [Figure 11](#), and on metallographic sections, grain boundaries only become apparent on etching. Although grain boundaries are regions of imperfection and of crystallographic mismatch, they are nevertheless quite strong, and metals do not normally fail intergranularly. Indeed, grain boundaries act as barriers to the movement of dislocations, and a fine-grained pure metal will normally be considerably stronger than a single-crystal or a coarse-grained material.

A grain boundary is a planar defect in a crystal and as such has a higher energy than the surrounding crystal. By way of comparison, the free surface energy of copper is about  $1200\text{--}1800\text{ nJ mm}^{-2}$ , the grain boundary energy is about  $300\text{--}500\text{ nJ mm}^{-2}$ , while the stacking-fault energy is about  $80\text{--}100\text{ nJ mm}^{-2}$ .

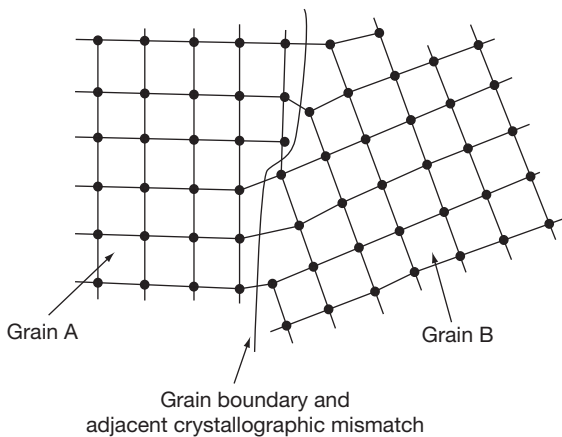


**Figure 11** High-angle grain boundary.

#### 1.03.1.6 Annealing: Recovery and Recrystallization

It must be emphasized that many of the crystalline defects already discussed are metastable and tend to be eliminated on annealing at elevated temperatures. Thus, when a cold-worked metal is heated, the energy stored in the metal during the cold-working process is released; the dislocation tangles rearrange themselves, and the internal stresses, hardness, and strength of the metal are progressively reduced. The changes occurring during this process (which is known as recovery) do not affect the optical microstructure of the metal. Recovery is followed at higher temperatures by recrystallization. New grains are nucleated throughout the metal and grow; the heavily deformed high-dislocation-density cold-worked grains are replaced by new equiaxed low-dislocation-density grains. On prolonged heating at even higher temperatures, some of these grains grow at the expense of others, and a coarse-grained material (or even a single crystal) replaces the fine-grained recrystallized structure. The changes occurring during recrystallization are readily apparent in the optical microscope and are accompanied by a drastic softening of the metal.

#### 1.03.1.7 Macroscopic Defects in Metals

While vacancies, dislocations, etc. may be regarded as atomic defects, grains may be regarded as microscopic defects. There are also, however, what may conveniently be termed macroscopic defects in metals. Too often these are the result of poor design, poor processing or production, poor welding, careless

handling or operating. Examples of these would be sharp re-entrant corners, crevices, casting defects, rolled-in mill-scale, rough-sheared edges, poorly machined surfaces, weld defects, surface scratches, etc. However, by far the most important macroscopic defect, which is inherent in the uses to which metals are put, and the ways in which they are formed, is the presence of stresses, particularly tensile stresses. These stresses may be either applied, resulting from the fact that the metal is being used in a load-bearing capacity, or residual. Residual stresses may either be microstresses arising, for example, from dislocations piled up against a grain boundary or, much more importantly, macrostresses. Residual macrostresses arise from a very wide range of effects, for example, forming, heat treating, machining, welding, and assembling operations can all give rise to high residual tensile stresses over relatively large regions.

#### 1.03.1.8 Structure of Metal Surfaces and Surface Defects

So far the structure of pure metals has been discussed with reference to bulk characteristics and continuous crystals. However, corrosion is essentially a surface phenomenon, and it is necessary to consider how the structure and defects already described interact with free surfaces. At this stage, it is convenient to consider only a film-free metal surface, although of course, in most corrosion phenomena the presence of surface films is of the utmost importance. Furthermore, it is at free surfaces that the hard sphere model of metals first begins to become inadequate, particularly when surface films are considered, or in aqueous environments, where an electrical double layer exists.

**Figure 12(a)** shows schematically a smooth metal surface, although it should always be borne in mind that even a high-quality electropolished surface will not be flat but will have a roughness of about 5 nm or so high, while the roughness on a high-quality machined surface may be about 1  $\mu\text{m}$  or so high. In most real materials, there will be grain boundaries meeting the surface as shown in **Figure 12(a)**. Furthermore, it is extremely unlikely that the plane of the metal surface will coincide with a low-index low-energy high-atomic-density close-packed plane, as in grain *B*. In most cases, the plane of the metal surface will be a high-index high-energy low-atomic-density plane, as in grains *A* and *C*.

On an atomic scale, metal surfaces are usually described in terms of the terrace–ledge–kink model shown in **Figure 12(b)**. Essentially, it is suggested that

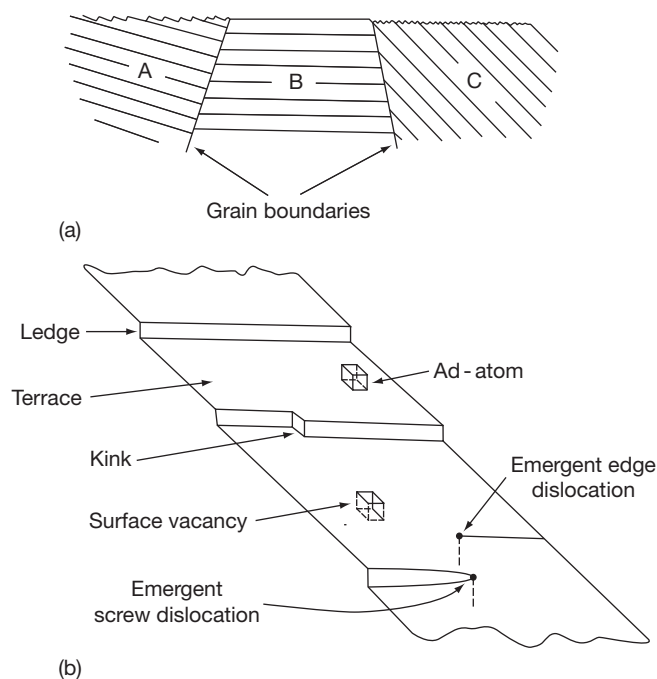


**Figure 12** (a) Grains of different orientation intersecting a free surface and (b) the terrace-ledge-kink model of a free metal surface.

clean metal surfaces consist of low-energy low-index terraces separated by ledges of monatomic height, which occasionally contain monatomic kinks.

By their nature, dislocations cannot end suddenly in the interior of a crystal; a dislocation line can only end at a free surface or a grain boundary (or form a closed loop). Where a screw dislocation intersects a free surface, there is inevitably a step or ledge in the surface, one atomic layer high, as shown in Figure 6(c). Furthermore, the step need not necessarily be straight and will, in fact, almost certainly contain kinks.

The coordination number of an atom lying in a (111) surface of an f.c.c. crystal is 9, compared with the bulk value of 12; an atom at a step in the surface has a co-ordination number of 7 while that of an atom at a kink in a step is only 6. The latter atom, therefore, is the most weakly bound to the metal crystal and is likely to be the first to be removed from the lattice in any active dissolution process. Clearly, however, this removal does not eliminate the kink and, in fact, it is impossible, even by repeated removal of atoms, to eliminate the step caused by a screw dislocation intersecting a free surface. There are, however, in addition to screw dislocations, many other causes of steps or ledges on metal surfaces, for example, low-index planes intersecting the surface at an acute angle (see grain A in Figure 12(a)).

As shown in Figure 12(b), an edge dislocation intersecting a free surface does not cause a step. However, the atoms adjacent to the core of the dislocation, being in nonequilibrium positions, have a higher energy than other atoms in the surface. The emergent ends of both edge and screw dislocations thus represent potential sites for preferential dissolution. Finally, there may be vacancies in the surface and ad-atoms on the surface (Figure 12(b)).

### 1.03.2 Structure of Alloys

The discussion so far has been limited to the structure of pure metals and to the defects which exist in crystals composed of atoms of one element only. Of course, pure metals are comparatively rare, and all commercial materials contain impurities, including in many cases, deliberate alloying additions. In the production of commercially pure metals and alloys, impurities are inevitably introduced into the metal, for example, manganese, silicon, and phosphorus in mild steel and iron and silicon in aluminum alloys. However, most commercial materials are not even nominally pure metals but are alloys in which deliberate additions of one or more elements have been made, usually to improve some property of the metal;

examples are the addition of carbon or nickel and chromium to iron to give, respectively, carbon and stainless steels and the addition of copper to aluminum to give a high-strength age-hardenable alloy.

### 1.03.2.1 Components and Phases

Impure metals and alloys exhibit all the structural features and crystal defects of the pure metals already discussed. In addition, however, impure metals and alloys exhibit many structures that are not observed in pure metals and which, in many instances, have an extremely important effect on the properties, particularly the corrosion resistance. However, before dealing with the structure of impure metals and alloys, it is necessary to consider the concept of metallurgical components, phases, constituents, and equilibrium phase diagrams.

The fundamental difference between pure metals and impure metals and alloys arises from the fact that there is only one atomic species present in the former, while there are two or more present in the latter; thus, a pure metal is a single-component system, a pure binary alloy is a two-component system, while impure metals and alloys, strictly speaking, are multi-component systems. It is, however, usually valid to neglect the impurities and, for example, to consider a commercial brass as a binary Cu–Zn alloy, that is, as a two-component system.

Gibbs' phase rule, as applied to metallurgical systems (i.e., under conditions of constant pressure) indicates that pure metals, being single-component systems, can only coexist as two phases in equilibrium at a single temperature. Thus pure copper, for example, exhibits three phases, namely solid f.c.c. copper, liquid copper, and gaseous copper. Any two of these phases, say solid and liquid copper, can coexist in equilibrium at only one temperature, that is, the melting point of copper. Pure iron exhibits four phases, namely two solid phases (f.c.c. and b.c.c. iron (see Table 1)) and a liquid and a gaseous phase. Alloys, on the other hand, being multicomponent systems, can exhibit two or more phases in equilibrium over a range of temperatures. The phases which are present in an alloy and their composition and distribution markedly affect many of the properties of the alloy, including its corrosion resistance.

### 1.03.2.2 Solid Solutions

When a pure metal *A* is alloyed with a small amount of element *B*, the result is ideally a homogeneous random

mixture of the two atomic species *A* and *B*, which is known as a solid solution of *B* in *A*. The solute *B* atoms may take up either interstitial or substitutional positions with respect to the solvent atoms *A*, as illustrated in Figures 13(a) and 13(b), respectively. Interstitial solid solutions are only formed with solute atoms that are much smaller than the solvent atoms, as is obvious from Figure 13(a); for the purpose of this section, only three interstitial solid solutions are of importance, that is, Fe–C, Fe–N, and Fe–H. On the other hand, the solid solutions formed between two metals, as for example in Cu–Ag and Cu–Ni alloys, are nearly always substitutional (Figure 13(b)). Occasionally, substitutional solid solutions are formed in which the distribution of *B* in *A* is not random (Figure 13(c)), and such solid solutions are said to be ordered and exhibit a superlattice. Order–disorder transitions are observed with temperature changes. Superlattices are observed in the Cu–Au, Cu–Zn, and Fe–Ni systems.

There are a number of differences between interstitial and substitutional solid solutions, one of the most important of which is the mechanism by which diffusion occurs. In substitutional solid solutions, diffusion occurs by the vacancy mechanism already discussed. Since the vacancy concentration and the frequency of vacancy jumps are very low at ambient temperatures, diffusion in substitutional solid solutions is usually negligible at room temperature and only becomes appreciable at temperatures above about  $0.5T_M$ , where  $T_M$  is the melting point of the solvent metal (K). In interstitial solid solutions, however, diffusion of the solute atoms occurs by jumps between adjacent interstitial positions. This is a much lower energy process that does not involve

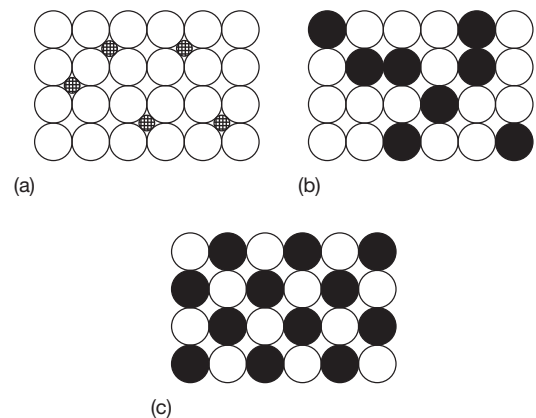


**Figure 13** (a) Interstitial solid solution, (b) random substitutional solid solution, and (c) an ordered substitutional solid solution forming a superlattice.



vacancies, and it therefore occurs at much lower temperatures. Thus, hydrogen is mobile in steel at room temperature, while carbon diffuses quite rapidly in steel at temperatures above about 370 K.

### 1.03.2.3 Segregation at Dislocations and Grain Boundaries

In practice, the distribution of solute atoms in a solid solution is not ideally homogeneous. There is almost invariably a stress field around any solute atom in a solid solution, and there is therefore, a tendency for these atoms to migrate to regions of the crystal lattice that are already strained, in particular to grain boundaries and to dislocations. Thus, in impure metals and alloys, there is an inherent tendency for impurities and alloying additions to segregate at grain boundaries and around the cores of dislocations. Segregation of carbon and nitrogen to dislocations in steels has a very significant effect on their mechanical properties and is particularly responsible for their sharp yield point; similar segregation may also affect the corrosion behavior of cold-worked steels. The segregation of impurities and alloying elements to grain boundaries is clearly of relevance in any consideration of the strength and reactivity of grain boundaries and, in particular, of intergranular corrosion, temper embrittlement, etc.

In addition, it has fairly recently been recognized that impurities and alloying elements will also tend to segregate to free surfaces. The implications of this for corrosion resistance and particularly for passive-film formation have received relatively little attention.

### 1.03.2.4 Limited and Complete Solid Solubility

Just as the saturated solubility of sugar in water is limited, so the solid solubility of element *B* in metal *A* may also be limited, or may even be so low as to be negligible, as for example with lead in iron or carbon in aluminum. There is extensive interstitial solid solubility only when the solvent metal is a transition element and when the diameter of the solute atoms is  $<0.6$  of the diameter of the solvent atom. The Hume-Rothery rules state that there is extensive substitutional solid solubility of *B* in *A* only if:

- The atomic diameters of *A* and *B* do not differ by more than 15%.
  - The two elements have similar electronegativity.
- (Note: electronegativity is the power of an

element to attract electrons to itself when present in a molecule or in an aggregate of unlike atoms; it is a different property from the electrode potential, which depends on the free energy difference between an element in its standard state and a compound or ion in solution.) In addition, a metal of a lower valency tends to dissolve a metal of a higher valency more readily than vice versa.

However, just as two liquids may be completely miscible and form a complete range of solutions from one pure liquid to the other, so certain metals, for example, copper and nickel, exhibit complete solid solubility over the whole range of compositions from pure copper to pure nickel. Clearly, for two metals to be soluble in each other over the whole compositional range, they must have the same crystal structure, that is, they must be isomorphous.

### 1.03.2.5 Intermediate Phases and Intermetallic Compounds

When metal *A* is alloyed with enough element *B* to exceed the solid solubility of *B* in *A*, a new phase is formed. This may be the other terminal solid solution of *A* in *B*. Alternatively, an intermediate solid-solution phase, with a crystal structure different from that of either of the terminal solid solutions, may be formed over a range of compositions. An example of this is the so-called  $\beta$ -phase in brasses, which is the stable phase at room temperature over the composition range 47–50% Zn. In some alloys, intermediate phases are formed that are best regarded as compounds. Examples are  $\text{Fe}_3\text{C}$  (cementite) in the Fe–C system and the intermetallic compounds  $\text{MgNi}_2$  and  $\text{Mg}_2\text{Ni}$  formed in the Mg–Ni system. While solid solutions are stable over a range of compositions, compounds have a unique composition; cementite, for example, corresponds to Fe–25 at.% C (Fe–6.7 wt.% C).

## 1.03.3 Equilibrium Phase Diagrams

In alloys, as in pure metals, the stable phase or phases change with changing temperature. Furthermore, in alloys, the stable phase or phases, and the composition of these phases, changes with the composition of the alloys. These changes are best represented by equilibrium phase diagrams. These define the stability and composition of the phases that can occur in an alloy system as a function of temperature and alloy composition, under conditions of constant pressure. Phase diagrams are in many ways analogous to



Pourbaix diagrams, which define the stability of phases in a metal/water system as a function of potential and pH, and like  $E$ -pH diagrams, phase diagrams have certain limitations. First, it must be emphasized that they are equilibrium phase diagrams and that they only predict the stability and composition of phases under equilibrium conditions. They neither give any indication of how rapidly equilibrium will be achieved in practice, nor do they give any indication of the distribution of the phases at equilibrium. Somewhat analogously,  $E$ -pH diagrams give no information about the rate at which a particular metal will corrode or the protectiveness of a particular passive film. Second, equilibrium phase diagrams give no information whatsoever about the existence of metastable phases, some of which are of the utmost practical significance. These limitations become particularly important under conditions of rapid temperature change. Phase diagrams, in contrast to  $E$ -pH diagrams, are always determined experimentally, although they can be explained, and to a certain extent, qualitatively predicted from thermodynamic data and considerations. Nevertheless, in spite of these limitations, phase diagrams are an extremely important and useful metallurgical tool.

### 1.03.3.1 Binary Isomorphous Phase Diagrams

Although ternary and quaternary phase diagrams are beyond the scope of this section, it is appropriate to

deal with the various types of binary phase diagrams by referring to some specific alloys. The simplest phase diagram refers to an isomorphous alloy system in which there is complete solid solubility. By way of example, the Cu–Ni phase diagram is shown in **Figure 14**. This phase diagram indicates that at 1600 K, an alloy containing 70% Cu is a liquid (point *a* in **Figure 14**). On slow cooling, this alloy starts to solidify when the liquidus line is reached, that is, point *b* at about 1500 K. At this point, grains of a solid solution containing about 53% Cu are nucleated from the liquid containing 70% Cu and start to grow. As the temperature continues to fall, the composition of the liquid follows the liquidus line while that of the solid falls along the solidus line, until at 1470 K the alloy consists of a mixture of a solid solution containing 62% Cu and a liquid containing 78% Cu (**Figure 14**). Furthermore, the fraction of solid in the two-phase mixture is given by the ratio of the lengths  $yz/xz$ , while the fraction of liquid is given by  $xy/xz$ . This is known as the lever rule. On further slow cooling, the solidus line is reached, that is, point *c* at about 1430 K, when solidification of the alloy is complete; the last liquid to freeze contains about 85% Cu, while the last solid to solidify contains 70% Cu. At 1300 K, for example, and indeed at all temperatures below the solidus, an alloy containing 70% Cu is a solid (point *d* in **Figure 14**). Clearly the phase change in this transformation is liquid  $\rightarrow$  solid. The microstructure of a homogeneous single-phase solid-solution alloy is

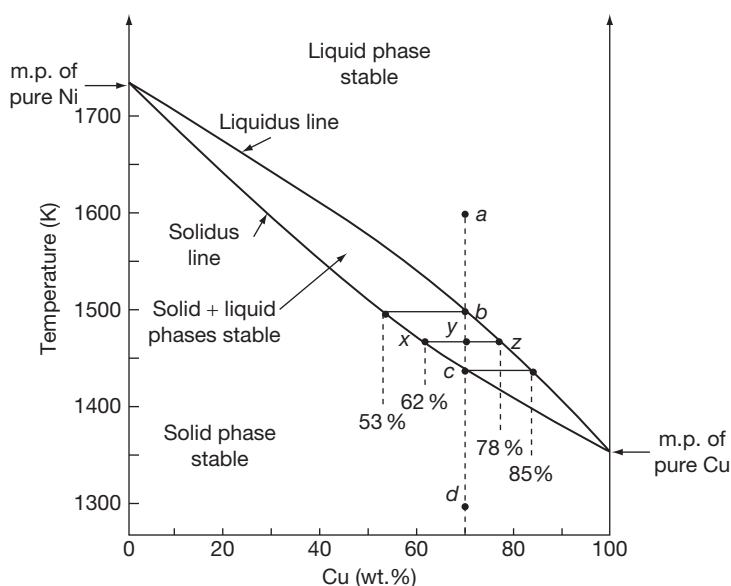


**Figure 14** Nickel–copper phase diagram.

indistinguishable from that of a pure metal, as shown in [Figure 4](#) (bottom).

### 1.03.3.2 Coring

If the alloy is cooled sufficiently slowly, the alloy itself and all the grains in it will be homogeneous after solidification. If, on the other hand, the alloy is cooled more rapidly, the grains will be cored, not homogeneous. During cooling, the composition changes in the solid phase involve solid-state diffusion; if the temperature falls too rapidly, therefore, there is insufficient time for diffusion. In the Cu–30Ni alloy referred to earlier, clearly the center of the grains, the first metal to have solidified, would be nickel rich (i.e., low in copper) while the grain boundary regions, the last metal to have solidified, would be copper rich. Coring is eliminated by annealing at high temperatures to permit diffusion and homogenization to take place.

### 1.03.3.3 Eutectic Phase Diagrams

The equilibrium phase diagram for Pb–Sb alloys represents a simple eutectic system and is shown in [Figure 15](#). This type of phase diagram is often observed when there is negligible solid solubility of the two metals in each other, and no intermediate phases are formed. The point *E* is the eutectic point,

$T_E$  the eutectic temperature, and  $C_E$  the eutectic composition, in this case approximately 520 K and 13% Sb, respectively. Like a pure metal, an alloy of eutectic composition freezes at a single temperature  $T_E$ , instead of over a temperature range, as in the case of the Cu–30Ni alloy already discussed. Unlike a pure metal, however, a eutectic alloy freezes to give a mixture of two phases, in this case Pb and Sb; in general terms, therefore, a eutectic reaction involves liquid  $\rightarrow$  solid  $\alpha$  + solid  $\beta$ .

A hypereutectic alloy containing, say, 50% Sb starts to freeze when the temperature reaches the liquidus line (point *a* in [Figure 15](#)). At this temperature, pure proeutectic Sb nucleates; as the temperature continues to fall, more antimony is deposited from the melt, and the composition of the liquid phase moves down the liquidus line to the eutectic point. When this is reached, the remainder of the melt solidifies. The microstructure of alloys of eutectic composition varies somewhat with the alloy system, but generally consists of an aggregate of small particles, often platelets, of one of the phases comprising the eutectic in a continuous matrix of the other phase. Finally, the microstructure of the hypereutectic 50% Sb alloy already mentioned consists of primary (proeutectic) antimony surrounded by the eutectic constituent, as illustrated in [Figure 16](#). This microstructure is clearly to be expected from the solidification sequence just described.

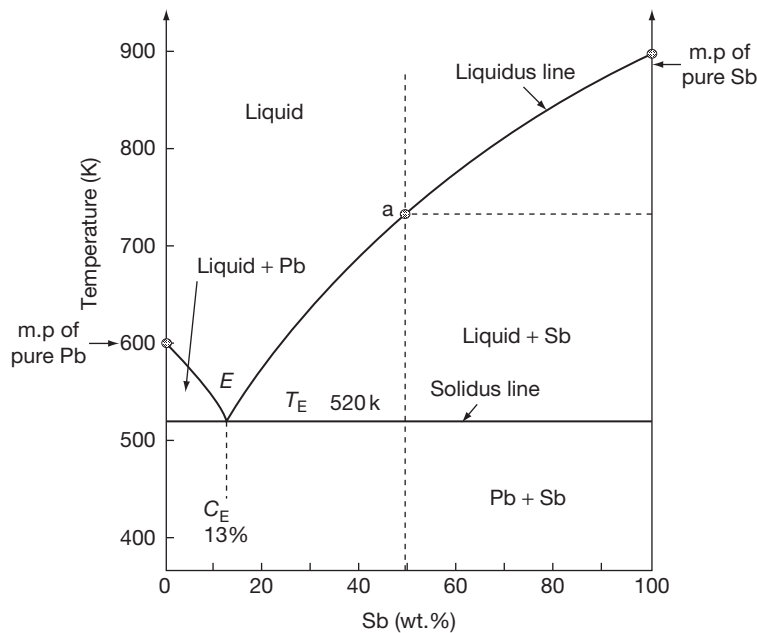


**Figure 15** Lead–antimony phase diagram.

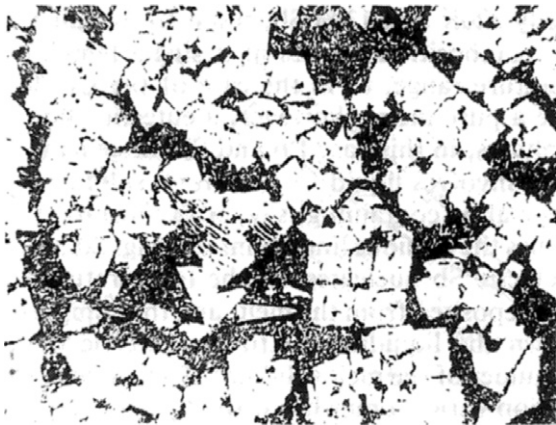


**Figure 16** Light micrograph showing the microstructure of a hyper-eutectic Pb-50Sb alloy ( $\times 50$ ).

#### 1.03.3.4 More Complex Binary Phase Diagrams

Most phase diagrams, however, are more complex than those shown in [Figures 14 and 15](#). Thus, in most eutectic systems, there is some appreciable solid solubility, as in the Ag-Cu phase diagram shown in [Figure 17\(a\)](#). At ambient temperatures, therefore, an Ag-50Cu alloy would contain two components (Ag and Cu), two phases (the  $\alpha$  and  $\beta$  solid solutions), and two constituents (primary proeutectic  $\beta$  and the eutectic mixture of  $\alpha + \beta$ ). Furthermore, in many alloy systems intermediate phases and/or intermetallic compounds are formed. [Figure 17\(b\)](#), for example, illustrates the Mg-Sn phase diagram; this exhibits two eutectic reactions and the intermetallic compound,  $\text{Mg}_2\text{Sn}$ . Finally, a number of other reactions, in addition to the eutectic reaction, are observed; of particular importance are (on cooling in all cases):

1. The eutectoid reaction: solid  $\alpha \rightarrow$  solid  $\beta +$  solid  $\gamma$ .
2. The peritectic reaction: liquid + solid  $\alpha \rightarrow$  solid  $\beta$ .
3. The peritectoid reaction: solid  $\alpha +$  solid  $\beta \rightarrow$  solid  $\gamma$ .

By way of example, the Cu-Zn phase diagram shown in [Figure 18](#) exhibits a number of different intermediate phases ( $\beta$ ,  $\gamma$ ,  $\delta$ , etc.) and a number of peritectic reactions and a eutectoid reaction. In many instances, it is not necessary to consider a complete phase diagram. Thus [Figure 19](#) illustrates the Al-rich end of the Al-Cu phase diagram and is used below in a discussion of precipitation hardening. Again, [Figure 20](#) shows the Fe-Fe<sub>3</sub>C phase diagram, the great practical importance of which is in no way reduced by the fact that one of the components in it, namely Fe<sub>3</sub>C (cementite), is a metastable compound. The true

equilibrium diagram, in which graphite appears in place of cementite, is of use only when cast irons are being considered, as opposed to steels. Other phase diagrams that are of particular significance are the iron-rich ends of the Fe-Ni and Fe-Cr systems, which are shown in [Figures 21\(a\) and 21\(b\)](#), respectively. It follows from the diagrams that Ni and C are austenite ( $\gamma$ -phase) stabilizers while Cr is a ferrite ( $\alpha$ -phase) stabilizer. The fact that the interstices in an f.c.c. structure are bigger than those in a b.c.c. structure accounts for the fact that C is much more soluble in f.c.c. iron (austenite) than in b.c.c. iron (ferrite) ([Figure 20](#)).

#### 1.03.4 The Fe-Fe<sub>3</sub>C Phase Diagram

Because of the great practical importance of steels, it is necessary to discuss the Fe-C system in rather more detail. The Fe-Fe<sub>3</sub>C phase diagram consists of the following three reactions

1. At 1766 K and 0.16% C the peritectic reaction:  
liquid Fe +  $\delta$  - Fe (b.c.c.)  $\rightarrow$   $\gamma$  - Fe (f.c.c.).
2. At 1420 K and 4.3% C the eutectic reaction: liquid Fe  $\rightarrow$   $\gamma$  - Fe (f.c.c.) + Fe<sub>3</sub>C.
3. At 996 K and 0.80% C the eutectoid reaction:  
 $\gamma$  - Fe (f.c.c.)  $\rightarrow$   $\alpha$  - Fe + Fe<sub>3</sub>C.

The peritectic transformation generally has little effect on the structure, properties, or corrosion resistance of steels at room temperature; an exception to this occurs in the welding of certain steels, when  $\delta$ -ferrite can be retained at room temperature and can affect corrosion resistance. Furthermore, since most steels contain less than about 1.0%C (and by far the greatest tonnage contains less than about 0.3% C), the eutectic reaction is of relevance only in relation to the structure and properties of cast irons, which generally contain 2-4%C. This discussion, therefore, will be limited to the eutectoid reaction that occurs when homogeneous austenite is cooled.

##### 1.03.4.1 Decomposition of Austenite

When austenite is cooled, the structures that result from the eutectoid reaction depend on the temperature at which the transformation takes place. In practice, of course, steels are generally continuously cooled at a rate that may vary from very rapid (quenching) to very slow (furnace cooling). However, it is useful and valid to simplify the situation by assuming that the transformation occurs isothermally. In other words, therefore, we shall consider initially,

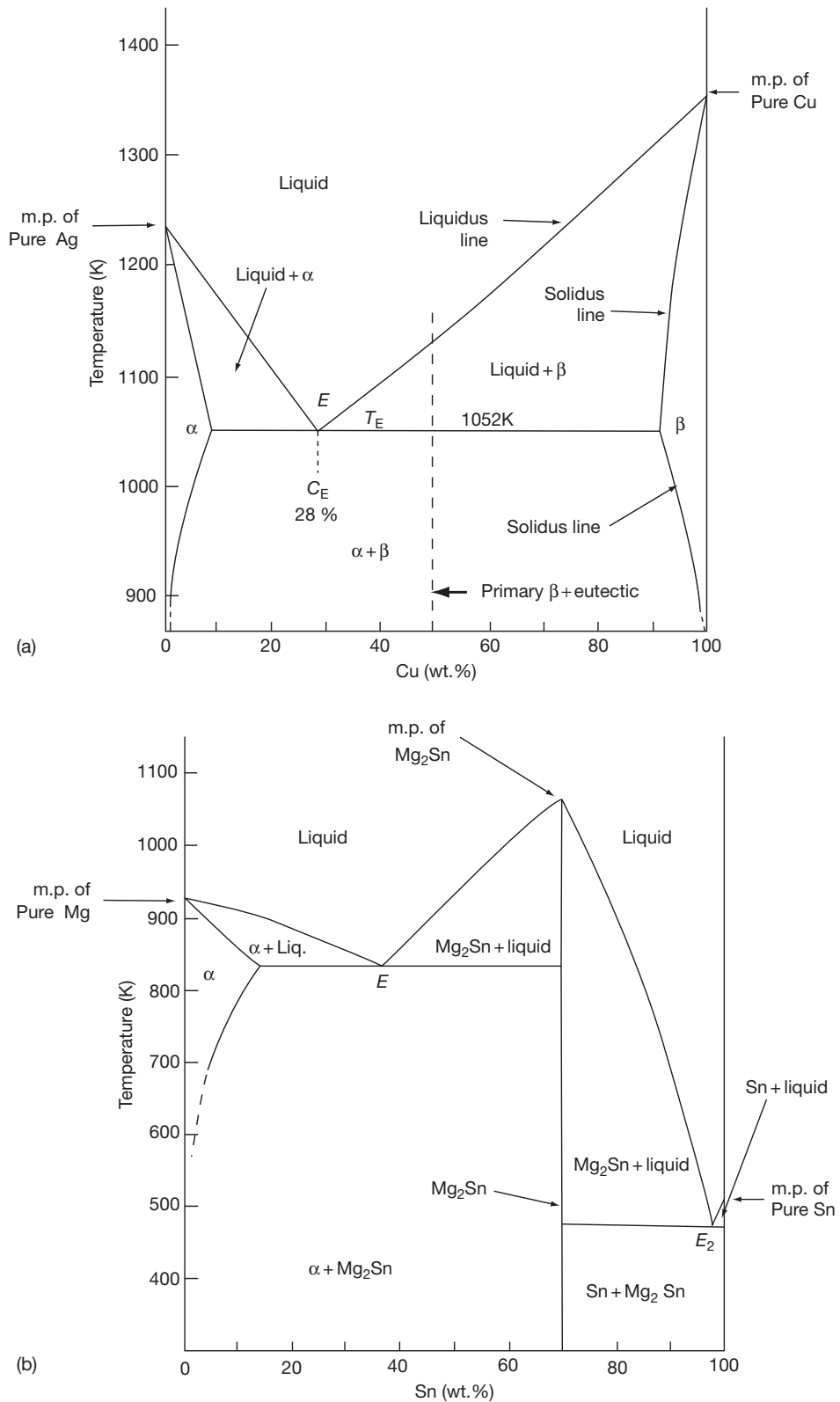


**Figure 17** (a) Silver–copper phase diagram and (b) magnesium–tin phase diagram.

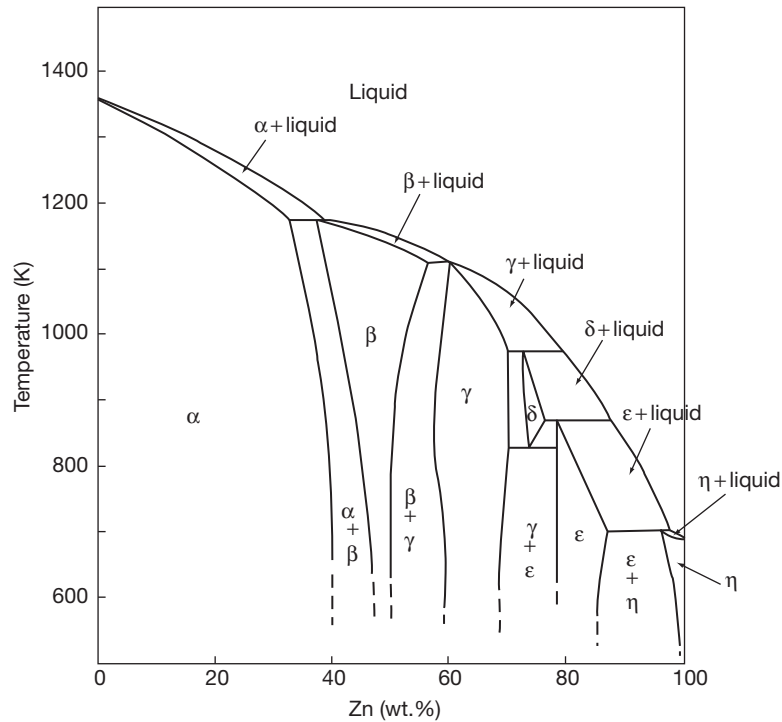


**Figure 18** Copper–zinc phase diagram.

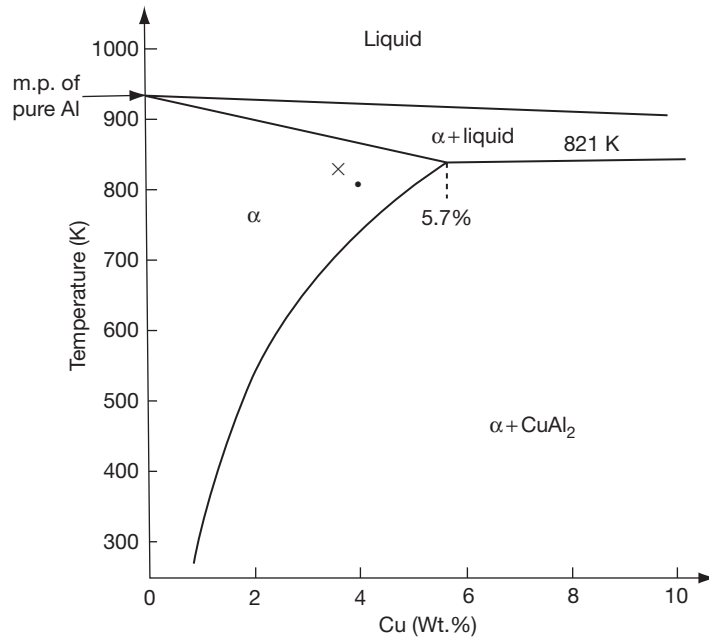


**Figure 19** Aluminum-rich end of the aluminum–copper phase diagram.

the reactions that occur when a steel containing 0.8% C (i.e., of eutectoid composition) is very rapidly quenched from, say, 1400 K to some temperature  $T < 996$  K, at which decomposition of the austenite

takes place. In general, the structures produced on slow continuous cooling approximate to those resulting from high temperature isothermal transformation, while rapid continuous cooling results in

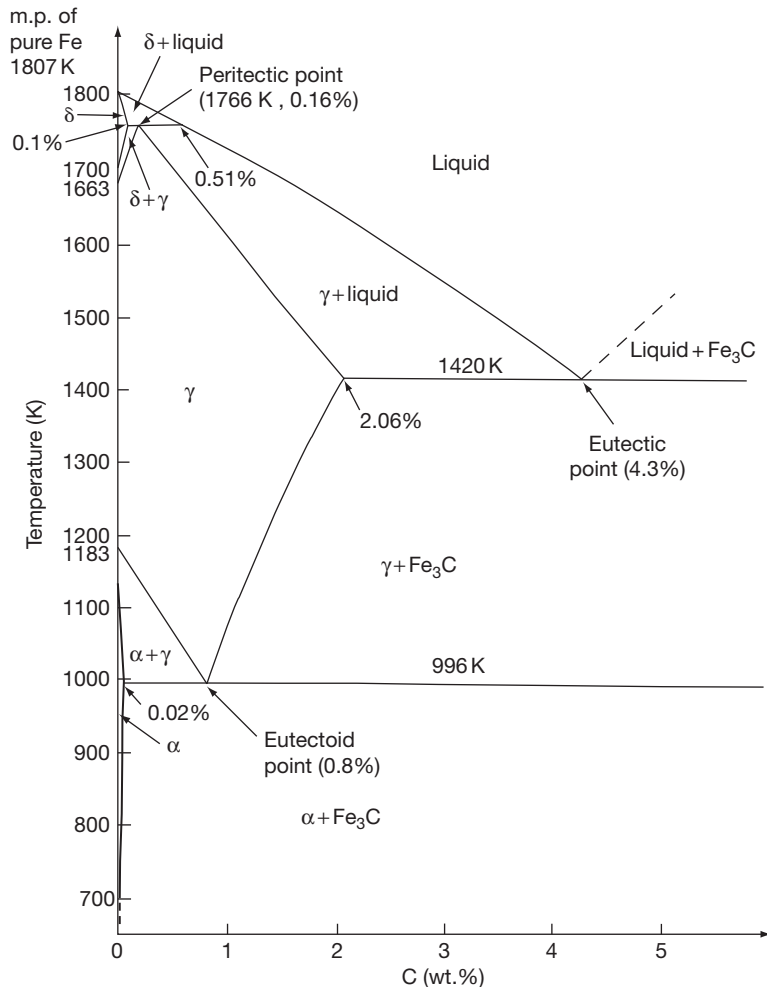


**Figure 20** Iron-rich end of the metastable Fe–Fe<sub>3</sub>C phase diagram.

structures that approximate to those obtained by intermediate-temperature isothermal transformation.

#### 1.03.4.2 Formation of Pearlite

If austenite is allowed to transform just below 996 K, the reaction product, as predicted by the Fe–Fe<sub>3</sub>C phase diagram, is the  $\alpha$  – Fe + Fe<sub>3</sub>C eutectoid. This eutectoid constituent is known as pearlite and consists of alternate platelets of ferrite ( $\alpha$ -Fe) and cementite (Fe<sub>3</sub>C), the former being the continuous phase. The decomposition of austenite to pearlite involves nucleation of pearlite, which occurs almost exclusively at austenite grain boundaries, followed by growth of pearlite; both processes involve the solid-state diffusion of carbon in iron. Immediately after quenching, therefore, the structure of the steel consists of untransformed austenite, as shown schematically in

**Figure 22(a).** At some later time, nucleation of a number of colonies of pearlite will have occurred at the austenite grain boundaries, as shown in **Figure 22(b)**; at this stage, about 10% of the austenite has transformed. At some still later time, growth of the pearlite will have occurred by nucleation of new  $\alpha$ -Fe and Fe<sub>3</sub>C platelets and by extensive edge-wise growth of existing platelets as shown in **Figure 22(c)**; at this stage, about 90% of the austenite has transformed and eventually, transformation will be complete.

In fundamental terms, the transformation temperature affects both the driving force for the decomposition of austenite and the diffusion rate of carbon. In effect, therefore, the transformation temperature alters both the rate of nucleation and the rate of growth. This in turn manifests itself in different transformation times at different temperatures. Furthermore, the spacing of the pearlite platelets is



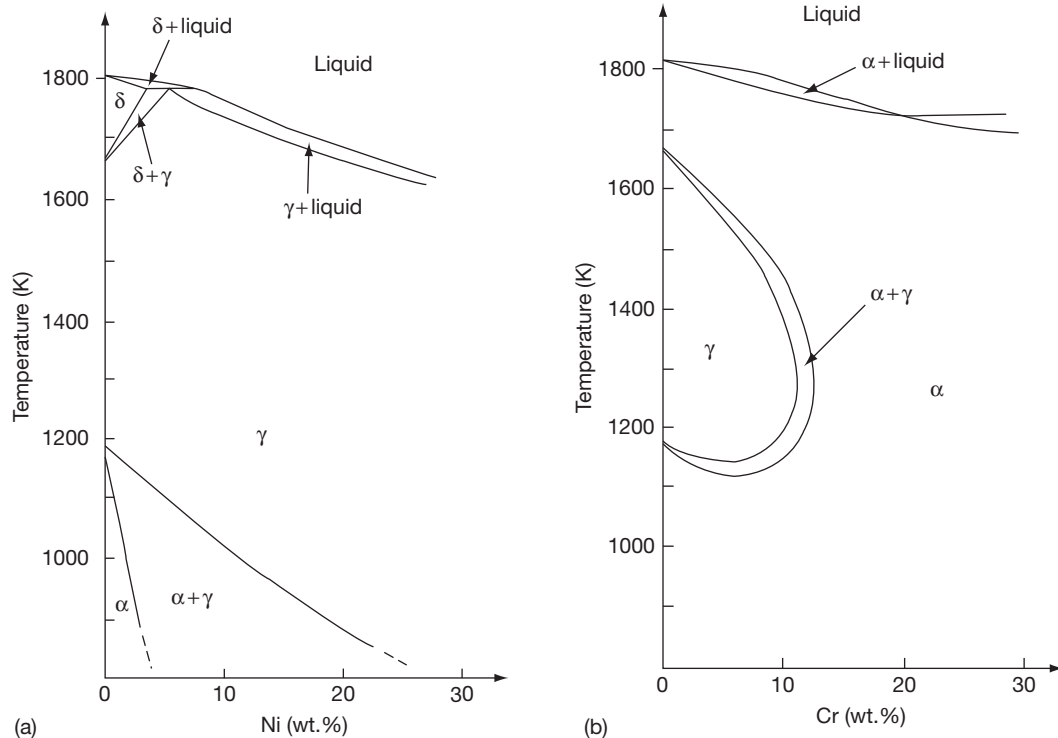


**Figure 21** (a) Iron-rich end of the iron–nickel phase diagram and (b) iron-rich end of the iron–chromium phase diagram.

characteristic of the temperature at which transformation occurred; the lower the transformation temperature the finer are the platelets, and the greater the hardness and the strength of the steel. The distinction between coarse and fine pearlite structures is shown in [Figures 22\(d\) and 22\(e\)](#), respectively; in practice, the platelets in very fine pearlite may not be resolvable with a light microscope. The rate of transformation of carbon steels is also markedly affected by the presence of other alloying elements. However, a detailed consideration of the transformation and structure of low-alloy steels is beyond the scope of this section.

#### 1.03.4.3 Formation of Bainite

At lower transformation temperatures ( $<770$  K approximately), a second reaction, the formation of bainite, intervenes. Like pearlite, the bainite constituent in steels consists of a mixture of ferrite and an iron carbide and is formed by a time-dependent nucleation and growth process involving diffusion of carbon. Bainite, however, grows as needle-like plates, which consist of very fine particles of carbide embedded in a ferrite matrix. The carbide particles can only be resolved in an electron microscope; in the light microscope, only the acicular bainite needles are

visible. The microstructure of a bainitic steel is shown schematically in [Figure 22\(f\)](#); the appearance of bainite, however, and the structure and composition of the carbides in it, vary somewhat with transformation temperature, bainite being much harder than pearlite.

#### 1.03.4.4 Formation of Martensite

Finally, at even lower transformation temperatures, a completely new reaction occurs. Austenite transforms to a new metastable phase called martensite, which is a supersaturated solid solution of carbon in iron and which has a body-centered tetragonal crystal structure. Furthermore, the mechanism of the transformation of austenite to martensite is fundamentally different from that of the formation of pearlite or bainite; in particular, martensitic transformations do not involve diffusion and are accordingly said to be diffusionless. Martensite is formed from austenite by the slight rearrangement of iron atoms required to transform the f.c.c. crystal structure into the body-centered tetragonal structure; the distances involved are considerably less than the interatomic distances. A further characteristic of the martensitic transformation is that it is predominantly athermal, as opposed to the isothermal transformation of austenite

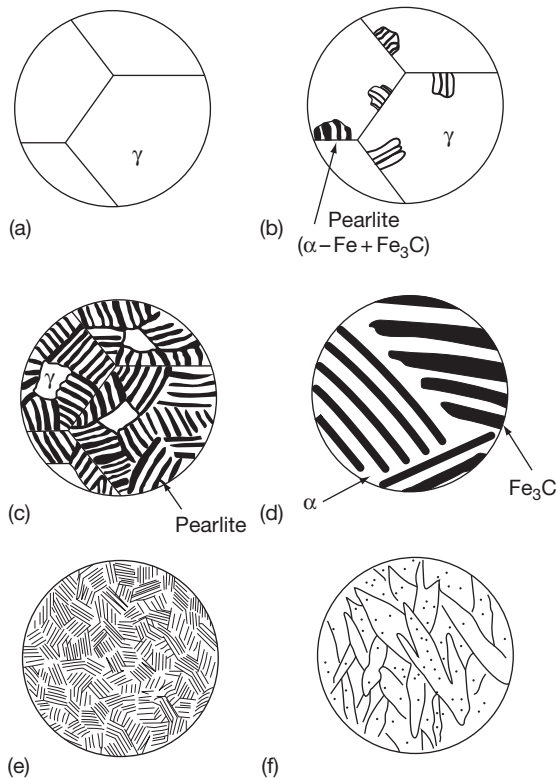


**Figure 22** Some of the pearlitic and bainitic microstructures observed in eutectoid steels after various heat treatments.

to pearlite or bainite. In other words, at a temperature midway between  $m_s$  (the temperature at which martensite starts to form), and  $m_f$  (the temperature at which martensite formation is apparently complete), the steel will consist of about 50% austenite and about 50% martensite; this transformation of 50% of the austenite to martensite is effectively instantaneous, and no matter how long the steel is held at this temperature, no further transformation will occur. **Figure 23** illustrates the microstructure of a fully martensitic steel. The martensite platelets are heavily twinned, although this is only apparent in an electron microscope. In fact, in a eutectoid steel, the  $m_f$  temperature is below room temperature although in a more common hypoeutectoid steel containing about 0.2% C,  $m_s \approx 720$  K and  $m_f \approx 550$  K. Other alloying elements also affect the temperature at which the martensite transformation takes place and usually decrease it.

#### 1.03.4.5 Isothermal Transformation Diagrams

Time–temperature–transformation (T–T–T) diagrams are used to present the structure of steels

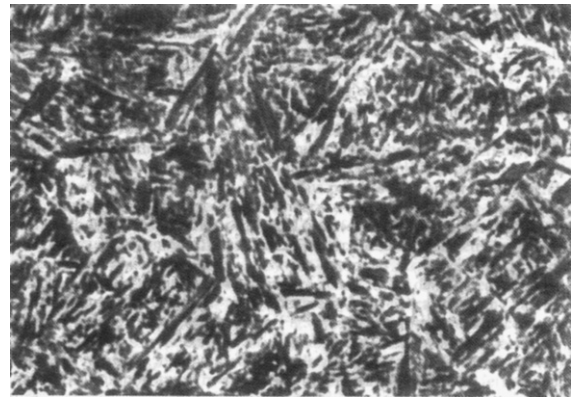


**Figure 23** Light micrograph showing the microstructure of a martensitic steel ( $\times 550$ ).

after isothermal transformation at different temperatures for varying times. The T–T–T diagram for a commercial eutectoid steel is shown in **Figure 24(a)**. Also shown on the curves are the points at which the microstructures illustrated in **Figures 22 and 23** are observed, and the thermal treatments producing these structures. When a steel partially transformed to, say, pearlite, is quenched from point *a* in **Figure 24(a)** to below  $m_f$ , the untransformed austenite transforms to martensite.

#### 1.03.4.6 Transformation of Hypo-Eutectoid Steels

As noted above, most steels are, in practice, hypo-eutectoid. Consider, by way of example, a low-alloy steel containing 0.3% C. The Fe–C phase diagram (**Figure 20**) indicates that as a steel of this composition is cooled below about 1080 K, the equilibrium state is a two-phase structure containing primary, pro-eutectoid ferrite and austenite. On further cooling to below 996 K, the equilibrium structure consists of pro-eutectoid ferrite and pearlite. These differences are reflected in the rather more complicated T–T–T diagram used for this steel, shown in **Figure 24(b)**.

Depending on the transformation temperature, the steel may transform to ferrite plus austenite ( $T_1$  in **Figure 24(b)**), to ferrite plus pearlite via ferrite plus austenite ( $T_2$ ), directly to ferrite plus pearlite ( $T_3$ ) or directly to ferrite plus bainite ( $T_4$ ). The pro-eutectoid ferrite morphology, like the pearlite morphology, varies with the isothermal transformation temperature and also with the carbon content of the steel. The ferrite nucleates heterogeneously on austenite grain boundaries. Any pro-eutectoid ferrite in slightly hypoeutectoid steels (about 0.6%),

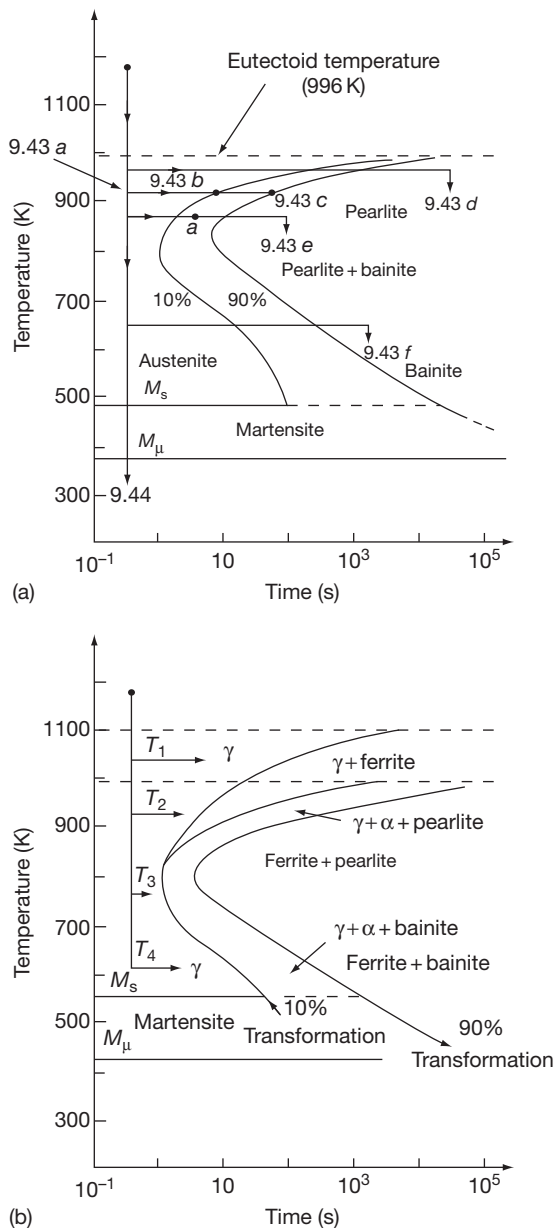


**Figure 24** Isothermal time temperature transformation curves for (a) a eutectoid steel and (b) a hypo-eutectoid steel.

therefore, tends to be distributed along the austenite grain boundaries, with the grain centers transforming later to pearlite, as shown schematically in [Figure 25\(a\)](#). At lower carbon contents, Widmanstätten pro-eutectoid ferrite is observed, as shown schematically in [Figure 25\(b\)](#), while in low-carbon steels, massive ferrite is observed ([Figure 25\(c\)](#)). It is important to reemphasize that these pro-eutectoid ferrite structures also vary with isothermal transformation temperature and therefore, in practice, with

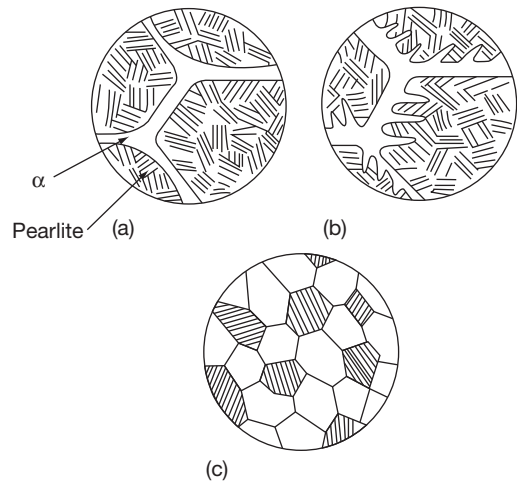


**Figure 25** Schematic illustration of some of the ferritic/pearlitic microstructures observed in hypo-eutectoid steels after various heat treatments.

cooling rate; they can also be altered by subsequent heat treatment and working. Grain-boundary and Widmanstätten ferrite are generally undesirable and result in poor mechanical properties. [Figure 25](#) illustrates some of the more important structures generally observed in two-phase alloys.

The higher the carbon content of a hypo-eutectoid steel, the more pearlite there will be in a ferritic/pearlitic structure and the greater will be the strength of the steel, other factors (grain-size, pearlite spacing, etc.) being equal.

#### 1.03.4.7 Tempering of Martensite

As-quenched martensite is not only extremely hard, but also extremely brittle. The hardness of as-quenched martensite, which also increases with increasing carbon content, is due partly to the strain involved in retaining the carbon in solid solution in body-centered tetragonal iron, and partly, in low-carbon martensites, to their very high dislocation density. The martensite reaction in steels is not reversible and on reheating as-quenched martensite ([Figure 26\(a\)](#)) to various temperatures below 996 K, the carbon tends to precipitate out of the solid solution; this process is known as tempering. On tempering at about 370–520 K, the carbon precipitates out as the so-called  $\epsilon$ -carbide, which may be written as  $\text{Fe}_{2.4}\text{C}$  and has a different structure from cementite. These carbides precipitate on certain crystallographic planes and on the twin boundaries in the martensite plates, forming what is known as a Widmanstätten structure, as shown schematically in [Figure 26\(b\)](#).

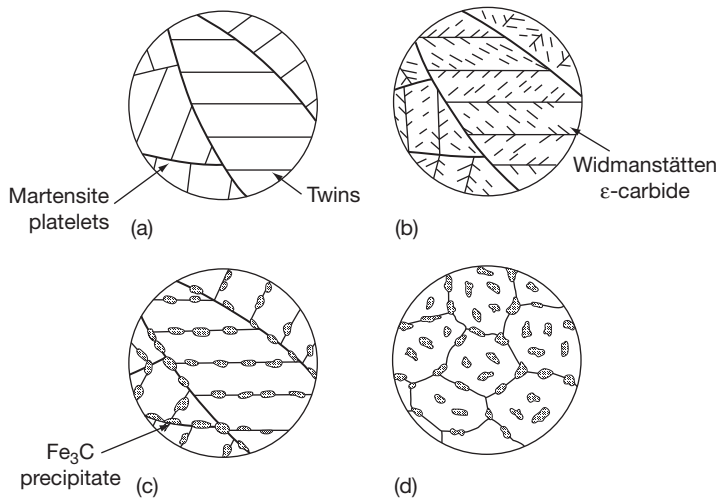


**Figure 26** Some of the microstructures observed during the tempering of martensite.

On tempering at 520–770 K, cementite particles are precipitated on twin boundaries and on boundaries between martensite platelets, leaving a matrix of ferrite as shown in [Figure 26\(c\)](#). Eventually, the cementite particles grow and become spheroidal in shape while the twinned structure breaks down and fine equiaxed ferrite grains are observed, as illustrated in [Figure 26\(d\)](#). On tempering, as the carbon precipitates out of the solid solution, the strength and hardness of the steel falls progressively, as shown in [Figure 27](#), while the toughness increases. Quenched and tempered low-alloy steels are widely used where high-strength high-toughness materials are required.

#### 1.03.4.8 Spheroidized Structures in Steels

On tempering or annealing martensite, bainite, or even pearlite at even higher temperatures (about 970 K), a structure consisting of coarse cementite spheroids (readily visible in a light microscope) in a ferrite matrix is obtained. This is the most stable of all ferrite/cementite aggregates, and it is also one of the softest.

The structures and phase transformations observed in steels have been dealt with in some detail not only because of the great practical importance of steels, but also because reactions similar to those occurring in steels are also observed in many other alloy systems, too. In particular, diffusionless transformations (austenite → martensite), continuous precipitation (austenite → pearlite), and discontinuous precipitation (austenite → bainite and tempering of martensite) are fairly common in other alloy systems.

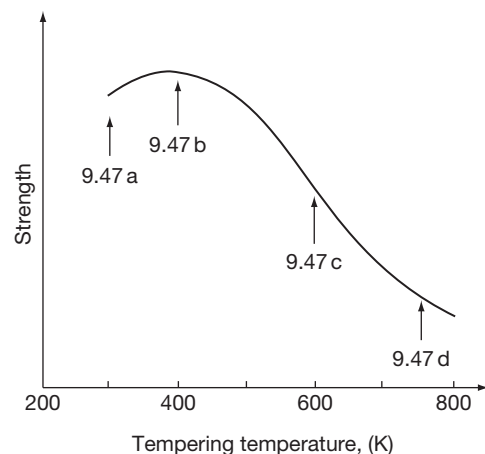


**Figure 27** Effect of tempering temperature on the strength and microstructure of martensite.

#### 1.03.5 Strengthening Mechanisms in Metals

Many of the ways of increasing the strength of metals have already been dealt with in passing. For example, cold working a metal increases its dislocation density and therefore, as already discussed, increases its strength. (The processes involved in the nucleation and multiplication of dislocations during cold working are very complex and beyond the scope of this section.) Substitutional solid solutions (e.g., austenitic stainless steels and brass) are normally stronger than the equivalent pure metals (i.e., iron and copper), as the lattice distortion involved hinders dislocation

movement. This is known as solid–solution hardening. Metals with fine grain structures, produced by grain-refining treatments, such as cold working followed by annealing to give recrystallization, are stronger than coarse-grained materials and single crystals, since grain boundaries act as barriers to dislocation movement. Steels may be quenched and tempered to produce high-strength and high-toughness materials. Clearly, all these involve altering the structure of the metal in some way. Another very important strengthening mechanism, namely precipitation hardening, also involves microstructural changes.

### 1.03.5.1 Precipitation Hardening

Precipitation hardening (also called age hardening and dispersion hardening) is particularly important in high-strength aluminum alloys, but it is also used to strengthen other alloys, notably certain steels and nickel-base alloys. Consider, by way of example, the Al–Cu phase diagram shown in [Figure 19](#). At about 820 K, the equilibrium structure of an Al–4Cu alloy (point *X* in [Figure 19](#)) is the single-phase  $\alpha$  solid solution of copper in aluminum, as shown in [Figure 28\(a\)](#). On annealing at this temperature, that is, on solution heat treating, this equilibrium state is

readily achieved. At room temperature, because the limit of solid solubility decreases with decreasing temperature, the equilibrium structure consists of the  $\alpha$ -solid solution plus the  $\text{CuAl}_2$  intermetallic compound. This equilibrium state may be achieved by very slowly cooling the alloy from 820 K to room temperature and consists of very coarse discontinuous precipitates of  $\text{CuAl}_2$  in an  $\alpha$  matrix, as shown in [Figure 28\(b\)](#). However, on quenching the alloy to room temperature, diffusion (and therefore nucleation and growth of  $\text{CuAl}_2$ ) is prevented, and the copper is retained in supersaturated solid solution, as shown in [Figure 28\(c\)](#). This supersaturated solid solution is relatively soft, weak, and ductile. If this metastable supersaturated solid solution is then aged, that is, heat treated at a relatively low temperature (370–520 K), the excess copper again precipitates out of the solid solution as  $\text{CuAl}_2$ . In this case, however, the  $\text{CuAl}_2$  particles are extremely fine, certainly submicroscopic, and under certain conditions, only just resolvable in the electron microscope. The precipitation sequence varies from alloy to alloy but is generally quite complex and involves a number of intermediate metastable precipitates. The initial precipitates or coherent zones formed during the early stages of aging (i.e., after relatively short times)

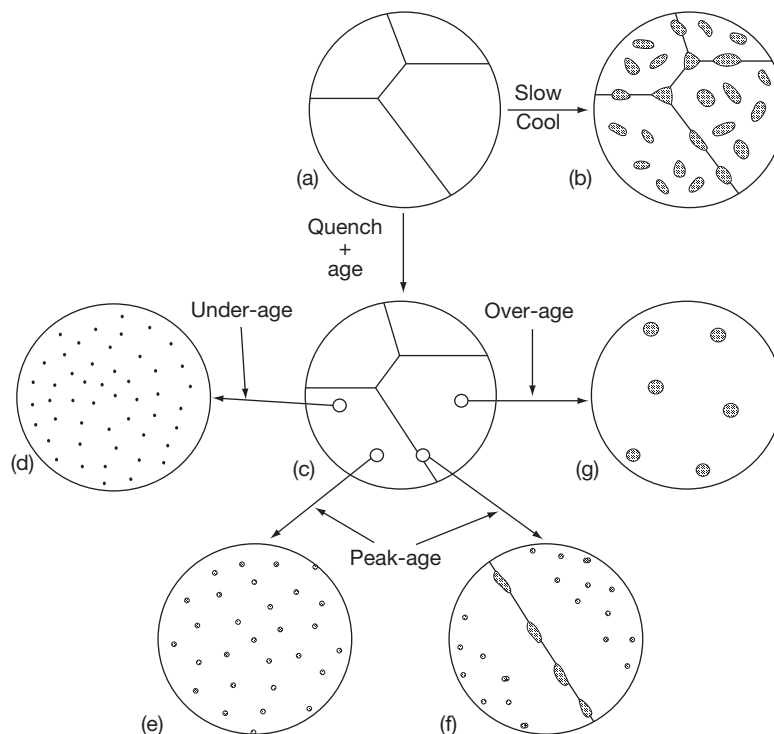


**Figure 28** Some of the microstructures observed during the heat treatment of precipitation-hardening aluminum alloys.



interact with dislocations and tend to hinder their movement. This underaged condition is therefore stronger than the as-quenched condition, but since the zones are extremely fine (**Figure 28(d)**) and are readily sheared by moving dislocations (**Figure 29(a)**), it is only moderately so. On further aging, somewhat coarser, semicoherent intermediate precipitates are formed (**Figure 28(e)**). These interact strongly with dislocations and, being too large to be sheared, form very effective barriers to dislocation motion. Dislocations can only move through the matrix by bowing round the precipitates and leaving behind dislocation loops, as shown in **Figure 29(b)**, and in this peak-aged condition, the alloy is strongest. If aging is continued, a relatively coarse dispersion of the equilibrium precipitate is formed. In this overaged condition (**Figure 28(g)**), the precipitates are too coarse and widely spaced to interact strongly with dislocation; they are relatively ineffective barriers to dislocation motion, and the alloy again has only intermediate strength. It should be emphasized, however, that even in the over-aged condition, the precipitates are still submicroscopic.

The rate at which aging occurs depends on the aging temperature. At very low aging temperatures, over-aging is not observed in a realistic timescale while at high aging temperatures, the strength falls off almost immediately. In general, the lower the aging temperature, the greater the peak hardness. These effects are illustrated schematically in **Figure 30**.

During aging, nucleation always occurs first at grain boundaries; the intergranular precipitates are therefore always coarser and more advanced than the intragranular precipitates. Furthermore, owing to vacancy and

solute depletion, there is always a precipitate-free zone adjacent to the grain boundary. The grain-boundary structure of a peak-aged high-strength precipitation-hardening aluminum alloy is therefore as shown schematically in **Figure 28(f)** and in the electron micrograph in **Figure 31**.

### 1.03.5.2 Complex Alloy Systems

Detailed consideration of the structure of many of the advanced and complex alloys that are of considerable technological importance (high-strength titanium alloys, nickel-base superalloys, etc.) is beyond the

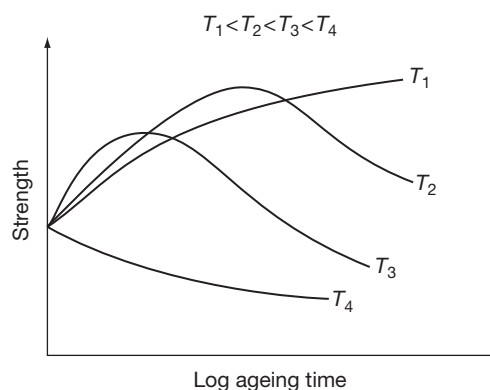


**Figure 30** Curves of strength against the logarithm of the ageing time for a precipitation-hardening aluminum alloy aged at different temperatures.

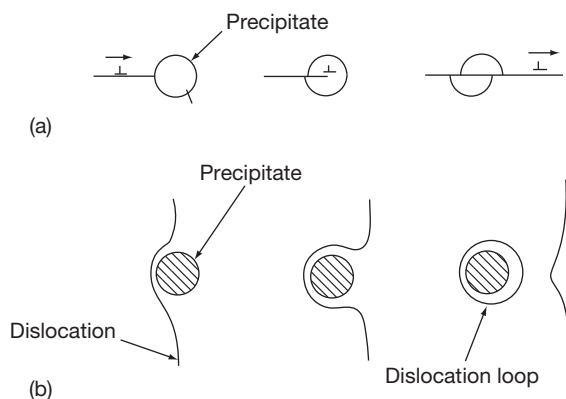


**Figure 29** (a) Dislocation shearing a precipitate particle and (b) a dislocation bowing round a precipitate particle.

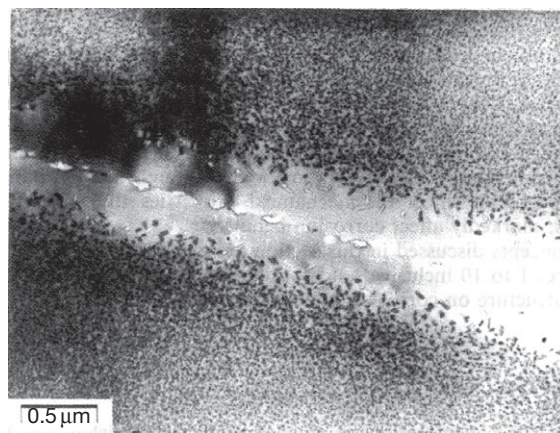


**Figure 31** Transmission electronmicrograph showing intergranular and intragranular precipitation and the precipitate-free zone adjacent to the grain boundary in a high-strength precipitation-hardening Al-Zn-Mg alloy ( $\times 24\,000$ , courtesy of G. Lorimer).



scope of this section, other than to point out that no new principles are involved. Certain titanium alloys, for example, exhibit a martensitic transformation, while many nickel-base superalloys are age hardening. Similarly, cast irons, although by no means advanced materials, are relatively complex.

### 1.03.5.3 Inclusions in Metals

In conclusion, it must be emphasized again that commercial materials are never pure metals or pure binary or ternary alloys. They always contain impurities that are not particularly beneficial to the properties of the material; however, so long as they are not positively detrimental (as in the case of carbon in certain austenitic stainless steels), their presence is tolerated as it would be uneconomical to remove them. Some of these impurities are in solid solution. Others, however, exist as inclusions that are quite unaffected by heat treatment, although they may be broken up by working. Examples are the Fe–Si-rich inclusions in aluminum alloys ([Figure 10](#)), manganese sulfide inclusions in steel, etc. However, although these impurities may have a negligible effect

on mechanical properties, they can, in certain instances, markedly affect corrosion behavior.

The concepts discussed in this section are dealt with in greater depth in References Reed-Hill,<sup>1</sup> Rollason,<sup>2</sup> Bailey,<sup>3</sup> Smallman,<sup>4</sup> Cottrell,<sup>5</sup> Cahn,<sup>6</sup> Chalmers,<sup>7</sup> McLean,<sup>8</sup> Shewman,<sup>9</sup> and Peckner,<sup>10</sup> inclusive.

### References

1. Reed-Hill, R. E. *Physical Metallurgy Principles*; van Nostrand Reinhold: New York, 1970.
2. Rollason, E. C. *Metallurgy for Engineers*; Edward Arnold: London, 1973.
3. Bailey, F. W. J. *Fundamentals of Engineering Metallurgy and Materials*; Cassell: London, 1972.
4. Smallman, R. E. *Modern Physical Metallurgy*; Butterworths: London, 1970.
5. Cottrell, A. H. *An Introduction to Metallurgy*; Edward Arnold: London, 1967.
6. Cahn, R. W., Ed. *Physical Metallurgy*; North-Holland: London, 1970.
7. Chalmers, B. *Physical Metallurgy*; John Wiley: New York, 1959.
8. McLean, D. *Mechanical Properties of Metals*; John Wiley: New York, 1962.
9. Shewman, P. G. *Transformations in Metal*; McGraw-Hill: New York, 1969.
10. Peckner, D., Ed. *The Strengthening of Metals*; Reinhold: New York, 1967.

## 1.06 Defects and Transport in Oxides and Oxide Scales

**B. Pieraggi**

Ecole Nationale Supérieure des Ingénieurs en Arts Chimiques et Technologique de Toulouse, Institut National Polytechnique de Toulouse, F-31077 Toulouse Cedex 04, France

© 2010 Elsevier B.V. All rights reserved.

1.06.1	Introduction	102
1.06.2	Crystal Defects	102
1.06.2.1	Point Defects: Thermal Defects and Constitutive Defects	102
1.06.2.2	Dislocations	104
1.06.2.3	Surfaces	107
1.06.2.4	Grain Boundaries and Interfaces	108
1.06.3	Point Defects in Ionic Crystals	110
1.06.3.1	Structure and Building Elements: Kröger–Vink Notation	110
1.06.3.2	Use of Kröger–Vink Notation: Formation Equilibriums of Frenkel and Schottky Disorders	111
1.06.3.3	Electronic Defects and Ionized Point Defects	112
1.06.3.4	Point Defect Equilibriums in Nonstoichiometric Oxides	113
1.06.3.4.1	p-Type oxides	113
1.06.3.4.2	n-Type oxides	114
1.06.3.5	Intrinsic Defect Equilibriums Close to Stoichiometry	114
1.06.3.6	Effect of Impurities on Defect Equilibriums	115
1.06.3.7	Extended Defects	115
1.06.4	Diffusion Laws and Mass Transport in Solid State	116
1.06.4.1	Diffusion Laws	116
1.06.4.2	Lattice Diffusion and Diffusion Mechanisms	117
1.06.4.3	Interdiffusion, Intrinsic Diffusion, and Kirkendall Effect in Binary Solid Solutions	118
1.06.4.4	Diffusion in Multiphase Systems	119
1.06.4.5	Interdiffusion in Ternary Systems	120
1.06.4.6	Short-Circuit Diffusion	121
1.06.5	Diffusion and Transport in Oxides	122
1.06.5.1	Chemical Diffusion in Nonstoichiometric Oxides	122
1.06.5.2	Diffusion Processes in Oxide Scales	123
1.06.5.3	Oxide Scale Microstructure and Diffusion Processes	124
1.06.5.4	Point Defects and Diffusion in Common Oxides	127
1.06.5.4.1	Nickel and cobalt monoxides	127
1.06.5.4.2	Iron oxides	128
1.06.5.4.3	Chromia	129
1.06.5.4.4	$\alpha$ -Alumina ( $\alpha$ -Al <sub>2</sub> O <sub>3</sub> )	129
1.06.6	Concluding Remarks	130
References		131

### Abbreviations

**DIGM** Diffusion-induced grain-boundary motion  
**PSZ** Partially-stabilized zirconia  
**SZ** Stabilized zirconia  
**TLK** Terrace-ledge-kink

### Symbols

**b** Burgers vector of a dislocation  
**n** Molar fraction of free electron (mol<sup>-1</sup>)  
**p** Molar fraction of positive hole (mol<sup>-1</sup>)  
**t** Time (s)

$x_i$	Mole fraction of species $i$ ( $\text{mole}^{-1}$ )
$C_i$	Molar concentration of $i$ ( $\text{mol m}^{-3}$ )
$D$	Diffusion coefficient ( $\text{m}^2 \text{s}^{-1}$ )
$J$	Diffusion flux ( $\text{mol m}^{-2} \text{s}^{-1}$ )
$K_r$	Equilibrium constant for the reaction $r$
$P$	Pressure (bar)
$Q$	Activation energy ( $\text{J mol}^{-1}$ )
$R$	Universal gas constant ( $8.314 \text{ J mol}^{-1} \text{ K}^{-1}$ )
$T$	Temperature (K)
$T_m$	Temperature of melting (K)
$\Delta_f G$	Molar free enthalpy of formation ( $\text{J mol}^{-1}$ )
$\Delta_f G_i$	Molar free enthalpy of formation of component $i$ (defect or compound) ( $\text{J mol}^{-1}$ )
$\Delta V_r$	Molar relaxation volume ( $\text{m}^3 \text{mol}^{-1}$ )
$\delta$	Departure from ideal stoichiometry ( $\text{mol}^{-1}$ )
$\phi$	Pilling–Bedworth ratio
$\xi$	Thickness (m)
$\Omega$	Molar volume ( $\text{m}^3 \text{mol}^{-1}$ )

### 1.06.1 Introduction

High temperature oxidation of many materials often results in the formation and growth of a continuous external oxide scale and/or in the internal oxidation of the less-noble constituents of the oxidized materials. Therefore, matter transport usually plays a very important role in scale growth and internal oxidation processes. Indeed, a growing external oxide scale separates its own substrate from the oxidizing chemical environment; thus, oxidant species and/or material constituents must be transported across the oxide scale during its growth. Similarly, internal oxidation involves the dissolution and diffusion of oxidant species within the substrate. Furthermore, heat-resisting metallic materials are protected against oxidation by the selective oxidation of their less-noble constituents, usually Cr and/or Al, leading to the growth of chromia or alumina scales that, in addition to matter transport across the scale, requires the diffusion of Al or Cr within the oxidized substrate toward the scale–substrate interface.

Therefore, processes and mechanisms of diffusion and mass transport in oxide scales and oxidized substrates are of prime importance in the understanding and modeling of the high temperature oxidation of materials. As diffusion and mass transport in solids require the presence of crystal defects, [Section 1.06.2](#) is devoted to a general description of common crystal defects. Point defects of ionic crystal are described in [Section 1.06.3](#). [Section 1.06.4](#) is devoted

to different aspects of diffusion and mass transport, including diffusion laws, diffusion in two-phase systems and in ternary systems, and short-circuit diffusion. Specific aspects of diffusion in oxide scales and defect structure, and diffusion in the most common oxides are reported in [Section 1.06.5](#) before some concluding remarks ([Section 1.06.6](#)).

### 1.06.2 Crystal Defects

The crystal structure of any solid chemical compound defines the perfect periodical arrangement of its chemical constituents. However, many physical and chemical processes would not be possible without the existence of local discontinuities in this perfect periodic arrangement; these local discontinuities form more or less extended defective zone or crystal defects. Different kinds of crystal defects are distinguished from their geometrical dimension  $D$ : 0D for point defects, 1D for linear defects, and 2D for planar defects. These different defects are briefly described in the following subsections.

#### 1.06.2.1 Point Defects: Thermal Defects and Constitutive Defects

Point defects are the simplest defects that can be found in any crystal phase. They are localized on single sites of the crystal structure; these sites can be regularly occupied by some chemical species or else regularly unoccupied sites of the vacant interstitial sublattice. [Figure 1](#) defines the simplest and common point defects that can be present in pure solid chemical elements; vacancies and interstitials can also be present in disordered solid solutions. More complex defects such as divacancies or disassociated interstitials can also be formed; they are not considered here.

Interstitial sites are defined from the crystal structure. The simplest case corresponds to the close-packed stacking of hard spheres leading to the

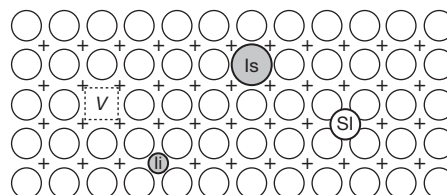


**Figure 1** Schematic representation of point defects in a pure solid chemical element: v, vacancy; Is, substitutional impurity; SI, self-interstitial; Ii, interstitial impurity; the crosses mark the vacant interstitial sites.

face-centered cubic (fcc) lattice or to the hexagonal close-packed (hcp) lattice. Two kinds of interstitial site, octahedral and tetrahedral, are usually distinguished in such close-packed structure. For an fcc lattice, there is one octahedral site and two tetrahedral sites per lattice site. For fcc pure metals such as Ni or  $\gamma$ -Fe, small impurity atoms such as C, H, or O, for example, would occupy the octahedral sites that are the larger ones. For MO oxides of rock salt structure such as NiO and FeO and for oxides  $M_3O_4$  ( $Fe_3O_4$ ) or  $AB_2O_4$  ( $NiCr_2O_4$ ) of spinel structure, oxygen anions also form a close-packed fcc lattice. In rock salt structure, metal cations are only localized over octahedral sites of the fcc anionic sublattice and the tetrahedral sites always remain empty. Thus, point defects of such MO oxides would be mainly vacant octahedral sites (cation vacancies) and oxygen vacancies or self-interstitials. For spinel structure, only one-half of the octahedral sites and one-eighth of the tetrahedral sites are occupied by metal cations, which permits more complex combinations of cationic point defects as briefly described in [Section 1.06.5.4.2](#).

Vacancies and self-interstitial defects are also called intrinsic defects, while substitutional or interstitial impurities are extrinsic defects. The amount of point defects in a crystal is usually defined by their concentration (defects per cubic meters), their site fraction or their molar fraction (defects per mole), which is also, the number of defects per mole of the considered crystal phase. The thermodynamic argument for the stability of defective crystals is well known and does not need to be repeated here. A detailed treatment of the thermodynamic of point defects can be found elsewhere.<sup>1,2</sup>

From the Gibbs phase rule, in unstressed state, pure solid chemical element, for example, pure Ni or Si, and disordered solid solutions of constant composition have no degree of freedom at constant temperature  $T$  and pressure  $P$ . The corresponding thermodynamic systems are invariant so that intrinsic point defects cannot be considered as being independent constituents of these systems; these defects are nonconservative species that need to be created/annihilated at sources or sinks.

By assuming that pressure  $P$  remains in a range such that its influence can be neglected, the mole fraction  $x_d$  of the intrinsic point defects  $d$  then only depends on temperature  $T$ :

$$x_d = \exp\left(-\frac{\Delta_f g_d}{RT}\right) \quad [1]$$

Although point defects are a characteristic of atomic level, their usual thermodynamic quantities are commonly expressed in molar quantities ( $J mol^{-1}$ ). Therefore, in [eqn \[1\]](#),  $\Delta_f g_d$  is the molar Gibbs energy of formation of intrinsic defects  $d$ . As shown by [eqn \[1\]](#), the mole fraction  $x_d$  increases with  $T$  and depends only on that external independent variable, which justifies that such intrinsic defects are also called thermal defects. Vacancies are the dominant point defect in common metals and alloys; enthalpy of formation and entropy of vacancies in pure metals have been reviewed by 'Kraftmaker'.<sup>3</sup> [Equation \[1\]](#) also means that the chemical potential of vacancy is null at equilibrium. For disordered solid solution, enthalpy of formation and entropy of point defects, particularly for vacancies, would depend on solid-solution composition. However, for ideal solid solutions, there is no interaction between solution constituents and therefore no local modification of the composition in the vicinity of point defects; the chemical potential of vacancy at equilibrium is thus independent of solid-solution composition and remains null. Therefore, the equilibrium vacancy molar fraction varies monotonically as a function of composition. The situation is more complex for non-ideal solid solutions where point defects would interact differently with solution constituents. For example, a constituent of larger atomic radius could trap vacancies to accommodate more easily the local volume change it introduces. Therefore, in nonideal solid solution, the dependence of defect molar fraction as a function of solution composition could be complex and the presence and rearrangement of point defects could favor localized composition change.

Under very high pressure or very large stress, the equilibrium mole fraction of intrinsic defects also depends on pressure and stress state.<sup>4</sup> For the simple case of a crystal submitted to a hydrostatic pressure  $P$ , the mole fraction of intrinsic defects varies as

$$x_d(P) = x_d(0) \exp\left(-\frac{P(\pm\Omega + \Delta v_r)}{RT}\right) \quad [2]$$

where  $\Omega$  is the crystal molar volume (the sign is '+' for vacancy formation and '-' for interstitial formation) and  $\Delta v_r$  is the molar relaxation volume, that is, 1 mol of the local volume variation resulting from the relaxation of the crystal lattice around a defect  $d$ . [Equation \[2\]](#) can be also applied to stressed crystals by replacing the pressure  $P$  by a stress tensor  $\sigma$  and the term  $(\pm\Omega + \Delta v_r)$  by a formation volume tensor  $v_f$ . Like pressure, a compressive stress has a positive sign, and hence, from [eqn \[2\]](#), hydrostatic pressure or compressive stress would decrease the equilibrium

molar fraction of vacancy while a tensile stress would increase it. An opposite influence would be observed with interstitial defects.

The situation is more complex for binary or multi-component compounds. Indeed, an  $n$ -ary compound, in an unstressed state and at constant  $T$ , has  $(n - 1)$  degree of freedom, that is, its composition depends on  $(n - 1)$  composition variables that can vary independently without affecting its crystal structure. The chemical formula or ideal stoichiometric composition of such a compound is fixed by its crystallographic structure, but, as there is  $(n - 1)$ -independent composition variables, the real chemical composition can differ from the ideal stoichiometric composition.

Several types of point defects can explain such a departure from ideal stoichiometric composition. **Figure 2** defines the main types of single intrinsic point defects that can be encountered in binary compounds. The point defects of such compounds are usually described by affecting a sublattice for each independent compound constituent. But, in addition to vacancies and interstitials associated to each sublattice, antisite defects can be also present in multi-component compounds. For a simple binary AB compound, an antisite defect corresponds to the wrong occupation of one crystal site as, for example, an atom A occupying a lattice site regularly occupied by an atom B, or inversely an atom B on a site of A. Such antisite defects are mainly observed in inter-metallic and covalent compounds; they cannot be stable in ionic compounds because of the large and repulsive electrostatic interactions they would induce.

Two simple examples are provided by the crystal structure of nickel oxide NiO (rock salt structure) and the simple cubic crystal structure of nickel aluminide  $\beta$ -NiAl. For NiO, its departure from the ideal stoichiometry is only due to a deficit in  $\text{Ni}^{2+}$  cations, its real chemical composition can be expressed as

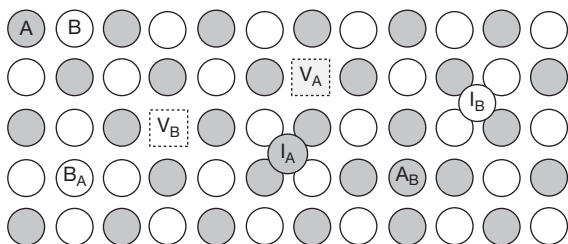


**Figure 2** Intrinsic point defects in a compound AB:  $V_A$ ,  $V_B$  and  $I_A$ ,  $I_B$  are, respectively vacancies and interstitials of sublattices A and B.  $A_B$  and  $B_A$  correspond to antisite defects.

$\text{Ni}_{1-\delta}\text{O}$  where  $\delta$  is the mole fraction of cation vacancies per mole of NiO. At constant  $T$ , the departure  $\delta$  varies as a function of one compositional variable that, in this case, is usually the activity (partial pressure) of oxygen. Therefore, these vacancies are not thermal defects; they are structurally linked to the crystal structure of NiO, which justifies their denomination of structural or constitutive defects.  $\beta$ -NiAl, contrary to NiO, is stable over a large range of chemical composition, including its stoichiometric composition. In that case, the type and concentration of structural point defects compatible with the conservation of crystal structure vary with the mole fraction of Al or Ni. For example, complex point defects such as triple defects associating one antisite Ni atom and two Ni vacancies can be found in stoichiometric  $\beta$ -NiAl, while Ni vacancies and antisite Ni atoms are the predominant defects in Al-rich and Ni-rich  $\beta$ -NiAl, respectively.

At constant temperature, the composition range over which a binary compound is stable, that is, the concentration limits of point defects, depends on the relative stability of this compound with respect to the closest adjacent compounds. A very stable compound, such as alumina, would have a very narrow stability range corresponding to very small departures from stoichiometry and very low defect concentrations. A less stable oxide, such as  $\text{Ni}_{1-\delta}\text{O}$ , would have larger stability range and thus larger defect concentration, in which case it is equal to  $\delta/\Omega$ .

### 1.06.2.2 Dislocations

Dislocations are linear defects involved in mechanical behavior, mass transport, and reactivity of materials.<sup>5</sup> In a crystal, a dislocation is a line that, on one slip plane, forms the boundary between a crystal region that has slipped and an adjacent unslipped region so that the glide of the dislocation line results in plastic deformation (**Figure 3(a)**). Such a definition has simple but important consequences. One of them is that any dislocation cannot simply end in the bulk of a crystal; a dislocation must have its extremities on a surface, an interface or a grain boundary or intersect two other dislocations to form a dislocation node or else form a dislocation loop. Dislocations are characterized by the direction of the dislocation line and the slip vector or Burgers vector  $\mathbf{b}$  defining the relative displacement of slipped and unslipped crystal regions. **Figures 3(b) and 3(c)** illustrates schematically the two limiting types or characters of dislocations:

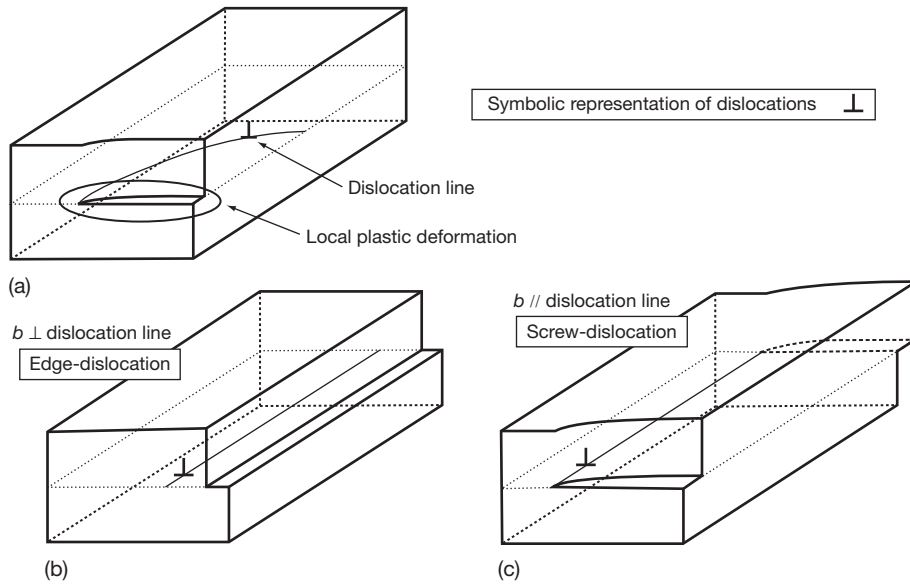


**Figure 3** Schematic definition of dislocations: (a) mixed dislocation, (b) edge dislocation, and (c) screw dislocation.

1. edge dislocations for which  $\mathbf{b}$  is normal to the dislocation line (**Figure 3(b)**),
2. screw dislocations for which  $\mathbf{b}$  is parallel to the dislocation line (**Figure 3(c)**).

A dislocation loop has a mixed character when its Burgers vector lies in the plane of the loop, some parts are edge and some parts are screw. Such a loop may glide in its own plane. On the contrary, when the Burgers vector is normal to the loop plane, the dislocation loop, named prismatic loop, is a pure edge dislocation and cannot glide.

Dislocations induce local displacements of lattice sites from their equilibrium position. These displacements result in strain and stress fields around each dislocation. The related elastic strain energy per unit length of dislocation line is proportional to  $b^2$  so that the dislocation lines tend to be straight to minimize the energy added to the crystal. One other consequence is that the Burgers vector  $\mathbf{b}$  of stable dislocations is the shortest translation vector of the crystal lattice, which permits to infer easily the possible Burgers vectors of dislocations for simple crystal lattices – as, for example, the fcc lattice of pure metals. These dislocations are called perfect dislocations. One perfect dislocation of Burgers vector  $\mathbf{b}_1$  can dissociate into two partial dislocations of Burgers vectors  $\mathbf{b}_2$  and  $\mathbf{b}_3$  separated by a bidimensional defect called stacking fault. The Burgers vectors  $\mathbf{b}_2$  and  $\mathbf{b}_3$  of such partial dislocations are a fraction of lattice

translation vectors, which justify their denomination of partial dislocations. Such a dislocation dissociation is energetically favorable, only if  $b_1^2 > b_2^2 + b_3^2$ . The example of fcc metals is well known and described in many basic textbooks.<sup>5</sup>

The definitions of perfect edge and screw dislocations emphasize their role in plastic deformation by dislocation glide. But, dislocation motion is not restricted to gliding and dislocation lines are usually not straight. Indeed, many irregularities are commonly observed along dislocation lines resulting from dislocation intersections and also from thermal activation.<sup>5</sup> These irregularities can be described as more or less sharp steps distributed along a dislocation line. One step lying in the dislocation slip plane forms a kink, but such a step forms a jog when it is normal to the slip line (**Figure 4**). Kinks and jogs can move by glide, the slip plane is then stepped for jogged dislocations. On the contrary, the displacement of a jog along one dislocation moves the dislocation line in a direction normal to its slip plane; such a movement is called climb. Climb occurs at jogs by the creation/annihilation of vacancies and interstitials. Jog moving along an edge dislocation line acts as a source or sink for vacancies and interstitials, as illustrated by **Figure 5**. The interactions among the jog, dislocation climb, and intrinsic point defects play an important role in the recovery and creep as well as in point defect equilibrium – and thus on transport processes – at high temperature, that is, at  $T > 0.4T_m$  for metallic materials.



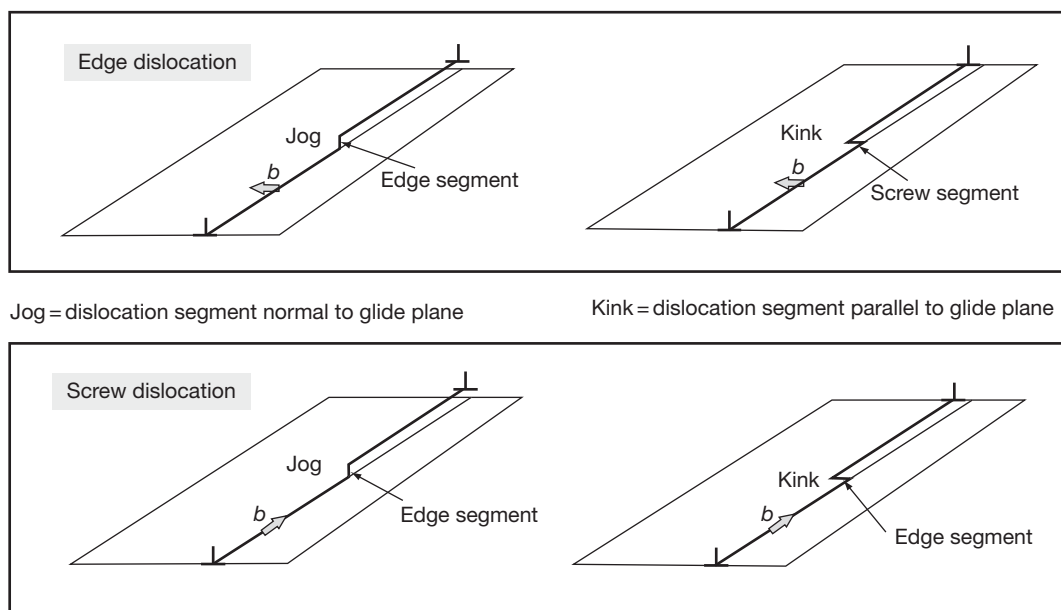


**Figure 4** Kink and jog on edge and screw dislocations.

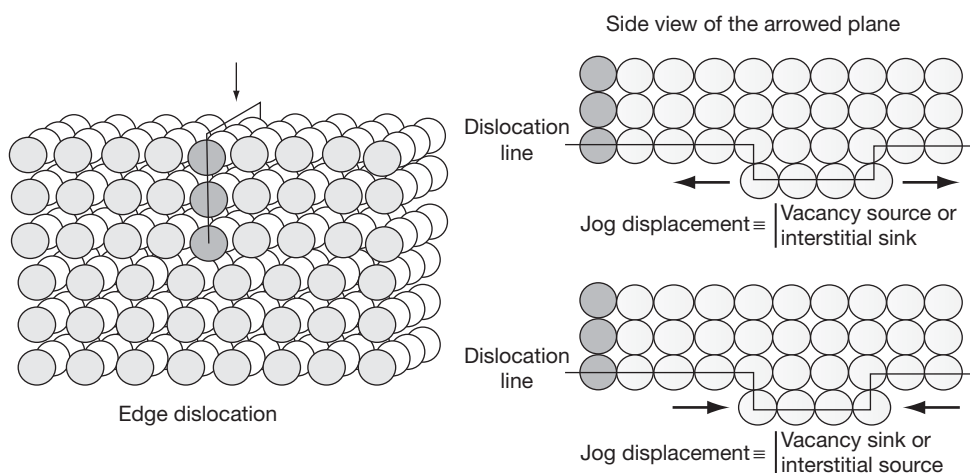


**Figure 5** Schematic representation of the sink/source action of an edge dislocation from climb by jog displacement along the dislocation line.

All the above definitions are valid for disordered metallic materials. The situation is often more complex for intermetallic, covalent, and ionic compounds. The ordered structure of intermetallic compounds like  $\beta$ -NiAl leads to perfect superdislocations that dissociate to form antiphase boundaries bounded by dissociated dislocations. In covalent compound, most of the binding energy is localized in the nearest-neighbor bonds; the structure of glide dislocations is thus complex and involves dangling bonds so that the glide of such dislocations results in the successive

breaking and reformation of chemical bonds. For ionic compounds, electrical neutrality and electrostatic interactions between ions of opposite charges results in quite complicated electrical effects for dislocations. **Figure 6** shows that a dislocation in a simple 2D ionic crystal induces a local charge at the dislocation emergence. Furthermore, for the dislocation shown in **Figure 6**, the glide along direction  $x$  will be easier than the glide along direction  $z$ . Indeed, the glide along  $x$  maintains a separation between ions of same sign, which is not the case of glide along  $z$

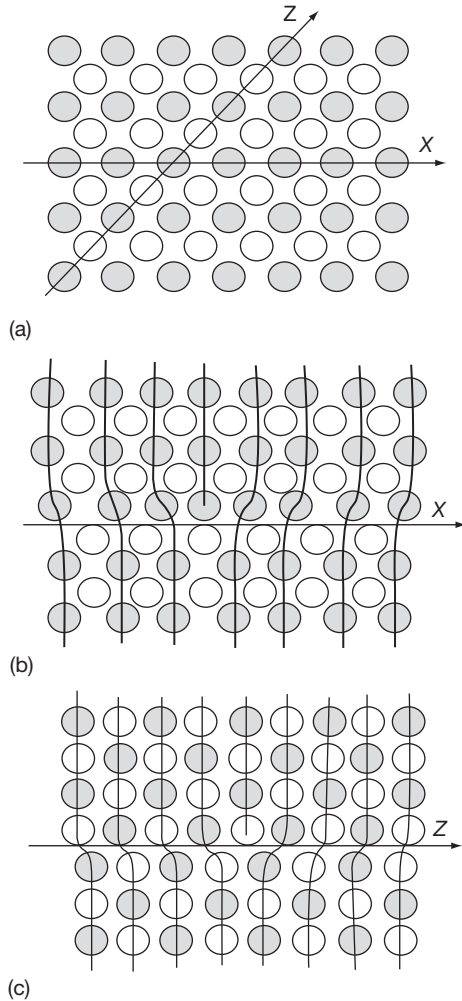


**Figure 6** Dislocation glide in an ionic compound: (a) possible compact glide directions, (b) dislocation formed by glide along z direction, and (c) dislocation formed by glide along x direction.

direction. Kinks and jogs are also observed for dislocations present in ionic materials; dislocation climb by the interaction of dislocations and point defects remain the rule, which is of great importance for high temperature deformation (creep) and mass-transport processes in ionic compounds.

### 1.06.2.3 Surfaces

Mass and energy exchanges between a solid phase and its environment always proceed from its surface. Many processes such as, for example, adsorption and segregation, surface chemical reactions or else nucleation and crystal growth depend on the structure and properties of surfaces.<sup>6</sup> Atoms, molecules, or ions on a crystal surface have not the same number of nearest neighbors than in the bulk of the crystal; the surface of a solid crystal phase is thus a discontinuity, and consequently, a bidimensional crystal defect. Moreover, such a difference in surface and bulk environment is at the origin of surface energy  $\gamma$ , expressed in Joules per square meter, or surface tension (then expressed in the equivalent unit of  $\text{N m}^{-1}$ ). For a solid, surface energy depends on the surface orientation; this dependence determines the equilibrium shape of the crystal by minimizing its total surface energy.

The most common model of ideal and unrelaxed surfaces for solid crystal phases is the terrace–ledge–kink (TLK) model schematized in Figure 7. According to this model, surfaces are classified into three categories: singular, vicinal, and rough. A singular surface corresponds to a surface orientation perfectly parallel to a crystal plane of low Miller index. Such a singular surface is formed by one single terrace, that is,

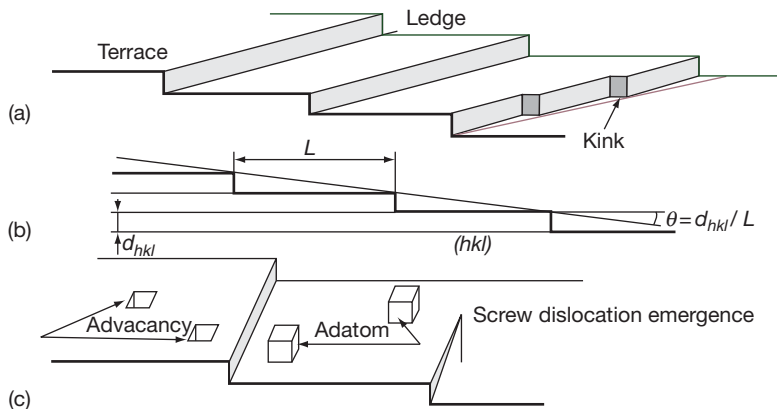


**Figure 7** TLK model of crystal surface: (a) definition of terraces, ledges, and kinks, (b) relation between surface disorientation and ledge spacing, and (c) surface point defects.

a surface essentially smooth on an atomic scale. Vicinal surfaces have an orientation close to a singular surface. For disorientations along only one direction, the departure from the exact orientation is accommodated by one set of ledges, that is, steps parallel to a low-index crystal direction and delimiting successive terraces. The height of ledges is usually equal to the interplanar spacing of reticular planes parallel to the terraces; thus, the height and spacing of ledges can be easily related to the angular disorientation of the vicinal surface relatively to the singular orientation of terraces. For vicinal surfaces disoriented in two directions, the departure from the ideal orientation of terraces is accommodated by ledges and kinks forming single steps along the ledges. The spacing between successive kinks is similarly related to the surface disorientation.

Ledges and kinks have an important role in surface reactivity; as schematized in **Figure 7**, adsorption or segregation on a terrace or at a ledge or a kink are not equivalent. Similarly, ledges and kinks are important in crystal growth processes and, more generally, surface defects play an equally important role in surface reactivity. The main surface defects are also described in **Figure 7**. The formation of these defects is thermally activated; more defects are formed as temperature increases, which results in the roughening of the surface becoming disordered and more reactive.

#### 1.06.2.4 Grain Boundaries and Interfaces

Grain boundaries and interfaces are surfaces where two single crystals of same nature and different orientation (grain boundary) or different nature and orientation (interface) join in a manner permitting some kind of matter continuity across these surfaces.<sup>7,8</sup> Such a surface introduces local discontinuities and thus must be considered as a bidimensional defect. By their shape, size, arrangement, and combination, grain boundaries and interfaces are important elements of the microstructure of materials and thus influence their properties. Microstructure is a non-equilibrium property of materials and as such is very sensitive to temperature, chemical composition, defect nature and concentration, mass transport processes, time, etc.

Similar to surface energy, grain-boundary energy results from the difference in local chemical environment between grain boundary and crystal, which in turn depends on the mutual orientation of the two adjacent crystals. For small disorientation, the

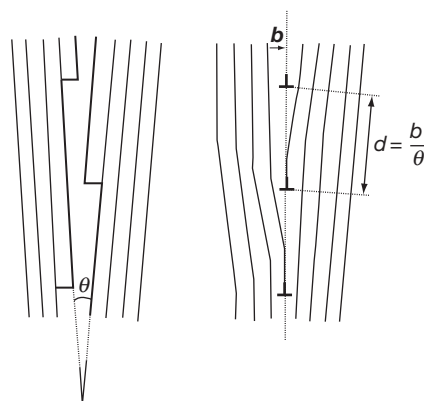


**Figure 8** Formation of a parallel array of edge dislocations at low-angle tilt boundary.

simplest grain boundary structure is obtained by joining two similar vicinal surfaces disoriented in one direction; that is, only formed of terraces and ledges, which, as shown in **Figure 8(a)**, is similar to a symmetric tilt rotation of axis parallel to the ledge direction. The resulting grain boundary is a low-angle tilt boundary that is formed by a set of parallel and equidistant edge dislocations of Burgers vector normal to the boundary plane (**Figure 8(b)**). One other simple structure is obtained by joining two similar singular surfaces slightly disoriented in a rotation of axis normal to these surfaces, which lead to a low-angle twist boundary formed by an array of screw dislocations of Burgers vectors parallel to the boundary. From these two limiting cases, any low-angle grain boundary, also called subboundary, may be described by a more or less complex array of edge and screw dislocations. For these subboundary models, dislocation spacing is inversely proportional to disorientation angle  $\theta$  so that they cannot hold when dislocation spacing is too small as that arise for  $\theta > 0.10$  rad.

However, the variation of grain-boundary energy as a function of a given disorientation angle shows minima for specific large disorientations. The simplest cases of such stable high-angle boundaries are twins similar to those usually observed for fcc or hcp metals. Several models were proposed to describe the structure of more general high-angle grain boundaries.<sup>7,8</sup> Dislocation models based on coincidence site lattice (CSL) are well adapted to high-angle boundaries near a twin boundary, but the description of grain boundary structure by polyhedral structural units is more realistic. The important point here is that, in addition to the orientation dependence

of grain-boundary structure and energy, there is a corresponding dependence of grain-boundary diffusivity upon disorientation.

The modeling of the structure of heterogeneous interfaces separating two different crystal phases is more complex. These interfaces are commonly classified into the three categories of coherent, semicoherent and incoherent interfaces. The coherent and semicoherent interfaces correspond to specific mutual orientations of the two adjacent crystal phases, which implies the parallelism of lattice planes and crystal directions. Independent of their structure, the mutual orientation expresses that two lattice planes and two crystal directions belonging to the specified lattice planes are both respectively parallel. For two crystals noted 1 and 2, such an orientation relationship is expressed in the following form:  $(b_1 k_1 l_1) [u_1 v_1 w_1] // (b_2 k_2 l_2) [u_2 v_2 w_2]$ , where the plane and direction indexes for crystal  $i$  must be such that  $b_i u_i + k_i v_i + l_i w_i = 0$  ( $i = 1, 2$ ) to express their parallelism.

**Figure 9** shows that, for the simplest case of two sets of parallel lattice planes of differing spacing, the disregistry of lattice planes can be accommodated by a parallel set of interfacial edge dislocations of Burgers vector parallel to the interface plane. These interfacial dislocations are named misfit dislocations. But, as lattice plane spacings are usually incommensurable, a small elastic deformation of both lattices is often required to permit their accommodation in the region of good fit, as exaggeratedly shown in **Figure 9**. The resulting stress field can influence the interface behavior and properties.

A relative twist rotation of the two sets of lattice planes can be accommodated by disorientation dislocations of Burgers vectors lying in the interface plane, that is, of screw character. More generally, as schematically shown in **Figure 10(a)**, any

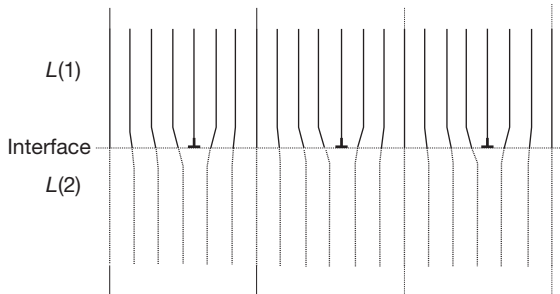


**Figure 9** Misfit dislocations formed at the interface separating two parallel lattices of different interplanar spacings.

heterogeneous interface can be modeled by a combination of misfit and disorientation dislocations, ledges and kink, and also a specific interfacial defect named disconnection<sup>9</sup> and symbolized by a dissymmetric dislocation symbol. Disconnections are defects specific to heterogeneous interface (**Figure 10(b)**), they have partly dislocation character and partly ledge character and are formed at the junction of two half planes of the same orientation; disconnections participate in lattice misorientations.

Surfaces, grain boundaries, and interfaces can also act as sources and sinks for vacancies and interstitials.<sup>10,11</sup> Like for edge dislocations, the displacement of kinks along a ledge or of jog along grain boundary or interface dislocations or else the displacement of interfacial ledges and kinks would result in the creation or annihilation of vacancies or interstitials.

*Remarks:* The intersection of three grain boundaries, named a triple junction, is a complex line defect. The structure and properties of these line defects are neither well known nor understood and appreciated. But, these defects are more open and disordered than dislocation or grain boundaries. Therefore, their role and contribution to mass transport is likely less negligible than considered till now, particularly for fine-grained materials such as oxide scales grown at intermediate temperatures where bulk diffusion is not predominant. Similar observations apply to triple junction line defects formed at the intersection of one grain boundary and one solid–solid interface.

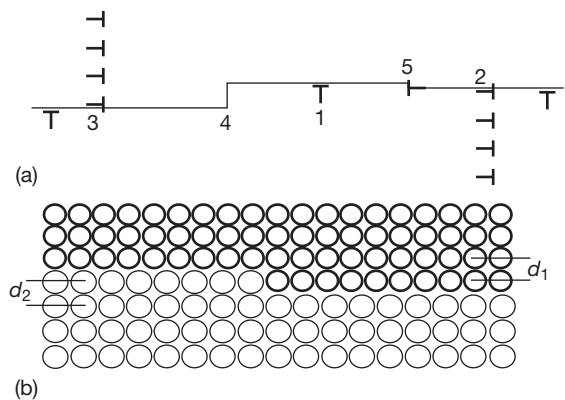


**Figure 10** Interfacial defects and disconnection: (a) interfacial line defects at a semi-coherent metal–oxide interface: 1, misfit dislocation; 2, misorientation dislocation with an extra half-plane in metal lattice; 3, misorientation dislocation with an extra half-plane in oxide lattice; 4, ledge; 5, disconnection. (b) Disconnection equivalent to a misorientation dislocation of Burgers vector modulus equal to  $d_2 - d_1$ .

### 1.06.3 Point Defects in Ionic Crystals

Binary ionic compounds are formed by interpenetrating anionic and cationic sublattices that contain point defects. Several textbooks provide a detailed treatment and analysis of point defect equilibria and defect-dependent properties of ionic compounds and metal oxides.<sup>12–15</sup>

Two kinds of point defect association permit to conserve the stoichiometry of a compound as illustrated in Figure 11 for an  $MX$  compound where  $M$  is a metal and  $X$  an oxidant. One association is the Frenkel defect or disorder consisting of the association of one cation vacancy and one interstitial cation. The other one is the Schottky disorder associating one cation vacancy and  $v$  anion vacancies for an  $MX_v$  compound. These two disorders are intrinsic defects. Indeed, an  $MX_v$  compound maintained at its ideal stoichiometry contains only Frenkel and/or Schottky disorders, but loses one degree of freedom so that the disorder concentration or its mole fraction only depends on temperature. As for pure elements, these thermal equilibria require operative sources or sinks of point defects. Departure of  $MX_v$  compounds from ideal stoichiometry arises from reactions with any phase – solid, liquid, or gaseous – containing  $M$  or  $X$  in a form different to  $MX_v$ ; these reactions obviously occur at the interface between  $MX_v$  and one of these other phases.

The thermal equilibrium of stoichiometric  $MX_v$  compound as well as the creation/annihilation of point defects from interfacial reactions can be treated with the usual concept of chemical reactions and the associated thermodynamic tools, that is, law of mass action, chemical potentials, and activities, but such a treatment requires a specific notation for point defects. This notation must permit to express reactions balanced with respect to conservation of matter, electrical neutrality, and lattice site ratio fixed by the exact stoichiometry of the considered compound.

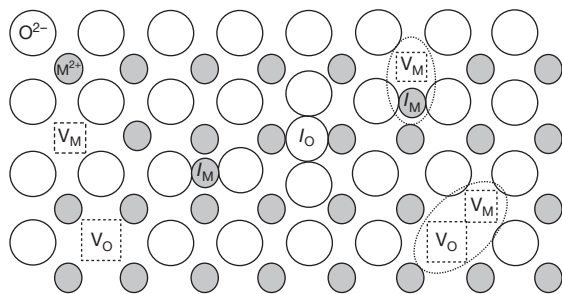


**Figure 11** Intrinsic point defects of a  $MO$  oxide.

#### 1.06.3.1 Structure and Building Elements: Kröger–Vink Notation

The commonly recommended and well-accepted notation for point defects has been suggested by Kröger and Vink and is, therefore, called Kröger–Vink notation. This notation is a symbolic representation of structure elements of defective crystals. A structure element is an atom, ion, molecule, or else vacancy or interstitial located on a specified lattice site of the perfect crystal lattice. The Kröger–Vink notation provides the following information on any kind of structure element:

1. the nature of the chemical species occupying one given lattice site in the real crystal,
2. the nature of the regular occupant of this given lattice site in the perfect crystal,
3. the effective electrical charge of the structure element.

The effective charge of a structure element is the difference between its charge in the real crystal and its charge in the neutral perfect crystal lattice. Positive effective charges are noted by dots and negative effective charges by commas or dashes; the sign ‘ $\times$ ’ is used for a null effective charge. A vacancy is represented by the symbol  $V$  and an interstitial is designed by the index  $i$  affected to any species occupying an insertion site. The sites of interstitial sublattice are all noted  $V_i$  as they are always empty in the perfect crystal. All these notations are illustrated and explained in Figure 12 while the notation of all possible neutral and charged single point defects of ionic compound  $MX_v$  is reported in Table 1. The use of Kröger–Vink notation is not restricted to ionic compounds; it can be extended to any kind of compounds; for nonionic crystal, the sign ‘ $\times$ ’ for null effective charge is then usually omitted.

The reaction of formation of intrinsic defects or the interfacial reactions between an ionic crystal and its environment often result in the formation or destruction of one or more building elements of the considered compound. A building element is a combination of structure elements that can be added or removed without affecting the ideal stoichiometry or, in other words, conserves the crystal structure by keeping the ratio between the different lattice sites constant. For example,  $M_M^{\times} + O_O^{\times}$  or  $V_M^{\times} + O_O^{\times}$  are additive building elements of oxide  $MO$ . Building elements relative to only one sublattice can also be defined; they must keep constant the total site

Form of Kröger-Vink notation :  $S_P^{q_{\text{eff}}}$

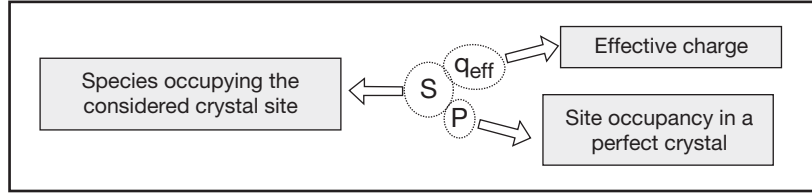
S = chemical symbol of the species localized on the considered lattice site in the real crystal

P = chemical symbol of the species localized on the considered lattice site in the perfect crystal

Additional symbols : V = vacancy

i = interstitial

$V_i$  = empty interstitial site



Effective charge = Site charge in the real crystal – Charge of the same site in the perfect crystal

Notation of effective charge : Positive effective charge : dot

Negative effective charge : comma

Neutral effective charge : cross

Additional symbols :  $h^*$  = electron hole

$e'$  = free electron

**Figure 12** Kröger-Vink notation of point defects.

**Table 1** Kröger-Vink notation of point defects in  $MO_v$  oxide

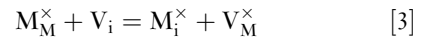
Defect type	Kröger-Vink notation
<i>Single point defect</i>	
Free electron	$e'$
Electron hole	$h^*$
Cationic impurity (charge $q > 2v$ )	$I_M^{(q-2v)}$
Cationic impurity (charge $q < 2v$ )	$I_M^{(2v-q) '}$
Neutral cation vacancy	$V_M^{\times}$
Ionized cation vacancy	$V_M^{n \bullet}$ ( $n \leq 2v$ )
Self-interstitial cation	$M_i^{n \bullet}$
Interstitial cationic impurity	$I_i^{q \bullet}$
Anionic impurity (charge $> 2$ )	$I_O^{(q-2) '}$
Anionic impurity (charge $< 2$ )	$I_O^{(2-q) \bullet}$
Neutral anion vacancy	$V_O^{\times}$
Ionized anion vacancy	$V_O^{n \bullet}$ ( $n \leq 2$ )
Self-interstitial anion	$O_i^{n '}$
Interstitial anionic impurity	$I_i^{q '}$
<i>Combined defects (<math>v</math> = integer number)</i>	
Schottky	$V_M^{2v '} + v V_O^{2 \bullet}$
Frenkel (or Frenkel-cation)	$M_i^{2 \bullet} + V_M^{2v '}$
Anti-Schottky	$M_i^{2 \bullet} + v O_i^{2v '}$
Anti-Frenkel (or Frenkel-anion)	$O_i^{2 '} + V_O^{2 \bullet}$

number of the considered sublattice to maintain the crystal structure and its stoichiometry; for the cation sublattice of  $MO$ , subtractive building elements such as  $V_M^{\times} - M_M$  or  $M_i^{\times} - V_i$  are compatible with this constraint.

### 1.06.3.2 Use of Kröger-Vink Notation: Formation Equilibria of Frenkel and Schottky Disorders

The aim of this section is to illustrate the use of Kröger-Vink notation on simple examples of Frenkel and Schottky disorders formed from only neutral defects and to underline some difficulties and limits of this notation.

The formation of cationic Frenkel disorders in  $MX_v$  only affects the cation sublattice. By using Kröger-Vink notation, the formation reaction of this disorder is



A similar disorder may also affect the anion sublattice (anionic Frenkel or anti-Frenkel disorder). Equation [3] fulfills the conditions of matter and lattice site balances. However, the law of mass action cannot be directly applied to eqn [3]. Indeed, like for an ionic solution for which it is not possible to vary the amount of only one ionic species while keeping all the other ones constant, it is not possible to maintain constant the number of regularly occupied cationic sites or the number of empty interstitial sites of the cation sublattice and to simultaneously create a cation vacancy or an interstitial cation. Equation [3] shows that the chemical potential, and thus the activity, of individual structure elements cannot be defined and expressed in their usual form. However, eqn [3] can be transformed to



$$0 = (M_i^\times - V_i) + (V_M^\times - M_M^\times) \quad [4]$$

where 0 represents the perfect lattice. The chemical potential and activity of subtractive building elements appearing in eqn [4] can then be defined and thus the law of mass action can be applied to this equation leading to

$$K_{FC} = a_{(M_i^\times - V_i)} a_{(V_M^\times - M_M^\times)}$$

where  $K_{FC} = \exp(-\Delta g/RT)$  is the equilibrium constant for the formation of cationic Frenkel disorder and  $\Delta g$  the molar free energy of formation of this disorder at temperature  $T$ . The number of each subtractive building element is equal to the number of each associated point defects. Therefore, by assuming that the mole fractions of cation vacancies and interstitials are very small, an ideal behavior may be assumed and the activity of the building elements can be taken as equal to their mole fraction and therefore to the mole fraction of the associated point defects, so that

$$K_{FC} = x_{M_i^\times} x_{V_M^\times} \quad [5]$$

Although incorrect, the application of mass action law to eqn [3] leads to eqn [5] by assuming that defective and regular structure elements form a dilute ideal solid solution, the activity of regular structure elements (solvent) is then equal to 1 while the activity of defective structure elements (solutes) is equal to their mole fraction.

Both cationic and anionic sublattices are involved in the formation equilibrium of Schottky disorders. The following formation equilibrium expresses that  $v$  independent anionic structure elements and one cationic structure element combine to form a new  $MX_v$  unit and equivalent number of vacancies

$$M_M^\times + vX_X^\times = V_M^\times + vV_X^\times + MX_v \quad [6]$$

or, in the form of subtractive building elements

$$0 = (V_M^\times - M_M^\times) + v(V_X^\times - X_X^\times) + MX_v \quad [6']$$

But, eqn [6] can be simplified by considering that there is no formal difference between the  $MX_v$  unit and the additive building element  $M_M^\times + vX_X^\times$ , which leads to the following equilibrium reaction for the formation of Schottky disorders:

$$0 = V_M^\times + vV_X^\times \quad [7]$$

A similar equilibrium, usually named anti-Schottky disorder, involves only interstitial defects. Under the same restrictive conditions as for Frenkel disorders, the mass action law applied to eqn [6'] or to eqn [7] leads to

$$K_{SV} = x_{V_M^\times} \cdot (x_{V_X^\times})^v \quad [8]$$

$K_{SV}$  is the equilibrium constant for Schottky disorders involving vacancies ( $K_{Si}$  would be used for anti-Schottky disorders).

Therefore, for the sake of simplicity, but keeping in mind that such a procedure is not thermodynamically correct, the law of mass action will be applied to equilibrium reactions, written by using the Kröger–Vink notation with the restriction that the defect mole fractions remain sufficiently small to allow the assumption of ideal behavior.

### 1.06.3.3 Electronic Defects and Ionized Point Defects

In semiconductors and ionic compounds, the energy levels of the outer electrons form two energy bands: the valence and conduction bands separated by a forbidden band or gap. At 0 K, the valence band contains all the outer electrons while the conduction band is empty. Similar to the formation of a Frenkel defect, as the temperature increases, the energy of electrons increases up to a limit to permit the jump of electrons from the valence band to the conduction band. Such a jump creates a free or excess electron occupying a regular empty level of the conduction band and a vacant electronic level, or electron hole, in the valence band. Free electrons and electron holes are mobile electronic defects of, respectively, negative and positive effective charges. Thus, according to Kröger–Vink notation, free electrons are noted as  $e'$  and electron holes – also called positive holes – are noted as  $h'$ . The equilibrium of electronic defects is then:

$$0 = e' + h' \quad [9]$$

The equilibrium constant  $K_e$  is:

$$K_e = np = \exp\left(-\frac{E_g}{RT}\right)$$

where  $n$  and  $p$  are, respectively, the molar fraction of electronic defects  $e'$  and  $h'$ , and  $E_g$  the energy gap.

Point defects and electronic defects can interact to form ionized point defects. Compared with perfect crystal, point defects are in an excited state of higher energy: their outer electrons occupy energy levels localized in the forbidden bands. There are two kinds of such levels: the donor levels close to the conduction band and the acceptor ones close to the valence band; the donor levels easily release electrons to the conduction band while acceptor levels easily accept electrons from the valence band.

For example, a neutral cationic interstitial  $M_i^\times$  induce a local excess of electrons and then acts as a donor. For a monovalent metal, the ionization equilibrium is

$$M_i^\times = M_i^\bullet + e' \quad [10]$$

For a divalent metal, there are two ionization equilibria, one similar to eqn [10] and the other

$$M_i^\bullet = M_i^{\bullet\bullet} + e' \quad [10']$$

On the contrary, a neutral cation vacancy induces a local electron deficit and acts as an acceptor

$$V_M^\times = V_M' + h \quad [11]$$

Similarly, a neutral anion vacancy acts as a donor and a neutral anionic interstitial as an acceptor

$$V_X^\times = V_X^\bullet + e' \quad [12]$$

$$X_i^\times = X_i' + h \quad [13]$$

Other ionization equilibria are possible depending on the oxidation state of the metallic and/or oxidant constituents of  $MX_v$ . The mass action law is applicable to all these ionization equilibria, which permits, in combination with the equilibrium of electronic defects and the condition of electrical neutrality, to determine the equilibrium molar fractions of ionized and electronic defects.

#### 1.06.3.4 Point Defect Equilibria in Nonstoichiometric Oxides

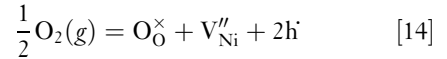
For any oxide  $MO_v$ , departure from ideal stoichiometry results in an O/M ratio not equal to  $v$ . This ratio is greater than  $v$  for metal deficit ( $M_{1-\delta}O_v$ ) or oxygen excess ( $MO_{v+\delta}$ ) and smaller than  $v$  for metal excess ( $M_{1+\delta}O_v$ ) or oxygen deficit ( $MO_{v-\delta}$ ). The departure from stoichiometry  $\delta$ , and thus the equilibrium molar fractions of ionic point defects and electronic defects, depends on temperature and oxygen or metal activity. But,  $\delta$  is usually expressed as a function of  $T$  and oxygen partial pressure  $P_{O_2}$ .

A specific type of point defect is commonly predominant in nonstoichiometric oxides such as nickel oxide  $Ni_{1-\delta}O$  or zirconia  $ZrO_{2-\delta}$ . Equations [10]–[13] show that the ionization of point defects results in the formation of electronic defects; therefore, the predominance of one specific ionized point defect induces the predominance of one specific type of electronic defect. Thus, as the mobility of electronic defects is much higher than that of ionic defects or species, most of nonstoichiometric oxides behave like semiconductors. Nonstoichiometric oxides are p-type semiconductors if the dominant electronic defects are

positive holes and inversely n-type semiconductors if free electrons are dominant.

##### 1.06.3.4.1 p-Type oxides

Common p-type oxides present a metal deficit or an oxygen excess. Nickel oxide  $Ni_{1-\delta}O$  is a typical example of a metal-deficient oxide. Over a large range of oxygen partial pressure, numerous experimental evidences have revealed that doubly charged Ni cation vacancies  $V_{Ni}''$  are the predominant point defects in nonstoichiometric  $Ni_{1-\delta}O$ . The formation of these vacancies can be represented by the following equilibrium:



The dependence of molar fraction, ( $x_{V_{Ni}''} = \delta$ ), of  $V_{Ni}''$  and  $h$  on  $P_{O_2}$  is obtained from the mass action law applied to this formation equilibrium

$$K_{VC2} = \frac{x_{V_{Ni}''} \cdot p^2}{P_{O_2}^{1/2}} \quad [15]$$

where  $K_{VC2}$  is the equilibrium constant. The condition of electrical neutrality implies

$$2x_{V_{Ni}''} = p$$

These two relations give

$$x_{V_{Ni}''} = \left( \frac{K_{VC2}}{2^2} \right)^{1/3} P_{O_2}^{1/6}$$

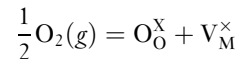
This result can be extended to cation vacancies of any charge  $q \leq 2v$  that can appear in nonstoichiometric  $M_{1-\delta}O_v$  oxides:

$$x_{V_M^{q/}} = \left( \frac{K_{VCq}}{q^q} \right)^{1/(q+1)} P_{O_2}^{v/2(q+1)} \quad [16]$$

and

$$p = qx_{V_M^{q/}}$$

The charge of predominant defects may vary with  $P_{O_2}$  depending on the free energy of formation of these defects or, which is equivalent, the equilibrium constants associated to their ionization equilibrium. For example, the cation vacancies of p-oxide  $M_{1-\delta}O$  may be neutral, singly charged, or doubly charged, so that  $\delta = x_{V_M^\times} + x_{V_M'} + x_{V_M}''$ . The molar fractions can be calculated from the three simultaneous equilibria



$$V_M^\times = V_M' + h$$

$$V_M' = V_M'' + h$$

and the condition of electrical neutrality

$$p = x_{V'_M} + 2x_{V''_M}$$

This last equation determines the two domains where one charged defect dominates

$$x_{V'_M} \ll 2x_{V''_M} \Rightarrow x_{V''_M} = p/2$$

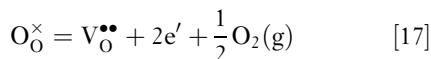
$$x_{V''_M} \ll x_{V'_M} \Rightarrow x_{V'_M} = p$$

This procedure, known as Brouwer's approximation, can be applied to any combination of ionized points defects; it simplifies greatly the calculation of defect equilibria and their representation.

Oxides with oxygen excess caused by interstitial anions are also p-type semiconductors. However, because of the large size of oxygen anions compared to metal cations, such p-type oxides are rather uncommon in usual high temperature materials.

#### 1.06.3.4.2 n-Type oxides

Zirconium oxide  $ZrO_{2-\delta}$  and zinc oxide  $Zn_{1+\delta}O$  are typical of n-type oxides. For  $ZrO_{2-\delta}$ , the formation of doubly charged oxygen vacancies is expressed by the equilibrium



The dependence of molar fraction of  $V_O^{\bullet\bullet}$  and  $e'$  on  $P_{O_2}$  is obtained from the law of mass action

$$K_{V2a} = nx_{V_O^{\bullet\bullet}}P_{O_2}^{1/2}$$

and the condition of electrical neutrality

$$n = 2V_O^{\bullet\bullet}$$

These two relations give

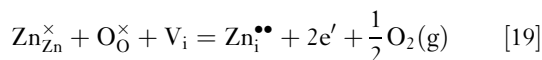
$$x_{V_O^{\bullet\bullet}} = \left( \frac{K_{V2a}}{2^2} \right)^{1/3} P_{O_2}^{-1/6}$$

where  $K_{V2a}$  is the equilibrium constant.

Again, this result can be extended to oxygen vacancies of charge  $q$  ( $0 \leq q \leq 2$ )

$$x_{V_O^{q\bullet}} = \left( \frac{K_{VAq}}{q^q} \right)^{1/(q+1)} P_{O_2}^{-1/2(q+1)} \quad [18]$$

Oxides like  $Zn_{1+\delta}O$  with charged interstitial cations are also n-type semiconductors. The formation equilibrium of doubly charged interstitials  $Zn_i^{\bullet\bullet}$  is



where  $V_i$  is a vacant site of the interstitial cation sublattice. Comparison of eqns [17] and [19] permits to easily understand that the mole fraction of charged

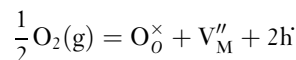
interstitial cations is expressed by a relation similar to eqn [18], with an equilibrium constant  $K_{iCn}$ . Equations [16] and [18] show that the mole fractions of ionic and electronic defects increase in p-type oxides and decrease in n-type oxides, at increasing  $P_{O_2}$ .

#### 1.06.3.5 Intrinsic Defect Equilibria Close to Stoichiometry

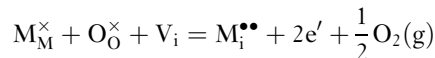
The nature of the dominant defect may vary depending on  $P_{O_2}$ . Some amphoteric p-type oxides can present a metal excess at low  $P_{O_2}$  and a metal deficit at higher  $P_{O_2}$ . Reverse situation may be encountered for n-type oxides with an oxygen deficit at low  $P_{O_2}$  and an oxygen excess at higher  $P_{O_2}$ .

Considering the case of an oxide MO with predominant fully ionized cationic defects, the defect equilibria to be considered are:

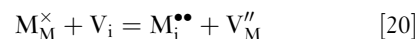
- formation of doubly charged cation vacancies (equilibrium constant  $K_{VC2}$ )



- formation of doubly charged interstitial cations (equilibrium constant  $K_{iC2}$ )



and the electronic equilibrium (eqn [9]) as both  $e'$  and  $h$  are involved in ionic defect equilibria. The combination of these three equilibria gives the equilibrium formation of a cationic Frenkel disorder (equilibrium constant  $K_{FC}$ )



The condition of electrical neutrality is

$$2x_{M_i^{\bullet\bullet}} + h = 2x_{V_M^{\bullet\bullet}} + e' \quad [21]$$

At the stoichiometric composition, molar fractions  $p$  and  $n$  of electronic defects are equal,  $p = n = K_e^{1/2}$ , and similarly the molar fractions of ionic defects,  $x_{M_i^{\bullet\bullet}} = x_{V_M^{\bullet\bullet}} = K_{FC}^{1/2}$ , which from eqns [16] and [18] corresponds to  $(P_{O_2})_{\text{stoi}} = K_{iC2}/K_{VC2}$ . In the vicinity of their stoichiometric composition, such oxides could have different behavior and properties depending on the relative magnitude of the equilibrium constants  $K_e$  and  $K_{FC}$ . Two different situations are possible:

1.  $K_e \gg K_{FC}$ ; in that case,  $x_{M_i^{\bullet\bullet}} \ll h$  and  $x_{V_M^{\bullet\bullet}} \ll e'$  and therefore the equality  $p = n = K_e^{1/2}$  hold on a more or less large range of  $P_{O_2}$  while  $x_{V_M^{\bullet\bullet}}$  and  $x_{M_i^{\bullet\bullet}}$  remain small but vary as a function of  $P_{O_2}$ ,

2.  $K_e \ll K_{FC}$ , which implies  $x_{M_i^{\bullet\bullet}} \gg h'$  and  $x_{V_M''} \gg e'$ ; then, the equality  $x_{M_i^{\bullet\bullet}} = x_{V_M''} = K_{FC}^{1/2}$  is verified while  $p$  and  $n$  vary with  $P_{O_2}$ .

In case (1), the electronic defects predominate; such oxides are intrinsic electronic oxides; their electrical conductivity is purely electronic and independent of  $P_{O_2}$ . For the opposite case (2), the ionic defects are predominant; these oxides are intrinsic ionic oxides. Their electrical conductivity can present a significant ionic component but the electronic component is usually not negligible because of the higher mobility of electronic defects.

Out of the vicinity of stoichiometric composition, all the ionic and electronic defects coexist but their molar fraction strongly depends on  $P_{O_2}$ . From eqns [19] and [16], cation vacancies and electron holes, of molar fractions  $h' = 2x_{V_M''}$ , are predominant at  $P_{O_2}$  significantly higher than  $(P_{O_2})_{stoi}$ . Similarly, from eqns [20] and [18], interstitial cations and free electrons, of molar fractions  $2x_{M_i^{\bullet\bullet}} = e'$ , are predominant at  $P_{O_2}$  lower than  $(P_{O_2})_{stoi}$ .

### 1.06.3.6 Effect of Impurities on Defect Equilibria

The above simplified treatment of ionic and electronic defects in oxide only considers perfectly pure oxides, which is a rather uncommon case, particularly for oxide scale grown on a metallic alloy. Indeed, the molar fractions of ionic and electronic defects are strongly affected by the presence of small amounts of impurities of different oxidation state. In some instances, the effect of impurities may be so large that it can induce an inversion of the type of predominant defects.

The influence of a trivalent impurity, like chromium, on the molar fraction of ionic defects in a nonstoichiometric p-type oxide such as nickel oxide  $Ni_{1-\delta}O$  is a typical and well-known example. Chromium cations  $Cr^{3+}$  are in substitution in the cationic sublattice and constitutes a new structure element  $Cr_{Ni}^{\bullet}$ . The condition of electrical neutrality is then

$$x_{Cr_{Ni}^{\bullet}} + p = 2x_{V_{Ni}''} \quad [22]$$

For  $Ni_{1-\delta}O$ , the departure to stoichiometry  $\delta$ , and thus the mole fraction of electron holes, is lower than  $10^{-3}$  at temperatures lower than  $1300^\circ C$ . Therefore, a molar fraction of Cr higher than  $10^{-2}$  is sufficient to induce a significant increase of vacancy and electron hole molar fractions. Indeed, for a mole fraction  $x_{Cr_{Ni}^{\bullet}} \gg p$ , eqns [16] and [22] leads to

$$x_{V_{Ni}''} = \frac{x_{Cr_{Ni}^{\bullet}}}{2} \text{ and } p = \left( \frac{2K_{VC2}}{x_{Cr_{Ni}^{\bullet}}} \right)^{1/2} P_{O_2}^{1/4}$$

Depending on  $x_{Cr_{Ni}^{\bullet}}$  and  $P_{O_2}$ , the molar fraction  $p$  can reach very small values so that the intrinsic electronic equilibrium should be taken into account. Free electrons may become predominant, resulting in an inversion from p-type to n-type oxide. A similar analysis can be performed for the influence of monovalent impurities such as Li or Na. A sufficiently large amount of such impurities may induce an inversion of the type of major ionic defect from cation vacancies to interstitial cations.

This analysis can also be extended to nonstoichiometric n-type oxides. A typical example is given by zirconia  $ZrO_{2-\delta}$ . Its tetragonal and cubic crystal structures can be stabilized (SZ) or partially stabilized (PSZ) by the addition of CaO or  $Y_2O_3$ . A large increase in anion vacancies and an inversion from n-type to p-type are induced by these additions; ionic defects are predominant, and SZ and PSZ are extrinsic ionic oxides.

For all the possible situations, the effect of impurities can be summarized as follows:

- For p-type oxides, the addition of cations of higher oxidation degree induces a decrease of positive holes and an increase of cation vacancies for oxides  $M_{1-\delta}O_v$ , or of oxygen interstitials for  $MO_{v+\delta}$ ; cations of lower oxidation degree have the reverse effect.
- For n-type oxides  $M_{1+\delta}O$ , the addition of cations of higher oxidation degree induces an increase in free electrons and a decrease in anion vacancies for  $MO_{v-\delta}$  oxides or cation interstitials for  $M_{1+\delta}O$  oxides, cations of lower oxidation degree has the reverse effect.

### 1.06.3.7 Extended Defects

At sufficiently high molar fractions, the interactions between point defects may lead to the formation of more complex defects. The most common example is wüstite,  $Fe_{1-\delta}O$ , where cation vacancies form ordered defect clusters. However, the formation of these defect clusters is directly linked to the large departure  $\delta$  (up to 0.15) of  $Fe_{1-\delta}O$  from stoichiometry. Such defect clusters are not observed in oxides, such as CoO and NiO, of smaller stoichiometry departure; for CoO,  $\delta$  remains smaller than  $10^{-2}$  up to about  $1400^\circ C$  and is 10–100 smaller for NiO.

Other complex defect structures are known to be present in oxides like  $TiO_2$  and derived suboxides

$\text{Ti}_n\text{O}_{2n-1}$ , and also in many other oxides of transition metals. However, up to now, these complex defects and/or oxide structures have not been observed in oxide scales grown from high temperature oxidation of metallic materials.

#### 1.06.4 Diffusion Laws and Mass Transport in Solid State

The growth of a single oxide scale or a complex corrosion scale both require the diffusion of molecular and/or ionic chemical species through the growing scale and/or the diffusion within the oxidized or corroded substrate of their chemical components toward the scale–substrate interface as usually required for the selective oxidation of the less-noble substrate component or deeper into the substrate for the more noble components. Diffusion is commonly driven by the concentration gradients of diffusing species, as expressed by diffusion laws. However, transport phenomena induced by internal or external forces can interact with concentration gradients to accelerate or slow down the motion of mobile chemical species. Useful definitions of terms specific to diffusion and matter transport in solid state are given in Kizikyalli *et al.*<sup>16</sup>

##### 1.06.4.1 Diffusion Laws

Matter movement by diffusion and/or transport in a phase is quantified by the flux of moving species, that is, a number of species per time unit and per unit area normal to the movement direction. Referring this movement relatively to a defined reference frame, the total flux  $\mathcal{J}_k$  of any species  $k$  along a direction  $x$  is given by

$$\mathcal{J}_k = -D_k \frac{\partial C_k}{\partial x} + \bar{v} C_k \quad [23]$$

Fluxes and concentrations are functions of time  $t$  and abscissa  $x$ . Equation [23] is a general form of the well-known Fick's first law evidencing the two components of total flux  $\mathcal{J}_k$  (in  $\text{mol m}^{-2} \text{s}^{-1}$ ):

1. the diffusion component is expressed by the term  $-D_k(\partial C_k/\partial x)$ , where  $D_k$  (in  $\text{m}^2 \text{s}^{-1}$ ) is the diffusion coefficient of species  $k$  and  $C_k$  (in  $\text{mol m}^{-3}$ ) its local concentration;
2. the transport component, induced by internal or external forces, corresponds to the term  $\bar{v} C_k$  where  $\bar{v}$  is the average displacement rate of all species moving relative to the reference frame.

The relative influence of these two terms is illustrated in Figure 13 that corresponds, for example, to the

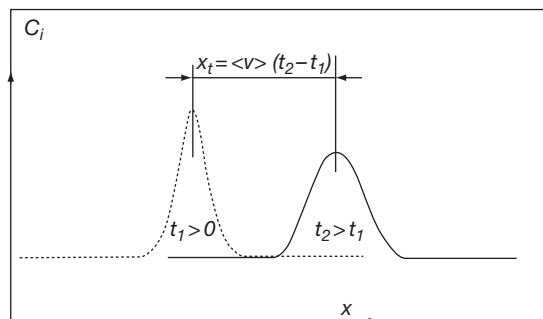


**Figure 13** Diffusive and displacement components of flux relative to the fixed frame ( $x, C$ ).

broadening of a drop of colored solute in a slowly flowing fluid. The concentration profile of the colored solute at time  $t_2 > t_1$  is the sum of the two contributions of eqn [23]: broadening of the concentration profile due to the diffusion under the only influence of concentration gradient and displacement  $x_t$  of this concentration profile with the fluid flow under a force such as, for example, the gravitation force.

The displacement rate  $\bar{v}$  depends on the force  $f$  acting on the moving species as expressed by the Nernst–Einstein relation

$$\bar{v} = D \frac{f}{RT} \quad [24]$$

However, in many practical situations, there is no external or internal force acting on the moving species. Equation [23] reduces to the common form of Fick's first law

$$\mathcal{J}_k = -D_k \frac{\partial C_k}{\partial x} \quad [25a]$$

Equations [23] and [25a] are only useful in conditions such that  $\partial C_k/\partial x$  remains constant (stationary state) or can be easily assessed as in the growth of an oxide scale on a metal when both metal–scale and scale–gas interfaces are assumed to remain in equilibrium (pseudo stationary state) as the oxidation proceeds.

For all other situations, the resolution of diffusion problems required to solve the Fick's second law, the general diffusion equation expressing the conservation of matter:

$$\frac{\partial C_k}{\partial t} = -\frac{\partial \mathcal{J}_k}{\partial x} \quad [25b]$$

For a pure diffusion process and constant diffusion coefficient  $D_k$ , this equation transforms into

$$\frac{\partial C_k}{\partial t} = D_k \frac{\partial^2 C_k}{\partial x^2} \quad [26]$$



In eqns [23]–[26], the use of molar concentration in the expression of the local composition is essentially a practical choice. A more formal, and physically more correct, expression links the diffusion coefficient  $D_k$  to the chemical potential of species  $k$ . Indeed, Fick's laws apply only to systems assumed in local equilibrium, that is, such that the thermodynamic properties of all system constituents are determined from all the state variables required for a complete description of the system equilibrium states, independent of the local gradient of these state variables.

Equation [26] can be solved analytically. The solution depends on the initial and limit conditions; many textbooks describe the most common solutions.<sup>17–20</sup> For the general case of concentration-dependent diffusion coefficients, the solving of the general diffusion equation [25b] required the use of numerical methods that are now implanted in many types of mathematical software.

#### 1.06.4.2 Lattice Diffusion and Diffusion Mechanisms

In many cases of diffusion in a crystal phase, one constituent forms an immobile sublattice that determines a fixed frame of reference where eqns [25] and [26] can be applied to diffusing species. For a given crystal phase, site-to-site jumps of diffusing species are the most common elementary steps of diffusion processes, but such jumps must preserve the major characteristics of the crystal structure of the phase. Therefore, the diffusion of atoms, molecules, or ions within a crystal phase is only possible in the presence of crystal defects. The simplest situation is the diffusion of small interstitial impurities within a fixed host lattice. Interstitial species then jump from one interstitial site to one of the closest adjacent interstitial sites. A common example of simple interstitial diffusion is the diffusion of interstitial oxygen atoms dissolved in  $\alpha$ -Ti or  $\alpha$ -Zr during their oxidation at high temperature. The host lattice can be also assumed immobile for the diffusion of highly diluted substitutional impurities. One impurity atom, ion, or molecule occupying a lattice site having one vacancy for nearest neighbor can jump to exchange its position with this vacancy. Such a vacancy exchange results in the motion of vacancies in a direction opposite to the diffusion of substitutional impurities. The dilute substitutional impurities can be replaced by some specific marked species of one constituent of the host lattice. For example, radioisotope  $^{63}\text{Ni}$  can be introduced in pure nickel or nickel compounds

such as NiO. These marked species can also exchange their position with adjacent vacancies of Ni lattice or cation sublattice of NiO, thus leading to random displacements and dispersion of marked species under the only influence of thermal activation. Such a diffusion process is named self-diffusion. Therefore, for a system remaining in local equilibrium, the self-diffusion coefficient  $D_{\text{sd}}$  can be expressed as the product of vacancy molar fraction  $x_v$  and vacancy diffusivity  $D_v$

$$D_{\text{sd}} = x_v D_v \quad [27]$$

However, vacancy diffusivity  $D_v$  is not formally equivalent to a diffusion coefficient because vacancies are nonconservative species of concentration remaining constant and equal to its equilibrium value everywhere as imposed by the assumption of local equilibrium. Equation [27] remains valid for the self-diffusion in a given sublattice as, for example, the self-diffusion of cation in the cationic sublattice of an ionic compound. However, for the diffusion of marked species or dilute impurities, the analysis is more complex than reflected by eqn [27]. Indeed, the environment of marked or impurity species changes after their jump so that all jump directions are not equivalent for such species, which leads to the introduction of a correlation factor taking into account this effect that is neglected in eqn [27].

The interstitial and vacancy exchange mechanisms are the two basic mechanisms of lattice or bulk diffusion. They are valid for many kinds of materials; however, other elementary mechanisms involving more complex defects or jump sequences may be encountered in specific situations such as, for example, diffusion in intermetallic compounds, or diffusion under high energetic fluxes as occurring in materials used in nuclear power plants. Such complex diffusion processes are out of the scope of this chapter.

Both interstitial and substitutional diffusion mechanisms involve atomic jumps requiring the overcoming of an energy barrier. Diffusion is thus a thermally activated process and the temperature dependence of diffusion coefficient is then expressed by the well-known Arrhenius relation

$$D = D_0 \exp\left(-\frac{Q_D}{RT}\right) \quad [28]$$

where  $Q_D$  is the activation energy for the diffusion of a given species. The order of magnitude of diffusion coefficients for solids varies in the range  $10^{-23}$  to  $10^{-8} \text{ m}^2 \text{ s}^{-1}$  depending on  $T$ . In metals, the diffusion of interstitial species, such as C, O, or N, is faster than



the diffusion of substitutional species. Diffusion in covalent or ionic solids is of several orders of magnitude slower than the diffusion in metallic materials.

Diffusion coefficients are important and useful properties of materials, particularly at high temperature. For self-diffusion in pure metals and some classes of materials, empirical correlations permit a rough estimate of the activation energy and the diffusion coefficient at melting point as a function of crystal structure and chemical bond.<sup>21</sup>

The knowledge of diffusion coefficients allows the calculation of the nominal diffusion length,  $\bar{l}_D = (Dt)^{1/2}$ , which provides an estimation of the size of the domain affected by the considered diffusion process. Solids or diffusion couples of size much greater than  $\bar{l}_D$  along the diffusion direction are usually qualified as infinite solids for diffusion along two opposite directions, or semi-infinite solids for diffusion along only one direction.

#### 1.06.4.3 Interdiffusion, Intrinsic Diffusion, and Kirkendall Effect in Binary Solid Solutions

In an inhomogeneous, disordered, substitutional binary solid solution, both constituents  $i$  ( $i = A$  or  $B$ ) are usually able to diffuse, via the vacancy exchange mechanism, within the unique crystal lattice of such a solid solution. This diffusion process is called interdiffusion. The well-known experiments of Smigelkas and Kirkendall for the diffusion in  $\alpha$ -brass have demonstrated that Zn and Cu diffuse simultaneously at different rates and that the faster diffusivity of Zn must be compensated by a displacement of the host lattice evidenced by the displacement of inert markers within the diffusion zone. This phenomenon, named Kirkendall effect, is schematized in Figure 14 for two constituents A and B of constant partial molar volumes. In Figure 14(a), the initial position of the contact surface is marked by fixed inert markers. As the partial molar volume of both constituents is assumed constant, the total volume of the diffusion couple remains constant; then, the fixed markers determine also the origin of the frame of reference centered on the number of moles or number-fixed frame denoted N-frame, also defined as the Matano plane M. Under this assumption of constant couple volume, this frame is immobile and its origin can also be taken at one extremity of the diffusion couple, which justify the denomination of laboratory-fixed frame of reference sometimes used for the N-frame. Moving inert markers determine the actual position

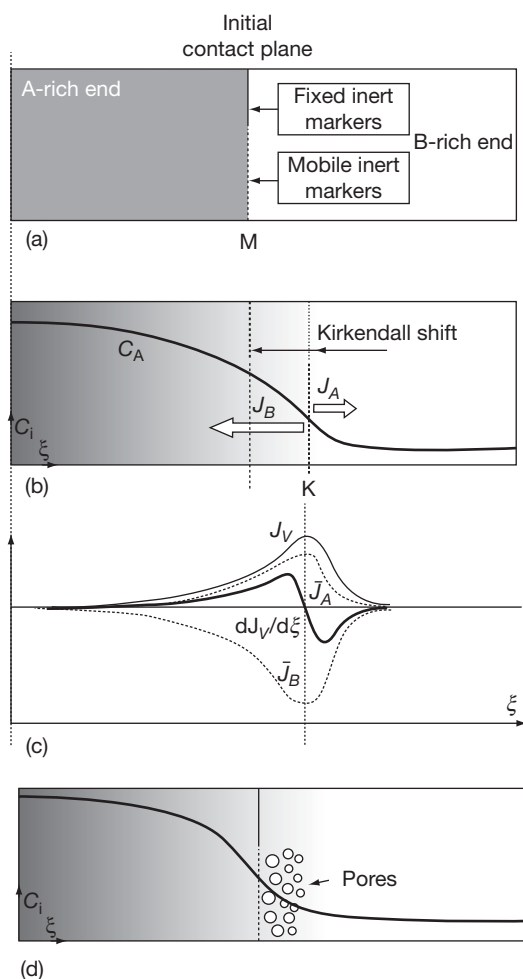


**Figure 14** Kirkendall effect in a homogeneous binary A–B diffusion couple: (a) initial diffusion couple before diffusion annealing, (b) concentration profile and markers position after diffusion annealing, (c) variation of diffusion fluxes and vacancy source/sink density ( $dJ_v/d\xi$ ), and (d) pore formation in the absence of vacancy sink.

of the initial contact surface after diffusion annealing (Figure 14(b)) and, therefore, visualize the drift of lattice planes within the diffusion zone; they mark the origin K, also named Kirkendall plane, of the lattice-fixed frame of reference, denoted K-frame. N- and K-frames are the more commonly considered frames of reference. The form of Fick's first law and the meaning of the corresponding diffusion coefficient depend on the chosen reference frame; a detailed analysis can be found in diffusion textbooks.<sup>17,19</sup>

When using N-frame, only one diffusion coefficient, denoted  $\tilde{D}$  and named interdiffusion coefficient, is needed for the analysis of concentration profiles of both constituents and the calculation of interdiffusion fluxes  $\tilde{J}_i$  from Fick's first law;  $\tilde{D}$  is

a function of composition. Thus, the interdiffusion flux of constituents  $i$  ( $i = A$  or  $B$ ),  $\tilde{J}_i$  must be expressed by

$$\tilde{J}_i = \bar{J}_i + v_K C_i \quad [29]$$

- $\bar{J}_i$  is the diffusion flux of  $i$  relative to the moving lattice (K-frame), it is thus named intrinsic diffusion flux; Fick's first law leads to  $\bar{J}_i = -\bar{D}_i(\partial C_i/\partial x)$ , where  $\bar{D}_i$  is the intrinsic diffusion coefficient of species  $i$ ; and
- $v_K C_i$  is the transport term,  $v_K$  is the displacement rate of the moving lattice relative to the N-frame.

The conservation of matter in the N-frame implies that  $\tilde{J}_A + \tilde{J}_B = 0$ . This relation combined with relation [28], applied to A and B constituents, lead to the Darken equations

$$v_K = (\bar{D}_A - \bar{D}_B) \frac{\partial x_A}{\partial x} \quad [30a]$$

$$\tilde{D} = x_B \bar{D}_A + x_A \bar{D}_B \quad [30b]$$

where  $x_A$  is the molar fraction of A.

The intrinsic diffusion coefficient  $\bar{D}_i$  is equivalent to the self-diffusion coefficient  $D_i$  of  $i$  in the crystal lattice of the considered solid solution. The Kirkendall effect is one consequence of the difference in intrinsic diffusivities of chemical constituents of substitutional solid solutions (nonreciprocal diffusion). The relative displacement of N- and K-frames is caused by the internal chemical forces resulting from the interactions between the constituents of nonideal solid solutions, which lead to the following relation between  $\bar{D}_i$  and  $D_i$

$$\bar{D}_i = D_i \left( 1 + \frac{\partial \ln \gamma_i}{\partial x_i} \right) \quad [31]$$

where  $\gamma_i$  and  $x_i$  are the activity coefficient and molar fraction of constituent  $i$ . Therefore, when the two constituents form an ideal solid solution, there is no relative displacement of N- and K-frames, that is, no Kirkendall effect.

This classical treatment of Kirkendall effect in binary homogeneous systems assumes that the difference between the intrinsic diffusion fluxes of the two substitutional constituents is compensated by the action of local vacancy sinks and sources that maintain the system in local equilibrium. This local action is formally equivalent to an intrinsic vacancy flux  $\bar{J}_v$  permitting the conservation of lattice sites, which is expressed by the relation

$$\bar{J}_A + \bar{J}_B + \bar{J}_v = 0$$

But local equilibrium implies that the vacancy concentration remains equal to its equilibrium value within all the diffusion couple. To achieve this requirement, the density of vacancy sources or sinks must be greater or equal to the divergence of the equivalent vacancy flux (Figure 14(c)). This action of vacancy sources and sinks result in the lattice drift characteristic of the Kirkendall effect in stress-free homogeneous diffusion couples. For species such as chemical elements, a Fickian diffusion flux is always the consequence of a gradient of chemical potential or concentration but such a gradient is not required for the apparent migration of vacancies that are annihilated at sinks and created elsewhere at sources and *vice versa*.

On the side of the faster diffusing species, when the density of vacancy sinks is not sufficient, the difference in the diffusion fluxes of substitutional chemical species would induce local vacancy supersaturation and associated build-up of local stress states within the diffusion zone. Return to local equilibrium in a stress-free state would be achieved by the nucleation of pores leading to the well-known Kirkendall porosity (Figure 14(d)). All the intermediate situations between complete or null Kirkendall shift are possible depending on local stress states and density, distribution and efficiency of vacancy sinks. Therefore, local stress states, composition-dependent volume changes, geometry, and size of the diffusion zone are among the parameters and phenomena that can interfere with nonreciprocal diffusion and must be considered in a detailed analysis and understanding of the behavior of systems when such a diffusion process occurs. Furthermore, when the partial molar volume of solution constituents are not constant and varies as a function of local composition, the total volume of the diffusion couple varies continuously as the diffusion proceeds. In addition to the increased difficulty in the analysis of diffusion profiles and fluxes, such a volume variation is also a source of local stresses that can interfere with diffusion processes and system behavior.

#### 1.06.4.4 Diffusion in Multiphase Systems

Diffusion in multiphase systems is often only focused on the growth kinetics of intermediate phases.<sup>22</sup> But, the Kirkendall effect is not restricted to diffusion couples constituted of one single phase; it may also occur in diffusion couples associating several phases.

For a two-phase diffusion couple constituted of two adjacent  $\alpha$  and  $\beta$  phases of an A–B binary system,

the initial contact plane can be evidenced, as for a homogenous couple, by the position of a fixed inert marker. This situation is more complex for mobile inert markers that are linked to the displacement of lattice planes. In a two-phase diffusion couple, the shift of lattice planes induced by nonreciprocal diffusion is different within the two contacting phases. Therefore, the displacement of lattice planes in both phases cannot be referred to only one frame of reference, which implies that each phase requires one specific lattice-fixed frame of reference.<sup>23</sup>

The difference in intrinsic diffusivity within both  $\alpha$  and  $\beta$  phases requires, as for a homogeneous diffusion couple, the action of vacancy sink/source distributed within these two phases. But, the differences in the required vacancy sources and sinks in each phase implies that the same  $\alpha/\beta$  interface must be able to either create or annihilate vacancies depending upon the intrinsic diffusion coefficients and the initial composition of contacting  $\alpha$  and  $\beta$  phases.<sup>23</sup> Vacancy creation or annihilation must be considered as an inherent interfacial activity in any diffusion-driven phase transformation involving substitutional solid solutions or ordered compounds with diffusion via vacancies. Interfacial defects such as misfit and misorientation dislocations would provide the vacancy sources or sinks required by such an interface action.<sup>10,11</sup>

But, for a phase transformation totally or partially driven by solid-state diffusion, the role of the interface is not limited to the creation or annihilation of vacancies involved in the diffusion process, the interface has several other roles to play. For one phase growing at the expense of one other phase, the interface needs to satisfy several interrelated requirements to accommodate:

- the change in chemical composition and eventually in chemical bonding,
- the mismatch in crystal structure and molar volume, and
- the difference in phase growth or recession rate and interface displacement rate by annihilating or creating the point defects involved in the diffusion processes.

If one of these requirements is not realized, the interface and the reacting phases would not be in a state of local equilibrium. Additional constraints must then be considered and, therefore, additional state variables must be introduced to describe and quantify the properties of contacting phases and the system evolution. These constraints can be local stresses or

constraints related to interface reactions, diffusion fluxes and interface movement.

#### 1.06.4.5 Interdiffusion in Ternary Systems

Interdiffusion in ternary, and higher systems, is more complex than in binary systems. Fick's laws remain valid for the diffusion in such systems. But, for a nonideal solid solution, the flux and gradient of each component are coupled with the fluxes and gradients of all other components. Therefore, the diffusion in ternary systems cannot be treated as a simple extension of binary diffusion. The interactions between the constituents of a nonideal solid solution imply that the diffusion flux of a given constituent cannot be expressed from only one diffusion coefficient.<sup>18,19</sup> A  $(2 \times 2)$  diffusion matrix must replace the single diffusion coefficient of binary systems. Furthermore, the terms of this diffusion matrix depends on the choice of one of the constituents as solvent, but the concentration profiles of each constituent are obviously independent of this choice. The interactions between the diffusing species are expressed by the off-diagonal elements of the diffusion matrix and are the cause of the complex shape of concentration profiles and diffusion paths that are commonly observed in ternary diffusion experiments.

One additional complication in ternary diffusion arises from the extra degree of freedom of ternary systems compared to binary systems. This extra degree of freedom permits the occurrence of two-phase fields in diffusion couples which also results in large variation in the morphology and microstructure of diffusion zones. Therefore, for multiphase diffusion in ternary systems, the correlation between the phase diagram, the diffusion path, the morphology and microstructure of a diffusion zone are much more complicated than for multiphase binary diffusion.<sup>22</sup>

Equation [28] remains valid for diffusion in a ternary, disordered, substitutional solid solution.<sup>19</sup> Like for binary diffusion, the difference in intrinsic diffusivities of the constituents of a ternary solid solution requires the action of vacancy sources or sinks for maintaining the systems in local equilibrium, which means that the Kirkendall effect also occurs in ternary diffusion. For diffusion in multiphase ternary systems, interfaces would have to likely act as vacancy sources or sinks, but the situation, particularly the microstructure of diffusion zone, is more complex than for binary systems and would require a specific and detailed analysis that still need to be carried out.

#### 1.06.4.6 Short-Circuit Diffusion

For most common materials, self-diffusion and diffusion of solute elements cannot be limited to diffusion in bulk crystals for which point defects are the only defects involved in diffusion processes. Internal defects like dislocations, grain boundaries or triple junctions and interfaces are always present in common materials and are characterized by a disturbed and more open structure along which diffusion is easier. Thus, these internal defects are preferred diffusion paths leading to short-circuit diffusion. Local strains and stresses associated with these defects can be partially minimized or relaxed by the positive (attractive) or negative (repulsive) segregation of diffusing solutes. Segregation of diffusing species often interferes with diffusion processes and must not be neglected. This influence is well documented in the case of grain-boundary diffusion.<sup>24</sup> Diffusion along free surfaces is not considered here because surface diffusion processes and mechanisms are rather different compared to internal diffusion. The influence of short circuits on the diffusion flux of a given solute is schematized in **Figure 15** for a slab of material such that the common operating short circuits, that is, dislocations, grain boundaries, and triple junctions, denoted by their respective index d, gb, and tj, are parallel to the diffusion direction. Each short circuit is then characterized by diffusion coefficients  $D_d$ ,  $D_{gb}$ , and  $D_{tj}$  higher than  $D_b$ , the solute diffusion coefficient in the bulk phase.

Assuming that the boundary conditions are different but constant on each slab side and not affected by the emergence of internal defects, the total solute

flux  $\mathcal{J}_t$  through such a slab is the sum of the solute flux for each diffusion path

$$\mathcal{J}_t = \mathcal{J}_b + \mathcal{J}_d + \mathcal{J}_{gb} + \mathcal{J}_{tj}$$

For cross-sectional fraction areas  $f_b$ ,  $f_d$ ,  $f_{gb}$ , and  $f_{tj}$  of each diffusion path and constant diffusion coefficients, Fick's first law lead to the following expression of the total solute flux

$$\mathcal{J}_t = - \left( f_b D_b + f_d D_d + f_{gb} D_{gb} + f_{tj} D_{tj} \right) \frac{\Delta C}{w}$$

This relation shows that the total flux can be expressed by using an apparent diffusion coefficient  $D_{app}$  averaging the contribution of all the diffusion paths

$$D_{app} = f_b D_b + f_d D_d + f_{gb} D_{gb} + f_{tj} D_{tj} \quad [32]$$

The dislocation density  $\rho_d$  and the average grain size  $d_{gb}$  must be known for the evaluation of fraction areas  $f_d$ ,  $f_{gb}$ , and  $f_{tj}$  and of the contribution of each diffusion path. Therefore, no quantitative analysis of short-circuit diffusion can be performed without an accurate analysis of these microstructural characteristics. For the calculation of these fraction areas, a value of 0.5 nm is usually taken for the radius of dislocation cores and the thickness of grain boundaries. The relative magnitude of these diffusion coefficients is usually in the following order

$$D_b < D_d < D_{gb} < D_{tj}$$

Only bulk and grain-boundary diffusion are usually considered in the common situation encountered in oxidation of pure metals or selective oxidation of alloys.

**Equation [30]** is a generalization of the Hart's equation. However, for non-steady-state conditions, the use of  $D_{app}$  for the calculation of diffusion fluxes or concentration profiles from Fick's second law is only valid when the nominal diffusion length of bulk diffusion greatly exceeds the average grain size or the average dislocation spacing, which is a common situation for the diffusion in a growing oxide scale and/or its substrate. Triple junctions are very efficient short circuits but their influence is only noticeable for grain size smaller than about 100 nm<sup>25</sup>; therefore, one can wonder if this contribution can be neglected for fine-grained oxide scales often formed at low or intermediate temperatures.

The diffusion mechanisms along dislocations, grain boundaries, or triple junctions are neither completely known nor understood. These mechanisms are likely based on atomic jumps involving vacancies and/or interstitials although the meaning of point defects associated with dislocations, grain boundaries, or triple junctions need to be clarified. Furthermore, the

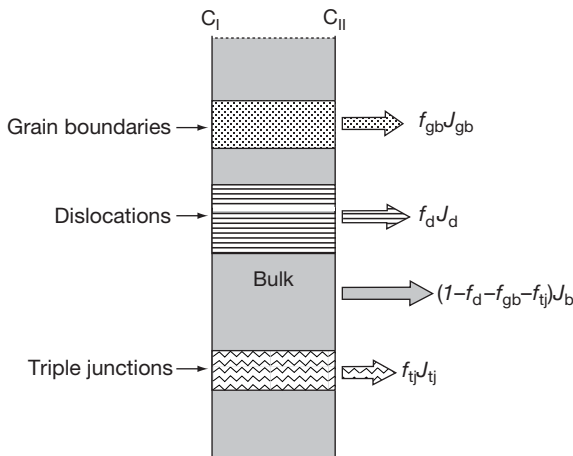


**Figure 15** Schematic representation of total diffusion flux through a slab with different kinds of short circuit.

experimental determinations of solute diffusion permit only the measurement of a diffusivity parameter that includes the diffusion coefficient, the segregation factor and the thickness or cross-section area of the considered short circuit. All these factors may interfere and caution must be taken in using diffusion coefficients calculated by taking arbitrary values of segregation factors or defect width or section. The situation is even more complex for ionic compounds for which local space charges may also interfere with the diffusion processes. Experimental determinations have shown that diffusion along dislocations and grain boundaries are thermally activated and their activation energies are usually lower than that for bulk diffusion because short-circuit diffusion is easier than bulk diffusion. Therefore, as schematically illustrated in **Figure 16** for grain-boundary diffusion and bulk diffusion, short-circuit diffusion is predominant at low temperatures. It is often quoted that the transition temperature for the predominance of grain-boundary diffusion is about  $0.5T_m$  (K), where  $T_m$  is the melting temperature of bulk phase. However, it can be deduced from eqn [30] that this transition temperature would, in fact, depend on the value of fraction area  $f_{gb}$ , and thus of scale microstructure.

Finally, it must be emphasized that experimental measurements and usual treatments of dislocation and grain-boundary diffusivities are valid for stationary dislocations and grain boundaries. In many practical situations encountered in high temperature oxidation or corrosion, these defects would move and their size and density would vary, sometimes strongly, as a function of time and temperature. In that case, solute drag

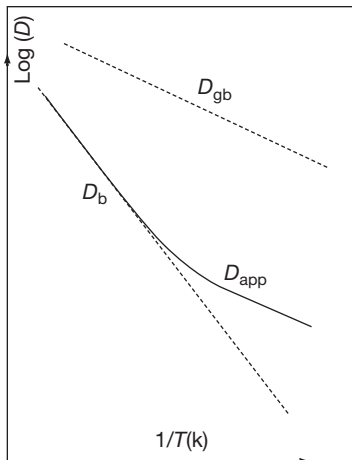


**Figure 16** Arrhenius representation of bulk, grain boundary and apparent diffusion coefficients (the gb area fraction is assumed constant).

by moving internal defects can result in a large increase of apparent diffusion flux. In addition, the analysis can be complicated by the occurrence of specific phenomena such as diffusion-induced grain-boundary motion (DIGM) that can be observed in alloys or materials experiencing large concentration changes across moving grain boundaries.<sup>26</sup>

## 1.06.5 Diffusion and Transport in Oxides

### 1.06.5.1 Chemical Diffusion in Nonstoichiometric Oxides

The diffusion process induced in nonstoichiometric oxides and ionic compounds by a chemical potential gradient is named chemical diffusion. In common nonstoichiometric oxides, there is usually only one type of dominant point defect localized on one specific sublattice. Therefore, the diffusion process is restricted to the cationic sublattice for dominant defects such as cation vacancies or interstitials, and to the anionic sublattice for dominant anionic defects.

For an oxide like  $M_{1-\delta}O_v$  that contains  $\delta$  cation vacancy per mole of oxide, the cation concentration  $C_M$  is proportional to the departure from stoichiometry  $\delta$ :  $C_M = (1-\delta)/\Omega_{MO_v}$ , where  $\Omega_{MO_v}$  is the molar volume of oxide  $MO_v$ . Thus, Fick's first law, applied in the laboratory frame of reference, implies that the cation flux is proportional to the  $\delta$  gradient

$$\tilde{J}_M = \frac{\tilde{D}}{\Omega_{MO_v}} \frac{\partial \delta}{\partial x} \quad [33]$$

By taking care of the expression for cation and anion molar fractions in a nonstoichiometric oxide and neglecting the diffusion coefficient of anionic species, eqns [16], [30], and [31] lead to the following expression of  $\tilde{D}$

$$\tilde{D} = (1 + q) \frac{D_M}{\delta} \quad [34]$$

where  $D_M$  is the self-diffusion coefficient of cation and  $q$  the absolute value of the effective charge of cation vacancies. By introducing the cation vacancy diffusivity  $D_{V_M}$  through eqn [27], the chemical diffusion coefficient is then related to the cation vacancy mobility, which does not depend on the vacancy molar fraction

$$\tilde{D} = (1 + q) D_{V_M} \quad [35]$$

The form of this relation is general and applies to any kind of point defect by simply replacing  $D_{V_M}$  by the diffusivity  $D_d$  of the predominant defect involved in the diffusion process.



Therefore, from these relations between chemical diffusion and defect diffusivity, transport in an ionic compound can be expressed only in terms of fluxes of point defects that are the primary mobile species.

Concentration gradients and transport of charged species (ions, points and electronic defects) induce internal electric fields within ionic compounds and oxides. For an internal electric field strength  $E$ , the force  $f$  acting on transported species of charge  $q$  is  $f = qE$ . The flux of each species  $i$  can then be expressed from eqns [23] and [24]

$$\tilde{J}_i = -D_i \frac{\partial C_i}{\partial x} + D_i C_i \frac{q_i E_i}{RT} \quad [36]$$

But, the condition of electrical neutrality implies that there is no net current flow within the oxide scale, which lead to the equation:  $\sum q_i \tilde{J}_i = 0$ . However, solving this equation by using the expression [36] for the fluxes of all charged species leads again to eqn [35].

When an external electric field is applied to an ionic compound or an oxide initially at equilibrium, the only driving force for the diffusion/transport of charged species is that induced by the electric field. The Nernst–Einstein relation [24] leads to the expression of the flux of each charged species that is related to their electrical mobility and to the expression of the contribution of the species  $i$  to the electric conductivity

$$\sigma_i = q^2 F \frac{C_i D_i}{RT} \quad [37]$$

where  $F$  is the Faraday constant ( $F = eN_A$ ). The total conductivity is the sum of the contribution of all the charged species. The mobility of electronic defects is largely higher than the mobility of ionic defects and thus the total conductivity is mainly electronic except in the case of some intrinsic ionic oxides. However, for nonstoichiometric oxides, the variations of electric conductivity with oxygen partial pressure  $P_{O_2}$  permit the determination of the type and charge of the predominant ionic defect as the molar fractions of electronic and ionic defects vary similarly as a function of  $P_{O_2}$  (cf. Section 1.06.2.4). A detailed treatment of diffusion in oxides and its relation to electric conductivity can be found in textbooks.<sup>1,12–15</sup>

Predominant defects are involved in mass transport. But minority point defects can be involved in other important properties of compounds. This is, for example, the case of deformation by creep at high temperature of ionic compounds that involves dislocation climb. Dislocation climb in an oxide requires the simultaneous movement of cationic and anionic species and is thus controlled by the transport rate of the slowest species, that is, the one associated to the minority defect.

### 1.06.5.2 Diffusion Processes in Oxide Scales

The diffusion and transport process occurring in an oxide scale can be illustrated by considering the behavior of such a scale when the chemical potential of one scale constituent differs on both its faces. This

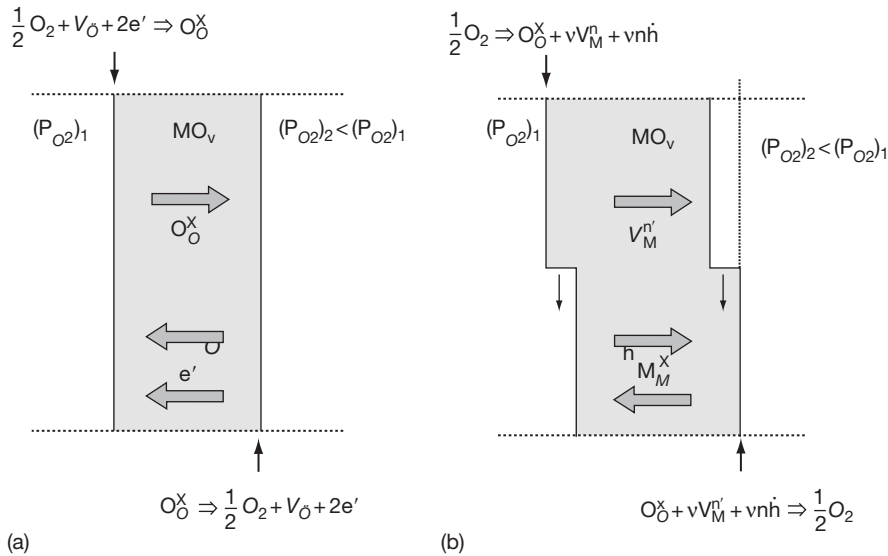


**Figure 17** Diffusion fluxes and defect creation/annihilation for an  $MO_n$  oxide scale maintained in a constant oxygen gradient: (a) n-type oxide with anion vacancies and (b) p-type oxide with cation vacancies.



situation is schematized in **Figure 17** for an  $\text{MO}_x$  scale separating two environments of differing oxygen partial pressure. Both sides of the oxide scale are assumed to be in equilibrium so that a gradient in the concentration of predominant defects is established within the scale. Corresponding flux of point defects can be easily calculated from eqns [33], [34], and [16] or [18] when only one type of point defect is predominant. The calculation is more complex for oxides in which anionic and cationic species are able to diffuse simultaneously.

In the case of predominant anion vacancies, as shown in **Figure 15(a)**, the cation sublattice is not affected by the oxygen gradient so that there is no transport of cationic species and the oxide scale remains stationary. The reactions occurring on the faces of the oxide scale can be represented by the oxidation/reduction equilibrium [17] but the oxidation reaction occurs only on the high  $P_{\text{O}_2}$  and results in the annihilation of anion vacancies while the opposite reduction reaction occurs on the low  $P_{\text{O}_2}$  side and expresses the formation of anion vacancies. A constant concentration gradient of oxygen vacancies (and free electrons) is then established so that anion vacancies are continuously created at the low  $P_{\text{O}_2}$  side and annihilated at the high  $P_{\text{O}_2}$  side, which results in a constant flux of anion vacancy and a constant counter flux of oxygen anions. Therefore, in such a situation, the oxide scale acts simply as a permeable membrane that controls the oxygen flux from the high  $P_{\text{O}_2}$  compartment toward the low  $P_{\text{O}_2}$  one.

This situation is different for an oxide with predominant cation vacancies (**Figure 17(b)**). Indeed, the oxidation/reduction equilibrium expressed by eqn [14] involves species belonging to both anionic and cationic sublattices and results not only in the creation/annihilation of cation vacancies but also in the creation (oxidation reaction) of one new structural unit of the oxide lattice on the high  $P_{\text{O}_2}$  side and the destruction of one such unit on the low  $P_{\text{O}_2}$  side (reduction reaction). These simultaneous reactions of creation/destruction of structural unit of oxide lattice result in a net shift of the oxide scale toward the high  $P_{\text{O}_2}$  side.<sup>1</sup> This translation of the oxide scale can be seen as the movement of ledges operating the advance of oxide lattice planes on the oxidation side and their recession on the reduction side, as schematically shown in **Figure 17(b)**. This steady-state shift of cationic oxide scales under a constant potential gradient of oxygen is an illustration of the Kirkendall effect in ionic compounds. Again, a constant concentration gradient of cation vacancies (and electron holes) is established through the oxide

scale and cation vacancies are continuously created at the high  $P_{\text{O}_2}$  side and annihilated at the low  $P_{\text{O}_2}$  side, which results in a constant flux of cation vacancies and an opposite constant flux of cations that causes the observed shift of the oxide scale toward the high  $P_{\text{O}_2}$  side.

This analysis can be extended to the case of two oxides, AO and BO, forming a solid solution (A,B)O where A and B cations are randomly distributed over the cationic sites of their common crystal structure; charged cation vacancies are assumed to be the predominant point defects in pure oxides and their solid solutions. In an oxygen potential gradient, the same causes producing the same effect, a shift of the crystal lattice toward the high  $P_{\text{O}_2}$  side is again observed. But, the mobility of A and B cations are usually not equal so that the faster cations, for example A cations, move faster toward the high  $P_{\text{O}_2}$  side, which results in an enrichment in A at this side, regardless of the relative thermodynamic stability of AO and BO; this process is named kinetic demixing and results in a steady-state demixing profile established through the oxide scale.<sup>1</sup>

### 1.06.5.3 Oxide Scale Microstructure and Diffusion Processes

The growth of an oxide scale on a pure metal or an alloy fits into the general category of diffusion-driven phase transformation. This general statement does not mean that diffusion is the only process governing or controlling the growth kinetics. Indeed, many other processes, linked to the role and movement of gas–oxide and/or oxide–metal interfaces, can be involved in oxide scale growth, as briefly described in **Section 1.06.3.5** for a general  $\alpha$ – $\beta$  transformation.

The understanding of growth mechanisms and kinetics of an oxide scale always requires the knowledge of diffusion and transport modes within this oxide scale. Such information can be obtained by the use of inert markers and/or diffusion tracers, but the morphological and microstructural features of oxide scales can also provide quite useful information.

As for multiphase diffusion in a binary system, a Kirkendall frame of reference (K-frame) can be defined for the metal and oxide lattices. For pure metals or ideal solid solutions, the initial unoxidized surface determines the location of metal K-frame (denoted  $K_M$ ) and the Matano plane (denoted M). The location of oxide K-frame (denoted  $K_{\text{Ox}}$ ) depends on the growth process.

One difficulty for the oxidation of metals or alloys is linked to the large volume change usually induced

by the transformation of a metal into its oxide. This volume change is characterized by the well-known Pilling and Bedworth ratio (PBR)  $\phi$ . For the growth of the oxide  $\text{MO}_x$ , this ratio is given by  $\phi = (v_{\text{MO}_x}/\bar{v}_M)$ , where  $v_{\text{MO}_x}$  is the molar volume of the growing oxide, assumed pure, and  $\bar{v}_M$  the partial molar volume of metal  $M$  at the oxide–metal interface.

In many cases, this volume variation is totally accommodated or assumed to be accommodated by an elongation parallel to the growth direction. **Figure 18** schematizes, for the oxidation of a pure metal, the three different situations that can be observed in such an ideal case depending on the location of the reactions associated with the growth of the oxide lattice;  $M$  defines the position of Matano plane and  $K_M$  and  $K_{Ox}$  the position of Kirkendall planes, respectively associated to the metal and oxide lattices. The thickness of oxidized metal is equal to  $\xi_M$  and the oxide scale thickness  $\xi_{Ox}$  is then such that the ratio  $\xi_{Ox}/\xi_M$  is equal to the PBR  $\phi$ . For the three situations of **Figure 18**, the recession of metal lattice obviously occurs at the oxide–metal interface. **Figure 18(a)** shows the relative location of  $M$ ,  $K_M$ , and  $K_{Ox}$  planes for a scale of pure p-type oxide for which the oxide lattice growth occurs at the gas–oxide interface. **Figure 18(b)** defines the same location for a scale of pure n-type oxide for which the oxide lattice growth and the metal lattice recession occur simultaneously along the oxide–metal interface. The typical examples corresponding respectively to the situations depicted by **Figures 18(a)** and **18(b)** are the

oxidation of pure nickel (p-type oxide) or pure zirconium (n-type oxide) in a temperature range such that the bulk diffusion of cations or anions is the only limiting growth process. In that case, the oxide scales are characterized by a homogeneous and regular microstructure consisting of columnar grains for both NiO and  $\text{ZrO}_2$  scales but with a smaller grain size, in a section parallel to the oxide–scale interface, for  $\text{ZrO}_2$  scales. The difference in grain size is likely due to the location of lattice growth reaction. Indeed, NiO grains grew at the oxide–gas interface where they are free to expand, which explains also their faceted morphology. On the contrary, for  $\text{ZrO}_2$  scales, the lattice growth reaction is localized at the oxide–scale interface, the expansion of oxide grains is thus limited by the previously formed oxide; furthermore, the first formed oxide is not affected by its subsequent growth, which explains that the external morphology of such oxide scales reproduces the initial microstructure and/or morphology of its metal substrate. The smaller grain size of these scales may be also due to the continuous nucleation of new oxide grains at the scale–substrate interface and/or to local stresses and strain associated with the large value of PBR  $\phi$ .

**Figure 19** can help for a better understanding of the processes leading to the situation of **Figure 18(c)**. Indeed, **Figure 19** reveals the similar microstructures of a NiO scale (**Figure 19(a)**), grown at  $800^\circ\text{C}$ ,<sup>27</sup> and of a CoSi layer formed in a  $\text{Co}_2\text{Si}/\text{CoSi}_2$  diffusion couple (**Figure 19(b)**).<sup>28</sup> Both NiO scale and

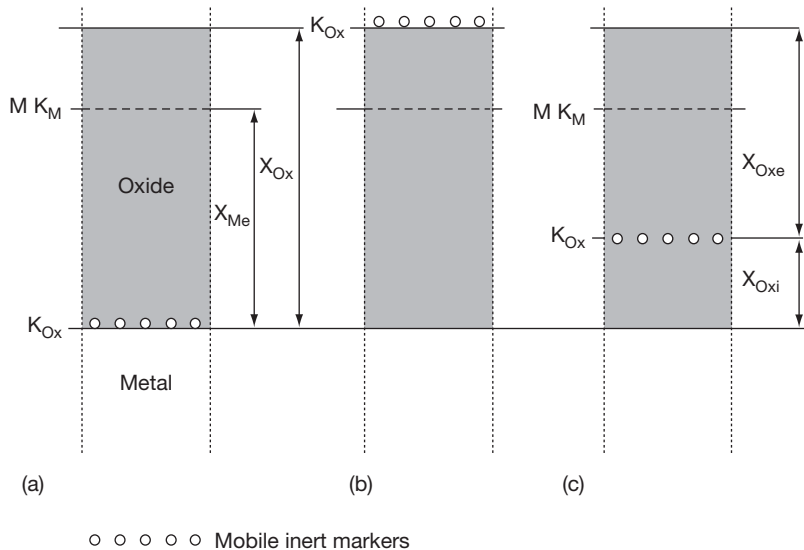


**Figure 18** Relative positions of  $M$ ,  $K_M$ , and  $K_{Ox}$  reference planes during the growth of an oxide scale by the oxidation of a pure metal: (a) scale growth occurring only at the external gas–oxide interface, (b) scale growth occurring only at the internal oxide–metal interface, and (c) scale growth occurring at both interfaces.

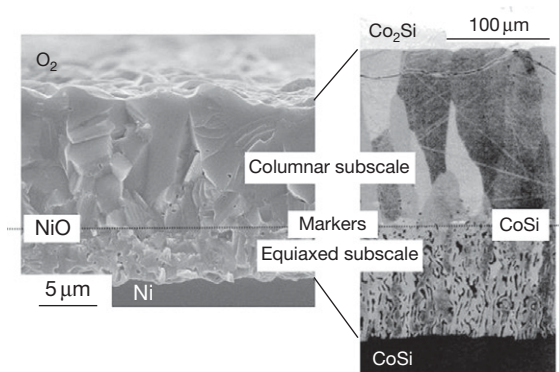


**Figure 19** Similarity of the microstructure of a NiO scale grown on a high-purity nickel<sup>27</sup> and of a CoSi layer grown between CoSi<sub>2</sub> and Co<sub>2</sub>Si. Reproduced from Paul, A.; van Dal, M. J. H.; Kodentsov, A. A.; van Loo, F. J. J. *Acta Mater.* **2004**, 52, 623–630.

CoSi layer are characterized by a duplex microstructure formed by two sublayers of, respectively, equiaxed and columnar microstructure.

The growth of the columnar CoSi sublayer combines the diffusion of Si from CoSi<sub>2</sub> toward Co<sub>2</sub>Si and its reaction at the Co<sub>2</sub>Si/CoSi. Simultaneously, the counter diffusion of Co and its reaction at the CoSi–CoSi<sub>2</sub> interface leads to the growth of the equiaxed CoSi sublayer. Inert markers, initially located at the Co<sub>2</sub>Si–CoSi<sub>2</sub> interface, are always located along the internal interface separating the columnar and equiaxed sublayers and they define the location of the Kirkendall plane of CoSi phase.<sup>28</sup>

Such a duplex microstructure is commonly observed for NiO scales grown at a temperature lower than 1000 °C.<sup>27,29</sup> For these duplex scales, inert marker location and <sup>18</sup>O experiments have shown that the growth of the external columnar subscale is associated to the outward diffusion of Ni cations and occurs at the scale–gas interface while the inward diffusion of oxygen is involved in the growth of the inner equiaxed subscale. Therefore, the internal interface between equiaxed and columnar sublayers marks also the initial location of the Ni surface before the formation and growth of NiO scales. These two examples clearly show that similar growth processes lead to similar microstructures. The microstructure of a growing phase directly depends on the nature of diffusing species and on the localization of growth reactions as observed in many examples of solid-state and solid–gas reactions and its microstructure differs on both sides of its Kirkendall plane.<sup>22,28</sup> Therefore, metallographic examinations of oxide scales provide also an easy way to determine

the location of K<sub>Ox</sub>. **Figure 18(c)** then corresponds to a mixed case such that oxide lattice growth occurs simultaneously at both gas–oxide and oxide–metal interfaces. The oxide scale fraction growing at the external gas–oxide interface has a thickness  $\xi_{\text{oxe}}$  and the fraction growing at the internal oxide–metal interface a thickness  $\xi_{\text{oxi}}$ . For diffusion-controlled scale growth, the relative magnitude of  $\xi_{\text{oxe}}$  and  $\xi_{\text{oxi}}$  is directly proportional to the relative magnitude of intrinsic diffusivity of species involved in the growth process, as observed in many examples of solid-state reactions.<sup>22</sup>

For a pure metal, the position of M and K<sub>M</sub> planes always coincides with the position of the initially nonoxidized metallic surface. Therefore, after the growth of an oxide scale, the position of these reference planes can be accurately determined relative to a fixed reference plane such as, for example, the specimen mid-plane or any marked plane far enough from the scale–metal interface supposed to be fixed and not affected by the lattice movements induced by scale growth. These displacements can be rationalized by a factor  $\Gamma$  that defines the displacement  $\xi$  of any reference plane of the oxide scale as a function of the thickness of oxidized metal  $\xi_m$ :  $\xi = \Gamma \xi_m$ <sup>30</sup>; the factor  $\Gamma$  is defined as positive for outward displacement. For the general case of simultaneous growth at the external gas–scale interface and at the internal scale–substrate interface, the factor  $\Gamma$  is given by

$$\Gamma = \phi(1 - f_c) - 1 \quad [37a]$$

The term  $f_c$  in relation [37a] is the fraction of cationic scale growth;  $f_c$  is equal to the ratio  $\xi_{\text{oxe}}/\xi_{\text{ox}}$ . Relation [37a] is easily checked from the displacement of K<sub>Ox</sub> plane for pure cationic (**Figure 18(a)**) or pure anionic (**Figure 18(b)**) growth.

**Figure 18** and relation [37a] remain valid for the selective oxidation of ideal disordered solid solutions; the value of  $\phi$  is then that of the selectively oxidized constituent. Indeed, the total volume of an ideal solid solution does not depend on the spatial distribution of its constituents because the partial molar volume of each constituent is constant and equal to its own molar volume. Therefore, there is no difference between pure metal and ideal solid solution regarding the definition and location of planes M and K<sub>M</sub>. This situation is more complex for nonideal solid solutions as the partial molar volume of each constituent varies as a function of composition. Selective oxidation of one constituent of a solid solution results in concentration gradients of all constituents in the alloy underlying the oxide scale and the resulting local variations of partial molar volumes is the

cause of local volume changes, which in turn results in local deformation and stress fields. Unfortunately, an accurate evaluation of such volume changes and related deformation field requires data that are often not available. Many oxide scales present a duplex microstructure similar to NiO scale of [Figure 19](#). This is the case of  $\alpha$ -alumina scales grown on FeCrAlY alloys oxidized at high temperature ( $T > 1000\text{--}1100^\circ\text{C}$ ); they are formed of an equiaxed outer subscale and a columnar inner subscale.<sup>31</sup> Like for NiO scales, this duplex microstructure is representative of the simultaneous occurrence of two growth processes, the surface separating these two subscales defines the location of  $K_{\text{ox}}$ -plane, that is, the initial location of the metal surface. But, the microstructure of alumina scales grown on high temperature alloys depends strongly on many parameters such as oxidation temperature, oxygen partial pressure or alloy composition and more particularly of the presence of reactive element such as Y, Zr, Hf, etc. Furthermore, the influence of these parameters on the nature and concentration of predominant point defects and electronic defects, diffusion mechanisms, and processes is yet neither well known nor understood. For many oxide scales, a detailed analysis and understanding of correlations between scale growth microstructure, growth mechanisms and diffusion processes is needed and is still far away to be possible. Several experimental methods now commonly used in solid-state electrochemistry can offer new insights in oxide-scale properties and scale-growth mechanism. This is notably the case of impedance spectroscopy<sup>32</sup> and photoelectrochemical spectroscopy.<sup>35</sup> Impedance spectroscopy is a powerful tool that can permit to analyze the influence of many parameters such as scale composition, scale thickness, scale microstructure, and grain size. Photoelectrochemical spectroscopy permits the determination of the local electronic properties of oxide scales, which is of particular importance for a better understanding of growth mechanisms. These techniques are particularly interesting at temperatures where bulk diffusion is not the limiting process as shown by the results obtained on the oxidation of zirconium alloys<sup>33</sup> or pure nickel.<sup>34</sup>

#### 1.06.5.4 Point Defects and Diffusion in Common Oxides

Many works have been devoted to the study of bulk and grain-boundary self-diffusion in ionic compounds, particularly in oxides and sulfides that are

commonly found in high temperature oxidation or corrosion of metallic materials.<sup>12–14</sup> But, only few very common oxides such as NiO monoxide, iron oxides, chromia, and alumina are briefly considered in this section. By its importance in the manufacturing of integrated circuits and its protective role in the oxidation behavior of some iron-based materials, silica is also a very common oxide. However, silica scales are amorphous and diffusion processes in amorphous solids are not considered here. Most of the studies devoted to point defects and diffusion processes in oxides are often based on measurements of electrical conductivity, scale growth kinetics or else concentration profiles of marked species. For bulk diffusion, the equations reported in [Section 1.06.5.1](#) permit the interpretation of experimental data regarding the diffusion mechanisms and the nature and ionization degree of defects involved in diffusion processes. But, it must be kept in mind that diffusion data obtained from oxide single crystals, very pure oxides and/or oxide samples of controlled, homogeneous and regular microstructure are not always useful for the understanding and analysis of diffusion and transport processes in oxide scales grown on complex metallic materials.

##### 1.06.5.4.1 Nickel and cobalt monoxides

Both  $\text{Ni}_{1-\delta}\text{O}$  and  $\text{Co}_{1-\delta}\text{O}$  are p-type oxides of rock salt structure. Cation vacancies and positive holes are the predominant point and electronic defects; the departure from stoichiometry  $\delta$  is significantly smaller for NiO. The self-diffusion coefficients of cations were determined from tracer experiments and from the analysis of scale-growth kinetics at temperatures higher than  $1000^\circ\text{C}$ . The agreement between these independent determinations is excellent. The growth of NiO and CoO scales at high temperatures is one of the best examples of scale growth controlled by bulk diffusion according to the Wagner theory as demonstrated by the recent work of Mrowec and Gresik<sup>36</sup> on the oxidation of high-purity nickel at temperatures higher than  $1100^\circ\text{C}$ . In this temperature range, NiO scales are characterized by a homogeneous microstructure consisting of large columnar grains such that the contribution of grain-boundary diffusion can be readily neglected. The following equations express the departure from stoichiometry and the variation of self-diffusion coefficient of Ni cations as a function of  $T$  and  $P_{\text{O}_2}$

$$\delta = 0.153 \left( \frac{P_{\text{O}_2}}{P^0} \right)^{1/6} \exp \left( -\frac{9620}{T} \right) \quad [38]$$

$$D_{\text{Ni}}(\text{cm}^2\text{s}^{-1}) = 9.3 \times 10^{-3} \left( \frac{P_{\text{O}_2}}{P^0} \right)^{1/6} \times \exp\left(-\frac{27\,900}{T}\right) \quad [39]$$

Chemical diffusion coefficient  $\tilde{D}$  in NiO can be deduced from eqns [34], [38], and [39];  $\tilde{D}$  and cation vacancy diffusivity, calculated from eqn [35], are independent of  $P_{\text{O}_2}$  and thus of the vacancy molar fraction. Diffusion data in NiO have been recently reviewed by Monceau.<sup>37</sup> Few measurements of self-diffusion coefficient of oxygen anions were performed at temperatures higher than 1100 °C; their values are more than five orders of magnitude smaller than self-diffusion coefficients of Ni. Other data were obtained from high temperature creep behavior of NiO, which is controlled by the diffusion of oxygen.

At temperatures lower than 1000 °C, the influence of grain-boundary diffusion cannot be neglected.<sup>38</sup> The grain-boundary self-diffusion of cations and anions in NiO scales has been extensively investigated and discussed.<sup>27,29,37,38</sup> However, the morphology and microstructure of NiO scales vary strongly as a function of time and temperature<sup>27</sup>; therefore, the only influence of grain-boundary diffusion is likely not sufficient for a detailed understanding of experimental scale-growth kinetics and complex evolutions of oxide-scale morphology and microstructure at  $T < 1000$  °C.

#### 1.06.5.4.2 Iron oxides

Three oxides can be found in iron–oxygen systems: wüstite  $\text{Fe}_{1-\delta}\text{O}$ , magnetite  $\text{Fe}_3\text{O}_4$ , and hematite  $\text{Fe}_2\text{O}_3$ . Pure wüstite is only stable at temperatures higher than 570 °C and reduced  $P_{\text{O}_2}$ . Therefore, oxide scales grown on pure Fe above 570 °C is, from pure iron substrate up to oxygen gas phase, formed of successive three sublayers of wüstite, magnetite, and hematite. The relative thicknesses of these sublayers are almost independent of temperature and show very clearly that diffusion is largely faster in wüstite (95% of the total scale thickness) than in magnetite (4%) and hematite (1%).

Like CoO and NiO, wüstite  $\text{Fe}_{1-\delta}\text{O}$  is a p-type oxide of rock salt structure but it differs by its larger departure from stoichiometry  $\delta$  that can reach a value as high as about 0.15. The defects responsible for Fe self-diffusion in  $\text{Fe}_{1-\delta}\text{O}$  are, like for NiO and CoO, cation vacancies but Fe self-diffusion in wüstite is about four orders of magnitude faster than Ni self-diffusion in NiO. Furthermore, contrary to NiO and CoO, Fe self-diffusion coefficients are

nearly independent of  $\delta$ ; the formation of highly stable defect clusters combining cationic vacancies and interstitials interferes with the diffusion processes that are therefore more complex than in NiO or CoO. The main point defect of anionic sublattice are oxygen interstitials but the variation of oxygen self-diffusion as a function of temperature and  $P_{\text{O}_2}$  is complex and not yet understood. In wüstite, oxygen self-diffusion is several orders of magnitude slower than iron self-diffusion.

Magnetite  $\text{Fe}_3\text{O}_4$  has a spinel crystal structure where the octahedral and tetrahedral sites of the fcc sublattice of oxygen anions can be occupied by  $\text{Fe}^{2+}$  and  $\text{Fe}^{3+}$  cations. The distribution of  $\text{Fe}^{2+}$  and  $\text{Fe}^{3+}$  cations over octahedral and tetrahedral sites is a function of temperature.

Magnetite is stoichiometric at room temperature and  $\text{Fe}^{3+}$  cations are equally distributed over tetrahedral and octahedral sites while  $\text{Fe}^{2+}$  cations are only in octahedral sites. This distribution of  $\text{Fe}^{2+}$  and  $\text{Fe}^{3+}$  cations corresponds to the inverse spinel structure. At temperatures higher than about 900 °C, the distribution of  $\text{Fe}^{2+}$  and  $\text{Fe}^{3+}$  cations is randomized over tetrahedral and octahedral sites and the departure from stoichiometry increases as temperature increases.

The predominant point defects are in the cationic sublattice; their nature is thus defined relatively to the normal site occupancy of one-half of octahedral sites and one-eighth of tetrahedral sites but defects localized on octahedral and tetrahedral sites are not equivalent and must be distinguished. Cation vacancies and interstitials are localized on the same sites and are formed when the proportions of occupied sites are respectively smaller (vacancy) or higher (interstitial) than 1/2 and 1/8. The majority defects are neutral cation interstitials ( $\text{Fe}_{3+\delta}\text{O}_4$ ) at low  $P_{\text{O}_2}$  close to the wüstite–magnetite equilibrium and neutral cation vacancies ( $\text{Fe}_{3-\delta}\text{O}_4$ ) at higher  $P_{\text{O}_2}$  close to the magnetite–hematite equilibrium. The formation equilibria of these defects lead to defects concentration varying as  $P_{\text{O}_2}^{2/3}$  for vacancies and  $P_{\text{O}_2}^{-2/3}$  for interstitials.<sup>39</sup>

The variation of iron self-diffusion coefficient as a function of  $P_{\text{O}_2}$  is similar and expressed by the following relation<sup>40</sup>

$$D_{\text{Fe}}(\text{cm}^2\text{s}^{-1}) = 4 \times 10^{-11} \left( \frac{P_{\text{O}_2}}{P^0} \right)^{2/3} \exp\left(-\frac{16\,800}{T}\right) + 8 \times 10^7 \left( \frac{P_{\text{O}_2}}{P^0} \right)^{-2/3} \exp\left(-\frac{73\,800}{T}\right)$$



The minimum of iron self-diffusion coefficients is not observed for the stoichiometric composition where the molar fraction of cation vacancies and interstitials are equal. This minimum corresponds to a  $P_{O_2}$  value such that vacancies molar fraction is higher than interstitials molar fraction, which means that interstitials are more mobile than vacancies. Oxygen self-diffusion is two orders of magnitude slower than iron self-diffusion and varies also as a function of  $P_{O_2}$  indicating that the nature of predominant anionic point defects varies also with  $P_{O_2}$ ; the interpretation of the observed variations involve the formation of complex point defects at high  $P_{O_2}$ .

The crystal structure of hematite  $Fe_2O_3$  is, like  $Cr_2O_3$  and  $\alpha-Al_2O_3$  of corundum type. Corundum structure can be described as a close packing of anions, cations occupying two-thirds of the octahedral sites.  $Fe_2O_3$  is known to be an oxygen-deficient oxide with very small departure from stoichiometry. Its defect structure is very sensitive to metallic impurities; it changes from oxygen vacancies and n-type conductivity to interstitial cations and p-type conductivity at about 800 °C. Iron and oxygen self-diffusion are apparently of the same order of magnitude but the works devoted to the influence of  $P_{O_2}$  on defect structure and self-diffusion in  $Fe_2O_3$  cannot be interpreted on the basis of simple defect structure and lead to rather different interpretations.

#### 1.06.5.4.3 Chromia

Heat-resisting alloys are commonly classified as chromia-forming or alumina-forming alloys according to the nature of the protective oxide scale formed upon their high temperature oxidation. However, at  $P_{O_2}$  close to atmospheric pressure, the oxidative evaporation of  $Cr_2O_3$  in volatile  $CrO_3$  chromic oxide limits the uses of chromia-forming alloys to about 1000 °C.  $Cr_2O_3$ , like hematite, has the corundum structure but a much more narrow range of nonstoichiometry because of its greater thermodynamic stability.  $Cr_2O_3$  is an electronic semiconductor that can be either a p-type or an n-type semiconductor depending on  $T$ ,  $P_{O_2}$ , and doping impurities. The influence of these parameters on the nature of predominant defect is complex and not yet fully understood. It is still the subject of many controversies, particularly for the role of reactive elements (RE) such as Y, Ce, etc. that modify the transport properties of  $Cr_2O_3$ , and therefore, the growth mode, the growth kinetics, and the microstructure of  $Cr_2O_3$  scales.

The variations of electrical conductivity, chromium and oxygen self-diffusion and scale-growth

kinetics as a function of  $P_{O_2}$  are complex and difficult to interpret and to compare, particularly because of their rather wide scattering. However, many data are consistent with a defect structure based on the predominance of  $V_{Cr}'''$  cation vacancies at  $P_{O_2}$  close to atmospheric pressure and on the predominance of interstitial cations  $Cr_i^{3\bullet}$  at very low  $P_{O_2}$ , close to  $Cr_2O_3$ -Cr equilibrium, although anion vacancies may be important minority defects at these low  $P_{O_2}$  in agreement with experimental data showing that bulk chromium and oxygen self-diffusion coefficients are of the same order of magnitude.<sup>41</sup> At intermediate  $P_{O_2}$ , free electrons and electron holes are the major defects;  $Cr_2O_3$  then behaves as an intrinsic electronic semiconductor. These differences in defect structure as a function of  $P_{O_2}$  must have a marked influence on the microstructure of  $Cr_2O_3$  scales but there is much less work on the characterization of  $Cr_2O_3$  scales than on NiO or  $\alpha-Al_2O_3$  scales.

Grain-boundary diffusion play also an important role in the growth of  $Cr_2O_3$  scales, particularly at temperatures lower than 1000 °C. Grain-boundary diffusion of cations appears usually faster than anion diffusion. But more data on the influence of  $T$ ,  $P_{O_2}$  and RE on grain-boundary self-diffusion of chromium and oxygen are needed for a better understanding of diffusion process involved in the growth of  $Cr_2O_3$  scales.

#### 1.06.5.4.4 $\alpha$ -Alumina ( $\alpha-Al_2O_3$ )

Alumina of corundum structure,  $\alpha-Al_2O_3$ , is the most protective and stable oxide among all the oxides commonly encountered in high temperature oxidation. Therefore,  $\alpha-Al_2O_3$  is also the most important oxide from the technological view point of oxidation resistance and behavior of heat-resisting alloys. Unfortunately, despite all the work conducted over its point defect structure and transport properties, there remain major problems in the understanding of  $\alpha-Al_2O_3$  properties and behavior that are still the subject of discussion and controversy as illustrated by a recent review.<sup>42</sup>

The great thermodynamic stability of  $\alpha-Al_2O_3$  results in a so narrow nonstoichiometry range that there is no accurate determination of its extent. As a consequence, the transport properties of  $\alpha-Al_2O_3$ , as determined from electrical conductivity, tracer diffusion or scale-growth kinetics, are controlled by extrinsic defects associated to cationic impurities. This strong influence of impurities likely explains the wide scattering of experimental data usually observed among the numerous studies devoted to  $\alpha-Al_2O_3$ .



One other characteristic of the transport properties of  $\alpha$ -Al<sub>2</sub>O<sub>3</sub> is the large value of the experimental activation energy reported for the bulk self-diffusion of O and Al. For oxygen diffusion, mainly studied by means of <sup>18</sup>O tracer, the reported activation energies range between 570 and 640 kJ mol<sup>-1</sup>. The absence of natural Al isotope explains why there is only one study which used<sup>26</sup> Al markers, an artificial isotope, to measure the self-diffusion coefficient of Al.<sup>43</sup> The reported activation energy of Al self-diffusion is also high and found to be equal to 510 kJ mol<sup>-1</sup>, a value close to the activation energy of O self-diffusion. Surprisingly, the activation energy for the diffusion of many foreign metallic cations is smaller, usually comprised between 260 and 300 kJ mol<sup>-1</sup>, a value close to the mean activation energy of  $\alpha$ -Al<sub>2</sub>O<sub>3</sub> scale-growth kinetics reported by Hou<sup>44</sup> from a compilation of growth kinetics of numerous Ni-based and Fe-based alumina-forming alloys.

To add to the complexity of transport processes in  $\alpha$ -Al<sub>2</sub>O<sub>3</sub>, the experimental activation energies of grain boundary self-diffusion of O and Al are significantly higher than the activation energies for bulk self-diffusion, a rather uncommon situation. Indeed, the reported activation energies for grain-boundary diffusion are higher than 800 kJ mol<sup>-1</sup> for both O and Al. But, despite all the studies devoted to the oxidation behavior of alumina-forming alloys, there is no convincing explanation of the different activation energies for oxidation and diffusion. The complexity of  $\alpha$ -Al<sub>2</sub>O<sub>3</sub> growth is also reflected in the diversity of microstructures observed for  $\alpha$ -Al<sub>2</sub>O<sub>3</sub> scales that can be equiaxed, columnar, or duplex depending on *T*, *P*<sub>O<sub>2</sub></sub>, and alloying elements such as RE or Pt. These different microstructures must correspond to different growth mechanisms and diffusion processes. But, a more detailed analysis of the correlation between scale microstructure, growth mechanisms and diffusion processes remains to be done.

A better understanding of defect structure and transport properties of  $\alpha$ -Al<sub>2</sub>O<sub>3</sub> could be obtained from theoretical calculations permitting the determination of the enthalpy of formation of different point defects. But, the various calculation methods and interaction potentials used in these calculations lead to somewhat differing results. The most recent calculation has shown that Schottky defects, formed by the combination  $2V_{Al}^{3'} + 3V_O^{2\bullet}$ , are the dominant intrinsic point defects in stoichiometric  $\alpha$ -Al<sub>2</sub>O<sub>3</sub><sup>45</sup> but this result is not in agreement with previous results leading to a predominance of Frenkel pairs.<sup>46</sup> However, because of the extrinsic behavior of

$\alpha$ -Al<sub>2</sub>O<sub>3</sub>, the development of such calculations would be very useful and would lead to more consistent results and thus to a better understanding of defect structure and transport properties of  $\alpha$ -Al<sub>2</sub>O<sub>3</sub>.

## 1.06.6 Concluding Remarks

Mass-transport processes are of fundamental importance for the understanding and modeling of high temperature oxidation and corrosion behavior of materials but, as roughly shown in [Section 1.06.5.4](#), the defect structure and transport properties of most common and important oxides are far from being well known and understood. The increased capability of theoretical treatments would likely permit a more accurate modeling of chemical bonding, point defect structure and intrinsic and extrinsic behavior of common oxides in the coming years.

However, very few scale-growth kinetics can be perfectly described from the only knowledge of defect structure and bulk transport properties of the growing scale. For example, the oxidation of high-purity nickel in pure and dry oxygen is certainly the simplest situation that can be encountered in the field of high temperature oxidation of metallic materials but, at temperature lower than 1000 °C, NiO growth kinetics are several orders of magnitude faster than expected from the extrapolation of high temperature data.

Grain-boundary diffusion is currently invoked to explain faster growth kinetics at intermediate temperatures; there are indeed many experimental evidences confirming the major role of short-circuit diffusion in scale growth. But our understanding of the structure and properties of oxide grain boundaries, particularly their defect structure and the influence of intergranular segregations, needs to be considered and greatly improved without ignoring the influence of triple junctions. Furthermore, this knowledge would be useful for the analysis and modeling of the complex time-dependent evolutions of oxide-scale morphology and microstructure that interfere with short-circuit diffusion.

Surface and grain boundary are common planar defects; the interface separating two crystal phases is also a planar defect that, like surfaces and grain boundaries, can play a role in the creation or annihilation of point defects involved in scale growth or in diffusion processes within the oxidized substrate. There are many examples of solid-state reactions for which solid–solid interfaces and interfacial reactions play a major role.<sup>47</sup> In the field of high temperature

oxidation, one well-known example is provided by the oxidation of silicon. Indeed, molecular oxygen diffuses through the thin silica layer and reacts with the silicon substrate at the silica-silicon interface; this interfacial reaction is the controlling step for the growth of the very thin silica layers now required in the manufacturing of integrated circuits. Therefore, the roles of scale-substrate interfaces need to be more particularly analyzed in relation with some specific topics related to oxide-scale processes such as interface displacement, growth stresses and injection of point defects (vacancy or interstitial). In addition, the development of experimental techniques and methods permitting an accurate determination of the relative movement of M,  $K_M$ , and  $K_{Ox}$  planes would help in the modeling of scale-growth mechanisms. The development of such models combining diffusion processes and interface action could lead to a new approach to questions linked to the effect of impurities and of their segregation, the effect of reactive element and thus a better understanding of the dynamical behavior of scale-substrate interface during scale growth, which could open up new opportunities for the control of oxidation behavior of high temperature materials and the improvement of their oxidation resistance.

## References

- Schmalzried, H. *Chemical Kinetics of Solids*; VCH: Weinheim, 1995.
- Hillert, M. In *Phase Equilibria, Phase Diagrams and Phase Transformations*; Cambridge University Press: Cambridge, 1998; Chapter 16, pp 427–457.
- Kraftmaker, Y. *Phys. Rep.* **1998**, 299, 79–188.
- Aziz, M. *Appl. Phys. Lett.* **1997**, 70, 2810–2812.
- Hull, D.; Bacon, D. J. *Introduction to Dislocations*, 4th ed.; Butterworth-Heinemann: Oxford, 2001.
- Hudson, J. B. *Surface Science: An introduction*; John Wiley: New York, 1998.
- Howe, J. M. *Interface in Materials: Atomic Structure, Thermodynamics and Kinetics of Solid-Vapor, Solid-Liquid and Solid-Solid Interfaces*; John Wiley: New York, 1997.
- Sutton, A. P.; Balluffi, R. W. *Interfaces in Crystalline Materials*; Oxford University Press: Oxford, 2006.
- Pond, R. C.; Hirth, J. P. *Solid State Phys.* **1997**, 47, 287–365.
- Hirth, J. P. *Metall. Trans. A* **1991**, 22A, 1331–1339.
- Pieraggi, B.; Rapp, R. A.; van Loo, F. J. J.; Hirth, J. P. *Acta Metall. Mater.* **1990**, 38, 1780–1790.
- Kofstad, P. *Non Stoichiometry, Diffusion and Electrical Conductivity in Binary Metal Oxides*; Wiley Interscience: New York, 1972.
- Mrowec, S. *Defects and Diffusion in Solids*; Elsevier: Amsterdam, 1980.
- Smyth, D. M. *The Defect Chemistry of Metal Oxides*; Oxford University Press: Oxford, 2000.
- Maier, J. *Physical Chemistry of Ionic Materials: Ions and Electrons in Solids*; John Wiley & Sons: New York, 2004.
- Kizikyalli, N.; Corish, J.; Metselaar, R. *Pure Appl. Chem.* **1999**, 71, 1307–1325.
- Philibert, J. *Atom Movements, Diffusion and Mass Transport in Solids*; Les Editions de Physique/Les Ulys 1991.
- Kirkaldy, J. S.; Young, D. J. *Diffusion in the Condensed State*; The Institute of Metals: London, 1987.
- Glicksman, M. E. *Diffusion in Solids*; John Wiley & Sons: New York, 2000.
- Ghez, R. *Diffusion Phenomena*; Kluwer Academic/Plenum Press: New York, 2001.
- Brown, A. M.; Ashby, M. F. *Acta Metal* **1980**, 28, 1085–1101.
- van Loo, F. J. J. *Prog. Solid State Chem.* **1990**, 20, 47–99.
- van Loo, F. J. J.; Pieraggi, B.; Rapp, R. A. *Acta Metall. Mater.* **1990**, 38, 1769–1779.
- Mishin, Y.; Herzig, C.; Bernardini, J.; Gust, W. *Int. Mater. Rev.* **1997**, 42, 155–178.
- Wang, H.; Yang, W.; Ngan, A. H. W. *Scripta Mater.* **2005**, 52, 69–73.
- Shewmon, P. *Diffusion in Solids*, 2nd ed.; The Minerals, Metals and Materials Society: Warrendale, 1989.
- Peraldi, R.; Monceau, D.; Pieraggi, B. *Oxid. Met.* **2002**, 58, 249–273.
- Paul, A.; van Dal, M. J. H.; Kodentsov, A. A.; van Loo, F. J. J. *Acta Mater.* **2004**, 52, 623–630.
- Haugrud, R. *Corr. Sci.* **2003**, 45, 211–235.
- Manning, M. I. *Corr. Sci.* **1979**, 21, 301–316.
- Nychka, J. A.; Clarke, D. R. *Oxid. Met.* **2005**, 63, 323–352.
- Maier, J. *Solid State Electrochemistry: Thermodynamics and Kinetics of Charge Carriers in Solids*. In *Modern Aspects of Electrochemistry N° 38*; B.E., Kluwer Academic/Plenum Publishers: New York, 2005.
- Vermoyal, J. J.; Frichet, A.; Dessemond, L. J. *Nuclear Mat.* **2004**, 328, 31–45.
- Liu, H.; Mojica-Calderon, C.; Lyon, S. B.; Stack, M. M. *Solid State Ionics* **1999**, 126, 363–372.
- Wouters, Y.; Marchetti, L.; Galerie, A.; Bouvier, P.; Petit, J. P. *Analysing Thermal Oxidation using MicroPhotoElectrochemistry (MPEC)*. In *Local Techniques for Corrosion Research (EFC45)*; Woodhead Publishing: Cambridge, 2007.
- Mrowec, S.; Grzesik, Z. J. *Phys. Chem. Sol.* **2004**, 65, 1651–1657.
- Monceau, D.; Peraldi, R.; Pieraggi, B. *Defect Diffusion Forum* **2001**, 194–199, 1675–1682.
- Atkinson, A. *Rev. Modern Phys.* **1985**, 57, 437–470.
- Martin, M. *Solid State Phenomena* **1992**, 21–22, 1–56.
- Amani, B.; Addou, M.; Monty, C. *Defect Diffusion Forum* **2001**, 194–199, 1051–1056.
- Tsai, S. C.; Huntz, A. M.; Dolin, C. *Mater. Sci. Eng. A* **1996**, A212, 6–13.
- Doremus, R. H. *J. Appl. Phys.*, **2006**, 100, 101301/17.
- Le Gall, M.; Lesage, B.; Bernardini, J. *Phil. Mag. A* **1994**, 70, 761–763.
- Hou, P. Y. *J. Am. Ceram. Soc.* **2003**, 86, 660–668.
- Sun, J.; Stimer, T.; Matthews, A. *Surf. Sci. Coatings* **2006**, 201, 4201–4204.
- Lagerlöf, K. D. P.; Grimes, R. W. *Acta Mater.* **1998**, 46, 5689–5700.
- Dybkov, V. I. *Reaction-diffusion and solid-state chemical kinetics*; IPMS Publications: Kyiv, 2002.

## 1.07 Mechanisms and Kinetics of Oxidation

**S. Chevalier**

Institut Carnot de Bourgogne, UMR 5209 CNRS, University of Bourgogne, 9 Avenue Savary, BP 47870, 21078 Dijon cedex, France

© 2010 Elsevier B.V. All rights reserved.

1.07.1	Introduction	133
1.07.2	Thermodynamics	134
1.07.3	Kinetics	135
1.07.4	Diffusion	137
1.07.5	How to Investigate the High Temperature Corrosion Process	139
1.07.5.1	Surface Preparation	139
1.07.5.2	High Temperature Corrosion Investigations	139
1.07.5.3	High Temperature Corrosion Products Characterization	140
1.07.5.4	Prediction and Modeling of High Temperature Oxidation	142
1.07.6	High Temperature Oxidation Behavior of Metals and Alloys	144
1.07.6.1	Description of Chromia- and Alumina-Forming Materials	144
1.07.6.2	Oxide Scale Spallation: Mechanical Properties and Stress	144
1.07.6.3	Role of Minor Elements	146
1.07.6.4	Reactive Element Effect (REE)	146
1.07.6.4.1	Influence of RE on oxide scale growth kinetics	148
1.07.6.4.2	Influence of RE on oxide scale adherence	148
1.07.6.4.3	Location of RE in oxide scales	148
1.07.6.4.4	Influence of RE on oxide scale growth mechanism	148
References		148

### Glossary

**Alumina ( $\text{Al}_2\text{O}_3$ )** Aluminum oxide.

**Alumina (transient)** Different phases of alumina ( $\gamma\text{-Al}_2\text{O}_3$ ,  $\delta\text{-Al}_2\text{O}_3$ ,  $\theta\text{-Al}_2\text{O}_3$ ) able to transform into the stable alumina phase,  $\alpha\text{-Al}_2\text{O}_3$ .

**Alumina-forming (alloy)** Alloy able to form an alumina scale.

**Aluminide** Intermetallic compound containing aluminum (examples  $\text{FeAl}$ ,  $\text{TiAl}$ ,  $\text{NbAl}_3$ , ...).

**Aluminization** Surface treatment consisting of forming aluminide diffusion coating via a cementation process.

**Arrhenius plot** Relationship between reaction rate and temperature,  $k = k_0 \exp(-E/RT)$  with  $E$  activation energy.

**Cyclic oxidation** Discontinuous oxidation corresponding to periods at temperature followed by rapid cooling to room temperature.

**Diffusion** Transport or migration of atoms, ions or molecules in a solid, liquid or gaseous media.

**Diffusion (coefficients of)**  $D_{\text{app}}$  is apparent diffusion coefficient,  $D_V$  is volume diffusion

coefficient,  $D_{\text{gb}}$  is grain boundary diffusion coefficient.

**Isothermal oxidation** Continuous oxidation at a fixed temperature.

**Marker (isotopic marker)** Two stage oxidation experiment consisting of oxidizing a metallic substrate at high temperature in  $^{16}\text{O}_2$ , then in  $^{18}\text{O}_2$ , and locating oxygen isotopes across the thermally grown oxide scale.

**Pilling–Bedworth (ratio)** Oxide volume relative to native metal volume.

**Residual stress** Stress taking into account growth stress as well as thermal stress.

**Silica ( $\text{SiO}_2$ )** Silicon oxide.

**Spallation** Detachment of oxide scales during cooling from oxidation to room temperature.

**Thermogravimetry** Continuous weight change measurement as a function of oxidation time.

**Wagner's theory** Theory which relates kinetic parameters to diffusion of species across a growing scale.

**Zirconia ( $\text{ZrO}_2$ )** Zirconium oxide.

## Abbreviations

<b>AES</b>	Auger electron spectroscopy
<b>AFM</b>	Atomic force microscopy
<b>AISI 304</b>	Austenitic stainless steel mainly composed of (in wt%) Fe–18Cr–10Ni
<b>EDX</b>	Energy dispersive X-ray analysis
<b>EPMA</b>	Electron probe micro analysis
<b>FIB</b>	Focused ion beam
<b>MOCVD</b>	Metal-organic chemical vapor deposition
<b>PIPS</b>	Precision ion polishing system, ion milling using low angle Ar guns
<b>PLS</b>	Photoluminescence spectroscopy
<b>RE</b>	Reactive element
<b>REE</b>	Reactive element effect
<b>SEM</b>	Scanning electron microscopy
<b>SIMS</b>	Secondary ion mass spectrometry
<b>SNMS</b>	Secondary neutral mass spectrometry
<b>TEC</b>	Thermal expansion coefficient in °C <sup>-1</sup> or K <sup>-1</sup>
<b>TEM</b>	Transmission electron microscopy
<b>XPS</b>	X-ray photoelectron spectroscopy
<b>XRD</b>	X-ray diffraction

## Symbols

$\mu_{\text{products}}$	Chemical potential of corrosion products
$\mu_{\text{reactants}}$	Chemical potential of reactants
$\Delta_r G^0$	Variation of standard free enthalpy of reaction
$\Delta_r H^0$	Variation of standard enthalpy of reaction
$\Delta m/A^0$	Weight gain per unit area
$\Delta_r S^0$	Variation of standard entropy of reaction
<b>F17Ti</b>	Ferritic stainless steel mainly composed of (in wt%) Fe–17Cr–0.4Ti
$G_r$	Free enthalpy of reaction
$k_p$	Parabolic rate constant
$k_l$	Linear rate constant
$K$	Equilibrium constant
<b>Y<sub>3</sub>Al<sub>5</sub>O<sub>12</sub></b>	Garnet (called YAG for yttrium aluminum garnet)

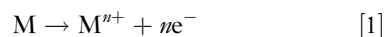
## 1.07.1 Introduction

As is evident, humans need oxygen to survive. This is a paradox because this fundamental molecule can be very aggressive against most metallic materials. Even if air contains only 20% of oxygen, it is enough to provoke large-scale degradation of materials.

This degradation is directly connected to their conditions of use. The failures caused by the

oxidation process can be very different depending on whether the materials are subjected to acids or salts in wet conditions, to dry conditions but at high temperature (over 500 °C) or to different aggressive atmospheres (O<sub>2</sub>, hot corrosion, sulfur, chloride, ...). Whatever the exposed conditions, the materials degrade and disintegrate more or less, following different mechanisms.<sup>1,2</sup>

The understanding of the mechanisms which control these different types of corrosion is fundamental to try to improve the corrosion resistance of materials and to extend their lifetime under such severe conditions. One rule is clearly established about the corrosion process; one cannot suppress corrosion. Thermodynamic data show that the formation of corrosion products is energetically favored, following the chemical reaction:



Moreover, these chemical reactions are also largely dependent upon the corrosion rates. Thus, both thermodynamics and kinetics need to be considered while studying the corrosion process; they have to be carefully controlled to try to protect the base material. That is the reason why the best protection consists of decreasing the corrosion rates.

This chapter focuses on the description of fundamentals for high temperature oxidation. Specific attention will be paid to the high temperature oxidation mechanisms (from thermodynamics, kinetics, and diffusion points of view) and mainly how to relate these mechanisms to the improvement in oxidation resistance. The better the knowledge of the high temperature oxidation mechanisms is, the better is the improvement in the high temperature performance of metallic material.

High temperature oxidation performances are based on the formation of a protective oxide scale which acts as a diffusion barrier, separating the base materials from the aggressive atmospheres.<sup>3–7</sup> It is most of the time a huge challenge, because an effective barrier has to be dense and homogeneous, to cover the entire alloy surface, to possess mechanical properties matching those of the base materials, to consume the least possible metal,<sup>8</sup> to remain stable, to be able to resist complex atmospheres (presence of water vapor for example<sup>9–11</sup>) and above all to keep adherent to the substrate, even after thermal shocks.

Materials able to form protective chromia, Cr<sub>2</sub>O<sub>3</sub>, alumina, Al<sub>2</sub>O<sub>3</sub>, or silica, SiO<sub>2</sub> layers are the best candidates to be used at high temperatures in oxidizing atmospheres. These refractory oxides grown on

Fe-, Co-, or Ni-based alloys possess high melting points. Cr (12 wt%) and Al (5 wt%) are necessary to form chromia on chromia-forming alloys and to form alumina on alumina-forming alloys, respectively. The growth rate of chromia scales is much faster than that of alumina scales<sup>12</sup> and, at temperatures over 1000 °C, chromium oxides (especially CrO<sub>3</sub>) start to become volatile.

As a matter of fact, chromia and alumina scales should only be employed in adequate temperature ranges,  $T \leq 1000$  °C for Cr<sub>2</sub>O<sub>3</sub> and  $T \leq 1300$  °C for Al<sub>2</sub>O<sub>3</sub>, under isothermal exposures, that is, continuous maintenance at temperature, or under thermal cycling conditions, that is, successive exposure at oxidizing temperature followed by rapid cooling. During cycling, the oxide scales tend to spall, losing any protective effect. Thermal stresses generated during cooling and due to differences between the thermal expansion coefficient of the base metal and that of the oxide scale are mainly responsible for oxide scale spallation.<sup>13</sup> The thermal and/or residual stresses are known to play a huge role during the oxidation of metallic alloys.<sup>4,14–20</sup>

A recent study showed that the amplitude of oxide scale spallation could not be directly related to the residual stresses in the oxide layers.<sup>21</sup> It is also proposed that vacancy coalescence at the metal–oxide interface, as a result of the oxide scale growth, can create pores and cavities and therefore weaken scale adhesion.<sup>22</sup>

It appears clearly that one has to consider not only the chemical evolution of the oxide scale during its growth, but also its mechanical evolution, as well as the close relationship it establishes with the base metallic material. All these considerations are usually named ‘physical-chemistry’ of the oxide scales.

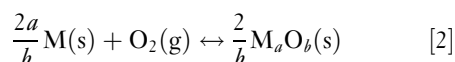
The proposed situation is the simplest one, as pure oxide scales grown on model materials are being considered. In fact, commercial alloys contain a lot of elements added to increase the mechanical properties, to stabilize the austenitic phase instead of the ferritic phase, to avoid or fix carbide formation (formation of  $\sigma$  phases for example) or to increase their corrosion resistance at ambient or high temperature. The minor element additions perturb the oxide scale formation because they may form mixed oxides, such as spinel or perovskite oxides; these oxides are known to possess poor resistance to high temperature oxidizing atmospheres compared to chromia or alumina scales. Most of the added elements segregate at the interfaces, at the oxide

grain boundaries, sometimes within the oxide grains, or form mixed oxides. Some of them, called reactive elements or rare earths (RE), have considerable effects on the high temperature oxidation behavior of alloys. Their addition in small quantities is enough not only to greatly decrease the oxidation rates, but above all to drastically increase the oxide scale adherence to the base material.

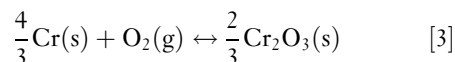
The present chapter helps define adequate ways to study high temperature corrosion processes. Thermodynamics, metallurgy, kinetics and diffusion, experimental tools, and the effect of complex atmospheres will be described to answer the still open question: how to improve high temperature corrosion resistance of metals in aggressive atmospheres? Some solutions will be proposed in order to limit the degradation of metallic materials when exposed in such atmospheres at high temperature.

## 1.07.2 Thermodynamics

Thermodynamics can be considered the driving force for the degradation of metals and alloys in corrosive atmospheres. Effectively, pure metals or metallic elements that constitute alloys are not stable in a reactive gaseous atmosphere. Then, if one considers that the gas is oxygen, a pure metal (M) transforms to oxide (M<sub>a</sub>O<sub>b</sub>), following the chemical reaction:



In case of chromia formation for example, the chemical reaction becomes:



The free enthalpy of the reaction is expressed by:

$$G_r = \sum \mu_{\text{products}} - \sum \mu_{\text{reactants}} \quad [4]$$

where  $\mu_{\text{products}}$  and  $\mu_{\text{reactants}}$  are the chemical potential of the corrosion products and the reactants, respectively.

By detailing each chemical potential, this equation can be written:

$$G_r = \frac{2}{b}\mu_{M_aO_b}^0 + \frac{2}{b}RT \ln(a_{M_aO_b})^{2/b} - \frac{2a}{b}\mu_M^0 - \frac{2a}{b}RT \ln(a_M)^{2a/b} - \mu_{O_2}^0 - RT \ln \frac{P_{O_2}}{P^0} \quad [5]$$

If one assumes that:

$$\Delta_r G^0 = \frac{2}{b} \mu_{M_a O_b}^0 - \frac{2a}{b} \mu_M^0 - \mu_{O_2}^0 \quad [6]$$

$a_{M_a O_b} = 1$  (oxide is pure),  $a_M = 1$  (metal is pure), and  $P^0 = 1$  atm.

The classical expression of the free enthalpy of reaction is:

$$G_r = \Delta_r G^0 + RT \ln \frac{1}{P_{O_2}} = \Delta_r G^0 + RT \ln K \quad [7]$$

with  $K$  the equilibrium constant.

When the equilibrium is reached,  $G_r = 0$  and then,

$$\Delta_r G^0 = -RT \ln K = RT \ln P_{O_2} \quad [8]$$

Then,

$$\ln P_{O_2} = \frac{\Delta_r G^0}{RT} \quad [9]$$

This expression means that for a partial pressure of oxygen below this critical value (value obtained when the equilibrium is reached), the metal does not oxidize. For a partial pressure of oxygen over this value, the metal can be totally oxidized.

Another possibility for expressing the variation of the reaction standard free enthalpy is:

$$\Delta_r G^0 = \Delta_r H^0 - T \Delta_r S^0 \quad [10]$$

with  $\Delta_r H^0$  being the variation of the standard enthalpy of the reaction and  $\Delta_r S^0$  being the variation of the standard entropy of the reaction.

These two expressions [8] and [10] allow a combination of the oxidation temperature together with the partial pressure of oxygen. Then, two diagrams will indicate the evolution of a metal or an alloy in an oxidizing atmosphere at high temperature: phase diagrams and Ellingham diagrams.<sup>6,7,23</sup>

Phase diagrams give the phases that can be formed depending on the temperature or the pressure. Then, if for one component (an oxide in our case), several crystallographic phases can be formed, the use of phase diagrams allows the identification of the one that is thermodynamically stable for a fixed temperature. As an example, zirconia ( $ZrO_2$ ) has three allotropic structures: cubic, tetragonal, and monoclinic, which transform to each of them on decreasing the temperature, as shown in the Zr–O phase diagram.<sup>24</sup>

Ellingham diagrams are useful for comparing the thermodynamic stability of two oxides formed from two different metals. Their use is crucial in the case of oxidation of alloys (i.e., those which contain

different minor elements), in order to know which oxides are the most thermodynamically stable.

However, this approach needs the system to be at equilibrium; most of the time, this situation is not obtained in real systems. Thermodynamics has some limits in the understanding of the corrosion behavior of metals and alloys at high temperatures. Further details on the thermodynamics of gas–metal reactions can be found in **Chapter 1.09, Thermodynamics and Theory of External and Internal Oxidation of Alloys**.

### 1.07.3 Kinetics

A kinetics approach is complementary to a thermodynamics approach, because it gives information about the rate of oxidation of a metal or an alloy. One can talk about heterogeneous kinetics because a metallic surface reacts with a gas, oxygen for example.<sup>25</sup> The mechanisms occurring during high temperature oxidation are complex. **Figure 1** describes some aspects of the reaction between a metallic surface and oxygen

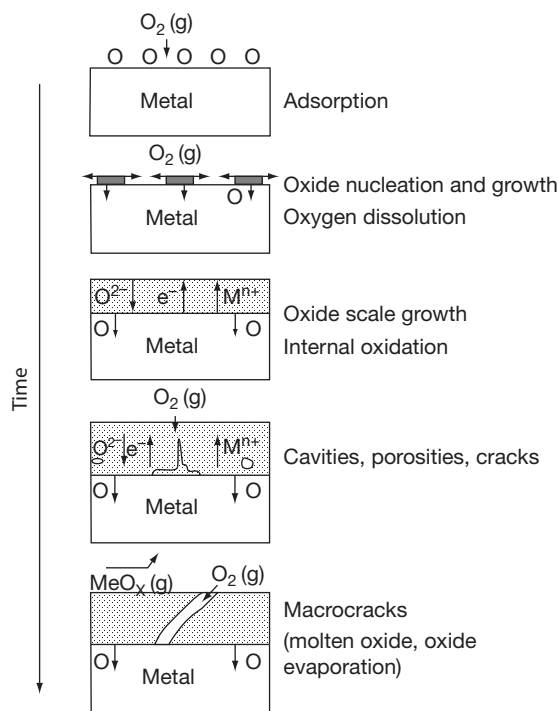


**Figure 1** Schematic representation of the reaction between a metallic surface and oxygen at high temperature. Adapted from Kofstad, P. *High Temperature Corrosion*; Elsevier Applied Science, 1988; Sarrazin, P.; Galerie, A.; Fouletier, J. *Les mécanismes de la corrosion sèche. Une approche cinétique*; EDP Sciences, 2000.



at high temperature.<sup>6,7,26</sup> The main steps of the oxidation process can be described as follows:

- oxygen adsorption at the metal surface,
- oxide nucleation with formation of a bidimensional layer
- tridimensional growth of oxide with formation of a thin oxide layer,
- diffusion of species (from metal or from gas) across the growing scale,
- apparition of cracks or microcracks in the base metal and/or in the oxide scale,
- development of cracks at the metal–oxide interface, which can lead to scale spallation and loss of protectiveness.

Two limiting cases can be observed during the growth of an oxide layer:

- growth of a dense oxide layer, for which the transport of species takes place by solid state diffusion,
- growth of a porous oxide scale, for which the transport of species takes place by gaseous diffusion.

One can associate two kinetic regimes to these two limiting cases (Figure 2)<sup>27</sup>:

- a parabolic regime, for which in planar symmetry, diffusion of species across a growing scale is the limiting step in the oxidation process. In that case,

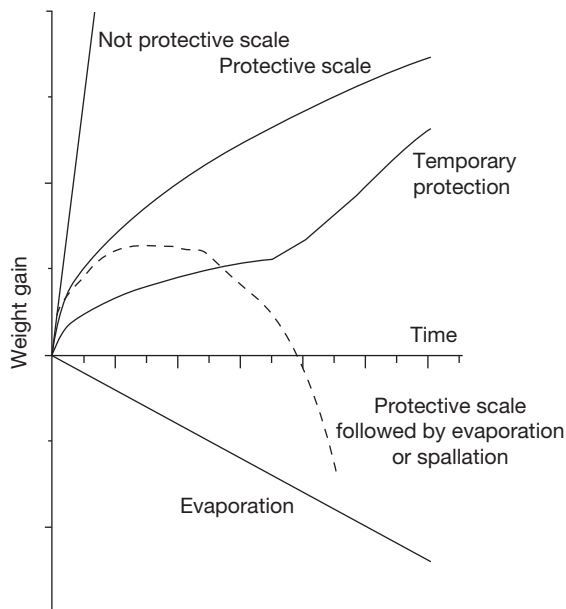


**Figure 2** Schematic representation of kinetics observed during high temperature oxidation. Adapted from Antoni, L.; Galerie, A. Corrosion sèche des métaux, Techniques de l'Ingénieur, M4 228, p 9.

the relationship between the weight gain per unit area ( $\Delta m/A$ ) and the exposure time ( $t$ ) is:

$$\left(\frac{\Delta m}{A}\right)^2 = k_p t \quad [11]$$

with  $k_p$  the parabolic rate law constant ( $\text{g}^2 \text{cm}^{-4} \text{s}^{-1}$ ). The parabolic rate law constant can be also expressed in square centimeter per second, by using:

$$k_c = \left(\frac{M_{M_aO_b}}{bM_O\rho_{M_aO_b}}\right)^2 k_p \quad [12]$$

where  $M_{M_aO_b}$  and  $M_O$  are the molar mass of  $M_aO_b$  and O, respectively, and  $\rho_{M_aO_b}$  is the oxide density.

The plot of  $\Delta m/A = f(t^{1/2})$  or  $(\Delta m/A)^2 = f(t)$  allows us to determine the domain where the parabolic rate law is verified, and also to calculate the value of  $k_p$ . The first plot is preferable because it improves the accuracy by minimizing the errors in  $\Delta m/A$ :

- a linear regime, for which a chemical reaction at one of the interfaces (gas–oxide and/or metal–oxide) is the limiting step in the oxidation process. In that case, the relation becomes:

$$\left(\frac{\Delta m}{A}\right) = k_l t \quad [13]$$

with  $k_l$  the linear rate law constant ( $\text{g cm}^{-2}$ ).

When a good protection against high temperature oxidation is observed, the parabolic rate law is verified. Conversely, poor oxidation resistance corresponds to a linear rate law (Figure 2).

Other kinetics laws can be found during the growth of oxide scales at high temperature:

- Cubic law, for which

$$\left(\frac{\Delta m}{A}\right)^3 = k_c t \quad [14]$$

- Power law, for which

$$\left(\frac{\Delta m}{A}\right)^n = k_n t \quad [15]$$

with  $1 < n < 3$ .

This last law corresponds to an intermediate case between the three previous cases. When  $2 < n < 3$ , the kinetic law is generally called subparabolic, which means deviation from a real parabolic law. It can be caused by the evolution of grain size during the high oxidation process, by scale cracking, oxidation of reactive element, or incorporation of metal precipitates.<sup>28</sup>

Other laws were identified in specific cases (thin films, beginning of the oxidation process, or low oxidation temperatures). They are:

- Logarithmic law, for which

$$\left(\frac{\Delta m}{A}\right) = A + B \ln t \quad [16]$$

- Inverse-logarithmic law, for which

$$\left(\frac{\Delta m}{A}\right) = C - D \ln t \quad [17]$$

Some specific cases are also obtained when mixed kinetics laws are observed, especially when chemical reaction at interface(s) takes place together with diffusion of species across the growing scale. In that case, the kinetics regime can be described by:

$$t = A + B\left(\frac{\Delta m}{A}\right) + C\left(\frac{\Delta m}{A}\right)^2 \quad [18]$$

where  $A$ ,  $B$ , and  $C$  are constants;  $B$  corresponds to  $1/k_p$  and  $C$  to  $1/k_p$ .

A particular case corresponds to successive rate laws: parabolic then linear, which signifies a protective oxidation behavior followed by a loss of protectiveness. Both regimes are separated by a transient period. This case, illustrated in **Figure 2**, is typical of what happens during the growth of zirconia on Zr or zircaloy.<sup>29–31</sup>

The plot of instantaneous  $k_p$  can also give crucial information, especially on the evolution of phases in the oxide scale.<sup>32,33</sup> This is particularly true for alumina-forming alloys, because of the presence of several alumina phases ( $\theta$ ,  $\gamma$ ,  $\delta$ ,  $\alpha$ - $\text{Al}_2\text{O}_3$ <sup>34,35</sup>). The plot of instantaneous  $k_p$  versus time indicates the evolution of  $k_p$  values; a constant  $k_p$  value is indicative of a stationary oxidation regime, which can be associated with the formation of a stable oxide phase, whereas an evolution of  $k_p$  with time suggests the presence of a transient phase ( $\theta$ - $\text{Al}_2\text{O}_3$  for example). The so-plotted curves are then helpful in determining the time necessary to form a protective stable oxide phase ( $\alpha$ - $\text{Al}_2\text{O}_3$  for example).

Wagner developed a theory relating the parabolic rate law constants to the diffusion coefficient of species: anions ( $\text{O}^{2-}$ ,  $\text{S}^{2-}$ , ...) and cations ( $\text{Cr}^{3+}$ ,  $\text{Al}^{3+}$ , ...).<sup>36</sup> Then, for an oxide,  $\text{M}_a\text{O}_b$ , Wagner's oxidation theory gives:

$$k_c = \frac{1}{2} \int_{p_{\text{O}_2}}^{p_{\text{O}_2}'} \left[ D_{\text{anion}} + \left(\frac{b}{a}\right) D_{\text{cation}} \right] d \ln P_{\text{O}_2} \quad [19]$$

with  $k_c$ , the parabolic rate law constant ( $\text{cm}^2 \text{s}^{-1}$ ),  $a = 2$  and  $b = 3$  (for  $\text{Cr}_2\text{O}_3$  for example),  $p_{\text{O}_2}$  is the partial pressure of oxygen for the oxide decomposition at the metal–oxide interface, and  $p_{\text{O}_2}'$  is the partial pressure of oxygen at the gas–oxide interface.

This theory can be adjusted in order to fit realistic situations and to consider short-circuit diffusion paths for example. In the case of diffusion across chromia and alumina scales in the temperature range 800–1200 °C, these short-circuit paths are usually oxide grain boundaries.

### 1.07.4 Diffusion

The diffusion short-circuits for diffusion within oxide scales in the temperature range from 800 to 1000 °C are considered to be oxide grain boundaries. According to Harrison,<sup>37</sup> three diffusion regimes could be identified. The A regime is defined by  $\sqrt{Dt} \gg d$ ,  $d$  being the oxide grain size; in that case, the volume penetration is superior to the short-circuit size, especially the grain boundaries. The C regime claims that the penetration is continuous at the grain boundaries ( $\sqrt{Dt} \ll \delta$ ,  $\delta$  being the grain boundary width). Finally, the B regime is an intermediate regime where three processes participate in diffusion: volume, grain boundary, and lateral diffusion ( $\delta \ll \sqrt{Dt} \ll d/2$ ).

Marker experiments made during oxidation in  $^{18}\text{O}_2$  lead to the determination of oxygen diffusion coefficients via oxide grain boundaries and via the oxide bulk. Taking into consideration the plots of  $\ln [^{18}\text{O}] = f(x)$ , the first part of the curve corresponds to the apparent diffusion of oxygen (**Figure 3**). From the three diffusion regimes, the B regime is usually chosen for the study of intergranular diffusion.<sup>38,39</sup> In this

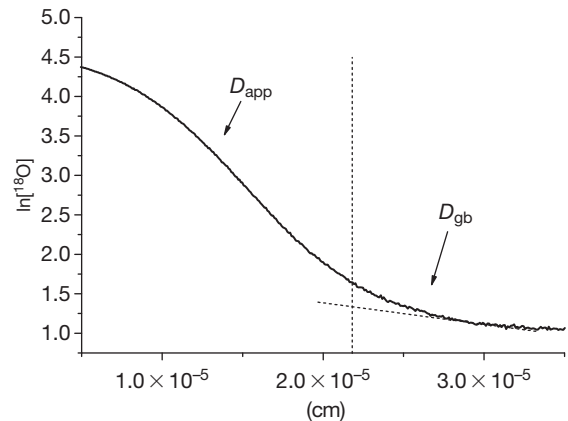


**Figure 3** Plot of  $\ln [^{18}\text{O}] = f(x)$  showing the zones where apparent and oxide grain boundary diffusion predominate.

regime,  $\delta \ll \sqrt{Dt} \ll d/2$  with  $\delta$  being the grain boundary width and  $d$  being the oxide grain size.

The apparent diffusion of oxygen corresponds to diffusion in the bulk and the oxide grain boundaries. It is expressed in the case of dislocation and bulk diffusion<sup>40</sup> but can be used in the case of grain boundary and bulk diffusion,<sup>41,42</sup> if we assume that the beginning of the oxygen distribution profile corresponds to  $D_{app}$  (A regime)<sup>38</sup>:

$$D_{app} = (1 - f)D_b + fD_{gb} \quad [20]$$

where  $f$  is the fraction of sites associated to the grain boundaries;  $f$  can be expressed as:

$$f = \frac{3\delta}{\phi} \quad [21]$$

where  $\delta$  is the grain boundary width (generally assumed to be 1 nm) and  $\phi$  is the average oxide crystallite size.

$D_{app}$  is determined from the second Fick's law solution:

$$\frac{C(x, t) - C_s}{C_0 - C_s} = \text{erf}\left(\frac{x}{2\sqrt{D_{app}t}}\right) \quad [22]$$

$C_s$  is the oxygen 18 concentration at the oxide scale surface,  $C_0$  is the natural concentration of oxygen 18 within the oxide layer (0.2 at.%<sup>43</sup>), and  $t$  is the diffusion time.

This model which associates the beginning of the distribution profile to an apparent diffusion coefficient has been recently discussed by Fielitz *et al.*<sup>44</sup> who proposed that the first part of the oxygen diffusion profile in polycrystalline mullite corresponded to the bulk diffusion coefficient in the B regime and not to the apparent diffusion coefficient.

The second part of the diffusion curve,  $\ln[^{18}\text{O}] = f(x)$ , led to determination of the oxygen grain boundary diffusion coefficient (Figure 3). By applying the model developed by Suzuoka<sup>45,46</sup> and Whipple–Le Claire<sup>47–49</sup>  $D_{gb}$  is expressed by:

$$D_{gb}\delta = 0.661\sqrt{\frac{4D_b}{t}}\left(-\frac{\partial \ln C}{\partial x^{6/5}}\right)^{-5/3} - D_{app} \quad [23]$$

where  $(\partial \ln C / \partial x^{6/5})$  is the slope of the curve  $\ln[^{18}\text{O}] = f(x^{6/5})$ .

By combining eqns [22] and [25], one obtains the following relation:

$$(1 - f)D_b + \frac{0.661f}{\delta}\sqrt{\frac{4D_b}{t}}\left(-\frac{\partial \ln C}{\partial x^{6/5}}\right)^{-5/3} - D_{app} = 0 \quad [24]$$

This relation allows the determination of the oxygen bulk diffusion coefficient,  $D_b$ . Using  $D_{app}$  and  $D_b$ , the relation [20] leads to the calculation of  $D_{gb}$ .

This calculation takes into consideration the oxide scale roughness.<sup>50</sup> The principle for determining the oxygen diffusion coefficients is the same, but the fraction of sites associated with grain boundaries is given by:

$$f_r = \frac{\phi/2}{\phi/2 + 2R_a} \times \frac{3\delta}{\phi} \quad [25]$$

where  $R_a$  is the average roughness of the oxide scale.

Cation diffusion has also to be taken into account during oxide scale growth. Chromium 54 can be used as an isotopic marker in chromia (made of  $^{56}\text{Cr}_2^{16}\text{O}_3$ ), and also in alumina (made of  $^{27}\text{Al}_2^{16}\text{O}_3$ ). As a matter of fact and taking into account the fact that both chromium and aluminum cations diffuse in the same way, the results obtained for chromium diffusion coefficients in alumina scales are applied for aluminum cation diffusion coefficients in the same scale. Indeed, the use of a chromium isotope as a diffusive species is easier than the use of aluminum, which has no natural isotope; one can only use an artificial aluminum isotope,  $^{26}\text{Al}$ , which is radioactive and very expensive. Very few studies have used this radioactive tracer.<sup>51,52</sup>

In the case of  $^{54}\text{Cr}$  or  $^{26}\text{Al}$ , the solution of the second Fick's law corresponding to a thin deposited layer is:

$$C(x) = C_0 \exp\left(-\frac{x^2}{4D_{app}t}\right) \quad [26]$$

The procedure is the same as that applied for the determination of oxygen diffusion coefficients. The first part of the plot  $\ln[C_{\text{isotope}}] = f(x)$  corresponds to  $D_{app}$  and the second part to  $D_{gb}$ .<sup>53</sup>  $D_{app}$  is calculated from the slope of  $\ln[C_{\text{isotope}}] = f(x^2)$ , whereas  $D_{gb}$  is determined from the Whipple–Le Claire model.

Figure 4<sup>50,54–60</sup> is an illustration of oxygen and chromium diffusion coefficients determined in thermally grown  $\text{Cr}_2\text{O}_3$  scales formed on chromia-forming alloys. It appears clearly that, in thermally grown  $\text{Cr}_2\text{O}_3$ , the grain boundary diffusion coefficients ( $D_{gb}^{\text{Cr}}$  and  $D_{gb}^{\text{O}}$ ) are higher than the bulk diffusion coefficients (Figure 4), in the considered temperature range. The large discrepancy in the diffusion coefficient values depends on the nature of the chromia-forming materials and on the presence or not of a reactive element.

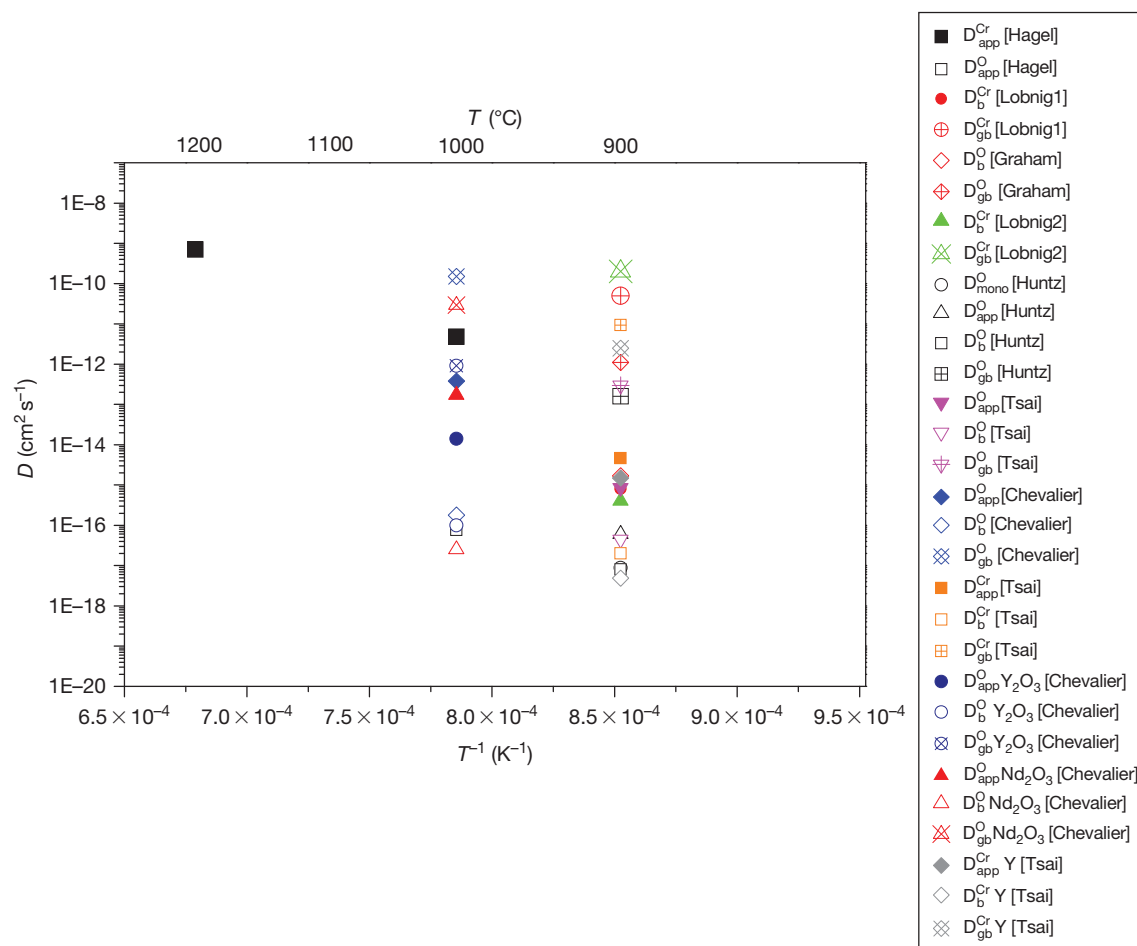


**Figure 4** Comparison of oxygen or chromium diffusion coefficients in thermally grown chromia scales doped or not by RE ( $D_{\text{app}}^{\text{O}}$  is the apparent oxygen diffusion coefficient,  $D_{\text{V}}^{\text{O}}$  is the volume oxygen diffusion coefficient,  $D_{\text{gb}}^{\text{O}}$  is the grain boundary oxygen diffusion coefficient,  $D_{\text{app}}^{\text{Cr}}$  is the apparent chromium diffusion coefficient,  $D_{\text{V}}^{\text{Cr}}$  is the volume chromium diffusion coefficient,  $D_{\text{gb}}^{\text{Cr}}$  is the grain boundary chromium diffusion coefficient). The samples doped with RE are indicated by  $\text{Y}_2\text{O}_3$ ,  $\text{Nd}_2\text{O}_3$ , or Y.

## 1.07.5 How to Investigate the High Temperature Corrosion Process

### 1.07.5.1 Surface Preparation

Particular attention has to be paid to the preparation of samples. Depending on the study, one has to ask if it is necessary to polish the surfaces (if the answer is positive, then one has to ask: ‘up to which finishing grade? Is it necessary to achieve a mirror-like finish?’) or to use sand blasting to prepare the surfaces or to degrease in ethanol or acetone (is it necessary to use an ultrasonic bath, deionized water?).

At this step in the preparation, the sample surface area has to be precisely determined, because all mass gain or loss will be divided by the sample surface area in order to make comparisons between tests.

### 1.07.5.2 High Temperature Corrosion Investigations

The tools used to investigate the high temperature reactivity of metallic materials are numerous: they can be basic (tubular or muffle furnaces, thermogravimetric devices,<sup>61,62</sup> ...) or more elaborate (corrosion under stress application,<sup>63</sup> oxidation with 18 oxygen,<sup>64–68</sup> ...).

For isothermal oxidation tests, the use of a thermobalance is of great interest, because it gives information about kinetics for more or less long exposures (see Figure 2). However, for most isothermal oxidation tests the duration in a thermobalance is relatively short (from 24 to 200–300 h typically) compared to real time in service conditions. Discontinuous

experiments can be used for long oxidation times; these allow the introduction of many samples (10–50 for example) all together in the same furnace (a muffle furnace is the most used) at a fixed temperature and removal of specimens after various times. By weighing each sample after such exposures, kinetic curves can be built for long periods (several thousands hours).

However, failure of oxide scales mainly occurs when the materials are subjected to thermal cycling conditions. The stresses, induced by temperature drops and rises, promote cracks and spalling, followed by drastic enhancement of the damage caused by the corrosive atmospheres.<sup>69–74</sup> Since thermal cycling treatments are usually more severe than isothermal oxidation, cyclic oxidation tests are widely performed in order to test the scale adherence under such severe conditions.<sup>75–85</sup> Cyclic oxidation experiments can be performed in a thermobalance (this means that the furnace or the sample is moved to produce cycling, but the sample is continuously weighed<sup>86</sup>), although, usually, net and gross weights are collected after automatic or manual cycles. The net weight gain corresponds to the specimen weight excluding any spalled scale. The gross weight gain corresponds to the specimen weight including any spalled scale collected in the crucible. The difference between the net and the gross weight gains indicates the proportion of spalled oxide scale. The results in **Figure 5** give an illustration of plots of net and gross weights for aluminide diffusion coatings on Fe–Cr alloys, which indicate cyclic behavior with and without spallation.<sup>1</sup>

### 1.07.5.3 High Temperature Corrosion Products Characterization

The complete understanding of oxide scale growth mechanisms needs a very careful analysis of the corrosion products. **Figure 6** illustrates most of the possibilities for characterizing thermally grown oxide scales.<sup>1,87</sup> Scanning electron microscopy (SEM) coupled with energy dispersive X-ray analyses (EDX) is probably the most useful analytical tool for observing oxide scales at the microscopic level. Coupled with XRD, it gives much necessary information about thermally grown oxide scales. However, one has also to consider optical microscopy; this gives more macroscopic information, which is often sufficient for evaluating the oxidation behavior of metals and alloys. Another convenient tool for studying oxide scales is transmission electron microscopy (TEM), which allows observations of the scale

morphology at the nanometric scale, in association with local chemical analyses and microdiffraction.<sup>88</sup> Unfortunately, two main difficulties limit the use of this technique:

- sample preparation is very delicate and needs long and difficult manipulations,<sup>88–90</sup> even though the use of a focused ion beam (FIB) drastically increases the chance of success for sample preparation<sup>91–97</sup>),
- the correspondence between the nanometric and the macrometric scale is often difficult and needs repeated observations.

These parameters are the reasons why TEM observations are usually the last step in the characterization process, which logically evolves from macro- to nanoscale, and not the opposite!

A second very promising tool is the use of two stage oxidation experiments in  $^{16}\text{O}_2/^{18}\text{O}_2$ . This method consists of using an oxygen isotope,  $^{18}\text{O}$ , as a marker in a preformed  $^{16}\text{O}$  containing layer. The principle is to oxidize the metallic substrate first under a  $^{16}\text{O}_2$  atmosphere; the reaction chamber is evacuated and  $^{18}\text{O}_2$  is introduced for the second step of the test, without temperature modification. The technique has been largely used not only to study oxide scale growth mechanisms, but also to determine oxygen diffusion coefficients in many chemical systems.<sup>44,98–102</sup> The method can be extended to marker experiments in water vapor by making successive exposure to  $\text{H}_2\ ^{16}\text{O}/\text{H}_2\ ^{18}\text{O}$ .<sup>103</sup> The oxygen isotope distributions are followed using secondary ion mass spectrometry (SIMS) or secondary neutral mass spectrometry (SNMS). Very careful analyses of the oxygen isotope distribution profiles allow determination of the oxygen diffusion coefficients in growing scales. **Figure 7** shows three limiting cases corresponding to the diffusion of cations (**Figure 7(a)**), to the diffusion of anions (**Figure 7(b)**) and to mixed diffusion (**Figure 7(c)**). Bulk and grain boundary diffusion coefficients for oxygen were calculated using the models proposed by Suzuoka<sup>45,46</sup> and Whipple–Le Claire.<sup>47,48</sup>

More recently, other characterization tools have been used in the field of high temperature corrosion. These give complementary information and, together with ‘more classical’ analyses, they allow the determination and understanding of oxide scale growth mechanisms. Among these techniques, Raman spectroscopy,<sup>104–108</sup> photoluminescence spectroscopy (PLS),<sup>35,109–114</sup> X-ray photoelectron spectrometry (XPS),<sup>34,35,115–117</sup> and photoelectrochemistry<sup>118–121</sup> are probably the most interesting tools.

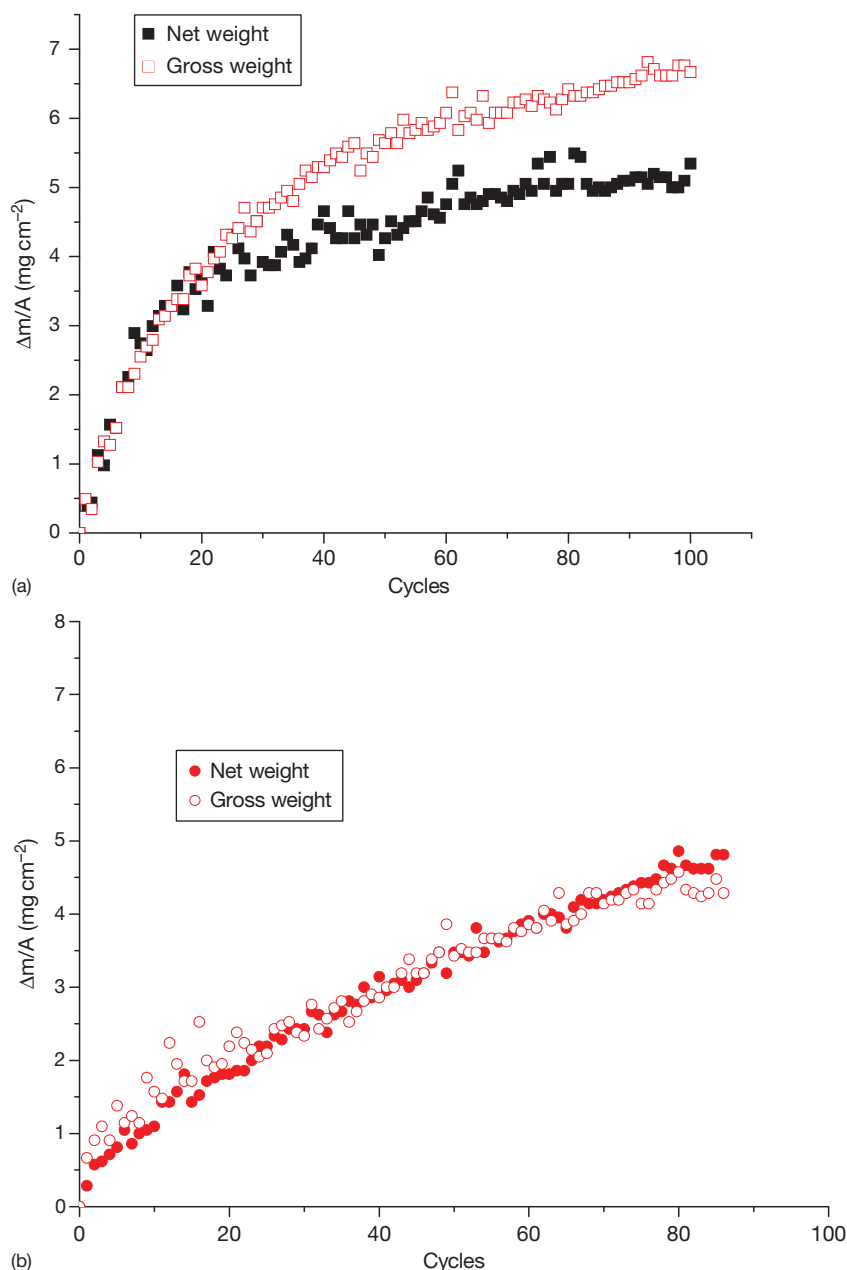


**Figure 5** Cyclic oxidation kinetics (24 h cycle at 1000 °C); case of aluminized diffusion coatings: (a) the deviation between gross and net weights means oxide spallation and (b) when doped with  $Y_2O_3$ , there is no spallation. Reproduced from Chevalier, S. *Traitements de surface et nouveaux matériaux: quelles solutions pour lutter contre la dégradation des matériaux à haute température?*; Les Editions Universitaires de Dijon, 2007.

Generally, the study of the corrosion products is performed ‘*ex situ*,’ which means after the specimen has cooled down to room temperature. How can one be sure that what is observed at room temperature is representative of what happened at the oxidation temperature? *In situ* analyses are able to follow the oxidation reactions at the oxidation temperature.

X-ray diffraction devices equipped with high temperature furnaces were developed in order to follow the evolution of crystallographic phases during the oxidation process of metallic substrates and of the underlying substrate microstructure under oxidizing conditions.<sup>122</sup> The technique is also able to follow growth stress evolution during the establishment of



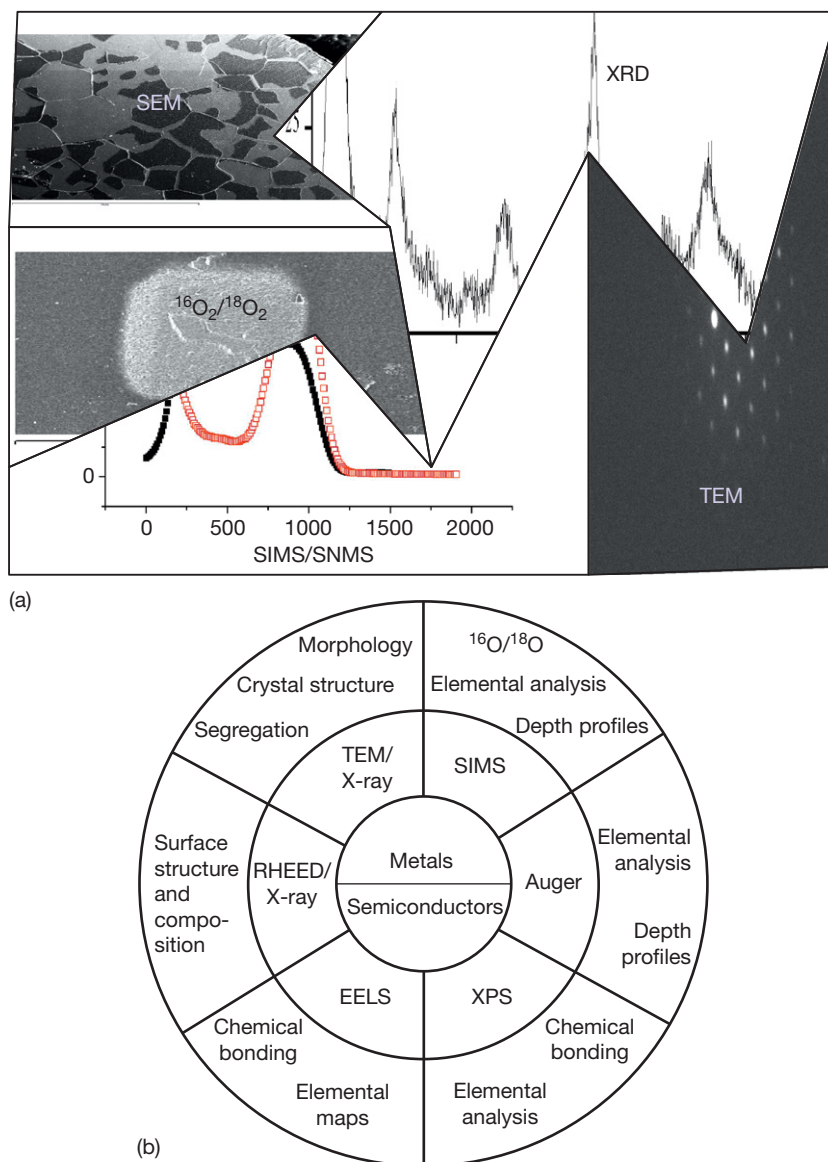


**Figure 6** Illustration of characterization tools to analyze thermally grown oxide scale. Part (a) adapted from Chevalier, S. *Traitements de surface et nouveaux matériaux: quelles solutions pour lutter contre la dégradation des matériaux à haute température?*; Les Editions Universitaires de Dijon, 2007 and part (b) adapted from Graham, M. J. *Mater. High Temp.* **2000**, 17, 1.

the growing scales.<sup>123,124</sup> More recently, texture analyses of the oxide scale as well as of the metallic substrate has been followed during the formation and growth of the corrosion products. These ‘*in situ*’ characterizations are very useful for understanding the oxide scale growth mechanisms, for understanding the role played by minor elements on their formation and for linking the chemical properties of the scale to its mechanical properties. Figure 8 gives an illustration of the use of *in situ* XRD; it allows one to follow the phase formation and transformation

during oxidation at 950 °C of a  $\text{Y}_2\text{O}_3$  coated-Fe–30Cr alloy. It shows that the peak corresponding to the substrate (Fe–30Cr) disappears after 60 min of oxidation, which corresponds to the formation of  $\text{YCrO}_3$ .

#### 1.07.5.4 Prediction and Modeling of High Temperature Oxidation

In order to prevent high temperature degradation due to oxidation, predictive modeling has been

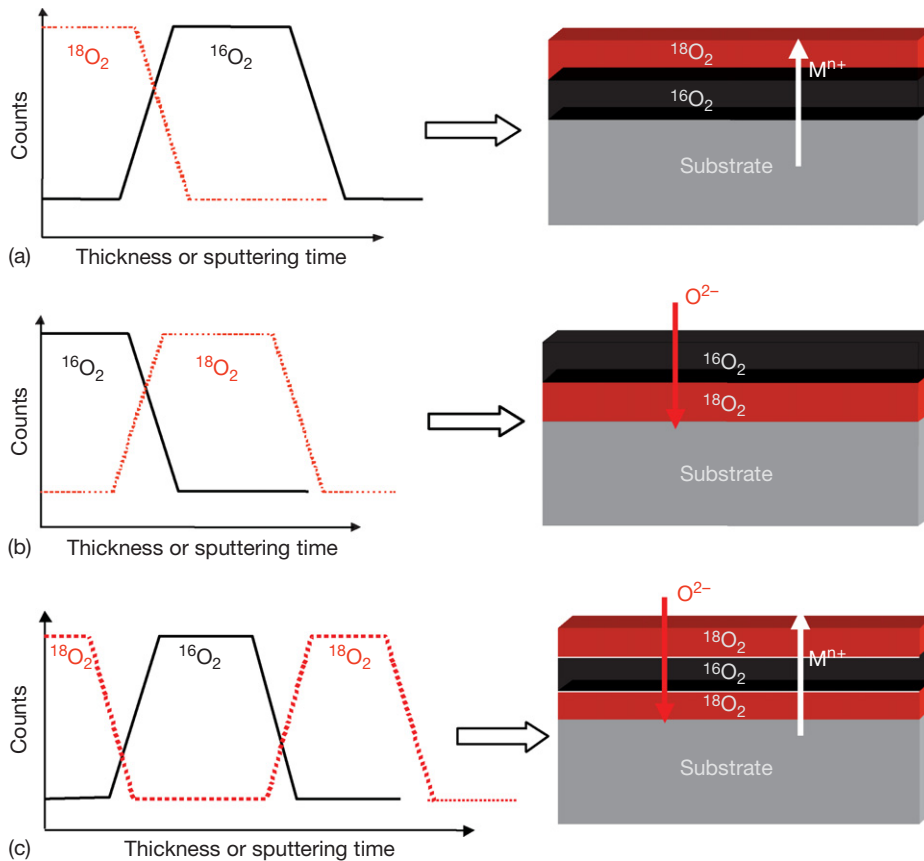


**Figure 7** Three main cases encountered during two stage oxidation experiments. The location of  $^{18}\text{O}$  compared to the  $^{16}\text{O}$  containing scale leads to the understanding of thermally grown oxide scales, (a) diffusion of cation, (b) diffusion of anion, and (c) mixed diffusion.

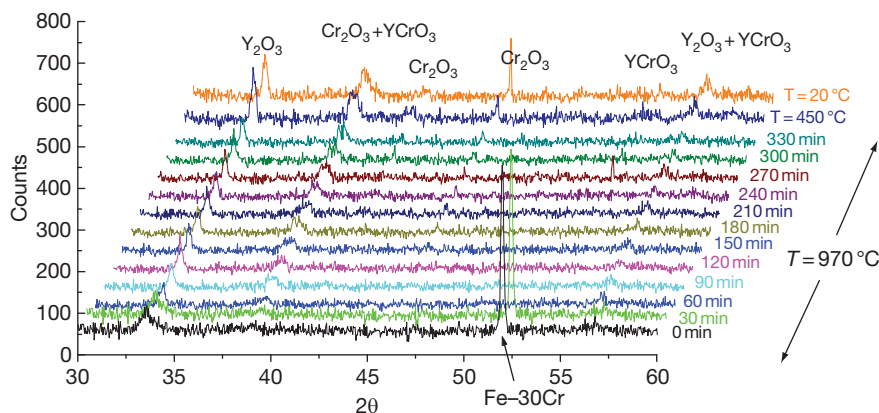


**Figure 8** *In situ* XRD following phase formation and transformation during oxidation at 950 °C of a  $\text{Y}_2\text{O}_3$  coated-Fe-30Cr alloy. Adapted from Chevalier, S. *Traitements de surface et nouveaux matériaux: quelles solutions pour lutter contre la dégradation des matériaux à haute température?*; Les Editions Universitaires de Dijon, 2007.

developed. This aspect is of particular interest for industrialists who need to target several thousands of hours in service condition. For alumina-forming alloys, it was shown that there was a critical Al level

below which an alumina scale was no more able to grow and form a protective oxide scale. For a binary alloy, this critical value was established from Wagner's theory as:<sup>125</sup>

$$c_B = f \left( \sqrt{\frac{k_c}{2\tilde{D}}} \right) \text{ with } f(u) = \pi^{1/2} u (1 - \operatorname{erf} u) \exp u^2 \quad [27]$$

with  $k_c$  ( $\text{cm}^2 \text{s}^{-1}$ ) the parabolic rate constant and  $\tilde{D}$  ( $\text{cm}^2 \text{s}^{-1}$ ) the interdiffusion coefficient of aluminum and iron.

When the Al concentration reaches this critical value, a catastrophic oxidation phenomenon occurs, because of the formation of iron and chromium oxides, which soon leads to complete destruction of the samples. Recently, Strehl *et al.*<sup>126</sup> also proposed a method, based on Wagner's theory, to determine the critical Al concentration leading to catastrophic oxidation. They found that this critical value was dependent on temperature and varies from 0 wt% at 1000 °C to 3 wt% at 1300 °C. Quakkers and Bongartz<sup>127</sup> established predictive diagrams for the life time of metallic materials. The proposed diagrams were obtained from kinetic considerations:

$$t_B = 4.4 \times 10^{-3} (C_0 - C_B) \rho d k^{-1/n} (\Delta m^*)^{-1/(n-1)} \quad [28]$$

where  $t_B$  corresponds to the start of catastrophic oxidation,  $k$  and  $n$  are kinetic constants and exponents established from  $\Delta m^* = \Delta m/S = kt^n$ ,  $C_0$  is the initial aluminum concentration,  $C_B$  is the critical Al concentration,  $\rho$  is the alloy density,  $d$  is the sample thickness, and  $\Delta m^*$  is the total weight gain measured during the thermal treatment. This modeling was in agreement with experimental data in order to predict the beginning of oxide scale spallation in Fe–Cr–Al foils at 1100 °C.<sup>128</sup>

Recent models developed by Monceau<sup>129,130</sup> and Smialek<sup>131</sup> predict the life time for alloys exposed to cyclic tests. The correlation between modeling and experimental data is clear, despite simple hypotheses.

## 1.07.6 High Temperature Oxidation Behavior of Metals and Alloys

### 1.07.6.1 Description of Chromia- and Alumina-Forming Materials

In the real world, it is rare to find pure metals; most of the time, alloys, which contain minor elements, such as Cr, Al, Si, Ti, etc., are used. Generally speaking, steels are iron-based and contain between 0.02 and 2.06 wt% carbon. Cast-irons correspond to a level of

C over 2.06 wt%. Other alloys used at high temperatures are usually Ni- or Co-base.

In the field of high temperature oxidation, the classical alloys are chromia-forming (i.e., being able to form a chromia,  $\text{Cr}_2\text{O}_3$ , layer) or alumina-forming (i.e., being able to form an alumina,  $\text{Al}_2\text{O}_3$ , layer). These oxide scales, together with silica,  $\text{SiO}_2$ , layers, are the most protective scales for protection against high temperature degradation. These refractory oxides have high melting points (2330 °C for  $\text{Cr}_2\text{O}_3$ , 2054 °C for  $\text{Al}_2\text{O}_3$  and 1713 °C for  $\text{SiO}_2$ <sup>132,133</sup>) and grow on Fe-, Ni-, or Co-base alloys, which contain at least 12 wt% Cr for the chromia-forming alloys,<sup>134</sup> associated with at least 5 wt% Al for the alumina-forming alloys.<sup>135</sup> One has also to distinguish ferritics (containing elements able to stabilize the  $\alpha$ -Fe phase, such as Cr) from austenitic steels (containing elements able to stabilize the  $\gamma$ -Fe phase, such as Ni).<sup>1,136</sup> Some steels can be also martensitic or duplex in nature. The properties of the different categories of steel depend on minor element additions. As an example, **Figure 9** gives a comparison of thermal expansion coefficients, TEC, for different materials and oxides.<sup>137</sup> The formation of a continuous silica layer is guaranteed in the case of silicides,  $\text{MoSi}_2$  or  $\text{FeSi}_2$ , but their physical and chemical properties are very different from those of chromia- and alumina-forming alloys. In many cases, Si is added as a minor element to the latter alloys and contributes to the formation of a discontinuous scale below the main oxide scales.<sup>138</sup>

As indicated previously, chromia- and alumina-forming materials usually guarantee the establishment of parabolic regimes, which are the most protective. One can note that the parabolic rate law constants for alumina-forming alloys are lower than those for chromia-forming alloys (**Figure 10**).<sup>12</sup> This means that the oxidation rate is lower when an alumina scale grows on an alloy surface. Growth of  $\text{SiO}_2$  scales result in similar parabolic rate constants as those of  $\text{Al}_2\text{O}_3$  scales.

### 1.07.6.2 Oxide Scale Spallation: Mechanical Properties and Stress

When they are used under appropriate conditions (maximum temperatures of 1000 and 1300 °C, for M–Cr and M–Cr–Al, respectively),  $\text{Cr}_2\text{O}_3$  and  $\text{Al}_2\text{O}_3$  scales possess the main protective properties needed for high temperature service conditions, at least under isothermal conditions (for a fixed temperature without thermal shocks). When exposed to thermal cycling

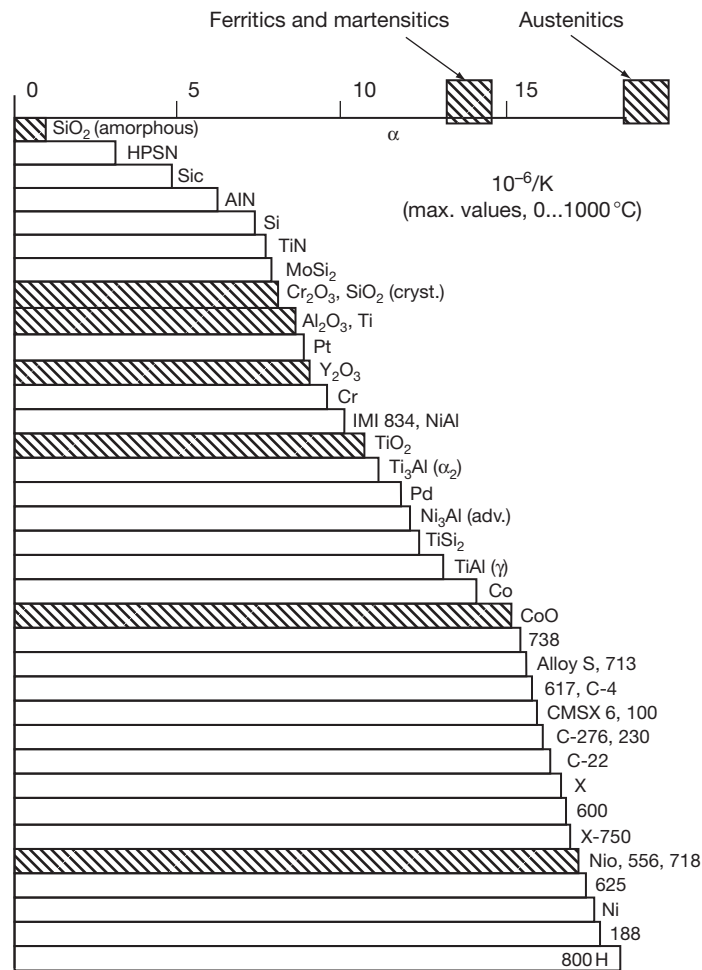


**Figure 9** Comparison of thermal expansion coefficients of different materials and oxides. Reproduced from Schuetze, M. In Proceedings of the Euroconference 2000 ProEnMach, Clausthal-Zellerfeld, Germany, 20–22 Juillet 2000.

(repeated heating and cooling), the adherence of the oxide scales is often poor and limits the life time of alloys considerably.<sup>139–142</sup> The more the amplitude of the thermal shocks, the more is the tendency for the oxide scale to spall off or crack, making the underlying substrate free of any protection. The reasons why the oxide layers detach from the substrates are mainly due to the difference in TEC between the oxides and the substrates (Figure 9), which generates thermal stress. Various stresses are able to develop in the oxide scales: growth stress, thermal stress, and residual stress (as a first approximation, residual stress can be ascribed to the addition of both growing and thermal stress). They play a considerable role in the high temperature corrosion mechanisms and their determination gives fundamental information on the way to increase the corrosion resistance.<sup>4,143–150</sup> Another reason for stress

generation in thermally grown oxide scales is associated with the volume change between the oxide and the native metal; this change is characterized by the Pilling–Bedworth ratio (PBR) and corresponds to the growth stress within the scale.<sup>151,152</sup> Table 1 gives values of PBR for different oxides.<sup>152</sup> When  $PBR < 1$ , the volume of oxide is lower than the volume of metal and tensile stress appears in the oxide scale. When  $PBR > 1$ , the volume of oxide is higher than the volume of metal and compressive stress appears in the oxide scale. Several complementary models deal with growth stresses and attribute them to microstructural and/or diffusion considerations,<sup>153–157</sup> but are based on the general models established in the past.<sup>151,158</sup>

Geometry is also a parameter that influences the mechanical properties of the scale and has a huge

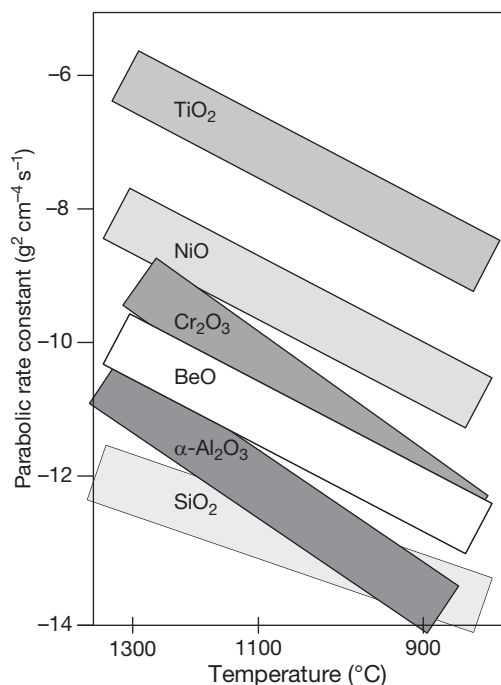


**Figure 10** Parabolic rate constants in oxide scales. Adapted from Hindam, H.; Whittle, D. P. *Oxid. Met.* **1982**, *18*, 245.

**Table 1** Pilling–Bedworth ratio for different oxides

Oxides	Pilling–Bedworth ratio
K <sub>2</sub> O	0.45
MgO	0.81
Na <sub>2</sub> O	0.97
Al <sub>2</sub> O <sub>3</sub>	1.28
ThO <sub>2</sub>	1.3
ZrO <sub>2</sub>	1.56
Cu <sub>2</sub> O	1.64
NiO	1.65
TiO <sub>2</sub>	1.76
CoO	1.86
Cr <sub>2</sub> O <sub>3</sub>	2.07
Ta <sub>2</sub> O <sub>5</sub>	2.5
Nb <sub>2</sub> O <sub>5</sub>	2.68
V <sub>2</sub> O <sub>5</sub>	3.19
WO <sub>3</sub>	3.3

impact on the oxide scale adherence.<sup>152</sup> The stress generated in an oxide scale as is thermally grown on a tube is not the same as that in an oxide grown on a flat coupon.<sup>159</sup>

However, the amplitude of oxide spallation cannot be always ascribed to residual stress in the scale.<sup>160</sup> Oxide spallation is also strongly connected to the process of growth of the oxide scale. During its thermal growth, cation vacancies are generated at the

metal–oxide interface; if they coalesce together, cavities are formed, weakening the interface.<sup>161</sup>

It appears then clearly that it is necessary to consider the chemical evolution of the oxide scale together with its mechanical evolution, as well as its relationships with the underlying substrate.

### 1.07.6.3 Role of Minor Elements

As indicated by their name, alloys contain minor element additions which improve their mechanical properties, their corrosion resistance, etc. As a matter of fact, thermally grown oxide scales are never pure chromia or alumina. By reacting with them, mixed oxides are formed; these include the spinel phase, (Mn,Cr)<sub>3</sub>O<sub>4</sub>,<sup>162,163</sup> perovskite, MCrO<sub>3</sub>,<sup>164–168</sup> or MAIO<sub>3</sub>,<sup>169</sup> or garnet, Y<sub>3</sub>Al<sub>5</sub>O<sub>12</sub>.<sup>170–173</sup> Nevertheless, these phases are usually less protective than chromia or alumina. Some additions have a particularly large influence on the high temperature performance of alloys; so-called reactive elements (RE), decrease the oxidation rate and strongly increase the oxide scale adherence.<sup>1,6,174</sup>

### 1.07.6.4 Reactive Element Effect (REE)

The beneficial effect of the RE on the high temperature resistance of alloys has been known for more than 50 years.<sup>175,176</sup> Even if the reasons why REs are so efficient are not fully understood, several hypotheses have been proposed in order to explain their beneficial effects. According to the large numbers of published papers on this problem, there is probably no single theory that is able to explain their role, irrespective of the tested materials, the native oxide scale, or the nature of the oxidizing atmosphere.<sup>177</sup> As an example, some RE additions give the well-known beneficial effect, whereas others can have a detrimental influence on the oxidation performance of the alloy.

A decrease in the oxidation rate and an improvement in the oxide layer adherence are usually the final result arising from RE additions.<sup>1,178</sup> Generally, REs favor the nucleation and the growth of scales.<sup>179–183</sup> They decrease the oxide grain size, and consequently change scale plasticity<sup>184,185</sup> and creep,<sup>186,187</sup> which can modify the growth and/or thermal stresses generated within the scale during its growth or on cooling to room temperature.<sup>188–190</sup> They prevent the detrimental sulfur effect<sup>191–193</sup> and suppress dislocation climb in the metal and, then, limit cation transport (poisoned interface model).<sup>194,195</sup> REs can also influence the

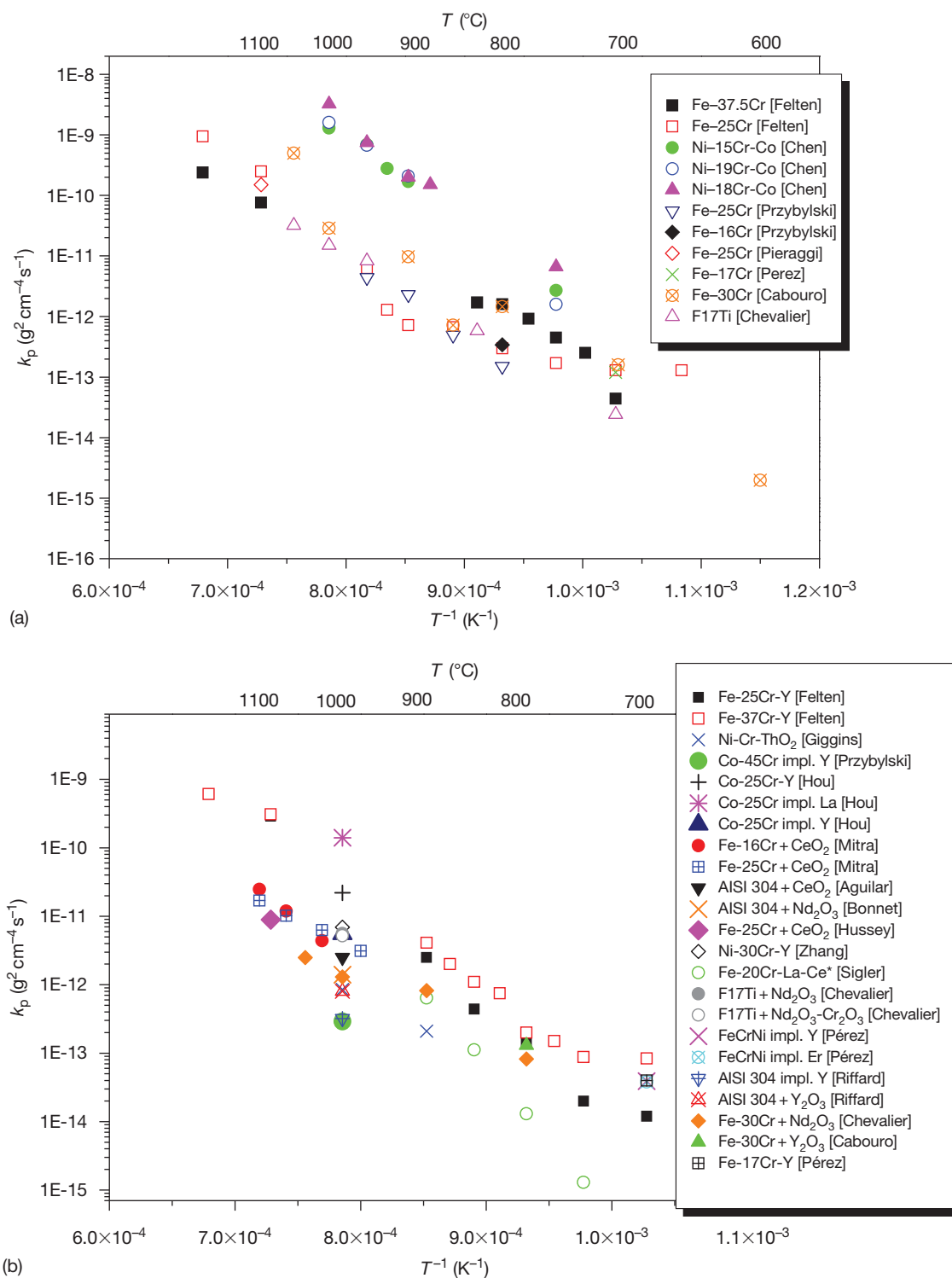


**Figure 11** Parabolic rate constants established for the growth of chromia scales: (a) undoped and (b) RE doped alloys. (\*Atmosphere  $\text{N}_2 + \text{H}_2\text{O} + \text{CO}_2$ ).



formation and/or transformation of transient phases, especially in alumina-forming alloys.<sup>196,197</sup>

#### 1.07.6.4.1 Influence of RE on oxide scale growth kinetics

The RE influence on oxide scale growth rate is shown clearly on the kinetic curves for chromia-forming materials. The oxidation rate can be divided by a factor of 100 in the presence of the RE. The comparison of  $k_p$  values shown in Figures 11(a) and 11(b)<sup>198–214</sup> illustrates this decrease. The influence of RE on alumina growth rates is much more limited.<sup>215</sup>

The quantity of RE introduced in the alloys plays a considerable role on the oxidation rates. When added in amounts above a critical content, the RE leads to negative effects, including a large increase in the oxidation rate.<sup>216,217</sup> This ‘overdoping’ effect is probably due to an increase in oxygen diffusion due to the presence of oxygen vacancies in the RE oxides (REO).

#### 1.07.6.4.2 Influence of RE on oxide scale adherence

The most spectacular effect of RE introduction on oxide scale behavior is their much improved adherence to the underlying substrate.<sup>213,218–220</sup> Cyclic oxidation tests clearly show the resistance to spallation, since the oxide layers formed on the RE doped steels remain adherent to the alloys, even after many cycles (see example in Figure 5).

#### 1.07.6.4.3 Location of RE in oxide scales

The RE is usually very difficult to detect within the oxide scale. Their presence at the surface of oxide layers as perovskite phases,  $\text{MCrO}_3$ <sup>164,221–224</sup> or  $\text{MAIO}_3$ ,<sup>225</sup> garnets<sup>217,226–228</sup> or as not well defined phases ( $\text{CeTi}_{21}\text{O}_{28}$ ,<sup>229</sup>  $\text{NdTi}_{21}\text{O}_{38}$ ,<sup>213</sup>  $\text{YAl}_x\text{O}_y$ <sup>230,231</sup>) has been observed after long exposures in oxidizing atmospheres at high temperature.

The precise location of the RE within the oxide scale needs to be observed in TEM cross-sections.<sup>232–247</sup> Most of the TEM analyses have revealed the RE at the oxide grain boundaries within the thermally grown scale as well as at the metal–oxide interface. The RE solubility in  $\text{Cr}_2\text{O}_3$  and in  $\text{Al}_2\text{O}_3$  is very low (around 10 wt ppm for Y in  $\text{Al}_2\text{O}_3$ <sup>248</sup>).

Previous results have shown that the efficient dopant in thermally grown oxides (those for which the oxidation rate is decreased, the oxide scale adherence is improved and the oxide grain morphology is changed) usually segregates to the oxide grain boundaries. Nevertheless, other dopants, such as Ti, Nb, Ta, Ca, are found to segregate at the oxide grain

boundaries but without giving any beneficial improvement in the oxide layer performances at high temperature.<sup>249,250</sup> The dopant size could play a role in its efficiency in increasing the oxidation resistance. However, the results are mainly contradictory. For example, no relationship could be found between the kinetics ( $k_p$  and mass gain) of REO coated-ferritic steels and the corresponding RE ionic radius.<sup>1,251</sup>

#### 1.07.6.4.4 Influence of RE on oxide scale growth mechanism

The main consequence of the RE segregation at the oxide grain boundaries is a change in the oxide scale growth mechanism. The transport of oxygen becomes predominant in RE doped chromia layers,<sup>252–255</sup> as well as in alumina scales.<sup>256–260</sup>

Isotopic marker experiments in  $^{16}\text{O}_2/^{18}\text{O}_2$  demonstrate the change in the oxide growth mechanism of RE doped oxides. The presence of the  $^{18}\text{O}$  peak below the  $^{16}\text{O}$  on SIMS profiles shows that oxygen transport is the main diffusion process during the scale growth.<sup>261</sup>

As a consequence, the morphology and the size of the oxide grains forming the scale change. Indeed, the annihilation of cation diffusion promotes the formation of equiaxed chromia grains,<sup>262,263</sup> instead of columnar grain for the undoped steels, and thin columnar alumina grains for alumina scales, instead of coarse oxide grains.<sup>264,265</sup>

The segregation of RE at oxide grain boundaries leads also to a decrease in the oxygen diffusion coefficient<sup>1,215</sup> even if the results appear somewhat contradictory.

The change in the oxide scale growth mechanism associated with the decrease in the oxygen diffusion are the main reasons why REs lead to improved adhesion and slower growth rates for chromia scales and improved adhesion for alumina scales.

## References

1. Chevalier, S. Traitements de surface et nouveaux matériaux: quelles solutions pour lutter contre la dégradation des matériaux à haute température? Les Editions Universitaires de Dijon, 2007.
2. Huntz, A. M.; Pieraggi, B. *Oxydation des métaux et alliages*; Lavoisier: Paris, 2003.
3. Bénard, J. *L'oxydation des métaux*; Gauthier-Villars et Cie: Paris, 1962.
4. Béranger, G.; Colson, J. C.; Dabosi, F. *Corrosion des Matériaux à Haute Température*; Les Editions de Physique, Ecole d'Hiver du CNRS: Piau-Engaly, 1985.

5. Caillet, M.; Galerie, A.; Audisio, S.; Mazille, H. *La protection contre la corrosion*; Les Editions de Physique: Paris, 1987.
6. Kofstad, P. *High Temperature Corrosion*; Elsevier Applied Science, 1988.
7. Sarrazin, P.; Galerie, A.; Fouletier, J. *Les mécanismes de la corrosion sèche. Une approche cinétique*; EDP Sciences, 2000.
8. Green, A.; Bastow, B. In Proceedings of the 2nd International Conference on the Microscopy of Oxidation; Newcomb, S. B., Bennett, M. J., Eds.; Maney Publishing, 1993; p 137.
9. Jianian, S.; Longjiang, Z.; Tiefan, L. *Oxid. Met.* **1997**, *48*, 347.
10. Yurek, Z. *Solid State Phenom.* **1995**, *41*, 185.
11. Henry, S. PhD Thesis, INPG, Grenoble, 2000.
12. Hindam, H.; Whittle, D. P. *Oxid. Met.* **1982**, *18*, 245.
13. Schütze, M. Proceedings of the Euroconference 2000 ProEnMach Clausthal-Zellerfeld: Germany, 20–22 Juillet, 2000.
14. Tien, J. K.; Davidson, J. M. In *Stress Effects and the Oxidation of Metals*; Cathcart, J. V., Ed.; AIME: New York, 1975; p 200.
15. Delaunay, D.; Huntz, A. M.; Lacombe, P. *Corros. Sci.* **1980**, *20*, 1109.
16. Huntz, A. M. *Mater. Sci. Technol.* **1988**, *4*, 1079.
17. Huntz, A. M.; Schuetze, M. *Mater. High Temp.* **1994**, *12*, 151.
18. Evans, H. E. *Mater. High Temp.* **1994**, *12*, 219.
19. Evans, H. E. *Int. Mater. Rev.* **1995**, *40*, 1.
20. Schuetze, M. *J. Corros. Sci. Eng.* **2003**, *6*; <http://www.umist.ac.uk/corrosion/JCSE/>
21. Tolpygo, V. K.; Clarke, D. R. *Mater. Sci. Eng. A* **2000**, *278*, 142.
22. Brumm, M. W.; Grabke, H. J. *Corros. Sci.* **1993**, *34*, 547.
23. Gaboriaud, R. *Thermodynamique: Éléments fondamentaux de l'énergétique et de la cinétique chimique*; Ellipses: Paris, 1998.
24. Levin, E. M.; McMurdie, H. F. *Phase Diagrams for Ceramists*; The American Ceramic Society, 1975; p 17.
25. Barret, P. *Cinétique hétérogène*; Gauthier-Villars: Paris, 1973.
26. Soustelle, M. *Modélisation macroscopique des transformations physico-chimiques*; Masson: Paris, 1990.
27. Antoni, L.; Galerie, A. *Corrosion sèche des métaux, Techniques de l'Ingénieur*, 2003, M4 228, p 9.
28. Quadackers, W. J.; Naumenko, D.; Wessel, E.; Kochubey, V.; Singheiser, L. *Oxid. Met.* **2004**, *61*, 17–37.
29. Cox, B. J. *Nucl. Mater.* **2005**, *336*, 331.
30. Pétigny, N.; Barberis, P.; Lemaignan, C.; Valot, C. H.; Lallemand, M. J. *J. Nucl. Mater.* **2000**, *280*, 318.
31. Tupin, M.; Pijolat, M.; Valdivieso, F.; Soustelle, M.; Frichet, A.; Barberis, P. *J. Nucl. Mater.* **2003**, *317*, 130.
32. Monceau, D.; Pieraggi, B. *Oxid. Met.* **1999**, *50*, 477.
33. Cadoret, Y.; Monceau, D.; Bacos, M. P.; Josso, P.; Maurice, V.; Marcus, P. *Oxid. Met.* **2005**, *64*, 185.
34. Chevalier, S.; Molins, R.; Heintz, O.; Larpin, J. P. In Proceedings of the 6th International Conference on the Microscopy of Oxidation, Birmingham, England; Tatlock, G. J., Evans, H. E., Eds.; **2005**; p 365.
35. Chevalier, S.; Galerie, A.; Heintz, O.; Chassagnon, R.; Crisci, A. *Mater. Sci. Forum* **2008**, *595–598*, 915.
36. Wagner, C. J. *Electrochem. Soc.* **1952**, *99*, 369.
37. Harrison, L. G. *Trans. Faraday Soc.* **1961**, *57*, 1191.
38. Philibert, J. *Diffusion et transport de matière dans les solides*; Les Editions de Physique, 1990; p 227.
39. Philibert, J.; Vignes, A.; Bréchet, Y.; Combrade, P. *Métallurgie: Du Minéral au Matériau*; Masson, **1998**, p 389.
40. Hart, E. W. *Acta. Metall.* **1957**, *5*, 597.
41. Smeltzer, W. W.; Haering, R. R.; Kirkaldy, J. S. *Acta Metall.* **1961**, *9*, 880.
42. Atkinson, A.; Taylor, R. I.; Hughes, A. *Philos. Mag. A* **1982**, *45*, 823.
43. Lederer, C. M.; Hollander, J. M.; Perlman, I. *Table of Isotopes*, 6th ed.; Wiley: New-York, 1967.
44. Fielitz, P.; Borchardt, G.; Schmücker, M.; Schneider, H. *Solid State Ionics* **2003**, *160*, 75.
45. Suzuoka, T. *Trans. Jpn. Inst. Met.* **1961**, *2*, 25.
46. Suzuoka, T. *J. Phys. Soc. Jpn.* **1964**, *19*, 839.
47. Whipple, R. T. P. *Philos. Mag.* **1954**, *45*, 1225.
48. Le Claire, A. D. *Philos. Mag.* **1962**, *7*, 141.
49. Nowick, A. S.; Burton, J. J. Eds. *Diffusion in Solids*; Academic Press, 1975.
50. Tsai, S. C.; Huntz, A. M.; Dolin, C. *Oxid. Met.* **1995**, *43*, 581.
51. Le Gall, M.; Lesage, B.; Bernardini, J. *Philos. Mag. A* **1994**, *70*, 761.
52. Fielitz, P.; Borchardt, G.; Schücker, M.; Schneider, H. *Solid State Ionics* **2006**, *177*, 493.
53. Tsai, S. C.; Huntz, A. M.; Dolin, C. *Mater. Sci. Eng. A* **1996**, *212*, 6.
54. Chevalier, S.; Bonnet, G.; Borchardt, G.; Colson, J. C.; Larpin, J. P. *Ceram. Polish Ceram. Bull.* **2000**, *61*, 177.
55. Hagel, W. C.; Seybolt, A. U. *J. Electrochem. Soc.* **1961**, *108*, 1146.
56. Hagel, W. C. *J. Am. Ceram. Soc.* **1965**, *48*, 70.
57. Lobnig, R. E.; Schmidt, H. P.; Hennesen, K.; Grabke, H. *J. Oxid. Met.* **1992**, *37*, 81.
58. Graham, M. J.; Eldridge, J. I.; Mitchell, D. F.; Hussey, R. *J. Mater. Sci. Forum* **1989**, *43*, 207.
59. Huntz, A. M. *J. Phys. III France* **1995**, *5*, 1729.
60. Tsai, S. C.; Huntz, A. M.; Philibert, J. *Defects Diffusion Forum* **1997**, *143–147*, 1195.
61. Nicholls, J. R. In *Guidelines for Methods of Testing and Research in High Temperature Corrosion*; Grabke, H. J., Meadowcroft, D. B., Eds.; **1995**, p 11.
62. Grabke, H. J. In *Guidelines for Methods of Testing and Research in High Temperature Corrosion*; Grabke, H. J., Meadowcroft, D. B., Eds.; **1995**, p 52.
63. Gosmain, L. Ph.D. Thesis, Université de Bourgogne, Dijon, 2001.
64. Jedlinski, J. *Solid State Phenom.* **1992**, *21–22*, 335.
65. Göbel, M. Ph.D. Thesis. Technische Universität Clausthal, Clausthal-Zellerfeld, 1997.
66. Åkerman, T. *Oxid. Met.* **1998**, *50*, 167.
67. Berger, P.; Gaillet, L.; El Tahann, R.; Moulin, G.; Viennot, M. *Nucl. Instr. Meth. Phys. Res. B* **2001**, *181*, 382.
68. Alibhai, A. A.; Chater, R. J.; McPhail, D. S.; Shollock, B. A. *Appl. Surf. Sci.* **2003**, *203–204*, 630.
69. Delaunay, D.; Huntz, A. M.; Lacombe, P. *Corros. Sci.* **1980**, *20*, 1109.
70. Huntz, A. M. *Mater. Sci. Technol.* **1988**, *4*, 1079.
71. Huntz, A. M.; Schütze, M. *Mater. High Temp.* **1994**, *12*, 151.
72. Evans, H. E. *Mater. High Temp.* **1994**, *12*, 219.
73. Evans, H. E. *Int. Mater. Rev.* **1995**, *40*, 1.
74. Evans, H. E. In Proceedings of the Workshop on Cyclic of High Temperature Materials; Schütze, M., Quadackers, W. J., Eds.; IOM Communications, 1999; Vol. 27, p 3.
75. Moon, C. O.; Lee, S. B. *Oxid. Met.* **1993**, *39*, 1.
76. Smialek, J. L.; Jayne, D. T.; Schaeffe, J. C.; Murphy, W. H. *Thin Solid Films* **1994**, *253–285*.
77. Jedlinski, J.; Bennett, M. J.; Evans, H. E. *Mater. High Temp.* **1994**, *12*, 169.

78. Pennefather, R. C.; Boone, D. H. *Surf. Coat. Technol.* **1995**, 76–77, 47.
79. Chan, K. W. *Metal. Mater. Trans.* **1997**, 28A, 411.
80. Gleeson, B.; Harper, M. A. *Oxid. Met.* **1998**, 49, 373.
81. Strehl, G.; Al-Badairy, H.; Rodriguez, L. M.; Klöwer, J.; Borchardt, G.; Tatlock, G.; Criado, A. J. In Proceedings of the Workshop on Cyclic of High Temperature Materials; Schütze, M., Quadakkers, W. J., Eds.; IOM Communications, 1999; Vol. 27, p 82.
82. Chevalier, S.; Bonnet, G.; Valot, C.; Colson, J. C.; Larpin, J. P. In Proceedings of the Workshop on Cyclic of High Temperature Materials; Schütze, M., Quadakkers, W. J., Eds.; IOM Communications, 1999; Vol. 27, p 421.
83. Amano, T.; Watanabe, T.; Michiyama, K. *Oxid. Met.* **2000**, 53, 451.
84. Baleix, S.; Bernhart, G.; Lours, P. *Mater. Sci. Eng.* **2002**, A327, 155.
85. Kulinska, A.; Choux, C.; Chevalier, S. *Intermetallics* **2008**, 16, 1.
86. Vangeli, P. In ; Proceedings of the Workshop on Cyclic of High Temperature Materials; Schütze, M., Quadakkers, W. J., Eds.; IOM Communications, 1999; Vol. 27, p 198.
87. Graham, M. J. *Mater. High Temp.* **2000**, 17, 1.
88. Rhüle, M.; Schumann, E. In *Guidelines for Methods of Testing and Research in High Temperature Corrosion*; Grabke, H. J., Meadowcroft, D. B., Eds.; EFC Publication 14, Maney Publishing, 1995, p 177.
89. Amelinckx, S. van Dyck, D. van Landuyt, J.; van Tendeloo, G. Eds. *Handbook of Microscopy: Applications in Materials Science, Solid-State Physics and Chemistry* Wiley-VCH, 1997, p 751.
90. Baunier, L. *Préparation des échantillons, Ecole Thématique: Microscopie des Défauts Cristallins*; St Pierre d'Oléron, 2001; p 393.
91. Langford, R. M.; Rogers, M. *Micron* **2008**, 39, 1325.
92. Przybylski, K.; Chevalier, S.; Juzon, P.; Galerie, A.; Borchardt, G.; Heintz, O.; Larpin, J. P. *Mater. Sci. Forum* **2008**, 595–598, 1103.
93. Tortorelli, P. F.; More, K. L.; Specht, E. D.; Pint, B. A.; Zschack, P. *Mater. High Temp.* **2003**, 20, 57.
94. Fukuda, K.; Takao, K.; Hoshi, T.; Usui, Y.; Furukimi, O. *Mater. High Temp.* **2003**, 20, 73.
95. Mayer, J.; Penkalla, H. J.; Dimiyati, A.; Dani, M.; Untoro, P.; Naumenko, D.; Quadakkers, W. J. *Mater. High Temp.* **2003**, 20, 167.
96. Ford, S.; Young, D. J.; McGrouther, D.; Munroe, P. R. In Proceedings of the 6th International Conference on The Microscopy of Oxidation, Birmingham, England.; Tatlock, G. J., Evans, H. E., Eds.; **2005**; p 183.
97. Svensson, H.; Stiller, K. In Proceedings of the 6th International Conference on The Microscopy of Oxidation, Birmingham, England; Tatlock, G. J., Evans, H. E., Eds.; **2005**; p 237.
98. Kilo, M.; Borchardt, G.; Lesage, B.; Kaitasov, O.; Weber, S.; Scherrer, S. *J. Eur. Ceram. Soc.* **2000**, 20, 2069.
99. Schmidt, H.; Borchardt, G.; Weber, S.; Scherrer, S.; Baumann, H.; Müller, A.; Bill, J. *J. Appl. Phys.* **2000**, 88, 1827.
100. Kilo, M.; Borchardt, G.; Lesage, B.; Weber, S.; Scherrer, S.; Schroeder, M.; Schulz, O.; Martin, M. *Electrochem. Soc. Proc.* **2001**, 16, 275.
101. Kilo, M.; Weller, M.; Borchardt, G.; Damson, B.; Weber, S.; Scherrer, S. *Defects Diffusion Forum* **2001**, 194–199, 1039.
102. Legros, C.; Lesage, B.; Kilo, M.; Strehl, G.; Borchardt, G.; Carry, C. *Key Eng. Mater.* **2002**, 206–213, 401.
103. Bamba, G.; Wouters, Y.; Galerie, A.; Borchardt, G.; Shimada, S.; Heintz, O.; Chevalier, S. *Scr. Mater.* **2007**, 57, 671.
104. Mougin, J.; Le Bihan, T.; Lucazeau, G. *J. Phys. Chem. Solids* **2001**, 62, 553.
105. Bouvier, P.; Godlewski, J.; Lucazeau, G. *J. Nucl. Mater.* **2002**, 300, 118.
106. Kemdehoundja, M.; Dinhut, J. F.; Grosseau-Poussard, J. L.; Jeannin, M. *Mater. Sci. Eng. A* **2006**, 435–436, 666.
107. Kadleikova, M.; Breza, J.; Vesely, M. *Microelectr. J.* **2001**, 32, 955.
108. Krishnan, R.; Kesamoorthy, R.; Dash, S.; Tyagi, A. K.; Raj, B. *Scr. Mater.* **2003**, 48, 1099.
109. Tolpygo, V. K.; Clarke, D. R. *Mater. High Temp.* **2000**, 17, 59.
110. Peng, X.; Clarke, D. R.; Wang, F. *Oxid. Met.* **2003**, 60, 225.
111. Laxman, S.; Franke, B.; Kempshall, B. W.; Sohn, Y. H.; Giannuzzi, L. A.; Murphy, K. S. *Surf. Coat. Technol.* **2004**, 177–178, 121.
112. Murphy, K. S.; More, K. L.; Lance, M. J. *Surf. Coat. Technol.* **2001**, 146–147, 152.
113. Sohn, Y. H.; Vaidyanathan, K.; Ronski, M.; Jordan, E. H.; Gell, M. *Surf. Coat. Technol.* **2001**, 146–147, 102.
114. Mu, N.; Izumi, T.; Zhang, L.; Gleeson, B. *Mater. Sci. Forum* **2008**, 595–598, 239.
115. Kuiry, S. C.; Seal, S.; Fei, W.; Quick, N. *Oxid. Met.* **2003**, 59, 543.
116. Berthomé, G.; N'Dah, E.; Wouters, Y.; Galerie, A. *Mater. Corros.* **2005**, 56, 389.
117. Maurice, V.; Despert, G.; Zanna, S.; Josso, P.; Bacos, M. P.; Marcus, P. *Acta Mater.* **2007**, 55, 3315.
118. Petit, J. P.; Mermoux, M.; Wouters, Y.; Galerie, A.; Chemarin, C. *Mater. Sci. Forum* **2004**, 461–464, 681.
119. Wouters, Y.; Bamba, G.; Galerie, A.; Mermoux, M.; Petit, J. P. *Mater. Sci. Forum* **2004**, 461–464, 830.
120. Wouters, Y.; Marchetti, L.; Galerie, A.; Petit, J. P. *Corros. Sci.* **2008**, 50, 1122.
121. Wouters, Y.; Galerie, A.; Petit, J. P. *Mater. Sci. Forum* **2008**, 595–598, 1181.
122. Chevalier, S.; Strehl, G.; Borchardt, G.; Larpin, J. P.; Le Coze, J. *Mater. Technol.* **2003**, 7–8–9, 71.
123. Bernard, F. PhD Thesis, Université de Bourgogne, Dijon, 1993.
124. Valot, C. PhD Thesis, Université de Bourgogne, Dijon, 1995.
125. Moulin, G.; Huntz, A. M.; Lacombe, P. *Acta Metall.* **1980**, 28, 745.
126. Strehl, G.; Beaven, P.; Lesage, B.; Borchardt, G. *Mater. Corros.* **2006**, 56, 778.
127. Quadakkers, W. J.; Bongartz, K. *Mater. Corros.* **1994**, 45, 232.
128. Klöwer, J. *Mater. Corros.* **1998**, 49, 758.
129. Poquillon, D.; Monceau, D. *Oxid. Met.* **2003**, 59, 409.
130. Kartono, R.; Monceau, D.; Young, D. J. *Scr. Mater.* **2007**, 57, 647.
131. Smialek, J. L. *Acta Mater.* **2004**, 52, 2111.
132. [www.matweb.com](http://www.matweb.com)
133. Materials database from NIMS, [www.NIMS.jp](http://www.NIMS.jp)
134. Barralis, J.; Maeder, G. *Précis métallurgie: Elaboration, Structures-Propriétés, Normalisation*; Nathan: Paris, 1997.
135. Lacombe, P.; Baroux, B.; Béranger, G. *Les aciers inoxydables*; Les Editions de Physique: Paris, 1990.
136. Philibert, J.; Vignes, A.; Bréchet, Y.; Combrade, P. *Métallurgie: du minéral au matériau*; Masson: Paris, 1998.

137. Schuetze, M. In Proceedings of the Euroconference 2000 ProEnMach Clausthal-Zellerfeld: Germany, 20–22 Juillet, 2000.
138. Mikkelsen, L.; Linderth, S.; Bilde-Sorensen, J. B. *Mater. Sci. Forum* **2004**, 461–464, 117.
139. Schütze, M.; Quadakkers, W. J. *Cyclic Oxidation of High Temperature Materials*; IOM Communications: London, 1999.
140. Schütze, M.; Malessa, M. *Mater. Corros.* **2006**, 57, 5.
141. Osgerby, S.; Pettersson, R. *Mater. Corros.* **2006**, 57, 14.
142. Niewolak, L.; Malessa, M.; Coleman, S. Y.; Quadakkers, W. J.; Schütze, M. *Mater. Corros.* **2006**, 57, 31.
143. Tien, J. K.; Davidson, J. M. In *Stress Effects and the Oxidation of Metals*; Cathart, J. V., Ed.; AIME: New York, 1975; p 200.
144. Delaunay, D.; Huntz, A. M.; Lacombe, P. *Corros. Sci.* **1980**, 20, 1109.
145. Huntz, A. M. *Mater. Sci. Technol.* **1988**, 4, 1079.
146. Huntz, A. M.; Schütze, M. *Mater. High Temp.* **1994**, 12, 151.
147. Evans, H. E. *Mater. High Temp.* **1994**, 12, 219.
148. Evans, H. E. *Int. Mater. Rev.* **1995**, 40, 1.
149. Schütze, M. J. *Corros. Sci. Eng.*; 2003, 6 <http://www.umist.ac.uk/corrosion/JCSE/>.
150. Mougin, J.; Lucazeau, G.; Galerie, A.; Dupeux, M. *Mater. Sci. Eng. A* **2001**, 308, 118.
151. Pilling, N. B.; Bedworth, R. E. *J. Inst. Met.* **1923**, 1, 529.
152. Béranger, G.; Huntz, A. M.; Pieraggi, B. In *Corrosion des Matériaux à Haute Température*; Béranger, G., Colson, J. C., Dabosi, F., Eds.; Les Editions de Physique, Ecole d'Hiver du CNRS: Piau-Engaly, 1985; p 227.
153. Bernstein, H. L. *Metall. Trans. A* **1987**, 18, 975.
154. Evans, H. E. *Intern. Mater. Rev.* **1995**, 40, 1.
155. Bull, S. J. *Oxid. Met.* **1998**, 49, 1.
156. Tolpygo, V. K.; Dryden, J. R.; Clarke, D. R. *Acta Mater.* **1998**, 46, 927.
157. Clarke, D. R. *Acta Mater.* **2003**, 51, 1393.
158. Rhines, F. N.; Wolf, J. S. *Metall. Trans.* **1970**, 1, 1701.
159. Rosenband, V.; Gany, A. *Corros. Sci.* **1995**, 37, 1991.
160. Tolpygo, V. K.; Clarke, D. R. *Mater. Sci. Eng. A* **2000**, 278, 142.
161. Brumm, J. M. W.; Grabke, H. J. *Corros. Sci.* **1993**, 34, 547.
162. Fergus, W. *Mater. Sci. Eng. A* **2005**, 397, 271.
163. Quadakkers, W. J.; Greiner, H.; Hänsel, M.; Pattanaik, A.; Khanna, A. S.; Malléner, W. *Solid State Ionics* **1996**, 91, 55.
164. Riffard, F.; Buscail, H.; Caudron, E.; Cuffe, R.; Issartel, C.; Perrier, S. *Appl. Surf. Sci.* **2002**, 199, 107.
165. Seybolt, A. U. *Corros. Sci.* **1966**, 6, 263.
166. Downham, D. A.; Shendye, S. B. *Oxid. Met.* **1995**, 43, 411.
167. Cristobal, M. J.; Gibson, P. N.; Stroosnijder, M. F. *Corros. Sci.* **1996**, 38, 805.
168. Paul, A.; Odiozola, J. A. *Mater. Sci. Eng. A* **2001**, 300, 22.
169. Tien, J. K.; Pettit, F. S. *Metall. Trans.* **1972**, 3, 1587.
170. Cuffe, R.; Buscail, H.; Caudron, E.; Riffard, F. *Mater. Sci. Forum* **2001**, 369–372, 311.
171. Kim, K. Y.; Kim, S. H.; Kwon, K. W.; Kim, I. H. *Oxid. Met.* **1994**, 41, 179.
172. Pint, B. A.; Hobbs, L. W. *J. Electrochem. Soc.* **1994**, 141, 2443.
173. Pint, B. A. *Mater. Sci. Forum* **1997**, 251–254, 397.
174. Lang, E. Ed. *The Role of Active Elements in the Oxidation Behaviour of High Temperature Metals and Alloys*; Elsevier Applied Science, 1989; p 33.
175. Pfeil, L. B. U.K. Patent 459848, 1937.
176. Pfeil, L. B. U.K. Patent 574088, 1945.
177. Quadakkers, J.; Singheiser, L. *Mater. Sci. Forum* **2001**, 369–372, 77.
178. Lang, E. Ed. *The Role of Active Elements in the Oxidation Behaviour of High Temperature Metals and Alloys*; Elsevier Applied Science, 1989; p 111.
179. Stringer, J.; Wright, I. G. *Oxid. Met.* **1972**, 5, 59.
180. Stringer, J.; Wilcox, B. A.; Jaffee, R. I. *Oxid. Met.* **1972**, 5, 11.
181. Whittle, D. P.; Stringer, J. *Philos. Trans. R. Soc. Lond. A* **1980**, 295, 309.
182. Yedong, H.; Stott, F. H. *Corros. Sci.* **1994**, 36, 1869.
183. Ramanarayanan, T. A.; Ayer, R.; Petkovic-Luton, R.; Leta, D. P. *Oxid. Met.* **1988**, 29, 445.
184. Zhang, Y.; Gerberich, W. W.; Shores, D. A. *J. Mater. Res.* **1997**, 12, 697.
185. Zhu, D.; Stout, J. H.; Nelson, J. C.; Shores, D. A. *Mater. Sci. Forum* **1997**, 251–254, 437.
186. Tolpygo, V. K.; Dryden, J. R.; Clarke, D. R. *Acta Mater.* **1998**, 46, 927.
187. Tolpygo, V. K.; Clarke, D. R. *Oxid. Met.* **1998**, 49, 187.
188. Huntz, A. M. *Mater. Sci. Eng. A* **1987**, 87, 251.
189. Forest, C.; Davidson, J. H. *Oxid. Met.* **1995**, 43, 479.
190. Sarioglu, C.; Stiger, M. J.; Blachere, J. R.; Janakiraman, R.; Schumann, E.; Ashary, A.; Pettit, F. S.; Meier, G. H. *Mater. Corros.* **2000**, 51, 358.
191. Funkenbusch, A. W.; Smeggil, J. G.; Bornstein, N. S. *Metal. Trans. A* **1985**, 16, 1164.
192. Lees, D. G. *Oxid. Met.* **1987**, 27, 75.
193. Smialek, J. L. In Proceedings of the International Conference on the Microscopy of Oxidation; Bennett, M. J., Lorimer, G. W., Eds.; **1990**; p 258.
194. Pieraggi, B.; Rapp, R. A. *J. Electrochem. Soc.* **1993**, 140, 2844.
195. Pieraggi, B.; Rapp, R. A.; Hirth, J. P. *Oxid. Met.* **1995**, 44, 63.
196. Rommerskirchen, I.; Kolarik, V. *Mater. Corros.* **1996**, 47, 625.
197. Montealegre, M. A.; Gonzalez-Carrasco, J. L. *Intermetallics* **2003**, 11, 169.
198. Chen, J. H.; Rogers, P. M.; Little, J. A. *Oxid. Met.* **1997**, 47, 381.
199. Felten, A. J. *J. Electrochem. Soc.* **1961**, 108, 490.
200. Pérez, J.; Cristobal, M. J.; Hierro, M. P.; Arnau, G.; Botella, J. *Oxid. Met.* **2000**, 54, 87.
201. Brylewski, T.; Prazuch, J.; Przybylski, K. *Ceram. Polish Ceram. Bull.* **2000**, 61, 221.
202. Brylewski, T.; Nanko, M.; Maruyama, T.; Przybylski, K. *Solid State Ionics* **2001**, 143, 131.
203. Pieraggi, B.; Rapp, R. A. *J. Phys. IV* **1993**, 3, 275.
204. Cabouro, G.; Caboche, G.; Chevalier, S.; Piccardo, P. *J. Power Sources* **2006**, 156, 39.
205. Giggins, C. S.; Pettit, F. S. *Metall. Trans.* **1971**, 2, 1071.
206. Przybylski, K.; Garratt-Reed, A. J.; Yurek, G. J. *J. Electrochem. Soc.* **1988**, 135, 509.
207. Hou, P. Y.; Stringer, J. *Oxid. Met.* **1988**, 29, 45.
208. Mitra, S. K.; Roy, S. K.; Bose, S. K. *Oxid. Met.* **1990**, 34, 101.
209. Bonnet, G.; Larpin, J. P.; Colson, J. C. *Solid State Ionics* **1992**, 51, 11.
210. Hussey, R. J.; Papaioannou, P.; Mitchell, D. F.; Graham, M. J. *Mater. Sci. Eng. A* **1989**, 120, 147.
211. Zhang, Y.; Zhu, D.; Shores, D. A. *Acta Metall. Mater.* **1995**, 43, 4015.
212. Sigler, D. R. *Oxid. Met.* **1996**, 46, 335.
213. Chevalier, S.; Bonnet, G.; Larpin, J. P.; Colson, J. C. *Oxid. Met.* **1997**, 47, 53.

214. Riffard, F.; Buscail, H.; Caudron, E.; Cuffe, R.; Issartel, C.; Perrier, S. *Appl. Surf. Sci.* **2002**, *199*, 107.
215. Chevalier, S. In *Developments in High-Temperature Corrosion and Protection of Materials*; Gao, W., Li, Z., Eds.; Woodhead Publishing: Cambridge, England, 2008; Chapter 10.
216. Klöwer, J.; Li, J. G. *Mater. Corros.* **1996**, *47*, 545.
217. Klöwer, J. *Mater. Corros.* **2000**, *51*, 373.
218. Chevalier, S.; Bonnet, G.; Larpin, J. P.; Colson, J. C. *Corros. Sci.* **2003**, *45*, 1661.
219. Chevalier, S.; Larpin, J. P. *Mater. Sci. Eng. A* **2003**, *363*, 116.
220. Chevalier, S.; Dawah Tankeu, A. P.; Buscail, H.; Issartel, C.; Borchardt, G.; Larpin, J. P. *Mater. Corros.* **2004**, *55*, 610.
221. Seybolt, A. U. *Corros. Sci.* **1966**, *6*, 263.
222. Downham, D. A.; Shendye, S. B. *Oxid. Met.* **1995**, *43*, 411.
223. Cristobal, M. J.; Gibson, P. N.; Stroosnijder, M. F. *Corros. Sci.* **1996**, *38*, 805.
224. Paul, A.; Odriozola, J. A. *Mater. Sci. Eng. A* **2001**, *300*, 22.
225. Tien, J. K.; Pettit, F. S. *Metall. Trans.* **1972**, *3*, 1587.
226. Kim, K. Y.; Kim, S. H.; Kwon, K. W.; Kim, I. H. *Oxid. Met.* **1994**, *41*, 179.
227. Pint, B. A.; Hobbs, L. W. *J. Electrochem. Soc.* **1994**, *141*, 2443.
228. Pint, B. A. *Mater. Sci. Forum* **1997**, *251–254*, 397.
229. Aguilard, G. Ph.D. Thesis Université de Bourgogne, Dijon, 1992.
230. Pint, B. A.; Garratt-Reed, A. J.; Hobbs, L. W. *J. Am. Ceram. Soc.* **1998**, *81*, 305.
231. Wu, Y.; Hagihara, K.; Umakoshi, Y. *Intermetallics* **2004**, *12*, 519.
232. Yurek, G. J.; Przybylski, K.; Garratt-Reed, A. J. *J. Electrochem. Soc.* **1987**, *134*, 2643.
233. Przybylski, K. *Mater. Sci. Eng. A* **1989**, *121*, 509.
234. Przybylski, K.; Yurek, G. J. *Mater. Sci. Forum* **1989**, *43*, 1.
235. Chevalier, S.; Bonnet, G.; Przybylski, K.; Colson, J. C.; Larpin, J. P. *Oxid. Met.* **2000**, *54*, 527.
236. Ul-Hamid, A. *Oxid. Met.* **2002**, *58*, 23.
237. Przybylski, K.; Garratt-Reed, A. J.; Pint, B. A.; Katz, E. P.; Yurek, G. J. *J. Electrochem. Soc.* **1987**, *134*, 3207.
238. Pint, B. A.; Garratt-Reed, A. J.; Hobbs, L. W. In Proceedings of the 2nd International Conference on the Microscopy of Oxidation; Newcomb, S. B., Bennett, M. J., Eds.; **1993**; p 463.
239. Schumann, E.; Yang, J. C.; Graham, M. J.; Rhüle, M. *Mater. Corros.* **1995**, *46*, 218.
240. Schumann, E.; Yang, J. C.; Graham, M. J.; Rühle, M. *Mater. Corros.* **1996**, *47*, 631.
241. Pint, B. A.; Garratt-Ree, A. J.; Hobbs, L. W. *J. Phys. IV* **1993**, *3*, 247.
242. Pint, B. A.; Alexander, K. B. In Proceedings of the 3rd International Conference on the Microscopy of Oxidation; Newcomb, S. B., Little, J. A., Eds.; **1996**; p 153.
243. Pint, B. A.; Alexander, K. B. *J. Electrochem. Soc.* **1998**, *145*, 1819.
244. Mennicke, C.; Schumann, E.; Le Coze, J.; Smialek, J. L.; Meier, G. H.; Rhüle, M. In Proceedings of the 3rd International Conference on the Microscopy of Oxidation; Newcomb, S. B., Little, J. A., Eds.; **1996**; p 95.
245. Newcomb, S. B.; Dunin-Borkowski, R. E.; Boothroyd, C. B.; Czyrska-Filemonowicz, A.; Clemens, D.; Quadakkers, W. J. In Proceedings of the 3rd International Conference on the Microscopy of Oxidation; Newcomb, S. B., Little, J. A., Eds.; **1996**; p 166.
246. Kohn, M.; Ishikawa, S.; Ishi, K.; Satoh, I. In Proceedings of the 3rd International Conference on the Microscopy of Oxidation; Newcomb, S. B., Little, J. A., Eds.; **1996**; p 55.
247. Molins, R.; Germidis, A.; Andrieu, E. In Proceedings of the 3rd International Conference on the Microscopy of Oxidation; Newcomb, S. B., Little, J. A., Eds.; **1996**; p 3.
248. Sato, E.; Carry, C. *J. Am. Ceram. Soc.* **1996**, *79*, 2156.
249. Pint, B. A.; Alexander, K. B. In Proceedings of the 3rd International Conference on the Microscopy of Oxidation; Newcomb, S. B., Little, J. A., Eds.; **1996**; p 153.
250. Pint, B. A.; Alexander, K. B. *J. Electrochem. Soc.* **1998**, *145*, 1819.
251. Chevalier, S.; Larpin, J. P. *Acta Mater.* **2002**, *50*, 3105–3114.
252. Quadakkers, W. J.; Speier, W.; Holzbrecher, H.; Nickel, H. In Proceedings of the International Conference on the Microscopy of Oxidation; Bennet, M. J., Lorimer, G. W., Eds.; **1990**; p 149.
253. Papaioacovou, P.; Hussey, R. J.; Mitchell, D. F.; Graham, M. J. *Corros. Sci.* **1990**, *30*, 451.
254. Hussey, R. J.; Sproule, G. I.; Graham, M. J. *J. Phys. IV* **1993**, *3*, 241.
255. Quadakkers, W. J.; Norton, J. F.; Penkalla, J.; Breuer, U.; Gil, A.; Rieck, T.; Hänsel, M. In Proceedings of the 3rd International Conference on the Microscopy of Oxidation; Newcomb, S. B., Little, J. A., Eds.; **1996**; p 221.
256. Quadakkers, W. J.; Speier, W.; Holzbrecher, H.; Nickel, H. In Proceedings of the International Conference on the Microscopy of Oxidation; Bennet, M. J., Lorimer, G. W., Eds.; **1990**; p 149.
257. Jedlinski, J.; Borchardt, G. *Oxid. Met.* **1991**, *36*, 317.
258. Czyrska-Filemonowicz, A.; Szot, K.; Wasilkowska, A.; Ennis, P. J.; Breuer, U.; Gil, A.; Quadakkers, W. J. In Proceedings of the 3rd International Conference on the Microscopy of Oxidation; Newcomb, S. B., Little, J. A., Eds.; **1996**; p 185.
259. Quadakkers, W. J.; Clemens, D.; Bennett, M. J. In Proceedings of the 3rd International Conference on the Microscopy of Oxidation; Newcomb, S. B., Little, J. A., Eds.; **1996**; p 195.
260. Chevalier, S.; Przybylski, K.; Borchardt, G.; Larpin, J. P. *Mater. Sci. Forum* **2004**, *461–464*, 53.
261. Chevalier, S.; Bonnet, G.; Borchardt, G.; Colson, J. C.; Larpin, J. P. *Mater. Sci. Forum* **2001**, *369–372*, 327.
262. Pint, B. A.; Garratt-Reed, A. J.; Hobbs, L. W. *Mater. High Temp.* **1995**, *13*, 3.
263. Turker, M.; Hugues, T. A. *Oxid. Met.* **1995**, *44*, 505.
264. Turker, M.; Hugues, T. A. *Oxid. Met.* **1995**, *44*, 505.
265. Chevalier, S.; Przybylski, K. Unpublished results.



## 1.09 Thermodynamics and Theory of External and Internal Oxidation of Alloys

**B. Gleeson**

Department of Mechanical Engineering and Materials Science, The University of Pittsburgh, 647 Benedum Hall, Pittsburgh, PA 15261, USA

© 2010 Elsevier B.V. All rights reserved.

1.09.1	Introduction	180
1.09.2	Pure Metal Reactions	181
1.09.2.1	Thermodynamics of a Single-Oxidant Reaction	181
1.09.2.2	Thermodynamics of Dual Oxidant Reactions	184
1.09.2.3	Kinetics of Scale Formation	186
1.09.2.3.1	Parabolic rate law	186
1.09.2.3.2	Linear rate law	187
1.09.2.3.3	Logarithmic rate law	187
1.09.2.4	Transport Properties of Metal Oxides	187
1.09.2.5	Wagner's Theory of Metal Oxidation	188
1.09.3	Alloy Reactions	190
1.09.3.1	Thermodynamics of Alloy Oxidation	190
1.09.3.2	Criterion for the Sustained Exclusive Growth of a Protective Scale	191
1.09.3.3	Internal Oxidation	192
1.09.3.4	Transition from Internal Oxidation to External Scale Formation	193
1.09.4	Epilogue	193
References		193

### Symbols

$a_i$  Chemical activity of phase or component  $i$   
 $D_i$  Diffusion coefficient of component  $i$  ( $\text{m}^2 \text{s}^{-1}$ )  
 $K$  Equilibrium constant for a given reaction  
 $k_l$  Linear rate constant ( $\text{m s}^{-1}$ ) or ( $\text{kg m}^{-2} \text{s}^{-1}$ )  
 $k_p$  Parabolic rate constant ( $\text{m}^2 \text{s}^{-1}$ ) or ( $\text{kg}^2 \text{m}^{-4} \text{s}^{-1}$ )  
 $N_i$  Mole fraction of component  $i$   
 $P_i$  Partial pressure of gaseous species  $i$   
 $R$  Universal gas constant ( $8.314 \text{ J mol}^{-1} \text{ K}^{-1}$ )  
 $T$  Temperature (K)  
 $t$  Time (s)  
 $V_m$  Molar volume of metal or alloy ( $\text{m}^3 \text{mol}^{-1}$ )  
 $X$  Thickness of metal consumed due to scaling (m)  
 $x$  Scale thickness (m)  
 $\Delta G^\circ$  Gibbs free enthalpy in the standard state ( $\text{J mol}^{-1}$ )  
 $\Delta W$  Weight change ( $\text{kg m}^{-2}$ )  
 $\gamma_i$  Chemical activity coefficient of solute  $i$   
 $\nu$  Stoichiometric factor for the oxide  $\text{BO}_\nu$

### 1.09.1 Introduction

High temperature corrosion plays an important role in the selection of materials in modern industry. Numerous commercial processes such as electric power generating plants, aerospace, gas turbines, heat-treating, and mineral and metallurgical processing operate at temperatures exceeding  $\sim 500^\circ\text{C}$ .<sup>1</sup> Oxidation is often the most important high temperature corrosion reaction in these commercial processes. Indeed, most high temperature alloys are designed to react with the oxidizing environment in such a way that a protective oxide scale forms.<sup>2</sup> The degradation resistance of a high temperature alloy depends on sustaining the formation of this protective scale.

The properties of the scale determine the extent to which protection can be provided. Ideally, the scale should exhibit a slow growth rate, good adherence to the alloy substrate, a high stability, and be continuous and free of defects such as microcracks or large



voids. In general, a chromia, alumina, or silica scale can meet these requirements for high temperature oxidation resistance, with chromia-forming alloys being the most extensively used in high temperature industrial applications.

Almost all theoretical treatments of high temperature corrosion assume local equilibrium. In the majority of cases, this proves to be a reasonable assumption, although it is usually insufficient for predicting the nature and phase constitution of the reaction product. This is because reaction kinetics dictate the pathway for scale development. The following discusses key fundamental aspects associated with the thermodynamics and kinetics of high temperature corrosion. From a thermodynamic standpoint, it will be shown that relative partial pressures of the gaseous components in the reacting atmosphere are important for predicting the composition of the product scale. From a kinetic standpoint, it will be shown that limiting equations can be established for predicting both scaling kinetics and critical concentrations in the alloy for transitioning to and sustaining protective scaling behavior.

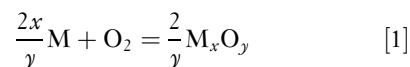
## 1.09.2 Pure Metal Reactions

In the context of this discussion, the metal and gas react to form a solid surface scale. The prototypical gas will be oxygen; however, it should be realized that the fundamental treatments equally apply to other gases, such as sulfur and nitrogen. Moreover, the oxidant may be simple, like  $O_2$ ,  $S_2$ , and  $N_2$ , or it may be more complex, like  $H_2O$ ,  $H_2S$ , and  $NH_4$ . For the sake of clarity, the following discussion will consider oxide-scale formation. An oxide scale may be a single layer or it may be comprised of two or more layers of varying compositions that depend on the temperature and oxidizing conditions. There are two important factors in discussing the oxidation of metals: thermodynamics and kinetics. Metallic elements react with oxygen to form oxides if it is energetically feasible. Thermodynamics show whether or not a reaction can take place. When the oxidation reaction is possible, kinetics shows how fast the reaction will be. In practical applications, kinetics is of more importance because it determines the extent of metal consumption and the overall reaction pathway (i.e., assemblage and structure of the reaction product). Oxidation theory of pure metals provides the foundation for understanding the more complicated processes associated with alloy oxidation.

### 1.09.2.1 Thermodynamics of a Single-Oxidant Reaction

Consider the high temperature reaction of a metal,  $M$ , with an oxidant gas, in this case oxygen. The metal initially absorbs oxygen and then chemical reaction ensues to form an oxide. For the metals of relevance to this review, the resulting oxide is solid. Thus, the oxide first nucleates and then grows to form a scale on the metal surface. Depending on its growth kinetics, the scale may or may not protect the underlying metal.

The formation of an oxide may be generally described by the reaction



Presented in this manner, the high temperature oxidation of metals may seem to be among the simplest of reactions; however, the reaction path and behavior often involve a number of phenomena and processes that depend on a variety of factors.<sup>3,4</sup> In fact, at the same temperature for a given gas-metal reaction, one can observe drastically different rates of reaction (linear, parabolic, or any other rate) when the gaseous composition of the atmosphere is altered and the relative partial pressures of the gaseous components are different.<sup>5</sup>

Under equilibrium conditions, the law of mass action for reaction [1] gives<sup>6</sup>

$$K_1 = \frac{a_{M_xO_y}^{2/y}}{a_M^{2x/y} a_{O_2}} \quad [2]$$

where  $K_1$  is the temperature-dependent equilibrium constant and  $a_i$  is the chemical activity of species  $i$ . In most cases, the solids (metal and oxide) are assumed to be in their pure standard state, so that their activities are defined as unity. At relatively high temperatures and moderate pressures, the oxidant gas can be treated as being ideal; that is, the activity of oxygen can be approximated by its partial pressure in atmospheres. Thus, eqn [2] simplifies to

$$K_1 = 1/P_{O_2} \quad [3]$$

where  $P_{O_2}$  is the oxygen partial pressure.

Thermodynamically, reaction [1] for any metal can take place spontaneously from left to right when its overall Gibbs free energy change,  $\Delta G$ , is negative. For reaction [1], the Gibbs free energy change under isobaric conditions is given as:

$$\Delta G = \Delta G^\circ + RT \ln K_1 \quad [4]$$

where  $\Delta G^\circ$  is the standard Gibbs free energy of formation of the oxide at absolute temperature

$T$  and  $R$  is the gas constant. If  $\Delta G = 0$ , the system is at equilibrium, and if  $\Delta G > 0$ , the reaction is thermodynamically unfavorable. At equilibrium ( $\Delta G = 0$ ),

$$\Delta G^\circ = -RT \ln K_1 = RT \ln P_{O_2} \quad [5]$$

Thus, knowing that at equilibrium both the forward and reverse reaction rates are equal, the dissociation pressure of the oxide can be defined from [5] as:

$$P_{O_2}^{\text{diss}} = \exp\left(\frac{\Delta G^\circ}{RT}\right) \quad [6]$$

The metal  $M$  can only be oxidized to the oxide  $M_xO_y$  at the temperature  $T$  if the ambient partial pressure of oxygen is larger than the dissociation pressure defined by eqn [6].

For the usual conditions of constant temperature and pressure, the auxiliary function  $\Delta G^\circ$  is usually described by the simple relation

$$\Delta G^\circ = \Delta H^\circ - T\Delta S^\circ \quad [7]$$

where  $\Delta H^\circ$  is the enthalpy of reaction and  $\Delta S^\circ$  is the entropy change under standard-state conditions. Tabulated values of  $\Delta H^\circ$  and  $\Delta S^\circ$  for the determination of  $\Delta G^\circ$  at any given temperature are readily available.<sup>7-9</sup> A small selection of useful values is given in Table 1.

Equation [7] shows that a plot of  $\Delta G^\circ$  versus  $T$  gives a straight line. This line would change in slope when a new phase forms (i.e., at melting or boiling temperature). A Gibbs energy–temperature diagram,

**Table 1** Standard energies of reaction<sup>7,8</sup> for pure solid metal (except liquid Al) and various common gasses

Reaction	$\Delta G^\circ = \Delta H^\circ - T\Delta S^\circ$ ( $J mol^{-1}$ )	
	$\Delta H^\circ$ ( $J mol^{-1}$ )	$-T\Delta S^\circ$ ( $J mol^{-1} K$ )
$\frac{2}{3}Al(l) + \frac{1}{2}O_2 = \frac{1}{3}Al_2O_3$	-565 900	128
$Co + \frac{1}{2}O_2 = CoO$	-233 886	70.7
$3CoO + \frac{1}{2}O_2 = Co_3O_4$	-183 260	148.1
$\frac{2}{3}Cr + \frac{1}{2}O_2 = \frac{1}{3}Cr_2O_3$	-373 420	86
$Fe + \frac{1}{2}O_2 = FeO$	-264 890	65.4
$3FeO + \frac{1}{2}O_2 = Fe_3O_4$	-312 210	125.1
$2Fe_2O_3 + \frac{1}{2}O_2 = 3Fe_2O_4$	-249 450	140.7
$Mn + \frac{1}{2}O_2 = MnO$	-412 304	72.8
$Ni + \frac{1}{2}O_2 = NiO$	-234 345	84.3
$\frac{1}{2}Si + \frac{1}{2}O_2 = \frac{1}{2}SiO_2$	-451 040	86.8
$H_2 + \frac{1}{2}O_2 = H_2O$	-246 440	54.8
$CO + \frac{1}{2}O_2 = CO_2$	-282 420	86.8
$O_2 + \frac{1}{2}S_2 = SO_2$	-362 420	72.4
$NiO + Cr_2O_3 = NiCr_2O_4$	-1 376 880	332
$NiO + Al_2O_3 = NiAl_2O_4$	-1 933 667	408

The calculated  $\Delta G^\circ$  value would be for the mole numbers shown in the particular reaction considered.

usually called an Ellingham diagram,<sup>6</sup> summarizes the temperature dependence of  $\Delta G^\circ$  for various common oxidation reactions at a standard state ( $p_{O_2} = 1$  atm). Such a diagram is shown in Figure 1 for oxides.

The Ellingham diagram in Figure 1 shows the relative thermodynamic stability of the indicated oxides. The lower the line on the diagram, the more negative the standard free energy of formation and, hence, the more stable the oxide. For example, the lines for  $Al_2O_3$ ,  $SiO_2$ , and  $Cr_2O_3$  are lower than those for  $FeO$ ,  $NiO$ , and  $CoO$  in the Ellingham diagram, so the former oxides are more stable and therefore meet an important criterion for being protective scales. It is further seen in Figure 1 that the  $\Delta G^\circ$  versus  $T$  lines for most of the oxides are parallel and positively sloped. This is a consequence of the fact that the entropy of a gas is much larger than that of a solid. Thus, for the metal oxidation reactions represented by eqn [1],

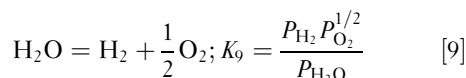
$$\Delta S^\circ = \frac{2}{y}S_{M_xO_y}^\circ - \frac{2x}{y}S_M^\circ - S_{O_2}^\circ \approx -S_{O_2}^\circ. \quad [8]$$

It follows from eqn [7] that  $\partial \Delta G^\circ / \partial T = -\Delta S^\circ \approx S_{O_2}^\circ$ , which is greater than zero.

The  $P_{O_2}$  can be read directly from Figure 1 by using the  $P_{O_2}$  scale along the bottom and the right side of the diagram. A straight line drawn from the index point labeled 'O' (at  $\Delta G^\circ = 0$ ,  $T = 0$  K) at the upper left of the diagram, through a specific temperature point on an oxide line, intersects the  $P_{O_2}$  scale at the dissociation oxygen partial pressure ( $P_{O_2}^{\text{diss}}$ ) for that oxide at that particular temperature. Accordingly, the oxides lower on the diagram are more stable and consequently have lower  $P_{O_2}^{\text{diss}}$  values. For instance, from Figure 1, it is found that the dissociation pressure for  $NiO$  is  $\sim 10^{-10}$  atm at  $1000^\circ\text{C}$ , while that for  $Cr_2O_3$  is  $\sim 10^{-22}$  atm, and for  $SiO_2$  and  $Al_2O_3$ , it is  $10^{-26}$  and  $10^{-34}$  atm, respectively. The significance of this is that it is difficult thermodynamically to preclude the oxidation of Cr, Si, and Al.

Similar free-energy diagrams, which can be interpreted in exactly the same way, have been constructed for sulfides, carbides, and nitrides.<sup>5</sup> Moreover, Lou *et al.*<sup>10</sup> presented an excellent review on the use of Ellingham diagrams for treating gas–solid reactions.

Low oxygen partial pressures are in practice achieved using oxygen-bearing gas mixtures. The most common gas mixtures are  $H_2O/H_2$  and  $CO_2/CO$ . The partial pressures of oxygen are then established from the equilibria:



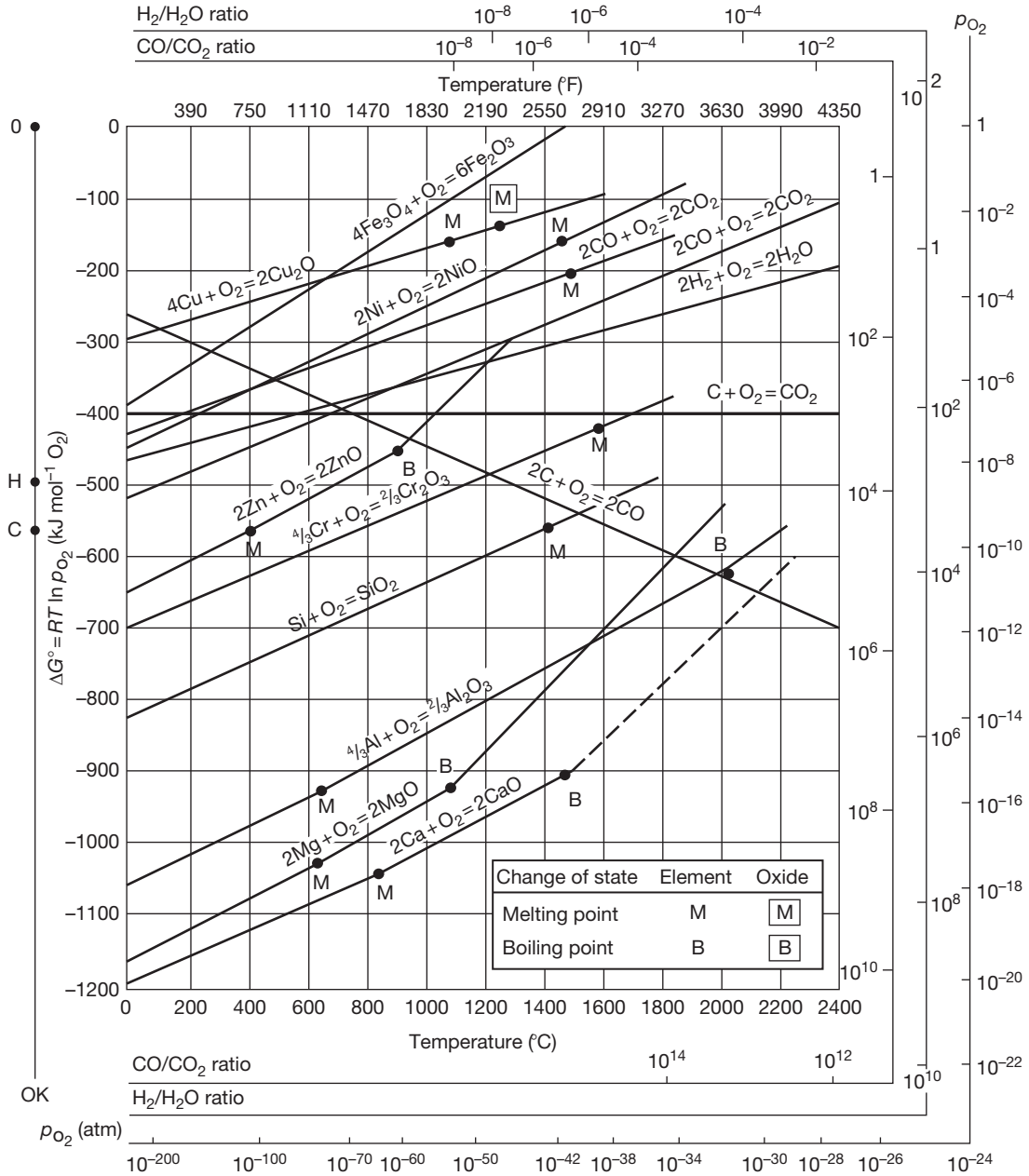


**Figure 1** Ellingham diagram showing the standard Gibbs energies of formation of selected oxides as a function of temperature. Reproduced from Gaskell, D. R. *Introduction to the Thermodynamics of Materials*, 5th ed.; Taylor & Francis: New York, 2008.

and

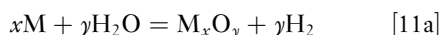
$$CO_2 = CO + \frac{1}{2} O_2; K_{10} = \frac{P_{CO} P_{O_2}^{1/2}}{P_{CO_2}} \quad [10]$$

where  $K_9$  and  $K_{10}$  are the temperature-dependent equilibrium constants for reactions [9] and [10], respectively. Thus, the  $P_{O_2}$  may be determined from

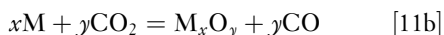
these equilibrium constants if the equilibrium  $P_{CO}/P_{CO_2}$  or  $P_{H_2}/P_{H_2O}$  ratios are known. In oxygen-lean gases containing both H<sub>2</sub>O and CO<sub>2</sub>, the  $P_{O_2}$  is usually determined by the H<sub>2</sub>–H<sub>2</sub>O reaction [9] since steam is more reactive than CO<sub>2</sub>. Moreover, for a controlled laboratory experiment, it is preferred practice to facilitate the equilibrium by using a

platinum-containing catalyst in the reaction zone of the furnace.

In addition to the direct oxidation with oxygen, the overall metal oxidation reactions in these gas mixtures are:



and



From **Figure 1**, the  $H_2/H_2O$  and  $CO/CO_2$  ratios can be obtained by using the same method as for determining  $P_{O_2}^{diss}$ , using the index points labeled 'H' and 'C' at the left of the diagram instead of point 'O.'

The growth of a scale is usually sufficiently slow for local equilibrium to be closely approached. In fact, it is found that the Gibbs phase rule<sup>6</sup> can be applied to rationalizing the phase assemblage of a growing scale. Specifically, the Gibbs phase rule under isothermal and isobaric conditions is given as

$$P + F = C \quad [12]$$

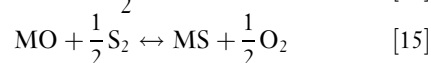
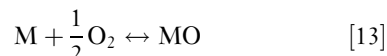
where  $P$  is the number of phases at a given location in the scale,  $F$  represents the degrees of freedom, and  $C$  number of components in the system. For the oxidation of a pure metal,  $C = 2$  (i.e., metal and oxygen), and for diffusion to occur there must be a gradient in the chemical activity across the scale, so that  $F = 1$ . Thus,  $P = 1$ , meaning that only one phase can exist at a given plane (parallel to the metal/scale interface) within the scale. In practical terms, this means that a metal capable of forming multiple oxides must form those oxides as distinct scale layers. For example, at 1 atm  $O_2$  and temperatures above 560°C, pure iron oxidizes to form a triple-layered scale in the sequence  $Fe|FeO|Fe_3O_4|Fe_2O_3|O_2$ , with the oxide position being dictated by the necessity for the oxygen content to progressively increase when traversing from the iron to the oxygen at the scale surface. A similar line of reasoning can be used to show that a pure metal oxidized isothermally will not form internal oxide precipitates, but instead must form an external product.

### 1.09.2.2 Thermodynamics of Dual Oxidant Reactions

The thermodynamic aspects of multioxidant corrosion have been discussed by Giggins and Pettit.<sup>11</sup> Often, however, the complexity of a given process environment precludes an accurate determination

of which type of corrosion should predominate. In such cases, it may be necessary to conduct field-exposure tests to properly evaluate the corrosion behavior of the candidate alloys. Even so, the assumption of thermodynamic equilibrium provides a reasonable starting point for assessment.

Quite often, two-dimensional phase stability diagrams are used to assess the high temperature corrosion of a metal  $M$  exposed to a dual-oxidant atmosphere. To illustrate this, the possible reactions of  $M$  exposed to oxidizing-sulfidizing atmosphere are determined by considering the following:



The equilibrium from reactions [13] and [14] defines the critical  $P_{O_2}^*$  and  $P_{S_2}^*$  values (i.e., dissociation pressures) for  $M/MO$  and  $M/MS$  equilibrium, respectively, while reaction [15] defines critical  $P_{S_2}/P_{O_2}$  ratios for  $MS/MO$  equilibria. With regard to the latter, it can be easily shown for reaction [15] that  $\log(P_{S_2}) = \log(P_{O_2}) - 2\log K_{15}$ , where  $K_{15}$  is the equilibrium constant for this reaction. Thus, a plot of  $\log(P_{S_2})$  versus  $\log(P_{O_2})$  should have a line of slope equal to the unity that separates  $MS$  stability from  $MO$  stability. **Figure 2** shows the general construction of an  $M-S-O$  phase-stability diagram. It is noted that a more complete diagram may include higher-order oxides and sulfides, as well as sulfates ( $MSO_4$ ).<sup>11</sup> Only the simpler diagram is discussed here since the main important points can still be made.

The diagram in **Figure 1** shows the stability range of a metal and its oxide and sulfide products as a function of the two principal reactants: oxygen and

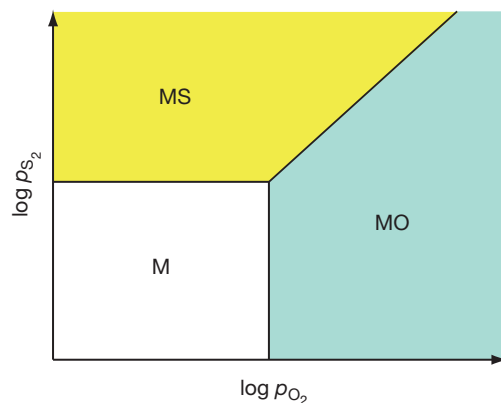


**Figure 2** Schematic representation of a simple phase-stability diagram for a metal and its oxide and sulfide.

sulfur. A given atmosphere is defined by either equilibrium or nonequilibrium  $P_{O_2}$  and  $P_{S_2}$  values and would therefore be represented by a point in the stability diagram. The location of that point identifies the phase that is in stable equilibrium with that particular atmosphere. However, as shown in **Figure 3**, other phases can form even if only oxide stability is predicted. This depends on the reacting gas, the  $P_{O_2}$ – $P_{S_2}$  combination, and whether the scale develops open pathways for gaseous penetration (e.g., microcracks). Internal sulfidation is particularly apt to occur in  $SO_2$ -containing atmospheres due to the local equilibrium dictated by the reaction  $O_2 + \frac{1}{2} S_2 \rightarrow SO_2$ , which has an equilibrium constant denoted as  $K_3$ . As indicated in **Figure 3**, the formation of an internal sulfide beneath an external oxide scale can only be completely avoided if

$$P_{SO_2} < K_3 P_{O_2}^* \sqrt{P_{S_2}^*} \quad [16]$$

Although phase-stability diagrams are very useful for interpreting reaction products and gaining insights into reaction pathways, they do not have any predictive capabilities from a practical standpoint.

On the basis of equilibrium thermodynamics of reaction [15], the transition from sulfidation to oxidation of metal M should occur when

$$\left(\frac{P_{O_2}}{P_{S_2}}\right)^{1/2} > K_{15} \quad [17]$$

The thermodynamic boundary separating sulfide and oxide stability in a phase stability diagram is determined by replacing ‘>’ with ‘=’ in eqn [17]. **Figure 4** shows the phase-stability diagram for the Type 310 stainless steel at 875 °C.<sup>12</sup> Superimposed on this diagram are experimental data indicating the

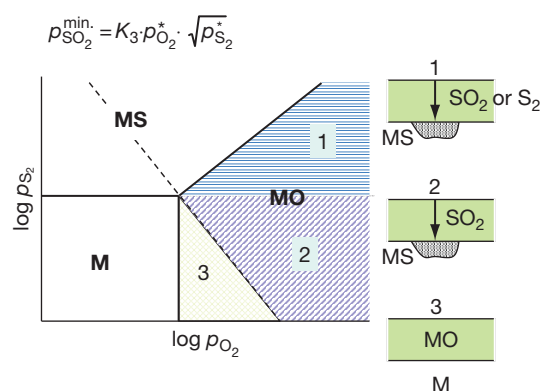


**Figure 3** Application of the phase-stability diagram in identifying possible modes of attack.

type of scale formed on 310 under different  $P_{O_2}$ – $P_{S_2}$  combinations. It is seen that sulfide-to-oxide transition at a given  $P_{S_2}$  actually occurs at a higher  $P_{O_2}$  than that predicted from equilibrium calculations. The experimentally-determined boundary is dictated by kinetic factors and, accordingly, is referred to as the kinetic boundary. For the case of the 310 stainless steel shown in **Figure 4**, the actual  $P_{O_2}$  values for the transition from chromium–sulfide to chromium–oxide formation are about three orders of magnitude higher than the equilibrium values. The kinetic factors which influence the location of the kinetic boundary include composition and surface finish of the alloy, and gas composition. Although theoretical prediction of the location of a kinetic boundary is not possible, LaBranche and Yurek<sup>13</sup> showed that for  $H_2$ – $H_2O$ – $H_2S$  gas mixtures there is a critical  $H_2O/H_2S$  ratio associated with the kinetic boundary. The value of this ratio is dictated by the competitive formation of the oxide and the faster-growing sulfide. It was found by LaBranche and Yurek that oxide formation on pure chromium at 900 °C could only occur when the area fraction of  $Cr_2O_3$  was greater than  $\sim 0.9$  in the early stages of exposure, which corresponds to  $H_2O/H_2S > 10$ .

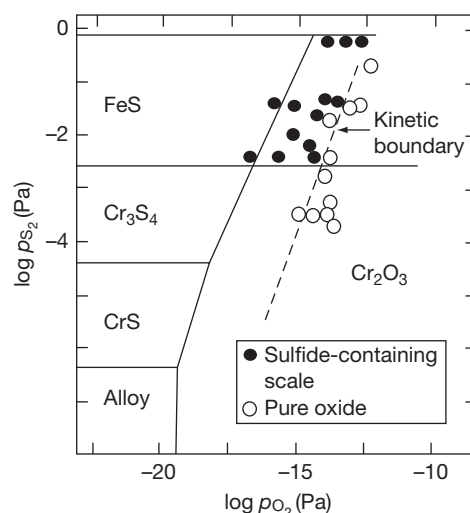


**Figure 4** Thermodynamic phase-stability diagram for type 310 stainless steel at 875 °C, showing the experimentally-determined kinetic boundary. Reproduced from Stroosnijder, M. F.; Quadackers, W. J. *High Temp. Technol.* **1986**, 4, 141.



### 1.09.2.3 Kinetics of Scale Formation

The reaction of a metal with an oxidant to form a product scale is concomitant with a weight gain due to pick-up of the oxidant (e.g., grams of oxygen gained). Accordingly, the scaling rate may be quantified by the change in the scale thickness,  $x$  (cm), or by weight gain,  $\Delta W$  ( $\text{mg cm}^{-2}$ ). In the case of oxidation, these two parameters are directly related by

$$x = \frac{V_{\text{ox}}}{\gamma M_{\text{O}}} \Delta W \quad [18]$$

where  $V_{\text{ox}}$  is the molar volume of oxide in  $\text{cm}^3 \text{mol}^{-1}$ ,  $\gamma$  is the stoichiometric amount of oxygen in oxide  $\text{M}_x\text{O}_y$ , and  $M_{\text{O}}$  is the atomic weight of oxygen.

The formation of oxide scale is also related to the consumption of metal, and the relationship between  $\Delta W$  and the thickness of the metal consumed ( $X$ ) is given by

$$X = \frac{V_{\text{m}}}{\gamma M_{\text{O}}} \Delta W \quad [19]$$

where  $V_{\text{m}}$  is the molar volume of metal in  $\text{cm}^3 \text{mol}^{-1}$  and  $\gamma$  is the stoichiometric factor for the oxide scale product (i.e.,  $\gamma = y/x$  for  $\text{M}_x\text{O}_y$ ). For most metals, the oxidation rates follow one or more of the three possible kinetic laws: linear, logarithmic, and parabolic. These kinetic laws are discussed in the following.

Formation of an oxide scale will separate the two reactants, metal and gaseous oxygen. In order for the reaction to proceed further, at least one of the reactants must progress through the scale to form more oxide at the oxide/gas, oxide/metal, or both interfaces. The mechanisms by which the reactants progress through the scale can therefore be an important part of the overall mechanism and kinetics by which high temperature oxidation reaction proceeds. Another aspect of the oxidation process, which can sometimes be rate controlling, is the kinetics of the interfacial reaction steps.

#### 1.09.2.3.1 Parabolic rate law

At high temperature, initial scale growth is usually very rapid; however, the reaction rate will eventually decrease when scale thickness reaches  $\sim 0.5 \mu\text{m}$  and the transport of reacting species through the scale becomes rate controlling. When the rate-controlling step in the oxidation process is the diffusion of reactant(s) through the oxide layer and with the boundary conditions for diffusion being time independent, the scaling kinetics will follow the parabolic rate law. Parabolic kinetics results from the fact that the scale

thickness,  $x$ , increases with time,  $t$ , and, since this corresponds to the increasing diffusion distance, the oxidation rate decreases. Thus, the instantaneous oxidation rate is quite simply inversely proportional to the oxide thickness, that is,

$$\frac{dx}{dt} = \frac{k'_{\text{p}}}{x} \quad [20]$$

where  $k'_{\text{p}}$  is a proportionality constant. Integration of eqn [20] gives

$$x^2 = k_{\text{p}} t + C \quad [21]$$

where  $k_{\text{p}}$  is taken to be the parabolic rate constant ( $k_{\text{p}} = 2 k'_{\text{p}}$ ) with typical units of  $\text{cm}^2 \text{s}^{-1}$ . Another form of the parabolic rate equation is given by the weight gain ( $\text{g cm}^{-2}$ ):

$$\Delta W^2 = k_{\text{p}} t + C \quad [22]$$

where the units of  $k_{\text{p}}$  in this case are  $\text{g}^2 \text{cm}^{-4} \text{s}$ .

The parabolic rate law is the standard for analysis of high temperature oxidation kinetics, in which diffusion through the relatively thick scale controls reaction rates. The diffusion-controlled scale-thickening process is thermally activated, meaning that the rate increases exponentially with temperature, as given by the Arrhenius equation:

$$k_{\text{p}} = k_0 \exp\left(\frac{-Q}{RT}\right) \quad [23]$$

Here,  $k_0$  is a constant that is a function of the oxide composition and the gas pressure, and  $Q$  is the activation energy for oxide-scale growth. Figure 5<sup>1</sup> shows the temperature dependence of the  $k_{\text{p}}$  values for the oxides of Fe, Co, Ni, Cr, Al, and Si. The figure shows a range of  $k_{\text{p}}$  values for  $\text{Al}_2\text{O}_3$  and  $\text{Cr}_2\text{O}_3$  growth because these oxides do not show intrinsic behavior and are instead very sensitive to impurities (i.e., doping).

Deviations from parabolic kinetics are generally analyzed in terms of chemical and metallurgical effects on the rates of the relevant diffusing process(es). The parabolic rate law will not hold in the very early stages of oxidation, before the scale has developed sufficient continuity and thickness. In the case of hafnium and zirconium, the time exponent in eqn [21] is found to be  $\sim 3$  (cubic kinetics) rather than 2 (parabolic kinetics) at high temperatures. This has been attributed to the simultaneous dissolution of oxygen into the substrate metal during oxidation.<sup>14</sup> It has also been shown for  $\text{NiO}$ -<sup>15</sup> and  $\text{Al}_2\text{O}_3$ -scale<sup>16</sup> growth that subparabolic kinetics can occur if both short-circuit diffusion through the scale predominates and the average grain size of the scale increases with oxidation time.



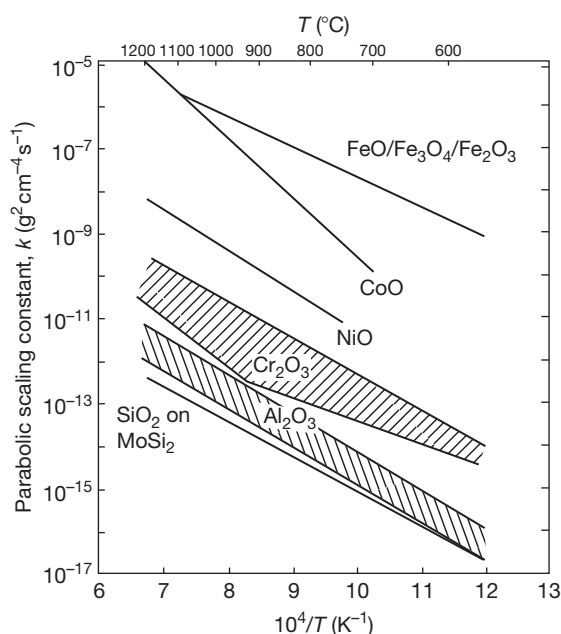


**Figure 5** Parabolic oxidation rate constant for various oxide scales as a function of temperature. Reproduced from Gleeson, B. In *Corrosion and Environmental Degradation*, Vol. II: Volume 19 of the Materials Science and Technology Series; Schütze, M., Ed.; Wiley-VCH: Weinheim, Germany, 2000.

### 1.09.2.3.2 Linear rate law

Under certain conditions, the oxidation of a metal proceeds at a constant rate according to a linear rate law, that is,

$$x = k_l t \quad [24]$$

where  $x$  is the scale thickness and  $k_l$  is the linear rate constant. A linear rate law may result when a phase-boundary reaction controls the kinetics rather than a transport process. An example is  $\text{CO}_2$  dissociation at the scale surface controlling the oxidation kinetics of steel in a  $\text{CO}_2$ -rich atmosphere.<sup>17</sup>

Linear kinetics is also possible if the oxide is volatile or molten, if the scale spalls or cracks, or if a porous, nonprotective oxide forms on the metal.<sup>4</sup> Since the rate of oxidation never slows down, consumption of the metal occurs in a relatively short time in comparison to a metal scaling according to parabolic kinetics. Examples of metals that scale in a nonprotective, linear manner due to continual scale cracking are Nb and Ta.<sup>18</sup>

In the early stages of a metal oxidation process, the scale may be sufficiently thin that linear oxidation kinetics prevails. As the scale thickens, a transition to parabolic kinetics will usually ensue.<sup>19</sup> Conversely,

microcracking and porosity may develop as the scale thickens, reducing the protectiveness of the oxide. The parabolic rate law may then fail, and the kinetics approaches linearity at some time after the start of reaction and scale growth. That is, a constant oxidation rate can develop after a period of parabolic behavior. In this special case of parabolic scaling superimposed on a relatively constant rate of scale cracking and healing, the overall kinetics is said to be 'paralinear'.<sup>20</sup>

### 1.09.2.3.3 Logarithmic rate law

At low temperatures (e.g.,  $T < 300\text{--}400^\circ\text{C}$ ), oxidation rates are often inversely proportional to time, that is,

$$\frac{dx}{dt} = \frac{k}{t} \quad [25]$$

where  $k$  is a constant. Integration of [25] leads to the logarithmic rate law

$$x = k_a \log(k_b t + 1) \quad [26]$$

where  $k_a$  and  $k_b$  are constants. Logarithmic oxidation is usually obeyed for relatively thin scales at low temperatures.

### 1.09.2.4 Transport Properties of Metal Oxides

Metallic oxides are seldom stoichiometric, meaning that the metal-to-oxygen atom ratio is not exactly that given by the stoichiometric chemical formula, even though the compound is electrically neutral. The same can be stated for sulfides and nitrides, but the focus here will be on oxides as the prototypical systems. The ionic charge imbalance in a nonstoichiometric oxide is compensated by electronic charges, that is, electron and electron holes. As a consequence, nonstoichiometric oxides exhibit both electronic and ionic conductivities. These conductivities are temperature dependent, which, from the electronic standpoint, classifies the nonstoichiometric oxides as semiconductors.

Electronic semiconductors are categorized as n-type (excess of electrons) or p-type (excess of electron holes). The n-type oxides may have either an excess of cation interstitials or an excess of oxygen vacancies (i.e., a deficiency in filled sites on the oxygen sublattice,  $\text{MO}_{1-x}$ ) as the principal ionic defects. Some examples of n-type oxides are  $\text{TiO}_2$ ,  $\text{Fe}_2\text{O}_3$ ,  $\text{NiFe}_2\text{O}_4$ ,  $\text{ZnO}$ ,  $\text{Al}_2\text{O}_3$ , and  $\text{SiO}_2$ .<sup>18</sup> For n-type oxides, the principal ionic defect concentration,  $C_i$  is found to be proportional to the negative power of the oxygen partial pressure<sup>21</sup>:

$$C \propto P_{\text{O}_2}^{-1/n} \quad [27]$$

where  $n$  is a positive integer which depends upon the charge of the ionic defect in the oxide and the oxide's stoichiometry.

The p-type oxides may have either an excess of cation vacancies (i.e., a deficiency in filled sites on the metal sublattice,  $\text{M}_{1-x}\text{O}$ ) or an excess of oxygen interstitials. Some common p-type oxides include NiO, CoO, FeO,  $\text{FeCr}_2\text{O}_4$ ,  $\text{CoCr}_2\text{O}_4$ , and  $\text{NiAl}_2\text{O}_4$ . For p-type oxides, the principal ionic defect concentration is related to the oxygen partial pressure by<sup>21</sup>:

$$C \propto P_{\text{O}_2}^{1/n} \quad [28]$$

During the oxidation process, ions transport by two ways: the cation migrates outward to scale/gas interface and the anion migrates inward to metal/scale interface (Figure 6). Thus, two reactions could potentially happen at the two interfaces to result in scale growth, although it is typically found that one reaction predominates. In other words, either metal or oxygen diffusion predominates in the thickening of a given oxide scale.

For the defective structures treated so far, it has been assumed that the oxides are pure; however, it is thermodynamically impossible to produce perfectly pure compounds or materials. It is therefore necessary to consider the effects of impurities on the defective structure of oxides. It is noted, however, that the presence of impurities can sometimes be neglected if the intrinsic defect concentration in the host oxide is relatively large. As an example of the so-called 'doping effect',<sup>21</sup> the following is found for a p-type, metal-deficient oxide  $\text{M}_{1-x}\text{O}$ :

- The addition of substitutionally dissolved foreign cations of lower valence increases the concentration of electron holes and decreases the concentration of cation vacancies.
- The addition of substitutionally dissolved foreign cations of higher valence decreases the concentration of electron holes and increases the concentration of cation vacancies.

Thus, for the p-type, metal-deficient NiO, doping with  $\text{Cr}^{3+}$ , will cause an increase in the nickel vacancy concentration, which in turn will cause an increase in the effective diffusivity of nickel in the NiO. This increase in diffusivity is manifested as an increase in the  $k_p$  for NiO-scale growth. Indeed, it is found experimentally that NiO grows faster on dilute Ni-Cr alloys than on pure Ni.<sup>22</sup>

### 1.09.2.5 Wagner's Theory of Metal Oxidation

Carl Wagner's theory of metal oxidation<sup>23,24</sup> provides a fundamental understanding of the essential features of the high temperature growth of a continuous scale. The model ideally assumes that the scale is dense, single-phase, continuous, and adheres to the metal over the entire metal surface. The basic assumption of the theory is that lattice diffusion of the reacting atoms or ions through the dense scale is rate controlling (i.e., the microstructure of the oxide scale was not considered). Figure 7 gives a set-up of the model.<sup>14</sup>

As indicated in Figure 7, the scale growth involves fluxes of both ionic and electronic charged species. The driving forces for these fluxes are related to the chemical potential gradient and electrostatic field that develop in the growing scale. The relative

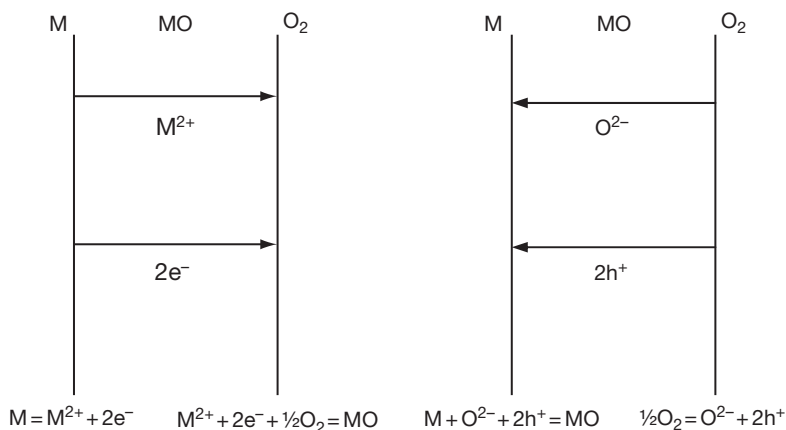


**Figure 6** Ionic and electronic transport processes and interfacial reactions in the growth of a nonstoichiometric oxide scale MO.

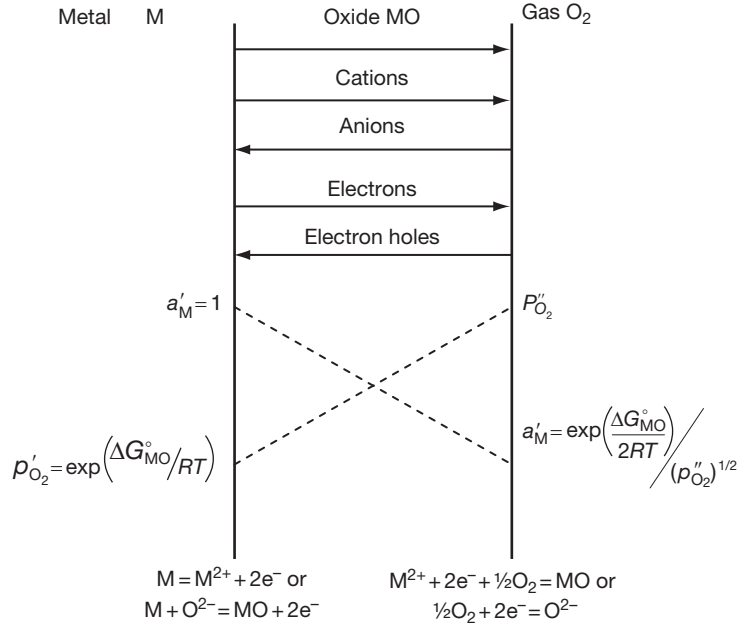


**Figure 7** Transport processes according to Wagner's theory. Adopted from Birks, N.; Meier, G. H. *Introduction to High Temperature Oxidation of Metals*; Edward Arnold: London, 1983.

migration rates of cations, anions, electrons, and electron holes must also be balanced such that no net charge build up occurs within the scale.

Wagner derived an expression for the parabolic rate constant in terms of the electronic and ionic conductivities of the oxide or, alternatively, in terms of the self-diffusion coefficients of the reacting ions in which parameters can be measured relatively easily. Limiting cases of Wagner's derivation are as follows<sup>14</sup>:

$$k' = \frac{1}{RT} \int_{\mu'_M}^{\mu'_M} D_M d\mu_M \quad [29]$$

and

$$k' = \frac{1}{RT} \int_{\mu''_X}^{\mu'_X} D_X d\mu_X \quad [30]$$

where  $k'$  is the parabolic rate constant with units of  $\text{cm}^2 \text{s}^{-1}$ ,  $D_M$  and  $D_X$  are the self-diffusion coefficients for metal, M, and nonmetal, X, through the scale, respectively, and  $\mu_M$  and  $\mu_X$  are the chemical potentials for the metal and nonmetal. Equation [29] is valid when cation diffusion predominates and eqn [30] is valid when anion diffusion predominates. The good agreement between parabolic rate constants calculated from diffusivities and the oxidation rate constants measured experimentally have provided validation for Wagner's theory.<sup>25,26</sup>

Because the diffusion flux within the oxide is proportional to the defect concentration, eqn [28] can be used for a p-type oxide to arrive at the following relation for the oxidation rate:

$$k' \propto [(P_{O_2}^o)^{1/n} - (P_{O_2}^i)^{1/n}] \quad [31a]$$

where  $P_{O_2}^o$  and  $P_{O_2}^i$  are the oxygen pressures at the scale/gas interface and metal/scale interface respectively, and  $n$  is an integer related to the cation vacancy or oxygen interstitial charge. For an n-type oxide, use of eqn [27] gives:

$$k' \propto [(P_{O_2}^i)^{-1/n} - (P_{O_2}^o)^{-1/n}] \quad [32a]$$

where in this case  $n$  is related to the oxygen vacancy or cation interstitial charge. In most cases, the ambient oxygen pressure  $P_{O_2}^o$  is much greater than  $P_{O_2}^i$ , which is the dissociation pressure ( $P_{O_2}^{\text{diss}}$ ). Thus, eqns [31a] and [32a] can be approximated to give

$$k' \propto (P_{O_2}^o)^{1/n} \text{ for a p-type scale} \quad [31b]$$

and

$$k' \propto (P_{O_2}^i)^{-1/n} \text{ for a n-type scale} \quad [32b]$$

These equations show that the growth rate of a p-type oxide is directly dependent on the oxygen partial pressure in the atmosphere. By contrast, the

growth rate of an n-type oxide is independent of the external oxygen partial pressure.

Oxides formed in practice are usually more complex than what was assumed by Wagner. First, a multilayer scale can form on a number of metals, such as Fe, Cu, and Co. For instance, and as discussed earlier, a three-layered  $\text{FeO}/\text{Fe}_3\text{O}_4/\text{Fe}_2\text{O}_3$  scale forms on iron above  $\sim 570^\circ\text{C}$  at atmospheric pressure. Treatments of the growth kinetics of multilayered scales have been presented by a number of authors.<sup>27–30</sup> In general, these treatments relate overall oxidation scaling kinetics to the intrinsic growth rates of the individual layers in the scale. Second, scales forming on metal surfaces are usually polycrystalline in structure, and in many cases, these structures are fine-grained. The activation energy for grain-boundary diffusion is lower than that for lattice diffusion by up to a factor of three. As a consequence, grain-boundary diffusion will tend to predominate at lower temperatures and can cause the scaling kinetics to be orders of magnitude higher than what would be predicted based on lattice diffusion.<sup>26</sup>

As indicated above, Wagner's theory considered the ideal case of scale formation in which the scale is assumed to be a compact and perfectly adherent barrier, that is, free of voids, pores, and fissures. The assumptions made by Wagner were indeed appropriate; however, deviations from Wagner's theory have been shown.<sup>31</sup> Many studies have shown that pores form and develop preferentially along grain boundaries in the scale.<sup>32,33</sup> The presence of voids in scales clearly represents a deviation from ideal scale growth. In some extreme cases, it may be necessary to take into account the void volume fraction in Wagner's model; but often the void formation may be considered to be a secondary process that does not significantly affect the overall scaling kinetics.

As the scale grows, stresses develop due to differences in the molar volume of metal and oxide(s). The resulting growth stresses are typically compressive.<sup>34,35</sup> More significant stresses can develop under thermal cycling conditions due to a mismatch in the coefficient of thermal expansion (CTE) between oxide scale and metal. Increasing stresses may eventually result in crack formation and even scale detachment.<sup>35</sup> Cracking of a protective oxide scale can result in the parabolic oxidation kinetics being interrupted by a sudden increase in rate when the gas can react directly with the metal surface. As oxide begins to cover the metal surface again, parabolic oxidation is resumed. The overall oxidation of the metal becomes approximately a parabolic process of periodic cracking and healing of a protective oxide.

### 1.09.3 Alloy Reactions

The fundamentals of pure-metal oxidation provide a basic understanding of alloy oxidation, but the latter is generally much more complex as a result of some, or all, of the following<sup>14</sup>:

- The various metal components in an alloy will have different affinities for oxygen, as indicated in the Ellingham diagram in [Figure 1](#).
- More oxides may be formed, including ternary and higher oxides.
- A degree of solid solubility may exist between the oxides.
- The various metal ions will have different mobilities in the oxide phases.
- The various metals will have different diffusivities in the alloy.
- The extra degree of thermodynamic freedom provided by an additional metal component in the alloy may result in subsurface oxide precipitation (i.e., internal oxidation).

When it is considered that scales can crack, contain voids, spall, and even form multiple layers of irregular thickness, the situation becomes even more complex. The following provides a brief overview of the fundamental aspects of alloy oxidation.

#### 1.09.3.1 Thermodynamics of Alloy Oxidation

As in the case of a pure metal, alloy oxidation is driven by an overall decrease in free energy. However, the alloy components are not in their pure state, which corresponds thermodynamically to their chemical activities being less than unity. For dilute solution of metallic component B in A, the average solvent A atom exists essentially in the same chemical surrounding environment as in its pure state, with only a small number of neighboring solute B atoms. Thus, in the limit of a very dilute solution, the A atoms follow Raoult's law,<sup>6</sup> such that:

$$\lim_{N_A \rightarrow 1} a_A = N_A \quad [33]$$

where  $a_A$  and  $N_A$  are the chemical activity and mole fraction of solvent A, respectively. Also, according to Henry's law, the chemical activity of solute B is given as:

$$\lim_{N_B \rightarrow 0} a_B = \gamma_B N_B \quad [34]$$

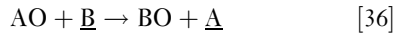
where  $\gamma_B$  is the activity coefficient of solute B for the A–B system. It can be easily shown that the dissociation  $P_{\text{O}_2}$  for an AO scale in contact with an A–B alloy is

greater than what would be calculated for AO in contact with pure A. Specifically,

$$\frac{P_{O_2}}{P_{O_2}^*} = \left( \frac{1}{a_A} \right)^2 \quad [35]$$

where  $a_A$  is the activity of A in the A–B alloy, and  $P_{O_2}$  and  $P_{O_2}^*$  are the dissociation pressures for the A–B alloy and pure A, respectively.

It is typically the activity of the solute that is most important when assessing the thermodynamics of alloy oxidation; although, the results are often of limited utility. This can be shown as follows. Consider the oxidation of an A–B alloy in which the solute B forms a more stable and protective oxide. Assuming that the only stable oxides are AO and BO and that these oxides are insoluble in one another, the important reaction to consider is



where  $\underline{B}$  and  $\underline{A}$  correspond to B and A in the alloy solution. The law of mass action for this reaction gives

$$K_{36} = \frac{a_A}{a_B} \approx \frac{N_A}{\gamma_B N_B} \quad [37]$$

Thus, reaction [36] will only proceed to the right if  $\frac{a_A}{a_B} < K_{36}$ , which means that there is a critical  $a_B$ , or conversely  $N_B$ , for this to occur. In most practical cases of interest, the solute–metal oxide BO is significantly more stable than the base-metal oxide AO, causing  $K_{36}$  to be much larger than unity. This, in turn, results in a very small minimum  $N_B$  value for BO to be thermodynamically stable in contact with the A–B alloy. In the case of an Ni–Cr alloy,  $N_{Cr}$  must be greater than  $\sim 10^{-9}$  at 1000 °C for the displacement reaction  $3NiO + 2\underline{Cr} \rightarrow Cr_2O_3 + 3\underline{Ni}$  to be thermodynamically stable.<sup>36</sup> Such a low Cr content is orders of magnitude below what is necessary kinetically to sustain Ni–Cr/ $Cr_2O_3$  stability, let alone to kinetically establish a continuous  $Cr_2O_3$  scale. For the latter, the critical Cr mole fraction,  $N_{Cr}^{crit}$ , in Ni–Cr alloy exposed to air at 1000 °C is experimentally found to be  $\sim 0.2$ .<sup>37</sup>

### 1.09.3.2 Criterion for the Sustained Exclusive Growth of a Protective Scale

If a continuous  $BO_v$  scale on an A–B alloy is established under a particular set of conditions, it may be necessary to determine if its growth can be sustained under a different set of conditions. (The stoichiometric factor  $v$  for the oxide  $BO_v$  will be used for the

remainder of this chapter in order to provide more general kinetic-based expressions.) An example of this could be the preoxidation of an alloy at a low  $P_{O_2}$  followed by in-service exposure to a higher  $P_{O_2}$  and/or different temperature. The sustained growth of a continuous  $BO_v$  scale requires a sufficient supply of B from within the alloy to the alloy/scale interface. The resulting subsurface concentration gradient of solute B is represented schematically in Figure 8, in which  $N_B^i$  is the mole fraction of B in the alloy at the alloy/scale interface. The maximum possible rate of B supply in the alloy can be imposed by setting  $N_B^i$  equal to zero, thereby producing the steepest possible diffusion gradient of B. Under steady-state conditions, this maximum rate of B supply would have to equal the rate of B consumption due to  $BO_v$  scale growth. Determination of the minimum B content in the alloy,  $N_{B(min)}^o$ , necessary for the sustained exclusive growth of a  $BO_v$  scale on an A–B alloy was originally considered by Wagner,<sup>38</sup> who further assumed that: (1) the diffusion coefficient of B in the alloy,  $D_B$ , is independent of concentration; (2) the  $BO_v$  scale obeys parabolic thickening kinetics with a rate constant  $k_p$ ; (3) solvent metal A is insoluble in  $BO_v$ ; and (4) the recession of the alloy/scale interface may be neglected. Wagner derived the criterion

$$N_{B(min)}^o > \frac{V_m}{vM_O} \left( \frac{\pi k_p}{2D_B} \right)^{\frac{1}{2}} \quad [38]$$

where  $V_m$  is the equivalent molar volume of the alloy and  $M_O$  is the atomic weight of the oxidant, which is oxygen in this discussion ( $M = 16 \text{ g mol}^{-1}$ ). Many researchers have used the criterion in eqn [38] to predict the minimum content of B necessary for a bare alloy to form an exclusive  $BO_v$  scale layer. However, this is not a correct use of the criterion, since its derivation was based on supply rather than establishment. The

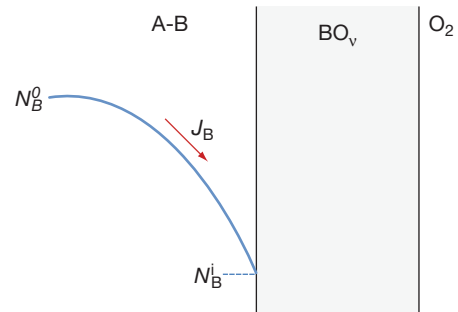


**Figure 8** Schematic representation of the concentration profile of B in a binary alloy A–B which is forming an exclusive scale layer of  $BO_v$ .

criterion given in [38] gives only the minimum possible B content in the alloy necessary to supply B at a sufficient rate to the alloy/scale interface for the sustained growth of an established  $\text{BO}_v$  scale layer. The actual B content necessary for both the establishment and sustained growth of a  $\text{BO}_v$  scale will very likely be higher than  $N_{\text{B(min)}}^0$  owing to transient and kinetic effects.

### 1.09.3.3 Internal Oxidation

Internal oxidation is used here in a generic sense to represent a process in which a diffusing oxidant from the surface reacts with a less-noble solute component in the alloy to form discrete particles.<sup>39</sup> Internal oxidation is not desired because it changes the optimized mechanical properties of an alloy and may result in internal stress and weakening of the grain boundary.

For a dilute binary alloy A–B, the dissolved oxygen atoms can react with less-noble B atoms in the alloy in the manner,



The necessary condition for  $\text{BO}_v$  formation in the alloy may be formulated in terms of the equilibrium solubility product  $K_{\text{sp}}$ , such that:

$$[a_{\text{B}}][a_{\text{O}}]^v > K_{\text{sp}} \quad [40]$$

The degree to which the solubility product must be exceeded (i.e., the degree of supersaturation) before precipitation occurs depends on a number of factors, such as the stability, composition, and crystal structure of the precipitating  $\text{BO}_v$  phase. For instance, if the crystal structure and lattice dimensions of  $\text{BO}_v$  are such that it can form a coherent interface with the alloy matrix, then only a small degree of supersaturation is likely to be necessary for  $\text{BO}_v$  precipitation. In general, the greater the stability of  $\text{BO}_v$ , the lower will be its  $K_{\text{sp}}$  value. It is for this reason that the internal precipitates commonly observed in oxidized high temperature alloys are of the stable oxides  $\text{Al}_2\text{O}_3$ ,  $\text{SiO}_2$ ,  $\text{TiO}_2$ , and  $\text{Cr}_2\text{O}_3$ .<sup>40,41</sup> Multiple internal oxidation zones can also develop if more than one reaction product is stable.<sup>42,43</sup> The sequence of the thermodynamically possible phases progresses from metal-rich in the innermost zone of the alloy to oxidant-rich at the surface.

The internal oxidation zone extends to the depth at which the activity of dissolved oxygen becomes too small for the formation of the oxide  $\text{BO}_v$ . The kinetics of internal oxidation are generally found to be

diffusion-controlled and the depth of the internal oxidation zone,  $\xi$ , in an alloy undergoing no external scale formation can be described by the following kinetic expression, assuming no enrichment of B in the internal oxidation zone<sup>44,45</sup>:

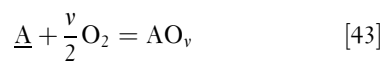
$$\xi = \left( \frac{2N_{\text{O}}^s D_{\text{O}} t}{vN_{\text{B}}^0} \right)^{1/2} \quad [41]$$

where  $N_{\text{O}}^s$  is the solubility of the oxidant in the alloy,  $D_{\text{O}}$  is the diffusivity of the oxidant in the alloy,  $N_{\text{B}}^0$  is the initial solute concentration in the A–B alloy, and  $t$  is the time. The product  $N_{\text{O}}^s D_{\text{O}}$  is the oxygen permeability in alloy. The solubility of oxygen in the alloy depends upon the oxygen partial pressure at the alloy surface in accordance with Sievert's law,<sup>6</sup> that is,

$$N_{\text{O}}^s \propto P_{\text{O}_2}^{1/2} \quad [42]$$

Thus, the depth of internal oxidation would be expected to decrease with decreasing  $P_{\text{O}_2}$  in the manner  $\xi \propto P_{\text{O}_2}^{1/4}$ .

The above discussion considers only internal precipitation in the absence of external scale formation. In the case of  $\text{AO}_v$  scale formation, the value of  $N_{\text{O}}^s$  is no longer fixed by the environment but is instead fixed by the equilibrium between at the alloy/scale interface (assuming no through-scale access by the oxidant) according to the reaction,



The effective thickness of the internal precipitation zone in the situation of concurrent  $\text{AO}_v$ -scale formation decreases in a most pronounced manner from that predicted in the absence of an external scale at large  $k_{\text{p}}$  and  $N_{\text{B}}^0$  values.<sup>46</sup> A large  $k_{\text{p}}$  value for  $\text{AO}_v$ -scale growth corresponds to a large amount of metal recession, which means the total attack is still high, even though the internal precipitation zone is relatively low.

The preceding theoretical considerations are based on models assuming predominant lattice diffusion of both oxygen and the alloying element. As such, the theoretical treatments are only expected to apply to relatively high temperatures or to very large-grained materials, with the extreme being single crystals. As the temperature is reduced, grain-boundary effects will become increasingly important. This is due to relatively rapid diffusion along grain boundaries, enhanced concentration or segregation of the oxidant and the alloying element at grain boundaries, and a preferred tendency for nucleation at grain boundaries.<sup>4</sup>



### 1.09.3.4 Transition from Internal Oxidation to External Scale Formation

The transition from internal to external oxide formation typically occurs with a relatively small increase in the alloy content of the less-noble component B in the A–B alloy, at which oxidation leads to the formation of a surface scale of  $\text{BO}_b$ , and the alloy no longer undergoes internal oxidation. Considering again the alloy system A–B, there are two limiting possible situations: one is when only one of the components can oxidize and the other is when both of the components can oxidize. For the first case, if the oxygen partial pressure is low (i.e., below the stability of  $\text{AO}_b$  formation), the component B in the alloy surface nucleates as  $\text{BO}_b$  in an A-rich matrix. If B can diffuse fast enough to reach the surface and maintain a sufficient supply for  $\text{BO}_b$  formation, a complete surface layer of  $\text{BO}_b$  will be established. However, if this condition is not met, then  $\text{BO}_b$  will precipitate as internal particles within the alloy. So, the internal or external formation of  $\text{BO}_b$  depends on the balance between the outward flux of B and the inward flux of atomic oxygen into the alloy.

Wagner<sup>47</sup> proposed that the condition for the transition from internal to external  $\text{BO}_b$  formation occurs when a critical volume fraction of  $\text{BO}_b$ ,  $f^*$ , is attained. Under this condition, the influx of oxygen is so restricted that sideways growth of the internal  $\text{BO}_b$  precipitates is kinetically favored to the extent that  $\text{BO}_b$  eventually forms as a continuous layer on the alloy surface. Under conditions of no or a negligibly small rate of metal recession, the following criterion for the transition from internal to external  $\text{BO}_b$  formation was obtained:

$$N_{\text{B}^*}^{\text{o}} \geq \left[ f^* \left( \frac{V_{\text{m}}}{V_{\text{ox}}} \right) \pi \frac{N_{\text{O}}^{\text{s}} D_{\text{O}}}{2vD_{\text{B}}} \right]^{1/2} \quad [44]$$

where  $N_{\text{B}^*}^{\text{o}}$  is the critical mole fraction of B in the alloy,  $V_{\text{m}}$  is molar volume of the alloy,  $V_{\text{ox}}$  is molar volume of the oxide, and  $D_{\text{B}}$  is the diffusion coefficient of solute B in the alloy. Rapp<sup>44</sup> reported excellent agreement between experimental and reasonably predicted values of  $N_{\text{B}^*}^{\text{o}}$  as a function of oxygen partial pressure in Ag–In alloys oxidized at 550°C. The value of  $f^*$  is usually taken to be 0.3 in accordance with the results from this study by Rapp.

From the criterion given by eqn [44], it is seen that  $N_{\text{B}^*}^{\text{o}}$  can be decreased by decreasing the product of  $N_{\text{O}}^{\text{s}}$  and  $D_{\text{O}}$  (i.e., decreasing the permeability of oxygen) and/or increasing  $D_{\text{B}}$ . Indeed, the direct and indirect control of these variables in numerous

experimental studies conducted over the past 40 years have validated this criterion.<sup>1</sup>

### 1.09.4 Epilogue

Advances in the high temperature stability of materials are critically needed to realize the full performance and potential of many current and future commercial systems. These advances must lead to significantly enhanced capabilities that will allow high temperature components to operate robustly for prolonged periods in harsh environments, such as those involving aggressive gases, deposits, photon or radiation fluxes, stresses, high or low pressures, or some combination of these conditions. For example, coal gasification, biomass conversion, and gas-cooled nuclear reactor systems typically produce complex, multioxidant gaseous environments that can be highly aggressive from the standpoint of surface degrading structural components. The resulting multioxidant process environments are often non-equilibrium and can involve both gaseous and deposit-induced attack. Fundamentally, the high temperature stability of a material in an aggressive environment relates to reactions and transport at and across its external surfaces. Similar to what was discussed in this chapter, these reactions are defined in terms of some combination of chemical potential, temperature and pressure and can be highly complex. Different processes, many of them coupled, are involved from the onset of reaction, that is, the absorption and dissociation of gaseous molecules at the surface, to the steady-state growth of a protective surface scale that develops. Indeed, the ability to control the growth and stability of this scale and to predict its behavior under different types of extreme chemical environments for extended periods of time will require a much greater basic understanding of the underlying reactions and transport processes involved. The basic starting points have been presented in this chapter, but still much more research and development are needed to improve the reliability and durability of materials exposed to aggressive conditions.

## References

1. Gleeson, B. In *Corrosion and Environmental Degradation, Vol. II: Volume 19 of the Materials Science and Technology Series*; Schütze, M., Ed.; Wiley-VCH: Weinheim, Germany, 2000.

2. Lai, G. Y. *High-Temperature Corrosion of Engineering Alloys*; ASM International: Materials Park, OH, 1990.
3. Kofstad, P. *High Temperature Oxidation of Metals*; John Wiley and Sons: New York, 1966.
4. Young, D. *High Temperature Oxidation and Corrosion of Metals*; Elsevier: Amsterdam, 2008.
5. Alcock, J. C. B.; Easterbrook, E. Thermodynamics and Kinetics of Gas-Metal Systems. In *Corrosion, Volume 1: Metal/Environment Reactions*, 3rd ed.; Shreir, L. L., Jarman, R. A., Burstein, G. T., Eds.; Butterworth-Heinemann: London, 1994.
6. Gaskell, D. R. *Introduction to the Thermodynamics of Materials*, 4th ed.; Taylor & Francis: New York, 2008.
7. Kubaschewski, O.; Alcock, C. B. *Metallurgical Thermochemistry*, 5th ed.; Pergamon Press: Oxford, 1979.
8. Barin, I.; Platzki, G. *Thermochemical Data of Pure Substances*; VCH: Weinheim, 1995.
9. JANAF Thermochemical Data, Army-Navy-Air Force Thermochemical Panel, Dow Chemical Company, Midland, MI, 1962–1963.
10. Lou, V. L. K.; Mitchell, T. E.; Heuer, A. H. *J. Am. Ceram. Soc.* **1984**, 68, 49.
11. Giggins, C. S.; Pettit, F. S. *Oxid. Met.* **1980**, 14, 363.
12. Stroosnijder, M. F.; Quadakkers, W. J. *High Temp. Technol.* **1986**, 4, 141.
13. LaBranche, M. H.; Yurek, G. J. *Oxid. Met.* **1987**, 28, 73.
14. Birks, N.; Meier, G. H. *Introduction to High Temperature Oxidation of Metals*; Edward Arnold: London, 1983.
15. Peraldi, R.; Monceau, D.; Pieraggi, B. *Oxid. Met.* **2002**, 58, 275.
16. Naumenko, D.; Gleeson, B.; Wessel, E.; Singheiser, L.; Quadakkers, W. J. *Metall. Mater. Trans. A* **2007**, 38A, 2974.
17. Lee, V. H. J.; Gleeson, B.; Young, D. J. *Oxid. Met.* **2005**, 63, 15.
18. Bradford, S. A. Fundamentals of Corrosion in Gases. In *Metals Handbook*, 9th ed.; *Corrosion*; ASM International: Metals Park, OH, 1987; Vol. 13.
19. Pettit, F. S.; Wagner, J. B. *Acta Met.* **1964**, 12, 35.
20. Sheasby, J. S.; Smeltzer, W. W. *Oxid. Met.* **1981**, 15, 215.
21. Kofstad, P. *Nonstoichiometry, Diffusion and Electrical Conductivity in Binary Metal Oxides*; Wiley-Interscience: New York, 1972.
22. Giggins, C. S.; Pettit, F. S. *Trans. AIME* **1969**, 245, 2495.
23. Wagner, C. Z. *Phys. Chem.* **1933**, 21, 25.
24. Wagner, C. *Atom Movements*; ASM: Cleveland, 1951; p 153.
25. Raynaud, G. M.; Clark, W. A. T.; Rapp, R. A. *Metall. Trans. A* **1984**, 15A, 573.
26. Atkinson, A. *Rev. Mod. Phys.* **1985**, 57, 437.
27. Garnaud, G.; Rapp, R. A. *Oxid. Met.* **1977**, 11, 193.
28. Hsu, H. S. *Oxid. Met.* **1986**, 26, 315.
29. Gesmundo, F.; Viani, F. *Corros. Sci.* **1978**, 18, 217.
30. Wang, G.; Gleeson, B.; Douglass, D. L. *Oxid. Met.* **1989**, 31, 415.
31. Yurek, G. J. *Corrosion Mechanisms*; Marcel Dekker Inc.: New York, 1987; p 397.
32. Dravinieks, A.; McDonald, H. J. *Electrochem. Soc.* **1948**, 94, 139.
33. Mrowec, S. In *Proceedings of JIM International Symposium on High Temperature Corrosion of Metals and Alloys*; Mt Fuji, Japan, 17–20 November 1982; p 115.
34. Stringer, J. *Corros. Sci.* **1970**, 10, 1970, 513.
35. Schütze, M. *Protective Oxide Scales and Their Breakdown*; Institute of Corrosion and Wiley Series on Corrosion and Protection; John Wiley & Sons Ltd: England, 1991.
36. Birks, N.; Rickert, H. J. *Inst. Met.* **1963**, 91, 1963, 308.
37. Wood, G. C.; Wright, I. G.; Hodgkiess, T.; Whittle, D. P. *Werkst. Korros.* **1970**, 20, 900.
38. Wagner, C. J. *Electrochem. Soc.* **1952**, 99, 369.
39. Douglass, D. L. *Oxid. Met.* **1995**, 44, 81.
40. Gleeson, B.; Harper, M. A. *Oxid. Met.* **1998**, 49, 373.
41. Wei, F. I.; Stott, F. H. *High Temp. Technol.* **1989**, 7, 59.
42. Schnaas, A.; Grabke, H. J. *Oxid. Met.* **1978**, 12, 387.
43. Kane, R. H. *Corrosion* **1981**, 37, 187.
44. Rapp, R. A. *Corrosion* **1965**, 21, 382.
45. Wagner, C. Z. *Elektrochem.* **1959**, 63, 772.
46. Gesmundo, F.; Viani, F. *Oxid. Met.* **1986**, 25, 269.
47. Wagner, C. Z. *Elektrochem.* **1959**, 63, 772.

## 1.08 Stress Effects in High Temperature Oxidation

**M. Schütze**

Karl Winnacker Institut der DECHEMA e.V., Theodor-Heuss-Allee 25, D-60486 Frankfurt am Main, Germany

© 2010 Elsevier B.V. All rights reserved.

1.08.1	Introduction	154
1.08.2	Scale Stresses Arising from Oxide Growth	155
1.08.2.1	Intrinsic Growth Stresses in Oxide Scales	155
1.08.2.1.1	Experimental observations	155
1.08.2.1.2	Modeling	160
1.08.2.2	Geometrically Induced Growth Stresses	161
1.08.2.3	Other Types of Growth Stresses	161
1.08.3	Thermally Induced Scale Stresses Resulting from Temperature Changes	162
1.08.3.1	Experimental Observations	162
1.08.3.2	Modeling	164
1.08.4	The Effect of Stresses on the Integrity of the Oxide Scale	164
1.08.4.1	Measured Critical Strain Values to Scale Failure	164
1.08.4.2	Model Considerations	167
1.08.5	Maintaining the Protective Effect of Oxide Scales Even After Mechanical Failure under Stresses	171
1.08.5.1	Healing of Cracks or other types of Damage in the Protective Oxide Scale	171
1.08.5.2	The Influence of Subsurface Zone Depletion on Maintaining the Protective Effect of Oxide Scales Under Stresses	173
1.08.6	Concluding Remarks	176
References		177

### Glossary

**Acoustic emission** Acoustic signals ('noise')

arising from the generation of transient elastic waves produced by sudden redistribution of stress in a material (e.g., cracking, micro-cracking, and dislocation movement).

**Buckling** Failure by elastic instability under the effect of compressive stresses where the structural member (e.g., scale) bends sideways in the center of an unattached area.

**Coefficient of thermal expansion (CTE)** Degree of expansion/contraction divided by the change in temperature.

**Creep** Time-dependent plastic deformation at high temperatures ('flow').

**Depletion** Drop in element concentration in an alloy during high temperature exposure. For example, by the consumption of this element for surface oxide formation.

**Elastic modulus/Young's modulus** (1) Slope of the stress-strain curve in elastic

deformation, (2) resistance of a material against elastic deformation.

**Healing** Closure of cracks or other defective sites in a layer or oxide scale by diffusion or scale growth processes.

**Microcracking** Formation of cracks or crack networks where the single cracks are in the range of microns, or less.

**Growth stresses** Mechanical stresses originating from scale or layer growth directly due to volume changes.

**Protrusions** Local extension of the surface scale into the metal substrate.

**Poisson ratio** Ratio of transverse strain (contraction strain) divided by the extension strain (axial strain).

**Physical defect** Defects in a physical structure (material), for example, pores, voids, crevices, cracks, etc.

**Residual stress** Stresses remaining in a structure even after removing external load.

**Subsurface zone** Area in a material directly underneath the surface.

**Thermogravimetry** Test procedure in which the mass change of a specimen due to high temperature corrosion is recorded by a balance.

**Thermocycling** Test procedure in which a specimen is subjected to regularly repeated temperature cycles.

## Abbreviations

**COSIM** Computer code for predicting oxide spallation

**CTE** Coefficient of thermal expansion

**DTMO** Differential test in monofacial oxidation

**NASA** National Aeronautics and Space Administration

**ODIN** Computer code for predicting alloy depletion

**PBR** Pilling-Bedworth-ratio

**RT** Room temperature (ambient temperature)

**XRD** X-ray diffraction

## Symbols

$c$  Physical defect size

$d_{\text{met}}$  Thickness of the metal substrate

$d_{\text{ox}}$  Oxide scale thickness

$r$  Interfacial amplitude

$t$  Time

$t_{\text{B}}$  Time to the beginning of breakaway oxidation

$A_{\text{o}}$  Length of a defect free interface

$A_{\text{sep}}$  Separated length of an interface

$C_{\text{c}}$  Minimum alloy concentration to form a protective oxide scale (critical concentration limit)

$D$  (inter-)Diffusion coefficient

$E^*$  Effective elastic (Young's) modulus

$E_{\text{met}}$  Elastic (Young's) modulus of the metal

$E_{\text{ox}}$  Elastic (Young's) modulus of the oxide

$G_{\text{c}}$  Critical surface energy

$K$  Stress intensity factor

$K_{\text{c}}$  Fracture toughness

$k_{\text{i}}$  Oxidation rate constant for the recession of the oxide/metal interface

$K_{\text{Ic}}$  Fracture toughness under mode I load

$N_{\text{A},\text{b}}$  Atom fraction of element B in an alloy

**PBR** Value of the Pilling-Bedworth-Ratio

$R$  Radius of a scale delamination

$T$  Temperature

$\nu_{\text{met}}$  Poisson ratio of the metal

$\nu_{\text{ox}}$  Poisson ratio of the oxide

$\alpha_{\text{m}}$  Mean coefficient of thermal expansion (CTE) of a multi-scale system

$\alpha_{\text{met}}$  Coefficient of thermal expansion (CTE) of the metal

$\alpha_{\text{ox}}$  Coefficient of thermal expansion (CTE) of the oxide

$\epsilon_{\text{c}}$  Critical strain to failure

$\delta_{\text{el}}$  Elastic strain

$\epsilon_{\text{ext}}$  External strains resulting from component operation

$\epsilon_{\text{geo}}$  Geometrically induced oxide growth strains

$\epsilon_{\text{int}}$  Intrinsic oxide growth strains

$\epsilon_{\text{ox}}$  Strain in the oxide

$\epsilon_{\text{pl}}$  Plastic strain

$\epsilon_{\text{therm}}$  Thermally induced oxide strains from temperature changes

$\dot{\epsilon}$  Strain rate

$\dot{\epsilon}_{\text{c}}$  Critical strain rate for scale crack healing

$\lambda$  'Wave length' of an interface

$\sigma$  Elastic stress

$\sigma_{\text{c}}$  Critical stress for failure

$\sigma_{\text{ext}}$  External stresses resulting from component operation

$\sigma_{\text{geo}}$  Geometrically induced oxide growth stresses

$\sigma_{\text{int}}$  Intrinsic oxide growth stresses

$\sigma_{\text{ox}}$  Stress in the oxide

$\sigma_{\text{therm}}$  Thermally induced oxide stresses from temperature changes

$\omega$  Stress relaxation factor

$\Delta T$  Temperature change

$\gamma_{\text{i}}$  Intrinsic surface energy

$\gamma_{\text{o}}$  Fracture surface energy

## 1.08.1 Introduction

The role of stresses in oxidation is of significance because these stresses can determine the lifetime of a high temperature component from a corrosion point of view.<sup>1</sup> High temperature corrosion resistance is based on the protective effect of dense, slowly growing, and adherent oxide scales, that is, if any chemical or mechanical damage occurs to these scales, the corrosion resistance of the materials will be endangered. This chapter deals with the key aspects describing scale integrity under the effect of stresses, also taking into account the role of the superimposed oxidation processes. The latter is important as, at elevated temperature, stresses and oxidation should not be looked at separately as they are active simultaneously and interact with each other.

Therefore, not only the topics of mechanical scale failure (cracking, spalling, delamination, etc.), but also the mechanisms of scale damage healing and metal subsurface zone depletion are addressed.

An example where the whole complexity of this interaction becomes evident is the so-called 'break-away mechanism' by which the protective period in oxidation ends and the nonprotective period starts.<sup>2</sup> From a technical point of view this is the end of the lifetime of a component, at least under the aspect of high temperature corrosion. Although the breakaway effect can also be described solely based on chemical mechanisms (loss of chemical stability of the protective oxide),<sup>3</sup> under industrial conditions mechanical stresses are always present and the breakaway effect is considerably determined from a joint interaction of chemical and mechanical mechanisms.<sup>3,4</sup> In the simplest case the latter may be initiated from (intermediate) cooling, but also at constant operation temperature oxide growth stresses can reach critical limits where the integrity of the scales is endangered.<sup>5</sup>

Generally, the following stresses in oxidation can be distinguished<sup>1</sup>:

1. Intrinsic growth stresses  $\sigma_{\text{int}}$  resulting from the chemical nature of the oxidation process. These can arise when new oxide is formed inside the existing oxide, for example, by counter diffusion of oxide forming species. Other sources of such stresses can be epitaxial relationships between metal surface and oxide in particular at the beginning of oxidation or phase transformations in the oxide scale, the metal, or coating subsurface zone.
2. Geometrically induced growth stresses  $\sigma_{\text{geo}}$  resulting from particular narrow surface curvatures where effects of the differences in volume of oxide formed and metal consumed come into play.
3. Thermally induced stresses  $\sigma_{\text{therm}}$  resulting from temperature changes and the different values of the coefficients of thermal expansion (CTE) for metal/alloys and oxides.
4. External stresses  $\sigma_{\text{ext}}$  resulting from operation, for example, centrifugal stresses, gravity, constraints in structures, etc.

All these stresses have to be accommodated by elastic or plastic/creep deformation in the oxide/metal system. Otherwise, if critical stress values are exceeded, mechanical failure of the scale results as a stress relief mechanism. In this case, however, the protective effect of the scale may be lost unless it can be restored by scale healing mechanisms.

Equation [1] summarizes this situation in terms of the strain values resulting from the different types of stresses:

$$\varepsilon_{\text{int}} + \varepsilon_{\text{geo}} + \varepsilon_{\text{therm}} + \varepsilon_{\text{ext}} = \varepsilon_{\text{el}} + \varepsilon_{\text{pl}} \quad [1]$$

Failure occurs when the elastically stored energy in the form of ('elastic') stress  $\sigma$  reaches or exceeds a critical value  $\sigma_c$ :

$$\sigma = E_{\text{ox}} \varepsilon_{\text{el}} \geq \sigma_c \quad [2]$$

where  $E_{\text{ox}}$  is the elastic modulus of the oxide scale.

Failure occurs in terms of strains when

$$\varepsilon_{\text{int}} + \varepsilon_{\text{geo}} + \varepsilon_{\text{therm}} + \varepsilon_{\text{ext}} = \varepsilon_{\text{el}} + \varepsilon_{\text{pl}} = \varepsilon_c \quad [3]$$

where  $\varepsilon_c$  is the critical strain for the different failure mechanisms (see Section 1.08.4). As will be shown later, oxide scales usually behave in a brittle manner, even at service temperatures of high temperature components, so that at mechanical scale failure  $\varepsilon_{\text{pl}} \ll \varepsilon_{\text{el}}$  or  $\varepsilon_c \approx \varepsilon_{\text{el}}$ .

In addition to the failure mechanism,  $\varepsilon_c$  is also a function of the oxide/metal system and the oxidation parameters. High values of  $\varepsilon_c$  automatically mean high tolerance of the system against failure by mechanical stresses.

The following sections deal in some detail with the key issues of the role of stresses in oxidation. For an even more detailed description of this topic, the reader is referred to a textbook which is devoted solely to this field.<sup>1</sup>

## 1.08.2 Scale Stresses Arising from Oxide Growth

### 1.08.2.1 Intrinsic Growth Stresses in Oxide Scales

#### 1.08.2.1.1 Experimental observations

Most standard investigations of the oxidation behavior of materials do not take into account that the formation of growth stresses in the scales may take place during the oxidation process.<sup>6</sup> The existence of such stresses has, however, already become evident in an optical observation of the oxide scale surfaces as shown as an example in Figure 1.<sup>7</sup> In this example the scale shows a perpendicular arrangement of waves that have partially detached from the substrate. The formation of such waves is an indication that additional volume had been created in the existing oxide which had to be accommodated by a stress relaxation mechanism like detachment. This situation has been observed by a number of authors.<sup>8-15</sup>

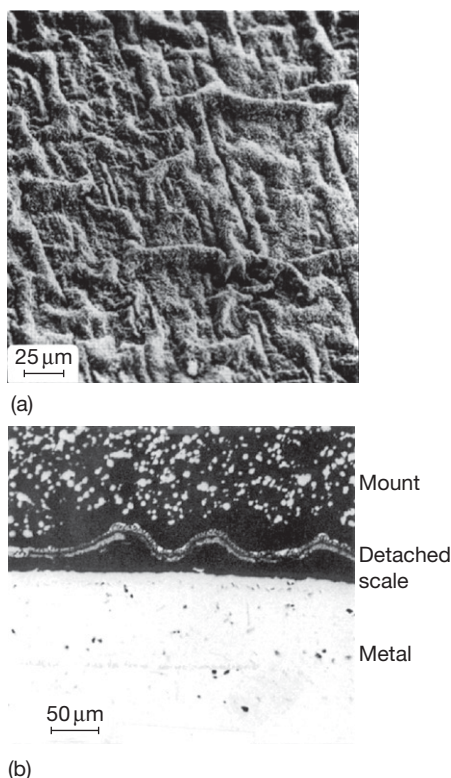


**Figure 1** 'Wave' formation in the oxide scale due to lateral growth stresses on a heat resistant 18 Cr steel after 100 h oxidation at 1000 °C in air.<sup>7</sup> (a) SEM image of the surface and (b) optical micrograph of a cross-section.

As the example in **Figure 1** shows, the formation of waves was possible without damage to the existing oxide so that its protective effect remained.

Thermogravimetric investigations of the oxidation of pure chromium revealed that such (isothermal) growth stresses could even be sufficiently high to crack the existing oxide and initiate the formation of new oxide on the fresh metal surface exposed underneath the waves.<sup>8,9</sup> This becomes evident in the mass change versus time curve shown in **Figure 2**. After each cracking process, the start of a new parabolic partial curve is observed and in the extreme case of very high growth stresses at the highest test temperature, in these investigations the cracking frequency has become so high that a quasilinear mass change curve is found.

Besides the phenomenological observations, a number of measurements have been performed in order to quantify the level of these growth stresses. The measurement techniques reported in the literature are the following:

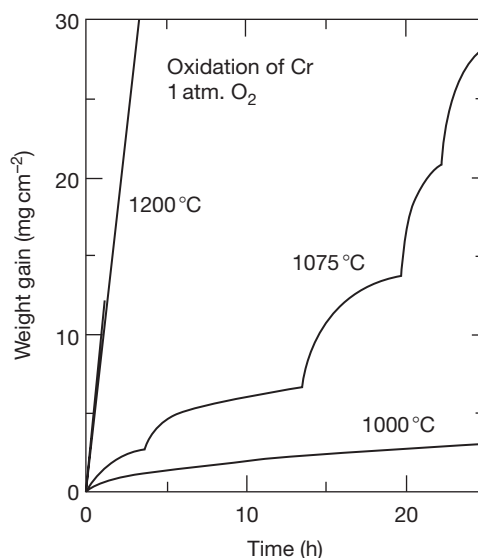


**Figure 2** Repeated cracking of scales leading to a sequence of 'parabolic' stages in the overall oxidation of pure Cr at 1000–1200 °C in O<sub>2</sub>.<sup>8,9</sup>

1. Measurement of the bending of a thin metal strip which is protected on one side and oxidized on the other side.<sup>16–22</sup> This test is sometimes called differential test in monofacial oxidation (DTMO).<sup>21,22</sup>
2. Measurement of the bulging of a thin metal plate protected on one side and oxidized on the other side.<sup>23</sup>
3. Measurement of the change in diameter of a helix or a spiral made of a thin metal strip oxidized either on one side<sup>24,25</sup> or on both sides.<sup>26</sup> On the spiral, the length change can also be measured.
4. Measurement of the increase in length of thin metal strips or tubes resulting from creep and elastic deformation of the substrate due to the stresses from the oxide growth.<sup>27–30</sup>
5. Measurement of the curvature or a radius change of a U-shaped thin foil specimen.<sup>31</sup> A somewhat similar method is the catenary method which makes use of a wire sample suspended as a catenary between two supports and where a change in the shape of the catenary curve is recorded during oxidation.<sup>32</sup>
6. Measurement of the bending of an oxidized strip as one of the sides is polished away stepwise and the thickness is progressively reduced.<sup>33</sup>
7. Measurement of the frequency shift due to scale stresses in Raman spectroscopy/photo luminescence.<sup>34–39</sup>



8. Using changes in the photocurrent due to stresses by applying a microphotoelectrochemistry technique.<sup>39</sup>
9. Measurement of the distortion of the oxide lattice using X-rays.<sup>40–45</sup>
10. Measurement by using synchrotron radiation instead of standard X-ray sources which allows one to study thinner oxides and with greater time resolution.<sup>45,46</sup>

In particular, the foil bending measurements can be combined with acoustic emission recording, which allows the detection of any cracking or delamination processes resulting from the build-up of scale stresses.<sup>5,21,22</sup> All these measurements have been described in great detail in the respective publications where the drawbacks and the advantages of the different methods are also discussed. In the following section, only the results from measurements are addressed.

One of the systems that has been investigated in some detail is NiO on nickel or Ni–Cr.<sup>20,21,47–49</sup> The reason for this is that a single phase oxide of significant thickness is formed, which allows nickel oxide scales to be looked at as a model system. A typical example of the course of the stress curves as a function of oxidation time is given in [Figure 3\(a\)](#). In many cases, such curves start with a very short tensile period before they change into a steeply increasing compressive slope, which reaches a maximum and then falls off slightly. Often after longer times, the level of stress starts to oscillate around a certain value as is also indicated in this example for the two polycrystalline nickel versions. Interestingly the oxide formed on the nickel single crystal shows a further increase of the growth stresses which falls together with the effect that no acoustic emission occurs for the single crystal specimen while on the two polycrystalline specimens significant acoustic emission takes place, starting after ~10 h of exposure, [Figure 3\(b\)](#). Acoustic emission is an indication that, evidently, micro cracking and oxide delamination has taken place because of the formation of growth stresses allowing direct access of oxygen through the scale to the oxide/metal interface and the formation of new fine-grained oxide at these positions. As a consequence, the typical two layered structure on nickel is formed as an oxide scale while on the single crystal nickel only a single oxide layer appears. In Przybilla and Schütze,<sup>21</sup> this could be explained in a model by the presence of impurities in the polycrystalline nickel materials which facilitates interfacial delamination while the nickel single crystal was ultra pure

and the oxide scale was adherent. This effect was later also confirmed by Huntz *et al.*<sup>48</sup> The maximum growth stress values which were observed in these tests were around –550 MPa at 900 °C.

Much higher stresses are reported, for example, for chromia layers growing at 750 °C in pure oxygen.<sup>38</sup> In this case, values of up to –2.4 GPa were reached as measured by Raman spectroscopy. Similar values were measured under the same conditions for steels of the composition Fe–18Cr and Fe–18Cr–TiNb. For the oxide scales on pure iron or mild steel, respectively, different values were observed for magnetite and hematite in the same oxide scale.<sup>45</sup> In magnetite, these stresses reached values of tensile nature up to 135 MPa at 400 °C while those in the same scale for hematite were compressive and went up to –270 MPa. Interestingly when oxidizing gray cast iron the stresses in both partial layers were of compressive nature at 400 °C. For magnetite, they reached –60 MPa, while for hematite the maximum was around –570 MPa. In all cases, there was first an increase up to a maximum in the value of the stresses while during further oxidation, a decrease or an oscillation around a certain level occurred. This was similar to the observations described for NiO on polycrystalline Ni in [Figure 3](#).

The largest number of investigations on oxide growth stresses focused on the behavior of alumina scales on iron or nickel based substrates. In most cases, surprisingly high compressive stress values were found, which make it hard to believe that the oxide scale could survive such stresses without any mechanical damage. As an example, a tensile stress value of 600 MPa on  $\beta$ -NiAl alloys that had been oxidized at 1100 °C can be quoted.<sup>46</sup> It should, however, be mentioned that large contradictions also occur between the measured values of different investigations. As an example, the measurements by Hou *et al.*<sup>50</sup> can be quoted with much lower values, which were explained by stress relaxation processes. Hou *et al.*<sup>50</sup> also reveals that in the early stages the growth stress in  $\theta$ -Al<sub>2</sub>O<sub>3</sub> is compressive and is converted into tensile stresses when the formation of  $\alpha$ -Al<sub>2</sub>O<sub>3</sub> begins. Only when a complete  $\alpha$ -Al<sub>2</sub>O<sub>3</sub> layer had formed at the metal/oxide interface did the stresses in  $\alpha$ -Al<sub>2</sub>O<sub>3</sub> become compressive, reaching a steady state level around –75 MPa at 1100 °C. Other sources report growth stresses on NiAl oxidized at 1100 °C in the range of around zero.<sup>44</sup>

For FeCrAl(Y) alloys and iron-based aluminides extremely high stresses had been found, for example, up to –1.6 GPa.<sup>51</sup> Surprisingly there is, however, a big

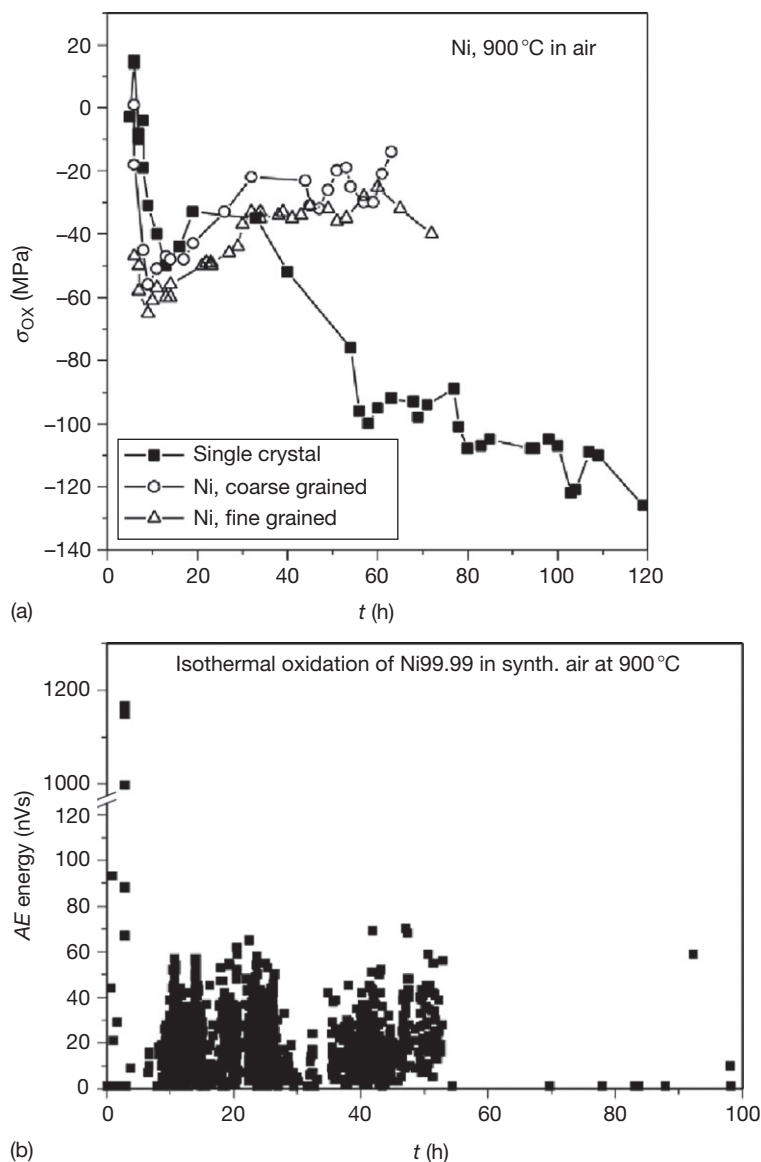


**Figure 3** (a) Growth stress in NiO scales on nickel as a function of oxidation time at 900 °C in air as determined by XRD measurements<sup>21,49</sup> (single crystal = 99.9999% Ni, Ni coarse or fine grained = 99.99% Ni). (b) Acoustic emission activity in a plain oxidation test with Ni99.99 at 900 °C in air. Reproduced from Przybilla, W.; Schütze, M. *Oxid. Met.* **2002**, 58, 103–145.

scatter between very high compressive and very high tensile stresses, depending also on the measurement technique. While in high temperature X-ray measurements compressive values as high as  $-1.7$  GPa were observed,<sup>44</sup> similar investigations at the same temperature by synchrotron X-ray radiation led to tensile stresses of the same order of magnitude.<sup>46</sup> Tensile growth stresses of  $\sim 1$  GPa were also observed by Mennicke *et al.*<sup>52</sup> which addresses, however, also the point that significant stress relaxation may take place

during isothermal, and in particular, thermocycling oxidation of the materials. Interestingly Mennicke *et al.*<sup>52</sup> also detected that there is no significant difference in the growth stresses as well as in the residual stresses after cooling or with regard to stress relaxation during thermocycling, between oxides formed on Y-doped and undoped FeCrAl materials. Evidently, the presence of a reactive element in this case did not lead to a change of the oxidation mechanism in a way that influences the intrinsic growth stress situation.

Limited information is available on  $\text{TiO}_2$  as well as  $\text{TiO}_2/\text{Al}_2\text{O}_3$  mixtures on titanium and titanium aluminides, respectively. While for titania the values are compressive and exceed  $-1000$  MPa,<sup>39</sup> those of the mixed oxide scale on the titanium aluminides can be compressive as well as tensile, both in the range of  $\sim 100$  MPa.<sup>22</sup>

In **Table 1** a rather incomplete summary of the existing information in the literature on the level

of intrinsic growth stresses in oxides is attempted, which indicates that there is still a significant scatter between the data and definitely more work is needed to get a clearer view of the role and the level of intrinsic growth stresses in oxide scales.

Finally an interesting aspect, which was observed for ferritic steels forming Cr-rich oxide scales, is addressed. Here it turned out that water vapor-containing environments lead to higher compressive

**Table 1** Results from growth stress measurements of oxide scales

Oxide	Substrate	Temperature (°C)	Max. abs. value <sup>a</sup> (MPa)	Technique	Ref.
NiO	Ni	627	-90		53
	Ni	1027	+12/+110		53
	Ni	940	+1365		53
	Ni Grade A	900	+20		54
	Ni SX 99.999	900	-130/+15	X-ray	49
	Ni 99.99	900	-55/+15	X-ray	49
	Ni 99.0	900	-65/+15	X-ray	49
	Ni 99.99	900	-550/+250	DTMO	21
	Ni 99.0	900	-400/+300	DTMO	21
	Ni 99.99	800	-1500/+700	DTMO	21
Fe <sub>2</sub> O <sub>3</sub>	Mild Steel	400	-270	X-ray	45
	Grey Cast Iron	400	-5770	X-ray	45
Fe <sub>3</sub> O <sub>4</sub>	Mild Steel	400	+135	X-ray	45
	Grey Cast Iron	400	-60	X-ray	45
Cr <sub>2</sub> O <sub>3</sub>	Cr 99.7	750	-2400	Raman	38
	Fe-18Cr	750	-2800	Raman	55
	Fe-18Cr-TiNb	750	-2200	Raman	55
	Cr	875	+200		19
	Cr	940	-350		1
θ-Al <sub>2</sub> O <sub>3</sub>	β-NiAl	1000/1100	-480	Synchrotron	50
α-Al <sub>2</sub> O <sub>3</sub>	β-NiAl	1000/1100	-75/+500	Synchrotron	50
Al <sub>2</sub> O <sub>3</sub>	NiAl	1100	0	X-ray	44
	FeCrAlY	1100	-1300/-200	X-ray	44
	FeCrAl	1100	-400	X-ray	44
	FeCrAlY	1000	-1700/-500	X-ray	44
	FeCrAl	1000	-1000	X-ray	44
	FeCrAlY	1100	+1100/+500	Synchrotron	46
	FeCrAlY	1000	+500	Synchrotron	46
	FeCrAlY	1200	+800/+100	Synchrotron	46
	Kanthal	1000	+260	Synchrotron	46
	Kanthal	1200	-150	Synchrotron	46
	NiAl	1100	+600/-300	Synchrotron	46
	NiAl + Hf	1100	+500		46
	FeNiCrAl	1000	-400	DTMO	18
	FeNiCrAlY	1000	-80	DTMO	18
	FeCrAl	1300	-340	DTMO	56
TiO <sub>2</sub>	Ti99.6		-1000	Raman	39
TiO <sub>2</sub> /Al <sub>2</sub> O <sub>3</sub>	TiAl2Cr	800	+100/-100	DTMO	22
	TiAl	900	-130	DTMO	22
Cr-(Fe)-oxide	P91 steel	650/dry air	-200	DTMO	5
	P91 steel	650/10% H <sub>2</sub> O	-1200	DTMO	5
	Nf 616	650/dry air	-120	DTMO	5
	Nf 616	650/10% H <sub>2</sub> O	-900	DTMO	5

<sup>a</sup>Max. abs. value means that this was the highest value measured independent of the stress direction. The latter is indicated by the (+) or (-) sign: (+), tensile; (-), compressive.

stresses than dry air.<sup>5</sup> While the stresses in dry air oscillate around a constant value over oxidation time, there is a significant stress relaxation in the humid environment, which leads after a while to a drop of the growth stresses to values close to those in dry air.

### 1.08.2.1.2 Modeling

The earliest attempt to model the formation of growth stresses in oxide scales during the oxidation process, dates back to 1923 and was performed by Pilling and Bedworth.<sup>57</sup> In their model, they described the volume change that is involved in the transition from the metal lattice to the cation lattice of the oxide when only the oxygen anions are diffusing during the oxide growth process. The ratio of the volume of the oxide formed by the oxidation process to the metal consumed in this reaction is termed the Pilling–Bedworth ratio (PBR). Values of the PBR are given in **Table 2** for several oxides and metal substrates. The key assumption in this model is that the oxide scales grow inwardly and they would be compressed if the PBR were greater than one. Tensile stresses would develop in the oxide if the PBR were less than one. Consequently, if oxide scales grow outward by the diffusion of metal cations, the oxide scale must remain free of growth stresses as the new oxide grows freely on the scale surface. Assuming inward scale growth will occur, the resulting strain

in the oxide can be calculated according to the following equation<sup>60</sup>:

$$\varepsilon_{\text{ox}} = \omega[(\text{PBR})^{1/3} - 1] \quad [4]$$

where the factor  $\omega$  is introduced to take account of possible stress-reducing processes. Assuming elastic behavior, the corresponding growth stress in the oxide would be:

$$\sigma_{\text{ox}} = \frac{-E_{\text{ox}}}{1 - \nu_{\text{ox}}} \varepsilon_{\text{ox}} \quad [5]$$

where  $E_{\text{ox}}$  is the elastic modulus of the oxide, and  $\nu_{\text{ox}}$  is the Poisson ratio.

The PBR values have been used for many years, and are sometimes still used, to explain the formation of growth stresses in oxide scales. Nowadays, however, it is generally agreed that this model is too simplistic an explanation, especially because it does not take into account the outward growth of oxides by metal cation transport, which is a dominant mechanism for many technical alloys. In the meantime a number of more sophisticated models have been developed<sup>61</sup> describing, for example, the formation of growth stresses based on the formation of new oxide in the existing oxide scale, as shown in **Figure 4**.<sup>2</sup> The first model of this type was developed by Rhines and Wolf, based on the assumption that counter diffusion takes place in the oxide scale with the inward movement of oxygen along grain boundaries and the outward movement of metal cations within the oxide grains.<sup>142</sup> The reactions of the two species at the oxide grain boundaries would lead to the formation of new oxide at these positions with a volume increase that also generates strains in a lateral direction. As counter diffusion of the oxide-forming species during scale growth has also been shown in several

**Table 2** PBR values for some technically important oxides and metal substrates<sup>2,17,57–59</sup>

System	PBR
$\alpha\text{-Al}_2\text{O}_3/\text{Al}$	1.28
$\text{CoO}/\text{Co}$	1.86
$\text{Cr}_2\text{O}_3/\text{Cr}$	2.07
$\text{Cr}_2\text{O}_3/\text{Fe-25Cr-20Ni}$	2.1
$\text{CuO}/\text{Cu}$	1.70
$\text{FeCr}_2\text{O}_4/\text{Fe-18Cr-8Ni}$	2.1
$\text{Fe}(\text{FeCr})_2\text{O}_4\text{spinel}/\text{Fe-Cr}$	2.1
$\text{FeO}/\alpha\text{-Fe}$	1.68
$\text{Fe}_2\text{O}_3/\alpha\text{-Fe}$	2.14
$\text{Fe}_2\text{O}_3/\text{Fe}_3\text{O}_4$	1.02
$\text{Fe}_3\text{O}_4/\alpha\text{-Fe}$	2.1
$\text{Fe}_3\text{O}_4/\text{FeO}$	1.2
$\text{MgO}/\text{Mg}$	0.84
$\text{MnO}/\text{Mn}$	1.77
$\text{MoO}_3/\text{Mo}$	3.27
$\text{NiO}/\text{Ni}$	1.65
$\text{SiO}_2/\text{Si}$	2.15
$\text{TiO}_2/\text{Ti}$	1.73
$\text{ZrO}_2/\text{Zr}$	1.57

Reproduced from Kofstad, P. *High Temperature Corrosion*; Elsevier Applied Science: London, 1988.

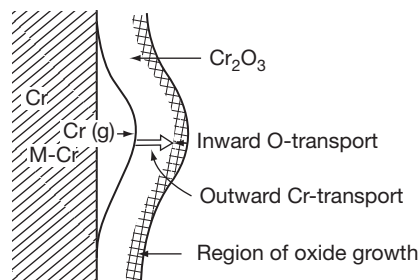


**Figure 4** Schematic representation of the growth of chromia scales by counter transport of oxygen and chromium in the scale. Reproduced from Kofstad, P. *High Temperature Corrosion*; Elsevier Applied Science: London, 1988.

investigations by isotope and SIMS measurements,<sup>62</sup> this approach has also become the basis for many of the more advanced and more recent models in the literature.<sup>63–65</sup> Clarke was able to express the growth strain rate in terms of a number of parameters including the parabolic rate constant, the scale thickness, and the oxide grain size.<sup>63</sup> This lateral growth strain rate increases with the parabolic rate constant and decreases with increasing oxide grain size and scale thickness. While these models in several cases can predict the measured order of magnitude of scale stresses correctly, they still have the problem that any stress relaxation process, which will inevitably take place under practical conditions, is not reflected. Nevertheless, all these models can help a better understanding of the complex situation in the oxidation of particular technical alloys, which is in most cases away from the simple parabolic growth mechanism usually described in textbooks.

### 1.08.2.2 Geometrically Induced Growth Stresses

On curved substrate surfaces, the growth of oxide scales can lead to growth stresses originating from the surface geometry. The reason is that metal is consumed by the oxidation process so that the original metal surface recedes and at the same time there is a difference between the original metal volume consumed by the oxidation process and the volume of the resulting oxide, see PBR. **Figure 5** illustrates the potential situations that can exist, based on the extreme cases of scale growth by cation diffusion alone and by anion diffusion alone for  $PBR > 1$ .<sup>66</sup>

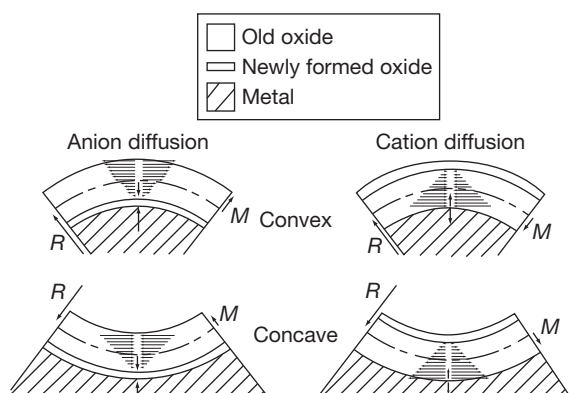


**Figure 5** Growth stresses in the oxidation of curved surfaces. Reproduced from Christl, W.; Rahmel, A.; Schütze, M. *Oxid. Met.* **1989**, *31*, 1.

In the case of anion diffusion, the new oxide is formed at the interface between oxide scale and metal. As most of the technical oxides have a  $PBR > 1$ , it means that additional volume is created at the interface, which shifts the existing oxide scale outward. As a consequence, tensile stresses will arise in circumferential direction on convex surfaces, while compressive stresses will be present perpendicular to the interface between oxide and metal. The circumferential stresses are the highest in the 'oldest' part of the oxide, which is the one on the scale surface. The part that was formed last is almost stress-free with regard to the circumferential direction. On concave surfaces the same situation leads to compressive circumferential and perpendicular stresses, as shown in the lower left part of **Figure 5**. For cation diffusion, new oxide is formed on top of the existing oxide and is, thus, the stress-free part of the system. The oldest part is at the oxide/metal interface and, thus, shows the highest circumferential stresses. These are compressive for convex surfaces and tensile for concave surfaces. The stresses perpendicular to the oxide/metal interface are tensile in both cases.

As described by Schütze,<sup>1</sup> these scale stresses can be calculated quantitatively, based on the oxidation rate data and the surface curvature. The general tendency is that the higher the oxide growth rate and the smaller the surface curvature radius, the more marked will be the oxide scale stresses resulting from the geometrical situation. As a result, fast-growing oxide scales, especially at sharp edges, are greatly endangered from high geometrical growth stresses. As will be shown later, tensile stresses especially can lead to delamination of the scale or scale cracking, so that low curvature radii such as edges can always be sites of preferred attack by high temperature corrosion as the protective oxide scale may suffer damage at these spots first.

### 1.08.2.3 Other Types of Growth Stresses

Among the stresses arising from oxide growth, there are many other sources of stress that can be considered intrinsic growth stresses, but are of significance only in very specific cases. In the literature, the role of epitaxial stresses has been discussed often, where stresses develop as a consequence of the difference in lattice parameters of the oxide and the substrate. Such stresses should be maximum at the oxide/metal phase boundary and will fall off toward the oxide surface.<sup>67</sup> It can be expected that with the increasing thickness of the oxide scale, such epitaxial

stresses will have less significance, which means that they play a role only in extremely thin films and at low temperatures.<sup>58</sup>

Another cause for growth stresses in oxide scales can be changes in the oxide composition.<sup>68</sup> For example, it has been observed that for various Fe–Cr alloys, the transition from initially formed (Cr, Fe)<sub>2</sub>O<sub>3</sub> to a scale with increasing Cr and decreasing Fe content, leads to the formation of tensile stresses in course of time.<sup>69</sup> The explanation for this effect was a decrease in atomic volume associated with this transition. Another example is the change from the transient alumina scales consisting of  $\theta$ -Al<sub>2</sub>O<sub>3</sub>, at the beginning of oxidation to the later  $\alpha$ -Al<sub>2</sub>O<sub>3</sub>, which, due to the different crystal structures, also induces stresses in the oxide, which usually lower the compressive stress level in the scale.<sup>50</sup> Further effects can be present in the case of phase changes in the metal subsurface zone where for example, the consumption of aluminum by oxidation and, thus, a phase change from  $\beta$ -NiAl to  $\gamma$ -NiAl leads to a volume change.<sup>70</sup> The situation of stresses induced by selective internal oxidation is discussed by Hänse *et al.*<sup>71</sup> also. Although such stresses are present in the metal subsurface zone they will have an effect on the oxide scale itself. Such internal oxides or oxide protrusions of the scale/metal interface can introduce stresses not only by the growth of the oxide under isothermal conditions but also during cooling, leading to detrimental local stress concentrations.<sup>72</sup> Another source of local differences in (growth) stress levels can be multiphase substrates on which different types of surface oxides are formed, with locally different oxide growth rates.<sup>72</sup>

Finally, it should be mentioned that the involvement of volatile species in the oxidation process can also have a dramatic effect on the stress situation in the oxide scale. This is particularly known as the so-called active oxidation, which takes place in oxidizing halogen-containing environments.<sup>73–75</sup> In this case, volatile metal halides, which are formed at the oxide/metal interface by the reaction of halogen from the gas phase with the metal migrate in an outward direction through the oxide scale and, with increasing oxygen partial pressure, are deposited as solid oxides within the scale. As a result, additional volume is created within the existing oxide scale, leading to high compressive stresses followed by the cracking and opening up of the oxide scale for further ingress of halogens to the metal. These very high growth stresses are the reason why a protective effect of the oxide scale cannot be maintained under halogenizing conditions.

Dissolution and precipitation processes in the oxide have also been speculated to create growth stresses that can lead to cracking and by this to a change in the oxidation kinetics. An example for this is the mixed TiO<sub>2</sub>/Al<sub>2</sub>O<sub>3</sub>-oxide scale on intermetallic titanium aluminides, where the initially formed Al<sub>2</sub>O<sub>3</sub> barrier in the scale becomes dissolved after a while and reprecipitated as discrete Al<sub>2</sub>O<sub>3</sub> particles in a TiO<sub>2</sub> matrix. This process seems to lead to precipitation stresses and microcracking in the scale after an incubation period, and initiates the so-called breakaway effect, where the oxidation rates increase significantly compared to the former protective period.<sup>76</sup>

### 1.08.3 Thermally Induced Scale Stresses Resulting from Temperature Changes

#### 1.08.3.1 Experimental Observations

The CTE of substrate material and oxide scale are usually different from each other and during temperature changes these differences can lead to significant stresses in the oxide/metal system. **Table 3** shows a compilation of measured and theoretically calculated CTE data. This compilation should serve as orientation as the CTEs are a function of temperature with, in most cases, a more or less linear dependency where the higher CTE values are at the higher temperature. **Table 3** reports the maximum values found in the literature. For a more exact quantitative consideration of the stress situation in oxide/metal systems during temperature changes, it is recommended that the reader either refers to the original literature or measures the CTE data in laboratory tests. As high temperature components have to be cooled down from their operation temperature during inspection intervals or if they are subjected to thermocyclic operation, it is necessary to regard the role of temperature induced stresses in the oxide/metal system in some depth. As general experience shows, these stresses are the most critical for the protective effect of the oxide scales and can reach values as high as 3 GPa and even more.<sup>78</sup>

For thermally grown oxide scales, the temperature-induced stress cannot be measured directly, as discussed in **Section 1.08.1**. After a temperature change new stresses develop in the scale; however, these new thermal stresses are added on top of the preexisting intrinsic growth stresses, geometrically induced growth stresses, and external stresses (see eqns [1]–[3]). Moreover, stress relaxation phenomena



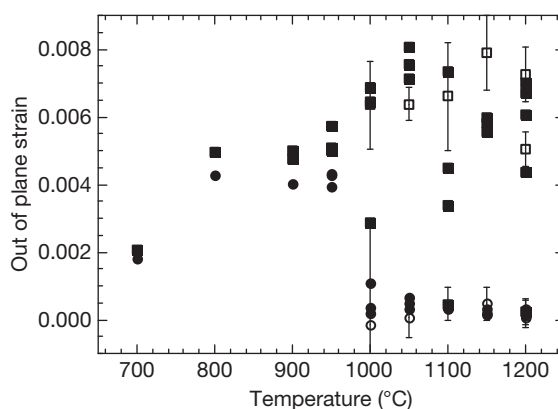
**Table 3** Orientational ('maximum') values of the coefficients of thermal expansion (CTE) for several technically relevant substrates, coatings, and oxide phases

	CTE $\alpha$ ( $10^{-6}$ K)		CTE $\alpha$ ( $10^{-6}$ K)
SiO <sub>2</sub> (amorphous)	0.9	Incoloy 956	15.0
HPSN	3.0	738	15.3
Si	4.6	Alloy S, 713	15.4
SiC	4.9	NiPt39Al	15.6
AlN	6.2	617, Hast C-4	15.6
TiN	7.8	CMSX 6, IN 100	15.8
MoSi <sub>2</sub>	7.9	Hast C-276, 230	15.9
Cr <sub>2</sub> O <sub>3</sub> , SiO <sub>2</sub> (cryst.)	8.1	Hast C-22	16.1
Al <sub>2</sub> O <sub>3</sub>	8.4	NiCrAlY	16.4
Ti	8.6	Hast X	16.5
Pt	8.8	600	16.6
Y <sub>2</sub> O <sub>3</sub>	8.9	X-750	16.7
Cr	9.5	NiO, 556, 718	17.1
IMI 834, NiAl	9.9	625	17.2
TiO <sub>2</sub>	10.5	Ni	17.5
Ti <sub>3</sub> Al ( $\alpha$ 2)	10.9	188	17.8
RuAl	11.0	Austenitic steels	17.0–19.0
Pd	11.6	800H	18.3
Ni <sub>3</sub> Al	11.9		
NiCo17Cr14AlY	18.5		
TiSi <sub>2</sub>	12.1	Fe <sub>3</sub> Al	19.5
TiAl	12.9	FeAl <sub>2</sub>	19.5
Ferritic steels	12.0–14.0	FeAl	21.8
Co	13.9	Fe–28Al–2Cr	22.5
CoAl	14.0	Al	23.8
FeCrAlY	14.5	Fe–28Al–5Cr–0.1Zr	24.0
CoO	14.9	Fe <sub>2</sub> Al <sub>5</sub>	24.2

Reproduced from Schütze, M.; Malessa, M.; Rohr, V.; Weber, T. *Surf. Coat. Technol.* **2006**, 201, 3872–3879.

such as scale microcracking, detachment, and plastic deformation of the substrate also change the scale stress state. The superposition of all these stress generators and relaxors are sometimes called the 'residual' scale stress, which is often measured at room temperature (RT) after high temperature exposure by Raman spectroscopy, optical fluorescence spectroscopy, and X-ray diffraction (XRD).<sup>79–86</sup> The measured RT residual stresses, even though they are not a direct measure of temperature-induced stress, provide insight into the scale stress situation, which has been demonstrated for the reactive element effect<sup>79–81</sup> and some sample geometry effects.<sup>82–84</sup>

An example for the case of the reactive element effect is given in **Figure 6** where the Raman technique

**Figure 6** A comparison of out-of-plane Al<sub>2</sub>O<sub>3</sub> residual scale strains after cooling as a function of oxidation temperature, as determined by XRD (open circles and open squares) and Raman spectroscopy (full circles and full squares). The materials investigated were FeCrAl (circles) and FeCrAl + 0.1Zr (squares).

was also verified by XRD measurements. At exposure temperatures above  $\sim 1000$  °C the alloy without the reactive element Zr spalls, after cooling to RT, and the measured strains go to zero. The alloy with Zr does not spall after cooling and the scale strain remains high. At temperatures below 1000 °C there is no significant difference in the strain levels between the two alloys. This aspect of the reactive element effect has been experimentally confirmed for the reactive elements Zr, Y, and Hf in a variety of FeCrAl, NiCrAl, NiCoCrAl, and NiAl alloys.<sup>79–81</sup> The transition temperature (1000 °C in **Figure 6**) above which the reactive element effect is observed can differ from alloy to alloy, for example on NiCoCrAl and even some FeCrAl. The reactive element effect is observed at temperatures above 1100 °C.<sup>79–81</sup> This is caused by the variation in thermal strain due to the different CTEs of the respective alloys as shown in **Table 3**. Generally speaking, the higher the alloy CTE the lower the exposure temperature required to produce an influence of the reactive element effect.

The Raman technique has also been used to investigate the role that sample geometry plays in residual stresses.<sup>82–84</sup> These investigations show that the higher compressive residual stresses are found in the sample center and decrease as the sample edge or corner is approached.<sup>82</sup> The stress analysis performed by finite element modeling shows that the stress component perpendicular to the sample surface is near zero at the sample center and becomes increasingly more tensile as the sample edge or

corner is approached. This tensile stress, if large enough, is expected to cause scale spallation at the edges and corners of samples.

### 1.08.3.2 Modeling

A quantitative assessment of the level of stresses induced by temperature changes can be performed using the following equation<sup>87</sup>:

$$\sigma_{ox} = \frac{-E_{ox}\Delta T(\alpha_{met} - \alpha_{ox})}{(E_{ox}/E_{met})(d_{ox}/d_{met})(1 - \nu_{met}) + (1 - \nu_{ox})} \quad [6]$$

where  $E_{met}$ ,  $E_{ox}$  are the elastic moduli of the metal and the oxide, respectively,  $\nu_{met}$ ,  $\nu_{ox}$  are the Poisson ratios of the metal and oxide, respectively,  $d_{met}$ ,  $d_{ox}$  are the thickness of the metal substrate and the oxide scale, respectively, and  $\alpha_{met}$ ,  $\alpha_{ox}$  are the thermal expansion coefficients of metal and oxide. The elastic moduli and, as already mentioned, in most cases also the CTE, are not independent of temperature, so eqn [6] is accurately applicable only for limited temperature intervals. For larger temperature changes  $\sigma_{ox}$  has to be calculated by making a summation of the incremental values over small temperature intervals. Equation [6] can be simplified if thin oxide scales on thick substrates are considered:

$$\sigma_{ox} = \frac{-E_{ox}\Delta T(\alpha_{met} - \alpha_{ox})}{1 - \nu_{ox}} \quad [7]$$

In the case of multilayer oxide scales, where the different layers have different CTE, the stress  $\sigma_i$  of each individual layer  $i$  of  $n$  layers can be calculated by<sup>88</sup>

$$\sigma_i = \frac{E_i}{1 - \nu_i} \Delta T \frac{\alpha_m - \alpha_i}{1 - \alpha_i \Delta T} \quad [8]$$

where  $\alpha_m$  is the mean thermal expansion coefficient of the combined scale:

$$\alpha_m = \frac{\sum_i^n d_i E_i \alpha_i / [(1 - \nu_i)(1 - \alpha_i \Delta T)]}{\sum_i^n d_i E_i / [(1 - \nu_i)(1 - \alpha_i \Delta T)]} \quad [9]$$

Also for thermally induced stresses, the surface curvature may play a role for the sign and the level of the thermally induced stresses (Figure 7). In most cases, the CTE of the oxide scale will be lower than that of the metal substrate (left part of Figure 7) so that on convex surfaces compressive stresses will be found in the circumferential direction and tensile stresses perpendicular to the oxide/metal interface. On concave surfaces, the circumferential stresses are compressive and those at the oxide/metal interface in the

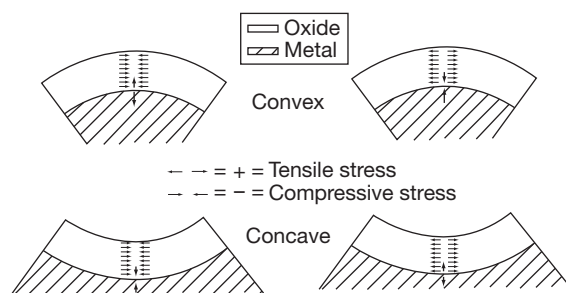


**Figure 7** Direction of the cooling stresses on curved surfaces.<sup>1</sup> Left part:  $\alpha_{met} > \alpha_{ox}$ . Right part:  $\alpha_{met} < \alpha_{ox}$ .

perpendicular direction also become compressive. The case where the CTE of the oxide is higher than that of the metal is shown in the right part of Figure 7.

The situation where the CTE of the oxide is higher than that of the substrate metal occurs only in some specific situations. One of these situations can be found in the unalloyed or low alloy steels where, due to the change from the normal to the inverse spinel structure in magnetite or chromium-iron spinels, a large variation of the value of the CTE takes place (see Figure 8). Such cases require a more sophisticated quantitative treatment, which is described elsewhere.<sup>1,66</sup> As a result, a rather complex stress distribution in the multilayer oxide scale can be observed, leading to a locally different sensitivity to cracking or spalling of the oxide layer system.<sup>1</sup>

## 1.08.4 The Effect of Stresses on the Integrity of the Oxide Scale

### 1.08.4.1 Measured Critical Strain Values to Scale Failure

Since the protective effect of a dense surface oxide scale guarantees the corrosion resistance of the technical high temperature materials under service conditions, one of the key issues is to maintain the integrity of the scales or at least to know the mechanical limits before failure of the scales occurs. This failure can consist of various forms of damage depending on the prevailing stress situation in the scale/metal composite system, the mechanical properties and structure of the scale, and the temperature and deformation rates:

1. fracture of a scale or a component of the scale perpendicular to the direction of tensile stress,
2. fracture of the scale or a component of the scale by the action of shear or buckling stresses in the scale,

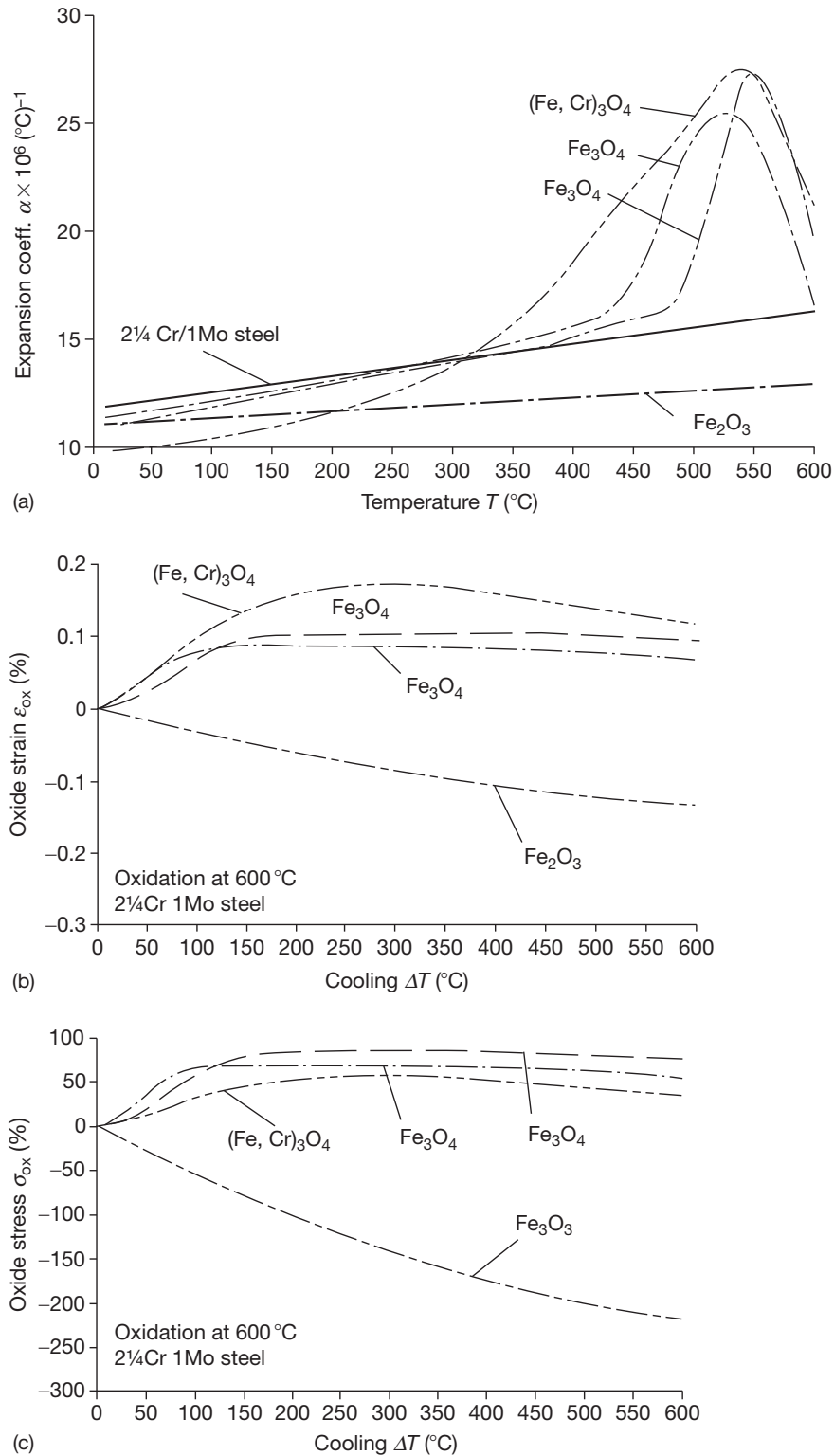


**Figure 8** Role of differences in CTE values for the example of the oxide scale formed on a 2.25 Cr1Mo steel at 600 °C in air.<sup>1,66</sup> (a) Variation with temperature of CTE,<sup>89,90</sup> (b) strains in the oxide on cooling from 600 °C, and (c) stresses in the oxide on cooling from 600 °C.

3. formation of microcracks in the scale,
4. disbonding of the scale from the metal or separation along the interfaces between the components of the scale,
5. spalling of parts of the scale under compressive stresses.

Before these failure situations are addressed by model considerations in [Section 1.08.4.2](#), it will be helpful to look at experimental data on the strains to scale failure.

The measurement of critical strains to scale failure requires some experimental effort. The most critical part in these measurements is to record the moment of scale failure either by optical or acoustic means. The most elegant technique has been proved to be the acoustic emission analysis, which has been applied to the measurement of scale failure in a number of investigations.<sup>1</sup> The simplest way would be to attach an acoustic waveguide to the specimen by clamping or spot welding in order to lead the signals from the hot zone of the test environment to the colder part outside the test rig and a piezoelectric transducer. In equipment that is more sophisticated, large size specimens that reach out into the colder part where the piezoelectric transducer can be attached directly.<sup>66</sup> If the respective parameters are known, especially the CTE, even the cooling step after oxidation can be used to assess critical strains for scale failure together with temperature and acoustic signal recording.<sup>1</sup> More accurate methods, however, are based on tensile or compressive testing machines in which simple uniaxial tension and compression or more sophisticated four point bending tests can be performed. Both types of tests have been used successfully and are described in detail in the literature.<sup>1,91–93</sup> An example of the test arrangement for a tensile test is shown in [Figure 9](#).<sup>7</sup>

The critical strain values to scale failure existing in the literature from such measurements have been summarized elsewhere<sup>92</sup> and are shown in [Table 4](#). It turns out that, with the exception of nickel oxide on nickel, under compressive strains where a specific stress relief mechanism of simultaneous microcracking and crack healing in the scale ('pseudoplasticity') comes into play,<sup>93</sup> almost all other values lie in the range between 0 and ~1%. This confirms the brittleness of the protective oxide scales indicating that oxides, even if they are grown as metal oxide scales on metallic substrates, show ceramic nature. Also, the fracture toughness values which can be derived from these critical strain values (see [Section 1.08.4.2](#)) as shown in [Table 5](#)<sup>92</sup>

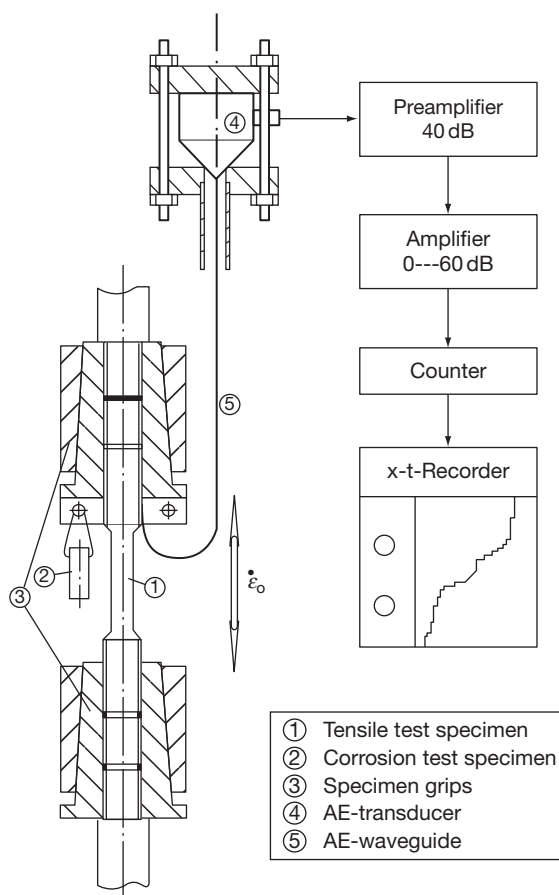


**Figure 9** Schematic of a test arrangement for measuring critical strains to oxide scale failure at oxidation temperature in a furnace using a tensile test machine equipped with an acoustic emission measurement device and a waveguide. Reproduced from Schütze, M. *Oxid. Met.* **1985**, 24, 199–232.

confirm the brittleness of oxide scales. These values can be used for model-based assessments of critical failure strains (see [Section 1.08.4.2](#)).

Besides the standard tensile or compression test, or the rather universal four point bending test, a number of special tests for scale adhesion measurements have been developed. These have been described elsewhere.<sup>1,106,107</sup> Most of these techniques are only applicable at RT since they rely on the strength of an organic glue. Recently a new type of test has been developed, which is called the 'inverted blister test'.<sup>107</sup> In this case, the energy that is necessary to enlarge an area of detached scale by increasing the hydrostatic pressure in a complex arrangement through a central hole so that the substrate metal (which is a thin foil)

**Table 4** Experimental data on scale failure strains given in the literature

Oxide	Substrate	Temperature (°C)	$\epsilon_c$ (%)	Mode	Ref.
Al <sub>2</sub> O <sub>3</sub>	18CrAl steel	800	0.08–0.16	Tensile	7
Al <sub>2</sub> O <sub>3</sub>	FeCrAlY	RT	0.4–1.3	Tensile	94
Al <sub>2</sub> O <sub>3</sub>	FeCr alloy	RT	0.05	Tensile	95
Al <sub>2</sub> O <sub>3</sub>	MA 956	600	0.5–0.6	Tensile	96
Al <sub>2</sub> O <sub>3</sub>	FeCr alloy	RT	–1.4	Compressive	95
Cr <sub>2</sub> O <sub>3</sub>	AISI 310	RT	0.78–0.95	Tensile	97
Cr <sub>2</sub> O <sub>3</sub>	Alloy 800	800	0.09–0.50	Tensile	7
Cr <sub>2</sub> O <sub>3</sub>	Nimonic 75	700	0.002–0.005	Tensile	98
Cr <sub>2</sub> O <sub>3</sub>	Nimonic 75	800	0.005–0.008	Tensile	98
Cr <sub>2</sub> O <sub>3</sub>	Nimonic 75	1000	0.013–0.018	Tensile	98
Cr <sub>2</sub> O <sub>3</sub>	AISI 310	RT	–(0.29–0.79)	Compressive	97
Cr <sub>2</sub> O <sub>3</sub>	Alloy 800	RT	–(0.6–0.8)	Compressive	1, 97
NiO	Pure Ni	800	0.2–0.7	Tensile	1
NiO	Pure Ni	800	0.13–0.48	Tensile	7
NiO	Pure Ni	900	0.04–0.11	Tensile	99
NiO	Pure Ni	RT	–(0.9–2.2)	Compressive	1
NiO	Pure Ni	RT	–(0.8–2.7)	Compressive	93
NiO	Pure Ni	400	–(0.8–2.0)	Compressive	93
NiO	Pure Ni	600	–(0.7–4.0)	Compressive	93
NiO	Pure Ni	800	–(1.2–3.2)	Compressive	93
FeO	Low alloy steel	600–900	0.01–0.02	Tensile	89
Fe <sub>3</sub> O <sub>4</sub>	Mild steel	RT	0.05–0.08	Tensile	89
Fe <sub>3</sub> O <sub>4</sub>	Pure iron	RT	0.1–0.33	Tensile	89
Fe <sub>3</sub> O <sub>4</sub>	Pure iron	RT	0.1–0.13	Tensile	89
Fe <sub>3</sub> O <sub>4</sub>	Pure iron	300	0.05–0.08	Tensile	89
Fe <sub>3</sub> O <sub>4</sub>	AISI 316	RT	0.11–0.20	Tensile	89
Fe <sub>3</sub> O <sub>4</sub>	AISI 316	800	0.17–0.31	Tensile	89
Fe <sub>3</sub> O <sub>4</sub> /Fe <sub>2</sub> O <sub>3</sub>	Mild steel	RT	0.15–0.45	Tensile	100
Fe <sub>3</sub> O <sub>4</sub> /Fe <sub>2</sub> O <sub>3</sub>	Mild steel	550	0.05–0.42	Tensile	100
Fe <sub>3</sub> O <sub>4</sub> /Fe <sub>2</sub> O <sub>3</sub>	2.25Cr1Mo steel	600	0.1	Tensile	89
Fe <sub>3</sub> O <sub>4</sub> /Fe <sub>2</sub> O <sub>3</sub>	AISI 316	RT	0.13–0.22	Tensile	89
Fe <sub>3</sub> O <sub>4</sub> /Fe <sub>2</sub> O <sub>3</sub>	AISI 316	600	0.27–0.35	Tensile	89
Fe <sub>3</sub> O <sub>4</sub> /Fe <sub>2</sub> O <sub>3</sub>	Mild steel	500	0.01–0.02	Tensile	98
FeO/Fe <sub>3</sub> O <sub>4</sub> /Fe <sub>2</sub> O <sub>3</sub>	Mild steel	600	0.01–0.02	Tensile	98
FeO/Fe <sub>3</sub> O <sub>4</sub> /Fe <sub>2</sub> O <sub>3</sub>	Mild steel	700	0.02–0.03	Tensile	98
FeO/Fe <sub>3</sub> O <sub>4</sub> /Fe <sub>2</sub> O <sub>3</sub>	Mild steel	800	0.03–0.06	Tensile	98
Fe <sub>3</sub> O <sub>4</sub> /Fe <sub>2</sub> O <sub>3</sub>	Mild steel	RT	–(0.18–0.55)	Compressive	101
Fe <sub>2</sub> O <sub>3</sub>	2.25Cr1Mo steel	600–300	–0.6	Compressive	66
TiO <sub>2</sub> /Al <sub>2</sub> O <sub>3</sub>	Ti50Al	900	0.15–0.50	Tensile	102
TiO <sub>2</sub> /Al <sub>2</sub> O <sub>3</sub>	Ti50Al2Nb	900	0.15–1.30	Tensile	102
TiO <sub>2</sub> /Al <sub>2</sub> O <sub>3</sub>	Ti47Al1Cr Si	900	0.6–1.7	Tensile	99

Reproduced from Schütze, M.; Ito, S.; Przybilla, W.; Echsler, H.; Bruns, C. *Mater. High Temp.* **2001**, 18, 39–50.

deforms plastically (forming a growing blister at the detached area) and separates from the oxide, is measured. Although this test looks intriguing, it is not easy to use.

Hou *et al.*<sup>108</sup> contains a number of adhesion energy data with a scatter even within one metal/oxide system of up to three orders of magnitude. This shows the difficulties of such types of measurements. Much of the scatter will certainly also arise from the presence and the level of impurities at the oxide/metal interface. Sulfur especially is known to play

a detrimental role on scale adhesion as it weakens the interface and enhances interfacial pore formation.<sup>109–111</sup> For example, in NiAl, increasing the interface sulfur content from zero to ~2.5% reduced the interfacial strength by a factor of ~10.

#### 1.08.4.2 Model Considerations

Because oxide scales are brittle phases even at high temperatures, as is obvious from the experimental data, a model description of scale failure is possible,

**Table 5** Oxide fracture toughness data calculated from critical strain and defect data given in the literature

Oxide	Substrate	Temperature (°C)	$K_{Ic}$ (MPa m <sup>1/2</sup> )	Mode	Ref.
Al <sub>2</sub> O <sub>3</sub>	Bulk	RT	3.0–6.0	Bending test	99
Al <sub>2</sub> O <sub>3</sub>	Bulk	RT	2.5	Calculated from $\gamma_0$	103, 104
Al <sub>2</sub> O <sub>3</sub>	FeCrAl	RT	0.4	Through scale	95
Al <sub>2</sub> O <sub>3</sub>	Kanthal APM	700	1.0	Through scale	105
Al <sub>2</sub> O <sub>3</sub>	18CrAl steel	800	0.3–1.0	Through scale	104
Al <sub>2</sub> O <sub>3</sub>	MA 956	1100	0.4–1.7	Through scale, initiation at macro pores	105
Al <sub>2</sub> O <sub>3</sub>	MA 956	1100	0.6–2.1	Through scale, initiation at macro pores	105
Cr <sub>2</sub> O <sub>3</sub>	Bulk	RT	1.8	Calculated from $\gamma_0$	103, 104
Cr <sub>2</sub> O <sub>3</sub>	Nimonic 75	700	1.8–2.5	Through scale	98
Cr <sub>2</sub> O <sub>3</sub>	Nimonic 75	800	2.0–3.2	Through scale	98
Cr <sub>2</sub> O <sub>3</sub>	Nimonic 75	900	4.0–5.5	Through scale	98
Cr <sub>2</sub> O <sub>3</sub>	Alloy 800	800	1.2	Through scale	104
NiO	Bulk	RT	1.2	Calculated from $\gamma_0$	103, 104
NiO	Nickel	RT	0.5	Through scale	98
NiO	Nickel	RT	0.3–0.4	Through scale, initiation at pores	99
NiO	Nickel	RT	0.75–1.3	Through scale, initiation at microcracks	99
NiO	Nickel	RT	3.6	Scale detachment, parallel to interface	99
NiO	Nickel	800	2.6–6.0	Through scale	104
NiO	Nickel	900	1.2	Through scale	98
FeO	Bulk	RT	0.9	Calculated from $\gamma_0$	103, 104
Fe <sub>3</sub> O <sub>4</sub>	Bulk	RT	1.4	Calculated from $\gamma_0$	103, 104
Fe <sub>3</sub> O <sub>4</sub>	2.25Cr1Mo steel	600	0.2	Through scale	104
Fe <sub>3</sub> O <sub>4</sub>	Bulk	RT	1.6	Calculated from $\gamma_0$	103, 104
FeO/Fe <sub>3</sub> O <sub>4</sub>	Pure iron	570	2.0	Through scale	98
FeO/Fe <sub>3</sub> O <sub>4</sub>	Pure iron	670	2.2–4.0	Through scale	98
FeO/Fe <sub>3</sub> O <sub>4</sub>	Pure iron	740	2.3–5.3	Through scale	98
FeO/Fe <sub>3</sub> O <sub>4</sub>	Pure iron	800	5.8–9.3	Through scale	98
FeCr <sub>2</sub> O <sub>4</sub>	Bulk	RT	1.5	Calculated from $\gamma_0$	103, 104
Fe <sub>2</sub> MnO <sub>4</sub>	Bulk	RT	0.8	Calculated from $\gamma_0$	103, 104
TiO <sub>2</sub>	Titanium	RT	1.3	Through scale	103, 104
TiO <sub>2</sub> /Al <sub>2</sub> O <sub>3</sub>	Ti47Al1CrSi	RT	0.2	Scale detachment, parallel to interface	99
TiO <sub>2</sub> /Al <sub>2</sub> O <sub>3</sub>	Ti47Al1CrSi	700	1.2	Scale detachment, parallel to interface	99
TiO <sub>2</sub> /Al <sub>2</sub> O <sub>3</sub>	Ti50Al	900	1.5–3.0	Through scale	102
TiO <sub>2</sub> /Al <sub>2</sub> O <sub>3</sub>	Ti50Al2Nb	900	1.0–3.3	Through scale	102
TiO <sub>2</sub> /Al <sub>2</sub> O <sub>3</sub>	Ti47Al1CrSi	900	2.7–7.0	Through scale	99
TiO <sub>2</sub> /Al <sub>2</sub> O <sub>3</sub>	Ti47Al1CrSi	900	1.4–4.0	Scale detachment, parallel to interface	99
SiO <sub>2</sub>	Bulk	RT	0.9	Calculated from $\gamma_0$	103, 104
MnO	Bulk	RT	0.9	Calculated from $\gamma_0$	103, 104
CoO	Bulk	RT	1.0	Calculated from $\gamma_0$	103, 104

Reproduced from Schütze, M.; Ito, S.; Przybilla, W.; Echsler, H.; Bruns, C. *Mater. High Temp.* **2001**, 18, 39–50.

based on fracture mechanics approaches. Such approaches always assume that so-called physical defects (pores, voids, micro cracks, etc.) are present in a structure and are responsible for its failure. From this assumption, a critical stress  $\sigma_c$  can be calculated from the critical surface energy  $G_c$  which is released by the growth of the existing physical defect,

$E^*$  which is the effective Young's modulus (calculated from the values of different phases if the crack passes along the phases<sup>112,113</sup>) and  $c$ , which characterizes the size of the physical defect:

$$\sigma_c = \left( \frac{E^* G_c}{\pi c} \right)^{1/2} \quad [10]$$



Assuming linear elastic behavior, the numerator in eqn [10] can be replaced by the fracture toughness  $K_{Ic}$ .

$$K_c = (E_{ox}^* G_c)^{1/2} \quad [11]$$

which is valid for the plain stress situation that usually predominates in thin scales. In the case of plain strain, the right hand side of eqn [11] must be multiplied by the factor  $1/\sqrt{(1-\nu^2)}$ . The fracture toughness  $K_c$  or  $K_{Ic}$  is a material property characterizing the resistance of the oxide to crack growth. Crack growth starts to occur once the stress intensity factor  $K$  at the tip of the defect in the scale reaches or exceeds the value of this fracture toughness. Values of the fracture toughness are given in Table 5. If the fracture toughness and the size of the physical defects in the oxide scale or the scale/metal system are known, critical strain values can be assessed by model equations at which damage to the scale occurs. The respective equations for the different damage situations are summarized here and represented schematically in Figure 10.

1. Through scale cracking (tensile):

$$\varepsilon_c^t = \frac{K_{Ic}}{f E_{ox} \sqrt{\pi c}} \quad [12]$$

2. Beginning of interfacial crack growth/delamination (compressive)<sup>115</sup>

$$-\varepsilon_c^i = \frac{K_{Ic}}{f \sqrt{\pi c}} \frac{(1 + \frac{r}{d})(1 + \nu_{ox})}{2 E_{ox}} \quad [13]$$

3. Buckling (compressive)<sup>116</sup>

$$-\varepsilon_c^b = \frac{1.22}{1 - \nu_{ox}^2} \left( \frac{d}{R} \right)^2 \quad [14]$$

4. Crack deflection at scale buckles toward surface (compressive)<sup>10</sup>

$$-\varepsilon_c^{bf} = 3.6 \left( \frac{d}{R} \right)^2 \quad [15]$$

5. Spalling (compressive)<sup>116</sup>

$$-\varepsilon_c^s = \sqrt{\frac{2\gamma_o}{d E_{ox} (1 - \nu)}} \quad [16]$$

$\varepsilon_c$  is the critical strain in the oxide (i.e., the strain parallel to the oxide/metal interface) at which the respective type of failure occurs.  $K_{Ic}$  is the mode I (i.e., plain tensile straining) fracture toughness of the plane in which failure starts,  $E_{ox}$  is the Young's

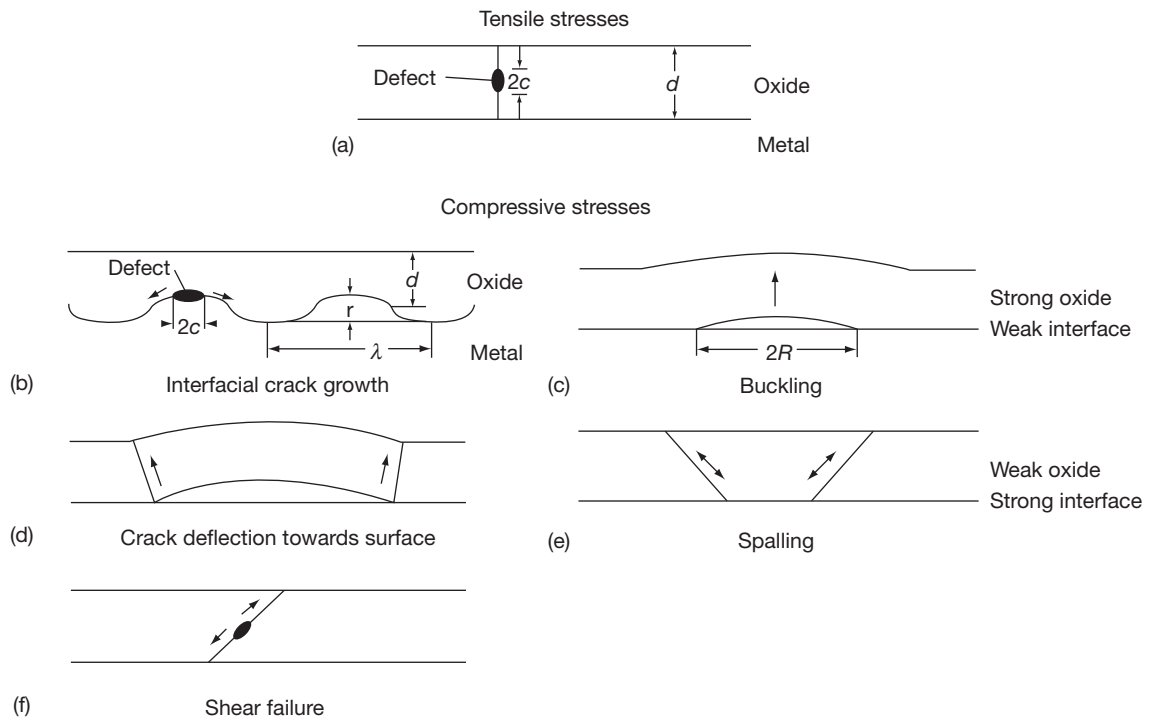


**Figure 10** Schematic of the different potential modes of scale failure. Reproduced from Schütze, M. In *High Temperature Corrosion of Advanced Materials and Protective Coatings*; Saito, Y., et al. Ed.; North Holland: Amsterdam, 1992; 29.

modulus of the oxide, and  $2c$  is the size of an embedded physical defect (pore, void, microcrack, etc.) which is responsible for failure. The size of a surface defect would be  $c$ .  $f$  is a geometrical factor (for embedded defects  $f = 1$ ) and  $d$  is the scale thickness. The remaining parameters are the interfacial roughness (amplitude  $r$ ), the Poisson ratio  $\nu_{\text{ox}}$ , and the radius of an already existing delamination  $R$ . Finally,  $\gamma_0$  is the surface energy needed for the creation of two new surfaces by cracking or detachment. This energy is an effective energy, which is influenced by the geometrical parameters of the failure plane in the following way<sup>103,117</sup>:

$$\gamma_0 = \gamma_i \left( 1 + \frac{0.1 E_{\text{ox}} r}{2 \gamma_i \lambda} \right) \left( \frac{A_0 - A_{\text{sep}}}{A_0} \right) \quad [17]$$

where the additional parameter  $\lambda$  represents the ‘wavelength’ of a rough interface,  $A_0$  the surface without separations and  $A_{\text{sep}}$  that part of the surface where delaminations/separations already exist (i.e.,  $A_{\text{sep}}$  is an equivalent to  $c$ ).  $\gamma_i$  is the intrinsic surface energy, which is a material’s parameter and, thus, similar to  $K_{\text{Ic}}$  independent of the microgeometry:

$$K_{\text{Ic}} = \sqrt{2 \gamma_i E_{\text{ox}}} = \sqrt{G_c E_{\text{ox}}^*} \quad [18]$$

Equation [16] actually corresponds to the original equation of U.R. Evans.<sup>118</sup> However, as shown by eqns [17] and [18] this rather simple equation should be extended by micromechanics parameters.

It should be mentioned here that for the size of physical defects also, especially where size depends on the oxidation process, some kinetic data exist in the literature, at least to a small extent.<sup>21,99,102</sup> Furthermore, these values can also be determined from metallographic examinations of oxidized specimens. The same is valid for the other geometrical parameters such as scale thickness and waviness of the oxide/metal interface.

Sometimes there is a criticism that the physical defect sizes needed for scale failure, particularly for the buckling situation, are much larger than is commonly observed on scales in metallographic investigations, that is, the scales fail before the appearance of critical physical defect sizes. As the literature shows, critical buckling constellations can grow from many small cavities to the necessary size.<sup>119</sup> Furthermore, small defects can interact with each other in a mechanical sense if they are lying close enough to each other so that a much larger ‘effective’ defect size determines the failure behavior of the scale.<sup>1</sup> Rules on how to calculate the effective physical defect size are given elsewhere.<sup>1,120</sup>

A number of Young’s moduli and Poisson ratios are given in Tables 6 and 7. Further values of the elastic constants, especially for elevated temperatures, can be found elsewhere.<sup>1</sup>

Figures 11 and 12 show how the model equations can be used to calculate the dependency of the critical strain to failure on the respective scale parameters. Assuming a physical defect size of  $\sim 1 \mu\text{m}$  or less, this results in critical strain values of a few tenths of a percent under tensile strain for  $\text{Al}_2\text{O}_3$ ,  $\text{Cr}_2\text{O}_3$ , and  $\text{Fe}_3\text{O}_4$  (see Figure 11). A comparison with actually measured critical strain values in Table 4 shows that this is very much in the same order of magnitude and confirms that the model approaches are suitable for a first assessment of the sensitivity to mechanical failure of such oxide scales.

**Table 6** Surface fracture energies, elastic moduli, and fracture toughness values at room temperature (RT) (calculated from atomistic data)

Oxide	$\gamma_i$ ( $\text{J m}^{-2}$ )	$E_{\text{ox}}$ (MPa)	$K_{\text{Ic}}$ ( $\text{MPa m}^{1/2}$ )
FeO	3.0	130 000	0.9
CoO	3.0	156 000	1.0
NiO	3.6	191 000	1.2
MnO	2.7	148 000	0.9
$\text{Fe}_3\text{O}_4$	4.5	208 000	1.4
$\text{FeCr}_2\text{O}_4$	5.0	233 000	1.5
$\text{Fe}_2\text{MnO}_4$	3.0	108 000	0.8
$\text{Al}_2\text{O}_3$	7.7	419 000	2.5
$\text{Cr}_2\text{O}_3$	5.8	283 000	1.8
$\text{Fe}_2\text{O}_3$	6.0	219 000	1.6
$\text{Y}_2\text{O}_3$	4.8	123 000	1.1
$\text{SiO}_2$	4.4	85 600	0.9

Reproduced from Robertson, J.; Manning, M. I. *Mater. Sci. Technol.* **1990**, 6, 81–91.

**Table 7** Values of Poisson ratios  $\nu_{\text{ox}}$  at RT

Oxide	$\nu$
$\text{Al}_2\text{O}_3$	0.24
$\text{Cr}_2\text{O}_3$	0.29
FeO	0.36
$\text{Fe}_2\text{O}_3$	0.19
$\text{Fe}_3\text{O}_4$	0.29
NiO	0.32
$\text{SiO}_2$	0.07
$\text{TiO}_2$	0.28
CoO	0.36
MnO	0.34
$\text{FeCr}_2\text{O}_4$	0.31
$\text{MnFe}_2\text{O}_4$	0.39
$\text{Y}_2\text{O}_3$	0.38

Reproduced from Robertson, J.; Manning, M. I. *Mater. Sci. Technol.* **1990**, 6, 81–91.

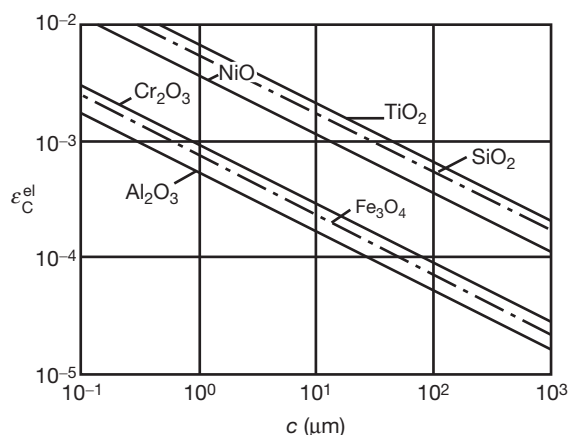


**Figure 11** Strain values to scale cracking  $\varepsilon_c$  under tensile stress for different oxides as a function of the physical defect size  $c$  calculated using eqn [12]. Reproduced from Schütze, M. *Oxid. Met.* **1995**, *44*, 29–61.

Similar values are observed for the beginning of crack growth (scale detachment) along the metal/scale interface, as represented in Figure 12. These values are slightly lower than those observed in experimental investigations for global scale failure under compression, which is, however, sensible, as the beginning of crack growth or delamination along the scale/metal interface is not yet the complete failure by spalling or detachment of large parts of the scale. Therefore, the situation in Figure 12 represents rather a conservative approach to scale failure under compressive stresses. See Schütze<sup>1,104</sup> for an in-depth discussion of the models available for the theoretical description of scale failure occurs. Schütze<sup>1</sup> also contains a discussion of the influence of oxide creep, if existing, on the critical strains to failure. It can, however, be stated here that this influence is limited and only becomes evident at very low defect or grain sizes of the oxide. For most technical situations, the oxide scale will behave in a brittle manner as described by the model equations shown, even at the operation temperature of a high temperature component.

### 1.08.5 Maintaining the Protective Effect of Oxide Scales Even After Mechanical Failure under Stresses

#### 1.08.5.1 Healing of Cracks or other types of Damage in the Protective Oxide Scale

As the discussion on the cracking behavior of oxide scales shows that brittle failure is to be expected, it is

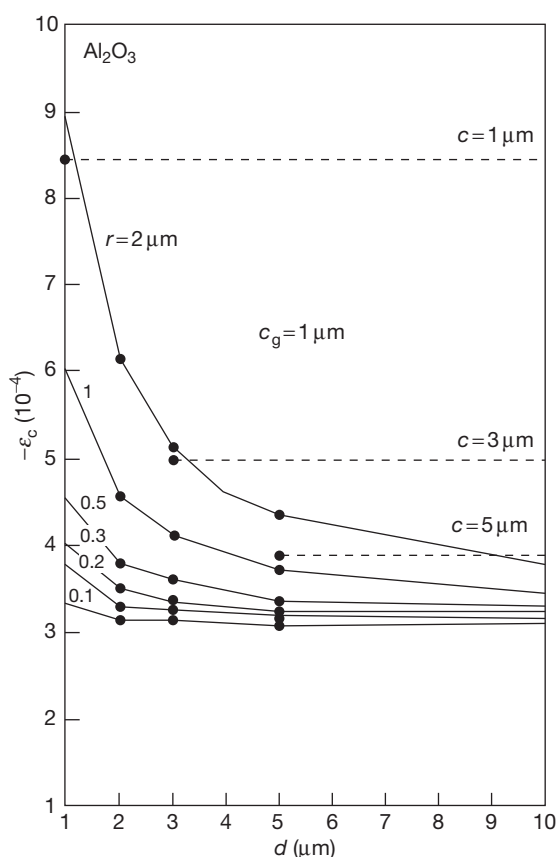


**Figure 12** Strain values to the beginning of scale delamination  $\varepsilon_c$  under compressive stress for  $\text{Al}_2\text{O}_3$  and a physical defect size  $c_g = 1 \mu\text{m}$  at the scale/metal interface calculated using eqn [13].  $r$  denotes the 'interfacial amplitude' (see Figure 10(b)). Reproduced from Schütze, M.; Ito, S.; Przybilla, W.; Echsler, H.; Bruns, C. *Mater. High Temp.* **2001**, *18*, 39–50.

even more important to discuss the mechanism of oxide damage healing. It can be stated that all current technical metallic alloys would not survive for a long time in operation, from a high temperature corrosion point of view, if healing of oxide scale damage did not take place. The reason is that in almost all cases of high temperature, service strains or stresses of the types described so far (be it external or internal stresses of the system) will arise and endanger the integrity of the brittle oxide scale. What distinguishes a growing 'ceramic' oxide scale from a 'dead' artificially applied ceramic layer is that, during high temperature exposure, the oxidation process and, thus, the growth of the oxide scale, continues. At the same time, this growth process represents the healing potential of the oxide/metal system, which allows it

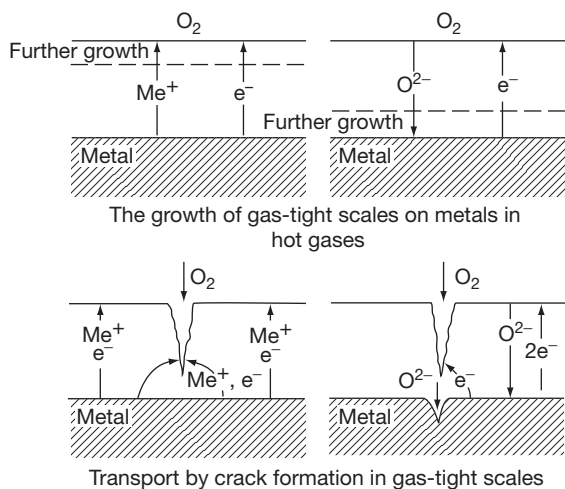


**Figure 13** The two extreme cases of material transport through oxide scales (inward growth and outward growth) and their effect on scale crack healing. Reproduced from Bruch, U.; Döhle, K.; Pütz, J.; Rahmel, A.; Schütze, M.; Schuhmacher, K. D. *Proceedings of the International Congress on Metallic Corrosion*; NRC, Ottawa, 1984; Vol. 3, 325–329.

to protect itself even after intermediate mechanical damage.

The principles of the crack healing process are illustrated schematically in **Figure 13**. As the diffusion length at a crack is shorter than in the undamaged part of the oxide scale, this means that the local oxide growth rates will also be higher than in the rest of the scale. With increasing time and continuously increased thickening at these damaged spots, the overall scale becomes smooth again so that with time the crack is closed. **Figure 14** shows that this is not a theoretical consideration alone but that cracks can be closed almost completely by this healing process, leaving only scars in the oxide surface, which are hard to detect by optical means, (**Figure 14(c)**). As observed in experiments, healing of oxide cracks requires that a certain critical deformation rate of the substrate is not exceeded.<sup>122</sup> Otherwise the crack faces of the oxide scale would move apart at a higher rate than can be accommodated by the oxidation process from the faces of the scale crack. **Figure 15**

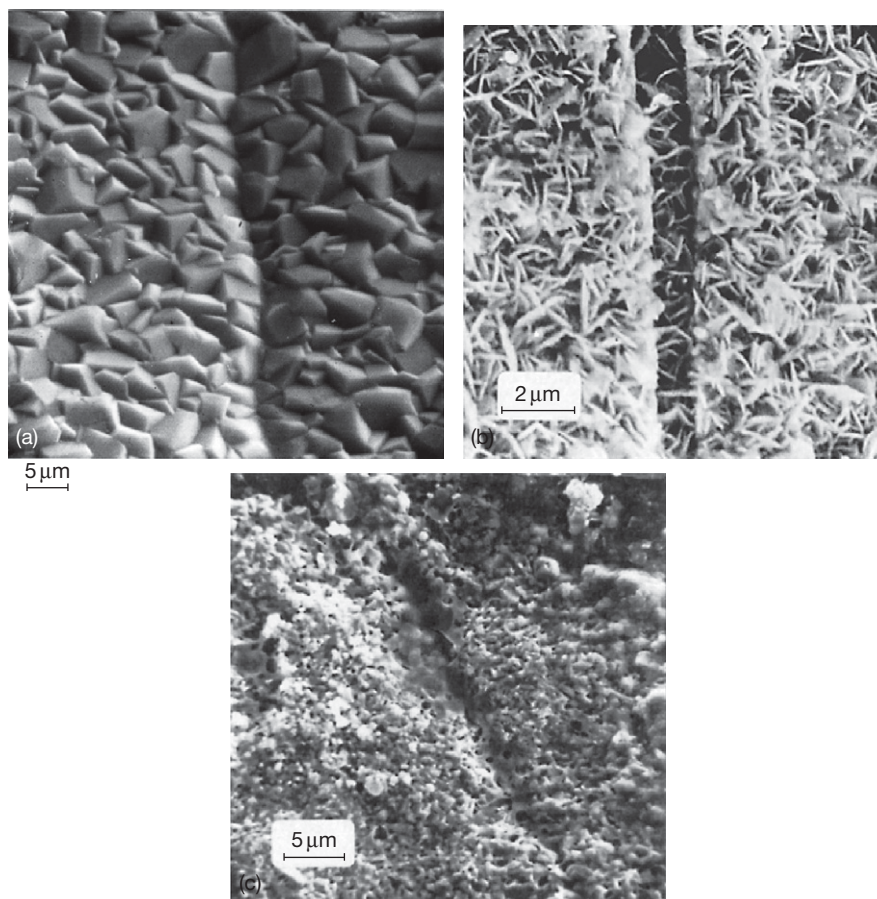


**Figure 14** Examples of healed scale cracks in SEM surface investigations. (a) NiO scale on Ni99.2 after oxidation and straining at 800 °C, (b) oxide scale on Alloy 800H after oxidation and straining at 800 °C, and (c) same scale as (b) but later stage in the healing process.

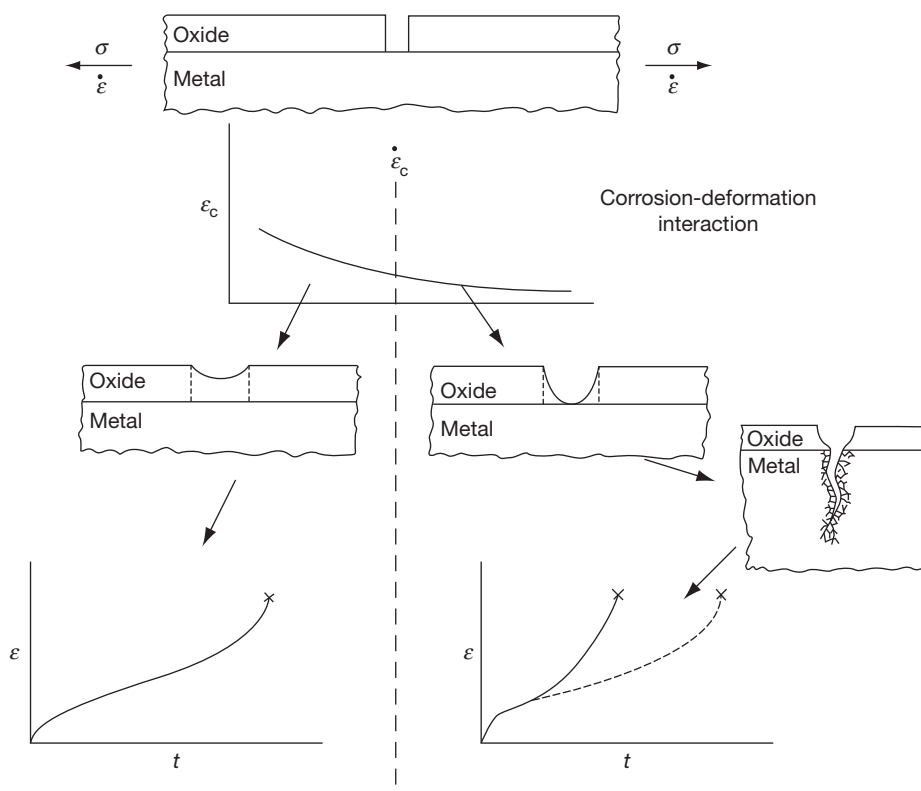


**Figure 15** Schematic illustration of the role of a critical deformation rate  $\dot{\epsilon}_c$  of the substrate for scale crack healing.

Left: below  $\dot{\epsilon}_c$  instant healing of the scale crack is possible and in the creep curve  $\epsilon-t$  no acceleration of creep due to corrosion damage occurs. Right: above  $\dot{\epsilon}_c$  healing is impeded and internal corrosive attack at the unprotected site reduces the load bearing metal cross-section ending up in accelerated creep.

illustrates this schematically, indicating that above this critical strain rate, crack healing would be impeded and internal corrosion in particular along grain boundaries could facilitate crack formation in the metal subsurface zone as observed by Wagner.<sup>123</sup> At lower strain rates, the healing process would be able to close the cracks again, restoring the protective effect of the scale. This situation has been modeled by superimposing the oxidation process on the movement of crack phases by continued deformation and the details of this model development as described by Barbehön *et al.*<sup>124</sup> The model calculations provided quantitative values of the critical strain rates, which were in the range of  $10^{-6}$  to  $10^{-8} \text{ s}^{-1}$  and in good agreement with the experimentally determined values.<sup>1,102</sup>

#### 1.08.5.2 The Influence of Subsurface Zone Depletion on Maintaining the Protective Effect of Oxide Scales Under Stresses

Contrary to what is required by the theoretical models of oxidation<sup>125</sup> it is usual that significant depletion

of the protective scale-forming alloy takes place in the metal subsurface zone directly underneath the oxide scale. Evidently, in most technical cases, an equilibrium situation is not achieved and the oxidation process requires a faster supply of scale forming species from the substrate than can be achieved by the alloy. As shown in Figure 16 this is at least true for many of the technical alloys in their normal operating temperature range (further examples are given elsewhere<sup>1,4</sup>). This may be different at very high temperatures and for materials with high self-diffusion coefficients of the scale forming elements, where the level of this element is equal over the whole material thickness (i.e., no gradient), for example, FeCrAl alloys at 1200 °C.<sup>127</sup>

The drop in the alloy concentration directly underneath the oxide scale means that it is no longer the original alloy that was in contact with the oxide scale or the environment, if the oxide scale fails. In order to make this aspect clearer one should take a look at Figure 17, which shows the parabolic rate constant as a function of the chromium content in iron chromium steels at 1000 °C.<sup>128</sup> From this figure

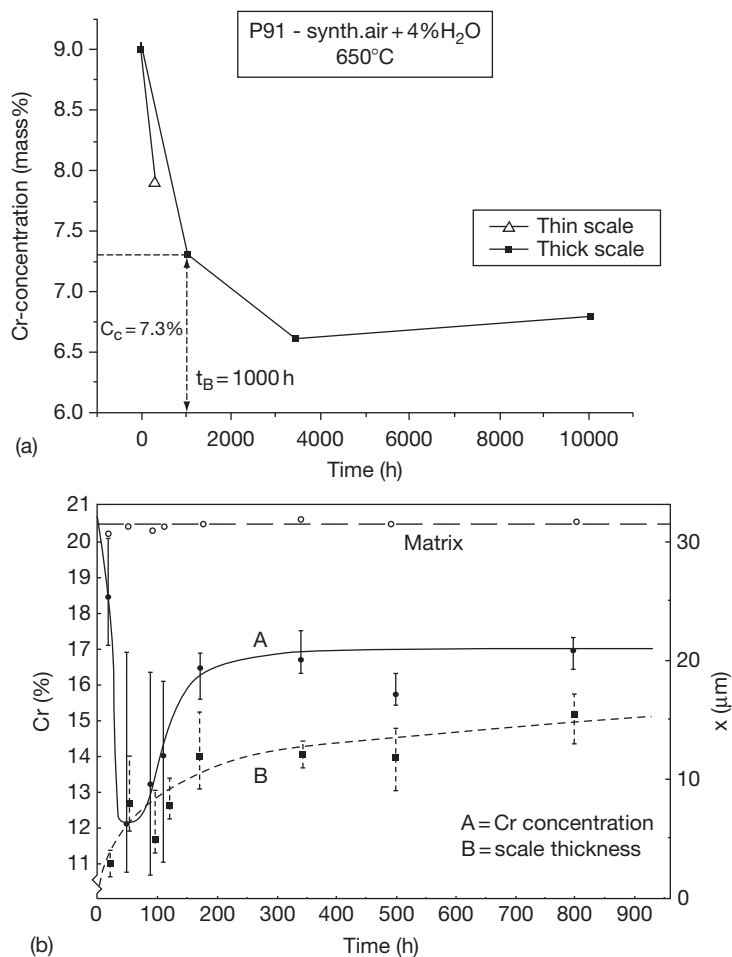


**Figure 16** Cr depletion during oxidation as a function of oxidation time measured by EPMA directly underneath the oxide scale in the metal subsurface zone. (a) P91 in air with 4% water vapor at 650 °C,<sup>4</sup> (b) alloy 800 in laboratory air at 800 °C,<sup>126</sup> A = Cr concentration, B = oxide scale thickness.

it becomes clear that steel, containing originally 20% of chromium which forms a more or less pure chromia scale, would behave much worse after significant depletion of chromium in the metal subsurface zone if the scale should crack or spall. At these spots, a material with significantly lower chromium concentration would be exposed to the oxidizing environment and, consequently, fast-growing iron-rich oxides would grow at these spots strongly deteriorating the protective effect of the scale. For this, it is not necessary that the scale is cracked by external stresses; even intrinsic growth stresses or geometrically induced growth stresses can lead to scale damage as shown in Figure 18, where nodule formation of fast-growing iron-rich oxides has taken place at machining marks on an undeformed specimen of 9% chromium steel, which protruded through the

thin chromium-rich oxide scale on the original surface.<sup>129</sup> As can be seen from Figure 16 and also Schütze<sup>4</sup> for this kind of material a steep drop in the chromium content takes place during oxidation.

Generally, four different cases can be distinguished with regard to the influence of depletion in the metal subsurface zone on the healing capability of damaged oxide scales. This is summarized schematically in Figure 19 for the example of chromia formers. In case (a) subsurface zone depletion takes place at a measurable rate but the values do not fall below the critical Cr-limit, which is necessary to form the protective scale. This situation guarantees the long-term healing capability of the oxide/metal system under operation. In case (b) there is a steep drop in the concentration of the protective scale forming the alloy at the beginning of oxidation but



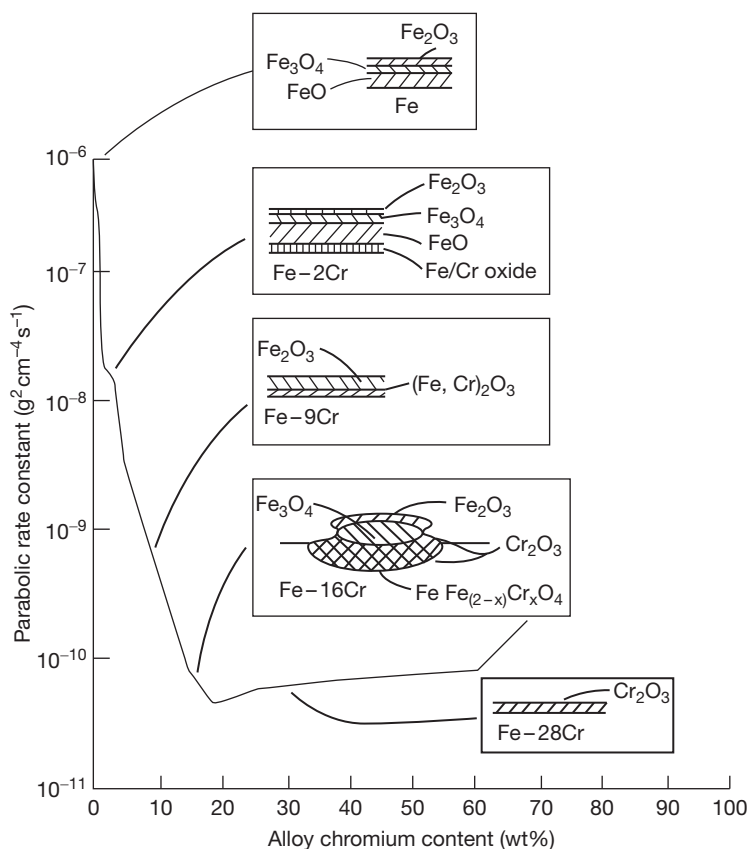


**Figure 17** Schematic showing the effect of Cr in Fe–Cr alloys on oxidation rate and oxide scale structure at 1000 °C in oxygen. Reproduced from Whittle, D. P.; Wood, G. C.; Evans, D. J.; Scully, D. B. *Acta Metall.* **1967**, *15*, 1747.

rediffusion of this element from the metal interior fills the reservoir directly underneath the oxide scale again so that the critical limit is undercut only temporarily. If oxide scale cracking can be avoided in this first period of exposure time, then the healing capability would be restored and would last for the rest of the lifetime of the component. Case (c) represents the situation where rediffusion from the metal interior is not able to fill the alloying reservoir in the metal subsurface zone to the extent which allows protective healing of the oxide scale, and case (d) shows the even worse situation where the composition of the subsurface zone falls below the thermodynamic stability limit of the oxide scale in contact with the metal substrate. In the latter case, therefore, even without any mechanical damage to the oxide scale, the scale would no longer be stable from a chemical point of view and would be converted into a nonprotective type of oxide.

The situation of subsurface zone depletion and rediffusion from the metal interior has been modeled

by a number of authors and for different material systems.<sup>130–138</sup> Two of these models have been converted into an open source code software tool. The first is called COSIM and is available from NASA.<sup>139</sup> The second is called ODIN<sup>140</sup> and allows the treatment of the situation of two-dimensional structures, which is of importance at edges and corners. As discussed in [Section 1.08.2](#), these sites are most endangered from the viewpoint of the stress situation in the oxide scale. A pragmatic diagram has been developed by Whittle using Wagner's considerations on the formation of a continuous protective oxide scale,<sup>141</sup> ([Figure 20](#)).<sup>142</sup> Further details are given elsewhere.<sup>1</sup> The diagram in [Figure 20](#) marks four regions with increased healing potential. In region (1), the chromium content is not sufficient to establish a protective chromia scale. In region (2), a protective scale can be established but after the first cracking or spalling the amount of chromium would not be sufficient for protective healing. This region would correspond to cases (c) and (d) in [Figure 19](#).

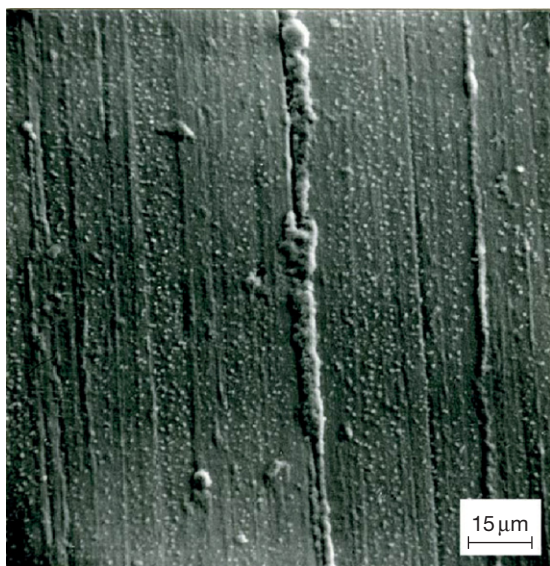


**Figure 18** Oxide nodule formation by faster growing Fe-rich Cr-(Fe)-oxide at machining marks on an undeformed specimen of a 9% Cr steel after 850 h in isothermal oxidation at 650 °C in air. Reproduced from Wulf, G. L.; McGirr, M. B.; Wallwork, G. R. *Corros. Sci.* **1969**, 9, 739.

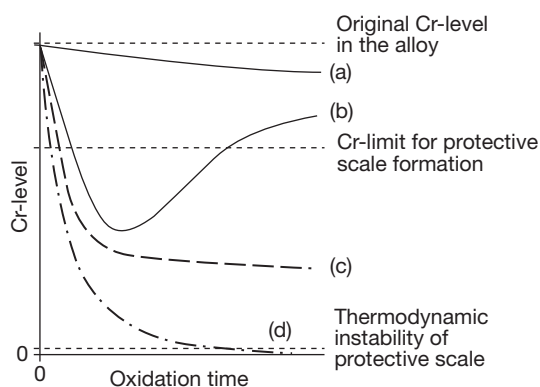


**Figure 19** Schematic of the four cases of subsurface zone depletion of the protective scale forming element (in this example Cr for chromia formers): (a) Drop of the alloy concentration at a slow rate. The concentration does not fall below the Cr-limit for protective scale formation. (b) Temporary drop below the protective limit but rediffusion from the alloy interior = temporary jeopardizing of the protective effect. (c) Final drop below the protective limit but not below the thermodynamic stability limit of the oxide on the alloy; in case of scale damage the protective effect would be finally lost. (d) Same situation as (c) but drop below the thermodynamic stability limit = 'chemical destruction' of the protective scale without the need of superimposed stresses.

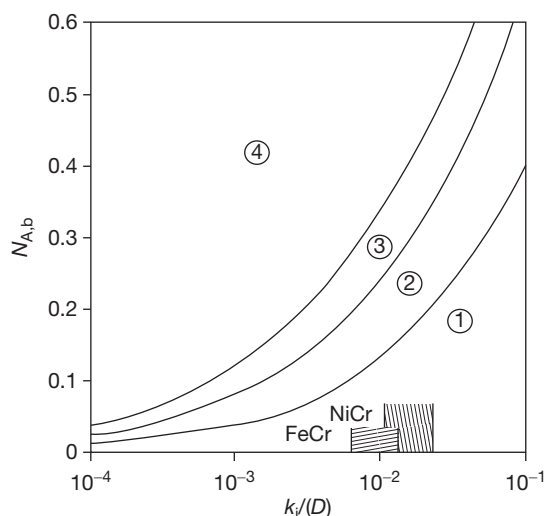


**Figure 20** Critical values for the atom fraction  $N_{A,b}$  of the protective scale-forming element A as a function of the  $k_i/D$ .<sup>142</sup> This figure is an example for chromia formers.  $k_i$  = oxidation rate constant for the recession of the oxide/metal interface,  $D$  = interdiffusion coefficient of A in the alloy, also shown are the bandwidths of the  $k_i/D$  ratio for Fe–Cr and Ni–Cr alloys (see text for explanation).

Region (3) shows the area in which healing can take place at least once after cracking or spalling and only region (4) guarantees repeated protective healing for longer operation times. The latter region would be equivalent to case (a) in Figure 19. Similar diagrams can of course be established also for alumina formers and help in the assessment of the choice of the right material for long-term operation. All these models can be used for a first theoretical assessment of the healing potential of materials. In most cases, very reasonable results can be expected. There is still, however, a need for a broader experimental basis to verify these models.

### 1.08.6 Concluding Remarks

It is the aim of this chapter to illustrate the important role of the mechanical aspects of oxidation behavior, particularly oxidation resistance of metallic materials at high temperatures. In a number of cases where the observed oxidation behavior could not be explained by the classical models of oxidation theory, the presence of stresses in the oxide/metal system was the reason for the discrepancies. As shown in the

relatively concise treatment of this topic in this chapter, a number of well-elaborated models describing the role of stresses, and also the healing of scale damage and subsurface zone depletion for the protective effect of the oxide scales, exist. Furthermore, a limited number of experimental data are available to characterize at least the more common situations, but at this point more work is needed. The model basis is now sufficiently broad to develop comprehensive computer codes regarding the complex synergistic interplay of the different chemical and mechanical mechanisms. This has indeed been started<sup>141</sup> and may in the near future allow a better quantification of the role of stress effects in oxidation, especially under industrial conditions. At the same time, the basis of experimentally determined data that can be fed into computer calculations has to be broadened. This chapter provides a general understanding of this rather complex situation in which stresses and oxidation interact with each other, leading sometimes to unexpected oxidation behavior. For a more detailed treatment of the topic the reader is referred to the textbook literature.<sup>1</sup>

## References

- Schütze, M. *Protective Oxide Scales and Their Breakdown*; John Wiley: Chichester, 1997.
- Kofstad, P. *High Temperature Corrosion*; Elsevier Applied Science: London, 1988.
- Evans, H. E.; Donaldson, A. T.; Gilmour, T. C. *Oxid. Met.* **1999**, 52, 379–402.
- Schütze, M.; Renusch, D.; Schorr, M. *Mater. High Temp.* **2005**, 22, 113–120.
- Donchev, A.; Fietzek, H.; Kolarik, V.; Renusch, D.; Schütze, M. *Mater. High Temp.* **2005**, 22, 139–146.
- Isecke, B.; Schütze, M.; Strehblow, H. H. In *Springer Handbook of Materials Measurement Methods*; Czichos, H., Saito, T., Smith, L., Eds.; Springer Verlag: Berlin, 2006; Chapter 12: Corrosion.
- Schütze, M. *Oxid. Met.* **1985**, 24, 199–232.
- Kofstad, P.; Lillerud, K. P. *J. Electrochem. Soc.* **1980**, 127, 240.
- Lillerud, K. P.; Kofstad, P. *J. Electrochem. Soc.* **1980**, 127, 2397.
- Evans, A. G.; Crumley, G. B.; Demaray, R. E. *Oxid. Met.* **1983**, 20, 193.
- Caplan, D.; Sproule, G. I. *Oxid. Met.* **1975**, 9, 459.
- Ecer, G. M.; Meier, G. H. *Oxid. Met.* **1979**, 13, 119.
- Golightly, F. A.; Stott, F. H.; Wood, G. C. *Oxid. Met.* **1976**, 10, 163.
- Golightly, F. A.; Wood, G. C.; Stott, F. H. *Oxid. Met.* **1978**, 14, 217.
- Miner, R. G.; Nagarajan, V. *Oxid. Met.* **1981**, 16, 313.
- Pawel, R. E.; Cathcart, J. V.; Campbell, J. J. *J. Electrochem. Soc.* **1963**, 110, 551.
- Stringer, J. *Corros. Sci.* **1970**, 10, 513.
- Delaunay, D.; Huntz, A. M.; Lacombe, P. *Corros. Sci.* **1980**, 20, 1109.
- Zhao, J. G.; Huntz, A. M. *J. Mater. Sci.* **1984**, 19, 3166.
- Huntz, A. M.; Calvarin Amiri, G.; Evans, H. E.; Cailletaud, G. *Oxid. Met.* **2002**, 57, 499.
- Przybilla, W.; Schütze, M. *Oxid. Met.* **2002**, 58, 103–145.
- Przybilla, W.; Schütze, M. *Oxid. Met.* **2002**, 58, 337–359.
- Tylecote, R. F. *Mem. Sci. Rev. Metall.* **1965**, 62, 241.
- Jaenicke, W.; Leistikow, S. Z. *Phys. Chem.* **1958**, 15, 175.
- Jaenicke, W.; Leistikow, S.; Städler, A. *J. Electrochem. Soc.* **1964**, 111, 1031.
- Engell, H.; Wever, F. *Acta Metall.* **1957**, 5, 695.
- Buresch, F. E.; Bollenrath, F. J. *Nucl. Mater.* **1967**, 24, 270.
- Cathcart, J. V.; Liu, C. T. *Oxid. Met.* **1973**, 6, 123.
- Roy, C.; Burgess, B. *Oxid. Met.* **1970**, 2, 235.
- Donaldson, A. T.; Evans, H. E. *J. Nucl. Mater.* **1981**, 99, 38.
- Kang, K. J.; Hutchinson, J. W.; Evans, A. G. *Acta Mater.* **2003**, 51, 1283–1291.
- Zhao, J. G.; Zhang, Y. T. *Mater. Sci. Eng. A* **1989**, 120, 245.
- Huntz, A. M.; Zhao, J. G.; Boumazza, A.; Moulin, G. *Mater. Sci. Technol.* **1988**, 4, 470.
- Vosberg, V. R.; Fischer, W.; Berger, M. G.; Clemens, D.; Quadackers, W. J.; Nickel, H. *Fresenius J. Anal. Chem.* **1996**, 355, 745–747.
- Zouboulis, E.; Renusch, D.; Grimsditch, M. *Appl. Phys. Lett.* **1998**, 72, 1.
- Birnie, J.; Graggs, C.; Gardiner, D. J.; Graves, P. R. *Corros. Sci.* **1992**, 33, 1.
- Tolpygo, V. K.; Clarke, D. R. *Mater. High Temp.* **2000**, 17, 59–70.
- Mougin, J.; Rosman, N.; Lucazeau, G.; Galerie, A. J. *Raman Spectrosc.* **2001**, 32, 739–744.
- Wouters, Y.; Galerie, A.; Bouvier, P.; Mermoux, M.; Petit, J. P. *Microscopy of Oxidation*; Science Reviews: Strixton, UK, 2005; Vol. 6, pp 145.
- Lawless, K. R.; Gwathmey, A. T. *Acta Metall.* **1956**, 4, 153.
- Pyun, Y. J.; Homma, T.; Takakuwa, K. *J. Jpn. Int. Metall.* **1983**, 47, 663.
- Liu, C.; Lebrun, J. L.; Huntz, A. M.; Sibieude, F. Z. *Metallk.* **1993**, 84, 140.
- Goedjen, J. G.; Stout, J. H.; Guo, Q.; Shores, D. A. *Mater. Sci. Eng. A* **1994**, 177, 115.
- Sarioglu, C.; Schumann, E.; Blachere, J. R.; Pettit, F. S.; Meier, G. H. *Mater. High Temp.* **2000**, 17, 109–115.
- Corkovic, S.; Pyzalla, A. R. *Mater. Corr.* **2004**, 55, 341.
- Tortorelli, P. F.; More, K. L.; Specht, E. D.; Pint, B. A.; Zschack, P. *Mater. High Temp.* **2003**, 20, 303–309.
- Calvarin-Amiri, G.; Huntz, A. M. *R. Molins Mater. High Temp.* **2001**, 18, 91–99.
- Huntz, A. M.; Lefevre, A.; Andrieux, M.; Severac, C.; Moulin, G.; Molins, R.; Jomard, F. *Microscopy of Oxidation*; Science Reviews: Strixton, UK, 2003; Vol. 5, pp 393.
- Gnäupel-Herold, T.; Reimers, W. In *Proceedings of the International Conference on Residual Stresses*; Frisson, T., Odin, M., Anderson, A., Eds.; Linköping University: Linköping, Sweden, 1997.
- Hou, P. Y.; Paulikas, A. P.; Veal, B. W. *Microscopy of Oxidation*; Science Reviews: Strixton, UK, 2005; Vol. 6, pp 373.
- Echslar, H.; Alija Martinez, E.; Singheiser, L.; Quadackers, W. J. *Mater. Sci. Eng. A* **2004**, 384, 1–11.
- Mennicke, C.; Clarke, D. R.; Rühle, M. *Oxid. Met.* **2001**, 55, 551–569.
- Homma, T.; Pyun, P. J. *High Temperature Corrosion*; Jap. Int. Metals: Tokyo, 1983; 161.

54. Liu, C.; Huntz, A. M.; Lebrun, J. *Mater. Sci. Eng. A* **1993**, *160*, 113.
55. Galerie, A.; Toscan, F.; Dupeux, M.; Mouglin, J.; Lucazeau, G.; Valot, C.; Huntz, A. M.; Antoni, L. *Mater. Res.* **2004**, *7*, 83–88.
56. Dionnet, B. PhD Thesis, University of Limoges, 1993.
57. Pilling, N. B.; Bedworth, R. E. *J. Inst. Metals* **1923**, *29*, 529.
58. Hancock, P.; Hurst, R. C. *Adv. Corros. Sci. Technol.* **1974**, *4*, 1.
59. Weast, R. C. *Physical Constants of Inorganic Compounds Handbook of Chemistry and Physics*, 6th ed.; CRC, 1984; B68, B161.
60. Bernstein, H. L. *Metall. Trans.* **1987**, *A18*, 975.
61. Stott, F. H.; Atkinson, A. *Mater. High Temp.* **1994**, *12*, 195–207.
62. Chevalier, S.; Strehl, G.; Favergeon, J.; Desserrey, F.; Weber, S.; Heintz, O.; Borchardt, G.; Larpin, J. P. *Mater. High Temp.* **2003**, *20*, 253–259.
63. Clarke, D. R. *Acta Mater.* **2003**, *51*, 1393–1407.
64. Krishnamurthy, R.; Srolovitz, D. J. *Acta Mater.* **2003**, *51*, 2171–2190.
65. Limarga, A.; Wilkinson, D. S.; Weatherly, G. L. *Scripta Mater.* **2004**, *50*, 1475–1479.
66. Christl, W.; Rahmel, A.; Schütze, M. *Oxid. Met.* **1989**, *31*, 1.
67. Taniguchi, S. *Trans IDIJ* **1985**, *25*, 3.
68. Appleby, W. K.; Tylecote, R. F. *Corros. Sci.* **1970**, *10*, 325.
69. Howes, V. R.; Richardson, C. N. *Corros. Sci.* **1969**, *9*, 385.
70. Singheiser, L. Forschungszentrum Jülich, Private communication.
71. Hänsel, M.; Boddington, C. A.; Young, D. J. *Corros. Sci.* **2003**, *45*, 967–981.
72. Quadackers, W. J.; Tyagi, A. K.; Clemens, D.; Anton, R.; Singheiser, L. In *Elevated Temperature Coatings: Science and Technology III*; Hampikian, J. M., Dahotre, N. B., Eds.; The Minerals, Metals and Materials Society: Warrendale, 1999; pp 119–138.
73. Lee, Y. Y.; McNallan, M. J. *Metall. Trans.* **1987**, *18A*, 1099.
74. Bramhoff, D.; Grabke, H. J.; Schmidt, H. P. *Werkst. Korr.* **1989**, *40*, 642.
75. Schwalm, C.; Schütze, M. *Mater. Corros.* **2000**, *51*, 34, 73, 161.
76. Schmitz-Niederau, M.; Schütze, M. *Oxid. Met.* **1999**, *52*, 225–240.
77. Schütze, M.; Malessa, M.; Rohr, V.; Weber, T. *Surf. Coat. Technol.* **2006**, *201*, 3872–3879.
78. Huntz, A. M.; Schütze, M. *Mater. High Temp.* **1994**, *12*, 151–161.
79. Rensch, D.; Grimsditch, M.; Koshelev, I.; Veal, B. W. *Oxid. Met.* **1997**, *48*, 471.
80. Uran, S.; Grimsditch, M.; Veal, B.; Paulikas, P. *Oxid. Met.* **2001**, *56*, 551–569.
81. Koshelev, I. K.; Paulikas, A. P.; Uran, S.; Beno, M. B.; Jennings, G.; Linton, J.; Veal, B. W. *Oxid. Met.* **2003**, *59*, 469–481.
82. Rensch, D.; Muralidharan, G.; Uran, S.; Grimsditch, M.; Veal, B. W.; Wright, J. K.; Williamson, R. L. *Oxid. Met.* **2000**, *53*, 171.
83. Uran, S.; Veal, B. W.; Grimsditch, M.; Pearson, J.; Berger, A. *Oxid. Met.* **2000**, *54*, 73–85.
84. Wright, J. K.; Williamson, R. L.; Rensch, D.; Grimsditch, M.; Veal, B. W.; Hou, P. Y.; Cannon, R. M. *Mater. Sci. Eng. A* **1999**, *262*, 246.
85. Lipkin, D. M.; Clarke, D. R.; Hollatz, M.; Bobeth, M.; Pompe, W. *Corros. Sci.* **1997**, *39*, 231.
86. Tolpygo, V. K.; Dryden, J. R.; Clarke, D. R. *Acta Mater.* **1998**, *46*, 927.
87. Tien, J. K.; Davidson, J. M. In *Stress Effects and the Oxidation of Metals Proceedings*; Cathcart, J. V., Ed.; TMS-AIME: New York, 1975; p 200.
88. Metcalfe, E.; Manning, M. I. The spalling of steam grown oxide from austenitic and ferritic alloys. Report RD/L/R/ 1966 Central Electricity Generating Board, CERL, Leatherhead, 1977.
89. Armitt, J.; Holmes, D. R.; Manning, M. I.; Meadowcroft, D. B.; Metcalfe, E. The spalling of steam grown oxide from superheater and reheater tube steels. Report FP686 EPRI, Palo Alto, 1978.
90. Manning, M. I.; Metcalfe, E. Steamside spalling from Type 316 superheater and reheater tubes. Report RD/L/ N15/75 Central Electricity Generating Board, CERL, Leatherhead, 1975.
91. Saunders, S. R. J.; Nagl, M. M.; Schütze, M. *Mater. High Temp.* **1994**, *12*, 103–109.
92. Schütze, M.; Ito, S.; Przybilla, W.; Echsler, H.; Bruns, C. *Mater. High Temp.* **2001**, *18*, 39–50.
93. Küppenbender, I.; Schütze, M. *Oxid. Met.* **1994**, *42*, 109–144.
94. Golightly, F. A.; Stott, F. H.; Wood, G. C. *Werkstoffe Korr.* **1979**, *30*, 487–491.
95. Banks, J. P.; Gohil, D. D.; Evans, H. E.; Hall, D. J.; Saunders, S. R. J. In *Materials for Advanced Power Engineering*; Contouradis, D., et al. Ed.; Kluwer Academic: Dordrecht, 1994; pp 1543–1552.
96. Guttman, V.; Mediavilla, A.; Ruano, O. *Mater. High Temp.* **1993**, *11*, 42–50.
97. Nagl, M. M.; Saunders, S. R. J.; Guttman, V. *Mater. High Temp.* **1994**, *12*, 163–168.
98. Hancock, P.; Nicholls, J. R. *Mater. High Temp.* **1994**, *12*, 209–218.
99. Bruns, C.; Schütze, M. *Oxid. Met.* **2001**, *55*, 35–68.
100. Nagl, M. M.; Evans, W. T.; Hall, D. J.; Saunders, S. R. J. *J. Phys. III* **1993**, *3*, 933–941.
101. Nagl, M. M.; Evans, W. T.; Saunders, S. R. J.; Hall, D. J. *Mater. Sci. Technol.* **1992**, *8*, 1043–1049.
102. Schmitz-Niederau, M.; Schütze, M. *Oxid. Met.* **1999**, *52*, 241–276.
103. Robertson, J.; Manning, M. I. *Mater. Sci. Technol.* **1990**, *6*, 81–91.
104. Schütze, M. *Oxid. Met.* **1995**, *44*, 29–61.
105. Hukelmann, F. Doctoral Thesis, Technical University of Clausthal, 2000.
106. Hou, P. Y.; Atkinson, A. *Mater. High Temp.* **1994**, *12*, 119–125.
107. Mouglin, J.; Dupeux, M.; Galerie, A.; Antoni, L. *Mater. Sci. Technol.* **2002**, *18*, 1217–1220.
108. Hou, P. Y.; Saunders, S. R. J. *Mater. High Temp.* **2005**, *22*, 121–129.
109. Hou, P. Y.; Priimak, K. *Oxid. Met.* **2005**, *63*, 113–129.
110. Funkenbusch, A. W.; Smeggil, J. G.; Bornstein, N. S. *Metall. Trans.* **1985**, *16A*, 1164.
111. Smialek, J. L. *Metall. Trans.* **1991**, *22A*, 739.
112. Suga, T. Doctoral Thesis University of Stuttgart **1983**.
113. Suga, T.; Kvernes, I.; Ellsner, G. Z. *Werkstofftechn.* **1984**, *15*, 371.
114. Schütze, M. In *High Temperature Corrosion of Advanced Materials and Protective Coatings*; Saito, Y., et al. Ed.; North Holland: Amsterdam, 1992; 29.
115. Evans, H. E.; Mitchell, G. P.; Lobb, R. C.; Owen, D. R. J. *Proc. R. Soc. London A* **1993**, *440*, 1.
116. Evans, A. G.; Hutchinson, J. W. *Acta Metall.* **1989**, *37*, 909.
117. Evans, U. R. *An Introduction to Metallic Corrosion*; Arnold Publishers: London, 1948.
118. Zimmermann, D.; Tolpygo, V. K.; Rühle, M.; Clarke, D. R. *Z. Metallk.* **2003**, *94*, 157–162.

119. Hancock, P.; Nicholls, J. R. *Mater. Sci. Technol.* **1988**, *4*, 398.
120. Schütze, M. *Oxid. Met.* **1986**, *25*, 409.
121. Bruch, U.; Döhle, K.; Pütz, J.; Rahmel, A.; Schütze, M.; Schuhmacher, K. D. *Proceedings of the International Congress on Metallic Corrosion*; NRC, Ottawa, 1984; Vol. 3, 325–329.
122. Schütze, M. *Werkstoffe Korros.* **1987**, *38*, 597.
123. Wagner, C. Z. *Elektrochemie* **1959**, *63*, 772.
124. Barbehön, J.; Rahmel, A.; Schütze, M. In *High Temperature Alloys for Gas Turbines and Other Applications*; Betz, W., et al. Ed.; D. Reidel Publishers: Dordrecht, 1986; 1267.
125. Quadackers, W. J.; Bongartz, K. *Mater. Corr.* **1994**, *45*, 232–241.
126. Wright, I. G. In *Metals Handbook* 9th ed., ASM International: Metals Park, 1987; Vol. 13, Corrosion, 97.
127. Barbehön, J.; Rahmel, A.; Schütze, M. *Oxid. Met.* **1988**, *30*, 85.
128. Whittle, D. P.; Wood, G. C.; Evans, D. J.; Scully, D. B. *Acta Metall.* **1967**, *15*, 1747.
129. Wulf, G. L.; McGirr, M. B.; Wallwork, G. R. *Corros. Sci.* **1969**, *9*, 739.
130. Evans, H. E.; Lobb, R. C. *Corros. Sci.* **1984**, *24*, 223.
131. Nicholls, J. R., et al. In *Lifetime Modelling of High Temperature Corrosion Processes*; Schütze, M., Quadackers, W. J., Nicholls, J. R., Eds.; EFC-Publication No. 34: Maney, Leeds, 2001.
132. Wright, I. G.; Pint, B. A.; Hall, L. M.; Tortorelli, P. F. In *Lifetime Modelling of High Temperature Corrosion Processes*; Schütze, M., Quadackers, W. J., Nicholls, J. R., Eds.; EFC-Publication No. 34: Maney, Leeds, 2001; p 339–358.
133. Nesbitt, J. A. In *Lifetime Modelling of High Temperature Corrosion Processes*; Schütze, M., Quadackers, W. J., Nicholls, J. R., Eds.; EFC-Publication No. 34: Maney, Leeds, 2001; pp 359–378.
134. Evans, H. E.; Taylor, M. E. *Oxid. Met.* **2001**, *55*, 17–34.
135. Pragnell, W. M.; Evans, H. E. *Oxid. Met.* **2006**, *66*, 209–230.
136. Renusch, D.; Echsler, H.; Schütze, M. *Mater. Sci. Forum* **2004**, *461–464*, 729–736.
137. COSIM – A finite difference computer model to predict tenary concentration profiles associated with oxidation and interdiffusion of overlay coated substrates. Funding No. WU-714-04-20-00. Contact: J.A. Nesbitt, NASA John Glenn Research Centre, Cleveland.
138. Pragnell, W. M. PhD thesis, University of Birmingham, 2005.
139. Wagner, C. J. *Electrochem. Soc.* **1952**, *99*, 369.
140. Whittle, D. P. *Oxid. Met.* **1972**, *4*, 171.
141. Schütze, M.; Malessa, M.; Renusch, D.; Tortorelli, P. F.; Wright, I. G.; Dooley, R. B. *Mater. Sci. Forum* **2006**, *522–523*, 393–400.
142. Rhines, F. N.; Wolf, J. S. *Metall. Trans.* **1970**, *1*, 1701.

## 1.10 Oxidation of Metals and Alloys

**P. Y. Hou**

Lawrence Berkeley National Laboratory, Materials Sciences Division, 1 Cyclotron Rd., Berkeley, CA 94720, USA

© 2010 Elsevier B.V. All rights reserved.

<b>1.10.1</b>	<b>Introduction</b>	196
<b>1.10.2</b>	<b>Oxidation of Nickel, Cobalt, and Iron</b>	197
1.10.2.1	Nickel	197
1.10.2.1.1	Transient stage oxidation	197
1.10.2.1.2	Oxide structures	197
1.10.2.1.3	Growth rate and transport processes through NiO	199
1.10.2.2	Cobalt	200
1.10.2.3	Iron	201
<b>1.10.3</b>	<b>Oxidation of Refractory Metals and Their Alloys</b>	203
1.10.3.1	Oxidation of Ta, Nb, Mo, and W Metals	203
1.10.3.1.1	Tantalum and niobium	203
1.10.3.1.2	Tungsten and molybdenum	205
1.10.3.2	Oxidation of Refractory Alloys	206
1.10.3.3	Coatings on Refractory Metals and Alloys for Oxidation Protection	207
<b>1.10.4</b>	<b>Oxidation of Silica-Forming Alloys</b>	208
1.10.4.1	Si-Containing Alloys	208
1.10.4.2	Silicides	209
<b>1.10.5</b>	<b>Oxidation of Chromia-Forming Alloys</b>	211
1.10.5.1	Transport Properties and Oxidation Rates	211
1.10.5.2	Cr <sub>2</sub> O <sub>3</sub> Layer Development on Alloys	213
1.10.5.3	Scale Morphology and Breakaway Oxidation	214
<b>1.10.6</b>	<b>Oxidation of Alumina-Forming Alloys</b>	215
1.10.6.1	Scale Development	216
1.10.6.2	Oxidation Rates	218
1.10.6.3	Oxide Growth Mechanism	219
1.10.6.4	Scale Adhesion	223
<b>1.10.7</b>	<b>Effect of Minor Alloying Elements and Impurities</b>	224
1.10.7.1	Reactive Elements	224
1.10.7.1.1	Promoted selective oxidation	226
1.10.7.1.2	Decreased growth rate and changed growth direction	226
1.10.7.1.3	Improved scale adhesion	228
1.10.7.2	Nonmetallic Impurities	230
1.10.7.2.1	Sulfur	230
1.10.7.2.2	Other impurities	231
<b>1.10.8</b>	<b>Concluding Remarks</b>	232
<b>References</b>		232

### Abbreviations

**AE** Acoustic emission

**AES** Auger electron spectrometry

**EDS** Energy dispersive spectroscopy

**EELS** Electron energy loss spectroscopy

**ppm** Parts per million

**RE** Reactive element

**SEM** Secondary electron microscopy

**SIMS** Secondary ion mass spectrometry

**SNMS** Secondary neutral mass spectrometry

**STEM** Scanning transmission electron microscopy

**TEM** Transmission electron microscopy



**UHV** Ultra high vacuum  
**YAG** Yttrium aluminum garnet

### Symbols

***b*** Oxide grain size  
***D*** Diffusivity  
 **$\Delta G$**  Gibb's free energy  
 **$k_p$**  Parabolic rate constant  
 **$p_{O_2}$**  Partial pressure of oxygen  
***R*** Gas constant  
***T*** Temperature  
 **$\delta$**  Grain boundary width

## 1.10.1 Introduction

This chapter provides an overview of the corrosion behavior of different metals and alloys where oxygen is the only oxidant. Isothermal oxidation studies conducted in air and oxygen are considered, but any effects due to the presence of nitrogen in air, or humidity in the atmosphere are not included; these topics are covered in **Chapter 1.13, Nitridation of Alloys** and **Chapter 1.17, Oxidation in Steam and Steam/Hydrogen Environments**. Only pure metals and model alloys are discussed to illustrate the oxidation process; the behavior of more complicated commercial alloys is addressed in **Chapter 1.23, High Temperature Corrosion of Chromia-forming Iron, Nickel and Cobalt-base Alloys** and **Chapter 1.24, High Temperature Corrosion of Alumina-forming Iron, Nickel and Cobalt-base Alloys**. The principles that govern many aspects of high temperature oxidation that are considered in this chapter, such as oxidation kinetics, transport mechanisms through oxides, defect formation, stress generation and relaxation, microstructural evolution, and scale failure mechanisms, are thoroughly covered elsewhere in this volume. In this chapter, only experimental results on these phenomena will be summarized, without details of mechanistic discussions. The purpose here is to provide a short view of the current understanding of the oxidation behavior of a range of metals and alloys. More extensive discussions can also be found in textbooks on the oxidation of metals and alloys.<sup>1-3</sup>

The chapter is divided into sections on similar types of oxides that are formed on metals and alloys. The oxidation of Ni, Co, and Fe is first summarized, followed by that of refractory metals (Nb, Mo, Ta, W)

and their alloys, and then by  $SiO_2$ -,  $Cr_2O_3$ -, and  $Al_2O_3$ -forming alloys. In each section, results on the nucleation, growth and protectiveness of the oxide formed are presented with the following topics covered whenever data are available: initial stage scale development, oxidation rates, transport mechanisms and dominating diffusion paths, development of oxide phases including oxide phase transformation, and evolution of scale microstructure and its relationship to the growth mechanism and scaling rate. A section (**Section 1.10.7.2**) on impurity segregation (mainly S, but also C) at different oxide-alloy interfaces, and its effect on oxide scale adhesion is included. The data cover a range of  $Al_2O_3$ -forming alloys, with or without Pt or reactive elements (REs), and some  $Cr_2O_3$ -forming alloys. In **Section 1.10.7.1**, the RE effect on  $Cr_2O_3$ - and  $Al_2O_3$ -forming alloys, and some work with NiO on Ni, is presented. Mechanisms that have been proposed for the RE effects on oxide nucleation, growth and adhesion are briefly reviewed.

**Figure 1** compares the range of oxidation rates at different temperatures for the major oxides discussed in this chapter. Above 1100 °C, the oxide on Si has the slowest growth rate, but the establishment of a protective surface  $SiO_2$  layer is difficult; more details are presented in **Section 1.10.4**. The kinetics for

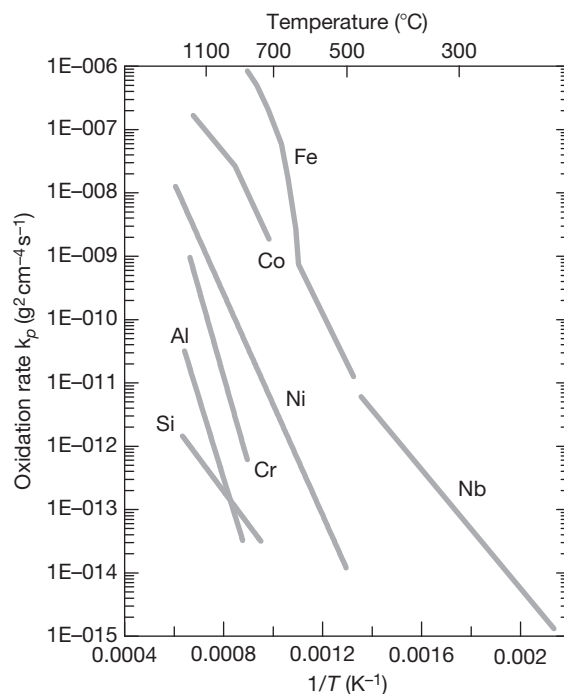


**Figure 1** Summary of parabolic oxidation rate constants for some of the metals discussed in this chapter.

refractory metals, such as Nb, are only parabolic at low temperatures. Linear kinetics and oxide volatilization are often observed at higher temperatures (Section 1.10.3). The rate for Co oxidation shows two activation energies that are associated with the formation of  $\text{Co}_3\text{O}_4$  above a growing CoO layer at lower temperatures; more details are discussed in Section 1.10.2.2. For iron, the lower temperature rate is dominated by the growth of magnetite ( $\text{Fe}_3\text{O}_4$ ), while, at high temperatures, above  $\sim 570^\circ\text{C}$ , the rate is mainly dominated by the growth of the very nonstoichiometric wustite ( $\text{FeO}$ ); since deviation from stoichiometry decreases with increasing temperature, the activation energy is seen to diminish with temperature. Details of iron oxidation are presented in Section 1.10.2.3.

## 1.10.2 Oxidation of Nickel, Cobalt, and Iron

The high temperature oxidation behaviors of Fe, Ni, and Co are similar in that the oxide growth is mainly controlled by the outward diffusion of cations because they form oxides that are metal-deficient at high temperatures and over a wide range of oxygen partial pressures.<sup>4</sup> From studies of nonstoichiometry, electrical conductivity, and self-diffusion coefficients, the predominant point defects in the major oxides formed on these metals are determined to be metal vacancies. Among these metals, iron oxidizes the fastest, as iron oxide and, hence, has the highest concentration of defects and the highest diffusion rate. The next lowest rate is for Co and then Ni (see Figure 1).

As Ni forms only one oxide, NiO, over a wide range of temperatures and oxygen potentials,<sup>5</sup> it is relatively the simplest system. Consequently, it has often been chosen as a model to study the fundamentals of high temperature metal oxidation, where oxide growth is controlled by cation diffusion. In this section, Ni oxidation is discussed first and in detail, because many concepts applicable to Ni are also relevant to the other metals, for example, initial stage of oxidation, metal and oxygen transports, the importance of oxide grain boundaries as transport paths, the generation of oxidation stresses and the development of duplex structures. Specific characteristics for Co and Fe oxidation follow.

### 1.10.2.1 Nickel

Nickel forms only one oxide, NiO, over a wide range of temperatures and oxygen potentials,<sup>5</sup> and much is

known of its oxidation mechanism and the scale microstructure that develops.<sup>6–12</sup>

#### 1.10.2.1.1 Transient stage oxidation

According to the surface studies of Mitchell *et al.*,<sup>13,14</sup> the initial stage oxidation of Ni proceeds in three stages. The first is the chemisorption of oxygen and the formation of a two-dimensional oxygen surface structure, which is different for different Ni orientations. The second involves nucleation and lateral growth of NiO. Nucleation occurs on sites that are present at the onset of oxidation, but such sites were not identified; lateral growth takes place at the periphery of nuclei by direct capture of oxygen from the gas phase. Stage 3, which starts before the completion of stage 2, involves logarithmic thickening of the oxide nuclei (up to their tested temperature of  $300^\circ\text{C}$ ). The nucleation and growth kinetics depend on temperature and the partial pressure of oxygen, but not significantly on metal orientation. At higher oxidation temperatures, however, the shape, size, and density of NiO nuclei have been found to depend strongly on Ni orientation,<sup>15</sup> in agreement with later results<sup>16,17</sup> showing that substrate orientation can strongly affect oxide grain size and oxide-scale thickness within a wide range of oxidation temperatures, from  $450$  to  $1200^\circ\text{C}$ .

#### 1.10.2.1.2 Oxide structures

The structure of NiO can be either simplex (single layer), which consists of a layer of columnar grains, or duplex (double layer), which has a columnar outer layer similar to that on the simplex scale, and an equiaxed, fine-grained, porous inner layer; examples of these are shown in Figure 2. In both structures, the columnar grains are textured,<sup>18,19</sup> where the degree of texture becomes more apparent for thicker scales. There have been experimental indications that the type of texture varies with Ni orientation,<sup>20,21</sup> and these differences may create different NiO grain boundary characters, thus affecting the oxidation rate.<sup>20</sup> However, the mechanism by which a different texture develops and exactly how it affects transport through the oxide is not yet clear. Even with an apparently single layer of columnar NiO, TEM studies<sup>22</sup> have found that a layer of fine-grained oxide with differently orientated grains can exist at the oxide-metal interface, where the oxide grains are only submicron in size. The reason for their formation is not clear; it is also not known if such a layer exists under all oxidation conditions. The

consequence of having this layer of fine-grained oxide at the interface may be to relax the growth and even the thermal stresses, since these fine grains may exhibit superplasticity.

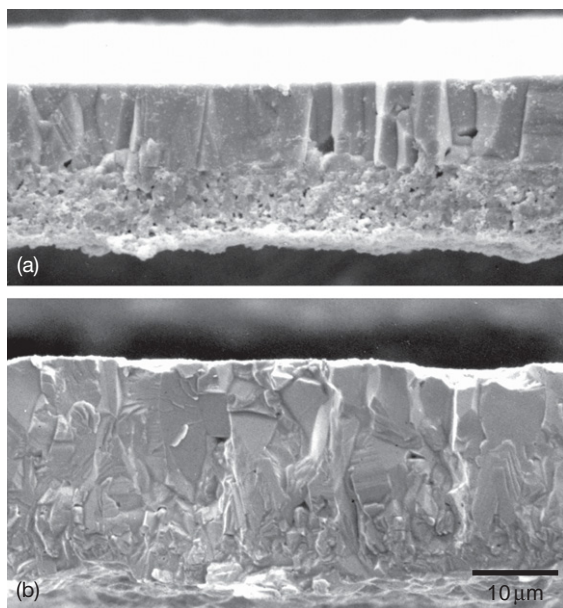


**Figure 2** Typical NiO microstructure (a) duplex, columnar outer and fine grained, porous inner layers formed on normal purity Ni, 99.6–99.7%. (b) Single columnar layer formed on high-purity Ni, >99.95%. Reproduced from Hou P. Y.; Cannon, R. M. *Mater. Sci. Forum* **1997**, 251–254, 325–332.

It is not known if the fine-grained oxide layer at the oxide–metal interface is the prelude to the thicker inner scale that is observed in a duplex structure. The thickness ratio of the inner and outer layers has been noted to depend on the oxidation temperature, the surface preparation<sup>23</sup> and, most importantly, the metal purity. For a given oxidation condition, less pure Ni is more prone to develop duplex scales than high purity Ni<sup>24, 25</sup>; furthermore, the duplex structure is always found on dilute Ni-based alloys.<sup>10, 26</sup> Smoother surfaces and higher temperatures tend to decrease the duplex layer formation. **Figure 3** illustrates the range of temperatures and times at which different microstructures of NiO develop on high purity Ni.<sup>17</sup> At 900 °C or above (up to 1200 °C), the scale is one single compact layer, but, at temperatures below ~850 °C, it can be duplex or a porous single layer, depending on the oxidation time. In both cases, the first formed scale is a single layer, but less dense oxide forms at higher temperatures; with time, the scale can become duplex, where an inner, more fine-grained layer develops. Greater amounts of porosity are often found in the inner layer of the duplex structure. The mechanisms by which they develop are not clear, although several have been proposed; a review of these proposals can be found in the article by Kyung and Kim.<sup>27</sup> Some of these mechanisms attribute oxide growth stress as the cause for the onset of a porous, and eventually duplex, scale

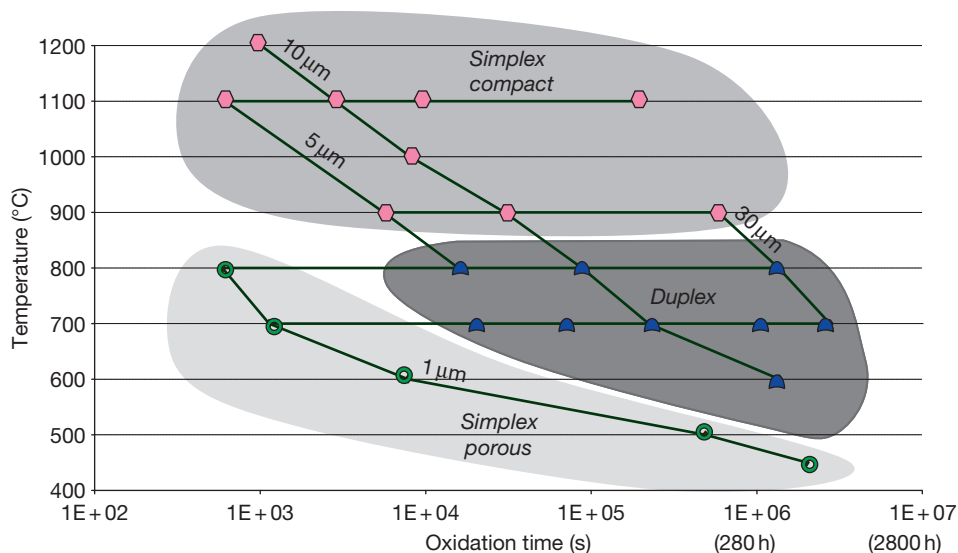


**Figure 3** Formation of different NiO microstructures in relation to oxidation temperature, time, and oxide scale thickness. Oxidation was carried out on high purity Ni (>99.999%) in oxygen, after polishing to a 0.25 μm diamond surface finish and annealing at 1350 °C in Ar–5% H<sub>2</sub>. Reproduced from Peraldi, R.; Monceau, D.; Pieraggi, B. *Oxid. Met.* **2002**, 58, 249–273.

formation<sup>28–30</sup>; others point to the importance of the inward transport of oxygen through the initially formed single layer.<sup>31,32</sup> For whatever reason porosities are present in the oxide, a quasiequilibrium model of gaseous transport through these pores was developed to explain the formation of the inner layer.<sup>33,34</sup> In the case of Ni oxidation, it was suggested by Caplan *et al.*<sup>35</sup> that the duplex structure was also related to carbon impurity in the Ni. It was found that carbon, segregated at Ni grain boundaries, could induce grain boundary cavitation as a result of metal creep under the oxide growth stress. These cavities were then incorporated into the oxide as the oxidation front progressed inward. In nondecarburized Ni, cavities that formed inside the oxide contained C-containing gases, so CO–CO<sub>2</sub> was suggested to act as a carrier gas for the inward transfer of oxygen across these cavities.

#### 1.10.2.1.3 Growth rate and transport processes through NiO

The growth of NiO at 700–1300 °C generally follows parabolic kinetics, although, usually, these are only exactly parabolic at temperatures above ~1000 °C. Reported parabolic rate constants have recently been compiled by Peraldi *et al.*<sup>36</sup> over a wide range of temperatures, with data from different surface preparations, metal purities and orientations and partial pressures of oxygen. There has not been enough work done in the low-temperature range (<500 °C), and existing data show too much discrepancy to warrant a clear understanding of the behavior in this temperature regime. Oxidation rate values at very high temperatures (>1000 °C) have much less scatter than at intermediate temperatures (from 500 to 1000 °C). Furthermore, the activation energy for all the high temperature data are similar, ranging between 180 and 240 kJ mol<sup>-1</sup>, which is similar to the activation energy for Ni lattice diffusion, at 154–254 kJ mol<sup>-1</sup>. Tracer studies by Atkinson *et al.*<sup>37</sup> have also shown that NiO growth above 1000 °C is controlled by Ni lattice diffusion, but the growth is dominated by Ni grain boundary diffusion below this temperature.<sup>38</sup> In the intermediate temperature range, a decrease in the rate constant is often observed with oxidation time,<sup>38–40</sup> which can be attributed to a decreased grain boundary area due to grain growth,<sup>41</sup> attesting to the tracer studies<sup>38</sup> that oxide growth is dominated by grain boundary, rather than lattice, diffusion. Results from different works in this regime displayed greater scatter; some data showed apparently slower oxidation

rates and lower activation energies than those at the high temperatures. These differences may be due to differences in sample purity, orientation and surface treatment, all of which have been reported to affect NiO growth rates. Impurities from the Ni, or minor alloying elements incorporated into the NiO, can change its defect concentration and, hence, affect the Ni cation transport rates.<sup>42,43</sup> Experimental measurements,<sup>44</sup> however, indicate that impurities often decrease the grain boundary diffusion rate of Ni. Thus, it would appear that the effects of impurities in increasing the oxidation rate of Ni most probably result from an altered oxide microstructure. Indeed, the most significant way the oxidation rate can be affected seems to be a change in the microstructure of the NiO scale, from simplex to duplex,<sup>12</sup> where the inner layer of the duplex scale is often fine-grained and porous.

Although the overall growth of the NiO scale is largely controlled by the outward diffusion of Ni through lattice or grain boundary diffusion *via* nickel vacancies,<sup>2</sup> a noticeable degree of oxygen diffusion through the scale is often observed. As seen from the oxygen isotope studies conducted by Atkinson *et al.*<sup>7</sup> (Figure 4), the thicker the inner layer, the more inward penetration of oxygen, and the inner layer thickness is directly related to Ni purity. Gaseous transport of oxygen is believed to occur through a porous oxide, whether in a porous simplex scale or in a porous inner layer in a duplex scale and, hence, contributes to, and increases, the oxidation rate. The oxygen tracer studies show that most of the inner layer growth takes place at or near the scale–metal interface *via* oxygen inward transport through the scale.<sup>37</sup> The path for oxygen transport, particularly through the outer layer, has been suggested, by Atkinson *et al.*,<sup>37</sup> to be microcracks or fissures, in the scale caused by growth stresses. The conclusion was made simply because the rate of oxygen transport is too fast to be accounted for by solid state diffusion.

The topic of stresses in thermally grown NiO can be dated back to 1947 when Evans<sup>45</sup> reported the observations of buckling and curling of NiO scale after its removal from the underlying Ni substrate. This indicated the presence of a compressive residual stress in the NiO film, and a possible stress gradient through it, with higher compression at the scale–metal interface.<sup>46</sup> Later studies<sup>47</sup> further demonstrated the existence of a compressive growth stress by measuring the degree of Ni elongation during oxidation. Others<sup>48</sup> have come to the same conclusion by

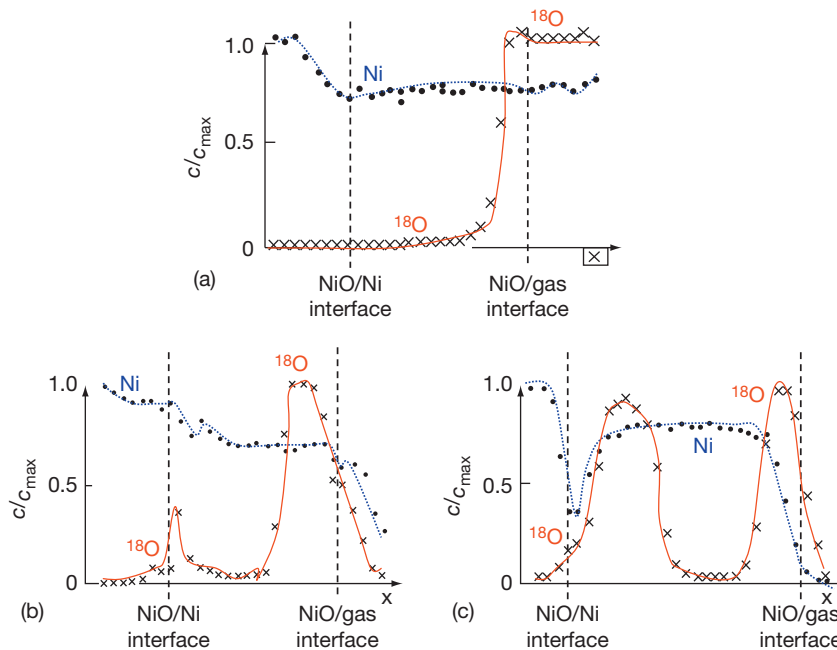


**Figure 4** Ni and  $^{18}\text{O}$  traces through NiO scales formed at  $1000^\circ\text{C}$  on (a)  $\{100\}$  Ni crystal, (b) 99.998% high-purity polycrystalline Ni, and (c) 99% low-purity polycrystalline Ni. Each specimen was first oxidized in  $^{18}\text{O}_2$  then in equal amount of time in  $^{18}\text{O}_2$ , under 50 torr of total oxygen pressure. (After Atkinson, Taylor and Goode<sup>7</sup>).

studying the flexure of thin strips of Ni samples as a result of oxide growth. More recent studies using *in situ* X-ray diffraction techniques, however, have found the growth stress to be slightly tensile<sup>49–51</sup> at  $900^\circ\text{C}$ , but compressive at lower temperatures, that is,  $800^\circ\text{C}$ <sup>52</sup> and  $600^\circ\text{C}$ .<sup>51</sup>

An implication consistent with the stress studies seems to be that the first formed simplex scale is under compression, but the growth stress in duplex NiO scales is mildly tensile near the outer surface and strongly compressive near the scale–metal interface, with the total net stress still being compressive.<sup>25</sup> The tensile stress in the outer duplex layer may assist microcrack formation, although direct observations of these gaseous transport paths have not been made. Acoustic emission studies conducted at 800 and  $900^\circ\text{C}$ <sup>53</sup> have shown some activities during Ni oxidation, indicating possible cracking of the oxide. However, the experiment was done on a thin film of Ni that was allowed to bend during oxidation, in order to determine the level of growth stress. It is unclear how the bending of the sample under the oxide growing condition affected the AE signals. Since oxidation is a dynamic process, where cracks can form and heal at any time within the scale, it may be impossible to identify

these fast gaseous transport paths, if they do exist, unless microstructures can be studied *in situ* at the oxidation temperatures.

### 1.10.2.2 Cobalt

Three cobalt oxides exist, namely  $\text{Co}_3\text{O}_4$ ,  $\text{Co}_2\text{O}_3$ , and  $\text{CoO}$ , and have respectively the spinel, hexagonal, and cubic structures.  $\text{Co}_2\text{O}_3$  is unstable above  $300^\circ\text{C}$ , so is not found in oxidation products of Co, where tests are usually conducted between 400 and  $1400^\circ\text{C}$ .<sup>5</sup> From the results reported in the review by Wood *et al.*,<sup>5</sup> average activation energies are calculated to be  $107 \pm 26 \text{ kJ mol}^{-1}$  between 500 and  $800^\circ\text{C}$ , and  $213 \pm 47 \text{ kJ mol}^{-1}$  between 800 and  $1400^\circ\text{C}$ . Clearly, there is a sharp, but unexplained, increase in oxidation rate with temperature above  $600\text{--}700^\circ\text{C}$ . Kofstad<sup>2</sup> has compiled some of these oxidation rates, between 800 and  $1150^\circ\text{C}$ , and noted yet another change in activation energy at about  $950^\circ\text{C}$ , which is associated with the formation of  $\text{Co}_3\text{O}_4$ . The activation energy for self-diffusion of Co in  $\text{CoO}$  in the range  $800\text{--}1300^\circ\text{C}$  is 144 or  $160 \text{ kJ mol}^{-1}$ ,<sup>4,54</sup> which lies in the range of oxidation activation energies. These results suggest that  $\text{CoO}$  growth is controlled by cation movement via vacant lattice sites.



Above  $\sim 900\text{--}950^\circ\text{C}$ , only CoO is formed, but below this temperature,  $\text{Co}_3\text{O}_4$  can exist as a thin layer at the scale–gas interface above the CoO. The proportion of  $\text{Co}_3\text{O}_4$  in the scale seems to increase with decreasing temperature, from 800 to  $600^\circ\text{C}$ .<sup>55</sup> The relative thickness of the two layers is a function not only of temperature, but also of the partial pressure of oxygen. These dependencies, from 500 to  $900^\circ\text{C}$ , have been summarized by Hsu and Yurek.<sup>56</sup> Both layers grow by cation outward diffusion, with probably lattice and grain boundary diffusion dominating in the CoO and  $\text{Co}_3\text{O}_4$  layers respectively, due to the difference in grain size between the two layers. The growth rate of CoO at  $600^\circ\text{C}$  has been found to be about five times greater than that of  $\text{Co}_3\text{O}_4$ ,<sup>57</sup> so the overall oxidation rate is usually considered to be controlled by the growth of the CoO layer. It should also be noted that, once a complete  $\text{Co}_3\text{O}_4$  layer exits at the surface, the overall oxidation rate becomes independent of the ambient oxygen pressure, as the partial pressure of oxygen at the CoO/ $\text{Co}_3\text{O}_4$  interface is given by the decomposition pressure of  $\text{Co}_3\text{O}_4$  in equilibrium with CoO.

Like NiO, the CoO layer can be single- or double-layered.<sup>55</sup> It also appears that a double-layered structure is favored with alloying addition in dilute Co alloys,<sup>58</sup> while pure Co tends to form a single layer.<sup>59</sup> Pt markers placed on the sample surface prior to oxidation reside at the inner–outer oxide layer interface,<sup>55,60,61</sup> suggesting that, analogous to NiO, the outer layer grows by the outward movement of cobalt ions and the inner one by the inward diffusion of oxygen gas or anions. More recent work using the  $^{18}\text{O}$  isotope<sup>62</sup> has confirmed these earlier studies; between 1000 and  $1300^\circ\text{C}$ . The CoO formed on dilute Co–Cr alloys develop duplex structures, where the inner layer thickness increased with increasing Cr content. Growth of the scale is dominated by cation outward transport, but oxygen inward diffusion becomes more apparent with a thicker inner layer.

### 1.10.2.3 Iron

The rate of iron oxidation is governed by the stabilities of its various oxide phases, FeO,  $\text{Fe}_3\text{O}_4$ , and  $\text{Fe}_2\text{O}_3$ , which are in turn a function of the oxidation temperature and the ambient partial pressure of oxygen. The temperature and  $p\text{O}_2$  ranges at which each of these oxides are stable is shown in Figure 5 so, at  $900^\circ\text{C}$  and  $10^{-18}$  atm, for example, iron will not be oxidized, because none of its oxides is thermodynamically stable under such a condition. In air or oxygen

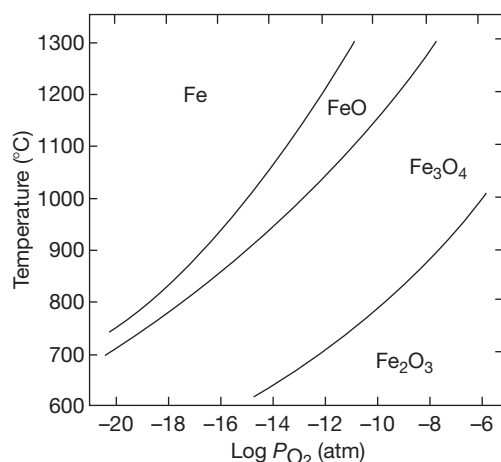


**Figure 5** Regions of stability for different iron oxides as a function of oxygen partial pressure and temperature.

Reproduced from Kofstad, P. *High Temperature Corrosion*; Elsevier Applied Science: London, UK, 1988.

and above  $570^\circ\text{C}$ , the oxide scale is multilayered, consisting of hematite ( $\text{Fe}_2\text{O}_3$ ) at the scale–gas interface, magnetite ( $\text{Fe}_3\text{O}_4$ ) in between and wustite (FeO) at the scale–metal interface. Below  $570^\circ\text{C}$ , wustite is unstable, so the scale only consists of  $\text{Fe}_2\text{O}_3$  and  $\text{Fe}_3\text{O}_4$ . While these observations are true for bulk scales, FeO has been found to be stable in very thin films at temperatures down to  $400^\circ\text{C}$ <sup>63</sup> and within narrow cracks at  $500^\circ\text{C}$ .<sup>64</sup> A cross-section of a scale formed at  $525^\circ\text{C}$  is given in Figure 6, where the scale consists only of  $\text{Fe}_3\text{O}_4$  and  $\text{Fe}_2\text{O}_3$ , and the  $\text{Fe}_3\text{O}_4$  layer is seen to consist of two different layers.<sup>65</sup> Similar to NiO and CoO, duplex  $\text{Fe}_3\text{O}_4$  or FeO layers are often observed, and the amount of porosity in them increases with oxide thickness.

Wustite is metal deficient,  $\text{Fe}_{1-y}\text{O}$ . The nonstoichiometry,  $y$ , is a function of the partial pressure of oxygen and temperature. Between 800 and  $1250^\circ\text{C}$ , it varies from 0.05 at the iron–wustite phase boundary to about 0.1–0.15 (higher at higher  $p\text{O}_2$ ) at the wustite–magnetite boundary.<sup>66–70</sup> Unlike CoO and NiO, the deviation from stoichiometry decreases with increasing temperature at a constant partial pressure of oxygen, which means that the enthalpy of defect formation is negative. Magnetite has the spinel structure. At  $p\text{O}_2$  values above the stoichiometric composition, the oxide is metal deficient ( $\text{Fe}_{3-y}\text{O}_4$ ), where  $y$  increases with increasing  $p\text{O}_2$  and decreases with increasing temperature, as occurs for wustite. At lower  $p\text{O}_2$  values, the oxide has a cation excess, with the dominant defect being iron ions on interstitial sites.<sup>71</sup> Because of these properties, Fe



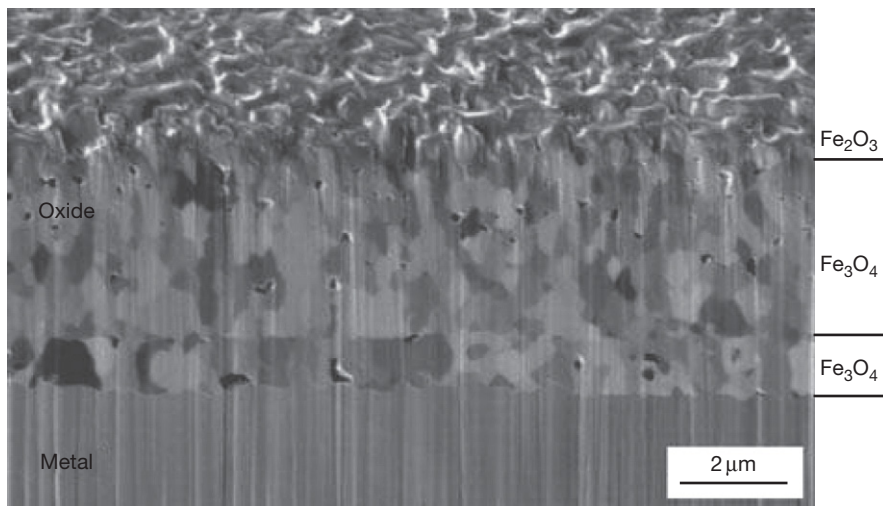


**Figure 6** Focus ion beam image of ion milled cross-section of oxide formed on iron after 1 hr oxidation in oxygen at 525 °C. The oxide is seen to consist of three layers, with the top being hematite and the bottom two magnetite. Reproduced from Jonsson, T.; Jardnas, A.; Svensson, J. -E.; Johansson, L. -G.; Halvarsson, M. *Oxid Met.* **2007**, 67, 193–214.

diffusion in magnetite as a function of  $pO_2$  shows a minimum near its stoichiometric composition for each temperature.<sup>72</sup> Among the three iron oxides,  $Fe_2O_3$  has the smallest degree of nonstoichiometry.

Both FeO and  $Fe_3O_4$  grow predominantly by cation transport of  $Fe^{2+}$  in FeO and  $Fe^{2+}$  and  $Fe^{3+}$  in  $Fe_2O_3$ . The dominant transport path in FeO seems to be Fe lattice diffusion,<sup>73</sup> but oxide grain boundaries have been shown to be more important for  $Fe_3O_4$  below 600 °C, and at all temperatures for  $Fe_2O_3$ .<sup>74–76</sup> The measured activation energy for  $Fe_2O_3$  growth is about 169–222 kJ mol<sup>-1</sup>,<sup>77</sup> which is much lower than that expected from measurements of tracer diffusivities of iron or oxygen.<sup>78</sup> Oxygen tracer diffusion studies on the growth of  $Fe_2O_3$  during the oxidation of iron at 550 °C have shown that, while the primary diffusion species through the oxide is Fe ions, fast, inward oxygen diffusion occurs down cracks in the scale.<sup>79</sup> A simplified schematic diagram for the diffusion-controlled growth of multilayered scales on iron above 570 °C is illustrated in Figure 7, and the reactions that occur at each interface are noted. The range of oxidation rates, in an Arrhenius plot, can be found in Figure 1. Above 570 °C, a distinct break associated with the formation of FeO in the scale occurs. The activation energy above this temperature is not constant, because of the large change in stoichiometry of FeO with temperature.

A strong orientation relationship exists between the iron surface and the composition and thickness of the initial oxide that forms. The first-formed oxide layer, at around 200 °C, consists of  $Fe_2O_3$  and

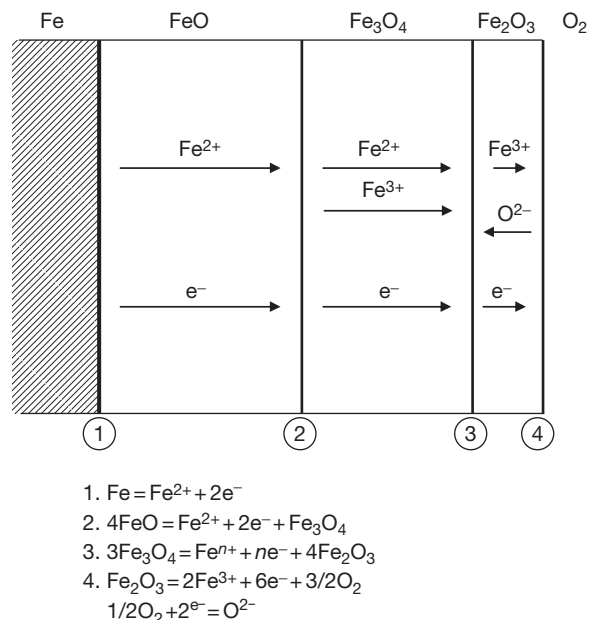


**Figure 7** Schematic illustration of the oxide layers formed upon iron oxidation above 570 °C, the dominant diffusing species through each layer and the reactions that take place at each interface are indicated.

$Fe_3O_4$ ,<sup>80</sup> where a higher proportion of  $Fe_3O_4$  exists on the lower index planes close to (100), (110), and (111), than on the higher index planes. The initial oxide composition and thickness are also found to depend on surface preparation and the presence of impurities<sup>81</sup>; for example, on cold-worked surfaces, the scale tends to contain less  $Fe_3O_4$ .<sup>82</sup> Between 350

and 500 °C,  $\text{Fe}_3\text{O}_4$  nucleates first, and then grows laterally over the entire surface.<sup>83</sup> Subsequent growth of the  $\text{Fe}_3\text{O}_4$  layer follows parabolic kinetics, where the rate is dominated by the diffusional transport of  $\text{Fe}^{2+}$  and  $\text{Fe}^{3+}$  ions through oxide grain boundaries. With time, and if the  $p\text{O}_2$  is sufficiently high,  $\text{Fe}_2\text{O}_3$  nucleates in the  $\text{Fe}_3\text{O}_4$  surface.<sup>84</sup> When the  $\text{Fe}_2\text{O}_3$  overgrows to form a continuous layer, the overall oxidation rate is substantially decreased, because the growth rate of  $\text{Fe}_2\text{O}_3$  is slower than that of  $\text{Fe}_3\text{O}_4$ , and growth of the  $\text{Fe}_3\text{O}_4$  layer is decreased due to the lower effective  $p\text{O}_2$  at the  $\text{Fe}_3\text{O}_4/\text{Fe}_2\text{O}_3$  interface. Therefore, the oxidation of iron often shows an unusual dependence on oxygen pressure, with a higher overall oxidation rate at lower  $p\text{O}_2$  values, due to a slower rate of  $\text{Fe}_2\text{O}_3$  nucleation, so a complete surface layer of  $\text{Fe}_2\text{O}_3$  is achieved less easily to help impede the faster growth of  $\text{Fe}_3\text{O}_4$ .

It is well known that most technical steels oxidize faster in the presence of water vapor than in dry air. The reasons are currently under intense investigation. For unalloyed iron, a strong water vapor effect is not always observed. The difference in behavior between dry and moist environments seems to be affected by the oxidation temperature,<sup>85,86</sup> as well as the experimental procedure and the purity of the samples.<sup>87</sup> When a water vapor effect was observed, it appears that the oxide scale is more plastic when it was formed in the presence of moisture.<sup>85,87</sup>

### 1.10.3 Oxidation of Refractory Metals and Their Alloys

Refractory metals are by definition metals with high melting points. If this were the only criterion, that is, melting point greater than 1925 °C,<sup>88–90</sup> eleven metals would fall into this category. Other definitions are more restrictive and include the requirements that the metal has a body-centered-cubic (bcc) crystal structure and forms oxides whose melting points are lower than that of the metal.<sup>89</sup> These are niobium (Nb), tantalum (Ta), molybdenum (Mo), tungsten (W), and rhenium (Re), in increasing melting points that range from 2468 to 3180 °C. Although the high melting points make these metals attractive candidates for high temperature applications, their usage has been limited due to several problems, such as insufficient yield strength at high temperatures, difficulties in fabrication and poor oxidation resistance. Even at 300 °C, oxidation can be significant (Figure 1); above 1100 °C, the rates are simply too

high to completely preclude their use. Alloying has improved the high temperature strengths, as well as the oxidation resistances, allowing refractory alloys to be used in a number of high temperature structural applications, principally in areas of propulsion and energy conversion, such as rockets and reentry systems.<sup>91</sup> Among the five metals listed above, Nb, Ta, Mo, and W have received greater attention in research and have wider industrial applications; therefore, these will be the ones discussed here.

#### 1.10.3.1 Oxidation of Ta, Nb, Mo, and W Metals

Although these are simple metals, their oxidation behaviors are very different and more complicated than those of Fe, Ni, and Co described in the previous section. This is because in addition to the usual complications associated with oxidation, such as oxide nucleation, growth and diffusion processes in the oxide and the metal, these metals can have relatively high oxygen solubility, and large numbers of oxides that can form under different temperatures and oxygen pressures and, in some cases, are volatile, especially oxides of Mo and W. The equilibrium vapor pressures of some refractory metal oxides at  $p\text{O}_2 = 1$  atm are summarized<sup>92</sup> in Figure 8. Most studies on the oxidation of refractory metals, including reaction mechanisms, metal recession rates and their  $p\text{O}_2$  dependence, were performed prior to 1970, and a thorough description can be found in Ref. 2. This section only briefly summarizes the unique oxidation behavior of these metals and discusses their alloys and coatings or surface treatments that have been attempted to improve oxidation resistance.

##### 1.10.3.1.1 Tantalum and niobium

Tantalum forms only one thermodynamically stable solid oxide,  $\text{Ta}_2\text{O}_5$ . However, nucleation of this oxide appears to be difficult, especially at lower temperatures and oxygen pressures. As a result, oxidation of Ta during the initial stage involves extensive dissolution of oxygen in the metal and the formation of different metastable  $\text{TaO}_x$  type oxides at different temperatures. Between 300 and 500 °C, the oxides grow in the form of platelets on the metal surface and extend into the metal along preferred crystallographic orientations.<sup>93,94</sup> As temperature increases,  $\text{Ta}_2\text{O}_5$  begins to nucleate on the surface platelets but, below 800 °C, it is not able to develop into a dense surface layer; reaction is believed to be controlled by oxygen-chemisorption equilibrium and the nucleation and growth of  $\text{Ta}_2\text{O}_5$ , leading to a porous surface film

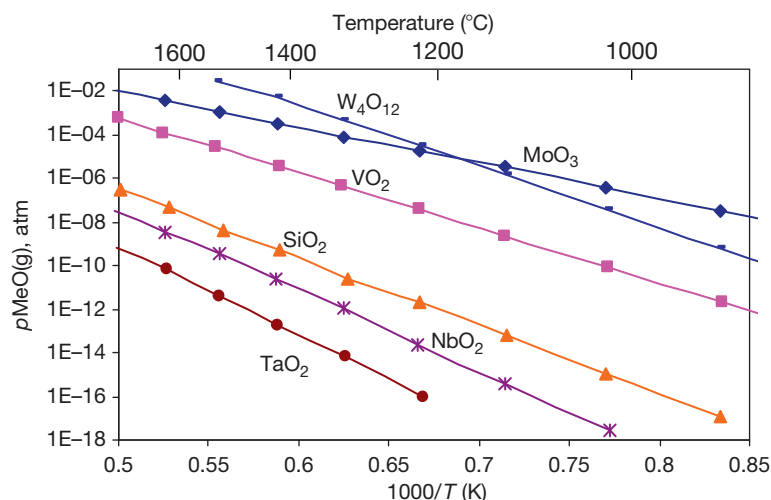


**Figure 8** Equilibrium vapor pressure of some refractory metal oxides and silicon dioxide at  $pO_2 = 1$  atm. Reproduced from Ramberg, C. E.; Beatrice, P.; Kurokawa, K.; Worrell, W. L. In *High Temperature Silicides and Refractory Alloys*; Proceedings of the Material Research Society Symposium, Boston, MA, Nov.–2 Dec. 1993; Briant, C.L., Petrovic, J. J., Bewlay, B. P., Vasudevan, A. K., Lipsitt, H. A., Eds.; Material Research Society: Pittsburgh, PA, 1994; pp 243–253.

and a linear oxidation rate.<sup>94</sup> A consequence of oxygen dissolution into the metal is metal embrittlement, which can be significant and should not be ignored.<sup>95</sup>

Above 800 °C, between 1 atm to 0.01 torr  $O_2$ , a complete  $Ta_2O_5$  layer can develop after an initial incubation time that is associated with the nucleation and growth of  $Ta_2O_5$  in similar ways as at lower temperatures.<sup>96</sup> Growth of the first formed  $Ta_2O_5$  layer exhibits parabolic kinetics, which should be dominated by oxygen inward transport through the scale. This conclusion, although made only from the morphology of the scale, is consistent with the oxidation pressure dependence of the rate constants.<sup>96</sup> Since conductivity experiments show that  $Ta_2O_5$  exhibits p-type conductivity at pressures close to 1 atm  $O_2$  and n-type conductivity at lower oxygen pressures,<sup>97</sup> it was concluded that transport through the compact  $Ta_2O_5$  predominantly occurs *via* oxygen vacancies at lower  $pO_2$  and by interstitials at higher  $pO_2$ . After the short parabolic period, the oxidation rate becomes linear.<sup>96</sup> This behavior was interpreted to involve a repetitive, continuous, and probably statistically distributed cracking of the scale down to the metal, whereby exposing the metal–oxide interface beneath the cracks to oxygen. Oxygen then chemisorbs on the freshly exposed metal surface and reaction rates again become dominated by the nucleation and regrowth of  $Ta_2O_5$ . Indeed, substantial amounts of compressive growth stresses have been found during oxidation up to 550 °C by deflection of Ta, as well as Nb.<sup>98</sup> The sources of the stresses are

oxygen dissolution during the initial stage and oxide film formation afterwards. The stress distribution across the scale to the metal region affected by oxygen dissolution cannot be determined from the bending test, but tensile stress can develop in the oxide film at some stage if there is compression in the substrate near the oxide–metal interface, and this tensile stress can easily induce scale fracture. Under compression, oxides are less easy to crack, but scale failure, especially by buckling of the surface film, is common under biaxial compression. The fact that blisters were found on the oxides formed on Ta and Nb<sup>99</sup> suggests this kind of failure.

Above 1050 °C, the post-parabolic oxidation rate is no longer linear, but decreases with time,<sup>100</sup> probably due to increased sintering of the oxide grains that densify the film, and enhanced plasticity to relieve some of the growth stresses that cause cracking. At temperatures greater than 1200 °C, however, reaction rates at 1 atm oxygen can be so fast that severe sample heating or even ignition can occur. Above ~1500 °C, evaporation of TaO and  $TaO_2$  becomes important.

The oxidation behavior of niobium is in many ways analogous to that of tantalum, but the behavior is even more complex due to the fact that Nb forms several stable oxides: NbO,  $NbO_2$ , which has the rutile structure, and several polymorphs of  $Nb_2O_5$ . During the initial stage, oxidation proceeds principally by dissolution of oxygen in the metal, and this is subsequently followed by the formation of NbO,  $NbO_2$  or a mixture of both. At higher temperatures, ~450–500 °C, a

surface layer of  $\text{NbO}_2$  forms at low  $p\text{O}_2$  ( $\sim 10^{-4}$  to  $10^{-5}$  torr)<sup>101,102</sup> and  $\text{Nb}_2\text{O}_5$  develops near atmospheric pressures.<sup>103,104</sup> Both types of oxides can be protective for a period of time, showing parabolic growth rate controlled by the inward diffusion of oxygen, but the surface layer eventually breaks down, giving rise to linear kinetics, where the rate is controlled by oxygen adsorption and the nucleation and growth of Nb oxide at the oxide-metal interface. Usually, oxidation kinetics are parabolic to paralinear over the temperature range 400–600 °C, but linear from 700 to 900 °C.<sup>105</sup> Like Ta, oxidation can only be studied in low  $p\text{O}_2$  environments above 1200 °C, because the rate is too rapid near atmospheric pressure.<sup>102</sup> At and above 1500 °C, oxidation is affected by the presence of liquid  $\text{Nb}_2\text{O}_5$ , which melts at 1490 °C; at even higher temperatures, evaporation of  $\text{Nb}_2\text{O}_5$  becomes increasingly important.

#### 1.10.3.1.2 Tungsten and molybdenum

When W is heated in the temperature range ~200–700 °C in oxygen, it grows a multilayered oxide film

that desorbs above ~900 °C into predominantly volatile  $\text{WO}_2$ , with very small amounts of WO and  $\text{WO}_3$ .<sup>106</sup>  $\text{WO}_{3-x}$  forms in the temperature range 568–908 °C, and its growth rate has been expressed as:  $D = 6.83 \times 10^{-2} \exp(-29890/RT)$ , with the activation energy given in calories per mole.<sup>107</sup> Growth of the  $\text{WO}_{3-x}$  film was determined to be dominated by oxygen diffusion via oxygen vacancies. At higher temperatures (~1100–2900 °C),<sup>108</sup> the oxidation rate is dominated by the formation of a variety of volatile products, namely  $\text{WO}_2$ ,  $\text{W}_2\text{O}_6$ ,  $\text{WO}_3$ , and  $\text{W}_3\text{O}_9$ , where the polymeric oxides,  $(\text{WO}_2)_2$  and  $(\text{WO}_3)_2$ , are believed to form through the interaction between  $\text{WO}_2$  molecules. Due to the extensive volatilization, the oxidation of tungsten is dominated by the adsorption and dissociation of oxygen, the surface interaction of oxygen atoms with the metal and the subsequent desorption of tungsten oxide.<sup>109</sup> The reaction rates are a strong function of not only temperature, but also oxygen pressure, as illustrated in Figure 9, where the experimental data are those from Bartlett.<sup>110</sup>

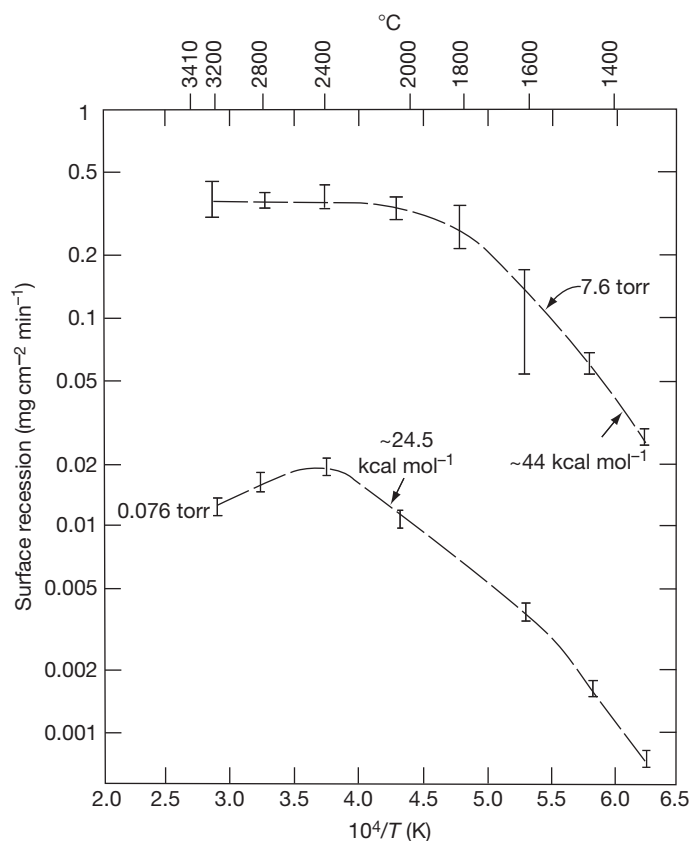


**Figure 9** Tungsten surface recession rate as a function of temperature under high and low oxygen partial pressures. Reproduced from Kofstad, P. *High Temperature Corrosion*; Elsevier Applied Science: London, UK, 1988.

Under low oxygen pressures, generally below  $\sim 10^{-4}$  atm,<sup>111</sup> the oxidation rate is governed by surface processes or reactions; above  $\sim 1300^\circ\text{C}$ , the oxide evaporates as soon as it is formed, and the metal remains free of surface oxide during oxidation.<sup>112</sup> The metal recession rate is slower at higher pressures, because a surface boundary layer exists, which limits the rate of oxygen arrival at the metal surface. Furthermore, the surrounding gas acts as a blanket that reflects escaping molecules back to the surface; the fraction of this back-reflection process is a function of the total gas pressure of the system. Consequently, metal recession rates are slower than expected from surface reactions alone. Furthermore, the high pressure regime is affected by the gas flow rate, because the thickness and effect of the boundary layer are decreased with higher flows.

The oxidation of Mo is similar to that of W. At  $190^\circ\text{C}$  in air, molybdenum is coated with an oxide film, which hinders further oxidation up to  $350^\circ\text{C}$ . Over  $350^\circ\text{C}$ , oxidation recommences. At  $500^\circ\text{C}$ , the rate increases quickly as  $\text{MoO}_3$  sublimates intensively, exposing the metal. When oxidized in air, molybdenum oxides show valencies of 4 and 6.<sup>113</sup> Oxidation behaviors at higher temperatures are dictated again, as with W, by volatilization of oxides. The principal products are the gaseous dioxide and trioxide,  $\text{MoO}_2$  and  $\text{MoO}_3$ , respectively. Between  $\sim 1200$  and  $2300^\circ\text{C}$ ,<sup>114</sup> the trioxide was found to be the more important species at lower temperatures, and the dioxide was the dominant product at higher temperatures. At the lowest temperatures and highest oxygen pressures, small amounts of polymeric oxides,  $(\text{MoO}_2)_2$  and  $(\text{MoO}_3)_2$  were also detected.

### 1.10.3.2 Oxidation of Refractory Alloys

The focus of this section is not to review the effect of alloying additions on the oxidation of refractory metals, but to discuss advances made that can improve the oxidation behavior and, hence, the usefulness of this class of material.

Some of the investigators, who studied the oxidation behavior of refractory metals prior to 1970, also examined the oxidation mechanism of some refractory alloys. For example, W addition to Ta has been studied to evaluate its effect on Ta oxidation; the amount of W added varied from 10 wt%<sup>115–117</sup> to 50 wt%.<sup>118</sup> In most cases, no significant beneficial effects were found, except at  $1200^\circ\text{C}$ , where 50 wt% W was reported to decrease the Ta oxidation rate by nearly a factor of 10, but the effect quickly diminished at higher

temperatures.<sup>117</sup> Dilute Nb–Hf and Nb–Zr alloys, often considered for applications where strength and resistance to alkali metals are required, have also been studied.<sup>119,120</sup> Although the oxidation rate in air can be decreased with the addition of Hf or Zr, the benefit is not significant. Furthermore, internal oxide precipitates of Hf and Zr develop, and they may further embrittle the alloy. Careful heat treatments can control the size, morphology, and distribution of the internal particles, allowing them to produce a strengthening effect in the alloy,<sup>119</sup> but this type of controlled morphology is difficult to maintain in long-term applications. Also, protective surface oxides do not form on alloys such as Ta–8W–1Re–0.7Hf–0.25C and Mo–36Re (all in wt%); with the Mo–Re alloy, weight gains associated with the formation of  $\text{MoO}_2$  were found at temperatures above  $400^\circ\text{C}$  for  $P_{\text{O}_2} < 10^{-3}$  Pa ( $10^{-5}$  torr) in vacuum, but weight losses took place with evaporation of  $\text{MoO}_3$  at  $10^{-2}$  Pa.<sup>121</sup> Oxygen dissolution and internal oxidation were also reported to affect the mechanical property of these alloys.<sup>122</sup> The oxidation rate of Nb in air from  $800^\circ\text{C}$  to above  $1000^\circ\text{C}$  can be decreased by alloying with Hf, Zr, W, Mo, Ti, or Ta.<sup>123</sup> However, the preferred fabricable alloys still require further protection by coating.

The development of oxidation resistant Nb alloys that can be used for aerospace applications had received considerable interest,<sup>124</sup> since Nb is less dense but stronger than Ni-based superalloys at high temperatures. Attempts have been made by alloying to promote the formation of an  $\text{Al}_2\text{O}_3$  scale as a protective layer. Svedberg<sup>125</sup> conducted an extensive investigation of the oxidation resistance of Nb-alloys in air at  $1200^\circ\text{C}$  and found the slowest rate for NbAl<sub>3</sub>, which developed an alumina inner layer adjacent to the metal–oxide interface and an NbAlO<sub>4</sub> outer layer at the oxide–gas interface. The oxidation rate was approximately parabolic, but the rate constant was still 2 orders of magnitude higher than that of NiAl, which forms a protective alumina scale in  $\text{O}_2$  at  $1200^\circ\text{C}$ . Perkins and Meier<sup>126</sup> have also studied factors affecting the selective oxidation of Al and the formation of protective alumina scales on Nb–Al alloys. It was shown that protective alumina scales are not formed on NbAl<sub>3</sub> in air at  $1350^\circ\text{C}$  due to the formation of an Al-depleted Nb<sub>2</sub>Al layer at the scale–alloy interface. Protective alumina scales can be formed on Nb–Al alloys with 37.5–50 at.% Al in air at  $1400$ – $1600^\circ\text{C}$  by adding Ti to increase the solubility and diffusivity of Al and adding Cr and/or V to decrease the solubility–diffusivity product of O in the alloy. An alloy with 25.4Nb–29.1Ti–2.8Cr–3.5V–39.2Al



(wt%) was developed and was able to form a protective alumina scale in air at temperatures above 1000 °C that was even stable up to 1400 °C. Furthermore, this alloy oxidized with kinetics comparable to those of NiAl.<sup>127</sup> However, the melting point of the alloy was relatively low, about 1600 °C, which resulted in poor mechanical strengths at high temperatures. Attempts to raise the melting point were made by replacing Nb (melting point ~2500 °C) with Ta (m.p. ~3000 °C), and led to an increase in the alloy melting point by ~300 °C. However, the microstructures of the Ta–Al–Ti–V–Cr alloys are thermally unstable. Technical efforts have also been made to improve the strength and oxidation resistance of the Nb–Al–Ti–V–Cr alloys by adding dispersion particles.<sup>128</sup> It was found that Al<sub>2</sub>O<sub>3</sub> and Y<sub>2</sub>O<sub>3</sub> were thermally and chemically stable with respect to Nb alloys, but SiC, Nb<sub>5</sub>Si<sub>3</sub> and AlN reacted extensively with the alloys at high temperatures.

Some efforts have also been carried out through alloying of Cr to produce a refractory metal based alloy that is a good Cr<sub>2</sub>O<sub>3</sub> former,<sup>129</sup> but the results have not been successful, mainly due to the difficulties in controlling the alloy microstructure and also from the formation of volatile oxides, especially those of W and Mo.

In general, despite quite a bit of effort and some limited successes, successful development of high temperature refractory-based alloys with the ability to form a protective oxide scale over an extended period has not been achieved. Even though some of these alloys have potentially useful properties, the alloying elements usually lead to detrimental effects in at least one crucial alloy property.<sup>130</sup> These drawbacks have severely limited the applicability of refractory alloys. One approach to improve the oxidation resistance has been to use coatings, and these will be briefly discussed in the next section.

### 1.10.3.3 Coatings on Refractory Metals and Alloys for Oxidation Protection

Coatings, whether applied as an external layer, or produced in the alloy surface region, have been used to improve the oxidation resistance of refractory alloys. In some cases, they are very effective.<sup>131</sup> These include MoSi<sub>2</sub>,<sup>132,133</sup> niobium silicide, both in its pure form and alloyed with Fe and Cr,<sup>130</sup> (Mo,W)(Si,Ge)<sub>2</sub>,<sup>134</sup> and aluminides.<sup>127</sup> The oxidation behavior of some of the silicides is described in [Section 1.10.4.2](#). Although these coatings can, for the most part, provide adequate oxidation protection, they tend to be very brittle. Even

a small mismatch in the thermal expansion coefficients between the base metal and the coating can lead to cracks, especially when the coating is under residual tension. The cracks can heal under some conditions, but often they allow oxygen penetration into the base metal, which then oxidizes rapidly. Consequently, the use of coatings to protect these metals is not always an adequate solution to the oxidation problem.

Other types of coatings have continually been evaluated, but have showed little success. On tungsten, amorphous W–N–Ni coatings with different N and Ni contents have been demonstrated to improve the oxidation resistance up to 800 °C,<sup>135</sup> by forming two nickel-rich, external oxide layers of NiO and NiWO<sub>4</sub>. The oxidation rate was controlled by the outward diffusion of either Ni<sup>2+</sup> or W<sup>6+</sup> ions through the oxide layers. However, for the coating to remain effective, it has to stay amorphous. Crystallization induced a dimensional stress capable of destroying the protective oxide layers. FeCrAl-, SiCrFe-, and MoSi<sub>2</sub>-based coatings have been deposited onto molybdenum with various techniques (plasma spraying, slurry deposition and physical vapor deposition) to different thicknesses with a range of varying thermal post-treatments.<sup>136</sup> The best coating lifetime, however, was only a few thousand hours at 1200 °C and a few hundred hours at 1450 °C under isothermal oxidation tests in air. Although a noticeable improvement from uncoated metal, durability has not been proved for these coated systems for them to be used reliably in engineering applications.

Surface treatments have included laser alloying, ion implantation and aluminizing, all of which aim at modifying the surface composition of an alloy so that it can develop a protective oxide scale, while not changing the alloy bulk properties. Ion implantation of different species can have a beneficial influence on the thermal oxidation kinetics of niobium in pure oxygen at temperatures below 500 °C.<sup>137</sup> Si and Al were most beneficial. However, the treatment only delayed the appearance of the linear catastrophic kinetics, but showed no long-term effects. When Al or Si powders were deposited onto niobium by laser melting, forming aluminized or siliconized surface coatings, the effect was longer lasting, but the coatings still failed with time.<sup>138</sup> Likewise, coatings produced by pack cementation with Cr and Al also failed under longer times and at higher temperatures; one of the reasons for the failure was interdiffusion, where the scale forming element is lost from the coating by diffusing into the alloy, while alloying elements diffuse into the coating and change its oxidation



properties. Diffusion barriers have been tested to show some success. When a Re–Ni film that contained more than 70 at% Re was applied onto a Nb–5Mo–15W (wt%) alloy via electroplating, followed by pack cementation with Cr and Al, the alloy was able to develop a protective  $\text{Al}_2\text{O}_3$  scale, with a Re–Cr rich  $\sigma$ -phase layer in the inner layer of the coating, which decreased the mutual diffusion between the outer Al reservoir layer and the alloy substrate.<sup>139</sup> However, the most severe condition tested so far was isothermal oxidation at 1100 °C for 100 h in air. No cyclic oxidation tests have been performed to evaluate the durability of the coating.

#### 1.10.4 Oxidation of Silica-Forming Alloys

Pure silica ( $\text{SiO}_2$ ) is one of the most impermeable oxides at high temperatures. The low activation energy for the diffusion of oxygen in  $\text{SiO}_2$  makes it a more protective oxide scale than  $\text{Al}_2\text{O}_3$  at temperatures above  $\sim 1080$  °C (see Figure 1). However, this rate can increase by a factor of 2–8 in the presence of water vapor or certain impurities such as Na or Al.<sup>140,141</sup> More than 15 different crystalline forms of  $\text{SiO}_2$  have been reported.<sup>142</sup> Silica also exists in amorphous form (quartz glass). In both crystalline and vitreous (fused) quartz, tracer studies have shown that the diffusivity of oxygen is much faster than that of silicon.<sup>143</sup> The diffusion rate of oxygen in fused quartz, is around  $10^{-13} \text{ cm}^2 \text{ s}^{-1}$  at 1200 °C, and about 1.5 orders of magnitude lower at 1000 °C.<sup>144,145</sup> Formation of volatile  $\text{SiO}$ , however, should limit the application of  $\text{SiO}_2$ -forming alloys in environments of low oxygen activity.<sup>146</sup>

##### 1.10.4.1 Si-Containing Alloys

Silicon additions to Fe, Co, and Ni-based alloys have strong adverse effects on their mechanical properties; therefore, like Al, only small amounts can be added. Similar to aluminum, the presence of a third element in the alloy, such as Cr, can greatly enhance  $\text{SiO}_2$  formation, where a  $\text{SiO}_2$  healing layer is often found beneath either a  $\text{Cr}_2\text{O}_3$  healing layer or an external  $\text{Cr}_2\text{O}_3$  scale. (An example of a partial  $\text{SiO}_2$  healing layer beneath an external  $\text{Cr}_2\text{O}_3$  can be seen in Figure 10.) According to Stott *et al.*,<sup>147</sup> healing layers of  $\text{SiO}_2$  are harder to establish than  $\text{Al}_2\text{O}_3$  because the Gibbs free energy of formation ( $\Delta G$ ) for  $\text{SiO}_2$  and  $\text{Cr}_2\text{O}_3$  are closer than that between  $\text{Al}_2\text{O}_3$  and  $\text{Cr}_2\text{O}_3$  ( $-125$ ,  $-162$ , and  $-202 \text{ kcal mol}^{-1} \text{ O}_2$  at 1000 °C, respectively, for  $\text{SiO}_2$ ,  $\text{Cr}_2\text{O}_3$ , and  $\text{Al}_2\text{O}_3$ ). The smaller differences in  $\Delta G_{\text{SiO}_2}$  and  $\Delta G_{\text{Cr}_2\text{O}_3}$  give rise to a lower driving force for  $\text{SiO}_2$  nucleation at, or near, the scale–alloy interface, resulting in a lower density of internal oxide precipitates, hence making the formation of a healing layer more difficult.

Experimentally, it has been suggested that  $\text{SiO}_2$  forms as a complete layer beneath a  $\text{Cr}_2\text{O}_3$  scale when a 20Cr–25Ni–Nb stainless steel containing 0.45–0.75 wt% Si was oxidized at 750–900 °C.<sup>148</sup> However, there was no strong evidence indicating that this layer was not partial, but complete at the interface. Later work on the same 20Cr–25Ni–Nb alloy oxidized at 825 °C in  $\text{CO}_2$ , has shown by TEM that the silica layer at the interface was amorphous.<sup>149</sup> The addition of various amounts of Si to a similar steel, 20Cr–25Ni–TiN, oxidized at 850 °C in  $\text{CO}_2$ -based gas containing 2% CO showed a minimum parabolic rate at  $\sim 0.9$  wt% Si, and X-ray mapping of polished scale cross-sections showed the presence of a silica interlayer between the external  $\text{Cr}_2\text{O}_3$  and the alloy.<sup>150</sup> However,

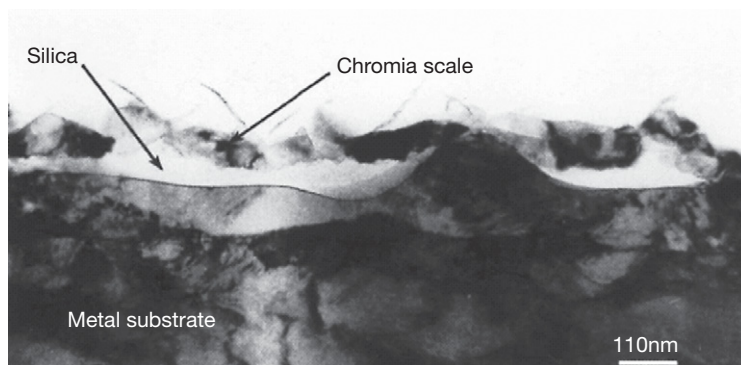


**Figure 10** Cross-sectional transmission electron micrograph showing  $\text{SiO}_2$  healing layer beneath an external  $\text{Cr}_2\text{O}_3$  scale formed on commercial Ni–20 wt% Cr alloy containing 1.3 wt% Si, oxidized in air for 2 min at 950 °C. Reproduced from Ahmad, B.; Fox, P. *Oxid. Met.* **1999**, 52, 113.

the decrease in alloy oxidation rate was no more than 2.5 times, and this rate was considered to be controlled by Cr diffusion through the  $\text{SiO}_2$  layer. For example,  $\text{Cr}_2\text{O}_3$  internal oxides were often found beneath the silica interlayer, suggesting that the layer did not form continuously over the entire alloy surface. Similar base metal cation transport through  $\text{SiO}_2$  layers was also proposed for Fe–14 and –20 wt% Si alloys,<sup>151</sup> where Fe seemed to diffuse through an apparently complete  $\text{SiO}_2$  layer to form  $\text{Fe}_2\text{O}_3$ , resulting in a linear oxidation rate.

Whether the  $\text{SiO}_2$  layer, formed at the oxide–alloy interface, is continuous or intermittent is often considered to depend on the Si concentration in the alloy, as well as the oxidation time and temperature. For example, Douglass and Armijo<sup>152</sup> reported that an almost continuous  $\text{SiO}_2$  layer formed after oxidizing Ni–20Cr–1Si (wt%) at 1200 °C for 2 weeks, while Saito and Maruyama<sup>153</sup> observed a continuous  $\text{SiO}_2$  layer on a similar Ni–20Cr–1Si alloy oxidized for 50 h at 1250 °C. However, the method of detection can affect these results. While most works rely on microprobe or EDS/SEM analyses, where relatively thick (close to a micron) layers are observed, much thinner films can be detected by STEM. An amorphous silica healing layer, a few nanometers thick, has been found on a Ni–20Cr–1Si (wt%) alloy after only 5 min oxidation at 950 °C in air.<sup>154</sup> Upon oxidation, the initial scale consisted almost exclusively of  $\text{Cr}_2\text{O}_3$ . Thin, partial layers of silica were detected at the metal–oxide interface (Figure 10) after 2 min at 950 °C, and they thickened locally with oxidation times. After >25 min, these regions spread along the metal–oxide interface until an almost continuous silica layer had formed.

Healing layers of silica have also been reported in Ni–Si alloys.<sup>155</sup> The addition of 1 wt% Si had little effect on the oxidation rate of nickel at 1000 °C, but was sufficient to establish a partial-healing layer of amorphous  $\text{SiO}_2$ . The layer was incorporated into the inner part of the duplex NiO scale but did not react with the oxide. Increasing the silicon concentration to 4 or 7% facilitated the development of apparently continuous amorphous  $\text{SiO}_2$  layers at the base of the scale, resulting in decreased rates of oxidation. However, these layers were unable to prevent the continued transport of  $\text{Ni}^{2+}$  ions into the NiO scale and oxygen into the alloy. Furthermore, the  $\text{SiO}_2$  layers provided planes of weakness that resulted in considerable damage under thermal stresses during cooling, causing severe scale spalling, where failure occurred within the  $\text{SiO}_2$  layer.

The structure of the  $\text{SiO}_2$  that formed during high temperature oxidation seemed to be amorphous at or

below 1000 °C,<sup>149,154</sup> but a crystalline form of either cristobalite or tridimite developed at ~1100 °C, depending on alloy composition and oxidation time.<sup>156</sup> In general, the amorphous phase is favored at low temperatures and is the first formed phase, while crystalline forms are favored at high temperatures or after longer time periods. Transformation from amorphous to the cristobalite phase involves a substantial volume change, which generates higher stresses within the silica layer that may contribute to the often observed preferential spalling.<sup>157</sup>

In summary, even though  $\text{SiO}_2$  can provide effective protection against high temperature oxidation, Si added to Fe-, Co-, or Ni-based alloys is not able to develop into protective  $\text{SiO}_2$  scales in the same way that Cr and Al can in forming  $\text{Cr}_2\text{O}_3$  and  $\text{Al}_2\text{O}_3$ . In most cases, the  $\text{SiO}_2$  may not be a complete layer that acts as a diffusion barrier. Even if it were, base metal cations and oxygen seem to diffuse rather rapidly through it, which may involve transport through short-circuit paths, such as cracks and pores.<sup>158</sup> Furthermore, the presence of a  $\text{SiO}_2$  layer, whether partial or complete, often has a detrimental effect on oxide scale adhesion, where preferential cracking and spalling take place within this layer.

#### 1.10.4.2 Silicides

Because of their high melting points and low densities, silicides have long been considered for high temperature applications, but their poor ductility is a major drawback, which has hampered their development as high temperature structural components.<sup>159,160</sup> When a protective  $\text{SiO}_2$  scale can form, the silicides should also possess adequate oxidation resistance. From thermodynamic considerations, most Si-rich  $\text{M}_x\text{Si}_y$  silicides, where M = Ti, V, Nb, Ta, Cr, Mo, W, Mn, Tc, Re, Fe, Ru, Os, Co, Rh, Ir, Ni, Pd, or Pt, are predicted to be capable of forming protective  $\text{SiO}_2$  layers at temperatures greater than 900 °C.<sup>161</sup> However, like the Si-containing alloy discussed above, kinetic considerations ultimately determine whether or not a protective  $\text{SiO}_2$  scale will develop. Higher temperatures and longer oxidation times usually favor the formation of a complete surface  $\text{SiO}_2$  layer; for example,  $\text{SiO}_2$  was found to cover the entire  $\text{MoSi}_2$  surface at temperatures greater than 1000 °C, but at lower temperatures, portions of the surface were covered by  $\text{MoO}_3$ .<sup>162</sup>

The high temperature oxidation and corrosion of some silicides, namely  $\text{MoSi}_2$ ,  $\text{Mo}_5\text{Si}_3$ ,  $\text{TiSi}_2$ ,  $\text{Ti}_5\text{Si}_3$ ,  $\text{V}_5\text{Si}_3$ ,  $\text{Cr}_3\text{Si}$ , and Fe and Ni silicides have recently

been summarized by Brady *et al.*<sup>163</sup>; emphasis was placed on Mo and Ti silicides, because their oxidation behaviors have been most extensively studied. Readers interested in the details of silicide oxidation should refer to this publication. Only brief summaries are given here.

During the initial stages of silicide oxidation, oxides of the metal and silica usually form simultaneously. For example, TaSi<sub>2</sub> or NbSi<sub>2</sub>, upon oxidation, form mixed oxides of both silica and Ta<sub>2</sub>O<sub>5</sub> or Nb<sub>2</sub>O<sub>5</sub>.<sup>164,165</sup> Diffusion across the surface scale at this point is therefore not dictated by the transport through SiO<sub>2</sub>, but through the mixed MeO<sub>x</sub>-SiO<sub>2</sub> layer. Although the Nb and Ta silicides could eventually be protected by a thick mixed-oxide layer, spallation problems due to growth stresses become critical as scale thickness increases, and the oxide scales on TaSi<sub>2</sub> and NbSi<sub>2</sub> can crack extensively.<sup>164,165</sup> In some systems, the mixed oxide layer can be rather protective. Several studies<sup>166,167</sup> have suggested that the oxidation kinetics of TiSi<sub>2</sub> are parabolic, due to the formation of a protective scale that consists of a silica layer near the silicide-scale interface and islands of TiO<sub>2</sub> at the scale-gas interface. Ti, which is soluble in SiO<sub>2</sub> up to ~10 at.%,<sup>168</sup> apparently diffuses to the outer surface, forming islands of TiO<sub>2</sub> and leaving a protective silica-titania glass on the inside. In other systems, the metal oxide that coexists and continues to grow with the SiO<sub>2</sub> may eventually disrupt the protectiveness of the silica.<sup>169-171</sup>

Many of the metal oxides can be volatile under some oxidation conditions, which complicates the scale development process. Equilibrium vapor pressures of some refractory metal oxides, together with SiO<sub>2</sub>, are presented in Figure 8. Mo and W oxides, for example, are highly volatile. As these oxides, initially formed with silica on MoSi<sub>2</sub> or WSi<sub>2</sub>, volatilize, the scale layer becomes more silica-rich and oxygen transport to the silicide-scale interface decreases. This decrease in oxygen transport and the associated decrease in the oxygen activity at the silicide-scale interface continue as the metal oxides continue to volatilize. Eventually, the oxygen activity at the interface decreases to a value where the base metal oxide is unstable, then the Mo or W silicide is protected by a relatively pure SiO<sub>2</sub> layer.<sup>172, 173</sup> This process is favored as the oxidation temperature is raised. At temperatures >1200 °C, volatilization is rapid, and the silica layer can be purified within the first hour of oxidation.<sup>174</sup>

Pesting is often a problem with molybdenum silicides, where extensive oxidation disintegrates the silicide to powder or fragments. For MoSi<sub>2</sub>, this occurs in the temperature range ~300–550 °C.<sup>163</sup>

The rapid disintegration is usually preceded by an incubation period,<sup>175</sup> the duration of which is affected by microstructure, applied stress, temperature, and oxygen partial pressure. The susceptibility to pesting seems to depend on the material microstructure and stoichiometry. When the MoSi<sub>2</sub> is dense with small amounts of connected porosity, and is free of cracks, pesting does not occur.<sup>176-179</sup>

An example of the pesting behavior and its sensitivity to specimen porosity is seen in Figure 11, from Kurokawa *et al.*,<sup>179</sup> where noticeable pesting of the porous sample took place shortly after 56 h at 500 °C, leading to total disintegration of the sample after 100 h, but weight gain of the dense sample was less than  $2 \times 10^{-3} \text{ g cm}^{-2}$  up to the end of the test, at ~111 h. The oxides that formed in various stages of disintegrated MoSi<sub>2</sub> are MoO<sub>3</sub> and amorphous SiO<sub>2</sub>.<sup>177,180,181</sup> Pest disintegration appears to be caused by the formation of voluminous Mo oxides in extended defects. This introduces stresses that provide the driving force for fast crack propagation and fragmentation of the relatively brittle solid. It appears that susceptibility to pesting increases with Mo concentration for Mo:Si ratios >0.5 and decreases when MoSi<sub>2</sub> is Si-rich (68–70 at.%).<sup>181</sup>

Mo-Si-B alloys, with melting points above 2000 °C, are being considered for high temperature applications, such as turbine blade materials.<sup>182</sup>

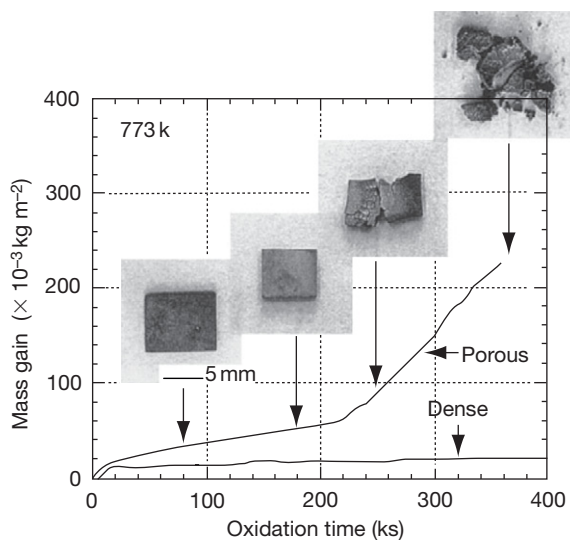


**Figure 11** Oxidation kinetics of dense and porous MoSi<sub>2</sub> at 500 °C in air, and the appearance of the porous sample at four different times. Reproduced from Kurokawa, K.; Houzumi, H.; Saeki, I.; Takahashi, H. *Mater. Sci. Eng. A* **1999**, 261, 292–299.

Several compositions of this alloy are able to develop a protective surface borosilicate glass that offers good oxidation resistance at high temperatures. The development of this glass layer is similar in principle to the oxidation of  $\text{MoSi}_2$ . Above  $800^\circ\text{C}$ , the first formed oxides are rich in  $\text{MoO}_3$ , which volatilizes, while the silicon and boron oxides slowly form a complete layer of borosilicate. Once this silicate layer is established, the rate of alloy recession is decreased. However, development of the protective silicate layer is very sensitive to the oxidation temperature, alloy composition, particularly the B to Si ratio, and other factors.<sup>183</sup> Increasing the B/Si ratio decreases the viscosity of the glass and allows it to cover the surface of the sample faster, but this also increases the oxygen diffusivity through the glass and lowers the high temperature oxidation performance. Furthermore, at low temperatures,  $\sim 650\text{--}750^\circ\text{C}$ , the formation of a protective borosilicate layer is slow compared to the loss of Mo by the formation and volatilization of  $\text{MoO}_3$ , and this leads to pesting of the material.<sup>184,185</sup> Current efforts in improving the oxidation resistance of these alloys involve the development of coatings.<sup>186</sup>

### 1.10.5 Oxidation of Chromia-Forming Alloys

Chromium oxidizes at high temperatures to form one oxide, the corundum  $\text{Cr}_2\text{O}_3$ , which consists of hexagonally close-packed oxygen ions with Cr cations occupying two-thirds of the octahedral sites. The structure is the same as  $\alpha\text{-Al}_2\text{O}_3$  and  $\alpha\text{-Fe}_2\text{O}_3$ .  $\text{Cr}_2\text{O}_3$  reacts with oxygen to form volatile  $\text{CrO}_3$  according to the equation  $0.5\text{Cr}_2\text{O}_3 + 0.75\text{O}_2 = \text{CrO}_3$ , at temperatures above  $850\text{--}900^\circ\text{C}$ ; the reaction rate increases with increasing partial pressure of oxygen in the atmosphere and with increasing gas flow rates<sup>187</sup>; it becomes rather pronounced at temperatures above  $1000^\circ\text{C}$ ,<sup>188</sup> thus limiting the use of  $\text{Cr}_2\text{O}_3$  forming alloys to temperatures less than  $900^\circ\text{C}$ . In the presence of moisture,  $\text{Cr}_2\text{O}_3$  reacts with water vapor to form a number of volatile chromium hydroxides.<sup>189</sup> The reaction rates depend on temperature, total pressure, partial pressure of water and the reaction gas flow rate. These volatilization reactions have been shown to cause severe problems in solid oxide fuel cell environments, where  $\text{Cr}_2\text{O}_3$  forming alloys are being considered as a low-cost interconnect material.<sup>190–193</sup> The most common and extensively used  $\text{Cr}_2\text{O}_3$ -forming alloys are stainless steels. Ferritic

steels have the base composition of Fe–Cr with 13–18 wt% Cr to ensure the formation of a slow growing scale of  $\text{Cr}_2\text{O}_3$ , or mixed Fe–Cr spinel and  $\text{Cr}_2\text{O}_3$ , for corrosion protection. Common austenitic steels contain higher concentrations of Cr (18–30 wt%) and an austenite stabilizer, such as Ni or Mn. The present chapter describes the development, growth and adhesion of  $\text{Cr}_2\text{O}_3$  scales observed for Cr and model  $\text{Cr}_2\text{O}_3$ -forming alloys.

#### 1.10.5.1 Transport Properties and Oxidation Rates

$\text{Cr}_2\text{O}_3$  is an electronic semiconductor.<sup>4</sup> It changes from a p-type to an n-type semiconductor from near-atmospheric oxygen pressures to oxygen activities close to the Cr/ $\text{Cr}_2\text{O}_3$  interface. There are evidences<sup>4</sup> showing that Cr self-diffusion (mainly lattice diffusion) depends on oxygen activity, and it can vary by 3–4 orders of magnitude under a given temperature. The dominant defect structures may be Cr vacancies or interstitials respectively, at high and low oxygen activities.<sup>194</sup> Earlier diffusion studies by Hagel and Seybolt<sup>195</sup> on sintered polycrystalline  $\text{Cr}_2\text{O}_3$  showed a three orders of magnitude higher Cr diffusivity over that of oxygen. Compared with Cr diffusion rates found in single crystal  $\text{Cr}_2\text{O}_3$ ,<sup>196</sup> which is nearly five orders of magnitude lower than the rates reported by Hagel and Seybolt, the earlier rates should be dominated by short circuit diffusion, mainly via oxide grain boundaries.<sup>74</sup> Consequently, growth of  $\text{Cr}_2\text{O}_3$  scales has often been considered to be dominated by cation outward transport, mainly through  $\text{Cr}_2\text{O}_3$  grain boundaries.<sup>197</sup> Location of inert markers subsequent to oxidation of essentially  $\text{Cr}_2\text{O}_3$ -forming alloys seems to support this conclusion,<sup>198</sup> where markers that had been deposited on specimen surfaces prior to oxidation resulted near the scale–metal interface after oxidation, suggesting an outward growth mechanism.

More recent diffusion studies,<sup>199</sup> utilizing oxygen and chromium isotopes,  $^{18}\text{O}$  and  $^{54}\text{Cr}$  respectively, showed that the rates of O and Cr bulk diffusion are similar, but Cr grain boundary diffusion is greater than that of oxygen. The parabolic oxidation rate constants calculated from these diffusion data agreed with experimentally determined values, but suggested that  $\text{Cr}_2\text{O}_3$  scale growth is in fact controlled by counter diffusions of oxygen and chromium along oxide grain boundaries. Moreover, SIMS studies<sup>200</sup> on different areas of  $\text{Cr}_2\text{O}_3$  showed different transport properties on the same sample of Cr after it was



oxidized in natural oxygen ( $^{16}\text{O}$ ) and then, without cooling to room temperature, in oxygen enriched in  $^{18}\text{O}$ . Results showed that, in some places, the oxide grew primarily by chromium transport while, in others, it grew primarily by oxygen transport and, in still others, it grew by a mixture of both. It was postulated that these apparent different transport processes were related to different degrees of high *versus* low angle oxide grain boundaries, presuming that the two have different transport properties, whether intrinsic or due to different degrees of impurity segregation.

Above  $700^\circ\text{C}$  in air or atmospheric oxygen, the kinetics of  $\text{Cr}_2\text{O}_3$  growth are generally interpreted as parabolic, although periodic increases in the reaction rates have been observed in some cases<sup>201</sup>; these will be treated later under breakaway oxidation. The parabolic oxidation rates on Cr metal prior to 1980 had been compiled by Hindam and Whittle,<sup>202</sup> with data scattered between the two solid lines in Figure 12; all of the experiments included here were conducted in oxygen. Reported rates from more recent studies also fall within this wide band of scattered data. It is rather astonishing that such a large range of rates, over three orders of magnitude, can exist for a simple metal. The most likely explanation for these differences may

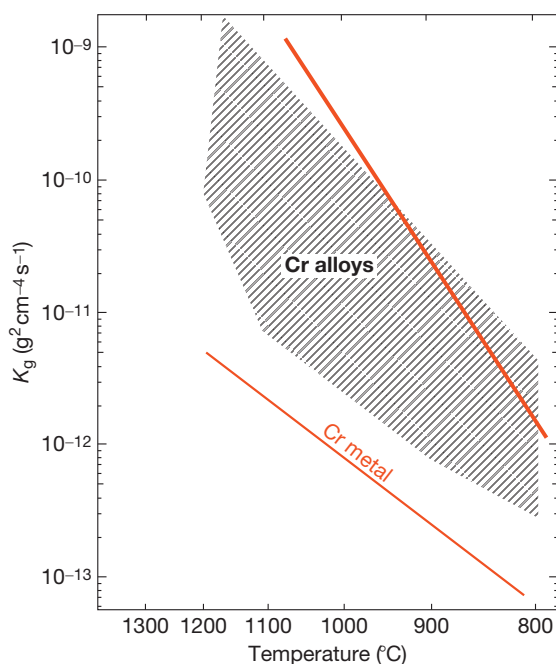


**Figure 12** Range of parabolic rate constants from the oxidation of pure Cr (bonded between the solid lines) and binary Co, Ni and Fe–Cr alloys (the shaded area), compiled by Hindam and Whittle.<sup>202</sup>

be the relative adhesion of the  $\text{Cr}_2\text{O}_3$  scale, resulting in different degrees of scale buckling and convolution during oxidation, or even local breakaway resulting in small nodule formation (see Figure 13 for typical microstructures). Buckling, driven by the compressive growth stress in the oxide film,<sup>203</sup> often occurs; an example is given in Figure 14. These buckles increase the amount of oxide per unit area of metal, hence giving rise to an apparent increase in oxidation rate. Continued scale growth beneath a buckle is achieved by Cr vapor transport,<sup>204</sup> which can be faster than solid state diffusion through the scale. Several other factors may also contribute to the scatter. Formation of volatile oxide species, especially at higher temperatures, can be a problem. Although most studies corrected for the sample weight loss due to  $\text{CrO}_3$  formation, the possible effect of water vapor and the formation of other volatile species were not considered. Metal purity can also be a contributor to rate variations. Dissolution of metallic impurities in  $\text{Cr}_2\text{O}_3$  can exert a doping effect, that is, changing its defect concentration and, hence, its oxidation kinetics. Nonmetallic impurities, such as S and C, have also been suggested to affect the transport rate through  $\text{Cr}_2\text{O}_3$ .<sup>205,206</sup> However, it is also possible that these impurities caused a decrease in scale adhesion, consequently, leading to increases in the rate by forming more convoluted or buckled oxides. Different surface treatments, such as electropolishing, etching or mechanical abrasion, have also been shown to have profound effects on subsequent oxidation rates,<sup>207</sup> mainly due to the development of very different oxide grain sizes on these surfaces.<sup>208</sup> Likewise, sample pretreatment, such as annealing, cold working, rolling, etc., or the rate at which specimens are heated to the oxidation temperature can all have an effect, since they can influence the development and

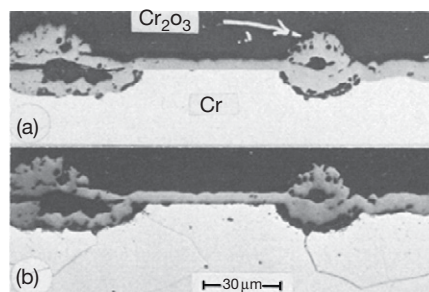


**Figure 13** Optical micrograph of polished cross-section of etched Cr oxidized for 42 h at  $1200^\circ\text{C}$ , giving examples of localized oxide nodule, or ridge, formation on pure Cr. Reproduced from Caplan, D.; Sproule, G. I. *Oxid. Met.* **1975**, 9, 459–472.

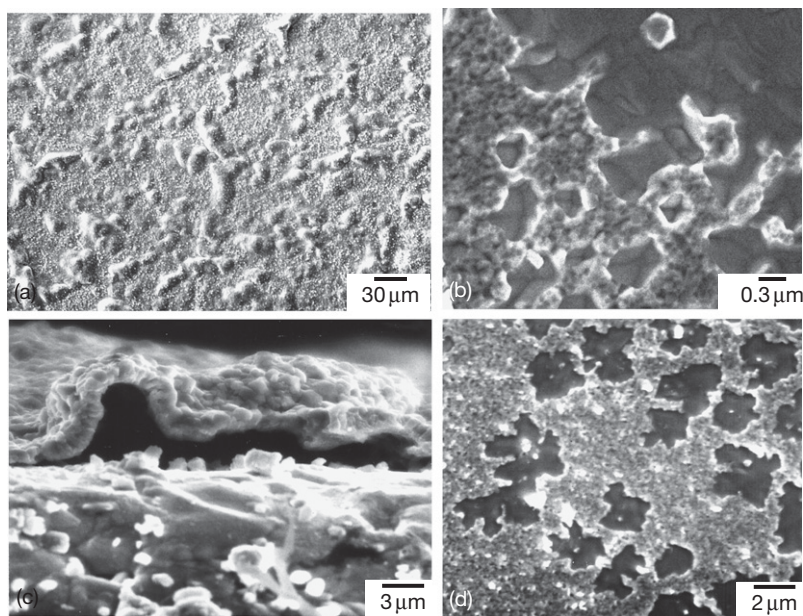


**Figure 14** Examples of buckled  $\text{Cr}_2\text{O}_3$  scale formed on commercial grade 99.8% Cr at  $1000^\circ\text{C}$ . (a) Scale surface and (c) cross-section after oxidation for 30 min. (b) and (d) are metal surfaces after scale removal and oxidation for 5 and 10 min, respectively.

grain size of the first formed  $\text{Cr}_2\text{O}_3$ . Although it appears that the grain size and microstructure of the  $\text{Cr}_2\text{O}_3$  scale dictates its growth rates, no clear correlations can be identified between the rate and the various factors mentioned above.

The oxidation rates of  $\text{Cr}_2\text{O}_3$  forming alloys of Ni, Co, or Fe–Cr have also been compiled by Hindam and Whittle,<sup>202</sup> and those data are also plotted, as a shaded band, in **Figure 12**. It is seen that, even with different base metals, less scattering occurs during alloy oxidation. This is probably related to better  $\text{Cr}_2\text{O}_3$  adhesion on alloys than on Cr. It is also possible that base metals incorporated into these  $\text{Cr}_2\text{O}_3$  scales dominate other impurities that might influence the oxidation rate. Both Ni and Co have small, but significant solubility in  $\text{Cr}_2\text{O}_3$ , while  $\text{Fe}_2\text{O}_3$  and  $\text{Cr}_2\text{O}_3$  are completely isomorphous.

#### 1.10.5.2 $\text{Cr}_2\text{O}_3$ Layer Development on Alloys

When a Cr-containing alloy is oxidized, its oxidation rate usually changes with its Cr concentration, as illustrated in **Figure 15** for binary Co–Cr alloys.<sup>209</sup> The rate increases with the first few percent of Cr addition, due to duplex scale formation and the increased oxidation rate from oxygen inward transport, as described for Ni and Co alloys in **Section 1.10.2**. Afterwards, the

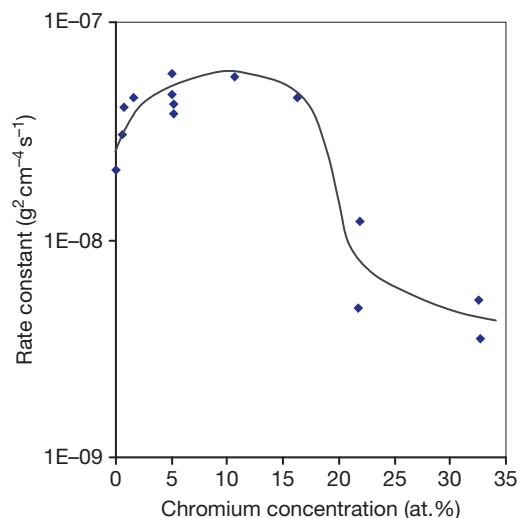


**Figure 15** The change of oxidation rate, at  $1000^\circ\text{C}$  760 torr oxygen, of Co–Cr as a function of alloy Cr concentration. Data from Wright and Wood<sup>209</sup> include parabolic rate constants from initial and steady states.

rate constant is rather unaffected by additional Cr until a critical Cr concentration is reached. This is the concentration necessary to form a complete  $\text{Cr}_2\text{O}_3$  layer, whether as an external surface layer or a healing layer beneath some base metal oxides. Once the  $\text{Cr}_2\text{O}_3$  layer is formed, the oxidation rate



becomes dominated by its subsequent growth. Ni–Cr and Fe–Cr alloys behave similarly.<sup>210</sup>

The minimum Cr concentration necessary for the establishment of a continuous Cr<sub>2</sub>O<sub>3</sub> layer is usually around 13–25 wt% in oxygen at atmospheric pressure. However, this selective oxidation process depends heavily not only on partial pressures of oxygen, but also on oxidation temperature; sample surface treatments and substrate grain size are also influencing factors. Consequently, alloys with compositions around the narrow transition range can develop non-protective or protective scales with minor changes in operating conditions. For example, a Ni–14.6 wt% Cr<sup>211</sup> can either form a protective Cr<sub>2</sub>O<sub>3</sub> scale or a Ni-rich oxide, depending on how it was heated to the oxidation temperature. The former protective scale developed when heating was done in vacuum ( $\sim 10^{-5}$  torr), but the latter behavior was found when the sample was heated in air, attesting to the  $p_{O_2}$  dependence of the selective oxidation process. Fine-grained<sup>212</sup> or cold-worked alloys<sup>213</sup> can also assist the establishment and maintenance of the Cr<sub>2</sub>O<sub>3</sub> layer, often at Cr concentrations lower than otherwise predicted. This is because alloy grain boundaries are faster diffusion paths, so the healing Cr<sub>2</sub>O<sub>3</sub> layer is preferentially established at the intersections of these grain boundaries with the surface. The effect has been clearly demonstrated on a Ni–Cr alloy.<sup>214</sup> For Fe–Cr alloys with comparable compositions to Ni–Cr, Cr<sub>2</sub>O<sub>3</sub> is more readily established initially because of the greater alloy interdiffusion coefficient in the bcc Fe–Cr structure compared with that in the fcc Ni–Cr structure, and the lower oxygen solubility and diffusivity in Fe–Cr. Consequently, less Fe than Ni oxides are present above the Cr<sub>2</sub>O<sub>3</sub> layer formed on Fe–Cr and Ni–Cr respectively. Detailed discussions of the selective oxidation process and factors affecting it can be found elsewhere in this volume.

### 1.10.5.3 Scale Morphology and Breakaway Oxidation

The first-formed, thin Cr<sub>2</sub>O<sub>3</sub> scales are uniform and adherent. However, under these apparently adherent scales are often debonded areas or faceted interfacial voids (**Figure 14(b)**), which can be seen after the scale has been spalled away from the force of a scratch. The debonded areas had a smooth, often thermally etched appearance, where the scale and substrate were not in intimate contact at the reaction temperature, and their fraction increased with oxidation time (**Figure 14(d)**). Elsewhere, the metal

surface exhibits oxide grain ‘imprints,’ where the scale had maintained contact with the alloy. It is evident that the fraction of these debonded areas can be significant, and the extent of scale detachment is found to be strongly related to alloy purity.<sup>215</sup>

With longer oxidation times, Cr<sub>2</sub>O<sub>3</sub> scales formed on Cr can be heavily buckled (or convoluted) or show localized nodule formation (**Figures 13, 14(a), and 14(c)**). Development of the nodules seen in **Figure 13** has been shown to be related to oxide grain size. When the Cr surface was etched prior to oxidation, large grained Cr<sub>2</sub>O<sub>3</sub> developed on some metal orientations, while finer grained oxide formed on other orientations and on alloy grain boundaries.<sup>208</sup> The fine grained oxide grew considerably faster, and apparently inward and outward from the original alloy surface, and is most likely due to faster transport rates via oxide grain boundaries. Both kinds of oxide, thin film or nodule, remained in good contact with the metal. However, such good contacts are not often observed. Typically, scale buckling occurs, as seen in **Figure 14** in plan view and in cross-section. The buckles appeared to have formed preferentially along alloy grain boundaries, similar to those observed by Howes,<sup>216</sup> who in a later paper<sup>217</sup> investigated buckling above alloy grain boundaries under a scanning electron microscope. It was suggested that the preferential separation was due to faster Cr boundary diffusion from the alloy, hence higher cation vacancy flux, but not all grain boundaries developed buckles, so the exact reason why scales are buckled on some locations but not on others is not clear. Depending on the sample surface treatment, oxidation conditions and probably other factors, such as metal purity, the extent of buckling can be rather severe, resulting in very convoluted oxides. Cracking of these extremely convoluted, or buckled oxides can occur at the oxidation temperature and allow oxygen access to the bare metal surface underneath; repeated cracking and healing at temperature eventually leads to the formation of a multilayered oxide, as shown in **Figure 16**. In the case of chromium-containing alloys, this process is unlikely, except for high Cr contents,<sup>218,219</sup> because selective oxidation of Cr to form Cr<sub>2</sub>O<sub>3</sub> leads to an appreciable Cr depletion in the alloy beneath the scale–alloy interface. When the protective Cr<sub>2</sub>O<sub>3</sub> is damaged, base metal oxides may develop, resulting in the formation of large nodules that are usually double layered, with an outer layer of almost purely base metal oxide, and an inner layer of mixed base metal and Cr oxides. Depending on the growth rate of the base

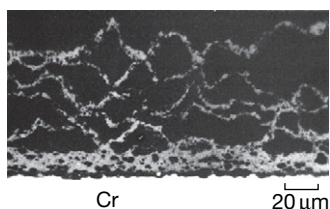


**Figure 16** Optical micrograph showing layers of  $\text{Cr}_2\text{O}_3$  scales formed on Cr metal after oxidation at  $1090^\circ\text{C}$  for 21 h. Reproduced from Caplan, D.; Sproule, G. I. *Oxid. Met.* **1975**, *9*, 459–472.

metal oxide and the diffusion rate of Cr in the alloy, a healing layer of  $\text{Cr}_2\text{O}_3$  may again form at the base of the nodule and thus stop its growth. Otherwise, the fast growing nodule continues to grow vertically and laterally, and eventually destroys the protective  $\text{Cr}_2\text{O}_3$  scale.

Associated with the failure of the protective  $\text{Cr}_2\text{O}_3$  layer to allow fast base metal oxide growth are accelerated oxidation kinetics that can be observed as a fast increase in specimen weight gain, and called ‘breakaway oxidation.’ When the  $\text{Cr}_2\text{O}_3$  forms again as a healing layer, the oxidation rate can revert to that dominated by  $\text{Cr}_2\text{O}_3$  scale growth. In cases where breakaway and healing happen continuously at different locations, the weight gain may still show an apparent parabolic behavior, but with a much faster rate than that found for  $\text{Cr}_2\text{O}_3$  only. Breakaway oxidation usually occurs more easily on Fe–Cr than Ni–Cr or Co–Cr alloys,<sup>220</sup> due to a poorer scale adhesion on Fe–Cr alloys, for reasons that are not clear. When breakaway does happen for Ni–Cr alloys,<sup>211</sup> the situation is worse, because chromium depletion at the alloy–oxide interface is greater and longer lasting than for Fe–Cr alloys.

The driving force for buckling has to be the compressive stress that develops in the  $\text{Cr}_2\text{O}_3$  film.<sup>203</sup> Although earlier works have concluded that oxidation stresses are negligible compared with thermal stresses,<sup>221,222</sup> direct measurements of stresses in  $\text{Cr}_2\text{O}_3$  at oxidation temperatures have been achieved more recently. Using *in situ* Raman spectroscopy, Kitamura *et al.*<sup>223</sup> determined that the growth stress in  $\text{Cr}_2\text{O}_3$  formed at  $900^\circ\text{C}$  in air is highly compressive, with a maximum level of  $700 \pm 100$  MPa. Although still a fraction of the thermal stress, measured to be about 3500 MPa, the magnitude is higher than that observed on any  $\text{Al}_2\text{O}_3$  forming alloys, recently performed with *in situ* synchrotron X-ray techniques.<sup>224,225</sup> A study by Zhu *et al.*<sup>226</sup> using hot stage X-ray diffraction, also reported compressive

stresses in  $\text{Cr}_2\text{O}_3$ , although the level was not as high as that found by Kitamura *et al.*<sup>223</sup> Counter diffusion of oxygen and chromium and internal oxide growth resulting from these fluxes has been suggested<sup>47</sup> to be the cause of such stresses.

More severe  $\text{Cr}_2\text{O}_3$  buckling and convolution have been observed on Cr oxidized at low  $p\text{O}_2$  values.<sup>194</sup> The scales were heavily wrinkled or even totally detached from the metal except at specimen corners. It was suggested that the difference in behavior in lower  $p\text{O}_2$  is due to a higher oxide plasticity at low oxygen pressures. The greater plasticity would indeed allow the scale to deform without cracking, but there still appears to exist a higher driving force that causes the greater deformation. It is possible that higher growth stresses were generated at lower  $p\text{O}_2$ . If the stress generation mechanism was that of internal growth, as proposed by Rhines and Wolf,<sup>47</sup> it is possible that the relative diffusion rates of Cr and O may differ under different  $p\text{O}_2$  values.

### 1.10.6 Oxidation of Alumina-Forming Alloys

At temperatures above  $900^\circ\text{C}$ , alloys or coatings that develop  $\text{Al}_2\text{O}_3$  scales are most commonly employed for practical applications, due to the relative ease with which alumina can develop into a complete layer and the slow growth rate and long-term chemical stability of  $\text{Al}_2\text{O}_3$ . There are mainly two types of commercial  $\text{Al}_2\text{O}_3$ -forming alloys: the aluminides, such as FeAl and NiAl, and the MCrAl type alloy that is often the base of superalloys, where ‘M’ represents the base metal and can be a mixture of Fe, Ni, and Co. For the aluminides, at least  $\sim 19$  at.% Al is needed to achieve the selective oxidation of Al to develop a protective  $\text{Al}_2\text{O}_3$  scale and suppress the oxidation and growth of iron oxides<sup>227,228</sup>;  $\sim 22$  at.% Al is needed for Ni–Al, where a thin layer of Ni-containing oxide, NiO and/or  $\text{NiAl}_2\text{O}_4$ , is present at the scale outer surface and the  $\text{Al}_2\text{O}_3$  forms at the scale–alloy interface as a healing layer. In accordance with the theory on selective oxidation, these critical Al compositions can vary depending on oxidation temperature and environment, and also on alloying additions. The addition of about 18–20 at.% Cr in MCrAl type alloys decreases the amount of Al necessary to establish the protective  $\text{Al}_2\text{O}_3$  layer to no more than 10 at.%. Iron aluminides have limited industrial usage, due to their low high temperature strengths.<sup>163</sup> Platinum is often added to nickel

aluminides<sup>229</sup> to enhance the oxidation resistance, mainly by increasing the  $\text{Al}_2\text{O}_3$  scale adhesion. Small amounts of Ti, Zr, Hf, Y, or a combination of these are added to MCrAl type alloys also to enhance  $\text{Al}_2\text{O}_3$  adhesion; these are the so-called 'REs,' which have higher oxygen affinities than Al, and their effects on the oxidation behavior of  $\text{Al}_2\text{O}_3$ -forming alloys will be presented in [Section 1.10.7.1](#).

### 1.10.6.1 Scale Development

Only  $\text{Al}_2\text{O}_3$  is formed on  $\beta$ -NiAl<sup>230–232</sup> and  $\beta$ -FeAl<sup>233</sup> at elevated temperatures ( $>800^\circ\text{C}$ ). On  $\gamma'$ -Ni<sub>3</sub>Al, an external layer of Ni-rich oxide, either NiO and/or NiAl<sub>2</sub>O<sub>4</sub>, is always present, beneath which is the  $\text{Al}_2\text{O}_3$  layer.<sup>234–236</sup> Unlike Ni<sub>3</sub>Al, Fe<sub>3</sub>Al alloys do not seem to develop a noticeable Fe-rich surface layer.<sup>237,238</sup> When such alloys are heated slowly to  $1100^\circ\text{C}$  in air,<sup>239</sup> the first detected oxide, using Raman spectroscopy, was  $\text{Fe}_2\text{O}_3$ , whose intensity increased from  $500$  to  $700^\circ\text{C}$ , then dropped to zero with continued oxidation at higher temperatures. Above  $900^\circ\text{C}$ , the scale consisted of only  $\text{Al}_2\text{O}_3$  and  $\text{Fe}_2\text{O}_3$  was no longer detected. This difference between the Fe-based and the Ni-based alloys is believed to be associated with faster diffusion rates of Al relative to Fe in Fe<sub>3</sub>Al than of Al compared to Ni in Ni<sub>3</sub>Al.<sup>238</sup>

On MCrAl type alloys, the addition of Cr promotes  $\text{Al}_2\text{O}_3$  formation, by the well-known third element

effect,<sup>240</sup> where the alloy is suggested to initially develop  $\text{Cr}_2\text{O}_3$ , causing a decrease in the partial pressure of oxygen at the scale–alloy interface to facilitate the  $\text{Al}_2\text{O}_3$  formation. Therefore, steady-state scales that form on these alloys are always almost pure  $\text{Al}_2\text{O}_3$ . However, the initial scale still has appreciable amounts of the base metals, because all metals and alloys exposed in the ambient atmosphere contain a thin layer of native oxide that is a few nanometers thick. An example is given in [Figure 17\(a\)](#) for FeCrAl where the surface oxide consists of an outer layer rich in Fe and an inner layer slightly enriched with Cr. When the alloy is heated to elevated temperatures in air or oxygen, this native oxide quickly thickens and aluminum starts to enrich at the scale–alloy interface ([Figure 17\(b\)](#)). Further oxidation results in a fully established aluminum oxide layer at the scale–alloy interface ([Figure 17\(c\)](#)). Subsequent scale growth only involves thickening of this alumina layer, where all the initially formed Fe and Cr oxides become incorporated into the  $\text{Al}_2\text{O}_3$  layer. Integrating the depth profile curves in [Figure 17](#) over distance shows that the initial stage oxide clearly contains high levels of base metals, in this case Fe and Cr, whose concentrations decrease as the scale develops into a complete layer of the thermodynamically most stable oxide, in this case  $\text{Al}_2\text{O}_3$ .<sup>241</sup> This process of initial stage base metal oxidation and the subsequent incorporation of their oxides into the final scale are expected for all alloys.<sup>242</sup> The amount that is incorporated depends

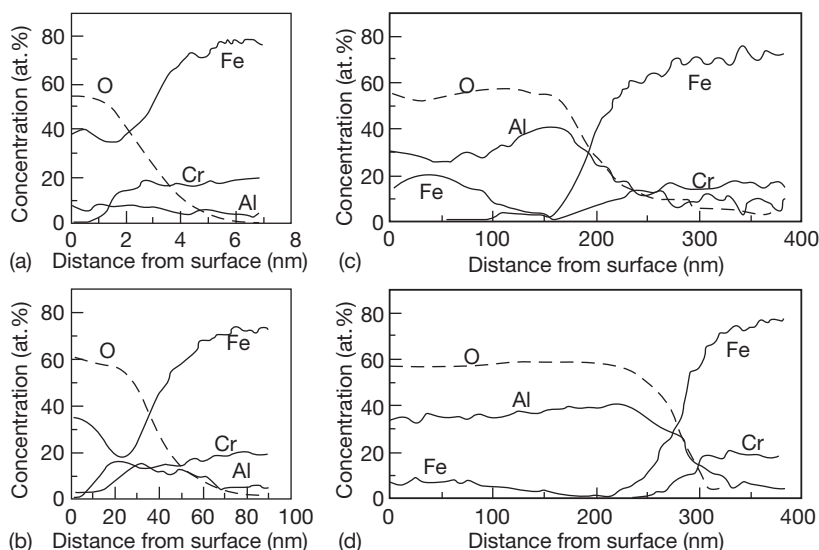


**Figure 17** Auger depth profiles through the surface oxide on a FeCrAl alloy (a) the native oxide prior to oxidation, (b)–(d) oxides formed after the alloy was introduced into a  $1000^\circ\text{C}$  furnace and oxidized in air for 1, 3, and 11 min, respectively. Reproduced from Hou, P. Y. *J. Am. Ceram. Soc.* **2003**, *86*, 660–668.

strongly on the alloy composition, the oxidation temperature and the partial pressure of oxygen in the environment, or sometimes even on the alloy surface finish.<sup>243</sup> The behavior of FeCrAl similar to that reported here has been shown using other surface techniques<sup>244,245</sup>; NiCrAl<sup>246</sup> also forms transient Ni and Cr oxides. The effect of these base metals in Al<sub>2</sub>O<sub>3</sub> on its transport, and hence growth properties, are addressed later in this section.

When Al<sub>2</sub>O<sub>3</sub> is first developed, regardless of the alloy system, it is never the thermodynamically most stable  $\alpha$  form, especially upon heating, but consists of alumina that have often been identified as the cubic  $\theta$ <sup>230,231</sup> or  $\gamma$ <sup>232,235,247–250</sup> phase, or a mixture of the two.<sup>230,252</sup> The more stable hexagonal  $\alpha$ -Al<sub>2</sub>O<sub>3</sub> phase later nucleates at the transition alumina–alloy interface,<sup>249–251</sup> while the initially formed transition alumina transforms to the  $\alpha$  form with time. The development of  $\alpha$ -Al<sub>2</sub>O<sub>3</sub> is faster at higher temperatures<sup>252</sup> and with the presence of Cr<sup>253</sup> and/or Fe<sup>238,239</sup> in the alloy, but seems slower with higher concentrations of Al or the presence of a RE, such as Hf, Y or Zr.<sup>254</sup>

The first-formed alumina are often referred to as ‘transition’ or ‘metastable’ alumina. At present, there are no clear indications as to why a certain form of transition alumina is formed; either  $\theta$  or  $\gamma$  has been found without any systematic differences in alloy type, oxidation temperature, detection methods or oxidation environment, for example, the presence of moisture. Even the  $\delta$ <sup>230</sup> and  $\kappa$  phases have been reported in some cases. Since there are many polymorphs of alumina, and many routes by which one phase can transform to the other,<sup>255</sup> it is possible that many different types of alumina can be present during the initial stage of oxidation.<sup>256</sup> TEM studies<sup>230,232,235,236</sup> often showed that the transition alumina formed epitaxially, having a cube-on-cube orientation relationship with the alloy, while the degree of preferred orientation decreased with oxidation time. Limited high-resolution TEM studies<sup>257</sup> indicated that the interface between the transition alumina and the alloy, in this case a single crystal NiAl, was coherent, but became incoherent once  $\alpha$ -Al<sub>2</sub>O<sub>3</sub> nucleated. The morphology of the transition aluminas is often described as platelet or needle-like. TEM analyses<sup>258,259</sup> have identified the plane of the platelets to be (110), whether they are  $\theta$  or  $\gamma$ -Al<sub>2</sub>O<sub>3</sub>; and the platelets are often heavily twinned along the [111] direction.<sup>259</sup> This structure is probably related to the high compressive growth stresses present in the initially formed transition alumina layer,<sup>260</sup> whereas twinning and needle-like growth are means to relieve

the growth stress. Surface smoothing of the platelets occurs with time as a spheroidization phenomenon driven by a decrease in surface energy.<sup>258</sup>

When  $\alpha$ -Al<sub>2</sub>O<sub>3</sub> is nucleated at the transition alumina–alloy interface, its orientation is random, and it forms an incoherent interface with the alloy.<sup>232</sup> On FeCrAl type alloys, these nuclei are finer grained<sup>250,261</sup> than those on NiAl<sup>260,262</sup> or NiPtAl,<sup>263</sup> where they tend to form large circular plates that extend faster laterally than vertically<sup>260,262,264</sup>; an example of these circular plates found on Ni–55 at.% Al is shown in **Figure 18(a)**. The number density of these circular plates depends on the alloy grain orientation<sup>260</sup> and increases on rougher surfaces.<sup>263</sup> The first formed  $\alpha$ -Al<sub>2</sub>O<sub>3</sub> is always under tension,<sup>224,225,260</sup> which can be as high as 400–600 MPa. Since there is  $\sim 5\%$  volume shrinkage associated with the  $\theta$ -to- $\alpha$  transformation, this result indicates that most of this alpha phase is developed by oxide phase transformation, rather than from oxidation, that is, growth of a new oxide grain at the interface. The high tensile stress, which exceeds the

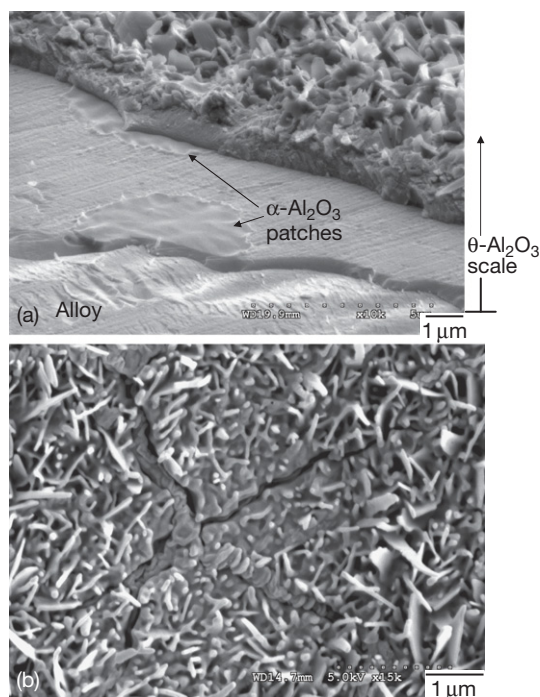


**Figure 18** Examples of alumina scale morphology resulting from the transformation of  $\theta$  to  $\alpha$  alumina during oxidation with SEM micrographs showing (a) cross-section of scale formed on Ni–55 at.% Al, 1100 °C, 40 min. (b) Surface of oxide on the same alloy after 11 h at 1100 °C. Reproduced from Hou, P. Y.; Paulikas, A. P.; Veal, B. W. *Mater. High Temp.* **2006**, *22*, 373–381.



toughness limit of  $\alpha$ -Al<sub>2</sub>O<sub>3</sub>,<sup>265</sup> often causes cracking of the first-formed  $\alpha$ -Al<sub>2</sub>O<sub>3</sub> grains. Ridges of oxides, which are associated with  $\alpha$ -Al<sub>2</sub>O<sub>3</sub> grain boundaries, develop and fill the cracks after the transformation is completed (Figure 18(b)). The alpha nuclei eventually impinge and develop into a complete  $\alpha$ -Al<sub>2</sub>O<sub>3</sub> layer above the alloy, and subsequent scale growth becomes dominated by the transport of O and Al through this alpha layer, while the initially formed transition alumina transform to the  $\alpha$ -Al<sub>2</sub>O<sub>3</sub> phase with time.

When Cr and/or Fe are present in the alloy, the transformation to  $\alpha$ -Al<sub>2</sub>O<sub>3</sub> is accelerated. Since Cr<sub>2</sub>O<sub>3</sub> and Fe<sub>2</sub>O<sub>3</sub> have the same corundum structure as  $\alpha$ -Al<sub>2</sub>O<sub>3</sub>, they have been suggested to serve as templates that facilitate the nucleation and growth of the  $\alpha$  phase at a temperature below which this transition happens in the bulk at 1000 °C.<sup>239,253</sup> TEM studies have found small particles of  $\alpha$ -Al<sub>2</sub>O<sub>3</sub> present in the first-formed transition alumina layer on FeCrAl<sup>250</sup> and Fe<sub>3</sub>Al<sup>238</sup> alloys. Although it is not clear how their formation is related to the Cr<sub>2</sub>O<sub>3</sub> and/or Fe<sub>2</sub>O<sub>3</sub> that were present on the alloy surface at the onset of oxidation, their presence in the initial Al<sub>2</sub>O<sub>3</sub> layer must also help to facilitate the alumina transformation and the development of a complete  $\alpha$ -Al<sub>2</sub>O<sub>3</sub> layer.

#### 1.10.6.2 Oxidation Rates

Oxidation of alumina scales usually follows parabolic kinetics, indicating diffusion-controlled growth. The growth rate of the transition alumina is about 1 order of magnitude faster than that of the  $\alpha$ -Al<sub>2</sub>O<sub>3</sub>.<sup>248</sup> Due to the phase transformation and the different growth rates of the different aluminas, oxidation kinetics usually show two parabolic stages separated by a gradual transition.

The parabolic rate constants of many binary and ternary Al<sub>2</sub>O<sub>3</sub>-forming alloys, known prior to 1982, have been compiled by Hindam and Whittle.<sup>202</sup> Their summary included alloys that contained a RE, such as Y, Ce, or Th, and contributions from transitional alumina phases were not always eliminated. It was also noted that, in some cases, strict parabolic behavior was not observed, so the rate constants were only determined from the weight change near maximum exposure times. Despite these reservations, all the data fell in a scatter band of about 16, with scale thickness for a given time varying by a factor of 4. The scatter is much smaller than that observed for Cr<sub>2</sub>O<sub>3</sub> scales (Figure 12), probably

because transport through Al<sub>2</sub>O<sub>3</sub> scales is less sensitive to impurities.

As common base metals such as Fe, Ni, Co, and Cr can be incorporated into the Al<sub>2</sub>O<sub>3</sub> scale during initial stage oxidation, and some of these elements have been shown to have a profound effect on the high temperature creep properties of Al<sub>2</sub>O<sub>3</sub>,<sup>266–271</sup> hence affecting O and/or Al transport; it is worthwhile to examine whether these incorporated base metals affect oxidation rates. Before that, one needs to realize how much of these base metals are present in a growing  $\alpha$ -Al<sub>2</sub>O<sub>3</sub> scale and whether they segregate at the grain boundaries. TEM studies have found a decrease from 4 to 0.3 at.% Fe and Cr in the scale as it increases from 0.4 to 5  $\mu$ m for Al<sub>2</sub>O<sub>3</sub> scales grown on FeCrAl alloy at 1000–1200 °C,<sup>272</sup> indicating that the scale becomes purer as it thickens with oxidation time. In other words, all these impurities were incorporated during the initial stage, attesting to the protectiveness of the Al<sub>2</sub>O<sub>3</sub> scale. The Fe and Cr concentrations in the Al<sub>2</sub>O<sub>3</sub> appeared uniform when relatively large areas, that is, 14  $\mu$ m<sup>2</sup>, were examined, but they varied greatly from point to point under a 17 nm beam size. This kind of distribution was also found for Ni and Cr in Al<sub>2</sub>O<sub>3</sub> formed on NiCrAl.<sup>293</sup> These local high concentrations probably resulted from small grains of base metal oxides or spinels left from the initial stage of oxidation. The lattice parameter of  $\alpha$ -Al<sub>2</sub>O<sub>3</sub> grains within the scale was enlarged with higher concentrations of Fe, Ni, and Cr,<sup>272</sup> suggesting that at least some of these elements are dissolved in the Al<sub>2</sub>O<sub>3</sub>. Point analyses made at many grain boundaries and within the grains adjacent to the boundary found 38% of the boundaries with higher concentrations of Fe, but none had higher concentrations of Cr. Since Cr<sub>2</sub>O<sub>3</sub> forms a complete solid solution with Al<sub>2</sub>O<sub>3</sub>,<sup>273</sup> Cr is expected to dissolve in Al<sub>2</sub>O<sub>3</sub> and not segregate on grain boundaries. Fe may have segregated, but its segregation may be charge related, hence  $p$ O<sub>2</sub> dependent. Recent work by Harmer *et al.*<sup>274</sup> using EELS shows that Fe<sup>2+</sup> segregates at Fe-doped Al<sub>2</sub>O<sub>3</sub> grain boundaries, but not Fe<sup>3+</sup>. The behavior is consistent with the fact that Fe<sup>3+</sup> has an appreciable solubility in Al<sub>2</sub>O<sub>3</sub>, about 3–5 at.%,<sup>275</sup> but the solubility is only a few parts per million for Fe<sup>2+</sup>.<sup>276</sup>

In order to better correlate alloy composition to oxidation rates, data cited in the Hindam and Whittle paper<sup>202</sup> are reevaluated, and those representing steady-state growth rates from Ni-, Fe-, or Pt-based alloys that are undoped with REs are compared with more recently published results.<sup>277–302</sup> These rates

are plotted in **Figure 19** as a function of the inverse of the oxidation temperature. All the studies included here are from laboratory tests performed on high purity binary M–Al or ternary M–Cr–Al type alloys, so M (Fe, Ni, or Pt) and Cr should be the most abundant impurities incorporated in the  $\text{Al}_2\text{O}_3$  scale. Most tests were carried out at one atmosphere oxygen, but some in air. Different symbols in **Figure 19** distinguish different types of alloys. The data showed much scatter from study to study even for alloys with the same composition. Some general trends, however, seem apparent. PtAl alloys, on average, tend to have the slowest oxidation rates, but this conclusion is not supported by all the PtAl data. The presence of Cr does not seem to make any difference to oxidation rates. The Fe-based alloys seem to oxidize with the highest rates, which would agree with the higher creep rates observed for Fe-doped  $\text{Al}_2\text{O}_3$ .<sup>266</sup> However, the higher oxidation rates may also be related to increases in surface area that resulted from wrinkling of the scale and the underlying alloy.<sup>303,304</sup> FeCrAl and  $\text{Fe}_3\text{Al}$  type alloys are especially prone to wrinkling. Such increase in surface area can be as high as 10%,<sup>304</sup> but none of the oxidation rates cited here had been corrected for it.

In summary, the growth rates of  $\alpha\text{-Al}_2\text{O}_3$  scales from 1000 to 1300 or 1400 °C on Fe-, Ni-, Co-, and

Pt-based binary or ternary alloys without any RE addition can vary over two orders of magnitude, with an average activation energy of about  $240\text{ kJ mol}^{-1}$ . Although base metal components are incorporated in the growing alumina during the initial stage of oxidation, and depending on their size and solubility in  $\text{Al}_2\text{O}_3$ , may segregate to oxide grain boundaries, their effect on oxidation rates seems small. In a way, this is surprising, because  $\text{Al}_2\text{O}_3$  is a very stoichiometric oxide, whose transport property is dictated by impurity contents.<sup>305</sup> No explanations are apparent for the large variation in reported oxidation rates. Perhaps part of this scatter is indeed due to the presence of different types and/or amounts of impurities under different test conditions. To date, there is no good understanding of which impurities these may be. Tolpygo *et al.*,<sup>306</sup> for example, have shown that grit blasted coating surfaces develop much thicker  $\text{Al}_2\text{O}_3$  scales (by a factor of  $\sim 3$ ) than other surfaces, due to the incorporation of impurities, such as Li, Na, K, Ca, Mg, and/or Si, in the surface

### 1.10.6.3 Oxide Growth Mechanism

The transition alumina has been shown to grow predominantly by aluminum outward transport.<sup>231,307</sup> From several earlier inert Pt marker studies,<sup>301,308</sup>  $\alpha\text{-Al}_2\text{O}_3$  was believed to grow predominantly by O inward diffusion, since markers that were placed on the alloy surface prior to oxidation remained on the scale surface afterwards, indicating inward growth of the scale. The minor amount of aluminum outward transport is believed to contribute to lateral growth of the scale, causing extensive scale convolution, or wrinkling<sup>298</sup>; an example is given in **Figure 20**. Based on the degree of such a convolution, whether the scale is detached from the substrate or wrinkled with it, the extent of lateral growth on polycrystalline FeCrAl alloy, for example, can be as high as 20–50%.<sup>303,304</sup> This shows that the amount of Al outward transport is not trivial. More recent two-stage oxidation studies using  $^{18}\text{O}/^{16}\text{O}$ <sup>309–315</sup> indicated clearly that a considerable amount of Al outward transport indeed occurs during scale growth. In this type of study, the oxidation at each stage is done in an atmosphere enriched with one of the oxygen isotopes. The isotope distribution throughout the scale is subsequently determined using spectroscopic methods. Secondary ion mass spectroscopy (SIMS) is the most commonly employed technique.<sup>311,313–315</sup> Secondary neutral mass spectroscopy<sup>312</sup> (SNMS) and other techniques<sup>309,310</sup> have also been used.

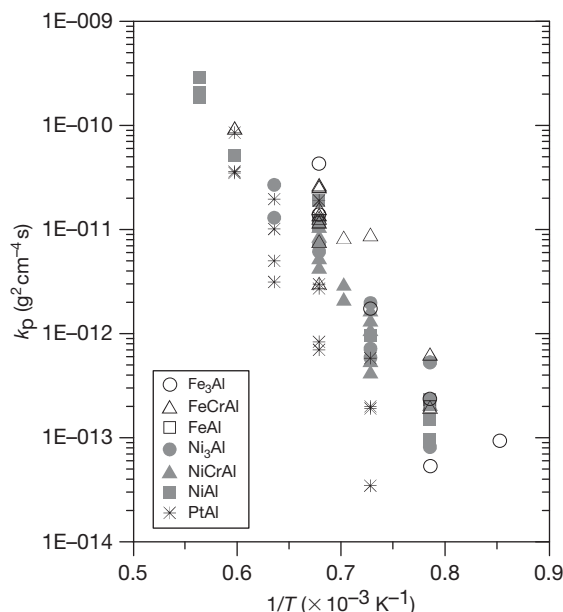


**Figure 19** Parabolic rate constants showing the  $\text{Al}_2\text{O}_3$  scale growth rate on different Fe, Ni, and Pt-based alloys. Reproduced from Hou, P. Y. *J. Am. Ceram. Soc.* **2003**, *86*, 660–668.



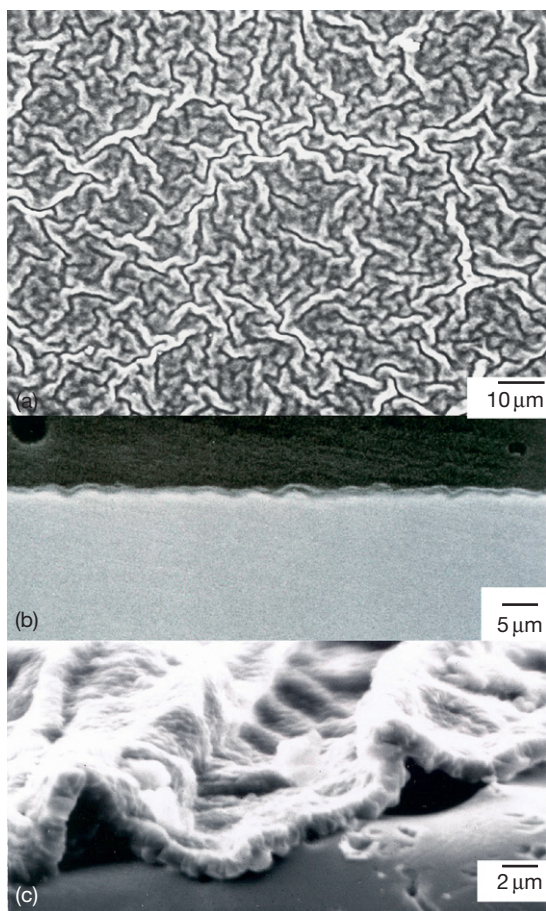


**Figure 20** Wrinkling of alumina scale formed on FeCrAl at 1000 °C in oxygen: (a) oxide surface and (b) polished cross-section after 3 h, (c) fractured cross-section after 120 h.

From the location and the distribution profiles of the second stage isotope, the dominant transport species and its path can be determined.<sup>37,310,316</sup> A typical profile from the results of Quakackers *et al.*<sup>312</sup> is presented in **Figure 21** as an illustration. The alumina scale was formed at 1000 °C on a FeCrAl alloy after oxidation first in  $^{16}\text{O}_2$  for 2.5 h to ensure a completely transformed and stable  $\alpha\text{-Al}_2\text{O}_3$  layer, then without cooling, the specimen was continually oxidized in  $^{18}\text{O}_2$  for 5 h to allow new oxides to grow so its location could be determined later. A large peak of the second isotope, in this case  $^{18}\text{O}$ , is present at the scale–gas interface. Portions of it come from oxygen isotope exchange but, due to the slow rate of this process,<sup>37</sup> its contribution should be small. The majority of  $^{18}\text{O}$  found at the outer surface is therefore due to new oxide formation from Al that diffused through the scale and reacted with oxygen from the atmosphere. A significant amount of  $^{18}\text{O}$  also exists within the first

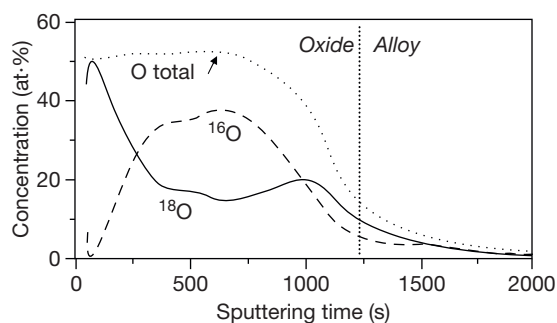


**Figure 21** An example of oxygen isotope profiles from Quadackers *et al.*<sup>312</sup> after two-stage oxidation of an FeCrAl alloy oxidized at 1000 °C first in  $^{16}\text{O}_2$  for 2.5 h, then in  $^{18}\text{O}_2$  for 5 h.

formed oxide and at the scale–alloy interface. This is the result of oxygen diffusion through the  $\text{Al}_2\text{O}_3$  scale forming new oxides at the scale–alloy interface. If the outer and inner portions are integrated and their areas compared, one obtains an outward to inward growth ratio of 0.45. This method is of course not quantitatively precise, but can be used to compare the effect of dopants on the transport properties through alumina scales.

Although the isotope studies clearly show that  $\alpha\text{-Al}_2\text{O}_3$  grows mainly by oxygen inward transport, but with an appreciable amount of Al outward transport, the transport path, that is, lattice, grain boundary or other short circuit diffusion paths, cannot be revealed. The grain size of transition alumina that grows initially on alloy surfaces upon oxidation is extremely fine, in the range of a few nanometers.<sup>238,246</sup> Even with more mature scales, that is,  $\alpha\text{-Al}_2\text{O}_3$ , that have grown to several microns thick, the oxide grain size is still no more than 1 or 2  $\mu\text{m}$ .<sup>281,282</sup> Owing to these small grain sizes, and the slow oxygen lattice diffusivity found by tracer studies,<sup>317</sup> grain boundaries have always been considered the dominant transport paths through alumina scales. More recently, microstructural evidence has also shown the importance of grain boundary transport through  $\alpha\text{-Al}_2\text{O}_3$  scales.<sup>263</sup> While some oxide ridges, such as those shown in **Figure 18**, develop during the initial stage from alumina transformation, continued ridge growth can still occur through an adherent  $\alpha\text{-Al}_2\text{O}_3$  layer. Furthermore, polished cross-sections, as seen in **Figure 22**, often show thicker scales above and below an  $\text{Al}_2\text{O}_3$  grain boundary,<sup>263</sup> giving clear indications that this is the preferred transport path through the scale, and growth of the oxide took place at the scale–alloy interface and on the oxide surface, as suggested by oxygen tracer studies.

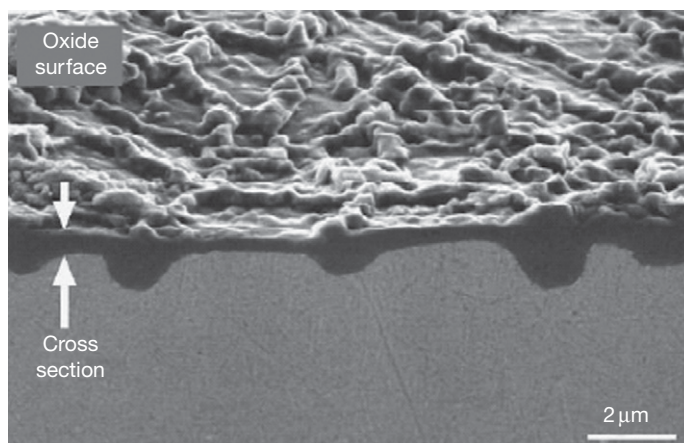


**Figure 22** SEM image of polished cross-section of alumina formed on NiPtAl, showing oxide ridges above and below the alumina grain boundary. Oxidation was carried out at 1200 °C for 50 h in air. Reproduced from Tolpygo, V. K.; Clarke, D. R. *Mater. High Temp.* **2000**, *17*, 59–70.

The growth of an  $\text{Al}_2\text{O}_3$  oxide scale that follows parabolic kinetics is controlled by the diffusion of O and Al through the scale layer according to the following equation

$$k_p = \int_{P_{\text{O}_2}} \left[ 1.5 \left( D_L^{\text{Al}} + \frac{\delta D_b^{\text{Al}}}{d} \right) + \left( D_L^{\text{O}} + \frac{\delta D_b^{\text{O}}}{d} \right) \right] d \ln P_{\text{O}_2} \quad [1]$$

where  $k_p$  is the parabolic rate constant,  $d$  is the oxide grain size and  $D_s$  are the respective diffusivities. Assuming the  $D_s$  are not functions of  $P_{\text{O}_2}$  and that the contribution from lattice diffusion is insignificant, an effective diffusivity,  $D_{\text{eff}}$ , which is a combination of the boundary diffusivities of Al and O, can be obtained as

$$D_{\text{eff}} = k_p d / \ln P_{\text{O}_2} \quad [2]$$

The  $P_{\text{O}_2}$  is the oxygen potential difference across the alumina scale. The parabolic rate constant,  $k_p$ , in its usual units of  $\text{g}^2 \text{cm}^{-4} \text{s}^{-1}$ , can be converted to the units of  $D_s$  in  $\text{cm}^2 \text{s}^{-1}$  using the density of alumina. Assuming thermodynamic equilibrium at the  $\text{Al}_2\text{O}_3$ –alloy interface, the  $P_{\text{O}_2}$  there would be that of the dissociation pressure of  $\text{Al}_2\text{O}_3$  at the oxidation temperature. From most reported microstructure of oxide scales, the average oxide grain size can be taken as roughly 0.5, 1, 1.5, and 2  $\mu\text{m}$  respectively for oxidation at 1000, 1100, 1200, and 1300 °C. The range of  $D_{\text{eff}}$  thus calculated using eqn [2] from the range of  $k_p$ s shown in Figure 19 is presented as a shaded area in Figure 23. On this figure are also plotted different cation and anion diffusivities experimentally determined in bulk alumina. A grain boundary width,  $\delta$ , of

10 nm is chosen to convert grain boundary diffusivity, usually presented as  $\delta D$  with units of  $\text{cm}^3 \text{s}^{-1}$ .

Oxygen diffusion from tracer studies in single crystals undertaken by several investigators<sup>317–321</sup> all agree within an order of magnitude and with similar activation energies. Good agreement was also found with  $D_L^{\text{O}}$  obtained from dislocation loop annealing studies by Lagerloff *et al.*<sup>322</sup> The apparent oxygen diffusivity determined on polycrystalline  $\text{Al}_2\text{O}_3$  by Oishi and Kingery<sup>317</sup> showed enhanced rates by 1–2 orders of magnitude; the lower temperature branch may be related to impurities, but the exact reason is unknown. To deduce a boundary diffusivity from these data is not straightforward, as the study only measured the total uptake of  $^{18}\text{O}$ . The boundary diffusion of oxygen obtained by Prot and Monty<sup>323</sup> has a drastically different activation energy from that of Oishi and Kingery.<sup>317</sup> Tracer studies of Al diffusion have been limited due to the low activity of  $^{26}\text{Al}$ . The only data are from Paladino and Kingery<sup>324</sup> and a more recent work by Le Gall *et al.*<sup>325</sup> Although Paladino and Kingery<sup>324</sup> used polycrystalline  $\text{Al}_2\text{O}_3$ , the grain size was 130–200  $\mu\text{m}$  and the behavior was believed to be of bulk diffusion. In that case, this result should be comparable to those from Le Gall *et al.*,<sup>325</sup> whose study was performed on single crystal  $\text{Al}_2\text{O}_3$ , but was slightly contaminated with Si.<sup>320</sup> Yet the two sets of data differ by nearly four orders of magnitude. The discrepancy between these two tracer studies may lie in the difference in the Si content of their samples, or simply due to experimental difficulties using the  $^{26}\text{Al}$  tracer. These results show that diffusion data on  $\text{Al}_2\text{O}_3$  are

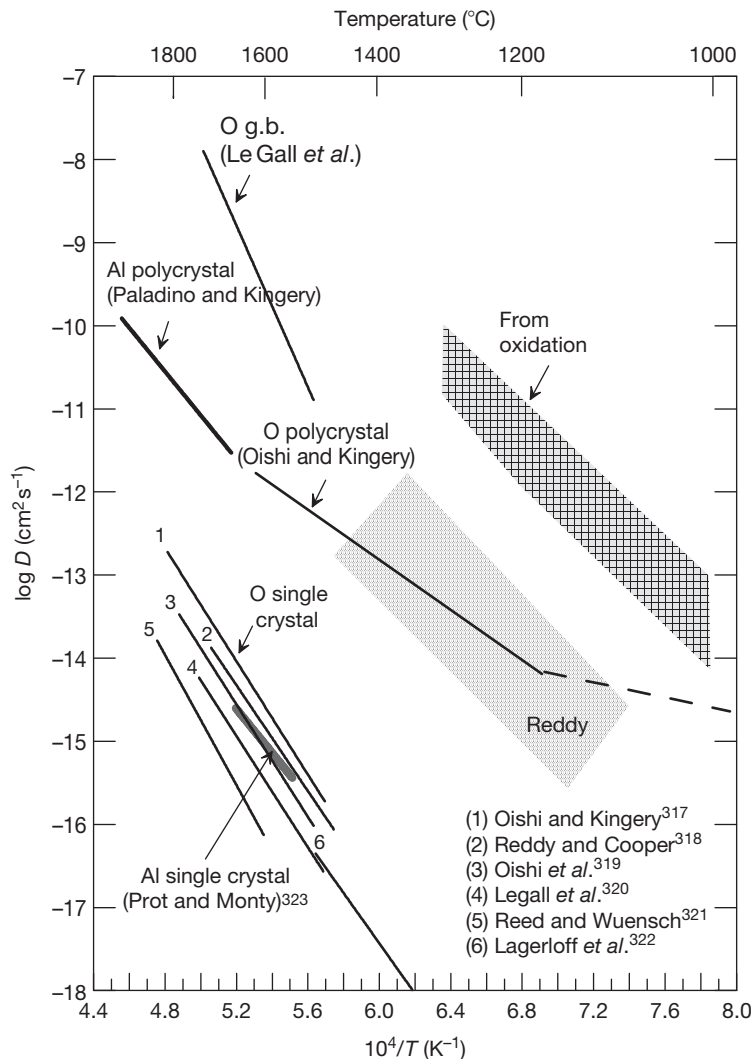


**Figure 23** Comparison of diffusion rates calculated from oxidation kinetics with published tracer diffusivity data.

rather scattered. One can only conclude that  $D_{gb}^O$  (oxygen boundary diffusion) is much faster than that of  $D_L^O$ , and the same may be true for Al. A conclusion on the relative magnitude of the Al and O boundary diffusivity is more difficult. They may be more comparable than the difference between Al and O lattice diffusions. These general conclusions agree qualitatively with the current view on O and Al transports through  $Al_2O_3$  scales, and also with diffusion rates compiled from creep and sintering studies.<sup>326</sup> However, qualitatively, diffusivities from creep tend to be at least an order of magnitude higher than the rates determined from tracer studies. This could be either due to contributions from other deformation mechanisms, such as basal slip and cavitation, or from trivial amounts of grain boundary migration that perturb the tracer

profiles, giving rise to a higher  $D_L$ , thereby causing deconvolution to yield ratios of  $D_b/D_L$  that are too low by a few orders of magnitude.<sup>327</sup>

Oxidation studies are usually performed at much lower temperatures than creep, sintering or tracer diffusion studies, making direct comparisons less straight forward, where diffusivities are extrapolated assuming activation energies to be constant over a wide range of temperatures. The effective diffusivity determined from the range of  $k_p$ s from  $\alpha-Al_2O_3$  scale growth (shaded band in Figure 23) is seen to lie slightly above the available  $\delta D_b^{Al}$  values from tracer studies. Compared to  $\delta D_b^O$ , it is more than two orders of magnitude higher than most of the tracer data, except the calculated lower temperature branch of Oishi and Kingery.<sup>317</sup> These comparisons suggest that

Al boundary transport in  $\text{Al}_2\text{O}_3$  scale growth is not trivial, which agrees with the results of two-stage oxidation studies using  $^{18}\text{O}_2/^{16}\text{O}_2$ <sup>310</sup> and with the conclusion obtained from oxide wrinkling analysis<sup>328</sup> and oxide microstructures.<sup>263</sup>

#### 1.10.6.4 Scale Adhesion

Although  $\text{Al}_2\text{O}_3$  grows slowly to offer good oxidation protection, it spalls extensively during cooling on alloys that do not contain any RE. Part of the reason is the high thermal stress, as high as several gigapascals,<sup>329</sup> that exists between  $\text{Al}_2\text{O}_3$  and these  $\text{Al}_2\text{O}_3$ -forming alloys, and partly due to a weak  $\text{Al}_2\text{O}_3$ -alloy interface. Unlike  $\text{Cr}_2\text{O}_3$ ,  $\text{Al}_2\text{O}_3$  almost always fails adhesively, where the oxide delaminates along the interface, exposing bare alloy surfaces after scale spallation. Interfacial pores are often present after oxidation, acting as interfacial defects, which can further deteriorate scale adhesion. Sulfur impurity is known to weaken the interface and REs to strengthen it. These effects are discussed in detail in the next section. Discussion of  $\text{Al}_2\text{O}_3$  adhesion here only involves alloys without any RE addition.

Intermetallic alumina formers, such as NiAl and FeAl, are particularly susceptible to forming large cavities at the scale-alloy interface. Several experimental studies on NiAl<sup>232,235,330–332</sup> and FeAl<sup>333–335</sup> have investigated the pore formation behavior in these systems. On NiAl,<sup>331</sup> more voids were observed on the Ni-rich alloys, where diffusion of Ni in the alloy is much faster than that of Al. The authors attributed the pore formation mechanism to the Kirkendall effect, where the different Ni and Al diffusion rates can cause a net flux of vacancy to the scale-alloy interface, which condenses out into voids. Indeed, the mechanism of pore formation has often been attributed to vacancy condensation. These can be vacancies that arrive at the scale-alloy interface from the growing scale as a result of cation outward transport,<sup>336,337</sup> or from any unequal diffusion of the alloying elements in the substrate,<sup>338</sup> such as that from the Kirkendall effect. It has been suggested<sup>339,340</sup> that vacancies can be injected into the metal to be annihilated or to form voids there. However, if the oxide-metal interface acts as a perfect vacancy sink, such rejection should not take place; instead, vacancies will be annihilated at the scale-metal interface.<sup>341,342</sup> Harris,<sup>343</sup> on the other hand, disputed the vacancy condensation model entirely and suggested that tensile stress induced in the alloy by the compressive growth stress in the oxide caused voiding. Similar views are shared

by others,<sup>344</sup> suggesting that interfacial pore formation is a result of uneven stress distribution at the scale-alloy interface.

Although the exact mechanism of void formation is still not established, it is clear that on Ni or Fe aluminides, voids almost 10 times larger than the oxide grain size and as deep as the scale thickness can exist from the very beginning of oxidation,<sup>335</sup> even during the heating stage; an example is shown in Figure 24. On FeAl, it has been shown that most voids nucleated during the initial stage of oxidation, where the first-formed transition alumina grew predominantly by cation outward transport. Moreover, the density of these voids increased dramatically with the presence of surface impurities, such as C, Cl, P, S, or a combination of these.<sup>345</sup> Impurities, whether present at the alloy surface prior to oxidation or inside the alloy that diffuses to the surface during oxidation, have been suggested to enhance pore formation by lowering the metal surface energy.<sup>346</sup>

Other than the often large pores found at oxide-metal interfaces, various types of porosity have also been reported within the  $\text{Al}_2\text{O}_3$  scale. One particularly common appearance is a row of fine pores at the boundary between the first-formed outer transition

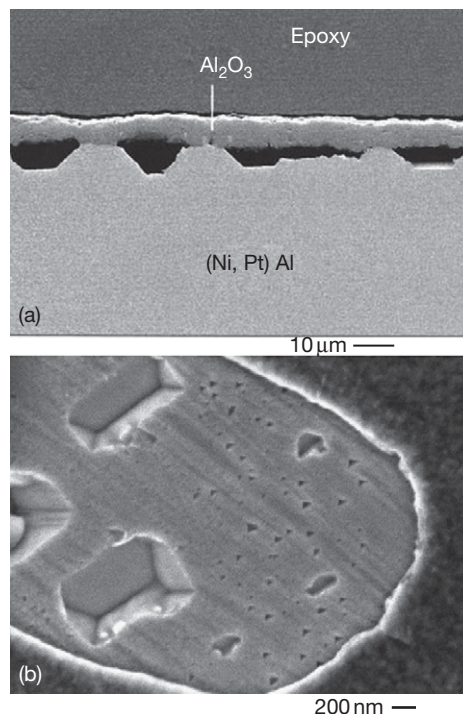


**Figure 24** Examples of voids formed at the alumina-aluminide interfaces: (a) on a Ni-44Al-6Pt-3.5Co-1.5Cr (at. %) alloy after 300 h at 1150 °C,<sup>385</sup> and (b) on Fe-40Al after 3 min at 1000 °C.<sup>335</sup>



alumina layer and the subsequently developed  $\alpha$ - $\text{Al}_2\text{O}_3$  inner layer. These pores most likely resulted from the alumina transformation that is associated with a volume reduction. Other types of small pores, some at  $\text{Al}_2\text{O}_3$  grain boundaries, especially at triple point junctions, and some even at oxide grain centers, are commonly observed. A few explanations have been given for their occurrence,<sup>246,328,332</sup> but there has not been much discussion on this topic. As most of these pores are small, about a fraction of the alumina grain size, and randomly distributed inside the scale, they usually do not contribute to scale failure.

Buckling of  $\text{Al}_2\text{O}_3$  scales at the growth temperature, as often found with  $\text{Cr}_2\text{O}_3$  scales, is rarely observed, except after extensive scale convolution,<sup>347</sup> sometimes referred to as rumpling<sup>348</sup> or wrinkling.<sup>349</sup> In the beginning of the convolution, the oxide remains attached to the alloy at all locations, and the alloy and scale wrinkle together. An example of such morphology is seen in **Figure 20(b)**. The compressive growth stress in the oxide is believed to be the driving force<sup>266,350,351</sup> that causes an initially planar oxide–alloy interface to convolute as a stress relaxation mechanism. With further oxidation, the rumpling amplitude increases and its wavelength decreases. This phenomenon seems to occur only for Fe-based  $\text{Al}_2\text{O}_3$  formers without a RE addition, such as FeAl and FeCrAl<sup>352</sup>; some believe the process is related to the alloy's mechanical properties, but others have suggested that it may be related to the rates of interface diffusion.<sup>351,352</sup> It is important to note that this type of wrinkling happens at the oxidation temperature, with only a small contribution during the first few hundred degrees of cooling.<sup>353</sup> The phenomenon is very different from that observed on coatings during thermal cycling oxidation.<sup>354,355</sup> A consequence of the wrinkling morphology is the establishment of very uneven stress distribution along the oxide–metal interface.<sup>353</sup> High tensile stress thus present at the peaks can cause scale separation from the alloy, and after prolonged oxidation, this indeed occurs. Therefore, even though a convoluted, rough interface like the ones discussed here can impede crack propagation,<sup>356</sup> the outcome is that it provides a tensile stress component at the interface that can act as a crack initiator.

### 1.10.7 Effect of Minor Alloying Elements and Impurities

The most beneficial minor alloying additions in combating high temperature oxidation are the so-called

'REs',<sup>357</sup> such as Y, Ce, Hf, and Zr. They are often added in the alloy and found in the protective oxide scales. Studies have shown that they segregate strongly at alumina and chromia grain boundaries and alter the scale growth process.<sup>358,359</sup> The first part of this section describes the RE effects and discusses some of the mechanisms that have been proposed to explain these effects.

Impurities that are incorporated into the growing scale can come from many different sources. An apparent one is the common surface contaminants that are present before oxidation, such as Na and K,<sup>360</sup> but their concentrations are usually low and can vary significantly from test to test. The most abundant impurity sources are base metal components (discussed in the previous section), such as Fe, Ni, or Co, which are incorporated as oxides during the initial stage of oxidation.<sup>241,361</sup> Nonmetallic impurities that are present in almost all commercial grade alloys may segregate to the scale–alloy interface during oxidation. In particular, the segregation of sulfur is believed to greatly deteriorate scale adherence.<sup>362,363</sup> This phenomenon is also addressed in this section, after the discussion on RE effects.

#### 1.10.7.1 Reactive Elements

The addition of oxygen active elements, such as Y, Hf, Ce, or Zr, is known to have profound beneficial effects on the oxidation behavior of  $\text{Cr}_2\text{O}_3$ - and  $\text{Al}_2\text{O}_3$ -forming alloys. This so-called 'RE effect' was discovered 70 years ago<sup>364</sup> and was first termed the rare earth effect, because rare earth metals added as melt deoxidants to Nichrome (Ni–20 wt% Cr) heating elements were found to increase cyclic lifetimes substantially by increasing the adhesion of  $\text{Cr}_2\text{O}_3$  scale to the alloy. The amounts of the rare earth additions were 0.01–0.5 wt%. In a later patent,<sup>365</sup> it was found that elements from groups IIA, IIIA, IVA, and VA of the periodic table could produce similar beneficial effects. Indeed, subsequent work carried out by various other investigators confirmed that a wide range of additions affect  $\text{Cr}_2\text{O}_3$ - and  $\text{Al}_2\text{O}_3$ -forming alloys similarly, as long as the additions form a more stable oxide than  $\text{Cr}_2\text{O}_3$  or  $\text{Al}_2\text{O}_3$ .

Early results have been extensively reviewed by Whittle and Stringer,<sup>357</sup> where they concluded that the effects on  $\text{Cr}_2\text{O}_3$ -forming alloys are fourfold; they (1) enhance the selective oxidation of chromium, (2) decrease the oxide growth rate, (3) change the oxide growth mechanism from predominantly cation outward to oxygen inward transport and (4) improve the oxide scale adhesion. For  $\text{Al}_2\text{O}_3$ -forming alloys,

however, the effect was only to improve the scale adhesion. This last conclusion arises because the ratio of cation to anion transport is much lower in  $\text{Al}_2\text{O}_3$  than  $\text{Cr}_2\text{O}_3$ ; also,  $\text{Al}_2\text{O}_3$  growth rate is significantly lower than that of  $\text{Cr}_2\text{O}_3$ , so any effect on cation transport and oxidation rate would be small and, therefore, difficult to measure. Furthermore, most  $\text{Al}_2\text{O}_3$ -forming alloys studied prior to that time were MCrAl type alloys, where M was Fe, Ni or Co. These alloys already have Cr as an added third

element to help promote  $\text{Al}_2\text{O}_3$  formation; hence, any effect of RE, on the selective oxidation of Al, could not be observed. Advances with improved analytical techniques and studies of NiAl and FeAl alloys have since shown that actually effects (1) and (2) also apply to  $\text{Al}_2\text{O}_3$  formers.<sup>366</sup> Each of these effects is described and discussed separately later in this section. Other than these, RE additions also alter the oxide grain structure from equiaxed to columnar<sup>367</sup> (an example can be seen on [Figure 25](#)), and the average oxide

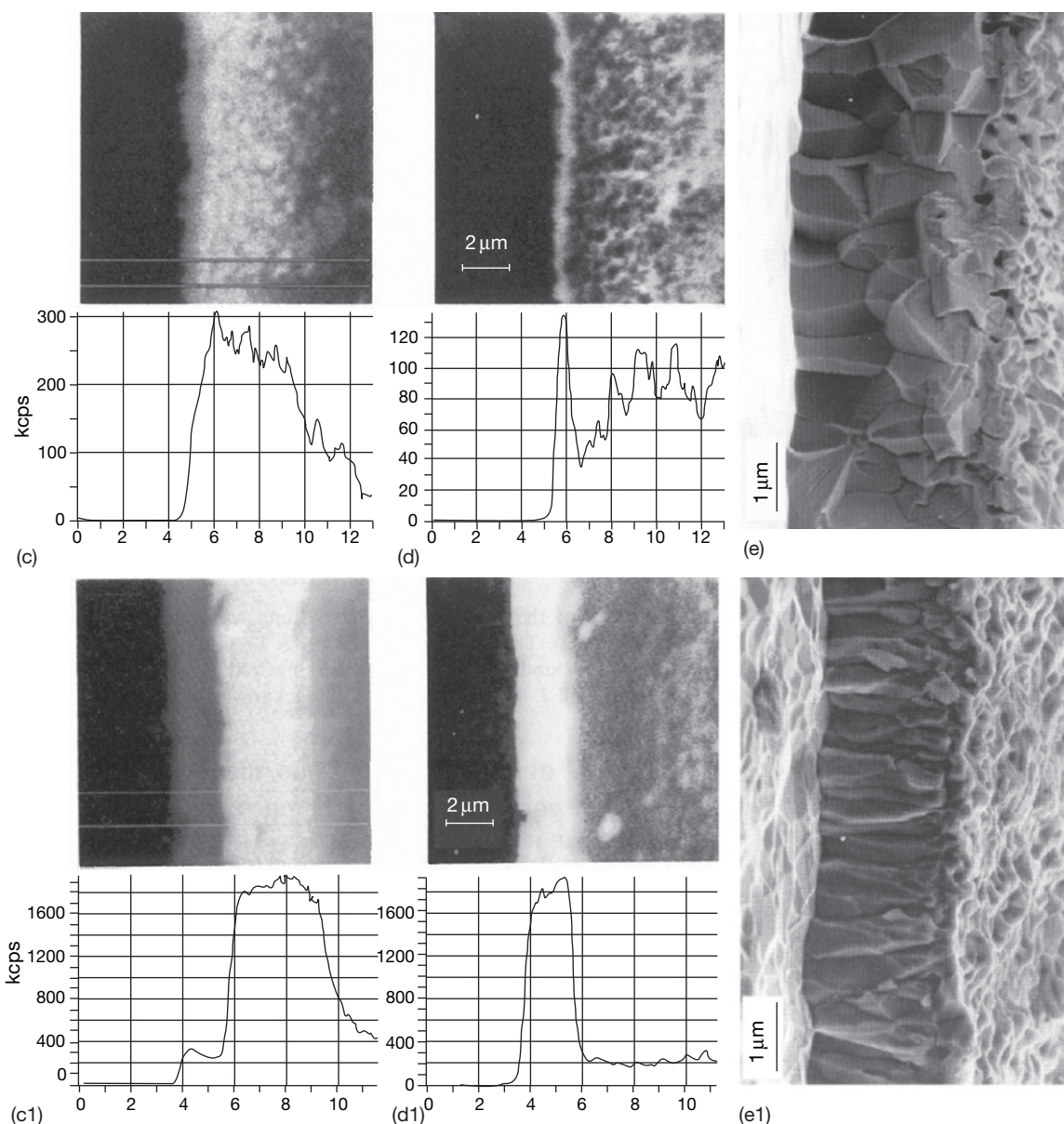


**Figure 25** Effect of Y addition (bottom set of figures) in FeCrAl on oxygen transport and oxide microstructure.<sup>315</sup> (a) and (c) are map and line traces of  $^{16}\text{O}$ ; (b) and (d) are those for  $^{18}\text{O}$ . The specimens were oxidized at  $1200^\circ\text{C}$  first for 1.5 h in  $^{16}\text{O}_2$ , then 3.5 h in  $^{18}\text{O}_2$ .



grain size is decreased by about a factor of 1.5–2. The RE effects are most pronounced between 1000 and 1200 °C. At 900 °C or below, they become marginal; above 1300 °C (tested for  $\text{Al}_2\text{O}_3$  formers), the effects break down.

Other than alloying additions of REs, a fine dispersion of a few volume percent of RE oxide particles, usually incorporated by mechanical alloying, are just as effective. Furthermore, superficially applied RE or RE oxide,<sup>368</sup> via ion-implantation or a thin coating of RE oxides or nitrates that convert to the oxides, seems equally effective. However, these surface applications, although sometimes useful for mechanistic studies,<sup>369,370</sup> are not effective for long-term applications that are often required for industrial usage, due to insufficient supply of the RE. The distribution<sup>368</sup> and concentration<sup>278</sup> of RE in alloys are extremely critical for their effectiveness on oxidation. While earlier studies usually use a few tenths of a weight percent, more recent works suggest that a more favorable concentration may be only a few hundred parts per million.<sup>371</sup> Whether this range of concentration is ‘optimal’ for all applications and systems is, however, questionable. The most favorable concentration may depend on the type of RE, the alloy system, the oxidation conditions or a combination of them. Overdoping of RE can produce detrimental rather than beneficial effects. Excess RE in the alloy can form a second phase, such as Y garnet, which oxidizes to YAG that promotes internal oxidation and acts as a crack initiator, hence decreases scale adhesion. An uneven distribution of RE oxide dispersions is also undesirable, for it causes nonuniform oxidation, where areas without any RE oxides can exhibit fast and nonprotective oxidation behavior.

The relative effectiveness of the different REs is unknown, although there do appear to be differences. It is also not yet clear whether one type of RE is more effective in a certain type of alloy system, although the same RE incorporated in different types of alloys can show different effects.<sup>372</sup> Hafnium, for example, has been shown to be exceptionally effective in NiAl alloys, decreasing the oxidation rate by almost a factor of 10.<sup>372</sup> The early patent<sup>365</sup> also noted that the effectiveness of RE decreased on passing from group II to group V, but increased with increasing atomic weight within a particular group, which is similar to recent suggestions made by Pint and Alexander,<sup>283</sup> pointing out that the relative effectiveness may be related to the atomic size of these elements. In summary, the relative effectiveness of REs and their optimal concentrations in a given alloy

system and for a given application is still an open question and is currently under investigation. Another question worth pursuing is the benefits of codoping,<sup>373</sup> that is, adding more than one type of RE in an alloy. This may be the future area for optimization of the RE effect for commercial applications.

#### **1.10.7.1.1 Promoted selective oxidation**

The beneficial effect of REs on selective oxidation is to decrease the amount of Cr or Al in the alloy necessary to develop the protective  $\text{Cr}_2\text{O}_3$  or  $\text{Al}_2\text{O}_3$  scales. For alloys that already have sufficient amounts of Cr or Al, the effect is to decrease the time required for these scales to be established, hence decreasing the amount of base metal oxide formation. RE oxide dispersions seem to be more effective than RE additions in this respect, while surface applied RE or RE oxides do not show the same effectiveness.<sup>374</sup>

It has been suggested that RE or its oxides in the alloy increase Cr diffusion,<sup>375</sup> or acts as preferential nucleation sites,<sup>376</sup> to promote the establishment of the  $\text{Cr}_2\text{O}_3$  layer. However, diffusion studies<sup>377</sup> on  $\text{Y}_2\text{O}_3$ - and  $\text{ThO}_2$ -containing Ni–Cr and Co–Cr alloys have shown that the presence of RE dispersions alone does not enhance the diffusivity of chromium in the alloy; rather, Cr diffusion increases with a decrease in alloy grain size. Indeed, both RE and their oxide dispersions tend to stabilize a fine alloy grain size; this has been shown for  $\text{Cr}_2\text{O}_3$ -<sup>378</sup> and  $\text{Al}_2\text{O}_3$ -forming alloys.<sup>379</sup> Furthermore, subgrain structures created by the oxide dispersions can also enhance diffusion.<sup>377,380</sup> It is known that a  $\text{Cr}_2\text{O}_3$  layer develops on Ni–Cr alloys more readily over alloy grain boundaries than over the bulk of the grains, and on cold-worked surfaces than on polished ones.<sup>381</sup> Therefore, it appears that the major effect of RE or RE oxides is to decrease the alloy grain size, thus allowing faster diffusion of the scale-forming element from the bulk to promote an earlier development of a protective scale.

#### **1.10.7.1.2 Decreased growth rate and changed growth direction**

Above 900 °C, RE additions can decrease the growth rate of  $\text{Cr}_2\text{O}_3$  scales by nearly an order of magnitude.<sup>357</sup> While the oxidation rates of undoped alloys are approximately parabolic, those doped with RE are often described as asymptotic or cubic. Similar decreases can be achieved by surface-applied RE or RE oxides, or even with RE implanted into an

existing thin oxide film,<sup>370,382</sup> suggesting that RE incorporation into the oxide is essential in decreasing the scale growth rate. Below 900 °C, the effect is minimal, with an approximately twofold decrease in rates.<sup>383</sup>

When rates on RE-doped and undoped Al<sub>2</sub>O<sub>3</sub>-forming alloys are compared and plotted over a wide temperature range, the data are scattered over about two orders of magnitude and show no apparent effect of RE on scale growth rate.<sup>202,241,357</sup> Therefore, earlier reviews<sup>202,357</sup> have concluded that RE has no effect on Al<sub>2</sub>O<sub>3</sub> scale growth rate. However, the scatter may be related to differences in the process of adding RE to the alloys, and the different experimental conditions and procedures. If data with or without RE additions obtained from the same research group on the same type of alloy are compared,<sup>241</sup> the results show a consistent decrease in oxidation rate with the addition of RE (Table 1). In this summary, no distinction was made on the different types of RE, even though some RE may be more effective than others in some cases. Some of the rates were averaged from several tests of an undoped alloy, or from alloys doped with different REs, giving rise to the relatively large error bars. Still, a clear trend can be seen from these results showing that all RE additions in Ni- and Fe-based alloys decrease the oxidation rate by about a factor of two. On the PtAl alloy, the addition of Zr decreased the rate by a factor of four, but only one set of data exist for this alloy, so it would be premature to conclude that the RE effect on scale growth rate is greater on Pt-based than on Ni- or Fe-based alloys.

Other than the decrease in rate, RE additions also affect the relative transport rates of oxygen and Cr or Al through the scale. The effect was more prominent for Cr<sub>2</sub>O<sub>3</sub>-forming alloys, so it was often realized with earlier Pt marker studies.<sup>384</sup> Not until oxygen isotopes were used, was the effect also verified for Al<sub>2</sub>O<sub>3</sub>-forming alloys, where a noticeable amount of Al outward

transport is decreased with the addition of REs; an example can be seen in Figure 25. An estimate from the relative percentage of the two oxygen isotope distributions, averaged over seven data sets over the temperature range of 900–1100 °C,<sup>241</sup> showed that the outward transport of Al is decreased by about a factor of four. These oxygen tracer studies, performed on different types of alloys with different REs, showed similar results. However, microstructural observations on the extent of grain boundary ridge development on Al<sub>2</sub>O<sub>3</sub> surfaces showed obvious differences between the type of alloy and RE.<sup>385,386</sup> These studies were made during a second stage oxidation after polishing the top layer of the first-formed oxide. In the first study, it was found that different REs behaved similarly on FeCrAl-based alloys, but 0.05 at.% addition of Zr in Ni–50Al was more effective in decreasing Al outward transport than the same amount of Y addition. In a second, more quantitative study, Y was found to be more effective on FeCrAl-based alloys than Zr. It was concluded that the ratio of inward diffusion of oxygen to outward diffusion of aluminum depends not only on the oxidation temperature, but also on the RE dopant, as well as its form in the alloy. There are apparent discrepancies between the two reports, but the results are interesting in that they point to possible different degrees of the RE effect in different systems.

Utilizing analytical TEM, Yurek and coworkers investigated oxide scales in cross-sectional samples and first demonstrated that RE segregates to Cr<sub>2</sub>O<sub>3</sub><sup>359</sup> and Al<sub>2</sub>O<sub>3</sub><sup>358</sup> grain boundaries. A similar segregation has since been observed for many RE-containing alloys, where different REs, such as Y, Zr, Hf, La, and Ti, added in different forms (metallic, oxide dispersion, ion-implantation, or surface coating) and in different types of alloys, have been found to segregate at Al<sub>2</sub>O<sub>3</sub> grain boundaries.<sup>237,281–283,358,387–392</sup> The amount that is segregated has been quantified to

**Table 1** Effect of RE addition on oxidation rates

Alloy system	Oxidation condition	Rate w/o RE	RE type	Rate with RE	Refs
NiAl	1200 °C	$(1.4 \pm 0.4) \times 10^{-11}$	Ti, La, Zr, Hf, Y	$(8.0 \pm 4.1) \times 10^{-12}$	277, 279, 280, 283, 387
Ni <sub>3</sub> Al		$7.1 \times 10^{-12}$	Y	$(4.3 \pm 3.1) \times 10^{-12}$	
Fe <sub>3</sub> Al		$(1.3 \pm 0.2) \times 10^{-11}$	Hf, Zr, Y	$(4.9 \pm 2.4) \times 10^{-12}$	
FeCrAl		$(1.8 \pm 0.6) \times 10^{-11}$	Nb, Ti, Sc, Hf, Gd, Ba, Nd, La, Zr, Y	$(7.1 \pm 2.8) \times 10^{-12}$	
PtAl		$(1.6 \pm 0.4) \times 10^{-11}$	Zr	$4.1 \times 10^{-12}$	287, 290
FeCrAl		$7.8 \times 10^{-12}$	Y	$4.1 \times 10^{-12}$	
FeCrAl	1150 °C	$8.5 \times 10^{-12}$	Ti	$2 \times 10^{-13}$	
NiCrAl	1100 °C	$1.1 \times 10^{-12}$	Y, Hf	$(4.5 \pm 2.1) \times 10^{-13}$	

be about 0.2 monolayer.<sup>392</sup> When the segregation was followed as a function of oxidation temperature and time,<sup>393</sup> it was determined that the RE not only segregates at  $\text{Al}_2\text{O}_3$  grain boundaries, but also diffuses through it to the scale surface, where it can precipitate out as fine oxide particles.

Based on the segregation result, and the change in the oxygen isotope distribution, Yurek and coworkers<sup>358</sup> proposed that the presence of RE at the oxide interface decreases cation grain boundary diffusion, but probably does not affect oxygen diffusion; consequently, scale growth becomes dominated by oxygen inward transport. This proposal has been explained in detail by Pint,<sup>393</sup> stating that the oxygen potential across the scale drives the RE to diffuse from the alloy, through the scale to the outer surface, where the diffusion path is the oxide grain boundaries, and this is where RE segregates. Although there are ample evidences of RE segregation to growing  $\text{Cr}_2\text{O}_3$  and  $\text{Al}_2\text{O}_3$  oxide grain boundaries, creep studies have also indicated that RE additions to sintered  $\text{Al}_2\text{O}_3$  significantly decreased the creep rate,<sup>270,271</sup> implying a decrease in Al grain boundary diffusivity, the exact mechanism by which RE at oxide grain boundaries affects cation, but not anion, diffusion is not known. Analysis of the effect of impurities on grain boundary structure<sup>394,395</sup> may shed some light on the boundary diffusional processes. Another question worth considering, which may be closely related to the transport mechanism of cations and anions in oxide grain boundaries, is why Al and O do not react at the boundary, as both diffuse through it. Such a reaction should result in internal plating of oxide at the grain boundary, or lateral growth,<sup>47</sup> which would generate in-plane compressive stress. It is possible that once such stress is generated, it prevents further reaction, until the stress is relieved. Clarke,<sup>396</sup> using a dislocation climb model, has determined for  $\text{Al}_2\text{O}_3$  scale that only  $10^7$  molecules per micron length of grain boundary can generate  $\sim 0.5$  GPa of growth stress.

#### **1.10.7.1.3 Improved scale adhesion**

The most industrially relevant beneficial effect of the RE additions is the improved scale adhesion, especially for  $\text{Al}_2\text{O}_3$ -forming alloys and coatings. It has been demonstrated repeatedly that additions of RE or RE oxides in the alloy greatly increase the spallation resistance of  $\text{Al}_2\text{O}_3$  and  $\text{Cr}_2\text{O}_3$  scales during cooling, thereby significantly increasing the lifetime of an alloy or coating under cyclic oxidation conditions. Associated with the greater spallation resistance are noticeable microstructural changes, particularly at

the scale–alloy interface. Chromia scales without any RE tend to detach from the alloy at the oxidation temperature, leading to widespread buckling, and, hence, cracking and spalling during cooling. Alumina scales, on the other hand, often develop many discrete interfacial voids, which act as defects to assist in scale failure, or become wrinkled, as often seen in Fe-based alloys, which give rise to tensile stresses at some locations at the interface that lead to scale delamination. Apart from these microstructure changes, there are also significant chemical changes at the scale–alloy interface, which can significantly affect the strength of the interface. This effect will be discussed in more detail later in this section under the ‘sulfur effect.’ Surface additions of REs or RE oxides have been shown to exert a similar beneficial effect on  $\text{Cr}_2\text{O}_3$  scale adhesion,<sup>397</sup> but do not seem to do so on  $\text{Al}_2\text{O}_3$ -forming alloys.<sup>398</sup>

Many earlier explanations of the possible role of REs in improving scale adhesion have been summarized and described.<sup>357,366,399–401</sup> A few of them are no longer being considered, except for special cases. For example, in the case of fine-grained scales that develop on nanocoatings,<sup>402,403</sup> that is, alloy coatings consisting of columnar grains with grain widths in the tens of nanometer range, the small grains are envisaged to be highly plastic and, hence, are able to relieve much of the growth stress and decrease the driving force for spallation. However, recent *in situ* stress measurements using synchrotron radiation have shown that the magnitude of the growth stress is far less important than the interface chemistry or microstructure in dictating scale failure.<sup>404</sup> Oxide pegging, where fine stringers of  $\text{Al}_2\text{O}_3$  oxide grow internally from the external scale into the substrate, have been suggested to impede crack propagation due to the large interfacial contact areas associated with the peg microstructure, and to relieve stresses by the two-phase peg-containing region.<sup>405</sup> Morphology of the pegs is critical to their effectiveness,<sup>406</sup> where a fine and more uniform distribution of small pegs is much more efficient in combating scale spallation than large ones, which are even capable of initiating scale failure. Although pegging may be important, there are several alloy systems, including  $\text{Cr}_2\text{O}_3$ -forming alloys, which do not form any pegs, but still remain adherent under severe cyclic oxidation conditions.

To date, the most accepted mechanism by which RE affects scale adhesion is related to the chemical change that occurs at the scale–alloy interface when RE is present. This can be a decrease in interface

S concentration and/or the presence of RE at the interface. The proposed mechanism related to sulfur segregation<sup>362,407,408</sup> is usually known as the ‘sulfur effect.’ The hypothesis is that the oxide–metal interfaces are intrinsically strong, but the indigenous sulfur that is present in metals and alloys, possibly as low as around 5–30 ppm, segregates to the interface during oxidation, thus weakening the bonding and rendering the scale nonadherent. The role of the REs, as a result of their strong sulfide-forming ability, is to react and tie up the sulfur, thereby preventing it from segregating to the interface.

There has been some debate on whether it is possible for a large and negatively charged sulfur ion to segregate to an intact oxide–metal interface.<sup>346</sup> Indeed, if the interface were always coherent, it might not have enough space to accommodate a large segregand, especially one that is negatively charged as are the oxygen ions in the oxide. However, oxide–metal interfaces are not always coherent; coherency is often lost after prolonged oxidation.<sup>409</sup> At such interfaces, as with high angle grain boundaries,<sup>410,411</sup> segregation may be easier. When  $pO_2$  and interfacial strains are taken into consideration, first principle calculations show that S segregation to  $Al_2O_3/Ni(Al)$  interfaces is in fact thermodynamically favored.<sup>412</sup> Ample evidences also exist from Auger analysis studies, showing that sulfur can indeed segregate to growing oxide–metal interfaces,<sup>413,414</sup> not only on interfacial void surfaces, but also on intact interfaces. The latter location was further vindicated when sulfur was detected by analytical transmission electron microscopy (TEM) on cross-sectional specimens of  $Cr_2O_3$ <sup>415</sup> and  $Al_2O_3$ <sup>416–419</sup> scales, indicating that true interfacial segregation of S to an oxide–metal interface is possible, even though such detection is often difficult, due to beam-induced desorption.<sup>417</sup>

The effect of S segregation on interfacial strength has been demonstrated experimentally on  $Al_2O_3$  grown on  $NiAl$ <sup>420</sup> and on diffusion bonded  $Al_2O_3$  on  $Ni$ ,<sup>421</sup> showing greatly decreased interfacial strength with submonolayer of S coverage. Furthermore, first principle calculations also demonstrated a large bond-weakening effect of S at oxide–metal interfaces.<sup>412</sup> When an alloy is desulfurized, for example by a high temperature  $H_2$ -annealing process, its ability to retain the scale under severe thermal cycling conditions is also greatly improved. This conclusion has been repeatedly demonstrated for  $Al_2O_3$ -forming alloys,<sup>363</sup> and also for  $Cr_2O_3$ -forming alloys.<sup>422</sup> These results further attest to the detrimental effect of S on scale adhesion.

Although it is clear that S can segregate at oxide–metal interfaces and weaken the interfacial strength, the role of the RE is still uncertain. The presence of RE in the alloy can indeed prevent S segregation to the interface,<sup>423</sup> but by what mechanism? It is conceivable that RE can getter sulfur by forming a sulfide, but RE oxide dispersions are equally effective in improving scale adhesion. The RE oxides are more stable than their sulfides, so the gettering mechanism does not seem to apply. Since REs are known to segregate to oxide–alloy interfaces,<sup>237,392</sup> as they do to oxide grain boundaries, it has been suggested<sup>393,424</sup> that RE at the interface prevents S from segregating there, by blocking available sites for S segregation, similar to surface site competition or poisoning. Pieraggi *et al.*<sup>424,425</sup> further suggested that the segregated large RE ions can pin interfacial dislocations, which are necessary in annihilating interfacial point defects generated by the scale growth process. Blocking these interfacial reaction steps can then retard the scaling kinetics and even alter the scaling mode, for example, from predominantly cation transport to that of anion transport. This ‘poisoned interface’ model attempts to explain the RE effects on scale growth kinetics, transport process and adhesion. However, there has not been convincing experimental evidence to support it.

The presence of RE at the interface may exert a bond strengthening effect. This has been demonstrated experimentally<sup>423</sup> on  $Fe_3Al$ -based alloys that were undoped, doped with Zr and desulfurized. When interfacial composition and strength were compared, it was found that, although eliminating the sulfur in the alloy greatly improved scale adhesion, the presence of RE at the interface further strengthened the scale–alloy interface. The bond strengthening effect of RE at  $Al_2O_3$ -metal interfaces has also been established by earlier theoretical analyses,<sup>426</sup> and, recently, by more rigorous first principle calculations.<sup>427</sup>

All the above discussions on the RE effect have been based mainly on  $Al_2O_3$ - and some on  $Cr_2O_3$ -forming alloys. A few studies have also been done on the oxidation of nickel and other pure metals.<sup>428</sup> For the work on nickel, surface application techniques were often used, such as sol–gel coatings of RE oxides<sup>429</sup> or ion-implantation of REs.<sup>430</sup> The observed effects are not as strong as those reported for  $Al_2O_3$ - and  $Cr_2O_3$ -forming alloys. Oxidation rates are usually decreased by 2–3 times and the oxide grain sizes are also decreased, by a factor of  $\sim 2$ . Since the adhesion of  $NiO$  on  $Ni$  is usually good, it is not clear if these surface-applied REs affect  $NiO$  adhesion.

### 1.10.7.2 Nonmetallic Impurities

#### 1.10.7.2.1 Sulfur

The segregation of indigenous sulfur impurity from an alloy to the scale–alloy interface during high temperature oxidation is often considered the major cause that weakens the interface, a conclusion drawn mainly from works performed on  $\text{Al}_2\text{O}_3$ -forming alloys.<sup>362,363,408,431</sup> The originally proposed hypothesis<sup>362,408,431</sup> states that the oxide–metal interface is intrinsically strong, but is weakened by the segregation of indigenous sulfur, which is often present in the alloy in parts per million levels, hence making the scale nonadherent. Evidence of the detrimental effect of sulfur on scale adhesion has been provided by the performance of many different desulfurized or low S alloys.<sup>292,432,433</sup> When the sulfur content in the alloy is decreased to less than 3 ppm or so, often by a high temperature  $\text{H}_2$ -annealing process, scale spallation under thermal cycling can be significantly decreased.<sup>433</sup>

The proposed ‘sulfur effect’ shows how interface chemistry may affect scale adhesion. Sulfur is well known to segregate to alloy grain boundaries and weaken them,<sup>434</sup> and theoretical studies have shown bond weakening effects of S on  $\text{Al}_2\text{O}_3$ –metal interfaces.<sup>412,426</sup> Limited mechanical testing on the strength of diffusion-bonded  $\text{Al}_2\text{O}_3$ –metal interfaces in the presence of a foreign element has also demonstrated strong effects of interface chemistry.<sup>435,436</sup> However, most of these studies did not characterize the effect that these segregands had on interface microstructure, particularly on the defect type, size, and distribution. This is especially important, as more debonded areas seem to exist when impurities are present at these interfaces.<sup>412,435</sup> As all commercial metals and alloys contain parts per million levels of nonmetallic impurities that readily segregate to surfaces when the alloy is heated; it is often assumed that the same kind of segregation takes place at oxide–metal interfaces. Whether this is always the case is not obviously clear. Some researchers have questioned whether it is energetically favorable for a large and electronically negative sulfur to segregate to an oxide–metal interface.<sup>346,437</sup>

Studies of the chemical changes at  $\text{Al}_2\text{O}_3$ –alloy interfaces as a function of oxidation time have in recent years been carried out for MCrAl type of alloys, where M is Fe<sup>414,438</sup> or Ni,<sup>413</sup> iron aluminides,<sup>439–441</sup> nickel aluminides,<sup>420,442</sup> or NiPtAl<sup>443,444</sup>; a few studies have also been conducted on  $\text{Cr}_2\text{O}_3$ /NiCr<sup>445</sup> and  $\text{Cr}_2\text{O}_3$ /Cr.<sup>446</sup> In most cases, the interfacial chemistry

was evaluated using conventional Auger electron microscopy (AES) with a typical probe size of about 1  $\mu\text{m}$ , after spalling the oxide scale in ultrahigh vacuum (UHV) by scratching an oxidized specimen surface,<sup>420, 438,443,445,446</sup> or bending a thin strip of oxidized sample.<sup>414</sup> The chemical composition of the alloy surface was then examined. With the scratch technique, the underside of the oxide, or the oxide side of the interface, could also be examined, and that location was always found to be free from segregands. Any impurity, if present at the interface, resided on the alloy side after scale spallation. One of these studies also utilized a field emission AES,<sup>439</sup> of probe size  $\sim 30\text{ nm}$ , and verified that sulfur was indeed present at the interface, rather than at small interfacial void surfaces. Furthermore, the amount of interface sulfur was found to be significantly higher than that calculated from interface sweeping, that is, accumulation of impurity atoms in the alloy onto the moving oxide–metal interface when it advances into the alloy as a result of an inwardly grown scale. Occasionally, sulfur could also be detected by using scanning electron transmission microscopy (STEM) on thin cross-sectional samples,<sup>415–419</sup> but such detection is usually difficult, partly due to the small amount of S segregated at the interface, and partly to S desorption under the electron beam.<sup>417</sup> However, results from these few TEM investigations have further demonstrated that sulfur can segregate to intact oxide–alloy interfaces that are pore-free.

AES studies of the build-up of sulfur as a function of oxidation time on several  $\text{Al}_2\text{O}_3$ –alloy interfaces are summarized in **Figure 26**, where each datum point was obtained from a different specimen oxidized for a given time. Although sulfur was found to be the major segregand at these scale–alloy interfaces, the segregation behavior, in terms of rate and amount, varied significantly for different alloys and differed from surface segregation. A few general conclusions can be made from these interfacial segregation results: (i) On MCrAl type alloys, the amount of interfacial sulfur is high due to strong co-segregation of S with Cr<sup>413,438</sup>; cosegregation of C also occurs on FeCrAl during cooling, but not on NiCrAl, due to the faster C diffusion rate in the bcc FeCrAl than in the fcc NiCrAl. (ii) On Fe or Ni aluminides, S is only present at the  $\text{Al}_2\text{O}_3$ –alloy interface when a complete layer of  $\alpha\text{-Al}_2\text{O}_3$  is developed.<sup>413,420</sup> On FeAl, the amount saturated at the  $\text{Al}_2\text{O}_3$ –alloy interface is about 0.5 monolayer, while much higher concentrations are found on surfaces of interfacial voids due to



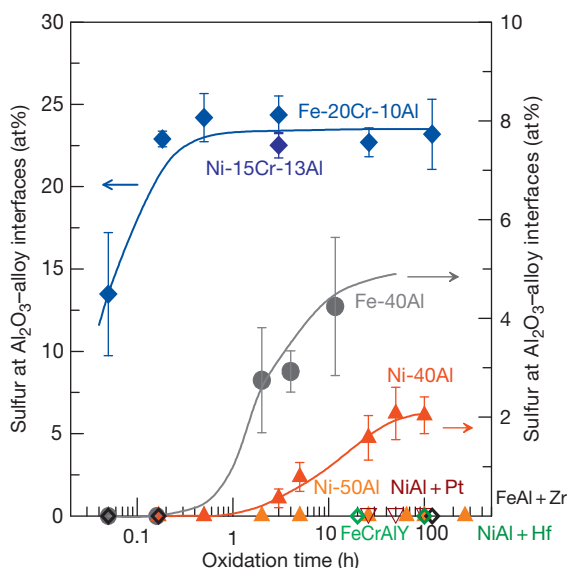


**Figure 26** Summary of the amount of sulfur detected at different alumina-alloy interfaces as a function of oxidation time.

cosegregation of Al and S.<sup>439</sup> On NiAl, the saturation level is lower, only about 0.2 monolayer, which may be related to the lower level of sulfur impurity in nickel aluminides compared with that in iron aluminides (a few parts per million *vs.* tens of parts per million). (iii) Segregation on NiAl depends on alloy stoichiometry, in that no S segregates at  $\alpha$ -Al<sub>2</sub>O<sub>3</sub>/Ni-50Al interfaces, but small amounts are present at  $\alpha$ -Al<sub>2</sub>O<sub>3</sub>/Ni-40Al.<sup>420</sup> Finally, Pt<sup>443</sup> and REs (Hf, Zr, and Y)<sup>423</sup> prevent S segregation to the interface. Mechanical testing on some of these alloy systems directly related the amount of S at the interface to interfacial strengths,<sup>420,423</sup> and found that the strength decreases most sharply with the first few submonolayers of sulfur. Another related detrimental effect of sulfur on scale adhesion is its ability to enhance interfacial void formation, probably by decreasing the energy of void nucleation by decreasing the metal surface energy when S is segregated to a void embryo.<sup>332,345</sup> In fact, different types of common surface impurities, such as C, P, Cl, and Na, have also been shown to greatly increase the interfacial pore density on FeAl.<sup>345,447</sup>

Although it is now clear that sulfur, as an impurity in the alloy, can segregate to the growing oxide-metal interface to enhance interfacial void formation and decrease the interfacial bond strength, a few studies have shown a surprising beneficial effect of sulfur. For example, under steam oxidation environments, Cr cosegregated with S to the alloy surface, a high Cr

ferritic steel, and promoted the formation of a protective Cr<sub>2</sub>O<sub>3</sub> layer.<sup>448</sup> In FeCrAl, samples containing greater than 100 ppm sulfur seemed to develop Al<sub>2</sub>O<sub>3</sub> scales that were more adherent than those with 3 or 30 ppm S.<sup>449</sup> It is not clear if this ‘improved adhesion’ is related to the formation of a thin layer of sulfide at the Al<sub>2</sub>O<sub>3</sub>-alloy interface; the mechanism is rather unclear and the method of determining scale adhesion not quantitative.

Sulfur has also been suggested to affect the growth mechanism of Al<sub>2</sub>O<sub>3</sub> or Cr<sub>2</sub>O<sub>3</sub> scales. Some studies have reported that the effect of excess sulfur, in the alloy or from the oxidizing atmosphere, is to produce a less protective surface oxide film, as seen from the outgrowth of Cr<sub>2</sub>O<sub>3</sub> nodules on a layer of Al<sub>2</sub>O<sub>3</sub> on a NiCrAl alloy,<sup>450</sup> or an Al<sub>2</sub>O<sub>3</sub> layer that was more easily cracked at the oxidation temperature.<sup>432</sup> These results can be explained by the less adherent scales that usually form in the presence of sulfur. However, in other cases where scale damage or breakaway was not apparent or not studied, excess sulfur seemed to affect transport rates through the oxide, giving rise to thicker scales with higher S concentrations in the alloy.<sup>417</sup> Consequently, sulfur in the oxide scale, particularly at grain boundaries, was suggested to enhance cation outward transport,<sup>415,417,451</sup> where S acts as an electron donor and increases the number of Al vacancies.<sup>451</sup> However, the exact effect of S on oxide growth rates is not fully substantiated, for there are cases where sulfur was detected everywhere within the oxide layer, but it did not show any effect on scale growth rate.<sup>418</sup>

#### 1.10.7.2.2 Other impurities

For all of the metals discussed in this chapter under most conditions, oxidation rates are controlled by diffusional transport across the oxide scale. Therefore, impurities that are incorporated into the growing oxide must have an effect on the rates of cation and/or anion diffusion, on oxide creep and perhaps also on the oxide microstructure. These impurities can be segregated at oxide grain boundaries, as in the case of REs (Section 1.10.7.1), or dissolve in the oxide, to affect grain boundary transport, diffusional creep, and/or change the oxide defect concentration, thereby affecting the rates of cation or anion transport through the oxide film. For NiO, it is clear that impurities enhance duplex scale formation<sup>452</sup> (see Section 1.10.2.1), in ways that are still not clearly understood.

Although the type and concentration of impurities must be important in high temperature oxidation,



evaluations of their effects have not been made systematically. Ample examples on the effect of impurities, whether on sample surfaces from the environment<sup>306,345</sup> or from within the alloy,<sup>453,454</sup> serve to underline their importance, as well as the complexity of the oxidation process.

### 1.10.8 Concluding Remarks

Oxidation is considered by some as a perfect topic for teaching material science, because it covers all aspects of the field, from basic thermodynamics to gas–solid interaction, defect chemistry, similar and dissimilar interfaces, bulk and short circuit diffusions, phase transformation, deformation, fracture mechanics and more. Indeed, the oxidation of even pure metals and simple binary alloys involves extremely complicated processes, many of which are interrelated. The summary given here and the many references cited are intended to provide future researchers with a foundation of the extensive works that have been done, so that the same conclusions need not be repeated. In every section of this chapter, many questions obviously remain for future scientists to unravel. It is important to bear in mind that quantitative analysis is extremely important. Although some aspects of the oxidation processes are difficult to quantify, one should strive to do it as much as possible, even if semiquantitatively. It is also important to always consider the *dynamic* nature of the oxidation process and take notice of the knowledge gained from other disciplines, as oxidation covers a wide range of scientific principles.

What is most lacking in past research, in my view, is the understanding of the coupling of different phenomena and the identification of the generality of certain phenomenon, that is, how and/or whether an experimentally observed trend for one system applies to others. An example of this is the sulfur effect, which has been extensively studied and substantiated for  $\text{Al}_2\text{O}_3$  formers, but it is not certain if the same applies for  $\text{Cr}_2\text{O}_3$ ,  $\text{NiO}$ ,  $\text{Fe}_2\text{O}_3$ , or other systems. Related to this question is the nature of the oxide–metal interface on different types of alloys. There seems to be a myth that interfaces formed on alloys whose scales grow mainly by anion transport are stronger than those that grow by cation transport. Quantitative experimental work has to be conducted to provide answers. First principle calculations may also be employed to help elucidate many questions related to metal–oxide interfaces and how structure

and chemistry affect their strength. The above example is only one of many that can be raised. While engineering investigations are often system specific, scientific research should provide knowledge that has broad relevance. Coupling of phenomena is an area that has received little attention. For example, it has been proposed<sup>328</sup> that the magnitude of the oxidation stress should be related to the oxide microstructure and *vice versa*. How structure and chemistry affect stress generation and how the stress in turn affects structure due to relaxation are questions that remain unclear. Many such *couplings* can be identified. Studying them undoubtedly raises the level of experimental difficulty, but with increasingly advanced instrumentation and theoretical tools, new results and insights should be attainable.

### References

1. Kubaschewski, O.; Hopkins, B. E. *Oxidation of Metals and Alloys*, 2nd ed.; Academic Press: New York, 1962.
2. Kofstad, P. *High Temperature Corrosion*; Elsevier Applied Science: London, UK, 1988.
3. Birks, N.; Meier, G. H.; Pettit, F. S. *Introduction to the High-Temperature Oxidation of Metals*, 2nd ed.; Cambridge University Press: Cambridge, UK, 2006.
4. Kofstad, P. *Nonstoichiometry, Diffusion, and Electrical Conductivity in Binary Metal Oxides*; Wiley-Interscience: London, 1972; Chapter 11, pp 221–257.
5. Wood, G. C.; Wright, I. G.; Ferguson, J. M. *Corros. Sci.* **1965**, 5, 645–661.
6. Vasyutinskiy, B. M.; Kartmazov, G. N. *Fiz. Metal Metalloved* **1963**, 15, 132.
7. Atkinson, A.; Taylor, R. I.; Goode, P. D. *Oxid. Met.* **1979**, 13, 519–537.
8. Harris, A. W.; Atkinson, A. *Oxid. Met.* **1990**, 34, 229–258.
9. Sawhill, H. T.; Hobbs, L. W.; Tinker, M. T. *Adv. Ceram.* **1983**, 6, 128–138.
10. Moon, D. P. *Oxid. Met.* **1989**, 31, 71–89.
11. Kim, C. K.; Fan, S. K.; Hobbs, L. W. In *Microscopy of Oxidation*; Bennett, M. J., Lorimer, G. W., Eds.; Institute of Metals: London, UK, 1991; pp 374–380.
12. Peraldi, R.; Monceau, D.; Pieraggi, B. *Mater. Sci. Forum* **2001**, 369–372, 189–196.
13. Mitchell, D. F.; Sewell, P. B.; Cohen, M. *Surf. Sci.* **1976**, 61, 355.
14. Mitchell, D. F.; Graham, M. J. *Surf. Sci.* **1982**, 114, 546–562.
15. Martius, U. M. *Can. J. Physics* **1956**, 33, 466–472.
16. Balmain, J.; Savall, C.; Molins, R.; Severac, C.; Haut, C.; Huntz, A. M. *Mater. Sci. Forum* **2001**, 369–372, 125–132.
17. Peraldi, R.; Monceau, D.; Pieraggi, B. *Oxid. Met.* **2002**, 58, 249–273.
18. Ueno, T. *Trans. Jpn. Inst. Met.* **1973**, 14, 267.
19. Lebrun, J. L.; Huntz, A. M.; Beranger, G.; Aubry, A.; Zhao, J. G. In *Residual Stresses in Science and Technology*; Ceck, G., Denis, D., Simon, A., Eds.; Elsevier Science: London, UK, 1988; p 135.
20. Czerwinski, F.; Zhilyaev, A.; Szpunar, J. A. *Corr. Sci.* **1999**, 41, 1703–1713.
21. Desserrey, F.; Valot, C.; Montesin, T.; Larpin, J. P. *Mater. Sci. Forum* **2002**, 408–412, 1007–1012.

22. Hobbs, L. W.; Sawhill, H. T.; Tinker, M. T. *Rad. Effects* **1983**, 74, 291–297.
23. Homma, H.; Khoi, N. N.; Smeltzer, W. W.; Embury, J. D. *Oxid. Met.* **1971**, 3, 463–473.
24. Kim, C. K.; Fan, S. K.; Hobbs, L. W. In *Microscopy of Oxidation*; Bennett, M. J., Lorimer, G. W., Eds.; Institute of Metals: London, UK, 1991; pp 374–380.
25. Hou, P. Y.; Cannon, R. M. *Mater. Sci. Forum* **1997**, 251–254, 325–332.
26. Stawbridge, A.; Stott, F. H.; Wood, G. C. *Corros. Sci.* **1993**, 35, 855–862.
27. Kyung, H.; Kim, C. K. *Mater. Sci. Eng.* **2000**, B76, 173–183.
28. Mrowec, S. *Corros. Sci.* **1967**, 7, 563.
29. Evans, A. G.; Rajdev, D.; Douglass, D. L. *Oxid. Met.* **1972**, 4, 151.
30. Kofstad, P. *Oxid. Met.* **1985**, 24, 265.
31. Atkinson, A.; Smart, D. W. *J. Electrochem. Soc.* **1988**, 135, 2886.
32. Robertson, J.; Manning, M. I. *Mater. Sci. Technol.* **1988**, 4, 1064.
33. Gibbs, G. B.; Hales, R. *Corros. Sci.* **1977**, 17, 487.
34. Yurek, G. J.; Schmalzried, H. *Ber. Bunsenges. Phys. Chem.* **1975**, 79, 255.
35. Caplan, D.; Hussey, R. J.; Sproule, G. I.; Graham, M. J. *Oxid. Met.* **1980**, 14, 279–299.
36. Peraldi, R.; Monceau, D.; Pieraggi, B. *Oxid. Met.* **2002**, 58, 275–295.
37. Atkinson, A.; Taylor, R. I.; Goode, P. D. *Oxid. Met.* **1979**, 13, 519–543.
38. Atkinson, A.; Taylor, R. I.; Hughes, A. E. *Philos. Mag. A* **1982**, 45, 823–833.
39. Gulbransen, E. A.; Andrew, K. F. *J. Electrochem. Soc.* **1954**, 101, 128.
40. Herchl, R.; Khoi, N. N.; Homma, T.; Smeltzer, W. W. *Oxid. Met.* **1972**, 4, 35.
41. Rhines, F. N.; Connell, R. G., Jr. *J. Electrochem. Soc.* **1977**, 124, 1122.
42. Horn, I. Z. *Metallkunde* **1949**, 40, 73.
43. Wood, G. C.; Stott, F. H.; Forrest, J. E. *Werk. Korr.* **1977**, 28, 395–404.
44. Atkinson, A.; Taylor, R. I. *J. Phys. Chem. Solids* **1986**, 47, 315.
45. Evans, U. R. *Symposium on Internal Stresses in Metals and Alloys*, London, 1947, pp 291–310.
46. Ueno, T. *Trans. Jpn. Inst. Met.* **1974**, 15, 167–172.
47. Rhines, F. N.; Wolf, J. S. *Metall. Trans.* **1970**, 1, 1701–1710.
48. Ueno, T. *Jpn. J. Appl. Phys.* **1975**, 14, 2081–2082.
49. Liu, C.; Huntz, A. M.; Lebrun, J. L. *Mater. Sci. Eng. A* **1993**, 160, 113–126.
50. Goedjen, J. G.; Stout, J. H.; Guo, Q.; Shores, D. A. *Mater. Sci. Eng. A* **1994**, 177, 115–124.
51. Homma, T.; Pyun, Y. J. In *Proceedings of JIMIS-3: High Temperature Corrosion Trans. Jpn. Inst. Met., Suppl.* **1983**, 161–166.
52. Wolf, J. S.; Cavin, B. In *Advances in X-ray Analysis*; Golfrich, J. V., et al. Ed.; Plenum, 1994; p 449.
53. Przybilla, W.; Schutze, M. *Oxid. Met.* **2002**, 58, 103–145.
54. Carter, R. E.; Richardson, F. D. *J. Met* **1954**, 6, 1244.
55. Phalnikar, C. A.; Evans, E. B.; Baldwin, W. M. *J. Electrochem. Soc.* **1956**, 103, 367–429.
56. Hsu, H. S.; Yurek, G. J. *Oxid. Met.* **1982**, 17, 55–76.
57. Martin, M.; Hilbrandt, N.; Koops, U. In *Proceedings of the Symposium on High Temperature Corrosion and Materials Chemistry*; Electrochemical Society: Pennington, NJ, 1998; pp 106–117.
58. Kofstad, P. K.; Hed, A. Z. *J. Electrochem. Soc.* **1969**, 116, 224–229.
59. Pettit, F. S.; Wagner, J. B. *Acta Metall.* **1964**, 12, 41.
60. Wagner, C.; Koch, E. Z. *Phys. Chem.* **1936**, 1332, 439.
61. Mrowec, S.; Werber, T. *Roczniki Chem.* **1962**, 36, 159.
62. Przybyski, K.; Szwagierczak, D. *Oxid. Met.* **1982**, 17, 267–295.
63. Gulbransen, E. A.; Ruka, R. *Trans. AIME* **1950**, 188, 1500.
64. Pinder, L. W. C.E.G.B. Report, MID/SSD/80/0050/R, August 1980.
65. Jonsson, T.; Jardnas, A.; Svensson, J. -E.; Johansson, L. -G.; Halvarsson, M. *Oxid. Met.* **2007**, 67, 193–214.
66. Vallet, P.; Raccach, P. *Mem. Sci. Rev. Metall.* **1965**, 67, 1.
67. Swaroop, B.; Wagner, J. B., Jr. *Trans. AIME* **1967**, 239, 215.
68. Bransky, I.; Hed, A. Z. *J. Am. Ceram. Soc.* **1968**, 57, 231.
69. Fender, B. E.; Riley, F. D. *J. Phys. Chem. Solids* **1969**, 30, 793.
70. Giddings, R. A.; Gordon, R. S. *J. Am. Ceram. Soc.* **1973**, 56, 111.
71. Dieckmann, R. In *High Temperature Corrosion*; Rapp, R. A., Ed.; NACE: Houston, TX, 1983; p 70.
72. Dieckmann, R. In *Oxidation of Metals and Associated Mass Transport*; Dayananda, M. A., Rothman, S. J., King, W. E., Eds.; Metallurgical Society: Warrendale, PA, 1986; p 7.
73. Garnaud, G.; Rapp, R. A. *Oxid. Met.* **1977**, 11, 193.
74. Atkinson, A. *Rev. Mod. Phys.* **1985**, 57, 437–470.
75. Atkinson, A.; Taylor, R. I. *High Temperature – High Pressure* **1985**, 14, 469.
76. Atkinson, A.; Taylor, R. I. *J. Phys. Chem. Solids* **1985**, 46, 469.
77. Channing, D. A.; Graham, M. J. *Corros. Sci.* **1972**, 12, 271.
78. Channing, D. A.; Dickerson, S. M.; Graham, M. J. *Corros. Sci.* **1973**, 13, 933.
79. Francis, R.; Lees, D. G. *Corros. Sci.* **1976**, 16, 847.
80. Sewell, P. B.; Cohen, M. J. *Electrochem. Soc.* **1964**, 111, 501–508.
81. Caplan, D.; Graham, M. J.; Cohen, M. *Corros. Sci.* **1970**, 10, 1.
82. Svedung, I.; Hammar, B.; Vannerberg, N. G. *Oxid. Met.* **1973**, 6, 21.
83. Howe, C. I.; McEnany, B.; Scott, V. D. *Corros. Sci.* **1985**, 25, 195.
84. Boggs, W. E.; Kachik, R. H.; Pellisier, G. E. *J. Electrochem. Soc.* **1965**, 112, 539.
85. Rahmel, A.; Robolski, J. *Corros. Sci.* **1965**, 5, 333.
86. Fukumoto, M.; Hayashi, S.; Maeda, S.; Narita, T. *J. Inst. Met.* **2001**, 65, 115.
87. Tuck, C. W.; Odgers, M.; Sachs, K. *Corros. Sci.* **1969**, 9, 271.
88. Wittnauer, J. J. *Met* **1900**, 42, 7.
89. Buckman, R. W., Jr. In *Alloying*; Walter, J. L., Jackson, M. R., Sims, C. T., Eds.; ASM International: Metals Park, 1988; p 419.
90. Pugh, J. J. *Met.* **1958**, 212, 335.
91. Nieh, T. G.; Wadsworth, J. In *High Temperature Silicides and Refractory Alloys*; Proceedings of the Matererial Research Society Symposium; Briant, C. L., Petrovic, J. J., Bewlay, B. P., Vasudevan, A. K., Lipsitt, H. A., Eds.; Mater. Res. Soc.: Pittsburgh, PA, 1994; Vol. 322, p 315.
92. Ramberg, C. E.; Beatrice, P.; Kurokawa, K.; Worrell, W. L. In *High Temperature Silicides and Refractory Alloys*; Proceedings of the Matererial Research Society Symposium, Boston, MA, Nov.–2 Dec. 1993; Briant, C. L., Petrovic, J. J., Bewlay, B. P., Vasudevan, A. K., Lipsitt, H. A., Eds.; Material Research Society: Pittsburgh, PA, 1994; pp 243–253.
93. Kofstad, P. J. *Inst. Met.* **1962**, 90, 253–264.

94. Pawel, R. E.; Cathcart, J. V.; Campbell, J. J. *Acta Metall.* **1962**, 10, 149.
95. Pint, B. A.; DiStefano, J. R. *Oxid. Met.* **2005**, 63, 33–55.
96. Kofstad, P. J. *Electrochem. Soc.* **1963**, 110, 491.
97. Kofstad, P. J. *Electrochem. Soc.* **1962**, 109, 776.
98. Pawel, R. E.; Campbell, J. J. *Acta Metall.* **1966**, 14, 1827.
99. Cathcart, J. V.; Campbell, J. J.; Smith, G. P. *J. Electrochem. Soc.* **1958**, 105, 442.
100. Kofstad, P. J. *Less Common Met.* **1963**, 5, 158.
101. Inouye, H. In *Cohimbium Metallurgy*; AIME Metallurgical Society Conferences, 10; Douglass, D. L., Kunz, F. W., Eds.; Interscience Publishers: New York, 1961.
102. Kofstad, P.; Espevik, S. J. *Electrochem. Soc.* **1965**, 112, 153.
103. Earl, A.; Gulbransen, A.; Andrew, K. F. J. *Electrochem. Soc.* **1958**, 105, 4–9.
104. Sheasby, J. S.; Wallwork, G. R.; Smeltzer, W. W. *J. Electrochem. Soc.* **1966**, 113, 1255.
105. Strafford, K. N. *Corros. Sci.* **1979**, 19, 49–62.
106. King, D. A.; Madey, T. E.; Yates, J. T., Jr. *J. Chem. Phys.* **1971**, 55, 3247–3253.
107. Sikka, V. K.; Rosa, C. J. *Corros. Sci.* **1980**, 20, 1201–1219.
108. Schissel, P. O.; Trulson, O. C. J. *Chem. Phys.* **1965**, 43, 737–743.
109. Walsh, P. N.; Quets, J. M.; Graff, R. A. J. *Chem. Phys.* **1967**, 46, 1144–1153.
110. Bartlett, R. W. *Trans. Metal Soc., AIME* **1964**, 230, 1097.
111. Bartlett, R. W. *Trans. Metall. Soc. AIME* **1964**, 230, 1097.
112. Perkins, R. A.; Crooks, D. D. J. *Met.* **1961**, 13, 490.
113. Zhetbaev, A. K.; Ibragimov, S. H. S. H.; Shokanov, A. K. J. *Phys.* **1980**, 41, 387–388.
114. Berkowitz-Mattuck, J. B.; Cuchler, A.; Engelke, J. L.; Goldstein, N. J. *Chem. Phys.* **1963**, 39, 2722–2730.
115. Voitovich, R. F. *Fiz. Metal. Metalloved* **1961**, 12, 376.
116. Kofstad, P. J. *Inst. Met.* **1962–63**, 91, 411.
117. Dooley, R. B.; Stringer, J. J. *Less Common Met.* **1971**, 25, 15–26.
118. Klopp, W. D.; Maykutii, D. J.; Jaffee, R. I. *Trans. Am. Soc. Met.* **1961**, 53, 637.
119. Corn, D. L.; Douglass, D. L.; Smith, C. A. *Oxid. Met.* **1991**, 35(1–2), 139–173.
120. DiStefano, J. R.; Chitwood, L. D. J. *Nucl. Mater.* **2001**, 295, 42–48.
121. DiStefano, J. R.; Chitwood, L. D. AIP Conference Proceedings, no. 552, 2001; pp 1076–1081. [Conference Paper; Journal Paper].
122. DiStefano, J. R.; Pint, B. A.; DeVan, J. H. *Int. J. Refract. Met. Hard Mater.* **2000**, 18(4–5), 237–243.
123. Babitzke, H. R.; Siemens, R. E.; Asai, G.; Kato, H. Bureau of Mines Report of Investigations 6558, US Department of the Interior, 1964.
124. Nieh, T. G.; Wadsworth, J. In *High Temperature Silicides and Refractory Alloys*; MRS Proceedings; Briant, C. L., Petrovic, J. J., Bewlay, B. P., Vasudevan, A. K., Lipsitt, H. A., Eds.; **1993**; Vol. 322, p 315.
125. Svedberg, R. C.; Foroulis, Z. A.; Pettit, F. S. *J. Electrochem. Soc.* **1976**, 331.
126. Perkins, R. A.; Meier, G. H. J. *Met.* **1990**, 42, 17–21.
127. Perkins, R. A.; Chiang, K. T.; Meier, G. H. *Scripta Metall.* **1988**, 22, 419–424.
128. Lee, J. S.; Stephens, J. J.; Nieh, T. G. In *High Temperature Niobium Alloys*; Stephens, J. J., Ahmad, I., Eds.; TMS: Warrendale, PA, 1991; p 143.
129. Diliberto, S.; Rapin, C.; Steinmetz, P.; Vilasi, M.; Berthod, P. J. *Mater. Sci.* **2003**, 38, 2063–2072.
130. Perkins, R. A.; Meier, G. H. J. *Met.* **1990**, 42, 17.
131. Wittenauer, J. J. *Met.* **1990**, 42, 7.
132. Wadsworth, J.; Nieh, T. G.; Stephens, J. J. *Int. Met. Rev.* **1988**, 33, 131.
133. Ux, M.; Wittenauer, J. P. J. *Met.* **1992**, 44, 25.
134. Mueller, A.; Ge, W.; Rapp, R. A.; Courtright, E. L. *J. Electrochem. Soc.* **1992**, 139, 1266–1275.
135. Louro, C.; Cavaleiro, A. J. *Mater. Proc. Tech.* **1999**, 92–93, 162–168.
136. Martinz, H. -P.; Rieger, M. *Mater. Sci. Forum* **1997**, 251–254, 761–768.
137. Pons, M.; Caillet, M.; Galerie, A. *Mater. Chem. Phys.* **1986**, 15, 45–60.
138. Pons, M.; Caillet, M.; Galerie, A. *Mater. Chem. Phys.* **1987**, 16, 423–432.
139. Fukumoto, M.; Matsumura, Y.; Hayashi, S.; Sakamoto, K.; Kasama, A.; Tanaka, R.; Narita, T. *Oxid. Met.* **2003**, 60, 355.
140. Deal, B. E.; Grove, A. S. J. *Appl. Phys.* **1965**, 36, 3770.
141. Opila, E. J. J. *Am. Ceram. Soc.* **1994**, 77, 730.
142. Duquesnoy, A.; Marion, F. C. R. *Hebd. Seances Acad. Sci.* **1963**, 256, 2862.
143. Kroger, F. A. In *High Temperature Corrosion*; Rapp, R. A., Ed.; NACE: Houston, 1983; p 89.
144. Sucov, E. W. J. *Am. Ceram. Soc.* **1965**, 46, 190.
145. Haul, R.; Dumbgen, Z. *Elektrochem* **1962**, 66, 636.
146. Robinson, R. C.; Smialek, J. L. J. *Am. Ceram. Soc.* **1999**, 82, 1817–1825.
147. Stott, F. H.; Wood, G. C.; Stringer, J. *Oxid. Met.* **1995**, 44, 113–145.
148. Evans, H. E.; Hilton, D. A.; Holm, R. A.; Webster, S. J. *Oxid. Met.* **1980**, 14, 235.
149. Bennett, M. J.; Desport, J. A.; Labun, P. A. *Math. Phys. Sci.* **1987**, 412, 223–230.
150. Evans, H. E.; Hilton, D. A.; Holm, R. A.; Webster, S. J. *Oxid. Met.* **1983**, 19, 1.
151. Adachi, T.; Meier, G. H. *Oxid. Met.* **1987**, 27, 347.
152. Douglass, D. L.; Armijo, J. S. *Oxid. Met.* **1970**, 2, 207.
153. Saito, Y.; Maruyama, T. *Mater. Sci. Eng.* **1987**, 87, 275.
154. Ahmad, B.; Fox, P. *Oxid. Met.* **1999**, 52, 113.
155. Stott, F. H.; Gabriel, G. J.; Wood, G. C. *Oxid. Met.* **1987**, 28, 329–345.
156. Adachi, T.; Meier, G. H. *Oxid. Met.* **1987**, 27, 347.
157. Saito, Y.; Maruyama, T.; Amano, T. *Mater. Sci. Eng.* **1987**, 87, 275–280.
158. Meier, G. *Mater. Sci. Eng.* **1989**, 120, 1.
159. Sauthoff, G. *Intermetallics*; VCH: New York, 1995; pp 99–117.
160. Willaims, J. C. In *Structural Intermetallics*; Nathal, M. V., Darolia, R., Liu, C. T., Martin, P. E., Miracle, D. B., Wagner, W., Yamaguchi, M., Eds.; TMS: Warrendale, PA, 1997; pp 3–8.
161. Jiang, H.; Petersson, C. S.; Nicolet, M. A. *Thin Solid Films* **1986**, 140, 115.
162. Meier, G. H. *Mater. Corros.* **1996**, 47, 595.
163. Brady, M. P.; Pint, B. A.; Tortorelli, P. F.; Wright, I. G.; Hanrahan, R. J., Jr. In *Corrosion and Environmental Degradation; Materials Science and Technology; Vol II*, Schutze, M., Ed.; Wiley-VCH: Germany, 2000, pp 296–308.
164. Lublin, P.; Sama, L. *Am. Ceram. Soc.* **1967**, 46, 1083.
165. Lavendel, H. W.; Elliot, A. G. *Trans AIME* **1967**, 239, 143.
166. Schwettmann, F. N.; Graff, R. A.; Kolodney, M. *J. Electrochem. Soc.* **1971**, 118, 1973–1977.
167. Abba, A.; Galerie, A.; Caillet, M. *Oxid. Met.* **1982**, 17, 43–54.
168. Evans, D. L. J. *Am. Ceram. Soc.* **1970**, 53, 418.
169. Meschter, P. J. *Metall. Trans. A* **1992**, 23A, 1763.
170. Glushko, P. I.; Postogvard, G. I.; Pugachev, N. S.; Dudnik, S. F.; Podtykan, V. P. *Prot. Met.* **1977**, 13, 187.
171. Melsheimer, S.; Fietzek, M.; Kolarik, V.; Rahmel, A.; Schutze, M. *Oxid. Met.* **1997**, 47, 139.

172. Berkowitz-Mattuck, J.; Dils, R. R. *J. Electrochem. Soc.* **1965**, *112*, 583.
173. Mochizuki, T.; Kashiwagi, M. *J. Electrochem. Soc.* **1980**, *127*, 1128.
174. Ramberg, C. E.; Worrell, W. L. *J. Am. Ceram. Soc.* **2001**, *84*, 2607–2616.
175. Aitken, E. A. In *Intermetallic Compounds*; Westrook, J. H., Ed.; Wiley: New York, 1967; p 491.
176. Berkowitz-Mattuck, J. B.; Blackburn, P. E.; Felten, E. J. *Trans. AIME* **1965**, *233*, 1093.
177. Berztiss, D. A.; Cerchiara, R. R.; Gulbransen, E. A.; Pettit, F. S.; Meier, G. H. *Mater. Sci. Eng. A* **1992**, *155*, 165.
178. Yanagihara, K.; Przybylski, K.; Maruyama, T. *Oxid. Met.* **1997**, *47*, 277.
179. Kurokawa, K.; Houzumi, H.; Saeki, I.; Takahashi, H. *Mater. Sci. Eng. A* **1999**, *261*, 292–299.
180. Bartlett, R. W.; McCamont, I. W.; Gage, P. R. *J. Am. Ceram. Soc.* **1965**, *48*, 551.
181. McKamey, C. G.; Tortorelli, P. F.; DeVan, J. H.; Carmichael, C. A. *J. Mater. Res.* **1992**, *7*, 2747.
182. Dimiduk, D. M.; Perepezko, J. H. *MRS Bull* **2003**, *28*, 639.
183. Thom, A. J.; Summers, E.; Akinc, M. *Intermetallics* **2002**, *10*, 555.
184. Supatarawanich, V.; Johnson, D. R.; Liu, C. T. *Intermetallics* **2004**, *12*, 721.
185. Parthasarathy, T. A.; Mendiratta, M. G.; Dimiduk, D. M. *Acta Metall.* **2002**, *50*, 1857.
186. Sakidja, R.; Rioult, F.; Werner, J.; Perepezko, J. H. *Scripta Mater.* **2006**, *55*, 903.
187. Young, C. T.; Tenney, D. R.; Herring, H. W. *Metall. Trans.* **1975**, *6A*, 2253.
188. Caplan, D.; Cohen, M. *J. Electrochem. Soc.* **1961**, *108*, 438.
189. Opila, E. J.; Jacobson, N. S. In *Fundamental Aspects of High Temperature Corrosion*; Shores, D. A., Rapp, R. A., Hou, P. Y., Eds.; The Electrochemical Society: Pennington, NJ, 1997; Vol. 96–26, pp 269–280.
190. Kofstad, P.; Bredesen, R. *Solid State Ionics* **1992**, *52*, 69.
191. Huang, K.; Hou, P. Y.; Goodenough, J. B. *Solid State Ionics* **2000**, *129*, 237.
192. Brylewski, T.; Nanko, M.; Maruyama, T.; Przybylski, K. *Solid State Ionics* **2001**, *143*, 131.
193. Quadackers, W. J.; Piron-Abellan, J.; Shemet, V.; Singheiser, L. *Mater. High Temp.* **2003**, *20*, 115–127.
194. Kofstad, P.; Lillerud, K. P. *J. Electrochem. Soc.* **1980**, *127*, 2410–2419.
195. Hagel, W. C.; Seybolt, A. U. *J. Electrochem. Soc.* **1961**, *108*, 1146.
196. Atkinson, A.; Taylor, R. I. In *Proceedings of the 3rd International Conference on Nonstoichiometric Compounds*, State College: PA, 1984.
197. Hughes, A. E.; Atkinson, A.; Chadwick, A. T. In *Defect Properties and Processing of High-Technology Nonmetallic Materials*; North-Holland: New York, NY, 1984; pp 27–37.
198. Giggins, C. S.; Pettit, F. S. *Metall. Trans.* **1971**, *2*, 1071.
199. Tsai, S. C.; Huntz, A. M.; Dolin, C. *Mater. Sci. Eng. A* **1996**, *212*, 6–13.
200. Dong, W.; Bishop, H. E.; Johnson, D.; Lees, D. G.; Lorimer, G. W. *Oxid. Met.* **2000**, *54*, 509.
201. Lillerud, K. P.; Kofstad, P. *J. Electrochem. Soc.* **1980**, *127*, 2397–2410.
202. Hindam, H.; Whittle, D. P. *Oxid. Met.* **1982**, *18*, 245–262.
203. Evans, A. G.; Cannon, R. M. *Mater. Sci. Forum* **1989**, *43*, 243–268.
204. Kofstad, P.; Lillerud, K. P. *Oxid. Met.* **1982**, *17*, 177.
205. Ben Abderrazik, G.; Moulin, G.; Huntz, A. M. *Oxid. Met.* **1990**, *33*, 191–235.
206. Fox, P.; Lees, D. G.; Lorimer, G. W. *Oxid. Met.* **1991**, *36*, 491.
207. Caplan, D.; Harvey, A.; Cohen, M. *Corros. Sci.* **1963**, *3*, 161.
208. Caplan, D.; Sproule, G. I. *Oxid. Met.* **1975**, *9*, 459–472.
209. Wright, I. G.; Wood, G. C. *Oxid. Met.* **1977**, *11*, 163.
210. Wood, G. C.; Hodgkiess, T.; Whittle, D. P. *Corros. Sci.* **1966**, *6*, 129–147.
211. Wood, G. C.; Hodgkiess, T. *J. Electrochem. Soc.* **1966**, *113*, 319.
212. Moulin, P.; Armanet, F.; Beranger, G.; Lacombe, P. *Mere. Sci. Rev. Metall.* **1977**, *74*, 143.
213. Warzee, M.; Maurice, M.; Sonnen, C.; Waty, J.; Berge, P. H. *Rev. Met.* **1964**, *61*, 593.
214. Stott, F. H.; Bartlett, P. K. N.; Wood, G. C. *Mater. Sci. Eng.* **1987**, *8*, 163.
215. Hou, P. Y. unpublished results.
216. Howes, V. R. *Corros. Sci.* **1968**, *8*, 221.
217. Howes, V. R. *Corros. Sci.* **1968**, *8*, 729.
218. Mortimer, D.; Post, M. L. *Corros. Sci.* **1968**, *8*, 499.
219. Wood, G. C.; Whittle, D. P. *J. Electrochem. Soc.* **1968**, *115*(126), 133.
220. Wood, G. C. *Oxid. Met.* **1970**, *2*, 11–57.
221. Daghigh, S.; Lebrun, J. L.; Huntz, A. M. *Mater. Sci. Forum* **1997**, *251*, 381–388.
222. Hou, P. Y.; Stringer, J. *Act. Metall.* **1991**, *39*, 841–849.
223. Kitamura, K.; Nishiyama, Y.; Otsuka, N.; Kudo, T. *Mater. Sci. Forum* **2006**, *522–523*, 489–495.
224. Tortorelli, P. F.; More, K. L.; Specht, E. D.; Pint, B. A.; Zschack, P. *Mater. High Temp.* **2003**, *20*, 303–310.
225. Hou, P. Y.; Paulikas, A. P.; Veal, B. W. *Mater. Sci. Forum* **2004**, *461–464*, 671–680.
226. Zhu, D.; Stout, J. H.; Nelson, J. C.; Shores, D. A. *Trans. Tech. Pub.* **1997**, *251–254*, 437–444.
227. Tortorelli, P. F.; Natesan, K. *Mater. Sci. Eng.* **1998**, *A258*, 115.
228. DeVan, J. H.; Tortorelli, P. F. *Corros. Sci.* **1993**, *35*, 1065.
229. Pint, B. A.; Wright, I. G.; Lee, W. Y.; Zhang, Y.; Pruessner, K.; Alexander, K. B. *Mater. Sci. Eng. A* **1998**, *245*, 201.
230. Doychak, J.; Smialek, J. L.; Mitchell, T. E. *Metall. Trans. A* **1989**, *20*, 499.
231. Rybicki, G. C.; Smialek, J. L. *Oxid. Met.* **1989**, *31*, 275.
232. Yang, J. C.; Nadarzinski, K.; Schumann, E.; Rühle, M. *Scripta Metall.* **1995**, *33*, 1043.
233. Smialek, J. L.; Doychak, J.; Gaydosh, D. J. *Oxid. Met.* **1990**, *34*, 259.
234. Kuenzly, J. D.; Douglass, D. L. *Oxid. Met.* **1974**, *8*, 139.
235. Doychak, J.; Rühle, M. *Oxid. Met.* **1989**, *31*, 431.
236. Schumann, E.; Rühle, M. *Acta Metall. Mater.* **1994**, *42*, 1481.
237. Alexander, K. B.; Prussner, K.; Hou, P. Y.; Tortorelli, P. F. In *Microscopy of Oxidation*; Newcomb, S. B., Little, J. A., Eds.; The Institute of Metals, 1997; Vol. 3, pp 246–264.
238. Zhang, X. F.; Thaidigsmann, K.; Ager, J.; Hou, P. Y. *J. Mater. Res.* **2006**, *21*, 1409–1419.
239. Rensch, D.; Grimsditch, M.; Koshelev, I.; Veal, B. W.; Hou, P. Y. *Oxid. Met.* **1997**, *48*, 471.
240. Wagner, C. *Corros. Sci.* **1965**, *5*, 751.
241. Hou, P. Y. *J. Am. Ceram. Soc.* **2003**, *86*, 660–668.
242. Wood, G. C.; Hodgkiess, T. *Nature* **1966**, *211*, 1358–1361.
243. Sauer, J. P.; Rapp, R. A.; Hirth, J. P. *Oxid. Met.* **1982**, *18*, 285–294.
244. Jedlinski, J.; Borchardt, G.; Bernaski, A.; Scherrer, S.; Ambos, R.; Rajchel, B. In *Microscopy of Oxidation*; Newcomb, S. B., Bennett, M. J., Eds.; The Institute of Metals, 1993; Vol. 2, pp 445–454.
245. Quaddackers, W. J.; Elschner, A.; Speier, W.; Nickel, H. *Appl. Surf. Sci.* **1991**, *52*, 271–287.

246. Smialek, J. L.; Gibala, R. *Metall. Trans. A* **1983**, *14A*, 2143–2161.
247. Pint, B. A. In *Fundamental Aspects of High Temperature Corrosion*; Shores, D. A., Rapp, R. A., Hou, P. Y., Eds.; Electrochemical Society, 1996; pp 74–85.
248. Brumm, M. W.; Grabke, H. J. *Corros. Sci.* **1992**, *33*, 1677–1690.
249. Yang, J. C.; Schumann, E.; Levin, I.; Rühle, M. *Acta Mater.* **1998**, *46*, 2195–2201.
250. Andoh, A.; Taniguchi, S.; Shibata, T. *Mater. Sci. Forum* **2001**, 369–372, 303–310.
251. Yang, J. C.; Nadarzinski, K.; Schumann, E.; Rühle, M. *Scripta Metall.* **1995**, *33*, 1043–1048.
252. Sigler, D. R. *Oxid. Met.* **1991**, *36*, 57–80.
253. Hagel, W. C. *Corrosion* **1965**, *21*, 316.
254. Jedlinski, J. *Oxid. Met.* **1993**, *39*, 55–60.
255. Frémy, N.; Maurice, V.; Marcus, P. *Surf. Interf. Anal.* **2002**, *34*, 519–523.
256. Doychak, J.; Rühle, M. *Oxid. Met.* **1989**, *31*, 431–452.
257. Yang, J. C.; Schumann, E.; Mülleijans, H.; Rühle, M. *J. Phys. D: Appl. Phys.* **1996**, *29*, 1716–1724.
258. Doychak, J. K. Doctoral thesis, Case Western Reserve University: Cleveland, OH, 1986.
259. Yang, J. C.; Schumann, E.; Levin, I.; Rühle, M. *Acta Metall.* **1998**, *46*, 2195–2201.
260. Hou, P. Y.; Paulikas, A. P.; Veal, B. W. *Mater. High Temp.* **2006**, *22*, 373–381.
261. El Kadiri, H.; Molins, R.; Bienvenu, Y.; Horstemeyer, M. F. *Oxid. Met.* **2005**, *64*, 63–97.
262. Lipkin, D. M.; Schaffer, H.; Adar, F.; Clarke, D. R. *Appl. Phys. Lett.* **1997**, *70*, 2550–2552.
263. Tolpygo, V. K.; Clarke, D. R. *Mater. High Temp.* **2000**, *17*, 59–70.
264. Steiner, C. J. -P.; Hasselman, D. P. H.; Spriggs, R. M. *J. Am. Ceram. Soc.* **1971**, *54*, 412–413.
265. Schutze, M. In *Proceedings of the Workshop on High Temperature Corrosion of Advanced Materials and Protective Coatings*; Saito, Y., Onay, B., Maruyama, T., Eds.; Elsevier Science, 1992; pp 39–49.
266. Lessing, P. A.; Gordon, R. S. *J. Mater. Sci.* **1977**, *12*, 2291–2302.
267. Ikuma, Y.; Gordon, R. S. *J. Am. Ceram. Soc.* **1983**, *66*, 139–147.
268. Hollenberg, G. W.; Gordon, R. S. *J. Am. Ceram. Soc.* **1973**, *56*, 140–147.
269. Sugita, T.; Pask, J. A. *J. Am. Ceram. Soc.* **1970**, *53*, 609–613.
270. Cho, J.; Harmer, M. P.; Chan, H. M.; Richman, J. M.; Thompson, A. M. *J. Am. Ceram. Soc.* **1997**, *80*, 1013–1017.
271. Wang, C. M.; Cho, J.; Chan, H. M.; Harmer, P.; Richman, J. M. *J. Am. Ceram. Soc.* **2001**, *84*, 1010–1016.
272. Hou, P. Y.; Zhang, X. F.; Cannon, R. M. *Scripta Metall.* **2004**, *51*, 45–49.
273. Levin, E. M.; Robbins, C. R.; McMurdie, H. F. Eds. *Phase Diagram for Ceramists*; The American Ceramic Society, 1964; p 309.
274. Drahush, M. D.; Chan, H. M.; Rickman, J. M.; Harmer, M. P. *J. Am. Ceram. Soc.* **2005**, *88*, 3369–3373.
275. Muan, A. A. *J. Sci.* **1958**, *256*, 413–422.
276. Novokhatskii, I. A.; Velov, B. F.; Gorokh, A. V.; Savinskaya, A. A. *Russ. J. Phys. Chem.* **1965**, *39*, 1498–1499.
277. Wright, I. G.; Pint, B. A.; Tortorelli, P. F. *Oxid. Met.* **2001**, *55*, 333–337.
278. Pint, B. A.; More, K. L.; Tortorelli, P. F.; Porter, W. D.; Wright, I. G. *Mat. Sci. Forum* **2001**, 369–372, 411–418.
279. Pint, B. A.; Garratt-Reed, A. J.; Hobbs, L. W. In *Microscopy of Oxidation*; Newcomb, S. B., Bennett, M. J., Eds.; The Institute of Materials, 1993; Vol. II, pp 463–475.
280. Pint, B. A.; Hobbs, L. W. *Proc. Electrochem. Soc.* **1992**, 92–100.
281. Pint, B. A.; Hobbs, L. W. *Oxid. Met.* **1994**, *41*, 203–233.
282. Pint, B. A.; Garratt-Reed, A. J.; Hobbs, L. W. *J. Phys. IV.* **1993**, C9-3, 247–256.
283. Pint, B. A.; Alexander, K. B. *J. Electrochem. Soc.* **1998**, *145*, 1819–1829.
284. Sheasby, J. S.; Jory, D. B. *Oxid. Met.* **1978**, *12*, 527–539.
285. Felten, E. J.; Pettit, F. S. *Oxid. Met.* **1976**, *10*, 189–223.
286. Giggins, C. S.; Pettit, F. S. *J. Electrochem. Soc.* **1971**, *118*, 1782–1790.
287. Tien, J. K.; Pettit, F. S. *Metall. Trans.* **1972**, *3*, 1587–1599.
288. Pettit, F. S. *AIME Met. Soc. Trans.* **1967**, *239*, 1296–1305.
289. Stasik, M. S.; Pettit, F. S.; Meier, G. H.; Ashary, A.; Smialek, J. L. *Scripta Metall. Mater.* **1994**, *31*, 1645–1650.
290. Sarioglu, C.; Stiger, M. J.; Blachere, J. R.; Janakiraman, R.; Schumann, E.; Ashary, A.; Pettit, F. S.; Meier, G. H. *Mater. Corros.* **2000**, *51*, 358–372.
291. Hindam, H. M.; Smeltzer, W. W. *J. Electrochem. Soc.* **1980**, *127*, 1622–1630.
292. Smialek, J. L. *Metall. Trans. A* **1978**, *9A*, 309–320.
293. Smialek, J. L.; Gibala, R. In *High Temperature Corrosion*; Rapp, R. A., Ed.; NACE: Houston, TX, 1981; pp 274–283.
294. Nanko, M.; Ozawa, M.; Maruyama, T. *J. Electrochem. Soc.* **2000**, *147*, 283–288.
295. Xu, C. H.; Gao, W.; Gong, H. *Intermetallics* **2000**, *8*, 769–779.
296. Kuenzly, J. D.; Douglass, D. L. *Oxid. Met.* **1974**, *6*, 139–178.
297. Kumar, A.; Nasrallah, M.; Douglass, D. L. *Oxid. Met.* **1974**, *8*, 227–263.
298. Golightly, F. A.; Stott, F. H.; Wood, G. C. *J. Electrochem. Soc.* **1979**, *126*, 1035–1042.
299. Kahn, A. S.; Lowell, C. E.; Barrett, C. A. *J. Electrochem. Soc.* **1980**, *127*, 670–679.
300. Nicolas-Chaubet, D.; Haut, C.; Picard, C.; Millot, F.; Huntz, A. M. *Mater. Sci. Eng. A* **1989**, *120–121*, 83–89.
301. Amano, T.; Yajima, S.; Saito, Y. *Trans. Jpn. Inst. Met.* **1979**, *20*, 431–441.
302. Amano, T.; Yajima, S.; Saito, Y. *Trans. Jpn. Inst. Met.* **1985**, *26*, 433–443.
303. Hou, P. Y.; Cannon, R. M.; Zhang, H.; Williamson, R. L. In *Fundamental Aspects of High Temperature Corrosion*; ECS Fall Meeting, San Antonio, TX, 6–11 October 1996; Shores, D. A., Rapp, R. A., Hou, P. Y., Eds.; Electrochemical Society: Pennington, PA, 1997; ECS Proceedings, Vol. 96-26, pp 28–40.
304. Tolpygo, V. K.; Clarke, D. R. *Acta Metall.* **1998**, *46*, 5135–5166.
305. Kroger, F. A. *Ann. Rev. Mater. Sci.* **1977**, *7*, 449–475.
306. Tolpygo, V. K.; Clarke, D. R.; Murphy, K. S. *Metall. Trans. A* **2001**, *32*, 1467–1478.
307. Jedlinski, J.; Borchardt, G.; Mrowec, S. *Solid State Ionics* **1992**, *50*, 67–74.
308. Hindam, H. M.; Smeltzer, W. W. *Oxid. Met.* **1980**, *14*, 337–349.
309. Young, E. W. A.; De Wit, J. H. W. *Solid State Ionics* **1985**, *16*, 39–46.
310. Reddy, K. P. R.; Smialek, J. L.; Cooper, A. R. *Oxid. Met.* **1982**, *17*, 429–449.
311. Jedlinski, J.; Borchardt, G. *Oxid. Met.* **1991**, *36*, 317–337.
312. Quadackers, W. J.; Elschner, A.; Speier, W.; Nickel, H. *Appl. Surf. Sci.* **1991**, *52*, 271–287.
313. Prescott, R.; Mitchell, D. F.; Sproule, G. I.; Graham, M. J. *Solid State Ionics* **1992**, *53–56*, 229–237.
314. Pint, B. A.; Martin, J. R.; Hobbs, L. W. *Oxid. Met.* **1993**, *39*, 167–195.

315. Mennicke, C.; Schumann, E.; Ruhle, M.; Hussey, R. J.; Sproule, G. I.; Graham, M. J. *Oxid. Met.* **1998**, *49*, 455–466.
316. Basu, S. N.; Halloran, J. W. *Oxid. Met.* **1987**, *27*, 143–155.
317. Oishi, Y.; Kingery, W. D. *J. Chem. Phys.* **1960**, *33*, 480–486.
318. Reddy, K. P. R.; Cooper, A. R. *J. Am. Ceram. Soc.* **1982**, *65*, 634–638.
319. Oishi, Y.; Ando, V.; Suga, N.; Kingery, W. D. *J. Am. Ceram. Soc.* **1983**, *66*, C130–C131.
320. Le Gall, M.; Huntz, A. M.; Lesage, B.; Monty, C.; Bernardini, J. *J. Mater. Sci.* **1995**, *30*, 201.
321. Reed, D. J.; Wuensch, B. J. *J. Am. Ceram. Soc.* **1980**, *63*, 88–92.
322. Lagerlof, K. P. D.; Peltka, B. J.; Mitchell, T. E.; Heuer, A. H. *Rad. Effects* **1983**, *74*, 87–107.
323. Prot, D.; Monty, C. *Philos. Mag.* **1996**, *73*, 899–917.
324. Paladino, A. E.; Kingery, W. D. *J. Chem. Phys.* **1962**, *37*, 957–962.
325. Le Gall, M.; Lesage, B.; Bernardini, J. *Philos. Mag.* **1994**, *70*, 761–773.
326. Cannon, R. M.; Rhodes, W. H.; Heuer, A. H. *J. Am. Ceram. Soc.* **1980**, *63*, 46–53.
327. Glaeser, A. M.; Evans, J. W. *Acta Metall.* **1986**, *34*, 1545.
328. Cannon, R. M.; Hou, P. Y. In *High Temperature Corrosion and Materials Chemistry*; Hou, P. Y., McNallan, M. J., Oltra, R., Opila, E. J., Shores, D. A., Eds.; The Electrochemical Society, 1998; pp 594–607.
329. Lipkin, D. M.; Clarke, D. R. *Oxid. Met.* **1996**, *45*, 267–280.
330. Hutchings, R.; Loretto, M. H.; Smallman, R. E. *Met. Sci.* **1981**, *15*, 7.
331. Brumm, M. W.; Grabke, H. J. *Corros. Sci.* **1993**, *34*, 547.
332. Pint, B. *Oxid. Met.* **1997**, *48*, 303.
333. Rommelskirchen, I.; Eltester, B.; Grabke, H. J. *Mater. Corros.* **1996**, *47*, 646.
334. Xu, C. H.; Gao, W.; Gong, H. *High Temp. Mater. Proc.* **2000**, *19*, 371.
335. Hou, P. Y.; Niu, Y.; Van Lienden, C. *Oxid. Met.* **2003**, *59* (1/2), 41–61.
336. Dravnieks, A.; McDonald, H. J. *J. Electrochem. Soc.* **1948**, *94*, 139.
337. Dobson, P. S.; Smallman, R. E. *Proc. R. Soc. Lond. A* **1966**, *293*, 423.
338. Kumar, A.; Nasrallah, M.; Douglass, D. L. *Oxid. Met.* **1974**, *8*, 227.
339. Hales, R.; Smallman, R. E.; Dobson, P. S. *Proc. R. Soc. Lond. A* **1968**, *307*, 71.
340. Douglass, D. L. *Mater. Sci. Eng.* **1969**, *3*, 255.
341. Evans, H. E. *Mater. Sci. Technol.* **1988**, *4*, 1089.
342. Pieraggi, B.; Rapp, R. A.; Hirth, J. P. *Oxid. Met.* **1995**, *44*, 63.
343. Harris, J. *Acta Metall.* **1978**, *26*, 1033.
344. Zimmermann, D.; Bobeth, M.; Ruhle, M.; Clarke, D. R. *Zeit. Metall.* **2004**, *95*, 84–90.
345. Hou, P. Y.; Van Lienden, C. *Mater. High Temp.* **2003**, *20*, 357.
346. Grabke, H. J.; Wiemer, D.; Viehhaus, H. *Appl. Surf. Sci.* **1991**, *47*, 243.
347. Hou, P. Y.; Stringer, J. *J. Phys.* **1993**, *4*(C9), 231–240.
348. Golightly, F. A.; Stott, F. H.; Wood, G. C. *Oxid. Met.* **1976**, *10*, 163.
349. Tolpygo, V. K.; Clarke, D. R. *Acta Mater.* **1998**, *46*, 5153.
350. Wood, G. C.; Stott, F. H. *Mater. Sci. Technol.* **1987**, *3*(7), 519.
351. Suo, Z. *J. Mech. Phys. Solids* **1995**, *43*, 829.
352. Yang, Z. G.; Hou, P. Y. *Mater. Sci. Eng. A* **2005**, *391*(1/2), 1–9.
353. Wright, J. K.; Williamson, R. L.; Renusch, D.; Veal, B.; Grimsditch, M.; Hou, P. Y.; Cannon, R. M. *Mater. Sci. Eng. A* **1999**, *262*, 246.
354. Balint, D. S.; Xu, T.; Hutchinson, J. W.; Evans, A. G. *Acta Metall.* **2006**, *54*, 1815–1820.
355. Davis, A. W.; Evans, A. G. *Metall. Trans.* **2006**, *A37A*, 2085–2095.
356. Schutze, M.; Saito, Y.; Onay, B.; Maruyama, T. *Proceedings of the Workshop on High Temperature Corrosion of Advanced Materials and Protective Coatings*; Saito, Y., Onay, B., Maruyama, T., Eds.; Elsevier Science, 1992; pp 39–49.
357. Whittle, D. P.; Stringer, J. *Philos. Trans. R. Soc. London A* **1980**, *295*, 309.
358. Przybylski, K.; Garrett-Reed, A. J.; Pint, B. A.; Katz, E. P.; Yurek, G. J. *J. Electrochem. Soc.* **1987**, *134*, 3207.
359. Cotell, C. M.; Yurek, G. J.; Hussey, R. J.; Mitchell, D. F.; Graham, M. J. *Oxid. Met.* **1990**, *34*, 173–200.
360. Tolpygo, V. K.; Grabke, H. J. *Scripta Metall.* **1998**, *38*, 123–129.
361. Delaunay, D.; Huntz, A. M.; Lacombe, P. *Corros. Sci.* **1984**, *24*, 13–25.
362. Funkenbusch, A. W.; Smeggil, J. G.; Bornstein, N. S. *Metall. Trans.* **1985**, *16A*, 1164–1166.
363. Smialek, J. L. *Metall. Trans.* **1991**, *22A*, 739–752.
364. Pfeil, L. B. U.K. Patent No. 459848, 1937.
365. Pfeil, L. B. U. K. Patent No. 574088, 1945.
366. Pint, B. A. In *Proceedings of John Stringer Symposium on High Temperature Corrosion*; ASM Materials Solution Conference, Indianapolis, IN, 5–8 November 2001; Tortorelli, P., Wright, I. W., Hou, P. Y., Eds.; ASM International: OH, 2003; pp 52–62.
367. Pint, B. A. In *Fundamental Aspects of High Temperature Corrosion*; Shores, D. A., Rapp, R. A., Hou, P. Y., Eds.; Electrochemical Society, 1997; Vol. 96–26, pp 74–85.
368. Stringer, J.; Hou, P. Y. In *Proceedings of the Symposium on Corrosion and Particle Erosions at High Temperatures*; TMS Annual Meeting, Las Vegas, NV, 27 February–3 March; Srinivasan, V., Vedula, K., Eds.; 1989; pp 383–401.
369. Jedlinski, J.; Godlewski, K.; Mrowec, S. *Mater. Sci. Eng. A* **1989**, *120–121*, 539–543.
370. Hou, P. Y.; Brown, I.; Stringer, J. *Nucl. Inst. Meth. B* **1991**, *59/60*, 1345–1349.
371. Pint, B. A. *J. Am. Ceram. Soc.* **2003**, *86*, 686–695.
372. Pint, B. A. *Oxid. Met.* **1998**, *49*, 531–559.
373. Pint, B. A.; More, K. L.; Wright, I. G. *Mater. High Temp.* **2003**, *20*, 375–386.
374. Hou, P. Y.; Stringer, J. *Oxid. Met.* **1988**, *29*, 45–73.
375. Davis, H. H.; Graham, H. C.; Kvernes, I. A. *Oxid. Met.* **1971**, *3*, 431.
376. Stringer, J.; Wilcox, B. A.; Jaffee, R. L. *Oxid. Met.* **1972**, *5*, 11.
377. Seltzer, M. S.; Wilcox, B. A.; Stringer, J. *Met. Trans.* **1972**, *3*, 2391; Seltzer, V. J. *Metall. Trans.* **1972**, *3*, 2357.
378. Nanni, P.; Stoddart, C. T. H.; Hondros, E. D. *Mater. Chem.* **1976**, *1*, 297.
379. Pint, B. A.; Leibowitz, J.; DeVan, J. H. *Oxid. Met.* **1999**, *51*, 183–199.
380. Pint, B. A.; Garratt-Reed, A. J.; Hobbs, L. W. *Mater. High Temp.* **1995**, *13*, 3–16.
381. Giggins, C. S.; Pettit, F. S. *Trans. TMS–TIME* **1969**, *245*, 2509.
382. Li, M. S.; Qian, Y. H.; Zhou, Y. C. *Oxid. Met.* **2004**, *61*, 529.
383. Huang, K.; Hou, P. Y.; Goodenough, J. B. *Mater. Res. Bull.* **2001**, *36*, 81–95.
384. Giggins, C. S.; Pettit, F. S. *Met. Trans.* **1971**, *2*, 1071.
385. Tolpygo, V. K.; Clarke, D. R. *Mater. High Temp.* **2003**, *20*, 261–271.



386. Nychka, J. A.; Clarke, D. R. *Oxid. Met.* **2005**, *63*, 325–352.
387. Dickey, E. C.; Pint, B. A.; Alexander, K. B.; Wright, I. G. *J. Mater. Res.* **1999**, *14*, 4531–4540.
388. Ishii, K.; Kohno, M.; Ishikawa, S.; Satoh, S. *Mater. Trans., JIM (Japan)* **1997**, *38*, 787–792.
389. Mennicke, C.; Schumann, E.; Le Coze, J.; Smialek, J. L.; Meier, G. H.; Ruhle, M. In *Microscopy of Oxidation*; Newcomb, S. B., Little, J. A., Eds.; Institute of Materials: UK, 1997; Vol. 3, pp 95–104.
390. Ramanarayanan, T. A.; Raghavan, M.; Petkovic-Luton, R. *Oxid. Met.* **1984**, *22*, 83–100.
391. Versaci, R. A.; Clemens, D.; Quadackers, W. J.; Hussey, R. *Solid State Ionics* **1993**, *59*, 235–242.
392. Schumann, E.; Yang, J. C.; Ruhle, M.; Graham, M. J. *Oxid. Met.* **1996**, *46*, 37–49.
393. Pint, B. A. *Oxid. Met.* **1996**, *45*, 1–37.
394. Duffy, D. M.; Tasker, P. W. *Philos. Mag. A* **1984**, *50*, 155–169.
395. Lartigue-Korinek, S.; Dupau, F. *Acta Metall. Mater.* **1994**, *42*, 293–302.
396. Clarke, D. R. *Acta Metall.* **2003**, *51*, 1393–1407.
397. Hou, P. Y.; Stringer, J. J. *Electrochem. Soc.* **1987**, *134*, 1836–1849.
398. Hou, P. Y.; Shui, Z. R.; Chuang, G. Y.; Stringer, J. *J. Electrochem. Soc.* **1992**, *139*, 1119–1126.
399. Wood, G. C.; Stott, F. H. In *High Temperature Corrosion*; Rapp, R. A., Ed.; NACE, 1981; p 227.
400. Prescott, R.; Graham, M. J. *Oxid. Met.* **1992**, *38*(3/4), 233–254.
401. Strawbridge, A.; Hou, P. Y. *Mater. High Temp.* **1994**, *12*, 177–182.
402. Yang, S. L.; Wang, F. H.; Niu, Y.; Wu, W. T. *Mater. Sci. Forum* **2001**, 369–372, 361–368.
403. Wu, Y. N.; Qin, M.; Feng, Z. C.; Liang, Y.; Sun, C.; Wang, F. H. *Mater. Lett.* **2003**, *57*(16–17), 2404–2408.
404. Hou, P. Y.; Paulikas, A. P.; Veal, B. W. *Mater. Sci. Forum* **2006**, 522–523, 433–440.
405. Hindam, H.; Whittle, D. P. *Trans. Jpn. Inst. Met. Suppl.* **1983**, 261.
406. Allam, I. A.; Whittle, D. P.; Stringer, J. *Oxid. Met.* **1978**, *12*, 35; **1979**, *13*, 381.
407. Ileda, Y.; Nii, K.; Yoshihara, K. *Trans. Jpn. Inst. Met. Suppl.* **1983**, *24*, 207.
408. Lees, D. G. *Oxid. Met.* **1987**, *27*, 75.
409. Hou, P. Y.; Bennett, M. J.; Ruhle, M. In International Workshop on High Temperature Oxidation; Gorisch, Germany, 15–19 August 1994, Douglass, D. L., Kofstad, P., Rahmel, A., Wood, G. C., Eds.; *Oxid. Met.* **1996**, *45*, pp 529–620.
410. Balluffi, W. In *Interfacial Segregation*; Johnson, W. C., Blakely, J. M., Eds.; ASM: Metals Park, OH, 1997; pp 193–237.
411. Seah, P.; Hondros, E. D. *Proc. R. Soc. Lond. A* **1973**, *335*, 191–212.
412. Zhang, W.; Smith, J. R.; Wang, X. G.; Evans, A. G. *Phys. Rev. B* **2003**, *67*, 245414.
413. Hou, P. Y. *J. Corr. Sci. Eng.* **2003**, *6*, Paper 75.
414. Al-Badary, H.; Tatlock, G.; Le Coze, J. In *Microscopy of Oxidation*; Newcomb, J. B., Little, J. A., Eds.; The Institute of Metals, 1997; Vol. 3, pp 105–114.
415. Fox, P.; Lees, D. G.; Lorimer, G. W. *Oxid. Met.* **1991**, *36*, 491–503.
416. Hou, P. Y.; Prüßner, K.; Fairbrother, D. H.; Roberts, J. G.; Alexander, V. *Scripta Metall.* **1999**, *40*, 241–247.
417. Prussner, K.; Schumann, E.; Ruhle, M. In *Proceedings of the Symposium Fundamental Aspects of High Temperature Corrosion*; Shores, D. A., Rapp, R. A., Hou, P. Y., Eds.; Electrochemical Society: Pennington, NJ, 1997; pp 344–351.
418. Molins, R.; Rouzou, I.; Hou, P. Y. *Mater. Sci. Eng. A* **2007**, *454–455*, 80–88.
419. Prüßner, K.; Schumann, E.; Rühle, M. In *Fundamental Aspects of High Temperature Corrosion*; Shores, D. A., Rapp, R. A., Hou, P. Y., Eds.; The Electrochemical Society, 1996; p 344.
420. Hou, P. Y.; Priimak, K. *Oxid. Met.* **2005**, *63*, 113–130.
421. Kiely, J. D.; Yeh, T.; Bonnell, D. A. *Surf. Sci.* **1997**, *393*, L126.
422. Hou, P. Y.; Smialek, J. L. *Scripta Metall.* **1995**, *33*, 1409–1416.
423. Hou, P. Y. *Oxid. Met.* **1999**, *52*, 337–351.
424. Pieraggi, B.; Rapp, R. A. *Mater. High Temp.* **1994**, *12*, 229–235.
425. Pieraggi, B.; Rapp, R. A.; Hirth, J. P. *Oxid. Met.* **1995**, *44*(1–2), 63–79.
426. Hong, Y.; Anderson, A. B.; Smialek, J. L. *Surf. Sci.* **1990**, *230*, 175–183.
427. Yong, J.; Smith, J. R.; Evans, A. G.  $\gamma$ -Ni/Al<sub>2</sub>O<sub>3</sub> Adhesion: Aluminum Activity and Impurity Effects, Presented at the Workshop on Science and Technology of Thermal Barrier Systems, University of California, Santa Barbara, CA, 9–11 January 2007.
428. Strawbridge, A.; Rapp, R. A. *J. Electrochem. Soc.* **1994**, *141*, 1905–1915.
429. Czerwinski, F.; Szpunar, J. A.; Smeltzer, W. W. *J. Electrochem. Soc.* **1996**, *143*, 3000–3007.
430. George, P. J.; Bennett, M. J.; Bishop, H. E.; Cotell, C. M.; Garratt-Reed, A. J. *Surf. Coat. Technol.* **1992**, *51*(1–3), 45–51.
431. Ikeda, Y.; Nii, K.; Yoshihara, K. *Trans. Jpn. Inst. Met. Suppl.* **1983**, *24*, 207.
432. Smeggil, J. G. *Mater. Sci. Eng.* **1987**, *87*, 261–265.
433. Smialek, J. L.; Jayne, D. T.; Schaeffer, J. C.; Murphy, W. H. *Thin Solid Films* **1994**, *235*, 285–292.
434. Seah, P.; Hondros, E. D. *Proc. R. Soc. Lond. A* **1973**, *335*, 191–212.
435. Lipkin, D. M.; Clarke, D. R.; Evans, A. G. *Acta Met.* **1998**, *46*, 4835–4850.
436. Bonnell, D. A.; Kiely, J. *Phys. Stat. Sol.* **1998**, *166*, 7–17.
437. Grabke, H. J.; Wagemann, B. *Oxid. Met.* **1995**, *43*, 97–114.
438. Hou, P. Y. *Mater. Corros.* **2000**, *51*, 329.
439. Hou, P. Y.; Moskito, J. *Oxid. Met.* **2003**, *59*(5/6), 559–574.
440. Hou, P. Y. *J. Mater. Sci. Lett.* **2000**, *19*, 577–578.
441. Hou, P. Y. *Mater. Sci. Forum* **2001**, 369–372, 23.
442. Rivoaland, L.; Maurice, V.; Josso, P.; Bacos, M. -P.; Marcus, P. *Oxid. Met.* **2003**, *60*, 137–157.
443. Hou, P. Y.; McCarty, K. F. *Scripta Metall.* **2006**, *54*, 937–941.
444. Cadoret, Y.; Bacos, M. -P.; Josso, P.; Maurice, V.; Marcus, P.; Zanna, S. *Mater. Sci. Forum* **2004**, 461–464, 274.
445. Hou, P. Y.; Stringer, J. *Oxid. Met.* **1992**, *38*, 323–345.
446. Hou, P. Y. In *High Temperature Corrosion and Materials Chemistry*; Hou, P. Y., McNallan, M. J., Oltra, R., Opila, E. J., Shores, D. A., Eds.; The Electrochemical Society, 1998; pp 198–210.
447. Hou, P. Y. In *Proceedings of the John Stringer Symposium on High Temperature Corrosion*; ASM Materials Solution Conference, Indianapolis, IN, Nov. 5–8, 2001; Tortorelli, P., Wright, I. W., Hou, P. Y., Eds.; ASM International: OH, 2003; pp 164–173.
448. Murata, Y.; Nakai, M.; Nagai, K.; Morinaga, M.; Sasaki, Y.; Hashizume, R. *Mater. Sci. Forum* **2006**, 522–523, 147–154.

- 
449. Amano, T.; Watanabe, T.; Michiyama, K. *J. Jpn. Inst. Met.* **1997**, *61*, 1077–1085.
450. Quadakkers, W. J.; Wasserfuhr, C.; Khanna, A. S.; Nickel, H. *Mater. Sci. Technol.* **1988**, *4*(12), 1119–1125.
451. Huang, T. T.; Richter, R.; Chang, Y. L.; Pfender, E. *Metall. Trans. A* **1985**, *16A*, 2051–2059.
452. Molins, R.; Andrieux, M.; Huntz, A. M. *Mater. High Temp.* **2005**, *22*, 335–342.
453. Ben Abderrazik, G.; Moulin, G.; Huntz, A. M. *Oxid. Met.* **1990**, *33*, 191–235.
454. Mayer, J.; Penkalla, H. J.; Dimyati, A.; Dani, M.; Untoro, P.; Naumenko, D.; Quadakkers, W. J. *Mater. High Temp.* **2003**, *20*, 413–419.

## 1.11 Sulfidation and Mixed Gas Corrosion of Alloys

**R. John**

Shell Global Solutions (US) Inc., Westhollow Technology Center, P.O. Box 4327, Houston, TX 77210, USA

© 2010 Elsevier B.V. All rights reserved.

<b>1.11.1</b>	<b>Sulfidation</b>	240
1.11.1.1	Types of Equipment and Processes	240
1.11.1.2	Corrosion Mechanism	240
1.11.1.3	Compilations of Sulfidation Corrosion Rate Predictions	243
1.11.1.4	Time Dependence to Predict Sulfidation	243
1.11.1.5	Laboratory Simulation	245
<b>1.11.2</b>	<b>Corrosion by Mixed Gases</b>	245
1.11.2.1	Thermochemical Calculations to Predict Oxide–Sulfide–Carbide–Nitrides on Alloys	247
1.11.2.2	Sulfidation/Oxidation by CO–CO <sub>2</sub> –COS and H <sub>2</sub> –H <sub>2</sub> O–H <sub>2</sub> S Gases	249
1.11.2.3	Thermochemistry and Corrosion Mechanism	250
1.11.2.4	Laboratory Simulation	250
1.11.2.5	Kinetics	254
1.11.2.6	Corrosion Influenced by Gas History	259
<b>1.11.3</b>	<b>Oxidation/Nitridation by N<sub>2</sub>–O<sub>2</sub> Gases</b>	260
1.11.3.1	Types of Equipment and Processes Where Nitridation Occurs	260
1.11.3.2	Thermochemistry and Corrosion Mechanism	262
1.11.3.3	Predicting Corrosion Product and Alloy Phase Formation in Nitriding/Oxidizing Conditions	262
<b>1.11.4</b>	<b>Oxidation/Carburization by CH<sub>4</sub>–H<sub>2</sub>O Gases</b>	265
1.11.4.1	Types of Equipment and Processes Where Carburization Occurs	265
1.11.4.2	Thermochemistry and Corrosion Mechanism	265
1.11.4.3	Corrosion Products Prediction	266
<b>1.11.5</b>	<b>Summary</b>	267
<b>References</b>		270

### 1.11.1 Sulfidation

#### 1.11.1.1 Types of Equipment and Processes

Corrosion of metals and alloys used in equipment processing high temperature, corrosive, gases containing sulfur, H<sub>2</sub>S, and COS is a concern in processes used in gas processing, combustion gas process heaters, petroleum refineries (hydrocracking, coking, vacuum flashing, hydrotreating, and catalytic reforming) coal/coke/oil gasification, petrochemical production, gasification of black liquor in pulp/paper production, and fossil fuel-fired power generation. Corrosion is often the phenomenon, which defines the maximum allowable temperature or maximum allowable gas species concentrations for metals and alloys in equipment.

#### 1.11.1.2 Corrosion Mechanism

The key variables, which influence the kinetics are exposure time, partial pressures  $P_{H_2}$  and  $P_{H_2S}$  (for H<sub>2</sub>

and H<sub>2</sub>S gases) or  $P_{CO}$  and  $P_{COS}$  (for CO and COS gases), alloy composition and temperature. Sulfidation corrosion forms sulfide corrosion products, damages the metal and alloy by losses in wall thickness (penetration), and occurs upon exposure of metals to gases containing sulfur, COS, or H<sub>2</sub>S. Sulfidation by H<sub>2</sub>S is predominately discussed in this chapter. Sulfidation reduces the useful thickness of the metal by the formation of surface sulfide scale and internal sulfide phases. The sum of these two thicknesses is defined as the total metal penetration. The first step in determining the potential for equipment to sulfide is to assume that sulfidation is the dominant corrosion mechanism. The key indicator of sulfidation is that most of the corrosion products are sulfides. Sulfides will be found on the exposed surface and within the alloy microstructure near to the surface, depending upon the alloy and exposure conditions. X-ray analyses by diffraction and fluorescence of a surface scale sample are common methods to determine the presences of sulfides. An alternate

method is to evaluate the thermochemical interactions between the alloy and gas, and the compounds formed. Surface metal loss (scaling) by sulfidation can be detected by methods, which measure the metal thickness, such as ultrasonic and mechanical methods. Sound metal loss by internal sulfidation can only be detected by metallography, as shown schematically in **Figure 1**.

The time dependence of sulfidation has been controversial<sup>1-5</sup> with reports of a parabolic time dependence (metal loss proportional to  $\text{time}^{0.5}$ ), linear time dependence (metal loss proportional to time), power law dependence (metal loss proportional to  $\text{time}^x$ ), and various combinations of these dependencies. If the corrosion product sulfide scale remains undisturbed on the alloy surface and sufficient time has passed (in excess of 1000 h), currently available information suggests that the time dependence is parabolic. Removal or cracking of the surface sulfide scale tends to increase the rate of sulfidation, because the presence of the scale is a partial barrier, which tends to slow the sulfidation rate as time passes. The idealized time parabolic dependence of sulfidation of G10200 carbon steel at 350 °C in 0.05 atm  $\text{H}_2\text{S}$  in  $\text{H}_2$  after several thousand hours is shown in **Figure 2**. Some studies suggest an initial linear time dependence for several thousand hours. Sulfidation data measured after several hundred hours (as is often the case for available data) are unlikely to be useful in estimating sulfidation corrosion rates for long-term service. Sulfidation data are properly used when the time dependence is considered.

Increasing the concentration of  $\text{H}_2\text{S}$  tends to increase the sulfidation rate of alloys. **Figure 3** shows

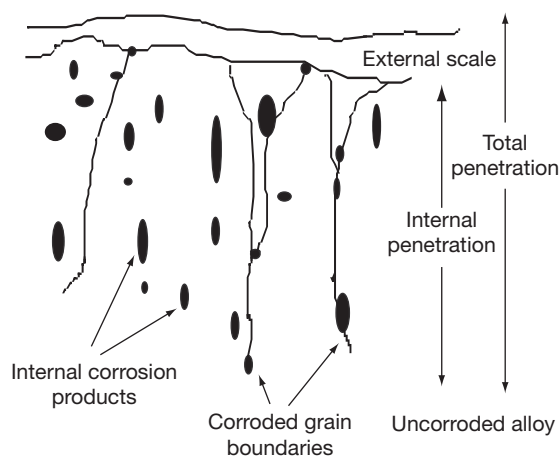


**Figure 1** Schematic view of total penetration measurement for a typical corrosion product morphology.

the effect of several alloys widely used in process equipment. Dashed lines represent extrapolations of the available data, while solid lines represent interpolations of the available data. The line for carbon steel stops for low concentrations of  $\text{H}_2\text{S}$  because  $\text{FeS}$  is not stable at low concentrations of  $\text{H}_2\text{S}$  (as shown in **Figure 4**), and the carbon steel cannot corrode at combinations of sufficiently high temperature and sufficiently low partial pressure of  $\text{H}_2\text{S}$ . It is incorrect to indicate that steels with significant concentrations of Cr cannot corrode at conditions representing low  $\text{H}_2\text{S}$  concentrations and high temperatures indicated by this line. This is because alloys with Cr form  $\text{CrS}$  at lower  $\text{H}_2\text{S}$  concentrations and higher temperatures

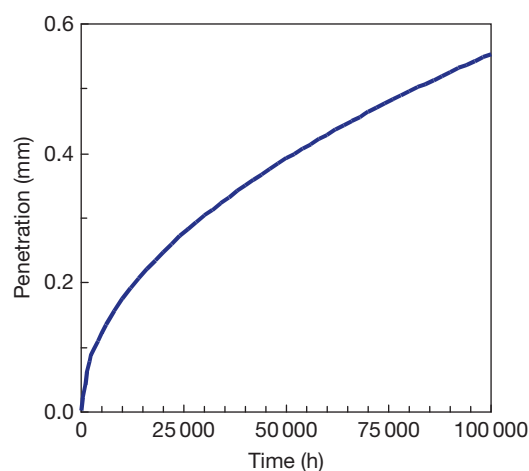


**Figure 2** Effect of time upon the sulfidation corrosion of carbon steel (G10200) after 1 year in 0.05 atm  $\text{H}_2\text{S}$  and  $\text{H}_2$  at 623 K.

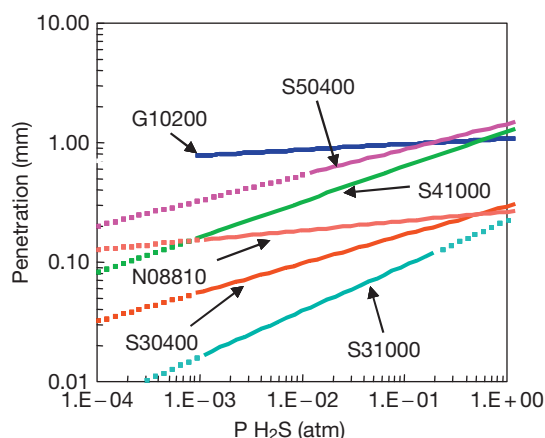


**Figure 3** Effect of  $\text{H}_2\text{S}$  partial pressure upon the sulfidation corrosion after 1 year in  $\text{H}_2$ - $\text{H}_2\text{S}$  gases at a total pressure of 1 atm at 723 K.

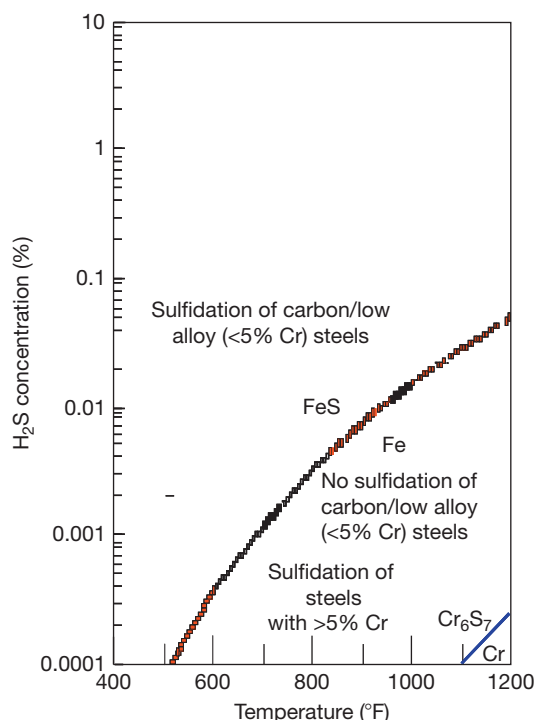


**Figure 4** Conditions for possible sulfidation, based upon  $\text{H}_2\text{S}$  concentrations in  $\text{H}_2$ – $\text{H}_2\text{S}$  gases and temperatures above the FeS/Fe line for carbon/low alloy (<5% Cr) steels and above the  $\text{Cr}_6\text{S}_7$ /Cr line for alloys with >5% Cr, 400–1200 °F (204–648 °C, 473–921 K).

than that needed to form FeS on steels. **Figure 4** shows the limits of  $\text{H}_2\text{S}$  concentration and temperature corresponding to sulfide corrosion products of Fe and Cr, as shown beneath the lines. Alloys with greater than 5% Cr can corrode in conditions where low alloy steels cannot corrode. The corrosion rates may be low (such as 0.025–0.25 mm year<sup>-1</sup>) but still significant for conditions where steels are traditionally thought to be immune to sulfidation. The ranges of  $\text{H}_2\text{S}$  concentration represented in **Figures 3 and 4** span the low  $\text{H}_2\text{S}$  range of catalytic reformers to the high  $\text{H}_2\text{S}$  concentrations expected in modern hydro-treaters in crude oil distillation equipment in petroleum refineries. These curves are in good agreement with the traditional data.<sup>1–5</sup>

Sulfidation caused by sulfur-containing compounds in liquid hydrocarbons in the absence of a gas phase (such as that found in petroleum distilling units) is not discussed in this chapter. The sulfur concentrations in liquid hydrocarbons and the sulfur evolvable as gaseous  $\text{H}_2\text{S}$  have not yet been clearly related. However, the effective  $\text{H}_2$  and  $\text{H}_2\text{S}$  concentrations are likely dominant variables in the liquid hydrocarbons. If the

effective gas concentration of  $\text{H}_2\text{S}$  could be estimated, the approach discussed should be suitable for estimating the metal losses, as related to the maximum allowable temperatures/ $\text{H}_2\text{S}$  concentrations and appropriate materials of construction.

High-Ni alloys used either as base metals or as welding filler metals are a special concern in sulfidation conditions. Sulfidation of high-Ni alloys can be especially rapid and yield corrosion rates greater than 2.5 mm year<sup>-1</sup> if the temperature exceeds 530 °C, which is the melting point of a potential corrosion product which forms as a mixture of Ni and nickel sulfide. A reasonable approach for high-Ni alloys is that they should not be used in sulfidation conditions when metal temperatures will exceed 530 °C. High-Ni alloys with high-Cr levels (such as N06625 or N08825) can be very suitable, with low corrosion rates at lower temperatures.<sup>6–8</sup> The phase behaviors of FeS and NiS are described in **Figures 5–8**.

The first step in assessing the rate of sulfidation is to evaluate the potential for the formation of sulfide corrosion products. Confirmation of formation of sulfides on existing equipment or a thermochemical evaluation of the corrosive gas to produce sulfides may be done by the analyses of corrosion products, use of well-known compilations,<sup>7–13</sup> or ASSET program.<sup>10</sup> Once sulfidation is expected, one can predict sulfidation rates by using either the traditional sulfidation curves for corrosion in  $\text{H}_2\text{S}$ – $\text{H}_2$  gases or the curves of the type shown in previous work,<sup>7–13</sup> including the effects of temperature, gas composition, and alloy composition.

Most corrosion data for alloys exposed to high temperature gases have been reported in terms of weight change/area for relatively short exposures and inadequately defined exposure conditions. The weight change/area information is not directly relatable to the thickness of corroded metal (penetration), which is often needed to assess the strength of the equipment components. Corrosion is best reported in penetration units, which indicate the sound metal loss, as discussed earlier.<sup>12,13</sup> Corrosion in high temperature gases is affected by key parameters of the corrosive environments such as temperature, alloy composition, time, and gas composition. Summaries of metal penetrations are used in this chapter, which goes beyond the traditional corrosion weight change data by reporting total metal penetration for an extensive number of alloys over a wide range of conditions. Compositions of some alloys discussed in this chapter are shown in **Table 1**.

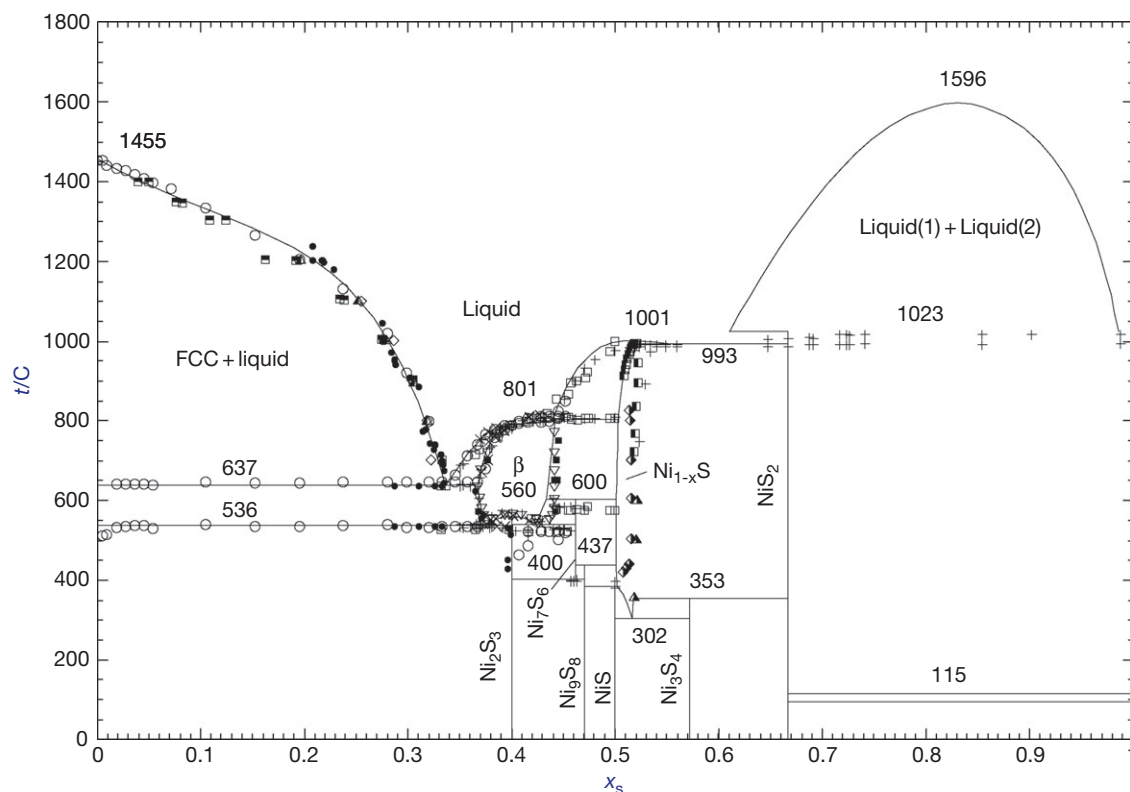


**Figure 5** Calculated condensed phase diagram with experimental data for Ni-S system.

### 1.11.1.3 Compilations of Sulfidation Corrosion Rate Predictions

Sulfidation rate data for some commercial alloys are summarized in **Figures 9–12**. **Figure 9** shows sulfidation predictions of several simple metals (copper, carbon steel, and nickel). **Figure 10** shows sulfidation predictions of a range of alloys often used in these types of conditions. **Figure 11** shows sulfidation predictions of some of the most resistant alloys available. **Figure 12** shows sulfidation predictions of several alloys similar to the 18% Cr–8% Ni steels. These steels experience different sulfidation rates, even though the Cr and Ni concentrations are similar. The different concentrations of Mo, Ti, and Nb among these alloys do significantly influence the sulfidation kinetics which is not well known; it is widely assumed that these steels corrode with kinetics similar to the common 18% Cr–8% Ni steel UNS S30400.

The effects of temperature and  $H_2S$  concentration upon sulfidation of steels often used in oil refining services are shown in **Figures 3 and 9–12**, which represent metal losses expected after 1 year of exposure. Increasing the temperature and  $H_2S$  concentration

increase the sulfidation rate. Temperature increases of  $50^\circ C$  will typically double the sulfidation rate, while increasing the  $H_2S$  concentration by a factor of 10 may be needed to double the sulfidation rate. Therefore, likely changes of  $H_2S$  concentrations in processes are generally less significant, in terms of influencing corrosion, than the likely temperature variations. Increasing the Cr content of the alloy greatly slows the sulfidation, as seen in progression from 9% Cr (S50400), 12% Cr (S41000), 18% Cr (S30400), 20% Cr (N08810), and 25% Cr (N08825 and N06625). The ranges of  $H_2S$  concentration represented in these figures span the low  $H_2S$  range of catalytic reformers to the high  $H_2S$  concentrations expected in modern hydrotreaters. These curves are in good agreement with the traditional data.<sup>8–13</sup>

### 1.11.1.4 Time Dependence to Predict Sulfidation

A large compilation of test data was evaluated with respect to the time dependence of the corrosion. The following rate equation can be used to calculate corrosion by sulfidation.<sup>8</sup> The equation incorporates the



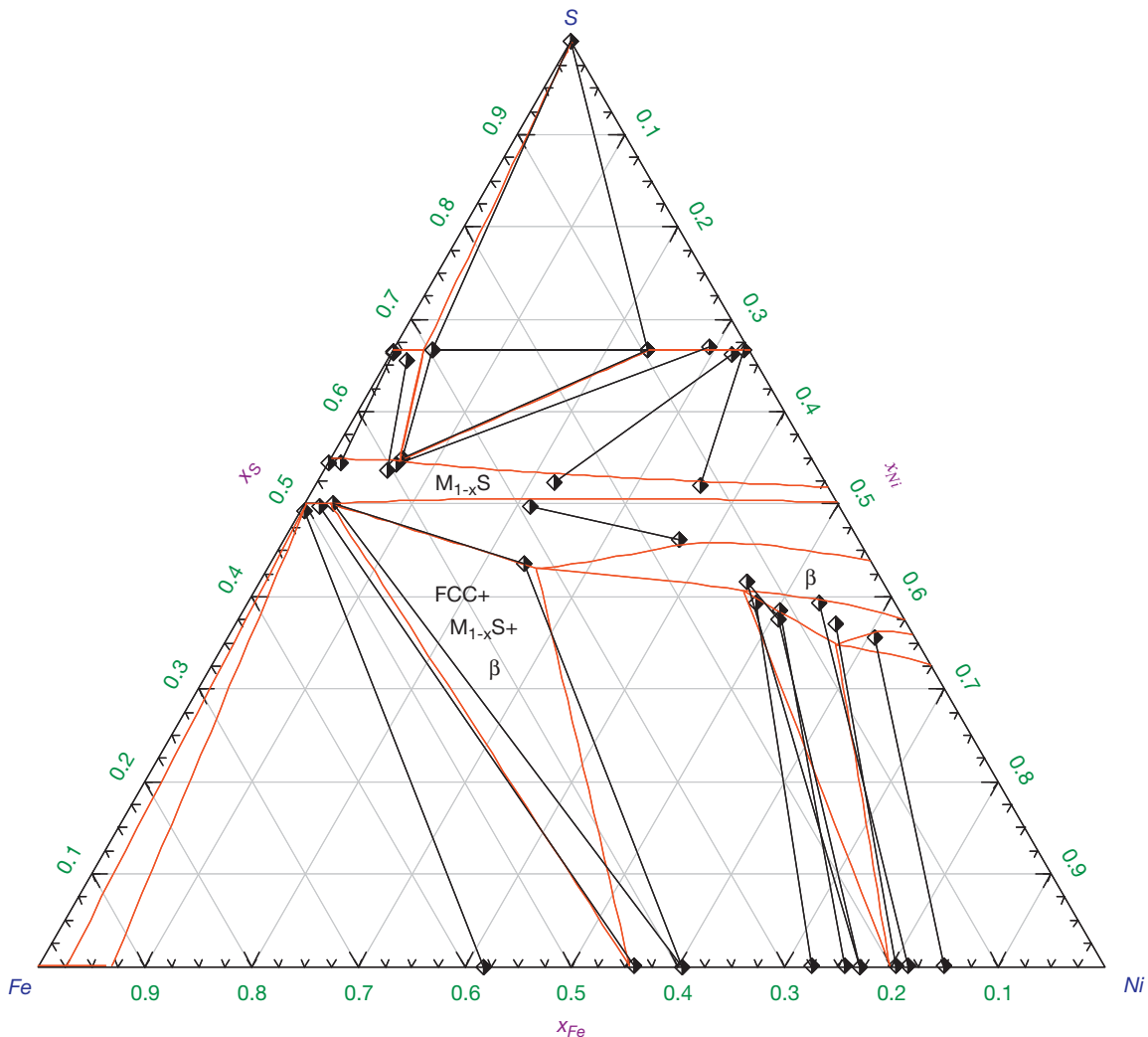


**Figure 6** Calculated isotherm of the Fe-Ni-S system at 998 K.

well-known time parabolic and linear behaviors, which have been observed. Parabolic behavior occurs initially and then tends towards linear time dependence as the surface scales crack or partially spall as they thicken and become less adherent. The transition towards linear dependence often results from development of an effective steady-state thickness of surface corrosion product, as caused by cracking, spalling, or other failure mechanisms.

$$\log((\text{Penetration}/\text{Hours}^{0.5}) + (M \times \text{Hours})) \\ = A + B \times \log(P_{\text{H}_2\text{S}}) + C \times \log(P_{\text{H}_2}) + D/T \quad [1]$$

In this equation, penetration represents sound metal loss by corrosion,  $T$  is the absolute temperature, and  $P_{\text{H}_2\text{S}}$  and  $P_{\text{H}_2}$  represent the partial pressures of the respective species.  $A$ ,  $B$ ,  $C$ ,  $D$ , and  $M$  are constants that

are calculated separately for each alloy. The form of the equation includes both linear and parabolic time dependencies. The  $M$  factor empirically describes how much time passes before the time dependence becomes linear and varies for each alloy.

Graphical illustrations of correlations for a couple of example alloys (S30400 and N08810) are shown in [Figure 13](#). These alloys are fairly typical and in that Fe-Ni-Cr alloys are widely used in many different types of process equipment, and they are also well correlated with the methodology described in this article. In fact, the data are well correlated over about three orders of magnitude of variation in the measured corrosion for wide ranges in the important environmental variables of temperature, partial pressure of  $\text{H}_2$ , and partial pressure of  $\text{H}_2\text{S}$ .

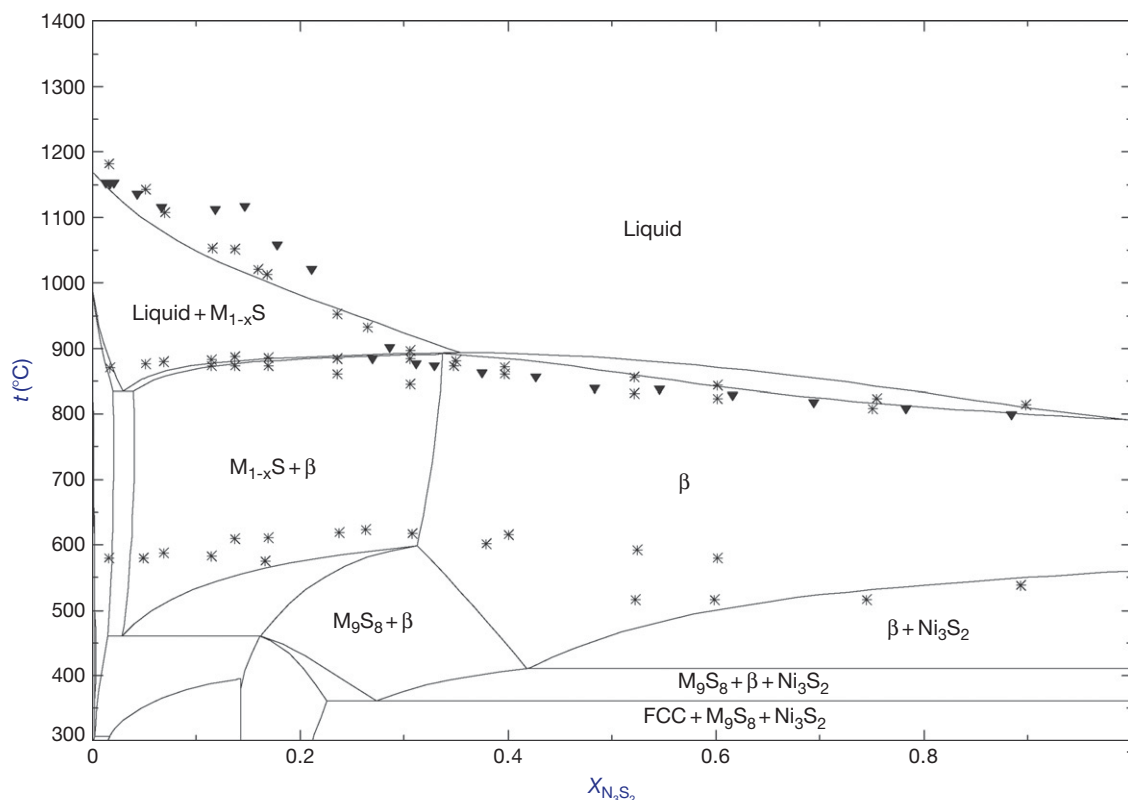


**Figure 7** Calculated section of the FeS–Ni<sub>3</sub>S<sub>2</sub> with experimental data.

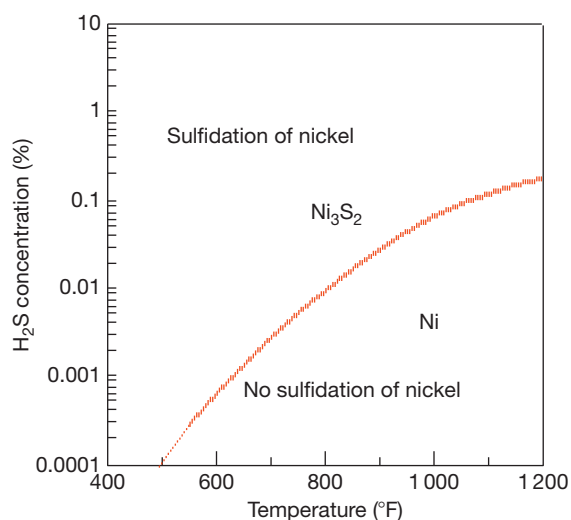


**Figure 8** Conditions for possible sulfidation of nickel based upon combinations of H<sub>2</sub>S concentrations in H<sub>2</sub>–H<sub>2</sub>S gases and temperatures above the Ni/Ni<sub>3</sub>S<sub>2</sub> line for Ni-base alloys. 400–1200 °F (204–628 °C).

#### 1.11.1.5 Laboratory Simulation

Laboratory simulation of sulfidation corrosion is generally carried out with flowing H<sub>2</sub>–H<sub>2</sub>S gases or CO–COS gases at constant temperature, starting with a polished metal surface. The combination of gas flow rate and H<sub>2</sub>S (or COS) concentration must be high enough to prevent significant consumption of H<sub>2</sub>S during the test exposures. Post-exposure examination is carried out with weight change and microscopic methods to assess the amount of metal consumed by scale formation and also the amount of the metal containing internal corrosion products.

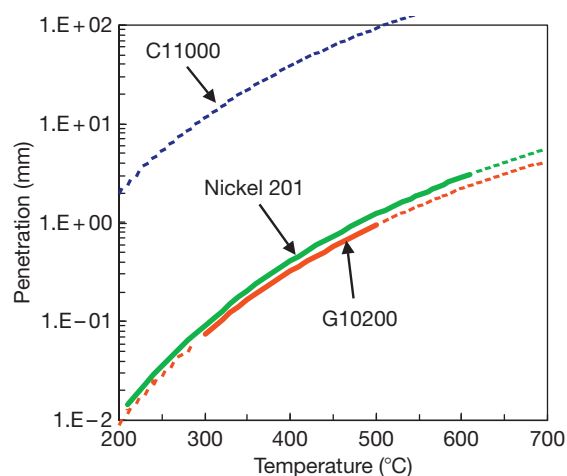
#### 1.11.2 Corrosion by Mixed Gases

The corrosion mechanism names for mixed gas corrosion indicate the stable alloy corrosion products formed and result from a competition between the different possibilities and are named after the corrosion

**Table 1** Compositions of alloys discussed

UNS	Fe	Cr	Ni	Co	Mo	Al	Si	Ti	W	Mn	Cu	RE	Nb
S30415	69.66	18.30	9.50	0.00	0.42	0.00	1.23	0.00	0.00	0.56	0.23	0.05	0.00
S30815	65.60	20.90	11.00	0.00	0.00	0.00	1.77	0.00	0.00	0.64	0.00	0.00	0.00
N06025	9.45	25.35	62.63	0.00	0.00	2.09	0.06	0.14	0.00	0.09	0.01	0.00	0.00
S41000	86.50	12.30	0.50	0.00	0.10	0.00	0.60	0.00	0.00	0.00	0.00	0.00	0.00
G10200	99.42	0.00	0.00	0.00	0.00	0.00	0.04		0.00	0.38	0.00	0.00	0.00
S30400	71.07	18.28	8.13	0.14	0.17	0.00	0.49	0.00	0.00	1.48	0.19	0.00	0.00
S31000	52.41	24.87	19.72	0.05	0.16	0.00	0.68	0.00	0.00	1.94	0.11	0.00	0.00
S31600	68.75	17.00	12.00	0.00	2.25	0.00	0.00	0.00	0.00	0.00	0.00	0.00	0.00
S34700	68.14	17.75	10.75	0.00	0.00	0.00	0.55	0.00	0.00	1.80	0.00	0.00	0.96
S44600	74.12	24.36	0.36	0.02	0.20	0.00	0.33	0.00	0.00	0.45	0.10	0.00	0.00
R30188	1.32	21.98	22.82	38.00	0.00	0.00	0.37	0.00	14.55	0.82	0.00	0.04	0.00
N07214	2.49	16.04	76.09	0.14	0.10	4.71	0.10	0.00	0.10	0.20	0.00	0.00	0.00
N06230	1.30	21.90	59.70	0.28	1.20	0.38	0.42	0.02	14.20	0.49	0.01	0.00	0.00
R30556	32.50	21.27	21.31	18.09	2.88	0.17	0.33	0.00	2.38	0.96	0.00	0.00	0.00
N06600	7.66	15.40	75.81	0.00	0.00	0.32	0.16	0.00	0.00	0.29	0.32	0.00	0.00
N06601	13.53	23.48	60.00	0.06	0.16	1.26	0.50	0.27	0.00	0.31	0.38	0.00	0.00
N06617	0.76	22.63	53.20	12.33	9.38	1.15	0.15	0.27	0.00	0.02	0.05	0.00	0.00
N06625	2.66	21.74	62.79	0.00	8.46	0.10	0.41	0.19	0.00	0.10	0.00	0.00	3.52
N08810	44.22	21.22	31.71	0.00	0.00	0.33	0.60	0.41	0.00	0.92	0.51	0.00	0.00
C11000	0.00	0.00	0.00	0.00	0.00	0.00	0.00		0.00	0.00	100.00	0.00	0.00
N08120	34.53	25.12	37.44	0.11	0.37	0.11	0.57	0.02	0.10	0.73	0.18	0.00	0.66
N12160	8.00	28.00	34.30	27.00	0.00	0.00	2.70	0.00	0.00	0.00	0.00	0.00	0.00
S67956	75.22	19.40	0.28	0.05	0.00	4.50	0.11	0.33	0.00	0.09	0.00	0.00	0.00
N02270	0.00	0.00	99.99	0.00	0.00	0.00	0.00	0.00	0.00	0.00	0.00	0.00	0.00

RE means rare earth elements.

**Figure 9** Effect of temperature upon sulfidation of some simple metals after 1 year in 0.5 atm  $H_2$  and 0.05 atm  $H_2S$ .

products, which dominate. Examples are: sulfidation/oxidation means that sulfides and oxides form, oxidation/carburization means that carbides and oxides form, oxidation/nitridation means that nitrides and oxides form, and so on. Corrosion leads to the

formation of corrosion products, which leads to metal loss (penetration), and occurs upon exposure of metals to gases, which contain the reactive species needed to form the corrosion products. An X-ray analysis by diffraction of a surface scale sample is a common method to determine the identity of corrosion products. An alternate method is to evaluate the gas composition. Surface metal loss (scaling) can be detected by methods, which measure the metal thickness, such as ultrasonic and mechanical methods. Sound metal loss by internal corrosion can only be detected by metallography, as schematically shown in [Figure 1](#).

The time dependence of high temperature corrosion is controversial<sup>3-5</sup> and depends on the combination of alloy, temperature, time, and corrosion mechanism. Reported time dependencies include: parabolic (metal loss proportional to  $time^{0.5}$ ), linear (metal loss proportional to time), power law (metal loss proportional to  $time^x$ ), and various combinations of these dependencies. If the corrosion product scale remains undisturbed on the alloy surface and sufficient time has passed (in excess of 1000 h), a reasonable approximation is that the time dependence is parabolic. Removal or cracking

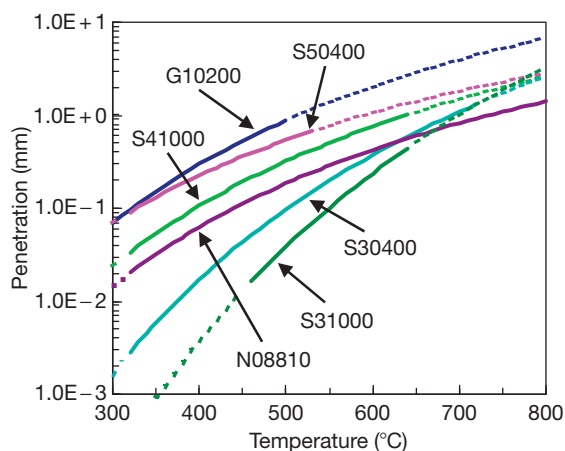


**Figure 10** Effect of temperature upon sulfidation corrosion of some alloys commonly used in sulfidizing conditions after 1 year at 0.5 atm  $H_2$  and 0.05 atm  $H_2S$ .

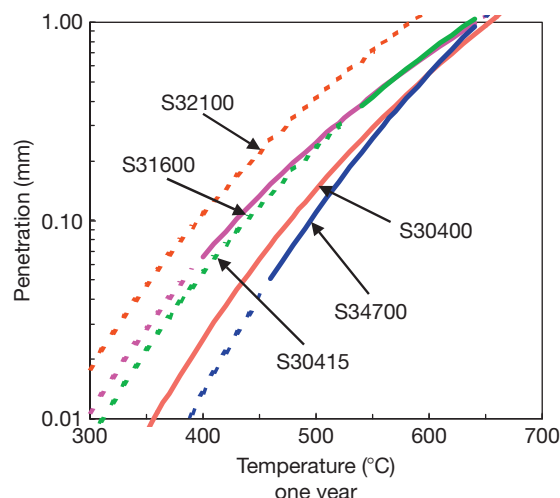


**Figure 12** Effect of temperature upon sulfidation corrosion of '18-8' steels exposed to 0.5 atm  $H_2$  and 0.05 atm  $H_2S$  after 1 year.

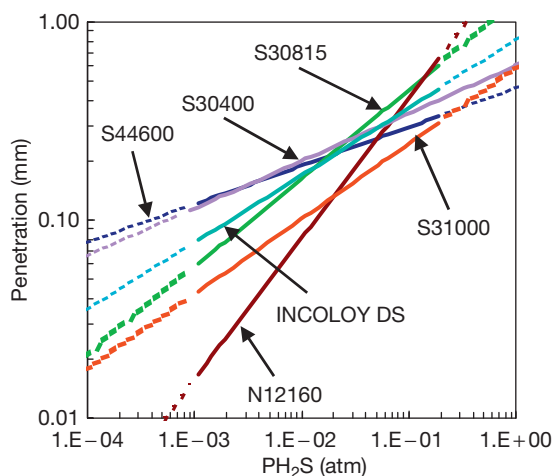


**Figure 11** Effect of  $H_2S$  partial pressure upon sulfidation corrosion of some very resistant alloys at 550°C after 1 year.

of the surface scale will tend to increase the rate of corrosion, because the presence of the scale is a partial barrier, which tends to slow corrosion as time passes, but corrosion still continues. Some studies suggest initial linear time dependence for several thousand hours. Corrosion data measured after hundreds of hours (as is often the case for available data) are unlikely to be useful in estimating sulfidation corrosion rates for long-term service. Corrosion data are properly used when the time dependence is considered. The corrosion mechanisms considered and some of the important variables are listed below:

- Sulfidation/oxidation by  $CO-CO_2-COS$  and  $H_2-H_2O-H_2S$  gases – key variables, which influence the kinetics, are exposure time,  $P_{O_2}$ ,  $P_{S_2}$ , alloy composition, and temperature;
- Oxidation/nitridation by  $O_2-N_2$  gases – key variables, which influence the kinetics, are exposure time, partial pressures of  $O_2$  and  $N_2$ , alloy composition, and temperature;
- Oxidation/carburization by  $CH_4-H_2O$  gases – key variables, which influence the kinetics, are exposure time,  $P_{O_2}$ , activity of carbon ( $a_C$ ), alloy composition, and temperature.

### 1.11.2.1 Thermochemical Calculations to Predict Oxide-Sulfide-Carbide-Nitrides on Alloys

Since many alloys may be used in a wide range of gases, which can induce corrosion producing mixtures of corrosion products, it is wise to examine the types and combinations of potential corrosion products. One approach is to use thermochemical calculations to predict the stable corrosion products defined by equilibrium reactions between the alloy, gas, and alloy temperature. The surface of equipment exposed to large amounts of flowing gas can be approximated by a small amount of alloy exposed to a large amount of gas. For example, a ratio of 1 mol alloy to 1000 mol of gas will not deplete the gas of important corrosives in the calculation. This

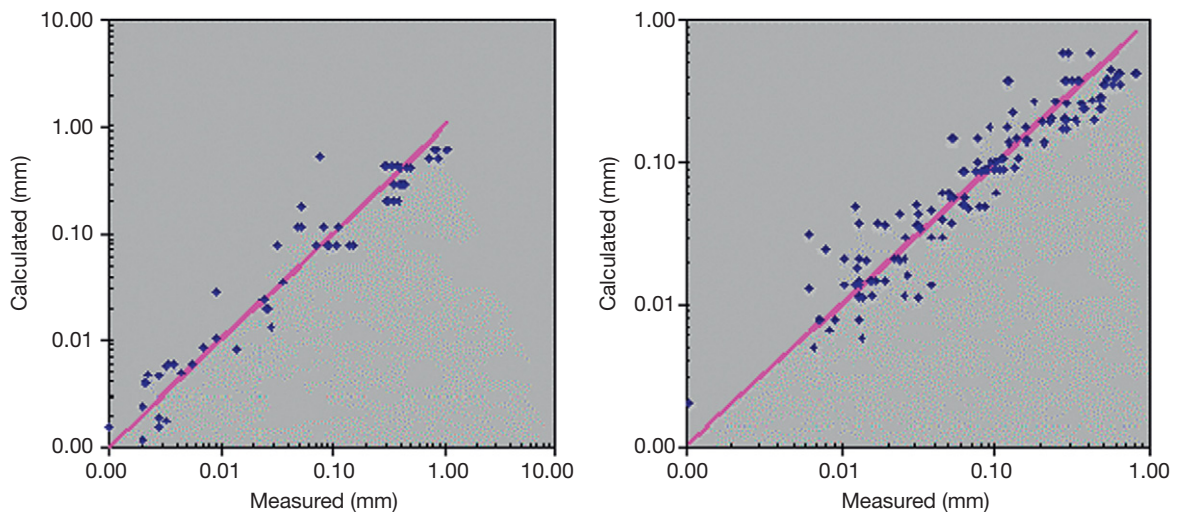


**Figure 13** Example of correlations of sulfidation data for S30400 (left) and N08810 (right) using the formalism described in this chapter. Corrosion by mixed gases.

approach ignores differing reaction and diffusion rates of the species in the alloys and corrosion products. The calculation also assumes that the major elements in the alloys will determine the type of dominant corrosion products, which is typically true and will ignore any subtleties of corrosion product morphologies and kinetics.

To this end, a capability to perform thermochemical models for complex corrosion product phases was developed to enable the required calculations. The elements considered in the thermochemical calculations are:

W–La–Mo–Nb–Cu–Ni–Co–Fe–Mn–Cr–  
Ti–Ar–Cl–S–Si–Al–F–O–N–C–H

With all of the known corrosion product phases having been analyzed in terms of the thermochemical solution behaviors of the known species in each phase, the assumption of pure and single component condensed phases, which is a common assumption, is no longer required. In order to structure the calculations, the thermochemical literature was extensively reviewed. Thermochemical data such as free energies of formation, heat capacities, heats of mixing, heats of fusion, heats of evaporation, and second-order phase transition were also considered and compiled. Models were then constructed to describe the solution thermodynamics of the complex sulfide, alloys, carbides, oxides, and intermetallic phases, as described.<sup>22–24</sup> The elements considered to occur in the solution phases, are:

- Al–Co–Cr–Fe–Mn–Ni–Si–Ti in oxides,
- Fe–Ni–Co–Cr in sulfides,
- W–Mo–Nb–Cu–Ni–Co–Fe–Mn–Cr–Ti–Si–Al in carbides and nitrides,
- W–La–Mo–Nb–Cu–Ni–Co–Fe–Mn–Cr–Ti–Si–Al–N–C in the alloy liquid and solid-solution phases.

The effort included development of mathematical models, based on the known solutions and described the thermodynamic properties as functions of temperature and composition. The models were optimized using all the available thermodynamic and phase diagram data from the literature in order to obtain a set of model parameters for the two-component, three-component, and higher-order subsystems. The resulting models were then used to estimate the thermodynamic properties of the *N*-component solutions from the database of parameters for lower-order subsystems. Examples of the species groupings are listed below:

- Spinel – ( $\text{Fe}^{2+}$ ,  $\text{Fe}^{3+}$ ,  $\text{Co}^{2+}$ ,  $\text{Co}^{3+}$ ,  $\text{Cr}^{2+}$ ,  $\text{Cr}^{3+}$ ,  $\text{Ni}^{2+}$ , Mg, Al) [ $\text{Fe}^{2+}$ ,  $\text{Fe}^{3+}$ ,  $\text{Co}^{2+}$ ,  $\text{Co}^{3+}$ ,  $\text{Cr}^{3+}$ ,  $\text{Ni}^{2+}$ , Mg, Al]<sub>2</sub>O<sub>4</sub>;
- Corundum –  $\text{Fe}_2\text{O}_3$ – $\text{Cr}_2\text{O}_3$ – $\text{Al}_2\text{O}_3$ ;
- Monoxide –  $\text{FeO}$ – $\text{CoO}$ – $\text{NiO}$ – $\text{CaO}$ – $\text{MgO}$ – $\text{ZnO}$ – $\text{CuO}$ .

For oxide phases in the Fe–Co–Ni–Cr–O system, thermodynamic data are available mainly for the following subsystems:

- Fe–O, Co–O, Ni–O, Cr–O
- Fe–Cr–O, Fe–Ni–O, Fe–Co–O

The models were evaluated by comparison to the available thermodynamic and phase equilibrium data. Comparison between the model results and known phase diagrams indicated that the model predictions could reproduce the measured data within the experimental error limits from 25 °C to above the liquidus temperatures at all compositions and oxygen partial pressures from metal saturation to equilibrium with oxygen. Examples of the high-quality fits of the thermochemical models to the measured data are shown in **Figures 5–7**. The model for the sulfide liquid phase contains Fe–Ni–Co–Cr–S and uses the quasichemical model pair approximation<sup>22–24</sup> to take into account strong short-range ordering. For solid nonstoichiometric sulfide solutions in the Fe–Ni–Co–Cr–S system, appropriate thermodynamic models were developed. Parameters of these models were optimized to reproduce all solid–solid and solid–liquid phase equilibria.

The main data that were considered in the models were:

- Solid sulfide/liquid sulfide equilibrium, partial pressure data of S in the liquid sulfide over the whole composition range from pure metals to sulfur-rich liquid
- Sulfur activity over the liquid sulfide and over solid (Fe, Ni)S solutions
- Sulfide/metal/oxide/gas equilibria
- Heats of mixing, heat content, heat capacities, etc.
- Metal activity data
- Metal–liquid sulfide equilibrium data
- Liquid–oxide equilibrium data.

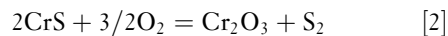
This technology is embodied in the ASSET (Alloy Selection System for Elevated Temperatures) technology and is widely available.<sup>10,25,32,33</sup>

### 1.11.2.2 Sulfidation/Oxidation by CO–CO<sub>2</sub>–COS and H<sub>2</sub>–H<sub>2</sub>O–H<sub>2</sub>S Gases

Sulfidation corrosion in the presence of oxidizing gases is called sulfidation/oxidation, which occurs when both sulfide and oxide corrosion products form. The key variables, which influence the kinetics, are exposure time, partial pressures of O<sub>2</sub> and S<sub>2</sub>, in gases like CO–CO<sub>2</sub>–COS or H<sub>2</sub>–H<sub>2</sub>O–H<sub>2</sub>S or CO–CO<sub>2</sub>–COS–H<sub>2</sub>–H<sub>2</sub>O–H<sub>2</sub>S, alloy composition, and temperature. The corrosion leads to metal losses by both surface scaling and internal corrosion product formation (penetration).

Significant research has been carried out over the last 20 years by investigators such as Perkins,<sup>14,15</sup> Natesan,<sup>16–18</sup> Bakker,<sup>19</sup> and John<sup>20,21</sup> to define how the gas composition influences the kinetics of alloy corrosion in sulfidizing/oxidizing conditions. It is well accepted that the thermochemical interactions of the alloys and the exposure conditions influence the stabilities (and formation) of the corrosion products and the rates of corrosion. The referenced studies and others show that the corrosion products, which form may not necessarily be those expected, are based upon simplified thermochemical expectations using Fe–S–O, Cr–S–O, and Ni–S–O systems for the computations and assuming pure component corrosion products. In fact, gas mixtures corroding real alloys expected to form pure Cr<sub>2</sub>O<sub>3</sub>-type corrosion products actually require gas P<sub>O<sub>2</sub></sub> values of 2 or 3 orders of magnitude greater than the calculated value thought to form Cr<sub>2</sub>O<sub>3</sub>. This has been interpreted to be a ‘kinetic boundary,’ meaning that an excess P<sub>O<sub>2</sub></sub> value is needed to precipitate and grow the Cr<sub>2</sub>O<sub>3</sub>. This is different in concept from a thermochemical criterion for the relative stabilities of corrosion products, as defined by combinations of P<sub>O<sub>2</sub></sub> and P<sub>S<sub>2</sub></sub>, at a given temperature. It was suggested that the high growth rates of sulfides cause high P<sub>O<sub>2</sub></sub>s required to form the Cr<sub>2</sub>O<sub>3</sub>-rich corrosion products. However, thermochemical calculations possible with the models now available can calculate the real corrosion product compositions. These thermochemical solution calculations now suggest that the ‘kinetic boundaries’ are really equilibrium phase boundaries, when the real phase compositions and thermochemistry are considered.

On the basis of the logic presented above, the strategy adopted by John<sup>20,21</sup> has been used to correlate sulfidation/oxidation corrosion with the relative stabilities of the Cr<sub>2</sub>O<sub>3</sub> and CrS phases as expressed in terms of P<sub>O<sub>2</sub></sub> and P<sub>S<sub>2</sub></sub>, as shown below:



$$\frac{P_{\text{O}_2}^{3/2} K_2}{P_{\text{S}_2}} = \frac{A_{\text{Cr}_2\text{O}_3}}{A_{\text{CrS}^2}} \quad [3]$$

where K<sub>2</sub> is the equilibrium constant for reaction [2]. A measure of the relative stability of Cr<sub>2</sub>O<sub>3</sub> and CrS (or the activity factor AF), is defined below:

$$\text{AF} = \log(A_{\text{CrS}^2}/A_{\text{Cr}_2\text{O}_3}) \quad [4]$$

where A indicates the activity of the subscripted species. High AF values correspond to high activities of CrS (A<sub>CrS</sub>) values and rapid corrosion, while low AF values reflect low A<sub>CrS</sub> values and slow corrosion.



It has been experimentally well demonstrated that sulfidation/oxidation kinetics correlate with AF and that sulfidation/oxidation kinetics are parabolic with time, a parabolic rate constant is written in terms of the gas composition, as related by eqns [3] and [4] and then used to correlate corrosion by sulfidation/oxidation with exposure conditions:

$$\log(K_p) = A + B(\log(P_{S_2}) - 1.5\log(P_{O_2})) + C/T \quad [5]$$

where  $K_p$  is a parabolic rate constant for the reactions leading to total penetration,  $A$ ,  $B$ , and  $C$  are experimentally determined constants, and  $T$  is temperature. This relationship has been demonstrated to correlate alloy corrosion by sulfidation/oxidation for many different alloys over wide ranges of temperatures and gas compositions.<sup>8–10,20,21</sup> An example of this type of correlation between measured corrosion and exposure conditions is shown in Figure 14 for a common heat-resistant alloy N06600. Once these types of correlations for an alloy are established, alloy corrosion in sulfidation/oxidation conditions can be made for many alloy/condition combinations. The utility of these correlations is obvious. Accurate predictions of sulfidation/oxidation for wide ranges of conditions in terms of gas composition, temperature, and time can be made and expressed in very practical engineering units related to change in wall thickness.

### 1.11.2.3 Thermochemistry and Corrosion Mechanism

The utility to predict the formation of alloy corrosion products is illustrated in Figures 15–17. The results compare very well with practical experience and summarize the stable corrosion products for ranges of gas compositions and temperatures. Nickel-base alloys like N06600 and N06625 form liquid sulfide at temperatures slightly above 1100°F (866 K), while an Fe–Cr–Ni stainless steel like S30400 and a heat-resistant Ni–Cr–Co alloy like N12160 form liquid sulfide corrosion products only at much higher temperatures. Nickel-base alloys form liquid nickel sulfide corrosion products, if any portion of the corrosion product layer is in conditions, which stabilize the liquid. Through the thickness of the corrosion product, one might think of a gradient of  $H_2S$ , as the corroding alloy at the alloy/corrosion product interface consumes sulfur species. Increasing the amount of Cr will increase the amount of oxide in the corrosion product for a nickel-base alloy (as found in N06025) but will not prevent the formation of the liquid sulfide. An iron-

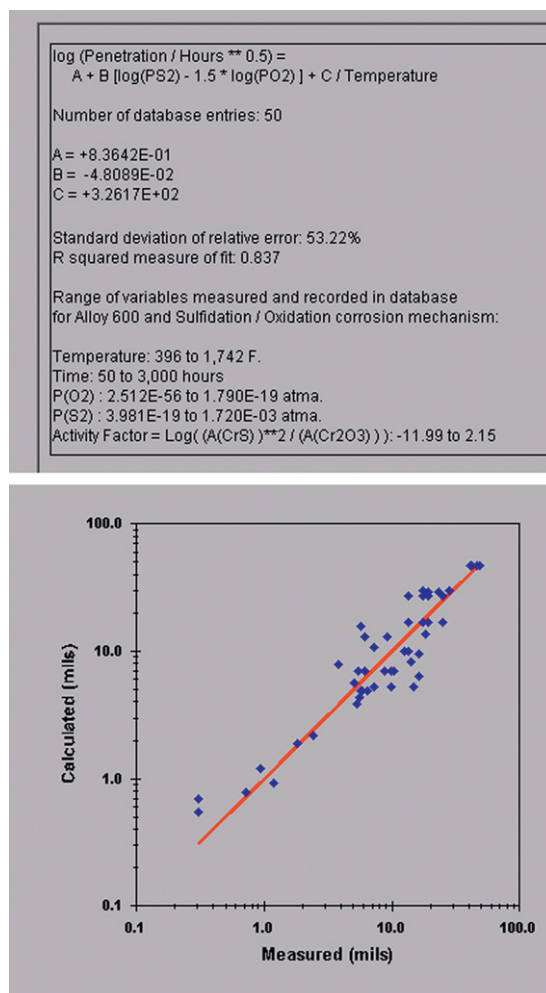


**Figure 14** Illustration of sulfidation/oxidation correlation for alloy N06600 in various combination of exposure conditions, in terms of temperature, time,  $P_{O_2}$  and  $P_{S_2}$ .

based stainless steel, like S30400, does not form liquid sulfide, but does form large amounts of solid sulfides. A Ni–Cr–Co alloy like N12160 with high concentrations of Cr, Si, and Co shows large concentrations of oxides and no liquid sulfide formation, until higher  $H_2S$  concentrations are present, which should be excellent for resistance to corrosion in these conditions, as is the case for the Ni–Cr–Co alloy.

### 1.11.2.4 Laboratory Simulation

It is important to remember that the usual goal of laboratory corrosion tests is to produce information, which will help decisions related to industrial equipment. Industrial equipment often requires lifetimes of years at high pressures, high temperatures

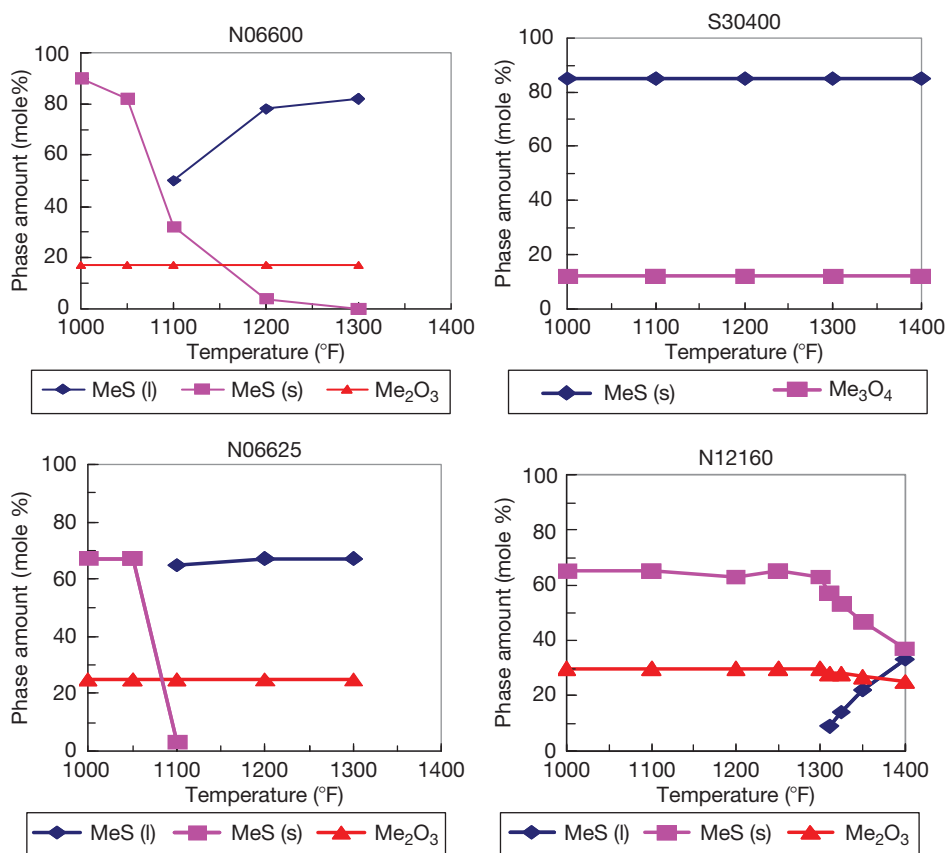


**Figure 15** Calculated corrosion products for a small amount of alloy exposed to a large amount of 5% H<sub>2</sub>–65% H<sub>2</sub>–30% H<sub>2</sub>O at 1 atm, 1000–1400 °F (811–1033 K).

and requires considerable expense and time to fabricate. Laboratory tests aim to quickly and cheaply define the likely corrosion phenomena and kinetics prior to building the industrial equipment. For the case of sulfidizing/oxidizing conditions, some important issues will now be discussed, including the effects of temperature, exposure time, and gas composition.

Laboratory corrosion tests often intend to accelerate corrosion relative to exposures in industrial equipment and to speed assessment of many alloys and their corrosion with coupons. This is cheaper, faster, and more reliable than gathering corrosion data by inspecting full-scale equipment in operating processes. Examples of process equipment where sulfidation/oxidation may occur are processes in petroleum refining such as hydrocrackers, hydrotreaters, coal/coke/oil gasifiers, crude-oil distilling columns, vacuum flashers, sulfur-removal plants, coking units, and flexicokers. Corrosion will be discussed in terms of the total metal penetration, which is defined as the sum of the metal lost by surface scale formation plus the thickness of the subsurface metal layer that is

affected by the corrosion exposure. Such a subsurface layer may have internal precipitates of corrosion products, pores, voids, or cracks, which have been produced by reaction with the corrosive environment. This is illustrated in the schematic view of a cross section of a corroded alloy shown previously in Figure 1. Some of the alloys studied are shown in Table 1.

Many process gases contain H<sub>2</sub>–H<sub>2</sub>O–H<sub>2</sub>S gas mixtures, which will determine the partial pressures of O<sub>2</sub> and S<sub>2</sub> ( $P_{O_2}$  and  $P_{S_2}$ ) and which are in turn well known to determine the sulfidation/oxidation corrosion behaviors for Cr-containing alloys. As the following reactions show, chemical thermodynamics can be used to calculate the  $P_{O_2}$  and  $P_{S_2}$  values for C-based gases (CO–CO<sub>2</sub>–COS):



$$K_{eqn[6]} = \frac{P_{CO_2}}{P_{O_2}^{1/2} P_{CO}} \quad [7]$$

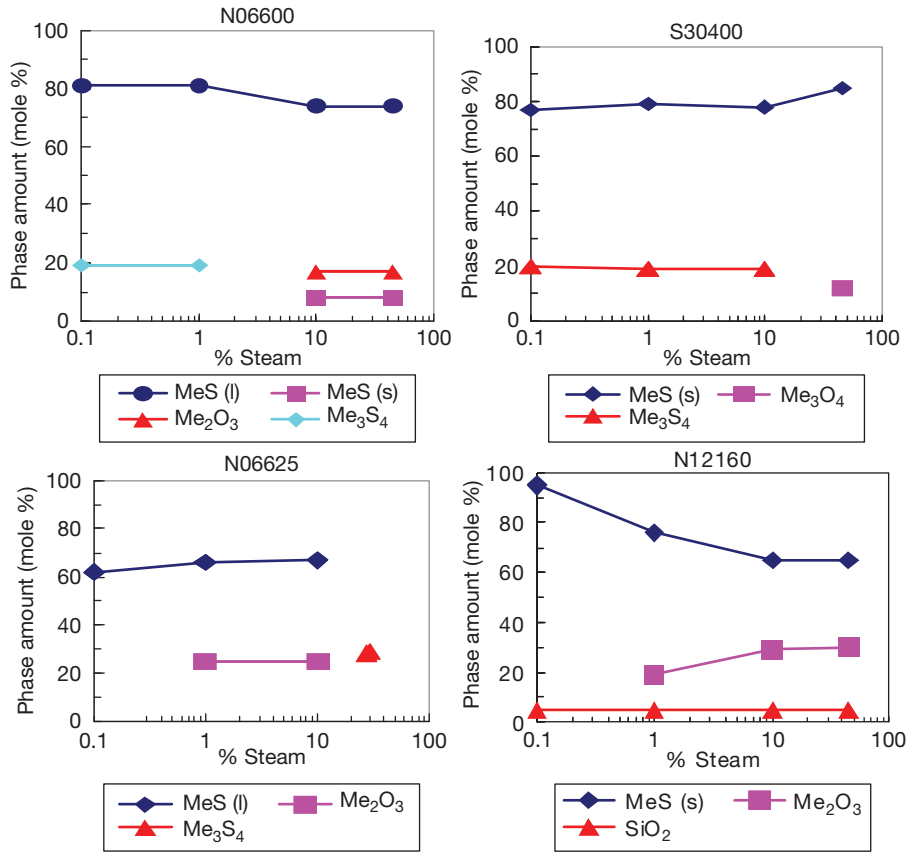


**Figure 16** Calculated corrosion products for a small amount of alloy exposed to a large amount of gas of 5% H<sub>2</sub>S, 50% H<sub>2</sub>, and X% H<sub>2</sub>O at 1 atm at 921 K.

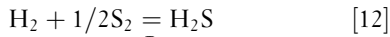
$$P_{O_2} = \frac{P_{CO_2}^2}{K_{eqn[6]}^2 P_{CO}^2} \quad [8]$$



$$K_{eqn[9]} = \frac{P_{COS}}{P_{S_2}^{1/2} P_{CO}} \quad [10]$$

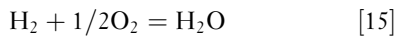
$$P_{S_2} = \frac{P_{COS}^2}{K_{eqn[9]}^2 P_{CO}^2} \quad [11]$$

While the  $P_{O_2}$  and  $P_{S_2}$  values can be calculated for H-based gases (H<sub>2</sub>-H<sub>2</sub>O-H<sub>2</sub>S):



$$K_{eqn[12]} = \frac{P_{H_2S}}{P_{S_2}^{1/2} P_{H_2}} \quad [13]$$

$$P_{S_2} = \frac{P_{H_2S}^2}{K_{eqn[13]}^2 P_{H_2}^2} \quad [14]$$



$$K_{eqn[15]} = \frac{P_{H_2O}}{P_{O_2}^{1/2} P_{H_2}} \quad [16]$$

$$P_{O_2} = \frac{P_{H_2O}^2}{K_{eqn[15]}^2 P_{H_2}^2} \quad [17]$$

where  $K_{eqn}$  values are the equilibrium constants for the reaction number indicated.

The H-based gases are found in many industrial processes. However, use of these gases as test gases in small-scale laboratory testing involves some practical difficulties, including producing, handling, and controlling small amounts of H<sub>2</sub>O vapor (steam). Using H<sub>2</sub>O in the test gases requires attention to several concerns: continuous production of small quantities of steam and heat tracing of the test apparatus to prevent steam condensation during the tests. Condensation of the steam would change the gas composition and the corrosion conditions in the tests. H<sub>2</sub>-H<sub>2</sub>O-H<sub>2</sub>S gases are widely used in corrosion testing. However, there is an alternative.

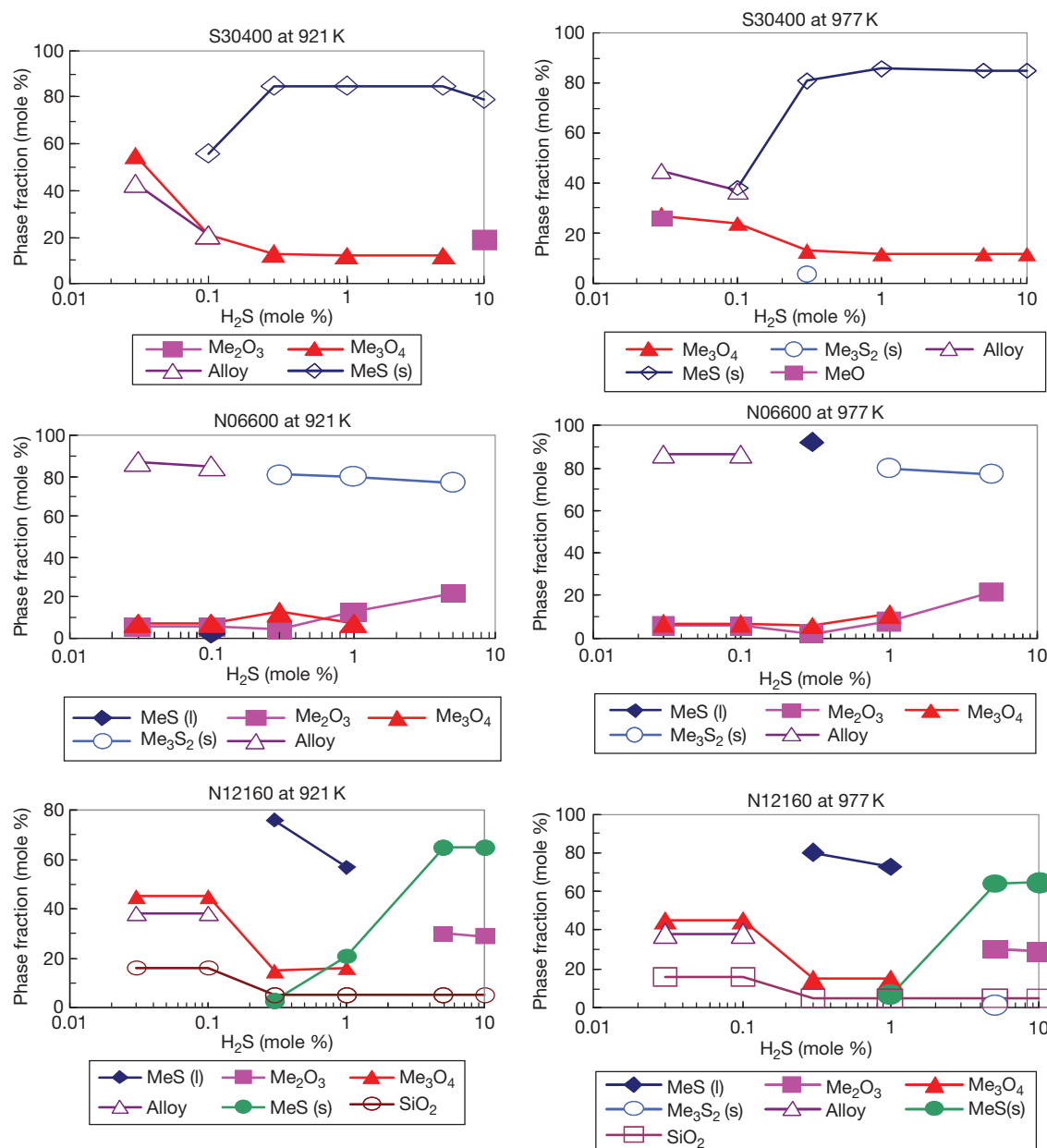


**Figure 17** Effect of  $H_2S$  concentrations upon formation of liquid corrosion products for several alloys exposed to  $X\%$   $H_2S$ , 60%  $H_2$ , 30%  $H_2O$ , and balance Ar at 1 atm.

We can also use  $CO-CO_2-COS$  gases to simulate the  $P_{O_2}$  and  $P_{S_2}$  values of the  $H_2-H_2O-H_2S$  gases. Use of  $CO-CO_2-COS$  gases, rather than  $H_2-H_2O-H_2S$  gases avoids the difficulties of managing steam in small amounts and losses due to condensation. The ambition is to make laboratory tests easier and more reliable, particularly during long-term corrosion tests.

C-based gases can simulate the  $P_{O_2}$  and  $P_{S_2}$  values and corrosion behaviors of H-based gases. An example of a comparison of some values of  $P_{O_2}$  and  $P_{S_2}$  for a C-based gas of 32%  $CO-1\%$   $COS$ -balance  $CO_2$  at 1 atm, which was chosen to simulate the H-based gas of 10%  $H_2-10\%$   $H_2S-25\%$   $H_2O$ -balance Ar at 1 atm is shown in Table 2. The  $P_{O_2}$  and  $P_{S_2}$  values closely match

between the C- and the H-based gases. **Figure 18** illustrates the excellent agreement for  $P_{O_2}$  and  $P_{S_2}$  values between these C- and H-based gases over the temperatures of 1200–1800 °F (648–982 °C) for the example compositions shown. C-based and H-based gases can interchangeably simulate equivalent thermochemistries of the corrosive conditions, as defined in terms of  $P_{O_2}$  and  $P_{S_2}$ . **Figure 19** shows that the AF values for C-based and H-based gases can also be closely matched. It is not important that the values of AF,  $P_{O_2}$ , and  $P_{S_2}$  in the laboratory test conditions exactly match the

conditions of industrial interest, because correlations between these variables can be defined and used to interpolate/extrapolate/predict corrosion for ranges of conditions of interest, once a correlation is established.

### 1.11.2.5 Kinetics

It is not sufficient to only confirm that AF,  $P_{O_2}$ , and  $P_{S_2}$  thermochemical values of gases can be correlated between H-based and C-based gases in order to assure that corrosion is adequately related between the gas

**Table 2** Summary of calculations comparing  $P_{S_2}$ ,  $P_{O_2}$ , and AF values in C-based and H-based gases, where AF(activity factor) =  $\log((a_{CrS})^2)/(a_{Cr_2O_3})$ , corrosion correlates with,  $\log(\text{Penetration/Hours}^{0.5}) = A + B[\log(P_{S_2}) - 1.5\log(P_{O_2})] + C/\text{absolute temperature}$

		Temperature (°F)			
		1200	1400	1600	1800
H <sub>2</sub> -H <sub>2</sub> S-H <sub>2</sub> O gases	$P_{S_2}$ atm	8.3 E-06	1.0 E-04	7.5 E-04	3.3 E-03
	$P_{O_2}$ , atm	3.0 E-22	3.2 E-19	8.5 E-17	7.8 E-15
	AF	-7.54	-6.51	-5.69	-5.04
	MeS	79	79	79	79
	Me <sub>2</sub> O <sub>3</sub>	18	18	18	18
CO-COS-CO <sub>2</sub> gases	$P_{S_2}$ atm	9.7 E-05	9.7 E-05	5.9 E-04	1.7 E-03
	$P_{O_2}$ , atm	4.9 E-23	1.4 E-19	8.0 E-17	1.5 E-14
	AF	-6.37	-5.99	-5.76	-5.76
	MeS	79	79	79	85
	Me <sub>2</sub> O <sub>3</sub>	18	18	18	0
	Me <sub>3</sub> O <sub>4</sub>	0	0	0	11

The table is calculated for 10% H<sub>2</sub>-10% H<sub>2</sub>S-25% H<sub>2</sub>O-balance Ar and 32% CO-1% COS-balance CO<sub>2</sub> at 1 atm and corrosion product quantities are calculated for UNS S34700.

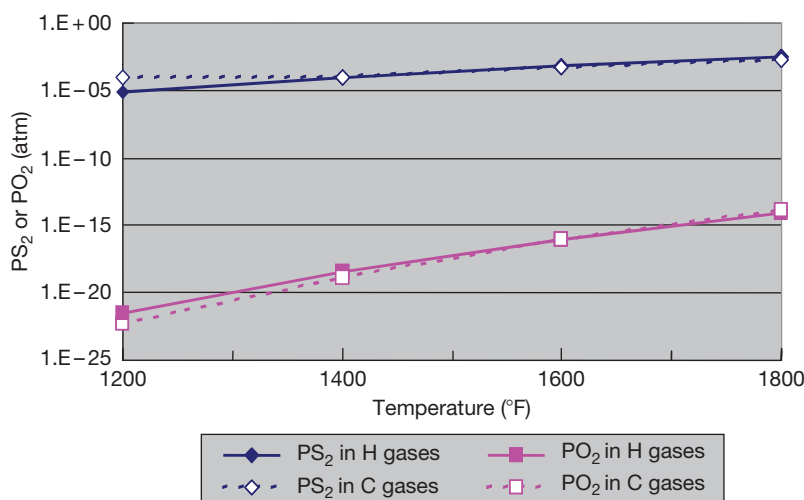


**Figure 18** Summary of calculations comparing  $P_{S_2}$  and  $P_{O_2}$  values in C- and H-based gases where C-based gas means CO-CO<sub>2</sub>-COS and H-based gas means H<sub>2</sub>-H<sub>2</sub>O-H<sub>2</sub>S.

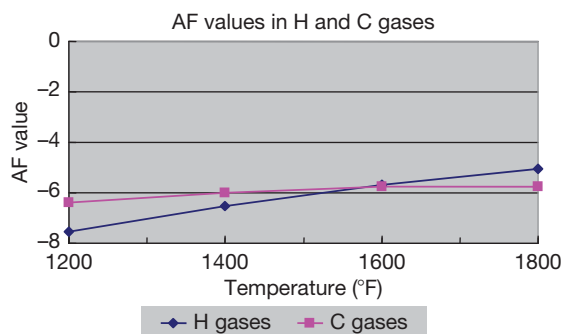


**Figure 19** Summary of calculations comparing AF in C- and H-based gases where C-based gas means CO–CO<sub>2</sub>–COS and H-based gas means H<sub>2</sub>–H<sub>2</sub>O–H<sub>2</sub>S.

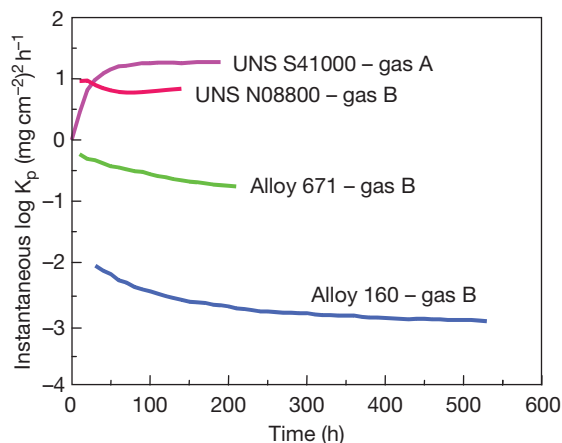


**Figure 20** Effect of time upon the instantaneous parabolic rate constants for sulfidation/oxidation of several alloys at 600 °C. Gas A is 2% CO–2% COS–balance CO<sub>2</sub> and Gas B is 48% CO–48% CO<sub>2</sub> and 4% COS.

types. The relation between measured corrosion kinetics for the gas types and their compositions must also be examined. Many studies either suggest or assume that the time dependence of the extent of hot gas corrosion is parabolic. Figure 20 shows that the measured values of the instantaneous parabolic rate constants for a number of alloys exposed to sulfidizing/oxidizing conditions can vary greatly from the initial exposure time. It may take up to 500 h before the parabolic rate constant becomes constant (meaning it is independent of time). Exposure times greater than 500 h may be needed to measure real parabolic rate constants useful to predict very long-time corrosion behavior. Indeed, after the initial time of changing kinetics, the long-term corrosion behavior can be

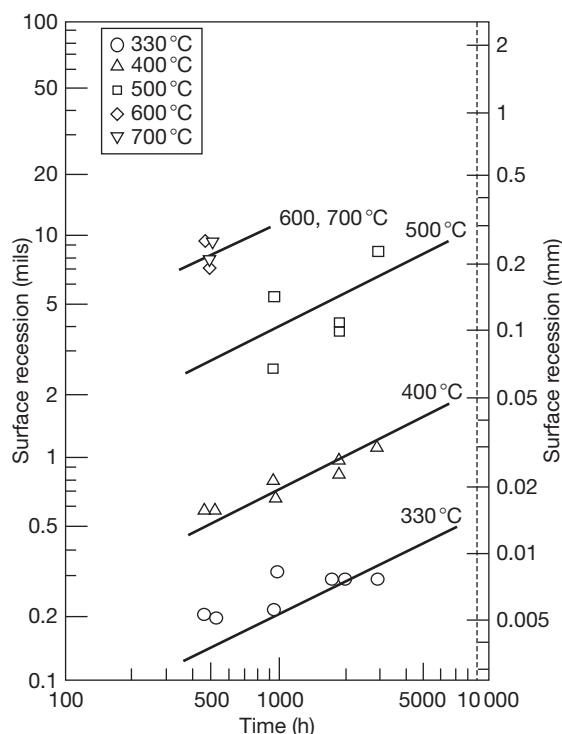


**Figure 21** Sulfidation/oxidation corrosion of alloy UNS N06625 in a gas of initial composition of 0.1% H<sub>2</sub>S–79.1% H<sub>2</sub>–20.8% CO at 1 atm.

shown to be parabolic for many thousands of hours for many Fe–Ni–Cr heat resistance alloys, with an example shown in Figure 21.

Once the time dependence is understood, the next question becomes whether real corrosion behavior in equilibrium and nonequilibrium H-based and C-based gases can be correlated in the same way. This question arises because many industrial processes handle gases, which are not equilibrated and alloy corrosion occurs by contact with nonequilibrium gases. Nonequilibrium gases occur when the combinations of gas flow rates, temperatures, and gas phase reaction rates do not allow sufficient time to equilibrate the gases.

Corrosion in equilibrated and nonequilibrated gas compositions has been compared. Previous corrosion tests<sup>25,26</sup> showed that if the  $P_{O_2}$  and the  $P_{S_2}$  values are matched between CO–CO<sub>2</sub>–COS gases and H<sub>2</sub>–H<sub>2</sub>O–H<sub>2</sub>S gases, then the corrosion behaviors of Fe–Ni–Cr alloys are equivalent in terms of the corrosion products formed, corrosion product morphologies, and the measured corrosion kinetics. This is illustrated in Figure 22, where the gas compositions of various C-based and H-based gases at equilibrium and not at equilibrium were used to



expose N08800. All the different types of gases induce similar corrosion behavior, once the AF (or  $P_{O_2}$  and  $P_{S_2}$  values) are considered. These gases cover variations of about 10 orders of magnitude in both  $P_{O_2}$  and  $P_{S_2}$ . The open symbols are C-based gases, while the closed symbols are H-based gases. The solid points are equilibrium gases and open points are nonequilibrium gases. Figure 22 shows that there is no distinction between the C-based and H-based gases, in terms of correlating  $P_{O_2}$  and the  $P_{S_2}$  with corrosion behavior for alloy UNS N08800. This is true for a variation of nearly six orders of magnitude change in the gravimetric parabolic rate constants for

alloy N08800, showing that C-based and H-based gases can be used interchangeably to simulate corrosion conditions, as long as the  $P_{O_2}$  and  $P_{S_2}$  values are assessed. This approach has been used for a large number of heat-resistant alloys based on various combinations of Fe–Ni–Cr–Co–Al.

After demonstrating that AF (or  $P_{O_2}$  and  $P_{S_2}$  values) can define the corrosion condition for the alloy; an alternative approach is to prepare the phase stability diagram shown in Figure 23. The diagram includes iso-AF lines, which suggest lines of equal corrosion kinetics, as defined by AF (or  $P_{O_2}$  and  $P_{S_2}$ ) values. The next step is to then add isocorrosion contours, which

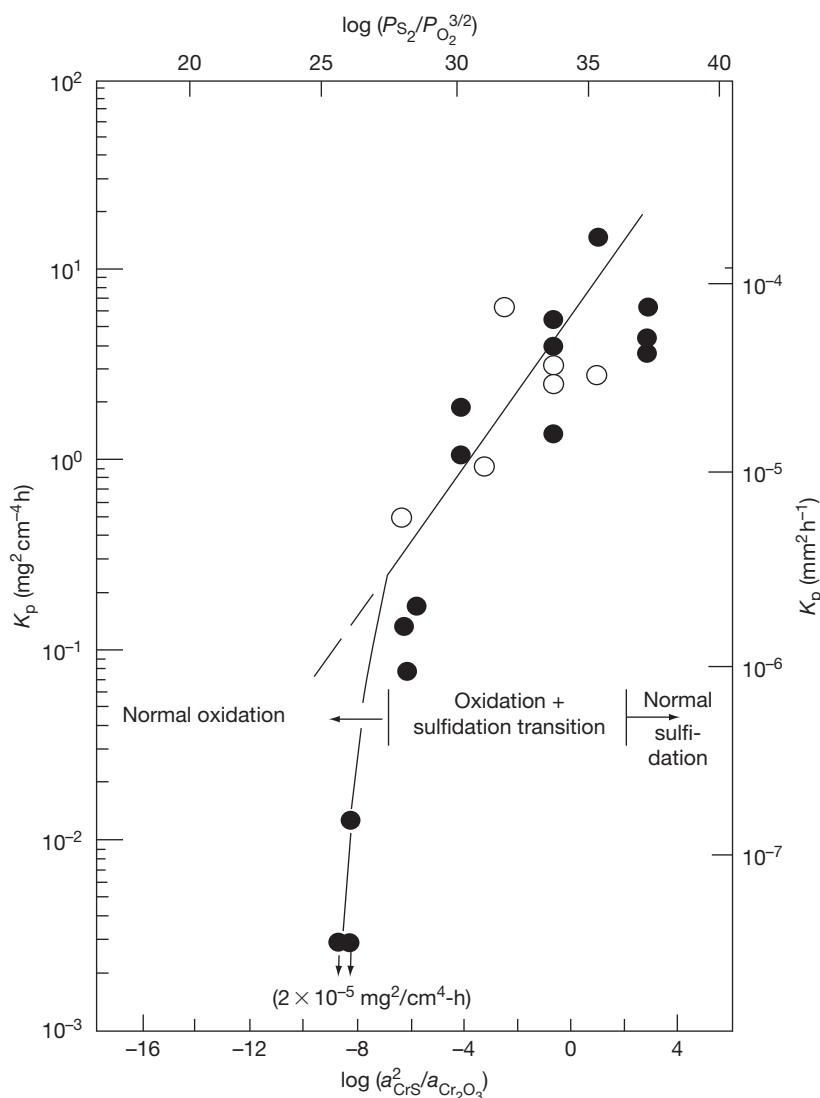


**Figure 22** Effect of gas composition expressed in terms of AF (comparing C-based and H-based gases) upon the instantaneous parabolic rate constant ( $K_p$ ) for UNS N08800 exposed to sulfidizing/oxidizing conditions at 600 °C.

are parallel to the phase boundary between the CrS and Cr<sub>2</sub>O<sub>3</sub> phase fields for the diagram for Cr–S–O–C at 600 °C, as shown in **Figure 24**. This accomplishment is quite remarkable in using thermochemical information on corrosion product stability diagrams to compile and correlate corrosion kinetics of real engineering alloys in complex gases. Indeed, a collection of these types of diagrams could be constructed for numerous combinations of alloys and exposure conditions of gas compositions and temperatures. However, the utility represented in ASSET,<sup>10,25,32,33,52,53</sup> avoids the cumbersome preparation of many diagrams and allows accurate predictions as needed.

One concern with CO–CO<sub>2</sub>–COS gases in laboratory tests is that compositions and temperatures must be maintained to keep carbon activities ( $a_C$ ) < 1, in order to avoid carbon deposition, which could present practical problems in terms of unexpected changes in the gas composition and potential plugging of gas flow lines. A potential reaction between CO and CO<sub>2</sub>, which can lead to carbon deposition, is shown below.



$$a_C = \frac{P_{\text{CO}}^2}{K_{\text{eqn}[18]} P_{\text{CO}_2}} \quad [19]$$

where  $a_C$  is the activity of solid C described in reaction [18] and calculated in eqn [19]. In order for the CO–CO<sub>2</sub>–COS gases to adequately simulate the corrosivity of the H<sub>2</sub>–H<sub>2</sub>O–H<sub>2</sub>S gases, conditions must also not allow solid carbon to form. This can be confirmed experimentally by analyses of the corrosion products and can also be assessed by calculating the stabilities of the potential phases, while considering oxides, carbides, sulfides, and alloy phases. Formation of carbides in conditions which induce sulfidation/oxidation is rare, since oxides and sulfides are usually much more stable than carbides. Safety and toxicity concerns with COS are similar to those with H<sub>2</sub>S, and the methods to remove COS and H<sub>2</sub>S from exiting test gases by passage through aqueous NaOH solutions before exhausting them into the atmosphere. Performing these types of corrosion tests requires careful control of the test atmosphere. For example, the air must be adequately removed from the test chamber before the high temperature test gas contacts the alloy coupons. The test chamber must be purged with gases

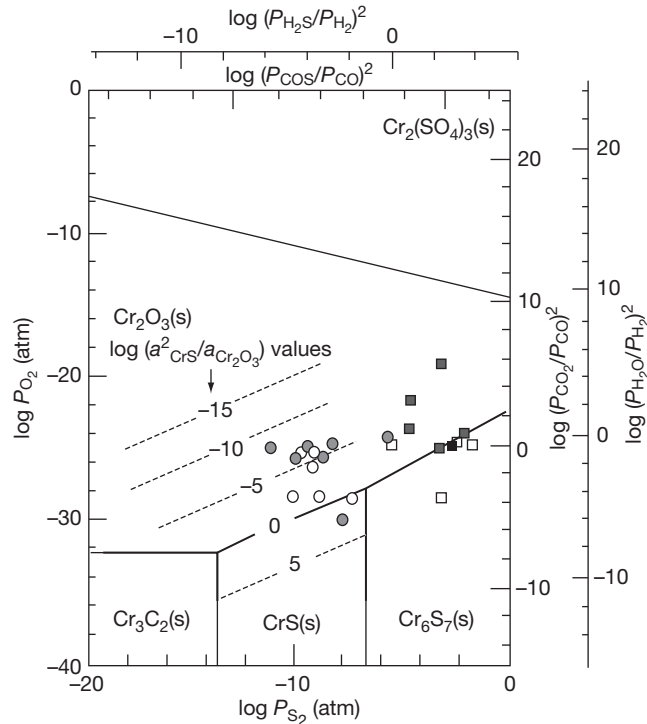


**Figure 23** Calculated thermochemical phase stability diagram for C–S–O system at 600 °C. Round points represent H-based gases and square points represent C-based gases. Solid points represent equilibrium gases and open points are nonequilibrium gases.

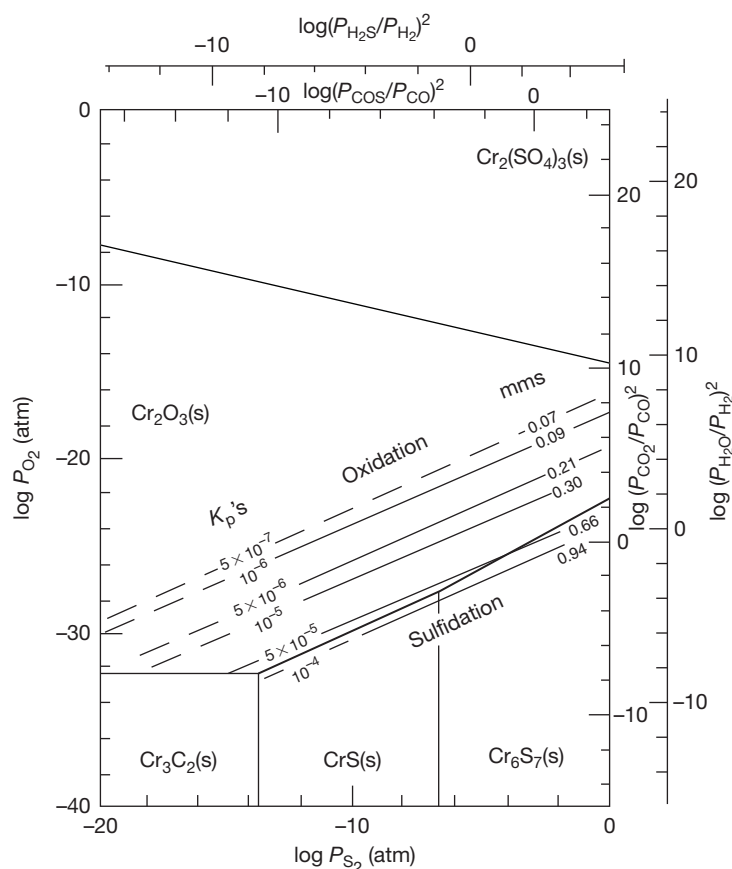


**Figure 24** Isocorrosion contours for alloy N08800 on the calculated Cr–S–O thermochemical phase stability diagram at 600 °C. Values for  $K_p$ 's in square millimeter per hour and metal loss (in mm) after 1 year of exposure are shown.

like  $N_2$  or inert gases until the  $O_2$  decreases to values below 0.001 atm. Then,  $H_2$  can be introduced to the test chamber at temperatures above 1000 °F to scavenge the remaining low levels of  $O_2$  by reaction to form  $H_2O$  before the corrosion test exposure starts.

Another concern that might be raised is whether C-based gases can adequately simulate H-based gases in terms of any potential effects of water vapor upon the corrosion behavior. The reported observations to date suggest that the effects of water vapor upon oxidation are associated with oxidizing conditions where volatile, oxidized, hydrated species form. The conditions that produce sulfidation/oxidation have  $P_{O_2}$  values of perhaps  $10^{-25}$  to  $10^{-10}$  atm, and the majority of corrosion products are sulfides. The  $P_{O_2}$  values are well below those associated with conditions showing oxidation to be affected by water vapor.

Let us examine the utility of these concepts. The presence of oxidizing gases such as  $H_2O$  or  $CO_2$  slows the sulfidation rate because they increase the stability of slow-growing oxide corrosion products. The

corrosion can be much slower than expected if only  $H_2S$ – $H_2$  were present. This can be important because gases, sometimes thought to contain only  $H_2S$ – $H_2$ , also contain some  $H_2O$  vapor, because of exposure of the gas to liquid water. A gas exposed to water at room temperature (from processes such as a water wash) may contain up to 2–3% water in the gas, if saturated with water at room temperature. Sulfidation rates predicted using only the  $H_2S$ – $H_2$  concentrations would overestimate the corrosion, if  $H_2O$  were really present. This slower corrosion rate by sulfidation/oxidation can be predicted using the approaches described in this article. This is illustrated in **Figures 25 and 26** for several alloys at 600 °C in sulfidizing/oxidizing gases. The extent of corrosion occurring at the right-hand  $P_{O_2}$  in **Figure 26** and the low AF values in **Figure 26** corresponds to simple oxidation, while progression to the left-hand side of the axis corresponds to lower  $P_{O_2}$ s and the high values of AFs are expected in  $O_2$ -depleted conditions. When the  $P_{O_2}$  becomes low enough and oxides are no longer stable, sulfidation

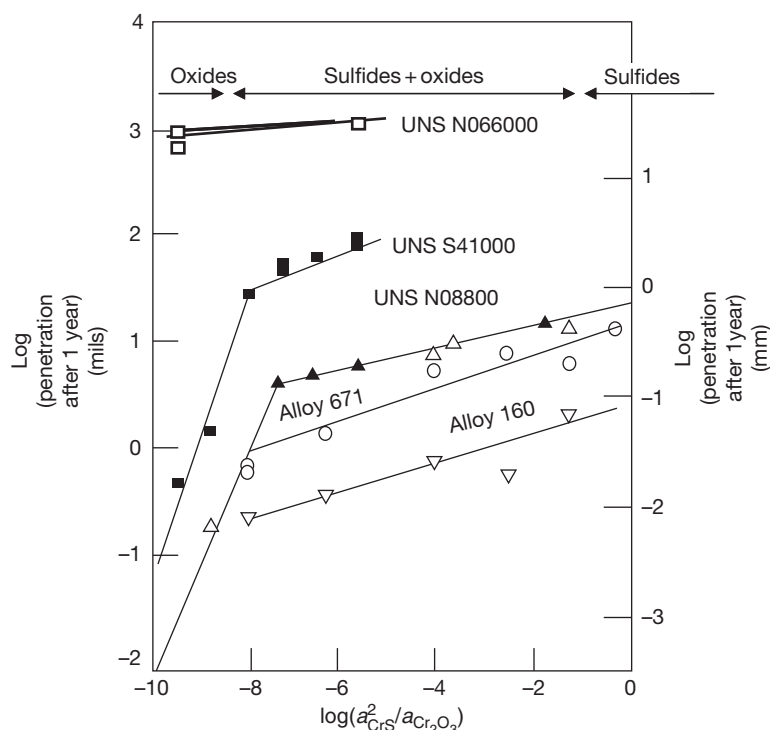


**Figure 25** Influence of gas composition measured in terms of AF upon corrosion of high-chromium alloys corroding by sulfidation/oxidation.

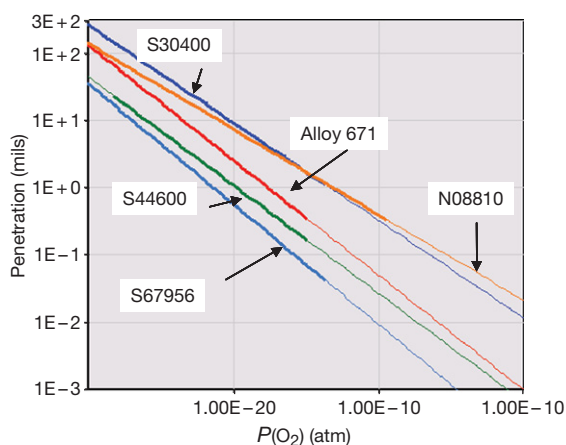


**Figure 26** Effect of  $O_2$  partial pressure upon sulfidation/oxidation of alloys after 1 year of time and exposure to  $S_2$  partial pressure of  $10^{-7}$  atm at  $700^\circ C$ .

becomes the dominant corrosion mechanism. The minimum corrosion in this scenario is oxidation in  $O_2$ -containing gases and the maximum corrosion is sulfidation in  $H_2S$ - $H_2$  gases. Several alloys are shown in Figure 26, with both thick and thin portions of the lines. The thick portions represent predictions based upon interpolations for conditions for which there

are compiled corrosion data for that alloy. The thin portions of the lines represent corrosion predictions based upon extrapolations for conditions outside the data represented by the data compilation. Figures 25 and 26 clearly show that data compilations for a number of commercially important alloys can represent many orders of magnitude of variation in the exposure conditions, as summarized in terms of the  $P_{O_2}$ ,  $P_{S_2}$ , temperature and exposure time. Figure 27 shows how variations in steam concentrations can affect the sulfidation/oxidation of S30400, which is typical for many alloys. Figure 28 shows an example of a correlation for sulfidation/oxidation for alloys S30400.

#### 1.11.2.6 Corrosion Influenced by Gas History

Another way to examine the approach to equilibrium for an alloy corroding by sulfidation/oxidation is to examine how promptly changes in gas composition influence subsequent alloy corrosion behavior, since the gas thermochemistry should determine the alloy corrosion behavior. Data reported some time ago<sup>21</sup> for sulfidation/oxidation of UNS N08800 exposed to gases, which induced sulfidation/oxidation, showed

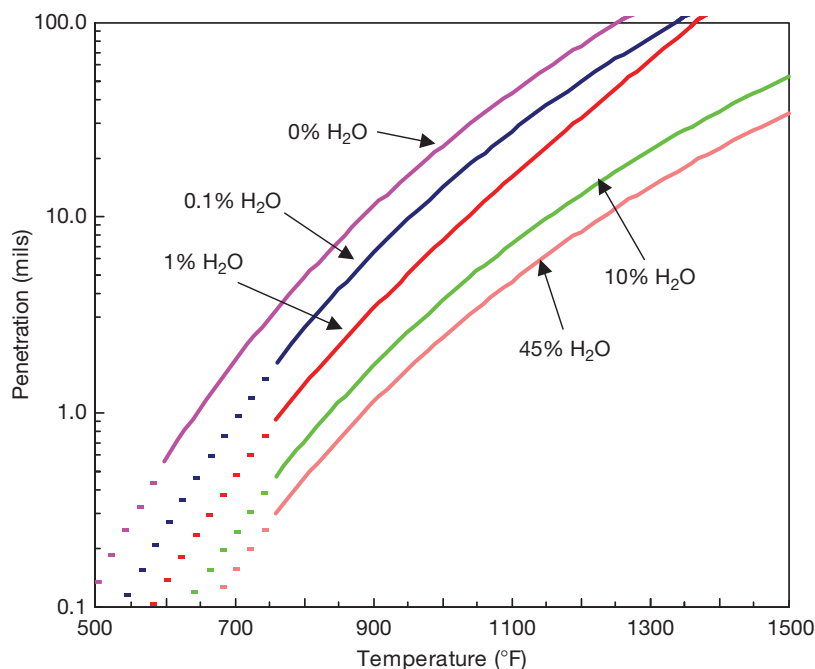


**Figure 27** Effect of temperature and steam concentration upon metal penetration by sulfidation/oxidation of S30400 after 1 year in 5%  $\text{H}_2\text{S}$ , 50%  $\text{H}_2\text{O}$ , X%  $\text{H}_2\text{O}$  and balance Ar.

that corrosion kinetics changed promptly as the gas composition and temperature were changed to correspond to that measured when the alloy had always been exposed to that environment. The previous exposure history of the corroding alloy had no effect upon the corrosion behavior after a few hundred hours. This was demonstrated by comparing the parabolic rate constants for the time periods corresponding to the same gaseous exposure, independently of the prior exposure. The alloy corrosion kinetics change within only a hundred hours to match those expected for the new gaseous exposure. There have been several examples of summing the expected amounts of corrosion expected because of different portions of complex exposure as if they were produced by individual exposures.

### 1.11.3 Oxidation/Nitridation by $\text{N}_2$ – $\text{O}_2$ Gases

#### 1.11.3.1 Types of Equipment and Processes Where Nitridation Occurs

Stainless steels and other heat-resistant alloys are used because of their excellent corrosion resistances and mechanical properties in different kinds of service, such as vessels and pipelines in oil and gas equipment and other components. Their high temperature corrosion behaviors depend upon the composition of the

gases and temperatures. Surface scales and internal (subsurface) oxidation are both possible and seen in many different applications. Corrosion by both nitridation and oxidation are possible when alloys are exposed to atmospheres rich in nitrogen at temperatures higher than 1000 °F (537 °C), nitrides such as  $\text{CrN}$  and  $\text{Fe}_4\text{N}$  may form and affect the alloy mechanical properties. Nitridation is similar to carburization in that both are high temperature corrosion mechanisms for metals and alloys which do not produce surface scales and do not cause losses in wall thickness, as experienced by other high temperature corrosion mechanisms, such as oxidation and sulfidation. The main consequence of nitridation (like carburization) is embrittlement of the alloys making them vulnerable to fracture. There is also a slight increase in volume (decrease in density) as the nitrogen dissolves into the alloy (or carbon in the case of carburization). The interstitial solution of the nitrogen into the austenite phase distorts the lattice.<sup>41–44</sup>

The high temperature oxidation of UNS 30400 steel and other stainless steels in the presence of 60%  $\text{H}_2$ –40%  $\text{N}_2$ ,  $\text{NH}_3$ – $\text{H}_2\text{O}$  mixtures, and other  $\text{H}_2$ – $\text{N}_2$  mixture, has already been studied by several authors from the phase transformation point of view.<sup>45–47</sup> It is also well known that nitrogen and carbon dissolving into alloys increase hardness yield strength, tensile strength, and wear resistance<sup>48</sup> and

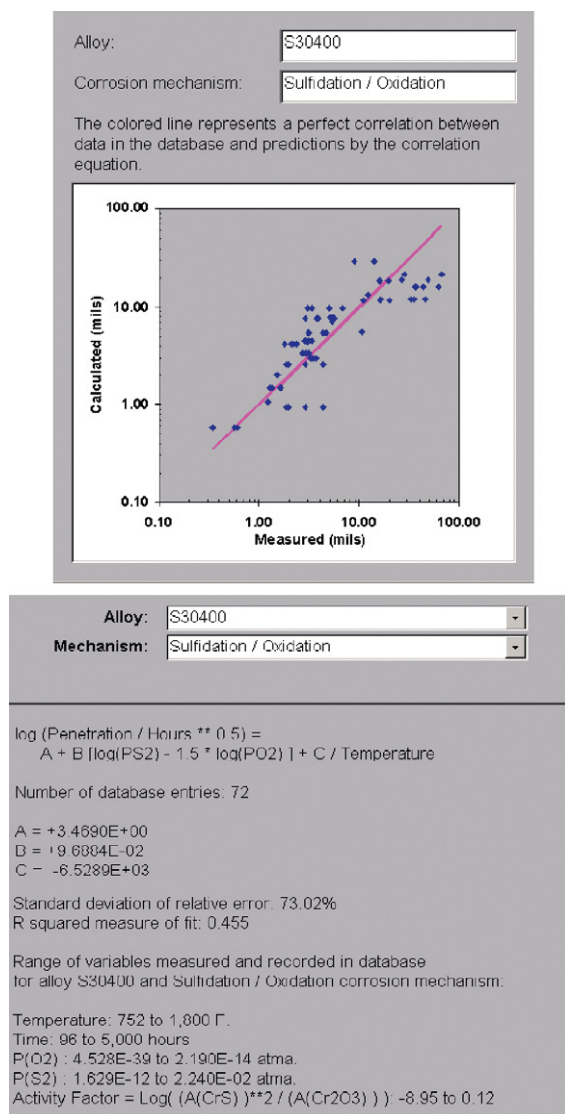


**Figure 28** Example of the analysis of the sulfidation/oxidation corrosion database for S30400 and the quality of the corrosion correlation.

lower toughness. Nevertheless, there is almost no previous work dealing with the conditions, which define the competition between nitridation and oxidation at high temperatures for these materials. Nitridation primarily forms internal nitride corrosion products and can be described in terms of sound metal loss (penetration) by measuring the depth of the formation of the internal nitrides. The process occurs upon exposure of metals in gases containing pure  $N_2$ ,  $N_2 + H_2$ ,  $NH_3$ , air, and mixtures of  $O_2$ -depleted air and other gases at temperatures above 300–430 °C (600–800 °F). This corrosion

depends upon the gas composition, alloy composition, time, and temperature.<sup>42,44</sup>

A recent corrosion evaluation study was performed on stainless steel tubes used in as a component part in a reactor.<sup>41</sup> The material was UNS S30400 and was exposed to a nitriding, carburizing, and oxidizing environment, containing mainly  $NH_3$  and  $CO_2$ , at temperatures between 390 and 450 °C. The atmosphere had a high nitridation potential. Alloy nitrides were stable and formed. The authors explained that the corrosion process includes ingress (solution) of nitrogen into the steel and then formation of a nitrided layer, once the solubility products of the nitrides are exceeded. This formation of CrN particles at temperatures above 425 °C in the near-surface layer causes a volume expansion of about 11% and a corresponding increase in compressive stresses in the surface that can lead to crack formation. Temperatures lower than 425 °C lower the Cr mobility, even if the  $N_2$  concentration in the atmosphere is high.

Issartel *et al.*<sup>45,46</sup> analyzed this occurrence of nitridation and the effect of the temperature upon spalling in terms of the corrosion products formed in UNS S30400 stainless steel in air at 800 and 900 °C (1122 and 1652 °F) by using X-ray diffraction and SEM. Their results support the presence of austenite at lower than expected temperatures in a nontreated sample because the nitridation treatment on the steel surface produced a solid solution of N in the austenite. In this case, no nitrides form in the alloy surface. Riffard *et al.*<sup>47</sup> used *in situ* X-ray diffraction to follow the formation of nitrides at the testing temperature. At the beginning of the oxidation test, CrN formed together with  $Fe_2O_3$ .  $Cr_2O_3$  quickly appears and leads to a protective oxide scale formation growing according to a parabolic rate law. During oxidation, *in situ* X-ray diffraction also shows that  $Fe_2O_3$  transforms to  $FeCr_2O_4$ . These results confirm that nitridation enhances internal oxidation at high temperature.

Internal nitridation is also observed on numerous commercial high temperature alloys.<sup>49–51</sup> In the case of nickel-base alloys, which are often used for high temperature applications, internal nitridation is aided by repeated spalling and cracking of the protective oxide made of either  $Al_2O_3$  or  $Cr_2O_3$ . Nitrogen penetrates into the near-surface area of the alloy and forms stable nitrides, such as, TiN and AlN.<sup>51</sup> These surface precipitates embrittle the high temperature and low-temperature mechanical properties of the material. Additionally, dissolution of the high-volume fraction of the initial small precipitates of the cubic  $\gamma'$ -phase



occurs [ $\text{Ni}_3(\text{Al}, \text{Ti})$ ], which provides the excellent creep resistance of Ni-base superalloys at high temperature. Formation of nitrides can reduce creep and stress rupture properties of Ni-base superalloys at high temperatures, lowering the maximum allowable stress and/or temperature for a particular application.

The transition from oxidation to nitridation in  $\text{O}_2$ - $\text{N}_2$  gases of varying composition for several different types of alloys (Fe-Cr alloy UNS 410000, Fe-Ni-Cr alloy UNS 30400 and Ni-Cr-Al alloy UNS N07214) is a function of temperature,  $\text{O}_2$  partial pressure, and alloy composition in  $\text{O}_2$ - $\text{N}_2$  gases at 1600 °F. The stable alloy phases and corrosion products were calculated by ASSET<sup>52-54</sup> by thermochemical equilibrium calculations for varying gas compositions. The predictions of the phase behavior were compared to and agreed with experimental observations made with carefully exposed coupons of the alloys.<sup>53,54</sup>

### 1.11.3.2 Thermochemistry and Corrosion Mechanism

Oxidation/nitridation by  $\text{O}_2$ - $\text{N}_2$  gases occurs in various industrial equipment involved in fossil fuel combustion, fertilizer manufacturing, or ammonia production. The key variables influencing the kinetics are exposure time, partial pressures of  $\text{O}_2$  and  $\text{N}_2$ , alloy composition, and temperature. The effects of variation from a high  $P_{\text{O}_2}$  to low  $P_{\text{O}_2}$  can induce changes in the corrosion products and rates of corrosion. The oxidation behavior can vary from predominantly surface oxidation (scaling) to oxidation by internal oxidation as the  $P_{\text{O}_2}$  decreases depending upon alloy composition. Progression to lower levels of  $P_{\text{O}_2}$  will induce nitridation to dominate over oxidation. These observations impact how laboratory tests can best simulate corrosion behavior by oxidation or nitridation and also in terms of applications where low levels of  $P_{\text{O}_2}$  may be different from the expected in  $\text{O}_2$ - $\text{N}_2$  gases.

### 1.11.3.3 Predicting Corrosion Product and Alloy Phase Formation in Nitriding/Oxidizing Conditions

Three different alloys were investigated: two iron-base stainless steels, under the specification AISI 304 (UNS S30400) and 410 (UNS S41000), and a nickel-base alloy named 214 (UNS N07214). The nominal chemical compositions of these alloys are reported in Table 1. The stable corrosion products

for conditions of interest were predicted using ASSET and are the likely surface corrosion products for the alloys exposed to the  $\text{O}_2$ - $\text{N}_2$  gases. Corrosion data reported in the literature have been compared to these predictions, in terms of corrosion product formation and the metal losses observed.

Figures 29 and 30 show the calculated phases for UNS S30400 and UNS S41000 stainless steels, as functions of the  $\text{O}_2$  partial pressure (in  $\text{O}_2$ - $\text{N}_2$  gases) at 1 atm and 1600 °F (871 °C). The results show that both alloys form the  $\text{M}_2\text{O}_3$  phase at  $\text{O}_2$  partial pressures higher than 0.001 atm. The corrosion products are about 75%  $\text{Fe}_2\text{O}_3$  and 25%  $\text{Cr}_2\text{O}_3$ . Alloy UNS S30400 has around 8 wt% Ni and differs from UNS S41000 in that a significant fraction of the spinel phase  $(\text{Fe}/\text{Ni})_3\text{O}_4$  forms over a broad range of  $\text{O}_2$  partial pressures, as shown in Figure 29. The 0.5 wt% Ni composition in the alloy UNS S41000 is insufficient to contribute to the significant formation of the spinel phase  $(\text{FeNi}_2\text{O}_4)$ , which occurs for only a very narrow range of  $\text{O}_2$  partial pressure.

In the case of stainless steel UNS S30400 shown in Figure 29, levels of  $\text{O}_2$  between 0.04 and 0.0634 atm induce formation of an MeO phase (where Me is mostly Fe with small amounts of Cr and Ni). Lower levels of  $\text{O}_2$  tend to produce some  $\text{M}_2\text{O}_3$  phase (where M is mostly Cr) with a maximum content of 15%; then, this phase decreases slowly. For this alloy, very low levels of  $\text{O}_2$  tend to form nitrides. Chromium nitrides formation ( $\text{CrN}$  and  $\text{Cr}_2\text{N}$ ) starts at 0.0125 atm of  $\text{O}_2$  and continue to increase in concentration at lower  $P_{\text{O}_2}$ s until the Cr reacts to make nitride.

For the UNS S41000 stainless steel shown in Figure 30, a comparable result was observed. There is more MeO phase ( $\text{FeO}$ ) – maximum 85% at an  $\text{O}_2$  partial pressure of  $64 \times 10^{-5}$  atm – and the presence of this phase increases at 0.075–0.0275 atm  $\text{O}_2$ . At  $\text{O}_2$  partial pressures below  $3 \times 10^{-5}$  to  $15 \times 10^{-5}$  atm  $\text{O}_2$ , the formation of iron ferrite forms with the reduction of austenite. This steel has 12.3 wt% of Cr. At very low levels of  $\text{O}_2$ , the formation of nitrides starts. As seen from Figure 30, the UNS S41000 stainless steel forms Cr nitrides ( $\text{CrN}$  and  $\text{Cr}_2\text{N}$ ) but less than the values found in UNS S30400. The lower Cr content (12.0 wt %) of UNS S41000 naturally forms less nitride phase than UNS S30400 which has a higher Cr content (18.4 wt%). At even lower partial pressures of  $\text{O}_2$  ( $5 \times 10^{-6}$  atm), the amount of  $\text{Cr}_2\text{N}$  decreases to 3–4%.

Increasing the amount of Ni, as found in the alloy UNS N07214 increases the amount of oxides, which depend upon the presence of nickel, such as MeO oxides, where Me can be Fe or Ni. Figure 31 illustrates

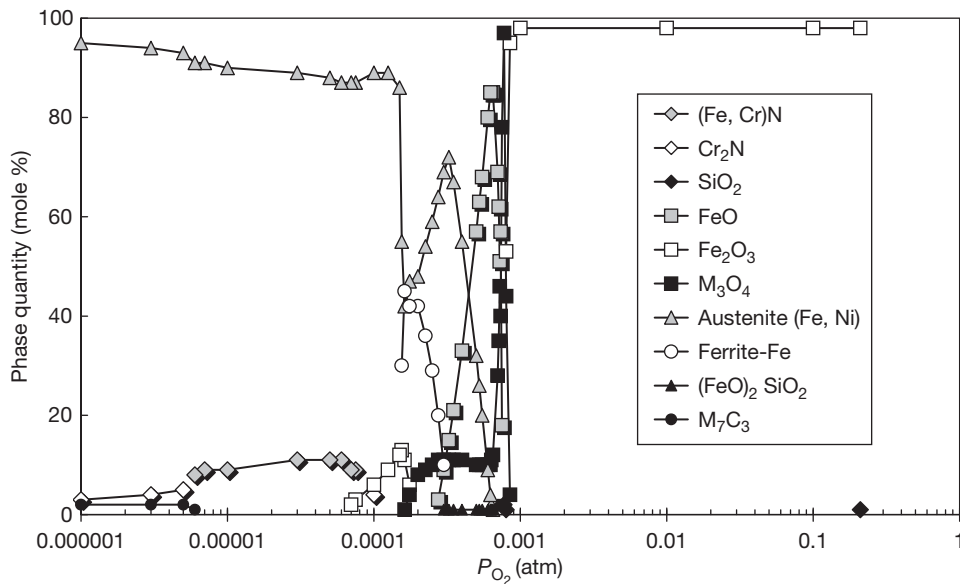


**Figure 29** Effect of  $O_2$  partial pressure upon the stable phases for UNS S30400 stainless steel exposed to  $O_2$ - $N_2$  gases at 1 atm and 871 °C (1600 °F).

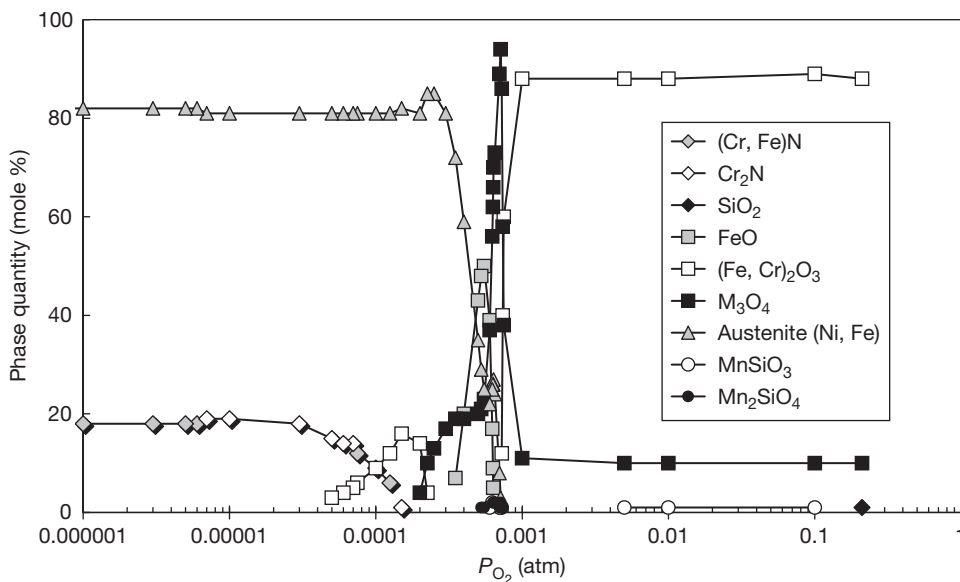


**Figure 30** Effect of  $O_2$  partial pressure upon the stable phases for UNS S41000 stainless steel exposed to  $O_2$ - $N_2$  gases at 1 atm and 871 °C (1600 °F).

this by showing stable NiO at  $O_2$  partial pressures above  $6 \times 10^{-3}$  atm and spinel phases consisting of  $NiCr_2O_4$  and  $NiO \cdot Al_2O_3$  at  $O_2$  partial pressures between  $3 \times 10^{-3}$  and  $6 \times 10^{-3}$  atm, as shown in [Figure 31](#).

Because alloy 214 (nickel-base UNS N07214) has a high Ni content (76 wt%) and low Fe content (2.5 wt%), the results are very different. [Figure 31](#) shows the effect of the  $O_2$  partial pressure at 1 atm

and 1600 °F (871 °C). At  $O_2$  partial pressures above 0.006 atm of  $O_2$ , NiO is the dominant phase (80 wt%), but this phase decreases dramatically at lower  $O_2$  partial pressures and disappears at 0.003 atm of  $O_2$ . The reduction in the amount of NiO occurs simultaneously with an increase in the amount of the Ni-rich austenite phase. It is well known that the oxidation rates of nickel alloys such as UNS N07214

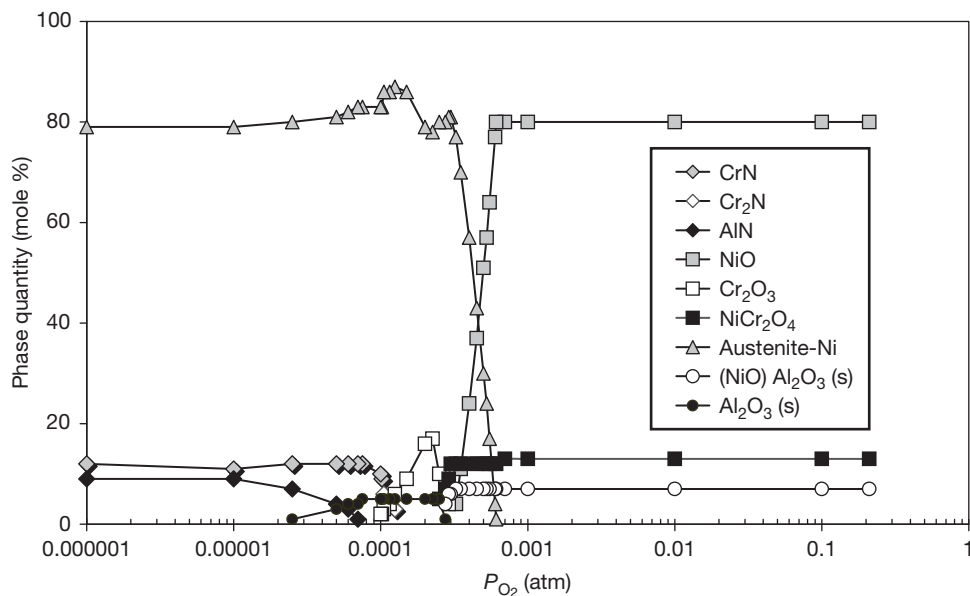


**Figure 31** Effect of  $O_2$  partial pressure upon the stable phases for nickel-base alloy UNS N07214 exposed to  $O_2$ - $N_2$  gases at 1 atm and 871 °C (1600 °F).

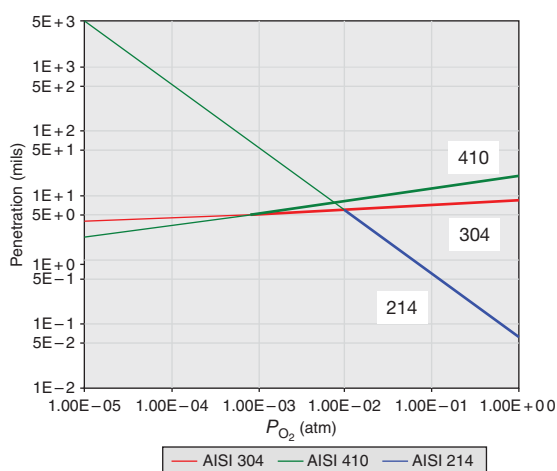


**Figure 32** Predicted effect of  $P_{O_2}$  upon oxidation corrosion of UNS S30400, UNS S41000, and UNS N07214 at 871 °C (1600 °F) after 1 year of exposure time (obtained by using ASSET predictions). The thickened portion of each line correspond to interpolations of actual data (corrosion rates) obtained in the range of pressure from 1 to 0.001 atm for 304 and 410; and from 1 to 0.01 atm for 214.

depend strongly upon the  $O_2$  partial pressure in the gas. Low  $O_2$  partial pressures (about 0.01 atm, and less) favor subsurface oxidation and rapid total penetration. At  $25 \times 10^{-3}$  atm and above of  $O_2$ , the formation of  $Cr_2O_3$  and  $Al_2O_3$  occurs while  $NiCr_2O_4$  and the  $NiO \cdot Al_2O_3$  (spinel structure) cannot form. At  $10^{-3}$  atm of  $O_2$  and less, nitrides became stable.

Low levels of  $O_2$  and high levels of  $N_2$ , such as found in  $3 \times 10^{-3}$  atm  $O_2$  and 0.997 atm  $N_2$  increase the stability of the austenite phase (FCC), since nitrogen is well known as an austenite stabilizer. This behavior was observed in the stainless steels considered in this study at 1600 °F (871 °C). The  $N_2$  partial pressure of about 1 atm in the gas phase when  $O_2$  partial pressures are sufficiently low ( $10^{-4}$  to  $3 \times 10^{-3}$  atm), allows formation of nitrides – mostly in the form of  $CrN$  and  $Cr_2N$  with limited solubility for Fe into the nitride phases. These compounds can be detected by bulk analysis of the corrosion product scale with X-ray diffraction.

**Figure 32** shows the predicted effect of  $O_2$  (in  $O_2$ - $N_2$  gases) at 871 °C (1600 °F) after 1 year of exposure time obtained by using ASSET for UNS S30400, UNS S41000, and UNS N07214. Stainless steels UNS S30400 and UNS S41000 have comparable penetrations under different  $O_2$  partial pressures. Penetration of UNS S30400 is almost independent of  $O_2$  while penetration of UNS S41000 slightly decreases when  $O_2$  concentration decreases. In the case of nickel-base alloy UNS N07214, the penetration decreases with increasing  $O_2$  concentration and internal oxidation is the dominant oxidation mechanism. These predicted rates are based on the correlations of measured oxidation data. The corrosion rates were predicted for 1.0 to 0.001 atm, as indicated in the bold lines in **Figure 32**.

As shown in **Figure 33**, the influence of  $O_2$  concentration upon oxidation is complex over the

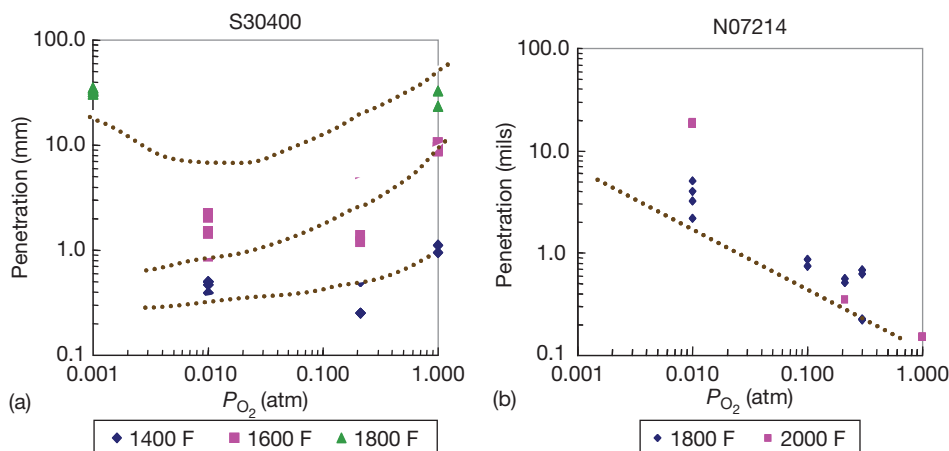


**Figure 33** Effect of  $O_2$  partial pressure upon metal penetration of (a) UNS S30400 and (b) UNS N07214 exposed to different temperatures for 1000 h.

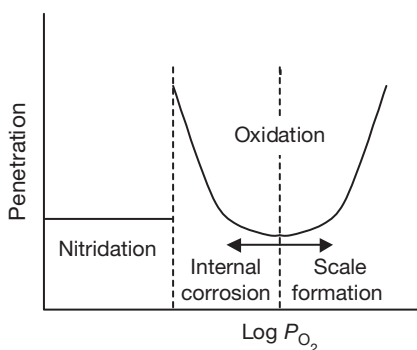


**Figure 34** Schematic representation of the transition from oxidation to nitridation, for a fixed temperature, exposure time, and alloy.

temperature range of 871–1177 °C (1400–2000 °F) for alloys exposed to different  $O_2$  concentrations at a constant exposure time of 1000 h. Alloys S30400 and S41000 show higher penetrations at higher  $P_{O_2}$ s and lower  $P_{O_2}$ s, with a minimum at some intermediate  $P_{O_2}$ . Microstructures show that penetration for these alloys is mostly scale formation at high  $P_{O_2}$ s, while internal oxidation dominates at low  $P_{O_2}$ s. The minimum penetration at some intermediate  $P_{O_2}$  is caused by the transition between dominance by scale formation and internal oxidation.

$Al_2O_3$ -forming alloys such as N07214 exhibit slower oxidation as the  $O_2$  concentration increased the amount of oxide present as  $Al_2O_3$ – $Cr_2O_3$ – $Fe_2O_3$ . **Figure 34** illustrates the different types of corrosion expected over a range of  $N_2$ – $O_2$  gas composition. Internal oxidation competes with scaling as defined

by the  $P_{O_2}$ . At low  $O_2$  pressures, such as  $10^{-4}$  atm of  $O_2$ , nitrides form and grow within the metal matrix.

#### 1.11.4 Oxidation/Carburization by $CH_4$ – $H_2O$ Gases

##### 1.11.4.1 Types of Equipment and Processes Where Carburization Occurs

Corrosion of metals and alloys used in equipment processing high temperature, corrosive, gases containing carbon, hydrocarbons and gases like CO or  $CO_2$  have the potential to induce carburization. Examples of some processes might be gas processing, combustion gas process heaters, petroleum refineries (hydrocracking, coking, vacuum flashing, hydrotreating, and catalytic reforming) coal/coke/oil gasifying, petrochemical production, gasification of black liquor in pulp/paper production, and fossil fuel-fired power generation. Carburization may limit the maximum allowable temperature or maximum allowable gas species concentrations for metals and alloys in equipment.

##### 1.11.4.2 Thermochemistry and Corrosion Mechanism

Oxidation/carburization by  $CH_4$ – $H_2O$ , CO, or  $CO_2$  gases is possible. The key variables influencing the kinetics are exposure time,  $P_{O_2}$ , activity of carbon ( $a_C$ ), partial pressure of  $H_2S$ , alloy composition, and temperature. Alloys exposed to mixtures of C– $CH_4$ – $H_2O$  can experience corrosion by oxidation and carburization. The transition between carburization and

oxidation behaviors of commercial alloys will be discussed.

In carburizing atmospheres, carbon is transferred from the environment into metal components. This process is carburization, which is a high temperature corrosion phenomenon.<sup>57–66</sup> This can change mechanical properties of metals and alloys mostly at temperature  $>800^{\circ}\text{C}$  when carbon diffuses into alloys and react with metals to form internal carbide precipitates.

A result of carburization is an increase in hardness of the carburized materials. Low alloy steels are often exposed to carbonaceous environments to produce hard surfaces to increase wear resistance, corrosion resistance, and abrasion resistance. So, with the proper heat treatment in a gas atmosphere, the consequence of carburization is beneficial.

Carburization is also a corrosion process that affects high temperature alloys, especially in petrochemical industry processes. It is a common contribution to failure of ethylene pyrolysis tubes and can degrade the corrosion resistance and mechanical properties of metals and alloys. In some cases, coke deposition occurs at the inner walls of tubes during hydrocarbon cracking. The decoking process is used to remove coke deposits. Steam or steam–air mixtures are often used to remove coke. The removal processes oxidize the coke to CO and  $\text{CO}_2$  and by thermal shocking/spalling of the deposits. The decoking process also introduces oxidation as a corrosion concern.

Carburization occurs when carbon enters the surface layer of a metal or alloy. The dissolved carbon remains in solution or reacts with the metal to form carbides. Both mechanisms strengthen or harden the surface of the metal. In most cases, carburization leads to precipitation of carbides like  $\text{M}_{23}\text{C}_6$  and  $\text{M}_7\text{C}_3$  inside the alloy surface. The internal carbide formation causes a volume increase of the carburized zone and potential cracking which leads to deterioration of mechanical properties of metals. The increased carbon levels also lead to loss of ductility, which can lead to various forms of fracture.

The carburization rate of an alloy is affected by alloy composition, exposure gas composition, temperature, and time. This chapter discusses carburization in terms of the total sound metal loss (penetration), which is the sum of surface metal loss by scaling plus internal carburization.

#### 1.11.4.3 Corrosion Products Prediction

ASSET was used to calculate stable corrosion products and alloy phases of several alloys exposed to  $\text{CH}_4\text{--H}_2\text{O}$  gas mixtures at  $1800^{\circ}\text{F}$  ( $982^{\circ}\text{C}$ ). Three alloys are summarized: UNS S34700, UNS S44600, and UNS N06025. UNS S34700 is an Fe–Cr–Ni stainless steel stabilized with small additions of niobium and tantalum. The alloy exhibits an excellent resistance to intergranular corrosion and can be used for prolonged service from  $800$  to  $1500^{\circ}\text{F}$  ( $427\text{--}816^{\circ}\text{C}$ ). UNS S44600 is an Fe–Cr ferritic heat-resisting alloy with excellent resistance to oxidation and to various forms of hot corrosion. The alloy is most commonly used for service between  $1500$  and  $2200^{\circ}\text{F}$  ( $815$  and  $1200^{\circ}\text{C}$ ). UNS N06025 is a high carbon Ni–Cr–Fe alloy with additions of Al, Ti, Y, and Zr. The alloy exhibits exceptional resistance to oxidation at high temperatures and possesses very good high temperature carburization resistance. This alloy can be used for pressure vessels with service temperatures up to  $1150^{\circ}\text{C}$ .

Corrosion products and alloy phases were calculated at  $1800^{\circ}\text{F}$  ( $982^{\circ}\text{C}$ ) under various  $\text{CH}_4\text{--H}_2\text{O}$  gas mixtures by assuming that equilibrium conditions are satisfied, as shown in **Figure 35** for alloy UNS S34700, **Figure 36** for alloy UNS S44600, and **Figures 37 and 38** for alloy UNS N06025. Each figure shows the stable corrosion products such as oxides and carbides, the alloy phases and their relative phase amounts.

The effect of gas composition on  $\text{Me}_3\text{O}_4$  (spinel) composition was investigated. The concentration of metals (Fe, Cr, and Ni) in spinel were calculated, as shown in **Figure 35** for UNS S34700, **Figure 36** for UNS S44600, and **Figure 37** for UNS N06025. For these three alloys, the amount of spinel increases with increasing  $\text{H}_2\text{O}$  in gas mixture. The major metals in the spinel are Fe and Cr. For UNS S34700 and UNS S44600, the concentration of Fe in spinel increases with increasing  $\text{H}_2\text{O}$  and the concentration of Cr in spinel ( $\text{Me}_3\text{O}_4$ ) decreases with increasing  $\text{H}_2\text{O}$ . For UNS S44600, which is a nickel-based alloy, the concentration of Ni in spinel ( $\text{Me}_3\text{O}_4$ ) increases with increasing  $\text{H}_2\text{O}$ .

Carburization tests were performed on several alloys at  $1800^{\circ}\text{F}$  ( $982^{\circ}\text{C}$ ) for 720 h under different gas atmospheres. One group of samples was under flowing pure  $\text{CH}_4$  gas, which decomposed to produce massive amounts of solid carbon. The other group was under  $\text{H}_2\text{--}1.2\% \text{CH}_4$ , which yields a carbon activity of one at the test temperature of  $1800^{\circ}\text{F}$  ( $982^{\circ}\text{C}$ ).

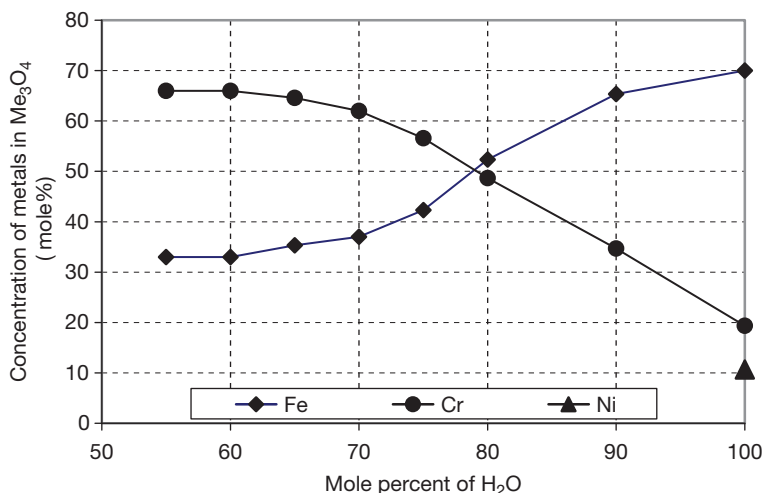


**Figure 35** Effect of gas composition upon  $\text{Me}_3\text{O}_4$  composition in alloy UNS S34700 at 1800 °F (982 °C).

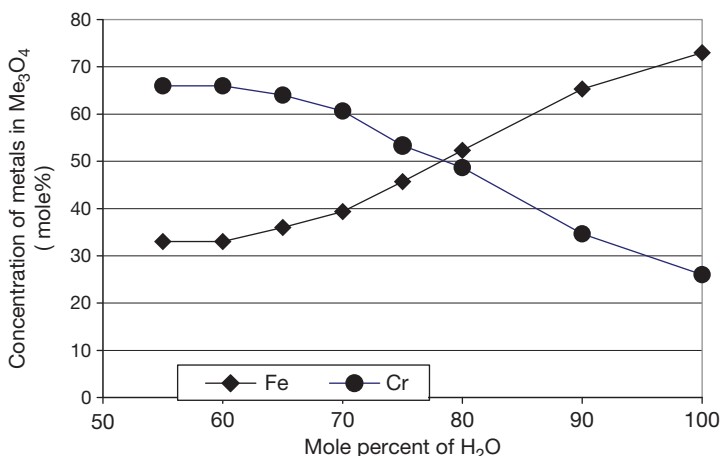


**Figure 36** Effect of gas composition upon  $\text{Me}_3\text{O}_4$  composition in alloy UNS S44600 at 1800 °F (982 °C).

The carburization corrosion rates were measured and shown in Figure 39 for samples under  $\text{H}_2$ -1.2%  $\text{CH}_4$  gas mixtures and Figure 40 for samples under pure  $\text{CH}_4$ . Also carburization rates for 1 year were calculated based on the measured corrosion rates for 720 h and assuming parabolic kinetics for 1 year, as shown in Figures 39 and 40. The carburization results show that UNS S34700 has better carburization resistance than UNS S44600 and UNS N06025 in both testing gas environments.

The carburization corrosion rates for alloys in pure  $\text{CH}_4$  are much higher than those in  $\text{H}_2$ -1.2%  $\text{CH}_4$ . Under pure  $\text{CH}_4$  gas atmosphere at 1800 °F (982 °C), tested alloys were heavily coated with solid carbon on the surface and their carburization rates are much higher than the same samples in the

$\text{H}_2$ -1.2%  $\text{CH}_4$  gas mixture. Carbon activity would have been one if the gas mixture had been at equilibrium. Since available data for well-known alloys like UNS N08810, HP, and HK show increasing carburization at higher carbon activities, the carbon activity must have been larger than one in the pure  $\text{CH}_4$  gas atmosphere and the gas must not have been at equilibrium at 1800 °F (982 °C).

### 1.11.5 Summary

The various corrosion mechanisms are named for the corrosion products that form in high temperature gas phase corrosion of metals and alloys, which occur in a variety of industrial processes. The thermochemistry



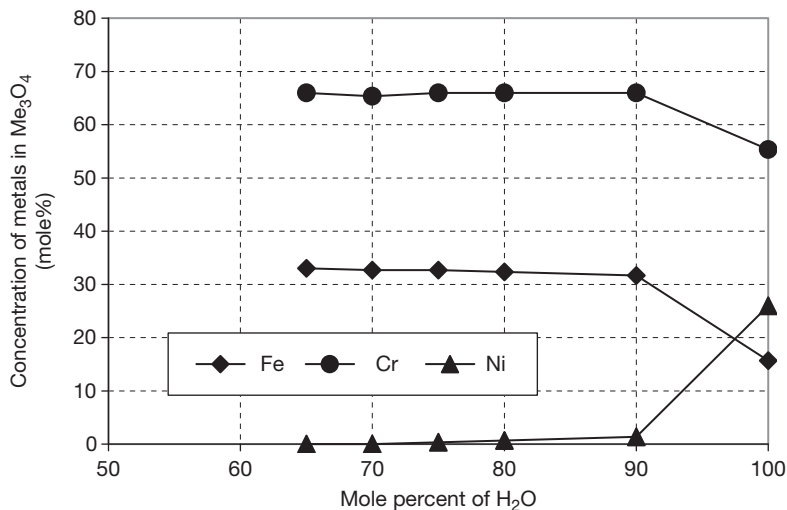


**Figure 37** Effect of gas composition upon  $\text{Me}_3\text{O}_4$  composition in alloy UNS N06025 at 1800 °F (982 °C).

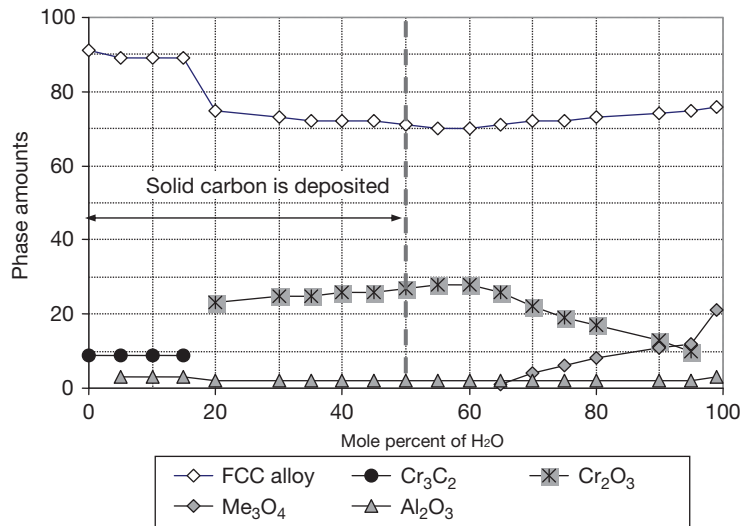


**Figure 38** Equilibrium corrosion products of UNS N06025 under  $\text{CH}_4\text{-H}_2\text{O}$  gas mixture atmospheres at 1800 °F (982 °C).

of the interactions between the alloying elements and the species in the gas phase determines which corrosion products form. In most instances, increasing the temperature increases the rate of corrosion. However, the effect of changes in the gas species concentrations upon the rate of corrosion may have nonobvious effects upon the rate of corrosion, particularly when corrosion is producing a mixture of corrosion products. Much of the effects of mixed gas corrosion can be thought of in terms of a competition between the different corrosion products, which likely impact corrosion behaviors in various ways. Effects of changing gas species concentrations upon corrosion for

mixed gas corrosion have been discussed for several classes of corrosion mechanisms. Any changes in gas composition, which induce greater stability of slower growing corrosion products, will tend to slow the rate of corrosion in mixed gases. For example, increasing the  $P_{\text{O}_2}$  in a gas, which is causing sulfidation/oxidation, will tend to favor slower oxide growth at the expense of growth of faster growing sulfides, thereby, slowing the rate of corrosion. This chapter has reviewed the current knowledge of how thermochemistry in terms of the  $P_{\text{O}_2}$  and  $P_{\text{S}_2}$  values of gases can describe corrosion behaviors for sulfidation/oxidation conditions and can even be used to select a test

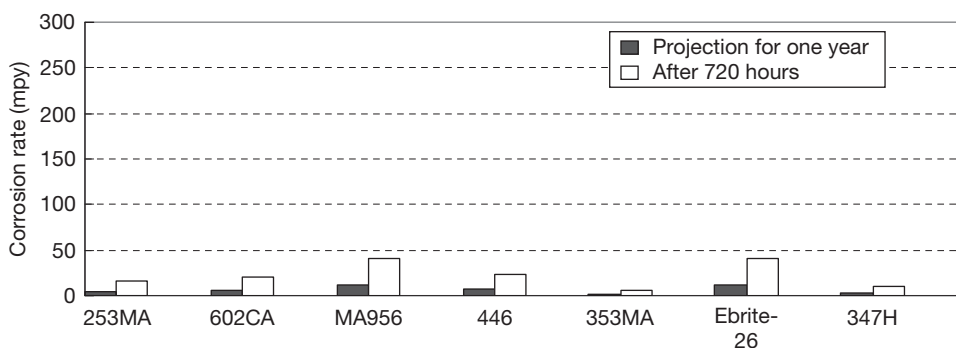


**Figure 39** Carburization rates for alloys in H<sub>2</sub>-1.2% CH<sub>4</sub> at 1800 °F (982 °C).

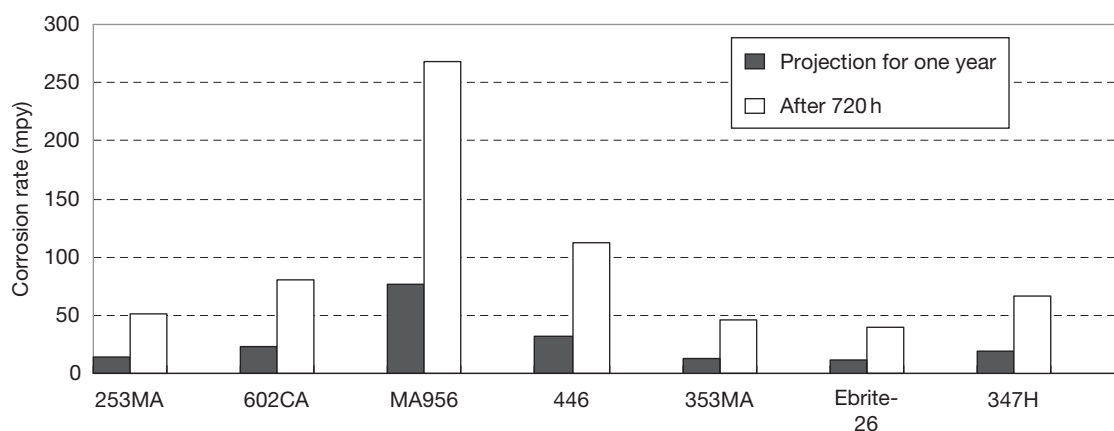


**Figure 40** Carburization rates for alloys in CH<sub>4</sub> at 1800 °F (982 °C).

gas which is very different from the industrial gas in question. Industrial corrosion in H<sub>2</sub>-H<sub>2</sub>O-H<sub>2</sub>S gases can be simulated in laboratory tests using CO-CO<sub>2</sub>-COS, which are suggested because they are experimentally more convenient. Test exposure times must be long enough to achieve long-term corrosion behavior, as measured by the time needed for the parabolic rate constant to become independent of time, which is at least 500 h at 600 °C for a number of alloys discussed. Once long-time (time independent) parabolic time dependence is achieved, then the extent of corrosion over thousands of hours can be well correlated with a parabolic time dependence. Once the effects of gas composition, exposure time, and temperature are well understood for a given alloy and corrosion mechanism, it is also possible to predict alloy corrosion for many hot-gas corrosion mechanisms for wide ranges of conditions using correlations, even considering changing gaseous and temperature

exposures, by summing the corrosion expected in the various sets of exposure conditions.

Corrosion can be well discussed and used in terms of total metal penetration, which is the sum of metal thickness lost by scale formation plus the metal thickness affected by internal corrosion product formation. Alloys vary widely in their relative amounts of total metal penetration for various corrosion mechanisms and exposure conditions, which is due to either internal penetration or scale formation.

The corrosion behaviors of alloys vary from surface to internal corrosion and were studied by assessing the stable corrosion products and alloy phases as functions of the ambient gas composition. There are transitions in corrosion behavior as the gas exposure changes, causing changes in the stable corrosion products. The metal loss information for alloys in several corrosive environments was reviewed and advice given on how to predict the probable corrosion

mechanism and amount of metal penetration as functions of the important variables. A new capability was developed and reviewed with the ability to predict formation of the basic types of corrosion products and thickness losses by corrosion for wide ranges of conditions of gas composition, temperatures, and times for many alloys.

## Acknowledgments

Support by the following organizations are recognized and appreciated: US Department of Energy – Office of Industrial Technologies via cooperative agreement DE-FC02-00CH11020, Shell Global Solutions (US) Inc.; Shell International E&P Inc, Arthur L. Young of Humberside Solutions Ltd., Arthur D. Pelton of Centre for Research in Computational Thermochemistry in Université de Montréal, William T. Thompson of the Royal Military College of Canada, Oak Ridge National Laboratory, Foster Wheeler Development Corporation, KEMA, Caterpillar, Special Metals Corporation, Texaco, Haynes International, Usinor Industrieel, Kvaerner Pulpung Oy, Materials Technology Institute of the Chemicals Process Industries (MTI), Dupont, Exxon/Mobil, Rolled Alloys, VDM Fluor Daniel and Air Products. The experimental testing effort owes its deepest gratitude to Owen Kriegel and Paul F. Schmidt of Shell Global Solutions (US) Inc and research staff at ORNL. Data contributions from Haynes International, VDM and Special Metals Corporation are acknowledged. Ian G. Wright of Oak Ridge National Laboratory is thanked for his many contributions. Technical contributions from Yali Li and Juan Gonzalez are acknowledged.

## References

- Haycock, E. W. In *High Temperature Metallic Corrosion of Sulphur and Its Compounds*; Foroulis, Z. A., Ed.; Electrochemical Society: Princeton, NJ, 1970; p 110.
- Haycock, E. W.; Sharp, W. H. Corrosion of ferrous alloys by H<sub>2</sub>S at high temperatures, Session from the 24th Meeting of the American Petroleum Institute, New York 1959.
- Guzeit, J. In *Process Industries Corrosion – The Theory and Practice*; National Association of Corrosion Engineers: Houston, TX, 1986.
- Backensto, E. B.; Drew, R. E.; Stapleford, C. C. In *Corrosion*; NACE, 1956; Vol. 12, p 22.
- Sorell, G.; Hoyt, W. B. In *Corrosion*; NACE, 1956; Vol. 12, p 213t.
- Lai, G. Y. *High-Temperature Corrosion of Engineering Alloys*; ASM International: Materials Park, OH, 1990; Literature from Haynes International Marketing, “Technical Information, Oxidation Resistance of Haynes High Temperature Alloys”.
- Stoklosa, A.; Stringer, J. *Oxid. Met.* **1977**, *11*, 263.
- John, R. C.; Pelton, A. D.; Young, A. L.; Thompson, W. T.; Wright, I. G.; Besmann, T. M. Assessing corrosion in oil refining and petrochemical processing, Presented at Symposium on High Temperature Corrosion in Energy Related Systems, Angra dos Reis, Rio de Janeiro, 1–4 September 2002.
- John, R. C.; Fort, W. C., III; Tait, R. A. *Mater. High Temp.* **1993**, *11*, 124.
- John, R. C.; Young, A. L.; Thompson, W. T. *Corrosion/97*; National Association of Corrosion Engineers: Houston, TX, 1997; Paper 142.
- Lai, G. Y. In *Corrosion/84*; National Association of Corrosion Engineers: Houston, TX, 1984; Paper 73. Data from brochures Haynes 188 and Pocket Guide to Haynes Alloys from Cabot Corp, 1986.
- John, R. C. Second International Conference on Heat Resistant Materials, Gatlinburg, TN, 11–14 September 1995.
- John, R. C. In *Corrosion/96*; National Association of Corrosion Engineers: Houston, TX, 1996; Paper 171.
- Perkins, R. A. In *High Temperature Corrosion*; Rapp, R. A., Ed.; National Association of Corrosion Engineers: Houston, TX, 1981; pp 345–353.
- Perkins, R. A. Proceedings of the Third Annual Conference on Materials for Coal Conversion and Utilization. U. S. Department of Energy, CONF-781018, October, 1978.
- Natesan, K.; Chopra, O. K. In Proceedings of the Conference on Properties of High-Temperature Alloys; Foroulis, Z. A., Pettit, F. S., Eds.; The Electrochemical Society: New Jersey, 1976; pp 493–510.
- Natesan, K. In *High Temperature Corrosion*; Rapp, R. A., Ed.; National Association of Corrosion Engineers: Houston, TX, 1981; pp 336–344.
- Baxter, D. J.; Natesan, K. In *High Temperature Corrosion in Energy Systems*; Rothman, M. F., Ed.; TMS-AIME/MSD-ASM: Detroit, 1985, pp 237–252.
- Bakker, W. T. Mixed oxidant corrosion in nonequilibrium syngas at 540 °C; Electric Power Research Institute: Palo Alto, CA, 1995.
- John, R. C. In *High Temperature Corrosion in Energy Systems*; Rothman, M. F., Ed.; TMS-AIME/MSD-ASM: Detroit, 1985, pp 501–514.
- John, R. C. In *High Temperature Materials/Corrosion – Fundamental Aspects of High Temperature Corrosion II*, Shores, D. A., Yurek, G. J., Eds.; Electrochemical Society, 1987, pp 86–99.
- Waldner, P.; Pelton, A. D. *J. Phase Equilib. Diff.* **2005**, *26*, 23–28.
- Waldner, P.; Pelton, A. D. Thermodynamic modeling of the Ni–S system, in press.
- Waldner, P.; Pelton, A. D.; Thermodynamic modeling of the Fe–Ni–S system, in press.
- John, R. C. In *Life Prediction of Corrodible Structures*; NACE, ISBN 1-877914-60-6 1994; Vol. 1.
- John, R. C. Meeting of Electrochemical Society, 4–9 May 1986; paper no. 358.
- John, R. C. *Fundamental Aspects of High Temperature Corrosion – II, Simultaneous Sulphidation and Oxidation of Alloy 800 in Mixed Gases*; Electrochemical Society, 1987; p 86.
- Natesan, K. In *High Temperature Corrosion*; Rapp, R. A., Ed.; NACE: Houston, TX, 1983; p 336.
- Baxter, D. J.; Natesan, K. *Oxid. Met.* **1989**, *31*, 305.
- Rhamel, A.; Schorr, M.; Valesco-Tellez, A.; Pelton, A. *Oxid. Met.* **1987**, *27*, 199.

31. Perkins, R. A.; Morse, G.; Coons, W. C. Materials for syngas coolers, Report AP-2518, EPRI Research Report 1654-5, Palo Alto, CA, August 1982.
32. John, R. C.; Thompson, W. T.; Karakaya, I. In *Corrosion/88* 1988; Paper 136.
33. John, R. C.; Pelton, A. D.; Young, A. L.; Thompson, W. T.; Wright, I. G. MS&T Conference, Cincinnati, OH, 15–19 October 2006.
34. Kofstad, P. *High temperature Corrosion*; Elsevier Applied Science, 1988.
35. *Process Industries Corrosion*; National Association of Corrosion Engineers, 1975.
36. Norton, J. F.; Bakker, W. T. Eds. *Materials for Coal Gasification Power Plant*; Butterworth-Heinemann, 1993.
37. Bakker, W. T.; Dapkunas, S.; Hill, V. Eds. *Materials for Coal Gasification*; ASM International, 1988.
38. Embury, J. D. Ed. *High Temperature Oxidation and Sulphidation Processes*; Pergamon Press, 1990.
39. Rapp, R. A. Ed. *High Temperature Corrosion*; National Association of Corrosion Engineers, 1983.
40. Streiff, R.; Stringer, J.; Krutenat, R. C.; Caillet, M. Eds. *High Temperature Corrosion – Advanced Materials and Coatings*; Elsevier Science, 1989.
41. Grabke, H. J. *Mater. Corros.* **2005**, 56(6), 384–388.
42. Grabke, H. J.; Strauss, S.; Vogel, D. *Mater. Corros.* **2003**, 54(11), 865–901.
43. Kothari, D. C.; et al. *Mater. Sci. Eng. A* **1989**, 116, 89–95.
44. Agudo, L.; Sanchez, C.; Nachez, L.; Feugeas, J. N.; Staia, M. H. *Revista de la Facultad de Ingeniería, Universidad Central de Venezuela* **2005**, 20(1), 71–76.
45. Issartel, C.; et al. *Corros. Sci.* **2004**, 46(9), 2191–2201.
46. Issartel, C.; Buscail, H.; Caudron, E.; et al. *Appl. Surf. Sci.* **2004**, 225, 14–20.
47. Riffard, F.; Buscail, H.; Caudron, E.; Cuffe, R.; Issartel, C.; Perrier, S. *J. Phys. IV* **2004**, 118, 369–375.
48. Rawers, J. C. *Proc. Inst. Mech. Eng. L J. Mater. Des. Applic.* **2004**, 218(L3), 239–246.
49. Han, S.; Young, D. J. *Oxid. Met.* **2001**, 55(3–4), 223–242.
50. Krupp, U.; Christ, H.-J. *Oxid. Met.* **1999**, 52(3–4), 277–298.
51. John, R. C. In *Proceedings of the 4th International Symposium on High Temperature Corrosion and Protection of Materials*, Les Embiez, France, 20–24 May 2000.
52. John, R. C.; Pelton, A. D.; Young, A. L.; Thompson, W. T.; Wright, I. G. Predicting equipment lifetimes with high temperature corrosion data, Presented at the 6th International Symposium on High Temperature Corrosion and Protection of Materials, Les Embiez, France, 16–21 May 2004; *Proceedings of the Material Science Forum*, 2004; Vols. 461–464, 599–610.
53. Thompson, W. T.; Bale, C. W.; Pelton, A. D. Facility for the analysis of chemical thermodynamics (FACT), Ecole Polytechnique, Royal Military College of Canada in Kingston, McGill University Montreal, Montreal, 1985.
54. Christ, H. J.; Berchtold, L.; Sockel, H. G. *Oxid. Met.* **1986**, 26(1–2), 45–76.
55. Pedraza, F.; Grosseau-Poussard, J. L.; Abrasonis, G.; Rivière, J. P.; Dinhut, J. F. *J. Appl. Phys.* **2003**, 94(12), 7509–7519.
56. Udyavar, M.; Young, D. J. *Corros. Sci.* **2000**, 42, 961–883.
57. Grabke, H. J. *Carburization: A High Temperature Corrosion Phenomenon*; MTI, 1998.
58. Kofstad, P. *High Temperature Corrosion*; Elsevier Applied Science, 1988.
59. Grabke, H. J.; Muller, E. M.; Speck, H. V.; Konczos, G. *Steel Res.* **1985**, 56(5), 275–282.
60. Grabke, H. J.; Müller-Lorenz, E. M.; Schender, A. *ISIJ Int.* **2001**, 41, S1–S8.
61. John, R. C.; Pelton, A. D.; Young, A. L.; Spencer, P.; Thompson, W. T. Alloy Carburization at Temperatures of 1200–2100°F (650–1150°C); NACE – Corrosion, 2003, Paper 03474.
62. Nava Paz, J. C.; Grabke, H. J. *Oxid. Met.* **1993**, 39(5/6), 437–456.
63. Ben-Haroe, I.; Rosen, A.; Hall, I. W. *Mater. Sci. Technol.* **1993**, 9, 620–626.
64. Bullock, E.; Frampton, P. D.; Norton, J. F. *Microstruct. Sci.* **1981**, 9, 215–224.
65. Klöwer, J. *Mater. Corros.* **1996**, 47, 685–694.
66. Driver, D.; Barrand, P. J. *Iron Steel Inst.* **1964**, 202, 614–615.

## 1.12 Carburization and Metal Dusting

**D. J. Young**

School of Materials Science and Engineering, University of New South Wales, UNSW Sydney, NSW 2033, Australia

© 2010 Elsevier B.V. All rights reserved.

1.12.1	Introduction	273
1.12.2	Gaseous Carbon Activities	274
1.12.3	Carburization	274
1.12.4	Internal Carburization of Model Alloys	276
1.12.4.1	Reaction Morphologies and Thermodynamics	276
1.12.4.2	Carburization Kinetics	277
1.12.4.3	Carbide Microstructures and Distributions	280
1.12.5	Internal Carburization of Heat-Resisting Alloys	282
1.12.5.1	Effect of Carbon	283
1.12.5.2	Effect of Molybdenum	283
1.12.5.3	Effect of Silicon	283
1.12.5.4	Effect of Niobium and Reactive Elements	284
1.12.5.5	Effect of Aluminum	284
1.12.5.6	Alloying for Carburization Protection	284
1.12.6	Metal Dusting of Iron and Ferritic Alloys	285
1.12.6.1	Metal Dusting of Iron	285
1.12.6.2	Iron Dusting in the Absence of Cementite	288
1.12.6.3	Effects of Temperature and Gas Composition on Iron Dusting	288
1.12.6.4	Dusting of Low-Alloy Steels	290
1.12.6.5	Dusting of Ferritic Chromium Steels	291
1.12.6.6	Dusting of FeAl and FeCrAl Alloys	292
1.12.7	Dusting of Nickel and Austenitic Alloys	293
1.12.7.1	Metal Dusting of Nickel	293
1.12.7.2	Dusting of Nickel Alloys in the Absence of Oxide Scales	296
1.12.7.3	Effects of Temperature and Gas Composition on Nickel Dusting	297
1.12.7.4	Dusting of Austenitic Alloys	297
1.12.8	Protection by Oxide Scaling	298
1.12.8.1	Protection by Adsorbed Sulfur	300
1.12.8.2	Protection by Coatings	300
1.12.9	Conclusions	301
References		301

### Abbreviations

**EDS** Energy dispersive spectrometry (of X-rays)

**FIB** Focused ion beam

**ppm** Parts per million (concentration)

**SAD** Selected area diffraction

**TEM** Transmission electron microscopy

### Symbols

$\alpha$  Ferrite; solubility

$\gamma$  Austenite

$\gamma_i$  Activity coefficient of species  $i$

$\varepsilon$  Tortuosity factor, reflecting diffusional blocking by precipitate

$\nu$  Stoichiometric coefficient

$a_i$  Activity of species  $i$

**erf** Error function

**erfc** Complementary error function

$g$  Critical volume fraction necessary to form external scale (of oxide or carbide)

$k_d$  Metal disintegration (dusting) rate constant

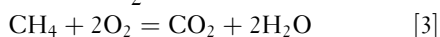
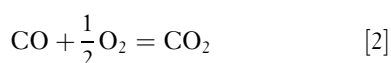
$k_p^{(i)}$  Parabolic rate constant for internal carburisation

$r_n$  Rate constant for reaction  $n$

$t$	Time
$w/o$	Weight percent
$x$	Position co-ordinate
$A$	Surface area
$B_i$	Mobility of species $i$
$D_i$	Diffusion coefficient of species $i$
$E_A$	Activation energy for kinetic process
$\Delta G_f^\circ$	standard Gibbs free energy of formation
$\Delta \bar{H}_C$	Partial molar enthalpy of carbon dissolution
$K_n$	Equilibrium constant for reaction $n$
$K_{sp}$	Solubility product
$N_i$	Mol fraction of species $i$
$N_i^{(o)}$	Original mol fraction of species $i$ in solid prior to diffusion
$N_i^{(s)}$	Mol fraction of species $i$ at surface of alloy
$Q$	Activation energy for diffusion
$R$	General gas constant
$\Delta S_C^{xs}$	Partial molar excess entropy of carbon dissolution
$T$	Temperature
$V_i$	Molar volume of species $i$
$W$	Weight
$X$	Scale thickness
$X_i$	Width of internal precipitation zone

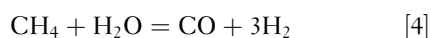
### 1.12.1 Introduction

Carbonaceous gases are generated by the combustion of fossil fuels: coal, oil, and natural gas. The reactions



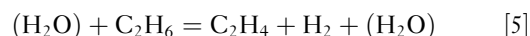
are often carried out using excess air, so that the exhaust gases contain free molecular oxygen plus  $CO_2$  and  $H_2O$ . Despite the use of excess air or oxygen, locally reducing conditions can form and persist in large-scale combustion units. Such conditions can lead to carbon attack, as will be discussed in the following sections.

A number of other high temperature processes are conducted under reducing conditions so as to produce hydrogen or CO, rather than their oxidation products. Steam reforming of natural gas



at temperatures around 800–900 °C is widely used to produce hydrogen. This process is carried out by

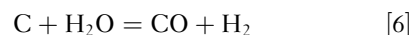
passing the gases through catalyst beds in externally heated alloy tubes. Somewhat similar tubular reactors are used in the pyrolysis or ‘steam cracking’ process for making ethylene or propylene; for example,



In this case, the steam is added as a diluent in order to reduce the amount of solid carbon produced by gas-phase pyrolysis.

Feedstock materials, hydrocarbons, have been rising in price, and the need for improved process efficiencies has led to higher operating temperatures. Simultaneously, tube wall thicknesses have been reduced to improve heat transfer. Thus, process engineering changes have led to higher tube metal temperatures and reduced load-bearing sections. These increased demands on material properties have been met by a series of advances in alloy design. The tubes are centrifugally cast, austenitic chromia formers. Their compositions have evolved from the old HK 40 grade (Fe–25Cr–20Ni), through the HP grades (Fe–25Cr–35Ni) to high-nickel alloys containing 45% or even 60% Ni. The increased alloy levels have provided significant improvements in creep properties, but the materials are still subject to corrosion by carbon.

The process of coal gasification is of potential importance in achieving high-efficiency electric power generation. Steam is contacted with coal at high temperature, producing synthesis gas



Although coal gasification has been employed for a long time, its use on the scale and at the intensity required to support gas turbine-driven power generation is relatively new. However, the carbon corrosion mechanisms can be expected to be related to those observed in steam reforming and steam cracking plants.

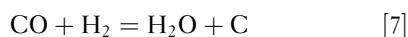
Under combustion conditions, the oxygen potential is usually high enough to guarantee oxide scale formation. The questions of interest then concern interaction of  $CO_2$  with the oxide. In contrast, synthesis gas and other carbonaceous gases handled in the chemical and petrochemical industries are characterized by high  $a_C$  values and low oxygen potentials. Typically, these gases are oxidizing to chromium and aluminum, but not to iron or nickel. The questions of interest, therefore, concern the ability of  $Cr_2O_3$  and  $Al_2O_3$  scales to exclude carbon from the alloy, and the consequences of oxide scale failure when carbonaceous gas species contact the metal surface.



We consider first the simple case where the oxygen potential is so low that no oxide forms, and corrosion by carbon alone results. If the carbon activity,  $a_C$ , is less than 1, but large enough to stabilize a metal carbide, the reaction is described as carburization. Such reactions are rapid and destructive. However, if the gas is supersaturated with respect to carbon ( $a_C > 1$ ), an even greater threat emerges. Catalysis of carbon deposition by the metal can lead to its disruption and fragmentation in an extremely rapid corrosion process known as metal dusting. Dusting mechanisms are different for ferritic and austenitic alloys, and they are discussed separately. Alloy design strategies for slowing carburization and metal dusting are shown to be of limited value. However, alloying to achieve protective oxide formation can delay carbon access to the metal. This approach is discussed together with other surface treatments in the final section of this chapter.

### 1.12.2 Gaseous Carbon Activities

The common gas-phase processes producing carbon are the synthesis gas reaction



the Boudouard reaction



and hydrocarbon cracking, for example,



The standard free energies of these reactions are listed in [Table 1](#). It is necessary to recognize that all three reactions are very slow as homogenous gas-phase processes. They will not reach equilibrium in a typical laboratory reactor, unless catalyzed. Although many materials of practical interest – iron, nickel, cobalt, and their alloys – are catalytically active to these reactions, their oxide scales are inert.

**Table 1** Gas phase equilibria relevant to carburizing

Reaction	$\Delta G_f^\circ = A + BT(J)$	
	A	B
$\text{CO} + \text{H}_2 = \text{H}_2\text{O} + \text{C}$	–134 515	142.37
$2\text{CO} = \text{CO}_2 + \text{C}$	–170 700	174.5
$\text{CH}_4 = 2\text{H}_2 + \text{C}$	+87 399	–108.74

As seen in [Figure 1](#), temperature effects are very different for these carbon-producing reactions. Thus, methane, and hydrocarbons in general, can produce significant carbon activities only at high temperatures. On the other hand, the synthesis gas and Boudouard reactions produce increasing carbon activities as the temperature is lowered.

It is because these gases are difficult to equilibrate that they can become supersaturated with respect to carbon; that is,  $a_C > 1$ . An example is synthesis gas produced in a steam reforming unit, which will normally have  $a_C < 0.5$ . As the gas is cooled from reaction temperature, however, the rate of reaction [7] is so slow that the gas fails to adjust its composition by depositing carbon. The gas-phase carbon activity calculated from

$$a_C[7] = \frac{K_7 p_{\text{H}_2} p_{\text{CO}}}{p_{\text{H}_2\text{O}}} \quad [10]$$

can then be much greater than 1. It is recognized that the same gas also produces carbon via reaction [8], and one can calculate

$$a_C[8] = \frac{K_8 p_{\text{CO}}^2}{p_{\text{CO}_2}} \quad [11]$$

In general,  $a_C[7] \neq a_C[8]$ , because the gas is not at equilibrium. In this situation, it is appropriate to consider reactions [7]–[9] as separate, independent processes, as will be demonstrated in [Sections 1.12.6](#) and [1.12.7](#). Nonetheless, because reaction [7] is usually faster than [8], it is common to calculate  $a_C$  from [eqn. \[1\]](#).

Carburization experiments require  $a_C \leq 1$ . The use of  $\text{CH}_4/\text{H}_2$  gas mixtures to control carbon activity is inadvisable at temperatures below  $\sim 1000^\circ\text{C}$ , because of the slow rate of reaction [9] and the usually brief residence time of a laboratory reactor. It is preferable to use mixtures of  $\text{H}_2$  and  $\text{C}_3\text{H}_6$ , as the latter pyrolyzes readily.

### 1.12.3 Carburization

Carbides are much less stable than oxides, as seen from the examples in [Table 2](#). Thermodynamic data for other carbides can be found in a review by Shatynski.<sup>1</sup> Of the common alloy base metals, nickel and cobalt do not form carbides under the conditions of interest. Iron forms cementite,  $\text{Fe}_3\text{C}$ , at temperatures below  $763^\circ\text{C}$  only if  $a_C > 1$ . Exposure of these metals to reducing carbonaceous gases leads to dissolution of carbon at the metal surface and its

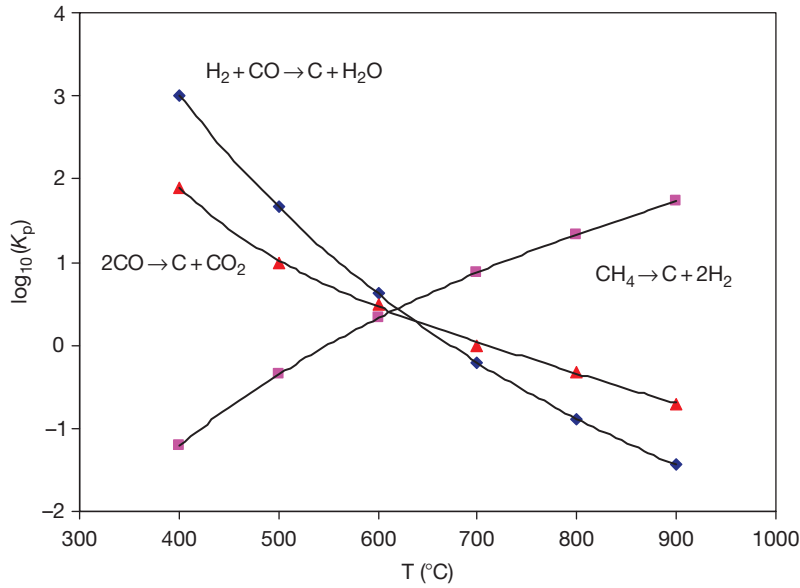


**Figure 1** Equilibrium constants for gas-phase carbon producing reactions.

**Table 2** Properties of metal carbides

Carbide	$\Delta G_f^\circ = A + BT(J)$		$V_{MC_y}^*$ (cm <sup>3</sup> )	MP (°C)
	A	B		
Cr <sub>23</sub> C <sub>6</sub>	-411 200	-38.7	7.91	1580
Cr <sub>7</sub> C <sub>3</sub>	-174 509	-25.5	8.26	1665
Cr <sub>3</sub> C <sub>2</sub>	-84 353	-11.53	8.98	1895
NbC	-130 122	+1.67	13.47	3480
SiC	-113 386	+75.7	13.70	2700
Al <sub>4</sub> C <sub>3</sub>	-266 520	+96.2	15.24	~1400
Fe <sub>3</sub> C	29 037	-28.0	8.31	1650

\*Volume per mole of metal

diffusion inwards, but no carbide phase is formed if  $a_C < 1$ . If the metal surface is at equilibrium with the gas phase, the surface concentration of dissolved carbon  $N_C^{(s)}$  (mole fraction), can be found from the relationship

$$N_C^{(s)} = K a_C \quad [12]$$

Data for carbon dissolution in iron and nickel is summarized in **Table 3**, where the carbon solubility in nickel is seen to be much lower than in  $\gamma$ -Fe. If inward carbon diffusion causes no phase change in the solvent metal, and if furthermore  $D_C$  is independent of composition, then the resulting carbon concentration profile is found by solving Fick's second law to obtain

**Table 3** Partial molar enthalpy and entropy for carbon dissolution in metal

Metal	$\Delta \bar{G}_C$ (kJ mol <sup>-1</sup> )	$\Delta S_C^{xs}$ (J mol <sup>-1</sup> K <sup>-1</sup> )	Ref
Ni	54	5	2
$\gamma$ -Fe	44.04	17.62	3

$$\frac{N_C - N_C^{(o)}}{N_C^{(s)} - N_C^{(o)}} = \operatorname{erfc}\left(\frac{x}{2\sqrt{D_C t}}\right) \quad [13]$$

Here,  $N_C^{(o)}$  represents the original carbon level in the metal prior to carburization. The rate at which the carburization zone widens is given approximately by

$$X_i^2 = 4D_C t \quad [14]$$

As  $D_C$  values in austenite are high, the process is fast. Using data for  $D_C$ ,<sup>4, 5</sup> it is found that carbon penetrates about 3 mm into each of  $\gamma$ -Fe and Ni in 24 h at 1000 °C.

The heat-resisting alloys used in contact with carbon-rich gases are usually chromia formers. As seen in **Table 2**, chromium also forms reasonably stable carbides. It is commonly observed<sup>6-8</sup> that exposure of these alloys to gas compositions such that no chromia scale can form leads to internal chromium carbide precipitation, rather than external scale formation. The conditions under which this

reaction morphology develops are now examined using model Fe–Cr, Ni–Cr, and Fe–Ni–Cr alloys, for which the necessary data is available.

## 1.12.4 Internal Carburization of Model Alloys

### 1.12.4.1 Reaction Morphologies and Thermodynamics

Chromium carbides are the expected reaction products and their formation within the alloy is the outcome of competition between rival processes. Scale formation is favored by rapid diffusion of chromium from the alloy to its surface, whereas internal precipitation is favored by rapid carbon ingress. Wagner's analysis<sup>9</sup> of this situation allows calculation of the minimum value of  $N_{Cr}^{(o)}$  at which scaling is favored over internal precipitation

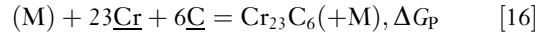
$$N_{Cr}^{(o)} = \left( g_{CrC_v} \frac{\pi}{2v} \frac{V_A}{V_{CrC_v}} \frac{N_C^{(s)} D_C}{D_{Cr}} \right)^{1/2} \quad [15]$$

where  $g$  is the critical volume fraction necessary to form a continuous carbide layer,  $V_A$  and  $V_{CrC_v}$  are the molar volumes of alloy and carbide,  $D_C$  and  $D_{Cr}$  are the diffusion coefficients in the alloy of the indicated solutes, and  $v$  is the stoichiometric constant for the carbide  $CrC_v$ . Choosing Nimonic 75 (approximately Ni–20Cr) as a basis for calculation, we can specify  $V_A = 6.58 \text{ cm}^3 \text{ mol}^{-1}$ . Values for carbon permeability ( $N_C^{(s)} D_C$ ) and  $D_{Cr}$  listed in Table 4, together with  $V_{CrC_v}$  from Table 2 and the supposition  $g = 0.3$ , lead to estimates of  $N_{Cr}^{(o)} = 15, 20$ , and 37 required to form scales of  $Cr_3C_2$ ,  $Cr_7C_3$ , and  $Cr_{23}C_6$ , respectively, at 1000 °C. Of course, values of  $N > 1$  lack physical significance and result from inaccuracies in the data. The conclusion is simply that Ni–Cr alloys are unlikely to form carbide scales exclusively, because the inward carbon flux is so high and the molar volume of chromium carbide is small.

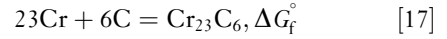
**Table 4** Permeability data for carburization

Alloy	$T$ (°C)	$N_C^{(s)} D_C$	$D_{Cr}$
$\gamma$ -Fe	900	$4.3 \times 10^{-9}$	$4.4 \times 10^{-13}$
	1000	$1.4 \times 10^{-8}$	$3.7 \times 10^{-12}$
	1100	$5.5 \times 10^{-8}$	$2.3 \times 10^{-11}$
Ni	900	$7.9 \times 10^{-10}$	$8.0 \times 10^{-13}$
	1000	$3.6 \times 10^{-9}$	$7.2 \times 10^{-12}$
	1100	$1.4 \times 10^{-8}$	$4.7 \times 10^{-11}$

The conditions necessary for carbide precipitation are now examined more closely. In the case of  $Cr_{23}C_6$ , we can write



the free energy change for which can be calculated from data for carbide formation



and alloy component dissolution



in the solvent metal, M. Thus,

$$\Delta G_p = \Delta G_f^\circ - 23\Delta \bar{G}_{Cr} - 6\Delta \bar{G}_C \quad [20]$$

and we evaluate the carbide solubility product

$$N_{Cr}^{23} N_C^6 = K_{sp} = \exp[(\Delta G_f^\circ - 23\Delta \bar{H}_{Cr} - 6\Delta \bar{H}_C)/RT] \quad [21]$$

with  $\bar{H}_i$  being the partial molar heat of dissolution. A similar treatment for  $Cr_7C_3$  leads to the result

$$N_{Cr}^7 N_C^3 = K_{sp} = \exp[(\Delta G_f^\circ - 7\Delta \bar{H}_{Cr} - 3\Delta \bar{H}_C)/RT] \quad [22]$$

Standard values (Table 2) for  $\Delta G_f^\circ$ , carbon solubility data for  $\gamma$ -Fe and Ni (Table 3), and activity coefficient data for Fe–Cr<sup>10</sup> and Ni–Cr<sup>11</sup> allow calculation of carbide solubility product values shown in Tables 5 and 6.

Carbon solute levels in  $\gamma$ -Fe and Ni in equilibrium with  $a_C = 1$  are also shown in the tables, along with the corresponding minimum chromium concentrations necessary to stabilize each carbide. Iron base alloys are predicted on this basis to be more susceptible to internal carbide precipitation. This prediction is tested by comparing the calculated minimum  $N_{Cr}$  values required for carbide precipitation with the

**Table 5** Chromium carbide precipitation in Fe–Cr alloys

Alloy	900 °C	1000 °C	1100 °C
$N_C^{(s)}(\gamma\text{-Fe})$	0.057	0.066	0.098
$K_{sp}(Cr_{23}C_6)$	$1 \times 10^{-29}$	$3.6 \times 10^{-27}$	$2.6 \times 10^{-24}$
$N_{Cr}(\text{min})$	0.12	0.14	0.17
$K_{sp}(Cr_7C_3)$	$3 \times 10^{-16}$	$3.8 \times 10^{-15}$	$3.4 \times 10^{-14}$
$N_{Cr}(\text{min})$	0.02	0.03	0.03

**Table 6** Chromium carbide precipitation in Ni–Cr alloys

Alloy	900 °C	1000 °C	1100 °C
$N_{\text{C}}^{(\text{s})}$	0.007	0.011	0.016
$K_{\text{sp}}(\text{Cr}_{23}\text{C}_6)$	$9.9 \times 10^{-26}$	$8.4 \times 10^{-24}$	$3.7 \times 10^{-22}$
$N_{\text{Cr}}(\text{min})$	0.29	0.32	0.34
$K_{\text{sp}}(\text{Cr}_7\text{C}_3)$	$9.8 \times 10^{-14}$	$9.4 \times 10^{-13}$	$6.5 \times 10^{-12}$
$N_{\text{Cr}}(\text{min})$	0.10	0.13	0.17

**Table 7** Internal carbides found in Ni–Cr and Fe–Cr at 1000 °C at ambient  $a_{\text{C}} = 1$ 

Alloy	$N_{\text{Cr}}^{(\text{o})}$	Surface carbides	Internal carbides	Ref.
Ni–Cr	0.11	None	None	12
	0.22	$\text{Cr}_3\text{C}_2$	$\text{Cr}_7\text{C}_3$	12
	0.33		$\text{Cr}_7\text{C}_3$	13
Fe–Cr	0.05	$\text{M}_3\text{C}$	$\text{M}_7\text{C}_3^{\text{a}}$	14
	0.08	$\text{M}_3\text{C}$	$\text{M}_7\text{C}_3$	14
	0.11	$\text{M}_3\text{C}$	$\text{M}_7\text{C}_3$	14
	0.18	$\text{M}_7\text{C}_3$	$\text{M}_7\text{C}_3 + \text{M}_{23}\text{C}_6$	14
	0.26	$\text{M}_7\text{C}_3$	$\text{M}_7\text{C}_3 + \text{M}_{23}\text{C}_6$	14

<sup>a</sup>M: chromium-rich (Cr + Fe).

experimental results for 1000 °C summarized in **Table 7**. The appearance of the carbide precipitation zones in Fe–Cr alloys is illustrated in **Figure 2**. As predicted, Fe–Cr alloys of high chromium content formed both carbides, whereas Ni–Cr formed only  $\text{Cr}_7\text{C}_3$ . Furthermore, the prediction that no carbide should form in Ni–Cr with  $N_{\text{Cr}}^{(\text{o})} < 0.13$  is borne out.

The success of this simple thermodynamic treatment indicates that local equilibrium is attained, and a steady-state diffusion description should be applicable. However, whilst the assumption that the chromium carbides are pure phases – the basis for eqns. [21] and [22] – is reasonable for the Ni–Cr–C system, it is a poor approximation for Fe–Cr–C. As seen in the phase diagram of **Figure 3**, iron solubilities in the carbides are high, and cannot be neglected. It is possible to calculate  $K_{\text{sp}}$  values for the mixed carbides  $(\text{Cr,Fe})_{23}\text{C}_6$  and  $(\text{Cr,Fe})_7\text{C}_3$ , but a simpler approach is to construct diffusion paths representing the locus of phase constitutions along lines through the reaction zone. As  $D_{\text{C}} \gg D_{\text{Cr}}$ , these paths are constructed on the basis that only carbon diffuses and hence the  $N_{\text{Cr}}/N_{\text{Fe}}$  ratio remains unchanged within the reaction zone.

The diffusion path in **Figure 3** for  $N_{\text{Cr}}^{(\text{o})} = 0.08$  is seen to cross the  $\gamma + \text{M}_7\text{C}_3$  two-phase region, corresponding to internal precipitation of this carbide,

before entering the single-phase  $\text{M}_3\text{C}$  zone, in agreement with experimental observation (**Table 7**). An alloy with  $N_{\text{Cr}}^{(\text{o})} = 0.18$  is seen to develop a carbon diffusion path which crosses successive two-phase regions  $\gamma + \text{M}_{23}\text{C}_6$  and  $\gamma + \text{M}_7\text{C}_3$  before entering the single-phase  $\text{M}_7\text{C}_3$  field. Again, this corresponds with the experimental observation (**Table 7**) of two internal precipitation zones, with  $\text{M}_{23}\text{C}_6$  forming in the inner (lower  $a_{\text{C}}$ ) zone.

As iron solubility in the carbides increases with  $a_{\text{C}}$ , the Fe/Cr ratio in the precipitates is predicted to decrease with increasing depth within the precipitation zone. Microanalysis in a transmission electron microscope of carbides precipitated within an Fe–Ni–Cr alloy<sup>16</sup> revealed the partitioning of chromium between precipitate and matrix in the carburized alloy. As seen in **Figure 4**, the results are in reasonable agreement with measured equilibrium values, and again it is concluded that local equilibrium is achieved throughout the precipitation zone. Two more important inferences can be drawn from the phase diagram of **Figure 3**. Carburization is predicted to transform the alloy matrix of a high-chromium Fe–Cr alloy from ferrite to austenite as a result of chromium depletion and carbon saturation. As shown in **Figure 2**, this transformation is observed at the precipitation front. Secondly, if  $N_{\text{Cr}}^{(\text{o})}$  is less than  $\sim 0.4$ , then  $(\text{Fe,Cr})_3\text{C}$  is predicted to form at or near the alloy surface if the gas phase  $a_{\text{C}}$  value is high enough. This is important in metal dusting reactions (**Section 1.12.6**), but can be ignored when studying carburization reactions at  $a_{\text{C}} \leq 1$ . Furthermore, in austenitic alloys the nickel content destabilizes  $\text{Fe}_3\text{C}$ , and the phase is not observed.

#### 1.12.4.2 Carburization Kinetics

Internal carburization is a particular form of internal oxidation, and its kinetics can therefore<sup>6–8,12</sup> be described using Wagner's theory.<sup>9</sup> Because  $N_{\text{C}}^{(\text{s})} D_{\text{C}} \gg N_{\text{Cr}}^{(\text{o})} D_{\text{Cr}}$ , the rate at which the carbide precipitation zone deepens is given by

$$X_i^2 = 2k_{\text{p}}^{(\text{i})} t \quad [23]$$

$$k_{\text{p}}^{(\text{i})} = \frac{\epsilon N_{\text{C}}^{(\text{s})} D_{\text{C}}}{v N_{\text{M}}^{(\text{o})}} \quad [24]$$

where  $N_{\text{M}}^{(\text{o})}$  is the original alloy concentration of metal M which forms carbide  $\text{MC}_v$ . Thus, carburization rates are predicted to vary inversely with concentration of reactive solute metal. Data for a series of Fe–Cr

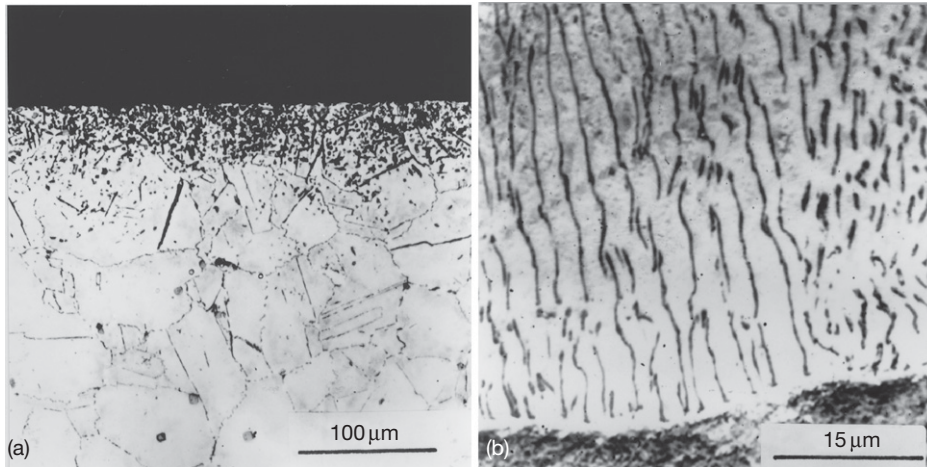


**Figure 2** Internal carburization of Fe–Cr at 1000 °C (a) Fe–7.5Cr forms  $M_7C_3$  precipitates and (b) Fe–17Cr forms innermost zone of  $M_{23}C_6$  precipitates.<sup>14</sup>

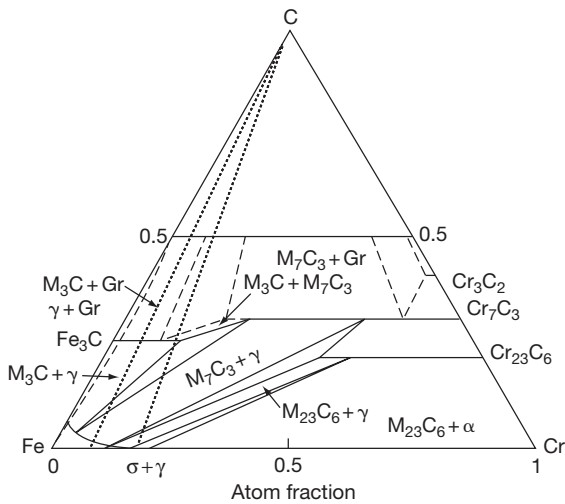


**Figure 3** Isothermal section at 1000 °C of the Fe–Cr–C phase diagram.<sup>15</sup> Dotted lines show carburization diffusion paths for  $D_C \gg D_{Cr}$ .

alloys<sup>14,17</sup> is shown in **Figure 5**. The kinetics are seen to be parabolic, and plots of  $k_p^{(i)}$  against  $1/N_{Cr}^{(o)}$  are linear except at high  $N_{Cr}^{(o)}$  values. The slopes of these lines were used together with  $v = 0.71$  (for  $(Cr_{0.6}Fe_{0.4})_7C_3$  formed by low-chromium alloys) and the assumption  $\epsilon = 1$  to calculate carbon permeabilities. Comparison in **Table 8** with values found from  $N_C^{(s)}$ <sup>3</sup> and  $D_C$ <sup>4</sup> measurements shows good agreement, demonstrating the utility of **eqn. [24]** in describing carburization rates. This is at first sight surprising, as **eqn. [24]** is based on the assumption that  $K_{sp} \ll 1$ , and the

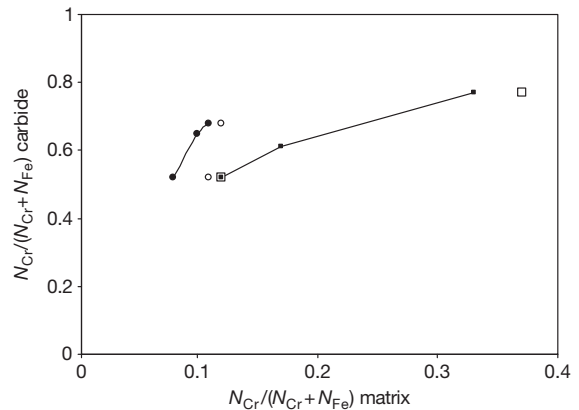


**Figure 4** Partitioning of Cr between precipitates and matrix in carburized alloy<sup>16</sup> (filled symbols) and in equilibrium studies<sup>15</sup> (open symbols). Circles for  $M_7C_3$  and squares for  $M_{23}C_6$ .

concentration of chromium in the matrix being close to zero. However, as will be seen in **Section 1.12.4.3**, the effect on carburization rates is small.

A further prediction of **eqn. [24]** is that carburization rates are determined by the permeability of the metal matrix, regardless of the identity of the precipitating carbide, providing that changes in the stoichiometric coefficient  $v$  are taken into account. Permeability values calculated for nickel by Allen and Douglass<sup>12</sup> from their carburization measurements of Ni–V, Ni–Cr, and Ni–Nb alloys are seen in **Table 9** to be in approximate agreement with each other and with values found from independently

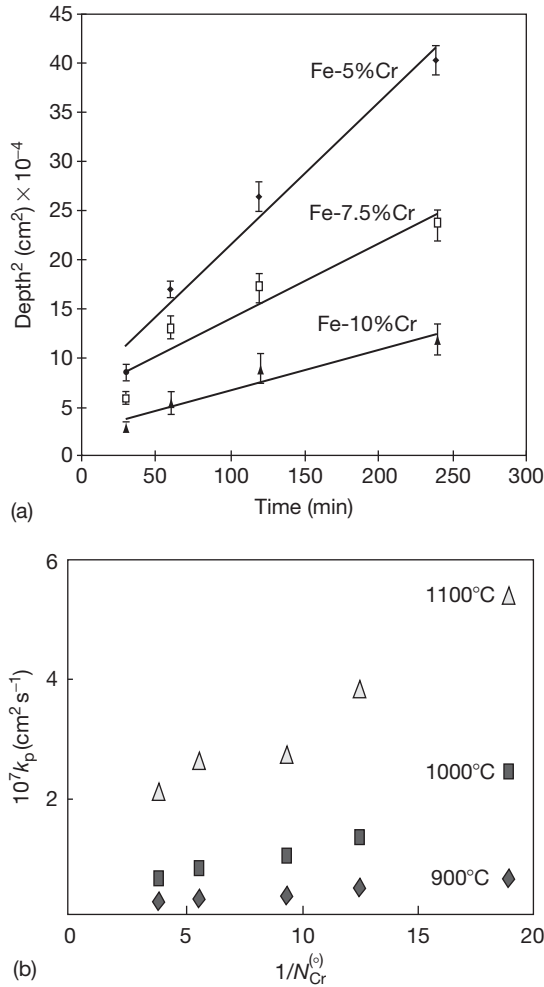


**Figure 5** Carburation of Fe–Cr alloys (a) representative kinetics at 1000 °C and (b) effect of alloy chromium content on carburization rate.<sup>14,17</sup>

measured values of  $N_C^{(s)}$ <sup>2</sup> and  $D_C$ .<sup>5</sup> It is concluded that internal carburization of both Fe and Ni base alloys is controlled by interstitial diffusion of carbon through the depleted metal matrix lattice. The temperature effect on the rate is described by the empirical equation:

$$k_p^{(i)} = k_o^{(i)} \exp(-E_A/RT) \quad [25]$$

Logarithmic differentiation of eqn. [24] yields

$$E_A = \Delta \bar{H}_C + Q \quad [26]$$

where  $Q$  is the activation energy of diffusion. In the case of Fe–Cr alloys, the extent of iron dissolution in the carbides varies with temperature as does the

**Table 8** Carbon permeabilities  $N_C^{(s)}D_C$  (cm² s⁻¹) in Fe–Cr

	900 °C	1000 °C	1100 °C
Carburization kinetics	$6.6 \times 10^{-9}$	$2.5 \times 10^{-8}$	$6.2 \times 10^{-8}$
From $N_C^{(s)}$ and $D_C$	$4.3 \times 10^{-9}$	$1.4 \times 10^{-8}$	$5.5 \times 10^{-8}$

**Table 9** Carbon permeabilities ( $N_C^{(s)}D_C$ ) ( $10^{10}$  cm² s⁻¹) deduced from carburization kinetics of Ni–base alloys<sup>12</sup>

Alloy	$T$ (°C)			
	700	800	900	1000
Ni–12V	0.40	2.2	11	44
Ni–20Cr	0.21	0.8	8	55
Ni–3Nb	0.30		6	14
From $N_C^{(s)}$ and $D_C$	0.19	1.6	7	36

stability of the carbides, and the simple description of eqn. [26] cannot be expected to apply. In the case of Ni–Cr alloys, however, nickel dissolves to only a small extent in the carbides, and  $Cr_7C_3$  is the only stable internal carbide over a wide range of temperature for  $N_{Cr}^{(0)} \approx 0.2$ . The value of  $E_A = 190$  kJ mol⁻¹ measured by Allen and Douglass<sup>12</sup> for Ni–20Cr agrees with the prediction of eqn. [26] based on  $\Delta \bar{H}_C = 54$  kJ mol⁻¹<sup>(2)</sup> and  $Q = 138$  kJ mol⁻¹<sup>(5)</sup>.

Chromia-forming alloys are usually based on Fe–Ni, and the applicability of eqn. [24] to Fe–Ni–Cr model alloys is now tested. Carburization of 25Cr alloys at 1000 °C and  $a_C = 1$  produces two reaction zones. Diffraction studies identified the near-surface zone precipitates as  $M_7C_3$ , and those in the inner zone as  $M_{23}C_6$ . Carburization kinetics of a series of Fe–Ni–Cr alloys have been found<sup>18</sup> to be parabolic at 1000 °C, and the rate constants are seen in Figure 6 to vary considerably with alloy nickel content. If nearly all the chromium is precipitated as carbide, then the reaction is sustained by carbon dissolution in and diffusion through the remaining Fe–Ni matrix. Ignoring the dissolution of some of the iron into carbide, we approximate the matrix as having the same  $N_{Ni}/N_{Fe}$  ratio as the parent alloy. On this basis, one can use values of  $N_C^{(s)}$  measured by Wada *et al.*<sup>2</sup> for Fe–Ni alloys and for  $D_C$  measured by Bose and Grabke<sup>19</sup> to predict carburization rates from eqn. [24]. Measured and predicted rates were found<sup>18</sup> to agree very well. It is therefore concluded that the Wagner theory provides a satisfactory basis for describing the carburization of alloy compositions close to those of



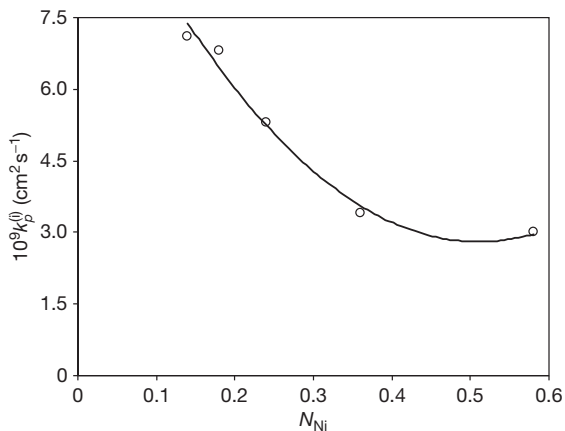


**Figure 6** Variation of carburization rate at 1000 °C with Ni content of Fe–Ni–25Cr alloys.<sup>18</sup>

commercial heat-resisting alloys. Before going on to consider practical alloys, it is worth considering the microstructures and distributions of carbide precipitates.

#### 1.12.4.3 Carbide Microstructures and Distributions

Particles of  $M_7C_3$  precipitated in austenite are globular, and develop no rational orientation relationship with the matrix. In contrast,  $M_{23}C_6$  possesses a cubic structure and develops a strong cube-in-cube orientation relationship with the fcc  $\gamma$ -matrix<sup>20</sup>

$$[001]_{\gamma}[001]_{M_{23}C_6} : (100)_{\gamma}(100)_{M_{23}C_6} \quad [27]$$

Usually, the  $M_{23}C_6$  precipitates are small, cuboidal, or needle-shaped particles (e.g., **Figure 7**). The small precipitate size reflects the fact that they grew for only a short time: a result of the continued nucleation of new particles as the reaction front advanced into the alloys. This in turn was due to rapid carbon diffusion, which quickly produced sufficient supersaturation to favor homogeneously distributed nucleation. In other circumstances, the same carbide can form elongated lamellar or lath shaped precipitates oriented parallel to the reaction direction (**Figure 7**). As the value of  $k_p^{(i)}$  is 30–50% higher when the aligned microstructure is adopted, the reasons for its development are of interest.

Lamellar or cellular  $M_{23}C_6$  microstructures have been reported to develop in ferritic alloys,<sup>14,16,21,22</sup> in high-nickel austenitics,<sup>18</sup> and in a variety of heat-resisting alloys carburized at low temperatures.<sup>23,24</sup> It is also observed in previously nitrided Fe–Ni–Cr

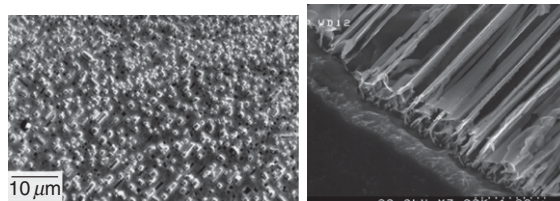
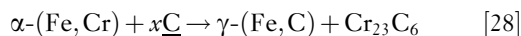


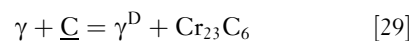
**Figure 7** Cuboidal and lath-shaped  $M_{23}C_6$  precipitates at the reaction front in Fe–20Ni–25Cr carburized at 1000 °C.

alloys.<sup>18,20</sup> A distinctive common feature in these cases is the formation of a grain boundary at the carbide precipitation front. In the case of ferritic alloys (**Figure 2(b)**), the boundary corresponds to the phase transformation



In high-nickel alloys, lamellar carbides develop in colonies in the alloy interior. It seems likely that they nucleated at alloy grain boundaries and then grew into the adjacent grain in a discontinuous precipitation process which is now described.

A clear view of the boundary at the carbide precipitation front is shown in **Figure 8** for an Fe–20Ni–25Cr alloy first subjected to a brief period of internal nitridation to form a boundary just beneath the surface. Subsequent carburization led to the pictured microstructure: the dark grain on the right is unreacted austenite, the light grain on the left is chromium-depleted matrix, and the precipitates are  $M_{23}C_6$ . The selected area diffraction pattern shows the same cube-in-cube orientation relationship [27] between precipitate and matrix. The crystallographically oriented sides of the precipitates were always the close-packed (111) planes. No rational orientation relationships were found between unreacted austenite and either reacted austenite or carbide. Microanalysis results in **Figure 8** show a step function change in  $N_{Cr}$  at the austenite/depleted austenite grain boundary, but no sign of lateral diffusion within the matrix. The mechanism is that of discontinuous precipitation<sup>20,25</sup>



where  $\gamma^D$  denotes depleted austenite. The change in crystallographic orientation from parent  $\gamma$  to product  $\gamma^D$  is obvious in **Figure 8**. This reorientation resulted from the free energy reduction achieved when the austenite formed coherent interfaces with the precipitates which grew approximately unidirectionally, parallel to the carbon diffusion direction.

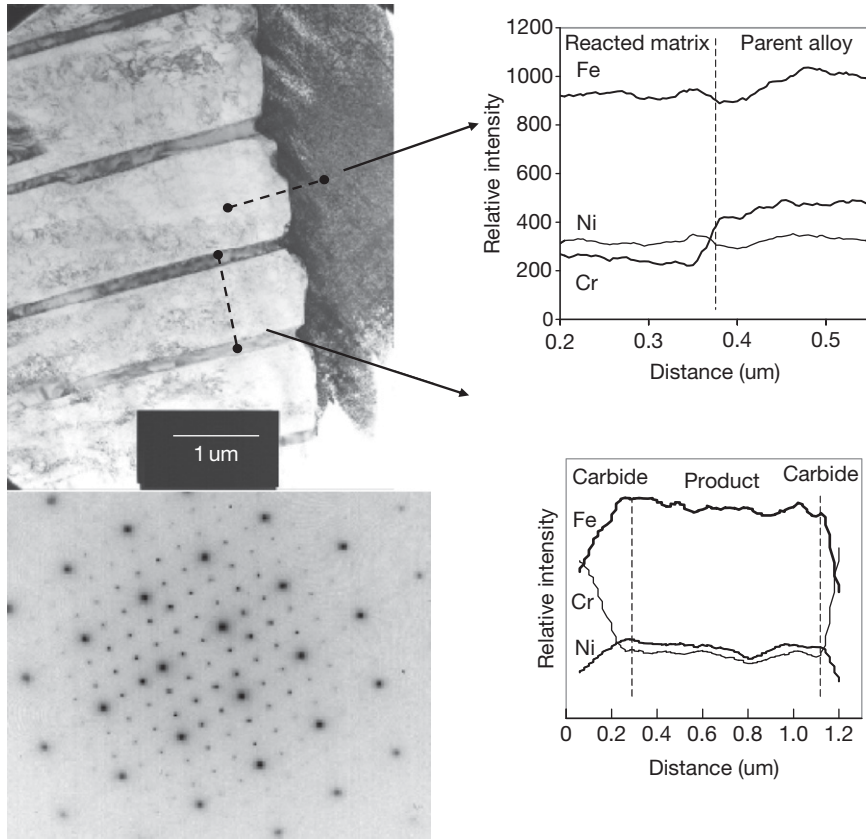


**Figure 8**  $M_{23}C_6$  precipitation front in Fe–20Ni–25Cr after brief prenitridation and subsequent carburization at 1000 °C,  $a_C = 1$ .<sup>20,25</sup>

The incoherency of the  $\gamma/\gamma^D$  interface is evident in its curvature, and this provided rapid chromium diffusion towards the advancing carbide precipitate tips, sustaining their growth and producing the discontinuous change in  $N_{Cr}$  seen at the interface.

It is concluded that lamellar carbide precipitates develop when a grain boundary is present. The boundary provides more rapid chromium diffusion to the precipitates, favoring their continued growth rather than nucleation of new ones. As seen in **Figure 5(b)**, carburization rates for Fe–Cr alloys with high  $N_{Cr}$  values are higher than predicted by **eqn. [24]**. These are the alloys which form lamellar precipitates, and the acceleration is attributed to boundary diffusion of carbon along the multiple carbide–austenite interfaces. As  $N_C^{(s)} D_C$  in austenite is in any case large, the increase in rate is relatively small: 30% faster in Fe–Cr and 30–50% faster in Fe–Ni–Cr alloys at 1000 °C.

Carbide precipitate distributions are nonuniform, because  $K_{sp}$  is not small. Thus, as depth within the

precipitation zone increases,  $a_C$  and  $N_C$  decrease causing  $N_{Cr}$  to increase according to the solubility product equilibria [21] and [22]. As a result, the amount of chromium precipitated is less. The qualitative effect on carburization rate can be seen from **eqn. [24]**: because the effective value of  $N_{Cr}^{(o)}$  is lowered, the penetration rate is faster. This effect has been analyzed<sup>26,27</sup> for the general case of low-stability precipitates. Deviation from the Wagner assumption of vanishingly small  $K_{sp}$  values is expressed via a solubility parameter

$$\alpha = 1 - N_{Cr}^{(s)}/N_{Cr}^{(o)} \quad [30]$$

where  $N_{Cr}^{(s)}$  is the matrix equilibrium chromium concentration at the surface of the reacted alloy. If  $\alpha = 1$ ,  $K_{sp} = 0$  and the Wagner model applies; if  $\alpha = 0$ , no precipitation occurs and an error function solution describes the carbon profile. Considering Fe–Cr alloys, we find from **eqn. [22]** and the data of **Table 5** that  $N_{Cr}^{(s)} = 0.028$ . Taking a representative value of

$N_{\text{Cr}}^{(0)} = 0.25$ , then a value of  $\alpha = 0.9$  is arrived at. For this value, Ohriner and Morall<sup>26</sup> calculate that  $k_p^{(i)}$  is increased by a factor of 2 above that predicted from eqn. [24]; that is, the penetration depth is increased by  $\sim 40\%$ . However, uncertainties in measured values of  $D_C$ ,  $N_C^{(s)}$ , and  $k_p^{(i)}$  total at least this amount. A similar conclusion is reached for  $\text{Cr}_{23}\text{C}_6$  precipitation. It is, therefore, concluded that despite the approximate nature of its assumptions, the simple result eqn. [24] provides good order of magnitude prediction for model alloy carburization. A more precise prediction can be made using the numerical treatment of the Ohriner–Morall theory developed by Christ.<sup>28</sup>

### 1.12.5 Internal Carburization of Heat-Resisting Alloys

Many laboratory studies of the carburization of heat-resisting alloys have been reported.<sup>6–8,28–45</sup> These are in general agreement with the findings from industrial exposures<sup>46</sup> that carburization rates vary with Fe/Ni ratio and decrease with increased levels of Cr, Nb, Si, and sometimes W and Ti.

The usual appearance of a cast heat-resistant alloy after carburization is shown in Figure 9. Murakami's etch reveals finely precipitated, cuboidal  $\text{M}_{23}\text{C}_6$  particles in the inner zone and coarser, spherical  $\text{M}_7\text{C}_3$  particles near the surface. The original cast alloy structure is seen to the right: austenite dendrites with primary interdendritic  $\text{M}_{23}\text{C}_6$ . Near the carburization front, preferential precipitation is seen along dendrite boundaries. Some fragmentary external carbide scale is also seen. This is usually  $\text{Cr}_3\text{C}_2$  on

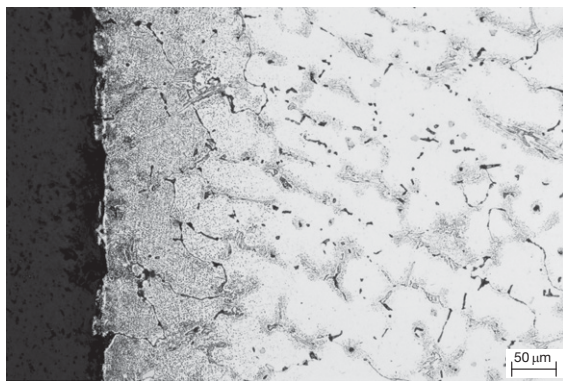


**Figure 9** Cast alloy Fe–45Ni–19Cr after carburization for 24 h at 900 °C.

high-nickel alloys and  $\text{M}_7\text{C}_3$  on low-nickel materials. The difference arises from the changed Fe/Cr ratios.<sup>35</sup> Thus, reaction morphologies are consistent with local equilibrium. Moreover, as the internal carburization kinetics are parabolic, it is clear that the process is diffusion controlled.

Despite the complexity of these alloys, their relative performance under nonoxidizing conditions can be understood in terms of Wagner's equation [24]. The procedure is to model the heat-resisting alloys as Fe–Ni–Cr ternaries, and approximate the carburization zones as chromium carbide precipitates in an Fe–Ni matrix. Carburization rates are then predicted from eqn. [24] to change with carbon permeability,  $N_C^{(s)} D_C$ . This permeability shows a minimum at Ni/Fe  $\approx 4:1$ ,<sup>2,10</sup> which was shown by Rahmel *et al.*<sup>47</sup> to be reflected in relative penetration depths of a range of alloys. Clearly, the Fe/Ni ratio has a significant effect on carburization rate. However, this approach neglects the effect of  $N_M$ , and a more detailed calculation is required.

The quantity  $N_M$  represents mainly chromium. In calculating its value, the alloy chromium content must, therefore, be corrected for the amount already removed from the matrix into interdendritic carbide during casting. This is done on the assumption that all of the alloy carbon was precipitated as pure  $\text{Cr}_{23}\text{C}_6$ . Added contributions to  $N_M$  are calculated on the basis of NbC and other MC carbide formation, as well as the molybdenum carbides  $(\text{Mo}_2\text{Fe})\text{C}$  and  $(\text{CrMoFe})\text{C}$ . As seen earlier, the application of eqn. [24] is nonetheless an approximation because  $\text{M}_7\text{C}_3$  and  $\text{M}_{23}\text{C}_6$  carbides contain substantial levels of iron.<sup>15</sup> Consequently, the value of  $N_M$  calculated as described above is an underestimate. On the other hand, however, an overestimate of  $N_M$  results from the error in the mass balance underlying eqn. [24]. This latter error arises because the solubility products of  $\text{Cr}_7\text{C}_3$  and  $\text{Cr}_{23}\text{C}_6$  are large, and significant levels of chromium remain unreacted in the depleted matrix.

Carburization leads to approximately equimolar amounts of  $\text{M}_7\text{C}_3$  and  $\text{M}_{23}\text{C}_6$ ; hence, a value of  $v = 0.345$  is used in eqn. [24]. No value for  $\epsilon$  is available. Predicted  $k_p$  values based on  $\epsilon = 1$  are compared in Table 10 with measured<sup>40</sup> quantities for a selection of alloys. It is seen that close order of magnitude agreement is achieved for the 30, 35, and 45 Ni grades, but not for the 60Ni grades. The latter contain aluminum, and will be discussed below. We consider first the effects of other alloy components.

**Table 10** Carburization rate constants ( $k_p$ ) ( $10^7 \text{ cm}^2 \text{ s}^{-1}$ ) for heat-resisting alloys

Cast Alloy	1100 °C		1000 °C		900 °C	
	Measured	Calc	Measured	Calc	Measured	Calc
Fe-30Cr-30Ni (Nb, Ti, Zr)	1.45	2.05	0.13	0.33	0.10	0.11
Fe-25Cr-35Ni (Nb)	0.64	2.15	0.28	0.37	0.18	0.10
Fe-26Cr-36Ni (Nb, low C)	0.44	1.32	0.17	0.24	0.06	0.06
Fe-35Cr-45Ni	0.44	0.50	0.10	0.08	0.04	0.03
Fe-19Cr-45Ni (Mo, Hf)	0.41–0.43	0.99	0.13–0.22	0.18	0.05–0.08	0.03
Fe-30Cr-45Ni (Hf)	0.63	0.62	0.10–0.15	0.15	0.04–0.05	0.02
Fe-25Cr-60Ni-2.4Al	0.14	0.87	0.04	0.17	0.03	0.03
Fe-25Cr-60Ni-3.6Al	0.01	0.95	0.01	0.19	0.02	0.03
Fe-25Cr-60Ni-4.8Al	0.02	0.90	ND	0.18	ND	0.03
602CA (2.3 Al, wrought)	0.14	0.82	0.04	0.17	0.03	0.03

ND, not determined.

### 1.12.5.1 Effect of Carbon

Cast alloys usually contain high levels of carbon, which segregates as  $\text{M}_{23}\text{C}_6$  during alloy solidification, thereby affecting  $N_M$  as described above. The success of this description is tested by comparing carburization rates for the alloy Fe-25Cr-35Ni-Nb with high and low carbon. At 1000 °C, the ratio  $k_p(\text{High C})/k_p(\text{Low C})$  predicted from eqn. [24] to be 1.5 compares well with the measured value of 1.7. Agreement at the other temperatures is also good. It is concluded that the method used to calculate the effect of original alloy carbon is successful. On this basis, it would follow that cast alloys have lower carburization resistance than their wrought (low carbon) equivalents. In fact, the opposite effect is found,<sup>8,38</sup> as a result of rapid grain boundary diffusion of carbon in wrought alloys.

### 1.12.5.2 Effect of Molybdenum

Molybdenum can be added for solution strengthening of an alloy, and is also a carbide former. Two alloys containing 24Cr, 32Ni, 0.8Nb, and 0.44C, with and without the addition of 3 w/o Mo were found<sup>38</sup> to carburize at  $a_C = 1$  at significantly different rates. The carbides  $\text{Mo}_3\text{C}$  and  $\text{Cr}_7\text{C}_3$  are of comparable stability, and can therefore co-exist if the metals are at similar activity levels. In fact, the carbides  $(\text{Mo}_2\text{Fe})\text{C}$ ,  $(\text{CrFeMo})\text{C}$ , and  $\text{Cr}_7\text{C}_3$  were all identified by X-ray diffraction analysis of the carburized alloy C. Equation [24] is now used to test the possibility that precipitation of molybdenum carbides slows the rate.

A level of 3 w/o molybdenum, forming a carbide of stoichiometry  $\text{Mo}_{1.5}\text{C}$  (an average of the two observed carbides), is equivalent in its consumption

of carbon to a level of 2.5 w/o chromium, forming  $\text{Cr}_7\text{C}_3$ . The value of  $N_M$  in the molybdenum-bearing alloy is on this basis calculated to be 13.6% higher than for the comparison alloy. Taking into account the effects of alloy compositional changes in  $D_C$ ,  $N_C$ , and  $N_M$  gives predicted relative reductions in the  $k_p$  values when Mo is added of 40% at 900 °C, 23% at 1050 °C, and 10% at 1150 °C. The measured reductions were 44% at 900 °C, 24% at 1050 °C, and 16% at 1150 °C. This suggests that eqn. [24] enables the effect of molybdenum to be modeled, subject to the reliability of the  $N_C$  and  $D_C$  data. Furthermore, it also predicts correctly the effect of temperature on the efficacy of this element in reducing carburization.

### 1.12.5.3 Effect of Silicon

It has long been known<sup>29</sup> that silicon slows carburization, even under gas conditions where no silicon-rich oxide can form. The stability of  $\text{SiC}$  is a great deal less than that of  $\text{Cr}_{23}\text{C}_6$  and  $\text{Cr}_7\text{C}_3$  and no  $\text{SiC}$  will form in these chromium-rich alloys. Increasing the alloy silicon content therefore has no effect on  $N_M$ . Under the reducing conditions of these experiments no  $\text{SiO}_2$  is formed, and the beneficial effects to be expected of silicon on carburization rates under reducing conditions, therefore, result from modification of the carbon solubility and/or diffusivity. These modifications are due to thermodynamic interaction between the dissolved silicon and carbon.

Silicon is known to reduce both  $N_C^{(s)}$  and  $D_C$ . Roy *et al.*<sup>48</sup> have examined the effect of silicon on carbon diffusion in Fe-Si-C. A comparison of carburization rates of two cast heat-resisting steels which differed only in their silicon levels showed<sup>38</sup> that increasing the silicon level decreased the rate by more than



would be predicted from Roy's diffusion data. The other major contributory factor is the depression of carbon solubility by silicon. The effect has been measured in liquid iron alloys, where the resulting change in carbon solubility is significant, but no data directly applicable to heat-resisting alloys is available.

#### 1.12.5.4 Effect of Niobium and Reactive Elements

Niobium is often added to cast heat resistant alloys for strengthening purposes. It is also found in some wrought alloys, where it improves weldability. Reactive elements such as Ce and Hf are added to modify carbide shapes and to improve oxide scale spallation resistance. All are strong carbide formers and have strong effects on carburization resistance. The benefits of niobium have been reported several times.<sup>8,45,49</sup> The variation of  $k_p^{(i)}$  with niobium concentrations is shown in Figure 10 for several heat-resisting alloys. The effect of niobium can be distinguished from variations in  $N_C^{(s)}D_C/D_M$  also plotted in this figure. Even if all the alloy niobium was available in solution to precipitate NbC, the effect of adding 1–2 w/o Nb on  $N_M$  is very small, much less than the substantial reductions in  $k_p^{(i)}$  seen at higher niobium levels.

Similar effects have been noted for additions of Ce<sup>39</sup> and Hf.<sup>40</sup> These elements are present at low concentrations, typically around 0.1–1.0 w/o, and their effect on the value of  $N_M$  is negligible. Nonetheless, their addition is found to reduce carburization rates substantially. It is possible that carbides of Nb, Ce, and Hf precipitate preferentially at sites where interference with carbon diffusion is maximal. As carbon penetration is more rapid at primary carbide/

dendrite boundaries (Figure 9), reactive metal carbide precipitation at these interfaces could exercise a disproportionate effect on the overall rate.

#### 1.12.5.5 Effect of Aluminum

The 60Ni alloys in Table 10 were predicted from eqn. [24] to carburize at rates similar to the 45Ni alloys. At 900 °C, the wrought alloy 602 CA and two cast versions reacted at close to the predicted rates. At higher temperatures, the rates were much slower than predicted. The explanation is clear from the micrographs of Figure 11, where a protective, external scale is seen to form on high- $N_{Al}$  alloys. The scale was  $\alpha$ -Al<sub>2</sub>O<sub>3</sub>, which is thermodynamically stable at the water vapor impurity levels which are unavoidable in reaction gases. However, external scale formation is possible only when a sufficient flux of alloy solute aluminum is available, and internal oxidation can be avoided (see eqn. [15]). This flux increases with both alloy  $N_{Al}$  and temperature, through its effect on  $D_{Al}$ , qualitatively accounting for the observed pattern of behavior. When this scale formed, it functioned as a barrier limiting carbon access to the underlying metal. Thus, at 900 °C, no alumina formed and the 60Ni alloys all carburized at the expected rates. At 1000 and 1100 °C, alumina scales grew on all alloys, and carburization was slowed. The scale was discontinuous on the low-aluminum alloys, and carburization was not completely suppressed. A minimum aluminum content of ~4 w/o was required to achieve complete protection.

#### 1.12.5.6 Alloying for Carburization Protection

The kinetics of alloy carburization are very well described by diffusion theory, and a rational approach to alloy design is therefore available. Unfortunately, however, most methods of suppressing internal attack on chromia-forming alloys are either impractical or only modestly successful. It is not possible to adjust chromium levels to achieve exclusive external carbide growth. Modifications of alloy carbon permeability through adjusting the Fe/Ni ratio or alloying with other metals yield only small improvements in carburization rates. Silicon decreases carbon solubility and diffusivity quite strongly, but metallurgical limits on alloy silicon concentrations mean that only modest improvements in carburization resistance can be obtained. The only really successful alloy additive

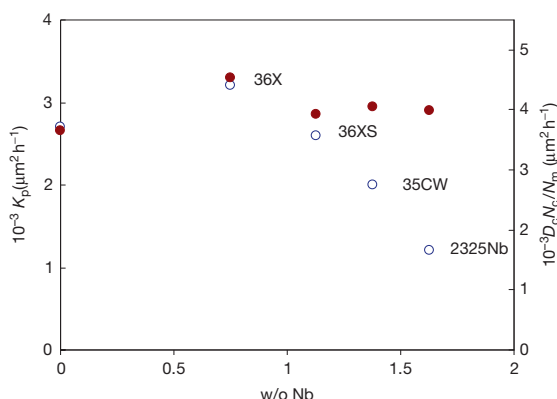


**Figure 10** Carburization rate constants for commercial 25Cr–35Ni alloys at 1000 °C as a function of niobium content (○) compared with  $N_C^{(s)}D_C/N_M$  (●). Data from Ref. 8.

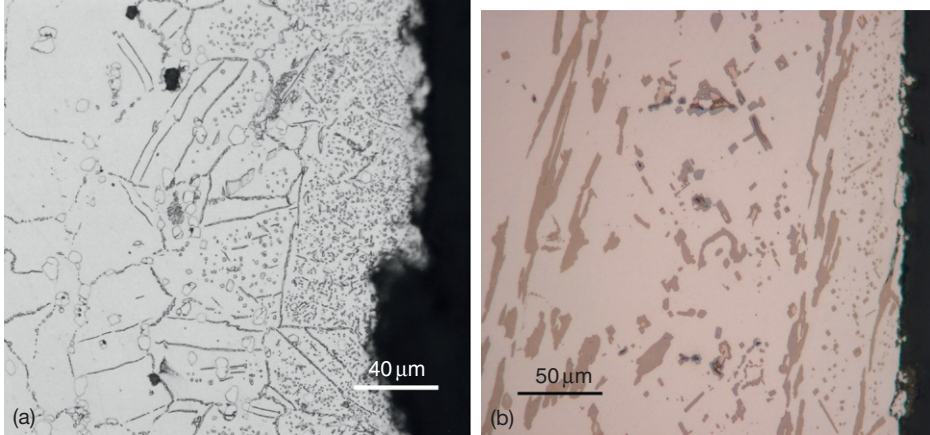


**Figure 11** Effect of  $\text{Al}_2\text{O}_3$  formation on carburization of 60Ni alloys (a) low-Al at 900 °C and (b) high Al at 1100 °C.

is aluminum, and it functions by forming an oxide scale. The general question of protection against carburization by oxide scale formation is considered in [Section 1.12.8](#).

### 1.12.6 Metal Dusting of Iron and Ferritic Alloys

Metal dusting is a catastrophic form of corrosion in which metals exposed to carbon-supersaturated gas disintegrate, forming metal-rich particles (the ‘dust’) dispersed in a voluminous carbon deposit. Early reports of industrial failures<sup>50–53</sup> were followed by the laboratory research of Hochman<sup>54–56</sup> concerning the dusting of iron, nickel, cobalt, and chromia-forming ferritic and austenitic alloys. Subsequently, work by Grabke<sup>57–61</sup> quantified and extended Hochman’s observations. The description of the process, as provided by Hochman and Grabke, for pure iron is shown schematically in [Figure 12](#).

#### 1.12.6.1 Metal Dusting of Iron

When iron is exposed to carbon-rich gas at oxygen potentials too low to form iron oxide, the metal catalyzes reactions such as [\[7\]–\[9\]](#), but the resulting carbon is dissolved in the metal. Hochman and Grabke suggested that this leads to carbon supersaturation of the iron, and the subsequent precipitation of metastable  $\text{Fe}_3\text{C}$  phase which they observed. The appearance of the cementite is shown in [Figure 13](#). According to the proposed mechanism, once the iron surface is covered with cementite, carbon deposits on

the carbide. The carbon activity at the cementite surface is then supposed to be unity (rather than the supersaturated value of the gas phase); the cementite becomes unstable and decomposes via the reaction



producing finely divided iron and carbon. The iron particles produced in this way are catalytically active, and lead to accelerated carbon deposition. The kinetics of carbon deposition were observed<sup>61</sup> in the short term to follow the quadratic rate law

$$\Delta W_{\text{C}}/A = k_{\text{C}}t^2 \quad [32]$$

where  $\Delta W_{\text{C}}/A$  is the carbon weight per unit area, before becoming approximately linear. The form of [eqn. \[32\]](#) was explained by Grabke *et al.*<sup>61</sup> as being due to the generation of catalytically active particles by metal consumption in the dusting process:

$$\Delta W_{\text{M}}/A = k_{\text{d}}t \quad [33]$$

where  $\Delta W_{\text{M}}/A$  is the metal wastage expressed as a mass loss per unit area. If the catalytic particles are of uniform surface area and activity, then the rate of carbon deposition is proportional to the mass of metal consumed

$$\frac{d(\Delta W_{\text{C}}/A)}{dt} = k \times k_{\text{d}}t \quad [34]$$

Integration of this expression yields [eqn. \[32\]](#). In the long term, individual particles are encapsulated by carbon and deactivated as catalysts. The rate at which this happens approximately balances the rate of new particle generation, as coking rates become approximately constant.



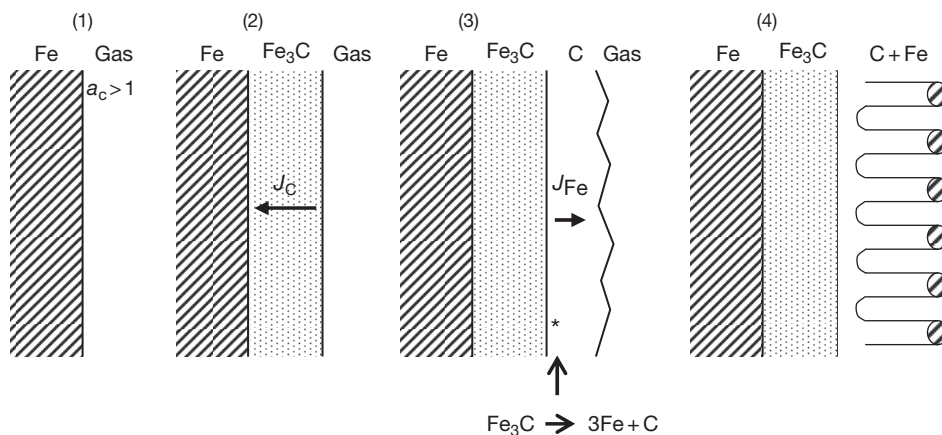


**Figure 12** Hochman–Grabke model for dusting of pure iron.

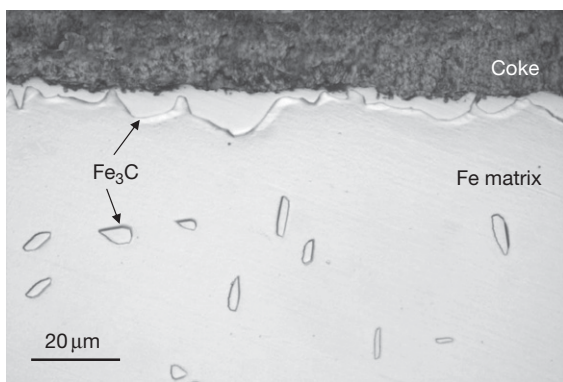


**Figure 13** Cementite produced by reaction of pure iron with  $\text{CO}/\text{H}_2/\text{H}_2\text{O}$  ( $a_{\text{C}} = 2.9$ ,  $p_{\text{O}_2} = 2 \times 10^{-23}$  atm).<sup>62</sup>

Transmission electron microscopy (TEM)<sup>63–66</sup> has revealed that the carbon at the cementite surface is mainly graphite at temperatures above  $\sim 500^\circ\text{C}$ . It was suggested that the iron resulting from cementite decomposition dissolved in the graphite, diffused outwards and precipitated as metal particles which catalyzed further carbon deposition. The evidence for this was the measurement by EDS of a small concentration of iron in the graphite. However, it is difficult to understand the driving force which would cause iron to diffuse from a low-activity source, the cementite, towards a high activity destination, metallic iron particles.

Further examination of the particles by both X-ray and electron diffraction<sup>23,67–70</sup> has established that they are  $\text{Fe}_3\text{C}$ . As seen in **Figure 14**, much of the coke deposit is filamentary. These filaments usually carry faceted  $\text{Fe}_3\text{C}$  particles at their tips. The particles are oriented with their  $[001]$  direction parallel to

the carbon tube axis.<sup>71</sup> This allows  $\text{Fe}_3\text{C}$  planes in the  $\{010\}$  and  $\{100\}$  families to be parallel to the tube axis. The  $d$ -spacing of the  $(020)$  plane is 0.337 nm and that of the  $(300)$  plane is 0.169 nm. These correspond closely to the  $(0002)$  and  $(0004)$   $d$ -spacings of graphite (0.337 and 0.168 nm, respectively). Accordingly, it is suggested that alignment of these planes with the graphite basal planes, which form the multiple walls of the nanotube, leads to formation of low-energy graphite–carbide interfaces and a preferred growth orientation for the carbon tubes.

A mass transport model for filamentary coke deposit is shown in **Figure 14(c)**. The exposed  $\text{Fe}_3\text{C}$  facets are in contact with the gas, and catalyze carbon production. This carbon diffuses through the particle to the  $\text{Fe}_3\text{C}$ –graphite interface where growth of the carbon tube continues. The model is analogous to that originally proposed by Baker *et al.*<sup>72</sup> for catalysis of carbon filaments grown by metallic particles. There remains, however, the question of how the  $\text{Fe}_3\text{C}$  particles are formed.

If iron does, in fact, dissolve in graphite, it could diffuse outward if a carbon activity gradient was in effect, as illustrated in **Figure 15(a)**. The iron flux is given by

$$J_{\text{Fe}} = B_{\text{Fe}} N_{\text{Fe}} \frac{\partial \mu_{\text{C}}}{\partial x} \quad [35]$$

and results from the thermodynamic Fe–C interaction. Here,  $B_{\text{Fe}}$  is the mobility of iron in graphite. When the solute iron reaches a position at which  $a_{\text{C}}$  is high enough to stabilize cementite, that phase precipitates. To test this model, one needs values for iron solubility and its diffusion coefficient in graphite, and these are lacking. It is clear that an extremely high value for  $D_{\text{Fe}}$  would be required to explain why the decomposition

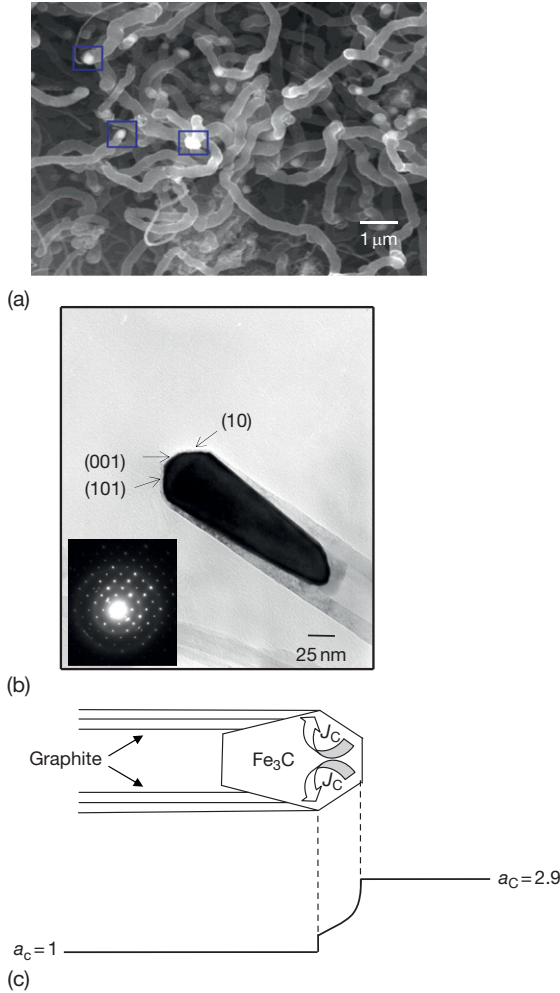


**Figure 14** Coke filaments with Fe<sub>3</sub>C particles at their tips (a) SEM view, (b) TEM image, and (c) mass transfer model.

reaction [31] leads to 75 at % iron, but produces none of that phase at the decomposition site.

Studies of cementite decomposition in CH<sub>4</sub>-H<sub>2</sub> gas mixtures<sup>73</sup> have shown that the reaction products are iron and graphite. In that case, the reaction is controlled by the diffusion of carbon through the product ferrite, driven by the carbon activity gradient between the high value at the Fe<sub>3</sub>C/Fe phase boundary and its value of unity at the Fe/C(gr) boundary:

$$\text{Rate} = D_C \left( C^{\text{Fe}_3\text{C}/\text{Fe}} - C^{\text{C}/\text{Fe}} \right) \quad [36]$$

where  $C^{\text{Fe}_3\text{C}/\text{C}}$  and  $C^{\text{C}/\text{Fe}}$  are carbon concentrations at the ferrite–cementite and ferrite–graphite interfaces,  $D_C$  is the carbon diffusion coefficient in ferrite, and the variation in the diffusion path length is ignored. The concentration of carbon is related to

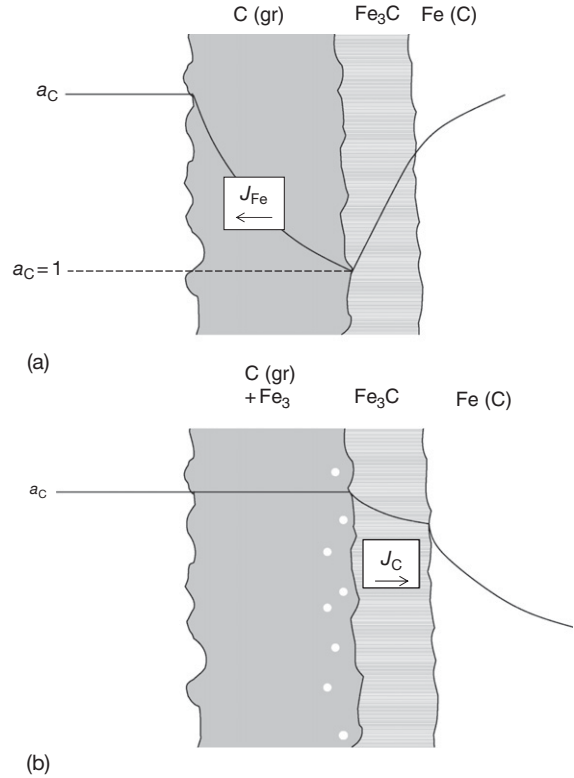


**Figure 15** Mass transport models for metal dusting when cementite is formed: (a) cementite decomposition and iron diffusion through graphite and (b) cementite disintegration coupled with inward graphite growth.

its activity by a coefficient  $\gamma_C$ , with  $a_C = \gamma_C C$ . Approximating  $\gamma_C$  as a constant and setting  $a_C = 1$  at the iron–graphite interface, we obtain

$$\text{Rate} = D_C \left( a_C^{\text{Fe}_3\text{C}/\text{Fe}} - 1 \right) / \gamma_C \quad [37]$$

Using standard data for  $D_C$ <sup>74</sup> and  $a_C^{\text{Fe}_3\text{C}/\text{Fe}}$ <sup>75</sup> it is found that the temperature dependence of cementite decomposition predicted by eqn. [37] is in very good agreement with experimental observation (Figure 16). Cementite decomposition by that mechanism is clearly not occurring in the iron dusting reaction depicted in Figures 13 and 14.

The alternative mechanism of Fe<sub>3</sub>C particle production is mechanical disintegration resulting from volume expansion.<sup>67,76</sup> Because Fe<sub>3</sub>C is a carbon diffuser,<sup>77,78</sup> the cementite layer grows inward and is consequently under compressive stress. Precipitation of graphite could occur at internal defects in a nucleation and growth process.<sup>67</sup> Such a process would be similar to the way carbon forms and grows at the rear

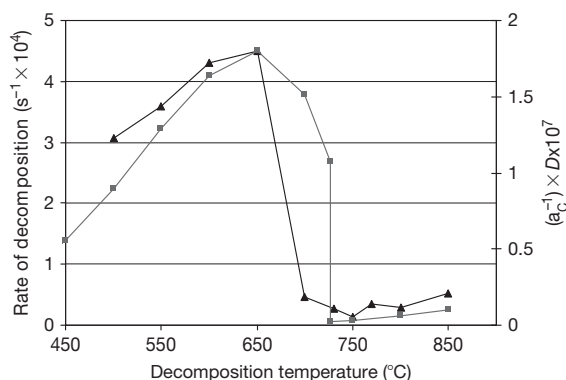


**Figure 16** Rate of  $\text{Fe}_3\text{C}$  decomposition measured (▲) in  $\text{H}_2/\text{CH}_4$  and calculated (■) from  $D_C$  and  $a_C$  in ferrite.<sup>73</sup>

of  $\text{Fe}_3\text{C}$  particles (Figure 14). Growth of these precipitates could then disrupt the cementite surface. Examination of the  $\text{C}(\text{gr})/\text{Fe}_3\text{C}$  interface in Figure 17 shows that graphite is growing into the cementite layer, and that nanoparticles of  $\text{Fe}_3\text{C}$  are detached from the bulk carbide. For these to exist,  $a_C$  must be high enough to stabilize the phase. It is therefore concluded that the graphite layer does not function as an effective barrier to the gas, and that  $a_C$  at the coke–cementite interface is probably close to the value in the ambient gas.

This conclusion is supported by the observation<sup>79</sup> that the surface cementite layer continues to thicken, and that the carbon content of the iron specimen increases as dusting proceeds. It is clear that carbon is diffusing through the cementite scale and into the iron, and that the description of Figure 15(b) applies. However, these experiments were of limited duration (up to ~40 h) and at a single temperature. Once the iron sample reaches a steady state of carbon supersaturation, the mechanism may well change<sup>80</sup> when an inward flux of carbon is no longer possible. Moreover, it is likely that the mechanism changes with gas composition and temperature. Zhang *et al.*<sup>81</sup> have reported that at  $T = 700^\circ\text{C}$ , and low  $p_{\text{CO}}$  values, the surface  $\text{Fe}_3\text{C}$  scale decomposes to form a surface layer of ferrite. At still higher temperatures, no cementite layer is seen, and graphite deposits directly into the metal.

### 1.12.6.2 Iron Dusting in the Absence of Cementite

Given the important role played by cementite in the dusting of iron, it is reasonable to enquire whether dusting might be prevented if  $\text{Fe}_3\text{C}$  formation was suppressed. Cementite can be destabilized with

respect to graphite by alloying with silicon to raise the solute carbon activity. Unfortunately, silicon also oxidizes in the gases under discussion, as will be discussed in the following sections. Germanium, on the other hand, forms a much less stable oxide, and by virtue of its chemical similarity to silicon, might be expected to suppress  $\text{Fe}_3\text{C}$  formation. This is indeed the case, as shown in Figure 18, where graphite is seen to be growing directly into a ferritic  $\text{Fe-Ge}$  alloy, in the absence of any cementite. The nanoparticulate material near the disintegrating interface is also  $\alpha\text{-Fe}(\text{Ge})$ , as are the particles found on coke filaments.

Alloying with germanium suppressed  $\text{Fe}_3\text{C}$  formation, but did not prevent metal dusting. Instead, dusting occurred more rapidly by the growth of graphite directly into the alloy. Metal particles were formed by disintegration of the bulk metal, as the graphite grew inwards. Again it is suggested that this was a consequence of the volume expansion accompanying nucleation and growth of graphite within the metal. This process was more rapid than the corresponding one involving  $\text{Fe}_3\text{C}$ . It is noteworthy that the  $\text{Fe-Ge/graphite}$  interface morphology is similar to that developed between nickel and graphite (where no carbide forms) during dusting (see Section 1.12.7). However, the dusting rate was much faster for the ferritic material. It is concluded that suppression of  $\text{Fe}_3\text{C}$  formation does not prevent dusting when this alternative mechanism is available.

### 1.12.6.3 Effects of Temperature and Gas Composition on Iron Dusting

As noted by Grabke,<sup>82</sup> iron dusting and coking kinetics are very complex, and more detailed studies are needed to arrive at a comprehensive, self-consistent picture. As seen in Figure 19, somewhat different temperature dependencies have been reported under different gas conditions. Grabke *et al.*<sup>61</sup> considered the temperature dependence at  $T < 540^\circ\text{C}$  to reflect rate control by cementite decomposition, which is independent of gas composition. Ramarayanan *et al.*<sup>65,84</sup> identified two temperature regimes:  $T < 450^\circ\text{C}$  where the coke was amorphous and the rate was controlled by physical disintegration of  $\text{Fe}_3\text{C}$ , and  $450 < T < 570^\circ\text{C}$  where the chemical decomposition of  $\text{Fe}_3\text{C}$  was thought to become important. Its rate increased as the graphitization of coke increased with temperature, which was thought to provide a diffusion pathway for dissolved iron. The decline in dusting rates reported by Ramarayanan *et al.* at  $T > 570^\circ\text{C}$  was attributed by them to a

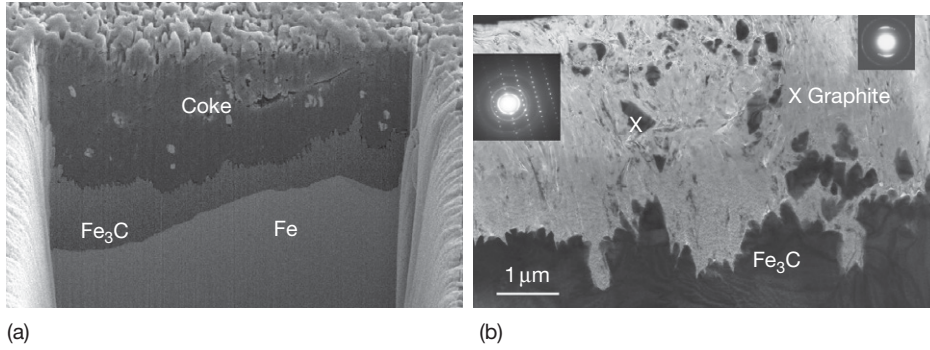


**Figure 17** Graphite–cementite interface developed during dusting of iron at 680 °C: (a) FIB milled section and (b) TEM bright field with SAD identifying nanoparticles as  $\text{Fe}_3\text{C}$ .<sup>62</sup>

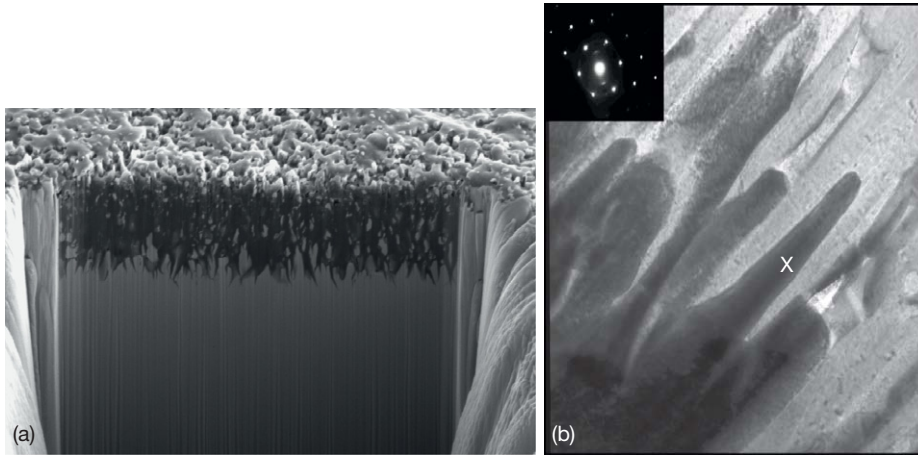


**Figure 18** Fe–10Ge alloy after 10 h reaction in  $\text{H}_2/\text{H}_2\text{O}/\text{CO}$  ( $a_{\text{C}} = 2.9$ ,  $p_{\text{O}_2} = 2 \times 10^{-23}$  atm): (a) FIB cross-section and (b) TEM cross-section with SAD identifying  $\alpha\text{-Fe}$ .<sup>62</sup>

decrease in  $a_{\text{C}}$  with increasing temperature. Muller-Lorenz and Grabke<sup>83</sup> observed an increased dusting rate in the range 540–620 °C, reporting it to vary with the product  $p_{\text{CO}}p_{\text{H}_2}$ , and concluded that carbon transfer was rate-controlling.

Part of the reason for this confusion is the way in which  $a_{\text{C}}$  varies with temperature (Figure 1) and gas composition (eqns. [10] and [11]) in  $\text{CO}/\text{H}_2/\text{H}_2\text{O}$  gas mixtures. Thus, the driving force for carbon precipitation ( $a_{\text{C}} - 1$ ) is related to gas composition variables which themselves appear in kinetic expressions. Distinguishing the two effects can be difficult, and is impossible if the gas compositions are not carefully controlled. Thus, the use of  $\text{CO}/\text{H}_2$  gases without  $\text{H}_2\text{O}$  to buffer the composition means that  $a_{\text{C}}$  is uncontrolled, and will vary with the extent of carbon deposition. As carbon deposition rates are rapid

around 550 °C, both  $a_{\text{C}}$  and  $p_{\text{CO}}$  can vary considerably in a nominal  $\text{CO}-\text{H}_2$  gas mixture.

The dependence of both coking and dusting rates on the composition of  $\text{CO}/\text{H}_2/\text{H}_2\text{O}$  gases determined by Muller-Lorenz and Grabke<sup>83</sup> is shown in Figure 20. Similar results were found for iron dusting at 550 °C by Chun *et al.*<sup>65</sup> In both cases it was concluded that the rate-determining step in the dusting process was reaction [7] leading to

$$\text{Rate} = r_7 p_{\text{CO}} p_{\text{H}_2} \quad [38]$$

However, this analysis neglects the effect of  $a_{\text{C}}$ . Experiments<sup>85</sup> in which  $a_{\text{C}}$  was constant revealed that keeping the product  $p_{\text{CO}}p_{\text{H}_2}$  constant, but varying the individual partial pressures changed both coking and dusting rates. Obviously, the simple description of eqn. [38] fails.

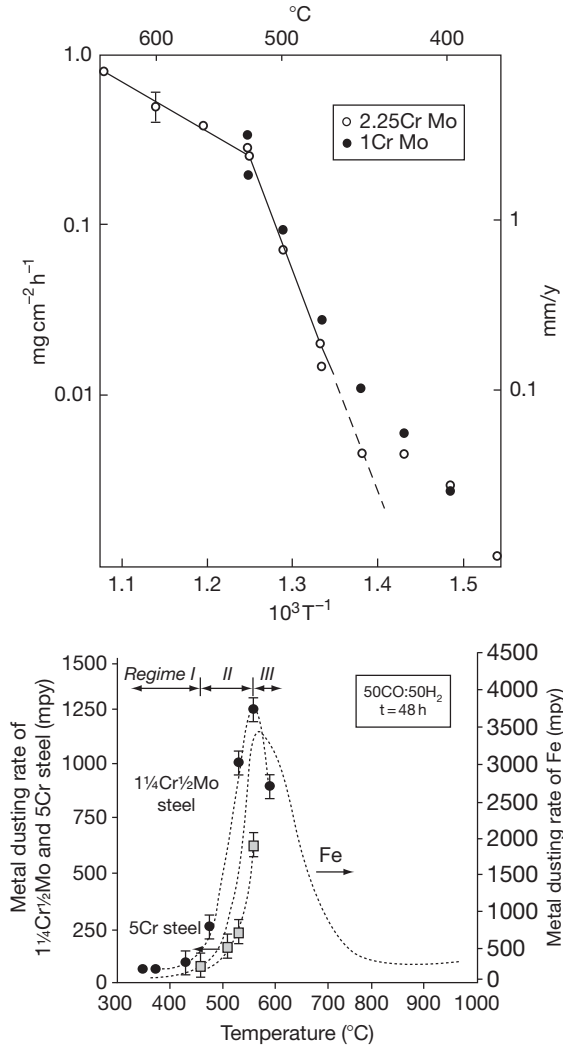


**Figure 19** Temperature effects on metal dusting for iron and low-alloy steels: LHS in CO/H<sub>2</sub>/H<sub>2</sub>O<sup>83</sup>; RHS in CO–H<sub>2</sub>.<sup>84</sup>

Considering the coking process first, it is seen that the Boudouard reaction [8] is likely to be important at high  $p_{\text{CO}}$  values. Furthermore, when  $p_{\text{H}_2}$  is high, it is likely that methanation (the reverse process in [9]) will occur under catalyzed conditions. Ignoring the reverse reactions in [7] and [8] along with the forward process [9], we can write

$$\frac{d(\Delta W_C/A)}{dt} = r_7 p_{\text{CO}} p_{\text{H}_2} + r_8 p_{\text{CO}}^2 - r_{-9} p_{\text{H}_2}^2 \quad [39]$$

where  $r_i$  are the rate constants. As seen in Figure 21, this expression is successful in describing coking rates with  $r_7 = 35.5$ ,  $r_8 = 4.5$ , and  $r_{-9} = 5.6 \text{ mg cm}^{-2} \text{ atm}^{-2} \text{ h}^{-1}$ . It is concluded that coke deposition can be described in terms of gas–solid kinetics.

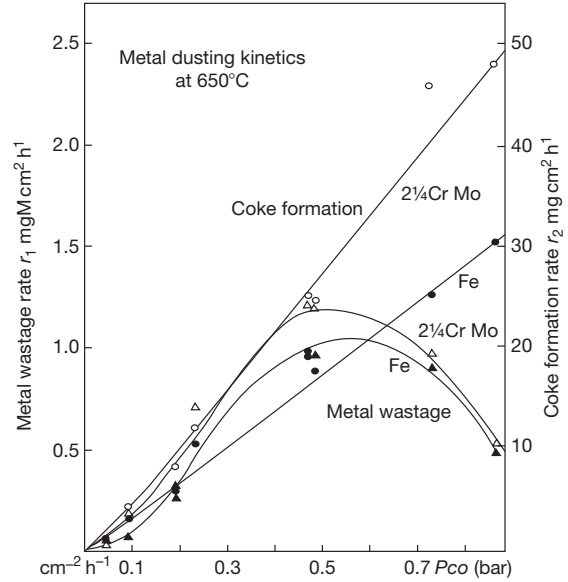


**Figure 20** Dependence of coking and dusting rates on  $p_{\text{CO}}$  in H<sub>2</sub>/CO/H<sub>2</sub>O mixtures.<sup>83</sup>

More information is required on the variation of dusting kinetics with gas composition. Available data for dusting in CO/H<sub>2</sub>/H<sub>2</sub>O mixtures at 500°C<sup>86</sup> indicates the rate increases with  $a_{\text{C}}$ . Data at 550°C<sup>84</sup> for metal consumption rates of iron exposed to CO/H<sub>2</sub> mixtures reveal a maximum at  $p_{\text{CO}} = 0.5 \text{ atm} = p_{\text{H}_2}$ . If the unavoidable water vapor impurity level was the same in all gases used, then  $a_{\text{C}} = K_7 p_{\text{CO}} p_{\text{H}_2} / p_{\text{H}_2\text{O}}$  also had its maximum at this composition.

#### 1.12.6.4 Dusting of Low-Alloy Steels

Dusting of 2¼Cr–1Mo and 1Cr–½Mo steels is seen in Figures 19 and 20 to be similar to pure iron in rate and dependence on temperature and gas composition. Reaction morphologies are also similar,<sup>82</sup> and it may be concluded that mechanisms are the same. The reasons for the slightly faster dusting rates observed on 2¼Cr–1Mo steel have not been established. However, it is to be noted that in CO/H<sub>2</sub>/H<sub>2</sub>O gases, the  $p_{\text{O}_2}$  values are high enough to oxidize the chromium. Although no Cr<sub>2</sub>O<sub>3</sub> scales can form on such a dilute alloy, conversion of the steel surface to Fe<sub>3</sub>C may lead to encapsulation of chromium-rich oxide particles. These might act as nuclei for graphite precipitates, thereby accelerating the cementite disintegration.

Addition of silicon to iron has two effects: a partial destabilization of Fe<sub>3</sub>C with respect to C(gr) and the promotion of SiO<sub>2</sub> formation at the oxygen potentials



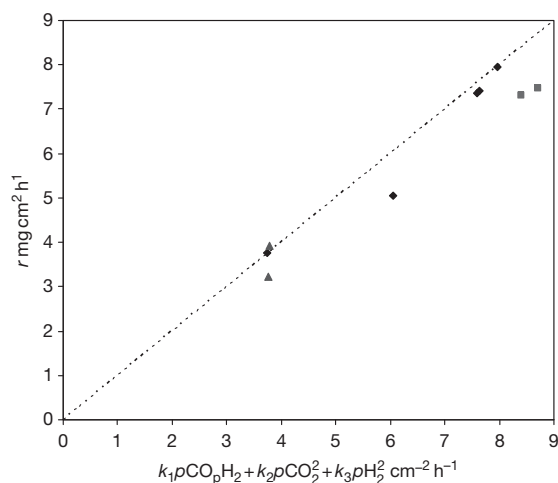


**Figure 21** Variation of coking rates on iron according to eqn. [38].<sup>85</sup>

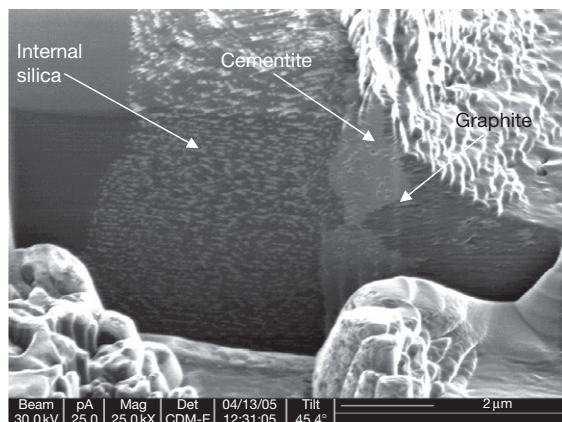


**Figure 22** FIB image of Fe-xSi after dusting in CO/H<sub>2</sub>/H<sub>2</sub>O ( $a_C = 2.9$ ,  $p_{O_2} = 10^{-23}$  atm) at 680 °C.<sup>87</sup>

of CO/H<sub>2</sub>/H<sub>2</sub>O gases. At low-silicon alloy levels, the SiO<sub>2</sub> forms as a dendritic internal precipitate rather than an external scale (Figure 22). Thus, the SiO<sub>2</sub> provides little or no protection against carbon access to the metal. The Fe<sub>3</sub>C layer formed by Fe-Si alloys is thinner than on iron, coking is faster, and metal wastage is also more rapid.<sup>87</sup> The internal SiO<sub>2</sub> precipitates are incorporated into the Fe<sub>3</sub>C scale as it grows into the alloy. These might act as graphite nucleation sites, thereby accelerating cementite disintegration and dusting.

#### 1.12.6.5 Dusting of Ferritic Chromium Steels

The behavior of these alloys when exposed to CO/H<sub>2</sub>/H<sub>2</sub>O gas mixtures depends on whether a chromia

scale is formed and retained. If the alloy chromium level is too low to form a Cr<sub>2</sub>O<sub>3</sub> scale, the steel will dust at essentially the same rate as a 2 $\frac{1}{4}$ Cr-1Mo steel.<sup>88</sup> If the steel forms a continuous, adherent chromia scale, resistance to dusting under isothermal conditions is very good, because the scale prevents carbon entry. The factors determining the success or otherwise of a steel in resisting dusting are those governing its ability to quickly form a continuous Cr<sub>2</sub>O<sub>3</sub> scale by diffusing chromium to the surface.

The effect of temperature on  $D_{Cr}$  is clear from the studies of Grabke *et al.*<sup>60</sup> Steels containing 17 and 26 Cr showed complete resistance to dusting at 650 and 600 °C, but underwent a slight extent of attack at 550 °C. Thus, the susceptibility to dusting increased as the temperature and  $D_{Cr}$  decreased. The effective value of  $D_{Cr}$  can be increased at the low temperatures involved here by creating a deformed and fine-grained alloy surface. This is done by surface grinding, shot peening, etc., and has been shown<sup>88</sup> to lead to better dusting resistance. In the absence of such treatment (or after its effects have been annealed out), the ferritic nature of the alloy is itself important, because of the higher  $D_{Cr}$  value compared to austenitic materials. A comparison of the dusting performance of model ferritic and austenitic 25Cr alloys in Figure 23 illustrates this point. These alloys had been electropolished to remove any cold-worked surface material, so that alloy chromium transport was via lattice diffusion.

Alloys which successfully develop continuous, protective chromia scales are nonetheless subject to long-term dusting attack. Under isothermal exposure conditions, growth stress accumulation in the scale leads ultimately to mechanical failure. A series of such events can exhaust the capacity of an alloy to regrow its protective scale, and metal dusting ensues.<sup>88,89</sup> Discontinuous exposures combine the effects of accumulated growth stress and occasional thermal shock. These have also been shown to produce alloy depletion and eventual dusting.<sup>60,82,88,90</sup> Short-term thermal cycling experiments induce the same failure mode, and are useful as accelerated corrosion tests.<sup>91</sup> In all cases, the chromia scale breaks down locally, allowing carbon to enter the chromium-depleted metal. Rapid inward diffusion of carbon leads to internal precipitation of chromium carbides, thereby preventing any subsequent rehealing of the scale. The depleted iron matrix forms a surface cementite layer<sup>23,92</sup> which disintegrates producing numerous cementite particles which catalyze further coke deposition.<sup>23</sup> This localized attack produces a



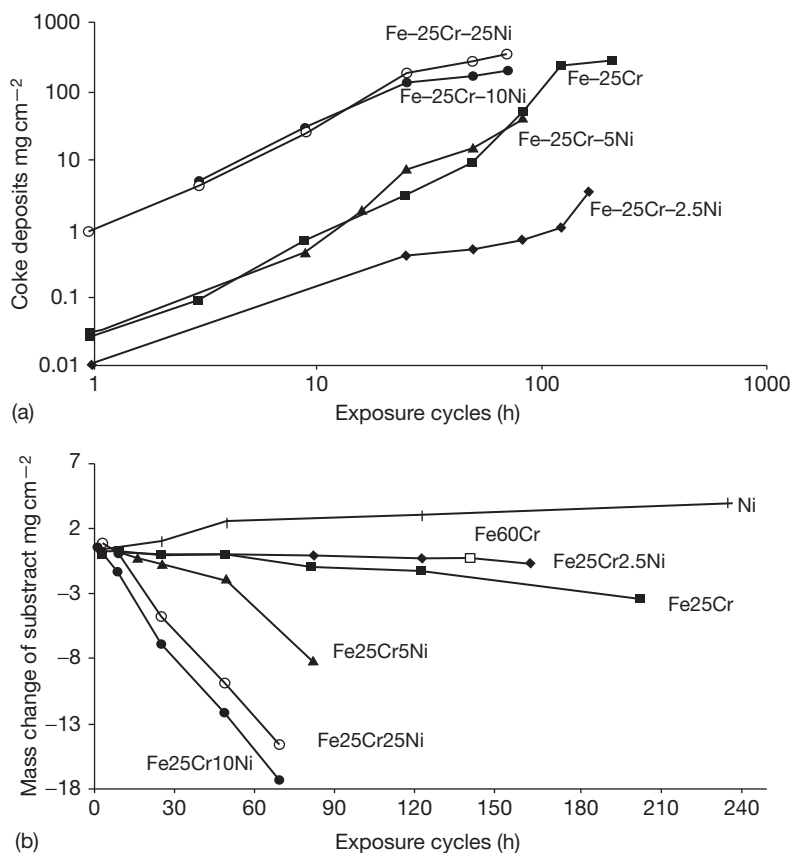


**Figure 23** Coke deposition and metal wastage kinetics for electropolished 25Cr alloys at 680 °C in CO/H<sub>2</sub>/H<sub>2</sub>O ( $a_C = 2.9$ ,  $p_{O_2} = 10^{-23}$  atm).<sup>23</sup>

pitted surface (Figure 24). As the reaction proceeds, more pits form and they widen and coalesce until the attack becomes general.

If the alloy chromium level is high enough, dusting of ferritics can be prevented. An Fe-60Cr alloy survived one thousand 1-h cycles at 680 °C, forming only Cr<sub>2</sub>O<sub>3</sub>,<sup>23</sup> which was impermeable to carbon. Furthermore, the chromia was catalytically inactive, and no coke deposited.

#### 1.12.6.6 Dusting of FeAl and FeCrAl Alloys

Iron aluminides and FeCrAl alloys are able to develop alumina scales, and their ability to resist dusting is, therefore, of interest. The high-diffusion coefficients characteristic of the ferritic FeCrAl materials (typically Fe-20Cr-5Al) means that they are able to reheal scales quickly, thereby preserving the surface barriers to carbon entry.

Dusting of the intermetallic Fe<sub>3</sub>Al at 650 °C in CO-H<sub>2</sub>-H<sub>2</sub>O was investigated by Strauss *et al.*,<sup>93</sup>

who reported extensive attack at localized pits. After addition of 2.2% Cr to the alloy, dusting was confined to the unpolished specimen edges. With 4.8% Cr and 0.15% Zr, pitting was completely suppressed, and only a thin coke layer formed. Dusting was associated with formation of a surface layer of Fe<sub>3</sub>C. Further work on Fe-15Al and Fe-26Al by Schneider and Zhang<sup>94,95</sup> showed that dusting was also associated with internal precipitation of the  $\kappa$ -carbide, Fe<sub>3</sub>AlC<sub>x</sub>. Attack on Fe-15Al was general, but was reduced to localized pitting by alloying with 2.9% of Nb or Ta, and almost stopped by adding 2% of either V or Ti. Increases in temperature or alloy aluminum content led to reduced dusting rates. As pointed out by the authors, the observations are consistent with protection against dusting due to Al<sub>2</sub>O<sub>3</sub> scale formation. However, at the relatively low temperature of 650 °C, the binary intermetallic does not reliably form a continuous scale. Alloy additions of Cr, Nb, Ta, V, and Ti all improve alumina scale formation. Nonetheless, once the scale is

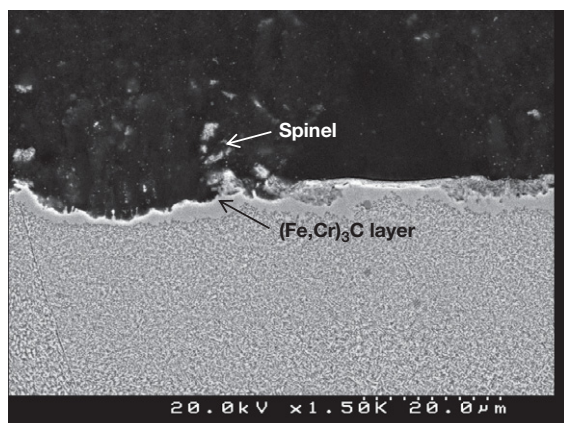


**Figure 24** Onset of dusting for Fe–25Cr reacted at 680 °C in CO/H<sub>2</sub>/H<sub>2</sub>O ( $a_C = 2.9$ ,  $p_{O_2} = 10^{-23}$  atm) showing local internal carburization, surface cementite layer and its disintegration.

damaged, rapid carbon entry leads to internal carburization of the alloy and prevents subsequent alumina rehealing. The mechanism is, thus, very similar to that of attack on ferritic Fe–Cr alloys.

The FeCrAl materials provide much better dusting resistance. Baker and Smith<sup>90</sup> reported that an oxide dispersion-strengthened alloy, MA956, demonstrated very good dusting resistance at 621 °C up to 9000 h in a CO–H<sub>2</sub>–H<sub>2</sub>O gas which was oxidizing to aluminum. Good performance has also been reported<sup>80,91</sup> for FeCrAl materials at 650 °C in similar atmospheres. Internal precipitation of the  $\kappa$ -carbide was observed after several thousand hours,<sup>80</sup> and filamentary coke growth was catalyzed by Fe<sub>3</sub>C particles<sup>91</sup> when the scale was damaged by repeated thermal shocks.

### 1.12.7 Dusting of Nickel and Austenitic Alloys

Metal dusting of nickel and austenitic alloys differs from the reaction of ferritic materials in that cementite is not formed and the corresponding nickel carbide is unstable. An examination of the dusting behavior of pure nickel provides a good basis for understanding the reaction of austenitic, heat-resisting alloys.

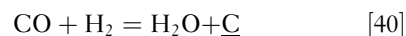
#### 1.12.7.1 Metal Dusting of Nickel

Exposure of nickel to carbon-rich gases at oxygen potentials where the metal does not oxidize leads to

catalysis of reactions [7]–[9] producing carbon. Hochman<sup>56</sup> and Schneider *et al.*<sup>95</sup> reported the rate of carbon uptake to be much slower than the corresponding process on iron. The kinetics are approximately linear<sup>94,95</sup> after an induction period of length varying with temperature and gas composition. Metal consumption kinetics have not been measured directly. It is usually assumed that the carbon deposit contains an approximately constant nickel concentration (1–2 w/o), and on this basis linear dusting kinetics would be deduced. Chun *et al.*<sup>96</sup> measured metal surface recession after 7 h reaction in unbuffered CO/H<sub>2</sub> gas mixture of proportions 25:1, and found average rates to be of order 1 mm year<sup>−1</sup> at temperatures above 600 °C.

Reaction morphologies vary with ambient conditions, and the available information is incomplete. The 25:1 CO/H<sub>2</sub> gas produced external attack, whereas at a CO to H<sub>2</sub> ratio of 1:1, extensive internal graphitization also resulted. The appearance of coarse-grained nickel after exposure to a CO/H<sub>2</sub>/H<sub>2</sub>O gas is shown in Figure 25. Cold working the metal surface prior to reaction induced recrystallization of the near-surface region, and graphite formation at the multiple grain and sub-grain boundaries. It is clear that carbon dissolves in the nickel and diffuses inwards, supersaturating the metal until graphite precipitates nucleate and grow at favorable sites. Nava Paz and Grabke<sup>58</sup> reported earlier that CO/H<sub>2</sub>/H<sub>2</sub>O mixtures with low  $p_{CO}$  led to internal graphitization, whereas high  $p_{CO}$  mixtures induced surface deposition.

Coke accumulated on the external nickel surface in three forms: a more-or-less uniform layer on to the surface, clusters of approximately spherical particles, and filaments.<sup>97</sup> The spheres contain nickel particles and the filaments carry particles at their tips. The presumed correlation between coke mass and metal consumption is seen to be reasonable. Nickel is catalytically active to all of reactions [7]–[9], and it was proposed long ago<sup>72</sup> that reactions such as



where  $\underline{C}$  represents dissolved carbon, occur on the bare facets of the nickel particles. The carbon then diffuses rapidly through the particle and precipitates at the rear faces, causing elongation of the carbon filament. If the exposed nickel faces cannot dissolve carbon quickly enough, the particle is encapsulated with graphite, forming a roughly spherical particle. The accumulation of the outer, loose-coke deposit is thereby explained. Of more interest, however, is the

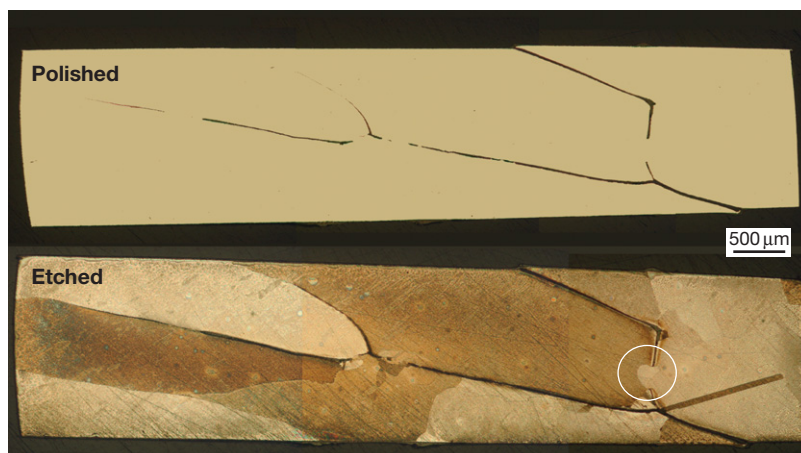


**Figure 25** Graphitization of nickel exposed to CO/H<sub>2</sub>/H<sub>2</sub>O ( $a_C = 19$ ) for 100 h at 650 °C.

development of coke at the metal surface, and the way in which parent metal is ‘dusted’ to form the catalytic nanoparticles.

Zeng and Natesan<sup>98</sup> used Raman spectroscopy, which is sensitive to the degree of carbon crystallinity, to show that the surface carbon layer was more graphitic than the outer coke. Grabke *et al.*,<sup>99,100</sup> Pippel *et al.*,<sup>64</sup> and Chun *et al.*<sup>96</sup> all used TEM to examine the nickel–carbon interface. These authors agreed that the carbon was graphite, that the graphite basal planes were oriented approximately normal to the nickel surface when dusting occurred, and that nickel was dissolved (1–2 w/o) in the graphite. The mechanism deduced from these observations was one of outward diffusion of solute nickel through the graphite, followed by precipitation of nickel particles in the outer regions of the graphite layer. The fundamental difficulty with this mechanism is essentially the same as was identified earlier in the iron dusting case. No driving force is apparent for mass transfer from bulk nickel to particulate metal, which would presumably be at a higher energy level as a result of its surface area.

A TEM image of the graphite layer and nickel concentrations analyzed within it using EDS<sup>101</sup> are shown in Figure 26(b). Very little concentration gradient is apparent, suggesting either that no diffusion occurs or that  $D_{Ni}$  in graphite is extremely high. Examination of the microstructure in Figure 26 shows that in fact nickel nanoparticles are distributed throughout the graphite layers. Thus, the surface layer is a two-phase, two-component material in which isothermal diffusion could not occur if local equilibrium was in effect. It is nonetheless possible

that a single-phase graphite–nickel solution might form under other reaction conditions and the nickel diffusion model could apply. In the example of Figure 26, it appears that mechanical disintegration of the metal is a consequence of the inward growth of graphite and the accompanying volume expansion. Such a process was in fact deduced from the original electron microscopy studies,<sup>64,96,99,100</sup> and the proposed diffusion of nickel through graphite is of secondary importance.

The mechanism of graphite nucleation and growth is of fundamental importance to the dusting process. It is proposed<sup>96,99,102</sup> that the free edges of graphite basal planes act as attachment sites for carbon atoms, permitting their extension into the metal (Figure 27, left). The supply of carbon necessary for this process can only be maintained if direct gas access to the metal continues throughout the reaction. Even when the surface is covered with graphite and coke, no effective barrier to the gas is formed. Most of the coke is obviously porous, and even the more dense graphite layer is extensively fissured.

The factors controlling graphite formation on nickel have been investigated intensively because carbon fouling (coking) of industrial nickel catalysts is an important practical problem. Direct surface observation<sup>103</sup> using low energy electron diffraction showed that a preferred epitaxial relationship developed between the graphite basal plane (0001) and Ni(111) faces. A computer simulation of this arrangement is shown in Figure 27 (right). Electron diffraction<sup>104</sup> confirmed that (111), (113), and (220) nickel faces were found at filament–metal interfaces. The same preferred epitaxies are observed in metal dusting.

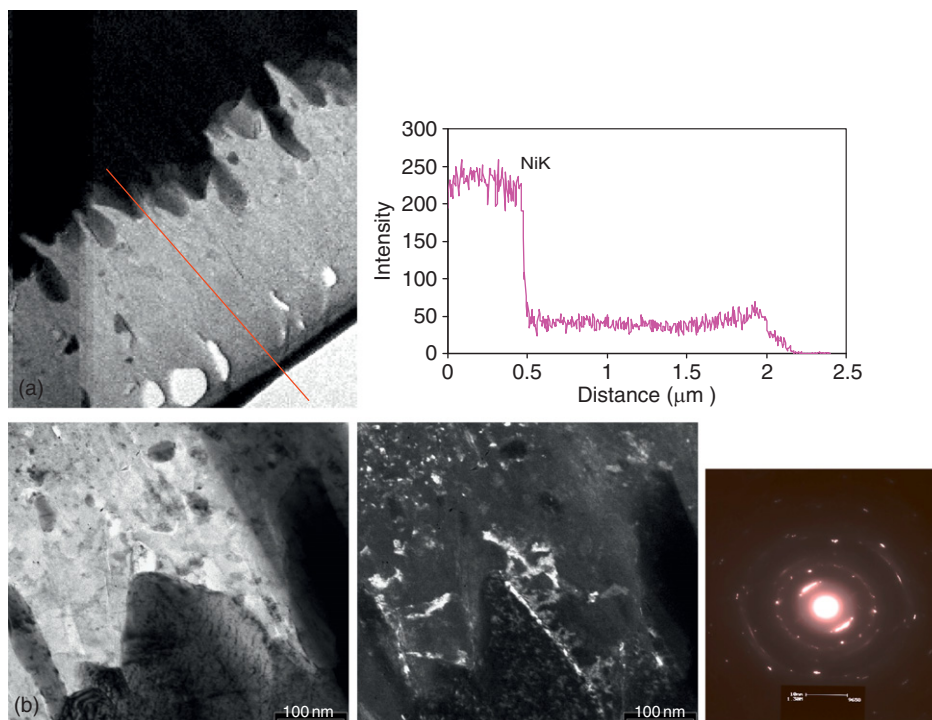


**Figure 26** (a) TEM bright field view and EDS line scan through uniform graphite layer on nickel and (b) bright and dark field images using (111) nickel reflection reveal particulate metal in graphite ( $\text{CO}/\text{H}_2/\text{H}_2\text{O}$ ,  $a_{\text{C}} = 19$ ,  $T = 680^\circ\text{C}$ ).<sup>101</sup>

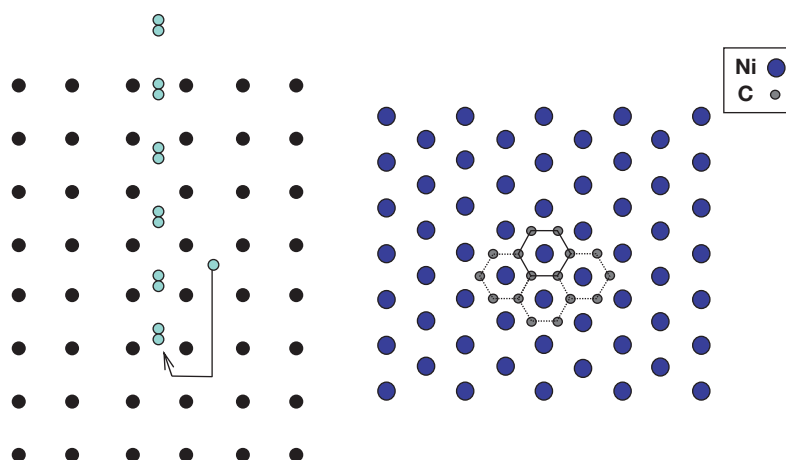


**Figure 27** Left: Schematic view of graphite growth into nickel. Right: Computer simulation of the epitaxial relationship between the graphite basal plane and a Ni(111) surface.

Examination by TEM of reacted nickel single crystal and polycrystalline surfaces<sup>64,96,100</sup> revealed that graphite basal planes developed parallel to nickel (111) and (110) surfaces, but at right angles to a (100) surface. In the short term, no dusting occurred at the (111) or (110) surfaces, but on the (100)

surface graphite grew into the nickel, causing its disintegration. This pattern of behavior is clearly consistent with the reaction model of Figure 27, which requires the graphite basal planes to be oriented at an angle to the surface. Of course, the model is somewhat over simplified. Consider, for example,



a (111) surface which is in fact intersected by planes such as (11 $\bar{1}$ ), providing favorable inward growth directions for graphite. These will be accessible at surface jogs, kinks, etc., and dusting does, in fact, ultimately commence on these surfaces.<sup>64,96,100</sup>

**Figure 28** shows graphite growing into the metal, along nickel (111) and (11 $\bar{3}$ ) planes. Penetration of graphite basal planes between adjacent planes of the nickel lattice destroys its structure. It has been suggested<sup>98,101</sup> that the graphite nucleates within the metal interior. This is self evidently the case for internal graphitization (**Figure 25**). Such a process is analogous to the dissolution–precipitation mechanism producing carbon filaments from nickel nanoparticles. Some insight into the process can be gained from a consideration of alloying effects.

### 1.12.7.2 Dusting of Nickel Alloys in the Absence of Oxide Scales

The dusting of austenitic Ni–Fe alloys at 650 °C in CO/H<sub>2</sub>/H<sub>2</sub>O gases such that no oxidation occurred was studied by Grabke *et al.*,<sup>105</sup> who found that both coking and metal wastage rates increased monotonically with iron concentration. The changes in coking rate reflected a combination of changing catalytic activity and dust particle size. Regardless of alloy iron content within the range 0–70%, the reaction

morphologies were the same as for pure nickel. The dependence of dusting rate on alloy composition can be understood in part from carbon permeability data. The higher permeability of iron-rich alloys would provide a greater flux to the graphite nucleation and growth sites, supporting more rapid graphitization and metal dusting. On this basis, however, pure nickel would be predicted to dust more rapidly than alloys with ~80% Ni, which have the lowest  $N_C^{(s)}D_C$  values. In fact, the metal dusted more slowly than the alloy. More information is required for high Ni/Fe ratios, which are typical of Inconel alloys.

Alloying copper with nickel has been found<sup>106,107</sup> to decrease coking and dusting rates sharply (**Figure 29**). The coke deposit on alloys containing at least 10 w/o copper consisted solely of filaments. Thus, metal wastage via the process leading to graphite particle clusters was suppressed. Copper is known to be immune to dusting attack, but its effect on nickel alloy dusting was much greater than one of simple dilution. Similar results have been reported<sup>108–110</sup> for the effect of copper on catalytic coking by nickel. This can be understood<sup>108,110,111</sup> if the catalytically active sites consist of  $\gamma$  near-neighbor atoms. Then the carbon deposition rate on an alloy,  $r$ , is described by

$$r = r_{\text{Ni}}(1 - N_{\text{Cu}})^{\gamma} \quad [41]$$

where  $r_{\text{Ni}}$  is the rate on pure nickel. The effect of copper can be described by this equation with  $\gamma = 18$ , as shown by the calculated lines in **Figure 29**.

A catalytic site of 18 near-neighbor atoms is physically unrealistic if surface reactions of simple molecules (e.g., eqn. [40]) are involved. However, if graphite nucleation is the process being catalyzed, then a stable

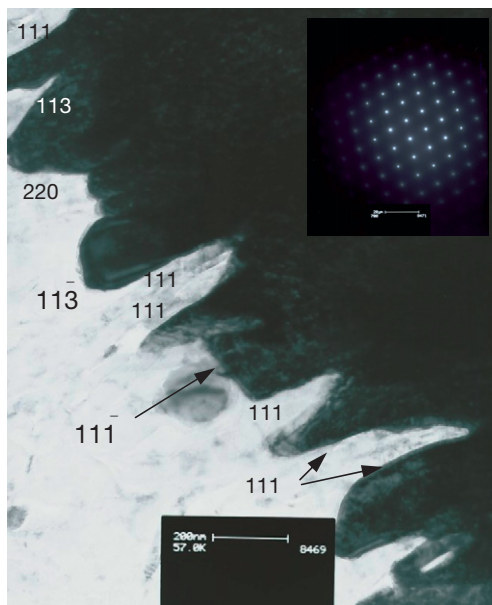


**Figure 28** Nickel facets at graphite–metal reaction front determined by SAD.<sup>101</sup>

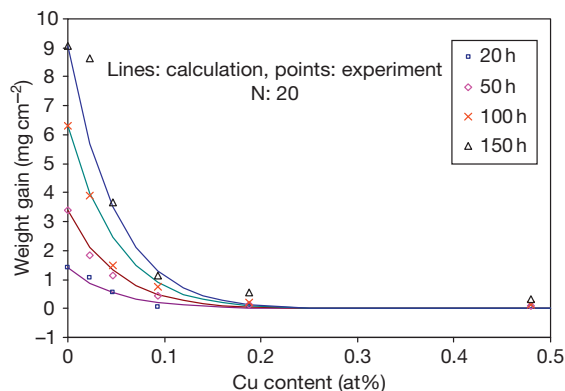


**Figure 29** Carbon uptake on Ni–Cu alloys at 680 °C in CO/H<sub>2</sub>/H<sub>2</sub>O ( $a_C = 19$ ). Continuous lines calculated from eqn. [41].<sup>106</sup>

nucleus presumably requires at least one hexagonal carbon ring. As seen in Figure 27 (right), it would require 7 near-neighbor nickel atoms on a free surface or 14 atoms on adjacent (111) planes for internal nucleation. It is therefore concluded that the copper effect is consistent with internal graphite nucleation.

Copper alloying also affects carbon solubility in the metal. The solubility is reported<sup>112</sup> to be reduced from a maximum of 0.18% in nickel to  $\sim 0.01\%$  in Ni–90Cu. However, Mclellan and Chrashka<sup>113</sup> showed that carbon solubility was unaffected by the presence of up to 40% copper. More information is required for carbon permeability, but on the basis of existing data, graphite nucleation appears to be more strongly affected.

### 1.12.7.3 Effects of Temperature and Gas Composition on Nickel Dusting

Average metal recession rates in a 50–50 mixture of CO–H<sub>2</sub> were found<sup>96</sup> to increase with temperature to a maximum at about 800 °C, and to remain constant at higher temperatures. The carbon activity in those experiments was uncontrolled, and interpretation of the high temperature results is therefore difficult. The low-temperature results were correlated with an observed increase in carbon graphitization with increasing temperature. Chun *et al.*<sup>96</sup> suggested that dusting was controlled by outward diffusion of nickel dissolved in graphite, and therefore accelerated with increased graphitization of the coke. However, it could also be argued that only graphite, and not amorphous carbon, was capable of growing into the metal, because graphite can develop a crystallographic orientation relationship with the metal. Increasing graphitization would, therefore, increase the extent of nickel disintegration. Carbon uptake rates in a gas mixture of H<sub>2</sub>–24CO–2H<sub>2</sub>O were found by Schneider *et al.*<sup>99</sup> to have a maximum at about 625 °C, and decreased sharply at higher temperatures, reflecting the lower carbon activities reached at higher temperatures in a gas of fixed composition.

Direct measurements of the dependence of metal consumption (i.e., dusting) rates on gas composition are lacking, but data is available for coking rates. At a fixed temperature of 650 °C, carbon uptake rates vary with gas composition in a complex way. Experiments in which  $p_{\text{CO}}$  and  $a_{\text{C}}$  (as calculated from eqn. [10]) were varied independently<sup>97</sup> showed that carbon uptake rates were not directly related to  $a_{\text{C}}$ . Using instead an elementary kinetic description for reactions [7]–[9], one arrives at eqn. [39]. Figure 30 demonstrates the

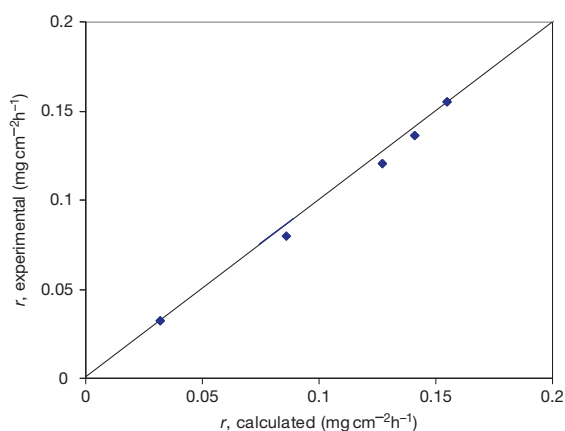


**Figure 30** Carbon uptake kinetics on nickel according to eqn. [39].<sup>97</sup>

success of this description with  $r_7 = 0.73$ ,  $r_8 = 0.06$ , and  $r_{-9} = 0.27 \text{ mg cm}^{-2} \text{ atm}^{-2} \text{ h}^{-1}$ . This indicates that coke formation is controlled by the CO + H<sub>2</sub> reaction [7] at moderate  $p_{\text{CO}}$  levels and by the Boudouard reaction [8] at high  $p_{\text{CO}}$  levels. The methanation process is important when  $p_{\text{H}_2}$  is significant. It needs to be recognized that different dependencies are likely at different temperatures, and that the relationship between coking and dusting rates is likely also to be temperature dependent. More work is required to obtain a full understanding of the effects of environmental variables on nickel dusting.

### 1.12.7.4 Dusting of Austenitic Alloys

Grabke *et al.*<sup>102,105</sup> found that the dusting of binary Fe–Ni alloys varied in reaction morphology and rate with nickel content. Essentially, low-nickel content alloys behaved like pure iron, forming a surface layer of cementite, whereas high-nickel alloys graphitized directly without forming carbide. The nickel level necessary to suppress cementite formation at 650 °C was reported as 30%<sup>105</sup> and also as 5–10%.<sup>102</sup>

The dusting of austenitic chromia-forming alloys is prevented for so long as the oxide scale acts as a barrier to carbon ingress.<sup>56</sup> The onset of dusting has been characterized by Grabke *et al.*<sup>58,60,105</sup> and the general features of the process are now clear. Selective oxidation of chromium produces a chromium-depleted sub-surface alloy region. Local scale damage allows gas access to the metal. If sufficient chromium remains, the Cr<sub>2</sub>O<sub>3</sub> scale reheals; if not, other reactions follow. If  $p_{\text{O}_2}$  is too low for nickel or iron oxides to form, carbon enters the alloy, precipitating chromium carbides.



At these low-temperatures,  $D_{Cr}$  is small, and the carbides are very fine. Removal of chromium from the matrix renders future oxide healing of the surface impossible, and gas access to the chromium-depleted surface continues. The metal is essentially an Fe–Ni alloy, and at high-nickel levels it undergoes graphitization and disintegration in the same way as pure nickel.

Thermal cycling dusting studies<sup>23</sup> on model Fe–xNi–25Cr alloys revealed considerable variation in metal wastage rate with nickel content (Figure 23). A 2.5Ni alloy was ferritic, and formed a surface layer of  $M_3C$ , which disintegrated into cementite dust. Alloys with 5 and 10Ni had duplex  $\alpha + \gamma$  microstructures, in which the austenite was clearly carburized more rapidly than the ferrite. Dusting produced nanoparticles of  $M_3C$  from the 5Ni alloys and both  $M_3C$  and austenite from the 10Ni alloy. A 25Ni alloy was fully austenitic, and disintegrated to yield austenite dust. This shift from carbide to austenite particles with increasing nickel levels is the same as that of binary Fe–Ni alloys,<sup>102,105</sup> and reflects the mechanism of attack on chromium depleted surfaces.

The variation of dusting rate with Fe/Ni ratio shown in Figure 23 reflects mainly the difference in  $D_{Cr}$  accompanying the change from ferritic to austenitic structures. Because the alloy surfaces were electropolished and any cold-worked surface regions removed, chromium was available to the surface only via lattice diffusion. Thus, rehealing was more effective, and frequency of dusting initiation less, in the alloy sequence  $\alpha > (\alpha + \gamma) > \gamma$ . At still higher nickel levels, improved performance resulted from the lowering of alloy carbon permeability.

A growing body of results on the dusting resistance of austenitic alloys is becoming available. It is generally agreed<sup>60,90,105,114</sup> that higher nickel levels are beneficial and that a minimum chromium level of about 25% is required.<sup>114,115</sup> At these levels, scale breakdown allows formation of two internal carbide zones, usually spheroidal  $M_7C_3$  near the surface and lamellar or Widmanstätten  $M_{23}C_6$  at greater depths.<sup>23,116</sup> Alloy additions of silicon and aluminum improve the ability of the scale system to exclude carbon by forming oxide subscales.<sup>59,90,117–119</sup> Additions of carbide forming metals (Mo, W, Nb) form stable carbides. Their ability to getter carbon allows unreacted chromium to reheat the surface scale, delaying the onset of dusting.<sup>119</sup> However, subsequent oxidation of these refractory metal carbides leads to volume expansion, and disruption of the protective scale.<sup>120</sup> It has been shown<sup>121</sup> that additions of copper improve the dusting resistance of 310 stainless steel and

alloy 800, just as copper decreases the dusting of nickel itself. This effect is limited by the alloy solubility for copper, which increases with nickel concentration.

Szkalos *et al.*<sup>24,80,122</sup> have pointed out that the fine internal carbides formed after scale failure can be oxidized *in situ*, leading to disruption of the metal and contributing to the dusting process. This is, in fact, the ‘green rot’ corrosion process,<sup>123</sup> in which the large volume expansion accompanying carbide oxidation fractures the metal. Under dusting conditions, this could occur simultaneously with graphitization of the chromium-depleted surface metal. The two possible reactions for internal carbides near the surface are the oxidation process and simple dissolution, providing a chromium flux toward the surface. The competition between the two processes will depend on oxygen and carbon permeabilities, and  $D_{Cr}$  within the subsurface alloy region. Rates of carbon and oxygen dissolution into the region are also likely to depend on gas compositions.

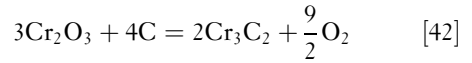
### 1.12.8 Protection by Oxide Scaling

As noted earlier, industrial gas streams which cause carburization are almost always oxidizing to chromium, and therefore also to silicon and aluminum. Heat-resisting alloys used at temperatures up to about 1000 °C are usually chromia formers, and the protective nature of their scales is what preserves the alloys from carburization. Using radioactive  $^{14}C$ , Wolf and Grabke<sup>124</sup> showed that the solubility of carbon in  $Cr_2O_3$  and  $Al_2O_3$  at 1000 °C is below the detectability limit of 0.01 ppm. Nonetheless, chromia scales grown on alloy surfaces can be permeable to carbon, presumably by transport through defects or along internal surfaces. Grabke *et al.*<sup>125</sup> showed that radio-tracer carbon in a  $CO/CO_2/H_2/H_2O$  gas mixture slowly permeated scales on preoxidized Fe–Cr alloys. Simultaneous internal carburization and external  $Cr_2O_3$  growth has been observed<sup>126</sup> on Fe–28Cr exposed to  $CO/CO_2$  at 900 °C. However, a Ni–28Cr alloy reacted in the same way formed no internal carbides, indicating a more gas-tight scale.

Cast heat-resisting steels form scales consisting of mixed carbides and oxides, the proportion of oxide increasing with ambient  $p_{O_2}$ . At high-oxygen activities, the scale is mainly  $Cr_2O_3$  with an outermost layer of manganese-rich spinel and, depending on alloy silicon levels, a more or less continuous  $SiO_2$  layer at the alloy–scale interface. For as long as they maintain their mechanical integrity, these scales completely block carbon access to the underlying

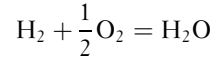
alloys. The appearance of scales grown at 1000 °C, low  $p_{O_2}$  values and  $a_C = 1$  and the corresponding diffusion paths mapped on the thermochemical diagram are shown in **Figure 31**. The scale grown at  $p_{O_2} = 10^{-22}$  atm is a mixture of oxide (dark) and carbide (light) with a sublayer of  $SiO_2$  (black). The protectiveness of these scales depends on alloy silicon content, as shown in **Figure 32**, where a level of about 1.8 w/o is seen to reduce the carburization rate dramatically at 1050 °C. Kane<sup>29</sup> reported a value of 2 w/o at 1093 °C. At  $p_{O_2} = 10^{-24}$  atm,  $Cr_2O_3$  is unstable, but  $SiO_2$  still forms (**Figure 31**). Exposure to these conditions<sup>127</sup> led to a scale of carbide over a thin silica layer at the alloy surface. This scale was not protective, and alloys carburized rapidly, even at silicon levels up to 2.4 w/o. It is concluded that conditions producing both  $SiO_2$  and  $Cr_2O_3$  are necessary to provide a carbon-resistant scale.

The location of the stability boundary between chromium carbide and oxide shown in **Figure 31** is temperature dependent:



$$\Delta G^\circ = 3192100 - 797.3T \quad [43]$$

In the presence of a coke deposit,  $a_C = 1$ , and the value of  $p_{O_2}$  corresponding to the equilibrium [42] is calculated to be as shown in **Figure 33**. In a steam cracking reactor, the  $H_2/H_2O$  ratio is approximately 1. The equilibrium  $p_{O_2}$  values calculated for



are seen to be much higher than the  $Cr_3C_2/Cr_2O_3$  values, and the oxide is stable. However, as pointed out by Grabke *et al.*,<sup>6</sup> the oxygen activity beneath a carbon deposit can be a great deal less. If the carbon deposit is gas tight, then the gas species will be CO and  $CO_2$ , with the ratio  $p_{CO}^2/p_{CO_2}$  set through the Boudouard equilibrium [42] with unit carbon activity. If the total pressure  $p_{CO} + p_{CO_2} = 1$  atm, the corresponding  $p_{O_2}$  is found from the thermodynamics

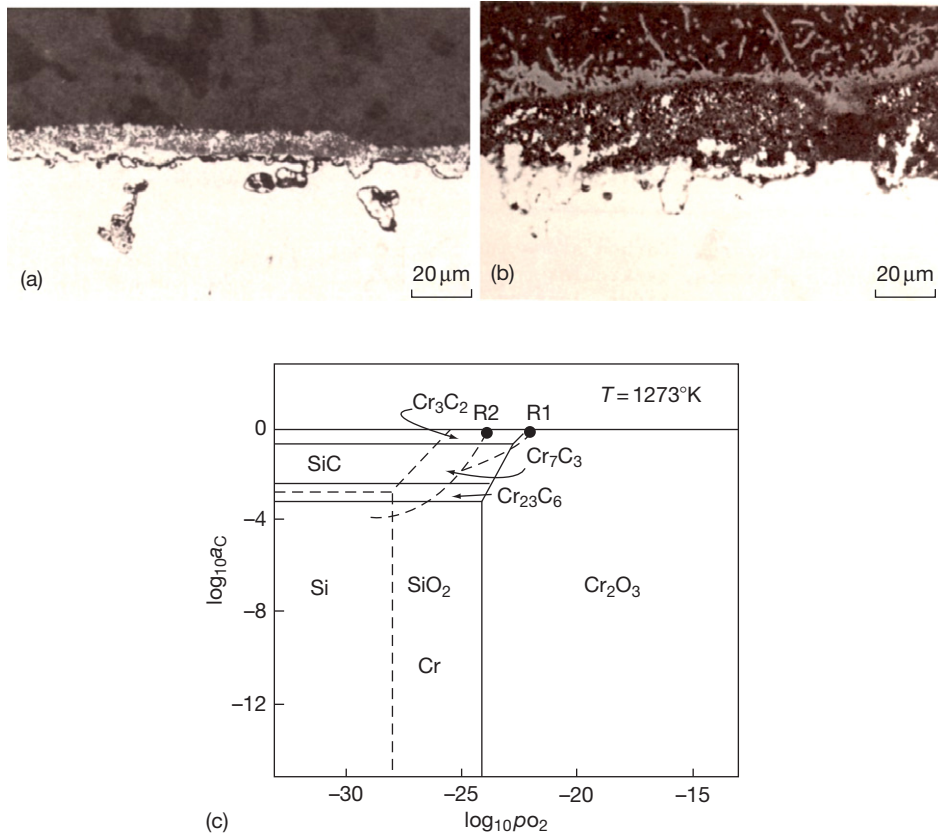


**Figure 31** Scales grown on 25Cr-35Ni heat-resisting steels at 1000 °C and  $a_C = 1$ , (a),  $p_{O_2} = 10^{-22}$  atm, (b)  $p_{O_2} = 10^{-24}$  atm<sup>127</sup> and (c) diffusion paths.

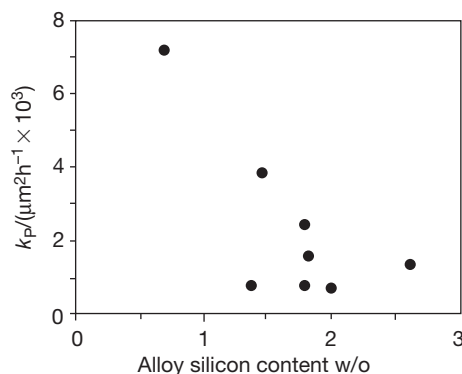
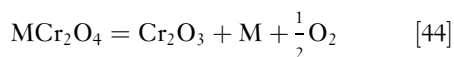


**Figure 32** Dependence of carburization rate on alloy silicon content at 1050 °C,  $a_C = 1$ ,  $p_{O_2} = 3 \times 10^{-20}$  atm.<sup>128</sup>

of [2] to be low at high temperatures (Figure 33). If  $T \geq 1100^\circ\text{C}$ , carbon will reduce the oxide and degrade the protective nature of the scale.

Both  $\text{Cr}_2\text{O}_3$  and  $\text{Al}_2\text{O}_3$  scales provide effective barriers to carbon entry and metal dusting, but will eventually fail by cracking or spallation. If sufficient chromium or aluminum remains at the alloy surface, then scale rehealing occurs. If not, carbon dissolves in the depleted alloy and diffuses inward, to precipitate carbides.<sup>129</sup> At high carbon activities, metal dusting follows. The competition between outward metal diffusion to form a scale and inward carbon diffusion should in principle be described by an equation such as eqn. [15]. Unfortunately, no rigorous test of this description is available. Qualitative support is provided by the finding<sup>91,130</sup> that several heat-resisting alloys can be ranked in metal dusting resistance during temperature cycling according to their  $N_{\text{Cr}}^{(o)} D_{\text{Cr}} / N_{\text{C}}^{(s)} D_{\text{C}}$  values.

A practical problem arises in the use of oxide scales for protection against carbon. Preoxidation procedures used to develop a chromia scale prior to service can also develop an outer scale layer of spinel,  $\text{MCr}_2\text{O}_4$ . If subsequent service conditions provide an oxygen potential below the spinel stability level, it is reduced leaving particles of metal,



These particles act as catalytic sites, accelerating the onset of coking. This in turn can lead to scale disintegration and the commencement of dusting. Exposing austenitic chromia formers to oxidizing and carburizing conditions has been shown<sup>131</sup> to lead to rapid scale failure, accelerated carburization, and in some cases the commencement of dusting. In order to avoid this effect it is necessary to adjust the

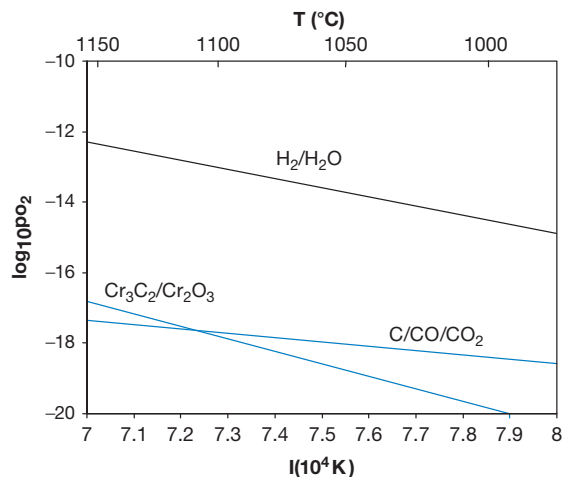


**Figure 33** Thermodynamics of oxide to carbide conversion compared with  $\text{CO}/\text{CO}_2$  mixture at  $p_T = 1$  atm in equilibrium with graphite, and with oxygen potential controlled by  $\text{H}_2/\text{H}_2\text{O}$  equilibrium in steam cracking furnaces.

preoxidation conditions so that the oxides formed at that stage are stable during subsequent service.

#### 1.12.8.1 Protection by Adsorbed Sulfur

The introduction of gaseous sulfur species such as  $\text{H}_2\text{S}$  to industrial process steams is widely practiced in order to minimize carburization and metal dusting. Sulfur adsorbs on the metal surface, impeding carbon access.<sup>34,132,133</sup> Under these conditions, rehealing of damaged oxide scales is favored over carbon penetration. The effect increases with  $p_{\text{S}_2}$ , but the sulfur pressure must be kept below the value at which  $\text{CrS}$  can form.

Adsorbed sulfur also provides protection against metal dusting, delaying the onset of the process and allowing more time for oxide rehealing. Data assembled by Schneider *et al.*<sup>134</sup> for the effect on iron is shown in Figure 34. The  $\text{H}_2\text{S}/\text{H}_2$  ratios required to yield protection increase with temperature because sulfur adsorption is strongly exothermic. In the case of iron, sulfur adsorbs on cementite and prevents the nucleation of graphite.

#### 1.12.8.2 Protection by Coatings

As is clear, long-term protection against metal dusting and carburization can only be achieved by forming a stable oxide scale which is capable of rapid rehealing. Coatings with high concentrations of scale forming elements can be used to provide this

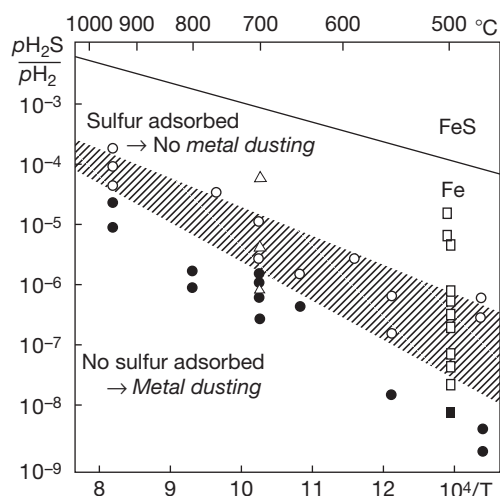


**Figure 34** Effect of sulfur on metal dusting. The hatched region represents the transition to an iron surface saturated with sulfur.<sup>134</sup>

protection. Chemical vapor deposition<sup>135–140</sup> and flame spraying<sup>141</sup> have been used to produce carburization resistant coatings, and their utility under metal dusting conditions has also been tested.<sup>142</sup> Aluminum diffusion coatings were found to be protective for a series of ferritic steels (2.25–28Cr) and the austenitic alloy 800. However, long-term exposure led to pore development under the scale and cracking. Silicon diffusion coatings did not develop protective scales. A flame sprayed  $\gamma$ -TiAl coating was successful on a ferritic material, but failed on alloy 800 as a result of thermal mismatch. This work showed that alumina scales provided better protection against carbon than did chromia.

### 1.12.9 Conclusions

Carburization reactions at  $a_C \leq 1$  are described by the classical theory of internal oxidation. Local equilibrium is achieved within the reacting alloy, solid-state diffusion of dissolved carbon controls the rate, and parabolic kinetics result. Wagner's diffusion theory provides good quantitative predictive capability, despite the approximate nature of some of its assumptions.

Metal dusting reactions at  $a_C > 1$  proceed according to complex mechanisms which are still not fully defined. Local equilibrium is not achieved within the gas or at the gas–solid interface. It is, therefore, necessary to consider both the thermodynamic state of the gas and the kinetics of the several parallel gas–solid reactions possible. This requires specification of

the complete gas composition, including minority species, as well as temperature. Considerably more work is needed to define temperature and gas composition effects on dusting rates.

Ferritic materials at moderate temperatures form  $\text{Fe}_3\text{C}$ . This phase is either disintegrated by precipitation within it of graphite or, in other gases, decomposed to yield metallic iron. Unfortunately, the boundaries between the two regimes are still not defined. Austenitic materials form no iron carbide, and are disintegrated by precipitation and growth of graphite within the metal. A similar mechanism operates for ferritic materials when cementite formation is prevented by high temperatures or alloying.

Protection against carburization and dusting requires the provision of a surface barrier between metal and gas, either an adsorbed sulfur layer or an oxide scale. When attack by carbon does occur, it is catastrophically rapid. For this reason, protective measures must be employed, and their continued effectiveness monitored.

### References

1. Shatynski, S. R. *Oxid. Met.* **1978**, *13*, 105.
2. Wada, T.; Wada, H.; Elliott, J. F.; Chipman, J. *Met. Trans.* **1971**, *2A*, 2199.
3. Wada, T.; Wada, H.; Elliott, J. F.; Chipman, J. *Met. Trans.* **1972**, *3*, 2865.
4. Smith, R. P. *Acta Met.* **1953**, *1*, 578.
5. Grabke, H. J.; Peterson, E. M. *Scripta Met.* **1978**, *12*, 1111.
6. Grabke, H. J.; Gravenhorst, U.; Steinkusch, W. *Werkst. u. Korros.* **1976**, *27*, 291.
7. Schnaas, A.; Grabke, H. J. *Oxid. Met.* **1978**, *12*, 387.
8. Smith, G. M.; Young, D. J.; Trimm, D. L. *Oxid. Met.* **1982**, *18*, 229.
9. Wagner, C. Z. *Elektrochem.* **1959**, *63*, 772.
10. Kubaschewski, O.; Alcock, C. B. *Metallurgical Thermochemistry*, 5th ed.; Pergamon: Oxford, 1983.
11. Mazandarany, F. N.; Pehlke, R. D. *Met. Trans.* **1973**, *4A*, 2070.
12. Allen, A. T.; Douglass, D. L. *Oxid. Met.* **1999**, *51*, 199.
13. Ramanarayanan, T. A.; Slolovitz, D. J. *J. Electrochem. Soc.* **1985**, *132*, 2268.
14. Ahmed, O.; Young, D. J. In *High Temperature Corrosion and Materials Chemistry*; McNallan, M. J., Opila, E. J., Maruyama, T., Narita, T., Eds.; The Electrochemical Society, Inc.: Pennington, NJ, 2000; Vol. II; p 77.
15. Benz, R.; Elliott, J. F.; Chipman, J. *Met. Trans.* **1974**, *5*, 2235.
16. Ford, S. Ph.D. Thesis, University of New South Wales, 2005.
17. Young, D. J.; Ahmed, O. *Mater. Sci. Forum* **2001**, 369–372, 93.
18. Udyavar, M.; Young, D. J. *Corros. Sci.* **2000**, *42*, 861.
19. Bose, S. K.; Grabke, H. J. *Z. Metallk.* **1978**, *69*, 8.
20. Ford, S.; Young, D. J.; McGrouther, D.; Munroe, P. R. *Mater. High Temp.* **2005**, *22*, 351.
21. Bunin, K. P. *Izv. Chern. Metall.* **1973**, *2*, 123.
22. Mozchan, V. I. *Izv. Chern. Metall.* **1979**, *8*, 92.

23. Toh, C. H.; Munroe, P. R.; Young, D. J. *Oxid. Met.* **2002**, 58, 1.
24. Szakalos, P.; Lundberg, M.; Petterson, R. *Corros. Sci.* **2006**, 48, 1679.
25. Ford, S.; Munroe, P. R.; Young, D. J. In *John Stringer Symposium*; Tortorelli, P. F., Wright, I. G., Hou, P. Y., Eds.; ASM International: Materials Park OH, 2003; p 77.
26. Ohriner, E. K.; Morall, J. E. *Scripta Met.* **1979**, 13, 7.
27. Kirkaldy, J. S. *Canad. Met. Q.* **1969**, 8, 35.
28. Christ, H. J. *Mater. Corros.* **1998**, 49, 258.
29. Kane, R. H. *Corrosion* **1981**, 37, 187.
30. Chu, W. F.; Rahmel, A. *Oxid. Met.* **1981**, 15, 331.
31. Roach, D. B.; Wright, I. G. *The Study of the Carburisation Resistance of Heat Resistant Casting Alloys*; 1st Interim Report on Project No 60, Batelle, Columbus Labs, OH, 1974.
32. Ledgerf, K.; Rahmel, A.; Schorr, H. *Werkst. Korros.* **1980**, 31, 121.
33. Ramanarayanan, T. A.; Petkovic-Luton, R. *Corrosion* **1981**, 37, 712.
34. Barnes, J.; Corish, J.; Norton, J. F. *Oxid. Met.* **1986**, 26, 333.
35. Kinniard, S. P.; Young, D. J.; L Trimm, D. *Oxid. Met.* **1986**, 26, 417.
36. Mitchell, D. R. G.; Young, D. J. *Foundry Trade J.* **1992**, 166, 253.
37. Mitchell, D. R. G.; Young, D. J. *J. Mat. Sci. Lett.* **1993**, 12, 1076.
38. Mitchell, D. R. G.; Young, D. J.; Kleeman, W. *Mater. Corros.* **1998**, 49, 231.
39. Becker, P.; Ouamara, F.; Young, D. J. In *High Temperature Corrosion Materials Chemistry IV*; Opila, E., Hou, P., Moruyama, T., Pieraggi, B., Schifler, D., Wachina, E., Eds.; The Electrochemical Society, Inc.: Pennington, NJ, 2003; p 178.
40. Becker, P.; Young, D. J. *Oxid. Met.* **2007**, 67, 267.
41. Klower, J.; Heubner, U. *Mater. Corros.* **1998**, 49, 237.
42. Young, D. J. *Mater. Corros.* **1999**, 50, 675.
43. Forseth, S.; Kofstad, P. *Mater. Corros.* **1998**, 49, 266.
44. Grabke, H. J. *Carburisation – A High Temperature Corrosion Phenomenon*; MTI Publication No. 52, Materials Technology Institute of the Chemical Processing Industries: St. Louis, MI, 1997.
45. Grabke, H. J.; Wolf, I. *Mater. Sci. Eng.* **1987**, 87, 23.
46. Lewis, H. B. *Corros.* **1968**, 3, 166.
47. Rahmel, A.; Grabke, H. J.; Steinkusch, W. *Mater. Corros.* **1998**, 49, 221.
48. Roy, S. K.; Grabke, H. J.; Wepner, W. *Arch. Eisenhüttenwes.* **1980**, 51, 91.
49. Hemptenmacher, J.; Grabke, H. J. *Werkst. Korros.* **1983**, 34, 333.
50. Camp, E.; Phillips, C.; Cross, L. *Corrosion* **1954**, 10, 149.
51. Hubbell, W. G. *The Iron Age* **1946**, 157, 56.
52. Burns, L. *Corrosion* **1950**, 6, 169.
53. Lefrancois, P. A.; Hoyt, W. B. *Corrosion* **1963**, 19, 360t.
54. Hochman, R. F. *Proc. 3<sup>rd</sup> Int. Cong. Met. Corrosion*, University of Moscow Press, 1969.
55. Hochman, R. F.; Klett, M. G. *Proc. 5<sup>th</sup> Int. Cong. Met. Corrosion*, NACE: Houston, TX, 1974.
56. Hochman, R. F. In *Proc. Symp. Properties of High Temperature Alloys with Emphasis on Environmental Effects*; Foroulis, Z. A., Pettit, F. S., Eds.; Electrochemical Society: Pennington, NJ, 1977; p 571.
57. Grabke, H. J.; Hemptenmacher, J.; Munker, A. *Werkst. Korros.* **1984**, 35, 543.
58. Nava Paz, J. C.; Grabke, H. J. *Oxid. Met.* **1993**, 39, 437.
59. Grabke, H. J.; Krajak, R.; Nava Paz, J. C. *Corros. Sci.* **1993**, 35, 1141.
60. Grabke, H. J.; Krajak, R.; Muller-Lorenz, E. M. *Werkst. Korros.* **1993**, 44, 89.
61. Grabke, H. J.; Bracho-Troconis, C. B.; Muller-Lorenz, E. M. *Werkst. Korros.* **1994**, 45, 215.
62. Motin, M. A. A.; Munroe, P. R.; Brady, M. P.; Young, D. J. *Scripta Mater.* **2007**, 56, 281.
63. Pippel, E.; Woltersdorf, J.; Grabke, H. J.; Strauss, S. *Steel Research* **1995**, 66, 217.
64. Pippel, E.; Woltersdorf, J.; Schneider, R. *Mater. Corros.* **1998**, 49, 309.
65. Chun, C. M.; Mumford, J. D.; Ramanarayanan, T. A. J. *Electrochem. Soc.* **2002**, 149, B348.
66. Schmid, B.; Walmsley, J. C.; Grong, O.; Odegard, R. *Met. Mat. Trans. A* **2003**, 34, 345.
67. Zeng, Z.; Natesan, K.; Maroni, V. A. *Oxid. Met.* **2002**, 58, 147.
68. Zhang, J.; Schneider, A.; Inden, G. *Corros. Sci.* **2003**, 45, 1329.
69. Zhang, J.; Schneider, A.; Inden, G. *Corros. Sci.* **2003**, 45, 281.
70. Zhang, J.; Schneider, A.; Inden, G. *Mater. Corros.* **2003**, 54, 770.
71. Toh, C. H.; Munroe, P. R.; Young, D. J. *Mater. High Temp.* **2003**, 20, 527.
72. Baker, R. T. K.; Barber, M. A.; Harris, P. S.; Yeates, F. S.; Waite, R. J. *J. Catal.* **1972**, 26, 51.
73. Longbottom, R. J.; Ostrovski, O.; Zhang, J.; Young, D. J. *Met. Mat. Trans. B* **2007**, 38, 175.
74. Smith, R. P. *Transactions, AIME* **1962**, 224, 105.
75. Turkdogan, E. T. *Physical Chemistry of High Temperature Technology*; Academic Press: New York, 1980.
76. Koszman In *Proc. Symp. on High Temp. Gas-Metal Reactions in Mixed Environments*; Jansson, S. A., Foroulis, Z. A., Eds.; Met. Soc. AIME: New York, 1973; p 155.
77. Ozturk, B.; Fearing, V. L.; Ruth, J. A.; Simkovich, G. *Met. Trans. A* **1982**, 13, 1871.
78. Schneider, A.; Inden, G. *Calphad* **2007**, 31, 141.
79. Young, D. J.; Motin, M. A. A.; Zhang, J. Defects and Diffusion, accepted for publication.
80. Szakalos, P. *Mater. Corros.* **2003**, 54, 752.
81. Zhang, J.; Schneider, A.; Inden, G. *Mater. Corros.* **2003**, 54, 763.
82. Grabke, H. J. *Mater. Corros.* **2003**, 54, 736.
83. Muller-Lorenz, E. M.; Grabke, H. J. *Mater. Corros.* **1999**, 50, 614.
84. Chun, C. M.; Ramanarayanan, T. A. *Oxid. Met.* **2004**, 62, 71.
85. Yin, H. ME Thesis, University of New South Wales 2006.
86. Schneider, Vielhaus, H.; Inden, G.; Grabke, H. J.; Muller-Lorenz, E. M. *Mater. Corros.* **1998**, 49, 336.
87. Motin, M. A. A. PhD Thesis, University of New Southwales 2009.
88. Grabke, H. J.; Muller-Lorenz, E. M.; Eltester, B.; Lucas, M.; Monceau, D. *Steel Research* **1997**, 68, 179.
89. Frabiezewski, A. S.; Watkins, W. R.; Hoffman, J. J.; Dean, S. W. *Corrosion 2000*; NACE: Houston, TX, 2000; paper no. 532.
90. Baker, B. A.; Smith, G. D. *Corrosion 2000*; NACE: Houston, TX, 2000; paper no. 257.
91. Toh, C. H.; Munroe, P. R.; Young, D. J.; Fogar, K. *Mater. High Temp.* **2003**, 20, 129.
92. Grabke, H. J. *Mater. Corros.* **1998**, 49, 303.
93. Strauss, S.; Krajak, R.; Palm, M.; Grabke, H. J. *Mater. Corros.* **1996**, 47, 701.
94. Schneider; Zhang, J. *Mater. Corros.* **2003**, 54, 778.
95. Schneider; Zhang, J. *J. Corros. Sci. Eng.* **2003**, 6, paper H043.

96. Chun, C. M.; Mumford, J. D.; Ramanarayanan, T. A. *J. Electrochem Soc.* **2000**, *147*, 3680.
97. Zhang, J.; Young, D. J. *Corros. Sci.* **2007**, *49*, 1496.
98. Zeng, Z.; Natesan, K. *Chem. Mater.* **2003**, *15*, 872.
99. Schneider, R.; Pippel, E.; Woltersdorf, J.; Strauss, S.; Grabke, H. J. *Steel Research* **1997**, *68*, 326.
100. Wei, Q.; Pippel, E.; Woltersdorf, J.; Strauss, S.; Grabke, H. J. *Mater. Corros.* **2000**, *51*, 652.
101. Zhang, J.; Munroe, P. R.; Young, D. J. *Acta Mater.* **2008**, *56*, 68.
102. Pippel, E.; Woltersdorf, J.; Grabke, H. J. *Mater. Corros.* **2003**, *54*, 747.
103. Shelton, J. C.; Patil, H. R.; Blakely, J. M. *Surf. Sci.* **1974**, *43*, 493.
104. Yang, R. T.; Chen, J. P. *J. Catal.* **1972**, *26*, 51.
105. Grabke, H. J.; Krajak, R.; Muller-Lorenz, E. M.; Strauss, S. *Mater. Corros.* **1996**, *47*, 495.
106. Zhang, J.; Cole, D. M. I.; Young, D. J. *Mater. Corros.* **2005**, *56*, 756.
107. Shihyama, Y.; Otsuka, N. *Mater. Sci. Forum* **2006**, *522–523*, 581.
108. Bernardo, C. A.; Alstrup, I.; Rostrup-Nielsen, J. R. *J. Catal.* **1985**, *96*, 517.
109. Alstrup, Tavares, M. T.; Bernardo, C. A.; Sorensen, O.; Rostrup-Nielsen, J. R. *Mater. Corros.* **1998**, *49*, 367.
110. Tavares, M. T.; Alstrup, I.; Bernardo, C. A. *Mater. Corros.* **1999**, *50*, 681.
111. Dalmon, J. A.; Martin, G. A. *J. Catal.* **1998**, *49*, 367.
112. DKI German Copper Institute Booklet: *Copper nickel alloys: Properties, Processing, Application*. [http://www.copper.org/applications/cuni/txt\\_DKI.html](http://www.copper.org/applications/cuni/txt_DKI.html).
113. McLellan, R. B.; Chraska, P. *Mater. Sci. Eng.* **1970**, *6*, 176.
114. Grabke, H. J.; Muller-Lorenz, E. M.; Klower, J.; Agarwal, D. C. *Mater. Performance* **1998**, *37*, 58.
115. Maier, M.; Norton, J. F.; Puschek, P. *Mater. High Temp.* **2000**, *17*, 347.
116. Perkins, R. A.; Coons, W. C.; Radd, F. J. In *Properties of High Temperature Alloys*; Foroulis, Z. A., Pettit, F. S., Eds.; Electrochemical Society, Inc.: Princeton, NJ, 1976; p 733.
117. Maier, M.; Norton, J. F. *Corrosion* **99**; NACE: Houston, TX, 1999; paper 75.
118. Zeng, Z.; Natesan, K.; Grimoditch, M. *Corrosion* **2004**, *60*, 632.
119. Strauss, S.; Grabke, H. J. *Mater. Corros.* **1998**, *49*, 321.
120. Litz, J.; Rahmel, A.; Schorr, M. *Oxid. Met.* **1988**, *29*, 95.
121. Zhang, J.; Young, D. J. *Corros. Sci.* **2007**, *49*, 1450.
122. Szakalos, P.; Pettersson, R.; Hertzman, S. *Corros. Sci.* **2002**, *44*, 2253.
123. Betteridge, W. *The Nimonic Alloys*; E. Arnold: London, 1959.
124. Wolf; Grabke, H. J. *Solid State Commun.* **1985**, *54*, 5.
125. Grabke, H. J.; Ohla, K.; Peters, J.; Wolf, I. *Werkst. Korros.* **1983**, *34*, 495.
126. Zheng, X. G.; Young, D. J. *Oxid. Met.* **1994**, *42*, 163.
127. Tomas, P.; Young, D. J.; L Trimm, D. In *Proc. Int. Congress Met. Corros.* National Research Council of Canada: Ottawa, 1984; Vol. 1; p 58.
128. Mitchell, D. R. G.; Young, D. J.; Kleeman, W. *Corrosion* **92**; NACE: Houston, TX, 1992; paper 302.
129. Dillinger, L.; Buchheit, R. D.; Van Echo, J. A.; Roach, D. B.; Hall, A. M. *Microstructures of Heat-Resistant-Alloys*; Steel Founders' Society of America: Rocky River, OH, 1970.
130. Young, D. J. *Mater. Sci. Forum* **2006**, *522–523*, 15.
131. Harper, M. A.; Ducasse, M.; Young, D. J. *Corrosion* **1995**, *51*, 191.
132. Grabke, H. J.; Peterson, E. M.; Srinivasan, S. R. *Surface Sci.* **1977**, *67*, 501.
133. Grabke, H. J.; Moller, R.; Schnaas, A. *Werkst. Korros.* **1979**, *30*, 794.
134. Schneider; Viefhaus, H.; Inden, G.; Grabke, H. J.; Muller-Lorenz, E. M. *Mater. Corros.* **1998**, *49*, 336.
135. Southwell, G.; MacAlpine, S.; Young, D. J. *J. Mater. Sci. Eng.* **1987**, *88*, 81.
136. Ganser, B.; Wynns, K. A.; Kurlekar, A. *Mater. Corros.* **1999**, *50*, 700.
137. Rapp, R. A. *Corrosion* **89**; NACE: Houston, TX, 1989; paper 532.
138. Streiff, R. In *Elevated Temperature Coatings: Science and Technology II*; Dahotre, N. B., Hampikian, J. M., Eds.; TMS, 1996; p 407.
139. Wachtell, R. L. In *Science and Technology of Surface Coating*; Chapman, B. N., Anderson, J. C., Eds.; Academic Press: London, 1974; p 105.
140. Kung, S. C.; Rapp, R. A. *Oxid. Met.* **1989**, *32*, 89.
141. Schutze, M. German Patent: DE 197 43 421.5 (1998).
142. Rozado, C.; Schutze, M. *Mater. Corros.* **2003**, *54*, 831.



## 1.13 Nitridation of Alloys

**U. Krupp**

Faculty of Engineering and Computer Sciences, University of Applied Sciences Osnabrück, Albrechtstraße 30, 49076 Osnabrück, Germany

© 2010 Elsevier B.V. All rights reserved.

1.13.1	Introduction	304
1.13.2	Thermodynamics and Kinetics of Nitridation Processes	305
1.13.2.1	Nitrogen-Containing Gas Atmospheres	305
1.13.2.2	Diffusion-Controlled Internal Nitridation	306
1.13.2.3	Influence of the Chemical Composition – Thermodynamics of Internal Nitridation	308
1.13.2.4	The Transition from Internal to External Nitridation	309
1.13.3	Internal Nitridation of Heat-Resistant Alloys	310
1.13.3.1	Internal Nitridation of Fe- and Ni-Based Superalloys	310
1.13.3.2	Mechanical Effects on Internal Nitridation Kinetics	311
1.13.3.3	Protection Against Internal Nitridation Attack	312
1.13.4	Modelling and Computer Simulation of Internal Nitridation	313
1.13.5	Concluding Remarks	314
	References	315

### Abbreviations

**CALPHAD** Calculation of phase diagrams  
**CSL** Coincident site lattice

### Symbols

$c_i$  Concentration of a species  $i$   
 $c_B^\xi$  Concentration of the nitride-forming alloying element B at the reaction front  $\xi$   
 $c_B^0$  Initial concentration of the nitride-forming alloying element B in the alloy  
 $c_N^0$  Nitrogen concentration at the surface (can be set equal to the max. nitrogen solubility in the alloy)  
 $c_N^\xi$  Nitrogen concentration at the reaction front  $\xi$   
 $D_i$  Diffusivity of a species  $i$  ( $\text{m}^2 \text{s}^{-1}$ )  
 $g^*$  Critical volume fraction for the transition from internal to external oxidation/nitridation  
 $j_{\text{bulk}}$  Diffusive flux through the bulk ( $\text{m}^{-2} \text{s}^{-1}$ )  
 $j_{\text{if}}$  Diffusive flux along interfaces (precipitates, grain or phase boundaries) ( $\text{m}^{-2} \text{s}^{-1}$ )  
 $j_{\text{prec}}$  Diffusive flux through the precipitates ( $\text{m}^{-2} \text{s}^{-1}$ )  
 $K$  Equilibrium constant  
 $L_{\text{SP}}$  Solubility product  
 $P$  Permeability ( $\text{m}^2 \text{s}^{-1}$ )  
 $p(\text{H}_2)$  Hydrogen partial pressure (Pa)  
 $p(\text{NH}_3)$  Ammonia partial pressure (Pa)  
 $p(\text{N}_2)$  Nitrogen partial pressure (Pa)

$p(\text{O}_2)$  Oxygen partial pressure (Pa)  
 $R$  Universal gas constant ( $\text{J mol}^{-1} \text{K}^{-1}$ )  
 $t$  Exposure time (s)  
 $T$  Temperature (K, °C)  
 $x, y$  Coordinates (m)  
 $V_i$  Molar volume of a species  $i$  ( $\text{m}^3 \text{mol}^{-1}$ )  
 $\Delta G_0$  Standard free energy of formation ( $\text{J mol}^{-1}$ )  
 $\varepsilon$  Labyrinth factor  
 $\gamma$  Parameter  
 $\nu$  Stoichiometric coefficient  
 $\xi$  Depth of the internal reaction front (precipitation depth) (m)

### 1.13.1 Introduction

Nitridation of alloys refers mostly to a kind of surface-modification process applied to high-strength steels, to improve wear and fatigue resistance (case hardening).<sup>1</sup> Here, the nitridation process is carried out in an ammonia-containing atmosphere, exhibiting high nitrogen activity, leading to the formation of Fe nitrides, as well as V, Cr, and Al nitrides, in the case of alloy steels. However, nitrogen-based gas atmospheres are often considered inert and used for welding and heat-treatment purposes. Nitridation as a kind of high temperature corrosion becomes relevant for technical components operating at temperatures well above 800°C, for example, gas-turbine blades or tubes

in power generation and chemical industry. At these temperatures, dissociation of  $N_2$  into atomic nitrogen at metal surfaces is sufficient, so that alloying elements with a high affinity to nitrogen, such as Ti, Al, and Cr, can form nitrides. Provided that diffusive penetration of nitrogen is fast, the nitrides form internally; it is a form of corrosive attack that is very similar to internal oxidation and has been termed internal nitridation.<sup>2</sup> **Figure 1** shows an example of internal nitridation leading to failure of a natural-gas-fired burner tube made of the Ni-base alloy 601.

In most technical cases, internal nitridation has been observed in heat-resistant alloys together with superficial oxide-scale formation and internal oxidation. Hence, quantitative prediction of the degree of nitridation attack requires a thorough analysis of the relevant diffusive transport mechanisms and the thermodynamic stabilities of the species participating in the high temperature corrosion processes. The relationship between the gas atmosphere and the formation of metal nitrides is discussed in [Section 1.13.2](#), while [Section 1.13.3](#) focuses on some implications during internal corrosion reactions occurring during the operation of components made of technical heat-resisting alloys. [Section 1.13.4](#) provides an insight into applying computer modeling to complex internal-corrosion processes.

## 1.13.2 Thermodynamics and Kinetics of Nitridation Processes

### 1.13.2.1 Nitrogen-Containing Gas Atmospheres

The risk of nitridation of alloys is prevalent in atmospheres with high nitrogen activities  $a_N$ , that is, nitrogen-based atmospheres ( $N_2$ ) or, in particular, ammonia-bearing atmospheres ( $NH_3$ ) with nitrogen

activities up to the range of  $a_N = 10^{10}$ . The resulting atomic-nitrogen concentration at the metal surface can be calculated using the following equations<sup>2</sup>:

$$\frac{1}{2}N_2 \rightleftharpoons N_{\text{dissolved}}, \quad c(N_{\text{dissolved}}) = K\sqrt{p(N_2)} \quad [1]$$

$$NH_3 \rightleftharpoons \frac{3}{2}H_2 + N_{\text{dissolved}},$$

$$c(N_{\text{dissolved}}) = K \frac{p(NH_3)}{p(H_2)^{3/2}} \quad [2]$$

It should be mentioned that at moderate and low temperatures atomic nitrogen (eqn [2]) recombines to form molecular  $N_2$ . Hence, nitridation requires either a high flux of nitriding gas or high temperatures.

The relevant nitride-forming alloying elements Ti, Al, and Cr are at the same time prone to oxidation. The formation of the respective nitrides or oxides depends on the standard free energy of formation (cf. [Section 1.13.2.3](#)) and the relationship between the nitrogen and oxygen partial pressures. With the help of thermodynamic data for the stability of the different oxide and nitride compounds, this relationship can be represented by means of stability diagrams.

The competitive situation between oxidation and nitridation is prevalent during high temperature exposure to gases containing both oxygen and nitrogen. This is the case for air and for nearly all combustion atmospheres. In the case of cracks in thermally-grown oxide (TGO) scale and/or metal substrate, the nitrogen activity can reach much higher values than the oxygen activity, which is reduced due to oxidation. This can lead to situations where locally the  $p(N_2)/p(O_2)$  ratio reaches values at which Al, Ti, and Cr form nitrides instead of oxides.<sup>3,4</sup> An example of such a situation is shown in [Figure 2](#).

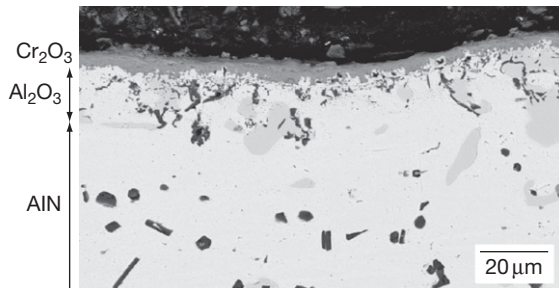


**Figure 1** Internal-oxidation and -nitridation attack of a failed natural-gas burner tube of alloy 601 operated at  $T = 1100^\circ\text{C}$ .

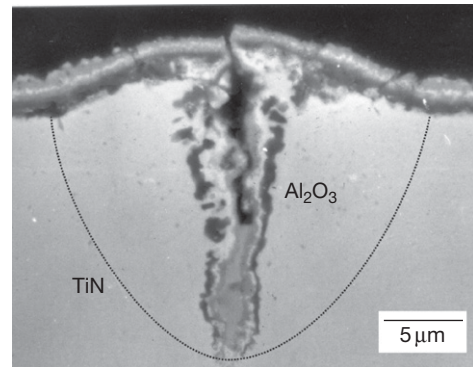


**Figure 2** Crack in the superalloy CMSX-6 caused by fatigue at  $950^\circ\text{C}$  showing internal oxidation and nitridation.

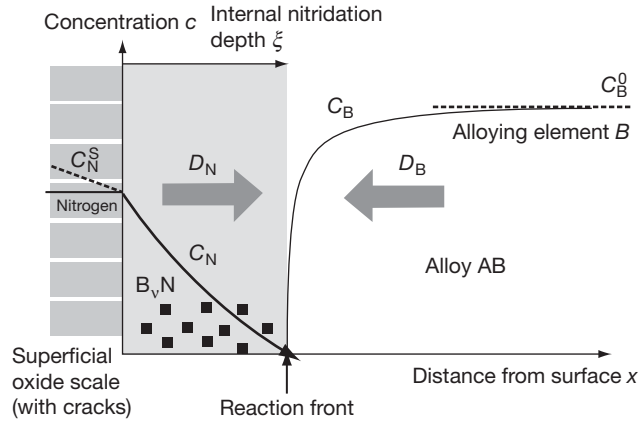


**Figure 3** Concentration profiles during internal precipitation of  $B_vN$  according to Wagner's classical theory of internal oxidation.

### 1.13.2.2 Diffusion-Controlled Internal Nitridation

Provided that the degree of  $N_2$  dissociation at the metal surface is fast enough, that is,  $p(N_2)$  can be assumed to be equal to the nitrogen concentration in the gas phase, the nitridation process is determined by inward diffusion of nitrogen into the alloy and outward diffusion of the nitride-forming alloying element, cf. **Figure 3**. Under these conditions, the nitrogen concentration at the surface is constant ( $c_N(x=0) = c_N^s$ ), while the concentration of the nitride-forming alloying element far away from the internal-nitridation zone is always equal to the nominal bulk concentration ( $c_B(x > \xi) = c_B^0$ ). In the most simple case of just one nitride compound precipitating in a specimen or component where two- or three-dimensional geometrical features are negligible, the nitridation process can be described by Fick's second law of diffusion with  $c_N$ ,  $c_B$ ,  $D_N$ ,  $D_B$  being the concentrations and diffusivities of nitrogen N in the alloy and the nitride-forming alloying element B, respectively:

$$\frac{\partial c_{N/B}}{\partial t} = D_{N/B} \frac{\partial^2 c_{N/B}}{\partial x^2} \quad [3]$$

In general, internal nitridation can be treated in an analogous way to internal oxidation, where the classical theory of Carl Wagner<sup>5</sup> can be applied. Assuming parabolic progress of the internal-nitridation depth  $\xi$ , that is,

$$\xi(t) = 2\gamma\sqrt{D_N t} \quad [4]$$

the diffusion [equation \[3\]](#) can be coupled with the concentrations  $c_N^\xi$  and  $c_B^\xi$  at the reaction front  $\xi$  based on the

solubility product  $L_{SP} = c_B c_N$  of the respective nitride compound  $B_vN$  (cf. **Figure 3** and [Section 1.13.2.3](#))

$$c_N(x, t) = c_N^s - \frac{c_N^s - c_N^\xi}{\text{erf} \gamma} \text{erf} \left( x / 2\sqrt{D_N t} \right) \quad [5]$$

$$c_B(x, t) = c_B^0 - \frac{c_B^0 - c_B^\xi}{\text{erfc} \left( \gamma \sqrt{\frac{D_N}{D_B}} \right)} \text{erfc} \left( x / 2\sqrt{D_B t} \right) \quad [6]$$

and taking into account that the diffusive flux of nitrogen and the nitride-forming alloying element at the reaction front must be equivalent (according to the stoichiometry  $B_vN$ ).

$$\lim_{\varepsilon \rightarrow 0} \left[ -D_O \left( \frac{\partial c_N}{\partial x} \right)_{x=\xi-\varepsilon} = v D_B \left( \frac{\partial c_B}{\partial x} \right)_{x=\xi+\varepsilon} \right] \quad [7]$$

For nitride compounds of high stability, like the common ones TiN and AlN, the concentrations  $c_N^\xi$  and  $c_B^\xi$  can be neglected, that is,  $L_{SP} = 0$  (type I behavior). Furthermore, interstitial nitrogen diffusion (cf. [Table 1](#)) should be by orders of magnitude faster than substitutional diffusion of the metallic alloying elements, that is,  $D_B/D_N \ll c_N^\xi/c_B^0 \ll 1$ . According to Wagner's theory of internal oxidation, the internal-nitridation depth can be calculated as

$$\xi^2(t) = 2 \underbrace{\frac{c_N^\xi D_N}{v c_B^0}}_{k_N} t \quad [8]$$

with  $k_N$  being the nitridation constant. Even though [eqn \[8\]](#) provides a good estimate for many internal carburization, oxidation, and nitridation phenomena, technical corrosion processes involve mostly simultaneous formation of various compounds of different

thermodynamic stability,<sup>6,7</sup> for example, in NiCrAlTi alloys, the progress of the internal TiN precipitation front is governed by the consumption of nitrogen due to CrN/Cr<sub>2</sub>N and AlN formation and the surface nitrogen concentration  $c_N^s$ , which might be decreasing because of the possible growth of an outer Al<sub>2</sub>O<sub>3</sub> and/or Cr<sub>2</sub>O<sub>3</sub> scale. This is schematically represented in **Figure 4**.

The problem becomes more complex when nitrides of moderate or low thermodynamic stability like CrN, Cr<sub>2</sub>N, or Fe nitrides have to be accounted for. For such situations, where the solubility product  $L_{SP}$  is considerably high (eqn [9]), the theory of Laflamme and Morral<sup>8</sup> (type II behavior) or numerical approaches<sup>9,10</sup> (**Section 1.13.4**) should be considered.

$$0 < L_{SP}/c_N^s c_B^0 < 1 \quad [9]$$

In most studies, nitrogen diffusion coefficients were not determined directly, but by evaluating nitridation kinetics,<sup>11</sup> for example, experimental determination of the permeability  $P = c_N D_N$  by measuring the precipitation depth  $\xi$ <sup>12</sup> (cf. eqn [8]). Diffusion data for nitrogen in Ni and  $\gamma$ -Fe alloys are given in **Table 1**.

**Table 1** Diffusion coefficients ( $m^2 s^{-1}$ ) for nitrogen in Ni alloys and Fe–20Ni

	<i>N in Ni alloys</i>	<i>N in Fe–20Ni</i>
700 °C	$9.5 \times 10^{-13}$ to $2.3 \times 10^{-12}$	$1.2 \times 10^{-12}$
800 °C	$3.2 \times 10^{-12}$ to $8.5 \times 10^{-12}$	$3.9 \times 10^{-12}$
900 °C	$1.4 \times 10^{-11}$ to $4.0 \times 10^{-11}$	$1.5 \times 10^{-11}$
1000 °C	$2.2 \times 10^{-11}$ (24)	–

Source: Douglass, D. L. *J. Met.* **1991**, 11, 74–79.

The assumption that internal nitridation is governed by bulk diffusion of nitrogen according to Fick's second law is an oversimplification. As demonstrated by Stott and Wood,<sup>13</sup> for internal oxidation, the diffusive flux  $j$  of nitrogen through the precipitation zone should be threefold (cf. **Figure 4**): bulk diffusion through the solvent  $j_{bulk}$ , diffusion through the precipitates  $j_{prec}$  (should be negligible), and diffusion along the precipitate/bulk interfaces or grain boundaries  $j_{if}$ . Since the flux contributions have to be multiplied by the respective diffusion area, the blocking effect of the precipitates ( $j_{prec} \cong 0$ ) plays an important role for the transition from internal nitridation to external nitride-scale formation (cf. **Section 1.13.2.4**). A phenomenological approach to account for the flux-blocking effect of the internal precipitates was suggested by Schnaas and Grabke<sup>14</sup> using a labyrinth factor  $\varepsilon$  in eqn [8]:

$$\xi^2(t) = 2 \frac{\varepsilon c_N^s D_N}{v c_B^0} t \quad [10]$$

Douglass<sup>11</sup> reports diffusion coefficients for nitrogen in nickel being two orders of magnitude higher than for oxygen and attributes this observation to trapping effects, where a higher binding energy between oxygen atoms and the traps could exist.

It has been observed in several studies<sup>15,16</sup> that internal nitridation (similar to internal oxidation<sup>17–19</sup>) does not only imply diffusion of the reacting species, but also mechanical stresses arising from the higher specific volumes of the nitride compounds as compared to the substrate. This leads to a flux of the nonreacting alloying elements towards the surface,

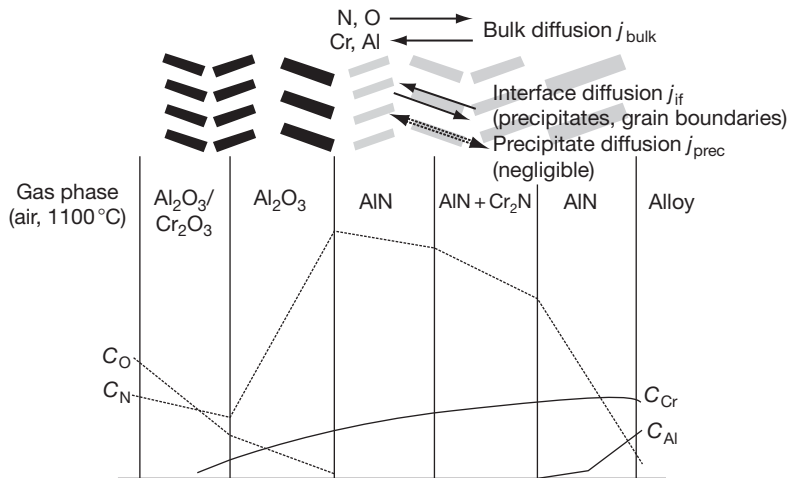


**Figure 4** Schematic representation of the concentration profiles during oxidation and nitridation of Ni–Cr–Al alloys<sup>6</sup> and relevant diffusion fluxes.<sup>13</sup>

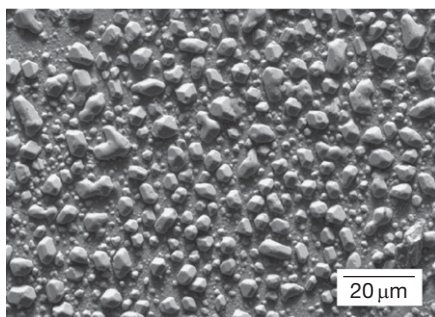


**Figure 5** Formation of solvent surface protrusions after internal nitridation of Ni-10Cr-2Ti for 150 h at 1100 °C in low-oxygen N<sub>2</sub>-45% He-5% H<sub>2</sub> atmosphere.

where they form protrusions (Figure 5). Hence, internal nitridation kinetics must be influenced by additional factors like Nabarro–Herring creep,<sup>18</sup> dislocation pipe diffusion,<sup>18</sup> and/or grain-boundary sliding.<sup>19</sup>

### 1.13.2.3 Influence of the Chemical Composition – Thermodynamics of Internal Nitridation

Although diffusive fluxes are relevant for the lateral progress of the reaction front, the kind of nitride that is formed depends on thermodynamic-stability conditions: local thermodynamic equilibrium can be assumed in cases of sufficiently high reaction rates. Figure 6(a)<sup>20</sup> represents the condition for thermodynamic equilibrium in terms of the standard free energy of formation  $\Delta G_0$ , which is correlated with the equilibrium nitrogen partial pressure  $p(\text{N}_2)$ :

$$\ln p(\text{N}_2)_{\text{equ}} = \frac{-\Delta G_0}{RT} \quad [11]$$

In addition to the technically most relevant nitrides Fe<sub>4</sub>N,  $\epsilon$ -Fe<sub>2-3</sub>N, TiN, AlN, CrN, and Cr<sub>2</sub>N, in Ni-based alloys with high Cr contents, the ternary  $\pi$  phase can also occur.<sup>21-23</sup> The  $\pi$  phase of a stoichiometry of Cr<sub>10</sub>Ni<sub>7</sub>N<sub>3</sub> is formed by a peritectic reaction of Cr<sub>2</sub>N with Ni.<sup>22</sup> An estimation of the nitrides/oxides being formed for given nitrogen and oxygen partial pressures  $p(\text{O}_2)$  and  $p(\text{N}_2)$ , respectively, is possible with the help of thermodynamic stability diagrams. An example for the system Ni–Cr–Al–Ti–N–O is shown in Figure 6(b). To account for complex higher-order interaction terms determining the internal-corrosion behavior of complex technical alloys, the CALPHAD method, implemented,

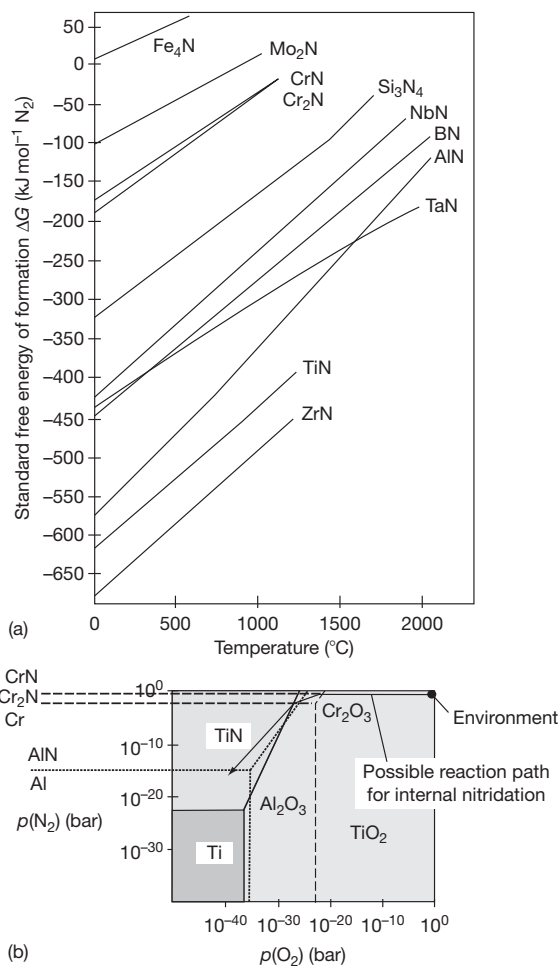


**Figure 6** (a) Standard free energy diagram of selected nitridation reactions and (b) stability diagram for nitridation and oxidation in N<sub>2</sub>/O<sub>2</sub> gas mixtures (1000 °C).

for example, in the software packages FactSage™, ChemApp™, and ThermoCalc™, is applied.

In general, from the thermodynamic point of view, the susceptibility to nitridation depends on (i) the concentration of the nitride-forming elements, and, in particular, on (ii) the nitrogen concentration being dissolved in the alloy. Although the nitrogen solubility in steels at elevated temperatures is rather high (in the order of 10<sup>-1</sup> at.%), it drops substantially when increasing the Ni or Co content in the alloys. This was shown by Barnes and Lai<sup>2</sup> experimentally and by Krupp *et al.*<sup>12,24</sup> by means of CALPHAD calculations, using the thermodynamic software ChemApp™. It should be mentioned that the solubility data reported for nitrogen in Ni alloys show large scatter, ranging from 0.0015 at.% (Wriedt and Gonzalez<sup>25</sup> for



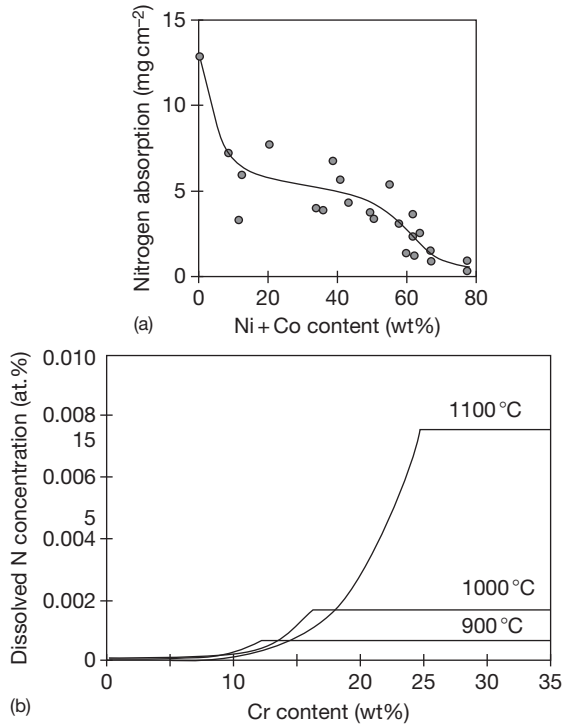


**Figure 7** Effect of the chemical composition of (a) the nitridation resistance of Ni-, Fe-, and Co-base alloys<sup>2</sup> and (b) the nitrogen solubility in Ni-xCr alloys (ChemApp<sup>TM</sup> calculation according to Gorr *et al.*<sup>24</sup>).

pure Ni) and 0.004 at.% (Chang<sup>26</sup> derived from measurements (LECO nitrogen analyzer) for Ni-10%Cr) to 0.16 at.% (Allen and Douglass for Ni-V<sup>27</sup> alloys). **Figure 7** shows data for the nitrogen concentration absorbed or dissolved in Ni-containing alloys.

The low nitrogen solubility in Ni-based alloys, which can be assumed to be equal to the maximum N concentration in the alloy surface layer ( $c_N^s$ ), is directly related to the susceptibility to internal nitridation, where, according to eqn [8], the precipitation depth depends on the permeability  $c_N^s D_N$ , the exposure time  $t$ , and the concentration of the nitride-forming alloying element  $c_B^0$ . These relationships are represented by results obtained for the nitridation of various Ni-xCr-yTi model alloys,<sup>12</sup> as shown in **Figure 8**.

#### 1.13.2.4 The Transition from Internal to External Nitridation

Assuming eqn [8] to be valid, the mole fraction of nitrides  $B_vN$  in the internal-nitridation zone is

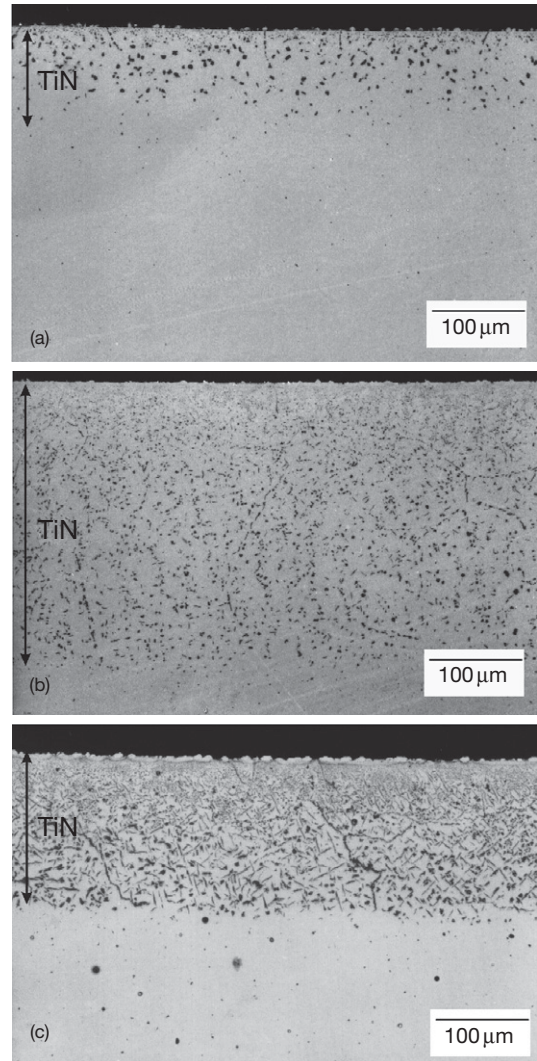


**Figure 8** Internal-nitridation attack (TiN) of Ni-xCr-yTi model alloys after 100 h exposure at 1100 °C to low-oxygen N<sub>2</sub>-45%He-5%H<sub>2</sub> atmosphere: (a) 5 wt% Cr-2 wt% Ti, (b) 20 wt% Cr-2 wt% Ti, (c) 20 wt% Cr-6 wt% Ti.<sup>12</sup>

approximately equal to the original mole fraction  $c_B^0$  of the nitride-forming alloying element B. However, if the diffusivity of B is not negligible as compared to the nitrogen diffusivity, that is,  $D_N c_N^s \leq D_B c_B^0$ , then the mole fraction of nitrides  $B_vN$  in the internal-nitridation zone becomes substantially higher than  $c_B^0$ . According to Wagner,<sup>5</sup> coalescence of the nitride precipitates into a compact nitride scale can be expected once a critical volume fraction  $g^*$  of the nitrides (typical values:  $g^* = 0.2, \dots, 0.3$ ) is exceeded, corresponding to a solute concentration



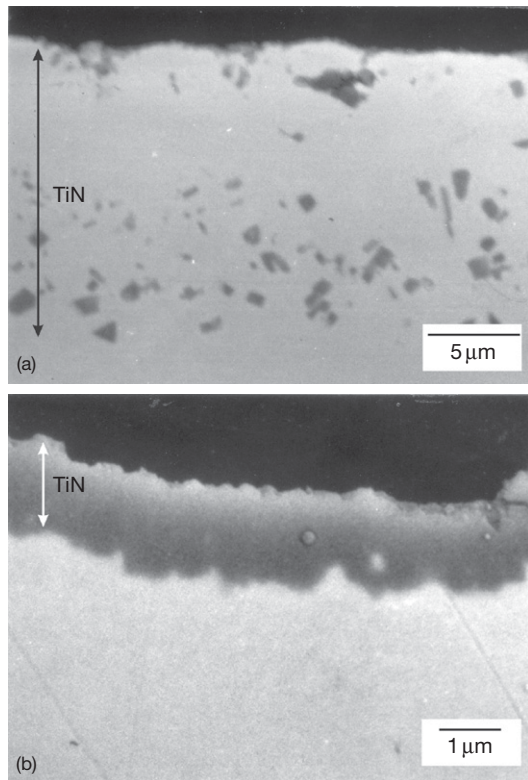


**Figure 9** Internal-nitridation attack (TiN) of Ni- $\gamma$ Ti model alloys after 800 h exposure at 900 °C to low-oxygen  $N_2$ -45% He-5%  $H_2$  atmosphere: (a) 2 wt% Ti and (b) 6 wt% Ti.

$$c_B^0 < \frac{\pi g^* D_N V}{2v D_B V_{B,N}} c_N^s \quad [12]$$

for which internal nitridation instead of superficial nitride-scale formation occurs, with  $V$  and  $V_{B,N}$  being the molar volumes of the alloy and the nitride compound, respectively. Hence, the critical solute concentration  $c_B^0$  increases with (i) increasing nitrogen solubility  $c_N^s$ , (ii) increasing nitrogen diffusivity  $D_N$ , and (iii) decreasing solute diffusivity  $D_B$ . This is the reason why for Ni-6Ti with very low N solubility, superficial TiN-scale formation was observed (Figure 9, Ni-2Ti shows little internal-nitridation attack under the same conditions), while Ni-20Cr-6Ti shows deep internal-nitridation attack (cf. Figure 8).

Equation [12] has to be considered when designing alloys to form superficial nitride scales for improved wear resistance at elevated temperatures. However, in such cases, the high specific volume of the nitrides compared with that of the substrate alloy, needs to be taken into account (cf. Section 1.13.3.1).

### 1.13.3 Internal Nitridation of Heat-Resistant Alloys

#### 1.13.3.1 Internal Nitridation of Fe- and Ni-Based Superalloys

Because of the very low nitrogen solubility in Ni compared to Fe, Ni-based alloys, for example, alloy 600 and 601,<sup>2,28</sup> exhibit a substantially higher resistance to internal nitridation than Fe-based alloys, such as alloy 800/800H or AISI 314.<sup>2,29</sup> In the case of  $NH_3$ -containing atmospheres, the high temperature corrosion behavior of both, Ni- and Fe-based alloys can be catastrophic, generally leading to external and/or internal nitridation attack.<sup>30</sup> Very high nitrogen activities in combination with some amount of oxygen lead to the formation of nonprotective porous oxide-nitride scales. According to Strauß *et al.*,<sup>31</sup> in low- and high-alloy Cr steels, sponge-like scales of  $Fe_3O_4$  or  $FeCr_2O_4$  are formed in 70%  $NH_3$ -30%  $H_2O$  atmosphere being obviously permeable for  $NH_3$  with the consequence of strong internal nitridation in the form of needle-like Cr nitrides. Because of the high specific volume of the Cr nitrides, compressive stresses are induced in the internal-nitridation zone, leading to intercrystalline cracks and a disintegration of the polycrystalline microstructure. Ni alloys may form very instable  $Ni_3N$  that releases gaseous nitrogen when decomposing, leading to pore formation. In the case of Cr-containing Ni-based alloys, the combination of pores and internal Cr nitrides causes fast surface-layer degradation in ammonia atmosphere.<sup>31</sup>

Since Cr nitrides are of only moderate thermodynamic stability, their formation is limited to atmospheres with very high nitrogen activities or alloys containing Cr concentrations above ~20 wt%, hence exposure of most technical NiCr alloys to air does not cause any nitridation. However, alumina-forming superalloys, often alloyed with Ti for  $\gamma'$  strengthening, often show massive internal nitridation under service conditions, for example, gas-turbine blades operating in air or combustion atmosphere.<sup>32</sup> Below a superficial  $Cr_2O_3$  scale, the oxygen partial pressure drops to a value sufficient only for the formation of  $Al_2O_3$  and  $TiO_2$ . On the other hand,  $Cr_2O_3$  is observed to be permeable to atomic nitrogen;<sup>33</sup> hence the ratio  $p(N_2)/p(O_2)$  increases below the chromia scale. For conditions where no dense  $Al_2O_3$  sub-scale can be formed because of overall or local depletion of the Al concentration below a critical value, a situation that is often promoted by service under thermal-cycling conditions, further penetration of nitrogen is possible, allowing stable AlN and TiN

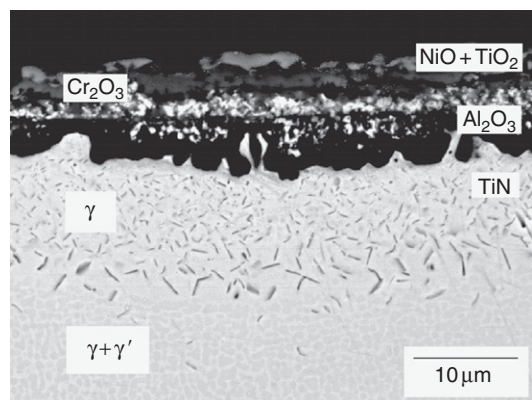


**Figure 10** Internal nitridation in the single-crystalline Ni-base superalloy SRR99 after 100 h exposure at 1000 °C to air.

precipitates to be formed according to the local combination of  $p(\text{N}_2)$  and  $p(\text{O}_2)$  (cf., thermodynamic stability diagrams, [Figure 6\(b\)](#)). The process of internal nitridation of alumina-forming Ni- or Fe-based superalloys is shown for the single-crystalline superalloy SRR99, as an example, in [Figure 10](#).

For superalloys with Cr concentrations not above 20 wt% and nitrogen activities below  $a_{\text{N}} = 1$ , occurrence of only the most stable nitride TiN, the somewhat less stable nitride AlN, and, depending on the gas and alloy composition, NbN and VN,<sup>27</sup> is possible.

In cast Ni-based superalloys, for example, the single-crystalline alloys used for the first stages gas-turbine blades, the susceptibility to internal nitridation varies locally due to dendritic segregations. The high nitrogen diffusivity (cf. [Section 1.13.2.2](#)) leads to a fast progress of the internal-precipitation front, which is accompanied by a dissolution of the strengthening  $\gamma'$  phase ( $\text{Ni}_3(\text{Al}, \text{Ti})$ ) due to the nitridation (and oxidation-) caused consumption of the  $\gamma'$ -forming alloying elements Al and Ti (see [Figure 10](#)). A particular deep dissolution can be observed in alloys where the  $\gamma'$  phase is stabilized by a high Ti content ( $c_{\text{Ti}} > 2$  wt%).

Even though it can be assumed that internal nitridation of superalloys is controlled by nitrogen diffusion, the parabolic rate law was shown in an explicit way only for model systems or in pure nitriding gas atmospheres.<sup>6,12</sup> It can be assumed that the morphology of the internal reaction products itself is of significance for the precipitation kinetics. The AlN precipitates are by orders of magnitude larger than the TiN precipitates (see [Figures 10 and 14](#)).

Hence, the formation of AlN nuclei requires much higher supersaturation and particle growth must be partly controlled by Al diffusion in a much more pronounced way than is the case for TiN precipitates.

Ni-based alloys with Cr concentrations above ~20wt% are prone to the formation of a third group of nitrides:  $\text{Cr}_2\text{N}$  and the ternary  $\pi$  phase ( $\text{Cr}_{10}\text{Ni}_7\text{N}_3$ , cf. [Section 1.13.2.3](#)). The  $\pi$ -phase nitrides reported by several authors<sup>21–23</sup> are of coarse morphology and were discussed as a possible strengthening phase in the bulk<sup>34</sup> or as surface layer of heat-resistant alloys.

### 1.13.3.2 Mechanical Effects on Internal Nitridation Kinetics

Generally, the mechanisms governing internal-corrosion cannot be analyzed without taking mechanical stresses into account. In particular, large, needle-like precipitates act as crack initiation sites and cause an embrittlement of the internally-corroded surface layer. According to a study by Klöwer *et al.*,<sup>29</sup> the small sub-micrometer TiN precipitates are much less harmful than the blocky AlN precipitates. However, in cases where the initial Ti concentration is rather high ( $c_{\text{Ti}} \geq 2$  wt%), the alloy grain boundaries can be completely covered by TiN, leading to intercrystalline cracking as shown for a nitrided model alloy in [Figure 11\(a\)](#). Hence, nitridation leads to a dangerous decrease in the ductility of technical high temperature alloys.

As a second effect, the nitridation reaction is accompanied by a strong increase in the specific volume  $v$  of the nitrides, for example,  $v_{\text{CrN}} = 0.17 \text{ cm}^3 \text{ g}^{-1}$ ,  $v_{\text{AlN}} = 0.19 \text{ cm}^3 \text{ g}^{-1}$ ,  $v_{\text{TiN}} = 0.31 \text{ cm}^3 \text{ g}^{-1}$ , as compared to the specific volume of Ni-base superalloys,  $v_{\text{Ni-base}} \cong 0.13 \text{ cm}^3 \text{ g}^{-1}$ . This volume increase has been shown by various authors to cause damage in the form of cracks or grain disintegration<sup>14,31</sup> and/or to drive outward solvent diffusion leading to substrate-metal protrusions.<sup>15–19</sup> [Figure 11\(b\)](#) shows the tip of a wedge-shaped specimen of the Ni-based superalloy CMSX-4 after thermal cycling at 1100 °C (1 h dwell times interrupted by 15 min cooling periods).<sup>35</sup> The combination of geometry-induced growth stresses and differences in the coefficient of thermal expansion ( $\text{CTE}_{\text{oxide}} \ll \text{CTE}_{\text{alloy}}$ ) led to repeated spalling of the alumina scale, near-surface depletion of the Al reservoir, and, eventually, strong internal-oxidation and nitridation attacks in combination with cracks and fast oxidation of the solvent ('breakaway' oxidation).

As mentioned earlier, stress-driven and stress-enhanced diffusion contributes vitally to the kinetics

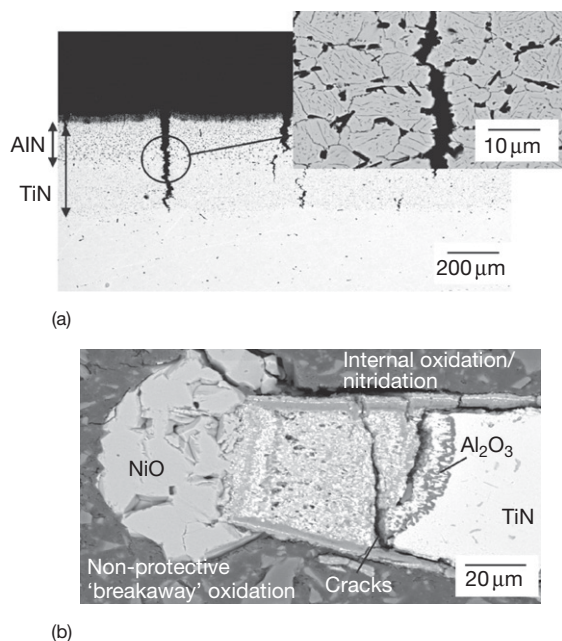


**Figure 11** Cracks in an internally nitrided surface layer in alloy 80A (100 h, 1000 °C, low-oxygen  $N_2$ –45% He–5%  $H_2$  atmosphere) due to tensile testing and (b) ‘breakaway oxidation’ and internal oxidation/nitridation of a wedge-shaped specimen of the single-crystalline Ni-base superalloy CMSX-4 after thermal cycling exposure at 1100 °C – 1 h dwell times in air.

of internal nitridation. Figure 5 shows NiCr protrusions on top of an internally nitrided Ni–10Cr–2Ti alloy. Chang *et al.*<sup>15</sup> could prove the direct relationship between the depth of internal TiN precipitation and the degree of coverage by surface protrusions. The most probable mechanism for the respective outward transport of solvent has been assumed to be dislocation-pipe diffusion<sup>15,18</sup> rather than Nabarro–Herring creep or grain-boundary sliding. Furthermore, it was shown by Krupp *et al.*<sup>36</sup> and Dong *et al.*<sup>37</sup> that the internal-nitridation rate was substantially increased when superimposing a mechanical creep load (Figure 12); again, this can be attributed to dislocation-pipe diffusion, contributing to internal precipitation when the dislocation density is increasing due to dislocation creep.

### 1.13.3.3 Protection Against Internal Nitridation Attack

In the literature on high temperature corrosion of technical superalloys, there is agreement that a dense and adherent  $Al_2O_3$  scale provides the most effective protection against internal nitridation. Nitrogen permeation is obviously very slow. However, it should be mentioned that in a nitrogen-based atmosphere with

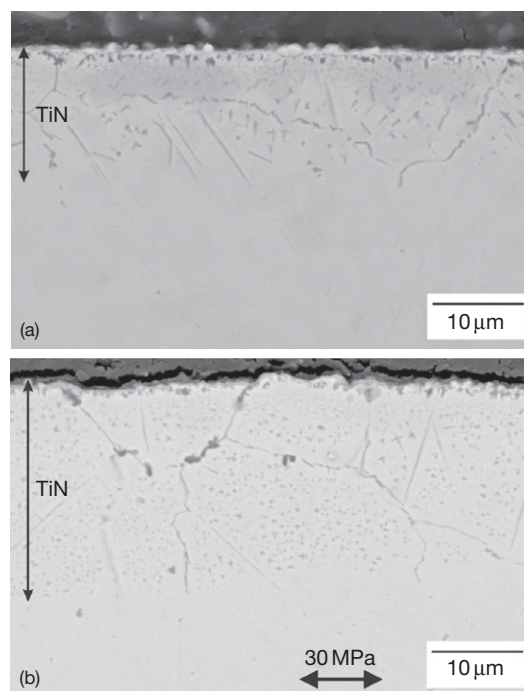


**Figure 12** Internal nitridation within (a) a mechanically unloaded specimen and (b) a creep-loaded specimen ( $\sigma = 30$  MPa) of the Ni-base superalloy alloy 80A exposed at  $T = 900$  °C for  $t = 48$  h to low-oxygen  $N_2$ –45% He–5%  $H_2$  atmosphere.

very low oxygen partial pressures in the range of  $p(O_2) < 10^{-23}$  bar, a very thin alumina scale of sub-micrometer thickness is formed, which is not able to block nitrogen permeation.<sup>4</sup> Even though pre-oxidation of an alumina-forming alloy or any other alloy that has been aluminized could prevent internal oxidation, there is still the risk of local spalling and/or cracking of the scale. If under service conditions no healing layer can be formed, such a situation would cause a transition to internal oxidation and nitridation.

As a second possibility to protect a material against internal nitridation, nitride-forming alloying elements, such as Ti and Al, should be avoided. However, this is difficult because of the high significance of Al for alumina-scale formation and  $\gamma'$  stabilization. The latter effect,  $\gamma'$  destabilization because of Al and Ti reduction, can be partly accommodated by adding Ta and Nb, though the latter also is a nitride former.<sup>27</sup> Similar to many alloying elements in high-alloyed Ni-based superalloys, the risk of brittle-phase formation, for example, by high Nb concentrations, needs to be taken into account when considering new alloy compositions. Attempts to replace Al as the most



effective TGO former at very high temperatures, for example, by Si, has never been successful; hence, even for coated alloys, a minimum Al concentration for healing-layer formation must be maintained.

In the case of polycrystalline alloys, the susceptibility to internal-oxidation and internal-nitridation attack might be reduced by grain-boundary-engineering-type processing. It was shown for oxidation of alloy 718 in air that by increasing the fraction of low-energy CSL boundaries (coincident site lattice) the oxidation rate was reduced.<sup>38</sup> There is a chance that a combination of near-surface grain refinement and high temperature exposure could (i) reduce the ratio between the inward oxygen flux and the outward aluminum flux, that is, promoting superficial  $\text{Al}_2\text{O}_3$  formation even at low initial Al concentrations, and (ii) reduce the inward nitrogen flux by an increasing number of CSL boundaries exhibiting low grain-boundary diffusivity.

#### 1.13.4 Modelling and Computer Simulation of Internal Nitridation

According to the preceding sections, internal nitridation is governed by solid-state diffusion of the reacting metallic and nonmetallic species (i) through a superficial oxide scale, (ii) through an internal-precipitation zone, and (iii) through the substrate alloy. In general, this problem can be treated by the diffusion differential equation for all the species participating in the nitridation process, using either the gradients in the chemical potential or, in a simplified way, the concentration gradients.<sup>9,10,39</sup> In the latter case, the equations need to be coupled with a mass balance and a Gibbs-energy criterion, accounting for the local solubility product, that is, the concentrations of the diffusing species in thermodynamic equilibrium.

Possible ways to solve the diffusion equation

$$\frac{\partial c}{\partial t} = \nabla(D\nabla c) \quad [13]$$

numerically are provided by the finite-difference and the finite-element method. Although the latter one is of a large flexibility with respect to diffusion in complex geometries, the finite-difference approach is easier to handle and to link with computational thermodynamics. Here, the derivatives in eqn [13] (simplified for two-dimensional diffusion problems) are replaced by difference quotients using time steps of a length  $\Delta t$  and location steps of flexible widths  $\Delta x$  and  $\Delta y$ , respectively,

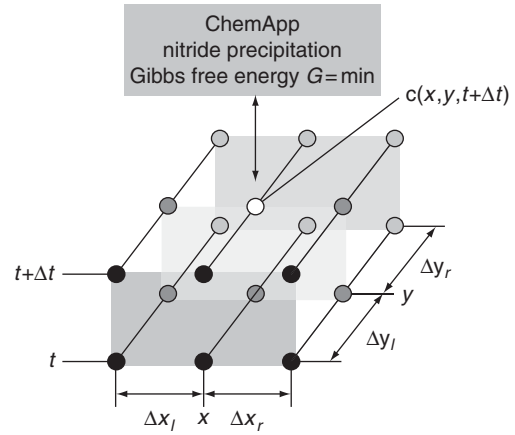


**Figure 13** Schematic representation of the two-dimensional finite-difference mesh (Crank–Nicolson scheme) for simulation of internal-corrosion processes in combination with ChemApp™.

according to the Crank–Nicolson scheme (Figure 13, l = left-hand side, r = right-hand side)<sup>40</sup>.

$$\begin{aligned} \frac{c(x, y, t + \Delta t) - c(x, y, t)}{\Delta t} = & \frac{D_x(x, y)}{2} \left( \frac{c(x - \Delta x, y, t) - 2c(x, y, t) + c(x + \Delta x, y, t)}{\Delta x_l(x, y) \cdot \Delta x_r(x, y)} \right. \\ & + \frac{c(x - \Delta x, y, t + \Delta t) - 2c(x, y, t + \Delta t) + c(x + \Delta x, y, t + \Delta t)}{\Delta x_l(x, y) \cdot \Delta x_r(x, y)} \Big) \\ & + \frac{D_y(x, y)}{2} \left( \frac{c(x, y - \Delta y, t) - 2c(x, y, t) + c(x, y + \Delta y, t)}{\Delta y_l(x, y) \cdot \Delta y_r(x, y)} \right. \\ & + \frac{c(x, y - \Delta y, t + \Delta t) - 2c(x, y, t + \Delta t) + c(x, y + \Delta y, t + \Delta t)}{\Delta y_l(x, y) \cdot \Delta y_r(x, y)} \Big) \end{aligned} \quad [14]$$

Equation [14] applied simultaneously to all the species involved in the internal-nitridation process allows the stepwise solution of two-dimensional diffusion problems in a two-dimensional area with location-dependent diffusion coefficients accounting for the different diffusion paths, that is, bulk diffusion, grain-boundary-diffusion, etc. Coupling of the equations can be established by the integrable thermodynamics interface ChemApp™, which represents the thermodynamic software FactSage™. The interface recalculates the set of concentrations at a certain time step according to thermodynamic equilibrium until the diffusion calculation continues.

The numerical approach can be applied to solve complex internal-nitridation phenomena, which cannot be treated by Wagner's classical theory of internal oxidation, for example, (i) internal precipitation of compounds of moderate thermodynamic stability such as Cr nitrides (cf. Figure 14(a)), (ii) simultaneous internal

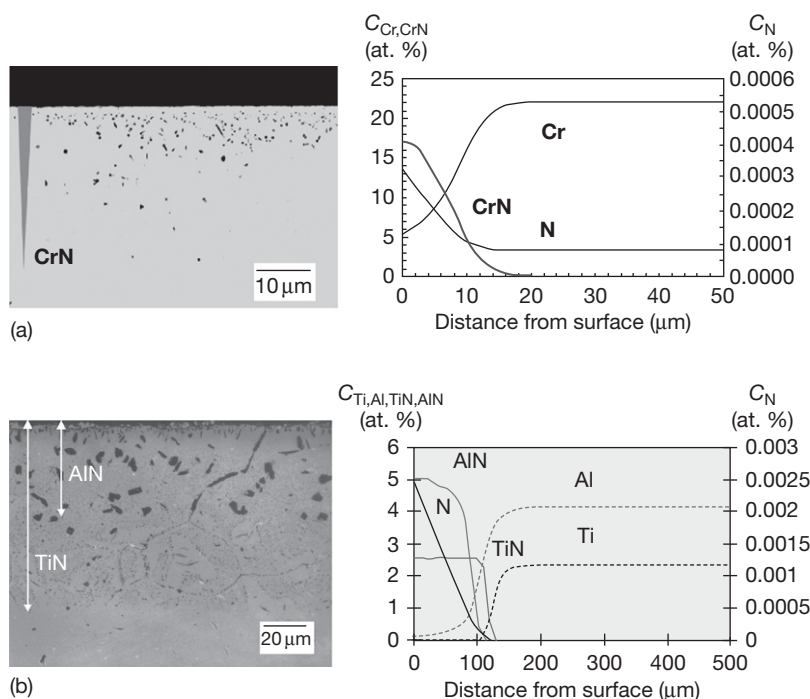


**Figure 14** Cross-sectional view and simulated concentration profiles of (a) internal precipitation of CrN in Ni-20Cr (800 °C, 200 h) and (b) simultaneous internal precipitation of TiN and AlN in Ni-20Cr-2Al-2Ti (1100 °C, 150 h) in both cases exposure to low-oxygen  $\text{N}_2$ -45%  $\text{He}$ -5%  $\text{H}_2$  atmosphere.

and/or intergranular precipitation of more than one nitride and/or oxide compound (cf. [Figure 14\(b\)](#)), or (iii) internal corrosion as a consequence of local damage of a superficial oxide scale by cracking or spalling.

### 1.13.5 Concluding Remarks

Although for many technical applications nitridation treatments are used to produce wear-resistant surface layers on steels, in high temperature corrosion, the term nitridation refers to a deep embrittlement attack caused by nitride compounds. Nitridation occurs not only in ammonia atmospheres with a high nitrogen activity but also in pure nitrogen or even in air or combustion atmospheres at temperatures above 800 °C, where  $\text{N}_2$  dissociation is fast enough to allow atomic nitrogen to penetrate into the metal surface by solid-state diffusion. The nitridation rate depends mainly on the diffusivity of nitrogen in the alloy and the thermodynamic stability of the nitrides being formed internally; the precipitation depth as a function of exposure time follows in many cases a parabolic rate law as was proposed by Wagner<sup>5</sup> for internal oxidation. Most technical applications of heat-resistant alloys with alloying elements of high

nitrogen affinity, such as Al, Ti, Cr, Nb, and V, imply superimposition of oxidizing and nitriding environments. Hence, whether a superficial oxide scale can protect the substrate against internal corrosion attack depends strongly on the mechanical integrity of the scale and the ability to form a healing layer by means of sufficient supply of the oxide-forming alloying element to the metal surface. Here, the critical factors are (i) the local ratio between the oxygen and the nitrogen activity, and (ii) the solute concentration being required for transition from internal oxidation to external scale formation. These factors may change when mechanical stresses are superimposed, which arise due to thermal cycling or due to volume changes caused by internal precipitation. The mutual interactions between the diffusivity of the reacting species through a superficial oxide scale and the metallic bulk, the thermodynamics and nucleation kinetics of nitrides, and the parameters caused by the service conditions, that is, temperature changes, composition of the gas phase, etc., are complex and only touched upon in this chapter. A thorough analysis is not possible by means of an analytical approach; it requires a numerical treatment taking the various aspects of solid-state reactions into account.

## Acknowledgments

The author acknowledges the experimental and theoretical work of Dr. S.Y. Chang, Dr. R. Orosz, Dr. V. Braz da Trindade Filho, and Dr. U. Buschmann, as well as the strong support by Prof. Dr. H.-J. Christ, head of Institut für Werkstofftechnik of the University of Siegen, Germany, where a great part of the research work discussed in this chapter was carried out. The research was financially supported by Deutsche Forschungsgemeinschaft and the European Commission, which is gratefully acknowledged.

## References

- Gupton, P. S. *The Heat Treatment Source Book*; ASTM: Metals Park, 2001.
- Lai, G. L. *High-Temperature Corrosion of Engineering Alloys*; ASM International, Materials Park, 1990.
- Bennett, M. J.; Nichols, J. R.; Borchardt, G.; Strehl, G. *Mater. High. Temp.* **2002**, 19, 117–125.
- Krupp, U.; Christ, H.-J. *Met. Mat. Trans.* **2000**, 31, 47–56.
- Wagner, C. Z. *Elektrochem.* **1959**, 63, 772–782.
- Han, S.; Young, D. J. *Oxidat. Met.* **2001**, 55, 223–242.
- Young, D.J. In *Proceedings Corrosion Science in the 21st Century*, 7–11 July 2003, Manchester, UK; J. Corros. Sci. Eng [online].
- Lafamme, G. R.; Morral, J. E. *Acta Met.* **1978**, 26, 1791.
- Nesbitt, J. *Oxidat. Met.* **1995**, 44, 309–338.
- Engström, A.; Höglund, L.; Ågren, J. *Met. Mat. Trans.* **1994**, 25, 1127–1134.
- Douglass, D. L. *J. Met.* **1991**, 11, 74–79.
- Krupp, U.; Christ, H.-J. *Oxidat. Met.* **1999**, 52, 277–298.
- Stott, F. H.; Wood, G. C. *Mater. Sci. Technol.* **1988**, 4, 1072–1078.
- Schnaas, A.; Grabke, H. J. *Werkst. Korrosion* **1978**, 29, 635–644.
- Chang, S. Y.; Krupp, U.; Christ, H.-J. *Mater. Sci. Eng.* **2001**, 301, 196–206.
- Kodentsov, A. A.; van Dal, M. J. H.; Cserhati, C.; Daróczy, L.; van Loo, F. J. *Acta Mater.* **1999**, 11, 3169.
- Douglass, D. L. *Oxidat. Met.* **1995**, 44, 81–111.
- Yi, C.; Guan, S. W.; Smeltzer, W. W.; Petric, A. *Acta Met. Mater.* **1994**, 42, 981–990.
- Stott, F. H.; Shida, Y.; Whittle, D. B.; Wood, G. C.; Bastow, B. D. *Oxidat. Met.* **1982**, 18, 127.
- Bürgel, R. *Handbuch Hochtemperatur-Werkstofftechnik*; Vieweg: Braunschweig Wiesbaden, 1998.
- Krupp, U.; Chang, S. Y.; Christ, H.-J. *Z. Metallkunde*, **2000**, 12, 2006–2012.
- Kodentsov, A. A.; Van Dal, M. J. H.; Cserhati, C.; Daróczy, L. *Acta Mater.* **1999**, 47, 3169–3180.
- Ono, N.; Kajihara, M.; Kikuchi, M. *Met. Trans. A* **1992**, 23, 1389–1393.
- Gorr, S.; Chang, S.Y.; Krupp, U.; Christ, H.-J. Unpublished data.
- Wriedt, H. A.; Gonzalez, O. D. *Trans. AIME* **1961**, 221, 532.
- Chang, S. Y., PhD thesis, University of Siegen, 2001.
- Allen, A. T.; Douglass, D. L. *Oxidat. Met.* **1999**, 52, 505–536.
- Tjokro, K.; Young, D. J. *Oxidat. Met.* **1995**, 44, 453–474.
- Klöwer, J.; Brill, U.; Rockel, M. *Mater. Corros.* **1997**, 48, 511–517.
- Rubly, R. P.; Douglass, D. L. *Oxidat. Met.* **1991**, 35, 259–278.
- Strauß, S.; Grabke, H. J.; Vogel, D. *Mater. Corros.* **2003**, 54, 895–902.
- Barnes, J.; Lai, G. Y. In *Proceedings Corrosion and Particle Erosion at High Temperatures*; Srinivasan, V., Vedula, K., Eds.; TMS: Warrendale, 1989; 617.
- Krupp, U.; Chang, S.-Y.; Christ, H.-J. In *Proceedings EFC-Workshop Life Time Modelling of High-Temperature Corrosion Processes*; Schütze, M., Quadakkers, W. J., Nichols, J. R., Eds.; EFC Publications No. 34, 2001; pp 148–164.
- Brill, U. Habilitation thesis, RWTH Aachen Technical University Aachen, Germany, 1997.
- Orosz, R.; Krupp, U.; Christ, H.-J. *Mater. Corros.* **2006**, 57, 154–158.
- Krupp, U.; Orosz, R.; Christ, H.-J.; Buschmann, U.; Wiechert, W. *Mater. Sci. Forum* **2004**, 461–464, 37–44.
- Dong, J. X.; Sawada, K.; Yokokawa, K.; Abe, F. *Scripta Mater.* **2001**, 44, 2641–2646.
- Krupp, U.; Wagenhuber, Ph. E. G.; Kane, W. M.; McMahon, C. J., Jr. *Mater. Sci. Technol.* **2005**, 21, 1247–1254.
- Krupp, U.; Christ, H. J. *Oxidat. Met.* **1999**, 52, 299–319.
- Krupp, U.; Trindade, V. B.; Christ, H.-J.; Buschmann, U.; Wiechert, W. *Mater. Corros.* **2006**, 57, 263–268.



## 1.14 Corrosion in Molten Salts

**M. Spiegel**

Salzgitter-Mannesmann-Forschung GmbH, Ehinger Strasse 200, 47259 Duisburg, Germany

© 2010 Elsevier B.V. All rights reserved.

1.14.1	Introduction	316
1.14.2	Principles and Mechanisms of Corrosion in Sulfate Melts	317
1.14.2.1	Thermodynamic Considerations	317
1.14.2.2	Solubility of Gases in Sulfate Melts	317
1.14.2.3	Oxidizing and Reducing Reactions of Sulfate Melt Species	317
1.14.3	Principles and Mechanisms of Corrosion in Carbonate Melts	319
1.14.3.1	Solubility of Gases	319
1.14.3.2	Oxidizing and Reducing Reactions of Carbonate Melt Species	319
1.14.4	Solubility of Oxides in Sulfate and Carbonate Melts	320
1.14.5	Corrosion Mechanisms in Sulfate Melts: The Rapp and Goto model	322
1.14.6	Methods of Investigation of Corrosion in Molten Salts	323
1.14.6.1	Electrochemical Techniques	323
1.14.6.2	Other Methods	325
1.14.7	Examples of Hot-Salt Corrosion in Industrial Practice	325
1.14.7.1	Gas Turbines: Corrosion Beneath Na <sub>2</sub> SO <sub>4</sub> Deposits	325
1.14.7.2	Waste Incineration: Corrosion in Chloride Melts	326
1.14.7.3	Corrosion in Molten Carbonate Fuel Cells	328
References		330

### Abbreviations

**CE** Counter electrode  
**RE** Reference electrode  
**WE** Working electrode

### Symbols

**$a_i$**  Activity of species  $i$   
 **$E$**  Voltage (V, mV)  
 **$I$**  Current (A cm<sup>-2</sup>)  
 **$K$**  Equilibrium constant  
 **$M^{n+}$**  Cation of charge  $n+$   
 **$n$**  Charge  
 **$p_i$**  Partial pressure of species  $i$   
 **$Z$**  Complex resistivity ( $\Omega$ )

### 1.14.1 Introduction

Molten salts are present in many technical processes. As sulfate- and chloride-containing deposits on boiler tubes from conventionally-fired plants such as waste-, biomass-, and coal-fired boilers, they are responsible

for severe corrosion-induced failures. For many years, salt deposits on gas turbines (especially Na<sub>2</sub>SO<sub>4</sub>) were identified as the major corrosive species that limit the lifetime of the turbine blades. Molten salts are also present as electrolytes, for example, ((Li,K)<sub>2</sub>CO<sub>3</sub>) in molten carbonate fuel cells. As the economic impact of corrosion due to molten salts (i.e., hot corrosion) is significant, great research efforts have been conducted on the mechanisms and prevention of molten salt-induced corrosion.

High temperature corrosion processes beneath molten salts are generally complicated as many different steps are involved. The metal is separated from the gas phase by the melt and transport of oxidizing species from the gas phase to the metal–melt interface that occurs. Hence, the solubility of gases in the salt is an important factor in hot corrosion. Subsequent to diffusional transport of the dissolved gas species through the molten salt, interfacial reactions take place at the metal–melt interface and corrosion products are formed, partially soluble in the salt, and transported towards lower concentrations by diffusion in the salt film.

The nature of the molten salts is generally ionic and the corrosion process involves electrochemical reactions, that is, oxidation of the metal and reduction

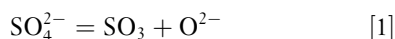
of melt components and dissolved gases. This requires investigation by electrochemical techniques. The complexity of the corrosion mechanism and the interdependence of many physical and chemical steps require a systematic description of the processes involved. Due to the different chemical and electrochemical properties of a particular melt, it is impossible to give a general approach, as this is the case for oxidation processes.

As a consequence, the following chapters look much more deeply into corrosion mechanisms in sulfate and carbonate melts, as examples of very different mechanisms involved.

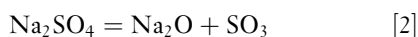
## 1.14.2 Principles and Mechanisms of Corrosion in Sulfate Melts

### 1.14.2.1 Thermodynamic Considerations

Sulfate melts contain  $\text{SO}_4^{2-}$  oxyanions. According to the models of Flux<sup>1</sup> and Flood and Forland and Motzfeld,<sup>2</sup> the  $\text{SO}_4^{2-}$  anion dissociates, giving  $\text{SO}_3$  and  $\text{O}^{2-}$  ions, eqn [1]:



As cations (e.g.,  $\text{Na}^+$ ) are also present in the melt, equilibrium [1] can be written as eqn [2]:



The *basicity* of the melt is defined by the  $p(\text{O}^{2-})$  value, eqn [3]:

$$p\text{O}^{2-} = -\log a_{\text{O}^{2-}} \quad [3]$$

According to eqn [3], a small  $p\text{O}_2$  value is given by a high  $\text{O}^{2-}$  activity and the melt is defined to be basic. Correspondingly, a high  $p\text{O}_2$  value is given by a small  $\text{O}^{2-}$  activity and the melt is defined to be acidic.

The overall basicity of the melt can be changed by the gas phase composition. From eqn [2], it becomes clear that:

$$a(\text{O}^{2-}) = Kp(\text{SO}_3)^{-1} \quad [4]$$

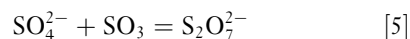
Hence, by variation of  $p(\text{SO}_3)$  in the gas phase, the value of  $a(\text{O}^{2-})$  is increased.

### 1.14.2.2 Solubility of Gases in Sulfate Melts

From eqn [4], it becomes immediately clear that the melt chemistry is influenced by variations in the gas phase in the atmosphere, especially by variations in  $p(\text{O}_2)$  and  $p(\text{SO}_3)$  values. In order to reach chemical equilibrium through the whole melt film, the gases

under consideration need to be soluble in the molten salt, where they can act as oxidizing agents for the metal and, therefore, detrimentally influence the corrosive nature of the salt.

Experimental investigations of the solubility of  $\text{O}_2$  and  $\text{SO}_2$  in molten  $\text{Na}_2\text{SO}_4$  were carried out by Andresen *et al.*<sup>3</sup> For  $\text{O}_2$  and  $\text{SO}_2$ , a low solubility was observed, following Henry's law. Flood and Forland<sup>2</sup> published some work on the solubility of  $\text{SO}_3$  in the melt. At low concentration of  $\text{SO}_3$ , the solubility follows Henry's law but, at higher concentrations, deviation from Henry's law was observed according to a reactive solubility of  $\text{SO}_3$  with the sulfate ion, eqn [5]:

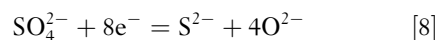
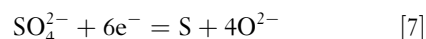
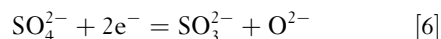


In summary, the solubility of  $\text{O}_2$  and  $\text{SO}_2$  in  $\text{Na}_2\text{SO}_4$  is negligibly low, whereas the solubility of  $\text{SO}_3$  is significantly high.

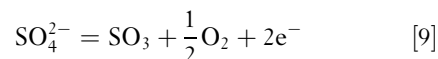
### 1.14.2.3 Oxidizing and Reducing Reactions of Sulfate Melt Species

From an electrochemical point of view, the corrosion process is only possible if the anodic oxidation of the metal as it occurs in corrosion is forced by a complementary cathodic reduction of either the melt components or the dissolved gases. In order to study the electrochemical behavior of a sulfate melt, polarization experiments in a pure  $\text{Na}_2\text{SO}_4$  melt have been performed with noble metal electrodes when the following anodic and cathodic reactions were identified, eqns [6]–[11]:

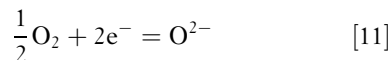
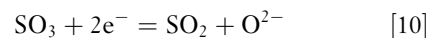
Reduction (cathodic) reactions (increasing overpotential):



Oxidation (anodic) reactions:



Reduction of  $\text{SO}_3$  and  $\text{O}_2$ , produced by equilibrium eqn [1], is also possible:



The decomposition of the sulfate as described previously only occurs in highly basic melts under

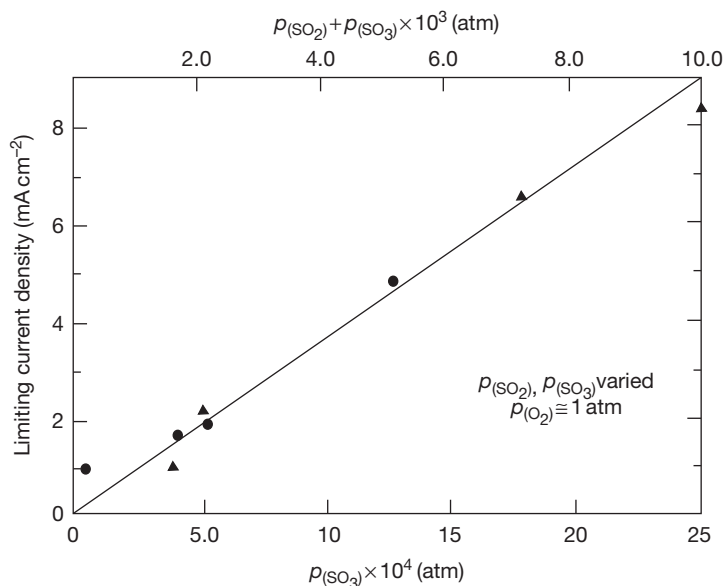


**Figure 1** Limiting diffusion current at Pt electrodes beneath a thin  $\text{Na}_2\text{SO}_4$  melt as a function of  $p(\text{SO}_2, \text{SO}_3)$  at constant  $p(\text{O}_2)$  at  $896^\circ\text{C}$ .

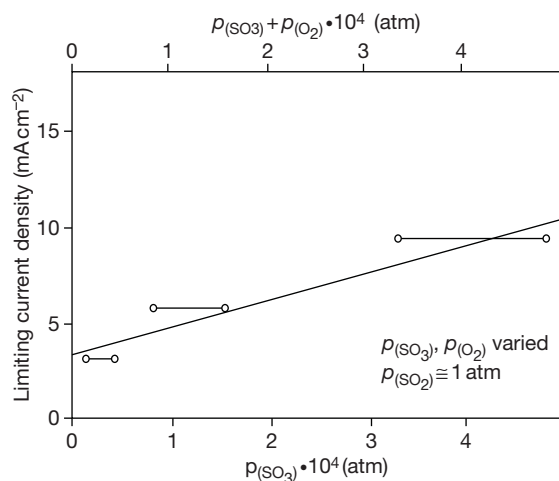


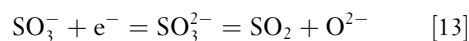
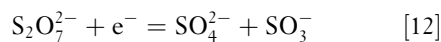
**Figure 2** Limiting diffusion current at Pt electrodes beneath a thin  $\text{Na}_2\text{SO}_4$  melt as a function of  $p(\text{SO}_3)$  at constant  $p(\text{SO}_2, \text{O}_2)$  at  $896^\circ\text{C}$ .

reducing conditions or at high cathodic or anodic overpotentials. In principle, this is possible in deep melts or if the melt is trapped in pores within the oxide scale.

The situation is completely different if gas species are dissolved in the melt. This has been shown by measurements of the limited diffusion current in a thin  $\text{Na}_2\text{SO}_4$  film at  $896^\circ\text{C}$ .<sup>4</sup> The experiments were carried out in an  $\text{O}_2 - (\text{SO}_3 + \text{SO}_2)$  gas mixture,

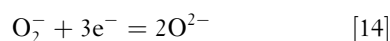
showing that the limiting diffusion current increases with increasing  $p(\text{SO}_3, \text{SO}_2)$  values at constant  $p(\text{O}_2)$  (Figure 1) and also increases with increasing  $p(\text{SO}_3)$  values at constant  $p(\text{O}_2, \text{SO}_2)$  (Figure 2).

As  $\text{SO}_3$  is dissolved as  $\text{S}_2\text{O}_7^{2-}$  in the melt, the major oxidizing species in a thin  $\text{Na}_2\text{SO}_4$  melt film in the presence of  $\text{SO}_3$  is  $\text{S}_2\text{O}_7^{2-}$  ions. The reduction reactions were investigated by chronopotentiometric measurements in a  $\text{Na}_2\text{SO}_4$  melt at  $900^\circ\text{C}$  in an  $\text{O}_2 + 1\%$  ( $\text{SO}_2 + \text{SO}_3$ ) atmosphere<sup>5</sup> and the results show two transition times (Figure 3), attributed to the following reduction steps, eqns [12] and [13]:



The reduction of  $\text{O}_2$  is also possible in an  $\text{O}_2^-$  and  $\text{SO}_3^-$  containing atmosphere, but to a much smaller extent, due to the low solubility of  $\text{O}_2$  in the sulfate melt.

For very basic melts without  $\text{SO}_2/\text{SO}_3$  being present in the gas atmosphere, the reduction of oxygen ions occurs, as shown by chronopotentiometric measurements in a  $\text{Na}_2\text{SO}_4$  melt, with the addition of 5 mol%  $\text{Na}_2\text{O}_2$  in air at  $900^\circ\text{C}$ . Two major reactions were identified, eqns [14] and [15]:



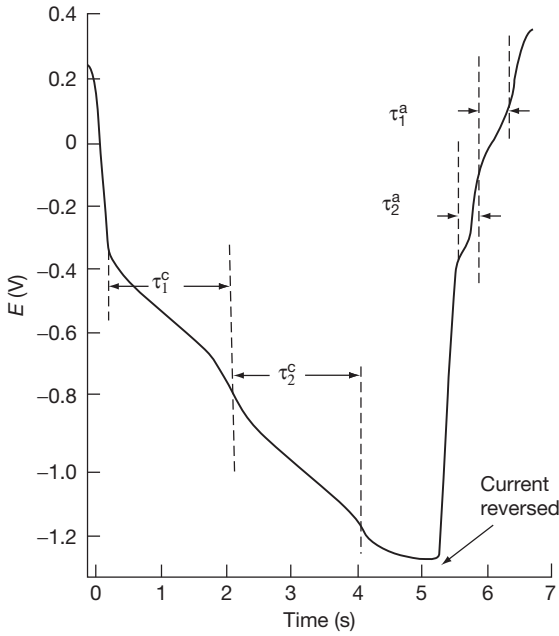
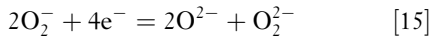


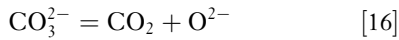
**Figure 3** Chronopotentiometric curve for  $\text{Na}_2\text{SO}_4$  in  $\text{O}_2$  + 1% ( $\text{SO}_2$  +  $\text{SO}_3$ ) at  $900^\circ\text{C}$ .



In general, corrosion mechanisms in sulfate melts mainly involve gaseous species dissolved in the molten salt. The same is true for molten carbonates, which is considered in the next section.

### 1.14.3 Principles and Mechanisms of Corrosion in Carbonate Melts

Molten carbonates are also oxyanion melts, containing  $\text{O}^{2-}$  ions, stemming from the dissociation of the carbonate ions, eqn [16]:



In accordance with the definition of the acid/base characteristic of sulfate melts, the basicity of carbonate melts is defined by eqn [17]:

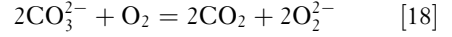
$$p\text{O}^{2-} = -\log a_{\text{O}^{2-}} \quad [17]$$

#### 1.14.3.1 Solubility of Gases

The dissolution of oxygen in carbonate melts takes place by a chemical reaction between the  $\text{O}_2$  molecules and the basic component of the melt (i.e.,  $\text{Na}_2\text{O}$ ); hence, it does not obey Henry's Law. Based

on impedance measurements in a  $(\text{Li},\text{K})_2\text{CO}_3$  melt at  $615\text{--}800^\circ\text{C}$ , the following reduction steps for oxygen species take place by dissolution in the carbonate melt,<sup>6</sup> eqns [18] and [19]:

1. Peroxide mechanism:



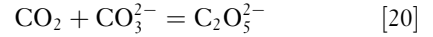
Peroxide ions are mainly present in K-rich melts.

2. Superoxide mechanism:



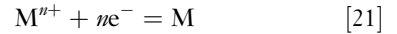
The superoxide mechanism does not take place in pure  $\text{Li}_2\text{CO}_3$  melts, that is, superoxide-ions are not present in predominately Li-rich melts.

According to experiments by Cleas *et al.*<sup>7</sup> in a molten  $\text{Na}_2\text{CO}_3\text{--K}_2\text{CO}_3$  melt at  $800^\circ\text{C}$ , the solubility of  $\text{CO}_2$  in carbonate melts is rather high. The results of cyclovoltametric experiments indicate a very weak anodic reduction peak for  $\text{CO}_2$  to  $\text{CO}$ , but a significant solubility of  $\text{CO}_2$  in the carbonate melt by chemical reaction of  $\text{CO}_2$  with the carbonate ion, according to eqn [20]:

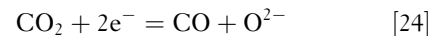
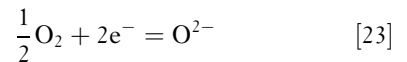
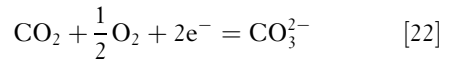


#### 1.14.3.2 Oxidizing and Reducing Reactions of Carbonate Melt Species

Anodic polarization of a carbonate melt with inert Au-electrodes is limited by the oxidation of the carbonate ion according to the reaction given in eqn [16]. The cathodic process is generally the deposition of alkali-metal according to:



There is also evidence that, when in contact with  $\text{O}_2$ - and  $\text{CO}_2$ -containing gases, some contributions to the cathodic current are due to the following reduction reactions, eqns [22]–[24]:



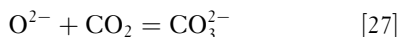
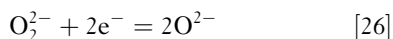
Special interest has to be paid to the electrochemical behavior of oxygen species, stemming from the reactive dissolution of oxygen in the carbonate.<sup>8</sup>

The following reduction steps take place after reactive dissolution by the peroxide and superoxide mechanisms in a  $(\text{Li,K})_2\text{CO}_3$  melt at 615–800 °C for oxygen species, eqns [25]–[30]:

1. Peroxide mechanism:



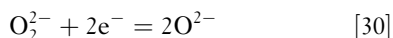
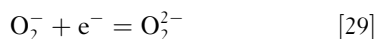
peroxide reduction steps:



2. Superoxide mechanism:



superoxide reduction steps:



Hence, in corrosion studies in oxygen-containing environments, the reduction of oxygen species is the relevant reduction reaction.

#### 1.14.4 Solubility of Oxides in Sulfate and Carbonate Melts

Metal surfaces are protected by a dense and adherent oxide layer, formed upon high temperature oxidation. Corrosive attack of metals and alloys in molten salts is due to the solubility of oxide scales by basic and acidic dissolution whereas the solubility of oxides is a function of melt basicity and depends on the chemical composition of the passive layer.

By a combination of thermodynamic stability diagrams of the salt phase to be investigated and the oxide phase under consideration, phase stability diagrams can be constructed to predict the behavior of any oxide in any molten salt. Figure 4 shows the Na–Fe–S–O phase diagram for prediction of corrosion of iron in a  $\text{Na}_2\text{SO}_4$  melt at 1200 K. This diagram was constructed from superposition of the Na–S–O- and Fe–S–O-stability plots. The diagram shows clearly the basic corrosion products:  $\text{NaFeO}_2$  at high  $a(\text{Na}_2\text{O})$  and the acidic corrosion products  $\text{FeSO}_4$  and  $\text{Fe}_2(\text{SO}_4)_3$  at low  $a(\text{Na}_2\text{O})$ .

In order to investigate the solubilities of oxides in molten salts as a function of melt basicity, experiments were carried out by Rapp *et al.*<sup>8</sup> in molten

$\text{Na}_2\text{SO}_4$  at 1200 K. The melt basicity was fixed by a variation in the gas atmosphere, that is,  $p(\text{SO}_2)$  and  $p(\text{O}_2)$ , and by the addition of  $\text{Na}_2\text{O}_2$  to the molten salt. Figure 5 shows solubility plots for various oxides in molten  $\text{Na}_2\text{SO}_4$  at 1200 K as a function of melt basicity, that is,  $-\log a(\text{Na}_2\text{O})$ . The characteristic shape of the plots represents the amphoteric dissolution behavior of oxides in molten sulfates. Basic solubility occurs at high  $a(\text{Na}_2\text{O})$  (left hand side of each curve), acidic solubility occurs at low  $a(\text{Na}_2\text{O})$  (right hand side of each curve). A characteristic minimum is

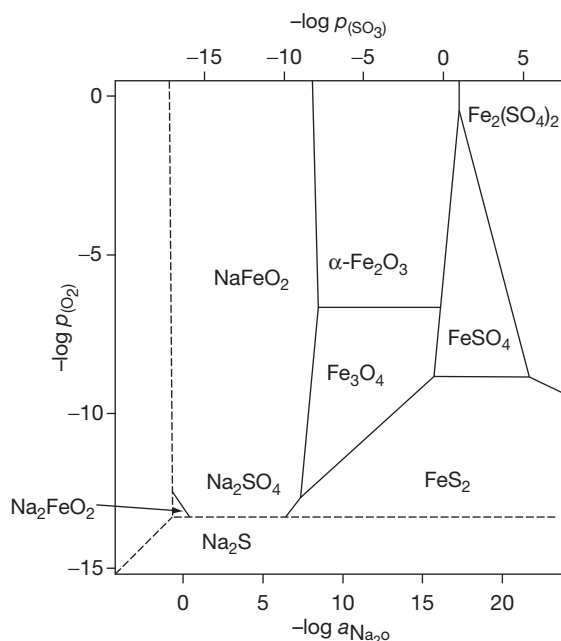


**Figure 4** Na–Fe–S–O phase diagram for prediction of corrosion of iron in a  $\text{Na}_2\text{SO}_4$  melt at 1200 K.

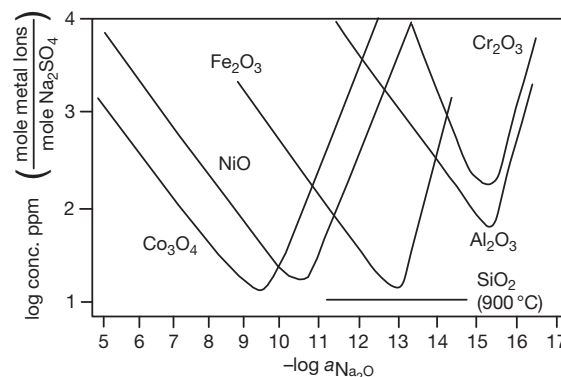
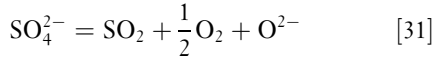


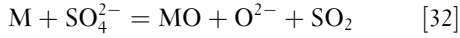
**Figure 5** Solubility plots of various oxides in molten  $\text{Na}_2\text{SO}_4$  at 1200 K as a function of melt basicity, for example,  $a(\text{Na}_2\text{O})$ .

reached, where the dissolution mechanism changes from basic to acidic.

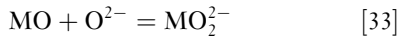
Basic dissolution of oxide scales occurs when oxide ions are present in the molten salt from the dissociation of the sulfate ion according to the reaction given in eqn [31]:



During oxidation of the bare metal surface by  $\text{SO}_4^{2-}$  in a basic melt, metal oxide and additional oxide ions are formed according to eqn [32]:



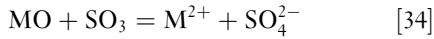
Hence, the  $\text{O}^{2-}$  ion concentration on top of the metal oxide is higher than in the entire melt and dissolution of oxide takes place according to eqn [33]:



In the case of basic dissolution, the metal oxide is dissolved as a complex oxide ion.

Such dissolution reactions were investigated by Rapp and coworkers<sup>12</sup> for several oxides, such as  $\text{Al}_2\text{O}_3$ ,<sup>9</sup>  $\text{Fe}_2\text{O}_3$ ,<sup>10</sup>  $\text{Cr}_2\text{O}_3$ ,<sup>11</sup>  $\text{NiO}$ , and  $\text{Co}_3\text{O}_4$ , in a  $\text{Na}_2\text{SO}_4$  melt at 1200 K.

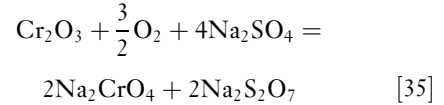
Acidic dissolution occurs by  $\text{SO}_3$ , which is dissolved in the molten sulfate as  $\text{S}_2\text{O}_7^{2-}$  ions. In principle, the following reaction takes place, eqn [34]:



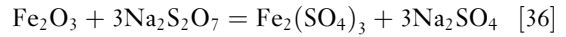
The oxides are dissolved as metal ions in the sulfate melt and metal sulfates are formed.

Hwang and Rapp<sup>13</sup> have shown that the solubility of different oxides is not independent and a synergistic effect is observed, showing accelerated dissolution of both oxides with respect to the single oxide phase. At 1200 K,  $\text{Fe}_2\text{O}_3$  and  $\text{Cr}_2\text{O}_3$  powder were dissolved in a  $\text{Na}_2\text{SO}_4$  melt with a certain basicity, given by an atmosphere of oxygen containing 1 vol.%  $\text{SO}_2$ . In Figure 5, this condition is placed between the solubility minima of  $\text{Cr}_2\text{O}_3$  and  $\text{Fe}_2\text{O}_3$  in the melt.

Hence,  $\text{Cr}_2\text{O}_3$  is dissolved by basic fluxing, eqn [35]:



The presence of  $\text{Na}_2\text{S}_2\text{O}_7$  leads to acidic fluxing of the  $\text{Fe}_2\text{O}_3$ , according to eqn [36]:



The accelerated dissolution is due to the short diffusion distance for  $\text{SO}_3$  in the melt.

As in the case of sulfates, the solubility of oxides in carbonate melts also depends on the partial pressure of  $\text{CO}_2$  in the gas phase, that is, on the basicity of the melt. As  $\text{NiO}$  is the cathode material in molten carbonate fuel cells, its solubility is of major interest and has been investigated in detail. Figure 6 shows the solubility plot for  $\text{NiO}$  in a  $(\text{Li}_{0.62}\text{K}_{0.38})_2\text{CO}_3$  mixture as a function of  $p(\text{CO}_2)$  in the gas phase at temperatures of 923–1023 K.<sup>14</sup>

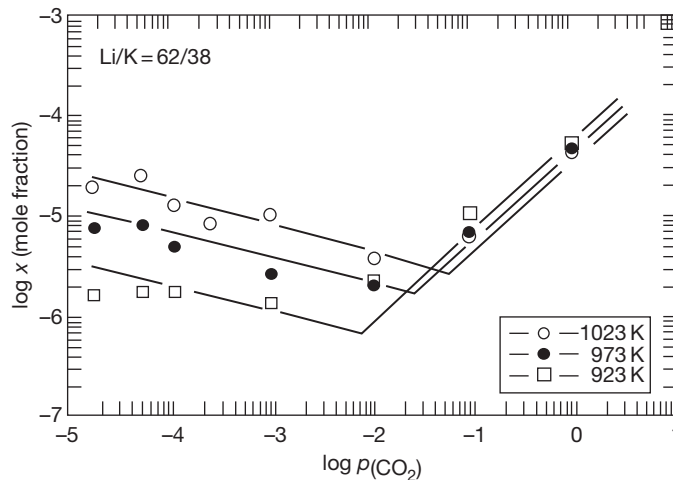
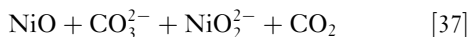


**Figure 6** Solubility plot of  $\text{NiO}$  in a  $(\text{Li}_{0.62}\text{K}_{0.38})_2\text{CO}_3$  mixture as a function of  $p(\text{CO}_2)$  in the gas phase at temperatures of 923–1023 K.

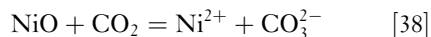


Two different solubility regimes are observed, showing a negative slope (low  $p(\text{CO}_2)$ ) and a positive slope (high  $p(\text{CO}_2)$ ). These two regimes correspond to the basic (low  $p(\text{CO}_2)$ ) dissolution and acidic dissolution (high  $p(\text{CO}_2)$ ) of NiO in the carbonate melt, according to eqns [37] and [38]:

basic dissolution:

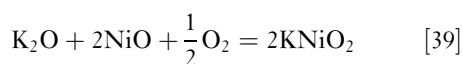


acidic dissolution:



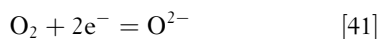
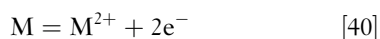
Further investigations of the basic dissolution of NiO in other carbonates have shown that the solubility also depends on the nature of the carbonate. The solubility of NiO at 910 °C in a  $\text{CO}_2\text{--O}_2\text{--Ar}$  atmosphere is highest for  $\text{Rb}_2\text{CO}_3$  and lowest for  $\text{Na}_2\text{CO}_3$ , especially in the acidic regime.<sup>15</sup>

Evidence is also given to the fact that the basic solubility of NiO in  $\text{K}_2\text{CO}_3$  melts at constant  $p(\text{CO}_2)$  depends slightly on the  $p(\text{O}_2)$  value in the gas phase. This dependence is due to the following basic dissolution reaction:

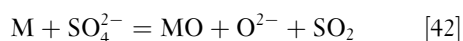


### 1.14.5 Corrosion Mechanisms in Sulfate Melts: The Rapp and Goto model

As discussed earlier, the oxidation of the metal beneath a highly basic molten sulfate film generates  $\text{O}^{2-}$ -ions at the oxide–melt interface by the reduction of  $\text{O}_2$  or by the reduction of the sulfate-ion, eqns [40]–[42].

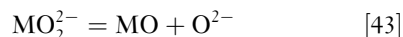


and:



Accordingly, the region close to the oxide surface is much more basic than the entire salt film and basic dissolution of the oxide occurs. In the ideal case, the dissolved species form a separate layer, comparable to a Nernst concentration interface. From this interface, transport of the dissolved oxide species and also oxidant gas occur within their concentration gradients in

the melt film towards the melt/gas or the gas/oxide interface. In addition to the concentration gradient in the melt film, a basicity gradient also exists, from regions of high  $p(\text{O}^{2-})$  at the melt/oxide interface to low  $p(\text{O}^{2-})$  at the melt/gas interface. By reaching regions of low  $p(\text{O}^{2-})$ , the solute is no longer stable and precipitation of solid oxide occurs by the reverse of the dissolution reactions, eqn [43]:



This precipitation creates a permanent sink for the solute, promoting the continuous flux of the dissolved oxide in the melt film. On the other hand, the consumption of oxidant gas  $\text{O}_2$  by the formation of  $\text{O}^{2-}$  ions and subsequent dissolution reaction at the melt–oxide interface creates the gradient for oxidant diffusion. Figure 7 shows a schematic plot of the gradients and transport processes within the melt film.

Rapp and Goto<sup>16</sup> analyzed the basic fluxing conditions and developed a criterion for the continuous fluxing of oxide scales, eqn [44]:

$$\left(\frac{d_{(\text{sol.})}}{dx}\right)_{x=0} < 0 \quad [44]$$

As long as the negative solubility gradient (Rapp–Goto criterion) is valid, basic fluxing proceeds and the rate of the corrosion process is enhanced.

An important proof of the Rapp–Goto criterion was given later by Otsuka and Rapp,<sup>17</sup> who performed an electrochemical experiment (potentiometric measurements) on preoxidized nickel at 1173 K in an  $\text{O}_2\text{--}0.1\% \text{SO}_2$  gas atmosphere and covered by a thin film of  $\text{Na}_2\text{SO}_4$ . The authors continuously recorded the basicity and oxygen activity of the melt as a function of time. Figure 8 shows the results, plotted on the Ni–Na–S–O phase diagram. At the beginning of the corrosion reaction, the melt was found to be basic.

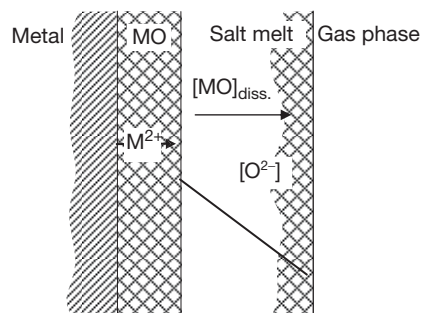


**Figure 7** Schematic plot of the solubility gradient and transport processes within the melt film. The oxide precipitates at the melt–gas interphase.

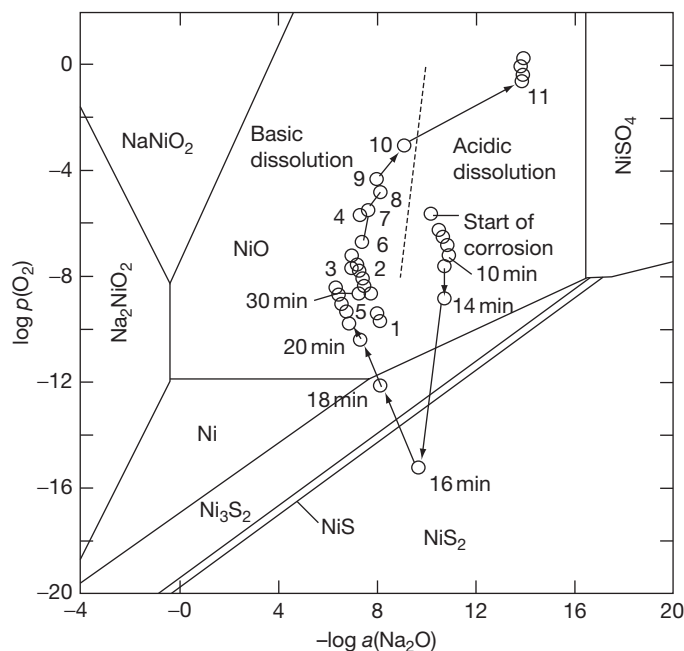


**Figure 8** Basicity and oxygen activity measurements during corrosion of preoxidized Ni beneath a  $\text{Na}_2\text{SO}_4$  film at 1173 K in  $\text{O}_2\text{-SO}_2$ , plotted in the Ni-Na-S-O phase diagram.

During the corrosion reactions, the basicity of the melt increases and Ni-sulfide becomes stable. As the composition of the gas atmosphere was not changed, the results show quite clearly that the local chemistry of the melt is influenced by the local corrosion reactions.

Acidic fluxing requires a higher  $p(\text{SO}_3)$  value in the gas phase and/or some alloying elements such as Co or Ni, from which molten eutectic mixtures are able to form with the sulfate deposit (alloy-induced acidic fluxing). The main feature of acidic fluxing is the solubility of certain metal sulfates, formed by reaction of the alloying elements and  $\text{SO}_3$  from the gas phase, within the salt deposit. Generally, no sulfide formation occurs by acidic fluxing.

### 1.14.6 Methods of Investigation of Corrosion in Molten Salts

#### 1.14.6.1 Electrochemical Techniques

Being electrochemical in nature, fundamental studies of hot corrosion mechanisms require electrochemical techniques. The simplest electrochemical measurement is polarization of the sample and the measurement of the induced current. As in aqueous corrosion, polarization studies provide information mainly about the potential dependent behavior of a piece of metal in the melt, that is, active dissolution, the passive range

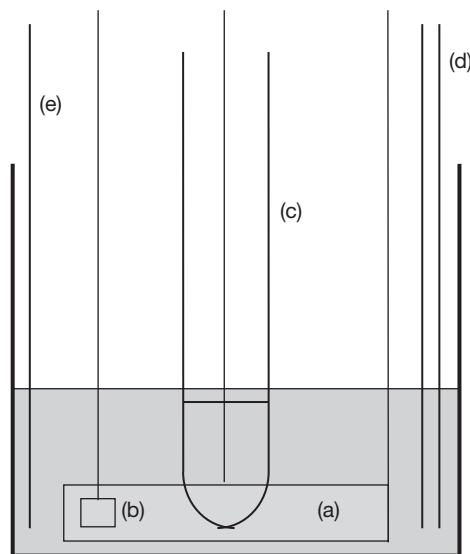


**Figure 9** Typical set-up of the inner crucible of a high temperature electrochemical cell with counter-electrode (a), the working-electrode (b), the reference electrode (c), the gas inlet tube (d), and the thermocouple (e).

and breakthrough potentials. For such studies, the melt is placed in an alumina crucible, situated in a vertical, closed-end furnace, as shown in [Figure 9](#).

In order to avoid electronic distortions from the furnace heating wires, a cylindrical vessel made of stainless steel is usually placed between the alumina

crucible and the furnace. The vessel is electrically connected to the furnace in order to avoid electrical charges on the surface. The alumina crucible is closed by a heat-resistant pyrex-glass flange with spaces for the electrodes, the thermocouple and the gas-inlet tube. The electrode wires and the thermocouple are shielded by small-diameter alumina tubes. These *alumina tubes* are fixed with cation fittings in the glass flange.

For the polarization studies, a three electrode set-up is necessary, consisting of a working electrode (WE), a counter electrode (CE), and a reference electrode (RE). The WE is usually the metal to be investigated or, for studies of the polarization behavior of the melt itself, Au or Pt are appropriate; the latter are also suitable for the counter electrode.

The main difference in aqueous corrosion studies is the design of the reference electrodes. The most useful types are closed-end tubes of either internally-platinized  $Y_2O_3$ -stabilized  $ZrO_2$ , mullite or glass membranes, depending on the composition of the melt and the temperature. Glass membranes, especially Pyrex<sup>®</sup>, Supremax<sup>®</sup> and Duran 50<sup>®</sup>, are  $Na^+$  and  $K^+$  ion-conducting membranes and are also useful for studies in molten salts, especially at temperatures up to 700 °C. Similar to the mullite reference electrode, a silver wire is dipped into the molten chloride or sulfate to be investigated; usually this melt additionally contains  $AgCl_2$  or  $Ag_2SO_4$  in concentrations of 1–10 mol%.<sup>18</sup>

For example, Figure 10 shows a polarization curve for a 2.25Cr–1Mo–steel in a eutectic (Ca–K–Na) sulfate mixture at 850 °C in an  $N_2$ –5 vol.%  $O_2$  gas mixture, using a mullite–Ag/AgSO<sub>4</sub> reference electrode. After an active region, the material behaves in a passive

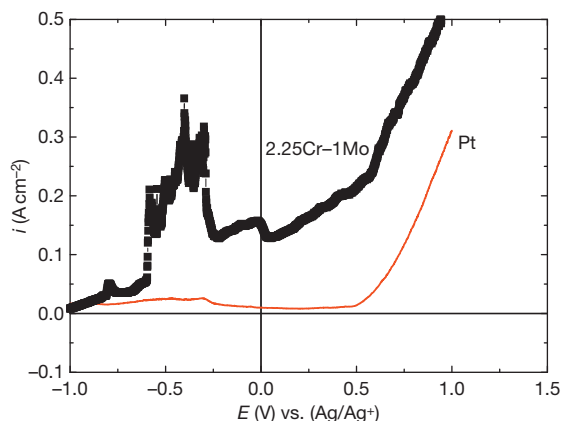
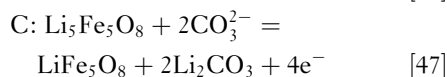
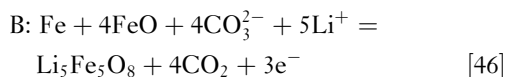
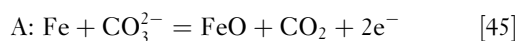


**Figure 10** Polarization curve of a 2.25Cr–1Mo–steel in a eutectic (Ca–K–Na)–sulfate mixture at 850 °C in an  $N_2$ –5 vol.%  $O_2$  gas mixture; the curve for Pt is shown for comparison.

manner in the potential range of approximately  $-0.25$  to  $0.25$  V; this is followed by an increasing current. Investigation of the sample within the passive region shows the formation of a porous  $Fe_2O_3$  scale on the metal surface.<sup>19</sup>

Extended investigations are possible by using cyclic voltammetry. Figure 11 shows a cyclic voltammogram of pure iron in a eutectic 62 wt%  $Li_2CO_3$ –38 wt%  $K_2CO_3$  melt at 650 °C in synthetic air, containing 25 vol.%  $CO_2$ . The details regarding reference electrode and set-up are described elsewhere.<sup>20</sup> Upon anodic polarization, the voltammogram shows three different anodic peaks (A, B, C) and two cathodic peaks (D, E).

According to detailed investigation by SEM and XRD on samples, held at different anodic potentials, the following reactions were identified:



Impedance spectroscopic measurements are occasionally used in molten-salt corrosion studies. In general, most of the impedance spectra emphasize diffusion-controlled kinetics for the active corrosion of metals in molten salts. This behavior is expected as the activation energy for charge-transfer reactions is easily reached at higher temperatures.

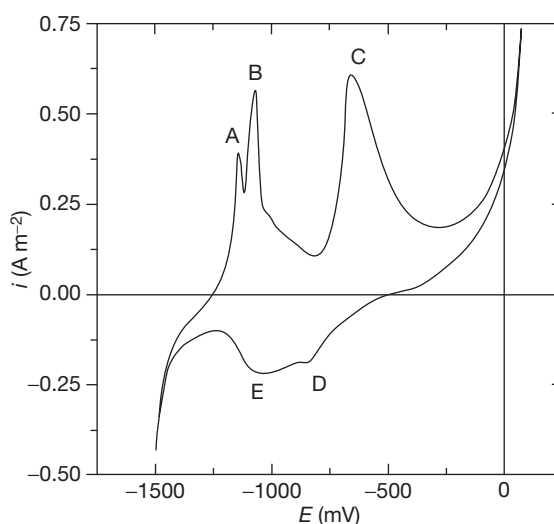


**Figure 11** Cyclic voltammogram of pure iron in a eutectic 62 wt%  $Li_2CO_3$ –38 wt%  $K_2CO_3$  melt at 650 °C in synthetic air, containing 25 vol.%  $CO_2$ .

The paper by Zheng *et al.*<sup>21</sup> gives some theoretical impedance models for hot corrosion of metals in molten salts. In general, the authors propose large semicircles in the Nyquist plot for nonactive metals, resulting from a rate-limiting charge-transfer reaction. For active metals, the total impedance may result from the scaling of the metals when the Nyquist plot should show two capacitance loops, *and* with the rate-limiting step being the charge-transfer reaction. For porous scales on the surface, a line should be shown in the low frequency range; this is related to a diffusion-controlled process.

One example is the hot corrosion of a preoxidized nickel specimen under a thin  $\text{Na}_2\text{SO}_4$  melt film in a 0.1 wt%  $\text{SO}_2$ - $\text{O}_2$  gas mixture at 1200 K.<sup>22</sup> By variations in the oxide scale thickness and the purity of the material, different regimes of corrosion were investigated, that is, the passive state, the pseudopassive state and the active state. The passive state for 99.9975% of pure nickel, preoxidized in pure  $\text{O}_2$  for 2 h at 1200 K, is controlled by diffusion of  $\text{S}_2\text{O}_7^{2-}$  ions in the salt melt. The corresponding Nyquist plots of impedance data show linear behavior in the low frequency range with a slope of  $45^\circ$ , as shown in Figure 12.

#### 1.14.6.2 Other Methods

Multisample exposure tests are the most useful tests for estimating long-term corrosion data behavior of a certain material by fitting the corrosion data to general kinetic laws. The furnace set-up, used for the tests, is connected to a gas-flow device. In addition, salt needs to be deposited on the sample surface. This can be done by different techniques:

- evaporation of the salt with subsequent condensation on the cooler sample surface (Dean test)

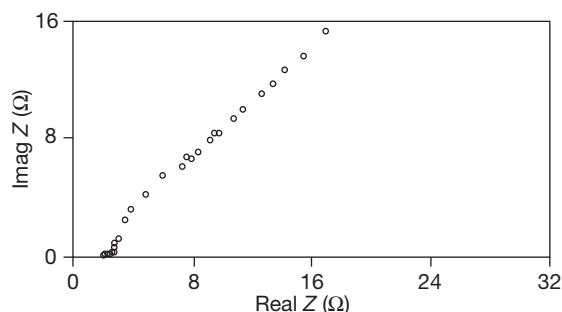


**Figure 12** Nyquist plot of impedance data of the passive state of 99.9975% pure nickel in a  $\text{Na}_2\text{SO}_4$  melt in an 0.1 wt%  $\text{SO}_2$ - $\text{O}_2$  gas mixture at 1200 K, showing linear behavior in the low frequency range, with a slope of  $45^\circ$ .

- full salt immersion (crucible test, thick salt film)
- surface coverage of the sample (thin salt film)
- slurry or from an aqueous solution (thin salt film)

Determination of the extent of corrosion can be obtained by measurements of the scale thickness or of the remaining metal thickness or by the determination of the total weight loss after removal of the corrosion products. The last method is particularly favored if a high amount of oxide is dispersed in the solidified salt.

According to the standard guidelines for exposures of samples coated with thin salt films, as developed in the TESTCORR project,<sup>23</sup> the extent of corrosion should be determined on a logarithmic time scale, that is, after 1, 3, 10, 30, 100, 300, and 1000 h of exposure and redeposition of salt should be made *after* every 20 h.

In order to study short-term kinetics, thermogravimetric experiments are useful; these allow the identification of possible incubation times or the influence of gas phase composition. However, it has to be shown that the overall mass change is not influenced by reactions of the salt itself, for example, significant evaporation or reaction of the salt with the gas phase.

### 1.14.7 Examples of Hot-Salt Corrosion in Industrial Practice

#### 1.14.7.1 Gas Turbines: Corrosion Beneath $\text{Na}_2\text{SO}_4$ Deposits

The need for the early work on hot corrosion beneath  $\text{Na}_2\text{SO}_4$  melts was based on gas-turbine blade failures as a consequence of  $\text{Na}_2\text{SO}_4$  deposition. It has been established that deposition of  $\text{Na}_2\text{SO}_4$ , formed by salt from the air and sulfur from the fuel, is responsible for these kinds of attack. Especially the work by Goebel and Pettit<sup>24</sup> as well as by Bornstein and DeCrescente<sup>25,26</sup> recognized that the formation of sulfides on the metallic engine parts results from the presence of a thin salt film on the metal surface. As a consequence, extensive research was conducted on alloys coated with  $\text{Na}_2\text{SO}_4$  and how they reacted in different environments. In the following discussion, some general principles on the reaction mechanisms will be discussed. The corrosion kinetics of metals are significantly enhanced by several orders of magnitude compared to the oxidation without any salt, as shown in Figure 13 for nickel reaction beneath a  $\text{Na}_2\text{SO}_4$  deposit at 900 °C in an  $\text{O}_2$ - $\text{SO}_2$  containing atmosphere.<sup>27</sup>

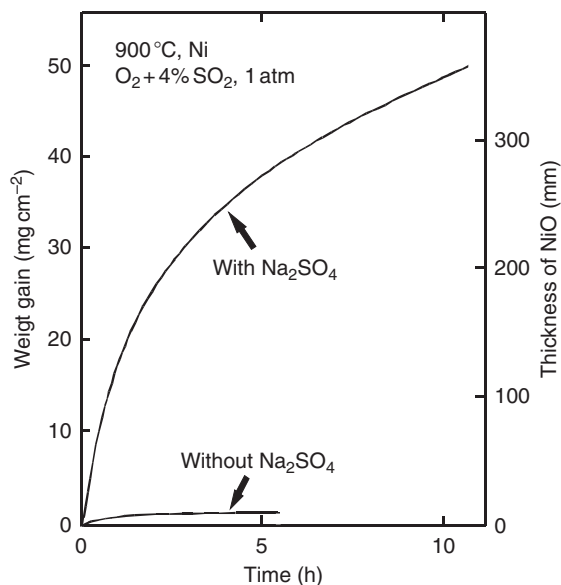


**Figure 13** Comparison of the reaction kinetics of pure nickel with and without deposit of  $\text{Na}_2\text{SO}_4$  in 1 atm  $\text{O}_2$ -4%  $\text{SO}_2$  at 900 °C. Reproduced from Edeleanu, C.; Littlewood, R. *Electrochim. Acta* **1960**, 3, 195.

Two main corrosion mechanisms have been identified: Type I and Type II hot corrosion. Type I usually occurs at temperatures above the melting point of  $\text{Na}_2\text{SO}_4$  ( $T > 884^\circ\text{C}$ ); here, the undie oxide scale is dissolved in the salt melt due to basic fluxing (see Section 1.14.4). Type II hot corrosion occurs at temperatures below the melting point of  $\text{Na}_2\text{SO}_4$ . One example for this is the corrosion of nickel beneath a solid  $\text{Na}_2\text{SO}_4$  salt deposit in  $\text{SO}_3$ -containing gas. In the early stages of corrosion, a  $\text{Na}_2\text{SO}_4$ - $\text{NiSO}_4$  solid solution is formed:



In the preceding reaction, the amount of  $\text{NiSO}_4$  increases, the  $\text{Na}_2\text{SO}_4$ - $\text{NiSO}_4$  mixture starts to melt and accelerated corrosion is observed. The melting point of the mixture strongly depends on the  $p(\text{SO}_3)$  value in the gas phase, that is, it decreases with the increasing value of  $p(\text{SO}_3)$  and the melting point of the  $\text{Na}_2\text{SO}_4$ - $\text{NiSO}_4$  mixture decreases,<sup>28,29</sup> Figure 14.

In aircraft engines, *mostly* Type II hot corrosion is mainly observed in nickel- and cobalt-based materials. Extensive studies were preformed on Co-Cr, Co-Al, Ni-Cr, Ni-Cr-Al, and Co-Cr-Al-Y alloys.<sup>35,36</sup> A detailed corrosion mechanism for Co-based alloys in  $\text{O}_2^-$  and  $\text{SO}_3^-$  containing gases was presented by Luthra.<sup>30</sup> In this model, the  $\text{SO}_3$  is dissolved in the melt and transported via  $\text{SO}_4^{2-}$  ions from the melt-gas to the melt-oxide interface at which  $\text{CoSO}_4$  is

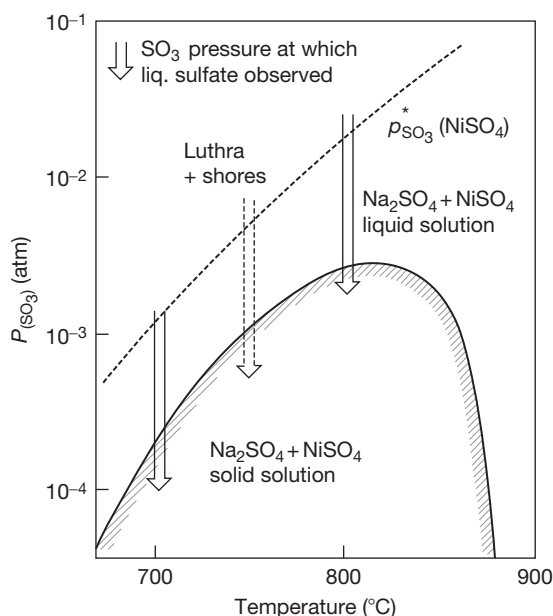


**Figure 14** Comparison of the theoretical values of the critical  $\text{SO}_3$  pressure needed to form a  $\text{Na}_2\text{SO}_4 + \text{NiSO}_4$  melt with the lowest pressures occurring where a molten sulfate was observed and 'hot corrosion' was initiated.<sup>28,29,34,35</sup>

formed. In only  $\text{O}_2$ -containing gases,  $\text{Co}^{2+}$  ions are dissolved from the oxide and transported to the melt-gas interface at which they are oxidized by  $\text{O}_2$  to  $\text{Co}^{3+}$  ions and  $\text{Co}_3\text{O}_4$  is formed. Some  $\text{Co}^{3+}$  ions also diffuse back to the melt-oxide interface where they are reduced to  $\text{Co}^{2+}$  ions again. Alloying elements Mo, W, and, also, V (present as a fuel impurity) form the acidic oxides:  $\text{MoO}_3$ ,  $\text{WO}_3$ , and  $\text{V}_2\text{O}_5$ . The effect of  $\text{NaVO}_3$  on the acidic fluxing of  $\text{CeO}_2$ ,  $\text{HfO}_2$ , and  $\text{Y}_2\text{O}_3$  was studied in detail by Zhang and Rapp.<sup>31</sup> The authors show that fluxing was accelerated by the presence of acidic solutes in the melt. This behavior was shown to result from complexing reactions between the solute  $\text{VO}^{3-}$  ions and oxide ions, provided by the acidic dissolution of ceria in the respective oxide.

#### 1.14.7.2 Waste Incineration: Corrosion in Chloride Melts

In waste-fired boilers, solid and molten salts are formed by condensation of aerosols within the flue gas on cooled material surfaces that function as heat-exchanger tubes. The presence of salts accelerates the corrosion process, especially if they are associated with the formation of molten phases on the material surface or in the oxide scales.



**Figure 15** shows a characteristic failure situation, in which the salt-covered part of the tube is significantly damaged.

The molten phases are mainly chlorides, such as KCl, NaCl,  $\text{ZnCl}_2$ , and  $\text{PbCl}_2$ .<sup>32</sup> Due to the significant amount of heavy metals, these salt mixtures form molten eutectics at temperatures as low as 250 °C, as shown in **Table 1**.

A typical salt melt-induced attack of a superheater tube ( $T \approx 550^\circ\text{C}$ ) from a waste-fired boiler is shown in **Figure 16**. The morphology of the scale is typical for molten salt attack, that is, a thick and dense chromium-rich oxide scale in contact with the metal and iron-oxide and nickel-oxide precipitates in the former molten salt.<sup>33</sup>

The behavior of metals and their oxides in molten chlorides has not been studied as extensively as in sulfate systems. Chloride melts are mostly simple

ions and initially free of oxygen, which is different from sulfates. In some cases, molecular species exist, for example  $\text{AlCl}_3$  or  $\text{HgCl}_2$ .

Theoretical thermodynamic considerations by Edeleanu and Littlewood<sup>34</sup> have shown that the corrosion tendency of a metal in chloride melts depends on the stability of the specific metal chloride. Furthermore, the solubility of the metal chloride or metal oxide depends on the total pressure and, more importantly, on contaminants in the molten salt, especially oxygen. In pure chloride melts, a passivation of the metal is impossible, because most of the metal chlorides are soluble. Electrochemical experiments on iron and nickel in a KCl–NaCl melt at 700 °C in argon showed a very negative corrosion potential with respect to platinum and no passivation of the metal was observed. As corrosion products,  $\text{Fe}_3\text{O}_4$ ,  $\text{Fe}_2\text{O}_3$ , and NiO were observed on top of the melt–gas interface.<sup>36</sup> Obviously, oxidation of the soluble metal chlorides occurs in contact with the oxygen-containing gas.

The cathodic reaction during metal oxidation is the reduction of contaminants in the melt, especially dissolved oxygen. Ishitsuka und Nose<sup>35</sup> studied the solubility of some metal oxides in pure NaCl–KCl melts at 727 °C and in NaCl–KCl– $\text{Na}_2\text{SO}_4$ – $\text{K}_2\text{SO}_4$  melts at 550 °C. The basicity of the melt was set at  $-\log a_{\text{O}^{2-}}^2 = -2$  for basic,  $-\log a_{\text{O}^{2-}}^2 = -7$  for intermediate and  $-\log a_{\text{O}^{2-}}^2 \geq 17$  for acidic conditions. The results show a typical amphoteric solubility, as already known from sulfate melts. For some oxides, no solubility minima were observed, that is, for example, NiO/ $\text{Cr}_2\text{O}_3$  is thought to be dissolved as chromate, corresponding to a basic solubility.

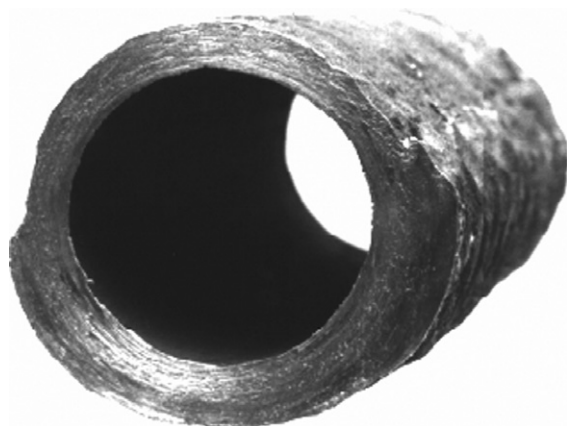


**Figure 15** Characteristic failure situation of a superheater tube from a waste-fired boiler. The ash-covered part of the tube is significantly damaged.

**Table 1** Eutectic mixtures and melting points of salts found in deposits from waste fired plants

Composition (wt%)	Melting point (°C)
48ZnCl <sub>2</sub> –52KCl	250
82ZnCl <sub>2</sub> –18KCl	262
84ZnCl <sub>2</sub> –16KCl	262
73ZnCl <sub>2</sub> –27PbCl <sub>2</sub>	300
31NaCl–69PbCl <sub>2</sub>	410
21KCl–79PbCl <sub>2</sub>	411
17NaCl–83PbCl <sub>2</sub>	415
39ZnCl <sub>2</sub> –50KCl–11PbCl <sub>2</sub>	275
35ZnCl <sub>2</sub> –48NaCl–17PbCl <sub>2</sub>	350
16NaCl–40KCl–44PbCl <sub>2</sub>	400
K <sub>2</sub> SO <sub>4</sub> –Na <sub>2</sub> SO <sub>4</sub> –ZnSO <sub>4</sub>	384
KCl–ZnCl <sub>2</sub> –K <sub>2</sub> SO <sub>4</sub> –ZnSO <sub>4</sub>	292

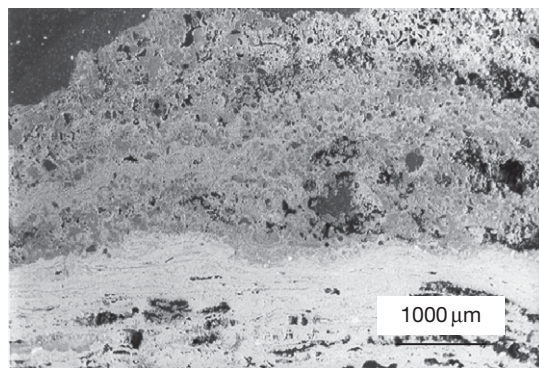


**Figure 16** Typical melt-induced attack of a superheater tube ( $T \approx 550^\circ\text{C}$ ) from a waste-fired boiler. The morphology of the scale is typical for molten salt attack that is, a thick and dense chromium-rich oxide scale in contact with the metal and iron-oxide and nickel-oxide precipitates in the molten salt.



In summary, it seems to be evident that corrosion in chloride melts is based on the solubility of metals and oxides as metal chlorides in the molten salt.

In deposits from waste incineration, mainly KCl–ZnCl<sub>2</sub> mixtures are present in the ashes and fast corrosion occurs at relatively low temperatures. The main corrosion mechanism is dissolution of metal in the molten salt as soluble metal chlorides. **Figure 17** shows a schematic plot of the mechanisms involved, as described by Ruh.<sup>36</sup>

At the metal–salt interface, the metal is dissolved as metal chloride by forming a ternary eutectic with the salt deposit. The concentration of dissolved metal chloride is high at the inner interface and low at the salt–gas interface. As a consequence, the metal

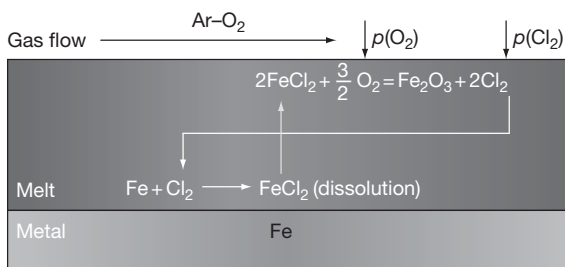


**Figure 17** Reaction scheme for the mechanisms involved in chloride-induced corrosion beneath a molten ZnCl<sub>2</sub>–KCl eutectic from deposits in waste-incineration plants.

chloride diffuses outward towards the oxygen-containing gas and is oxidized to oxide again.

It has been found that iron-based low alloyed steels show much more corrosion than nickel-based materials. The proposed model is supported by thermodynamic calculations of the solubility of iron, chromium, and nickel beneath a ZnCl<sub>2</sub>–KCl melt. **Figures 18–20** show ternary phase diagrams for the FeCl<sub>2</sub>–ZnCl<sub>2</sub>–KCl, CrCl<sub>2</sub>–ZnCl<sub>2</sub>–KCl, and NiCl<sub>2</sub>–ZnCl<sub>2</sub>–KCl systems at 320 °C.

The solubility of FeCl<sub>2</sub> is quite high whereas the solubility of CrCl<sub>2</sub> is low and almost no solubility occurs for NiCl<sub>2</sub>. This reflects the stability of the different alloys based on the corrosion mechanism as described above.

### 1.14.7.3 Corrosion in Molten Carbonate Fuel Cells

Molten carbonate fuel cells are high temperature fuel cells, working at 650 °C with a molten 62 wt% Li<sub>2</sub>CO<sub>3</sub>–38 wt% K<sub>2</sub>CO<sub>3</sub> eutectic mixture as the electrolyte, CO<sub>2</sub> and O<sub>2</sub> as oxidant gases and H<sub>2</sub> as the fuel. The relevant reactions are:

Cathode:

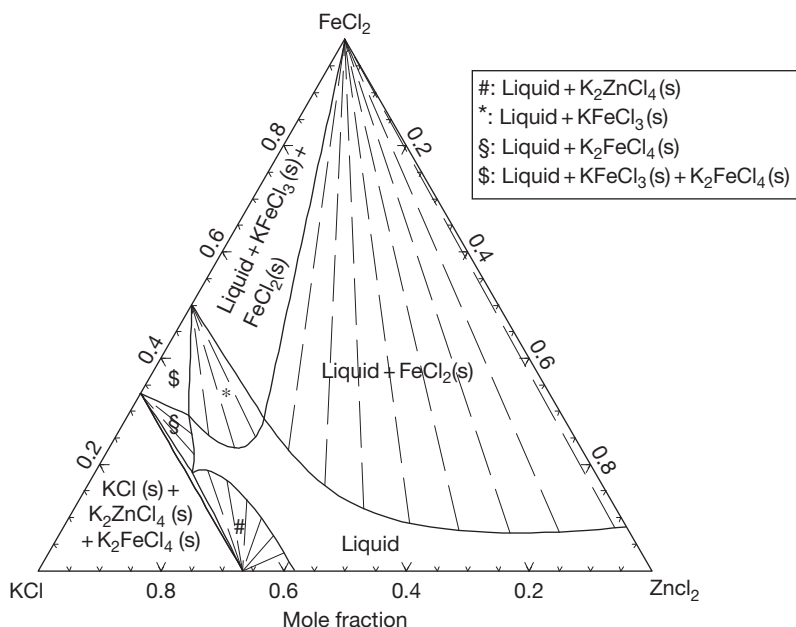
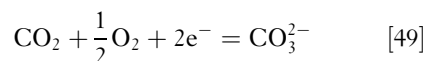


**Figure 18** Solubility of FeCl<sub>2</sub> in a ZnCl<sub>2</sub>–KCl eutectic mixture at 320 °C.

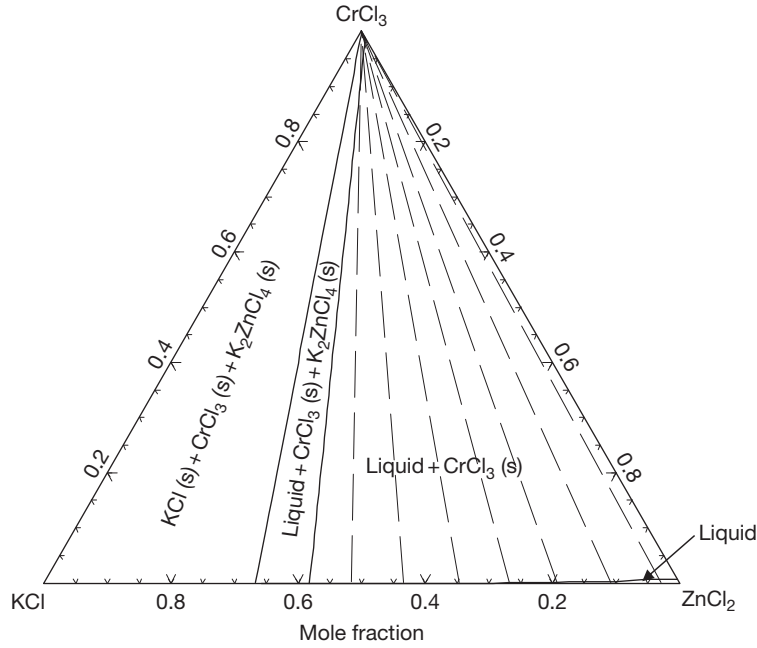


**Figure 19** Solubility of  $\text{CrCl}_2$  in a  $\text{ZnCl}_2$ - $\text{KCl}$  eutectic mixture at  $320^\circ\text{C}$ .

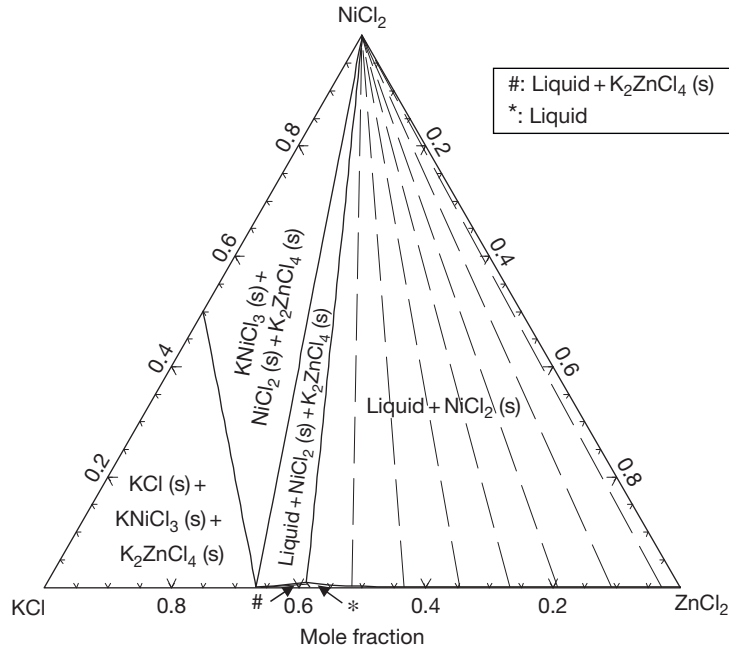
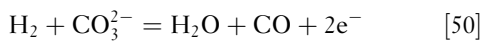


**Figure 20** Solubility of  $\text{NiCl}_2$  in a  $\text{ZnCl}_2$ - $\text{KCl}$  eutectic mixture at  $320^\circ\text{C}$ .

Anode:



In practice, the stack technology is applied, by stapling some of the modules to a bigger device.

The main corrosion problems occur at the cathodic side, where  $\text{NiO}$  is used as the cathode material and stainless steel as the current collector. Both parts are in contact with the gas phase ( $\text{O}_2$ ,  $\text{CO}_2$ ) and the molten carbonate, leading to hot corrosion

attack. NiO forms as the cathode materials starts to dissolve in the melt and reprecipitates in the electrolyte, leading to a short circuit and breakdown of the cell voltage. Furthermore, corrosion of the cathodic-current collector by the molten carbonate occurs and the cell voltage decreases due to the growth of poorly-conducting oxide phases, that is,  $\text{LiCrO}_2$ . Laboratory research is still going on in order to find metallic materials with good corrosion resistance, that form corrosion products with reasonable electric conductivity, such as spinels, doped with Co and/or Mn.

## References

1. Lux, H. Z. *Elektrochem. Angew. Phys. Chem.* **1939**, 45, 303.
2. Flood, H.; Forland, T.; Motzfeld, K. *Acta Chem. Scand.* **1952**, 6, 257.
3. Andresen, R. E. *J. Electrochem. Soc.* **1979**, 126, 328.
4. Shores, D. A.; Fang, W. C. *J. Electrochem. Soc.* **1981**, 128, 346.
5. Fang, W. C.; Rapp, R. A. *J. Electrochem. Soc.* **1983**, 130, 2335.
6. Nishina, T.; Uchida, I.; Selman, J. R. *J. Electrochem. Soc.* **1994**, 141, 1191.
7. Claes, P.; Thirjon, B.; Glibert, J. *Electrochim. Acta* **1996**, 41, 141.
8. Rapp, R. A. *Corrosion* **1986**, 42, 568.
9. Jose, P. D.; Gupta, D. K.; Rapp, R. A. *J. Electrochem. Soc.* **1985**, 132, 735.
10. Zhang, Y. S.; Rapp, R. A. *J. Electrochem. Soc.* **1985**, 132, 734.
11. Zhang, Y. S. *J. Electrochem. Soc.* **1986**, 133, 655.
12. Gupta, D. K.; Rapp, R. A. *J. Electrochem. Soc.* **1980**, 127, 2194.
13. Hwang, Y.-S.; Rapp, R. A. *J. Electrochem. Soc.* **1990**, 137, 1276.
14. Ota, K.; Mitsushima, S.; Kato, K.; Kamiya, N. In *Proceedings of the second Symposium in MCFC-Technology*; Electrochemical Society, 1990; Vol. 90-16, 318.
15. Orfield, M. L.; Shores, D. A. *J. Electrochem. Soc.* **1988**, 135, 1662.
16. Rapp, R. A.; Goto, K. In *Proceedings of the Fused Salt Symposium*; Braunstein, J., Ed.; The Electrochemical Society: Princeton, NJ, 1979; Vol. 2.
17. Otsuka, N.; Rapp, R. A. *J. Electrochem. Soc.* **1990**, 137, 46.
18. Lee, K. N.; Shores, D. A. *J. Electrochem. Soc.* **1990**, 137, 859.
19. Spiegel, M. *Proceedings EUROCORR'00*, London, 2000.
20. Biedenkopf, P.; Spiegel, M.; Grabke, H. *J. Mater. Corros.* **1997**, 48, 731.
21. Zheng, C. L.; Eang, W.; Wu, W. T. *Corros. Sci.* **2001**, 43, 787.
22. Wu, Y. M.; Rapp, R. A. *J. Electrochem. Soc.* **1991**, 138, 2683.
23. Tomkings, A. B., et al. TESTCORR, Code of Practice, ERA Report 2000-0546, 2001, Unpublished data.
24. Goebel, J. A.; Pettit, F. S. *Metall. Trans.* **1970**, 4, 1943.
25. Bornstein, N. S.; DeCrescente, M. A. *Trans. Met. Soc. AIME* **1969**, 24, 1947.
26. Bornstein, N. S.; DeCrescente, M. A. *Metall. Trans.* **1971**, 2, 2875.
27. Lillerud, K. P.; Kofstad, P. *Oxid. Met.* **1984**, 21, 233.
28. Luthra, K. L.; Shores, D. A. *J. Electrochem. Soc.* **1980**, 127, 2202.
29. Luthra, K. L. *Metall. Trans. A* **1982**, 13, 1647, 1843, 1853.
30. Luthra, K. L. *J. Electrochem. Soc.* **1985**, 132, 1293.
31. Zhang, Y. S.; Rapp, R. A. *Corrosion* **1987**, 43, 384.
32. Spiegel, M. *Mater. Corros.* **1999**, 50, 373.
33. Spiegel, M. *Mater. Corros.* **2000**, 51, 303.
34. Edeleanu, C.; Littlewood, R. *Electrochim. Acta* **1960**, 3, 195.
35. Ishitsuka, T.; Nose, K. *Mater. Corros.* **2000**, 51, 177.
36. Ruh, A.; Spiegel, M. *Corros. Sci.* **2006**, 48, 679.

## 1.16 Types of Environments

**B. A. Baker**

Special Metals Corporation, 3200 Riverside Drive, Huntington, WV 25705, USA

© 2010 Elsevier B.V. All rights reserved.

1.16.1	Introduction	399
1.16.2	Oxidizing Environments	400
1.16.3	Nitridation	400
1.16.4	Environments Promoting Carbon Ingress	401
1.16.5	Environments Containing Halides	402
1.16.6	Sulfur-Containing Environments	403
1.16.6.1	Coal-Fired Boiler Corrosion	404
1.16.6.2	Oil-Fired Boiler Corrosion	404
1.16.7	Molten Metals	405
1.16.8	Molten Salts	405
References		405

### Abbreviations

**AHF** Anhydrous hydrofluoric acid

**LME** Liquid metal embrittlement

**MSW** Municipal solid waste

### 1.16.1 Introduction

High temperature corrosion in gaseous environments is commonly interpreted as that taking place above the temperature at which corrosive liquids may condense, causing dew point corrosion. While most high temperature corrosion processes typically take place at quite high temperatures, above about 450 °C, such phenomena can take place at even lower temperatures. For example, formation of pyrosulfates of potassium and sodium can contribute significantly to corrosion rate in coal-fired boiler furnace walls within the temperature range of ~250–350 °C.<sup>1</sup>

While interaction with gaseous environments comprises much of the breadth of knowledge of high temperature corrosion, interdiffusion can occur between high temperature materials and other solids, for example, between a silicon carbide furnace hearth and a furnace belt carrying product through the furnace, or between a graphite sample holder and metallic furnace components. Contact with molten materials may occur, such as interaction between alkali salts of sulfur or halides and metal alloys, which can result in the formation of lower-melting eutectics. Processes governing corrosion resulting from contact with

molten salts are analogous to aqueous corrosion processes in that an electrolyte is present; galvanic effects may thus be operable. Lower-melting metals and alloys are another source of possible corrosion.

Laboratory studies have contributed significantly over the years to deepen the knowledge base of high temperature corrosion processes. Prediction of corrosion rates for many high temperature corrosion phenomena may be performed based upon the modeling of the kinetics of governing reactions; predictive software tools have been developed which provide this function for a wide range of high temperature alloys.<sup>2</sup>

Extraneous factors, which may be difficult to simulate in the laboratory, often account for the difficulty in mimicking commercial processes. Such factors include, but are not limited to, pressure, gas velocity, impurities, and mechanical and thermal stress.

*Pressure:* The effect of pressure upon the mobility of reacting ions through a surface layer such as an oxide is not pronounced. However, if the dissociation pressure of a corrosion product is within the given range of conditions, then pressure may exert a profound effect. The effect of temperature is far more prominent, typically.

*Gas velocity:* Very high velocity gas streams may promote erosion; this, in conjunction with corrosive species which may be present, can result in accelerated wastage rates via an erosion–corrosion mechanism. Conversely, exposure of materials high in molybdenum or vanadium to stagnant high temperature oxidizing atmospheres can lead to what is termed ‘catastrophic oxidation’ – molybdenum trioxide, MoO<sub>3</sub>, melts

at 795 °C and vanadium pentoxide,  $V_2O_5$ , melts at 690 °C. If adequate gas flow is not provided, these oxides do not volatilize and serve to promote additional oxidation.<sup>3,4</sup>

*Impurities:* Simulation of industrial corrosion environments is frequently very difficult because of the improbability of pinpointing the concentration of various low-level impurities. This often stems from a lack of knowledge about the specific nature of the industrial environment.

*Stress:* Stress-accelerated grain boundary oxidation has been found to contribute to cracking phenomena in high temperature materials. For example, Soontrapa<sup>5</sup> documented a case occurring in an age-hardenable Fe–Ni material. Interaction between this mechanism and stress-corrosion cracking in simulated primary water at 360 °C, mimicking conditions found in a pressurized water reactor, has been reported by Panter<sup>6</sup>; cracking in austenitic stainless steels at 610 °C has also been attributed to this mechanism.<sup>7</sup>

Thermal cycling can produce stresses sufficient to cause cracking and buckling of corrosion layers, possibly leading to eventual spalling of the corrosion layer completely from the surface. The tendency for this to occur can depend upon the differential expansion coefficients between the oxide and substrate as well as the strength of the oxide itself versus that of the substrate. Subsurface oxides can serve to provide mechanical stability during thermal cycling as well.

### 1.16.2 Oxidizing Environments

Oxidation is certainly the most important mode of high temperature corrosion. While certain processes do involve simple oxidation by air, such as the external surfaces of electrically heated components, it is more common that oxidizing species are accompanied by other reacting components from the atmosphere. The combustion of natural gas is one very common example, where typically a percentage of excess air is employed, producing a gas which contains primarily  $O_2$ ,  $N_2$ ,  $H_2O$ ,  $CO_2$ , and  $CO$ . While the majority of the oxidizing potential is provided by  $O_2$  in such an atmosphere, other species may have very meaningful effects upon observed oxidation behavior. For example, water vapor is known to have a significant effect upon ferritic and austenitic stainless steel oxidation behavior, in the formation and volatilization of  $CrO_2(OH)_2$ .<sup>8–11</sup> In cases where combustion is carried out with a substoichiometric air-to-fuel ratio, the oxygen pressure becomes a function of the  $pCO/$

$pCO_2$  and  $pH_2/pH_2O$  ratios. In such ‘reducing’ combustion atmospheres, oxidation, while occurring concurrently, may not often be the predominant mode of corrosion. For example, if the sulfur level in the combusted fuel is sufficiently high, sulfidation could become the principal mode of corrosion.

Oxidation in pure steam is a significant consideration in the specification of materials for steam superheater tubes and steam header pipes in power generating plants. Recent advances in power plant design have targeted very high steam temperatures up to 760 °C and increased pressure levels in boosting the efficiency of future plants. Oxidation rates of austenitic stainless steels and even nickel-based alloys are concerns under these conditions.<sup>12,13</sup>

Some industrial processes utilize pure oxygen at elevated temperatures; for example, conversion of titanium tetrachloride to titanium oxide. Pure oxygen rather than air can be utilized for combustion of coal and other fuels (oxy-fuel combustion) in the interest of reducing  $NO_x$  levels in emissions, and producing a purified  $CO_2$  stream for enhanced utilization or disposal.<sup>14</sup> Reforming processes, which involve combining a hydrocarbon feedstock (typically methane) with steam to produce syngas and ultimately hydrogen, can also utilize oxygen in place of a fraction of supplied steam.

### 1.16.3 Nitridation

Nitridation can give concurrent results with oxidation in air, or in combustion environments employing air as the oxidizing gas. This is predominant in materials having additional elements such as aluminum, titanium, and niobium – nitrides formed are typically internal – for which nitride formation is particularly thermodynamically favorable. Such nitridation can occur under static conditions, but is more prevalent upon exposure to dynamic loading conditions. Internal nitrides are often found to be associated with the tips of creep cracks formed in air or combustion environments.<sup>15</sup> In nickel-based alloys, the diffusivity of nitrogen is determined to be nearly two orders of magnitude greater than that of oxygen.<sup>16</sup> This explains the observation of internal nitrides extending to greater depths than internal oxides after exposure to such environments.

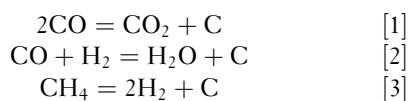
Nitrogen or cracked ammonia is often used as a protective atmosphere during the heat treatment of stainless steels. Sintering of powder metal components is performed in a nitrogen-based atmosphere.

Purposeful nitridation of the surface of metallic components is frequently carried out to impart strength and wear resistance. Furnace components exposed repeatedly to the same nitriding atmosphere must possess good resistance. Typically, in nitrogen and ammonia-based environments, alloys high in nickel content (having low nitrogen solubility and diffusivity) and low in elements which are strong nitride formers (aluminum, titanium, niobium, chromium) are favored for sustained service. Uncracked ammonia is a particularly harsh nitriding environment. Interaction of the uncracked ammonia with the metal surface results in direct diffusion of nascent nitrogen. Ammonia, which has been dissociated into  $H_2$  and  $N_2$ , possesses less nitriding potential compared to pure nitrogen.

A mixture of nitrogen and water vapor is utilized in processes employing the Kalina Cycle. Corrosion effects in such atmospheres have been studied by Grabke.<sup>17</sup> Interestingly, the performance of austenitic stainless steels was found to supersede the performance of nickel-based materials in this specific environment.

#### 1.16.4 Environments Promoting Carbon Ingress

Carburization, a high temperature form of corrosion promoted by carbon ingress and subsequent internal carbide precipitation, may proceed via one of the following reactions resulting in carbon formation:



High temperature carburization in hydrocarbon-based environments is encountered commonly in heat treatment processes. Here again, materials having high nickel content (low carbon solubility and diffusivity) and low levels of strong carbide formers (chromium, titanium, niobium, tungsten, molybdenum) are commonly favored. High levels of aluminum or silicon can enhance the performance in such environments as well, where even very low levels of oxygen may allow the formation of a protective scale.

Environments that are concurrently oxidizing and carburizing allow for a wider range of material usage, if the oxygen pressure is high enough to promote the formation of chromium oxide. For example, Fe–Ni–Cr materials, often having chromium levels at or above 25% and silicon additions, are commonly

used as radiant tubes in ethylene-cracking furnaces. Under normal operating conditions, chromium oxide protects the tubes against rapid carburization in the carburizing–oxidizing environment at the ID of the tubes. At very high temperatures, at and above  $\sim 1100^\circ C$  where chromium oxide is not stable, silicon oxide can afford protection, as shown by Nishiyama.<sup>18</sup> Coke formation also occurs in the ethylene cracking environment. Laboratory testing to truly simulate such an environment would thus need to incorporate an atmosphere for which the carbon activity exceeds unity. Production of carbon fiber products also typically involves exposure to solid carbon deposits at elevated temperatures.

Steam reformers, converting natural gas or other hydrocarbon feed stocks to a gas rich in hydrogen and carbon monoxide, can promote carburization if temperatures exceed the normal  $700\text{--}850^\circ C$ , or if carbon activity becomes excessive in the normally oxidizing gas atmosphere.<sup>19</sup>

Gas carburizing of steels takes place in an endothermic combustion environment with added hydrocarbons. Such atmospheres typically have a carbon activity below unity. Carburization of furnace components such as supporting grates, fans, and radiant furnace tubes is often observed; heat treatment baskets and belts are also affected.

Another form of carburization, termed ‘green rot’ involves alternating exposure of a nickel-based material having an intermediate chromium level (first encountered with 80% Ni–20% Cr heating element materials) to a nonoxidizing (reducing) carburizing atmosphere followed by an environment containing sufficient oxygen to oxidize chromium. Internal carbides formed during the reducing cycle are subsequently preferentially oxidized upon exposure to the oxidizing environment. This phenomenon has been combated by the use of nickel-based materials having higher Cr levels, or niobium addition.

Carbon dioxide cooled nuclear reactors, which operate at temperatures lower than the helium-cooled variant, can experience carburization of components, despite the fact that the  $CO_2$  environment is oxidizing and has low carbon activity. This occurs at the oxide scale–metal interface if  $CO_2$  penetrates the scale.<sup>19</sup> Numerous reactors employing  $CO_2$  cooling are in operation in the United Kingdom.

Carburization can occur in coal combustion and coal gasification processes, despite the fact that the prevailing form of attack is typically sulfidation, often via contact with incompletely combusted carbonaceous material at elevated temperatures.



Metal dusting is a form of carburization which occurs when carbon activity exceeds unity at intermediate temperatures,  $\sim 400\text{--}800^\circ\text{C}$ . The most frequently encountered occurrence of this phenomenon is seen in processes which form syngas via the combination of steam and hydrocarbon feedstock (reforming) at high temperature ( $750\text{--}850^\circ\text{C}$ ). The resulting syngas mixture contains  $\text{H}_2$ ,  $\text{CO}$ ,  $\text{CO}_2$ , and  $\text{H}_2\text{O}$  as well as residual  $\text{CH}_4$  and other hydrocarbons. Industrial processes involving syngas production include production of hydrogen, fertilizers, and synthetic fuels as well as gasification of various feedstocks including coal and biomass. Typically, higher ratios of  $p\text{CO}/p\text{CO}_2$  and  $p\text{H}_2/p\text{H}_2\text{O}$  produce higher calculated carbon activity and consequently higher propensity for metal dusting. Carbon activity, by virtue of reactions [1] and [2], rises as temperature is lowered; at some point as temperature drops, sluggish kinetics result in decreased metal dusting activity. Nickel-based alloys having high levels of oxide scale forming elements, chromium and aluminum, and low iron content tend to exhibit the most favorable performance in these environments. Environments with very high CO levels encountered in iron ore reduction promote metal dusting as well. Metal dusting corrosion is also encountered occasionally in the heat treating industry. Petroleum refineries experience metal dusting in hydrodealkylation processes and catalyst regeneration systems. Nuclear plants employing  $\text{CO}_2$  for cooling can experience metal dusting as well. Metal dusting can occur in molten carbonate and solid oxide fuel cells. Exposure in hydrocarbon-based environments can also result in metal dusting attack.<sup>20</sup>

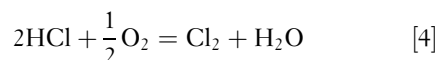
Incorporation of even ppm levels of  $\text{H}_2\text{S}$  into environments, known to promote metal dusting, has been found to suppress the phenomenon.<sup>20,21</sup>

### 1.16.5 Environments Containing Halides

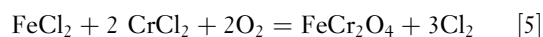
Chlorine and hydrogen chloride are found in numerous industrial processes. Concentrations, which may have an impact upon high temperature corrosion behavior, range from ppm levels to pure gas streams. Other gaseous components can have an effect on material performance; environments which contain oxygen and/or water vapor can accelerate corrosion behavior for some materials.

Municipal solid waste (MSW) combusted to produce electrical power typically contains sufficient

chloride-containing plastic materials (primarily PVC) to promote a severe form of corrosion on the fireside wall of waterwall and superheater tubing. Metal temperatures range typically from  $400$  to  $650^\circ\text{C}$ . Deposition of alkali chlorides (often containing heavy metals such as lead and zinc), which may be molten or partially molten, onto metal surfaces results in the formation of metal chlorides. In addition, the flue gas contains  $\text{HCl}$  vapor. The  $\text{HCl}$  vapor can react with oxygen in the oxidizing combustion environment to form chlorine gas, according to the following equation:



Volatilized metal chlorides, formed via interaction with the generated chlorine, may react with oxygen in the flue gas to form additional chlorine, creating a self-sustaining mechanism:



Vapor pressures for various metal chlorides as a function of temperature are shown in Figure 1.<sup>22</sup>

Typical MSW combustion gas also contains  $\text{SO}_2$ ; residual levels of  $\text{HCl}$  in the gas commonly range from  $400$  to  $600$  ppm, whereas  $\text{SO}_2$  levels are typically in the range of  $100\text{--}200$  ppm. It is generally agreed that the mechanism of corrosion in MSW boilers is related primarily to the presence of chlorine-containing species. To combat this form of corrosion, metallic coatings are typically applied via weld overlay or thermal spray onto the fireside tube surface. These materials are typically Ni–Cr–Mo alloy systems. At temperatures above  $800^\circ\text{C}$  in oxidizing–chloridizing atmospheres, the high vapor pressure of molybdenum oxychlorides makes molybdenum-containing materials a less desirable choice.<sup>23</sup> At such high temperatures, Ni–Cr–Al materials typically exhibit better performance.

Combustion of biomass in boilers can have a mechanism of corrosion in waterwalls and superheaters similar to that seen in MSW boilers. Wood and straw products, for example, contain significant levels of potassium and chlorine, producing  $\text{KCl}$  in the gas phase. Condensation on cooler metal surfaces from the gas phase in turn can create more complex alkali salts with alloying elements from the metal substrate. As in MSW boilers, metallic coatings are typically applied by weld overlay, thermal spray, etc. Materials utilized to combat the intermediate-temperature form of chloride salt attack are also typically Ni–Cr–Mo alloy systems.

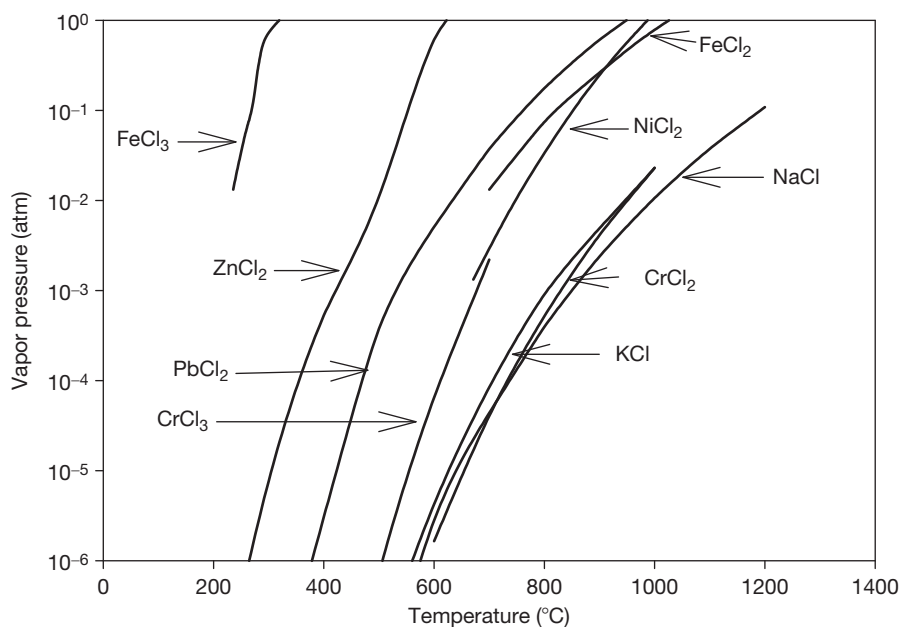


**Figure 1** Vapor pressure versus temperature for metal chlorides.

Production of ethylene dichloride, an intermediate of vinyl chloride monomer, involves creation of chlorine-bearing high temperature environments.

Production of titanium and silicon dioxides involves oxidation of a chloride precursor at high temperature.

Formation of metal chlorides from ores is a common step in metals production, capitalizing upon the very high vapor pressure of many metal chlorides.

Chemical vapor deposition processes may incorporate the utilization of high temperature HCl vapor.

Certain coals can contain low levels of chlorine, which can exacerbate coal ash corrosion effects in boiler tubing and superheater tubing.<sup>24</sup> Chloride layers have been discovered at the scale-to-metal interface in exposed tubes. Even a very modest quantity of chlorine at high temperatures can evoke severe corrosion effects because of the previously described self-perpetuating mechanism.

Fluorine can promote very severe forms of corrosion as well. Anhydrous hydrofluoric acid (AHF) is used in the alkylation catalysis for gasoline manufacture and for the manufacture of chlorofluorocarbon refrigerants and propellants. Uranium oxide is fluorinated at high temperatures with hydrofluoric acid to produce  $\text{HF}_6$ . Centrifuging then typically follows for the separation of  $\text{HF}_6$  containing U235 from that incorporating U238. Production of modern refrigerants involves elevated-temperature exposure to chlorine- and fluorine-containing environments.

Bromine and iodine have similar effects, though less severe than those of chlorine or fluorine.

### 1.16.6 Sulfur-Containing Environments

Sulfidation occurs in a variety of forms and environments, and can result from a number of different sulfur-containing species. Exposure to  $\text{H}_2$ - $\text{H}_2\text{S}$  gas mixtures in refining environments is a classical form of sulfidation. Exposure of nickel-containing materials in such an environment above the Ni-NiS eutectic melting temperature ( $\sim 645^\circ\text{C}$ ) can have catastrophic results. However, at lower temperatures, nickel-based materials can provide very good performance. Attack rate is dependent simply on the partial pressure of sulfur, determined by the  $p_{\text{H}_2}/p_{\text{H}_2\text{S}}$  ratio. These conditions are encountered in petroleum refining in hydrotreating, hydrocracking, and hydrodesulfurising processes.

Environments containing significant partial pressures of both sulfur and oxygen are termed sulfidizing-oxidizing; this is typical of most sulfur-containing environments. Corrosion behavior is dictated by both the oxygen and sulfur partial pressures. Again, in general, high nickel alloys are not desired for such environments; however, with sufficient levels of scale-forming elements such as chromium or aluminum, protection can be afforded. An example of such an environment

would be that produced by the combustion of natural gas containing significant levels of  $\text{H}_2\text{S}$ . Commercial food preparation operations involving meat products can produce sulfidation–oxidation in oven components by virtue of the sulfur present in the disulfide bonds of proteins. Oil-fired boilers commonly burn low-grade fuel containing significant sulfur levels.

#### 1.16.6.1 Coal-Fired Boiler Corrosion

The sulfur content of coal used for energy generation can be as high as 5% or more, producing combustion gases containing  $\text{H}_2\text{S}$ ,  $\text{SO}_2$ , and  $\text{SO}_3$  and resulting in the deposition of flue ash containing alkali sulfate salts onto metal surfaces cooler than the gas (furnace walls, superheaters and reheaters). These salts may react with  $\text{SO}_2$  or  $\text{SO}_3$  to form pyrosulfates or more complex alkali–iron trisulfates. Low-melting combinations of the various species may be formed. For example, potassium sulfate ( $\text{K}_2\text{SO}_4$ ) and potassium pyrosulfate ( $\text{K}_2\text{S}_2\text{O}_7$ ) form a molten salt mixture at  $407^\circ\text{C}$  when the  $\text{SO}_3$  concentration is 150 ppm. The mode of sulfidation promoted by deposits containing such salt mixtures is commonly termed ‘coal-ash corrosion.’

While the sulfidizing–oxidizing environments noted so far are typically strongly oxidizing in nature, certain environments exhibit a higher ratio of sulfur pressure to oxygen pressure. These types of environments are generated by combustion under significantly substoichiometric conditions. Typically, oxides afford protection to the point where breakaway corrosion initiates, followed by significant sulfidation attack. Coal gasification processes typify this type of environment. Low- $\text{NO}_x$  burners in coal combustion operate under conditions which produce a reducing environment in the vicinity of the burners, with metal temperatures possibly as high as  $600^\circ\text{C}$ . This can result in the presence of  $\text{H}_2\text{S}$  rather than  $\text{SO}_2$  in the combustion gas. High wastage rates of waterwall tubes in such boilers can result. Weld overlays are applied to combat corrosion; Ni–Cr–Mo welding products are commonly utilized. Thermal spray coatings and chromium/chromium–silicon coatings are also often utilized.

Blowing deposits from superheaters and reheaters using steam soot blowers is commonly employed, which promotes a form of erosion–corrosion. Water lances or water canons may be used to remove slag deposits from waterwalls via thermal shock. This can contribute to circumferential cracking by a mechanism involving corrosion-assisted thermal fatigue.

Steam superheaters and reheaters in coal-fired boilers are subject to severe coal-ash corrosion problems as well, because of deposition of combustion ash containing sulfate salts. Temperatures are significantly higher than that at the waterwall surface. Such conditions often necessitate not only high-strength austenitic materials for tubing, but also consideration of protective claddings. Nickel–chromium materials have been found to perform well; tubes clad with a 50Ni–50Cr material are often utilized.

Recent interest in developing the technology required for the construction and operation of coal-fired plants having steam temperatures of up to  $760^\circ\text{C}$  has necessitated consideration of a different class of materials. Elevating the operating temperature of the waterwall and superheaters will have an effect upon coal-ash corrosion dynamics. One recent study by McDonald involved insertion of a test loop into the low- $\text{NO}_x$  boiler burning Ohio coal containing 3% sulfur, in the interest of simulating conditions in a superheater operating at temperatures higher than conventional; at  $1050\text{--}1210^\circ\text{F}$ .<sup>25</sup> Results indicated that the conditions were harsh for many materials and that, tubes weld-overlaid or clad with Ni–Cr materials having very high Cr levels exhibited the most favorable performance.

#### 1.16.6.2 Oil-Fired Boiler Corrosion

Fuel oils consisting of residuals from petroleum refining cause oil-ash corrosion in boilers. Compounds formed from residual vanadium, sulfur, and sodium account for this mode of corrosion. Vanadium forms  $\text{V}_2\text{O}_5$ ; similarly, sodium forms sodium oxide ( $\text{Na}_2\text{O}$ ) or sodium sulfate ( $\text{Na}_2\text{SO}_4$ ). These compounds can combine to form fused salts that can have very low melting temperatures.<sup>26</sup> The resulting molten vanadate compounds cause fluxing of otherwise protective oxide scales, promoting very aggressive corrosion attack and metal wastage. The concentration of  $\text{SO}_3$  in the flue gas exerts significant influence upon the stability of the fused vanadate salts, as discussed by Seiersten and Kofstad.<sup>27</sup> As in coal-fired boilers, Ni–Cr overlay coatings are commonly applied over the ferritic or austenitic steels used in steam superheaters and reheaters in the interest of optimizing corrosion resistance.

The mode of corrosion resulting from exposure to deposited sulfate is termed ‘Type I’ hot corrosion in gas turbines, whereby sulfur-containing salts become molten, resulting in dissolution of protective oxides, and resultant ingress of sulfur and formation of internal sulfides. Type I hot corrosion occurs typically in the temperature range of  $850\text{--}950^\circ\text{C}$ , and primarily

in aerospace applications. Coatings are normally used for protection of metallic components against this mode of corrosion; for example nickel- and cobalt-based MCrAlY systems have been used with success. Cobalt-based coatings offer particularly good resistance to Type I hot corrosion. Type II hot corrosion, also resulting from sulfate salt deposition, typically occurs at temperatures below 800 °C. This form of hot corrosion results from localized formation of low-melting eutectics, resulting in localized pitting with the absence of gross sulfide formation, and is more commonly encountered in land-based and marine gas turbine applications. Typically, cobalt-based coatings are not as resistant to Type II hot corrosion as nickel-based coatings.

### 1.16.7 Molten Metals

Liquid metals are often considered for use as heat transfer media, because of their attractive physical properties – high thermal conductivity and heat capacity. Also, their operating pressures are very low compared to water. Lead, lead–bismuth, and sodium have all been considered as coolants for nuclear reactors. Sodium metal is used to fill hollow high-performance engine valve stems, in the interest of transmitting heat along the valve stem and to the cooling jacket. The properties of molten potassium make it suitable as the working fluid for a two-phase Rankine cycle, enabling operation at temperatures higher than that for typical steam-based systems.<sup>28</sup>

Solar Stirling engines have employed the use of sodium as the working fluid as well. The range of heat capacities and boiling points for the various metals used for heat transfer applications serve to dictate the range for the use. For example, lead is useful up to 500 °C, sodium 700 °C, and lithium 1300 °C.<sup>29</sup>

Molten aluminum is an extremely harsh environment for all types of metals and alloys.

Molten zinc is commonly used in the hot-dip galvanizing process for coating steel for corrosion resistance enhancement. Galvanizing tanks and handling accessories require resistance.

When under stress, metals may become susceptible to liquid metal embrittlement (LME). Instances of LME are often associated with welding, brazing, or soldering.

### 1.16.8 Molten Salts

Molten-salt technology is critical for several industries.<sup>30</sup> As with molten metals, molten salts are utilized

in nuclear and solar energy systems as a medium for heat transfer and storage because of high thermal conductivity and heat capacity. A mixture of sodium and potassium nitrates has been used for energy storage in solar collectors.

Extraction of aluminum is performed by dissolving alumina in cryolite. Extraction of various reactive metals, such as titanium, magnesium, sodium and others is accomplished using molten salts, often chlorides.

Molten salt batteries use molten salts as an electrolyte. They are used in services where very high power density is required. These characteristics make such batteries a promising technology for powering electric vehicles. Operating temperatures as high as 700 °C, however, pose significant challenges.

Molten carbonate fuel cells are currently being developed for natural gas and coal-based power plant applications, as well as other industrial and military applications. These fuel cells do not require an external reformer to produce hydrogen. Instead, fuels are converted to hydrogen within the fuel cell itself.

Molten salts are used frequently in the heat treating industry for case hardening, annealing and stress relieving, quenching and tempering, as well as cleaning. As corrosion rate in molten salts is typically a form of oxidation, attack is commonly exacerbated at the salt-to-air interface.

In the chemical industry, molten salts are used for cracking and catalysis, curing and vulcanizing plastics, synthesis of organics and gases, and in pyrolysis of scrap and hazardous materials.

## References

1. Reid, W. T. *External Corrosion and Deposits*; American Elsevier: New York, 1971.
2. John, R. C., et al. *Mater. Sci. Forum* **2004**, 461–464, 599–610.
3. Meijering, J. K.; Rathenau, G. W. *Nature* **1950**, 165, 240.
4. Brennor, S. S. J. *Electrochem. Soc.* **1955**, 102(1), 16.
5. Soontrapa, C. Master's Thesis, Massachusetts Institute of Technology, 2005.
6. Panter, J.; Viguer, B.; Cloué, J. M.; Foucault, M.; Combrade, P.; Andrieu, E. J. *Nucl. Mater.* **2006**, 348(1–2), 213–221.
7. Le Calvar, M.; Scott, P. M.; Magnin, T.; Rieux, P. *Corrosion* **1998**, 54(2), 101–105.
8. Asteman, H.; Svensson, J. E.; Johansson, L. G.; Norell, M. *Oxid. Met.* **2000**, 54(1–2), 11–26.
9. Young, D.; Pint, B. *Oxid. Met.* **2006**, 66(3–4), 137–153.
10. Peraldi, R.; Pint, B. A. *Oxid. Met.* **2004**, 61(5–6), 463–483.
11. Rakowski, J. M. J. *Eng. Gas Turbines Power* **2004**, 126(4), 768–873.

12. Program on Technology Innovation. Oxide Growth and Exfoliation on Alloys Exposed to Steam EPRI, Palo Alto, CA, 2007; 1013666.
13. Holcomb, G. R. *Oxid. Met.* **2008**, 69(3–4), 163–180.
14. Natesan, K.; Rink, D. L. In Proceedings of the 21st Annual Conference on Fossil Energy Materials, Oak Ridge National Laboratory/U.S. Department of Energy, April 30 to May 2, 2007.
15. Welker, M.; Rahmel, A.; Schütze, M. *Metall. Trans. A* **1989**, 20A, 1541–1551.
16. Douglass, D. L. *JOM*; **1991**, 74.
17. Grabke, H. J.; Strauss, S.; Vogel, D. *Mater. Corros.* **2003**, 54(11), 895.
18. Nishiyama, Y.; Otsuka, N.; Nishizawa, T. *Corrosion* **2003**, 59(8), 689–700.
19. Grabke, H. J. *Carburisation – A High Temperature Corrosion Phenomenon*; Materials Technology Institute of the Chemical Process Industries: St. Louis, MO, 1998.
20. Grabke, H. J. In *European Corrosion Congress, Eurocorr'99*; Aachen, September 1999.
21. Grabke, H. J.; Müller-Lorenz, A.; Schneider, A. *ISIJ Int.* **2001**, 41(Supplement), S1–S8.
22. Brandes, E. A.; Brook, G. B. Eds. *Smithells Metals Reference Book*; Butterworth-Heinemann: Oxford, 1992.
23. Oh, J. M.; McNallan, M. J.; Lai, G. Y. *Metall. Trans. A* **1986**, 17A, 1087–1094.
24. Effect of Coal Chlorine on Waterwall Wastage in Coal-Fired Boilers with Staged Low NO<sub>x</sub> Combustion Systems, EPRI, Palo Alto, CA; American Corporation, St. Louis, MO; Dairyland Power Cooperative, La Crosse, WI, 2002, 1004082.
25. McDonald, D. K. Coal Ash Corrosion Resistant Materials Testing Program Evaluation of the First Section Removed in November 2001, The Babcock and Wilcox Company, submitted to DOE (DE-FC26-99FT40525) and OCDO (CDO/D-98-2).
26. Reid, W. T. *External Corrosion Deposits in Boilers and Gas Turbines*; Elsevier: Amsterdam, 1971.
27. Siersten, M., Kofstad, P. *High Temp. Technol.* **1987**, 5(3), 115.
28. Radovanovic, M. *Fluidized Bed Combustion*; Taylor & Francis: London, 1986; 267.
29. Baboian, R. *Corrosion Tests and Standards: Application and Interpretation*, 2nd ed.; ASTM International: West Conshohocken, PA, 2005.
30. Lovering, D. G. Ed. *Molten Salt Technology*; Plenum Press: New York, 1982; 1.

## 1.18 Fireside Corrosion

**N. Otsuka**

Corporate R&D Laboratories, Sumitomo Metal Industries, Ltd., 1-8 Fusocho, Amagasaki, Japan

© 2010 Elsevier B.V. All rights reserved.

<b>1.18.1</b>	<b>Introduction</b>	459
1.18.1.1	Fuel Chemistry	459
1.18.1.2	Flue Gas Composition	460
1.18.1.3	Combustion Conditions	461
1.18.1.4	Deposit Chemistry	461
<b>1.18.2</b>	<b>Gas-Phase Corrosion</b>	464
1.18.2.1	Oxidizing Conditions	464
1.18.2.2	Reducing Conditions	465
<b>1.18.3</b>	<b>Molten Salt Corrosion in Power Generating Systems</b>	468
1.18.3.1	Vanadium Attack	470
1.18.3.2	Sulfate-Induced Corrosion	472
1.18.3.3	Fireside Corrosion Induced by Chlorine in Fuel	477
<b>References</b>		481

### Glossary

**Acidic dissolution (of metal oxides)** A dissolution reaction to form acidic solutes such as  $\text{Fe}_2(\text{SO}_4)_3$ ,  $\text{NiSO}_4$ ,  $\text{Cr}_2(\text{SO}_4)_3$ . See basic dissolution.

**Basic dissolution (of metal oxides)** A dissolution reaction to form basic solutes such as  $\text{NaFeO}_2$ ,  $\text{NaNiO}_2$ ,  $\text{Na}_2\text{CrO}_4$ . See acidic dissolution.

**Basicity (of fused sodium sulfate)** Defined as  $-\log a_{\text{Na}_2\text{O}}$ . The basicity of sodium sulfate is affected by the  $\text{SO}_3$  concentration of the ambient gas atmosphere.

**Biomass** Plant matter grown for use as a biofuel. Biomass is grown from several plants, including switchgrass, hemp, corn, willow, and sugarcane. Chips of wood are also included.

**Bitumen** A mixture of organic liquids that are highly viscous, black, sticky, entirely soluble in carbon disulfide, and composed primarily of highly condensed polycyclic aromatic hydrocarbons.

**Bituminous coal** A relatively hard coal containing a tar-like substance called bitumen. It is of higher quality than lignite coal but of poorer quality than anthracite coal.

**Black liquor** A solvent of the cooking process for Kraft pulping. Black liquor is rich in sodium and organic portions such as lignin and

hemicelluloses. It is fired in boilers to obtain heat and to recover sodium as sodium sulfide and sulfates from it.

**Borio index** An index obtainable from coal chemistry. This index is used to estimate the relative severity of high-S coal regarding the fireside corrosion of metal components.

**Catastrophic oxidation** See hot corrosion.

**Fireside corrosion** A type of corrosion encountered for high temperature metal components exposed to hot combustion gases.

**Fluxing of oxide scale** A reaction that takes place when protective oxide scales form on high temperature steels and alloys come in contact with molten salts. Protective metal oxides dissolve in molten salts and lose their protection against corrosive environments.

**High temperature hot corrosion (HTHC)** See Type I hot corrosion.

**Hot corrosion** An accelerated (or catastrophic) oxidation of metals and alloys whose surface is coated with fused salt and/or corrosive slag films in high temperature gaseous environments.

**Kinetic boundary (of  $\text{Cr}_2\text{O}_3$  protection)** A boundary shown in the  $P_{\text{O}_2}$ – $P_{\text{S}_2}$  phase stability diagram of chromium which



separates the regime of the uniform formation of protective  $\text{Cr}_2\text{O}_3$  scale from that of the formation of fast-growing Cr/Fe sulfide scale on high temperature stainless steels and alloys.

**Lignite coal** Often referred to as brown coal, which is the lowest rank of coal and used almost exclusively as fuel for steam-electric power generation. It is brownish-black and has a high inherent moisture content, sometimes as high as 66%, and very high ash content compared to bituminous coal. It is also a heterogeneous mixture of compounds for which no single structural formula will suffice.

**Low-temperature hot corrosion (LTHC)** See Type II hot corrosion.

**Naphtha** A group of various liquid hydrocarbon intermediate-oil-refining products used primarily as feedstock for producing a high-octane gasoline component via the catalytic reforming process. Naphtha is also used in the petrochemical industry for producing olefins in steam crackers and in the chemical industry for solvent applications.

**Oil ash corrosion** See vanadium attack.

**Orimulsion** A new type of fossil fuel coming from vast reserves of bitumen in the Orinoco Belt in Venezuela. This fuel is dispersed by water in a condition of emulsion.

**Oxidizing gas** A gas atmosphere containing oxidizing gas species such as  $\text{O}_2$ ,  $\text{CO}_2$ ,  $\text{SO}_x$ , and  $\text{H}_2\text{O}$ . Generally, oxidation of steels and alloys takes place upon exposure to this environment.

**Reheater** A heat exchanger made of steel tubes which are used in steam generating boilers to reheat steam coming from a steam turbine in order to be used again in a steam turbine. Their metal temperature is among the highest in boiler tubes, and they are prone to fireside corrosion.

**Reducing gas** A gas atmosphere containing reducing gas species such as  $\text{H}_2$ , CO, and hydrocarbon ( $\text{CH}_4$ , etc). For some combustion gases where sulfur-bearing gas species such as  $\text{H}_2\text{S}$  are included, sulfidation (see sulfidation below) may take place for steels and alloys upon exposure to this gas atmosphere.

**Salt-fluxing model** A corrosion mechanism based on the destructive dissolution of originally protective metal oxide scale into thin fused salt film, followed by reprecipitation of these metal oxides as thick, porous, nonprotective reaction products.

**Sulfidation** A type of corrosion caused by reaction of metal and alloys with sulfur-bearing species such as gaseous hydrogen sulfide or liquid alkali sulfates. The major reaction products are metal sulfides.

**Superheater** A heat exchanger made of steel tubes which are used in steam generating boilers in order to raise the temperature and pressure of steam (to superheat) to be used in steam turbines. Their metal temperature is among the highest in boiler tubes, and they are prone to fireside corrosion.

**Syngas (or synthetic gas)** A gas mixture containing CO and  $\text{H}_2$ . Syngas is used as a fuel gas for combustion or as a raw material to obtain ammonia, methanol, and hydrogen.

**Type I (or high temperature) hot corrosion** Occurs at a relatively high temperature (900–1000 °C) at which pure  $\text{Na}_2\text{SO}_4$  (melting point 884 °C) is liquid.

**Type II (or low-temperature) hot corrosion** Occurs at 600–750 °C, well below the melting point of pure sodium sulfate (884 °C). This corrosion results from the reaction of protective oxide scale with liquid phase of sodium and potassium complex metal sulfates.

**Vanadium attack** A type of corrosion caused by the reaction of molten vanadate compounds with protective metal oxide scales. The major degradation reaction is the dissolution of the protective metal oxide scales into molten oxides, and fast transport of the dissolved oxygen in molten oxide layer from flue gas to metal surface supports the corrosion reaction.

## Abbreviations

**BLRB** Black liquor recovery boiler

**HTHC** High temperature hot corrosion

**LTHC** Low temperature hot corrosion

**MSW** Municipal solid waste

**ppm** parts per million

**PVC** Polyvinyl chloride plastic

## Symbols

$k_p$  Parabolic rate constant ( $\text{cm}^2 \text{s}^{-1}$ )

$-\log a_{\text{Na}_2\text{O}}$  Basicity of melt

$P_{\text{O}_2}$  Oxygen partial pressure (atm)

$P_{\text{S}_2}$  Sulfur partial pressure (atm)

type of fuel, combustion conditions, and design factors of respective system. In this chapter, fireside corrosion is explained from the point of fuel chemistry, and the effect of combustion conditions and design factors on corrosion is emphasized. Corrosion resistance of steels and alloys is introduced as well.

### 1.18.1 Introduction

Fireside corrosion is often encountered in metal components of energy-converting systems which are aimed at generating steam and electricity upon combusting fossil fuel such as coal and oil, biomass, municipal and industrial solid waste. Turbine blades and vanes, boiler tubes and plate-fin type heat-exchangers, hangers and tube supports, etc., which are exposed to hot combustion gases, are the major concerns. Corrosion is normally influenced by the

#### 1.18.1.1 Fuel Chemistry

Examples of elemental analyses of major fuels used for generating electricity are shown in [Table 1](#). Fuels consist of combustible elements such as carbon and hydrogen, with slight addition of impurities such as nitrogen, sulfur, and chlorine. In this table, municipal solid waste (MSW) burnt in waste incinerators and black liquor fired in Kraft pulping mill are shown for comparison. From the point of fireside corrosion, vanadium, sulfur, and chlorine in fuel are the important impurity elements.<sup>1</sup> Alkali metals

**Table 1** Elemental analyses of major fuel (wt.%, example)

Element	Heavy oil	Coal	Natural gas <sup>a</sup>	Municipal solid waste <sup>b</sup>	Black liquor <sup>c</sup>
Ultimate					
C	85	76.2	76.5	22	28.4
H	12	5.13	23.5	8.7	5.2
O	0.35	6.15	—	60.4	44.3
N	0.2	1.63	—	0.3	—
S	2.4	1.73	—	0.02	2.7
Cl	—	0.275	—	0.4	3.0
Ash	0.05	8.89	—	8.18	—
Metals					
Fe	—	1.1	—	0.2	—
V	0.01	—	—	—	—
Ca	—	0.1	—	0.9	—
Mg	—	0.04	—	0.1	—
Na	50 ppm	0.03	—	0.06	13.0
K	50 ppm	0.03	—	0.04	3.4
Zn	—	—	—	70 ppm	—
Pb	—	—	—	10 ppm	—
Heat value <sup>d</sup>	10 400	7509	10 800	2440	3700

<sup>a</sup>Liquefied natural gas (LNG):  $\text{CH}_4$ –6%  $\text{C}_2\text{H}_6$ –4%  $\text{C}_3\text{H}_8$ –2%  $\text{C}_4\text{H}_{10}$ .

<sup>b</sup>51 wt.% water involved.

<sup>c</sup>For closed cycle,  $\text{S}/\text{Na}_2 = 0.3$ , 20% water involved.

<sup>d</sup> $\text{kcal kg}^{-1}$ , high-heat value.

Source

Heavy oil: Thermal and Nuclear Power Engineering Society, *The Thermal and Nuclear Power*, **1988**, 39, 1453–1485.

Coal: Blough, J. L.; Stanko, G. J. In *Fireside Corrosion testing of Candidate Superheater Tube Alloys, Coatings, and Claddings-Phase II*, Corrosion/97, NACE International: Houston, TX, 1997; Paper no. 140.

MSW: Otsuka, N. In *Thermodynamic Equilibrium Calculations of Deposits on Superheater Tubes in Waste Incinerators*, Corrosion/2000; NACE International: Houston, TX, 2000; Paper 00229.

Black Liquor: Pejryd, L.; Hupa, M. In *Bed and Furnace Gas Composition in Recovery Boilers-Advanced Equilibrium Calculations*, Proceedings of TAPPI Pulping Conference, 1984; pp 579–590.

Reproduced from Otsuka, N. *Corr. Sci.* **2002**, 44, 265–283.

sodium and potassium, along with alkali earth metals calcium and magnesium, relate to corrosion as well. In the case of oils used in utility and industrial boilers, various types of oils such as crude oil, heavy oil, light oil, and naphtha, or mixtures of these are combusted. Similarly, with respect to coals, lignite, bituminous, anthracite coals, etc. with varying sulfur and chlorine contents, are fired. Therefore, a large variety does exist in the fuel chemistry. For most of the oils fired in boilers, vanadium is included typically from 0 to as high as 300 ppm<sup>1</sup> (parts per million by weight). Sulfur content ranges from 0.1 to 3.2 wt%<sup>2</sup>, and sodium and potassium, from 0 to 100 ppm.<sup>1</sup> Sulfur concentration generally correlates with vanadium content; high-sulfur oil contains high concentration of vanadium.<sup>2</sup> Chlorine content of oil is in most cases low, up to 100 ppm.<sup>3</sup> For fuel coal, sulfur and chlorine are the significant impurities relevant to corrosion. Similar to oil, their composition varies depending on their origin and how they are blended. Sulfur is generally present from less than 0.5% to 3% (in extreme cases up to 7%),<sup>1</sup> while chlorine, from less than 0.01% to as much as 0.8%.<sup>1</sup> Fuel coal contains sodium from 0 to 700 ppm while potassium from 0 to 2500 ppm.<sup>4</sup> Vanadium content of coal is generally negligible. In contrast, natural gas does not virtually contain impure elements of vanadium, sulfur, and chlorine. This is considered one major reason why fireside corrosion in gas-fired boilers and turbines is slight. For municipal solid waste (MSW), almost half of their weight is water, and they contain chlorine in the order of 1000 ppm. The sources of chlorine are inorganic, primarily as NaCl and organic such as polyvinyl chloride plastic (PVC). Note that sulfur concentration of waste is minor. Heavy metals such as lead and zinc in waste are noticed as well. Black liquor is a solvent of cooking process for Kraft pulping and is rich in sodium with organic portion such as lignin and hemicelluloses. This fuel, burnt in boilers to recover sodium and heat, contains large amounts of sulfur and chlorine. Ranges of chlorine and sulfur contents of various fuels are illustrated in **Figure 1**. From the point of chlorine and sulfur concentrations, coal and black liquor are categorized as high-chlorine high-sulfur fuel, oil as high-sulfur low-chlorine fuel, municipal solid waste as high-chlorine low-sulfur fuel, and natural gas as low-chlorine low-sulfur fuel. According to the literature,<sup>5</sup> biomass fuel can be categorized as low-sulfur medium-chlorine fuel, since their sulfur content ranges from 0.02% to 0.1%, whereas chlorine, from 0.01% to just below 1%.

### 1.18.1.2 Flue Gas Composition

Examples of flue gas composition in boilers firing various types of fuels are presented in **Table 2**. These values may vary depending on the location of boilers, combustion conditions such as air-fuel ratio as described in the following section, and the degree of combustion reactions proceeding toward the final thermodynamic equilibrium conditions. Note that the flue gas of heavy oil contains SO<sub>2</sub> of the order of 0.1%; that of coal has similar SO<sub>2</sub> concentration with slight HCl; those of natural gas and black liquor are virtually free of SO<sub>2</sub> and HCl; and that of municipal solid waste contains HCl of the order of 0.1% with traces of SO<sub>2</sub>.

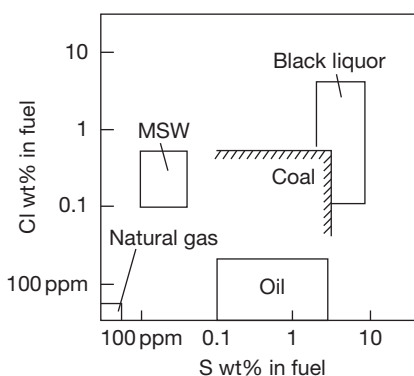


**Figure 1** Chlorine and sulfur contents of major fuels.

**Table 2** Flue gas composition for complete combustion (vol. %, example)

	Heavy oil	Coal	Natural gas	Municipal solid waste	Black liquor
O <sub>2</sub>	3	4.2	3.3	9.0	1.2
CO <sub>2</sub>	14.5	13.6	9.1	10.9	14.2
H <sub>2</sub> O	10.5	5.5	16.7	19.5	16.8
SO <sub>2</sub>	0.1	0.12	–	19 ppm	–
HCl	–	0.02	–	0.11	4 ppm

Data taken from

Heavy Oil: Thermal and Nuclear Power Engineering Society, *Therm. Nucl. Power* **1988**, 39, 1453–1485.

Coal: Calculated for the coal in **Table 1** for air-fuel ratio of 13 in weight at 1300 °C.

Natural gas: Calculated for the natural gas in **Table 1** for air-fuel ratio of 20 in weight.

MSW: Kawahara, Y.; Hagiwara, H.; Nakamura, M.; Shibuya, E.; Yukawa, K. In *An Evaluation of Corrosion Resistant Alloys by Field Corrosion Test in Japanese Refuse Incineration Plants*, CORROSION/95; NACE International: Houston, TX, 1995; Paper no. 564.

Black Liquor: Calculated for the black liquor in **Table 1** for air-fuel ratio of 3.77 in weight at 1000 °C.

### 1.18.1.3 Combustion Conditions

Flue gas composition is significantly affected by the combustion conditions. Concentration of gaseous species upon firing 1.7% S coal (chemical composition is given in Table 1) was calculated at 1300 °C, assuming thermal equilibrium, and presented in Figure 2 as a function of air–fuel ratio. In this chapter, air–fuel ratio is defined by the ratio of their weights; air–fuel ratio of 10 represents combustion of 100 g fuel with 1000 g air. Where combustion takes place in complete or in air-excess conditions such as for the air–fuel ratio of more than 10, oxidizing gas species such as O<sub>2</sub>, SO<sub>2</sub>, and NO prevail. Complete combustion is termed here when carbon and hydrogen in fuel is totally oxidized to carbon dioxide and water vapor, and no additional oxygen is present in the flue gases. This corresponds to air–fuel ratio of 10 in Figure 2. In contrast, when combustion reactions proceed in air-deficient conditions where air–fuel ratio is less than 10, reducing gas species such as CO, H<sub>2</sub>, and H<sub>2</sub>S replace the oxidizing gas species of O<sub>2</sub>, SO<sub>2</sub>, and NO. This is termed the partial combustion. Concentration of CO<sub>2</sub> and H<sub>2</sub>O is not significantly affected by the air–fuel ratio. Carbon dioxide and water vapor can coexist with oxidizing gas species of O<sub>2</sub> and SO<sub>2</sub> and reducing gas species of CO and H<sub>2</sub>. Normally, from the point of combustion

efficiency, fuel is fired in slightly air-excess conditions. Therefore, except at locations where equilibrium is not established, flue gas generally oxidizes the metal components. Partial combustion is encountered for gasification process of coal and residual oil. For these cases, flue gas, called synthetic gas (syngas) in some cases, is generally reducing, and contains gaseous H<sub>2</sub>S, resulting from sulfur in fuel. For some industrial boilers, slightly air-deficient combustion is favored at their furnaces, in order to minimize formation of gaseous nitrogen oxides. Gaseous H<sub>2</sub>S exists in the flue gases locally. Oxygen and sulfur partial pressures of these combustion gases are calculated as a function of air–fuel ratio at 1300 °C and presented in Table 3. As expected, low  $P_{O_2}$ –high  $P_{S_2}$  gas atmospheres are indicated upon combustion at low air–fuel ratio, whereas high  $P_{O_2}$ –low  $P_{S_2}$  gas atmospheres are characterized for combustion at high air–fuel ratio. Therefore, from the equilibrium point of view, corrosion environments for air-excess combustion are categorized as ‘oxidizing,’ while that for partial combustion as ‘sulfidizing’ when fuel contains considerable amounts of sulfur. The effect of temperature on flue gas composition upon combusting 1.7% S coal is basically minor for conditions of air-excess combustion (Table 4 for air–fuel ratio of 12), but slight changes are noticed for conditions of partial combustion (Table 5 for air–fuel ratio of 6).

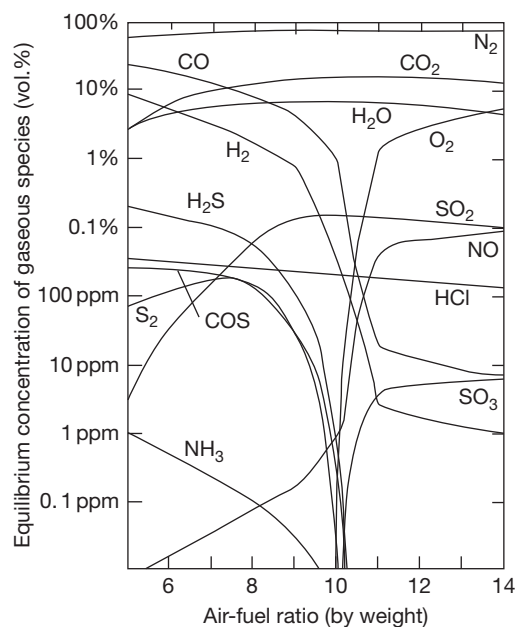


**Figure 2** Equilibrium concentration of gaseous species in flue gas upon combustion of 1.7% S coal at 1300 °C. Calculated based on the coal chemistry presented in Table 1. Air–fuel ratio is given by weight; for example, air–fuel ratio of 10 represents combustion of 100 g coal with 1000 g air.

### 1.18.1.4 Deposit Chemistry

Fireside corrosion of metal components is significantly affected, in many cases, by the chemical and physical properties of deposits piled up on metal surface from flue gas. Usually, chemical and physical properties of these deposits vary drastically,

**Table 3** Equilibrium oxygen partial pressure  $P_{O_2}$  and sulfur partial pressure  $P_{S_2}$  of flue gases upon combustion of 1.7% S coal as a function of air–fuel ratio at 1300 °C (calculated)

Air–fuel ratio	$P_{O_2}$	$P_{S_2}$
5	$3 \times 10^{-12}$	$8 \times 10^{-5}$
6	$2 \times 10^{-11}$	$1 \times 10^{-4}$
7	$8 \times 10^{-11}$	$2 \times 10^{-4}$
8	$3 \times 10^{-10}$	$2 \times 10^{-4}$
9	$2 \times 10^{-9}$	$3 \times 10^{-5}$
10	$5 \times 10^{-8}$	$4 \times 10^{-8}$
11	0.01	$4 \times 10^{-19}$
12	0.03	$8 \times 10^{-20}$
13	0.04	$3 \times 10^{-20}$

Coal composition is taken from Table 1. Air–fuel ratio is defined by weight; for example, air–fuel ratio of 10 represents combustion of 100 g coal with 1000 g air.

**Table 4** Equilibrium flue gas composition upon combusting 1.7% S coal in an air-excess condition (vol.%, air–fuel ratio of 12, calculated)

Temperature (°C)	N <sub>2</sub>	O <sub>2</sub>	CO <sub>2</sub>	H <sub>2</sub> O	SO <sub>3</sub> (ppm)	SO <sub>2</sub>	NO (ppm)	OH (ppm)	CO (ppm)	H <sub>2</sub> (ppm)	P <sub>S<sub>2</sub></sub> <sup>a</sup>
200	76.4	2.8	14.7	5.9	1252	–	–	–	–	–	$3 \times 10^{-86}$
400	76.4	2.8	14.7	5.9	1239	0.001	–	–	–	–	$6 \times 10^{-56}$
600	76.4	2.8	14.7	5.9	787	0.04	3	–	–	–	$6 \times 10^{-40}$
800	76.4	2.8	14.7	5.9	152	0.11	27	–	–	–	$4 \times 10^{-31}$
1000	76.3	2.9	14.7	5.9	31	0.12	134	4	–	–	$2 \times 10^{-25}$
1200	76.3	2.9	14.7	5.9	9	0.12	425	30	3	–	$2 \times 10^{-21}$
1400	76.3	2.9	14.7	5.9	4	0.12	1022	144	43	5	$2 \times 10^{-18}$

<sup>a</sup>Partial pressure. Coal composition is taken from Table 1. Air–fuel ratio is defined by weight; for example, air–fuel ratio of 12 represents combustion of 100 g coal with 1200 g air.

depending on the type of fuel and location of the component in the system. A layered structure is usually observed for these deposits,<sup>6,7</sup> with different chemistry and porosity in each position. Deposit chemistry of the innermost layer, which contacts directly the metal to its oxide scale, is considered important to examine the corrosion. Examples of the deposit chemistry obtained for superheater tubes of boilers firing various fuels are presented in Table 6. Tube deposit of heavy oil is rich in vanadium and sulfur, and the major constituents are Na<sub>2</sub>SO<sub>4</sub> and V<sub>2</sub>O<sub>5</sub> (explained later). Tube deposit of coal comprises ash constituents of silicon and aluminum oxides, and sulfur compounds such as (Na,K)<sub>2</sub>SO<sub>4</sub><sup>7</sup> are also indicated. For those firing municipal solid waste, chlorides of sodium and potassium with slight inclusion of lead and zinc salts are characterized. Deposit of black liquor consists of mixtures of sodium and potassium sulfates, carbonates, and chlorides. Corrosive compounds in these deposits can be predicted to a certain extent, from the fuel chemistry, assuming that the corrosive compounds are vanadium oxides, sodium and potassium salts such as sulfates, chlorides, and carbonates, and compounds of heavy metals such as lead and zinc.<sup>8</sup> This is schematically illustrated in Figure 3. This sketch is constructed with the assumption that combustion terminates at thermodynamic equilibrium, and deposition of corrosive salts such as sulfates and chlorides takes place by vapor condensation from flue gas on metal surface. For example, in the case of high-Cl high-S coal, sodium and potassium in the fuel do not react with chlorine, but they preferentially react with sulfur to generate sulfate salts.<sup>8</sup> Chlorine in coal reacts to form gaseous HCl. Therefore, sodium/potassium chlorides are normally not found in their tube deposits. Similarly, for municipal solid waste, sodium, potassium, lead, and zinc

react primarily with sulfur to form their sulfates, and the remaining react with chlorine to generate their chlorides. Hence, upon firing municipal solid waste, SO<sub>x</sub> concentration in flue gas is generally very low, since sulfur in waste is totally captured upon reaction to form sulfate salts. The important point is that the chemical affinity of sulfur to react with sodium and potassium is much greater than that of chlorine; for fuel abundant in sulfur, there is no chance for chlorine to react with sodium/potassium to form their chlorides, and for this fuel chloride salts are generally not incorporated in the deposits. For black liquor, abundant sodium enables reaction with sulfur and chlorine in the fuel to form its sulfide and chloride. In this case, sulfur and chlorine in the fuel are completely consumed, and the remaining sodium can react with carbon to form its carbonate. Therefore, in tube deposits of black liquor recovery boilers sulfates, chlorides, and carbonates are present. In this way, one may predict the deposit chemistry, to the first-order approximation, upon knowing the fuel chemistry of the respective system. Critical temperature at which the corrosive salts in the deposits start to melt varies with the salt systems. For V<sub>2</sub>O<sub>5</sub>–Na<sub>2</sub>SO<sub>4</sub> salt mixtures relating to oil deposits, this is reported to be 600 °C<sup>9</sup>; for Na<sub>2</sub>SO<sub>4</sub>–K<sub>2</sub>SO<sub>4</sub>–Fe<sub>2</sub>O<sub>3</sub> salt mixtures representing coal deposits, it is recognized as 552 °C<sup>10</sup>; for (Na,K)<sub>2</sub>SO<sub>4</sub>–(Na,K)Cl (–(Na,K)<sub>2</sub>CO<sub>3</sub>) salt mixtures relevant to black liquor deposits, it is estimated to be around 500 °C<sup>11</sup>; for sulfates and chlorides of sodium, potassium, and heavy metals such as lead and zinc representing municipal solid waste deposits, it can be as low as 300 °C.<sup>12</sup> Involvement of chloride salts of sodium and potassium in the deposits generally lowers their melting points, and its effect on temperature is drastic for sulfates and chlorides of heavy metals such as lead and zinc.

**Table 5** Equilibrium flue gas composition upon combusting 1.7% S coal in a partial combustion condition (vol.%, air-fuel ratio of 6, calculated)

Temperature (°C)	N <sub>2</sub>	CO <sub>2</sub>	CO	CH <sub>4</sub>	H <sub>2</sub> O	H <sub>2</sub>	H <sub>2</sub> S	SO <sub>2</sub>	COS	NH <sub>3</sub>	P <sub>O<sub>2</sub></sub> <sup>a</sup>	P <sub>S<sub>2</sub></sub> <sup>a</sup>
200	73.7	15.3	5 ppm	0.46	10.2	0.08	0.24	–	2 ppm	11 ppm	4 × 10 <sup>–45</sup>	3 × 10 <sup>–14</sup>
400	72.9	16.1	0.35	0.68	7.7	2	0.24	–	26 ppm	34 ppm	3 × 10 <sup>–32</sup>	2 × 10 <sup>–11</sup>
600	67.5	12	10.2	0.23	3	6.8	0.21	–	0.02	23 ppm	3 × 10 <sup>–25</sup>	2 × 10 <sup>–9</sup>
800	64.9	7.9	17	12 ppm	3	6.9	0.19	–	0.02	6 ppm	8 × 10 <sup>–20</sup>	2 × 10 <sup>–7</sup>
1000	64.9	7	18	–	3.9	6	0.19	–	0.02	2 ppm	1 × 10 <sup>–15</sup>	5 × 10 <sup>–6</sup>
1200	64.9	6.4	18.6	–	4.6	5.4	0.17	9 ppm	0.03	–	1 × 10 <sup>–12</sup>	6 × 10 <sup>–5</sup>
1400	64.9	5.9	19.1	–	5	4.9	0.13	0.01	0.02	–	2 × 10 <sup>–10</sup>	2 × 10 <sup>–4</sup>

<sup>a</sup>Partial pressure. Coal composition was taken from [Table 1](#). Air–fuel ratio is defined by weight; for example, air–fuel ratio of 6 represents combustion of 100 g coal with 600 g air.



**Table 6** Composition of Superheater Deposits (wt%, example)

	Heavy oil	Coal			Municipal solid waste	Black liquor
		Outer layer	Intermediate layer	Inner layer		
Si as SiO <sub>2</sub>	–	23.5	23.3	7.6	15.3	–
Al as Al <sub>2</sub> O <sub>3</sub>	–	14	11.5	1.7	9.5	–
Fe as Fe <sub>2</sub> O <sub>3</sub>	11.2	36	11	70.5	1.8	–
Ti as TiO <sub>2</sub>	–	0.9	< 0.1	< 0.1	1.4	–
Ca as CaO	1.17	1.3	< 0.1	< 0.1	17.4	–
Mg as MgO	0.88	1.3	1.1	< 0.1	2.9	–
Na as Na <sub>2</sub> O	17.8	0.3	1.7	0.15	8.4	44.3
K as K <sub>2</sub> O	–	2.9	13.5	1.3	12.3	5.2
V as V <sub>2</sub> O <sub>5</sub>	49.7	–	–	–	–	–
Ni as NiO	2.24	< 0.1	< 0.1	0.3	–	–
Cr as Cr <sub>2</sub> O <sub>3</sub>	–	< 0.1	< 0.1	7.0	1.2	–
Pb as PbO	–	–	–	–	0.1	–
Zn as ZnO	–	–	–	–	1.0	–
C as CO <sub>2</sub>	1.6	–	–	–	0.4	14.3
S as SO <sub>3</sub>	21.6	7.3	27.5	10.0	15	34.6
Cl	–	0.02	< 0.01	< 0.01	9.2	1.5
pH	3.8	3	2.2	4.3	8.2	–
Water soluble %	–	9	45.4	9.0	–	–

Data taken from

Heavy oil: superheater deposit for 1.6–1.8%S, 130–150ppm V<sub>2</sub>O<sub>5</sub>, from Fukahori, K.; Uera, H.; Harada, Y. *The Thermal and Nuclear Power*, **1977**, 28, 639–649. Coal: Blazewicz, A.J.; Gold, M. ASME publication, 79-WA/Fu-6, 1980. Municipal solid waste: Otsuka, N. CORROSION/97, paper no.157, NACE: Houston Texas, 1997. Black liquor: Backman, R.; Skrifvars, B.-J.; Hupa, M.; Siiskonen, P.; Mäntyniemi, J. *J.Pulp and Paper Sci.*, **1996**, 22, J119–J126.

## 1.18.2 Gas-Phase Corrosion

In this section, fireside corrosion caused not by slag deposits but by gaseous species in flue gas is explained. Gas-phase corrosion can be separated into two categories, that is, high temperature oxidation in oxidizing gas atmospheres and sulfidation in reducing gas atmospheres.

### 1.18.2.1 Oxidizing Conditions

In most energy-converting systems, combustion is conducted under slightly excess-air conditions and their flue gases normally contain oxidizing gas species such as O<sub>2</sub>, CO<sub>2</sub>, H<sub>2</sub>O, and SO<sub>x</sub>. From engineering point of view, scaling of metal components exposed to these oxidizing gas atmospheres can generally be predicted from the available data reported in air, since the effects of CO<sub>2</sub> and SO<sub>x</sub> on scaling is in most cases minor.<sup>13</sup> Approximate temperature limits of steels and alloys considered to be applicable for these oxidizing gas conditions are summarized and shown in Table 7. For carbon steel and low-alloyed steels of up to 5% Cr, exposing these steels to flue gases of higher temperature results in heavy scaling, and metal loss due to scaling increases exponentially upon raising the oxidation temperature. This

behavior is shown in Figure 4. For steels of more than 9%Cr, stainless steels, and nickel-base alloys, uniform formation of Cr<sub>2</sub>O<sub>3</sub> scale is established at lower temperatures, and their weight gains are slight. Above a critical temperature, which depends on respective alloy system, breakaway oxidation results for these steels and alloys and Cr<sub>2</sub>O<sub>3</sub> scale loses its protection to high temperature oxidizing gases.<sup>14</sup> Temperature limits shown in Table 7 for stainless steels and nickel-base alloys are determined from the onset of breakaway oxidation. Parabolic rate constants of major metal oxide scales are summarized in Figure 5. Among the metal oxide scales which can uniformly form on metal surfaces, the growth rates of Cr<sub>2</sub>O<sub>3</sub>, Al<sub>2</sub>O<sub>3</sub>, and SiO<sub>2</sub> are relatively low, compared to those of Fe<sub>3</sub>O<sub>4</sub>, CoO, and NiO. Therefore, these metal oxide scales can be used as ‘protective’ oxide scales for steels and alloys as far as breakaway oxidation does not take place. The effect of water vapor on oxidation of engineering steels and alloys forming Cr<sub>2</sub>O<sub>3</sub> scale must be pointed out. As shown in Figure 6, water vapor in flue gas atmosphere can significantly enhance the breakaway oxidation, especially of stainless steels.<sup>14</sup> For some stainless steels, oxidation experiments conducted in laboratory air during hot, wet season (e.g., P<sub>H<sub>2</sub>O</sub> of 0.1 atm at 40°C with 100% humidity) can be different from those performed in cold, dry air

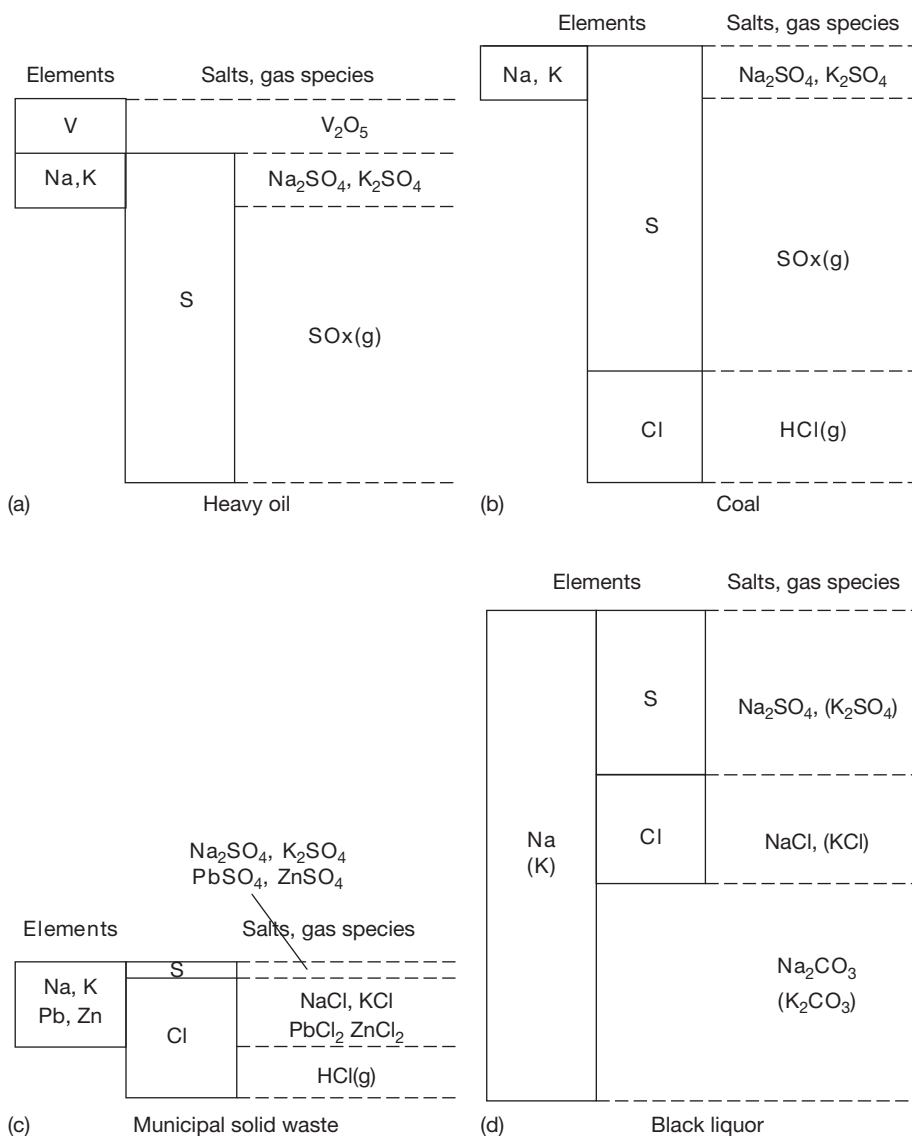


**Figure 3** A simplified relationship between the elements in fuel and corrosive salts in tube deposits.

(e.g.,  $P_{H_2O}$  of 0.006 atm at  $0^\circ\text{C}$  with 100% humidity). Partial pressure of water vapor as a function of dew point of flue gas can be found in the literature.<sup>15</sup> Since flue gases resulting from combustion of natural gas contain greater amount of water vapor, its effect on oxidation of steels and alloys should be examined carefully. Oxidation rates of boiler tube materials exposed to 100% steam, often used to estimate the metal temperatures for ferritic steels, are summarized in the literature.<sup>16</sup>

### 1.18.2.2 Reducing Conditions

For gasifiers of coal, residual-oil, etc., combustion is regulated under air-deficient conditions. In these

cases, reducing gas species of  $H_2$  and  $CO$  coexist with  $CO_2$  and  $H_2O$ , in flue gases and  $H_2S$  is incorporated when fuel contains sulfur.<sup>17</sup> For high temperature components exposed to these gas mixtures, sulfidation of steels and alloys occurs. For reducing conditions, gas atmospheres are normally high in  $P_{S_2}$  and low in  $P_{O_2}$ , and simultaneous formation of metal sulfides and oxides takes place. Since the driving force for the formation of metal oxide scale is small, uniform formation of protective metal oxide scales is relatively difficult to be established. In these cases, formation of metal sulfides overwhelms that of metal oxides, since the growth rate of metal sulfide scales is generally much higher than those of metal oxide scales.<sup>18,19</sup> Corrosion rates are

**Table 7** Approximate temperature limits (°C) in air

Steel	Composition (wt%)	Fontana & Green	Morris		Kane
			Intermittent service	Continuous service	
Plain carbon	0.1C	480	—	—	510
T12	1Cr–0.5Mo	—	—	—	565
T22	2.25Cr–1Mo	—	—	—	580
T5	5Cr–0.5Mo	620	—	—	620
T9	9Cr–1Mo	670	—	—	650
AISI type 410	11Cr	760	815	705	700
AISI type 430	17Cr	840	870	815	840
AISI type 442	21Cr	950	1035	980	—
AISI type 446	25Cr	1030	1175	1095	—
AISI type 304, 321, 347	18Cr–8Ni–(Ti,Nb)	900	870	925	900
AISI type 316	18Cr–10Ni–2Mo	900	870	925	—
AISI type 309	23Cr–12Ni	1090	980	1095	1040
AISI type 310	25Cr–20Ni	1150	1035	1150	1090
Hastelloy X	Ni-base superalloy	1200	—	—	—
Hastelloy C	Ni-base superalloy	1150	—	—	—
Cr		900	—	—	—
Ni		780	—	—	—
Cu		450	—	—	—
Brass	70Cu–30Zn	700	—	—	—

Temperature below which oxidation rate is negligible. Negligible is defined as less than about  $0.31 \text{ mg cm}^{-2} \text{ h}^{-1}$  (for weight gain, Fontana & Greene). For Morris and Kane, criteria is not presented.

Source: Fontana, M. G.; Greene, N. D. *Corrosion Engineering*; McGraw-Hill, 1967; p 369.

Morris, L. A. *Met. Eng. Q. Am. Soc. Met.* **1968**, 8, 30–47.

Kane, R. H. In *Process Industries Corrosion*; Moniz, B. J., Pollock, W. I., Eds.; NACE: Houston, TX, 1986; pp 45–65.

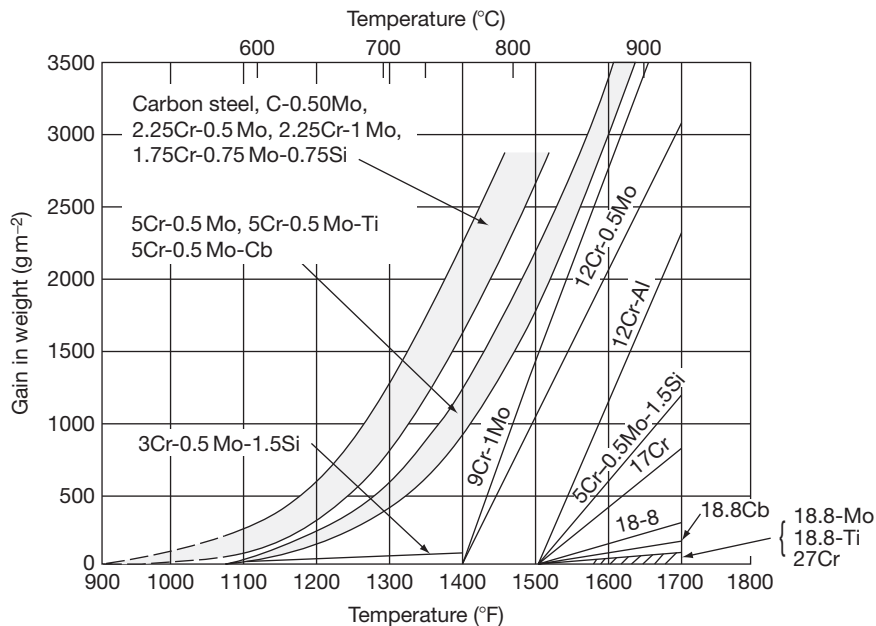


**Figure 4** Oxidation behavior of engineering steels and alloys exposed to air for 1000 h. Reproduced from Kane, R. H. In *Process Industries Corrosion – The Theory and Practice*, Moniz, B. J., Pollock, W. I., Eds.; NACE: Houston, TX, 1986; pp 45–65.

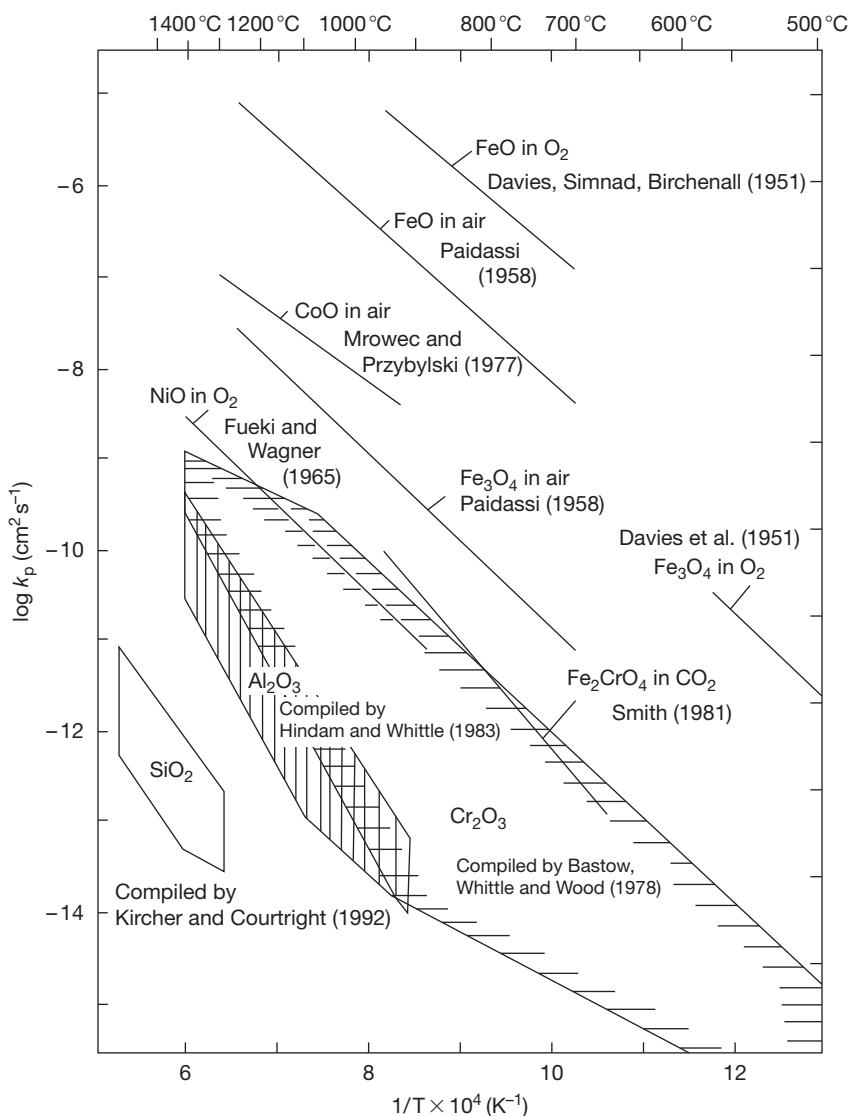


**Figure 5** Parabolic rate constants (in scale thickness) of major oxide scales. Data were taken from Davies, M. H.; Simnad, M. T.; Birchenall, C. E. *J. Met.* **1951**, 889–896; Paidassi, J. *Rev. Metall.* **1957**, LIV, 569–585; Mrowec, S.; Przybylski, K. *Oxid. Met.* **1977**, 11, 365–381; Fueki, K.; Wagner, J. B. *J. Electrochem. Soc.* **1965**, 112, 384–388; Smith, A. F. *Werkst. Korros.* **1979**, 30, 100–104; Hindam, H.; Whittle, D. P. *Oxid. Met.* **1982**, 18, 245–284; Bastow, B. D.; Whittle, D. P.; Wood, G. C. *Oxid. Met.* **1978**, 12, 413–438; Kircher, T. A.; Courtright, E. L. *Mater. Sci. Eng. A* **1992**, 155, 67–74.

influenced not by slow-growing metal oxide scales but by fast-growing metal sulfide scales. Therefore, sulfidation can cause serious corrosion damage for metal components. In order to estimate the sulfidation rates of industrial steels and alloys, data taken from simple binary  $\text{H}_2\text{S}/\text{H}_2$  gas mixtures are often referred,<sup>20</sup> since these data are considered to indicate the maximum corrosion rates of steels and alloys in respective  $P_{\text{S}_2}$  gas atmospheres. Iso-corrosion rate curves of engineering steels are presented in Figure 7 as a function of temperature and  $\text{H}_2\text{S}$  concentration in

$\text{H}_2\text{S}-\text{H}_2$  gas mixture of naphtha desulfurizers. These data represent exclusive formation and growth of sulfide scales where formation of protective oxide scales is minimized. For certain flue gas system containing not only  $\text{H}_2\text{S}$  and  $\text{H}_2$  but also some oxidizing gas species of  $\text{CO}_2$  and  $\text{H}_2\text{O}$ , formation of the protective  $\text{Cr}_2\text{O}_3$  scale may result for stainless steels and nickel-base alloys, if thermodynamic condition favors. Once formation of uniform  $\text{Cr}_2\text{O}_3$  scale is achieved, sulfidation by  $\text{H}_2\text{S}$  is hindered, and steels and alloys are protected by the uniform  $\text{Cr}_2\text{O}_3$  scale. In coal

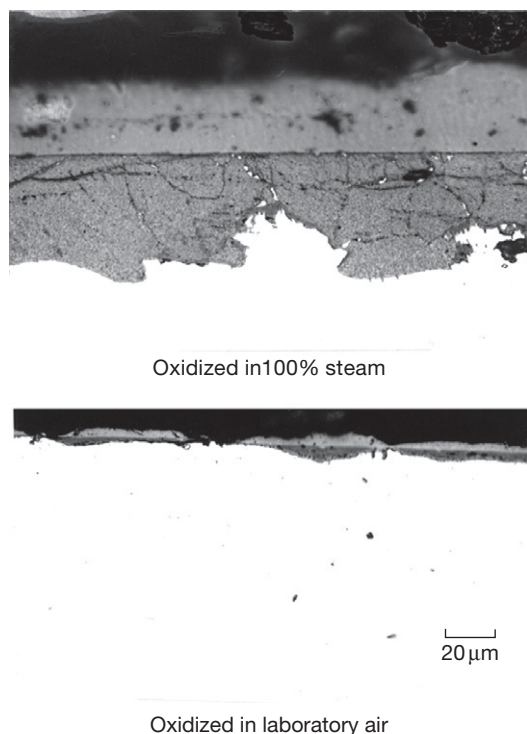


**Figure 6** Cross section of TP321H steel (18% Cr–8% Ni–0.4% Ti) reacted with 100% steam (top) and laboratory air (bottom) at 650 °C for 1000 h under atmospheric condition.

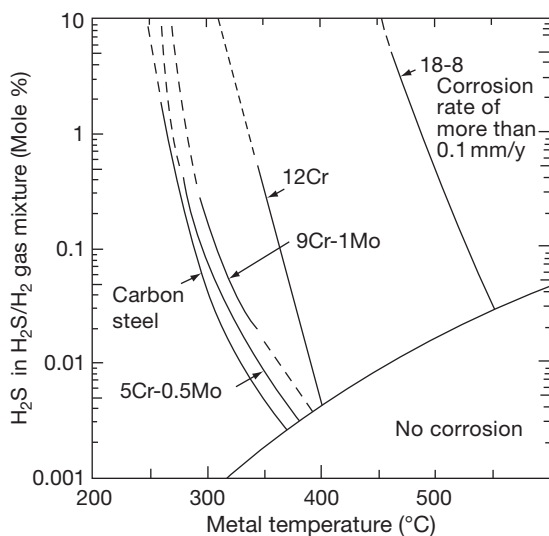


**Figure 7** Isocorrosion rate curves of engineering steels for high temperature  $H_2S/H_2$  corrosion in naphtha desulfurizers. Corrosion rate of  $0.1 \text{ mm year}^{-1}$ . Adapted from Gutzeit, J. In *Process Industries Corrosion – The Theory and Practice*; Moniz, B. J., Pollock, W. I., Eds.; NACE: Houston TX, 1986; pp 367–372.

gasifiers,  $P_{S_2}-P_{O_2}$  boundary of uniform formation of  $Cr_2O_3$  scale on steels and alloys deviates from that predicted from the thermodynamics. This boundary is referred as the kinetic boundary of  $Cr_2O_3$  scale, shown in **Figure 8** for example. Higher oxygen potential (or lower sulfur potential) is needed to secure the uniform formation of  $Cr_2O_3$  scale, since greater driving force is needed for the growth of  $Cr_2O_3$  to compete with that of the fast-growing metal sulfides.

### 1.18.3 Molten Salt Corrosion in Power Generating Systems

In this section, fireside corrosion caused predominantly by molten salts is outlined. High temperature metal components subject to fireside corrosion in energy-converting systems are exposed to hot combustion gases, and their metal temperatures are normally lower than the ambient flue gases, especially for heat exchanger materials placed in hot combustion gases to obtain heat from them. Depending on fuel chemistry, sodium/potassium sulfates and their chlorides, vanadium oxides, and chlorides and sulfates of heavy metals such as lead and zinc, which are present as vapor phases in flue gases, are considered as corrosive salts. They tend to vapor-condense on ‘cold’ metal surface from surrounding hot gas atmospheres. These vapor-condensed salts concentrate at the innermost metal-side of the deposit layer, since these sites are the coldest location in the deposits and hence the driving force for vapor-condensation of these salts is considered the greatest. For conditions where these salts become molten, reaction of these salts with protective metal oxide scales may initiate and fluxing reaction would take place, resulting in degradation of these protective metal oxide scales.<sup>6,21</sup> Metal oxide scales, initially formed as protective oxide layer on metal surfaces by gas-phase reaction, react with fused salts and dissolve into the salts. These dissolved metal ions precipitate out as oxide particles at the gas-side of the salt layer. Hence, once fluxing of metal oxide scale initiates, protective metal oxide scale is converted into porous, nonprotective oxide particles. At the reaction front, oxidation of metal constituents takes place in much higher rates than the case where the formation of protective oxide scales is established. At these sites, sulfidation as well as chlorination may simultaneously occur depending on the chemistry of molten salts. Since the final product of this corrosion is generally metal oxides, the overall reaction of molten salt corrosion can be interpreted as ‘oxidation’ of metals. This is

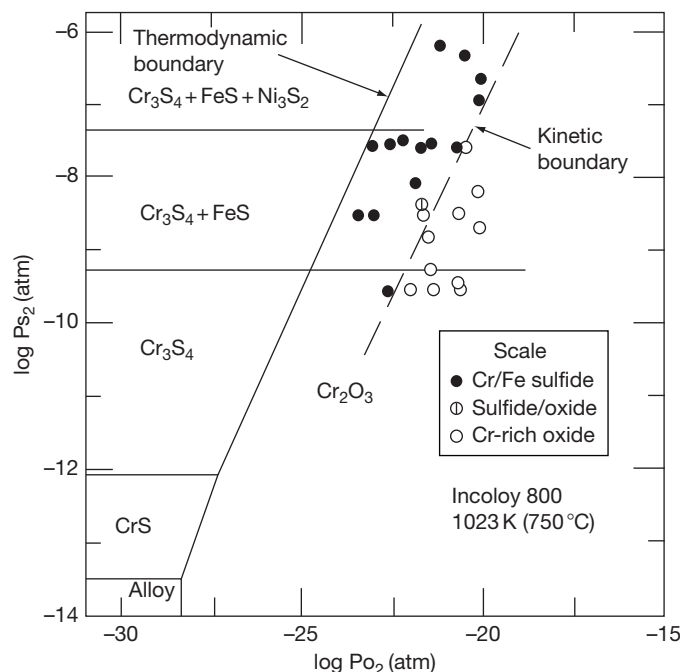


**Figure 8** Kinetic boundary of  $\text{Cr}_2\text{O}_3$  protection found for Alloy 800 as a function of oxygen and sulfur partial pressures in sulfidizing gas atmospheres at  $750^\circ\text{C}$ . Reproduced from Natesan, K. In *High Temperature Corrosion*, 2–6 March 1981, San Diego, CA; Rapp, R. A., Ed.; NACE: Houston, TX, 1981; pp 336–344.

one reason why the molten salt corrosion is termed as ‘accelerated oxidation’ or ‘catastrophic oxidation.’<sup>6</sup> In molten salt corrosion, severe corrosion does not take place when the surrounding gas atmosphere does not contain any oxygen, even though sufficient amounts of molten salts are present on metal surfaces. Generally, oxygen is the predominant oxidant for fireside corrosion, while carbon dioxide and water vapor are not that influencing. The role of molten salts is interpreted to enable fluxing of metal oxide scales,<sup>21</sup> and the ability to facilitate fast transportation of oxygen in molten salt layer to reaction sites is another important property of molten salts to maintain the high reaction rates of this corrosion.<sup>9</sup> A schematic behavior of molten salt corrosion is presented in Figure 9. Frequently, incubation time is experienced at the beginning of the corrosion,<sup>6</sup> where the corrosion rates remain relatively low. In this period, formation of protective oxide scales and condensation of corrosive salts are considered to take place. For conditions where salts become fused, that is, metal temperatures exceed that of the melting points of the salt mixture, accelerated oxidation takes place, and fireside corrosion initiates. When the metal temperatures remain lower than the melting point of the salt mixture, accelerated oxidation does not take place, and corrosion remains slight. Therefore, it is of

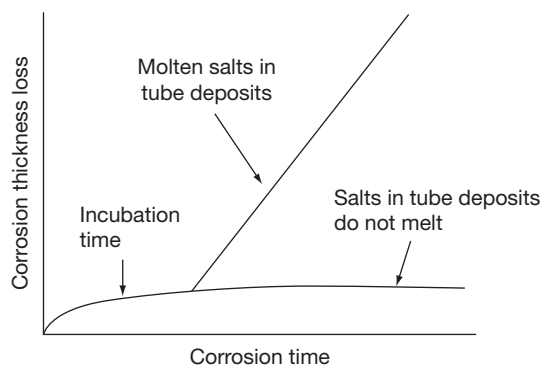


**Figure 9** Schematic corrosion behavior caused by fused salts.

great importance to know the melting point of the deposits and to compare it with the metal temperature of the component. Finally, the importance of flue gas temperature on corrosion should be pointed out. It is generally accepted that the corrosion rate of this type depends not only on metal temperature, but also on flue gas temperature to which the metal components are exposed. Exposing metal components to flue gas of higher temperature generally result in higher corrosion rates.<sup>22,23</sup> This is interpreted from greater concentration of corrosive salts in the deposits, since the



flue gas of higher temperature normally contains higher concentration of vapor species of corrosive salts, and the driving force for vapor-condensation of these salts onto metal surface is apparently greater than those exposed to flue gas of low temperatures, which is attributed to the temperature difference between the flue gas and the base metal.<sup>8</sup>

### 1.18.3.1 Vanadium Attack

Vanadium attack, referred as oil ash corrosion as well, has been recognized as severe fireside corrosion for boiler tubes, turbine components, furnace tubes, and reformer tubes in boilers, combustors, and reformers which fire oil containing vanadium.<sup>3,9</sup> Oil, rich in vanadium and sodium of approximately more than 1–10 ppm, is recognized to have potential corrosivity to metals.<sup>24</sup> Vanadium reacts with oxygen in combustion air to form  $V_2O_3$ ,  $V_2O_4$ , and finally volatile  $V_2O_5$  in flue gases.<sup>2</sup> Gaseous  $V_2O_5$  vapor condenses on metal surface as ash deposits. Depending on the deposition rates of  $V_2O_5$  and of other vapor-condensed species such as  $Na_2SO_4$ , etc., the deposit chemistry varies, but vanadium (as oxide) can constitute up to 80% of the deposits although vanadium concentration in fuel is typically less than 300 ppm.<sup>3</sup> In many cases, vanadium oxides react with other constituents such as sodium to form low melting point compounds. This is shown in Figure 10. Note that for  $Na_2O-V_2O_5$  system, melting points can be as low as 530–540 °C, which corresponds to the metal temperature of superheater and reheater tubes in practical boilers.<sup>3</sup> In addition to vanadium pentoxide, sodium vanadates of  $Na_2O-V_2O_4-5V_2O_5$ ,  $4Na_2O-V_2O_4-11V_2O_5$ ,  $Na_2O-V_2O_5$ , and  $3Na_2O-V_2O_5$  can be involved in superheater and reheater deposits. Melting points of superheater and reheater deposits taken from 350–500 MW boilers firing oil of 30–40 ppm V, 8–15 ppm Na, and 1–1.5% S are plotted as a function of  $(Na + S)/V$  atomic ratio of their deposits and shown in Figure 11.<sup>25</sup> Clearly, vanadium-rich deposits start to melt at 480–500 °C, whereas those lean in vanadium remain solid until heated to above 800 °C. Sulfate-rich deposits have normally high melting points.

Vanadium attack is interpreted to result from fluxing of protective metal oxide scales and fast transfer of dissolved oxygen in molten oxide layer.<sup>9</sup> A laboratory corrosion test revealed that accelerated corrosion of TP304 stainless steel occurred when reacted with pure molten  $V_2O_5$ , but the corrosion rate even increased when sodium sulfate was added to vanadium pentoxide; maximum corrosion resulted

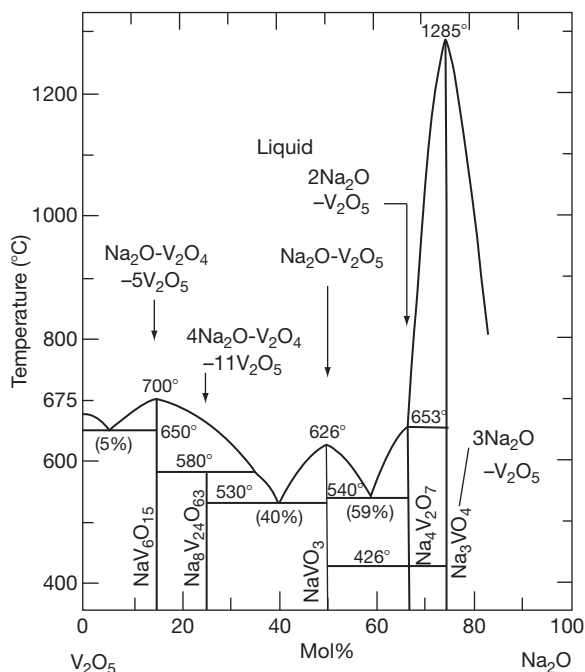
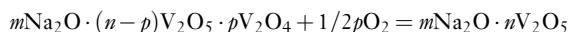


**Figure 10** Melting point of  $Na_2O-V_2O_5$  system. Reproduced from Roth, R. S.; Dennis, J. R.; McMurdie, H. F. *Phase Diagrams for Ceramists*; The American Ceramic Society, 1987; Vol. VI, p 98.

for  $V_2O_5$ –20 mol%  $Na_2SO_4$  salt mixture.<sup>9</sup> This was explained from the ability for vanadium pentoxide–alkali salt mixtures to absorb oxygen. Indeed, vanadium pentoxide–alkali salt mixtures absorb oxygen upon heating from solid to liquid phase through the reversible change from vanadylvanadate to alkali acid vanadates, according to the following equation<sup>9</sup>



Capability to accommodate great amount of oxygen in the melt and ability for fast diffusion of oxygen through its layer to metal surface seem to be the characteristics of this liquid phase.

The effect of metal temperature on corrosion is significant. In order to minimize the corrosion, limiting metal temperature to below the critical temperature, which relates to the melting points of the ash deposits, is considered an effective measure to alleviate the corrosion.<sup>3</sup> The effect of flue gas temperature on corrosion is reported to be important as well. When placing heat-exchanger tubes and plates to flue gases of higher temperature, vapor-deposition of corrosive vanadium and sodium compounds enhances, and concentration of these compounds on metal surface

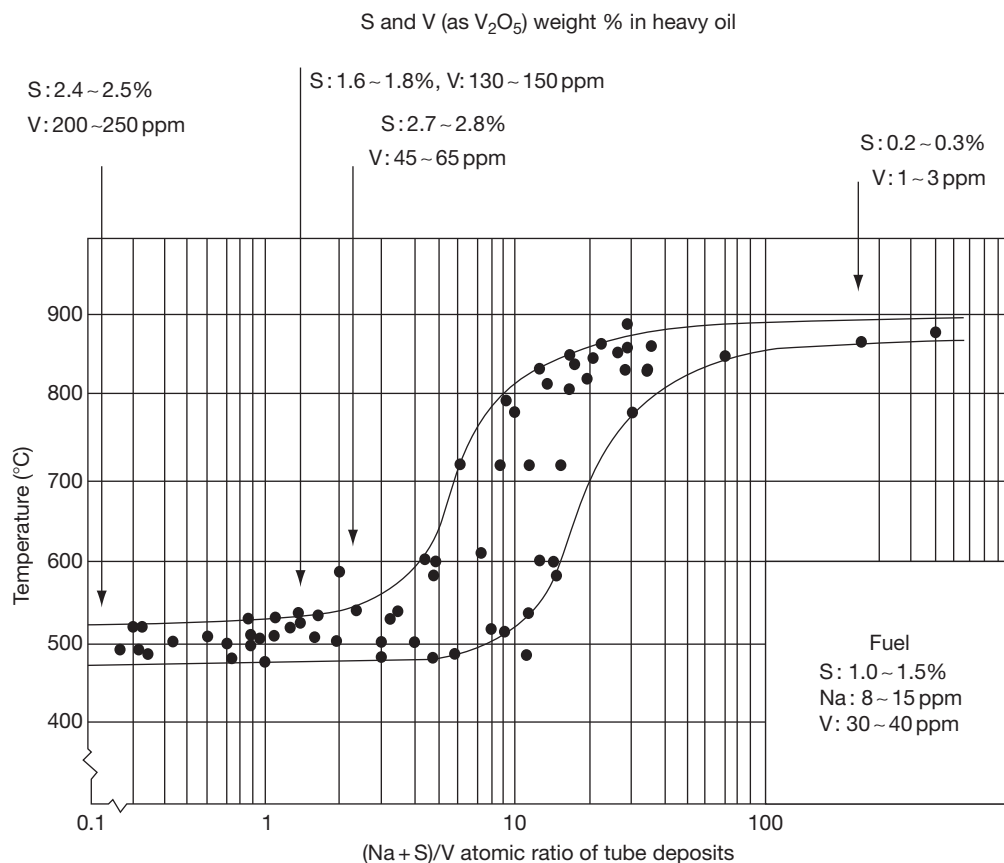


**Figure 11** Melting point of tube deposits taken from superheater and reheater tubes of 350–500 MW boilers firing heavy oil. Steam temperatures were 540–571 °C. Reproduced from Harada, Y.; Nakamori, S. *Boushoku Gijutsu* **1980**, 29, 615–621.

increases. This facilitates formation of molten salts at these sites, and the corrosion aggravates accordingly. For boiler tubes, regions of gas and metal temperatures where corrosion may occur are empirically recognized in practice. This is presented in [Figure 12](#). This criterion depends on several factors such as fuel chemistry, boiler design, and combustion conditions, but in order to increase metal temperature, the lowering of the flue gas temperature is generally needed. Lowering excess air used for combustion of oil should have a certain effect to reduce the corrosion rate, since removing ‘free’ oxygen in the flue gas obviously would help in minimizing supply of major oxidizing gas species of the corrosion reaction. However, using low excess combustion air is reported not always successful when applied to practical power plants, because of the complexity of combustion and flue gas mixing in real boilers.<sup>3</sup> The effect of inhibitors and fuel additives on corrosion has been widely recognized, and addition of inhibitors to fuel oil is successfully applied to some boilers in practice.<sup>25</sup>

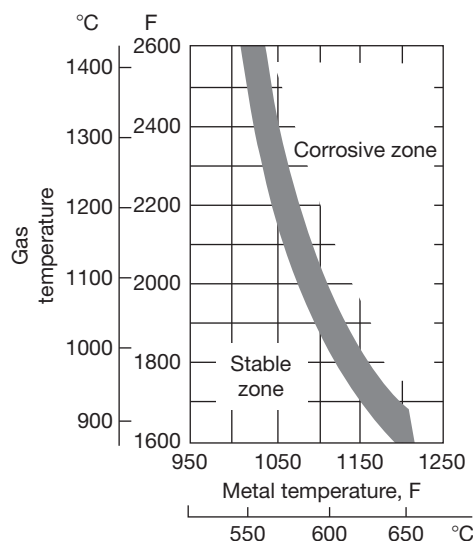


**Figure 12** Regions where boiler tubes are subject to fireside corrosion as a function of tube metal temperature and flue gas temperature. Reproduced from Hansen, W. H.; Kessler, G. W. *Trans. ASME* **1965**, 210–214.

These inhibitors are designed to react with vanadium to form compounds of high melting points. Out of a number of inhibitors, MgO and its derivatives are used in practice because of its effectiveness and relatively low cost.<sup>3,25</sup> For example, addition of water-soluble  $\text{Mg}(\text{OH})_2$  to fuel oil, at an atomic Mg/V ratio of 2, is reported to have been successful in reducing the corrosion rate of TP321H (18% Cr–10% Ni–0.4% Ti) superheater tubes in a practical boiler to about one-third, the steam temperature of which was 571 °C.<sup>25</sup>

According to Figure 13, high-chromium steels and alloys seem to have better resistance to vanadium attack. Nickel-based alloys have generally higher corrosion rates than the iron-based alloys, suggesting that nickel is detrimental compared to iron. For boiler tube application, high-Cr ferritic steels of 9% Cr and 12% Cr are reported to have better resistance than the austenitic 18-8 stainless steels.<sup>26,27</sup> This is interpreted to be attributed, again, to nickel in 18-8 steels, since nickel is a harmful alloying element to combat the corrosion, the reason for which still seems to remain unclear.

Recently, a new type of fossil fuel coming from vast reserves of bitumen existing in the Orinoco Belt

in Venezuela has become recognized as an useful fuel to generate electricity.<sup>28</sup> This fuel, arising from the technology for dispersing natural bitumen in water, is called orimulsion. Orimulsion contains water of around 30 wt%. An example of the elemental analysis is 60.1% carbon, 10.1% hydrogen, 26.4% oxygen, 0.35% nitrogen, 2.85% sulfur, and 0.2% ash (by weight).<sup>28</sup> It should be noted that this fuel contains vanadium of 310 ppm and sodium of 30 ppm. Vanadium attack on metal components is predicted. Field tests were conducted in real boilers firing orimulsion, and fireside corrosion of boiler materials turned out to be not that severe. This was attributed to high concentration of magnesium in the fuel, that is, 370 ppm, which acted as inhibitor to raise the melting points of the ash deposits, and hence alleviating corrosion for metal components. Information on the concentration not only of corrosive impurities but also of other impurities such as alkali earth elements is needed to evaluate the corrosivity of fuel.

### 1.18.3.2 Sulfate-Induced Corrosion

Fireside corrosion has often been encountered in blades and vanes of land-based and aircraft gas

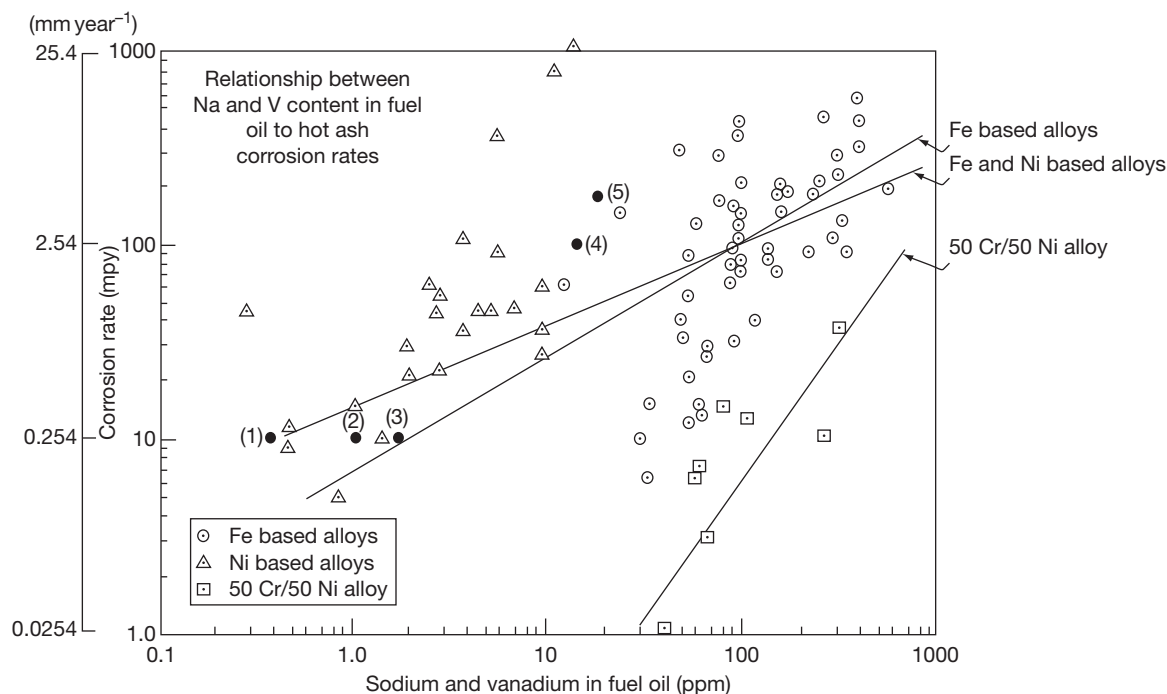
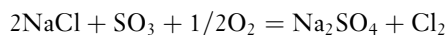


**Figure 13** Relationship between Na + V content in fuel oil to corrosion rates. Reproduced from Demo, J. J. *Mater. Perform.* 1980, 9–15. Data of iron-based alloys are from boiler and furnace/reformer tubes, those of nickel-base alloys predominantly from turbine blades, and those of 50Cr–50Ni alloy from tube supports and hangers. Solid marks with numbers represent industrial and semiworks experience points of iron-based reformer alloys.

turbines because of thin film of pure liquid sodium sulfate, which is vapor-condensed from flue gas onto metal surface.<sup>6,21</sup> The source of sodium comes from either the fuel or the air intake. Sodium, commonly present in sea salt as sodium chloride, reacts with sulfur in fuel to form sodium sulfate, according to the well-known reaction<sup>6</sup>:



At turbine conditions, sodium chloride is considered thermodynamically unstable. Metal temperatures of the components are generally above the melting point of sodium sulfate, that is, 884 °C. This is often termed as Type I hot corrosion or high temperature hot corrosion (HTHC).<sup>21</sup> For utility boilers firing high-sulfur coal, fireside corrosion of superheater and reheater tubes can take place. This is categorized as Type II hot corrosion, or low-temperature hot corrosion (LTHC), since this corrosion occurs in the temperature range of 600–750 °C, well below the melting point of pure sodium sulfate.<sup>21,29</sup> In this section, fireside corrosion of Type II hot corrosion is introduced firstly.

It is well recognized that for boilers firing pulverized coal of high sulfur concentration, external corrosion of superheater and reheater tubes takes place.<sup>7,10,29,30,31</sup> The corrosion rate of boiler tubes starts to significantly increase at around 565 °C (1050 °F) when the metal temperature exceeds the melting point of their tube deposits, exhibits a maximum at around 650–700 °C, and decreases drastically upon further increase in the metal temperature.<sup>7,10</sup> The drastic decrease in the corrosion rate at above 700 °C is interpreted to be from the solidification of liquid phases, the temperature of which depends upon the partial pressure of SO<sub>3</sub> in flue gas and the chemistry of the complex sulfates.<sup>32</sup> Hence, the corrosion behavior is characterized as 'bell-shaped' form.<sup>7,10</sup> Corrosion rate of tube steels is influenced not only by the metal temperature, but also by the flue gas temperature, suggesting a great effect of vapor-condensation of corrosive salts from flue gas on metal surface.<sup>23</sup> This is shown in Figure 14. Tube deposits contain corrosive salts of sodium and potassium sulfates and iron oxide (hematite, Fe<sub>2</sub>O<sub>3</sub>), in addition to ash constituents such as complex oxides of aluminum, silicon, etc. Sodium and potassium sulfates can form complex sulfates of low melting-points upon reaction with hematite, that is, sodium and potassium iron trisulfates of (Na,K)<sub>3</sub>Fe(SO<sub>4</sub>)<sub>3</sub>. Under a simulated flue gas atmosphere of 0.25% SO<sub>2</sub>–3.6% O<sub>2</sub>–15.0% CO<sub>2</sub>–balance N<sub>2</sub>, sodium iron

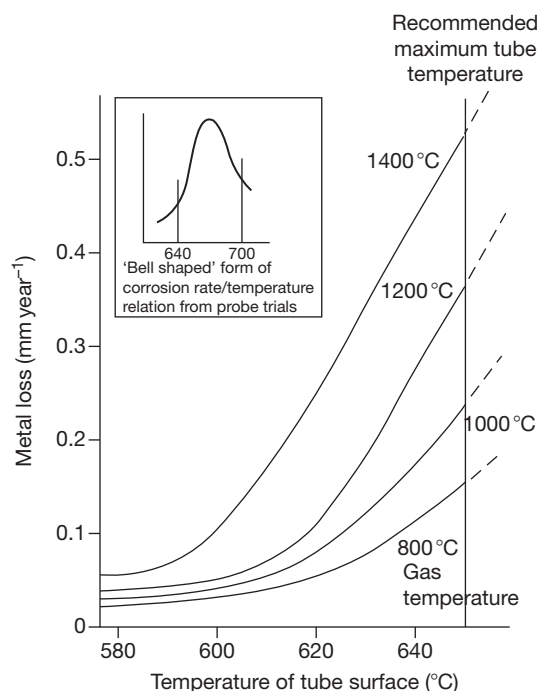


**Figure 14** An example of the corrosion rates of superheaters and reheaters as a function of tube surface temperature and flue gas temperature. The inset shows the 'bell-shaped' corrosion behavior of this type of corrosion. Reproduced from Cutler, A. J. B.; Flatley, T.; Hay, K. A. *Metallurgist and Materials Technologist*, **1981**, February, 69–81.

trisulfate, Na<sub>3</sub>Fe(SO<sub>4</sub>)<sub>3</sub> becomes fused at 624 °C, whereas potassium iron trisulfate, K<sub>3</sub>Fe(SO<sub>4</sub>)<sub>3</sub>, at 618 °C.<sup>10</sup> The melting point of these complex sulfates is affected by the sodium–potassium ratio, and the lowest melting-point 552 °C is obtained for compounds between 1:1 and 2:1 molar mixture of potassium to sodium iron trisulfates.<sup>10</sup> Hence, for most laboratory tests simulating fireside corrosion of Type II attack, synthetic ash of Na<sub>1.5</sub>K<sub>1.5</sub>Fe(SO<sub>4</sub>)<sub>3</sub> (1.5 mol Na<sub>2</sub>SO<sub>4</sub>–1.5 mol K<sub>2</sub>SO<sub>4</sub>–1 mol Fe<sub>2</sub>O<sub>3</sub> mixture) is used as predominant corrosives to simulate this environment.<sup>33</sup> It should be noted that these sodium and potassium complex iron trisulfates are stable only in gas atmospheres containing SO<sub>2</sub>. Temperature range for the liquid-phase stability of these complex sulfates seems to be affected by SO<sub>2</sub> (and therefore SO<sub>3</sub>) concentration in the flue gases. For example, temperature regime where severe corrosion occurs for TP321H steel (18% Cr–10% Ni–0.4% Ti) becomes broader when exposed to gas atmospheres of higher SO<sub>2</sub> concentration. This is shown in Figure 15.<sup>33</sup> For flue gas of low SO<sub>2</sub> concentration,

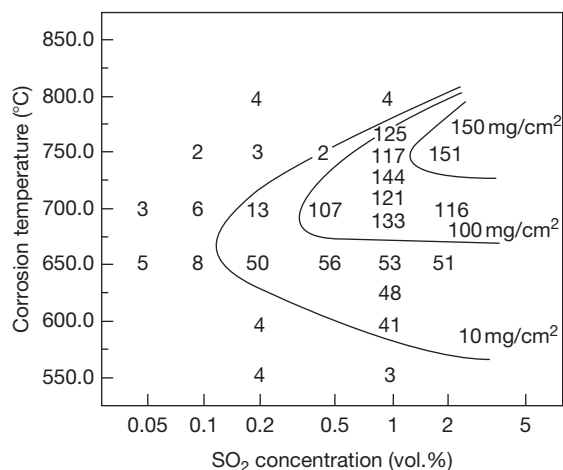


**Figure 15** The effect of SO<sub>2</sub> vol.% in gas atmosphere on high temperature corrosion of TP321H steel specimen reacted with 1.5 mol Na<sub>2</sub>SO<sub>4</sub>–1.5 mol K<sub>2</sub>SO<sub>4</sub>–1 mol Fe<sub>2</sub>O<sub>3</sub> in x% SO<sub>2</sub>–5% O<sub>2</sub>–15% CO<sub>2</sub>–N<sub>2</sub>. Numbers in the figure designate corrosion weight loss. Reproduced from Fukuda, S. T.; Hamada, H.; Sakaguchi, Y. In Proceedings of the 32th Meeting of the Japanese Society of Corrosion Engineering, 1985, August, Sapporo, B-302, pp 239–246.

sulfates of potassium and sodium do not seem to react with iron oxides to form stable complex sodium and potassium iron trisulfates, and these ash deposits remain solid at tube metal temperatures. This result clearly demonstrates the importance of SO<sub>2</sub> (and therefore SO<sub>3</sub>) concentration in flue gases, since one can predict the occurrence/absence of fireside corrosion of superheater and reheater tubes of coal-fired boilers, when the SO<sub>2</sub> concentration of flue gas is specified. Therefore, for firing low-S coal where the SO<sub>2</sub> concentration of flue gas is less than 0.1%, sulfate-induced corrosion is expected to be slight.

There is an index representing the corrosivity of high-S coal of 1.4–8.2% S (proximate, by weight) from the coal chemistry. This index is often referred to as the Borio index, determined from the concentration of acid-soluble alkali and alkali earth elements (in ppm), and Fe<sub>2</sub>O<sub>3</sub> (in wt%) of coal.<sup>4</sup> Procedure to obtain this index is shown in Figure 16. In order to obtain acid-soluble sodium and potassium concentrations in coal, precise measurement seems to be necessary. Test procedure for this is described in the literature as follows,<sup>4</sup> ‘set 2 g portion of coal sample (~70% through 200 mesh) to a 250-m L Erlenmeyer flask and add 40 m L of 5% HCl solution. Fix air condenser and digest the sample for 16 h at a gentle boil. After digestion, filter through #40 Whatman filter paper of 15 cm into 100-ml volumetric flask. Wash filter

and contents at least four times with small amounts of water, and make it up to 100 ml volume. This solution should be carefully measured.’<sup>4</sup> As expected, corrosivity of high-S coal is related to the concentration of acid-soluble sodium and potassium compounds, hematite content, and calcium and magnesium contents. To combat the corrosion, high-Cr steels and alloys perform well, which will be explained later in detail.

The mechanism of Type II hot corrosion seems to resemble that of Type I hot corrosion. Therefore, corrosion reaction offered for Type I hot corrosion is explained. For Type I hot corrosion observed at turbine blades and vanes, corrosion products consist generally of relatively thin outer oxide layer, a thick mixed oxide/metal layer, and a thin metal zone containing sulfides below the mixed oxide/metal layer.<sup>6</sup> Sulfides are generally rich in chromium, but in some cases nickel-rich or cobalt-rich sulfides are found for materials which experienced rapid degradation, presumably, due to liquid formation of Ni–Ni<sub>3</sub>S<sub>2</sub> or Co–Co<sub>4</sub>S<sub>3</sub> eutectics.<sup>6</sup> The eutectic temperatures are 645 and 877 °C, for Ni–Ni<sub>3</sub>S<sub>2</sub> and Co–Co<sub>4</sub>S<sub>3</sub> eutectics respectively.<sup>34</sup> Early interpretation of this corrosion was derived to explain the formation of sulfides in the base metal and called the sulfidation model.<sup>34</sup> According to this model, corrosion can be divided into two stages. At a triggering stage, which is ‘sporadic and unpredictable,’ reduction of sodium sulfate by an unspecified reducing agent generates elemental sulfur, which reacts with base metal components to form their sulfides. Hence, for this model, oxidizing agent is considered sodium sulfate. These metal sulfides react with base metal elements to form low melting point eutectics such as Ni–Ni<sub>3</sub>S<sub>2</sub>. At an enhanced oxidation stage, metal is penetrated by the metal–metal sulfide liquid eutectics, and oxidation of these liquid eutectics by oxygen was proposed to proceed more rapidly than the sulfur-free alloy. Formation and enhanced oxidation of metal–metal sulfide eutectics was the early mechanism. Since chromium sulfides are normally present in the corrosion products of the degraded turbine blades and vanes, and metal–metal sulfide eutectics such as Ni–Ni<sub>3</sub>S<sub>2</sub>, etc. are not always indicated,<sup>6</sup> more generalized interpretation seems to be necessary. Chromium does not form any metal–metal sulfide eutectic. Recent understanding of this type of corrosion is based on destructive dissolution of originally protective metal oxide scale into thin fused salt film, followed by reprecipitation of these metal oxides as thick, porous, nonprotective reaction products.<sup>21</sup> This is called the salt-fluxing model. The overall reaction is again accelerated/catastrophic

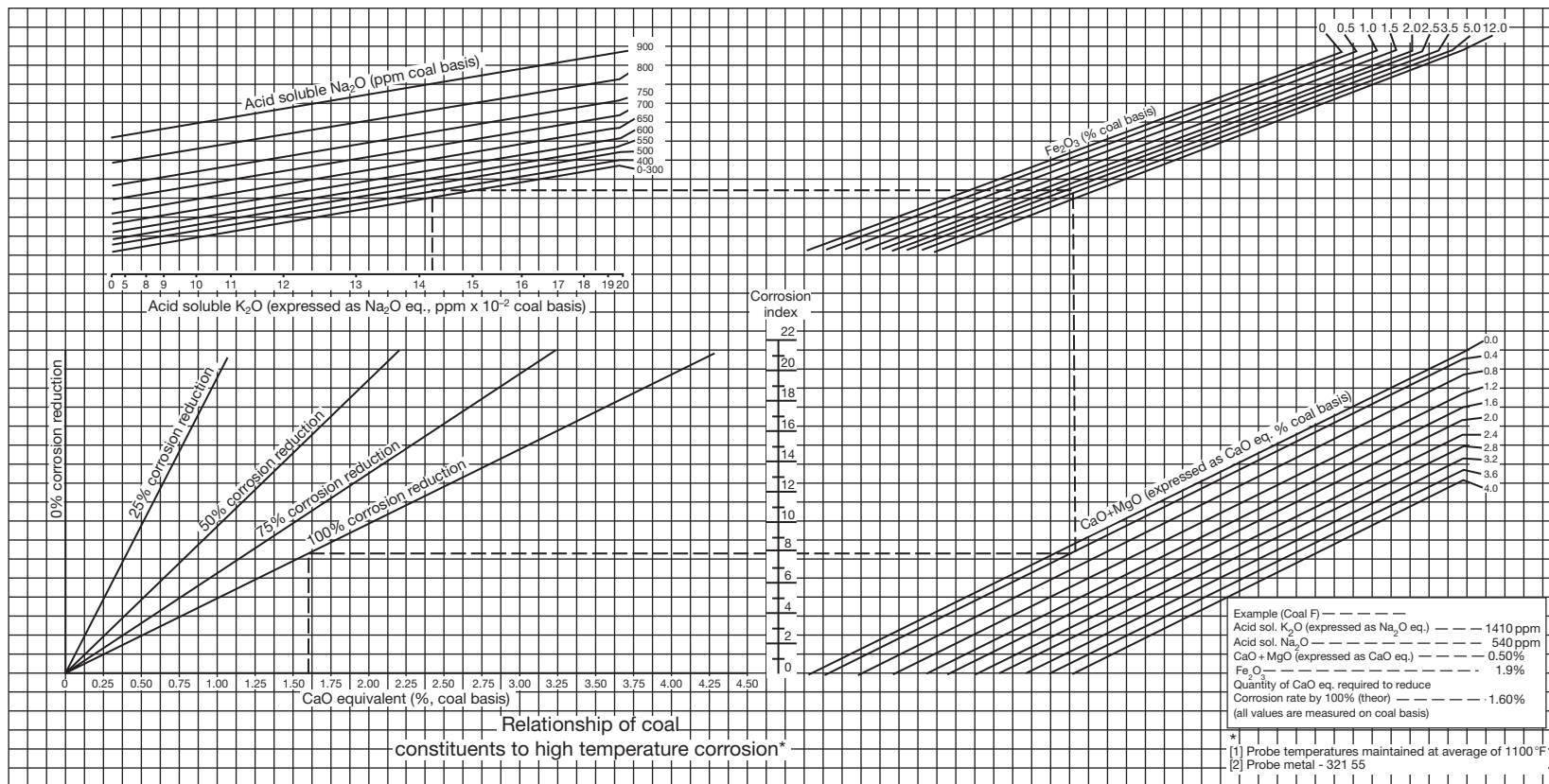
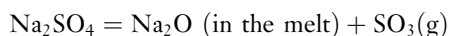


Figure VII-13. Relationship of coal constituents to high temperature corrosion VII-29

**Figure 16** Relation of coal constituents to high temperature corrosion of boiler tubes. Reproduced from Borio, R. W.; Wilson, E. B. The control of high temperature fire-side corrosion in utility coal-fired boilers, OCR R6D Report No. 41, April 1969, Office of Coal Research, Department of the Interior, Washington, DC.



oxidation of metals, and deterioration of protective metal oxide scale through dissolution/fluxing reactions is an important step for initiating and maintaining the corrosion. Oxygen in flue gas is necessary to maintain the corrosion; without oxygen, reaction cannot proceed even when abundant fused salts are present on metal surfaces. The fluxing reactions of metal oxide scales are significantly affected by the 'basicity' of fused salts, which is defined as  $-\log a_{\text{Na}_2\text{O}}$  for pure sodium sulfate.<sup>21</sup> Basicity of sulfate melts is affected by the activity of  $\text{SO}_3$  in flue gas, according to the following reaction:



This is similar to the thermal stability of the complex sodium/potassium iron trisulfates where the stability of its liquid phase is influenced by  $\text{SO}_3$  concentration.<sup>33</sup> It should be pointed out that basicity of fused sulfate salts is influenced by the partial pressure not of  $\text{SO}_2$ , but of  $\text{SO}_3$ . Generally,  $\text{SO}_3$  concentration of flue gas is approximately two orders of magnitude less than  $\text{SO}_2$  (see Table 4, for example).

Solubility of major metal oxides in fused sodium sulfate at 927 °C is presented in Figure 17.<sup>21</sup> Clearly, solubility of metal oxides depends on the basicity of sulfate melt, and two types of dissolution reactions are noticed, except for  $\text{SiO}_2$ . The one is categorized as the acidic dissolution, which takes place in an acidic melt lean in  $\text{O}^{2-}$  ion.<sup>21</sup> For  $\text{NiO}$ , for example, the reaction is written as  $\text{NiO} = \text{Ni}^{2+} + \text{O}^{2-}$ . The other one is termed as the basic dissolution, which occurs in a basic melt rich in  $\text{O}^{2-}$  ion. The reaction is designated as  $2\text{NiO} + \text{O}^{2-} + 1/2\text{O}_2 = 2\text{NiO}_2^-$ .

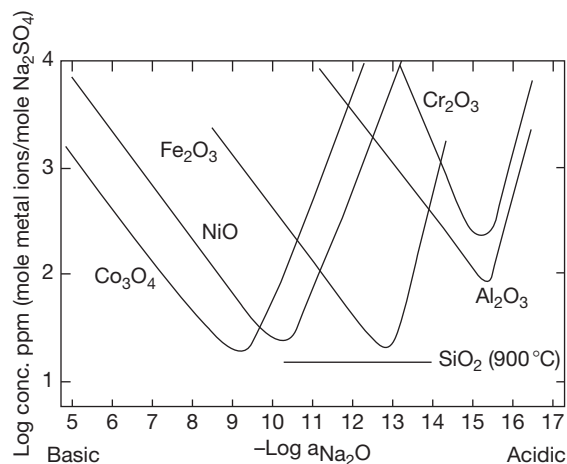
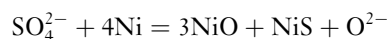


**Figure 17** Oxide solubility of major oxides in fused  $\text{Na}_2\text{SO}_4$  at 927 °C and 1 atm  $\text{O}_2$ . Reproduced from Rapp, R. A. *Corrosion* 1986, 42, 568–577.

In order to establish self-sustaining hot corrosion of steels and alloys, it seems necessary for fused sodium sulfate to locate its melt chemistry at a specific condition where simultaneous dissolution and reprecipitation of metal oxide scales are sustained. The basicity at which self-sustaining hot corrosion can occur may depend upon the alloy system; for pure nickel, this corresponds to the basicity at which basic dissolution of  $\text{NiO}$  is secured.<sup>35</sup> One explanation for it may be provided by the solubility gradient model, which can be found in the literature.<sup>36</sup> For fused salt film of sodium sulfate, maintaining its melt basicity in basic conditions is considered rather difficult since the melt chemistry enabling  $\text{NiO}$  basic dissolution is quite far from the melt conditions equilibrated with acidic flue gas atmosphere containing  $\text{SO}_3$ . In acidic melts, pure nickel, if protected by dense metal oxide scales, did not produce any rapid attack.<sup>35</sup> Current understanding for this is to incorporate the effect of sulfidation reaction of the base metal by fused sodium sulfate, which generates  $\text{O}^{2-}$  ion and shifts its basicity to more basic conditions.<sup>21</sup> For pure nickel, the sulfidation reaction is given by the following equation:



Direct contact of fused salts with the base metal, presumably at cracks, flaws, and grain boundaries of its protective oxide scale results in altering the basicity to more basic, where self-sustaining corrosion is facilitated. Since formation of protective oxide scales is considered to precede vapor-condensation of molten salts, 'incubation time' is usually required for fused salts to permeate the protective oxide scale<sup>37</sup> and to arrive at the point where direct contact of fused salt and base metal becomes possible. For acidic melts, oxide solubility is the lowest for  $\text{Cr}_2\text{O}_3$  and  $\text{Al}_2\text{O}_3$ , as shown in Figure 17. Therefore, these metal oxide scales, along with  $\text{SiO}_2$ , is expected to function as protective oxide scales in acidic melts. This may be one reason why the steels and alloys forming uniform  $\text{Cr}_2\text{O}_3$ ,  $\text{Al}_2\text{O}_3$ , and  $\text{SiO}_2$  scales have good resistance to hot corrosion. On the contrary, molybdenum, tungsten, and vanadium, commonly added to strengthen their alloys, are regarded as harmful alloying elements for hot corrosion.<sup>38</sup> Oxides of these alloying elements can be categorized as 'acidic' oxides, which are thermodynamically stable in acidic melts. Thermodynamic stability of major metal oxides relevant to alloy constituents of high temperature materials is calculated at 927 °C,  $P_{\text{O}_2}$  of 1 atm and shown in Figure 18. In this figure, unit activities of condensed phases in mutual equilibrium are assumed. Oxides of

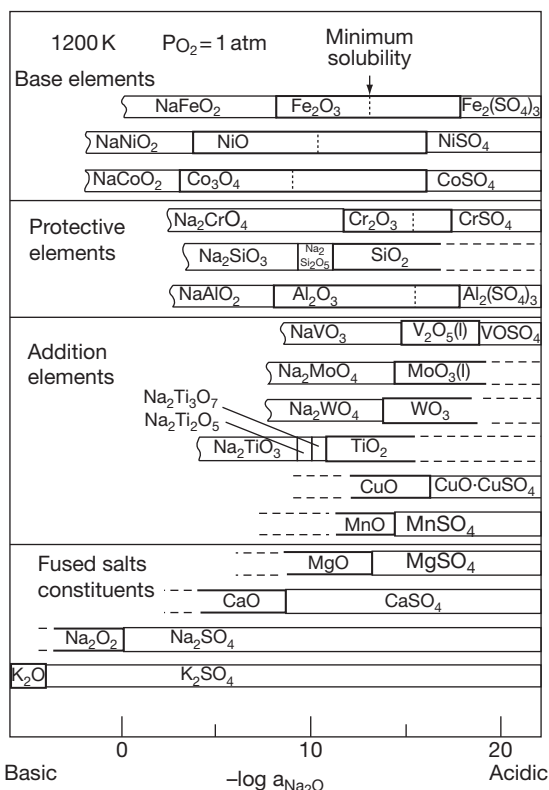
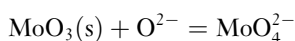


**Figure 18** Basicity of major oxides at 1200 K,  $P_{O_2} = 1$  atm relevant to high temperature corrosion.

molybdenum, tungsten, and vanadium are stable in acidic melts, while oxides of sodium and potassium are stable in basic melts. In 'neutral' melts, basic dissolution may take place for acidic oxides; described for molybdenum oxide as follows:



This reaction shifts the basicity of molten salts to more acidic. At the reaction front of metal/salt interface of nickel-base alloys containing molybdenum and the like, oxidation and subsequent dissolution of these alloying elements may take place simultaneously and a very acidic condition can be established locally, which forces acidic fluxing of otherwise protective  $Cr_2O_3$  and  $Al_2O_3$  scales. This may be one explanation for the detrimental effect of molybdenum and tungsten on corrosion.

For Type II hot corrosion, the beneficial effect of chromium on corrosion is prominent as well, as shown in Figure 19 for example. High-Cr alloys such as alloy 671 are used to combat fireside corrosion in these environments. It should be pointed out that for 18-8 stainless steel family additional elements of molybdenum and titanium to steels degrade their

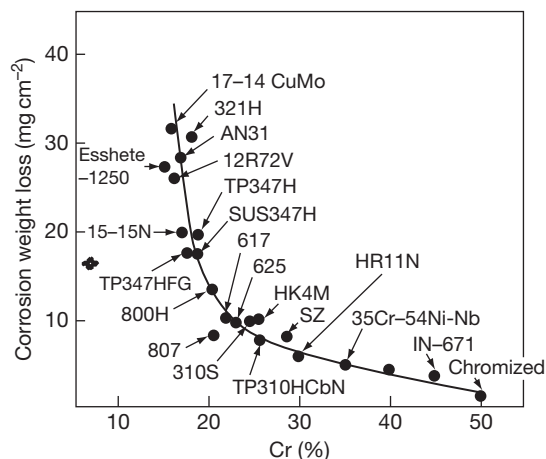


**Figure 19** Laboratory corrosion test results of high temperature steels and alloys. The test was conducted at 650 °C for 5 h in 1%  $SO_2$ -5%  $O_2$ -15%  $CO_2$ - $N_2$ . Test specimens were reacted with 1.5 mol  $Na_2SO_4$ -1.5 mol  $K_2SO_4$ -1 mol  $Fe_2O_3$  salt mixture by salt-coating method.

corrosion resistance, whereas with niobium the opposite occurs. The beneficial effect of niobium on corrosion seems to remain unclarified, although recent modern 18-8 stainless steel tubes contain small amount of niobium.

This explanation is valid for fireside corrosion encountered in components exposed to environments firing fossil fuel containing sulfur. In general cases,  $SO_2$  concentration in these flue gases lies in the range of less than several thousand parts per million, and  $SO_3$  concentration in the range of less than 100 ppm. However, for extreme cases such as boilers firing solid sulfur,  $SO_3$  concentration of flue gas may surpass hundreds of parts per million, and fused-salt corrosion attributed to liquid sodium/potassium pyrosulfates of  $Na_2S_2O_7$  and  $K_2S_2O_7$  can take place.<sup>39</sup> Since the melting point of  $Na_2SO_4$ - $Na_2S_2O_7$  and  $K_2SO_4$ - $K_2S_2O_7$  systems is reported to be low, down to around 400 °C (Figure 20), fireside corrosion resulting from the formation of liquid phase of sodium and potassium pyrosulfates can occur for boiler tubes. Again, it must be pointed out that these liquid phases are only stable for conditions where  $SO_3$  (not  $SO_2$ ) concentration in flue gas exceeds 200 ppm for potassium pyrosulfate and 2000 ppm for sodium pyrosulfate, which is very rare for boilers firing conventional fuel.

### 1.18.3.3 Fireside Corrosion Induced by Chlorine in Fuel

Fireside corrosion relating to chlorine in fuel is encountered for boiler components in waste incinerators and

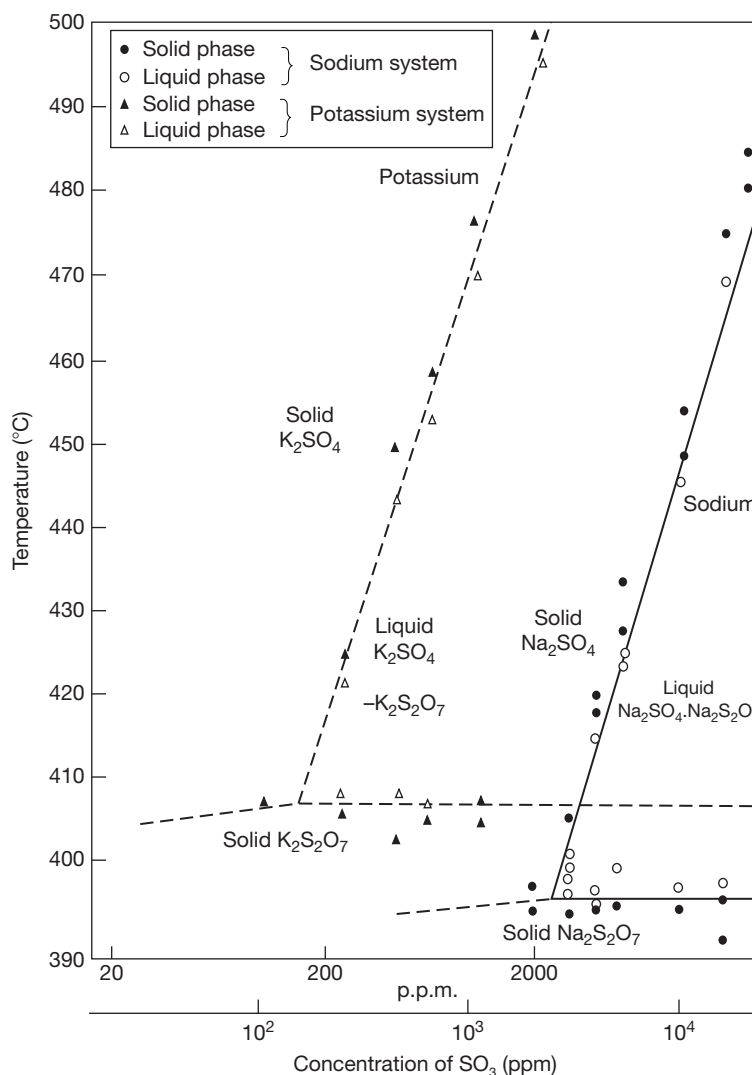


**Figure 20** Temperature range of liquid  $\text{K}_2\text{S}_2\text{O}_7$ – $\text{K}_2\text{SO}_4$  and  $\text{Na}_2\text{S}_2\text{O}_7$ – $\text{Na}_2\text{SO}_4$  in the presence of various partial pressures of  $\text{SO}_3$ . Reproduced from Coats, A. W.; Dear, D. J.; Penfold, D. J. *Inst. Fuel* **1968**, 129–132.

in black liquor recovery boilers (BLRB). It is generally accepted that chloride salts, deposited on metal surface via vapor-condensation, play an important role in corrosion.<sup>40</sup> In order to deposit chloride salts from flue gas on metal surface, chloride vapor species must be present in flue gas atmospheres.

Fireside corrosion of waste incinerators has been intensively studied for steel tubes of their heat recovery boilers.<sup>40–42</sup> Except for aqueous corrosion experienced at below the dew-point temperatures, corrosion can start at above 320 °C, which is indeed surprisingly low compared to other types of fireside corrosion encountered in real systems. A schematic temperature dependence of boiler tubes on corrosion

in waste incinerators is presented in [Figure 21](#).<sup>41</sup> Since hydrogen chloride is always present in flue gases in the order of hundreds and thousands of parts per million, the early interpretation of corrosion was the gas-phase attack of metals by hydrogen chloride.<sup>42</sup> Since one of the reaction products can be highly volatile iron trichloride ( $\text{Fe}_2\text{Cl}_6$ , boiling point 315 °C, see [Figure 22](#)), corrosion products are expected not to function as corrosion barrier for boiler tubes, and high corrosion rates can be expected even at low temperatures. However, laboratory tests examining gas-phase corrosion of tube steels by hydrogen chloride turned out that its corrosion rate is significantly low at 400 °C, which cannot explain

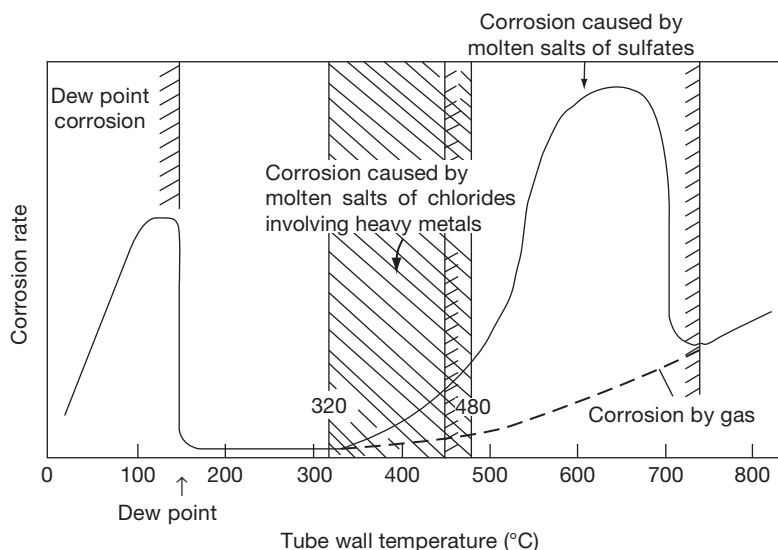


**Figure 21** Corrosion behavior of carbon steel boiler tube in waste incinerator as a function of tube wall temperature (schematic). Adapted from Von Faßler, K.; Leib, H.; Spahn, H. *Mitteilungen der VGB* 1968, 48, 126–139.

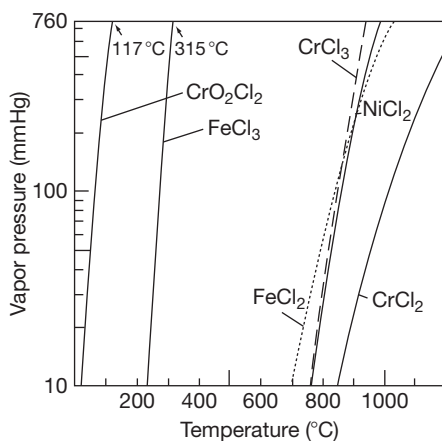
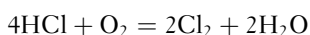


**Figure 22** Vapor pressure of Fe, Cr, and Ni chlorides. Data taken from Kubaschewski, O.; Alcock, C.B. *Metallurgical Thermochemistry*, 5th ed.; Pergamon Press, 1979.

the corrosion occurring in real boilers.<sup>43</sup> Therefore, gas-phase corrosion by chlorine was proposed instead as the root cause for the corrosion since the corrosion rate of tube steel by chlorine gas is appreciably higher than hydrogen chloride.<sup>41</sup> Gaseous chlorine is never found in furnace flue gases. Therefore, local formation of chlorine gas in tube deposits through the following Deacon reaction:



was suggested.<sup>41</sup> Tube deposits were explained to function as catalyst of the Deacon reaction. Sulfur

may corrode steels through the formation of sodium and potassium pyrosulfates  $((\text{Na,K})_2\text{S}_2\text{O}_7)$  of low melting points, which react with tube steels (and their protective oxide scales) to form liquid alkali iron trisulfates  $((\text{Na,K})_3\text{Fe}(\text{SO}_4)_3)$  at below 500 °C.<sup>41</sup> Gas-phase corrosion by chlorine, and corrosion by liquid phases are the early mechanisms.<sup>40,41</sup> According to this mechanism, corrosion of carbon steel boiler tubes by chlorine and sulfur occurs simultaneously. Corrosion products of these reactions are the corresponding iron chlorides ( $\text{FeCl}_2$ ,  $\text{Fe}_2\text{Cl}_6$ ), iron oxides ( $\text{Fe}_3\text{O}_4$ ,  $\text{Fe}_2\text{O}_3$ ), and iron sulfide ( $\text{FeS}$ ) for steel boiler tubes.<sup>40</sup>

According to the Deacon reaction, increasing corrosion temperature should result in lowering the partial pressure of  $\text{Cl}_2$ , and hence would lead to a decrease in the corrosion rate of tube materials. However, in real furnaces, severe fireside corrosion of boiler tubes normally occurs when metal temperature of tube steels exceeds certain critical temperature, which depends on several factors such as tube location, operational conditions, boiler design, waste chemistry, etc.<sup>44</sup> This is apparently inconsistent with the model based on the Deacon reaction. In addition, in order to stabilize molten phases of pyrosulfate salts, high concentration of gaseous  $\text{SO}_3$  (of more than several hundreds parts per million) is needed in the ambient flue gases (see Figure 20), which is apparently not the case in real waste incinerators. The concentration of  $\text{SO}_3$  in flue gas of waste incinerators is normally below ppm level. Extensive field

tests conducted in the late 1990s revealed that fire-side corrosion of boiler tubes becomes significant for the area where their metal temperatures exceed the melting point of tube deposits.<sup>12,46</sup> Most slag deposits contain not only sodium and potassium chlorides, but also chlorides and sulfates of heavy metals such as lead, zinc, tin, which can lower the melting point of tube deposits, down to below 300 °C.<sup>12</sup> Therefore, the corrosion can be interpreted as molten salt corrosion as well. In many cases, molten phase is indicated in tube deposits where fireside corrosion is prominent. Similar to fused sodium sulfate, acid–base equilibrium for chloride melts with hydrogen chloride and water vapor in flue gas is proposed,<sup>46</sup> and solubility measurements of major metal oxides in eutectic NaCl–KCl and NaCl–KCl–Na<sub>2</sub>SO<sub>4</sub>–K<sub>2</sub>SO<sub>4</sub> melts as a function of the melt ‘basicity’ were performed experimentally.<sup>47</sup> Since tube deposits in waste incinerators generally contain considerable amounts of solid ash constituents such as CaSO<sub>4</sub>, Al<sub>2</sub>O<sub>3</sub>, and SiO<sub>2</sub>, which do not melt at tube metal temperatures, tube deposits are expected to be in partial fusion when corrosion reaction takes place. Laboratory test revealed that the corrosion rate of tube materials drastically increases when the tube deposits start to melt, and the enhanced corrosion rate is influenced by the volume fraction of fused salts in tube deposits.<sup>48</sup> For more molten phases in the deposit, higher corrosion rate is expected. This is schematically illustrated in Figure 23. Therefore, enrichment of heavy metals such as lead and zinc in tube deposits will not only

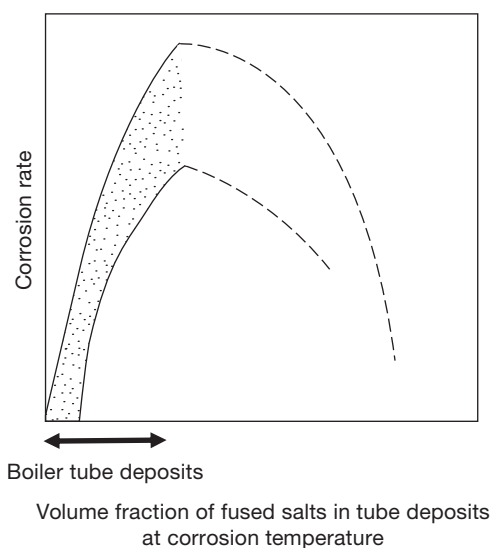


**Figure 23** A schematic illustration explaining the effect of volume fraction of fused salts on corrosion.

lower the melting points of the deposits, but may also augment the volume fraction of molten phases at a certain temperature, resulting in an increased corrosion rate for boiler tubes.

Generally, among iron, chromium, and nickel, iron and chromium have poor resistance to high temperature chlorine environments. This is interpreted from the ability to form highly volatile chlorides at low temperatures, for example, iron trichloride for iron and chromium oxychloride for chromium. This is shown in Figure 22. Corrosion resistance of steels and alloys in waste incinerators seems to follow this trend, and high-Ni alloys have normally good resistance to the environment. However, according to the field tests, chromium seems to be effective as well, which is different from the argument of chloride volatility. Nickel-base alloys with high chromium seem to perform well. It is interesting to note that the effect of molybdenum on corrosion is beneficial, which is opposite to those experienced for sulfate-induced corrosion. Corrosion resistance of steels and alloys seems to increase with increasing their Cr + Mo + Ni concentration, shown in Figure 24 for example. High-Cr, high-Ni, high-Mo alloys such as alloy 625 (22% Cr–61% Ni–9% Mo) are recognized to be resistant in this environment.

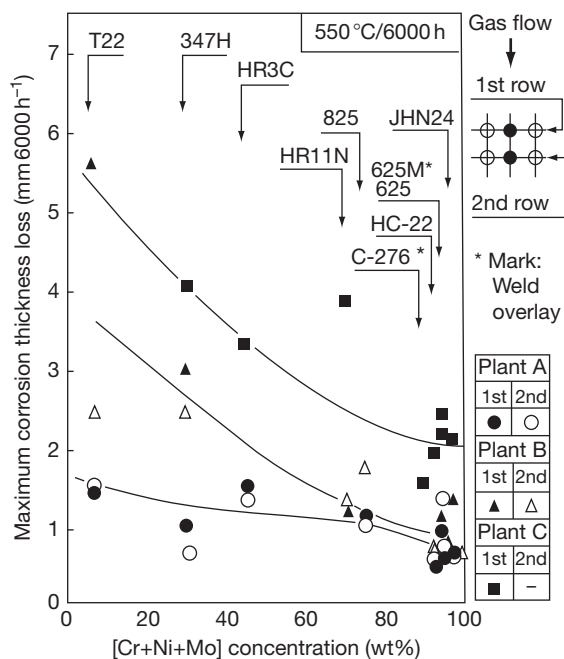


**Figure 24** Tube wall thickness loss of corrosion probes as a function of alloy Cr + Mo + Ni concentration after exposure at 550 °C for 6000 h in waste incinerators. Reproduced from Kawahara, Y.; Orita, N.; Nakamura, M.; Ayukawa, S.; Hosoda, In *Corrosion 97*; NACE: Houston, TX, 1999; paper no. 91.

For black liquor recovery boilers, chloride salts are incorporated in superheater and reheater tube deposits, similar to those in waste incinerators.<sup>49</sup> However, their melting points are generally above 500 °C, considerably higher than the waste incinerators. This is attributed to the absence of heavy metals such as zinc and lead in the fuel. For black recovery boilers, stress corrosion cracking of their floor tubes seems to be the major concern.<sup>50</sup>

## References

- Stringer, J. *Mater. Perform.* **1993**, 53–59.
- Fukahori, K.; Uera, H.; Harada, Y. *Therm. Nucl. Power* **1977**, 28, 33–43.
- Paul, L. D.; Seeley, R. R. In *Corrosion/90*; NACE: Houston, TX, 1990; Paper no. 267.
- Borio, R. W.; Wilson, E. B. The control of high-temperature fire-side corrosion in utility coal-fired boilers, OCR R6D Report No.41, April 1969, Office of Coal Research, Department of the Interior: Washington, DC.
- Simms, N. J.; Kilgallon, P. J.; Oakey, J. E. In *Materials for Advanced Power Engineering 2006*, Proceedings of the 8th Liège Conference Part III, Forschungszentrum Jülich GmbH Zentralbibliothek, Verlag, 2006; pp 1503–1512.
- Stringer, J. *Ann. Rev. Mater. Sci.* **1977**, 7, 477–509.
- Nelson, W.; Cain, C., Jr. *Trans. ASME, Series A* **1960**, 82, 194–204.
- Otsuka, N. *Corros. Sci.* **2002**, 44, 265–283.
- Cunningham, G. W.; Brasunas, A. *Corrosion* **1956**, 12, 389t–405t.
- Cain, C.; Nelson, W. *Trans. ASME, Series A* **1961**, 83, 468–474.
- Levin, E. M.; Robbins, C. R.; McMurdie, H. F. *Phase Diagrams for Ceramists*; The American Ceramic Society, 1964; Vol. I, p 495.
- Daniel, P. L.; Paul, L. D.; Barna, J. In *Corrosion/1987*; NACE: Houston, TX, 1987; Paper no. 400.
- Edström, J. O. *JISI* **1957**, 185, 450–466.
- Kofstad, P. *High Temperature Corrosion*; Elsevier Applied Science, 1988.
- Weast, R. C.; Astle, M. J.; Beyer, W. H. *CRC Handbook of Chemistry and Physics*, 68th ed., CRC Press: Boca Raton, FL, 1987; pp D189–D190.
- Armitt, J.; Holmes, R.; Manning, M. I.; Meadowcroft, D. B.; Metcalfe, E. The spalling of steam-grown oxide from superheater and reheater tube steels, EPRI FP-686, TPS 76-655, Final Report, February 1978.
- Bakker, W. T. Mixed oxidant corrosion in nonequilibrium syngas at 540 °C EPRI TR-104228, March 1995.
- Mrowec, S.; Werber, T. In *Corrosion of Metals*; Department of Commerce, National Technical Information Service, 1978; Chapter 13, pp 444–474.
- Young, D. J. *Rev. High-Temp. Mater.* **1980**, 4(4), 299–346.
- Gutzeit, J. In *Process Industries Corrosion – The Theory and Practice*; Moniz, B. J., Pollock, W. I., Eds.; NACE: Houston, TX, 1986; pp 367–372.
- Rapp, R. A. *Corrosion* **1986**, 42, 568–577.
- Hansen, W. A.; Kessler, G. W. *Trans. ASME* **1965**, 87, 210–214.
- Cutler, A. J. B.; Flatley, T.; Hay, K. A. *Metallurgist and Materials Technologist*, 1981, February, pp 69–81.
- Demo, J. J. *Mater. Perform.* **1980**, 19, 9–15.
- Harada, Y.; Nakamori, M. *Boushoku Gijutsu* **1980**, 29, 615–621.
- Alexander, P. A.; Marsden, R. A.; Nelson-Allen, J. M.; Stewart, W. A. J. *Inst. Fuel* **1964**, 37, 59–69.
- Holland, N. H. J. *Inst. Fuel* **1970**, 43, 97–103.
- Marruffo, F.; Chirinos, M. L.; Sarmiento, W.; Hernandez-Carstents, E. In *17th Congress of the World Energy Council, Division II*, 13–18 September; World Energy Council: Houston, TX, 1988; Vol. 73, pp 73–87.
- Plumley, A. L.; Jonakin, J.; Vuia, R. E. A review study of fire-side corrosion in utility and industrial boilers, Presented at Corrosion Seminar at MacMaster University and Engineering Institute of Canada, Hamilton, Ontario, 19–20 May 1966.
- Blazewicz, A. J.; Gold, M. *An ASME Publication 79-WA/Fu-6*, The American Society of Mechanical Engineers, 1979.
- Blough, J. L.; Stanko, G. J.; Bakker, W. T. In *Ultra-Supercritical Power Plants*, CORROSION/2000, NACE: Houston, TX, 2000, Paper no. 250.
- Luthra, K. L.; Shores, D. A. J. *Electrochem. Soc.* **1980**, 127(10), 2202–2210.
- Fukuda, Y.; Sato, T.; Hamada, H.; Sakaguchi, Y. In *Proceedings of the 32th Meeting of the Japanese Society of Corrosion Engineering*, August 1985, Sapporo, B-302, pp 239–246.
- Simons, E. L.; Browning, G. Y.; Liebafsky, H. A. *Corrosion* **1955**, 11, 505t–514t.
- Otsuka, N.; Rapp, R. A. J. *Electrochem. Soc.* **1990**, 137, 46–52.
- Rapp, R. A.; Goto, K. S. In *Proceedings of the 2nd International Symposium on Molten Salts*; Braunstein, J., Ed.; The Electrochemical Society: Pennington, NJ, 1979; pp 159–177.
- Pettit, F. S.; Meier, G. H. In *Oxidation and Corrosion of Superalloys*; Superalloys 85, The Metallurgical Society of AIME: Warrendale, PA, 1985; pp 651–687.
- Goebel, J. A.; Pettit, F. S.; Goward, G. W. *Met. Trans.* **1973**, 4, 261–278.
- Coats, A. W.; Dear, D. J. A.; Penfold, D. J. *Inst. Fuel* **1968**, 41, 129–132.
- Krause, H. H. J. *Mater. Energy Syst.* **1986**, 7(4), 322–332.
- Von Fäbller, K.; Leib, H.; Spähn, H. *Mitteilungen der VGB* **1968**, 48(2), 126–139.
- Von Huch, R. *Brennst.-Wärme-Kraft* **1966**, 18, 76–79.
- Brown, M. H.; DeLong, W. B.; Auld, J. R. *Ind. Eng. Chem.* **1947**, 39, 839–844.
- Wright, I. G.; Krause, H. H.; Dooley, R. B. In *Corrosion/95*; NACE: Houston, TX, 1995; Paper no. 562.
- Krause, H. H.; Wright, I. G. In *Corrosion/95*; NACE: Houston, TX, 1995; Paper no. 561.
- Otsuka, N.; Kudo, T. In *High Temperature Corrosion of Advanced Materials and Protective Coatings*; Saito, Y., Önay, B., Maruyama, T., Eds.; North-Holland: Tokyo, Japan, 1992; pp 205–211.
- Ishitsuka, T.; Nose, K. *Mater. Corros.* **2000**, 51, 177–181.
- Otsuka, N.; Tsukaue, Y.; Nakagawa, K.; Kawahara, Y.; Yukawa, K. In *Corrosion/97*; NACE: Houston, TX, 1997; paper no.157.
- Tran, H. N.; Barham, D.; Hupa, M. *Mater. Perform.* **1988**, 27(7), 40–45.
- Barna, J. L.; Mattie, R. J.; Rogan, J. B.; Allison, S. F. *Pulp Paper* **1989**, 63(6), 90–98.



## 1.15 High Temperature Tribocorrosion

**I. A. Inman, P. S. Datta, and H. L. Du**

Ellison Building, Northumbria University, Newcastle upon Tyne, NE1 8ST, UK

**C. Kübel**

Group Leader Electron Microscopy, Forschungszentrum Karlsruhe, Institute for Nanotechnology, Postfach 3640, 76021 Karlsruhe, Germany

**P. D. Wood**

Ricardo Plc, Shoreham Technical Centre, Shoreham-by-Sea, West Sussex, BN43 5FG, UK

© 2010 Elsevier B.V. All rights reserved.

<b>1.15.1</b>	<b>Introduction</b>	336
<b>1.15.2</b>	<b>Wear Theory</b>	336
1.15.2.1	Early Wear Theory	336
1.15.2.1.1	Archard and Hirst – Distinction between mild and severe wear	336
1.15.2.1.2	Classification by mechanism	338
1.15.2.2	‘Two and Three Body’ Wear	340
1.15.2.2.1	Overview	340
1.15.2.2.2	Surface films and preoxidation – Third body or not?	341
1.15.2.2.3	Behavior of particles at the interface	342
1.15.2.2.4	The effect of forces of attraction between third bodies	343
1.15.2.3	Mild Wear and Mechanisms of Compact Oxide Formation	344
1.15.2.3.1	Introduction to compacted oxides or ‘glazes’	344
1.15.2.3.2	Quinn’s oxidational wear model	345
1.15.2.3.3	Modification of Quinn’s oxidational wear model for discontinuous contact	346
1.15.2.4	Effect of Load and Sliding Speed	347
1.15.2.4.1	Early work	347
1.15.2.4.2	Wear of cobalt-based alloys	349
1.15.2.4.3	The effect of load and sliding speed – Stellite 6	351
1.15.2.5	Effect of a Second Phase on Wear	353
<b>1.15.3</b>	<b>High Temperature Wear Behavior of Advanced Materials</b>	354
1.15.3.1	Oxide Dispersion Strengthened (ODS) Alloys	354
1.15.3.1.1	Introduction	354
1.15.3.1.2	Observations on high temperature wear behavior of some ODS alloys	354
1.15.3.1.3	Effects of load	358
1.15.3.2	Intermetallics	359
1.15.3.2.1	Introduction	359
1.15.3.2.2	Wear of TiAl – Metallic counterfaces	360
1.15.3.2.3	Wear of TiAl – Ceramic counterfaces	362
1.15.3.3	Nimonic Alloys	364
1.15.3.3.1	Incoloy 800HT counterface	364
1.15.3.3.2	Stellite 6 counterface	366
1.15.3.3.3	Effect of Nimonic material processing route on wear	371
1.15.3.3.4	Nimonic 80A sliding wear – Comparisons between various wear rig configurations	371
1.15.3.3.5	Si <sub>3</sub> N <sub>4</sub> counterface	371
1.15.3.4	Effects of Environmental Variables	371
1.15.3.4.1	Oxygen levels and partial pressure	371
1.15.3.4.2	Effect of water vapor and relative humidity	373
1.15.3.4.3	Other atmospheres	373
1.15.3.5	Effects of Pretreatment of Sliding Surfaces	374
1.15.3.5.1	Preoxidation	374
1.15.3.5.2	Presliding	375

1.15.3.5.3	Ion implantation	375
<b>1.15.4</b>	<b>'Glaze' Formation – Microscale and Nanoscale Investigations</b>	376
1.15.4.1	Introduction	376
1.15.4.2	Microscale Studies of 'Glaze' Formation	376
1.15.4.3	Third Body Interaction in Relation to Compact Oxide Formation	377
1.15.4.4	Nanoscale Investigations of 'Glaze' Formation	379
1.15.4.4.1	Wear data	381
1.15.4.4.2	Studies of wear-affected surfaces produced during sliding of Nimonic 80A against Stellite 6 at 20 °C	383
1.15.4.4.3	Nano-scale microscopy of 'glazed' layers formed during high temperature sliding wear at 750 °C	387
1.15.4.4.4	Other systems	389
<b>1.15.5</b>	<b>Wear Maps: A Useful Design Aid for Selecting Wear-Resistant Materials and Surfaces</b>	389
1.15.5.1	Introduction	389
1.15.5.2	Work by Lim	392
1.15.5.3	Dissimilar Interfaces	393
1.15.5.3.1	Oxide chemistry	396
<b>1.15.6</b>	<b>Summary</b>	396
<b>References</b>		396

---

## Glossary

**Abrasion** The removal of material from a solid surface by the mechanical action of another solid. The second solid may be in the form of a second body (the opposing sliding surface) or third body (wear debris).

**Abrasive wear** The removal of surface material from an object by the action of another agent or medium. This may be the surface of another object or by hard particles trapped between the two interacting surfaces – referred to as 'two body' and 'three body' abrasion respectively. The hard particles or surface must be 1.3 times harder than the soft material from which material is removed.

**Adhesion/cohesion** The action of intermolecular forces at surfaces or interfaces in close contact, holding those surfaces together. Such forces may include chemical bonding (chemical adhesion), intersolubility (diffusive adhesion), Van der Waals forces (dispersive adhesion) and electrostatic forces (electrostatic adhesion). Surface interlocking may also occur (mechanical adhesion) via material filling surface voids or pores. Adhesion is of greater influence during contact of clean metallic surfaces (and thus during severe wear), as there are no contaminants to prevent this contact.

Adhesion is also more effective in a vacuum, where there is no surrounding atmosphere to affect it. Adhesion is normally used to describe attraction between dissimilar molecules and cohesion between like molecules.

**Asperity** A protruding, raised area of (sliding) surface.

**Block-on-cylinder** A test configuration used to study unidirectional sliding wear, with the 'block' (either stationary or in reciprocating motion) as the sample material and the 'cylinder' (normally rotating) as the counterface.

**Coefficient of friction** Dimensionless value describing the resistance experienced by two surfaces in movement against each other. The higher the value, the greater the ability to resist movement. The 'frictional force' is that which needs to be applied to overcome this resistance to movement.

**Compacted oxide layer** Often wear-protective layers of oxide are formed as a 'tribocorrosion' product, when two metals (or a metal and ceramic) are slid against each other at high temperature in an oxygen-containing atmosphere.

**Compacted particles** Debris forming a compacted oxide layer.

**Counterface (countersurface)** The material or surface sliding against the sample.

**Critical oxide thickness ( $\xi$ )** According to Quinn's oxidation wear model,<sup>1</sup> this is the maximum thickness of compacted oxide layer or 'glaze' that can develop and remain mechanically stable. Beyond this, the oxide becomes unstable, generating a wear particle.

**Critical transition temperature** The minimum temperature according to Jiang<sup>2</sup> at which sintering can occur within a compacted oxide layer, allowing a solid wear-protective layer (or 'glaze') to form on top of it before it is broken down.

**Cross-slip** Transfer of (screw) dislocation glide from one slip plane to another during deformation.

**Cutting** The physical deformation due to a harder asperity or third body being pushed through a softer material where adhesion is high. The movement of the harder material over the softer material results in the creation of a deeper groove upon the sample surface than seen with 'wedge-forming' or ploughing, with long strips of debris forming at the point of contact.

**Dissimilar interface system** A configuration where the sample and counterface are of different materials.

**Ejection** The removal of wear debris from the sliding wear interfaces such that it can no longer play an 'active' part in the wear process.

**Fretting** Damage due to repeated relative motion of sliding surfaces against each other, for example, due to vibration or oscillation.

**Glaze** Compacted oxide layer, usually referring to a more wear protective, sintered form generated (normally) at elevated temperatures.

**High angle annular dark field in STEM** Images formed by gathering scattered electrons with an annular dark field detector. An 'annular dark field' (ADF) image generated only by very high angle, incoherently scattered electrons, is highly sensitive to variations in atomic number of the elements in the sample (Z-contrast images) and is hence known as 'high angle annular dark field' or HAADF.

**HIPped (hot isostatically pressed)** A method of alloy or material production by powder metallurgy methods, using a combination of temperature and (isostatic) pressure to produce the final item.

**Intermetallic** Materials composed of defined proportions of two or more metallic elements and possibly one or more nonmetallic elements. Such materials typically have a highly ordered crystal lattice structure composed of the constituent parts, but not necessarily the same as any of the constituent parts.

**Ion-implantation** The implantation of ions of one material into the crystal lattice of another solid, thereby bringing about a desired change in the physical properties of that solid (i.e., doping).

**Material transfer** Transfer of material at the wear interface from one wear surface to the other.

**Mechanical alloying** The mixing of two or more solid phase materials to produce material of different composition and possibly phase to either of the original materials. During sliding wear (i.e., severe wear), this may happen where the two parent sliding surfaces are of different composition, due to material transfer between and mixing at the sliding interface. This mechanically alloyed material may then potentially readhere to either parent sliding surface.

**Mild wear** Wear in which direct contact between the sliding surfaces are separated by corrosion debris (generally oxide), often less than 1  $\mu\text{m}$  diameter. This debris may take the form of compacted oxide or 'glaze' layers. Where the two sliding surfaces are metallic, the debris being generally nonmetallic prevents adhesion and (metallic) transfer. Coefficient of friction values are thus usually much lower. Wear values are generally, but not always, lower than severe wear, however, such debris can act abrasively and instead enhance wear.

**'Orowan' stress** The stress required to bow a dislocation between particles or impurities, acting as obstacles within a crystal lattice.

**Oxide dispersion strengthened (ODS) alloy** An alloy in which a fine dispersion of oxides have been introduced, to strengthen the material

by interfering with the operation of slip systems during material deformation.

**Phase transition** Thermally or mechanically induced change in crystallographic structure, for example, from 'face-centered cubic' to 'body-centered cubic' in iron or mild steel, or 'face-centered cubic' to 'hexagonal close-packed' in cobalt-rich alloys

**Pin-on-disk** A test configuration used to study sliding wear, with the 'pin' (or in some cases 'button' or 'coupon') as the sample material and the 'disk' as the counterface. The 'pin' may be held stationary against a rotating 'disk' to study unidirectional sliding wear, or moved backwards and forward against a stationary 'disk' to study reciprocating or fretting wear.

**Ploughing** A general term, covering the three related terms of 'ploughing,' 'wedge-forming' and 'cutting,' being defined as the physical deformation due to a harder material ploughing through a softer material or rather the work required to carry this out. Ploughing is also referred to more specifically as the physical deformation due to a harder material being pushed through a softer material where adhesion forces are weak. The grooves created are shallower than with 'cutting' or 'wedge-forming,' with lower penetration of the harder asperity or third body into the softer material. Formation of wear debris particles cannot be clearly seen at the point of contact.

**Positron annihilation (PA)** A major technique in Materials Science, originally applied in condensed-matter physics, now widely used in metals and alloys to provide information on defect structures.

**Retention** The continued residency of wear debris at the wear interface, such that it may continue to play an active part in the wear process.

**'Run-in' wear** A normally brief period of severe wear due to initial metal-to-metal contact almost always observed before mild wear is established.

**Sample** The material or surface undergoing wear testing.

**Scanning electron microscopy (SEM)** A type of microscope in which the surface of a sample is scanned with a high energy beam of electrons. An image of the sample surface is

created from secondary electrons that are ejected from it.

**Scanning transmission electron microscopy (STEM)** A variation of TEM in which the electrons pass through the specimen and the electron optics focus the beam into a narrow spot over the sample in a raster. The rastering of the beam across the sample is used to perform various analyses such as annular dark field (ADF) imaging, energy dispersive X-ray (EDX) analysis and electron loss spectroscopy (EELS) simultaneously, allowing direct correlation of image and quantitative data.

**Scanning tunneling microscopy (STM)** An imaging technique based on the concept of quantum tunneling. In STM a conducting surface is brought very near to the surface (metallic/semiconductor) when a bias between the two allows electrons to tunnel through the vacuum between them. At low voltage the tunneling current is a function of local density of states (LODS) at the Fermi level of the sample. The changes in current accompanying the tip movement over the surface are translated into an image.

**Scanning tunneling spectroscopy (STS)** A technique employed within an STM, to probe the local density of electronic states, and band gap of surfaces and materials on surfaces at the atomic scale. The technique allows observation of changes in constant current topographies with tip-sample bias, local measurements of  $I/V$  curves and tunneling conductance  $dI/dV$ . This allows investigations of small areas (5 Å diameter, the area in which the tunneling current flows).

**Scuffing** Roughening of surfaces by plastic flow, whether or not there is material loss or transfer.

**Selected area diffraction pattern (SAD)** This technique is generally performed inside a TEM, in which electrons pass through a thinned sample (see 'TEM'). As the wave length (a fraction of a nanometer) and the spacing between atoms are comparable, the atoms act as diffraction gratings to the electrons. Some of the electrons are scattered to particular angles determined by the material crystal structures (allowing

identification and analysis) and form a spot pattern image on the TEM screen.

**Severe wear** The wear encountered typically where two metallic surfaces are in direct sliding contact, without an intervening compacted oxide or 'glaze' layer, or other protective coating. Such wear is characterized by high coefficient of friction values, high levels adhesion, plastic deformation and to varying degrees (mainly metallic), material transfer between the surfaces. Also typical of severe wear is the generation of large, flat, angular, generally metallic wear debris with sizes of up to 0.1 mm (or greater) due to 'delamination.'

**Slip direction** The direction on the slip plane with the highest linear density.

**Slip plane** The crystallographic close packed plane in which dislocation movement can occur.

**Slip system** A combination of slip planes and directions defined by crystallographic arrangement (i.e., body-centered cubic, face-centered cubic, hexagonal close-packed).

**'Third body'/'three body' wear** The interaction of two wear surfaces during sliding, in combination with a third agent (i.e., debris). This third agent may be termed 'active' (it is retained between the wear surfaces and modifies the wear process) or 'passive' (it is ejected and has no effect).

**Torque transducer** A device for measuring torque in a rotating system. In tribology, changes in torque due to sliding surface contact can be used to determine the coefficient of friction.

#### **Transmission electron microscopy (TEM)**

A widely used technique in Materials Science where an electron beam is transmitted through a thinned sample placed in vacuum with a typical energy of 100–400 keV. The electron beam is then focused by a series of magnetic field lenses into a typical spot of diameter 1–10 nm. A TEM image is created from those electrons that pass through the sample.

**Tribocorrosion, tribo-oxidation** The enhanced generation of corrosion product (normally oxide) during sliding wear. The conjoint action of tribology and corrosion/oxidation.

**Tribology** The study of the science and technology of interacting surfaces in relative motion, and including the related subjects of lubrication, friction and wear. Derived from the Greek verb τριβο ('tribo'), meaning 'to rub.'

**'Two body' wear** The interaction of two wear surfaces during sliding, in the absence of a third agent (i.e., wear debris) between the wear surfaces.

**Unidirectional sliding** Where the sample and counterface move in only one direction relative to each other.

**Van der Waals' forces** Attractive forces between unbonded atoms and molecules (significant for very small particles of less than 5  $\mu\text{m}$  in diameter).

**Vickers hardness number (VHN)** A parameter defining the hardness of an engineering material. The Vickers hardness number is that obtained by application of a predefined load through a diamond pyramidal (or Vickers) indenter. The size of the indent created is used to obtain a measure of materials' hardness.

**Wear behavior, wear regime, wear mechanism** The type of wear observed (i.e., mild or severe wear).

**Wear debris** The material removed from sliding surfaces during wear. This may be metallic (dominant during severe wear) or oxide (dominant during mild wear).

**Wear map, wear mechanism map** A plot that shows the effect on wear mechanism of two or more sliding variables (i.e., load, temperature, sliding speed), allowing prediction of wear mechanism where the values of these variables are known.

**Wear rate** The rate of material removal during sliding.

**Wear volume** The volume of material removed during sliding.

**Wedge-forming** The physical deformation due to a harder asperity or third body being pushed through a softer material where adhesion is moderate. Material is pushed up ahead of asperities on the counterface, resulting in a grooved wear scar with transverse cracks. The depth of groove created is lower than for the 'cutting' model, but higher than for 'ploughing.'

**Symbols**

<b><i>d</i></b>	Distance for which sliding contact is maintained
<b><i>f</i></b>	Mass fraction of oxide
<b><i>p</i></b>	Mean pressure (load/area)
<b><i>r</i></b>	Distance affecting mutual action of Van der Waals' forces
<b><i>t</i></b>	i) Time of sliding ii) Time required to grow oxide layer of critical thickness
<b><i>v</i></b>	Speed
<b><i>A</i></b>	i) True area of contact ii) Hamaker constant
<b><i>A<sub>p</sub></i></b>	Arrhenius constant
<b><i>D</i></b>	Depth of wear
<b><i>E</i></b>	Activation energy for bonding
<b><i>F</i></b>	i) Force of attraction ii) Contact frequency
<b><i>H</i></b>	i) Material indentation hardness ii) Indentation hardness
<b><i>K<sub>a</sub></i></b>	Probability of a wear particle being generated
<b><i>K<sub>p</sub></i></b>	Oxidation rate (parabolic rate constant)
<b><i>K<sub>1</sub></i></b>	'K factor' ( $K_1 = K_a/H$ )
<b><i>K<sub>1c</sub></i></b>	Fracture toughness
<b><i>L</i></b>	Sliding distance
<b><i>P</i></b>	Applied load
<b><i>Q<sub>p</sub></i></b>	Activation energy for oxidation
<b><i>R</i></b>	i) Radius of particle of sphere ii) Gas constant
<b><i>T, T<sub>0</sub></i></b>	Temperature in Kelvin (absolute temperature)
<b><i>V</i></b>	Sliding speed
<b><i>W</i></b>	Work volume
<b><i>γ</i></b>	Surface energy
<b><i>γ<sub>0</sub></i></b>	Surface energy at standard temperature and pressure
<b><i>ρ</i></b>	Oxide average density
<b><i>τ</i></b>	Length of time of each encounter (contact between surfaces)
<b><i>ξ</i></b>	Critical oxide layer thickness
<b><i>Δm</i></b>	Growth of oxide per unit area
<b><i>1/K<sub>a</sub></i></b>	Number of encounters (contacts between surfaces) required to generate an oxide layer of critical thickness

**1.15.1 Introduction**

High temperature wear is a serious problem in many situations, including power generation, transport, materials processing, and turbine engines.<sup>3–7</sup> Such wear is accentuated by faster surface oxidation kinetics, loss of mechanical hardness and strength of materials

forming the contacting surfaces, and changes in adhesion between these surfaces caused by the joint action of temperature and tribological parameters. Efforts to prevent wear have included the use of oxidation resistant and thermally stable materials, coatings, and materials with preoxidized surfaces.<sup>3–10</sup> However, the choices of coatings and materials are severely restricted by high temperature environmental conditions.<sup>3–5</sup>

An alternative method of generating wear-resistant surfaces on coated and uncoated materials is to take advantage of certain events that accompany the high temperature wear process, such as oxidation, debris generation, and elemental transfer between contacting surfaces.<sup>3–5,11</sup> These events under certain conditions of temperature, pressure, and speed can lead to 'glaze' formation on contacting surfaces, enhancing resistance to further wear.<sup>2–5,11–30</sup> Although 'glaze' formation and the general issues relating to wear at elevated temperatures have been extensively studied,<sup>2–5,11–30</sup> it is still difficult to predict the precise conditions that promote 'glazed' surface formation. Many aspects of high temperature wear, including debris generation, debris oxidation, material transfer between surfaces, and enhanced elemental diffusion, still need clarification. At present, there is incomplete understanding of the formation, nature, microstructure, and defect structure of high temperature wear-resistant surface 'glaze.'

This chapter is not intended to catalogue all previous work. Instead, the objective is to concentrate on generic principles, modeling, and scientific theories, which where possible will facilitate understanding of the high temperature wear process. There is a heavy reliance on the information generated in the authors' own laboratory, where extensive use has been made of current microscopical techniques.

The chapter is structured as follows: [Section 1.15.2](#) deals with some general principles of wear, [Sections 1.15.3](#) and [1.15.4](#) consider published research while [Section 1.15.5](#) discusses some results of nanoscale investigations of 'glaze' formation; [Section 1.15.6](#) concludes with some final remarks.

**1.15.2 Wear Theory****1.15.2.1 Early Wear Theory****1.15.2.1.1 Archard and Hirst – Distinction between mild and severe wear**

In 1956, Archard and Hirst<sup>31,32</sup> categorized wear into two groups: mild wear and severe wear.

'Mild wear' occurs when the debris produced (generally oxide) prevents direct metal-to-metal contact. Although Quinn<sup>33</sup> does not specifically mention



the oxidation reaction in his review of oxidational wear when discussing the definition of mild wear, the majority of studies into sliding wear have concentrated on the oxidation reaction. Debris produced is of very small size ( $<1\text{ }\mu\text{m}$ ) and complete coverage is not necessarily achieved, with oxide in many cases only forming on load-bearing areas such as asperities. Electrical contact resistance is high because of the presence of the oxide on the wear surfaces.

The absence of such oxides allows contact between the metallic interfaces, with adhesion, plastic deformation, and, to varying degrees, material transfer between the surfaces. This is typical of the 'severe wear' situation, examples of which have already been observed in the lower temperature sliding wear of

Incoloy MA956 against Incoloy 800HT, in the work of Wood<sup>3</sup> and Rose<sup>4</sup> (these authors refer to these alloys as MA956 and Incoloy 800); the  $270^\circ\text{C}$  case shown in Figure 1 is one such example. Debris particles tend to be large, flat and angular, up to  $0.1\text{ mm}$  or greater. Contact resistance on surfaces that have undergone severe wear tends to be very low, due to the exposure of the metallic surface.

Temperature affects the nature of wear as it influences the kinetics of oxidation. Other factors such as relative humidity<sup>34</sup> and partial pressure of oxygen also affect the nature of wear as explained by Lancaster<sup>26</sup> and Stott *et al.*<sup>14,35</sup> Figure 2 shows a smaller range of severe wear in an oxygen atmosphere at  $300^\circ\text{C}$ , compared to that in air.

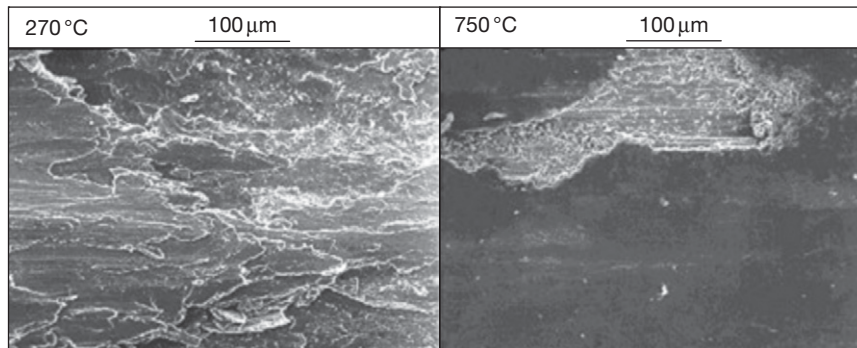


**Figure 1** Wear surfaces produced during the sliding of Incoloy MA956 against Incoloy 800HT at  $270^\circ\text{C}$ <sup>4</sup> (load =  $7\text{ N}$ , sliding speed =  $0.654\text{ m s}^{-1}$ , sliding distance =  $9418\text{ m}$ ). At  $270^\circ\text{C}$ , a highly worn, heavily deformed surface is produced. There is direct metal-to-metal contact, allowing high levels of adhesion accompanied by plastic deformation, material transfer and the production of large flat angular debris. At  $750^\circ\text{C}$ , a compacted oxide layer has been created from the debris, giving physical protection via enhanced hardness and also separating the metallic surfaces, preventing contact and adhesion.

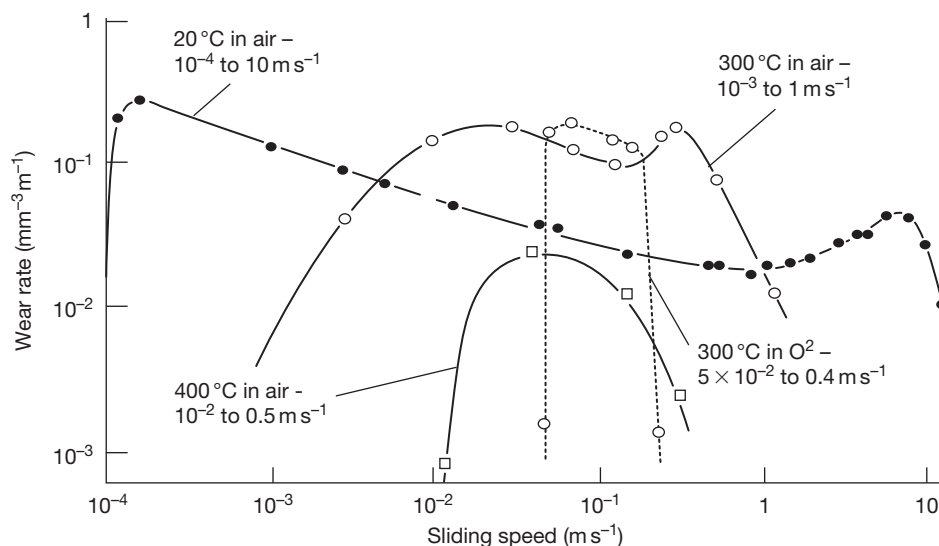


**Figure 2** Variation in wear rate with sliding speed at  $20^\circ\text{C}$ ,  $300^\circ\text{C}$ , and  $400^\circ\text{C}$  in air and also  $300^\circ\text{C}$  in pure oxygen for  $\alpha/\beta$  brass sliding against steel<sup>26</sup> (approximate sliding speed ranges for severe wear at each temperature given in italics).

The model that Archard and Hirst<sup>31</sup> proposed assumes a true area of contact, occurring between a small number of asperities on the contacting surfaces. The true area of contact can be calculated by eqn [3]:

$$A = P/H \quad [1]$$

where  $P$  is the applied load and  $H$  is the indentation hardness of the material. If  $W$  is the worn volume and  $L$  is the sliding distance producing the wear, then  $W/L$  is dependent on, and is therefore proportional to, the area of the friction junctions or true area of contact.

$$W/L \propto A \quad \text{or} \quad W/L = K_a L \quad [2]$$

This gives:

$$W/L = K_a P/H \quad \text{or} \quad W = K_a PL/H \quad [3]$$

the dimensionless parameter  $K_a$  being the constant of proportionality and also the probability of a wear particle being generated. It is also referred to as the 'wear coefficient.' An alternative form ( $K_1 = K_a/H$ ) is:

$$W = K_1 PL \quad [4]$$

$K_1$  being referred to as the 'K factor.'<sup>31</sup> Taking eqn [3] and rearranging allows  $K_a$  to be expressed in terms of wear depth, sliding velocity, and pressure.

Dividing by the apparent area of contact gives:

$$d/L = p(K_a/H) \quad [5]$$

where  $d$  is the depth of wear (volume divided by area) and  $p$  is the mean pressure (load over area). If  $v$  is sliding speed and  $t$  is the time of sliding,  $L = vt$ , then

$$d/vt = p(K_a/H) \quad \text{or} \quad t = dH/K_a p v \quad [6]$$

$$K_a = dH/pvt \quad [7]$$

The above implies that the level of wear is proportional to the sliding distance and applied load; Archard and Hirst showed this to be true over a limited range<sup>31</sup> (Figure 3).

The Archard model<sup>31</sup> is effective assuming that there are no changes in the wear surface as a result of the sliding process. However, changes do occur in many cases, leading to changes in wear rate resulting from little or no variation in experimental or operational parameters,<sup>27,28,36,37</sup> and thus, changes in  $K_a$  value may be observed. Previous experimental work<sup>3-5</sup> has demonstrated that such changes can occur, with changes in friction being coincident with a switch from early severe wear to mild oxidational wear, without any alteration of experimental parameters. This was usually denoted by decreases in the mean coefficient of friction and also in the variability of the

coefficient of friction versus time trace. For example, during early severe wear at 750 °C, mean values typically between 0.7 and 1 could be obtained for Nimonic 80A versus Incoloy 800HT. On reaching the mild wear stage, values of between 0.4 and 0.5 were typically obtained.

A direct link between hardness and wear rate is not always observed. Archard and Hirst proposed the theory of mild and severe wear discussed in this section, to resolve these difficulties.<sup>31</sup>

#### 1.15.2.1.2 Classification by mechanism

Many approaches to classifying wear have been attempted; Quinn's 1983 review<sup>33</sup> lists a number of these and tries to classify them under Archard and Hirst's mild and severe wear<sup>31</sup> headings (Table 1). For example, Burwell and Strang<sup>38</sup> propose seven different classifications of mild and severe wear, which Quinn argues are actually special cases of Archard and Hirst's mild and severe wear (with many of their classifications, including elements of both).<sup>31</sup> Ludema<sup>39</sup> talks in terms of 'scuffing' ('roughening of surfaces by plastic flow, whether or not there is material loss or transfer') and 'run-in,' Quinn seeing 'scuffing' as a form of adhesive wear and 'run-in' as corrosive or mild wear (due to the generation of oxides on the wear surface). Finally, Tabor<sup>40</sup> does not distinguish between adhesive and corrosive wear, preferring to classify both as adhesive wear, with Burwell and Strang's remaining mechanisms being referred to as 'nonadhesive wear' (surface fatigue, abrasion, and fretting) or a mixture of both (cavitation and erosion).

The classification of wear mechanisms clearly remains a matter of debate, although Quinn<sup>33</sup> proposes that each of the forms of wear described should be considered in terms of either mild or severe wear in any given situation. However, it is the view of the current authors that it is not possible to talk simply in terms of mild and severe wear. For example, when material is lost by abrasion, the loss of material by the ploughing action of asperities on a wear surface does not necessarily require adhesion or corrosion to remove material. Also, loss of material by delamination wear is a fatigue-related process, caused by repeated loading and unloading of surface layers as asperities of the opposite surface pass over it, assisting the propagation of subsurface cracks, eventually leading to material loss. Although adhesion or reaction with a corrosive environment may accelerate the process, again neither is necessary for fatigue and crack propagation to occur.

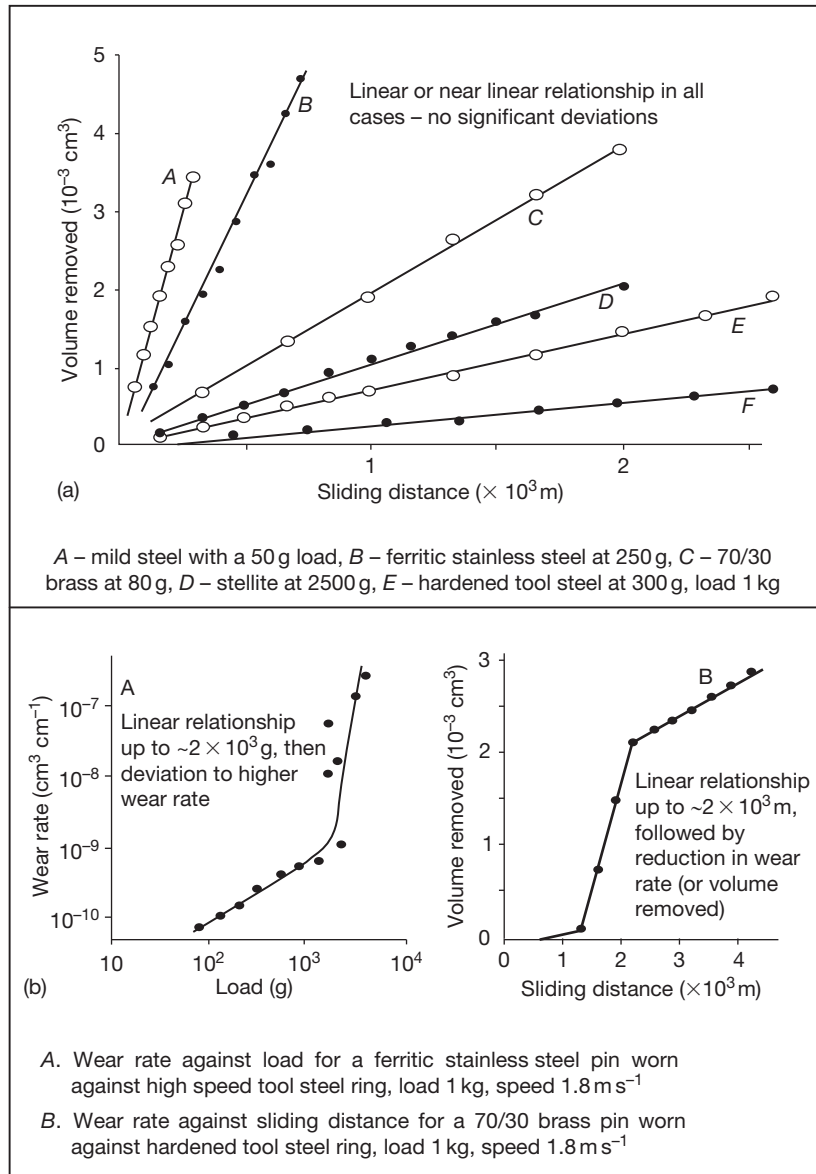


**Figure 3** Experimental data from Archard and Hirst's Work on like-on-like sliding at  $1.8 \text{ m s}^{-1}$ . Reproduced from Archard, J. F.; Hirst, W. *Proc. Royal Soc. London A* **1956**, 236, 397–410.

**Table 1** Quinn's comparison of the various classifications of wear

Burwell and Strang [25]	Tabor	Ludema	Quinn [16]
<div style="display: inline-block; vertical-align: middle;">           { Adhesive wear Corrosive wear Surface fatigue (pitting) Abrasion Fretting Cavitation Erosion }         </div>	Adhesive wear	Scuffing "Run-in"	Severe wear Mild wear
	Nonadhesive wear	Mechanisms of scuffing and "run-in"	Mechanisms of mild and severe wear
	{ Mixtures of adhesive and non-adhesive wear }	Not covered in Ludema's review	

Source: Reproduced from Quinn, T. F. J. *Tribol. Int.* **1983**, 16, 257–270.

The different behaviors of oxide debris are not accounted for either. Inman *et al.*<sup>5,21–24</sup> observed that during sliding wear, an oxide could either be protective or abrasive or even in limited quantities affect the severe wear process. It was thus suggested that mild and severe wear could be subcategorized into ‘standard severe wear’ (no oxide present, adhesion and delamination dominating), ‘abrasion-assisted severe wear’ (oxide abrasively assists the adhesion/delamination dominated wear process), ‘protective mild wear’ (oxide prevents metallic contact and forms a protective layer as loose debris or ‘glaze’), and ‘abrasive mild wear’ (oxide debris prevents metallic contact, but remains loose and promotes wear by abrasion).<sup>24</sup> Another suggested classification system is that of Rabinowicz,<sup>41</sup> who identifies abrasive and fatigue wear, as well as adhesive and corrosive wear, as distinct categories of wear in their own right. Each of these four categories of wear is now discussed.

### 1.15.2.2 ‘Two and Three Body’ Wear

#### 1.15.2.2.1 Overview

Much of the discussion so far has been concerned with what happens when two surfaces move relative to one another, generating wear debris. The consideration of wear without the interaction of debris is referred to as ‘two body’ wear. However, the generation of debris particles introduces a ‘third body’ into the sliding process, which can then go on to have a significant effect on the wear process.

This debris may be retained within the interface area, where it may become an ‘active’ participant<sup>42</sup> in the wear process or may be ejected immediately after its formation, in which case, it is referred to as ‘passive’ debris. Active debris tends to be fine and may be a mixture of metallic and oxide particles. On the other hand, ‘passive’ debris particles are in general much larger and, because of their immediate removal from the wear interface on formation, may retain much of their original form and structure. In metallic wear, ‘passive debris’ is more likely to be metallic.

The work of Rose<sup>4</sup> and Inman *et al.*<sup>5,21–23</sup> clearly illustrates this difference. For sliding of Nimonic 80A and Incoloy MA956 versus Stellite 6, at lower temperatures (390 °C and lower at 0.654 m s<sup>−1</sup>, 270 °C and lower at 0.905 m s<sup>−1</sup>), debris particles tended to be of a fine nature; these were largely retained at the interface, commuted, and converted to a layer of loose, discrete (usually) oxide particles. The retention of this debris as a ‘third body’ then acted to keep the interfaces separated and wear values low. This is an example of ‘active’ debris.

At intermediate temperatures up to 630 °C for Nimonic 80A versus Stellite 6 and 510 °C for Incoloy MA956 versus Stellite 6, debris was ejected as larger metallic particles that did not remain at the wear interface and thus did not separate the two wear surfaces. This is an example of ‘passive’ debris.

At higher temperatures, larger amounts of fine oxide debris were generated; in the case of Incoloy MA956 versus Stellite 6, this again separated the interfaces and also formed protective compacted oxide or ‘glaze’ layers. Nimonic 80A slid against Stellite 6 also formed protective layers at 0.314 m s<sup>−1</sup>; however, at 0.654 and 0.905 m s<sup>−1</sup>, wear levels increased because of oxide debris acting abrasively against the Nimonic 80A surface. These latter observations are once again examples of ‘active’ debris.

In addition to promoting mild wear, the negative effect of abrasion has also been noted; as with hard and soft surfaces in the two body wear models already discussed, for a third body to have an abrasive effect at the wear interface possibly leading to increased wear, it is normally expected that the hardness of the third body will be at least 1.3 times greater than that of either of the contacting materials.<sup>33</sup>

Active participation of third bodies has been noted by other researchers, notably Iwabuchi *et al.*,<sup>43–45</sup> who studied the effects of the introduction of iron oxide (Fe<sub>2</sub>O<sub>3</sub>) particles to the wear interface, noting that, where the particles were supplied under fretting test conditions, the severe running-in wear volume for a standard carbon steel (S45C) was decreased 10-fold.<sup>45</sup> Increased surface roughness also proved to be a positive factor in that the particles were more effectively retained. Introduction of a large enough quantity of Fe<sub>2</sub>O<sub>3</sub> particles eliminated the severe wear running in stage.

Iwabuchi also studied the effects of particle size<sup>43</sup> and found that with a surface roughness of maximum asperity height 20 μm, a particle size of 0.3 μm (the smallest studied) was found to give the lowest wear rate during mild wear. However, particle sizes of 1 μm were observed to decrease the wear rate in the severe wear stage the most. Ideally, the same size particle would result in both; for practical use to be made of such observations, a compromise needs to be made. It is also to be noted that Iwabuchi expressed uncertainty as to whether the 0.3 μm particle size is the most effective only for the 20 μm maximum asperity height or for other asperity heights as well.

The current authors suggest that the optimum size will vary and also change as the wear test proceeds, for the simple reason that, as the larger asperities are

removed, until such time as an oxide layer forms, the particle size that can be contained in the recesses will also decrease. Conversely, during severe wear, roughening of the wear surface may allow for a larger particle size to be retained. A limiting factor is that there will probably be an upper limit of particle size, partially due to comminution and ejection of larger debris and also a limit to the size of particle that can convert from metal to oxide.

Iwabuchi also points out that the tendency to form a protective compacted layer of oxide is affected by other parameters; varying test parameters such as load and sliding speed showed that, for certain conditions, the oxide particles acted as an abrasive and increased the wear rate. Figure 4 is a wear map of load versus amplitude, where different combinations of load and amplitude produce different outcomes as regards the influence of the introduced oxide particles.<sup>42</sup> For very low loads and amplitudes, the introduction of the oxide particles has a positive effect, lowering the level of wear. For medium loads and amplitudes, the oxides have a negative effect and wear levels are higher because of the abrasive action of the oxides. Moreover, increasing load for moderate amplitude or amplitude for moderately high load again results in a positive influence and wear levels are low.

Leheup and Pendlebury<sup>46</sup> took a different approach, by the use of an interfacial air flow in a like-on-like 'cup-on-flat surface' sliding test at various

temperatures for Fe–18% Cr–9% Ni stainless steel. The effect of temperature was quite marked, with removal of the debris at room temperature leading to increased wear. At temperatures of 400 and 500 °C, formation of compacted oxide layers did still occur; this was considered to be due to the ready sintering and adherence of the loose oxide particles at these temperatures. The attractive effects of Van der Waals' forces (acting to retain smaller particles between the wear surfaces) were also considered, as detailed in Sections 1.15.2.2.3 and 1.15.2.2.4. Colombie *et al.*<sup>47</sup> obtained similar results with increased wear on blowing nitrogen through the wear interface at frequent intervals; the more frequent the intervals, the greater the observed wear. Magnetic fields can also have an effect with ferromagnetic materials; Hiratsukam *et al.*<sup>48</sup> showed that the field direction could influence whether debris was retained (thus decreasing wear) or ejected (thus increasing wear).

Rigney<sup>49</sup> also questioned the validity of the traditional models of wear if they do not take into account third bodies resulting from transfer and mixing; in addition to separating or screening 'first bodies' (sample and counterface), third bodies can have other effects as they are able to flow and transmit load, accommodate velocity gradients, and are also created, destroyed, and regenerated during sliding. Resulting behavior can depend on dimensions, compositions (may be the same as either of the 'first body' materials or a mixture of both), properties (the materials may undergo stresses close to their mechanical limits), and hardness. Chemical composition is a key to the observed properties of the third body.

Despite the evidence, it is still the case that many models of wear do not take into account the action of the third body, with debris assumed to be ejected on formation. Much work has been done using experimental rigs in which debris is retained at the wear interface, including fretting wear and much of the pin-on-disk work.<sup>1,2,6,10,14,17–19,33,35,43,46,50–71</sup> Even in situations where ejection is favored, such as the block-on-cylinder approach,<sup>3,4</sup> debris has remained at the interface and has played a significant part in the promotion of mild wear.

#### 1.15.2.2.2 Surface films and preoxidation – Third body or not?

Also absent from the traditional models, is consideration of the effect of any surface films, adsorbed gases or other volatile species that may be present in most situations. Clearly, the wear process will be affected by the nature of the surfaces.<sup>72,73</sup>

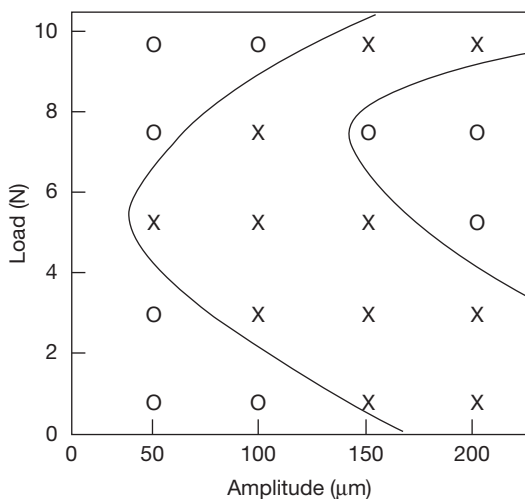


**Figure 4** Effectiveness of wear reduction on S45C plain carbon steel due to the introduction of  $\text{Fe}_2\text{O}_3$  particles.<sup>42</sup> (○) Positive effect, oxide separates wear surfaces and wear is low, (×) negative effect, oxide acts as an abrasive and increases wear.



This is also true for preoxidized films,<sup>3,48,49,52</sup> where early metal-to-metal contact has been decreased or eliminated to varying degrees, followed by earlier formation of compacted oxides in a number of cases. Although not a 'third body' in their own right (they are directly attached to one or both 'first body' surfaces at the beginning of sliding), the sliding action will create extra loose material from the surface oxide layer, which will proceed to act as a third body where retention is preferred over ejection.

#### **1.15.2.2.3 Behavior of particles at the interface**

The behavior of third body material at the wear interface goes beyond just acting as an agent for separation of the sliding surfaces or removing material from them. Rigney's observations<sup>49</sup> on load transmission, velocity gradients and debris particle creation, destruction, and regeneration are one example of this.

In addition, the particles may undergo varying degrees of motion at the interface because of the movement of the sliding surfaces. Halliday and Hirst<sup>53</sup> noted accumulation and 'rolling' of debris particles during fretting corrosion tests on mild steel specimens, which they commented as being responsible for the decrease in friction during testing. They also noted that some sliding debris must be present, as the observed coefficient of friction would have been in the region of 0.002 for rolling alone, rather than the values near or below 0.05 observed after the run-in phase was completed. Halliday and Hirst also established that the presence of the oxide particles prevented wear due to welding (adhesion) of the surfaces together.

Conversely, Suh and Sin<sup>74</sup> noted an increase in friction and wear by ploughing due to the presence of debris particles; this was confirmed by the removal of the debris, after which the coefficient of friction fell from a high 'steady-state' value and gradually rose again as further debris was generated. It is to be commented here, that Suh and Sin used a unidirectional crossed rotating-cylinder-on-stationary-cylinder configuration, while Halliday and Hirst conducted tests with an 'oscillatory-cylinder-on-two-block-fretting-wear' configuration. Thus, it would have been likely that debris retention in Halliday and Hirst's work would have been much greater, allowing for the observed generation of Fe<sub>2</sub>O<sub>3</sub> oxide particles.

Also, Suh and Sin's work<sup>74</sup> largely describes a metal-metal interaction, with most testing being carried out in a purified argon atmosphere. Even where an inert atmosphere is not used (as with AISI 1020

steel), there was nothing to suggest the generation of oxide debris and thus all interactions can be assumed to be metal-metal in their case. Hence, a direct comparison between their work and that of Halliday and Hirst may not be wholly appropriate. However, Rose<sup>4</sup> and Inman *et al.*<sup>5,21,22,24</sup> report high levels of wear for Nimonic 80A versus Stellite 6 at elevated temperature, where only oxide debris was generated during all but the earliest part of the sliding process. Here, it is the oxide debris that acts as a third body and aids material removal.<sup>5,21,22,24</sup>

Rice *et al.*<sup>75</sup> showed that the effects of debris parameters on coefficient of friction are more important than asperity parameters. On modeling and comparing the influence of variations in density and size of particles at the interface with that of asperities on coefficient of friction, the sensitivity of coefficient of friction to changes in particle density and size was much the greater.

When particle parameters alone were considered, it was observed that increases in density lead to a much faster increase in the coefficient of friction to a high steady state value. Increased particle sizes also lead to increases in the coefficient of friction values, or conversely, smaller particle sizes are preferred for a lower friction regime. Of most interest in the work of Rice *et al.*,<sup>75</sup> was the observation that, if particle density was increased while particle size was decreased (which could be regarded as analogous to particle break-down early in the wear process), then there was a sharp increase in friction, followed by a steady decrease with time.

It is to be noted that Suh and Sin,<sup>74</sup> Rice *et al.*<sup>75</sup> did not consider the movement of debris, as the debris was 'entrapped.' However, their approach<sup>75</sup> does allow for estimation of friction where particle size means that movement is not a primary consideration; Hesmat<sup>76</sup> proposes a lower size limit of 20 μm for debris to be a contributor to abrasive wear. At higher values, the results of Suh and Sin<sup>74</sup> and Rice *et al.*<sup>75</sup> are, therefore, more applicable.

Debris movement for smaller particles is clearly a key consideration, as the fall in friction due to, for instance, rolling invalidates any models that fail to consider it. Jiang *et al.*<sup>19</sup> proposed the following series of mechanisms for wear debris movement under sliding conditions, each mechanism accounting for a different mode of perceived particle movement (Figure 5).

1. *Rotating:* A particle is entrapped in front of another fixed or immovable particle or object. It cannot move from its current position when impacted by



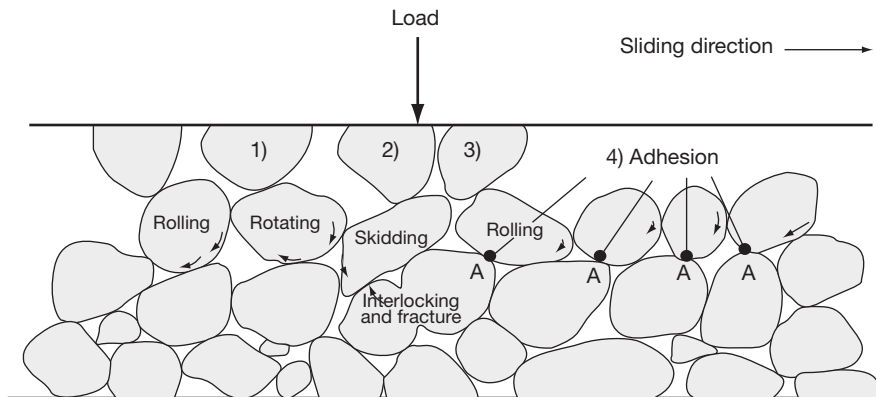


**Figure 5** Mechanisms of possible movement of particles during sliding of particulate materials.<sup>19</sup> 1 – Rotating, 2 – relative skidding, 3 – rolling, 4 – adhesion or sintering affected rolling mechanism.

an asperity from the opposite surface and is only able to rotate around its own center.

2. *Relative skidding*: A fixed or locked grain in one half of the sliding pair slides or 'skids' against a fixed grain attached to the opposite surface.
3. *Rolling*: The particles are able to freely move or roll along with the opposite sliding surface (and are not entrapped by it as with the 'rotation' mechanism).
4. *Adhesion or sintering affected rolling mechanism*: Adhesion developing between adjacent particles hinders the rolling of particles, affecting (increasing) friction compared with the 'free' rolling mechanism.

The mechanisms of movement can change and any particle may be subject to a different mechanism at different time points. It is also possible that a particle will become 'interlocked' or 'entrapped'<sup>54</sup> and be unable to move, and thus be liable to fracture, due to a build-up of stress upon it. Further appraisal of these mechanisms<sup>54</sup> does not specifically mention the fourth mechanism, adhesion and sintering general factors affecting the resulting particle layer as a whole.

It is also possible that for a given range of particle sizes, powder 'flow' may occur. Hesmat<sup>76</sup> observes that particles of an intermediate size, between 5 and 20  $\mu\text{m}$ , may undergo 'quasihydrodynamic flow' under sliding conditions. Larger particles will behave as *in situ* elastic bodies and contribute to abrasive wear, while smaller particles will compact and behave as a nearly solid body, moving along with the 'first body' interface and protecting it. At these smaller sizes, Van der Waals' forces and other attractive forces will become important factors and inhibit the flow process.

However, it is to be pointed out that the debris particles produced using the block-on-cylinder configuration,<sup>3,4</sup> in the 5–20  $\mu\text{m}$  size range specified by Hesmat for flow, were noted to be highly irregular in shape, being 'flat and angular' as a result of delamination wear. Also, they were metallic, meaning that adhesion between metallic surfaces would also be a major influence; Hesmat's work was with oxide particles. The combination of these influences would thus inhibit any flow process and eliminate the quasihydrodynamic flow region; high levels of metallic wear were observed<sup>3,4</sup> during the 'severe wear' stages, with associated high levels of adhesion due to transfer and back-transfer of material between metallic interfaces. Where oxidative wear did occur, particles were 5  $\mu\text{m}$  in size or less, when, as Hesmat points out, Van der Waals' and other attractive forces and compaction come into play. This means that quasihydrodynamic flow cannot play a significant part in the sliding wear process as observed between the selected test alloys in the current configuration, favoring ejection of material from the wear interface. Hesmat's lower limit of 20  $\mu\text{m}$  for abrasive wear could, therefore, be revised downward to the 5  $\mu\text{m}$  upper limit for forces of attraction and compaction.

#### 1.15.2.2.4 The effect of forces of attraction between third bodies

As already noted,<sup>76</sup> attractive forces such as Van der Waals' forces become a factor when considering very small particles (for oxides, 5  $\mu\text{m}$  or less). Electrostatic forces between particles, and between particles and tribosurfaces, also exist, but these are only about 1% of Van der Waals' forces for nonconductive solids.<sup>77</sup>

If  $F$  is the force of attraction and assuming the particle is spherical, this can be directly related to particle size by:

$$F = \frac{AR}{6r^2} \quad [8]$$

where  $A$  is the Hamaker constant;  $R$ , the radius of the particle or sphere;  $r$  is the equilibrium separation.

The Hamaker constant<sup>50</sup> is dependent on the surface energy of the sphere:

$$A = 9\pi r^2 \gamma \quad [9]$$

where  $r$  is the distance affecting mutual action of Van der Waals' forces (which can be estimated at 0.3–0.5  $\mu\text{m}$ ), and  $\gamma$  is the surface energy.

Van der Waals' forces are extremely short ranged in nature, produced by dipole induction between neighboring bodies. This accounts for the attraction observed between the smaller wear particles (<5  $\mu\text{m}$ )<sup>76</sup> and the wear surfaces.<sup>78</sup>

Surface energy is temperature-dependent, thus making the Hamaker 'constant' and the force of attachment  $F$  temperature-dependent. An Arrhenius relationship exists between surface energy and temperature:

$$\gamma = \gamma_0 \exp\left(-\frac{E}{RT}\right) \quad [10]$$

where  $R$  is the gas constant;  $E$ , the activation energy for 'bonding'; and  $T$  is the absolute temperature.

The amount of work done in relation to wear is fairly minimal, compared with the formation of compacted oxides and 'glazes,' as discussed in [Section 1.15.2.3](#), with the work of Hesmat<sup>76</sup> being one of the more comprehensive studies of the potential behavior of debris and particles at the wear interface in relation to their size. It is suggested, here, that the role of Van der Waals' forces in the accumulation and grouping together of particles is perhaps more important, especially at more elevated temperatures. For sintering and fusion of finer oxide particles to form glazes, an attractive force must be present to hold the particles in position long enough to allow significant sintering reactions to occur.

The importance of sintering in the formation of debris layers in itself cannot be ignored. Zhou *et al.*<sup>79</sup> showed that for iron, nickel, and iron–25% nickel powders, significant sintering can occur on raising the temperature above room temperature (denoted by the significant shrinkage of specially prepared compacts), where the particle size is defined as 'ultra-fine,' in this case, 30–40 nm. In comparison, more

traditional fine particles of around 5  $\mu\text{m}$  did not show a significant response (in terms of shrinkage) until above 500 °C. This does not mean that sintering did not occur with the larger particles; it is more that a greater response was obtained for the smaller particles because of their greater relative surface area, and hence, the contact area. With particles of 300–400 nm, a ready sintering response may be detectable in a wear situation.

The effect of shrinkage of the compacts, as occurs in all powder compacts on sintering, is worth noting. As sintering and thus shrinkage undoubtedly occur in accumulations of wear debris at not-necessarily-greatly-elevated temperatures, this will no doubt have an influence on the formation of compacted oxide layers during the wear process. To date, no attempt has been made to address this issue or its importance on the sliding wear process.

### 1.15.2.3 Mild Wear and Mechanisms of Compact Oxide Formation

#### 1.15.2.3.1 Introduction to compacted oxides or 'glazes'

As stated in [Section 1.15.2.1](#), Archard and Hirst<sup>31,32</sup> defined mild wear as that occurring where the surface is extremely smooth and consisting partially or wholly of the product of reaction between the material under sliding and the surrounding atmosphere or fluid. An oxidation reaction is required for the creation of the corrosion product, although, as already stated, the corrosion product itself need not necessarily be an oxide.

The term 'glaze' is misleading, as it implies a glassy amorphous material, which was thought to be the case until Lin *et al.*<sup>6</sup> proved it to be crystalline by means of electron diffraction; the term 'compacted oxide layer' is a more accurate description. 'Glaze' and 'compacted oxide' tend to be used fairly interchangeably throughout literature, and despite the crystalline nature of these surfaces, the term 'glaze' has remained in common use. More recently, Datta *et al.*<sup>15,80</sup> have demonstrated that the compacted oxide layers formed in some systems and under certain conditions have a nanocrystalline structure and are highly disordered as discussed further in [Section 1.15.4.3](#).

Compacted oxide layers tend to form under conditions of moderately high temperature, low loading, and usually low sliding speed. For a compacted oxide layer to form and a resultant decrease in wear to occur, many researchers specify that a minimum temperature that is dependent on conditions and

alloy composition must be exceeded. With increasing temperature, the formation of these compacted oxides becomes more rapid, with a consequent decrease in the 'severe wear' running in period, the debris from which can be a major source of material needed for the formation of the compacted oxide layers. Compacted oxide formation is not restricted to low sliding speed, as the effect of frictional heating due to high sliding speed can raise the temperature above the critical temperature required for the formation of the compacted oxide layers.

Many researchers have extensively studied the decrease in wear by the formation of compacted oxides at high temperatures. In addition to Archard and Hirst,<sup>31,32</sup> others such as Lancaster,<sup>26</sup> Bhansali,<sup>81</sup> Razavizadeh and Eyre,<sup>82</sup> Stott *et al.*,<sup>2,6,10,14,17–19,35,50,55–61</sup> Quinn<sup>1,33,62–64</sup> and Garcia,<sup>83</sup> have contributed to the knowledge of compacted oxide formation. Recent work<sup>3–5,20–25</sup> has additionally concentrated on the sliding of dissimilar interfaces and their effects on the mode of wear. The key issues on oxide formation are discussed as follows.

Wear that is dependent on the tendency to oxidation is highly dependent on temperature. The tendency to oxidation with respect to temperature can be described by the following Arrhenius type equation:

$$K_p = A_p \exp\left(\frac{Q_p}{RT_0}\right) \quad [11]$$

where  $K_p$  is the oxidation rate,  $A_p$  is the Arrhenius constant,  $Q_p$  is the activation energy (for oxidation),  $R$  is the gas constant, and  $T_0$  is the absolute temperature in Kelvin.

Stott in conjunction with Lin and Wood,<sup>6,55–59</sup> and later Glascott and Wood<sup>10,50,54,60,61</sup> proposed various modes and mechanisms of 'glaze' formation based on the generation and behavior of oxide debris at the sliding interface. Jiang *et al.* building on studies of third body interactions<sup>19</sup> (later revised by Stott<sup>54</sup>) and adhesive processes between particles,<sup>17</sup> proposed a descriptive model for debris behavior at the sliding interface,<sup>2</sup> based on their generation, commutation, sintering to form 'glaze' layers (above a critical temperature), layer break-up, and debris removal. These mechanisms and modes of formation are discussed in more detail in [Section 1.15.4](#).

### 1.15.2.3.2 Quinn's oxidative wear model

Quinn's model of wear<sup>62</sup> assumes a dependence upon the wear rate of oxide film formation on the wear interface. At a critical thickness  $\xi$ , the oxide layers are no longer able to withstand the forces acting

tangentially on them, and suffer failure and break away. Combining Quinn's and Archard's models<sup>31</sup> allows the critical thickness to be used to relate wear rate to material oxidation rate, showing an increase in wear rate with temperature.

From Archard's wear [equation \[5\]](#), the wear volume  $W$  is related to the applied load  $P$  and the total sliding distance  $L$ , giving

$$W = \frac{K_a PL}{H} \text{ or } W = K_a AL \left( A = \frac{P}{H} \right)$$

$K_a$  can be regarded as the probability of a wear particle being generated in any given encounter (assuming unit sliding distance in the following derivation, making  $W$  the wear rate). Thus,  $1/K_a$  is the number of encounters required to produce a wear particle.

In oxidative wear, a wear particle cannot be produced until the critical thickness for mechanical stability  $\xi$  is reached; thus  $1/K_a$  is the number of encounters required to generate an oxide layer of this thickness. If  $t$  is the time required to grow the layer and  $\tau$  is the length of time of each encounter, then

$$t = \frac{\tau}{K_a} \quad [12]$$

If  $V$  is the sliding speed and  $d$  is the distance along which the sliding contact is maintained, then

$$t = \frac{\tau}{V} \quad [13]$$

and [eqn \[14\]](#) can be modified to

$$t = \frac{\tau}{VK_a} \quad [14]$$

In a given time period  $t$ , the growth of oxide per unit area will be  $\Delta m$ . Assuming parabolic oxidation

$$\Delta m^2 = K_p t \quad [15]$$

where  $K_p$  is the parabolic rate constant. If  $f$  is the mass fraction of oxide, that is, oxygen, and  $\rho$  is the oxide average density, then

$$\Delta m = f \xi \rho \quad [16]$$

and

$$f^2 \xi^2 \rho^2 = K_p t \quad [17]$$

Substituting [eqn \[2\]](#) into [eqn \[16\]](#) gives

$$K_a = \frac{dK_p}{V f^2 \xi^2 \rho^2} \quad [18]$$

The rate constant can normally be calculated using an Arrhenius relationship, as described by eqn [13]:

$$K_p = A_p \exp\left(\frac{Q_p}{RT_0}\right)$$

where  $A_p$  is the Arrhenius constant,  $Q_p$  is the activation energy (in this case for oxidation),  $R$  is the gas constant, and  $T_0$  is the absolute temperature of reaction. Thus

$$K_a = \frac{dA_p \exp(Q_p/RT_0)}{Vf^2\xi^2\rho^2} \quad [19]$$

Substituting into Archard's equation<sup>31</sup> gives a final expression for wear rate:

$$W = \frac{dAA_p \exp(Q_p/RT_0)}{Vf^2\xi^2\rho^2} \quad [20]$$

This expression relates directly to the oxidational properties of the materials, plus the critical environmental variables affecting the wear process, such as temperature at the interface at the time of contact and sliding speed relative to the opposing interface, as well as the critical thickness of the oxide. Knowing the critical thickness of the oxide<sup>62</sup> and the static oxidation properties of the wearing materials, wear rate prediction can be easily achieved.

However, there are many complications that can prevent the accurate prediction of the wear rate:

- The difficulty in estimating the wear interface temperature, particularly in the presence of oxides;

- The slower heat flow from the wear interface and thus higher interface temperature, caused by lower thermal conductivity of the oxides;
- The presence of multilayer scales (formed particularly at high temperature, e.g., with iron), preventing the calculation of the temperature based on the oxide type generated<sup>33</sup>;
- The expected presence of increased levels of surface defects at the contacting surfaces, increasing the oxidation rate constant.
- The continued removal of oxides, leading to exposure of fresh surfaces and a decrease in oxide thickness (hence diffusion distance), thereby enhancing the tribooxidation rate; and
- The presence of defects such as cracks and grain boundaries, allowing ingress of oxygen (in ion and molecular form), leading to an enhanced oxidation rate.

A schematic presentation of Quinn's models<sup>84</sup> is shown in **Figure 6**.

#### 1.15.2.3.3 Modification of Quinn's oxidation wear model for discontinuous contact

The validity of Quinn's model<sup>1</sup> is conditional upon the maintenance of contact between the two surfaces, which is clearly often not the case. Quinn's model was further modified by Garcia *et al.*<sup>83</sup> to take into account discontinuous contacts between the contacting surfaces.

For this modified model, it is assumed that  $1/K_a$  contact events are required for  $\xi$ , the critical oxide

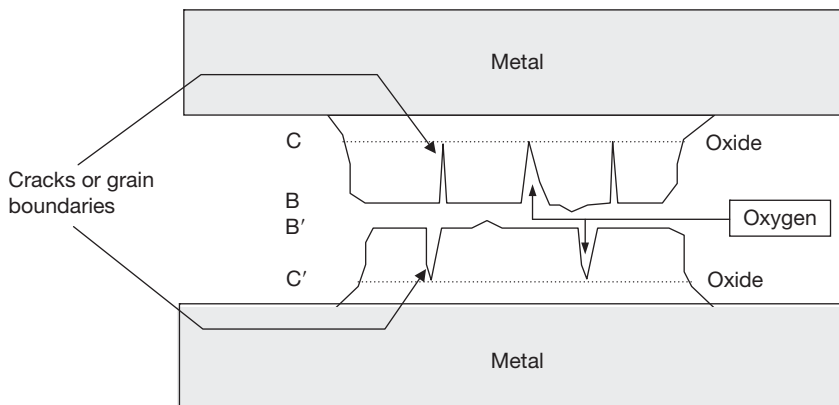


**Figure 6** Oxygen transport between oxide plateaux and cracks in the oxides.<sup>84</sup> Quinn's oxidation model supposes that any oxygen species would have to diffuse right from the surface of the oxide (B or B') to the metal. The presence of cracks and grain boundaries act as points of ingress for oxygen ions and in the case of cracks, molecular oxygen. This means that the distance for diffusion is significantly less where cracks in the outer layers of oxide are prevalent. Diffusion need only take place across the underlying oxide from the crack tips (C and C') to the metal and thus the rate of oxidation is greater.

thickness, to be achieved; this is the same as for Quinn's model. However, in this case, the time required to reach this critical thickness depends on the contact frequency  $F$ , which is the inverse of the elapsed time between two contacts at a given point between the contacting surfaces; while this can clearly be related to the sliding speed, the frequency of contact can also be changed by varying the length of the wear track without any need to vary the sliding speed. It is clear that each asperity will not make contact each time the disk rotates; however, Garcia<sup>83</sup> comments that the probability of a contact (and hence a wear particle being generated) is included in the statistical meaning of the wear coefficient,  $K_a$ .

Therefore

$$t = \frac{1/K_a}{F} = \frac{1}{FK_a} \quad [21]$$

The constant of proportionality  $K_a$  in Archard and Hirst's model<sup>31</sup> is thus defined by

$$K_a = \frac{K_p}{Ff^2\xi^2\rho^2} \quad [22]$$

and substituting the rate constant as defined by eqn [11] gives

$$K_a = \frac{A_p \exp(Q_p/RT_0)}{Ff^2\xi^2\rho^2} \quad [23]$$

Substituting into Archard's equation [5]

$$W = \frac{K_a PL}{H} \text{ or } W = K_a AL \left( A = \frac{P}{H} \right)$$

gives a final expression for wear rate (again as the sliding distance  $L$  is assumed to be 1, the wear volume  $W$  can be taken to represent the wear rate), the frequency of contact events being the determining parameter for the input of energy for oxide growth, rather than the sliding speed:

$$W = \frac{AA_p \exp(Q_p/RT_0)}{Ff^2\xi^2\rho^2} \quad [24]$$

The validity of Garcia's model<sup>83</sup> is dependent upon a wear particle being generated on any given contact. For this to work, it is necessary for a wear particle to be generated each time a contact is made; this in itself is highly improbable. However, the lower level of data scatter achieved by Garcia's discontinuous contact model indicates that this alternative frequency-based

approach provides a good approximation in circumstances where Quinn's model is less effective in predicting wear rates (i.e., where contact is not maintained).

### 1.15.2.4 Effect of Load and Sliding Speed

#### 1.15.2.4.1 Early work

A significant contribution to the effects of load and sliding speed came from Welsh's work<sup>27,28</sup> on low-carbon steels using a pin-on-rotating-ring (cylinder) configuration with applied loads of up to 2 kgf and sliding speeds of up to  $2.66 \text{ m s}^{-1}$ . The wear process was characterized by two transitions:  $T_1$ , which is mild-to-severe at low load and sliding speed, and  $T_2$ , which is severe-to-mild at high load and sliding speed. Increasing the sliding speed decreased the critical load at which these transitions occurred (Figure 7), the lower transition being eliminated in some cases, leaving only the severe wear to mild wear transition. In extreme cases, these transitions could be decreased enough to be eliminated from the experimental data – mild wear could be observed over the whole range. The variation in the upper transition from the intermediate severe wear back to higher speed mild wear was observed to be the more sensitive to the sliding speed.

Low-speed, low-load mild wear was attributed to the presence of loose oxide debris at the sliding interface and intermediate severe wear to direct metal-to-metal wear. The mild wear encountered at high speed and high load was attributed to hardening, accompanied by the development of an adherent oxide film, as a result of frictional heating. The hardening came about as a result of the low-carbon steels undergoing phase changes, due to high localized temperatures around points of contact being sufficient to produce a transformation to austenite, followed by rapid cooling by conduction of heat into the bulk metal producing a structure at the surface not too dissimilar to martensite.

A critical hardness had to be exceeded by these phase changes for mild wear to be reestablished under high-speed, high-load conditions; the transition back from severe wear to mild wear is in fact a two part transition, with  $T_2$  referring to the point where sufficient phase hardening occurs to suppress severe wear without the intervention of an oxide film (the development of which further acts to protect the wear surface) and a  $T_3$  transition approximately matching the point where permanent phase change hardening occurs.

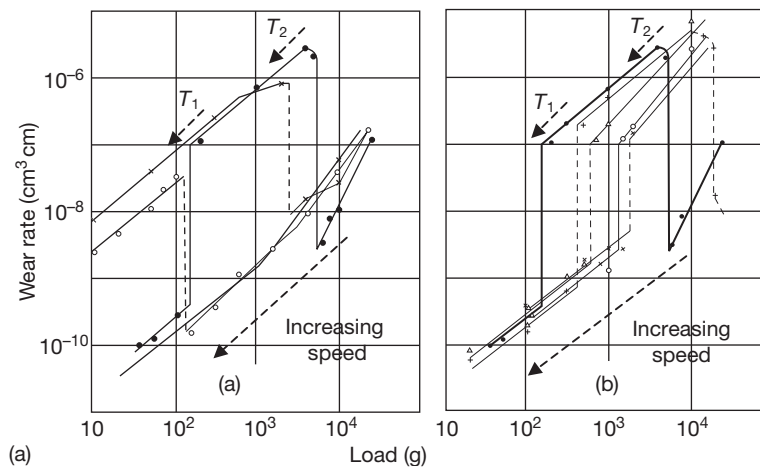


**Figure 7** Effect of sliding speed on wear rate/load – 0.52% carbon steel.<sup>27</sup> (a) 1.00–2.66  $\text{m s}^{-1}$  (● – 1.00  $\text{m s}^{-1}$ ; × – 1.33  $\text{m s}^{-1}$ ; ○ – 2.00  $\text{m s}^{-1}$ ; + – 2.66  $\text{m s}^{-1}$ ), (b) 0.17–1.00  $\text{m s}^{-1}$  (× – 0.017  $\text{m s}^{-1}$ ; ○ – 0.067  $\text{m s}^{-1}$ ; ▽ – 0.33  $\text{m s}^{-1}$ ; + – 0.66  $\text{m s}^{-1}$ ; ● – 1.00  $\text{m s}^{-1}$ ).  $T_1$  – Transition from low speed, low load mild wear to severe wear.  $T_2$  – Transition from severe wear to high speed, high load mild wear. (Arrows show movement of transitions with increasing sliding speed).

Subramanian<sup>85</sup> conducted a series of sliding tests of an Al–12.3 wt% Si alloy in pin form against various rotating ‘ring’ counterfaces, including mild steel in the rolled condition, quenched and tempered die steel and copper with varying levels of aluminum, during which the sliding speed was increased at various times. The wear rate of the Al–12.3 wt% Si alloy pin (Figure 8) decreased with increased sliding speed up to a critical value of usually  $1 \text{ m s}^{-1}$ , regardless of counterface material or applied pressure used. Further increases in speed above this critical value led to progressive increases in wear.

Subramanian explains the decrease in wear with increasing sliding speed is due to increasing strain rates and due to increased hardness and flow strength of the wear surface. The true area of contact is thus and with a lower level of contacts between the wearing surfaces, a lower wear rate results. In competition with this is the effect of increased temperature because of frictional heating (which was observed to occur), softening the material at the wear interface. This results in an increase in the true area of contact and thus an increase in the wear rate. Subramanian does not go into detail with his reasoning; however, the softening of the material must allow for deformation and ‘spreading’ of asperities and also increased contact at other points.

Changes in wear mechanism were observed at Subramanian’s  $1 \text{ m s}^{-1}$  transition, with equiaxed particles produced below this critical or ‘transition’ speed, compaction of these particles and delamination of the compacted particles around the transition speed, and

delamination or plastically deformed material at higher speeds. It is not stated whether the particles produced at any particular speed are metallic or oxide.

The critical speed was observed to be dependent on counterface material and a higher transition was noted for harder, more thermally conductive alloys. Decreased mutual solubility also led to a higher transition speed.

Welsh<sup>27,28</sup> discusses the existence of lower limits of load and speed, marking the transition from mild to severe wear and also an upper limit, marking the transition back to mild wear. So,<sup>86</sup> on the other hand, discusses only a single limit or critical value for both load and speed for the transition from mild wear at low speeds and loads, to severe wear at high speeds and loads. Comparison with the work of Welsh would make So’s transition equivalent to the lower transition, with no mention of an upper transition despite the use of higher sliding speeds. So quotes values of  $400^\circ\text{C}$  and 5 MPa contact pressure as being limiting conditions for mild wear for many steels. In one test of note, a high carbon steel sample underwent a mild-to-severe wear transition at a contact pressure of 4.43 MPa, on raising the sliding speed from 3 to 4  $\text{m s}^{-1}$ . A Stellite sample remained in the mild wear state at a contact pressure of 8.85 MPa (just under twice as much pressure) under similar conditions. As So used a pin-on-disk configuration, compared to the pin-on-rotating-cylinder configuration of Welsh, this may account for the differences in results; the pin-on-disk configuration may not have generated sufficiently severe conditions for the upper transition to occur.



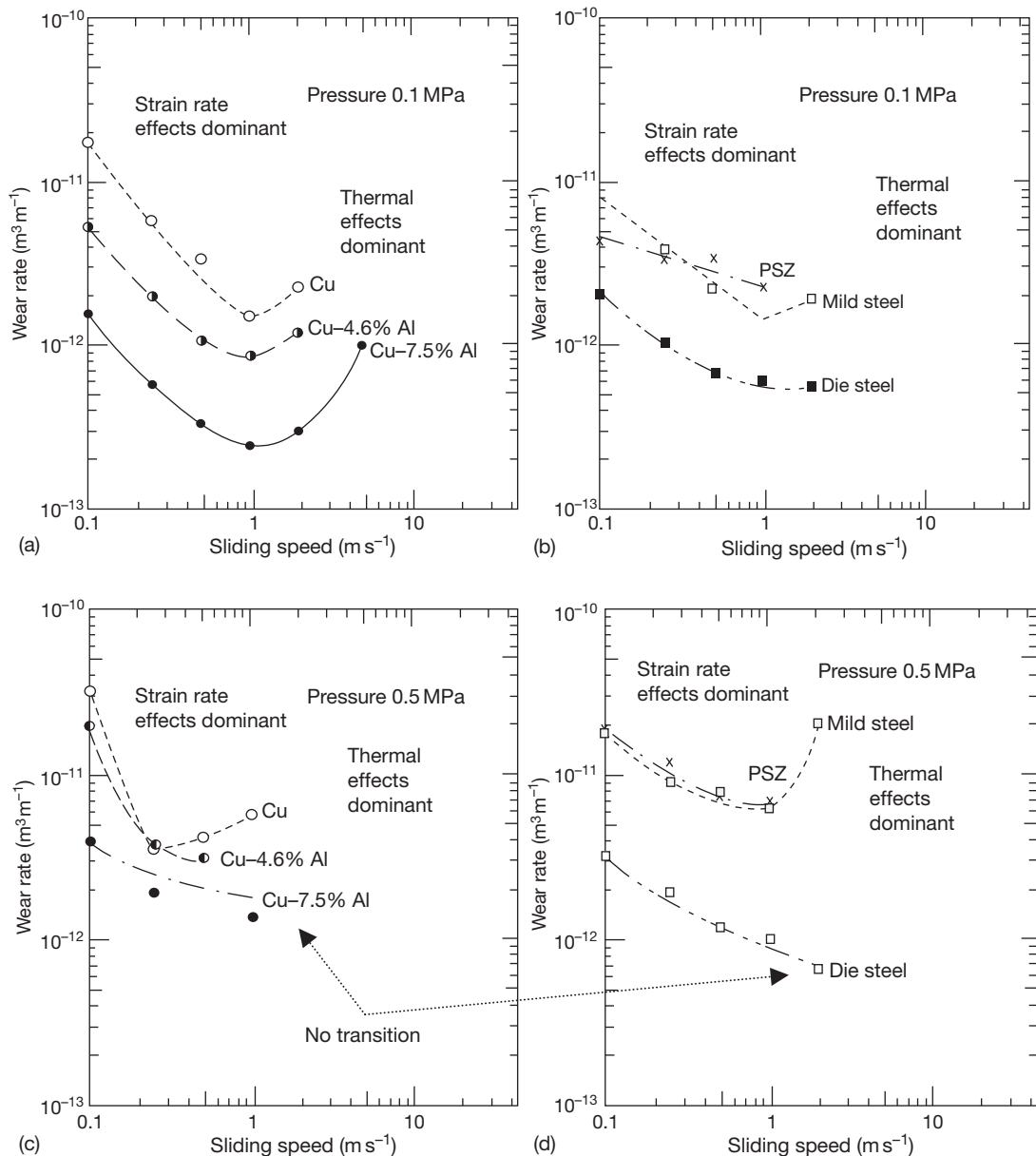


**Figure 8** Effect of sliding speed on wear rate of Al-12.3 wt% Si versus various counterface materials.<sup>85</sup> (a) Cu, Cu-4.6 wt% Al, and Cu-7.5 wt% Al counterfaces, applied pressure 0.1 MPa, (b) mild steel, die steel, and partially stabilized zircona counterfaces, applied pressure 0.1 MPa, (c) Cu, Cu-4.6 wt% Al, and Cu-7.5 wt% Al counterfaces, applied pressure 0.5 MPa, (d) mild steel, die steel, and partially stabilized zircona counterfaces, applied pressure 0.5 MPa.

Most load and sliding speed work done to date has concentrated on what happens at room temperature, with little work at elevated temperature. One example is the work of Rose,<sup>4</sup> where a series of experiments were conducted at 750 °C with loads between 7 and 25 N, during which an apparent transition from mild-to-severe wear was noted at 15 N, when Nimonic 80A was worn against Incoloy 800HT. Also, when

Incoloy MA956 was worn against Stellite 6 or Incoloy 800HT, at 25 N, the 'glaze' layer formed on the Incoloy MA956 was beginning to show signs of breaking away (as described later).

#### 1.15.2.4.2 Wear of cobalt-based alloys

Valuable information can be gleaned from work on cobalt-based alloys. The most comprehensive work

carried out on the sliding wear of cobalt was that by Buckley,<sup>87</sup> who compared the sliding wear of cobalt with that of copper in vacuum. Lower friction and adhesion levels noted for cobalt were attributed to its hexagonal close-packed structure, compared to copper's face-centered cubic structure.

The observed increase in friction and cohesion for cobalt tested at temperatures  $\geq 300^\circ\text{C}$ , with complete welding at  $450^\circ\text{C}$ , was considered to result from a phase change from hexagonal close-packed to face-centered cubic because of increased temperature (to above  $417^\circ\text{C}$ ; the phase change temperature for cobalt), caused by frictional heating.

The differences between the sliding behavior of metals in hexagonal close-packed phase and face-centered cubic phase are due to the greater number of active slip systems available in face-centered cubic structures. There are 12 primary slip systems within a typical face-centered cubic metal (4 slip planes each with 3 slip directions), which are all crystallographically similar, compared to only three primary slip systems in cobalt, these being based on the basal plane with the highest atomic density (i.e., 1 slip plane with 3 slip directions). Cross slip is also more difficult, as with hexagonal close-packed structures such as cobalt, screw dislocations are required to move out of the primary basal glide plane onto planes that, unlike face-centered cubic structures, are crystallographically different. Hexagonal close-packed materials are thus less deformable.

The effect of these hexagonal close-packed structures on wear was further elaborated on by Persson<sup>88,89</sup> on studying the low friction tribological properties of Stellite 21 and Stellite 6. Persson comments that although a metastable face-centered cubic structure may be retained in both Stellite alloys down to room temperature, transformation to a hexagonal close-packed structure can be induced by application of sufficiently high shear stresses (i.e., during sliding). A thin, easily sheared layer can develop at the sliding surface due to the shear-induced alignment of the hexagonal close-packed basal plane parallel to the direction of sliding.<sup>89</sup> This alignment significantly reduces friction and improves galling resistance, with shear and adhesive transfer restricted to this layer. This sliding regime persists even as this layer is removed, as it is easily regenerated. Also, the removal of material in such thin sections may at least in part explain the ready generation of fine Stellite 6-sourced Co-based oxide debris observed elsewhere.<sup>3-5,20-25</sup> These sections may be more easily commutable to a small size and oxidized, providing a ready supply of material for 'glaze' formation.

The formation of compacted oxide layers during like-on-like fretting wear tests of cobalt-based Stellite 31, between room temperature and  $800^\circ\text{C}$  ( $293\text{--}1074\text{K}$ ), was observed by Stott *et al.*<sup>90</sup> The formation of these oxides was by a similar route to that observed for iron-based and nickel-based alloys, with alloying components present in the oxides to roughly the same proportions as the original alloy.

At temperatures between room temperature and  $300^\circ\text{C}$ , Stellite 31 undergoes a much lower level of wear than do various nickel- and iron-based alloys, which Stott also attributes to the smaller number of slip planes in the hexagonal close-packed structure of cobalt. He specifies an initial period of low wear for up to an hour, followed by the production of a bright, rough metallic wear scars showing characteristics of abrasion and evidence of material transfer. This he attributes to a probable change in phase from hexagonal close-packed to face-centered cubic and thus a loss in wear resistance. Later, the bright worn surface is lost with increasing amounts of oxide being produced, although the load-bearing areas remain metallic.

Both the 'phase changes' and oxide production have been attributed to temperature increases at the wear interface. However, the phase transformation temperature for cobalt is  $417^\circ\text{C}$ ; Stellite 31 contains 26% chromium, which has the effect of significantly raising the hexagonal close-packed to face-centered cubic transition temperature; 20% Cr is estimated to raise the transition temperature to  $847^\circ\text{C}$  (expressing uncertainty as to the effects of the other alloying components). This suggests a far greater influence due to frictional heating and localized flash temperatures due to asperity interactions; for a phase change to readily occur, the temperature at the immediate interface would have to reach  $500^\circ\text{C}$  above ambient. In a fretting wear situation, it is difficult to see how this could occur.

However, the level of alteration of temperature for any phase transitions will also depend on the effects of other alloying components in cobalt-based alloys. As already stated, chromium will raise the transition temperature quite dramatically. Other works<sup>68,87-89</sup> suggest that tungsten and molybdenum also raise this transition, while nickel and iron (also, magnesium and carbon<sup>88,89</sup>) have the effect of stabilizing the higher temperature face-centered cubic structure (due to increases in stacking fault energy<sup>88,89</sup>) and suppressing this transition. It is possible that the presence of nickel to 10.5% and iron to 2% may be sufficient to retard the effect of the chromium and

7.5% tungsten to a much lower level. Thus, a much smaller increment in temperature due to frictional heating and flash temperatures may be needed to effect any phase transition, confirming the conclusion that the damage observed can be attributed to phase changes, and hence, a decrease in resistance to deformation.

Stott *et al.*<sup>90</sup> observed that compacted oxide formation was not accompanied by any decreases in friction observed during similar experimentation with nickel-based alloys at elevated temperatures. With friction levels already low due to the hexagonal close-packed structure, it is possible that no significant difference between the friction levels before and after elimination of metallic contact by higher temperature 'glaze' formation may be discerned.

The face-centered cubic to hexagonal close-packed transformation observed in Co-based alloys is considered a martensitic transformation.<sup>91</sup> Attempts to utilize Co-free hard wearing alternatives making similar use of the austenite–martensite transition in Fe-based alloys have been limited by typical upper useful temperatures of  $\sim 180^\circ\text{C}$ <sup>88,89</sup> (not discussed in the current work).

#### 1.15.2.4.3 The effect of load and sliding speed – Stellite 6

Following on from previously discussed work (Section 1.15.2.4.1) with a Stellite material,<sup>86</sup> So *et al.* went on to test Stellite 6 clad mild steel against AISI 4140 and 4340 steels in the martensitic phase, first as the pin material (4.75 mm in diameter) and then the disk material.<sup>30</sup> Measured hardness values were 580 Vickers hardness number (VHN) for the Stellite 6 layer and 750 VHN for the steels, increasing to 970 VHN after an unspecified heat treatment followed by water quenching, with test loads of up

to 156.8 N and sliding speeds of up to  $4\text{ m s}^{-1}$  used. After sliding for up to 10 000 m, the Stellite 6 layer was observed to be mostly covered by an oxide layer reported to consist of  $\text{W}_3\text{O}$ ,  $\text{CrO}$ , and  $\text{Co}_2\text{O}_3$ . Where this oxide layer spalled, a new oxide film was observed to replace it readily. This applied for all combinations of loads (19.6, 39.2, 78.4, and 156.8 N) and sliding speeds (1, 2, 3, and  $4\text{ m s}^{-1}$ ), with the exception of the most severe tested combination, 156.8 N and  $4\text{ m s}^{-1}$ , when severe wear was observed for the Stellite 6 as the pin material. The experimental data obtained from these tests are presented in Figure 9.

The steels underwent increased wear compared to the Stellite 6, despite being of much greater hardness, and So *et al.* concluded that the oxide layer formed on the Stellite 6 must be tougher than that formed on the steels. When used as a disk material, only a thin layer of oxide material was formed on the AISI 4340, compared to the thicker layer formed on the Stellite 6; the wear rate of the steel was seven times that of the Stellite 6 laser-clad pin. As the pin material, severe wear was observed for the AISI 4140 steel, the rate of wear being 10 times higher than that of the Stellite 6 laser-clad disk. For all but the highest load, the wear rate of the Stellite 6 pin actually decreased when the sliding speed was increased from 1 to  $2\text{ m s}^{-1}$ , with only a slight increase at intermediate loads on raising the sliding speed to  $4\text{ m s}^{-1}$  (Figure 9). At the lowest load used, the decrease in wear continued up to  $4\text{ m s}^{-1}$ .

The increasing wear rate for specimens under a load of 156.8 N was ascribed to softening of material due to the higher flash temperatures encountered, especially at higher sliding speed. The higher flash temperatures also led to changes in the oxide phases that were reported to form on the respective wear surfaces. A shift was noted from  $\text{Fe}_2\text{O}_3$  to  $\text{FeO}$  on the steels and from  $\text{W}_3\text{O}$ , through  $\text{Co}_2\text{O}_3$ ,  $\text{CrO}$ ,  $\text{Cr}_2\text{O}_3$ ,

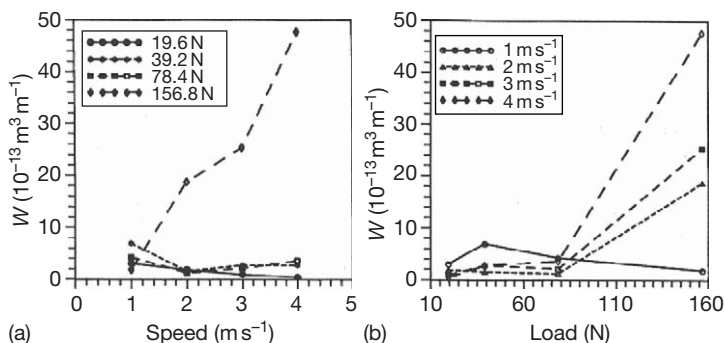


**Figure 9** Variation in wear rate ( $W$ ) with sliding speed (a) and load (b) for the rubbing of laser-clad Stellite 6 pins with AISI 4340 steel disks. Reproduced from So, H. *Wear* **1996**, 192, 78–84.

to  $\text{Cr}_5\text{O}_{12}$  on the laser-clad Stellite 6 layer with increasing temperature; this was accompanied by a decrease in friction. So does not offer an explanation for the change in oxide with temperature, though as for the oxidation of iron, it appears that this can be attributed to changes in oxidation state of the chromium in Stellite 6, with preferential oxidation of tungsten and cobalt respectively at lower temperatures. It is curious to note here that, in the work of Wood<sup>3</sup> and Rose,<sup>4</sup> no such shift was observed for Stellite 6, with  $\text{Cr}_2\text{O}_3$ ,  $\text{Co}_3\text{O}_4$ , or a combined oxide of the two being consistently observed from XRD results. No evidence of tungsten phases was found, although this could be attributed to the sensitivity of the measurement and characterization equipment.

Also of note was the fact that the oxide layers formed in So's work were more reminiscent of those created at higher ambient temperature in the work of Wood and Rose ( $>510^\circ\text{C}$ ), indicating extremely high temperatures at the points of contact. So's measurements indicate a rapid rise in temperature with increasing load and speed (speed having less of an effect than load). So comments that, under the most severe conditions ( $156.8\text{ N}$  and  $4\text{ m s}^{-1}$ ), the mean surface temperature at the point of contact reaches over  $700^\circ\text{C}$  and, because of this, wear becomes severe due to softening. This may be more to do with the load and speed conditions than to temperature (even accounting for phase transitions), as Wood and Rose tested Incoloy MA956 and Nimonic 80A against Stellite 6 at an ambient temperature of  $750^\circ\text{C}$ , with oxide layers being obtained in both cases on the Stellite 6 counterface.

This implies that So has underestimated the temperature at the sliding interface in this case. The softening may again be attributable to phase changes from hexagonal close-packed to face-centered cubic. In the case of Stellite 6, there are far fewer alloying additions to offset the effects of chromium (present at 27%) and tungsten (5%) on this transition. The transition between the two phases for 27% chromium is  $\sim 880\text{--}900^\circ\text{C}$ ,<sup>5,92</sup> almost  $200^\circ\text{C}$  higher than So's  $700^\circ\text{C}$  estimate.

Crook and Li<sup>69</sup> carried out a comparative 'like-on-like' sliding study of Stellite 6 and a number of other hard-facing alloys of various cobalt contents, including Stellite 1 (with higher levels of carbon, chromium, and tungsten than Stellite 6), Stellite 2006 (a 33% cobalt-iron-chromium alloy), Haynes No. 716 (a nickel-iron-chromium alloy with 11% cobalt), and Haynes No. 6 (a nickel-chromium alloy with no cobalt). They observed that in general the

higher the cobalt content, the better was the resistance to metal-metal wear at temperatures up to  $750^\circ\text{C}$ . Where no cobalt was present within the alloy, wear rates were observed to be highest. Above this temperature (at  $1000^\circ\text{C}$ ), all alloys exhibited low wear with a protective oxide layer forming across the wear surface. Increases in wear were observed for all combinations with increased contact pressure, though at high load, increases became less severe for cobalt-chromium and cobalt-iron-chromium alloys. Of particular note is the response to increasing the sliding speed by an order of 10 from the  $7.06 \times 10^{-4}\text{ m s}^{-1}$  used for all their other tests, to  $7.88 \times 10^{-3}\text{ m s}^{-1}$ , carried out at  $500^\circ\text{C}$  and  $20.69\text{ MPa}$ . For the high cobalt-chromium alloys, including Stellite 1 and Stellite 6, there was a slight decrease in the observed wear rate. Where cobalt levels were low or non-existent, the converse was true and increases in wear were observed.

Crook and Li<sup>69</sup> attributed the superior wear resistance of the cobalt-chromium alloys, first, to the superior galling resistance, and second, to the tendency of alloys when in the face-centered cubic form to undergo phase changes and become hexagonal close-packed, which as discussed earlier is less prone to deformation, due to a smaller number of available slip planes. Conversely, they point out that high nickel alloys have a poor galling resistance, yet specifically quote the work of Stott *et al.*<sup>55,56,58</sup> as examples of nickel-chromium alloys, in particular, exhibiting low levels of wear and developing 'glaze' during the wear process at high temperature.

In both experimental programs, a low amplitude 'button-on-disk' system suitable for fretting wear studies was used. However, Stott *et al.* concentrated solely on one material (Nimonic 80A), whereas Crook and Li's comparative work on a range of alloys showed that, although wear was still low for nickel-chromium alloys, the wear resistances were inferior to those of cobalt-containing alloys. In both cases, it is not possible to say that in an extreme high wear environment (e.g., high speed, high load) similar observations of low wear would be made. In the case of Stellite 6, So's work<sup>30</sup> does indicate continued low wear rates during moderately high speed, high load unidirectional sliding wear (up to  $156.8\text{ N}$  and  $4\text{ m s}^{-1}$ , with frictional temperatures of up to  $700^\circ\text{C}$  being generated); however, if the works of Wood<sup>3</sup> and Rose<sup>4</sup> are considered, high rates of wear are observed with Nimonic 80A at elevated temperature ( $750^\circ\text{C}$ ,  $0.654\text{ m s}^{-1}$ ,  $7\text{ N}$ ,  $9418\text{ m}$  sliding distance) when

undergoing unidirectional wear against a Stellite 6 counterface. Even in a like-on-like situation, wear properties of Nimonic 80A are inferior to those of Stellite 6.<sup>4,93</sup>

#### ***The presence of carbides in Stellite 6***

In both the work of Stott<sup>90</sup> and So,<sup>86</sup> no mention was made of the effect of carbides that would have formed with both Stellite 31 and especially Stellite 6, carbon being present to 0.5% and 1.1%, respectively. In the cast form, carbon combines with chromium to form a chromium carbide phase at the grain boundaries; in Stellite alloys, these are of the form  $M_7C_3$  and  $M_{23}C_6$ .<sup>30</sup> In the wrought and hot isostatically pressed forms, these carbides instead form discrete particles dispersed evenly in the microstructure (the effect of Stellite processing or carbide position on sliding wear has not, to the knowledge of the authors, been investigated).

The presence of these hard, difficult-to-deform carbides may have had a number of effects on both sets of experimental work. First, they may have further inhibited deformation of the mainly cobalt matrix during sliding wear, over and above the effect expected from the hexagonal close-packed structure, blocking the operation of the fewer slip planes present. Second, the removal of material from the Stellite alloys may have released some of these carbides into the sliding interface, increasing the levels of wear observed due to increased abrasion effects. The enhanced wear of the AISI 4140 and 4340 steels, when worn against Stellite 6 clad mild steel in So's work<sup>30</sup> may have in addition been partially attributable to this.

There is also the possibility that the carbides (up to 30  $\mu\text{m}$  in size) within the Stellite 6 may affect the formation of 'glaze' (only a few micrometers thick) on opposing wear surfaces<sup>4</sup> as the Stellite 6 is worn down and the carbides are exposed; Inman,<sup>5</sup> however, suggested that the exposed carbides are not hard enough to do this. The possible effects of carbides are discussed in more detail in [Sections 1.15.2.5](#) and [1.15.3.3.2](#).

#### **1.15.2.5 Effect of a Second Phase on Wear**

The role of second phases in the wear process is often neglected in wear studies. In many studies, experimentation has concentrated only on single-phase alloys. However, second phases are used in many alloys for various reasons, including enhancement of strength and creep resistance, especially in high temperature

systems where the properties of the metallic matrix can become less robust.

During the wear process, where second phases are harder than the matrix material, it is not sufficient to assume that their presence will have no effect on the wear process and that they will simply be 'worn away' with the matrix as sliding proceeds; this only occurs if the second phase is of similar or lesser hardness. Vardavoulas<sup>94</sup> studied a number of steels into which hard ceramic phases of various sizes were introduced; these included titanium carbide (modified to a much finer carbon nitride phase by nitrogen annealing), copper phosphide, and alumina. It is assumed following that the substrate metal is oxidized and is the main source of compacted oxide or oxide debris and, thus, the oxide-metal interface is effectively moving into the metal.

If the sizes of the second phase particles are less than the critical oxide thickness ( $\xi$  from Quinn's oxidation wear theory<sup>62</sup>), then these particles pass into the oxide layer as the metal is oxidized. They may not protrude above the surface of the oxide layer and thus cannot directly protect the matrix or impinge on the counterface material. The particles are lost as the oxide layer breaks up at the critical thickness to form debris. The only contribution may be to enhance the load-carrying capacity of the metallic matrix in supporting the oxide film.

Where the second phase particle size is only slightly greater than the critical oxide thickness (between  $\xi$  and  $3\xi$ ), there is a transition in the wear mechanism – this is referred to as the 'first stage' – while a small quantity of the second phase may be removed with the oxide, as it breaks up, most will remain embedded in the substrate or matrix. These particles protrude above the nominal surface of the interface and the counterface slides over them. This continues until the oxide layer can reform and during this stage of wear, the matrix cannot influence the wear process; this is the 'second stage.'

The mechanical properties of the second phase particles influence what happens next during the 'second stage.' If the particles are able to resist the sliding action, then the matrix will be protected for a prolonged period and the 'second stage' is extended. Enhanced wear of the counterface material by abrasion may occur in this stage. If they are unable to resist the sliding process and fail under the load from the counterface, then contact between matrix and counterface is quickly restored and the 'first stage' of wear will be repeated. A further possibility is detachment of second phase particles as the oxide



breaks up, with these particles acting as third body abrasives; this occurs where cohesion between matrix and second phase is poor.

If the mean particle size is much greater than the critical oxide thickness, the particles show increased efficiency in providing oxidational wear protection to the material subject to wear. After break up of the oxide layer (end of the 'first stage'), the harder second phase particles remain embedded in the matrix. Again, the main interaction is between the particles and the counterface, and this process controls the wear mechanism; the matrix plays no direct part. The majority of the particles are surrounded by the matrix; thus, break up is more difficult and detachment is almost impossible. While this means that the matrix is well protected against wear, the counterface may undergo high rates of wear and thus become the main source of debris. The inference here is that the first stage cannot resume until these larger particles wear to near the level of the rest of the sample surface; as other particles will continue to be exposed elsewhere on the surface, first stage wear with protective oxide layer formation cannot readily happen and severe wear will continue.

On the basis of the apparent failure of carbides in Stellite 6 to disrupt 'glaze' formation for certain wear combinations, Inman<sup>5</sup> suggested that the second phase particles must also be harder than the generated 'glaze' on the opposing sliding surface (Section 1.15.3.3.2). If this is not so, the second phase particles may wear in preference to the 'glaze' layer and not promote its break-up. This may prove beneficial, with a harder second phase conferring wear resistance but allowing protective 'glazes' to form. Tribaloy alloys, consisting of a hard Laves intermetallic second phase in a Ni-based or more notably a Co-based matrix,<sup>95</sup> are possible examples (not discussed in the current work).

### **1.15.3 High Temperature Wear Behavior of Advanced Materials**

#### **1.15.3.1 Oxide Dispersion Strengthened (ODS) Alloys**

##### **1.15.3.1.1 Introduction**

This section discusses the HT wear behavior of ferritic ODS alloys, Incoloy MA956, and its variants. The section starts with a brief introduction to ODS alloys to provide a context and facilitate interpretation of the experimental observations on their HT wear characteristics.

Ni-base-Inconel alloys MA 6000, MA754, MA758, and MA760, and Fe-base Incoloy MA956, PM2000, and PM2000SD are well-known examples of ODS superalloys. Such ODS alloys possess good high temperature strength and resistance to HT corrosion and oxidation. They derive their strength from the insoluble, deformation resistant and thermally stable dispersoids such as  $Y_2O_3$  (as used in Incoloy MA956)<sup>96</sup> introduced during fabrication by mechanical alloying. This process offers great opportunities in the selection of dispersoids–matrix combination. Strengthening by insoluble, deformation resistant and inert dispersoids is far more effective than other methods such as solid solution and precipitation hardening, as thermodynamics imposes limitation on their continued effectiveness. At certain critical temperatures, solubility limits may be exceeded, leading to the onset of precipitation and eventually Oswald ripening of the precipitates.

During high temperature deformation, most ODS alloys exhibit a threshold stress  $\sigma_0$  below which creep becomes negligible; the threshold stress  $\sigma_0$  is less than Orvan stress  $\sigma_{or}$ . Several models, such as dislocation climb and dislocation detachment (local climb), have been advanced to explain the existence of the threshold stress. None of these models have been universally accepted.

To increase the temperature capability of ODS alloys, the powder produced by mechanical alloying is subjected to hot extrusion and the fine grained extruded structure is then subjected to a high temperature secondary recrystallization anneal.

The overall enhancement of HT capability may be associated with:

- large grain size produced by secondary recrystallization;
- high GAR (grain aspect ratio) produced by recrystallization under a high temperature gradient and minimizing the detrimental effect of transverse grain boundary effect;
- formation of serrated grain boundaries allowing grain interlocking; and
- minimum grain boundary hardening.

##### **1.15.3.1.2 Observations on high temperature wear behavior of some ODS alloys**

There is no evidence to suggest any improved wear resistance conferred by alloy pretreatment for the three near-identical ODS alloys, Incoloy MA956, PM2000, and PM2000SD<sup>3</sup> (Figure 10). Testing against various counterfaces (Stellite 6 and  $Si_3N_4$ )



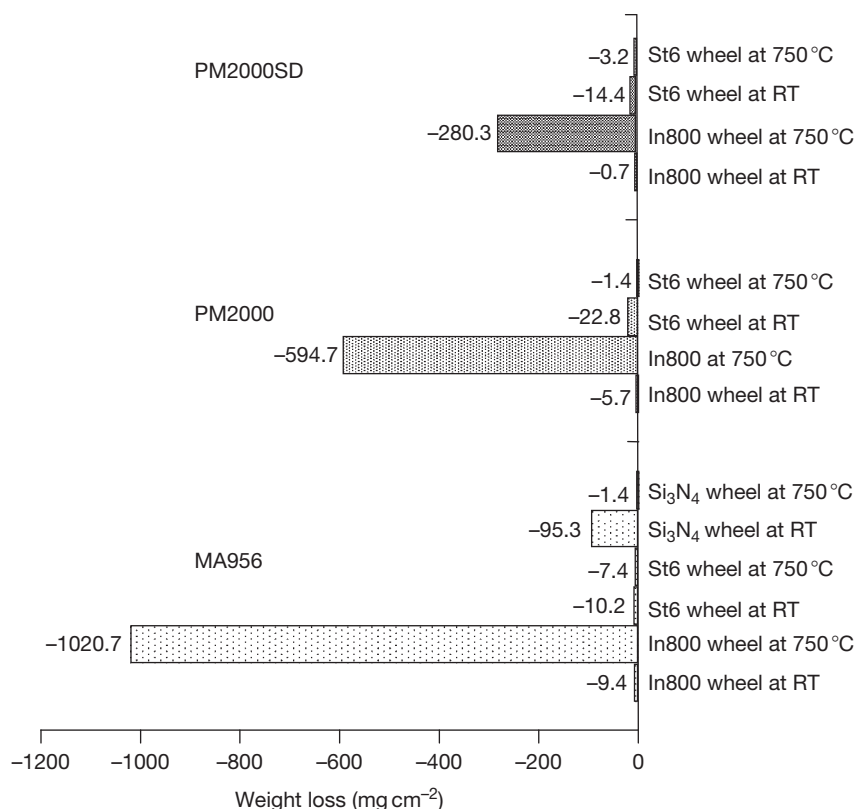


**Figure 10** Weight change of the ODS alloys worn against various counterfaces at room temperature and 750 °C<sup>3</sup> (sliding speed 0.654 m s<sup>-1</sup>, load 7 N).

and at various temperatures (room temperature to 750 °C) does not indicate a definitive trend in relation to grain size and hardness.

#### **Incoloy 800HT counterface**

Only on sliding against Incoloy 800HT there is an apparently strong preference towards lower grain size and increased hardness (Table 2) favoring higher wear.<sup>3</sup> The severity of wear was of the order PM2000SD, PM2000, and Incoloy MA956.

Poor wear resistance and high friction coefficient characterize the wear behavior of the ODS alloys worn against Incoloy 800HT at 750 °C (reciprocating rig, 0.314, 0.654, and 0.905 m s<sup>-1</sup> sliding speed, 7 N load) as indicated by higher weight losses compared to that at room temperature (Figure 10 – 0.654 m s<sup>-1</sup>).<sup>3</sup> The apparent improved wear resistance observed at room temperature is attributable to transfer<sup>3–5</sup> and work hardening of a layer of Incoloy 800HT or back-transferred Incoloy MA956,<sup>5</sup> protecting the ODS alloy surface from sustained wear (Figure 11(a) – 0.654 m s<sup>-1</sup>).

**Table 2** Description and properties of the ODS alloys investigated

Alloy	Description	Hv 500g	Av. grain size (μm)
Ma956	ODS alloy strengthened through a yttria dispersion in Fe–Cr–Al matrix	303	3000
PM2000	ODS alloy strengthened through a yttria dispersion in Fe–Cr–Al matrix	311	500
PM2000SD	ODS alloy strengthened through a yttria dispersion in Fe–Cr–Al matrix. Rolled at higher temperature than PM2000 imparting greater ductility	363	80

Reproduced from Wood, P. D. Ph.D. Thesis, Northumbria University, UK, 1997.

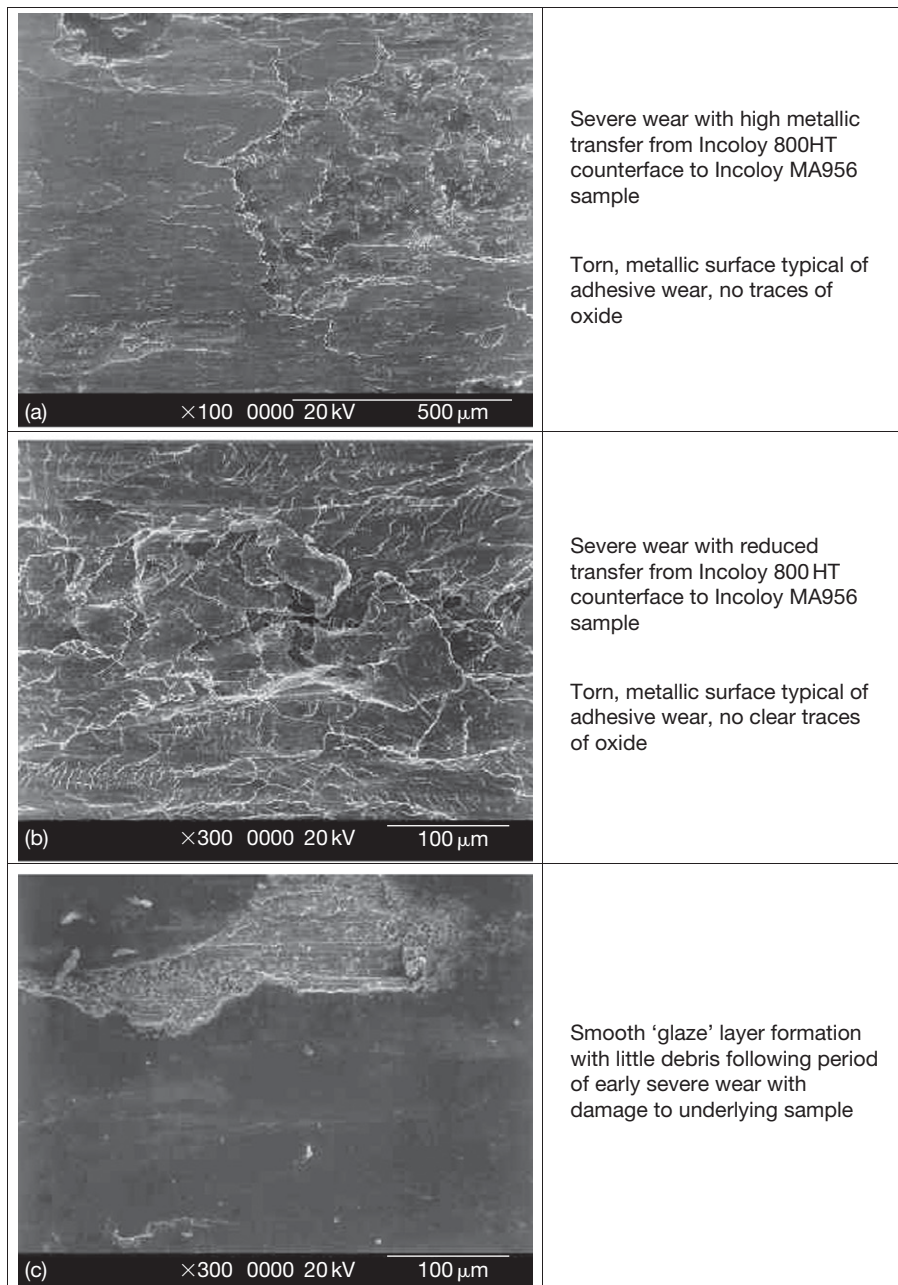
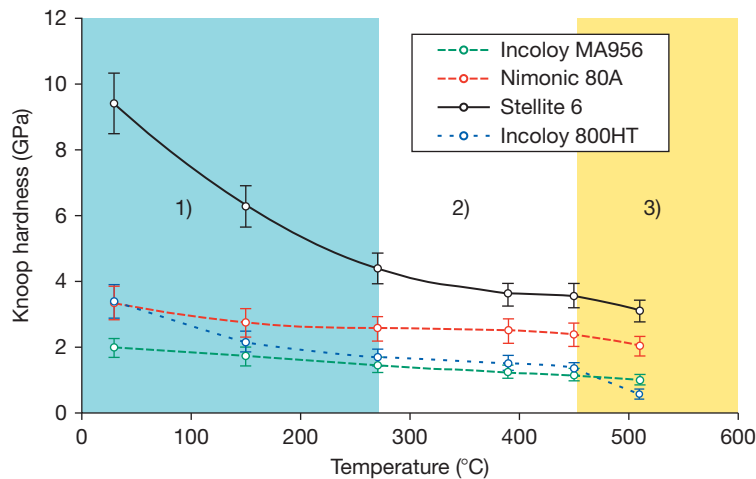


**Figure 11** SEM micrographs of Incoloy MA956 wear surfaces after sliding at  $0.654 \text{ m s}^{-1}$  against an Incoloy 800HT counterface at room temperature, 510 and  $750^\circ\text{C}$  (sliding distance 9418 m).<sup>4</sup> (a) Room temperature (shown), also typical of  $270^\circ\text{C}$ , (b)  $510^\circ\text{C}$  (also typical of 390, 450, 570, and  $630^\circ\text{C}$ ), (c)  $750^\circ\text{C}$  (shown), also typical of  $690^\circ\text{C}$ .

The loss of strength and hardness suffered by the ODS alloys at higher temperatures<sup>10–12</sup> (Figure 12) probably undermines the ability of the alloy to support the process of 'glaze' development. Severe wear continues (Figure 11(b) –  $0.654 \text{ m s}^{-1}$ ) and the low levels of oxide produced act only to inhibit metallic adhesion, preventing the formation of the protective

metallic transfer layer seen at room temperature<sup>5</sup> and wear thus increases with temperature. Some transfer of Incoloy 800HT material still occurs at high temperature; however, continued sliding removes this layer.<sup>3,5</sup> Such transfer tends to be greater at higher sliding speeds, and hence, the weight loss is lower at  $0.905 \text{ m s}^{-1}$  than at



	Mean Knoop hardness (GPa)			
Temperature (°C)	Stellite 6	Nimonic 80A	MA956	Incoloy 800
30	9.39	3.33	1.99	3.38
150	6.28	2.75	1.71	2.16
270	4.37	2.58	1.45	1.68
390	3.61	2.50	1.24	1.52
450	3.55	2.37	1.16	1.34
510	3.08	2.01	0.97	0.55

**Figure 12** Mean Knoop hardness (hot hardness, 50 g load, 12 s dwell time) from room temperature to 510 °C,<sup>4</sup> with wear regimes with respect to temperature identified for the Nimonic 80A/Stellite 6 and Incoloy MA956/Stellite 6 systems.<sup>4,5</sup> 1. Low-temperature oxidative wear, moderate falls (large for Stellite 6) in hardness. 2. Low-temperature oxidative wear at 0.314 m s<sup>-1</sup>, metallic severe wear only at 0.905 m s<sup>-1</sup>, little change in hardness. 3. 'Glaze' formation for Nimonic 80A vs. Stellite 6 at 0.314 m s<sup>-1</sup> with high oxidative wear replacing metallic severe wear at 0.905 m s<sup>-1</sup>. Also, early 'glaze' formation for Incoloy MA956 versus Stellite 6, with extended early severe wear at 0.905 m s<sup>-1</sup>.

0.314 m s<sup>-1</sup><sup>5</sup> Only at 690 and 750 °C (Figure 11(c) – 0.654 m s<sup>-1</sup> example shown) is an oxide<sup>3</sup> or 'glaze',<sup>4,5</sup> layer able to develop on the Incoloy MA956 surface (sourced from the Incoloy MA956) after an initial period of severe wear.<sup>5</sup>

#### Stellite 6 counterface

The improved wear resistance of ODS alloys when worn against Stellite 6 coincides with rapid oxide development; such oxide is sourced from both sample and counterface. At low temperature, this debris remains loose and does not readily form 'glaze' (Figures 13(a) and 14(a)). At high temperature, it sinters rapidly to form more extensive 'glaze' layers (Figures 13(c) and 14(c)).<sup>3-5</sup> The relative contributions of sample- and counterface-sourced debris

(at least for Incoloy MA956 versus Stellite 6) have been observed to depend on sliding speed.<sup>5,23</sup> A slow sliding speed (0.314 m s<sup>-1</sup>)<sup>5</sup> favors greater Stellite 6 wear and thus higher levels of Co-based oxide debris. Faster sliding speeds (0.654 m s<sup>-1</sup><sup>4</sup> and especially, 0.905 m s<sup>-1</sup>)<sup>5</sup> encourage greater Incoloy MA956 wear and thus higher levels of Fe and Cr oxide contribution (Figure 15). At 750 °C, the presence of Co in the debris promotes more rapid 'glaze' formation<sup>23</sup> and prevents continued early wear.

Only at intermediate temperatures (390 and 450 °C)<sup>4,5</sup> and at 0.654 and 0.905 m s<sup>-1</sup> does the oxide fail to separate wear surfaces and allow severe wear to occur (Figure 14(b)). Below these temperatures, the oxide separates the surfaces even in the

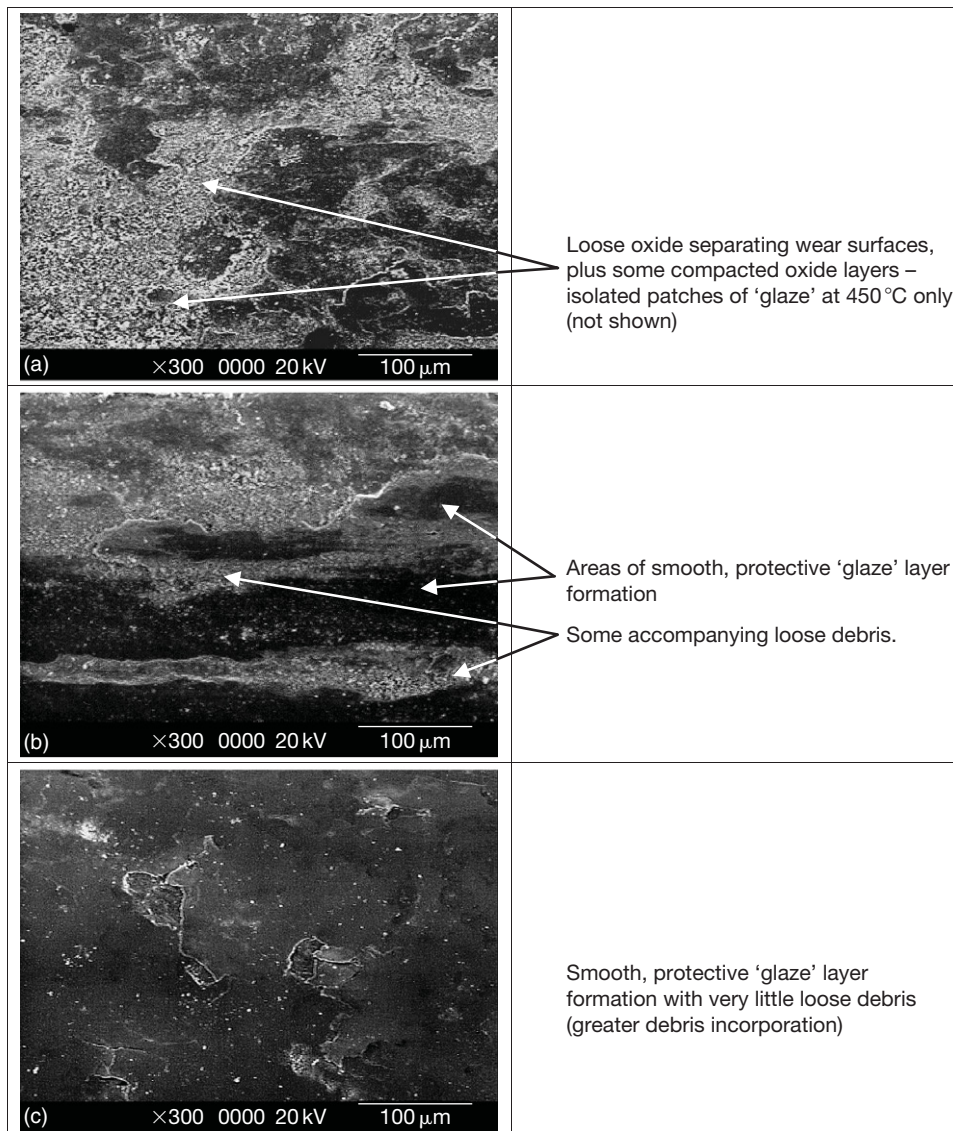


**Figure 13** SEM micrographs of Incoloy MA956 wear surfaces after sliding at  $0.314 \text{ m s}^{-1}$  against a Stellite 6 counterface at room temperature, 510, and 750 °C.<sup>23</sup> (a) Room temperature (shown), also typical of 270, 390, and 450 °C, (b) 510 °C, and (c) 750 °C (shown), also typical of 570, 630, and 690 °C.

form of the aforementioned loose debris. At progressively higher temperatures, severe wear is increasingly restricted to only the initial sliding period as continued sliding promotes debris sintering and ‘glaze’ formation. Above 630 °C, ‘glaze’ development is so rapid that severe wear is all but eliminated. No severe wear is observed at  $0.314 \text{ m s}^{-1}$ , with the loose debris progressively developing into ‘glaze’ as sliding temperature is increased<sup>5</sup> (Figure 13 shows the debris (a) loose at room temperature, (b) partially forming a ‘glaze’ layer at 510 °C, and (c) forming a comprehensive ‘glaze’ layer at 750 °C).

#### 1.15.3.1.3 Effects of load

Rose<sup>4</sup> also examined the effect of load (7–25 N,  $0.654 \text{ m s}^{-1}$  only) on the sliding behavior of Incoloy MA956 when slid against Incoloy 800HT and Stellite 6 counterfaces at 750 °C (Figure 16). ‘Glaze’ layers were observed for all loads up to 20 N for both counterfaces and no change in oxide behavior was observed with increasing load (although greater material working was reported as being necessary to provide material for ‘glaze’ when an Incoloy 800HT counterface was used). No significant increases in weight loss were observed with increasing load up to 20 N (Figure 17). These



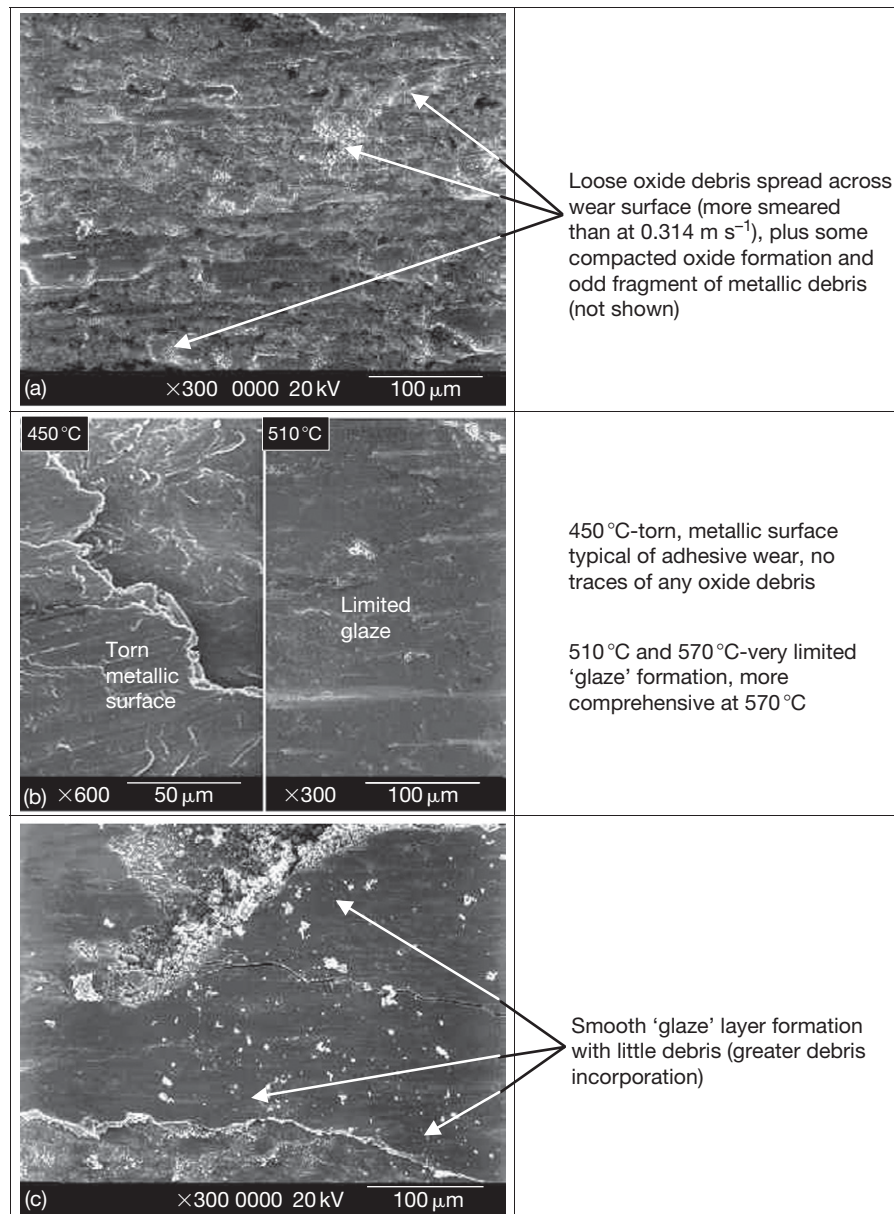


**Figure 14** SEM micrographs of Incoloy MA956 wear surfaces after sliding at  $0.654 \text{ m s}^{-1}$  against a Stellite 6 counterface at room temperature, 450, 510, and 750 °C<sup>4</sup> (also representative of  $0.905 \text{ m s}^{-1}$ ).<sup>23</sup> (a) Room temperature (shown), also typical of 270 and 390 °C, (b) 450 °C (left) and 510 °C (right – also typical of 570 °C), (c) 750 °C (shown), also typical of 630 and 690 °C.

observations were irrespective of whether the 'glaze' was primarily Stellite 6-counterface sourced or Incoloy MA956-sample sourced (when the counterface was Incoloy 800HT). Higher losses were reported at 25 N (most noticeably with an Incoloy 800HT counterface – [Figure 17](#)) and, although 'glaze' layers still formed, the Incoloy MA956 sample substrate was unable to provide sufficient support for the 'glaze' layer to remain protective.

### 1.15.3.2 Intermetallics

#### 1.15.3.2.1 Introduction

Strong, predominantly metallic bonding between unlike atoms leads to the formation of intermetallics and intermetallic compound phases. From such bonding comes crystal structure, ordering, high strength at low and high temperature, low ductility, and low  $K_{IC}$ , particularly at low temperature.

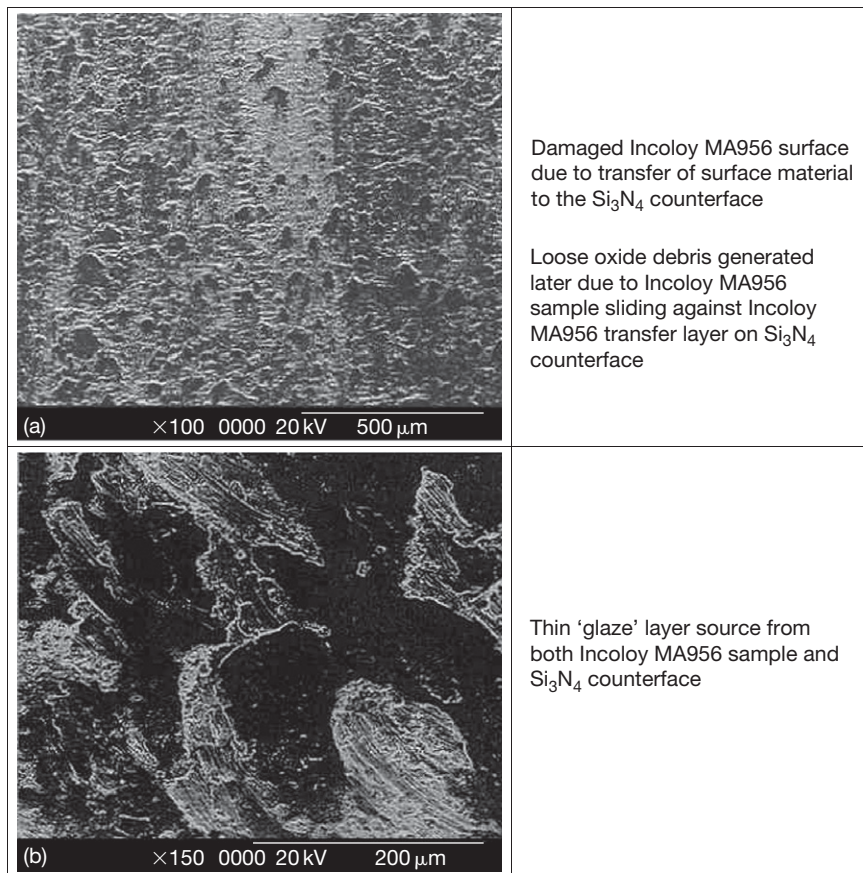


**Figure 15** SEM micrographs of Incoloy MA956 wear surfaces after sliding at  $0.654 \text{ m s}^{-1}$  against a  $\text{Si}_3\text{N}_4$  counterface at (a) room temperature and (b)  $750^\circ\text{C}$  (load 7 N, sliding distance 9418 m). Reproduced from Wood, P. D. Ph.D. Thesis, Northumbria University, UK, 1997.

The low ductility, low  $K_{1c}$ , and high strength of intermetallics stem from such critical factors as complex crystal structures, the large Burgers Vector, high lattice stress, the inadequate slip systems and the inability to cross slip. The complex interplay between these parameters makes the prediction of intermetallic wear behavior difficult.

The expected improvement in wear resistance from high strength, ordering and an adequate slip system may be off-set by low  $K_{1c}$  and low fracture strain. The advantage in providing high wear resistance due to ordering may eventually be lost by the destruction of this ordering due to elemental diffusion from the counterface into the intermetallic lattice. At elevated temperature, increased  $K_{1c}$  and fracture strain are likely to improve the wear resistance; however, some of the effects of these parameters may be masked by the formation of wear resistance surface 'glaze' layers.

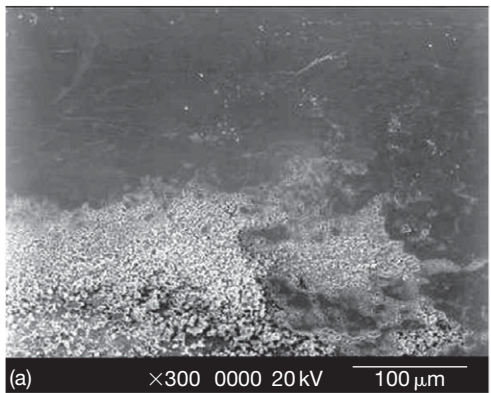
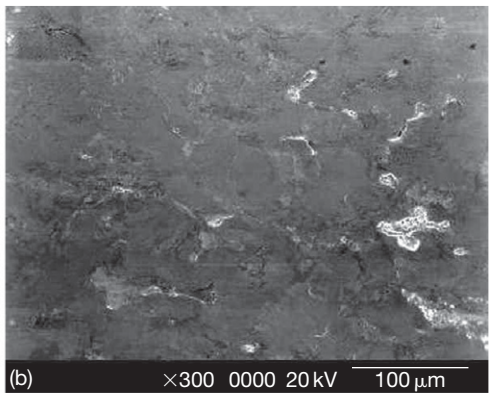
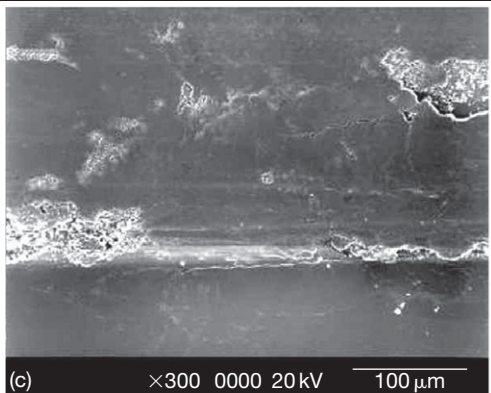
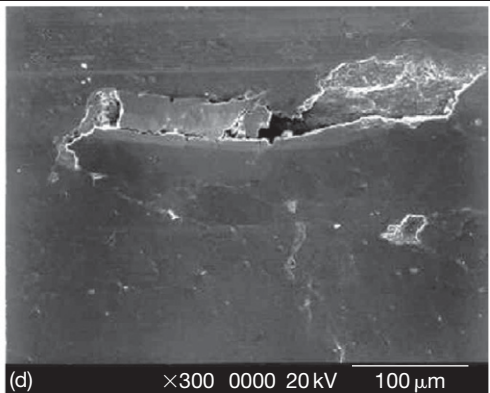
#### 1.15.3.2.2 Wear of TiAl – Metallic counterfaces

In discussing intermetallic wear resistance, attention is focused on TiAl and TiAl-based intermetallics because of increasing interest in using these materials in many industrial applications, including automotive, aerospace, and power generation.

TiAl when worn against Incoloy 800HT at room temperature ('reciprocating-block-on-rotating-cylinder' rig, load 7 N, sliding speed  $0.654 \text{ m s}^{-1}$ ) shows a similar wear pattern to the ODS and Nimonic alloys, and involves a similar mechanism<sup>3</sup>; the transfer of Incoloy 800 to the TiAl surface, followed by work hardening of the transferred layer, and formation of a wear-resistant oxide layer ( $\text{NiCr}_2\text{O}_4/\text{Fe}_2\text{O}_3$ ). The development of this hardened, wear-resistant layer causes some improvement in wear resistance without any observable 'glaze' formation (Figure 18(a)).

In contrast, 'glaze' formation has been observed in the same system at  $750^\circ\text{C}$  (7 N,  $0.654 \text{ m s}^{-1}$ ), the 'glaze'



Incoloy 800HT counterface		Stellite 6 counterface	
 <p>(a) ×300 0000 20 kV 100 μm</p>	<p>Smooth compacted oxide / 'glaze' layers with a little loose debris (underlying sample damaged due to early severe wear)</p>	 <p>(b) ×300 0000 20 kV 100 μm</p>	<p>Smooth compacted oxide / 'glaze' layers</p>
 <p>(c) ×300 0000 20 kV 100 μm</p>	<p>Smooth compacted oxide / 'glaze' layers and a little loose debris, with some cracking due to high load (underlying sample damaged due to early severe wear)</p>	 <p>(d) ×300 0000 20 kV 100 μm</p>	<p>Smooth compacted oxide / 'glaze' layers, with some cracking due to high load</p>

**Figure 16** SEM micrographs of Incoloy MA956 worn against an Incoloy 800HT counterface at applied loads of (a) 7 N and (b) 25 N, and against a Stellite 6 counterface at applied loads of (c) 7 N and (d) 25 N (750 °C, sliding speed 0.654 m s<sup>-1</sup>, sliding distance 9418 m). Reproduced from Rose, S. R. Ph.D. Thesis, Northumbria University, UK, 2000.

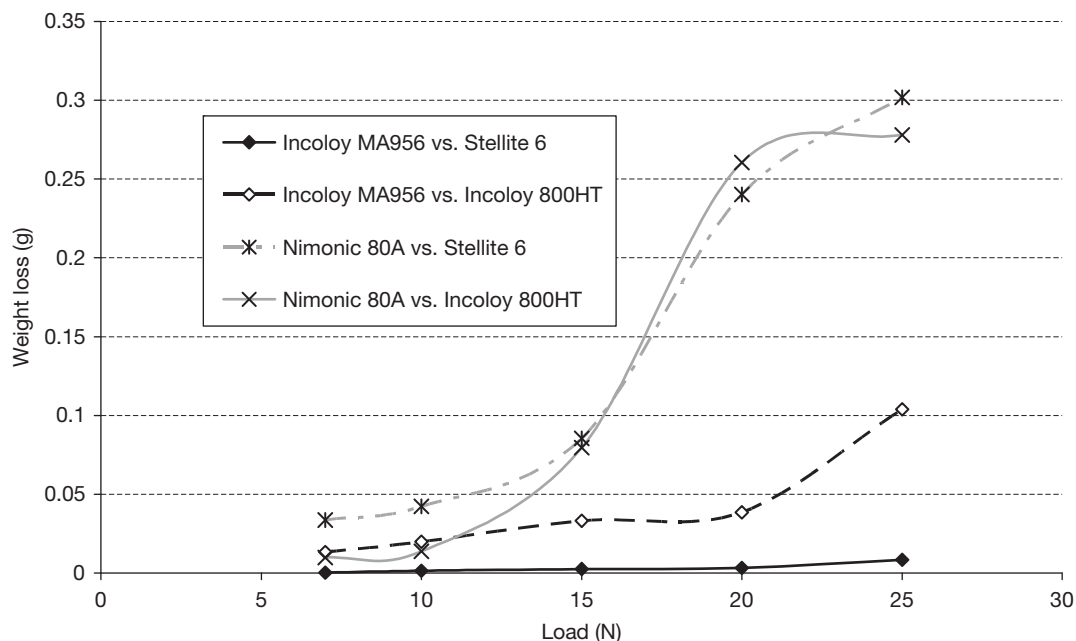


**Figure 17** Weight losses for Incoloy MA956 and Nimonic 80A worn against Incoloy 800HT and Stellite 6 counterface at applied loads of between 7 and 25 N (750 °C, sliding speed  $0.654 \text{ m s}^{-1}$ , sliding distance 9418 m). Reproduced from Rose, S. R. Ph.D. Thesis, Northumbria University, UK, 2000.

(Figure 18(b)) containing mainly oxidized Fe/Ni/Cr material from Incoloy 800 with little Ti and Al.<sup>3</sup> These observations are in conflict with other work where the 'glaze' contained the elements of TiAl. It is believed that the use of a different test system ('pin-on-disk' rather than 'block-on-cylinder') in the latter work accounts for this difference. The role of TiAl is considered to provide a deformation and wear-resistant substrate for the 'glaze' to develop, to reside, and to be sustained.

When worn against Stellite 6 ( $7 \text{ N}$ ,  $0.654 \text{ m s}^{-1}$ ),<sup>3</sup> initial transfer of Stellite 6-based material on the TiAl surface results initially in a like-on-like sliding regime, with the Stellite 6 counterface sliding against this transferred layer. At room temperature (Figure 18(c)), instability of this layer leads to a continual process of transfer and removal from both surfaces and a loose oxide containing Ti and Al from the TiAl, and Co and Cr from the Stellite 6 is generated. Only at 750 °C (at  $0.314 \text{ m s}^{-1}$ ,<sup>97</sup> as well as  $0.654 \text{ m s}^{-1}$ )<sup>3</sup> does the transferred Stellite 6 material form a primarily Co–Cr-oxide 'glaze' layer on the TiAl surface (Figures 18(d) and 19(a)), this layer being thinner than that created when sliding against Incoloy 800HT.

#### 1.15.3.2.3 Wear of TiAl – Ceramic counterfaces

TiAl suffers moderate wear when slid against a silicon nitride interface at room temperature ( $0.654 \text{ m s}^{-1}$ ).

While the debris generated (sourced from both sample and counterface) forms loose oxide platforms (or 'plateaux' – Figure 20(a)), these are formed and removed as sliding continues and do not form a wear protective layer. The high TiAl wear has been attributed to the elements of the counterface material interfering with the ordered structure of the intermetallic, as small atomic radii Si and N enter the lattice and increase its susceptibility to wear. A mixture of abrasive and adhesive wear with some evidence of stick-slip, possibly due to high mutual chemical compatibility between the  $\text{Si}_3\text{N}_4$  and the TiAl, has been reported<sup>98</sup> ( $\text{Si}_3\text{N}_4$  has been previously observed to have high mutual chemical compatibility with both Ti and Al<sup>99</sup>), leading to moderate wear of the TiAl and high wear of the  $\text{Si}_3\text{N}_4$ . In contrast, TiAl undergoes lower wear when slid against silicon nitride at 750 °C (at  $0.314$ <sup>97</sup> and  $0.654 \text{ m s}^{-1}$ ),<sup>3</sup> due to the rapid formation of a thin wear-resistant oxide layer (Figures 19(b) and 20(b)). The formation of this layer, sourced from both the TiAl and  $\text{Si}_3\text{N}_4$ , prevents substantial wear. It is suggested that any high mutual compatibility enhances the very early stages of wear, providing the necessary material for the wear-resistant layer.

TiAl undergoes higher wear when worn against  $\text{Al}_2\text{O}_3$  at room temperature<sup>97</sup> with enhanced material removal by abrasion, the debris from which does not form a protective layer. The material generated from

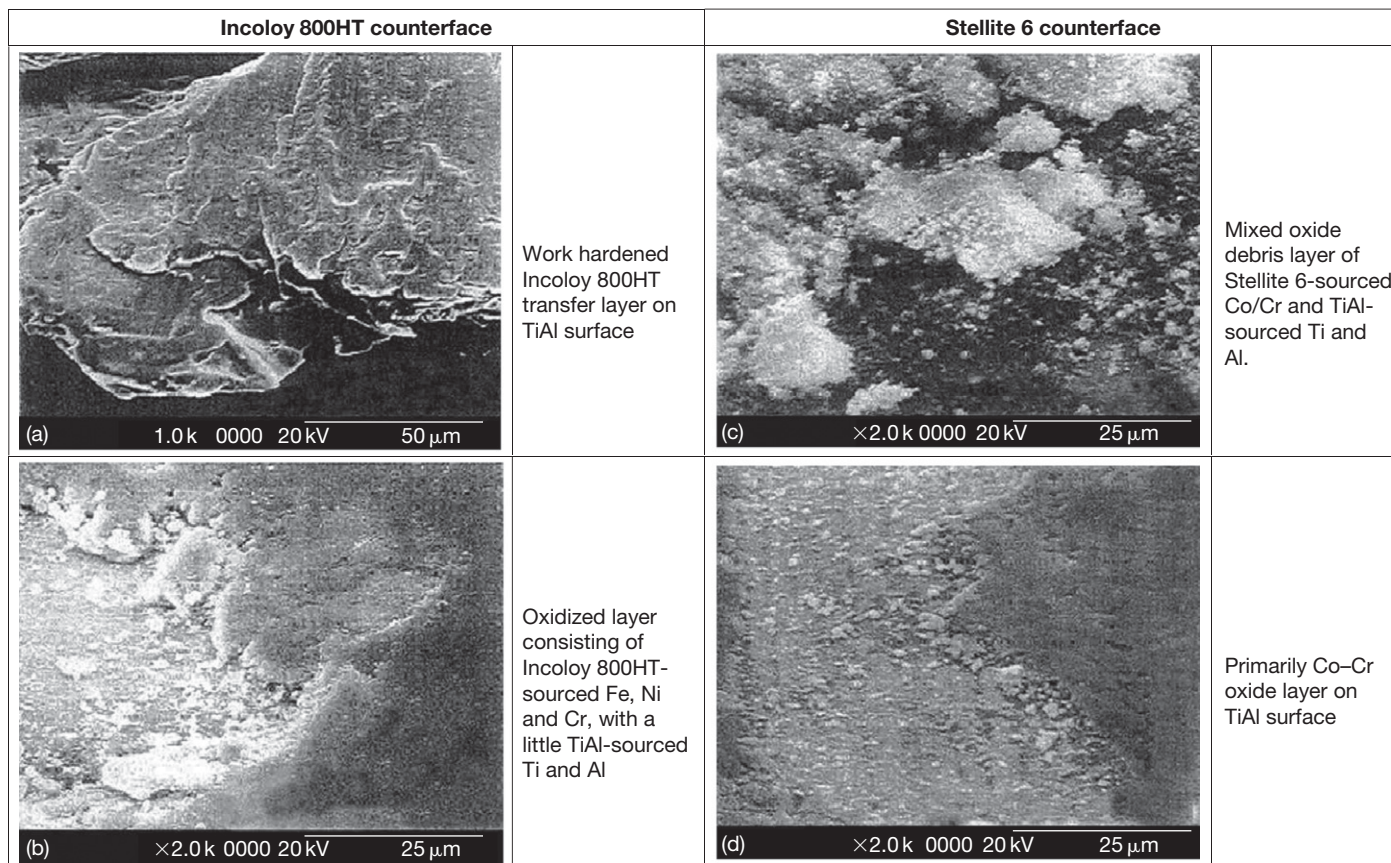


**Figure 18** SEM micrographs of TiAl worn against an Incoloy 800HT counterface at (a) room temperature and (b) 750 °C, and against a Stellite 6 counterface at (c) room temperature and (d) 750 °C, sliding speed  $0.654 \text{ m s}^{-1}$  (load 7 N, sliding distance 9418 m). Reproduced from Wood, P. D. Ph.D. Thesis, Northumbria University, UK, 1997.



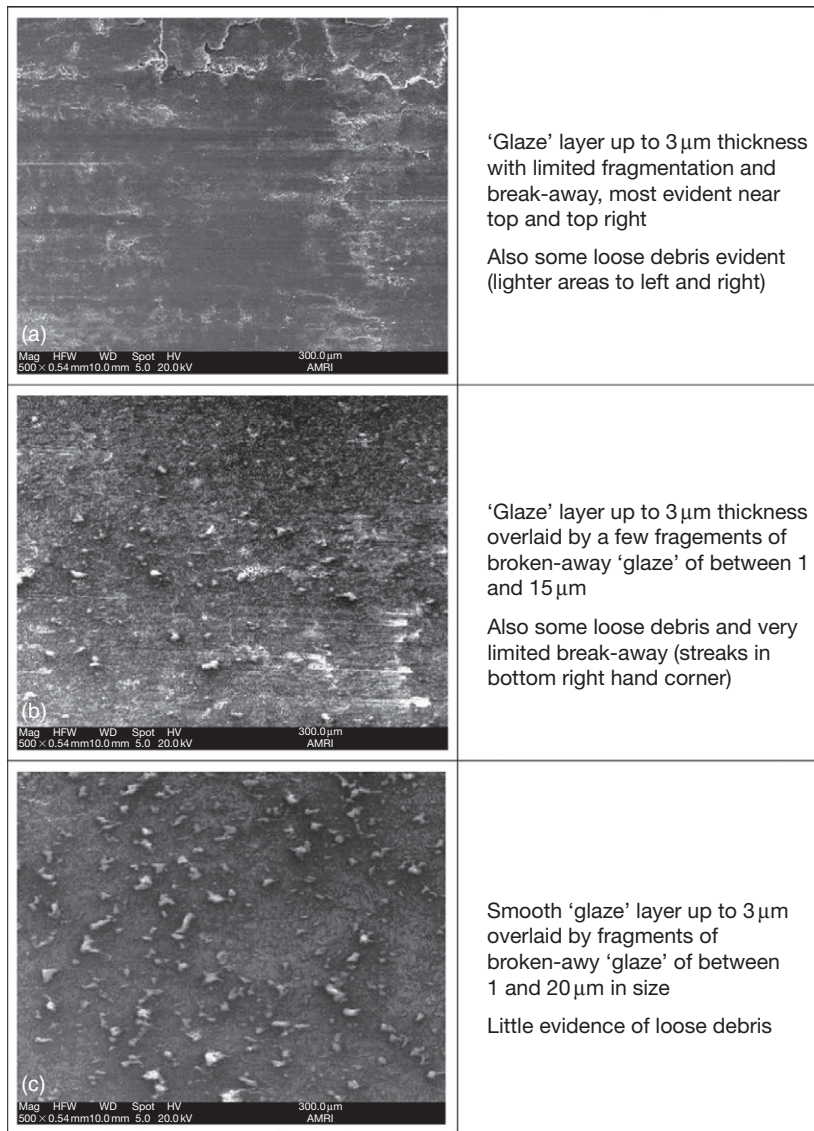


**Figure 19** SEM micrographs of  $\gamma$ -TiAl wear scar surfaces after wear against Stellite 6,  $\text{Si}_3\text{N}_4$  and  $\text{Al}_2\text{O}_3$  counterfaces at 750 °C, sliding speed 0.314 m s<sup>-1</sup> (load 7 N, sliding distance 4522 m).<sup>97</sup> (a) Stellite 6 counterface, (b)  $\text{Si}_3\text{N}_4$  counterface, and (c)  $\text{Al}_2\text{O}_3$  counterface.

an initial period of high TiAl-wear against  $\text{Al}_2\text{O}_3$  at 750 °C,<sup>97</sup> however, readily forms a 'glaze' layer (Figure 19(c)) which provides some protection for the TiAl surface and prevents excessive wear. However, despite the 'glaze' layer, the abrasive nature of the oxide generated (a mixture of Ti and Al oxides) still promotes continued material removal. In contrast, the  $\text{Al}_2\text{O}_3$  undergoes little wear at both room temperature<sup>99</sup> and 750 °C,<sup>97</sup> with it having no potential chemical compatibility with TiAl; hence, no adhesive mechanism can occur.

### 1.15.3.3 Nimonic Alloys

#### 1.15.3.3.1 Incoloy 800HT counterface

Wood<sup>3</sup> reported a correlation between Nimonic 80A cast, Nimonic 80A HIPped, and Nimonic 90 when tested against different counterfaces at various temperatures (0.654 m s<sup>-1</sup>, 7 N load and reciprocating-block/sample-on-rotating cylinder/counterface configuration). The results of room temperature tests seemed to be greatly influenced by the degree of material transfer to the Nimonic surface, this transfer

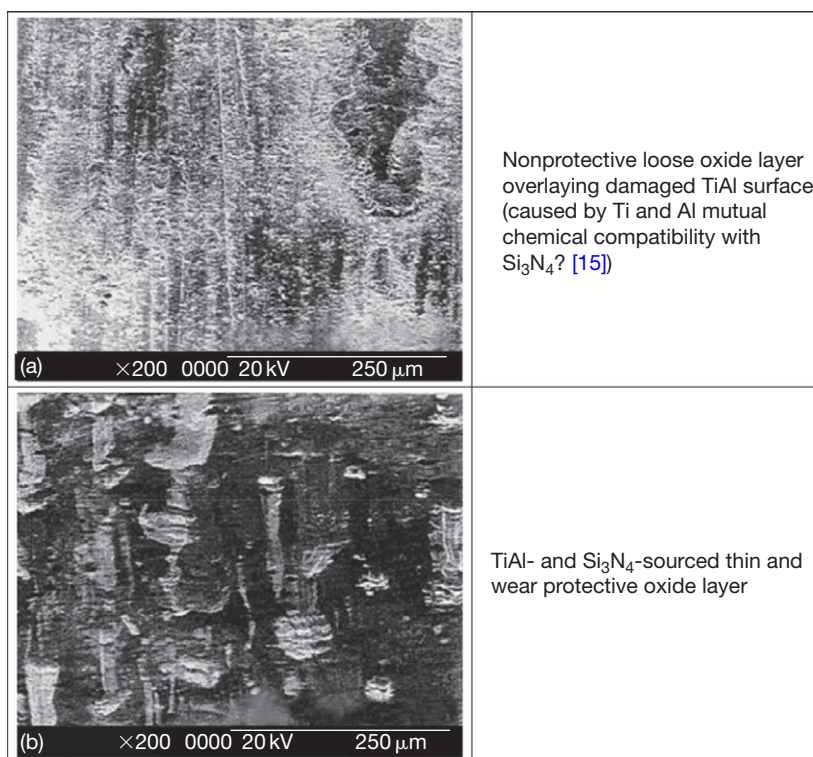


**Figure 20** SEM micrographs of TiAl worn against a  $\text{Si}_3\text{N}_4$  counterface at (a) room temperature and (b) 750 °C, sliding speed  $0.654 \text{ m s}^{-1}$  (load 7 N, sliding distance 9418 m). Reproduced from Wood, P. D. Ph.D. Thesis, Northumbria University, UK, 1997.

itself being influenced by counterface hardness; the softer the counterface the higher the amount of transfer.

Metallic transfer readily occurred from the relatively soft Incoloy 800HT counterface onto the surfaces of each of the Nimonic materials at room temperature. The transferred material formed a wear-resistant layer which protected the Nimonic material surfaces and led to very small weight changes. Inman<sup>5</sup> later reported the development of metallic transfer layers at  $0.314$  and  $0.905 \text{ m s}^{-1}$  (Figures 21 and 22 – greater transfer was observed at  $0.905 \text{ m s}^{-1}$ ) when Nimonic 80A was slid against Incoloy 800HT; these layers were work hardened.

At 750 °C, the Nimonic alloys showed a large range of behaviors when tested against the same three counterfaces.<sup>3</sup> When slid against Incoloy 800HT, mainly Incoloy 800HT-sourced layers that protected the Nimonic alloys against wear, together with low weight changes, were observed. Rose<sup>4</sup> and Inman<sup>5</sup> additionally reported ‘glaze’ overlying any transferred material when Nimonic 80A was worn against Incoloy 800HT at this temperature.

Rose ( $0.654 \text{ m s}^{-1}$ )<sup>4</sup> and Inman ( $0.314$  and  $0.905 \text{ m s}^{-1}$ )<sup>5</sup> examined temperatures between room temperature and 750 °C (Figures 21 and 22), with Rose<sup>4</sup> noting that Incoloy 800HT-sourced transfer layers continued to be observed up to 570 °C. Inman<sup>5</sup> reported the development of transfer layers up to 750 °C, observing an increase in transfer with sliding speed. At  $0.314 \text{ m s}^{-1}$ , transfer was less, due to increased amounts of oxide that interfered with metallic adhesion, but did not form ‘glaze.’ At  $0.905 \text{ m s}^{-1}$ , transfer was greater than at either  $0.314$  or  $0.654 \text{ m s}^{-1}$ ; any surface oxidation was more readily removed, allowing greater adhesion of transferred material.

‘Glaze’ layers were observed only between 630 and 750 °C,<sup>4,5</sup> with its formation being favored by increased test temperature<sup>4,5</sup> and lower sliding speed (due to decreased material removal).<sup>5</sup> These ‘glaze’ layers were reported to form after transfer from the Incoloy 800HT counterface to the Nimonic 80A surface<sup>5</sup>; effectively, the ‘glaze’ was generated by ‘like-on-like’ sliding of the transfer layer against the Incoloy 800HT counterface.

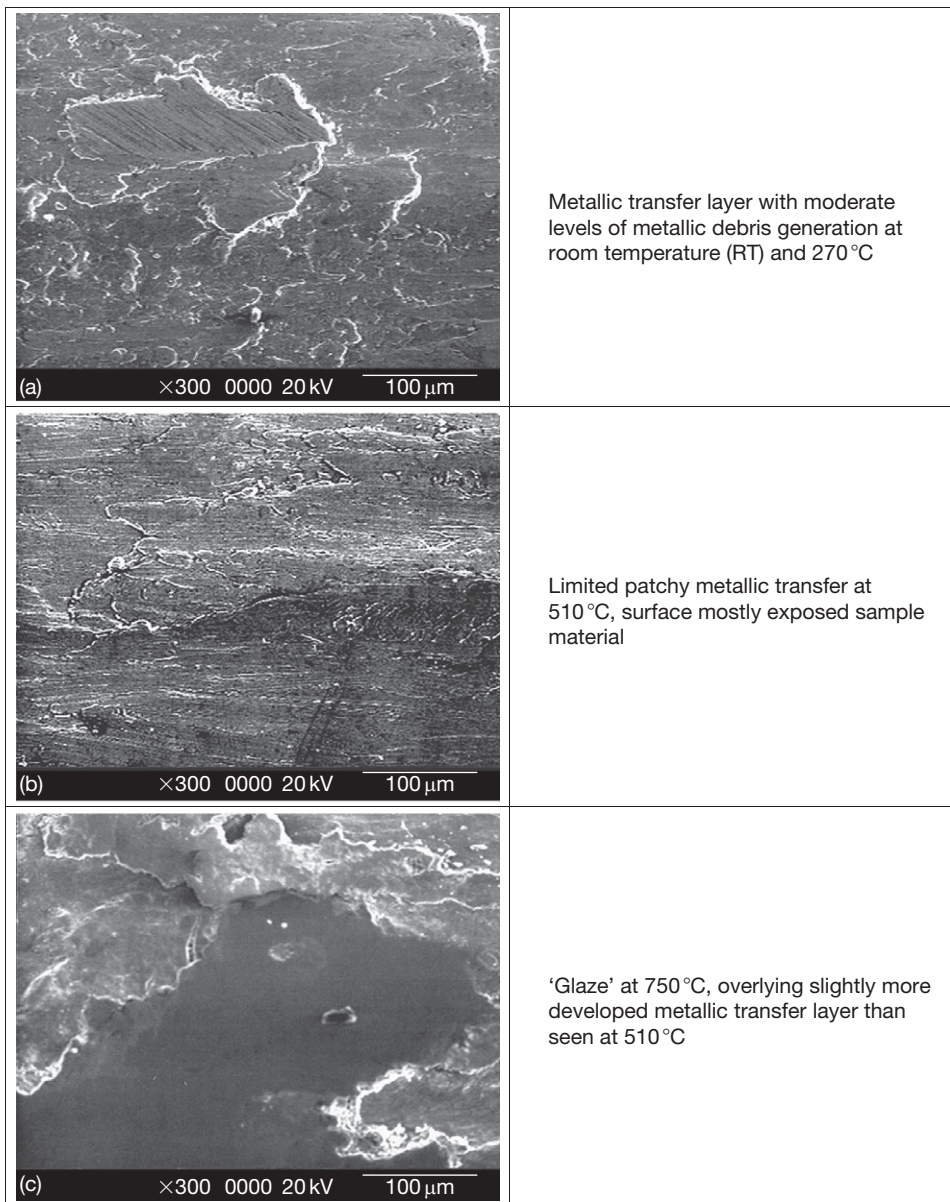


**Figure 21** SEM micrographs of Nimonic 80A wear surfaces after sliding at  $0.314 \text{ m s}^{-1}$  (load 7 N, sliding distance 4522 m) against an Incoloy 800HT counterface at room temperature, 270, 570, and 750 °C.<sup>5</sup> (a) Room temperature (shown), also typical of 270 °C, (b) 510 °C (shown), also typical of 390, 450, 570, and 630 °C, and (c) 750 °C (shown), also typical of 690 °C.

#### **Effects of load**

Rose<sup>4</sup> also examined the effect of load (7–25 N,  $0.654 \text{ m s}^{-1}$  only) on sliding behavior for Nimonic 80A when slid against Incoloy 800HT at 750 °C. Limited compacted oxide layers formed at 7 N (**Figure 23(a)**) and 10 N load, protecting the Nimonic 80A surface. At loads between 15 and 25 N (**Figure 23(b)**), an abrasive, oxidative wear regime dominated, with no debris build-up or layer formation; the behavior of the oxide

changed from protective to abrasive due to the increased load. This was reflected by a rapid increase in weight loss above 15 N (**Figure 17**).

#### **1.15.3.3.2 Stellite 6 counterface**

Wood ( $0.654 \text{ m s}^{-1}$ , 7 N load)<sup>3</sup> reported only limited material transfer from the harder Stellite 6 counterface to the Nimonic material surfaces at room temperature. Thin mixed oxide layers were formed on the Nimonic



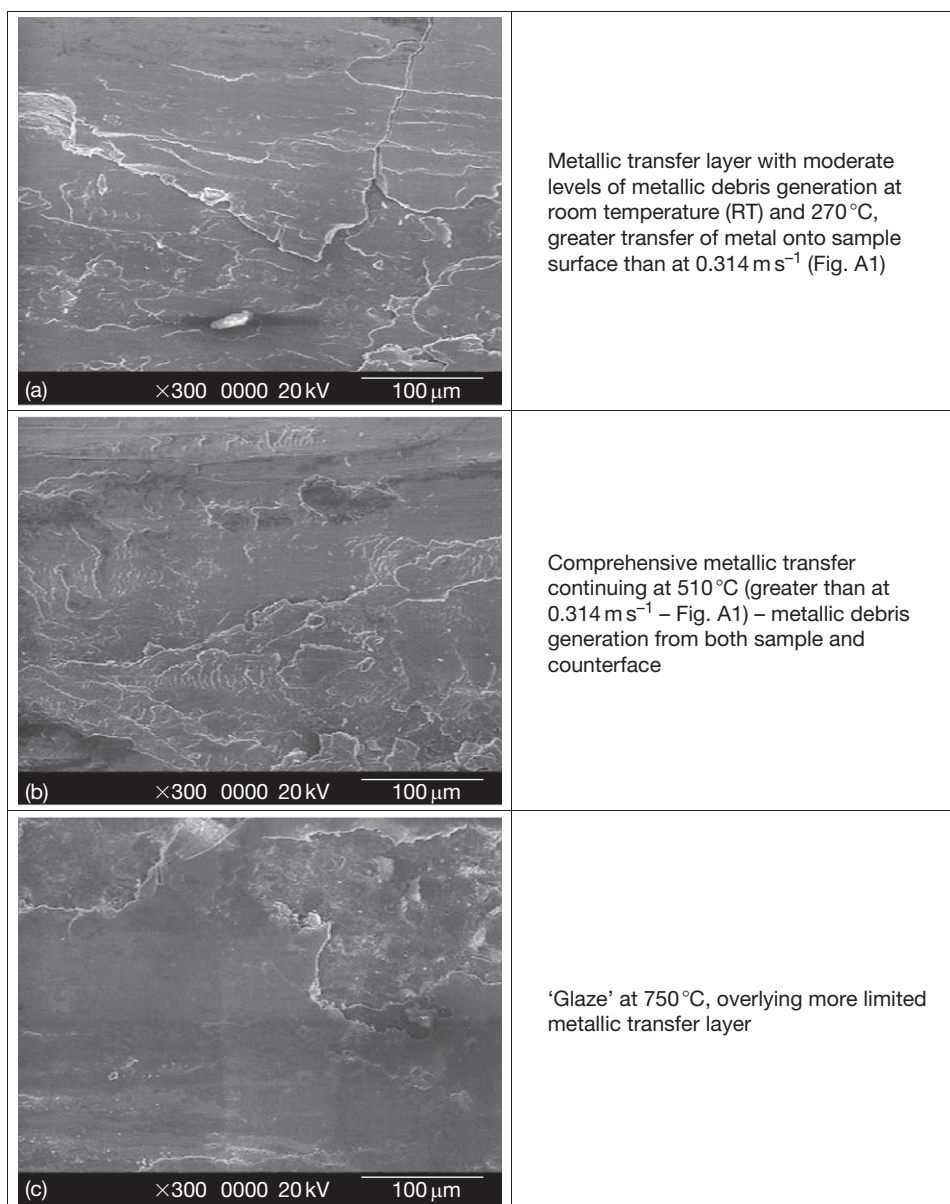


**Figure 22** SEM micrographs of Nimonic 80A wear surfaces after sliding at 0.905 m s<sup>-1</sup> (load 7 N, sliding distance 4522 m) against an Incoloy 800HT counterface at room temperature, 270, 570, and 750 °C.<sup>5</sup> (a) Room temperature and 270 °C (shown), also typical of 390 °C, (b) 570 °C (shown), also typical of 450, 510, and 630 °C, and (c) 750 °C (shown), also typical of 690 °C.

surfaces; these contained material from both the Nimonic and Stellite 6 wear surfaces and provided only limited protection. Testing of Nimonic 80A against a Stellite 6 counterface at 0.654 m s<sup>-1</sup>(<sup>4</sup>) and at 0.314 and 0.905 m s<sup>-1</sup>(<sup>5,21,22</sup>) (Figures 24(a) and 25(a)) resulted in preferential wear of the Stellite 6 counterface, generating loose Co–Cr-based oxides. This debris

separated the wear surfaces, preventing metallic contact; a low temperature mild wear regime resulted.

Behavior at intermediate and high temperature depended significantly on sliding speed. At 0.314 m s<sup>-1</sup>(<sup>5,21,22</sup>) the loose debris mild wear regime (Figure 24(a)) continued up to 450 °C. Increased sintering was observed at 390 °C, isolated 'glaze' at

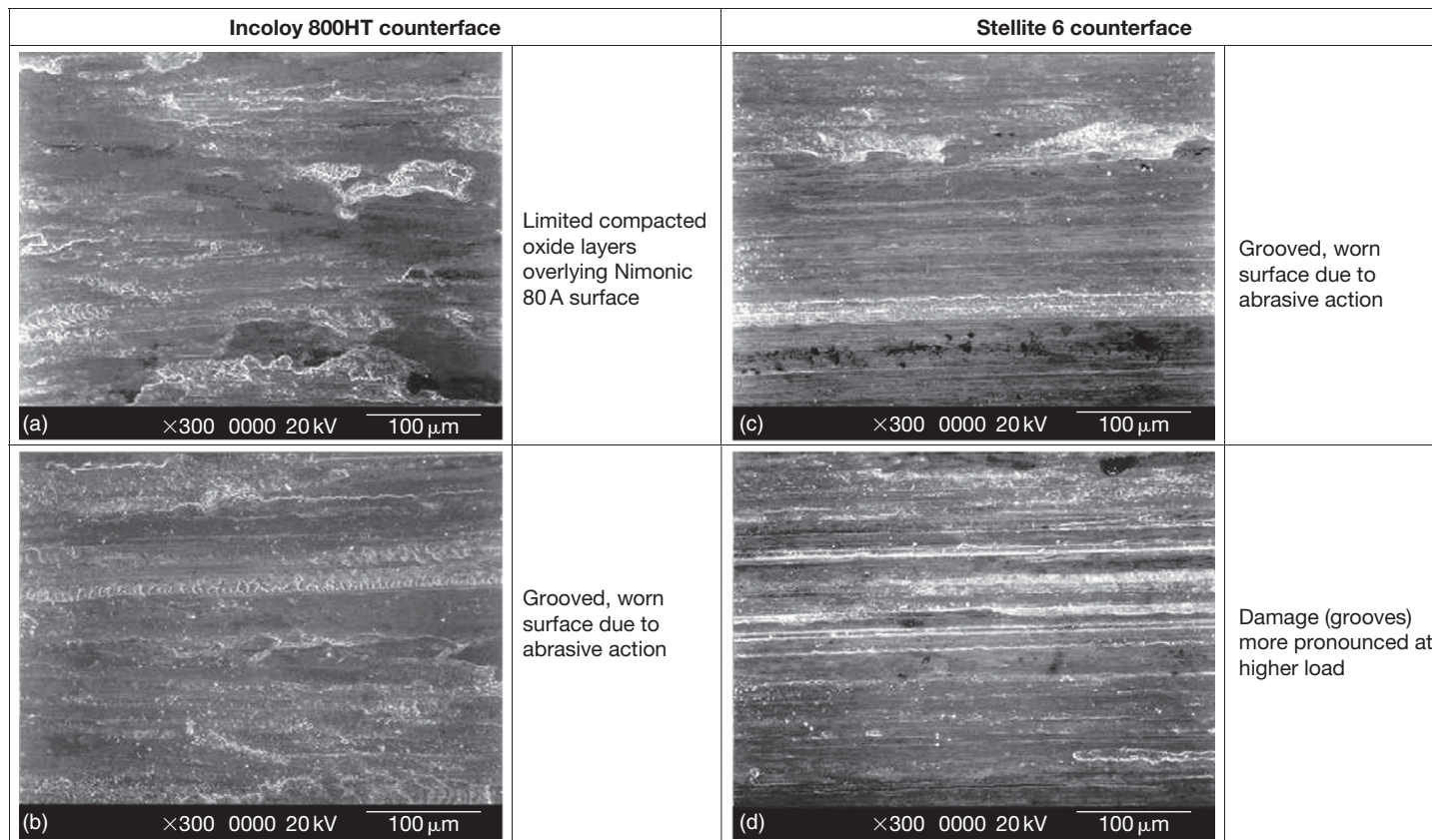


**Figure 23** SEM micrographs of Nimonic 80A worn against an Incoloy 800HT counterface at applied loads of (a) 7 N and (b) 25 N, also against a Stellite 6 counterface at applied loads of (c) 7 N and (d) 25 N (750 °C, sliding speed  $0.654 \text{ m s}^{-1}$ , sliding distance 9418 m). Reproduced from Rose, S. R. Ph.D. Thesis, Northumbria University, UK, 2000.

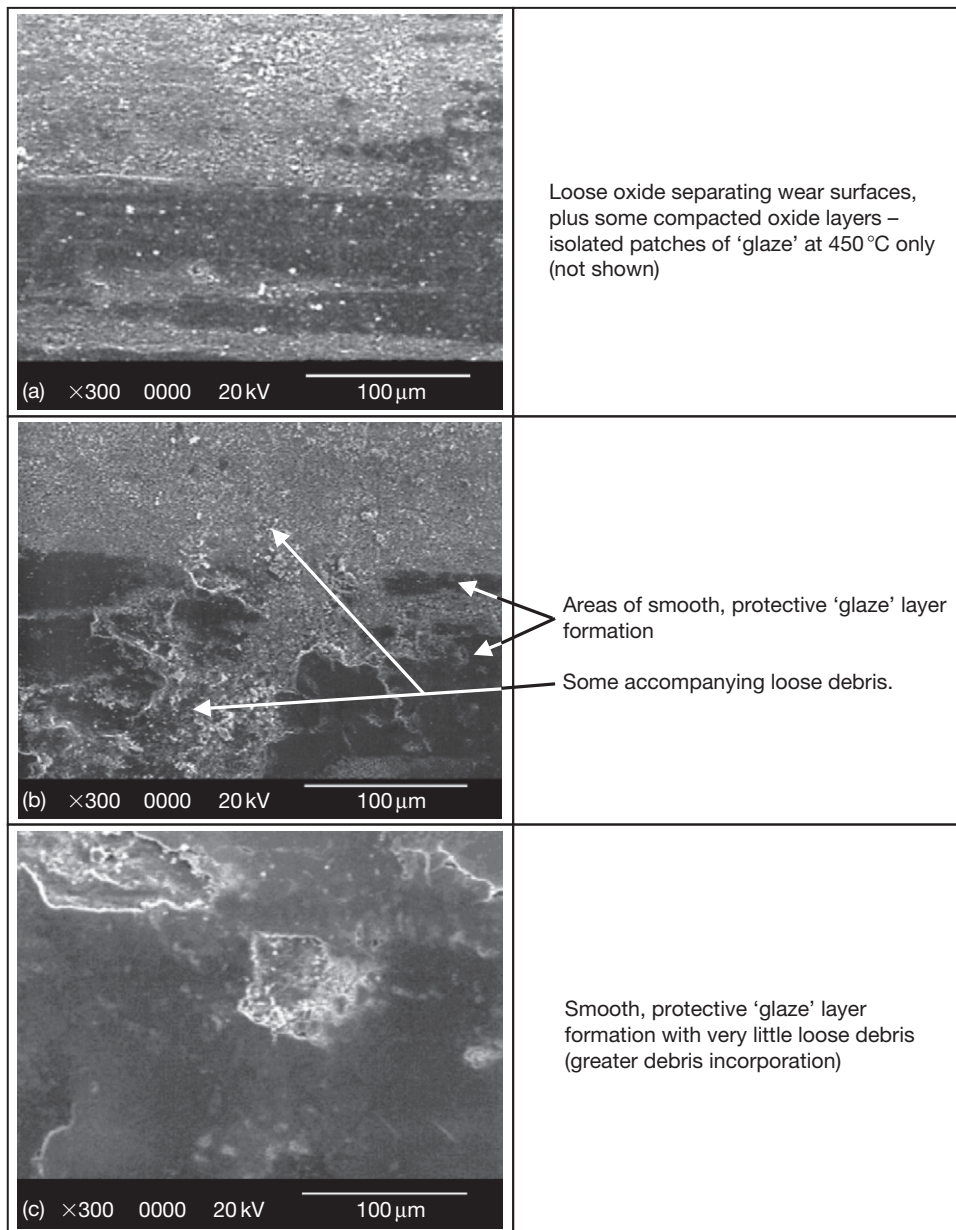


**Figure 24** SEM micrographs of Nimonic 80A wear surfaces after sliding at  $0.314 \text{ m s}^{-1}$  (load 7 N, sliding distance 4522 m) against a Stellite 6 counterface at room temperature, 510 and 750 °C.<sup>22</sup> (a) Room temperature (shown), also typical of 270, 390, and 450 °C and (b) 510 °C, (c) 750 °C (shown), also typical of 570, 630, and 690 °C.

450 °C, with increasingly comprehensive ‘glaze’ formation above 510 °C (Figure 24(b)) and most notably between 630 and 750 °C (Figure 24(c)).<sup>5,21,22,24</sup>

The loose debris mild wear regime was observed up to 390 °C at  $0.654 \text{ m s}^{-1}$ <sup>(4)</sup> and 270 °C at  $0.905 \text{ m s}^{-1}$ <sup>(5,21,22)</sup>; at higher temperatures, there was a transition to intermediate severe wear. Such severe wear was observed at  $0.654 \text{ m s}^{-1}$  up to 570 °C,<sup>4</sup> without any evidence of oxide (Figure 25(b)); only

metallic debris sourced from the Nimonic 80A was generated by delamination wear. At 630 °C, however, oxide was observed and this assisted severe wear by abrasion.<sup>5,21,22,24</sup> A similar pattern was observed at  $0.905 \text{ m s}^{-1}$ <sup>(5,21,22)</sup> though enhanced frictional heating led to oxide generation at 570 °C as well as 630 °C.

On increasing temperature to 690 and 750 °C, further increases in oxide production were sufficient to separate completely the Nimonic 80A sample and



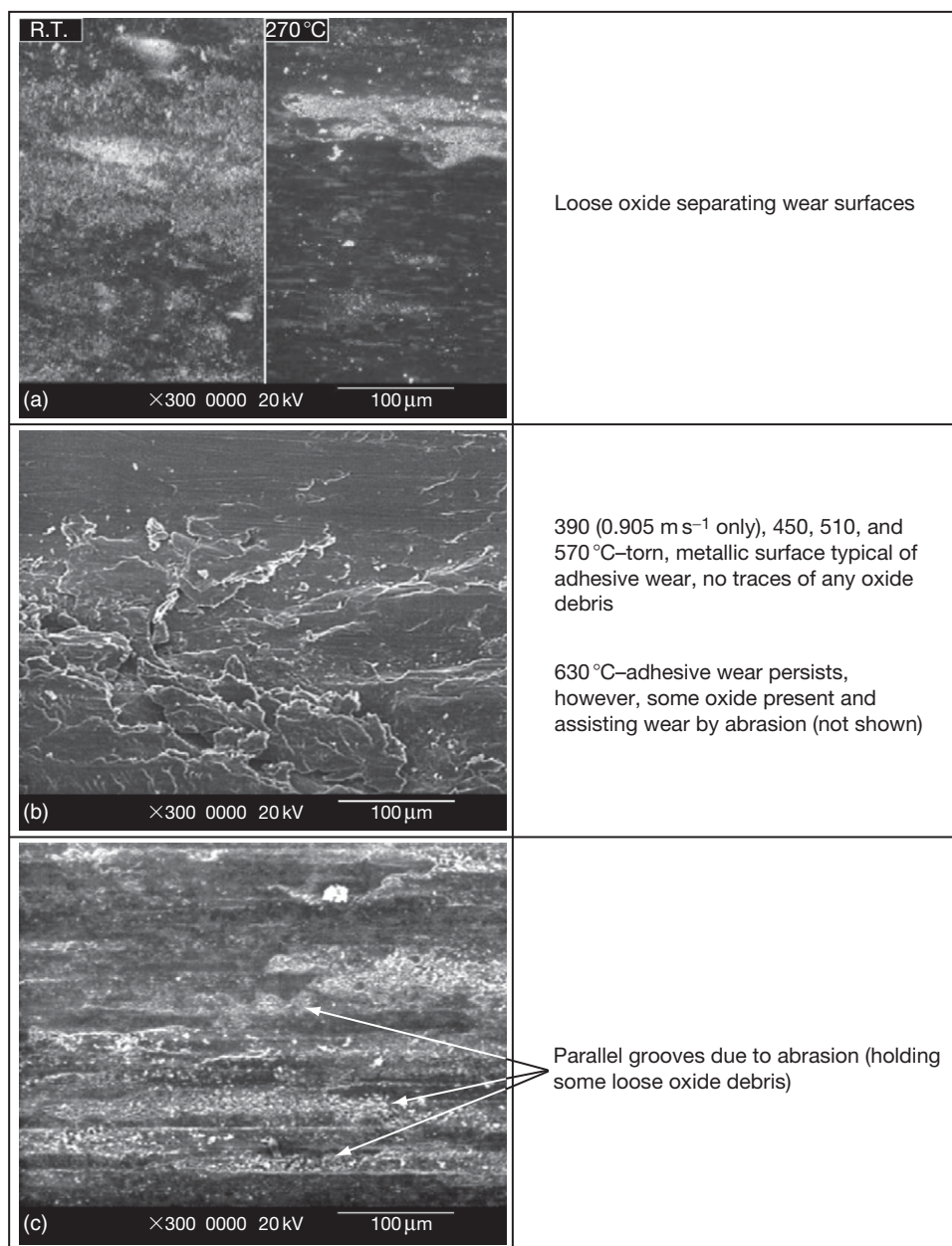


**Figure 25** SEM micrographs of Nimonic 80A wear surfaces after sliding at 0.654 m s<sup>-1</sup> (load 7 N, sliding distance 4522 m) against a Stellite 6 counterface at room temperature, 270, 570, and 750 °C (also typical of 0.905 m s<sup>-1</sup>).<sup>22</sup> (a) Room temperature and 270 °C (shown), also typical of 390 °C (0.654 m s<sup>-1</sup> only), (b) 570 °C (shown), also typical of 390 (0.905 m s<sup>-1</sup> only) 450, 510, and 630 °C, and (c) 750 °C (shown), also typical of 690 °C.

Stellite 6 counterface; a mild wear regime was thus established. However, high wear rates continued; although technically a mild wear regime, the high wear rates indicates that the oxide was not protective. Two slightly different forms of oxidational behavior were observed, depending on researcher. At 0.654 m s<sup>-1</sup>, Wood<sup>3</sup> reported the formation of a poorly

adherent 'glaze' that was continuously removed. In contrast, Rose<sup>4</sup> reported no 'glaze' formation on Nimonic 80A and the generation of only loose oxides that acted abrasively (NiO and Cr<sub>2</sub>O<sub>3</sub>), thereby enhancing removal from the Nimonic 80A surface. These latter observations were confirmed by Inman<sup>5,22,24</sup> at both 0.654 m s<sup>-1</sup> (Figure 25(c)) and 0.905 m s<sup>-1</sup>, who

observed greater oxide generation at  $0.905 \text{ m s}^{-1}$  but still without 'glaze' layer formation.

Rose<sup>4</sup> stated that layers were unable to form due to insufficient debris adhesion to the Nimonic 80A sample surfaces and lack of debris cohesion, caused by the ploughing of sample surfaces by hard carbide particles in the Stellite 6 counterface. However, Inman<sup>5</sup> argued that the carbides were not hard enough to have this ploughing effect and inhibit the development of oxide layers; it was possible that the carbides were softer than the 'glaze' layers and wore in preference to them. This inability of the Nimonic 80A-sourced NiO and  $\text{Cr}_2\text{O}_3$  oxides to form a 'glaze' was instead attributed to their relatively poor sinterability. If this failure to form 'glaze' layers had been due to carbide ploughing, then these layers would not have formed in other systems involving Stellite 6. For example, Stellite 6-sourced Co–Cr layers formed in the Nimonic 80A/Stellite 6 (counterface) system at  $0.314 \text{ m s}^{-1}$ .<sup>5,22,24</sup> Also, Incoloy MA956-sourced Fe–Cr-based layers formed at  $0.905 \text{ m s}^{-1}$  in the Incoloy MA956/Stellite 6 (counterface) system.<sup>5,23</sup>

Inman *et al.*<sup>22</sup> collated the available data to create a temperature versus sliding speed wear map for the Nimonic 80A versus Stellite 6 (counterface) system (later further developed by Inman and Datta<sup>24</sup>), covering a variety of different modes of wear behavior that are dependant on load–sliding speed combination. This is discussed further in [Section 1.15.5.3](#).

#### Effects of load

Rose also studied the effect of load on sliding behavior for Nimonic 80A worn against Stellite 6 at  $750^\circ\text{C}$ .<sup>4</sup> At all loads (7–25 N), the wear mechanism remained predominantly oxidational, with elements of abrasive wear, regardless of applied load ([Figures 23\(c\) and 23\(d\)](#)); no compacted debris layers were formed across the range of loads (7–25 N) at  $750^\circ\text{C}$ . There was no evidence that changing load had any significant effect on wear regime in this case; however, the grooves on the damaged surface became more pronounced at high load. This was reflected by increased weight loss at high load ([Figure 17](#)).

#### 1.15.3.3.3 Effect of Nimonic material processing route on wear

Very similar wear properties were observed for Nimonic 80A (cast) and Nimonic 80A (HIPped)<sup>3</sup> and it was not possible to conclude that processing route affected wear resistance. Wear behavior was also similar for Nimonic 90, the only exception being the enhanced wear resistance of Nimonic 90 over Nimonic 80A (cast) at  $750^\circ\text{C}$  ([Figure 26](#)).

#### 1.15.3.3.4 Nimonic 80A sliding wear – Comparisons between various wear rig configurations

The apparently poor sintering and 'glaze' forming characteristics of NiO and  $\text{Cr}_2\text{O}_3$  generated from Nimonic 80A (at  $0.654$  and  $0.905 \text{ m s}^{-1}$ )<sup>4,5,21,22,24</sup> at first seems to contradict the extensive studies carried out into 'glaze' formation with Nimonic 80A-based systems by Jiang *et al.*<sup>2,16–19</sup> However, the last group used lower sliding speeds with a like-on-like reciprocating 'pin-on-disk' configuration (mean sliding speed  $83 \text{ mm s}^{-1}$ ); such systems have a higher degree of debris retention, providing greater opportunity for the oxide debris to sinter together to form 'glaze' layers. The 'block-on-cylinder' configuration used by Rose<sup>4</sup> and Inman *et al.*<sup>5,21,22,24</sup> is a unidirectional sliding wear system that promotes debris mobility and ejection over retention, especially at higher sliding speeds. The decreased residency and greater mobility of the debris do not allow sufficient contact time between debris particles for sintering and welding processes to occur, as is necessary for 'glaze' formation.

#### 1.15.3.3.5 $\text{Si}_3\text{N}_4$ counterface

Wood ( $0.654 \text{ m s}^{-1}$ , 7 N load)<sup>3</sup> reported limited material transfer from the harder  $\text{Si}_3\text{N}_4$  counterface to the Nimonic material surfaces at room temperature. Thin mixed oxide layers were formed on the Nimonic surfaces; these contained material from both wear surfaces that provided only limited protection.

Wood<sup>3</sup> observed a very different wear resistance when Nimonic 80A (cast) and Nimonic 90 were worn against  $\text{Si}_3\text{N}_4$  at  $750^\circ\text{C}$ . Nimonic 80A (cast) showed very poor resistance, with no 'glaze' formation in contrast to Nimonic 90 where 'glaze' formation and very low weight losses were observed. Wood attributed the difference to the presence of Co in the Nimonic 90, which somehow improved 'glaze' adhesion and/or strength on the Nimonic 90 surface.

### 1.15.3.4 Effects of Environmental Variables

#### 1.15.3.4.1 Oxygen levels and partial pressure

Even in environments with low oxygen partial pressure<sup>19,100</sup> (effectively removing much of the oxygen from the system), stable oxide layers are still able to form. Under vacuum, increasing pressure from high vacuum conditions to  $10^{-2} \text{ Pa}$  was enough to result in a decrease in friction in sliding of an iron–chromium alloy. Buckley<sup>101</sup> noted during the like-on-like sliding of clean iron that a pressure of 400 Pa (or 3 Torr) was

sufficient to prevent seizure. Lancaster<sup>26</sup> noted that, at 300 °C, the range of sliding speeds over which severe wear was observed when a 60/40 brass was slid against tool steel was greatly in an oxygen atmosphere compared to the level of wear observed in air (Figure 2).

Barnes *et al.*<sup>100,102,103</sup> investigated the effects of partial pressure on iron–chromium alloys, ranging from pure iron to iron–40% chromium (Figure 27). Initial work in a normal atmosphere indicated high friction and seizure at 450 °C for iron and between 500 and 600 °C (rising slightly with

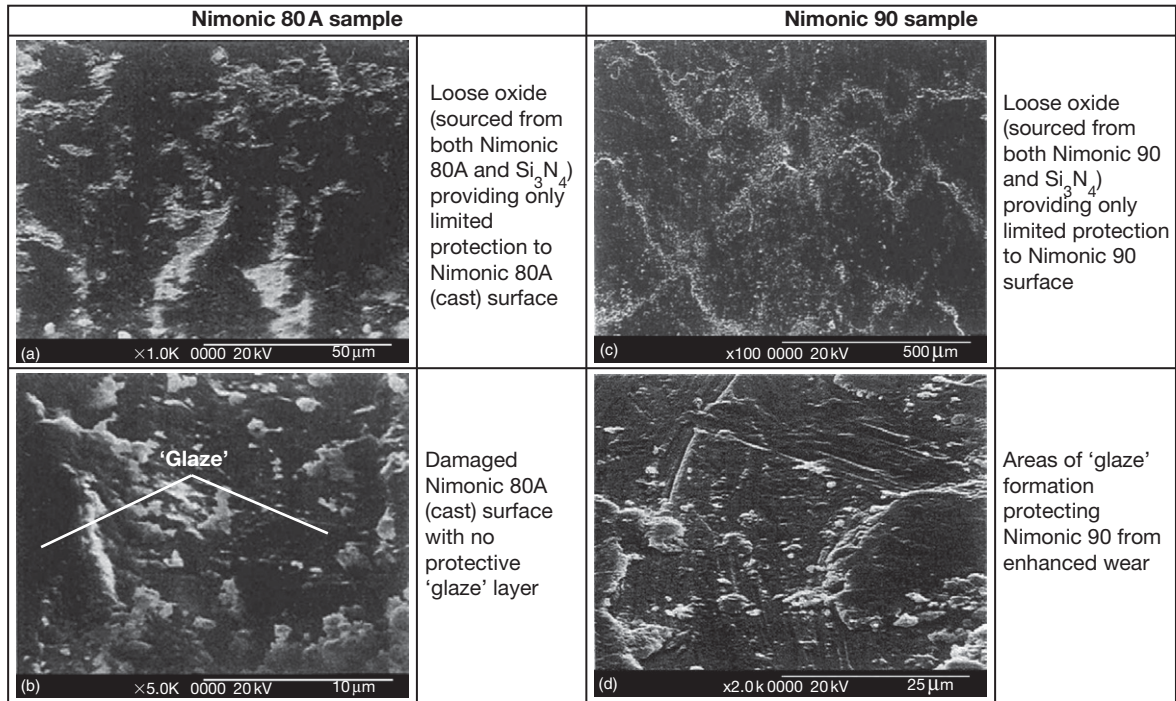


**Figure 26** SEM micrographs of Nimonic 80A (cast) at (a) room temperature and (b) 750 °C, also Nimonic 90 at (c) room temperature and (d) 750 °C, worn against a Si<sub>3</sub>N<sub>4</sub> counterface, sliding speed 0.654 m s<sup>-1</sup> (load 7 N, sliding distance 9418 m). Reproduced from Wood, P. D. Ph.D. Thesis, Northumbria University, UK, 1997.

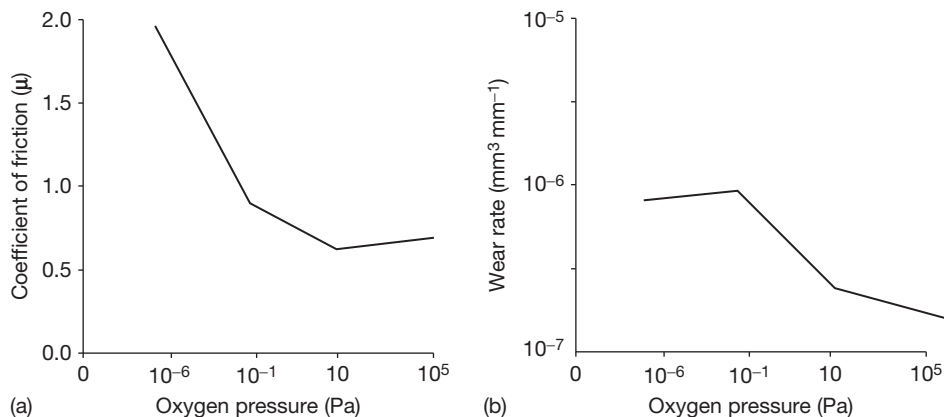


**Figure 27** Variation of coefficient of friction (a) and wear rate (b) of Fe–4.9% Cr with oxygen partial pressure during like-on-like sliding at 20 °C. Reproduced from Barnes, D. J.; Wilson, J. E.; Stott, F. H.; Wood, G. C. *Wear* 1977, 45, 634–640.



chromium content) for various iron–chromium alloys; the only exception to this was Fe–40% Cr where there was no seizure up to the maximum test temperature of 850 °C.

Adhesive wear and seizure (here defined as the coefficient of friction rising above a nominal value of 3.5) were dominant at oxygen partial pressures of  $10^{-6}$  and  $10^{-5}$  Pa, despite there apparently being sufficient oxygen present to prevent this. On raising the partial pressure to  $10^{-4}$  Pa, however, significant amounts of oxide were observed and areas of compacted debris had developed. These ‘islands’ were specified as the reason for the switch from severe to mild wear, with even more rapid development of these oxides on raising the partial pressure to  $10^{-1}$  Pa. The compacted debris was either completely oxidized or oxide-covered metallic debris; its formation was accompanied by decreases in friction (Figure 27). However, despite the presence of this oxide debris, the wear rate remained high until the oxygen partial pressure reached 1 Pa or above.

Changes in partial pressure were also made during sliding tests,<sup>100</sup> with oxygen in some cases being removed from the wear system (the pressure was from  $10^{-1}$  to  $10^{-6}$  Pa). When this occurred, the oxide debris and the compacted oxide layers remained at the wear interface, showing continued stability and wear resistance even without a continued supply of oxygen.

#### 1.15.3.4.2 Effect of water vapor and relative humidity

The presence of water vapor in the atmosphere can have a positive or negative effect on oxide development, depending on relative humidity levels and materials. For mild steel a decrease in wear was observed with increasing relative humidity under fretting conditions<sup>104,105</sup> and similarly with carbon steel under sliding wear conditions.<sup>17</sup> It has been suggested that adsorbed moisture might have a dual effect,<sup>106</sup> in that on the debris surface, it might act as a lubricant, promoting speedier debris dispersal and, thus, less abrasive wear. From this, it was proposed that the hydrated form of the iron oxide that develops in the presence of the moisture might be a less abrasive medium. Such debris does, however, have the potential to enhance interface contact and bring about adhesive wear.

Experimental work by Bill<sup>107</sup> demonstrated that this could be the case, with the relationship between relative humidity and wear rates becoming quite complex. Iron showed a significant increase in wear

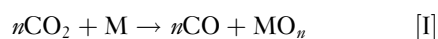
rate on raising the relative humidity from 0 to 10%, followed by a rapid decrease and minimum values in the region of 50–70%, then by a small increase towards atmospheric saturation. Increasing wear was demonstrated for titanium at up to 30% relative humidity, followed by an erratic decline in wear values up to saturation levels. Nickel showed a sharp decrease in wear levels between 0 and 10% relative humidity, followed by increasing wear with relative humidity up to saturation.

Oh *et al.*<sup>17</sup> suggested a transition from severe to mild wear with increasing relative humidity for carbon steels. At low relative humidity, severe wear was encountered, with total losses amounting to between 0.130 and 0.190 g. This remained the case up to 50% relative humidity. The level of wear dropped rapidly after this ‘transition point,’ with mild wear being observed at relative humidity levels of 70% and losses totaling no more than 0.002 g. The amounts of carbon in the steel were observed to affect this transition, which occurred at higher values with increasing carbon content. Friction was also observed to fall rapidly, from between 0.62 and 0.68 at 35% relative humidity to between 0.44 and 0.48 at 70% relative humidity.

#### 1.15.3.4.3 Other atmospheres

The wear process in atmospheres other than air or oxygen will depend on whether the atmosphere is oxidizing or reducing. In most practical situations, corrosion product will not form in a reducing (non-oxidizing) atmosphere and, thus, the formation of wear protective layers is not possible. Only the presence of adsorbed gases or other volatiles will act to separate the wear surfaces, adhesion, and therefore, levels of wear and friction.<sup>108</sup>

In other oxidizing atmospheres, only carbon dioxide has been examined to any significant extent. Sullivan and Granville<sup>51</sup> showed that a compacted oxide layer was formed when a Fe–9% Cr steel was tested in a pin-on-disk rig in carbon dioxide, between 200 and 550 °C. Smith<sup>109</sup> observed the formation of compacted oxides on wear testing of 316 stainless steel in carbon dioxide at temperatures between 20 and 600 °C. The carbon dioxide acted as the oxidizing agent in each case:



with the wear mechanisms being very similar to those in air.

Research in other environments is extremely limited. Bill<sup>107</sup> obtained ‘prodigious amounts of black debris’ on testing titanium in supposedly pure dry

nitrogen. It may be that this is removed oxide that was present prior to sliding (or formed during sliding by reaction with the trace oxygen invariably present in bottled gases) or even a mixture of metallic titanium and oxide. The possibility of titanium nitride is extremely unlikely, if not impossible, due to the tests being carried out at room temperature. However, no attempt was made to analyze the debris or explain the result.

### 1.15.3.5 Effects of Pretreatment of Sliding Surfaces

#### 1.15.3.5.1 Preoxidation

Stott and Mitchell<sup>52</sup> carried out preoxidation (oxidation prior to commencement of sliding) on Jethete M152 (a high chromium steel) and 321 stainless steel. Elimination of metal-to-metal contact was observed immediately on commencement of sliding in the case of Jethete M152 and also the immediate establishment of compacted oxide in the case of the 321 stainless steel. They concluded that the preoxidation provided an extra supply of oxide debris that led to the more rapid establishment of 'glaze' surfaces.

Iwabuchi *et al.*<sup>65</sup> studied the effects of preoxidation of a number of samples of S45C carbon steel; for each sliding test, a moving disk specimen was rotated against a fixed ring specimen, with both preoxidized samples and nonoxidized samples undergoing unidirectional sliding for 1000 m at room temperature. The preoxidation treatment was carried out at 300 °C for 5 min, 1 h, or 3 h. Times of 5 min and 1 h did result in progressive decreases in wear (Figure 28); however, increasing the time to 3 h produced no further improvement. The observed decreases in wear occurred because of break-down of the oxide layer to form debris, the presence of which prevented metal contact and adhesion.

Iwabuchi *et al.* conducted similar experiments with 304 stainless steel specimens,<sup>65</sup> with specimen configurations identical to those for S45C plain carbon steel. Preoxidation was carried out at 300 °C for times of up to 10 h. Although there was some scatter in the data after 300 m of sliding, there was no evidence of any effect of preoxidation on overall wear, regardless of the time of preoxidation and it was concluded that preoxidation had no effect under the prescribed test conditions. This was due to 'selective oxidation' of chromium at the surface;

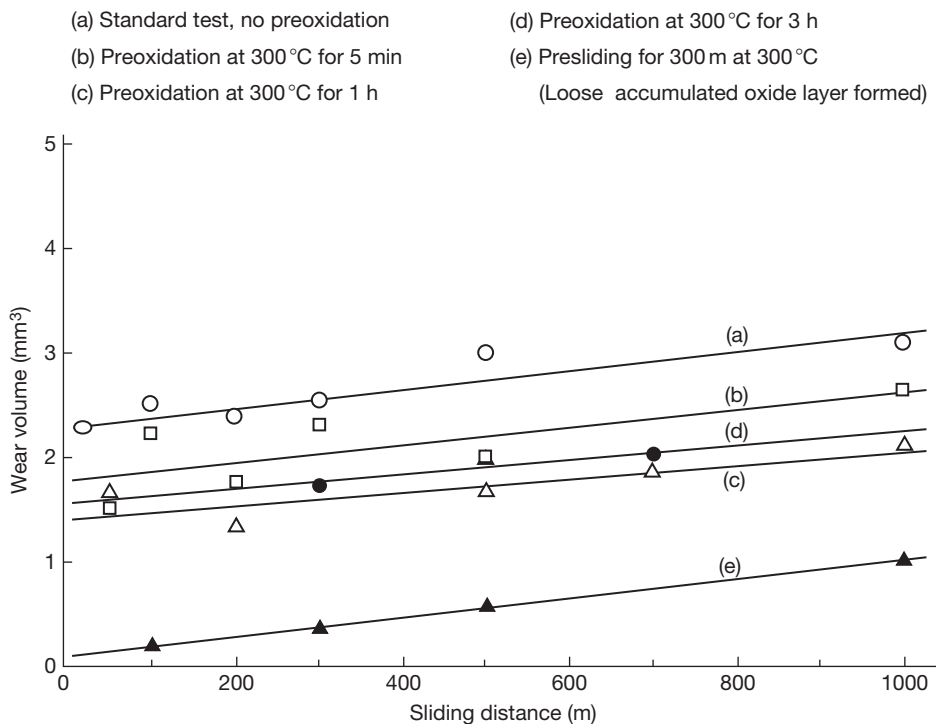


**Figure 28** Effects of preoxidation and presliding on wear of S45C at 20 °C.<sup>34</sup> (a) Standard test, no preoxidation, (b) preoxidation at 300 °C for 5 min, (c) preoxidation at 300 °C for 1 h (loose accumulated oxide layer formed), (d) preoxidation at 300 °C for 3 h, and (e) presliding for 300 m at 300 °C.

this decreased the level of oxidation of the stainless steel, with the result that there was insufficient oxide to decrease the severe wear rate by debris generation from this layer.

Thus, although preoxidation can decrease or eliminate early metal-metal contact, this cannot be guaranteed. Under certain circumstances, possibly due to the effects of variations in alloy composition on the nature of the surface oxidation, the production of suitable surface oxide required for the promotion of early 'glaze' formation may not occur.

#### 1.15.3.5.2 Presliding

Iwabuchi *et al.*<sup>65</sup> additionally looked at samples of S45C carbon steel that had undergone presliding for 300 m at 300 °C; this was sufficient to create an accumulated loose oxide layer. Subsequent tests indicated the complete elimination of the severe wear regime (Figure 28), with only mild wear being observed, regardless of test temperature. In the case of preoxidation, the oxide layer served at best only to reduce (dependent on combination) the severe wear 'run-in' period (Section 1.15.3.5.1).

A decrease in severe wear was also observed when 304 stainless steel underwent presliding for 100 m at room temperature, due again to the presence of an accumulated loose oxide layer. In both cases, the availability of preexisting oxide debris acted to prevent contact between the metallic interfaces.

Presliding was additionally carried out for 304 stainless steel over a distance of 300 m at room temperature, 200, and 400 °C (at which temperature the oxide layer formed was a 'glaze'), with the severe wear stage being eliminated in each case during subsequent sliding. The presence of accumulated oxide from presliding did not, however, lead to a decrease in the rate of wear during mild wear.

#### 1.15.3.5.3 Ion implantation

Langguth *et al.*<sup>66</sup> carried out oxygen ion implantation on a series of chromium and carbon steels (AISI 52100, AISI 440B, AISI M2) and 321 stainless steel, followed by a series of sliding experiments using a pin-on-disk rig. A sliding speed of  $28 \times 10^{-3} \text{ m s}^{-1}$  was used over a sliding distance of 400 m, with relative humidity at 30% or 80%.

In general, recorded levels of wear for the ion-implanted samples were much lower than for their untreated equivalents (Table 3). This was due to the oxygen in the surface layers assisting the formation of oxidized debris and, thus, decreasing the initial

**Table 3** Wear rates of case-hardened steels before and after implantation of oxygen ions, 400 m sliding distance

		Wear rate ( $10^{-16} \text{ m}^3 \text{ m}^{-1}$ )			
		Steel ball		Tungsten carbide ball	
		30% RH	80% RH	30% RH	80% RH
AISI 52100					
Untreated		1000	100	17.5	17.5
Implanted		1	3.4	1.8	0.3
AISI 440B					
Untreated		19	25	34	85
Implanted		1.4	2.5	2.8	1.8
AISI M2					
Untreated		11.5	2.9	11.2	20
Implanted		3.3	1.9	1.6	3.3

Ion implantation conditions  $5 \times 10^{17} \text{ cm}^{-2}$ , 50 keV; test conditions in air at 30% or 80% relative humidity RH,  $28 \times 10^{-3} \text{ m s}^{-1}$ . Reproduced from Stott, F. H.; Wood, G. C. *Tribol. Int.* **1978**, 11, 211–218.

severe wear period. Certain aspects of heat treatment of the alloys and the sliding conditions were observed to affect this. For example, in the case of the chromium and carbon steels, the improvement in wear resulting from oxygen ion implantation was noticeably less for AISI 52100 and AISI 440B in the annealed form compared to the martensitic form; this can be seen from the data in Tables 3 and 4. Relative humidity has a marked effect, as in the case of AISI 52100 steel, where the oxygen ion implanted material actually undergoes a higher level of wear than the untreated material. These observations were attributed to the higher plasticity of the annealed samples.

A change in the form of the debris was also observed, from a smooth oxide layer for the martensitic samples to loose debris for the annealed samples. The one exception was for AISI 440B steel, where the decrease was greater in the annealed state and sliding was accompanied by a change in the state of the oxide debris from the loose form to the oxide layer form.

In comparison to standard preoxidation treatment (Table 4), wear tended to be less, with the exception of annealed AISI 52100, where the preoxidized samples produced superior results, regardless of the levels of relative humidity.

Langguth *et al.* note also that implantation has been tried using different ions, including nitrogen, carbon, and boron, with varying degrees of success, though not to the same extent as oxygen, as these alternatives do not promote wear track oxidation.

**Table 4** Wear rates of case-hardened steels before and after implantation of oxygen ions, 100 m sliding distance

	Wear rate ( $10^{-16} \text{ m}^3 \text{ m}^{-1}$ )			
	Steel ball		Tungsten carbide ball	
	30% RH	80% RH	30% RH	80% RH
AISI 52100				
Untreated	611	7.7	38	1.5
Implanted	68	11.2	38	2.2
Oxidized	1.1	0	0.8	0.8
AISI 321				
Untreated	1400	72	4000	32
Implanted	215	72	2000	16
Oxidized	140	72	0	32
AISI 440B				
Untreated	98	9.1	42	42
Implanted	33	0.2	84	42

Ion implantation conditions  $5 \times 10^{17} \text{ cm}^{-2}$ , 50–100 keV in case of AISI 52100; test conditions in air at 30% or 80% relative humidity RH,  $28 \times 10^{-3} \text{ m s}^{-1}$ . Reproduced from Stott, F. H.; Wood, G. C. *Tribol. Int.* **1978**, *11*, 211–218.

## 1.15.4 ‘Glaze’ Formation – Microscale and Nanoscale Investigations

### 1.15.4.1 Introduction

It is clearly recognized that ‘glaze’ formation on the contacting surfaces affords significant protection against wear damage and degradation. The generation of HT wear-resistant surfaces *in situ* overcomes the serious limitations on materials and coatings imposed by HT wear conditions. ‘Glaze’ formation is very useful as it takes advantage of important events that accompany the processes of HT wear, such as oxidation, debris generation, and elemental transfer between the contacting surfaces.<sup>3–6,14,110</sup> These events, under certain conditions of temperature, pressure, and speed<sup>3–6,14,20–22,24,25,111</sup> lead to the formation of surfaces with self-functionalized HT wear resistance. Although the phenomenon of ‘glaze’ formation and related general issues of HT wear have been extensively studied, it is still not possible to predict the precise conditions which promote ‘glazed’ surfaces.

Here, it has been recognized that a step forward would be to gain detailed knowledge of ‘glaze’ layer microstructure and nanoscale structure evolution so that the precise mechanisms of ‘glaze’ formation can be established. This section summarizes and updates the studies carried out on ‘glaze’ formation during wear of various systems. It has been written with

emphasis on generic principles and wear systems have been selected that facilitate the mechanistic understanding of the ‘glaze’ formation process.

### 1.15.4.2 Microscale Studies of ‘Glaze’ Formation

From a study of mainly nickel- or nickel–iron-based alloys containing significant quantities of chromium in like-on-like sliding, and in some cases, cobalt, it was established by Stott *et al.*<sup>6</sup> that the oxides formed have elemental ratios that differ little from the original base alloys. It was thus concluded that the observed low wear and friction arise from the physical properties and condition of the glaze, rather than their chemical compositions.

Further research<sup>6,50,55–59</sup> allowed the identification of the following modes of compacted layer formation.

- The first mode is characterized by the formation of transient oxides, followed by the oxide thickening by continued oxidation by oxygen diffusion to the substrate–oxide interface and through physical defects.
- The second mode of formation is characterized by two stages. Stage one involves the formation of an insufficiently thick layer due to unfavorable temperature and low alloy strength, possibly involving an extended preglaze or severe run-in period. Stage two involves the formation of a sufficiently thick oxide layer through continued break-up and consolidation of ‘glaze’ debris produced in stage one.
- In the third mode, the ‘glaze’ does not remain stable during sliding and areas of compacted oxide continually break down and reform.

Stott *et al.*<sup>10,50,55,61,112</sup> later produced a further set of three modified mechanisms, based on their studies of the elevated temperature (200–600 °C) fretting wear of iron-based alloys. These mechanisms<sup>50</sup> were seen as limiting cases for oxide debris generation, after which the build-up of oxide to form compacted layers continued:

- *Oxidation–scrape–reoxidation*. This involves a two-stage process. In the first step, oxide generation takes place in the areas of contact between the two sliding surfaces, with general oxidation over the apparent sliding area of contact and, also, at asperity contacts where temperatures exceed the general temperature in the region of the sliding area of contact. In the second stage, this oxide is removed by subsequent traversals of the sliding interfaces, exposing fresh

metal for further oxidation. The debris formed may then be either completely removed from the interface, act as a third body abrasive, thereby contributing to the wear process or be compacted to form a wear-protective oxide layer.

- **Total oxidation:** Under certain conditions, particularly high ambient temperatures, oxide generated during sliding or even present prior to the commencement of sliding, is not completely removed by subsequent traversals of the sliding interfaces, allowing the oxide to thicken with time. Provided this layer is coherent and adherent to the metal substrate and can withstand the stresses of sliding, a plastically deformed wear-protective oxide layer can develop.
- **Metal debris:** Debris particles generated during the early stages of wear are broken up by the sliding action, with any fresh areas of exposed metal being subject to further oxidation. There may be a high level of oxidation of the debris surfaces, due to the relatively large exposed surface area of metal.

Enhanced oxidation is promoted by heat of deformation and increased energy of the particles due to increased defect density and surface energy (the exposed surface area of debris material will increase as particle size decreases). There is also an input due to the heat of oxidation, promoting oxidation of the metallic particles, the finer particles undergoing complete and spontaneous oxidation. The resulting oxide can later develop into a wear-protective layer.

The formation of compacted layers has also been observed by Wood *et al.*,<sup>3,12</sup> Rose,<sup>4</sup> Inman *et al.*,<sup>5,21–25</sup> Datta *et al.*,<sup>20</sup> and Du *et al.*<sup>110</sup>

The third mechanism proposed in Stott's original work is similar to that of Lin and Wood,<sup>6</sup> both depending on the generation of larger debris from the wear substrate and the comminution of this debris to fine oxide particles as the wear process continues to develop.

The one major difficulty with these mechanisms is that they were developed from work on low speed reciprocating sliding wear, where frictional heating is not such an important factor.<sup>61</sup> At sliding speeds of greater than  $1 \text{ m s}^{-1}$ ,<sup>104</sup> frictional heating increasingly becomes an issue.

#### 1.15.4.3 Third Body Interaction in Relation to Compact Oxide Formation

In Section 1.15.2.2.3, a brief discussion was made of four mechanisms of particle behavior at the sliding

interface, as proposed by Jiang *et al.*<sup>19</sup> – these included (1) rotation, (2) skidding, (3) rolling, and (4) adhesion/sintering affected rolling (Figure 5). Jiang *et al.* observed that the friction levels for mechanism (4) are highly dependent on the adhesion force between particles in the sliding system. While this adhesion force is weak, friction levels for mechanism (4) are lower than those for mechanism (2); however, increasing this adhesion force above a critical level results in a situation where the reverse is the case. Skidding then becomes the dominant mechanism, with no relative movement between neighboring particles – an increase in adhesion force locks them in place. A stable compact layer can result and, at higher temperatures, a wear-resistant 'glaze type' layer is possible (with the particles locked together, there is sufficient time for sintering). Stott's later modification of this approach<sup>111</sup> (the inclusion of adhesion and sintering effects in rotation, skidding and rolling mechanisms) better recognizes the fact that adhesion and sintering has a more general effect on the various particles making up the particle layer, regardless of whether they are entrapped or in relative motion.

Adhesive forces and sintering tend to take effect at more elevated temperatures, as demonstrated by experimental work carried out by Jiang *et al.*<sup>17</sup> on the sliding wear of Nimonic 80A at 20, 150, and 250 °C. At 20 °C, a thick layer of compacted, fine wear debris was formed, with some evidence of solidification and sintering in some areas; however, these layers were found to be predominantly particulate in nature. There is a transition from metal–metal wear to contact between these primarily oxide particle layers, at which point increases in contact resistance and decreases in levels of wear are coincident. At 250 °C, sintering becomes a significant factor and there is a tendency to form smooth 'glaze' layers on top of these compacted oxide layers. The 150 °C case was intermediate, with some development of smooth load-bearing areas between the particulate layers. Removal of this more loosely compacted material by ultrasonic cleaning in acetone left behind the more compacted debris, load-bearing areas.

These observations clearly indicate that temperature is a major driving force for adhesion between particles and formation of load-bearing compacted debris layers. This was demonstrated further<sup>17</sup> by a heat treatment for 90 min at 600 °C, for samples preslid at 20 °C. The compacted layers formed during the sliding phase of the test became solidly sintered together as a result of the subsequent



heating of the samples. The effect of a very small particle size would be to increase the available surface energy, due to the resultant increase in relative surface area. This would act to drive the adhesion and sintering processes and allow for observable sintering at temperatures where sintering of the larger particles used in powder technology applications would not be noticeable. As adhesion itself is temperature-dependent, increases in temperature due to ambient or frictional heating would accelerate the adhesion and, therefore, the sintering process. An Arrhenius relationship<sup>1</sup> influences the process

( $K_p = A_p \exp(Q_p/RT_0)$ ). Shrinkage and thermal stress-induced cracks were, however, observed on layers sintered at 600 °C.

From experimental observations, Jiang *et al.* proposed a descriptive model of the sliding wear process.<sup>2,112</sup> Figure 29 shows this diagrammatically, with possible modifications to it for the reincorporation of debris for broken-down compacted oxide and 'glaze' layers:

1. Generation of wear particles due to the relative movement of the metal surfaces;

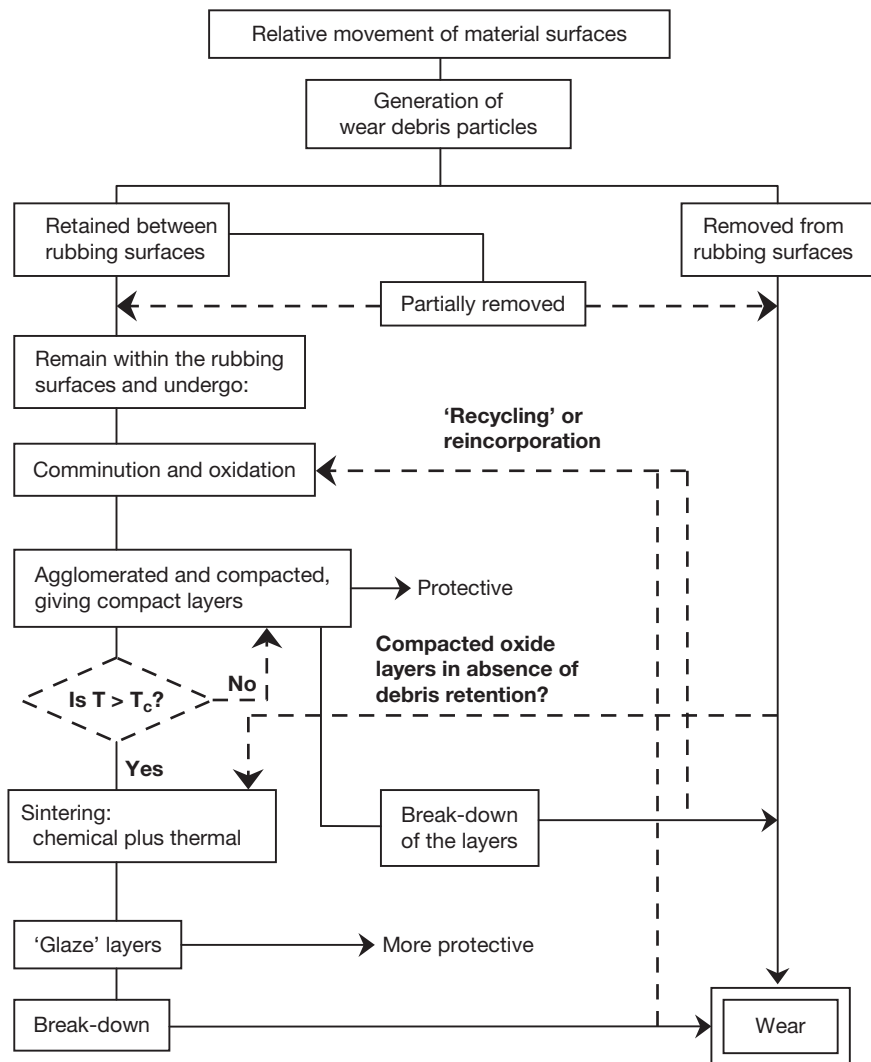


**Figure 29** 'Modified' version of Jiang's diagrammatic representation of sliding wear processes at various temperatures.<sup>2,5</sup> The original diagrammatic representation<sup>2</sup> does not contain any 'feedback' loops to account for recycling of broken down 'glaze' layers and debris. A decision box is inserted to describe what happens with the actual contact temperature  $T$  in relation to Jiang's critical temperature  $T_c$ . Also, what happens in the case of partial retention, plus the formation of compact layers when there is no significant debris retention, are not covered. Suggested modifications are indicated in bold. Reproduced from Inman, I. A. Ph.D. Thesis, Northumbria University, UK, 2003; published by 'Dissertation.com', 2006.

2. Removal of some particles from the wear tracks to form loose wear particles;
3. Retention of other particles within the wear track;
4. Comminution of the retained particles by repeated plastic deformation and fracture, with particles freely moving between the rubbing surfaces and undergoing partial or even complete oxidation, due to continued exposure of fresh metallic surfaces during comminution;
5. Continued fragmentation and agglomeration at various sites on the wear surfaces, due to adhesion forces between solid surfaces originating from surface energy and the formation of relatively stable compact layers.

This has two effects, that is:

1. First, material loss is reduced by a material recycling effect of the wear debris particles. Material breaking away from the compacted debris may rejoin it.
2. Second, due to heavy deformation and oxidation of the wear debris particles, the layers formed are hard and wear-protective.

Two competitive processes then occur during subsequent sliding, that is:

- (a) The compacted layers are continually broken down, the debris generated promoting wear (though, again, reincorporation may occur).
- (b) Continuing sintering and cold welding between particles within the layers, leading to further consolidation.

For the latter case to predominate, the temperature must be high enough (in excess of a critical temperature) to encourage the sintering processes required to ensure the formation of a solid wear-protective layer on top of the compacted particle layers before the layers are broken down. The effects of this can be seen in the experimental work of Jiang *et al.* – at 20 °C, this critical temperature was not reached and the debris, although undergoing compaction, did not sinter to form a ‘glaze’ layer. At 250 °C, ‘glaze’ was clearly visible, while at 150 °C, closer to and possibly just above the critical temperature, more limited sintering meant; although some ‘glaze’ areas were formed, there were also substantial areas of loose debris still present.

Also of note is the formation of compacted debris layers close to the center of the wear scars, the location of highest debris retention,<sup>18</sup> where coverage by high resistance compacted layers was estimated to be 20–50%.

Jiang estimated also that, to cause a transition from severe to mild wear, only 20% of the surface needed to be covered by ‘glaze’-type layers, compared to a value of greater than 30% for nonglaze compacted layers, demonstrating that ‘glaze’ layers offer more physical protection.

Jiang’s model is based on experimental work done on fretting wear systems and Rose<sup>4</sup> questioned the applicability of Jiang’s model in a low debris retention system. However, Jiang does account for debris removal from the system leading to wear as would occur in, for example, high-speed unidirectional sliding<sup>3–5,20–25,110</sup> or debris removed by introduced interfacial airflow.<sup>46</sup> Also, in Rose’s own ‘reciprocating-block-on-rotating-cylinder’ experimental work (a higher speed unidirectional sliding configuration), examples of debris retention with ‘glaze’ formation and compacted layers do occur (i.e., Incoloy MA956 vs. Stellite 6), despite the more adverse sliding conditions. However, as Rose points out, there are examples where compacted oxide layers do form and there is no significant third body debris retention,<sup>3–5,23,58</sup> thus suggesting that Jiang’s model requires further modification to account for this; Figure 29 includes some suggestions by Inman<sup>5</sup> to cover these points.

#### 1.15.4.4 Nanoscale Investigations of ‘Glaze’ Formation

This section reports recent findings on the evolution of structures and substructures of ‘glaze’ layers at the nanoscale level,<sup>20,25,113</sup> from extensive research carried out in the authors’ laboratory. Data relating to transmission electron microscopy (TEM) and scanning tunneling microscopy (STM) studies are presented in Figures 30–44. Scanning tunneling spectroscopy (STS) and current imaging tunneling spectroscopy (CITS) data are not shown here.

The work presented here is generic in nature, but refers to a particular system in order to facilitate understanding of the underlying mechanisms for nanostructure evolution in the surface ‘glaze’ layers and their improved HT wear resistance. In this case, the ‘Nimonic 80A (sample) versus Stellite 6 (counterface)’ system is considered, using a counterface surface sliding speed of 0.314 m s<sup>−1</sup>, with a 7 N applied load and total sliding distance of 4522 m.<sup>5,23–25</sup> The sample also underwent a reciprocating action against the counterface for a distance of 12 mm, three times a minute, thereby limiting debris retention to between 20 and 30% (most of the debris was allowed to escape).

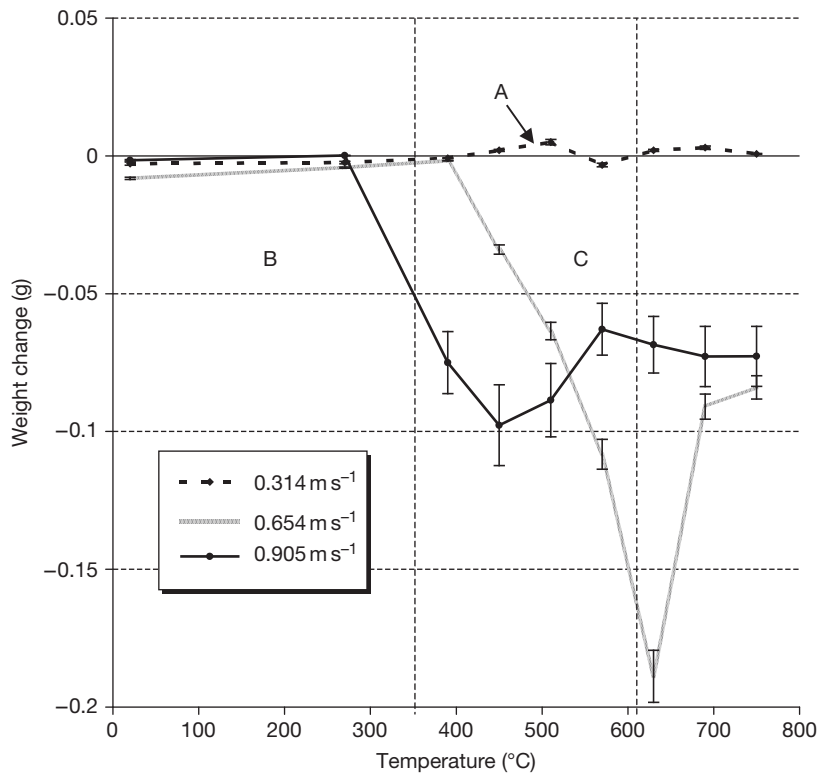


**Figure 30** Weight change versus temperature for Nimonic 80A slid against Stellite 6 at 0.314, 0.654, and 0.905  $\text{m s}^{-1}$  (load 7 N, sliding distance 4522 m).<sup>22</sup> At 0.314  $\text{m s}^{-1}$ : (A) Loose oxide debris spread across wear surface, plus some compacted oxide formation, room temperature to 390 °C; smooth 'glaze' layers with only a little loose debris (450 °C to 750 °C). At 0.654 and 0.905  $\text{m s}^{-1}$ : (B). Loose oxide debris spread across wear surface, plus some compacted oxide formation (room temperature and 270 °C at both 0.654  $\text{m s}^{-1}$  and 0.905  $\text{m s}^{-1}$ , also 390 °C at 0.654  $\text{m s}^{-1}$ ). (C) Torn, metallic surface typical of adhesive wear, no traces of any oxide debris (390 °C to 510 °C) or only very limited oxide debris formation (at 0.905  $\text{m s}^{-1}$  – 570 °C; at 0.654  $\text{m s}^{-1}$  and 0.905  $\text{m s}^{-1}$  – 630 °C). (D) Loose oxide but with no compact oxide layers at 0.654  $\text{m s}^{-1}$  and only isolated build-ups of oxide at 0.905  $\text{m s}^{-1}$ ; fine parallel grooves in direction of sliding on Nimonic 80A surface (690–750 °C).

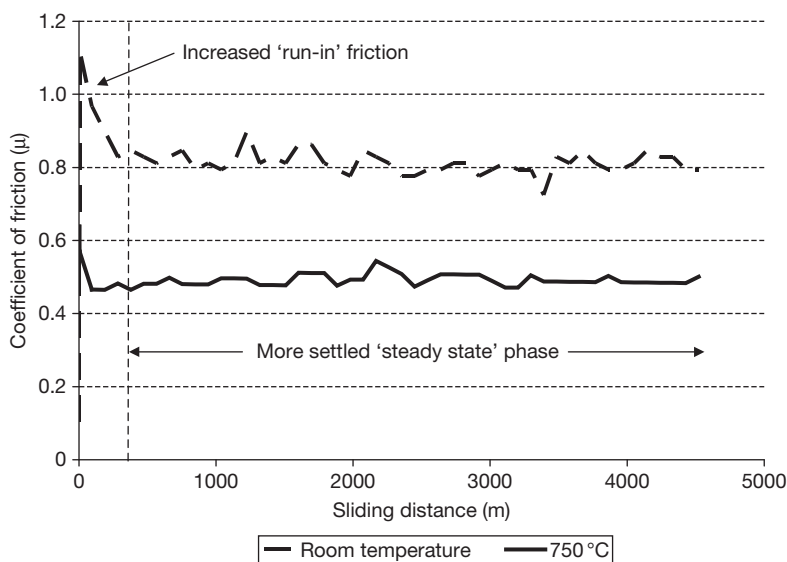


**Figure 31** Coefficient of friction versus time for Nimonic 80A versus Stellite 6 at 0.314  $\text{m s}^{-1}$ , room temperature and 750 °C.<sup>5,21,25</sup>

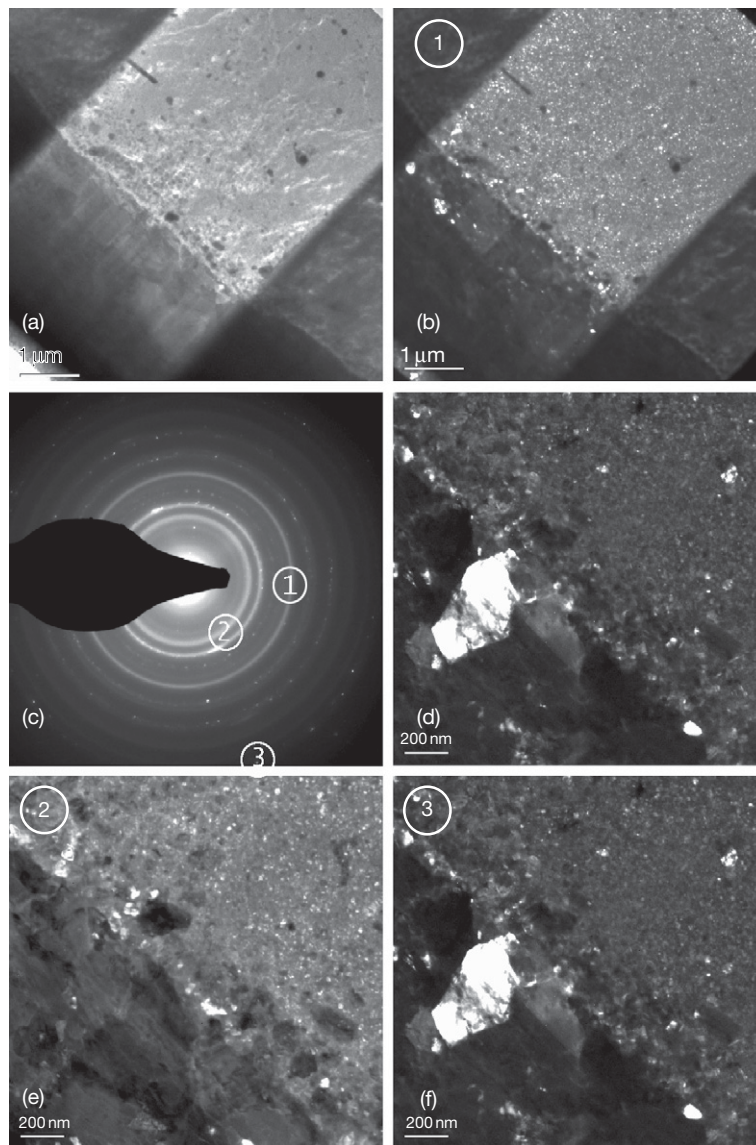


**Figure 32** TEM overview of a cross-section of the wear affected surface (Nimonic 80A vs. Stellite 6,  $0.314 \text{ m s}^{-1}$ ,  $20^\circ\text{C}$ , load 7 N, sliding distance 4522 m): (a) bright-field overview image of the Nimonic 80A and the 'glaze' layer; (b) dark-field image of the nanocrystalline 'glaze' layer (obtained with a  $10 \mu\text{m}$  objective aperture as indicated in the SAD pattern by ①); (c) selected area diffraction (SAD) pattern of the cross-section; (d) bright-field image of the interface; (e) dark-field image of the nano-crystalline 'glaze' layer close to the interface (as indicated in the SAD pattern by ②); (f) dark-field image of a larger crystal in the Nimonic 80A close to the interface (as indicated in the SAD pattern by ③). Reproduced from Du, H. L.; Datta, P. K.; Inman, I.; Geurts, R.; Kübel, C. *Mater. Sci. Eng. A* **2003**, 357, 412–422.

#### 1.15.4.4.1 Wear data

**Figure 30** displays the wear data for the Nimonic 80A/Stellite 6 system as a function of temperature at  $0.314 \text{ m s}^{-1}$ . Weight changes after 4522 m of sliding were extremely low for all temperatures, with the largest mean change being  $0.002(4) \text{ g}$  at  $270^\circ\text{C}$ . Slight gains were observed for all test temperatures between

$450$  and  $750^\circ\text{C}$ , with maxima in the mean values at  $510$  and  $630^\circ\text{C}$  of  $0.001(1)$  and  $0.001(4) \text{ g}$  respectively. It should be noted that the wear data at  $570^\circ\text{C}$  show a departure from the general trend and repeated experiments indicate the  $570^\circ\text{C}$  situation needs further attention. The following discussion focuses on the situation at room temperature and  $750^\circ\text{C}$ .

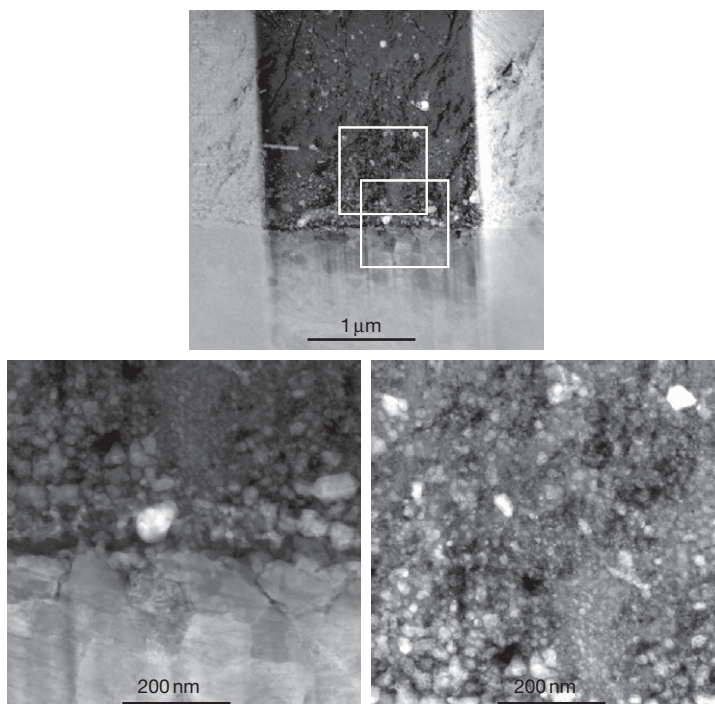


**Figure 33** HAADF-STEM (200 mm camera length) overview image and close-up of the interface and the nanocrystalline 'glaze' layer (Nimonic 80A vs. Stellite 6,  $0.314 \text{ m s}^{-1}$ ,  $20^\circ\text{C}$ , load 7 N, sliding distance 4522 m). Reproduced from Du, H. L.; Datta, P. K.; Inman, I.; Geurts, R.; Kübel, C. *Mater. Sci. Eng. A* **2003**, 357, 412–422.

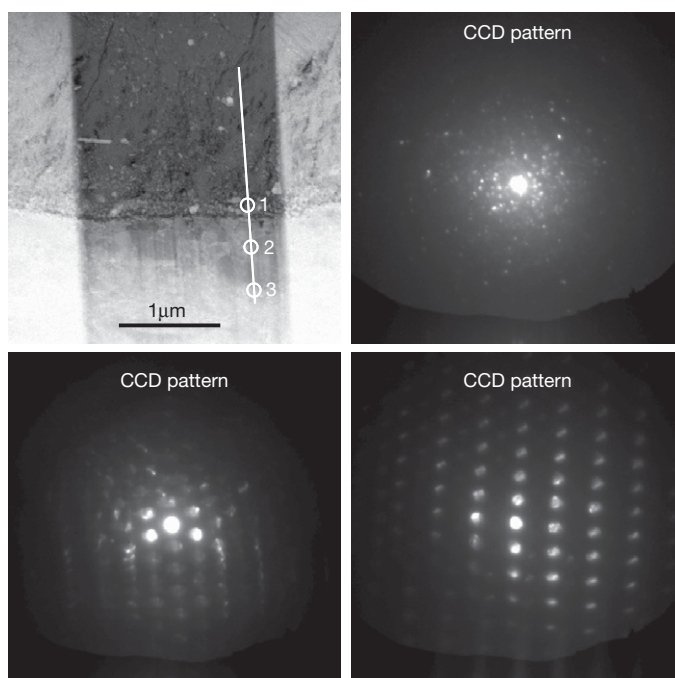


**Figure 34** HAADF-STEM overview image with examples from a CCD line trace (Nimonic 80A vs. Stellite 6,  $0.314 \text{ m s}^{-1}$ ,  $20^\circ\text{C}$ , load 7 N, sliding distance 4522 m). Reproduced from Du, H. L.; Datta, P. K.; Inman, I.; Geurts, R.; Kübel, C. *Mater. Sci. Eng. A* **2003**, 357, 412–422.



The coefficient of friction values measured during the tests showed an initial period of rapid change, before, in many cases, settling down into a 'steady state' situation with less variation. The data in **Figure 31** show no significant changes with time after an initial peak at the very beginning of the test. This indicates the rapid onset of debris generation (up to 450 °C) or 'glaze' layer formation (~450 °C and above, almost immediate at 750 °C), with the lack of frictional variation during the 'steady state' stage being due to the continued presence of debris or 'glaze' on the worn surfaces (**Figure 24**). Coefficient of friction levels (**Figure 31**) are significantly lower for 'glaze' covered surfaces (i.e., 750 °C) than for loose debris covered surfaces (i.e., room temperature).

#### **1.15.4.4.2 Studies of wear-affected surfaces produced during sliding of Nimonic 80A against Stellite 6 at 20 °C**

##### **Scanning electron microscopy (SEM)**

The top layer of the wear surface after sliding at 20 °C (**Figure 24**) consisted of a loosely bound noncompacted oxide that was easily detachable by brushing or light polishing. Underneath this layer, there was a more compacted layer that was not clearly apparent using optical and scanning electron microscopy.<sup>113</sup>

Analysis of the surfaces reveals the presence of oxygen and elements from Nimonic 80A (typically Ni/Cr) and Stellite 6 (Co/Cr). The results indicate elemental transfer from the counterface to the specimen and mixing of the transferred and host element oxides. In this section, attention is focussed on the surface layers produced at 20 °C.<sup>113</sup>

##### **Transmission electron microscopy (TEM)**

**Figure 32(a)** shows a cross-sectional TEM image of the wear-affected Nimonic 80A surface, revealing the interface between the Nimonic 80A substrate and the compact 'glaze' layer (the loosely bound uncompacted oxide debris layer was not visible in this area).<sup>113</sup> The associated selected area diffraction (SAD) pattern (**Figure 32(c)**) is dominated by Debye rings and some well-defined Bragg reflections. Dark-field images (**Figures 32(e) and 32(f)**) reveal that the latter correspond to irregular shaped Nimonic 80A crystals of several hundred nanometres diameter, in a layer up to 1 µm from the 'glaze' layer/substrate interface. The 'glaze' layer shows a very different morphology, consisting of small and misoriented crystals

produced by fragmentation (**Figures 32(b) and 32(e)**), of typical diameter of 5–20 nm. Although the adhesion between the 'glaze' layer and Nimonic 80A substrate was generally good, cracks were visible in some areas.

**Figure 33** shows a HAADF-STEM overview image of the FIB prepared cross-section described in the previous paragraph.<sup>113</sup> This is consistent with the structural variations observed by TEM. Two different areas are revealed for the substrate: a uniform 'bulk' area and a large grained structure about one micron below the interface with the 'glaze' layer. The latter exhibits a fine-grained structure (5–20 nm) with irregular shaped grain boundaries. The particles are larger close to the interface (up to about 50 nm). Furthermore, the strong Z-dependence of the HAADF-STEM image reveals several metal particles in the (oxidized) 'glaze' layer as well as low-density material at the interface.

**Figure 34** shows examples from a STEM line trace of nano-diffraction patterns, taken using a ~30 nm probe.<sup>113</sup> As previously, only small randomly oriented crystals are observed in the 'glaze' layer and at the interface. The larger grains in the alloy exhibit various crystallographic orientations; some of them well defined and similar to those expected for Nimonic 80A.

**Figure 35** shows EDX analyses of the 'glaze' layers, together with their reference areas.<sup>113</sup> The quantification is based on theoretical k-factors and uses a thickness correction for an estimated 150 nm sample thickness (EELS thickness measurements indicate a thickness of 2–3 nm mean free path). Quantitative analysis of the Nimonic 80A layer (Area 1) gives the characteristic composition of the bulk alloy (**Table 5**), apart from a slightly higher silicon concentration and a small amount of cobalt.

Analysis of the 'glaze' layer shows that it is essentially oxidized Stellite 6, with a significant contribution of between 15–20% Ni from the Nimonic 80A.

The interface layer consists of a mixture of Nimonic 80A and Stellite 6, with a higher than average titanium concentration.<sup>113</sup> HAADF-STEM EELS/EDX line traces across the interface (**Figure 36**) show the transition between the 'glaze' layer and the Nimonic 80A substrate, based on the cobalt and nickel concentrations; the composition of the 'glaze' layer is locally inhomogeneous (**Figures 36 and 37**). There are some variations in the chromium, cobalt and oxygen concentrations as well as a few distinct particles with a high nickel concentration. Nevertheless, the overall concentrations are relatively uniform throughout the 'glaze' layer, for example, no nickel

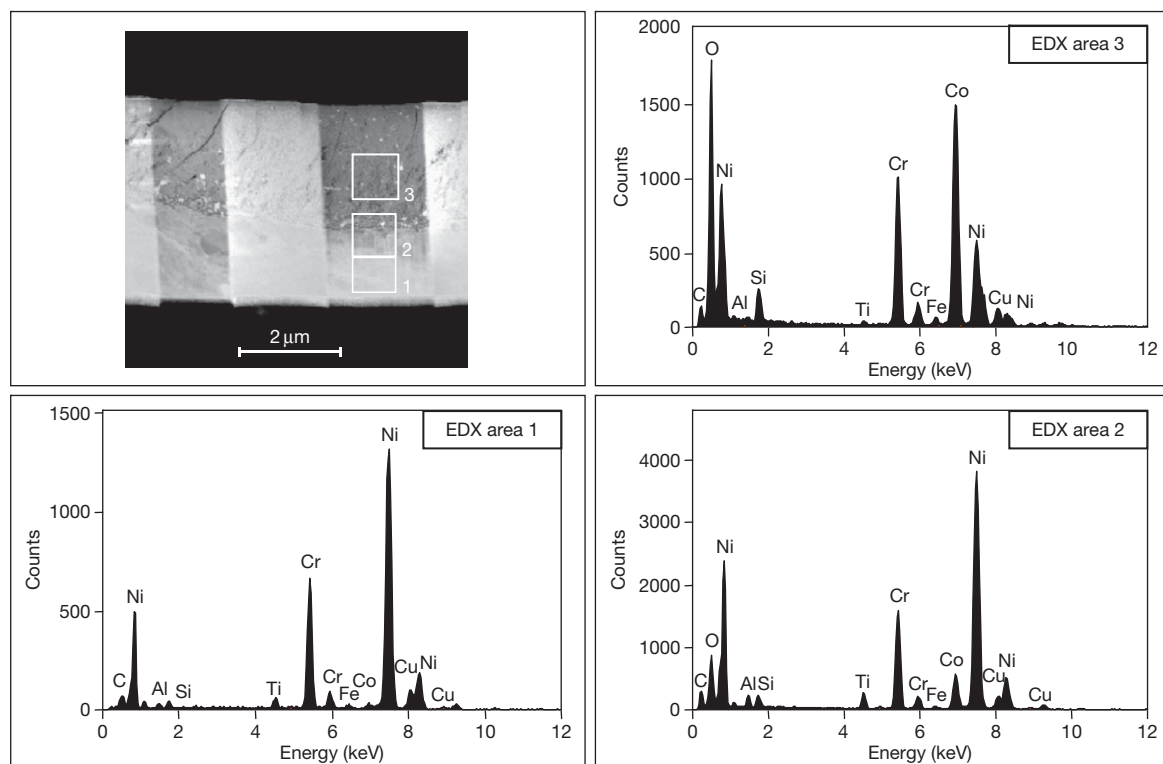


**Figure 35** HAADF-STEM (200 mm camera length) overview image and local EDX analysis (Nimonic 80A vs. Stellite 6,  $0.314 \text{ m s}^{-1}$ ,  $20^\circ\text{C}$ , load 7 N, sliding distance 4522 m). Reproduced from Du, H. L.; Datta, P. K.; Inman, I.; Geurts, R.; Kübel, C. *Mater. Sci. Eng. A* **2003**, 357, 412–422.

concentration gradient was observed. The line traces further reveal the preferential formation of titanium and aluminum oxides in a  $\sim 100 \text{ nm}$  thick layer at the interface. Slight chromium depletion is observed in the substrate close to the interface, with a corresponding chromium enrichment in the first  $\sim 300 \text{ nm}$  of the 'glaze' layer.

Similar areas of enrichment/depletion have been found at other locations along the interface; an example is given at a higher spatial resolution in [Figure 37](#).<sup>113</sup> Furthermore, this line trace also confirms aluminum enrichment at the interface; moreover, this  $\text{Al}_2\text{O}_3$  layer is between the  $\text{TiO}_2$  layer and the Nimonic 80A substrate. Aluminum (in  $\text{Al}_2\text{O}_3$ ) enrichment is further responsible for the dark areas in the HAADF-STEM image, leading from the interface into the substrate ([Figure 26](#)).

The atomic numbers of chromium (24), cobalt (27) and nickel (28) are similar and compositional variations of these main elements do not explain the strong contrast observed in the HAADF-STEM image ([Figure 38](#)).<sup>113</sup> However, the EDX/EELS line

traces reveal a low oxygen concentration for the bright areas, indicating that the image mostly reflects the oxidation state. Furthermore, a low oxygen concentration coincides with a low chromium concentration; local EDX analysis shows a low chromium and oxygen concentration for the particles that appear bright in the image. This implies that some of the nickel and cobalt particles are not completely oxidized.

EDX line traces in an area up to about one micron below the interface reveal the preferential segregation of light elements, especially aluminum and in some cases titanium ([Figure 39](#)).<sup>113</sup> This segregation is also visible in the HAADF-STEM images as thin lines ( $<10 \text{ nm}$  diameter) oriented parallel to the interface ([Figures 33–39](#)). It is noted that the peaks of Ti and Al are overlapped away from the interface, which indicates the presence of sub-microscopic  $\gamma'$ -phase,  $\text{Ni}_3\text{Al}$  or  $\text{Ni}_3(\text{TiAl})$  particles, as expected following ageing.<sup>113</sup>

These results clearly indicate the formation of a wear-resistant nanostructured surface during sliding wear of Nimonic 80A against Stellite 6 at  $20^\circ\text{C}$  using

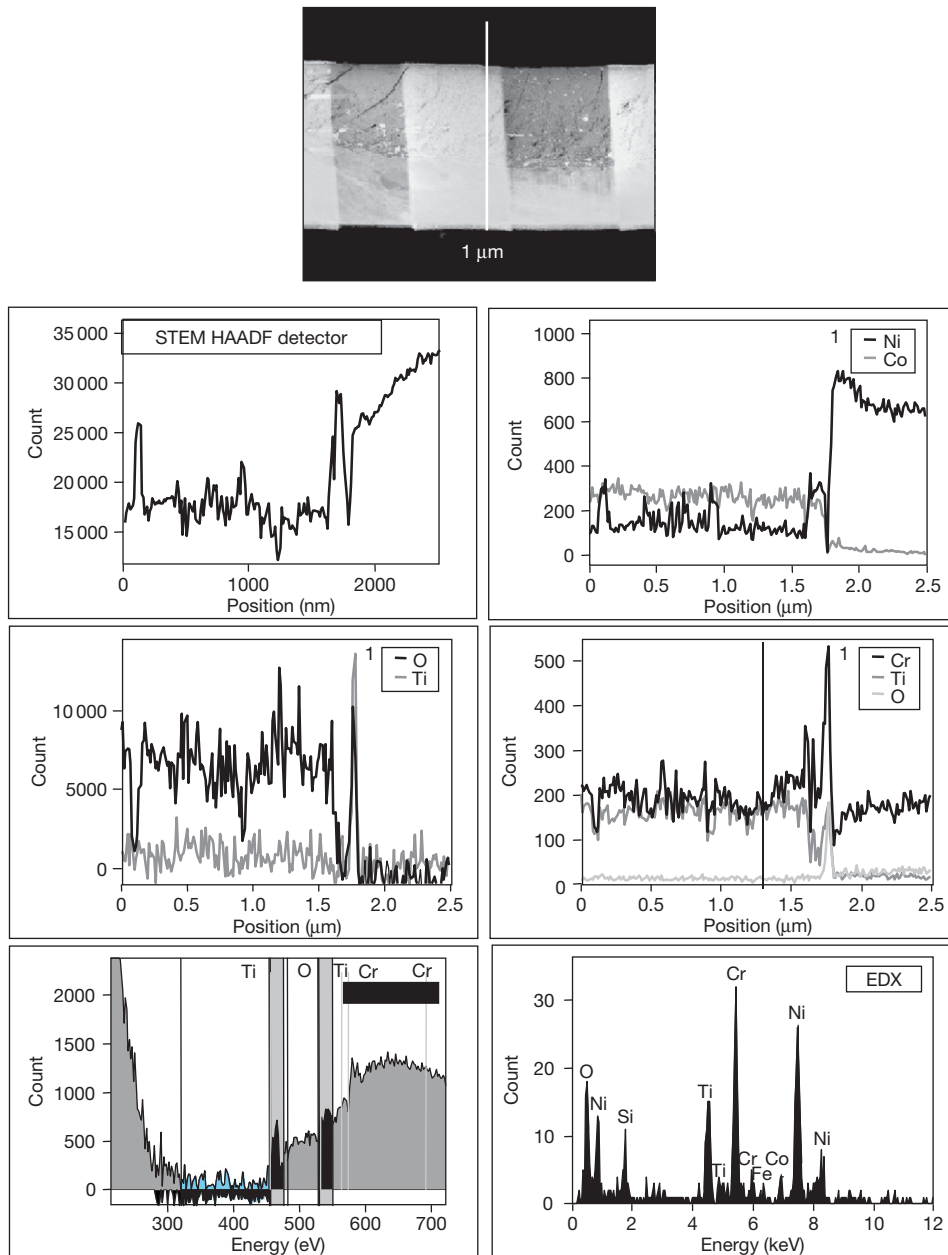


**Figure 36** HAADF-STEM EELS/EDX line trace revealing the compositional variations of the wear affected surface (Nimonic 80A vs. Stellite 6,  $0.314 \text{ m s}^{-1}$ ,  $20^\circ \text{C}$ , load 7 N, sliding distance 4522 m); line trace performed with 1 nm probe size and spectra collected every 10 nm. Reproduced from Du, H. L.; Datta, P. K.; Inman, I.; Geurts, R.; Kübel, C. *Mater. Sci. Eng. A* **2003**, 357, 412–422.

a speed of  $0.314 \text{ m s}^{-1}$  under a load of 7 N.<sup>113</sup> The analyses reveal the complex structure of this surface, which consists of multiple layers:

1. A loose, uncompacted, highly oxidized layer.
2. A nano-crystalline (5–20 nm grain diameter) compacted layer mostly consisting of oxides of elements originating both from Stellite 6 and Nimonic 80A.

3. Larger particles with a diameter of up to 50 nm were observed in a layer of about 300 nm at the base of the 'glaze' layer. The compositions indicate

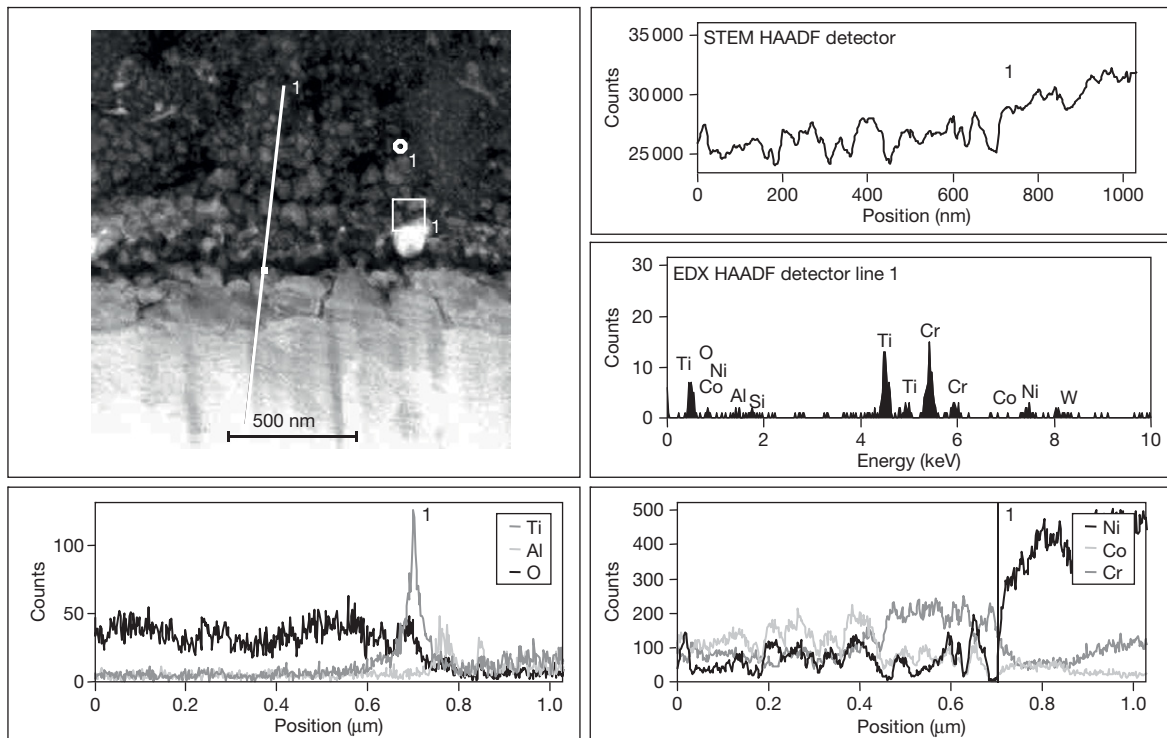


**Figure 37** HAADF-STEM (200 mm camera length) overview and EDX line trace revealing the compositional variations of the wear interface structure (Nimonic 80A vs. Stellite 6,  $0.314 \text{ m s}^{-1}$ ,  $20^\circ\text{C}$ , load 7 N, sliding distance 4522 m); the line trace was performed with a 1 nm probe size and spectra collected every 2 nm. Reproduced from Du, H. L.; Datta, P. K.; Inman, I.; Geurts, R.; Kübel, C. *Mater. Sci. Eng. A* **2003**, 357, 412–422.

the presence of elements from both Stellite 6 and Nimonic 80A, but chromium enriched.

4. The chromium-rich phase gradually gave way to a titanium (oxide)-rich phase of about 100 nm thickness, followed by an aluminum (oxide)-rich phase of about 50 nm thickness, at the interface with the Nimonic 80A substrate.
5. Adjacent to the interface with the 'glaze' layer, the Nimonic 80A substrate exhibited a large-grained structure (of diameter of several hundred nanometres). Slight chromium depletion was observed. The precipitation lines (diameter  $< 10 \text{ nm}$ ) indicated that aluminum-, and in some cases titanium-, enriched phases formed near the large-grained structures. The larger dark areas perpendicular to the interface were also due to aluminum enrichment.
6. A uniform 'bulk' Nimonic 80A composition was observed at depths greater than one micron below the interface.

The first key process in the development of nano-structured 'glaze' layers involves oxidation of the

contacting surface/particles subjected to high mechanical stress due to rotation of the counterface. The 'glaze' layer, consisting mainly of the oxides of the elements originating from the contacting surfaces, acted as a barrier that separated the substrate from the environment. Although the mechanical effect would continue to influence the 'glaze' layer and subsurface deformation, the subsequent oxidation process is controlled by oxygen species and substrate element diffusion, and the thermodynamic nature of the relevant oxides. The observed sequential existence of the oxides  $\text{Cr}_2\text{O}_3/\text{TiO}_2/\text{Al}_2\text{O}_3/\text{substrate}$  at the interface can be understood in terms of thermodynamics. [Figure 40\(a\)](#) indicates the oxidation tendencies of relevant elements.<sup>113</sup> The dissociation partial pressures for  $\text{Al}_2\text{O}_3$ ,  $\text{TiO}_2$ ,  $\text{Cr}_2\text{O}_3$ ,  $\text{NiO}$ , and  $\text{Co}_3\text{O}_4$  follow the same trend in the range of temperatures  $25\text{--}1000^\circ\text{C}$ .  $\text{Al}_2\text{O}_3$ ,  $\text{TiO}_2$  and  $\text{Cr}_2\text{O}_3$  are more likely to develop with increasing temperatures. Although the temperature generated was not measured, the relatively fast kinetics of oxidation, as evidenced by the rapid formation of the 'glaze' layer, indicates the generation of relatively high temperatures, sufficient for such oxidation to occur.

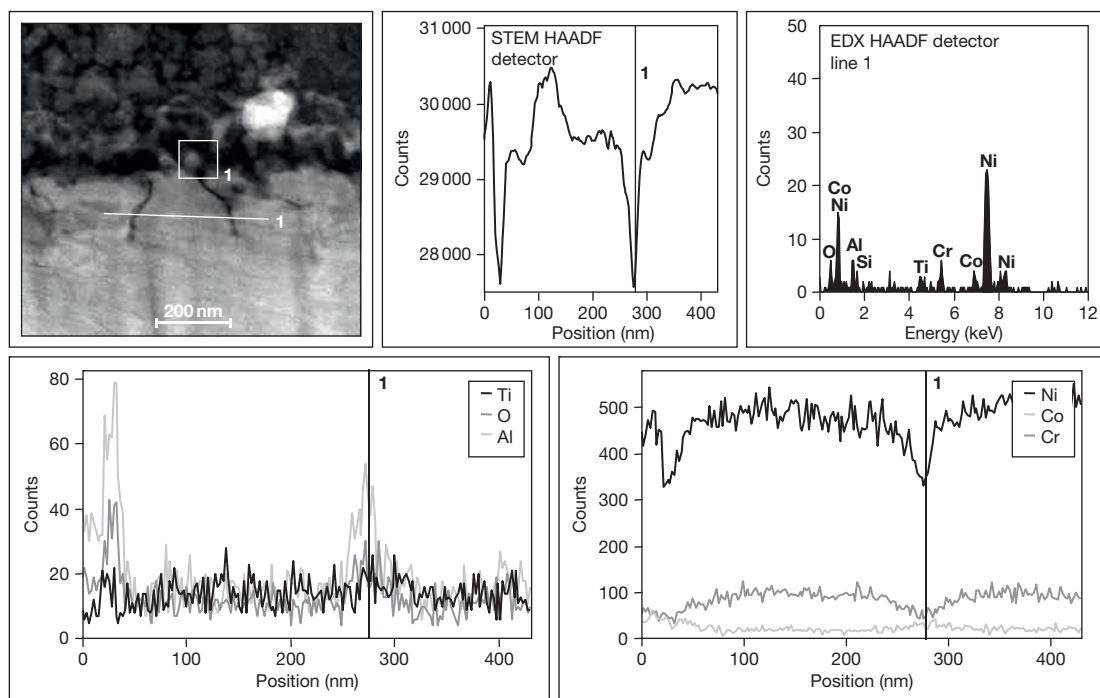


**Figure 38** HAADF-STEM (50 nm camera length) overview and EDX line trace revealing the aluminum (oxide) segregation at the top of the Nimonic 80A phase (Nimonic 80A vs. Stellite 6,  $0.314 \text{ m s}^{-1}$ ,  $20^\circ \text{C}$ , load 7 N, sliding distance 4522 m); the line trace was performed with a 1 nm probe size and spectra collected every 2 nm. Reproduced from Du, H. L.; Datta, P. K.; Inman, I.; Geurts, R.; Kübel, C. *Mater. Sci. Eng. A* **2003**, 357, 412–422.

Additionally, it is apparent that the high Cr activity in both counterface and sample materials leads to the formation of  $\text{Cr}_2\text{O}_3$  preferentially in the early stages of the process. When oxygen diffuses inwards, Ti in the  $\gamma'$  phase is favorably oxidized. The formation of  $\text{TiO}_2$  gives rise to a decrease in Ti activity and, correspondingly, the Al activity in the  $\gamma'$  phase increases and  $\text{Al}_2\text{O}_3$  becomes a favorable product, as described for oxidation of TiAl in air.<sup>115,116</sup> NiO and  $\text{Co}_3\text{O}_4$  are much less stable than  $\text{TiO}_2$  and  $\text{Al}_2\text{O}_3$ , which is the reason why some particles of Ni and Co have not been oxidized in the wear process. These oxides ( $\text{TiO}_2$  and  $\text{Al}_2\text{O}_3$ ) formed beneath the 'glaze' layer, play an important role in providing support additional to that provided by the substrate, to sustain the 'glaze' layer and prevent it from collapsing.<sup>4</sup>

#### 1.15.4.4.3 Nano-scale microscopy of 'glazed' layers formed during high temperature sliding wear at $750^\circ \text{C}$

The spectrum from EDX analysis of the surface generated under sliding wear at  $0.314 \text{ m s}^{-1}$  and  $750^\circ \text{C}$  for 4522 m, Figure 40(b), reveals the

dominant presence of Co, Ni, Cr and O on the 'glaze' surface.<sup>20,25</sup> Quantification of the results on average gives 34.2% Co, 36.2% Cr, 16.7% Ni, 3.8% Si, and 1.3% Fe (all at%). However, analysis by TEM-EDS showed some location-to-location variation. The dominant phases identified by XRD included  $\text{CoCr}_2\text{O}_4$  and  $\text{Ni}_{2.9}\text{Cr}_{0.7}\text{Fe}_{0.36}$ .

Figure 41(a) is a cross-sectional composite TEM micrograph of the surface formed during wear.<sup>20,25</sup> It reveals the surface layer (glazed surface), the deformed substrate and the 'glazed' layer/substrate interface. The wear-affected region (total thickness  $\sim 3 \mu\text{m}$ ) consists of three layers; the top-most layer (the 'glaze' layer) has a uniform grain structure of size 5–15 nm, some of the grains displaying contrast, while the dislocation density in this area is low. The interfacial layer consists of grains of 10–20 nm and has a higher dislocation density. The layer just beneath the interfacial layer shows subsurface deformation and elongated grains. The SAD pattern from the 'glaze' layer (Figure 42) consists of spots arranged in concentric circles, indicating the presence of small grains with high angle boundaries, multiple boundaries and large misorientations



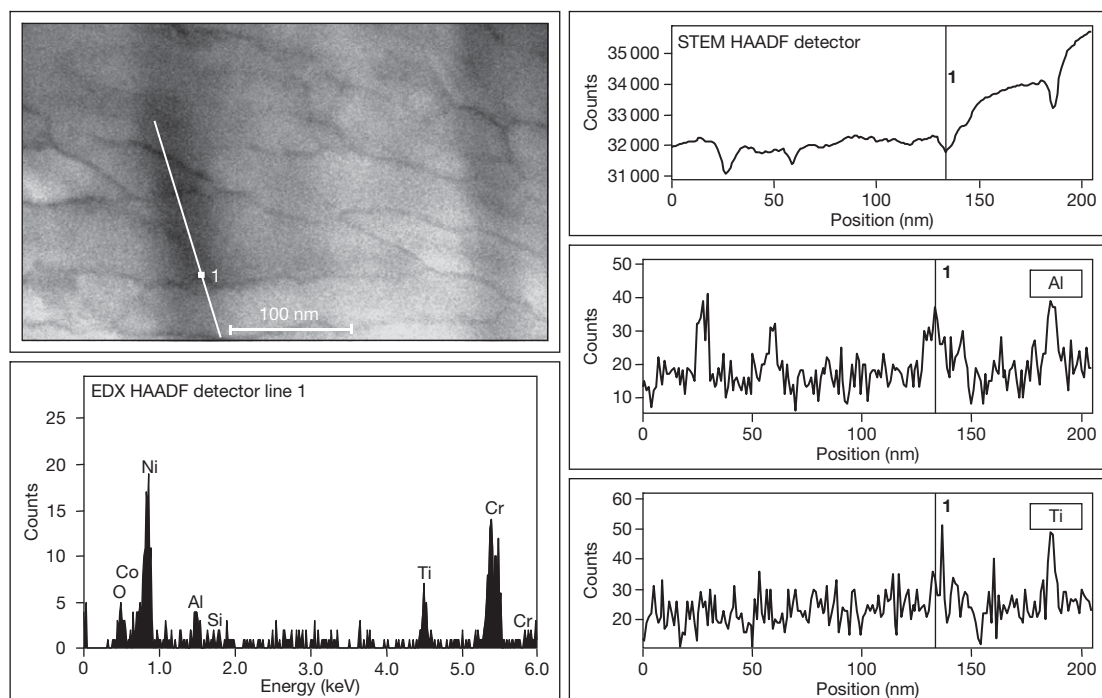


**Figure 39** HAADF-STEM (50 mm camera length) overview and EDX line trace revealing the precipitation of light elements (aluminum and titanium) in the Nimonic 80A close to the wear interface (Nimonic 80A vs. Stellite 6,  $0.314 \text{ m s}^{-1}$ ,  $20^\circ\text{C}$ , load 7 N, sliding distance 4522 m). Reproduced from Du, H. L.; Datta, P. K.; Inman, I.; Geurts, R.; Kübel, C. *Mater. Sci. Eng. A* **2003**, 357, 412–422.

(formation of misorientated lattice-fragmentation). The poorly-defined irregular boundaries indicate nonequilibrium high-energy configuration. The indexed SAD pattern also revealed the presence of oxides of Ni, Cr, and Co (indexing not shown here).

Sub-surface deformation is illustrated in **Figure 41(b)**.<sup>20,25</sup> Dislocations, present as networks inside the deformed (elongated) grains, have been observed in the deformed substrate. Shearing deformation took place in the substrate as a response to the sliding process.

The present results clearly indicate the formation of a nano-structured ‘glaze’ oxide layer during high temperature sliding wear under the specified conditions. The creation of nano-structures is confirmed by the STM topography, indicating grains of between 5 and 10 nm (**Figure 43**).<sup>5,20,21,25</sup> These results again demonstrate that such a nano-structured surface is extremely effective in conferring high resistance to wear.

It has been indicated by various authors<sup>5,20,21,110</sup> that, in many systems, surfaces with ultra-fine structure are generated during high temperature sliding wear. Mechanical mixing involving repeated welding, fracture and re-welding of the debris generated from

both contacting surfaces is responsible for the generation of the ultrafine structured surfaces. Moreover, the detailed TEM studies presented here has enabled understanding of the formation mechanisms of wear-resistant nano-structured surfaces.

It is clear that the initial processes responsible for generating the ‘glazed’ layer at both  $20$  and  $750^\circ\text{C}$  are ‘deformation of the surface,’ ‘intermixing of the debris generated from the wear and the counterface surfaces,’ ‘oxidation,’ ‘further mixing,’ and ‘repeated welding and fracture.’ These processes are aided by high temperature oxidation and diffusion. The positron annihilation studies confirmed the presence of vacancy clusters consisting of five vacancies.<sup>110</sup>

The next stage in the process involves deformation of oxides and generation of dislocations, leading to the formation of sub-grains. These sub-grains are then further refined, with increasing misorientation resulting in nano-structured grains with high angle boundaries (a process called ‘fragmentation’), a non-equilibrium state indicated by poorly defined and irregular grain boundaries. High internal stress is created inside the grains; the dislocation density and arrangement depend on the grain size, with smaller

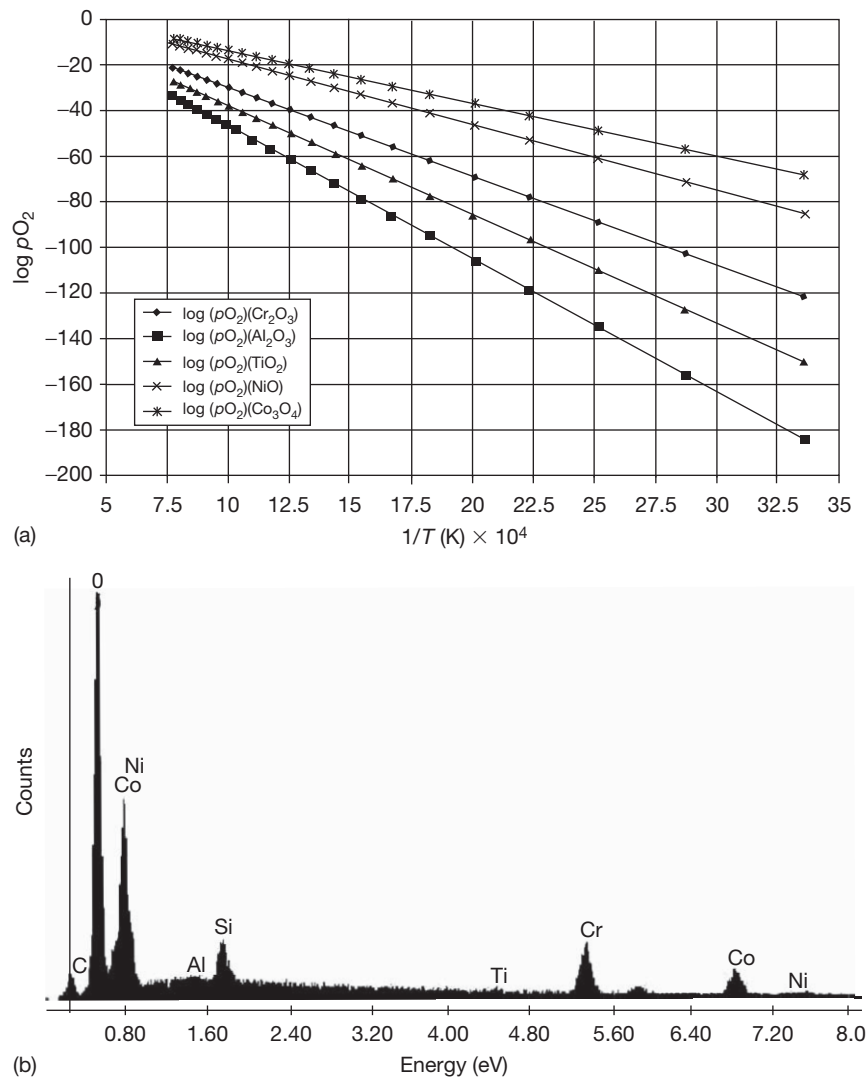


**Figure 40** Plots showing (a) dissociation partial pressures of  $Al_2O_3$ ,  $TiO_2$ ,  $Cr_2O_3$ ,  $NiO$ , and  $Co_3O_4$  versus reciprocals of temperatures<sup>20</sup> and (b) EDX surface spectrum for Nimonic 80A vs. Stellite 6 ( $0.314 \text{ m s}^{-1}$ ,  $750^\circ\text{C}$ , load 7 N, sliding distance 4522 m).<sup>20, 25</sup>

grains containing fewer dislocations. The process leads to the formation of high energy grain boundaries with a high defect density.<sup>117–123</sup>

#### 1.15.4.4.4 Other systems

Such nanostructured 'glaze' layers are not unique to Nimonic 80A when slid against Stellite 6 ( $0.314 \text{ m s}^{-1}$ , 7 N load, 4522 m sliding distance). For example, using AFM, Incoloy MA956 has also been shown to form nanostructured 'glaze' layers when slid against Stellite 6<sup>23</sup> and Incoloy 800HT at  $750^\circ\text{C}$  (Figure 44).<sup>114</sup> In the case of the Incoloy MA956/Stellite 6 system, this nanostructured 'glaze' formed has been found to originate from both Co–Cr-dominated oxide debris at  $0.314 \text{ m s}^{-1}$  and

Fe–Cr-dominated debris at  $0.905 \text{ m s}^{-1}$ ; the sliding speed and composition having no noticeable effect on 'glaze' structure with this latter system.

### 1.15.5 Wear Maps: A Useful Design Aid for Selecting Wear-Resistant Materials and Surfaces

#### 1.15.5.1 Introduction

Lancaster,<sup>26</sup> Welsh,<sup>27,28</sup> So,<sup>29,30</sup> Rose,<sup>4</sup> Inman,<sup>5,21–24</sup> and others<sup>42,85</sup> have shown that various combinations of load, temperature and sliding speed can

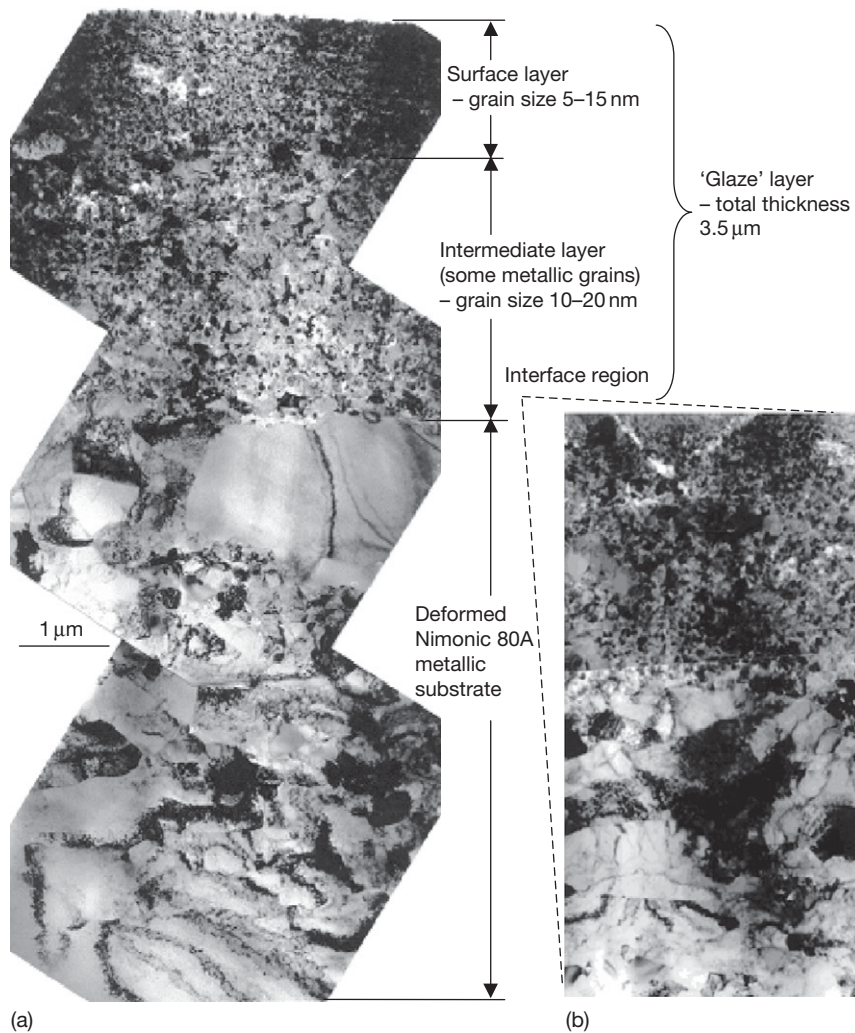


**Figure 41** Nanoscale characterization of 'glaze' layers formed (Nimonic 80A vs. Stellite 6,  $0.314 \text{ m s}^{-1}$ ,  $750^\circ\text{C}$ , load 7 N, sliding distance 4522 m) showing TEM bright field images of (a) a wear-induced polycrystalline 'glaze' layer plus substrate deformation and (b) the interface of the 'glaze' layer and deformed substrate.<sup>5,20,21,25</sup>

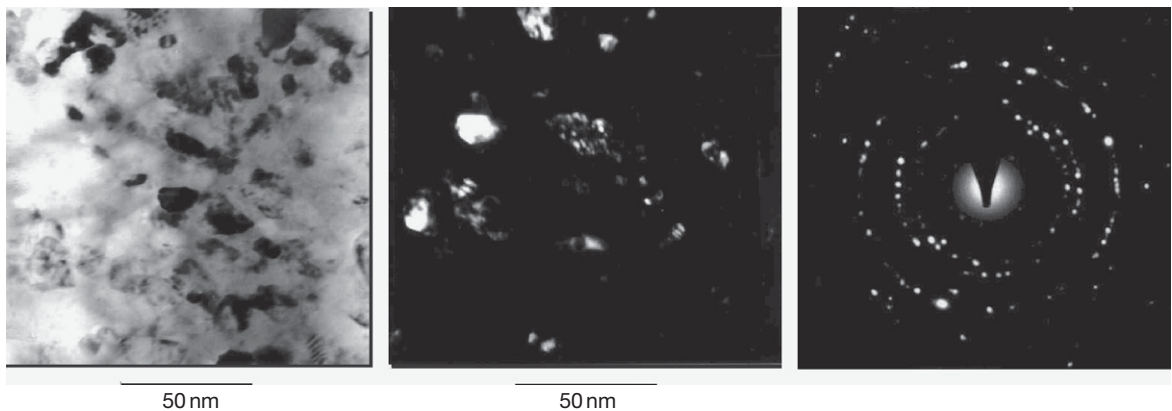


**Figure 42** TEM morphological and structural details of the 'glaze' layer formed (Nimonic 80A vs. Stellite 6,  $0.314 \text{ m s}^{-1}$ ,  $750^\circ\text{C}$ , load 7 N, sliding distance 4522 m).<sup>20,25</sup>

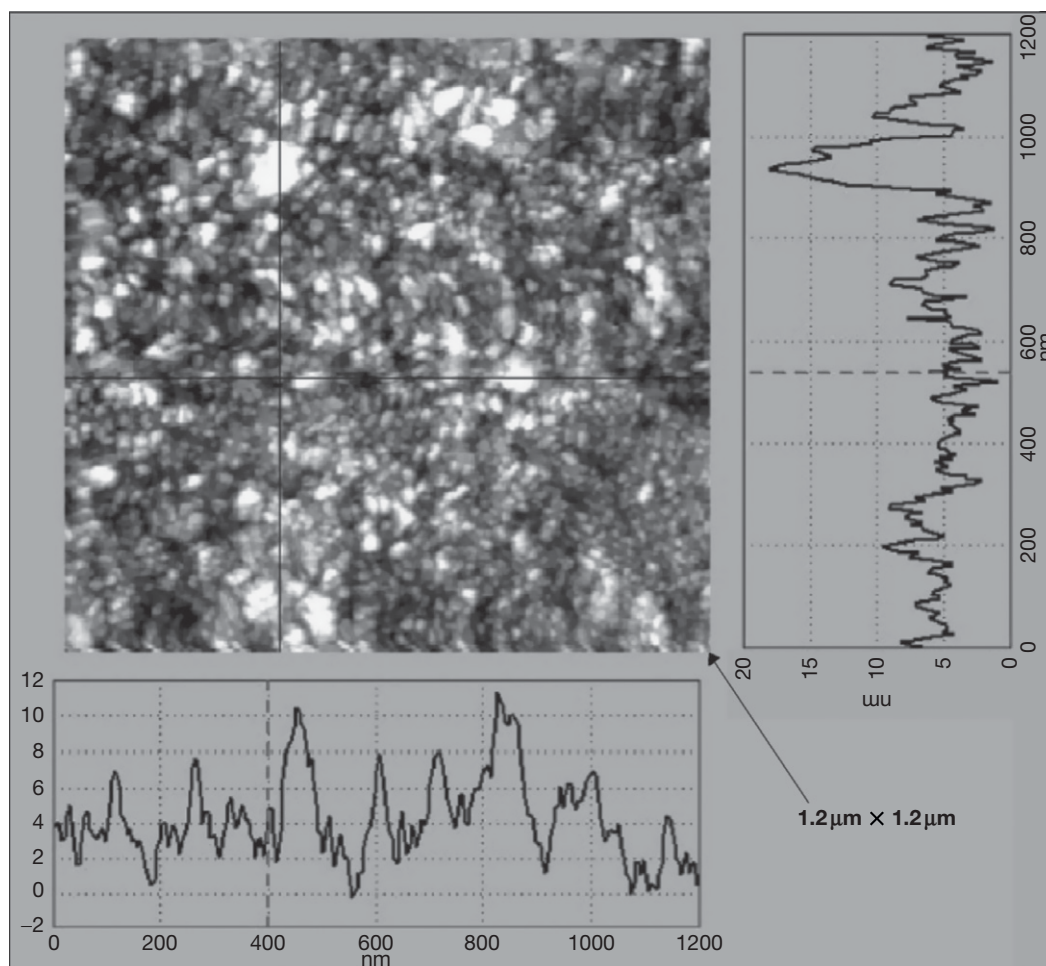


**Figure 43** STM surface line profile results on the 'glaze' layer formed on Nimonic 80A (Stellite 6 counterface,  $0.314 \text{ m s}^{-1}$ ,  $750^\circ\text{C}$ , load 7 N, sliding distance 4522 m).<sup>5,20,21,25</sup>

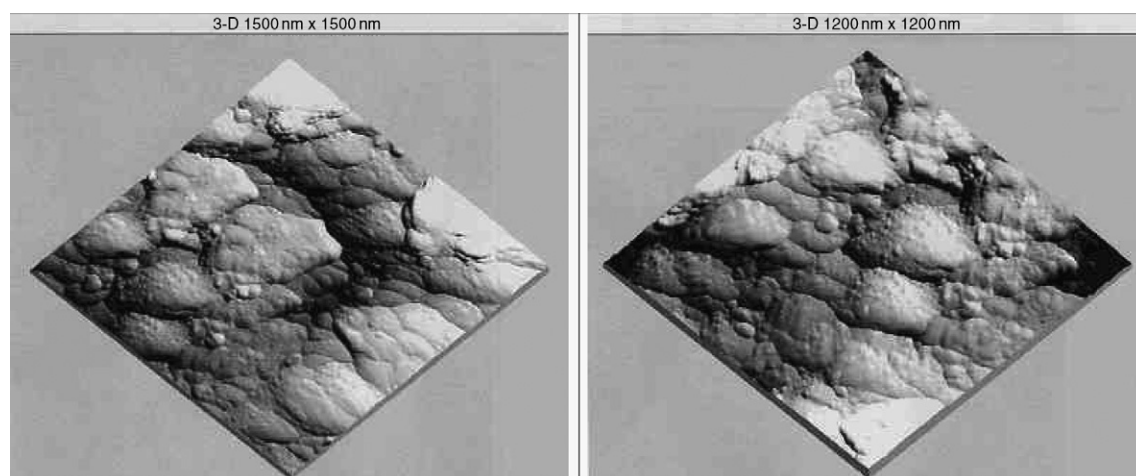


**Figure 44** AFM image of 'glaze' layer surfaces produced on Incoloy MA956 (slid against Incoloy 800HT) at  $750^\circ\text{C}$  and sliding speeds of (a)  $0.314 \text{ m s}^{-1}$  and (b)  $0.905 \text{ m s}^{-1}$ . Reproduced from Inman, I. A. Nano-scale studies of 'glaze' layers formed on Incoloy MA956 when slid against Incoloy 800HT at  $750^\circ\text{C}$ , Northumbria University, 2003, Unpublished work.



significantly affect wear behavior, regardless of whether or not a protective 'glaze' can form.

Several authors have also constructed wear maps in an attempt to present wear data in a more easily understood format, allowing prediction of likely wear mode under specified sliding conditions. Lim<sup>124,125</sup> (Figure 45), Childs<sup>126</sup> (Figure 46(a)), and more recently, Riahi and Alpas,<sup>128</sup> Chen and Alpas,<sup>129</sup> Yang *et al.*,<sup>130</sup> Grimanellis and Eyre,<sup>131,132</sup> and Elleuch *et al.*<sup>133</sup> have constructed wear maps for various sliding

systems based on load/pressure and sliding speed. Other wear-related parameters have also been used and Kato and Hokkirigawa<sup>127</sup> developed an abrasive wear map using 'degree of penetration (of asperities)' and 'shear strength at the contact interface' as key parameters (Figure 46(b)). Adachi *et al.*<sup>134</sup> used 'severity of contact' and 'thermal severity of contact' for ceramic wear.

The following section discusses recent developments in high temperature wear maps made by the present authors, following a brief review of earlier work by Lim.

**Table 5** Quantification of the EDX spectra in Figure 35

Element	Area 1 (Nimonic 80 A substrate)		Area 3 (Glaze layer)	
	wt. %	at. %	wt. %	at. %
Al	0.7	1.4	0.4	0.9
Si	0.7	1.3	1.1	2.3
Ti	1.8	2.1	0.4	0.5
Cr	18.7	20.2	25.0	27.4
Fe	0.7	0.7	1.4	1.4
Co	1.0	0.9	49.8	48.2
Ni	76.6	73.4	19.0	18.4
W	–	–	2.9	0.9

### 1.15.5.2 Work by Lim

Lim<sup>124</sup> attempted to collate the available data for mild steels into a single comprehensive wear map (Figure 45) using dimensionless parameters of normalized velocity versus normalized load. This showed that the selection of sliding conditions and configuration can greatly affect the wear behavior and transitions observed, with load, sliding speed, and temperature potentially having a large influence on the boundaries between the different modes of wear.

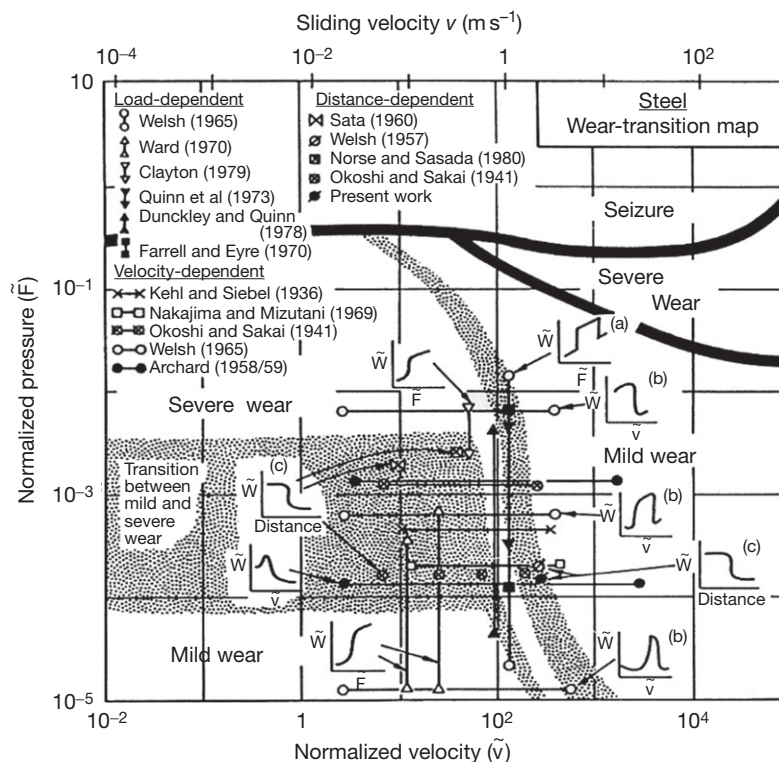


**Figure 45** Wear transition map for steels showing regions of mild and severe wear – sliding conditions corresponding to different types of wear transitions observed are also indicated. Reproduced from Lim, S. C. *Tribol. Int.* **1998**, 31(1–3), 87–97.



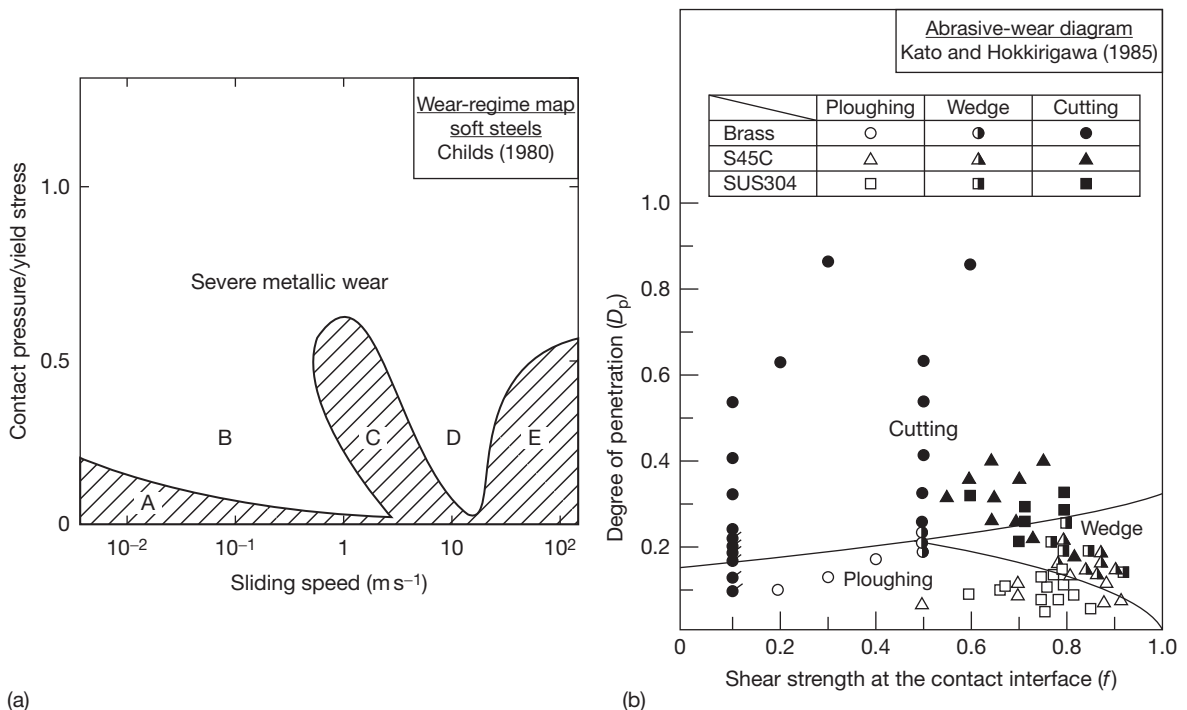


**Figure 46** Examples of 'alternative parameter' wear maps: (a) Childs soft steels wear-regime map<sup>126</sup>, and (b) Kato and Hokkirigawa's abrasive-wear diagram for brass, S45C medium carbon steel and SUS304 stainless steel. Reproduced from Kato, K.; Hokkirigawa, K. In *Proceedings of the Eurotrib'85*; Elsevier: Amsterdam, 1985; Vol. 4, Section 5.3, pp 1–5.

For example, it can be seen that, if a relatively high fixed load is used, with increasing sliding speed, a transition from severe-to-mild wear is observed.<sup>27</sup> More complex forms result at lower loads when sliding speeds are at much higher values.<sup>27,32</sup> Similarly, if speed is fixed at an arbitrarily low value, increasing load may see a switch from mild to severe wear<sup>124</sup> while a higher speed can result in a more complex curve.<sup>27</sup> To summarize, when two surfaces are worn against each other, the outcome can be a variety of apparently contradictory results. Thus, mapping is necessary to understand the relative behaviors in different tests and the potential outcome under a given set of sliding conditions.

### 1.15.5.3 Dissimilar Interfaces

As discussed previously, Inman *et al.*<sup>5,22,23</sup> studied the effects of temperature and sliding speed on several superalloys using dissimilar interfaces. This section refers specifically to Nimonic 80A<sup>22</sup> and Incoloy MA 956<sup>23</sup> worn against Stellite 6. For both systems, the data have been used to create simple 'temperature versus sliding speed' wear maps<sup>22,23</sup> (Figures 47 and 48). The weight change data are presented in Figures 30 and 49.

For both systems,<sup>23</sup> mild wear with low weight loss dominates at  $0.314 \text{ m s}^{-1}$  regardless of temperature (Figures 47 and 48). Up to  $450^\circ\text{C}$ , a low temperature mild wear regime occurs, with the wear surfaces separated by a layer of Co–Cr oxide particles (i.e., loose debris – Figures 13(a) and 24(a) – potentially underlain by a more compacted layer – Section 1.15.4.3.2), primarily sourced from the Stellite 6. Increased agglomeration and sintering of the debris has been observed at  $390^\circ\text{C}$ , with isolated patches of 'glaze' at  $450^\circ\text{C}$  (although most of the oxide remained as loose debris). Mild wear persists between  $510^\circ\text{C}$  (Figures 13(b) and 24(b)) and  $750^\circ\text{C}$  (Figures 13(c) and 24(c)), with the still Stellite 6-sourced oxide sintering to form comprehensive 'glaze' layers with nanostructured surfaces<sup>5,20,21,23,25</sup> (discussed in Section 1.15.4.4); with extremely low weight change with some very slight weight gains due to oxide development (Figures 47 and 48). At all temperatures, there was virtually no initial severe wear period, with sufficient Co–Cr oxide debris forming extremely rapidly.

The Nimonic 80A versus Stellite 6 system<sup>22</sup> is characterized by three distinct wear regimes at  $0.654 \text{ m s}^{-1}$  (Figure 47); up to  $390^\circ\text{C}$ , a low temperature 'low weight loss' mild wear regime (Figure 30) was observed, with a

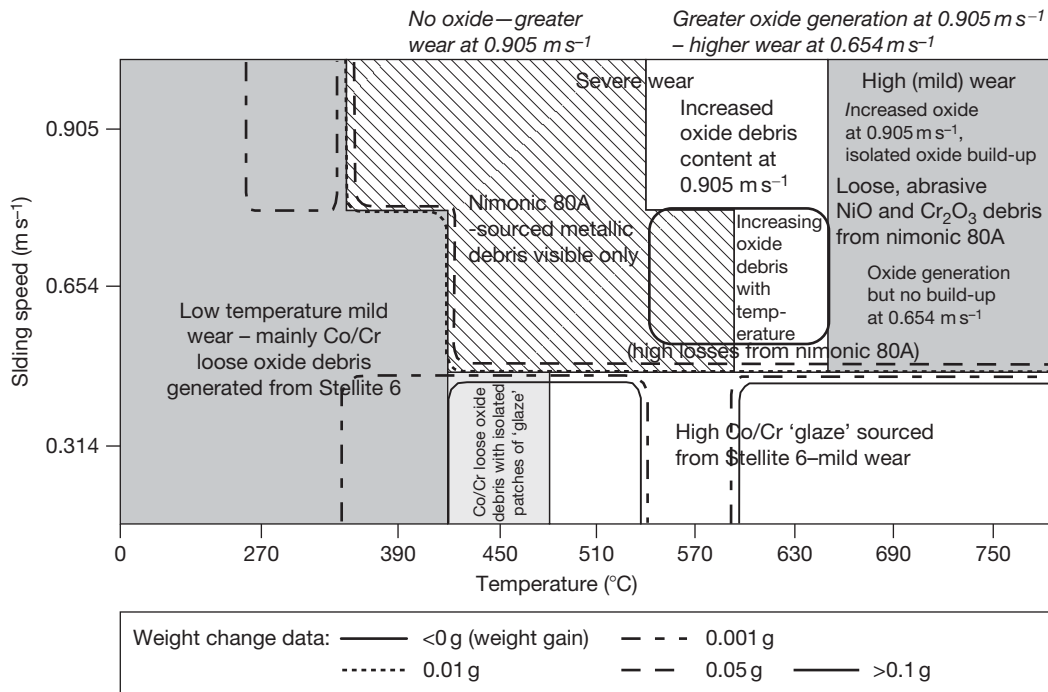


**Figure 47** Wear map for Nimonic 80A versus Stellite 6 (load 7 N, sliding distance 4522 m), with weight loss (contour) data superimposed. Reproduced from Inman, I. A.; Rose, S. R.; Datta, P. K. *Wear* **2006**, 260, 919–932.

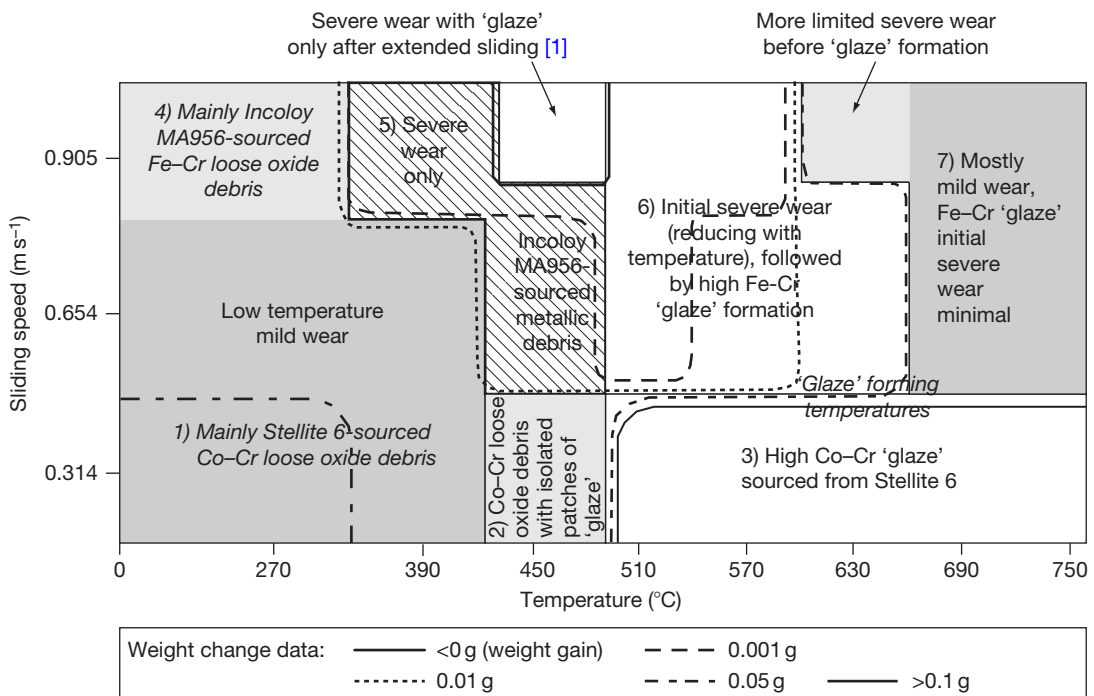


**Figure 48** Wear map for Incoloy MA956 slid against a Stellite 6 counterface (load 7 N), with weight loss (contour) data superimposed. Reproduced from Inman, I. A.; Rose, S. R.; Datta, P. K. *Tribol. Int.* **2006**, 39, 1361–1375.

layer of Stellite 6-sourced Co–Cr oxide particles separating the wear surfaces (**Figure 41(a)**). A metallic severe wear (especially of the Nimonic 80A) regime dominated between 450 and 630 °C (**Figure 25(b)**) with no visible oxide between 450 and 570 °C. This severe wear regime was also observed at 630 °C, now accompanied by a small amount of NiO and Cr<sub>2</sub>O<sub>3</sub> generated by thermal and frictional heating; however, this oxide was insufficient to impede metal-to-metal contact and may instead have assisted wear by abrasion.

A mild oxidational wear regime was evident at 690 and 750 °C, although Nimonic 80A weight losses (**Figure 30**) remained high due to abrasion. This abrasion was caused by large amounts of Nimonic 80A-sourced NiO and Cr<sub>2</sub>O<sub>3</sub>, which (unlike Co–Cr oxides generated at 0.314 m s<sup>-1</sup>) showed little tendency to sinter and form ‘glaze.’

The sliding behavior at 0.905 m s<sup>-1</sup> exhibited the same three sliding regimes observed at 0.654 m s<sup>-1</sup>.<sup>22</sup> However, greater frictional heating resulted in a downward shift in the low-temperature-mild-wear-to-severe-wear transition from 390–450 to 270–390 °C. Increased amounts of loose NiO and Cr<sub>2</sub>O<sub>3</sub> debris occurred at 570 °C upwards, but not sufficient to

lower the severe-wear-to-abrasive-mild-wear transition from 690 °C.

The behavior for the Incoloy MA956 versus Stellite 6 system follows the same general pattern at 0.654 and 0.905 m s<sup>-1</sup> as that of Nimonic 80A versus Stellite 6<sup>23</sup> (**Figure 48**). However, in this case, the high temperature mild wear regime confers protection, with the mixed Fe–Cr and Co–Cr oxides at 0.654 m s<sup>-1</sup> or the largely Fe–Cr oxides at 0.905 m s<sup>-1</sup> readily sintering to form ‘glaze’ layers. Such ‘glaze’ is observed from 510 °C upwards (450 °C after extended sliding at 0.905 m s<sup>-1</sup>), after a period of early severe wear (**Figure 14(b)**) that decreases in length with increasing temperature. At and above 630 °C, rapid ‘glaze’ formation (**Figure 14(c)**) almost completely eliminates early severe wear (**Figure 49**).

A later study by Inman and Datta<sup>24</sup> looked to improve Nimonic 80A versus Stellite 6 wear map resolution between 630 and 750 °C by adding extra test sliding speeds. Rudimentary wear maps were also developed separately for Nimonic 80A and Incoloy MA956 as sample materials versus an Incoloy 800HT counterface.<sup>5</sup>

Such sliding studies indicate the potential for complex behavior during sliding of dissimilar

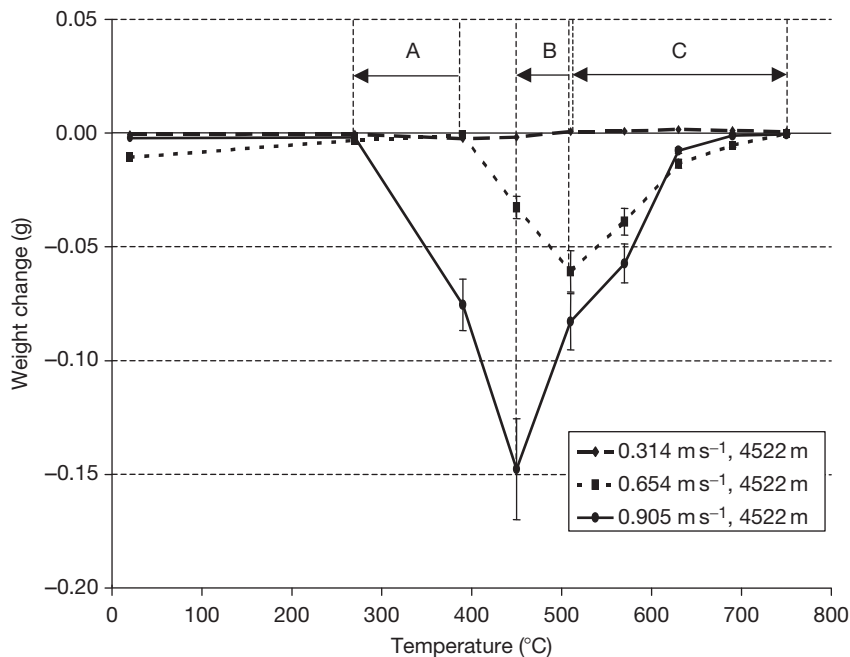


**Figure 49** Weight change versus temperature for Incoloy MA956 slid against Stellite 6 at 0.314, 0.654, and 0.905 m s<sup>-1</sup> (load 7 N, sliding distance 4522 m) – effect on transition temperatures on increasing sliding speed from 0.654 to 0.905 m s<sup>-1</sup> are indicated.<sup>23</sup> (a) Decrease in low temperature mild to severe wear transition from 390 °C at 0.654 m s<sup>-1</sup> to 270 °C at 0.905 m s<sup>-1</sup>, (b) Decrease in temperature of first appearance of ‘glaze’ from 510 °C at 0.654 m s<sup>-1</sup> to 450 °C after extended sliding at 0.905 m s<sup>-1</sup>, and (c) More rapid ‘glaze’ formation at 0.905 m s<sup>-1</sup>.

materials. In such cases, the necessity for mapping wear behavior to assist prediction of mild or severe wear is important, if potentially catastrophic material failure is to be avoided.

#### 1.15.5.3.1 Oxide chemistry

These studies also indicate that the readiness for a wear-generated oxide to form 'glaze' layers depends not just upon the sliding conditions, but also on the chemical composition of the oxide. For example, Co–Cr-based oxides readily form wear protective 'glaze' layers at high temperature,<sup>3,20–25</sup> while Fe–Cr-based oxides<sup>3,23</sup> can also form fairly robust wear protective layers under adverse sliding conditions. NiO and Cr<sub>2</sub>O<sub>3</sub> oxides produced from Nimonic 80A do not too readily sinter together to develop into 'glaze' and can actually enhance wear by abrasion<sup>3,6,7</sup>; however, NiO (produced from Nickel 200)<sup>3</sup> has been shown to easily form a 'glaze' in the absence of Cr<sub>2</sub>O<sub>3</sub>.

### 1.15.6 Summary

In writing this chapter strong emphasis has been placed on scientific principles underpinning the phenomenon of high temperature wear. At the outset a review of some of the well-known and relevant wear theories and models, supported by experimental findings on conventional and advanced materials, has been presented. This background information has provided a framework to discuss new areas of high temperature wear. In this context the high temperature wear behavior of those materials which have provided new information has been considered. Particular attention has been focused on high temperature wear behavior of oxide dispersion strengthened and Nimonic alloys, and inter-metallic materials involving like-on-like and unlike-on-unlike combinations. The most significant part of this chapter includes the exposition of the phenomena of glaze formation at fundamental levels. Here the novel aspect is the inclusion of nanoscale elaboration of the processes of glaze formation underpinned by fundamental information gathered from TEM and STM/STS investigations. In this area significant reliance has been placed on the authors' own research.

### References

1. Quinn, T. F. J. *Wear* **1992**, 153, 179–200.
2. Jiang, J.; Stott, F. H.; Stack, M. M. *Wear* **1995**, 181–183, 20–31.
3. Wood, P. D. Ph.D. Thesis, Northumbria University, UK, 1997.
4. Rose, S. R. Ph.D. Thesis, Northumbria University, UK, 2000.
5. Inman, I. A. Ph.D. Thesis, Northumbria University, UK, 2003; published by 'Dissertation.com', 2006.
6. Stott, F. H.; Lin, D. S.; Wood, G. C. *Corros. Sci.* **1973**, 13, 449–469.
7. Johnson, M.; Moorhouse, P.; Nicholls, J. R. DTI Industry Valve Project 1990; pp 61–68.
8. Aoh, J.-N.; Chen, J.-C. *Wear* **2001**, 250–251, 611.
9. Singh, J.; Alpas, A. T. *Metall. Mater. Trans. A* **1996**, 27, 3135–3148.
10. Stott, F. H.; Glascott, J.; Wood, G. C. *Wear* **1984**, 97, 93–106.
11. Gee, M. G.; Jennett, N. M. *Wear* **1995**, 193, 133–145.
12. Wood, P. D.; Datta, P. K.; Burnell-Gray, J. S.; Wood, N. *Mater. Sci. Forum* **1997**, 251–254, 467–474.
13. Wisbey, A.; Ward-Close, C. M. *Mater. Sci. Technol.* **1997**, 13, 349–355.
14. Jiang, J.; Stott, F. H.; Stack, M. M. *Wear* **1997**, 203–204, 615–625.
15. Li, X. Y.; Tandon, K. N. *Wear* **2000**, 245, 148–161.
16. Jiang, J.; Stott, F. H.; Stack, M. M. *Wear* **2004**, 256, 973–985.
17. Jiang, J.; Stott, F. H.; Stack, M. M. *Tribol. Int.* **1998**, 31–5, 245–256.
18. Jiang, J.; Stott, F. H.; Stack, M. M. *Tribol. Int.* **1997**, 30–7, 517–526.
19. Jiang, J.; Stott, F. H.; Stack, M. M. *Wear* **1994**, 176, 185–194.
20. Datta, S.; Inman, I.; Du, H. L.; Luo, Q. Microscopy of 'glazed' layers formed during high temperature wear, Invited Talk at the Institute of Materials, Tribology Meeting, London, November 2001.
21. Inman, I. A.; Datta, S.; Du, H. L.; Burnell-Gray, J. S.; Pierzgalski, S.; Luo, Q. *Tribol. Int.* **2005**, 38, 812–823.
22. Inman, I. A.; Rose, S. R.; Datta, P. K. *Wear* **2006**, 260, 919–932.
23. Inman, I. A.; Rose, S. R.; Datta, P. K. *Tribol. Int.* **2006**, 39, 1361–1375.
24. Inman, I. A.; Datta, P. S. *Wear* **2008**, 265, 1592–1605.
25. Inman, I. A.; Datta, S.; Du, H. L.; Burnell-Gray, J. S.; Pierzgalski, S.; Luo, Q. *Wear* **2003**, 254, 461–467.
26. Lancaster, J. K. *Proc. Royal Soc. London A* **1962**, 273, 466–483.
27. Welsh, N. C. *Philos. Trans. A* **1965**, 257, 31–50.
28. Welsh, N. C. *Philos. Trans. A* **1965**, 257, 51–70.
29. So, H. *Tribol. Int.* **1996**, 25(5), 415–423.
30. So, H. *Wear* **1996**, 192, 78–84.
31. Archard, J. F.; Hirst, W. *Proc. Royal Soc. London A* **1956**, 236, 397–410.
32. Archard, J. F.; Hirst, W. *Proc. Royal Soc. London A* **1957**, 238, 515–528.
33. Quinn, T. F. J. *Tribol. Int.* **1983**, 16, 257–270.
34. Oh, H.-K.; Yeon, K.-H.; Kim, H. Y. *J. Mater. Process. Technol.* **1999**, 95, 10–16.
35. Stott, F. H.; Wood, G. C. *Tribol. Int.* **1978**, 11, 211–218.
36. Bowden, F. P.; Tabor, D. *Friction, An Introduction to Tribology*; Heinemann: London, 1973.
37. Eyre, T. S.; Maynard, D. *Wear* **1971**, 18, 301–310.
38. Burwell, J. T.; Strang, C. D. *J. Appl. Phys.* **1952**, 23, 18–28.
39. Ludema, K. Scuffing, run-in and the function of surface films, particularly oxides; Review Paper for Interdisciplinary Collaboration in Tribology Project, NASA-Lewis, 1981.
40. Tabor, D. Proceedings of the International Conference on Wear of Materials, St. Louis, Missouri in April 1977; ASME, 1978; pp 1–10.
41. Rabinowicz, E. C. *Friction and Wear of Materials*; Wiley: New York, 1965.

42. Blau, P. J. *Wear* **1981**, 72, 55–66.
43. Iwabuchi, A. *Wear* **1990**, 151, 301–311.
44. Iwabuchi, A.; Kubosawa, H.; Hori, K. *Wear* **1988**, 128, 123–137.
45. Iwabuchi, A.; Kubosawa, H.; Hori, K. *Wear* **1990**, 139, 319–333.
46. Leheup, E. R.; Pendlebury, R. E. *Wear* **1991**, 142, 351–372.
47. Colombie, C.; Berthier, Y.; Floquet, A.; Vincent, L. *Trans. ASME* **1984**, 106F, 194–201.
48. Hiratsukam, K.; Sasada, T.; Norose, S. *Wear* **1986**, 110, 251–261.
49. Rigney, D. A. *Wear* **2000**, 245, 1–9.
50. Stott, F. H.; Glascott, J.; Wood, G. C. *Proc. Royal Soc. London A* **1985**, 402, 167–186.
51. Sullivan, J. L.; Granville, N. W. *Tribol. Int.* **1984**, 17, 63–71.
52. Stott, F. H.; Mitchell, D. R. G. In *Surface Engineering*; Datta, P. K., Gray, J. S., Eds.; Vol. 1: Fundamentals of Coatings; Royal Society of Chemistry, 1993; pp 141–150.
53. Halliday, J. S.; Hirst, W. *Proc. Royal Soc. London A* **1956**, 236, 411–425.
54. Stott, F. H. *Tribol. Int.* **2002**, 35, 489–495.
55. Lin, D. S.; Stott, F. H.; Wood, G. C.; Wright, K. W.; Allen, J. H. *Wear* **1973**, 24, 261–278.
56. Lin, D. S.; Stott, F. H.; Wood, G. C. *Trans. ASLE* **1973**, 17 (4), 251–262.
57. Stott, F. H.; Lin, D. S.; Wood, G. C. Proceedings of the 5th European Congress on Corrosion, 1973; pp 452–455.
58. Stott, F. H.; Lin, D. S.; Wood, G. C. *Nat. Phys. Sci.* **1973**, 242, 75–77.
59. Stott, F. H.; Lin, D. S.; Wood, G. C.; Stevenson, C. W. *Wear* **1976**, 36, 147–174.
60. Stott, F. H.; Glascott, J.; Wood, G. C. *Wear* **1984**, 97, 155–178.
61. Stott, F. H. *Tribol. Int.* **1998**, 31, 61–71.
62. Quinn, T. F. J. *Wear* **1971**, 18, 413–419.
63. Quinn, T. F. J. *Wear* **1996**, 199, 169–180.
64. Quinn, T. F. J. *Wear* **1994**, 175, 199–208.
65. Iwabuchi, A.; Hori, K.; Kudo, H. Proceedings of the International Conference on Wear of Materials, New York 1987; pp 211–220.
66. Langgath, K.; Kluge, A.; Rysse, H. *Wear* **1992**, 155, 343–351.
67. Mølgaard, J. *Wear* **1976**, 40, 277–291.
68. Kuzucu, V.; Ceylan, M.; Çelik, H.; Aksoy, I. J. *Mater. Process. Technol.* **1997**, 69, 257–263.
69. Crook, P.; Li, C. C. *Wear of Materials*; ASME, 1983; pp 272–279, Publ. No. 110254.
70. Bartsch, M.; Wasilkowska, A.; Czyrska-Filemonowicz, A.; Messerschmidt, U. *Mater. Sci. Eng. A* **1999**, 272, 152–162.
71. Fujita, A.; Shinohara, M.; Kamada, M.; Yokota, H. *Isij Int.* **1998**, 38, 291–299.
72. Soda, N.; Sasada, T. *ASME Trans. J. Lubr. Technol.* **1978**, 100(4), 492–499.
73. Wu, W.-Z.; Xing, J.-D.; Su, J.-Y. *Wear* **1997**, 210, 299–303.
74. Suh, N. P.; Sin, H. C. *Wear* **1981**, 69, 91–114.
75. Rice, S. L.; Moslehy, F. A.; Zhang, J. In *Proceedings of the 18th Leeds-Lyon Symposium on Tribology*, 3–6 September 1991, Lyon, France; Dowson, D., Ed.; Elsevier, 1991; pp 463–467.
76. Hesmat, H. *Tribol. Trans.* **1991**, 34(3), 433–439.
77. Ludema, K. C. In *Proceedings of the 18th Leeds-Lyon Symposium on Tribology*, 3–6 September 1991, Lyon, France; Dowson, D., Ed.; Elsevier, 1991; pp 155–160.
78. Shaw, D. J. *Colloid and Surface Chemistry*, 4th ed.; Butterworth Heinemann, 1992.
79. Zhou, Y. H.; Harmelin, M.; Bigot, J. *Scr. Metall.* **1989**, 23, 1391–1396.
80. Datta, P. K.; Du, H. L.; Kuzmann, E.; Inman, I. A. Near surface structural changes of 'glaze' layers formed during high temperature sliding wear, to be published in *Wear*.
81. Bhansali, K. J. *Wear* **1980**, 160, 95–110.
82. Razavizadeh, K.; Eyre, T. S. *Wear* **1982**, 79, 325–333.
83. Garcia, I.; Ramil, A.; Celis, J. P. *Wear* **2003**, 254, 429–440.
84. Mølgaard, J.; Srivastava, V. K. *Tribol. Int.* **1983**, 16, 305–314.
85. Subramaniam, C. *Scr. Metall.* **1991**, 25, 1369–1374.
86. So, H. *Tribol. Int.* **1996**, 25(5), 415–423.
87. Buckley, D. H. *Cobalt* **1968**, 38, 20–28.
88. Persson, D. H. E. Licentiate of Philosophy Dissertation, Uppsala University, 2003.
89. Persson, D. H. E. Ph.D. Thesis, Uppsala University, 2003.
90. Stott, F. H.; Stevenson, C. W.; Wood, G. C. *Met. Technol.* **1977**, 4, 66–74.
91. Antony, K. C. J. *Met.* **1983**, 35(2), 52–60.
92. Brandes, E. A.; Brook, G. B. *Smithells Metals Reference Book*, Butterworth Heinemann, 1992.
93. Inman, I. A. High temperature 'like-on-like' sliding of Nimonic 80A under conditions of limited debris retention, Northumbria University, 2003, Unpublished work.
94. Vardavoulas, M. *Wear* **1994**, 173, 105–114.
95. Wood, P. D. Unpublished work.
96. Incoloy Alloy MA956; Special Metals Corporation, Publ. No. SMC-008.
97. Inman, I. A. The effects of pre-oxidation on the high temperature wear of  $\gamma$ -TiAl, Internal report, Northumbria University/University of Birmingham, 2005.
98. Li, C. X.; Xia, J.; Dong, H. *Wear* **2006**, 261, 693–701.
99. Takadom, J.; Houmid-Bennani, H.; Mairey, D. J. *Eur. Ceram. Soc.* **1998**, 18, 553–556.
100. Barnes, D. J.; Wilson, J. E.; Stott, F. H.; Wood, G. C. *Wear* **1977**, 45, 634–640.
101. Buckley, D. H. Influence of chemisorbed films on adhesion and friction of clean iron, NASA Center for Aerospace Information, NASA-TN-D-4775, 1968.
102. Barnes, D. J.; Stott, F. H.; Wood, G. C. *Wear* **1977**, 45, 199–209.
103. Barnes, D. J.; Wilson, J. E.; Stott, F. H.; Wood, G. C. *Wear* **1977**, 45, 97–111.
104. Feng, J.-M.; Uhlig, H. H. *J. Appl. Mech.* **1954**, 21(4), 395–400.
105. Wright, K. H. R. *Proc. Inst. Mech. Eng.* **1952–1953**, 1B (11), 556–574.
106. Waterhouse, R. B. *Fretting Corrosion*; Pergamon Press: New York, 1972.
107. Bill, R. C. *Wear of Materials*; ASME: New York, 1979; pp 356–370.
108. Hutchings, I. M. *Tribology: Friction and Wear of Engineering Materials*; Edward Arnold, 1992.
109. Smith, A. F. *Tribol. Int.* **1986**, 19, 65–71.
110. Du, H. L.; Datta, P. K.; Inman, I. A.; Kuzmann, E.; Suvegh, K.; Marek, T.; Vértés, A. *Tribol. Lett.* **2005**, 18(3), 393–402.
111. Chattopadhyay, B.; Wood, G. C. *Oxidat. Met.* **1970**, 2, 373–399.
112. Stott, F. H. *Tribol. Int.* **2002**, 35, 489–495.
113. Du, H. L.; Datta, P. K.; Inman, I.; Geurts, R.; Kübel, C. *Mater. Sci. Eng. A* **2003**, 357, 412–422.
114. Inman, I. A. Nano-scale studies of 'glaze' layers formed on Incoloy MA956 when slid against Incoloy 800HT at 750°C, Northumbria University, 2003, Unpublished work.



115. Du, H. L.; Aljarany, A.; Datta, P. K.; Burnell-Gray, J. S. *Corros. Sci.* **2005**, *47*, 1706–1723.
116. Aljarany, A. A. Ph.D. Thesis University of Northumbria, UK, 2002.
117. Gleiter, H. *Prog. Mater. Sci.* **1989**, *33*, 223–315.
118. Valiev, R. Z.; Islamgaliev, R. K.; Alexandrov, I. V. *Prog. Mater. Sci.* **2000**, *45*, 103–189.
119. Lowe, T. C.; Valiev, R. Z. *JOM* **2000**, *52*, 27–28.
120. Ghosh, A. K.; Huang, W. In *Investigations and Applications of Severe Plastic Deformation*; Lowe, T. C., Valiev, R. Z., Eds.; Kluwer Academic, 2000; pp 29–36.
121. Mishra, R. S.; McFadden, S. X.; Mukherjee, A. K. *Mater. Sci. Forum* **1999**, *304–306*, 31–38.
122. Mishra, R. S.; Mukherjee, A. K. In *Superplasticity and Superplastic Forming*; Ghosh, A. K., Bieler, T. R., Eds.; TMS Warrendale, 1998; pp 109–116.
123. Mishra, R. S.; McFadden, S. X.; Mukherjee, A. K. In *Investigations and Applications of Severe Plastic Deformation*; Lowe, T. C., Valiev, R. Z., Eds.; Kluwer Academic, 2000; pp 231–240.
124. Lim, S. C. *Tribol. Int.* **1998**, *31*(1–3), 87–97.
125. Lim, S. C. *Tribol. Int.* **2002**, *35*(11), 717–723.
126. Childs, T. H. C. *Tribol. Int.* **1980**, *13*, 285–293.
127. Kato, K.; Hokkirigawa, K. In *Proceedings of the Eurotrib'85*; Elsevier: Amsterdam, 1985; Vol. 4, Section 5.3, pp 1–5.
128. Riahi, A. R.; Alpas, A. T. *Wear* **2003**, *255*, 401–409.
129. Chen, H.; Alpas, A. T. *Wear* **2000**, *246*, 106–116.
130. Yang, S. H.; Kong, H.; Yoon, E.-S.; Kim, D. E. *Wear* **2003**, *255*, 883–892.
131. Grimaldis, D.; Eyre, T. S. *Wear* **2007**, *262*, 93–103.
132. Grimaldis, D.; Eyre, T. S. *Surf. Coat. Technol.* **2006**, *201–6*, 3260–3268.
133. Elleuch, K.; Elleuch, R.; Mnif, R.; Fridrici, V.; Kapsa, P. *Tribol. Int.* **2006**, *39–4*, 290–296.
134. Adachi, K.; Kato, K.; Chen, N. *Wear* **1997**, *203–204*, 291–301.

## 1.20 Gas Turbine Oxidation and Corrosion

**J. R. Nicholls and N. J. Simms**

Cranfield University, Cranfield, Bedfordshire MK43 0AL, UK

© 2010 Elsevier B.V. All rights reserved.

1.20.1	Introduction	518
1.20.2	Gas Turbine Operating Conditions	520
1.20.3	Gas Turbine Hot Gas Path Components and Materials	522
1.20.4	Oxidation and Thermal Cycling	524
1.20.4.1	Oxide Formation and Spallation	524
1.20.4.1.1	Oxidation processes	524
1.20.4.1.2	Modeling oxide growth and spallation	526
1.20.4.2	Thermal Barrier Coating Systems	527
1.20.4.2.1	Damage mechanisms	527
1.20.4.2.2	Modeling TBC spallation	529
1.20.5	Hot Corrosion	529
1.20.5.1	Hot Corrosion Mechanisms	530
1.20.5.2	Deposit Formation and Fuel Specifications	532
1.20.5.3	Damage Locations	535
1.20.5.4	Rates of Hot Corrosion Attack and Modeling Hot Corrosion Processes	535
1.20.6	Current/Future Issues	538
1.20.7	Summary	538
References		539

### Abbreviations

**APS** Air plasma spray  
**CVD** Chemical vapor deposition  
**EBPVD** Electron beam physical vapor deposition  
**EFC** European Federation of Corrosion  
**EPSRC** Engineering and Physical Sciences Research Council (United Kingdom)  
**EU** European Union  
**FOD** Foreign object damage  
**HP** High pressure  
**HRSG** Heat recovery steam generator  
**HVOF** High velocity oxy-fired  
**IGCC** Integrated gasification combined cycle  
**ISO** International Organization for Standardisation  
**LPPS** Low pressure plasma spray  
**NGV** Nozzle guide vane  
**NMAB** National Materials Advisory Board (USA)  
**NRC** National Research Council (USA)  
**PLPS** Photoluminescence piezospectroscopy  
**TBC** Thermal barrier coating  
**TGO** Thermally grown oxide

### Symbols

$y$  Reciprocal value of the C to H ratio in mol  
**A/F** Air to fuel mass flow ratio  
**MO** Metal oxide  
**S/F** Steam (water) to fuel mass flow ratio  
 $X_A$  Contaminant concentration in inlet air (ppm) by weight  
 $X_F$  Contaminant concentration in fuel (ppm) by weight  
 $X_S$  Contaminant concentration in injected steam or water (ppm) by weight  
 $X_T$  Total contamination in fuel equivalent (ppm) by weight  
 $\lambda$  Amount of excess air: actual mass flow divided by the air mass flow for stoichiometric combustion

### 1.20.1 Introduction

Gas turbines have been developed rapidly over the last 60 years, with applications currently ranging from aeroengines to marine propulsion to industrial mechanical power to utility scale electrical power generation.<sup>1,2</sup> Whatever be the intended application

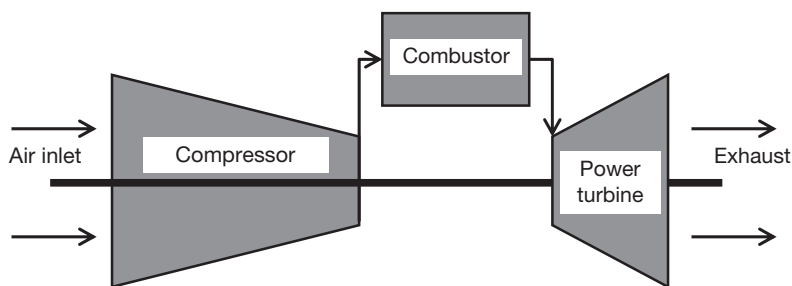


**Figure 1** Schematic diagram of simple cycle gas turbine showing fundamental components.

of the gas turbine, the basic features and principles of operation are common. **Figure 1** illustrates the fundamental parts of a gas turbine.

Details of the operation of gas turbines (which use the Brayton cycle) are available from numerous sources<sup>1,2</sup> but can be summarized as follows for the purposes of this chapter:

- air enters the gas turbine through the compressor;
- the air is compressed (and heated adiabatically) as it passes through a series of vane/rotor stages of the compressor;
- this air is passed into combustion chamber(s) where fuel is introduced and burnt raising the temperature of the gas stream;
- this hot, high pressure gas stream is then passed through the power turbine where its temperature and pressure are reduced as it passes through a series of vane/rotor stages which drive both the compressor and mechanical/electrical power conversion unit.

The Carnot efficiency of the gas turbine (as with any heat engine) is related to the difference between the maximum and minimum absolute temperatures of the working fluid (in which case, the inlet and outlet temperatures of the power turbine are divided by the inlet temperature). For a current gas turbine with an inlet temperature of 1400 °C (1673 K) and an exit temperature of 600 °C (873 K), this would give a Carnot efficiency of ~48%. Real cycle efficiencies are always lower than Carnot efficiencies, and in this case, for a simple cycle gas turbine, the efficiency would be closer to ~38–40%.<sup>3</sup> If the inlet temperature is to be raised to ~2100 °C or ~2373 K (just below stoichiometric combustion for maximum flame temperature<sup>1</sup> – a near impossible achievement) and the exit temperature remains at 600 °C (~873 K), then the maximum thermal efficiency will be ~63%, without dropping the exit temperature to extract energy from this lower grade heat source.

Thus, within these constraints, there are several routes to improve the efficiency of gas turbines:

- increasing the power turbine inlet temperature; this is the traditional route with limitations being set by the materials of construction for the hot gas path, but now also being set by cooling technologies and thermal barrier coating (TBC) performance;
- lower the exit temperature;
- using the heat in the exit gases in another way; for example, by passing the gases through a heat recovery steam generator (HRSG) to generate steam which is then passed through steam turbine to generate power (i.e., using a conventional Rankine cycle); the overall system is known as a combined cycle, and overall efficiencies for such systems have been reported to exceed 60%.

In addition, there are several other variations of gas turbine cycles that continue to be investigated:

- Indirect firing; where the compressed air is heated by an external heat source via heat exchangers before passing through the power turbine;
- Oxy-firing; where the fuel is burnt with oxygen to generate a combusted gas stream of mostly CO<sub>2</sub> and steam, from which the steam can be condensed to produce a CO<sub>2</sub> rich gas stream for recycling into the compressor or for storage (after further cleanup).

In terms of the sizes of gas turbines:

- the largest utility power turbines are rated at ~340 MWe in simple cycle mode and 530 MWe in combined cycle mode<sup>4</sup>;
- jet engines are rated in terms of their thrust, with the largest generating up to 100 000 lbs.<sup>1</sup>

From the foregoing, it is evident that materials in gas turbines need to be capable of operating at high bulk temperatures with high static and fluctuating stresses, while by also withstanding the surrounding environments. The environments generated within

the hot gas paths of gas turbines can be both physically and chemically aggressive, with particles producing erosion or deposition while gaseous and vapor-phase species may produce different forms of deposition, as well as oxidation and hot corrosion. The balance between these various degradation mechanisms is component and turbine dependent (as are the temperatures and stresses involved).

Thus, from a generic materials point of view, issues of concern for gas turbine hot gas path components include:

- creep,
- fatigue (thermal, low cycle, and high cycle),
- thermal cycling,
- oxidation,
- hot corrosion,
- erosion/foreign object damage (FOD),
- synergistic oxidation/corrosion/mechanical property interactions.

This chapter focuses on the oxidation and hot corrosion performance of materials in a range of different gas turbines and on how thermal cycling, erosion, and mechanical loading affect this performance.

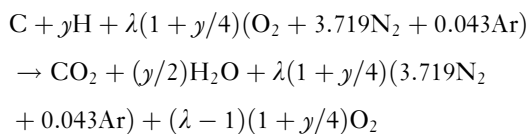
### 1.20.2 Gas Turbine Operating Conditions

Gas turbines have conventionally been fired using hydrocarbon fuels (such as diesels, jet fuels, and natural gases) burnt using air as the oxidant. More recent fuels have included syngases produced by coal or biomass gasification processes. In addition, use of oxygen as the oxidant is now being actively investigated for utility gas turbines as one potential route to enable CO<sub>2</sub> capture technologies to be introduced.

In all cases, the basic reaction of the fuels with the oxidant can be summarized as:



or



where  $y$  is the reciprocal value of the C to H ratio in mol,  $\lambda$  is the amount of excess air actual mass flow divided by the air mass flow for stoichiometric combustion.

Excess air is always used in the process to ensure that the fuel is completely consumed, to reduce the temperature of the combusted gas stream, and to increase the mass flow through the power turbine. This produces a high temperature combusted gas stream that is oxidizing. For some industrial gas turbines, water/steam is also added to increase the mass flow through the power turbine and/or reduce NO<sub>x</sub> emissions<sup>5–9</sup> (in some cases, steam-cooled components also exhaust into the main combusted gas flow).

However, unwanted products of combustion processes can be produced:

- CO from incomplete combustion of the fuel;
- NO<sub>x</sub> from thermal deposition of air or fuel-derived nitrogen species;
- SO<sub>x</sub> from oxidation of fuel borne impurities.

Various approaches have been developed to control these unwanted combustion products, such as improved combustor design, staged combustion, water injection, etc. Not all are appropriate (or feasible) for every gas turbine application, so their use varies. However, increasingly stringent environmental regulations are being developed and applied in various countries; especially to utility scale gas turbines.

Unfortunately, the combusted fuel gas stream also includes species derived from minor and trace elements in the fuels and oxidant streams: these elements commonly include sulfur, alkali metals, chlorine, magnesium, calcium, lead, vanadium, etc. However, when gasification processes are considered, even more elements can be involved, including cadmium and arsenic.<sup>10</sup> These various elements can combine to cause hot corrosion damage to the hot gas path of the gas turbine. The reactions involved, their effects, and methods to limit them (including fuel specifications) are described in detail in [Section 1.20.5](#).

During the last 60 years, there has been a continuous drive to increase the efficiencies of all types of gas turbine, but they still fall short of the Carnot theoretical optimum, which would be achieved at stoichiometric combustion combined with no mechanical losses. As a result, the firing temperatures and pressures of gas turbines have increased steadily ([Figure 2](#)). Current industrial gas turbines for power generation applications have firing temperatures of up to ~1430 °C and pressures of up to ~34 bar, while for jet engine applications, firing temperatures are up to ~1550 °C and pressures up to ~45 bar.<sup>1</sup>

[Figure 3](#) illustrates the temperature and pressure variations expected through a generic gas turbine. There are wide variations in the actual

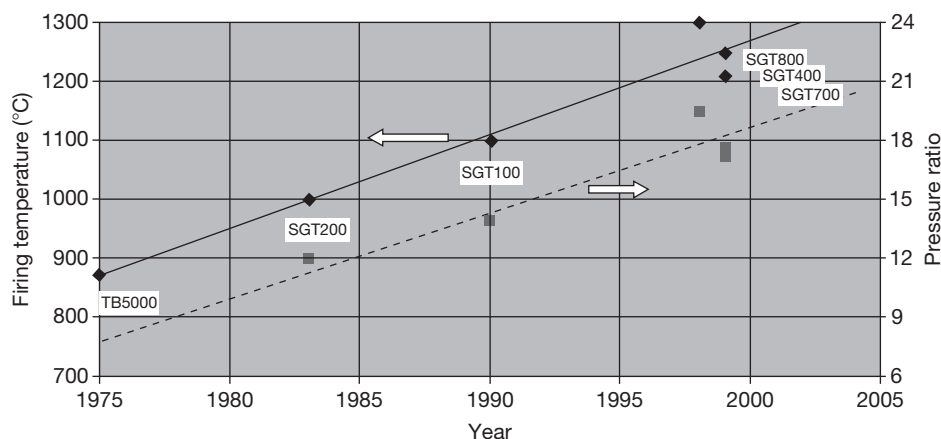


**Figure 2** Increase in turbine entry temperatures and pressure ratios over time for Siemens industrial gas turbines (4–50 MW). Reproduced from Hannis, J. M. In *Power Generation in an Era of Climate Change*; Proceedings of the 7th International Charles Parsons Turbine Conference; Strang, A. et al. Eds.; IOM Communications, 2007; pp 37–49.

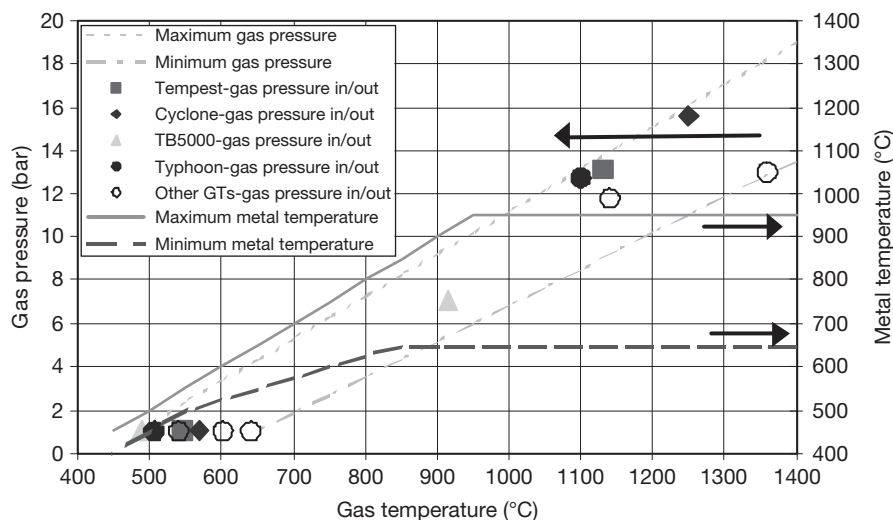


**Figure 3** Variation in temperature and pressure of the gas stream passing through typical industrial gas turbines. Reproduced from Simms, N. J.; Nicholls, J. R.; Oakey, J. E. In *Lifetime Modelling of High Temperature Corrosion Processes*; Schütze, M. et al. Eds.; Maney, 2001; pp 379–397, EFC No. 34.

temperatures and pressures that are produced by different gas turbines. This results from a number of factors such as:

- power requirement of the turbine,
- design approach,
- duty and cycle required,
- materials/lifting restrictions.

The gas turbines used for the different applications outlined in the introduction, while obviously related by their basic principles of operation, have different detailed requirements. For example (Figure 4), civil aeroengines go through a routine cycle on every flight

(with flight times of up to ~12 h), with peak operating temperatures for short periods during takeoff and landing. In contrast, industrial gas turbines designed for utility scale electrical power generation should be ramped slowly to their optimum operating temperature and then ideally remain there for hundreds if not thousands of hours. Other differences include weight limitations and the various contaminants that can enter the gas turbines during their operation. Thus the gas turbine usage defines the maximum gas temperature and pressure, duty cycle, operating time at temperature, number of shut-down cycles, and material operating environment.



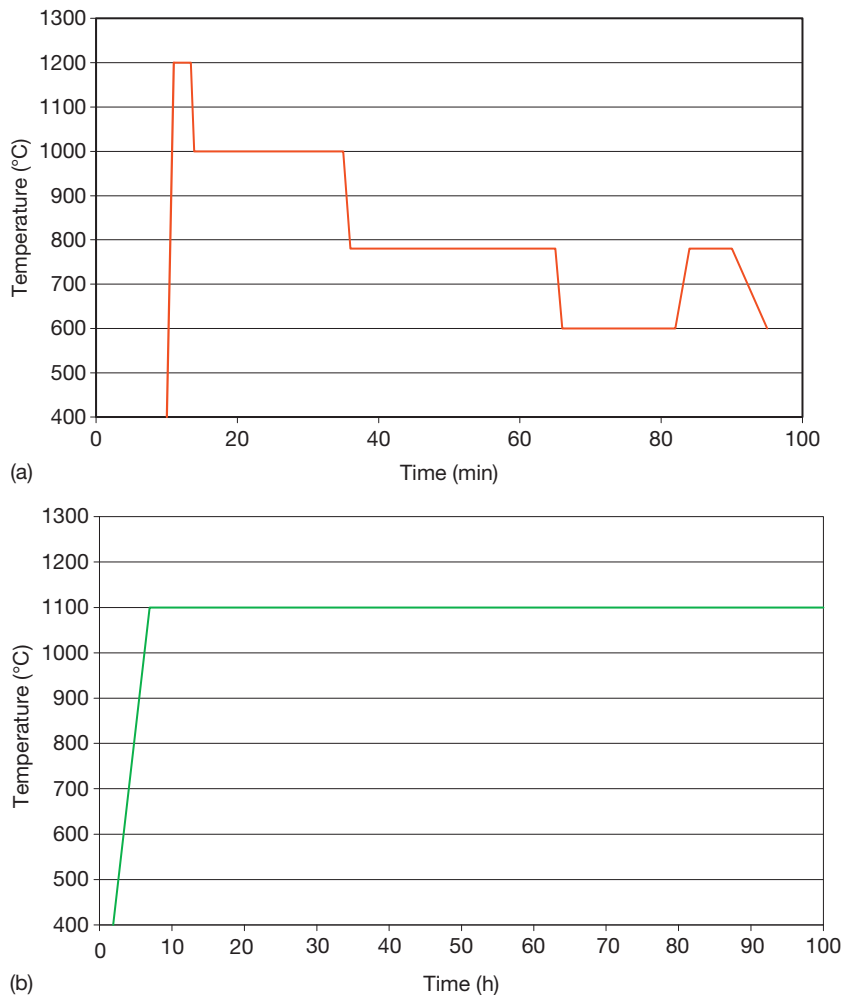


**Figure 4** Examples of gas temperature cycles for an aeroengine flight and an industrial gas turbine.<sup>12</sup> (a) Example of short duration aeroengine cycle (Note: 4000–7500 cycles between overhauls, depending on cycle duration). (b) Example of industrial gas turbine cycle (Note: desired component lives of >24 000 h).

### 1.20.3 Gas Turbine Hot Gas Path Components and Materials

As efficiencies of all types of gas turbines increase with firing temperature and pressure, there has always been a drive for the hot gas paths to use materials close to their mechanical and environmental operating limits.<sup>1,2</sup> However, viable component lives for the hot gas path of the gas turbines have only been achieved as a result of significant materials developments coupled with improved manufacturing methods and engine designs (specifically efficient cooling). Originally steel parts were used, but as the severity of operating conditions was increased, it was necessary to invent and develop whole series of nickel-based and cobalt-based superalloys with

improved mechanical properties and thermal stabilities. As these compositions have been progressively optimized, new materials have been developed with improved high temperature mechanical properties (Figure 5). Until the 1970s, such improvements in high temperature mechanical properties could be coupled to improved oxidation and hot corrosion resistance,<sup>2,14</sup> with alloys being designed to have sufficient chromium and aluminum contents to form self-protective oxide scales. However, more recent alloy developments, targeted at improved mechanical properties, could only be achieved to the detriment of oxidation and hot corrosion resistance of these alloys. Thus there is now a requirement for many hot gas path components to be coated to enable them to resist the surrounding environments and

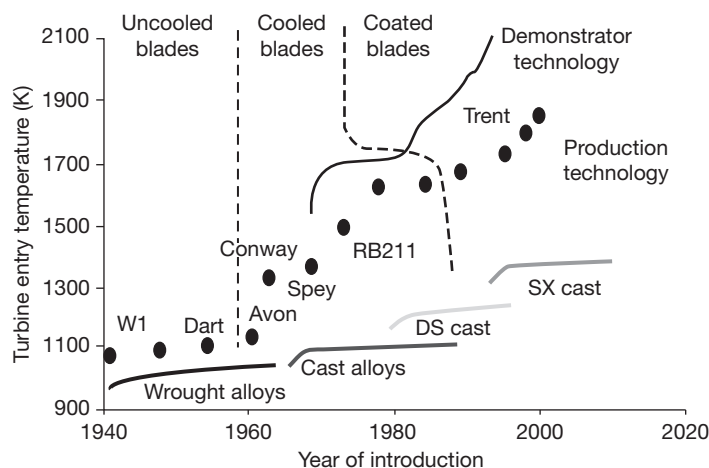


**Figure 5** Improvements in materials strength with time and new alloy development. Reproduced from Rickerby, D. S.; Hicks, M. A. In *Power Generation in an Era of Climate Change*, Proceedings of the 7th International Charles Parsons Turbine Conference; Strang, A. *et al.* Eds.; IOM Communications, 2007; pp 229–240.

to permit economically viable component lives. Higher temperature alloy mechanical performance, as well as associated engine capability, has also been enhanced through improvements in casting technologies. These have permitted a change in the microstructure of nickel-based superalloys from equiaxed to directionally solidified and single-crystal blade materials (eliminating the grain boundaries that partly dictate high temperature creep damage). Originally these casting technologies were developed for small aero-engine blades, but now larger industrial gas turbine blades/vanes can also be processed.<sup>3</sup>

The development of a range of increasingly sophisticated component cooling technologies (including air impingement, film cooling, etc. [Figure 6](#)) has enabled gas stream temperatures to be decoupled from metal temperatures along the gas turbine hot gas path. Most of the cooling systems rely on air diverted from selected locations in the air compressor, but there are some land-based gas turbines that use steam cooling. The use of such cooling technologies has enabled gas temperatures to be progressively increased, much further than would be expected from alloy developments.

The introduction of cooled components has allowed the adoption and development of TBCs as part of the turbine thermal management system. These low conductivity ceramic coatings protect the underlying metallic materials from the surrounding high temperature gas streams and allow a balance between component life, component operating temperature, and cooling air requirements to be addressed. The principal of TBCs is illustrated in [Figure 7](#). The use of advanced air cooling technologies coupled with

TBCs means that first stage blades/vanes can now be operated at gas temperatures in excess of the melting points of the alloys used for these components.<sup>3,4</sup>

Critical components within the hot gas path of gas turbines include:

- combustor can/tiles/transitions ducts,
- vanes and blades (both in multiple stages),
- seals,
- discs.

Examples of alloys used for these components are given in [Table 1](#).

A wide range of coatings have been developed and used for protection along the gas turbines hot gas path. The different routes for coating application that have developed are favored by different gas turbine manufacturers. Thus, the situation of using a ‘standard’ coating for protection against hot corrosion damage has not developed. Instead, there are several coatings from the different classes of coating materials available that are currently being used ([Table 2](#)):

- Overlay coatings:
  - typically Ni–Co–15–23% Cr–8–12% Al–0.1–0.9% Y,
  - applied by high velocity oxy-fuel (HVOF) or low pressure plasma spray (LPPS) coating processes,
  - some newer coatings also include Re, Hf, Ta, or Si in some combination.
- Diffusion coatings:
  - Aluminizing, chromizing, or chrome-aluminizing;

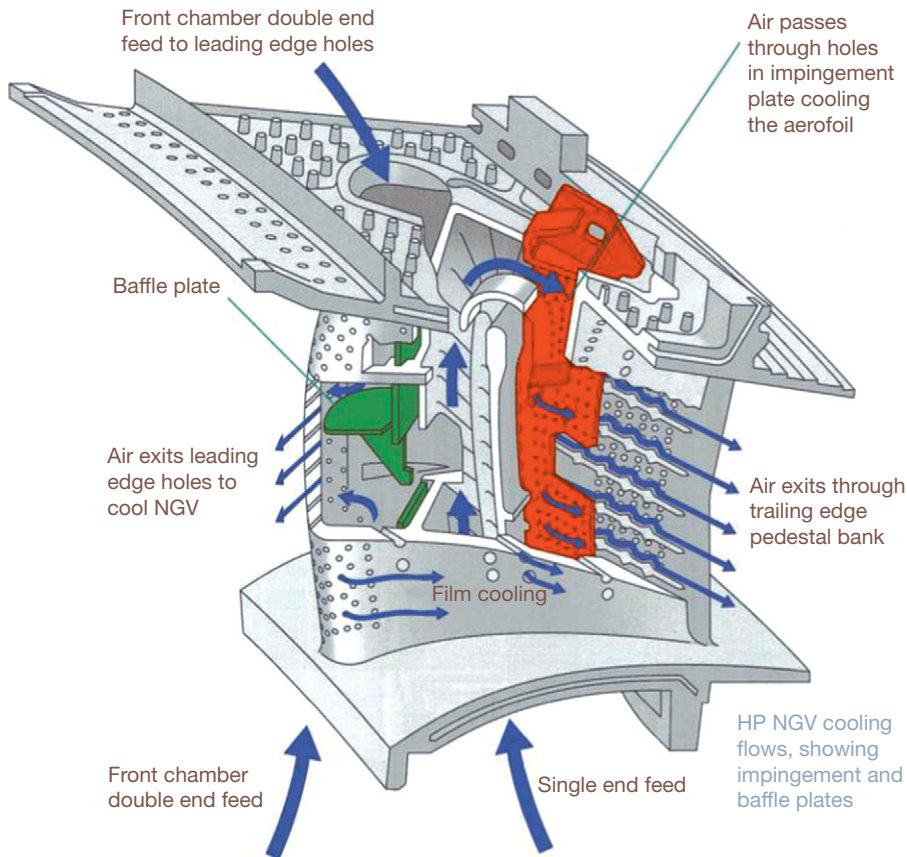


**Figure 6** Example of air cooling systems in advanced gas turbine aerofoil.<sup>1</sup> Courtesy of Rolls Royce.

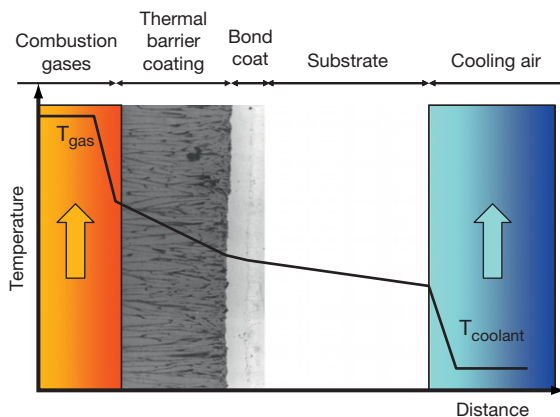


**Figure 7** Principal of operation of thermal barrier coatings (TBCs).

- Chemical vapor deposition (CVD) processes applied by in-pack, above pack or gaseous routes;
- Gaseous routes enable coating of internal cooling passages in advanced aero-foil designs;

- Platinum-aluminizing;
- Electroplate of platinum followed by CVD aluminizing process.
- Slurry coatings;
- Silicon-aluminizing.
- Coating performance varies with base alloy compositions, which have a notable effect in terms of hot corrosion resistance, with such coatings on lower Cr-based alloys performing significantly worse than on higher Cr substrates.

## 1.20.4 Oxidation and Thermal Cycling

### 1.20.4.1 Oxide Formation and Spallation

#### 1.20.4.1.1 Oxidation processes

Gas turbine materials will oxidize in the combustion gases produced in all gas turbine systems. The earlier superalloys were relatively rich in chromium and so formed slow growing protective  $\text{Cr}_2\text{O}_3$  scales at their temperatures of use. However, as component

**Table 1** Examples of materials used in gas turbine hot gas path components (in wt%)

	<i>Ni</i>	<i>Co</i>	<i>Fe</i>	<i>Cr</i>	<i>Al</i>	<i>Ti</i>	<i>Mo</i>	<i>W</i>	<i>Others</i>
CMSX-4	Bal	9.0		6.5	5	1	0.6		0.1 Hf
IN738LC	Bal	8.5		16	3.4	3.4	1.7	2.6	1.7 Ta, 0.9 Nb
GTD111	Bal	9.5		14	3	4.9	1.5	3.8	2.8 Ta
IN939	Bal	19		22.5	1.9	3.7		2.0	1.4 Ta, 1.0 Nb
IN6203	Bal	19		22	2.3	3.5		2.0	1.1 Ta, 0.8 Nb, 0.8 Hf
GTD222	Bal	14		22.5	1.2	2.3		2.0	1.0 Ta, 0.8 Nb
IN792	Bal	9.0		12.4	3.1	4.5	1.9	3.8	3.9 Ta
FSX-414	10	Bal	1	29				7.5	
MarM 247	Bal			8.3	5.5	1	0.7	10	1.5 Hf
Hastelloy X	Bal								
Haynes 230	Bal		<3	22	0.3		2	14	
RR1000	Bal	18.5		15	3	3.6	5		2 Ta, 0.5 Hf
IN718	Bal		18.5	19	0.5	0.9	3		5.1 Nb
Astroloy	Bal	15		15	4.4	3.5	5.2		
Waspalloy	Bal	13.5	<2	19.5	1.4	3	4.3		
U500	Bal	19	4	19	3	3	4		
U720Li	Bal	15		16	2.5	5	3	1.2	
Haynes 214	Bal		3	16	4.5				0.1 Zr, 0.01 Y
PM2000			Bal	20	5.5	0.5			0.5 Y as Y <sub>2</sub> O <sub>3</sub>
Aluchrom YHf	0.2		Bal	20	5.8				0.5 Y, 0.05 Hf, 0.05 Zr

**Table 2** Examples of gas turbine coating compositions (wt%)

<i>Overlays</i>	<i>Ni</i>	<i>Co</i>	<i>Cr</i>	<i>Al</i>	<i>Y</i>	<i>Other</i>
Amdry 963	Bal	–	25	6	0.4	
Amdry 995	32	Bal	21	8	0.5	
Amdry 997	Bal	23	20	8.5	0.6	4 Ta
LCO22	32	Bal	21	8	0.5	
CT102	32	Bal	21	8	0.6	
CT103	Bal	22	17	12	0.6	
CT104	Bal	23	22	11	0.4	4 Hf, 0.4 Si
GT29	–	Bal.	29.0	6.0	0.3	
SV20	Bal	–	25	5.5	0.7	1 Ta, 2.7 Si
SV30	Bal.	–	25.0	5.0	0.7	0.1 Ta, 0.35 Ti
SC2231	30	Bal	28	8	0.5	0.5 Si
SC2453	Bal	10	28	12	0.6	3 Re
<i>Diffusion</i>	<i>Description</i>					
Aluminized	Applied in-pack, above pack or by gas phase CVD					
Chromized	Applied in-pack, above pack or by gas phase CVD					
RT22	Variations on platinum electro-plate followed by aluminizing					
CN91						
MDC150						
SermaLoy 1515	Slurry application					

temperatures rose, so did the rate of Cr<sub>2</sub>O<sub>3</sub> formation, and other oxidation mechanisms, such as formation of volatile oxide and oxyhydroxide species in the fast flowing combustion gases, also became significant.<sup>2,15</sup>

The development of superalloys for high metal temperatures resulted in materials with progressively less chromium and more aluminum. This resulted in alloys that formed slower growing Al<sub>2</sub>O<sub>3</sub> scales at high temperatures that were not volatile in the surrounding gas streams.<sup>2</sup>

At temperatures higher than ~950–1000 °C, α-Al<sub>2</sub>O<sub>3</sub> scales are the preferred scale to be formed. Considerable research targeted at a range of base alloys and different applications has been carried out on the growth of these scales over the year.<sup>2,16</sup> However, at lower metal temperatures, more complex oxides may form on the surfaces of superalloys: various transition aluminas (e.g., θ- or γ-Al<sub>2</sub>O<sub>3</sub>) as well as mixed (Cr, Al)<sub>2</sub>O<sub>3</sub> oxides, spinel oxides of Cr and/or Al with base metal oxides, and oxides of other minor alloying elements that are present in these complex superalloy materials may form.

In general, the combination of metal temperature and a ‘clean’ oxidizing environment (i.e., a combustion gas stream with trace metal contaminants at too low a level to cause any hot corrosion) will result in the formation of slow-growing stable oxide scales for the appropriate blade and vane materials, plus any coating system, in the gas turbine hot gas path (but it should be noted that such materials will vary between gas turbine manufacturers, and with the intended use of gas turbine).

There will, therefore, be a difference between gas turbines: the higher peak temperatures of

aeroengines will encourage  $\alpha$ -Al<sub>2</sub>O<sub>3</sub> scale formation, compared to industrial machines operating close to oxide transition temperature. Another important difference in the exposure conditions will be number and severity of thermal cycles. Aeroengine temperatures are cycled much more frequently and rapidly than industrial gas turbines. As a result, the slow-growing scales may spall from the component surfaces and a new oxide will form during the next period of operation: whether this is the same oxide or not will depend on the composition of the underlying alloy/coating.

The coating of superalloys with most overlay and diffusion coatings (Table 2) results in a surface relatively rich in aluminum, which assists in the formation, retention, and reformation of a slow-growing Al<sub>2</sub>O<sub>3</sub>-based (or at least alumina rich) oxide scale. Overlay coatings traditionally include 'reactive elements' such as Y or Hf that are well known to enhance the adhesion of alumina scales (see Chapter 1.23, **High Temperature Corrosion of Chromia-forming Iron, Nickel and Cobalt-base Alloys**). Scales can develop through transient oxides (i.e., various Al<sub>2</sub>O<sub>3</sub>) and other oxides (e.g., NiO, spinels) and multiple oxide layer developments (e.g., undergrowths of Cr<sub>2</sub>O<sub>3</sub> and  $\alpha$ -Al<sub>2</sub>O<sub>3</sub>) before reaching a slow growing stable structure (e.g., Figure 8). This development depends on the exposure temperature and coating-base alloy composition.

Diffusion coatings have also progressively developed to assist in the growth and retention of alumina scales, in this case, using metals such as Pt and Pd. These coatings will also develop scales through the formation of transient oxides (i.e., various Al<sub>2</sub>O<sub>3</sub>) and other oxides (e.g., NiO) and multiple oxide layer developments (i.e., undergrowth of  $\alpha$ -Al<sub>2</sub>O<sub>3</sub>) before reaching a slow growing stable structure. As for overlay coatings, this development depends on the exposure temperature and coating-base alloy composition.

At high temperatures, coatings will degrade by interdiffusion with the substrate as well as surface oxidation; this can be particularly important for aluminum which tends to diffuse inwards as well as being consumed due to oxidation. The development of diffusion barriers to reduce or prevent such inwards diffusion is an active research topic.

#### 1.20.4.1.2 Modeling oxide growth and spallation

Oxide growth and spallation models have been developed for alumina type oxide scales by several research groups around the world, most notably: NASA,<sup>18</sup> Jülich-Cranfield<sup>19,20</sup> and Toulouse.<sup>21</sup> These models are essentially all empirical, but are based on the mathematical understanding of oxidation processes:

- The NASA cyclic oxidation and spallation (COSP) model is based on rate constants determined from mass change data and uses these combined with idealized parameters that describe the spallation process to predict the damage to a metal in terms of mass change or metal loss for different time periods, cycle durations, etc.
- The Toulouse  $p$ - $k_p$  model uses a spalling probability ( $p$ ) and parabolic rate constant ( $k_p$ ) to predict the mass change of materials as a function of time and temperature.
- The Jülich-Cranfield model uses the concept of an aluminum reservoir to calculate the metal loss due to alumina growth and spallation. Spallation processes are assumed to commence after some critical mass gain (or oxide thickness) which is influenced by thermal cycling.

Continuous oxide growth and coating interdiffusion models are being developed by several research groups, most notably NASA,<sup>22</sup> DTU,<sup>23</sup> and Toulouse.<sup>24,25</sup> These use various finite difference or finite element methods, in some cases combined

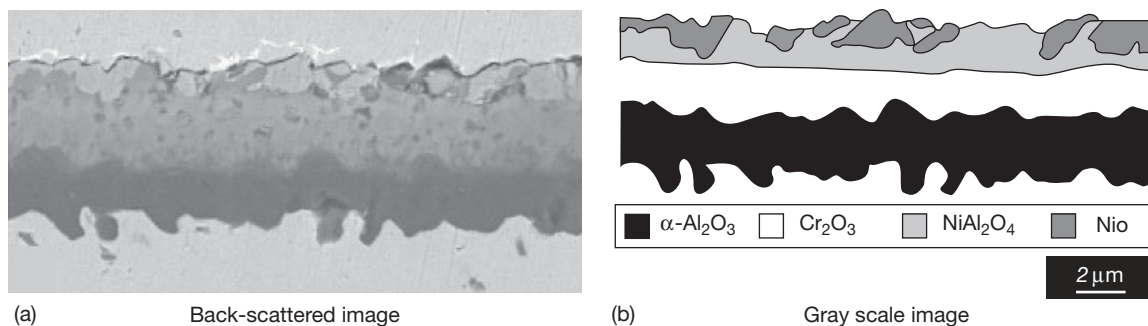


**Figure 8** Scale grown on Ni-27Cr-8Al at 1353 K.<sup>17</sup> (a) Back-scattered image and (b) grey scale image.



with thermodynamic phase predictions, to calculate elemental profiles throughout the oxide–coating–substrate system as a function of time and temperature, again using the ideal  $\alpha$ -Al<sub>2</sub>O<sub>3</sub> scale formation.

### 1.20.4.2 Thermal Barrier Coating Systems

#### 1.20.4.2.1 Damage mechanisms

Two types of TBCs are now frequently found in gas turbines. These are generally classified by their application routes: air plasma sprayed (APS) and electron beam physical vapor deposition (EB PVD) (Figure 9). However, currently their compositions are generally the same:  $\sim 7$  wt% Y<sub>2</sub>O<sub>3</sub>–balance ZrO<sub>2</sub>. New thermal barrier ceramics are also being researched,<sup>27</sup> but a review of these is beyond the scope of this chapter.

Both types of TBCs are applied to gas turbine components after they have had a bond coating applied. The purpose of this bond coating is to encourage and maintain the formation of a stable  $\alpha$ -Al<sub>2</sub>O<sub>3</sub> scale at the interface between metal and ceramic,

as well as to provide a transition zone between the metal and the ceramic layer. Thus bond coat materials are often classically established environmental protection coatings, for example, a platinum aluminide diffusion coating system or an MCrAlY overlay coating. However, bond coatings for APS and EB PVD TBCs require different initial characteristics to enable the coatings to be successfully applied. APS TBCs generally need to be applied to deliberately roughened bond coat surfaces to provide mechanical keying, whereas EBPVD TBCs are usually applied to smoother, polished, or media finished bond coat surfaces.

The spallation of TBCs after exposure at high temperature is now well recognized as the life-limiting factor dictating TBC performance and has been frequently reported.<sup>28</sup> However, the causes of this spallation remain controversial (e.g., Figure 10). Features reported include<sup>28</sup>:

- spallation is usually observed on samples/components after the growth of  $\sim 5$ – $10$   $\mu\text{m}$  of oxide scale;
- cracks grow roughly parallel to the bond coat/thermally grown oxide/TBC interfaces, before large areas of TBC spall;
- cracks may grow:
  - in TBC near TGO interface (between bond-coat peaks, or not),
  - within the TGO,
  - along bond coat/TGO interface, depending on the system;
- bondcoat/TGO/interfaces may roughen with exposure (for EBPVD TBCs on Pt–Al bond coats);
- mixed oxides (Cr,Al)<sub>2</sub>O<sub>3</sub> or spinels (e.g., (Ni,Co)Cr<sub>2</sub>O<sub>4</sub>) may form above or below the stable alumina scales in areas close to crack growth.

Both academic and industrial research is actively continuing in this area, but has moved from characterization towards methods of finding damaged TBCs nondestructively and also developing predictive models for TBC spallation (see below). But it is worth noting that there are many significant differences between the preparation and processes used for applying bond coatings, initiating the growth of thermally grown oxide and applying the TBC layer that are used by different coating companies, all of which may interact and therefore influence susceptibility to TBC spallation.

Particular interest has been taken in finding ways of detecting the cracks in/close to TGO using non-destructive inspection methods, before the cracks have a chance to coalesce and cause TBC spallation

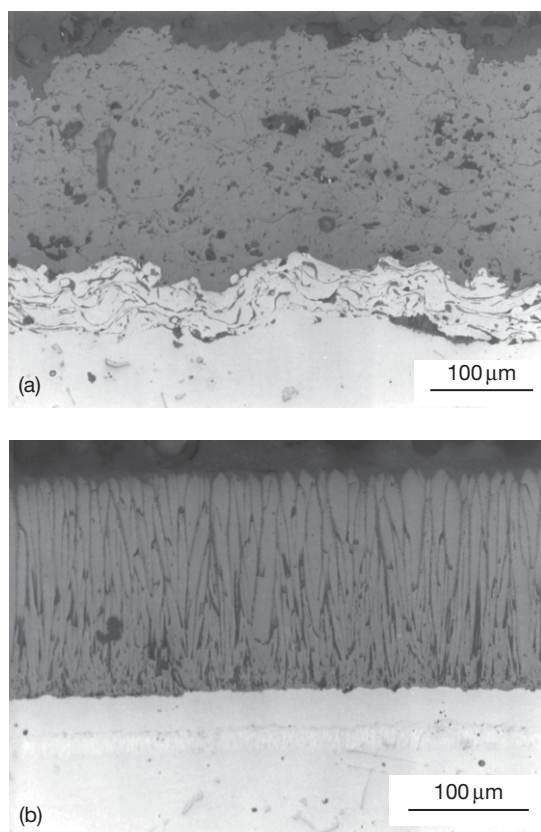


**Figure 9** Two main types of TBCs.<sup>26</sup> (a) Air plasma sprayed thermal barrier coating (APS TBC) and (b) electron beam physical vapor deposition thermal barrier coating (EB PVD TBC).

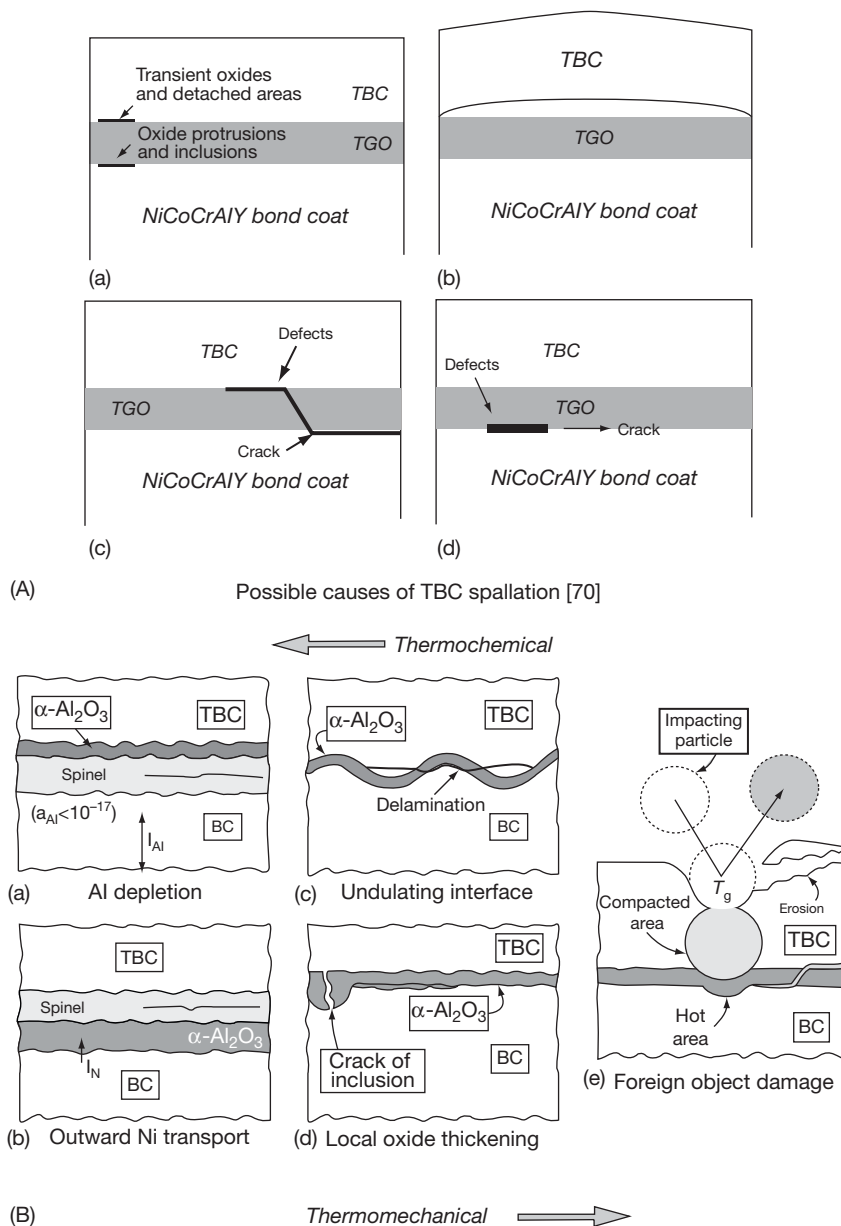


**Figure 10** Schematic diagrams of alternative views of the causes of TBC spallation. (A) Possible causes of TBC spallation<sup>29</sup> and (B) possible causes of TBC spallation. Reproduced from Simms, N. J.; Kilgallon, P. J.; Roach, C.; Oakey, J. E. In *Microscopy of Oxidation*, Proceedings of 5th International Conference, Newcomb, S. and Tatlock, G. Eds.; Science Reviews, 2003; pp 273–280.

to occur. Promising nondestructive techniques currently include<sup>30</sup>:

- images produced by differential heat conduction (using lasers or other heat sources) – essentially relying on cracked regions of the coating system not allowing heat to pass through as readily as fully adherent coated regions;
- photoluminescence piezospectroscopy (PLPS) – this uses lasers to excite the  $\text{Cr}^{3+}$  contaminant ions that are always present in  $\text{Al}_2\text{O}_3$  oxide scales in these material systems and detects the shift in the characteristic peaks produced: the greater the shift the more stressed the TGO. This technique can be used to examine a coated TBC component and to detect variations in stresses in the TGO (cracked areas

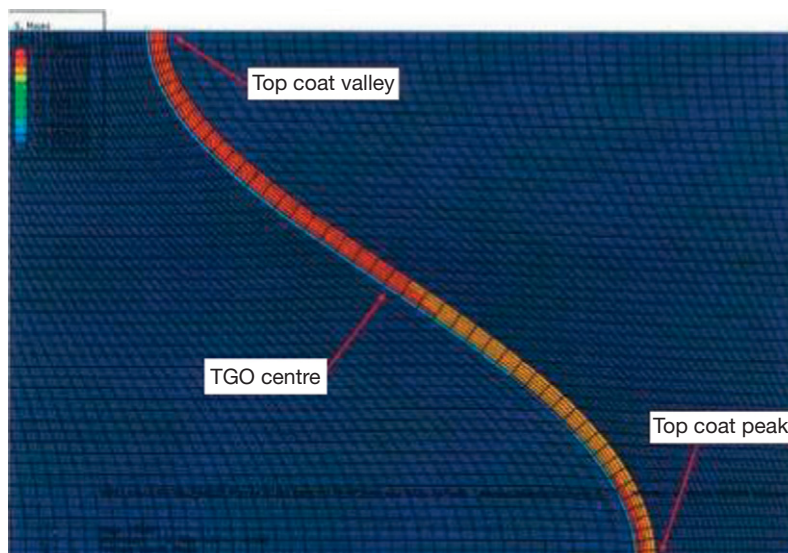


**Figure 11** Finite element approach to TBC spallation modeling as a function of TGO growth. Reproduced from Hermosilla, U. PhD Thesis, Nottingham University 2008; UK EPSRC Supergen Plant Life Extension Consortium.

showing up as low stressed TGO). This technique works better on EB-PVD TBCs than APS TBCs due to the columnar microstructure of the former that allows light signals to pass through more easily.

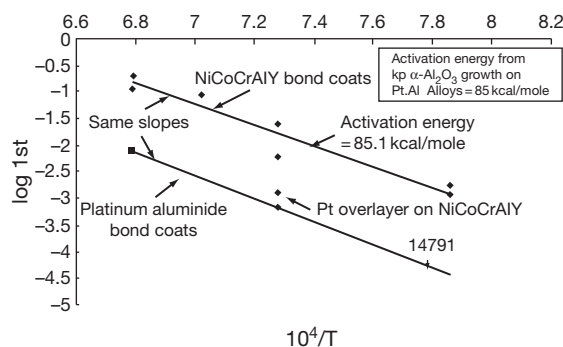
#### 1.20.4.2.2 Modeling TBC spallation

Several industrial and academic research groups are working on the development of models to predict spallation of TBCs.<sup>31–37</sup> There are essentially two distinct approaches:

- Finite element modeling of a selected area of an idealized TBC system to predict development of stresses around TGO as it grows (e.g., [Figure 11](#)); these models are being developed by several EU and US research groups.<sup>32–34,36,37</sup>
- Phenomenological approaches based on observation of the performance of many TBC-coated samples under a range of conditions to identify the most important variables and their effects as a function of exposure time and temperature (e.g., [Figure 12](#)); these types of models are being developed particularly by Dechema and Cranfield in Europe<sup>31,35</sup> and Pittsburg in USA.<sup>29</sup>

### 1.20.5 Hot Corrosion

Although oxidation of gas turbine hot gas path materials is rarely life-limiting, unless localized overheating has occurred (e.g., following TBC spallation), the hot corrosion of these materials can occur much

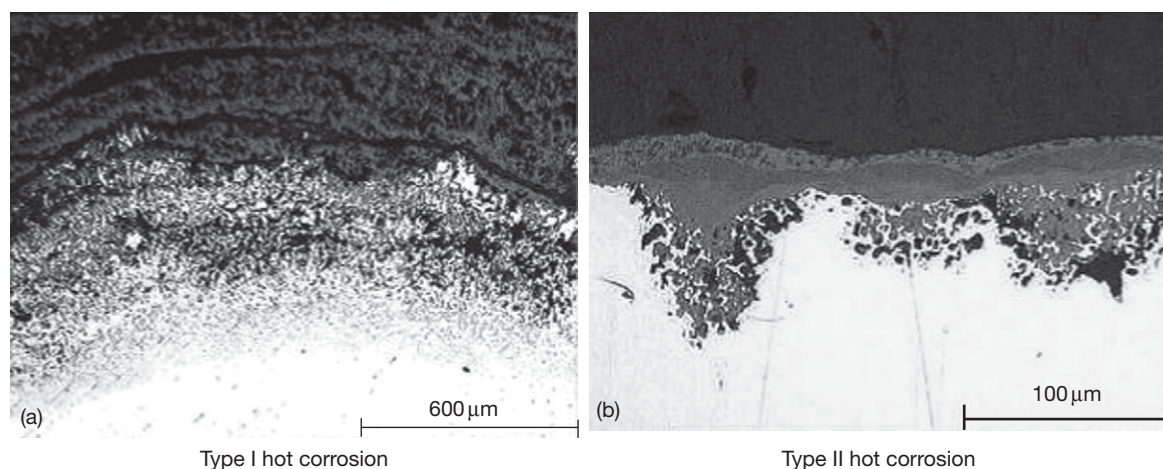


**Figure 12** Observations of TBC spallation that form a basis for analytical approaches to life modeling. Reproduced from Yanar, N. M.; Kim, G.; Hamano, S.; Petit, F. S.; Meier, G. H. In *Microscopy of Oxidation*, Proceedings of 5th International Conference, Newcomb, S. and Tatlock, G., Eds.; Science Reviews, 2003; pp 249–260.

more rapidly and can be life limiting for all components. As a result, hot corrosion of gas turbine hot gas path materials has been the subject of active research and industrial experience for more than 50 years.<sup>2</sup> The potential problems that may be encountered in gas turbines fired on conventional natural gas, diesel, and jet fuels have been well characterized,<sup>2,15,38–45</sup> and fuel standards derived ([Table 3](#)). In recent years, the ranges of fuels that need to be considered have widened in response to changes in availability and price. In addition, investigations have also been carried out into the potential effects on gas turbines from using fuel gases derived from solid fuels (e.g., gasification of coal and/or biomass).<sup>47</sup>

**Table 3** Fuel specifications<sup>46</sup>

Fuel type	True distillates		Ash-forming fuels	
	Kerosene	No.2 Distillate	Blended residuals and crude	Heavy residuals
Sulfur (%)	0.01/0.1	0.1/0.8	0.2/3	0.5/4
Ash (as delivered) (ppm)	1/5	2/50	25/200	100/1000
Ash (inhibited) (ppm)	—	—	25/250	100/7000
<i>Trace metal contaminants (untreated) (ppm)</i>				
Sodium + potassium	0/0.5	0/1	1/100	1/350
Vanadium	0/0.1	0/0.1	0.1/80	5/400
Lead	0/0.5	0/1	0/1	0/25
Calcium	0/1	0/2	0/10	0/50

**Figure 13** Typical appearance of type I and type II hot corrosion during their propagation stages.<sup>50</sup> (a) Type I hot corrosion and (b) type II hot corrosion.

These studies have successfully identified the causes of hot corrosion and some methods to limit the damage caused. A considerable amount of data on hot corrosion damage for a wide range of materials, under different exposure conditions, has been generated during the course of research projects and industrial usage.<sup>2,42</sup> This dataset has permitted, experimentally determined, safe operating conditions to be produced. However, the development of quantitative predictive models for hot corrosion damage to materials of current interest in gas turbines is an on-going activity,<sup>48,49</sup> with some embryonic models produced for these complex corrosion phenomena.

#### 1.20.5.1 Hot Corrosion Mechanisms

Hot corrosion of materials in a power turbine occurs when a liquid deposit forms on the surface of a component. After a period of incubation as the deposit forms on the surface and reacts with the initially protective oxide, hot corrosion reactions move into their more rapid propagation stages. There are

two widely recognized forms of hot corrosion, distinguished by their propagation modes in gas turbines (Figure 13)<sup>2,15,38–45</sup>:

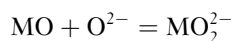
- Type I hot corrosion has traditionally been observed in a temperature band between the melting point of the surface deposit and vapor deposition dew point for the deposit (above this dew point deposit is unstable and will evaporate). An example of this could be the formation of sodium sulfate deposits. This form of corrosion damage is characterized by the appearance of internal sulfide phases in a zone of selective alloy depletion beneath a fairly smooth scale–metal interface. The typical temperature ranges quoted for this type of attack are typically 750–900 °C. This form of attack has been called high temperature hot corrosion.
- Type II hot corrosion occurs at a lower range of temperatures (typically quoted as 600–750 °C). This form of attack relies on the formation of a complex mixed metal sulfate deposit: an example of this could be the formation of a mixed nickel



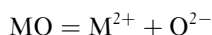
sulfate–sodium sulfate deposit. Such deposits are not very stable and require the presence of significant levels of  $\text{SO}_3$  to stabilize them (hence the term ‘gas phase induced acidic fluxing’). The corrosion occurs over the stability range of the liquid deposit from its melting point to its dissociation temperature. The attack is characterized by the formation of pitted or uneven surfaces with layers of corrosion products/deposits on the surface and no subsurface depletion zones or internal sulfide formations (although a layer of sulfides may be observed at the metal–scale interface). This form of attack has been called low temperature hot corrosion.

The mechanisms of hot corrosion are generally believed to be a result of the interaction of the surface oxide scales at first and then of the underlying alloys with molten surface deposits.<sup>2,15,38,39,42</sup> These are commonly described as fluxing mechanisms. Both acidic and basic fluxing reactions are possible depending on the deposit composition and the composition of oxide/underlying coating/alloy.

In basic fluxing, oxide ions are produced in a deposit of  $\text{Na}_2\text{SO}_4$  by removal of oxygen and sulfur from the deposit by reaction with underlying coating/alloy. Then, the oxide scales (e.g.,  $\text{MO}$ ) that form can react with the oxide ions via reactions such as<sup>2,15,38</sup>:



In acidic fluxing, the oxide scale dissolves to donate oxide ions to the deposit melt<sup>2,15,38</sup>:



Acidic conditions can be developed in a molten deposit by at least two different processes, leading to the terminology gas phase acidic fluxing and alloy-induced acidic fluxing.

As a result of these different possible hot corrosion mechanisms, the solubility of commonly formed oxides in molten deposits by acidic and basic reactions has been the subject of several studies (e.g., **Figure 14**).

In practice, the temperature ranges of type I and type II hot corrosion are affected by the composition of deposits formed. For example, the presence of potassium in a deposit can significantly lower the melting point of the deposit and lower the temperature range for type I when compared to sodium sulfate alone (**Figure 15**). Similarly,  $\text{NaCl}$  may also lower deposit melting points<sup>51</sup> and also assist the breakdown of any protective oxide scales.

Other elements can also affect the melting ranges of these deposits: these may be contaminants from

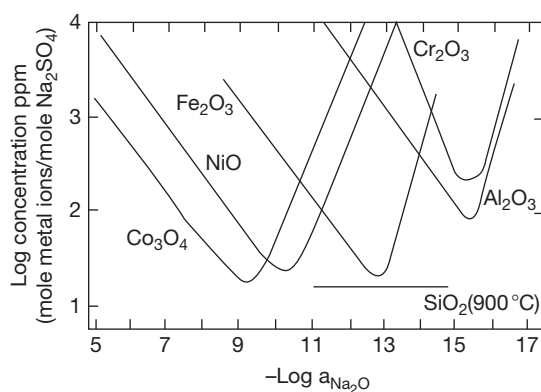


**Figure 14** Oxide solubility in molten  $\text{Na}_2\text{SO}_4$  at 927 °C. Reproduced from Sims, C. T.; Stoloff, N. S.; Hagel, W. C. Eds. *Superalloys*; Wiley: New York, USA, 1987; Vol. II.

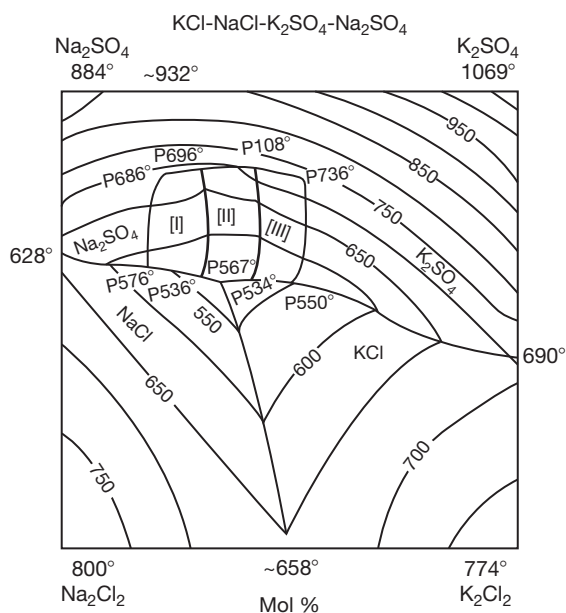


**Figure 15**  $\text{Na}_2\text{SO}_4$ – $\text{K}_2\text{SO}_4$ – $\text{NaCl}$ – $\text{KCl}$  phase diagram. Reproduced from *Phase Diagrams for Ceramists*; American Ceramic Society, 1964.

combustion gas stream (e.g., calcium, magnesium, lead, or chlorine) or elements from the components being corroded (e.g., molybdenum or tungsten). Some of these elements may also participate in the hot corrosion reactions between the deposit and the component materials.

Along with the distinctive propagation morphologies of types I and II hot corrosion, it is also possible for an intermediate form of attack to develop which has some of the features of both. This has been described as mixed mode attack or a transition-type



attack. It is characterized by the formation of layered corrosion products/deposit on the component surface and intermittent areas of internal sulfides/depletion zones and an uneven scale/metal interface. This form of attack has been observed at temperatures between traditional type I and type II corrosion regimes.

An alternative mode of hot corrosion attack is seen in turbines in which the combustion gas stream contains vanadium (usually a contaminant that arrives via a fuel oil). This form of hot corrosion also depends on the formation of liquid deposits on the surfaces of components, but these low-melting-point deposits do not require the presence of high levels of  $\text{SO}_3$ . In the presence of sodium-containing deposits, mixed deposits, for example, sodium vanadyl vanadate may form with melting points as low as  $535^\circ\text{C}$ .<sup>51</sup> These sodium vanadate compounds can flux the protective oxide from component surfaces and then continue with a fluxing reaction with the metallic substrates below. It has been found that this form of hot corrosion can be suppressed by deliberately adding dopants (such as magnesium or chromium compounds) to the fuel; these are designed to react with the vanadium species as they pass through the combustion process and deposit onto component surfaces as solid deposits with high melting points that remain stable and unreactive.

### 1.20.5.2 Deposit Formation and Fuel Specifications

For hot corrosion to occur, a liquid or partially molten deposit must be created on the surface of components. Such deposits can be formed by a number of different mechanisms,<sup>52,53</sup> but all require the combusted gas streams passing through the gas turbine hot gas path to contain both trace metal species (such as alkali metals) and reactive gas species (such as  $\text{SO}_2/\text{SO}_3$ ). The source of the contaminants may be either the fuel or the oxidant (usually air) or component coolant (usually air, but sometimes steam in large land based gas turbines) or a mixture of all three. For example:

- Sea salt contains a mixture of metal chlorides and lower levels of sulfates: these contaminants may enter a turbine through its air inlet, pass through the compressor and the combustor before entering the power turbine. The salts may build up as deposits on the compressor vanes/blades before shedding and passing further into the turbine as particles, or may pass through as vapor or aerosols.
- Gas turbine fuels usually contain sulfur compounds together with a number of trace metal species; in the combustor, these contaminants can join those exiting in the compressor and react as they pass through the combustor and power turbine.
- Salts entering the compressor can be diverted from the main air flow into smaller flows that are used to cool components in the power turbine; these salts do not get the chance to react with the fuel derived contaminants as they pass through the combustor, so different compositions of deposits can form from this contaminant routing.

For gas turbines that operate under steady conditions (i.e., some larger land-based gas turbines), it is possible to use knowledge of these conditions to calculate the total contaminants entering the system (whether from fuel or oxidant or coolant) giving rise to an equivalent fuel contaminant level<sup>49,54,55</sup>:

$$X_T = (A/F)X_A + (S/F)X_S + X_F$$

where  $X_T$  is the total contamination in fuel equivalent (ppm) by weight;  $A/F$  is the air to fuel mass flow ratio;  $S/F$  is the steam (water) to fuel mass flow ratio;  $X_A$  is the contaminant concentration in inlet air (ppm) by weight;  $X_S$  is the contaminant concentration in injected steam or water (ppm) by weight;  $X_F$  is the contaminant concentration in fuel (ppm) by weight.

This approach provides a method of assessing potential corrosiveness of gas streams within the gas turbine and is one route to setting specifications for safe operation of such turbines.

It is also possible to consider how the various contaminant species that enter the power turbine can deposit out onto components. There are several well-known deposition processes (and associated models<sup>52,53,56–62</sup>) that can occur within a gas turbine hot gas path (illustrated schematically in **Figure 16** for an aerofoil):

- Direct inertial impact ion; larger particles ( $>5\ \mu\text{m}$ ) from the gas stream impact on components instead of following the gas flows around them; depending on their properties and the surface condition of the components, these particles may stick to the component surface, bounce off (or partially stick).
- Eddy diffusion; smaller particles may become entrained in the turbulent eddies that can form in certain locations in the gas paths (e.g., towards the trailing edge of aerofoil suction surfaces, or around blade platforms, disc edges, seals, etc.); these particles can then impact on component surfaces, and again depending on their properties and the surface

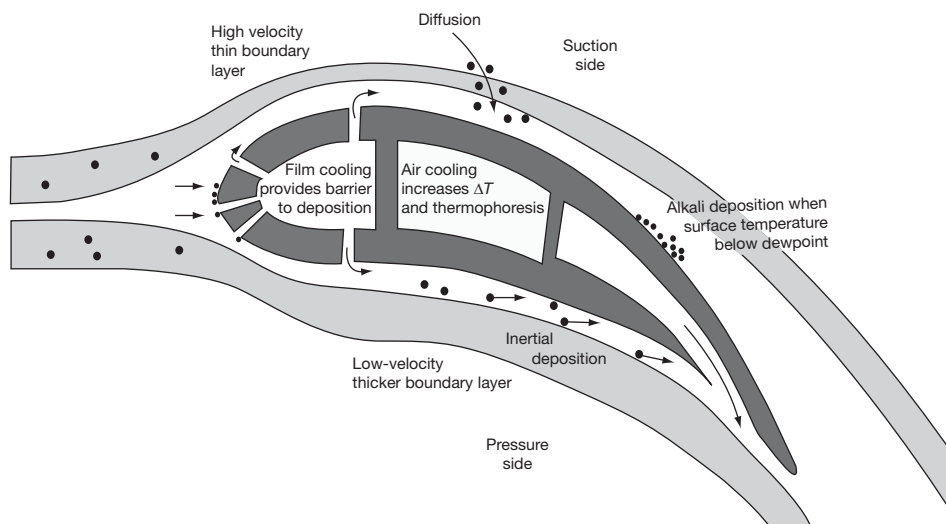


**Figure 16** Potential deposition around a gas turbine aerofoil surface. Reproduced from Grimthorpe Topping Cycle Project, UK DTI Clean Coal Programme, Summary Report 1995.

condition of the components, these particles may stick to the component surface, bounce off (or partially stick). It is quite likely that the composition of the particles will vary with size, so this may cause the behavior of larger and smaller particles to differ, as well as the differences in impact conditions.

- Vapor deposition; this transfers trace elements from the bulk gas stream to the surface of components; however, there are several variations of this type of process which include:
  - condensation of a vapor of a particular species from a hot gas stream onto a cooler metal surface (e.g., gaseous sodium sulfate condensing out as solid or liquid sodium sulfate);
  - condensation of a vapor of a particular species from a hot gas stream into a solid or liquid of another species on a cooler surface (e.g., gaseous sodium hydroxide or sodium chloride condensing out as solid or liquid sodium sulfate); reaction with  $\text{SO}_2/\text{SO}_3$  could happen during the condensation process or on the component surface after condensation;
  - these can be complex processes that depend on the activities and relative stabilities of all the contaminants involved in the gas stream and at the surface of the components, as well as the temperature differences between the bulk gas stream and component surface, system pressure, boundary layer thickness, and other flow related parameters.

Other deposition processes such as Brownian diffusion or thermophoresis (i.e., diffusion along a

temperature gradient) are well known but are believed to be less probable in the environments present within a gas turbine.

It is clear from the brief descriptions of the different types of deposition processes above that the deposition mechanisms that will operate will depend on a large number of potential variables that include ones resulting from (a) the composition of the combusted gas flow and (b) gas turbine component operations/geometry.

Combusted gas stream factors (local to area of deposit formation):

- trace metal contaminant levels,
- $\text{SO}_2/\text{SO}_3$  levels,
- particle sizes,
- particle composition.

Gas turbine component operations and geometrical factors (local to area of deposit formation):

- bulk gas temperatures,
- component temperatures,
- difference between bulk gas and metal temperatures,
- gas pressure,
- component shape and size, affecting:
  - gas flows around component,
  - development of eddy flows,
  - development and thickness surface boundary layers.

The source of the contaminant can alter the form in which it enters the gas turbine, passes through it and deposits onto components in the power turbine.

For example, sodium chloride can enter the system from the fuel or combustion air, pass through the combustor as a vapor or as particles (or both), and then deposit via direct inertial impaction, eddy impaction, and/or vapor condensation on different areas of an aerofoil.

For a given gas turbine design, only factors related to the combusted gas stream composition may be open to an operator to control (and so minimize deposition and hot corrosion). Gas turbine manufacturers, some gas turbine operators, and standards bodies have all considered the potential damage that can be caused to gas turbines by fuel contaminants. As a result, a number of fuel specifications have been produced that include limitations on elements related to hot corrosion (the fuel standards also include limitations on many other fuel properties for other purposes). Examples of such fuel specifications are given in [Table 3](#). All these specifications have the aim of reducing the damage caused by contaminants to levels acceptable to gas turbine manufacturers or users.

Along with controlling the contaminants entering the gas turbine hot gas path via the fuel, for many gas turbines (land and marine based systems), it is also possible to limit the contaminants entering the system via the combustion air (using air filters to remove particles and aerosols). For aeroengines, the contaminants entering the system via the air intakes depend on the types of flight path, its height, and location in the world: for example, for civil jet engines, island hopping with short flights at low altitudes over the sea versus long haul flights with long periods at high altitudes.<sup>63</sup>

In addition, it should also be recognized that contaminants can be accidentally put onto gas turbine components via cleaning fluids, greases, and other lubricants used during component manufacturing, inspection and/or assembly. However, every effort should obviously be made to avoid this deposit formation route wherever possible.

Fuel specifications have been derived mainly from experience with traditional gas turbine fuels such as diesels, jet fuels, heavy fuel oils and natural gas. However, in recent years, economic and environmental/regulatory pressures have encouraged the development of power systems that use a wider range of fuels, as well as new types of power systems<sup>3,14,60,64–66</sup>:

- Integrated gasification combined cycles (IGCC) in which solid fuels such as coal, biomass, and waste products are gasified, and then the fuel gases (or syngases) produced cleaned up and passed into a gas turbine for combustion and power generation;

- Pressurized combustion systems (such as pressurized fluidized bed combustion) in which solid fuels are burnt, and then the hot pressurized gas stream produced cleaned and passed through the power turbine part of the gas turbine (in some cases, the compression part could be used to produce the pressurized air stream needed for the combustion process);
- Use of natural gases with increasingly high H<sub>2</sub>S levels (beyond the range of previously acceptable gas compositions);
- Natural gases or syngases are processed to reduce their carbon contents and enhance their hydrogen contents;
- Bio-oil fuels;
- Gas turbines fired using oxygen and any of the other potential fuels to produce a combusted gas stream of mostly CO<sub>2</sub> and steam, from which the steam can be condensed to produce a CO<sub>2</sub> rich gas stream for recycling into the compressor or for storage (after further cleanup).

All these systems can be expected to have similar contaminants (e.g., S, Cl, alkali metals, Ca, Pb, V) to those traditionally found in the various oil or natural gas systems fired on air. However, both the absolute and relative levels of these contaminants will be different in each of the different systems, as a result of different fuels being used in them. In addition, other trace metals (e.g., Cd, Sb, Zn), which may give rise to vapor phase species when different fuels are gasified, may affect the deposition and hot corrosion processes in the gas turbines that use the fuel gases produced.<sup>49,50,60,64</sup> Coal, biomass, and waste products have significantly different compositions to each other, and these variations persist to differing degrees for each element/fuel utilization process by the time the fuel gas streams reach the gas turbine.

Thus, new gas turbine fuel specifications will be needed for new types of fuels that are being considered. These are currently under active consideration and in some cases research.<sup>14,49,50,60,62</sup> However, in considering the use of gas turbines for new applications, it is necessary to consider both the composition of the combusted gas stream expected in the power turbine and detailed design of gas turbine as both should be optimized for the new gas turbine applications, to minimize deposition and subsequent hot corrosion (as well as allowing for new bulk gas compositions in some of the novel power generating cycles).

### 1.20.5.3 Damage Locations

The potential locations for hot corrosion along the gas turbine hot gas path are controlled by deposition processes (outlined in [Section 1.20.4](#)) and the heat transfer processes between bulk gas stream and various components that enclose it. Heat transfer processes (via radiation, convection, and conduction mechanisms) cause unique distributions of metal temperatures to be set up on each type of component; for example, the vanes and blades at each stage of any turbine will have different temperature distributions. The air-cooled vanes/blades in the higher pressure stages may have wider temperature distributions than the ‘uncooled’ vanes/blades in lower pressure stages. However, the temperature profiles on cooled vanes/blades depend on the cooling methods used (e.g., convection cooling, film cooling), details of the blade designs, and whether TBCs are used. Thus, the surface temperature distributions on all components along a gas turbine hot gas path are unique (and are often commercially sensitive). [Figure 17](#) gives examples of predicted temperature distributions on a cooled and an uncooled turbine aerofoil surface.

It is quite possible for cooled blades or vanes in the higher pressure stages to have the combination of surface temperature and deposition conditions to cause oxidation as well as type I and type II hot

corrosion in different areas of components. It should be noted that as operating temperatures are slowly being raised, potential areas for damage are not restricted to aerofoil surfaces traditionally considered. In addition, platforms, shrouds, roots, and shanks may also develop hot corrosion damage as may internal cooling air passages. In future advanced gas turbines, one may expect that even outer parts of discs and seals may also suffer from oxidation or corrosion damage as the gas temperatures and component operating temperatures are raised further.

### 1.20.5.4 Rates of Hot Corrosion Attack and Modeling Hot Corrosion Processes

The rates of hot corrosion attack on a component depend on the alloy and coating used as well as on exposure conditions (including local environment). As a result of the potential for hot corrosion to be a life-limiting failure mechanism for some hot gas path components within gas turbines, there have been many studies of the mechanisms of hot corrosion damage in gas turbines over the years.<sup>2,15,38–45</sup> Failed or damaged components from operating gas turbines have confirmed that the various potential hot corrosion mechanisms are all possible in practice and have enabled these potential problems to be well characterized. Thus, operating experience and research studies have identified the main factors that will influence the rates of hot corrosion; in no particular order, these are<sup>2,15,38–45</sup>:

- metal temperature,
- gas temperature,
- gas pressure,
- rate of deposit formation (or deposition flux),
- deposit composition,
- gas composition,
- component geometry,
- alloy composition,
- coating composition,
- exposure time (hot corrosion damage goes through an incubation stage before reaching the characteristic propagation stage).

Some of these factors relate more to deposition processes than hot corrosion processes, but are necessary to set up conditions needed for hot corrosion to proceed.

Unfortunately, each type of component in every gas turbine operating with different fuels provides a different combination of exposure conditions. Thus carrying out systematic studies on all the different

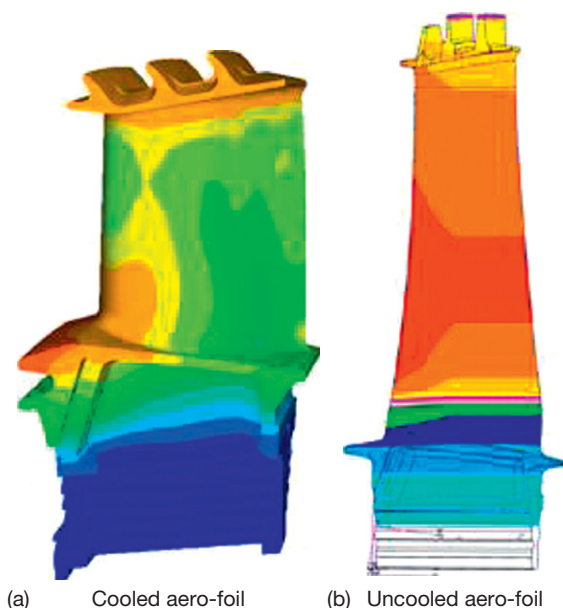


**Figure 17** Examples of temperature distributions on (a) cooled and (b) uncooled gas turbine aerofoil surfaces. Courtesy of Siemens Industrial Turbo-Machinery Ltd.

potential variables is not a viable option. However, information is available from:

- manufacturers and operators of fleets of gas turbines, that use fuels from different sources and turbines sited or operated in different locations;
- rainbow trials of components in operating gas turbines;
- burner rigs:
  - high velocity,
  - low velocity,
- laboratory tests:
  - deposit recoat methods,
  - dean rig,
  - buried in ash methods.

Moving down the above list, control over some of the exposure variables generally increases and their cost decreases, but their relevance to gas turbine service also decreases unless care is taken to match exposure conditions to particular in-service conditions. In addition it is necessary to ensure that materials performance data is produced in a form that is useful for comparison with component performance determined from use in real environments (i.e., metal loss data rather than weight change data).

**Figure 18** illustrates hot corrosion damage found for two example gas turbine materials in burner rig studies carried out to compare the performance of base alloys and coatings under well-characterized operating conditions.

Such studies have confirmed that base alloys containing higher chromium (e.g., IN939, IN6203DS, IN738LC, and FSX-414) tend to perform well under hot corrosion conditions. Such materials are still used for components in many turbines. However, gas turbines that use high component operating temperatures have moved to using single crystal superalloys for blades and vanes in the higher pressure stages. These lower chromium materials (e.g., CMSX-4) do not have good hot corrosion resistance, so they require coating to provide them with the required surface protection.<sup>14,49,50</sup>

**Figure 19** gives a qualitative indication of the relative performance of different coating types (dating from the late 1980s).<sup>69,70</sup> The introduction of single crystal materials with poor hot corrosion performance and the differences between type I and type II hot corrosion mechanisms, that are now known, have complicated this picture.

Quantitative data on hot corrosion of gas turbine substrate materials and coatings under well-characterized conditions are not frequently reported due to the difficulties of carrying out such experimental programs and the commercial sensitivities of the results if they are targeted at particular operating conditions or materials systems.<sup>14</sup>

However, over the last 15 years, a series of experimental programs have been carried out at Cranfield University with the aim of generating systematic data sets of the performance of generic gas turbine materials (e.g., IN738LC and CMSX-4) under ranges of

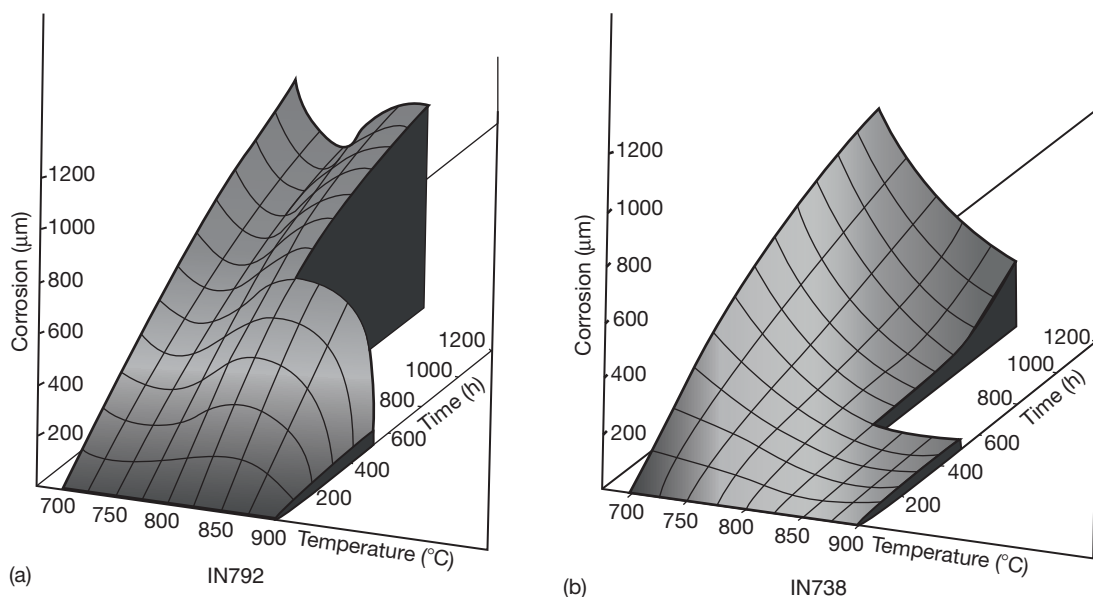


**Figure 18** Examples of hot corrosion performance of two example materials in burner rig tests as a function of metal temperature and exposure time.<sup>67</sup> (a) IN792 and (b) IN738.

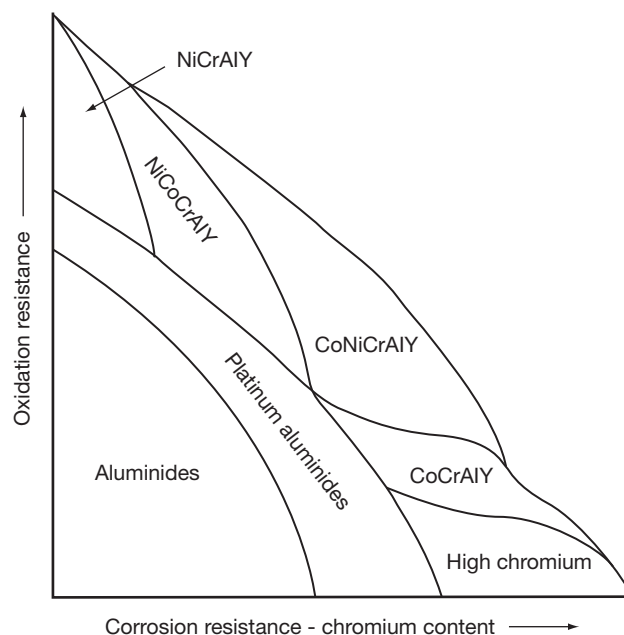


exposure conditions that reflect hot corrosion conditions in industrial and aeroengines that have been accelerated to differing degrees. These datasets are in the form of metal losses determined at a number of locations to give a cumulative probability distribution for the damage observed under specific exposure conditions. The methods being used for this work have been included in EU guidelines for hot corrosion testing that now form parts of draft ISO

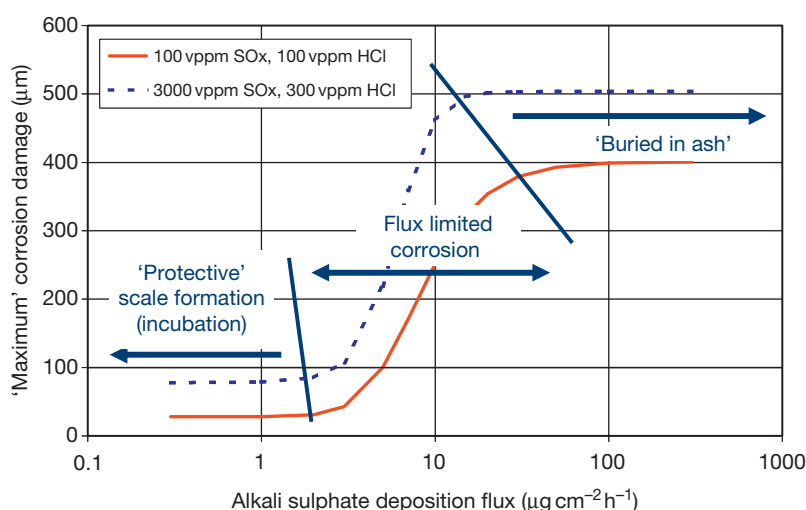
standards. The datasets generated illustrate some of the features of hot corrosion damage in gas turbine environments (Figures 20 and 21).

Figure 20 illustrates three different regimes for hot corrosion damage<sup>11,47,48,50</sup>:

- At low deposition fluxes; accelerated oxidation processes are observed and the hot corrosion is still in an incubation phase after this exposure time (500 h);



**Figure 19** Qualitative indication of the relative performance of different coating types.<sup>27,68–70</sup>



**Figure 20** Dependency of type II hot corrosion damage as a function of deposition flux for IN738LC. Reproduced from Simms, N. J.; Nicholls, J. R.; Oakey, J. E. In *Lifetime Modelling of High Temperature Corrosion Processes*; Schütze, M. et al. Eds.; Maney, 2001; pp 379–397, EFC No. 34.

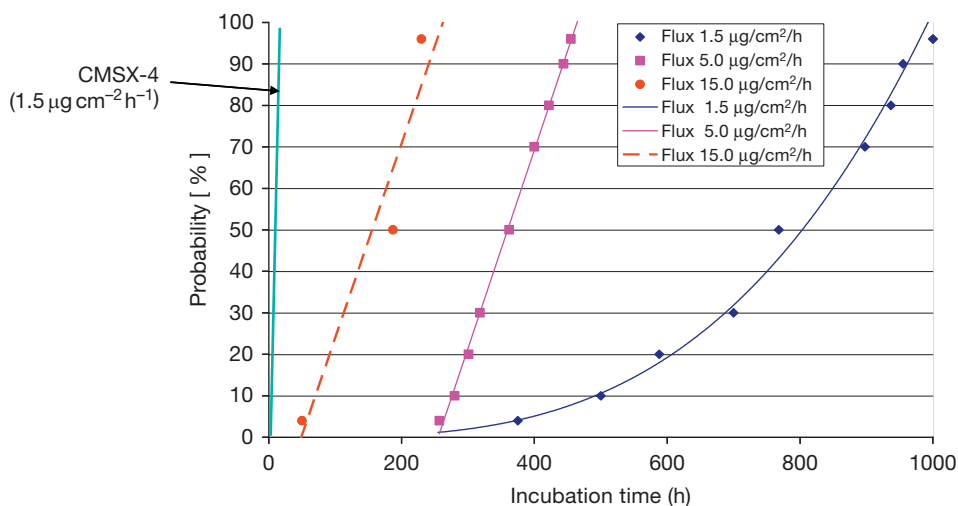


**Figure 21** Dependence of type II hot corrosion incubation times on deposition flux for CMSX-4 and IN738LC. Reproduced from Nicholls, J. R.; Simms, N. J.; Encinas-Oropesa, A. In *Materials Issues Governing the Performance of Advanced 21st Century Energy Systems*; Levi, T. et al. Eds.; Science Reviews, 2008; pp 35–48.

- At intermediate deposition fluxes; corrosion rates are proportional to deposition fluxes;
- At high deposition fluxes; corrosion rates are not sensitive to deposition flux as it is no longer the rate limiting process in hot corrosion reactions (this is equivalent to previous and older 'buried in ash' test methods).

Figure 21 illustrates the much shorter incubation times found for the single crystal material CMSX-4 when compared to that of the older alloy IN738LC.<sup>48</sup> In addition, the effect of increasing deposition flux on the reduction of incubation times for the IN738LC is shown.

In such laboratory tests, the exposure conditions have been adjusted to accelerate the hot corrosion damage relative to that expected in operating gas turbines. However, by determining the sensitivity of the damage to changes in exposure conditions, it is possible to determine the expected degree of acceleration linked to specific operating conditions and then compare the data generated to that observed in practice under service conditions.

The overall data set being generated by this work is being used to produce empirical-mechanistic based models of hot corrosion damage to assist with the assessment and prediction of component lives within the hot gas paths of gas turbines.

### 1.20.6 Current/Future Issues

The development of gas turbine technologies for many different potential applications is a continuing

process. In terms of hot corrosion, there are several issues that are believed to be of increasing interest in the near future<sup>3,14,60,64–66</sup>:

- Corrosion of internal blade cooling passages (from contaminants in the cooling air);
- Deposit-induced corrosion damage below blade platforms/on disc rims (due to increasing component temperatures);
- Much higher SO<sub>x</sub> levels than traditionally considered (from dirtier/cheaper fuels) modifying type I and type II hot corrosion reactions;
- Gasifier fuel gas derived deposits with calcium, magnesia, alumina, silica, and iron compounds;
- Effects of novel environments (e.g., high steam levels from H<sub>2</sub> firing, or high CO<sub>2</sub>/steam mixtures from oxy-fired systems) combined with traditional gas turbine degradation issues;
- Interaction between mechanical properties (e.g., fatigue) and hot corrosion;
- Development of single crystal alloys with compositions that produce higher hot corrosion resistance.

### 1.20.7 Summary

Gas turbines are currently used in a wide variety of applications: from jet engines to large-scale power generation. Each of these applications presents its own particular set of challenges for the use of specific gas turbine designs. However, many of these systems experience damage related to oxidation and hot

corrosion in the hot gas paths of gas turbines. These various forms of damage are related to a combination of operating conditions of the particular gas turbine and its components together with contaminants entering hot gas paths via air or fuel streams. The various forms of oxidation and hot corrosion that are expected under such exposure conditions are well known and are characterized with qualitative description of the potential mechanisms developed mostly during the 1970s. However, quantitative data on the various damaging reactions are less readily available, and models to enable the prediction of such damage are subjects of current research activity. The use of new materials designed for strength rather than corrosion resistance is proving to be problematic for some gas turbine applications. The on-going wish to increase gas turbine efficiencies and at the same time widening the range of potential fuels and including new types of power generation system, to meet environmental and regulatory wishes, is presenting a new series of challenges in terms of the oxidation and hot corrosion performance of components in various gas turbine hot gas paths.

## References

- Rolls Royce: The jet engine. Rolls Royce, 2005.
- Sims, C. T.; Stoloff, N. S.; Hagel, W. C. Eds. *Superalloys*; Wiley: New York, USA, 1987; Vol. II.
- Hannis, J. M. In *Power Generation in an Era of Climate Change*; Proceedings of the 7th International Charles Parsons Turbine Conference; Strang, A. et al. Eds.; IOM Communications, 2007; pp 37–49.
- Data sheet for SGT5-8000H; Siemens AG, 2007.
- Pavri, R.; Moore, G. D. *General Electric Reference Document, GER-4211*, 2001.
- De Backer, W.; Bopp, C. In Proceedings of ASME TURBOEXPO 2000, Munich, Germany 2000; Paper 2000-GT-0307.
- Ingistov, S. Proceedings of ASME TURBOEXPO 2000, Munich, Germany, 2000; Paper 2000-GT-305.
- Horlock, J. H. Proceedings of ASME TURBOEXPO 2001, New Orleans, Louisiana, 2001; Paper 2001-GT-0343.
- Bhargava, R.; Meher-Homji, C. B. In Proceedings of ASME TURBOEXPO 2001, Amsterdam, The Netherlands 2002; Paper 2002-30560.
- Bradshaw, A.; Simms, N. J.; Nicholls, J. R. *Fuel* **2008**, 87, 3529–3536.
- Simms, N. J.; Nicholls, J. R.; Oakey, J. E. In *Lifetime Modelling of High Temperature Corrosion Processes*; Schütze, M. et al. Eds.; Maney, 2001; pp 379–397, EFC No. 34.
- ADSEALS – Investigation in advanced high temperature seals, European Union FP5 project, G4RD-CT-2000-00185, 2004.
- Rickerby, D. S.; Hicks, M. A. In *Power Generation in an Era of Climate Change*, Proceedings of the 7th International Charles Parsons Turbine Conference; Strang, A. et al. Eds.; IOM Communications, 2007; pp 229–240.
- Simms, N. J.; Bale, D. W.; Baxter, D.; Oakey, J. E. In *Materials for Advanced Power Engineering 2002*, Lecomte-Beckers, J. et al. Eds.; Jülich, 2002; p 73, 675–690.
- Birks, N.; Meier, G. H.; Petit, F. S. *Introduction to the High Temperature Oxidation of Metals*; Cambridge University Press: Cambridge, 2006.
- Schütze, M. et al. Eds. *Lifetime Modelling of High Temperature Corrosion Processes*; Maney, 2001, EFC No. 34.
- Nijdam, T. J.; van der Pers, N. M.; Sloof, W. G. In *Novel Approaches to Improving High Temperature Corrosion Resistance*; Schütze, M. and Quadakkers, W. J., Eds.; Woodhead, 2008; pp 582–598, EFC No. 47.
- Smialek, J. L.; Nesbitt, J. A.; Barrett, C. A.; Lowell, C. E. In *Cyclic Oxidation of High Temperature Materials*; Schütze, M. et al. Eds.; IOM Communications, 1999, Chapter 9, EFC No. 27.
- Nicholls, J. R.; Newton, R.; Bennett, M. J.; Evans, H. E.; Al-Badair, H.; Tatlock, G. J.; Naumenko, D.; Quadakkers, W. J.; Strehl, G.; Borchardt, G. In *Lifetime Modelling of High Temperature Corrosion Processes*; Schütze, M. et al. Eds.; Maney, 2001; pp 83–106, EFC No. 34.
- Nicholls, J. R. In *Life Assessment of Hot Section Gas Turbine Components*; Townsend, R. et al. Eds.; IOM Communications, 2000; pp 135–154.
- Poquillon, D.; Monceau, D. *Oxid. Met.* **2003**, 59, 409.
- Nesbitt, J. A. In *Lifetime Modelling of High Temperature Corrosion Processes*; Schütze, M. et al. Eds.; Maney, 2001; pp 359–378, EFC No. 34.
- Dahl, K. V.; Hald, J. In *Materials for Advanced Power Engineering 2006*; Lecomte-Beckers, J. et al. Eds.; Jülich, 2006; pp 675–690.
- Bertrand, N.; Desgranges, C.; Nastar, M.; Girardin, G.; Poquillon, D.; Monceau, D. *Mater. Sci. Forum* **2008**, 595–598, 463–472.
- Bacos, M. P.; Josso, P.; Vialas, N.; Poquillon, D.; Pieraggi, B.; Monceau, D.; Nicholls, J. R.; Simms, N.; Encinas-Oropesa, A.; Ericsson, T.; et al. *Appl. Therm. Eng.* **2004**, 24, 1745–1753.
- Simms, N. J.; Kilgallon, P. J.; Roach, C.; Oakey, J. E. In *Microscopy of Oxidation*, Proceedings of 5th International Conference, Newcomb, S. and Tatlock, G. Eds.; Science Reviews, 2003; pp 273–280.
- Nicholls, J. R. *Mater. Res. Soc. Bull.* **2003**, 28(9), 659–670.
- Newcomb, S. and Tatlock, G. Eds.; *Microscopy of Oxidation*; Proceedings of 5th International Conference Science Reviews, 2003.
- Yanar, N. M.; Kim, G.; Hamano, S.; Petit, F. S.; Meier, G. H. In *Microscopy of Oxidation*, Proceedings of 5th International Conference, Newcomb, S. and Tatlock, G., Eds.; Science Reviews, 2003; pp 249–260.
- Osgerby, S.; Rinaldi, C.; De Maria, L. In *Materials for Advanced Power Engineering 2006*; Lecomte-Beckers, J. et al. Eds.; Jülich, 2006; pp 217–232.
- Renusch, D.; Schütze, M. *Mater. Sci. Forum* **2008**, 595–598, 151–158.
- Busso, E. P.; Lin, J.; Sakurai, S.; Nakayama, M. *Acta Mater.* **2001**, 49, 1515.
- Busso, E. P.; Evans, H. E.; Wright, L.; McCartney, L. N.; Nunn, J. E.; Osgerby, S. *Mater. Corros.* **2008**, 59(7), 556–565.
- Hermosilla, U. PhD Thesis, Nottingham University 2008; UK EPSRC Supergen Plant Life Extension Consortium.
- Nicholls, J. R. *DARP: Advanced Aero-engine Materials (ADAM) – Next Generation Single Crystal and Lifting Methodologies*; GR/S26149/01, Final Report, EPSRC, 2007.
- Padture, N. P.; Gell, M.; Jordan, E. H. *Science* **2002**, 296, 280–284.

37. He, M. Y.; Hutchinson, J. W.; Evans, A. G. *Mater. Sci. Eng. A* **2003**, 345, 172–178.
38. Kofstad, P. *High Temperature Corrosion*; Springer, 1988.
39. Giggins, C. S.; Pettit, F. S. Hot Corrosion of Metals and Alloys – A unified Theory, PWA Report No. FR-11545, 1979.
40. *Corrosion*, 9th ed.; ASM International: Ohio, USA, 1987; Vol. 13, ISBN 0-87170-007-7.
41. Stringer, J.; Wright, I. G. *Oxidation Metals* **1995**; 44(1/2), 265–308.
42. Special Issue on Hot-salt corrosion standards, test procedures and performance, *High Temp. Technol.* **1989**, 7(4).
43. Rapp, R. A. *Corros. Sci.* **2002**, 44, 209–221.
44. Rapp, R. A.; Goto, K. S. In *Symposium on Fused Salts*; Braunstein, J., Selman, J. R., Eds.; The Electrochemical Society, 1979; p 159.
45. Shores, D. A. In *High Temperature Corrosion*; Rapp, R. A., Ed.; NACE, 1983; p 493.
46. Foster, A. D.; von Doering, H. E.; Hilt, M. B. *Fuels Flexibility in Heavy Duty Gas Turbines*; GE: Schenectady, NY, 1983; GER3428a.
47. Simms, N. J.; Nicholls, J. R.; Oakey, J. E. *Mater. Sci. Forum* **2001**, 369–372, 833–840.
48. Nicholls, J. R.; Simms, N. J.; Encinas-Oropesa, A. In *Materials Issues Governing the Performance of Advanced 21st Century Energy Systems*; Levi, T. et al. Eds.; Science Reviews, 2008; pp 35–48.
49. Bordenet, B.; Bossman, H. P. *Mater. Sci. Forum* **2004**, 461–464, 907–916.
50. Simms, N. J.; Encinas-Oropesa, A.; Nicholls, J. R. *Mater. Sci. Forum* **2004**, 461–464, 941–948.
51. *Phase Diagrams for Ceramists*; American Ceramic Society, 1964.
52. Hamed, A.; Tabakoff, W.; Wenglarz, R. J. *Propul. Power* **2006**, 22(2), 350–360.
53. Young, J. B.; Wu, Z. Particulate and vapour deposition in gas turbines fired on coal-derived gases, Final report DTI Cleaner Coal R&D Programme. Project 142, 2004.
54. Foster, A. D.; et al. Fuels flexibility in heavy-duty gas turbines, General Electric Reference Document, GER-3428a; GE: Schenectady, NY, 1983.
55. Wolf, J.; Werning, H. J. Proceedings of VGB Conference on 'Corrosion and Corrosion Protection in Power Plant Technology 1995 (VGB, 1995), paper 27.
56. Fackrell, J. E.; Tabberer, R. J.; Young, J. B.; Fantom, I. R. ASME International Gas Turbine & Aeroengine Congress, The Hague, 1994; Paper 94-GT-177.
57. Fackrell, J. E.; Tabberer, R. J.; Young, J. B. In *The Impact of Ash Deposition in Coal Fired Plants*; Williamson, J. et al. Eds.; Taylor and Francis, 1994; pp 123–134.
58. Hepworth, J. K.; Fackrell, J. E.; Pinder, L. W.; Wilson, J. D. In *Life Assessment of Hot Section Gas Turbine Components*, Townsend, R. et al. Eds.; IOM Communications, 2000; pp 281–292.
59. Simms, N. J.; Oakey, J. E.; Stephenson, D. J.; Smith, P. J.; Nicholls, J. R. In Proceedings 8th International Conference on Erosion by Liquid and Solid Impact; *Wear* **1995**; 186–187(Part 1), 247–255.
60. DeCorso, M.; Newby, R.; Anson, D.; Wenglarz, R.; Wright, I. Coal/biomass fuels and the gas turbine: Utilization of solid fuels and their derivatives; ASME, Paper 96-AT-76, 1996.
61. Fackrell, J. E.; Tabberer, R. J.; Young, J. B.; Wu, Z. Gas turbines fired on coal-derived gases – Modelling of particulate and vapour deposition, UK DTI Report No. COAL R280, DTI/Pub URN 05/661, March 2005.
62. Grimethorpe Topping Cycle Project, UK DTI Clean Coal Programme, Summary Report 1995.
63. Leggett, A. J.; Simms, N. J.; Rickerby, D. S. In *Power Generation in an Era of Climate Change*, Proceedings of the 7th International Charles Parsons Turbine Conference; Strang, A. et al. Eds.; IOM Communications, 2007; pp 241–251.
64. Wenglarz, R.; Oakey, J. E. In *Materials for Advanced Power Engineering 2006*, Lecomte-Beckers, J. et al. Eds.; Jülich, 2006; pp 233–244.
65. Ruth, L. A. In *Life Cycle Issues in Advanced Energy Systems*, Norton, J. F. et al. Eds.; Science Reviews, 2003; pp 7–14.
66. Paisley, M. A.; Welch, M. J. In ASME Turbo Expo 2003; ASME, 2003; GT2003-38294.
67. High Temperature Corrosion of Aerospace Alloys, AGARD-AG-200, 1975.
68. *Coatings for High Temperature Structural Materials*, NMAB report of the NRC; National Academic Press: Washington DC, 1996.
69. Mom, J. A. NLR Report MP 81003U, Amsterdam, 1981.
70. Novak, R. C. Coating development and use: Case studies. *Presentation to the Committee on Coating for High-Temperature Structural Materials*; National Materials Advisory Board; National Research Council: Irvine; California, April 18–19, 1944. Cited in references [27] and [68].

## 1.21 Design of High Temperature Alloys

**P. F. Tortorelli and M. P. Brady**

Oak Ridge National Laboratory, Oak Ridge, TN 37831-6115, USA

© 2010 Elsevier B.V. All rights reserved.

1.21.1	Introduction	541
1.21.2	Protective Oxidation	542
1.21.3	Selective Oxidation and Establishment of a Protective Scale on an Alloy	543
1.21.4	Minimizing Oxide Growth and Improving Scale Adhesion by Alloying	546
1.21.5	Maximizing Oxidation Lifetime	547
1.21.6	Alloy Selection for Specific Environments	549
1.21.7	Conclusions	555
References		555

### Abbreviations

**AA** Accelerated attack

**AAS** Accelerated attack with spallation

**POS** Protective oxide scale

### Symbols

***d*** Specimen thickness

***D<sub>AB</sub>*** The alloy interdiffusion coefficient in binary alloy A–B where B is the metal that forms the protective oxide  $B_xO_y$

***D<sub>O</sub>*** Diffusion coefficient of oxygen in alloy A–B

***k*** Rate constant where  $(kt)^n$  is the rate equation for B consumption by oxidation

***M*** Mass conversion factor for metal and oxide

***N<sub>B</sub><sup>\*</sup>*** Concentration of B needed to form protective  $B_xO_y$

***N<sub>B,c</sub>*** Critical concentration below which a protective  $B_xO_y$  cannot be maintained

***N<sub>B</sub>*** Concentration of B in the bulk alloy A–B

***N<sub>O,s</sub>*** Solubility of oxygen in alloy A–B

***t*** Time of exposure

***t<sub>b</sub>*** Time to breakaway

***x*** Depth of internal oxidation

***ρ*** Alloy density

protective surface layer. Such surface layer formation involves a complex interplay of reactive and diffusive processes, mediated by both material and environmental factors. There are well known principles to overcome this design problem, particularly for the simpler alloy systems that exhibit behaviors that are a close match to the assumptions made to produce analytical expressions of reaction rates and species fluxes.<sup>1</sup> However, designing of alloys for maximal corrosion resistance at high temperatures is often a qualitative endeavor, due to the large set of possible alloy and environmental permutations that make quantification and prediction difficult. Therefore, material specifications for corrosion resistance are often based on empirical databases and experiences that lack the quantification needed for directly linking materials selection to the component design lifetime. Nevertheless, there are a number of cases where alloy composition can be manipulated, based on an underlying understanding of corrosion principles and their verification, to derive good or excellent corrosion behavior in appropriate high temperature environments. In this chapter, certain approaches based on some of these basic principles and empirical findings will be reviewed with selected alloy systems and environments used as examples. Many more specific examples of alloy design or optimization for high temperature corrosion resistance can be found in other chapters of this book.

The essence of the alloy design effort for high temperature corrosion resistance is to achieve a continuous and protective surface layer or scale. Once a layer of this type is established, the access of the alloy to the environment is effectively isolated and, thereafter, is controlled by the transport properties and

### 1.21.1 Introduction

The design of alloys for corrosion resistance at high temperatures involves specification and manipulation of alloy composition and microstructures that assure preferential formation and long-term stability of a

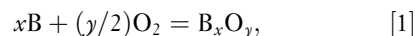


stability of the surface scale as long as its integrity is maintained. This type of scale is most often an oxide because virtually all high temperature, technically relevant environments contain reactive oxygen. Further, at equivalent gas activities and, frequently at very small concentrations of  $O_2$  in many mixed-gas environments, oxides are more thermodynamically stable than their equivalent carbides, nitrides, sulfides, etc. It is important to note, though, that the approaches to alloy design for protective scale formation described here, while typically discussed in terms of oxides, are also applicable to situations where other reactive species are present, that is, the formation of surface or internal carbides, nitrides, sulfides, etc. by ‘oxidation,’ a chemical process by which the valence state of the metal species is increased. Such product formation can be of interest as a synthesis route to functional surface structures<sup>2</sup> but, at elevated temperatures in most technically-relevant environments, these nonoxide phases are less stable than their equivalent oxides and hence, can subsequently be converted to oxides. Even if thermodynamic stability is achieved, most nonoxides, and many oxides, cannot meet the other key criterion of protective scale formation: the kinetic standard of a slowly thickening layer that, by itself, is an effective permeation barrier between the reactive environmental species and the alloy on which it is growing. For temperatures in excess of 600 °C, the protective oxides relevant for alloys in service applications are  $Cr_2O_3$ ,  $Al_2O_3$ , and, to a lesser extent,  $SiO_2$  (as evidenced by the fact that most ‘heat-resistant’ alloys rely on these surface oxides for corrosion resistance). At lower temperatures, iron, nickel, cobalt, and zirconium oxides can be considered protective, but in this chapter, design examples focus on the former three types. Under certain conditions, protective oxides can also serve as efficient barriers to environmental species other than oxygen (such as water vapor, carbon, or sulfur), thus alloys designed to form these surface layers may have attractive applications in high temperature mixed-gas environments (see [Section 1.21.6](#) on alloy selection for specific environments).

### 1.21.2 Protective Oxidation

For this study, binary alloys, generally denoted as A–B, will be considered with other major alloying elements being treated as minor additions to the binary system, and with oxides as the exclusive form

of protective scales for the reasons discussed above. In this hypothetical A–B alloy notation scheme, element A is typically a base metal such as Fe, Ni, or Co, while B forms the desired protective oxide:



with possible modification of the oxide by other major and minor alloying elements. Principal examples of B would be Al, Cr, and Si for  $Al_2O_3$ ,  $Cr_2O_3$ , and  $SiO_2$ , respectively. The desired design goal is to formulate an alloy composition and microstructure that will produce a continuous layer of  $B_xO_y$  at the expense of less protective base metal A oxides. To assure this,  $B_xO_y$  must be thermodynamically stable in the subject environment, and, typically, have significantly greater stability than the oxide(s) of A. This thermodynamic tendency can be readily assessed qualitatively in terms of the (negative) free energies of formation ( $\Delta G$ s) as a function of temperature. Such an Ellingham diagram is schematically shown in [Figure 1](#) for representative metal oxides. From an empirical alloy design experience, preferential formation of  $B_xO_y$  is found to be easier in alloy systems for which the difference between  $\Delta G$ s of the A and B oxides is large. Hence, it is much easier to assure  $Al_2O_3$  formation on Ni–Al than on Ti–Al. However, kinetic factors rather than thermodynamic factors are often more important in determining whether a continuous protective scale can be established.

In the present context, ‘protective’ has several attributes. First,  $B_xO_y$  must form preferentially, and

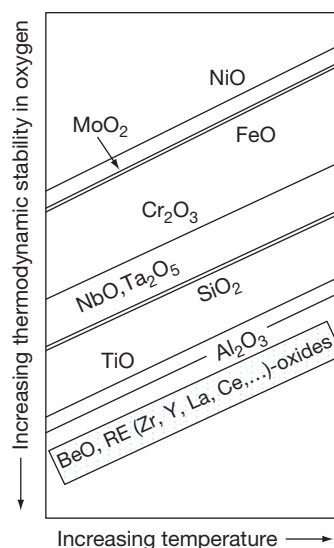


**Figure 1** Schematic representation of free energies of formation of oxides of interest. Increasing stability means larger negative energies.

reduce the permeation between the reactive species in the environment and in the alloying elements – that is, both the solubility and diffusivity of anionic species (from the environment) and cationic species (from the alloy substrate) in the oxide scale must be low. Therefore, the product must be continuous across the alloy surface and exhibit long-term stability in the environment. Note that this does not necessarily mean that no other products can grow or exist. Rather, the protective layer must form in a way that it rapidly controls the transport across the entire surface of the alloy – see, for example, **Figure 2**, which shows the development of a continuous  $\text{Al}_2\text{O}_3$  scale on a Nb–33Ti–40Al (wt%) alloy under the fast-growing Nb-rich transient (nonprotective) oxides. The protective scale should also be dense (no interconnected porosity or large pores), mechanically sound (no through cracks), and adherent to the alloy substrate on which it grows. This last attribute, strong adhesion to the alloy, is often problematic even when other chemical and physical characteristics are met; these oxides tend to have coefficients of thermal expansion (CTEs) that are quite different from those of the alloy and, thus, large stresses (typically compressive) are encountered upon cooling from high temperature such that spallation of the scale eventually occurs.<sup>3</sup> This is a disruptive event; the protective scale regrows during the next heating cycle (hopefully) and accelerates the metal wastage (as well as the attendant subsurface depletion of B) due to reinitiation of the product growth process.<sup>4</sup> Stresses can also develop in the scale due to the growth process itself<sup>5</sup> but, typically, these are not of the same order of magnitude as the thermal stresses on cooling, at least at a steady state.

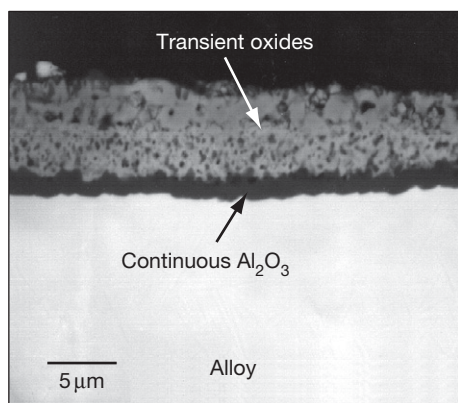


**Figure 2** Scanning electron micrograph of cross-section of Nb–33Ti–40Al (at. %) exposed at 1400 °C in air for 15 min. Reproduced from Brady, M. P.; Gleeson, B.; Wright, I. G. *JOM* 2000, 52, 16–21.

### 1.21.3 Selective Oxidation and Establishment of a Protective Scale on an Alloy

Managing the inherent instability of a metallic material in a reactive environment so as to limit the amount of metal wastage through control of thermodynamic and kinetic factors is the goal of alloy design for high temperature applications. This is first attempted by the application of well founded, although somewhat idealized, fundamental principles of selective oxidation of alloys that effect preferential formation of a continuous protective scale ( $\text{B}_x\text{O}_y$ ) on alloy A–B. (Some guidelines for choosing  $\text{B}_x\text{O}_y$  for a given set of environmental factors are discussed below.) For a single-phase alloy, A–B, the formalism is based on pioneering work of Wagner,<sup>6</sup> further studied and elaborated by a host of others.<sup>7,8</sup> For multiphase alloys, the development of relevant principles is more recent<sup>9–11</sup> and takes advantage of analytical advances originating from more extensive work on single-phase alloy oxidation. The treatment in this section follows the outline of a recent description of principles for protective scale formation on alloys by Brady *et al.*<sup>12</sup> Specific application of these approaches to intermetallics can be found in Brady and Tortorelli.<sup>13</sup>

As an illustration and reference to the discussion that follows, it is appropriate to consider the schematic descriptions of the two limiting cases, namely, fully nonprotective behavior (**Figure 3**, left side) and the best possible outcome for the alloy design process being addressed here (**Figure 3**, right side) under conditions where  $\text{O}_2$  is the reactive species, A and B oxides are mutually insoluble, and the oxygen partial pressure is sufficiently high to oxidize either both A and B or just B. In the former (nonprotective) limiting case, internal oxidation of B occurs, with the possible formation of rapidly growing A oxides while, in the latter limiting case, a slowly growing, exclusive, continuous, adherent  $\text{B}_x\text{O}_y$  layer develops.

In the former case, the depth of internal oxidation,  $x$ , at time  $t$  can be described functionally as<sup>14</sup>

$$x^2 \propto (N_{\text{O},s}/N_{\text{B}}D_{\text{AB}})^2 D_{\text{O}} t \quad [2]$$

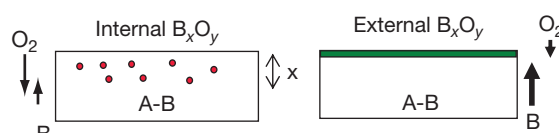


**Figure 3** Schematic illustration of internal oxidation and external scale formation by selective oxidation.

where  $D_O$  is the diffusion coefficient of oxygen in A–B,  $N_{O,s}$  is the solubility of oxygen in A–B,  $N_B$  is the concentration of B in the bulk alloy, and  $D_{AB}$  is the alloy interdiffusion coefficient. From a practical alloy design viewpoint, the extent of internal oxidation can be decreased most directly by increasing the concentration of B. Internal oxidation can also be decreased by decreasing the permeability of oxygen in A–B ( $N_{O,s}D_O$ ) via ternary and higher-order alloying additions. Microstructure can impact the extent of internal oxidation if the morphology of these internal oxides enhances the transport of oxygen along their interfaces with the alloy matrix (increased  $D_O$ ).<sup>15</sup> It is this type of mechanism that can explain the presence of stable (essentially inert)  $Al_2O_3$  reinforcements in a  $Ni_3Al$  matrix composite structure that compromises the otherwise good oxidation resistance of the aluminide.<sup>16</sup>

From the Wagner perspective, as  $N_B$  is increased, the volume fraction of internal  $B_xO_y$  precipitates increases to the point where an external layer of  $B_xO_y$  forms (Figure 3, right side). Under this assumption, the critical concentration needed for external formation of  $B_xO_y$ ,  $N_B^*$ , is a function of metal and oxygen diffusivities in the alloy, and the solubility of oxygen<sup>6</sup> such that

$$N_B^* \propto N_{O,s}(D_O/D_{AB})^{1/2} \quad [3]$$

Therefore, external  $B_xO_y$  formation is favored (that is, the critical concentration of B is decreased) by compositional and microstructural conditions that decrease the solubility and inherent diffusivity of the oxidizing species in the alloy and/or increase the mobility of the metallic elements (cf. Figure 3). One way to preferentially increase the effective value of  $D_{AB}$  and, thus, decrease the value of  $N_B^*$ , is to provide a greater density of short-circuit diffusion paths – for example, by decreasing the grain size<sup>17</sup> or increasing the dislocation density at the alloy surface.<sup>18</sup> Although such structural pathways may not be stable over long periods of time at elevated temperature, their existence during the period when the  $B_xO_y$  layer is being established is critical and effective.

In theory, ternary and higher order alloying additions that decrease the solubility of the environmental species in the alloy should, using eqns [2] and [3], decrease the value of  $N_B^*$  and promote protective scale formation. Obviously, the opposite is also true: compositional modifications that increase reactant solubility in the alloy can increase  $N_B^*$  to a value greater

than  $N_B$  such that an exclusive protective scale does not form. Therefore, it is important from an alloy design viewpoint to be aware of how alloying (for whatever purpose) affects this solubility term to avoid unintended deleterious effects on the ability of an alloy to develop a protective surface product.

It is well known that protective scale development can be promoted by the ‘third-element effect,’ defined generically as an alloying addition that decreases the amount of B needed to form a protective layer of  $B_xO_y$  ( $N_B^*$ ). This can be an important design principle if it is necessary to minimize the concentration of B to achieve other desirable properties of the alloy (for example, decreasing the aluminum concentration to avoid brittleness). For example, such an effect has been observed for (Ni,Co,Fe)–Al–Cr alloys, where the addition of Cr lowers the  $N_{Al}^*$  value for protective  $Al_2O_3$  formation, and is, in fact, the basis for the design of commercial heat-resistant alloys.<sup>19</sup>

There are several mechanistic variants to the third-element effect. The ‘classic’ version is generally associated with a secondary gettering mechanism,<sup>1,20</sup> whereby X is added to A–B such that its oxide is of intermediate stability compared to that of the oxides of A and B, and decreases the effective partial pressure at the metal–oxide scale interface such that continuous  $B_xO_y$  layer formation can occur. A second type of third-element effect can be considered to be the influence of an alloying addition on early-stage oxidation, such that a transient oxide can preferentially nucleate the growth of  $B_xO_y$ .<sup>21,22</sup> Additionally, just as microstructure can enhance metal diffusivity in the alloy lattice (see above discussion), a third element can be used to influence diffusional effects so that protective oxide layer formation is promoted ( $D_{AB}$  is increased and/or  $N_{O,s}$  and  $D_O$  are decreased).<sup>23</sup>

The activity(ies) of the reactant(s) in the subject environment must be a part of alloy design considerations for protective scale development.<sup>12</sup> For example, an alloy with  $N_B > N_B^*$  at a given reactant (oxygen) partial pressure may not be able to form a protective  $B_xO_y$  layer at higher pressures where the oxygen solubility in A–B increases in accordance with Sievert’s law and possibly raises the value of  $N_B^*$  above that of  $N_B$  (eqn [3]) or where the higher pressures result in altering the nature and/or stability of the competing A oxides. Similar considerations must be given to service temperature, which not only affects the reactant solubility in the alloy, but also other factors that influence the value of  $N_B^*$ .

Despite the importance of multiphase alloys to real-world applications, relatively little work in high temperature corrosion has been dedicated to comprehensive studies of such materials.<sup>9–11,24–28</sup> Nevertheless, some important and intriguing implications of alloy design have begun to emerge from developments in the understanding of how multiphase alloys oxidize. In this regard, two limiting cases of high temperature oxidation of a multiphase alloy<sup>9</sup> are shown in **Figure 4**. In (a), the component phases react independent of each other, and this can result in corrosion behavior that is worse than that displayed by either phase singly, and is certainly inferior to the other limiting case where the phases act together to form a continuous, exclusive protective layer, as depicted in (b) of **Figure 4**. In the latter case, a solute-rich phase acts as an efficient source or ‘reservoir’ of B, resulting in a subscale zone that is depleted of this component. The important factors include size, shape, distribution, volume fraction, and composition(s) of the minority phase(s). Normally, a finer dispersion of such phases is more efficient in promoting protective scale formation.<sup>24,29</sup> A striking example of this is shown in **Figure 5**, where the as-cast version of an alloy of Fe–15Cr–0.5C (wt%) composition did not form a protective  $\text{Cr}_2\text{O}_3$ , but a version of the same alloy with a refined dispersion of carbides did.<sup>29</sup>

A second approach using alloys to form a reservoir phase is best exemplified by the addition of Cr to  $\gamma\text{-TiAl}$ , facilitating the formation of a protective layer of  $\text{Al}_2\text{O}_3$ . Without a minimum of 8–10 at.% Cr in place of Ti, 60–70 at.% Al was needed for a protective alumina scale to form.<sup>30</sup> Because Cr is significantly more noble in oxygen than Ti or Al, this alloying benefit was not the traditional third-element

secondary-gettering mechanism described earlier. Rather, the addition of Cr introduced a second (Laves) phase,  $\text{Ti}(\text{Cr},\text{Al})_2$ , which promoted the formation of a protective  $\text{Al}_2\text{O}_3$  layer by equilibrating with, and stabilizing, the  $\gamma\text{-TiAl}$  phase that acted as an effective Al reservoir and did not transform to the less oxidation-resistant  $\alpha_2\text{-Ti}_3\text{Al}$  phase due to Al depletion.<sup>31,32</sup> Such an example highlights the variety of phase stability relationships in multiphase alloys that can be exploited as design routes to protective scale formation. Similar approaches based on thermodynamic and kinetic pathway factors are currently being exploited, for example, in the design of multiphase coatings used as bond coats in thermal barrier systems<sup>33</sup> or as alloy templates for synthesizing composite structures by controlling gas–metal reactions.<sup>2,13</sup>

This section has briefly described the underlying principles for the promotion of a protective scale via alloying or microstructural manipulation. These serve as a qualitative guide in assuring that the selective oxidation process produces the desired surface layer, as opposed to internal oxidation or a mixed external scale that is not truly protective. For an A–B alloy, this is achieved by considering conditions that minimize the solubility and diffusion of environmental reactants in the alloy and maximize the flux of B to the reacting surface – by increasing its initial concentration, its availability, or its mobility. Once a protective scale is formed, there are other considerations for maximizing the corrosion resistance and component lifetime; these are discussed below in terms of alloying for minimizing the scale growth and spallation as well as for materials selection for specific environments.

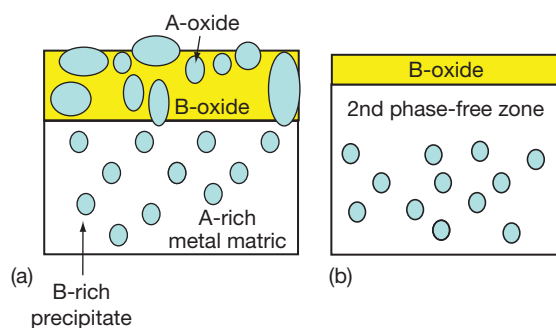


**Figure 4** Schematic depiction of (a) independent and (b) cooperative oxidation based on concepts presented in Gesmundo, F.; Gleeson, B. *Oxid. Met.* **1995**, *44*, 211–238.

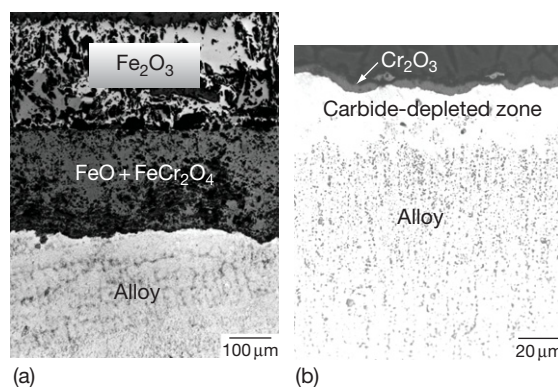


**Figure 5** Cross-sectional micrographs of Fe–15Cr–0.5C (wt%) steel exposed at 850 °C for 72 h in 1 atm  $\text{O}_2$  (a) as-cast and (b) hot-forged. Reproduced from Durham, R. N.; Gleeson, B.; Young, D. J. *Oxid. Met.* **1998**, *50*, 139–165.

### 1.21.4 Minimizing Oxide Growth and Improving Scale Adhesion by Alloying

It is now a known fact that dilute additions of reactive, or rare-earth elements (REs) can substantially decrease the oxide scale growth rate and improve the scale adhesion of alloys that form protective layers of chromia or alumina.<sup>34–38</sup> Oxides of REs are highly stable (see Figure 1) and are readily taken up into the protective oxide layer, where they can help decrease the steady-state growth rate.<sup>35</sup> These active elements can also improve the scale adhesion, in many cases by offsetting the detrimental effects of indigenous impurities, such as sulfur.<sup>35,39</sup> Therefore, the most oxidation-resistant commercial alloys contain minor (<0.1 wt%) concentrations of REs. As an example, Figure 6 illustrates the beneficial effects of certain RE additions on cyclic oxidation lifetime for two  $\text{Al}_2\text{O}_3$ -forming alloy systems.

While all these active elements qualitatively respond in a similar manner upon exposure to an oxidizing environment, there are differences in the effectiveness of specific REs. Different effects on oxidation behavior are observed depending on the RE chosen,

the way it is added to or incorporated into the alloy, and its concentration (see Figure 6), as well as how it is dispersed in the alloy matrix.<sup>35–38</sup> These additions can add significant costs to alloy production and, because of their reactivity, REs can be difficult to control to specified levels during processing, especially for coatings,<sup>40,41</sup> where laboratory-scale benefits have not yet been scaled up for commercialization. It is, therefore, particularly important to weigh all factors affecting the RE concentration and incorporation into the alloy, some of which (such as the use of multiple REs and the effects of other minor alloy constituents – see below) have only been widely discussed relatively recently.

The choice of a particular RE can be guided by empirical findings or rules. For example, as single additions, Hf and Zr are preferable for aluminides, while Y is superior in Ni–Cr–Al and Fe–Cr–Al alloys.<sup>37</sup> For chromia-forming alloys, La seems to be preferred based on its large ion size and its higher solubility, particularly in ferritic alloys.<sup>42</sup> In this regard, the low solubility of Y in many alumina-forming alloys limits its effectiveness.<sup>37,43</sup> When a RE exceeds its solubility limit, it can be more readily internally oxidized given

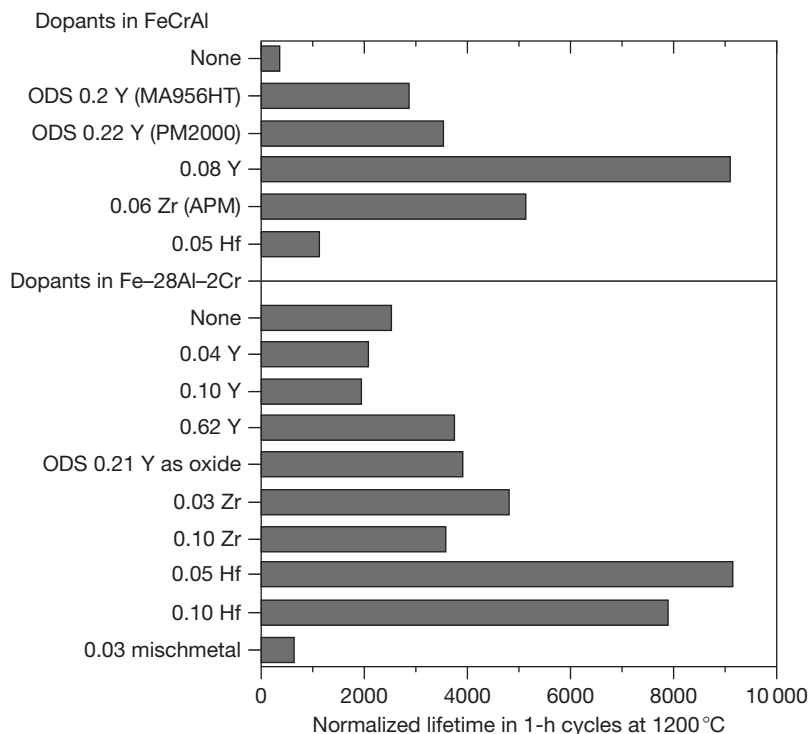


**Figure 6** Effect of various RE additions to a base Fe–20Cr–10Al or Fe–28Al–2Cr (at.%) alloy in terms of normalized oxidation lifetime for 1-h thermal cycles at 1200 °C. Reproduced from Pint, B. A. In *Proceedings of John Stringer Symposium*; Tortorelli, P. F., Hou, P. Y., Wright, I. G., Eds.; ASM International: Materials Park, OH, 2003; pp 9–19.



the active nature of these elements (**Figure 1**). This can compromise the oxidation resistance and/or mechanical integrity (if extreme). The effective use of a RE requires optimization of its concentration.<sup>38</sup>

**Figure 6** clearly indicates that the oxidation resistance is quite sensitive to RE concentrations.

The use of two reactive elements (so-called ‘co-doping’) is often more effective than the use of a single RE,<sup>38,43–45</sup> at least for alumina-forming alloys. Several commercial alumina-forming alloys and coatings contain multiple REs.<sup>43,44</sup> It is thought (at least for Fe–Cr–Al alloys) that co-doping allows Y to be fully effective by keeping it below its solubility limit and then supplementing it with a more soluble RE, such as Hf or Zr. Thus, in general, it appears that co-doping allows the total RE concentration to be decreased while maintaining good scale adhesion, and low oxide growth rates. In many cases, this then decreases the amount of internal oxidation relative to the single dopant case.<sup>43</sup>

It is clear that attention to microalloying additions and/or impurity control is important in maximizing the oxidation resistance of alloys using REs. Sulfur (and possibly other) impurities can have a detrimental effect on scale adhesion.<sup>4,46–48</sup> Further, such indigenous impurities, as well as purposeful additions for microstructural tailoring and properties enhancement (such as carbon, nitrogen, boron, etc.), can mitigate the positive effects of REs on oxidation resistance.<sup>38,45,49,50</sup> For example, in Hf-doped NiAl, the Hf/C ratio has been found to be important in optimizing scale adhesion.<sup>49,50</sup> **Figure 7** shows that NiAl suffered greater scale spallation with decreasing Hf/C ratios. It has been suggested that, if the Y:S and/or Hf:C ratios are  $<1$ , the alloy will have less than optimal performance.<sup>38</sup> Therefore, the active nature of REs makes alloy design with these elements a delicate optimization process.

It should be emphasized that, while effective when concentrations are optimized for given levels of impurities or microalloying additions, REs generally do not promote protective scale formation, that is, they do not make marginal  $\text{Al}_2\text{O}_3$  or  $\text{Cr}_2\text{O}_3$ -forming compositions into robust ones.<sup>37</sup> Other approaches, as outlined in the previous sections, must be used. In this regard, however, any indirect effects of RE additions need to be evaluated and separated from the direct influence of RE's on scale growth and adherence. For example, a sufficient concentration of RE-rich precipitates in the alloy matrix can result in a finer grain size and, this in itself, can promote protective scale development (as discussed in a preceding section).<sup>37</sup>

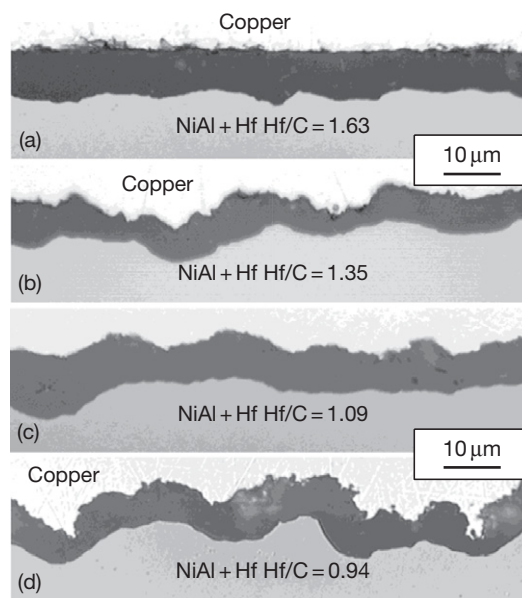


**Figure 7** Polished cross-sections of the  $\text{Al}_2\text{O}_3$  scale formed on coatings of NiAl+Hf with differing Hf/C ratios, after 10 100-h thermal cycles at  $1200^\circ\text{C}$ . Reproduced from Pint, B. A. In *Proceedings of John Stringer Symposium*; Tortorelli, P. F., Hou, P. Y., Wright, I. G., Eds.; ASM International: Materials Park, OH, 2003; pp 9–19.

There are potential detrimental effects of other alloying elements on oxidation resistance if they are sufficiently active. For example, single additions of 1 at.% Re, Ti, Ta, or Cr (commonly present in coatings and Ni-base superalloys) were found to degrade the oxidation resistance of Hf-doped NiAl.<sup>50</sup> The Re and Cr additions formed precipitates in the alloy and negatively affected the oxide–metal adhesion, while the Ti and Ta were oxidized and incorporated into the scale as potential sites for scale breakdown.<sup>51,52</sup> On the contrary, certain precious metal additions to NiAl can improve the oxidation resistance by improving the scale adhesion,<sup>53,54</sup> presumably by mitigating the detrimental effect of sulfur, and promoting alumina formation on low-Al ( $\gamma+\gamma'$ ) substrates.<sup>33</sup>

### 1.21.5 Maximizing Oxidation Lifetime

There has been an increasing focus on oxidation lifetime, particularly in terms of approaches used for predicting it accurately for a given material and exposure condition.<sup>55</sup> The primary reason for this trend is that lifetime values can lead to quantification of oxidation behavior in a way that can be better used by researchers, engineers, systems designers, plant

operators, etc. As the most corrosion-resistant materials have very long lifetimes, verified life prediction models provide a way to predict end of life without necessarily having to conduct extensive, extended exposures. Also, lifetime models can provide guidance to the alloy design process by quantifying the effect of specific approaches taken to improve high temperature corrosion resistance. Some trends based on these are discussed in this section.

Usually, lifetime is defined as the time-to-break-away ( $t_b$ ) – the time at which the protective scale fails and cannot be reformed, thereby resulting in the growth of faster-growing, nonprotective products. The cross-sectional image in **Figure 8** captures the process at  $t_b$ , that is, the transition from protective to nonprotective behavior, and illustrates the radical difference in the nature of the respective aluminum and iron oxides. After 1101 h, the protective  $\text{Al}_2\text{O}_3$  layer on the right-hand side of the image in **Figure 8** reached the point where it could no longer be maintained by the supply of remaining Al from the alloy.<sup>56</sup> Therefore, iron oxides formed and rapidly consumed the remaining metal. Following Quadakkers *et al.*,<sup>57,58</sup> the time-to-breakaway for alloy A–B that forms a protective  $\text{B}_x\text{O}_y$  layer can be expressed as:

$$t_b = [(N_B - N_{B,c})/100 \cdot d/2 \cdot \rho \cdot M^{-1} \cdot k^{-1}]^{1/n} \quad [4]$$

where  $N_B$  is the initial B concentration,  $N_{B,c}$  is the critical concentration below which a protective  $\text{B}_x\text{O}_y$  layer cannot be maintained (different from  $N_B^*$ ),  $d$  is the thickness of the specimen,  $\rho$  is the alloy density,  $M$  is the mass conversion factor for metal and oxide, and  $k$  is the rate constant, where  $(kt)^n$  is the rate for consumption of B by oxidation. This  $k$  represents the total consumption of B by oxide growth as well as spallation. It can also be dependent (inversely) on  $d$  for thin cross-sections.<sup>59</sup>

From an alloy design viewpoint, oxidation lifetime can be increased by any approach (discussed above

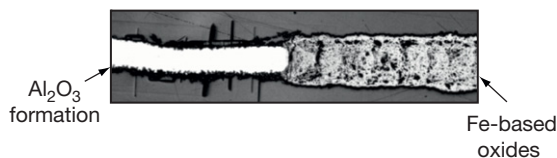


**Figure 8** Cross-sectional image of an Fe-28Al-5Cr-0.2Zr (at.%) alloy exposed in air for 1101 h at 1300°C. Other data from these exposures reported in Bennett, M. J.; DeVan, J. H.; Tortorelli, P. F. *The Oxidation Behavior of Iron Aluminides in Air at 1300°C*. In *Microscopy of Oxidation 3*; Newcomb, S. B., Little, J. A., Eds.; The Institute of Materials: London, 1997; pp 233–245.

or elsewhere in this book), that slows the rate of scale growth or spallation (decreases  $k^n$ ) or enhances the promotion of a protective layer (decreases  $N_{B,c}$ ). In addition,  $t_b$  can be increased by increasing the concentration of B, assuming no alteration of other factors (e.g., solubilities or  $D_{AB}$ ) that would destabilize the stability of the protective  $\text{B}_x\text{O}_y$  layer. However, increasing B can affect physical or mechanical properties that, in turn, can influence the lifetime through effects on  $k$ . For example, for Fe–Al systems, simply increasing the concentration of Al can actually decrease the lifetime. This is because the ordered structures at higher Al levels result in significantly higher values of alloy CTE than those of other iron-based alumina-forming alloys (see **Figure 9**).<sup>60</sup> Therefore, greater compressive stresses are experienced by the scales on cooling, leading to higher spallation rates and, thus, higher values of  $k$ . Hence, iron aluminides do not necessarily show substantially greater lifetimes than Fe–Cr–Al alloys despite much greater values of  $N_B$ .<sup>56</sup>

The critical concentration for maintaining the ability to reform a protective layer,  $N_{B,c}$ , is dependent on the failure mode of the  $\text{B}_x\text{O}_y$  layer (intrinsic chemical failure or mechanically-induced chemical failure).<sup>61</sup> Intrinsic failure is when the actual level of B falls below the equilibrium value for formation of the protective oxide by continued selective oxidation; here,  $N_{B,c}$  can be quite low and only achieved under very limited circumstances when the alloy is very

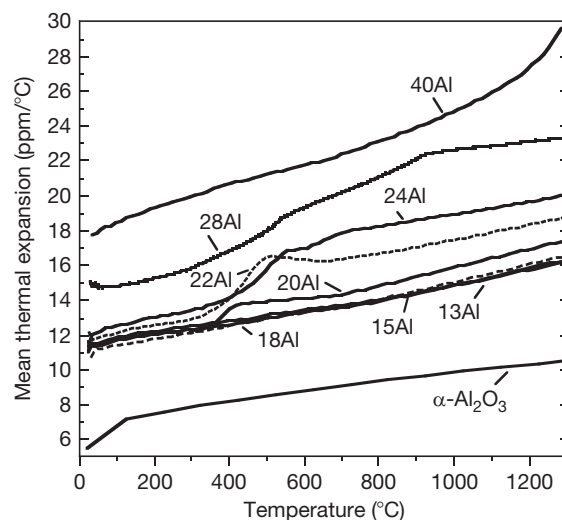


**Figure 9** Mean thermal expansion coefficient versus temperature for  $\alpha\text{-Al}_2\text{O}_3$  and various Fe–Al alloys. Reproduced from Pint, B. A.; Porter, W. D.; Wright, I. G. *Mater. Sci. Forum* **2008**, 595–598, 1083–1092.

thin (to relieve stresses readily by creep) and temperatures very high.<sup>61–63</sup> The mechanically induced chemical failure mode is the more typical one and occurs when the concentration of B becomes lower than the value needed for kinetically controlled scale rehealing, and the accumulated strain energy is sufficient for scale cracking and/or decohesion.<sup>3</sup> It may, therefore, be possible to use alloying additions to control this process and lower  $N_{B,c}$  (raise  $t_b$ ). For alumina forming alloys, Cr can increase the lifetime by allowing  $\text{Cr}_2\text{O}_3$  scales to extend protection after  $\text{Al}_2\text{O}_3$  scales can no longer form (intrinsic failure mode)<sup>61</sup> or to promote reestablishment of the latter by a type of third-element effect (mechanically induced chemical failure mode).<sup>63</sup> In this regard, alloying additions or heat treatments that affect the mechanical strength of the substrate can also influence oxidation lifetime by modifying the effective strain energy available for protective scale breakdown<sup>37,64</sup> as reflected by  $k$  (and  $n$ ) in eqn [4]. This is another example of unintended, or secondary, consequences of alloy manipulation via effects on chemical, physical, or mechanical factors that affect either the ability to form a protective scale or to reform it after a failed event.

There are additional concerns about the lifetime of corrosion-resistant coatings designed for use at high temperatures. Because of the dependence of  $t_b$  on the total amount of B available for protective oxide scale (POS) formation (manifested through  $d$  in eqn [4]), coatings, particularly thin ones, have limited reservoirs of B. Additionally, the depletion of B by oxidation ( $k$ ) is accompanied by loss of B by back-diffusion from the coating into the substrate on which it is deposited.<sup>65</sup> Alloy manipulation can be used to control this process to a certain extent.<sup>33</sup> Barrier layers at the coating–substrate interface may also have to be considered to prevent undesirable (from an oxidation perspective) alloying of the coating by elements diffusing from the substrate.<sup>66</sup> As discussed above, it is often difficult to synthesize coatings in a controlled manner with appropriate levels and distributions of REs; so attempts to minimize  $k$  in order to maximize lifetime are rather more limited in these cases.

### 1.21.6 Alloy Selection for Specific Environments

Most high temperature environments involve more than one potential reactant. In many mixed reactants involving  $\text{O}_2$ ,  $\text{N}_2$ ,  $\text{H}_2\text{O}$ ,  $\text{S}_2$ ,  $\text{CO}$ , etc., the reaction of alloys can be quite complex, with multiple types of

internal precipitates and limited means to predict and control their formation.<sup>67,68</sup> However, in other cases of multiple reactive species, reactions with oxygen still predominate and can be used constructively to promote the formation of a POS that is an effective barrier to other reactive species in the environment. This is usually enabled, at least in part, by the greater stability of oxides relative to other products so that oxide formation is possible even at very low oxygen partial pressures. A good example in this regard is the preferential establishment of a protective  $\text{Al}_2\text{O}_3$  layer even under the so-called ‘reducing’ sulfidizing environments, where the partial pressure of oxygen ( $p_{\text{O}_2}$ ) is of the order of  $10^{-20}$  atm while  $p_{\text{S}_2}$  is  $\sim 12$ – $14$  orders of magnitude greater.<sup>69</sup> Under these conditions, approaches to promote the stability, exclusiveness, integrity, and maintenance of POSs can still have a role in alloy design and selection for mixed-oxidant environments. Some examples of alloy selection for specific environments are given below. Further details of the relevant corrosion processes are described in other chapters of this book.

*Air/Nitridation.* Because of the typically greater stability of the oxides, the alloys that form protective  $\text{Al}_2\text{O}_3$ ,  $\text{SiO}_2$ , and/or  $\text{Cr}_2\text{O}_3$  scales often perform well in air with little interference from nitrogen. However, subscale nitride formation is possible if there is a way for the nitrogen to penetrate the oxide scale or disrupt its ability to form a continuous surface layer, or if the scale is mechanically breached and cannot heal. (This is true, of course, for many oxygen-second oxidant systems.) For example, Fe-based  $\text{Al}_2\text{O}_3$ -forming alloys usually perform similarly in oxygen and air but, recently, Pint *et al.* reported (nonclassical) internal oxidation and nitridation of Fe–Al alloys upon air exposure.<sup>70</sup> This accelerated attack was eliminated by additions of REs or Ti to the Fe–Al alloy, by promoting a less defective scale. For TiAl intermetallics, TiN formation during the initial stages of oxidation in air has been shown to disrupt the continuity of the  $\text{Al}_2\text{O}_3$  layer, resulting in less protective (alumina + titania)-based mixed-oxide scales.<sup>71</sup> The addition of Ag or Cr to TiAl helps promote continuous  $\text{Al}_2\text{O}_3$  layer formation and ameliorates this problem in part by modifying the nature of the compositional changes at the alloy–scale interface during the initial stages of oxidation which can otherwise trigger local TiN formation, and prevent the development of continuous alumina layers.<sup>32,72</sup>

The participation of nitrogen as a reactant for air exposures can also be triggered by the presence of

ambient water vapor in the environment. As an example, while  $\text{Cr}_2\text{O}_3$  formed on a Cr–Nb alloy in both dry and humid air, subsurface nitridation only occurred in the latter case (Figure 10).<sup>73</sup> Similar behavior was also observed for a gamma-based Ti–Al–Cr alloy, with a borderline Cr content to promote alumina scale formation; protective  $\text{Al}_2\text{O}_3$  formed in dry air at 1000 °C, but subscale nitridation was observed after exposure to humid air.<sup>32</sup> For Cr–Nb at 950 °C, little difference between dry and humid air was observed, but significant subscale nitridation was observed when the oxygen and sulfur impurities in the alloy were decreased, with possible synergistic effects between S and water vapor.<sup>73</sup> Experience suggests that such complicated effects tend to occur in alloy composition ranges which fall near the kinetic boundary for continuous, POS formation.

As already noted, internal nitridation can occur in air environments if a continuous, protective oxide layer cannot form or is breached. It can also be observed in nitrogen-rich environments that are reducing with respect to even the most stable oxides. Under such conditions, alloys with elements that minimize nitrogen solubility and diffusivity are less susceptible to attack (eqn [2]). In this regard, nickel and cobalt have strong beneficial effects, with the added advantage that neither Ni nor Co tend to form thermodynamically stable nitrides under most technologically relevant nitrogen-containing environments.<sup>74,75</sup> This impact of low nitrogen permeability is illustrated in Figure 11, which shows nitrogen uptake as a function of the sum of Ni and Co concentrations in Fe–Ni–Co alloys and in Figure 12, where reaction rates of internal nitridation are shown

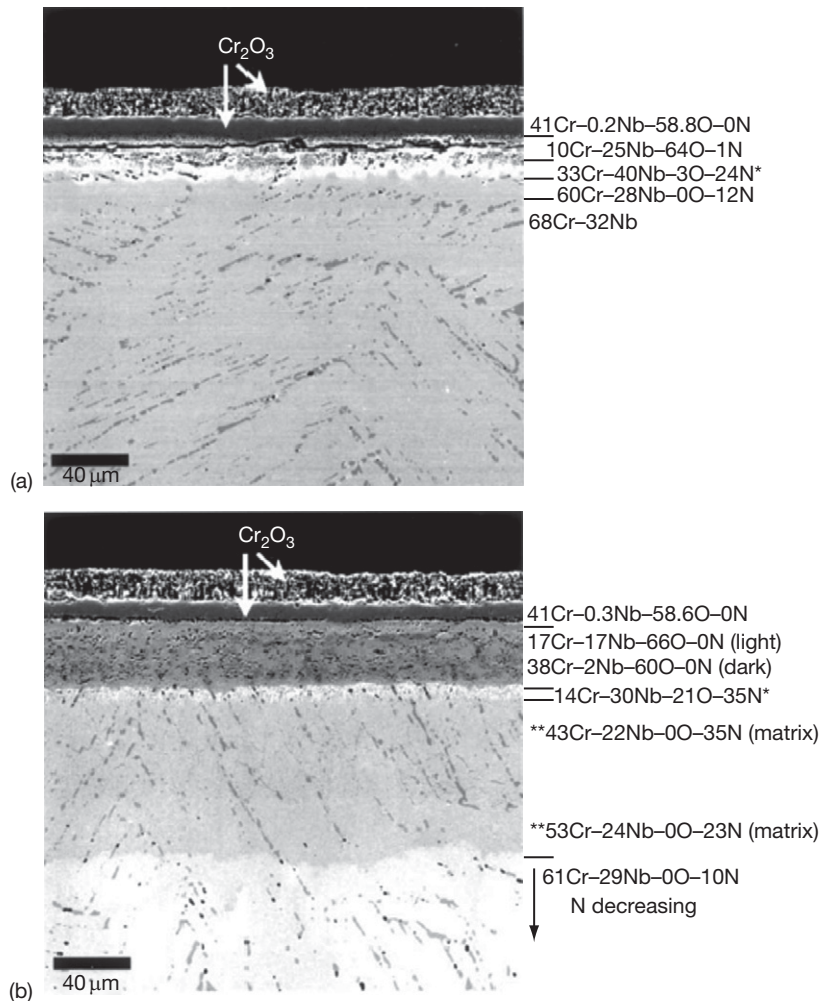


**Figure 10** Cross-sectional micrographs of Cr–Nb (at.%) oxidized for 24 h at 1100 °C. (a) filtered dry air (b) humid air. Reproduced from Brady, M. P.; Tortorelli, P. F.; Walker, L. R. *Oxid. Met.* **2002**, 58, 297–318.



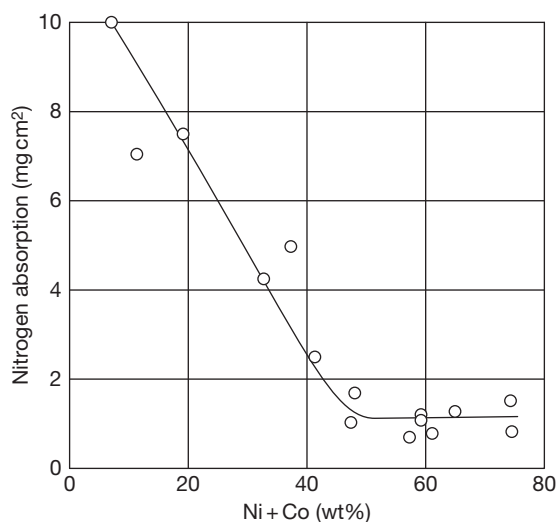


**Figure 11** Effect of Ni + Co content in Fe-Ni-Co alloys on nitridation at 650 °C for 168 h (NH<sub>3</sub>). Data of Barnes and Lai as shown in Lai, G. Y. *High Temperature Corrosion of Engineering Alloys*; ASM International: Materials Park, OH, 1990.

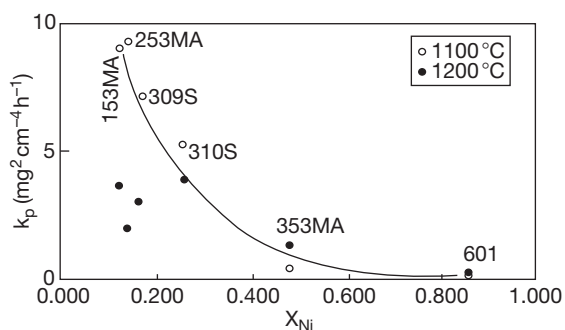


**Figure 12** Parabolic rate constants for nitridation in NH<sub>3</sub> as a function of Ni concentration in various alloys. Reproduced from Tjokro, K.; Young, D. J. *Oxid. Met.* **1995**, *44*, 453–474.

to decrease strongly with nickel concentration of the alloy. Under these special circumstances, alloying additions of Cr, Al, or Ti will lead to internal precipitation of their respective nitrides and, therefore, will compromise the nitridation resistance of the nickel or cobalt. In particular, the introduction of Cr in Ni–Al or Ni–Ti base alloys strongly increased the amount of internal attack due to increased nitrogen permeability.<sup>76</sup>

**Carburization and Metal Dusting.** Like many cases of nitridation, carburization is manifested as an internal precipitate formation (of carbides), ahead of the alloy–scale interface. Chromia-forming materials are often used for service where carburization can occur due to the many options available among such

alloys to combine good oxidation resistance with attractive high temperature mechanical properties at relatively low alloy cost. Resistance to attack derives from the development and maintenance of a continuous Cr<sub>2</sub>O<sub>3</sub> scale. Consequently, alloy design approaches that generally promote chromia formation are also a benefit in carburizing environments. Alloying that leads to the development of an Al<sub>2</sub>O<sub>3</sub> or SiO<sub>2</sub> layer or sub-layer can proffer greater protection under carburization conditions that are too severe for chromia-forming alloys.<sup>77,78</sup> Recently, it was shown that increasing the nickel content of Fe–Cr–Ni alloys from 30–35 wt% to 45% or greater, significantly decreased the carburization rate due to decreased carbon solubility and diffusivity in the alloy (eqn [2]).<sup>78</sup> Furthermore, the addition of a few % Al to 60% Ni alloy increased the carburization resistance substantially due to alumina scale formation at higher temperatures.<sup>78</sup>

Metal dusting is a catastrophic form of metal degradation in carbonaceous environments that occurs over a lower temperature range (typically 400–800 °C), but accompanied by higher carbon activities than the carburization phenomenon described above.<sup>79,80</sup> It can result in the disintegration of alloy into powder, and occurs for nickel- as well as iron-based alloys (although it is less severe in the former case). As indicated above, alloying or microstructural approaches that promote the exclusive formation of a robust protective chromia scale improve the resistance to metal dusting, including the use of cold work or surface deformation to increase outward Cr diffusivity in the alloy.<sup>81</sup> Alloys with ≥26 wt% Cr and a few % of Si or Al should show improved resistance to metal dusting.<sup>77</sup> It is expected that silica or alumina scales should resist the uptake of carbon more than chromia scales and, therefore, be suitable for metal dusting resistance. Indeed, any alloy improvements that extend the time for localized oxide scale breakdown, and the initiation of metal dusting at such locations, will also confer a benefit from any processes that can be used to reoxidize a component during operational shutdowns.<sup>82</sup> Alloying Ni with Cu has been found to improve the resistance to metal dusting.<sup>83</sup> Rates of reaction of Ni–Cu alloys decreased significantly with increasing Cu up to 10 wt% with virtually no metal dusting at 20% Cu. Because Cu appears to be noncatalytic towards carbon deposition and has virtually no solubility for C, its positive effect on dusting of Ni–Cu alloys probably relates to a dilution effect.<sup>83</sup>

**Sulfidation.** Pure sulfidation, that is gas–metal reaction in an environment completely devoid of oxygen,



poses a challenge for the design of traditional heat-resistant high temperature alloys that normally depend on the development of  $\text{Cr}_2\text{O}_3$ ,  $\text{Al}_2\text{O}_3$ , or  $\text{SiO}_2$  scales.<sup>84</sup> This is because the growth rates of many metal sulfides are quite high (due to their highly defective structures) and they cannot function as protective scales. On the contrary, refractory metal sulfides based on Mo or Nb are slow growing,<sup>84</sup> but little success in alloying Fe–Al with Mo or Nb has been reported.<sup>77</sup> The most promising system is Fe–Al–Mo, due to the formation of a protective layer of  $\text{Al}_{0.55}\text{Mo}_2\text{S}_4$ .<sup>85</sup>

As mentioned earlier in this section, there are applications in which the environment is highly sulfidizing, but there is a presence of oxygen ( $p_{\text{O}_2}$  of the order of  $10^{-18}$ – $10^{-24}$  atm or perhaps even lower). Under these circumstances, there are greater opportunities for design of more practical alloy systems. This is because  $\text{Al}_2\text{O}_3$  and  $\text{SiO}_2$  are thermodynamically/kinetically stable at these oxygen partial pressures, while  $\text{Cr}_2\text{O}_3$  may or may not be.<sup>86</sup> At 700 °C with  $p_{\text{S}_2} \sim 10^{-8}$  atm and  $p_{\text{O}_2} \sim 10^{-20}$ – $10^{-24}$  atm, chromia scales can form on Fe–Cr(–Ni) alloys, at least at the highest oxygen pressures, with scales formed on Fe–Cr ( $\text{M}_2\text{O}_3$  type with low Fe levels,  $M$  = metallic element) being significantly more protective than those on Fe–Cr–Ni ( $\text{M}_3\text{O}_4$ , with higher Fe contents).<sup>86</sup> Consequently, minor alloying elements that promote exclusive formation of  $\text{M}_2\text{O}_3$ -type scales (Si, Al) also improved sulfidation resistance.<sup>86</sup>

Work over a number of years has consistently shown that alumina-forming materials have significantly better resistance to corrosion under highly sulfidizing conditions than chromia-forming alloys,<sup>69,87–89</sup> particularly for iron-based systems. Figure 13 compares mass change data at 800 °C for model Fe–Cr–Ni (stainless steel) and FeCrAl alloys with that of an Fe–28Al (at.%) alloy in a  $\text{H}_2\text{S}$ – $\text{H}_2$ – $\text{H}_2\text{O}$  gas mixture, where  $p_{\text{O}_2}$  was  $\sim 10^{-22}$  and  $p_{\text{S}_2} \sim 10^{-6}$  atm. The exceptionally low rate of reaction in this very aggressive environment is due to the formation of a protective  $\text{Al}_2\text{O}_3$  scale for the iron aluminide while sulfides formed on the other alloys. Additions of Cr to the base Fe–28Al composition increased the rate of reaction at a concentration level of 4% and above.<sup>69</sup> The presence of REs in alumina-forming alloys was reported to have a beneficial effect on sulfidation resistance by improving the scale integrity.<sup>90</sup> In contrast, no influence of REs on sulfidation behavior of chromia-forming systems, where scale breakdown was not by mechanical disruption of the oxide scale, was found.<sup>90</sup>

Recent work with TiAlCr alloys in  $\text{H}_2\text{S}$ – $\text{H}_2$ – $\text{H}_2\text{O}$  environments indicated that, in contrast to Fe–Cr–Al

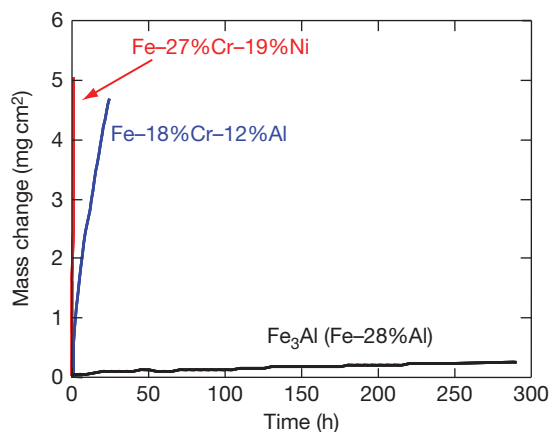


**Figure 13** Mass change of Fe-based alloys in  $\text{H}_2$ – $\text{H}_2\text{S}$ – $\text{H}_2\text{O}$  at 800 °C ( $p_{\text{O}_2} \sim 10^{-22}$  and  $p_{\text{S}_2} \sim 10^{-6}$  atm). Concentrations are in at.%. Reproduced from DeVan, J. H. In *Oxidation of Intermetallics*; Grobstein, T., Doychak, J., Eds.; TMS: Warrendale, PA, 1989; pp 107–115.

alloy systems, alloying approaches that promote exclusive formation of protective  $\text{Al}_2\text{O}_3$  layers in this system result in good sulfidation resistance.<sup>91</sup> This is speculated to result, in part, from the unusual mechanism of the third-element effect in the Ti–Al–Cr system, mechanistically based on sub-scale alloying depletion effects during reaction rather than the more classical gettering type behavior for Fe–Cr–Al.<sup>25</sup> There have been other reports of good sulfidation resistance for coatings based on Ti–Al,<sup>92</sup> and a low reaction rate for Ti–6Al–4V.<sup>93</sup>

Alloys that form  $\text{SiO}_2$  scales also show some promise for the highly sulfidizing-oxidizing environments described above. Good resistance of  $\text{MoSi}_2$  to Ar– $\text{H}_2$ – $\text{H}_2\text{S}$  has been reported,<sup>92</sup> presumably due to the slow reaction rate of Mo in sulfur<sup>84</sup> and the lack of a stable sulfide of Si. More recently, work with multiphase Mo–Si–B alloys in the same mixed sulfidizing-oxidizing gas as used for the data in Figure 13 showed low reaction rates at 800 °C, with the formation of  $\text{MoSi}_2$  and  $\text{SiO}_2$  scales.<sup>94</sup> Despite the susceptibility of nickel to reaction with sulfur or  $\text{SO}_2$ , silica scales seemed to proffer good sulfidation resistance to iron and nickel silicides.<sup>95</sup>

As  $p_{\text{S}_2}$  is decreased and  $p_{\text{O}_2}$  increased,  $\text{SO}_2$  becomes the dominant reactive species. Such environments are typically found in combustion of sulfur-bearing fuels. Under these conditions, chromia is often stable, although its range of stability is usually determined by kinetic factors.<sup>96</sup> However, the overall corrosion resistance still involves approaches for manipulating alloy composition and microstructure

to promote the formation and maintenance of a protective  $\text{Cr}_2\text{O}_3$ -(rich) scale, as discussed above. Many studies of sulfidation and POS breakdown under such oxidizing-sulfidizing conditions have been conducted.<sup>74,77,96</sup> Alloys that form protective  $\text{Al}_2\text{O}_3$  and  $\text{SiO}_2$  scales can, in theory, show good resistance to corrosion by  $\text{SO}_2$ . On the other hand, nickel aluminides were not particularly resistant to corrosion in the presence of  $\text{SO}_2$ ,<sup>97</sup> although iron aluminides should be.<sup>89</sup> If conditions are such that sulfate salts deposit on alloys, chromia scales are most resistant compared to  $\text{Al}_2\text{O}_3$  and  $\text{SiO}_2$  scales under the so-called type II hot corrosion conditions (lower temperature mode), while alumina scales can be preferable for resistance to type-I attack.<sup>98</sup>

**Water vapor.** The effects of water vapor ( $\text{H}_2\text{O}$ ) on high temperature oxidation have received increasingly greater attention. In large part, this is because most power-generation applications (gas turbines, combustion and steam-generation systems, solid oxide fuel cells, etc.) involve environments with relatively high levels of  $\text{H}_2\text{O}$ . As such, there is a critical need for materials that are relatively nonreactive with water vapor under the aggressive conditions imposed by the increased operating temperatures and pressures needed to achieve high power-generation efficiencies and decreased emissions. As described elsewhere in this book, the presence of water vapor in the environment typically leads to higher oxidation rates, particularly for chromia- or silica-forming alloys where  $\text{H}_2\text{O}$  can dramatically enhance oxide volatilization and/or impact oxide structure/stability and solid-state transport properties.<sup>99,100</sup> In particular, water vapor results in the formation of volatile oxyhydroxides, which can significantly compromise the formation of POS by constant thinning of the oxide surface layer due to volatilization.<sup>99</sup> Because chromia has the highest volatilization susceptibility of the major high temperature protective oxides,<sup>100</sup> Mn is added to chromia-forming steels to decrease the rate of volatilization substantially by promoting the development of  $(\text{Cr,Mn})_3\text{O}_4$  surface layers.<sup>101</sup> In contrast to  $\text{Cr}_2\text{O}_3$  and  $\text{SiO}_2$  scales,  $\text{Al}_2\text{O}_3$  scales are far more stable in  $\text{H}_2\text{O}$ -containing environments (see **Table 1**)<sup>100</sup> and, as discussed below, are generally less susceptible to accelerated oxidation in the presence of water vapor.

Accelerated oxide scale growth rates, decreased time-to-breakaway (associated with formation of iron oxide nodules), and increased spallation susceptibility under thermal-cycling conditions have been widely reported for water vapor effects on chromia-forming

**Table 1** Approximate upper use temperature ( $^{\circ}\text{C}$ ) for oxides based on partial pressure of all volatile species equal to  $1 \times 10^{-7}\text{MPa}$

	<b>Air: 0.1 MPa total <math>2.1 \times 10^{-2}</math> MPa <math>\text{O}_2</math> <math>10^{-3}</math> MPa <math>\text{H}_2\text{O}</math></b>	<b>0.1 MPa total <math>10^{-2}</math> MPa <math>\text{O}_2</math> <math>10^{-3}</math> MPa <math>\text{H}_2\text{O}</math></b>	<b>1 MPa total 0.1 MPa <math>\text{O}_2</math> 0.1 MPa <math>\text{H}_2\text{O}</math></b>
$\text{Cr}_2\text{O}_3$	1122	1042	499
$\text{SiO}_2$	1575	1370	967
$\text{Al}_2\text{O}_3$	*	1864	1345

\*limited by melting point of oxide rather than volatility.

Source: Adapted from Opila, E. J.; Jacobson, N. S.; Myers, D. L.; Copland, E. H. *JOM* **2006**, 58, 22–28.

ferritic and austenitic steels, which are extensively used in the  $\sim 500$ – $800^{\circ}\text{C}$  range (see other chapters in this book).<sup>102–110</sup> However, proper alloying can improve oxidation resistance of these chromia-forming alloys in the presence of water vapor. This is shown schematically for Cr and Ni in **Figure 14**, which indicates the compositional regions where behavior associated with development of a POS consisting of Cr-rich  $(\text{Cr,Fe})_2\text{O}_3$  was observed at 650 and  $800^{\circ}\text{C}$ .<sup>106</sup> As expected normally (cf. eqn [2]), increasing Cr has a beneficial effect on promoting POS formation in water vapor-containing environments. At levels above  $\sim 16$  wt% Cr, increasing the Ni level in the alloy also provides some improvement in oxidation resistance in the presence of water vapor.<sup>106</sup> While increasing the Cr levels above those shown in **Figure 14** may improve the oxidation resistance even more, the onset of brittle sigma phase formation in the alloy and its detrimental effect on the mechanical properties must be considered.<sup>109</sup> As discussed in the previous sections, a finer alloy grain size can help promote POS formation on an alloy.<sup>17</sup> This has been observed in water vapor-containing environments for chromia-forming alloys.<sup>111</sup>

Minor individual alloying additions of Mn (0.1–3.5 wt%), Si (0.2%), Ti, and B to form  $\text{TiB}_2$  ( $\leq 1\%$ ), and Nb and C to form NbC ( $\leq 1\%$ ) in model Fe–16 wt% Cr base alloys have been reported to have a beneficial effect on oxidation resistance in air +10%  $\text{H}_2\text{O}$ .<sup>111</sup> The effects of Ti and Nb may result, in part, by decreasing the alloy grain size by formation of  $\text{TiB}_2$  and NbC, which retard the grain growth during alloy processing. No beneficial effect of RE-type additions (0.3% La, 0.1% Y, 0.03% Zr) on oxidation resistance in water vapor was noted.<sup>111</sup> As mentioned previously, Mn additions to Fe–Cr alloys in sufficient concentrations to promote a Cr–Mn spinel layer can be beneficial by decreasing oxide volatilization.<sup>101</sup> Additions of Mn and Si to Fe–20Cr–20Ni (wt%)

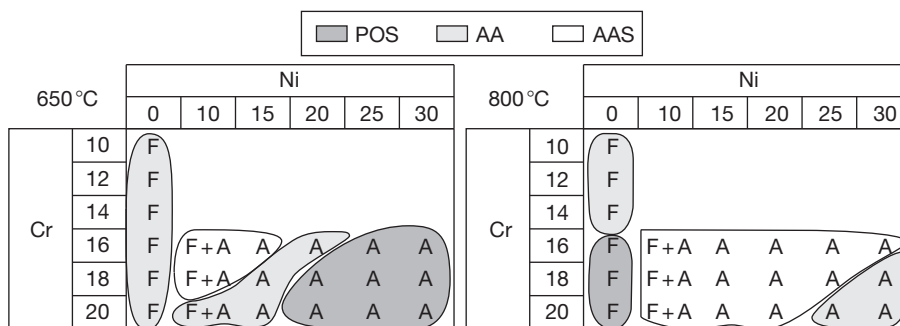


**Figure 14** Maps of three behaviors (POS – protective oxide scale, AA – accelerated attack, AAS – accelerated attack with spallation) as a function of Ni and Cr concentrations (wt%) in Fe-based alloys (F – ferritic, A – austenitic). Based on observations for 100 1-h thermal cycles in air + 10 vol. % H<sub>2</sub>O at indicated temperatures. Reproduced from Peraldi, R.; Pint, B. A. *Oxid. Met.* **2004**, 61, 463–483.

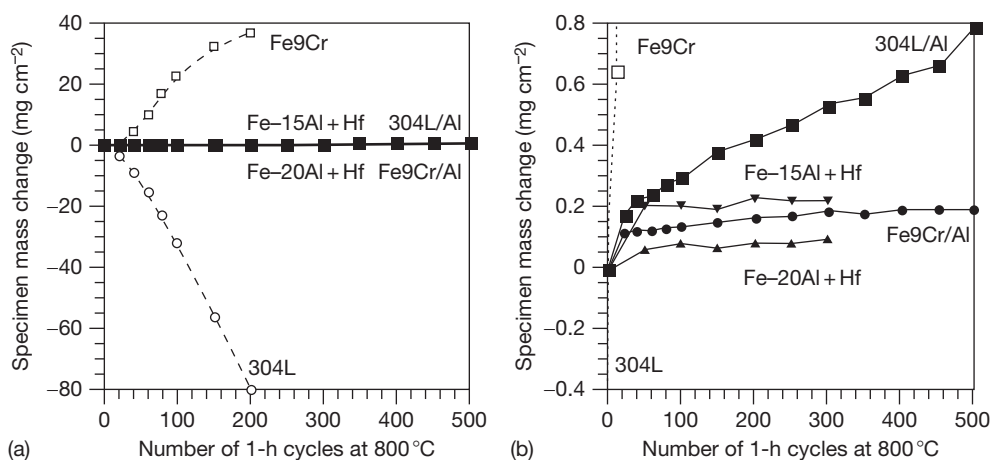


**Figure 15** Mass changes for 1-h thermal cycles at 800°C in air + 10 vol. % H<sub>2</sub>O. Selected data from (a) are shown in (b) over a smaller ordinate range. 'Fe9Cr/Al' and '304L/Al' denote data for aluminized Fe-9Cr-1Mo steel and type 304L stainless steel, respectively. Concentrations are in wt%. Reproduced from Zhang, Y.; Pint, B. A.; Haynes, J. A.; Tortorelli, P. F. *Oxid. Met.* **2004** 62, 103–120.

have been reported to have a positive effect on oxidation in air+10% H<sub>2</sub>O, with the best performance observed when both elements were present.<sup>111</sup> Henry *et al.* have also indicated a positive effect of Si on oxidation resistance in water vapor.<sup>105</sup> However, recent work of Hammer *et al.* indicates an opposite effect for Si because of the presence of SiO<sub>2</sub> at the oxide–metal interface,<sup>109</sup> a reason suggested by Pint *et al.* for its beneficial effect.<sup>111</sup> These observations illustrate the need to balance the effect of Si as an alloying addition to chromia-forming alloys (for water vapor-containing environments as well for oxidizing conditions, in general). The formation of a silica layer beneath the chromia scales can decrease the overall scale growth rate relative to that of chromia, but only if the Si concentration is insufficient to form a brittle continuous subscale that promotes scale spallation.<sup>112,113</sup>

Kvernes *et al.* found that additions of Al to a Fe-13Cr alloy eliminated the detrimental influence of water vapor in the oxidizing environment (studied up to 2.3% H<sub>2</sub>O) if present in sufficient concentration to form a continuous protective layer of Al<sub>2</sub>O<sub>3</sub> (1% Al was needed at 680°C and 4 at.% 980°C).<sup>102</sup> While there are some reported detrimental effects of H<sub>2</sub>O on Al<sub>2</sub>O<sub>3</sub>-forming alloys,<sup>114</sup> these are relatively minor compared to those reported for chromia- and silica-forming alloys, and protective alumina scales provide substantially improved resistance for alloys in water vapor-containing environments.<sup>115,116</sup> For example, Figure 15 shows the mass changes of an Fe–Al alloy and ferritic, and austenitic steels (Fe-9Cr and type 304L stainless steel) with and without an aluminized coating in air + 10% H<sub>2</sub>O under cyclic oxidation exposures at 800°C. Both the Fe–Al alloy

and the aluminized specimens (which developed Fe–Al-based surface compositions) showed excellent oxidation resistance despite the presence of H<sub>2</sub>O, whereas the uncoated chromia-forming steels oxidized rapidly.

Given the attractiveness of alumina-forming alloys for water vapor (and other) applications, the alloy design problem, therefore, becomes one of assuring the development and maintenance of protective Al<sub>2</sub>O<sub>3</sub> scales and devising routes to achieving adequate strength and ductility, particularly under creep conditions, at higher temperatures and H<sub>2</sub>O pressures envisioned for advanced uses of such materials. In this system, increasing the Al content (that is, increasing  $N_B$ ) is limited because aluminum stabilizes the body-centered cubic form of Fe, which inherently exhibits poor high temperature creep strength. (Austenitic Ni-base alumina-forming alloys are available, but their high cost limits their use to a small subset of higher performance applications.) To this end, there has been some recent progress in the design of creep-resistant, alumina-forming austenitic stainless steels based on Fe–(20–25)Ni–(12–15)Cr–(2–4)Al (wt%) with fine dispersions of MC (M = Nb, V, Ti) and intermetallic B<sub>2</sub>–NiAl and Fe<sub>2</sub>Nb Laves precipitates.<sup>117–119</sup> At ~600–800 °C, Nb was found to promote Al<sub>2</sub>O<sub>3</sub> layer development, while both Ti and V had the reverse effect for the range of compositions with good creep resistance.<sup>118</sup> In order to maintain a single-phase austenitic matrix microstructure, these compositions contain lean levels of Al and Cr (via a third-element effect) for protective Al<sub>2</sub>O<sub>3</sub> scale formation. Therefore, under certain conditions, enhanced internal oxidation and a transition to nonprotective Fe-based oxide nodule formation were observed in water vapor-containing environments compared to exposures in dry air.<sup>119</sup> Enhanced internal oxidation of chromia-forming alloys in the presence of water vapor has also been reported.<sup>110</sup> This effect has been speculated to be the result of hydrogen ingress into the alloy from decomposition of the water vapor, possibly shifting the balance of internal/external oxidation by increasing the oxygen solubility (cf. eqns [2] and [3]).<sup>110</sup>

### 1.21.7 Conclusions

Given the vast number of possible alloy and environmental combinations, this chapter has focused on general principles and illustrative (but far from exhaustive) examples related to the formation of the most protective scales needed for corrosion resistance

of alloys used at high temperatures, Cr<sub>2</sub>O<sub>3</sub>, Al<sub>2</sub>O<sub>3</sub>, and SiO<sub>2</sub>, with emphasis on the first two. At its essence, alloy design for high temperature corrosion resistance relates to the tailoring of composition and microstructure to promote the preferential formation of the desired POS by selective oxidation, and its subsequent stability and integrity, while balancing the effects on other properties. The attractiveness of alumina as a protective scale for higher temperatures as well as in a variety of aggressive multireactant environments (e.g., water vapor, sulfur) is evident, but widespread applications of appropriate compositions await further alloy and/or coating development that must optimize high temperature corrosion resistance, desired mechanical performance, and/or physical properties.

The goal of the alloy design or materials selection processes should, in most cases, be to maximize the overall oxidation lifetime by accounting for all factors (thermodynamic, kinetic, mechanical, physical, metallurgical, etc.) that influence it. Looking into the future, it is hoped that understanding and control of these factors can be developed to the point that improved lifetime prediction will enable quantification of the effectiveness of various alloying schemes for given application environments and component designs. To this end, it is anticipated that the ability to describe adequately and manipulate reaction product development and kinetic pathways for complex, multiphase alloys and material systems in multireactant, high temperature environments will provide the foundation for approaches to be successful and efficient in alloy design, and selection for a variety of future applications.

This research was sponsored by the U.S. Department of Energy under Contract No. DE-AC05-00OR22725. By accepting the article for publication, the publisher acknowledges that the United States Government retains a nonexclusive, paid-up, irrevocable, worldwide license to publish or reproduce the published form of this work, or allow others to do so, for United States Government purposes.

### References

1. Stott, F. H.; Wood, G. C.; Stringer, J. *Oxid. Met.* **1995**, *44*, 113–145.
2. Brady, M. P.; Tortorelli, P. F.; More, K. L.; Payzant, E. A.; Armstrong, B. L.; Lin, H. T.; Lance, M. J.; Huang, F.; Weaver, M. L. *Mater. Corros.* **2005**, *56*, 748–755.
3. Schütze, M. *Protective Oxide Scales and their Breakdown*; John Wiley and Sons: Chichester, 1997.

4. Smialek, J. *JOM* **2000**, 52, 22–25.
5. Stott, F. H.; Atkinson, A. *Mater. High Temp.* **1994**, 12, 195–207.
6. Wagner, C. Z. *Elektrochem.* **1959**, 63, 772–790.
7. Whittle, D. P. In *High Temperature Corrosion*; Rapp, R. A., Ed.; National Association of Corrosion Engineers: Houston, TX, 1981; pp 171–183.
8. Stott, F. H. *Rep. Prog. Phys.* **1987**, 50, 861–913.
9. Gesmundo, F.; Gleeson, B. *Oxid. Met.* **1995**, 44, 211–238.
10. Gesmundo, F.; Castello, P.; Viani, F. *Oxid. Met.* **1996**, 46, 383–398.
11. Gesmundo, F.; Niu, Y. *Oxid. Met.* **1998**, 50, 1–26.
12. Brady, M. P.; Gleeson, B.; Wright, I. G. *JOM* **2000**, 52, 16–21.
13. Brady, M. P.; Tortorelli, P. F. *Intermetallics* **2004**, 12, 779–789.
14. Rapp, R. A. *Corrosion* **1965**, 21, 382–401.
15. Stott, F. H. *Mater. Charact.* **1992**, 28, 311–325.
16. Tortorelli, P. F.; DeVan, J. H.; McKamey, C. G.; Howell, M. *Ceram. Trans.* **1991**, 19, 961–968.
17. Yurek, G. J.; Eisen, D.; Garratt-Reed, A. *Metall. Trans. A* **1982**, 13, 473–485.
18. Caplan, D. *Corros. Sci.* **1966**, 6, 509–515.
19. Wright, I. G. Oxidation of Iron-, Nickel-, and Cobalt-Base Alloys, Metals and Ceramics Information Center Report MCIC-72-07 (Columbus, OH, Battelle Columbus Laboratories, 1972).
20. Wagner, C. *Corros. Sci.* **1965**, 5, 751–764.
21. Renusch, D.; Veal, B.; Natesan, K.; Grimsditch, M. *Oxid. Met.* **1996**, 46, 365–381.
22. Niu, Y.; Wang, S.; Gao, F.; Zhang, Z. G.; Gesmundo, F. *Corros. Sci.* **2008**, 50, 345–356.
23. Guan, S. W.; Smeizer, W. W. *Oxid. Met.* **1994**, 42, 375–391.
24. Wang, Ge; Gleeson, B.; Douglass, D. L. *Oxid. Met.* **1991**, 35, 333–348.
25. Gesmundo, F.; Viani, F.; Niu, Y. *Oxid. Met.* **1994**, 42, 409–429.
26. Gesmundo, F.; Niu, Y.; Douglass, D. L. *Oxid. Met.* **1994**, 42, 465–484.
27. Gesmundo, F.; Viani, F.; Niu, Y. *Oxid. Met.* **1996**, 45, 51–76.
28. Carter, P.; Gleeson, B.; Young, D. *Acta Mater.* **1996**, 44, 4033–4038.
29. Durham, R. N.; Gleeson, B.; Young, D. J. *Oxid. Met.* **1998**, 50, 139–165.
30. Perkins, R. A.; Meier, G. H. In *Proceedings of the Industry-University Advanced Materials Conference II*; Smith, F. W., Ed.; Advanced Materials Institute: Denver, 1989; pp 92–99.
31. Brady, M. P.; Smialek, J. L.; Terepka, F. *Scripta Met.* **1995**, 32, 1659–1664.
32. Brady, M. P.; Smialek, J. L.; Smith, J.; Humphrey, D. L. *Acta Mater.* **1997**, 45, 2357–2369.
33. Gleeson, B.; Mu, N.; Hayashi, S. J. *Mater. Sci.* **2009**, 44, 1704–1710.
34. Whittle, D. P.; Stringer, J. *Philos. Trans. Royal Soc. London* **1980**, 295(A), 309–329.
35. Pint, B. A. *Oxid. Met.* **1996**, 45, 1–37.
36. Quadakkers, W. J.; Singheiser, L. *Mater. Sci. Forum* **2001**, 369–372, 77–92.
37. Pint, B. A. In *Proceedings of John Stringer Symposium*; Tortorelli, P. F., Hou, P. Y., Wright, I. G., Eds.; ASM International: Materials Park, OH, 2003; pp 9–19.
38. Pint, B. A. *J. Am. Ceram. Soc.* **2003**, 86, 686–695.
39. Sigler, D. R. *Oxid. Met.* **1993**, 40, 555–583.
40. Warnes, B. M. *Surf. Coat. Technol.* **2001**, 146–147, 7–12.
41. Naveos, S.; Oberlaender, G.; Cadoret, Y.; Josso, P.; Bacos, M. P. *Mater. Sci. Forum* **2004**, 461–464, 375–382.
42. Quadakkers, W. J.; Malkow, T.; Phon-Abellan, J.; Flesch, U.; Shemet, V.; Singheiser, L.; McEvoy, A. J., Ed.; In *Proceedings of the 4th European Solid Oxide Fuel Cell Forum*; Elsevier: Amsterdam, 2000; Vol. 2, pp 827–836.
43. Pint, B. A.; More, K. L.; Wright, I. G. *Mater. High Temp.* **2003**, 20, 375–386.
44. Gupta, D. K.; Duvall, D. S. In *Superalloys*; Gell, M., et al. Eds.; TMS: Warrendale, PA, 1984; pp 711–720.
45. Kochubey, V.; Al-Badair, H.; Tatlock, G.; Le-Coze, J.; Naumenko, D.; Quadakkers, W. J. *Mater. Corros.* **2005**, 56, 848–853.
46. Funkenbush, A. W.; Smeggil, J. G.; Bornstein, N. S. *Met. Trans.* **1985**, 16A, 1164–1166.
47. Sigler, D. R. *Metals* **1989**, 32, 337–355.
48. Smialek, J. L.; Jayne, D. T.; Schaeffer, J. C.; Murphy, W. H. *Thin Solid Films* **1994**, 253, 285–292.
49. Wright, I. G.; Pint, B. A. In *Proceedings of SF2M*; Journées d'automne, Soc. Française de Metallurgie et de Matériaux: Paris, 2000; pp 86–87.
50. Pint, B. A.; More, K. L.; Wright, I. G. *Oxid. Met.* **2003**, 59, 257–283.
51. Pint, B. A.; Wright, I. G.; Lee, W. Y.; Zhang, Y.; Prüßner, K.; Alexander, K. B. *Mater. Sci. Eng.* **1998**, A245, 201–211.
52. Wright, I. G.; Pint, B. A.; Lee, W. Y.; Alexander, K. B.; Prüßner, K. In *High Temperature Surface Engineering*; Nicholls, J., Rickery, D., Eds.; Institute of Materials: London, 2000; pp 95–113.
53. Haynes, J. A.; More, K. L.; Pint, B. A.; Wright, I. G.; Cooley, K.; Zhang, Y. *Mater. Sci. Forum* **2001**, 369–372, 679–686.
54. Cadoret, Y.; Bacos, M. P.; Josso, P.; Maurice, V.; Marcus, P.; Zanna, S. *Mater. Sci. Forum* **2004**, 461–464, 247–254.
55. Schütze, M. Quadakkers, W. J.; Nicholls, J. R. Eds. *Lifetime Modeling of High Temperature Corrosion Processes*; Maney Publishing: London, 2001.
56. Bennett, M. J.; DeVan, J. H.; Tortorelli, P. F. The Oxidation Behavior of Iron Aluminides in Air at 1300°C In *Microscopy of Oxidation 3*; Newcomb, S. B., Little, J. A., Eds.; The Institute of Materials: London, 1997; pp 233–245.
57. Quadakkers, W. J.; Bongartz, K. *Mater. Corros.* **1994**, 45, 232–241.
58. Guruppa, I.; Weinbruch, S.; Naumenko, D.; Quadakkers, W. J. *Mater. Corros.* **2000**, 51, 101–108.
59. Huczowski, P.; Shemet, V.; Piron-Abellan, J.; Singheiser, L.; Quadakkers, W. J.; Christiansen, N. *Mater. Corros.* **2004**, 55, 825–830.
60. Pint, B. A.; Porter, W. D.; Wright, I. G. *Mater. Sci. Forum* **2008**, 595–598, 1083–1092.
61. Evans, H. E.; Donaldson, A. T.; Gilmour, T. C. *Oxid. Met.* **1999**, 52, 379–402.
62. Newton, R.; et al. In *Modeling of High Temperature Corrosion Processes*; Schütze, M., Quadakkers, W. J., Nicholls, J. R., Eds.; Maney Publishing: London, 2001; pp 15–36.
63. Nicholls, J. R.; Newton, R.; Bennett, M. J.; Evans, H. E.; Al-Badair, H.; Tatlock, G. J.; Naumenko, D.; Quadakkers, W. J.; Strehl, G.; Borchardt, G. In *Modeling of High Temperature Corrosion Processes*; Schütze, M., Quadakkers, W. J., Nicholls, J. R., Eds.; Maney Publishing: London, 2001; pp 83–106.
64. Evans, H. E. *Inter. Mater. Rev.* **1995**, 40, 1–40.
65. Nesbitt, J. A. *Oxid. Met.* **1995**, 44, 309–338.
66. Haynes, J. A.; Zhang, Y.; Cooley, K. M.; Walker, L.; Reeves, K. S.; Pint, B. A. *Surf. Coat. Technol.* **2004**, 188–189, 153–157.
67. Giggins, C. S.; Pettit, F. S. *Oxid. Met.* **1980**, 14, 363–413.
68. Young, D. J.; Watson, S. *Oxid. Met.* **1995**, 44, 239–264.



69. DeVan, J. H. In *Oxidation of Intermetallics*; Grobstein, T., Doychak, J., Eds.; TMS: Warrendale, PA, 1989; pp 107–115.
70. Pint, B. A.; Dwyer, M. J.; Deacon, R. M. *Oxid. Met.* **2008**, 211–231.
71. Dettenwanger, F.; Schumann, E.; Rühle, M.; Rakowski, J. M.; Meier, G. H. *Oxid. Met.* **1998**, 50, 269–307.
72. Shemet, V.; Tyagi, A. K.; Becker, J. S.; Lersch, P.; Singheiser, L.; Quadakkers, W. J. *Oxid. Met.* **2000**, 54, 211–235.
73. Brady, M. P.; Tortorelli, P. F.; Walker, L. R. *Oxid. Met.* **2002**, 58, 297–318.
74. Lai, G. Y. *High Temperature Corrosion of Engineering Alloys*; ASM International: Materials Park, OH, 1990.
75. Tjokro, K.; Young, D. J. *Oxid. Met.* **1995**, 44, 453–474.
76. Krupp, U.; Christ, H.-J. *Oxid. Met.* **1999**, 52, 277–298.
77. Gleeson, B. In *Materials Science and Technology: Corrosion and Environmental Degradation*; Shütze, M., Ed.; Wiley-VCH: Weinheim, 2000; Vol. 2, Chapter 5.
78. Becker, P.; Young, D. J. *Oxid. Met.* **2007**, 67, 267–277.
79. Hochman, R. F. In *Properties of High Temperature Alloys*; Foroulis, Z. A., Pettit, F. S., Eds.; The Electrochemical Society: Pennington, NJ, 1976; pp 715–732.
80. Nava Paz, J. C.; Grabke, H. J. *Oxid. Met.* **1993**, 39, 437–456.
81. Grabke, H. J.; Müller-Lorenz, E. M.; Strauss, S.; Pippel, E.; Woltersdorf, J. *Oxid. Met.* **1998**, 50, 241–254.
82. Zeng, Z.; Natesan, K. *Oxid. Met.* **2006**, 66, 1–20.
83. Zhang, J.; Cole, D. M. I.; Young, D. J. *Mater. Corros.* **2005**, 56, 756–764.
84. Mrowec, S. *Oxid. Met.* **1995**, 44, 177–209.
85. Gleeson, B.; Douglass, D. L.; Gesmundo, F. *Oxid. Met.* **1990**, 34, 123–150.
86. Wright, I. G.; Srinivasan, V.; Vedula, K. M. *Mater. High Temp.* **1993**, 11, 159–166.
87. Green, S. W.; Stott, F. H. *Oxid. Met.* **1991**, 36, 239–252.
88. Stott, F. H.; Chuah, K. T.; Bradley, L. B. *Mater. Corros.* **1996**, 47, 695–700.
89. Tortorelli, P. F.; Natesan, K. *Mater. Sci. Eng. A* **1998**, 258, 115–125.
90. Stott, F. H.; Chong, F. M. F.; Stirling, C. A. *Mater. Sci. Forum* **1989**, 43, 327–362.
91. Brady, M. P.; Tortorelli, P. F.; More, K. L.; Walker, L. R. Oak Ridge National Laboratory, *Oxid. Met.* 2009 (in press).
92. Schütze, M.; Nöth, M. NACE Paper 517, Proceedings of Corrosion/98; NACE International: Houston, TX, 1998.
93. Du, H. L.; Datta, P. K.; Lewis, D. B.; Burnell-Gray, J. S. *Oxid. Met.* **1996**, 45, 507–527.
94. Tortorelli, P. F.; Schneibel, J. H.; More, K. L.; Pint, B. A. *Mater. Sci. Forum* **2004**, 461–464, 1063–1070.
95. Kim, G. M.; Meier, G. H. Breakdown Mechanisms of  $\text{Al}_2\text{O}_3$ ,  $\text{Cr}_2\text{O}_3$ , and  $\text{SiO}_2$  Scales in  $\text{H}_2/\text{H}_2\text{O}/\text{H}_2\text{S}$  Environments, Oak Ridge National Laboratory report, ORNL/Sub-83–43346/02, 1989.
96. Baxter, D. J.; Natesan, K. *Oxid. Met.* **1989**, 31, 305–313.
97. Natesan, K. *Oxid. Met.* **1988**, 30, 53–83.
98. Nicholls, J. R. *JOM* **2000**, 52, 28–35.
99. Opila, E. J. *J. Am. Ceram. Soc.* **1994**, 77, 730–736.
100. Opila, E. J.; Jacobson, N. S.; Myers, D. L.; Copland, E. H. *JOM* **2006**, 58, 22–28.
101. Stanislawski, M.; Wessel, E.; Hilpert, K.; Markus, T.; Singheiser, L. *J. Electrochem. Soc.* **2007**, 154, A295–A306.
102. Kvernes, I.; Oleveira, M.; Kofstad, P. *Corros. Sci.* **1977**, 17, 237–252.
103. Asteman, H.; Svensson, J.-E.; Norell, M.; Johansson, L.-G. *Oxid. Met.* **2000**, 54, 11–26.
104. Rakowski, J. M.; Pint, B. A. NACE Paper 00–517, Proceedings of Corrosion 2000; NACE International: Houston TX, 2000.
105. Henry, S.; Galerie, A.; Antoni, L. *Mater. Sci. Forum* **2001**, 369–372, 353–360.
106. Peraldi, R.; Pint, B. A. *Oxid. Met.* **2004**, 61, 463–483.
107. Pint, B. A. Paper GT2005–68495, Proceedings of ASME Turbo Expo 2005; ASME International: New York, 2005.
108. Ehlers, J.; Young, D. J.; Smaardijk, E. J.; Tyagi, A. K.; Penkalla, H. J.; Singheiser, L.; Quadakkers, W. J. *Corros. Sci.* **2006**, 48, 3428–3454.
109. Hammer, J. E.; Laney, S. J.; Jackson, R. W.; Coyne, K.; Pettit, F. S.; Meier, G. H. *Oxid. Met.* **2007**, 67, 1–38.
110. Essuman, E.; Meier, G. H.; Zurek, J.; Hänsel, M.; Quadakkers, W. J. *Oxid. Met.* **2008**, 69, 143–162.
111. Pint, B. A.; Peraldi, R.; Maziasz, P. J. *Mater. Sci. Forum* **2004**, 461–464, 815–822.
112. Bennett, M. J.; Desport, J. A.; Labun, P. A. *Oxid. Met.* **1984**, 22, 291–306.
113. Hoelzer, D. T.; Pint, B. A.; Wright, I. G. *J. Nucl. Mater.* **2000**, 283–287, 1306–1310.
114. Maris-Sida, M. C.; Meier, G. H.; Pettit, F. S. *Metall. Mater. Trans. A* **2003**, 34A, 2609–2619.
115. Zhang, Y.; Pint, B. A.; Haynes, J. A.; Tortorelli, P. F. *Oxid. Met.* **2004**, 62, 103–120.
116. Pint, B. A.; Shingledecker, J. P.; Brady, M. P.; Maziasz, P. J. paper GT2007–27916, Proceedings of the ASME Turbo Expo 2007; ASME International: New York, 2007.
117. Yamamoto, Y.; Brady, M. P.; Lu, Z. P.; Maziasz, P. J.; Liu, C. T.; Pint, B. A.; More, K. L.; Meyer, H. M.; Payzant, E. A. *Science* **2007**, 316, 433–436.
118. Brady, M. P.; Yamamoto, Y.; Santella, M. L.; Pint, B. A. *Scripta Mater.* **2007**, 57, 1117–1120.
119. Brady, M. P.; Yamamoto, Y.; Santella, M. L.; Maziasz, P. J.; Pint, B. A.; Liu, C. T.; Lu, Z. P.; Bei, H. *JOM* **2008**, 60, 12–18.

## 1.19 High Temperature Corrosion Issues for Metallic Materials in Solid Oxide Fuel Cells

L. Singheiser, P. Huczowski, T. Markus, and W. J. Quadackers

Forschungszentrum Jülich, IEF2, Jülich, Germany

© 2010 Elsevier B.V. All rights reserved.

1.19.1	Introduction	483
1.19.2	Metallic Materials for High Temperature Applications	484
1.19.3	Chromium-Base Metallic Interconnectors	485
1.19.4	Volatile Cr Species	485
1.19.5	Behavior of Cr-Based Alloys in H <sub>2</sub> /H <sub>2</sub> O-Based Gases	488
1.19.6	Mixed Gas Corrosion of Cr-Based Alloys	489
1.19.7	Oxidation Rates of Chromium-Based Alloys	490
1.19.8	Electronic Conductivity of Chromia-Based Scales	492
1.19.9	High-Chromium Ferritic Steels	492
1.19.10	Behavior of High-Cr Ferritic Steels in Anode Gas	494
1.19.11	Ferritic Steels in Anode Gases Containing Carbonaceous Gas Species	497
1.19.12	Ferritic Steels Designed for SOFC Application	499
1.19.13	Effect of Component Thickness on Oxidation Behavior	502
1.19.14	Oxidation Behavior of Ferritic Steels Under Dual Atmosphere Conditions	507
1.19.15	Interaction of Chromia-Forming Interconnects with Cathode Side Materials	507
1.19.16	Protection Methods to Minimize Cr Vaporization	509
1.19.17	Interaction of Chromia-Forming Interconnects with Anode Side Materials	510
1.19.18	Interaction of Metallic Interconnects with Glass Sealants	512
References		514

### Symbols

**a** Activity

**C<sub>B</sub>** Critical chromium concentration in the component (wt%)

**ΔV<sup>F</sup>** Volume change associated with the formation of the relevant point defect (cm<sup>3</sup>)

**C<sub>v</sub>** Vacancy concentration ((z) cm<sup>-3</sup>)

**C<sub>v</sub><sup>o</sup>** Equilibrium concentration of vacancies in the unstressed state ((z) cm<sup>-3</sup>)

**C<sub>0</sub>** Initial chromium concentration in the component (wt%)

**d** Component thickness (mm)

**D** Diffusivity (m<sup>2</sup> s<sup>-1</sup>)

**D** Interdiffusion coefficient of volatile species in laminar boundary layer (cm<sup>2</sup> s<sup>-1</sup>)

**D<sub>o</sub>** Oxygen grain boundary diffusion coefficient (m<sup>2</sup> s<sup>-1</sup>)

**J** Mass flux (mg cm<sup>-2</sup> h<sup>-1</sup>)

**k** Oxidation rate constant (mg cm<sup>-2</sup> h<sup>-n</sup>)

**k'** Parabolic oxidation rate constant (cm<sup>2</sup> s<sup>-1</sup>)

**K** Equilibrium constant of the reaction

**K<sub>P</sub>** Parabolic oxidation rate constant (mg<sup>2</sup> cm<sup>-4</sup> s<sup>-1</sup>)

**K<sub>P</sub>'** Apparent oxidation rate constant (g<sup>2</sup> cm<sup>-4</sup> s<sup>-1</sup>)

**L** Characteristic length (cm)

**M** Molecular weight of volatile species (g mol<sup>-1</sup>)

**n** Oxidation rate exponent

**p** Vapor pressure bar (Pa)

**P** Partial pressure of volatile species (atm)

**r** Grain size (μm)

**R** Gas constant ((cm<sup>3</sup> atm) K<sup>-1</sup> mol<sup>-1</sup>)

**Re** Reynold's number

**Sc** Schmidt number

**t** Time (h, s)

**t<sub>B</sub>** Time to breakaway (h)

**T** Temperature (K, °C)

**x** Oxide scale thickness (cm, μm)

**δ** Grain boundary width (nm)

**ρ** Alloy density (mg cm<sup>-3</sup>)

**σ** Electrical conductivity (S cm<sup>-1</sup>)

**σ<sub>h</sub>** Hydrostatic component of the stress tensor (Pa)

**σ<sub>xx</sub>** Biaxial compressive stress (Pa)

**Δm** Oxygen uptake per unit area (Weight change) (mg cm<sup>-2</sup>)

**Δm\*** Critical weight change at which the onset of scale spallation occurs (mg cm<sup>-2</sup>)

$\Delta H$  Enthalpy ( $\text{kJ mol}^{-1}$ )  
 $\Delta H^*$  Activation enthalpy ( $\text{kJ mol}^{-1}$ )  
 $\Delta S^*$  Activation entropy ( $\text{kJ mol}^{-1} \text{K}^{-1}$ )  
 $\Delta V^*$  Activation volume ( $\text{m}^3 \text{mol}^{-1}$ )  
 $\Delta \mu_o$  Oxygen – potential gradient across the scale ( $\text{J mol}^{-1}$ )

### 1.19.1 Introduction

A solid oxide fuel cell (SOFC) is an electrochemical device that converts the chemical energy in fuels into electrical energy by utilizing the natural tendency of oxygen and hydrogen to react.<sup>1</sup> Fuel cells are able to convert hydrogen-based fuels with higher efficiency compared to engines and thermal power plants. Compared with other fuel cell systems, the main advantage of the SOFC is its ability to use not only hydrogen but also the currently available fossil fuels (such as methane, butane, or even gasoline and diesel), thus reducing operating costs and flexibility. SOFCs possess no moving parts, so the cells are free of

vibration, and therefore, the noise pollution commonly associated with power generation is eliminated.

In an SOFC system, the single cell is constructed with an electrolyte arranged between two porous electrodes (Figure 1). When the oxygen in the flowing air at the cathode side contacts the cathode–electrolyte interface, it catalytically acquires electrons from the cathode and splits into oxygen ions. The oxygen ions diffuse into the electrolyte material and migrate to the anode side of the cell where they react with the fuel at the anode–electrolyte interface thereby giving off water (and/or carbon dioxide if a CO-containing fuel is used), heat, and electrons. The electrons are transported through the anode to the external circuit and back to the cathode, providing a source of useful electrical energy in an external circuit.<sup>1</sup>

Two possible design configurations for SOFCs have been considered, they are: the tubular and the planar design, the latter drawing more attention because it allows higher power densities than the tubular configuration. In the planar design, the components are assembled in flat stacks, with air and fuel flowing through channels, in most cases built into the

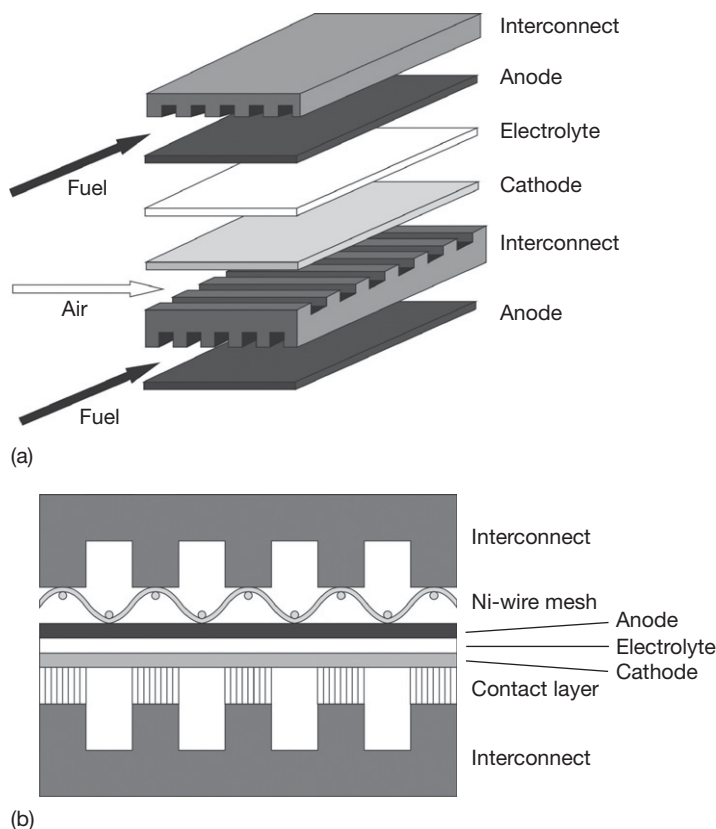


**Figure 1** Schematic configuration of a planar SOFC stack (a) and schematic cross-section showing means of contacting between interconnect and electrodes (b).

interconnect (**Figure 1**). In an SOFC stack, the interconnect thus provides the separation of the gas atmospheres, acts as current collector, and provides the electrical connection between the various single cells.<sup>1</sup> In most planar designs, two additional components are present to improve the electrical contact between the interconnect and the anode and cathode, respectively (**Figure 1**):

- a Ni-wire mesh at the anode side,
- a ceramic contact layer with high electronic conductivity at the cathode side.

The most important properties required for the interconnector material are high electronic conductivity, thermal stability in the cathode and anode side gas at the high-service temperatures (650–1000 °C), and a thermal expansion coefficient (**Table 1**) similar to that of the ceramic, electro-active components. Most designs use yttria-stabilized zirconia (YSZ) as electrolyte, (La,Sr)MnO<sub>3</sub> as cathode, and Ni/ZrO<sub>2</sub>-cermet as anode.<sup>2,3</sup> Ceramic, perovskite type materials on the basis of La-chromite have been shown to possess the property combination required for SOFC interconnects.<sup>3–5</sup> However, in planar cell designs, the interconnector also acts as the mechanical support for the thin electroactive ceramic parts and it is the

gas-proof separation between fuel gas and oxidant. Besides, it distributes the gases in co-, cross, and/or counter flow and acts as the construction connection to the external inlets and outlets. Therefore, the use of metals has a number of significant advantages over La-chromite-based ceramics,<sup>6–9</sup> because they are easier, and therefore cheaper to fabricate than ceramics, they are less brittle, easier to machine, and they can be joined with a number of standard welding and brazing techniques. Additionally, they possess higher electrical and thermal conductivities than most ceramics.

### 1.19.2 Metallic Materials for High Temperature Applications

When using metallic interconnect materials, it has to be considered that the reaction with the anode and cathode side service environments at the high operating temperatures may not only lead to dimensional changes and loss in load-bearing cross sections of the components but also to the formation of oxide scales on the component surface<sup>10,11</sup> which mostly possess low electrical conductivities. The use of noble metals could avoid these problems, however, because of the limited availability and high cost, this solution has been abandoned for large scale application, and conventional high temperature alloys<sup>12,13</sup> have received by far the most attention as possible candidate metallic interconnector materials.

From the viewpoint of oxidation resistance, alloys of the type NiCrAl, CoCrAl, and especially FeCrAl would be the materials to be chosen as construction materials for interconnects.<sup>10</sup> These types of high temperature alloys are able to form extremely slowly growing alumina scales on the material surface upon high temperature exposure. Alumina-forming intermetallics on the basis of NiAl have been considered as interconnector materials<sup>14</sup> because they not only possess superior oxidation resistance but also the required low thermal expansion coefficient. However, like all alumina-forming metallic materials, they have a major drawback; that is, the surface oxide scales possess an extremely low electronic conductivity<sup>15–17</sup> and the use of such materials would thus require measures to overcome this problem by developing special stack designs to assure suitable, long-term stable electrical connections of the interconnector with anode and cathode.

The second type of surface oxide scale which is potentially suitable to provide oxidation/corrosion protection to high temperature alloys is silica.

**Table 1** Thermal expansion coefficients (between RT and 1000 °C) of ceramic materials used in SOFCs compared with that of a Cr-based alloy and a high-Cr ferritic steel

Material	TEC (10 <sup>-6</sup> K <sup>-1</sup> )
8YSZ-	10.5
Ni-YSZ-Cermet	11–12
(La,Sr)MnO <sub>3</sub>	11–14
LaCrO <sub>3</sub>	9.5
(La,Sr)CrO <sub>3</sub>	11
LaCoO <sub>3</sub>	20–23
(La,Sr)CoO <sub>3</sub>	18–23
(La,Ca)(Cr,Co)O <sub>3</sub>	9.5–23
Cr-based ODS alloy	9–10
Ferritic steel Crofer 22 APU	12

Source: Minh, N. Q. *J. Am. Ceram. Soc.* **1993**, 176(3), 563–588.  
 Steele, B. C. H. *Solid State Ionics* **2000**, 134, 3–20.  
 Singhal, S. C. In *Solid Oxide Fuel Cell (SOFC-V)*; Stimming, U., Singhal, S. C., Tagawa, H., Lehnert, W., Eds.; The Electrochemical Society Proceedings Series, Pennington, NJ, 1997; p 88, PV 97-40.  
 Stolten, D.; Späh, R.; Schamm, R.; In *Solid Oxide Fuel Cell (SOFC-V)*; Stimming, U., Singhal, S. C., Tagawa, H., Lehnert, W., Eds.; The Electrochemical Society Proceedings Series, Pennington, NJ, 1997; p 88, PV 97-40.  
 Quadackers, W. J.; Piron-Abellan, J.; Shemet, V.; Singheiser, L. *Mater. High Temp.* **2003**, 20(2), 115–127.

However, the formation and long-term stability of a protective silica scale requires quite a large amount of silicon additions in nickel-, cobalt-, or iron-based alloys. This leads, in nearly all cases, to substantial embrittlement, thus making the alloys unsuitable as construction materials. Besides, silica has a very low electronic conductivity, leading to similar problems in SOFC application as mentioned above for alumina surface scales.

Most commercially available high temperature alloys rely on the formation of chromia-based surface scales for their oxidation resistance during the high temperature service. Chromia provides less oxidation/corrosion protection than alumina or silica,<sup>11</sup> however, its electronic conductivity in the envisaged SOFC operation temperature range of  $\sim 600\text{--}1000^\circ\text{C}$  is orders of magnitude larger than that of alumina or silica. Due to the required similarity of the thermal expansion coefficient with that of the commonly used electroactive ceramic cell materials,<sup>18,19</sup> the chromia-forming alloys, most frequently studied for SOFC interconnector application, are based on the binary alloy system Fe–Cr. The thermal expansion coefficient in Fe–Cr alloys decreases with increasing chromium content<sup>20</sup> and consequently, chromium-based materials have in most cases been considered for application in zirconia electrolyte-based SOFC concepts.<sup>6,21–23</sup> If a slightly higher thermal expansion coefficient is tolerable (typically  $12 \times 10^{-6} \text{ K}^{-1}$ ), for example, the case in Ni-cermet anode-based cell concepts or in cells using ceria as electrolyte, high-chromium ferritic steels are commonly considered as construction material for the interconnect.<sup>20</sup>

### 1.19.3 Chromium-Base Metallic Interconnectors

The chromia scales forming on pure chromium and chromium-based alloys at high temperatures exhibit slow growth rates. However, when formed during exposure in air or oxygen, the scales tend to buckle and possess poor adherence to the metallic substrate. The buckling is related to substantial compressive growth stresses in combination with vacancy condensation at the scale–metal interface. Tracer studies using <sup>18</sup>O isotopes revealed that the latter is related to outward chromium diffusion being the dominating transport mechanism in chromia scales whereas the contribution of oxygen transport is substantially smaller.<sup>24–27</sup> The buckling that occurs at oxidation temperature as a result of lateral growth<sup>24</sup> has frequently

been attributed to oxide formation within the scale resulting from the parallel diffusion of chromium and oxygen along chromia grain boundaries.<sup>11,25</sup>

An improvement in scale adherence and reduction in scale growth rate can be obtained by the addition of the so-called reactive elements (REs) such as Y, La, Ce, and Zr, either in metallic form or in the form of an oxide dispersion.<sup>28–31</sup> This RE-imparted change of the most important oxide scale properties is frequently claimed to be related to a suppression of the outward transport of chromium ions.<sup>27–31</sup>

A major drawback of metallic chromium is its high ductile to brittle transition temperature (DBTT) which is known to be significantly affected by interstitially dissolved gaseous impurities such as oxygen and nitrogen.<sup>23</sup> Extensive research work at Plansee led to the development of oxide dispersion strengthened (ODS) chromium which showed substantially improved mechanical properties compared to conventional chromium alloys.<sup>6,7</sup> The ODS materials are manufactured by elemental mixing of the starting powders (abbreviated as MIX alloy) or by mechanical alloying (MA), that is, by high-energy ball milling of chromium and oxide powders in a nonoxidizing environment.<sup>23,32</sup> The latter process can produce a very finely distributed oxide dispersion (typical size  $\approx 15 \text{ nm}$ ) embedded in the chromium matrix, compared to the coarser dispersions in MIX materials, as shown in Figure 2.<sup>6,7</sup> The alloys manufactured from the compacted powders possess superior mechanical properties, especially with respect to creep resistance (Figure 3). The improvement in ductility depends on a number of factors, for example, dispersion type and distribution. A substantial ductility increase of Cr was obtained by using MgO dispersions,<sup>33</sup> however, no further data on other mechanical properties have yet been reported. The commercial dispersion strengthened Cr alloys especially developed for SOFC application mostly contain a few percent of iron to adjust the thermal expansion coefficient as close as possible to that of the yttria-stabilized zirconia electrolyte.<sup>6,7</sup> As mentioned above, the RE-oxide dispersion not only improves the mechanical properties but also decreases the oxide growth rate and improves the adherence of the oxide to the metallic substrate.<sup>28–32</sup>

### 1.19.4 Volatile Cr Species

During the operation of planar SOFCs with Cr-based interconnects, rapid degradation of the cell performance has frequently been found and was claimed to



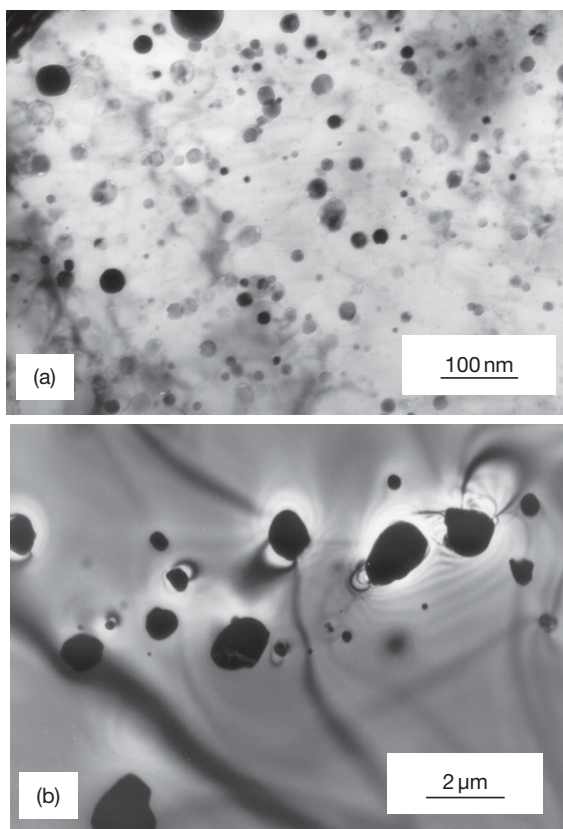


**Figure 2** TEM pictures showing distribution of  $\text{Y}_2\text{O}_3$  dispersions in Cr-based ODS alloys, manufactured by (a) mechanical alloying (MA) and (b) elemental mixing (MIX) of the metal and oxide powders. Reproduced from Quadackers *et al. Mater. High Temp.* **2003**, 20(2), 115–127.

be caused by the release of gaseous Cr species, designated in the following sections as ‘Cr vaporization’,<sup>34</sup> from the metallic materials. The volatile Cr species are reduced at the triple-phase boundaries between cathode, electrolyte, and air thereby forming solid  $\text{Cr}_2\text{O}_3$  and other Cr-rich phases which inhibit the electrochemical processes of the cell. This effect is often called ‘poisoning’ of the cathode and/or the cathode–electrolyte interface. A detailed description of the degradation mechanisms was given by Hilpert *et al.*<sup>35</sup> and Jiang *et al.*<sup>36</sup>

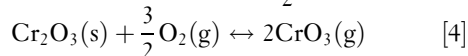
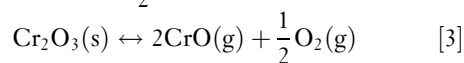
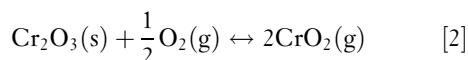
The gas on the cathode side of the SOFC is in most cases normal air which contains the usual minor amounts of water vapor. Several authors have shown that even small amounts of water vapor may substantially increase the ‘Cr vaporization’ in the high temperature environment. Chromia are known to react with water vapor at elevated temperatures to

form volatile (oxy-) hydroxide species, however, the published data on the actual thermodynamic stability of these vapor species still show major differences. The rate of material loss by volatilization is highly dependent on the partial pressures of the volatile species as well as the gas flow rate. It is known that under laminar flow conditions, which are representative of many power generation and propulsion environments, the rate of material loss,  $\mathcal{J}$  (in  $\text{mg cm}^{-2} \text{h}^{-1}$ ) by evaporation, is given by the following expression<sup>37</sup>:

$$\mathcal{J} = 0.664 \text{ Re}^{1/2} \text{ Sc}^{1/3} \frac{DPM}{LRT} \quad [1]$$

where the terms are:  $\mathcal{J}$  is the mass flux ( $\text{mg cm}^{-2} \text{h}^{-1}$ ); Re, the Reynold’s number; Sc, the Schmidt number;  $D$ , the interdiffusion coefficient of volatile species in laminar boundary layer ( $\text{cm}^2 \text{s}^{-1}$ );  $P$ , the partial pressure of volatile species (atm);  $M$ , the molecular weight of volatile species ( $\text{g mol}^{-1}$ );  $L$ , the characteristic length (cm);  $R$ , the gas constant ( $\text{cm}^3 \text{atm K}^{-1} \text{mol}^{-1}$ );  $T$  is the absolute temperature (K).

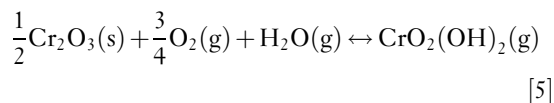
At high temperatures in dry air, the  $\text{Cr}_2\text{O}_3$  surface scale present on Cr or Cr-based alloys evaporates according to the following reactions, forming volatile  $\text{CrO}$ ,  $\text{CrO}_2$ , and  $\text{CrO}_3$ :



Ebbinghaus *et al.*<sup>38</sup> summarized and evaluated the available literature data and found  $\text{CrO}_3(\text{g})$  to be the most abundant vapor species formed upon vaporization in dry air.

In the development of SOFCs that use chromia-forming alloys or conductive chromia-containing ceramics as interconnect, the loss of chromium in the presence of air and water vapor has frequently been identified as a major cause for cell degradation. Therefore, a detailed knowledge on the vaporization behavior and equilibria of chromia in the cathode side environments, especially in the presence of water vapor, is of great importance.

It has been experimentally proven that in wet air the volatile  $\text{CrO}_2(\text{OH})_2$  is formed by the reaction<sup>35,39</sup>:



At the cathode–electrolyte interface, the

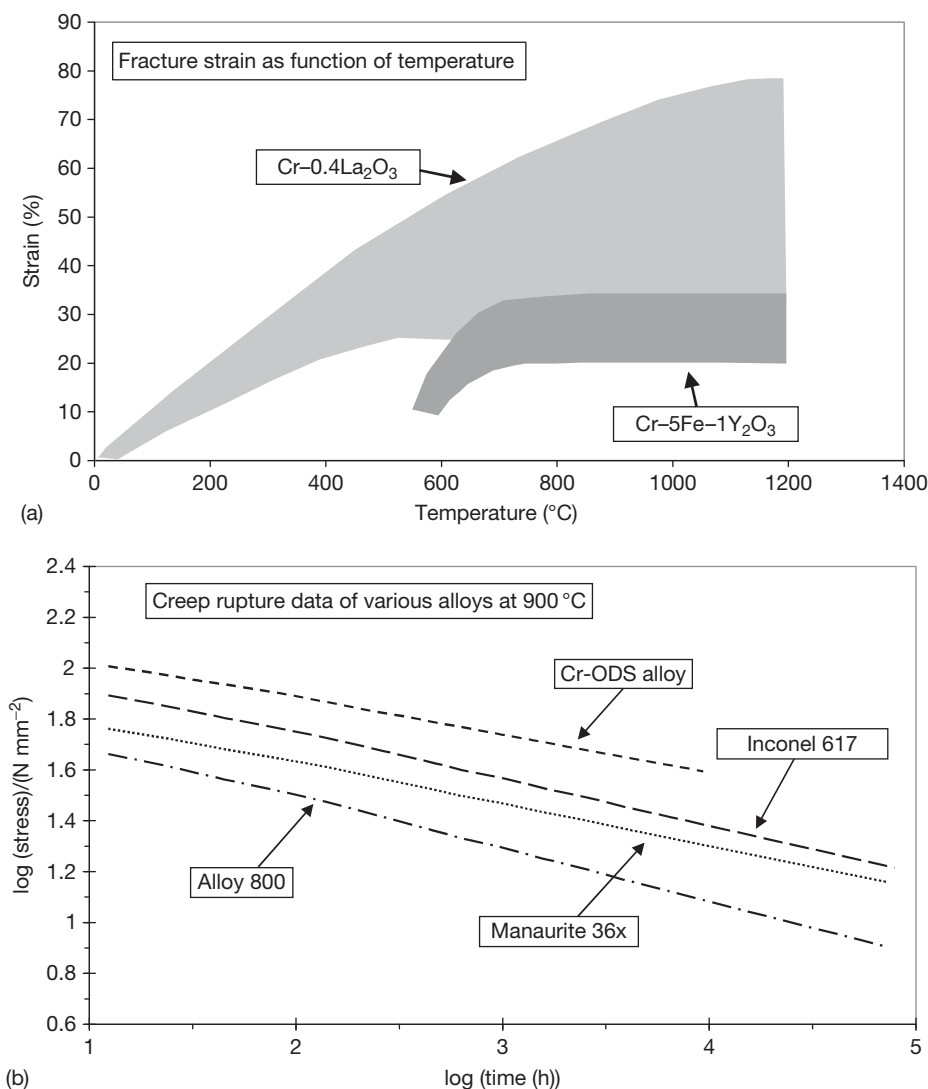
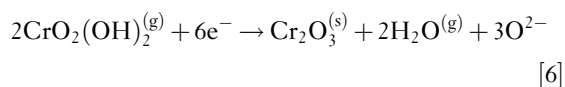


**Figure 3** Typical mechanical properties of Cr-based ODS alloys. Reproduced from Quadakkers, W. J.; Greiner, H.; Köck, W. In *Proceedings of the First European Solid Oxide Fuel Cell Forum*, Bossel, U., Ed.; European SOFC Forum, Dr. Ulf Bossel, Morgenacher Str. 2F, CH-5452: Oberrohrdorf, Switzerland, 1994; Vol. 2, p 525.

oxyhydroxide reacts according to:



Ebbinghaus<sup>38</sup> derived thermodynamic data for a large number of volatile chromium oxyhydroxides in 1993 using the limited available experimental data at that time, in combination with the molecular constant method. Empirical relationships were employed, where needed, to estimate unknown molecular properties, which in some cases resulted in large uncertainties of

the derived thermodynamic data. Assuming the validity of eqn [5], the equilibrium constant  $K_p$  of the reaction can be calculated from experiments using the vapor transpiration method. Stanislawski *et al.*<sup>40</sup> have carried out equilibrium vaporization experiments with  $\text{Cr}_2\text{O}_3(\text{s})$  in humid air under SOFC-relevant conditions. The data derived are confirmed by the work of Opila *et al.*<sup>41</sup> The results are shown in Figure 4. For comparison, the calculated equilibrium constants according to the thermodynamic database IVTANTHERMO,<sup>42</sup> as well as the data from Ebbinghaus<sup>38</sup> and the experimental results from Gindorf *et al.*<sup>43</sup> are shown. From those results, the

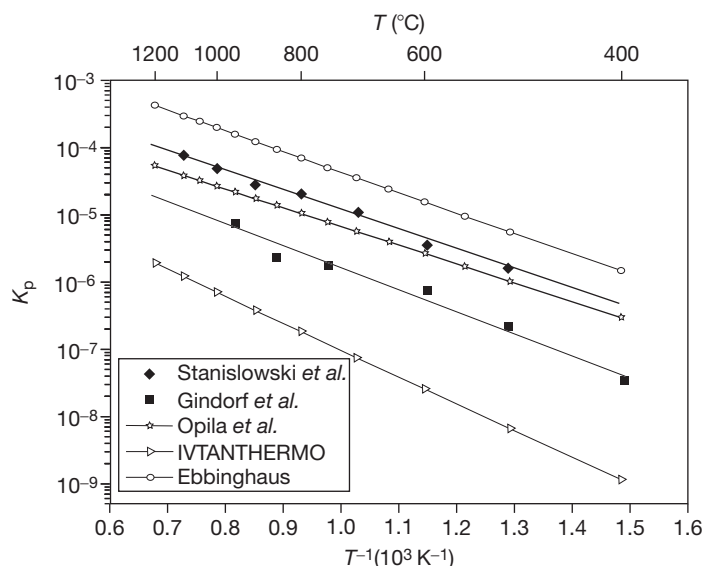


**Figure 4** Equilibrium constant for reaction [5], comparing the data of various authors. Reproduced from Stanislawski, M.; Wessel, E.; Hilpert, K.; Markus, T.; Singheiser L. *JES* **2007**, 154(4), A295–A306.

enthalpy and entropy of formation for the volatile species  $\text{CrO}_2(\text{OH})_2(\text{g})$  can be calculated. The recommended value resulting from the aforementioned comparison is  $\Delta H_{f,298}^0 = -767.7 \pm 11 \text{ kJ mol}^{-1}$ .

In technical systems, the actually occurring chromium evaporation also depends on a number of other factors such as the morphology of the outer oxide layer as well as its growth mechanism and its adherence to the metallic material. Therefore, the actual chromium release from Cr-based alloys under operating conditions may quantitatively differ from that measured for pure chromia samples.

Although the significance of reaction [6] occurring at the triple-phase boundaries has been identified in a number of studies, several authors have claimed that the driving force for cell degradation is related to spinel formation in the cathode. This occurs by the reaction of volatile Cr species with elements such as Mn, Co, and Fe present in the perovskite type cathode and/or contact layer. The extent of degradation thus depends on the cathode composition.<sup>36</sup> Several protection methods have been proposed to minimize evaporation of volatile Cr-species, such as coating of the interconnector with La-chromite<sup>44</sup> or -manganite,<sup>45</sup> metallic layers,<sup>46</sup> oxide layers,<sup>46</sup> or aluminum surface enrichment to promote alumina surface scale formation on interconnector areas, where electrical conductivity is not a major issue.<sup>46,47</sup> This subject will be extensively treated in Section 1.19.16.

### 1.19.5 Behavior of Cr-Based Alloys in $\text{H}_2/\text{H}_2\text{O}$ -Based Gases

Several reviews on oxidation of chromium in oxygen or air have been published and substantial information can be found in text books.<sup>10,11,48,49</sup> Far less information is available on behavior of Cr and Cr alloys in SOFC-relevant anode side  $\text{H}_2/\text{H}_2\text{O}$ -based gases. Hänsel *et al.*<sup>50</sup> found the oxidation rate of Cr-based ODS alloys at 950–1050 °C in an  $\text{Ar}/\text{H}_2/\text{H}_2\text{O}$ -mixture (equilibrium oxygen partial pressure  $\sim 10^{-15}$  bar at 1000 °C) to be higher than in high- $p_{\text{O}_2}$  environments (air,  $\text{Ar}/\text{O}_2$ ), whereby the difference could only partly be explained by formation of volatile oxides and hydroxides in the high- $p_{\text{O}_2}$  gases (Figure 5). In the  $\text{Ar}/\text{H}_2/\text{H}_2\text{O}$ -environment, where the formation of volatile Cr species is negligible, the alloys tended to form whisker type oxide morphologies, the extent of whisker formation being decreased by an ‘optimum’ addition of a reactive element (oxide dispersion).

Chromia scales formed on Cr-based ODS alloys in  $\text{Ar}/\text{H}_2\text{O}/\text{H}_2$  are far less voided and exhibit substantially better adherence to the metallic substrate than those formed in air or oxygen.<sup>24,50</sup> This effect of atmosphere composition on scale adhesion is even more dramatic in the case of non-RE-doped alloys and elemental chromium. Water vapor can eliminate or at least decrease oxide porosity by providing rapid gas phase transport of oxygen within the void space. As proposed earlier,<sup>51</sup> the oxygen transport is facilitated

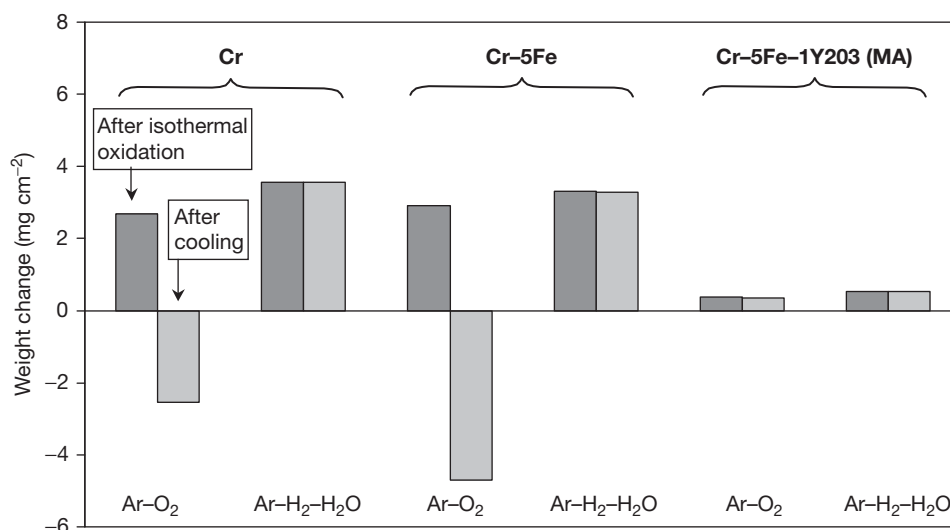


**Figure 5** Weight changes of Cr, Cr-5Fe, and the ODS alloy Cr-5Fe-Y<sub>2</sub>O<sub>3</sub> after isothermal oxidation in Ar-20% O<sub>2</sub> and Ar-4% H<sub>2</sub>-2% H<sub>2</sub>O at 1000 °C and after subsequent cooling to room temperature. The results illustrate, especially for the RE-free materials, the importance of the test atmosphere for oxide adherence. Reproduced from Hänsel, M.; Quadackers, W. J.; Singheiser, L.; Nickel, H. *Report Forschungszentrum Jülich, Jülich FRG, Jül-3583*, 1998; ISSN 0944-2952.

by the reaction between H<sub>2</sub>O<sup>(g)</sup> and oxide. Water vapor reacts with the oxide on the side of the cavity nearest to the metal, whereas the formed hydrogen reacts with the outer surface of the void. These redox reactions are coupled with gas phase mass transfer, and the inward oxygen transport through the scale via this mechanism leads to new oxide formation at the scale-metal interface, reducing the probability of void formation and subsequent scale detachment.<sup>52</sup> Enhanced inward oxygen transport, which was proven by two-stage oxidation tests using Ar-H<sub>2</sub>-H<sub>2</sub><sup>18</sup>O,<sup>53</sup> accounts satisfactorily for the observed decrease in the scale porosity and improved scale adhesion. The change in the dominating growth mechanism of chromia in the high- and low-*p*O<sub>2</sub> environments is accompanied by a substantial change in oxide grain size, the grains being much smaller when formed in the low *p*O<sub>2</sub> environment. More detailed information on the differences in chromia scale formation in low- and high-*p*O<sub>2</sub> gases can be found in the chapter 'Oxidation in Steam and Steam/Hydrogen Environments.'

### 1.19.6 Mixed Gas Corrosion of Cr-Based Alloys

During service in the SOFC cathode side environment, the reaction of oxygen with the surface of the Cr-based interconnect may be affected by the presence of nitrogen and/or water vapor. Especially, for

non-RE-doped chromium and chromium alloys, reaction with nitrogen is of major concern because it leads to environmentally induced embrittlement during high temperature exposure.<sup>23</sup> This is caused by nitrogen dissolution in the metal or the alloy as well as by nitride formation beneath the chromia scale (Figure 6). The sensitivity for nitrogen uptake depends on the gas tightness of the chromia layer because nitrogen transport between gas atmosphere and metal or alloy is known to occur via gas molecules rather than via solid state diffusion through the scale. Generally, it can be said that the thick chromia scales formed on non-RE-doped Cr and Cr alloys are more permeable for nitrogen than the thinner, that is, more protective, scales on RE- or RE-oxide-doped metals or alloys. This observation in fact indicates that also in a purely oxidizing environment, the protective properties of the chromium oxide layer are to a large extent determined by its ability to prevent molecular transport of oxidizing species rather than by the exact concentration of point defects in the chromia lattice.

The second reactive gaseous species which is of importance during air oxidation of Cr-based materials is water vapor. As extensively described in the previous section, the first well-known effect of water vapor is that it promotes the formation of volatile chromium oxyhydroxides.<sup>35,38,39,54</sup> A second, less apparent effect was observed by Hänsel *et al.*<sup>50</sup> The authors found the scale growth rate in the temperature range 950–1050 °C to be enhanced if water vapor was

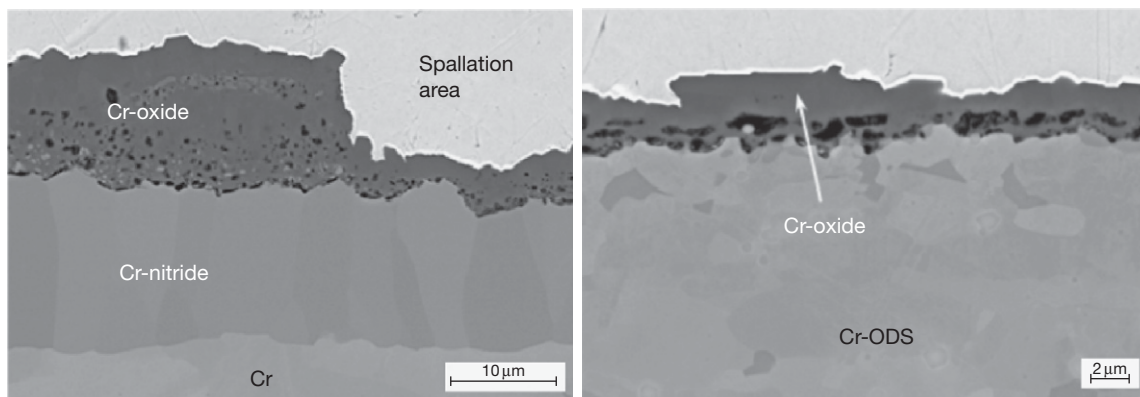


**Figure 6** Metallographic cross-sections (SEM images) of Cr and Cr ODS alloy after 1000 h oxidation at 800 °C in air.

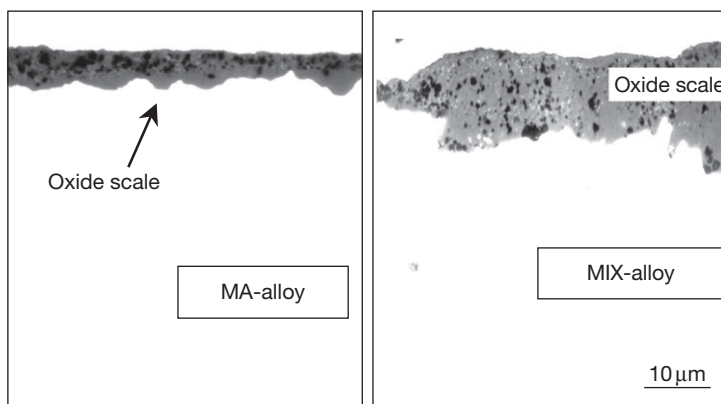


**Figure 7** Oxide scales on Cr-based ODS alloys, manufactured by different processes (cf. Figure 2) after 1000 h exposure in a  $\text{H}_2\text{O}-\text{H}_2$  mixture at 950 °C. Reproduced from Hänsel, M.; Quadakkers, W. J.; Singheiser, L.; Nickel, H. *Report Forschungszentrum Jülich, Jülich FRG, Jül-3583*, 1998; ISSN 0944-2952.

present in air or  $\text{Ar}-\text{O}_2$ , and this effect was related to the enhanced oxidation of cracks which formed in the chromia layers as a result of growth stresses even during the isothermal oxidation. The enhanced oxidation may therefore be related to a dissociation mechanism occurring in voids and cracks,<sup>51</sup> similar to that described in the previous section.

Depending on the cell operating conditions and the actually used fuel, the mixed gas corrosion of Cr-based alloys also has to be considered in the anode side gas. If carbon-containing gas species such as CO and/or  $\text{CH}_4$  are present, all Cr-based alloys tend to form a subscale layer containing Cr-carbide, that is, mainly  $\text{Cr}_2\text{C}_3$ , sometimes in combination with  $\text{Cr}_7\text{C}_3$ .<sup>21,55</sup> In the case of a  $\text{CH}_4$ -based test gas, the carbides exist as a near-continuous layer,<sup>21</sup> whereas in the case of a CO-based gas, the subscale layer mainly consists of an oxide-carbide mixture.<sup>55</sup> The extent of

carbon attack, which occurs by molecular transport of the carbon-containing gas species through the oxide scale, decreases with the decreasing growth rate of the oxide layer.<sup>55</sup> This again is a strong indication that in the case of chromia scales, protectiveness means to a large extent resistance against molecular transport from the gaseous atmosphere to the metal or alloy. In the case of Cr-ODS alloys, the protective scale properties depend on the dispersion type, and even more on the dispersion distribution<sup>50,55,56</sup> and thus on the alloy manufacturing process (Figures 7 and 8).

### 1.19.7 Oxidation Rates of Chromium-Based Alloys

If chromia growth proceeds by diffusion of point defects in the oxygen and/or chromium sublattice,



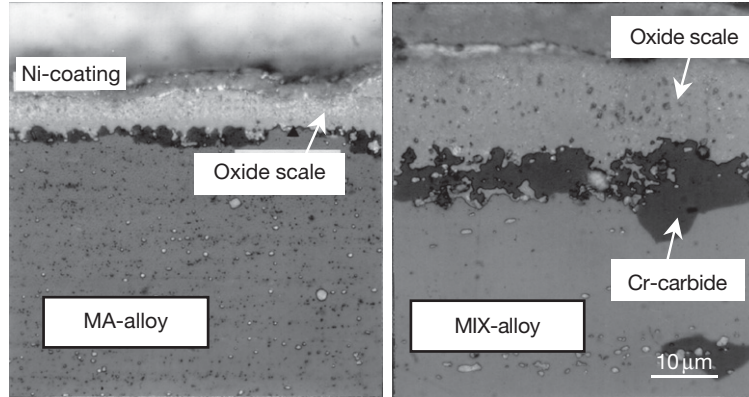


**Figure 8** Oxide scales on Cr-based ODS alloys, manufactured by different processes (cf. Figure 2) after 1000 h exposure in a CO-containing H<sub>2</sub>O–H<sub>2</sub> mixture at 950 °C. Reproduced from Hänsel, M.; Quadakkers, W. J.; Singheiser, L.; Nickel, H. *Report Forschungszentrum Jülich, Jülich FRG, Jül-3583*, 1998; ISSN 0944-2952.

scaling rates could be calculated by Wagner theory,<sup>11</sup> if the self-diffusion coefficients of chromium and oxygen were known. Lattice self-diffusion coefficients of both chromium and oxygen in chromia are reported to be extremely small, whereby the literature data show considerable scatter. At 1100 °C, the self-diffusion coefficients are in the range  $10^{-17}$  to  $10^{-18} \text{ cm}^2 \text{ s}^{-1}$ .<sup>57–59</sup> These low values indicate that it is extremely difficult to achieve true equilibrium, and this might be an important reason for the discrepancies in the literature diffusion data.

The oxidation rate of Cr-based ODS alloys is substantially slower than that of pure Cr or Cr alloys without addition of a RE (oxide).<sup>48–50</sup> It is difficult to give a quantitative figure of this reduction in oxidation rate by the RE addition because Cr as well as Cr-based alloys frequently do not exhibit the classical parabolic time dependence for oxide scale growth. Classical Wagner's oxidation theory<sup>11</sup> predicts the scale growth to obey a parabolic time dependence, if oxidation is controlled by diffusion of metal and/or oxygen ions through the oxide lattice:

$$x^2 = K' t \quad [7]$$

in which  $x$  is the scale thickness,  $t$  the time, and  $k$  the parabolic oxidation rate constant. Expressed as oxygen uptake per unit area ( $\Delta m$ ), eqn [7] is mostly written in the following form:

$$(\Delta m)^2 = K_p t \quad [8]$$

For Cr, Cr alloys, and especially Cr-based ODS alloys, eqn [8] is not often followed<sup>50,51,60</sup> because the assumptions made to describe scale growth by eqn [8] are mostly not completely fulfilled.<sup>61–63</sup> Chromia

growth proceeds to a large extent via rapid diffusion paths, such as oxide grain boundaries,<sup>26,27,58</sup> the density of which is in most cases not time-independent. For ODS alloys, the parabolic rate constant  $K'$  (in  $\text{cm}^2 \text{ s}^{-1}$ ) for such cases can be written as<sup>62</sup>:

$$K' \sim \frac{D_o \delta}{r} \frac{\Delta \mu_o}{RT} \quad [9]$$

in which  $D_o$  is the oxygen grain boundary diffusion coefficient;  $\delta$ , the grain boundary width;  $r$ , the grain size; and  $\Delta \mu_o$ , the oxygen-potential gradient across the scale. In many cases,  $r$  increases in scale growth direction, and/or with oxidation time.<sup>62,63</sup> This frequently leads to a  $K'$ -value which decreases with increasing oxidation time (Figure 9).

Another factor which has to be considered in evaluating oxide growth rates is that the scales are not completely gas-tight due to the formation of micro voids and micro cracks and consequently, molecular gas transport contributes to the growth process. Furthermore, the above-mentioned formation of volatile oxides and/or hydroxides can affect chromia growth, especially, at high temperatures in oxygen-rich environments (see previous sections).

In the case of ODS alloys, it has to be considered that the desired low oxide growth rate of the scales requires the RE to become incorporated in the surface oxide layer.<sup>31,64</sup> This occurs by embedding the dispersions in the inwardly growing oxide scale and subsequent diffusion of the RE to the oxide grain boundaries.<sup>60</sup> Consequently, the beneficial effect does not immediately become apparent but appears only after a certain oxidation time, with the consequence that a rapid oxide growth rate occurs which then subsequently decreases to very low values.<sup>50,60,62,63</sup>

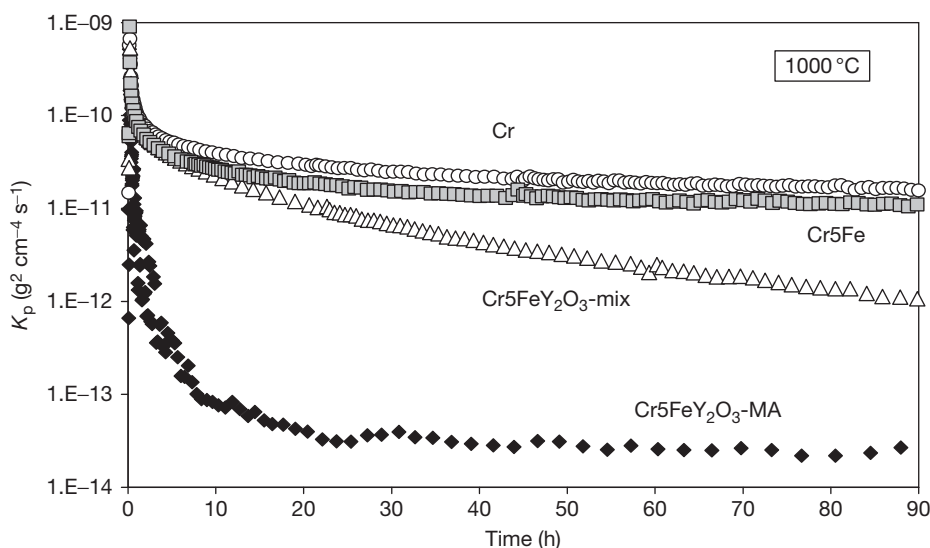


**Figure 9** Typical time dependence of the apparent oxidation rate  $K_p'$  during isothermal oxidation of Cr and Cr alloys in Ar/H<sub>2</sub>/H<sub>2</sub>O at 1000 °C. Reproduced from Hänsel, M.; Quadackers, W. J.; Singheiser, L.; Nickel, H. *Report Forschungszentrum Jülich, Jülich FRG, Jül-3583*, 1998; ISSN 0944-2952.

As a reduction in scale growth rate in a RE (oxide) containing Cr alloy requires the RE to become incorporated into the scale,<sup>64,65</sup> the RE-imparted reduction in chromia growth rate is strongly affected by size and distribution of the oxide dispersion.<sup>50</sup> Small dispersoid sizes and small distances between the dispersoids are required to obtain an optimum growth rate reduction. The oxidation rates of the ODS alloys thus depend on the manufacturing process.<sup>50</sup> In fact, tracer studies using <sup>18</sup>O<sub>2</sub> revealed that even by the optimum dispersion distribution, which can be achieved in commercial alloys, the resulting RE distribution in the growing scale does not completely block outward chromium transport. A virtually complete suppression of outward growth can be obtained by a strong surface enrichment of the RE, for example, by applying a RE-oxide coating or by RE-ion implantation.<sup>65,66</sup>

### 1.19.8 Electronic Conductivity of Chromia-Based Scales

Chromia is an electronic conductor and at high temperatures (>1000 °C) the electrical conductivity is found to be independent of the oxygen partial pressure.<sup>67–69</sup> At lower temperatures, the concentration of electronic defects due to the intrinsic electronic equilibrium becomes so small that the chromia changes into an extrinsic electronic conductor, the electronic conductivity being dominated by the

presence of impurities or dopants.<sup>68–73</sup> The electrical conductivity of bulk chromia samples at 800–1000 °C (Figure 10) has been reported to be in the range  $1 \times 10^{-2}$  to  $5 \times 10^{-2}$  S cm<sup>-1</sup>,<sup>68–71,74</sup> although lower values have also been found.<sup>75–77</sup> Below 1000 °C Mg-doped chromia is a p-type conductor, whereby the electronic conductivity only marginally depends on oxygen partial pressure.<sup>68</sup> In H<sub>2</sub>–H<sub>2</sub>O mixtures, the conductivity is affected by dissolved protons,<sup>68,70</sup> whereas in TiO<sub>2</sub>-doped chromia, no effect of hydrogen on conductivity is detected.<sup>69</sup> In the temperature range 400–1000 °C, the Ti-doped chromia is an n-type conductor at low oxygen partial pressures and a p-type conductor at near atmospheric oxygen partial pressure. Nagai *et al.*<sup>75,78,79</sup> found the electronic conductivity to increase by Y<sub>2</sub>O<sub>3</sub> or La<sub>2</sub>O<sub>3</sub> doping and decrease with increasing oxygen partial pressure, although this effect is not very pronounced, especially at high temperatures (Figure 11). The highest increase of the conductivity was observed for doping by NiO, whereby in this case no oxygen partial pressure dependence was found. Also doping by CeO<sub>2</sub> or Fe<sub>2</sub>O<sub>3</sub> increased the conductivity, however, the effect was much smaller than that observed for NiO-doping.

### 1.19.9 High-Chromium Ferritic Steels

High-chromium ferritic steels are to be preferred over Cr-based (ODS) alloys if lower SOFC service

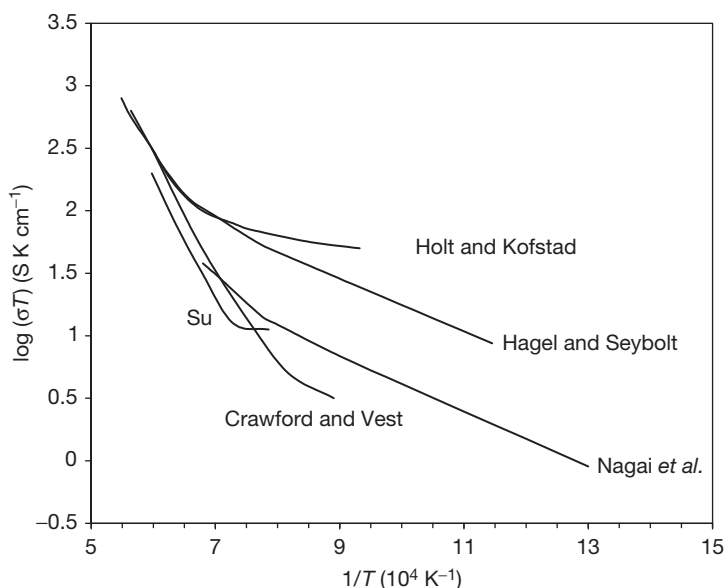


**Figure 10** Electrical conductivity of  $\text{Cr}_2\text{O}_3$  as function of reciprocal temperature in air (derived from Holt,<sup>68–71</sup> Hagel and Seybolt,<sup>74</sup> Nagai and Fujikawa,<sup>75</sup> Su,<sup>76</sup> and Crawford and Vest<sup>77</sup>).

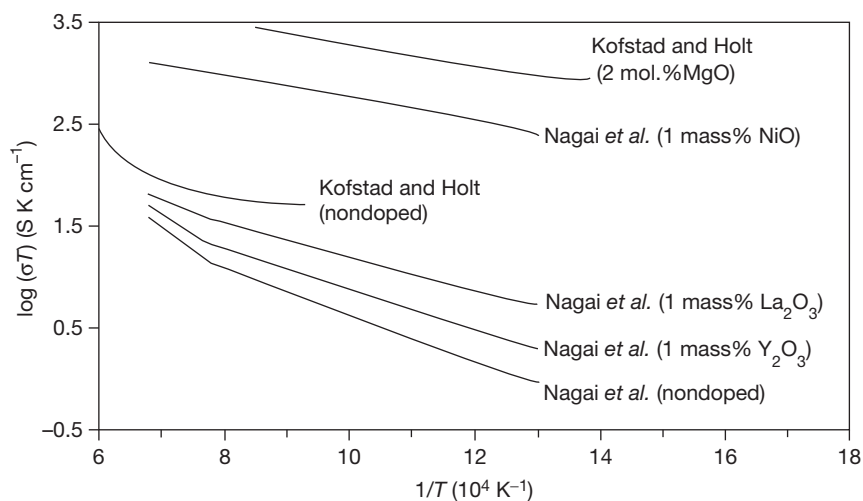


**Figure 11** Effect of dopants on electrical conductivity of  $\text{Cr}_2\text{O}_3$  as a function of reciprocal temperature (derived from Nagai and Fujikawa,<sup>75</sup> Nagai and Ohbayashi,<sup>78</sup> Nagai *et al.*<sup>79</sup>).

temperatures ( $<900^\circ\text{C}$ ) prevail, especially in the case of anode-supported cell designs, in which the CTE is mainly governed by the anode rather than the electrolyte. In commercially available ferritic steels, for high temperature application, the Cr content varies between  $\sim 7$  and  $28\text{ mass\%}$  (Table 2). During air exposure, for example, in the temperature range  $700\text{--}1000^\circ\text{C}$ , the oxide scale composition strongly varies with Cr concentration and the oxidation

resistance generally increases with increasing Cr content.<sup>80</sup> On low-Cr steels ( $<5\%$  Cr), the scales consist of nearly pure Fe-oxide accompanied by internal oxide precipitates of  $\text{Cr}_2\text{O}_3$  and/or  $\text{FeCr}_2\text{O}_4$ -spinel. With increasing Cr content, the scales become richer in spinel and chromia, which is accompanied by a decrease of the scale growth rate. Formation of a highly protective, single-phase chromia layer requires a chromium content of  $\sim 17\text{--}20\%$ , the

**Table 2** Main alloying elements in selected commercially available, high-Cr ferritic steels

Material	Commercial name	DIN-Nr.	Composition of Cr, Al, Si, Mn, and others (mass%)				
X10CrAl7	Ferrotherm 4713	1.4713	6–8	0.5–1	0.5–1	–	
X10Cr13	Nirosta 4006	1.4006	11.9	<0.02	0.49	0.30	
	–	1.4509	15–16	<1.25	<0.5	<1	Ti/Nb
X10CrAl18	Ferrotherm 4742	1.4742	17.3	1.04	0.93	0.31	
X10CrAl24	Ferrotherm 4762	1.4762	23.5	1.82	1.01	0.38	
			24.4	1.38	1.14	0.54	
Fe-25Cr-Mn	RA 446	–	24.2	–	0.43	0.67	
Fe-26Cr-1Mo	E Brite	–	25.8	–	0.24	0.02	
X18CrN28	Sandvik 4C54	1.4749	26.5	<0.01	0.47	0.70	
Fe-29Cr-4Mo-Ti	Al29-4C	–	27.3	–	0.26	0.28	Ti

exact concentration depending on surface treatment, minor alloying additions, environment, and impurities (e.g., C, S, P). The critical Cr content for obtaining protective chromia scale formation on ferritic steels increases with increasing temperature.

Minor alloying additions of Mn, Ti, Si, and Al may substantially alter the oxidation behavior of commercial ferritic steels (Figure 12). During high temperature exposure, the two first mentioned elements tend to become incorporated in the scale,<sup>81</sup> although titanium can also be present in the form of internal titania precipitates in the subsurface region. Titanium can become dissolved in chromia at low oxygen partial pressures, that is, in the inner part of the scale, whereas at higher oxygen partial pressures, that is in the outer part of the scale, it tends to become reprecipitated. It is therefore frequently found in the form of titania crystals at the scale–gas interface.<sup>81</sup> The incorporation of Ti into the oxide scale tends to increase the chromia growth rate, especially at higher temperatures. Mn possesses only a small solubility in chromia and it is frequently found in the form of a Cr–Mn-spinel layer in the outer part of the oxide scale.

Oxides of Si and Al mostly prevail as internal oxides rather than being incorporated into the external scale. This is related to the higher thermodynamic stability of those oxides compared to that of chromia. If the Al and/or Si contents in the steel are increased to ~1%, the internal silica and/or alumina precipitation can change into protective, external scale formation, which is accompanied by a strong decrease in oxidation rate.<sup>80</sup> The exact Si and/or Al levels, at which this effect occurs, depend on temperature, Cr content, concentrations of minor alloying additions, and component surface treatment. The latter effect was, for example, clearly demonstrated during air oxidation at 800 °C of an 18Cr, 1Al steel (DIN designation 1.4742) which formed

poorly protective Fe- and Cr-rich heterogeneous oxide mixtures accompanied by internal oxidation and nitridation of aluminum on coarse ground surfaces but tended to form a protective alumina scale on polished surfaces.<sup>80,82,83</sup>

This finding illustrates that only slight changes in alloy composition, service temperature, or design-related parameters can fundamentally change the oxidation properties of high-chromium ferritic steels (Figure 12). Additionally, a change from one oxide scale type into another may occur during long-term service due to the depletion of minor alloying elements such as Al, Si, Mn, and/or Ti in the alloy matrix because of their low concentrations.

External silica scale formation is rarely observed during oxidation of commercial ferritic steels. Sometimes silica, mostly in the amorphous state, locally forms relatively dense subscales at the interface between alloy and chromia-based external layer (Figure 13). This effect is frequently accompanied by an increased tendency of the oxide scales to spallation during thermal cycling, probably due to the extremely small thermal expansion coefficient (CTE) of the silica compared to that of the alloy and/or due to the transformation, for example, into cristoballite.

As already mentioned before, the formation of alumina or silica in the form of a closed (sub-) layer is generally not desired in SOFC application, because it can dramatically increase the contact resistance between the interconnector and the electrodes or contact materials.

#### 1.19.10 Behavior of High-Cr Ferritic Steels in Anode Gas

A change of the test atmosphere from air to an anode gas simulating H<sub>2</sub>O–H<sub>2</sub> mixture for high-Cr ferritic

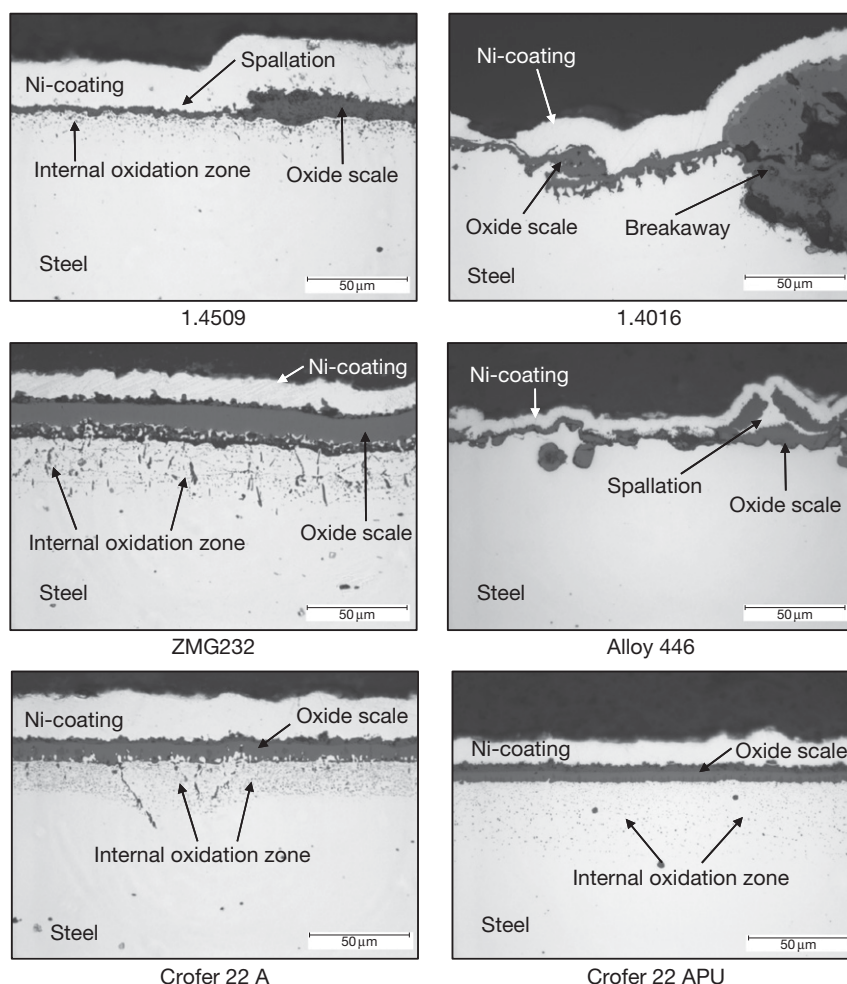


**Figure 12** Different types of oxide scale formation on high-Cr ferritic steels after 1000 h oxidation at 900 °C in air.

steels has similar effects as described for the Cr-based alloys. The morphology of the chromia and spinel-rich surface layers is slightly modified<sup>84</sup> and the adherence of the scale is improved.<sup>80</sup> The oxide growth rates of ferritic steels with Cr contents above about 20% in H<sub>2</sub>O–H<sub>2</sub> mixtures are generally similar or slightly smaller than those in air. This observation seems at first sight to be surprising because chromia scales on Cr-based alloys showed an opposite gas composition dependence of the oxidation rates, as described in [Section 1.19.5](#). The behavior of the high-chromium ferritic steels in anode and cathode side gases was shown<sup>85</sup> to be governed by the differences in growth mechanisms of a Cr–Mn–spinel layer which forms on top of the inner chromia scale. In anode gas, the spinel tends to be stoichiometric MnCr<sub>2</sub>O<sub>4</sub>, whereas in air it is Mn<sub>1+x</sub>Cr<sub>2–x</sub>O<sub>4</sub>. The latter grows by the outward lattice diffusion of cations

whereas the spinel in simulated anode gas grows via grain boundary diffusion<sup>86</sup> resulting in plate and whisker type oxide morphologies and microvoids at the chromia–spinel interface (**Figures 14 and 15**). Further details can be found in the section on ‘Oxidation in Steam and Steam/Hydrogen Environments.’

Due to the substantially lower equilibrium oxygen partial of the anode gas compared to that of the cathode side environment, the thermodynamic driving force for oxide formation in anode gas is in fact substantially smaller than that in the cathode gas. In ferritic steels with Cr contents which are lower than ~20%, the anode side environment can, for instance during the transient stages of oxidation, suppress formation of oxides with low thermodynamic stability.<sup>80</sup> This may for such steels result in a type and morphology of external and internal oxide formation which completely differs from that occurring during air or oxygen



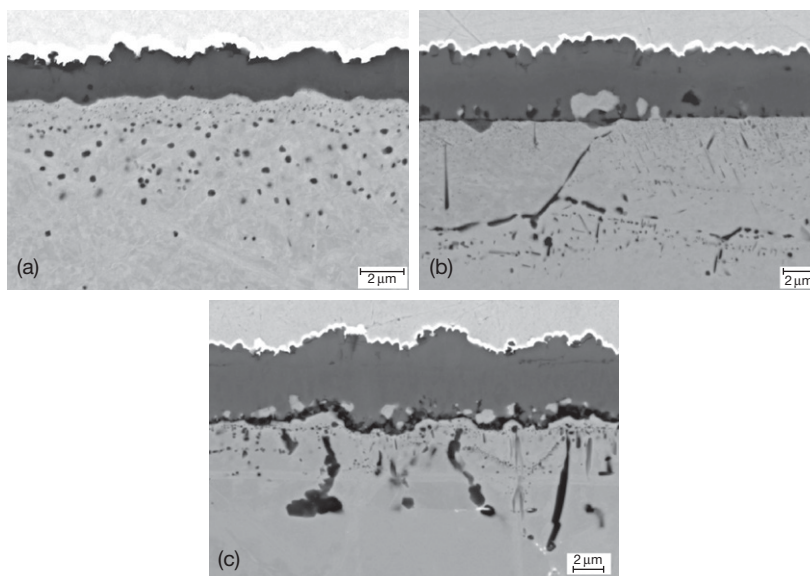


**Figure 13** Oxide scale formation on ferritic steels with 22% Cr after 1000 h exposure at 800 °C in air showing effect of Si/Al content: (a) 0.01% Si/Al, (b) 0.1% Si/Al, and (c) 0.4% Si/0.2% Al. Reproduced from Quadackers *et al. Mater. High Temp.* **2003**, 20(2), 115–127.

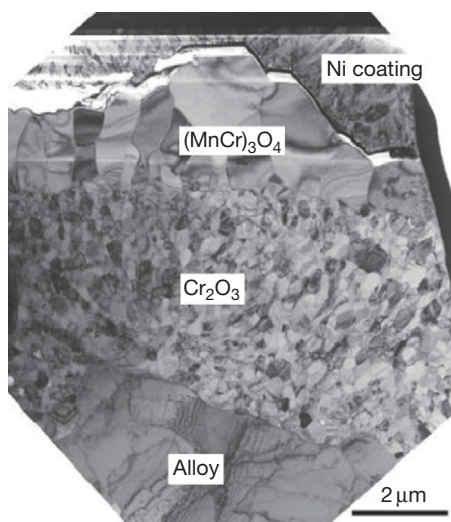


**Figure 14** TEM bright field image of oxide scale (spinel + chromia) on high-Cr ferritic steel after exposure in air at 900 °C for 1000 h. Reproduced from Essuman *et al. Corros. Sci.* **2008**, 50, 1753–1760.

exposure.<sup>80</sup> This, however, does not mean that the oxidation rates are generally smaller in anode than in cathode gas. An example of higher growth rates in anode gas was already illustrated for the case of pure chromia scales formed on chromium-based alloys (Section 1.19.5) and was also found to occur in the case of Mn-free, high-purity Fe–Cr and Ni–Cr model alloys with Cr contents well above 20%.

A more dramatic effect of atmosphere dependence of oxidation rates can be found for ferritic steels with intermediate Cr contents of 10–20%. In atmospheres in which water vapor is the main oxidizing species, the tendency to form a protective external chromia-based scale is substantially suppressed compared to that during air or oxygen exposure.<sup>88,89</sup> Presence of high amount of water vapor thus shifts the critical Cr content for obtaining protective chromia scale formation towards higher concentrations. This has as a result, that a steel with an intermediate Cr content, which may form a protective chromia-based scale during air or oxygen exposure, may form a poorly protective, Fe-base oxide scale during exposure in a high water vapor-containing environment. The tendency to nonprotective scale formation is suppressed by the small size of alloy grain and surface deformation of the steel. Details on the mechanisms of nonprotective scale formation in wet gases can be found in the chapter on ‘Oxidation in Steam and Steam/Hydrogen Environments.’

The formation of poorly protective, Fe-rich oxides will, of course, occur only if the equilibrium oxygen partial pressure in the gas is higher than the dissociation pressures of the Fe oxides. In an H<sub>2</sub>–H<sub>2</sub>O gas mixture at typical SOFC temperatures in the range 600–900 °C, this is the case if the H<sub>2</sub>/H<sub>2</sub>O ratio is lesser than ~1. Thus, if pure hydrogen is used as fuel in an SOFC stack with an intermediate Cr content,

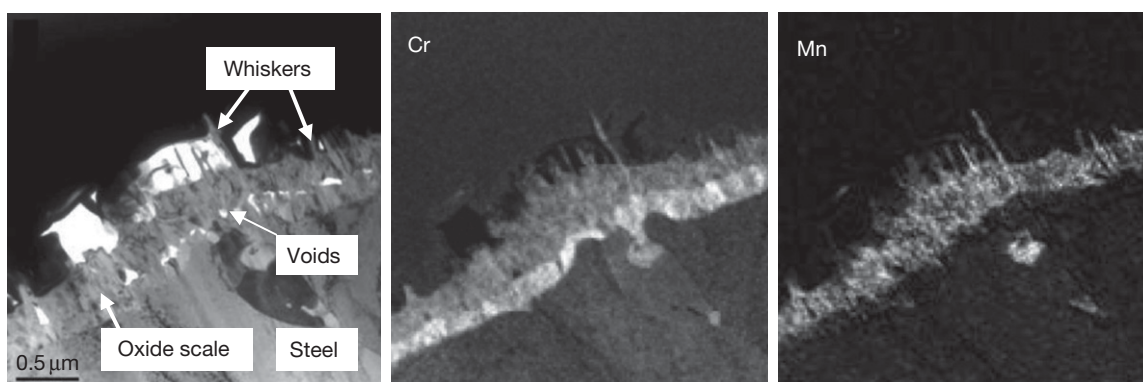


**Figure 15** TEM bright field image and EELS maps for Mn and Cr of the oxide scale on high-Cr ferritic steel during 15 h exposure at 800 °C in Ar-4% $\text{H}_2$ -2%  $\text{H}_2\text{O}$ . Reproduced from Essuman *et al. Corros. Sci.* **2008**, 50, 1753–1760.

ferritic interconnect, the poorly protective oxides will not form in areas near the gas entrance of the stack but only in gas flow direction nearer to the gas outlet, the critical areas being determined by the actually applied fuel utilization.

### 1.19.11 Ferritic Steels in Anode Gases Containing Carbonaceous Gas Species

Applying internal or external reforming, SOFCs can handle a variety of fuels containing carbon-containing gas species. The simulated anode gas will then contain gas species such as CO,  $\text{CO}_2$ , and/or  $\text{CH}_4$  in addition to  $\text{H}_2$  and  $\text{H}_2\text{O}$ .

The carbon transfer which may occur from the service environment to the alloy can, depending on the prevailing gas composition, the temperature, and the properties of the interconnect material, result in a number of material degradation mechanisms, that is, carburization, metal dusting, and C deposition. The latter two effects occur only if the C activity of the environment is larger than unity. Thereby C deposition may hamper the cell performance, for example, by blocking narrow gas passages, but it does not necessarily affect the properties of the interconnect adversely. Metal dusting, however, is a process which commonly results in a very rapid damage of metallic materials. The mechanisms of the metal dusting process are still a subject of scientific debate and a detailed description of it falls outside the scope of this chapter. The reader is referred to a number of references<sup>90,91</sup> in which the various steps in the degradation process are described.

**Table 3** Typical gas composition at SOFC gas inlet and gas outlet (assuming 80% fuel utilization) when using reformed gasoline as fuel

Gas species	Gas composition (vol.%)	
	Stack inlet	Stack outlet
$\text{H}_2$	20	4
CO	22	4.4
$\text{N}_2$	52	52
$\text{CO}_2$	3	20.6
$\text{H}_2\text{O}$	2.5	18.5
$\text{CH}_4$	0.5	0.2

When using carbonaceous fuels, the interconnect may be subjected to environments in which the oxygen partial pressure and the carbon activity substantially change as a function of time. For illustration, we use the application of an SOFC stack in mobile application using reformed gasoline as fuel (Table 3).

During the heating process of the stack to the operation temperature, the interconnect is subjected to a gas with a high-carbon activity and thus a substantial danger for occurrence of metal dusting exists, especially in the temperature range 400–650 °C (Figure 16). When reaching the SOFC operation temperature of 800 °C, the carbon activity is lower than unity and metal dusting attack is no longer possible. Due to the electrochemical reactions occurring at the anode side of the cell, the concentrations of CO,  $\text{CH}_4$ , and  $\text{H}_2$  decrease in gas flow direction, whereas the concentrations of  $\text{CO}_2$  and  $\text{H}_2\text{O}$  increase. As shown in the Cr–O–C stability diagram in Figure 17, chromia is the stable phase in equilibrium with the gas atmospheres at 800 °C. However, it is well established<sup>55,90</sup> that under such conditions, formation of internal Cr carbide, for example,  $\text{Cr}_{23}\text{C}_6$ , may occur even if the equilibrium

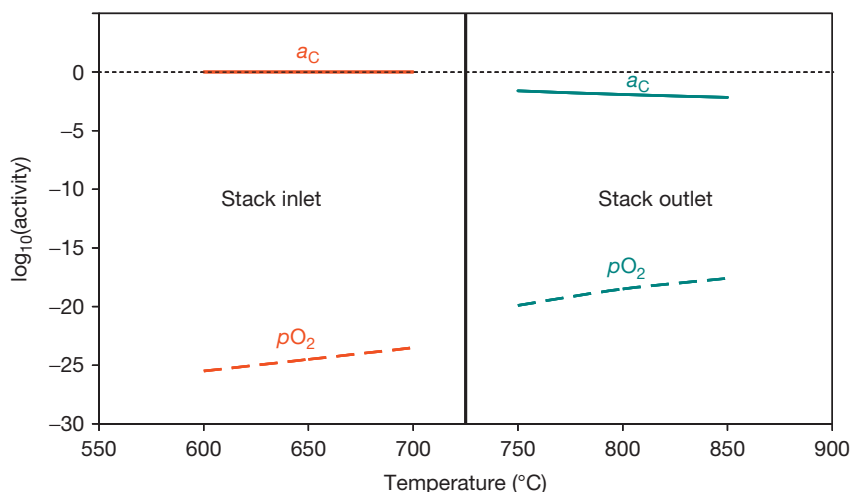


**Figure 16** C activities and oxygen partial pressures of gases in Table 3 as a function of temperature.

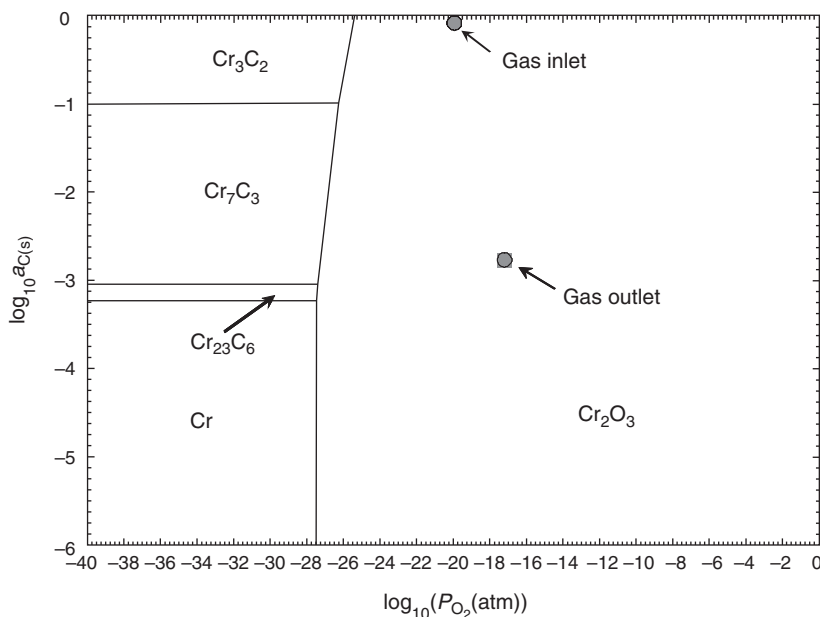


**Figure 17** Cr–O–C stability diagram at 800°C and the location of the equilibrium oxygen partial pressures and carbon activities of the atmospheres in Table 3.

carbon activity in the gas is smaller than the activity required to form the carbide. This is related to a decrease in oxygen partial pressure and a parallel increase in carbon activity upon molecular transport of the gaseous carbonaceous species through the surface oxide layer.<sup>90</sup>

Internal carburization in the case of ferritic steels does not generally result in formation of a continuous subscale carbide layer, but in formation of finely distributed carbide precipitates in the alloy matrix.

The formation of these Cr-rich carbides ( $\text{Cr}_{23}\text{C}_6$  and/or  $\text{Cr}_7\text{C}_3$ ) leads to material embrittlement and additionally depletes Cr from the ferritic matrix in the surface-near region of the alloy. The latter may result in a reduced Cr availability for transport to the surface required for protective scale formation and thus in a deterioration of the steel oxidation resistance.

During stack operation, the steel interconnect may thus be subjected to service environments

which, from the viewpoint of thermodynamic driving forces, cycle between metal dusting and oxidizing/carburizing conditions. It is generally accepted that metal dusting as well as internal carburization can be prevented by the presence of a protective surface oxide layer which prohibits molecular transport of carbonaceous species to the metal surface. The resistance against metal dusting and carburization thus increases with increasing protective properties of the surface oxide layer. Ferritic steels with Cr contents well above 20% showed higher metal dusting and carburization resistance under SOFC conditions than lower Cr steels and, for example, 18–20% Cr austenitics.<sup>92</sup>

### 1.19.12 Ferritic Steels Designed for SOFC Application

The optimum steel composition for an SOFC interconnector will depend on the used cell design (e.g., electrolyte or anode supported concept) and the service conditions (temperature, thermal cycling, fuel gas composition, and required service life).<sup>93</sup> If a YS–ZrO<sub>2</sub> electrolyte-supported design is considered, a low thermal expansion coefficient of  $\sim 10 \times 10^{-6} \text{ K}^{-1}$  is a crucial requirement for the interconnector. Using binary Fe–Cr alloys with Cr contents commonly present in ferritic steels (see Table 2), such a low value cannot be achieved.<sup>20</sup> Some authors, therefore, alloyed steels on the basis of Fe–20% Cr with large amounts of refractory elements such as Mo or W<sup>94,95</sup> to decrease the CTE. The oxidation resistance could be improved by adding small amounts of REs. However, it has to be demonstrated whether the scaling rates are sufficiently small for the materials to be used in SOFCs with the required high-application temperature of 1000 °C in electrolyte-supported designs.

Substantially lower service temperatures between 600 and 800 °C seem to be more appropriate if ferritic steels are to be used as interconnectors. In this temperature range, for example, ceria should be used as electrolyte<sup>3</sup> or an anode-supported cell design allowing an extremely thin YS–ZrO<sub>2</sub> electrolyte should be applied.<sup>82,83</sup> The choice of such concepts would require interconnectors with CTEs similar to that of the Ni/ZrO<sub>2</sub>-anode, that is, in the range  $11\text{--}12 \times 10^{-6} \text{ K}^{-1}$ . Such CTE values can be achieved by ferritic steels with Cr contents of  $\sim 20\%$ .

Quadackers *et al.*<sup>96,97</sup> studied the suitability of model steels with Cr contents of 16–25% and evaluated the effect of various RE additions to achieve an

optimum combination of low scale growth rate and excellent scale adherence. La appeared to be the preferred RE addition, mainly because it does not, contrary to other commonly used REs, form intermetallic compounds with iron. This allows La to become evenly distributed in the alloy rather than being precipitated in the form of intermetallics on the alloy grain boundaries, for example, observed if Y or Ce additions<sup>98</sup> are being used. The actual scale growth rate strongly depends on commonly present minor alloying additions/impurities such as Mn and Ti (Figures 18 and 19). Although in RE-doped steels, very protective behavior can be obtained if the Cr content is just 16–18%, a substantially higher level was chosen to obtain a larger ‘Cr reservoir’ to counteract the danger for the occurrence of breakaway oxidation due to the presence of high water vapor contents in the anode gas,<sup>99</sup> Cr loss due to interaction with contacting materials<sup>100</sup> or rapid exhaustion of the Cr reservoir in very thin interconnects. Small amounts of Mn and Ti were added to obtain external spinel formation which is known to decrease the formation of volatile Cr species.<sup>43,97,101</sup> Minor Ti additions were added to obtain fine internal oxide precipitates of titania (Figure 20) which results in strengthening of the surface-near alloy region thus reducing the tendency for occurrence of surface wrinkling caused by relaxation of oxidation-induced stresses during thermal cycling. By defining low Al and Si contents (Table 4), formation of oxide scales with a very low electrical resistance was obtained for alloys of the type FeCrMn(La/Ti) (Figures 21 and 22). The low Al/Si content also prevents extensive internal oxide formation which was found to affect not only the mechanical properties of the surface-near regions but also the growth rate of the external chromia scale. The latter is related to a volume increase imparted by the internal oxide formation resulting in outward metal flow and inclusions of metallic nodules in the scale.<sup>86,102</sup>

Further indications for development of steels which are especially designed for SOFC application are described elsewhere,<sup>103–105</sup> however, no detailed information in respect to steel composition prevail. Recently, developments on the basis of 22% Cr-containing ferritic steels with systematic variations of minor alloying additions were described.<sup>106</sup> Honnegger *et al.*<sup>107</sup> developed high-Cr ferritic materials for SOFC application that were produced by powder metallurgical techniques, thus allowing incorporation of oxide dispersions to achieve dispersion strengthening. The mechanical alloying

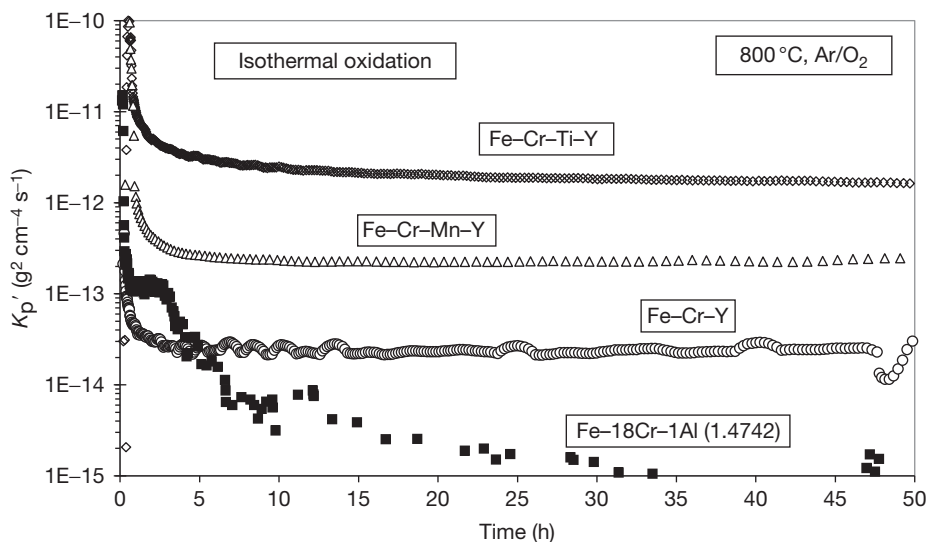


**Figure 18** Apparent oxidation rate  $K_p'$  as function of time for various types of FeCr alloys during isothermal oxidation at 800 °C in Ar/oxygen. Reproduced from Piron-Abellan, J.; Quadackers, W. J. Development of ferritic steels for application as interconnect materials for intermediate temperature solid oxide fuel cells (SOFCs), Report Forschungszentrum Jülich, Jül-4170, March 2005; ISSN 0944-2952.

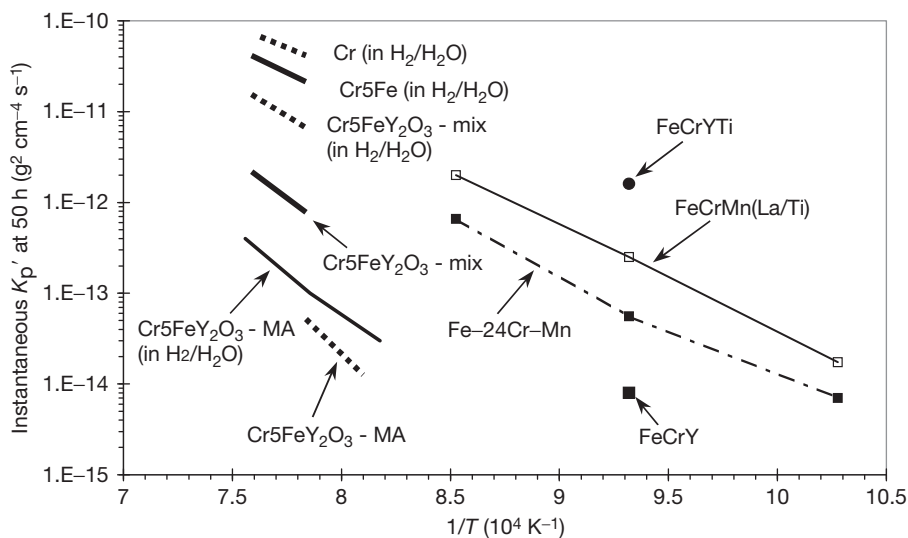


**Figure 19** Instantaneous apparent oxidation rates at 50 h of FeCr-RE and FeCrMn(La/Ti) alloys during isothermal oxidation at various temperatures compared with data of various Cr alloys. If not indicated, data relate to exposures in Ar/20% O<sub>2</sub> (compiled from Refs. 24, 50, 85).

process allows to produce materials with substantially higher concentrations of REs (here Y) than can be obtained by conventional alloy manufacturing methods (Table 4). Therefore, the ferritic ODS steels generally exhibit lower oxidation rates than RE containing wrought alloys produced by conventional methods. A high RE content in the surface regions

can also be obtained by applying a RE-containing coating. In this way, the oxidation rate of a commercial, ferritic 18% Cr steels can substantially be decreased.

A major disadvantage of high-Cr ferritic steels is their tendency to form  $\sigma$ -phase and  $\alpha'$  precipitates at lower temperatures. As both processes lead to



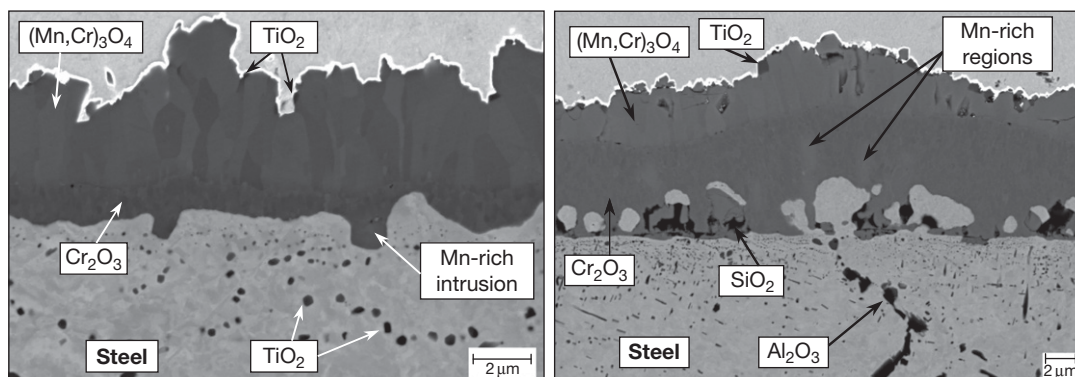


**Figure 20** Cross sections of oxide scales on type FeCrMn(La/Ti) steels after 6000 h exposure in air at 800 °C showing effect of minor Al/Si additions. Left: Crofer 22APU, right: Crofer 22A. (Mark the differences in magnification). Reproduced from Huczowski, P.; Christiansen, N.; Shemet, V.; Niewolak, L.; Piron-Abellan, J.; Singheiser, L.; Quadackers, W. J. *Fuel Cells* 2006, 2, 93–99.

**Table 4** Compositions of selected ferritic steels specially developed for SOFC application

Steel	Composition (mass%)									
	Fe	Cr	Mn	Ti	La	Si	Al	Ni	Zr	Others
Crofer 22A	Bal.	22	0.4	0.05	0.09	<0.01	<0.01	<0.002	—	
Crofer 22APU	Bal.	22	0.4	0.06	0.07	0.11	0.12	0.16	—	
Crofer 22H	Bal.	22	0.4	0.06	0.09	0.3	0.01	0.1	—	Nb, W
ZMG232	Bal.	22	0.5	—	—	0.36	0.19	0.31	0.13	
Sanergy HT	Bal.	22	<0.5	—	—	<0.3	—	—	—	Nb, Mo, Ce
IT11	Bal.	26	0.04	0.2	—	—	0.03	—	—	Mo; Y <sub>2</sub> O <sub>3</sub>

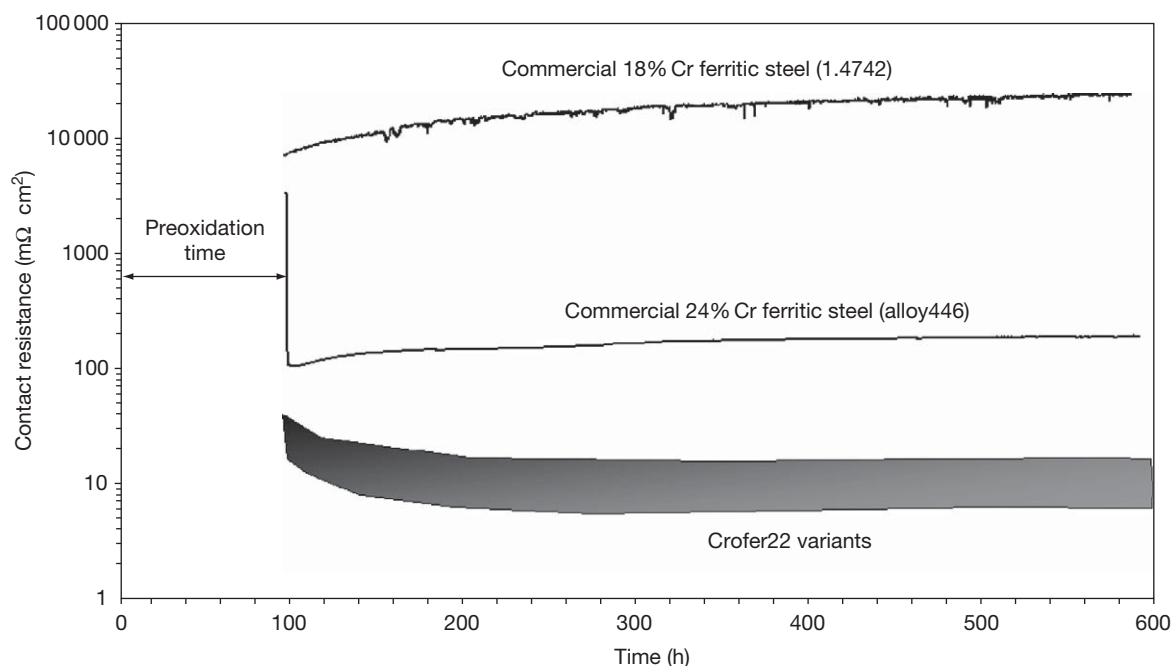


**Figure 21** Contact resistance of various steels during isothermal exposure at 800 °C in air. Reproduced from Piron-Abellan, J.; Quadackers, W. J. Development of ferritic steels for application as interconnect materials for intermediate temperature solid oxide fuel cells (SOFCs), Report Forschungszentrum Jülich, Jül-4170, March 2005; ISSN 0944-2952.

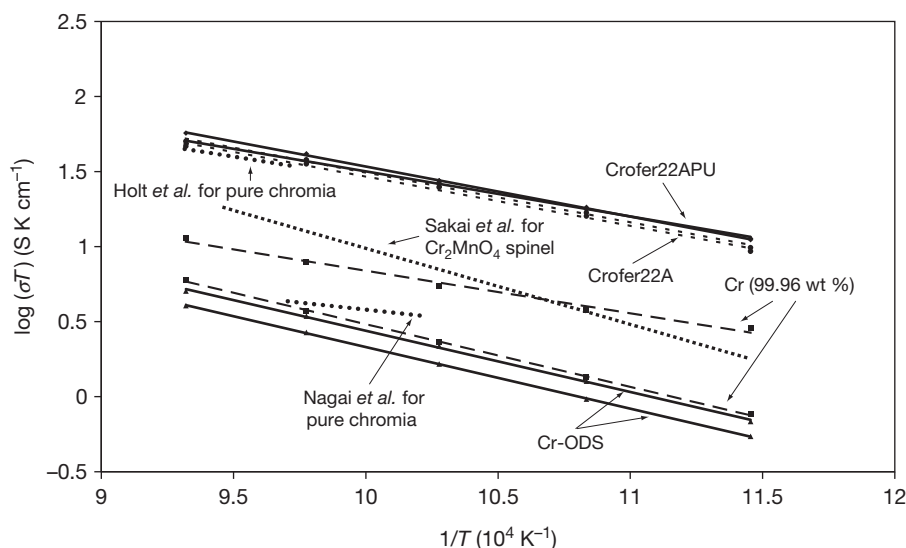


**Figure 22** Temperature dependence of ‘apparent’ conductivity for various steels during exposure at 800 °C in air. Reproduced from Huczowski, P.; Christiansen, N.; Shemet, V.; Niewolak, L.; Piron-Abellan, J.; Singheiser, L.; Quadackers, W. J. *Fuel Cells* **2006**, 2, 93–99.

embrittlement of the steels, the exact alloy composition has to be carefully adapted to the actual envisaged application temperature. For instance, steels with a Cr content of more than 25% are prone to  $\sigma$ -phase formation even at temperatures as high as 800 °C, whereby the  $\sigma$ -phase formation is known to be promoted, for example, by alloying additions of Mo and Si. Hammer *et al.*<sup>102</sup> illustrated that the  $\sigma$ -phase nucleation is not only affected by the alloy purity but also by the actual prevailing service environment. Steels with Cr contents substantially lower than 20% behave more ‘forgiving’ in respect to embrittling precipitate formation. However, they are prone to breakaway oxidation in high water vapor-containing anode side gases.<sup>108</sup> They also may easily run into breakaway oxidation in cathode side gases in the case of thin components, as will be illustrated in the next section.

### 1.19.13 Effect of Component Thickness on Oxidation Behavior

Especially in mobile applications of SOFCs, a reduction in weight of the fuel cell stack is a major design requirement. Weight reduction can be achieved by reducing the interconnect thickness from the common few millimeters to a few tenths of a millimeter. When using such thin components of high-chromium ferritic steels, it has to be considered that the

long-term formation of protective chromia-based oxide scales is not only governed by the alloy chromium content but also by the chromium reservoir in the prevailing interconnect. The growth of the chromia-based surface scale consumes chromium from the metallic material with the result that after long-term service, the initial chromium concentration in the component ( $C_0$ ) may decrease to such a low level ( $C_B$ ) that the growth of the protective scale can no longer be sustained. The time until depletion of the chromium content down to this critical concentration will be shorter in thin than in thick components. Huczowski *et al.*<sup>109</sup> used a simplified expression derived from studies on breakaway oxidation of alumina-forming FeCrAl alloys to predict the time ( $t_B$ ) until the occurrence of breakdown of the protective chromia scale for selected high-chromium ferritic steels as a function of temperature and component thickness (Figure 23)

$$t_B = \left[ 2.3 \times 10^{-3} (C_0 - C_B) \frac{\rho d}{k} \right]^{1/n} \quad [10]$$

Here  $k$  and  $n$  are the oxidation parameters;  $d$ , the component thickness; and  $\rho$ , the alloy density. In deriving this expression, it was assumed that the chromium depletion profiles beneath the oxide scales are virtually ideally flat. Experimental data showed that in the temperature range 800–900 °C, this assumption was a close description of the actual

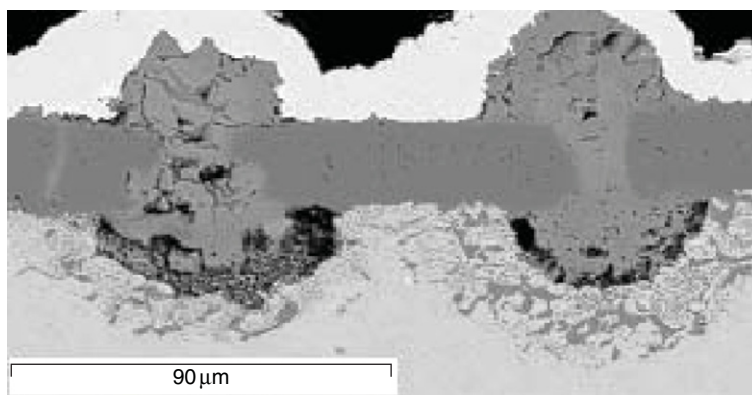
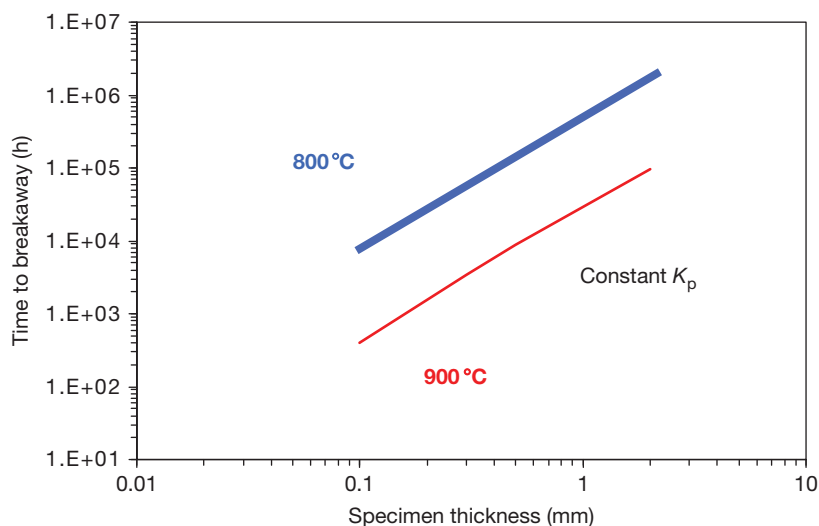


**Figure 23** Upper figure shows calculated life time for plate material of Crofer 22A in air at 800 and 900 °C (ignoring scale spalling and thickness dependence of  $K_p$ ). Lower figure shows example for loss of protective scale properties for 0.2 mm specimen after 1000 h at 900 °C. Reproduced from Huczowski, P.; Quadackers, W. J. Effect of geometry and composition of Cr steels on oxide scale properties relevant for interconnector applications in solid oxide fuel cells (SOFCs), Report Forschungszentrum Jülich, Energy Technology; 2007; Vol. 65, ISBN 978-3-89336-484-8.

occurring profiles because the ratio between oxidation rate  $k$  (in  $\text{cm}^2 \text{s}^{-1}$ ) and diffusion coefficient ( $D$ ) of chromium in the ferritic steel is quite small.<sup>109</sup>

For cases in which oxide scale spallation occurred, a modified expression based on observations for FeCrAl alloys<sup>110,111</sup> may be derived:

$$t_B = 2.3 \times 10^{-3} (C_0 - C_B) \rho d(k)^{-1/n} (\Delta m^*)^{(1/n)-1} \quad [11]$$

Here,  $\Delta m^*$  is the critical weight change at which the onset of scale spallation occurs.

A major finding of Huczowski *et al.*<sup>112</sup> was that, in these life time calculations, it had to be taken into account that not only the time until occurrence of breakaway oxidation depended on component thickness but also the intrinsic oxidation rates of the

alloys. Figure 24 shows mass change data for the high-Cr ferritic steel Crofer 22 A<sup>109,112</sup> during cyclic oxidation at 900 °C for specimens of different thickness. The thickening rate of the two-phase oxide layer consisting of  $\text{Cr}_2\text{O}_3$  and  $\text{MnCr}_2\text{O}_4$  appears to increase with decreasing specimen thickness. This is confirmed by the metallographic cross sections in Figure 25 which shows that the difference in overall scale thickness on high-chromium ferritic steels is mainly related to the difference in thickness of the inner chromia layer, whereas the thickness of the outer spinel layer differs only marginally.<sup>109,112</sup> A second effect of specimen thickness is that the extent of internal oxidation may become limited by the reservoir of the minor elements Ti and Al in the

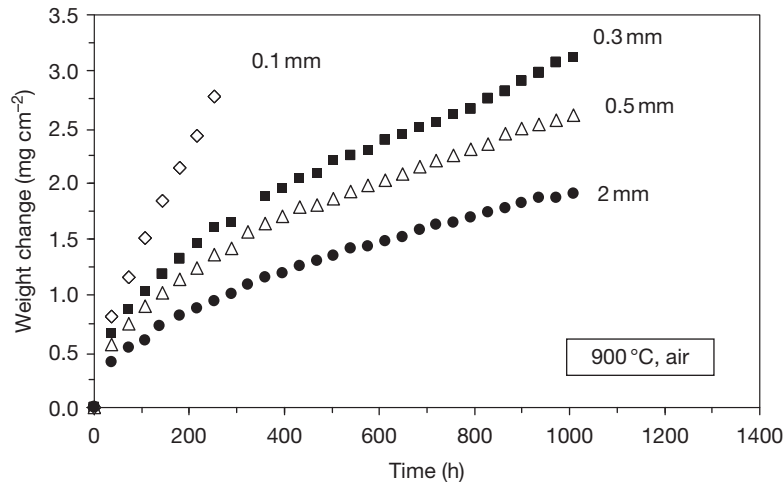


**Figure 24** Weight change during cyclic air oxidation of ferritic steel Crofer 22 A at 900 °C showing effect of specimen thickness on oxidation rate. Reproduced from Huczkwski, P.; Quadakkers, W. J. Effect of geometry and composition of Cr steels on oxide scale properties relevant for interconnector applications in solid oxide fuel cells (SOFCs), Report Forschungszentrum Jülich, Energy Technology; 2007; Vol. 65, ISBN 978-3-89336-484-8.

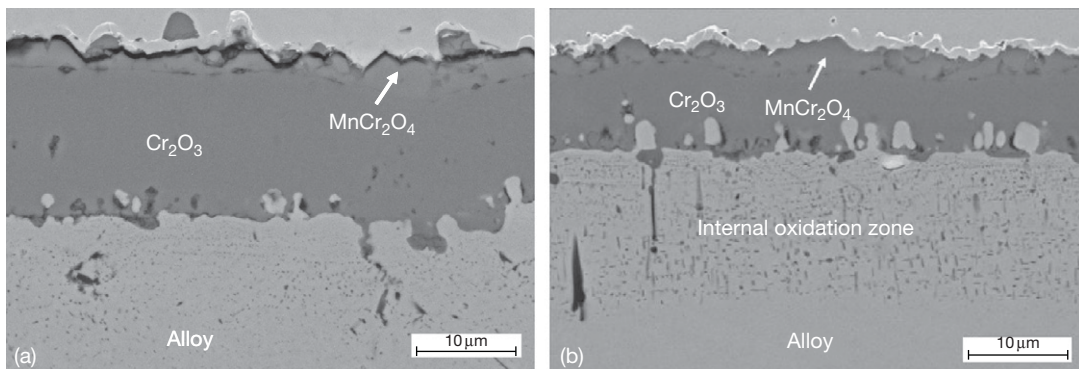


**Figure 25** Metallographic cross sections (SEM images) of Crofer 22 A after 1000 h cyclic oxidation at 900 °C in air: (a) 0.3 mm thick specimen and (b) 2 mm thick specimen. Reproduced from Huczkwski, P.; Quadakkers, W. J. Effect of geometry and composition of Cr steels on oxide scale properties relevant for interconnector applications in solid oxide fuel cells (SOFCs), Report Forschungszentrum Jülich, Energy Technology; 2007; Vol. 65, ISBN 978-3-89336-484-8.

component (Figure 25). At 800 °C, the thickness dependence of the oxidation rate is less pronounced than at 900 °C, but is still clearly seen and of technical importance (Figure 26).

First attempts to explain the specimen thickness dependence of the oxidation rates related to depletion of major (Cr) and minor alloying elements (Al, Si, La, Ti, and/or Mn) as well as scale microcracking occurring during thermal cycling.<sup>109,112</sup> However, more recent experimental results for the ferritic steels<sup>113</sup> in combination with data for Ni-base alloys<sup>114</sup> indicate that all these factors quantitatively affect the oxidation rates, however, they do not seem to be the main reason for the oxidation rate dependence on specimen

thickness. Strong indications were found that the difference in growth rate of the chromia-based scales on thick and thin specimens is the result of compressive growth stresses in the scales which can relax by plastic deformation of the substrate for thin specimens but are maintained at significant levels for thick specimens.

For an oxide under a biaxial compressive stress  $\sigma_{xx}$ , the diffusivity may be written as<sup>114,115</sup>:

$$D = A \exp\left(\frac{\Delta S^*}{R}\right) \exp\left(\frac{-\Delta H^*}{RT}\right) \exp\left(\frac{\frac{2}{3}\Delta V^* \sigma_{xx}}{RT}\right) \quad [12]$$

in which  $\Delta H^*$  and  $\Delta S^*$  are the *activation enthalpy* and *entropy*, respectively,  $\Delta V^*$  is the *activation volume*, and  $A$  is a pre-exponential constant. Additionally, there is

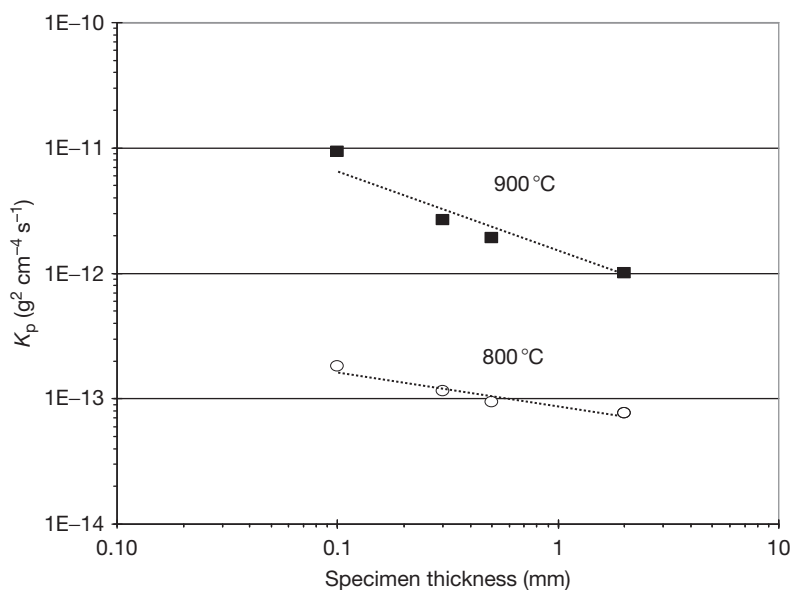


**Figure 26** Measured  $K_p$  values as a function of specimen thickness during cyclic oxidation of high-Cr ferritic steel Crofer 22 A in air. Reproduced from Huczowski, P.; Quadackers, W. J. Effect of geometry and composition of Cr steels on oxide scale properties relevant for interconnector applications in solid oxide fuel cells (SOFCs), Report Forschungszentrum Jülich, Energy Technology; 2007; Vol. 65, ISBN 978-3-89336-484-8.

the possibility of a stress gradient over the oxide scale whereby both cations and anions are transported from regions where the stress is compressive to regions where the stress is tensile resulting in a net transport of oxide into the tensile regions. The vacancy concentration can be written as

$$C_V = C_V^0 \exp\left(\frac{\sigma_h \Delta V^F}{RT}\right) \quad [13]$$

where  $C_V^0$  is the equilibrium concentration of vacancies in the unstressed state and  $\Delta V^F$  is the volume change associated with the formation of the relevant point defect. Of course, in the case of oxidation, the rate is controlled by the faster diffusing ion. An estimate of the reduction caused by the effect of an assumed compressive stress<sup>116–118</sup> revealed for chromia that the effect of stress on the defect concentrations may be more significant than the direct effect on diffusivity.<sup>114</sup>

This explanation for the effect of specimen thickness on oxidation rate implies that occurrence of the effect depends on the extent of growth stress development in the scale. This explains the observation that the specimen thickness dependence differs from environment to environment and is, for instance, far less pronounced in anode than in cathode gas.<sup>86</sup> The explanation also implies that an increase in creep strength of the ferritic steel would decrease the tendency for the oxidation rates to increase with

decreasing component thickness. Studies on steel compositions such as Crofer 22H which were modified by adding the solid solution strengthening element tungsten in combination with the Laves phase forming element niobium, indeed showed that, especially the oxidation rates of thin components of a few tenths of a millimeter at 800 °C were markedly reduced compared to corresponding specimens made of high-purity, high-chromium ferritics (Figure 27(a)).

A further beneficial property of this type of creep-resistant steels of the type Crofer22H (Table 4),<sup>119,120</sup> is that the Laves phase was found to dissolve substantial amounts of silicon,<sup>121</sup> an element which is commonly added in minor amounts as deoxidant of the alloy melt. As explained above, these minor additions (commonly a few tenths of a percent) of silicon in conventional alloys result, during high temperature exposure, in undesired internal oxidation and/or formation of a silica sublayer beneath the chromia scale. The incorporation of silicon in the Laves phase leads to a decreased activity of this element in the steel matrix with the result that no internal oxidation of silicon occurs (Figure 27(b)) if the niobium/silicon ratio is carefully adjusted.<sup>119</sup> In parallel, the incorporation of silicon stabilizes the Laves phase with the result that the adverse effect of niobium on the chromia growth rate is suppressed. This finding allowed the definition of ferritic steel compositions that contained a minor



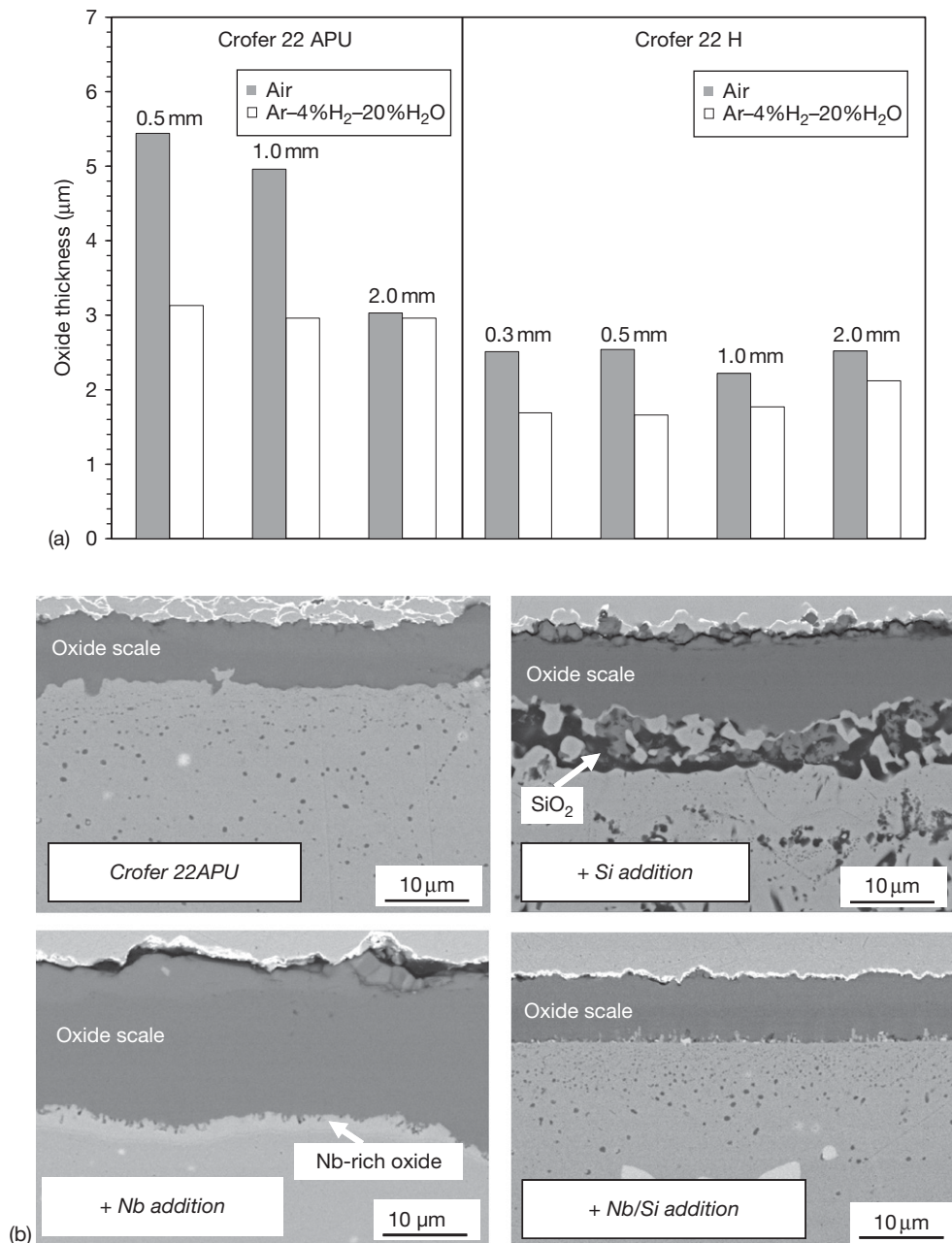


**Figure 27** (a) Oxide thicknesses on Crofer 22 APU and Crofer 22 H after 1000 h discontinuous oxidation at 800 °C (100 h cycles) in different gases. (b) Effect of Si, Nb, and combined Si/Nb addition on oxide scale formation (1000 h, 900 °C, air) on Crofer22 type materials. Alloy designated as 'Nb/Si addition' corresponds to Crofer 22H in Table 4. Reproduced from Froitzheim, J. Ferritic steel interconnectors and their interactions with Ni base anodes in solid oxide fuel cells (SOFC), RWTH Aachen, Report Forschungszentrum Jülich, Energy and Environment, Vol. 16, 2008; ISBN 978-3-89336-540-1.

amount of silicon which are desired from the viewpoint of alloy manufacturing by conventional methods, but did not exhibit the disadvantageous effect of silicon on the oxide scale formation mechanisms. In this way,

oxidation properties could be obtained for components of a few millimeter thickness which were similar to those of the high-purity steels thus allowing to decrease the alloy manufacturing costs compared to

those of the high-purity, single-phase ferritic steels.<sup>122</sup> For components with a thickness of a few tenths of a millimeter, this creep resistant steel showed lower oxidation rates than the high-purity steel.

#### 1.19.14 Oxidation Behavior of Ferritic Steels Under Dual Atmosphere Conditions

Most laboratory oxidation testing of candidate materials for interconnect application is based on short- or long-term exposures in cathode gas and various types of anode gases. However, in reality, the metallic interconnect is simultaneously exposed to air at the cathode side and fuel at the anode side and thus experiences a chemical potential gradient from the fuel side to the air side. A number of investigations have shown that under such conditions, the oxidation behavior of metallic interconnects on the cathode side may differ from that observed during normal air oxidation.<sup>123,124</sup> Especially, ferritic stainless steels with relatively low Cr contents of less than ~20%, under dual atmosphere conditions, show a tendency to form oxide scales with less protective properties than formed during normal air oxidation. The 17% Cr ferritic steel AISI 430 exhibited hematite nodules on the air side of an air–hydrogen sample during isothermal exposure at 800 °C, whereas no hematite formation was seen on the air–air sample. The oxidation behavior on the hydrogen side of the air–hydrogen sample was similar to that on the hydrogen–hydrogen sample. The detrimental effects of the dual exposures are far less pronounced in the case of steels with higher Cr contents, such as Crofer 22APU or E-brite, although a modification of the outer spinel layer was observed<sup>125,126</sup> and some Fe-oxide formation was found at higher exposure temperatures. Dual atmosphere effects were observed for austenitic stainless steels,<sup>127</sup> Ni–Cr-base alloys,<sup>128</sup> alumina-forming alloys<sup>125</sup> as well as pure metals such as nickel or silver.<sup>125,129</sup> The observations are in qualitative agreement with observations of Nakagawa *et al.*<sup>130</sup> when studying the oxidation behavior of martensitic steels under conditions in which the inner surface of a tube was exposed to steam and the other side to air.

The poorer oxidation resistance of ferritic steels with relatively low Cr contents under dual atmosphere conditions is commonly attributed to the transport of hydrogen through the metal substrate from the fuel side to the air side. Hydrogen permeation through metallic materials at high temperatures

is known to be very fast<sup>131</sup> but may be substantially reduced by presence of protective, perfectly gas-tight surface oxide layers of chromia.<sup>131</sup> The modified air side oxidation behavior of ferritic steels under dual atmosphere conditions is similar to that found when such steels are exposed to wet air<sup>88,132</sup> or wet oxygen.<sup>133</sup> The extent of enhanced attack depends on steel composition, interconnect thickness as well as exact composition of the anode gas environment and tends to be reduced by a preoxidation treatment.

#### 1.19.15 Interaction of Chromia-Forming Interconnects with Cathode Side Materials

In evaluating the growth rates and the electronic properties of the surface scales of metallic interconnectors, it has to be borne in mind that parts of the interconnects are at the cathode side in direct contact with the cathode or with ceramic contact materials.

The cathode and contact materials are in most cases La-based perovskites. Due to interaction between these compounds and the interconnect, two important processes can occur: a change of the oxide composition on the interconnect surface and/or a change in the alloy composition in the surface-near region of the interconnect, mainly due to Cr transport into the perovskite.<sup>106,134</sup> These processes can change the contact resistance as well as the oxidation resistance of the interconnect.<sup>134,135</sup> With perovskite type contact materials commonly used in SOFCs, formation of spinel layers (e.g.,  $\text{CoCr}_2\text{O}_4$ ,  $\text{MnCr}_2\text{O}_4$ ) is frequently observed at the interface between the surface oxide film and the perovskite.<sup>134–138</sup>

The changes in interface composition can affect the contact resistance in a positive as well as negative way. The relatively pure chromia layers formed on Cr-based (ODS) alloys are frequently reported to exhibit high contact resistances which can even be at 1000 °C in the range  $\Omega\text{cm}^2$ .<sup>139</sup> Larring and Norby<sup>140</sup> observed, for contact layers of Sr-doped La-manganite and La-cobaltite on a Cr-ODS alloy at 900 °C, an extrapolated contact resistance of  $24\text{ m}\Omega\text{cm}^2$  after 10 000 h. It was claimed that the formation of CoMn-spinel at the interface reduced the transport of Cr from the interconnector into the perovskite. This chromium transport has been shown to at least partly occur via volatile species,<sup>141</sup> as already discussed in Section 1.19.4. Due to the significance of this effect for cell performance, some authors

tried to select the composition of the perovskite-based contact layer in such a way that it not only acted as contacting material but also as 'gettering agent' for the evaporating chromium species. Other authors proposed that a dense and gas-tight Cr-free spinel layer can be formed on top of a protective chromia scale by reaction of manganese, which outwardly diffuses through the chromia scale on the ferritic steel, with contact layers containing large amounts of spinel-forming elements such as Co or Ni (Figure 28). The dense, Cr-free spinel layer, formed by interdiffusion, acts as barrier against vapor-phase transport of volatile chromium oxides and hydroxides.<sup>101,140,142</sup>

Several authors found that Sr or Ca dopants added to increase the electrical conductivity of contact layers on the basis of La-manganite, -chromite, and -cobaltite are easily transported from the cathode or contact layer in the direction of the Cr-based or ferritic steel interconnect surface.<sup>141,143</sup> This not only alters the initial electrical conductivity of the perovskite contact layer but also that of the chromia surface scale (Figure 29) due to formation of compounds such as  $\text{SrCrO}_4$  and/or  $\text{Sr}_3\text{Cr}_2\text{O}_8$ .

In the case of ferritic steels, the chemical compatibility between alloy and perovskite mainly depends on the relative thermodynamic stability of the mixed

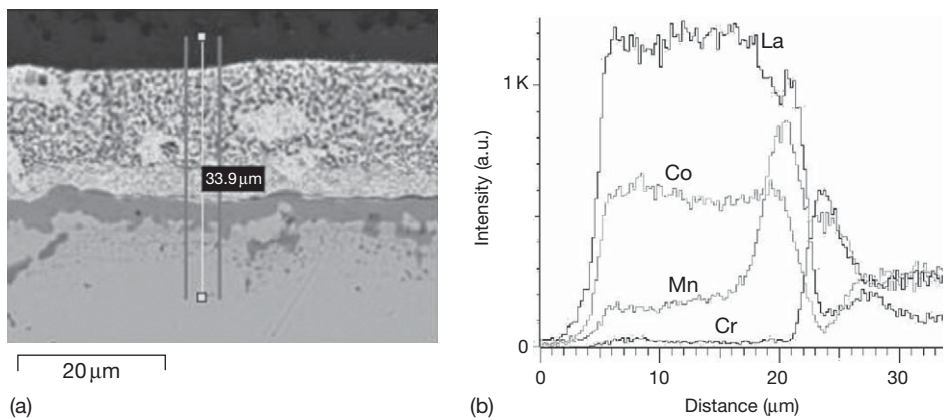


**Figure 28** Interface between steel of the type FeCrMn(La/Ti) and  $\text{LaCoO}_3$  contact layer after 1000 h exposure at 800 °C in air. (a) SEM cross section and (b) element profiles measured along trace indicated in (a). Reproduced from Quadakkers, W. J.; Piron-Abellan, J.; Shemet, V.; Singheiser, L. *Mater. High Temp.* **2003**, 20(2), 115–127.

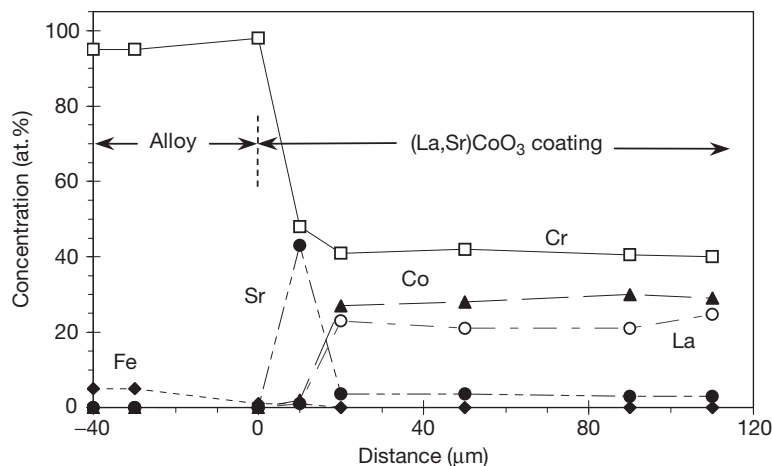


**Figure 29** Element profiles measured near interface between Cr-ODS alloy and  $(\text{La,Sr})\text{CoO}_3$  contact layer after 500 h exposure at 950 °C in air. Reproduced from Quadakkers, W. J.; Piron-Abellan, J.; Shemet, V.; Singheiser, L. *Mater. High Temp.* **2003**, 20(2), 115–127.

oxides (e.g., spinels) which can form due to reaction of Cr from the alloy with the B-type elements (Co, Mn, Cr, Fe, Cu, etc.) in the perovskite contact layer.<sup>80,134–136</sup> From this viewpoint, it seems obvious that manganites and especially chromites provide the best compatibility with the ferritic steels, whereas cobaltites and ferrites tend to result in extensive reaction with the ferritic steel, thereby decreasing its oxidation resistance.<sup>80,144–148</sup> Also, the presence of Cu in the perovskite substantially enhances the oxidation rates of interconnector steels.<sup>149</sup>

The effect of these interface reactions on the contact resistance cannot simply be correlated with the thickness of the reaction layer. The resistance depends on the type of perovskite used and also on perovskite and oxide layer morphology. The results are also affected by the way in which the perovskite is applied, that is, to a bare or to a preoxidized metal. Indications were found that the dense inner chromia layer frequently present at the interface with the alloy possesses a higher specific resistivity than the outer mixed oxide layers (e.g., of the spinel type) formed either due to oxidation of steel alloying elements or due to reaction of the chromia layer with perovskite constituents. Several surface modifications were therefore proposed to decrease the scale growth rate or to modify the composition of the inner chromia layer. To achieve this goal, a number of methods such as RE implantation or application of RE-nitrate solutions have been used, sometimes in combination with Ni deposition to increase chromia conductivity.<sup>66,150–153</sup>

From the viewpoint of long-term stack performance, it has to be considered that the electronic conductivity of actually formed reaction products alone does not govern the relevant contact resistance of the interface between interconnector and contact layer. The reaction between the perovskite and the chromia-based surface scales may also lead to morphological changes of the perovskite layer near the interface with the surface oxide. These morphological changes sometimes, for example, result in substantial void formation which increases the overall contact resistance. Therefore, a number of authors<sup>154</sup> considered the use of Co–Mn or Co–Mn–Fe-spinels as possible contact layer materials. These spinels were found to exhibit less extensive reactions with the steel surfaces than most perovskites, thus ensuring a slower increase in contact resistance during long-term cell operation. Yang *et al.*<sup>155</sup> used a combination of Co-based spinels and RE-oxides, the latter being added to improve the adherence of the oxide scale to the steel surface.

### 1.19.16 Protection Methods to Minimize Cr Vaporization

Different strategies are used to minimize the cell degradation as a result of the Cr release from metallic interconnector materials in SOFCs. They include a decrease in the operation temperature of the SOFC, the application of less Cr-sensitive cathode materials, the design of alternative multilayer interconnects, the development of interconnect alloys with a lower Cr release, and the use of barrier coatings against Cr release.

It has been observed that the Cr vaporization can be reduced by the formation of outer spinel layers formed on the inner protective chromia scale on high temperature alloys<sup>97</sup> and therefore, ferritic interconnect steels such as Crofer 22APU, with defined additions of Mn and Ti in combination with reactive elements (REs) such as Y, Ce, Zr, or La, have been developed (Table 4). A number of studies on Cr vaporization of a number of these steels are available.<sup>40,43</sup> The potential of the Cr retention capability of alloys with different types of oxide layers on the outer surface, such as for example  $(\text{Cr,Mn})_3\text{O}_4$  layers or other oxide scales, is described elsewhere.<sup>156</sup> The Cr vaporization rates of ferritic stainless steels, specifically developed for application as interconnector materials in SOFCs such as Crofer 22 APU, ZMG 232, and IT-10 and IT-11, are very similar. These alloys form a well-adhering outer  $(\text{Cr,Mn})_3\text{O}_4$ -spinel layer that reduces Cr vaporization rates in humid air at 800 °C by 61–75% compared to alloys which form pure chromia scales such as Cr-based ODS alloys or E-Brite. Substantially lower oxidation rates were found for Fe-, Ni-, or Co-base alloys with relatively low Cr contents. This type of alloys formed thicker oxides of the base material (e.g., Co-oxide on Co-based alloy) on top of the inner chromia layer, however, with the disadvantage of high oxidation rates.

For electrically insulating SOFC components, alumina-forming alloys are sometimes considered. At high temperatures, these alloys at their surfaces form slow-growing alumina scales which possess far better protective properties and resistance against Cr evaporation than chromia-forming materials. However, due to the low electronic conductivity of alumina, these materials do not seem to be suitable as construction materials for interconnectors.

Numerous authors aimed to reduce the Cr vaporization from ferritic steels by development of coating systems which possess sufficient electronic conductivity at the SOFC operating temperature.<sup>43,137,141,148,157,158</sup>

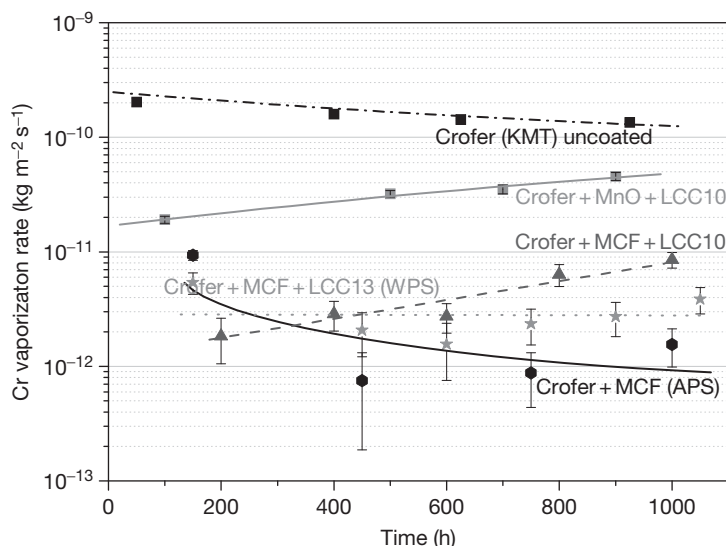


**Figure 30** Cr evaporation rate of Crofer 22 APU with and without various types of coatings during exposure in wet air at 800 °C.<sup>158</sup> LCC: La-base perovskite; MCF: Mn/Co/Fe-spinel.

The coatings mostly are perovskites layers on the basis of (La,Sr)MnO<sub>3</sub>, (La,Sr)CoO<sub>3</sub>, and (La,Sr)CrO<sub>3</sub> or combinations of these (Figure 30). There were also attempts to use reactive coatings of La<sub>2</sub>O<sub>3</sub> and SrO, that is, compounds which form protective (La,Sr)CrO<sub>3</sub> layers by reaction with Cr in the steel.<sup>48</sup> The most common coating techniques used to apply such protection layers are vacuum plasma spraying (VPS), air plasma spraying (APS), and wet powder spraying.<sup>43,48,140,141</sup>

Sputtered ceramic Cr barrier coatings of La<sub>0.8</sub>Sr<sub>0.2</sub>CrO<sub>3</sub>, La<sub>0.99</sub>(Cr<sub>0.77</sub>Mg<sub>0.05</sub>Al<sub>0.18</sub>)O<sub>3</sub>, La<sub>0.80</sub>Sr<sub>0.20</sub>MnO<sub>3</sub>, and La<sub>0.65</sub>Sr<sub>0.30</sub>MnO<sub>3</sub> on substrates of Crofer 22 APU showed only a minor reduction of the Cr release. This is mainly related to the formation of pores due to crystallization of the amorphous sputter coatings during high temperatures exposure. The LSM coatings showed a high tendency to spallation after thermal cycling, which might be prevented by a proper adjustment of the manufacturing parameters such as the thickness of the coating. In general, the practical application of perovskite type Cr retention layers seems to be questionable due to high costs and difficulties with the fabrication of dense coatings.

Promising results have been obtained with coatings on the basis of spinel type oxides, for example, on the basis of Co and/or Ni. The coatings were either directly applied in the form of respective oxides or as metallic coatings of Co or Ni with a thickness of about 10 μm. The metallic layers are transformed into oxides during high temperature exposure and form the spinel layers by reactions

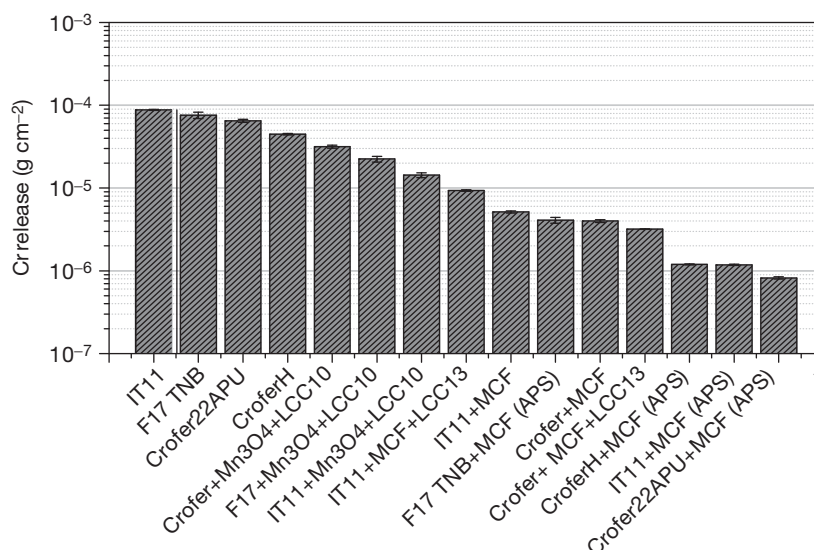
with the chromia-based surface scales present on the ferritic steels. With such coatings, Cr retentions of more than 99% up to the maximum test time of 1200 h at 800 °C in humid air could be achieved. The coatings seem to be applicable for a wide range of stainless steels and fulfill the requirements for mobile and stationary long-term applications. These types of coatings were found to possess electronic conductivities which are 1–2 orders of magnitude larger than that of Cr<sub>2</sub>O<sub>3</sub> and even tend to reduce the oxidation of the ferritic substrate.

Figure 31 shows a comparison of the chromium release during 1000 h exposure in wet air at 800 °C for different types of ferritic steels with and without various types of coatings. It is obvious that suitable coating compositions can effectively reduce the chromium release by approximately two orders of magnitude provided that they can be applied in the form of a dense layer with suitable adhesion to the metallic substrate.

### 1.19.17 Interaction of Chromia-Forming Interconnects with Anode Side Materials

At the anode side, the interconnect is in direct contact with the Ni/ZrO<sub>2</sub> cermet anode or, in most cases, with a Ni wire mesh which provides the electrical contact between the interconnect and the anode. If, for instance, the Ni net is spot welded to the





**Figure 31** Total Cr release during 1000 h exposure in air with standard humidity of 60% rel. at 25 °C. LCC: Perovskite type coating; MCF: Mn/Co/Fe-spinel coating. Reproduced from Trebbels, R. Ph.D. Thesis, RWTH Aachen, 2009.

interconnector, excellent contact resistance values are initially observed. In the case of a Cr-based interconnector, however, interdiffusion can result in excessive Kirkendall-void formation at the Cr–Ni interface, eventually resulting in deterioration of the contact. Ni plating of the interconnector has been applied to reduce this problem,<sup>135</sup> however, extensive outward diffusion of Cr into the Ni with subsequent chromia formation on the Ni layer has been found to occur after long-term exposure.

Interdiffusion between a ferritic steel interconnect and the spot-welded nickel wire mesh will lead to Ni transport into the steel resulting in local austenite formation (Figure 32), thereby changing the steel oxidation resistance as well as the thermal expansion coefficient. As a result of interdiffusion these property changes will be of special concern if very thin interconnects are being used.

Vice versa, transport of Fe, Cr, and other steel constituents into the wire mesh renders the latter as an alloy which will tend to form surface oxide layers in the anode side environment resulting in a decreased catalytic activity.<sup>159</sup>

Preoxidation layers have been examined as possible barriers to minimize interdiffusion processes between the ferritic steel and the Ni wire mesh or the Ni/ZrO<sub>2</sub>-anode. However, the preformed oxide scales tended to become dissociated at the Ni–steel interfaces,<sup>160,161</sup> so after longer exposure time, the unwanted interdiffusion processes appeared again

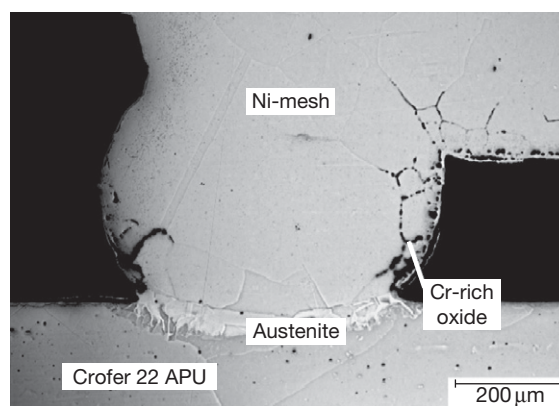


**Figure 32** Ni mesh in direct contact with the interconnect plate of an SOFC stack after 3000 h at 800 °C. Reproduced from Brandner, M.; Bram, M.; Froitzheim, J.; Buchkremer, H.P.; Stover, D. *Solid State Ionics* **2008**, 179(27–32), 1501–1504.

(Figure 33). A number of externally applied diffusion barrier layers have been proposed and quite promising results were obtained with sputtered ceria layers.<sup>162,163</sup> The intrinsic electronic conductivity of ceria in the low-*p*O<sub>2</sub> anode gas is substantially smaller than that of Ni, but it is sufficiently high to obtain low contact resistance values because layers of only a few micrometer thickness appeared to be sufficient to virtually completely suppress the interdiffusion phenomena.<sup>87</sup> During long-term operation, however, the outward growing Cr–Mn-spinel oxide

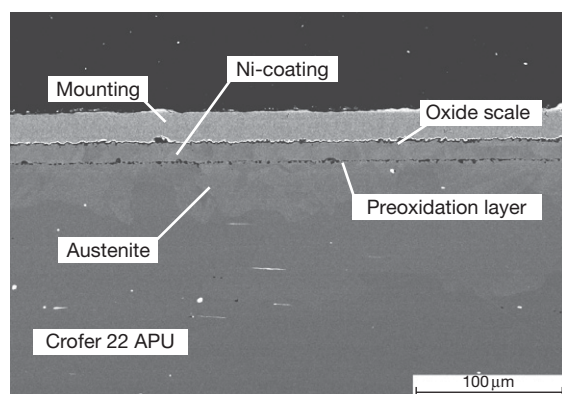


**Figure 33** Cross section of sample with a Ni coating on (100 h) preoxidized Crofer 22 APU after 1000 h exposure in Ar-4H<sub>2</sub>-2H<sub>2</sub>O at 800 °C showing austenite formation, dissociation of the preformed oxide layer, and chromia formation on top of the Ni coating. Reproduced from Froitzheim, J.; Niewolak, L.; Brandner, M.; Singheiser, L.; Quadakkers, W. J. *J. Fuel Cell Sci. Technol.* in press 6(4).

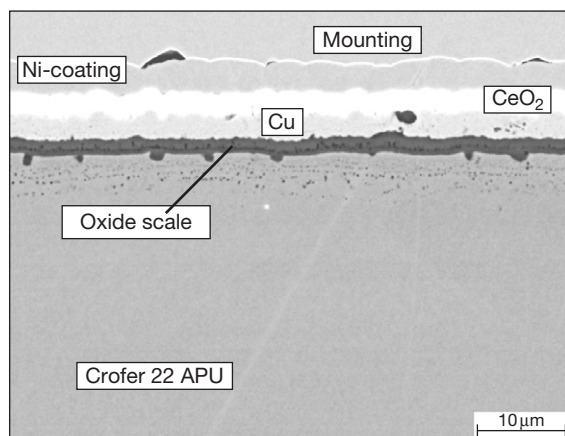


**Figure 34** Cross section of multilayer ceria/Cu coating between preoxidized Crofer 22 APU and Ni layer after 1000 h of exposure in Ar-4H<sub>2</sub>-2H<sub>2</sub>O at 800 °C. Reproduced from Froitzheim, J.; Niewolak, L.; Brandner, M.; Singheiser, L.; Quadakkers, W. J. *J. Fuel Cell Sci. Technol.* in press 6(4).

on the steel deteriorated the chemical contact between oxide scale and ceria layer. An improvement of the electrical contact could be obtained by applying a duplex layer of ceria and copper on a preoxidized ferritic steel (Figure 34). The high oxygen solubility in Cu prevented the dissociation of the oxide layer and the geometrical deterioration of the contact was reduced because the geometrical irregularities were compensated by plastic deformation of the Cu layer.<sup>87</sup>

### 1.19.18 Interaction of Metallic Interconnects with Glass Sealants

Most glass sealants used in solid oxide fuel cells are based on the system, barium-calcium-aluminosilicate (BCAS).<sup>164–167</sup> The glasses frequently contain further minor amounts of other oxides, for instance, to increase the wetting properties. The extent of the reaction of high-chromium ferritic steels with the glass ceramics depends on the exposure conditions and the distance of the interface of sealing glass and ferritic steel to the ambient air.<sup>168–170</sup> Near the triple-phase boundary, steel/glass/air volatile chromium species react with BaO, thereby forming BaCrO<sub>4</sub> (Figure 35). In the interior seal regions, hardly any access of oxygen from the air is possible and thus only a very minor reaction with the steel surface occurs and the chromium tends to slightly dissolve into the glass. The extent of reaction depends on the steel composition. Crofer 22 APU was found to exhibit better chemical compatibility and bonding with the BCAS-based glass-ceramics than most other ferritic steels due to the growth of its specific oxide scale on the alloy during high temperature exposure.<sup>170</sup> A further suppression of interface reactions and BaCrO<sub>4</sub> formation was obtained when an alumina-forming alloy was used.<sup>169</sup> Thus, one approach to improve the sealing effectiveness is to engineer the alloy surface, for example, by local aluminizing<sup>171</sup> in places where electrical conductivity is not required.

More severe reactions may occur if the glass contains minor amounts of wetting agents in the form of thermodynamically less stable oxides such as PbO or ZnO. Depending on the ferritic steel composition, the use of such glasses may result in rapid short circuiting of SOFC stacks by excessive iron oxide formation on the ferritic steels near the triple-phase boundary air/glass/metal.<sup>172–175</sup> It was however found that the trigger of this detrimental effect occurred near the triple-phase boundary at the anode side of the stack. Here, the less stable oxides were reduced to, for example, metallic Pb, which possesses a substantial vapor pressure ( $\sim 10^{-4}$  bar at 800 °C) at the prevailing high service temperature of 800–900 °C. As confirmed by laboratory tests,<sup>159</sup> the presence of Pb vapor resulted in severe grain boundary attack in the high-chromium ferritic steels accompanied by excessive internal oxidation of chromium (Figure 36). Due to the low  $p_{\text{O}_2}$  in the anode side gas, no external iron oxide formation occurred. However, the internal oxidation resulted in a large volume increase and thus in a local bulging of the steel. In the actual SOFC stack,

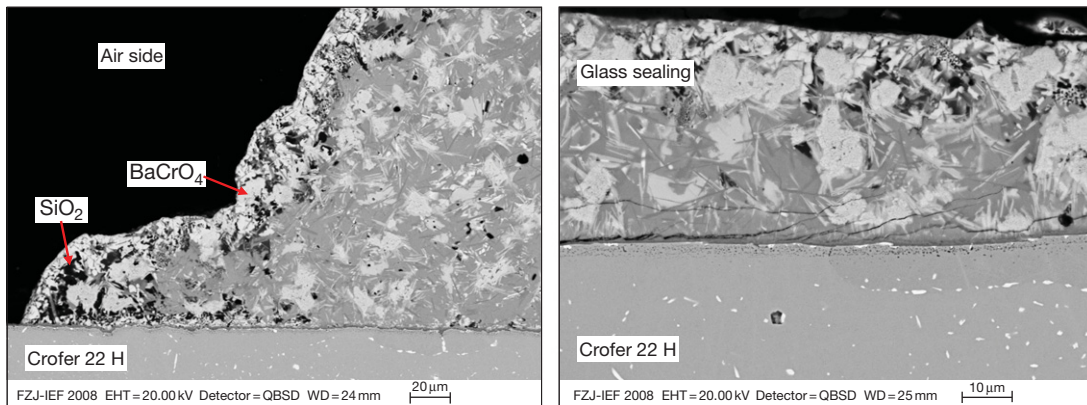


**Figure 35** SEM/BSE pictures of glass/metal microstructure on cathode side (left) and interseal region (right) of SOFC stack after 1000 h operation at 800 °C. Reproduced from Shemet, V.; Quadakkers, W. J. Unpublished results.

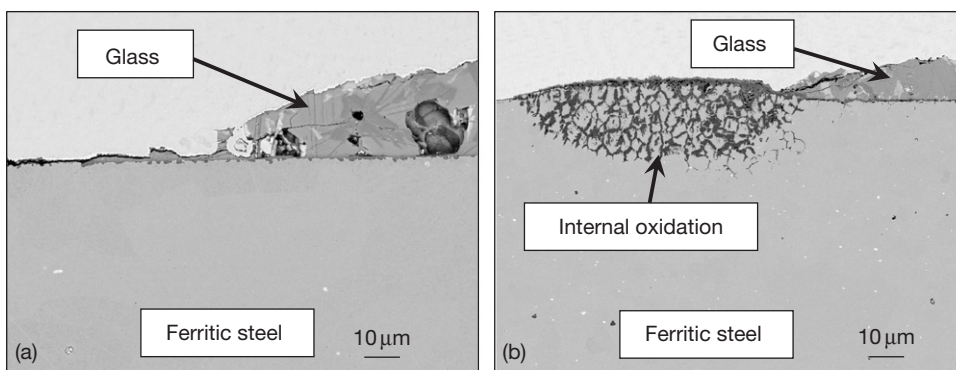


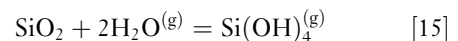
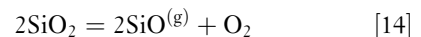
**Figure 36** Interaction of ferritic steel with PbO-containing BCAS glass at 800 °C in (a) air and (b) Ar–H<sub>2</sub>–H<sub>2</sub>O. Reproduced from Shemet, V.; Quadakkers, W. J. Unpublished results.

this initiated a cracking at/near the steel–glass interface which allowed the Pb vapor-triggered internal oxidation to propagate in the direction of the triple-phase boundary glass/steel/air. When reaching this point, the chromium-depleted steel matrix started to form rapidly growing iron-base oxide which eventually ‘bridged’ the small distance between two interconnector plates. The high electronic conductivity of the Fe-base oxide in this way resulted in a short circuiting of the stack.

The rate at which this Pb vapor-induced reaction occurred, appeared to depend on the amount of the minor alloying additions Si and Al in the ferritic steel. Concentrations of a few tenths of a percent results, as explained in [Section 1.19.9](#), in formation of internal silicon- and aluminum oxides. The minor volume increase imparted by this effect leads to outward metal flow, noticeable by formation of metallic nodules in the surface oxide scale<sup>86,102</sup> and is accompanied by formation of micro cracks. The latter can act as channels for transport of Pb vapor through the oxide

scale towards the steel surface resulting in the above described enhanced oxidation attack. High-purity steels (for instance Crofer 22APU) with very low Al and Si contents in the range 0.01% were less prone to Pb vapor attack than steels (such as, e.g., Crofer 22A) with more common Al/Si contents of ~0.1%.

A further effect imparted by an indirect interaction of the steel with the ceramic sealant is related to the high silicon content of the glass. In dry and wet gases, silicon may form a number of volatile oxides and (oxy-)hydroxides



It is apparent that [reaction \[14\]](#) is only significant in low- $p\text{O}_2$  environments. [Reactions \[15\] and \[16\]](#) are independent of  $p\text{O}_2$  and the vapor pressure of the volatile species is proportional to  $p^2(\text{H}_2\text{O})$  and  $p(\text{H}_2\text{O})$ ,



respectively.<sup>176</sup> Due to these volatile species, silicon-containing oxides are frequently found at the external surface at the anode side of ferritic steel interconnects after long-term stack operation, mainly in the form of Mn-silicate.<sup>177</sup> For further details on the formation of volatile silicon-containing species, see the chapter on 'Oxidation in Steam and Steam/Hydrogen Environments.'

## References

- Singhal, S. C. *MRS Bull.* **2000**, 25(3), 16–21.
- Minh, N. Q. *J. Am. Ceram. Soc.* **1993**, 76(3), 563–588.
- Steele, B. C. H. *Solid State Ionics* **2000**, 134, 3–20.
- Singhal, S. C. In *Solid Oxide Fuel Cell (SOFC-V)*; Stimming, U., Singhal, S. C., Tagawa, H., Lehnert, W., Eds.; The Electrochemical Society Proceedings Series: Pennington, NJ, 1997; p 88, PV 97-40.
- Stolten, D.; Späh, R.; Schamm, R. In *Solid Oxide Fuel Cell (SOFC-V)*; Stimming, U., Singhal, S. C., Tagawa, H., Lehnert, W., Eds.; The Electrochemical Society Proceedings Series: Pennington, NJ, 1997; p 88, PV 97-40.
- Quadackers, W. J.; Piron-Abellan, J.; Shemet, V.; Singheiser, L. *Mater. High Temp.* **2003**, 20(2), 115–127.
- Köck, W.; Martinz, H.; Greiner, H.; Janousek, M. In *Solid Oxide Fuel Cells (SOFC IV)*; Dokiya, M., Yamamoto, O., Tagawa, H., Singhal, S. C., Eds.; The Electrochemical Society Proceedings Series: Pennington, NJ, 1995; p 841, PV 95-1.
- Yang, Z. *Int. Mater. Rev.* **2008**, 53(1), 39–54.
- Stöver, D.; Diekmann, U.; Flesch, U.; Kabs, H.; Quadackers, W. J.; Tietz, F.; Vinke, I. In *Solid Oxide Fuel Cells (SOFC VI)*; Singhal, S. C., Dokiya, M., Eds.; The Electrochemical Society Proceedings Series: Pennington, NJ, 1999; p 812, PV 99-19.
- Lai, G. *High Temperature Corrosion of Engineering Alloys*; ASM International: Materials Park, OH, 1990.
- Kofstad, P. *High Temperature Corrosion*; Elsevier Applied Sciences/Chapman and Hall: London, 1988.
- England, D.; Virkar, A. V. *J. Electrochem. Soc.* **1999**, 146(9), 3196.
- Wersing, W.; Ivers-Tiffée, E.; Schiesl, M.; Greiner, H. In Proceedings of the International Symposium on Solid Oxide Fuel Cells; Nagoya, Japan, 13–14 November 1989; Yamamoto, O., Dokiya, M., Tagawa, H., Eds.; Science House: Tokyo, Japan, 1989; p 33.
- Yamamoto, O. *Electrochim. Acta* **2000**, 45, 2423.
- Kofstad, P. In *Proceedings of the 2nd European Solid Oxide Fuel Cell Forum*; Thorstensen, B., Ed.; European SOFC Forum: Switzerland, 1996; Vol. 2, p 479.
- Kofstad, P. In *Proceedings of the 17th Riso International Symposium on Materials Science: High Temperature Electrochemistry, Ceramics and Metals*; Poulsen, F., Bonanos, N., Linderth, S., Mogenson, M., Zachau-Christiansen, B., Eds.; Riso National Laboratory: Roskilde, Denmark, 1996; p 55.
- Kofstad, P.; Bredesen, R. *Solid State Ionics* **1992**, 52, 69.
- Matsuzaki, Y.; Yasuda, I. *Solid State Ionics* **2000**, 132, 271.
- Yasuda, I.; Baba, Y.; Ogiwara, T.; Yakabe, H.; Matsuzaki, Y. In *Solid Oxide Fuel Cells (SOFC VII)*; Yokokawa, H., Singhal, S. C., Eds.; The Electrochemical Society Proceedings Series: Pennington, NJ, 2001; p 130, PV 2001-16.
- Malkow, T.; Crone, U. v. d.; Laptev, A. M.; Koppitz, T.; Breuer, U.; Quadackers, W. J. In *Solid Oxide Fuel Cells (SOFC V)*; Stimming, U., Singhal, S. C., Tagawa, H., Lehnert, W., Eds.; The Electrochemical Society Proceedings Series: Pennington, NJ, 1997; p 1245, PV 97-40.
- Thierfelder, W.; Greiner, H.; Köck, W. In *Solid Oxide Fuel Cells (SOFC V)*; Stimming, U., Singhal, S. C., Tagawa, H., Lehnert, W., Eds.; The Electrochemical Society Proceedings Series: Pennington, NJ, 1997; p 1306, PV 97-40.
- Schmidt, H.; Brückner, B.; Fischer, K. In *Solid Oxide Fuel Cells (SOFC IV)*; Dokiya, M., Yamamoto, O., Tagawa, H., Singhal, S. C., Eds.; The Electrochemical Society Proceedings Series: Pennington, NJ, 1995; p 869, PV 95-1.
- Quadackers, W. J.; Greiner, H.; Köck, W. In *Proceedings of the First European Solid Oxide Fuel Cell Forum*; Bossel, U., Ed.; European SOFC Forum, Dr. Ulf Bossel, Morgenacher Str. 2F, CH-5452: Oberrohrdorf, Switzerland, 1994; Vol. 2, p 525.
- Quadackers, W. J.; Norton, J. F.; Penkalla, H. J.; Breuer, U.; Gil, A.; Rieck, T.; Hänsel, M. In *Proceedings of the 3rd International Conference on Microscopy of Oxidation, Cambridge, 16–18 September 1996*; Newcomb, S. B., Little, J. A., Eds.; The Institute of Materials, 1996; p 221.
- Graham, M.; Hussey, R. *Oxid. Met.* **1995**, 44, 339–374.
- Cotell, C.; Yurek, G.; Hussey, R.; Mitchel, D.; Graham, M. *J. Electrochem. Soc.* **1987**, 134, 1871.
- Quadackers, W. J.; Holzbrenner, H.; Briefs, K. G.; Beske, H. In *Proceedings of the Europ. Coll. on the Role of Active Elements in the Oxidation Behaviour of High Temperature Alloys, 12–13 December 88*; Petten, N. L., Lang, E., Ed.; European Communities, 1988; p 155.
- Hou, P.; Stringer, J. *Oxid. Met.* **1992**, 38, 323.
- Whittle, D.; Stringer, J. *Philos. Trans. Roy. Soc. London A* **1980**, 295, 309.
- Golightly, F.; Stott, H.; Wood, G. *Oxid. Met.* **1976**, 10(3), 163.
- Pint, B. *Oxid. Met.* **1996**, 45, 1.
- Quadackers, W. J.; Greiner, H.; Köck, W.; Buchkremer, H. P.; Hilpert, K.; Stöver, D. In *Proceedings of the 2nd European Solid Oxide Fuel Cell Forum*; Thorstensen, B., Ed.; European SOFC Forum, Dr. Ulf Bossel, Morgenacher Str. 2F, CH-5452: Oberrohrdorf, Switzerland, 1996; Vol. 2, p 297.
- Brady, M. P.; Wright, I. G.; Anderson, I. M.; Sikka, V. K.; Ohriner, E. K.; Walls, C.; Westmoreland, G.; Weaver, M. L. In *Ductilization of Cr via Oxide Dispersions*; Proceedings of the 15th International Plansee Symposium; Plansee, AG, Reutte, Kneringer, G., Rodhammer, P., Wildner, H., Eds.; 2001; pp 108–110–13.
- Badwal, S. P. S.; Deller, R.; Foger, K.; Ramprakash, Y.; Zhang, J. P. *Solid State Ionics* **1997**, 99, 297.
- Hilpert, K.; Das, D.; Miller, M.; Peck, D. H.; Weiß, R. *J. Electrochem. Soc.* **1996**, 143, 3642.
- Jiang, S. P.; Zhang, J. P.; Apateanu, L.; Foger, K. *J. Electrochem. Soc.* **2001**, 148, 447.
- Odell, S. P.; Ding, G. L.; Tewari, S. N. *Metall. Mater. Trans. A* **1999**, 30A, 2159–2165.
- Ebbinhaus, B. B. *Comb. Flame* **1993**, 93, 119.
- Das, D.; Miller, M.; Nickel, H.; Hilpert, K. In *Proceedings of the First European Solid Oxide Fuel Cell Forum*; Bossel, U., Ed.; European SOFC Forum, Dr. Ulf Bossel, Morgenacher Str. 2F, CH-5452: Oberrohrdorf, Switzerland, 1994; Vol. 2, p 703.

40. Stanislawski, M.; Wessel, E.; Hilpert, K.; Markus, T.; Singheiser, L. *JES* **2007**, 154(4), A295–A306.
41. Opila, E. J.; Myers, D. L.; Jacobson, N. S.; et al. *J. Phys. Chem. A* **2007**, 111, 1971–1980.
42. Yungman, V. S.; Medvedev, V. A.; Veits, I. V. and Bergman, G. A.; Eds. *IVTANTHERMO – A Thermodynamic Database and Software System for the Personal Computer*; CRC Press/Begell House: Boca Raton, FL, 1993.
43. Gindorf, C.; Singheiser, L.; Hilpert, K. *Steel Res.* **2001**, 72, 528.
44. Gindorf, C.; Hilpert, K.; Nabielek, H.; Singheiser, L.; Ruckdäschel, R.; Schiller, G. In *Proceedings of the Fourth European Solid Oxide Fuel Cell Forum*; McEvoy, J., Ed.; European SOFC Forum, Dr. Ulf Bossel, Morgenacher Str. 2F, CH-5452: Oberrohrdorf, Switzerland, 2000; Vol. 2, p 845.
45. Batawi, E.; Plas, A.; Straub, W.; Honegger, K.; Diethelm, R. In *Solid Oxide Fuel Cells (SOFC VI)*; Singhal, S. C., Dokiya, M., Eds.; The Electrochemical Society Proceedings Series: Pennington, NJ, 1999; p 767, PV 99-19.
46. Quadackers, W. J. *German Patent DE 195 47 699 C2*; 1995.
47. Quadackers, W. J.; Baumanns, F.; Nickel, H. *German Patent DE 44 10 711*; 1995.
48. Linderth, S. *Mater. Processes* **1998**, 17, 217.
49. Linderth, S.; Hendriksen, P.; Mogensen, M.; Langvad, N. J. *Mater. Sci.* **1996**, 31(9), 5077.
50. Hänsel, M.; Quadackers, W. J.; Singheiser, L.; Nickel, H. *Report Forschungszentrum Jülich, Jülich FRG, Jül-3583*, 1998; ISSN 0944-2952.
51. Rahmel, A.; Tobolski, J. *Corros. Sci.* **1965**, 5, 333.
52. Young, D. J. *Mater. Sci. Forum* **2008**, 595–598, 1189–1197.
53. Zurek, J.; Young, D. J.; Essuman, E.; Hänsel, M.; Penkalla, H. J.; Niewolak, L.; Quadackers, W. J. *Mater. Sci. Eng. A* **2008**, 477, 259–270.
54. Miyake, Y.; Yasuo, T.; Taniguchi, Y.; Kadowaki, M.; Kawamura, H.; Saitoh, T. In *Proceedings of the 4th International Symposium on Solid Oxide Fuel Cells (SOFC IV)*; Dokiya, M., Yamamoto, O., Tagawa, H., Singhal, S. C., Eds.; The Electrochemical Society Proceedings Series: Pennington, NJ, 1995; p 100, PV 95-1.
55. Quadackers, W. J.; Hänsel, M.; Rieck, T. *Mater. Corros.* **1998**, 49, 252.
56. Crone, U. v. d.; Hänsel, M.; Quadackers, W. J.; Vaßen, R. *Fresenius J. Anal. Chem.* **1997**, 358, 230.
57. Atkinson, A.; Taylor, R. In *Transport in Non-Stoichiometric Compounds*; Simkovich, G., Stubican, G., Eds.; NATO ASI Series, Series B: Physics Col. Vol. 129, Plenum Press: New York, 1984; p 285.
58. Sabioni, A.; Huntz, A.; Millot, F.; Monty, C. *Philos. Mag. A* **1992**, 66, 351.
59. Sockel, H.; Saal, B.; Heilmayer, M. *Surf. Interf. Anal.* **1988**, 12, 531.
60. Gil, A.; Penkalla, H. J.; Hänsel, M.; Norton, J.; Köck, W.; Quadackers, W. J. *IX Conference on Electron Microscopy of Solids, 6–9 May 1996*, Krakow-Zakopane, Poland 1996, Fotobit: Krakow, Poland; p 441.
61. Quadackers, W. J. *J. Phys. IV* **1993**, 3(part I), 177.
62. Quadackers, W. J. *Werkst. Korros.* **1990**, 41, 659.
63. Bongartz, K.; Quadackers, W. J.; Pfeifer, J. P.; Becker, J. S. *Surf. Sci.* **1993**, 292, 196.
64. Quadackers, W. J. *Mater. Sci. Forum* **2001**, 369–372, 77.
65. Hou, P.; Brown, I.; Stringer, J. *Nucl. Instrum. Meth. B* **1991**, 59/60, 1345.
66. Quadackers, W. J.; Breuer, U.; Tyagi, A.; Gil, A.; Stroosnijder, M. F.; Becker, S.; Hänsel, M. Report, Forschungszentrum Jülich, Jülich, FRG, Jül-1372, p. 97, ISSN 0944-2952.
67. Park, J. H.; Natesan, K. *Oxid. Met.* **1990**, 33(1/2), 31.
68. Holt, A.; Kofstadt, P. *Solid State Ionics* **1994**, 69, 137.
69. Holt, A.; Kofstadt, P. *Solid State Ionics* **1999**, 117, 21.
70. Holt, A.; Kofstadt, P. *Solid State Ionics* **1997**, 100, 201.
71. Holt, A.; Kofstadt, P. *Solid State Ionics* **1994**, 69, 127.
72. Liu, H.; Stack, M.; Lyon, S. *Solid State Ionics* **1998**, 109, 247.
73. Huczowski, P.; Christiansen, N.; Shemet, V.; Niewolak, L.; Piron-Abellan, J.; Singheiser, L.; Quadackers, W. J. *Fuel Cells* **2006**, 2, 93–99.
74. Hagel, W. C.; Seybolt, A. U. *J. Electrochem. Soc.* **1961**, 108(12), 1146–1152.
75. Nagai, H.; Fujikawa, T. *Trans. JIM* **1983**, 24(8), 581.
76. Su, M. Y. *Diss. Abstr. Int.* **1988**, 48, 3049.
77. Crawford, J. A.; Vest, R. W. *J. Appl. Phys.* **1964**, 35(8), 2413–2418.
78. Nagai, H.; Ohbayashi, K. *J. Am. Ceram. Soc.* **1989**, 72, 400.
79. Nagai, H.; Ishikawa, S.; Amano, N. *Trans. JIM* **1985**, 26(10), 753.
80. Malkow, Th.; Quadackers, W. J.; Singheiser, L.; Nickel, H. Report Forschungszentrum, Jülich, Jülich, FRG, Jül-3589, 1998; ISSN 0944-2952.
81. Ennis, P. J.; Quadackers, W. J. In *Proceedings of the Conference High Temperature Alloys – Their Exploitable Potential*, JRC Petten, NL, 15–17 October 1985; Marriot, J. B., Merz, M., Nihoul, J., Ward, J. O., Eds.; Elsevier Applied Science: London, 1987; p 465.
82. Buchkremer, H. P.; Diekmann, U.; Stöver, D. In *Proceedings of the 2nd European Solid Oxide Fuel Cell Forum*, Thorstensen, B., Ed.; European SOFC Forum, Dr. Ulf Bossel, Morgenacher Str. 2F, CH-5452: Oberrohrdorf, Switzerland, 1996; Vol. 2, p 221.
83. De Haart, L.; Vinke, I. C.; Janke, A.; Ringel, H.; Tietz, F. In *Solid Oxide Fuel Cells (SOFC VII)*; Yokokawa, H., Singhal, S. C., Eds.; The Electrochemical Society Proceedings Series: Pennington, NJ, 2001; p 111, PV 2001-16.
84. Horita, T.; Xiong, Y.; Yamaji, K.; Sakai, N.; Yokokawa, H. In *Proceedings of the 5th European Solid Oxide Fuel Cell Forum*, Huijsmans, J., Ed.; European SOFC Forum, Dr. Ulf Bossel, Morgenacher Str. 2F, CH-5452: Oberrohrdorf, Switzerland, 2002; Vol. 1, p 401.
85. Piron-Abellan, J.; Quadackers, W. J. Development of ferritic steels for application as interconnect materials for intermediate temperature solid oxide fuel cells (SOFCs), Report Forschungszentrum Jülich, Jül-4170, March 2005; ISSN 0944-2952.
86. Huczowski, P.; Ertl, S.; Piron-Abellan, J.; Christiansen, N.; Hoefler, T.; Shemet, V.; Singheiser, L.; Quadackers, W. J. *Mater. High Temp.* **2005**, 22(3/4), 253–262.
87. Froitzheim, J. Ferritic steel interconnectors and their interactions with Ni base anodes in solid oxide fuel cells (SOFC), RWTH Aachen, Report Forschungszentrum Jülich, Energy and Environment, Vol. 16, 2008; ISBN 978-3-89336-540-1.
88. Fujii, C. T.; Meussner, R. A. *Corros. Iron & Steel* **1964**, 111, 1215–1221.
89. Essuman, E.; Meier, G. H.; Zurek, J.; Hänsel, M.; Quadackers, W. J. *Oxid. Met.* **2008**, 69, 143–162.
90. Grabke, H. J. *Mater. Corros.* **2003**, 54(10), 736–746.
91. Young, D. J. *Mater. High Temp.* **2007**, 24(3), 225–232.
92. Huczowski, P.; Quadackers, W. J. Unpublished results.
93. Dulieu, D.; Cotton, J.; Greiner, H.; Honegger, K.; Scholten, A.; Christie, M.; Seguelong, T. In *3rd European*



- SOFC Forum; Stevens, P., Ed.; European Fuel Cell Forum: Oberrohrdorf, Switzerland, CH-5452, 1998; p 447.
94. Ueda, M.; Taimatsu, H. In *Proceedings of the Fourth European Solid Oxide Fuel Cell Forum*, McEvoy, J., Ed.; European SOFC Forum, Dr. Ulf Bossel, Morgenacher Str. 2F, CH-5452: Oberrohrdorf, Switzerland, 2000; Vol. 2, p 837.
  95. Ueda, M.; Kadowaki, M.; Taimatsu, H. *Mat. Trans. JIM* **2000**, 41(2), 317–322.
  96. Quadackers, W. J.; Malkow, T.; Piron-Abellan, J.; Flesch, U.; Shemet, V.; Singheiser, L. In *Proceedings of the Fourth European Solid Oxide Fuel Cell Forum*, McEvoy, J., Ed.; European SOFC Forum, Dr. Ulf Bossel, Morgenacher Str. 2F, CH-5452: Oberrohrdorf, Switzerland, 2000; Vol. 2, p 827.
  97. Piron-Abellan, J.; Shemet, V.; Tietz, F.; Singheiser, L.; Quadackers, W. J. In *Solid Oxide Fuel Cells (SOFC VII)*; Yokokawa, H., Singhal, S. C., Eds.; The Electrochemical Society Proceedings Series: Pennington, NJ, 2001; p 811, PV 2001-16.
  98. Bredesen, R.; Kofstad, P. In *Proceedings of the 17th Risø International Symposium on Materials Science: High Temperature Electrochemistry, Ceramics and Metals*; Poulsen, F., Bonanos, N., Linderth, S., Mogenson, M., Zachau-Christiansen, B., Eds.; Risø National Laboratory: Roskilde, Denmark, 1996; p 187.
  99. Quadackers, W. J.; Thiele, M.; Ennis, P. J.; Teichmann, H.; Schwarz, W. In *Proceedings of the EUROCORR 97, Trondheim, Norway, 22–25 September 1997*, European Federation of Corrosion, 1997; Vol. II, p 35.
  100. Huang, K.; Hou, P.; Goodenough, J. *Solid State Ionics* **2000**, 129, 237.
  101. Pirón-Abellán, J.; Tietz, F.; Shemet, V.; Gil, A.; Ladwein, T.; Singheiser, L.; Quadackers, W. J. In *Proceedings of the 5th European Solid Oxide Fuel Cell Forum*, Huijsmans, J., Ed.; European SOFC Forum, Dr. Ulf Bossel, Morgenacher Str 2F, CH-5452: Oberrohrdorf, Switzerland, 2002; Vol. 1, p 248.
  102. Hammer, J. E.; Laney, S. J.; Jackson, R. W.; Coyne, K.; Pettit, F. S.; Meier, G. H. *Oxid. Met.* **2007**, 67(1/2), 1–38.
  103. Ghosh, D.; Tang, E.; Perry, M.; Prediger, D.; Pastula, M.; Boersma, R. In *Solid Oxide Fuel Cells (SOFC VII)*; Yokokawa, H., Singhal, S. C., Eds.; The Electrochemical Society Proceedings Series: Pennington, NJ, 2001; p 101, PV 2001-16.
  104. Kung, S.; Cal, T.; Moris, T.; Barringer, E.; Elangovan, S.; Hartvigsen, J. In *Proceedings of the 2000 Fuel Cell Seminar*, Portland OR, 30 October–2 November 2000; **2000**; p 585.
  105. Krumpelt, M.; Ralph, J.; Cruse, T.; Bae, J.-M. In *Proceedings of the 5th European Solid Oxide Fuel Cell Forum*, Huijsmans, J., Ed.; European SOFC Forum, Dr. Ulf Bossel, Morgenacher Str 2F, CH-5452: Oberrohrdorf, Switzerland, 2002; Vol. 1, p 215.
  106. Uehara, T.; Ohno, T.; Toji, A. In *Proceedings of the 5th European Solid Oxide Fuel Cell Forum*, Huijsmans, J., Ed.; European SOFC Forum, Dr. Ulf Bossel, Morgenacher Str 2F, CH-5452: Oberrohrdorf, Switzerland, 2002; Vol. 1, p 281.
  107. Honegger, K.; Plas, A.; Diethelm, R.; Glatz, W. In *Solid Oxide Fuel Cells (SOFC VII)*; Yokokawa, H., Singhal, S. C., Eds.; The Electrochemical Society Proceedings Series: Pennington, NJ, 2001; p 803, PV 2001-16.
  108. Ehlers, J.; Quadackers, W. J. Oxidation von 9–12% Cr-Stählen in wasserdampfhaltigen Atmosphären bei 550 bis 650°C, Report Forschungszentrum Jülich, Jülich, FRG, Jül-3883, ISSN 0944–2952, June 2001.
  109. Huczowski, P.; Christiansen, N.; Shemet, V.; Piron Abellan, J.; Singheiser, L.; Quadackers, W. J. *Mater. Corros.* **2004**, 55(11), 825–830.
  110. Quadackers, W. J.; Bongartz, K. *Werkst. Korros.* **1994**, 45, 232–241.
  111. Gurrappa, I.; Weinbruch, S.; Naumenko, D.; Quadackers, W. J. *Mater. Corros.* **2000**, 51, 224–235.
  112. Huczowski, P.; Christiansen, N.; Shemet, V.; Piron Abellan, J.; Singheiser, L.; Quadackers, W. J. *J. Fuel Cell Sci. Technol.* **2004**, 1, 30.
  113. Huczowski, P.; Quadackers, W. J. Effect of geometry and composition of Cr steels on oxide scale properties relevant for interconnector applications in solid oxide fuel cells (SOFCs), Report Forschungszentrum Jülich, Energy Technology; 2007; Vol. 65, ISBN 978-3-89336-484-8.
  114. Zurek, J.; Meier, G. H.; Essuman, E.; Hänsel, M.; Singheiser, L.; Quadackers, W. J. *J. Alloys Comp.* **2009**, 450–458.
  115. Mehrer, H. *Defect Diffus. Forum* **1996**, 57, 129–130.
  116. Huntz, A.-M.; Daghigh, S.; Piant, A.; Lebrun, J. L. *Mater. Sci. Eng. A* **1998**, 248, 44.
  117. Galerie, A.; Toscan, F.; Dupeux, M.; Mouglin, J.; Lucazeau, G.; Valot, C.; Huntz, A.-M.; Antoni, L. *Mater. Res.* **2004**, 7, 81.
  118. Gray, S.; Berriche-Bouhanek, K.; Evans, H. E. *Mater. Sci. Forum* **2004**, 755, 461–464.
  119. Froitzheim, J.; Meier, G. H.; Niewolak, L.; Ennis, P. J.; Hattendorf, H.; Singheiser, L.; Quadackers, W. J. *J. Power Sources* **2008**, 178, 163–173.
  120. Quadackers, W. J.; Niewolak, L.; Ennis, P. J. Patent number(s): WO2007093148-A1; DE102006007598-A1. Application date, 18 February 2006 (DE), PCT/DE2007/000166.
  121. Niewolak, L.; Huczowski, P.; Froitzheim, J.; Ennis, P. J.; Singheiser, L.; Quadackers, W. J. In *Proceedings of the 7th European SOFC Forum*, 3–7 July 2006, Lucerne, CH, CD-ROM, Paper B084.
  122. Niewolak, L.; Quadackers, W. J. Unpublished results.
  123. Yang, Z.; Walker, M. S.; Singh, P.; Stevenson, J. W. *Electrochem. Solid State Lett.* **2003**, 6, B35–B37.
  124. Nakagawa, K.; Matsunaga, Y.; Yanagisawa, T. *Mater. High Temp.* **2003**, 20, 67–73.
  125. Yang, Z.; Xia, G.-G.; Walker, M. P.; Wang, C.-M.; Stevenson, J. W.; Singh, P. *Int. J. Hydrogen Energy* **2007**, 32, 3770.
  126. Yang, Z.; Walker, M. S.; Singh, P.; Stevenson, J. W.; Norby, T. J. *Electrochem. Soc.* **2004**, 151, B669–B678.
  127. Ziomek-Moroz, M.; Cramer, S. D.; Holcomb, G. R.; Covino, B. S., Jr.; Bullard, S. J.; Singh, P. In *Corrosion 2005*; NACE International: Houston, TX, 2005; Paper no. 10.
  128. Yang, Z.; Xia, G.-G.; Singh, P.; Stevenson, J. W. *J. Power Sources* **2006**, 160, 1104–1110.
  129. Jackson, R. W.; Pettit, F. S.; Meier, G. H. *Journal of Power Sources* **2008**, 185(2), 1030–1039.
  130. Nakagawa, K.; Matsunaga, Y.; Yanagisawa, T. *Mater. High Temp.* **2001**, 18, 51–56.
  131. Hecker, R.; Stover, D.; Jonas, H.; Buchkremer, H. P. *J. Nucl. Mater.* **1990**, 171(1), 84–93.
  132. Wood, G. C.; Wright, I. G.; Hodgkiess, T.; Whittle, D. P. *Werkst. Korros.* **1970**, 21, 900–910.
  133. Ehlers, J.; Young, D. J.; Smaardijk, E. J.; Tyagi, A. K.; Penkalla, H. J.; Singheiser, L.; Quadackers, W. J. *Corros. Sci.* **2006**, 48, 3428–3454.
  134. Tietz, F.; Simwonis, D.; Batfalsky, P.; Diekmann, U.; Stöver, D. In *Degradation Phenomena during Operation of Solid Oxide Fuel Cells*, Proceedings of the 12th IEA Workshop on SOFCs: Materials and Mechanisms;

- Nisancioglu, K., Ed.; International Energy Agency, 1999; p 3.
135. Teller, O.; Meulenberg, W.; Tietz, F.; Wessel, E.; Quadackers, W. J. In *Solid Oxide Fuel Cells (SOFC VII)*; Yokokawa, H., Singhal, S. C., Eds.; The Electrochemical Society Proceedings Series: Pennington, NJ, 2001; p 895, PV 2001-16.
136. Batfalsky, P.; Buchkremer, H.-P.; Froning, D.; Meschke, F.; Nabielek, H.; Steinbrech, R. W.; Tietz, F. In *Proceedings of the 3rd International Fuel Cell Conference*; New Energy and Industrial Technology Development Organization (NEDO) and Fuel Cell Development Information Center (FCDIC), Japan, 1999; p 349.
137. Urbanek, J.; Miller, M.; Schmidt, H.; Hilpert, K. In *Proceedings of the 2nd European Solid Oxide Fuel Cell Forum*, Thorstensen, B., Ed.; European SOFC Forum, Dr. Ulf Bossel, Morgenacher Str. 2F, CH-5452: Oberrohrdorf, Switzerland, 1996; Vol. 2, p 503.
138. Quadackers, W. J.; Mallener, W.; Grübmeier, H.; Wallura, E. In *Proceedings of the 5th IEA Workshop on SOFC: Materials, Process Engineering and Electrochemistry*, Jülich Germany, 2–4 March 1993, Forschungszentrum Jülich, Jülich, FRG **1993**; p 87; ISBN 3-89336-127-8.
139. Badwal, S.; Deller, R.; Föger, K.; Ramprakash, Y.; Zhang, J. *Solid State Ionics* **1997**, 99, 297.
140. Larring, Y.; Norby, T. J. *Electrochem. Soc.* **2000**, 147, 3251.
141. Quadackers, W. J.; Greiner, H.; Hänsel, M.; Pattaniak, A.; Khanna, A. S.; Mallener, W. *Solid State Ionics* **1996**, 91, 55.
142. Tietz, F.; Mohsine, Z.; Quadackers, W. J.; Shemet, V. U.S. Patent, US 7,407,717, B2, PCT/DE2004/000024, Application Data 18 February 2003.
143. Kadowaki, T.; Shiomitsu, T.; Matsuda, E.; Nakagawa, H.; Tsuneizumi, H.; Maruyama, T. *Solid State Ionics* **1993**, 67, 65.
144. Maruyama, T.; Ioue, T.; Nagata, K. In *Solid Oxide Fuel Cells (SOFC IV)*; Dokiya, M., Yamamoto, O., Tagawa, H., Singhal, S. C., Eds.; The Electrochemical Society Proceedings Series: Pennington, NJ, 1995; p 889, PV 95-1.
145. Oishi, N.; Namikawa, T.; Yamazaki, Y. *Surf. Coatings Technol.* **2000**, 132, 58.
146. Yoo, Y.; Dauga, M. In *Solid Oxide Fuel Cells (SOFC VII)*; Yokokawa, H., Singhal, S. C., Eds.; The Electrochemical Society Proceedings Series: Pennington, NJ, 2001; p 837, PV 2001-16.
147. Godfrey, B.; Föger, K.; Gillespie, R.; Bolden, R.; Badwal, S. J. *Power Sources* **2000**, 86, 68.
148. Hou, P.; Huang, K.; Bakker, W. In *Solid Oxide Fuel Cells (SOFC VI)*; Singhal, S. C., Dokiya, M., Eds.; The Electrochemical Society Proceedings Series: Pennington, NJ, 1999; p 737, PV 99-19.
149. Tietz, F.; Sebold, D. *Mater. Sci. Eng. B* **2008**, 150(2), 135–140.
150. Ager, F. J.; Respaldiza, M.; Botella, J.; Soares, J.; Da Silva, M.; Benitez, J.; Adriozaola, J. *Acta Mater.* **1996**, 44, 675.
151. Ruiz, M.; Heredia, A.; Botella, J.; Adriozaola, J. *J. Mater. Sci.* **1995**, 30(20), 5146.
152. Brylewski, T.; Nanko, M.; Maruyama, T.; Przybylski, K. *Solid State Ionics* **2001**, 143, 131.
153. Quadackers, W. J. German Patent DE 19 54 66 14, 1995; Quadackers, W. J.; Hänsel, M. German Patent DE 19 60 98 13, 1996.
154. Montero, X.; Jordan, N.; Piron-Abellan, J.; Tietz, F.; Stover, D.; Cassir, M.; Villarreal, I. *J. Electrochem. Soc.* **2009**, 156(1), B188–B196.
155. Yang, Z. G.; Xia, G. G.; Nie, Z. M.; et al. *Electrochem. Solid State Lett.* **2008**, 11(8), B140–B143.
156. Stanislawski, M.; Froitzheim, J.; Niewolak, L.; Quadackers, W. J.; Hilpert, K.; Markus, T.; Singheiser, L. *J. Power Sources* **2007**, 164, 578–589.
157. Batawi, E.; Honegger, K.; Diethelm, R. In *Proceedings of the 6th IEA Workshop on Advanced SOFC*, published by ENEA, Energy Department, 22–29 February 1994; Rome, Italy, p 175.
158. Trebbels, R. Ph.D. Thesis, RWTH Aachen, 2009.
159. Shemet, V.; Quadackers, W. J. Unpublished results.
160. Ertl, S. T. Ph.D. Thesis, RWTH Aachen, 2006.
161. Froitzheim, J.; Niewolak, L.; Brandner, M.; Singheiser, L.; Quadackers, W. J. *J. Fuel Cell Sci. Technol.* in press 6(4).
162. Brandner, M.; Bram, M.; Froitzheim, J.; Buchkremer, H. P.; Stover, D. *Solid State Ionics* **2008**, 179(27–32), 1501–1504.
163. Brandner, M.; Niewolak, L.; Froitzheim, J.; Quadackers, W. J.; Bram, M. Patent number(s): DE102006056251-A1; WO2008064938-A1.
164. Menzler, N. H.; Sebold, D.; Zahid, M.; Gross, S. M.; Koppitz, T. *J. Power Sources* **2005**, 152(1), 156–167.
165. Weil, K. S. *JOM* **2006**, 58, 37–44.
166. Eichler, K.; Solow, G.; Otschik, P.; Schafferath, W. *J. Eur. Ceram. Soc.* **1999**, 19, 101–104.
167. Sohn, S.-B.; Choi, S.-Y.; Kim, G.-H.; Song, H.-S.; Kim, G.-D. *J. Amer. Ceram. Soc.* **2004**, 87, 254–260.
168. Yang, Z.; Meinhart, K. D.; Stevenson, J. W. *J. Electrochem. Soc.* **2003**, 150, A1095–A1101.
169. Yang, Z.; Stevenson, J. W.; Meinhart, K. D. *Solid State Ionics* **2003**, 160, 213–225.
170. Yang, Z.; Xia, G.-G.; Meinhart, K. D.; Weil, K. S.; Stevenson, J. W. *J. Mater. Eng. Perform.* **2004**, 13, 327–334.
171. Yang, Z.; Coyle, C. A.; Baskaran, S.; Chick, L. A. US Patent, 6,843,406, 2005.
172. Haanappel, V. A. C.; Shemet, V.; Vinke, I. C.; Quadackers, W. J. *J. Power Sources* **2005**, 141, 102–107.
173. Haanappel, V. A. C.; Shemet, V.; Vinke, I. C.; Gross, S. M.; Koppitz, Th.; Menzler, N. H.; Zahid, M.; Quadackers, W. J. *J. Mater. Sci.* **2005**, 40, 1583–1592.
174. Haanappel, V. A. C.; Shemet, V.; Gross, S. M.; Koppitz, Th.; Menzler, N. H.; Zahid, M.; Quadackers, W. J. *J. Power Sources* **2005**, 150, 86–100.
175. Menzler, N. H.; Batfalsky, P.; Blum, L.; Bram, M.; Gross, S. M.; Haanappel, V. A. C.; Malzbender, J.; Shemet, V.; Steinbrech, R. W.; Vinke, I. *Fuel Cells* **2007**, 7(5), 356–363.
176. Opila, E. J.; Jacobson, N. S.; Myers, D. L.; Copland, E. H. *JOM* **2006**, 58, 22–28.
177. Niewolak, L.; Shemet, V. Forschungszentrum Jülich, 2008, Unpublished results.

## 1.22 High Temperature Corrosion of Low Alloy Steels

**L. W. Pinder**

E.ON Engineering Limited Technology Centre, Ratcliffe on Soar, Nottingham, NG11 0EE

**K. Dawson and G. J. Tatlock**

Department of Engineering, University of Liverpool, Liverpool, L69 3GH

This article is a revision of the Third Edition article 7.2 by L. W. Pinder, volume 1, pp 7:16–7:52, © 2010 Elsevier B.V.

1.22.1	Introduction	558
1.22.2	Factors Governing Oxidation Behavior	559
1.22.3	The Oxidation of Iron	560
1.22.4	General Alloying Effects on Oxidation	562
1.22.5	Effects of Specific Alloying Elements on the Oxidation of Iron	564
1.22.5.1	Carbon	564
1.22.5.2	Aluminum	565
1.22.5.3	Silicon	566
1.22.5.4	Manganese	567
1.22.5.5	Sulfur	567
1.22.5.6	Phosphorus	567
1.22.5.7	Nickel	567
1.22.5.8	Chromium	567
1.22.5.9	Molybdenum	568
1.22.5.10	Boron	568
1.22.5.11	Others	569
1.22.5.12	Effects of Heat Flux and Cold Work	569
1.22.6	Stress Effects	570
1.22.6.1	Growth Stresses	570
1.22.6.2	System-Applied Stresses	571
1.22.6.3	Thermal Stresses	571
1.22.7	Commercial Low-Alloy Steels in Air or Oxygen	572
1.22.8	Industrial Environments	572
1.22.8.1	Steam	572
1.22.8.2	Combustion Gases	575
1.22.8.3	Chemical Environments	576
1.22.8.4	CO/CO <sub>2</sub>	578
References		579

### 1.22.1 Introduction

Low alloy steels are generally considered to comprise plain carbon steels and steels with a total alloying content of up to 12 wt%. This group of steels is exploited for many applications, including those in the heavy engineering industries. While these materials are often selected based on mechanical properties, extensive use in high temperature applications often involving harsh environments including power generation and the petrochemical industries demands a degree of oxidation resistance. Emerging industries creating energy from waste and biofuels have introduced more varied and complex environments to

which steels may be exposed. Novel manufacturing techniques such as mechanically alloyed steels produced via powder metallurgy techniques are also offering new groups of steels designed for utilization in high temperature applications.

The drive for increased efficiency in power generation requires higher operating temperatures. Low alloy ferritic steels with attractive mechanical properties, including low coefficients of thermal expansion, have been optimized for high temperature performance. Since they possess adequate creep strength for their designed capability, the service life of these Fe–Cr alloys is now often limited by their steam-side oxidation resistance.

Alloying additions of Si, Al, and Cr which form stable, slow growing, protective scales on steels are extensively used; however, these additions can be financially inhibitive and/or detrimental to mechanical properties. In terms of low alloy steels in general, the restricted quantities (12 wt%) of alloying additions may not enable the most protective form of oxide to grow.

The extent to which low alloy steels react to high temperature corrosive environments is the subject of this chapter. In view of the commercial importance of these steels, the published literature on this topic is extensive and being continually enlarged. The reader is encouraged to refer to many excellent papers and current issues of journals, referenced at the end of the chapter, for more detailed and contemporary information on the topic.

### 1.22.2 Factors Governing Oxidation Behavior

In the absence of stress, the survival of a given component is largely determined by the extent to which the material of construction reacts with the environment in which it resides. This can largely be categorized by the extent to which the following two criteria are satisfied:

1. Is the material thermodynamically stable in the environment?
2. If not, will the reaction rate between the environment and the material be slow enough to give an acceptable life?

In the vast majority of cases at elevated temperatures, the answer to the first question is 'no.' With the exception of gold and platinum, which are generally too expensive for large-scale industrial use, are in short supply, and do not have the required mechanical properties, most materials will react to some degree with their environment. Most highly alloyed steels and superalloys satisfy the second criterion for a wide range of high temperature environments. However, these materials may be far too expensive for large-scale industrial applications. The oxidation behavior of most metals and alloys in a high temperature environment is, therefore, governed by the degree of protection afforded by any oxide scale that forms.<sup>1</sup> This depends upon the oxide melting point, its mechanical integrity, and the rate of diffusion of elemental species present within both the environment and the alloy, through the oxide scale.

In certain cases (e.g., Cr above 1000 °C), the CrO<sub>3</sub> oxide that forms is volatile, and clearly affords no

protection to the substrate.<sup>1</sup> In other cases, a solid oxide scale forms that may, or may not, be continuous. The extent to which a solid surface scale protects the metal depends upon the extent of surface coverage. This behavior can largely be categorized according to whether the volume of oxide produced is less or greater than the volume of metal consumed during the oxidation reaction. This principle was originally advanced by Pilling and Bedworth,<sup>2</sup> with the oxide: metal volume ratio being known as the Pilling Bedworth Ratio (PBR), where

$$\text{PBR} = \frac{\text{Volume of oxide produced}}{\text{Volume of metal consumed}}$$

If the PBR is less than unity, the oxide will be non-protective and oxidation will follow a linear rate law, governed by surface reaction kinetics. However, if the PBR is greater than unity, then a protective oxide scale may form and oxidation will follow a reaction rate law governed by the speed of transport of metal or environmental species through the scale. Then the degree of conversion of metal to oxide will be dependent upon the time for which the reaction is allowed to proceed. For a diffusion-controlled process, integration of Fick's First Law of Diffusion with respect to time yields the classic Tamman relationship,<sup>3</sup> commonly referred to as the Parabolic Rate Law:

$$x^2 = Kt \quad [1]$$

where  $x$  is a measure parameter,  $K$  is the rate constant, and  $t$  is time. The progress of oxidation ( $x$ ) is generally measured by weight gain, weight loss, scale thickness, or retreat of the metal surface. However, other parameters, such as loss of oxidant in the environment, may be used. The time interval may be measured in seconds, hours, thousands of hours and years. As a consequence, many different units of the measured oxidation parameter and the time period have been reported in the literature, leading to many differing units for the quoted rate constant.

In some circumstances, the reaction rates may not be exactly parabolic, and even initially parabolic rates may be influenced by changes within the oxide scale with time. As an oxide scale grows, the build-up of inherent growth stresses, externally applied strains, and chemical changes to either the oxide scale or the metal may all compromise the initial protection offered by the scale, leading to scale breakdown and ultimately to a partial or complete loss of protection; parabolic or linear kinetics may ensue. In other circumstances, as will be seen later in this chapter, very small additions of contaminants to the

environment may radically modify the oxidation response, by either favoring nonprotective scales from the outset or causing rapid breakaway corrosion following an initially protective period. Hence, there are many hidden dangers in extrapolating short-term oxidation kinetic data to long periods, and great care is required when utilizing published oxidation data to assess potential corrosion rates and component lives in industrial environments.

The temperature dependence of a diffusion-controlled reaction is typically described by the Arrhenius relationship:

$$K = a \exp \left( \frac{-Q}{RT} \right) \quad [2]$$

where  $a$  is a constant,  $Q$  is the activation energy,  $R$  is the gas constant, and  $T$  is the temperature (K). Hence the rate constant ( $K$ ) will be influenced by the temperature of exposure because of the increased ion mobility at higher temperatures, via the activation energy term. Again, great care is required when extrapolating data beyond the temperature range of the initial experimental data. Sharp changes in the Arrhenius slope may occur with the appearance of a new, thermodynamically favored, species within the scale. In addition, an Arrhenius plot of the temperature dependence of the reaction rate may reveal curvature because of the progressive change from one rate determining process to another. Both the features are observed in the Arrhenius plot for low-alloy steels (Figure 1).

### 1.22.3 The Oxidation of Iron

For iron in most oxidizing environments, the PBR is approximately 2.2 and the scale formed is protective. The oxidation reaction forms a compact, adherent scale, the inner and outer surfaces of which are in thermodynamic equilibrium with the metal substrate and the environment respectively, and ion mobility through the scale is diffusion controlled.

The rate of oxidation of iron is then governed by the stabilities of the various phases, which are in turn a function of the temperature and oxygen partial pressure of the environment. Examination of the Fe–O<sub>2</sub> phase diagram (Figure 2) reveals that the principal solid oxide phases below 570 °C will be Fe<sub>3</sub>O<sub>4</sub> (magnetite) and Fe<sub>2</sub>O<sub>3</sub> (haematite). Above 570 °C, FeO (wüstite) appears as a third phase within the scale. These phases are present within the scale as individual layers, with the layer sequence dictated by the equilibrium oxygen partial pressure ( $p_{O_2}$ ) for phase stability

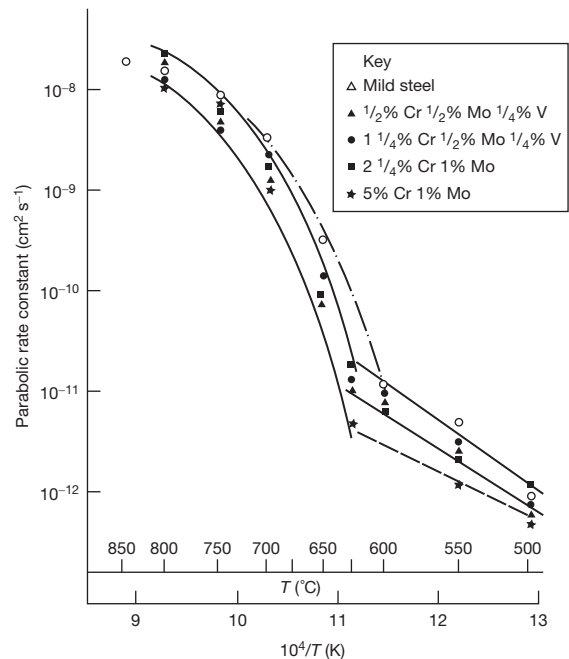


**Figure 1** Arrhenius plot for the oxidation of mild steel and low-alloy steels in air showing a sharp break in the slope and curvature due to the appearance of FeO in the scale above 570 °C.

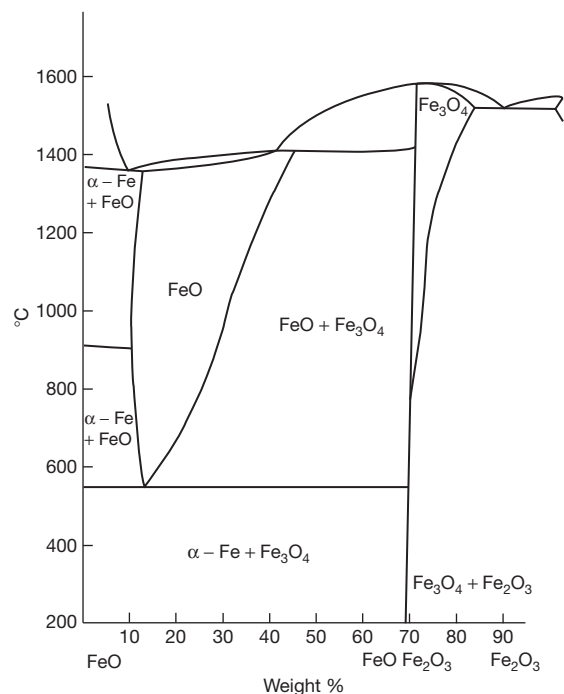


**Figure 2** Fe–O phase diagram showing the principal solid phases stable on iron and wide stoichiometry limits of FeO. Adapted from White, J. CEBG Private Communication.



prevailing at the given temperature. Hence, the oxide phase stable at the lowest  $pO_2$  (FeO at  $>570^\circ\text{C}$ ) is found closest to the metal substrate, whereas the phase stable at the highest  $pO_2$  ( $\text{Fe}_2\text{O}_3$ ) is found closest to the oxidizing environment. If, however, the  $pO_2$  of the environment is low enough, only FeO will be formed. At intermediate values of the  $pO_2$ ,  $\text{Fe}_3\text{O}_4$  will also form, and for most industrial environments, the  $pO_2$  is sufficient for the formation of an outer layer of  $\text{Fe}_2\text{O}_3$ . While these observations are true for bulk scales, FeO has also been found to be stable in very thin films at temperatures down to  $400^\circ\text{C}$ <sup>4</sup> and within narrow cracks at  $500^\circ\text{C}$ .<sup>5</sup>

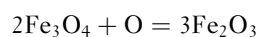
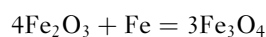
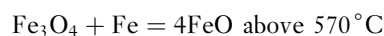
In the initial stages of oxidation, nucleation of oxide occurs at favored crystallographic sites, followed by preferential lateral spread from these nuclei to form a continuous thin film over the iron surface. At low temperatures ( $<200^\circ\text{C}$ ), thin films, tens of nanometers thick, form exceedingly rapidly. Ion mobility is driven by space charges between gas-oxide and oxide-metal interfaces. As the scale thickens, the initial rapid growth rate is superseded by an extremely slow, logarithmic or inverse logarithmic growth law.

For iron oxidizing at temperatures between  $350$  and  $500^\circ\text{C}$ ,  $\text{Fe}_3\text{O}_4$  nucleates first and grows laterally over the surface.<sup>6</sup> Once complete coverage is achieved, the  $\text{Fe}_3\text{O}_4$  thickens parabolically. Ultimately, nucleation and lateral overgrowth by  $\text{Fe}_2\text{O}_3$  occur, slowing the growth rate of the  $\text{Fe}_3\text{O}_4$  appreciably, because of the lower effective  $pO_2$  at the  $\text{Fe}_3\text{O}_4$  surface, that is, the  $pO_2$  falls from that of the environment to that governed by the equilibrium between  $\text{Fe}_3\text{O}_4$  and  $\text{Fe}_2\text{O}_3$  at the prevailing temperature. Both FeO and  $\text{Fe}_3\text{O}_4$  nucleate first and grow out of the surface of pure Fe and Fe-3%Cr alloy at  $700$ – $800^\circ\text{C}$  in low pressure  $O_2$  ( $10^{-3}$  Pa).<sup>7,8</sup> While  $\text{Fe}_2\text{O}_3$  is thermodynamically stable, it can form only when the oxygen available for  $\text{Fe}_2\text{O}_3$  growth has increased sufficiently. Initially, the available oxygen is continually depleted by the formation of  $\text{Fe}_3\text{O}_4$ . The length of this induction period prior to  $\text{Fe}_2\text{O}_3$  growth is a direct function of the prevailing  $pO_2$ , being 3 h at 40 Pa, but only 1 min at 101 kPa.<sup>7</sup>

Above  $570^\circ\text{C}$ , a distinct break occurs in the Arrhenius plot for iron, corresponding to the appearance of FeO in the scale. The Arrhenius plot is then nonlinear at higher temperatures. This curvature is due to the wide stoichiometry limits of FeO: limits that diverge progressively with increasing temperature. Diffraction studies have shown that complex clusters of vacancies exist in  $\text{Fe}_{(1-x)}\text{O}$ .<sup>9,10</sup> Such defect clustering is more prevalent in oxides

that demonstrate a high degree of nonstoichiometry; with vacancy-hole complexes possibly being present at the higher deviations.<sup>11</sup> Single defects occur only when these oxides are closest to their stoichiometric composition. These considerations lead to a complex dependence of the cation diffusion coefficient on the oxide stoichiometry,<sup>12</sup> and hence on temperature.

Mass transport measurements have shown that cation transport predominates in FeO ( $\text{Fe}^{2+}$ ) and  $\text{Fe}_3\text{O}_4$  ( $\text{Fe}^{2+}$ ,  $\text{Fe}^{3+}$ ), whereas anion transport predominates in  $\text{Fe}_2\text{O}_3$  ( $\text{O}^{2-}$ ). This leads to the well-accepted growth scheme for multilayered scale growth on iron as shown in Figure 3, the governing equations for individual layer growth being



It was originally considered that the growth of these layers was largely controlled by lattice diffusion, following the theories expounded by Wagner.<sup>13,14</sup> However, experimental work has shown that, for  $\text{Fe}_3\text{O}_4$  below  $600^\circ\text{C}$  and  $\text{Fe}_2\text{O}_3$  at all temperatures, theoretical calculations of oxide growth, using lattice diffusion coefficients are unable to predict the growth rates observed in practice.<sup>15,16</sup> Tracer studies during the growth of  $\text{Fe}_3\text{O}_4$  on Fe at  $500^\circ\text{C}$  have shown that  $\text{Fe}_3\text{O}_4$  growth is dominated by outward diffusion of Fe ions along short-circuit paths in the oxide.<sup>17</sup> These short-circuit paths are largely considered to be the oxide grain boundaries.<sup>15</sup> For  $\text{Fe}_3\text{O}_4$  above  $600^\circ\text{C}$ , the observed parabolic growth rate constants are within

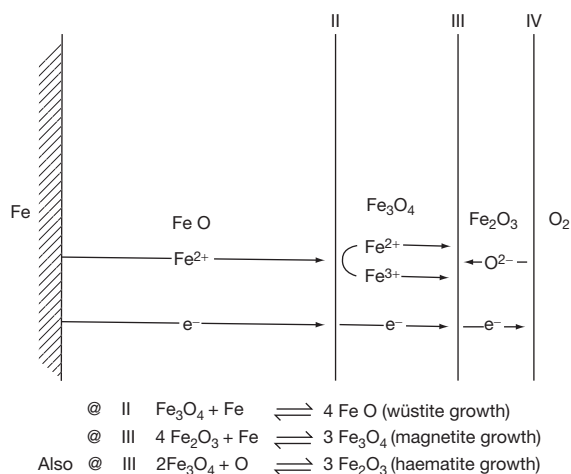


**Figure 3** Simplified scheme for the diffusion-controlled growth of multilayered scales on pure iron and mild steel above  $570^\circ\text{C}$ .

an order of magnitude of those calculated from tracer diffusion of Fe in  $\text{Fe}_3\text{O}_4$ .<sup>18</sup> A similar correspondence between theory and practice has been found for the growth of  $\text{Fe}_3\text{O}_4$  by the solid state reactions from FeO and  $\text{Fe}_2\text{O}_3$  between 600 and 1200 °C.<sup>18</sup> The growth rate of FeO is within 10% of the theoretical rate expected from Fe lattice diffusion, calculated according to the Wagner theory.<sup>19</sup>

The measured activation energy for  $\text{Fe}_2\text{O}_3$  growth is of the order of 169–222 kJ mol<sup>-1</sup>.<sup>20</sup> This activation energy is much lower than that expected from measurements of the tracer diffusion of Fe or O<sup>21</sup> and the measured rate constant for  $\text{Fe}_2\text{O}_3$  growth is approximately ten times greater than that calculated according to Wagner.<sup>13</sup> O<sup>18</sup> tracer diffusion studies of the growth of  $\text{Fe}_2\text{O}_3$  during the oxidation of Fe at 823 K have shown that, although the primary diffusion species through the crystal lattice is Fe ions, fast, inward O<sub>2</sub> diffusion occurs down cracks in the scale.<sup>22</sup>

The oxidation rate of pure Fe in O<sub>2</sub> has been shown to be affected by the specimen shape and the original surface profile.<sup>23</sup> For iron oxidizing in O<sub>2</sub>, 50:50 O<sub>2</sub> + H<sub>2</sub>O and O<sub>2</sub> + CO<sub>2</sub> rough surfaces have been found to oxidize more slowly than smooth surfaces, since surface irregularities hinder the oxide flow.<sup>23,24</sup> The oxide is unable to deform sufficiently to maintain intimate contact with the metal surface such that porous scales are formed.<sup>25</sup>

For the oxidation of pure Fe at 500 °C, the early reaction rate is more rapid on cold-rolled than annealed surfaces. On cold-worked surfaces, the scale tends to be rough and poorly adherent and contains less  $\text{Fe}_3\text{O}_4$ .<sup>26</sup> Cold-work enhances the oxidation rate by mopping up vacancies so that pore-free scales are formed which maintain contact with the substrate.<sup>27–31</sup> One of the authors<sup>32</sup> has found an effect of stored cold-work during the oxidation of fracture surfaces at 600 °C, which disappears with increasing oxidation because of the effect of surface annealing and consumption of the cold-worked layer by oxidation. At long oxidation times (>200 h), the oxidation rate of a fracture surface becomes indistinguishable from that of an annealed emery-ground surface.<sup>32</sup> At temperatures above approximately 625 °C, there is no effect of cold-work.<sup>23</sup>

#### 1.22.4 General Alloying Effects on Oxidation

The general requirements for higher temperature alloys is that they should be cheap, should possess adequate mechanical strength, should be resistant to

chemical degradation by the environment, and should be easily fabricated. These requirements are often conflicting, and a compromise is required for alloy design. Simple iron alloys form oxides that are not normally protective enough at temperatures above about 550 °C.<sup>33</sup> Therefore, the addition of other elements is needed to form a more protective scale. These elements usually comprise chromium, aluminum, and/or silicon. For these elements to confer adequate protection, the scale that they develop should be stoichiometric (to minimize ionic transport rates), free of gross defects, stress free at temperature, should resist spalling, and should not be volatile by further reaction with the environment.<sup>34</sup>

It has already been shown that bulk lattice diffusion is not generally considered to be the rate-controlling process for the oxidation of iron in most real situations. Hence, the classical Wagner treatment, whereby the valency of the alloying element increases or decreases the number of lattice defects, provides little clue as to the overall effects of alloying elements on the oxidation of iron alloys. Rather, studies have shown that the effects of alloying elements on the oxidation of iron alloys are largely brought about by their mobility (or lack of mobility) in the iron oxide lattice, and the effect this has on scale morphology, phase structure, and oxide plasticity. The addition of even small quantities of alloying elements can profoundly influence the scale morphology produced and hence the subsequent oxidation behavior.

The  $\text{Fe}_3\text{O}_4$  unit cell comprises an inverse spinel structure, with  $\text{Fe}^{2+}$  and  $\text{Fe}^{3+}$  cations occupying octahedral and tetrahedral interstitial sites within a close-packed oxygen lattice. The occupation of an interstitial site is accompanied by a specific site energy and particular cations show a preference for occupation of that site in which they sit most comfortably, that is, the lowest-energy site (Figure 4). The difference between the potential energy of a cation in a preferred site to that in a nonpreferred site is termed the crystal field preference energy<sup>35</sup> (CFPE) and is principally determined by the number of electrons on the d-shell. The direction of travel of a cation through the magnetite lattice is via alternate octahedral–tetrahedral–octahedral site transfers.<sup>36</sup> These interstitial sites are interconnected by saddle points within the lattice, and in order to transfer from one interstitial site to another, the diffusing ion must acquire enough energy to surmount this energy barrier and pass through the saddle point. If the direction of movement of the cation is from a favored to a nonfavored site, additional energy is required to overcome the CFPE. If, however, the direction of cation

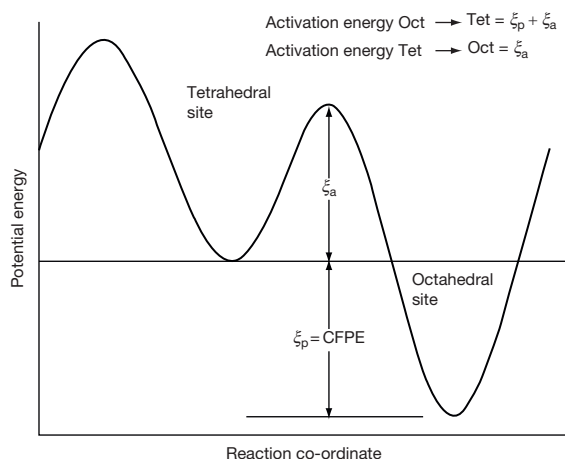


**Figure 4** Potential energy/lattice position diagram for occupation of interstitial sites in Fe<sub>3</sub>O<sub>4</sub> lattice alloying element cations.

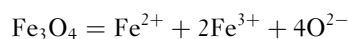
movement is in the opposite direction, there is a net reduction in the total lattice energy equivalent to the CFPE. It is apparent that, if the cation shows a high CFPE between interstitial sites, then cation transfer is much easier in one direction than the other and diffusion of the cation through the lattice will be severely hindered. The CFPE for Cr, Mo, and V in octahedral sites in magnetite is high, whereas that for Mn is virtually identical to that of Fe, both of which are very low. Hence Cr, Mo, and V are virtually immobile in the magnetite lattice, while Mn is found throughout the scale at atom ratios to the iron similar to those found in the original metal.<sup>37,38</sup>

As a result of this lack of mobility of certain alloying elements, a new phase layer appears in the scale. This new layer grows inward from the original metal surface, is in intimate contact with the substrate alloy,<sup>39</sup> and has an alloying element composition approximately 1.5 times that of the original metal.<sup>37</sup> Moreau<sup>40</sup> identified this inward growing layer on Fe–Cr steels as FeCr<sub>2</sub>O<sub>4</sub> globules within a wüstite matrix. Further, Rahmel<sup>39</sup> determined that the inner layer of four-layered scales grown on iron alloys containing Cr, Mo, V, and Si consisted of FeO containing (Fe, X)<sub>3</sub>O<sub>4</sub>, where X is Cr, Mo, V, or Si. The oxygen transport through the inner layer is thought to take place via pores within the inner layer, since solid-state diffusion of oxygen through the magnetite lattice is five orders of magnitude too low,<sup>41</sup> and grain boundary diffusion is also too low, to account for the observed growth rates.<sup>42</sup> The oxygen pathways are now thought to comprise grain boundary triple points and transient microvoids, continuously created and rearranged by creep.<sup>43</sup>

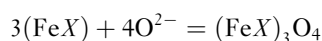
At temperatures below approximately 600 °C, numerous studies have shown that the thickness of the inward growing layer approximates to that of the outwardly growing magnetite + hematite scale, with the location of the spinel–magnetite interface approximately located at the original metal surface.<sup>34,37,44–46</sup> Hence, the new spinel formed approximately balances the volume of metal consumed, implying equal amounts of oxygen and cation transport in duplex film growth<sup>34</sup> and also implying that the rate of growth of the two scales are linked to one another. Moreover, it is now considered that the overall growth rate is mainly determined by the rate of cation diffusion outward through the outer layer, since the cations must first diffuse out to provide space for inner layer growth. Hence, the extent of inner layer growth is dictated by the recession of the oxide–metal interface.

These observations have been rationalized by Robertson and Manning,<sup>43</sup> who suggest that, for single-layer growth, the metal ions are transported as metal vacancies to the scale–metal interface. This interface consists of incomplete planes of metal atoms, or ledges, on which there are incomplete rows or jogs, analogous to interfacial edge dislocations. A metal vacancy in the oxide, on arrival at the interface, aligns with a jog atom on the metal surface. Oxidation then occurs when the jog atom moves into the oxide and annihilates the vacancy. Repetition of this process causes continual stripping of the metal ledge and allows oxide to fall into the space created (analogous to the climb of an edge dislocation). The surrounding oxide lattice then relaxes, maintaining adhesion. Since Cr is much less mobile in Fe<sub>3</sub>O<sub>4</sub> than Fe, a Cr ion tends to remain at the site where it first enters the oxide and inhibits dislocation movement.<sup>47</sup> This prevents the scale falling into the space created by the outward diffusion of Fe ions and microvoids (a few atom sites) are formed at the scale–metal interface. This initiates duplex growth by creating the space required for inner layer growth, without compromising adhesion.

For many low-alloy steels, therefore, the scale phase sequence is as shown in Figure 5 and the governing equations for individual layer growth are similar to those for pure iron, with the addition of



at the spinel–magnetite interface and



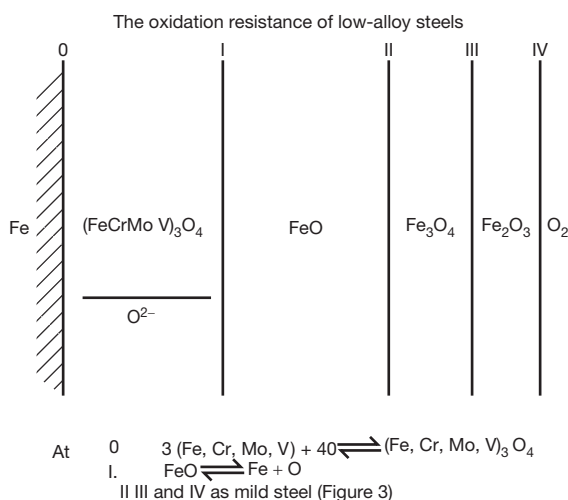
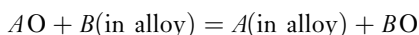


**Figure 5** Simplified scheme for the diffusion-controlled growth of multilayered scales containing spinel layers on low-alloy steels.

at the metal–spinel interface. The  $\text{Fe}^{2+}$  and  $\text{Fe}^{3+}$  ions diffuse through the overlying magnetite (or wüstite) to promote higher oxide reduction as before. The  $\text{O}^{2-}$  ions percolate through pores and microfissures in the underlying spinel to promote growth of the spinel layer.

With some alloying elements, for example, Si and Al, the concentration of element required in the lattice to form their own oxide is so low that preferential formation of pure  $\text{Al}_2\text{O}_3$  or  $\text{SiO}_2$ , which are both highly protective, may occur. For the reaction



the limiting mole fraction ( $N_A$ ) of  $A$  required for protection is given by

$$\frac{N_A}{1 - N_A} = \exp \frac{1}{RT} (\Delta G_{A\text{O}} - \Delta G_{B\text{O}}) \quad [3]$$

where  $\Delta G_{A\text{O}}$  and  $\Delta G_{B\text{O}}$  are the free energies of formation of the oxides  $A\text{O}$  and  $\text{BO}$ , respectively.

Provided the mole fraction of  $A$  does not fall below  $N_A$ , the oxide  $A\text{O}$  will be formed exclusively. The important criterion is the ratio of the oxidation parabolic rate constant to that of the diffusion coefficient of  $A$ .<sup>48</sup> For Al in Fe, the parabolic rate constant is very low, while the diffusion coefficient is relatively high, whereas the diffusion coefficient of Cr is much lower. Hence, the bulk alloy composition of Al in iron required for the exclusive formation of  $\text{Al}_2\text{O}_3$  at any given temperature is lower than the Cr concentration required for the exclusive formation of  $\text{Cr}_2\text{O}_3$ .

By adding a third element ( $C$ ), it is possible to increase the likelihood of forming compound  $\text{BO}$ , at a lower concentration than would be required in the pure binary alloy  $A$ – $B$ , provided that the third element  $C$  has an affinity for O intermediate between that of  $A$  and  $B$ .<sup>49</sup> If the mobility of  $B$  in the ternary alloy is high enough and element  $C$  has sufficient thermodynamic activity in the alloy to form  $\text{CO}$ , then the potential of O may be lowered to such an extent that  $\text{BO}$  forms more readily, that is, element  $C$  acts as a getter for element  $B$ . Such behavior is characteristic of, for instance, Fe–Al–Si and Fe–Cr–Si alloys.

### 1.22.5 Effects of Specific Alloying Elements on the Oxidation of Iron

Although in reality, binary low alloy steels are rarely used in industry, the effects of single element additions to iron will be discussed. However, the effects of further additions whether intentional or as impurities to form ternary, quaternary or multi-element alloys can be large and may alter the behavior of the previous system to which they were added to a great extent.

#### 1.22.5.1 Carbon

The addition of carbon to iron principally affects the subsequent oxidation response via the oxidation of the carbon in the steel to form  $\text{CO}$  and  $\text{CO}_2$ . Runk and Kim<sup>50,51</sup> and latterly Nosek and Werber<sup>52</sup> have all reported similar observations on the oxidation of Fe–C alloys at temperatures up to 400 °C. It appears that magnetite nucleates first over the ferrite, the growth reaction obeying two-stage logarithmic kinetics with electron transfer through the scale being the rate-controlling process. Due to the formation of a kinetic barrier of  $\text{CO}$  and  $\text{CO}_2$  at the carbide–oxide interface, only a thin film (15 nm) of randomly oriented crystallites of  $\gamma$ - $\text{Fe}_2\text{O}_3$  of approximately 7 nm mean grain diameter form over the cementite. Continued oxidation results in grain growth in the  $\gamma$ - $\text{Fe}_2\text{O}_3$  due to strain-induced grain boundary migration and a transition from  $\gamma$ - to  $\alpha$ - $\text{Fe}_2\text{O}_3$ . This latter transformation is accompanied by a 2.3% volume decrease, which causes cracking and allows the carbon oxides to escape. Ultimately, lateral magnetite overgrowth of the cementite occurs, and once  $\text{Fe}_3\text{O}_4$  has spread over the whole surface, protective kinetics prevail, since the magnetite is impermeable to the carbon oxides.

Bohnenkamp and Engell<sup>53</sup> and Caplan *et al.*<sup>54,55</sup> have also reported rapid carbon loss from the steel during the initial stage of oxidation at higher

temperatures ( $\sim 850^\circ\text{C}$ ) followed by a much lower, or zero, loss of carbon later. Caplan *et al.* measured the  $\text{CO}_2$  evolution by infrared gas analysis and reported that the percentage of carbon loss from 0.1% C, 0.4% C, 0.8% C, and 1.2% C steels was overall very small and may be redistributed in the metal. There was no carbon loss detected at  $700^\circ\text{C}$ . The overall oxidation rates were all found to be parabolic at  $850^\circ\text{C}$  and less than the oxidation rate of pure Fe. In the Fe–C alloys, the individual phases of  $\text{FeO}$ ,  $\text{Fe}_3\text{O}_4$ , and  $\text{Fe}_2\text{O}_3$  were found to be less regular than those of pure Fe and were often highly porous.

Malik<sup>56</sup> reported that, at temperatures between 600 and  $850^\circ\text{C}$ , in 101 kPa oxygen, the oxidation rate of Fe–5% *M*–C steels (where *M* was Si, Ti, V, Nb, Ta, Cr, W, or Ni) fell as the carbide stability increased. The oxidation of all of the alloys obeyed parabolic kinetics, although some breakaway occurred following an incubation period. This breakaway was attributed to scale disruption, as a result of  $\text{CO}_2$  evolution, with the carbon loss being most rapid during the first 5 min. Although the amount of carbon loss increased with the carbon content of the alloy, as did the oxidation rate constant, the total carbon loss was very much lower than that available. Those alloys forming a pure carbide phase were found to have a lower oxidation rate than those alloys comprising a solid solution phase or cementite. All of the binary Fe–5% *M* alloys displayed a similar reaction rate, which was approximately one order of magnitude lower than that of pure Fe, because of the formation of mixed oxides or spinels in the scale. The Fe–5% *M*–C alloys always showed two-layered scales, with an inner mixed oxide or spinel overlaid with  $\text{Fe}_2\text{O}_3$ . The scales formed on the high-carbon alloys were generally more compact and adherent (following initial scale disruption by C loss) because of carbide dispersion improving scale integrity. Malik<sup>56</sup> argued that the carbide-forming elements retard the diffusion of carbon in austenite, reducing the overall scaling rate. In non-carbide-forming alloys, such as Ni and Si, the oxidation rate was greater because of a higher carbon mobility in the steel.

At  $850^\circ\text{C}$  and 1.2% C, the oxidation rate was found to be in the order Fe–Cr–C > Fe–C > Fe–Ni–C > Fe–Ti–C > Fe–Ta–C > Fe–Nb–C > Fe–V–C > Fe–W–C, which is nearly, but not exactly, the sequence of carbide stabilities.

### 1.22.5.2 Aluminum

On oxidation, aluminum forms the highly refractory, and hence protective,  $\text{Al}_2\text{O}_3$ . However, the addition

of aluminium to steels produces a dramatic change in their mechanical properties with a reduction in toughness and an increase in ductile-to-brittle transition temperature (DBTT), which is detrimental in many circumstances. There is a need, therefore, to realize the protective benefit of aluminum at as low a concentration as possible within the steel. Al compositions of 8 wt% results in severe embrittlement at room temperature, and the oxidation of iron–aluminum alloys has been reviewed in detail by Prescott and Graham.<sup>57</sup> At aluminum concentrations below 2.4 wt%, bulky stratified scales, comprising  $\text{Fe}_2\text{O}_3$  and  $\text{Fe}_3\text{O}_4$ , with an inner layer of  $\text{Al}_2\text{O}_3$  or  $\text{FeAl}_2\text{O}_4$  are formed at  $800^\circ\text{C}$ .<sup>58</sup> At 2.5% aluminum, large areas of  $\text{Al}_2\text{O}_3$  were always observed with iron oxide nodules. Formation of these iron oxide nodules is suppressed only when the aluminum content exceeds approximately 7 wt%.<sup>58–60</sup>

Ahmed and Smeltzer,<sup>61</sup> Pons *et al.*,<sup>62</sup> and Smith *et al.*<sup>63</sup> have all found that, at 1173 K, iron alloys containing around 5–6% aluminum initially form a rapidly growing duplex scale comprising an outer  $\alpha\text{-Fe}_2\text{O}_3$  layer overlaying an inner  $(\text{FeAl})_3\text{O}_4$  layer. However, with prolonged oxidation, an  $\text{Al}_2\text{O}_3$  layer eventually forms at the oxide–metal interface and precipitates within the alloy. The reaction rate gradually decreases as the  $\text{Al}_2\text{O}_3$  at, or near, the surface coalesces eventually to form a continuous film that virtually stops the outward diffusion of Fe ions. Electron backscattered Mössbauer spectroscopy studies have shown that the outer  $\text{Fe}_2\text{O}_3$  contains approximately 10%  $\text{Al}^{3+}$  and the inner layer comprises  $\text{Al}_2\text{O}_3$  with some  $\text{Fe}^{3+}$ .<sup>(64)</sup> The benefits afforded by alumina scale formation are well documented: slow growth as a result of low defect concentrations and stability at high temperature. A disadvantage associated with alumina scales on iron is the relatively poor scale adherence which can result in spallation of the protective layer.<sup>65</sup>

Alumina generally develops as either  $\alpha\text{-Al}_2\text{O}_3$  or  $\gamma\text{-Al}_2\text{O}_3$  during the oxidation of Fe–Al alloys.  $\alpha\text{-Al}_2\text{O}_3$  forms, and is stable at higher temperatures and is more desirable for conferring oxidation resistance.<sup>57</sup> Initial transient stages of alloy oxidation show scale compositions controlled by kinetics rather than those predicted by thermodynamics. The growth of convoluted transient scales containing all of the alloying elements is quickly replaced by a slow growing protective alumina scale dependent on composition and temperature. The critical Al content for the exclusive formation of  $\text{Al}_2\text{O}_3$  has been found to be raised by the presence of Ti and B.<sup>66</sup>



The beneficial effects of adding both aluminum and chromium to steels has been demonstrated by Tomaszewicz and Wallwork<sup>66</sup> during oxidation studies of Fe–Al–Cr alloys at 800 °C in pure oxygen at 26.6 kPa. They showed that Al acts as a primary getter for oxygen, nucleating  $\text{Al}_2\text{O}_3$ , with Cr acting as a secondary getter, nucleating  $\text{Cr}_2\text{O}_3$ . If there had been sufficient Cr and Al in the alloy, no iron oxides would have been formed. The total Al + Cr content to suppress nodule formation was found to be in the range of 7–8%, with 7% Al required at 0% Cr, but only 3% Al required at 5% Cr.

The diffusion coefficient for S in  $\text{Al}_2\text{O}_3$ <sup>67</sup> at 950 °C is approximately 100 times lower than that in  $\text{Cr}_2\text{O}_3$ .<sup>68</sup> Hence, for high temperature applications in S environments, aluminum confers a much greater degree of protection than that afforded by chromium.

### 1.22.5.3 Silicon

The addition of silicon to iron has been reported by many authors to confer significant corrosion protection. Rahmel and Tobolski<sup>69</sup> found that binary alloys containing up to 4% Si displayed a limiting corrosion rate due to the formation of an iron-silicate layer when exposed to pure oxygen,  $\text{O}_2 + \text{H}_2\text{O}$  or  $\text{CO}_2$  in the temperature range 750–1050 °C. However, Robertson and Manning<sup>70</sup> indicate that Fe–Si oxides are generally immiscible. Several authors<sup>71–74</sup> have reported that the corrosion protection apparent in Fe–Si alloys arises from the formation of a  $\text{SiO}_2$  healing layer, beneath the magnetite, which acts as a barrier to outward transport of metal ions. At the low oxygen potentials at the base of the scale, and for very thin films, charged effects in the amorphous  $\text{SiO}_2$  network and electronic carriers control the growth of the  $\text{SiO}_2$ .<sup>42,75</sup>

Adachi and Meier<sup>76</sup> studied the oxidation of Fe–Si alloys under isothermal and cyclic oxidation conditions, in air, between 900 and 1000 °C. They found that oxidation rates in air decreased with the silicon content, such that at 10 wt% Si the oxidation rate was lower than that conferred by Cr, because of the formation of a continuous film of  $\text{SiO}_2$ . The oxidation kinetics of these steels was found to be linear because of the diffusion of Fe through a film of  $\text{SiO}_2$  of constant thickness. Outward diffusing Fe subsequently dilutes the  $\text{SiO}_2$  to form  $\text{Fe}_2\text{SiO}_4$  and produced the  $\text{Fe}_2\text{O}_3$  as an outer layer. At greater than 10% Si,  $\text{SiO}_2$ , overlaid with  $\text{Fe}_2\text{O}_3$ , comprised the total scale.

At the low oxygen potentials found in  $\text{CO}/\text{CO}_2$  environments, the critical concentration of Si for the selective formation of a continuous film of  $\text{SiO}_2$  is

only approximately 0.05%.<sup>77</sup> However, at higher oxygen potentials, the higher growth rate of transient iron oxides suppresses the growth of this continuous  $\text{SiO}_2$  scale. Even at 5% Si in the steel, no continuous  $\text{SiO}_2$  layer formed during oxidation in air, whereas such a film was seen to form during oxidation in Ar at a  $p\text{O}_2$  of  $10^{-4}$ .

Logani and Smeltzer<sup>78–80</sup> have observed that, for Fe–1.5% Si at 1000 °C in  $\text{CO}/\text{CO}_2$ , the initial slow reaction rate was followed by regions of linear behavior because of the amorphous  $\text{SiO}_2$  film being consumed by the growth of wüstite–fayalite nodules during the early stages. These wüstite–fayalite nodules were nucleated at alloy grain boundaries and then grew laterally to inundate the  $\text{SiO}_2$  films over alloy grains.

During the oxidation of high Si content steels in high-pressure  $\text{CO}_2$ , the oxidation reaction can suddenly switch to a highly protective mode that proceeds extremely slowly after an initial incubation period.<sup>70</sup> This follows the formation of a healing layer, comprising a line of amorphous silicon-rich oxide along the oxide–metal interface with Cr enrichment to 30–40 at% just above the healing layer and Cr depletion in adjacent metal sites. Slowing of the oxidation reaction by the  $\text{SiO}_2$  permits selective oxidation of Cr. Cr and Si are then synergistic, with less Si being required in Cr-containing steels than in straight Fe–Si steels, because of secondary gettering. For Fe–Si, then, 2.5–3% Si is required for healing layer formation, irrespective of the temperature. For Fe–Cr–Si, however, the critical Si content decreases with increasing Cr content and temperature.

Silicon has a major effect on the rate of oxidation of iron. Yang *et al.*<sup>81</sup> found that small additions (less than 2 wt% Si) result in a marked decrease in the rate of oxidation up to 1000 °C in dry moving air, however, at 1200 °C the formation of a liquid phase resulting from the melt of FeO and  $\text{SiO}_2$  substantially increased the oxidation rate. Adachi and Meier<sup>76</sup> showed that the addition of 5 wt% Si is observed to decrease the oxidation rate of iron by more than two orders of magnitude and additions of 10 wt% Si or more results in oxidation rates slower than Fe–26 wt% Cr. Lashin *et al.*<sup>82</sup> studied Fe – 6 at.% Si steels at 500 °C – 540 °C in ambient air of various pressures. The tests were designed to show the oxidation behavior of steels intended for use in electro-magnetic applications.

Ishitsuka *et al.*<sup>83</sup> report a reduction in the steam side oxidation rate of 9Cr–0.5Mo–1.8W (P92) with increasing Si content. Improved oxidation resistance

was apparent at all temperatures investigated (500 °C, 550 °C, 600 °C, 650 °C and 700 °C). The largest reduction in corrosion rate was observed at 700 °C, oxidation rates at all other temperatures showed similar rate reductions. At 700 °C the remarkable reduction in oxidation rate was attributed to the formation of a protective amorphous SiO<sub>2</sub> film grown at the scale metal interface. At temperatures of 600 °C, or less, only dissolved silicon in the Fe–Cr spinel lattice contributes to the effect of silicon on oxidation rates.

#### 1.22.5.4 Manganese

Since Mn is both soluble in iron oxides and mobile to the same extent as Fe, the addition of Mn to steels has little effect on the overall scaling rate in air or oxygen. Jackson and Wallwork<sup>84</sup> have shown that between 20% and 40% manganese must be added to steel before the iron oxides are replaced by manganese oxides. However, Mn suppresses breakaway oxidation in CO/CO<sub>2</sub> possibly by reducing the coalescence of pores in the oxide scale. It also appears to be important in the healing of microcracks in protective chromia/spinel oxide scales formed on highly alloyed steels.<sup>85</sup>

The addition of up to 15% Mn to pure Fe, under sulfidizing conditions at 1073 K, leads to a small increase in the scaling rate.<sup>86</sup> At 2% Mn, MnS forms as stringers in the subscale, but these do not form a coherent layer even at a concentration of 15% Mn. The increase in scaling rate is possibly due to increased short-circuit diffusion, since metal diffusion in MnS is much slower than in FeS.<sup>87</sup>

#### 1.22.5.5 Sulfur

The presence of small quantities of S in steels has little effect on the initial scaling rates in air, but may be detrimental to long-term scale adhesion. Sulfur has, however, been shown to be detrimental to breakaway oxidation in CO/CO<sub>2</sub> environments.<sup>88</sup> However, it has been shown to reduce the total uptake of carbon in the steel under CO/CO<sub>2</sub><sup>89</sup> and reduce the scale thickening rate. In this context, free-cutting steels were found to oxidize at a significantly lower rate, as did steels subjected to pretreatment in H<sub>2</sub>S.

Modern steel making techniques are capable of routinely producing alloys of sulfur contents < 50 ppmw;<sup>90</sup> however, recent research by a number of groups<sup>91–93</sup> indicates that removing sulfur to extremely low levels may have a detrimental effect on the oxidation resistance of 9–12Cr steels in steam and it may, therefore, be necessary to intentionally add sulfur to these alloys.

#### 1.22.5.6 Phosphorus

Like sulfur, phosphorus appears to have only a small effect on the overall scaling of iron alloys in air. For example, minor additions (<0.1 wt%) have been shown to increase the oxidation resistance of iron at 500 °C, but above this amount the oxide layers begin to break and become nonprotective.<sup>94</sup> However, phosphorus may play a role in suppressing breakaway oxidation in carbon steels in CO/CO<sub>2</sub> environments. Donati and Garaud<sup>95</sup> found that the tendency for breakaway was lower over ferrite, where P segregates. To confirm this, the authors doped pure Fe with P and found that the breakaway rate slowed down at 350 ppm phosphorus and was totally suppressed at 900 ppm phosphorus. A similar benefit has been reported by Dewanckel *et al.*<sup>88</sup>

#### 1.22.5.7 Nickel

The addition of Ni to Fe dramatically reduces the oxidation rate due to the virtual insolubility of NiO in FeO.<sup>96</sup> The oxidation of iron nickel alloys in general was reviewed by Foley in 1962.<sup>97</sup> During the oxidation of Fe–Ni alloys, and in the absence of nickel oxide formation, Ni concentrates at the FeO–substrate interface as a result of Fe depletion. Oxidation rates decrease due to the reduced Fe activity at the base of the FeO scale and thus the stability of the FeO layer is diminished. Menzies and Lubkiewicz<sup>98</sup> found that the oxidation of an Fe–12%Ni alloy in O<sub>2</sub> obeyed parabolic kinetics at all temperatures between 700 °C and 1000 °C. At 700 °C, the Ni suppressed the formation of FeO, with the scale comprising only Fe<sub>3</sub>O<sub>4</sub> and Fe<sub>2</sub>O<sub>3</sub>. Progressive enrichment of Ni occurred in the alloy as the substrate was consumed by oxidation. When the concentration of Ni reached 50–60%, the Ni entered the spinel phase, leading to the formation of Ni<sub>(x)</sub>Fe<sub>(3-x)</sub>O<sub>4</sub> with x approximately equal to 0.24 near the alloy surface and less than 0.01 near the Fe<sub>2</sub>O<sub>3</sub>. At 900 °C – 1000 °C, the Ni entered the spinel in the early stages of oxidation, with x values of 0.4 at 900 °C. This led to a reduction in the parabolic rate constant. At 1000 °C FeO is the stable oxide phase formed on Fe–Ni alloys, even up to 80% Ni, since FeO is more stable than NiO.<sup>99</sup>

#### 1.22.5.8 Chromium

Of all of the alloying elements added to steels, Cr has been the most used for improving the corrosion properties. In terms of high temperature oxidation, steels

containing approximately 10% Cr are capable of forming a continuous, highly protective film of  $\text{Cr}_2\text{O}_3$ .<sup>33</sup> Rhys-Jones *et al.*<sup>100</sup> reported that the isothermal oxidation kinetics of Fe10Cr at 1000 °C were parabolic. However, significant reductions in the oxidation rate are also realized at lower Cr concentrations because of the formation of FeCr spinels<sup>101</sup> and the suppression of FeO formation to temperatures in excess of 570 °C.<sup>102</sup> At 700 °C, FeO exhibits a very narrow stability range on the Fe–Cr–O phase diagram (Figure 6) for Cr up to 6%.<sup>103</sup> The wüstite stability range is almost negligible on Fe–0.5% Cr because of the high reactivity of Cr toward  $\text{O}_2$  at 1000 °C. However, while  $\text{Cr}_2\text{O}_3$  is normally protective on steels in air or  $\text{O}_2$  up to approximately 900 °C, volatile  $\text{CrO}_3$  may form at higher temperatures.<sup>33</sup> Dewanckel *et al.*<sup>88</sup> found that although the addition of Cr to steels is normally considered beneficial, low quantities (<500 ppm Cr) were detrimental to the breakaway performance of low-alloy and carbon steels.

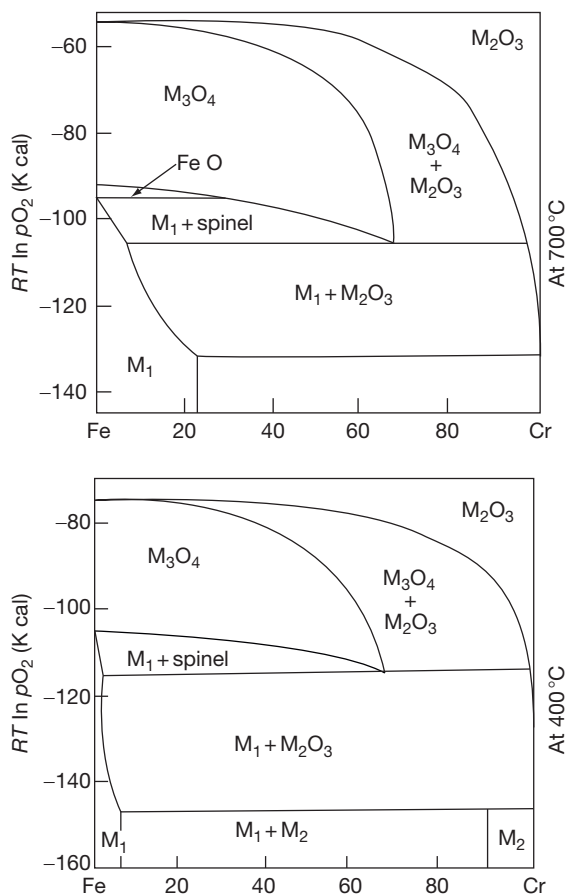


**Figure 6** Fe–Cr–O phase diagram for Fe–Cr alloys at 400 °C and 700 °C.

Many studies have shown that surface pretreatment of Fe–Cr alloys has a strong effect on the scale morphology and subsequent oxidation rate.<sup>27,104–106</sup> For instance, Caplan<sup>27</sup> indicated that several Fe–Cr alloys showed improvements in corrosion resistance because of cold work, with greater than 16% Cr required to show the optimum benefit. Khanna and Gnanamoorthy<sup>104</sup> examined the effect of cold work on 2.25% Cr–1% Mo steels at temperatures between 400 and 950 °C over 4 h in 1 atm  $\text{O}_2$ . They found that up to 90% reduction by cold rolling had a negligible effect on the oxidation rate up to 700 °C. However, above 700 °C there was a general reduction in the kinetics because of enhanced Cr diffusion in the alloy, leading to the formation of a Cr-rich spinel. In addition, they found that breakaway corrosion occurred at 900 °C on annealed samples, but this did not occur on samples that had been cold-worked. For Fe–10% Cr at 600 °C in air, Hossain found that the oxidation resistance increased with the degree of cold work.<sup>105</sup>

#### 1.22.5.9 Molybdenum

In the temperature range 500–1000 °C, additions of between 0.5% and 5.6% of Mo decreases the oxidation rate of iron by a factor of almost 10, with the maximum benefit being obtained at a concentration of approximately 2%.<sup>107</sup> Like many alloying elements, Mo promotes the formation of a duplex spinel–magnetite scale, with the Mo retained within the inner spinel layer.<sup>105</sup>

#### 1.22.5.10 Boron

Tsipas and Rus<sup>108</sup> and Suwattananont and Petrova<sup>109</sup> found that thermally diffusing boron into the surface of steel gave a boride layer with enhanced oxidation resistance at temperatures up to 900 °C by acting as a barrier to inward diffusing oxygen. Rowley *et al.*<sup>110</sup> also found that adding small amounts of boron to Fe–Cr alloys strongly affects the materials oxidation characteristics in super-heater steam. Enhanced manganese and/or chromium content of the oxide films in comparison to those seen in undoped 9Cr steels provides greater protection and hence a reduction in oxidation rates. Rowley proposes two likely models for boron doped oxide growth:

1. The possibility that Schottky electron emission from the metal substrate into the conduction band of the oxide layer and/or subsequent electron diffusion may control oxide growth kinetics.

These processes are governed by the space charge in the oxide film which is due to the electric field produced by an ionic defect gradient through the layer. Existing theories indicate that this mechanism is applicable for oxide thicknesses ranging from 5–100 nm in the temperature region 300–600 °C, both of these conditions are satisfied in the case of boron doped oxide films.

2. It is possible that a boron containing phase of low ionic conductivity is formed at grain boundaries. This may lead to a progressive reduction in ionic mobilities via a mechanism similar to that postulated for the reactive elements effect<sup>111</sup> (cited by Rowley *et al.*). Although boron does show a tendency to migrate to grain boundaries, it is experimentally observed that the limiting oxide thickness is reached extremely rapidly indicating an almost instantaneous formation of a blocking phase. Furthermore, the ultrafine grain size exhibited by boron doped oxides would provide a much larger number of short-circuit diffusion pathways than in control oxides. This suggests that ionic blocking must be extremely effective for this mechanism to be tenable.

#### 1.22.5.11 Others

Small additions of Ce have been shown to have a favorable influence on the oxide growth of several Fe–Cr alloys by improving scale adherence and acting as nucleation sites for  $\text{Cr}_2\text{O}_3$ .<sup>112</sup> In a  $\text{H}_2\text{--H}_2\text{O--CO--CO}_2$  atmosphere at 700 °C cerium levels as low as 0.024% reduce the carbon uptake of steels in carbonaceous atmospheres by several orders of magnitude. However, Sroda *et al.*<sup>113</sup> found additions of Ce to low alloy steels to have a negative effect on corrosion resistance at 500 °C, especially, in HCl containing atmospheres. The techniques used in the study did not enable the author to detect Ce in the oxide scale and thus it was not possible to determine the role of cerium in the corrosion process (although thermodynamic calculations show that the formation of cerium oxides is possible). Trace concentrations of As and Sn have been found to improve the breakaway properties of scales formed on mild and low-alloy steels in  $\text{CO/CO}_2$ , whereas Cu has been found to be detrimental.<sup>88</sup>

#### 1.22.5.12 Effects of Heat Flux and Cold Work

Another factor which has been largely ignored in earlier work is any influence of heat flux on the

oxidation behavior of boiler steels, for example. Most industrial components in service will be subjected to a thermal gradient across them, and the effect of this has been investigated recently by Fry *et al.*<sup>114,115</sup> They showed that the oxide grain size and morphology could change in subtle ways when subjected to a heat flux, and that this could have important implications under some conditions. Trindade *et al.*<sup>116</sup> have also shown that surface finish and cold work can influence the substrate grain size and hence the high temperature oxidation of pure Fe and 2.25Cr–1Mo steel. Decreasing grain size increases oxidation rates by facilitating oxygen diffusion down grain boundaries. Internal oxidation including the formation of  $\text{FeCr}_2\text{O}_4$  and  $\text{Cr}_2\text{O}_3$  along grain boundaries was observed. Oxidation kinetics decreased strongly with an increase in grain size as a result of the reduction of grain boundary density leading to less internal oxidation per unit volume. Fluctuation in grain size did not appear to affect the rate or structure of external oxide scales.

The effect of cold working on high temperature oxidation was also investigated. In agreement with Ostwald,<sup>117</sup> Trindade<sup>116</sup> suggests the increased dislocation density associated with cold working allows greater diffusion rates of chromium in bcc steel; this increased mobility enables Cr enrichment of the spinel layer in comparison to non-cold worked specimens. The increased Cr content within the spinel scale affords improved oxidation resistance. Recrystallization/recovery of specimens subjected to greater than 42% cold work resulted in low dislocation densities and polygonization; the ensuing fine grained low dislocation density microstructure led to an overall increase in oxidation rates.

Samples of pure iron were heat treated to establish microstructures of two different grain sizes and then oxidised in laboratory air at 550 °C for 72 h. Gold markers were used to indicate the position of the original metal surface and to define the mass transport direction. Studies reveal that the oxide scale in pure iron also grows by outward Fe migration and inward oxygen diffusion and that, similarly to 2.25Cr–1Mo steels, oxidation kinetics of pure iron also decrease with an increase in substrate grain size.

However, Caplan and Cohen<sup>30</sup> studied the effects of cold work on the oxidation rates of pure iron, where in contrast to the findings of cold worked 2.25Cr–1Mo steels, oxidation rates of cold worked pure Fe were observed to increase as a result of cold work. It was proposed that as iron diffused outwards, vacancies are annihilated at dislocations or lattice steps on the cold

worked Fe surface. As a result, the oxide layer remains in good contact with the Fe substrate in the absence of pore formation and rapid oxide growth ensues.

### 1.22.6 Stress Effects

While alloying elements may initially determine the protective nature of an oxide scale, the response of this oxide scale to stress is often crucial in determining the long-term oxidation performance of an alloy in an industrial environment.<sup>118</sup> The stresses in an oxide scale may arise both internally (because of growth stresses) and externally (because of applied stresses).<sup>119</sup> In general, oxide scales do not possess sufficient slip systems for plasticity and thus rely upon diffusion-controlled creep for plastic deformation and stress relief.<sup>120</sup> At temperatures below approximately 600 °C, only elastic deformation is possible and stress relief by cracking is likely to occur. If the scale-metal interface is strong, and the bulk oxide is weak, through-scale cracking results when the combined stresses exceed a critical value.<sup>121</sup> If the interface has a lower strength than the oxide bulk strength, decohesion occurs first. A minimum energy is required for cracking or decohesion.<sup>122,123</sup> Evans and Lobb<sup>121</sup> have calculated that cracking occurs when the strain energy per unit volume ( $w^*$ ) of oxide contained in layer thickness ( $z$ ) equals the work required for internal cracking ( $G_c$ ) or decohesion ( $G_d$ ). For internal cracking,

$$w^* = \frac{8PG_c}{fL} \sim \frac{4G_c}{fL} \quad [4]$$

where  $L$  is the side length of unit volume;  $f$ , the fraction of stored energy in the oxide;  $G_c$ , the energy for unit area of cracked oxide surface; and  $P$  is the geometric parameter ( $\sim 0.5$ ). For decohesion,

$$zw^* = \frac{G_d}{f} \quad [5]$$

where  $f$  is the energy/unit area of fresh metal at the oxide-metal interface.

Through-scale cracking may not necessarily be detrimental to an alloy if rapid scale healing can occur,<sup>124</sup> and scale delamination can reduce the total scaling rate if the scale remains adjacent to the alloy surface.<sup>119,125</sup> In this instance, scale separation confounds the transport of metal ions across the interface into the oxide. However, if through-scale cracking occurs in conjunction with delamination, scale spalling may follow,<sup>121</sup> with an attendant loss of

protection. For pure metals which oxidize in a parabolic manner, repetitive scale spalling may produce a much increased total metal loss over time, since the reaction kinetics continually revert to the initial rapid period of the oxidation curve and parabolic kinetics ensue.

The majority of heat-resisting alloys contain at least one element that is selectively oxidized (e.g., Cr, Si, Al). The resulting scale is highly protective, but depletion of the secondary element may occur if the diffusion rate of this element in the alloy is low. Then repetitious loss of the scale can be profoundly detrimental to long-term performance, since depletion of the alloying element near the surface may occur to such an extent that its concentration falls below the critical level for the exclusive reformation of the highly protective scale.<sup>126,127</sup>

#### 1.22.6.1 Growth Stresses

As indicated earlier, protective oxide scales typically have a PBR greater than unity and are, therefore, less dense than the metal from which they have formed. As a result, the formation of protective oxides invariably results in a local volume increase or a stress-free oxidation strain.<sup>128,129</sup> If lateral growth occurs, then compressive stresses can build up, and these are intensified at convex and reduced at concave interfaces by the radial displacement of the scale due to outward cation diffusion (Figure 7).<sup>48,129,130</sup>

The reduced oxidation near sample corners is related to these stress effects, either by retarded diffusion or by modified interfacial reactions.<sup>128</sup> Manning<sup>131</sup> described these stresses in terms of the conformational strain and distinguished between anion and cation diffusion, and concave and convex surfaces. He defined a radial vector  $M$ , describing the direction and extent of displacement of the oxide layer in order to remain in contact with the retreating metal surface, where

$$M = \frac{V_{ox}}{V_{me}} (1 - a) (1 - v) \quad [6]$$

and  $V_{ox}/V_{me}$  is the PBR,  $a$  is the amount of oxide formed at the surface, and  $v$  is the volume gain due to vacancy injection into the metal. If  $v$  is zero, the sign of  $M$  depends upon the predominance of anion ( $a = 0$ ) or cation ( $a = 1$ ) diffusion. The enforced radial displacement ( $\delta y$ ) of the oxide layer results in a tangential or radial reaction stress in both the oxide and the metal. The strain rate ( $\delta e/\delta t$ ) of the oxide layer



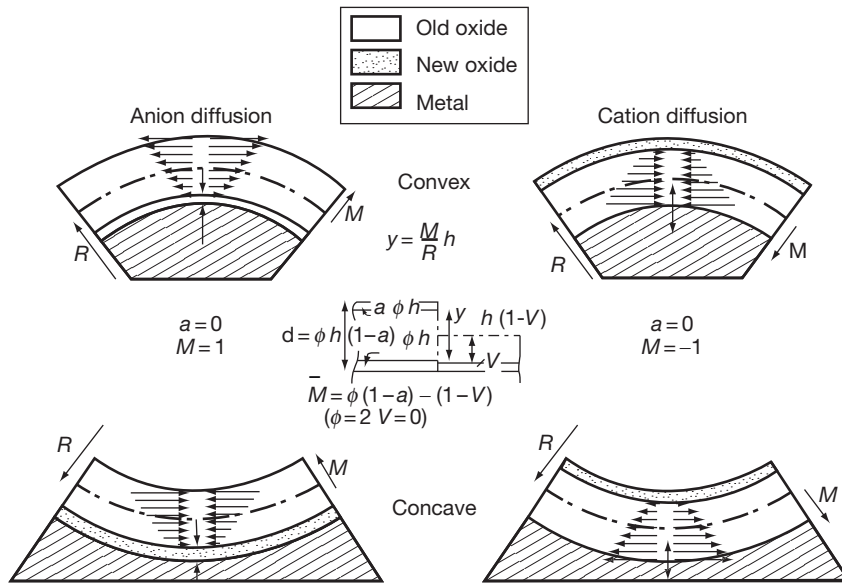


**Figure 7** Oxide growth stresses on curved surfaces. Reproduced from Hsueh, C. H.; Evans, A. G. *J. Appl. Phys.* **1983**, 54, 6672.

then depends upon the radius of curvature ( $R$ ) and the rate of metal loss ( $\delta b/\delta t$ ) as

$$\frac{\delta e}{\delta t} = \frac{M(\delta b)}{R(\delta t)} \quad [7]$$

This leads to high strains on regions of high curvature and zero strain on a flat surface. If new growth occurs stress free, then the oldest region of oxide will be the most highly stressed, this being located at the oxide surface for anion-controlled growth and at the oxide-metal interface for cation-controlled growth. Hsueh and Evans<sup>128</sup> carried out a similar analysis and calculated the distribution of radial and tangential stress within the oxide scale as a function of scale thickness and specimen geometry.

Whisker growth is a process often reported for the relief of compressive growth stresses during oxidation.<sup>132-134</sup> This whisker formation and scale buckling of thin hematite layers have been linked to the stresses arising from oxide formation at the magnetite-hematite interface as a result of the counter-current of cation and anion diffusion in both oxides.<sup>130</sup> Acoustic emission studies of 2.25% Cr-1% Mo steel at 900 °C have shown that, as the oxide thickness increases, growth stress builds up in the scale and is relieved by scale cracking.<sup>135</sup>

#### 1.22.6.2 System-Applied Stresses

The tensile failure strain of oxides grown on EN2 steel between 600 and 900 °C lies in the range  $1 \times 10^{-4}$  to

$2.5 \times 10^{-4}$ .<sup>(136)</sup> Components in service may be stressed beyond these failure strains, leading to scale cracking.

Ward *et al.*<sup>137</sup> have shown that, under cyclical loading, the oxidation rate of steels is similar to that under unstressed isothermal conditions, provided the fatigue stress is below the stress required to exceed the scale failure strain. If, however, the failure strain is exceeded, the oxidation rate is accelerated because of repetitive scale failure, and linear kinetics are observed.

Low-cycle fatigue loading of 9.5% Cr steel at 650 °C in air has been shown to enhance uniform scale formation as well as promote nodular scale formation at cracks.<sup>124</sup> However, no cracks were found in the scale after exposure, indicating that any cracks that form must heal very quickly. This healing of cracks was attributed to the overgrowth of the chromium-rich oxide by an iron-rich oxide.

#### 1.22.6.3 Thermal Stresses

Under thermal cycling conditions, the principal source of stress within the oxide scale is the temperature change.<sup>121</sup> Christl *et al.*<sup>125</sup> have noted that, when cooling 2.25% Cr-1% Mo steel from 600 °C in air, compressive stresses build up in the hematite, while tensile stresses build up in the magnetite and spinel layers. This arises because the thermal expansion coefficients of the individual oxide layers increase in the order  $\alpha_{\text{metal}} < \alpha_{\text{spinel}} < \alpha_{\text{magnetite}} < \alpha_{\text{hematite}}$ .<sup>119</sup>

Multilaminated scales have been reported following thermal cycling,<sup>138</sup> and Rolls and Nematollahi<sup>139</sup>

have studied the influence of thermal cycling on the oxidation of 1% Cr–0.5% Mo low-carbon steel. The oxidation kinetics were found to be mostly parabolic, with thin scales (10  $\mu\text{m}$ ) more prone to spalling than thick scales (20  $\mu\text{m}$ ). The authors reported that the higher the temperature drop on cycling, the greater the degree of scale disruption. They derived a qualitative relationship to describe this behavior:

$$Y = \frac{f(NO)}{x} \quad [8]$$

where  $Y$  is the degree of scale detachment,  $N$  is the number of cycles,  $x$  is the thickness, and  $O$  is the cooling rate. This implies that thicker scales cooled slowly show less detachment than thinner scales cooled rapidly. The oxide scale comprised spinel, magnetite, and wüstite, with only the spinel layer remaining adherent during thermal cycling. From this, the authors concluded that the bulk scale cohesive strength was less than the inner spinel adhesive strength. Scale detachment was observed at voids and microcracks produced at the outer–spinel interface during isothermal oxidation. Hence, the number of scale layers that became detached during thermal cycling was governed by the number of parallel rows of voids in the scale and not by the number of thermal cycles.

### 1.22.7 Commercial Low-Alloy Steels in Air or Oxygen

Simms and Little<sup>140</sup> have examined the early stages of scale growth on 2.25% Cr–1% Mo steel at 600 °C in dry flowing oxygen. Between 1 and 22 h, they found that a thick oxide layer spreads laterally over a thin oxide layer. After 50 h, no thin areas of oxide layer were left. Whiskers gradually developed on the outer surface and these were well defined after 100 h. Fracture sections of the oxide revealed that the thin scales were duplex, whereas the thicker scale was triplex, with a middle layer of  $\text{Fe}_3\text{O}_4$  which spread laterally with time. The authors concluded that the first phases to develop were fine equiaxed  $\alpha\text{-Fe}_2\text{O}_3$  overlying a doped spinel. Later, nucleation and lateral spread of coarse columnar grains of  $\text{Fe}_3\text{O}_4$  occurred between the two first-formed layers. The  $\text{Fe}_2\text{O}_3$  appears to reach a limiting thickness at which time  $\text{Fe}_3\text{O}_4$  nucleates.

One of the authors<sup>141</sup> has carried out exposures of a range of low-alloy steels (up to 5% Cr) in laboratory air between 500 and 850 °C. Plain carbon steel displayed a duplex scale, comprising 75%  $\text{Fe}_3\text{O}_4$  and

25%  $\text{Fe}_2\text{O}_3$  at all temperatures below 600 °C (Figure 8). Above 600 °C, a coarse, columnar-grained layer of FeO occupying approximately 90% of the scale thickness was observed. For the Cr-containing steels, a distinct spinel phase was observed at temperatures in excess of around 615 °C, with all of the Cr, Mo, and V incorporated within this layer, beneath the  $\text{Fe}_3\text{O}_4$  and  $\text{Fe}_2\text{O}_3$ . FeO was not observed in the scale until temperatures exceeded 650 °C, the FeO appearing as a fourth layer between the spinel and  $\text{Fe}_3\text{O}_4$  layers. Parabolic oxidation kinetics were observed for all steels at all temperatures. Below 600 °C, there was little difference in the oxidation kinetics between the chromium steels until the Cr level reached around 5%, this difference mainly arising because of an increasing activation energy for  $\text{Fe}_3\text{O}_4$  growth with increasing Cr content. There was no significant difference in the activation energy for  $\text{Fe}_2\text{O}_3$  growth, irrespective of the Cr content of the steel (Figure 9).

## 1.22.8 Industrial Environments

### 1.22.8.1 Steam

Many low alloy steels are utilized as pressure vessels in high temperature applications in a number of

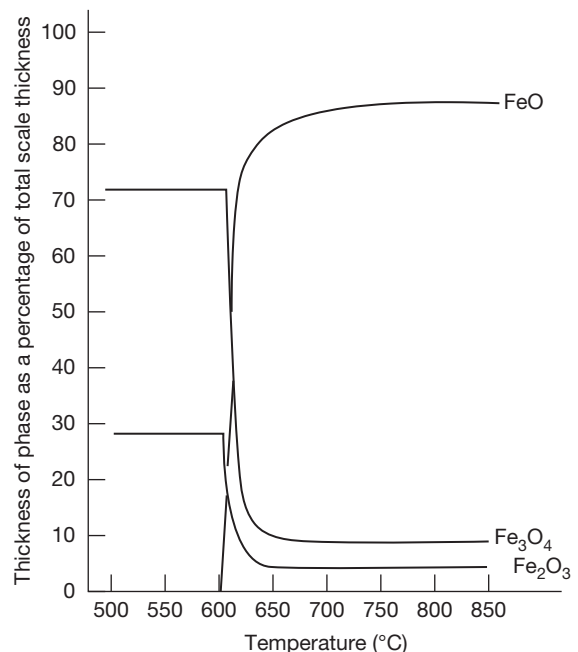


**Figure 8** Relative thickness of wüstite, magnetite and hematite on mild steel as a function of formation temperature.

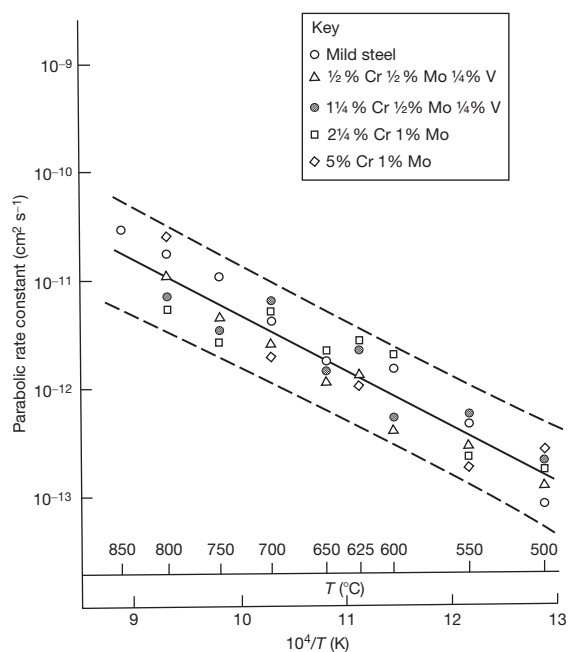


**Figure 9** Arrhenius plot for the hematite thickening rate on mild steel and low-chromium alloy steels in air.

diverse and often aggressive environments. Metal wastage by oxidation and corrosion reduces the load bearing cross sectional area of a vessel wall and can have grave consequences in terms of creep rupture life, especially of thin walled components. Different environment parameters including temperature, gas/fluid composition, pressure, flow rates and alloy composition will define the oxidation mechanisms and rate of material wastage. It is therefore imperative that a material gains protection from the formation of a stable slow growing oxide scale. Wright and Pint<sup>142</sup> predict that in steam environments the protective behavior associated with the formation of a complete  $\text{Cr}_2\text{O}_3$  layer is not necessarily observed in FeCr alloys with Cr contents below 20%.

Jonsson *et al.*<sup>143</sup> compared the oxidation of iron at 600 °C in dry  $\text{O}_2$  and wet  $\text{O}_2$  (40%  $\text{H}_2\text{O}$ ) where a three layer scale is formed consisting of a haematite outer layer, a magnetite middle layer and a wüstite inner layer forming the metal–scale interface. All three layers grow with time, but with different growth rates, the overall rate being roughly parabolic in both environments. While the detrimental effects of water vapour on oxidation rates are well reported, there is no consensus regarding the causes of this effect, however, recent investigations into the effect of hydrogen-accelerated oxidation on scale growth and morphology has

offered a possible insight into the increased steam side oxidation of low alloy steels.<sup>144–146</sup>

In recent years the group of modified 9%Cr steels has been developed for utilization in high temperature environments including power generation. Although the mechanical properties of these steels have been optimized, it is now appreciated that steam side oxidation of these alloys may be the factor that limits their maximum service temperature. Oxide growth rates have been shown to increase exponentially with temperature<sup>142</sup> up to 700 °C, where the isothermal oxidation rates are observed to be parabolic. However, investigations (COST-522, Europe's Thermie and the U.S. Vision 21 programs) aimed at improving thermodynamic efficiency by increasing service temperatures suggested that linear kinetics prevailed at temperatures above 700 °C for steels with Cr contents in the range 1–15 wt%.<sup>142,147</sup>

9% Cr ferritic martensitic steels show acceptable oxidation resistance in dry air at high temperatures due to the formation of a protective scale; between 400 °C and 600 °C the scale comprises of  $\text{FeO}$ ,  $\text{Fe}_2\text{O}_3$ , and  $\text{Cr}_2\text{O}_3$ . However, operation atmospheres composed of water vapour or steam + oxygen are much more corrosive than dry air. Subsequent scales that grow are less protective than  $\text{Fe}_2\text{O}_3$ , or  $\text{Cr}_2\text{O}_3$ . Sanchez *et al.*<sup>148</sup> predicts the formation of  $\text{Fe}_3\text{O}_4$ ,  $\text{Fe}_2\text{O}_3$  and  $(\text{FeCr})_3\text{O}_4$  scales in 100%  $\text{H}_2\text{O}$  atmosphere at 650 °C on 9%Cr steels, in contrast, at 800 °C the scale is mainly composed of  $\text{Fe}_3\text{O}_4$  and  $(\text{FeCr})_3\text{O}_4$ .

Itagaki *et al.*<sup>149</sup> found that an addition of 3%Pd to steel NF616 (similar to modified 9Cr–1Mo) gave significant improvements in oxidation resistance in steam at 650 °C as the growth of a Cr rich  $(\text{Fe}_2\text{Cr})_2\text{O}_3$  rhombohedral structured oxide was observed in the absence of a magnetite layer. Czyska-Filemonowicz *et al.*<sup>150</sup> state that oxidation (weight gain) of P91 steel can increase 30 fold in atmospheres containing water vapour compared to dry air.

Tuurna *et al.*<sup>151</sup> also studied the effects of water vapour on the high temperature oxidation of low alloy steels. Tests on 2.25Cr–1Mo steels at constant temperature (550 °C) with variable moisture content (5%–10%–15%) revealed an increasing linear relationship between moisture content and mass gain after 360 hours. Further tests at fixed moisture (15%) and variable temperature result in a steep increase in oxidation occurring at higher temperatures as the oxide scale becomes nonprotective; the use of 2.25Cr–1Mo steels is thus restricted to temperatures below 580 °C.

Nakai *et al.*<sup>152</sup> report the effects of preoxidation of Fe, 10%Cr, 0.08%C ternary alloy on subsequent steam

oxidation.<sup>143</sup>  $\text{Cr}_2\text{O}_3$  scales containing a small amount of  $\text{Fe}_2\text{O}_3$  are formed during preoxidation offering short term improvements in oxidation resistance. After long-term oxidation in steam nodular like oxides are formed on the preoxidised specimen showing a clear resemblance both chemically and structurally to the oxides formed on non-preoxidised specimens.

It is understood that hydrogen dissolves inward when steam oxidation takes place on the surface of steels.<sup>145,146,152</sup> Thus it appears that hydrogen plays an important role in the accelerated growth of the oxide scale when the steels are exposed to a wet gas atmosphere. Nakai *et al.*<sup>152</sup> proposes a model, where hydrogen dissolves as a proton ( $\text{H}^+$  ion) in  $(\text{Fe}, \text{Cr})_3\text{O}_4$  modifying the point defect structure inducing significant changes in the ionic diffusivity in the oxide. For example, the dissolved hydrogen will decrease the diffusion rate of Cr ions in  $(\text{Fe}, \text{Cr})_3\text{O}_4$ . The ensuing inhibited ionic Cr supply to the oxide layer results in the attendant decrease of the Cr concentration in  $(\text{Fe}, \text{Cr})_3\text{O}_4$ . Subsequently an apparent increase in the diffusion rate of Fe ions in the oxide is observed. As the oxidation rate of Fe–Cr steels is determined mainly by the Fe diffusivity in the  $(\text{Fe}, \text{Cr})_3\text{O}_4$  layer,<sup>153</sup> hydrogen dissolution induces the accelerated growth of the oxide scale on the steels.

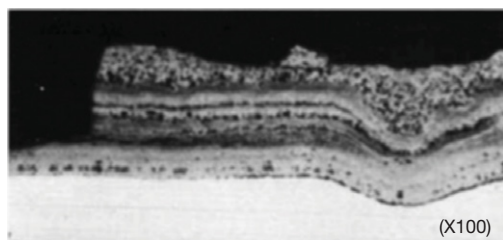
Low alloy steels containing a maximum Cr content of 9 wt% but excluding T/P91 display similar scale morphologies and tendency/mechanisms to spallation showing a laminated oxide scale. The initial formation of a magnetite outer layer and an inner spinel layer is followed by the formation of similar underlying duplex layers (Figure 10), possibly as a result of delamination of the original scale at the oxide–substrate interface.<sup>90</sup> Repetition of this process develops a multilayered scale consisting of repeated duplex magnetite and spinel layers, successive duplex layers becoming noticeably thinner. Exfoliation of

these scales has a propensity to occur along a plane between one of the sets of duplex layers or at the scale–metal interface and is likely to be a mechanism of stress relief. There is evidence that there are conditions where the scales formed on ferritic steels in steam can remain perfectly adherent for long times; for instance, from tests in a side loop on an operating boiler, Griess and Maxwell<sup>154</sup> reported that alloy T22 formed adherent scales throughout exposures for 28kh in 105 bar steam at 482 °C; at 538 °C exfoliation initiated after approximately 12kh. Alloys 9Cr–1Mo (0.46Si), 9Cr–2Mo, and Sandvik HT9 (11.4Cr) followed essentially the same kinetic behavior (and rates) as T22, but exhibited no signs of exfoliation at 482 and 538 °C after exposures of 28kh, 19kh, and 28kh, respectively.

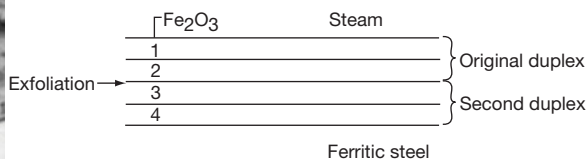
The laminated scales of low alloy steels are rarely observed on T/P91 steel, instead a largely duplex scale is observed with an incomplete outer layer of haematite. The duplex layer consists of an outer magnetite layer underlayered with a spinel layer rich in Cr, Si and Mo in comparison to the alloy composition.

12%Cr alloy steels display duplex oxide scale similar to those initially formed on the lower alloy ferritic steels. The outer scale is predominantly magnetite and the inner layer is a Cr rich spinel. The inner layer shows morphology similar to that often observed in P91 scales of incomplete Cr rich bands.

As quoted in the EPRI report on oxidation of alloys in steam<sup>90</sup> “There are five possible scenarios by which the scale morphologies observed on ferritic steels in steam might develop. Thus, it is suggested that the development of the (initial) double-layered scales on ferritic steels in steam (under isothermal conditions before the onset of any transition to multi-layered scales) involves the following steps; note that, in order to reflect the uncertainty in the dominant transport modes in these scales, five possible pathways for oxide growth are suggested (Figure 11)”:



(a)



(b)

**Figure 10** (a) A cross section from a 2.25Cr–1Mo steel tube oxidised in steam. (b) A schematic representation defining the duplex layered system.<sup>155</sup>

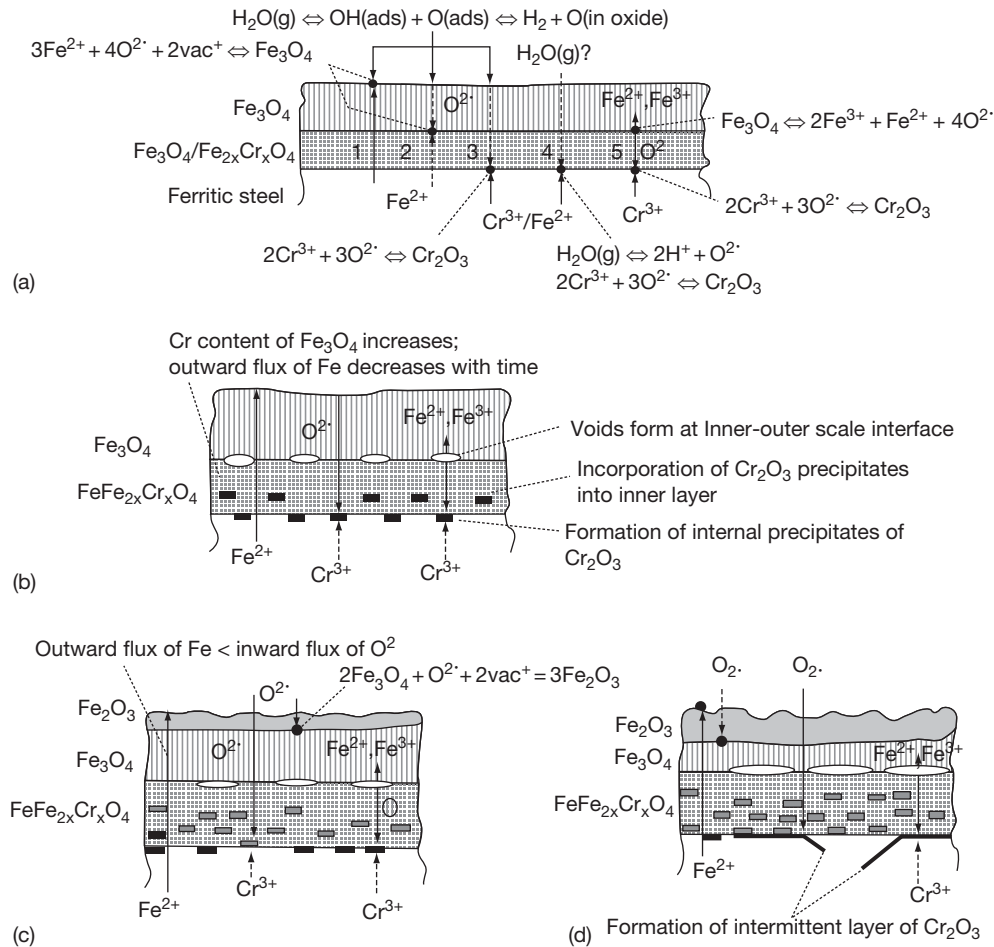


**Figure 11** Schematic representation of the oxidation mechanisms observed in low alloy steels containing chromium.<sup>158</sup>

Path 1: outward diffusion of iron ions, which react at the oxide-steam interface with oxygen from the dissociation of steam to form fresh magnetite.<sup>156,157</sup>

Path 2: dissociation of steam at the oxide-steam interface, and diffusion of oxygen ions inwards via defects in the oxygen lattice, or “hydrogen defects”<sup>159</sup>; these react with iron ions diffusing from the alloy to form new oxide at the interface between the inner and outer oxide layers.

Path 3: dissociation of steam at the oxide-steam interface, and diffusion of oxygen ions inwards to the alloy-oxide interface, where they react with chromium in the alloy to form discrete internal particles of chromia.

Path 4: suggests that molecular steam is transported through the scale, dissociating in the scale (in this case at the alloy-oxide interface) to form iron or chromium oxides. This path is considered to be

unlikely, unless the scale has significant, interconnected porosity.<sup>160</sup>

Path 5: which involves the dissociation of magnetite at the interface with the inner and outer layers,<sup>160,161</sup> with the iron ions released diffusing to the oxide-gas interface to react and form new oxide, and the released oxygen diffusing to the alloy-oxide interface to react with Cr in the alloy to form internal particles of  $\text{Cr}_2\text{O}_3$  (or Fe–Cr spinel).<sup>162</sup>

This whole area of steam oxidation has been reviewed recently by Wright and Dooley.<sup>162</sup>

### 1.22.8.2 Combustion Gases

A considerable amount of work has been carried out investigating the corrosion of steels in the gases produced during the combustion of fossil fuel due to



extensive use of low-alloy steels as heat exchanger tubes in power generation. Combustion gases contain many species, such as CO, CO<sub>2</sub>, SO<sub>2</sub>, SO<sub>3</sub>, H<sub>2</sub>S, and HCl, arising from elements within the fuel. The different combinations of operating temperature and chemical stoichiometry of combustion reactions lead to many possible complex corrosion reactions.

In coal-fired power stations, severe corrosion of the steam-generating tubes in the furnace walls has been attributed to reducing conditions with high  $p\text{CO}$ , low  $p\text{O}_2$ , high  $p\text{HCl}$ , and high local heat fluxes and flame impingement.<sup>163,164</sup> In areas of high corrosion, large concentrations of CO are almost always present, and thick Fe<sub>3</sub>O<sub>4</sub> scales, with islands and bands of FeS are observed.<sup>163,164</sup> Under the most severe reducing conditions, thick columnar scales of almost pure FeS have been observed.<sup>164</sup> The high corrosion rate areas are also subject to a significant flux of sulfur-bearing carbonaceous material in the flame envelope<sup>163</sup> which may locally exacerbate reducing conditions and raise the  $p\text{H}_2\text{S}$ .<sup>164</sup> Outside the high corrosion rate areas, the furnace atmospheres are found to be relatively O<sub>2</sub>-rich and the corrosion scales comprise protective Fe<sub>3</sub>O<sub>4</sub>.<sup>163</sup>

The emergence in recent times of biomass fuels intended to reduce the reliance on fossil fuels for steam power generation has introduced new challenges to the corrosion engineer. The use of biomass fuels based on a wide range of agricultural waste products, such as straw, forestry waste, sawdust, and purpose grown crops including coppiced willow and miscanthus have been investigated.<sup>165</sup> Concerns over potential high rates of metal wastage have been raised as the fireside environment is known to be particularly aggressive since it often contains HCl and different alkali salts which condense on heat exchanger surfaces promoting corrosion. Presently, it is necessary to operate biomass and energy from waste plants at lower temperatures than traditional coal fired systems so that tolerable corrosion rates prevail.<sup>166</sup> However, proposed methods of modifying combustion gas chemistry where corrosive KCl is converted to the far less corrosive K<sub>2</sub>SO<sub>4</sub> by the addition of sulphur may enable higher service temperatures to be attained.<sup>167</sup>

Similarly, refuse incineration plants are now based on the Waste-to-Energy concept, and it is necessary to optimize thermal transfer between combustion gases and water vapour. A significant problem with these installations concerns the fireside corrosion of the tubes. Combustion of waste generates highly corrosive flue gas often containing HCl, SO<sub>2</sub>, NaCl, KCl, alkali and heavy metal chlorides and

ashes containing chlorides and sulphates. *Wright and Krause*<sup>168,169</sup> predict corrosion by either combustion gases and/or molten deposits; erosion corrosion is also problematic due to flow rates and the presence of silica and alumina-silica particulates.

Fluidized-bed systems produce higher combustion intensities at lower temperatures than combustion of pulverized fuel in conventional fossil-fuel-fired boilers. The mineral matter for corrosion does not form fused salts and is not expected to release corrosive species. Fluidized bed combustors can, therefore, burn lower grade, cheaper fuel in smaller plant with better pollution control than traditional boilers.<sup>170</sup>

Minchener<sup>171</sup> reports that the bubble phase of atmospheric fluidized bed combustion has a  $p\text{O}_2$  in the range  $2 \times 10^{-1}$  to  $2 \times 10^{-2}$ . Combustion in the dense phase is substoichiometric, with the  $p\text{O}_2$  as low as  $10^{-13}$ , and SO<sub>2</sub> and SO<sub>3</sub> present in the range 500–5000 ppm. Low Cr–Mo steels show heavy scaling in these conditions, whereas 9–12% Cr steels show good resistance to sulfidation up to 650 °C. Roberts *et al.*,<sup>172</sup> however, report that for pressurized fluidized-bed combustion, ferritic steels at or below 9% Cr show heavy general corrosion above 540–560 °C.

### 1.22.8.3 Chemical Environments

The oil industry frequently uses stainless steels or exotic bonded alloys for the processing of crude oil in the temperature range 200–600 °C. These materials are very expensive and there is a strong economic incentive for finding cheaper alloys that are resistant to H<sub>2</sub>S and some gaseous organic sulfides arising from the S content of the crude oil.<sup>173</sup>

Metal sulfides show the same type of predominant defects as metal oxides, that is, cations in Fe<sub>(1-x)</sub>S, Cr<sub>(2+x)</sub>S<sub>3</sub>. The defect concentration in most sulfides is much higher than those in the corresponding oxides, but the defect mobilities are only slightly higher. Thus, the higher diffusivities and growth rates are determined by the higher defect concentrations. Cr and Al only slightly reduce the corrosion rate, and much higher Al is needed than that required for oxidation protection. Very protective scales are formed only at a S pressure lower than that for the formation of the base-metal sulfide.<sup>174</sup>

Mrowec *et al.*<sup>175</sup> examined the resistance to high temperature corrosion of Fe alloys with Cr contents between 0.35 and 74 at% Cr in 101 kPa S vapor. They found that the corrosion was parabolic, irrespective of the temperature or alloy composition, and noted

that sulfidation takes place at a rate five orders of magnitude greater than oxidation at equivalent temperatures. At less than 2% Cr, the alloys formed  $\text{Fe}_{(1-x)}\text{S}$  growing by outward diffusion of Fe ions, with traces of  $\text{FeCr}_2\text{S}_4$  near the metal core.

Narita and Nishida<sup>176</sup> examined the sulfidation of low Cr–Fe alloys at 700–900 °C in 101 kPa of pure S. They found that the addition of small quantities of Cr significantly decreased the corrosion rate because of the formation of  $\text{FeCr}_2\text{S}_4$  in the inner reaches of the scale. The scale comprised an outer FeS layer, with an inner layer of FeS,  $\text{FeCr}_2\text{S}_4$ , and  $\text{Cr}_3\text{S}_4$  in varying amounts depending upon the Cr content. The corners of specimens corroded more rapidly than flat faces because of breakaway conditions. At low Cr contents, the rate was increased, but above 4–6% Cr the parabolic rate constant decreased. Above 7.4% Cr, an intermediate layer containing  $\text{FeCr}_2\text{S}_4$  and varying amounts of  $\text{Cr}_3\text{S}_4$ , the proportion of the latter increasing with increasing Cr content, formed between the inner and outer layers.

In view of this potentially rapid degradation of Cr-containing steels by high temperature sulfidation in petrochemical and coal gasification reactors, Al is much used in the Fe alloys for these applications.<sup>177–180</sup> Al in Fe reduces the sulfidation rate in  $\text{S}_2$  vapor by up to two orders of magnitude<sup>181</sup> because of the high thermodynamic stability of aluminum sulfide relative to iron sulfide, the low rate of sulfidation of Al compared with pure Fe and the large PB ratio of  $\text{Al}_2\text{S}_3$  (3.7). The addition of 5% Al in Fe in 101 kPa  $\text{S}_2$  vapor between 500 and 700 °C resulted in the rate of reaction decreasing by a factor of 10. Parabolic kinetics were observed, with the inner layer of a duplex FeS scale containing a finely dispersed  $\text{Al}_2\text{S}_3$  phase which acts as a diffusion barrier to  $\text{Fe}^{2+}$  migration. Increasing the temperature to 800 °C resulted in a rapid take off of the corrosion rate, with catastrophic corrosion rates above 800 °C due to the large volume of  $\text{Al}_2\text{S}_3$  causing an increase in scale porosity.

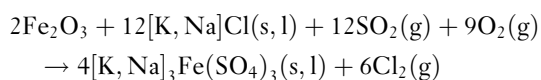
Condit *et al.*<sup>182</sup> examined the sulfidation of several Fe–Cr–Al alloys under a variety of sulfidizing conditions. They noted that, in the early stages of sulfidation, a thin compact inner layer forms that is high in Cr and Al. Subsequently, a thicker microcrystalline outer layer forms with a uniform Fe, Cr, and Al composition. Formation of the outer compact layer was favored by increasing  $p\text{S}_2$  and decreasing temperature, with the layer forming much more rapidly in  $\text{H}_2\text{S}$  than in pure  $\text{S}_2$ . The sublayer disappeared more or less rapidly depending upon the alloy composition.

The authors propose three stages for scale development. First, a thin compact layer forms because of the penetration of S into the alloy with preferential formation of sulfide from those metals with the highest affinity for S.  $\text{Fe}_{(1-x)}\text{S}$  also forms because of the abundance of Fe in the alloy.

The outer layer then dissociates to release sulfur, which dissolves in the grain boundaries of the alloy to form Cr and Al sulfides. The Fe released by this dissociation sulfidizes again at the interface between the two layers. The volume increase associated with the conversion of metal to sulfide generates a mechanical stress that causes the outer layer to break up and permits permeation of S. This initiates a second stage, where growth of the scale is linear and comprises a porous outer layer, with FeS,  $\text{Cr}_2\text{S}_3$ , and  $\text{Al}_2\text{S}_3$  evenly distributed, possibly as  $\text{FeCr}_2\text{S}_4$ ,  $\text{FeAl}_2\text{S}_4$ , and  $\text{FeCr}_{(x)}\text{Al}_{(2-x)}\text{S}_4$ . S then diffuses through the pores to the scale–metal interface. The third stage comprises the formation of an outer compact layer of  $\text{Fe}_{(1-x)}\text{S}$  and continued thickening of the inner layer.

Addition of Cr to Fe–Al alloys aids the formation of Cr sulfides and  $\text{Al}_2\text{S}_3$ , which together markedly reduce the sulfidation rate.<sup>173</sup> Between 2% and 5% Cr then, more than 3% Al is required to obtain protection. At 9% Cr, however, only 1% Al is needed to give protection, since the Cr is sufficiently active to lower the S potential seen by Al (secondary gettering). Thus, all Fe–Cr–Al alloys initially form FeS, Cr sulfides, and  $\text{Al}_2\text{S}_3$ . The Cr and Al are then exposed to a much lower  $p\text{S}_2$  at the scale–metal interface and Cr sulfides and  $\text{Al}_2\text{S}_3$  grow preferentially if their activity is high enough. Ultimately, a protective layer of  $\text{Al}_2\text{S}_3$  or  $\text{Al}_2\text{S}_3$  + Cr sulfides develops at the scale–metal interface and the reaction rate decreases substantially.

Karlson *et al.*<sup>183</sup> found, from on-site experience of cement-producing plant, that corrosion of Fe surfaces may occur in gases containing  $\text{O}_2$ ,  $\text{SO}_2$ , and alkali chlorides such as NaCl and KCl between 300 and 500 °C. They reported that the corrosion rates may be extraordinarily high (5–10 mm month<sup>−1</sup>) implying liquid-phase corrosion. Laboratory simulation of the plant conditions demonstrated the need for both  $\text{SO}_2$  and the alkali chloride in the environment. The principal corrosion reaction was found to be



A thermodynamic evaluation of this equation indicated that the reaction could proceed with  $\text{SO}_2$  levels as low as 100 ppm.

#### 1.22.8.4 CO/CO<sub>2</sub>

Failures of mild steel components in Magnox reactors in the United Kingdom and Italy after approximately 5 years of operation alerted the world to the potential for breakaway oxidation of low-alloy steels in CO/CO<sub>2</sub> environments.<sup>95</sup> The CO<sub>2</sub>, 1% CO, 300 vppm CH<sub>4</sub>, 250 vppm H<sub>2</sub>O, 100 vppm H<sub>2</sub> environment used in CAGRs was selected on the need to minimize oxidation of the graphite reactor core and deposition of C from the coolant gas.<sup>184</sup> Corrosion rate tests of 15 000–20 000 h, in the limited range of conditions anticipated by the designers, showed that the maximum reduction in corrosion rate of ferritic steels in CO<sub>2</sub> at 600 °C is realized at around the 9% Cr level.<sup>185–187</sup> Therefore, 9Cr1Mo steel was chosen for the evaporator and primary superheater sections of the CAGR.<sup>185</sup> However, in the late 1960s, Taylor (reported in Holmes *et al.*) identified evidence for a significant change in the corrosion mechanism for 9% Cr steels at around 550 °C. This change could lead to rate inversion with increasing temperature in steels containing 0.7–0.8% Si, or breakaway in 0.4–0.5% Si steels.

Because of their importance to the nuclear power generation industry, these observations initiated a vast amount of research into the oxidation of low-alloy steels in CO/CO<sub>2</sub> environments. It is now clear that low-alloy steels exhibit three types of behavior when exposed to CO/CO<sub>2</sub>, that is, protective, transitional, and linear-breakaway (Figure 12), with the time to breakaway and the breakaway rate being of crucial importance in determining component life.

For mild and low-alloy steels in CO<sub>2</sub>, the first scale to form is a compact coarse columnar layer of

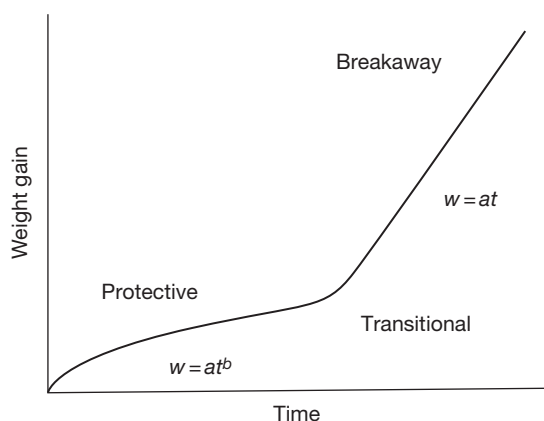


**Figure 12** Schematic diagram of stages of low-alloy steel oxidation in CO/CO<sub>2</sub>.

Fe<sub>3</sub>O<sub>4</sub>.<sup>188–190</sup> Growth of this layer is controlled by outward grain boundary diffusion of Fe ions.<sup>190–192</sup> The inward counter-current of vacancies is initially annihilated at the metal surface, but eventually vacancy condensation at the scale–metal interface gives decohesion, the scale develops microporosity, an inner layer grows within the space created by the departing metal ions and a duplex scale forms.<sup>193–195</sup> Then for Cr-containing steels, the protective scale comprises an outer, coarse columnar-grained magnetite layer and an inner, slightly porous, Cr-rich spinel of fine (0.1 μm) equiaxed grains.<sup>70,194,196</sup> As with low-alloy steels in other environments, the Cr is not mobile in the scale, but is oxidized *in situ*.<sup>195,196</sup> Studies have shown that the M<sub>3</sub>O<sub>4</sub> spinel nucleates at asperities on the surface and duplex growth is also known to be favored in the vicinity of inclusions and specimen corners.<sup>197</sup> Once initiated, the inner layer grows by inward diffusion of O, probably as CO<sub>2</sub>, down microfissures and micropores,<sup>17,136,196</sup> in both the lateral and vertical directions, until a complete layer is obtained.<sup>197</sup> The growth of this layer subsequently follows the parabolic rate law.

During this protective stage, decreasing the water and CO content of the gas appears to decrease the rate constant of Cr-containing steels,<sup>184</sup> but has little effect on the rate constant of carbon steels.<sup>193,198</sup> The rate constant of all steels has been found to decrease with decreasing temperature and increasing Si content.<sup>184,185,195,199</sup> Ferguson *et al.*<sup>198</sup> have also reported that increasing the S content of carbon steels reduces the parabolic rate constant.

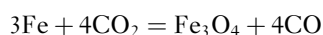
An increase in the Si content of the steel has been reported to give a significant increase in the duration of the protective regime for carbon steel.<sup>188,200,201</sup> A similar benefit has also been reported for Cr-containing steels.<sup>193,198,202</sup> Increases in the duration of the protective regime are also realized with reductions in the CO and H<sub>2</sub>O contents of the gas,<sup>198</sup> in the temperatures,<sup>185,193,198</sup> and for carbon steels, in the surface roughness,<sup>193</sup> or for 9Cr steels, with increased surface cold work. Robertson and Manning<sup>43</sup> found that breakaway may also be delayed by some S-containing gases.

Following the initial protective period, under certain conditions of temperature, alloy and gas composition,<sup>185</sup> the oxidation goes through a transitional stage into breakaway. Several authors have reported that breakaway oxidation is initiated once the scale reaches a critical thickness<sup>184,185</sup> or weight gain<sup>70</sup> and only occurs below an initially protective duplex layer.<sup>43,195</sup> Both single-layer protective and duplex-layer

protective scales have a PBR of 2.1, whereas breakaway scales show a PBR of approximately 2.7, containing around 23% porosity,<sup>195</sup> and graphitic carbon grains (up to 6% by weight) between the oxide grains.<sup>193,198</sup>

During this transitional period, and once full breakaway is established, growth occurs throughout the oxide and close to the scale–metal interface.<sup>203</sup> Growth below the oxidant surface requires oxidant transport through the scale, but solid-state lattice diffusion is much too slow to account for the rates observed.<sup>17</sup> Therefore, a porous scale is required. Mechanisms for pore growth have been postulated by several authors<sup>204–207</sup> who have suggested that the transition from single-layer to duplex growth is due to the initiation of pores within the scale. Then breakaway was thought to be caused by increased porosity giving unlimited access of oxidant to metal surface. However Atkinson<sup>47</sup> has shown single layer scales to be slightly porous. Robertson and Manning<sup>43</sup> have proposed that oxidant access is always available and the type of scale that develops is dependent upon conditions at the scale–metal interface. Breakaway occurs if space is created by continuous scale deformation or creep.<sup>208</sup>

The inward penetration of CO<sub>2</sub> via cracks and micropores gives



2CO = O<sub>2</sub> + 2C via the Boudouard reaction

at the scale–metal interface.<sup>136,196</sup>

The carbon initially diffuses into the steel, but ultimately, the steel may become saturated with C.<sup>208</sup> There is no detectable solubility of C in FeO, Fe<sub>3</sub>O<sub>4</sub>, MnO, or Cr<sub>2</sub>O<sub>3</sub>,<sup>209</sup> and C can only permeate through pores or faulty scales.<sup>112</sup> Thus, the C then deposits at the scale–metal interface and prevents the formation of a coherent protective layer once it reaches a critical activity.<sup>208</sup> Carbides in the steel have been found to be the preferred sites for breakaway. These are either pre-existing carbides or carbides precipitated by C injection during oxidation.<sup>190</sup> Precarburized or graphite-painted steel breaks away rapidly, as do thin foils, because of the smaller C sink available.<sup>190</sup> Pritchard *et al.*<sup>89</sup> reported that the proportion of C in the scale increased with scale thickness and water content of the gas and was higher in breakaway oxide. For 9% Cr steel, breakaway oxidation is associated with heavy carburization of the metal and C deposition within the oxide, with preferential breakaway occurring at corners and edges.<sup>196</sup>

For Fe in CO/CO<sub>2</sub> at atmospheric pressure, Surman<sup>210</sup> found that if

$$10^{-3} < \frac{p\text{CO}}{p\text{CO} + p\text{CO}_2} < 0.3$$

then the oxidation is parabolic and very little C deposition occurs. He concluded that magnetite is not sufficiently catalytic to promote the Boudouard reaction unless CO > 10% and moisture is present and surmised that H<sub>2</sub>O promotes the formation of a Boudouard catalyst. If the CO is greater than 0.4 in this expression, oxidation and carbon deposition occur simultaneously at a linear rate.<sup>211</sup>

German and Littlejohn<sup>193</sup> have observed that increasing the Si content of carbon steel reduces the linear rate constant during breakaway and Banks and Lorimer<sup>208</sup> have shown that Cr and Si reduce the creep rate of Fe<sub>3</sub>O<sub>4</sub>, thus reducing the postbreakaway rate of Cr-containing steels. However, Si has been reported as having no effect on the postbreakaway rate on 9Cr steels.<sup>184,199</sup> Small changes to the CO and H<sub>2</sub>O content of the environment and the temperature have no significant effect on the breakaway rate constant, but a large reduction in the CO can cause reversion to protective kinetics,<sup>211</sup> as does reducing the CO<sub>2</sub> pressure to atmospheric.<sup>212</sup> Increasing the CO switches breakaway on again.<sup>211</sup>

## References

- Holmes, D. R.; Stringer, J. In *Corrosion of Steels in CO<sub>2</sub>*; Holmes, D. R., Hill, R. B., Wyatt, L. M., Eds.; British Nuclear Energy Society: London, 1974; p 165.
- Pilling, N. B.; Bedworth, R. E. *J. Inst. Met.* **1923**, 29, 529.
- Tammann, G. Z. *Anorg. Allgem. Chem.* **1920**, 111, 78.
- Gulbrandsen, E. A.; Ruka, R. *Trans. AIME* **1950**, 188, 1500.
- Pinder, L. W. C.E.G.B Unclassified Report, MID/SSD/80/0050/R August 1980.
- Howe, C. I.; McEnany, B.; Scott, V. D. *Corr. Sci.* **1985**, 25(3), 195.
- Goursat, A. G.; Smeltzer, W. W. *Oxid. Met.* **1973**, 6(2), 101.
- Kuroda, K.; Labun, P. A.; Welsch, G.; Mitchell, T. E. *Oxid. Met.* **1983**, 19(3/4), 117.
- Koch, F.; Cohen, J. B. *Acta Crystallogr.* **1969**, B 25, 275.
- Cheetham, A. K.; Fender, B. E. G.; Taylor, R. I. *J. Phys. C.* **1971**, V, 2160.
- Catlow, C. R. A.; Mackrodt, W. C.; Norgett, M. J.; Stoneham, A. M. *Philos. Mag. A.* **1979**, 40(2), 161.
- Chen, W. K.; Peterson, N. L. *J. Phys. Chem. Solids* **1975**, 36, 1097.
- Wagner, C. Z. *Phys. Chem.* **1933**, B621, 25.
- Wagner, C. *Atom Movements*, ASM: Cleveland, **1951**, p 153.
- Atkinson, A. *Rev. Mod. Phys.* **1985**, 57, 437.
- Atkinson, A.; Taylor, R. I. *J. Phys. Chem. Solids* **1985**, 46, 469.
- Atkinson, A.; Taylor, R. I. *High Temperature – High Pressure* **1982**, 14, 571.

18. Dieckmann, R.; Kohne, M. *Phys Chem.* **1983**, 87, 495.
19. Garnaud, G.; Rapp, R. A. *Oxid. Met.* **1977**, 11, 193.
20. Channing, D. A.; Graham, M. J. *Corr. Sci.* **1972**, 12, 271.
21. Channing, D. A.; Dickerson, S. M.; Graham, M. J. *Corr. Sci.* **1973**, 13, 933.
22. Francis, R.; Lees, D. G. *Corr. Sci.* **1976**, 16, 847.
23. Rahmel, A. *Werkst. Korros.* **1965**, 16(10), 837.
24. Rahmel, A. *Korrosion* **1966**, 18, 41.
25. Eubanks, K. G.; Moore, D. G.; Pennington, W. A. *J. Electrochem. Soc.* **1962**, 109, 382.
26. Svedung, I.; Hammar, B.; Vannerberg, N. G. *Oxid. Met.* **1973**, 6(1), 21.
27. Caplan, D. *Corr. Sci.* **1966**, 6, 509.
28. von Fraunhofer, J. A.; Pickup, G. A. *Corr. Sci.* **1970**, 10, 253.
29. Janssen, S.; Lehtinen, B. *Metallurgie* **1967**, 7, 61.
30. Caplan, D.; Cohen, M. *Corr. Sci.* **1966**, 6, 321.
31. Price, W. R. *Corr. Sci.* **1967**, 7, 473.
32. Pinder, L. W. C.E.G.B Unclassified Report, MID/SSD/80/0057/R August 1980.
33. Stott, F. H. *Mat. Sci. Tech.* **1989**, 5(8), 743.
34. Atkinson, A. *Mat. Sci. Tech.* **1988**, 4(12), 1046.
35. Dunitz, J. D.; Orgel, L. E. *J. Phys. Chem. Solids* **1957**, 3, 318.
36. Azaroff, L. V. *J. Phys.* **1969**, 32, Part 9, 1658.
37. Cox, M. G. C.; MacEnany, B.; Scott, V. D. *Phil. Mag.* **1972**, 26, 839.
38. Hodge, J. D. *Electrochem. Soc.* **1978**, 125(2), 55c.
39. Rahmel, A. Z. *Electrochem.* **1962**, 66(4), 363.
40. Moreau, J. *Compte. Rendu.* **1953**, 236, 85.
41. Surman, P. L.; Castle, J. E. *Corr. Sci.* **1969**, 9, 771.
42. Atkinson, A. In *Oxidation of Metals and Associated Mass Transport*; Dayananda, M. A., et al. Ed.; The Metallurgical Society of the AIME: Warrendale, PA, 1987; p 29.
43. Robertson, J.; Manning, M. I. *Mat. Sci. Tech.* **1988**, 4, 1064.
44. Bruckman, A.; Emmerich, R.; Mrowec, S. *Oxid. Met.* **1972**, 5(2), 137.
45. Fromhold, A., Jr.; Sato, N. *Oxid. Met.* **1981**, 16(3/4), 203.
46. Harrison, P. L. *Oxid. Met.* **1984**, 22(1/2), 35.
47. Atkinson, A. *Philos. Mag. B* **1987**, 55, 637.
48. Whittle, D. P. *Acta Met.* **1967**, 15, 1421.
49. Wagner, C. *Corr. Sci.* **1965**, 5, 751.
50. Runk, R. B.; Kim, H. J. *Oxid. Met.* **1970**, 2(3), 285.
51. Kim, H. J.; Runk, R. B. *Oxid. Met.* **1970**, 2(3), 307.
52. Nosek, E.; Werber, T. *Oxid. Met.* **1986**, 25(3/4), 121.
53. Bohnenkamp, V. J.; Engell, H. J. *Arch. Eisenhuettenw.* **1962**, 33, 359.
54. Caplan, D.; Sproule, G. I.; Hussey, R. J.; Graham, M. J. *Oxid. Met.* **1979**, 13, 255.
55. Caplan, D.; Sproule, G. I.; Hussey, R. J.; Graham, M. J. *Oxid. Met.* **1978**, 12, 67.
56. Malik, A. U. *Oxid. Met.* **1985**, 25(5/6), 223.
57. Prescott, R.; Graham, M. J. *Oxid. Met.* **1992**, 38(1–2), 73–87.
58. Tomaszewicz, P.; Wallwork, G. R. *Oxid. Met.* **1983**, 19(5–6), 165–185.
59. Tomaszewicz, P.; Wallwork, G. R. *International Corrosion Conference Series*; 1983.
60. Boggs, W. E. *J. Electrochem. Soc.: Solid State Sci.* **1971**, 118, 906.
61. Ahmed, H. A.; Smeltzer, W. W. *J. Electrochem. Soc.* **1986**, 133(1), 212–216.
62. Pons, M.; Caillet, M.; Galerie, A. *Corros. Sci.* **1982**, 22(3), 239–249.
63. Smith, P. J.; Beauprie, R. M.; Smeltzer, W. W.; Stevanovic, D. V.; Thompson, D. A. *Oxid. Met.* **1987**, 28(5–6), 259–276.
64. Ahmed, H. A.; Underbill, R. P.; Smeltzer, W. W.; Brett, M. E.; Graham, M. J. *Oxid. Met.* **1987**, 28(5–6), 347–351.
65. Fox, P.; Tatlock, G. J. *Mater. Sci. Technol.* **1988**, 4, 439.
66. Tomaszewicz, P.; Wallwork, G. R. *Oxid. Met.* **1983**, 20(3–4), 75–109.
67. Wagner, J. B. In *Defects and Transport in Oxides*; Smeltzer, M. S., Jaffe, R. I., Eds.; Plenum Press: New York, 1974; p 283.
68. Seybolt, A. U. *Trans. Met. Soc. AIME* **1968**, 242, 752.
69. Rahmel, A.; Tobolski, J. *Werkst. Korros.* **1965**, 16(8), 662.
70. Robertson, J.; Manning, M. I. *Mater. Sci. Technol.* **1989**, 5(8), 741–753.
71. Darken, L. S. *Trans. AIME* **1942**, 150, 157–171.
72. Tuck, C. W. *Corros. Sci.* **1965**, 5(9), 631–634, IN3–IN7, 635–643.
73. Svedung, I.; Vannerberg, N. G. *Corros. Sci.* **1974**, 14(6), 391–399.
74. Wood, G. C.; Richardson, J. A.; Hobby, M. G.; Boustead, J. *Corros. Sci.* **1969**, 9(9), 659–668, IN7–IN12, 669–671.
75. Rochet, F.; Rigo, S.; Froment, M.; D'Anterrosches, C.; Maillot, C.; Roulet, H.; Dufour, G. *Philos. Mag. B.* **1986**, 55(2), 309.
76. Adachi, T.; Meier, G. H. *Oxid. Met.* **1987**, 27(5–6), 347–366.
77. Atkinson, A. *Corros. Sci.* **1982**, 22(2), 87–102.
78. Logani, R. C.; Smeltzer, W. W. *Oxid. Met.* **1971**, 3(3), 279–290.
79. Logani, R.; Smeltzer, W. W. *Oxid. Met.* **1969**, 1(1), 3–21.
80. Logani, R. C.; Smeltzer, W. W. *Oxid. Met.* **1971**, 3(1), 15–32.
81. Yang, C.-H.; Lin, S.-N.; Chen, C.-H.; Tsai, W.-T. *Oxid. Met.* **2009**, 72(3), 145–157.
82. Lashin, A.-R.; Schneeweiss, O.; Houbaert, Y. *Corros. Sci.* **2008**, 50(9), 2580–2587.
83. Ishitsuka, T.; Inoue, Y.; Ogawa, H. *Oxid. Met.* **2004**, 61(1–2), 125–142.
84. Jackson, P. R. S.; Wallwork, G. R. *Oxid. Met.* **1983**, 20(1–2), 1–17.
85. Huczowski, P.; Ertl, S.; Piron-Abellan, J.; Christiansen, N.; Höfler, T.; Shemet, V.; Singheiser, L.; Quadackers, W. J. *Mater. High Temp.* **2005**, 22(3–4), 253–262.
86. McAdam, G.; Young, D. J. *Oxid. Met.* **1987**, 28(3–4), 165–181.
87. Nishida, K.; Narita, T.; Tani, T.; Sasaki, G. *Oxid. Met.* **1980**, 14(1), 65–83.
88. Dewanckel, B.; Leclercq, D.; Dixmier, J.; Holmes, D. R. *Corrosion of unalloyed or low-alloyed steels in pressurized carbon dioxide*, 1974; p 3.
89. Pritchard, A. M.; Antill, J. E.; Cottell, K. R. J.; Peakall, K. A.; Truswell, A. E. In *Corrosion of Steels in CO<sub>2</sub>*; Holmes, D. R., Hill, R. B., Wyatt, L. M., Eds.; British Nuclear Energy Society: London, 1974; p 73.
90. *Program on Technology Innovation: Oxide Growth and Exfoliation on Alloys Exposed to Steam*; EPRI, Palo Alto, CA: 2007. 1013666.
91. Morinaga, M.; Murata, Y.; Hashizume, R.; Sawaragi, Y. *ISIJ Int.* **2001**, 41(3), 314–316.
92. Kutsumi, H.; Itagaki, T.; Abe, F. *Tetsu-To-Hagane/J. Iron Steel Inst. Jpn.* **2002**, 88(9), 520–525.
93. Greeff, A. P.; Louw, C. W.; Terblans, J. J.; Swart, H. C. *Corros. Sci.* **2000**, 42(6), 991–1004.
94. Vannerberg, N. G.; Svedung, I. *Corros. Sci.* **1971**, 11(12), 915–927.
95. Donati, G.; Garand. In *Corrosion of Steels in CO<sub>2</sub>*; Holmes, D. R., Hill, R. B., Wyatt, L. M., Eds.; British Nuclear Energy Society: London, 1974; p 28.
96. Menzies, L. A.; Tomlinson, W. J. *JISI* **1958**, 204, 1239.
97. Foley, R. T. *J. Electrochem. Soc.* **1962**, 109(4), 278–284.
98. Menzies, L. A.; Lubkiewicz, J. *Oxid. Met.* **1971**, 3(1), 41–58.
99. Dalvi, A. D.; Coates, D. E. *Oxid. Met.* **1972**, 5(2), 113–135.



100. Rhys-Jones, T. N.; Grabke, H. J.; Kudielka, H. *Corros. Sci.* **1987**, 27(1), 49–63, 65–73.
101. Wood, G. C. *Oxid. Met.* **1970**, 2(1), 11–57.
102. Yearian, H. J.; Randall, E. C.; Longo, T. A. *Corrosion* **1956**, 12, 515t–525t.
103. Douglass, D. L.; Gesmundo, F.; de Asmundis, C. *Oxid. Met.* **1986**, 25(3–4), 235–268.
104. Khanna, A. S.; Gnanamoorthy, J. B. *Oxid. Met.* **1985**, 23(1–2), 17–33.
105. Hossain, M. K. *Corros. Sci.* **1979**, 19(7), 1031–1045.
106. Caplan, D.; Sproule, G. I. *Oxid. Met.* **1975**, 9(5), 459–472.
107. Rahmel, A.; Jarger, W.; Becker, K. *Arch. Eisenhüttenwes* **1959**, 30, 351–359.
108. Tsipas, D. N.; Noguera, H.; Rus, J. *Mater. Chem. Phys.* **1987**, 18(3), 295–303.
109. Suwattananont, N.; Petrova, R. *Oxid. Met.* **2008**, 70(5), 307–315.
110. Rowley, P. N.; Brydson, R.; Little, J.; Saunders, S. R. J.; Sauer, H.; Engel, W. *Oxid. Met.* **1991**, 35(5), 375–395.
111. Hussey, R. J.; Mitchell, D. F.; Graham, M. J. *Werkst. Korros.* **1987**, 38(10), 575–583.
112. Wolf, I.; Grabke, H. J.; Schmidt, P. *Oxid. Met.* **1988**, 29(3–4), 289–306.
113. Sroda, S.; Baxter, D.; Arponen, M. *Mater. Corros.* **2005**, 56(11), 791–795.
114. Fry, A.; Banks, J.; Osgerby, S. The influence of heat flux on the oxidation of boiler steels. *Parson Conference*; 2007.
115. Fry, A. T.; Roberts, S.; Chapman, L. Measuring heat transfer through steam grown oxide scales. *NPL Measurement Note - DEPC(MN)043*, **2007**; p 9.
116. Trindade, V. B.; Borin, R.; Hanjari, B. Z.; Yang, S.; Krupp, U.; Christ, H. J. *Mater. Res.* **2005**, 8(4), 365–369.
117. Ostwald, C.; Grabke, H. J. *Corros. Sci.* **2004**, 46(5), 1113–1127.
118. Baxter, D. J.; Natesan, K. *Rev. High Temp. Mater.* **1983**, 5(3–4), 149–250.
119. Schutze, M. *Mater. Sci. Technol.* **1988**, 4, 407–414.
120. Stringer, J. *Corros. Sci.* **1970**, 10(7), 513–543.
121. Evans, H. E.; Lobb, R. C. *Corros. Sci.* **1984**, 24(3), 209–222.
122. Kubaschewski, O.; Hopkins, B. E. *Oxidation of Metals and Alloys* Butterworths: London, 1967; Vol. 50, pp 83–249.
123. Manning, M. I.; Metcalfe, E. In *EROCOR '77, Eur Congr on Met Corros, 92nd Event of the Eur Fed of Corros.* **1977**; pp 121–127.
124. Barbehön, J.; Rahmel, A.; Schütze, M. *Oxid. Met.* **1988**, 30(1–2), 85–94.
125. Christi, W.; Rahmel, A.; Schütze, M. *Oxid. Met.* **1989**, 31(1–2), 1–34.
126. Whittle, D. P. *Oxid. Met.* **1972**, 4(3), 171–179.
127. Deadmore, D. L.; Lowell, C. E. *Oxid. Met.* **1977**, 11(2), 91–106.
128. Hsueh, C. H.; Evans, A. G. *J. Appl. Phys.* **1983**, 54(11), 6672–6686.
129. Douglass, D. L. *Oxidation of Metals and Alloys*; American Society of Metals: Metals Park, OH, 1971; p 1137.
130. Mitchell, T. E.; Voss, D. A.; Butler, E. P. *J. Mater. Sci.* **1982**, 17(6), 1825–1833.
131. Manning, M. I. *Corros. Sci.* **1981**, 21(4), 301–316.
132. Evans, A. G.; Crumley, G. B.; Demaray, R. E. *Oxid. Met.* **1983**, 20(5–6), 193–216.
133. Norin, A. *Oxid. Met.* **1975**, 9(3), 259–274.
134. Appleby, W. K.; Tylecote, R. F. *Corros. Sci.* **1970**, 10(5), 325–341.
135. Jha, B. B.; Raj, B.; Khanna, A. S. *Oxid. Met.* **1986**, 26(3–4), 263–273.
136. Hancock, P.; Hurst, R. C. In *Corrosion of Steels in CO<sub>2</sub>*; Holmes, D. R., Hill, R. B., Wyatt, L. M., Eds.; British Nuclear Energy Society: London, 1974; p 320.
137. Ward, G.; Hockenhull, B. S.; Hancock, P. *Metall. Trans.* **1974**, 5(6), 1451–1455.
138. Forrest, J. E.; Bell, P. S. Relationship between the deformation of substrate and scale in the mechanism of multilayer oxide formation on low alloy ferritic steels; Commission of the European Communities, (Report) EUR, 1981.
139. Rolls, R.; Nematollahi, M. *Oxid. Met.* **1983**, 20(1–2), 19–35.
140. Simms, N. J.; Little, J. A. *Mater. Sci. Technol.* **1988**, 4(12), 1133–1139.
141. Pinder, L. W. C.E.G.B. Unclassified Report SSD/MID/R58/77, November 1977.
142. Wright, I. G.; Pint, B. A. In *NACE 2002*; 2002. Paper no. 02377.
143. Jonsson, T.; Pujilaksono, B.; Fuchs, A.; Svensson, J. E.; Johansson, L. G.; Halvarsson, M. In *7th International Symposium on High Temperature Corrosion and Protection of Materials*; Trans Tech Publications Ltd.: Les Embiez, France, 2008.
144. Yang, Z.; Xia, G.-G.; Walker, M. S.; Wang, C.-M.; Stevenson, J. W.; Singh, P. *Int. J. Hydrogen Energy* **2007**, 32(16), 3770–3777.
145. Nakagawa, K.; Matsunaga, Y.; Yanagisawa, T. *Mater. High Temp.* **2001**, 18, 51–56.
146. Nakagawa, K.; Matsunaga, Y.; Yanagisawa, T. *Mater. High Temp.* **2003**, 20, 67–73.
147. Fujii, C. T.; Meussner, R. A. *J. Electrochem. Soc.* **1964**, 111(11), 1215–1221.
148. Sánchez, L.; Hierro, M.; Pérez, F. *Oxid. Met.* **2009**, 71(3), 173–186.
149. Itagaki, T.; Kutsumi, H.; Haruyama, H.; Igarashi, M.; Abe, F. *Corrosion* **2005**, 61(4), 307–316.
150. Czyska-Filemonowicz, A.; Zielińska-Lipiec, A.; Ennis, P. J. *J. Achiev. Mater. Manufact. Eng.* **2006**, 19(2), 43–48.
151. Tuurna, S.; Yli-Olli, S. Heikinheimo. L. *Mater. Sci. Forum.*; 2008.
152. Nakai, M.; Nagai, K.; Murata, Y.; Morinaga, M. *Corros. Sci.* **2006**, 48(11), 3869–3885.
153. Fujikawa, H.; Otsuka, N. *Nippon Kagaku Kaishi/Chemical Society of Japan – Chem. Indust. Chemis. J.* **1998**, 1, 51–52.
154. Griess, J. C.; Maxwell, W. A. *The long-term oxidation of selected alloys in superheated steam at 482 and 538 °C.*; 1981.
155. Dooley, R. B.; Paterson, S. J.; Wright, I. G. Presented at a EPRI-NPL Workshop on Scale Growth and Exfoliation in Steam Plant.; National Physical Lab, 2003.
156. Gala, A.; Grabke, H. J. *Archiv. Fur. Das. Eisenhüttenwesen* **1972**, 43(6), 463.
157. Grabke, H. J.; Viehhaus, H. *Berichte Der Bunsen-Gesellschaft – Phys. Chem. Chem. Phys.* **1980**, 84(2), 152–159.
158. Wright, I. G.; Wood, G. C. *Dilute Fe–Cr alloys*; 1969.
159. Norby, T. In *3rd International Symposium on High Temperature Corrosion and Protection of Materials*; Editions Physique: Les Embiez, France, 1992.
160. Mayer, P.; Manolescu, A. V. In *International Corrosion Conference Series*; 1983.
161. Stott, F. H.; Wright, I. G.; Hodgkiess, T.; Wood, G. C. *Oxid. Met.* **1977**, 11(3), 141–150.
162. Wright, I. G.; Dooley, R. B. A review of the oxidation behaviour of structural alloys in steam; in press.
163. Clarke, F.; Morris, C. W. In *Corrosion Resistant Materials for Coal Combustion Systems*; Meadowcroft, D. B., Manning, M. I., Eds.; Applied Science Publishers: London, 1983; p 47.

164. Lees, D. G.; Whitehead, M. E. In *Corrosion Resistant Materials for Coal Combustion Systems*; Meadowcroft, D. B., Manning, M. I., Eds.; Applied Science Publishers: London, 1983; p 63.
165. Coleman, K. E.; Simms, N. J.; Kilgallon, P. J.; Oakey, J. E. *7th International Symposium on High Temperature Corrosion and Protection of Materials*; Trans Tech Publications Ltd.: Les Embiez, France, 2008.
166. Johansson, L. G.; Svensson, J. E.; Skog, E.; Pettersson, J.; Pettersson, C.; Folkesson, N.; Asteman, H.; Jonsson, T.; Halvarsson, M. J. *Iron Steel Res. Int.* **2007**, *14*(5 Suppl. 1), 35–39.
167. Henderson, P.; Szakálos, P.; Pettersson, R.; Andersson, C.; Högberg, J. *Mater. Corros.* **2006**, *57*(2), 128–134.
168. Krause, H. H. *Mater. Perform.* **1994**, *33*(3), 63–69.
169. Krause, H. H.; Wright, L. G. *Mater. Perform.* **1996**, *35*(1), 46–53.
170. Perkins, R. A. In *Corrosion Resistant Materials for Coal Combustion Systems*; Meadowcroft, D. B., Manning, M. I., Eds.; Applied Science Publishers: London, 1983; p 219.
171. Minchener, A. J. In *Corrosion Resistant Materials for Coal Combustion Systems*; Meadowcroft, D. B., Manning, M. I., Eds.; Applied Science Publishers: London, 1983; p 299.
172. Roberts, A. G.; Raven, P.; Lane, G.; Stringer, J. In *Corrosion Resistant Materials for Coal Combustion Systems*; Meadowcroft, D. B., Manning, M. I., Eds.; Applied Science Publishers: London, 1983; p 323.
173. Zelankof, P. D.; Simkovich, G. *Oxid. Met.* **1974**, *8*(5), 343–360.
174. Mrowec, S.; Przybylski, K. *Oxid. Met.* **1985**, *23*(3–4), 107–139.
175. Mrowec, S.; Walec, T.; Werber, T. *Oxid. Met.* **1969**, *1*(1), 93–120.
176. Narita, T.; Nishida, K. *Oxid. Met.* **1973**, *6*(3), 181–196.
177. Setterlund, R. B.; Prescott, G. R. *Corrosion* **1961**, *17*(6), 277–282.
178. Backensto, E.; Prior, B.; Sjöberg, J. E. *Corros. Sci.* **1962**, *18*, 253–258.
179. Malinowski, E. *Metal* **1962**, *94*(4).
180. Burns, F. J. *Corrosion* **1969**, *25*, 119.
181. Strafford, K. N.; Manifold, R. *Oxid. Met.* **1969**, *1*(2), 221–240.
182. Condit, R. H.; Hobbins, R. R.; Birchenall, C. E. *Oxid. Met.* **1974**, *8*(6), 409–455.
183. Karlsson, A.; Mäller, P. J.; Johansen, V. *Corros. Sci.* **1990**, *30*(2–3), 153–158.
184. Rowlands, P. C.; Garrett, J. C. P.; Garrett, F.; Hicks, F. G.; Lister, B. K.; Lloyd, B.; Twelves, J. A. In *Corrosion of Steels in CO<sub>2</sub>*; Holmes, D. R., Hill, R. B., Wyatt, L. M., Eds.; British Nuclear Energy Society: London, 1974; p 193.
185. Holmes, D. R.; Mortimer, D.; Newell, J. *Proc. BNES* **1974**, p 151.
186. Newell, J. E. *Nucl. Energy Int.* **1972**, *17*, 637.
187. Taylor, J. W.; Trotsenberg, P. V. In *Corrosion of Steels in CO<sub>2</sub>*; Holmes, D. R., Hill, R. B., Wyatt, L. M., Eds.; British Nuclear Energy Society: London, 1974; p 180.
188. German, P. A.; Littlejohn, A. C. In *Corrosion of Steels in CO<sub>2</sub>*; Holmes, D. R., Hill, R. B., Wyatt, L. M., Eds.; British Nuclear Energy Society: London, 1974; p 1.
189. Hussey, R. J.; Sproule, G. I.; Caplan, D.; Graham, M. J. *Oxid. Met.* **1977**, *11*, 65.
190. Gibbs, G. B.; Pendlebury, R. E.; Wooton, M. R. In *Corrosion of Steels in CO<sub>2</sub>*; Holmes, D. R., Hill, R. B., Wyatt, L. M., Eds.; British Nuclear Energy Society: London, 1974; p 59.
191. Atkinson, A.; Taylor, R. I. *High Temp. High Pressure* **1982**, *14*, 571.
192. Cox, M. G. C.; McEnaney, B.; Scott, V. D. *High Temp. High Pressure* **1982**, *14*, 247.
193. German, P. A.; Littlejohn, A. C. In *Corrosion of Steels in CO<sub>2</sub>*; Holmes, D. R., Hill, R. B., Wyatt, L. M., Eds.; British Nuclear Energy Society: London, 1974; p 1.
194. Hussey, R. J.; Sproule, G. I.; Caplan, D.; Graham, M. J. *Oxid. Met.* **1977**, *11*(2), 65–79.
195. Gibbs, G. B.; Pendlebury, R. E.; Wooton, M. R. In *Corrosion of Steels in CO<sub>2</sub>*; Holmes, D. R., Hill, R. B., Wyatt, L. M., Eds.; British Nuclear Energy Society: London, 1974; p 59.
196. Harrison, P. L.; Dooley, R. B.; Lister, S. K.; Meadowcroft, D. B.; Nolan, P. J.; Pendlebury, R. E.; Surman, P. L.; Wooton, M. R. In *Corrosion of Steels in CO<sub>2</sub>*; Holmes, D. R., Hill, R. B., Wyatt, L. M., Eds.; British Nuclear Energy Society: London, 1974; p 220.
197. Cox, M. G. C.; McEnaney, B.; Scott, V. C. In *Corrosion of Steels in CO<sub>2</sub>*; Holmes, D. R., Hill, R. B., Wyatt, L. M., Eds.; British Nuclear Energy Society: London, 1974; p 247.
198. Ferguson, J. M.; Garrett, F.; Lloyd, B. In *Corrosion of Steels in CO<sub>2</sub>*; Holmes, D. R., Hill, R. B., Wyatt, L. M., Eds.; British Nuclear Energy Society: London, 1974; p 15.
199. Grandison, N. O.; Facer, R. I. In *Corrosion of Steels in CO<sub>2</sub>*; Holmes, D. R., Hill, R. B., Wyatt, L. M., Eds.; British Nuclear Energy Society: London, 1974; p 208.
200. Ferguson, J. M.; Garrett, J. C. P.; Lloyd, B. In *Corrosion of Steels in CO<sub>2</sub>*; Holmes, D. R., Hill, R. B., Wyatt, L. M., Eds.; British Nuclear Energy Society: London, 1974; p 15.
201. Rowlands, P. C.; Garrett, J. C. P.; Popple, L. A.; Whittaker, A.; Hoaksey, A. *Nucl. Energy* **1986**, *25*(5), 267.
202. Rowlands, P. C.; Garrett, J. C. P.; Popple, L. A.; Whittaker, A.; Hoaksey, A. *Nucl. Energy* **1986**, *25*(5), 267–275.
203. Gleave, C.; Calvert, J. M.; Lees, D. G.; Rowlands, P. C. *Proc. R. Soc. London Ser. A* **1982**, *379*, 409.
204. Gibbs, G. B. *Oxid. Met.* **1973**, *7*(3), 173–184.
205. Gibbs, G. B.; Hales, R. *Corros. Sci.* **1977**, *17*(6), 487–497, 499–507.
206. Kofstad, P. *Oxid. Met.* **1985**, *24*(5–6), 265–276.
207. Mrowec, S. *Corros. Sci.* **1967**, *7*(9), 563–578.
208. Banks, P.; Lorimer, G. W. In *Materials to Supply the Energy Demand*; Hawbolt, E. B., Mitchell, A., Eds.; American Institute of mechanical Engineers: New York, 1982; p 231.
209. Wolf, I.; Grabke, H. J. *Solid State Commun.* **1985**, *54*(1), 5–10.
210. Surman, P. L. *Corros. Sci.* **1973**, *13*(11), 825–830, IN1–IN5, 831–832.
211. Surman, P. L.; Brown, A. M. In *Corrosion of Steels in CO<sub>2</sub>*; Holmes, D. R., Hill, R. B., Wyatt, L. M., Eds.; British Nuclear Energy Society: London, 1974; p 85.
212. Goodison, D.; Harris, R. J.; Goldenbaum, P. In *British Joint Corrosion Group Symposium on Metal–Gas Reactions in Atmospheres Containing CO<sub>2</sub>*; London, March 1967.

## 1.23 High Temperature Corrosion of Chromia-forming Iron, Nickel and Cobalt-base Alloys

**A. Galerie**

SIMaP, Grenoble INP/CNRS/UJF, Domaine Universitaire, BP 75, 39402 Saint Martin d'Hères, France

© 2010 Elsevier B.V. All rights reserved.

<b>1.23.1</b>	<b>Introduction</b>	583
<b>1.23.2</b>	<b>Underlying Principles of High Temperature Corrosion Protection by Chromium</b>	584
1.23.2.1	Various Types of Chromium-Containing Alloys	584
1.23.2.2	Growth of Cr-Containing Oxides	587
1.23.2.2.1	Chromia growth	588
1.23.2.2.2	Growth of spinel phases	588
1.23.2.3	Influence of Alloy Minor Elements	589
<b>1.23.3</b>	<b>High Temperature Oxidation Behavior of Chromium Alloys</b>	589
1.23.3.1	Oxidation of Martensitic and Ferritic Stainless Steels	589
1.23.3.2	Oxidation of Austenitic Stainless Steels (AISI 3XX Grades)	591
1.23.3.3	High Temperature Oxidation of Ni- and Co-Containing Alloys	592
1.23.3.3.1	Ni-Cr alloys	592
1.23.3.3.2	Ni-Fe-Cr alloys	593
1.23.3.3.3	Co-Cr alloys	593
1.23.3.3.4	Various comparisons between alloy grades	594
<b>1.23.4</b>	<b>Concluding Remarks</b>	597
<b>References</b>		605

### Abbreviations

**bcc** body-centered cubic  
**fcc** face-centered cubic  
**AISI** American Iron and Steel Institute  
**CTE** coefficient of thermal expansion  
**DIN** Deutsches Institut für Normung  
**EN** European norms  
**MICF** mechanically-induced chemical failure  
**REE** reactive element effect  
**SOFC** solid oxide fuel cell  
**UNS** Unified Numbering System

### Symbols

$\alpha$  bcc ferritic solid solution  
 $\gamma$  fcc austenitic solid solution  
 $\sigma$  brittle intermetallic sigma phase

### 1.23.1 Introduction

In industrial applications where high temperatures are required or produced, chromium-containing alloys are widely used. Based on iron and/or nickel,

and less often on cobalt, they can offer mechanical properties which can be adjusted to the situations they will encounter, with additional resistance to chemical attack by the various gaseous atmospheres.

Over the years, there have been arguments about who invented stainless steels, the first chromium-containing alloys. It seems that Pierre Berthier in France was the first to report ~1820 that addition of sufficient chromium to iron suppressed attack by water and acids. However, he could not, at that time, produce mechanically resistant steels. Harry Brearley of Sheffield was the first to produce a 13% Cr–0.24% C martensitic stainless steel in 1913 and to observe its excellent resistance to corrosion. It is amazing to note that this discovery was made as Brearley looked for better erosion (and not corrosion) resistance of gun barrels. More interesting is that his work was made in a technical laboratory cofinanced by two main Sheffield steel companies of the day. It seems however that the Krupp German company in Essen (first austenitic stainless steel patent: 1912) as well as Swedish steel-makers produced stainless steels at this time. In fact, all industrial countries could produce such materials after World War I. In 1924, grade 304 (18Cr–8Ni) was produced at Sheffield by W. H. Hatfield.

Concerning nickel based alloys, they were developed a decade later, for example, by Haynes International, USA. The term Superalloy appeared just after World War II for designing new alloys for aircraft engine applications.

Cobalt based alloys were also first produced at the beginning of the twentieth century, for example, by Stellite in 1907 in Canada.

The first published systematic comparative study of the behavior of numerous chromium-containing alloys by Hatfield appeared in the *Journal of the Iron and Steel Institute* in 1927.<sup>1</sup>

The same author published the first quantified values in 1928, using a 'scaling index' (SI) defined as the temperature giving a certain weight gain (in  $\text{g m}^{-2}$ ) at the end of a seven 6-h cycle oxidation run.<sup>2</sup> The higher the SI, the better the behavior of the alloys. His results for  $\text{SI}_{10}$  ( $10 \text{ g m}^{-2}$ ),  $\text{SI}_{20}$  ( $20 \text{ g m}^{-2}$ ), and  $\text{SI}_{100}$  ( $100 \text{ g m}^{-2}$ ) are presented in Table 1.

Nowadays, many results can be found either in the scientific literature or in technical notes provided by the steelmakers, giving the maximum service temperature acceptable for all commercial alloys. Figure 1 presents such data for isothermal oxidation

in air; it is generally considered that this maximum service temperature must be reduced by at least  $25^\circ\text{C}$  in cycling conditions, sometimes by larger values in more aggressive atmospheres (metal dusting or sulfidizing environments).

At present, simple scientific principles can explain the results of Hatfield; they are recalled in the following section.

### 1.23.2 Underlying Principles of High Temperature Corrosion Protection by Chromium

High temperature alloys must be protected in service by an external slow-growing oxide scale. In the case of chromium-containing alloys, this protective scale is based on chromia  $\text{Cr}_2\text{O}_3$ .

#### 1.23.2.1 Various Types of Chromium-Containing Alloys

As may be observed on Fe–Cr, Ni–Cr, and Co–Cr binary system phase diagrams (Figures 2–4),

**Table 1** Scaling indexes ( $^\circ\text{C}$ ) for a series of chromium-containing alloys

Cr	Ni	Si	Mn	Others	$\text{SI}_{10} (^\circ\text{C})$	$\text{SI}_{20} (^\circ\text{C})$	$\text{SI}_{100} (^\circ\text{C})$
0.1	0.1	0.25	0.82		<400	600	620
3.1	0.3	0.26	0.55	Mo	<500	600	640
3.1	0.9	0.22	0.61	Mo, V	<500	600	615
8.5	0.3	3.37	0.50		950	960	1010
9.0	0.4	0.19	0.48	Mo	<500	640	695
12.9	0.3	0.21	0.37		800	820	835
12.8	0.5	0.31	0.31		790	800	825
16.6	2.5	0.29	0.41		750	790	850
12.3	0.3	0.19	0.46	Mo	800	810	820
10.9	0.6	0.42	0.86	Mo, V	800	805	820
10.6	0.8	0.43	1.06	Mo, V, Nb	800	810	815
11.4	2.6	0.48	0.73	Mo, V, Nb	750	760	770
10.7	0.6	0.48	0.89	Mo, V, Nb, Co	800	810	825
15.9	4.0	0.55	0.26	Nb, Cu,	780	807	818
13.9	5.5	0.32	0.78	Mo, Nb, Cu	750	770	830
16.0	0.3	0.42	0.37		850	860	875
20.5	0.2	0.39	0.73		900	1000	1075
28.9	1.8	1.49	1.34	N	900	1120	1160
13.1	0.1	0.55	0.85	Al	1060	1100	1125
18.7	10.0	0.51	1.04		860	880	915
18.3	9.0	0.76	0.80	Ti	820	860	890
18.3	10.0	0.40	0.76	Nb	820	860	890
16.4	10.5	0.19	1.69	Mo	700	820	845
22.0	14.4	0.47	1.17		980	1060	1070
25.2	20.2	0.48	1.49		1030	1090	1180
20.3	33.5	0.60	1.12	Ti, Al	970	1010	1140

Oxidizing atmosphere: combustion gas with 50% excess air.

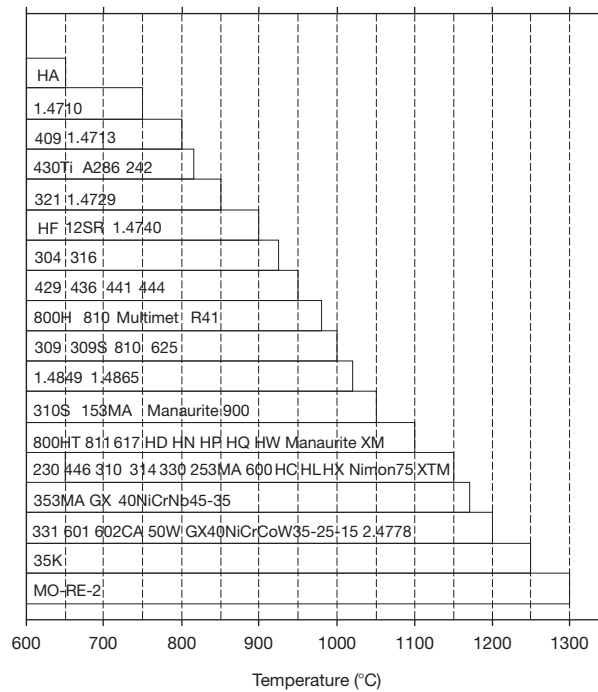


**Figure 1** Maximum isothermal service temperature for various chromia-forming alloys, estimated from literature and producer data.

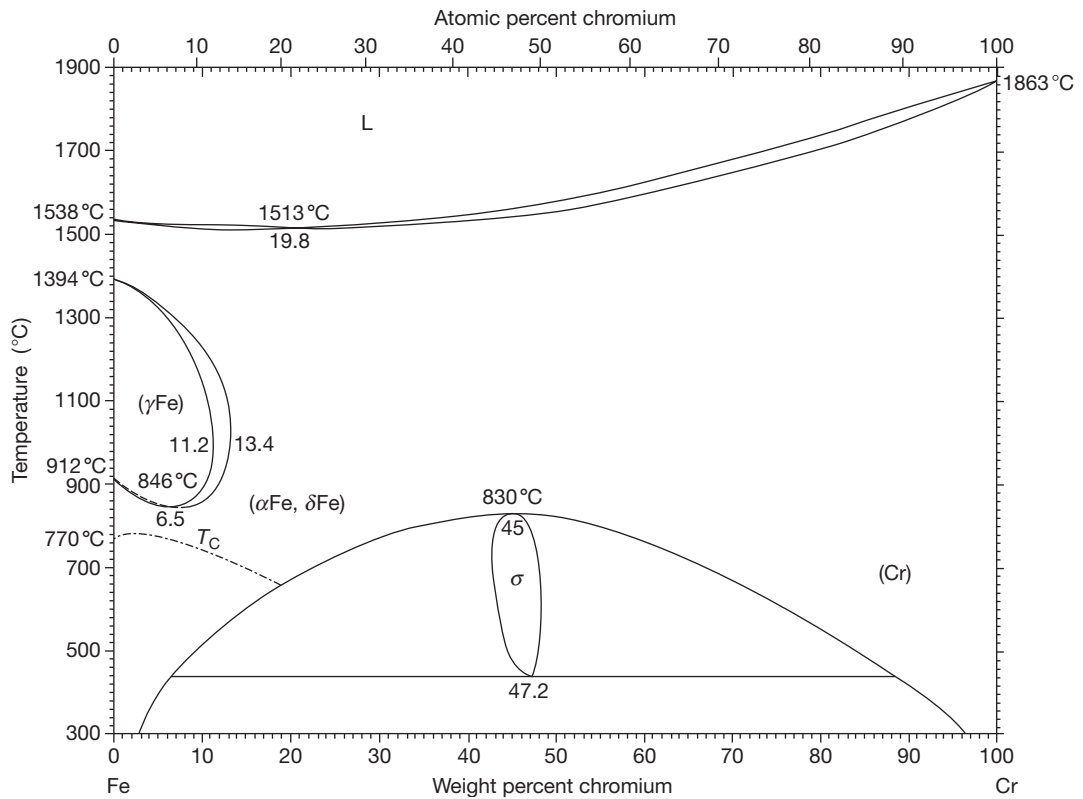


**Figure 2** Fe-Cr phase diagram.



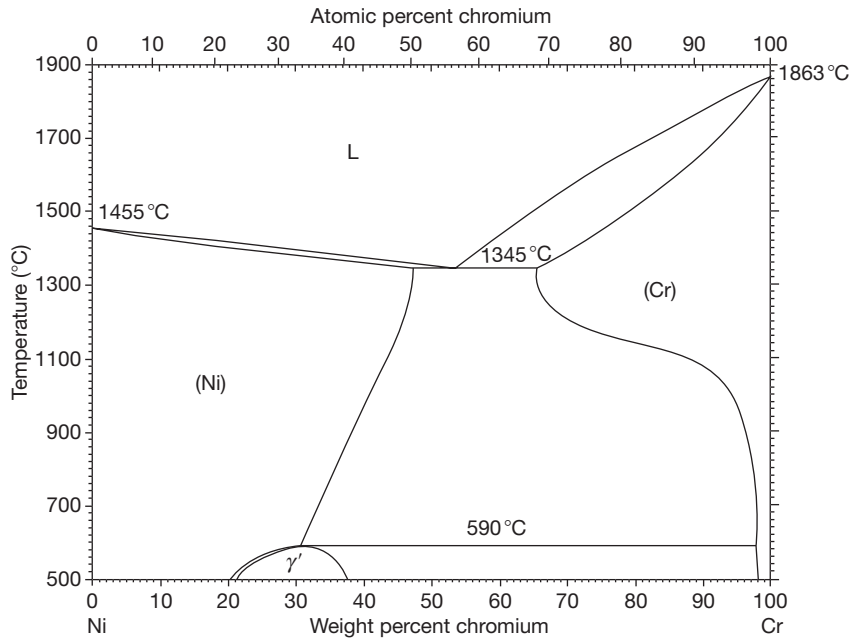


**Figure 3** Ni–Cr phase diagram.

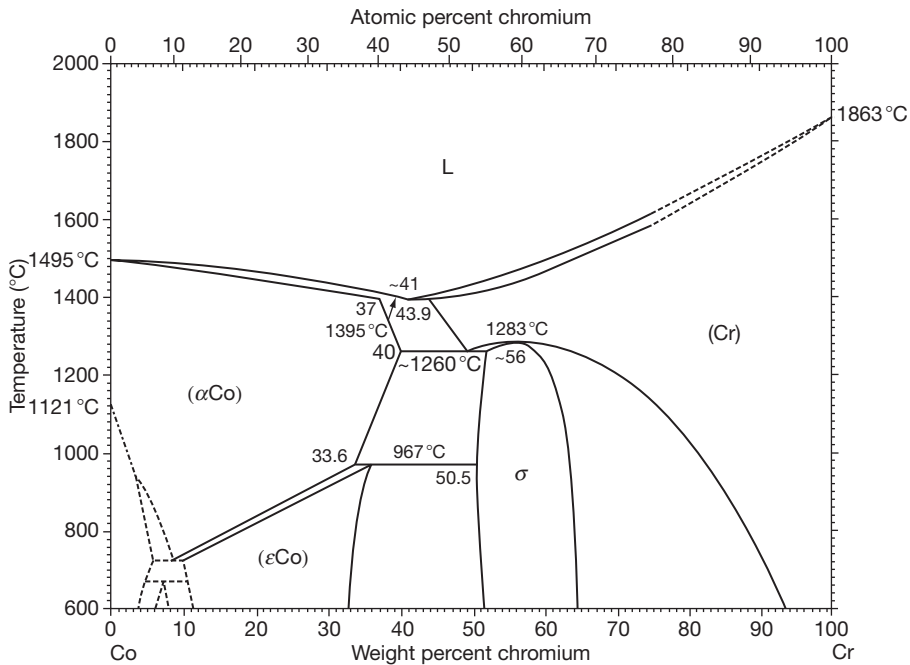


**Figure 4** Co–Cr phase diagram.

chromium is a highly soluble element in iron, nickel, and cobalt.<sup>3</sup> However, the intermetallic sigma phase may appear during long time anneal of iron–chromium alloys at medium temperatures

(700–1100 K), with very bad mechanical properties (high brittleness) and its formation must be avoided. Ternary or quaternary Fe–Ni–Co–Cr solid solutions are also stable.

The particular situation of iron, where bcc–fcc allotropic transformation occurs at 912 °C, has to be considered. Increasing chromium content of bcc Fe–Cr alloys to 5 wt% first reduces this value to ~850 °C before increasing it to ~1050 °C for 15 wt%. For higher Cr contents, the steels retain the bcc structure up to the melting temperature. Fe–Cr ferritic stainless steels with a chromium content falling in the  $\gamma + \alpha$  loop, if not ‘stabilized,’ undergo phase transformation on heating, leading to a biphasic structure. As described in the following, the appearance of the fcc  $\gamma$  phase significantly modifies two main properties of the alloy: diffusion coefficient of chromium and coefficient of thermal expansion (CTE).

Nickel is used as  $\gamma$ -promoter in chromium alloys, giving better mechanical properties than the ferritic structure. Considering not only the high price of nickel, but also the instability of its market, efforts have been made to replace it by other gamma-stabilizing elements. Manganese-containing austenitic stainless steels, such as 204Cu grade, have been produced and tested in high temperature situations.<sup>4</sup>

Carbon and nitrogen minor elements in Fe–Cr alloys are  $\gamma$ -stabilizers. Their concentration is therefore not strictly limited in austenitic alloys and can be adjusted according to the destination of the materials. Conversely, their amounts must be controlled in ferritic steels.

Metallic elements such as Ti, Nb, Mo, intrinsically ferrite promoters, have the additional property to strongly fix carbon and nitrogen as carbides, nitrides, and carbonitrides. Due to this fact, they increase the stability domain of ferrite and are largely used in ‘stabilized’ ferritic stainless steels.

Regarding these considerations, high temperature chromium-rich alloys are generally described as martensitic steels (iron based, with ferritic structure), stainless steels (iron based, with ferritic or austenitic structure) and refractory alloys (iron, nickel, or cobalt based, with austenitic structure).

Martensitic low chromium steel grades are first hardened by rapid cooling, and then tempered at a temperature in excess of the proposed service temperature. They are largely used for pressurized water or steam tubes, vessels and heat exchangers. Initially, based on the composition Fe–2.25Cr–1Mo (T22 steel), these grades had to follow the regular increase in temperature and pressure of processes to fit the required decrease in CO<sub>2</sub> emissions; they now include 9% Cr (T9 steel) and several similar grades with minor additions that increase their creep resistance in service (steels T91, T92, T911).

Chromium steels containing 12% Cr and more are usually qualified as stainless steels. Commercial grades are 12% and 17% Cr, with a new composition recently appeared at 14%. Higher chromium is also available, up to 30%. These alloys are ferritic or austenitic depending on the fraction of  $\gamma$ -stabilizing element (Ni or Mn). Both ferritic and austenitic stainless steels are protected in high temperature service by a chromia scale. However, that does not mean they can be used indifferently in any industrial situation. Austenitic stainless steels are preferably used when mechanical resistance at high temperatures is required, despite their higher price. Conversely, ferritic grades are used in situations where permanent or cyclic mechanical loading in service remains low. However, a careful design of parts made of ferritic grades may authorize their use in various industrial situations.

Due to their difference in crystallographic structure, ferritics, and austenitics do not allow identical chromium diffusion rates; the more open bcc ferritic structure allow quicker chromium diffusion than the compact fcc austenitic structure. As a result, alloy chromium depletion under chromia scales will be more marked, but to shorter depths, in austenitics.

A second property which makes ferritics and austenitics different is their CTE, which lies in the range  $(12\text{--}13) \times 10^{-6} \text{ K}^{-1}$  for the bcc grades and  $(19\text{--}20) \times 10^{-6} \text{ K}^{-1}$  for the fcc grades. Due to the lower CTE of chromia  $((8\text{--}12) \times 10^{-6} \text{ K}^{-1}$  according to various authors), chromia scales grown on austenitic stainless steels are subjected to more intense compressive stresses on cooling than the same scales on ferritics.

A particular phenomenon occurring during temperature increase (decrease) of the nonstabilized ferritic grades is the volume increase (decrease) associated with the ferrite–austenite transformation which can be deleterious for the integrity of the oxide scale, producing early breakaway corrosion in thermal cycling conditions.

Refractory alloys contain high chromium levels and strengthening elements to increase their mechanical properties at high temperatures. Based on the austenitic structure, they are mainly Fe or Ni-rich, and less often Co-rich.

### 1.23.2.2 Growth of Cr-Containing Oxides

To discuss the behavior of the various chromia-forming alloys used in high temperature industrial applications, several physical, chemical, and

mechanical mechanisms are of importance. Although they have been mostly described in other chapters, they are briefly recalled here for an efficient reading of this chapter.

### 1.23.2.2.1 Chromia growth

Regarding M–Cr–O systems (M = Fe, Ni, Co) subjected to oxidizing atmospheres, chromia  $\text{Cr}_2\text{O}_3$  is the most stable oxide. It is therefore expected to inhibit M oxidation by creating a chromia barrier to oxygen, lowering the oxygen chemical potential in contact with the alloy to a value too low for oxidation of the major element M. In fact, the minimum chromium content for effectively growing a chromia scale is  $\sim 14\%$  for iron, 20% for nickel, and 25% for cobalt.<sup>5</sup> Chromia is regarded as an amphoteric semiconductor, with predominant chromium interstitials at low oxygen potentials (i.e., near the metal–oxide interface) and predominant chromium vacancies at higher oxygen potentials (i.e., near the oxide–gas interface).<sup>6</sup> In all situations where chromium alloys are oxidized in air, chromia growth takes place by chromium transport through the scale. Inversion of transport may occur by blocking cation diffusion using yttrium or rare earth trace additions to the alloys, resulting in slower growth by oxygen transport (reactive element effect, REE). Water vapor or steam atmospheres also produce chromia scales where inward transport of H-assisted oxygen is predominant.<sup>7</sup>

Due to the high compactness of chromia, and also due to the necessity for less oxidizable Fe and Ni elements to enter it in the atomic state (atomic radius  $\sim 125$  pm compared to ionic (+II) radius  $\sim 77$  pm), this oxide is a good diffusion barrier for these major elements of stainless steels and refractory alloys. Conversely, Mn, Ti and, to a lesser extent, Nb, which are more oxidizable than chromium, rapidly diffuse through chromia scales as small cations ( $r_{\text{Mn}^{2+}} = 80$  pm,  $r_{\text{Ti}^{4+}} = 68$  pm).

The behavior of iron also has to be considered, as  $\text{Fe}^{3+}$  and  $\text{Cr}^{3+}$  ions are completely exchangeable in the rhombohedral chromia structure. All range of solid solutions between  $\text{Fe}_2\text{O}_3$  (hematite) and  $\text{Cr}_2\text{O}_3$  (chromia) are known, with the general formula  $\text{Cr}_{2-x}\text{Fe}_x\text{O}_3$ . In high temperature processes, it is of importance to limit the values of  $x$  to the minimum by rapidly heating the steels to 800 °C or using a reducing atmosphere for hematite during heating. This is of particular importance when iron-free surfaces are needed, for example, in the petrochemical industry where iron catalyzes graphite deposition (catalytic coking).

Maintaining protection against oxidation necessitates that chromia scales remain compact and adherent to the alloy substrates. Understanding the mechanisms of scale spallation was the subject of much work in the past decades.<sup>8,9</sup> Many results of stress measurements appear in the literature, showing mean values of 1–3 GPa compressive stresses in chromia scales, counterbalanced by tensile MPa values in the alloy substrates. However, it was experienced that oxide stress is not the key parameter in scale spallation, but that scale adhesion energy, defined as the metal–oxide interfacial fracture energy, was of greater importance.<sup>10</sup>

### 1.23.2.2.2 Growth of spinel phases

In any situation where a chromia scale cannot grow or be maintained on any Fe-containing alloy surface, magnetite enriched in chromium becomes the major oxidation product. This compound exhibits less protective properties than chromia, allowing outward transport of iron and inward transport of oxygen. That results in a typical duplex morphology where the external subscale is chromium free (hematite or magnetite) and the internal one has the limit stoichiometry of  $\text{FeCr}_2\text{O}_4$  (chromite spinel phase).

Iron chromite affords lower protection against oxidation compared to chromia, with larger mobility of oxide ions leading to more internal oxide growth.

Nickel–chromium spinel (nickel chromite  $\text{NiCr}_2\text{O}_4$ ) formation may occur concurrently with chromia on nickel based low chromium alloys, leading to some loss of protection. Increasing chromium content in the alloy tends to suppress this formation.

Manganese–chromium spinel (manganese chromite,  $\text{Mn}_{3-x}\text{Cr}_x\text{O}_4$ , with  $x$  generally between 1.5 and 2) is known to constitute the external part of the scale grown on high temperature alloys containing fractions of manganese, as low as 0.5%. This oxide overlays the internal chromia part of the scale and is the result of manganese diffusion from the alloy through this chromia part. The formation of this oxide is not considered as deleterious as it remains generally compact and adherent and it was even claimed that it is better resistant than chromia to chromium carbide transformation in high carbon activity atmospheres.<sup>11</sup> It also decreases chromia activity and consequently inhibits chromium (VI) vaporization.<sup>12,13</sup>

Competition between chromia and iron–nickel chromite is sometimes a key factor for long lasting use of high temperature alloys. Catastrophic break away oxidation occurs generally by local than by

generalized transformation of chromia to a spinel phase.<sup>14,15</sup> Factors that promote spinel appearance are

- high temperatures,
- low chromium and/or subsurface dechromization,
- thermal cycling, and
- water vapor atmospheres.

Promoting chromia growth may be obtained by increasing the chromium content of alloy or by any chemical or mechanical operation that enhances the number of fast diffusion paths for chromium from the alloy to the metal–oxide interface: laser glazing induced microcrystallization or work hardening generating high concentration of dislocations.

### 1.23.2.3 Influence of Alloy Minor Elements

Properties of today's industrial chromia-forming alloys are tailored to their exact application by adjusting the amount of minor metallic (Mn, Ti, Nb, Mo, Y, La, Ce, Zr) or nonmetallic (C, S, Si, B) elements.

The effect of manganese was described above. Titanium, in the form of carbide, nitride, carbonitride, and eventually excess solid solution Ti, slightly increases the parabolic rate constant of oxidation, but concurrently promotes scale adhesion,<sup>16</sup> due to TiO<sub>2</sub> precipitation at the alloy–scale interface. External diffusion of titanium through chromia may also occur, forming titania and/or Cr<sub>2</sub>TiO<sub>5</sub> surface nodules. Niobium in the form of carbide, nitride, carbonitride, but also of Fe<sub>2</sub>Nb intergranular intermetallic precipitates, may slowly oxidize to NbO at the alloy–scale interface and also slowly diffuse to the scale surface, forming NbO<sub>2</sub> (in solid solution with TiO<sub>2</sub> when this latter element is present). Molybdenum is not oxidized at the alloy–chromia interface, remaining as an intermetallic phase. Silicon and boron, more oxidizable than chromium, enrich as oxides at the metal–scale interface. Sulfur also segregates at this interface in the elementary form, strongly reducing scale adhesion.<sup>17</sup> Reactive elements (Y, La, Ce, Zr) decrease oxidation rates and promote scale adhesion. Mechanisms for that have been discussed at length. Interface sulfur removing and scale growth inversion are probably of major importance in these beneficial phenomena.

### 1.23.3 High Temperature Oxidation Behavior of Chromium Alloys

Oxidation, in its original meaning of oxygen fixation, is the most frequently encountered mode of high

temperature corrosion. All furnace elements working in air or combustion atmospheres are subject to oxide scale growth. It should be noted that oxidation, generally considered as a degradation mechanism, may be used as a beneficial phenomenon, as in stainless steel processing where iron–chromium thick scales formed during reheating before hot rolling consume surface defects and form a ductile lubricating coating preventing sticking between the metal and the roller.

#### 1.23.3.1 Oxidation of Martensitic and Ferritic Stainless Steels

Martensitic grades are possibly chromia-formers in oxygen or air in low aggressive conditions, but exhibit rapid chromia destabilization with increases in temperature and time. This destabilization, leading to the so-called breakaway corrosion, is also accelerated by thermal cycling. Post-breakaway scales exhibit classical duplex morphology, with internal Cr-containing magnetite subscale and external hematite. In water vapor or steam, chromia destabilization is easier and these grades can no longer be considered as chromia-formers. Duplex iron-rich scales are observed, as in air, generally with external magnetite instead of hematite due to low values of the oxygen chemical potential in the steam environment. For such a steam situation, an empirical law was proposed by Gabrel *et al.*<sup>18</sup> for the parabolic increase of scale thickness  $\zeta$

$$\zeta^2 = (8.099)^2 \times 2.35 \cdot 10^{10} \exp \left[ -\frac{16200}{8.32T} \right] (1 - \text{Si})^{187} (1 - \text{Cr})^{36.7} t$$

High chromium ( $\geq 18\%$ ) ferritic stainless steels (AISI 4XX grades) oxidize with near-parabolic slow growth of chromia-rich scales. The Fe/Cr ratio of the rhombohedral oxide increases with increasing temperature and oxidation time. For these grades, passive chromia scales can form for long periods, giving excellent oxidation resistance. As a consequence, increasing chromium concentration confers better oxidation resistance in isothermal conditions, as observed in [Figure 5](#). It is noted that small aluminum additions to ferritic stainless steels generate internal precipitation of alumina between the steel substrate and the chromia scale, leading to strong improvements in the oxidation behavior, as shown for the 12SR (12Cr–1Al) and 18SR (18Cr–2Al) in [Figure 5](#). Such alloys

are chromia-formers in air, but may become exclusively alumina-formers in high temperature situations of decreased oxygen chemical potential where chromia becomes unstable. Ferritic FeCrAls, exclusively alumina-formers need a minimum composition of 20Cr–4Al.

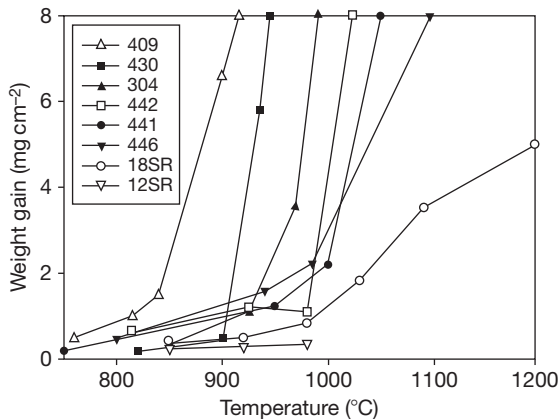


**Figure 5** Weight gains of various stainless steel grades after 100 h isothermal oxidation in air (data from producers).

**Table 2** Time to breakaway for cyclic oxidation of ferritic stainless steels (in and out 20 min cycles in laboratory air at 950 °C)

Steel grade	409	439	441	436
Composition	12 Cr	18 Cr	18 Cr–Ti, Nb	18 Cr–1 Mo
Time to breakaway (h)	150	900	>1200	>1200

**Table 3** Calculated partial pressures of gaseous chromium (VI) oxide or oxyhydroxide in equilibrium with solid  $\text{Cr}_2\text{O}_3$  or  $\text{MnCr}_2\text{O}_4$

Atmosphere	Solid compound	Predominant gas	900 (K)	1200 (K)	1500 (K)
$\text{N}_2 + 20\% \text{O}_2$	$\text{Cr}_2\text{O}_3$	$\text{CrO}_3$	$1.5 \times 10^{-8}$	$1.4 \times 10^{-6}$	$3.3 \times 10^{-5}$
$\text{N}_2 + 20\% \text{O}_2$	$\text{MnCr}_2\text{O}_4$	$\text{CrO}_3$	$5.0 \times 10^{-10}$	$1.1 \times 10^{-7}$	$4.3 \times 10^{-6}$
$\text{N}_2 + 20\% \text{O}_2 + 15\% \text{H}_2\text{O}$	$\text{Cr}_2\text{O}_3$	$\text{CrO}_2(\text{OH})_2$	$1.6 \times 10^{-7}$	$9.4 \times 10^{-7}$	$3.7 \times 10^{-6}$
$\text{N}_2 + 20\% \text{O}_2 + 15\% \text{H}_2\text{O}$	$\text{MnCr}_2\text{O}_4$	$\text{CrO}_2(\text{OH})_2$	$5.2 \times 10^{-9}$	$7.3 \times 10^{-8}$	$3.5 \times 10^{-7}$

Data for  $\text{CrO}_3$  from Barin,<sup>21</sup> for  $\text{CrO}_2(\text{OH})_2$  from Opila *et al.*<sup>22</sup> for  $\text{MnCr}_2\text{O}_4$  from Jung.<sup>23</sup> It is reminded that volatilization is assumed to be negligible for gas pressure <1 nbar and catastrophic for gas pressure >0.1 mbar.

**Table 4** Composition of ferritic grades specially adjusted to be used as SOFC interconnectors

Name	Cr	C	Si	Mn	Cu	Al	Ti	Ni	Others
CROFER22APU ThyssenKrupp	22	<0.03	<0.5	0.3–0.8	0.5	0.5	0.03–0.2		La 0.04–0.2
ZMG232	22	0.02	0.4	0.5		0.05		0.26	0.04 La, 0.22 Zr
Hitachi metals									
Fe–Cr–W	20		0.3			0.5			0.3 Zr
Sumitomo metals									7 W

In thermal cycling situations, good protection is obtained up to MICF (mechanically induced chemical failure), as proposed by Evans,<sup>19</sup> where breakaway oxidation occurs by forming nonprotective iron-rich oxides. In such thermal cycling situations, the same beneficial influence of chromium was noted, with also clear improvement by the ferrite stabilizers Ti and Nb (Table 2).<sup>20</sup> The 441 grade is commonly proposed for exhaust parts in the automotive industry.

High temperatures or water vapor in the gas may promote chromium (VI) oxide or oxyhydroxide volatilization, strongly impeded by manganese additions which form an external  $\text{MnCr}_2\text{O}_4$  spinel phase, decreasing chromium (III) oxide activity and therefore the gaseous chromium (VI) compound's partial pressure as seen in Table 3.

The growing interest in solid oxide fuel cells (SOFCs) working at intermediate temperatures (<800 °C) has led to increasing work on ferritic stainless steels which are possibly used as interconnectors, separating the cathode side (air) from the anode side (wet hydrogen) of the cell. Good technical solutions need decreased chromium (VI) poisoning of the cathode and manganese additions help by lowering the partial pressure of undesired gas species. Another important parameter for this application is the low contact resistance between scale and metal and elements forming internal oxide enrichment at the metal–scale interface (mainly Si and Al) must be avoided. Following these observations, special grades to be used in SOFCs have been produced and are now available in the market (Table 4).



### 1.23.3.2 Oxidation of Austenitic Stainless Steels (AISI 3XX Grades)

For temperatures lower than 800 °C, 18Cr–8Ni stainless steels 304 and 321 are commonly used. Increasing

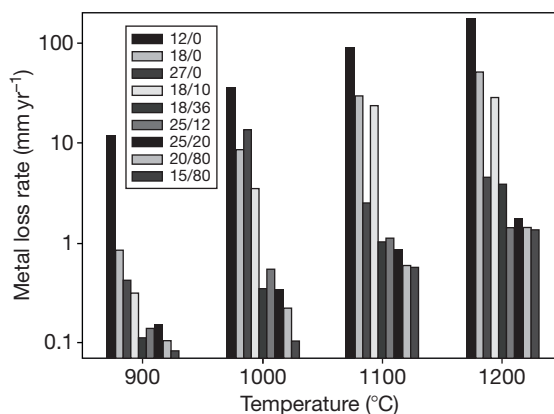


**Figure 6** Isothermal air behavior of various austenitic grades compared to three ferritics with equivalent chromium contents; legend: Cr/Ni in wt%. Redrawn from Brasunas, A. de S.; Gow, J. T.; Harder, O. E. *Proc. ASTM* 1946, 46, 870.

service temperature needs increased chromium up to 20–25%, with larger silicon additions up to 2–2.5% producing silica enrichment at the alloy–chromia interface, decreasing chromium incorporation into the scale. With such compositions, grades 309, 310, and 314 are known as ‘refractory stainless steels.’ All these grades are more mechanically resistant than ferritics and can be further strengthened by increasing carbon and/or nitrogen contents.

Care must be taken when using high chromium austenitic grades at intermediate temperatures where  $\sigma$ -FeCr may precipitate (310, 314, 253 MA grades, for example), leading to brittleness. Possible formation of this phase can be roughly predicted from the Fe–Ni–Cr phase diagram, with additional influence of minor elements by using empirical relations.<sup>24</sup>

In **Figure 6**, it is shown that the austenitic grades are more scaling resistant in isothermal conditions than the ferritic ones for equivalent chromium content.

In cyclic conditions, heavy spallation is observed clearly due to strong differential contraction on cooling. Here also, increasing nickel content leads to better behavior (**Figure 7**).

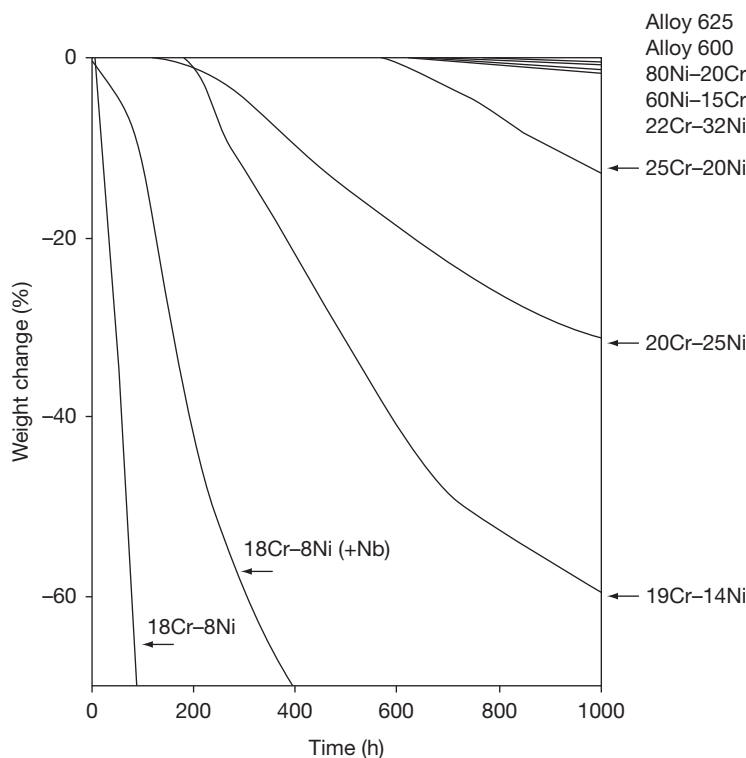


**Figure 7** Weight loss in cyclic conditions (15 min heating at 980 °C, 5 min cooling) of austenitic grades with different chromium and nickel contents. Adapted from Lai, G. A. *High Temperature Corrosion of Engineering Alloys*; ASM International: Metals Park, OH, 1990.

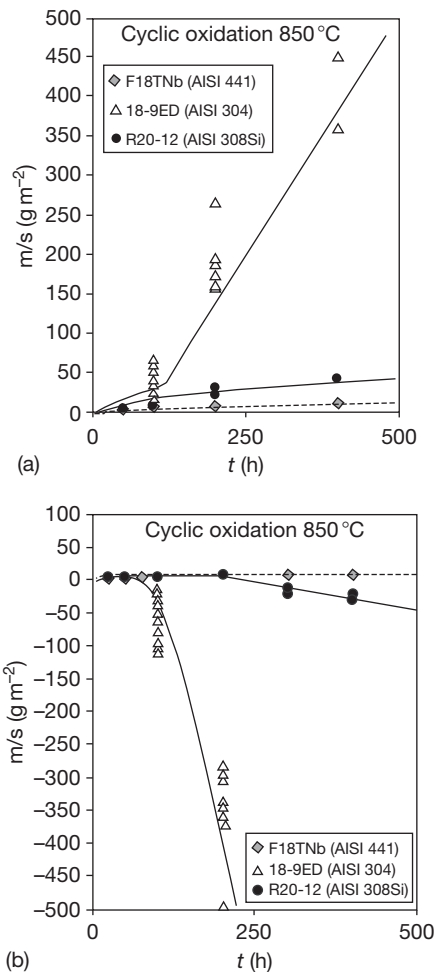


**Figure 8** Comparative air cyclic oxidation of ferritic and austenitic grades (20 min cycles). (a) gross mass gain; (b) mass change after descaling.

**Table 5** Weight changes of austenitic and (stabilized) ferritic grades of equivalent composition in air thermal cycling conditions

Alloy	Average composition	Cycling between 870 and 930 (°C)				Cycling between 980 and 1040 (°C)				
		288 cycles	480 cycles	750 cycles	958 cycles	130 cycles	368 cycles	561 cycles	753 cycles	1029 cycles
309	20 Cr, 12 Ni, 2 Si	0.3	-4.6	-23.7	-32.6	-24.2	-77.5	-178	-242	-358
310	25 Cr, 20 Ni, 2 Si	n.t. <sup>a</sup>	n.t.	n.t.	n.t.	1.5	-11.3	-29.3	-62.8	-107
442	20 Cr, 1 Mo, 1 Si	0.7	1.2	1.5	1.5	n.t.	n.t.	n.t.	n.t.	n.t.
446	25 Cr, 0.5 Si	0.3	0.4	0.3	0.1	0.4	0.5	-0.2	7.0	-19.4
18SR	18 Cr, 1 Si, 0.4 Ti, 2 Al	0.3	0.4	0.5	0.6	0.7	1.1	1.5	2.2	3.0

<sup>a</sup>n.t.: not tested.

Source: Reproduced from Lasday, S. B. *Ind. Heating* **1979**, 12. Reproduced from Lai, G. A. *High Temperature Corrosion of Engineering Alloys*; ASM International: Metals Park, OH, 1990.

An influence of steel structure on spallation appears also in the recent results from a study by Ugine & ALZ (today ArcelorMittal Stainless Europe) for exhaust systems (**Figure 8**),<sup>25</sup> confirming older results (**Table 5** and **Figure 9**) showing that ferritic stainless steels are better resistant in short cycle situations than austenitic ones. This is due to a lower thermal expansion coefficient which prevents high stress states from appearing during cooling. Ferritic materials also relax by high temperature creep, further decreasing oxide stress. However, the good behavior of ferritic stainless steels in cyclic conditions is lost as soon as they are used at temperatures entering the ( $\alpha + \gamma$ ) domain.

Internal alumina precipitation for the 18SR grade is also beneficial as seen in **Table 5**.

### 1.23.3.3 High Temperature Oxidation of Ni- and Co-Containing Alloys

#### 1.23.3.3.1 Ni-Cr alloys

Binary nickel–chromium alloys have been recognized very early as high temperature oxidation resistant. **Table 6** summarizes results published in 1957 showing the ability of Cr to drastically decrease the parabolic rate constant of nickel oxidation.<sup>28</sup> It can be noted that higher chromium is necessary when the temperature increases. Commercial alloys mainly contain 20–30% Cr to stabilize a protective chromia scale and always contain several minor additions to improve their mechanical and/or chemical properties: typical ‘Nichrome’ (UNS N06003, EN/DIN 2.4869) contains 1% Si and

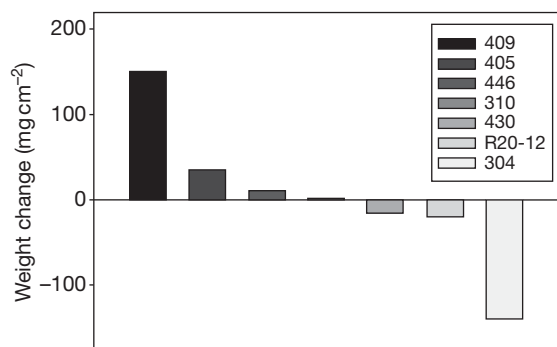


**Figure 9** Cyclic oxidation weight change of several ferritic and austenitic stainless steels after 400 cycles in air at 1000 °C (30 min in furnace, 30 min out). Reproduced from Kado, S., Yamazaki, T., Yoshida, K., Yabe, K., Kobayashi, H., *Trans. Iron Steel Inst. Jpn.* **1978**, 18, 387.

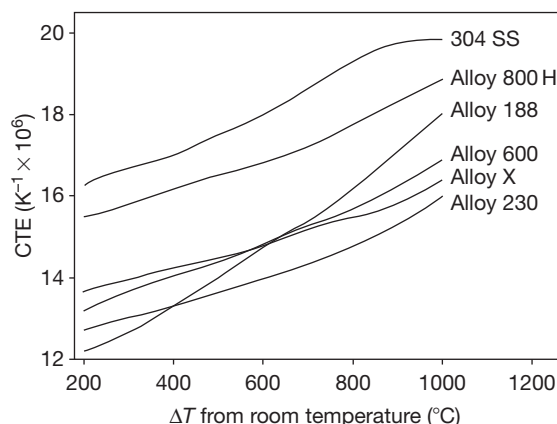


**Figure 10** Reduction of the coefficient of thermal expansion (CTE) by minor element additions for several chromia-forming alloys. Data from Haynes International.

**Table 6** Parabolic rate constant of oxidation in air or in pure oxygen (atmospheric pressure) of pure nickel and various nickel–chromium alloys

Chromium content (wt%)	Atmosphere	Temperature (°C)	Parabolic rate constant $\times 100$ ( $\text{g}^2 \text{cm}^{-4} \text{s}^{-1}$ )
0.0	Air	900	0.28
1.97	Air	900	4.9
4.12	Air	900	5.8
5.89	Air	900	8.2
8.0	Air	900	0.0
0.0	Oxygen	1000	3.48
0.3	Oxygen	1000	15.0
1.0	Oxygen	1000	25.8
3.0	Oxygen	1000	28.3
10.0	Oxygen	1000	5.55
0.0	Oxygen	1096	5.48
0.32	Oxygen	1096	23.6
0.92	Oxygen	1096	29.7
2.0	Oxygen	1096	39.6
3.45	Oxygen	1096	46.8
5.67	Oxygen	1096	58.5
7.64	Oxygen	1096	67.8
8.71	Oxygen	1096	30.8
11.1	Oxygen	1096	3.79
14.9	Oxygen	1096	0.35
20.0	Oxygen	1096	0.07

Source: Zima, G. E., *Trans. Am. Soc. Met.* **1957**, 49, 924.

0.01–0.04 reactive element, whereas Nimonic 75 contains 0.5% Ti.

Nickel–chromium alloys are mainly used in the form of wires for electrical heating and for making heat resistant parts in situations where mechanical considerations are low.

### 1.23.3.3.2 Ni–Fe–Cr alloys

Increasing nickel content from stainless steels stabilizes the gamma phase and prevents sigma phase formation. High mechanical resistance, particularly to creep in service, is realized by adding interstitial nonmetallic elements (C, N, B) and/or substitutional refractory elements (Mo, W, Ta, Nb) in solid solution in the  $\gamma$  phase. Carbide or intermetallic precipitation also participates in alloy strengthening.

Other effects of minor element additions are to slow down grain growth in service, to inhibit sigma phase formation and to lower the thermal expansion coefficient. **Figure 10** shows that Ni-base alloys (600, X, and 230) have naturally lower CTE than Fe-based (304, 800H) and also that the strongly-charged 230 alloy (14% W, 2% Mo) has lower CTE than Alloy X (9% Mo) and alloy 600 (no W, Mo). Decreasing CTE enhances resistance to scale spallation in thermal cycling service.

Scaling resistance of nickel-based alloys in oxidizing atmospheres is far better compared to stainless steels (**Figure 11**) and these grades are of major importance in all very high temperature processes using furnaces or combustion chambers for energy transformation and chemical or metallurgical reactions.

### 1.23.3.3.3 Co–Cr alloys

Industrial cobalt–chromium alloys are strengthened by solid solution and carbide formation. They present very good resistance to high temperature creep, even for temperatures above 1000 °C. Due to their high

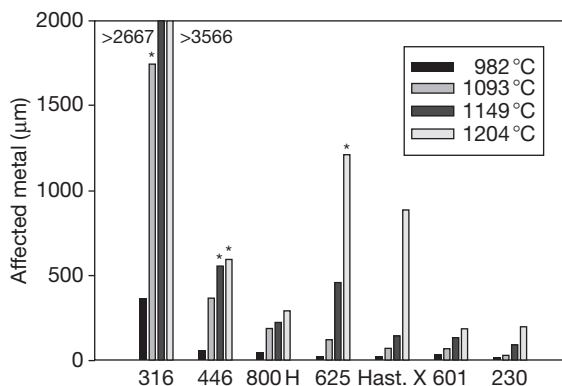


**Figure 11** Metal loss plus average internal penetration measured on various iron- and nickel-base alloys after 1008 h under flowing air ( $213.4 \text{ cm min}^{-1}$ ). Metal loss from weight gain, penetration from cross-section observations. Samples cycled to room temperature once a week. Asterisk: actual value larger. Data from Haynes International.

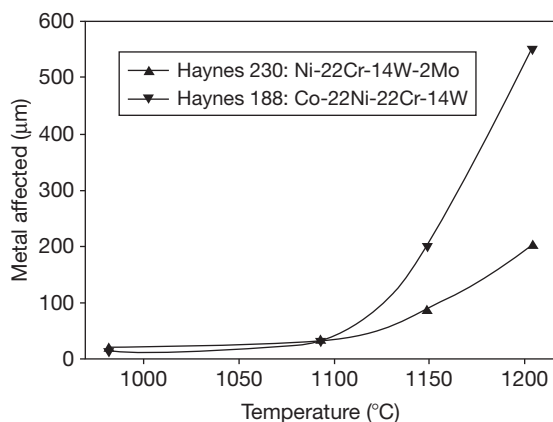


**Figure 12** Comparative oxidation damage of one nickel- and one cobalt-based alloy of approximate identical composition showing better performance of the nickel alloy at the highest temperatures.

chromium contents, they also resist oxidation well, but it was reported that alloy 188 is sensitive to water vapor in the oxidizing atmosphere which reduces its life time. They are of interesting use when nickel is prohibited, for example in sulfidizing situations where Ni-containing low melting temperature eutectics can form.

The drawback is that their market price is high. When no particular situation imposes the choice of cobalt, it seems preferable to use nickel alloys as shown in Figure 12.

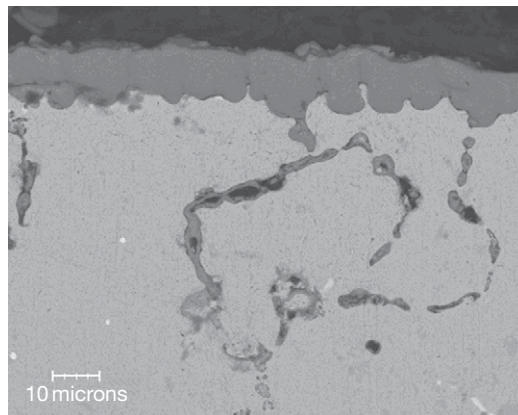


**Figure 13** Cross section of alloy HK40 oxidized at  $1100^\circ\text{C}$  in air for 50 h, showing large internal penetrations.

#### 1.23.3.3.4 Various comparisons between alloy grades

One point which may be emphasized concerns the high concentrations of minor oxidizable elements, particularly for Ni(Co)–Cr grades, which lead to internal inter- and intragranular oxidation to depths often much larger than the chromia scale thickness (Figure 13). This may be deleterious for the mechanical resistance of these alloys in situations where the total weight gain seems to be not catastrophic. For engineering comparison between different grades, figures concerning metal loss or scale thickness must necessarily be discussed together with the depth of the affected metal (Table 7).

As seen earlier, it is difficult to compare the resistance to high temperature oxidation of various industrial grades using only one parameter. Trying to overcome this difficulty, an important work done at NASA was presented by Barrett where not only kinetics were taken into account but also the visual aspect of the samples.<sup>27</sup> Many industrial alloys were submitted to 10 cycles of 1000 h each at  $982^\circ\text{C}$  in air. Kinetics were evaluated by determining linear ( $k_l$ ) and parabolic ( $k_p$ ) rate constants from weight change measurements according to

$$\Delta m/A = k_l t + k_p t^{1/2}$$

The attack parameter, called  $\text{KB}_3$ , was defined by

$$\text{KB}_3 = k_p + 100|k_l|$$

for positive values of  $k_p$ , or by

$$\text{KB}_3 = 250|k_l|$$

for negligible or negative values of  $k_p$ .

**Table 7** Comparative metal loss and depth of affected metal for Fe–Ni–Co grades after six 1-week cycles (data from Haynes International)

Alloy	T (°C)							
	980	1095	1150	1205				
	Metal loss (mm)	Affected metal (mm)	Metal loss (mm)	Affected metal (mm)	Metal loss (mm)	Affected metal (mm)	Metal loss (mm)	Affected metal (mm)
Iron base alloys								
253MA	0.033	0.074	0.018	0.210	0.210	0.41	0.465	0.73
310	0.009	0.029	0.023	0.033	0.075	0.113	0.2	0.26
316	0.315	0.365	>1.75	>1.74	>2.7	>2.67	>3.57	>3.57
330	0.010	0.109	0.02	0.170	0.041	0.221	0.096	–
446	0.035	0.060	0.335	0.370	>0.55	>0.551	>0.59	>0.592
556	0.010	0.027	0.027	0.065	0.237	0.296	>3.8	>3.8
800H	0.024	0.045	0.137	0.188	0.191	0.225	0.29	0.35
Multimet	0.100	0.033	0.226	0.295	>1.2	>1.2	>3.7	>1.7
RA 85H	0.013	0.210	0.074	0.660	0.092	>1.47	0.097	>1.47
Nickel base alloys								
214	0.002	0.005	0.002	0.003	0.004	0.008	0.005	0.018
230	0.006	0.018	0.011	0.032	0.058	0.087	0.11	0.201
263	0.018	0.145	0.089	0.361	0.18	0.409	>0.91	>0.91
600	0.008	0.023	0.027	0.041	0.044	0.073	0.13	0.213
601	0.013	0.033	0.031	0.066	0.061	0.135	0.11	0.191 <sup>a</sup>
617	0.080	0.033	0.015	0.046	0.028	0.086	0.27	0.32
625	0.008	0.018	0.083	0.122	0.405	0.462	>1.2	>1.21
HR-120	0.008	0.094	0.030	0.190				
HR-160	0.015	0.147	0.042	0.257	0.068	0.325	0.102	0.605
R-41	0.018	0.122	0.086	0.295	0.210	0.442	>0.73	>0.73
S	0.005	0.012	0.011	0.033	0.026	0.042	>0.81	>0.81
Waspaloy	0.015	0.079	0.036	0.137	0.079	0.231	>0.4	>0.4
X	0.009	0.024	0.038	0.069	0.114	0.148	>0.9	>0.89
Cobalt base alloys								
25	0.010	0.018	0.234	0.259	0.430	0.490	>0.96	>0.96
188	0.005	0.015	0.010	0.033	0.184	0.204	>0.55	>0.55

<sup>a</sup>Porosity formation in the metallic substrate.

In addition to  $KB_3$ , the post-test appearance of samples was ranked from 1 to 5:

rank 1: excellent,  
rank 2: good,  
rank 3: fair,  
rank 4: poor,  
rank 5: catastrophic

and the global rating parameter ( $KB_4$ ) was defined by

$$KB_4 = KB_3[1 + 0.1(\text{rank} - 1)]$$

Using this global parameter, the behavior of alloys in long term thermal cycling situations was ranked according to the following rule:

- $KB_4 > 0.2$ : excellent
- $0.2 < KB_4 < 0.5$ : good
- $0.5 < KB_4 < 1$ : fair

- $1 < KB_4 < 5$ : poor
- $KB_4 > 5$ : catastrophic.

The results for Fe-, Ni-, and Co-chromium containing alloys appear in [Figures 14–16](#) respectively.

None of the iron-base alloys were ‘excellent,’ with only four in the ‘good’ range. A minimum of 20% Cr seemed necessary for this ‘good’ ranking. Nickel-base alloys behave better, with four grades in the ‘excellent’ family and nine in the ‘good’ one. It should be observed that Hasteloy-S, which behaved the best, contains the reactive element (La) that improves scale adhesion, but Chromel-A, having a quite similar  $KB_4$ , does not. In fact, this test exhibiting very long isothermal periods and only a few thermal cycles was probably not discriminating in terms of scale spallation. Cobalt-base alloys presented the best behavior, with five alloys out of



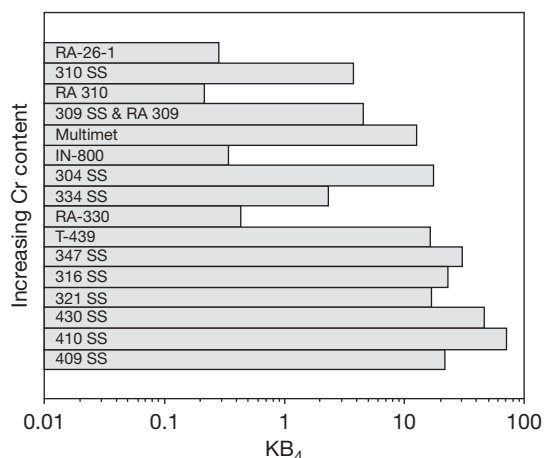


**Figure 14** KB<sub>4</sub> parameter for various iron-base chromia-forming alloys.

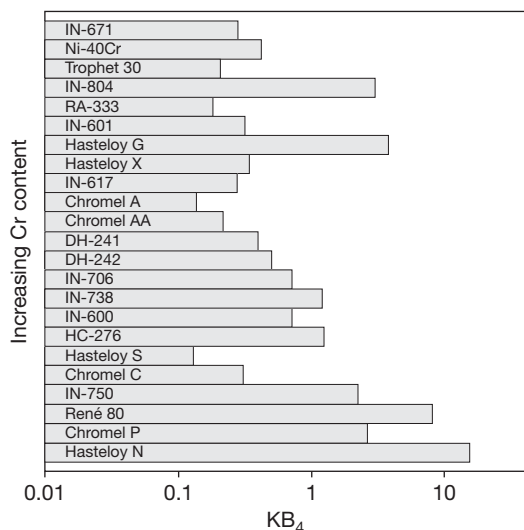


**Figure 15** KB<sub>4</sub> parameter for various nickel-base chromia-forming alloys.

eight tested ranking 'good' to 'excellent.' They all have high chromium content (25–28%). MAR-M-509 alloy, with 23.5% Cr has a 'fair' behavior probably due to 7% W and both alloys with lower chromium and higher W (WI-52 and L-605, 21Cr–11W and 20Cr–15W respectively) behaved 'catastrophic' and 'poor.'

It has to be reminded that the proposed test was performed at 982 °C, a temperature where chromia volatilization was not detrimental. The observation of the complete set of results also showed that alumina-forming alloys behaved much better than chromia-forming alloys, with 10 grades showing  $KB_4 < 0.1$ .

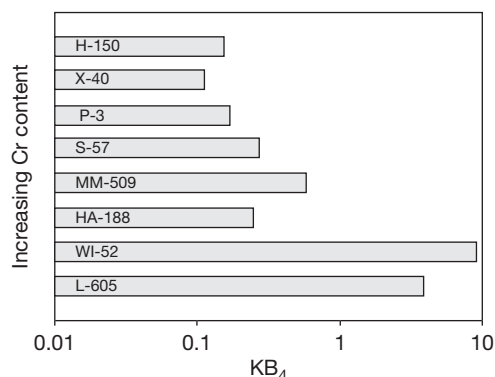


**Figure 16** KB<sub>4</sub> parameter for several cobalt-base chromia-forming alloys.

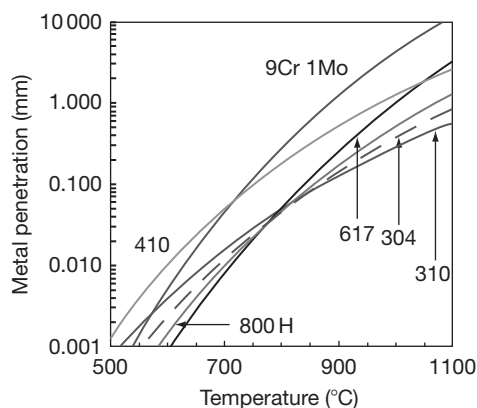


**Figure 17** Comparative metal penetration (metal loss + internal oxidation) of various alloys after 1 year oxidation in air as proposed by the ASSET system. Reproduced from John, R. C.; Pelton, A. D.; Thomson, W. T.; Young, A. L.; Wright, I. G. *High Temperature Corrosion Materials Chemistry III*. Electrochemical Society Meeting, March 25–30, 2001, Washington, DC, USA.

Another attempt to present comparative sets of results was initiated by SHELL under the name 'ASSET' (Alloy Selection System for Elevated Temperatures), in collaboration with several industrial and academic organizations in five countries.<sup>28</sup> This information system proposes a compilation of high temperature corrosion data, from literature and from specific testing, arranged so that engineering decisions can be made on lifetime, maximum temperature and influence of gas composition. In Figure 17 is presented the oxidation behavior of six common alloys exposed to air for 1 year. It is remarkable that, except the two ferritics (9Cr, 1Mo, and 410), all alloys behave similarly at 800 °C. Major differences are found at the lower and higher test temperatures,

with the worst alloys at 500 °C behaving the best at 1100 °C.

Attention has to be paid to transposition of oxidation data from laboratory tests to industrial practice. Alloys exposed in service to combustion atmospheres are better tested in burner rigs, a procedure really aggressive due to high rates of gas flow and possible particle impact. **Figure 18** shows comparative data from burner and furnace testing for various Fe-, Ni-, and Co-base alloys. It is clear that burner oxidation is more severe than still air by a factor extending from

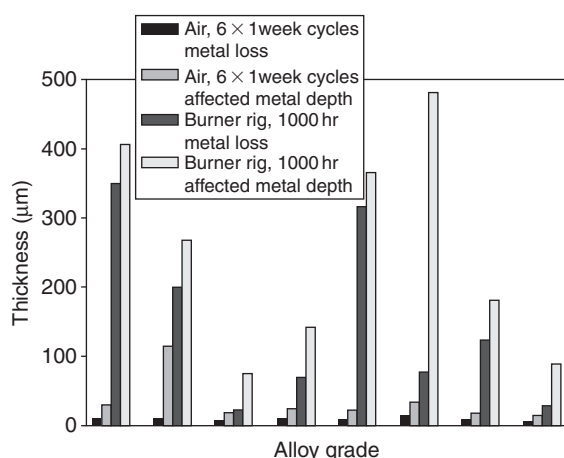


**Figure 18** Metal loss and average metal penetration for various alloys exposed to still air oxidation (980 °C, six 1-week cycles, conditions of **Table 7**) and burner test rig at 980 °C for 1000 h. Data from Haynes International.

3–5 for the best alloys to 15–40 for the worst ones. However, the general ranking of alloys established by furnace testing is not strongly modified.

### 1.23.4 Concluding Remarks

The number of technical chromia-forming alloys proposed on the market is very large (see **Appendices 1–6**) and the choice of the right material is generally very difficult. The first step to a right choice is the careful observation of the service conditions which will be supported by the alloy, with clear definition of the possible accidental situations. To select the best grade, laboratory tests have to be performed at a temperature and in an atmosphere as close as possible to the real ones, taking into account possible thermal cycling. Comparison with specimens exposed to the real industrial situations may validate the laboratory tests.

Attention has also to be paid to the desired shape, as all alloys are not available in all shapes, and sometimes, the shape influences the corrosion resistance.

The cost of the material is also an important parameter, and the technical engineers must always decide whether they want to use an expensive alloy which will function for a long time or a cheaper one which will have to be replaced after limited service.

A last criterion to have in mind is the availability of the chosen grade, which must be rapidly delivered and possibly by several suppliers to avoid a monopoly situation.

### Appendix 1 Denomination and composition of refractory ferritic stainless steels

Alloy	EN	UNS	Fe	Cr	Mo	Si	C	Ti	Others
409	1.4512	S40900	Bal	10.5–12.5					
430	1.4016	S43000	Bal	16–18	1	<1	<0.08	6(C+N)<Ti <0.65	
430Ti	1.4510	S43036	Bal	16–18	1	<1	<0.05	4(C+N) + 0.15–0.8	
436	1.4526	S43600	Bal	16–18	0.8–1.4	<1	<0.08		7(C+N) + 0.1–1 Nb
439	1.4510	S43035	Bal	17.5		0.35	0.02	0.4	
441	1.4509	S44100	Bal	17.5–18.5		<1	<0.03	0.1–0.6	3 C+0.3–1 Nb
442		S44200	Bal	18–23	1	1	0.2		
444	1.4521	S44400	Bal	17–20	1.8–2.5	<1	<0.025	4(C+N) + 0.15–0.8	0.45 (Ti+Nb)
446	1.4763	S44600	Bal	23–26	1.5	<1	<0.1		
CROFER 22APU	1.4760	S44535	Bal	20–24		<0.5	<0.03	0.03–0.2	0.04–0.2 La
ZMG232			Bal	22		0.4	0.02		0.04 La, 0.02 Zr
12SR				12		0.6	0.02	0.3	1.2 Al 0.6 Nb
18SR	1.4736		Bal	18		1	0.02	0.4	2 Al
R2012		S482800	Bal	20		2			

**Appendix 2** Denomination and composition of refractory austenitic stainless steels

<i>Alloy</i>	<i>EN</i>	<i>UNS</i>	<i>Fe</i>	<i>Ni</i>	<i>Cr</i>	<i>Mo</i>	<i>Si</i>	<i>C</i>	<i>Others</i>
302B/309	1.4828	S30900	Bal	8–10	19–21		1.5–2.5	<0.2	
308		S30800	Bal	10–12	19–21		1	0.08	
347	1.4550	S34700	Bal	9–13	17–19			<0.08	10 C<Nb+Ta<1
310/314	1.4841	S31400/S31000	Bal	19–22	24–26		1.5–2.5	<0.2	
25–20	1.4843			19–21	23–25		1.5–2.5	<0.1	<0.1 RE 0.3 Al
31	1.4562	N08031	Bal	30–32	26–28	6–7	<0.3	<0.015	1–1.4 Cu 0.15–0.25 N
33	1.4591	R20033	Bal	30–33	31–35	0.5–2	<0.5	<0.015	0.3–1.2 Cu 0.35–0.6 N
153MA	1.4818	S30415	Bal	9–11	18–20		1–2	0.04–0.08	0.03–0.08 Ce 0.12–0.2 N
204Cu		S20430	Bal	1.5–3	16–18	<1	<1	<0.15	0.05–0.25 N 2–4 Cu; 6.5–9 Mn
253MA	1.4835	S30815	Bal	10–12	20–22		1.4–2.5	0.05–0.12	0.03–0.08 Ce 0.12–0.2 N
304	1.4301	S30400	Bal	8–11	18–20		0.75	0.08	
309S	1.4833	S30908	Bal	12–14	22–24		<1	<0.15	
310S	1.4845	S31008	Bal	19–22	24–26		<1.5	<0.1	
316	1.4401	S31600	Bal	10–14	16–18	2–3	0.75	<0.08	
321	1.4878	S32100	Bal	9–12	17–19		<1	<0.1	0.5×(C–0.8)Ti
353MA	1.4854	S35315	Bal	34–36	24–26		1.2–2	0.04–0.08	0.053–0.08 Ce 0.12–0.2 N; 1.5 Mn
RA85H		S30615	Bal	14.5	18.5		3.5	0.2	1 Al

**Appendix 3** Denomination and composition of wrought refractory Fe–Ni–Cr alloys (balance: Fe)

<i>Alloy</i>	<i>EN</i>	<i>UNS</i>	<i>Ni</i>	<i>Co</i>	<i>Cr</i>	<i>Al</i>	<i>Mo</i>	<i>Si</i>	<i>C</i>	<i>Ti</i>	<i>Others</i>
	1.4872		6–8		24–26			<1	0.2–0.3		0.2–0.4 N; 8–10 Mn
	1.4877		31–33		26–28			<0.3	0.04–0.08		0.05–0.1 Ce; 0.6–1 Nb
	1.4887		33–37		20–23			1–2	<0.15		1–1.5 Nb; <0.11 N
30–20	1.4860		30–31		19.5–21.5	<0.3		1.8–3	<0.1		<0.1 RE
330	1.4886	N08330	33–37		17–20			1–2	<0.15		1.5 Mn; <0.11 N
556	1.4971 1.4833	R30556	20	18	22	0.2	3	0.4	0.1		2.5 W; 0.02 La; 0.6 Ta
800	1.4958	N08800	30–35		19–23	0.15–0.6		<1	<0.1	0.15–0.6	0.3–1.2 Ti+Al; 0.8 Mn
800H	1.4876	N08810	30–35		19–23	0.15–0.6		<1	0.05–0.1	0.15–0.6	0.3–1.2 Ti+Al; 0.9 Mn
800HT	1.4876	N08811	30–35		19–23	0.25–0.6		<1	0.06–0.1	0.25–0.6	0.85–1.2 Ti+Al; 0.9 Mn
803		S35045	32–37		25–29	0.15–0.6		<1	0.06–0.1	0.15–0.6	0.9 Mn
864		S35135	30–38		20–25	0.3	4–4.8	0.8	<0.08	0.6	0.4 Mn
903		N19903	38	15		0.7				1.4	3 Nb
907		N19907	38.4	13		0.03		0.15		1.5	4.7 Nb
A-286	1.4980	S66286	24–27		13.5–16	<0.35	1–1.5	<1	<0.08	1.9–2.35	<0.01 B; 1.3 Mn; 0.1–0.5 V
DS	1.4864	N08332	34.5–41		17–19			1.9–2.6	0.1	0.2	0.8–1.5 Mn; 0.5 Cu
Multimet		R30155	20	20	21		3	1	0.08		2.5 W; 1Nb+Ta
Nitronic 50		S20910	12.5		22		2.25				5 Mn; 0.3 N; 0.2 Nb; 0.2 V
Nitronic 60		S21800	8.5		17			4			8 Mn; 0.15 N

**Appendix 4** Denominations and composition of wrought refractory Ni-(Fe)-Cr alloys (balance: Ni)

<i>Alloy</i>	<i>EN</i>	<i>UNS</i>	<i>Fe</i>	<i>Co</i>	<i>Cr</i>	<i>Al</i>	<i>Mo</i>	<i>Si</i>	<i>C</i>	<i>Ti</i>	<i>Others</i>
Waspaloy	2.4654	N07001	<2	12–15	18–21	1.2–1.6		<0.75	0.02–0.1	2.75–3.25	Zr, B
X	2.4665	N06002	17–20	0.5–2.5	20.5–23.5	<0.25		<1	0.05–0.15		0.2–1 W
S		N06635	2		15.5	0.3		0.4	0.02		0.2 Mn; 0.05 La; 0.01 B; 0.8 W
Chromel A			0.5		20			1.4	0.03		0.2 Mn
Chromel AA			10		20			2	0.03		0.2 Mn
Chromel C			24		15			1.4	0.06		0.2 Mn
Chromel P			0.2		10			0.4	0.01		
G		N06007	20		22			0.4	0.03		1 Nb; 1 Ta; 1.3 Mn; 2 Cu; 0.5 W
N		N10003	<5		7			1	0.06		0.3 Cu
N4				7.5	9.8	4.2			0.06	3.5	0.5 Nb; 5 Ta; 0.15 Hf; 6 W
N6				12.5	4.2	5.75					5.4 RE; 7.2 Ta; 0.15 Hf; 6 W
Astroloy				17	15	4			0.06	3.5	0.03 B
X-750	2.4669	N07750	5–9		14–17	0.4–1		<0.5	<0.08	2.25–2.75	1(Nb+Ta); 0.5 Mn
HR-160	2.4880	N12160	2	30	2828			2.8	0.05	0.5	0.5 Mn
HR-120	2.4854	N08120	35		25	0.1		0.6	0.05	0.1	0.7 Nb; 0.7 Mn; 0.004 B
R-95				8	14	3.5			0.15	2.5	0.01 B; 0.05 Zr; 3.5 Nb; 3.5 W
R-41	2.4973	N07041	5	10	18	1.5		0.5	0.09	3.1	0.005 B
G-30		N06030	15	5	29.5			0.4	0.03		2 Cu; 2.5 W
G-3	2.4619	N06985	18–21	<5	21–23.5			<1	<0.015		<0.5(Nb+Ta); 2 Cu; <1.5 W
70–30	2.4658	N06003	<1		29–31	<0.2		1–1.5	<0.07		0.01–0.04 RE
45-TM	2.4889	N06045	21–25		26–29			2.5–3	0.05–0.12		0.03 Zr; Ce
59	2.4605	N06059	<1.5		22–24	0.1–0.4		<0.1	<0.01		
60–16	2.4867	N06004	Bal		14–17	<0.3		1–1.75	<0.1		<0.04 RE
80–20	2.4869	N06003	<1		19–21	<0.2		1–1.5	<0.08		0.01–0.04 RE
Nimonic 75	2.4951	N06075	<5		18–21			<1	0.08–0.15	0.2–0.6	0.3 Mn
Nimonic 80A	2.4952	N07080	<3	<2	18–21	1–1.8		<1	<0.1	1.8–2.7	0.3 Mn; 0.06 Zr; 0.003 B
Nimonic 90	2.4632	N07090	<1.5	15–21	18–21	1.2		<1	<0.13	2–3	0.3 Mn; 0.06 Zr; 0.003 B



Nimonic 105	2.4634		<1	18–22	14–15.7	4.5–9	4.5–5.5	<1	<0.12	0.9–1.5	0.3 Mn; 0.1 Zr; 0.005 B
Nimonic 115	2.4636		<1	13–15.5	14–16	4.5–5.5	3–5	<1	0.12–0.2	3.5–4.5	0.016 B; 0.04 Zr
214	2.4646	N07214	3.5		16	4.5			0.04		0.05 Y; 0.03 Zr
230	2.4633	N06230	<3		22	0.3	2	0.4	0.1		14 W; 0.02 La; 0.5 Mn; 0.004 B
242					8		25		0.03		14 W
Nimonic 263	2.4650	N07263	<0.7	19–21	19–21	<0.6	5.6–6.1	<0.4	0.04–0.08	1.9–2.4	0.4 Mn; 0.02 Zr; 0.001 B
333	2.4608	N06333	18	3	25		3	1.25	0.05		3 W
Udimet 400				14	17.5	1.5	4		0.06	2.5	0.5 Nb; 0.06 Zr; 0.008 B
Monel 400	2.4360	N04400	<2.5		0.1	0.02		<0.5	<0.3	0.4	28–34 Cu; 0.8 Mn
Udimet 500				18.5	18	2.9	4		0.08	2.9	0.05 Zr; 0.006 B
Udimet 520				12	19	2	6		0.05	3	1 W; 0.005 B
600	2.4816	N06600	6–10		14–17	<0.3		<0.5	<0.08	0.2–0.6	<1 Mn
601	2.4851	N06601	Bal		21–25	1–17		<0.5	<0.1	0.4	0.5 Mn
602CA	2.4633	N06025	8–11		24–26	1.8–2.4		<0.5	0.15–0.25	0.1–0.2	0.1 Zr; 0.001–0.1 Y
617	2.4663	N06617	<2	10–13	20–23	0.5–1.5	8–10	<0.7	0.05–0.1	0.2–0.6	
625	2.4856	N06625	<5	<1	20–23	<0.4	8–10	<0.5	<0.1	<0.4	3.5–4.15(Nb+Ta)
625LCF		N06626	<5	<1	20–23	<0.4	8–10	<0.15	<0.03	<0.4	3.5–4.15(Nb+Ta); <0.02 N
Udimet 630			18		18	0.5	3		0.03	1	6.5 Nb; 3 W
671					46	0.3			0.05	0.3	
686	2.4606	N06686	<5		19–23		15–17	<0.08	<0.01	0.02–0.25	3–4.4 W
690	2.4642	N06690	7–11		27–31			<0.5	<0.05		
693		N06693	2.5–6		27–31	2.5–4		<0.5	<0.15	<1	0.5–2.5 Nb
Udimet 700				17	15	4.3	5		0.06	3.5	0.08 Zr; 0.03 B
702		N09702	0.5		15.4	3.1			0.04	0.4	
706		N09706	39–44		14.5–17.5	<0.4		<0.35	<0.06	1.5–2	2.5–3.3(Nb+Ta)
Udimet 710				15	18	2.5	3		0.07	5	1.5 W; 0.02 B
718	2.4668	N07718	20–24	<1	17–21	0.2–0.8	2.8–3.3	<0.35	<0.08	0.65–1.15	4.75–5.5(Nb+Ta)
Udimet 720				15	16	2.5	3		0.03	5	1.3 W; 0.033 B; 0.03 Zr
751		N07751	5–9		14–17	0.9–1.5		<0.5	0.04	2–2.6	0.5 Mn; 0.7–1.2(Nb+Ta)
825	2.4858	N08825	<22		19.5–23.5	<0.2	2.5–3.5	<0.5	<0.05	0.6–1.2	1.5–3 Cu; 0.4 Mn

**Appendix 5** Denomination and composition of wrought refractory Co–Cr alloys (balance: Co)

<i>Alloy</i>	<i>EN</i>	<i>UNS</i>	<i>Fe</i>	<i>Ni</i>	<i>Co</i>	<i>Cr</i>	<i>Al</i>	<i>Mo</i>	<i>Si</i>	<i>C</i>	<i>Ti</i>	<i>Others</i>
25/L605	2.4964	R30605	<0.3	9–11	Bal	19–21			<0.3	0.05–0.15		14–16 W; 1–2 Mn
Belgian S-57					Bal	25	3					5 Ta; 0.5 Y
Belgian P-3			29.5	12	Bal	25				0.05		
6B	2.4683	R30188	3	3	Bal	30		<1.5	2	1.2		4.5 W; 2 Mn
150			20	1	Bal	28			0.7	0.08		0.6 Mn; 0.02 P; 0.002 S
188			<0.3	20–24	Bal	20–24			0.2–0.4	<0.15		13–16 W; <0.12 La; 0.004 B
MAR-M-918				20	Bal	20				0.05		7.5 Ta; 0.1 Zr
1233		R31231	3		Bal	26		5				2 W
S-816		R30816	4		Bal	20		4				4 Nb; 4 W
MP-35N		R30035			Bal	20		10				
Ultimet		R31233	3	9	Bal	25		5	0.3	0.06		2 W; 0.6 Mn

**Appendix 6** Denomination and composition of cast refractory Fe-, Ni-, and Co-base alloys

EN	UNS	Alloy	Fe	Ni	Co	Cr	Al	Mo	Si	C	Others
<b>Iron-base</b>											
1.4729			Bal			12–14			1–2.5	0.3–0.5	
1.4740			Bal			16–19			1–2.5	0.3–0.5	
1.4745			Bal			23–26			1–2.5	0.3–0.5	
1.4777			Bal			27–30			1–2.5	1.2–1.5	0.5–1 Mn
1.4743			Bal			17–19			1–2.5	1.4–1.8	
		HA	Bal			8–10		0.9–1.2	<1	<0.2	
1.4776	J92605	HC	Bal	<4		27–30			1–2.5	0.3–0.5	
1.4823	J93005	HD	Bal	3–6		25–28			1–2.5	0.3–0.5	
	J93403	HE	Bal	8–11		26–30			0.5–2	0.2–0.5	
1.4825	J92603	HF	Bal	8–10		17–19			0.5–2	0.15–0.35	
1.4826			Bal	9–11		21–23			1–2.5	0.3–0.5	
1.4832			Bal	13–15		19–21			0.5–2.5	0.15–0.35	
1.4855			Bal	23–25		23–25			1–2.5	0.3–0.5	0.8–1.8 Nb
1.4837	J93503	HH	Bal	11–14		24–27			1–2	0.3–0.5	
	J93503	HH1	Bal	12		26			1–2	0.4	0.5 Mn
	J94003	HI	Bal	14–18		26–30			0.5–2	0.2–0.5	
1.4848	J94224	HK	Bal	19–22		24–27			1–2.5	0.4–0.5	
	J94204	HK40	Bal	20		26			1.4	0.4	0.6 Mn
	J94604	HL	Bal	18–22		28–32			0.5–2	0.2–0.6	
	J94213	HN	Bal	23–27		19–23			1–2	0.2–0.5	
1.4852	J95705	HP	Bal	33–36		24–27			1–2.5	0.3–0.5	0.8–1.8 Nb
	J94605	HT	Bal	33–37		13–17			1.7	0.35–0.75	0.9 Mn
1.4865			Bal	36–39		18–21			1–2.5	0.3–0.5	
	N08004	HU	Bal	37–41		17–21			1–2.5	0.35–0.75	
1.4849			Bal	36–39		18–21			1–2.5	0.3–0.5	1.2–1.8 Nb
1.4859			Bal	31–33		19–21			0.5–1.5	0.05–0.15	0.5–1.5 Nb
1.4857			Bal	33–36		24–27			1–2.5	0.3–0.5	1.2–1.8 Nb
		GX40NiCrCo 20–20–20	Bal	18–22	18.5–22	19–22			<1	0.35–0.65	2–3 W; 0.75–1.25 Nb
<b>Nickel-base</b>											
			13–23-	Bal	14–16	24–26			1–2	0.45–0.55	4–6 W
			11–21	Bal		32.5–37.5			1.5–2	0.35–0.45	
	N08001	HW	12–28	Bal		12–18			1–2.5	0.35–0.65	1–1.5 Mn; 1.5–2 Nb
	N08006	HX	10–20	Bal		15–19			1–2.5	0.35–0.75	
		NA22H	24.4	Bal		25				0.55	
		GX40CrNiSiNb35–17	38–50	Bal		17–20			1–2.5	0.3–0.5	0.8–1.8 Nb
		GX40CrNiSi 35–17	40–45	Bal		16–18			1–2.5	0.3–0.5	0.8–1.8 Nb
1.4865		GX40CrNiSi 38–19	37–45	Bal		18–21			1–2.5	0.3–0.5	

Continued

## Appendix 6 Continued

EN	UNS	Alloy	Fe	Ni	Co	Cr	Al	Mo	Si	C	Others
Cobalt-base		GX40NiCrCoW35–25–15	22–33	Bal	14–16	24–26			1–2	0.45–0.55	4–6 W
		GX40NiCrNb 45–35	10–20	Bal		32.5–37.5			1.5–2	0.35–0.45	1–1.5 Mn 1.5–2 Nb
		B-1900		Bal	10	8	6	6		0.1	4.3 Ta; 1 Ti; 0.1 Nb; 0.08 Zr; 0.15 B
		1N-100		Bal	15	10	5.5	3		0.18	5.5 Ti; 1 V; 0.05 Zr; 0.015 B
		IN-713 LC		Bal		12	6	4.5		0.05	2 Nb; 0.6 Ti; 0.1 Zr; 0.01 B
		IN-738		Bal	8.5	16	3.4	1.7		0.17	3.4 Ti; 1.7 Ta; 0.9 Nb; 0.1 Zr; 0.01 B
		MAR-M-200		Bal	10	9	5			0.15	2 Ti; 1 Nb; 0.05 Zr; 0.015 B
		Rene´ 120		Bal	10	9	4.3	2			4 Ta; 4 Ti; 0.07 Zr; 0.015 B
		Rene´ 80		Bal	9.5	14	3	4		0.17	5 Ti; 0.03 Zr; 0.015 B
		TAZ-8A		Bal		6	6	4		0.13	8 Ta; 2.5 Nb; 1 Zr; 0.004 B
		TRW-VIA		Bal	7.5	6	5.4	2		0.13	9 Ta; 1 Ti; 0.5 Nb; 0.4 Hf; 0.13 Zr; 0.02 B
		WAZ-20		Bal			6.5			0.15	0.15 Zr
	N07765	IN-657		Bal		50				0.03	1.5 Mn
		X-40		10.5	Bal	26				0.5	
		WI-52			Bal	21				0.45	2 Nb
		MAR-M-509		10	Bal	24				0.6	3.5 Ta; 0.5 Zr; 0.2 Ti

## References

1. Hatfield, W. H. *J. Iron Steel Inst.* **1927**, 115, 517.
2. Hatfield, W. H. *J. Inst. Fuel* **1938**, 11, 245.
3. Massalski, T. B. *Binary Alloys Phase Diagrams*; ASM International: Materials Park, OH, USA, 1990.
4. Antoni, L. *Mater. Sci. Forum* **2001**, 369–373, 345–352.
5. Gleeson, B. In *Corrosion and Environmental Degradation*; Schütze, M., Ed.; Wiley-VCH: Weinheim, Germany, 2000; Vol. 2, pp 173–228.
6. Kofstad, P. *High Temperature Corrosion*; Elsevier, 1988.
7. Bamba, G.; Wouters, Y.; Galerie, A.; Borchardt, G.; Shimada, S.; Heintz, O.; Chevalier, S. *Scripta Mater.* **2007**, 57(8), 671–674.
8. Evans, H. E. *Int. Mater. Rev.* **1995**, 40(1), 1–40.
9. Schütze, M. In *Series on Corrosion and Protection*; Holmes, D. R., Ed.; John Wiley: Chichester, UK, 1997; Vol. 1.
10. Galerie, A.; Dupeux, M.; Wouters, Y.; Toscan, F. *Mater. Sci. Forum* **2006**, 522–523, 441–450.
11. European Patent 1,325,166 B1, 2006.
12. Holcomb, G. R.; Alman, D. E. *Scripta Mater.* **2006**, 54(10), 1821–1825.
13. Stanilowski, M.; Wessel, E.; Hilpert, K.; Markus, T.; Singheiser, L. J. *Electrochem. Soc.* **2007**, 154(4), A295–A306.
14. Essuman, E.; Meier, G. H.; Zurek, J.; Haensel, M.; Norby, T.; Singheiser, L.; Quadakkers, W. J. *Corros. Sci.* **2008**, 50(6), 1753–1760.
15. Halvarsson, M.; Tang, J. E.; Asteman, H.; Svensson, J. E.; Johansson, L. G. *Corros. Sci.* **2006**, 48, 2014–2035.
16. Toscan, F.; Antoni, L.; Wouters, Y.; Dupeux, M.; Galerie, A. *Mater. Sci. Forum* **2004**, 461–464, 705–712.
17. Belogolowsky, I.; Hou, P. Y.; Jacobson, C. P.; Visco, S. J. *J. Power Sources* **2008**, 182, 259–264.
18. Gabrel, J.; Coussement, C.; Verest, L.; Blum, R.; Chen, Q.; Testani, C. *Mater. Sci. Forum* **2001**, 369–372, 931–938.
19. Evans, H. E.; Donaldson, A. T.; Gilmour, T. C. *Oxid. Met.* **1999**, 52(5/6), 379–402.
20. Antoni, L.; Baroux, B. *La Revue de Métallurgie-CIT/ Science et Génie des Matériaux* **2002**, 177–188.
21. Barin, I. *Thermochemical Data of Pure Substances*; VCH: Weinheim, Germany, 1989.
22. Opila, E. J.; Myers, D. L.; Jacobson, N. S.; Nielsen, I. M. B.; Olminky, J. K.; Allendorf, M. D. *J. Phys. Chem.* **2007**, 111, 1971–1980.
23. Jung, I. H. *Solid State Ionics* **2006**, 177, 765–777.
24. Sourmail, T. *Mater. Sci. Technol.* **2001**, 17, 1–12.
25. Santacreu, P. O. *ArcelorMittal Stainless Europe*; personal communication, 2007.
26. Lai, G. A. *High Temperature Corrosion of Engineering Alloys*; ASM International: Metals Park, OH, 1990.
27. Barrett, C. A. 10 000 hour cyclic oxidation behavior at 982 °C (1800 °F) of 68 Co-, Fe- and Ni-base alloys; NASA Technical Memorandum 107394, 1997.
28. John, R. C.; Pelton, A. D.; Thomson, W. T.; Young, A. L.; Wright, I. G. *High Temperature Corrosion Materials Chemistry III*. Electrochemical Society Meeting, March 25–30, 2001, Washington, DC, USA.



## 1.25 High Temperature Corrosion of Intermetallic Alloys

**J. W. Fergus**

Materials Research and Education Center, 275 Wilmore Laboratories, Auburn University, Auburn, AL 36849, USA

© 2010 Elsevier B.V. All rights reserved.

<b>1.25.1</b>	<b>Introduction</b>	647
1.25.1.1	General Uses of Intermetallic Alloys	647
1.25.1.2	Common Intermetallic Alloys	647
1.25.1.2.1	Nickel aluminides	647
1.25.1.2.2	Iron aluminides	648
1.25.1.2.3	Titanium aluminides	649
<b>1.25.2</b>	<b>Oxidation</b>	649
1.25.2.1	Nickel and Iron Aluminides	650
1.25.2.1.1	Scale properties/structure	650
1.25.2.1.2	Effect of atmospheres/impurities	654
1.25.2.1.3	Effect of alloying additions	655
1.25.2.2	Titanium Aluminides	656
1.25.2.2.1	Scale properties/structure	656
1.25.2.2.2	Effect of atmosphere and pretreatment	657
1.25.2.2.3	Effect of alloying additions	658
1.25.2.3	Other Aluminides	659
<b>1.25.3</b>	<b>Hot Corrosion</b>	660
1.25.3.1	Sulfur-Containing Environments	660
1.25.3.1.1	Gaseous	660
1.25.3.1.2	Molten salts	661
1.25.3.2	Chlorine-Containing Environments	661
1.25.3.2.1	Gaseous	661
1.25.3.2.2	Molten salts	662
1.25.3.3	Others	662
<b>1.25.4</b>	<b>Coatings</b>	662
1.25.4.1	Aluminide Coatings with Same Base as Substrate	663
1.25.4.1.1	Simple aluminide coatings	663
1.25.4.1.2	Alloyed aluminide coatings	663
1.25.4.2	Aluminide Coatings with Different Base as Substrate	665
<b>1.25.5</b>	<b>Summary and Conclusions</b>	666
<b>References</b>		666

### Glossary

**B2** Crystal structure formed by NiAl and FeAl (see [Figure 1\(a\)](#)).

**Corundum** Crystal structure formed by  $\alpha$ -Al<sub>2</sub>O<sub>3</sub>.

**D0<sub>3</sub>** Crystal structure formed by Fe<sub>3</sub>Al (see [Figure 1\(d\)](#)).

**D0<sub>19</sub>** Crystal structure formed by Ti<sub>3</sub>Al (see [Figure 1\(e\)](#)).

**Hot corrosion** Corrosion in a high temperature environment where molten salts are present.

**Kirkendall effect** Vacancy formation in a diffusion couple because of differences in the interdiffusion coefficients of the two atoms.

**Laves phase** Intermetallic crystal structure.

**L1<sub>0</sub>** Crystal structure formed by TiAl (see [Figure 1\(b\)](#)).

**L1<sub>2</sub>** Crystal structure formed by Ni<sub>3</sub>Al (see [Figure 1\(c\)](#)).

**Pack cementation** Chemical vapor deposition process performed in a packed bed.

**Rutile** Crystal structure formed by  $\text{TiO}_2$ .

**Spinel** Crystal structure formed by  $\text{NiAl}_2\text{O}_4$  and other mixed oxides.

**X-phase** Mixed titanium–aluminum oxide phase.

**Z-phase** Mixed titanium–aluminum oxide phase.

## Abbreviations

**CVD** Chemical vapor deposition

**NCP** New cubic phase (formed in Ti–Al–O system)

**TBC** Thermal barrier coating

**TCP** Topographically close packed (phases)

**TGO** Thermally grown oxide

## 1.25.1 Introduction

Metal alloys, such as those discussed in the chapter on **High Temperature Corrosion of Alumina-forming Iron, Nickel and Cobalt-base Alloys** can be strengthened by the formation of intermetallic compounds, but alloys consisting entirely of intermetallic compounds are stronger. These intermetallic compounds typically have higher melting temperatures compared with their constituent metals, and are thus attractive materials for high temperature applications. The most widely used intermetallic compounds for high temperature applications are aluminides, because of their low densities and their ability, or at least potential, to form a protective alumina scale. Silicides are also used for some high temperature applications, but their oxidation behavior is similar to that of nonoxide ceramics, such as silicon carbide and silicon nitride, so they are discussed in the chapter on **High Temperature Corrosion of Ceramics and Refractory Materials**. Thus, the focus of this chapter is on the high temperature corrosion behavior of aluminide intermetallic alloys.

### 1.25.1.1 General Uses of Intermetallic Alloys

The low density of intermetallic aluminides is primarily due to their high aluminum content, which also promotes the formation of an aluminum scale for good high temperature corrosion resistance. Intermetallic compounds also have good high temperature strength and creep resistance, but the mechanical properties at low temperatures (including ambient room temperature) are inferior to those of metal alloys. In particular, intermetallic compounds tend to have low ductility

because of the difficulty of slip in their ordered structures, which leads to low fracture toughness and creates challenges in the fabrication of intermetallic alloys and their implementation in engineering structures. The synthesis of intermetallic alloys is complicated because of the larger differences in melting temperature among the constituent elements, which limits the available fabrication processes. In addition, the properties of intermetallic alloys depend strongly on small changes in composition, so compositional control during synthesis and processing is particularly important.

Despite these significant engineering challenges, the attractive high temperature properties of intermetallic alloys have led to their use in a variety of high temperature applications.<sup>1–3</sup> One of the most promising applications of intermetallic alloys is for components in aeroturbine engines, where increases in operating temperature and decreases in weight improve engine efficiency and performance. Although low density is particularly important in aerospace applications, intermetallic alloys have also been used in other applications, such as valves and turbocharger rotors in high-performance internal combustion engines for automotive applications.

### 1.25.1.2 Common Intermetallic Alloys

Many of the promising intermetallic aluminide alloys have been developed from the nickel- and iron-based high temperature alloys described in the chapter on **High Temperature Corrosion of Alumina-forming Iron, Nickel and Cobalt-base Alloys**. Intermetallic alloys have also been developed in the titanium–aluminum system. In all cases, the intermetallic compounds form ordered crystal structures, some examples of which are shown in **Figure 1**. Plastic deformation by dislocation movement in such ordered structures is more difficult than in disordered metallic structures, so these compounds have high strength and low ductility. Some of the characteristics of these widely used systems are described in the following sections.

#### 1.25.1.2.1 Nickel aluminides

Alloys based on both  $\text{NiAl}$  and  $\text{Ni}_3\text{Al}$  have been developed. As shown in **Figure 2**,  $\text{NiAl}$ , which forms the cubic B2 structure (**Figure 1(a)**), has a much wider range of stoichiometry than  $\text{Ni}_3\text{Al}$ , which forms the cubic  $\text{L}_{12}$  structure (**Figure 1(c)**).  $\text{Ni}_3\text{Al}$ -based alloys exhibit an anomalous temperature dependence of flow stress, in which the strength

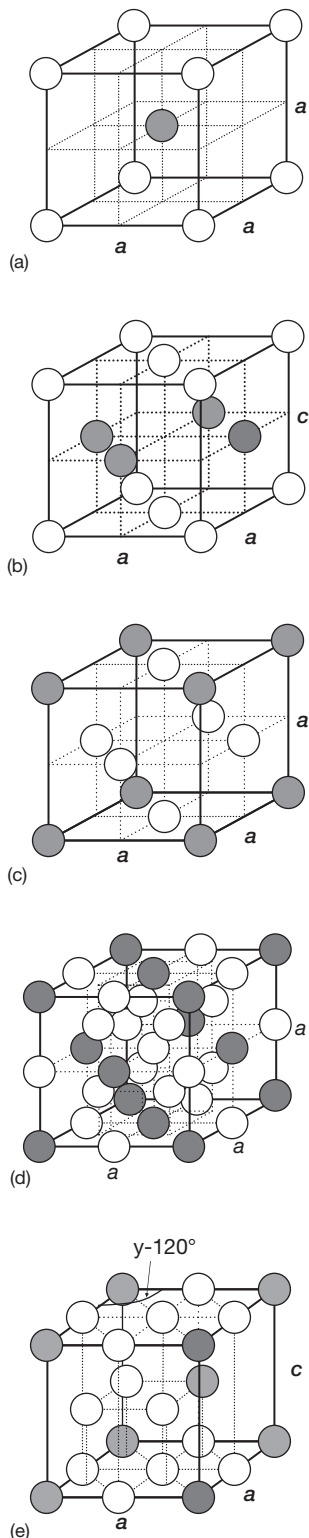


**Figure 1** Crystal structures of selected intermetallic compounds in the Ni–Al, Fe–Al, and Ti–Al systems. (a) B2 (NiAl, FeAl), Pearson symbol *cP2*, structure type CsCl, space group *Pm* $\bar{3}$ *m*. (b) *L1*<sub>0</sub> (TiAl), Pearson symbol *tP4*,

increases with increasing temperature up to about 700 °C and then decreases at higher temperatures. Polycrystalline Ni<sub>3</sub>Al is difficult to fabricate because of its low deformability. Although their ductility can be improved with boron, Ni<sub>3</sub>Al-based alloys have relatively large densities and do not offer significant advantages over nickel-based superalloys. NiAl-based alloys, however, have a higher aluminum content, which decreases density and also improves oxidation resistance. NiAl-based alloys have a higher melting temperature and better creep resistance compared to nickel-based superalloys. The strength can be improved with the addition of niobium or tantalum, which leads to the formation of Laves phases, and the ductility can be improved with alloying additions such as chromium, molybdenum, rhenium, and iron. However, the creep resistance of NiAl above 1000 °C is not good.

#### 1.25.1.2.2 Iron aluminides

The iron–aluminum system is similar to the nickel–aluminum system, in that both Fe<sub>3</sub>Al and FeAl compounds are formed. Like NiAl, FeAl forms the cubic B2 structure (Figure 1(a)), but Fe<sub>3</sub>Al forms the D0<sub>3</sub> structure (Figure 1(d)). The tendency towards ordering in the iron–aluminum system is not as strong as that in the nickel–aluminum system, as indicated by the large disordered ferrite region shown in the phase diagram in Figure 3. As in the nickel–aluminum system, the strengths of Fe<sub>3</sub>Al-based alloys increase with increasing temperature to about 500 °C and then decrease at higher temperatures. However, FeAl offers more advantages over superalloys than NiAl. In particular, the fracture toughness and specific properties of FeAl-based alloys are better than those of NiAl-based alloys, but ductility is low compared to metal alloys. The ductility can be improved with alloying additions such as zirconium. Another difference between the iron–aluminum and nickel–aluminum systems is that carbon is often used in the iron–aluminum system to improve strength through carbide strengthening.

structure type AuCu, space Group *P*<sub>4</sub>/*mmm*. (c) *L1*<sub>2</sub> (Ni<sub>3</sub>Al), Pearson symbol *cP4*, structure type Cu<sub>3</sub>Al, space group *Pm* $\bar{3}$ *m*. (d) D0<sub>3</sub> (Fe<sub>3</sub>Al), Pearson symbol *cF16*, structure type BiF<sub>3</sub>, space group *Fm* $\bar{3}$ *m*. (e) D0<sub>19</sub> (Ti<sub>3</sub>Al) Pearson symbol *hP8*, structure type Ni<sub>3</sub>Sn, space group *P63/mmc*. Reproduced from Villars P., Calvert L.D. (Eds.), *Pearson's Handbook of Crystallographic Data for Intermetallic Phases*, 2nd ed., ASM International, Materials Park, OH, 1991, with permission from ASM International.

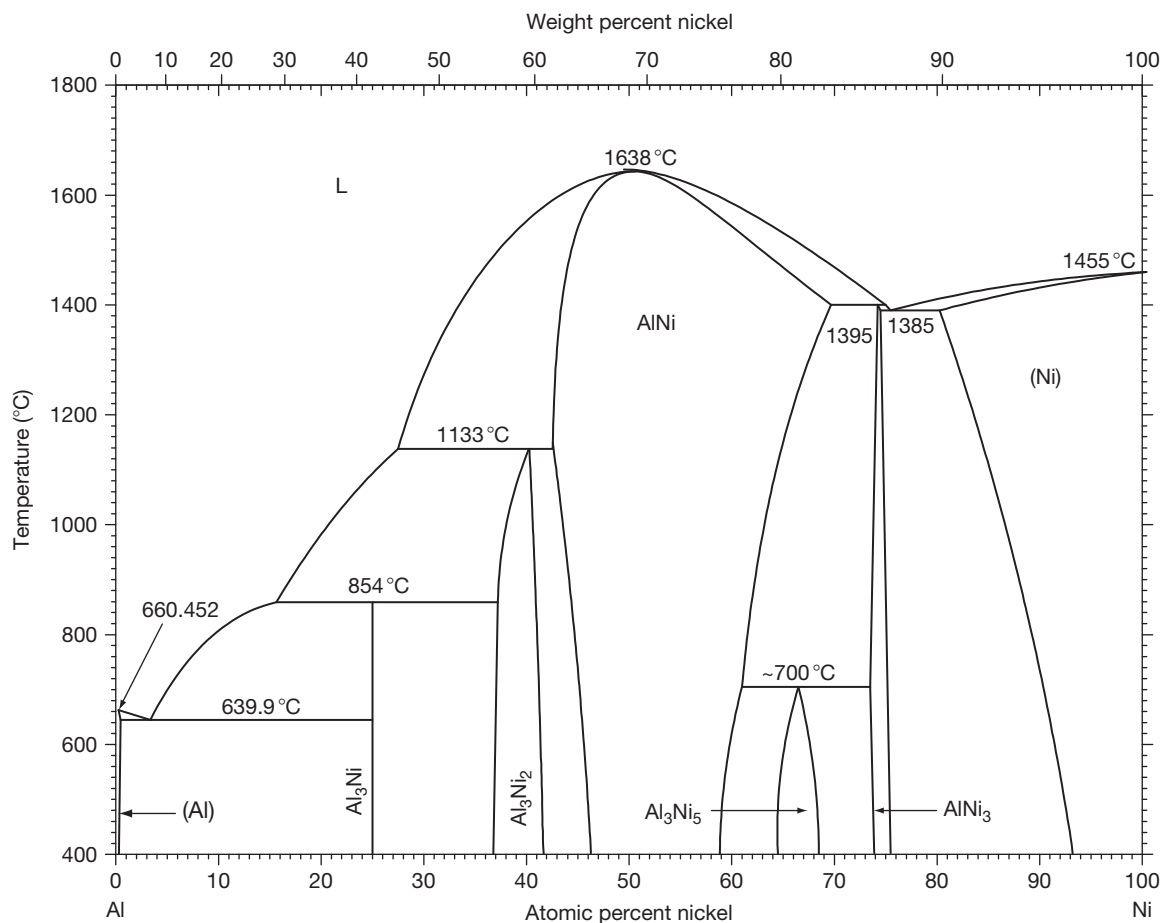


**Figure 2** NiAl phase diagram. Reproduced from *Binary Alloy Phase Diagrams*, 2nd ed., ASM International, Materials Park OH, 1996, with permission from ASM International.

### 1.25.1.2.3 Titanium aluminides

Titanium aluminide alloys have the lowest densities among the three common aluminide systems and thus offer the best specific properties. The phase diagram in [Figure 4](#) shows that Ti<sub>3</sub>Al and TiAl have similar ranges of stoichiometry. TiAl forms the tetragonal L1<sub>0</sub> structure ([Figure 1\(b\)](#)), while Ti<sub>3</sub>Al forms the hexagonal D0<sub>19</sub> structure ([Figure 1\(e\)](#)). Both Ti<sub>3</sub>Al- and TiAl-based alloys have been developed, but the best ductility is achieved with two-phase (Ti<sub>3</sub>Al + TiAl) alloys. Production of the desirable two-phase microstructure requires careful control of both the chemical composition and the heat treatment process. The aluminum content in Ti<sub>3</sub>Al is typically not sufficient for good oxidation resistance, so the most promising alloys consist entirely or mostly of the  $\gamma$ -phase (TiAl in the L1<sub>0</sub> structure). The mechanical properties can be improved by adding substitutional elements such as chromium, as well as interstitial elements such as carbon and boron. The

high reactivity of titanium creates challenges in attaining corrosion resistance, as will be discussed later, as well as in reliable alloy production.

## 1.25.2 Oxidation

A major difference between titanium aluminides and the other two common aluminide systems (nickel and iron) is that titanium is much more active than either iron or nickel. This is illustrated in the Ellingham diagram shown in [Figure 5](#). Titanium can change valence from Ti<sup>2+</sup> to Ti<sup>4+</sup>, so there are several titanium oxides, a few of which are included in [Figure 5](#). The two important titanium oxides are TiO, which is in equilibrium with titanium metal, and TiO<sub>2</sub>, which is stable in air. The free energy of TiO (per mole of oxygen) is about the same as that of Al<sub>2</sub>O<sub>3</sub>, indicating there is a strong competition between the formation of titanium and aluminum oxides on TiAl. In comparison,

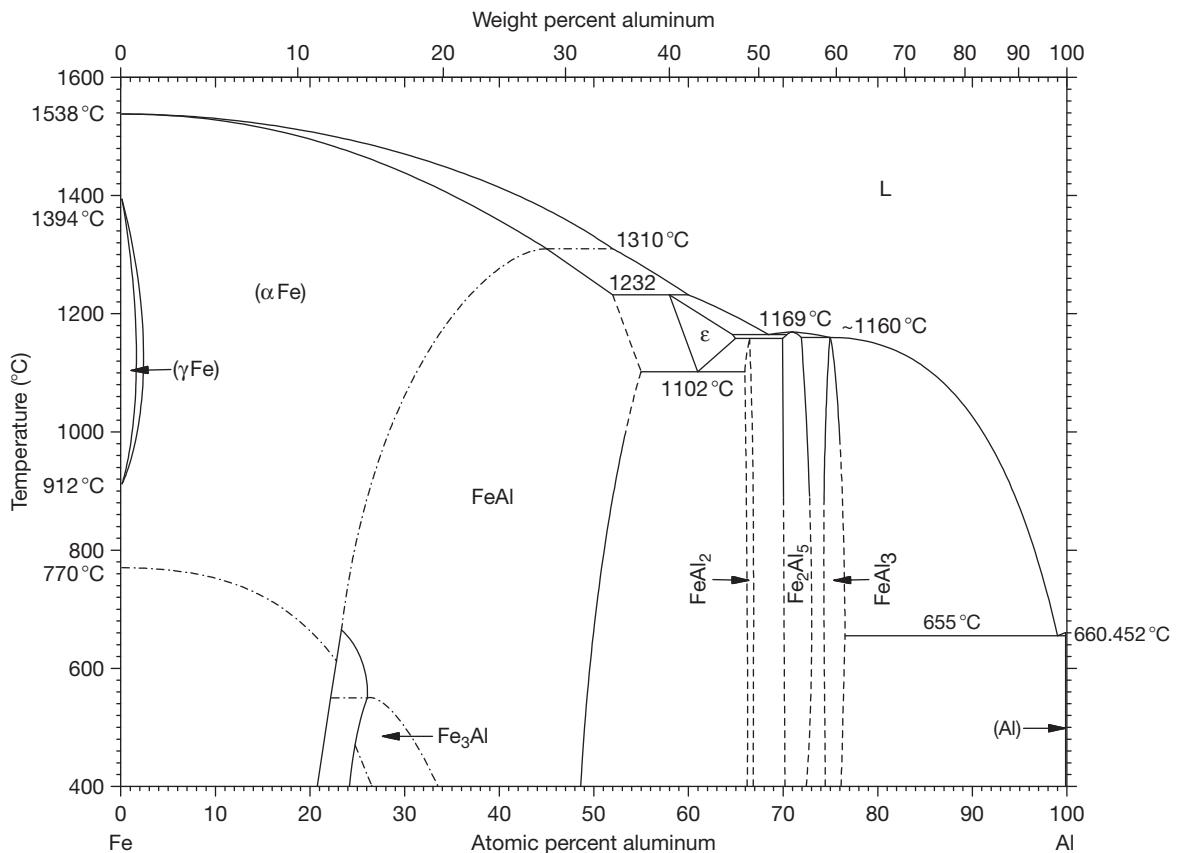


**Figure 3** FeAl phase diagram. Reproduced from *Binary Alloy Phase Diagrams*, 2nd ed., ASM International, Materials Park OH, 1996, with permission from ASM International.

nickel and iron oxides are much less stable than  $\text{Al}_2\text{O}_3$ , so the amount of aluminum in the alloy required for the formation of an  $\text{Al}_2\text{O}_3$  scale is much less in nickel and iron aluminides than in titanium aluminides. Because of this significant difference in oxide stabilities, nickel and iron aluminides have, in many ways, similar oxidation behavior and will be discussed together in the next section. This will be followed by a section on titanium aluminides, and then a section on some less commonly used aluminide alloys.

### 1.25.2.1 Nickel and Iron Aluminides

There are several general reviews of the oxidation of intermetallic alloys<sup>4-6</sup> as well as reviews that focus on either the nickel-aluminum<sup>7,8</sup> or iron-aluminum<sup>9</sup> system.

#### 1.25.2.1.1 Scale properties/structure

As a result of the large differences in oxide stability (Figure 5),  $\text{Ni}_3\text{Al}$ ,  $\text{NiAl}$ ,  $\text{Fe}_3\text{Al}$ , and  $\text{FeAl}$  are in equilibrium with  $\text{Al}_2\text{O}_3$ , so  $\text{Al}_2\text{O}_3$  is always present

in the scale formed during oxidation. However, nickel and iron oxides can also exist in the scale, either as pure oxides (e.g.,  $\text{NiO}$ ,  $\text{Fe}_2\text{O}_3$ ) or mixed oxides (e.g.,  $\text{NiAl}_2\text{O}_4$  spinel). In addition, with long-time exposure, the growth of an  $\text{Al}_2\text{O}_3$  scale depletes the alloy of aluminum, so the amount of aluminum required to maintain a protective scale is higher than the minimum for thermodynamic stability or initial alumina formation. Pettit<sup>10</sup> characterized the oxidation behavior of nickel-aluminum alloys and found that  $\text{Ni}_3\text{Al}$  alloys form a scale with alumina and  $\text{NiO}$  or the  $\text{NiAl}_2\text{O}_4$  spinel, whereas  $\text{NiAl}$  alloys form a protective alumina scale. Once the critical aluminum content for a protective alumina scale is reached, additional aluminum has little effect on the oxidation rate for short-term exposures. However, with longer exposures, the aluminum content of the alloy beneath the scale can decrease, which leads to an increase in the oxidation rate. Changes in the aluminum content can also affect the microstructure. For example, the decrease in the aluminum content in  $\text{FeAl}$  can lead to a disordered structure (i.e.,  $\text{FeAl}$

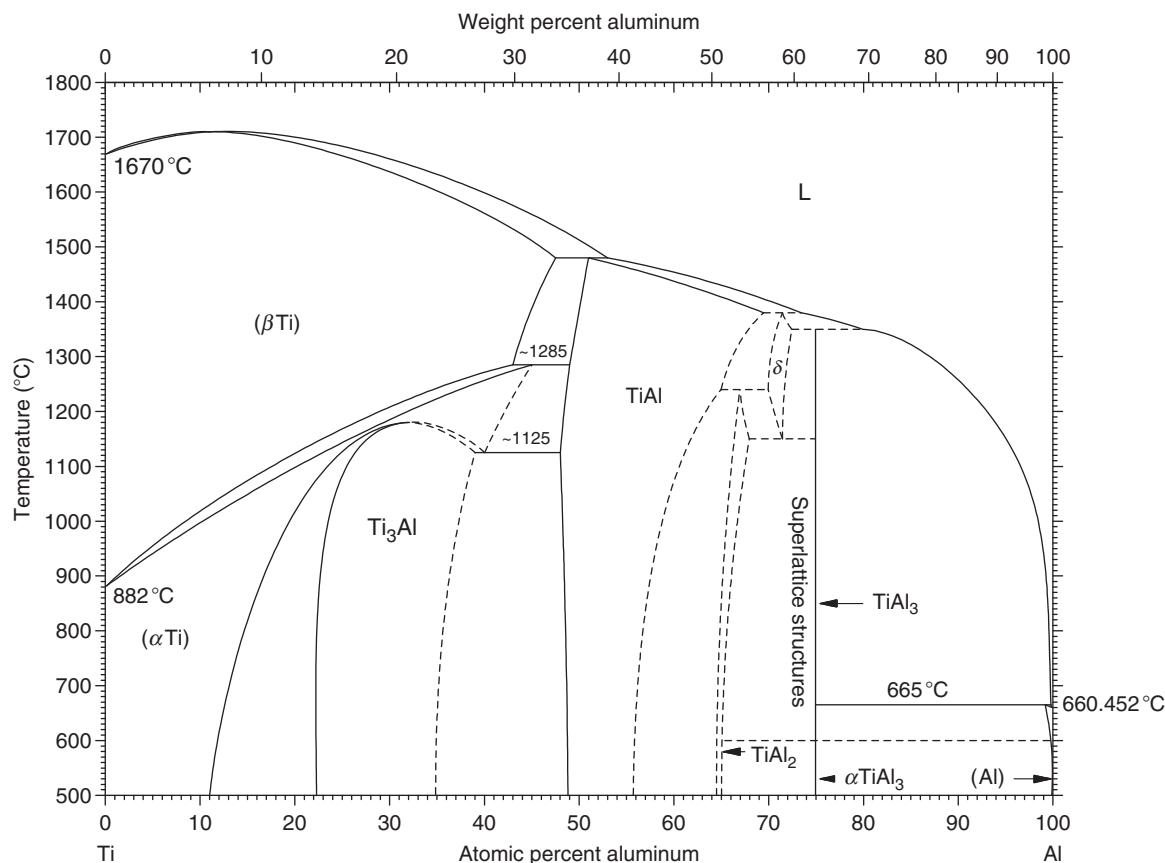


**Figure 4** TiAl phase diagram. Reproduced from *Binary Alloy Phase Diagrams*, 2nd ed., ASM International, Materials Park OH, 1996, with permission from ASM International.

to  $\alpha$ -Fe in **Figure 3**) below the oxide scale. Such changes can affect the oxidation behavior, as diffusion rates in the alloy will determine the magnitude of any changes in alloy composition at the alloy–scale interface, which determines the oxide phases formed in the scale.

In addition to alloy composition, microstructure also affects the oxidation behavior. For example, a finer alloy grain size can lead to reduced oxidation rates, because the diffusion of aluminum to replenish the aluminum used to form the alumina scale can reach the scale faster by grain boundary diffusion. A fine-grained microstructure has also been shown to improve the adherence of an alumina scale on NiAl.<sup>11</sup> Scale adherence is particularly important during thermal cycling, as thermal stresses are generated in the scale due to differences between the coefficients of thermal expansion of the scale and the alloy. However, stresses can be generated in the scale even in isothermal oxidation due to growth or transformation stresses in the oxides. In addition, porosity or

segregation of particular elements to the alloy–scale interface can lead to weakening of the interface.

Porosity is often formed beneath the scale formed on nickel and iron aluminide alloys. The formation of porosity is generally attributed to the coalescence of vacancies formed during the growth of alumina. **Figure 6** shows the transport processes that occur during the growth of an alumina scale on an aluminide alloy. Bulk alumina grows by the outward diffusion of aluminum through the inward diffusion of aluminum vacancies, which are created at the oxide surface from oxygen in the gas phase. The vacancies are filled by aluminum from the existing oxide, so that the new oxide is formed on the outer surface. The aluminum vacancies migrate to the alloy and are filled with aluminum from the alloy, which creates vacancies in the alloy. Once the concentration of these vacancies exceeds the maximum concentration in the alloy, pores will form.

The growth process at grain boundaries is generally attributed to the inward migration of oxygen rather than to the outward migration of aluminum.



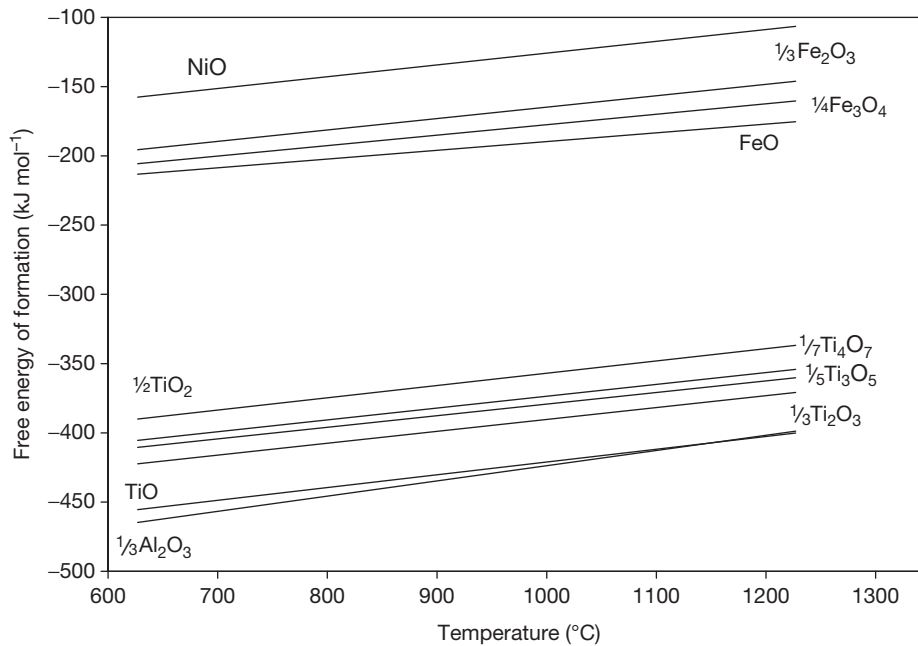


**Figure 5** Ellingham diagram for nickel, iron, titanium, and aluminum oxides. Data from Kubaschewski, O., Alcock, C. B. *Metallurgical Thermochemistry*, 5th ed., Pergamon Press, 1979; Chase M.W., Jr. (Ed.), NIST-JANAF Thermochemical Tables, 4th ed., J. Phys. Chem. Ref. Data, Monograph No. 9, 1998.

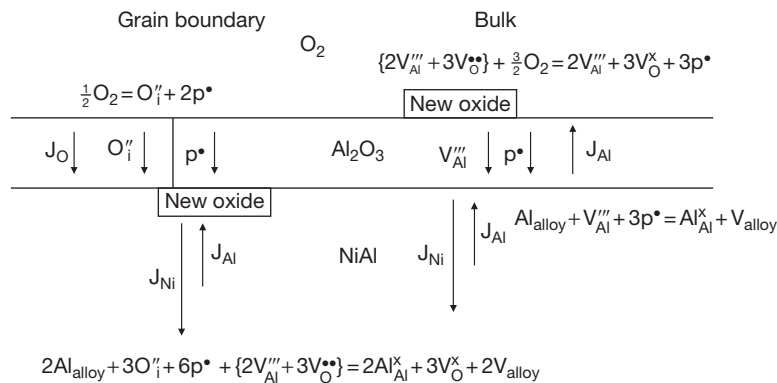


**Figure 6** Transport during growth of alumina scale on nickel aluminide alloys. The predominant inward diffusing oxygen species has not been determined, so oxygen interstitials are used as an example.

Although the specific oxygen defect by which oxygen is transported is not well established, for illustrative purposes, oxygen interstitials are shown in **Figure 6**. Regardless of the specific predominant oxygen defect, however, inward migration of oxygen will lead to the forming of new oxide at the alloy–scale interface. Inward-growing scales generally contain less porosity at the alloy–scale interface as compared to outward-growing scales. However, in the Ni–Al system, porosity can still form within the inward-growing scale. The formation of porosity is generally attributed to

the Kirkendall effect, as, for nickel-rich compositions, the diffusion constant for aluminum in NiAl is smaller than that for nickel in NiAl.<sup>12</sup> Thus, the diffusion of nickel away from the scale into the alloy is faster than the diffusion of aluminum from the bulk toward the scale, which leads to a net movement of mass away from the scale and the formation of vacancies in the metal beneath the scale. The concentration of vacancies continues to increase with increasing oxidation and eventually leads to the formation of pores. The Kirkendall effect can occur regardless of where

the new oxide forms. However, the Kirkendall effect does not occur for aluminum-rich compositions of NiAl, because, in this case, the diffusion of aluminum is not slower than that of nickel. This mechanism is supported by the observation that the number of voids formed decreases with decreasing grain size, as the larger amount of grain boundary diffusion in the finer grained material would reduce the amount of vacancies formed.<sup>13</sup>

The most important effect of the formation of porosity at the alloy–scale interface is that it weakens scale adhesion. The voids can act as stress concentrators and detachment of the oxide has been observed at the pores.<sup>14</sup> Pore formation does not, however, appear to significantly affect the oxidation rate. Although the loss of contact between the alloy and the scale at pores or voids might be expected to affect the scale growth, the  $\text{AlO}_x$  vapor pressure is large enough for vapor-phase transport of aluminum across the void to occur. The number and size of voids increase with oxidation time and the growth of voids in directions parallel to the surface is faster than that perpendicular to the surface.<sup>15</sup> Void formation has been attributed to the growth of the oxide around perturbations at the alloy–scale interface.<sup>16</sup>

Corundum ( $\alpha\text{-Al}_2\text{O}_3$ ) is the most stable form of alumina and the scale formed on nickel- and iron aluminide alloys is predominantly  $\alpha\text{-Al}_2\text{O}_3$ . However, the first alumina phase to form is generally one of the metastable alumina phases – usually  $\theta$  or  $\gamma$ , but occasionally  $\delta$ . These transient phases form on nickel and iron aluminide alloys, but are especially prevalent on NiAl. The crystallographic orientation of the  $\theta$ - or  $\gamma\text{-Al}_2\text{O}_3$  phases is typically aligned with that of the alloy, and the oxides can grow epitaxially, as observed by transmission electron microscopy<sup>17</sup> and low energy electron diffraction.<sup>18</sup> Epitaxial growth is maintained for a longer time on NiAl crystals with the (001) and (012) orientations as compared to those with (011) and (111) orientations.<sup>19</sup> The transient phases grow by outward diffusion of aluminum, but at a higher growth rate (with lower activation energy) as compared with  $\alpha\text{-Al}_2\text{O}_3$ .<sup>20,21</sup> The transport of aluminum in  $\theta\text{-Al}_2\text{O}_3$  is sufficiently high for the overall growth rate of the scale to be controlled in some cases by diffusion of aluminum from the bulk of the alloy to the alloy–scale interface, rather than the diffusion of aluminum through the scale to the surface.<sup>22</sup> As expected for meta-stable phases, the transient alumina phases are more prevalent at lower temperatures.<sup>23</sup> They are also more prevalent at low oxygen partial pressures and high

humidity. The transient alumina phases eventually transform to the more stable  $\alpha\text{-Al}_2\text{O}_3$  phase, which leads to a reduction in the oxidation rate, but volumetric changes associated with the phase transformation can generate stresses that can affect the morphology of the oxide scale.

The stresses generated in the  $\alpha\text{-Al}_2\text{O}_3$  are tensile, but relax with time.<sup>24</sup> Relaxation can occur by deformation in either the alloy or the oxide, and thus depends on the microstructure. Fine grains in either phase will enhance this deformation (i.e., creep of the oxide or grain-boundary sliding in the alloy), and thus accelerate relaxation of the stresses. The stresses can also lead to convolution of the alloy–scale interface, which is commonly referred to as rumpling.<sup>25</sup> Although the interface of the rumpled scale is irregular, contact is maintained between the alloy and the scale. The rumpling is associated with swelling of the scale, which is attributed to the different diffusion rates of nickel and aluminum in NiAl (i.e., the same Kirkendall effect that leads to void formation beneath the scale).<sup>26</sup> This has led to the suggestion that rumpling is initiated by swelling of individual grains in the alloy.

The  $\alpha\text{-Al}_2\text{O}_3$  forming from the transient oxides has been reported to nucleate at both the scale–gas interface<sup>27</sup> and at the alloy–scale interface.<sup>28</sup> After nucleation, the transformation progresses in directions both perpendicular to the surface (inward or outward) and parallel to the alloy surface (lateral) and can lead to the formation of ridges as illustrated in **Figure 7**.<sup>6</sup> The lateral growth of  $\alpha\text{-Al}_2\text{O}_3$  from the nucleation site results in low-angle grain boundaries, which are oriented radially from the nucleation site. The transformation of the transient alumina phase creates tensile stresses in the  $\alpha\text{-Al}_2\text{O}_3$  that can lead to the formation of radial cracks with associated accelerated growth, which can result in ‘spokes’ along the radial cracks (not shown in **Figure 7**). The outer ridges form because the transient phases in this region are the last to transform to  $\alpha\text{-Al}_2\text{O}_3$  and the higher growth rate of the transient oxides leads to a thicker scale in the region. The ridges do eventually transform to  $\alpha\text{-Al}_2\text{O}_3$  and high-angle grain boundaries are formed in the ridges at the boundaries between  $\alpha\text{-Al}_2\text{O}_3$  grown from adjacent nuclei. The high angle boundaries allow for more short-circuit migration of oxygen (as shown in **Figure 6**), so the growth rate of the ridges can continue to be higher than that inside the ridge, where only low-angle boundaries are present. The transformation stresses are relaxed with time and the scale eventually consists of columnar  $\alpha\text{-Al}_2\text{O}_3$  grains.

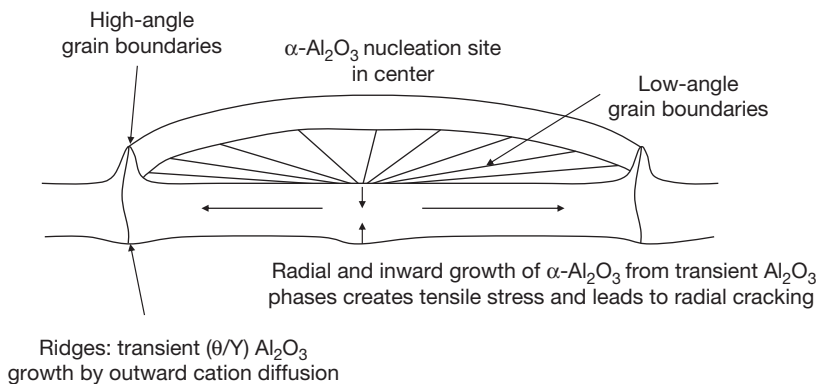


**Figure 7** Ridge formation in alumina scale formed on nickel aluminide alloys.<sup>6</sup>

In iron aluminides, the nucleation of  $\alpha\text{-Al}_2\text{O}_3$  can be enhanced by  $\text{Fe}_2\text{O}_3$ , which can be present in the oxide scale and act as a template or nucleation site for the  $\alpha\text{-Al}_2\text{O}_3$ . This transformation of the transient oxides to  $\alpha\text{-Al}_2\text{O}_3$  enhances rumpling or wrinkling of the scale. The degree of wrinkling increases with increasing temperature and aluminum content and also depends on the crystallographic structure (ordered or disordered) and orientation. Another difference between iron- and nickel aluminide alloys is that the  $\text{Fe}_2\text{O}_3$  formed on iron aluminides is often mixed with the alumina, whereas the  $\text{NiO}$  or spinel formed on nickel aluminides is usually located on the outer scale surface.

#### 1.25.2.1.2 Effect of atmospheres/impurities

In systems in which the active component provides the oxide for good corrosion resistance, such as nickel and iron aluminides, a reduced oxygen partial pressure is typically beneficial to the corrosion resistance, because it promotes the formation of the protective scale. If the oxygen pressure is sufficiently low, the oxide of the base metal could become unstable. However, even if the oxide of the base metal is stable, the dissolution of oxygen into the alloy is reduced at lower oxygen partial pressures, which reduces the formation of internal oxidation and promotes the formation of an external protective scale. Because the low oxygen partial pressure can promote a protective scale, preoxidation in low oxygen partial pressures is often used to improve the oxidation resistance. These trends apply to the nickel- and iron-aluminum systems as the amount of alumina in the scale is typically larger for oxidation in lower oxygen partial pressures, but there are exceptions. For example, the lower oxygen partial pressure stabilizes the transient oxides,

which, as discussed earlier, leads to higher growth rates. Nickel dissolves more readily in the transient oxides, so the outward diffusion of nickel is more prevalent in low oxygen partial pressures.<sup>29</sup> The dissolution of nickel has been postulated to increase the ionic transport number, but the effect on the parabolic rate constant is not significant.<sup>30</sup> At very low oxygen partial pressures, the formation of nickel oxide can be completely eliminated. Although this would seem to be beneficial, since alumina, rather than  $\text{NiO}$ , provides the good oxidation resistance, the absence of  $\text{NiO}$  can lead to higher stresses in the oxide scale.<sup>31</sup>

The presence of water vapor has less effect on the oxidation of alumina-forming alloys compared with its effect on chromia-forming alloys. Although water vapor often does not significantly affect the oxidation rate of aluminides, it can lead to increased spallation and oxidation rates for  $\text{NiAl}$ .<sup>32,33</sup> The increased spallation has been attributed to the hydration of the alumina scale. Hydrate phases are not stable at oxidation temperatures, but they can form during cooling and generate stresses in the scale, which promote scale spallation.<sup>32</sup> Although water vapor generally has little effect on the oxidation rate of iron aluminides, increased rates have been observed in some experiments.<sup>34</sup> Such variable results suggest that water vapor may influence transient phase transformations, which can be affected by minor changes in scale microstructure or morphology.

The most important impurity for the oxidation of alumina-forming oxides is sulfur, which can increase porosity at the alloy-scale interface and enhance crack propagation.<sup>35,36</sup> Sulfur diffuses to the scale and initially adsorbs to the surface of pores. Once a continuous alumina scale is formed, the sulfur segregation

expands to the alloy–scale interface. As increased porosity and sulfur segregation weaken the scale adherence, sulfur is detrimental to oxidation resistance. The diffusion rate of sulfur in NiAl decreases with increasing aluminum content; therefore the amount of segregation, and thus the associated detrimental effects, are greater for lower aluminum contents. In iron aluminides, sulfur initially adsorbs to the pore surface and subsequently cosegregates with aluminum. The presence of sulfur increases the scale convolution, which, as discussed earlier, results from growth and transformation stresses.

#### 1.25.2.1.3 Effect of alloying additions

The oxidation resistance of aluminide alloys can be improved with alloying additions. Reactive elements have been shown to be beneficial to the oxidation of aluminide alloys by reducing the amount of porosity that forms at the alloy–scale interface.<sup>37,38</sup> One of the mechanisms proposed for this beneficial effect of reactive elements is that the reactive elements segregate to the grain boundaries in the oxide scale and form oxides that block the outward diffusion of cations.<sup>36,38,39</sup> Decreasing the outward diffusion of cations leads to an increase in the proportion of growth by inward diffusion of oxygen, which, as discussed earlier, reduces the amount of porosity formed at the alloy–scale interface and thus improves scale adherence. This mechanism appears to be more prevalent in nickel aluminides compared to iron aluminides.

The reactive element most commonly added to aluminide alloys is yttrium, which can be added as a metallic alloy or as an oxide in oxide dispersion strengthened (ODS) alloys. In nickel aluminide alloys, the addition of yttrium can lead to the formation of a  $\text{NiY}_x$  phase, which promotes spinel formation and thus is detrimental to oxidation behavior. The formation of  $\text{NiY}_x$  is more likely when yttrium is added as a metallic alloy than when added as an oxide phase.<sup>40</sup> As too large an addition of yttrium can increase stresses in the oxide,<sup>41</sup> yttrium is most effective when added in small amounts as an oxide phase. At low temperatures, yttrium additions promote  $\alpha\text{-Al}_2\text{O}_3$  formation and thus decrease the oxidation rate. However, at high temperatures, where  $\alpha\text{-Al}_2\text{O}_3$  forms easily with or without yttrium additions, yttrium is detrimental by decreasing the grain size of the oxide scale, which increases the amount of short-circuit grain-boundary diffusion and thus increases the oxidation rate.<sup>42</sup>

Another common reactive element used with aluminide alloys is hafnium, which improves the adhesion of the oxide scale.<sup>43</sup> The improvement is

observed at temperatures lower than those at which the general reactive element effects are observed, and is attributed to the formation of hafnium oxides that protrude into the scale and provide anchors, which improve adhesion.<sup>44</sup> Hafnium also improves the plasticity of the scale, which increases the magnitude of stresses that can be accommodated without spallation. The addition of hafnium can significantly extend the lifetime of aluminide alloys, particularly when exposed to cyclic oxidation.<sup>45</sup>

Zirconium is also a commonly added alloy, and, like yttrium, can lead to the formation of an additional intermetallic compound,  $\text{NiZr}_5$ , which can lead to the formation of  $\text{ZrO}_2$  in the scale; therefore, the amount of zirconium added must be limited. Small amounts of zirconium can improve adherence and reduce oxide scale growth rate by increasing grain size. However, zirconium can also be detrimental by impeding the formation of  $\alpha\text{-Al}_2\text{O}_3$  and promoting outward scale growth, which increases growth rates. Zirconium is a strong carbide former, so if zirconium is added with carbon, which is commonly added to iron aluminides, the ratio of zirconium to carbon must be controlled, so that the appropriate amount of zirconium is available to beneficially affect the oxidation behavior.

Other reactive elements, such as titanium and cerium, have also been shown to decrease the oxidation rate, either by decreasing the outward diffusion of aluminum or by increasing the grain size of the oxide. However, not all reactive elements are beneficial to oxidation behavior; e.g., lanthanum leads to both a higher oxidation rate and lower scale adherence.

Transition metals are often used as alloying additions for aluminide alloys. Chromium is commonly added to intermetallic alloys to improve ductility and minimize environmentally assisted crack embrittlement. Chromium is beneficial to the alumina-forming nickel- and iron-based alloys, because it reduces the amount of aluminum required to avoid internal oxidation and form a protective scale. Chromium has a similar effect in  $\text{Ni}_3\text{Al}$  as it reduces the amount of aluminum required to maintain an effectively rehealing scale for long oxidation exposures. Chromium affects the transformation of  $\theta\text{-Al}_2\text{O}_3$  to  $\alpha\text{-Al}_2\text{O}_3$ , although the reported effects are mixed as chromium has been reported to both inhibit<sup>42</sup> and promote<sup>21</sup>  $\alpha\text{-Al}_2\text{O}_3$  formation. Chromium dissolves in  $\theta\text{-Al}_2\text{O}_3$ , which would explain the inhibitive effect, as the chromium diffusion may be required for  $\alpha\text{-Al}_2\text{O}_3$  formation.<sup>46</sup> At the same time, chromium appears to accelerate

nucleation of  $\alpha$ -Al<sub>2</sub>O<sub>3</sub>. The effects of chromium on the oxidation rate are likewise mixed as it has been reported to both increase and decrease the oxidation rate. Chromium can segregate to the alloy–scale interface and lead to additional phase formation, which decreases adherence and is therefore detrimental to oxidation resistance.

The effects of niobium and tantalum are more consistent than those of chromium. Like chromium, niobium and tantalum are added to improve the mechanical properties. In both cases, a mixed oxide, NiTa<sub>2</sub>O<sub>6</sub> or NiNb<sub>2</sub>O<sub>6</sub>, forms and is detrimental to oxidation resistance. However, if added in small amounts, niobium and tantalum improve the mechanical properties with an acceptably minimal effect on oxidation resistance. Although increasing the niobium content is detrimental to the oxidation resistance, very large niobium contents (i.e., NiAl + NbAl<sub>3</sub> alloys) can lead to the formation of Laves phases, which promote the formation of a protective alumina scale during oxidation.

Refractory metals, such as molybdenum, tungsten, and vanadium, are generally detrimental because of the formation of liquid or gaseous oxides. For example, although molybdenum does not significantly affect short-term oxidation behavior, for longer exposures, the formation of molybdenum oxide vapor phases is detrimental.

Noble metals, such as Pt, Re, and Rh, can be beneficial to the adherence of the oxide scale.<sup>6</sup> For example, the beneficial effect of platinum to the oxidation behavior of NiAl is generally attributed to its interaction with sulfur.<sup>47</sup> Platinum, like sulfur, segregates to the pore surfaces and alloy–scale interfaces. Any platinum present at these locations displaces sulfur, and thus decreases the detrimental effects associated with sulfur segregation. Platinum can also be detrimental by stabilizing  $\theta$ -Al<sub>2</sub>O<sub>3</sub>, which inhibits the formation of  $\alpha$ -Al<sub>2</sub>O<sub>3</sub>, thus increasing the oxidation rate.<sup>23</sup> However, because of the catastrophic effects of scale spallation, the beneficial effects of improved adherence can often outweigh the detrimental effects of increased growth rates. Scale spallation is particularly critical when the aluminide is used as a bond for thermal barrier coatings, which will be discussed in a later section. Large amounts of platinum additions can lead to the formation of a platinum aluminide phase (PtAl<sub>2</sub>), which minimizes depletion of aluminum from the alloy–scale interface. Maintenance of a sufficient aluminum level at the alloy–scale interface prevents the formation of Ni<sub>3</sub>Al, which can lead to local stresses at the

interface, and improves the long-term oxidation resistance of the alloy.

As mentioned earlier, carbon is used to strengthen iron aluminide alloys. Carbon is generally detrimental to oxidation resistance. The oxide scale formed on the carbide phase (Fe<sub>3</sub>AlC<sub>x</sub>) that strengthens the alloy is thicker than, but has the same morphology as, the scale formed on the metal phase. As mentioned earlier, when used with strong carbide formers (e.g., zirconium), the effects of carbide formation must be considered in optimizing the alloy composition.<sup>45</sup> Boron, another interstitial additional alloy, is also generally detrimental to oxidation behavior, but can be beneficial when added with others, such as zirconium or hafnium.

### 1.25.2.2 Titanium Aluminides

The high reactivity of titanium, relative to iron and nickel, creates additional challenges for the formation and maintenance of an alumina scale, because of the competition between aluminum and titanium for oxide formation. However, as mentioned earlier, titanium aluminides have excellent specific properties and so have been developed for aerospace application. There are several reviews of their oxidation behavior.<sup>48–51</sup>

#### 1.25.2.2.1 Scale properties/structure

The minimum aluminum content required for alumina formation on titanium aluminide alloys is much higher than that for alumina formation on nickel or iron aluminide alloys. TiAl is in equilibrium with TiO and Al<sub>2</sub>O<sub>3</sub>, but any lower compositions are not in equilibrium with Al<sub>2</sub>O<sub>3</sub>; so, even before any aluminum depletion occurs, TiAl is at the borderline aluminum composition for Al<sub>2</sub>O<sub>3</sub> formation. Thus, scales formed on titanium aluminides generally contain both aluminum and titanium oxides.

The typical scale morphology of the scale formed on TiAl is shown schematically in Figure 8.

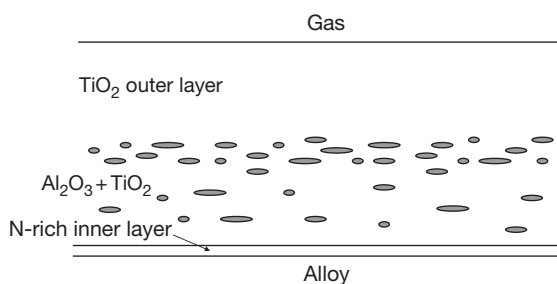


**Figure 8** Schematic of scale formed during oxidation of titanium aluminide alloys.

Although  $\text{TiO}$  is the titanium oxide in equilibrium with the alloy,  $\text{TiO}_2$  is stable in air. While there may be some titanium oxides with valence lower than +4 at the alloy–scale interface, the major portion of the titanium oxide is rutile  $\text{TiO}_2$ . Rutile is an oxygen-deficient oxide, for which the predominant ionic point defects are oxygen vacancies at high oxygen partial pressures and titanium interstitials at low oxygen partial pressures. Platinum marker experiments on the oxidation of pure titanium have shown that the new oxide forms in the middle of the oxide, indicating that the oxygen vacancies are predominant in the outer scale and titanium interstitials are predominant in the inner scale. The oxidation of titanium aluminide is further complicated, as the scale also contains aluminum oxides. As shown in **Figure 8**, the aluminum oxide is often dispersed in the rutile in the inner portion of the scale. The outer portion of the scale is usually  $\text{TiO}_2$ . Sometimes, as shown in **Figure 8**, there is a layer in the middle of the scale where the amount of alumina is higher than that in the inner portion of the scale. These layers could be in part due to the oxygen partial pressure dependence of the ionic point defects in rutile as described earlier. Although the defect chemistry has not been well established, platinum marker experiments have shown that, as in the case of pure titanium, the new oxide forms in the middle of the scale. There is typically an inner layer, which contains nitrogen if the oxidation is performed in air. This inner layer may also contain titanium in a lower valence and/or mixed oxides. The mixed titanium–aluminum oxide phases (X-phase, Z-phase, NCP) are not thermodynamically stable at the oxidation temperature, but can form at the interface and affect the oxidation behavior.

The growth rate of rutile is much higher than that of alumina, so an alumina scale is desired for oxidation resistance. A continuous alumina layer would provide the lowest oxidation rate and has been achieved on some titanium aluminide alloys. However, a mixed scale, as shown in **Figure 8**, is more typical and the growth rate of such a scale is between the rates for alumina and titania growth. Although increasing the amount of alumina is beneficial for oxidation resistance, the morphology is also important. For example, the more continuous the aluminum-rich layer in the middle of the scale (**Figure 8**), the slower is the growth rate. Thus, control of the oxidation rate of titanium aluminum alloys depends critically on the scale morphology. Because of the mixed scale that grows at a rate higher than pure alumina, the oxidation resistances of titanium aluminide alloys are generally

inferior to those of nickel and iron aluminides, so titanium aluminide alloys are usually considered for lower temperature applications.

#### **1.25.2.2.2 Effect of atmosphere and pretreatment**

The presence of a nitrogen-containing layer suggests that nitrogen may influence oxidation behavior. Nitrogen is often considered essentially inert for many oxidation processes. However, titanium, in particular, and aluminum to a lesser extent, are nitride formers, so nitrogen does affect oxidation behavior. The oxidation behavior of titanium aluminide alloys in air is different from that in argon–oxygen mixtures.<sup>49,50</sup> Although the results are somewhat varied, the oxygen rates in air are typically higher than those in oxygen without nitrogen for the same oxygen partial pressure. The detrimental effect of nitrogen is attributed to the nitrogen-containing layer promoting the formation of  $\text{TiO}_2$ . Although the nitride layer contains aluminum and titanium, the amount of titanium is typically higher than that of aluminum. Nitrogen has also been shown to be beneficial to the oxidation behavior of some alloys – particularly alloys with lower aluminum content. The beneficial effect of nitrogen is attributed to nitrogen doping the rutile and decreasing the concentration of the mobile defect, which decreases transport through the scale. Nitrogen may also promote the formation of alumina in the scale by reducing the titanium activity in the alloy.

Because of the delicate balance between alumina and titania formation, small changes can determine which phase nucleates and grows; subtle differences can therefore affect oxidation behavior. For example, surface finish has been shown to significantly affect the oxidation rate in oxygen, but not in air.<sup>52</sup> The surface finish most likely affects nucleation, which implies that the superior performance in oxygen is due to the formation of a phase that is inhibited by either the presence of nitrogen or the surface roughness. Such phenomena are difficult to characterize because they likely depend on transient phases and microstructures, which are not present when the sample characterization is performed after the oxidation experiment is completed.

The alloy microstructure also affects oxidation behavior. For the same alloy composition, the oxidation rate with a lamellar microstructure is lower than that for a duplex microstructure.<sup>53</sup> One of the challenges in the application of titanium aluminide alloys is control of the microstructure, as the microstructure also affects the mechanical properties. Production of



parts with the same microstructure throughout the sample, as well as between samples, is a significant engineering challenge. Microstructural inhomogeneities can lead to locally high corrosion rates or local mechanical weaknesses.

Water vapor in the atmosphere can increase the oxidation rate. This increase is generally attributed to increasing water vapor transport in the scale. Although water vapor does not significantly affect the growth of alumina, it does affect transport in rutile, which is generally the continuous phase in the oxidation scale and thus dominates the overall scale growth rate.

Preoxidation and presulfidation have been used to improve the oxidation resistance of titanium aluminide alloys. There are often conditions in which a protective scale would not form, but could be maintained if it had already formed. Under such conditions, a pretreatment in carefully controlled conditions can be used to form a protective scale, which subsequently grows at a slow rate.

#### 1.25.2.2.3 Effect of alloying additions

The aluminum content in titanium aluminide alloys is more critical than in nickel and iron aluminide alloys. The oxidation resistance of  $Ti_3Al$  is generally poor, and in binary titanium–aluminum alloys, at least 48–50 at% aluminum is generally required for good oxidation resistance. The amount of aluminum required, however, can be reduced with alloying additions.

The alloying addition most widely used for improving the oxidation resistance of titanium aluminide alloys is niobium. During oxidation, the alloy beneath the scale is enriched with niobium, but niobium is also incorporated in the scale. Several explanations for the beneficial effects of niobium additions have been proposed. One explanation is that niobium increases the activity of aluminum in the alloy, but this has not been supported by subsequent thermodynamic measurements of the aluminum activity.<sup>49</sup> Another explanation is that niobium increases the diffusion of aluminum and/or decreases the diffusion of oxygen in the alloy, which reduces the amount of internal oxidation of aluminum and promotes a more continuous alumina scale. The beneficial effect of niobium has also been attributed to niobium doping the rutile scale and decreasing the concentration of oxygen vacancies and/or titanium interstitials. Niobium has also been reported to improve the mechanical integrity of the scale, which improves the resistance to cyclic oxidation. Large amounts of niobium, however, can be detrimental if a  $Nb_2O_5$  phase forms in the oxide scale.

Another common alloying addition for titanium aluminide alloys is chromium, which is added primarily to improve the mechanical properties of the alloy. Small amounts of chromium lead to an increase in the oxidation rate. This increase is typically attributed to the chromium doping the rutile scale and increasing the concentration of oxygen vacancies and/or titanium interstitials. Larger amounts of chromium, however, are beneficial to oxidation resistance. The beneficial effect has been attributed to chromium increasing the aluminum activity in the alloy. While increases in the aluminum activity have been measured, the magnitude of the increase is not sufficient to explain the observed improvements. Another explanation is related to the formation of Laves phases, which form in alloys with high chromium content. The Laves phases have low oxygen solubility and lower titanium activity, both of which promote a more protective alumina scale.

Niobium and chromium are sometimes added together and, fortunately, the oxidation behavior appears to be dominated by niobium rather than by chromium. The oxidation rates of alloys with a combination of niobium and other alloying additions such as manganese, zirconia, and hafnium are also similar to those of alloys with niobium as the only alloying addition.

Like chromium, other transition metals, such as iron, nickel, manganese, and vanadium, are generally detrimental to the oxidation of titanium aluminide alloys, while refractory metals, such as tungsten and molybdenum, are beneficial. The beneficial effects of tungsten, like those of niobium, are attributed to decreasing the oxygen solubility in the alloy (to inhibit internal oxidation) and doping of the rutile (to reduce oxygen vacancies and/or titanium interstitial concentrations).

Silicon additions can be beneficial to the oxidation resistance of titanium aluminide alloys. If silicon is present in the alloy, silica will usually form in the scale. However, silica is often dispersed so that it is not effective for reducing the oxidation rate. In some cases, silicon additions lead to a continuous silica layer, which provides a barrier to oxygen diffusion and thus improves the oxidation resistance. However, this layer leads to stresses during thermal cycling and is thus detrimental to the cyclic oxidation resistance.

Noble metals have mixed effects on the oxidation of titanium aluminide alloys. Platinum and gold are detrimental to oxidation resistance, but silver is beneficial.<sup>54</sup> Silver promotes the formation of  $\theta-Al_2O_3$ , which, as discussed earlier, grows at a faster rate than  $\alpha-Al_2O_3$  and thus would seem to be detrimental. However, the  $\alpha-Al_2O_3$  formed from transient alumina

is continuous and the oxidation rate of the alloy is the same as that for the growth of an alumina scale. The beneficial effect of silver decreases with increasing temperature, presumably because it results from the transient formation of  $\theta$ - $\text{Al}_2\text{O}_3$ , which is metastable and thus becomes less prevalent with increasing temperature. The addition of small amounts (1–3%) of chromium to silver-doped alloys is detrimental to oxidation resistance, but with larger amounts (5–7%) the oxidation rate is reduced to that of an alumina-forming alloy.<sup>55</sup> The excellent oxidation resistance of these alloys, like the high-chromium-content alloys described earlier, is attributed to the presence of Laves phases in the alloy microstructure.

Reactive elements are used as alloying additions in titanium aluminide alloys, but not to the extent, or to the same beneficial effect, as in nickel and iron aluminide. Small amounts of reactive elements, such as zirconium, hafnium, and yttrium, are beneficial to oxidation resistance. Hafnium has been shown to improve scale adherence. Zirconium, while beneficial for short oxidation exposures, eventually leads to the formation of zirconia, the transformation of which creates stresses in the oxide scale.

One of the most successful recent approaches for improving the oxidation resistance of TiAl-based alloys is the addition of halogen elements, such as fluorine, chlorine, or bromine. The addition of the appropriate amount of a halogen element can lead to a continuous alumina scale and kinetics following the growth of an alumina scale. Various explanations have been proposed for the beneficial effect of halogen additions. One explanation is that chlorine doping of the scale decreases the oxygen vacancy and/or titanium interstitial concentration (i.e., the same as that of niobium and tungsten doping).<sup>56</sup> Other explanations are that the formation of  $\text{TiO}_2$  is inhibited by the presence of the halogen element<sup>57</sup> or by a reduction in titanium activity due to volatilization of titanium. The explanation that best illustrates the long-term effect is shown in Figure 9.<sup>58,59</sup> In this model, aluminum is transported from the alloy to the scale–gas interface in a gas phase that diffuses through pores or microcracks in the scale. Once the aluminum-containing vapor reaches the scale surface, it reacts with oxygen to form alumina and evolves chlorine, which can diffuse back to the alloy and form more of the aluminum-containing species. The chlorine that evolves is thus recycled and provides a mechanism for the transport of aluminum to heal pores and/or cracks in the scale. For this mechanism to work, chlorine partial pressure must be in a critical

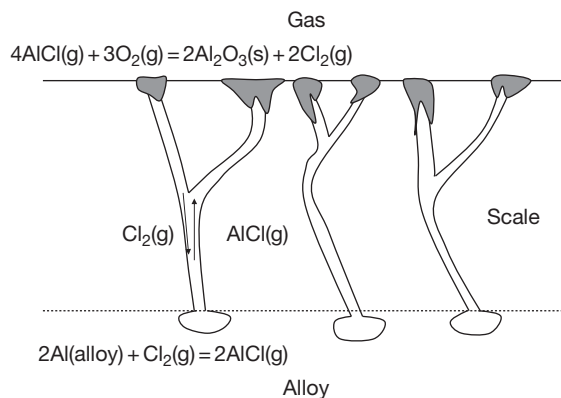


**Figure 9** Vapor transport mechanism for beneficial effect of halogen additions on the oxidation of titanium aluminide alloys.<sup>58,59</sup>

range: it must be high enough to transport sufficient aluminum to maintain the protective scale, but if it is too high, the partial pressure of a titanium chloride species may exceed that of the aluminum-containing species. When the pressure of the titanium species is too high the alumina forms in a whisker-like morphology, which does not provide adequate protection.

To impart its beneficial effect on oxidation resistance, the halogen element is needed only at the surface, so ion implantation is often used to add halogen elements to titanium aluminide alloys. The same is true for other alloying elements added for improved corrosion resistance, especially those which may have detrimental properties on the mechanical properties of the alloy. Thus, ion implantation is used to alloy titanium aluminide alloys with other metallic elements, as well as nonmetallic elements, such as phosphorous.<sup>60</sup> This technique minimizes the amount of alloying elements used by localizing the addition to the location at which the element is needed. This technique would not be effective for an element that is consumed during oxidation, as there is a limited source, which could become depleted after long exposures. However, in the case of halogen additions, the halogen element appears to be recycled, and ion implantation has been shown to improve oxidation resistance for long periods of time.

### 1.25.2.3 Other Aluminides

Most of the aluminide alloys used are from the nickel–, iron–, or titanium–aluminum system. However, there are a few other systems that have been developed, including aluminides of noble and active metals.

As described earlier, the beneficial effect of platinum additions to NiAl is due, in part, to the formation

of a platinum aluminide phase at the alloy–scale interface. Since platinum does not form a stable solid oxide, the only oxide that can form on a platinum aluminide alloy is alumina. The microstructure of the alumina scale is similar to that formed on NiAl, but the adhesion is better on platinum aluminide alloys.<sup>61</sup> The scale growth occurs predominately through short-circuit grain boundary diffusion, so the grain size of the oxide scale affects the oxidation rate. The adhesion can be further improved with zirconia additions, which segregate to the alloy–scale interface and lead to a convoluted, but strong, interface between the alloy and the scale.<sup>62</sup> A platinum aluminide coating is clearly expensive and thus is used in applications where a small amount of material is required, such as in a bond coat, which will be discussed in a later section.

Other noble metal aluminides include those of ruthenium and iridium. Ruthenium aluminide has better ductility than most aluminide alloys and has good oxidation resistance. The scale morphology suggests that the scale grows by outward diffusion of aluminum, although voids are not formed beneath the scale.<sup>63</sup> Two-phase Ru(Al) + RuAl are particularly attractive because of their good ductility. However, the oxidation resistance decreases as the amount of the metal phase increases, because the high oxygen diffusivity of the metallic phase leads to internal oxidation.<sup>64</sup> The oxidation resistance can be improved with platinum additions, but weight loss still occurs during cyclic oxidation.<sup>65</sup> Iridium aluminide is used because iridium has very low oxygen permeability and thus is an excellent oxygen barrier. The oxidation rates of iridium–aluminum alloys are representative of pure alumina scale growth.<sup>66</sup>

An aluminide alloy system that has been investigated because of its high melting point and low density is niobium aluminide.<sup>6</sup> However, niobium aluminides, even with large aluminum concentrations (e.g., NbAl<sub>3</sub>), form mixed oxide scales rather than alumina scales. In particular, the scales contain AlNbO<sub>4</sub> and Nb<sub>2</sub>O<sub>5</sub> and are thus not protective. Zirconium aluminide has been investigated but has poor oxidation resistance because of the formation of ZrO<sub>2</sub>. ZrO<sub>2</sub> not only has high oxygen permeability, but also undergoes phase transitions, which generate stresses in the oxide scale.

### 1.25.3 Hot Corrosion

The presence of other reactive species, such as sulfur and chlorine, in the environment can accelerate the

corrosion of intermetallic alloys. The corrosion can be enhanced if the additional species is in the gas phase, but corrosion is further accelerated if a condensed molten salt phase is formed.

#### 1.25.3.1 Sulfur-Containing Environments

The sulfidation behavior of intermetallic alloys has recently been reviewed.<sup>67</sup> The effects of sulfur on the corrosion rate depend on the oxygen partial pressure and whether a condensed phase is formed.

##### 1.25.3.1.1 Gaseous

The addition of SO<sub>2</sub> to an oxidizing environment does not significantly affect corrosion behavior. While the scale formed in SO<sub>2</sub> contains oxides and sulfides, scales formed in oxygen with SO<sub>2</sub> contain mostly oxides with little or no sulfides.<sup>68</sup> One notable difference between oxidation with and without sulfur is that silver, which as discussed earlier, is beneficial to the oxidation behavior of TiAl, is detrimental to the corrosion of TiAl in sulfur-containing atmospheres.

The corrosion behavior changes as the oxygen partial pressure is reduced. In H<sub>2</sub>–H<sub>2</sub>S–H<sub>2</sub>O mixtures, the oxygen partial pressure is typically sufficiently high for alumina to form and alumina is present in the outer portion of the scale. However, the inner portion of the scale consists of sulfides, which can be mixed, but usually contain little or no aluminum (e.g., TiS for TiAl<sup>69</sup> or FeS for FeAl<sup>70</sup>). As expected from the low aluminum content in the sulfides, increasing the aluminum content in the alloy increases the amount of alumina in the scale. For the corrosion of TiAl, TiO<sub>2</sub> is also formed in the scale. In addition, the rapid transport of titanium in the inner TiS layer leads to depletion of titanium in the alloy, so phases with higher aluminum content, such as TiAl<sub>2</sub> and TiAl<sub>3</sub>, form beneath the scale. The addition of niobium improves the sulfidation resistance of both FeAl and TiAl. Niobium oxides and sulfides form in the scale and the scale adherence is improved with niobium additions.<sup>71</sup>

With further decrease in the oxygen partial pressure in H<sub>2</sub>–H<sub>2</sub>S environments, the oxides become less stable and the scale consists almost entirely of sulfides. For FeAl alloys, FeS and mixed (Fe,Al)S phases are formed in sulfidizing environments. The predominant phase formed during sulfidation of NiAl is Ni<sub>3</sub>S<sub>2</sub>, which can also contain Al<sub>2</sub>S<sub>3</sub> or NiAl<sub>2</sub>S<sub>4</sub> inclusions. For low H<sub>2</sub>S levels the sulfidation rate is reasonably low, but as the H<sub>2</sub>S content increases a Ni–Ni<sub>3</sub>S<sub>2</sub> eutectic forms and leads to large (~4 orders of magnitude) increases in corrosion

rates. The addition of chromium leads to the formation of  $(\text{Cr},\text{Al})_3\text{S}_4$  and further degrades the sulfidation resistance.<sup>72</sup> Similarly, zirconium additions increase the amount of internal corrosion and increase the sulfidation rate. In general, nickel aluminides have poor sulfidation resistance.

TiAl forms a layered sulfide structure in low oxygen-partial-pressure sulfidizing atmospheres.<sup>73</sup> The scale typically contains  $\text{Ti}_3\text{S}_4$ , TiS, and  $\text{Al}_2\text{S}_3$ . The sulfide scale typically contains more titanium than aluminum, so the alloy beneath the scale is depleted in titanium, and aluminum-rich phases, such as  $\text{TiAl}_2$  and  $\text{TiAl}_3$ , form. Alloying addition affect the specific sulfide phases formed, but in most cases do not significantly affect the overall sulfidation rate. Silver and copper additions, however, increase the amount of sulfidation.

### 1.25.3.1.2 Molten salts

The corrosion behavior changes when sulfur is present in a condensed salt on the alloy surface. An oxide scale that is relatively stable in a gaseous environment may dissolve in the salt and lead to increased corrosion rates.

The reaction between FeAl and  $\text{Na}_2\text{SO}_4$  produces a complex mixture of oxygen- and sulfur-containing compounds (e.g.,  $\text{NaAlO}_2$ ,  $\text{NaAl}(\text{SO}_4)_2$ ,  $\text{Fe}_2\text{O}_3$ ,  $\text{Al}_2\text{O}_3$ ). The corrosion of the alloy occurs by dissolution of the oxide in the molten salt and internal sulfidation of the alloy. Corrosion resistance can improve with increasing temperature as the more rapid growth of the alumina results in a more protective scale.<sup>74</sup> Similarly, the addition of dispersed  $\text{Al}_2\text{O}_3$  to the alloy improves the corrosion resistance by stabilizing the  $\text{Al}_2\text{O}_3$  in the scale. Carbon additions have been shown to improve the corrosion resistance of FeAl by forming carbides that inhibit sulfur diffusion into the alloy. Boron additions, however, have mixed effects as they have been shown to be both beneficial and detrimental to hot corrosion resistance.

Aluminization of nickel-based superalloys has been used to improve hot corrosion resistance. The oxide scale formed on nickel aluminide alloys during hot corrosion in molten sulfates contains an outer layer of NiO or  $\text{NiAl}_2\text{O}_4$ . The latter has better hot corrosion resistance because of the lower solubility of the spinel, as compared to NiO, in the molten salt.<sup>75</sup> The resistance to molten sulfate corrosion can be improved with the addition of platinum, palladium, or chromium.

The oxide formed during the corrosion of titanium aluminide alloys in molten sulfates contains  $\text{TiO}_2$  and  $\text{Al}_2\text{O}_3$  with an inner layer of sulfides as

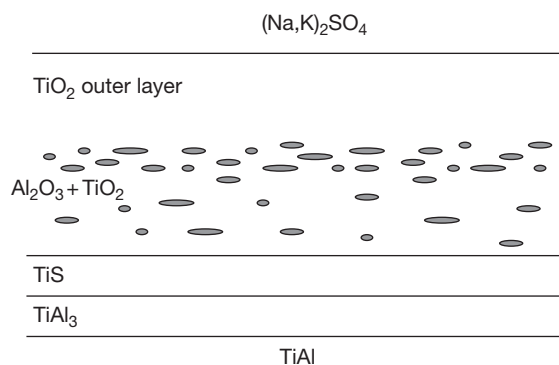


**Figure 10** Schematic of scale formed during corrosion of Ti-50Al in  $(\text{Na},\text{K})_2\text{SO}_4$  at 900 °C.<sup>76</sup>

shown schematically in Figure 10.<sup>76</sup> As with sulfidation in a gaseous environment, the scale contains more titanium than aluminum, so the alloy beneath the scale is depleted in titanium and a layer of  $\text{TiAl}_3$  is formed. Also, as with other sulfidation and oxidation processes, increasing the amount of aluminum in the alloy increases the amount of alumina in the scale and improves corrosion resistance. Niobium is beneficial to the oxidation resistance as it improves scale adherence.<sup>76</sup> Chromium aids the hot corrosion resistance, and, as will be discussed later, is often added to protect aluminide coatings. Vanadium additions, however, increase the amount of scale spallation and are thus detrimental.

### 1.25.3.2 Chlorine-Containing Environments

Chlorine enhances the corrosion rate of most materials and intermetallic alloys are no exception. Chlorine can be present in the gas phase or in a molten salt – either a chloride or mixed salt.

#### 1.25.3.2.1 Gaseous

The primary effect of chlorine in the gas-phase corrosion of aluminide alloys is the formation of volatile chloride species.<sup>77</sup> In particular, the vapor pressure of  $\text{AlCl}_3$  is relatively high and can lead to loss of aluminum and/or void formation in the scale, both of which are detrimental, as loss of aluminum decreases the amount of alumina in the scale, and void formation degrades scale adherence. The addition of zirconium has been shown to reduce the loss of aluminum and thus improve corrosion resistance. In some cases, the liquid chlorides can form from reaction with the chlorine in the gas and can enhance the corrosion rate.

### 1.25.3.2.2 Molten salts

Molten chlorides can also be formed from salts deposited on the alloy surface. For example, the reaction of titanium aluminides with sodium chloride results in the formation of  $\text{TiO}_2$ ,  $\text{Al}_2\text{O}_3$ , and  $\text{NaTiO}_2$ . The increase in corrosion rate due to the presence of sodium chloride is generally attributed to vapor phase transport via chloride gas species.<sup>78</sup> As discussed earlier, controlled amounts of chlorine, or other halogens, can improve the oxidation of titanium aluminide alloys, but for this beneficial effect to occur, the chlorine content must be limited so that transport of aluminum, but not titanium, occurs. The chlorine levels present during hot corrosion in  $\text{NaCl}$  are high enough for the transport of both titanium and aluminum from the alloy to the scale surface. Under these conditions, the alumina forms as whiskers, rather than as a protective layer, so the corrosion rate is increased.

Hot corrosion in lithium-containing chloride salts, such as  $\text{LiCl-Li}_2\text{O}$  or  $\text{KCl-Li}_2\text{O}$ , results in the formation of multiple mixed oxides. For  $\text{TiAl}$ , in addition to  $\text{TiO}_2$  and  $\text{Al}_2\text{O}_3$ ,  $\text{LiAlO}_2$  forms in the outer portion of the scale, while  $\text{Li}_2\text{TiO}_3$  forms in the inner portion of the scale.  $\text{LiAlO}_2$  also forms during corrosion of  $\text{NiAl}$  and  $\text{FeAl}$  in lithium-containing salts, but  $\text{NiAl}$  is more resistant than  $\text{FeAl}$  to chloride attack.<sup>79</sup>

The corrosion of titanium aluminide alloys in mixed sulfide-chloride molten salts is similar to that in chloride salts, although in some cases the corrosion in a molten chloride is faster than that in a mixed salt. The chloride vapor transport mechanism described above is active in the corrosion of  $\text{TiAl}$  in a mixed chloride-sulfide salt. Chromium and silver additions to  $\text{TiAl}$  improve the hot corrosion resistance by improving the adherence of the mixed oxide phase (Z-phase) formed at the alloy-scale interface.<sup>76,80</sup> The morphology of the scale formed on titanium aluminide containing 1–3% silver is shown in Figure 11.<sup>80</sup> Niobium, which, as discussed earlier, is generally beneficial to the corrosion of  $\text{TiAl}$ , can be detrimental when added in large amounts because of sulfide phase formation.

The corrosion of nickel aluminide alloys in mixed sulfide-chloride molten salts is similar to that in sulfide melts, presumably due to the absence of significant partial pressures of nickel chloride gas species to provide vapor phase transport analogous to that which occurs in titanium aluminide alloys. The oxide scale formed on nickel aluminide alloys consists of a layer of  $\text{NiO}$  and  $\text{Al}_2\text{O}_3$  above an inner layer of sulfides. The alloy beneath the scale is depleted in

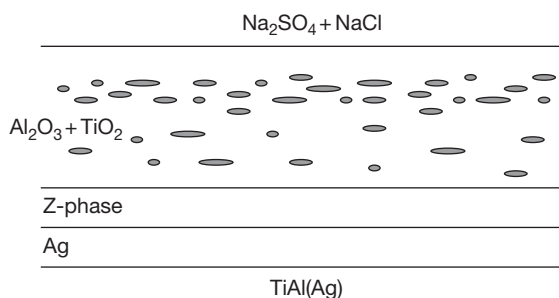


**Figure 11** Schematic of scale formed during corrosion of  $\text{Ti-48Al-(1-3)Ag}$  in  $\text{Na}_2\text{SO}_4 + \text{NaCl}$  at  $800^\circ\text{C}$ .<sup>80</sup>

aluminum and the scale is generally not protective. Silicon additions increase the amount of alumina, and thus improve the oxidation resistance. Oxide ( $\text{Y}_2\text{O}_3$ ) dispersions can also improve the corrosion resistance by improving scale adherence.<sup>81</sup>

### 1.25.3.3 Others

Molten carbonates can also lead to enhanced corrosion of aluminide alloys. Corrosion in lithium-containing carbonates is similar to that in other lithium-containing salts in that  $\text{LiAlO}_2$  is present in the corrosion scale. Because of their high aluminum content,  $\text{NiAl}$  and  $\text{FeAl}$  are used as replacements or coatings on stainless steels and superalloys in molten carbonate environments.

As mentioned earlier, vanadium is detrimental to the corrosion of  $\text{TiAl}$  in sulfate salts. Vanadium is also detrimental when present in a corrosive salt. Vanadium-containing salts are more corrosive than sodium chloride to iron aluminides. The scale formed in  $\text{V}_2\text{O}_5$ -containing salts consists of several mixed oxides and can be quite complex. For example, the weight loss of  $\text{FeAl}$  in a  $\text{V}_2\text{O}_5\text{-Na}_2\text{SO}_4$  mixture increases with increasing temperature up to about  $700^\circ\text{C}$  and then decreases at higher temperatures due to the formation of a more protective scale. The addition of  $\text{Al}_2\text{O}_3$  to the alloy provides some improvement in scale adherence.<sup>82</sup>

## 1.25.4 Coatings

Aluminide alloys are attractive as oxidation resistant coatings, because ductility, while desirable, is less critical in a coating than it is in a structural load-bearing member. Aluminide coatings can be used as coatings for other aluminide alloys with inferior oxidation resistance, but superior mechanical properties.



In addition, aluminide coatings can be applied to metallic alloys that have high ductility, but contain little or no aluminum and thus may have poor oxidation resistance. Coatings can be applied by a variety of techniques, some of which will be discussed in the chapter on **High Temperature Coatings: Protection and Breakdown**. However, diffusion coatings are widely used for aluminide intermetallic alloys and will be discussed in this chapter. Aluminum is typically supplied in a gaseous or liquid phase, but solid-state diffusion is required for the growth of the coating. For aluminide coatings of the same base alloy (e.g., NiAl on nickel-based alloys), only aluminum need be added to form an aluminide phase, although other elements are often added for improved properties. However, for aluminide coatings with a different base than the substrate (e.g., NiAl on steel), both elements of the aluminide phase (e.g., nickel and aluminum for NiAl on steel), must be provided, which complicates the coating process.

#### 1.25.4.1 Aluminide Coatings with Same Base as Substrate

Increasing the aluminum concentration at the surface is especially useful in the titanium–aluminum system, since, as discussed earlier, TiAl is a borderline alumina-former. The formation of TiAl<sub>3</sub> coatings on TiAl-based alloys can improve oxidation resistance.<sup>83</sup> A similar approach can be used in the nickel or iron systems, but an increase in the aluminum content of NiAl- or FeAl-based alloys is less critical, because, with the lower stability of the nickel- and iron-oxide phases, the alumina phase is more stable and the additional aluminum content only provides significant benefit for long exposure times when aluminum depletion occurs. However, aluminide coatings can significantly improve the oxidation resistance of metallic alloys with little or no aluminum. For example, aluminide coatings have been used for more than 30 years to improve the oxidation resistance of superalloys.<sup>84</sup> Such alloys contain several alloying additions, the concentrations of which can change during the diffusion process, and can lead to undesired microstructural changes, such as the formation of topographically close packed (TCP) phases.<sup>85</sup> Similarly, the corrosion resistance of steel can be improved by aluminization to form an iron aluminide coating. In this case, the presence of carbon, which can lead to undesired carbide precipitation, places restrictions on the coating process.<sup>86</sup> In the following sections, the application of aluminide coating processes to simple

and complicated alloy systems will be discussed. While alloying additions from the substrate alloy can complicate the coating process, the coating process can also be used to introduce desired alloying additions for improved coating performance.

##### 1.25.4.1.1 Simple aluminide coatings

The aluminum for growth of the aluminide coating can be introduced through several different methods. One method is to sputter an aluminum, or aluminum-containing, layer on the surface of the alloy. The sputtering process is typically followed by a high temperature anneal for diffusion of the aluminum into the alloy. Another method is to place the substrate in molten aluminum, which provides good contact with the alloy as well as protection from oxidation. The most common method for producing aluminide coatings, however, is pack cementation.

The pack in the pack cementation process consists of 10–30% of an aluminum source (aluminum metal or aluminum-containing alloy) and a few percent of an activator (typically a halide species), which are dispersed in an inert filler (typically alumina). Upon heating, aluminum halide gaseous species are formed and transport aluminum to the substrate material. Pure aluminum can be used as the aluminum source for process temperatures below the melting point of aluminum, while aluminum-containing alloys must be used for higher temperature deposition. Pack cementation processes are referred to as high activity or low activity, based on the aluminum activity in the aluminum source. Coatings formed in a high-activity process are inward-growing as aluminum diffuses into the alloy. Low-activity processes (e.g., Al/Ni < 1), however, result in the outward growth as both elements (e.g., Ni and Al) are deposited. The low-activity process is commonly referred to as chemical vapor deposition (CVD), as both, or all, components of the coating are deposited. One of the advantages of a low-activity process is that impurity elements, such as sulfur and phosphorus, are removed during the process, so that high-quality coatings are produced. The low-activity CVD process is more complicated, but provides flexibility to deposit a variety of coatings.<sup>87</sup>

##### 1.25.4.1.2 Alloyed aluminide coatings

As with bulk materials, the corrosion resistance of aluminide coatings can be improved with alloying additions, so the coating processes are often modified to incorporate other elements in the coating. One example is the introduction of chromium to improve



the resistance to corrosion in chlorine-containing environments. Chromium, as well as reactive element additions, can be deposited simultaneously with aluminum in a pack cementation process by using an alloy containing the desired elements as the source.<sup>88</sup> This process is complicated when steel is used as the substrate, because carbon in the steel reacts with chromium to form chromium carbides. For low carbon contents, the carbide particles form separate precipitates, but for higher carbon contents, even as low as 0.2%, a chromium carbide layer forms and disrupts the coating process. This problem can be overcome by using a two-step process, which is illustrated in [Figure 12](#).<sup>89</sup> In the first step, the pack is heated to a relatively low temperature where there is a significant partial pressure of the aluminum chloride vapor species, but the vapor species of the chromium chloride species is low, so that aluminum, but not chromium, is deposited. Aluminum stabilizes the ferrite structure, so dissolution of aluminum causes a phase change in the iron from austenite to ferrite. Because of the low carbon solubility of ferrite, carbon is rejected into the austenite layer below the ferrite. In the second step, the pack is heated to a higher temperature where the partial pressure of the chromium vapor species increases, so chromium is now deposited and diffuses in the ferrite. Because of the low concentration of carbon in the ferrite, chromium carbides do not form and a high-quality coating is produced. A similar process has been used with a nickel-based superalloy to produce a coating with an outer high-chromium layer, which provides good hot corrosion resistance.<sup>90</sup> Chromium, in larger amounts, can also improve the oxidation resistance of titanium aluminide alloys and is often incorporated in titanium aluminide coatings.

Another element that is commonly added to aluminide coatings is silicon. Silicon additions result in the

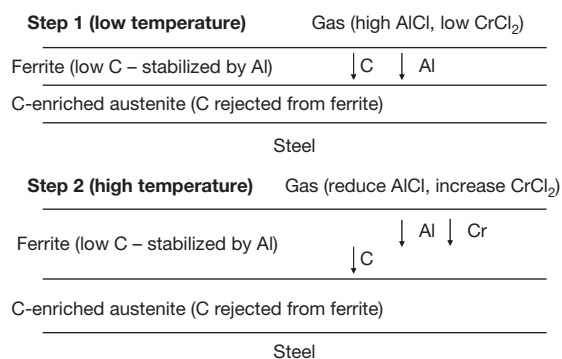


**Figure 12** Two-step process for codeposition of aluminum and chromium on steel.<sup>89</sup>

formation of silica, which provides excellent oxidation resistance because of its low oxygen permeability and is particularly resistant to acidic melts. Like chromium, silicon can be added in the pack cementation process, and, also like chromium, a two-step process can be used to produce a coating with the desired composition distribution.<sup>91</sup> Although silicon can be introduced through the vapor phase, the eutectic in the aluminum–silicon system provides an opportunity for the introduction of silicon and aluminum through liquid-phase processes. This includes simple dipping processes as well as surface melting processes, such as laser surface melting. Siliconizing is most widely used for titanium aluminide alloys. Although such processes can result in an outer titanium silicide layer, the scale formed during oxidation is similar to that formed on uncoated titanium aluminide alloys. The outer scales consist of titanium and aluminum oxides, but a silica layer is formed in the inner portion of the scale and improves the oxidation resistance.<sup>92</sup>

Aluminide coatings can also be used as the bond coating between superalloys and thermal barrier coatings (TBC). In this application, in addition to the inherent oxidation behavior, the interface between the thermally grown oxide (TGO) on the bond coating and the TBC must be strong, so that the TBC remains attached to the alloy during use (particularly during thermal cycling). Thus, the adherence of the scale is of greater importance than the growth rate, because a thicker TGO is less of a problem than the loss of the TBC. Because of the importance of adherence, one of the common additions to NiAl bond coating is platinum.<sup>93,94</sup> Platinum-containing coatings maintain good scale adherence even with significant amounts of sulfur, which, as discussed earlier, generally degrades scale adherence. Platinum is typically added as a coating prior to aluminization. There are several commercial pack cementation processes for producing platinum-containing coatings, including high-activity inward-growing coating with the substrate in the pack (e.g., Chromalloy RT22), high-activity inward-growing coating with the substrate above the pack (e.g., Howmet SS82A), and low-activity outward-growing coating (e.g., Thermatech MDC150L).<sup>95</sup> The addition of platinum eliminates void formation at the coating–TGO interface, but voids are observed at the alloy–coating interface, as shown schematically in [Figure 13](#).<sup>96</sup> Void formation beneath the scale can lead to spallation of the scale during thermal cycling, which is especially critical if the coating is used as a bond coat, since such spallation will lead to loss of the TBC. Void formation at the coating–scale interface has been

attributed to both the Kirkendall effect and stresses associated with the transformation of  $\beta$ -NiAl to  $\gamma'$ -Ni<sub>3</sub>Al.<sup>97</sup> The void formation at the alloy–coating interface is less critical than that at the coating–scale interface; as both NiAl and Ni<sub>3</sub>Al are more ductile than alumina, crack propagation is less likely.

As mentioned earlier, large amounts of platinum additions can lead to the formation of PtAl<sub>2</sub>, which in addition to improving the supply of aluminum needed to maintain an  $\alpha$ -Al<sub>2</sub>O<sub>3</sub> layer, also limits the transport of transition metal impurities outward from the aluminide coating into the scale. This is particularly important in coatings for superalloys, which contain elements that can degrade the corrosion protection provided by the coating.

Other noble metals used in NiAl bond coatings include rhenium and palladium. Rhenium acts like platinum in that it promotes the formation of an  $\alpha$ -Al<sub>2</sub>O<sub>3</sub> layer and forms a compound that acts as a diffusion barrier. Palladium helps to stabilize the NiAl phase and maintain sufficient aluminum in the scale. Noble metals can also be used with reactive elements. For example, hafnium and platinum have been used together, where, in addition to improving the oxidation resistance, the formation of a Hf–Pt layer provides a diffusion barrier to prevent loss of aluminum and incorporation of transition metals in the coating and scale.

Titanium aluminide alloys can also be used with TBCs. The TBC has relatively good adherence to the alloy, which is attributed to the better match in the coefficients of thermal expansion as compared to nickel-based superalloys. However, a bond coat, such as TiAlCr or TiAl<sub>3</sub>, is needed for long lifetimes.<sup>98</sup>

#### 1.25.4.2 Aluminide Coatings with Different Base as Substrate

Deposition of an aluminide phase of an element not in the substrate can provide useful properties, but is

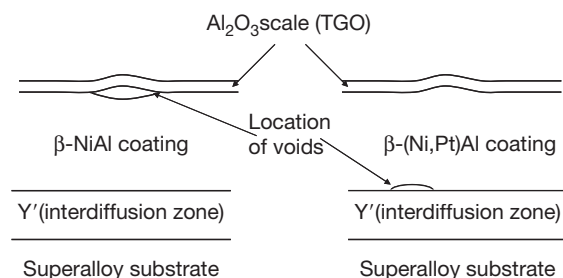


**Figure 13** Effect of platinum additions on pore formation in  $\beta$ -nickel aluminide coating after oxidation at 1150 °C.<sup>96</sup>

more complicated than simply increasing the aluminum content of the surface. For example, as discussed earlier, alumina is more stable on NiAl than on TiAl, so NiAl can provide improved long-term corrosion protection, but TiAl is less dense and has better specific strength. Titanium aluminide coated with NiAl combines the advantages of the two materials and can be produced by first electroplating the TiAl with nickel and then aluminizing the nickel layer by pack cementation.<sup>99</sup> The same process can be used for applying a NiAl coating to steel and allows for a reduction in the processing temperature to avoid grain growth or carbide formation in the steel substrate.<sup>100</sup> Similarly, steel, and other non-titanium alloys, can be coated with titanium aluminide by first depositing a layer of titanium and then aluminizing the titanium to form the corrosion resistant titanium aluminide coating.

An analogous process can be used to produce a ruthenium aluminide coating on a nickel-base superalloy.<sup>101</sup> In this case, the coating microstructure depends on whether the ruthenium layer is aluminized using a high-activity pack cementation process or a low-activity CVD process. As shown schematically in **Figure 14**, in a high-activity process, the coating grows by inward diffusion of aluminum, which results in an outer layer of RuAl and an inner layer of NiAl that are separated by a zone containing Ru(Al,Ta) precipitates. In a low-activity process, the coating grows by outward diffusion of aluminum, which results in an outer layer of NiAl. The coating with the outer NiAl layer has superior oxidation resistance. However, the presence of the inner RuAl layer is beneficial as it acts as a diffusion barrier, which can prevent undesired elements from the substrate from entering the outer coating and oxidation scale.

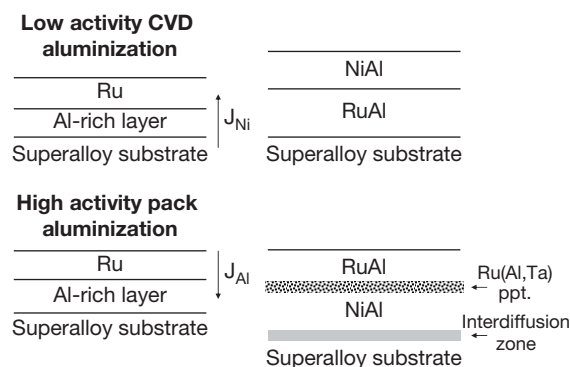


**Figure 14** Ruthenium-modified coatings by low-activity CVD aluminization and high-activity pack aluminization.<sup>101</sup>

### 1.25.5 Summary and Conclusions

Intermetallic aluminide alloys are attractive for high temperature applications. The corrosion resistance of aluminide alloys is achieved by the formation and maintenance of a protective alumina, or alumina-containing, scale. Of the three common aluminide systems, nickel, iron, and titanium, the formation of an alumina scale is most challenging on titanium aluminide alloys because of the thermodynamic stability of titanium oxide. However, titanium aluminide alloys also offer the greatest benefit in terms of improvements in specific properties. In addition to the initial thermodynamic stability of the oxides, long-term corrosion resistance requires maintenance of the protective scale in the presence of stresses (thermal and transformation) and changes in alloy composition with time. In applications where the intermetallic alloys have inadequate mechanical properties for use as structural components, they can be applied as coatings to provide corrosion resistance for structural alloys. Improvements in corrosion resistance can be achieved with alloying additions, but the effects of these elements on other factors, such as mechanical properties, cost, and manufacturability, must also be considered.

### References

1. Lasalmonie, A. *Intermetallics* **2006**, 14, 1126–1129.
2. Dimiduk, D. M. *Mater. Sci. Eng.* **1999**, A263, 281–288.
3. Stoloff, N. S.; Sikka, V. A. *Physical Metallurgy and Processing of Intermetallic Compounds*; Chapman & Hall: New York, NY, 1996.
4. Brady, M. P.; Gleeson, B.; Wright, I. G. *JOM* **2000**, 52(1), 16–21.
5. Meier, G. H.; Pettit, F. S. *Mater. Sci. Eng. A* **1992**, 153, 548–560.
6. Doychak, J. In *Intermetallics Compounds Principles and Practice. Vol. 1. Principles*; Westbrook, J. H., Fleischer, R. L., Eds.; John Wiley, 1995; pp 977–1016.
7. Cathcart, J. V. *Mater. Res. Soc. Proc.* **1985**, 39 (High-Temperature Ordered Intermetallic Alloys), 445–459.
8. Grabke, H. J. *Intermetallics* **1999**, 7, 1153–1158.
9. Tottorelli, P. F.; Natesan, K. *Mater. Sci. Eng. A* **1998**, 258, 115–125.
10. Pettit, F. S. *Trans. Metall. Soc. AIME* **1967**, 239, 2196–1305.
11. Godlewski, E. *Electrochem. Soc. Proc.* **2003**, 16 (High Temperature Corrosion and Materials Chemistry IV), 51–61.
12. Katsman, A.; Grabke, H. J.; Levin, L. *Oxidation of Metals* **1996**, 46, 313–331.
13. Liu, Z.; Gao, W. *Intermetallics* **2000**, 8, 1385–1391.
14. Choi, S. C.; Cho, H. J.; Kim, Y. J.; Lee, D. B. *Oxidation Metals* **1996**, 46, 51–72.
15. Hou, P. Y.; Niu, Y.; Van Lienden, C. *Oxidation Metals* **2003**, 59, 41–61.
16. Pint, B. A. *Oxidation Metals* **1997**, 47, 303–328.
17. Yang, J. C.; Nadarzynski, K.; Schumann, E.; Rühle, M. *Scripta Metall. Mater.* **1995**, 33, 1043–1048.
18. McCarty, K. F. *Surf. Sci.* **2001**, 474, L165–L172.
19. Doychak, J.; Smialek, J. L.; Mitchell, T. E. *Metall. Trans. A* **1989**, 20A, 499–518.
20. González-Carrasco, J. L.; Pérez, P.; Adeva, P.; Chao, J. *Intermetallics* **1999**, 7, 69–78.
21. Grabke, H. J.; Brumm, M.; Steinhorst, M. *Mater. Sci. Technol.* **1992**, 8, 339–344.
22. Rivoaland, L.; Maurice, V.; Josso, P.; Bacos, M. P.; Marcus, P. *Oxidation Metals* **2003**, 60, 159–178.
23. Cadoret, Y.; Monceau, D.; Bacos, M. P.; Josso, P.; Maurice, V.; Marcus, P. *Oxidation Metals* **2005**, 64, 185–205.
24. Heuer, A. H.; Reddy, A.; Hovis, D. B.; Veal, B.; Paulikas, A.; Vlad, A.; Rühle, M. *Scripta Mater.* **2006**, 54, 1907–1912.
25. Zhang, Z. G.; Hou, P. Y. *Mater. Sci. Eng. A* **2005**, 391, 1–9.
26. Tolpygo, V. K.; Clarke, D. R. *Acta Mater.* **2004**, 52, 5129–5141.
27. Doychak, J.; Rühle, M. *Oxidation Metals* **1989**, 31, 431–452.
28. Yang, J. C.; Schumann, E.; Levin, I.; Rühle, M. *Acta Mater.* **1998**, 46, 2195–2201.
29. Bobeth, M.; Pompe, W.; Schumann, E.; Rühle, M. *Acta Metall. Mater.* **1992**, 40, 2669–2676.
30. Balmain, J.; Huntz, A. M. *Oxidation Metals* **1996**, 45, 183–196.
31. Yi, H. C.; Smeltzer, W. W.; Petric, A. *Oxidation Metals* **1996**, 45, 281–299.
32. Kartono, R.; Young, D. J. *Electrochem. Soc. Proc.* **2004**, 16 (High Temperatures Corrosion and Materials Chemistry V), 43–55.
33. Pint, B. A.; Haynes, J. A.; Zhang, Y.; More, K. L.; Wright, I. G. *Surf. Coatings Tech.* **2006**, 201, 3882–3886.
34. Pint, B. A.; Regina, J. R.; Prussner, K.; Chitwood, L. D.; Alexander, K. B.; Tortorelli, P. F. *Intermetallics* **2001**, 9, 735–739.
35. Zhang, Z. F.; Thaidigsmann, K.; Ager, J.; Hou, P. Y. *J. Mater. Res.* **2006**, 21, 1409–1419.
36. Hou, P. Y. *J. Am. Ceram. Soc.* **2003**, 86, 660–668.
37. Kuenzly, J. D.; Douglass, D. L. *Oxidation Metals* **1974**, 8, 139–178.
38. Pint, B. A. *Oxidation Metals* **1996**, 45, 1–37.
39. Schumann, E.; Yang, J. C.; Rühle, M.; Graham, M. J. *Oxidation Metals* **1996**, 46, 37–49.
40. Pint, B. A.; Hobbs, L. W. *Oxidation Metals* **2004**, 61, 273–292.
41. Berlanga, M.; González-Carrasco, J. L.; Montealegre, M. A.; Muñoz-Morris, M. A. *Intermetallics* **2004**, 13, 205–212.
42. Montealegre, M. A.; Strehl, G.; González-Carrasco, J. L.; Borchardt, G. *Intermetallics* **2005**, 13, 896–906.
43. Taniguchi, S.; Shibata, T. In *Oxidation of High-Temperature Intermetallics*; Grobstein, T., Doychak, J., Eds.; The Minerals, Metals & Materials Society: Warrendale, PA, **1989**; pp 17–29.
44. Pint, B. A.; Wright, I. G. *Materials Science Forum* **2004**, 461–464 (High Temperature Corrosion and Protection of Materials 6, Part 2), 799–806.
45. Pint, B. A.; Schneibel, J. H. *Scripta Mater.* **2005**, 52, 1199–1204.
46. Pérez, P.; Adeva, P. *Oxidation Metals* **2006**, 65, 15–38.
47. Hou, P. Y.; McCarty, K. F. *Scripta Mater.* **2006**, 54, 937–941.

48. Fergus, J. W. *Mater. Sci. Eng. A* **2002**, 338, 108–125.
49. Brady, M. P.; Pint, B. A.; Tortorelli, P. F.; Wright, I. G.; Hanrahan, R. J., Jr. In *Corrosion and Environmental Degradation, Vol. II*; Schütze, M., Ed.; Wiley-VCH Verlag GmbH, Weinheim, Germany, 2000; pp 229–326.
50. Rahmel, A.; Quadackers, W. J.; Schütze, M. *Mater. Corros.* **1995**, 46, 271–285.
51. Leyens, C. In *Titanium and Titanium Alloys*; Leyens, C., Peters, M., Eds.; Wiley-VCH, 2003; pp 187, 230.
52. Haanappel, A. C.; Hofman, R.; Sunderkötter, J. D.; Glatz, W.; Clemens, H.; Stroosnijder, M. F. *Oxidation Metals* **1997**, 48, 263–287.
53. Dettenwanger, F.; Schumann, E.; Rühle, M.; Rakowski, J.; Meier, G. H. *Oxidation Metals* **1998**, 50, 269–307.
54. Shemet, V.; Tyagi, A. K.; Becker, J. S.; Lersch, P.; Singheiser, L.; Quadackers, W. J. *Oxidation Metals* **2000**, 54, 211–235.
55. Tang, Z.; Shemet, V.; Niewolak, L.; Singheiser, L.; Quadackers, W. J. *Intermetallics* **2003**, 11, 1–8.
56. Kumagai, M.; Shibue, K.; Kim, M. S.; Yonemitsum, M. *Intermetallics* **1996**, 4, 557–566.
57. Kim, Y. J.; Kim, I. B.; Kim, M. S.; You, B. D.; Han, W.; Hwang, W. S. *Metals Mater.* **2000**, 6, 455–459.
58. Donchev, A.; Richter, E.; Schütze, M.; Yankov, R. *Intermetallics* **2006**, 14, 1136–1142.
59. Donchev, A.; Gleeson, B.; Schütze, M. *Intermetallics* **2003**, 11, 387–398.
60. Yoshihara, M.; Taniguchi, S.; Zhu, Y. C. *Metall. Mater. Trans. A* **2003**, 34A, 2253–2261.
61. Felten, E. J.; Pettit, F. S. *Oxidation of Metals* **1976**, 10, 189–223.
62. Dickey, E. C.; Pint, B. A.; Alexander, K. B.; Wright, I. G. *J. Mater. Res.* **1999**, 14, 4531–4540.
63. Soldera, F.; Ilić, N.; Brännström, S.; Barrientos, I.; Gobran, H.; Mücklich, F. *Oxidation Metals* **2003**, 59, 529–542.
64. Ilić, N.; Soldera, F.; Mücklich, F. *Intermetallics* **2005**, 13, 444–453.
65. Cao, F.; Nandy, T. K.; Stobbe, D.; Pollock, T. M. *Intermetallics* **2004**, 15, 34–43.
66. Kuppusami, P.; Murakami, H. *Surf. Coatings Technol.* **2004**, 186, 377–388.
67. Natesan, K.; Datta, P. K. In *Intermetallic Compounds, Principles and Practice, Vol. 3*, Progress; Westbrook, J. H., Fleischer, R. L., Eds.; Wiley, 2002; pp 707–719.
68. Natesan, K. *Oxidation Metals* **1988**, 30, 53–83.
69. Kai, W.; Chang, M. T.; Bai, C. Y. *Oxidation Metals* **2001**, 56, 191–214.
70. Kai, W.; Huang, R. T. *Oxidation Metals* **1997**, 47, 59–86.
71. Kai, W.; Lee, S. H.; Chiang, D. L.; Chu, J. P. *Mater. Sci. Eng. A* **1998**, 258, 146–152.
72. Godlewska, E. *Mater. Corros.* **1997**, 48, 687–699.
73. Izumi, T.; Yoshioka, T.; Hayashi, S.; Narita, T. *Intermetallics* **2000**, 8, 891–901.
74. González-Rodríguez, J. G.; Luna-Ramírez, A.; Salazar, M.; Porcayo-Calderon, J.; Rosas, G.; Martínez-Villafañe, A. *Mater. Sci. Eng. A* **2005**, 399, 344–350.
75. Lee, W. H.; Lin, R. Y. *Mater. Chem. Phys.* **2003**, 77, 86–96.
76. Tang, Z.; Wang, F.; Wu, W. *Oxidation Metals* **1999**, 51, 235–250.
77. Kim, I.; Cho, W. D. *Mater. Sci. Eng. A* **1999**, 264, 269–278.
78. Nicholls, J. R.; Leggett, J.; Andrews, P. In *Oxidation of Intermetallics*; Grabke, H. J., Schütze, M., Eds.; Wiley-VCH Verlag GmbH: Weinheim, Germany, 1998; pp 329–344.
79. Li, Y. S.; Spiegel, M. *Corrosion Sci.* **2004**, 46, 2009–2023.
80. Zhang, K.; Gao, W.; Liang, J. *Intermetallics* **2004**, 12, 539–544.
81. Liang, J.; Gao, W.; Li, Z.; He, Y. *Mater. Lett.* **2004**, 58, 3280–3284.
82. Amaya, M.; Espinosa-Medina, M. A.; Porcayo-Calderon, J.; Martinez, L.; González-Rodríguez, J. G. *Mater. Sci. Eng. A* **2003**, 349, 12–19.
83. Gauthier, V.; Dettenwanger, F.; Schütze, M.; Quadackers, W. J. *Oxidation Metals* **2003**, 59, 233–255.
84. Lindblad, N. R. *Oxidation Metals* **1969**, 1, 143–170.
85. Rae, C. M. F.; Hook, M. S.; Reed, R. C. *Mater. Sci. Eng. A* **2005**, 396, 231–239.
86. Xiang, Z. D.; Datta, P. K. *Metall. Mater. Trans. A* **2006**, 37A, 3347–3358.
87. Warnes, B. M. *Surf. Coatings Tech.* **2003**, 163–164, 106–111.
88. Bianco, R.; Rapp, R. A. *J. Electrochem. Soc.* **1993**, 140, 1181–1190.
89. Zheng, M.; Rapp, R. A. *Oxidation Metals* **1998**, 49, 19–31.
90. Bai, C.-Y.; Luo, Y.-J.; Koo, C.-H. *Surf. Coatings Technol.* **2004**, 183, 74–88.
91. Brossard, J. M.; Hierro, M. P.; Trilleros, J. A.; Carpintero, M. C.; Sánchez, L.; Bolívar, F. J.; Pérez, F. J. *Surf. Coating Technol.* **2006**, 207, 5743–5750.
92. Xiong, H. P.; Mao, W.; Xie, Y.-H.; Ma, W.-L.; Chen, Y.-F.; Li, X.-H.; Li, J.-P.; Cheng, Y.-Y. *Acta Mater.* **2004**, 52, 2605–2620.
93. Pint, B. A. *Surf. Coatings Technol.* **2004**, 188–189, 71–78.
94. Pint, B. A.; Speakman, S. A.; Rawn, C. J.; Zhang, Y. *JOM* **2006**, 58(1), 47–52.
95. Angenete, J.; Stiller, K.; Langer, V. *Oxidation Metals* **2003**, 60, 47–82.
96. Zhang, Y.; Haynes, J. A.; Lee, W. Y.; Wright, I. G.; Pint, B. A.; Cooley, K. M.; Liaw, P. K. *Metall. Mater. Trans. A* **2001**, 32A, 1727–1741.
97. Angenete, J.; Stiller, K.; Bakchinova, E. *Surf. Coatings Technol.* **2004**, 176, 272–283.
98. Leyens, C.; Braun, R.; Fröhlich, M.; Hovsepian, P. *Eh. JOM* **2006**, 58(1), 17–21.
99. Izumi, T.; Nishimoto, T.; Narita, T. *Intermetallics* **2005**, 13, 727–732.
100. Xiang, Z. D.; Datta, P. K. *J. Mater. Sci.* **2005**, 40, 1959–1966.
101. Tryon, B.; Feng, Q.; Wellman, R. G.; Murphy, K. S.; Yang, J.; Levi, C. G.; Nicholls, J. R.; Pollock, T. M. *Metall. Mater. Trans. A* **2006**, 37A, 3347–3358.

## 1.17 Oxidation in Steam and Steam/Hydrogen Environments

**W. J. Quadakkers and J. Žurek**

Forschungszentrum Jülich, Institute of Energy Research (IEF-2), 52428 Jülich, Germany

© 2010 Elsevier B.V. All rights reserved.

<b>1.17.1</b>	<b>Introduction</b>	408
<b>1.17.2</b>	<b>Thermodynamic Considerations</b>	409
1.17.2.1	Thermodynamics of the Gas Atmosphere and Stability of Solid Oxides	409
1.17.2.2	Volatile Reaction Products in H <sub>2</sub> O-Containing Gases	409
1.17.2.3	Considerations for Material Testing in Steam Environments	411
<b>1.17.3</b>	<b>Growth Mechanisms of Oxide Scales</b>	413
1.17.3.1	Kinetics of Surface Reactions	413
1.17.3.2	Effect of Water Vapor and Hydrogen on Lattice Diffusion in Oxide Scales	415
1.17.3.3	Molecular Diffusion in Oxide Scales in Wet Gases	415
<b>1.17.4</b>	<b>Metallic High Temperature Components in Steam and Steam/Hydrogen Environments</b>	416
1.17.4.1	General Remarks	416
1.17.4.2	Oxidation of Chromium and High-Chromium Alloys	418
1.17.4.2.1	Oxidation of chromium	418
1.17.4.2.2	Oxidation of chromia-forming Fe- and Ni-based alloys	418
1.17.4.2.3	Mechanisms of chromia scale growth	419
1.17.4.2.4	Commercial chromia-forming Fe- and Ni-based alloys	422
1.17.4.2.5	Effect of common minor alloying additions	423
1.17.4.3	Effect of Environment on Scale Formation in Case of 'Borderline Alloys'	426
1.17.4.3.1	Nonprotective oxidation in water vapor	426
1.17.4.3.2	Internal oxidation of Cr as trigger for breakaway oxidation	427
1.17.4.3.3	Conditions for external chromia formation in dry and wet gases	427
1.17.4.3.4	Breakaway oxidation mechanisms of FeCr alloys in water vapor	430
1.17.4.3.5	Borderline NiCr alloys in water vapor	430
1.17.4.4	Oxidation of Ferritic and Austenitic Steels in Steam	431
1.17.4.4.1	General remarks	431
1.17.4.4.2	Steam oxidation mechanisms of 9–12% Cr steels	433
1.17.4.4.3	Void and gap formation	435
1.17.4.4.4	Long-term behavior	436
1.17.4.4.5	Temperature dependence of oxidation during long-term exposure	440
1.17.4.4.6	Austenitic steels	445
1.17.4.4.7	Effect of pressure on steam oxidation	449
1.17.4.5	Alumina-Forming Alloys and Coatings	449
1.17.4.5.1	$\alpha$ -Alumina scales	449
1.17.4.5.2	Metastable alumina	451
1.17.4.5.3	Borderline alumina forming alloys	452
<b>References</b>		454

### Abbreviations

**BC** Bond coat  
**EDX** Energy dispersive X-ray spectroscopy  
**IEP** Isoelectric point  
**ODS** Oxide dispersion strengthened  
**PSEs** Protective scale forming elements

**REs** Reactive elements

**SEM** Scanning electron microscopy  
**SNMS** Sputtered neutrals mass spectrometry  
**SOFC** Solid oxide fuel cell  
**TBC** Thermal barrier coating  
**TEM** Transmission electron microscopy

**XPS** X-RAY photoelectron spectroscopy**XRD** X-Ray diffraction**Symbols** **$h^*$**  Positive hole **$k_p(K_p)$**  Parabolic rate constant ( $\text{mg}^2 \text{cm}^{-4} \text{s}^{-1}$ ,  $\mu\text{m}^2 \text{h}^{-1}$ ) **$n$**  Oxidation rate exponent **$p$**  Vapor pressure (bar, Pa) **$p_i$**  Partial pressure of component (bar, Pa) **$t$**  Time (h, s) **$x$**  Material loss (cm,  $\mu\text{m}$ ) **$x$**  Oxide scale thickness (cm,  $\mu\text{m}$ ) **$A$**  Surface area ( $\text{m}^2$ ,  $\text{cm}^2$ ) **$\tilde{D}_{\text{Fe-Cr}}$**  Alloy interdiffusion coefficient ( $\text{m}^2 \text{s}^{-1}$ ) **$D_{\text{O}}$**  Diffusivity of oxygen ( $\text{m}^2 \text{s}^{-1}$ ) **$H_i^+$**  Interstitial proton **$J_{\text{O}_2}$**  Oxygen flux ( $\text{mol cm}^{-2} \text{s}^{-1}$ ) **$K_{15}$**  Equilibrium constant for reaction (15) **$K$**  Oxidation rate ( $\text{mm}^2 \text{h}^{-1}$ ) **$K'$**  Oxidation parameter **$M$**  Molecular mass ( $\text{g mol}^{-1}$ ) **$N_{\text{Cr}}^{(1)}, N_{\text{Cr}}^{(2)}$**  Critical Cr mole fraction for external scale formation **$N_{\text{O}}^{(s)}$**  Oxygen solubility ( $\text{mol/mol}$ ) **$Q$**  Activation energy ( $\text{J mol}^{-1}$ ) **$R$**  Universal gas constant ( $8.314 \text{ J mol}^{-1} \text{K}^{-1}$ ) **$T$**  Temperature (K,  $^{\circ}\text{C}$ ) **$V_{\text{Cr}}'''$**  Cr vacancy **$V_m$**  Molar volume of alloy ( $\text{cm}^3 \text{mol}^{-1}$ ) **$V_{\text{O}}''$**  Oxygen vacancy **$\Delta G^{\circ}$**  Standard free energy ( $\text{J mol}^{-1}$ ) **$\Delta m$**  Weight change ( $\text{mg cm}^{-2}$ )

environment as the main oxidizing gas species or in addition to larger amounts of 'free oxygen.' From the viewpoint of equilibrium oxygen partial pressure and oxygen/water vapor ratio, the service environments may be divided into four groups:

- A. Wet air or gases originating, for example, from combustion processes with a high oxygen (air) to fuel ratio. In such environments the oxygen content may be as high as 10–20%.<sup>2</sup>
- B. Combustion or exhaust gases originating from combustion processes with low oxygen (air) to fuel ratio. In such gases, which, for example, prevail in car exhaust gas or in the combustion gas of lignite/coal fired power plants, the oxygen content may be as low as 1% or even smaller.<sup>3</sup>
- C. Environments based on steam such as, for example, prevailing in chemical processes or in steam power plants.<sup>4</sup>
- D. Service environments that contain hydrogen in addition to water vapor which may prevail in chemical plants, gasification plants and (solid oxide) fuel cells.<sup>5</sup>

In the first two types of environments (A and B), the equilibrium oxygen partial pressure is hardly affected by the presence of water vapor, whereas in environments C and D it is mainly governed by the absolute water vapor partial pressure or the  $\text{H}_2\text{O}/\text{H}_2$  ratio. The equilibrium oxygen partial pressures in these environments are orders of magnitude smaller than in gases of type A and B. Consequently, oxide phases and vapor pressures of volatile species that form by reaction of metallic components with gases of group A and B may substantially differ from those formed in gases of groups C and D. When comparing the oxidation behavior of metallic materials in dry oxygen with that in water vapor-containing gases, it is therefore important to distinguish between the various types of water vapor-containing atmospheres.

The following sections deal with the oxidation properties of metallic construction materials in gases of type C and D. The main emphasis will be put on describing the oxidation mechanisms in these environments compared to the behavior in dry oxygen, oxygen-inert gas mixtures or air. The examples shown will mainly deal with alloy systems that are commonly used as construction materials in practical applications where typical application temperature ranges for the respective materials are being considered.

**Nomenclature**

In the following sections, the behavior of various materials in  $(\text{Ar}/\text{N}_2-\text{H}_2\text{O})$  and  $(\text{Ar}/\text{N}_2-\text{H}_2-\text{H}_2\text{O})$  is

**1.17.1 Introduction**

In practical applications, metallic construction materials for high temperature components are subjected to a large variety of service environments. Stability and growth rate of the oxide scales that form on the component surfaces during exposure are commonly described on the basis of equilibrium oxygen partial pressures of the various environments. However in many of these applications, water vapor has been found to substantially alter the technologically relevant properties, mainly growth rate and adherence, of the surface oxides.<sup>1</sup> Thereby it has to be considered whether water vapor can be present in the service

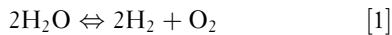


compared with that in air, oxygen or various mixtures of oxygen and inert gases. The equilibrium oxygen partial pressures of the two mentioned  $\text{H}_2\text{O}$ -containing gas types at, for example,  $800^\circ\text{C}$  are typically in the range  $10^{-8}$  to  $10^{-18}$  bar. This is obviously orders of magnitude lower than the  $p_{\text{O}_2}$  in the mentioned  $\text{O}_2$ -based gases. Therefore, in the following discussion the mentioned  $\text{H}_2$ -containing gases are frequently termed 'low- $p_{\text{O}_2}$  gases,' and the  $\text{O}_2$ -based environments 'high- $p_{\text{O}_2}$  gases.'

## 1.17.2 Thermodynamic Considerations

### 1.17.2.1 Thermodynamics of the Gas Atmosphere and Stability of Solid Oxides

In mixtures of hydrogen and water vapor, the oxygen partial pressure is substantially lower than in air where  $p_{\text{O}_2}$  is approximately 0.2 bar. The equilibrium oxygen partial pressure can be derived from:



and

$$p_{\text{O}_2} = \left\{ \exp \left( \frac{-\Delta G^\circ}{RT} \right) \right\} / \left( \frac{p_{\text{H}_2}}{p_{\text{H}_2\text{O}}} \right)^2 \quad [2]$$

in which  $\Delta G^\circ$  is the standard free energy of formation.<sup>6</sup>

In pure steam or Ar- $\text{H}_2\text{O}$  mixtures, the equilibrium hydrogen and oxygen partial pressures are

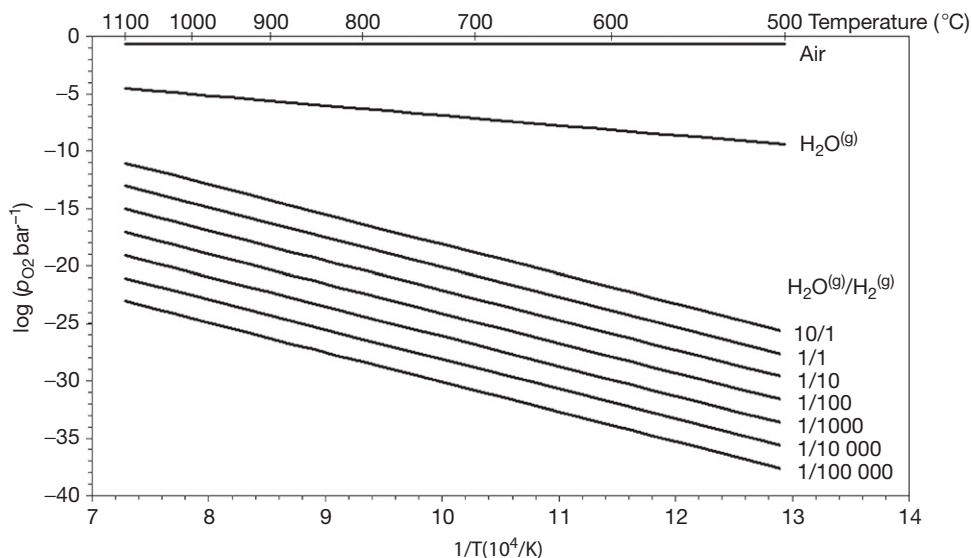
similar, but in the calculations the change in water vapor content due to formation of  $\text{H}_2$ ,  $\text{O}_2$ , and other gas species such as  $\text{HO}_2^{(\text{g})}$  and  $\text{OH}^{(\text{g})}$  has to be taken into account to calculate the oxygen partial pressure of the fully equilibrated gas or gas mixture. The equilibrium oxygen partial pressure in steam and in gases with various  $\text{H}_2/\text{H}_2\text{O}$  ratios in the temperature range  $500$ – $1100^\circ\text{C}$  is presented in **Figure 1**.

**Figure 2** compares the equilibrium oxygen partial pressure of an Ar-50 vol.%  $\text{H}_2\text{O}$  mixture and an Ar- $\text{H}_2\text{O}/\text{H}_2$  mixture ( $\text{H}_2\text{O}/\text{H}_2$  ratio = 1/1) with that of the dissociation pressures of selected oxides. It is apparent that oxides of Cr, Al, Si, and Ti are stable in both atmospheres in the temperature range  $500$ – $1100^\circ\text{C}$ . Fe will easily oxidize in Ar- $\text{H}_2\text{O}$  but only at lower temperatures in the Ar- $\text{H}_2$ - $\text{H}_2\text{O}$  mixture. In the latter gas, Ni and Co will not oxidize.

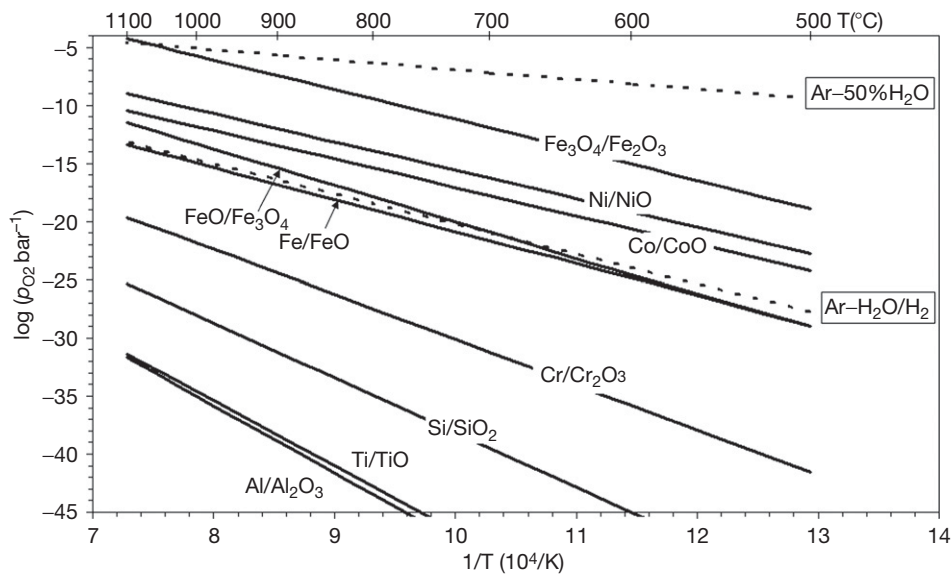
**Equation [2]** reveals that the equilibrium oxygen partial pressure of an  $\text{H}_2\text{O}/\text{H}_2$  mixture is governed by the  $\text{H}_2\text{O}/\text{H}_2$  ratio and thus independent of the total gas pressure. This is not the case in pure steam or in mixtures of water vapor with an inert gas.<sup>8</sup> In these gases, the equilibrium oxygen partial pressure increases with increasing total pressure (**Figure 3**).

### 1.17.2.2 Volatile Reaction Products in $\text{H}_2\text{O}$ -Containing Gases

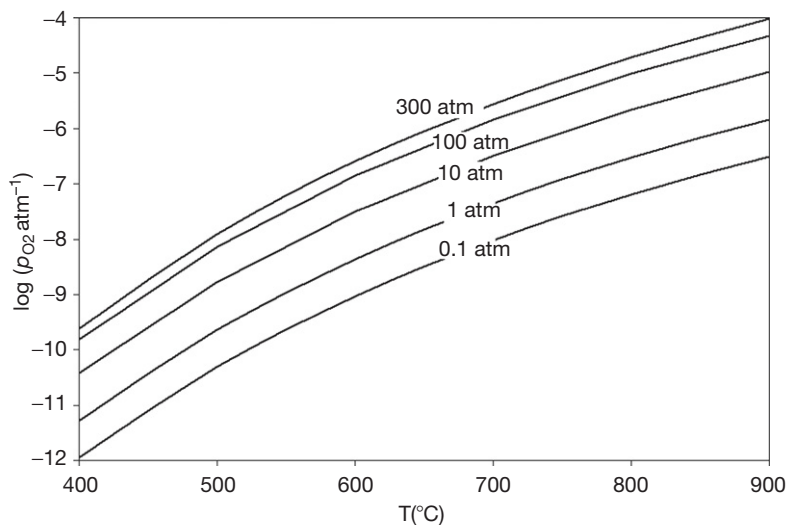
The oxidation behavior of metallic materials may be substantially affected by the formation of volatile oxides. Well known examples are  $\text{CrO}_3^{(\text{g})}$ , which



**Figure 1** Equilibrium oxygen partial pressure as function of temperature in various gas atmospheres (calculations carried out with the Program Fact Sage<sup>7</sup>).



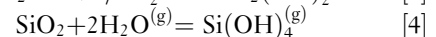
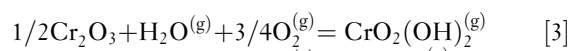
**Figure 2** Comparison of the equilibrium oxygen partial pressure of an Ar-50 vol.% H<sub>2</sub>O mixture and an Ar-H<sub>2</sub>O/H<sub>2</sub> mixture (H<sub>2</sub>O/H<sub>2</sub> ratio = 1:1) with that of the dissociation pressures of selected oxides (calculations carried out with the Program Fact Sage<sup>®</sup>).

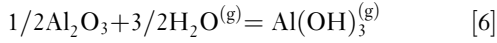
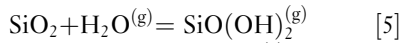


**Figure 3** Calculated equilibrium oxygen partial pressure in steam at various total pressures. Calculations carried out with the Program Fact Sage [7].

forms in equilibrium with Cr<sub>2</sub>O<sub>3</sub>, and SiO<sup>(g)</sup> in equilibrium with Si or SiO<sub>2</sub>. The vapor pressure of SiO<sup>(g)</sup> increases with decreasing  $p_{O_2}$ , whereas CrO<sub>3</sub><sup>(g)</sup> becomes more significant at high  $p_{O_2}$ . In case of competition between oxide scale growth and volatilization, a simple Tedmon model,<sup>9</sup> in which the overall rate of metal wastage is a function of the parabolic rate constant for oxide growth and the linear rate constant for volatilization, is frequently used to describe the observed kinetics. In the presence of

water vapor, a number of additional volatile species may form. For the three most important protective surface oxides on metallic materials, alumina, chromia, and silica, the following reactions in equilibrium with the respective oxide phases seem to be the most important ones:<sup>10</sup>





Various data sets<sup>11</sup> exist for vapor pressure data of these volatile oxyhydroxides, and in the case of  $\text{CrO}_2(\text{OH})_2$  this literature data substantially differ (Figure 4). More recent data show, for example, for the partial pressure of this oxyhydroxide at 850 °C in Air + 2%  $\text{H}_2\text{O}$ , a variation between  $10^{-8}$  and  $10^{-9}$  bar.<sup>12</sup> On the basis of own experimental data and an extensive evaluation of the various data sources, Opila<sup>11</sup> showed that the rates of evaporation increase in the following order:  $\text{Al}(\text{OH})_3^{(g)} < \text{Si}(\text{OH})_4^{(g)} < \text{CrO}_2(\text{OH})_2^{(g)}$ , as shown in Figure 5. It is apparent from eqn. [3] that the loss of chromium by volatilization

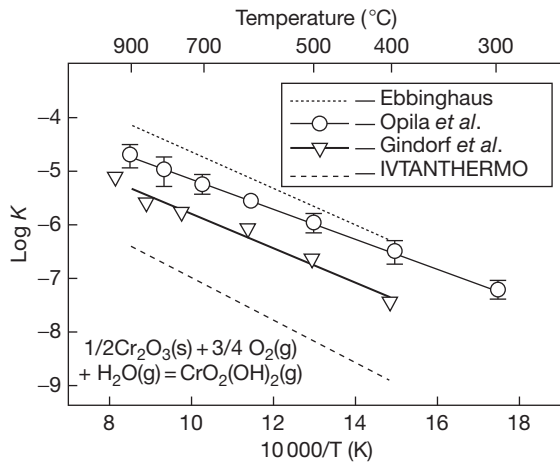


**Figure 4** Temperature dependence of the equilibrium constant  $K$  for the reaction  $1/2\text{Cr}_2\text{O}_3(\text{s}) + \text{H}_2\text{O}^{(g)} + 3/4\text{O}_2^{(g)} = \text{CrO}_2(\text{OH})_2^{(g)}$ . Compiled by Opila<sup>11</sup> using data from various sources.

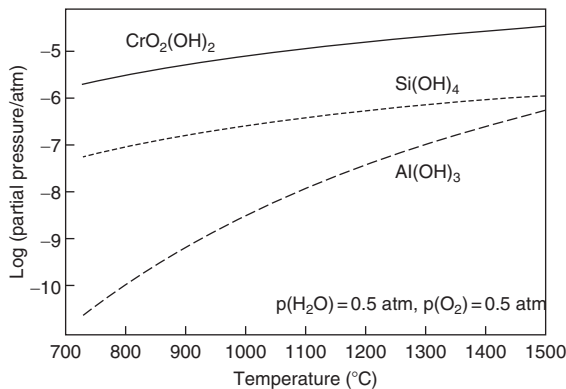


**Figure 5** Partial pressures of primary volatile species calculated for each oxide at 1 atm total pressure: 0.5 atm  $\text{O}_2$ , 0.5 atm  $\text{H}_2\text{O}$ .<sup>10</sup>

of  $\text{CrO}_2(\text{OH})_2^{(g)}$  should have a significant impact only on the oxidation process in gases in which partial pressures of both oxygen and water vapor are high,<sup>13</sup> and it should not be significant for the overall oxidation process in the low- $p_{\text{O}_2}$  gases considered in the present paper. In such gases, in fact  $\text{Cr}(\text{OH})_3^{(g)}$  is the most volatile chromium compound over the entire considered temperature range but the vapor pressure at 700 °C, for example, is only about  $10^{-13}$  atm. Galerie *et al.*,<sup>14</sup> Michalik *et al.*,<sup>15</sup> and Ehlers *et al.*<sup>16</sup> confirmed that at low- $p_{\text{O}_2}$   $\text{CrO}_2(\text{OH})_2$  does not possess sufficient volatility to be considered, for instance, as a possible cause of breakaway oxidation of ferritic steels in water vapor. Young and Pint<sup>17</sup> showed that the volatile Cr oxyhydroxide may become significant in high-pressure steam.

The data of Opila<sup>11</sup> shows that the reaction products of water vapor with chromia and silica have significant volatility at temperatures above about 800 °C, whereas for alumina this is the case only at temperatures in excess of 1400 °C. It is important to note that the vapor pressures of the most important volatile Al- and Si-containing species are independent of  $p_{\text{O}_2}$  (eqns [4] and [6]) and they can therefore be equally important for oxidation processes in  $\text{H}_2\text{O}$  ( $-\text{H}_2$ )-based gas mixtures and, for example, in wet air.

Also, volatilization of other alloying elements has been considered to play a role in the oxidation process in wet environments. For reaction of the ferritic 9% Cr steel P92 in oxygen/water vapor gas mixtures at 650 °C, formation of volatile species was considered by Milewska *et al.*<sup>18</sup> as function of  $p_{\text{O}_2}$  but with a constant water vapor content of 10%. At a low  $p_{\text{O}_2}$  of  $10^{-19}$  atm the most volatile species are  $\text{Fe}(\text{OH})_2^{(g)}$ ,  $\text{MoO}_2(\text{OH})_2^{(g)}$ , and  $\text{WO}_2(\text{OH})_2^{(g)}$ . With increasing  $p_{\text{O}_2}$  up to  $10^{-1}$  atm,  $\text{MoO}_2(\text{OH})_2^{(g)}$  and  $\text{WO}_2(\text{OH})_2^{(g)}$  remain the most volatile compounds but  $\text{CrO}_2(\text{OH})_2^{(g)}$  and  $\text{Mo}_3\text{O}_2^{(g)}$  also show significant volatility. The hydroxide  $\text{Fe}(\text{OH})_2^{(g)}$  as possible active volatile species in the oxidation of 9% Cr steels in presence of water vapor, especially at high total pressure, was also proposed by Thiele *et al.*,<sup>19</sup> Ehlers *et al.*,<sup>16</sup> and Davis and Dinsdale.<sup>8</sup> This was based on an evaluation by Surman and Castle,<sup>20</sup> but the authors indicated that better data was required to confirm its significance for oxidation processes.

### 1.17.2.3 Considerations for Material Testing in Steam Environments

When testing materials in water vapor-containing gases, impurities in the test gas may have an important effect on the equilibrium oxygen partial pressure

that establishes in the gas. If, for example, an inert gas such as Ar is bubbled through water at controlled temperature to establish a certain partial pressure of  $\text{H}_2\text{O}^{(\text{g})}$ , the equilibrium oxygen partial pressure of the gas mixture at temperatures between 500 and 900 °C is in the range  $10^{-9}$  to  $10^{-6}$  bars (Figure 6). Therefore, traces of oxygen as low as, for example, 1 ppm in the Ar carrier gas may, in this temperature range, substantially affect the equilibrium values. This will not be the case in (Ar)- $\text{H}_2$ - $\text{H}_2\text{O}$  mixtures containing a few percent of  $\text{H}_2$ . Hydrogen will at high temperature react with the  $\text{O}_2$  impurity such that the initial content of oxygen in the carrier gas will become insignificant for the overall equilibrium oxygen partial pressure. However, in pure steam or in Ar- $\text{H}_2\text{O}$  mixtures, not only traces of oxygen but also hydrogen in the initial gas mixture can have a substantial effect on the  $p_{\text{O}_2}$  of the equilibrated gas. For example, the presence of 1 ppm  $\text{H}_2$  in an Ar-4%  $\text{H}_2\text{O}$  gas mixture would, in a large temperature range, be sufficient to destabilize haematite, while traces of oxygen would have the opposite effect (Figure 6). It should be mentioned that traces of hydrogen may, for example, be present in the inert carrier gas, but may also originate from the reaction of the water vapor with the metallic material to be tested.<sup>21,22</sup> The latter effect was claimed to be responsible for differences in

oxide scale composition and thickness in the gas flow direction when testing ferritic steel specimens in slow-flowing Ar- $\text{H}_2\text{O}$  (Figure 7).<sup>22</sup> The effect did not occur if the test gas contained substantial amounts of hydrogen in addition to water vapor.<sup>23</sup>

The possible formation of volatile species due to reaction of oxides with water vapor has important implications for materials testing. Owing to its excellent thermal shock resistance, quartz is frequently used as construction material for reaction tubes and/or specimen holders in oxidation test facilities. In environments containing substantial amounts of water vapor, the formation of volatile Si-containing gas species such as, for example,  $\text{Si}(\text{OH})_4^{(\text{g})}$  can, however, substantially affect the oxidation process, as illustrated in Figure 8. In such test gases, reaction tubes and specimen holders should therefore, for instance, be made of alumina, in spite of problems that might occur due to the poorer thermal shock resistance of this material.

A further consequence of the  $\text{Si}(\text{OH})_4^{(\text{g})}$  formation is that materials or coatings that rely on formation of silica-based surface scales may not be suitable for material protection in steam environments. This is especially the case in high-pressure steam because eqn [4] shows that the vapor pressure of  $\text{Si}(\text{OH})_4^{(\text{g})}$  is proportional to  $[p_{\text{H}_2\text{O}}]^2$ .

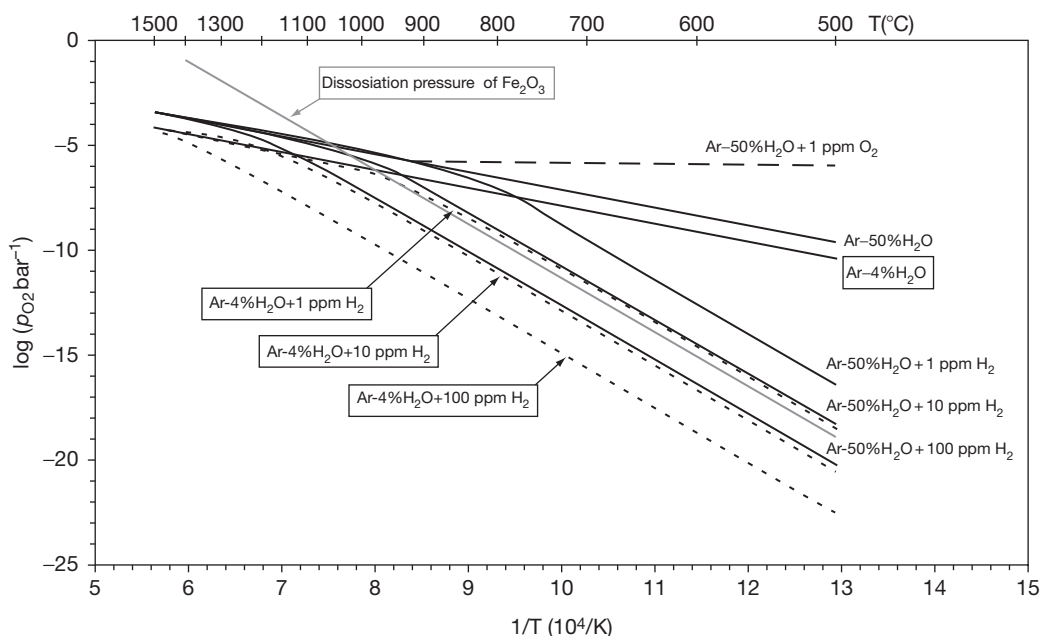


**Figure 6** Calculated equilibrium oxygen partial pressures in various Ar- $\text{H}_2\text{O}$ (- $\text{H}_2$ ) gas atmospheres compared with the dissociation pressure of  $\text{Fe}_2\text{O}_3$ , showing effect of trace amounts of  $\text{O}_2$  and  $\text{H}_2$ . Reproduced from Žurek, J.; Michalik, M.; Schmitz, F.; Kern, T. U.; Singheiser, L.; Quadackers, W. J. *Oxid. Met.* **2005**, 63(5/6), 401–422, calculated using FactSage.

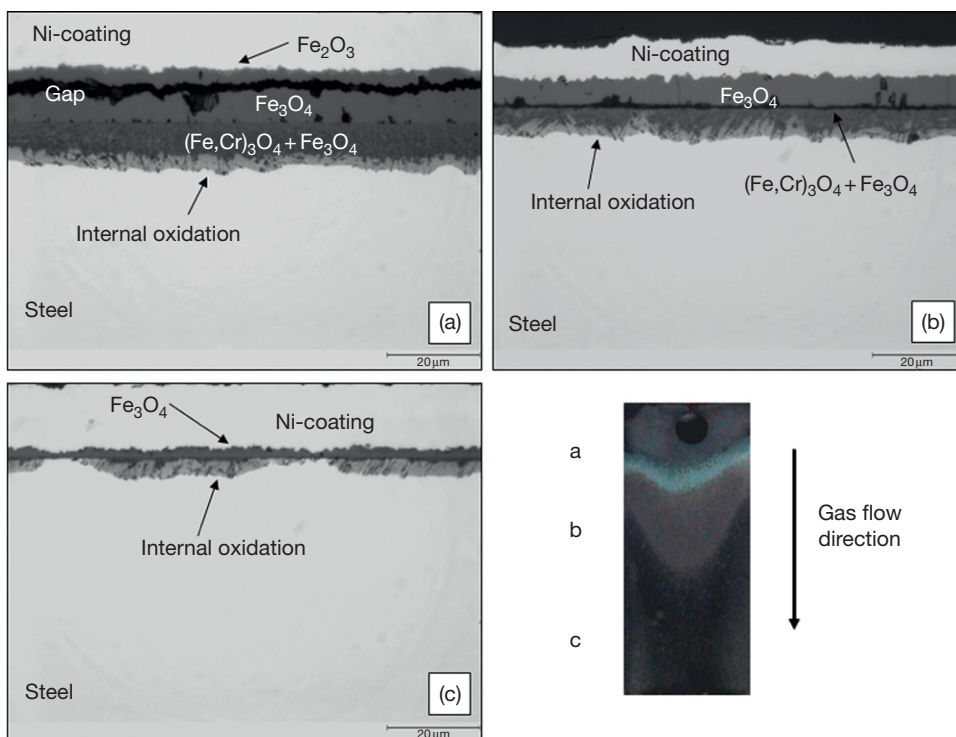


**Figure 7** Cross sections in different locations of rectangular specimen ( $20 \times 9 \times 2$  mm) oxidized for 5 h at  $15 \text{ l h}^{-1}$  gas flow in Ar-10%  $\text{H}_2\text{O}$  at  $650^\circ\text{C}$ . Macropicture shows the flow patterns and analysis areas. The specimen was placed in a reaction tube with a diameter of 10 mm and the linear gas flow rate was  $5.31 \text{ cm s}^{-1}$ .<sup>22</sup>

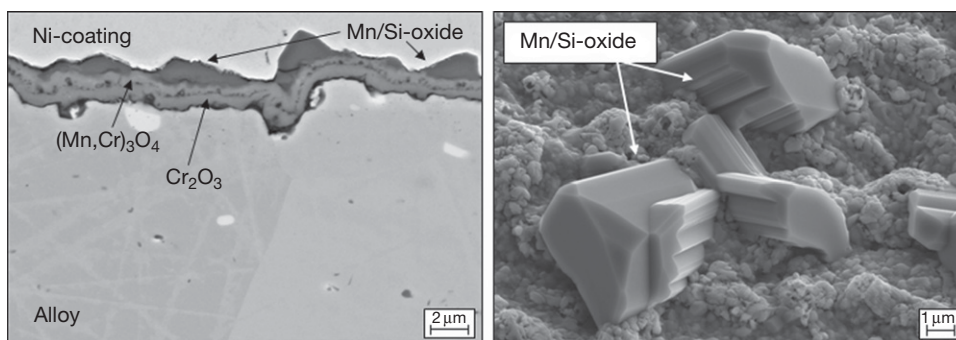


**Figure 8** Formation of mixed Mn/Si oxide on high-Cr ferritic steel during exposure in Ar- $\text{H}_2$ - $\text{H}_2\text{O}$  mixture with 18.5%  $\text{H}_2\text{O}^{(g)}$  at  $800^\circ\text{C}$  using a quartz reaction chamber.

### 1.17.3 Growth Mechanisms of Oxide Scales

#### 1.17.3.1 Kinetics of Surface Reactions

Upon long-term oxidation, the growth of oxide scales is frequently governed by solid-state transport processes within the scale. This results in an oxide thickening, which can, according to the classical oxidation theory developed by Wagner,<sup>6</sup> in many cases be described

by an approximate parabolic time dependence. However, especially in the early stages of oxidation, the kinetics of the surface reactions may be the rate-limiting step in the oxidation process.

Michalik *et al.*<sup>24</sup> studied the early stages of oxidation of Cr at  $1000^\circ\text{C}$  in an Ar-1%  $\text{O}_2$ -2%  $\text{H}_2\text{O}$  mixture using  $\text{H}_2^{18}\text{O}$  as tracer (Figure 9). The authors found that the chromia scale formation for up to exposure times of 3 h virtually contained only  $^{18}\text{O}$ , thus showing that in



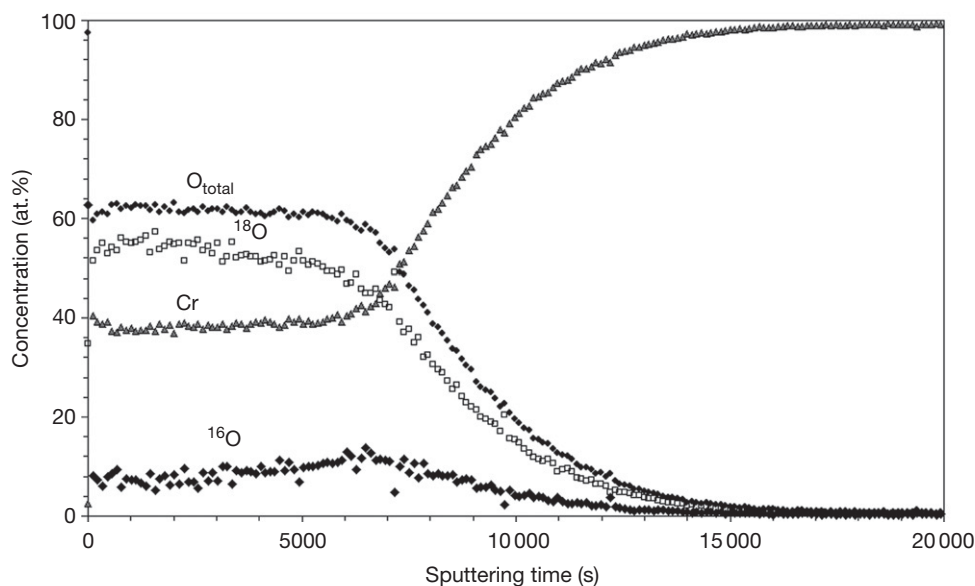


**Figure 9** SNMS depth profile after oxidation of chromium for 3 h in Ar-1%  $^{16}\text{O}_2$ -2%  $\text{H}_2^{18}\text{O}$  at 1000°C.<sup>24</sup>

this stage of the oxidation process oxygen transfer via  $\text{H}_2\text{O}^{(\text{g})}$  is much faster than that via  $\text{O}_2^{(\text{g})}$ . Also, Jacob *et al.*<sup>25</sup> reported for chromium oxidized in  $^{18}\text{O}_2/\text{H}_2^{16}\text{O}$  mixtures that oxygen derived from water vapor was the major component of the oxide even though the  $p_{\text{H}_2\text{O}}^{(\text{g})}/p_{\text{O}_2}^{(\text{g})}$  ratio was only 0.05 in that case.

In several studies it was found that whisker formation was promoted by the presence of water vapor.<sup>26,27</sup> Whiskers are believed to be formed at dislocations in the oxide<sup>28</sup> and have hollow cores such that rapid surface diffusion within the whisker can take place and their growth is then limited by the availability of oxidant at the whisker tip.<sup>28</sup> It was proposed<sup>26</sup> that the faster growth of whiskers in moist atmospheres is related to the generally faster dissociation of water molecules than for most other oxidant molecules.

Anghel *et al.*<sup>29</sup> studied the adsorption of  $\text{N}_2$ ,  $\text{H}_2$ , CO, and  $\text{H}_2\text{O}$  on oxidized Cr- and Zr-based materials in the temperature range 400–600 °C. When adding water vapor to CO gas, the dissociation rate of CO on Cr decreased, which can be interpreted as being the result of a blocking effect by water. On the basis of the results of these authors, the following ranking for the tendency of adsorption at high temperatures was made:  $\text{N}_2 < \text{H}_2 < \text{CO} < \text{H}_2\text{O}$ . This might explain the results of Michalik *et al.*,<sup>24</sup> who found pure Cr to form subscale nitrides during exposure at 1000 °C in  $\text{N}_2$ - $\text{O}_2$  but not in  $\text{N}_2$ - $\text{H}_2$ - $\text{H}_2\text{O}$ . Zheng and Young<sup>30</sup> found that for pure Cr at 900 °C subscale nitride formation occurred in  $\text{N}_2$ -CO-CO<sub>2</sub> but not in

$\text{N}_2$ - $\text{H}_2$ - $\text{H}_2\text{O}$  atmosphere with the same equilibrium oxygen partial pressure. The authors explained the results in terms of competitive adsorption of the various gas species on oxide surfaces and grain boundaries. Thus, as  $p_{\text{H}_2\text{O}}/p_{\text{O}_2}$  increases, preferential adsorption of  $\text{H}_2\text{O}$  becomes favored. Evidently, nitrogen can enter and penetrate dry  $\text{Cr}_2\text{O}_3$  grain boundaries, but cannot do so when large numbers of water molecules are present. This confirms the ability of  $\text{H}_2\text{O}^{(\text{g})}$  to interact with the interior of chromia scales modifying their transport properties.<sup>30</sup>

Akermark and Hultquist<sup>31</sup> showed that with an Fe-20% Cr-10% Al alloy oxidized at 920 °C, water dissociation rates decreased with decreasing oxidation rates, and they interpreted this as the result of fewer defects in the more mature alumina scale. In general, it appears that dissociation of a gas molecule such as  $\text{H}_2\text{O}^{(\text{g})}$  is favored by defects in the surface, and the stoichiometric oxides such as alumina may therefore be less active than, for example, FeO.

A number of authors have proposed that the relative acidity/basicity of oxides controls the reaction with water vapor,<sup>32</sup> where water vapor will react more strongly with more acidic oxides (Figure 10). The commonly used method of PZC (point of zero charge) or IEP (isoelectric point) is believed to yield a good relative assessment for oxide ranking, while use of chemical shift measurements by X-ray photoelectron spectroscopy (XPS) or heats of adsorption by calorimetry or gas chromatography yield better absolute values.<sup>33</sup>



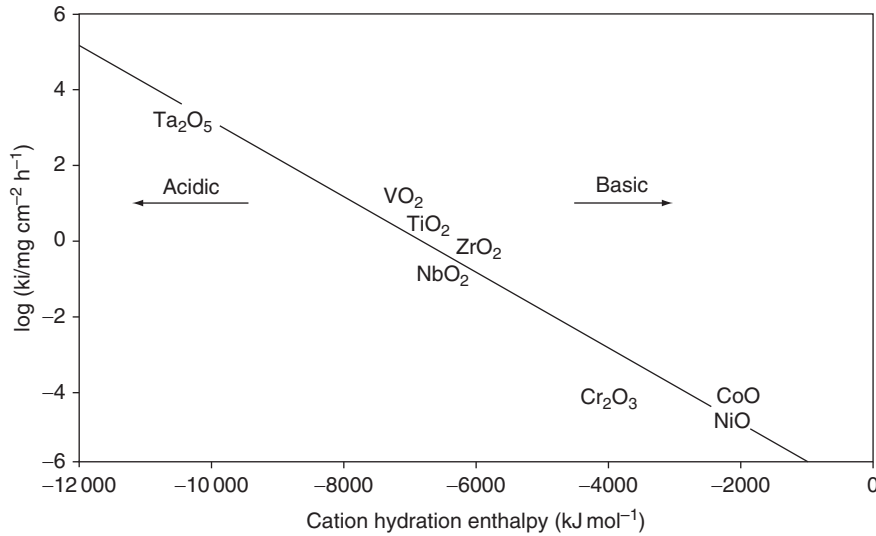
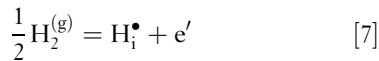


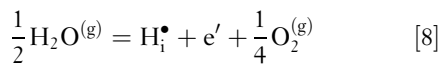
**Figure 10** Correlation between the oxidation rate of metals by water vapor at 800 °C and the hydration enthalpy of the corresponding cation.<sup>32</sup>

### 1.17.3.2 Effect of Water Vapor and Hydrogen on Lattice Diffusion in Oxide Scales

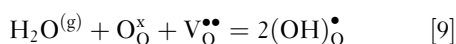
The possible effects of hydrogen/water vapor incorporation in the transport properties of oxides were considered by several authors. Hydrogen dissolves in the oxide as protons and is bound to oxide ions to form the substitutional hydroxide  $(\text{OH})_{\text{o}}^{\bullet}$ .<sup>34</sup> These defects may equivalently and more simply be described as interstitial protons  $\text{H}_{\text{i}}^{\bullet}$ . Generally it is found that the concentration of  $\text{H}_{\text{i}}^{\bullet}$  increases with increasing  $p_{\text{H}_2\text{O}}$  and decreasing temperature. The dissolution of protons in an oxide can be written as:



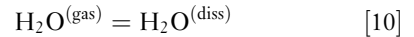
or, by considering gas equilibria,



Thus, at sufficiently low  $p_{\text{H}_2\text{O}}$  or  $p_{\text{H}_2}$ , protons are minority defects. The concentrations of native defects are independent of  $p_{\text{H}_2\text{O}}$  or  $p_{\text{H}_2}$  (at constant  $p_{\text{O}_2}$ ), while the concentrations of protons increase with  $p_{\text{H}_2\text{O}}^{1/2}$  or  $p_{\text{H}_2}^{1/2}$ . At higher  $p_{\text{H}_2\text{O}}$  or  $p_{\text{O}_2}$ , protons may become the dominant defect, compensated for by defect electrons, metal vacancies, oxygen interstitials or acceptor dopants. Many investigations focus on the equilibrium between water vapor, oxygen vacancies and protons as being the most likely:



which, in general, is exothermic so that protons are dominant at low temperatures and oxygen vacancies at high temperatures. It is also important to consider the parallel reaction of dissolution from the gas phase:



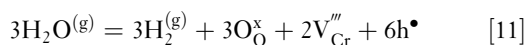
Thus, different types of hydrogen-containing species may be present simultaneously, that is, molecular water and OH groups, as is frequently found in glasses.<sup>35</sup> In close-packed structures such as alumina and chromia, dissolution of molecular water would be less favored. Transport of 'water' in oxide scales is claimed to occur by a proton 'hopping' process in which protons localized at oxide ions move by transfer from one oxygen to another. Since oxygen is available everywhere, the net effect of proton diffusion is diffusion of water, and since proton diffusion rates are high compared with those of metal or oxygen, diffusion of 'water' is easy. Although the general principles of the effects of protons can be outlined, the uncertainties regarding transport in the oxides scales of interest are such that it is not possible to predict with any certainty the effects of water vapor on lattice transport.

### 1.17.3.3 Molecular Diffusion in Oxide Scales in Wet Gases

Already in earlier studies it was claimed that, depending on the scale type, the oxidation kinetics in  $\text{H}_2\text{O}$ -containing gases at least partially depends on the ingress of water molecules through the oxides scales. For this to happen, 'microchannels' must be present,

or, as in the case of silica, an open network structure allows the transport of large molecular species.

It is important to consider gaseous or volatile species that might be created during oxidation reactions involving water vapor and how these are transported within the scale. A well-accepted process for vapor or gaseous transport is the dissociative mechanism first proposed by Rahmel and Tobolski.<sup>36</sup> This mechanism is applicable only for scales grown by cation transport and involves interaction with void formed by vacancy condensation.<sup>6</sup> If a void contains both hydrogen and water vapor, oxidation of the surface nearest the metal will occur by reaction with water to form new oxide and the gaseous reaction product hydrogen (Figure 11). Adapting this suggestion to  $\text{Cr}_2\text{O}_3$  and using the Kröger–Vink notation, one can write<sup>37</sup>



This process occurs in the forward direction, on the side of the cavity nearest the metal, and in the reverse direction at the outer surface of the cavity. It provides for rapid inward diffusion of oxygen while the void gradually moves outwards from the metal/oxide interface to the oxide/gas interface.

As mentioned in Section 1.17.2.2, Surman and Castle<sup>20</sup> and Ehlers *et al.*<sup>16</sup> have proposed that volatile  $\text{Fe}(\text{OH})_2^{(\text{g})}$  might participate in the scale-formation process in wet gases and might be an important factor for pore generation in an oxide formed on a 9% Cr steel in wet gas. Using available thermodynamic data, however, Ehlers *et al.*<sup>16</sup> calculated that the vapor pressure of  $\text{Fe}(\text{OH})_2^{(\text{g})}$  is too low to sustain the reaction, but pointed out that these data need verification. The process may be of more importance at high steam pressures.<sup>17</sup>

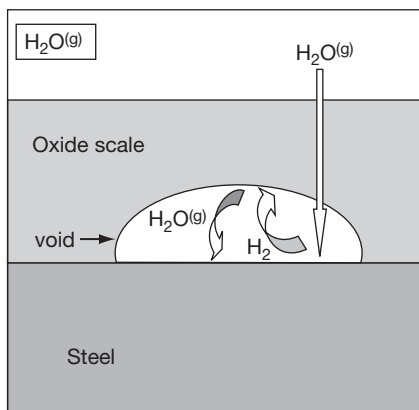


**Figure 11** Schematic illustration showing oxygen transfer across in-scale voids in water vapor-containing gas. (From Ref. 16 based on the Rahmel–Tobolski mechanism<sup>36</sup>).

Void transport by the Rahmel–Tobolski mechanism or generation of volatile  $\text{Fe}(\text{OH})_2^{(\text{g})}$  obviously requires water vapor to exist within the oxide scale. In addition to proton diffusion, the presence of cracks and fissures in the oxide is a possible mechanism to allow water ingress. Ehlers *et al.*<sup>16</sup> have found that scales grown in water vapor mixtures on the 9% Cr steel P91 are more permeable than those grown under dry conditions, which was demonstrated by  $^{16}\text{O}_2/\text{H}_2^{18}\text{O}$  studies (Figure 12). A competitive adsorption between water and oxygen occurred at inner surfaces, with water being preferentially adsorbed if the  $p_{\text{H}_2\text{O}}/p_{\text{O}_2}$  ratio is  $\geq 1$ .

### 1.17.4 Metallic High Temperature Components in Steam and Steam/Hydrogen Environments

#### 1.17.4.1 General Remarks

Nearly all high temperature metallic construction materials rely for their oxidation protection on chromia or alumina scales that form on the component surface during high temperature service. Only in a few cases, silica, mostly found as sublayer beneath chromia base scales, is of importance for metallic materials protection. Pure silica scales are of far more importance for environmental protection of a number of ceramic materials, for example, of the type Si nitride or carbide.

When comparing the behavior of metallic high temperature components in steam and steam/hydrogen gases with that in oxygen or air, the literature data indicate that the service environment may affect the growth of the protective scale (chromia or alumina) as well as that of the less protective oxides of the base elements (Fe, Ni, Co). Therefore, the effect of the environment on the overall material behavior of alloys with high concentrations of protective scale-forming elements (PSEs) chromium and aluminum may differ from that of lower alloyed materials that form oxide scales of the base elements or alloys that can be considered as ‘borderline’ alloys between protective and nonprotective behavior.

Figure 13 shows the qualitative dependence of the oxidation behavior of Fe-, Ni-, and Co-based alloys as a function of the amount of PSEs, as frequently measured when exposing the alloys to oxygen or air.<sup>6</sup> With small additions of PSEs (group I alloys), the total oxygen uptake frequently tends to be slightly higher than in case of pure base metal oxidation because of doping effects and/or occurrence of internal oxidation.<sup>6,38</sup> With a further increase in concentration of PSEs, the

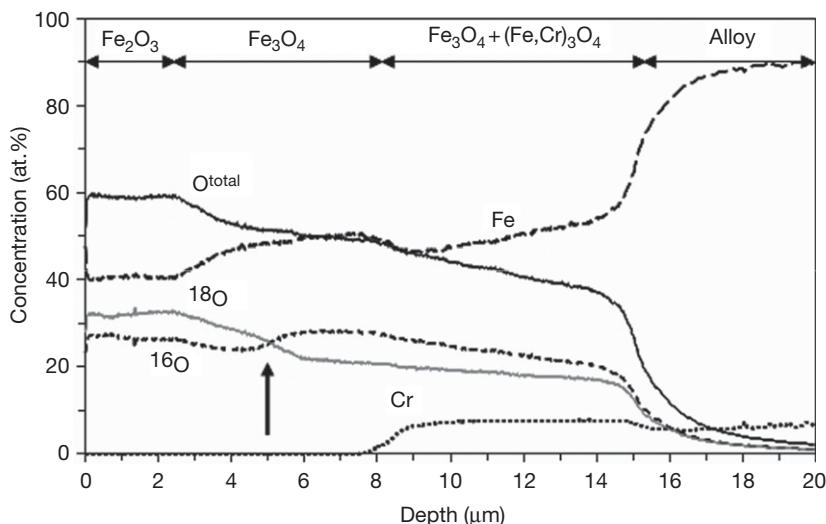


**Figure 12** MCs<sup>+</sup> secondary ion mass spectrometry profile of P91 steel after 30 h oxidation at 650 °C in N<sub>2</sub>-1% <sup>16</sup>O<sub>2</sub>-4% H<sub>2</sub><sup>18</sup>O showing differences in distribution of <sup>18</sup>O and <sup>16</sup>O in the Fe-based oxide scale. Arrow indicates location of gap in outer magnetite layer. Reproduced from Ehlers, J.; Young, D. J.; Smaardijk, E. J.; Tyagi, A. K.; Penkalla, H. J.; Singheiser, L.; Quadackers, W. J. *Corros. Sci.* **2006**, *48*, 3428–3454.

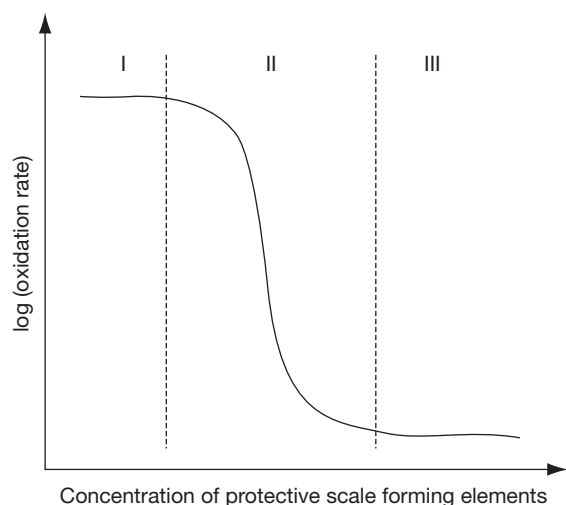


**Figure 13** Schematic illustration showing qualitatively the effect of Cr and/or Al content on the oxidation rates of Ni-, Fe- and Co-based alloys during exposure in air or oxygen. (The oxidation rates of group I and group III alloys are not necessary independent of the concentration of PSEs, as explained, for example, by Birks *et al.*<sup>6</sup>).

oxidation rate decreases as a result of the formation of larger amounts of more protective oxides in the surface scale. Above a critical concentration of the PSEs, the alloy starts forming a slowly growing scale of chromia or alumina. The exact concentration at which this fundamental change in oxidation mechanism occurs depends on numerous parameters such as temperature, time, gas composition, minor alloying additions, and

surface treatment. Alloys with a concentration of the PSE near the steep drop in oxidation rate (group II alloys) can thus be considered as ‘borderline’ alloys between protective and nonprotective scale formation.

The commercially available alloy systems for high temperature applications are mostly materials of group II and III in Figure 13. Therefore, in the following sections the effect of service environment on the behavior of these types of alloy systems will be described. First, chromia scale formation on pure Cr as well as high-Cr Fe- and Ni-based alloys (group III materials) will be discussed. Subsequently, the scale formation on corresponding ‘borderline alloys’ with intermediate Cr contents (group II) will be treated. Owing to its technological importance, special emphasis will be put on steam oxidation behavior of ferritic/martensitic and austenitic steels in the temperature range 550–650 °C. The final sections will deal with alumina-forming alloys and coatings, including the behavior of ‘borderline’ alumina formers.

### Nomenclature

In the following discussion the chromia and alumina scales will be frequently termed as ‘protective scales’ whereas the oxides of the base elements Fe, Ni, and, for example, Ti will be termed ‘nonprotective oxides.’ This expression is strictly speaking not correct because oxides with relatively high growth rates still offer protection of the metal or alloy. The expressions will, however, be used for convenience.

### 1.17.4.2 Oxidation of Chromium and High-Chromium Alloys

#### 1.17.4.2.1 Oxidation of chromium

In earlier studies, Quadakkers *et al.*<sup>39</sup> found the oxide scale on pure chromium in an Ar/H<sub>2</sub>/H<sub>2</sub>O mixture to grow faster than that formed in air. During cyclic oxidation, however, the overall oxidation resistance of the material was far better in Ar/H<sub>2</sub>/H<sub>2</sub>O because of the better adherence of the scales than that of the scales formed in air. The oxide scales formed in the low-*p*O<sub>2</sub> gas showed a smaller tendency to buckle, but a larger tendency to whisker formation, than found during air exposure.

The lower growth rate and/or poorer adherence might be related to the subscale nitride formation which is known to occur during air exposure of Cr. However, similar observations in respect to differences in adherence and growth rate were made by Hänsel *et al.*<sup>40</sup> when comparing the behavior in Ar-H<sub>2</sub>-H<sub>2</sub>O with that in Ar-O<sub>2</sub>. Hultquist *et al.*<sup>41</sup> found the chromia growth rates at 900 °C to be approximately doubled in 2% water vapor (20 mbar) compared with the rate in dry oxygen at the same total pressure. A similar acceleration was observed when the Cr contained dissolved hydrogen prior to exposure.<sup>42</sup> The adhesion of the scale was improved when it was formed in water vapor-containing atmospheres, and this was proposed to be related to a greater fraction of scale growth at the metal-oxide interface. The fact that adherence of chromia-based scales formed in Ar/H<sub>2</sub>/H<sub>2</sub>O is better than those formed in air or oxygen was also observed by Malkow *et al.*<sup>43</sup> for a number of high-Cr ferritic steels.

At higher levels of water vapor (Ar-15% H<sub>2</sub>O), Henry *et al.*<sup>44</sup> observed that the growth rate of chromia on pure chromium at 900 °C was higher than in an Ar-15% oxygen gas mixture. The authors proposed that the increased rate of growth was due to enhanced inward scale growth as a result of the smaller ionic radius of OH<sup>-</sup> (95 pm) compared with that of O<sup>2-</sup> (140 pm). It was also found that scale adhesion was significantly improved when water vapor was present compared with the case for dry oxygen. Hänsel *et al.*<sup>45</sup> showed that for Cr oxidized at 1000 °C the oxidation rates in Ar-H<sub>2</sub>-H<sub>2</sub>O mixtures were equal or greater than those in Ar-O<sub>2</sub> or Ar-O<sub>2</sub>/H<sub>2</sub>O and the formation of blades was observed at the oxide surface. They proposed a model in which oxide growth in Ar-H<sub>2</sub>-H<sub>2</sub>O was sustained by diffusion of chromium vacancies and adsorption of H<sub>2</sub>O on oxide exposed to low oxygen-activity gas led to the formation of

hydroxyl species. At high oxygen activities, molecular oxygen adsorbs preferentially on the entire surface, overwhelming any local variation due to catalysis of H<sub>2</sub>O dissociation. This explained the absence of whiskers in high-oxygen-content atmospheres.

Figure 14 shows results of Michalik *et al.*<sup>15</sup> comparing weight-change data after isothermal exposures of Cr in various low- and high-*p*O<sub>2</sub> gases. Also shown are the weight changes after cooling to room temperature. The data confirm that samples oxidized in low-*p*O<sub>2</sub> gases (Ar-H<sub>2</sub>O and Ar-H<sub>2</sub>-H<sub>2</sub>O) generally showed, during cooling, far less extensive scale spalling than samples oxidized in high-*p*O<sub>2</sub> gas. The most pronounced spalling was found for the specimen oxidized in Ar-20% O<sub>2</sub>. Figure 15 shows transmission electron microscopy (TEM) micrographs from cross sections of specimens oxidized in Ar-20% O<sub>2</sub> and Ar-2% H<sub>2</sub>O at 950 °C for 0.5 h. The oxide scale formed in the high-*p*O<sub>2</sub> gas exhibits pores and cracks, mainly at the alloy-oxide interface. The oxide formed during oxidation in the low-*p*O<sub>2</sub> gas appears to be very dense, the alloy-oxide interface is intact and the oxide adheres well to the metal (Figure 15(b)).

Michalik *et al.*<sup>15,24</sup> carried out two-stage oxidation tests with Cr at 1000 °C where the gas was, without intermediate cooling, changed from Ar-O<sub>2</sub> to Ar-H<sub>2</sub>-H<sub>2</sub>O. An oxide layer with a morphology typical for scales formed in Ar-H<sub>2</sub>-H<sub>2</sub>O was found at the scale/metal interface, beneath the buckled layer grown in Ar-O<sub>2</sub>.

The oxidation of Cr and chromia-forming alloys in dry, high-*p*O<sub>2</sub> gases is known to be influenced by reactive evaporation at the scale/gas interface which releases CrO<sub>3</sub><sup>(g)</sup> as the primary species,<sup>6</sup> whereas in the low-*p*O<sub>2</sub> gas the partial pressure of volatile Cr species should be extremely low.<sup>11,12</sup> The differences in oxide growth rates observed in the various environments might thus be related to differences in the formation of volatile species in Ar-O<sub>2</sub> and Ar(-H<sub>2</sub>)-H<sub>2</sub>O (see Section 1.17.2.2). However, Michalik *et al.*<sup>15</sup> illustrated that, under the used experimental conditions, this effect could not explain the observed differences in scale growth rates.

#### 1.17.4.2.2 Oxidation of chromia-forming Fe- and Ni-based alloys

Essuman *et al.*<sup>46</sup> studied the isothermal oxidation behavior of FeCr alloys at 900 °C in Ar-O<sub>2</sub> and Ar-H<sub>2</sub>-H<sub>2</sub>O. Energy dispersive X-ray (EDX) analysis showed that the surface oxide scales formed in both test gases on Fe-20% Cr consisted essentially of chromia, and no indication for the presence of Fe in the scale

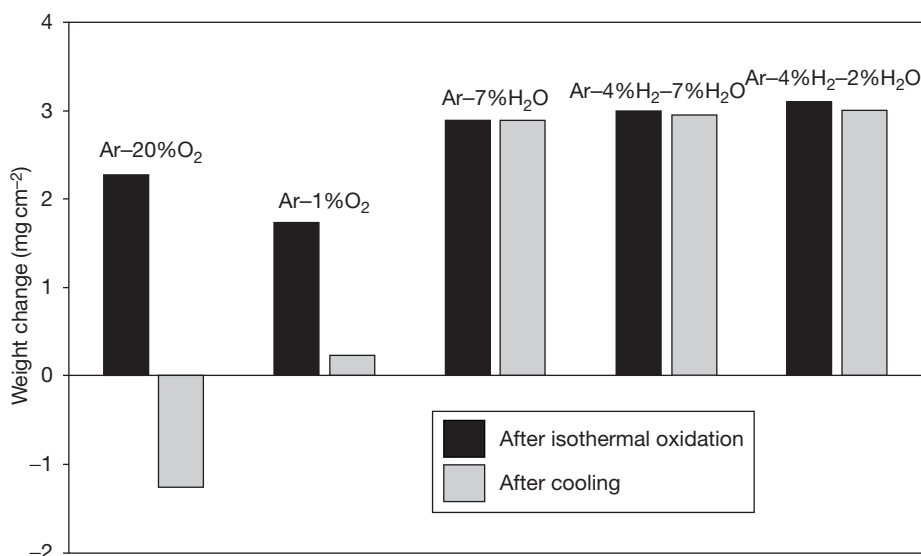


**Figure 14** Weight changes after 72 h isothermal oxidation and after subsequent cooling to room temperature of pure Cr in different high- and low- $p_{O_2}$  gases at 1000 °C. Reproduced from Michalik, M.; Hänsel, M.; Žurek, J.; Singheiser, L.; Quadackers, W. J. *Mater. High Temp.* **2005**, 22(3/4), 213–221.

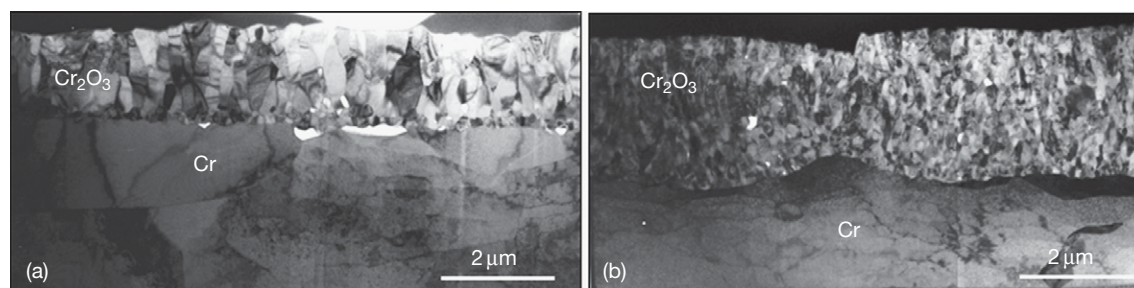


**Figure 15** TEM cross sections of oxide scales formed on pure chromium after 0.5 h oxidation at 950 °C in (a) Ar-20% O<sub>2</sub> and (b) Ar-2% H<sub>2</sub>O. Reproduced from Michalik, M.; Hänsel, M.; Quadackers, W. J. Report Forschungszentrum Jülich, **67** (2007), ISBN 978-3-89336-486-2.

could be found. As described above for pure Cr, the chromia scale that formed in the Ar-H<sub>2</sub>-H<sub>2</sub>O gas exhibited a higher growth rate than that that formed in Ar-O<sub>2</sub>.

**Figure 16** shows gravimetric data during isothermal oxidation of a binary Ni-25Cr alloy in low- $p_{O_2}$  gases Ar-(4% H<sub>2</sub>)-7% H<sub>2</sub>O and in Ar-20% O<sub>2</sub>. The growth rate in the latter gas was smaller than that in the low- $p_{O_2}$  gases and the scale was found to have developed voids and internal pores at and near the oxide-alloy interface. In contrast, the oxide grown on this alloy in Ar-4% H<sub>2</sub>-7% H<sub>2</sub>O was compact and closely adherent to the substrate.<sup>47</sup> The latter phenomenon had already been found in the earlier studies of Wood *et al.*<sup>48</sup> for scales grown on Fe-28% Cr in Ar-10% H<sub>2</sub>O compared to scales grown in oxygen.

#### 1.17.4.2.3 Mechanisms of chromia scale growth

The differences in chromia growth in the various gases appear to be similar for all three discussed materials, that is, Cr as well as high-Cr Ni- and Fe-based alloys. The scales exhibit higher growth rates but are more compact, show better adherence and frequently exhibit a flatter metal/scale interface when formed in low- $p_{O_2}$  gas.

The better adherence of the oxide in the low- $p_{O_2}$  gases might be related to the H<sub>2</sub>O/H<sub>2</sub> bridges in voids described by Rahmel and Tobolski (see [Section 1.17.3.3](#)). In Ar-O<sub>2</sub> the outward-growing scale will result in vacancy condensation, preferentially at the alloy/oxide interface, resulting in poor



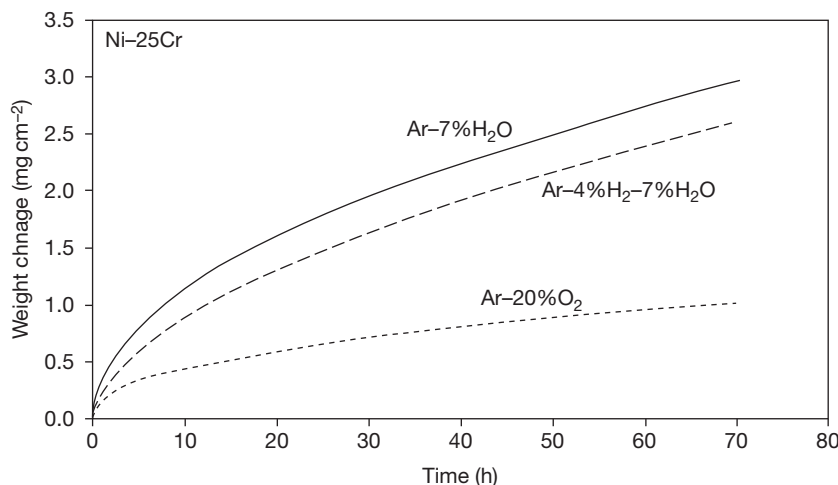


**Figure 16** Weight change versus time during isothermal oxidation of Ni-25Cr model alloy at 1050 °C in Ar-20% O<sub>2</sub>, Ar-7% H<sub>2</sub>O and Ar-4% H<sub>2</sub>-7% H<sub>2</sub>O. Reproduced from Essuman, E.; Meier, G. H.; Žurek, J.; Hänsel, M.; Norby, T.; Singheiser, L.; Quadakkers, W. J. *Corros. Sci.* **2008**, 50(6), 1753–1760.

adherence. The Rahmel–Tobolski mechanism provides an inward oxygen transport resulting in void healing and a net transport of the void away from the metal scale interface, which increases scale adherence. However, the mechanism cannot explain why, in fact, less voidage is seen in the scales formed in the low- $p_{\text{O}_2}$  gases (Figures 15 and 17).

The growth of chromia scales is generally believed to be controlled by boundary diffusion rather than lattice diffusion.<sup>37</sup> Nonetheless, if the mobile species are ionic and at local equilibrium with the surrounding oxide, then Wagner's description<sup>6,49</sup> of the dependence on  $p_{\text{O}_2}$  of scale growth rate can be applied, providing that a suitable effective diffusion coefficient is used. If the predominant defects are fully charged vacancies, then it is predicted for the parabolic rate constant  $k_p$ <sup>49</sup>

$$k_p \approx \text{const}(p_{\text{O}_2})^{\frac{1}{16}} \quad [12]$$

However, if the principal defects are interstitials and the ambient  $p_{\text{O}_2}$  value is significantly above the Cr/Cr<sub>2</sub>O<sub>3</sub> equilibrium value, then  $k_p$  is independent of  $p_{\text{O}_2}$ . Both predictions are not in agreement with the experimental observations.

From the TEM cross sections of the oxidized Cr (Figure 15) and Ni-25Cr specimens (Figure 17), it is apparent that the oxide scales formed in the high- $p_{\text{O}_2}$  gas show large grains with a columnar morphology which is typical, as frequently described by several authors,<sup>50</sup> for scales that mainly grow by outward cation diffusion. The oxides formed in the two low- $p_{\text{O}_2}$  gases are, however, extremely fine grained with a

small tendency for the grain size to increase towards the scale/alloy interface.

Figure 18 shows the distribution of oxygen isotopes in the scale formed on alloy Ni-25Cr during the two-stage oxidation in Ar-H<sub>2</sub>-H<sub>2</sub><sup>16</sup>O/H<sub>2</sub><sup>18</sup>O at 1050 °C. The small <sup>18</sup>O peak at the scale/alloy interface is a clear proof of inward transport of oxygen-bearing species along rapid diffusion paths, likely grain boundaries.<sup>51</sup> The continuously decreasing <sup>18</sup>O concentration in the outer part of the scale is, at least partly, related to extensive isotope exchange between <sup>18</sup>O at the grain boundaries and <sup>16</sup>O within the grains due to the extremely fine size of the chromia grains.<sup>51</sup> A similar difference in growth mechanism in a low- and high- $p_{\text{O}_2}$  environment was also found by Bamba *et al.*<sup>52</sup> for the alloy Fe-15Cr-0.5 Si at 850 °C.

In earlier studies it was proposed that the better adherence of chromia scales on pure chromium formed in water vapor-containing atmosphere may be related to enhanced scale plasticity.<sup>53,54</sup> It would seem that in terms of defect concentration the main effect of water vapor is to increase the concentration of the majority species so that one might not expect to see an effect on creep rates.<sup>27</sup> The improved plasticity in the low  $p_{\text{O}_2}$  gas could be related to the smaller chromia grain size compared to that formed on chromia in dry atmospheres. However, on the basis of the newer results, a more likely explanation is that the observed differences in adherence as well as growth rate of the scales found in the high- and low- $p_{\text{O}_2}$  gases are just a result of the difference in scale growth mechanisms. By the substantial inward



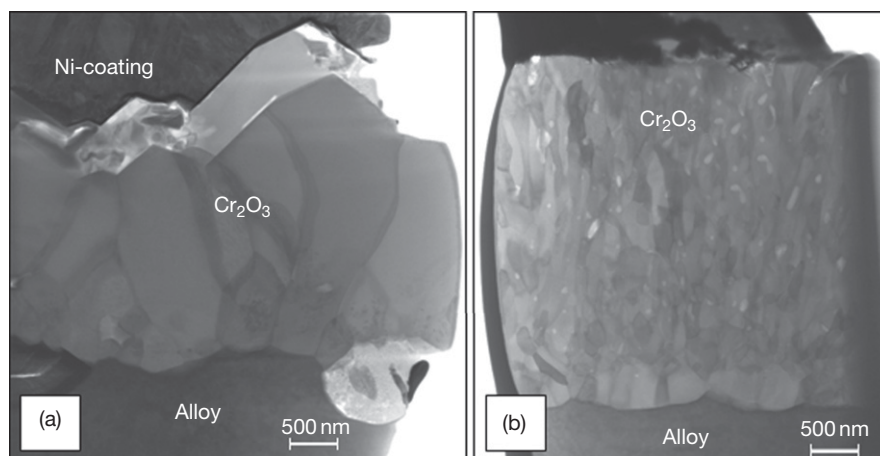


**Figure 17** TEM cross sections of oxide scales formed on Ni-25Cr model alloy during 4 h oxidation in (a) Ar-20% O<sub>2</sub> and (b) Ar-4% H<sub>2</sub>-2% H<sub>2</sub>O at 1050 °C.

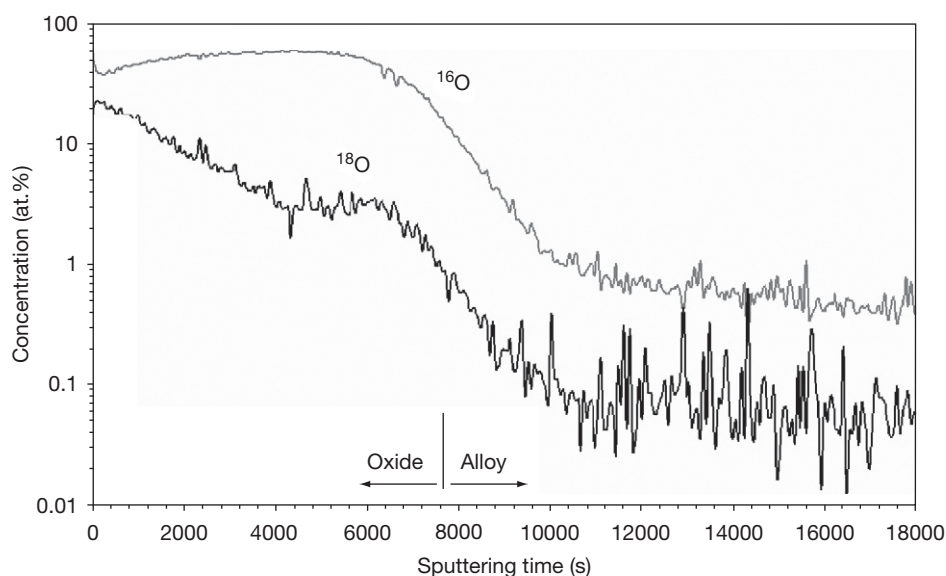


**Figure 18** Semi-logarithmic plot of the <sup>18</sup>O and <sup>16</sup>O profiles in the oxide scale on a Ni-25Cr model alloy after two-stage oxidation at 1050 °C: first stage 0.5 h in Ar-4% H<sub>2</sub>-2% H<sub>2</sub><sup>16</sup>O; second stage 2 h in Ar-4% H<sub>2</sub>-2% H<sub>2</sub><sup>18</sup>O. Reproduced from Żurek, J.; Young, D. J.; Essuman, E.; Hänsel, M.; Penkalla, H. J.; Niewolak, L.; Quadakkers, W. J. *Mater. Sci. Eng. A* **2008**, 477, 259–270.

oxygen transport in the low- $p_{\text{O}_2}$  gas, growth of voids as a result of vacancy condensation at the scale–metal interface is suppressed, resulting in better scale adherence. The extremely high grain boundary density favors inward oxygen transport, resulting in a higher oxide growth rate in the low- $p_{\text{O}_2}$  gas.

The remaining questions concern the mechanism whereby H<sub>2</sub>O<sup>(g)</sup> alters the grain size in the low- $p_{\text{O}_2}$  gas and the way in which inward oxygen transport occurs.<sup>37</sup> One possibility is that the presence of H<sub>2</sub>O adsorbed at the oxide grain boundaries hinders

their movement and thus grain growth. This would explain the extremely fine oxide grains formed in Ar(–H<sub>2</sub>)–H<sub>2</sub>O.<sup>51</sup> However, it could also be argued that the stronger contribution of inward scale growth might not be the result of the finer grain size: rather, the finer grain size could result from the modified scale growth process induced by H<sub>2</sub>O<sup>(g)</sup>. The available results do not allow a distinction to be drawn between the two possibilities. Nonetheless, it is clear that the effect of water vapor during oxidation in Ar(–H<sub>2</sub>)–H<sub>2</sub>O environments is twofold: water molecules

incorporated into the scale provide accelerated mass transport while simultaneously promoting the formation of a fine-grained, inwardly growing, and therefore better adhering, oxide scale.

#### 1.17.4.2.4 Commercial chromia-forming Fe- and Ni-based alloys

Nearly all commercially available chromia-forming alloys contain intentionally added alloying elements and impurities which may substantially affect the oxidation mechanisms and thus also differences in oxidation behavior in the mentioned low and high- $p_{O_2}$  gases. The alloying elements and impurities may, for example, lead to doping of the chromia layer and/or result in formation of other mixed oxides, for example, of the spinel type. Only a few systematic studies that deal with the effect of such impurities and minor alloying additions on the differences in the oxidation behavior in low- and high- $p_{O_2}$  gases are available.

England and Virkar<sup>55,56</sup> studied the oxidation of a series of thin-foil nickel-based alloys (Inconel 625, Inconel 718, Hastelloy X, and Haynes 230) in air and wet hydrogen ( $p_{O_2} = 10^{-21}$  to  $10^{-16}$  atm,  $p_{H_2O} = 0.07$  atm) at 700–1100 °C. At 800 °C the oxidation rate in wet hydrogen was increased by factors ranging between 8 and 30, but at 1100 °C the effect of wet hydrogen was to decrease the oxidation rate compared to that in air by factors ranging between 1.5 and 13. Hussain *et al.*<sup>57,58</sup> reported that Hastelloy C-4 formed a protective scale in 100% steam at all temperatures in the range 600–1200 °C, whereas the scale spalled when formed in air.

Extensive studies concerning the behavior of chromia forming-alloys, especially high-Cr ferritic steels, in low- and high- $p_{O_2}$  gases have been carried out in the development of solid oxide fuel cells

(SOFCs), as in these devices metallic interconnects are exposed on one side to the oxidant gas (mostly air) and on the other side to moist hydrogen-based environments. Figure 19 shows the oxide scales on a high-Cr ferritic steel Crofer APU (nominal composition in mass%, 22Cr–0.5Mn–Ti–La) after exposure for 1000 h at 800 °C in air and Ar–H<sub>2</sub>–H<sub>2</sub>O. In both cases a two-layered scale is formed consisting of Cr<sub>2</sub>O<sub>3</sub> and an outer Cr/Mn-spinel. During air exposure the spinel is present in the form of well-developed crystals, whereas in Ar–H<sub>2</sub>–H<sub>2</sub>O it possesses a blade-like morphology (Figure 20). The scale formed in the low- $p_{O_2}$  gas tends to form voids at/near the interface between the chromia and the spinel layer (Figure 19). Traces of Ti are frequently present in the scales: that is, dissolved in the Cr<sub>2</sub>O<sub>3</sub> near the scale–alloy interface and in form of TiO<sub>2</sub> particles near the scale–gas interface.<sup>59,60</sup> Presence of minor concentrations of Al and Si (a few tenths of a percent) results in internal oxide precipitates of those elements in the subsurface layer. In some cases the oxides contain traces of reactive elements (REs), for example, La or Y, which are added to the ferritic steels in metallic form or in the form of an oxide dispersion to lower the oxidation rates and/or improve the scale adherence.<sup>53,54</sup>

Contrary to the cases described in the previous section, the Cr-rich surface scales on the ferritic steel show a slightly slower growth rate in low- than in high- $p_{O_2}$  gas (Figure 19). This is in agreement with findings of other authors,<sup>60,61</sup> who observed that the growth rates of Cr-rich oxide scales on high-Cr ferritic steels at 800–900 °C in the H<sub>2</sub>/H<sub>2</sub>O-based gases are similar to, or smaller than, in air. The reason why these ferritic steels behave, in respect to gas composition dependence of the oxidation rate,

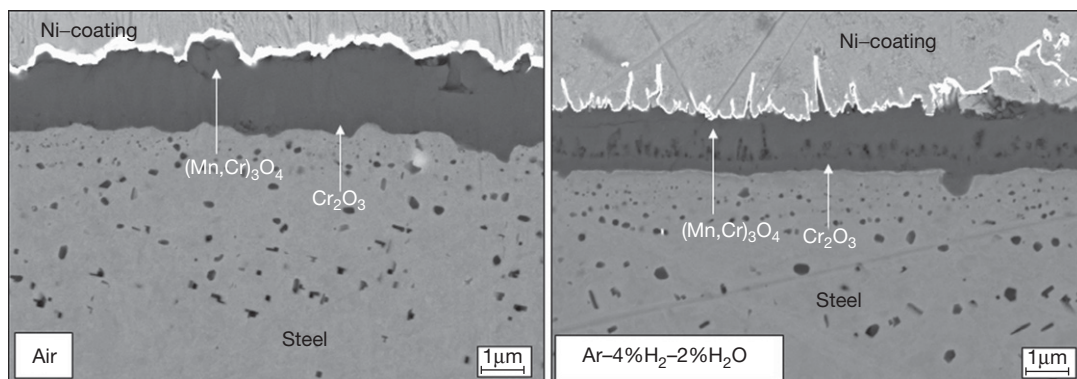


**Figure 19** SEM cross sections of high-Cr ferritic steel Crofer 22 APU after 1000 h oxidation at 800 °C in air and Ar–H<sub>2</sub>–H<sub>2</sub>O.<sup>59,60</sup>

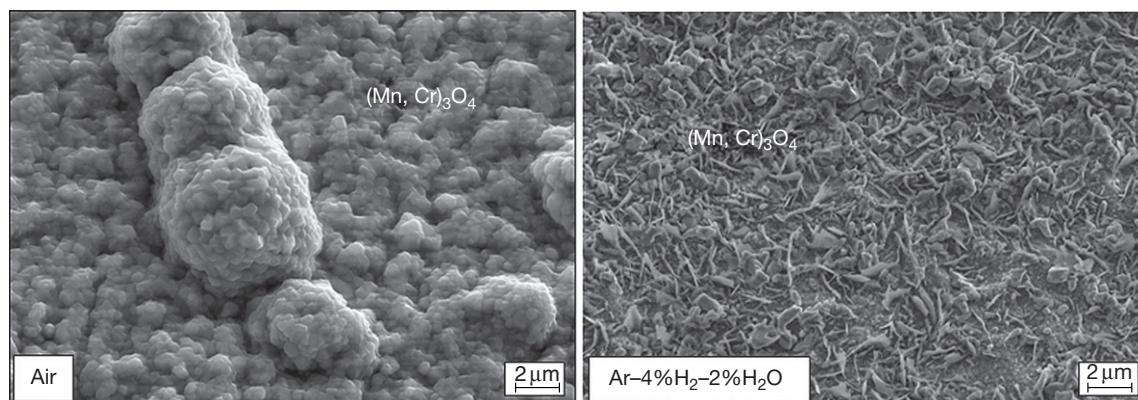


**Figure 20** Surface scale morphologies of high-Cr ferritic steel Crofer 22 APU after 1000 h exposure at 800 °C in air and Ar-H<sub>2</sub>-H<sub>2</sub>O. Adapted from Piron-Abellan, J.; Quadakkers, W. J. Report Forschungszentrum Jülich, Jül-4170, 2005; ISSN 0944-2952.

differently from that of Cr and model alloys of the type NiCr and FeCr (see [Sections 1.17.4.2.1](#) and [1.17.4.2.2](#)) cannot be unequivocally derived from the mentioned SOFC-related studies. Also, the differences in behavior mentioned above for the commercial Ni-based alloys are not immediately apparent from the respective papers. A likely explanation is that a change in scale growth mechanism imparted by one or more of the mentioned minor alloying additions (Mn, Ti, Si, Al, rare earths) results in a change of the gas composition dependence of the oxidation rate. Therefore, possible effects of some common minor alloying additions on the scale formation of chromia-forming alloys in low- and high- $p_{\text{O}_2}$  gases will be discussed in the following section.

#### 1.17.4.2.5 Effect of common minor alloying additions

**Figure 21** shows weight change data of a number of ternary Ni-25Cr-based model alloys in low- and high- $p_{\text{O}_2}$  gas after isothermal exposure at 1050 °C. Also presented are the weight changes after subsequent cooling to room temperature. The data shows that Y reduces, as frequently demonstrated,<sup>53,54</sup> the scale growth rate and spallation from the NiCr alloy during oxidation in Ar-O<sub>2</sub>. However, the Y addition has hardly any effect on the growth rate in the low- $p_{\text{O}_2}$  gas. The measured weight changes in this gas are even slightly higher than those of the corresponding Y-free alloy, which was found to be related to an additional oxygen uptake due to internal Y oxidation.<sup>51</sup> Like Ni-25Cr, the Ni-25CrY alloy showed a substantially higher oxide growth rate in Ar-H<sub>2</sub>O-H<sub>2</sub> than in Ar-O<sub>2</sub>. Apparently, the reactive element addition does not fundamentally alter the atmosphere dependence observed for Cr,

NiCr, and FeCr. This is in agreement with recent results from Essuman *et al.*,<sup>46</sup> who found for an Y<sub>2</sub>O<sub>3</sub> dispersion strengthened Ni-Cr-based alloy a similar atmosphere dependence of the oxidation rate as observed for Ni-25Cr.

The decreased growth rate and improved adherence of chromia scales grown in air and other oxygen-rich environments due to the Y addition is commonly explained by a reduction of outward cation diffusion as a result of Y segregation to the oxide grain boundaries.<sup>54</sup> The predominant inward grain boundary oxygen transport in combination with the high grain boundary density of the scales formed in Ar-4% H<sub>2</sub>-7% H<sub>2</sub>O ([Section 1.17.4.2.3](#)) has the result that Y-addition to the Ni-Cr alloy does not substantially alter the scale growth rate, unlike the effect observed during oxidation in O<sub>2</sub>-rich environments.

Mn addition apparently enhances the oxidation rate and decreases the scale adherence during Ar-O<sub>2</sub> exposure, but it decreases the growth rate in Ar-H<sub>2</sub>-H<sub>2</sub>O (**Figure 21**).<sup>51</sup> Similar low oxidation rates of the Mn-containing alloys were found during exposure in Ar-CO-CO<sub>2</sub>,<sup>62</sup> thereby indicating that the underlying mechanism is related to the low- $p_{\text{O}_2}$  rather than the presence of water vapor and/or hydrogen. The ternary NiCrMn alloy formed a double-layered oxide scale consisting of Cr<sub>2</sub>O<sub>3</sub> and a thin layer of Cr/Mn spinel in the outer part of the scale. In the case of Ar-20% O<sub>2</sub> exposure, the spinel layer was slightly thinner than that formed in Ar-4% H<sub>2</sub>-7% H<sub>2</sub>O; additionally, NiO was locally observed. The oxide scale formed on alloy NiCrMnY had a morphology similar to that on alloy NiCrMn; however, no clear indication of Ni-containing oxide was found during Ar-O<sub>2</sub> exposure, and the scale adherence was dramatically improved.

These results strongly indicate that the atmosphere dependence of the oxidation rate of the NiCrMn alloy and also that described in the previous section for the high-Cr ferritic steels are related to the formation of the Cr/Mn spinel on top of the chromia scale. Manganese has a higher solubility in  $\text{Cr}_2\text{O}_3$  at high oxygen potentials than at low  $p_{\text{O}_2}$  values.<sup>63</sup> One might speculate that in the low- $p_{\text{O}_2}$  gas Mn hinders inward oxygen transport by segregating at oxide grain boundaries. As far as known to the authors, this effect has not been studied extensively and no unequivocal evidence could be derived from previous work. Grain boundary segregation of Mn in the scale formed in the low- $p_{\text{O}_2}$  gas is not unlikely, considering the large size of the  $\text{Mn}^{+2}$  ion compared to that of  $\text{Cr}^{+3}$ .

On the basis of the phase diagrams (Figure 22) of Naoumidis *et al.*,<sup>63</sup> the spinel phase formed in the low- $p_{\text{O}_2}$  gas is stoichiometric  $\text{MnCr}_2\text{O}_4$ , whereas in high- $p_{\text{O}_2}$  gas it is  $\text{Mn}_{1+x}\text{Cr}_{2-x}\text{O}_4$ . This is confirmed by the secondary neutral mass spectrometry (SNMS) results in Figure 23 showing a nearly constant Cr/Mn ratio in the outer part of the oxide scale after exposure of a Mn-containing, high-Cr ferritic steel in  $\text{Ar-H}_2\text{-H}_2\text{O}$  but a changing ratio as function of depth, and thus as function of  $p_{\text{O}_2}$ , when formed in air. Retaining the double-layered oxide structure during longer time exposure in  $\text{Ar-H}_2\text{-H}_2\text{O}$  would require a balanced flux of Cr and Mn ions through the oxide scale. If, because of the low Mn concentration in the alloy the flux of Mn is reduced after longer

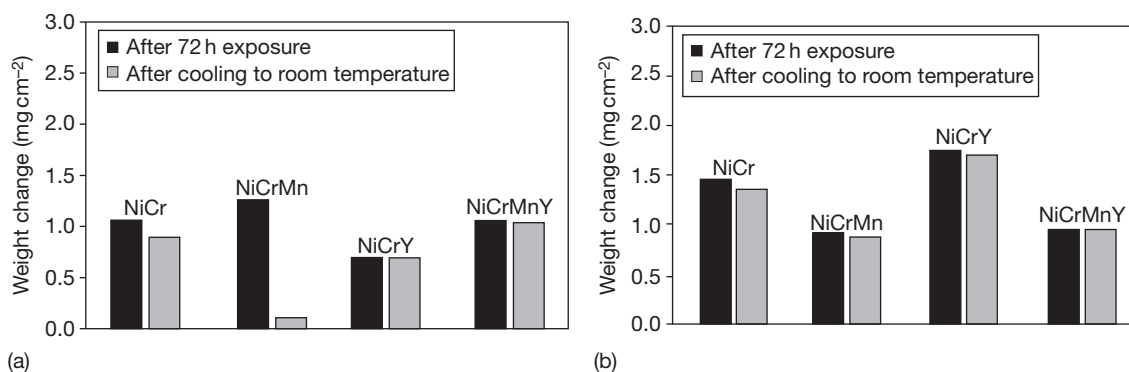


**Figure 21** Weight changes of Ni-25Cr-based model alloys after isothermal exposure at 1050 °C and after subsequent cooling to room temperature in (a) Ar-20%  $\text{O}_2$  and (b) Ar-4%  $\text{H}_2$ -7%  $\text{H}_2\text{O}$ . Mn and/or Y addition were 0.50 and 0.15% respectively. Reproduced from Žurek, J.; Young, D. J.; Essuman, E.; Hänsel, M.; Penkalla, H. J.; Niewolak, L.; Quadackers, W. J. *Mater. Sci. Eng. A* **2008**, 477, 259–270.

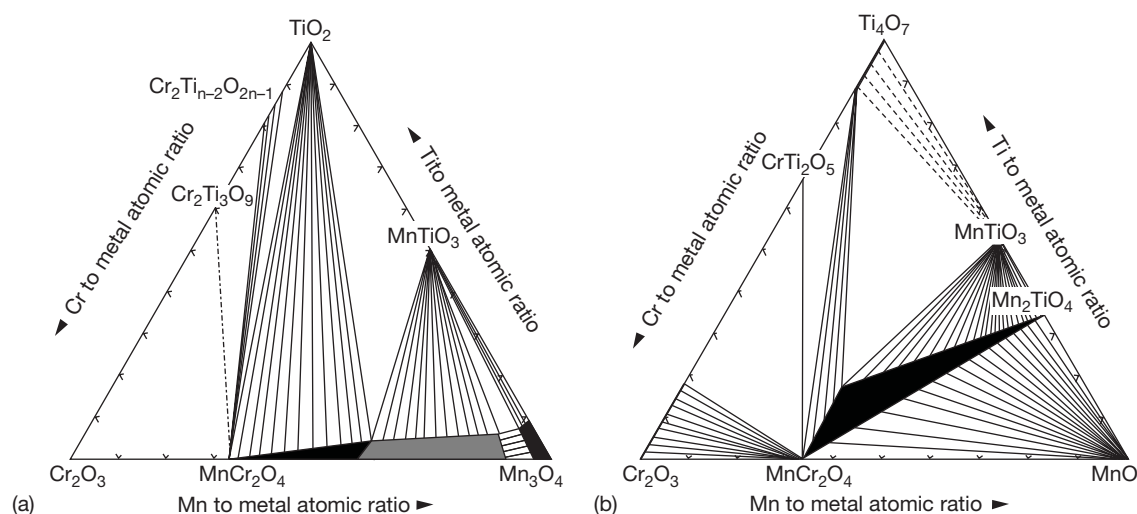


**Figure 22** Phase equilibria in the quasi-ternary system: (a)  $\text{Cr}_2\text{O}_3\text{-Mn}_3\text{O}_4\text{-TiO}_2$ , after annealing at 1000 °C in air; (b)  $\text{Cr}_2\text{O}_3\text{-MnO-Ti}_4\text{O}_7$  after annealing at 1000 °C in a gas with an equilibrium oxygen partial pressure of  $10^{-21}$  bar. Reproduced from Naoumidis, A.; Schulze, H. A.; Jungen, W.; Lersch, P. *J. Eur. Ceram. Soc.* **1991**, 7, 55–63.



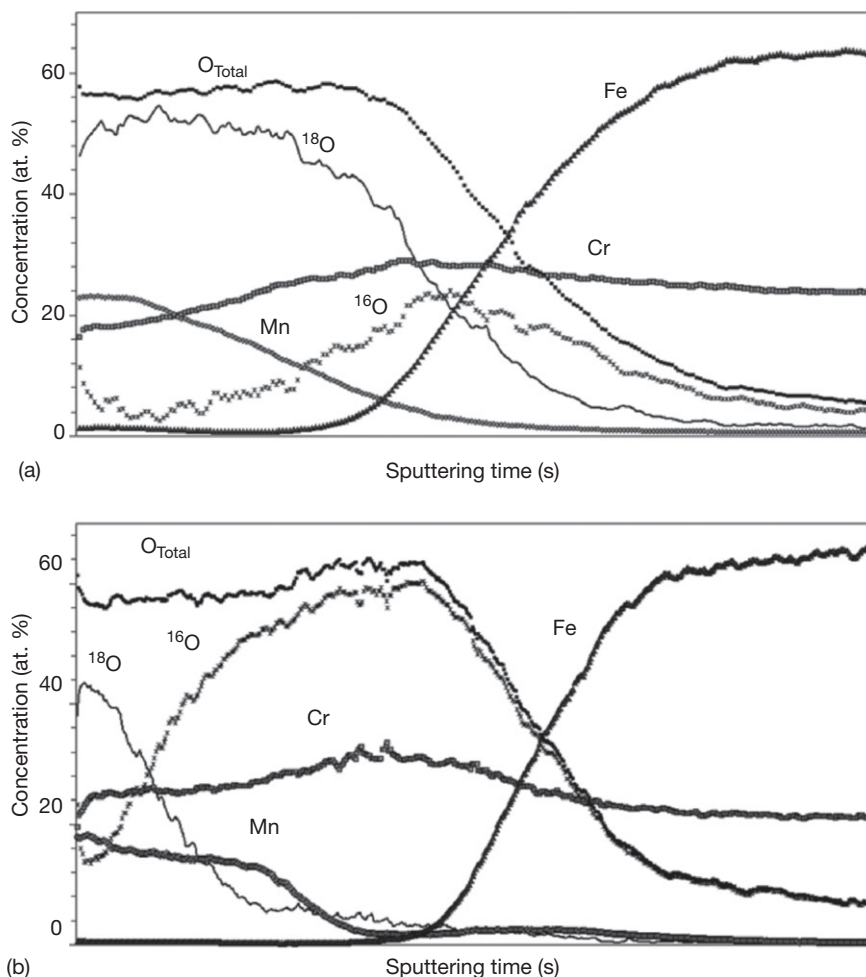


**Figure 23** SNMS profiles of high-Cr ferritic steel Crofer 22 APU after two-stage oxidation at 900 °C for (a) 2 h in Ar-20%  $^{16}\text{O}_2$ , 4 h in Ar-20%  $^{18}\text{O}_2$ ; (b) 2 h in Ar-4%  $\text{H}_2$ -2%  $\text{H}_2^{16}\text{O}$ , 4 h in Ar-4%  $\text{H}_2$ -2%  $\text{H}_2^{18}\text{O}$ . Reproduced from Ertl, S. T. Diss. RWTH Aachen, 2006.

exposure times,<sup>61</sup> a Mn deficit will occur in the spinel layer. In the  $p_{\text{O}_2}$  gradient existing in the scale, this will result in a vacancy flux from the spinel surface towards the spinel–chromia interface. Here these vacancies tend to condense and result in void formation, as illustrated in Figure 19. In air, the Mn deficit in the spinel may be compensated by Cr cations from the inner chromia layer. This would result in an enhanced outward flux of Cr, which could explain why during air exposure the presence of Mn in the alloy increases not only the overall thickness of the oxide but also that of the inner chromia scale.<sup>51</sup>

It should be mentioned that the rapid incorporation of Mn into the oxide layer may easily lead to complete exhaustion of the Mn reservoir in the test specimen. This effect, which will be especially pronounced at high oxidation temperatures and/or when

using thin components,<sup>61</sup> will obviously alter the described effect of Mn additions on the gas composition dependence of the oxide growth kinetics.

Figure 24 shows metallographic cross sections of a high-Cr ferritic steel with a very similar composition as that shown in Figure 19 but with minor additions of Si and Al, after exposure in air and  $\text{H}_2/\text{H}_2\text{O}$  at 800 °C. The volume increase accompanied by the internal oxide formation leads to outward metal flow<sup>61,64</sup> resulting in formation of metallic nodules in the scale and damage of the oxide scale.<sup>61</sup> In spite of this difference in scale morphology compared to that shown in Figure 19, both steels exhibit a double-layered surface oxide of  $\text{Cr}_2\text{O}_3$  and Cr/Mn spinel that exhibits a slightly higher growth rate in high – than in low –  $p_{\text{O}_2}$  gas. Apparently, the atmosphere dependence is mainly governed by presence of the Cr/Mn spinel and is not

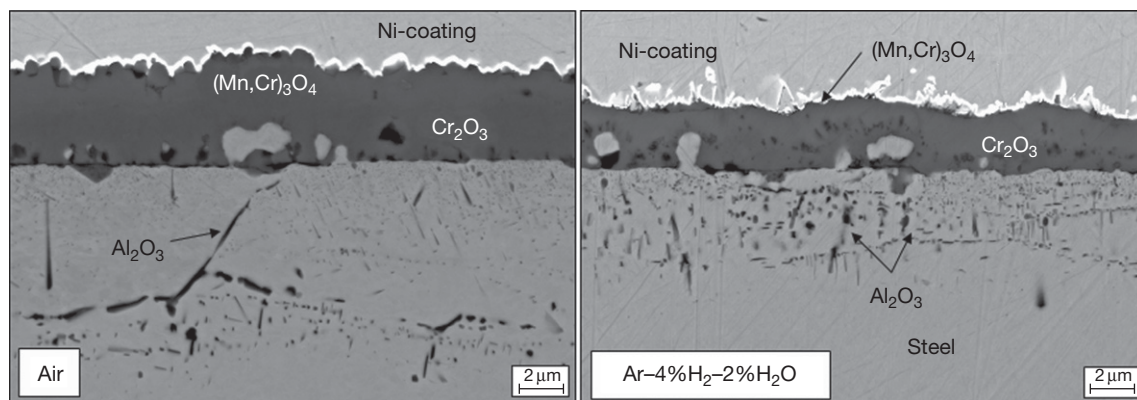


**Figure 24** Metallographic cross sections of high-Cr ferritic steel Crofer 22 A after 1000 h exposure in Air and in Ar-4% H<sub>2</sub>-2% H<sub>2</sub>O at 800 °C. The steel had a very similar composition as that shown in Figure 19; however, it contained 0.1% Al and 0.1% Si.

fundamentally affected by presence of the minor alloying additions (0.1%) of Al and Si. This may be different if higher amounts (e.g., a few tenths of a percent) of Si/Al are present. In that case, a more extensive internal oxidation and formation of metallic protrusions result in a more severe damage of the external scale with the result that molecular transport substantially contributes to the scale growth process.<sup>61</sup> It is obvious that then a substantially different atmosphere dependence may occur. This can be derived from results of Hammer *et al.*,<sup>65</sup> who studied the behavior of high-Cr ferritic steels containing Al and/or Si up to 1 wt% in low- and high- $p_{O_2}$  gas between 700 and 900 °C. For such alloys the gas composition dependence described earlier for alloys forming ‘ideal’ gas-tight two-layered spinel/chromia layers is not clearly observed.

Further studies on the effect of minor alloying additions on the oxidation behavior in low- and high- $p_{O_2}$  gases were carried out by Galerie *et al.*<sup>14</sup> The authors investigated the behavior of 18% Cr ferritic steels containing minor additions of Nb or Ti. Both elements affected the growth rate of the protective scale but did not fundamentally alter the relative differences between Ar-O<sub>2</sub> and Ar-H<sub>2</sub>O exposure.

#### 1.17.4.3 Effect of Environment on Scale Formation in Case of ‘Borderline Alloys’

##### 1.17.4.3.1 Nonprotective oxidation in water vapor

For iron–chromium alloys with intermediate Cr content in the range 8–20%, it has frequently been found that oxidation rates in water vapor may be several orders of magnitude higher than those found under

dry conditions.<sup>6,16,22,49,66–68</sup> These high rates are related to a change in oxide composition from a chromia base to an Fe-oxide base scale. They are sometimes preceded by an initial period of protection after which breakaway oxidation occurs as a consequence of failure of the protective chromium-rich oxide layer. Referring to Figure 13, the critical Cr content required for obtaining protective chromia scale formation in water vapor is thus higher than that required during O<sub>2</sub> or air exposure.

Ehlers *et al.*<sup>4</sup> suggested that during exposure of 9% Cr steels, in Ar-50% H<sub>2</sub>O at 600–650 °C, volatile Fe(OH)<sub>2(g)</sub> may form in the inner layers of the scale which is then converted to hematite or magnetite in the outer layers of the scale thereby contributing to the deterioration of the protective Cr-rich oxide. However, based on the available thermodynamic data, the vapor pressure of the hydroxide may be too low to provide sufficient mass transport by the volatile species.<sup>16</sup> Galerie *et al.*<sup>14</sup> showed that the first stage of breakaway of Fe-15% Cr at 800–1000 °C in Ar-15% H<sub>2</sub>O corresponds to a separation of the chromia scale from the alloy and consequently scale equilibration, allowing the formation of hematite at the metal–oxide interface. Then rapid growth of hematite at this interface disrupts the chromia scale and breakaway is initiated. The authors propose that the more acidic nature of hematite compared to chromia encourages more rapid dissociation of water and therefore continued hematite growth is favored, whereas in the absence of water vapor chromia would continue to form and protection is maintained. Fujii and Meussner<sup>68</sup> oxidized a range of FeCr alloys with up to 25% Cr at temperatures between 700 and 1100 °C in Ar-10% water vapor and observed a period of protective oxidation before occurrence of high



oxidation rates for the alloys with a Cr content greater than 20%. They proposed that the high rates of oxidation were related to hydrogen/water dissociation in pores (see [Section 1.17.3.3](#)) within the wüstite layer. Mikkelsen and Linderöth<sup>67</sup> explained the breakaway oxidation of Fe–22% Cr at 800 °C in a H<sub>2</sub>/Ar gas mixture (7:93) with addition of 12% water vapor to be the consequence of the stability of fast-growing wüstite, whereas with 1% water vapor wüstite is not stable. Hayashi *et al.*<sup>69</sup> observed for diluted Fe–Al alloys a very similar gas composition dependence as observed for Fe–Cr alloys by other authors.

Summarizing, it can be said that the breakaway type oxidation of ‘borderline’ FeCr-based alloys with intermediate contents of protective scale-forming elements exhibits a number of common features which strongly indicates that the responsible process is independent of the type of oxide formed. The mechanisms occurring at high temperatures (700–1000 °C) seem to be not fundamentally different from those at lower temperature (500–650 °C). Modified transport processes in, for example, wüstite due to presence of water vapor have clearly been verified, but are unlikely to be responsible for the initiation of breakaway because it also occurs at temperatures at which wüstite is unstable. A mechanism that explains the breakaway oxidation at higher as well as lower temperature will be discussed in the following sections.

#### 1.17.4.3.2 Internal oxidation of Cr as trigger for breakaway oxidation

**Figure 25** shows SEM cross sections of an Fe–10Cr model alloy after isothermal oxidation for 72 h at 900 °C in Ar–20% O<sub>2</sub>, Ar–4% H<sub>2</sub>–2% H<sub>2</sub>O and Ar–7% H<sub>2</sub>O. In Ar–O<sub>2</sub> the scale contains substantial amounts of Fe and consists of Fe<sub>2</sub>O<sub>3</sub> near the scale–gas interface, an intermediate layer of spinel, and a thin chromia layer in contact with the alloy. Apparently, significant transient oxidation occurred before the chromia became continuous, and thus Fe–10Cr can be considered as a ‘borderline alloy’ when exposed to Ar–O<sub>2</sub>.<sup>70</sup> In Ar–H<sub>2</sub>–H<sub>2</sub>O, only internal oxides, mainly of Fe/Cr spinel, have formed.<sup>62</sup> Very rapid oxidation occurred in Ar–H<sub>2</sub>O because the oxide scale consisted mainly of Fe-rich oxides. Similar observations were made at 1050 °C.<sup>46</sup>

These results clearly show that internal oxidation of Cr is promoted in the gases containing water vapor. In the gas with the highest oxygen potential (Ar–20% O<sub>2</sub>), a continuous external chromia layer develops

despite the presence of transient oxides. In the gas with the lowest oxygen potential (Ar–H<sub>2</sub>–H<sub>2</sub>O), the Cr is oxidized internally and no external Fe oxide scale is formed because of the low oxygen activity in the gas (**Figure 2**). This is contrary to Ar–H<sub>2</sub>O in which the alloy matrix, which is Cr-depleted due to the internal oxidation, oxidized because of the higher  $p_{O_2}$ , resulting in non-protective scale formation. A similar effect of water vapor on internal oxidation was found by Ani *et al.*<sup>71</sup> These authors studied the behavior of FeCr alloys at 800 °C in dry and wet gas ( $p_{H_2O} = 3 \times 10^{-3}$  bar) at a fixed low  $p_{O_2}$  of  $1.1 \times 10^{-9}$  bar. The transition from internal to external oxidation was shifted from 8% Cr in the dry gas to 12% Cr in the wet gas. In low Cr alloys, the depth of internal oxidation in the wet gas was substantially larger than in the dry gas.

These results thus indicate that the inward flux of oxygen in the FeCr alloys is greater in the water vapor-containing gases than in the dry gases. It is well known that hydrogen from water vapor readily permeates ferritic steels at high temperatures. Rahmel and Tobolski<sup>36</sup> observed hydrogen uptake in the samples oxidized in wet gases. Also a ‘dual atmosphere’ effect has been observed for ferritic steel interconnects in SOFCs where the oxidation on the cathode (air) side is influenced by the presence of a hydrogen/water vapor mixture on the anode (fuel) side.<sup>72</sup> Furthermore, the intrinsic diffusivity of hydrogen in bcc iron at 900 °C is approximately  $4 \times 10^{-3} \text{ cm}^2 \text{ s}^{-1}$ ,<sup>73</sup> which is 3 orders of magnitude larger than that of oxygen, which is  $2 \times 10^{-6} \text{ cm}^2 \text{ s}^{-1}$ .<sup>74</sup> The values in fcc iron are  $7 \times 10^{-5} \text{ cm}^2 \text{ s}^{-1}$  for hydrogen<sup>75</sup> and  $1.8 \times 10^{-7} \text{ cm}^2 \text{ s}^{-1}$  for oxygen.<sup>74</sup>

The reasons for the enhanced internal Cr oxidation by hydrogen incorporation into the alloy will now be discussed.

#### 1.17.4.3.3 Conditions for external chromia formation in dry and wet gases

The development and maintenance of a continuous external chromia scale require that two criteria are satisfied. First, the Cr concentration in the alloy must exceed that necessary for outward diffusion to prevent internal oxidation.<sup>76</sup> This criterion for the case of Fe–Cr alloys is:

$$N_{Cr}^{(1)} > \left[ \frac{\pi g^*}{3} N_O^{(S)} \frac{D_O V_m}{\tilde{D}_{Fe-Cr} V_{CrO_{1.5}}} \right]^{1/2} \quad [13]$$

where  $N_O^{(S)}$  is the oxygen solubility in the alloy,  $D_O$  is the diffusivity of oxygen in the alloy,  $\tilde{D}_{Fe-Cr}$  is the alloy

interdiffusion coefficient, and  $V_m$  and  $V_{CrO_{1.5}}$  are the molar volumes of the alloy and oxide, respectively. It was assumed here that the internal oxide was chromia. The factor  $g^*$  is generally approximated as about 0.3.<sup>77</sup> Equation [13] was derived under conditions where only Cr could oxidize. Under conditions where both Fe and Cr can oxidize, the transient oxidation of Fe must also be considered. Gesmundo and Viani<sup>78</sup> showed that the critical solute concentration increases as the rate constant for the growth of the transient, nonprotective oxide increases.

The second criterion is that, once a continuous external scale is formed, diffusion in the alloy must be rapid enough to supply the solute at least at the rate it is being consumed by scale growth.<sup>79</sup> This criterion may be expressed as:

$$N_{Cr}^{(2)} = \frac{V_m}{32v} \left( \frac{\pi k_p}{\tilde{D}_{Fe-Cr}} \right)^{1/2} \quad [14]$$

where  $k_p$  is the parabolic rate constant for growth of the external scale, measured in terms of scale thickness. Based on data Essuman *et al.*<sup>46</sup>, it was derived that, for example, at 900 °C  $N_{Cr}^{(1)}$  for FeCr alloys is  $\sim 0.03$ . Comparison of the results in Figures 25–27 shows that for the FeCr alloys the critical Cr content for external scale formation in Ar–20% O<sub>2</sub> at 900 °C is near 10 mass% ( $N_{Cr}^{(1)} \approx 0.11$ ). In Ar–H<sub>2</sub>–H<sub>2</sub>O, that

is, a gas in which Fe oxide can hardly form, it is apparently between 10 and 20 mass% ( $N_{Cr}^{(1)}$  between 0.11 and 0.21). In the wet gas Ar–H<sub>2</sub>O, in which Fe can easily oxidize, it is larger than 20 mass% ( $N_{Cr}^{(1)} > 0.21$ ).

Essuman *et al.*<sup>80</sup> have shown that for FeCr alloys the parameter regarding internal oxidation  $N_{Cr}^{(1)}$  (eqn [13]) moves to higher values as the temperature is increased (see Figure 27). Figure 27 shows that this is indeed the case for exposure in Ar–O<sub>2</sub> as well as in Ar–H<sub>2</sub>O. Thus, for Fe–20Cr, non-protective oxidation occurs in both gases at 1050 °C, only in Ar–H<sub>2</sub>O at 900 °C and in none of the gases at 800 °C.

Consideration of eqn [13] indicates that promoting internal oxidation by dissolution of hydrogen could result from a reduction of  $\tilde{D}_{Fe-Cr}$ ; however, based on data of Park *et al.*<sup>81</sup>, this seems to be unlikely. The second possibility is that water vapor is increasing the effective value of  $N_O^{(S)}$ . The rapid diffusion of hydrogen into the specimen may shift the H–O–H<sub>2</sub>O equilibrium such that a metastably high concentration of oxygen exists at the specimen surface and results in an increased inward flux of oxygen.<sup>46</sup> Considering the equilibration of water vapor at the specimen surface

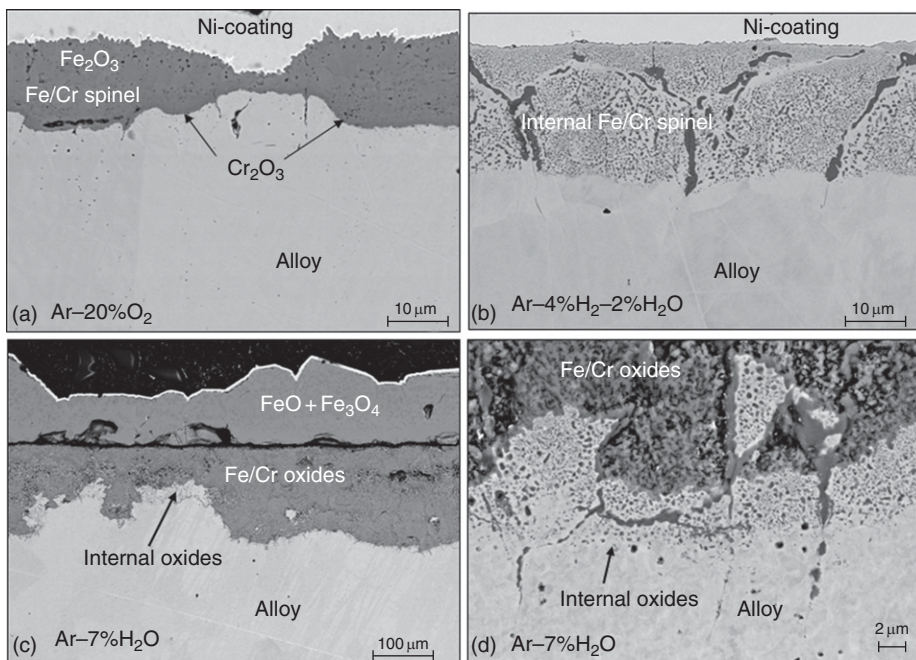


**Figure 25** Cross-section SEM micrographs of Fe–10Cr model alloy after isothermal oxidation for 72 h at 900 °C in various atmospheres: (a) Ar–20% O<sub>2</sub>; (b) Ar–4% H<sub>2</sub>–2% H<sub>2</sub>O; (c) Ar–7% H<sub>2</sub>O; (d) Ar–7% H<sub>2</sub>O high magnification of the internal oxidation zone in Fig. (c). Note the differences in magnification.<sup>46,62</sup>

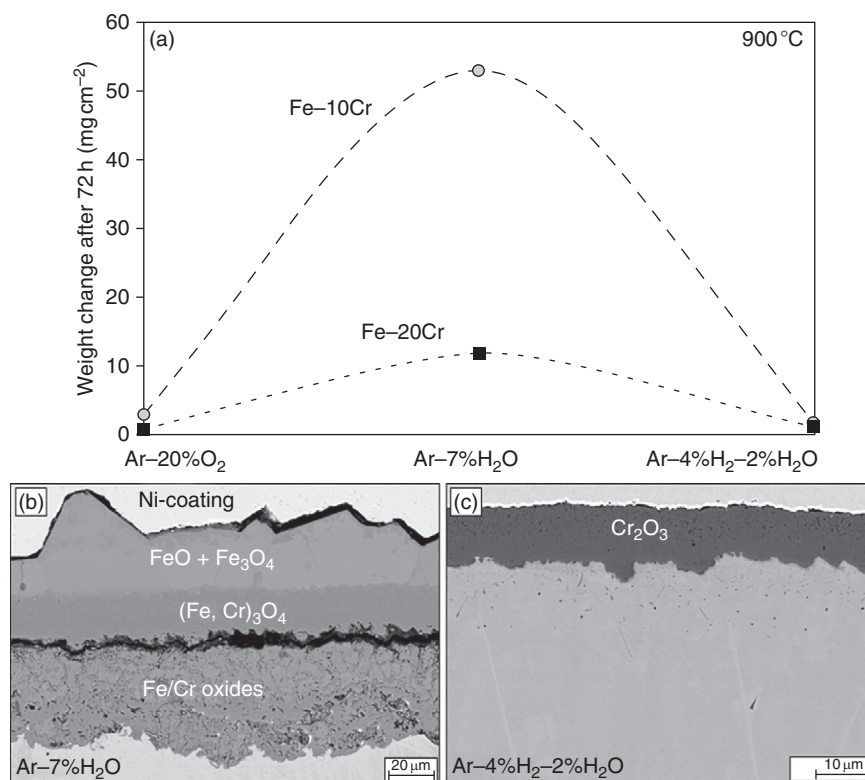


**Figure 26** (a) Weight change of Fe-10Cr and Fe-20Cr model alloys after 72 h isothermal exposure in different test environments at 900 °C. The dotted/dashed lines do not show the real dependence of the gas composition but are just inserted for easier visibility of the data points. SEM cross sections of the Fe-20Cr model alloy showing oxide scales formed during 72 h isothermal oxidation in (b) Ar-7% H<sub>2</sub>O, and (c) Ar-4% H<sub>2</sub>-2% H<sub>2</sub>O at 900 °C. [46,62](#)

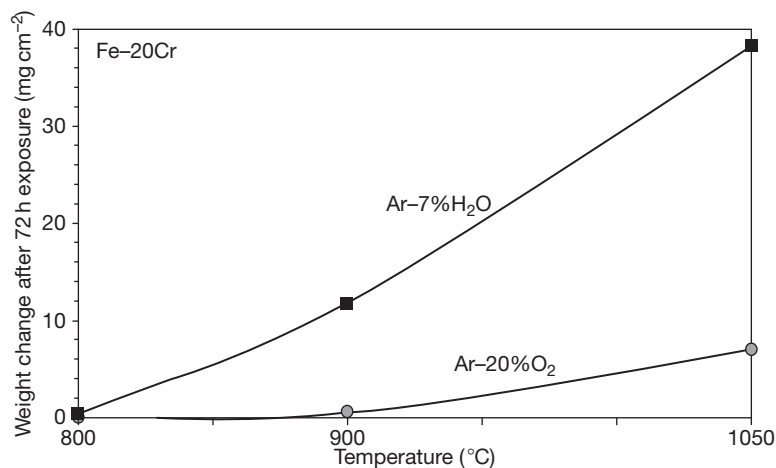


**Figure 27** Weight changes after 72 h isothermal oxidation of a binary Fe-20Cr model alloy in Ar-O<sub>2</sub> and Ar-H<sub>2</sub>O at different temperatures. Reproduced from Essuman, E.; Meier, G. H.; Žurek, J.; Hänsel, M.; Singheiser, L.; Quadakkers, W. J. *Mater. Sci. Forum* **2008**, 595–598, 699–706.

the concentration of oxygen at the metal surface may be expressed as:

$$N_{\text{O}} = K_{15} \frac{p_{\text{H}_2\text{O}}}{N_{\text{H}}^2} \quad [16]$$

If the hydrogen concentration is reduced by rapid inward diffusion, the gas phase will establish an increased concentration of dissolved oxygen, resulting in a concomitantly higher inward oxygen flux.

The final possibility is that the dissolved hydrogen increases the diffusivity of oxygen. It is known from studies on austenitic iron that lattice distortion produced by interstitials can affect diffusivities. For example, the intrinsic diffusivity of carbon increases with increasing carbon content, which is usually interpreted in terms of carbon interstitials expanding the Fe lattice and thus increasing their own mobility.<sup>82</sup> It is conceivable that the rapidly diffusing hydrogen interstitials expand the iron lattice sufficiently so that the diffusivity of the larger oxygen interstitials is increased.

#### 1.17.4.3.4 Breakaway oxidation mechanisms of FeCr alloys in water vapor

As stated in Section 1.17.4.3.1, enhanced, breakaway type oxidation of 'borderline' Fe(Ni)Cr-based alloys in water vapor-containing environments has been described in a large number of publications as well as in textbooks.<sup>1,6</sup> If enhanced internal oxidation of Cr due to dissolution of hydrogen in the alloy is the main reason for the occurrence of breakaway oxidation in steam or Ar–H<sub>2</sub>O, then this process will be promoted if molecules of water vapor or hydrogen have direct access to the steel surface. The significance of molecular transport of water vapor was identified by several authors as an important factor for the occurrence of breakaway in O<sub>2</sub>/H<sub>2</sub>O mixtures.<sup>16</sup> Ikeda *et al.*<sup>83</sup> proposed molecular transport as a major pre-requisite for the breakdown of initially protective scales on 5–30% Cr steels in O<sub>2</sub>–10 vol.% H<sub>2</sub>O at 750 and 900 °C. Similar conclusions were derived by Ehlers *et al.*<sup>16</sup> from thermogravimetry studies of a 9% Cr steel, where the gas was in situ changed from dry Ar–1% O<sub>2</sub> to an Ar–1% O<sub>2</sub>–7% H<sub>2</sub>O mixture at 650 °C. Galerie *et al.*<sup>14,32</sup> proposed that the change from a protective oxide scale formed in dry gas into breakaway-type oxidation of an Fe–15% Cr alloy at 800–1000 °C during subsequent exposure in wet gas was initiated by molecular transport of water vapor via microcracks.

In many of the studies in which Fe-rich, breakaway-type oxide scales were observed during exposure of Fe–Cr alloys in water vapor, a zone with internal precipitates of Cr-rich oxide was found (see Figure 25 and, e.g., Ueda *et al.*<sup>84</sup>). In classical oxidation theory, the presence of this zone can be described as a logical consequence of the formation of the nonprotective Fe-based oxide scale; that is, the oxygen partial pressure below that scale at the scale–alloy interface is sufficiently high for Cr to become

oxidized internally. Ehlers *et al.*<sup>4,16</sup> showed that an internal oxidation zone was present after 250 h oxidation of a 9% Cr steel in Ar–50% H<sub>2</sub>O at 650 °C. After subsequent exposure of the specimen in air, this internal oxidation zone vanished and a thin, protective, Cr-rich layer was formed at the scale–alloy interface and the scale growth rate in this second oxidation stage was extremely small. This change in composition and morphology of the inner interface upon changing from water vapor to a high-*p*O<sub>2</sub> atmosphere or vice versa can be explained by changes in transport processes in the scale by one or more of the mechanisms described in Section 1.17.3. However, based on the discussions in the previous sections, the main change in oxidation mechanism that occurs when changing from water vapor to a high-*p*O<sub>2</sub> gas is the decreased tendency of Cr to become internally oxidized. The formation of the rapid, breakaway-type, Fe-rich oxide scales when exposing 'borderline alloys' in water vapor is just a result of Cr depletion in the alloy matrix because Cr oxidizes internally rather than in the form of a protective external scale. This mechanism would be promoted by a direct reaction of H<sub>2</sub>O(g) molecules with the metal surface, thus explaining the observations described above that transport of H<sub>2</sub>O(g) through a preexisting scale is required to initiate breakaway oxidation. In H<sub>2</sub>O(g)/O<sub>2</sub>(g) mixtures, competitive adsorption of oxygen and water vapor molecules at external and internal surfaces of the oxide scale was found to govern the growth of the Fe-rich oxide scales at high H<sub>2</sub>O/O<sub>2</sub> ratios. It would therefore be expected that occurrence of breakaway oxidation is determined by the H<sub>2</sub>O(g)/O<sub>2</sub>(g) ratio in the gas, as was indeed experimentally observed for a 9% Cr steel at 600 °C.<sup>16</sup> Also, the oxidation behavior of Fe–Al alloys with Al contents of 5 wt% was found to depend on the H<sub>2</sub>O(g)/O<sub>2</sub>(g) ratio.<sup>85</sup>

#### 1.17.4.3.5 Borderline NiCr alloys in water vapor

Essuman *et al.*<sup>47</sup> studied the oxidation behavior of Ni–25Cr and Ni–20Cr as well as the 'borderline alloy' Ni–10Cr in various dry and wet Ar-based gas mixtures. Decreasing the oxygen content in dry gas from 20% to 1% was found to promote the selective oxidation of Cr in the 'borderline alloy' Ni–10Cr. It could be shown that this is related to a decrease of the NiO growth rate with decreasing oxygen partial pressure (Figure 28), which, according to Gesmundo



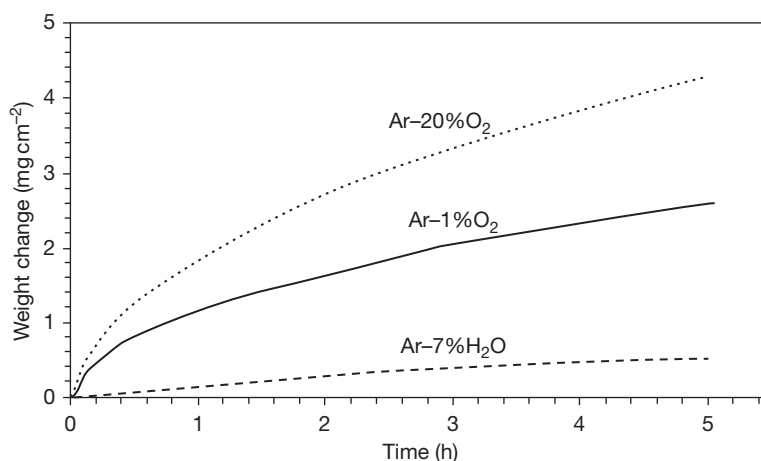


**Figure 28** Weight change versus time during isothermal oxidation of pure Ni at 1050 °C in Ar-20% O<sub>2</sub>, Ar-1% O<sub>2</sub> and Ar-7% H<sub>2</sub>O.

*et al.*,<sup>78</sup> promotes selective oxidation of Cr. Exposure in Ar-H<sub>2</sub>O would then be expected to result in a further improvement in selective oxidation due to the very slow growth rate of NiO in this low- $p_{O_2}$  gas.<sup>32</sup> However, the Cr-rich surface scale formed in Ar-H<sub>2</sub>O contained Ni-rich oxide. Also, internal oxides of Cr could be found. These results clearly indicated that, like in FeCr alloys, hydrogen promotes internal oxidation of Cr also in NiCr alloys.

In spite of this similarity in mechanism, the gas composition dependence of borderline NiCr alloys substantially differs from that of corresponding FeCr alloys, the most obvious difference being that the high oxidation rates observed for Fe-10Cr and Fe-20Cr in Ar-H<sub>2</sub>O<sup>46</sup> are not found for Ni-based alloys with the same Cr content (Figure 29). The reason is that the growth rate of NiO strongly decreases with decreasing  $p_{O_2}$ , with the result that in Ar-H<sub>2</sub>O the NiO growth rate is extremely small,<sup>32</sup> that is, in fact similar to that of chromia. Even if the Cr content was so low that a protective chromia scale could not form, the overall oxidation rate would still be quite low because of the very slow growth rate of NiO in Ar-H<sub>2</sub>O (Figure 28), and, obviously, in Ar-H<sub>2</sub>-H<sub>2</sub>O the NiO will not form at all.

Fe oxide exhibits quite high growth rates in Ar-H<sub>2</sub>O mixtures,<sup>14,16,36</sup> and for an Fe-10Cr alloy in Ar-H<sub>2</sub>O the enhanced internal oxidation of Cr will, thus, in contrary to Ni-10Cr, result in formation of rapidly growing Fe-rich oxide scales. The behavior of borderline FeCr alloys in Ar-H<sub>2</sub>O-H<sub>2</sub> mixtures strongly depends on the exact gas composition

because the equilibrium oxygen partial pressure in a gas with a H<sub>2</sub>O/H<sub>2</sub> ratio of 1 is very near to the dissociation pressure of Fe oxide (Figure 2).

#### 1.17.4.4 Oxidation of Ferritic and Austenitic Steels in Steam

##### 1.17.4.4.1 General remarks

A technologically important example in which 'borderline' FeCr- and FeNiCr-based alloys are subjected to steam at relatively high temperatures is encountered in many power generation systems. In conventional power plants, steam-carrying components are commonly designed using low-Cr (e.g., 2¼% Cr) steels. The behavior of this type of materials at steam temperatures up to  $\approx 530$  °C has frequently been described<sup>86,87</sup> and will not extensively be treated here. Increasing the steam temperature to 600 °C and even higher for obtaining higher energy conversion efficiencies requires construction materials that possess a higher creep strength than that of the low-Cr steels. This led to introduction of martensitic steels with Cr contents of 9–10% for tubing in heat exchanging components (e.g., T91, T92) as well as for various components in steam turbines.<sup>88</sup> Depending on the actual application, steels with higher Cr contents (e.g., 12% Cr in X20CrMoV12 1 or HCM 12) are considered (Table 1); however, these generally possess a lower creep strength than the 9% Cr steels.<sup>89</sup> Based on the results in the previous section, martensitic 9–12% Cr steels may, from the viewpoint of oxidation resistance, be considered as

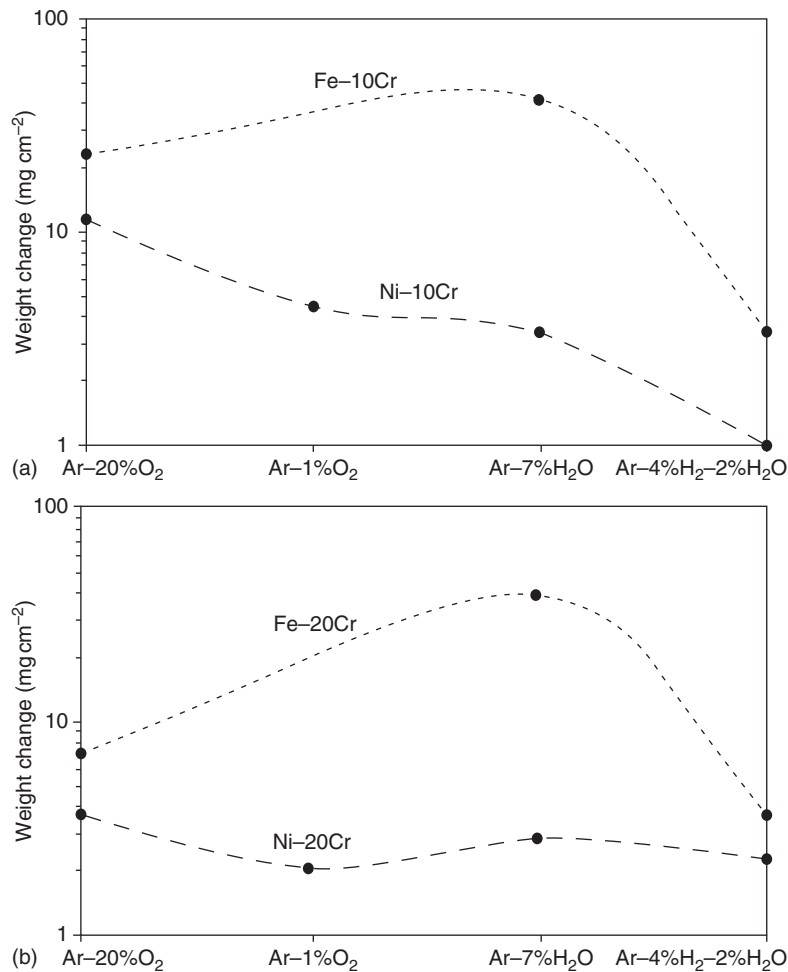


**Figure 29** Weight change of Ni-10Cr and Fe-10Cr (a), as well as Ni-20Cr and Fe-20Cr (b) after 72 h isothermal oxidation at 1050 °C in different test environments. Dotted/dashed lines do not present a real  $pO_2$  dependence of the oxidation rate; they are just inserted for clearer visibility of the data points.

**Table 1** Typical examples of ferritic, martensitic, and austenitic steels as well as Ni-based alloys presently considered as construction materials for steam-carrying components in fossil fuel-fired power plants

Steel designation	Nominal composition	Steel designation	Nominal composition
<i>Ferritic and martensitic steels</i>		<i>Austenitic steels</i>	
30CrMoNiV5-11	1Cr-1Mo	1.4910	17Cr-13Ni-Mo-N
HCM2S (T23)	2¼Cr-1.5W-V	Super 304H	18Cr-10Ni
NF616 (P92)	9Cr-2W-Mo-V-Nb-N	TP347HFG	18Cr-10Ni-Nb
P91	9Cr-1W-Mo-V-Nb-N	NF709	20Cr-25Ni
E911	9Cr-1Mo-1W-V-Nb-N	Save 25	23Cr-18Ni-3Cu-1.5W-Nb-N
X7CrCoNiMo10-6	10Cr-6Co-1Mo	HR3C	25Cr-20Ni-Nb-N
VM 12	11Cr-0.5Si-Mn	AC66	28Cr-32Ni-Ce-Nb
HCM 12	12Cr-1Mo-1W-V-Nb	<i>Ni-based alloys</i>	
HCM12A (P-122)	12Cr-1.5W-Mo-V-Nb-Cu-N	Alloy 617	22Cr-12Co-9Mo
X20CrMoV12-1	12Cr-1Mo-V	Alloy 740	24Cr-20Co-0.5Mo
AISI 430	17Cr-0.5Mn-0.5Si	Alloy 263	22Cr-20Co-0.6Al

Nominal concentrations of alloying additions given in mass%.



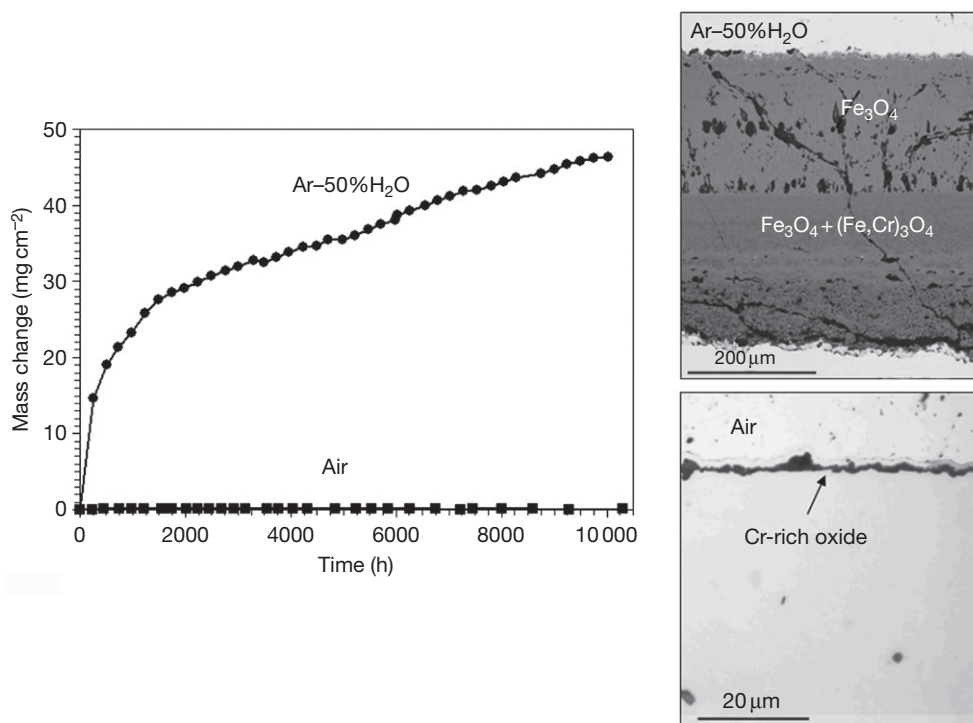


**Figure 30** Weight change versus time for oxidation of 9% Cr steel P92 during exposure at 650 °C in air and Ar-50% H<sub>2</sub>O. Metallographic cross sections show differences in scale morphology after 10 000 h exposure. Adapted from Ehlers, J.; Quadackers, W. J. Report Forschungszentrum Jülich, Jül-3883, 2001; ISSN 0944-2952.

'borderline' alloys. This is confirmed by the results in [Figure 30](#), which shows the weight change data of the 9% Cr steel P92 during exposure at 650 °C in air and in Ar-50% H<sub>2</sub>O.

#### 1.17.4.4.2 Steam oxidation mechanisms of 9–12% Cr steels

During exposure in (simulated) steam in the temperature range 550–650 °C, all ferritic 9–12% Cr steels tend to exhibit an incubation period in which the oxidation rates are very low ([Figure 31](#)). This incubation period can range from minutes to several hundreds of hours and it increases with increasing amount of protective scale-forming elements (e.g., Cr, Si) and the extent of cold work. In this oxidation stage, oxide layers of the type (Fe,Cr)<sub>2</sub>O<sub>3</sub> and/or Cr-rich (Fe,Cr)<sub>3</sub>O<sub>4</sub> covered by a hematite layer are formed.<sup>4,19,90</sup>

After longer exposure times, breakdown of this protective scale occurs, which is accompanied by formation of rapidly growing magnetite and a zone with internal Cr<sub>2</sub>O<sub>3</sub> precipitates ([Figure 31](#)).<sup>46</sup> At temperatures above approximately 580 °C, wüstite may be present near the scale–steel interface.<sup>16,84,87</sup> The inner and outer layers are separated by a gap,

probably caused by vacancy condensation resulting from the rapid outward growth of the outer magnetite layer ([Figure 31](#)). Further growth of the scale depends to a large extent on transport processes within this gap, likely by the so-called H<sub>2</sub>/H<sub>2</sub>O bridges (see [Section 1.17.3.3](#)). This explains why there is a relative movement of the 'transient gap' towards the magnetite layer in the outer part of the scale during prolonged exposure. As the overall scale thickness increases, the Fe activity at the scale–gas interface gradually decreases because of the increasingly difficult transport of Fe cations to the oxide surface as a result of the presence of the in-scale gap ([Figures 31 and 32](#)). This decrease in Fe activity in the outer scale eventually results in formation of hematite, that is, the oxide in equilibrium with the gas atmosphere ([Figure 32](#)), on top of the scale. The formation of hematite starts at the grain boundaries of the magnetite layer ([Figure 32\(b\)](#)). Additionally, molecular gas transport occurs through the outer scale.<sup>83</sup>

For a 10% Cr steel at 650 °C, time  $t_1$  in [Figure 31](#) is ~10–15 min and  $t_5$  ~5 h<sup>91</sup>. Exact times, however, differ with the water vapor content, exact steel composition and surface deformation, for example,

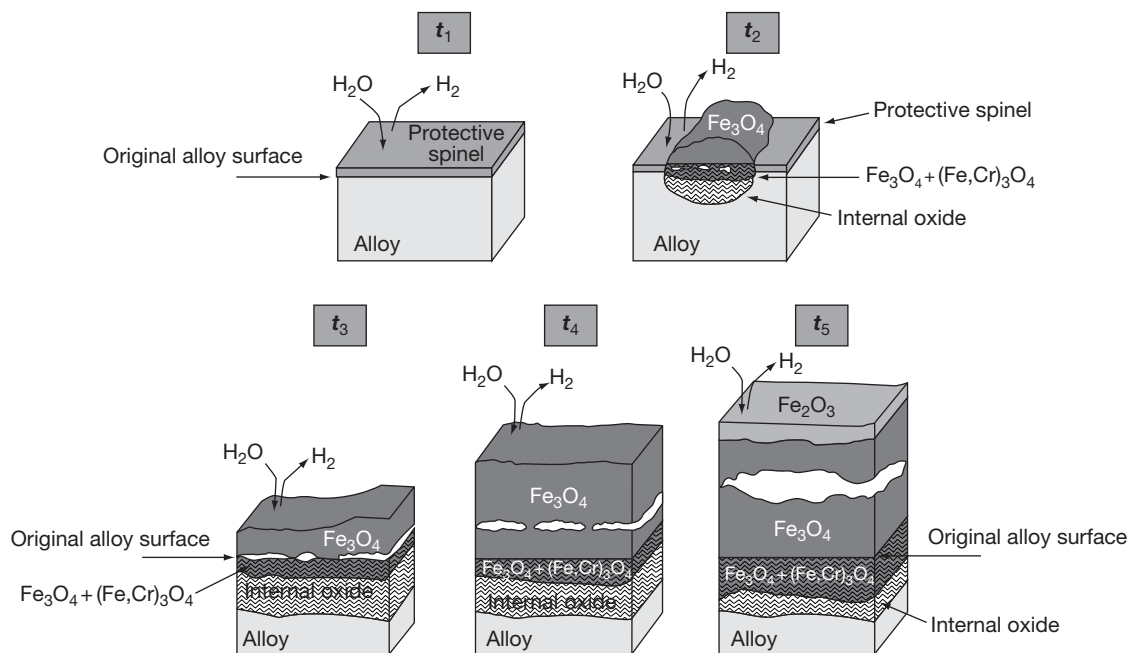


**Figure 31** Proposed mechanism for the oxide scale formation on ferritic 10% Cr steel in Ar-H<sub>2</sub>O mixtures. Times  $t_1, t_2, t_3, t_4, t_5$  represent subsequent time steps during the oxidation process. Reproduced from Quadakkers, W. J.; Ennis, P. J.; Žurek, J.; Michalik, M. *Mater. High Temp.* **2004**, 22(1/2), 37–47.

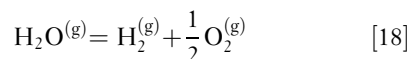
introduced by grinding or cold work. The depth of the internal oxidation zone tends to decrease with increasing temperature, as will be more extensively discussed later.

The change from protective to non-protective oxidation ( $t_1 \rightarrow t_2$  in Figure 31) can be explained by the enhanced oxygen transport in voids by H<sub>2</sub>/H<sub>2</sub>O as proposed by Fujii and Meussner.<sup>92</sup> During exposure in oxygen or air, and during the incubation period in wet gas ( $t_1$ , Figure 31), voids may be formed at the interface between steel and the protective Cr-rich oxide as result of vacancy condensation. In the case of Cr<sub>2</sub>O<sub>3</sub>,  $p_{O_2}$  at the scale–alloy interface at 650 °C is  $\sim 10^{-34}$  atm and the flux of oxygen ( $\mathcal{J}_{O_2}$ ) across a void can be calculated using the Hertz–Langmuir equation:<sup>93</sup>

$$\mathcal{J}_{O_2} = \frac{p}{(2\pi MRT)^{0.5}} \quad [17]$$

where  $p$  is the vapor pressure and  $M$  the mass of the gas molecules. The flux is found to be extremely low (in the range  $8 \times 10^{-34}$  g cm<sup>-2</sup> s<sup>-1</sup>), thus giving Cr sufficient time to diffuse from the bulk alloy towards the inner surface of the void, which can, therefore, heal by again forming a Cr-rich scale. Such a healing process could be illustrated by the TEM cross sections of an oxide scale on a 9% Cr steel after air

exposure at 650 °C.<sup>16</sup> If, however, H<sub>2</sub>O(g) is present in the void, its partial pressure will be determined by the equilibrium:



Calculating the equilibrium gas composition at a total pressure of 1 atm, assuming the gas Ar–50% H<sub>2</sub>O to be in equilibrium with the dissociation pressure of the oxide ( $10^{-34}$  atm), reveals for  $p_{H_2O}$  a value of  $10^{-6}$  atm. Putting this value in the Langmuir equation, it is found that an oxygen flux of  $5 \times 10^{-6}$  g cm<sup>-2</sup> s<sup>-1</sup> can be sustained. This is substantially larger than the actually observed oxidation rate in the wet gas. Thus, oxygen transport via the H<sub>2</sub>/H<sub>2</sub>O bridges<sup>36</sup> in voids within the scale can in principle explain the breakdown of the protective Cr-rich oxide and can account for the high oxidation rates in Ar–H<sub>2</sub>O.

However, based on the considerations in the previous sections, the change from protective to non-protective oxidation will likely be triggered by enhanced internal oxidation of Cr due to hydrogen dissolution in the alloy. Water vapor and hydrogen can be transported through the oxide layer, for example, via microcracks formed as a result of growth stresses.<sup>66</sup> Nakagawa *et al.*<sup>94</sup> considered the case where different oxidation processes were occurring on two sides of

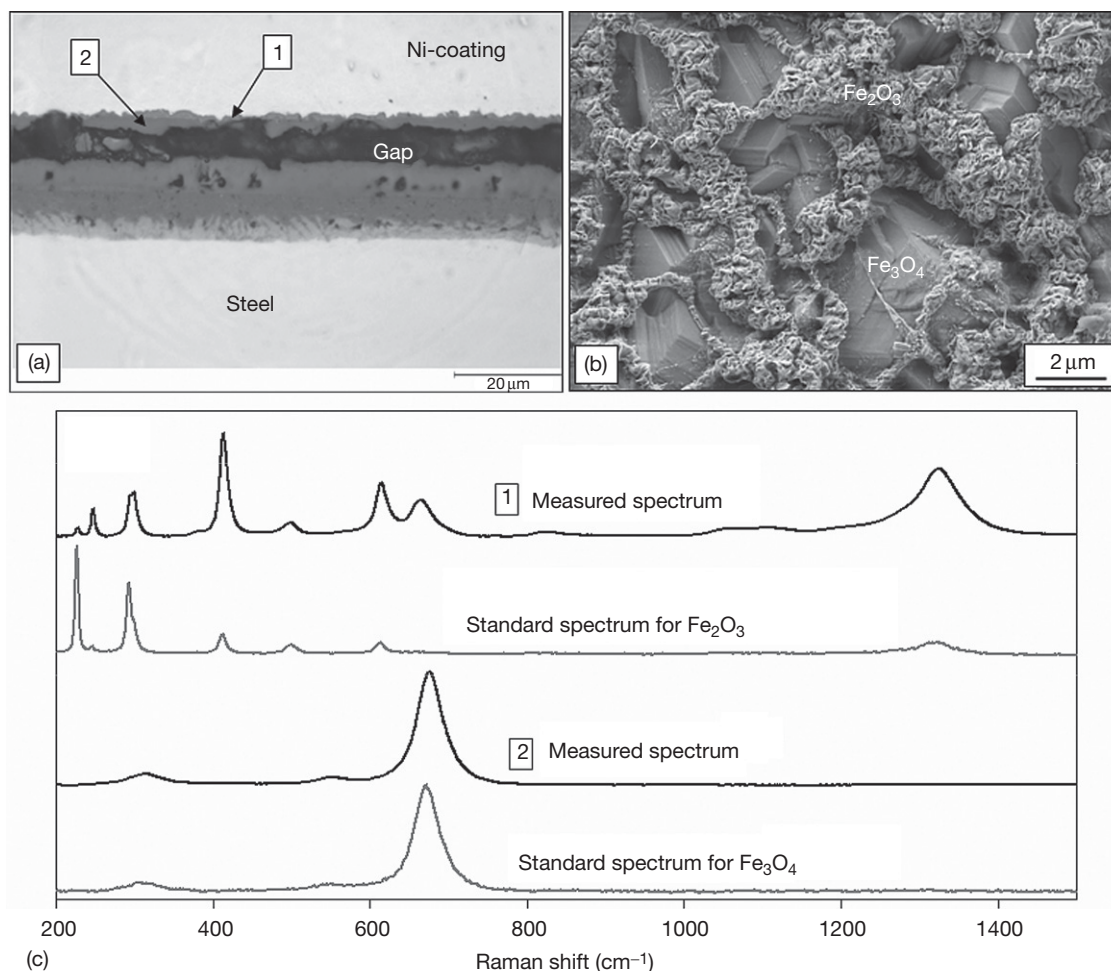


**Figure 32** Metallographic cross section (a) and SEM picture (b) of oxide surface of 10Cr-1Mo-1W (low Si) steel after 5 h oxidation in Ar-4% H<sub>2</sub>O at 650°C. Point 1 and 2 in (a) relate to Raman analyses in (c). Reproduced from Zurek, J.; Michalik, M.; Schmitz, F.; Kern, T. U.; Singheiser, L.; Quadakkers, W. J. *Oxid. Met.* **2005**, 63(5/6), 401–422.

ferritic steels when used as a boiler tube material for power stations. It was proposed that hydrogen generated on one side of the tube wall diffuses to the side with the higher  $p_{O_2}$  and deteriorates the protective properties of the air-formed chromia base scale. In many cases cited above, hydrogen diffusion into the metal was observed, a clear sign of direct reaction of the water vapor in the oxidation process.

#### 1.17.4.4.3 Void and gap formation

The oxide scales after oxidation of 9–10% Cr steels in water vapor contain nearly always a substantial amount of pores and/or microvoids (Figure 33), finally resulting in the formation of gaps that may promote spallation of the scales during thermal cycling. The main reason for void formation in the oxide scale given in the

literature is vacancy condensation as a result of the fast outward migration of metal ions through the scale.<sup>6,49</sup>

During long-term exposure, void formation seems to occur at different locations in the scale. First voids ('transient gap') start to form already after very short oxidation times as shown in Figure 31. If the isothermal exposure is continued, the 'transient' gap may heal by growth of the inner oxide scale as water vapor molecules gain access through the outer layer, and the gap may eventually completely close which results in a more or less compact scale. Transport of Fe cations to the surface then becomes again possible and thus the Fe activity at the oxide surface increases. At a sufficiently large flux of Fe cations, the outer hematite transforms into magnetite, and after longer times (at 650°C, for example, a few hundred hours)

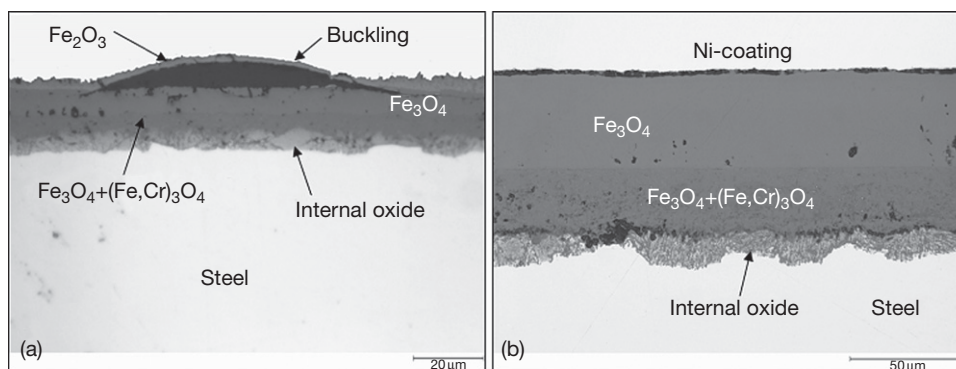


**Figure 33** (a) Isothermal oxidation of a 10Cr–Mo–W–Si steel at 625 °C in Ar–7% H<sub>2</sub>O showing buckling of oxide separation at hematite–magnetite interface, (b) oxidation of 10Cr–Mo–W–Si steel at 600 °C in Ar–50% H<sub>2</sub>O (intermediate cooling every 250 h) showing formation of compact oxide layer. No evidence of spalling was found up to the total exposure time of 1000 h. Reproduced from Quadakkers, W. J.; Ennis, P. J.; Žurek, J.; Michalik, M. *Mater. High Temp.* **2004**, 22(1/2), 37–47.

the scale appearance is then similar to that shown in [Figure 33\(b\)](#).

If a thermal cycle is introduced in the early stages of the oxidation process, that is, before healing of the ‘transient gap,’ scale spallation occurs. Further exposure then results in growth of the freely exposed magnetite layer eventually leading to a scale morphology similar to that shown in [Figure 33\(b\)](#). The question of whether spallation or healing of the outer layer above the gap occurs thus depends on the time at which, for a given temperature, the thermal cycle is introduced. This could be shown for a 10Cr–Mo–W–Si steel after exposures at 600 and 625 °C in Ar–H<sub>2</sub>O.<sup>91</sup> If the specimen was cooled after 70 h exposure, spallation of the top layer occurred because of the presence of the in-scale gap. If the first temperature cycle was introduced after 250 h, sufficient time was available for healing of the gap and thus excellent oxide adherence was found even after extended exposure for several thousand hours.

As long as the scale contains an outer hematite layer, local buckling by a separation at the magnetite–hematite interface is sometimes observed ([Figure 33\(a\)](#)). This might be related to a mechanism which is similar to that frequently described for oxide films on, for example, pure chromium,<sup>39</sup> that is, lateral growth of the scale due to in-scale oxide formation at scale grain boundaries. The cation and anion diffusion in the Fe<sub>2</sub>O<sub>3</sub> lattice are known to be much smaller than in magnetite and wüstite. Therefore, scale growth is likely to occur to a large extent via and at the oxide grain boundaries, and thus in-scale growth can occur by reaction of inwardly and outwardly moving species.

The time required for complete healing of the ‘transient’ gap tends to increase with decreasing temperature. After 550 °C exposure, remnants of the gap within the magnetite can sometimes be found up to quite long exposure times of more than 1000 h ([Figure 34\(a\)](#)), whereas after the same exposure time at higher temperatures only a dense magnetite layer, sometimes with isolated voids in the outer scale, is found ([Figure 34\(b\)](#)).

#### 1.17.4.4.4 Long-term behavior

The long-term behavior of the various types of commercially available martensitic Cr steels in steam in the temperature range 550–650 °C can be rationalized on the basis of a graph similar to that shown in [Figure 13](#). The borderline between the various oxidation regimes is substantially affected by alloying additions, as seen by the data in [Figure 35](#), with the result that a large variation in oxidation rates for group II alloys with the same Cr contents may be observed. As will be shown later, the exact location of the borderline between the various types of oxide scales depends on temperature. Taking these restrictions into account, it can be said that ferritic steels with a Cr content of less than approximately 8% (group I) exhibit at 600–650 °C high oxidation rates and the main oxide phases present in the surface scales are magnetite and (Fe,Cr) spinel. Steels of group III exhibit very low oxidation rates and the oxide scales mainly consist of Cr<sub>2</sub>O<sub>3</sub> and (Cr,Fe)<sub>2</sub>O<sub>3</sub>. The steels of group II are ‘intermediate cases’ because the oxidation rates and scale morphologies may substantially differ as a function of time, temperature, minor alloying additions, and surface treatment.



There is general consensus that steam-side oxidation of ferritic and martensitic boiler tubes occurs at a rate given by:

$$x = K' t^n \quad [19]$$

where  $x$  is the oxide scale thickness,  $t$  is the exposure time,  $n$  is the rate exponent, and  $K'$  is the proportionality coefficient, which is a function of temperature, alloy composition, oxygen partial pressure, stress level, and radius of curvature of the tubing. For tubing of ferritic/martensitic steels from groups I and II,  $n$  has been found to vary from 1/2 to 1/3, and is believed to be a function of time and temperature.<sup>88</sup>

During exposure of the ferritic steels of group I or II (Figure 35) for longer times of, for example, 1000 h

in the temperature range 600–650 °C, the outer magnetite layer is mostly compact and no hematite can be found (Figure 36). The magnetite frequently contains cracks perpendicular to the oxide surface, which are caused by tensile cracking during cooling due to the high thermal expansion coefficient of the magnetite.<sup>95</sup>

Upon prolonged exposure, the scales start to develop more and more microvoidage. This first occurs in the inner scale (Figure 36). Here the largest extent of void formation seems to develop at the interface between the internal oxidation zone, if present, and the inner oxide layer (Figure 36). The eventual pore morphology and distribution in the inner scale depend on the way in which the vacancies within the scale and/or at the scale–alloy interface

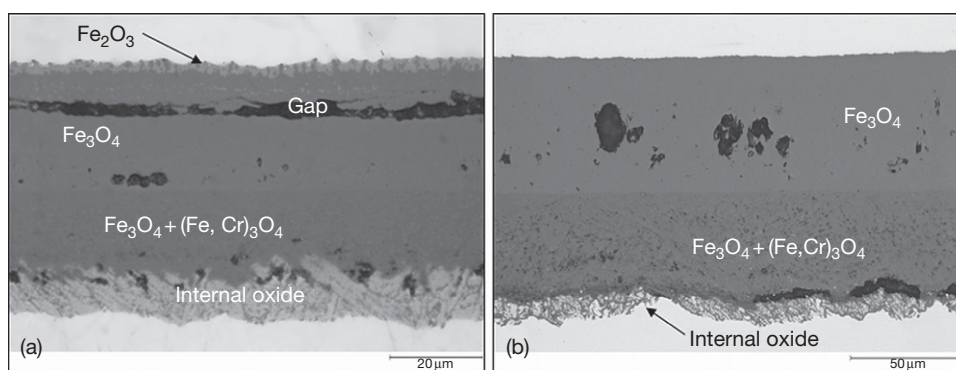


**Figure 34** Effect of temperature on morphology and void/gap formation of scale on 10Cr–1Mo–1W (low Si) steel during exposure in Ar–50% H<sub>2</sub>O for 1000 h: (left) 550 °C; (right) 600 °C. Note the differences in magnification. Reproduced from Quadackers, W. J.; Ennis, P. J.; Žurek, J.; Michalik, M. *Mater. High Temp.* **2004**, 22(1/2), 37–47.

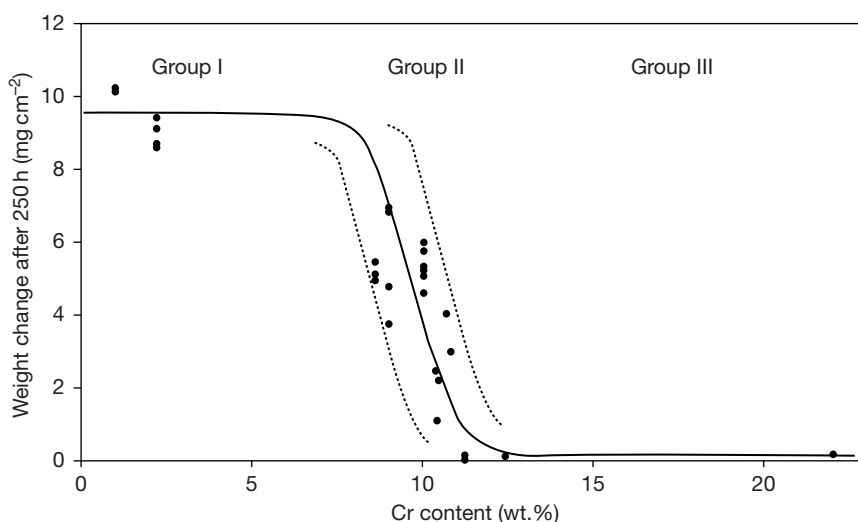


**Figure 35** Weight change of various ferritic and martensitic steels after 250 h oxidation in Ar–50% H<sub>2</sub>O at 600 °C, derived from data in Ehlers and Quadackers.<sup>4</sup> Designations ‘Group I–III’ are explained in the text.

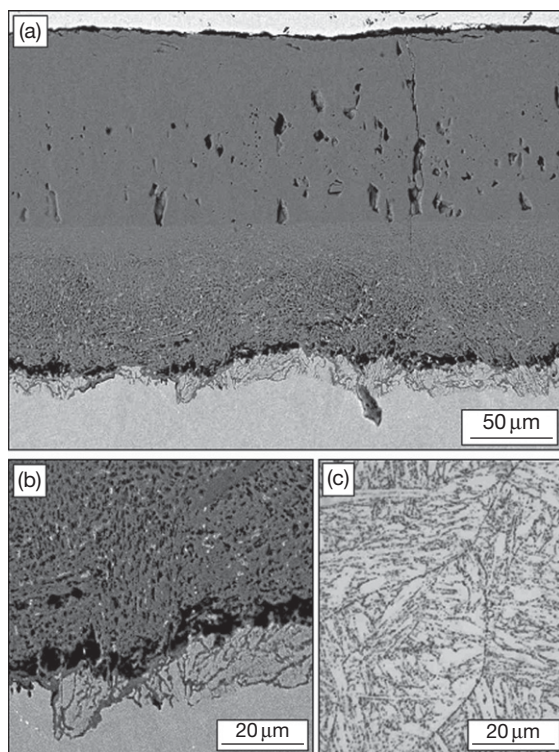


**Figure 36** Oxide scale formed on 10Cr-1Mo-1W steel during exposure for 1000 h in Ar-50% H<sub>2</sub>O at 650 °C: (a) overview; (b) higher magnification of scale-steel interface; (c) steel microstructure. Reproduced from Ehlers, R. J.; Ennis, P. J.; Singheiser, L.; Quadackers, W. J.; Link, T. In EFC Workshop 2001; Schütze, M.; Quadackers, W. J., Nicholls, J. R., Eds.; The European Federation of Corrosion Publications, 2001; Vol. 34, Paper 12, pp 178-193.

coalesce to voids. **Figure 36** shows a clear difference in pore morphology in the outer pure Fe<sub>3</sub>O<sub>4</sub> layer and in the inner two-phase layer consisting of Fe<sub>3</sub>O<sub>4</sub> + (Fe,Cr,Mn)<sub>3</sub>O<sub>4</sub> and in the internal oxidation zone adjacent to the alloy. Numerous tiny voids are present in the inner two-phase layer (**Figure 36**) which seem to be correlated with the (Fe,Cr,Mn)<sub>3</sub>O<sub>4</sub> bands embedded in the Fe<sub>3</sub>O<sub>4</sub> matrix.<sup>4</sup> Apparently, the interfaces between these bands and the magnetite act as nucleation sites for the voids. For a given alloy, the morphology and distribution of the ‘bands’ depend on temperature, as will be illustrated later.

This type of void formation, as well as the morphologies of the inner spinel layers and the zone of internal oxidation, is affected by the underlying steel microstructure (**Figure 37**), including carbides preferentially formed at steel grain boundaries and/or martensitic laths.<sup>96</sup> **Figure 38** compares the scale cross sections of a 10Cr-Mo-W steel with that of a Fe-9% Cr model alloy manufactured from

high-purity elements after 1000 h exposure in Ar-50% H<sub>2</sub>O. Although the thicknesses of the scales on the two materials do not substantially differ, the void and crack morphologies exhibit tremendous differences. The most striking difference is the large gap occurring in the case of the model alloy near the alloy-steel interface, but not in case of the commercial steel. This is likely related to differences in the mechanisms of vacancy condensation, due to the absence of carbide precipitates in the model alloy. This results in a concentration of the voidage at the scale-steel interface, whereas in case of the commercial steel the voids at first tend to be evenly distributed in the whole inner layer.

During long exposure of the commercial steels of group II, voidage also starts to occur in the outer magnetite layer (**Figure 36**). These voids can be unevenly distributed or they can coalesce to a gap at the interface between the inner and outer layers (**Figure 39(a)**). Indications have been found that the latter is caused by limitations of the cation transport in the inner scale. Here three possible reasons may be mentioned<sup>97</sup>:

1. The continuing formation of voids in the inner scale decreases the transport area available for cation diffusion.
2. The two-phase mixture of FeCr spinel and magnetite in the inner scale changes, near the interface between outer and inner scale, to a single-phase layer. Magnetite, which acts as ‘rapid diffusion path’ for Fe cations, vanishes with the result that the transport of Fe cations from the inner to the outer scale decreases.
3. The formation of a protective, Cr-rich spinel layer at the oxide-alloy interface.

The limitation of cation transport has the result that the growth rate of the outer magnetite in the existing oxygen activity gradient can no longer be sustained. Consequently, inwardly moving vacancies in the magnetite tend to condense at the interface between the inner and the outer layer resulting in void and gap formation (**Figure 39(a)**).

The formation of a Cr-rich layer at the oxide-alloy interface (No. 3 above) preferentially occurs at higher temperatures (at and above 600 °C) because then diffusion of Cr in the alloy and/or the rate of spinel formation are sufficiently fast. It is also favored by increasing the amounts of protective scale-forming elements (Cr, Si), and, therefore, the tendency for extensive void formation in the outer magnetite layer and/or at the interface between inner and outer scale



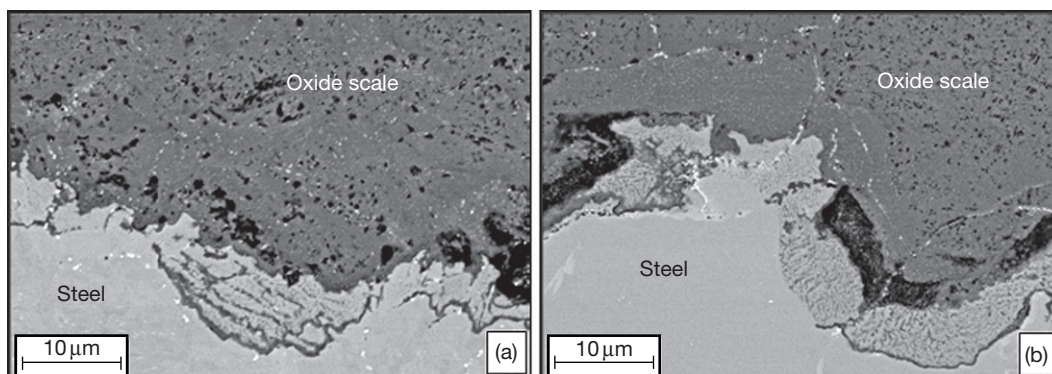


**Figure 37** Cross-sections of oxide scales on specimens of 9% Cr steel P92 after oxidation for 1250 h at 650 °C in Ar–50% H<sub>2</sub>O. Prior to exposure the specimens were heat-treated so that they had a martensitic (a) or ferritic (b) microstructure. Reproduced from Ehlers, R. J.; Ennis, P. J.; Singheiser, L.; Quadakkers, W. J.; Link, T. In EFC Workshop 2001; Schütze, M.; Quadakkers, W. J., Nicholls, J. R., Eds.; The European Federation of Corrosion Publications, 2001; Vol. 34, Paper 12, pp 178–193.

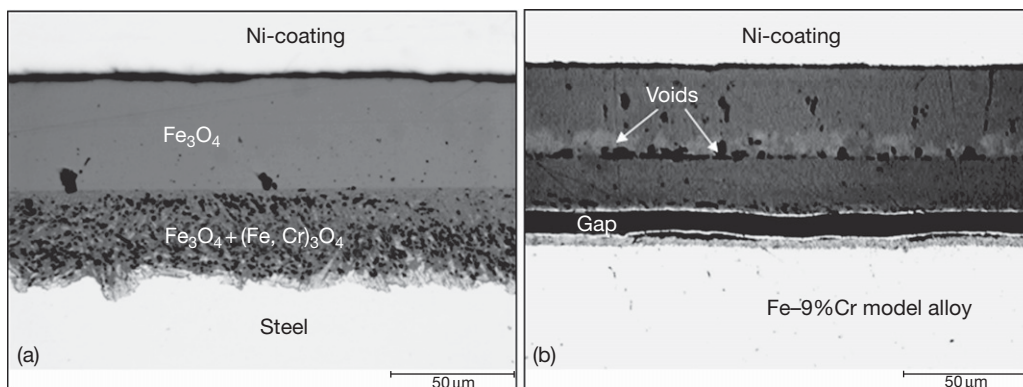


**Figure 38** Metallographic cross sections of oxide scales on (a) commercial 10Cr–Mo–W steel and (b) Fe–9% Cr model alloy (manufactured from high-purity materials) after 1000 h isothermal exposure in Ar–50% H<sub>2</sub>O at 625 °C, showing differences in void/gap formation in the scale. Reproduced from Quadakkers, W. J.; Ennis, P. J.; Żurek, J.; Michalik, M. *Mater. High Temp.* **2004**, 22(1/2), 37–47.

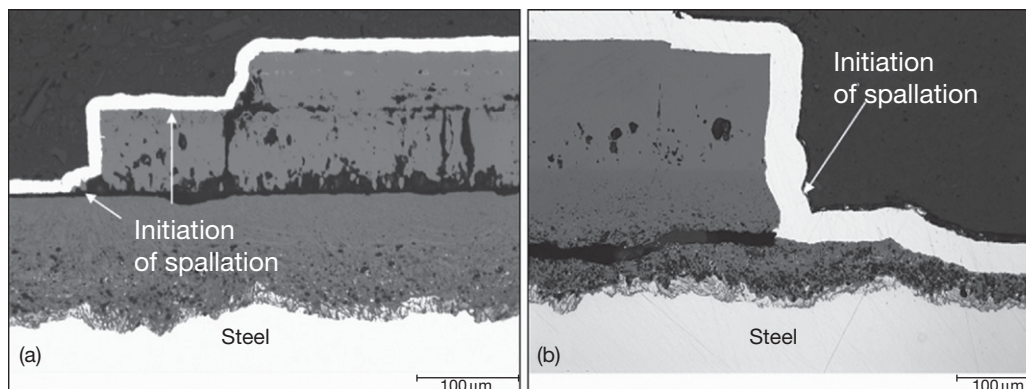


**Figure 39** Different types of scale spallation during oxidation on 10Cr–1Mo–1W low Si steel after long-term exposure in Ar–50% H<sub>2</sub>O at (a) 625 °C and (b) 650 °C.

will in principle be larger for steels of group II in **Figure 13** than for lower Cr steels (group I).

As explained in **Section 1.17.4.4.2**, extensive void/gap formation will eventually result in the formation of hematite on top of the outer magnetite layer. Macroscopic observation of hematite is thus frequently a strong indication for the formation of a heavily voided/cracked magnetite layer, which is expected to be prone to spallation. Nishimura *et al.*<sup>98</sup> described a similar mechanism for the hematite formation and claimed that the transformation of magnetite into hematite plays a role in oxide spalling. An interesting feature is that the outer surface of the hematite is in some cases flat; in other cases it exhibits a whisker type morphology, possibly related to a mechanism described in **Section 1.17.3.1** for whisker formation on chromia scales. The reasons for these differences in morphology of the hematite are, as far as known to the authors, not fully clarified.

On the basis of the described mechanisms of void/gap formation, it can generally be said that the crack initiation/propagation modes occurring can result in three different types of scale spallation: that is, spalling occurring in the outer magnetite layer (**Figure 39(a)**); near the interface between the oxide and the alloy or the internal oxidation zone (**Figure 39(b)**); or at the interface between inner and outer scale (**Figure 39(a)**). The latter mode preferentially occurs in case of group II alloys with higher Cr (and Si) contents and is similar to that frequently found for austenitic steels (see **Section 1.17.4.4.6**).

#### 1.17.4.4.5 Temperature dependence of oxidation during long-term exposure

Watanabe *et al.*<sup>99</sup> investigated the oxidation behavior of various steels in steam in an autoclave in the range 560–700 °C. Low alloy steels (group I) showed the same activation energy ( $Q$ ) for the oxidation rate constant, that is, 350–400 kJ mol<sup>-1</sup>, over the entire temperature range (**Figure 40**). On the other hand, the 9% Cr and 12% Cr steels (group II) showed a bilinear behavior. Below 600 °C they had the same  $Q$  but exhibited much lower values in the range 600–700 °C; the higher the Cr content, the lower the  $Q$  values. HCM12A had a  $Q$  value of 40 kJ mol<sup>-1</sup>.

The data show that the oxidation behavior of steels with Cr concentrations between 2 and 8% in superheated steam at temperatures below 600 °C is virtually independent of the Cr content.<sup>100</sup> The difference between 9% Cr steels and 12% Cr steels is also small at 600 °C but becomes marked at 650 °C.

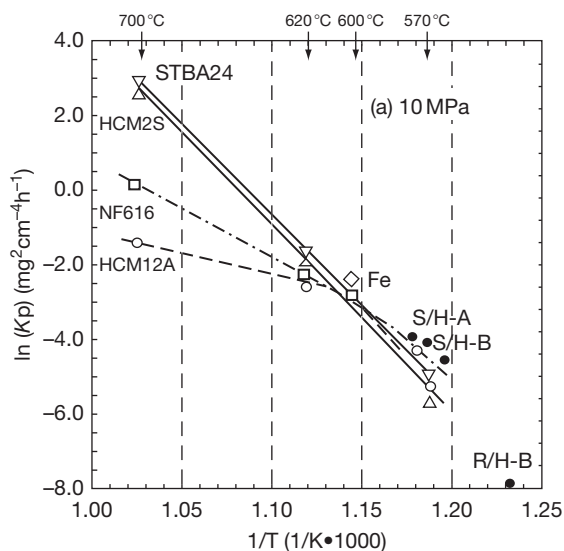


**Figure 40** Arrhenius-type plots of oxidation rate constant  $K_p$  measured at 10 MPa. Reproduced from Yi, Y. S.; Watanabe, Y.; Kondo, T.; Kimura, H.; Sato, M. *J. Pressure Vessel Technol.* **2001**, 123, 391–397.

A similar difference in temperature dependence of various steel types was found by Ehlers *et al.*<sup>4</sup> after exposure in Ar–50% H<sub>2</sub>O at 1 bar pressure. Also, the data from Husemann,<sup>101</sup> derived from service exposed tubes, show that at low temperatures (~550 °C) the oxidation rates of the 9% Cr steels are not substantially lower than those of the low alloy steels (**Figure 41**). These data also show that large differences in oxidation rates may occur between different batches of one steel, here shown for X20 ‘low Cr’ and ‘high Cr.’ This was also found by other authors during laboratory tests of 10.5% Cr and 11.3% Cr batches of this steel type (**Figure 41(c)**). The results in Refs. 4 and 101 indicate that at 550 °C a clear difference exists between low alloy steels and 12% Cr steel. This contradicts the results of Yi *et al.*<sup>100</sup>

The differences in temperature dependence of the oxidation rates for various steel types (**Figure 40**) are mainly related to the enhanced incorporation of chromium and other protective scale-forming elements into the scale upon temperature increase. The tendency to form surface scales which are richer in Cr upon increasing the temperature from, say, 550–650 °C is in some steels even more pronounced if the temperature is even further increased. This then has as result that the oxidation rate of, for example, P91 at 700 °C is, at least during short-term oxidation, smaller than at 600 °C.<sup>102</sup>

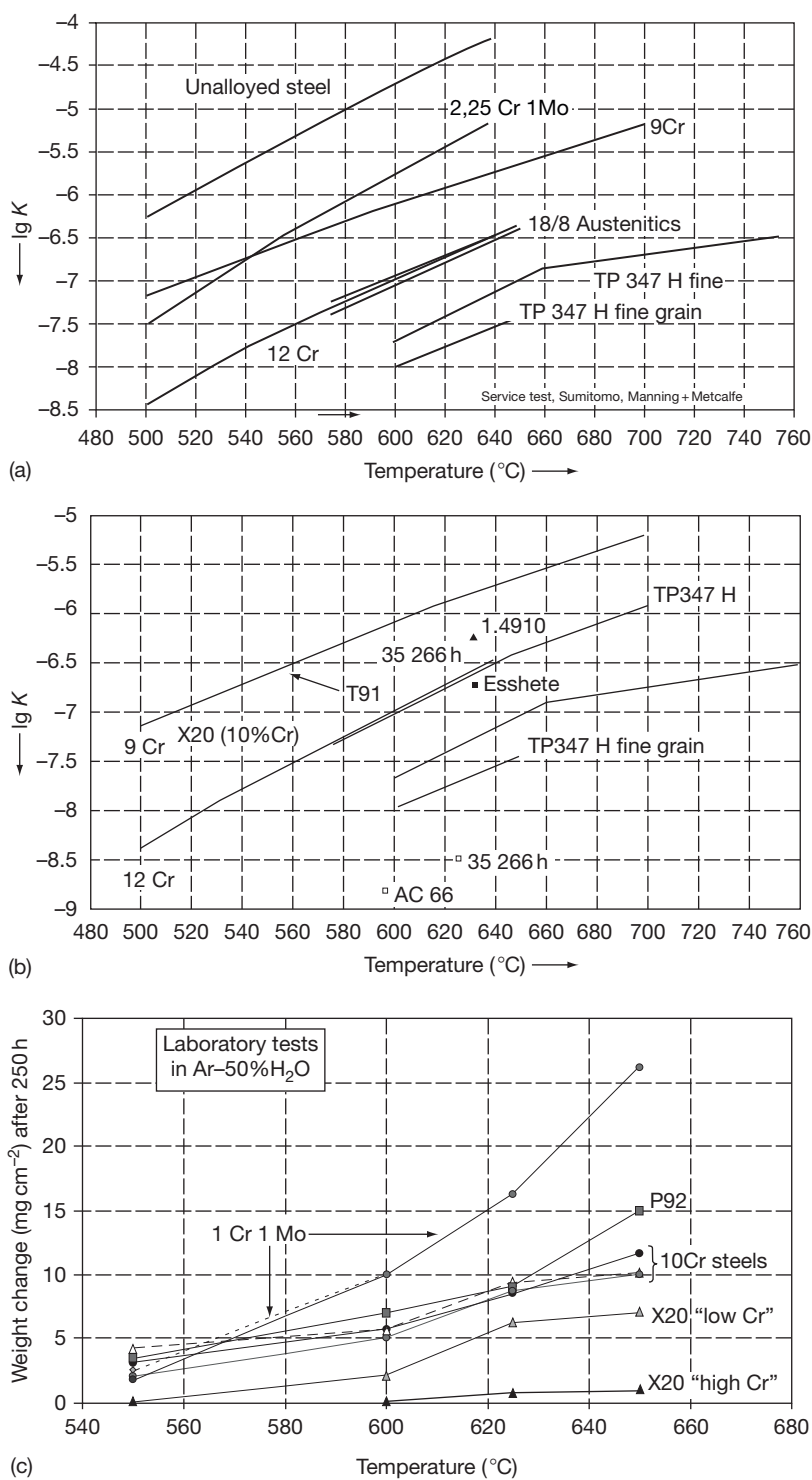


**Figure 41** (a, b) Oxidation rates for various steels derived from literature data and service-exposed tubes. The rate constant  $K$  here refers to the material loss  $x$  in mm defined as  $x^2 = Kt$  whereby  $t$  is the time in hours.<sup>101</sup> (c) Weight changes for various steels after laboratory tests of 250 h in Ar-50%  $\text{H}_2\text{O}$ .<sup>4</sup> Designation 'X20' relates to X20CrMoV12-1 (see Table 1).

Depending on the exact steel composition, a decreasing oxidation rate with increasing temperature can already occur at lower temperatures. **Figure 42** shows the mass change data after 1000 h exposure of different steels at different temperatures in Ar-50% H<sub>2</sub>O. Samples of 1Cr-Mo-V and 10Cr-Mo-W steels clearly exhibit increasing oxidation rates with increasing temperature (**Figure 42**). However, the 12% Cr steel exhibits lower oxidation rates at 625 °C than at 550 °C, whereas the Co-containing 11% Cr steel shows a quite complex temperature dependence (**Figure 42**). After 1000 h exposure at

625 °C, the weight changes are clearly lower than those observed after the 550 °C exposure, whereas at 600 °C the value is only slightly smaller than that at 550 °C. It is important to note that the high value at 600 °C was already reached after 250 h; in other words, the oxidation rate between 250 and 1000 h is as small as that observed at 625 °C.

**Figure 43** shows the oxide scales formed on the Co-containing steel after 1000 h of exposure at 550 and 600 °C. In agreement with the mass change data in **Figure 42**, the thicknesses of the scales formed at 550 and 600 °C are quite similar. However, the scale

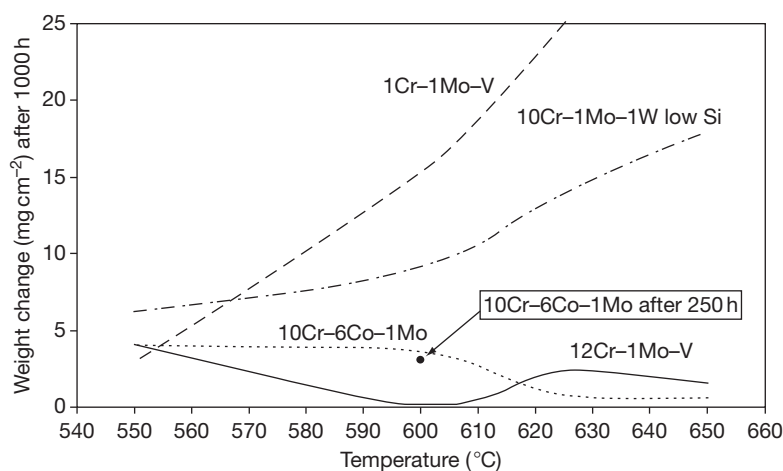


**Figure 42** Weight changes of four different ferritic steels after exposure for 1000 h in Ar-50% H<sub>2</sub>O showing different types of temperature dependence of the oxidation rates. Also inserted is the weight change of the 10Cr-6Co-1Mo steel after 250 h, showing that between 250 and 1000 h hardly any weight gain occurred. Reproduced from Žurek, J.; Wessel, E.; Niewolak, L.; Schmitz, F.; Kern, T. U.; Singheiser, L.; Quadakkers, W. J. *Corros. Sci.* **2004**, 46(9), 2301–2317.

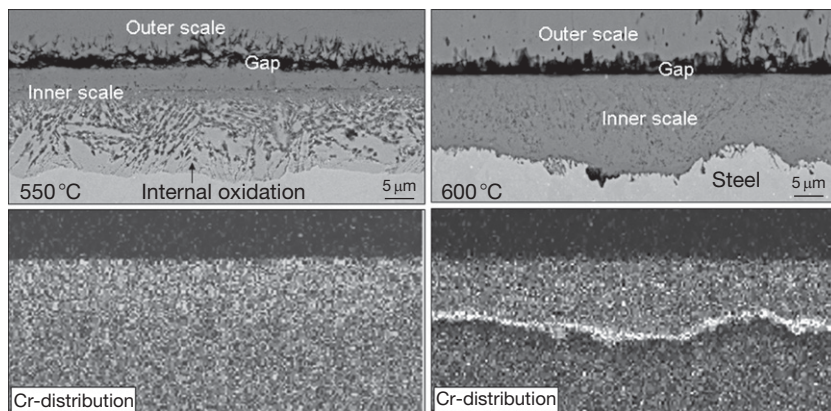


**Figure 43** Backscattered electron images and Cr distribution in scales formed on 10Cr-Co-Mo steel after 1000 h exposure in Ar-50% H<sub>2</sub>O at 550 and 600 °C showing the temperature dependence of Cr distribution in the inner scale. Reproduced from Žurek, J.; Wessel, E.; Niewolak, L.; Schmitz, F.; Kern, T. U.; Singheiser, L.; Quadakkers, W. J. *Corros. Sci.* **2004**, 46(9), 2301–2317.



morphologies show substantial differences. At 550 °C, the inner part of the scale exhibits a wide zone of internal oxide precipitates which are embedded in a Co-rich alloy matrix. After exposure at 600 °C, the internal oxidation zone is absent.

At 550 °C, chromium diffusion in the alloy and in the oxide is so slow that Cr can be considered as being virtually immobile. It becomes preferentially incorporated in the inner part of the scale as a result of oxidation of the Cr-rich carbides at the steel grain boundaries and/or martensite laths prevailing in the alloy.<sup>97</sup> The Cr-rich internal oxides become subsequently embedded in the scale by the inwardly moving oxidation front.<sup>96</sup> The Cr-rich bands in the inner scale thus exhibit a sort of ‘fingerprint’ of the typical microstructure in this type of steel (Figures 36(b) and 36(c)).

On the basis of the initial rapid mass change (Figure 42), the scale formation mechanism at 600 °C is more similar to that at 550 °C than that at 625 °C. However, after longer times the oxidation rate resembles that found at the higher temperatures, which means that somewhere in the scale a protective Cr-rich oxide becomes stabilized after about 250 h of exposure. The element mapping in Figure 43 shows that the overall Cr enrichment in the inner part of the scale is not very pronounced, but a strong enrichment

is visible in a narrow band near the scale–alloy interface. Beneath this, a Cr depletion in the alloy as a result of the selective oxidation of Cr is clearly visible. The enhanced diffusion and the associated increase in the selective oxidation of Cr become more pronounced if the temperature is increased to 625 °C. The Cr-rich oxide then becomes stabilized already in the very early stages of oxidation, resulting in an extremely slow oxidation rate during the whole 1000 h of exposure (Figure 42).

Qualitatively, these features in respect to the adverse temperature dependence of the oxidation behavior can also be observed in the case of the 12% Cr steel (Figure 42), in agreement with earlier findings of Haarmann *et al.*<sup>103</sup> for this type of steels. At 550 °C, the Cr-enriched regions almost exclusively consist of oxides initially formed on grain boundaries and martensite laths, thus expressing the original microstructure in the steel. After exposure at 625 °C, the alloy exhibits Cr-rich stringers in the inner oxide layer, arranged parallel to the initial steel surface, indicating more rapid Cr diffusion from the bulk alloy in the direction of the scale.<sup>104</sup> This preferential oxidation of Cr results in a Cr depletion beneath the Cr-rich spinel layer in the alloy. After continued Cr depletion, the growth of the Cr-rich spinel can eventually no longer be

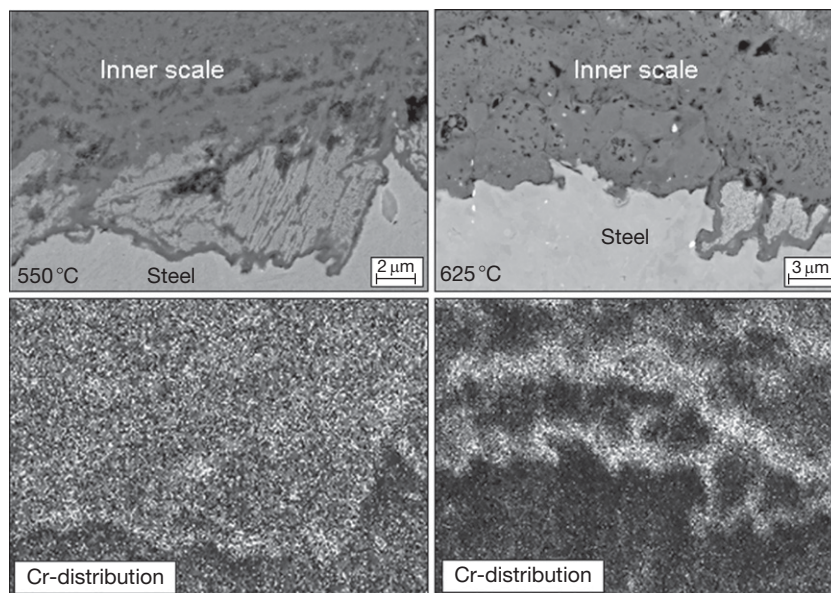


**Figure 44** Backscattered electron images and Cr distributions in inner scale formed on 12Cr–Mo–V steel after 1000 h exposure at 550 and 625 °C showing temperature dependence of Cr incorporation and distribution in inner scale. Reproduced from Z'urek, J.; Wessel, E.; Niewolak, L.; Schmitz, F.; Kern, T. U.; Singheiser, L.; Quadakkers, W. J. *Corros. Sci.* **2004**, 46(9), 2301–2317.

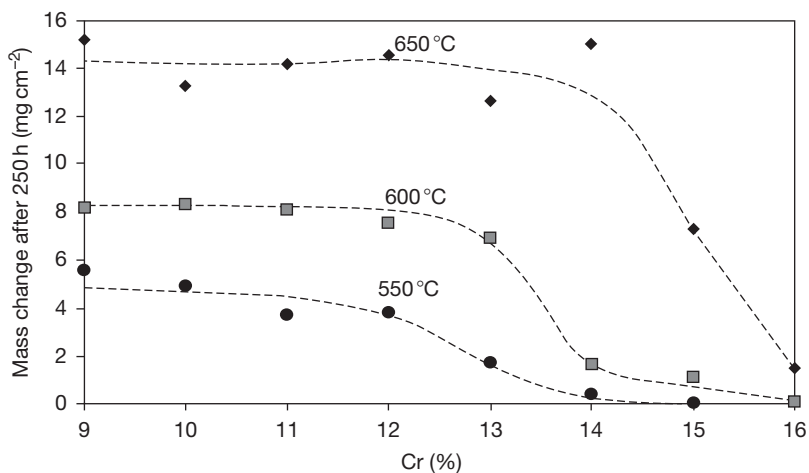


**Figure 45** Weight changes of binary Fe–Cr model alloys after 250 h exposure in Ar–50% H<sub>2</sub>O in the temperature range 550–650 °C. Adapted from Nieto-Hierro, L.; Quadakkers, W. J. Unpublished results, Forschungszentrum Jülich, FRG, 2006.

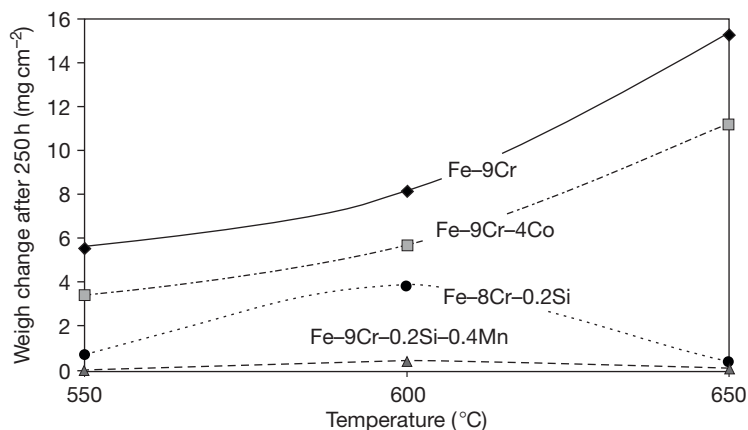


**Figure 46** Weight changes of Fe–Cr model alloys with various additions of minor elements, after 250 h exposure in Ar–50% H<sub>2</sub>O in the temperature range 550–650 °C. Derived from Nieto-Hierro and Quadakkers.<sup>105</sup>

sustained, and as a result Fe-rich oxides are subsequently formed. Repetition of this process leads to the microstructure in the inner part of the scale shown in Figure 44.

The adverse temperature dependence (Figure 42) can thus be expected in steels that exhibit a higher tendency to form protective Cr-rich scales (group II, Figure 13), that is, it increases with increasing amounts of elements (Cr, Si, etc.) that participate in the formation of protective scales.

The adverse temperature dependence, shown for two steels in Figure 42, in fact seems to contradict the results and considerations in Section 1.17.4.3.3 which showed that for binary FeCr alloys in the temperature range 800–1050 °C the tendency to form protective scales decreases with increasing temperature. The results obtained for high-purity Fe–Cr

model alloys in Figure 45 illustrate that this is also the case for steam oxidation in the temperature range 550–600 °C.<sup>105</sup> If a different temperature dependence is sometimes observed for the commercial ferritic steels, then apparently factors other than just temperature dependence of Cr and oxygen diffusion in the alloy affect protective scale formation. On the basis of studies with a number of ternary and quaternary model alloys, parameters that affect this process are alloying elements such as Si and Mn which participate in the oxidation process, C content in the alloy which apparently affects the Cr-distribution and activity, as well as enhanced dissolution of carbides with increasing temperature thereby ‘releasing’ Cr for diffusion. The results in Figure 46 confirm the significance of minor additions of Si and Mn for decreasing oxidation rates upon temperature increase.



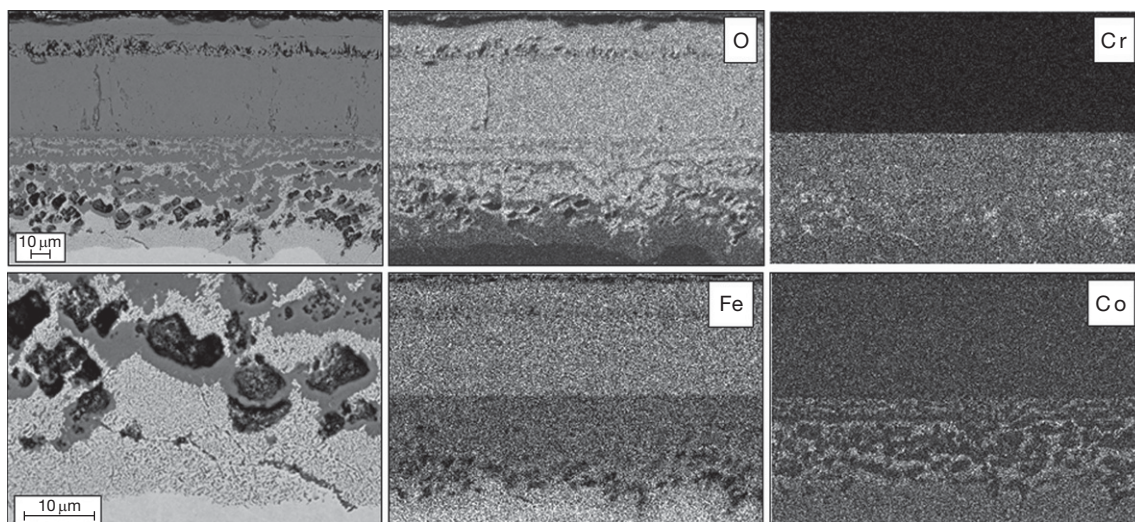


**Figure 47** Backscattered electron images (left) and X-ray mappings of oxide scale formed on model alloy Fe-9Cr-4Co after 1000 h of exposure at 650 °C in Ar-50% H<sub>2</sub>O. Pictures on left side show an overview of oxide scale and higher magnification of scale-steel interface, respectively. Adapted from Nieto-Hierro, L.; Quadackers, W. J. Unpublished results, Forschungszentrum Jülich, FRG, 2006.

For Si-containing steels, the occurrence of the adverse temperature dependence was also found by other researchers,<sup>106,107</sup> and a detailed description concerning the effect of Si for disappearance of the internal oxidation zone and the resulting formation of barrier layers was given by Ueda *et al.*<sup>84</sup> Single additions of other common alloying elements such as W, Co, and Nb did not fundamentally alter the  $T$ -dependence of the oxidation rates.<sup>4,105</sup> However, Co contents of more than 4% appeared to substantially affect the oxidation behavior of the Fe-Cr model as illustrated in **Figure 46**.

An Fe-9% Cr-4% Co model alloy forms at 650 °C an inner and outer scale (**Figure 47**), as shown for other steels before. However, here, the selective oxidation of Cr, and subsequently Fe, leads in the inner part of the scale to an apparent enrichment of Co in the remaining metallic regions due to the high dissociation pressure of Co oxide (**Figure 47**). X-ray diffraction (XRD) revealed even the presence of pure cobalt near the interface between inner and outer scale.<sup>105</sup> This results in a microstructure in which the transport of Fe cations is strongly hampered. In this way, sufficiently large additions of Co (e.g., 4%) substantially decrease the Cr content required to form protective Cr-rich oxide scales (**Figure 46**); however, no adverse temperature dependence is found.

#### 1.17.4.4.6 Austenitic steels

Attempts to further increase the steam temperature in power generation systems frequently requires the

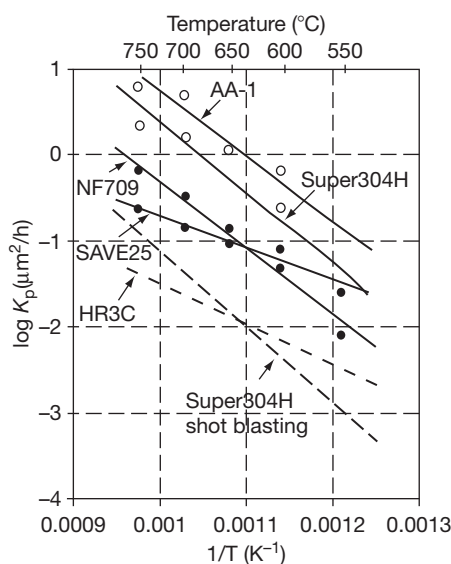


**Figure 48** Scale growth rate  $K_p$  of various austenitic steels versus reciprocal temperature during steam oxidation. Here  $K_p$  is defined as  $K_p = x^2/t$  with  $x$  the scale thickness and  $t$  the time. Reproduced from Muramatsu, K. In *Development of Ultrasupercritical Plant in Japan, Advanced Heat Resistant Steel for Power Generation*; Viswanathan, R., Nutting, J. W., Eds.; IOM Communications: London, UK, 1999; Book 708, pp 543–559.

highest temperature components to be designed using austenitic materials, sometimes from the viewpoint of mechanical properties and in other cases for obtaining improved steam oxidation resistance.

The various austenitic steels that are potentially suitable as construction materials for heat-exchanging components widely differ in composition, for example, in respect to Cr and Ni content (Table 1), and consequently steam oxidation resistance may substantially differ between various materials.

Depending on the composition, the commercially available austenitics may, in respect to steam oxidation resistance, be described as group II or group III alloys in Figure 13. Steels with Cr contents in the range 17–20% may be considered as group II alloys and thus show oxide scales that exhibit many features similar to those described for the high-Cr ferritics of group II. Muramatsu<sup>108</sup> found that the oxidation rates of the austenitic steels are characterized by a single

activation energy over the entire temperature range between 550 and 750 °C, whereas the activation energy  $Q$  decreases as Cr concentration increases (Figure 48).

Oxide scales formed on austenitic steels are sometimes more prone to spallation than those on ferritic or martensitic steels. Figure 49 shows the gross and net mass changes of an austenitic 25Ni–15Cr–Ti steel as a function of time during exposure in Ar–50% H<sub>2</sub>O in the temperature range 550–650 °C. As described for some of the high-Cr group II ferritics (Section 1.17.4.4.5), different from the materials studied by Muramatsu<sup>108</sup> this austenitic steel shows an ‘adverse temperature dependence’: the growth rate of the initially formed surface scale at 650 °C is

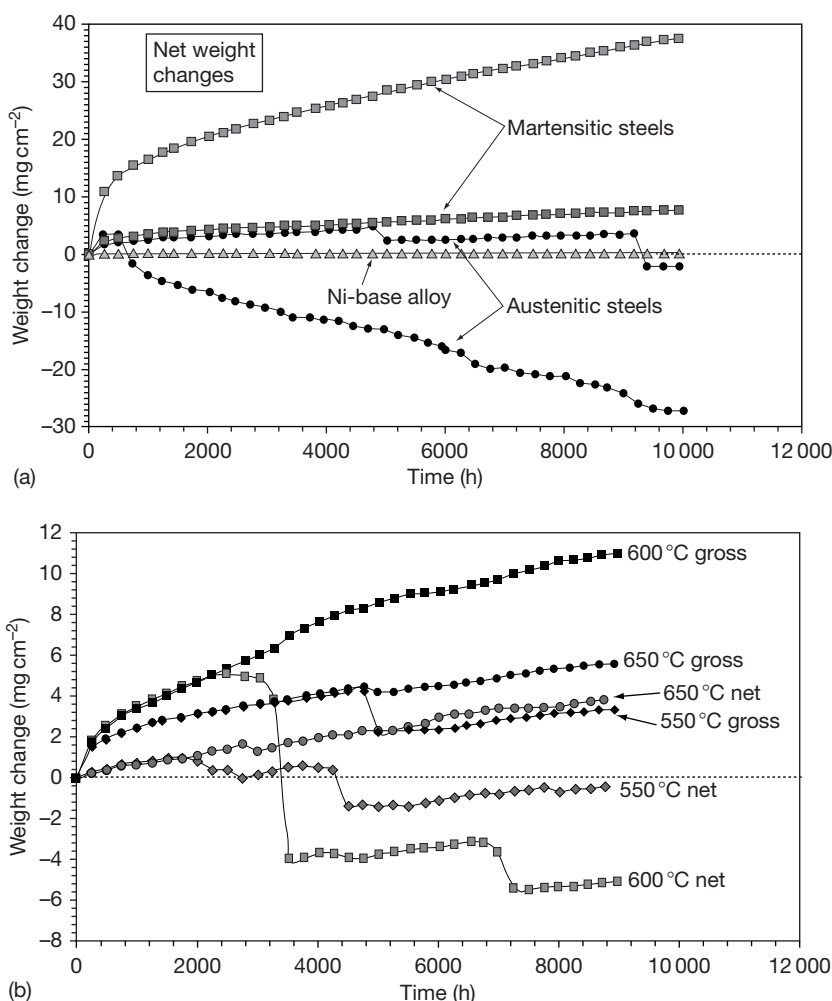


**Figure 49** Mass changes as function of time during oxidation in the temperature range 550–650 °C in Ar–50% H<sub>2</sub>O: (a) Typical examples showing differences in behavior of martensitic 9–10% Cr steels, austenitics and Ni-base alloy; (b) Temperature dependence for onset of scale spallation for austenitic steel 25Ni–15Cr–Ti. ‘Net’ and ‘gross’ weight changes correspond to specimen mass changes without and with spalled oxide, respectively.

smaller than that at 600 °C. The data illustrates that no clear correlation exists between the oxidation rate and the time for the onset of scale spallation. For example, at 600 °C, the first spallation occurs after 3000 h where the net mass change is  $\sim 5 \text{ mg cm}^{-2}$ , while at 650 °C spallation occurs after 5000 h, that is, when the mass change equals  $\sim 3.5 \text{ mg cm}^{-2}$ . At 550 °C, spallation starts to occur after 2000 h exposure, where the mass change exceeds  $\sim 1 \text{ mg cm}^{-2}$ . The onset of spallation can thus not easily be correlated with a critical thickness of the oxide scale.

The metallographic cross sections presented in **Figure 50** illustrate the typical scale morphologies on austenitic steels. Spallation generally occurs at the interface between the inner and the outer scale, that is, near the original metal surface. After the total outer scale has spalled, the scale regrowth is determined by transport processes in the thick inner scale and thus occurs at a rate similar to that prevailing just before the occurrence of spalling. Owing to the high Cr content, Fe diffusion in the inner scale is slow, and thus the regrown oxide exhibits features as described in the previous sections, which means that it mainly consists of hematite on top of a gap. The spalling rate is thus governed by an initial smaller weight loss, a slow scale re-growth and consequently a smaller weight loss during the following spalling steps. This is, for example, clearly illustrated by the 600 °C curve in **Figure 49**.

There are, however, a number of major differences in oxide scale formation between 17% and 20% Cr austenitic steels and most of the commercially available 9–12% Cr martensitic steels. The effect of carbide formation on martensite laths for the inner scale morphology does obviously not occur in the austenitic steels. Also, chromium diffusion in austenite is slower by approximately a factor 10 than in ferrite.<sup>104,109</sup> Therefore, the critical Cr content to

obtain protective chromia base scale formation will generally be higher for austenitic than for ferritic steels. In coarse-grained austenitics, the change from formation of Fe/Cr spinel to pure  $\text{Cr}_2\text{O}_3$  was reported to require a Cr content of 25% such as prevailing in HR3C.<sup>88</sup> Owing to the slow diffusion, Cr transport along grain boundaries in the alloy plays a more important role in austenitics for the overall scale formation than in case of ferritic steels. This has the result that the steam oxidation behavior can be strongly affected by the steel grain size or by ‘imperfections’ introduced by surface deformation (**Figure 51**). An interesting feature sometimes found in austenitic steels is that the depletion of Cr beneath a Cr-rich surface scale may differ from grain to grain (**Figure 52**).

Beneficial effects due to grain refining have been pursued as a proven method for improving oxidation resistance of austenitic steels. A typical example is TP347HFG, which has been applied widely in the grain-refined condition, and favorable service experience up to 50 000 h is available. Currently, the technique is being extended to other stainless steels such as SUPER304H. Sato *et al.*<sup>110</sup> have described substantial beneficial effects on oxidation resistance of austenitic stainless steels due to shot-blasting. This technique has been applied to conventional austenitic steels in Japan for more than 20 years. The effect of cold work pretreatment on the corrosion rate<sup>111</sup> is explained by the improved diffusivity of Cr in the defect structure, preferential oxidation, and formation of Cr-rich solid solution ( $\text{FeFe}_{2-x}\text{Cr}_x\text{O}_4$ ) spinel-type oxide scales.<sup>112</sup>

Another important feature is the role of Ni in the overall oxidation process. The thermodynamic driving force for oxidation of Ni in the steam environment is much smaller than that for Cr or Fe.

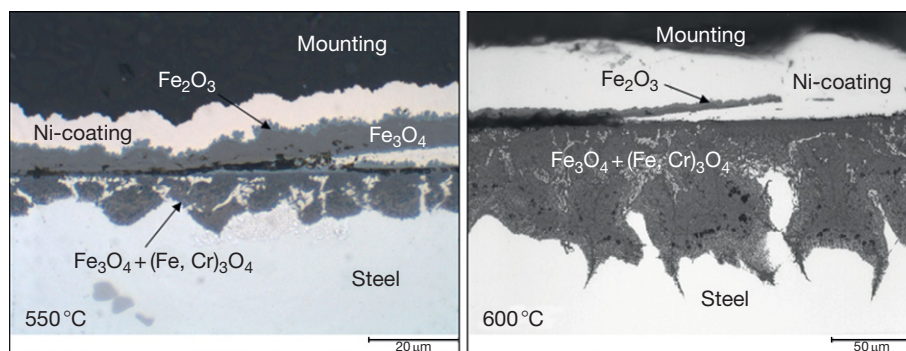


**Figure 50** Metallographic cross sections of 25Ni-15Cr-Ti after oxidation in Ar-50% H<sub>2</sub>O at 550 °C after 3000 h and 600 °C after 10 000 h.



Therefore, Ni is generally not present in the outer magnetite–hematite scale. As described for Co in Co-containing martensitic steels in [Section 1.17.4.4.5](#), Ni is frequently found in the inner scale where it sometimes prevails in metallic form ([Figure 53](#))

because in that area of the scale the oxygen partial pressure is apparently lower than the dissociation pressure of NiO or Ni/Fe/Cr spinel. The chromium and oxygen distribution clearly show that the steel initially formed a Cr-rich surface layer, remnants of

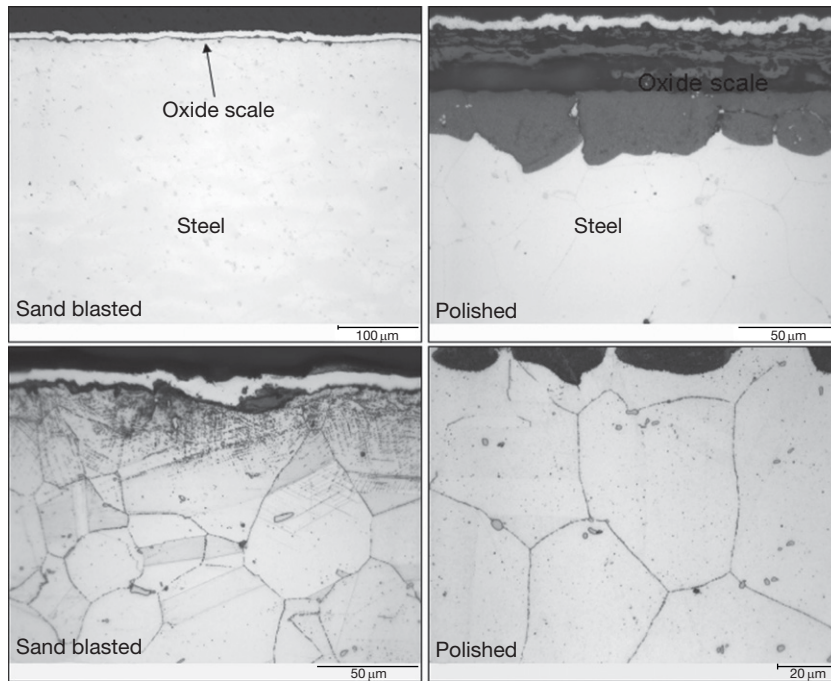


**Figure 51** Metallographic cross sections showing effect of surface treatment on oxide scale formation of austenitic steel TP347HFG during exposure in Ar–50% H<sub>2</sub>O for 1000 h at 625 °C. Adapted from Piron-Abellan, J.; Quadakkers, W. J. Unpublished results, Forschungszentrum Jülich, FRG, 2007.

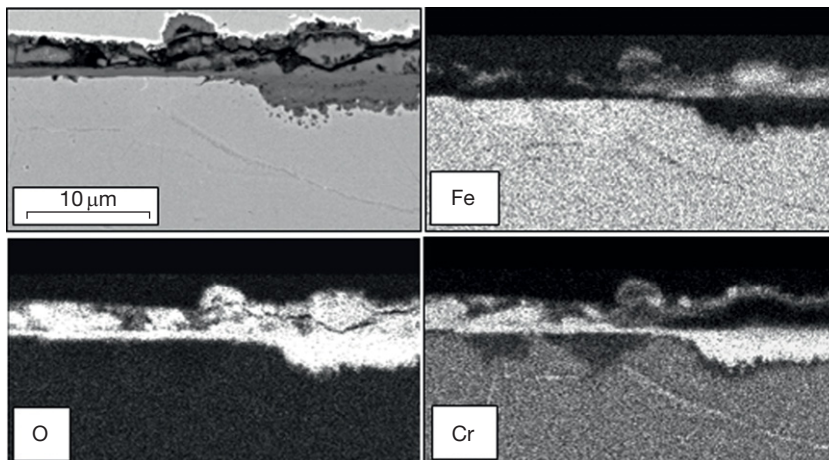


**Figure 52** Backscattered electron image and X-ray mappings of oxide scale on steel 310N (HR3C) after exposure at 600 °C for 10 000 h in Ar–50% H<sub>2</sub>O. Adapted from Piron-Abellan, J.; Quadakkers, W. J. Unpublished results, Forschungszentrum Jülich, FRG, 2007.

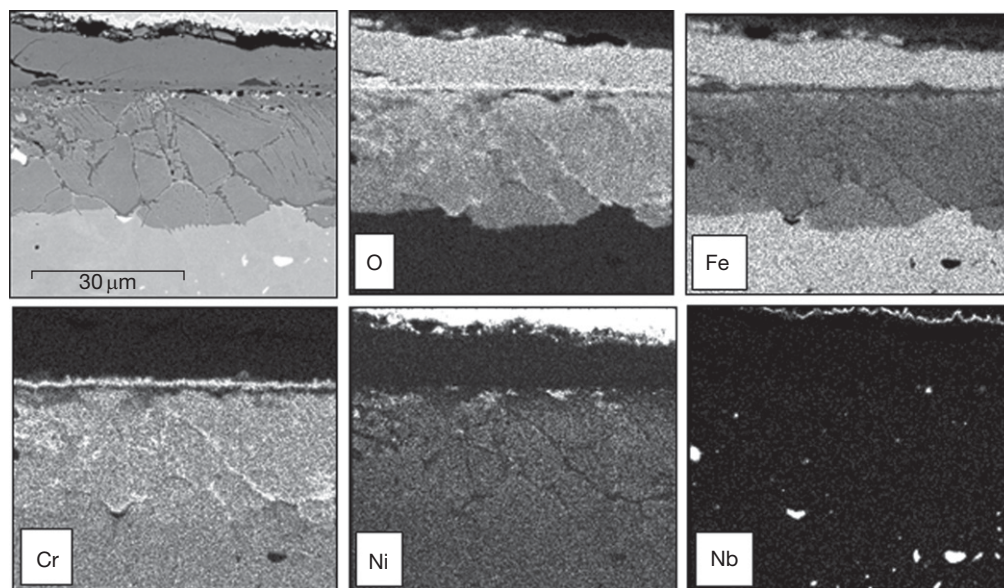


**Figure 53** Backscattered electron image and X-ray mappings of oxide scale on steel Super304H after exposure at 625 °C for 10 000 h in Ar–50% H<sub>2</sub>O. Adapted from Piron-Abellan, J.; Quadakkers, W. J. Unpublished results, Forschungszentrum Jülich, FRG, 2007.

which can be seen between the inner and outer layer. In the inner scale, Cr-rich oxide is present as continuous bands at the alloy grain boundaries and as internal oxides within the grains. Areas with Ni-rich alloy matrix prevail in the inner scale especially near the initial steel surface.

#### 1.17.4.4.7 Effect of pressure on steam oxidation

Data regarding the influence of pressure on steam oxidation behavior show a considerable amount of variation.<sup>113</sup> Otoguro *et al.*<sup>114</sup> measured the maximum scale thickness on four austenitic alloys (SUS347 HTB, 17/14CuMo, 20Cr/25Ni and 22Cr/35Ni) after exposure to steam for 500 h at 650 and 700 °C and pressures up to 35 MPa. On increasing the pressure at 650 °C, two of the alloys (SUS347 HTB, 17/14CuMo) investigated showed a decrease in scale growth rate of ~20%, one of the alloys (22Cr/35Ni) showed no influence of pressure on the scale thickness and one alloy (20Cr/25Ni) showed an increase in scale thickness by a factor of 4. The same trend in results was observed at 700 °C. Montgomery and Karlsson<sup>115</sup> have summarized the data on the influence of pressure on scale growth kinetics during exposure of martensitic steels to steam environments. The high-pressure data for HCM12 indicated a decrease in scale growth rate with increasing pressure, whereas the high-pressure data for P92

revealed either no effect of pressure or a change in the pressure effect with temperature depending on interpretation.

An apparent influence of steam pressure on the scale morphology is illustrated in [Figure 54](#) for a ferritic 12Cr–1Mo–V steel oxidized for 250 h at 650 °C. When exposed to Ar–50% H<sub>2</sub>O at ambient pressure, hematite was formed at the outer surface, whereas only magnetite was present after the high-pressure oxidation. However, the high-pressure exposure was carried out in an autoclave in stagnant gas, and the observed effect is probably due to a build-up of hydrogen in the sealed system. This leads to a decrease in oxygen partial pressure, thus inhibiting hematite formation, as explained in [Section 1.17.2.3](#). The build-up of H<sub>2</sub> may also have affected the high-pressure results of Yi *et al.*,<sup>100</sup> which were carried out in stagnant gas.

#### 1.17.4.5 Alumina-Forming Alloys and Coatings

##### 1.17.4.5.1 $\alpha$ -Alumina scales

There are conflicting reports about the behavior of alumina-forming alloys and coatings in water vapor-containing gases. In an extensive review of the effects of water vapor on the oxidation of metals,<sup>1</sup> it was concluded that water vapor had little effect on the oxidation behavior of alumina-forming alloys, although some evidence was cited that hydrogen defects were

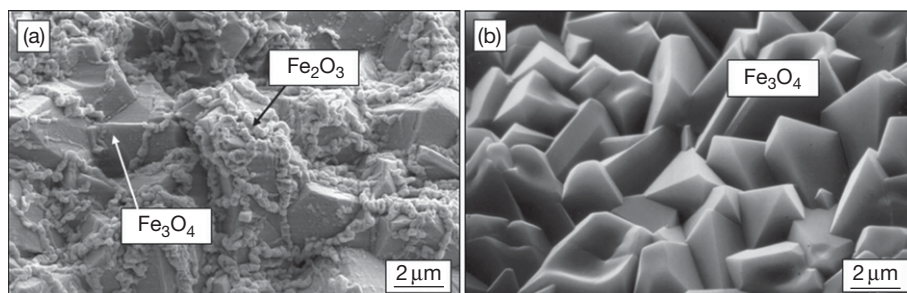


**Figure 54** Surface scale morphology of 12Cr–1Mo–V steel after 250 h exposure at 650 °C: (a) flowing Ar–50% H<sub>2</sub>O at 1 bar total pressure; (b) static steam at 300 bar total pressure. Adapted from Ehlers, J.; Quadackers, W. J. Report Forschungszentrum Jülich, Jül-3883, 2001.

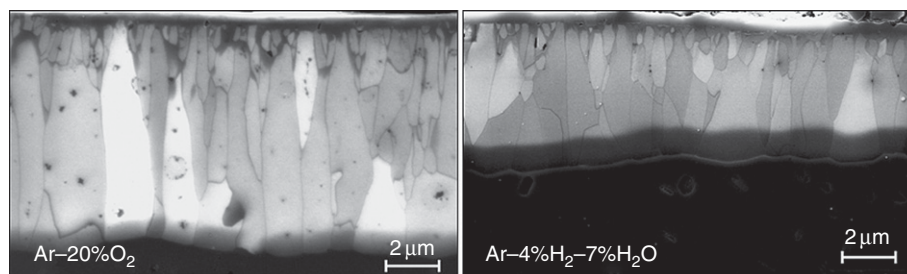


**Figure 55** In-lens SEM images of oxide scales formed on an FeCrAlY model alloy after 100 h isothermal oxidation in low- and high- $p_{\text{O}_2}$  gas at 1250 °C. Reproduced from Naumenko, D.; Quadackers, W. J. Unpublished results, Forschungszentrum Jülich, FRG, 2007.

present in Mg-doped alumina and that scale adhesion was reduced by water vapor. It should be noted that the mentioned studies mainly relate to wet air or wet oxygen rather than low- $p_{\text{O}_2}$  gases.

Kolb-Telieps *et al.*<sup>116</sup> showed the  $\alpha$ -alumina scale on an FeCrAlY alloy in the temperature range 1200–1300 °C to grow more slowly in Ar–H<sub>2</sub>–H<sub>2</sub>O mixtures than in Ar–O<sub>2</sub> or air (Figure 55). Kochubey *et al.*<sup>117</sup> found a  $p_{\text{O}_2}$  dependence of the sub-parabolic oxidation rates assuming oxygen grain boundary diffusion to be the dominating scale growth process whereby the oxide grains size increased in scale growth direction.<sup>118</sup> Also in a low- $p_{\text{O}_2}$  exhaust gas<sup>116</sup> and in H<sub>2</sub>/H<sub>2</sub>O-based shield gases,<sup>119</sup> the growth rate of  $\alpha$ -alumina on an Y-doped FeCrAl alloy was found to be smaller than that in air. In the low- $p_{\text{O}_2}$  exhaust gas, Naumenko *et al.*<sup>120</sup> found, however, the adherence of the scales to be worse than that of the scales formed in air or Ar–O<sub>2</sub>. Poorer scale adherence of alumina scales due to presence of water vapor therefore seems to be a feature which is independent of the  $p_{\text{O}_2}$  of the test gas. It was also observed by Janakiraman *et al.*<sup>121</sup> during oxidation of Ni-based superalloys and MCrAl coatings in wet air. Dieckmann<sup>35</sup> proposed hydrogen segregation at the oxide–metal interface to be a possible reason for

poor scale adherence. Kirchheim<sup>122–124</sup> actually observed hydrogen to segregate at metal–oxide interfaces during internal oxidation of Pd-based alloys. In recent studies, Smialek<sup>125</sup> attributed the poor alumina scale adherence in wet gases to hydrogen embrittlement of the scale–alloy interface.

Toscano *et al.*<sup>126</sup> studied the thermal cycling behavior of a thermal barrier coated (TBC) coated Ni-based alloy where the bond coat (BC) was a NiCoCrAlY alloy containing 10 mass% Al. The  $\alpha$ -alumina scale that formed during cyclic oxidation at the BC surface beneath the TBC appeared to grow faster in air than in Ar–H<sub>2</sub>–H<sub>2</sub>O. As a result, the life time of the TBC at 1100 °C, which was governed by spallation of the  $\alpha$ -alumina scale at the BC surface, was substantially longer in Ar–H<sub>2</sub>–H<sub>2</sub>O than in air.

This gas composition dependence was found only in case of optimized reactive element (RE) doped alloys or coatings which formed a scale that does not allow molecular gas transport. FeCrAl alloys that contained Zr (300 ppm) as a second RE in addition to Y developed in Ar–O<sub>2</sub> as well as in Ar–H<sub>2</sub>–H<sub>2</sub>O alumina scales, which exhibited substantial porosity. This was related to internal oxide particles of zirconia that became incorporated into the inwardly growing



$\alpha$ -alumina scale during long-term exposure.<sup>127</sup> Porosity appeared to develop at the interfaces between the alumina scale and the zirconia particles. Therefore the scale did not develop the ideal columnar, large-grained microstructure shown in Figure 55, and probably molecular transport participated in the scale growth process. This had the result that the  $p_{O_2}$  dependence of the oxidation rate was far less obvious than in case of the Zr-free alloy (Figure 56). At higher temperature (1300 °C) in low- $p_{O_2}$  gas, variations in oxide thickness over the specimen were found and locally the scale was even thicker than after Ar- $O_2$  oxidation (Figure 57). Indications were found that the Ar- $H_2$ - $H_2O$  exposure modified the internal oxidation of the Zr in a manner similar to that described for FeCr alloys in Section 1.17.4.3.2, and in this way the Ar- $H_2$ - $H_2O$  indirectly changed the alumina growth rate. The strong dependence of the  $\alpha$ -alumina growth rate on scale

morphology may be the reason for the fact that Ramnarayanan *et al.*<sup>128</sup> found in the oxidation of an FeCrAl-based oxide dispersion strengthened (ODS) alloy at 1000–1200 °C no clear effect of oxygen partial pressure on scale growth kinetics.

#### 1.17.4.5.2 Metastable alumina

Naumenko *et al.*<sup>129</sup> also studied the effect of gas composition on the oxidation of Y-doped FeCrAl alloys at lower temperatures. The authors found that the dependence of the oxidation behavior on gas composition in the temperature range 800–950 °C was completely different from that at temperatures well above 1000 °C. At the lower temperatures, the Ar- $H_2$ - $H_2O$  mixture tended to promote the formation of rapidly growing, metastable aluminum oxide phases (e.g.,  $\gamma$ ,  $\Theta$ ) compared to Ar- $O_2$

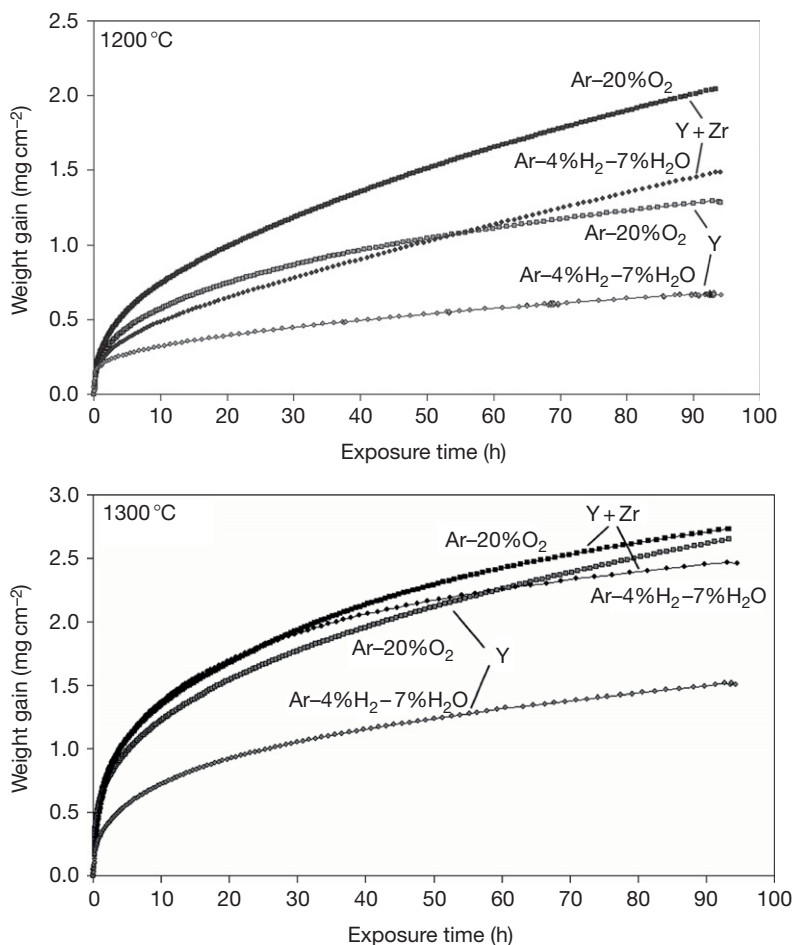


**Figure 56** Weight changes during isothermal oxidation of FeCrAlY alloy (Y content 500 ppm) without or with 300 ppm Zr in high and low- $p_{O_2}$  gas at 1200 and 1300 °C. Reproduced from Naumenko, D.; Quadackers, W. J. Unpublished results, Forschungszentrum Jülich, FRG, 2007.

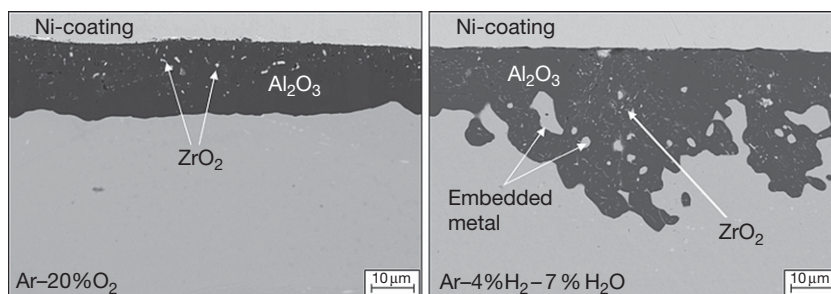


**Figure 57** SEM images of oxide scales on FeCrAlY + Zr alloy (compare [Figure 56](#)) after 100 h oxidation at 1300 °C in various atmospheres.<sup>117</sup> Reproduced from Kochubey, V. Ph.D. Thesis, Bochum University, 2005.

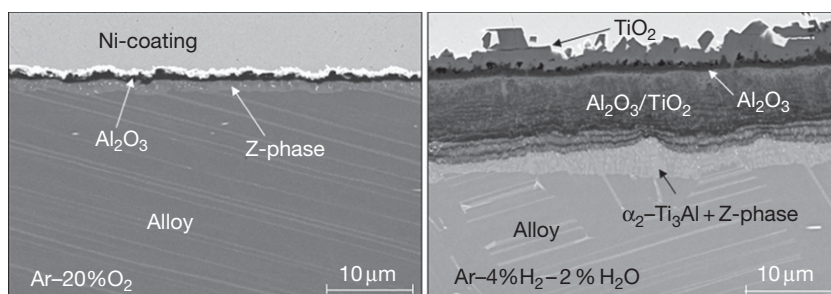


**Figure 58** Oxide scales on Ti-46.5Al-4(Cr, Nb, Ta, B) alloy after 96 h oxidation at 800 °C in Ar-20% O<sub>2</sub> and Ar-4% H<sub>2</sub>-2% H<sub>2</sub>O. Reproduced from Niewolak, L. Unpublished results, Forschungszentrum Jülich, FRG, 2003.

exposure. This effect was also found by Götlind *et al.*<sup>130</sup> when comparing the behavior of a commercial FeCrAl alloy in O<sub>2</sub> with that in O<sub>2</sub>-H<sub>2</sub>O, thereby indicating that presence of water vapor promotes metastable alumina growth, independent of the oxygen partial pressure in the gas. In a recent study, Lodziana *et al.*<sup>131</sup> demonstrated that strongly bonded hydroxide groups form on  $\Theta$ -Al<sub>2</sub>O<sub>3</sub> in the presence of water vapor. It was suggested that  $\gamma$ -Al<sub>2</sub>O<sub>3</sub>, when formed on FeCrAl alloys at 900 °C, can generate a strongly bonded surface hydroxide similar to  $\Theta$ -Al<sub>2</sub>O<sub>3</sub>. This is supported by the observation that  $\gamma$ -Al<sub>2</sub>O<sub>3</sub> powders can absorb significant amounts of water vapor (~3% by weight) at 900 °C.<sup>132</sup>

#### 1.17.4.5.3 Borderline alumina forming alloys

In earlier studies, Boggs<sup>133</sup> showed that the oxidation rate of Fe-5% Al was significantly increased at 800 °C when about 3% water vapor was present either alone or with oxygen.  $\gamma$ -Alumina formed initially in dry oxygen which later transformed to  $\alpha$ -alumina, with about 1% Fe-rich nodules. Hayashi *et al.*<sup>69</sup> found for an Fe-5% Al alloy at 800 °C a substantially lower growth rate in N<sub>2</sub>-20 vol.% O<sub>2</sub> than in N<sub>2</sub>-12.2 vol.% H<sub>2</sub>O. Malkow *et al.*<sup>43</sup> observed for an 18% Cr ferritic

steel containing 1.2% Al protective alumina scale formation after 1000 h exposure at 800 °C in air. However, in simulated SOFC anode gas (Ar-H<sub>2</sub>-H<sub>2</sub>O-(CO)), the alloy tended to form a Cr-rich surface oxide and internal oxidation of Al. The results for these borderline alloys might be related to enhanced internal oxidation of the protective scale-forming element Al due to hydrogen incorporation in the alloy, in a similar manner as described for FeCr alloys in [Section 1.17.4.3.2](#).

Another alloy system for which retarded protective alumina scale formation due to the presence of water vapor was described is the intermetallic phase  $\gamma$ -TiAl. On the basis of numerous studies,  $\gamma$ -TiAl can be considered as 'borderline alloy' because protective alumina scale formation in the temperature 700–900 °C has been shown to depend, for example, on the exact Al content, microstructure, surface treatment, alloying additions of, for example, Cr or Ag, and presence of microdopants such as halogens, etc.<sup>134–136</sup> Also, for this alloy system most of the studies in respect to the effect of water vapor relate to wet oxygen or wet air and only a few studies are available in low-*p*O<sub>2</sub> gases.

Niewolak<sup>137</sup> found protective alumina scale formation on a Ti-46.5Al-4(Cr, Nb, Ta, B) alloy after

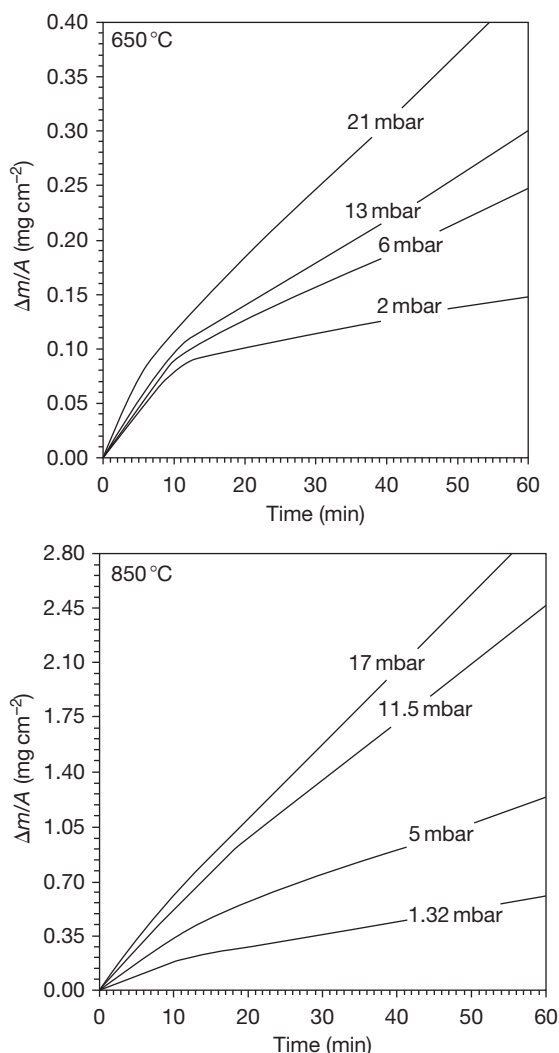


**Figure 59** Weight changes during isothermal oxidation of Ti in Ar-H<sub>2</sub>O showing influence of temperature and water vapor pressure. Reproduced from Wouters, Y.; Galerie, A.; Petit, J. P. *Solid State Ionics* **1997**, *104*, 89–96.

96 h of isothermal exposure at 800 °C in Ar–20% O<sub>2</sub> (Figure 58). However, when oxidized in Ar–4% H<sub>2</sub>–2% H<sub>2</sub>O, rapidly growing, mixed Al<sub>2</sub>O<sub>3</sub>/TiO<sub>2</sub> base scales were formed (Figure 58). As above, this effect might have been caused by an enhanced internal oxidation of Al due to hydrogen incorporation in the alloy. Considering the morphology of the mixed Al<sub>2</sub>O<sub>3</sub>/TiO<sub>2</sub> scales, also H<sub>2</sub>O/H<sub>2</sub> bridges (Section 1.17.3.3) in voids could principally explain this effect, although in this alloy system this mechanism seems unlikely. The oxygen partial pressure in a void at the scale–alloy interface will be extremely low, for instance, at 800 °C in the range 10<sup>–43</sup> atm. Therefore, the equilibrium water vapor partial pressure in that

void would only be 10<sup>–14</sup> atm. This would, using the Langmuir equation (Section 1.17.4.4.2), result in a maximum rate of oxygen transfer of 5 × 10<sup>–13</sup> g cm<sup>–2</sup> s<sup>–1</sup>, which is far too low to sustain the oxidation rates observed by Niewolak<sup>137</sup> in the wet gas.

Another possible explanation for the nonprotective scale formation in Ar–H<sub>2</sub>–H<sub>2</sub>O would be that water vapor increases the growth rate of the nonprotective oxide, here TiO<sub>2</sub>, thereby, according to Gesmundo *et al.* (Section 1.17.4.3.3), increasing the critical Al content required for protective scale formation. Such an explanation may be derived from the results of Wouters *et al.*,<sup>138</sup> who reviewed the oxidation behavior of Ti in H<sub>2</sub>O containing gas. For example, after 25 h oxidation of Ti at 850 °C, the mass gain was higher by about a factor of 3 in 20 mbar H<sub>2</sub>O compared with the rate in 20 mbar O<sub>2</sub>. In the temperature range 650–850 °C, the rate of oxidation was directly proportional to the water vapor content, and approximately parabolic kinetics were observed (Figure 59). Hydrogen was found in the metal after exposure and there was no change in the conductivity of the oxide, which remained n-type. Wouters *et al.*<sup>138</sup> proposed that the increased rate of oxidation results from incorporation of OH<sup>–</sup> in the titania lattice and the more rapid diffusion associated with the smaller ionic radius than the oxide ion.

Niewolak<sup>137</sup> investigated the oxidation kinetics of γ-TiAl alloys in a number of dry and wet, high- and low-*p*O<sub>2</sub> gases. He found, that the change from a protective alumina base scale to a poorly protective TiO<sub>2</sub>-rich oxide layer (Figure 58) also occurred when decreasing the oxygen content in dry Ar–O<sub>2</sub> gases from 20% to less than 5%. The results thus indicate that the gas composition dependence shown in Figure 59 is at least to certain extent related to the differences in oxygen partial pressures of the test gases. Several authors<sup>139–141</sup> have shown that the dominating point defects in TiO<sub>2</sub> are oxygen vacancies at high oxygen partial pressure, whereas titanium interstitials dominate at low *p*O<sub>2</sub>. At 800 °C the oxygen partial pressure at which this change from one dominating defect type to another occurs is ~10<sup>–3</sup> bar.<sup>142</sup> It has also been shown<sup>143–145</sup> that the solubility of Al in TiO<sub>2</sub> increases with decreasing oxygen partial pressure, a factor frequently illustrated to be of great importance for oxide scale formation on γ-TiAl-based alloys. Decreasing the oxygen partial pressure of the gas thus not only changes the growth rate of the ‘nonprotective’ oxide TiO<sub>2</sub> but also the competition between formation of the alumina scale and its dissolution in TiO<sub>2</sub>.

## References

- Douglass, D. L.; Kofstad, P.; Rahmel, A.; Wood, G. C. *Oxid. Met.* **1996**, 45(5/6), 529–620.
- Asteman, H.; Svensson, J. E.; Johansson, L. G.; Norell, M. *Oxid. Met.* **1999**, 52(1), 95–111.
- Thiele, M.; Quadakkers, W. J.; Schubert, F.; Nickel, H. Report Forschungszentrum Jülich, Jül-3712, 1999; ISSN 0944-2952.
- Ehlers, J.; Quadakkers, W. J. Report Forschungszentrum Jülich, Jül-3883, 2001; ISSN 0944-2952.
- Quadakkers, W. J.; Piron-Abellan, J.; Shemet, V.; Singheiser, L. *Mater. High Temp.* **2003**, 20(2), 115–127.
- Birks, N.; Meier, G. H.; Pettit, F. S. *Introduction to the High Temperature Oxidation of Metals*; Cambridge University Press: Cambridge, UK, 2006.
- Bale, C. W.; Pelton, A. D.; Thompson, W. J.; Eriksson, G.; Hack, K.; Chartrand, P.; Degterov, S.; Melancon, J.; Petersen, S. FactSage 5.3, Thermfact, 1976–2004.
- Davies, H.; Dinsdale, A. *Mater. High Temp.* **2005**, 22, 15–25.
- Tedmon, C. S. *J. Electrochem. Soc.* **1966**, 113(8), 766–768.
- Opila, E. J. *Mater. Sci. Forum* **2004**, 461–464, 765–774.
- Opila, E. J.; Jacobson, N. S.; Myers, D. L.; Copland, E. H. *JOM*, **2006**, 22–28.
- Stanislowski, M. Report Forschungszentrum Jülich, **54** (2006), ISBN 3-89336-432-2.
- Segerdahl, K.; Svensson, J. E.; Halvarsson, M.; Panas, I.; Johansson, L. G. *Mater. High Temp.* **2005**, 22, 69–78.
- Galerie, A.; Henry, S.; Wouters, Y.; Mermoux, M.; Petit, J. P.; Antoni, L. *Mater. High Temp.* **2005**, 21(4), 105–112.
- Michalik, M.; Hänsel, M.; Żurek, J.; Singheiser, L.; Quadakkers, W. J. *Mater. High Temp.* **2005**, 22(3/4), 213–221.
- Ehlers, J.; Young, D. J.; Smaardijk, E. J.; Tyagi, A. K.; Penkalla, H. J.; Singheiser, L.; Quadakkers, W. J. *Corros. Sci.* **2006**, 48, 3428–3454.
- Young, D. J.; Pint, B. A. *Oxid. Met.* **2006**, 66(3/4), 137–153.
- Milewska, A.; Hierro, M. P.; Trilleros, J. A.; Bolivar, F. J.; Pérez, F. J. *Mater. Sci. Forum* **2004**, 461–464, 321–326.
- Thiele, M.; Teichmann, H.; Schwarz, W.; Quadakkers, W. J. *VGB Kraftwerkstechnik* **1997**, 77(Heft 2), 135–140.
- Surman, P. L.; Castle, J. E. *Corros. Sci.* **1969**, 9, 771–777.
- Tomlinson, L.; Cory, N. J. *Corros. Sci.* **1989**, 29(8), 939–965.
- Żurek, J.; Michalik, M.; Schmitz, F.; Kern, T. U.; Singheiser, L.; Quadakkers, W. J. *Oxid. Met.* **2005**, 63(5/6), 401–422.
- Żurek, J.; Michalik, M.; Singheiser, L.; Quadakkers, W. J. *Mater. Sci. Forum* **2006**, 522–523, 155–162.
- Michalik, M.; Hänsel, M.; Quadakkers, W. J. Report Forschungszentrum Jülich, **67**(2007), ISBN 978-3-89336-486-2.
- Jacob, Y. P.; Haanappel, V. A. C.; Stroosnijder, M. F.; Buscail, H.; Fielitz, P.; Borchardt, G. *Corros. Sci.* **2002**, 44, 2027–2039.
- Raynaud, G. M.; Rapp, R. A. *Oxid. Met.* **1984**, 21(1/2), 89–102.
- Saunders, S. R. J.; Monteiro, M.; Rizzo, F. *Prog. Mater. Sci.* **2008**, 53(5), 775–837.
- Tallman, R. L.; Gulbransen, E. A. *J. Electrochem. Soc.* **1967**, 114(12), 1227–1230.
- Anghel, C.; Hörnlund, E.; Hultquist, G.; Limbäck, M. *Appl. Surf. Sci.* **2004**, 233, 392–401.
- Zheng, X. G.; Young, D. J. *Oxid. Met.* **1994**, 42(3/4), 163–190.
- Åkermark, T.; Hultquist, G. *Oxid. Met.* **1997**, 47(1), 117–137.
- Galerie, A.; Wouters, Y.; Caillet, M. *Mater. Sci. Forum* **2001**, 369–372, 231–238.
- Sun, C.; Berg, J. C. *Adv. Colloid Interf. Sci.* **2003**, 105(1–3), 151–175.
- Norby, T. *J. Phys. IV* **1993**, 3(C9), 99–106.
- Dieckmann, R. *Mater. High Temp.* **2005**, 22(172), 93–103.
- Rahmel, A.; Tobolski, J. *Corros. Sci.* **1965**, 5, 333–346.
- Young, D. J. *Mater. Sci. Forum* **2008**, 595–598, 1189–1197.
- Wood, G. C. *Oxid. Met.* **1970**, 2(1), 11–57.
- Quadakkers, W. J.; Norton, J. F.; Canetoli, S.; Schuster, K.; Gil, A. In 3rd International Conference on Microscopy of Oxidation; Newcomb, S. B., Little, J. A., Eds.; The Institute of Materials: Cambridge, 1996; pp 609–619.
- Hänsel, M.; Quadakkers, W. J.; Singheiser, L.; Nickel, H. Report Forschungszentrum Jülich, Jül-3583, 1998; ISSN 0944-2952.
- Hultquist, G.; Tventen, B.; Hörnlund, E. *Oxid. Met.* **2000**, 54(1/2), 1–10.
- Tveten, B.; Hultquist, G.; Norby, T. *Oxid. Met.* **1999**, 51(3), 221–233.
- Malkow, T.; Quadakkers, W. J.; Singheiser, L.; Nickel, H. Report Forschungszentrum Jülich, Jül-3589, 1998; ISSN 0944-2952.
- Henry, S.; Mouglin, J.; Wouters, Y.; Petit, J. P.; Galerie, A. *Mater. High Temp.* **2000**, 17(2), 231–235.
- Hänsel, M.; Quadakkers, W. J.; Young, D. J. *Oxid. Met.* **2003**, 59(3/4), 285–301.
- Essuman, E.; Meier, G.; Żurek, J.; Hänsel, M.; Quadakkers, W. J. *Oxid. Met.* **2008**, 69(3), 143–162.
- Essuman, E.; Meier, G. H.; Żurek, J.; Hänsel, M.; Norby, T.; Singheiser, L.; Quadakkers, W. J. *Corros. Sci.* **2008**, 50(6), 1753–1760.
- Wood, G. C.; Wright, I. G.; Hodgkiess, T.; Whittle, D. P. *Werkstoffe Korrosion*, **1970**, 21(11), 900–910.
- Kofstad, P. *High Temperature Corrosion*; Elsevier Applied Science: London, 1988.
- Przybylski, K.; Yurek, G. J. *J. Electrochem. Soc.* **1988**, 135(2), 517–523.
- Żurek, J.; Young, D. J.; Essuman, E.; Hänsel, M.; Penkalla, H. J.; Niewolak, L.; Quadakkers, W. J. *Mater. Sci. Eng. A* **2008**, 477, 259–270.
- Bamba, G.; Wouters, Y.; Galerie, A.; Borchardt, G.; Shimada, S.; Heintz, O.; Chevalier, S. *Scr. Mater.* **2007**, 57(8), 671–674.
- Whittle, D. P.; Stringer, J. *Philos. Trans. R. Soc. A* **1980**, 295, 309–329.
- Pint, B. A. In *John Stringer Symposium on High Temperature Corrosion*; Tortorelli, P. F., Wright, I. G., Eds.; ASM International: USA, 2003; pp 1–10.
- England, D. M.; Virkar, A. V. *J. Electrochem. Soc.* **1999**, 146(9), 3196–3202.
- England, D. M.; Virkar, A. V. *J. Electrochem. Soc.* **2001**, 148(4), A330–A338.
- Hussain, N.; Qureshi, A. H.; Shahid, K. A.; Chughtai, N. A.; Khalid, F. A. *Oxid. Met.* **2004**, 61(5), 355–364.
- Hussain, N.; Shahid, K. A.; Khan, I. H.; Rahman, S. *Oxid. Met.* **1994**, 41(3), 251–269.

59. Piron-Abellan, J.; Quadakkers, W. J. Report Forschungszentrum Jülich, Jül-4170, 2005; ISSN 0944-2952.
60. Huczowski, P.; Quadakkers, W. J. Report Forschungszentrum Jülich, 65, 2005; ISBN 978-3-89336-484-8.
61. Huczowski, P.; Ertl, S.; Pirón-Abellán, J.; Christiansen, N.; Höfler, T.; Shemet, V.; Singheiser, L.; Quadakkers, W. J. *Mater. High Temp.* **2006**, *22*, 253–262.
62. Żurek, J.; Quadakkers, W. J. Unpublished results, Forschungszentrum Jülich, FRG, 2007.
63. Naoumidis, A.; Schulze, H. A.; Jungen, W.; Lersch, P. *J. Eur. Ceram. Soc.* **1991**, *7*, 55–63.
64. Krupp, U.; Christ, H. J. *Oxid. Met.* **1999**, *52*(3), 277–298.
65. Hammer, J.; Laney, S.; Jackson, R.; Coyne, K.; Pettit, F.; Meier, G. *Oxid. Met.* **2007**, *67*(1), 1–38.
66. Schütze, M.; Rensch, D.; Schorr, M. *Mater. High Temp.* **2005**, *22*(1/2), 113–120.
67. Mikkelsen, L.; Linderroth, S. *Mater. Sci. Eng. A* **2003**, *361*(1–2), 198–212.
68. Fujii, C. T.; Meussner, R. A. *J. Electrochem. Soc.* **1964**, *111*(11), 1215–1221.
69. Hayashi, S.; Narita, T. *Oxid. Met.* **2001**, *56*(3), 251–270.
70. Essuman, E.; Meier, G. H.; Żurek, J.; Hänsel, M.; Singheiser, L.; Quadakkers, W. J. *Scr. Mater.* **2007**, *57*(9), 845–848.
71. Ani, M. H. B.; Ueda, M.; Kawamura, K.; Maruyama, T. In Proceedings of the European Corrosion Congress, Paper 183, Eurocorr 2007, 2007.
72. Yang, Z.; Xia, G.; Singh, P.; Stevenson, J. W. *Solid State Ionics* **2005**, *176*, 1495–1503.
73. Eichenauer, W.; Künzig, H.; Pebler, A. *Z. Metallk.* **1958**, *49*, 220.
74. Swisher, J. H.; Turkdogan, E. T. *Trans. Metall. Soc. AIME* **1967**, *239*, 426–431.
75. Fromm, E.; Gebhardt, E. *Gase und Kohlenstoff in Metallen*; Springer: Berlin, 1976.
76. Wagner, C. J. *Electrochem. Soc.* **1952**, *99*(10), 369–380.
77. Rapp, R. A. *Acta Metall.* **1961**, *9*(8), 730–741.
78. Gesmundo, F.; Viani, F. *Oxid. Met.* **1986**, *25*(5), 269–282.
79. Wagner, C. Z. *Elektrochem.* **1959**, *63*, 772.
80. Essuman, E.; Meier, G. H.; Żurek, J.; Hänsel, M.; Singheiser, L.; Quadakkers, W. J. *Mater. Sci. Forum* **2008**, *595–598*, 699–706.
81. Park, E.; Hüning, B.; Grabke, H. J.; Spiegel, M. *Defect Diffusion Forum* **2005**, *237–240*, 928–933.
82. Ågren, J. *Scr. Metall.* **1986**, *20*(11), 1507–1510.
83. Ikeda, Y.; Nii, K. *Trans. Nat. Res. Inst. Met.* **1984**, *26*(1), 52–62.
84. Ueda, M.; Nanko, M.; Kawamura, K.; Maruyama, T. *Mater. High Temp.* **2003**, *20*(2), 109.
85. Hayashi, S.; Narita, T. *Oxid. Met.* **2002**, *58*(3), 319–330.
86. Griess, J. C.; De Van, J. H. *Mater. Perform.* **1980**, *19*(6), 46–52.
87. Cory, N. J.; Herrington, T. M. *Oxid. Met.* **1987**, *28*(5), 237–258.
88. Viswanathan, R.; Sarver, J.; Tanzosh, J. M. *J. Mater. Eng. Perform.* **2006**, *15*(3), 255–274.
89. Ennis, P. J.; Quadakkers, W. J. *VGB PowerTech* **2001**, *8*, 87–90.
90. Mayer, P.; Manolescu, A. V. In *High Temperature Corrosion*; Rapp, R. A., Ed.; National Association of Corrosion Engineers, 1983; pp 368–379.
91. Quadakkers, W. J.; Ennis, P. J.; Żurek, J.; Michalik, M. *Mater. High Temp.* **2004**, *22*(1/2), 37–47.
92. Fujii, C. T.; Meussner, R. A. *J. Electrochem. Soc.* **1963**, *110*(12), 1195–1204.
93. Langmuir, I. *Phys. Rev.* **1913**, *5*(2), 329–342.
94. Nakagawa, K.; Matsunaga, Y.; Yanagisawa, T. *Mater. High Temp.* **2001**, *18*(1), 51–56.
95. Armitt, I.; Holmes, D. P. The spalling of steam grown oxide from superheater and reheater tube steels, Technical Planning Study 76-655, Final Report, EPRI, USA, 1978.
96. Ehlers, R. J.; Ennis, P. J.; Singheiser, L.; Quadakkers, W. J.; Link, T. In EFC Workshop 2001; Schütze, M., Quadakkers, W. J., Nicholls, J. R., Eds.; The European Federation of Corrosion Publications, 2001; Vol 34, Paper 12, pp 178–193.
97. Żurek, J.; Wessel, E.; Niewolak, L.; Schmitz, F.; Kern, T. U.; Singheiser, L.; Quadakkers, W. J. *Corros. Sci.* **2004**, *46*(9), 2301–2317.
98. Nishimura, N.; Komai, N.; Hirayama, Y.; Masuyama, F. *Mater. High Temp.* **2005**, *22*(1/2), 3–10.
99. Watanabe, Y.; Yi, Y. S.; Kondo, T.; Inui, K.; Kishinami, T.; Kimura, H.; Sato, M. In Proceedings of the 9th International Conference on Pressure Vessel Technology, ICPVT-9, Sydney, Australia; Price, J., Ed.; **2000**; pp 545–552.
100. Yi, Y. S.; Watanabe, Y.; Kondo, T.; Kimura, H.; Sato, M. *J. Pressure Vessel Technol.* **2001**, *123*, 391–397.
101. Husemann, R. U. *VGB Kraftwerkstechnik* **1999**, *10*, 146–149.
102. Ehlers, J.; Smaardijk, E. J.; Penkalla, H. J.; Tyagi, A. K.; Singheiser, L.; Quadakkers, W. J. In Proceedings of International Corrosion Congress, Cape Town, South Africa, 1999; Vol. 3, Paper 336.
103. Haarmann, K.; Vaillant, J. C.; Bendick, W.; Arbab, A. *The T91/P91 Book*; Vallourec & Mannesmann Tubes, 1999.
104. Piehl, C.; Tökei, Z.; Grabke, H. J. *Defect Diffusion Forum* **2001**, *194–199*, 1689–1694.
105. Nieto-Hierro, L.; Quadakkers, W. J. Unpublished results, Forschungszentrum Jülich, FRG, 2006.
106. Khanna, A. S.; Rodriguez, P.; Gnanamoorthy, J. B. *Oxid. Met.* **1986**, *26*(3), 171–200.
107. Ishitsuka, T.; Inoue, Y.; Ogawa, H. *Oxid. Met.* **2004**, *61*(1), 125–142.
108. Muramatsu, K. In *Development of Ultrasupercritical Plant in Japan, Advanced Heat Resistant Steel for Power Generation*; Viswanathan, R., Nutting, J. W., Eds.; IOM Communications: London, UK, 1999; Book 708, pp 543–559.
109. Peraldi, R.; Pint, B. A. *Oxid. Met.* **2004**, *61*(5), 463–483.
110. Sato, T.; Fukuda, Y.; Mitsuhara, K.; Sakai, K. In *Advances in Materials Technology for Fossil Power Plants*; Viswanathan, R., Gandy, D., Coleman, K., Eds.; ASM International, 2005.
111. Piron-Abellan, J.; Quadakkers, W. J. Unpublished results, Forschungszentrum Jülich, FRG, 2007.
112. Leistikow, S.; Wolf, I.; Grabke, H. J. *Werkstoffe Korrosion* **1987**, *38*, 556–562.
113. Osgerby, S.; Quadakkers, W. J. *Mater. High Temp.* **2005**, *22*(1/2), 27–33.
114. Otoguro, Y.; Sakakibara, M.; Saito, T.; Ito, H.; Inoue, Y. *Trans. Iron Steel Inst. Jpn.* **1988**, *28*, 761–768.
115. Montgomery, M.; Karlsson, A. *VGB Kraftwerkstechnik* **1995**, *75*(3), 258–264.
116. Kolb-Telieps, A.; Strehl, G.; Naumenko, D.; Quadakkers, W. J.; Newton, R. *High Temperature Corrosion of FeCrAlY/Aluchrom YHf in environments relevant to exhaust gas systems, Materials Aspects in Automotive Catalytic Converters*; Wiley-VCH: Weinheim, Germany, 2001.
117. Kochubey, V. PhD thesis, Bochum University, 2005.

118. Naumenko, D.; Gleeson, B.; Wessel, E.; Singheiser, L.; Quadakkers, W. J. *Metall. Mater. Trans.* **2007**, *38A*, 2974–2983.
119. Bennett, M. J.; Newton, R.; Nicholls, J. R. *Mater. High Temp.* **2003**, *20*(3), 347–356.
120. Naumenko, D.; Quadakkers, W. J. Unpublished results, Forschungszentrum Jülich, FRG, 2007.
121. Janakiraman, R.; Meier, G. H.; Pettit, F. S. *Metall. Mater. Trans. A* **1999**, *30A*, 2905–2913.
122. Kirchheim, R. *Acta Metall.* **1981**, *29*(5), 835–843.
123. Kirchheim, R. *Acta Metall.* **1981**, *29*(5), 845–853.
124. Kirchheim, R.; Hirth, J. P. *Scr. Metall.* **1982**, *16*(4), 475–478.
125. Smialek, J. L. *JOM* **2006**, 29–35.
126. Toscano, J.; Naumenko, D.; Gil, A.; Singheiser, L.; Quadakkers, W. J. *Mater. Corros.* **2008**, *59*(6), 501–507.
127. Wessel, E.; Kochubey, V.; Naumenko, D.; Niewolak, L.; Singheiser, L.; Quadakkers, W. J. *Scr. Mater.* **2004**, *51*(10), 987–992.
128. Ramanarayanan, T. A.; Ayer, R.; Petkovic-Luton, R.; Leta, D. P. *Oxid. Met.* **1988**, *29*(5), 445–472.
129. Naumenko, D.; Quadakkers, W. J.; Galerie, A.; Wouters, Y.; Jourdain, S. *Mater. High Temp.* **2003**, *20*(3), 287–293.
130. Götlind, H.; Liu, F.; Svensson, J. E.; Halvarsson, M.; Johansson, L. G. *Oxid. Met.* **2007**, *67*(5), 251–266.
131. Lodziana, Z.; Topsoe, N. Y.; Norskov, J. K. *Nat. Mater.* **2004**, *3*, 289–293.
132. Götlind, H. Thesis for the degree of doctor of engineering. Chalmers University of Technology: Göteborg, Sweden, 2614, 2007, ISBN 978-91-7291-933-4.
133. Boggs, W. E. *J. Electrochem. Soc.* **1971**, *118*(6), 906–913.
134. Niewolak, L.; Shemet, V.; Thomas, C.; Lersch, P.; Singheiser, L.; Quadakkers, W. J. *Intermetallics* **2004**, *12*(12), 1387–1396.
135. Donchev, A.; Richter, E.; Schütze, M.; Yankov, R. *Intermetallics* **2006**, *14*(10–11), 1168–1174.
136. Rakowski, J. M.; Meier, G. H.; Pettit, F. S.; Dettenwanger, F.; Schumann, E.; Rühle, M. *Scr. Mater.* **1996**, *35*(12), 1417–1422.
137. Niewolak, L. Unpublished results, Forschungszentrum Jülich, FRG, 2003.
138. Wouters, Y.; Galerie, A.; Petit, J. P. *Solid State Ionics* **1997**, *104*, 89–96.
139. Bak, T.; Nowotny, J.; Rekas, M.; Sorrell, C. C. *J. Phys. Chem. Solids* **2003**, *64*(7), 1043–1056.
140. Nowotny, J.; Bak, T.; Nowotny, M. K.; Sheppard, L. R. *Int. J. Hydrogen Energy* **2007**, *32*(14), 2630–2643.
141. Kofstad, P. *Nonstoichiometry, Diffusion and Electrical Conductivity in Binary Metal Oxides*; Wiley Interscience: New York, 1972.
142. Nowotny, J.; Radecka, M.; Rekas, M.; Sugihara, S.; Vance, E. R.; Weppner, W. *Ceram. Int.* **1998**, *24*(8), 571–577.
143. Rahmel, A.; Schütze, M.; Quadakkers, W. J. *Mater. Corros.* **1995**, *46*(5), 271–285.
144. Rahmel, A.; Spencer, P. J. *Oxid. Met.* **1991**, *35*(1), 53–68.
145. Becker, S.; Rahmel, A.; Schorr, M.; Schütze, M. *Oxid. Met.* **1992**, *38*(5), 425–464.



## 1.26 High Temperature Corrosion of Ceramics and Refractory Materials

**K. G. Nickel**

Applied Mineralogy, Institute for Geosciences, University Tübingen, Wilhelmstr. 56, D-72074 Tübingen, Germany

**P. Quirnbach and J. Pötschke**

Deutsches Institut für Feuerfest und Keramik GmbH, An der Elisabethenkirche 27, D-53113 Bonn, Germany

© 2010 Elsevier B.V. All rights reserved.

---

<b>1.26.1</b>	<b>Introduction</b>	670
<b>1.26.2</b>	<b>Differences between Metals and Ceramics</b>	670
<b>1.26.3</b>	<b>Corrosion Modes and Kinetics</b>	671
<b>1.26.4</b>	<b>Corrosion Measurement</b>	673
<b>1.26.5</b>	<b>Oxides</b>	674
1.26.5.1	Alumina	674
1.26.5.2	Zirconia	674
1.26.5.3	Cordierite	674
<b>1.26.6</b>	<b>Carbides</b>	675
1.26.6.1	Boron Carbide	675
1.26.6.2	Silicon Carbide	675
<b>1.26.7</b>	<b>Nitrides</b>	678
1.26.7.1	Silicon Nitride	678
1.26.7.2	Boron Nitride	679
1.26.7.3	Silico-Carbonitrides	680
<b>1.26.8</b>	<b>Titanium Compounds</b>	680
<b>1.26.9</b>	<b>Ultrahigh Temperature Ceramics</b>	680
<b>1.26.10</b>	<b>Refractories</b>	681
1.26.10.1	Chemical Dissolution	681
1.26.10.2	Erosion	681
1.26.10.3	Mechanical Wear	681
<b>1.26.11</b>	<b>Chemical Dissolution</b>	681
1.26.11.1	Diffusion/Blast Furnace	681
1.26.11.2	Marangoni Convection/SEN	682
1.26.11.3	Oxidation/Ladle	683
<b>1.26.12</b>	<b>Erosion</b>	684
1.26.12.1	Blast Wear/Pipes	684
1.26.12.2	Flowing Melts/Converter	684
<b>1.26.13</b>	<b>Mechanical Wear</b>	685
1.26.13.1	Thermal Shock Resistance/Ladle	685
1.26.13.2	Carbon Bursting/Blast Furnace	685
1.26.13.3	Destruction due to Impact/Converter	686
<b>1.26.14</b>	<b>Infiltration by Steel and Slag</b>	686
1.26.14.1	Basic Equations	686
<b>1.26.15</b>	<b>Examples</b>	687
1.26.15.1	Slag/MgO	687
1.26.15.2	Steel/MgO	687
1.26.15.3	Steel/MgO–C	688
<b>1.26.16</b>	<b>Concluding Remarks</b>	688
<b>References</b>		689

---

## Glossary

**Converter** The containment for the industrial conversion of ore to metal and its purification by slag formation.

**Ellipsometry** Measurement of the change of light polarization upon reflection or transmission. In corrosion, it is usually done in reflection and used to infer the thickness of a very thin layer (down to the angstrom-level) of reaction product.

**Flue gas** Exhaust gases from a fireplace, oven, furnace, or other production process.

**Hot corrosion** Historically evolved name for the attack of a material by or involving salt melts. A typical representative is a  $\text{Na}_2\text{SO}_4$  melt.

**Hydrothermal** Conditions which involve a water fluid at elevated temperatures. Commonly used for conditions above  $100^\circ\text{C}$  at pressures above the atmospheric pressure.

**Ladle** Container for transport and pouring of (metal) melts.

**Rate constant** Constant which relates the quantitative progress of a process, example, a growth of a layer on an infinite plate, to time.

**Slag** By-product of ore smelting or refining. It usually consists mainly of oxides, with or without other constituents like sulfides, phosphates, and metals.

**Steady-state conditions** Conditions in which a system has a constant behavior with time. In corrosion, this often implies that external conditions such as the atmospheric partial pressure of the attacking medium are kept constant and a dynamic equilibrium is established, where two or more reversible processes occur at one rate.

**Thermogravimetry** Continuous instrumental determination of mass changes of a sample as a function of time, with or without regular changes in temperature, pressure, or gas composition during the observed time.

**Wetting angle** Contact angle at which the liquid-vapor interface of a fluid and the solid-vapor interface of a contacting solid meet. Describes the tendency of the fluid to form a film (perfectly at  $0^\circ\text{C}$ ) or a ball resting on the surface (perfectly above  $150^\circ\text{C}$ ).

## Abbreviations

**SEN** Submerged entry nozzle

**SSiC** Pressureless sintered silicon carbide

## Symbols

**A** Surface area ( $\text{m}^2$ )

**a** Thermal diffusivity ( $\text{m}^2 \text{s}^{-1}$ )

**C<sub>0</sub>** Concentration of carbon in liquid iron (wt %)

**C<sub>S</sub>** Saturation concentration of carbon in liquid iron (wt %)

**D<sub>i</sub>** Diffusion coefficient of component *i* ( $\text{m}^2 \text{s}^{-1}$ )

**D<sub>p</sub>** Pore-diffusion coefficient ( $\text{m}^2 \text{s}^{-1}$ )

**E** Modulus of elasticity (GPa)

**G<sub>F</sub>** Crack energy ( $\text{J m}^{-2}$ )

**ΔG<sup>0</sup>** Free enthalpy in the standard state ( $\text{J mol}^{-1}$ )

**g** Acceleration of gravity ( $\text{m s}^{-2}$ )

**h** Height (m)

**h<sub>l</sub>** Diameter of the convection loop (m)

**h<sub>g</sub>** Characteristic length of the corrosion groove (m)

**K** Equilibrium constant

**k<sub>linear</sub>** Linear rate constant ( $\text{m s}^{-1}$  or  $\text{kg m}^{-2} \text{s}^{-1}$ )

**k<sub>log</sub>** Logarithmic rate constant

**k<sub>p</sub>** Parabolic rate constant ( $\text{m}^2 \text{s}^{-1}$  or  $\text{kg}^2 \text{m}^{-4} \text{s}^{-1}$ )

**l** Length (m)

**P<sub>i</sub>** Partial pressure of species *i*

**R** Universal gas constant ( $8314 \text{ J mol}^{-1} \text{ K}^{-1}$ )

**T** Temperature (K)

**t** Time (s)

**u** Stoichiometry factor

**V<sub>l</sub>** Molar volume of phase *l* ( $\text{m}^3 \text{mol}^{-1}$ )

**v** Flow velocity ( $\text{m s}^{-1}$ )

**Δw** Mass change ( $\text{kg m}^{-2}$ )

**x** Mass change per unit area ( $\text{kg m}^{-2}$ ) or scale thickness (m)

**α** Thermal expansion coefficient ( $\text{K}^{-1}$ )

**β** Mass transfer coefficients ( $\text{m s}^{-1}$ )

**γ** Labyrinth factor, tortuosity

**δ** Boundary layer of diffusion (m)

**δ<sub>Pr</sub>** Prandtl's boundary layer thickness (m)

**δ<sub>N</sub>** Nernst's diffusion-boundary-layer thickness (m)

**p<sub>c</sub>** Open porosity of the decarburized zone (%)

**ε<sub>c</sub>** Critical elongation

**ρ** Density ( $\text{kg m}^{-3}$ )

**η** Dynamic viscosity ( $\text{kg m s}^{-1}$ )

**μ** Poisson ratio

- $\nu$  Kinematic viscosity ( $\text{m}^2 \text{s}^{-1}$ )
- $\sigma$  Interfacial tension ( $\text{N m}^{-1}$ )
- $\sigma_c$  Critical stress (MPa)
- $\theta$  Wetting angle ( $^\circ$ )
- $\tau$  Correction time (s)

### 1.26.1 Introduction

Ceramics are nonmetallic–inorganic materials, which are usually made by forming from a mass or a powder and firing at high temperature, upon which the material becomes consolidated and obtains its properties. This implies that ceramics have thermal and chemical stability at the firing temperature in the firing environment. ‘High temperature’ is a very blurred term, but most people would accept temperatures above  $800^\circ\text{C}$  as high temperature. An exception is the behavior in hydrothermal conditions. Hot, pressurized water is very reactive and many compounds have a high level of solubility in it. For this reason, we will describe the hydrothermal behavior of ceramics at lower temperatures.

A classical division of ceramics is silicate, oxide, and nonoxide ceramics. Textbooks and handbooks on their properties and manufacture have been published<sup>1–4</sup> and contain chapters on their corrosion resistance.

Metals and intermetallics do survive at high temperatures in many environments only because they form phases, commonly oxides, which protect them from further attack. In this respect, many chapters in this book deal with ceramics. In order not to repeat too many issues, readers are referred to appropriate chapters, in particular the ones on **Oxidation of Metals and Alloys** and **High Temperature Coatings: Protection and Breakdown**. In this chapter, we will deal with bulk materials.

There are many applications of ceramics at high temperatures: one deals with materials that contain and protect from melts in the metal or glass industry, another is the function to transport or contain heat in predominantly gaseous environments. For some tasks, structural loads under adverse conditions have to be met, whereas for others, several forms of attack may occur, e.g., waste incineration. A rather new application is the use of SiC as an electronic material, commonly in the form of single crystal wafers. Although the use is at low or moderate temperatures, a high temperature treatment to produce insulating silica is a common step in the production of these new functional materials.

A refractory material is firstly a ceramic that has not reached the softening point, at which a special pyramid (Seeger-cone SK17) would bend when heated to  $1500^\circ\text{C}$ . However, the material has to fulfill other criteria at high temperatures to be called refractory, namely, it has to keep its shape, survive thermal fluctuations, and withstand attack by slags or melts for a sufficiently long time.<sup>5,6</sup> Refractories are in most cases porous composites, making the behavior complex.

There is an overlap in materials chemistry between refractories and technical ceramics. For example, alumina and silicon carbide are manufactured both as refractories and as dense, advanced engineering ceramics. For this reason, refractories are dealt with in the form of typical examples from the steel- and iron-making industries. Other applications have similar principal problems and, from a chemical point of view, are contained within the ceramics section.

### 1.26.2 Differences between Metals and Ceramics

In the corrosion of metals, we usually find oxidation of the metal to form some phase, which is then lost to the environment by spallation, dissolution, or some other mechanisms, resulting in mass loss or the formation of a surface layer, which can have protective characteristics. Basic cases like the oxidation of iron are well known<sup>7</sup> and may be described by simple laws such as a parabolic weight gain in certain regimes.

The complexities of scale evolution often necessitate a more complex modeling of the transport in oxide scales, and finite difference calculations are used to predict the process progression.<sup>8</sup>

The importance of the oxide development in silicon-based semiconductors has led to the development of sophisticated detailed models for high temperature oxidation, whether related to initial periods<sup>9</sup> or general laws.<sup>10</sup>

Ceramics are often oxides, carbides, or nitrides. In general, nonmetals have a higher electronegativity than metals. The bonding is mostly a mixed ionic–covalent one, but formally the electrons have to be assigned to the nonmetal. High temperature oxidation of these carbides and nitrides thus oxidizes the carbon or the nitrogen and leaves the metal or semiconductor in its oxidation state. Also, in contrast to metals, where often the metal is transported as an ion to the surface to become oxidized, in ceramics we usually have the transport of the corroding agent to

the scale–substrate interface where reaction occurs. The oxidation process is therefore better compared with semiconductors rather than with ordinary metals.

Oxide ceramics are stable in environments having sufficient oxygen; their corrosion is based on reactions that form other phases, becoming dissolved or evaporated.

### 1.26.3 Corrosion Modes and Kinetics

To understand the principles, we first assume the material to be single phased, isotropic, dense, and to have perfect surfaces. Just like metals, ceramics can show both active and passive corrosion behaviors. Unless retarding phases are formed, steady-state processes in active corrosion have simple and constant mass loss rates for a given set of physical boundary conditions. It does not matter whether the chemical reaction rate, the dissolution kinetics, or the diffusion from or into the corrosive medium is rate determining. The constancy of boundary conditions such as constant gradients in the attacking agent necessitates linear kinetics following eqn. [1], in which  $x$  denotes either the thickness of the layer lost or the mass of material loss per unit area,  $t$  the time, and  $k_{\text{linear}}$  is the linear rate constant:

$$x(\text{m or kg m}^{-2}) = k_{\text{linear}}(\text{ms}^{-1} \text{ or kg m}^{-2} \text{ s}^{-1}) \cdot t(\text{s}) \quad [1]$$

The time to reach those steady-state conditions is not covered by the model, so initial periods with differing rates are possible. In the initial period, transport-related problems are less likely to dominate, so formation or removal of surface adlayers may lead to incubation periods. Alternatively, the buildup of a gradient may be fast in the beginning and turn into a steady-state rate later.

The ease of this formulation hides the problems associated with it. Everything rests on the constancy of external conditions, and therefore the measured rates depend on a large number of boundary conditions. Laminar or turbulent flows of the attacking medium, convection or still conditions, and flow velocity of the attacking gas or fluid are only a few obvious parameters.

For polyphasic materials, the resistance against attack is usually different for the different phases. Here, eqn. [1] is only valid for each phase individually and only as long as the processes do not influence each other. The example of a preferential grain boundary phase attack is easy to understand. Here,

boundary phase removal concurrent with a more or less inert matrix material gives us the picture of increasing pathway lengths for the attacking agent with time. This is very likely to slow down the corrosion progress. In such cases, eqn. [1] is correct for neither the bulk material nor the individual phase.

Porous materials have another prominent problem: establishing contact with the medium so that the development of transport pathways becomes complex. Wetting behavior is of utmost importance, as it governs the penetration and hence the true contact surface. Wetting depends on surface energies and these are likely to change with time due to gradient developments, saturation effects, etc. Such problems are dealt with in detail in Section 1.26.14 on refractory corrosion in the form of typical examples and equations.

Although the chemical removal of phases is a corrosive process, it may well be influenced by erosive or mechanical stresses accompanying the attack. This is also described in the refractory section of this chapter (Section 1.26.10). At this point, we only want to hint that the formation of a solid reaction product during corrosion may not always retard the corrosion progress. Such a special form of active corrosion, which is particular to nonoxide ceramics, has been described for silicon carbide at very high temperatures,<sup>11</sup> where a high pressure of CO can create bubbles, which are easily removed by spallation and erosion.

The formation of solid phases during corrosion can often result in scales or layers. It depends on their physical nature whether they hamper the corrosion process or not. Oxide scales on nonoxide ceramics often do not have such a high mismatch in thermal expansion coefficients as oxidized metals. Hence, stresses in the scale can be lower and spallation is a less common phenomenon. Nonetheless, the oxides can undergo phase transitions with volume changes large enough to cause stresses and cracking during thermal cycling. Multiphase scales likewise can develop stresses that induce cracks. Bubbles are another way of potentially short-circuiting the scale.

In all such cases, eqn. [1] is also valid for passive corrosion, because the scale that develops is not protective. The equation has then positive constants for mass gain. Also in any real process where a scale becomes protective, there is an initial period, in which it is not thick enough to be rate determining. This has been established for the oxidation of silicon by Deal and Grove,<sup>10</sup> where the linear character of the initial period has been shown.

In both metals and ceramics, corrosion in which the transport of the reacting agent through a growing layer is governed by the diffusion of this agent or the reaction product through the scale, we have long-time behavior approximated by a simple parabolic law

$$x(\text{m or kg m}^{-2}) = \sqrt{k_p(\text{m}^2 \text{s}^{-1} \text{ or kg}^2 \text{m}^{-4} \text{s}^{-1}) \cdot t(\text{s})} \quad [2]$$

In eqns. [2]–[5],  $x$  now denotes either the thickness of the layer formed or the mass of material gained per unit area,  $t$  is the time, and  $k_p$  is the parabolic rate constant. Following the reasoning above, both parts of the process can be joined with the linear–parabolic model<sup>10</sup> to give

$$x^2 + Ax = B(t + \tau) \quad [3]$$

in which several physical parameter are contained in the factors  $A$  and  $B$  and a correction time  $\tau$  is introduced, which accounts for an initial scale thickness. By setting reasonable boundary conditions, it is found that  $B$  equals  $k_p$  for long times and thus eqn. [3] is approximated by eqn. [2],  $B/A$  equals  $k_{\text{linear}}$  and thus eqn. [3] is approximated by eqn. [1] for short times. Note that ‘short times’ is an expression relating to corrosion progress and can last, for example, for days at 700 °C in the oxidation of silicon.

It was claimed that the oxidation data for silicon can equally well be fitted by a simple power law<sup>12</sup>

$$x = at^b \quad [4]$$

This method has not been used extensively in the literature for oxidation of semiconductors or ceramics. The lack of a good physical explanation for the parameters of eqn. [4] is probably the main reason.

For easy fitting, a variant of eqn. [3] may be preferred:

$$\frac{x^2}{k_p} + \frac{x}{k_l} - \tau = t \quad [5]$$

A difference to be noted between ceramics and metals is that the corrosion progress  $x$  is not directly transferred from thickness to weight change units via densities  $\rho$ , because in nonoxides there is a loss of the accompanying light element. As described elsewhere,<sup>13</sup> a stoichiometry factor relating to the reaction equation

$$u = \frac{(n \cdot M)_{\text{Condensed product}}}{(n \cdot M)_{\text{Condensed product}} - (n \cdot M)_{\text{Material}}} \quad [6]$$

where  $n$  is the number of moles in the chemical reaction equation and  $M$  the molecular weight, has

to be calculated to relate rate constants to each other by eqn. [7]:

$$k_p(\text{m s}^{-1}) \frac{\rho_{\text{Product}}^2(\text{kg m}^{-3})^2}{u^2} = k_p(\text{kg}^2 \text{m}^{-2} \text{s}^{-1}) \quad [7]$$

A third basic law is the logarithmic or asymptotic law

$$x = c + k_{\log} \log(t) \quad [8]$$

This may be used for corrosion processes, which are effectively stopped by the formation of a material barrier during corrosion. It basically describes the decrease in the effective exposed surface area. The barrier may be a crystalline phase with a much lower diffusion coefficient.

Kinetic breaks are observed in cases where a physical effect interferes with the corrosion process. An example is the repeated cracking of the scale. If a critical thickness is responsible for the critical stress, which initiates the cracking process, pseudolinear behavior with a succession of periods of parabolic growth and intervening periods of renewal of short-circuiting paths follows.

Internal oxidation is observed in multiphase ceramics. A grain boundary phase is often the weakest material in terms of corrosion resistance and provides a transport path for the exchange of matter between the inside and the outside of the structure. The production of selectively corroded phases in the interior induces internal stresses because of volume increases. After a critical stress level is reached, mechanical failure of parts of the component near the surface may follow. If this cannot be healed during the process, a large new surface area is opened and a ‘break-away’ situation is likely, i.e., a change to fast linear corrosion.

Another typical break situation is observed in porous materials. The closure of pore openings by the formed scale diminishes the exposed surface markedly and almost instantaneously. A much slower progress follows after closure.

Simple basic laws of passive processes are only true for constant diffusion coefficients. In all cases, where extrinsic or intrinsic impurities, additives, etc., are present and enter the scale forming material, an influence on the diffusion coefficient must be envisaged. An increase or decrease in the coefficient causes the mass change curve to become steeper or flatter relative to parabolic behavior. Simulations show that for strong effects of this kind linear [1] or asymptotic behavior [7] is approximated.

Therefore, we have good reasons to envisage complex kinetic behavior during corrosion to be possible.



Complex strictly physical models are a matter of model calculations still and hard to generalize. Attempts to model complex situations by semi- or purely empirical curve fitting procedures, e.g., by using a multiple linear approach in the form

$$x = k_0 + k_{\text{lin}}t + k_p''\sqrt{t} + k_{\text{log}}\log(t) \quad [9]$$

have been proposed<sup>14, 15</sup> and shown to be quite successful. Attempts to introduce an even higher degree of sophistication made the equations less robust to the errors inherited from the uncertainties of measurement.<sup>16</sup>

A special case of complex kinetics arises from situations in which active and passive processes occur simultaneously. This has been discussed extensively because it is of great importance to applications such as gas turbines.<sup>17</sup> Corrosion in which a scale is formed and evaporated at the same time has a typical pattern in plots of mass change against time, because the initial gain will turn into a linear loss after longer times. Opila<sup>18</sup> has shown that the equation for metal oxidation with evaporation reported by Tedmon<sup>19</sup> in the form

$$t = \left[ \frac{u_1^2 k_p}{2k_1^2} \left[ -\frac{2k_1 \Delta w_1}{u_1 k_p} - \ln \left( 1 - \frac{2k_1 \Delta w_1}{u_1 k_p} \right) \right] \right] - \frac{\Delta w_2}{u_2 k_1} \quad [10]$$

where  $u_1$  and  $u_2$  are stoichiometric factors, which account for the mass balance of the appropriate reactions,  $\Delta w_1$  and  $\Delta w_2$  are weight gain and weight loss by scale growth and volatilization, respectively, is successful in describing this steady-state situation, leading to the establishment of a steady-state scale thickness and progressing corrosion of the material. The engineering basis for the loss function was also explored and simulated with parameters for the flow of fluids.<sup>20</sup>

### 1.26.4 Corrosion Measurement

In situ experiments of ceramic corrosion can only be done for simple cases. Simple oxidation of a nonoxide in a defined atmosphere can be followed continuously by thermogravimetry (TGA), which allows proper kinetic modeling. Resolution, accuracy, precision, and long-time stability of the apparatus have to be controlled. Other problems, e.g., contamination or the creation of local atmospheres, are identical to those discussed below.

Scale growth monitoring measurements, e.g., by ellipsometry, which are common for oxidation of silicon, have rarely been used in ceramics. Only in recent years, with SiC wafers for electronic applications becoming available, have such data been produced in greater numbers.

The most common experiments in ceramics corrosion are still exposures in special environments, followed by weighing and inspecting with microscopic and other available analytical techniques.

Melt corrosion is often studied by ordinary drop, crucible, and finger tests; these should only be used to rank materials, because they give qualitative data inside a narrow frame set by the standardized experimental setup.

Burner rigs are used to test for salt melt corrosion ('hot corrosion').<sup>21</sup> Salts are injected into the flame of a burner and deposited at constant rates onto samples, which are positioned and agitated in front of the apparatus exhaust.

Post-inspection of samples from furnace tests is most common for the investigation of interactions with gases. As a typical example for the contamination problems associated with the method, we can look at protective tubes made from alumina. Most gases, even expensive high-purity types, do contain water at the ppm-level. Unless the alumina tube was fired and flushed at high temperatures for times in the order of 1000 h, it may contaminate the sample with sodium, and as long as extreme measures have not been taken to dry the atmosphere (e.g., by  $\text{P}_2\text{O}_5$ ), there may be substantial contamination by alumina in the form of transfer as hydroxide.<sup>22</sup> In deliberately moistened atmospheres, the effect is quite high.<sup>23</sup> The effect on oxidation rates for silica formers has been shown to be extensive even for low contamination levels,<sup>24</sup> because the contaminants are good glass formers, and may change the properties of growing scales. Apart from contamination, local atmospheres may play a role, which may explain the observed influences of furnace size on experimental oxidation rates.<sup>25</sup>

High temperature experiments have always an extended level of contamination possibilities. An increased level of uncertainty in corrosion data comes also from sample inhomogeneities. Preferential corrosion of secondary or grain boundary phases is often calculated directly relative to the total sample surface and yields a corresponding bias in parameter evaluation. Adding the increased uncertainty levels of temperature measurement and physical side effects such as the relative large areas in the vicinity of an edge in the usually small

samples, it is plain that one has to allow for some systematic and statistical error in the experimental data.

## 1.26.5 Oxides

A number of oxides with high melting points could qualify as high temperature materials. Out of these only a small number is used as bulk engineering material, and therefore only alumina and zirconia are dealt with here in detail. The other oxides are either covered by the chapter on “Oxidation of Metals and Alloys” or are covered by the chapter on **Oxidation of Metals and Alloys** or are contained within the refractory sections of this chapter.

### 1.26.5.1 Alumina

The only form of alumina that is stable at high temperature is corundum or  $\alpha$ - $\text{Al}_2\text{O}_3$ . It is well known for its excellent chemical resistance, even at high temperatures. For this reason, it is a common tube material in high temperature furnace systems with oxidizing atmospheres. The applications at high temperature are often limited by other properties rather than corrosion, namely creep and poor mechanical properties.

Nonetheless, there are some restrictions for the use of alumina based on its chemical behavior. At temperatures of 1700 °C in Ar/ $\text{H}_2\text{O}$  mixtures, evaporation of alumina was reported and excessive grain growth may have enhanced the problems.<sup>26</sup> Reducing environments can also foster carbothermic reduction of alumina, e.g., in the presence of SiC,<sup>27</sup> but in general a good resistance to flue gases of the aluminum-remelting industry has been reported.<sup>28</sup> The attack by alkali metal vapors is impurity dependent.

Corrosion by aggressive gases can be estimated via calculation of the partial pressures of volatile species over alumina.<sup>29</sup> This has been shown for halogens<sup>30</sup> and is certainly true for other such agents. The vaporization in water containing systems is mainly in the form of  $\text{Al}(\text{OH})_3$ . Therefore, in high-velocity gas streams containing water, there is a limitation for long-time applications.

Solid-state reactions for silica are not restricted to phase equilibria with mullite, because the system is complicated and characterized by metastable immiscibility gaps at temperatures significantly below the eutectic value close to 1600 °C. Alumina is a common component in, and therefore can be dissolved by, silicate slags. For the details of the process dependencies, the reader is referred to example references.<sup>31</sup>

The corrosion resistance of alumina ceramics is strongly influenced by impurities because some of

these are incorporated as grain boundary phases with accordingly selective preferential damage. In particular, silica and alkalis are typical impurities for alumina in engineering ceramics and even small amounts have been shown to be responsible for the corrosion in hydrothermal conditions.<sup>32</sup> Similarly corrosion by salt melts is related to impurities and grain boundary phases.<sup>33</sup>

### 1.26.5.2 Zirconia

Zirconia ( $\text{ZrO}_2$ ) is a high temperature phase with a melting point above 2500 °C. Extremely high values even for the lowest eutectic temperatures in the binary systems with alumina and silica make it a prime material for refractory systems by itself or with those oxides. For many conditions, it will behave in an almost inert manner in contact with silica or alumina.

The section on thermal barrier coatings in this book discusses the corrosion aspects in those high temperature applications.

As a pure monolithic material, it is more problematic, because martensitic phase transformations with volume changes occur and tend to embrittle the material during thermal cycling. The addition of Mg, Ca, Y, and Ce stabilizes the higher temperature modifications (for a review on the basic science of these transformations see Hannink *et al.*<sup>34</sup>), and with appropriately high concentrations the cubic modification is stable down to room temperature.

In a stabilized modification, the use of zirconia as a refractory material is possible. Such refractories are susceptible to corrosion by slags, because slags with low basicity leach MgO, and highly basic slags can dissolve the material completely. Applications in remelting furnaces showed a good resistance to flue gases.

The stabilization can have deleterious effects on Ce-doped materials because the variation of external oxygen fugacity can induce corrosion due to a change in the oxidation state. Corrosion by water is a serious problem because even at low temperatures it can enter the structure of zirconia and destabilize the modifications. Appropriate phase transformations have been observed under hydrothermal conditions.<sup>35</sup>

### 1.26.5.3 Cordierite

Cordierite ( $\text{Al}_3\text{Mg}_2(\text{Si}_5\text{AlO}_{18})$ ) is a rock-forming mineral, and the pure Mg-end member of the solid solution with Fe melts incongruently at 1460 °C to yield mullite and liquid. It is a widely applied ceramic for soot filters or heat exchanger, because it

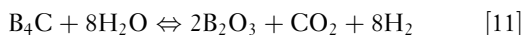
has a low thermal expansion coefficient and therefore is very tolerant to thermal shocks and cycling.

High temperature corrosion of cordierite is known from treatments with molten salts (hot corrosion).

## 1.26.6 Carbides

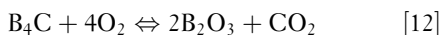
### 1.26.6.1 Boron Carbide

Hydrothermal corrosion of  $B_4C$  proceeds at low pressures and C:H-ratios according to reactions of the type



in which  $CO_2$  is replaced by methane or carbon monoxide under appropriate carbide/water ratios. In analogy with water vapor systems, reactions start at temperatures as low as 250 °C because no carbon layer is produced.

Experiments on the attack by oxygen on powders,<sup>36</sup> coatings, and sintered materials confirm that at low and moderate temperatures the oxidation yields boric acid



and the kinetics are governed by oxygen diffusion through it. In the high temperature regime, starting at about 800 °C, boric acid evaporates and the process becomes parabolic with an overall loss at longer times. Evaporation is stronger in wet atmospheres, because the reaction



dominates at temperatures below about 1000 °C with high partial pressures. Boron carbide was investigated in steam because it is an important material in the nuclear industry. The dependence of the kinetics on partial pressures of water and flow speed was confirmed and modeled.<sup>37</sup> It should be noted that many commercial bulk boron carbides contain impurities or additives, which strongly influence the process.<sup>38</sup>

### 1.26.6.2 Silicon Carbide

Corrosion data collections for SiC-based materials are found in a number of handbooks and textbooks,<sup>39–42</sup> are contained in specific conference proceedings<sup>14,43,44</sup> and a vast number of publications. The interest in the high temperature behavior of this material comes historically from its use as a refractory material, later from the structural engineering

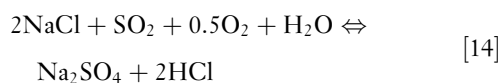
advanced ceramics, and in recent times, increasingly from the need to understand the behavior to obtain insulating parts within a semiconductor.

Hydrothermal corrosion is significant only at temperatures exceeding 500 °C, even though initial reactions may occur at 300 °C. The hydrothermal oxidation yields silica along with  $CH_4$ ,  $CO_x \pm C$ . The attack is commonly an active corrosion, because silica is dissolved in  $H_2O$ . The dissolution rate of silica is the key to the kinetics of the process and can be modified by increasing the pH of the water. The onset of hydrothermal oxidation in silicon nitride, likewise forming silica, is at much lower temperatures. The difference indicates protection by the formation of carbon layers at temperatures below about 500 °C, which has been observed for SiC-based fibers<sup>45</sup> and in halogen containing environments.<sup>46</sup>

Silicides are thermodynamically often more stable than SiC and a number of low-temperature eutectics exist with SiC. Therefore, metals can corrode SiC and a compilation<sup>41</sup> gives indications for reactions with Al (750 °C), Au (950 °C), Bi (600 °C), Cr (1000 °C), Cu (950 °C), Co (1150 °C), Fe (1000 °C), Li (815 °C), Mg (800 °C), Ti (575 °C), Mo (1200 °C), Nb (1300 °C), Ni (500 °C), Pd (600 °C), Ta (1200 °C), and W (1500 °C). Resistance to the attack was noted for Ag (962 °C), Ca (1180 °C), Cd (500 °C), Na (350 °C), Pb (815 °C), and Sn (600 °C).

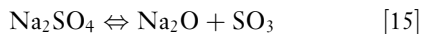
Most of those data were obtained in vacuum, where the wetting behavior, which is essential for the form and strength of attack, is different from oxidizing conditions. It should also be noted that SiC containing free Si reacts more readily than SiC. Temperatures of possible reactions may be evaluated with the aid of phase diagrams of the appropriate Si-metal system. In appropriate wear conditions, a reaction of SiC with a metal is therefore feasible.

For attack by salt melts (hot corrosion), the reviews by Jacobson and coworkers<sup>47–49</sup> are still fundamental. As explained in the appropriate chapter in this book, the attacking salts are best represented by  $Na_2SO_4$ , which forms in combustion environments by

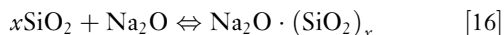


A first condition for a window of effective hot corrosion is given by the melting and dew points of  $Na_2SO_4$ . The melting point is 884 °C, the dew point varies with pressure, S content of the fuel, and NaCl concentration in the atmosphere. In gases with  $NaCl > 1$  ppm and combustion pressures of 100 bar, the dew point ranges between 1100 and 1200 °C (from eqn.[14]).

The corrosive effect is not a reaction with the sulfate. It is due to the activity of  $\text{Na}_2\text{O}$  from the decomposition



and reaction with the protective  $\text{SiO}_2$  scale



Therefore, other compounds releasing alkali oxide on decomposition, e.g.,  $\text{Na}_2\text{CO}_3$ , also cause hot corrosion.

Reaction [15] shows that a low  $P(\text{SO}_3)$  value drives reaction [16] to the right side, typical for the external  $P(\text{SO}_3)$  from the combustion of low-S fuels ( $<0.5\%$ , a condition met by many modern fuels) at temperatures of about  $1000^\circ\text{C}$ .

However, corrosion starts at the melting point of  $\text{Na}_2\text{SO}_4$ . Free carbon is often present in commercial SSiC (=pressureless sintered silicon carbide) and promotes the dissociation of  $\text{Na}_2\text{SO}_4$  by making the silicate melt more basic. Accordingly, very strong hot corrosion of SiC with free carbon is known.<sup>50</sup>

Even without free carbon hot corrosion of SiC should occur as an internally governed process analogous to studies<sup>51</sup> on  $\text{Si}_3\text{N}_4$ , because SiC may act as the reducing agent to promote sulfate dissociation directly or by establishing an oxygen gradient in the silica scale consumed by reaction [16].

Hot corrosion tests are often only qualitative. Even burner-rig methods have problems for quantifying the attack. In terms of degradation of the mechanical properties, it should be noted that hot corrosion

commonly causes pitting with a change in exposed surface and nonuniform attack. Pitting may not in all cases be a secondary phase problem, because it can be initiated by the immiscibility of two liquids.<sup>51</sup> It seems to be fairly difficult to model the damage by hot corrosion in a general way. One approach is to relate the pit diameter to strength data, i.e., to treat them as critical flaw sizes in the Griffith equation.

Hot corrosion protection has been investigated using mullite coatings.<sup>17</sup> Some temporary protection may even come from simple silica coatings.<sup>52</sup>

The corrosion of SiC by hot gases has been the subject of many studies. Active corrosion is a form of attack by gases, which do not form condensed species with Si at the temperatures of interest. Thus, halogens induce active corrosion, and calculated pressures of species such as  $\text{SiF}_4$  or  $\text{SiCl}_4$  over SiC will be as high as the concentration of F and Cl in the gas.

These pressures will be significantly decreased and the damage is less severe in the presence of oxygen, as evidenced by a study on  $\text{Cl}_2$  corrosion.<sup>53</sup>

Corrosion of pure SiC by  $\text{H}_2$  starts at temperatures above  $1300^\circ\text{C}$ , while grain boundaries and secondary phases in sintered SiC are attacked at temperatures as low as  $1000^\circ\text{C}$ .

The formation of silica is therefore essential for the stability of SiC. The boundary for active-to-passive oxidation is described in Figure 1. Wagner-type models predict the transition for diffusion-related situations and are relatively successful. From experimental evidence at temperatures of  $\sim 1760^\circ\text{C}$ ,<sup>54</sup>

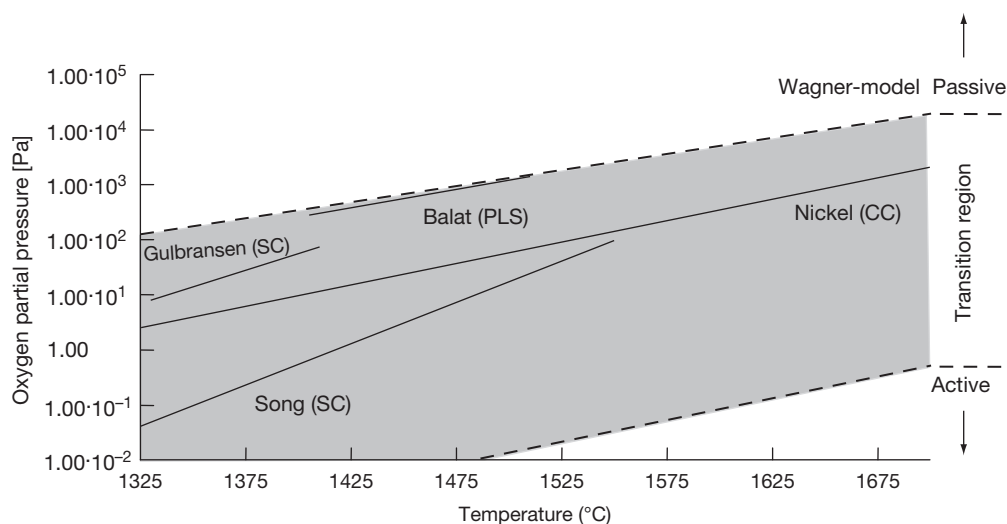


**Figure 1** Active-to-passive transition of SiC thermal oxidation calculated (CC) from Wagner-type models and volatility diagrams and experimental values on single crystals (SC) and SSiC (PLS), see Presser and Nickel.<sup>56</sup>

a secondary active-to-passive transition was formulated, at which the formed silica spalled because of a CO interface pressure exceeding ambient pressures.

Oxygen pressures in **Figure 1** should not be confused with data from  $\text{CO}_x$  experiments, because CO is a reactive and an oxidizing gas species for SiC<sup>41</sup> despite a low oxygen partial pressure. Therefore, active oxidation in CO is only observed at very high temperatures.<sup>55</sup>

The silica formation in the passive regime at high temperatures is in detail a complex process, which includes several stages of amorphous silica formation and its crystallization. A review will be given elsewhere.<sup>56</sup> At temperatures below about 1200 °C a linear-parabolic model in the sense of Deal and Grove<sup>10</sup> is necessary to explain the oxidation data, whereas at higher temperatures a simple parabolic law is usually sufficient.

The process is still not well understood, because the rate constants are clearly dependent on the exposed crystallographic face of SiC,<sup>57</sup> and at the same time it is believed that it depends on the diffusion of oxygen through silica, because the kinetics are parabolic and activation energies fit this process.<sup>58</sup> However, at temperatures above about 1300 °C, there are data sets indicating a high activation energy,

compatible with network oxygen diffusion in amorphous silica rather than molecular diffusion. It has been argued that this is related to extrinsic impurities from the experimental setups.<sup>59</sup>

In a plot compiling rate constants from a large number of data for fairly pure SiC (CVD, single crystals), including differing crystallographic faces, the situation is not so straight-forward,<sup>56</sup> but a fairly high spread of parabolic rates is evident (**Figure 2**).

Commercial qualities of sintered SiC often have low impurity or additive contents and have rates as low as pure materials, indicating extremely good oxidation resistance up to very high temperatures. This is certainly not really true for  $T$  above 1600 °C, because at very high temperatures the long-time kinetics are not adequately described by the parabolic law, the problem of active II oxidation is important and in addition bubble-and-pit formation, which is usually attributed to additives containing boron and/or aluminum, is likely to endanger applications (**Figure 3**). It should also be noted that bubble-and-pit formation can occur after an ‘incubation period’ of several 100 h at  $T > 1600$  °C, while oxidation studies run usually only for times <100 h. Therefore long-time studies may be necessary for a true qualification of SiC at extremely high temperatures.

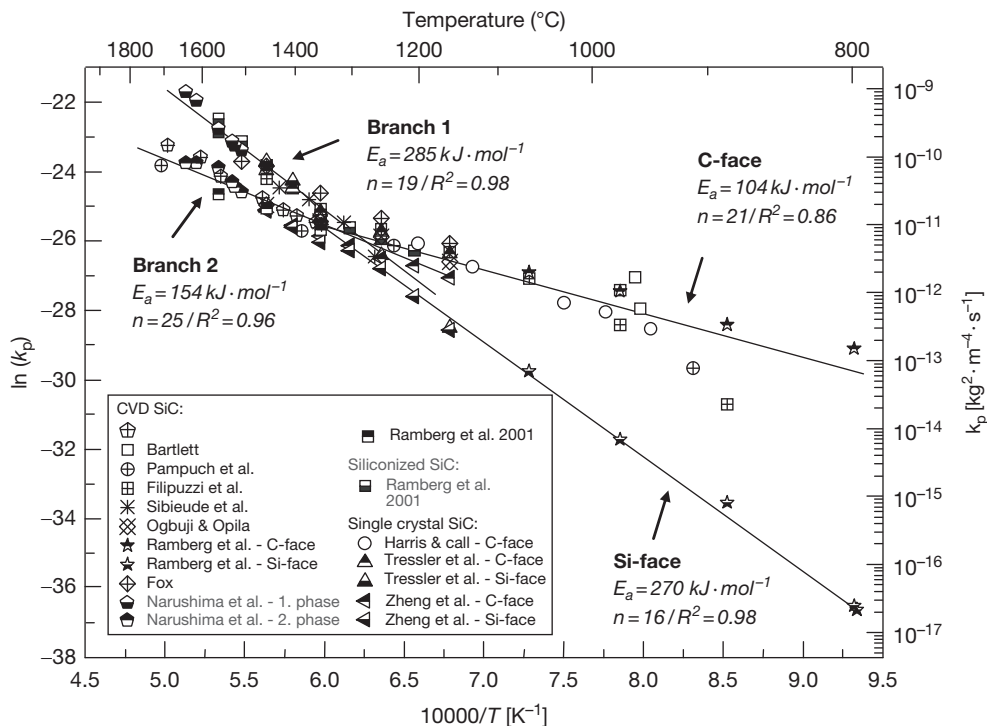


**Figure 2** Comparative plot of parabolic rate constants. The plot comes from Presser and Nickel<sup>56</sup> where the data sources are referenced.



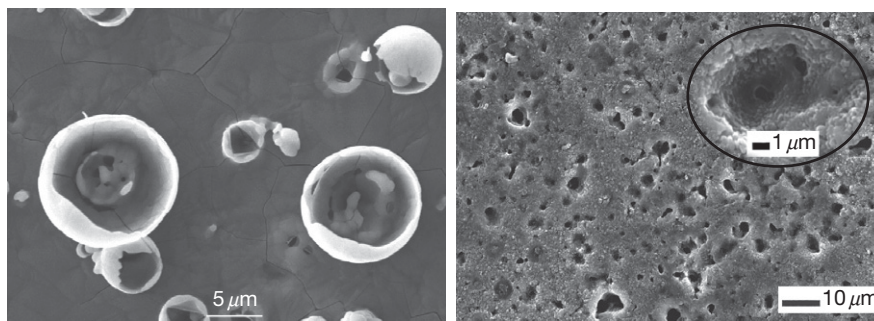


**Figure 3** Bubbles at the surface of SSiC oxidized at 1500 °C for 24 h under humid conditions and pits beneath (1500 °C, 50 h) revealed by HF-etching of oxidized SSiC from Ref. 100.

Furthermore, good resistance to oxidation by O<sub>2</sub> or air does not guarantee equally good behavior in complex industrial environments. Other components of the atmosphere or extrinsic impurities can change the behavior markedly and make a prediction difficult in cases of strong variations in temperature and gas composition, even though resistance of SiC-based materials to other aggressive environments, e.g., such as SO<sub>2</sub> or H<sub>2</sub>S, has been reported.<sup>14</sup>

For such environments, case studies give an indication but are not unambiguous.<sup>14</sup> SSiC was reported to resist flue gases of aluminum-remelting furnaces up to 1000 h without much change in strength in one study but had problems in others. The strength of SSiC was unchanged in nitrogen-based gases of the system N<sub>2</sub>–H<sub>2</sub>–CO, but decreased up to 50% in endothermic gases at 1200–1300 °C in long-time experiments.

Water enhances the oxidation of SiC only slightly, but the transport of extrinsic impurities because of water can strongly enhance oxidation and the limitations in applications with high gas flow rates because of vaporization of the silica scale inducing parabolic behavior are known.<sup>60</sup>

## 1.26.7 Nitrides

### 1.26.7.1 Silicon Nitride

Silicon nitrides are often discussed together with silicon carbides, because both materials are silica formers. For this reason, data collections and textbook sections are identical to those already cited for carbides.<sup>13,14,39,40,42–44</sup> For an additional, detailed study see Ref. 61. A typical difference from the silicon carbides is the much higher additive content of almost all commercial sintered silicon nitrides. Only liquid-phase sintered SiC types ('LP-SiC') have comparably high amounts.

Hydrothermal corrosion of silicon nitride starts at about 130 °C because of the high solubility of silica in water under high pressure. The reaction



does not passivate because the dissolution of NH<sub>3</sub> makes the solution caustic, which strongly enhances silica solubility. Therefore, reaction kinetics are linear and active corrosion prevails.

The hydrothermal corrosion of the grain boundary phase of Si<sub>3</sub>N<sub>4</sub> ceramics can be very strong and pit formation was observed at 300 °C and 8.6 MPa.<sup>62</sup> From experiments on hot isostatically pressed silicon nitride (HIPSIN), which were free of additives other than silica, we know that preferential hydrothermal leaching of silica as the grain boundary phase can cause grain dislodgment.<sup>63</sup>

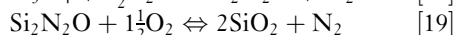
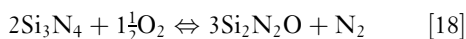
A compilation of data for the reactions of Si<sub>3</sub>N<sub>4</sub> with metals and alloys has been given in Ref. 64. The interaction is important for bonding to metals; often silicides or other ternary compounds are formed. The interaction of the related SiAlONs (silicon nitrides, which incorporate alumina and yttria in their lattice) and alloys was found to be similar. In inert gas atmosphere or under vacuum, Si<sub>3</sub>N<sub>4</sub> reacts readily with most transition elements below 1000 °C and with many other metals at various temperatures, while protection by silica in oxidizing conditions is effective for some conditions.<sup>64</sup>

Hot corrosion of Si<sub>3</sub>N<sub>4</sub> attacks the silica scale and the behavior is therefore similar to that of SiC, as confirmed by studies at NASA labs.<sup>48,65</sup> However, the initial process may be governed by intrinsic factors, because surface tension differences between sulfate and silicate melts result in a fractal pattern of hillocks of silicate melt beneath the sulfate. This was reported to enhance local corrosion and induce pit formation. The process slows down with time and

therefore  $\text{Si}_3\text{N}_4$ -based ceramics can serve well under hot corrosion conditions. Even though there is a degradation in mechanical properties similar to that of SiC,<sup>21,66</sup> the remaining strength after hot corrosion of the nitride is higher than that of SiC.

Active corrosion of  $\text{Si}_3\text{N}_4$  ceramics by hot gases is often stronger than comparable attack on SiC, because the grain boundary phase removal causes grain dislodgment and inhomogeneous internal corrosion. In particular, halogens create high partial pressures of Si-bearing species and accordingly strong active corrosion, but small amounts of oxygen or water can significantly decrease the effect of  $\text{Cl}_2$  or sulfidizing environments by silica formation. The active-to-passive transition occurs at similar conditions as the one for SiC (Figure 1).

From thermodynamic considerations<sup>67</sup> the passive oxidation of pure  $\text{Si}_3\text{N}_4$  should involve a two-step oxidation



forming a duplex layer in an oxygen potential gradient. A definitive proof for a sublayer of  $\text{Si}_2\text{N}_2\text{O}$  was only provided for pure nitrides,<sup>68</sup> but a superior

oxidation resistance for pure  $\text{Si}_3\text{N}_4$  compared with that for SiC at temperatures of about  $1500^\circ\text{C}$  is evident and contrasts with the behavior of sintered  $\text{Si}_3\text{N}_4$ . This is plain from Figure 4, which shows calculated critical times  $t_c$  for  $100\text{ }\mu\text{m}$  penetration on pure and sintered nitride and carbides, assuming parabolic growth and using the data compiled earlier.<sup>13</sup>

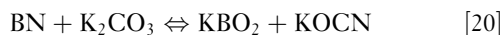
The presence of grain boundary phases is the main reason for the pronounced decrease in oxidation resistance. In detail, a number of processes, including the leaching of grain boundary constituents to the scale, crystallization, internal oxidation, bubble formation, and scale cracking, occur and vary with amount and exact composition of the additives. The discussion of such processes is referenced in the textbooks cited at the beginning of this chapter.

Again, it must be noted that the data in Figure 4 should serve as an indication only, because the values were calculated assuming a truly simple parabolic behavior, which is often not really fulfilled.

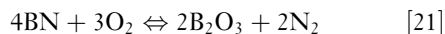
### 1.26.7.2 Boron Nitride

In hydrothermal conditions, BN is attacked at temperatures as low as  $150^\circ\text{C}$ , following linear kinetics.<sup>69</sup> Hexagonal BN is often applied in the production of the metal and for thermocouples in Fe alloy melts, which is ample evidence for a good corrosion resistance against metal melts and slags at much higher temperatures, namely alkali halides, lithium borate, and cryolite. This is due to the poor wetting behavior of such melts on BN.

Only molten alkali carbonates and hydroxides decompose boron nitride by the reactions of the type



The product of the oxidation of boron nitride at atmospheric and low pressures is boric acid



and therefore the material has a similarity to boron carbide. The melting point of boric acid at  $410\text{--}450^\circ\text{C}$  keeps the formed oxide liquid at high temperatures. Accordingly, at temperatures exceeding  $700^\circ\text{C}$ , there is parabolic oxidation with the loss of boria by evaporation.<sup>70</sup> Water enhances the evaporation process, because the partial pressure of hydrogen-bearing species is high<sup>71</sup> and the oxidation can be described as

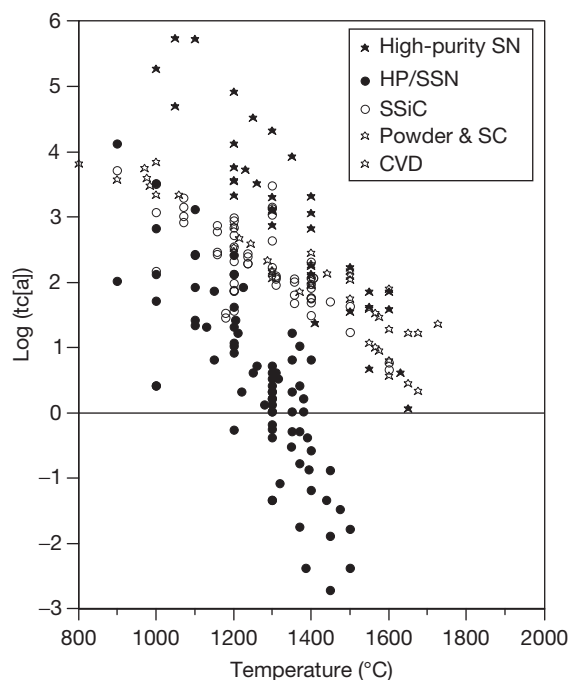
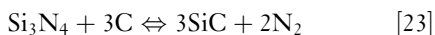


**Figure 4** Logarithm of calculated critical times in years for  $100\text{ }\mu\text{m}$  penetration for silicon nitrides (full symbols) and silicon carbides (open symbols) vs. temperature from compiled parabolic rate constants.<sup>13</sup>

### 1.26.7.3 Silico-Carbonitrides

The precursor-derived amorphous silico-carbonitrides have high thermal stabilities, a boron-containing type reportedly up to 2000 °C.<sup>72</sup>

Crystallization may induce detrimental reactions as was shown for pure carbonitrides at ≈1400–1500 °C.<sup>73</sup> Their nominal stoichiometry has C in addition to Si<sub>3</sub>N<sub>4</sub> and SiC and therefore the reaction



takes place at about the thermodynamically predicted temperature (≈1405 °C at 1 bar N<sub>2</sub>). Oxidized samples without such a reaction<sup>74</sup> were observed to survive because of an internal pressure buildup of several bars.

As suggested earlier,<sup>75</sup> carbonitrides are susceptible to hot corrosion because the excess carbon will tend to make a melt basic. In terms of oxidation resistance, the data<sup>76–78</sup> suggest that they have very low oxidation rates at temperatures up to 1600 °C. The problem of bubble formation seems to be avoidable by Al incorporation in the ceramic. However, the penetration rates are probably not much better than those for pure silicon nitrides, and the problem of parabolic behavior in fast-flowing gases is valid for these materials as well.

### 1.26.8 Titanium Compounds

TiC and TiN show a very wide range of stoichiometry and form solid solutions in the Ti–C–N system. Thermodynamic equilibria in water–carbide systems<sup>79</sup> indicated that carbon, corresponding oxides, CH<sub>4</sub>, CO<sub>2</sub>, CO, and H<sub>2</sub> are the main products of hydrothermal corrosion of metal carbides in the temperature range 300–1000 °C. No protective oxide layers were formed upon hydrothermal corrosion of carbides of transition metals, but Raman spectra from hydrothermally treated TiC powders demonstrated the presence of graphite.

Oxidation of TiN powders, films, and sintered bodies<sup>80,81</sup> showed that oxidation occurs at very low temperatures and becomes significant at about 500 °C, with the formation of TiO<sub>2</sub>. Scales from titania are usually not protective at temperatures above 800 °C, which limits the use of monolithic titanium compounds at high temperature.

TiB<sub>2</sub> forms titania and boria and is known primarily for coatings and composites. Oxidation of

TiB<sub>2</sub> is significant above 700 °C and shows parabolic kinetics at those temperatures.<sup>82</sup> In powder experiments, an onset of oxidation was found at 400 °C and TiBO<sub>3</sub> was an oxidation product at low temperatures.<sup>83</sup> At 950 °C, the evaporation of B<sub>2</sub>O<sub>3</sub> becomes significant and parabolic oxidation occurs. However, unlike for boron carbide and nitride, the kinetics become parabolic again at higher temperatures (>1200 °C). This is explained by the fact that, when B<sub>2</sub>O<sub>3</sub> is completely evaporated, the process is controlled by diffusion through the titanium dioxide film.

Impurities and metal binders were found to improve the oxidation resistance of TiB<sub>2</sub>, because the rutile scale sinters and becomes dense.<sup>84</sup>

The use of TiB<sub>2</sub> as a component of composites and their oxidation and corrosion behaviors are the subject of a large number of papers. The behavior can be fairly complex because other phases such as aluminum borates become stable and influence the behavior.

### 1.26.9 Ultrahigh Temperature Ceramics

With the realization of the limits of silica-forming ceramics in fast-flowing wet atmospheres, the search for so-called ‘ultrahigh temperature ceramics’ was started. The classes looked at were either the polymer-derived ceramics<sup>85,86</sup> or those forming very refractory oxides, particularly ZrO<sub>2</sub> or HfO<sub>2</sub>. However, the precursor-derived ceramics are silica formers, and therefore at least at temperatures above 1650 °C the problems of silica are inherent. The zirconia and hafnia formers have the problem of fast ionic oxygen transport and thus materials such as ZrB<sub>2</sub> or HfB<sub>2</sub> oxidize extremely fast<sup>87</sup> and are only candidates for very short-lived applications.

Together with the fact of decreasing mechanical properties for all metallic materials at very high temperatures, the only current vision is the development of composites, which are protected from oxidation by some sort of coating. Therefore, environmental barrier systems are a subject of current investigation. The old dream of a carbon-based system with its high temperature properties protected by coatings is still alive and investigated repeatedly with new approaches and systems. It must still be regarded as one of the most promising ways to maintain a strong system at very high temperatures!

## 1.26.10 Refractories

Formed and unformed refractory products have a wide process engineering spectrum of applicability and therefore satisfy various demands and reciprocal actions. The following text will present the corrosion of refractory materials with typical examples of the iron and steel industries. The effecting part-mechanisms can be compared with other industrial sectors and can be divided as follows.

### 1.26.10.1 Chemical Dissolution

The driving force is the existing thermochemical nonequilibrium between the two involved phases (liquid steel/slag/atmosphere – refractory lining) of a system. The thermodynamic stability of a phase (refractory material) is described by the free enthalpy of formation  $\Delta G$  and is heavily affected by the variables of temperature, pressure, and concentration. Besides the dissolution itself, reduction and oxidation processes as well as vaporization and evaporation play essential roles.

### 1.26.10.2 Erosion

The driving force is the flow of melts by gas flushing, vacuum treatment, tapping, and filling the metallurgical reactor respectively, and continuous casting and gases charged with solids. During the first process, a mostly predamaged structure is washed out. During the latter, the damage is affected by solid particles impacting onto the refractory lining because of their inertia, and which break off the material because of surface disruption.

### 1.26.10.3 Mechanical Wear

Thermal shocks and steep temperature gradients (e.g., during heating up, change of temperature when filling a ladle, etc.) cause thermal stresses and sometimes structure changes. Furthermore, the handling in steel plants (e.g., filling a converter with scrap, the cleaning process with skull breakout and removal of slag, the filling and transport of a ladle, etc.) cause wear by mechanical contacts.

These three mechanisms are superimposed and accelerated by infiltration, i.e., weakening the structure of the refractory materials by the ‘inner’ dissolution of the matrix. In practice, chemical dissolution, erosion, mechanical wear, and infiltration appear together with varying degrees of importance.

## 1.26.11 Chemical Dissolution

### 1.26.11.1 Diffusion/Blast Furnace

In a shaft-shaped, double conic built blast furnace, iron ore is constantly reduced to pig iron by carbon and carbon monoxide, respectively. The liquid iron drips into the hearth of the blast furnace, gathers on the ground, and is tapped periodically and in a batch wise manner into transport ladles. The fluid slag in the hearth floating on top of the pig iron fixes the impurities contained in the ore and is extracted continuously.

The hearth, which is water cooled via its outer wall, is lined with carbon and graphite containing bricks. The furnace lifetime is typically 10 years or more with a wall thickness of up to 2 m. In addition to high heat conductivity, another advantage of this lining is the nonwettability of the graphite by slag. No infiltration takes place.

Furthermore, the iron melt approaching from above is saturated with carbon, which strongly decreases attack of the lining. The saturation with carbon is also due to the presence of a bed of coke in the hearth, which is highly porous and filled with slag and pig iron. In addition elements such as Si and Mn accompanying the pig iron decrease the saturation concentration of carbon.<sup>88</sup>

Any iron melt not saturated in carbon causes a linear dissolution rate for a unidirectional water-cooled carbon plate described by the equation:

$$\frac{\Delta x}{\Delta t} = \beta \frac{\rho_{Fe}}{\rho_C} \cdot \frac{C_S - C_0}{100} \quad (\text{cm s}^{-1}) \quad [24]$$

where  $\beta$  is the mass transfer coefficient ( $\text{cm s}^{-1}$ );  $\rho_{Fe}$ , the density of liquid iron ( $6.67 \text{ g cm}^{-3}$ ),  $\rho_C$ , the density of carbon/graphite ( $2.25 \text{ g cm}^{-3}$ );  $C_S$ , the saturation concentration of carbon in liquid iron ( $1500^\circ\text{C}$ : 5.16 wt %);  $C_0$  is the concentration of carbon in liquid iron.

The mass transfer coefficient  $\beta$  is given by

$$\beta = \frac{D_C}{\delta} = \left( \frac{4D_C v}{\pi l_1} \right)^{1/2} \left( \frac{D_C}{v} \right)^{1/6} \quad (\text{cm s}^{-1}) \quad [25]$$

where  $D_C$  is the diffusion coefficient of carbon in liquid iron ( $10^{-4} \text{ cm}^2 \text{ s}^{-1}$ );  $\delta$ , the boundary layer of diffusion (cm);  $v$ , the flow velocity of the melt ( $\text{cm} \cdot \text{s}^{-1}$ );  $l_1$ , the diameter of the convection loop (assumption: 1 cm);  $v$  is the kinematic viscosity of liquid iron ( $10^{-3} \text{ cm}^2 \text{ s}^{-1}$ ).

A laminar flow is predominant (free convection,  $Re \leq 2100$ ) because of low temperature differences at

the phase interface ( $\Delta T < 1$  K). The speed of the convection loop moving at the phase interface can be estimated by using the Reynolds number  $Re$ :

$$v \leq \frac{Re \cdot \nu}{b_1} \quad (\text{cm s}^{-1}) \quad [26]$$

Using the above values, the flow velocity is  $u \leq 21 \text{ cm s}^{-1}$ . Inserting this upper limit in eqn. [25], a mass transfer coefficient  $\beta$  of  $0.035 \text{ cm s}^{-1}$  is obtained. For a temperature of  $1500^\circ\text{C}$ , the carbon concentration in the liquid iron will be  $5.15 \text{ wt } \%$ .<sup>89</sup> Then, eqn. [24] yields the linear dissolution rate:

$$\begin{aligned} \frac{\Delta x}{\Delta t} &= 0.035 \frac{6.67 \cdot 5.16 - 5.15}{2.25 \cdot 100} \\ &= 10^{-5} \text{ cm s}^{-1} \text{ or } 0.04 \text{ cm h}^{-1} \end{aligned} \quad [27]$$

At such a rate, the lining in the hearth of the blast furnace would be fully worn out within a few hours of operation. However, because of the above-described mechanisms, the presence of a coke bed and the decrease in the carbon saturation by the additional elements present in the pig iron, a long service life of up to 2 years is achievable.

### 1.26.11.2 Marangoni Convection/SEN

Preferential wear along the three-phase steel/slag/refractory material interface, such as at a submerged entry nozzle (SEN) used in a mould or in a ladle, can be explained by the temperature and particularly by the concentration-dependent interface phenomenon of Marangoni convection (Figure 5). The refractory material reacts with the steel and the slag. If it contains carbon, it dissolves in the steel which is constrained by the oxide in the refractory material. In turn, the dissolution of the oxide in the refractory material into the slag is constrained by the graphite. Nonetheless,  $\sim 0.1 \text{ wt } \%$  of carbon dissolves into the slag. Because of this reaction, a local concentration gradient develops at the steel/slag interface. For

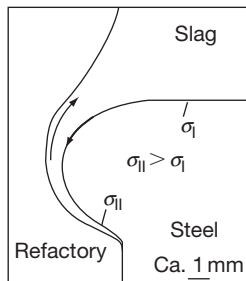


Figure 5 Advanced wear by Marangoni convection.

carbon-containing refractory material, there is a slightly increased carbon concentration in the region close to the three-phase interface, which makes the interfacial tension  $\sigma_{II}$  (Figure 5) higher than  $\sigma_I$ . A part of the carbon dissolved in the slag reacts with the steel, thereby forming carbon monoxide (CO) and this causes a locally decreased oxygen content at point II. The corresponding increase in the interfacial tension decreases the capillary activity of the slag and the steel tends to convect from point I to point II in order to decrease the interfacial tension there.

In a lot of cases, no infiltration occurs, because the corrosion progress is faster than the speed of infiltration. To estimate the extent of corrosive wear, one may use the approximation of eqn. [24]. The mass transfer coefficient  $\beta$  is estimated well by eqn. [25]. The flow velocity of the steel and slag along the phase interface is then<sup>90</sup>:

$$v_M = -\frac{b_g}{4\eta_s} \left( \frac{d\sigma}{dC} \text{grad } C + \frac{d\sigma}{dT} \text{grad } T \right) \quad (\text{cm s}^{-1}) \quad [28]$$

where  $b_g$  is the characteristic length of the corrosion groove (assumption:  $1 \text{ cm}$ ) and  $\eta_s$  is the dynamic viscosity of steel ( $1600^\circ\text{C}$ :  $0.04 \text{ g cm}^{-1} \text{ s}^{-1}$ ).

In this equation, the change in the interfacial energy of the steel/slag interface in relation to the oxygen content in the liquid steel is estimated as

$$\frac{d\sigma}{dC} = -\frac{200}{C_{[O]}^I} [\text{mN m}^{-1} \text{ wt } \%^{-1}] \quad [29]$$

the approximated concentration gradient of the oxygen along the phase interface is

$$\text{grad } C = \frac{C_{[O]}^I - C_{[O]}^{II}}{b_g} = 0.001 \text{ wt } \% \text{ cm}^{-1} \quad [30]$$

the change in the interfacial energy in relation to the temperature is<sup>91</sup>

$$\frac{d\sigma}{dT} = \sigma_T = -0.2 \text{ mN m}^{-1} \text{ K}^{-1} \quad [31]$$

and the approximated temperature gradient because of the heat removal to the refractory material is

$$\text{grad } T = \frac{T^I - T^{II}}{b} = 10 \text{ K cm}^{-1} \quad [32]$$

With an assumed oxygen content  $C_{[O]}^I = 0.004 \text{ wt } \%$  (40 ppm) in eqn. [19], the insertion of the values from eqns. [30]–[32] into eqn. [28] yields a flow velocity  $v_M$  of  $325 \text{ cm s}^{-1}$ .

Assuming that the back-flow velocity along the refractory material/slag interface is about the same



as  $v_M$ , the thickness of Prandtl's flow-boundary-layer  $\delta_{Pr}$  can be easily calculated:

$$\delta_{BL} = \left( \frac{\eta_{Sl} \cdot b}{\rho_{Sl} \cdot u_M} \right)^{1/2} \quad (\text{cm}) \quad [33]$$

where  $\eta_{Sl}$  is the dynamic viscosity of the slag ( $2 \text{ g cm}^{-1} \text{ s}^{-1}$ ,  $0.2 \text{ Pa s}^{-1}$ ) and  $\rho_{Sl}$  is the density of the slag ( $2.7 \text{ g cm}^{-3}$ ).

The thickness of the Nernst's diffusion-boundary-layer  $\delta_N$  is then

$$\delta_N = \left( \frac{\eta_{Sl}}{\rho_{Sl} D_{Sl}} \right)^{-1/3} \delta_{Pr} \quad (\text{cm}) \quad [34]$$

where  $D_{Sl}$  is the diffusion coefficient of the corrosion determining component ( $1650^\circ\text{C}$ :  $1 \times 10^{-7} \text{ cm}^2 \text{ s}^{-1}$ )

With these material values, we get  $\delta_{Pr} = 1.51 \times 10^{-2} \text{ cm}$  and  $\delta_N i = 1.67 \times 10^{-4} \text{ cm}$ . Accordingly, the mass transfer coefficient  $\beta$  is calculated by

$$\beta = \frac{D_{Sl}}{\delta_N} \quad (\text{cm s}^{-1}) \quad [35]$$

The result is  $\beta = 6 \times 10^{-4} \text{ cm s}$ . Assuming a slag whose starting content of  $\text{Al}_2\text{O}_3$  is  $\sim 13 \text{ wt } \%$ , and whose saturation concentration at  $1650^\circ\text{C}$  is in the range of  $60 \text{ wt } \%$   $\text{Al}_2\text{O}_3$ , the wear of a corundum-enriched, graphite-containing refractory material ( $\rho_R = 3.3 \text{ g cm}^{-3}$ ) due to Marangoni convection approximately amounts to

$$\begin{aligned} v_{\text{corr}} &= 360 \times 6 \times 10^{-4} \frac{2.7}{3.3} (60 - 12) \\ &= 8.5 \text{ mm h}^{-1} \end{aligned} \quad [36]$$

which is in accordance with laboratory experiments. The question is how to decrease this extremely severe corrosion. The process cannot be influenced easily. In the case of the continuous casting process, the concentration gradient and the temperature gradient are nearly fixed. The temperature and concentration dependency of the interfacial energy are natural values, and the same applies for the dynamic viscosity of the steel. Therefore, the only way left is to use a refractory material that is as chemically inert as possible.

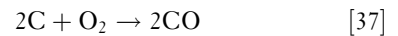
This is, for instance, achieved by the implementation of a sleeve made of  $\text{ZrO}_2$  at the three-phase interface of a SEN. According to eqn. [24], the slag and the mould powder, respectively, can be enriched with  $\text{Al}_2\text{O}_3$  up to a certain amount, in order to maintain the difference in the saturation concentration as small as possible.

### 1.26.11.3 Oxidation/Ladle

The crude steel coming from the melting aggregates (converter or electric arc furnace) is partially already post-treated during tapping into the ladle and then again within the ladle. This treatment, which is referred to as secondary metallurgy, includes the process steps<sup>92</sup> of degassing, decarburization, desulphurization, dephosphorization as well as removal of trace elements, fine adjustment of alloying contents, deoxidization, inclusion transformation, improvement in the purity levels as well as the solidifying structure, adjustment and homogenization of temperature and chemical composition.

To minimize the thermal stresses and the corresponding wear because of the actual temperature gradient when filling with crude steel ( $T$  up to  $1800^\circ\text{C}$ ), the cold ladle lined with  $\text{MgO-C}$  bricks is preheated for 2 hours in the steel mill. A newly lined ladle does not have a slag layer protecting the bricks against oxidation of the binding carbon (graphite, 5–15 wt %). As an instantaneous result of this pre-heating procedure, the graphite oxidizes. The carbon bonding and its advantageous properties such as the good thermal shock resistance and the nonwettability by slag are lost. At the same time, an enormous pore volume (about 35 vol %) is opened. Steel and slag can easily infiltrate into the microstructure and therewith lead to 'inner' dissolution.

The temporal progress of the reaction



in a  $\text{MgO-C}$  brick can be described by the following differential equation:

$$\frac{dx_i}{dt} = -2V_C D_P \frac{n_0 - n_i}{x_0 - x_i} \quad [38]$$

The sharp transition from the bright, decarburized outer zone to the black core suggests a topochemical reaction which is controlled by diffusion ( $\sqrt{t}$ -law). The determining factor is the pore-diffusion coefficient  $D_P$ <sup>93</sup>

$$D_P = D_{\text{O}_2} \gamma p_c \quad (\text{cm}^2 \text{ h}^{-1}) \quad [39]$$

with

$$D_{\text{O}_2} = 2.7 \times 10^{-2} T^{1.79} \quad (\text{cm}^2 \text{ h}^{-1}) \quad [40]$$

and

$$\gamma = 1.84 \times \sqrt{p_c} - 0.3 \quad [41]$$

where  $D_{O_2}$  is the diffusion coefficient of oxygen;  $T$ , the temperature ( $\approx 1373$  K);  $\gamma$ , the labyrinth factor; and  $p_c$  is the open porosity of the decarburized zone ( $\approx 0.35$ ).

The insertion of these values results in  $D_p = 3081 \text{ cm}^2 \text{ h}^{-1}$ . The solution of the differential equation [38] for an infinite plate is given by<sup>14</sup>

$$(1 - \phi)^2 = \tau \quad [42]$$

with

$$\phi = \frac{x_i}{x_0} \quad (x_i = x_0 \text{ at } t = 0) \quad [43]$$

where  $x_i$  is the position of the reaction front in the plate (cm) and  $x_0$  is the total thickness of the plate (cm).

$$\tau = \frac{t}{t_0} \quad [44]$$

where  $t$  is the time (h) and  $t_0$  is the time for total decarburization of a plate with  $x_0$  (h) and

$$t_0 = \frac{x_0^2}{2zV_C D_p (n_0 - n_i)} \quad (\text{h}) \quad [45]$$

where  $V_C$  is the mole volume of graphite ( $5 \text{ cm}^3 \text{ mol}^{-1}$ ),  $z$ , the geometry factor (infinite plate:  $z = 2$ );  $n_0$ , the oxygen content at the plate surface (20 vol %;  $2 \times 10^{-6} \text{ mol cm}^{-3}$ ); and  $n_i$  is the oxygen content at the reaction front ( $n_i \ll n_0$ ,  $n_i \rightarrow 0$ ).

A MgO–C brick with  $x_0 = 10 \text{ cm}$  would be totally decarburized within  $t_0 = 1014 \text{ h}$ . The time  $t$  required to decarburize 1 cm ( $x_i = 9 \text{ cm}$ ) of the brick results as follows:

$$\tau = \left(1 - \frac{9}{10}\right)^2 = 0.01 \quad [46]$$

$$\text{with } t = \tau t_0 = 0.01 \times 1014 \text{ h} = 10.14 \text{ h}$$

Numerous experiments demonstrated that the process is in fact controlled by diffusion and is extensively blocked by specific additives, such as  $>10 \text{ wt } \% \text{ ZrB}_2$ . However, the addition of 3 wt % metallic aluminum as an antioxidant has hardly any effect, since the porosity of the decarburized refractory material is high, and during the coke reaction at  $T \geq 800^\circ \text{C}$ , the metallic aluminum is consumed by the formation of  $\text{Al}_3\text{C}_4$ , and above  $1200^\circ \text{C}$  by spinel formation.

## 1.26.12 Erosion

### 1.26.12.1 Blast Wear/Pipes

Pneumatic conveying systems and pipes in thermo-technical aggregates are subject to severe wear

because of erosion. The reason for this is the segregation of a solid loaded gas flow because of the mass inertia of its solid particles. These particles impact mostly in areas of flow redirection (elbow) onto the refractory lining, whereby a cyclic mechanical stress occurs at permanently changing surface areas. For brittle materials, such as refractories, these alternating local impacts and corresponding multiaxial tensile and compression loads finally cause material removal by surface disruption. It should be noted that the resulting wear is always a system characteristic and is influenced by numerous factors.

At room temperature, the testing of refractory materials with respect to their wear by perpendicular impacting solid particles is performed according to ASTM C 704. For this purpose, 1000 g of SiC particles of predefined granularity are accelerated by a pressurized air flow within  $450 \pm 15 \text{ s}$  and shot over a distance of 203 mm perpendicular onto a surface of a test sample. The resulting wear volume (in  $\text{cm}^3$ ) is determined by weighing the geometrically well-defined sample.

However, the results thus achieved can hardly be transferred to the temperatures applied in operation. That is why a special experimental setup was developed, which is as far as possible in accordance with ASTM C 704 and whereby the wear by impacting particles can be determined at temperatures of up to  $1400^\circ \text{C}$ . The main item of this experimental setup is a ring burner by which the pressurized air flow, the blasting abrasive (SiC particles), and the test sample are heated to the relevant test temperature. It has been shown that the wear volume of heterogenic refractory materials decreases with an increase in temperature, which correlates quite well with the change in thermomechanical properties.

While brittle–elastic deformation behavior occurs at room temperature, viscoplastic deformation behavior is dominant at high temperatures, where molten phases from the binder phase are present. The local stress peaks, which are generated by the impacting SiC particles, are decreased by plastic deformation and by stress relaxation of the binder phase, respectively. In this context, particularly wear-resistant grains (SiC, corundum) incorporated inside the microstructure show no wear-reducing action.<sup>94</sup> Moreover, these grains break upon impact of a SiC particle because of their poor ductility.

### 1.26.12.2 Flowing Melts/Converter

During filling of a torpedo ladle or a converter with pig iron, or of a ladle with crude steel, the melt often ‘falls’ at about 2 m. Because of the high flow speed, the lining in the collision area of the melt

stream, which is possibly predamaged by chemical dissolution, thermal shock stress, or infiltration, is washed out. However, a quantitative prognosis is not possible. The same applies for the circulation current generated during gas stirring treatment within a converter or in a ladle. In connection with the high flow velocities of the melt, cavitation erosion might play a significant role, but this has not been examined further in the field of steel production.

## 1.26.13 Mechanical Wear

### 1.26.13.1 Thermal Shock Resistance/Ladle

In practice, mechanical wear as an instantaneous result of a poor thermal shock resistance is commonly found. During the filling of a ladle with crude steel, the lining is heated up rapidly from 1000 to 1800 °C within a few minutes. High tensile stresses develop in the surface, which frequently results in a single incipient crack, which can grow catastrophically. Off-bursts occur in the surface region of the lining, which is also referred to as 'spalling.' This mechanism is promoted by a modified structure of surface areas containing slag infiltrations.

An assessment of various refractory materials concerning their thermal shock resistance can be performed by the quick quenching of a 950 °C test sample by blowing pressurized air (DIN EN V 993-11) onto its surface, or by dipping the test sample into water (DIN 51068-1). Then tensile stresses occur, starting from the surface, which result in a large amount of incipient cracking. Usually, a catastrophic break does not occur.

No isothermal boundary conditions can be found in these cases and therefore a theoretical treatment becomes difficult. Modeling of 'quasistationary' crack propagation is possible, but during rapid heating up of a ladle lining, unstable crack propagation occurs. Therefore, characterization of the thermal shock resistance of refractory materials uses the resistance parameter  $R$  during unstable crack propagation and  $R_{st}$  during stationary crack propagation<sup>95</sup>:

$$R''' = \frac{G_F E}{\sigma_c^2} \approx L \text{ (mm)} \quad [47]$$

$$R_{st} = \sqrt{\frac{G_F}{\alpha^2 E}} \text{ (m}^{1/2} \text{ K)} \quad [48]$$

where  $G_F$  is the crack energy (J m<sup>-2</sup>);  $E$ , the modulus of elasticity (GPa);  $\sigma_c$ , the critical stress (MPa);  $\alpha$ , the thermal expansion coefficient (K<sup>-1</sup>); and  $L$  is the characteristic length (mm).

Both equations were derived from nonlinear fracture mechanics, which is necessary when dealing with refractory materials, since they have a very heterogeneous structure (grains, binder phase, pores). Together, both crack resistance parameters describe the so-called structure flexibility. From eqns. [47] and [48], it is plain that an increase in the required crack energy and the crack propagation work  $G_F$  with both unstable as well as 'quasistationary' crack propagation is advantageous in order to reach a high value for the respective resistance parameter and, therefore, to achieve a high thermal shock resistance.

This can be obtained in structures with coarse grains in a fine-grained matrix, where entanglement of the grains increases the crack length. The modulus of elasticity, however, has the opposite effect, which is dependent on the mechanism of the crack propagation alone. With unstable crack propagation, the crack itself and the incipient crack arising must be as big as possible to reach the area of the 'quasistationary' crack propagation without reaching the catastrophic breakpoint. In the area of the stationary crack propagation, the modulus of elasticity should be as small as possible, which calls for an optimization of the structure concerning both crack propagation mechanisms. A crack then gradually propagates with every higher and more critical temperature difference.

In spite of great experimental endeavor, no definite connection between the resistance parameters and the standard tests for judging the thermal shock resistance has been found.<sup>96</sup> At the moment, values must be inserted into the aforementioned equations, which have been measured isothermally.

Critical heating rates may be calculated according to the example of a hot plate made out of sintered corundum (99% Al<sub>2</sub>O<sub>3</sub>) at 1000 °C:

$$\dot{T} = \frac{\varepsilon_c (1 - 2\mu)}{3\alpha} \frac{16a}{x^2} \text{ (K s}^{-1}\text{)} \quad [49]$$

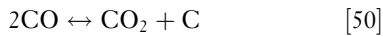
where  $\varepsilon_c$  is the critical elongation (0.001);  $\mu$ , the Poisson ratio (0.21);  $\alpha$ , the thermal expansion coefficient ( $1 \times 10^{-5}$  K<sup>-1</sup>);  $a$ , the thermal diffusivity ( $1 \times 10^{-6}$  m<sup>2</sup> s<sup>-1</sup>); and  $x$  is the thickness of the plate (0.02 m).

Inserting the values results in  $\dot{T} = 0.77$  K s<sup>-1</sup>. If the sample cools down/warms up faster, a breakage (crack) occurs.

### 1.26.13.2 Carbon Bursting/Blast Furnace

In industrial processes (chemical plants, blast furnace shaft) in the temperature range from 400 to 800 °C,

carbon bursting of refractory material in atmospheres containing CO is known. This phenomenon is due to the temperature dependence of the Boudouard equilibrium:



When crystalline graphite precipitates in refractory materials, it can create an enormous crystallization pressure, capable of bursting the structure. This precipitation is said to be catalytically promoted by metallic iron, hematite ( $\text{Fe}_2\text{O}_3$ ), and magnetite ( $\text{Fe}_3\text{O}_4$ ). In examination of the resistance to CO according to ASTM C 288, refractory materials are exposed to a pure CO atmosphere after a thermal pretreatment at 500 °C for 200 h.

A small amount of hydrogen ( $\sim 3\%$ ) accelerates the carbon precipitation and thus we assume a catalytic effect of hydrogen. After the test, a visual evaluation of the refractory material leading to a classification concerning its resistance to CO is performed. The resulting crystallization pressure ( $\pi - 1$ ) can be calculated using the following equation:

$$\pi - 1 = \frac{-\Delta G^0 - RT \ln K_C}{\Delta V_C \frac{R}{R^*}} \quad [51]$$

where  $\Delta G^0$  is the free enthalpy in the standard state (J/mol);  $R$ , the universal gas constant ( $8.314 \text{ J mol}^{-1} \text{ K}^{-1}$ );  $R^*$ , the gas constant ( $84.8 \text{ atm cm}^3 \text{ mol}^{-1} \text{ K}^{-1}$ );  $T$ , the temperature (K);  $K_C$ , the equilibrium constant; and  $\Delta V_C$  is the mole volume of graphite ( $5 \text{ cm}^3 \text{ mol}^{-1}$ ).

At 500 °C (773 K), magnetite is reduced to metallic iron, if the volumetric contents of CO and  $\text{CO}_2$  are equal; the formation of graphite results for the earlier stated reaction [50] with

$$K = \frac{P_{\text{CO}_2}}{P_{\text{CO}}} = 2 \quad \text{with } a_C = 1 \quad [52]$$

$$\begin{aligned} \Delta G^0 &= 169452 - 172.6T, \\ \Delta G^0(773\text{K}) &= -35522 \text{ J mol}^{-1} \end{aligned} \quad [53]$$

Inserting all values in eqn. [51] results in a crystallization pressure of 63 375.3 atm, corresponding to 62 150 bars, thereby destroying the structure of the refractory material.

### 1.26.13.3 Destruction due to Impact/Converter

In the converter, crude steel is produced by blowing oxygen onto and/or into the molten pig iron. In this

process, the dissolved carbon is oxidized to a certain amount. Iron and those elements accompanying the pig iron such as P, Si, and Mn are oxidized and form a slag. Temperatures of above 2000 °C are reached by strong exothermal reactions. It is, therefore, preferable that a large part of the crude steel charge is replaced by scrap steel, whose melting offers a cooling effect for the melt.

The lining of an emptied converter is  $\sim 1200$  °C at the hot bottom and is therefore under both thermal and mechanical stresses upon refilling with scrap steel.

To estimate the procedures during charging, the transmitted mechanical energy of a falling scrap piece  $mgb$  onto an impact area  $A$  is equated with the required crack energy  $nG_F$  for a number of  $n$  cracks. The prevailing impact area and the number of produced cracks are unknown, since the position of the scrap piece at the moment of impact is incidental and the shock wave spreads into the floor. It is assumed that a scrap piece falling from a height  $b = 4$  m with a mass  $m = 100$  kg influences a surface area  $A = 0.1 \text{ m}^2$ . The measured crack energy of the MgO–C material at 1200 °C is  $G_F = 500 \text{ J m}^{-2}$ . The number of emerging cracks is

$$n = \frac{mgb}{AG_F} = \frac{100 \times 9.81 \times 4}{0.1 \times 500} \approx 80 \quad [54]$$

and accordingly MgO–C material may break out of the surface. In the following refining process, temperatures of above 1800 °C develop, so there is also a good chance that cracks will heal again. To improve the structural flexibility of such stressed components, metallic aluminum powder and steel needles are added to the MgO–C material.<sup>97</sup>

## 1.26.14 Infiltration by Steel and Slag

### 1.26.14.1 Basic Equations

The contact of a pure oxide and a graphite-containing refractory material with liquid steel or slag in a thermodynamic equilibrium is described by wetting theory. The vectors of the surface tensions of the three involved phases acting at the point of contact of all three phases are in a mechanical equilibrium state:

$$\sigma_R - \sigma_S \cos \theta - \sigma_{R/S} = 0 \quad [55]$$

where  $\sigma_R$  is the surface tension of the refractory material ( $\text{mN m}^{-1}$ );  $\sigma_S$ , the surface tension of the

steel or slag ( $\text{mN m}^{-1}$ );  $\sigma_{\text{R/S}}$ , the interfacial tension between refractory material/steel or refractory material/slag ( $\text{mN m}^{-1}$ ); and  $\theta$  is the wetting angle ( $^\circ$ ).

The interactions of the three phases involved are characterized by the wetting angle of contact:

$$\cos\theta = \frac{\sigma_{\text{R}} - \sigma_{\text{R/S}}}{\sigma_{\text{S}}} \quad [56]$$

and

$$\theta > 90, \quad \text{if } \sigma_{\text{R}} - \sigma_{\text{R/S}} < 0 \text{ (non-wettability)}$$

$$\theta = 90, \quad \text{if } \sigma_{\text{R}} - \sigma_{\text{R/S}} = 0$$

$$\theta < 90, \quad \text{if } \sigma_{\text{R}} - \sigma_{\text{R/S}} > 0 \text{ (wettability)}$$

The wetting angle of contact  $\theta$  and the surface tension  $\sigma_{\text{S}}$  are the decisive values for the infiltration of a capillary or pore by steel or slag, which can be determined experimentally. The equilibrium of forces in a partly filled pore is then:

$$\rho_{\text{S}} g b = - \frac{4\sigma_{\text{S}} \cos\theta}{d} \quad [57]$$

where  $\rho_{\text{S}}$  is the density steel/slag ( $\text{kg m}^{-3}$ );  $g$ , the acceleration of gravity ( $\text{m s}^{-2}$ );  $b$ , the height of steel-/slag-column above the pore entry (m);  $d$  is the pore diameter (m).

If the wetting angle of contact  $\theta$  is smaller than  $90^\circ$ , capillary ascension is present. For instance, a liquid slag penetrates the pore or capillary system of an oxidic refractory material without the effect of any external force. In the case of liquid steel and oxide refractory material, capillary depression is present, since the wetting angle of contact is  $\theta > 90^\circ$ . Thus, an external (ferrostatic) pressure is necessary to allow the liquid steel to penetrate into the pore or capillary system. The same is true for a slag that does not wet the graphite binder phase of the oxide refractory material.

The infiltration speed of the slag or steel into the structure results from the Hagen–Poiseuille equation<sup>98</sup>:

$$\frac{dl}{dt} = \frac{d^2}{32\eta l} \left( \frac{4\sigma_{\text{S}} \cos\theta}{d} + \rho g b \right) \quad [58]$$

Integration leads to the penetration depth  $l$ , in relation to the time  $t$ :

$$l = \sqrt{\left( \frac{d\sigma_{\text{S}} \cos\theta}{4\eta_{\text{S}}} + \frac{d^2 \rho_{\text{S}} g b}{16\eta_{\text{S}}} \right) t} \quad [59]$$

where  $l$  is the penetration depth (m);  $\eta_{\text{S}}$ , the dynamic viscosity of steel/slag (Pa s); and  $t$  is the time (s).

## 1.26.15 Examples

### 1.26.15.1 Slag/MgO

A MgO brick in contact with a slag with a minimal surface energy at  $1600^\circ\text{C}$  ( $\sigma_{\text{S}} = 0.51 \text{ N m}^{-1}$ ,  $\eta_{\text{S}} = 1 \text{ Pa s}$ ) will show a penetration depth of 1 cm within a pore  $d = 50 \mu\text{m}$  according to eqn. [59] after an interaction period of 10 min. The dependence on the wetting angle disregarding a slag-column above the pore entry is outlined in Table 1. Note that this estimation is obtained with simplifications, namely that there is neither chemical interaction between the slag and the refractory material nor a temperature gradient within the inner structure.

### 1.26.15.2 Steel/MgO

Liquid steel ( $1600^\circ\text{C}$ :  $\sigma_{\text{S}} = 1.5 \text{ N m}^{-1}$ ,  $\eta_{\text{S}} = 6.8 \times 10^{-3} \text{ Pa s}$ ,  $\rho_{\text{S}} = 7.700 \text{ kg m}^{-3}$ ) and a MgO brick show completely different infiltration because of the wetting angle of  $\theta = 120^\circ$ . According to eqn. [57], steel can only penetrate into open pores, if their diameter is sufficiently large. For this, Table 2 gives the infiltration

**Table 1** Penetration depth of a slag in relation to the wetting angle of contact ( $d = 50 \mu\text{m}$  and  $t = 600 \text{ s}$ )

$(^\circ)$	$l \text{ (cm)}$
0	1.96
10	1.94
20	1.90
30	1.82
40	1.71
50	1.57
60	1.38
70	1.14
80	0.81
89	0.26
90	0

**Table 2** Infiltratable pore diameter  $d$  and penetration depth  $l$  in relation to the steel pool depth  $h$

$h \text{ (m)}$	$d \text{ (m)}$	$l \text{ (m). } d = 200 \text{ m}$
0.25	172	0.73
0.50	86	2.10
0.75	57	2.80
1.00	43	3.48
1.25	34	4.00
1.50	29	4.46
1.75	25	4.87
2.00	22	5.25
2.25	19	5.61
2.50	17	5.94
2.75	16	6.26
3.00	14	6.56



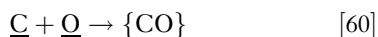
pore diameter  $d$  in relation to the depth of the steel pool,  $b$  (ferrostatic pressure). As we can see, the greater the depth, the higher the risk of infiltration of smaller pores.

Considering a depth,  $b$ , the penetration depth of the steel into a pore having a diameter of  $d = 200 \mu\text{m}$  after 10 min is calculated according to eqn. [59]. The penetration depth increases with a growing pool depth  $b$  and amounts to  $a$  about 2 m (see Table 2).

### 1.26.15.3 Steel/MgO–C

The graphitic binder phase of MgO–C bricks is resistant to slag because graphite is not wetted and only minimally dissolved. In contact with liquid steel, the situation is different. For example, carbon is soluble in iron at a temperature of  $1600^\circ\text{C}$ , up to 5.41 wt %. Therefore MgO–C should not be useful in practice and the question arises: ‘Why can MgO–C be used?’

1. From the Vatcher–Hamilton equilibrium between dissolved oxygen in iron and carbon<sup>88</sup>:



At  $1600^\circ\text{C}$  the partial pressure  $P_{\text{CO}}$  is

$$\underline{\text{C}} \cdot \underline{\text{O}} = 0.0024 P_{\text{CO}} \quad [61]$$

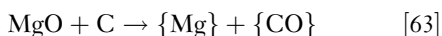
If a steel melt with a dissolved oxygen content of 30 ppm tries to enter into a pore and therefore comes into contact with the graphitic binder phase, the carbon activity  $a_{\text{C}}$  at this specific point is, thus, 1. Inserted into eqn. [45]

$$P_{\text{CO}} = \frac{1 \times 0.003}{0.0024} = 1.25 \text{ bar} \quad [62]$$

At the contact point, therefore, CO gas is produced, which separates the reaction partners from each other and retards the dissolution and the infiltration kinetically.

2. If steel would enter into the pore despite the CO cushion, the solubility of the carbon would be strongly decreased. The partial pressure  $P_{\text{CO}}$  inside the structure is only 0.05 bar. From eqn. [61], we have  $\underline{\text{C}} = 0.04 \text{ wt } \%$  for the dissolved carbon, which can be supported by experimental data.<sup>99</sup>

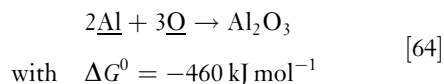
3. Furthermore, the formation of a MgO protective layer may take place because of the carbothermal reaction inside the structure:



Gaseous magnesium dissolves in the steel and reacts with the oxygen also dissolved in the steel in

order to form secondary MgO that precipitates at the interface (heterogeneous nucleation) and, thus, restrains further infiltration into the structure.

4. The carbon solubility in liquid iron is also affected by higher aluminum levels and the reaction thereof with oxygen. If the MgO–C material contains, for instance, metallic aluminum as an antioxidant, this metallic aluminum melts on contact with the steel and dissolves into the steel, infiltrating the open pores. During this process, an oxidation reaction according to the following equation occurs:



The equilibrium constant  $K$  of this reaction at  $1600^\circ\text{C}$  is

$$K = \frac{\underline{\text{Al}}^2 \cdot \underline{\text{O}}^3}{1} = e^{-\Delta G^0/RT} = 3 \times 10^{-13} \quad [65]$$

In general, the steel penetrating the pores contains 0.1 wt % of dissolved aluminum. The content of dissolved oxygen then in the equilibrium state is, according to eqn. [65],  $\sim 3 \text{ ppm}$ . As a consequence, the oxygen potential is decreased so that the bumping effect of the CO gas and the formation of a MgO protective layer are suspended. The infiltration and dissolution of the graphitic binder material are promoted. Accordingly, the content of carbon dissolved in the infiltrate, from eqn. [61], is

$$\underline{\text{C}} = \frac{0.0024 \times 0.05}{0.0003} = 0.4 \text{ wt } \% \quad [66]$$

which is much less than 5.4%.

In summary, infiltration influences the corrosion profoundly. It may have beneficial effects, if the reaction with the refractory material leads to a surface compaction (formation of an MgO protective layer) or to stiffening of the infiltrate (slag), but it also can have detrimental effects, if chipping (spalling) occurs.

### 1.26.16 Concluding Remarks

As can be seen from this chapter about ceramics and refractories, the subject is fairly complex, because often the interplay of physical boundary conditions and chemical interaction is governing corrosion processes. Furthermore, the microstructure of the materials, particularly when it comes to refractories, is likewise adding complexity, because several phases interact simultaneously and the ubiquitous porosity is

also causing problems in investigating the processes. Thus, despite its industrial importance there are a lot of things to be learned and certainly there are good possibilities to improve the corrosion resistance.

We are sure that the progress, which was made in the investigations of the technical ceramics and is described in the first parts of this chapter, will help both to extend the use of those materials in high temperature processes and to find economic viable solutions for the refractory world. Doing so could become a key issue in helping us to work more efficiently and less harmfully for our environment in many processes. The efforts to protect our climate could have a significant input from the work on corrosion resistant ceramics and refractories.

## References

- Kingery, W. D.; Bowen, H. K.; Uhlmann, D. R. *Introduction to Ceramics*, 2nd ed.; John Wiley: New York, 1976; 1038.
- Barsoum, M. W. *Fundamentals of Ceramics*; Drexel University: Philadelphia, 2002; 600.
- Richerson, D. W. *Modern Ceramic Engineering*, 3rd ed.; CRC Press, 2006; 707.
- Carter, C. B.; Norton, M. G. *Ceramic Materials Science and Engineering*; Springer: Berlin, 2007; 740.
- Carniglia, S. C.; Barna, G. L. *Handbook of Industrial Refractories Technology – Principles, Types, Properties and Applications* William Andrew Publishing: Noyes, USA, 1992.
- Schacht, C. *Refractories Handbook*; CRC, 2004; 520.
- Goursat, A. G.; Smeltzer, W. W. Oxidation of iron Rev. *High-Temp. Mater.* **1973**, 1(4), 351–395.
- Nesbitt, J. A. *Oxid. Metals* **1995**, 44(1/2), 309–338.
- Irene, E. A. *CRC Crit. Rev. Solid State Mater. Sci.* **1988**, 14(2), 175–223.
- Deal, B. E.; Grove, A. S. *J. Appl. Phys.* **1965**, 36(12), 3770–3778.
- Nickel, K. G. *J. Eur. Ceram. Soc.* **1992**, 9, 3–8.
- Reisman, A.; Nicollan, E. H.; Williams, C. K.; Merz, C. J. *J. Electron. Mater.* **1987**, 16(1), 45–55.
- Nickel, K. G.; Gogotsi, Y. G. In *Handbook of Ceramic Hard Materials*; Riedel, R., Ed.; VCH-Wiley: Weinheim, 2000; Vol. 1; pp 140–182.
- Nickel, K. G. *Corrosion of Advanced Ceramics – Measurement and Modelling*; Kluwer Academic Publisher: Dordrecht, NL, 1994; Vol. 267; 467.
- Nickel, K. G. *J. Eur. Ceram. Soc.* **2005**, 25(10), 1699–1704.
- Ogbuji, L. U. *J. T. J. Electrochem. Soc.* **1998**, 145(8), 2876–2882.
- Jacobson, N. S.; Fox, D. S.; Smialek, J. L.; Opila, E. J.; Tottorelli, P. F.; More, K. L.; Nickel, K. G.; Hirata, T.; Yoshida, M.; Yuri, I. In *Ceramic Gas Turbine Component Development and Characterisation*; Van Roode, M., Ferber, M. K., Richerson, D. W., Eds.; ASME Press: New York, 2003; pp 607–640.
- Opila, E. J.; Hann, R. E., Jr. *J. Am. Ceram. Soc.* **1997**, 80(1), 197–205.
- Tedmon, C. S. *J. Electrochem. Soc.* **1966**, 142(3), 925–930.
- Opila, E. J. *J. Am. Ceram. Soc.* **2003**, 86(8), 1238–1248.
- Baxter, D. J. In *Corrosion of Advanced Ceramics – Measurement and Modelling*; Nickel, K. G., Ed.; Kluwer Academic Publishers: Dordrecht, NL, 1994; Vol. NATO ASI E 267; pp 249–260.
- Opila, E. J. *J. Am. Ceram. Soc.* **1994**, 77(3), 730–736.
- Maier, N.; Nickel, K. G. *Key Eng. Mater.* **2006**, 326–328, 1780–1783.
- Opila, E. J. *J. Am. Ceram. Soc.* **1995**, 78(4), 1107–1110.
- Maeda, M.; Nakamura, K.; Tsuge, A. *J. Mater. Sci. Lett.* **1989**, 8, 195–197.
- Tai, W.-P.; Watanabe, T.; Jacobson, N. J. *Am. Ceram. Soc.* **1999**, 82(1), 245–248.
- Mah, T.; Keller, K. A.; Sambasivan, S.; Kerans, R. J. *J. Am. Ceram. Soc.* **1997**, 80(4), 874–878.
- Federer, J. I. In *Corrosion and Corrosive Degradation of Ceramics*; Tressler, R. E., McNallan, M., Eds.; Martinus Nijhoff: Boston, MA, 1990; pp 425–443.
- Jacobson, N.; Myers, D.; Opila, E.; Copland, E. J. *Phys. Chem. Solids* **2005**, 66(2–4), 471–478.
- Readey, D. W. *J. Eur. Ceram. Soc.* **1998**, 18, 2383–2387.
- Sarpoolaky, H.; Zhang, S.; Lee, W. E. J. *J. Eur. Ceram. Soc.* **2003**, 23, 293–300.
- Oda, K.; Yoshio, T. *J. Am. Ceram. Soc.* **1997**, 80(12), 3233–3236.
- Hirata, T.; Ota, S.; Morimoto, T. *J. Eur. Ceram. Soc.* **2003**, 23, 91–97.
- Hannink, R. H. J.; Kelly, P. M.; Muddle, B. C. *J. Am. Ceram. Soc.* **2000**, 83(3), 461–487.
- Herrmann, M.; Schilm, J.; Michael, G.; Seipel, B.; Nickel, K. G. *J. Eur. Ceram. Soc.* **2005**, 25(10), 1805–1812.
- Li, Y. Q. *Mater. Sci. Eng. A* **2007**, 444, 184–191.
- Steinbruck, M.; Veshchunov, M. S.; Boldyrev, A. V.; Shestak, V. E. *Nucl. Eng. Des.* **2007**, 237(2), 161–181.
- Gogotsi, Y. G.; Yaroshenko, V. P.; Porz, F. J. *Mater. Sci. Lett.* **1992**, 11, 308–310.
- Gogotsi, Y. G.; Lavrenko, V. A. *Corrosion of High-Performance Ceramics*; Springer Verlag: Berlin, F.R.G., 1992; 181.
- Morell, R. *Handbook of Properties of Technical & Engineering Ceramics* HMSO Books: London, 1987.
- Haase, V. In *Gmelins Handbuch der Anorganischen Chemie*; Schröder, F., Ed.; Springer: Berlin, 1986; Vol. B3; pp 325–395.
- Nickel, K. G.; Quirnbach, P. In *Technische Keramische Werkstoffe*; Kriegesmann, J., Ed.; Deutscher Wirtschaftsdienst: Köln 1991; pp 1–76.
- Tressler, R. E.; McNallan, M. *Corrosion and Corrosive Degradation of Ceramics* American Ceramic Society: Westerville, OH, 1990. Vol. 10; 493.
- Blachere, J. R.; Pettit, F. S. *High Temperature Corrosion of Ceramics*. Noyes Data Corporation: Park Ridge, NJ, 1989; 188.
- Gogotsi, Y. G.; Yoshimura, M. *J. Mater. Sci. Lett.* **1994**, 13, 395–399.
- Gogotsi, Y. G.; In-Deok, J.; McNallan, M. J. *J. Mater. Chem.* **1997**, 7(9), 1841–1848.
- Jacobson, N. S.; Smialek, J. L.; Fox, D. S. In *Handbook of Ceramics and Composites*; Cheremisinoff, N. P., Ed.; Marcel Dekker: New York, 1990; pp 99–136.
- Jacobson, N. S. *J. Am. Ceram. Soc.* **1993**, 76(1), 3–28.
- Jacobson, N. S.; Smialek, J. L.; Fox, D. S. In *Corrosion of Advanced Ceramics – Measurement and Modelling*; Nickel, K. G., Ed.; Kluwer Academic Publishers: Dordrecht, 1994; Vol. NATO ASI Series E 267; pp 205–222.
- Jacobson, N. S. *J. Am. Ceram. Soc.* **1985**, 68(8), 432–439.

51. Berthold, C.; Nickel, K. G. *J. Eur. Ceram. Soc.* **1998**, *5*, 2365–2372.
52. Nickel, K. G.; Berthold, C. In *High Temperature Corrosion and Materials Chemistry*; McNallan, M. J., Opila, E. J., Maruyama, T., Narita, T., Eds.; Electrochemical Society: Pennington, NJ, 2000; Vol. PV 99–38; pp 429–438.
53. Ip, S. Y.; McNallan, M. J.; Park, D. S. *J. Am. Ceram. Soc.* **1992**, *75*(7), 1942–1948.
54. Schneider, G. A.; Nickel, K. G.; Petzow, G. In *Physics and Chemistry of Carbides, Nitrides and Borides, NATO ASI Series E: 185*; Freer, R., Ed.; Kluwer Academic: Dordrecht, NL, 1990; pp 387–401.
55. Narushima, T.; Goto, T.; Yokoyama, Y.; Iguchi, Y. *J. Am. Ceram. Soc.* **1993**, *76*(10), 2521–2524.
56. Presser, V.; Nickel, K. G. *CRC Crit. Rev. Solid State Mater. Sci.* **2008**, *33*(1), 1–99.
57. Costello, J. A.; Tressler, R. E. *J. Am. Ceram. Soc.* **1986**, *69*(9), 674–681.
58. Ogbuji, L. U. J. T.; Opila, E. J. *J. Electrochem. Soc.* **1995**, *142*(3), 925–930.
59. Ramberg, C. E.; Worrell, W. L. *J. Am. Ceram. Soc.* **2001**, *84*, 2607–2716.
60. Opila, E. J. *J. Am. Ceram. Soc.* **1999**, *82*(3), 625–636.
61. Sangster, R. C.; Kämpf, P.; Nohl, U. *Silicon Suppl. B 5d2*; Springer-Verlag: Berlin, 1995; Vol. 15; 304.
62. Yoshio, T.; Oda, K. In *Corrosion and Corrosive Degradation of Ceramics*; Tressler, R. E., McNallan, M., Eds.; American Ceramic Society, 1990; pp 367, 386.
63. Oda, K.; Yoshio, T.; Miyamoto, Y.; Koizumi, M. *J. Am. Ceram. Soc.* **1993**, *76*(5), 1365–1368.
64. Sangster, R. C.; Bär, G. In *Gmelin Handbook of Inorganic and Organometallic Chemistry*; Schröder, F., Ed.; 8th ed.; Springer-Verlag: Berlin, 1995; Vol. Suppl. B 5d1; p 255.
65. Fox, D. S.; Smialek, J. L. *J. Am. Ceram. Soc.* **1990**, *73*(2), 303–311.
66. Fox, D. S.; Jacobson, N. S.; Smialek, J. L. In *Corrosion and Corrosive Degradation of Ceramics*; Tressler, R. E., McNallan, M., Eds.; Martinus Nijhoff: Boston, MA, 1990; pp 227–249.
67. Singhal, S. C. *Ceramurgia Int.* **1976**, *2*(3), 123–129.
68. Ogbuji, L.; Smialek, J. *J. Electrochem. Soc.* **1991**, *138* (10), 51–53.
69. Oda, K.; Yoshio, T. *J. Ceram. Soc. Jpn.* **1993**, *101*(8), 855–859.
70. Jacobson, N.; Farmer, S.; Moore, A.; Sayir, H. *J. Am. Ceram. Soc.* **1999**, *82*(2), 393–398.
71. Jacobson, N. S.; Eckel, A. J.; Misra, A. K.; Humphrey, D. L. *J. Am. Ceram. Soc.* **1990**, *73*(8), 2330–2332.
72. Riedel, R.; Kienzle, A.; Dreßler, W.; Ruwisch, L.; Bill, J.; Aldinger, F. *Nature* **1996**, *382*, 796–798.
73. Friess, M.; Bill, J.; Aldinger, F.; Szabo, D. V.; Riedel, R. *Key Eng. Mater.* **1994**, 89–9195–100.
74. Riedel, R.; Kleebe, H.-J.; Schönfelder, H.; Aldinger, F. *Nature* **1995**, *374*(6), 526–528.
75. Nickel, K. G. In *Precursor-Derived Ceramics*; Bill, J., Wakai, F., Aldinger, F., Eds.; VCH-Wiley: Weinheim, 1999.
76. Butcherit, E.; Nickel, K. G.; Müller, A. *J. Am. Ceram. Soc.* **2001**, *84*(10), 2184–2188.
77. Müller, A.; Gerstel, P.; Butcherit, E.; Nickel, K. G.; Aldinger, F. *J. Eur. Ceram. Soc.* **2004**, *24*, 3409–3417.
78. Wang, Y.; Fei, W.; An, L. *J. Am. Ceram. Soc.* **2006**, *89*(3), 1079–1082.
79. Jacobson, N. S.; Gogotsi, Y. G.; Yoshimura, M. *J. Mater. Chem.* **1995**, *5*(4), 595–601.
80. Gogotsi, Y. G.; Dransfield, G.; Porz, F. In *Microscopy of Oxidation*; Newcomb, S. B., Bennett, M. J., Eds.; The Institute of Materials: Cambridge, 1993; Vol. 2; pp 509.
81. Shimada, S.; Takada, Y.; Tsujino, J. *J. Eur. Ceram. Soc.* **2005**, *25*, 1765–1770.
82. Basu, B.; Raju, G. B.; Suri, A. K. *Int. Mater. Rev.* **2006**, *51* (6), 352–374.
83. Kulpa, A.; Troczynski, T. *J. Am. Ceram. Soc.* **1996**, *79*(2), 518–520.
84. Voitovich, V. B.; Lavrenko, V. A.; Adejev, V. M. *Oxid. Metals* **1994**, *42*(1), 145–161.
85. Raj, R.; Riedel, R.; Soraru, G. D. *J. Am. Ceram. Soc.* **2001**, *84*(10), 2158–2159.
86. Wang, Z. C.; Gerstel, P.; Kaiser, G.; Bill, J.; Aldinger, F. *J. Am. Ceram. Soc.* **2005**, *88*(10), 2709–2712.
87. Nguyen, Q. N.; Opila, E. J.; Robinson, R. C. *J. Electrochem. Soc.* **2004**, *151*(10), B558–B562.
88. Czichos, H. *HÜTTE - Die Grundlagen der Ingenieurwissenschaften*, 29th ed.; Springer-Verlag: Berlin, 1991; 1417.
89. Markert, J. Gravimetrische und elektrochemische Untersuchung der Reaktion zwischen Kieselsäure und Korund in desoxidierten Eisenschmelzen. RWTH Aachen, Aachen, 1977.
90. Levich, V. G. *Physicochemical Hydrodynamics*; Prentice Hall: Englewood Cliffs, NJ, 1962; pp 373–390.
91. Turkdogan, E. T. *Physicochemical Properties of Molten Slags and Glasses*; Metals Society: London, 1983; pp 163–174.
92. Eisenhüttenleute, V. D. *Stahlfibel*; Verlag Stahleisen mbH: Düsseldorf, 1989.
93. von Bogdandy, L. *Die Reduktion der Eisenerze*; Verlag Stahleisen mbH: Düsseldorf, 1967.
94. Brüggmann, C.; Krause, O.; Pötschke, J.; Simmat, R. In *High Temperature Abrasion Resistance of Cement-Based Refractories* 48th International Colloquium on Refractories, Aachen; 2005, pp 35–39.
95. Harmuth, H.; Tschegg, E. K. *Veitsch-Radex Rundschau* **1994**, *1–2*, 465–480.
96. Alapin, B.; Ollig, M.; Pötschke, J. In *Thermomechanical Properties of Selected Refractory Materials up to 1500 °C* 46th International Colloquium on Refractories, Aachen, D, 2003, pp 107–112.
97. Jansen, H. *Stahl und Eisen* **2005**, *125*(11), 43–49.
98. Lee, W. E.; Zhang, S. *Int. Mater. Rev.* **1999**, *44*(3), 77–104.
99. Ollig, M. Reaktionen kohlenstoffhaltiger MgO-Werkstoffe mit flüssigem Eisen. RWTH Aachen, Aachen, 2000.
100. Schumacher, C.; Nickel, K. G. *Ceram. Eng. Sci. Proc.* **2000**.

## 1.24 High Temperature Corrosion of Alumina-forming Iron, Nickel and Cobalt-base Alloys

**B. A. Pint**

Materials Science and Technology Division, Oak Ridge National Laboratory, Oak Ridge, TN 37831-6156, USA

© 2010 Elsevier B.V. All rights reserved.

<b>1.24.1</b>	<b>Introduction</b>	607
1.24.1.1	Functionality of Alumina-Forming Alloys	607
1.24.1.2	Other Applications for Thermally-Grown Alumina Layers	611
<b>1.24.2</b>	<b>Selective Oxidation</b>	612
1.24.2.1	M–Al Alloys	612
1.24.2.2	MCrAl and M–X–Al Alloys	613
1.24.2.3	Alloy Grain Size Effect	615
1.24.2.4	Precious or Platinum Group Metal (PGM) Effect	616
<b>1.24.3</b>	<b>Transient Oxidation</b>	617
1.24.3.1	Base Metal Oxide Formation	617
1.24.3.2	Cubic Alumina Phases	618
<b>1.24.4</b>	<b>Steady-State Oxidation</b>	621
1.24.4.1	Scale Growth Rate	621
1.24.4.2	Mechanism	624
1.24.4.3	Morphology	626
1.24.4.4	Adhesion	627
1.24.4.4.1	Reactive elements	628
1.24.4.4.2	Interstitials (S, C, etc.)	630
1.24.4.4.3	Precious metals	631
1.24.4.4.4	Role of CTE	631
1.24.4.4.5	Role of substrate strength	631
1.24.4.4.6	Effect of cycle frequency	632
1.24.4.5	Internal Oxidation	633
1.24.4.6	Comparison of Fe-, Ni-, and Co-Based Alumina Forming Alloys	634
<b>1.24.5</b>	<b>Breakaway Oxidation</b>	634
1.24.5.1	Failure Mechanisms	636
1.24.5.2	Unusual Failure Mechanisms	636
1.24.5.3	Strategies for Extending Lifetime	637
<b>1.24.6</b>	<b>Effect of Environment</b>	637
1.24.6.1	Water Vapor	637
1.24.6.2	Sulfur and Hot Corrosion	638
1.24.6.3	Carbon	639
1.24.6.4	Nitrogen	639
<b>1.24.7</b>	<b>Summary</b>	640
<b>References</b>		640

### Abbreviations

**COSIM** Coating oxidation and substrate interdiffusion model  
**COSP** Cyclic oxidation simulation program, NASA computer model  
**CTE** Coefficient of thermal expansion

**EPMA** Electron probe microanalysis using wavelength dispersive spectroscopy  
**NASA** National Air and Space Administration  
**ORNL** Oak Ridge National Laboratory  
**PM** Powder metallurgy  
**RE** Reactive element  
**SIMS** Secondary ion mass spectroscopy

## Symbols

$C_b$	Critical Al content of metal at breakaway oxidation, nominal or average
$C_{bi}$	Critical Al content at breakaway oxidation at the metal-oxide interface
$C_{min}$	Minimum initial Al content needed for alumina formation
$C_o$	Initial Al content
$d$	Specimen thickness
$D_{Al}$	Self-diffusion coefficient of aluminum
$D_o$	Self-diffusion coefficient of oxygen
$E_{ox}$	Elastic modulus of oxide
$M$	Metal: Fe, Ni or Co
$p'_{O_2}$	Partial pressure of oxygen at the metal-oxide interface, Al/Al <sub>2</sub> O <sub>3</sub> equilibrium
$p''_{O_2}$	Partial pressure of oxygen at the oxide-gas interface
$t_b$	Exposure time to breakaway oxidation
$t_z$	Exposure time to zero mass gain
$W^*$	Strain energy
$W_{ad}$	Work of adhesion
$[X]$	Concentration of element X, atom percent
$\alpha$	Coefficient of thermal expansion
$\gamma_{int}$	Surface energy of the metal-oxide interface
$\gamma_{met}$	Surface energy of the metal substrate
$\gamma_{ox}$	Surface energy of the oxide scale
$\rho$	Alloy density
$\nu$	Poisson's ratio
$\xi$	Scale thickness
$\xi_f$	Critical scale thickness at scale spallation
$\Delta\alpha$	Change in coefficient of thermal expansion
$\Delta T$	Change in temperature

## 1.24.1 Introduction

This chapter will discuss the oxidation behavior of alumina-forming alloys, particularly MCrAl and M(Al) where M is Fe, Ni and to a lesser extent, Co. (Information on intermetallic aluminides, such as NiAl, TiAl, or Fe<sub>3</sub>Al is included in **Chapter 1.25, High Temperature Corrosion of Intermetallic Alloys**) For the most part, these alloys owe their high temperature oxidation resistance to the formation of a dense, protective, external alumina scale; although some portion of the discussion will concern alloys that benefit from Al additions but do not exclusively form alumina scales. Compositions generally will be discussed in atomic percentage, with Al contents typically  $\leq 22\%$  in the binary

alloys. However, in **Table 1**, commercial alloy compositions are given in weight or mass percentage, which is the common convention, while **Table 2** provides compositions in atomic percentage. The oxidation behavior of alumina-forming alloys will be discussed in a general sense in **Sections 1.24.2–1.24.5** for air or oxygen environments. **Section 1.24.6** covers the behavior of these materials in different oxidants, for example, H<sub>2</sub>O, S, C, or N. This discussion assumes some basic knowledge of the high temperature oxidation concepts that were discussed in **Chapter 1.10, Oxidation of Metals and Alloys**. The terminology is defined in the Glossary. It is almost impossible to discuss the oxidation behavior of alumina-forming alloys without discussing the reactive element (RE) effect.<sup>1–11</sup> Low levels ( $\sim 0.1$  at.%) of RE dopants have a dramatic effect on oxidation performance and most commercial alloys contain one or more additions. The examples given will rely heavily on the oxidation database of the Corrosion Science and Technology Group in the Materials Science and Technology Division at Oak Ridge National Laboratory (ORNL) in Oak Ridge, TN.<sup>12</sup>

### 1.24.1.1 Functionality of Alumina-Forming Alloys

In a general sense, applications for alumina-forming alloys are only for the highest temperatures ( $>900^\circ\text{C}$ ) or most aggressive conditions. At lower temperatures, chromia-forming alloys, such as stainless steels, usually have sufficient high temperature oxidation resistance for most applications. In fact, Ni–Cr alloys are often discussed for applications as high as  $1200^\circ\text{C}$ .<sup>13</sup> However, metal consumption rates for Fe- and Ni-based chromia forming alloys become significant at temperatures above  $1000^\circ\text{C}$ .<sup>14</sup> These differences are not apparent at short intervals, but become more important after long intervals. **Figure 1** shows the total mass gain and the spalled mass of alloy coupons after 15 kh at  $1000^\circ\text{C}$  in laboratory air. (Total mass gain (i.e., specimen mass gain + spalled oxide) will be frequently used in this chapter as it is directly proportional to metal wastage and gives more information than just the specimen mass change which is typically lower than the total mass. Total mass is obtained by conducting the exposure in a preannealed alumina crucible.<sup>15</sup> The spalled mass can be larger than the total mass because the spalled mass includes the metal cations while the total mass reflects only O uptake.) One of the most



**Table 1** Alloy chemical compositions (mass or wt%) determined by inductively coupled plasma analysis and combustion analysis (interstitials)

Material	Fe	Ni	Al	Cr	Si	Ti	C	S	Other
<i>Commercial chromia-forming alloys</i>									
800H	43.2	33.8	0.7	19.7	0.3	0.5	0.08	<3	0.2 Mo, 1 Mn
330RA	42.6	35.9	0.1	19.0	0.1 <sup>a</sup>	0.1	0.06	<3	0.1 Mo, 1.5 Mn
45TM	23.7	47.8	0.1	27.4	0.2 <sup>a</sup>	0.1	0.08	<3	0.04 Ce, 0.02 La
X	17.9	46.8	0.1	22.1	0.3	0.01	0.07	<3	9.5 Mo, 1.8 Co, 0.6 W, 0.7 Mn
617	0.6	53.5	1.1	22.4	0.2	0.3	0.06	<3	12.5 Co, 9.2 Mo
556	31.3	22.2	0.1	21.6	0.3	0.03	0.11	3	18.5 Co, 3 Mo, 1 W, 0.3 Ta, 0.03 La
353MA	36.6	35.7	0.02	25.1	0.2	0.01	0.06	<3	0.05 Ce, 0.02La, 0.01 Nd
625	3.3	63.8	0.2	23.1	0.2	0.2	0.02	<10	8.9 Mo, 0.2 Nb
230	1.5	63.4	0.3	22.6	0.4	0.01	0.10	9	12.3 W, 1.4 Mo, 0.5 Mn, 0.01 La
602CA	9.5	62.3	2.4	24.9	0.08	0.15	0.19	<10	0.1 Zr, 0.1 Y
ODS Ni-25Cr (lab.)	0.5	74.2	0.01	24.3	0.06	<	0.04	220	0.08 Y, 0.6 O
<i>Commercial alumina-forming alloys</i>									
214	3.5	75.9	4.3	16.0	0.08	0.01	0.05	3	0.02 Zr, 0.004 Y
693	4.8	62.1	3.1	28.6	0.05	0.4	0.03	<3	0.6 Nb, 0.2 Mn, 0.05 Zr
702	0.04	81.9	2.9	14.7	0.01	0.3	<	<1	0.04 Mg, 0.02 Zr
René N5	0.07	63.5	6.3	6.8	0.07	0.01	0.05	4	7 Co, 6 Ta, 5 W, 3 Re, 0.2 Hf, 0.005 Y
Nimonic 105	0.8	53.0	4.9	15.5	0.13	1.36	0.14	20	19 Co, 4.7 Mo, 0.12 Zr
MA956	74.2	0.08	4.5	20.0	0.07	0.4	0.01	25	0.4 Y (oxide)
MA956HT	71.2	0.05	5.6	21.9	0.06	0.4	0.04	44	0.4 Y (oxide)
PM2000	73.2	0.02	5.5	20.1	0.02	0.4	0.01	31	0.4 Y (oxide)
ODM751	75.8	0.02	5.0	16.1	0.04	0.56	0.01	57	1.5 Mo, 0.4 Y
APM	73.3		5.5	20.4	0.2	0.03	0.03	10	0.1 Zr
APMT	69.2	0.2	5.0	21.1	0.6	0.02	0.03	<10	2.8 Mo, 0.2 Hf, 0.25 Y, 0.1 Zr
Ohmalloy 30	82.8	0.6	2.6	12.6	0.3	0.3	0.02	<3	0.4 Mn, 0.012 Mg
Ohmalloy 40	81.7	0.5	3.6	12.7	0.2	0.3	0.02	<3	0.4 Mn, 0.012 Mg
SUH21	78.6	0.1	3.0	17.7	0.3	0.1	0.01	<3	0.1 Mn, 0.01 Ce
Aluchrom YHf	72.9	0.1	6.1	20.3	0.2	<	0.02	<10	0.2 Mn, 0.06 Y, 0.05 Zr, 0.03 Hf

<sup>a</sup>Higher value in product literature.

&lt;Below the detectability limit of &lt;0.01% or &lt;0.001% for interstitials.

oxidation-resistant, commercial, chromia-forming alloys is the Ni-based, alloy 230, [Table 1](#). Even after 15 kh at 1000 °C (although there were only scale spallation-inducing, thermal cycles every 500 h, see [Section 1.24.4.4.6](#)), the mass gain for alumina-forming alloys (e.g., 214, MA956, PM2000, see [Table 1](#)) is not significantly lower than that for alloy 230. However, the amount of spalled oxide for the alumina-forming alloys is typically much lower ([Figure 1](#)). This has significant implications for extrapolations of oxidation-limited lifetimes for real applications where 40 kh is often considered a short interval between equipment overhauls and fossil or nuclear energy plant life can be 300 kh.<sup>16</sup> Also, alloy 230 was one of the best commercial alloys tested in the study. A number of chromia-forming alloys, particularly those without a RE addition (e.g., 330RA and 800H, while 230 contains La, [Table 1](#)) showed significantly more metal wastage in the study and a few had to be stopped early because of the degree of attack.

Above 1000 °C, the benefit of alumina-forming alloys becomes much more evident. Instead of just comparing the mass change of various alloys, consider the example of designing a heat exchanger where the wall thickness will determine the lifetime of the component. [Figure 2](#) shows the time to reach 20–40 mg cm<sup>-2</sup> total mass gains as a function of specimen thickness for alloy 230 (Ni–Cr, [Table 1](#)) at 1100 °C in laboratory air (exposed with 100 h per cycle). These times are compared with the times to breakaway oxidation ( $t_b$ , see [Section 1.24.5](#)) for oxide dispersed FeCrAl alloy MA956. As will be discussed in [Section 1.24.5](#), Ni-based alloys do not have such a definitive, binary-like, transition time and instead show an increase in the rates of mass gain and spallation. Thus, for a 2 mm thick alloy 230 specimen, almost 7 kh of exposure at 1100 °C was needed to reach 20 mg cm<sup>-2</sup> of total mass gain but in less than 1000 h more exposure, the mass gain increased to 40 mg cm<sup>-2</sup> ([Figure 2](#)). These times were not significantly different

**Table 2** Alloy chemical compositions (at.%) determined by inductively coupled plasma analysis and combustion analysis (interstitials)

Material	Fe	Ni	Al	Cr	Si	Ti	C	S	Other
<i>Commercial alumina-forming commercial alloys</i>									
214	3.4	70.5	8.7	16.7	0.16	0.01	0.23	5	0.012 Zr, 0.003 Y
693	4.7	57.7	6.2	30.0	0.10	0.47	0.12	<4	0.4 Nb, 0.2 Mn, 0.03 Zr
702	0.04	77.7	6.1	15.7	0.02	0.38	<	<1	0.09 Mg, 0.012 Zr
René N5	0.1	64.9	13.9	7.8	0.15	0.01	0.25	7	7 Co, 2 Ta, 2 W, 1 Re, 0.05 Hf, 0.003 Y
Nimonic105	0.8	49.6	10.0	16.4	0.25	1.56	0.64	34	17.8 Co, 2.7 Mo, 0.07 Zr
MA956	69.4	0.07	8.8	20.1	0.13	0.40	0.06	41	0.24 Y
MA956HT	65.7	0.04	10.7	21.7	0.11	0.43	0.17	71	0.23 Y
PM2000	67.8	0.02	10.6	20.0	0.04	0.44	0.03	50	0.23 Y
APM	68.1		10.7	20.4	0.43	0.03	0.13	16	0.06 Zr
APMT	65.2	0.1	9.7	21.3	1.11	0.02	0.13	<10	1.6 Mo, 0.15 Y, 0.07 Hf, 0.06 Zr
Ohmalloy 30	79.6	0.5	5.2	13.0	0.50	0.38	0.077	<4	0.03 Mg, 0.4 Mn
Ohmalloy 40	77.8	0.5	7.1	12.9	0.42	0.38	0.095	<4	0.03 Mg, 0.4 Mn
SUH21	75.0	0.1	5.9	18.1	0.55	0.12	0.04	<4	0.1 Mn, <0.01 Ce
Aluchrom YHf	67.3	0.1	11.7	20.1	0.35	<	0.09	<10	0.2 Mn, 0.036 Y, 0.028 Zr, 0.008 Hf
<i>Model alumina-forming alloys</i>									
NiAl + Hf	<	51.6	48.3	<	<	<	0.034	<4	0.056 Hf
Ni <sub>3</sub> Al + Hf	<	75.1	24.8	<	<	<	0.041	<4	0.057 Hf
Ni-22Al-5Pt + Hf	0.02	72.8	22.1	<	0.02	<	0.024	<10	5.0 Pt, 0.016 Hf
Ni-22Al-10Pt + Hf	0.02	68.1	21.7	0.01	<	<	0.012	<4	9.7 Pt, 0.39 Hf
NiCrAl + Hf	0.01	61.8	19.2	18.9	<	<	0.043	8	0.058 Hf
NiCrAl + Y	0.01	60.9	19.0	20.0	<	<	0.043	8	0.052 Y
NiCrAl + Y, Hf	0.01	61.4	18.9	19.5	0.02	<	0.042	5	0.046 Hf, 0.006 Y
NiCoCrAlY	0.02	40.4	23.5	17.4	<	<	0.042	8	0.147 Y
FeNiCrAl	56.5	18.7	5.1	15.0	0.29		0.39		2 Mn, 1.4 Mo, 0.6 Nb
FeCrAl	70.3	<	9.6	20.1	<	<	<	85	
FeCrAl-0.04Y	69.1	<	10.2	20.6	<	<	0.01	<10	0.041 Y
FeCrAl-0.08Y	69.8	<	9.9	20.2	<	<	<	16	0.082 Y
FeCrAl + Hf	70.1	<	10.0	19.8	<	<	0.044	41	0.053 Hf
FeCrAl + Mm	70.3	<	10.0	19.6	<	<	0.043	20	0.19 Ce, 0.007 Nd, 0.004 La, 0.006 Hf
FeCrAl + 0.04Hf, Y	70.1	0.01	9.8	20.1	<	<	0.037	16	0.035 Hf, 0.003 Y
FeCrAl + 0.02Hf, Y	69.6	0.01	10.1	20.3	<	<	0.010	16	0.018 Hf, 0.002 Y
FeCrAl + Al <sub>2</sub> O <sub>3</sub>	69.2	0.04	9.6	19.6	0.17	0.01	0.17	44	0.84 O
FeCrAl + Ho <sub>2</sub> O <sub>3</sub>	67.9	0.04	9.4	19.4	0.11	<	0.086	45	1.7 O, 0.9 N, 0.15 Ho
Fe-13Al + Hf	86.5	0.01	13.4	0.01	<	<	0.004	37	0.044 Hf
Fe-17Al + Hf	83.1	<	16.7	<	0.05	<	0.005	67	0.057 Hf
Fe-17Al + Y, Hf	82.8	<	17.1	<	0.02	<	0.009	8	0.023 Hf, 0.010 Y
Fe-17Al + Y, Ti	82.6	<	16.9	<	<	0.44	0.012	<	0.069 Y
Fe-17Al-10Cr + Y	72.5	<	17.4	10.0	0.05	<	0.014	<4	0.062 Y
Fe-18Al + Y	81.9	<	18.0	0.02	0.02	<	0.013	<15	0.057 Y
Fe-20Al + Hf	79.7	<	20.1	<	0.02	<	0.003	39	0.056 Hf
Fe-20Al + Y <sub>2</sub> O <sub>3</sub>	76.9	0.06	19.8	0.11	0.09	0.01	0.08	41	0.13 Y, 2.5 O, 0.4 N
Fe-40Al + Hf	60.5	<	39.5	<	<	<	0.007	21	0.047 Hf

<Below the detectability limit of <0.01% or <0.001% for interstitials.

for alloy 230 specimens that were <1 mm thick. In contrast, a drastic increase in the time to breakaway oxidation was observed for MA956 coupons in this exposure. The example of MA956 is given because a number of other alloys (typically with higher Al contents) have such high values for  $t_b$  that it is difficult to put them on the same plot with alloy 230.<sup>14</sup> It is easy to see that if one were designing a 1100 °C heat exchanger

with a minimum lifetime service of 25 kh it would be extremely difficult to predict any wall thickness of alloy 230 that would be applicable but an extrapolation of the MA956 data would suggest a minimum wall thickness of ~3 mm. Oxidation-limited lifetime predictions are further discussed in [Section 1.24.5](#).

The upper temperature limit for alumina-forming alloys is, of course, application dependent.

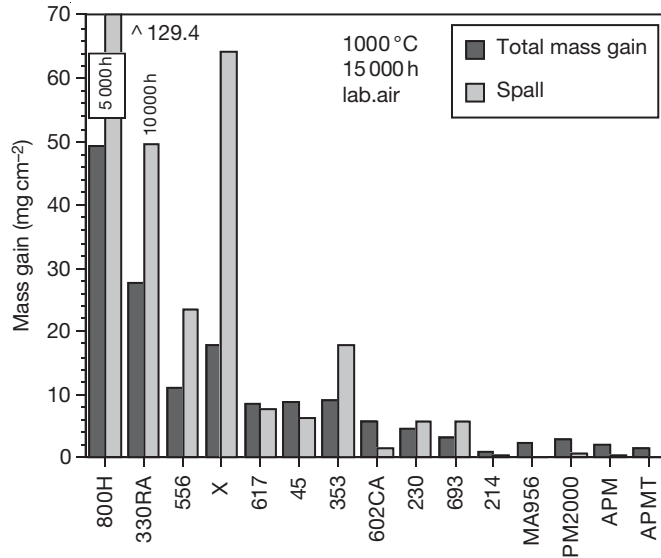


**Figure 1** Bar graph of the total mass gain (specimen mass gain + spalled oxide) and spalled oxide mass per unit area for various commercial alloy specimens (compositions in Table 1) at 1000 °C in laboratory air after 30, 500 h cycles (15 kh total exposure). Data from Pint<sup>12</sup> and Pint and Keiser.<sup>14</sup>

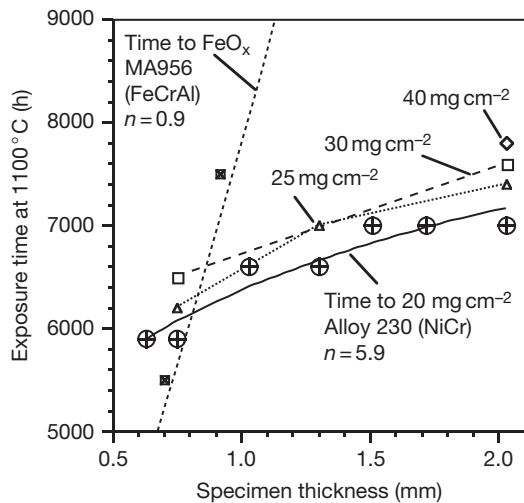


**Figure 2** Time to accelerated attack as a function of specimen thickness for NiCr alloy 230 and alloy MA956 (see Table 1 for compositions) for exposure in 100 h cycles at 1100 °C in laboratory air. For MA956, the time is for the onset of Fe-rich oxide formation and increases significantly with thickness. For NiCr, the times are to total mass gains of 20–40 mg cm<sup>-2</sup> that do not change significantly with thickness. Values of  $n$  are given for eqn [5]. Data from Pint<sup>12</sup> and Pint and Keiser.<sup>14</sup>

However, the lifetime predictions made by NASA using modeling methods like Cyclic oxidation simulation program (COSP)<sup>17</sup> for  $\beta$ -NiAl and NiAl + Zr, usually with criteria of 250  $\mu$ m metal consumption in <10 kh and 1 h thermal cycles, showed maximum

temperatures of  $\sim 1250$  °C for NiAl + Zr<sup>18</sup> which contains a substantially higher initial Al content ( $\sim 50$  at.%) than most alumina-forming alloys. Even with a longer cycle time between cooling to room temperature, the maximum temperature used to achieve respectable lifetimes will not be significantly higher. This is because scale spallation must also be considered. Specifically, the strain energy per unit volume ( $W^*$ ) is defined<sup>19</sup> as

$$W^* = E_{\text{ox}}(\Delta T \Delta \alpha)^2(1 - \nu) \quad [1]$$

(where  $E_{\text{ox}}$  is the elastic modulus of the oxide,  $\Delta T$  is the temperature drop,  $\Delta \alpha$  is the coefficient of thermal expansion (CTE) difference between metal and oxide, and  $\nu$  is Poisson's ratio) in a thick alumina scale ( $\xi > 10 \mu$ m) will exceed the work of adhesion ( $W_{\text{ad}}$ ), that is, the work needed to form unit area of oxide and metal interfaces from unit area of interface of the metal–oxide interface<sup>20</sup>:

$$W_{\text{ad}} = \gamma_{\text{ox}} + \gamma_{\text{met}} - \gamma_{\text{int}} - \xi W^* \quad [2]$$

where the  $\gamma$ 's are the surface energies of the oxide, metal and interface. This leads to spallation and the Al consumed to regrow the spalled oxide significantly increases the Al consumption rate, after spallation begins. For example, the time needed to form a 10  $\mu$ m thick alumina scale is  $\sim 200$  h at 1200 °C but  $\sim 10$  kh at 1050 °C. Thus, the prime temperature range of interest for commercial applications of alumina-forming alloys is  $\sim 1050$ –1250 °C.

Because of the high temperatures involved, applications for alumina-forming alloys are often limited by their creep strength. For ferritic alumina-formers such as FeCrAl, some of the primary applications are as heating elements (e.g., Kanthal alloys) and in foil (30–70  $\mu\text{m}$ ) form as catalyst supports in automotive applications<sup>21</sup> as well as catalytic combustion to lower emissions from turbine engines.<sup>22</sup> Some of the less discussed applications are: (1) dissipative resistor banks, which are used to eliminate excess electricity for regenerative braking of diesel electric locomotives,<sup>23</sup> (2) reinforcement for molded refractory products, and (3) thermal protection shields.

Oxide dispersion strengthened (ODS) FeCrAl alloys have been the subject of considerable research and will be discussed throughout this chapter. The use of yttria dispersions increases the creep strength of these materials but the drawback is that the powder metallurgy (PM) processing<sup>24</sup> increases their cost significantly. These alloys have been investigated for a variety of high temperature applications including heat exchangers running at  $\sim 1100^\circ\text{C}$ .<sup>25</sup> **Figure 3** gives the creep rupture life for 125  $\mu\text{m}$  thick PM2000 foil compared to 100  $\mu\text{m}$  thick Ni-based alloys. The higher creep strength of this material allows a wider range of applications to be considered. However, manufacturers (e.g., Plansee and Special

Metals) are discontinuing production because of the limited market. Less expensive dispersion strengthened alloys such as Kanthal alloys APM<sup>®</sup> and APMT<sup>®</sup> also have been developed and are more widely available. Because of their higher strength, dispersion strengthened alloys have better dimensional stability at high temperature and APMT is available in tube form. Because of its strength and oxidation resistance, APMT was selected as a heat shield material in the heat exchanger of a biomass gasifier.<sup>14</sup>

Nickel-based alumina-forming alloys generally have better high temperature strength than wrought ferritic alloys and can be considered for a broader range of applications. Alloys such as 214 have similar oxidation resistance as FeCrAl alloys and are available in foil form, as in **Figure 3**. The second-generation of single crystal (SX) and dispersion strengthened Ni-based super alloys contain  $\sim 11$ –13 Al and have fairly good oxidation resistance, even without a coating.<sup>16,27,28</sup> To further improve their oxidation resistance, Ni-based superalloys are often coated with a higher Al content NiAl or NiCoCrAl composition (dealt elsewhere in **Chapter 1.27, High Temperature Coatings: Protection and Breakdown**). When sufficient Al is added to an alloy for alumina scale formation, other properties such as strength, phase stability, and weldability may be adversely affected. Nevertheless, cast NiCrAlY alloys have been developed for steam reforming applications where the formation of a chemically inert alumina scale has an additional benefit of reducing surface coke formation.<sup>29</sup>

Cobalt-based alumina-forming alloys are also primarily used as coatings, especially for hot corrosion (see **Section 1.24.6.2**) or high temperature wear resistance applications. The addition of Co in MCrAlY coatings is known to change the phase composition and mechanical behavior.<sup>30,31</sup> Minimal research has been reported on Co-based alumina-forming alloys in the last 20 years and their application seems somewhat specialized and limited at present.

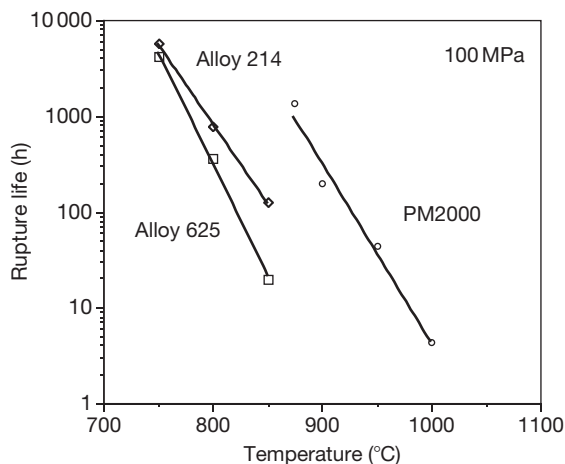


**Figure 3** Creep rupture life at 100 MPa for 100  $\mu\text{m}$  thick foil of Ni-base alloys 214 and 625 and for 125  $\mu\text{m}$  thick alloy PM2000 foil (alloy compositions in **Table 1**). Adapted from Pint, B. A.; Swindeman, R. W.; More, K. L.; Tortorelli, P. F. Materials selection for high temperature (750–1000°C) metallic recuperators for improved efficiency microturbines, ASME Paper #2001-GT-445, Presented at the International Gas Turbine and Aeroengine Congress and Exhibition, New Orleans, LA, June 4–7, 2001.

#### 1.24.1.2 Other Applications for Thermally-Grown Alumina Layers

One of the more interesting aspects of alumina-forming alloys is the usage of the alumina layer in other applications besides for oxidation resistance. After forming a dense-adherent alumina layer at high temperature, this layer could be used at lower temperatures where further alumina formation would be limited. Some of the properties of interest are electrical (insulating),

chemical inertness (for chemical processing applications) and wear resistance. Besides microelectronics, one application where alumina is attractive for its electrical resistance is, as a coating to decrease the magneto-hydrodynamic force in magnetic confinement fusion reactors. Alumina could be used as a coating or inside a flow channel insert.<sup>32</sup> Another property of interest is hydrogen or tritium permeability.<sup>33</sup> Alumina has a hydrogen permeability several orders of magnitude lower than most metals (**Figure 4**). Because of the recent interest in the use of hydrogen as a clean-burning fuel and in the use of more traditional weapons and nuclear energy applications (e.g., hydride fuels), permeation barriers are widely desired but frequently ineffective.<sup>35</sup> Also nuclear-related, alumina can be a corrosion barrier in liquid Pb (or Pb eutectics like Pb–Li or Pb–Bi) systems<sup>36</sup> but not liquid Li, which dissolves alumina<sup>37</sup> because of the thermodynamic stability of  $\text{LiO}_2$ .<sup>38,39</sup> Even with a decreased Li activity in Pb–Li eutectic, the Li can transform a pre-formed  $\alpha\text{-Al}_2\text{O}_3$  scale on alloy PM2000 to  $\text{LiAlO}_2$  after exposure to Pb–Li at 600–800 °C.<sup>40</sup>

### 1.24.2 Selective Oxidation

The first issue to consider as far as alumina-forming alloys are concerned is the need for selective oxidation of Al in the alloy to form alumina and the minimum alloy Al content,  $C_{\min}$ , needed to form alumina in the alloy. This minimum value is not necessarily equal to the minimum concentration

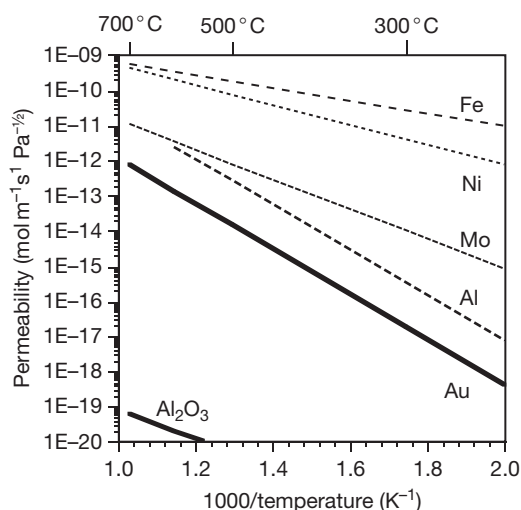


**Figure 4** Hydrogen permeability as a function of reciprocal temperature for various pure metals and alumina. Data from Fowler *et al.*<sup>33</sup> and Steward.<sup>34</sup>

needed to reform Al after an alumina scale had already been established,  $C_b$ .<sup>41,42</sup> The basic concept of selective oxidation was discussed in **Chapter 1.09, Thermodynamics and Theory of External and Internal Oxidation of Alloys**. For alumina-forming alloys, the general interest is the behavior of M–Al and M–X–Al, where X is normally Cr but can also be another element, such as Mn, with nobility between M and Al, the so-called third element.<sup>43</sup>

#### 1.24.2.1 M–Al Alloys

For Ni–Al alloys, an early work by Pettit<sup>44</sup> considered the thermodynamics of the system as well as experimental evidence which indicated that kinetic issues dominate  $C_{\min}$ . The thermodynamic calculations indicated <1 ppm Al at the alloy surface was needed for NiO or  $\text{NiAl}_2\text{O}_4$  (spinel) to be stable. However, experimental work, summarized in **Figure 5** showed that much higher Al contents were needed for transition from Al internal oxidation with an external NiO scale (Region I) to an external alumina formation (Region III) in 0.1 atm  $\text{O}_2$ . (An over-lying spinel layer is formed at up to ~40 at.% in the  $\beta$ -NiAl phase field.<sup>45</sup>) The effect of temperature was to slightly lower  $C_{\min}$  at higher temperatures. Even in a CO/ $\text{CO}_2$  mixture (2:1) where NiO was not stable, the

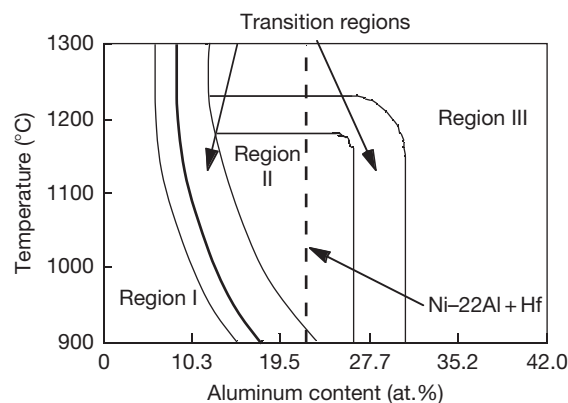


**Figure 5** Relationship between oxidation temperature and Al content on the reaction products formed on Ni–Al alloys oxidized in 0.1 atm  $\text{O}_2$ . The various regions are: I – primarily NiO + Al internal oxidation, II – initial spinel ( $\text{NiAl}_2\text{O}_4$ ) +  $\text{Al}_2\text{O}_3$  formation, but eventual NiO, III – primarily  $\text{Al}_2\text{O}_3$ . The bold line indicates the transition between internal and external oxidation in CO– $\text{CO}_2$  mixtures where  $\text{Al}_2\text{O}_3$  was the only stable oxide. Adapted from Pettit<sup>44</sup> with the Al content changed to atomic%. The dashed line is an observation for Ni–22Al + Hf where the initial  $\text{NiAl}_2\text{O}_4$  +  $\text{Al}_2\text{O}_3$  scale was stable for 1000 h at 1000–1200 °C. Pint, B. A. Unpublished oxidation data, ORNL, Oak Ridge, TN, 1994–2008.



solid bold line in **Figure 5** shows a fairly high Al content needed for transition from internal to external alumina formation. Thus, kinetic factors such as the scale growth rate and diffusivities in the metal and oxide dominate the selective oxidation process.

Values of  $C_{\min}$  for Fe–Al alloys have been reviewed<sup>46</sup> and **Figure 6** shows a summary of  $C_{\min}$  values found during oxidation in air or  $O_2$ .<sup>47–52</sup> As discussed by Pint *et al.*,<sup>51</sup> a distinct difference between complete alumina scale formation and Fe-rich oxide formation is clear at  $\geq 1000^\circ\text{C}$  but can be more difficult to differentiate at lower temperatures, especially at  $600\text{--}700^\circ\text{C}$  where an exclusive alumina scale is difficult to form on binary Fe–Al alloys and there is no significant difference in mass gain between high and low Al contents. One reason for the large range of values in **Figure 6** may be because of the interpretation. If the criterion is that no Fe-rich oxide formed using a visual assessment of scale color, then the contents of  $\sim 18\text{--}20\%$  Al are typically needed. However, the same requirement for Ni–Al alloys in air would require  $C_{\min} > 35\%$ . A more appropriate criterion is that a continuous alumina scale forms underneath the transient, base metal oxide. This is the criteria used in **Figure 5**. **Figure 7** gives an example for  $Y_2O_3$ -dispersed Fe–20Al where large faceted Fe-rich grains were observed at the gas

interface after oxidation at  $1100^\circ\text{C}$  but underneath is a fully-developed columnar alumina scale. Subsequent sections will discuss some of the other reasons for the scatter in **Figure 6**. Recent calculations by Zhang *et al.*<sup>53</sup> using relevant Fe–Al rate constants predicted much lower  $C_{\min}$  values ( $0.5\text{--}4.5\%$  depending on the assumptions) which does not agree with the experimental results summarized in **Figure 6**.

One issue that can affect  $C_{\min}$  is time, that is, the length of exposure, and whether the alloy can maintain the alumina scale during extended exposures. Region II in **Figure 5** indicates where an initial external alumina scale was not sustained and a faster growing NiO formed. The likely explanation was Al depletion in the metal which did not allow the sustained formation of alumina.<sup>44</sup> This point might be more relevant to the discussion of lifetime, i.e., the amount of time an alloy can sustain the formation of an alumina scale (discussed in **Sections 1.24.4.4 and 1.24.5**). Nevertheless, the usefulness of  $C_{\min}$  plots may be questionable if the specified level of Al cannot sustain alumina formation. For example, Hf-doped Fe–11Al at  $1200^\circ\text{C}$  (**Figure 6**) only survived for 300 h before breakaway oxidation.<sup>52</sup> Thus, these plots provide a defined minimum Al level and not a target Al content for alloy development.

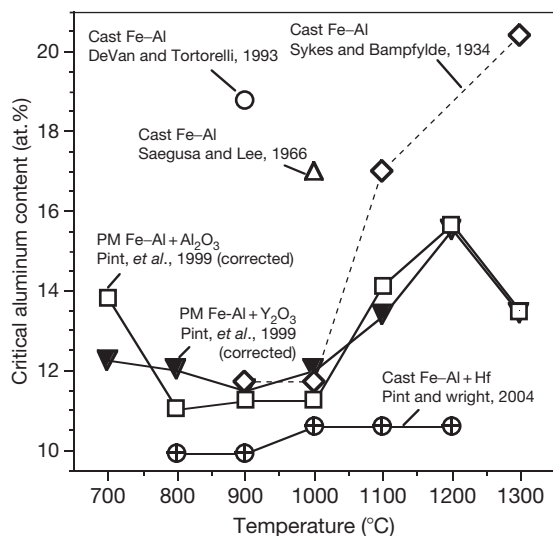


**Figure 6** Summary of critical Al contents for Fe–Al alloys from various studies. The values for powder metallurgy (PM) alloys<sup>51</sup> were decreased by  $\sim 2\%$  because this Al was tied up as oxides in these materials. Generally, these values were determined for exposures of  $\sim 100$  h. Data from Sykes and Bampfylde,<sup>47</sup> Saegusa and Lee,<sup>48</sup> Devan and Tortorelli,<sup>50</sup> Pint *et al.*,<sup>51</sup> and Pint and Wright.<sup>52</sup>

### 1.24.2.2 MCrAl and M–X–Al Alloys

Most commercial alumina-forming alloys are based on MCrAl rather than M–Al compositions. The main

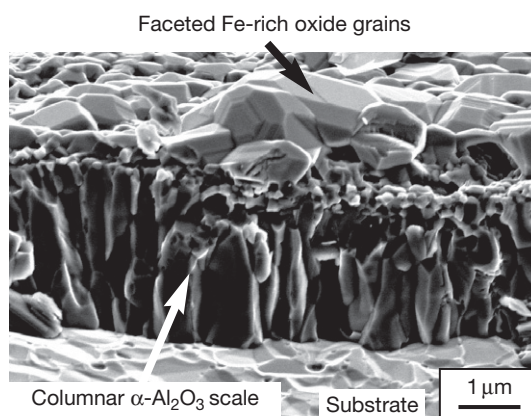


**Figure 7** SEM secondary electron image of scale fracture cross section after 100 h at  $1100^\circ\text{C}$  in air on Fe–20Al– $Y_2O_3$ . An outer Fe-rich oxide formed over the inner  $\alpha\text{-Al}_2O_3$  layer because of the relatively low Al content in this alloy. Adapted from Pint, B. A.; Leibowitz, J.; DeVan, J. H. *Oxid. Met.* **1999**, *51*, 181–197.

reason is that the addition of Cr (typically 10–25%, see Table 2) allows alloys with much lower Al contents to form a continuous alumina-scale than observed in M–Al compositions. Since Al tends to have detrimental effects on mechanical and fabrication (i.e., rolling, joining) properties, minimizing the Al content is often a goal in alloy development. The effect of Cr is described as a third element effect.<sup>43,53–55</sup> There is still a disagreement as to whether the third element (1) acts as an oxygen ‘getter,’ (2) changes the Al activity, (3) increases the Al diffusivity, (4) increases the volume of internal oxides in the alloy, (5) simply decreases the concentration of base metal in the alloy, and/or (6) acts by some other mechanism. Most agree that the third element effect is more complex than the early explanation of Wagner.<sup>54</sup>

To illustrate the performance of Ni–Cr–Al alloys (Figure 8) shows examples of Ni–(17–30)Cr alloys with various Al additions oxidized in 100-h cycles at 1200 °C. Lower Al additions, 2.5–4.8% such as in alloys 617 and 602CA resulted in high mass gains similar to alloy 230 without Al. Alloy 602CA does not form an external alumina layer at 1200 °C; only internal Al oxidation is observed.<sup>56</sup> However, the ~6% Al addition in alloys 702 and 693 resulted in a significantly lower mass gain after the initial transient formation of Ni- and Cr-rich oxides. Further increases in Al content, for example, alloy 214, decreased the transient (i.e., Ni-rich) oxide formation

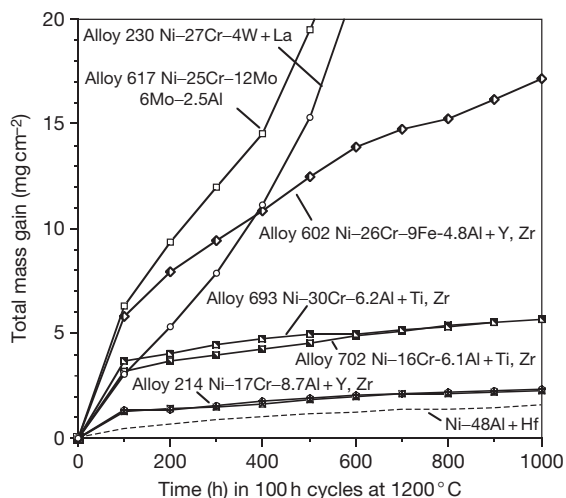


**Figure 8** Total mass gain (specimen + spalled oxide) during 100 h cycles at 1200 °C in laboratory air for various Ni–Cr and Ni–Cr–Al alloys (see Table 1). Generally, the mass gain decreases with Al content due to the formation of a protective alumina scale with NiAl + Hf having one of the slowest growth rates of any alumina-former. Data from Pint.<sup>12</sup>

and mass gain but did not decrease the long-term growth rate. With the presence of Cr in these alloys, the Al level needed for alumina formation, ~6%, is significantly lower than the Al levels discussed in binary Ni–Al alloys (Figure 5).

Composition effects can be summarized in so-called oxide maps.<sup>57–59</sup> Figure 9 shows a Ni–Cr–Al oxide map with some of the data points from Figure 8. The three oxide regions, very similar in composition to the work of Giggins and Pettit<sup>57</sup> (and not at all like Wallwork and Hed<sup>58</sup>) are: I – Ni-rich scale with Al internal oxidation, II – Cr-rich scale with Al internal oxidation (e.g., alloys 602 and 617), and III – continuous Al<sub>2</sub>O<sub>3</sub> scale. Obviously, the most oxidation-resistant alumina-forming alloys will be in region III.

A similar map was constructed for CoCrAl.<sup>57</sup> The main difference between CoCrAl and NiCrAl was that much higher Cr and Al contents were needed to achieve alumina scale formation, on the order of 20% Cr and 20% Al. The need for higher Cr and Al contents in Co-based alloys was also observed in a separate study.<sup>60</sup> Alloys based on TiCrAl are covered in a separate chapter.

Similarly to NiCrAl, in Fe-based alloys, as little as 13Cr is added to Ohmalloy<sup>®</sup> alloys combined with 5.2%Al to form alumina, Table 2.<sup>23</sup> In both Fe- and Ni-based alloys, a reasonable starting point for a standard alumina-forming MCrAl composition

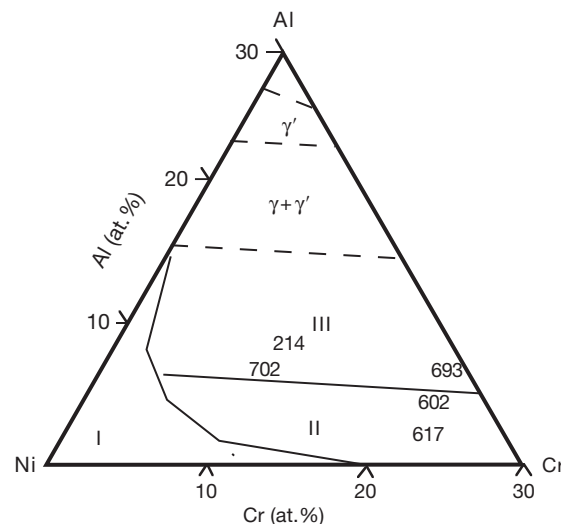


**Figure 9** Schematic of the oxide map for Ni–Cr–Al and the location of the commercial alloys from Figure 8. Region I is for alloys which form Ni-rich oxide and Al internal oxide, Region II alloys form a Cr-rich oxide and Al internal oxide, and Region III alloys are able to form a continuous alumina scale. Map based on Giggins and Pettit,<sup>57</sup> alloy data from Pint.<sup>12</sup>

is ~20% Cr and ~10% Al (~5 wt%). Obviously, lower Cr and Al contents can form alumina, as demonstrated by both commercial and laboratory alloys (Tables 1 and 2). Higher Cr contents (>25%) lead to a decrease in workability and ductility and in FeCrAlY to a decrease in the incipient melting temperature of any Y-rich precipitate.<sup>61</sup>

While Cr is the most popular third element addition, other elements are used or have been investigated. To replace Cr, Mn additions have been investigated in Fe-based alloys by several authors.<sup>62,63</sup> These austenitic alloys have good wear properties but their oxidation resistance, particularly above 900 °C, is compromised of the formation of Mn-rich oxides. The addition of Si has been investigated in Fe–Al alloys<sup>64</sup> and has been shown to exhibit a third element effect in Ni–Si–Al alloys.<sup>65</sup> (Large Si additions are mainly an academic exercise as Si has detrimental effects on ductility and fabricability.) In Fe–Al–Si alloys, higher Si contents led to a decrease in oxidation rate. Also, Ni additions to Fe–Al alloys have been attempted.<sup>66</sup> However, the addition of Ni did not appear to improve the oxidation behavior at 600–800 °C compared to binary Fe–Al.

Quaternary additions on selective oxidation have been explored. In the case of alumina-forming austenitics (AFA, see example in Table 2), where low levels by Al are needed to retain a fully austenitic matrix (and retain creep-resistance<sup>67,68</sup>), additions of Nb have been found to influence whether the alloy forms an alumina scale at 800 °C (Figure 10).<sup>69</sup> At constant 5 or

6 at.% Al in Fe–15Cr–19Ni, increasing the Nb content decreased the mass gain after 500 h at 800 °C. At low levels of Nb, mass losses were observed due to the formation of a thick Fe- and Cr-rich oxide. The effect of Y on selective oxidation also has been investigated. Castello and coworkers<sup>70</sup> reported improved selective oxidation in Ni–12.9Al–11.9Cr–7.5C–0.11Y compared to the Ni–Al + Cr<sub>3</sub>C<sub>2</sub> alloy without Y. They attributed the effect to Y reducing the growth rate of the initially-formed Cr-rich scale. Figure 6 shows that Hf-additions to Fe–Al alloys decreased the critical Al content needed to form alumina.<sup>52</sup> Studies of Y<sub>2</sub>O<sub>3</sub> additions in PM Fe–Al alloys did not find a benefit of Y on selective oxidation compared to PM alloys with an Al<sub>2</sub>O<sub>3</sub> dispersion.<sup>51</sup> Rather, the fine-grain size of the PM Fe–Al alloys was thought to influence selective oxidation.

### 1.24.2.3 Alloy Grain Size Effect

Alloy grain size effects on selective oxidation are not widely appreciated in high temperature oxidation but are extremely important and often ignored as specimen alloy grain size is not always specified in literature papers. Early work on chromia-forming stainless steels showed that a fine-grained substrate was more oxidation resistant.<sup>71–73</sup> More grain boundaries increased the flux of Cr to the surface along these fast diffusion paths. This concept was used in alumina-forming alloys by Maloney and Yurek<sup>74,75</sup> where rapid solidification was used to achieve a fine grain size in Fe–2.8Cr–4.7Al alloys and TiB<sub>2</sub> dispersions were used to stabilize the fine grains. As discussed in the previous section, these low levels of Cr and Al are well below commercial FeCrAl alloys, Table 2. Figure 11 shows the low mass gain at 600 °C and 700 °C for the fine-grained material compared to the conventionally-cast, coarse-grained Fe–2.8Cr–4.7Al specimens. While the TiB<sub>2</sub> additions may have contributed to the effect, Figure 12 shows a thicker oxide formed over a large grain in the TiB<sub>2</sub>-dispersed FeCrAl specimen. A thin Al-rich oxide (arrow) formed over the small grains in the substrate.

Goedjen and Shores<sup>76</sup> investigated the effect of grain size on NiCrAlY alloys. They found a decreased transient mass gain (i.e., less Ni-rich oxide formation) with finer grains but no change in the steady-state alumina scale growth rate. More recently, coating processes that produce fine-grained NiCrAl coatings have been found to have better selective oxidation.<sup>77,78</sup> Collectively, these results suggest that for low Al content alloys, reducing the grain size will improve

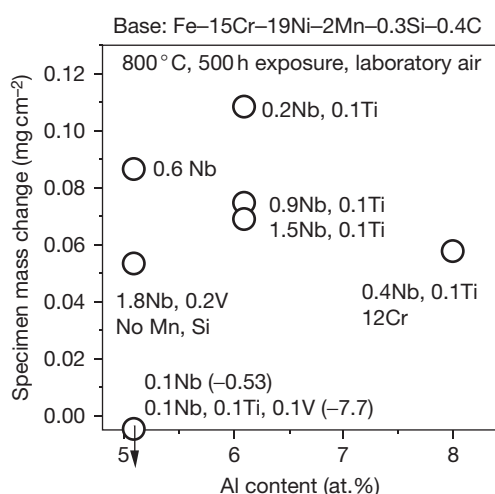


**Figure 10** Specimen mass gain for Fe–15 at.% Cr–19Ni alloys with various Al and carbide forming elements (Nb, Ti, V) after 500 h (5, 100-h cycles) in laboratory air at 800 °C. Data from Brady *et al.*<sup>69</sup>

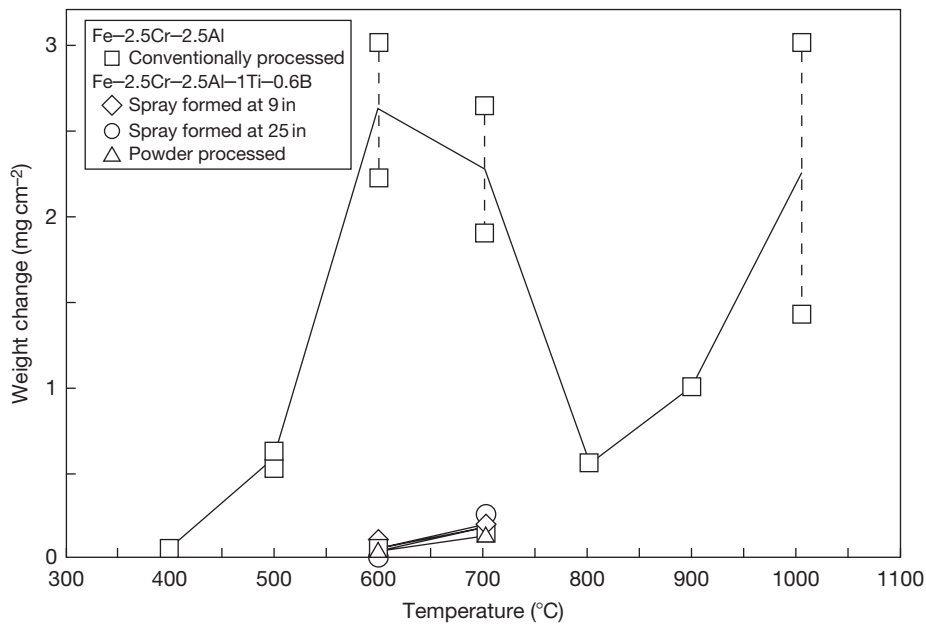


**Figure 11** Mass change for conventional processed and fine-grained Fe-2.5 wt% Cr-2.5Al (2.8 at.% Cr-4.7Al) alloys made by several spray and powder processes. By using  $\text{TiB}_2$  to keep a fine grain size, an Al-rich oxide was formed at 600–700 °C, thereby decreasing the mass gain of these alloys compared to conventional, coarse-grained material with the same Cr and Al content. Maloney, M. J. Ph.D. Thesis, Massachusetts Institute of Technology, Cambridge, MA, 1989, Maloney, M. J.; Yurek, G. J. In *Composites/Corrosion-Coatings of Advanced Materials*, Proceedings IMAM-4; Kimura, S., Kobayashi, A., Umekawa, S., Nii, K., Saito, Y., Yoshimura, M. Eds.; Materials Research Society: Pittsburgh, PA, 1989; Vol. 1, pp 383–388.

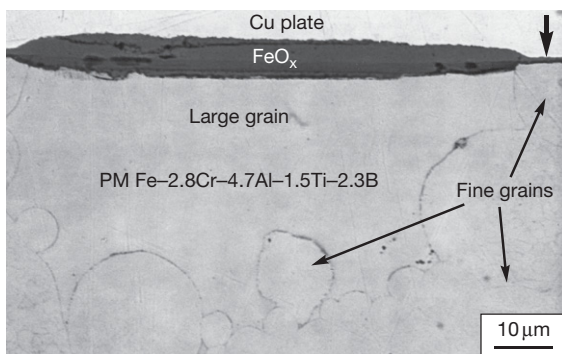


**Figure 12** SEM secondary electron image of a polished cross-section of Fe-2.8 at.% Cr-4.7Al-1.5Ti-2.3B after 50 h at 700 °C. A thick Fe-rich oxide formed over a large grain in the substrate, elsewhere a thin Al-rich oxide formed over the finer-grained regions (arrow). Adapted from Maloney, M. J. Ph.D. Thesis, Massachusetts Institute of Technology, Cambridge, MA, 1989.

the possibility of forming an alumina scale. Furthermore, this effect will probably be most critical at lower temperatures 600–1000 °C where selective alumina formation is more difficult because of slow diffusion rates and less critical at higher temperature >1100 °C where diffusion in the alloy is much faster.

#### 1.24.2.4 Precious or Platinum Group Metal (PGM) Effect

One of the more intriguing results of this decade in alumina-forming alloys is the work on  $\gamma$ - $\gamma'$  Ni-Pt-Al compositions.<sup>79–81</sup> The addition of a PGM such as Pt (or Ir, Pd, Rh, etc.)<sup>81–83</sup> to a base Ni-(16–22)Al alloy improves selective oxidation (i.e., decreases the formation of Ni-rich oxide) such that the alloy becomes a primary alumina former, similar to  $\beta$ -NiAl. However, TEM (or careful metallography) has found that a thin Ni-rich oxide layer does form on these alloys even with 30% Pt.<sup>82,83</sup> Improved selective oxidation had been previously observed in NiCrAl + Pt alloys by Felten,<sup>84</sup> Pt-containing superalloys by Tatlock and Hurd<sup>85</sup> and with Pt on the surface of MCrAl alloys.<sup>86</sup>

To illustrate the PGM effect on transient oxidation, **Figure 13** shows the mass gain after a 500 h isothermal exposure at 1000 °C as a function of PGM addition in cast Ni-22Al±Hf alloys.<sup>82,83</sup> The mass gain for Ni-48Al + Hf serves as a baseline for alumina formation with no Ni-rich oxide formation. The alloys without a PGM addition show a higher mass gain due to the formation of a Ni-rich scale with some contribution due to Hf internal oxidation.



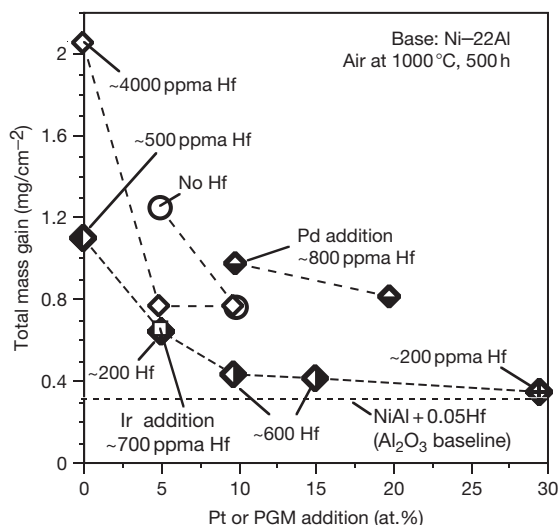


**Figure 13** Total mass gain (specimen + spalled oxide) after a 500 h isothermal exposure at 1000 °C in laboratory air for various precious metal (PM) and Hf additions to Ni-22Al alloys. Data from Pint *et al.*<sup>82,83</sup>

With increasing PGM content, the mass gain decreased. An Ir addition showed a similar benefit as Pt at the 5% level but 10–20% Pd, which is significantly less expensive than Pt, was not as effective due to formation of additional phases.<sup>83</sup> As an example of the alumina scale formed on these alloys, **Figure 14** shows scale cross-sections after 2000, 1-h cycles at 1100 °C. Without a Hf addition, the alumina scale on Ni-22Al-10Pt is similar in thickness to that formed on  $\beta$ -Ni-50Al-5Pt (**Figures 14(a) and 14(b)**). The addition of 0.4 Hf to Ni-22Al-10Pt decreased the oxide thickness but some internal oxidation of Hf was evident (**Figure 14(c)**).

The  $\gamma$ - $\gamma'$  Ni-Pt-Al compositions are primarily considered for coatings on NiCrAl-based superalloys but some effort has been dedicated to alloy development.<sup>87</sup> By suppressing the formation of Ni-rich oxides with the associated weak  $\text{Al}_2\text{O}_3$ - $\text{NiAl}_2\text{O}_4$  interface,<sup>88,89</sup> these compositions can be used as bond coatings in thermal barrier coatings (TBCs). Such  $\gamma$ - $\gamma'$  coatings are attractive because (1) they can be formed simply by interdiffusing a plated Pt layer into the surface of the super alloy (i.e., a Pt diffusion coating rather than a Pt-modified  $\beta$ -phase aluminide), (2) Al interdiffusion is less of an issue because the phase composition of the coatings is the same as the super alloy substrate<sup>79</sup> and Pt appears to decrease the Al activity in the coating,<sup>90</sup> thereby creating a chemical potential gradient for Al to diffuse from the substrate into the coating (rather than

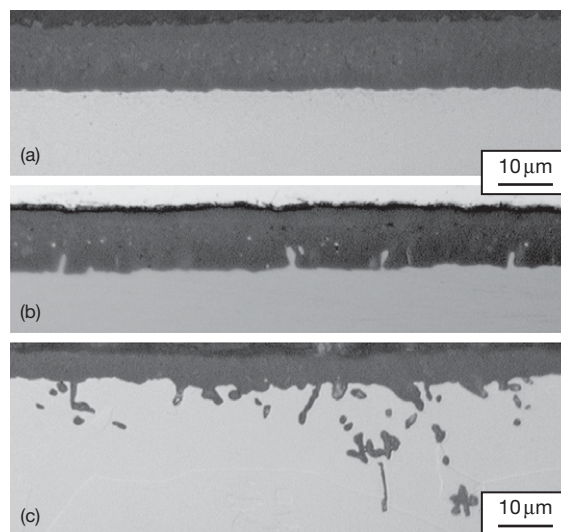


**Figure 14** Light microscopy of polished cross-sections after 2000, 1 h cycles at 1100 °C in O<sub>2</sub> (a) Ni-22Al-10Pt, (b) Ni-50Al-5Pt, and (c) Ni-22Al-10Pt + 0.4Hf. Adapted from Pint, B. A.; More, K. L.; Wright, I. G. *Oxid. Met.* in preparation.

out of an Al-rich coating), and (3) their high strength compared to  $\beta$ -NiAl and MCrAlY coatings<sup>82</sup> is thought to increase their resistance to thermal mechanical fatigue. When the  $\gamma$ - $\gamma'$  coating contains 5–10% Cr, either by interdiffusion from the substrate or by addition as a part of a secondary coating process, the hot corrosion resistance is improved.<sup>91</sup> One concern about these coatings is the depletion of Pt due to interdiffusion with the super alloy, which is significant at 1100 °C.<sup>92</sup>

## 1.24.3 Transient Oxidation

### 1.24.3.1 Base Metal Oxide Formation

As already discussed in the previous section on selective oxidation, during the initial or transient stage of oxidation, alumina-forming alloys will tend to form some base-metal oxide (e.g., NiO, FeO<sub>x</sub>, or M-Al-O spinel, etc.), see **Figure 7**. This is illustrated in **Figure 15** for Fe-Al alloys oxidized at 900 °C. The decreasing mass gain with increasing Al content is due to a decrease in the initial transient Fe-rich oxide formation.<sup>93</sup> Because of the subsequent slow alumina scale growth, the mass gain after 5 kh is dominated by the mass gain after the first 500 h exposure (triangles in **Figure 15**). In addition to the alloy composition, the transient oxide thickness and phase composition are affected by many factors associated with the



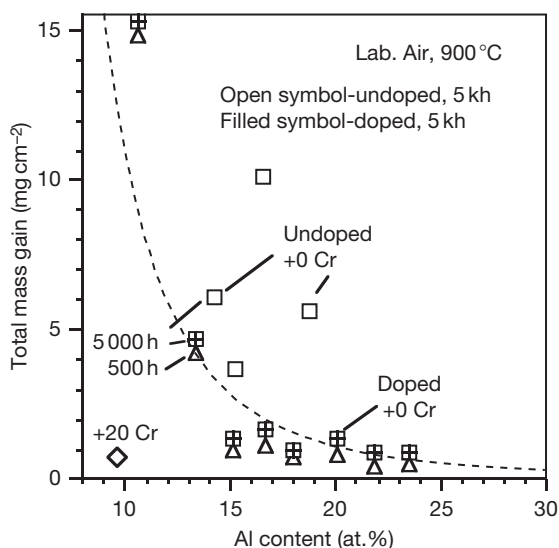


**Figure 15** Total mass gain (specimen + spalled oxide) after 1 or 10, 500-h cycles at 900 °C in air for Fe(Al) alloys as a function of Al content. The doped alloys contained Ti, Hf, Zr, or Y and the Fe–20Cr–10Al specimen contained no dopant. For doped Fe–Al alloys (dashed line fit), the majority of the mass gain occurred during the first 500 h (triangle) when Fe-rich oxide formed. The higher mass gains for the undoped Fe–Al alloys (open squares) were due to an internal oxidation/nitridation with nearly linear kinetics. This internal oxidation was not observed for FeCrAl. Data from Pint<sup>12</sup> and Pint *et al.*<sup>93</sup>

thermodynamics and kinetics of oxide formation. Examples of thermodynamic factors are temperature and the partial pressure of the oxygen (e.g.,  $\text{H}_2$ – $\text{H}_2\text{O}$  or  $\text{CO}$ – $\text{CO}_2$  gas mixtures). Some of the kinetic factors are heating rate, alloy grain size (affecting the flux of Al in the alloy) and surface preparation which can affect the number of fast-diffusion paths in the near surface region (e.g., grinding versus acid etching).

Oxidation temperature is a critical factor for transient oxide because of the slow-formation of alumina below 800 °C. (A slow heating rate to a higher temperature can have a similar effect.) Alumina may be the thermodynamically stable phase but kinetics often dominate, allowing rapid base-metal oxidation. A simple strategy to enhance alumina formation is to preoxidize at a higher temperature where an alumina scale forms more readily. Figure 16 gives an example of this strategy for alloy 214 foil ( $\sim 50 \mu\text{m}$  thick) preoxidized for 2 h at 1100 °C. Because of the difficulty in forming alumina at low temperatures, the parabolic rate constant after 5000 h was higher at 700 °C ( $8 \times 10^{-16} \text{ g}^2 \text{ cm}^{-4} \text{ s}^{-1}$ ) than at 800 °C ( $2 \times 10^{-16} \text{ g}^2 \times 10^{-16} \text{ g}^2 \text{ cm}^{-4} \text{ s}^{-1}$ ) (Figure 16(a)). The observed

mass gains reflect the formation of a Ni- and Cr-rich transient oxide which is nonuniform (e.g., Figure 16(b)). (Even at 1100 °C, a thin (0.5–1  $\mu\text{m}$ ) external layer of  $\text{Ni}(\text{Al,Cr})_2\text{O}_4$  formed on this alloy with only 8.7 at.% Al (see Table 2). But this exposure was sufficient to develop a continuous, underlying  $\alpha$ - $\text{Al}_2\text{O}_3$  layer.<sup>94</sup>) With the preoxidation ( $< 0.2 \text{ mg cm}^{-2}$  mass gain), no further mass gain was measured during 10 kh exposures in air at 700 or 800 °C.<sup>12</sup>

The differences in oxidation behavior among Co-, Ni-, and Fe-based alumina-forming alloys were studied at 1000 and 1200 °C by Stott *et al.*<sup>60</sup> The critical factors identified were  $D_{\text{Al}}$  and O permeability in the alloy. With similar Cr and Al contents, Co-based alloys formed thicker transient oxides that were attributed to the fast growth rate of CoO and the relatively slow Al diffusivity in Co-based alloys. (Stated differently, higher Cr and Al contents were needed in Co-based alloys to quickly form alumina.) The growth rate of FeO is faster, which is important at breakaway (see Section 1.24.5), but faster Al diffusivity in ferritic FeCrAl alloys resulted in rapid alumina formation. A less comprehensive study of Fe, Ni, and Co–Al alloys by Hagel found similar results.<sup>95</sup>

The work of Kear *et al.*<sup>96</sup> was one of the earliest microstructure studies of the transient stage oxidation of NiCrAl. By reducing the oxygen partial pressure, NiO and Ni-rich spinel-type oxide formation was suppressed at 1000 °C resulting in a mixture of  $\text{Cr}_2\text{O}_3$  and  $\text{Al}_2\text{O}_3$ . A subsequent characterization was reported by Smialek and Gibala.<sup>97</sup> On FeCrAl, there is typically very little transient base-metal oxidation. Quadakkers and coworkers<sup>98</sup> used the Fe and Cr in the outer scale to mark the original metal interface and study the alumina growth mechanism. Figure 17 gives an example of the type of transient scale on ODS FeCrAl after 2 h at 1000 °C in  $\text{O}_2$ .<sup>40</sup> The Fe and Cr maps (Figures 17(b) and 17(c)) show that Cr and Fe were concentrated in a thin ( $\sim 100 \text{ nm}$ ) outer layer after these conditions.

### 1.24.3.2 Cubic Alumina Phases

One of the most critical transient oxidation issues for alumina-forming alloys is the formation of metastable cubic  $\text{Al}_2\text{O}_3$  phases (e.g.,  $\gamma$ ,  $\delta$ ,  $\theta$  phases). Their formation can be considered as a transient phenomenon because, given time and temperature, these metastable phases generally transform to the stable  $\alpha$  phase. However, because these cubic phases are more defective than  $\alpha$ , they allow faster diffusion and grow at a faster rate.<sup>95,99,100</sup>

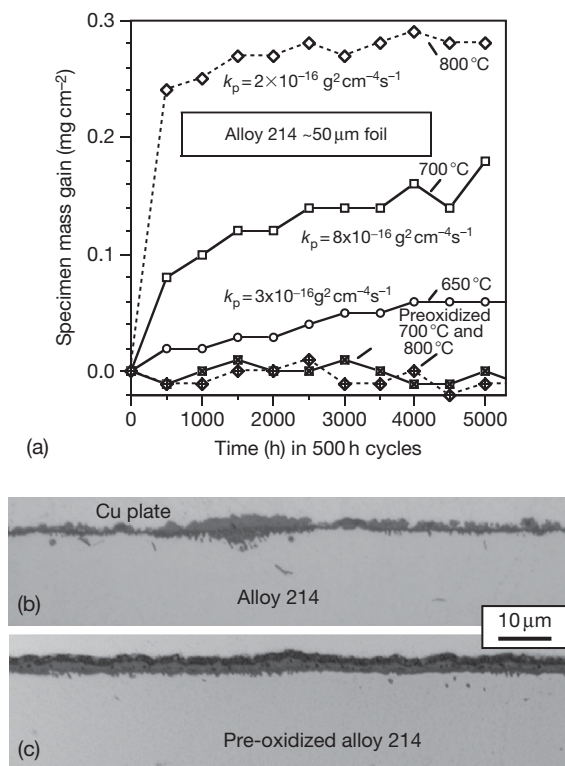


**Figure 16** (a) Specimen mass gains for alloy 214 (NiCrAl, see Table 2) foil (~50 μm) with and without preoxidation exposed for 500 h cycles in laboratory air at 650 °C, 700 °C, and 800 °C. Polished cross-sections for the specimens shown in (a) after exposure in laboratory air at 800 °C, (b) as-received foil specimen oxidized for 5000 h, and (c) preoxidized (2 h at 1100 °C in dry O<sub>2</sub>) foil after 10000 h. Data from Pint.<sup>12</sup>

The formation of cubic alumina phases on alumina-forming alloys was discussed in the early literature.<sup>95</sup> However, the possibility of forming these metastable phases, rather than α, was not discussed for many years and probably led to the controversy regarding the growth mechanism of alumina scales in the 1980s. The observation of growth by outward Al transport was assumed to be for an α-Al<sub>2</sub>O<sub>3</sub> scale but, based on the oxidation time and temperature, was likely θ-Al<sub>2</sub>O<sub>3</sub>.<sup>101</sup> This issue will be further discussed in Section 1.24.4.2.

The hallmark of cubic alumina phases is the gas-side blade or whisker morphology often observed. Much of the cubic alumina scale characterization work has been done on β-NiAl,<sup>102–105</sup> because of the cubic epitaxy with the β phase and because Fe and Cr in the substrate tend to help nucleate α phase.<sup>100,106</sup> However, at lower temperatures (<950 °C), cubic alumina scales form even on FeCrAl. Typical surface

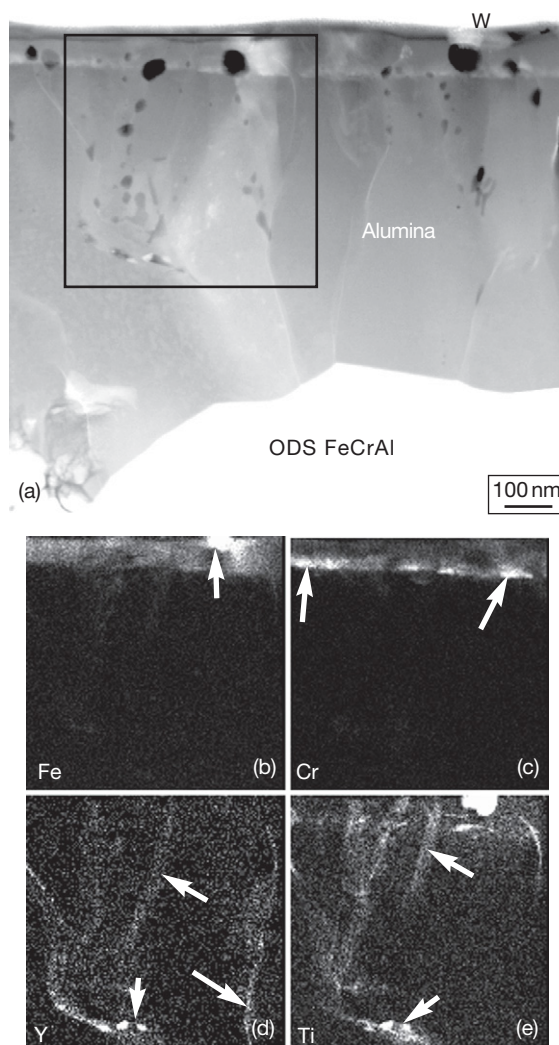


**Figure 17** Cross-section of the α-Al<sub>2</sub>O<sub>3</sub> scale formed on PM2000 (ODS FeCrAl, see Table 1) after 2 h at 1000 °C in dry O<sub>2</sub> (a), STEM high angle annular dark field image and EDS X-ray maps from the box in (a): (b) Fe, (c) Cr, (d) Y, and (e) Ti. Adapted from Pint, B. A.; More, K. L. *J. Nucl. Mater.* 2008, 376, 108–113.

morphologies on commercial FeCrAl foil are shown in Figure 18. The outward growing features are minor at 700 °C but are very evident at 800 °C (Figure 18(b)). After long-term exposure at 900 °C, there is little evidence of outward transport and the scale has completely transformed to α-Al<sub>2</sub>O<sub>3</sub> (Figure 18(c)). However, aluminized foils (aluminized to increase the Al reservoir) showed more distinct remnants of outward growth (Figure 18(d)). This is consistent with work on NiAl where surface enrichment of Al by ion implantation led to more cubic alumina formation.<sup>107</sup> Cubic alumina phases

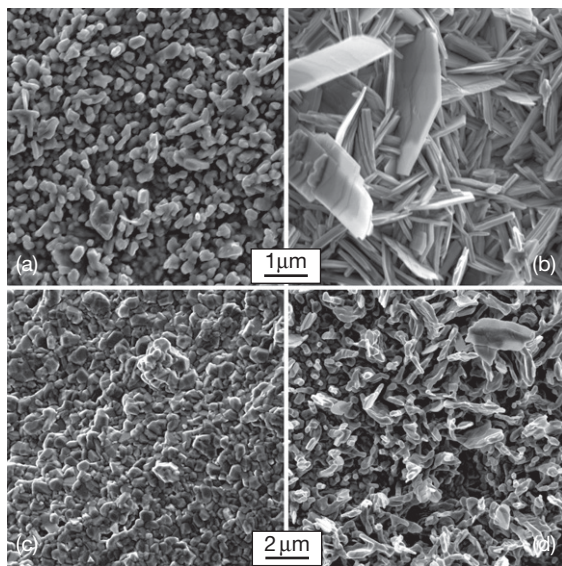


**Figure 18** SEM secondary electron plan view images of the alumina scale morphology formed on  $\sim 50 \mu\text{m}$  commercial FeCrAl foils after exposure in laboratory air: (a) FeCrAl + Y,Hf, 700°C 10 kh, (b) FeCrAl + Y,Hf, 800°C, 10 kh, (c) FeCrAl + Mm (mischmetal), 900°C, 50 kh, and (d) aluminized FeCrAl + Mm, 900°C, 50 kh. Adapted from Pint, B. A. Unpublished oxidation data, ORNL, Oak Ridge, TN, 1994–2008.

such as  $\theta$  also have been observed on bulk FeCrAl alloys at 900°C.<sup>104,108,109</sup> For Ni-based alloys, cubic aluminas are less common because they tend to form Ni-rich oxides first and the nucleation of alumina beneath this layer apparently favors  $\alpha\text{-Al}_2\text{O}_3$  formation. The alloy 214 (NiCrAl) foils in Figure 16 do not show the high parabolic rate constants observed on FeCrAl foils (Figure 19).

The study of the alumina phase may seem an academic exercise except that there is a strong effect on performance of commercial MCrAl foils in the 700–950°C temperature range. Figure 19 shows the kinetics for commercial aluminized FeCrAl foil oxidation in air at 700–900°C. At 900°C, the initial jump in mass gain is due to the initial formation of the cubic phase. Based on the mass gain, more Al was consumed during the first 500 h exposure than during the next 10 kh of exposure, after the cubic phase had transformed to a slower growing  $\alpha\text{-Al}_2\text{O}_3$  scale. Because of the faster growth of cubic-aluminas, the parabolic rate constant at 700°C ( $1 \times 10^{-15} \text{ g}^2 \text{ cm}^{-4} \text{ s}^{-1}$ ) is comparable to the rate at 900°C (Figure 19). At 800°C, where the blade structure was most evident (Figure 18(b)), the mass gain after 10 kh is higher than at 900°C, although the rate decreased significantly during the last 2.5 kh. All of these mass

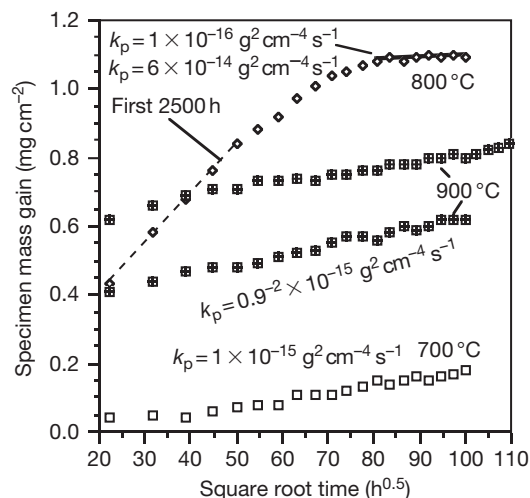


**Figure 19** Specimen mass gains for aluminized FeCrAl + Mm foil ( $\sim 50 \mu\text{m}$ ) exposed for 500 h cycles in laboratory air at 700, 800, and 900°C. The higher rate for cubic alumina phases is seen at 700°C and initially at 800°C. Data from Pint<sup>12</sup> and Dryepondt *et al.*<sup>110</sup>

gains are relatively low. However, with the foil there is a limited Al reservoir. Figure 20 shows the starting and final Al contents in these foils.<sup>110</sup> The starting Al profile in the aluminized FeCrAl is not flat because of the aluminization step. As expected, the Al content drops with exposure time at 900°C with very little Al remaining after 50 kh. However, because of the faster growth of the cubic alumina scale, the foil was almost completely depleted of Al after only 10 kh at 800°C (Figure 20) is similar to other observations for FeCrAl foils in this temperature range.<sup>111</sup>

Because of the use of these foils in automotive catalytic converters and other applications operating in this temperature range, there is considerable concern about the increasing Al depletion due to transient oxide formation. Various treatments have been developed to speed the transformation to an  $\alpha\text{-Al}_2\text{O}_3$  scale.<sup>112</sup> Small ion dopants such as Ti are known to speed the transformation from  $\theta$  to  $\alpha\text{-Al}_2\text{O}_3$ ,<sup>113,114</sup> Therefore, a  $\text{TiO}_2$  slurry was an effective surface modification.<sup>112</sup> Studies have shown a faster transformation to  $\alpha\text{-Al}_2\text{O}_3$  in the presence of  $\text{H}_2\text{O}$ ,<sup>112,115</sup> although an earlier study found the opposite effect.<sup>116</sup> Thus, a higher temperature pretreatment in  $\text{H}_2\text{-H}_2\text{O}$  is another strategy to quickly form an  $\alpha\text{-Al}_2\text{O}_3$  scale.

Once a continuous  $\alpha\text{-Al}_2\text{O}_3$  scale has formed, the transient stage of oxidation is completed and the steady-state period of oxidation begins.



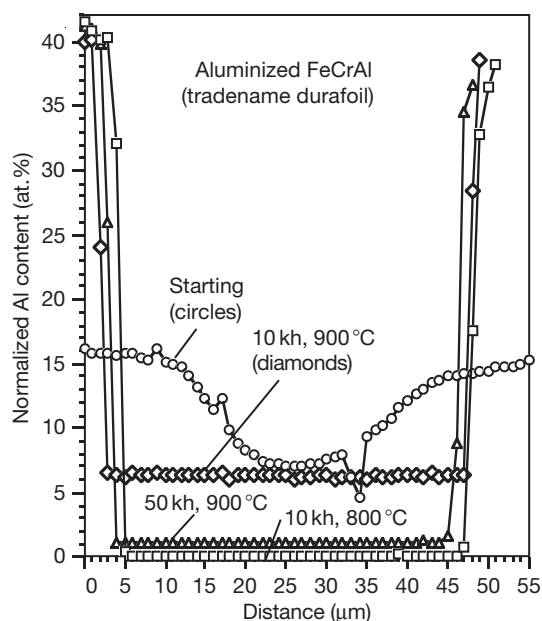


**Figure 20** Electron probe microanalysis using wavelength dispersive spectroscopy Al profiles of the aluminized FeCrAl + RE foil after various exposures in laboratory air. The higher depletion after 10 kh at 800 °C compared to 10 kh at 900 °C is consistent with the mass gain data in [Figure 19](#) and is attributed to the formation of a faster-growing metastable cubic alumina scale. Data from Pint<sup>12</sup> and Dryepondt *et al.*<sup>110</sup>

#### 1.24.4 Steady-State Oxidation

At the completion of the transient stage of oxidation, a complete alumina scale would have formed and subsequent oxidation should be controlled by the properties of this layer. This section will consider the performance of this layer and the factors that affect it. This will be a general discussion with examples given for various materials. The issues relevant to steady-state alumina formation have been reviewed several times.<sup>9,46,117</sup> Nominally, if the scale remains dense and adherent, steady-state oxidation should continue until the substrate is depleted in Al. This depletion will occur more rapidly if scale spallation occurs, requiring reformation of the oxide. Thus, adhesion of the oxide is also an important issue. Most commercial alumina-forming alloys contain a RE addition, for example, Y, Hf, Zr, La, Ce, etc. which strongly affects the steady state oxidation behavior. The role of RE additions will be discussed throughout. These dopants can be added as alloy additions, oxide dispersions or less effectively, as surface treatments or coatings such as slurries or ion

implantation.<sup>6,118</sup> The amount of addition can vary from the ppm level to 0.5% and one of the significant issues is optimizing the RE benefit to achieve the longest alloy lifetime.

##### 1.24.4.1 Scale Growth Rate

The previous section on transient cubic alumina formation began the discussion about growth rates. Starting with the derivation of Wagner,<sup>119</sup> the steady-state rate limiting step should be solid state diffusion through the alumina scale. Therefore, as the diffusion distance increases with time due to the formation of new oxide, the reaction kinetics are expected to be parabolic. Typically, parabolic rate constants have units in a form such as  $\text{g}^2 \text{cm}^{-4} \text{s}^{-1}$  for changes in mass data. The rate also could be expressed in terms of oxide thickness change or metal loss but mass change is the easiest parameter to quantify. For alumina in the temperature range of most interest (1050–1250 °C), the diffusion is along short-circuiting paths, likely the scale grain boundaries. As the oxide grain size increases with oxidation time, it has been argued that the kinetics are actually cubic.<sup>120,121</sup> The steady-state compressive growth stresses in an alumina scale<sup>122–124</sup> also could cause a change in the kinetics as Evans and coworkers argued for  $\text{ZrO}_2$ .<sup>125</sup> However, as will be shown for lifetime predictions of bulk alloys in the next section, the onset of scale spallation results in Al consumption kinetics which is nearly linear with time. Nevertheless, parabolic rate constants are a standard and conventional way to quantify and compare scale growth rates.

As a diffusion-controlled process, rate constants are expected to follow an Arrhenius-type relationship with temperature. [Figure 21](#) shows an Arrhenius plot of rate constants, mostly for RE-doped FeCrAl. As mentioned in the previous section, the rates are higher for cubic alumina scales such as  $\theta\text{-Al}_2\text{O}_3$ . Since cubic alumina is metastable, these scales are only present at lower temperatures, <1000 °C. At higher temperatures, only  $\alpha\text{-Al}_2\text{O}_3$  scales are formed. [Table 3](#) gives some values for FeCrAl with and without RE dopants and the associated activation energies over the range 1000–1300 °C. The activation energies for undoped  $\alpha\text{-Al}_2\text{O}_3$  are lower than that for RE-doped  $\alpha\text{-Al}_2\text{O}_3$ . The activation energy for  $\theta\text{-Al}_2\text{O}_3$  is also similar to undoped  $\alpha\text{-Al}_2\text{O}_3$ , 235  $\text{kJ mol}^{-1}$  for FeCrAl foils which is comparable to the  $\sim 200 \text{ kJ mol}^{-1}$  found for the cubic alumina scales formed on  $\beta\text{-NiAl}$ .<sup>99</sup>

**Table 3** Parabolic rate constants ( $\text{g}^2 \text{cm}^{-4} \text{s}^{-1}$ ) and activation energy ( $\text{kJ mol}^{-1}$ ) for several FeCrAl alloys. Data from Pint.<sup>129</sup>

Temperature	Undoped FeCrAl	0.08Y	0.038Hf + Y	0.020 Hf + Y
1000 °C	$3.1 \times 10^{-13}$	$(1.1\text{--}2.0) \times 10^{-13}$	$4.8 \times 10^{-14}$	$2.5 \times 10^{-14}$
1100 °C	$3.2 \times 10^{-12}$	$(4.2\text{--}4.4) \times 10^{-13}$	$1.4\text{--}3.7 \times 10^{-13}$	$0.98\text{--}1.5 \times 10^{-13}$
1200 °C	$1.4 \times 10^{-11}$	$7.5 \times 10^{-12}$	$5.6 \times 10^{-12}$	$3.5 \times 10^{-12}$
1300 °C	$(2.4\text{--}3.3) \times 10^{-11}$	$(3.6\text{--}4.4) \times 10^{-11}$	$2.2\text{--}2.3 \times 10^{-11}$	$1.1 \times 10^{-11}$
Activation energy ( $\text{kJ mol}^{-1}$ )	244	352	367	366

As can be seen in **Table 3**, RE additions can decrease the scale growth rate. However, this RE effect was not widely accepted until the past decade, particularly when it was discovered by Doychak<sup>126</sup> that Hf-doping in aluminides decreased the parabolic rate constant by a factor of 10.<sup>127–129</sup> One of the complicating factors is the additional mass gain in RE-doped alloys due to the internal oxidation of the RE addition. **Figure 22** illustrates this issue comparing the mass gains for FeCrAl and FeCrAl–0.08Y at 1100 °C. Little difference was observed after a 200 h exposure. However, for  $\text{Y}_2\text{O}_3$ -dispersed FeCrAl (PM2000) a slower rate was measured. For PM2000, there was no mass gain associated with the oxidation of Y because the Y was added to the alloy as an oxide. By minimizing the RE addition to limit internal RE oxidation, the rate constant was further decreased (**Figure 22**). **Figure 23** illustrates the effect on the oxide thickness after 1000 h at 1200 °C by minimizing the RE addition.<sup>94,129</sup> In these backscattered SEM images, the bright phases in the  $\alpha\text{-Al}_2\text{O}_3$  scale are RE-rich oxides which are defects in the scale allowing fast O transport.<sup>130</sup> Minimizing the RE addition, minimizes the number of these particles as well as RE-rich oxide penetrations that penetrate deeper into the substrate, typically referred to as pegs. Note that the lowest RE addition resulted in the thinnest alumina scale on FeCrAl (**Figure 23**).

Several RE optimization studies<sup>131–133</sup> have been conducted to determine the minimum alumina growth rate possible, as in **Figure 24**. With very low RE additions, little benefit was observed. With very high additions, the internal oxidation and entrapped RE-oxides increase the rate. However, the optimal RE levels found in laboratory scale heats may not be viable in commercial alloys with standard impurity levels of interstitials such as S, C, and N.<sup>10</sup> For ODS alloys, the level of  $\text{Y}_2\text{O}_3$  may be selected to optimize creep strength rather than a lower level that may minimize the oxidation rate.<sup>109,134</sup> The type of dopant can affect the oxidation rate. A clear effect of dopant ion size was found for chromia-forming alloys where larger ions decreased the rate more effectively

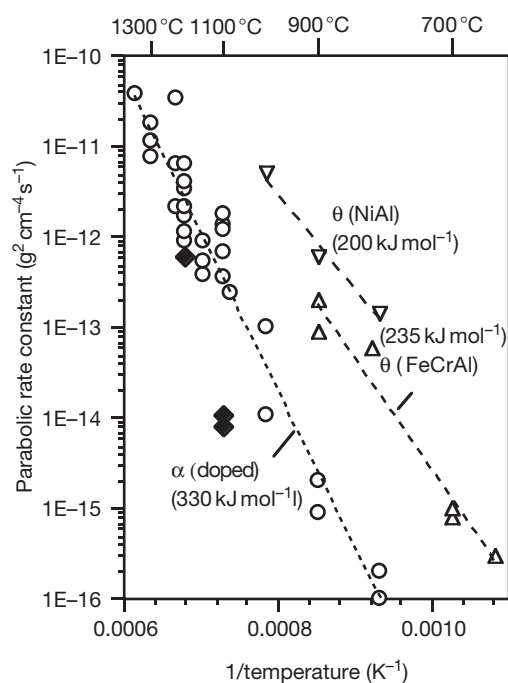


**Figure 21** Summary of parabolic growth rates reported in the literature for RE-doped FeCrAl and calculated activation energies. Rates can be split into those for  $\alpha\text{-Al}_2\text{O}_3$  and  $\theta\text{-Al}_2\text{O}_3$ . For comparison, the  $\theta\text{-Al}_2\text{O}_3$  rate data for NiAl is included.<sup>99</sup> The highlighted rates (diamonds) represent the lowest reported rates at 1100 °C and 1200 °C for Hf-doped NiAl. Other data points from Pint<sup>12</sup> and Pint.<sup>129</sup>

than smaller ions (**Figure 25**).<sup>11</sup> A similar relationship has not been established for alumina-forming alloys,<sup>135</sup> where ion size does not predict the strong beneficial effect of Hf. However, larger ions with high oxygen affinity, for example, Y, Zr, Hf, La, Ce, are all beneficial in reducing the scale growth rate. Smaller dopant ions such as Ti, Nb and Ta do not strongly affect the scale growth rate.<sup>135</sup>

As mentioned earlier, the parabolic rate constant is related to the rate of solid state ionic diffusion through the scale. However, there is no simple relationship and a number of authors have had difficulty relating the published  $\alpha\text{-Al}_2\text{O}_3$  diffusion data to alumina scale growth rates.<sup>136</sup> Using the derivation of



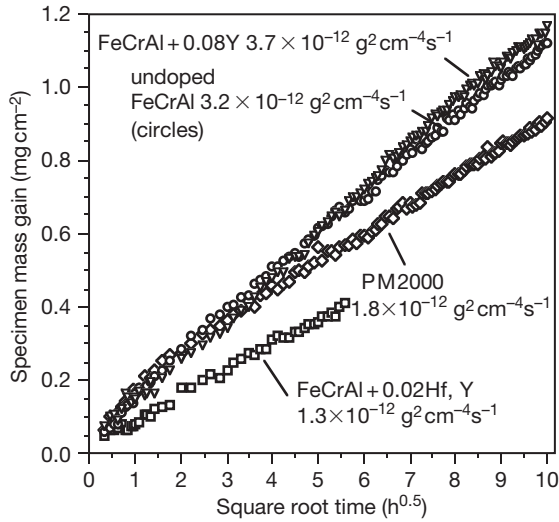


**Figure 22** Specimen mass gain for various FeCrAl alloys (Table 2) during isothermal oxidation at 1100 °C in dry flowing O<sub>2</sub>. The addition of Y did not decrease the reaction rate compared to undoped FeCrAl due to the additional mass gain associated with the internal oxidation of Y. When the addition is made as Y<sub>2</sub>O<sub>3</sub> or lower alloy additions, lower oxidation rates were measured. Data from Pint.<sup>12</sup>

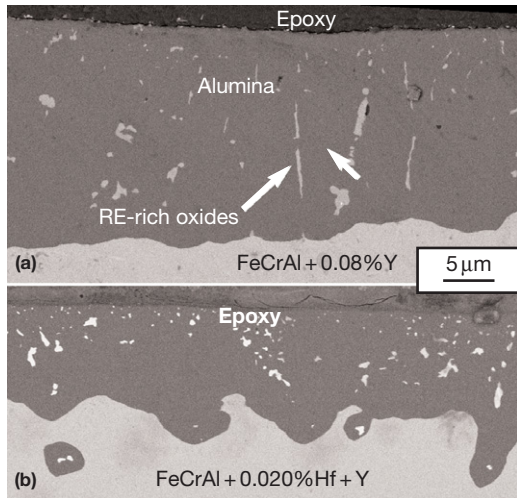


**Figure 23** SEM backscattered electron images of the polished cross-section of the scale formed after 10, 100 h cycles at 1200 °C on FeCrAl with additions of (a) 0.08% Y and (b) 0.020% Hf/Y. Adapted from Pint, B. A.; More, K. L.; Wright, I. G. *Mater. High Temp.* **2003**, *20*, 375–386.

Wagner<sup>119</sup> and the interpretation of Yurek,<sup>137</sup> the parabolic oxidation rate constant for the formation of Al<sub>2</sub>O<sub>3</sub> can be related to the solid state diffusion constant by the following equation for Al<sub>2</sub>O<sub>3</sub>:

$$k_p = \frac{1}{2} \int_{P''_{O_2}}^{P'_{O_2}} [3/2D_{Al} + D_O] d \ln P_{O_2} \quad [3]$$

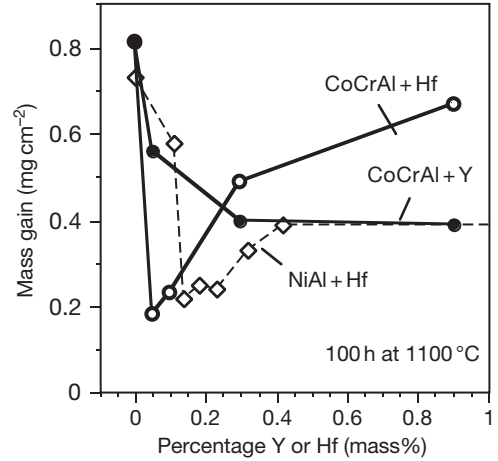


**Figure 24** Mass gain for CoCrAl and NiAl after 100 h at 1100 °C with various reactive element additions. CoCrAl data are from Figure 3 in Whittle and Stringer,<sup>1</sup> NiAl data are from Pint.<sup>12</sup>

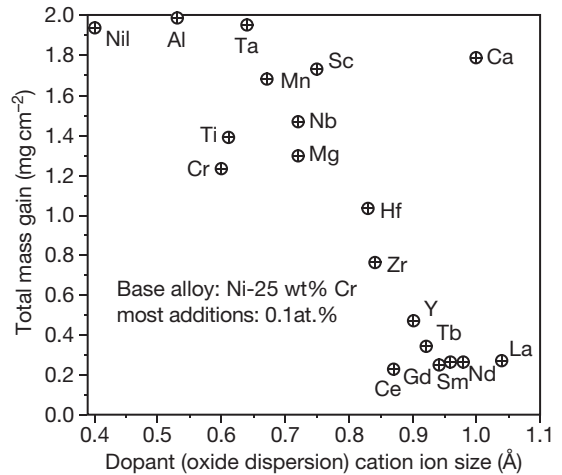


**Figure 25** Total mass gain for Ni-25 wt% Cr alloys with various oxide dispersions added at a nominal level of 0.1 cation% after 100 h at 1000 °C. The mass gain decreased for larger cation additions. The addition of an Al<sub>2</sub>O<sub>3</sub> dispersion had little effect on the scale growth rate. Data from Pint.<sup>11</sup>

where  $k_p$  is parabolic oxidation rate constant,  $P'_{O_2}$  is the decomposition pressure of Al<sub>2</sub>O<sub>3</sub>,  $P''_{O_2}$  is the ambient oxygen pressure, and  $D_{Al}$  and  $D_O$  are the respective self diffusion coefficients for aluminum and oxygen. This equation can be greatly simplified<sup>137</sup> given the observation that the alumina growth rate is independent of oxygen content in the environment,  $P''_{O_2}$ .<sup>108</sup> Extrapolating published diffusion rates for bulk  $\alpha$ -Al<sub>2</sub>O<sub>3</sub><sup>138,139</sup> to 1200 °C, Table 4

**Table 4** Parabolic rate constants at 1200 °C calculated from diffusion data from the literature<sup>138,139</sup> and compared to measured values for RE-doped and undoped alumina-forming alloys<sup>7,127,203</sup>

Predominant diffusion pathway and species	$k_g$ ( $g^2 cm^{-4} s^{-1}$ ) at 1200 °C
<i>Calculated</i>	
Grain boundary diffusion of O	$1.4 \times 10^{-12}$
Grain boundary diffusion of Al	$1.5 \times 10^{-11}$
Lattice diffusion of O	$9.3 \times 10^{-14}$
<i>Measured</i>	
RE-doped FeCrAl	$(3.0\text{--}4.4) \times 10^{-12}$
Hf-doped NiAl	$(0.76\text{--}1.0) \times 10^{-12}$
Undoped FeCrAl, or NiAl	$(0.9\text{--}1.4) \times 10^{-11}$

shows that parabolic rate constants can be calculated which are of the same order of magnitude as those measured.<sup>140</sup> A recent literature review concluded that diffusion in  $\alpha$ -Al<sub>2</sub>O<sub>3</sub> is not fundamentally well understood, making it difficult to correlate diffusion data with oxidation data.<sup>141</sup>

#### 1.24.4.2 Mechanism

While there was some confusion about the growth mechanism of Al<sub>2</sub>O<sub>3</sub> scales in the 1980s, the issue seems to be largely settled today. There were several complicating issues. First, Pt does not wet the surface of  $\alpha$ -Al<sub>2</sub>O<sub>3</sub> (based on work with Pt photolithographic markers<sup>142</sup>). Thus, traditional inert Pt markers used to determine the scale growth mechanism floated on the alumina scale surface whether the scale grew inward or outward. In all cases, the markers showed inward growth.<sup>61,143</sup> For Cr<sub>2</sub>O<sub>3</sub> scales, inert markers showed a predominant Cr outward growth without RE dopants and predominantly O inward growth with RE dopants and this was confirmed, without controversy, using <sup>18</sup>O tracer experiments.<sup>144,145</sup> Second, the transient, cubic Al<sub>2</sub>O<sub>3</sub> phase formation confused some of the early <sup>18</sup>O studies.<sup>101,146</sup> The issue was later clarified, showing that  $\theta$ -Al<sub>2</sub>O<sub>3</sub> scales predominantly grow by an Al outward mechanism,<sup>104</sup> which is intuitive given their morphology<sup>147</sup> (Figure 18(b)). Third, unlike Cr<sub>2</sub>O<sub>3</sub>, there is no distinct difference between undoped and RE-doped  $\alpha$ -Al<sub>2</sub>O<sub>3</sub>, both show some growth by inward O diffusion. With RE-doping, the outward Al transport is diminished and the scale grows predominantly by inward transport. This has been shown by several <sup>18</sup>O tracer studies.<sup>134,148–153</sup> An example of the tracer profiles is shown in Figure 26. The <sup>18</sup>O tracer was used first followed by <sup>16</sup>O. The first stage was 20 min at 1200 °C to ensure that the scale was

100%  $\alpha$ -Al<sub>2</sub>O<sub>3</sub>.<sup>150</sup> In the undoped scale (Figure 26(a)), the <sup>16</sup>O is enriched in both the inner and outer scale indicating both Al and O transport. With the addition of Zr, only a minor <sup>16</sup>O peak was observed at the specimen surface. A stronger <sup>16</sup>O peak was observed underneath the outer <sup>18</sup>O peak indicating predominantly inward O boundary transport.

The explanation for the RE effect on transport has long been thought to be the segregation of RE ions to scale grain boundaries in both alumina and chromia scales.<sup>8,154–157</sup> Segregation of dopant ions is commonly observed in bulk alumina because of the low solubility of many cations in the closed-packed  $\alpha$  lattice.<sup>158</sup> Examples of Y and Ti grain boundary segregation are shown in Figure 17. The mechanism by which RE ions inhibit cation transport could be blocking or site competition or a space charge effect.<sup>159</sup> However, the RE valence has not been shown to be an important variable.<sup>135</sup> A dynamic blocking mechanism was suggested, where large, slow-diffusing RE ions on the boundaries inhibit the diffusion of Al.<sup>8</sup> This mechanism is based on the observed outward transport of RE dopants during oxidation. Figure 27(a) shows a schematic of this phenomenon which is even observed on oxide-dispersed alloys like PM2000. After extended times at temperature, RE-rich oxide particles nucleate at the metal–oxide interface and grow during exposure.<sup>8,135,160</sup> Figures 27(b) and 27(c) show an example at 1100 °C where the faceted Y<sub>3</sub>Al<sub>5</sub>O<sub>12</sub> particles at the gas interface increase in volume with time and do not just coarsen. This mechanism explains why smaller dopants, Ti, Nb, and Ta, segregate to  $\alpha$ -Al<sub>2</sub>O<sub>3</sub> grain boundaries but do not have the same effect on the scale growth rate as larger RE dopants.<sup>135</sup> These smaller ions rapidly diffuse outward and thus do not effectively inhibit Al boundary transport.

Recently, there has been renewed interest in studying the effect of RE dopants on diffusion and sintering in bulk ceramics<sup>161,162</sup> because of the observation that RE dopants like Y and La strongly improve the tensile creep strength of polycrystalline alumina.<sup>163</sup> The boundary electronic structure model proposed as an alternative to a simple dopant ion sized model to explain the behavior of various dopants<sup>164</sup> may be relevant to the effect of RE dopants on scales. Similar to results for bulk ceramics, an increase in the creep resistance of Hf-doped alumina scales has recently been demonstrated.<sup>165</sup>

As mentioned previously, the O and/or Al transport is likely along the scale grain boundaries because bulk diffusion rates in  $\alpha$ -Al<sub>2</sub>O<sub>3</sub> are too slow to

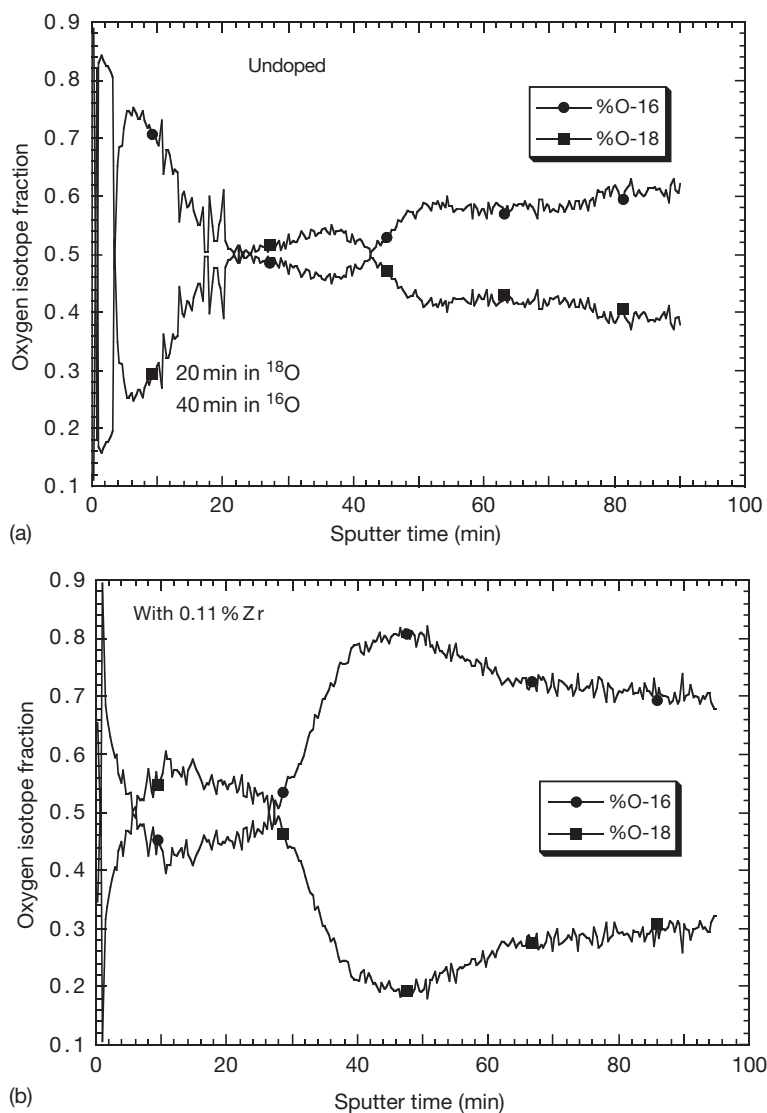


**Figure 26** Secondary ion mass spectroscopy (SIMS) sputter depth profiles of 100%  $\alpha$ - $\text{Al}_2\text{O}_3$  scales formed isothermally at 1200 °C after 20 min in  $^{18}\text{O}$  and 40 min in  $^{16}\text{O}$  on (a) undoped NiAl and (b) NiAl + 0.11%Zr. Data from Pint *et al.*<sup>150</sup>

account for the observed growth rates. **Figure 17** shows a typical cross-section of an alumina scale where very few dislocations or other defects were observed that might accommodate ionic transport. Atkinson and coworkers<sup>166</sup> calculated that a high dislocation density was needed for dislocation transport through the grains. It could be argued that the dislocations were present at a temperature but were annihilated during cooling.<sup>141</sup> However, the cooling rate for the thin scale is rapid which would not support this hypothesis. Experimental work has also indicated that, rather than neutral species, transport in alumina scales is via charged ions, that is,  $\text{O}^{-x}$  or  $\text{Al}^{+y}$ , as applied voltages have been shown to alter the

scale growth rate<sup>167–169</sup> and electrical properties measurements indicate that  $x$  is  $\sim 2$ .<sup>170</sup>

A final point about scale growth is that there is now considerable interest in studying scale growth stresses, particularly with the advanced characterization techniques now available for *in situ* measurements.<sup>124,165,171–174</sup> These *in situ* results are considerably better than measuring the stress after cooling to room temperature by photostimulated luminescence and attempting to separate the growth stress from the thermal stress.<sup>175,176</sup> This recent *in situ* work has confirmed the observation that these growth stresses can be tensile,<sup>171,172</sup> rather than the common assumption of compressive growth stresses.<sup>177</sup>

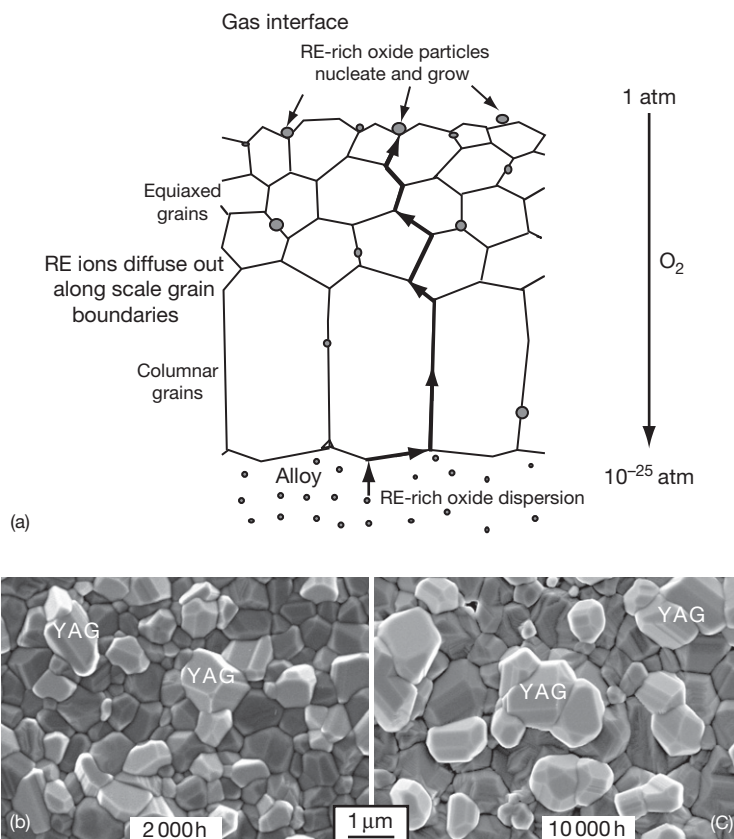


**Figure 27** (a) Schematic representation of the outward diffusion of RE ions from oxide particles in the substrate to incorporation in the scale.<sup>8</sup> (b) and (c) show plan view SEM secondary electron images of the scale formed on PM2000 (ODS FeCrAl) after exposures in air at 1100 °C for (b) 2000 h and (c) 10 000 h.<sup>12</sup> The size and volume fraction of Y-rich oxide particles such as Y<sub>3</sub>Al<sub>5</sub>O<sub>12</sub> (YAG) has increased with exposure time. Titanium, also present in the alloy, is highly enriched at the gas interface.

The stresses can also decay with time as they are accommodated by substrate or scale creep.<sup>165</sup> Nevertheless, these stresses are generally <10% of the thermal stresses generated on cooling due to the CTE mismatch between metal and scale (see [Section 1.24.4.4.4](#)). Thus, they are often ignored when calculating the effect of stress on adhesion, eqn [1].<sup>19</sup>

### 1.24.4.3 Morphology

**Figures 28 and 29** give some examples of typical scale morphologies on alumina-forming alloys that do not form a base metal transient oxide and are commonly observed in the literature.<sup>7,135,178–181</sup> The surface morphology of transient cubic aluminas was shown in [Figure 18](#). Without a RE addition, undoped  $\alpha$ -Al<sub>2</sub>O<sub>3</sub> often shows a wrinkled morphology with oxide whiskers at the gas interface<sup>7,117,143,178–181</sup> which hint at the outward transport of Al. As alumina scales are usually thin, the original surface roughness

(e.g., level of polishing for laboratory specimens) often affects the morphology.<sup>181</sup> At higher magnification, fine ridges can be seen that also suggest outward transport ([Figure 28\(a\)](#)). (These ridges are not the same as the ridges on  $\beta$ -NiAl formed by the  $\theta$ - $\alpha$  phase transformation.<sup>102</sup>) Undulations of the undoped oxide scales also occur on FeCrAl and Fe(Al), sometimes accompanied by equivalent deformation of the underlying metal but also due to the formation of interfacial voids.<sup>7,182–187</sup> The undulations are not found when undoped FeCrAl substrates have low S contents<sup>185</sup> or an Al<sub>2</sub>O<sub>3</sub> oxide dispersion is added ([Figure 29\(a\)](#)).<sup>187,188</sup> These differences suggest that the interfacial strength or mechanical properties of the oxide and scale may control this phenomenon.<sup>188</sup> In the cross-section, the scale typically has an equiaxed grain structure with or without wrinkles ([Figure 29\(a\)](#)).

With a RE addition, the surface ridges and whiskers are not present, indicative of the RE's role in



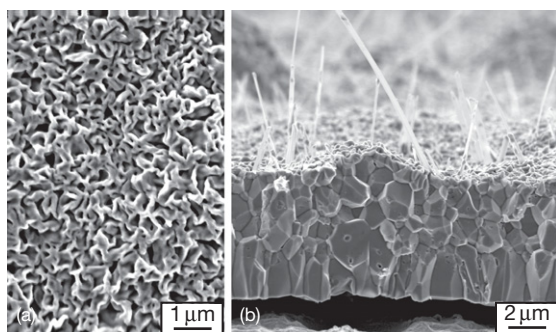


**Figure 28** SEM secondary electron images of the  $\alpha$ - $\text{Al}_2\text{O}_3$  scale formed on undoped FeCrAl at 1200 °C in dry flowing  $\text{O}_2$ . (a) Plan-view image of undoped FeCrAl after 2 h and (b) cross-section of the scale formed on  $\text{Al}_2\text{O}_3$ -dispersed FeCrAl after 100 h. In (a), the ridges can be referred to as intrinsic ridges to differentiate them from the extrinsic ridges formed on NiAl due to the alumina phase transformation. Adapted from Pint, B. A. Unpublished oxidation data, ORNL, Oak Ridge, TN, 1994–2008.

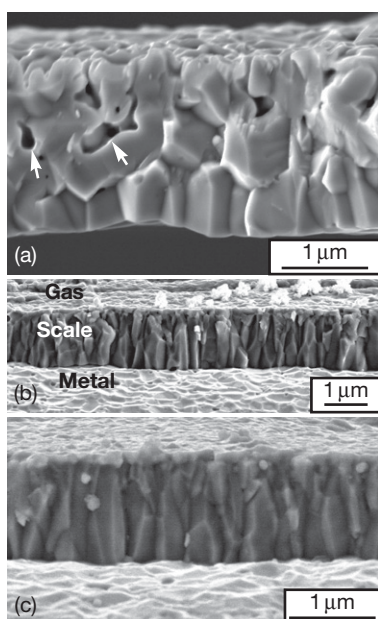


**Figure 29** SEM secondary electron images of fracture cross-sections of scales formed on oxide dispersed FeCrAl after 2 h at 1200 °C in dry flowing  $\text{O}_2$ . (a)  $\text{Al}_2\text{O}_3$ , (b)  $\text{Ho}_2\text{O}_3$ , and (c)  $\text{Er}_2\text{O}_3$ . Adapted from Pint, B. A. Unpublished oxidation data, ORNL, Oak Ridge, TN, 1994–2008; Pint, B. A.; Alexander, K. B. *J. Electrochem. Soc.* **1998**, *145*, 1819–1829. Arrows in (a) indicate internal voids.<sup>186</sup>

suppressing outward Al transport.<sup>148–153</sup> As shown in **Figure 27**, instead of ridges, fine RE-rich oxide particles form on the surface. Additions such as Ti will tend to make the surface grains more rounded and

less angular.<sup>135,189</sup> The most distinctive RE effect on morphology is on the grain structure where the change in growth mechanism results in a columnar grain structure with fine equiaxed grains near the gas interface.<sup>178</sup> In many alloys, the layer of equiaxed grains does increase in thickness with time because of the small amount of outward Al transport.<sup>190</sup> However, the scale thickening is predominantly due to an increase in the length of the columnar grains. Unlike some studies showing no texture, an x-ray pole figure on the scale formed on PM2000 at 1200 °C showed a preferred growth direction.<sup>191</sup> The grain structure of RE-doped  $\alpha$ - $\text{Al}_2\text{O}_3$  is remarkably similar independent of the RE type and substrate, that is, M–Al or M–Cr–Al, likely because the scales on all these substrates grow by a similar mechanism. Some less common RE dopants are shown in **Figure 29** to illustrate that a wide range of dopants produce similar effects. Varying the type and amount of dopant can alter the size and structure of the columnar grains.<sup>192</sup>

#### 1.24.4.4 Adhesion

The most critical performance issue for alumina-forming alloys in long-term high temperature applications is scale adhesion. Adherent scales grow with parabolic (or even cubic) kinetics which results in very slow Al consumption rates from the substrate. However, when the scale spalls, the oxide must regrow or heal the spalled region, resulting in a significant increase in the rate of Al consumption due to the initial high rate of oxidation. As described in **Section 1.24.1**, the major cause of scale spallation is the thermal or cooling stress due to the CTE mismatch ( $\Delta\alpha$ ) between the substrate and oxide, see **eqn [1]**. An additional issue is the formation of voids or other defects at the exposure temperature that lead to decohesion. Without defects, the scale will eventually reach a critical thickness,  $\zeta_f$ , where the strain energy ( $W^*$ ) is sufficient to cause spallation, **eqn [2]**. Defects will decrease the interfacial adhesion resulting in failure at a lower scale thickness.

For undoped alumina-formers, void formation at the metal–alumina interface is typically one of the critical issues that determines adhesion. Provenzano and coworkers<sup>193</sup> found in CoCrAl compositions that the interfacial void area increased with temperature from 700 to 1000 °C. Typically, these voids are thought to be formed by a Kirkendall-type mechanism either due to diffusion in the alloy or the oxide or both. Because of the outward transport of Al in the undoped scale, a counter current vacancy flux moves



towards the metal-scale interface. Also, because of the faster undoped scale growth rate, there is increased diffusion in the substrate with Al diffusing to the interface and other elements moving in the opposite direction. Contributing to the nucleation or growth of interfacial voids may be surface-active interstitial impurities such as S,<sup>186,194</sup> which will be discussed further in Section 1.24.4.4.2.

One problem with discussing scale adhesion is that it is difficult to quantify.<sup>195,196</sup> A well-formed scale is more tenacious than most epoxies used in quantifiable pull tests with an interface fracture toughness of  $>90$  MPa.<sup>197</sup> Specimen mass gain curves can be used with a decrease in mass suggesting spallation. However, consider some NiCrAl alloy examples in Figure 30. The specimens that spall and rapidly lose mass are obvious but a higher specimen mass gain does not necessarily indicate a more adherent oxide. A higher mass gain could indicate a faster growing oxide coupled with minor spallation. The lower mass gain for NiAl + Hf is due to a thinner, adherent oxide. Furthermore, some oxides remain attached but are friable and therefore not protective,<sup>198</sup> resulting in a false indication of adhesion. Many early RE optimization studies relied on a relatively short term cyclic oxidation data to conclude that a certain composition was superior.<sup>131,133</sup>

A more absolute way of quantifying scale adhesion is cyclically testing specimens through the steady-state oxidation period until they reach breakaway oxidation (see Section 1.24.5). Figure 31 shows the time to

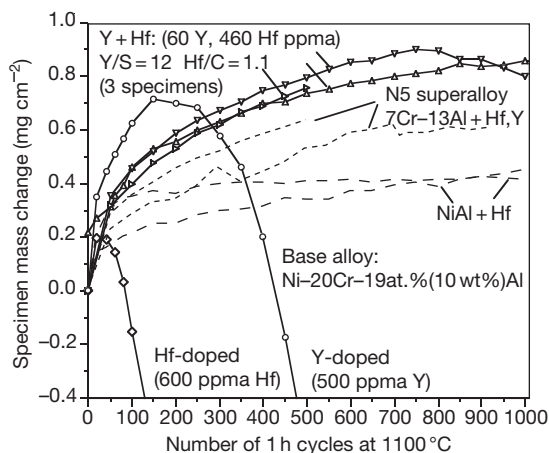


**Figure 30** Specimen mass change of various Ni-20Cr-19Al alloys during 1 h cycles at 1100 °C in dry flowing O<sub>2</sub>. The codoping of Y and Hf produced better scale adhesion compared to Hf or Y additions alone. Data from Pint<sup>12</sup> and Pint *et al.*<sup>94</sup>

breakaway for various FeCrAl models and commercial alloys, all with  $\sim 10\%$  Al. In order to accelerate the test, 1 h cycles were used at 1200 °C. The time has been normalized to a 1.5 mm thick specimen. Thus, all the specimens begin with a similar Al reservoir and the rate of scale growth and adhesion are thus key parameters in determining lifetime (see Section 1.24.5). An undoped wrought FeCrAl specimen, which spalls readily during thermal cycling, had a lifetime of only  $\sim 300$ , 1-h cycles. From Figure 31, it is obvious that RE additions play a critical role in increasing scale adhesion and thus increasing life.

#### 1.24.4.4.1 Reactive elements

The main beneficial effect of RE additions (e.g., Y, Zr, Hf, La, Ce) on alumina-forming alloys is the improvement in scale adhesion. Figure 31 shows that the addition of 0.08 Y increased the lifetime of FeCrAl by a factor of 30 compared to undoped FeCrAl. Most studies have observed a reduction in the interfacial void formation. A number of hypotheses have been proposed to explain the RE effect on void formation. Tien and Pettit<sup>143</sup> proposed that the RE dopants in the alloy formed a vacancy complex that prevented vacancies from coalescing at the metal scale interface. Using a similar logic, Kumar *et al.*<sup>199</sup> suggested that RE internal oxides in NiCrAl acted as a vacancy sink. However, there is no experimental evidence of these hypotheses. The formation of RE internal oxides or ‘pegs’ was thought to create a mechanical interlock that improved scale adhesion.<sup>61,131,132,200</sup> While a small number of

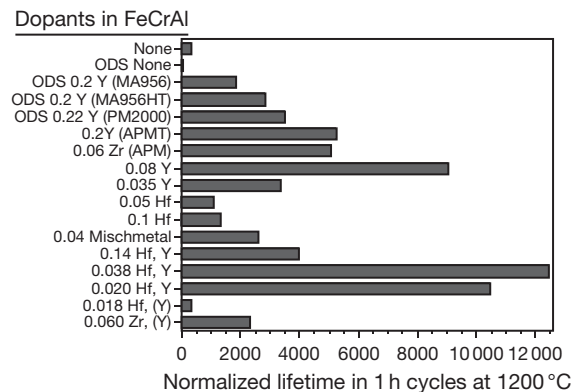


**Figure 31** Normalized time to breakaway oxidation (as an indicator of scale adhesion) for various FeCrAl alloys (see Table 2) at 1200 °C in 1 h cycles. The lifetime is normalized to a 1.5 mm thick specimen. Model wrought alloys doped with Y and Hf showed the longest lifetime. Data from Pint.<sup>12,129</sup>

pegs is likely to be beneficial in preventing interfacial (metal–scale) crack propagation, pegs are not necessary as ODS alloys achieve good scale adhesion without forming pegs. For example, the lifetimes for several ODS alloys are shown in **Figure 31**.

Another hypothesis was that the finer grained RE-doped alumina scale resulted in a more plastic oxide that accommodated the strain better.<sup>61,201</sup> Ironically, the recent work on RE-doped bulk alumina<sup>161,163,164</sup> and scales<sup>165</sup> has shown that RE-doping actually increased the creep strength by several orders of magnitude. The change in mechanical response of the oxide scale with Y doping can explain the higher residual stresses measured in Y-doped alumina scales.<sup>176</sup> Weaker, undoped scales can wrinkle to accommodate the growth stress at temperature.

One of the issues that confounded potential hypotheses to explain the role of RE additions was the reported benefit of *any* oxide dispersion, including  $\text{Al}_2\text{O}_3$  on scale adhesion.<sup>143,202</sup> This result could not be repeated in more recent work on  $\text{Fe}_3\text{Al}$ ,  $\text{NiAl}$ , or  $\text{FeCrAl}$ .<sup>135,188,203</sup> No benefit on scale adhesion, growth rate, or scale morphology was observed with only an  $\text{Al}_2\text{O}_3$  dispersion. In **Figure 31**, an  $\text{Al}_2\text{O}_3$  dispersion reduced the lifetime from 300 h for wrought undoped  $\text{FeCrAl}$  to 70 h.

A current interpretation<sup>8</sup> of the role of RE additions on scale adhesion involves several issues: (1) the inhibition of outward Al transport decreases the counter vacancy flux to the interface, (2) the segregation of RE ions to the interface decreases the interfacial energy ( $\gamma_{\text{int}}$ ), thereby increasing the critical scale thickness<sup>7,8,204</sup> (see eqn [2]), and (3) the RE addition prevents the interfacial segregation of S which has a detrimental effect on void growth. The observed outward flux of RE ions from the alloy into the scale results in RE ions segregated at the metal–scale interface.<sup>7,8</sup>

Mechanistically, the role of RE additions may be resolved, but, practically the issue of optimizing that benefit has not. The type of dopant, the amount, and the method of addition has still not been completely resolved. However, a few issues have been clarified. Surface doping with RE oxide coatings or ion implantation does not produce optimal benefits.<sup>6,118,205</sup> Alloy additions and oxide dispersions are clearly superior. Effective RE dopants have two qualities: large ion size and high oxygen affinity.<sup>135</sup> To avoid the issue of dopant solubility, which affects internal oxidation and other issues, a screening test was performed on various dopants added as oxide dispersions. **Figure 32** shows the 1200 °C, 1 h cycle

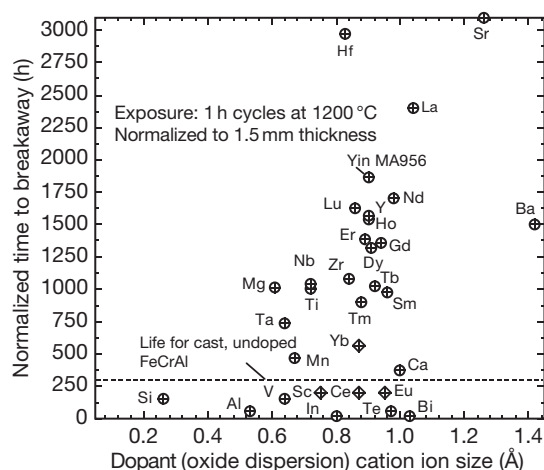


**Figure 32** Normalized time to breakaway oxidation (as an indicator of scale adhesion) at 1200 °C in 1 h cycles for various oxide (VN for V,  $\text{BaTiO}_3$  for Ba) dispersions (0.025–0.2 cation% additions) in  $\text{Fe-20Cr-10Al}$ . Lifetimes were normalized to a 1.5 mm specimen thickness. Low lifetimes for diamonds (Sc, Ce, Eu, and Yb) were attributed to over-doping with 0.2% additions. In general, all the lifetimes are somewhat lower than in commercial ODS alloys because of the laboratory processing. Data from Pint.<sup>11,12</sup> and Pint and Alexander.<sup>135</sup>

normalized lifetime for various dopants added as 0.2 cation% oxide dispersion additions to  $\text{FeCrAl}$ . (In general, the lifetimes for these laboratory-made alloys were not as good as that of the higher-quality commercial alloys (**Figure 31**).) There is a weak correlation between lifetime and larger ion size with many dopants not fitting this explanation. Several large ions, such as In, Te and Bi, have low oxygen affinity and never become incorporated into the oxide. Dopants such as Sc, Yb, Ce, Hf, La, and Eu produced negative effects with 0.2% additions associated with over-doping.<sup>135</sup> The data points for Hf and La, two of the highest lifetimes, were additions of 0.05%.

For alloy additions, **Figure 31** suggests that the best RE dopant is Y (compared to Hf, Zr, or mischmetal, a combination of Ce, La, and Nd). However, there was a considerable difference in lifetime between 0.08 and 0.035 Y additions. **Figure 33** shows lifetime as a function of specimen thickness for several Y additions. It is interesting to note that the lower Y contents, which would result in less internal oxidation, produced lower lifetimes than the specimens with 0.08% Y. A wider range of Y additions needs to be studied to resolve this issue and identify an optimum for lifetime. However, given the weak correlation with specimen thickness, these results suggest that the thicker specimens may become depleted in Y due to

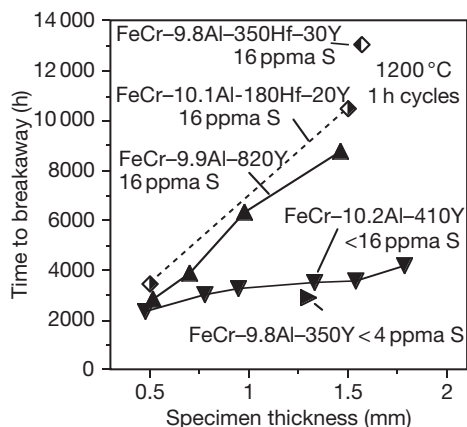


**Figure 33** Time to breakaway oxidation (i.e., Fe-rich oxide formation) at 1200 °C using 1 h cycles for various RE-doped FeCrAl alloys (dopant contents in ppm) as a function of specimen thickness. For both Y-doped and co-doped (Y and Hf) alloys, there is a decrease in lifetime with very low RE additions. Data from Pint.<sup>12</sup>

spallation and not get as full a benefit as with higher Y additions. A similar result has been observed with RE doping in NiCrAl coatings.<sup>206</sup>

**Figure 30** shows better spallation resistance for a NiCrAl with both Y and Hf compared to Y or Hf alone. **Figures 31 and 33** show the highest lifetimes for a combination of Y and Hf. This so-called co-doping results in low scale growth rates, minimal internal oxidation, and more optimal performance. Commercially, some alloys contain two or more dopants such as NiCrAl alloy 214 (Y and Zr), SX superalloys 1487 and N5+ (Hf and Y), and Aluchrom YHf (Y, Zr, Hf, and Ti) (**Tables 1 and 2**). A Pratt & Whitney NiCoCrAl coating (PWA286) also contains Y and Hf.<sup>207</sup> Co-doped alloys rely on a higher solubility dopant (Hf or Zr) along with lower levels of the low solubility Y dopant. Again, dopant depletion can be an issue because the lowest level of Y and Hf dopant did not produce the longest lifetime in a model FeCrAl alloy (**Figures 31 and 33**). Co-doping levels in model alloys were selected to match the alloy interstitial levels to achieve a  $[Y]/[S] > 1$  and a  $[Hf]/[C] > 1$ .<sup>129</sup> This interstitial-dopant ratio strategy was originally proposed by Sigler.<sup>208</sup> In commercial alloys, the interstitial levels are higher than in the laboratory, which may require slightly different doping strategies.<sup>10</sup> Trying to target narrow composition windows is probably not realistic for commercial production, particularly considering that a co-doped alloy with a  $Y/S < 1$  will have very poor performance lifetime, for example, FeCrAl with 0.018Hf(+Y) in **Figure 31**.

#### 1.24.4.4.2 Interstitials (S, C, etc.)

Identifying the detrimental role of S, and possibly other interstitials, has caused a major shift in the thought process on scale adhesion of alumina-forming alloys in the past 25 years.<sup>28,185,204,208–216</sup>

The early work by Smeggil and Smialek on NiCrAl and later on FeCrAl has resulted in almost every commercial high temperature alloy being produced with  $< 5$  ppm S, **Table 2**. While an early hypothesis<sup>217</sup> suggesting that S could explain all RE effects was disproved,<sup>8,204</sup> the current mechanistic understanding is that S segregates to the metal–scale interface thereby increasing the interface energy, which in turn increases the formation of interfacial voids and weakens the interface.<sup>186,194,218,219</sup> Sulfur segregates to all free surfaces<sup>220</sup> and alloy grain boundaries; thus, it is not surprising that a high S content in nano-grained FeCrAl did not have a detrimental effect on alumina scale adhesion.<sup>221</sup> The large number of alloy grain boundaries provided alternative locations for S segregation besides the metal–scale interface.

An alternative explanation, that other interstitial elements besides S, such as Na and Ca, has been proposed.<sup>222</sup> However, a follow-up study by Smialek<sup>223</sup> which examined 41 elements in a Ni-based superalloy found that hydrogen annealing of superalloys, which improved alumina scale adhesion, primarily lowered the S and C contents. It has been suggested that La additions to superalloys was beneficial in countering a detrimental effect of P.<sup>224</sup> However, a study of Ni–7Cr–13Al + Y alloys with intentional P additions (70 ppm) showed no effect on scale adhesion during 1 h cyclic testing at 1100 °C.<sup>12</sup>

A common RE–S explanation is that RE dopants ‘getter’ S away from the metal–scale interface by forming RE–S compounds.<sup>210</sup> However, this mechanism has not been proven for ODS alloys (which contain high S levels, **Table 2**) where dispersoids did not contain S and S was not found segregated to the dispersoid–alloy interface.<sup>8</sup> The observation of a Y–S compound<sup>225,226</sup> is not proof of a gettering mechanism, only that Y forms a stable sulfide. A segregation-based RE mechanism suggests that RE ions segregate to the metal–scale interface and lowers the energy such that S segregation is no longer thermodynamically favorable.<sup>8</sup> Whether this involves site competition for segregation or another mechanism is not known. Nevertheless, there is a clear relationship where the Y/S ratio needs to be greater than unity for good scale adhesion in FeCrAl and NiCrAl.<sup>28,129</sup>

#### 1.24.4.4.3 Precious metals

Alumina scale adhesion has been improved by Pt and other Pt group metals (PGMs).<sup>79,84–86,227–229</sup> The majority of observations have been for Ni-based alloys and coatings, especially  $\beta$ -NiAl. Pt additions also have been used to improve the performance of CoCrAlY coatings.<sup>227</sup> While the effect of Pt on adhesion is similar to RE additions as both are likely to lower the metal–scale interface energy, the mechanism is quite different as  $\sim 2$  at.% Pt or Ir is needed as an alloy addition to improve adhesion. Also, Pt does not alter the scale growth rate and does not become incorporated into the alumina scale or segregate to scale grain boundaries, even on Pt–Al alloys.<sup>230</sup>

There is some disagreement about the effect of Pt additions in FeCrAl-based alloys. One study suggested that PGM additions benefited scale adhesion on FeCrAl.<sup>229</sup> However, that result could not be reproduced with 0.1 or 3 at.% Pt additions.<sup>12</sup> Unlike in Ni-based compositions, the formation of a Pt-rich phase in FeCrAl + 3Pt, likely due to limited solubility of Pt in ferrite, may explain the lack of benefit compared to Ni- and Co-based alloys and coatings.

#### 1.24.4.4.4 Role of CTE

Thermal expansion mismatch between the metal and scale is a critical factor in understanding the oxidation resistance of various alumina-forming alloys. The effect is most evident in the Fe–Al system because of the very high CTE of the aluminide phases, particularly  $\beta$ -FeAl.<sup>52,128,231–233</sup> The difference in CTE can explain the scale spallation problems of RE-doped aluminides compared to ferritic FeCrAl and Fe(Al) alloys. The effect in RE-doped Fe–Al alloys can be quantified to a certain extent by using an approximation of the critical scale thickness,  $\xi_f$ , from eqns [1] and [2]:

$$\xi_f \propto (\Delta T \Delta \alpha)^{-2} \quad [4]$$

Above this thickness, the strain energy in the scale exceeds the interface strength and spallation occurs. Assuming that the Al content does not affect the interface or oxide properties, if  $\xi_f = 10 \mu\text{m}$  for FeCrAl, then it is only  $1 \mu\text{m}$  for  $\beta$ -phase Fe–40Al and  $2 \mu\text{m}$  for Fe<sub>3</sub>Al.<sup>233</sup>

Figure 34 gives some typical mean CTE values for alumina-forming alloys as a function of temperature. The values for NiAl, FeCrAl and Ni–22Al–5Pt are all remarkably similar at 1000–1200 °C and all these materials have the lowest CTE mismatch with

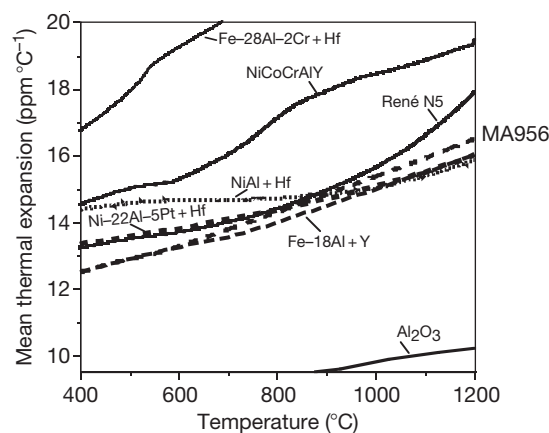


**Figure 34** Mean coefficient of thermal expansion as a function of temperature for several Ni- and Fe-based alloys (see Table 2) showing the difference between these metals and alumina. Data from Haynes *et al.*,<sup>30</sup> Pint *et al.*,<sup>82</sup> Wright *et al.*,<sup>232</sup> and Pint *et al.*<sup>233</sup>

$\alpha$ -Al<sub>2</sub>O<sub>3</sub>. Alloys that have a phase transformation such as NiCoCrAlY or  $\beta$ -FeAl have much higher CTE than the materials that remain a single phase across the 25–1200 °C temperature range.

For Ni-based alloys, it is difficult to draw an exact correlation between CTE mismatch and scale adhesion, again because it is difficult to quantify scale adhesion. One criterion used previously for lifetime modeling was the time to zero specimen mass gain,  $t_z$ , in a cyclic oxidation test.<sup>234</sup> For example, in Figure 31 the  $t_z$  for Hf-doped NiCrAl would be  $\sim 85$  h and  $\sim 425$  h for Y-doped NiCrAl. In Figure 35, the CTE mismatch is plotted versus  $t_z$  at 1150 °C for several Ni-based alloys.<sup>30</sup> The general trend in the data is that a smaller  $\Delta\alpha$  results in a longer  $t_z$ . The various NiCrAl and NiCoCrAlY compositions have a higher CTE and spall more readily. One complicating issue for this type of plot is that RE additions have a strong influence on scale adhesion (and thus  $t_z$ ) but have no effect on CTE.<sup>30</sup> Therefore, the horizontal arrows show the increase associated with RE-doping or RE optimization (in the case of NiCrAlYHf). The dashed line represents an assumed optimum for RE doping. (Note that the 2000 h value for Hf-doped NiAl was an approximation, the mass gain did not reach zero after 2000 h cycles at 1150 °C, although it was decreasing towards zero.<sup>12</sup>)

#### 1.24.4.4.5 Role of substrate strength

One of the alloys that does not fit the trend in Figure 35 is the single-crystal (SX) superalloy, N5, which contains both Y and Hf. There are two possible

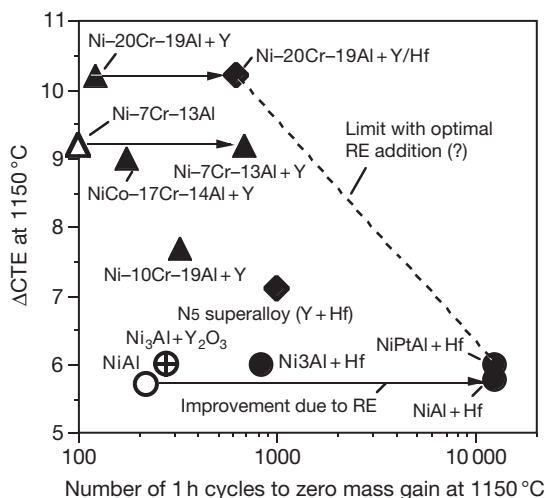


**Figure 35** Difference in CTE between the alloy and alumina at 1150 °C for various Ni-based alloys (see Table 2) plotted versus the number of 1 h cycles to zero mass gain at 1150 °C. The number of cycles reflects the relative scale adhesion of these materials. Intermetallic alloys have much lower CTE values than the multiphase NiCrAl alloys that undergo phase transformations between RT and 1150 °C. Adapted from Haynes, J. A.; Pint, B. A.; Porter, W. D.; Wright, I. G. *Mater. High Temp.* **2004**, 21, 87–94.

reasons for this deviation, one is that the spallation of the transient oxide on this alloy increases the specimen mass loss but does not actually reflect the adhesion of the alumina scale. The other possible reason is that this very strong SX substrate does not accommodate the stresses in the scale (e.g., by creep) like a weaker substrate, such as NiAl, resulting in earlier scale spallation.<sup>235,236</sup>

A substrate creep strength hypothesis has been used to explain the decreased alloy lifetimes of ODS FeCrAl alloys compared to weaker wrought FeCrAlY or Fe(Al)Y (Figures 31 and 36(a)).<sup>233</sup> One exception to this negative effect of alloy strength is the commercial FeCrAl alloys APM and APMT.<sup>233</sup> With the addition of Mo and lower Cr content, APMT has a higher creep strength than APM<sup>237</sup> but essentially no decrease in lifetime (Figure 36(a)). However, APMT also contains Y and Zr so that RE optimization compared to APM may be responsible for maintaining the cyclic oxidation lifetime.

Substrate strength also affects the performance of foil specimens. In this case, the thin metal section deforms due to stresses in the oxide and little scale spallation occurs in most cases. The compressive stress generated in the growing oxide can cause the foil to lengthen due to the tensile stress in the adjacent metal. This increase in length has been

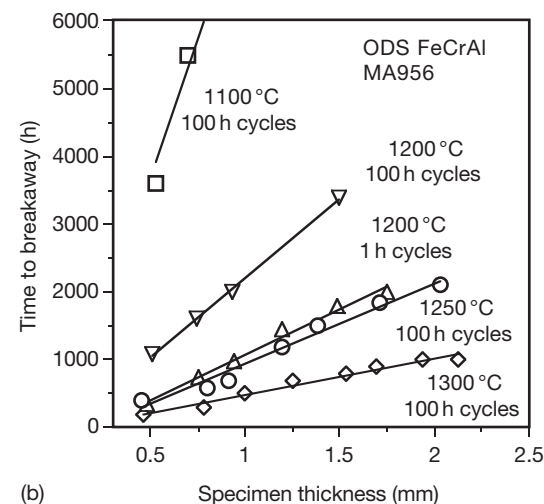
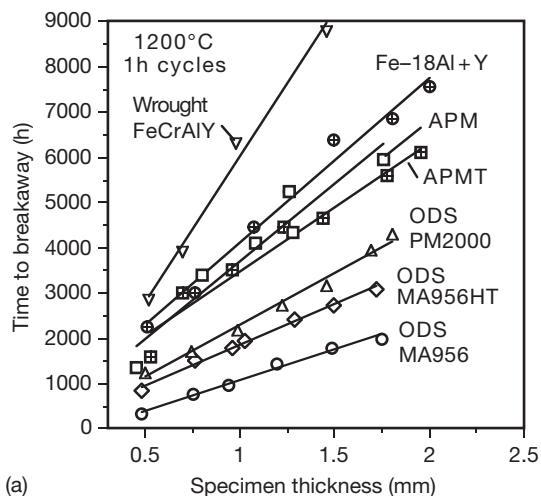


**Figure 36** Time to breakaway oxidation (i.e., Fe-rich oxide formation) as a function of initial specimen thickness (a) at 1200 °C using 1 h cycles for various FeCrAl and Fe-Al alloys (b) for alloy MA956 under various cyclic conditions (see Table 2 for compositions). Data from Pint<sup>12</sup> and Pint *et al.*<sup>233</sup>

characterized because it can be detrimental to the performance of FeCrAl catalyst supports.<sup>238</sup>

In general, it is difficult to quantify the mechanical effects of typical alumina-forming alloys because the tensile properties and creep (primary, as well as steady-state) rates are not commonly measured at the temperatures relevant for high temperature oxidation.<sup>187</sup>

#### 1.24.4.4.6 Effect of cycle frequency

A final note about adhesion is that increasing the cycle frequency, that is, reducing the time per cycle usually decreases scale adhesion by increasing the number of



thermal cycles per time period.<sup>15,198,234,239</sup> Figure 36(b) gives examples of the time to breakaway oxidation for ODS alloy MA956 under various cyclic conditions. Of course increasing the temperature decreases the lifetime using 100 h cycles at 1200–1300 °C. However, increasing the cycle frequency from 100 to 1 h per cycle at 1200 °C, produced a reduction in lifetime similar to increasing the test temperature by 50 °C. Figure 37 gives an example for FeCrAlY where during 100 h cycles to a total time of 5000 h cycles, virtually no scale spallation occurred. However, in 1 or 2 h cycles, spallation began after a few hundred hours. One-hour cycles are used in lifetime testing to accelerate the experiment by inducing scale spallation more quickly.

Exceptions to the inverse relationship between cycle frequency and scale adhesion were observed for some Ni-based superalloys.<sup>15</sup> This behavior was attributed to the spallation of transient scale during longer cycles but could also be due to the time-dependent growth of defects such as interfacial voids. In short cycles, the defect may never reach the critical size necessary to cause spallation or only cause small areas to spall. Longer cycles, with long holds at temperature, may allow defects to grow to a sufficient size or accumulate such that scale spallation occurs over large areas.

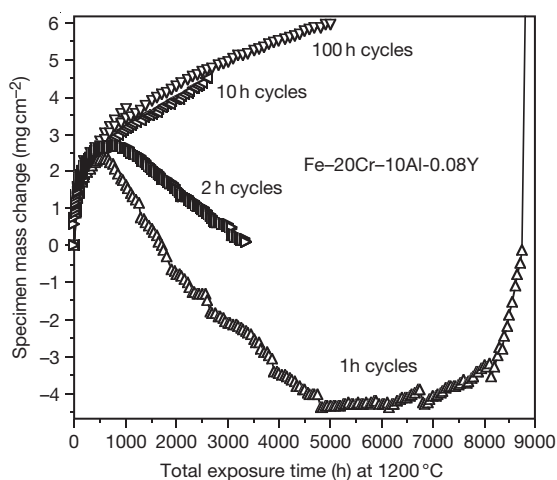


**Figure 37** Specimen mass change for FeCrAl-0.08Y as a function of total exposure time for various cycle frequencies of 1–100 h per cycle. In 100 h cycles, very little spallation was observed but reducing the cycle time increases the number of thermal cycles and increases the amount of spallation, particularly for 1 and 2 h cycles. Data from Pint<sup>12</sup> and Pint *et al.*<sup>15</sup>

#### 1.24.4.5 Internal Oxidation

The formation of oxide (or, more generally, any oxidation reaction product) within the alloy, beneath the external scale, is generally regarded as detrimental because it can degrade the mechanical properties of the substrate and interfere with the long-term chemical or mechanical stability of the protective external scale. For example, an internal oxide can help to nucleate a crack in the substrate. As also described previously (Section 1.24.4.1), internal oxidation generally increases the overall oxidation rate and can serve as fast transport paths for oxidants. The issue of internal oxidation of Al could be related to insufficient Al content to form an alumina scale, which essentially is a problem of low Al content alloys and/or alloys with poor selective oxidation.

Internal oxidation behavior has been studied on dilute M–Al alloys to understand the transition from internal to external oxidation. As oxidation is a diffusion controlled process, parabolic kinetics are generally observed.<sup>240,241</sup> The internal versus external oxidation condition given by Wagner<sup>240</sup> suggested that the oxidant solubility and diffusivity in the alloy were critical. Wolf and Evans<sup>242</sup> showed that the internal oxidation rate of Ni–Al alloys was nearly independent of the  $pO_2$  in the environment. Whittle *et al.*<sup>243</sup> found that the internal formation of  $Al_2O_3$  in dilute Ni–Al alloys accelerated O diffusion within the alloy, likely at the  $Al_2O_3$  precipitate–metal interface. This could explain the faster oxidation kinetics of dilute Ni–Al alloys compared to unalloyed Ni.<sup>244</sup>

In alloys with sufficient Al to form an external alumina scale, internal oxidation of Al has been observed in Fe(Al) + 0–5Cr alloys at 800–1000 °C in air.<sup>93</sup> Internal oxides as well as nitrides were observed on undoped alloys with defective alumina scales. It was concluded that the defective scale allowed N permeation through the scale into the substrate. The less-stable AlN precipitates were displaced by more-stable oxides and nitride formation moved further (deeper or laterally) into the substrate with time. The high mass gains (with linear kinetics) for the undoped ferritic Fe(Al) alloys are shown in Figure 15. Figure 15 also shows that internal oxidation did not occur in air for undoped Fe–20Cr–10Al.

Internal oxidation of other alloy elements may occur, typically only those with a higher affinity for O than Al such that oxidation will occur below the Al/ $Al_2O_3$  equilibrium  $pO_2$  at the metal–scale interface. All RE additions fall into this category.<sup>135</sup> The issue of RE internal oxidation has already been

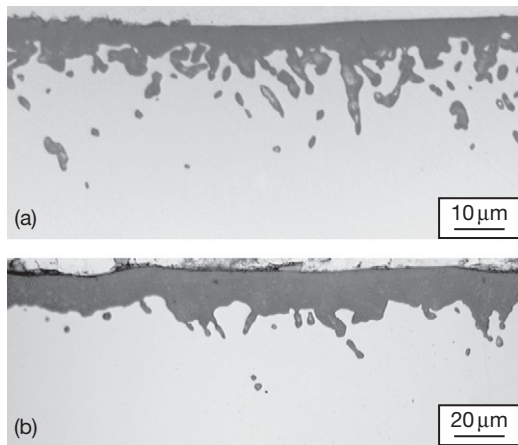


**Figure 38** Light microscopy of polished cross-sections of FeCrAl + 0.038(Y,Hf) after oxidation in laboratory air for (a) 5000 h at 1000 °C and (b) 100 h at 1300 °C.<sup>12</sup> More internal oxidation occurred at low temperature than at high temperature where a much thicker external oxide formed.

discussed in terms of minimizing the internal oxidation by reducing the RE addition (e.g., [Figure 23](#)). The effect of oxidation temperature on internal oxidation is complicated by the effects of solubility and diffusivity.<sup>240</sup> The solubilities and diffusivities of both O and the RE increase with temperature but at different rates. An example of the effect of temperature on internal oxidation is shown for FeCrAlYHf in [Figure 38](#). Over the range of 1000–1300 °C, it is difficult to make direct comparisons. However, relative to the external scale thickness, the internal attack at 1000 °C was deeper than at 1300 °C. The solubility of the particular RE addition in the alloy also could play a factor in the temperature effect.

For  $\gamma$ - $\gamma'$  NiPtAl alloys, the addition of Pt decreased the internal oxidation of Hf.<sup>80</sup> The effect was particularly strong with 10–15%Pt and Hf levels up to 0.4%. This Pt effect was attributed to Pt suppressing the Hf activity;<sup>80</sup> however, it could also be an effect of Pt on the O solubility.

#### 1.24.4.6 Comparison of Fe-, Ni-, and Co-Based Alumina Forming Alloys

Only a few authors have explicitly examined the differences in oxidation behavior due to the base metal.<sup>60,95</sup> In general, FeCrAl alloys are the best alumina-formers because they are single-phase, have a lower CTE, faster diffusion in the alloy (due to their bcc structure) and lower O solubility. This combination of diffusivity and solubility results in

lower Cr and Al additions needed to form alumina and better alumina adhesion. With two-phase alloys, the Al-poor phase will tend to form more base-metal oxide. Furthermore, alloy phase transformations typically increase the CTE. The low CTE of FeCrAl results in less thermal stress which drives scale spallation. Faster Al diffusion in the alloy minimizes Al concentration gradients in the alloy and decreases the critical Al content needed to form alumina. The rapid growth of FeO ( $\sim 10^6$  times faster than  $\text{Al}_2\text{O}_3$ ) results in more catastrophic failure at the end of life compared to NiCrAl (NiO forms  $\sim 10^3$  times faster than  $\text{Al}_2\text{O}_3$ ), however, the other factors tend to outweigh this problem.<sup>60</sup>

Several studies agree that the oxidation behavior of CoCrAl alloys are decidedly inferior to NiCrAl or FeCrAl.<sup>60,245</sup> For the formation of an alumina scale, Co-based alloys require higher Cr and Al contents because of the rapid growth of CoO ( $\sim 10^5$  times faster than  $\text{Al}_2\text{O}_3$ ) and the relatively low diffusivity in the alloy compared to Ni ( $\sim 10^2$  slower) and Fe-based ( $\sim 10^3$  slower) alloys.<sup>60</sup> In cyclic oxidation testing, CoCrAl alloys can be improved by RE additions.<sup>132,245,246</sup> However, their cyclic oxidation resistance is inferior to NiCrAl. The main interest for Co-based alumina-forming materials appears to be as coatings for Co-based alloys.

#### 1.24.5 Breakaway Oxidation

The final stage of oxidation is breakaway which is characterized by rapid oxidation due to the depletion of Al from the substrate and the formation of faster-growing reaction products. [Figure 39](#) shows a failed specimen of FeCrAl alloy APMT cycled to failure at 1200 °C using 1 h cycles. One edge had been completely consumed by Fe-rich oxide formation. Typical of many dispersion strengthened alloys,<sup>247</sup> the center contains Kirkendall voids due to the depletion of Al. In stronger ODS FeCrAl, the voids are often perfectly round. In weaker wrought FeCrAlY, more deformation of the substrate occurs and center voids are not very evident.

The time to breakaway,  $t_b$ , is thus the useful lifetime of a component with thickness,  $d$ . It was used in several figures in the previous section ([Figures 31–33](#) and [36](#)). A common model for lifetime of Fe-based alloys is based on the Al reservoir in the component and the rate of consumption of that reservoir<sup>41,42</sup>:

$$d\rho(C_0 - C_b) = A k t_b^n \quad [5]$$

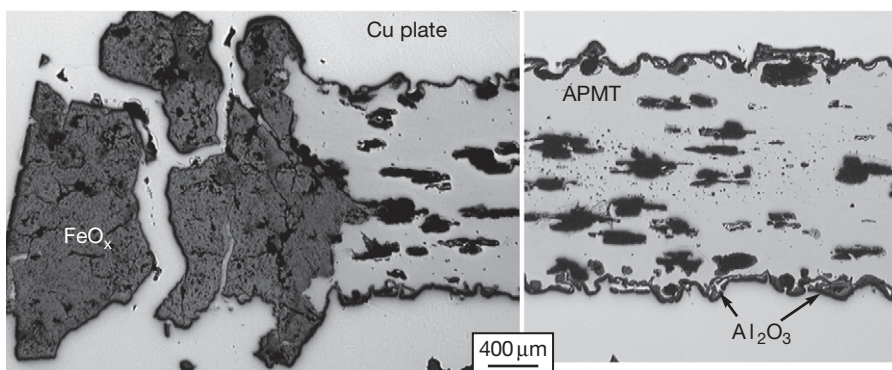


**Figure 39** Light microscopy of polished cross-sections of alloy APMT after cycling to failure in 1 h cycles at 1200 °C.<sup>12</sup> One edge has been consumed and only Fe-rich oxide remains. In the center of the specimen, large Kirkendall voids remain from the depletion of Al.

where  $\rho$  is the alloy density,  $C_0$  is the starting Al content in the alloy,  $C_b$  is the Al content where the material can no longer form a protective alumina scale,  $A$  is a constant,  $k$  is a rate constant, and  $n = 0.5$  for parabolic kinetics and 1 for linear kinetics. For FeCrAl-type alloys with  $\sim 20\%$  Cr,  $C_b$  is close to zero. With lower Cr contents,  $C_b$  increases to  $\sim 10\%$  Al in Fe–Al binary alloys.<sup>248,249</sup> This type of equation allows the lifetime to be predicted as a function of component thickness or for a thickness to be selected to achieve a desired service lifetime.

One of the key assumptions of the reservoir model is that there are no Al gradients in the substrate; this greatly simplifies behavior. It is a reasonable assumption for foil (e.g., Figure 20) and thin ( $<1$  mm) components.<sup>248</sup> However, for thicker components, Al gradients do occur and cause significant deviations in lifetime behavior.<sup>249</sup> For example, Figure 40 shows the gradients in several MA956 specimens oxidized to failure at 1200, 1250, and 1300 °C. The center of the specimen contained  $>1\%$  Al while the end of the specimen, near where the breakaway formation of Fe-rich oxide occurred, had  $\sim 0.1\%$  Al. Earlier studies suggested that  $C_b$  was a function of thickness.<sup>250</sup> While  $C_b$  effectively increases with thickness because of Al gradients in thick substrates, mechanistically, in all cases, the value of  $C_b$  at the metal–scale interface,  $C_{bi}$ , at breakaway is close to zero.<sup>249</sup>

Gradients also drive early failures in some materials (Figure 41). For Fe–17Al + Hf and NiCrAlY/Zr (alloy 214), increasing the specimen thickness resulted in virtually no increase in  $t_b$ . It was shown that Al gradients formed in Fe–17Al + Hf resulted in early failures for the thicker specimens.<sup>52,249</sup> A similar failure mechanism may occur on alloy 214,<sup>251</sup> but less characterization work was performed

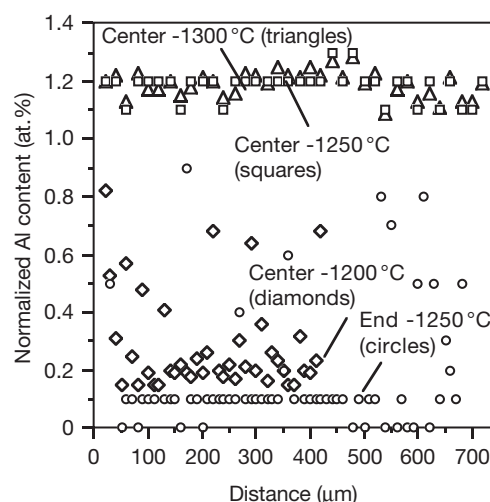


**Figure 40** EPMA Al line scans from two different MA956 (ODS FeCrAl) specimens oxidized to breakaway at 1200–1300 °C and metallographically sectioned. The center scans are across the entire specimen thickness near the center of the specimen while the end scan is from an end of the specimen with distance from the edge towards the center of the specimen. Data from Pint *et al.*<sup>249</sup>

on this alloy after cyclic oxidation. Specimen geometry (e.g., corners on thin specimens) can also lead to early failure. Therefore the specimen surface area to volume also can affect lifetime and round versus flat specimens may behave differently.<sup>252</sup>

As shown for alloy 214 (Figure 41), the behavior of Ni-based alumina-forming alloys<sup>12</sup> may not be explained well by the Quadakkers reservoir model. The slower diffusion of Al in austenitic alloys and the formation of multiple phases ( $\gamma$ ,  $\gamma'$ ,  $\beta$ ) in NiCrAl alloys may result in complications that are better modeled by a diffusion based model as suggested by Nesbitt and Heckel<sup>253</sup> or the spallation-based COSP

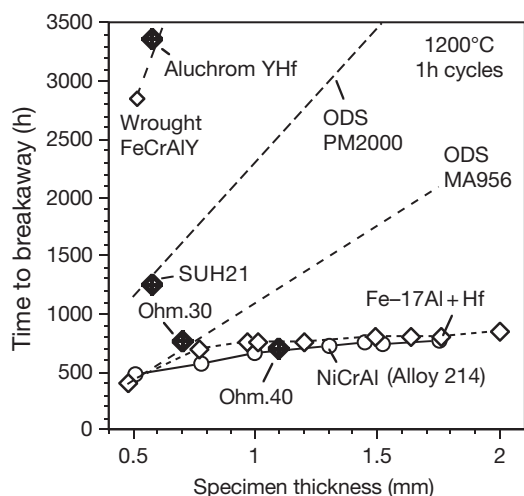


**Figure 41** Time to breakaway in 1 h cycles at 1200 °C versus specimen thickness for various alumina-forming alloys (see [Tables 1 and 2](#)). For alloy 214 and Hf-doped Fe-17Al, there was little increase in lifetime with specimen thickness due to the formation of alumina gradients. Data from Pint<sup>12</sup> and Pint et al.<sup>233</sup>

model.<sup>17</sup> These models and Nesbitt's COSIM (Coating Oxidation and Substrate Interdiffusion Model)<sup>254</sup> are well suited for studying the behavior of NiCrAl coatings where the Al content decreases both due to oxidation and interdiffusion with the coating substrate.

As shown in [eqn \[5\]](#), the consumption side of the equality is very simplistic. Parabolic kinetics would only be observed for alloys where no spallation occurred. As shown in [Figure 41](#) and in previous figures, the nearly linear relationship between specimen thickness and  $t_b$  suggests that linear kinetics, that is,  $n = 1$ , are more relevant. However, this approximation would overestimate the Al loss at early times, when the scale is adherent and Al consumption follows parabolic kinetics. A more complicated consumption equation probably involves several time stages with different  $k$  and  $n$  values for each stage.<sup>251</sup> If a critical scale thickness could be identified to determine the change from the protective scale phase to the spallation phase (with higher Al consumption and higher  $n$ ), such a model would be more mechanistic and accurate.

Other models are available to predict lifetime. The NASA-developed COSP model uses the scale growth and spallation rates to predict lifetime.<sup>17</sup> The spallation mass loss rate is attributed to an area fraction of spallation and regrowth. This model has been applied to an extensive oxidation database of typically Ni-based and ODS FeCrAl alloys that exhibit near-linear spallation rates. However, wrought

Fe-based alloys that do not spall as orderly cannot be modeled in this manner (compare Ni-base spall behavior in [Figure 30](#) to Fe-based spallation in [Figure 37](#)). In general, measuring the residual Al content and determining the rate of Al loss in the alloy is the most accurate method of predicting lifetime.<sup>255</sup>

#### 1.24.5.1 Failure Mechanisms

In practice, two types of oxidation-induced failure can be distinguished.<sup>256</sup> A chemical failure occurs when the substrate is sufficiently depleted in Al that it can no longer form alumina. The most extreme example of such a failure is for FeCrAl(+RE) foil where no scale spallation occurs because the foil can deform and accommodate strain energy from the scale. When the foil is depleted in Al, a chromia scale has been observed to form beneath the alumina scale.<sup>257</sup> As  $\text{Cr}_2\text{O}_3$  is less stable than  $\text{Al}_2\text{O}_3$ , normally this would not be thermodynamically possible. It occurs when Al is removed from the metal and the interface oxygen potential increases allowing  $\text{Cr}_2\text{O}_3$  to form.

Prior to a chemical failure, a mechanical failure can cause a premature failure by cracking the scale and requiring reformation of alumina at a bare interface.<sup>256</sup> The mechanical failure could be due to the typical thermal stress (which can induce scale spallation), an applied stress to the component in service or a one-time upset or impact which removes the surface oxide. In this case, the  $C_b$  at failure is higher, reducing  $t_b$ .

#### 1.24.5.2 Unusual Failure Mechanisms

Some unusual circumstances can cause early failure of alumina scales. Additional oxidants (discussed in the next section) can cause early failure as will environments that can otherwise degrade the alumina scale. As mentioned previously, the formation of Al concentration gradients in the alloy will result in earlier failures. This is generally not a problem for Fe-based alloys with relatively rapid Al diffusion (e.g., flat Al profiles in [Figures 20 and 40](#)). However, it appeared to be a problem for Fe-17Al + Hf, Ni-based alloy 214 (see [Figure 41](#)) and is likely a problem for Co-based alloys. There is little data in the literature for Ni- and Co-based alloys on residual Al profiles or lifetime as a function of specimen thickness.

Another unusual failure mechanism for Fe-based alloys has been attributed to the internal oxidation of Cr carbides on alloy grain boundaries resulting in



accelerated Fe-rich oxide formation at alloy grain boundaries, sometimes called ‘broccoli’ failures because of the eruption of the voluminous Fe-rich oxide.<sup>258</sup> This type of failure is found in alloys with higher C contents but no strong carbide former, for example, Y-doped FeCrAl and Fe–Al. The problem can be eliminated by the addition of a strong carbide former such as Hf or Ti, which is a common addition in commercial alloys, **Table 2**. For example, **Figure 42** shows the mass gain of ferritic Fe–17Al alloys tested at 1250 °C to accelerate their failure. With only Y or Y and Cr additions,  $t_b$  was relatively short compared to the specimen with a Hf addition. The early failures showed broccoli failures. However, when a small amount of Ti or Hf was added, the lifetime increased dramatically.

### 1.24.5.3 Strategies for Extending Lifetime

One goal of alloy development is to design alloys with longer lifetimes. Despite shortcomings, **eqn [5]** does focus attention on some of the key lifetime variables: the Al reservoir ( $C_0 - C_b$ ) and the Al consumption rate by oxidation ( $k$  and  $n$ ). It suggests that lifetime could be increased by decreasing the rate of consumption, or by increasing the Al reservoir either by increasing  $C_0$  or decreasing  $C_b$ . As discussed previously, the scale growth rate can be decreased by RE

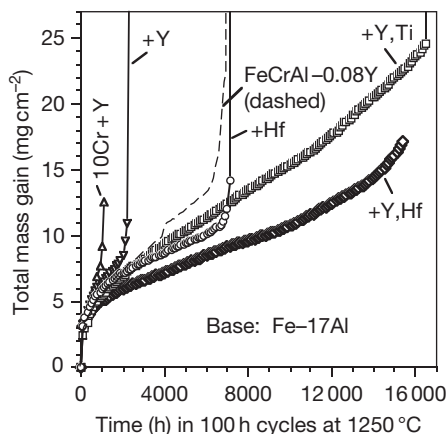


**Figure 42** Total mass gain (specimen + spalled oxide) for ferritic Fe–17Al alloys (see **Table 2** examples) during 100 h cycles at 1250 °C in laboratory air. Specimens of alloys with only Y additions showed relatively short times to breakaway oxidation due to ‘broccoli’ formation.<sup>258</sup> Specimens with strong carbide-forming elements: Hf, Y + Hf or Y + Ti, prevent this form of attack associated with accelerated oxidation of grain boundary carbides. The co-doped alloy specimens had a much longer time to breakaway oxidation. Data from Pint.<sup>12</sup>

optimization. However, in commercial alloys, the possibility of achieving narrow composition targets may be an unrealistic goal. In terms of increasing  $C_0$ , alloy mechanical properties and the phase equilibria limit the amount of Al that can be added without significant negative consequences to other properties. **Figure 41** shows the relatively low lifetimes for some commercial alloys, Ohmalloy 30 and 40 and SUH21, all with lower Al contents (**Tables 1 and 2**). However, these alloys are easier to fabricate, process and join than alloys with higher Al content such as ODS alloys and Aluchrom YHf. Also, FeCrAl alloys become very brittle above 12 at.% Al.<sup>61</sup> Decreasing  $C_b$  is virtually impossible for FeCrAl alloys because  $C_b$  is already close to zero. For ferritic Fe(Al) alloys with higher Al contents (up to 19%), attempts to lower  $C_b$  from ~10% for binary alloys have been unsuccessful.<sup>12</sup> Additions of ‘third elements’ Mn and Cr were explored with little success.<sup>12,233</sup> Manganese appears to become quickly incorporated into the scale near the end of life and Cr additions appear to increase the CTE resulting in increased spallation. A general strategy of lowering the CTE, possibly with refractory metal additions, may be possible but has not been successful for Fe-based alloys to date.<sup>233</sup> A low CTE Ni-based bond coating has been developed.<sup>259</sup>

### 1.24.6 Effect of Environment

The previous sections discussed the oxidation behavior of alumina-forming alloys in  $O_2$  or air with low levels of water vapor in the ambient laboratory environment. In practice, high temperature applications tend to involve more complex environments. However, because of the inherent chemical inertness (i.e., thermodynamic stability) of  $\alpha$ - $Al_2O_3$ , alumina-forming alloys tend to have an advantage over conventional chromia-forming alloys under these conditions.

#### 1.24.6.1 Water Vapor

In actual applications, particularly those involving combustion, water vapor is commonly found in the environment. While Kofstad called the effect of water vapor on oxidation a ‘forgotten’ problem in 1991,<sup>260</sup> it has become a significant topic for research in the past decade because of increases in temperature application and the desire to use new materials. Also, combustion of hydrogen or synthetic natural gas from coal would increase the water content in the combustion product from 10 to 15% for natural gas or jet fuel to 60% for hydrogen, making water vapor more of a



concern.<sup>261</sup> As shown by Opila,<sup>262</sup> chromia and silica scales readily form oxy-hydroxides in the presence of H<sub>2</sub>O and O<sub>2</sub> resulting in accelerated oxidation attack for chromia-forming alloys and silica-based ceramics.<sup>263,264</sup> For typical stainless steels at 650–800 °C, the Cr consumption becomes linear due to the evaporation.<sup>265</sup>

As  $\alpha$ -Al<sub>2</sub>O<sub>3</sub> is more stable than Cr<sub>2</sub>O<sub>3</sub> or SiO<sub>2</sub>, the reaction with water vapor is minimal until higher temperatures >1300 °C.<sup>262</sup> The effect of Al additions on resistance to water vapor is quite dramatic. Kvernes *et al.*<sup>266</sup> showed that small Al additions to Fe–Cr alloys were very effective in improving the oxidation resistance. Likewise, Pint *et al.*,<sup>267</sup> showed that additions of Al to austenitic Fe–15Cr–15Ni were very effective in reducing the detrimental role of water vapor. However, that study also showed that the addition of Al caused the formation of ferritic phases in the steel that decreased the 750 °C creep life by ~2 orders of magnitude, making the resulting alloy unacceptable for many applications. Recently, Brady and coworkers<sup>67–69</sup> showed that careful composition control and minor element additions could produce an Fe-based alumina-forming austenitic steel with very good creep strength and resistance to water vapor environments. This alloy is a potential solution to the problem of degradation of heat exchangers or recuperators for small turbines.<sup>268</sup> Compact, high-efficiency primary surface recuperators for these turbines require <100  $\mu$ m thick foil with good creep and oxidation resistance.

The excellent resistance of alumina scales to water vapor has led to extensive work on alumina-forming coatings on Fe-based alloys for combustion and steam environments. Thin coatings can improve oxidation resistance to steam for Fe–9Cr alloys for >40 kh at 650 °C.<sup>269</sup> Ferritic Fe(Al,Cr) weld overlaid coatings have shown promising results for boiler applications at <600 °C.<sup>270</sup> Coatings are further addressed in a separate chapter.

Several studies have examined the effect of water vapor on Ni-based alloys.<sup>261,271–274</sup> The general conclusions focused on three effects of water vapor on alumina-scales are: (1) Water vapor increases the spallation rate of alumina scales, particularly for marginally adherent scales. Smialek<sup>275</sup> suggested that this could be due to water vapor increasing the crack growth rate at the metal-scale interface. Figure 43 shows the specimen mass gain for NiAl + Hf and NiCrAlYHf specimens in dry O<sub>2</sub> and air with 10–90 vol.% H<sub>2</sub>O. For NiCrAlYHf, the drop in mass gain suggests scale spallation which increases with

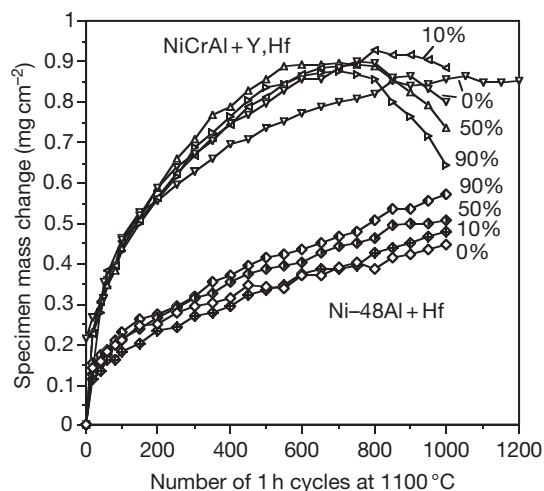


**Figure 43** Specimen mass gain for cast Ni–20Cr–10Al + Y,Hf and Ni–48Al–0.05Hf specimens (see Table 2) exposed to 1 h cycles at 1100 °C in dry O<sub>2</sub> or air with various vol% of H<sub>2</sub>O from 10 to 90%. The addition of water vapor caused a minor increase in the mass gain for Hf-doped NiAl and a slight increase in spallation (mass losses) after 800 cycles for NiCrAlYHf. Data from Pint<sup>12</sup> and Pint *et al.*<sup>261</sup>

H<sub>2</sub>O content. (2) A small increase in the oxidation rate. The mass gain of NiAl + Hf increases with H<sub>2</sub>O content suggesting a slight increase in the rate constant (Figure 43). This was also noted for Fe-based alloys.<sup>276</sup> (3) A decrease in selective oxidation. On low Al alloys, more Ni-rich spinel oxide was formed with the addition of water vapor. This is a particular concern for uncoated superalloys and  $\gamma$ – $\gamma'$  NiPtAl coatings with low Al content.<sup>82,261</sup> An explanation for this decrease based on H injection into the substrate may apply to both alumina- and chromia-forming alloys.<sup>277</sup> Nevertheless, for adherent alumina-forming alloys with adequate Al, these effects are relatively minor as shown by the data in Figure 43 where even 90% water vapor caused a minor effect at 1100 °C.

#### 1.24.6.2 Sulfur and Hot Corrosion

A wide range of environments contain sulfur, sulfur-containing compounds (i.e., hot corrosion) or, more commonly, mixtures of S and O such as in coal-fired combustion (SO<sub>x</sub>) or gasification (H<sub>2</sub>S, low  $p$ O<sub>2</sub>), which was extensively investigated in the 1980s. For purely sulfidizing and hot corrosion (salt) environments, alumina-forming alloys are only marginally effective since Al does not really form a selective, protective sulfide layer and can be fluxed away by sodium–sulfate salts. As a result, the sulfidation

reaction of the base metal is a key issue. Ni-based alumina-forming alloys will be catastrophically affected by the formation of a liquid Ni-S reaction product above 700 °C.<sup>278,279</sup> Cobalt-based alloys are thought to be more resistant to sulfidation. Therefore, CoCrAl alloys and coatings have been developed for their sulfidation and hot corrosion resistance.<sup>280,281</sup> For Fe-based alumina-formers, some improvement is associated with the addition of Al compared to FeCr alloys but the sulfidation rates are still relatively high.<sup>282</sup> For example, a 150 µm thick scale was formed in 7 h at 800 °C with a  $pS_2 = 0.1$  Pa.

For oxidizing-sulfidizing environments, the performance of Fe-based alumina-forming alloys in petroleum environments has been investigated for more than 40 years.<sup>283</sup> Since then a great deal of work has been conducted on Fe(Al) and FeCrAl alloys in low oxygen, high sulfur pressure environments.<sup>50,284–288</sup> Under these conditions, binary (low Cr) Fe-Al alloys are generally superior to FeCrAl alloys because of the possible sulfidation reaction with Cr. However, ~19%Al is needed in Fe(Al) for this sulfidation resistance.<sup>286</sup> A similar level of Al was needed at the surface of Fe-Al coatings for a protective scale to form.<sup>289</sup> However, these experiments were typically performed at ~800 °C. At lower temperatures, 400–600 °C, where reaction rates are lower and it is more difficult to form alumina, the presence of Cr may be beneficial and work better than Fe-Al materials. This has been observed for Fe<sub>3</sub>Al and FeCrAl porous metal filters used in sulfidizing environments.<sup>12</sup>

Several studies suggest that additions of Y and Zr are beneficial to corrosion resistance in sulfur-containing environments at 600–800 °C.<sup>284,285</sup> In some mixed O-S environments it is possible to form an alumina scale that could be protective. Another common strategy has been to preoxidize the alloy in an oxidizing environment prior to exposure to S-bearing gases, particularly for FeCrAl.<sup>290–292</sup> If metastable, cubic alumina phases form during preoxidation, the volume reduction and associated scale cracking during the transformation to  $\alpha$ -Al<sub>2</sub>O<sub>3</sub> will likely be detrimental to performance.<sup>292</sup> Thus, the preoxidation step must be controlled to assure an  $\alpha$ -Al<sub>2</sub>O<sub>3</sub> preoxidation scale. While preoxidation has been successful in laboratory tests, in practice it has been less effective. In some applications, the problem is probably due to the damage of the preoxidation scale during subsequent handling and joining.

Even when the alumina scale is adherent and dense, it has been shown that S will penetrate

alumina scales and S was found segregated to  $\alpha$ -Al<sub>2</sub>O<sub>3</sub> grain boundaries using STEM after exposure to a H<sub>2</sub>-H<sub>2</sub>O-H<sub>2</sub>S environment.<sup>293</sup> Cracks in the scale are another possible route for S penetration.

Hot corrosion, generally associated with Na<sub>2</sub>SO<sub>4</sub> salts, can be decreased by the formation of an adherent alumina scale. For example, on  $\gamma$ - $\gamma'$  NiPtAl compositions, preoxidation was very effective in reducing hot corrosion attack.<sup>91</sup> Therefore, RE additions and Pt may be somewhat beneficial in hot corrosion.<sup>294</sup> However, because of the fundamental fluxing reaction controlling hot corrosion,<sup>295</sup> Cr is much more effective than Al or Pt in reducing hot corrosion attack.<sup>296</sup>

#### 1.24.6.3 Carbon

For environments with high C activity where internal carburization and metal dusting occur,<sup>297</sup> alumina-forming alloys appear to be oxidation resistant. Compared to chromia-forming stainless steels, where the Cr<sub>2</sub>O<sub>3</sub> scale appears to allow the ingress of C, alumina scales appear to prevent C penetration.<sup>298,299</sup> The addition of Al or alumina-forming coatings appears to solve many C-related oxidation problems.

Again, the issue of alloy strength and joining is a critical one for alloy selections in many relevant applications. Alumina-forming alloys may not have the necessary strength or can be difficult to fabricate or join for commercial applications where high carbon activities are a concern. Recently, cast NiCrAlY alloy tubes have been developed for steam reforming applications.<sup>29</sup> The authors reported no major drop in creep strength or weldability. In addition, the relatively inert alumina scale had an additional benefit of reducing surface coke formation.

#### 1.24.6.4 Nitrogen

Nitrogen containing environments appear to be one condition that can cause problems for alumina-forming alloys. It appears that N can permeate through alumina scales and internally nitride alumina-forming alloys.<sup>93,299</sup> Most likely, the N permeation is not diffusion through dense alumina but penetration in the cracks in the scale. However, diffusion along  $\alpha$ -Al<sub>2</sub>O<sub>3</sub> grain boundaries, like S, cannot be ruled out. For Fe-based alumina-forming alloys, internal nitridation has been observed in atmospheres with predominantly N and low  $pO_2$ .<sup>299–301</sup> Both Al and Ti (when present) are internally nitride. Internal nitridation of Al is observed at higher  $pO_2$  levels when the Al content is decreased

during extended exposure. As mentioned previously, internal nitridation has been observed for undoped Fe(Al) alloys in air but not for undoped FeCrAl.<sup>93</sup>

For Ni-based alloys, Han and Young<sup>302</sup> found that internal oxidation and nitridation of Ni–Al–Cr alloys was a result of heavy spallation which depleted the alloy in Al and caused a phase transformation. The internal nitridation of Ni-based superalloys is commonly observed<sup>303</sup> and was briefly reviewed by Krupp and Christ.<sup>304</sup> Their study of model NiCrAlTi alloys concluded that higher Cr contents increased the N solubility and diffusivity in NiCrAlTi alloys.

Bennett and coworkers<sup>305</sup> also found internal nitridation of FeCrAl by ‘crevice corrosion.’ In this case, it was proposed that in crevices in components, O could be locally depleted in the gas due to reaction with the surrounding metal and stagnant flow. The resulting high N and low O environment could cause internal attack.

### 1.24.7 Summary

Alumina-forming alloys are the most oxidation resistant alloys due to their low oxidation rates and thermodynamically stable scale. However, because of the negative effects of Al on alloy mechanical properties, fabrication, and joining, alumina-forming alloys are not widely used except when needed in very high temperature applications or in particular environments such as those with water vapor (or steam) and high C activities. As application temperatures increase in search of higher generation and production efficiencies, the use of alumina-forming alloys or coatings will inevitably increase.

### Acknowledgments

The author would like to thank his colleagues at ORNL, acknowledge the discussions with I. G. Wright, appreciate the comments on the manuscript from M. P. Brady and P. F. Tortorelli, and gratefully acknowledge the assistance provided by the dedicated technical staff, L. D. Chitwood, G. W. Garner, J. L. Moser, H. F. Longmire and L. R. Walker for the experimental work. The manuscript preparation was sponsored by the U.S. Department of Energy, Fossil Energy Advanced Research Materials Program and work at the SHaRE User Facility by the Division of Scientific User Facilities, under contract DE-AC05-00OR22725 with UT-Battelle, LLC.

### References

- Whittle, D. P.; Stringer, J. *Philos. Trans. R. Soc. London, Ser. A* **1980**, 295, 309–329.
- Lang, E. Ed. *The Role of Active Elements in the Oxidation Behavior of High Temperature Metals and Alloys*; Elsevier Applied Science: London, 1989.
- King, W. E. Ed. *Material Science Forum 43, The Reactive Element Effect on High Temperature Oxidation – After Fifty Years*; Trans Tech Publications: Switzerland, 1989.
- Moon, D. P. *Mater. Sci. Technol.* **1989**, 5, 754–764.
- Strawbridge, A.; Hou, P. Y. *Mater. High Temp.* **1994**, 12, 177–1781.
- Pint, B. A. *Mater. Res. Bull.* **1994**, 19(10), 26–30.
- Pint, B. A.; Garratt-Reed, A. J.; Hobbs, L. W. *Mater. High Temp.* **1995**, 13, 3–16.
- Pint, B. A. *Oxid. Met.* **1996**, 45, 1–37.
- Stott, F. H. *Mater. Sci. Forum* **1997**, 251–254, 19–32.
- Quadackers, J.; Singheiser, L. *Mater. Sci. Forum* **2001**, 369–372, 77–92.
- Pint, B. A. In *Progress in Understanding the Reactive Element Effect Since the Whittle and Stringer Literature Review*, Proceedings of John Stringer Symposium on High Temperature Corrosion; Tortorelli, P. F., Wright, I. G., Hou, P. Y., Eds.; ASM International: Materials Park, OH, 2003; pp 9–19.
- Pint, B. A. Unpublished oxidation data, ORNL, Oak Ridge, TN, 1994–2008.
- Agarwal, D. C.; Brill, U. Performance of Alloy 602CA (UNS N06025) in high temperature environments up to 1200°C (~2200°F), NACE Paper 00-521, Houston, TX, Presented at NACE Corrosion 2000, Orlando, FL, March 2000.
- Pint, B. A.; Keiser, J. R. Alloy selection for high temperature heat exchangers, NACE Paper 06-469, Houston, TX, Presented at NACE Corrosion 2006, San Diego, CA, March 2006.
- Pint, B. A.; Tortorelli, P. F.; Wright, I. G. *Oxid. Met.* **2002**, 58, 73–101.
- Pint, B. A.; DiStefano, J. R.; Wright, I. G. *Mater. Sci. Eng. A* **2006**, 415, 255–263.
- Lowell, C. E.; Barrett, C. A.; Palmer, R. W.; Auping, J. V.; Probst, H. B. *Oxid. Met.* **1991**, 36, 81–112.
- Nesbitt, J. A.; Vinarcik, E. J.; Barrett, C. A.; Doychak, J. *Mater. Sci. Eng. A* **1992**, 153, 561–566.
- Evans, H. E.; Lobb, R. C. *Corros. Sci.* **1984**, 24, 209–222.
- Przybylski, K.; Yurek, G. J. *Mater. Sci. Forum* **1989**, 43, 1–74.
- Heck, R. M.; Farrauto, R. J. *Appl. Catal. A* **2001**, 221, 443–457.
- Kajita, S.; Dalla Betta, R. *Catal. Today* **2003**, 83, 279–288.
- Stainless Steel Ohmaloy® 30 and Ohmaloy® 40 Resistance Alloys*; ATI Allegheny Ludlum: Brackenridge, PA, 2007.
- Benjamin, J. S. *Metall. Trans.* **1970**, 1, 2943–2951.
- Nicholls, J. R.; Newton, R.; Simms, N. J.; Norton, J. F. *Mater. High Temp.* **2003**, 20, 93–108.
- Pint, B. A.; Swindeman, R. W.; More, K. L.; Tortorelli, P. F. Materials selection for high temperature (750–1000°C) metallic recuperators for improved efficiency microturbines, ASME Paper #2001-GT-445, Presented at the International Gas Turbine and Aeroengine Congress and Exhibition, New Orleans, LA, June 4–7, 2001.
- Wright, I. G.; Pint, B. A.; Lee, W. Y.; Alexander, K. B.; Prüßner, K. In *High Temperature Surface Engineering*; Nicholls, J., Rickerby, D., Eds.; Institute of Materials: London, UK, 2000; pp 95–113.

28. Smialek, J. L.; Pint, B. A. *Mater. Sci. Forum* **2001**, 369–372, 459–466.
29. Kirchheiner, R. R.; Becker, P.; Young, D. J.; Durham, R. Improved oxidation and coking resistance of a new alumina forming Alloy 60 HT for the petrochemical industry, NACE Paper 05-428, Houston, TX, Presented at NACE Corrosion 2005, Houston, TX, April 2005.
30. Haynes, J. A.; Pint, B. A.; Porter, W. D.; Wright, I. G. *Mater. High Temp.* **2004**, 21, 87–94.
31. Toscano, J.; Gil, A.; Huttel, T.; Wessel, E.; Naumenko, D.; Singheiser, L.; Quadakkers, W. J. *Surf. Coat. Technol.* **2007**, 202, 603–607.
32. Malang, S.; Deckers, H.; Fischer, U.; John, H.; Meyder, R.; Norajitra, P.; Reimann, J. J.; Reiser, H.; Rust, K. *Fusion Eng. Des.* **1991**, 14, 373–399.
33. Fowler, J. D.; Causey, R. A.; Chandra, D.; Elleman, T. S.; Verghese, K. J. *Vac. Sci. Technol.* **1976**, 13, 401–402.
34. Steward, S. A. Review of hydrogen isotope permeability through materials, LLNL Report #UCRL-53441, Lawrence Livermore National Laboratory, Livermore, CA, 1983.
35. Konys, J.; Aiello, A.; Benamati, G.; Giancarli, L. *Fusion Sci. Technol.* **2005**, 47, 844–850.
36. Müller, G.; Heinzl, A.; Konys, J.; Schumacher, G.; Weisenburger, A.; Zimmermann, F.; Engelko, V.; Rusanov, A.; Markov, V. J. *Nucl. Mater.* **2002**, 301, 40–46.
37. Lauf, R. J.; DeVan, J. H. *J. Electrochem. Soc.* **1992**, 139, 2087–2091.
38. Hubberstey, P.; Sample, T.; Terlain, A. *Fusion Technol.* **1995**, 28, 1194–1199.
39. Hubberstey, P. *J. Nucl. Mater.* **1997**, 247, 208–214.
40. Pint, B. A.; More, K. L. *J. Nucl. Mater.* **2008**, 376, 108–113.
41. Quadakkers, W. J.; Bennett, M. J. *Mater. Sci. Technol.* **1994**, 10, 126–131.
42. Quadakkers, W. J.; Bongartz, K. *Mater. Corros.* **1994**, 45, 232–241.
43. Stott, F. H.; Wood, G. C.; Stringer, J. *Oxid. Met.* **1995**, 44, 113–145.
44. Pettit, F. S. *Trans. Metall. Soc. AIME* **1967**, 239, 1296–1305.
45. Pint, B. A. *Surf. Coat. Technol.* **2004**, 188–189, 71–78.
46. Prescott, R.; Graham, M. J. *Oxid. Met.* **1992**, 38, 233–254.
47. Sykes, C.; Bampfylde, J. W. *J. Iron Steel Inst. Adv. Copy* **1934**, 12, 22.
48. Saegusa, F.; Lee, L. *Corrosion* **1966**, 22, 168–177.
49. Boggs, W. E. *J. Electrochem. Soc.* **1971**, 118, 906–913.
50. DeVan, J. H.; Tortorelli, P. F. *Corros. Sci.* **1993**, 35, 1065–1071.
51. Pint, B. A.; Leibowitz, J.; DeVan, J. H. *Oxid. Met.* **1999**, 51, 181–197.
52. Pint, B. A.; Wright, I. G. *Mater. Sci. Forum* **2004**, 461–464, 799–806.
53. Zhang, Z. G.; Gesmundo, F.; Hou, P. Y.; Niu, Y. *Corros. Sci.* **2006**, 48, 741–765.
54. Wagner, C. *Corros. Sci.* **1965**, 5, 751–764.
55. Zhang, X. J.; Wang, S. Y.; Gesmundo, F.; Niu, Y. *Oxid. Met.* **2006**, 65, 151–165.
56. Pint, B. A.; Paul, L. D. Oxidation behavior of welded and base metal UNS N06025, NACE Paper 07-470, Houston, TX, Presented at NACE Corrosion 2007, Nashville, TN, March 2007.
57. Giggins, C. S.; Pettit, F. S. *J. Electrochem. Soc.* **1971**, 118, 1782–1790.
58. Wallwork, G. R.; Hed, A. Z. *Oxid. Met.* **1971**, 3, 171–184.
59. Wallwork, G. R. *Rep. Prog. Phys.* **1976**, 39, 401–485.
60. Stott, F. H.; Wood, G. C.; Hobby, M. G. *Oxid. Met.* **1971**, 3, 103–113.
61. Wukusick, C. S.; Collins, J. F. *Mater. Res. Stand.* **1964**, 4, 637–646.
62. Sauer, J. P.; Rapp, R. A.; Hirth, J. P. *Oxid. Met.* **1982**, 18, 285–294.
63. De Freitas Cunha Lins, V.; Freitas, M. A.; De Paula e Silva, E. M. *Corros. Sci.* **2004**, 46, 1895–1907.
64. Boggs, W. E. *Oxid. Met.* **1976**, 10, 277–289.
65. Wu, Y.; Niu, Y. *Corros. Sci.* **2007**, 49, 1656–1672.
66. Sakiyama, M.; Tomaszewicz, P.; Wallwork, G. R. *Oxid. Met.* **1979**, 13, 311–330.
67. Yamamoto, Y.; Brady, M. P.; Lu, Z. P.; Maziasz, P. J.; Liu, C. T.; Pint, B. A.; More, K. L.; Meyer, H. M.; Payzant, E. A. *Science* **2007**, 316, 433–436.
68. Brady, M. P.; Yamamoto, Y.; Santella, M. L.; Maziasz, P. J.; Pint, B. A.; Liu, C. T.; Lu, Z. P.; Bei, H. *JOM* **2008**, 60(7), 12–18.
69. Brady, M. P.; Yamamoto, Y.; Santella, M. L.; Pint, B. A. *Scr. Mater.* **2007**, 57, 1117–1120.
70. Castello, P.; Stott, F. H.; Gesmundo, F. *Corros. Sci.* **1999**, 41, 901–918.
71. Merz, M. D. *Metall. Trans. A* **1979**, 10, 71–77.
72. Baer, D. R.; Merz, M. D. *Metall. Trans. A* **1980**, 11, 1973–1980.
73. Yurek, G. J.; Eisen, D.; Garratt-Reed, A. J. *Metall. Trans. A* **1982**, 13, 473–485.
74. Maloney, M. J. Ph.D. Thesis, Massachusetts Institute of Technology, Cambridge, MA, 1989.
75. Maloney, M. J.; Yurek, G. J. In *Composites/Corrosion-Coatings of Advanced Materials*, Proceedings IMAM-4; Kimura, S., Kobayashi, A., Umekawa, S., Nii, K., Saito, Y., Yoshimura, M., Eds.; Materials Research Society: Pittsburgh, PA, 1989; Vol. 1, pp 383–388.
76. Goedjen, J. G.; Shores, D. A. *Oxid. Met.* **1992**, 37, 125–142.
77. Wang, F. *Oxid. Met.* **1997**, 48, 215–224.
78. Chen, G.; Lou, H. *Oxid. Met.* **2000**, 54, 155–162.
79. Gleeson, B.; Wang, W.; Hayashi, S.; Sordelet, D. *Mater. Sci. Forum* **2004**, 461–464, 213–222.
80. Izumi, T.; Gleeson, B. *Mater. Sci. Forum* **2005**, 522–523, 221–228.
81. Kartono, R.; Young, D. J. *Mater. Corros.* **2008**, 59, 455–462.
82. Pint, B. A.; Haynes, J. A.; More, K. L.; Schneibel, J. H.; Zhang, Y.; Wright, I. G. In *Superalloys 2008*; Reed, R. C., et al. Eds.; TMS: Warrendale, PA, 2008; pp 641–650.
83. Pint, B. A.; More, K. L.; Wright, I. G. *Oxid. Met.* in preparation.
84. Felten, E. J. *Oxid. Met.* **1976**, 10, 23–28.
85. Tatlock, G. J.; Hurd, T. J. *Oxid. Met.* **1984**, 22, 201–226.
86. Fountain, J. G.; Golightly, F. A.; Stott, F. H.; Wood, G. C. *Oxid. Met.* **1976**, 10, 341–345.
87. Ballard, D. L.; Martin, P. L.; Gleeson, B.; Menon, S. Structure and oxidation behavior of PGM modified nickel-base alloys, Presentation at 18th AeroMat Conference and Expo, Baltimore, MD, ASM, June 2007.
88. Doychak, J.; Rühle, M. *Oxid. Met.* **1989**, 31, 431–452.
89. Pint, B. A.; Garratt-Reed, A. J.; Hobbs, L. W. *Oxid. Met.* **2001**, 56, 119–145.
90. Copland, E. J. *Phase Equilib. Diff.* **2007**, 28, 38–48.
91. Deodshimukh, V.; Mu, N.; Li, B.; Gleeson, B. *Surf. Coat. Technol.* **2006**, 201, 3836–3840.
92. Zhang, Y.; Haynes, J. A.; Pint, B. A.; Wright, I. G. *Surf. Coat. Technol.* **2005**, 200, 1259–1263.
93. Pint, B. A.; Dwyer, M. J.; Deacon, R. M. *Oxid. Met.* **2008**, 69, 211–231.

94. Pint, B. A.; More, K. L.; Wright, I. G. *Mater. High Temp.* **2003**, *20*, 375–386.
95. Hagel, W. C. *Corrosion* **1965**, *21*, 316–326.
96. Kear, B. H.; Pettit, F. S.; Fornwalt, D. E.; Lemaire, L. P. *Oxid. Met.* **1971**, *3*, 557–569.
97. Smialek, J. L.; Gibala, R. *Metall. Trans. A* **1983**, *14*, 2143–2161.
98. Quadakkers, W. J.; Elschner, A.; Speier, W.; Nickel, H. *Appl. Surf. Sci.* **1991**, *52*, 271–287.
99. Rybicki, G. C.; Smialek, J. L. *Oxid. Met.* **1989**, *31*, 275–304.
100. Brumm, M. W.; Grabke, H. J. *Corros. Sci.* **1992**, *33*, 1677–1690.
101. Young, E. W. A.; de Wit, J. H. W. *Oxid. Met.* **1986**, *26*, 351–361.
102. Doychak, J.; Smialek, J. L.; Mitchell, T. E. *Metall. Trans. A* **1989**, *20*, 499–518.
103. Prüßner, K.; Bruley, J.; Salzberger, U.; Zweggart, H.; Schumann, E.; Rühle, M. In *Microscopy of Oxidation 2*; Newcomb, S. B., Bennett, M. J., Eds.; Institute of Metals: London, 1993; pp 435–444.
104. Pint, B. A.; Martin, J. R.; Hobbs, L. W. *Solid State Ionics* **1995**, *78*, 99–107.
105. Yang, J. C.; Schumann, E.; Levin, I.; Rühle, M. *Acta Mater.* **1998**, *46*, 2195–2201.
106. Bye, G. C.; Simpkin, G. T. *J. Am. Ceram. Soc.* **1974**, *57*, 367–371.
107. Pint, B. A.; Jain, A.; Hobbs, L. W. In *High Temperature Ordered Intermetallics V, Symposium Proceedings*; Baker, I., Darolia, R., Whittenberger, J. D., Yoo, M. H., Eds.; Materials Research Society: Pittsburgh, PA, 1993; Vol. 288, pp 1013–1018.
108. Ramanarayanan, T. A.; Raghavan, M.; Petkovic-Luton, R. In *Proceedings of JIMIS-3, High Temperature Corrosion Transactions Supplement* Japan Institute of Metals: Tokyo, Japan, 1983; Vol. 24, pp 199–206.
109. Quadakkers, W. J.; Schmidt, K.; Grubmeier, H.; Wallura, E. *Mater. High Temp.* **1992**, *10*, 23–32.
110. Dryepont, S.; Pint, B. A.; Lara-Curzio, E. *Acta Mater.* in preparation.
111. Bennett, M. J.; Newton, R.; Nicholls, J. R.; Al-Badair, H.; Tatlock, G. J. *Mater. Sci. Forum* **2004**, *461–464*, 463–472.
112. N'Dah, E.; Galerje, A.; Wouters, Y.; Goossens, D.; Naumenko, D.; Kochubey, V.; Quadakkers, W. J. *Mater. Corros.* **2005**, *56*, 843–847.
113. Burtin, P.; Brunelle, J. P.; Pijolat, M.; Soustelle, M. *Appl. Catal.* **1987**, *34*, 225–238.
114. Pint, B. A.; Treska, M.; Hobbs, L. W. *Oxid. Met.* **1997**, *47*, 1–20.
115. Pijolat, M.; Dauzat, M.; Soustelle, M. *Thermochim. Acta* **1987**, *122*, 71–77.
116. Moseley, P. T.; Hyde, K. R.; Bellamy, B. A.; Tappin, G. *Corros. Sci.* **1984**, *24*, 547–565.
117. Hindam, H. M.; Whittle, D. P. *Oxid. Met.* **1982**, *18*, 245–284.
118. Hou, P. Y.; Shui, Z. R.; Chuang, G. Y.; Stringer, J. *J. Electrochem. Soc.* **1992**, *139*, 1119–1126.
119. Wagner, C. *Atom Movements*; American Society of Metals: Cleveland, OH, 1951; pp 153–173.
120. Quadakkers, W. J. *Mater. Corros.* **1990**, *41*, 659–668.
121. Quadakkers, W. J.; Naumenko, D.; Wessel, E.; Kochubey, V.; Singheiser, L. *Oxid. Met.* **2004**, *61*, 17–37.
122. Saunders, S. R. J.; Evans, H. E.; Li, M.; Gohil, D. D.; Osgerby, S. *Oxid. Met.* **1997**, *48*, 189–200.
123. Tolpygo, V. K.; Dryden, J. R.; Clarke, D. R. *Acta Mater.* **1998**, *46*, 927–937.
124. Hou, P. Y.; Paulikas, A. P.; Veal, B. W. *Mater. Sci. Forum* **2004**, *461–464*, 671–680.
125. Evans, H. E.; Norfolk, D. J.; Swan, T. J. *Electrochem. Soc.* **1978**, *125*, 1180–1185.
126. Doychak, J. In *Intermetallic Compounds, Principles*; Westbrook, J. H., Fleischer, R. L., Eds.; John Wiley & Sons: New York, NY, 1994; Vol. 1, pp 977–1016.
127. Pint, B. A.; Wright, I. G.; Lee, W. Y.; Zhang, Y.; Prüßner, K.; Alexander, K. B. *Mater. Sci. Eng. A* **1998**, *245*, 201–211.
128. Pint, B. A.; More, K. L.; Tortorelli, P. F.; Porter, W. D.; Wright, I. G. *Mater. Sci. Forum* **2001**, *369–372*, 411–418.
129. Pint, B. A. *J. Am. Ceram. Soc.* **2003**, *86*, 686–695.
130. Hindam, H.; Whittle, D. P. *J. Electrochem. Soc.* **1982**, *129*, 1147–1149.
131. Kvernes, I. *Oxid. Met.* **1973**, *6*, 45–64.
132. Allam, I. M.; Whittle, D. P.; Stringer, J. *Oxid. Met.* **1978**, *12*, 35–66.
133. Pivin, J. C.; Delaunay, D.; Roques-Carnes, C.; Huntz, A. M.; Lacombe, P. *Corros. Sci.* **1980**, *20*, 351–373.
134. Clemens, D.; Bongartz, K.; Speier, W.; Hussey, R. J.; Quadakkers, W. J. *Fresenius J. Anal. Chem.* **1993**, *346*, 318–322.
135. Pint, B. A.; Alexander, K. B. *J. Electrochem. Soc.* **1998**, *145*, 1819–1829.
136. Balmain, J.; Loudjani, M. K.; Huntz, A. M. *Mater. Sci. Eng. A* **1997**, *224*, 87–100.
137. Yurek, G. J. In *Corrosion Mechanisms*; Mansfeld, F., Ed.; Marcel Dekker: New York, 1987; pp 397–446.
138. Oishi, Y.; Kingery, W. D. *J. Chem. Phys.* **1960**, *33*, 480–486.
139. Paladino, A. E.; Kingery, W. D. *J. Am. Ceram. Soc.* **1962**, *37*, 957–962.
140. Pint, B. A.; Deacon, R. M. *J. Appl. Phys.* **2005**, *97*(11), 116111.
141. Heuer, A. H. *J. Eur. Ceram. Soc.* **2008**, *28*, 1495–1507.
142. Kim, C. K. *Oxid. Met.* **1996**, *45*, 133–152.
143. Tien, J. K.; Pettit, F. S. *Metall. Trans. A* **1972**, *3*, 1587–1599.
144. Cotell, C. M.; Yurek, G. J.; Hussey, R. J.; Mitchell, D. F.; Graham, M. J. *J. Electrochem. Soc.* **1987**, *134*, 1871–1872.
145. Cotell, C. M.; Yurek, G. J.; Hussey, R. J.; Mitchell, D. F.; Graham, M. J. *Oxid. Met.* **1990**, *34*, 173–200.
146. Jedlinski, J.; Borchardt, G.; Mrowec, S. *Solid State Ionics* **1992**, *50*, 67–74.
147. Felten, E. J.; Pettit, F. S. *Oxid. Met.* **1976**, *10*, 189–223.
148. Reddy, K. P. R.; Smialek, J. L.; Cooper, A. R. *Oxid. Met.* **1982**, *17*, 429–449.
149. Quadakkers, W. J.; Holzbrecher, H.; Briefs, K. G.; Beske, H. *Oxid. Met.* **1989**, *32*, 67–88.
150. Pint, B. A.; Martin, J. R.; Hobbs, L. W. *Oxid. Met.* **1993**, *39*, 167–195.
151. Versaci, R. A.; Clemens, D.; Quadakkers, W. J.; Hussey, R. *Solid State Ionics* **1993**, *59*, 235–242.
152. Prescott, R.; Mitchell, D. F.; Graham, M. J.; Doychak, J. *Corros. Sci.* **1995**, *37*, 1341–1364.
153. Mennicke, C.; Schumann, E.; Rühle, M.; Hussey, R. J.; Sproule, G. I.; Graham, M. J. *Oxid. Met.* **1998**, *49*, 455–466.
154. Ecer, G. M.; Singh, R. B.; Meier, G. H. *Oxid. Met.* **1982**, *18*, 55–81.
155. Kofstad, P. *Oxid. Met.* **1985**, *24*, 265–276.
156. Ramanarayanan, T. A.; Raghavan, M.; Petkovic-Luton, R. *J. Electrochem. Soc.* **1984**, *131*, 923–931.
157. Przybylski, K.; Garratt-Reed, A. J.; Pint, B. A.; Katz, E. P.; Yurek, G. J. *J. Electrochem. Soc.* **1987**, *134*, 3207–3208.
158. Li, C. W.; Kingery, W. D. In *Structure and Properties of MgO and Al<sub>2</sub>O<sub>3</sub> Ceramics, Advances in Ceramics*; American Ceramic Society: Columbus, OH, 1984; Vol. 10, pp 368–378.
159. Kingery, W. D. *Solid State Ionics* **1984**, *12*, 299–307.



160. Pint, B. A.; Garratt-Reed, A. J.; Hobbs, L. W. *J. Am. Ceram. Soc.* **1998**, *81*, 305–314.
161. Fang, J.; Thompson, A. M.; Harmer, M. P.; Chan, H. M. *J. Am. Ceram. Soc.* **1997**, *80*, 2005–2012.
162. Bedu-Amisssah, K.; Rickman, J. M.; Chan, H. M.; Harmer, M. P. *J. Am. Ceram. Soc.* **2007**, *90*, 1551–1555.
163. Cho, J.; Harmer, M. P.; Chan, H. M.; Rickman, J. M.; Thompson, A. M. *J. Am. Ceram. Soc.* **1997**, *80*, 1013–1017.
164. Yoshida, H.; Ikuhara, Y.; Sakuma, T. *Acta Mater.* **2002**, *50*, 2955–2966.
165. Veal, B. W.; Paulikas, A. P.; Gleeson, B.; Hou, P. Y. *Surf. Coat. Technol.* **2007**, *202*, 608–612.
166. Atkinson, A.; Taylor, R. I.; Hughes, A. E. *Philos. Mag. A* **1982**, *45*, 979–998.
167. Sheasby, J. S.; Jory, D. B. *Oxid. Met.* **1977**, *12*, 527–539.
168. Huntz, A. M.; Moulin, G.; Lesage, B. *Contribution of Combined Techniques for Studying Oxidation Mechanisms*, Proceedings of the 9th International Congress on Metallic Corrosion; National Research Council of Canada: Ottawa, Canada, 1984; Vol. 2, pp 400–405.
169. Nicolas-Chaubet, D.; Huntz, A. M.; Millot, F. *Coll. Phys.* **1990**, *51*, 1015–1020.
170. Ben Abderrazik, G.; Millot, F.; Moulin, G.; Huntz, A. M. *J. Am. Ceram. Soc.* **1985**, *68*, 307–314.
171. Tortorelli, P. F.; More, K. L.; Specht, E. D.; Pint, B. A.; Zsack, P. *Mater. High Temp.* **2003**, *20*, 303–310.
172. Veal, B. W.; Paulikas, A. P.; Hou, P. Y. *Nat. Mater.* **2006**, *5*, 349–351.
173. Hou, P. Y.; Paulikas, A. P.; Veal, B. W. *Mater. Sci. Forum* **2006**, *522–523*, 433–440.
174. Reddy, A.; Hovis, D. B.; Heuer, A. H.; Paulikas, A. P.; Veal, B. W. *Oxid. Met.* **2007**, *67*, 153–177.
175. Lipkin, D. M.; Clarke, D. R. *Oxid. Met.* **1995**, *45*, 267–280.
176. Christensen, R. J.; Tolpygo, V. K.; Clarke, D. R. *Acta Mater.* **1997**, *45*, 1761–1766.
177. Rhines, F. N.; Wolf, J. S. *Metall. Trans.* **1970**, *1*, 1701–1710.
178. Golightly, F. A.; Stott, F. H.; Wood, G. C. *Oxid. Met.* **1976**, *10*, 163–187.
179. Golightly, F. A.; Stott, F. H.; Wood, G. C. *J. Electrochem. Soc.* **1979**, *126*, 1035–1042.
180. Tolpygo, V. K.; Grabke, H. J. *Oxid. Met.* **1994**, *41*, 343–364.
181. Tolpygo, V. K. *Oxid. Met.* **1999**, *51*, 449–477.
182. Stott, F. H.; Wood, G. C.; Golightly, F. A. *Corros. Sci.* **1979**, *19*, 869–887.
183. Fox, P.; Tatlock, G. J. *Mater. Sci. Technol.* **1988**, *4*, 439–445.
184. Tolpygo, V. K.; Clarke, D. R. *Acta Mater.* **1998**, *46*, 5153–5166.
185. Mennicke, C.; Schumann, E.; Ulrich, C.; Rühle, M. *Mater. Sci. Forum* **1997**, *251–254*, 389–396.
186. Pint, B. A. *Oxid. Met.* **1997**, *48*, 303–328.
187. Dryepondt, S.; Pint, B. A. *Mater. Sci. Eng. A* **2008**, *497*, 224–230.
188. Pint, B. A. *Mater. Sci. Forum* **1997**, *251–254*, 397–404.
189. Pint, B. A.; Garratt-Reed, A. J.; Hobbs, L. W. *J. Phys. IV* **1993**, *3(C9)*, 247–255.
190. Nychka, J. A.; Clarke, D. R. *Oxid. Met.* **2005**, *63*, 325–352.
191. Lance, M. J.; Pint, B. A. Unpublished data; ORNL, Oak Ridge, TN, 1999.
192. Naumenko, D.; Kochubey, V.; Le Coze, J.; Wessel, E.; Singheiser, L.; Quadackers, W. J. *Mater. Sci. Forum* **2004**, *461–464*, 489–495.
193. Provenzano, V.; Sadananda, K.; Louat, N. P.; Reed, J. R. *Surf. Coat. Technol.* **1988**, *36*, 61–74.
194. Grabke, H. J.; Weimer, D.; Viehhaus, H. *Appl. Surf. Sci.* **1991**, *47*, 243–250.
195. Jedlinski, J.; Bennett, M. J.; Evans, H. E. *Mater. High Temp.* **1994**, *12*, 169–175.
196. Hou, P. Y.; Saunders, S. R. *J. Mater. High Temp.* **2005**, *22*, 121–130.
197. Hou, P. Y.; Priimak, K. *Oxid. Met.* **2005**, *63*, 113–130.
198. Stott, F. H.; Golightly, F. A.; Wood, G. C. *Corros. Sci.* **1979**, *19*, 889–906.
199. Kumar, A.; Nasrallah, M.; Douglass, D. L. *Oxid. Met.* **1974**, *8*, 227–263.
200. Giggins, C. S.; Kear, B. H.; Pettit, F. S.; Tien, J. K. *Metall. Trans.* **1974**, *5*, 1685–1688.
201. Antill, J. E.; Peakall, K. A. *J. Iron Steel Inst. Adv. Copy* **1967**, *205*, 1136–1142.
202. Kingsley, L. M.; Stringer, J. *Oxid. Met.* **1989**, *32*, 371–378.
203. Pint, B. A. *Oxid. Met.* **1998**, *49*, 531–560.
204. Hou, P. Y. *Oxid. Met.* **1999**, *52*, 337–351.
205. Hou, P. Y.; Stringer, J. *J. Phys. IV* **1993**, *3(C9)*, 231–240.
206. Quadackers, W. J.; Huczowski, P.; Naumenko, D.; Zurek, J.; Meier, G. H.; Niewolak, L.; Singheiser, L. *Mater. Sci. Forum* **2008**, *595–598*, 1111–1118.
207. Gupta, D. K.; Duvall, D. S. In *Superalloys*; Gell, M., et al. Eds.; TMS: Warrendale, PA, 1984; pp 711–720.
208. Sigler, D. R. *Oxid. Met.* **1989**, *32*, 337–355.
209. Ikeda, Y.; Nii, K.; Yoshihara, K. *Trans. Jpn. Inst. Met.* **1983**, *24*, 207–214.
210. Funkenbush, A. W.; Smeggil, J. G.; Bornstein, N. S. *Metall. Trans. A* **1985**, *16*, 1164–1166.
211. Smeggil, J. G.; Funkenbusch, A. W.; Bornstein, N. S. *Metall. Trans. A* **1986**, *17*, 923–932.
212. Smialek, J. L. *Metall. Trans. A* **1987**, *18*, 164–167.
213. Quadackers, W. J.; Wasserfuhr, C.; Khanna, A. S.; Nickel, H. *Mater. Sci. Technol.* **1988**, *4*, 1119–1125.
214. Smialek, J. L.; Jayne, D. T.; Schaeffer, J. C.; Murphy, W. H. *Thin Solid Films* **1994**, *253*, 285–292.
215. Meier, G. H.; Pettit, F. S.; Smialek, J. L. *Mater. Corros.* **1995**, *46*, 232–240.
216. Sarioglu, C.; Stinner, C.; Blachere, J. R.; Birks, N.; Pettit, F. S.; Meier, G. H. In *Superalloys*; Kissinger, R. D., Deye, D. J., Anton, D. L., Cetel, A. D., Nathal, M. V., Pollack, T. M., Woodford, D. A., Eds.; TMS: Warrendale, PA, 1996; pp 71–80.
217. Lees, D. G. *Oxid. Met.* **1987**, *27*, 75–81.
218. Hou, P. Y.; Stringer, J. *Oxid. Met.* **1992**, *38*, 323–345.
219. Hou, P. Y. *Annu. Rev. Mater. Res.* **2008**, *38*, 275–298.
220. Briant, C. L.; Luthra, K. L. *Metall. Trans. A* **1988**, *19*, 2099–2108.
221. Yang, S.; Wang, F. *Oxid. Met.* **2006**, *65*, 195–205.
222. Tolpygo, V. K.; Grabke, H. J. *Scr. Mater.* **1997**, *38*, 123–129.
223. Smialek, J. L. *Oxid. Met.* **2001**, *55*, 75–86.
224. Harris, K.; Wahl, J. B. In *Superalloys*; Green, K. A., Pollock, T. M., Harada, H., Howson, T. E., Reed, R. C., Schirra, J., Walston, S., Eds.; TMS: Warrendale, PA, 2004; pp 45–52.
225. Schumann, E.; Yang, J. C.; Graham, M. J. *Scr. Mater.* **1996**, *34*, 1365–1370.
226. Mendis, B. G.; Livi, K. J. T.; Hemker, K. J. *Scr. Mater.* **2006**, *55*, 589–592.
227. Lowrie, D.; Boone, D. H. *Thin Solid Films* **1977**, *45*, 491–498.
228. Allam, I. M.; Akuezue, H. C.; Whittle, D. P. *Oxid. Met.* **1980**, *14*, 517–530.
229. Amano, T.; Takezawa, Y.; Shiino, A.; Shishido, T. *J. Alloys Compd.* **2008**, *452*, 16–22.
230. Dickey, E. C.; Pint, B. A.; Alexander, K. B.; Wright, I. G. *J. Mater. Res.* **1999**, *14*, 4531–4540.
231. Smialek, J. L.; Doychak, J.; Gaydosh, D. J. *Oxid. Met.* **1990**, *34*, 259–275.

232. Wright, I. G.; Pint, B. A.; Tortorelli, P. F. *Oxid. Met.* **2001**, 55, 333–357.
233. Pint, B. A.; Porter, W. D.; Wright, I. G. *Mater. Sci. Forum* **2008**, 595–598, 1083–1092.
234. Smialek, J. L.; A Nesbitt, J.; Barrett, C. A.; Lowell, C. E. In *Cyclic Oxidation of High Temperature Materials*; Schütze, M., Quadakkers, W. J., Eds.; Institute of Materials: London, UK, 1999; pp 148–168.
235. Evans, H. E. *Int. Mater. Rev.* **1995**, 40, 1–40.
236. Nicholls, J. R.; Evans, H. E.; Saunders, S. R. *J. Mater. High Temp.* **1997**, 14, 5–13.
237. Jönsson, B.; Berglund, R.; Magnusson, J.; Henning, P.; Håttestrand, M. *Mater. Sci. Forum* **2004**, 461–464, 455–462.
238. Herbelin, J. M.; Mantel, M. *Mater. Sci. Forum* **1997**, 251–254, 349–356.
239. Lowell, C. E.; Deadmore, D. L. *Oxid. Met.* **1980**, 14, 325–336.
240. Wagner, C. J. *Electrochem. Soc.* **1952**, 99, 369–380.
241. Douglass, D. L. *Oxid. Met.* **1995**, 44, 81–111.
242. Wolf, J. S.; Evans, E. B. *Corrosion* **1962**, 18, 129–136.
243. Whittle, D. P.; Shida, Y.; Wood, G. C.; Stott, F. H.; Bastow, B. D. *Philos. Mag. A* **1982**, 46, 931–949.
244. Hindam, H. M.; Smeltzer, W. W. *J. Electrochem. Soc.* **1980**, 127, 1622–1635.
245. Barrett, C. A.; Lowell, C. E. *Oxid. Met.* **1978**, 12, 293–311.
246. Allam, I. M.; Whittle, D. P.; Stringer, J. *Oxid. Met.* **1979**, 13, 381–401.
247. Bennett, M. J.; Romary, H.; Price, J. B. In *Heat Resistant Materials*; Natesan, K., Tillack, D. J., Eds.; ASM: Materials Park, OH, 1991; pp 95–103.
248. Gurrappa, I.; Weinbruch, S.; Naumenko, D.; Quadakkers, W. J. *Mater. Corros.* **2000**, 51, 224–235.
249. Pint, B. A.; Walker, L. R.; Wright, I. G. *Mater. High Temp.* **2004**, 21, 175–185.
250. Wilber, J. P.; Bennett, M. J.; Nicholls, J. R. *Mater. High Temp.* **2000**, 17, 125–132.
251. Wright, I. G.; Pint, B. A.; Hall, L. M.; Tortorelli, P. F. In *Lifetime Modelling of High Temperature Corrosion Processes*; Schütze, M., Quadakkers, W. J., Nicholls, J. R., Eds.; Maney: London, 2001; pp 299–318.
252. Wright, I. G.; Peraldi, R.; Pint, B. A. *Mater. Sci. Forum* **2004**, 461–464, 579–590.
253. Nesbitt, J. A.; Heckel, R. W. *Oxid. Met.* **1988**, 29, 75–102.
254. Nesbitt, J. A. NASA Glenn Research Center: Cleveland, OH, 2000NASA/TM, 2000-209271.
255. Pint, B. A.; Walker, L. R.; Wright, I. G. *Mater. High Temp.* **2009**, in press.
256. Evans, H. E.; Donaldson, A. T.; Gilmour, T. C. *Oxid. Met.* **1999**, 52, 379–402.
257. Hiramatsu, N.; Stott, F. H. *Oxid. Met.* **1999**, 51, 479–494.
258. Kochubey, V.; Naumenko, D.; Wessel, E.; Le Coze, J.; Singheiser, L.; Al-Baidary, H.; Tatlock, G. J.; Quadakkers, W. J. *Mater. Lett.* **2006**, 60, 1564–1568.
259. Fritscher, K.; Leyens, C.; Peters, M. *Mater. Sci. Eng. A* **1995**, 190, 253–258.
260. Kofstad, P. In *Microscopy of Oxidation I*; Bennett, M. J., Lorimer, G. W., Eds.; Institute of Metals: London, 1991; pp 2–9.
261. Pint, B. A.; Haynes, J. A.; Zhang, Y.; More, K. L.; Wright, I. G. *Surf. Coat. Technol.* **2006**, 201, 3852–3856.
262. Opila, E. J. *Mater. Sci. Forum* **2004**, 461–464, 765–774.
263. Asteman, H.; Svensson, J.-E.; Johansson, L.-G.; Norell, M. *Oxid. Met.* **1999**, 52, 95–111.
264. Opila, E. J.; Hann, R. E., Jr. *J. Am. Ceram. Soc.* **1997**, 80, 197–205.
265. Young, D. J.; Pint, B. A. *Oxid. Met.* **2006**, 66, 137–153.
266. Kvernes, I.; Olivera, M.; Kofstad, P. *Corros. Sci.* **1977**, 17, 237–252.
267. Pint, B. A.; Peraldi, R.; Maziasz, P. J. *Mater. Sci. Forum* **2004**, 461–464, 815–822.
268. Pint, B. A.; More, K. L.; Trejo, R.; Lara-Curzio, E. *J. Eng. Gas Turbines Power* **2008**, 130, 012101.
269. Agüero, A.; Muelas, R.; Gutiérrez, M.; Van Vulpen, R.; Osgerby, S.; Banks, J. P. *Surf. Coat. Technol.* **2007**, 201, 6253–6260.
270. Regina, J. R.; DuPont, J. N.; Marder, A. R. *Oxid. Met.* **2004**, 61, 69–90.
271. Leyens, C.; Fritscher, K.; Gehrling, R.; Peters, M.; Kaysser, W. A. *Surf. Coat. Technol.* **1996**, 82, 133–144.
272. Janakiraman, R.; Meier, G. H.; Pettit, F. S. *Metall. Mater. Trans. A* **1999**, 30, 2905–2913.
273. Onal, K.; Maris-Sida, M. C.; Meier, G. H.; Pettit, F. S. *Mater. High Temp.* **2003**, 20, 327–337.
274. Maris-Sida, M. C.; Meier, G. H.; Pettit, F. S. *Metall. Mater. Trans. A* **2003**, 34, 2609–2619.
275. Smialek, J. L. *JOM* **2006**, 58(1), 29–35.
276. Al-Badair, H.; Tatlock, G. J. *Mater. High Temp.* **2000**, 17, 133–137.
277. Essuman, E.; Meier, G. H.; Zurek, J.; Hänsel, M.; Quadakkers, W. J. *Oxid. Met.* **2008**, 69, 143–162.
278. Alcock, C. B.; Hocking, M. G.; Zador, S. *Corros. Sci.* **1969**, 9, 111–122.
279. Vineberg, E. J.; Douglass, D. L. *Oxid. Met.* **1986**, 25, 1–28.
280. Wright, I. G. In *Proceedings of the 1974 Gas Turbine Materials in the Marine Environment Conference*; Fairbanks, J. W., Machlan, I., Eds.; Battelle: Columbus, OH, 1975; pp 357–377.
281. Nakamori, M.; Kayano, I.; Tsukuda, Y.; Takahashi, K.; Torigoe, T. *Mater. Sci. Forum* **1997**, 251–254, 633–640.
282. Narita, T.; Przybylski, K.; Smeltzer, W. W. *Oxid. Met.* **1984**, 22, 181–200.
283. Setterlund, R. B.; Prescott, G. R. *Corrosion* **1961**, 17, 103–108.
284. Huang, T. T.; Lin, Y. C.; Shores, D. A.; Pfender, E. *J. Electrochem. Soc.* **1984**, 131, 2191–2196.
285. Saxena, D.; Prakash, S.; Mehta, M. L.; Saraswat, I. P. *Oxid. Met.* **1987**, 28, 127–153.
286. DeVan, J. H.; Tortorelli, P. F. *Mater. High Temp.* **1993**, 11, 30–35.
287. Nyassi, A.; Larpin, J. P.; Bendriss, A. *Oxid. Met.* **1995**, 43, 543–560.
288. Banovic, S. W.; Du Pont, J. N.; Marder, A. R. *Metall. Mater. Trans. A* **2000**, 31, 1805–1817.
289. Pint, B. A.; Zhang, Y.; Tortorelli, P. F.; Haynes, J. A.; Wright, I. G. *Mater. High Temp.* **2001**, 18, 185–192.
290. Mari, P. A.; Chaix, J. M.; Larpin, J. P. *Oxid. Met.* **1982**, 17, 315–328.
291. Stott, F. H.; Chong, F. M. F.; Stirling, C. A. In *Proceedings of the 9th International Congress on Metallic Corrosion* National Research Council of Canada: Ottawa, Canada, 1984; Vol. 2, pp 1–16.
292. Taniguchi, S.; Shibata, T. *Oxid. Met.* **1989**, 32, 391–404.
293. Kim, Y.-K.; Przybylski, K.; Yurek, G. J. In *Fundamental Aspects of High Temperature Corrosion*; Shores, D., Yurek, G. J., Eds.; Electrochemical Society: Pennington, NJ, 1986; Vol. II, pp 259–281.
294. Schaeffer, J.; Kim, G. M.; Meier, G. H.; Pettit, F. S. In Lang, E., Ed.; *The Role of Active Elements in the Oxidation Behavior of High Temperature Metals and Alloys*; Elsevier Applied Science: London, 1989; pp 231–267.
295. Rapp, R. A. *Mater. Sci. Eng.* **1987**, 87, 319–327.
296. Leyens, C.; Wright, I. G.; Pint, B. A. *Mater. Sci. Forum* **2001**, 369–372, 571–578.

297. Grabke, H. J. *Mater. Corros.* **1998**, 49, 303–308.
298. Loudjani, M. K.; Pivin, J. C.; Huntz, A. M.; Davidson, J. H. *Corros. Sci.* **1988**, 28, 1075–1088.
299. Jönsson, B.; Svedberg, C. *Mater. Sci. Forum* **1997**, 251–254, 551–558.
300. Turker, M.; Hughes, T. A. In *Microscopy of Oxidation*; Newcomb, S. B., Bennett, M. J., Eds.; Institute of Metals: London, 1993; Vol. 2, pp 310–320.
301. Bennett, M. J.; Newton, R.; Nicholls, J. R. *Mater. High Temp.* **2003**, 20, 347–356.
302. Han, S.; Young, D. J. *Oxid. Met.* **2001**, 55, 223–242.
303. Stott, F. H.; Berg, S.; Sang, M.; Karim, N. In *High Temperature Materials for Power Engineering*; Bachelet, et al. Eds.; Kluwer Academic Publishers: Dordrecht, Netherlands, 1990; Vol. 1, pp 213–226.
304. Krupp, U.; Christ, H.-J. *Metall. Mater. Trans. A* **2000**, 31, 47–56.
305. Bennett, M. J.; Nicholls, J. R.; Borchardt, G.; Strehl, G. *Mater. High Temp.* **2002**, 19, 117–125.

## 1.27 High Temperature Coatings: Protection and Breakdown

**H. E. Evans**

School of Metallurgy and Materials, The University of Birmingham, Birmingham B15 2TT, UK

© 2010 Elsevier B.V. All rights reserved.

<b>1.27.1</b>	<b>The Need for Coatings</b>	692
<b>1.27.2</b>	<b>Underlying Requirements of Coatings</b>	693
1.27.2.1	The Protective Oxide Layer	693
1.27.2.2	Coating Composition and Solute Supply	694
<b>1.27.3</b>	<b>Examples of Main Coating Types</b>	696
1.27.3.1	Overlay Coatings	696
1.27.3.1.1	MCrAlY coatings	696
1.27.3.1.2	Examples of other metallic coatings	697
1.27.3.1.3	Oxide overlay coatings	698
1.27.3.2	SMART MCrAlY Overlay Coatings	699
1.27.3.3	Diffusion Coatings	700
1.27.3.3.1	Basic types	700
1.27.3.3.2	Aluminide coatings	701
1.27.3.3.3	Platinized coatings	702
1.27.3.3.4	Silicide diffusion coatings	702
1.27.3.4	Thermal Barrier Coatings	704
<b>1.27.4</b>	<b>Case Study I: Oxidation and Lining of MCrAlY Overlays</b>	705
1.27.4.1	Protective Oxidation	705
1.27.4.2	Spallation and Cracking of the Protective Alumina Layer	706
1.27.4.3	Aluminum Depletion	709
1.27.4.3.1	Uniform depletion	709
1.27.4.3.2	Diffusion cells and chemical failure	710
<b>1.27.5</b>	<b>Case Study II: Oxidation-Induced Failure of TBC Systems</b>	712
1.27.5.1	Failure Times under Oxidizing Conditions	712
1.27.5.2	Failure Characteristics	713
1.27.5.3	Strain Energy Considerations	715
1.27.5.4	Formation of Subcritical Cracks	716
1.27.5.4.1	Transformation strains	716
1.27.5.4.2	Mechanical instabilities	717
1.27.5.4.3	Roughness of the BC surface	718
1.27.5.4.4	Chemical failure	719
1.27.5.5	Surface Roughness: A Common Factor?	720
<b>References</b>		722

### Symbols

***a*** Amplitude of bond coat surface roughness (m)  
***b*** Wavelength of bond coat surface roughness (m)  
***C*** Concentration (at.%)  
***C<sub>Al</sub>*** Concentration of aluminum ( $\text{m}^{-3}$ )  
***C<sub>b</sub>*** Bulk concentration (at.%)  
***D*** Interdiffusion coefficient ( $\text{m}^2 \text{s}^{-1}$ )  
***D<sub>Al</sub>*** Interdiffusion coefficient for aluminum ( $\text{m}^2 \text{s}^{-1}$ )

***E<sub>m</sub>*** Young's modulus of the alloy or metallic coating (Pa or GPa)  
***E<sub>ox</sub>*** Young's modulus of the oxide (Pa or GPa)  
***f<sub>B</sub>*** Bulk fractional concentration of solute  
***f<sub>i</sub>*** Fractional concentration of solute at oxide-coating interface  
***f(x)*** Fractional concentration at position *x*  
***h*** thickness of oxide layer (m)  
***h<sub>o</sub>*** Preexisting oxide thickness (m)

$J_{Al}$	Flux of aluminum ( $m^{-2} s^{-1}$ )
$k_n$	Oxidation rate constant ( $m^n s^{-1}$ )
$k_p$	Parabolic oxidation rate constant ( $m^2 s^{-1}$ )
$k'_p$	Mass gain parabolic rate constant ( $g^2 m^{-4} s^{-1}$ or $mg^2 cm^{-4} s^{-1}$ )
$M_o$	Atomic weight of oxygen (kg)
$M_{ox}$	Molecular weight of the oxide (kg)
$n$	Dimensionless number
$R$	Radius of decohesion zone (m)
$t$	Exposure time (s)
$T$	Temperature (K)
$T_{ox}$	Oxidation temperature (K)
$\Delta T$	Amplitude of temperature change (K)
$\Delta T_b$	Critical temperature change for oxide buckling (K)
$\Delta T_c$	Critical temperature change for oxide spallation (K)
$v$	Volume of oxide formed per aluminum atom ( $m^3$ )
$w$	Half the specimen or cell thickness (m)
$W^*$	Strain energy ( $J m^{-3}$ )
$W_{Al}$	Atomic weight of aluminum (kg)
$W_{Al_2O_3}$	Molecular weight of alumina (kg)
$x$	Spatial coordinate and distance from the oxide-metal interface (m)
$x_h$	Section loss (m)
$\alpha_m$	Linear thermal expansion coefficient of alloy or coating ( $K^{-1}$ )
$\alpha_{ox}$	Linear thermal expansion coefficient of oxide ( $K^{-1}$ )
$\varepsilon$	Strain
$\phi$	Pilling-Bedworth ratio
$\gamma_F$	Effective fracture energy ( $J m^{-2}$ )
$\nu$	Poisson's ratio
$\rho_{Al_2O_3}$	Density of alumina ( $kg m^{-3}$ )
$\rho_m$	Density of the alloy ( $kg m^{-3}$ )
$\rho_{ox}$	Density of the oxide ( $kg m^{-3}$ )
$\sigma_{ox}$	In-plane oxide stress (Pa or MPa)

### 1.27.1 The Need for Coatings

High temperature superalloys, usually based on iron-, cobalt-, or nickel-rich compositions,<sup>1</sup> are optimized for mechanical properties, such as creep and fatigue resistance, since they are used for highly-stressed components. In all cases, however, these alloys will be exposed to oxidizing or hot-corrosion environments during service and will undergo some form of degradation process resulting from this interaction. The composition optimization required to achieve good mechanical properties, however, often conflicts with the requirements for

oxidation/hot-corrosion protection. As a result, the intrinsic protection capability of many superalloys is adequate only for short-term exposures and coatings are required to permit extended operation under service conditions. This point will be demonstrated in the later text for the particular case of Ni-based superalloys under oxidizing conditions.

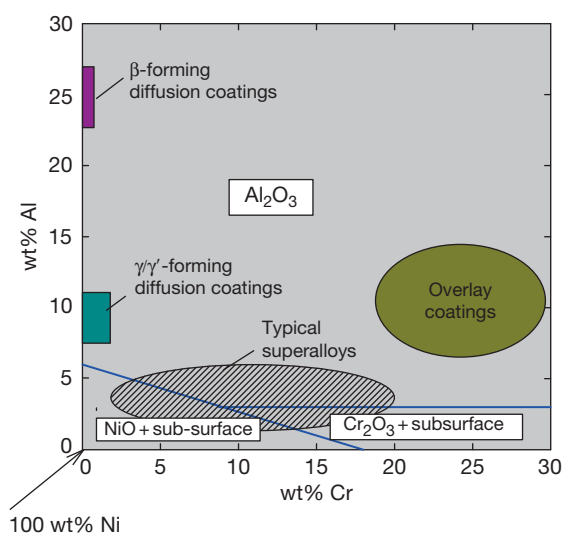
High-strength nickel-based alloys are used extensively for components in gas turbines; an excellent account of their development and properties is provided by Reed.<sup>1</sup> Single crystal alloys, for example, CMSX4, are used for high-pressure blades in aeroengines and in small ( $\sim 10$  MW) land-based turbines, but, in larger machines, polycrystalline alloys (e.g., IN738LC) are used. Some compositions of nickel-based alloys are given in Table 1. These are given in 'weight percentage' as is customary, but, in assessing the ability to form and maintain a protective alumina layer at high temperatures, it is the atomic percentage of available aluminum which is a key factor. For alloys having high nickel, chromium, and cobalt contents, the atomic concentration of aluminum is roughly twice the weight percentage value. In more complex alloys containing appreciable amounts of heavy elements such as tungsten, rhenium, or ruthenium, this factor is nearer 2.5. Thus, even though in most of the alloys (shown in Table 1) the aluminum concentration is  $\sim 5.6$  wt%, its atomic concentration increases from  $\sim 11$  at.% in simpler alloys such as RR2000 to  $\sim 13$  at.% in PWA1497. Much of this aluminum is associated with the strengthening  $\gamma'$  phase in these alloys.

The importance of both aluminum and chromium concentrations to the ability of a Ni-based alloy to form a protective alumina layer is summarized in Figure 1. This diagram is similar to that given by Evans and Taylor,<sup>2</sup> but has been modified to reflect the low-Cr compositions of the more recent alloys shown in Table 1 and to include  $\gamma/\gamma'$  coatings. For convenience in comparing between alloys, concentrations in weight percentage are used. The experimentally based lines shown in Figure 1 derive from the work of Giggins and Pettit<sup>3</sup> on NiCrAl alloys at temperatures within the range 1000–1200°C. They show that in simple Ni–Al binary alloys, at least 6 wt % aluminum is required to form an alumina layer at these temperatures. This critical value decreases with increasing alloy chromium content to  $\sim 3$  wt% aluminum at chromium contents  $\geq 10$  wt%. At low aluminum and chromium contents, that is, below the downward sloping line to the left-hand side of Figure 1, the principal surface oxide is expected to



**Table 1** Compositions (wt%) of some representative nickel-based superalloys

Alloy	Ni	Co	W	Cr	Al	Ta	Re	Hf	Ru	Ti	Mo	Nb
RR2000	Balance	15.0	–	10.0	5.5	2.8	–	–	–	4.0	3.0	–
IN738LC	Balance	8.5	2.6	16.0	3.4	1.7	–	–	–	3.4	1.7	0.9
CM186	Balance	9.3	8.5	6.0	5.7	3.4	3.0	1.4	–	0.5	0.2	–
CMSX4	Balance	9.8	6.4	6.4	5.6	6.5	3.0	0.1	–	1.0	0.6	0.4
CMSX10	Balance	3.0	5.0	2.0	5.7	8.0	6.0	0.03	–	0.2	2.9	–
PWA1497	Balance	16.5	6.0	2.0	5.6	8.3	6.0	0.15	3.0	–	2.0	–
TMS162	Balance	5.8	5.8	2.9	5.8	5.6	4.9	0.1	6.0	–	3.9	–

**Figure 1** A schematic map derived from Evans and Taylor,<sup>2</sup> based on experimental data<sup>3</sup> showing the type of oxide formed in the NiCrAl system over the temperature range 1000–1200 °C. Superimposed are the composition ranges of typical superalloys and coatings.

be NiO (in NiCrAl alloys), with internal oxidation of aluminum and chromium. To the right-hand side of **Figure 1**, corresponding to alloys of high chromium and low aluminum content, chromia will be the expected surface oxide and aluminum will oxidize internally.

Also shown schematically, as the cross-hatched ellipse in **Figure 1**, is the approximate range of aluminum and chromium contents often used in Ni-based superalloys. It is immediately apparent that they tend to lie on or near the bounding lines for protective alumina formation. In some cases, alumina formation can be expected but not in others. As a group, these Ni-based superalloys can be considered to be borderline alumina formers and nonprotective oxidation has been reported in this temperature range for IN738LC<sup>4,5</sup> and CMSX10.<sup>6</sup> The situation

is exacerbated with recent generations of alloys in which chromium levels have been decreased to ~2–2.5 wt% (**Table 1**), making it less favorable for a protective layer of alumina to form (see **Figure 1**). In addition, elements such as rhenium and ruthenium have been introduced, which have volatile oxides that can be released at high temperatures, at least in the absence of a protective surface oxide layer.

Another important consideration when assessing the oxidation resistance of an alloy is its ability to reform a protective alumina layer should that which formed initially spall or crack. This is an arduous requirement for borderline alloys, since the formation and growth of the original alumina layer is a process of selective oxidation and necessarily depletes the alloy of aluminum. Thus, even though an alumina layer may have formed initially on the superalloy, residual aluminum concentrations are unlikely to be able to maintain protective conditions when repeated spallation events occur.

It is for this combination of reasons that Ni-based superalloys operating at elevated temperatures, say  $\geq 1000$  °C, are coated with Al-rich layers. The composition ranges of two important classes of such coatings, overlays and diffusion coatings, are shown in **Figure 1**. These will be discussed shortly but, clearly, both types are designed to lie within the alumina-forming region in the diagram. It is the combination of high-strength superalloy and oxidation-resistant coating that permits component operation for extended periods at high temperatures.

## 1.27.2 Underlying Requirements of Coatings

### 1.27.2.1 The Protective Oxide Layer

High temperature coatings rely, for protection, on the formation of a dense and adherent surface oxide layer that is chemically stable, thickens slowly with time at temperature, and has good adherence to the coating.

These are, of course, the same requirements as are needed in the design of oxidation-resistant alloys in general, as discussed elsewhere in this book, and, as in that case, the choice is limited to chromia ( $\text{Cr}_2\text{O}_3$ ), silica ( $\text{SiO}_2$ ), and alumina ( $\alpha\text{-Al}_2\text{O}_3$ ).

Chromia layers are particularly useful in conferring protection against Type-II hot corrosion<sup>7</sup> and intermediate-temperature oxidation, say 600–800 °C, but can be converted to  $\text{CrO}_3$  at higher temperatures. The rate of formation of this gaseous oxide can be significant in both dry and moist air at temperatures  $\geq 950^\circ\text{C}$  and chromia-forming coatings have limited usage at high temperatures in such environments. Silica layers are capable of providing protection to very high temperatures, for example, *via* ceramic layers on carbon-based materials, to  $\sim 1800^\circ\text{C}$ .<sup>8</sup> They also suffer, however, from concerns with chemical stability in moist environments. Alumina layers do not suffer from such concerns and are the favored means of protection under Type-I hot-corrosion and high temperature oxidation conditions. The majority of coatings are now designed to form a continuous alumina layer under these conditions and to have sufficient aluminum content to provide a healing capability in the event of cracking or spallation of this layer. The majority of this chapter will place emphasis on the behavior of such alumina-forming coatings designed for use under high temperature oxidizing conditions, but interesting exceptions with commercial relevance are also included.

### 1.27.2.2 Coating Composition and Solute Supply

The initial priority of oxidation-resistant coatings is to form a protective layer that can be achieved simply by incorporating sufficient amount of the relevant element into the coating composition. However, this approach can impair physical and mechanical properties, for example, by decreasing melting temperatures or coating fracture toughness and ductility, and a balance must always be sought. The composition ranges of three types of alumina-forming coatings are shown in **Figure 1**, from which it is clear that all lie in the appropriate composition range for protective oxide formation. Detailed discussion of the coating types is provided later, but it is clear that aluminum concentrations of  $\sim 10\text{ wt}\%$  are typical for both the MCrAlY overlays and  $\gamma/\gamma'$  diffusion coatings. These compare with the minimum requirements for alumina formation (solid lines) of  $\sim 3$  and  $6\text{ wt}\%$  aluminum, respectively. The  $\beta$ -forming class of diffusion coating has substantially larger amounts of aluminum at  $\sim 25\text{ wt}\%$ .

It must be borne in mind, though, that the formation of the protective layer is a process of selective oxidation in which the solute atom is preferentially removed from the coating, oxidized, and incorporated into the oxide layer. This removal necessarily depletes the coating of the solute and will generate a concentration profile as shown schematically in **Figure 2** for the case of aluminum removal from, nominally, a NiCrAlY overlay coating. This is assumed to have had an initial aluminum concentration of  $10\text{ wt}\%$  and can be compared with the uncoated alloy having an initial concentration of  $5.6\text{ wt}\%$ .

The second requirement of a protective coating is that the residual solute concentration after initial formation of the surface layer is still sufficient to reform a protective layer in the event of cracking or spalling of this first-formed layer. As shown in **Figure 2**, the coating has sufficient aluminum, and hence even after alumina formation, there is still sufficient solute at the oxide–metal interface to reform this layer. By contrast, because the superalloy had barely sufficient aluminum to form the alumina layer initially, the interfacial concentration falls below the critical value after formation of the protective layer. Subsequent spallation of this layer would then mean that rapid oxidation of the alloy would take place until the local concentration had reached the critical value for reforming the alumina layer. The quantity of metal consumed is shown by the hatched area in **Figure 2** as  $\sim 7\text{ }\mu\text{m}$  but it will be much larger if spallation occurs later in life when more pronounced depletion has occurred. Typically, the thickness of this at-risk zone will increase parabolically with exposure time up to the first spallation event.

The shapes of the depletion profiles shown in **Figure 2** are determined by the need to maintain a mass balance at the oxide–metal interface, such that the flux of aluminum leaving the metal is equal to that required to produce the observed thickening rate of the oxide.<sup>9</sup> Considering the ideal case that the oxide thickness,  $b$ , increases parabolically with time,  $t$ , and forms at the start of the exposure period, the rate constant,  $k_p$ , is then defined as

$$k_p = b^2/t \quad [1]$$

This means that the flux of aluminum atoms,  $\mathcal{J}_{\text{Al}}$ , arriving at the oxide–metal interface is

$$\mathcal{J}_{\text{Al}} = -D_{\text{Al}} \left( \frac{\partial C_{\text{Al}}}{\partial x} \right)_{x=0} = \frac{1}{V} \left( \frac{d\xi}{dt} \right) = \frac{1}{2} k_p^{0.5} t^{-0.5} \quad [2]$$

where it is assumed, reasonably for protective conditions, that the recession of the oxide–metal interface is much smaller than the diffusion distances within

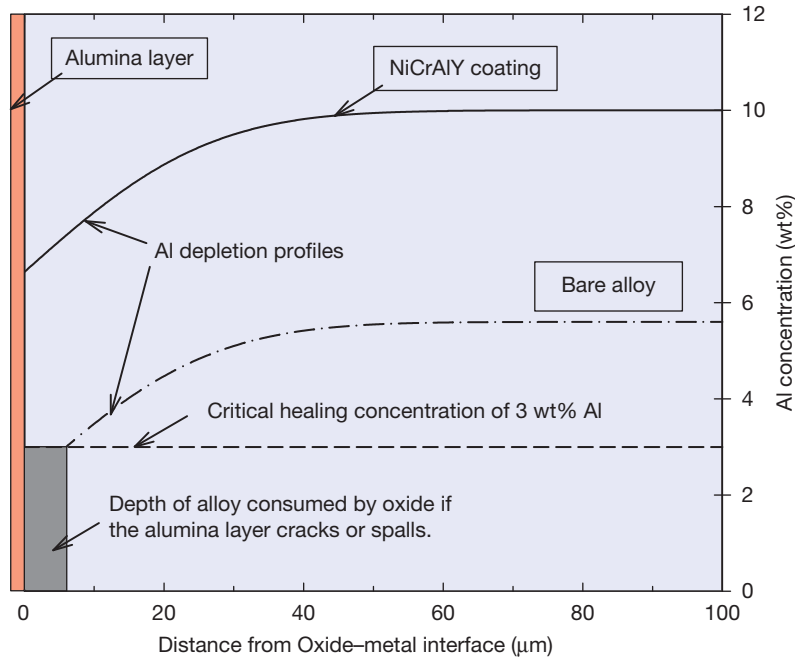


**Figure 2** Selective oxidation of aluminum from a NiCrAlY coating and superalloy produces depletion profiles in that element. They result in interfacial aluminum concentrations insufficient to reform the alumina layer on the superalloy without the prior consumption of some of the underlying metal. The critical interfacial concentration for reforming an alumina layer is taken as 3 wt%, that is, of similar magnitude to those shown as solid lines in Figure 1.

the coating. In eqn. [2],  $D_{Al}$  is the interdiffusion coefficient for aluminum within the coating,  $C_{Al}$  is the aluminum concentration (number/unit volume),  $x$  is the spatial coordinate measured from the oxide-metal interface, and  $V$  is the volume of oxide formed per aluminum atom. The depletion profile within the metal can then be obtained from solution of Fick's second law

$$\frac{\partial C_{Al}}{\partial t} = D_{Al} \frac{\partial^2 C_{Al}}{\partial x^2} \quad [3]$$

using eqn. [2] as a boundary condition, that is, the flux of aluminum at the oxide-metal interface varies as  $\bar{t}^{-1/2}$ . At relatively short exposure times, the depletion distance will be small compared with the thickness of the coating so that the latter can then be considered as semiinfinite. Under these conditions, the depletion profile is obtained as<sup>10</sup>

$$\frac{f(x) - f_i}{f_b - f_i} = \operatorname{erf} \left( \frac{x}{2(D_{Al}t)^{0.5}} \right) \quad [4]$$

where the  $f$ s are consistent concentration parameters, for example, weight (mass) fractions,  $f(x)$  is the value at distance  $x$ ,  $f_i$  is the value in the metal at the oxide-metal interface,  $f_b$  is the bulk value, and  $\operatorname{erf}$  is the error

function. The interfacial concentration,  $f_i$ , is constant provided that parabolic oxidation and semiinfinite conditions apply, but its value is directly related to the rate constant  $k_p$  and can be determined from the need to conserve the aluminum flux at the oxide-metal interface. For simplicity, taking  $f$  as a weight fraction, the interfacial concentration during the growth of alumina is given as<sup>11</sup>

$$f_i = f_b - \left[ \left( \frac{\pi k_p}{D_{Al}} \right)^{1/2} \left( \frac{\rho_{Al_2O_3} W_{Al}}{\rho_m W_{Al_2O_3}} \right) \right] \quad [5]$$

Here,  $\rho$  is density,  $W$  is molecular or atomic weight, the suffix 'm' is the coating, and  $Al_2O_3$  the oxide.

The concentration in the coating at its interface with the oxide will be maintained provided that there is sufficient aluminum reservoir and thickness of the coating to approximate to semiinfinite conditions. Protection should, thus, be provided by these generic coatings until end-of-life effects, initiated often by aluminum-reservoir depletion, intervene. At this stage, the interfacial concentration will begin to decrease and a level will eventually be reached where the protective alumina layer cannot be maintained. These issues will be discussed in detail in the following sections.

## 1.27.3 Examples of Main Coating Types

### 1.27.3.1 Overlay Coatings

#### 1.27.3.1.1 MCrAlY coatings

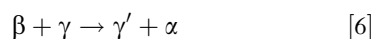
Overlay coatings consist of a discrete coating layer deposited onto the surface of the component, with little interdiffusion and chemical reaction with the alloy substrate. These overlay coatings are often metallic alloys, 150–300  $\mu\text{m}$  thick, based on MCrAlY compositions where M is Ni, Co, sometimes Fe, or a combination of these. Early development of these overlay coatings centered on cobalt-based materials containing 20–40 wt% Cr, 12–20 wt% Al, and 0.5 wt% Y.<sup>12</sup> On the basis of hot corrosion and mechanical property tests, an optimal composition of Co<sub>25</sub>Cr<sub>14</sub>Al<sub>0.5</sub>Y (wt%) was selected. This initial composition is similar to those of the more recent Co-based coatings, ATD 2B and ATD 5B, given in Table 2. Later trends, however, have been to replace some or all of the cobalt content with nickel in order to improve toughness and to limit interdiffusion effects when protecting high temperature Ni-based superalloys. There has also been a tendency to decrease aluminum content, again to improve coating toughness. A few examples of the composition of current MCrAlY overlay coatings are given in Table 2.

It is sometimes the case, as can be inferred from Table 2, that overlay coatings of the same or similar compositions have different designations, for example, LCO22 and CN122. This reflects the different possible deposition methods in commercial use. These include air plasma spraying (APS), argon-shrouded plasma spraying (ASPS), low-pressure plasma spraying (LPPS), high-velocity oxy-fuel (HVOF) spraying, electrodeposition, and physical vapor deposition (PVD) processes such as sputtering and electron beam (EB) PVD. Some of these methods

relate to the coatings shown in the table. Details of these techniques and the historical development of protective coatings can be found elsewhere.<sup>13–18</sup>

Even though the details of the coating techniques will be covered elsewhere in this book, it is important to note that different application methods will produce different coating structures as can be appreciated from Figure 3. In both of the plasma sprayed coatings, (a) and (b), the sequential spray runs are evident in the lateral dark stringers of oxide formed around individual alloy particles during the deposition process. These stringers can be continuous in the APS coating in which extensive oxidation in the air environment can result. Some oxide formation is inevitable also under LPPS, as can be appreciated from Figure 3(b), but in this case, continuous stringers are not usually formed (e.g., see Figure 4). These differences affect the longevity of the coatings, even for a given nominal composition, as will be discussed later with reference to aluminum reservoir issues. The EB-PVD coating, by contrast, forms as vertical columns with negligible oxidation. These vertical features can be seen on closer inspection in Figure 3(c), and their presence provides sites of potential mechanical weakness, which can be removed by postprocessing, for example, peening, to improve lateral bonding.

The MCrAlY coatings (shown in Table 2) have a nominal  $\beta/\gamma$  structure, where  $\beta$  can be NiAl or CoAl and  $\gamma$  is face-centered cubic Ni- or Co-rich solid solution. In practice, however, the actual microstructure will depend on cooling rate and temperature as well as on the detailed composition. Ni-rich phases, for example, can undergo the following four-phase reaction at  $\sim 980^\circ\text{C}$ <sup>19</sup>:



where  $\gamma'$  is the Ni<sub>3</sub>Al phase and  $\alpha$  is the  $\alpha$ -Cr solid solution. It can be appreciated that a given coating

**Table 2** Compositions (wt%) of some MCrAlY overlay coatings

Coating or feedstock	Al	Cr	Ni	Co	Fe	Y	Others
ATD 2B	12	23	–	Balance	–	0.3	
ATD 5B	11	18	–	Balance	–	0.5	
LCO 22	8	22	32	Balance	–	0.5	–
CN 122	8	22	32	Balance	–	0.5	–
LN 34	11	20	Balance	–	–	0.5	0.5Mo
ATD 8	11	24	–	–	Balance	0.6	–
Amdry 963	6	25	Balance	–	–	0.4	–
Amdry 995	8	21	32	Balance	–	0.5	–
Amdry 997	8.5	20	Balance	23	–	0.6	4Ta

LN and LCO coatings deposited by argon-shrouded plasma spraying, ATD deposited by EB-PVD, CN deposited by low-pressure plasma spraying, Amdry are feedstock powders.

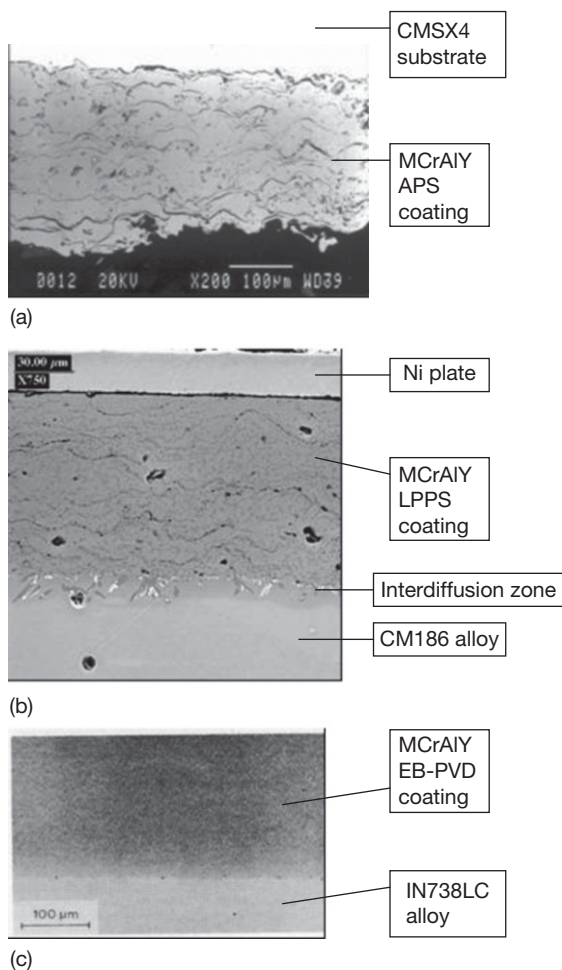


**Figure 3** Examples of the structure of MCrAlY coatings deposited by (a) APS,<sup>2</sup> (b) LPPS,<sup>2</sup> and (c) EB-PVD<sup>13</sup> techniques.

composition can have a  $\beta/\gamma$  microstructure at higher temperatures, but at lower temperatures – often corresponding to service conditions – can be  $\gamma'/\alpha$ . In reality, particularly if fairly rapid temperature changes take place, the microstructure may be non-equilibrium and contain a mixture of the various phases.<sup>20</sup> An example of a typical duplex microstructure is provided in **Figure 4**. Further complications may arise near the interface with the substrate alloy if  $\gamma'$ -stabilizing elements such as tantalum, titanium, and niobium have diffused into the coating; the  $\gamma'$  phase can then exist to temperatures above 980 °C at this location.

Reaction [6] is also accompanied by linear contraction strains of  $\sim 0.7\%$  and there has been concern that this could prejudice the integrity of the coating. There is no particular evidence for any deleterious

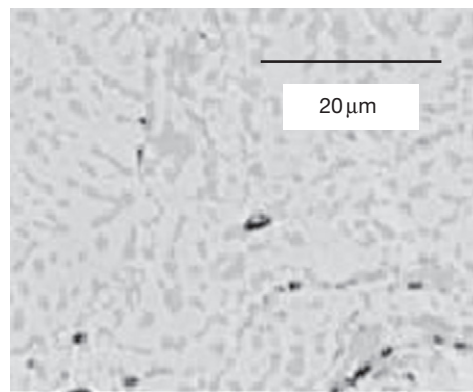


**Figure 4** The duplex microstructure of a LPPS CoNiCrAlY overlay coating. Courtesy of Dr. M.P. Taylor.

effect, however, possibly because the strains arise at temperatures where the coating is ductile and stress relaxation rates are high.<sup>21,22</sup> Nevertheless, the concern has been one of the historic factors influencing the incorporation of cobalt into many coating compositions in order to decrease the stability of the  $\gamma'$  phase. Even so,  $\gamma'$  phases have been reported<sup>20</sup> in Ni-based MCrAlY coatings containing 20 wt% Co.

Minor alloying additions, in addition to yttrium, have also been made to MCrAlY coatings either in attempts to improve alumina formation or adherence or to improve mechanical properties. Some examples include silicon<sup>23</sup> and hafnium<sup>24</sup> and also tantalum (**Table 2**), titanium,<sup>23</sup> molybdenum (**Table 2**), niobium, rhenium, and zirconium. These are often used in combinations, but detailed compositions of current coatings tend to be proprietary. MCrAlY coatings have also been modified by means of surface enrichment with silicon<sup>25</sup> and aluminum (e.g., GE coatings 29+ and 33+) and, in lower-density air plasma sprayed structures, by inward percolation of liquid  $\text{NiAl}_3$ .<sup>26</sup>

#### 1.27.3.1.2 Examples of other metallic coatings

Much effort has been made to deposit metallic coatings other than MCrAlYs in attempts to improve substrate properties<sup>15</sup>; some examples designed to confer oxidation resistance are given here.

Ti–Al alloys have considerable commercial potential because of their high specific creep strength, that is, the combination of good creep strength and low density. Their disadvantage lies in their poor oxidation resistance resulting from the competitive growth of alumina and rutile ( $\text{TiO}_2$ ). Both of these oxides are very stable, but the latter has a much higher growth rate than alumina and the combination makes it difficult to form and sustain protective conditions.



The situation can be improved by the application of surface coatings of increased aluminum to titanium ratios having greater propensity to form alumina. Interesting examples are the use of a sputtered Ti–51Al–13Cr (at.%) overlay<sup>27</sup> to improve oxidation performance of a near- $\alpha$  titanium alloy at 750 °C in air. A similar principle has been adopted<sup>28</sup> through the use of either graded or discrete sequential layers of Ti<sub>3</sub>Al, TiAl, and TiAl<sub>3</sub>, again on a near- $\alpha$  alloy. In an alternative approach,<sup>29</sup> it is recognized that at typical operating temperatures for Ti–Al (say 700–750 °C), it is not necessary to use an alumina layer for oxidation protection, since a chromia layer will provide the necessary improvements. As a consequence, it is possible to use Al-free chromia-forming coatings of high fracture toughness and ductility to confer oxidation protection.<sup>29</sup>

Overlay coatings may also allow the potential of other reactive alloys with attractive mechanical properties to be realized. Important examples are those alloys based on niobium, which have good creep properties at high temperature but poor oxidation resistance. Alumina-forming FeCrAlY and silica-forming SiCrAlY overlays, deposited by APS, can produce oxidation protection to molybdenum for significant periods, 300 and 2000 h, respectively, at 1200 °C.<sup>30</sup> An advanced coating architecture for the protection of a Nb–5Mo–15W alloy has been developed by Narita and coworkers,<sup>31</sup> in which the outer Al-rich reservoir within the coating is protected from interdiffusion by underlying Re–Cr-rich layers.

### 1.27.3.1.3 Oxide overlay coatings

Directly depositing a surface coating of a protective oxide layer ought, in principle, to be an attractive option, since it bypasses the need for the metallic element to be present in significant quantities in the underlying alloy. This is particularly the case for aluminum and silicon, whose presence in large amounts can impair the mechanical properties of the alloy.

A low-cost method for the deposition of an oxide coating is through the use of sol-gels.<sup>15,32</sup> In this, the coating is formed by evaporation of a colloidal suspension of oxide or hydroxide particles and subsequent consolidation of the deposit to form a dense layer. A common feature, though, is the formation of cracks during the curing process, which necessitates the use of multilayers to confer reasonable oxidation protection. Even so, crack-like defects will exist within the layer thickness, which will lead to decreased coating ductility. A better approach is to produce the oxide layer from the vapor phase and this has had considerable success with

the formation of silica coatings. An early evaluation of silica coatings, produced from silane onto a 9Cr ferritic steel, has been made by Crouch and Dooley.<sup>33</sup> Later developments have used plasma-assisted vapor deposition (PAVD) resulting from the decomposition of tetraethoxysilane. Very dense, uncracked, and adherent amorphous silica coatings up to 10  $\mu$ m thick have been produced by this method on, for example, Incoloy 800H,<sup>34</sup> IN 738LC<sup>35</sup> and 20Cr25Ni, Nb-stabilized austenitic steel.<sup>36</sup> The improvements in oxidation resistance obtained from these coatings have been substantial, for example, decrease by a factor of 5 in mass gain for IN 738LC after 5000 h exposure in air at 900 °C.<sup>35</sup>

A striking demonstration of the improvement obtained on the 20Cr25Ni austenitic steel at 1300 °C is given in Figure 5.<sup>37</sup> In this figure, the top micrograph shows how the entire cross-section of the uncoated specimen has been oxidized after 1 h exposure at this temperature in a CO<sub>2</sub>-based gas. In contrast, the silica-coated specimen (lower micrograph) is largely still intact. This example is particularly interesting, since the 20Cr25Ni, Nb-stabilized alloy is used as thin-walled (0.38 mm) tubes to contain UO<sub>2</sub> fuel in the UK's Advanced Gas-Cooled Reactors (AGRs). The test time and temperature used relate to postulated fault scenarios with restricted coolant flow.

These substantial improvements in oxidation resistance arise because the silica coating acts as a barrier both to the inward diffusion of oxygen and to

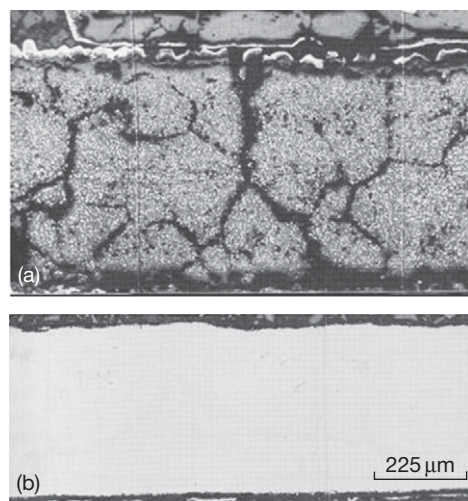


**Figure 5** Optical micrographs of cross-sections of specimens of a 20Cr25Ni, Nb-stabilized alloy after oxidation for 1 h at 1300 °C in a CO<sub>2</sub>/1% CO gas.<sup>37</sup> (a) Complete oxidation of the uncoated alloy and (b) relatively intact silica-coated specimen. The magnification is the same in each case.

the outward diffusion of the alloy constituents. A disadvantage, though, is that the coating offers no self-healing capability in the event that through-thickness cracks or localized spallation occurs. In other words, there is no reservoir of silicon available to reform the silica layer. Cracks in the layer will allow oxygen ingress to the underlying alloy and the continuing formation of nonprotective oxides.<sup>32</sup> The situation is aggravated in the case of amorphous silica because of its low linear thermal expansion coefficient of  $0.5 \times 10^{-6} \text{ K}^{-1}$ . Because the coating layer is much thinner than the metal thickness, it is reasonable to assume that the planar dimensions of the coating will follow those of the underlying alloy during a temperature change,  $\Delta T = (T - T_{\text{ox}})$ , (where  $T$  is the new temperature and  $T_{\text{ox}}$  is the original oxidation temperature). The in-plane strain,  $\varepsilon$ , within the coating is then given as

$$\varepsilon = \Delta T(\alpha_{\text{metal}} - \alpha_{\text{silica}}) \quad [7]$$

where  $\alpha$  is the respective thermal expansion coefficient. A detailed discussion of such mechanical issues has been given elsewhere,<sup>38</sup> but it is instructive here to calculate the thermal expansion strain in the silica coating of **Figure 5(b)**. Assuming that the silica layer was deposited at  $800^\circ\text{C}$ ,  $\Delta T = 500^\circ\text{C}$  for the temperature rise to the test temperature of  $1300^\circ\text{C}$ . Taking also  $\alpha_{\text{metal}} = 17.5 \times 10^{-6} \text{ K}^{-1}$  then gives a tensile in-plane strain within the silica coating of 0.85%. Interestingly, this is much higher than the fracture strain values at  $500^\circ\text{C}$  of 0.27–0.45% found by Crouch and Dooley<sup>33</sup> for sol-gel-deposited silica. It can be surmised from **Figure 5(b)** that the silica layer formed by PAVD remains uncracked, however, even after the  $500^\circ\text{C}$  temperature rise, since there is continued oxidation protection. It implies that the PAVD structure either contains fewer crack-like defects and, hence, has higher intrinsic ductility than the sol-gel equivalent or that creep processes at the oxidation temperature relax stresses at crack tips and, again, increase ductility.

Eventual degradation of the amorphous silica layer is associated both with its transformation to the crystalline state ( $\alpha$ -cristobalite) and with reaction with cations from the alloy.<sup>34</sup>

### 1.27.3.2 SMART MCrAlY Overlay Coatings

The compositions of current MCrAlY coatings (**Table 2**) reflect a compromise between the need to provide protection against low-temperature Type-II hot corrosion and intermediate-temperature oxidation

and the need to protect against Type-I hot corrosion and high temperature oxidation. In the former case, high chromium levels and chromia protective layers are optimum whereas, in the latter case, high aluminum concentrations and protective alumina layers are more effective.<sup>7,39</sup> These coatings respond reasonably but not as well as coatings designed for specific local conditions of temperature and environment within, say, a large land-based gas turbine. Furthermore, the range of protection afforded by these coatings is limited and hampers moves to a more flexible operating regime in which various alternative fuels could be employed, for example, ranging from natural gas through kerosene, diesel oils to gaseous fuels made from coal, biomass, or waste.

*SMART* MCrAlY overlay coatings have been designed<sup>40,41</sup> to address this problem of flexibility and also the need to increase fuel efficiency by higher-temperature operation. Under these aggressive conditions, high temperature oxidation and both Type-I and Type-II hot corrosion may be experienced across a single component. The intention is for *SMART* coatings to respond to the local environment and to generate the optimum protective system to it, that is, either a chromia or an alumina layer. The coatings are chemically graded to provide surface layers enriched in aluminum and chromium, respectively, overlying a MCrAlY overlay coating. The structure is shown schematically in **Figure 6**. The

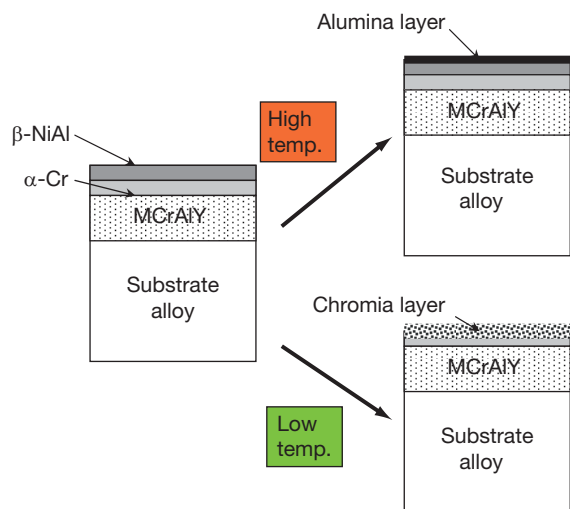


**Figure 6** Schematic diagram of the chemically-graded *SMART* coating structure showing the outer  $\beta$ -NiAl layer and the intermediate Cr-rich zone overlying the base MCrAlY coating. The right-hand figures show the expected response under different oxidation and hot-corrosion regimes.

outer layer consists of  $\beta$ -NiAl produced by aluminizing but before this treatment, the base MCrAlY coating had been pretreated to form an intermediate layer rich in chromium. Manufacturing details of this process are currently proprietary,<sup>41</sup> but it is the presence of this intermediate Cr-rich layer that distinguishes *SMART* coatings from over-aluminized variants, for example, GT33+, currently available.

Under high temperature oxidation or Type-I hot corrosion conditions, the outer layer of the *SMART* coating reacts to form an alumina layer and provide optimum protection. The Cr-rich intermediate layer acts as a diffusion barrier limiting interdiffusion and, particularly, the loss of aluminum from the outer layer into the base coating. Under Type-II hot corrosion conditions, say at 600–800 °C, the outer region of the coating forms an alumina layer sluggishly and is intended to be sacrificed to allow the corrosion front to encounter the intermediate Cr-rich layer at which a chromia protective layer will form. The rate of pitting attack, associated with Type-II corrosion, will then be substantially decreased at this stage.

Extensive testing of these coatings<sup>40,41</sup> under hot corrosion conditions has demonstrated that these concepts do work, as can be appreciated from the

montage of SEM micrographs of cross-sections of corroded specimens shown in Figure 7.<sup>40,41</sup> The test duration in all cases was 500 h in an air–400 vpm SO<sub>2</sub>/SO<sub>3</sub> environment and were recoated every 20 h in an 80% Na<sub>2</sub>SO<sub>4</sub>/20% K<sub>2</sub>SO<sub>4</sub> eutectic mix. Figure 7 shows a comparison of a *SMART* coating variant (SmC 155H) with a Pt-aluminized diffusion coating (RT22) and an over-aluminized CoNiCrAlY overlay coating in the as-produced condition and after testing at 700 and 800 °C. It can be seen that both commercial coatings have been severely corroded at both temperatures whereas the *SMART* variant is relatively unaffected at 800 °C and shows penetration only through the outer aluminized layer at the lower temperature.

### 1.27.3.3 Diffusion Coatings

#### 1.27.3.3.1 Basic types

Diffusion coatings are formed by direct interaction of the substrate alloy with elements, typically chromium, aluminum, and silicon, which are capable of forming protective oxide layers. Typically, coatings are produced through either immersion in a cementation-type pack or by vapor transfer of the

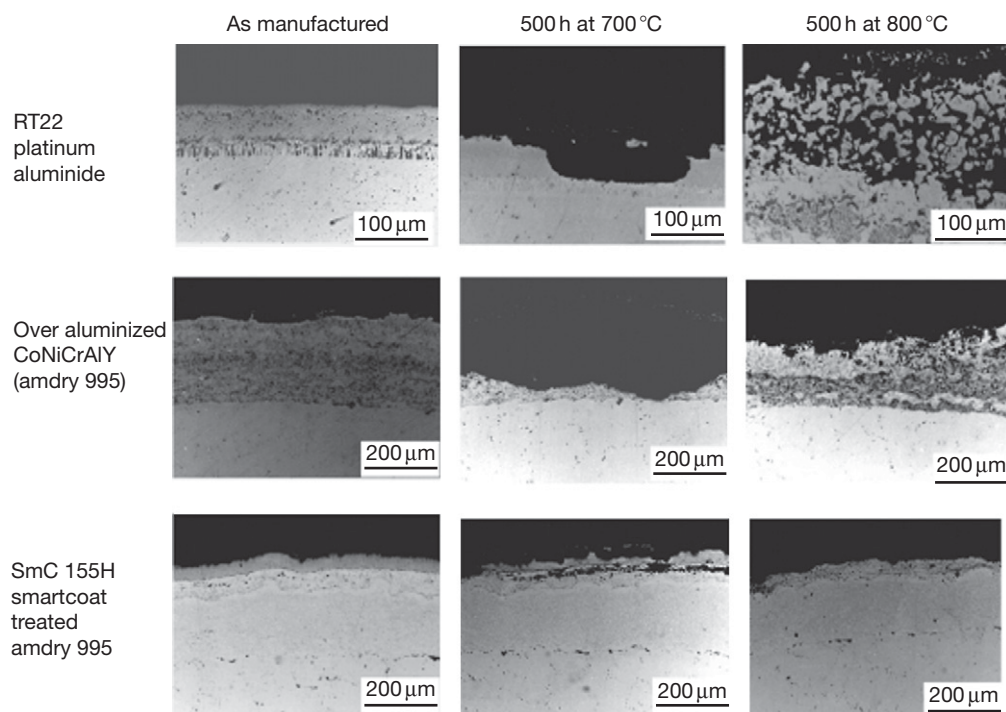


**Figure 7** Comparison of the corrosion morphology of a *SMART* coating variant with a RT22 (platinum-aluminide) coating and an over-aluminized MCrAlY coating.<sup>41</sup> See text for further details.

active species to the component remote from the pack at temperatures where concurrent diffusion in the alloy develops the coating layer. Details can be found elsewhere.<sup>13–18</sup> Unlike overlays, diffusion coatings produced by these methods have limited flexibility to vary composition, although it is possible to codeposit more than one reactive species, for example, Al/Cr,<sup>42</sup> Al/Si,<sup>43</sup> and Cr/Si<sup>44</sup> and to use predeposited layers, for example, platinum, to vary coating structure.<sup>45</sup> More flexibility with regard to coating composition can be achieved through the use of a slurry of reactive species, which can be painted or sprayed onto a work piece and subsequently diffusion annealed. By repetition of this process, multilayered coatings can be produced.<sup>46</sup> Important examples include Cr–Si- and Al–Si-rich compositions, for example, Sermaloy J and Sermetal 1515.

Chromizing can be used with both iron- and nickel-based alloys to provide protection at moderate temperatures (700 °C) against Type-II hot corrosion and intermediate-temperature oxidation. The concentration of chromium in the alloy surface can be raised to 40–80 wt% and this is sufficient to form a protective chromia layer. Chrome–aluminizing is also used to improve protection, particularly at slightly higher temperatures. It has become the case, however, as temperatures increase in the pursuit of improved fuel efficiency, that more attention has been paid to the production of aluminide layers and the subsequent formation of alumina protective layers.

### 1.27.3.3.2 Aluminide coatings

Important applications of aluminide coatings arise in the protection of Co- and, particularly, Ni-based superalloys, since both form aluminide phases which fix high concentrations of aluminum as a surface layer, typically 30–70  $\mu\text{m}$  thick. The coatings can be produced from packs of either high or low aluminum activity. The former is processed at lower temperatures and the latter at higher temperatures in the typical range 800–1100 °C. High-activity aluminizing results in the formation of a  $\text{Ni}_2\text{Al}_3$  layer produced predominantly by inward diffusion of aluminum. Constituents of the alloy can become incorporated within this layer, which has relatively poor toughness. Improvements result in subsequent heat treatment to convert the higher aluminide to  $\text{NiAl}$ . Low-activity processing results directly in the formation of a  $\text{NiAl}$  layer, which forms principally by the outward diffusion of nickel. This layer is then relatively free of alloy constituents (but can contain pack residues

unless formed by vapor deposition above pack) and exists over a wide range of stoichiometry<sup>47</sup> as shown schematically in Figure 1. These coatings provide good resistance to Type-I hot corrosion and to high temperature oxidation through the formation and maintenance of a protective alumina layer. Their disadvantage is that they are relatively thin and, although having higher aluminum contents than the thicker MCrAlY overlay coatings, have a smaller total reservoir of aluminum. Loss of aluminum through the oxidation process as well as by interdiffusion with the substrate alloy limits their effectiveness after extended periods at high temperatures, say >1050 °C.

A particularly successful modification to aluminide coatings has been the incorporation of platinum into the coating by deposition of a thin layer,  $\sim 10\ \mu\text{m}$  thick, prior to the aluminizing stage. The  $\beta$  layer which is formed, again  $\sim 50\ \mu\text{m}$  thick, has the composition (Ni, Pt)Al with platinum contents of  $\sim 8\ \text{at.}\%$ . This phase can also exist over a wide range of aluminum and platinum contents.<sup>47</sup> The microstructure of such a coating is shown in the as-received condition in Figure 8(a) as a bondcoat (BC) within a thermal

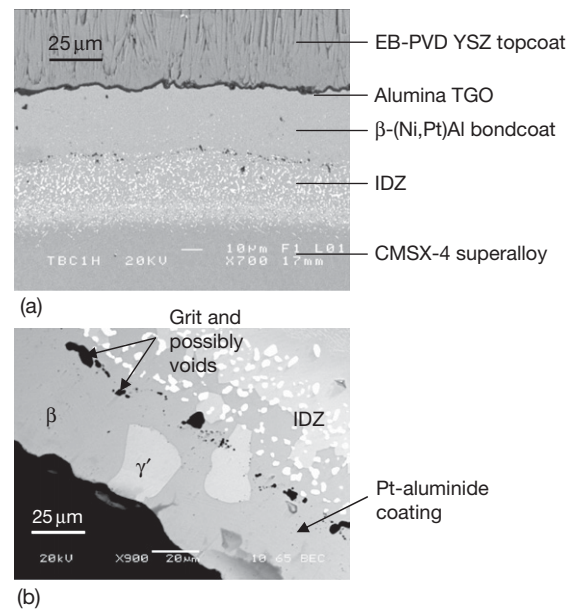
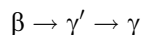


**Figure 8** Cross-section of Pt-aluminide diffusion coatings. (a) In the as-received condition as a bondcoat (BC) in a TBC system showing the fully  $\beta$ -(Ni, Pt)Al layer and an extensive interdiffusion zone (IDZ) and (b) after 100h oxidation at 1100 °C showing partial transformation of the original  $\beta$  phase to  $\gamma'$  resulting from aluminum depletion. Courtesy of Miss F. Schenach.



barrier coating (TBC) system, which will be described later. It can be seen that there is also an extensive interdiffusion zone beneath the  $\beta$  layer. This contains a dispersion of phases rich in alloy constituents such as tantalum and titanium.

The addition of platinum to the  $\beta$ -phase appears to improve the oxide spallation resistance of the coatings, possibly by decreasing the segregation of sulfur to the oxide–metal interface.<sup>48,49</sup> It also decreases the chemical activity of aluminum<sup>47</sup> and then should be expected to decrease the extent of aluminum loss by interdiffusion with the substrate alloy. The experimental evidence is ambiguous, however, because platinum additions also seem to increase the principal diffusion coefficient of aluminum.<sup>47</sup> Continued exposures at high temperature will inevitably result in aluminum depletion as a consequence of both alumina formation and interdiffusion and this will cause phase transformation within the coating along the sequence



An example of a Pt-aluminized coating with partial transformation to the  $\gamma'$  phase after oxidation at 1000 °C for 100 h is shown in **Figure 8(b)**. It should be noted, though, that both phases have adequate aluminum contents to maintain a protective alumina layer.

### 1.27.3.3.3 Platinized coatings

An important variation on the conventional Pt-aluminized coatings described above is to omit the aluminizing stage in coating manufacture but to retain the step of platinum deposition and subsequent inward diffusion into the Ni-based superalloy. This approach was patented in 1999 by Rolls-Royce and Chromalloy UK<sup>50</sup> and has subsequently been developed to the stage of commercial deployment as BCs in TBCs – see later text for a description of these. Unfortunately, few of the results of the underlying research work supporting this development have appeared in the open literature.<sup>51,52</sup>

The key requirement of the coating is that it should be capable of forming and maintaining a protective alumina layer. It is not intuitively obvious, however, that this should be so because no aluminum is added and, as is recalled from **Section 1.27.1 and 1.27.2**, the Ni-based superalloy has borderline properties in this respect. Nevertheless, a 50- $\mu\text{m}$ -thick  $\gamma/\gamma'$  surface zone of enhanced aluminum concentration is formed indicating that there must be an outward

flux of aluminum from the alloy into this zone. Concentrations of aluminum in the Ni–Al–Pt coating need to be  $\sim 10$  wt%, that is, approximately twice the base alloy concentration, to stabilize the  $\gamma/\gamma'$  phase structure at 1100 °C.<sup>47</sup> The likely range of aluminum contents within the coating, shown schematically in **Figure 1**, is similar to that of MCrAlY coatings and will be sufficient both to form an initial alumina layer and to reheal this in the event of its failure (**Figure 2**). The apparent ‘uphill’ diffusion of aluminum out of the alloy into the coating, that is, its diffusion against its concentration gradient, can be explained again by the strong bonding between platinum and aluminum. It must mean that the chemical activity of aluminum within the coating is lower than that within the alloy so that the enrichment within the coating is simply a consequence of aluminum diffusing down its activity gradient. As recognized,<sup>47</sup> the coating has a replenishing capability by being able to transfer aluminum into itself from the alloy, as the continued growth of the alumina layer removes aluminum from its outer surface.

### 1.27.3.3.4 Silicide diffusion coatings

Silicide coatings have the potential of offering significant improvements in oxidation and hot corrosion resistance through the formation of a protective layer of silica. Siliconizing of iron and simple carbon steels was achieved by Fitzer in 1954<sup>53</sup> using pack cementation. These coatings were found to improve resistance to both Type-I and Type-II hot corrosion. They consist principally of an outer layer of ferrite containing up to  $\sim 10$  wt% Si and are susceptible to cracking during mechanical and thermal loading.<sup>54</sup> Silicon-rich coatings on Ni-based alloys have been achieved using chemical vapor deposition (CVD)<sup>55</sup> but there are concerns with the Ni–Si system over the presence of relatively low melting temperature eutectics. NiSi, in particular, forms an eutectic with Ni<sub>2</sub>Si which melts at 943 °C. More attractive approaches for iron- and nickel-based alloys are likely to involve the incorporation of silicon into chromized or aluminized layers.<sup>36,56</sup>

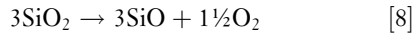
Direct reaction of silicon with the alloy substrate to form a high melting-point surface layer is of particular interest with molybdenum-,<sup>57</sup> niobium-,<sup>58</sup> and titanium-based<sup>57,59–62</sup> alloys. The last, in particular, are of current relevance in aeroengines because of their good density-compensated creep properties but are handicapped by poor long-term oxidation resistance.

A wide range of titanium silicides can be produced in sequential layers on the alloy surface by using a

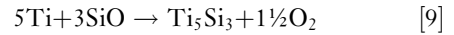


cementation pack, as shown by Cockeram and Rapp.<sup>57,61</sup> These coatings can be  $\sim 100\text{ }\mu\text{m}$  thick and substantially improve oxidation resistance, particularly when doped with germanium when oxidation rates in the temperature range  $700\text{--}1000\text{ }^\circ\text{C}$  are similar to those for the growth of silica itself (Figure 9). Protection is maintained even under thermal cycling but the layers are brittle and cracking should be expected. This is accentuated by the thickness of the coating which increases the probability of crack-like initiating defects being present.

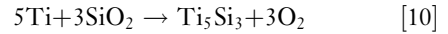
Thinner coatings ( $\sim 1\text{--}10\text{ }\mu\text{m}$ ) can be produced by siliconizing, in which the test piece is buried in silicon powder, at temperatures between  $800$  and  $1100\text{ }^\circ\text{C}$ .<sup>59,60</sup> Higher temperatures in this range favor the formation of the  $\text{Ti}_5\text{Si}_3$  phase rather than  $\text{TiSi}_2$  as the outermost layer produced in the cementation pack.<sup>57,61</sup> These thin  $\text{Ti}_5\text{Si}_3$  layers were uncracked and the layers again conferred significant improvements in oxidation resistance of the underlying Ti-rich alloy, as can be appreciated from Figure 9. A rather novel approach<sup>62</sup> to producing a thin,  $1\text{--}2\text{ }\mu\text{m}$ , layer of  $\text{Ti}_5\text{Si}_3$  is to use reaction (B) below to transport silicon to a Ti–Al test piece *via* gaseous SiO.



The subsequent reaction [9] produces the silicide:



The overall reaction is



This reaction will only proceed in the direction shown at low oxygen partial pressures, calculated by Gray *et al.*<sup>62</sup> at  $7.7 \times 10^{-22}$ . This seems to have been achieved in a sealed silica capsule, evacuated from an argon atmosphere, without the use of extraneous oxygen getters, such as titanium chips, but by using the  $\alpha_2$  phase of the alloy as an intrinsic getter. As with the above, a substantial improvement in oxidation resistance, a factor 5 in weight gain in this case, was achieved over the uncoated Ti–Al control over the test duration of 500 h at  $900\text{ }^\circ\text{C}$ . The parabolic rate constants of the more protective coatings are plotted in Figure 9 and compared with the behavior of unalloyed titanium<sup>63</sup> and pure silicon.<sup>64</sup> It can be seen that only the Ge-doped coatings actually achieve the level of protection expected of a pure silica layer.

Broadly similar behavior to the  $\text{Ti}_5\text{Si}_3$  coatings has been found by Taniguchi *et al.*<sup>65</sup> for the bulk phase. In this case, rutile ( $\text{TiO}_2$ ) had formed above the silica layer and clearly contributed to the weight

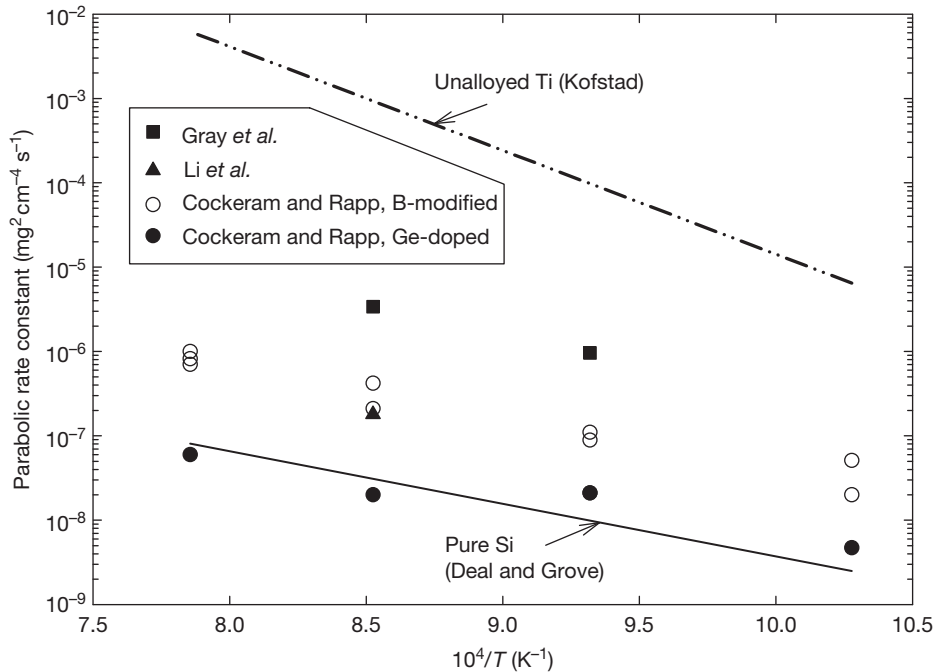


**Figure 9** Parabolic rate constants for some silicide-coated titanium-rich alloys compared with the behavior of unalloyed titanium and silicon.

gain of the specimen. An implication is that the beneficial influence of Ge-doping (Figure 9) arises by limiting the transport of titanium through the silica layer.

### 1.27.3.4 Thermal Barrier Coatings

When discussing the need for high temperature coatings in Section 1.27.1, emphasis on placed solely on achieving adequate oxidation and corrosion resistance. However, under modern turbine conditions and in other applications, such as diesel engines, it can also be necessary to protect the substrate alloys from combustion temperatures by means of TBCs. This developmental trend for aeroengines and associated Ni-based superalloys is shown in simplified form in Figure 10.

It can be seen how in the first 20 years or so, blade alloys had adequate properties in the wrought and unprotected form to satisfy turbine requirements. In the early 1960s, a significant change in blade design permitted the use of some intake air to provide cooling and this increased the turbine entry temperature (TET) significantly above the inherent capabilities of the substrate alloys. During this period from 1940 to approximately 1990, successive generations of superalloys were developed with improved mechanical properties and, hence, higher temperature capabilities. This has been shown simply as a linear trend in Figure 10 but more details can be found elsewhere.<sup>1</sup> The main change during this period was to move from wrought to cast, directionally-solidified structures.

The most recent development is the use of cast, single-crystal alloys, such as CMSX-4 (see Table 1), for blades which remain cooled and also are now coated with TBC systems. The use of these can improve engine efficiency and can also extend service lifetimes.<sup>66,67</sup> This same general developmental trend is mirrored in land-based turbines although TETs in these cases tend to be lower and the moves toward TBC usage lag behind those of aeroengines. A cross-section of a typical TBC system is shown schematically in Figure 11.

A TBC system consists of the outer thermal barrier topcoat which is attached to the alloy substrate by means of a mechanically-compliant, oxidation-resistant BC. The topcoat is generally zirconia, containing ~7–8 wt% yttria. This addition provides partial stabilization of the tetragonal (and cubic) zirconia phases and avoids the volume changes associated with the formation of the monoclinic phase. This yttria-stabilized zirconia (YSZ) layer (sometimes termed yttria partially stabilized zirconia (YPSZ)) has a low thermal conductivity,  $\sim 1 \text{ W m}^{-1} \text{ K}^{-1}$ , which is approximately an order of magnitude lower than that for alumina. It means that for cooled turbine blades, a temperature drop of perhaps  $150^\circ \text{C}$  can be obtained across a 250–300- $\mu\text{m}$ -thick topcoat during service which provides considerable benefit to the load-bearing capability of the Ni-based superalloy. It needs to be emphasized, however, that the YSZ topcoat is permeable to oxygen and will not provide oxidation protection. This is achieved by means of the BC which is intended to be alumina-forming and can be based on

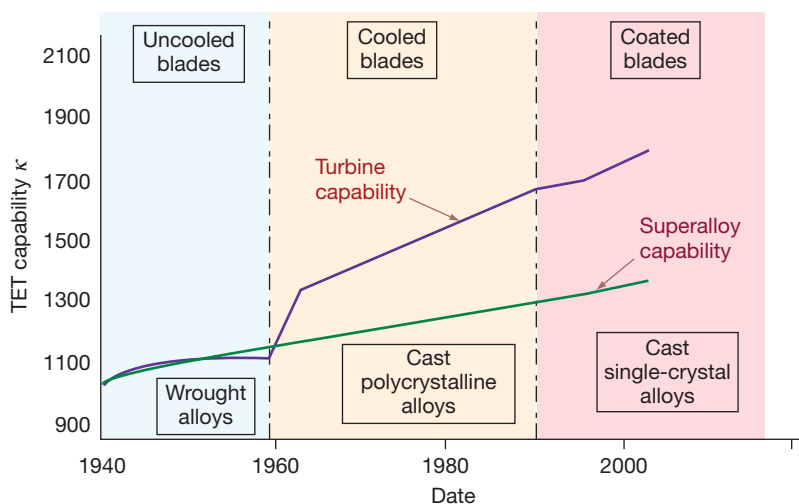


**Figure 10** A comparison of the historical increase in turbine entry temperature (TET) for aeroengines and the associated temperature capability of the alloys used for turbine blades.

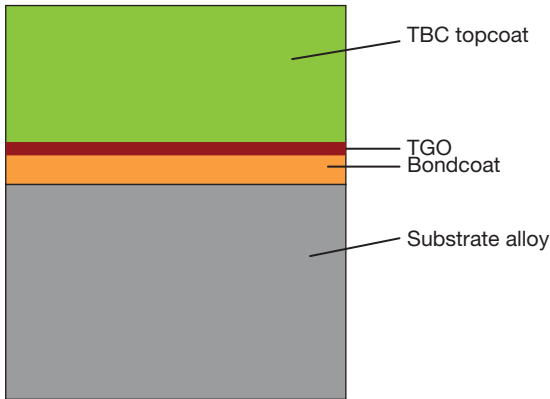


**Figure 11** Schematic cross-section of a thermal barrier coating system.

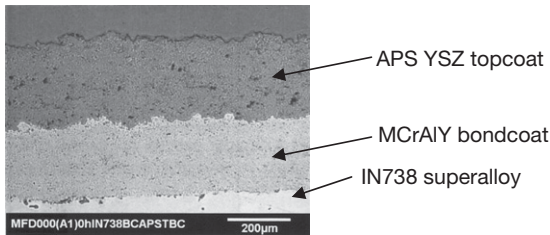


**Figure 12** Cross-section of a typical land-based TBC coating system consisting of an air plasma sprayed (APS) YSZ topcoat with a MCrAlY BC<sup>68</sup> on an IN738 Ni-based superalloy substrate. Note the relatively rough BC surface and the limited interdiffusion zone compared with the TBC system shown in Figure 8(a).

one of the MCrAlY overlays discussed previously or on diffusion coatings of the Pt-aluminide or platinized variants. The oxidation of these BCs forms a layer of thermally grown oxide (TGO) over time between the BC and TBC topcoat as shown schematically in Figure 11. As will be discussed in some depth in Section 1.27.5, the formation of the TGO plays a significant role in the failure by spallation of the TBC.

TBC systems used in practice on Ni-based superalloys for turbine applications tend to be of two distinct types. For large, land-based units, a system consisting of a MCrAlY BC, deposited by any of the processes discussed previously, with a YSZ topcoat produced by APS is usually used. An example of this system is shown in Figure 12. In smaller machines, such as aeroengines or, increasingly, small land-based turbines, YSZ layers deposited by electron-beam physical vapor deposition (EB-PVD) are favored. These TBC systems can use MCrAlY BCs also but more typically have Pt-aluminide or, in Rolls-Royce

aeroengines, platinized diffusion coatings. A typical cross-section of a system consisting of an EB-PVD topcoat and a Pt-aluminide diffusion BC is shown in Figure 8(a). The columnar nature of the EB-PVD topcoat is evident and can be contrasted with the splat structure of that produced by APS. A much more extensive interdiffusion zone than in the MCrAlY system is also formed during coating manufacture.

To date, the commercial exploitation of TBC systems has been dominated by applications using Ni-based alloys but there is also foreseeable potential for their use on other high temperature structural materials such as the Ti–Al series. Significant progress has already been made in the production of aluminide diffusion coatings on Ti-based alloys<sup>69–71</sup> and recently these have been used as a BC under an APS YSZ topcoat in a TBC system.<sup>72</sup>

## 1.27.4 Case Study I: Oxidation and Lifing of MCrAlY Overlays

### 1.27.4.1 Protective Oxidation

In the initial stages of exposure of a complex alloy such as the (Ni, Co)CrAlYs, all constituents which can oxidize will do so and nonprotective oxides such as NiO together with spinels such as NiCr<sub>2</sub>O<sub>4</sub> are likely to form. Eventually, however, a continuous  $\alpha$ -alumina layer will develop underneath these oxides and oxidation rates will rapidly decrease. The formation of metastable aluminas, even at the relatively low temperature of 950 °C, was not found in a study<sup>73</sup> using *in situ* high temperature XRD on a CoNiCrAlY coating. This transitional behavior may not be an issue with these systems at relevant operating temperatures although with FeCrAlY alloys at the slightly lower temperatures of 900 and 925 °C, the transition from  $\theta$ - to  $\alpha$ -alumina took tens of hours.<sup>74</sup>

The growth kinetics of the  $\alpha$ -alumina layer on MCrAlY-type alloys have been variously reported to be parabolic (eqn. [1])<sup>75,76</sup> or subparabolic<sup>77</sup> as in the general eqn. [11] for increase in oxide thickness,  $b$ , with exposure time,  $t$ , at a constant temperature.

$$b = b_0 + k_n t^{1/n} \quad [11]$$

Here,  $b_0$  is the preexisting oxide thickness at  $t = 0$ ,  $n$  is a time-invariant numerical constant, and  $k_n$  is the corresponding rate constant. Ideal parabolic conditions exist when  $b_0 = 0$  and  $n = 2$  (eqn. [1]) but subparabolic kinetics obtain when  $n > 2$ . The reasons for the differences in kinetics are poorly understood

although there are considerable implications for the longevity of the coatings. Subparabolic kinetics can arise, in principle, as a result of an increase with time of compressive growth stress within the oxide layer.<sup>38,78</sup> They will also arise<sup>79</sup> if oxide grain size increases during exposure and diffusion of reactive species occurs principally by grain boundary diffusion. It is also feasible, particularly with a stoichiometric compound such as alumina, that the gradual incorporation of coating or alloy (minor) constituents affects any doping of the oxide layer so as to decrease diffusion rates progressively with time. Apparent subparabolic kinetics will also occur in those systems and exposure conditions in which metastable alumina forms and transforms over time to the  $\alpha$  phase.<sup>80</sup> The situation is unclear and, for present purposes, it will be assumed that the  $\alpha$ -alumina layer grows parabolically with time with  $h_o = 0$  and  $n = 2$  in eqn. [11]. This assumption leads to conservative estimates of coating lifetimes.

The temperature dependence of the parabolic rate constant for the growth of a protective  $\alpha$ -alumina layer on various coating-type alloys is shown in Figure 13,<sup>75,76</sup> but expressed in terms of mass gain,  $\Delta m$ , per unit surface area. A reasonable mid-range expression for the rate constant,  $k'_p$ , from Figure 13 is

$$k'_p = 2.68 \times 10^4 \exp\left(-\frac{275\,000}{8.314T}\right), \text{mg}^2 \text{cm}^{-4} \text{s}^{-1} \quad [12]$$

where  $T$  is absolute temperature and the mass gain has been expressed in the more common units of  $\text{mg cm}^{-2}$ . This equation can be expressed in terms of the parabolic rate constant  $k_p$ , which uses oxide thickness rather than mass gain, by means of eqn. [13].

$$k_p = \left[ \frac{M_{\text{ox}}}{3M_o\rho_{\text{ox}}} \right]^2 k'_p \quad [13]$$

Here,  $\rho_{\text{ox}}$  is the density of  $\alpha$ -alumina (taken as  $4000 \text{ mg cm}^{-3}$ ),  $M_{\text{ox}}$  is the molecular mass of alumina and  $M_o$  is that of oxygen; the factor three arises because there are three oxygen atoms in  $\text{Al}_2\text{O}_3$ . This conversion equates  $1 \text{ mg cm}^{-2}$  mass gain to an  $\sim 5.3 \mu\text{m}$  thick layer of  $\alpha$ -alumina. Using eqn. [13] to substitute into eqn. [12] then gives:

$$k_p = 7.56 \times 10^{-7} \exp\left(-\frac{275\,000}{8.314T}\right) \text{m}^2 \text{s}^{-1} \quad [14]$$

The protection offered by the alumina layer can be appreciated by using eqn. [14] in eqn. [1] to show that the oxide thickness after 30000 h at  $1000^\circ\text{C}$  is still only  $\sim 20 \mu\text{m}$ . This corresponds to a section loss,  $x_h$ , of the coating of<sup>38</sup>

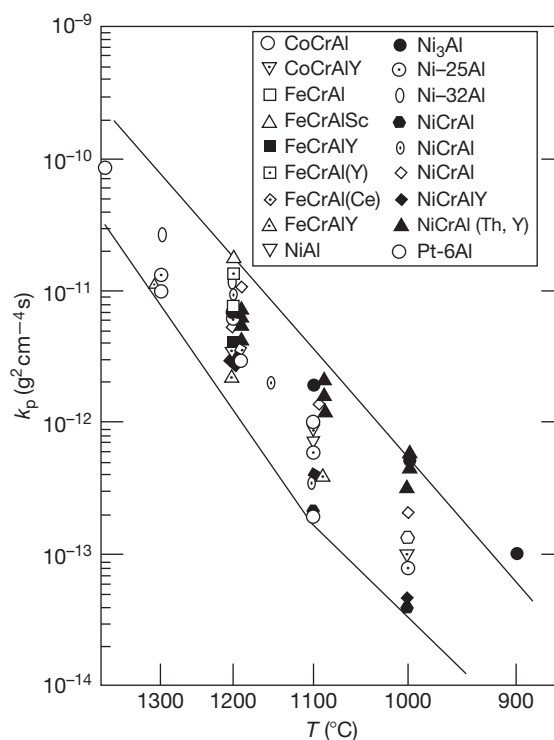


**Figure 13** Parabolic rate constants for the formation of alumina on coating-type alloys.<sup>76</sup>

$$x_h \approx \frac{b}{\phi} \approx \frac{20}{1.28} \approx 15.6 \mu\text{m} \quad [15]$$

where  $\phi$  is the Pilling–Bedworth ratio for alumina (1.28). This level of loss in an MCrAlY coating some  $200 \mu\text{m}$  thick after this exposure period would be excellent behavior but, unfortunately, other degradation processes also occur which limit lifetimes. Principal among these is the loss of aluminum from the coating and the consequences of this. Depletion will occur as a result of selective oxidation, as described in Section 1.27.2.2, and will increase with time at temperature. In addition, it will be exacerbated by spallation or cracking (and rehealing) of the protective oxide layer, geometrical factors, internal oxidation, and interdiffusion with the substrate alloy. All of these factors will be considered in this section.

#### 1.27.4.2 Spallation and Cracking of the Protective Alumina Layer

Spallation and cracking of the protective oxide layer results from the generation of strains and associated stresses arising from the oxide growth process,

from temperature changes or imposed upon the component. The issues are particularly complex since they depend on the nature of the oxidation process (the balance between growth by cation or anion fluxes), on the curvature of the substrate and on the elastic, plastic and, particularly, creep properties of the respective layers of the coating system. A background review is available<sup>38</sup> and phenomenological approaches to failure which combine strains from multiple sources have also been developed.<sup>81–83</sup> These predictive approaches have been formulated specifically for TBC systems but contain general principles.

This chapter emphasizes solely the influence of thermal strains in producing oxide spallation from a MCrAlY substrate in order to establish mechanisms. Strains deriving from oxide growth will be significant only if creep relaxation rates are low or, on curved surfaces, if the oxide thickness is of similar magnitude to the local radius of curvature.<sup>38</sup> For now they are neglected but, if significant, can simply be introduced as an additive term.<sup>82</sup> The implication is that the alumina–MCrAlY interface is sensibly flat, that is, there are no locations where the local radius of curvature is of similar magnitude to the oxide thickness. During cooling there are then negligible out-of-plane strains, provided the oxide remains adherent, but a substantial biaxial compressive in-plane strain can develop within the oxide layer. If elastic conditions are assumed, this strain corresponds to an in-plane oxide stress,  $\sigma_{ox}$ , given by<sup>84</sup>:

$$\sigma_{ox} = \frac{E_{ox} \Delta T (\alpha_m - \alpha_{ox})}{(1 - \nu) \left(1 + \frac{E_{ox} b}{E_m w}\right)} \quad [16]$$

Here,  $\Delta T (=T - T_{ox})$  is the temperature drop, taken as a negative quantity,  $E_{ox}$  and  $E_m$  are the Young's moduli of, respectively, oxide and metal;  $\alpha$  is the corresponding linear thermal expansion coefficient;  $\nu$  is the Poisson's ratio, assumed to be the same for oxide and metal;  $b$  is the oxide thickness, and  $w$  is half the specimen thickness. For thin oxides

relative to the metal substrate, the equation can be simplified to (compare eqn. [7]):

$$\sigma_{ox} = \frac{E_{ox} \Delta T (\alpha_m - \alpha_{ox})}{(1 - \nu)} \quad [17]$$

It is also reasonable to assume that the underlying superalloy is much thicker than the coating and, of course, the oxide so that the alloy's dimensional changes are imposed upon the oxide. This means that in eqn. [17], the expansion coefficient,  $\alpha_m$ , should be that for the superalloy rather than for the coating. Using representative values of,  $\nu = 0.3$ ,  $E_{ox} = 387$  GPa,  $\alpha_{ox} = 7.9 \times 10^{-6} \text{ K}^{-1}$ , and  $\alpha_m = 15.0 \times 10^{-6} \text{ K}^{-1}$  in eqn. [17] predicts a residual in-plane oxide stress of  $\sim -3.9$  GPa after a temperature drop of  $1000^\circ\text{C}$ . Values of stress of this magnitude have been measured in related alloys and coatings.<sup>68,85,86</sup> Since the values of expansion coefficients and Young's modulus are assumed to be independent of temperature, the elastic oxide stress varies proportionately with temperature change and will be tensile for temperature increases above the oxidation temperature.

Spallation under in-plane compression can occur by two nominally distinct routes depending on the relative strengths of oxide and oxide–coating interface,<sup>38,39</sup> as shown schematically in Figure 14. The critical stress for buckling of the oxide layer (Figure 14(a)) can be obtained from standard text<sup>87</sup> and converted<sup>38</sup> to a critical temperature drop,  $\Delta T_b$ , of

$$-\Delta T_b = \frac{1.22}{(1 - \nu^2)(\alpha_m - \alpha_{ox})} \left(\frac{b}{R}\right)^2 \quad [18]$$

where the symbols have the same meaning as previously and  $R$  is the radius of the circular zone of prior decohesion at the oxide–coating interface. It can be appreciated that for a given value of  $R$ , the temperature drop required to effect buckling increases with oxide thickness. For typical values of the various parameters, the zone diameter needs to be approximately at least  $20\times$  the thickness of the oxide layer

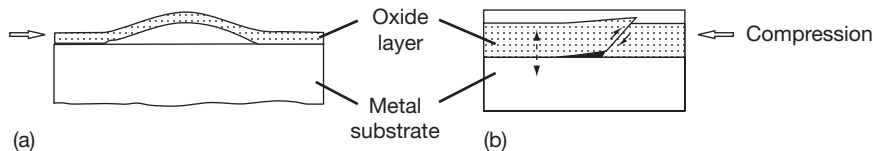


**Figure 14** Spallation of the oxide layer under in-plane compression from the metallic MCrAlY substrate can occur by either (a) a buckling or (b) a wedging process.



before the buckle configuration can develop. Thus, for a typical oxide thickness of 5  $\mu\text{m}$ , a circular interfacial zone of some 100  $\mu\text{m}$  would be required. This is a problematic issue since such large areas of decohesion are not seen at the alumina-MCrAlY interface in these simple overlay coatings. The intrinsically good adherence of the alumina layer is related to the addition of yttrium into these coatings which appears to mitigate the potentially harmful effects of sulfur segregation in lowering interface adhesion.<sup>88,89</sup>

In the presence of good adhesion between oxide and coating, a thick protective layer can develop but this, as found on related systems, still contains porosity and crack-like defects.<sup>90,91</sup> At some critical value of the compressive thermal stress generated during the cooling transient, a shear crack can be initiated from one or more of these defects, as shown schematically in Figure 14(b). Continued cooling and contraction of the oxide layer will produce further shear on the crack-like surface and the development of out-of-plane tensile stresses at the oxide-coating interface. A consequence is that a wedge crack will grow along this interface as cooling continues and may cause spallation of the overlying oxide layer. Extensive finite-element (FE) modeling of this wedging process has now been undertaken for chromia and alumina layers on various metallic substrates.<sup>92–94</sup> A consistent result from this work is that the growth rate of the interfacial wedge crack is significantly retarded during cooling as a result of the relaxation of crack-tip stresses by creep of the adjoining metal. Some results<sup>93</sup> for a 5- $\mu\text{m}$ -thick alumina layer on Haynes 214 are given in Figure 15. They show that the wedge crack nucleates quickly but its growth rate is then stopped until some lower temperature at which rapid propagation occurs over a narrow temperature range. This period of quiescence corresponds to the period of significant stress relaxation by alloy creep and its extent decreases with increased cooling rate, as shown.

The general behavior shown in Figure 15 can be approximated by the dashed horizontal and vertical lines superimposed, for clarity, only on the FE results for a cooling rate of  $10^4\text{ }^\circ\text{C h}^{-1}$ . They can be interpreted as showing that the oxide remains adherent to the alloy or coating until a critical temperature drop,  $\Delta T_c$ , at which stage the stored strain energy,  $W^*$ , per unit volume in the oxide layer is sufficient to produce decohesion of the oxide-metal interface. For a thin planar biaxially strained oxide layer of thickness  $b$ , the strain energy in the oxide layer per unit area of

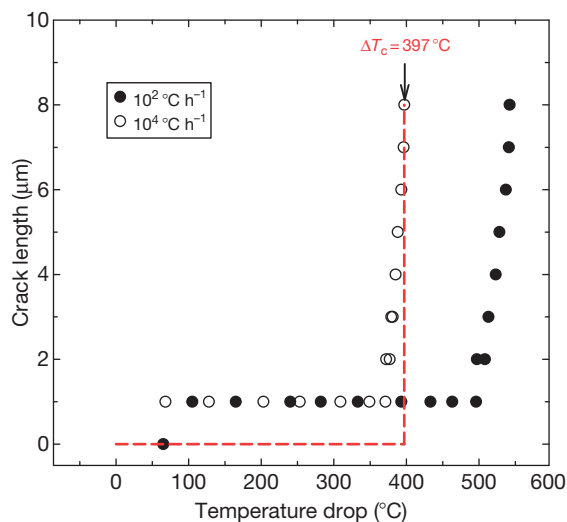


**Figure 15** Finite-element predictions of the kinetics of interfacial wedge crack growth for an alumina layer on Haynes 214 cooled from 1100  $^\circ\text{C}$  at the rates shown. The dashed line reflects ideal behavior for spallation to occur at a critical value of oxide strain energy.

oxide-metal interface at a temperature drop  $\Delta T$  is given as<sup>95</sup>:

$$bW^* = bE_{\text{ox}}(1 - \nu)(\Delta T)^2(\alpha_m - \alpha_{\text{ox}})^2 \quad [19]$$

Equating this to the fracture energy,  $\gamma_F$  of unit area of interface gives the critical temperature drop for spallation as:

$$-\Delta T_c = \left[ \frac{\gamma_F}{bE_{\text{ox}}(\alpha_m - \alpha_{\text{ox}})^2(1 - \nu)} \right]^{1/2} \quad [20]$$

This shows that the critical temperature drop decreases with oxide thickness, that is, spallation becomes easier for thicker oxides which is a common observation. It contrasts with the buckling mode (eqn. [18]) which becomes more difficult with increasing oxide thickness.

In applying eqn. [20] for prediction it should be noted that the fracture energy is an effective value since most of the strain energy is lost by creep relaxation during the cooling transient.<sup>92–94</sup> Its value can be obtained from eqn. [20] using the FE predictions of  $\Delta T_c$  and is always larger than the intrinsic fracture energy of the interface when relaxation processes are present. Thus, for the example shown in Figure 15,  $\gamma_F$  is calculated to be  $\sim 33\text{ J m}^{-2}$  for the higher cooling rate and  $\sim 62\text{ J m}^{-2}$  for the lower. Using a similar approach for a free-standing NiCrAlY coating,<sup>93</sup> the values of the effective fracture energy shown in

**Table 3** Estimated effective fracture energies,  $\gamma_F$ , for the spallation of a 5- $\mu\text{m}$ -thick alumina layer from a free-standing NiCrAlY coating<sup>92</sup>

Cooling rate ( $^{\circ}\text{C h}^{-1}$ ; $^{\circ}\text{C s}^{-1}$ )	Computed $\Delta T_c$ ( $^{\circ}\text{C}$ )	$\gamma_F$ ( $\text{J m}^{-2}$ )
$10^2$	745	40
$10^3$	620	28
$10^4$	550	22
$10^5$	382	10
$10^6$	314	7

**Table 3** are obtained as a function of cooling rate. This decrease of  $\gamma_F$  with increasing rate reflects the decreased contribution from creep relaxation and shows that no unique value of the fracture energy can be assumed. It is possible, however, to interpolate between these results for any given conditions within the range shown. The values of  $\gamma_F$  given in the table are typically 10–100 greater than the likely intrinsic interfacial fracture energy but are of similar magnitude to those measured by blister testing<sup>96</sup> and spallation<sup>93,94,97,98</sup> on other systems.

This discussion has highlighted the benefits of stress relaxation within the coating to the spallation resistance of the oxide during a simple cooling transient. It should not necessarily be generalized from this, however, that weak coatings should be preferred over strong. An important consideration is that creep relaxation during thermal cycling can generate a mechanical hysteresis loop<sup>94,99</sup> which can place the oxide layer into in-plane tension on the return to temperature. Consequent tensile cracking will, of course, impair the protective function of the oxide layer. Strong coatings are also desirable to maintain mechanical stability in rapidly rotating components. The balance of creep properties between high and low strength will depend on the application, for example, the magnitude of external stresses, the frequency of thermal cycling, the rate of change of temperature, and the presence of hold periods within the creep regime.

### 1.27.4.3 Aluminum Depletion

#### 1.27.4.3.1 Uniform depletion

The second main form of coating degradation is through the loss of aluminum and the consequent inability to maintain and reform the protective alumina layer. A general discussion of the depletion occurring as a result of the selective oxidation of aluminum has been given in [Section 1.27.2.2](#). It is

shown in that section, how the aluminum concentration can be decreased beneath the oxide but that the aluminum reservoir within the bulk of the coating could maintain concentrations sufficiently to ensure reformation of the alumina layer in the event of its spallation or cracking. Nevertheless, the depletion of aluminum by selective oxidation will destabilize Al-rich phases in the vicinity of the surface oxide. In particular, dissolution of the  $\beta$ -NiAl phase will occur in a zone near the alumina layer<sup>100,101</sup> and, as expected for parabolic oxidation kinetics, the depth of this  $\beta$ -free zone will thicken parabolically with time. In addition, loss of aluminum by interdiffusion with the substrate can also result in the formation of a  $\beta$ -free zone at this inner interface. With continued exposure, the entire coating can become free of the  $\beta$ -phase and this has been used as a failure condition for the coating.<sup>100</sup> This is a useful pragmatic approach but is conservative since sufficient aluminum will usually still be present to provide a rehealing capability.

Even so, substantial exposure periods can be obtained while still retaining some  $\beta$ -phase. Anton *et al.*,<sup>101</sup> for example, find a total  $\beta$ -depletion zone, from inner and outer coating surfaces, of 160  $\mu\text{m}$  in a 250- $\mu\text{m}$ -thick LPPS CoNiCrAlY coating after 10000 h at 1000  $^{\circ}\text{C}$ . This particular coating contained only 8 wt% Al but exhibited substantial interdiffusion with the IN738LC alloy substrate and formation of Kirkendall voids within the interdiffusion zone (IDZ). The extent of  $\beta$  depletion was decreased, as expected, by increasing the aluminum content to 12 wt% in a NiCoCrAlY coating but rhenium additions also decreased the extent of interdiffusion. In this case the total  $\beta$ -depletion zone was only  $\sim 75 \mu\text{m}$  after 10 000 h at 1000  $^{\circ}\text{C}$ .<sup>101</sup>

Although the extent of aluminum depletion resulting from selective oxidation can be predicted based on the concepts outlined in [Section 1.27.2.2](#), it is much more difficult to model the interdiffusion process. Analytical and numerical attempts have been made for MCrAlY systems<sup>83,102</sup> but it is difficult to deal with diffusion and concurrent precipitation without knowing the appropriate interaction terms for the diffusion coefficients or, equivalently, the chemical activities of the diffusing species. Taylor, *et al.*,<sup>102</sup> for example, report how the diffusion of aluminum from a LPPS CoNiCrAlY coating into a CM186 substrate alloy, in the early stages of exposure at 1200  $^{\circ}\text{C}$ , is limited by the formation of Al-rich phases, associated with tantalum, within the IDZ. With continued exposure and further aluminum

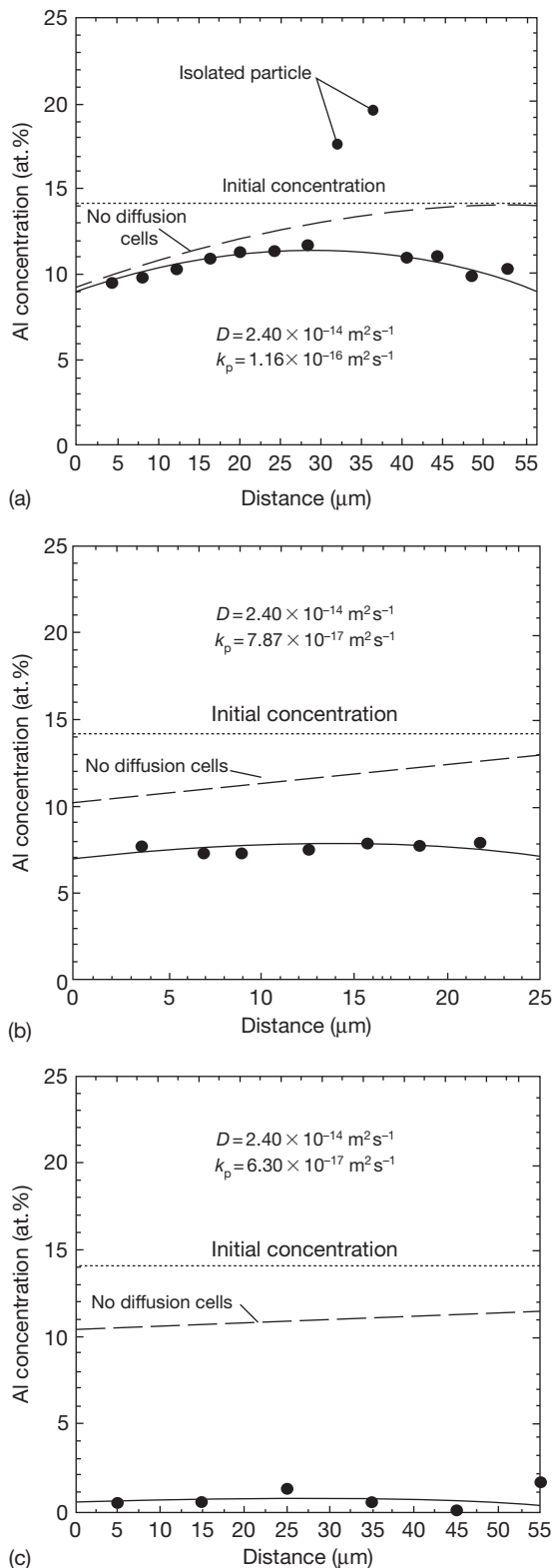


**Figure 16** Enhanced aluminum depletion measured in individual diffusion cells in an APS CoNiCrAlY coating.

depletion within the coating, these phases dissociate and act as a reservoir to resupply aluminum back into the coating. These counter-flows of diffusive flux reflect the changing aluminum activities within the coating and IDZ. They emphasize that, in such complex situations, modeling using single-valued diffusion coefficients and chemical potential gradients approximated by gradients in concentration can lead to erroneous results.

Interesting future developments to limit inter-diffusion are likely to involve the control of aluminum chemical activity within the coating<sup>103</sup> or the use of diffusion barriers such as  $\alpha$ -Cr or Re-based alloys.<sup>104</sup>

#### 1.27.4.3.2 Diffusion cells and chemical failure

In practice, exceptions to the ideal condition of uniform depletion will exist. These include the diffusional isolation of volumes of the coating as a result of internal oxidation or geometric factors. As highlighted in Figure 3, MCrAlY coatings deposited by plasma spraying in air (APS) are of relatively low density as a result of oxidation of the sprayed particles during coating formation. Bonding between the splats within the coating is impaired and internal oxidation at the splat surfaces can continue during subsequent exposure. APS and even HVOF coatings probably also suffer from this but to a lesser extent. The alumina layers formed internally in APS MCrAlY coatings have been shown<sup>105</sup> to act as diffusion barriers which isolate the splat volume from the reservoir of aluminum in the remainder of the coating. As a consequence, aluminum depletion within the relatively small splat volume occurs at a much greater rate than would be expected for the coating as a whole. This is shown in Figure 16 for an APS CoNiCrAlY coating oxidized in air at 1100 °C.<sup>105</sup> Here the measurements of aluminum concentration were obtained across separate diffusion cells which were located at the surface of the coating and bounded around their surface by an alumina layer. The lines in the figures are predictions from eqn. [21] which considers the cell to be approximated as a long 2-dimensional slab, on both flat surfaces on which alumina grows parabolically.

The points are measured using SEM/EDS and the solid line is the best-fit solution to eqn. [21] using the values shown for  $D$  and  $k_p$ . See text for more details. The dashed line is the expected depletion profile, using the same values of  $D$  and  $k_p$ , if diffusion cells were absent. Oxidation was performed in air for (a) 4 h, (b) 4 h, and (c) 100 h.<sup>105</sup>

$$C = C_b - \frac{50}{\phi} \left( \frac{\pi k_p}{D} \right)^{1/2} \sum_{n=0}^{\infty} \left[ \operatorname{erfc} \left( \frac{2nw+x}{2(Dt)^{1/2}} \right) + \operatorname{erfc} \left( \frac{2(n+1)w-x}{2(Dt)^{1/2}} \right) \right] \quad [21]$$

Here,  $C$  is the aluminum concentration in at.%,  $C_b$  is the initial value within the cell,  $D$  is the aluminum interdiffusion coefficient,  $2w$  is the cell width,  $x$  is the distance from the oxide–metal interface, and  $t$  is the exposure time. The predictions were made using a single-valued interdiffusion coefficient  $2.4 \times 10^{-14} \text{ m}^2 \text{ s}^{-1}$  (N.B. the sites were remote from any interdiffusion effects from the substrate) consistent with measurements on NiCrAl<sup>106</sup> and CoCrAl<sup>107</sup> systems. The corresponding  $k_p$  values to give the observed fit vary within a factor 2 but lie within the data spread of Figure 13 (shown there in terms of mass gain). The expected depletion profile without diffusion cells is shown by the dashed line. The agreement with the data is good and confirms that oxidation is continuing at similar rates at both the external and internal surfaces in these coatings. It can be seen that depletion is much more pronounced in the small cell of Figure 16(b) than in the larger one of Figure 16(a) even after 4 h at 1100 °C. After 100 h exposure, aluminum has been essentially consumed in the 55  $\mu\text{m}$  cell, Figure 16(c).

The decrease in aluminum concentration can make these cell volumes susceptible to chemical failure (CF) at which stage fast-growing nonalumina oxides will form. A framework theory of CF can be found elsewhere.<sup>108</sup> The cell will be susceptible to mechanically induced chemical failure (MICF) when the aluminum concentration anywhere within it (usually, at the center plane) falls below that needed to reform the alumina layer should the original crack or spall. Intrinsic chemical failure (InCF), unlike MICF, is a thermodynamic boundary at which the aluminum concentration at the oxide–metal interface falls to that below which alumina can be reduced by another of the coating constituents, chromia for example. This critical concentration is very close to zero for the reduction of alumina by chromium but there is experimental evidence for the formation of Cr-rich oxides beneath an alumina layer in NiCrAlY coatings.<sup>109</sup>

A CF map for MCrAlY coatings can be constructed using eqn. [21] as shown in Figure 17. The calculations were performed using  $D = 2.4 \times 10^{-14} \text{ m}^2 \text{ s}^{-1}$ , as above, and a mid-range value of  $k_p = 9.0 \times 10^{-17} \text{ m}^2 \text{ s}^{-1}$ . The threshold line for

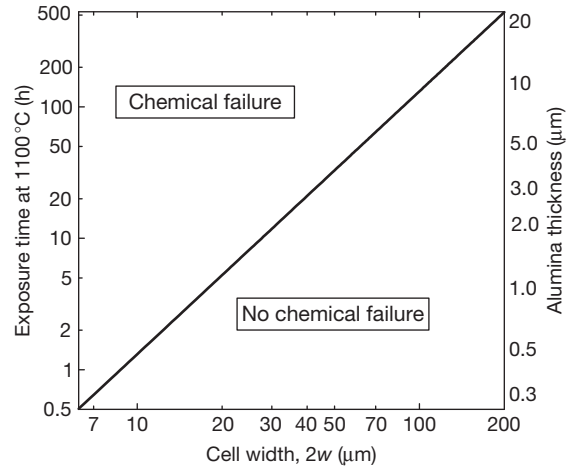


**Figure 17** A chemical failure (CF) map for a MCrAlY coating ( $M = \text{Co, Ni}$ ). The left-hand ordinate refers to exposure times at 1100 °C but the oxide thickness of the right-hand ordinate is independent of temperature.

initiating CF is relevant to the MICF condition assuming a critical aluminum concentration of 5 at.%. The exposure times shown as the left-hand vertical axis refer to 1100 °C but the oxide thicknesses (right-hand axis) apply at other temperatures also. Clearly, small cells are susceptible to early MICF leading to the consumption of the entire cell volume with the formation of porous and friable nonprotective oxides. For dense coatings, however, for example those produced by LPPS, internal oxidation is negligible and small diffusion cells do not form.<sup>110</sup>

MCrAlY coatings produced by spraying tend to have convoluted surfaces consisting of protuberances with dimensions relating to those of the original sprayed particles. They may also be postprocessed to change this topography but usually have a significant residual surface roughness. The significance is that a surface protuberance will have a surface-to-volume ratio larger than that of a flat coating. Aluminum depletion will then occur at an enhanced rate and early CF of the protuberance can be expected. Calculation of the rate of depletion is difficult to undertake analytically because the protuberance is not isolated from the bulk of the coating, as with the diffusion cells discussed earlier. Some resupply of aluminum will occur *via* the neck of the protuberance. Useful progress in prediction can be made, however, using numerical finite-difference methods and an example of some results, obtained using the 2-dimensional ODIN (Oxidation and INterdiffusion) code, is shown in Figure 18. These results apply to a

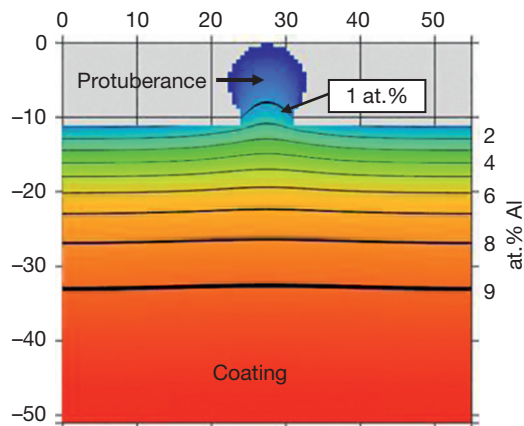


**Figure 18** Finite-difference predictions of the Al depletion produced in a surface protuberance of a MCrAlY coating after oxidation at 1100 °C for 1 h. The left-hand and top axes give distances in microns. The right-hand axis gives the aluminum concentration corresponding to the iso-concentration lines drawn on the figure. Courtesy of Dr. W.M. Pragnell.

100  $\mu\text{m}$  thick MCrAlY coating oxidized at 1000 °C for 1 h but with, for purposes of illustration, a relatively low initial concentration of 10 at.% Al. It can be appreciated that selective oxidation to form the alumina layer causes a significant decrease in aluminum content at the surface of the bulk coating with concentration increasing with distance from this interface. More details can be found elsewhere.<sup>111</sup> This level of depletion is similar to the schematic line for an uncoated alloy, of similar aluminum content, shown in Figure 2. In this particular example, there remains sufficient aluminum at depths of  $\sim 10\ \mu\text{m}$  to reform the protective alumina layer. This contrasts with the situation within the protuberance, however, where concentrations have dropped everywhere to  $< 1$  at.% after 1 h exposure. Early MIF of this is then likely and, indeed, was observed.<sup>111</sup> This failure time is somewhat less but of similar magnitude to that shown for diffusion cells in Figure 17.

## 1.27.5 Case Study II: Oxidation-Induced Failure of TBC Systems

### 1.27.5.1 Failure Times under Oxidizing Conditions

An overview of TBC systems and principal types has been given in Section 1.27.3.4. They are an essential part of present-day strategies to operate high temperature machinery, particularly aeroengines and gas turbines, with increased fuel efficiency and

longevity. In order to achieve this and to develop the full potential of TBC systems safely and reliably, it is necessary to understand and predict the degradation and failure processes within the system leading to spallation of the insulating topcoat. As a consequence, a tremendous amount of research activity has been undertaken worldwide, particularly in the last decade, to try and achieve these goals. At the time of writing, success has been elusive although large amounts of experimental data have been produced and a plethora of theoretical models have been suggested. It is beyond the scope of this present work to provide a detailed and comprehensive review of this large body of work which is often contradictory. Rather, a personal view will be presented which will attempt to identify key experimental observations and materials' properties and favor theoretical models which are consistent with these.

In some applications, for example, on rotating blades in gas turbines, TBC systems will experience mechanically-imposed strains in addition to those developed by the oxidation process. As discussed in relation to MCrAlY overlay coatings (Section 1.27.4.2), it may be feasible to sum these various strains and define a critical total value at which TBC failure will occur.<sup>81–83</sup> The approach is phenomenological in that no detailed mechanisms of failure are considered. It is, therefore, difficult to generalize complex situations where strains may be tensile or compressive and may act in different directions at different locations within the TBC system. Nevertheless, the approach does attempt to address the difficult subject of the interaction between applied external stresses and those produced by oxidation. For present purposes, however, as earlier with MCrAlY overlays, the intention is to examine only the role of oxidation and thermal loading in TBC failure.

It was pointed out in Section 1.27.3.4 that oxygen can penetrate the YSZ TBC layer and oxidize the underlying BC. The TGO, designed to be alumina, forms as an interlayer between the topcoat and BC as shown schematically in Figure 11. The development of this layer has been implicated in TBC spallation for many years and a simple failure criterion, used in practice, is to assume that spallation will occur at a critical TGO thickness. As shown in Figure 19, this can be a useful approach.

The time-to-failure data shown in Figure 19 derive from previous compilations,<sup>112,113</sup> but have been simplified to distinguish only between the common types of TBC system in commercial use: Pt-aluminide/EB-PVD YSZ, MCrAlY/EB-PVD YSZ, and MCrAlY/APS YSZ. Results on experimental



systems, which can show improved behavior to the above, have been omitted from this graph intentionally although they are prominent in current research literature. These include the use of platinum over- and under-layers to MCrAlY BCs,<sup>114</sup> preoxidation of MCrAlY BCs,<sup>115,116</sup> polishing of the BC surface,<sup>117</sup> and platinized BCs<sup>51,52</sup> see also [Section 1.27.3.3.3](#)). This body of work is of interest and may point the way to future improvements in TBC systems. The results have been omitted from [Figure 19](#) simply because they add other variables which will confuse the trends present in the failure-life compilation for conventional systems.

The data shown in [Figure 19](#) include results from tests ranging from nominally isothermal exposure to those using hourly thermal cycles, for which the accumulated time at peak temperature is used in the figure. A striking feature of the results is the very large scatter in lifetime – a factor 10 – at any given temperature. Within this scatter, there appears to be no systematic difference in behavior between the coating types or with the frequency of cycling.<sup>112</sup> This is a valuable working premise with which to find a path through the diverse competing models of failure. The solid line in the figure is the expected behavior if topcoat spallation occurred at a critical TGO thickness of 4  $\mu\text{m}$ . It is calculated from

eqn. [14], assuming an initially bare BC surface. It should be noted, though, that those systems with an EB-PVD topcoat will usually have a preformed alumina layer,  $\sim 0.5 \mu\text{m}$  thick on the BC surface. The agreement with the solid-line prediction is, nevertheless, quite reasonable and supports the use of this simple criterion as a pragmatic lifing method. It also supports the view,<sup>118,119</sup> that time and temperature are the principal parameters affecting lifetimes. The scatter can then be thought of as reflecting the underlying variability in the oxidation process together with the influence of uncontrolled variables, many of which are likely to arise from the manufacturing process. These will include BC surface roughness,<sup>112,113,117</sup> defects within the topcoat which may initiate interfacial cracks,<sup>120</sup> segregation of elements such as titanium from the substrate alloy,<sup>52</sup> and variable sulfur contents, particularly in Y-free BCs and alloys.<sup>91,121</sup>

### 1.27.5.2 Failure Characteristics

The failure times plotted in [Figure 19](#) refer to the loss of typically 20% or more of the area covered by the YSZ topcoat. Often this occurs by the spallation of the topcoat in sheets measuring some mm across as shown in [Figure 20](#).<sup>117</sup> The morphology of these failed regions in terms of the ratio of the diameter

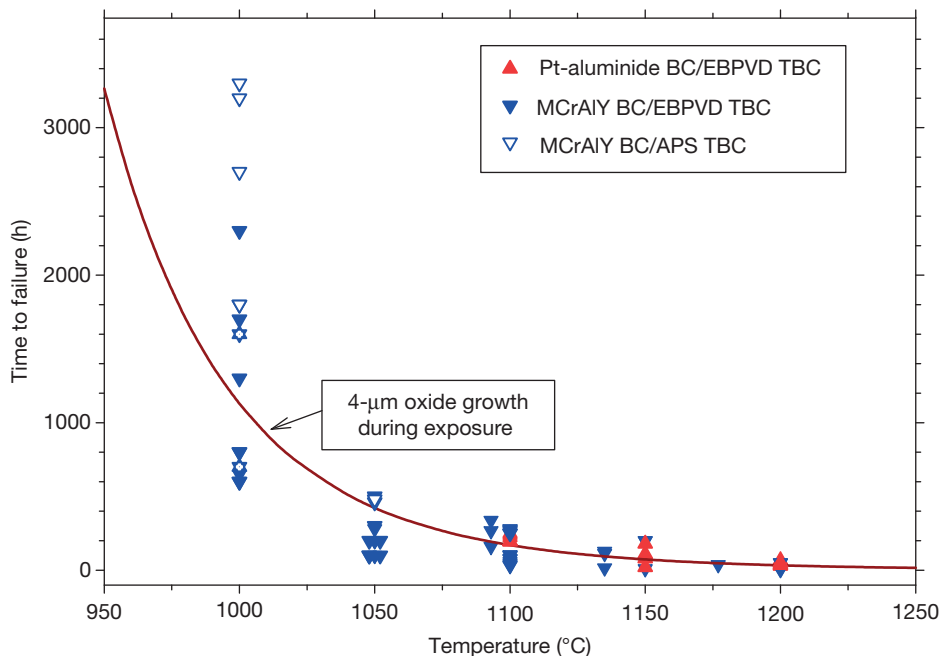


**Figure 19** The temperature dependence of the time to spallation of the ceramic topcoat in various TBC systems in general commercial use.



**Figure 20** Decohesion of large sheets of the YSZ TBC on a coated 25 mm diameter specimen.<sup>117</sup>

of the area of decohesion to the thickness of the coating ( $\sim 20$ ) is consistent with buckling occurring during cooling (Section 1.27.4.2). This is supported by examination of cross-sections of partially failed coatings<sup>122</sup> and by extensive modeling.<sup>123</sup> Edge cracking can also, in principle, produce spallation of large areas of the coating<sup>123</sup> but this appears to be a much more variable event than buckling. It has not occurred, for example, in the specimen shown in Figure 20 but there are other cases of laboratory samples where coating failure at edges has occurred<sup>117</sup> but also accompanied by failure remote from these sites.<sup>124</sup>

As discussed in Section 1.27.4.2, catastrophic buckling will occur during cooling only when a delamination zone of critical radius has formed under the coating. Preexisting zones of this size are not present in the as-manufactured coating and must form during the high temperature exposure. The relatively slow growth of these subcritical defects determines the life of the TBC system and, understandably, there has been much interest in techniques which can assess the extent of this damage nondestructively. Studies of the use of impedance spectroscopy have been made<sup>125</sup> but a more developed technique to date is that of laser-activated luminescence of trace  $\text{Cr}^{3+}$  ions within alumina. Application of this to TBC systems has been pioneered by Clarke and coworkers.<sup>126–128</sup> A particularly powerful aspect of the technique is its ability to determine regions in which the alumina TGO within TBC systems has relatively low stress after cooling to room temperature. By laser scanning the specimen, it is

possible to construct a map showing the extent of these low-stress regions as a function of exposure time. A particularly satisfying example is shown in Figure 21<sup>129</sup> for a platinized BC system exposed to repeated thermal cycles from 1150 °C.

The darker regions in this figure are those of relatively low in-plane compressive stress compared with the lighter regions. The low-stress regions can be interpreted as damaged, involving cracks at either the TGO–BC interface or within the TGO itself. For this particular example, it is clear that the extent of the damaged regions increases markedly only after 190 h leading to spallation of some of the TBC topcoat after 225 h.

The attractions of using this nondestructive technique to evaluate the residual life of TBC systems *in situ* within turbines are considerable but there are cautionary factors. The first to note is that although an EB-PVD YSZ topcoat is transparent to the laser light there is lateral spread of the beam so that return signals are obtained from an area of  $\sim 20$ – $60\ \mu\text{m}$  diameter.<sup>128,129</sup> It follows that early-stage cracks, perhaps  $5\ \mu\text{m}$  long, will not readily be detected. This may be why there appears to be an extensive damage-free period in the example shown in Figure 21 whereas, in reality, small cracks may already have nucleated. For APS topcoats, the applicability of the technique is less clear since the lateral splat boundaries now form internal interfaces across the path of the impinging laser beam and significant attenuation of the return signal is likely.

The other important consideration is the location of the spallation interface. In practice, cracks can form within the topcoat near the TGO, at the TGO–topcoat interface, within the TGO, and at the TGO–BC interface. The luminescence technique relates damage to a decrease in stress within the TGO and this will occur only if cracking occurs within the TGO itself or along its interface with the BC. Fracture damage occurring at the other locations will not be detected by the luminescence technique. For the example of the platinized BC shown in Figure 21, fracture damage did indeed develop both at the TGO–BC interface and within the TGO. The luminescence technique would detect this, subject to the limits on spatial resolution. There are many examples in the literature of crack formation in TBC systems and a perceived tendency for the spallation path to be at the TGO–BC interface in Pt-aluminide/EB-PVD YSZ systems. This is indeed frequently the case but it does not seem to be an intrinsic feature of this system, however, since fracture along the TGO–topcoat or within the topcoat

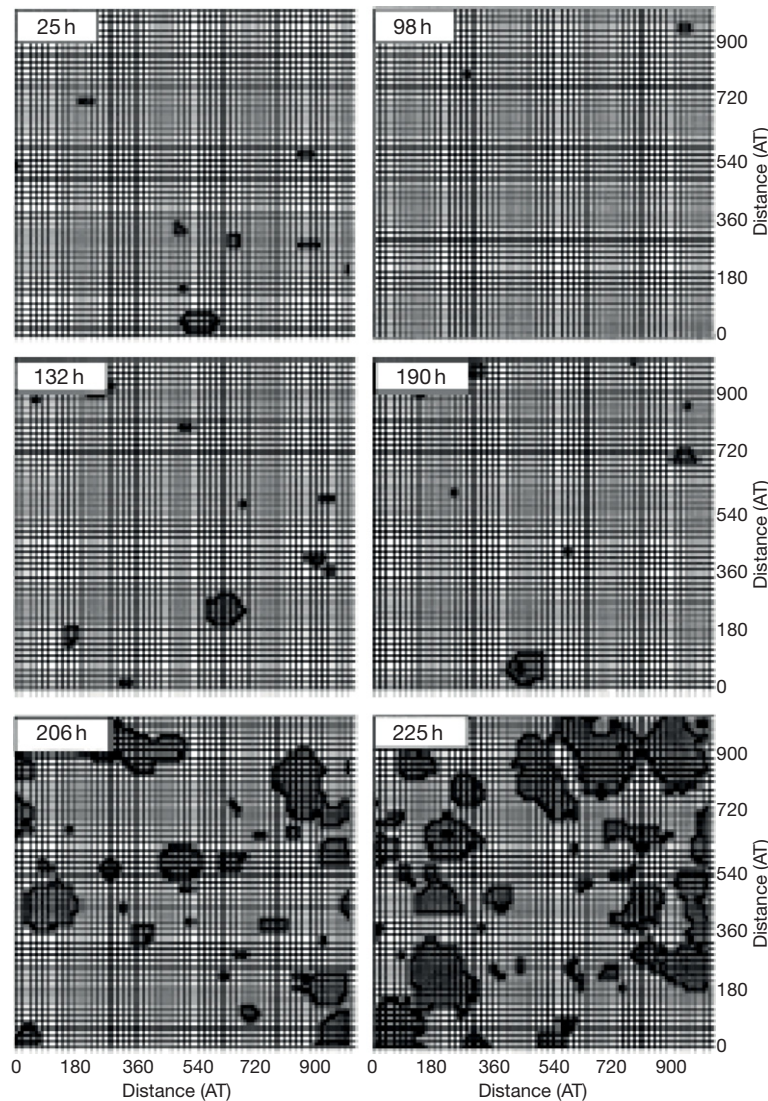


**Figure 21** Map showing the development of low-stress regions (dark areas) with increasing number of cycles, containing 1 h hold periods at 1150 °C, for a TBC system consisting of an EB-PVD YSZ topcoat and platinized BC. Note that a single specimen was examined sequentially but not the same area.<sup>129</sup>

has also been observed.<sup>117</sup> This cracking is often associated with BC protuberances, that is, with increased roughness of the BC. An example of the early stages of cracking within the topcoat of a (rough) Pt-aluminate/EB-PVD YSZ system is shown in [Figure 22](#).

By contrast, the perceived tendency with MCrAlY/APS YSZ systems is for the fracture path to lie mainly within the topcoat. Again, this is not an intrinsic property of the system but is associated with the generally rough BC surface. An example of multiple fracture sites, that is, within the topcoat, within the TGO and at the TGO–BC interface in such a system is shown in [Figure 23](#). Here, the principal

crack, marked A, is hundreds of microns long and lies at the base of the topcoat. It intersects sites, marked B, of porous nonprotective oxides resulting from CF. There is also a crack, marked C, along the TGO–BC interface which appears to be linked to an inclined shear crack traversing the thickness of the TGO. This is a similar morphology to that expected for wedge cracking ([Section 1.27.4.2](#)).

### 1.27.5.3 Strain Energy Considerations

The driving force for spallation within the TBC system is the release of the stored strain energy



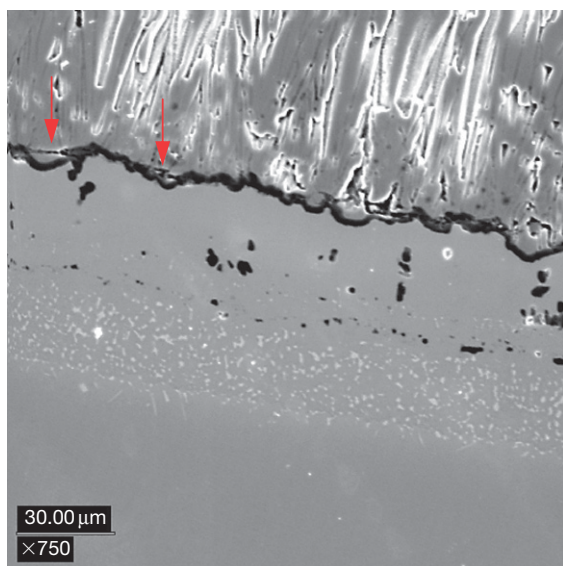


**Figure 22** SEM image of a section through a TBC system consisting of a Pt-aluminide bond coat with an EBPVD YSZ top coat that has been held at 1200 °C for 3 h. Small cracks have developed, arrowed, at the flanks of BC protuberances. Courtesy of Dr. M.P. Taylor.

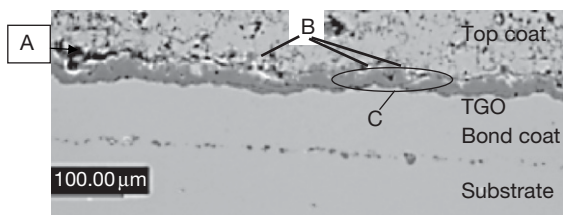


**Figure 23** Section through a TBC system consisting of an electroplated CoNiCrAlY BC and an APS topcoat after oxidation in air at 1100 °C for 600 h. Different cracking sites are indicated and described in the text. See text for discussion. Courtesy of Dr. M.P. Taylor.

within the respective layers. It is an analogous situation to the spallation of the alumina layer from a MCrAlY coating discussed in [Section 1.27.4.2](#). As in that case, [eqn. \[19\]](#) can be used as a first approach but it needs to be noted that this is a ‘thin-layer’ approximation which makes no allowance for any strain energy stored within the coating and alloy substrates. As pointed out earlier, it also assumes that negligible stress exists at the exposure temperature and that the strain energy derives only from thermal loading.

The stored energy within the topcoat will depend linearly on the in-plane Young’s modulus ([eqn. \[19\]](#)) but this parameter is not well defined, particularly for EB-PVD topcoats. Here the in-plane modulus will

vary through the coating thickness and is likely to reach its highest value at its base. Nevertheless, for purposes of illustration, consider a topcoat of thickness 200 μm with an average Young’s modulus of 50 GPa, which is representative of literature values. Using linear thermal expansion coefficients of  $12 \times 10^{-6} \text{ K}^{-1}$  for the topcoat and  $15 \times 10^{-6} \text{ K}^{-1}$  for the superalloy and 0.1 for the Poisson’s ratio of the topcoat within [eqn. \[19\]](#) yields a value for the stored strain energy within the topcoat of  $81 \text{ J m}^{-2}$  on cooling to 100 °C from 1100 °C. It is the release of this energy that will develop cracks at the TGO–topcoat interface or within the topcoat near the TGO. It should be noted that this strain energy may change with time as a result of sintering of the topcoat and an increase in its Young’s modulus<sup>130</sup> or it may decrease as a result of thinning due to chemical or physical erosion.<sup>131</sup>

The specific strain energy within the TGO will increase as the oxide thickens and, in principle, should be added to that within the topcoat to produce cracking either within the oxide layer or at the interface between the TGO and the coating. The strain energy within the TGO can be calculated from [eqn. \[19\]](#). For an oxide thickness of 4 μm, that is, corresponding to the failure line drawn in [Figure 19](#), and using similar parametric values as previously, gives a specific stored energy within the TGO of  $53 \text{ J m}^{-2}$ . The total energy available to produce fracture within the TGO or along the oxide–coating interface is then  $134 \text{ J m}^{-2}$  for the example used.

These values of specific strain energy should certainly be sufficient to produce cracking even with the dissipation of energy by creep anticipated for typical (MCrAlY) BCs – see, for example, [Section 1.27.4.2](#) and [Table 3](#). Interestingly, the stored energy within the topcoat is available to produce cracks within the TBC layer or at its interface with the TGO from the onset of exposure. The reason that cracking is deferred and that TBC systems survive beyond the first thermal cycle is that there must also develop a mechanism for producing cracking and releasing this energy. This is a product of the high temperature exposure and various suggested possibilities will be described briefly in the next section.

### 1.27.5.4 Formation of Subcritical Cracks

#### 1.27.5.4.1 Transformation strains

The removal of aluminum from the BC both by selective oxidation and interdiffusion will result in phase transformation and associated volume changes.

The most obvious of these, evident in **Figure 8(b)** for example, is the transformation from  $\beta$  to  $\gamma'$  phases. Tolpygo and Clarke<sup>132</sup> have estimated an associated volume contraction during this process of  $\sim 38\%$  and have suggested that this transformation strain could induce BC rumpling and decohesion. A difficulty with the calculation is that, in the vicinity of the TGO, the transformation occurs as a direct result of the removal and oxidation of aluminum. The volume change at this location should then also include the expansion arising from formation of alumina. When this is done,<sup>133</sup> the transformation (and concurrent oxidation), is found to produce a volume expansion, rather than contraction, which is of similar magnitude to that produced by direct oxidation of aluminum. Little effect of the  $\beta$  to  $\gamma'$  transformation on TGO adherence and mechanical stability of the BC surface should then be expected and this seems to be borne out by observations.<sup>134,135</sup> It can also be seen from **Figure 8(b)** that there is no marked indentation of the coating–oxide interface above the large  $\gamma'$  phase. It is worth noting, though, that at the inner surface of the BC where interdiffusion is occurring with the alloy substrate, the volume change associated with alumina formation should not be included in the calculation of total volume. The transformation may result in contraction strains in this case which could contribute to the cavity development sometimes found at these locations. It is not easy to calculate these transformation strains, however, since other, often poorly characterized, phases will form within the interdiffusion zone and the volume changes associated with these should also be taken into account.

Another transformation of interest is that of martensite formation of the  $\beta$  phase during cooling. This has been recognized for many years for  $\beta$ -NiAl<sup>136,137</sup> and has also recently been confirmed in  $\beta$ -(Ni, Pt)Al coatings.<sup>134,138,139</sup> Typical of martensitic transformations, a critical cooling rate is required but this seems remarkably low in this case where martensite has been found after air cooling<sup>138</sup> and even after furnace cooling.<sup>139</sup> The former, at least, is consistent with earlier observations on  $\beta$ -NiAl.<sup>140</sup> These recent results suggest that martensitic transformation of the  $\beta$ -(Ni, Pt)Al phase should be a common occurrence during cooling.

The formation of martensite will result in a volume change estimated at  $\sim -2\%$ , that is, a linear contraction of  $\sim 0.7\%$ .<sup>138,139</sup> Unlike the  $\beta \rightarrow \gamma'$  transformation discussed earlier, the expansion due to alumina formation will not mitigate this transformation strain and

out-of-plane tensile stresses may be produced across the TGO–BC interface at the transformation temperature of  $\sim 450\text{--}500^\circ\text{C}$ .<sup>139</sup> The magnitude of these is unclear since the strains may also be accommodated by void formation within the original  $\beta$  grain and some thermal or athermal relaxation may still be possible at this temperature. There is a strong circumstantial argument, however, that the transformation is not a significantly damaging event. If it were so, both Pt-aluminide and MCrAlY coatings would tend to fail before  $\beta$ -depletion had occurred. In practice, much of the life of MCrAlY coatings, for example, is spent with a  $\beta$ -depleted zone adjacent to the TGO layer. Platinized  $\gamma/\gamma'$  coatings, of course, never form the  $\beta$  phase.

#### 1.27.5.4.2 Mechanical instabilities

The alumina TGO layer is under compression during cooling and will also be so at temperature if growth stresses are compressive. The strain energy within the layer can be released and contribute to decohesion if the oxide layer can relax and extend to its stress-free dimensions. The linear relaxation strain per cooling transient will be no more than  $\sim 0.5\%$ , equivalent to an extension of  $0.1\text{ }\mu\text{m}$  over a  $20\text{ }\mu\text{m}$  distance. Large dimensional changes of the TGO layer over these small lengths would then require multiple thermal cycles.

One suggested mechanism is that of ratcheting.<sup>135,141</sup> The initiating event, in this case, is the formation of small cracks within the TBC above preexisting undulations of the BC, essentially as shown arrowed in **Figure 22**. These cracks remove mechanical constraint from the underlying TGO which, as discussed earlier, may be under a compressive growth stress at the oxidation temperature but will certainly experience large in-plane compressive stresses during cooling. Within the model, it is envisaged that, with increasing number of cycles, these stresses can drive the oxide layer as an indent into the BC and, in doing so, enlarge the crack at the base of the topcoat. The model seems feasible, in principle, and experimental support has been provided<sup>135</sup> although the incidence of failure by this route does not seem widespread. It is often observed, for example, that the main fracture site in TBC systems with such diffusion BCs is at the TGO–BC interface<sup>51,52,128</sup> rather than within the TBC topcoat. A key aspect is that there needs to be either a certain roughness to the BC surface so that cracks such as those in **Figure 22** can form or there needs to be a defect at the base of the topcoat which offers no



constraint to the downward migration of the TGO. The issue of surface roughness will be addressed in later sections.

There will probably exist a window of BC strengths within which the ratcheting process could occur. It is not possible to quantify this because modeling the progressive indentation is difficult and has tended to assume<sup>135,141</sup> that the BC deforms by athermal plasticity characterized by yield behavior. In fact, creep processes will dominate,<sup>142,143</sup> even during cooling.<sup>133</sup> Low creep strength is necessary to move the BC away from the indenting oxide but this deformation occurs at constant volume. There must, thus, also be an upwelling of the displaced matter against the TBC topcoat adjacent to the indent. In this case, the creep strength of the BC must be high enough to displace the topcoat upward and allow continued penetration of the indenting oxide layer into the BC. These two contradictory requirements of the BC creep strength may be satisfied only within a limited temperature and composition range.

Another interesting mechanical instability is rumpling. This has been recognized for some years and has been shown to occur in aluminized and Pt-aluminized coatings under thermal cycling conditions<sup>132,144,145</sup> but in the absence of a topcoat. It is manifested by a roughening of the specimen surface and is clearly associated with thermal cycling because isothermally-tested specimens do not show the phenomenon.<sup>144</sup> The basic underlying reasons for the surface instability are well understood<sup>146,147</sup> and are broadly the same as discussed above for the ratcheting process. In both cases, deformation of the coating permits the compressively stressed TGO to increase its length and, thereby, relax its strain energy. As pointed out earlier, this increase in length per temperature transient is small,  $\sim 0.5\%$ , and repeated thermal cycles are needed to produce readily observable deformation.

The rumpling process has been implicated<sup>147</sup> in failure of the TBC system because the instability would develop significant out-of-plane stresses in the vicinity of the TGO with associated crack initiation. Modeling of the process again assumes plastic yielding rather than creep behavior and, although the presence of the topcoat is considered, no mechanical constraint is attributed to it. This constraint will be present in real cases and, for the reasons given above when discussing ratcheting, is likely to limit the applicability of the process in TBC systems. Again, exceptions will arise when defects exist in the topcoat such that, locally, mechanical constraint is absent and upward displacement of the TGO and BC becomes feasible.

#### 1.27.5.4.3 Roughness of the BC surface

It has been known for some time that the roughness of the BC surface will have a significant influence on the development of stresses in the TBC system during cooling.<sup>148,149</sup> Various attempts have been made to evaluate these using FE methods<sup>113,130,133,150–153</sup> which incorporate materials' behavior of varying degrees of relevance. Most recently, it has also become clear that out-of-plane tensile stresses can also develop at the oxidation temperature as a consequence of the volume increase on oxide formation.<sup>112,113</sup>

The development of these numerical models has to some extent mirrored the expansion in computing power. Thus, initial approaches tended to assume entirely elastic behavior of the respective layers but, importantly, creep behavior has been subsequently incorporated and recognition made that the TGO thickens during exposure. The most recent models<sup>113,130,133</sup> incorporate creep of both BC and TGO, allow for growth of the latter together with the associated volume change at temperature during the computation. In addition, they permit densification of the YSZ topcoat, again during the simulated exposure time, and consider a variation in BC surface roughness. Some predicted results for two different BC-roughness geometries are shown in **Figure 24**.<sup>133</sup>

As described in the caption, the stress contours of **Figure 24** apply to the situation at the test temperature of  $1100^\circ\text{C}$ . For the case examined, the total thickness of the alumina TGO had increased to  $3.3\ \mu\text{m}$  during the simulated 100 h isothermal exposure at this temperature. The parameters  $b$  and  $a$  are the amplitude and half-wavelength, respectively, of the surface undulations shown in **Figure 24**. For the rougher surface, **Figure 24(a)**, out-of-plane tensile stresses of  $\sim 150\ \text{MPa}$ , have developed within the topcoat along the flank of the BC protuberance. For the less-rough surface, however (**Figure 24(b)**), these stresses are absent, showing the strong sensitivity of isothermal stress development to BC surface roughness. In both cases, tensile stresses also develop in the valleys of the undulations.

The out-of-plane tensile stresses on the flanks of the BC protuberance arise from continuity strains<sup>112</sup> which are required if the topcoat is to remain uncracked. Their origins can be understood by recognizing that the outward displacement due to the formation of the TGO is normal to the BC interface and, so, changes direction around the protuberance shown in **Figure 24**. The out-of-plane component, the  $x_{22}$  direction, of this displacement also varies around the protuberance and reaches a

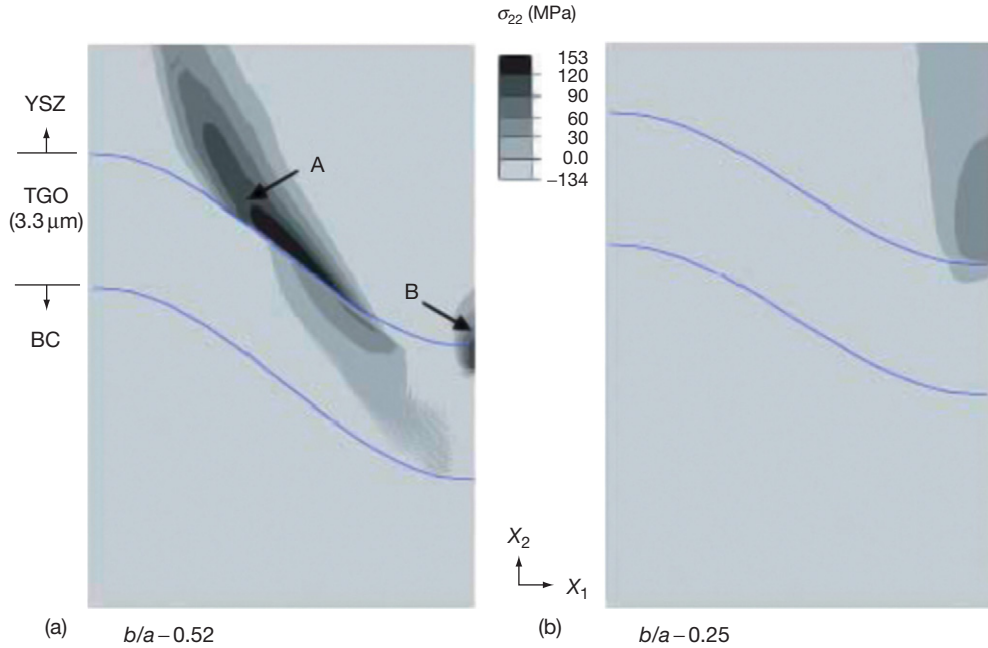


**Figure 24** FE predictions<sup>133</sup> of the  $\sigma_{22}$  stress contours at 1100 °C after 100 h oxidation at the same temperature for an EB-PVD YSZ TBC system containing a Pt-aluminide BC. Creep of the BC and TGO, sintering of the topcoat and outward strains due to TGO growth are considered in the stress analysis. The BC creep properties used were those of Taylor *et al.*,<sup>143</sup> The arrowed locations mark the general sites of high stress at the flank (a) and valley (b) regions.

minimum on its flank. To maintain continuity of the topcoat, tensile stresses must then develop to strain the topcoat in these locations to account for the out-of-plane deficit in the displacements resulting from oxide growth.

The effect, on the  $\sigma_{22}$  stress distribution, of cooling the specimen to 25 °C after the isothermal exposure for 100 h at 1100 °C is shown in **Figure 25**, again for the two BC surface roughnesses.<sup>133</sup> The out-of-plane flank stresses in the rougher specimen, **Figure 25(a)**, are largely unaffected by this transient and no new stress is developed in these locations in the less-rough specimen, **Figure 25(b)**. There is a large increase, however, in the tensile stress developed in the topcoat in the valley regions and across the TBC–TGO interface. For the rougher surface, this is ~700 MPa but is appreciably smaller (~200 MPa) for the smoother surface. Significant tensile stresses are also developed at the TGO–BC interface during cooling as a result of differential contraction strains between oxide and coating (see Ref. [37] for a general review of such issues). Broadly, the same behavior has also been found with MCrAlY BCs where, again, appropriate creep and oxide growth kinetics were incorporated into the FE modeling.<sup>113</sup>

These regions of high stress correspond to locations where cracks form in TBC systems. Examples of those found at flank and valley locations are arrowed in **Figure 22** and may well have formed at temperature. Crack initiation, presumably during cooling, has also been reported<sup>113</sup> at the TGO–BC interface at the peak of the BC protuberances. These nucleation processes will occur, however, only with relatively rough BCs. Cracking events should be less easy and TBC lifetimes would be expected to be longer with flatter BC surfaces. This has been clearly demonstrated recently by Yanar *et al.*<sup>117</sup> who found an approximate factor 10 increase in the lifetime of a NiCoCrAlY/EB-PVD YSZ system by hand polishing the BC prior to deposition of the topcoat.

#### 1.27.5.4.4 Chemical failure

A discussion of CF processes in relation to aluminum depletion and the endurance of overlay coatings has been given earlier in **Section 1.27.4.3.2**. Identical concepts apply to BCs in TBC systems but, in this case, spallation of the YSZ topcoat may be induced prior to complete CF of the BC.<sup>105</sup> This can arise because CF will result in the fast growth of nonalumina, break-away-type oxides which will produce upward displacements of the topcoat. This is an oxide-jacking

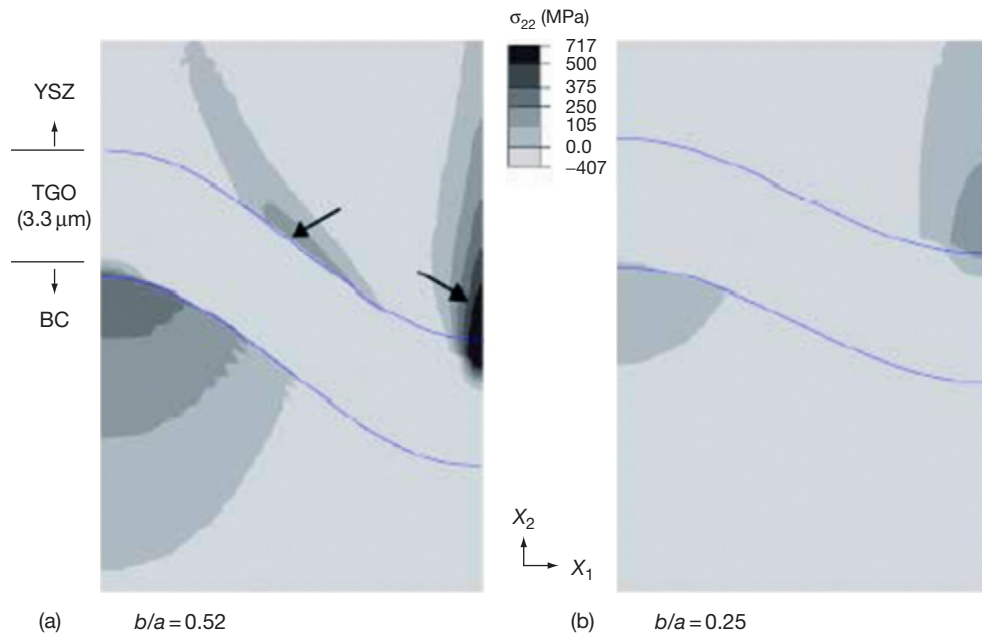


**Figure 25** FE contour plots of the  $\sigma_{22}$  stress for the same specimen as shown in Figure 24 but after cooling to 25 °C after exposure at 1100 °C for 100 h.<sup>133</sup> The arrows indicate the general areas in which out-of-plane stresses had developed prior to cooling.

process which will result in the development of out-of-plane tensile stresses within the topcoat when the CF sites are discrete (Figure 26). Possible localized sites for enhanced aluminum depletion and the early initiation of CF are diffusion cells (splats) within sprayed MCrAlY BCs,<sup>105</sup> protuberances (roughness) at the BC surface,<sup>109,111,153</sup> and locally thin cross-sections.

The jacking associated with the formation of the mound of fast-growing (Ni, Cr)-rich breakaway oxides, shown schematically in Figure 26, will tend to nucleate and propagate delamination cracks within the topcoat near the TGO. This process will occur at the oxidation temperature and will not need thermal cycles to produce this damage. It is likely that this type of process was responsible for the long crack (marked A) in the cross-section shown in Figure 23. This particular specimen had been exposed isothermally until the final cooling transient and several discrete regions of breakaway oxides (marked B), associated, in this case, with BC protuberances, had formed.

#### 1.27.5.5 Surface Roughness: A Common Factor?

A number of the degradation mechanisms described in Section 1.27.5.4 have been observed experimentally and, consequently, have validity. The

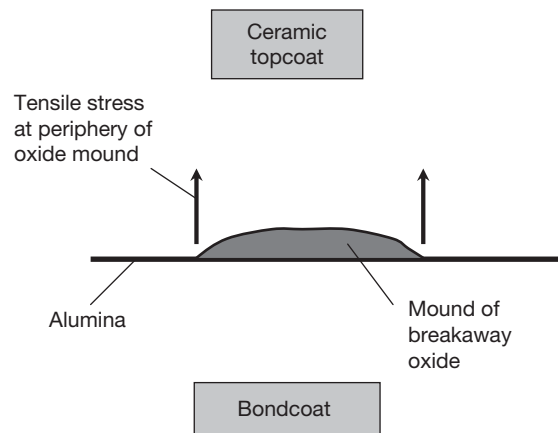


**Figure 26** A schematic diagram showing how the growth of fast-growing 'breakaway' oxides resulting from CF will generate out-of-plane tensile stresses within the topcoat.

importance of others (phase transformation strains, rumpling) to TBC failure is less clear and awaits more robust experimental support. Of those mechanisms which have been shown to nucleate and propagate subcritical cracks, some are either aided by or, indeed, require BC surface roughness (e.g., CF, out-of-plane tensile stress development at temperature or during cooling, ratcheting) and others (wedging) are likely to operate only on relatively flat interfaces. The

experiments of Yanar *et al.*,<sup>117</sup> in particular, show very well that decreasing the surface roughness of a MCrAlY BC can increase the lifetime of a TBC system by an order of magnitude. The improved behavior was similar in their experiments to the behavior of a Pt-aluminide BC which had similarly flat BC surfaces. As can be appreciated from Figure 22, however, flat Pt-aluminide BCs with EB-PVD topcoats need not always be the case and will depend on the extent of grit blasting performed by the manufacturer. The factor 10 improvement in lifetimes found by Yanar *et al.* is of the same order of magnitude found in the compilation of published lifetime results from commercial systems shown in Figure 19. It is certainly tempting to suggest that much of this scatter in lifetimes can be attributed to an uncontrolled variation in the surface roughness of the BCs. There will be other sources of scatter, inevitably included within these various tests, but the first-order importance of BC surface roughness to the scatter at any given temperature can be taken as a working hypothesis.<sup>113</sup>

The dependence of the various delamination mechanisms on surface roughness are only now being assessed quantitatively using realistic numerical models which, as described in earlier sections, allow for creep processes and the volume expansion due to oxide formation. Work in this area is incomplete but some rather qualitative trend lines are

shown schematically in Figure 27 which relates TBC lifetimes to the BC surface roughness.

Relatively flat surfaces (low values of  $b/a$ ) provide the longest lifetimes since opportunities for crack nucleation caused by continuity strains and CF will be limited. Studies of failure processes in such ideal structures are limited although in localized areas of otherwise rough BCs, wedge-type cracks have been found (Figure 23 but see also Section 1.27.4.2). The red line, representing continuity cracking in Figure 27, shows a decrease in lifetimes as BC roughness increases. It refers to the development of subcritical cracks at the flanks of BC protuberances at temperature, possible ratcheting nucleation, and the nucleation of cracks at the TGO/BC interface during cooling. The stresses produced increase with oxide thickness and, so, time at temperature is an important factor. They will also increase with the roughness factor  $b/a$  (Section 1.27.5.4.3)<sup>113</sup> and it is expected that TBC lifetimes will decrease as this increases. For large values of  $b/a$ , aluminum depletion within BC protuberances will be enhanced (e.g., Figure 18) and CF with the formation of breakaway-type oxides will take place. These will increase the stresses produced within the TBC layer at temperature and failure will occur earlier than in the absence of breakaway. This trend is shown as the downward-sloping blue line in Figure 27. Again, time at temperature will also be an

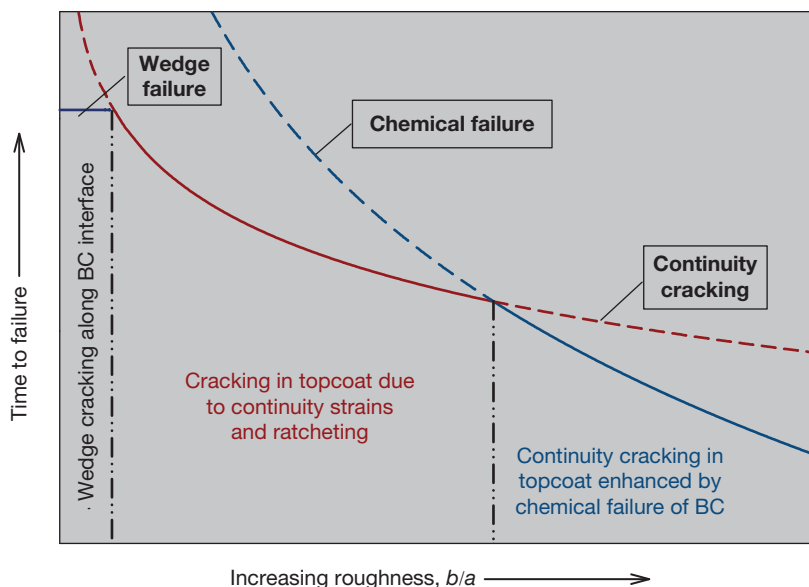


**Figure 27** A schematic map showing how variously proposed mechanisms for the nucleation and growth of subcritical cracks may depend on the surface roughness of the BC. The colored lines show possible dependences of continuity cracking and CF on roughness.

important parameter since the depletion of aluminum will be directly related to this.

As a final note of caution, it should be emphasized that the discussion in this section relates to typical laboratory experience in which the test specimens have relatively simple shapes. The map of Figure 27 then provides a mechanistic framework for these conditions but the concepts are also expected to be valid for service conditions although some modification might well be required. There may be thin regions, for example, within the complex geometry of actual components in which the local total aluminum reservoir is insufficient to maintain a protective TGO. Bulk depletion and breakaway oxidation could then occur prematurely and failure by this route might then be only weakly dependent on the surface roughness of the BC. In another example, local regions of components may be designed with a high radius of convex curvature and could develop significant out-of-plane tensile strains during cooling. These would contribute to the continuity strains developed solely from the surface roughness of the BC. As discussed earlier, similar issues would apply for the case of imposed service strains.

## References

1. Reed, R. C. *The Superalloys: Fundamentals and Applications*; Cambridge University Press: Cambridge, 2006.
2. Evans, H. E.; Taylor, M. P. *Proc. IMechE, Part G: J. Aerospace Eng.* **2006**, *220*, 1–10.
3. Giggins, G. S.; Pettit, F. S. *J. Electrochem. Soc.* **1971**, *118*, 1782–1790.
4. Bennett, M. J.; Tuson, A. T.; Knights, C. F.; Ayres, C. F. *Mater. Sci. Technol.* **1989**, *5*, 841–852.
5. Chan, W. Y.; Evans, H. E.; Ponton, C. B.; Nicholls, J. R.; Simms, N. J. *Mater. High Temp.* **2000**, *17*, 173–178.
6. Akhtar, A.; Hook, M. S.; Reed, R. C. *Metall. Mater. Trans. A* **2005**, *36A*, 3001–3017.
7. Luthra, K. L.; Shores, D. A. *J. Electrochem. Soc.* **1980**, *127*, 2202–2210.
8. Strife, J. R.; Sheehan, J. E. *Ceram. Bull.* **1988**, *67*, 369.
9. Wagner, C. J. *Electrochem. Soc.* **1952**, *99*, 369–380.
10. Crank, J. *The Mathematics of Diffusion*; Oxford University Press: Oxford, 1975.
11. Evans, H. E.; Hilton, D. A.; Holm, R. A.; Webster, S. J. *Oxid. Met.* **1980**, *14*, 235–247.
12. Talboom, F. T.; Elam, R. C.; Wilson, L. W. NASA Report CR7813, NASA: Houston, 1970.
13. Saunders, S. R. J.; Nicholls, J. R. *Mater. Sci. Technol.* **1989**, *5*, 780–798.
14. Mévrel, R. *Mater. Sci. Eng. A* **1989**, *120*, 13–24.
15. Hocking, G.; Vasantasree, V.; Sidkey, P. S. *Metallic and Ceramic Coatings*; Longman: Harrow, 1989.
16. Stern, K. H. Ed., *Metallurgical and Ceramic Protective Coatings*; Chapman and Hall: London, 1996.
17. Goward, G. W. *Surf. Coat. Technol.* **1998**, *108–109*, 73–79.
18. Coddet, C. *Mater. Sci. Forum* **2004**, *461–464*, 193–212.
19. Taylor, A.; Floyd, R. W. *J. Inst. Met.* **1952–53**, *81*, 451–464.
20. Muñoz-Arroyo, R.; Clemens, D.; Tietz, F.; Anton, R.; Quadackers, W. J.; Singheiser, L. *Mater. Sci. Forum* **2001**, *369–372*, 165–172.
21. Brindley, W. J.; Whittenberger, J. D. *Mater. Sci. Eng. A* **1993**, *163*, 33–41.
22. Taylor, M. P.; Evans, H. E.; Ponton, C. B.; Nicholls, J. R. *Surf. Coat. Technol.* **2000**, *124*, 13–18.
23. Fritscher, K.; Leyens, C.; Peters, M. *Mater. Sci. Eng. A* **1995**, *190*, 253–258.
24. Gupta, D. K.; Duval, D. S. *US Patent* **1986**, *4*, 585, 481.
25. Goebel, J. A.; Giggins, C. S.; Krasij, M.; Stringer, J. EPRI Report 2639SR; Palo Alto, CA, 1981.
26. Chan, W. Y.; Evans, H. E.; Ponton, C. B.; Nicholls, J. R.; Simms, N. J. *Mater. High Temp.* **2000**, *17*, 173–178.
27. Leyens, C.; van Liere, J.-W.; Peters, M.; Kaysser, W. A. *Surf. Coat. Technol.* **1998**, *108–109*, 30–35.
28. Leyens, C.; Peters, M.; Kaysser, W. A. *Mater. Sci. Forum* **1997**, *251–254*, 769–776.
29. Gray, S.; Ponton, C. B.; Jacobs, M. H.; Evans, H. E. *United States Patent* **2002**, *6*, 387, 541 B1, May 14.
30. Martinz, H.-P.; Rieger, M. *Mater. Sci. Forum* **1997**, *251–254*, 761–768.
31. Fukumoto, M.; Matsumara, Y.; Hayashi, S.; Sakamoto, K.; Kasama, A.; Tanaka, R.; Narita, T. *Oxid. Met.* **2003**, *60*, 335–346.
32. Bennett, M. J. In *Coatings for High Temperature Applications*; Lang, E., Ed.; Applied Science, 1983; pp 169, 192.
33. Crouch, A. G.; Dooley, R. B. *Corros. Sci.* **1976**, *16*, 341–347.
34. Coley, K. S.; Tuson, A. T.; Saunders, S. R. J.; Bennett, M. J.; Knights, C. F. *Mater. Sci. Eng. A* **1989**, *121*, 461–466.
35. Bennett, M. J.; Tuson, A. T.; Knights, C. F.; Ayres, C. F. *Mater. Sci. Technol.* **1989**, *5*, 841–852.
36. Pennisi, F. J.; Gupta, D. K. *Thin Solid Films* **1981**, *84*, 49–58.
37. Lobb, R. C.; Bennett, M. J. *Oxid. Met.* **1991**, *35*, 35–52.
38. Evans, H. E. *Int. Mater. Rev.* **1995**, *40*, 1–40.
39. Nicholls, J. R.; Lawson, K. J.; Al Yasiri, L. H.; Hancock, P. *Corros. Sci.* **1993**, *35*, 1209–1223.
40. Nicholls, J. R.; Simms, N. J.; Neseyif, S.; Ponton, C.; Evans, H. E.; Taylor, M. In *High Temperature Corrosion and Materials Chemistry*; The Electrochemical Society Proceedings; McNallan, M., Opila, E., Maruyama, T., Narita, T., Eds.; 2000; Vol. 99–38, pp 270–281.
41. Nicholls, J. R.; Simms, N. J.; Chan, W. Y.; Evans, H. E. *Surf. Coat. Technol.* **2002**, *149*, 236–244.
42. Choquet, P. A.; Naylor, E. R.; Rapp, R. A. *Mater. Sci. Eng. A* **1989**, *121*, 413–418.
43. Pérez, F. J.; Trilleros, J. A.; Hierro, M. P.; Milewska, A.; Carpintero, M. C.; Bolivar, F. J. *Mater. Sci. Forum* **2004**, *461–464*, 313–320.
44. Harper, M. A.; Rapp, R. A. In *Surface Modification Technologies*; Sudarshan, T. S., Bhat, D. G., Jeandin, M., Eds.; AIME, 1991; Vol. IV, 415–428.
45. Lehnert, G.; Meinhardt, H. *Surface Treatment* **1972**, *1*, 72.
46. Meelu, M. C.; McMordie, B. G.; Loretto, M. H.; Jones, A. In *The Processing, Properties and Applications of Metallic and Ceramic Materials*; Loretto, M. H., Beevers, C. J., Eds.; The University of Birmingham, Birmingham, UK, 1992; pp 1247–1252.
47. Gleeson, B.; Wang, W.; Hayashi, S.; Sordelet, D. *Mater. Sci. Forum* **2004**, *461–464*, 213–222.
48. Cadoret, Y.; Bacos, M.-P.; Josso, P.; Maurice, V.; Marcus, P.; Zanna, S. *Mater. Sci. Forum* **2004**, *461–464*, 247–254.



49. Zhang, Y.; Haynes, J. A.; Lee, W. Y.; Wright, I. G.; Pint, B. A.; Cooley, K. M.; Liaw, P. K. *Metall. Mater. Trans.* **2001**, 32A, 1727.
50. Rickerby, D. S.; Bell, S. R.; Wing, R. G. *United States Patent* **1999**, 5, 981 091, November 9.
51. Bouhanek, K.; Adesanya, O. A.; Stott, F. H.; Skeldon, P.; Lees, D. G.; Wood, G. C. *Mater. Sci. Forum* **2001**, 369–372, 615–622.
52. Adesanya, O. A.; Bouhanek, K.; Stott, F. H.; Skeldon, P.; Lees, D. G.; Wood, G. C. *Mater. Sci. Forum* **2001**, 369–372, 639–646.
53. Fitzer, E. *Archiv. Eisenhüttenwesen* **1954**, 25, 45–5.
54. Grünling, H. W.; Bauer, R. *Thin Solid Films* **1982**, 95, 3–20.
55. Itzhak, D.; Tuller, F. R.; Schieber, M. *Thin Solid Films* **1980**, 73, 379–384.
56. Young, S. G.; Deadmore, D. L. *Thin Solid Films* **1980**, 73, 373–378.
57. Cockeram, B. V.; Rapp, R. A. *Oxid. Met.* **1995**, 45, 375–425.
58. Gaillard-Allemand, B.; Vilasi, M.; Belmonte, T.; Steinmentz, J. *Mater. Sci. Forum* **2001**, 369–372, 727–734.
59. Li, X. Y.; Taniguchi, S.; Matsunaga, Y.; Nayagawa, K.; Fujita, K. *Intermetallics* **2003**, 11, 143–150.
60. Voytėch, D.; Kubatik, T.; Jurek, K.; Maixner, J. *Oxid. Met.* **2005**, 63, 305–323.
61. Cockeram, B. V.; Rapp, R. A. *Mater. Sci. Forum* **1997**, 251–254, 723–736.
62. Gray, S.; Jacobs, M. H.; Ponton, C. B.; Voice, W.; Evans, H. E. *Mater. Sci. Eng. A* **2004**, 384, 77–82.
63. Kofstad, P. *High Temperature Corrosion*; Elsevier, 1988.
64. Deal, B. E.; Grove, A. S. *J. Appl. Phys.* **1965**, 36, 3770–3778.
65. Taniguchi, S.; Minamida, T.; Shibata, T. *Mater. Sci. Forum* **1997**, 251–254, 227–234.
66. Wortman, D. J.; Nagaraj, B. A.; Dunderstadt, E. C. *Mater. Sci. Eng. A* **1989**, 121, 433–440.
67. Rhys-Jones, T. N.; Toriz, F. C. *High Temp. Technol.* **1989**, 7, 73–81.
68. Saunders, S. R. J.; Banks, J. P.; Chunnillal, C. NPL Report MATC(A)113, An evaluation of thermal barrier coated specimens exposed to long-term ageing tests, Teddington, July 2002.
69. Munro, T. C.; Gleeson, B. *Mater. Sci. Forum* **1997**, 251–254, 753–760.
70. Mabuchi, H.; Asai, T.; Nakayama, Y. *Scripta Metall.* **1989**, 23, 685–689.
71. Gauthier, V.; Dettenwanger, F.; Schütze, M.; Shemet, V.; Quadackers, W. J. *Oxid. Met.* **2003**, 59, 233–254.
72. Gauthier, V.; Dettenwanger, F.; Schütze, M. *Intermetallics* **2002**, 10, 667–674.
73. Czech, N.; Kolarik, V.; Quadackers, W. J.; Stamm, W. *Surf. Eng.* **1997**, 13, 384–388.
74. Naumenko, D.; Quadackers, W. J.; Galerie, A.; Wouters, Y.; Jourdain, S. *Mater. High Temp.* **2003**, 20, 287–293.
75. Hindam, H.; Whittle, D. P. *Oxid. Met.* **1982**, 18, 245–284.
76. Natesan, K.; Liu, Y. Y. *Mater. Sci. Eng. A* **1989**, 121, 571–580.
77. Clemens, D.; Vosberg, V. R.; Penkalla, H. J.; Breuer, U.; Quadackers, W. J.; Nickel, H. *Fresenius J. Anal. Chem.* **1997**, 358, 122–126.
78. Evans, H. E.; Norfolk, D. J.; Swan, T. J. *Electrochem. Soc.* **1978**, 115, 1180–1185.
79. Sabol, G. P.; Dalgaard, S. B. *J. Electrochem. Soc.* **1975**, 122, 316–317.
80. Pragnell, W. M.; Evans, H. E.; Naumenko, D.; Quadackers, W. J. *Mater. High Temp.* **2005**, 22, 561–566.
81. Miller, R. A. *Trans. ASME* **1987**, 109, 448–451.
82. Renusch, D.; Echsler, H.; Schütze, M. In *Lifetime Modelling of High Temperature Corrosion Processes*; Schütze, M., Quadackers, W. J., Nicholls, J. R., Eds.; Maney, Publishing: London, 2001; pp 324–336.
83. Renusch, D.; Echsler, H.; Schütze, M. *Mater. Sci. Forum* **2004**, 461–464, 729–736.
84. Tien, J. K.; Davidson, J. M. In *Stress Effects and the Oxidation of Metals*; Cathcart, J. V., Ed.; AIME, New York, 197; pp. 200–219.
85. Lipkin, D. M.; Clarke, D. R.; Hollatz, M.; Bobeth, M.; Pompe, W. *Corros. Sci.* **1997**, 39, 231–242.
86. Echsler, H.; Martinez, E. A.; Singheiser, L.; Quadackers, W. J. *Mater. Sci. Eng. A* **2004**, 384, 1–11.
87. Timoshenko, S. *Theory of Elastic Stability*; McGraw-Hill: New York, 1936; 367.
88. Hou, P. Y. *Mater. Sci. Forum* **2001**, 369–372, 23–28.
89. Smialek, J. L.; Pint, B. A. *Mater. Sci. Forum* **2001**, 369–372, 459–466.
90. Banks, J. P.; Gohil, D. D.; Evans, H. E.; Hall, D. J.; Saunders, S. R. J. In *Materials for Advanced Power Engineering*; Coutsouradis, D., et al., Eds.; Kluwer Academic: The Netherlands, 1994; Part II, pp 1543–1552.
91. Pint, B. A.; Wright, I. G.; Lee, W. Y.; Zhang, Y.; Prüßner; Alexander, K. B. *Mater. Sci. Eng.* **1998**, 245, 201–211.
92. Evans, H. E.; Mitchell, G. P.; Lobb, R. C.; Owen, D. R. J. *Proc. R. Soc. A* **1993**, 440, 1–22.
93. Evans, H. E.; Strawbridge, A.; Carolan, R. A.; Ponton, C. B. *Mater. Sci. Eng. A* **1997**, 225, 1–8.
94. Evans, H. E.; Osgerby, S.; Saunders, S. R. J. In *Proceedings of John Stringer Symposium on High Temperature Corrosion*; Tortorelli, P. F., Wright, I. G., Hou, P. Y., Eds.; ASM International: Ohio, 2003; pp 122–130.
95. Evans, H. E.; Lobb, R. C. *Corros. Sci.* **1984**, 24, 209–222.
96. Galerie, A.; Dupeux, M.; Wouters, Y.; Toscan, F. *Mater. Sci. Forum* **2006**, 522–523, 441–450.
97. Bouhanek, K.; Oquab, D.; Pieraggi, B. *Mater. Sci. Forum* **1997**, 251–254, 33–40.
98. Baleix, S.; Bernhart, G.; Lours, P. *Mater. Sci. Forum* **2001**, 369–372, 539–546.
99. Osgerby, S.; Berriche-Bouhanek, K.; Evans, H. E. *Mater. Sci. Eng. A* **2005**, 412, 182–190.
100. Chan, K. S.; Cheruvu, N. S.; Leverant, G. R. *Mater. Sci. Forum* **2001**, 369–372, 623–630.
101. Anton, R.; Birkner, J.; Czech, N.; Stamm, W. *Mater. Sci. Forum* **2001**, 369–372, 719–726.
102. Taylor, M. P.; Pragnell, W. M.; Evans, H. E. *Mater. Sci. Forum* **2004**, 461–464, 239–246.
103. Sato, A.; Harada, H.; Kawagishi, K. *Mater. Sci. Forum* **2006**, 522–523, 361–368.
104. Matsumaru, H.; Hayashi, S.; Narita, T. *Mater. Sci. Forum* **2006**, 522–523, 285–292.
105. Evans, H. E.; Taylor, M. P. *Oxid. Met.* **2001**, 55, 17–34.
106. Nesbitt, J. A.; Heckel, R. W. *Metall. Trans.* **1987**, 18A, 2075.
107. Roper, G. W.; Whittle, D. P. *Met. Sci.* **1981**, 15, 148.
108. Evans, H. E.; Donaldson, A. T.; Gilmour, T. C. *Oxid. Met.* **1999**, 52, 379–402.
109. Niranatlumpong, P.; Ponton, C. B.; Evans, H. E. *Oxid. Met.* **2000**, 53, 241–258.
110. Taylor, M. P.; Evans, H. E. *Mater. High Temp.* **2003**, 20, 461–466.
111. Taylor, M. P.; Pragnell, W. M.; Evans, H. E. *Mater. Corros.* **2008**, 59, 508–513.
112. Evans, H. E.; Taylor, M. P. *J. Corros. Sci. Eng.* **2003**, 6, Paper H011.

113. Busso, E. P.; Wright, L.; Evans, H. E.; McCartney, L. N.; Saunders, S. R. J.; Osgerby, S.; Nunn, J. *Acta Mater.* **2007**, *55*, 1491–1503.
114. Yanar, N. M.; Meier, G. H.; Pettit, F. S. *Scripta Mater.* **2002**, *46*, 325–330.
115. Lih, W.; Chang, E.; Wu, B. C.; Chao, C. H. *Oxid. Met.* **1991**, *36*, 221–238.
116. Nijdam, T. J.; Jeurgens, L. P. H.; Chen, J. H.; Sloof, W. G. *Oxid. Met.* **2005**, *64*, 355–377.
117. Yanar, N. M.; Pettit, F. S.; Meier, G. H. *Metall. Mater. Trans.* **2006**, *37A*, 1563–1580.
118. Tolpygo, V. K.; Clarke, D. R.; Murphy, K. S. *Surf. Coat. Tech.* **2001**, *146–147*, 124–131.
119. Kim, G. M.; Yanar, N. M.; Hewitt, E. N.; Pettit, F. S.; Meier, G. H. *Scripta Mater.* **2002**, *46*, 489–495.
120. Evans, A. G.; Mumm, D. R.; Hutchinson, J. W.; Meier, G. H.; Pettit, F. S. *Prog. Mater. Sci.* **2001**, *46*, 505–553.
121. Rouzou, I.; Molins, R.; Rémy, L.; Jomard, F. *Mater. Sci. Forum* **2004**, *461–464*, 101–108.
122. Padture, N. P.; Gell, M.; Jordan, E. H. *Science* **2002**, *296*, 280–284.
123. Choi, S. R.; Hutchinson, J. W.; Evans, A. G. *Mech. Mater.* **1999**, *31*, 431–447.
124. Nunn, J.; Saunders, S. R. J.; Banks, J. P. In *Microscopy of Oxidation* Tatlock, G. J., Evans, H. E., Eds.; Science Reviews, 2006; Vol 6, pp 219–226.
125. Md Shawkat Ali; Shenhua Song; Ping Xiao *J. Eur. Ceram. Soc.* **2002**, *22*, 101–107.
126. Christensen, R.; Lipkin, D. M.; Clarke, D. R.; Murphy, K. *Appl. Phys. Lett.* **1996**, *69*, 3754–3756.
127. Peng, X.; Clarke, D. R. *J. Am. Ceram. Soc.* **2000**, *83*, 1165–1170.
128. Tolpygo, V. K.; Clarke, D. R.; Murphy, K. S. *Surf. Coat. Technol.* **2001**, *146*, 124–131.
129. Selçuk, A.; Atkinson, A. A. *Acta Mater.* **2003**, *51*, 535–549.
130. Busso, E. P.; Qian, Z. Q. *Acta Mater.* **2006**, *54*, 325–338.
131. Wellman, R. G.; Nicholls, J. R. *Surf. Coat. Technol.*, **2004**, *177*, 80–88.
132. Tolpygo, V. K.; Clarke, D. R. *Acta Mater.* **2000**, *48*, 3283–3293.
133. Busso, E. P.; Qian, Z. Q.; Taylor, M. P.; Evans, H. E. *Acta Mater.*, in press.
134. Reid, M.; Pomeroy, M. J.; Robinson, J. S. *Mater. Sci. Forum* **2004**, *461–464*, 343–350.
135. Mumm, D. R.; Evans, A. G.; Spitsberg, I. T. *Acta Mater.* in press.
136. Rosen, S.; Goebel, J. A. *Trans. AIME* **1968**, *242*, 722.
137. Smialek, J. L. *Metall. Trans.* **1971**, *2*, 913.
138. Zhang, Y.; Haynes, J. A.; Pint, B. A.; Wright, I. G.; Lee, W. Y. *Surf. Coat. Technol.* **2003**, *163–164*, 19–24.
139. Chen, M. W.; Ott, R. T.; Hufnagel, T. C.; Wright, P. K.; Hemker, K. J. *Surf. Coat. Technol.* **2003**, *163–164*, 25–30.
140. Smialek, J. L.; Hehemann, R. F. *Metall. Trans.* **1973**, *4*, 1571.
141. Karlsson, A. M.; Hutchinson, J. W.; Evans, A. G. *Mater. Sci. Eng. A* **2003**, *351*, 244–257.
142. Pan, D.; Chen, M. W.; Wright, P. K.; Hemker, K. J. *Acta Mater.* **2003**, *51*, 2205–2217.
143. Taylor, M. P.; Evans, H. E.; Busso, E. P.; Qian, Z. Q. *Acta Mater.* **2006**, *54*, 3241–3252.
144. Deb, P.; Boone, D. H.; Manley, T. F. *J. Vac. Sci. Technol. A* **1987**, *5*, 3366–3372.
145. Tolpygo, V. K.; Clarke, D. R. *Acta Mater.* **2004**, *52*, 5129–5141.
146. Suo, Z. *J. Mech. Phys. Solids* **1995**, *43*, 829–846.
147. He, M. Y.; Evans, A. G.; Hutchinson, J. W. *Acta Mater.* **2000**, *48*, 2593–2601.
148. Miller, R. A.; Lowell, C. E. *Thin Solid Films* **1982**, *95*, 265–273.
149. Bartlett, A. H.; Maschio, R. D. *J. Am. Ceram. Soc.* **1995**, *78*, 1018–1024.
150. Chang, G. C.; Phucharoen, W.; Miller, R. A. *Surf. Coat. Technol.* **1987**, *32*, 307–325.
151. Freborg, A. M.; Ferguson, B. L.; Brindley, W. J.; Petrus, G. J. *Mater. Sci. Eng. A* **1998**, *245*, 182–190.
152. Kerkhoff, G.; Vaßen; Stover, D. In *Cyclic Oxidation of High Temperature Materials*; Schütze, M., Quadakkers, W. J., Eds.; IOM Communications: London, 1999; pp 373–382.
153. Hsueh, C.-H.; Haynes, J. A.; Lance, M. J.; Becher, P. F.; Ferber, M. K.; Fuller, E. R., Jr.; Langer, S. A.; Carter, W. C.; Cannon, W. R. *J. Am. Ceram. Soc.* **1999**, *82*, 1073–1075.

# COMPREHENSIVE CORROSION



ELSEVIER  
CORROSION  
ELSEVIER

# COMPREHENSIVE CORROSION



ELSEVIER  
CORROSION  
ELSEVIER

## 2.01 Principles of Corrosion in Liquids

**G. S. Frankel**

Fontana Corrosion Center, MSE The Ohio State University, Enarson Hall 154 W 12th Avenue, Columbus, OH 43210, USA

**R. A. Cottis**

Corrosion and Protection Centre, School of Materials, University of Manchester, P.O. Box 88, Sackville Street, Manchester M60 1QD, UK

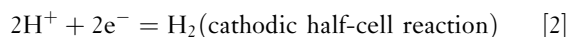
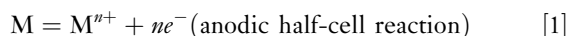
© 2010 Elsevier B.V. All rights reserved.

2.01.1	Thermodynamics	725
2.01.2	Kinetics	726
2.01.3	Passivity	727
2.01.4	Uniform Corrosion in Practice	727
2.01.5	Uniform Corrosion of Iron	728
2.01.6	Uniform Corrosion of Copper	729
2.01.7	Uniform Corrosion of Zinc	730
References		730

### 2.01.1 Thermodynamics

The corrosion reaction is an electrochemical cell. Like other electrochemical cells such as batteries, corrosion requires at least one anodic and one cathodic half reaction, where anodic reactions generate electrons and cathodic reactions consume electrons. In closed electrochemical cells, charge is conserved; there is no net generation or consumption of electrons.

For a generic metal  $M$  dissolving in an acidic solution, the dominant half reactions might be



Each half reaction will be in equilibrium (where the rates in the forward and reverse directions are equal) at a reversible potential. For half reactions in which all reactants and products are in their standard state, the reversible potential is given by the standard potential,  $E^\circ$ , which can be calculated from the difference in standard free energy of formation of the products and reactants,  $\Delta G^\circ$ , the number of electrons transferred in the half reaction,  $n$ , and Faraday's constant,  $F$ , according to

$$E^\circ = -\Delta G^\circ / nF \quad [3]$$

Reversible and standard potentials of any half reaction versus a suitable reference electrode are given. It is customary to use the standard hydrogen electrode (SHE) shown in eqn [2] as a universal reference when listing the potential of a half-cell. Under standard state conditions, the activity of the protons is unity,  $a_{H^+} = 1$ , and the partial pressure of hydrogen gas is one bar,  $P_{H_2} = 1$  bar (1 bar = 0.987 atm). The potential of the

SHE is arbitrarily set at zero,  $E_{SHE}^\circ \equiv 0$ . Correspondingly, this means that the free energy of protons in solution at unit activity is arbitrarily set to 0 as a reference point, which is required for any free energy scale.

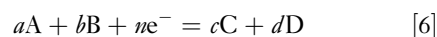
In the more general case where species are not present in their standard state concentrations, the reversible potential at equilibrium for a half reaction,  $E^{rev}$ , is given by the Nernst equation

$$E^{rev} = E^\circ + \frac{RT}{nF} \ln \left\{ \frac{\Pi(a_{ox})^j}{\Pi(a_{red})^k} \right\} \quad [4]$$

where  $R$  is the gas constant,  $T$  is temperature, and  $\Pi(a_{ox})^j$  and  $\Pi(a_{red})^k$  are the products of the activities of the oxidized and reduced species respectively, raised to a power equal to their stoichiometric coefficients in the half reaction equations. For dilute solutions, the activity coefficient is approximately equal to one. Therefore

$$a_A = \gamma_A c_A \approx c_A = [A] \quad [5]$$

where  $\gamma_A$  is the activity coefficient of species  $A$ , and  $c_A$  and  $[A]$  represent the concentration of species  $A$  in units of moles per liter. It should be noted that equating activity to concentration for dilute concentrations is a statement of Henry's law, which utilizes a hypothetical standard state of 1 mol  $l^{-1}$ . The Henrian activity is different than that obtained from Raoult's Law, which states that activity equals mole fraction (activity coefficient equals 1) when mole fraction is close to unity. Raoultian activity is used commonly in electrochemistry for gases and solvents. Thus, for the general half reaction





The Nernst equation is

$$E^{\text{rev}} = E^{\circ} + \left(\frac{RT}{nF}\right) \ln \left(\frac{[A]^a[B]^b}{[C]^c[D]^d}\right) \quad [7]$$

And at room temperature

$$E^{\text{rev}} = E^{\circ} + \left(\frac{0.059}{n}\right) \log \left(\frac{[A]^a[B]^b}{[C]^c[D]^d}\right)$$

The reversible potentials calculated from Nernst equations are important in corrosion, because half reactions will proceed in the net anodic (oxidizing) direction only at potentials more noble than the reversible potential. Similarly, cathodic (reducing) reactions will occur only at potentials less anodic than the reversible potential. Therefore, an analysis of the reversible potentials for two reactions provides insight into the thermodynamic likelihood for an electrochemical cell to proceed in the direction required for corrosion to occur: the reversible potential for the cathodic reaction must be higher than that for the anodic corrosion reaction.

### 2.01.2 Kinetics

Since electrochemical half reactions either generate or consume electrons, their rates can be assessed and measured as currents, or current densities when normalized to the area. As mentioned, an electrochemical half reaction will proceed in the net anodic or cathodic direction at potentials above or below the reversible potential respectively. At the reversible potential, the reaction proceeds in both directions

at the same rate, which when converted to the units of current density is called the exchange current density,  $i_0$ .

Electrochemical kinetics describe the rate of an electrochemical reaction as a function of the potential relative to the reversible potential or a reference electrode. In general, the rate of an electrochemical half reaction increases as the potential difference from the reversible potential increases. At a large enough potential difference from the reversible potential, the Tafel equation describes this relationship when the rate is limited by the transfer of charge across the interface:

$$E - E^{\text{rev}} = b \log(i/i_0) \quad [8]$$

where  $b$  is the Tafel slope. On a plot of  $E$  versus  $\log |i|$ , called an Evans diagram, this expression is a straight line with the slope of  $b$ . In Figure 1, the expression is plotted as  $\log |i|$  versus  $E$  and the slope is  $1/b$ :

$$\log i = \log i_0 + \frac{E - E^{\text{rev}}}{b} \quad [9]$$

As shown in Figure 1, the hydrogen evolution reaction, eqn [2], goes in the cathodic direction at potentials below the reversible potential for that reaction, which is given by the Nernst equation. The metal dissolution reaction goes in the anodic direction at potentials above the reversible potential for that reaction.

Many metals will dissolve by uniform corrosion when immersed in an acidic solution. In an acid, the primary cathodic reaction is often the hydrogen evolution reaction, and metal dissolution may be written as eqn [1]. Both reactions will occur on

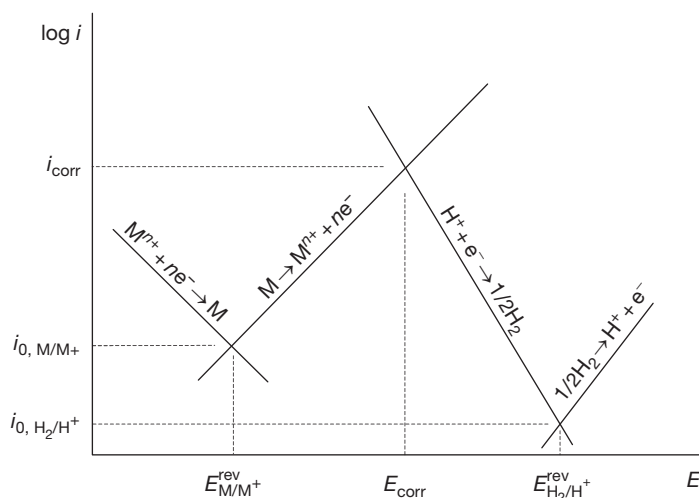


**Figure 1** Schematic Evans diagram for corroding active metal in an acid. Reproduced from Frankel, G. S.; Landolt, D. In *Corrosion and Oxide Films*, Stratmann, M., Frankel, G. S., Eds.; 2003; p. 38, with permission from Wiley-VCH Verlag GmbH & Co. KGaA.

the same surface at essentially the same potential. This potential is called a ‘mixed potential,’ because it is between the reversible potential of the two reactions. It is also called the open circuit potential (OCP) or for a corroding metal, the corrosion potential,  $E_{\text{corr}}$ .

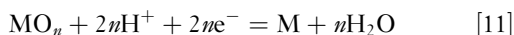
As shown in **Figure 1**,  $E_{\text{corr}}$  is the potential at which the anodic and cathodic current densities are equal, which is required for charge neutrality. For the more general case where there might be more than one anodic or cathodic reaction,  $E_{\text{corr}}$  at any point in time is the potential where the following is obeyed:

$$\sum i_a = \sum i_c \quad [10]$$

For uniform corrosion to occur, the anodic reaction must not be localized at specific spots on the surface of a sample. Instead, the anodic reaction must occur at multiple sites across the surface and continually move to new sites, thereby evenly removing material across the surface over time. Similarly, the cathodic reaction must not be localized. When these reactions remain at fixed locations, the attack is nonuniform, resulting in a localized form of attack such as pitting, crevice, or intergranular corrosion.

### 2.01.3 Passivity

Another form of nominally uniform attack involves a passive metal surface rather than the active dissolution described in the previous section. Passivity describes the relatively low rate of corrosion exhibited by metals covered by a thin oxide or hydroxide film, the passive film. Passive films are thermodynamically stable at high potentials for many metals. For example, the Nernst equation can be calculated for a reaction in which a metal oxide is formed from a metal in an aqueous solution:



$$E^{\text{rev}} = E^\circ - 0.059\text{pH} \quad [12]$$

where  $E^\circ = -(nG_{\text{H}_2\text{O}}^\circ - G_{\text{MO}_n}^\circ)/nF$  following **eqn [3]**. As indicated before, at potentials above this reversible potential, reaction [11] would tend to go in the anodic direction, from right to left or the opposite direction of what is written in **eqn [11]**, resulting in the formation of an oxide film. For many metals, this potential is below the potential for hydrogen evolution associated with proton or water reduction, and therefore, the passivation reaction will proceed spontaneously in aqueous solutions.

Passive films form spontaneously in the majority of practical environments on stainless steels, and

alloys of Al, Ni, and Ti. Fe spontaneously passivates at high pH or at high potentials. W, in contrast, spontaneously passivates at low pH. For many metals, including Al, Cu, and Zn, the passive oxide film is stable only in the mid-pH region. These metals are described as being amphoteric in nature.

Stainless steels are iron-based alloys with good corrosion resistance owing to the formation of a Cr-rich passive film. When Fe is alloyed with >13% Cr, such a protective passive film can form, thereby achieving the good corrosion protection associated with Cr while maintaining the mechanical properties of steel. Common grades of stainless steel contain 16–20% Cr, as well as other elements such as Ni and Mo.

Spontaneously formed passive films typically have a thickness of 2–4 nm, although they tend to thicken as the potential is increased. The protectiveness of passive films usually increases with potential, and the application of a high potential often improves the corrosion resistance by thickening the passive film. This is the basis for anodization, which is commonly performed on Al to thicken the aluminum oxide layer. At room temperature, the thickness increases by about  $1.2 \text{ nm V}^{-1}$ . Iron and nickel oxides are semi-conducting so that they support the oxygen evolution reaction at potentials above the reversible potential for that reaction, and therefore cannot be anodized to high potentials. Cr-rich passive films that form on Cr and Cr-containing alloys such as stainless steel dissolve at high potentials forming the soluble chromate ion (a process known as transpassive corrosion), and thus also cannot be anodized.

It should be noted that almost all metals and alloys that can be protected by a spontaneously formed passive film are susceptible to accelerated localized corrosion such as pitting or crevice corrosion as the result of localized breakdown of the otherwise protective passive film. Such breakdown requires the presence of an aggressive species, such as chloride ions, and is accelerated for many passive metals by the presence of high chloride concentration, high temperature, and high potentials.

### 2.01.4 Uniform Corrosion in Practice

Metals and alloys can corrode uniformly in one of three states:

- Active

In this case, the metal is in direct contact with the environment, the rate of corrosion being controlled by the kinetics of the anodic and cathodic

reactions, with a contribution (usually small except in pure waters) of solution resistance due to the separation between the instantaneous anodic and cathodic sites on the metal surface. It is normally only practicable to use alloys in this state if the rate of hydrogen evolution is low, which effectively limits alloy systems that can be used in this state in practice to those based on metals with an equilibrium potential that is not too far below that for hydrogen at the relevant pH (such as copper, nickel, and iron), or on metals that have a very low exchange current density for hydrogen evolution (such as lead and zinc). In aerated environments, it is common for the rate of corrosion to be controlled by the transport of oxygen to the metal surface, which leads to a typical uniform corrosion rate in air-saturated solutions such as seawater of  $0.1\text{--}1.0\text{ mm year}^{-1}$ , depending on the flow conditions. In stagnant liquids, soils and similar situations where the flow is restricted, when the surface is covered by a corrosion product film or when the solution has a low conductivity, such as many fresh waters, the corrosion rate will be lower.

- Immune

In this case the metal is the thermodynamically stable state and corrosion cannot occur at a significant rate (in an environment that is completely free of ions of the metal, there will be a very low corrosion rate as the metal oxidizes to a sufficient extent to achieve the metal ion concentration that is in equilibrium with the metal). In the presence of complexants or species that produce stable salts, the metal ion concentration may be maintained below the value that is in equilibrium with the metal, allowing corrosion to occur. Thus, in cyanide leaching of gold ores, gold ions are complexed by cyanide, allowing continuing corrosion of particles of metallic gold, with oxygen reduction as the cathodic reaction. In this condition, the metal is effectively corroding in the active state, although the kinetics will tend to be rather more complex.

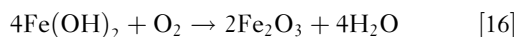
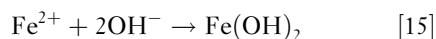
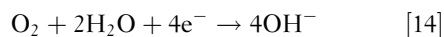
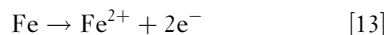
- Passive

In the case of passive metals, the corrosion rate is controlled by the properties of the passive film. This is usually an oxide or hydroxide, although passivation by salt films is also possible. The kinetics of passive corrosion have been studied in considerable detail in recent years, largely because of the requirements of nuclear waste disposal, for which some approaches depend on the corrosion performance of passive alloys over many thousands of years (see **Chapter 2.39, Predictive Modeling**

**of Corrosion** for a detailed discussion of this work). Other applications where the rate of passive corrosion is important are in the primary circuit of water-cooled nuclear reactors, where the release of radioactive transmutation products from the metals of construction of the reactor leads to significant safety hazards, and in biomedical applications where the release of metal ions (such as nickel and chromium) can lead to allergic or toxic effects on neighboring tissue. Otherwise, the rate of passive corrosion is usually not significant, and the various forms of localized corrosion tend to present much more serious problems for passive alloys.

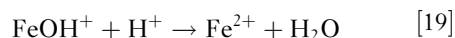
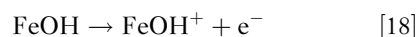
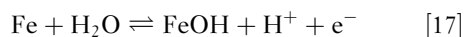
### 2.01.5 Uniform Corrosion of Iron

Unprotected iron will corrode and form rust in many environments. Lorenz and Heusler have provided a good summary of their work and others' on the mechanism of iron corrosion.<sup>1</sup> The reactions commonly used to describe this process in an aerated environment are



where the final iron oxide product, red rust, is usually a hydrated form of  $\text{Fe}_2\text{O}_3$  (usually assigned the formula  $\text{FeO}(\text{OH})$ ). However, it seems unlikely that solid  $\text{Fe}(\text{OH})_2$  is formed, as this would be expected to lead to a form of passivation, with an underlayer of  $\text{Fe}(\text{OH})_2$  covered by  $\text{Fe}_2\text{O}_3$ , and it is more likely that the oxidation of ferrous species to ferric occurs in solution, leading to precipitation of rust in solution away from the surface of the metal, resulting in the nonprotective corrosion product film that everyone is familiar with. In a deaerated aqueous environment (in the absence of oxygen), the cathodic reaction is hydrogen evolution via proton (eqn [2]) or water reduction and the ferric product will not form. The rate of reaction in this case is low in neutral or alkaline environments.

The mechanism of ferrous ion formation has been shown to be more complicated than eqn [13] as it involves multiple single electron transfer steps and depends on the pH of the environment:



The second charge transfer step (reaction [18]) is the rate-determining step, and in consequence, the rate of the overall reaction depends on the concentration of FeOH on the iron surface, and hence (by virtue of the equilibrium of reaction [17]) on the pH. Thus, in deaerated environments, the anodic and cathodic reaction kinetics both depend on pH; somewhat counter-intuitively, the rate of the anodic reaction at a constant potential decreases as the solution becomes more acidic (i.e., as the pH decreases), but this is countered in practice by the increase in the rate of the cathodic hydrogen evolution reaction due to the increased hydrogen ion concentration, which leads to an increase in the corrosion potential.

At high pH, iron spontaneously passivates as described earlier, forming a thin oxide layer. In neutral or acidic environments, passivity on Fe is only achieved by the application of a sufficiently high potential. If the potential is scanned, the polarization curve will exhibit an active-passive transition. In the active region, the current can be extremely high, approaching  $1 \text{ A cm}^{-2}$  (corresponding to a corrosion rate in the region of  $1 \text{ mm h}^{-1}$ ). In acidic solutions, a limiting current associated with mass-transport limited dissolution in the presence of a salt film on the surface can be observed over a range of potential. However, after the active-passive transition, the current density might drop by 4 orders of magnitude as a result of the formation of a thin passive film. On iron, the passive film has been found to be a bilayer, with an inner layer of  $\text{Fe}_3\text{O}_4$  and an outer layer of  $\gamma\text{-Fe}_2\text{O}_3$ .

Alloying of iron with carbon and other elements such as Mn and Si to make steel generally has a small influence on the corrosion rate, although sulfide inclusions (typically MnS) act as local sources of sulfide and other species that accelerate corrosion locally. However, alloying elements such as Cu, Cr, P, and Ni added in small quantities to create low-alloy steels can result in considerable improvement in corrosion resistance. One class of low-alloy steels specifically designed for improved atmospheric corrosion resistance is referred to as weathering steels.<sup>2</sup> The rust layer on weathering steels is more compact and protective than that formed on plain carbon steel, although not as thin and protective as the passive film formed on stainless steels having Cr content  $>13\%$ . The protectiveness of this compact thick film formed on weathering steels is improved by periodic drying, and hence, their primary use is in atmospheric exposure rather than immersed or buried conditions. However, under many atmospheric conditions, the oxide layer on

weathering steels provides sufficient protection even without painting, which is a huge advantage as the maintenance costs associated with repainting degraded structures can be eliminated.

## 2.01.6 Uniform Corrosion of Copper

Copper is a noble metal in that its reversible potential is higher than that for the hydrogen evolution reaction. Therefore, Cu is thermodynamically immune to corrosion in deaerated noncomplexing environments. This is the reason why, at the time of this writing, many countries are considering long-term disposal of high-level radioactive waste in Cu canisters that would be located in the anoxic (oxygen-free) saturated zone (below the water table) of a geologic formation. However, complexation of copper ions by, for instance, chloride or ammonia, or the presence of species, such as sulfide, that form copper salts that are more stable than the oxide, can decrease the reversible potential for Cu dissolution to the extent that it is below that of hydrogen evolution, rendering the Cu susceptible to corrosion even in anoxic environments.<sup>3</sup> Furthermore, Cu will corrode in the presence of oxygen and other oxidizing agents.

Cu is widely used in water distribution piping, both for hot and cold water. Cu water piping will occasionally fail by pitting corrosion. This form of attack is not well understood<sup>4</sup> (there appear to be several different mechanisms of pitting, at least some of which are microbially induced), and usually confined to certain districts or groups of houses. The concentrations of sulfate, chloride, hydroxide, carbonate, and bicarbonate ions can influence Cu pitting susceptibility.<sup>5</sup>

In aerated solutions, the surface of Cu is typically covered with a film of  $\text{CuO}$ , which provides marginal protection. In atmospheric conditions, Cu eventually develops a protective patina; in most atmospheres (where there is significant  $\text{SO}_2$  present as a result of pollution) this has the structure, composition, and characteristic green color of the mineral bronchite,  $\text{Cu}_4(\text{SO}_4)(\text{OH})_6$ .<sup>6,7</sup> The patina can also contain carbonate, or by the seashore, chloride.<sup>8</sup>

The corrosion rate of Cu in the atmosphere has been found to depend on the conditions existing during the initial period of the exposure. When the initial exposure was in the winter, the rate of corrosion over a period of years was greater than when the initial exposure was in the summer, indicating that the nature of the initial surface oxide film plays a critical role in the subsequent development of that film.

Cu is often alloyed for improved mechanical properties. Brasses and Al bronzes are susceptible to dealloying attack whereby the less noble alloying element is dissolved preferentially, leaving a porous structure with little mechanical strength. Dezincification is the most common form of dealloying, caused by the preferential dissolution of Zn from brass. A small addition of As to the alloy, only about 0.04%, will reduce the susceptibility to dezincification; additions of Sn, Sb, or P are also effective.<sup>9</sup>

### 2.01.7 Uniform Corrosion of Zinc

Zn is an active metal with good corrosion resistance in the atmosphere and in natural waters owing to the formation of a protective oxide or hydroxide surface film. This combination of low corrosion potential and low self corrosion rate makes it an ideal sacrificial anode for steel. Zn and Zn alloys are widely used as corrosion protective coatings on steel, often in combination with

paint overcoats. Most steel automotive body panels nowadays are galvanized prior to coating.

The pH of the environment has a large effect on the corrosion rate of Zn as Zn is amphoteric, corroding rapidly in low- and high-pH environments, but slowly in the pH range from about 6 to 12. As a result, the lifetime of galvanized layers is decreased in polluted locations where the mist and dew are acidic.

### References

1. Lorenz, W. J.; Heusler, K. E. In *Corrosion Mechanisms*; Mansfeld, F., Ed.; Marcel Dekker: New York, 1987.
2. Murata, T. In *Uhlig's Corrosion Handbook*, 2nd edn.; Revie, R. W., Ed.; John Wiley: New York, 2000.
3. Pourbaix, M. In *Lectures on Electrochemical Corrosion*; Plenum: New York, 1973.
4. Rushing, J. C.; Edwards, M. *Corr. Sci.* **2004**, *46*, 3069–3088.
5. Cong, H.; Michels, H. T.; Scully, J. R. *J. Electrochem. Soc.* **2009**, *156*, C16–C27.
6. Vernon, W. H. J.; Whitby, L. *J. Inst. Met.* **1929**, *42*, 181–202.
7. Vernon, W. H. J. *Whitby, J. Inst. Met.* **1930**, *44*, 389–408.
8. Vernon, W. H. J. *J. Inst. Met.* **1933**, *52*, 93–100.
9. Bengough, G. D.; May, R. *J. Chem. Soc.* **1924**, *32*, 81–269.



## 2.02 Passivity and Localized Corrosion

**G. T. Burstein**

Professor of Materials Chemistry and Corrosion, Department of Materials Science and Metallurgy, University of Cambridge, Pembroke Street, Cambridge CB2 3QZ, UK

This article is a revision of the Third Edition article 1.5 by G.T. Burstein, volume 1, pp 1:118–1:150, © 2010 Elsevier B.V.

2.02.1	Introduction	731
2.02.2	Determination of the Passive Corrosion Rate	734
2.02.3	The Polarization Curve	735
2.02.4	Mechanism and Kinetics of Passivation	737
2.02.5	Thermodynamics of Passivity	740
2.02.6	Chemical and Electrochemical Passivity	743
2.02.7	Passivation in Nonaqueous Liquids	744
2.02.8	Passivity of Alloys	744
2.02.9	Compositions of Passivating Oxide Films	746
2.02.10	Breakdown of Passivity and Pitting	747
References		751

### Abbreviations

**AC** Alternating current

**DC** Direct current

**SHE** Standard Hydrogen Electrode

### Symbols

***a*** Reaction coordinate

***A*** Constant

***B*** Constant

***E*** Electrochemical potential

***E*<sup>°</sup>** Standard equilibrium potential

***F*** The Faraday

***i<sub>b</sub>*** Backward current density

***i<sub>f</sub>*** Forward current density

***i<sub>pass</sub>*** Passive current density

***k*** Rate constant

***M*** Atomic weight of metal

***R*** Universal gas constant

***t*** Time

***T*** Temperature

***x*** Metal loss

***z*** Number of electrons released by oxidation

**$\Delta G^*$**  Change in Gibbs free energy

**$\eta$**  Overpotential

**$\rho$**  Density

### 2.02.1 Introduction

This article was first published in the 3rd edition; it is reprinted here in its entirety with only minor typographic corrections and a few editorial comments incorporated as footnotes.

Passivity is a state of low corrosion rate brought about under a high anodic driving force, or potential, by the presence of an interfacial solid film, usually an oxide. The phenomenon of passivity has been defined in a number of ways,<sup>1,2</sup> most of which are similar in meaning. Although from the more literal sense of the word, passivity could include metals immune from corrosion (such as gold in water); in the parlance of corrosion science, this is specifically excluded. Passive metals are thermodynamically unstable<sup>3</sup>: they possess a kinetic stability, which is engendered by a solid interfacial film, without which corrosion would occur. The oxide film, formed anodically through a mechanism very similar to that of the corrosion process, stifles the rate of further oxidation (corrosion and further passivation) by forming a barrier between the metal surface and its environment. So, many metallic structures and components depend on the state of passivity for their stability. From an engineering point of view, the phenomenon of passivity is a remarkable one due to its requirement of the extremely thin film to procure passivity.

The typical passivating oxide film on many metals is only 1–10 nm in thickness and is produced by the oxidation of the surface to a depth measured in monolayers of atoms. Without the passivating oxide film, many metallic structures would corrode at a very fast rate, phenomenological evidence for this being provided by the very fast rates at which localized corrosion (such as pitting corrosion or stress-corrosion cracking) can propagate when passivity is disrupted, and regeneration of the passivating oxide film cannot take place. This thin oxide film is the stabilizing barrier which separates the potentially active metal from the environment, for structures smaller than a hypodermic needle and larger than an aircraft. Not surprisingly, passivity and passivation have been examined extensively in the past for many decades using a large range of techniques; despite the great deal of information and knowledge that has thereby been generated, there are many questions that remain to be answered before a complete understanding of the subject is achieved.\* For example, since the advent of stainless steel, it has been realized that this important class of material owes its stainlessness to the surface oxide film, and even now, despite the large amount of research, using a wide range of *in situ* and *ex situ* techniques, the exact nature of this oxide film remains to be resolved. Passivity of iron has long been recognized<sup>6–8</sup>; the modern theories relating to the passivating oxide film are primarily due to Evans.<sup>9–12</sup>

Passivity of a metal lies in contrast to its activity, in which the metal corrodes freely under an anodic driving force. The passive state is well illustrated by reference to a classical polarization curve prepared potentiostatically or potentiodynamically (Figure 1). As the potential is raised (in the anodic or positive sense) above the equilibrium potential between the metal and its dissolved ions, the driving force toward oxidation and the rate of dissolution increase; in the classical case, it represents an exponential rise of current with potential according to the Tafel equation.<sup>13</sup> When the potential is high enough, a dramatic reduction in the dissolution rate occurs, and the rate of dissolution remains low with further increase in potential. The latter state is the state of passivity and the minimum potential at which the low oxidation

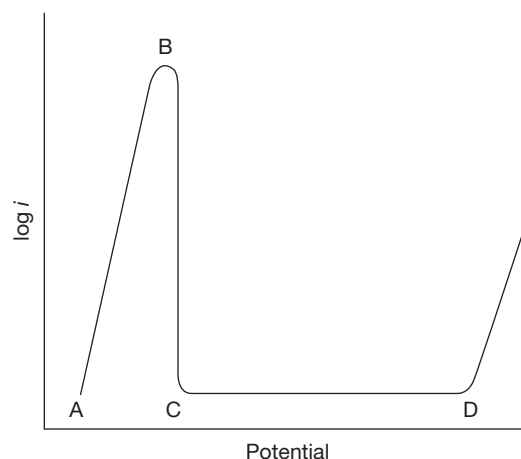
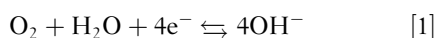


**Figure 1** Schematic anodic polarization curve for a metal. Region AB describes active dissolution of the metal. BC is the active–passive transition, with passivation commencing at B. Passivation is complete only at potentials higher than C. The metal is passive over the range CD.

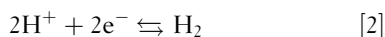
rate exists is the passivation potential. It is a feature of the passive state that the oxidation rate is independent of potential, or nearly so.<sup>14</sup> This feature does not define the state of passivity uniquely, as the diffusion-controlled dissolution reactions are also independent of potential, and passivity is not due to dissolution under diffusion control. Some surface films too, while displaying all the qualitative properties of passivity with respect to the polarization curve, allow a high corrosion current to pass, and cannot be regarded as passivating. An extreme example of this is the phenomenon of electropolishing, in which the rate of dissolution is controlled by the migration of ions through a viscous salt film layer, the rate is independent of potential, and the current density is high.<sup>14–17</sup> It is a primary requirement of passivity that the oxidation rate is small and it depends entirely on the application. The state of passivity is never perfect, and a passive metal always corrodes at a finite rate, albeit that this rate may be very low. The surface film forms a barrier between the metal and its environment, which retards further oxidation. Raising the potential in the passive state, while increasing the driving force toward oxidation, serves to thicken the surface oxide film, thereby increasing the barrier for further oxidation. It is this increase in the barrier film thickness with increase in potential that generates the potential independence of the oxidation rate as long as the metal remains passive. This phenomenon is used in high-voltage anodizing of some metals, in which highly resistive oxide films can be grown to a thickness of several hundred nanometers at high voltages.

\*Editor's note: This article embodies the state of the subject in about 1992. The subject has changed relatively little since then and most of the content is consistent with more recent work. For more recent reviews of passivity, the reader may consult 'argentumsolutions'<sup>4</sup> and Staehle *et al.*<sup>5</sup>

The above description of passivity refers to passivity stimulated by an externally applied potential. Passivity of real structures is, however, generally achieved in the absence of externally applied power (although it can be stimulated by application of an anodic voltage, a practice followed for anodic protection).<sup>18</sup> In the absence of an applied potential, the sink for the electrons generated by the anodic oxidation of the metal is a cathodic reaction which occurs on the passive metal surface itself. The cathodic reaction, thereby, provides the driving force. In aqueous systems, this is generally the reduction of dissolved oxygen or the reduction of water to hydrogen (or both simultaneously, depending on the potential involved) occurring on the passive oxide surface, as:



or



These same cathodic reactions also fuel the corrosion of metals if corrosion (rather than passivity) is the dominant process. It is to be noted that both cathodic reactions involve an increase in pH, while the anodic site tends to develop a decreased pH. These changes in pH over the anodic and cathodic sites can be important as they can lead to destabilization of the passive state. The state of passivity involving a cathodic reaction on the passive surface is sometimes referred to as 'chemical passivity,' as opposed to 'anodic passivity' or 'electrochemical passivity' (stimulated by an applied potential). The two phenomena are, however, very similar: both are electrochemical in nature. The only mechanistic difference lies in the fact that under chemical passivity, the transferred electrons must pass through the passivating oxide film from the metal atoms to the cathodic reactant, since the anodic reaction (metal oxidation) occurs at the metal–film interface, and the cathodic reaction occurs at the film–electrolyte interface. On the contrary, under externally applied anodic stimulation, the electrons are passed around an external circuit to a separate cathode. Electrons pass rather readily through most passivating oxide films, even those of high resistivity, because they are so thin. Other cathodic reactants may also behave as passivating agents. Their role varies depending on their nature. Thus, for example, the chromates added to the aqueous environment raise the potential of the metal by accelerating the cathodic reaction. If the potential is thereby raised into the passive regime, the metal is passivated essentially by the added chromate, which then functions as a corrosion

inhibitor. The reduced chromate also aids passivity by depositing Cr(III) into the passivating film. The earlier theory that only oxygen is required as an adsorbed layer for passivation is, of course, not tenable, since passivity can be achieved readily with alternative oxidizing agents, or with an applied potential in the absence of dissolved oxygen (or any other oxidizing agent): passivity is due to a surface film, usually an oxide, as a distinct solid phase and usually of thickness greater than one monolayer. The oxide ions required to form the film originate from water molecules, and the role of dissolved oxygen is merely that of an oxidizing agent.

Other corrosion inhibitors also enhance passivity without electrochemical reduction, by depositing insoluble oxidation products into the passivating film. For example, benzoate ions cause deposition of ferric benzoate into the oxide, but do not provide any cathodic reaction.

The phenomenon of chemical passivity can be considered by examining the polarization curves for the separate anodic and cathodic reactions, shown in **Figures 2 and 3**. The two forms of passivating agent, one that yields an accelerated cathodic reaction and the other providing insoluble reaction product, are both illustrated. Considering the fact that the anodic and cathodic reactions must occur at an equal rate, the point of intersection of these two kinetic lines in **Figures 2 and 3** describes the condition of the metal.

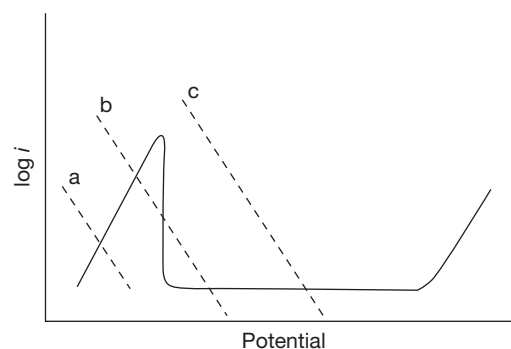


**Figure 2** Schematic anodic polarization curve for a passivable metal (solid line), shown together with three alternative cathodic reactions (broken line). Open-circuit corrosion potentials are determined by the intersection between the anodic and cathodic reaction rates. Cathode a intersects the anodic curve in the active region and the metal corrodes. Cathode b intersects at three possible points for which the metal may actively corrode or passivate, but passivity could be unstable. Only cathode c provides stable passivity. The lines a, b and c, respectively, could represent different cathodic reactions of increasing oxidizing power, or they could represent the same oxidizing agent at increasing concentration.

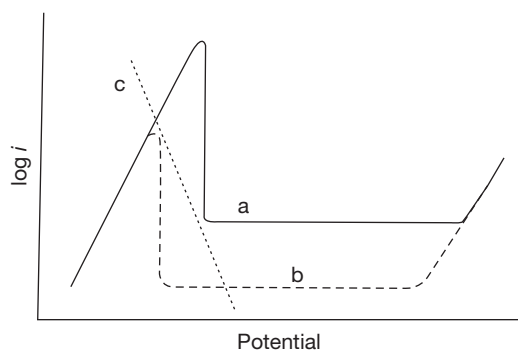
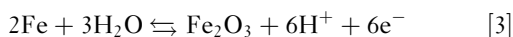


**Figure 3** Schematic anodic polarization curves for a passivable metal showing the effect of a passivating agent that has no specific cathodic action, but forms a sparingly soluble salt with the metal cation: (a) without the passivating agent and (b) with the passivating agent. The passive current density, the active–passive transition and the critical current density are all lowered in (b). The effect of the cathodic reaction c, is to render the metal active in case a, and passive in case (b).

To achieve chemical passivity, the potential must be sufficiently high to overcome the active loop (otherwise the oxidizing agent accelerates corrosion) and therefore, there must be sufficient cathodic reactant of sufficiently high driving force.

The process of formation of a passivating oxide film is anodic in nature; the driving force for its formation is raised by increasing the potential anodically across the metal–environment interface. Thus, for example, the driving force for formation of a passivating oxide film on iron by the reaction,



is raised as the potential is increased above the equilibrium potential between the metal and its oxide. Raising the potential, however, also raises the driving force toward oxidation of the metal, and thus, increases the propensity toward accelerated corrosion. The two processes of accelerated corrosion and passivation are, therefore, generally in competition, and the balance between the two can be quite delicate. Examples are abound, both in the laboratory and in the field, of passivity failure, leading frequently to rapid and sustained localized corrosion. Mechanisms describing the origins of stress-corrosion cracking and corrosion-fatigue inherently involve rupture of the passivating oxide film, and consequently, the rapid reactions that may ensue on the bare metal surface. The basis on which such forms of localized corrosion occur are well understood. In its passive state, the metal is thermodynamically very unstable. The conditions of the metal, the solution

and the potential dictate its state of passivity. If passivity is lost by whatever mechanism (e.g., by oxide film rupture or through reaction of local heterogeneities), the metal reacts anodically at high potential and therefore at a high rate, with the cathodic area occurring mainly on the surrounding undamaged passive surface. One consequence of such anodic reaction is the transport of ions to carry the current, and the generation of acidity through hydrolysis of the reaction products.<sup>19–23</sup> (Note that the reaction above describing ferric oxide formation on iron generates  $\text{H}^+$ .) If these processes generate a local solution of sufficient aggressiveness, then localized corrosion will ensue: the rate will be fast because of the high potential. If the local solution developed is not sufficiently aggressive or the reaction rate is not high enough (because the potential is too low), the site repassivates (i.e., it regenerates the passivating oxide film). These phenomena are dealt with in more detail below.

Passivity normally exists within a well defined potential range, below which the metal may activate and corrode, and above which it may transpassivate and corrode. The potential range is characteristic of the metal–environment system, and predominantly, of the available cathodic reaction. Because all anodic processes occurring through the passivating film, including the film growth, are controlled by the ionic conductance of the film,<sup>15,24</sup> a low ionic conductivity to metal cations as well as oxide ions is beneficial to passivity. Oxides of high ionic conductivity would grow to be thick, and thick oxide films are more likely to be mechanically unstable, because they are more crystalline, and more defective. The passivating film thickness is also controlled by the rate of dissolution of the oxide into the electrolyte. The electron conductivity of the oxide is of less consequence. Metals such as aluminum and tantalum, whose oxides are of low electronic conductivity, can be as passive as iron and copper, whose oxides are highly electronically conductive. Although passivity in an open circuit requires electron passage through the oxide, this is rarely a limiting step. Consideration of the variables associated with each system is therefore critical in determining the state of passivity.

## 2.02.2 Determination of the Passive Corrosion Rate

If a metal were perfectly passive and the solubility of its ions were zero, the passive corrosion rate would be

zero but it would take a long time to reach that state. This is never the case, and passivity always implies an ultimate steady state corrosion rate, and it is generally important to know that rate. This is determined as the passive current density,  $i_{\text{pass}}$ , through polarization experiments. The rate of penetration in the passive state is then  $dx/dt = Mi_{\text{pass}}/zF\rho$ , where  $M$  is the atomic weight of the metal,  $z$  is the electron number,  $F$  the Faraday constant, and  $\rho$  the density of the metal. Polarization curves as shown in Figure 1 are commonly measured by potential sweep measurements (at constant sweep rate,  $dE/dt$ ); such curves also yield a passive range of potentials. The value achieved, however, depends on the imposed potential sweep rate because at any potential the steady state value of  $i_{\text{pass}}$  takes some time to be reached. The time taken to reach the steady state, often overlooked or ignored in laboratory studies of passivity, can be measured in minutes, hours, or even days.<sup>†</sup> Fast sweep rates may, therefore, yield an erroneously high value. The passive current density is, thus, more accurately obtained at constant potential. A further feature, which can yield an erroneously low value of  $i_{\text{pass}}$ , is the presence of a cathodic reactant, such as oxygen. To overcome this, laboratory measurements are made in deaerated solution; full deaeration is, however, not possible. The lower the true passive current density, the greater is the inaccuracy in the measured value.

Measurement of  $i_{\text{pass}}$  at constant potential does not resolve this inaccuracy. The error can be recognized by measurement using a rotating disc or cylinder electrode. Variation in the rotation rate then alters the rate of oxygen transport, and an apparent reduction in  $i_{\text{pass}}$  is observed as the rotation rate increases. The constituent of passive corrosion rate forming a viably passive structure is to be questioned, and is dependent on the application. One of the most demanding states of passivity is that required by metallic surgical implant materials, where even small passive corrosion rates of metals (undamaging to the metal), which show toxicity in ionic form and whose ions are not excreted at the appropriate rate, may accumulate to significantly toxic levels. It is, nevertheless, quite common for the passive corrosion rate to be low, that a well engineered structure corroding in its passive state is visibly unchanged after very many years service.

<sup>†</sup>Editor's note: This is probably an understatement; work on Alloy 22, a highly corrosion resistant passive alloy, suggests that the passive corrosion rate falls over months or years.

### 2.02.3 The Polarization Curve

It is worthwhile to consider the general form of the anodic polarization curve, obtained when the potential of a metal is scanned in deaerated solution. Figure 4 shows a series of schematic curves which describe the onset of passivity (as shown in Figure 1) and the behavior of passive state. Such curves can only be determined potentiostatically or potentiodynamically; galvanostatic measurement of potential cannot provide the polarization curve of a passivating metal because the potential is a three-valued function of the current density. At low anodic potential (region AB) in solutions where the metal ion has appreciable solubility, the metal dissolves actively with the current rising exponentially with increase in potential (see Figure 1). Passivation commences at B and is completed at C; region BC comprises the active-passive transition. The passive current then continues to flow with further increase in potential, approximately independent of potential, until point D, F, H, or J depending upon the

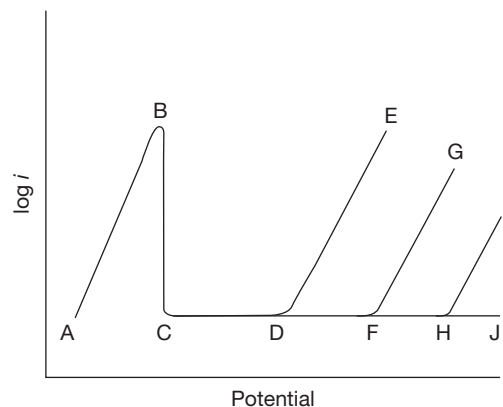


**Figure 4** Schematic anodic polarization curve of a metal showing possible behavior of the passive region. AB is the active region and BC the active-passive transition. The metal is passive at potentials more positive than C. If the solution contains aggressive anions such as chloride, passivity may breakdown at D (the pitting potential), and the current rises with further increase in potential (DE) as corrosion pits propagate and nucleate. The region DE is not necessarily linear. If pitting agents are absent, but the passivating film be transpassively dissolved, then transpassive corrosion commences at F, increasing in rate with increasing potential (FG). If the passivating film is chemically and electrochemically stable, and is conductive to electrons, oxygen evolution commences at H, and increases in rate to I. The metal remains passive. If the film is stable and insulating to electrons, oxide film growth continues with further increase in potential (HJ) and the metal remains passive.



properties of the passivating film with respect to the electrolyte solution.

In solutions with a sufficient concentration of aggressive ions, such as chloride, premature failure of passivity occurs with many metals (such as aluminum, iron, nickel, and their alloys) at point D, by the nucleation of pitting corrosion. Failure of passivity is localized, and the current rises with further increase in potential (region DE), as the pits grow and more pits form. Note that the current density is usually obtained by dividing the measured current by the surface area of the specimen being tested. When localized corrosion, such as pitting occurs, the actively dissolving area is found to be very small (else, corrosion cannot be termed localized). The current density measured as such does not, thus, represent the local corrosion rate, or the penetration rate, which is in fact much faster. The rise in mean current density in region DE of [Figure 4](#) is not necessarily an exponential function of the potential. The region accommodates an increasing number of pits with increase in potential, as well as their growing surface area, with time. This region also shows a significant noise in the measured current.

In the absence of aggressive anions, the passivating oxide film may begin to be oxidized at point F to produce a soluble anion, and passivity again fails, this time by oxidative dissolution. The current rises with further increase in potential (region FG) as the dissolution rate rises. This occurs, for example, with chromium and manganese by oxidation to  $\text{CrO}_4^{2-}$  and  $\text{MnO}_4^{2-}$  or  $\text{MnO}_4^-$ , respectively. If the oxide film is stable, and is also a good electron conductor, such as with iron and nickel in neutral or moderately alkaline solutions, then point H marks the potential at which the solution begins to be oxidized. In an aqueous solution, this is the oxidation of water to oxygen, for which the standard electrode potential is 1.228 V (SHE) at 25 °C. Subsequently, the rise of current with increase in potential in region HI describes the increasing rate of oxygen evolution. Passivity here is not disturbed (unless the oxide film is damaged mechanically by the oxygen bubbles). This process can only occur if the oxide film is an electron conductor, since the oxidation of water requires the withdrawal of electrons from the water molecules through the oxide to the metal: oxidation of water occurs at the film–electrolyte interface.

Finally, if the film is stable in solution, and is a poor electron conductor, as those formed on aluminum and tantalum in halide-free environments, oxygen evolution is not possible. Raising the potential

beyond point H in [Figure 4](#) causes the film to grow further, with the current continuing to be approximately independent of potential (region HJ). It is under these conditions that high-voltage anodizing can be adopted to produce relatively thick oxide films, as described below.

For metal–environment couples, where the passivating oxide film does not break down, does not oxidatively dissolve, and does not conduct electrons readily, the only mechanism for relaxing the increasing electric field as the potential is increased is the thickening of the oxide film. The process occurs by ion conduction through the film. In fact, if the potential of aluminum immersed in a suitable anodizing electrolyte is raised suddenly to a high value, transient evolution of oxygen bubbles is observed. The oxide is, of course, a dielectric, and the sudden potential jump imposes dielectric breakdown with conduction of electrons because of the increased electric field. The effect is rapidly quenched as the barrier oxide film grows simultaneously, relaxing the electric field.

In many cases, passivating and highly electrically insulating oxide films can be grown to thicknesses of several hundred nanometers, and even micrometers; such films can be observed readily in the scanning electron microscope.<sup>24–29</sup> The applied anodic voltages can be in the region of several tens, and even hundreds of volts, and can be applied as a DC current or voltage, or as an AC voltage, depending on the required properties of the oxide. The most widely anodized metal industrially is aluminum. Although AC anodizing of aluminum imposes a cathodic half-cycle for each anodic half-cycle, oxide film reduction does not occur, contrary to what might be expected. This is because the oxide film on aluminum is irreducible. In an appropriate electrolyte, the passivating oxide film can be induced to be overlaid with a much thicker microporous oxide layer. Electrolytes that induce formation of a porous overlayer tend to be more aggressive, for example, aluminum in sulfuric or phosphoric acid. Inevitably, the porous layer is underlaid with a nonporous barrier layer (otherwise the high applied voltage would induce vigorous oxygen evolution in those areas lacking the electron-insulating oxide). The barrier layer, which is the passivating component, is thus named because it carries most of the electric field and controls the film growth current. Its thickness increases linearly with the applied voltage, consistent with the behavior of other passivating oxide films. This duplex oxide film formed on aluminum finds wide technological

applications. Anodizing of titanium to appropriate oxide film thicknesses produces vigorous interference colors, a phenomenon exploited in the ingenious art of Pederferri.<sup>30</sup>

## 2.02.4 Mechanism and Kinetics of Passivation

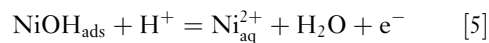
The basic mechanism of passivation is easy to understand. When the metal atoms of a fresh metal surface are oxidized (under a suitable driving force), two alternative processes occur. They may either enter the solution phase as solvated metal ions, passing across the electrical double layer, or may remain on the surface to form a new solid phase, the passivating film. The former case is active corrosion, with metal ions passing freely into solution via adsorbed intermediates. In many real corrosion cases, the metal ions, despite dissolving, are in fact not very soluble, or are not transported away from the vicinity of the surface very quickly, and may consequently deposit on the surface as an oxide or insoluble salt. Often these cases are not passivating because the insoluble corrosion product is deposited from the solution phase as a poorly adherent, loose, crystalline substance. Formation of rust on steel is one such example; blue and green deposits on corroded copper plumbing are another. Oxide films which are passivating are most commonly formed when they are generated directly on the metal surface without the constituent metal ions passing first into solution.<sup>31</sup> While the precise structures of passivating films remain contentious,<sup>32,33</sup> they are known to be coherent and continuous, necessarily so since any lack of continuity would provide paths for active dissolution leading to localized corrosion.

Formation of the first layer (a monolayer) of passivating oxide film on a denuded metal surface occurs easily by the loss of protons from the adsorbed intermediate oxidation products, such intermediates being common to both dissolution and passivation processes.<sup>34–42</sup> Thus, for example, the first oxidative step in the anodic oxidation of nickel is the formation of the unstable adsorbed intermediate NiOH by

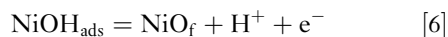


Similar initial reactions occur on many metals such as iron and cobalt. This intermediate can now react further in one of the two ways. Oxidation and protonation of the intermediate to Ni(II) leads to

dissolved nickel ions (active corrosion) which are unable to passivate the metal:



On the other hand, oxidation and deprotonation of the same intermediate leads directly to passivation by:



where the subscript 'ads' represents the adsorbed intermediate, 'aq' represents the aquated metal ion in solution, and 'f' represents the oxide film. These reactions are able to proceed because the solvent, water, is effectively an infinite source, and sink, for  $\text{H}^+$ . The intermediate  $\text{NiOH}_{\text{ads}}$  is common to both the dissolution and passivation reactions. It can be regarded as an hydroxide of Ni(I) or an adsorbed OH radical; the distinction probably is not important to the case of passivation. Because of subsequent reactions, it is better considered as the compound of univalent nickel. This intermediate does not exist as a bulk species. Its existence as an intermediate is undoubtedly due to the fact that it is adsorbed to the metal surface on one side, and carries the aqueous double layer on the other. The preferential occurrence of reactions [5] and [6] depends on the solution composition, its pH, the potential, and the temperature. It is apparent that the nickel atoms involved in going from Ni to NiO via steps [4] and [6] never leave the metal surface. Formation of NiO (or the hydrated form,  $\text{Ni}(\text{OH})_2$ ) by precipitation from the dissolved nickel ions formed in reaction [5] does not lead directly to passivity. For iron, formation of oxides from dissolved  $\text{Fe}^{2+}$  via precipitation from solution leads to nonprotective rust. (Brown rusts involve further oxidation of  $\text{Fe}^{2+}$  by dissolved oxygen). Such precipitated oxides are not usually passivating. The passivating oxide formed by reaction [6] can only occur when the equilibrium potential between the Ni and NiO is reached or exceeded. Higher oxides of nickel may also impart passivity once the appropriately higher equilibrium potential is exceeded.<sup>31</sup> Clearly, such oxides form preferentially in solutions where the oxide is effectively insoluble: for many metals these are solutions of neutral and mildly alkaline pH. Nevertheless, in acidic solutions where the oxide is thermodynamically unstable relative to the dissolved metal cation, passivation can still occur (and does so on many metals, including nickel), as exhibited by chromium. Cr(III) oxide is thermodynamically unstable in acidic systems,<sup>3</sup> but the metal is still very passive in sulfuric acid (at the appropriate potentials); the implication is that the dissolution of

the passivating oxide into acidic solutions, which must inevitably occur, is very slow, and the rate of corrosion of chromium in its passive state is undoubtedly controlled by this dissolution rate. (It is chiefly chromium (III) which gives rise to passivation of alloys containing sufficient quantities of Cr, such as stainless steels and nickel–chromium alloys.)

There are, in fact, many possible steps that could be included in the basic mechanisms described above, for example, involving adsorption processes for  $\text{H}_2\text{O}$  and  $\text{OH}^-$ , and interactions among the adsorbed species. The most widely studied is the reaction of iron, but similar steps are also encountered in the anodic oxidation of many metals. These mechanisms include the same basic steps as described above.<sup>34–42</sup>

The first monolayer is generally formed before any significant film thickening occurs, because of the very strong dependence of the film growth rate on the electric field across the reacting interface. A mechanism of the type shown in eqns [4] and [6] does not necessarily involve an oxide nucleation step. Rather, it is a random oxidation of the exposed surface metal atoms until the first monolayer of oxide is complete.<sup>41–44</sup> Such a model shows that passive films may, in fact, be amorphous, with no defined crystal structure. Alternatively for some metals, an initial nucleation step may occur with two-dimensional spreading of the oxide over the surface to produce expanding circular ‘pancakes’ of oxide which link when they impinge on one another. This mechanism, which involves different kinetics, has not been found in repassivation experiments involving mechanically stripped transition metal surfaces.<sup>41–44</sup> Growth of the first monolayer of the passivating oxide causes significant reduction in the rate of oxidation of the metal, but in general, the process does not stop there.

Once the metal surface has become covered with its first monolayer of the oxide film, the metal is then separated from its environment by that oxide, and film thickening ensues: metal cations or oxide anions (or both) are transported through the existing oxide film, thereby relaxing the electric field which drives the mobile ions, until a steady state is reached. Ion migration (or vacancy migration) under the electric field controls the film growth rate.<sup>14,24,45–48</sup> As the film thickens at constant potential, the relaxing electric field across it reduces the rate of field-assisted ion migration, and the rate of film growth declines. The steady state is reached when the rate of film thickening equals the rate of film dissolution into the environment, resulting in a net constant rate dissolution of metal. Different metals display different passive

corrosion rates, and it is the numerical value of this rate which dictates whether the metal can be regarded as sufficiently passive for specific engineering purposes. Highly passive metals usually carry very thin oxides, and the electric field sustained by the overall metal–oxide–film–electrolyte interphase region is very high. For example, at a potential of 0.2 V and an oxide film thickness of 2 nm the mean electric field is ca.  $108 \text{ V m}^{-1}$ . The precise distribution of this electric field, namely the fraction lying across the film and that lying across the two phase interfaces is not known, although several models exist.<sup>47–51</sup> Similarly, the identity of the transporting ions is often not known. Although bulk oxides can often be classified as cation-vacant, anion-vacant or containing excess ions interstitially, thus dictating the mode of ionic charge transport, passive films are so thin that properties of bulk oxides may not necessarily be applicable. The effect is strikingly realized when it is considered that many passivating oxide films are often no thicker than one or two unit cells of the equivalent bulk oxide, and their transport properties may consequently differ from those of the bulk material. Only in the model of Macdonald *et al.*<sup>50,51</sup> is such a distinction drawn for the corrosion and passivation characteristics, where the model predicts that the transport of metal cations across the oxide from the metal interface to the electrolyte interface causes dissolution, and the transport of oxide ions in the reverse direction causes film growth.

Derivation of the rate of oxide film growth proceeds as follows. When the metal carrying its oxide film is at its equilibrium potential, no overpotential exists across the oxide, and the rate at which ions move through the oxide from the metal to the electrolyte equals the rate at which they move back again. Expressed as current densities, the forward rate is  $i_f$  and the backward rate  $i_b$ ; these rates are equal at equilibrium. Ions moving through the film do so via vacancies (anionic or cationic, leading to anionic or cationic migration), or interstitially. They, thereby, encounter an energy barrier which they must surmount in order to move: the width of this energy barrier is the distance between anionic or cationic sites in the oxide lattice if the mechanism is by vacancy migration, or the distance between interstitial sites if the mobile ions move interstitially. This distance is  $2a$ . The height of the energy barrier is the activation energy,  $\Delta G^*$ . Thus, at equilibrium

$$i_f = i_b = zFk \exp \left[ -\frac{\Delta G^*}{RT} \right] \quad [7]$$

where  $k$  is the rate constant,  $z$  is the charge number,  $F$  is the Faraday constant,  $R$  is the gas constant, and  $T$  the temperature. Equation [7] is an expression of the Arrhenius equation.

We now apply an anodic overpotential  $\eta$ , for film growth, and for simplicity, we regard this overpotential as being distributed entirely across the oxide film. If the oxide film has a thickness  $x$ , then the electric field across the film is  $d\eta/dx$ , which equals  $\eta/x$  if the overpotential lies linearly across the oxide film. The potential drop across the distance  $2a$  (a single energy barrier) is then  $2a\eta/x$ . The activation energy in the forward direction (i.e., with the electric field) is thereby reduced by an amount  $a\eta zF/x$ , and that in the backward direction (i.e., against the electric field) increased by an amount  $a\eta zF/x$ . Thus, under the applied overpotential  $\eta$

$$\begin{aligned} i_f &= zFk \exp \left[ -\frac{(\Delta G^* - a\eta zF/x)}{RT} \right] \\ &= zFk \exp \left[ -\frac{\Delta G^*}{RT} \right] \exp \left[ \frac{a\eta zF}{xRT} \right] \end{aligned} \quad [8]$$

Similarly, in the backward direction

$$\begin{aligned} i_b &= zFk \exp \left[ -\frac{(\Delta G^* + a\eta zF/x)}{RT} \right] \\ &= zFk \exp \left[ -\frac{\Delta G^*}{RT} \right] \exp \left[ -\frac{a\eta zF}{xRT} \right] \end{aligned} \quad [9]$$

The following parameters are constants (at constant temperature) and are simplified to

$$A = zFk \exp \left[ -\frac{\Delta G^*}{RT} \right] \quad [10]$$

and

$$B = \frac{azF}{RT} \quad [11]$$

The net current density,  $i$ , in the forward direction (i.e., producing film growth) is

$$i = i_f - i_b \quad [12]$$

and

$$i = A \exp \left[ \frac{B\eta}{x} \right] - A \exp \left[ -\frac{B\eta}{x} \right] = 2A \sinh \left[ \frac{B\eta}{x} \right] \quad [13]$$

This is the general expression for film growth under an electric field. The same basic relationship can be derived if the forward and reverse rate constants,  $k$ , are regarded as different, and the forward and reverse activation energies,  $\Delta G^*$  are correspondingly different:

these parameters are equilibrium parameters, and are both incorporated into the constant  $A$ . The parameters  $A$  and  $B$  are constants for a particular oxide:  $A$  has units of current density ( $A m^{-2}$ ) and  $B$  has units of reciprocal electric field ( $m V^{-1}$ ). Equation [14] has two limiting approximations.

- (a) When the electric field,  $\eta/x$ , is large (high  $\eta$  and/or small film thickness,  $x$ ),  $2 \sinh y = \exp y$ , and

$$i = A \exp \left[ \frac{B\eta}{x} \right] \quad [14]$$

This is commonly known as the high field equation. It is similar to the Tafel equation for activation controlled electrochemical reactions with the additional feature that the potential driving the reaction lies across an oxide film of variable thickness,  $x$ , rather than across the double layer (of constant thickness). The kinetics of oxide film growth according to this equation approximates to (but are not identical to) inverse logarithmic film growth.<sup>46,52,53</sup> The passivity of most passive metals is associated with a high electric field since most passivating films are very thin. A high electric field implies either a thin passivating film ( $x$  is small) or a high overpotential ( $\eta$  is large), or both.

- (b) When the electric field is small (i.e.,  $\eta$  is small and/or  $x$  is large),  $\sinh y = y$ , and

$$i = \frac{2AB\eta}{x} \quad [15]$$

Equation [15] is ohmic ( $i \propto \eta$  for constant film thickness): the term  $x/2AB$  can be regarded as the film resistance. The equation is identical to parabolic film growth, for which the film thickens with the square root of time at constant potential.

Because passivating films are generally very thin, passivation is normally a high field process and eqn [14] can replace eqn [13]. The same relationships can be applied to high voltage anodizing of metals such as aluminum and titanium. However, under these conditions, the oxide sometimes assumes a duplex structure, with an inner barrier layer and an outer porous layer: for these, the film thickness  $x$ , relates to that of the barrier film only, since it is largely this part which carries the applied voltage. The relationships make no assumption about the identity of the mobile ion, and are equally applicable whether the anion or the cation is mobile within the film lattice causing film growth. Because the anodic current in the passive state is approximately independent of the potential in the steady state, the above kinetic equations

imply that the thickness of the passivating oxide film increases linearly with increase in the overpotential, and therefore with the applied potential. This has been confirmed by ellipsometric analysis of the oxide film.

As the film growth rate depends strongly on the electric field across it (eqn [14]), separation of the anodic and cathodic sites for metals in open circuit is of little consequence, provided film growth is an exclusive reaction. Thus, if one site is anodic, and the adjacent site cathodic, film thickening on the anodic site causes the two sites to swap roles so that the film on the former cathodic site also thickens correspondingly. Thus, the anodic and cathodic sites of the stable passive metal 'dance' over the surface. However, if a permanent separation of sites occur, where the anodic site has restricted access to the cathodic component in the electrolyte (as in a crevice), then breakdown of passivity and associated corrosion can follow. The kinetics outlined above, first observed empirically by Güntherschulze and Betz,<sup>54</sup> were modeled by Verwey<sup>45</sup> with the rate-controlling energy barrier being that between two adjacent cation sites within the oxide film. The same basic form can be derived if the rate-controlling energy barrier is that between a metal atom on the metal surface and an adjacent cation site in the film.<sup>14,46</sup> The rate is then limited by ion injection into the film rather than by ion migration through the film. It should also be noted that the above kinetic relationships can be modified to include the other processes occurring during anodic oxide film growth, such as space charges within the film and charging of the phase interfaces.<sup>47,48,55</sup>

The point defect model of Macdonald *et al.*<sup>51</sup> draws a distinction between cation and anion mobility, with mobile cations leading to metal dissolution and mobile anions (oxide ions) leading to passivity: this model has an inherent attraction of incorporating a mechanism for metal dissolution. The procedure leads to direct logarithmic film growth (at constant potential), as does the place exchange mechanism of Sato and Cohen.<sup>56</sup> Apart from the work of Macdonald,<sup>51</sup> the passive state dissolution rate has been studied far less than the oxide film growth rate, and it is not really known why the dissolution rate of the passivating oxide should be so slow. The process of oxide dissolution has been reviewed<sup>57</sup> and is complex. The complexity of the dissolution has been exemplified by Nii,<sup>58</sup> who showed that the rate of dissolution of nickel oxide particles (with no metal substrate) in aqueous solution is strongly dependent

on trace quantities (for concentrations down to  $\sim 10^{-6}$  M) of ionic impurities in the solution. The rate of dissolution of oxides is influenced by the polarization of the oxides, a notion clearly important to the passivity of metals.

The kinetics outlined above refer strictly to single crystals, with no metallurgical defects, such as grain boundaries. Polycrystalline metals and alloys contain many such defects, and their passivation is expected to be different, especially when the defects may contain high concentrations of impurity atoms, such as sulfur segregated in the grain boundaries in steels. The kinetics of passive oxide film growth, as measured electrochemically, may well be dominated by the passivation of the grain faces because of their overwhelmingly large surface area. However, the long-term stability of the passive state may become dominated by the grain boundaries (as in the case where intergranular corrosion occurs) or by inclusions, precipitates or other microscopic defects. This feature is very important in consideration of measured passive corrosion rates.

Determination of the kinetics of passivation can be carried out potentiostatically, provided any previously formed oxide film, such as that formed by prior exposure to air is first removed. Such removal can be achieved by the reduction at low potential for fairly noble metals, but cannot be readily achieved for the relatively base metals such as chromium, aluminum, or titanium. Some metals, such as iron, become charged with hydrogen during cathodic reduction of their oxide films, a process predicted by the thermodynamics of the two processes. Many alloys may undergo changes in surface composition and structure during applied electrochemical reduction, and subsequent reoxidation kinetics may not be representative of the true alloy surface. Under these conditions, the electrochemical kinetics of oxide film growth can only be determined if the preformed oxide film is stripped away mechanically, by cutting with an inert scribe, such as diamond, sapphire, or boron nitride.<sup>59–66</sup> Such techniques then allow measurement of the kinetics of passivation through potentiostatic current transients or through galvanostatic potential transients. Passivation in open circuit is also amenable to such examination.<sup>66</sup>

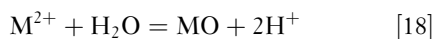
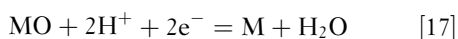
## 2.02.5 Thermodynamics of Passivity

The thermodynamics of passivity, primarily due to Pourbaix,<sup>3</sup> are usefully considered by examining the



equilibria between metals and their oxides in contact with water. Before doing so, however, it is worth bearing a number of points in mind. First, the passivating oxide film is in many cases so thin that its thermodynamics may not be identical to that of bulk oxides. This is already implicit in the discussion of the adsorbed NiOH intermediate in nickel oxidation. The matter is of particular importance when it is realized that the two faces of the oxide film, one in contact with the metal and the other in contact with the environment, are so very different. By nature, the passive film must therefore be regarded as being extremely anisotropic in the sense that its dimensions are very much larger in the two directions parallel to the metal surface than in the third dimension, which is perpendicular to the metal surface. Second, the electric field across any existing passivating oxide is very large in the direction perpendicular to the metal surface and insignificant in the parallel direction, adding to its anisotropy. Finally, in the case of engineering alloys such as stainless steels, it is frequently difficult to ascribe the passivating oxide film to a known stoichiometry or structure, and the use of thermodynamic data of known bulk oxides is open to question. This problem is clearly less pronounced for pure metals. Nevertheless, consideration of the thermodynamics of standard bulk metal oxides can still provide surprisingly good agreement with observation, and can often be used effectively and predictively.

As with all determinations of thermodynamic stability, we commence by defining all possible stable phases, and their standard chemical potentials. For most metals there are many such phases, including oxides, hydroxides, and dissolved ions. For brevity, only the minimum number of phases is considered. The simplest system is a metal M, which can oxidize to form a stable dissolved product,  $M^{2+}$  (corrosion), or to form a stable oxide MO (passivation). In aqueous environments, three equilibria can thereby be defined:



The equilibrium potentials ( $E$ ) for reactions [16] and [17] are then given, respectively, by the Nernst equation:

$$E = E^\circ - \frac{RT}{2F} \ln \frac{[M]}{[M^{2+}]} \quad [19]$$

$$E = E^\circ - \frac{RT}{2F} \ln \frac{[M][H_2O]}{[MO][H^+]^2} \quad [20]$$

where the brackets represent the activities of the components and  $E^\circ$  is the standard equilibrium potential (or standard electrode potential) for the reaction. The value of  $E^\circ$  is readily calculated from the standard chemical potentials of the relevant components. By defining the standard states of the metal, the oxide, and the solvent as the pure components (unit mole fraction), the only solution variables are the  $M^{2+}$  and  $H^+$  activities, provided the metal, the oxide and the water are pure. Thus, in decadic logs, eqns [19] and [20], respectively, are

$$E = E^\circ + \frac{2.303RT}{2F} \log[M^{2+}] \quad [21]$$

and

$$E = E^\circ + \frac{2.303RT}{2F} \text{pH} \quad [22]$$

For the nonelectrochemical reaction [18], the equilibrium constant ( $K$ ) for the reaction is written as

$$\text{pH} = -\frac{1}{2} \log K - \frac{1}{2} \log[M^{2+}] \quad [23]$$

The thermodynamic equilibria are then represented for fixed dissolved metal ion activity as a plot of  $E^\circ$  against the pH of the solution, as shown in **Figure 5**, noting that eqn [21] is independent of pH and eqn [23] is independent of potential. The Figure shows that oxide stability is achieved at potentials greater than  $E^\circ$  for reaction [22] and in solutions of pH greater than that described by eqn [23]. If the potential is greater than  $E^\circ$  for reaction [21] and the pH more acidic than that given by eqn [23] the metal corrodes to give  $M^{2+}$ . If the potential is low, the metal is immune to oxidation. The diagram thus describes the thermodynamically stable phases of the metal in terms of regions of passivity, corrosion and immunity as a function of  $E$  and pH. The position of the lines representing eqns [21] and [23] depends on the value of the selected  $M^{2+}$  activity. It is common (but not necessary) to adopt a concentration of  $10^{-6}$  M for this purpose, but the issue is critical in determining the relative thermodynamic stabilities of the dissolved component and the oxide. The fact that only equilibria with water are considered in the example specifies that any dissolved components present in solution have no effect on the reactions of the metal and its components. Reactive ions such as  $Cl^-$  dissolved in the solution modify the equilibria by their own free energy considerations. Although more complicated,

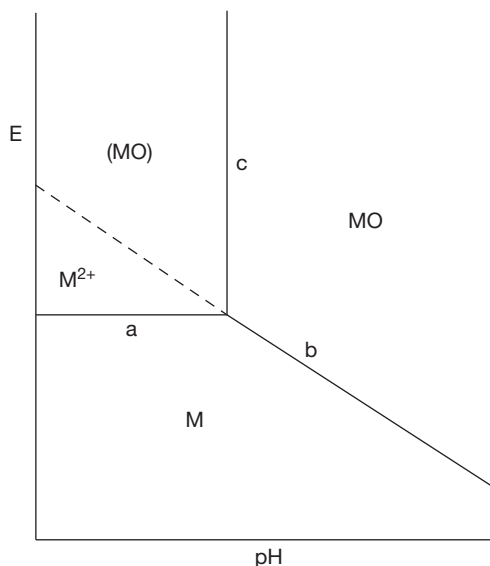


**Figure 5** Schematic potential–pH diagram for a metal M in equilibrium with water in the absence of complexing species. Line a represents eqns [16] and [21]. Line b represents eqns [17] and [22]. Line c represents eqns [18] and [23]. The stable phases are marked in bold. The metastable phase is in parentheses. The broken line is an extrapolation of eqn [22] and indicates possible metastable passivity.

such systems can nevertheless be thermodynamically calculated if the formation constants of the associated complexes and compounds can be defined.

The line representing eqn [22] is shown broken for pH more acidic than eqn [23]. The oxide is not thermodynamically stable in this region of pH, and for true thermodynamic equilibrium should not be shown at all. Many metals, however, still show a passive region in this state, provided the potential is higher than that given by eqn [22]. The origin of this is, of course, kinetic. If an oxide film does form, and if it is very slow to dissolve (it must dissolve since the oxide is unstable relative to the dissolved ion) then passivation ensues. The state has sometimes been referred to as ‘metastable passivity’.<sup>‡31</sup> While it might reasonably be rationalized that passivity is brought about by a very low solubility of the dissolved metal ion, thereby effectively preventing metal dissolution through formation of a sparingly soluble oxide layer, this is not a necessary condition for passivity. Certainly, a thermodynamically stable oxide layer is more likely to generate passivity. However, the existence of the metastable passive state implies that an oxide film may (and in many cases does)

still form in solutions in which the oxides are highly soluble. This occurs for example, on nickel, aluminum and stainless steel, although the passive corrosion rate in some systems can be quite high. What is required for passivity is the rapid formation of the oxide film and its slow dissolution, or at least the slow dissolution of metal ions through the film. The potential must, of course, be high enough for oxide formation to be thermodynamically possible. With these criteria, it is easily understood that a low passive current density requires a low conductivity of ions (but not necessarily of electrons) within the oxide.

It is not possible to predict thermodynamically whether or not a metastable passivating film forms in acidic solutions. Thus nickel, cobalt, and aluminum exhibit metastable passivity in acidic solution (although not necessarily practical); but cadmium does not. Metals which display metastable passivity, particularly in acidic solutions, often show polarization curves whose potential ranges can be correlated with the thermodynamic potentials of the potential–pH (Pourbaix) diagram (Figure 5). Thus, for example, nickel in sulfuric acid shows an active loop between the potentials represented by lines a and b in the Pourbaix diagram; as the potential is increased further, passivity commences when the potential exceeds approximately that described by eqn [22], observed as an active–passive transition. Because metastable passivity is a kinetic phenomenon, however, a significant overpotential may be required to produce it. Where more than one oxide may exist, it is not necessarily associated with the lowest metal oxidation state that provides the best state of passivity. On thermodynamic grounds alone, one predicts the classic form of the anodic polarization curve, in which the passive range of potential is preceded (at lower potential) by an active loop as shown in Figures 1–4. From the point of view of corrosion engineering for acidic systems, metastable passivity is of the utmost importance. Most structural metals designed for acidic environments are used in this state of metastable passivity. These are often chromium-containing alloys (stainless steels and nickel-based alloys), since chromium shows extremely good metastable passivity in acidic environments.

It is worth emphasizing that the position of lines representing equilibria with the dissolved species,  $M^{2+}$ , depend critically on the solubility of the ion, which is a function of pH. For example, iron in moderately alkaline solution is expected to be very passive,<sup>3</sup> and so it is in borate solutions (in the absence of aggressive ions). However, the anodic polarization curve still shows a small active loop at low potential.<sup>68</sup>

<sup>‡</sup>Editor’s note: This phenomenon has been analyzed in more detail by Macdonald.<sup>67</sup>

The form of [Figure 5](#) is common among many metals in solutions of acidic to neutral pH of non-complex anions. Some metals such as aluminum and zinc, whose oxides are amphoteric, lose their passivity in alkaline solutions, a feature reflected in the potential–pH diagram. This is likely to arise from the rapid rate at which the oxide is attacked by the solution, rather than from direct attack on the metal, although at low potential, active dissolution is predicted thermodynamically.<sup>3</sup> The reader is referred to the classical work of Pourbaix<sup>3</sup> for a full treatment of potential–pH diagrams of pure metals in equilibrium with water.<sup>8</sup>

### 2.02.6 Chemical and Electrochemical Passivity

Passivity is provided and maintained by the appropriate cathodic reaction such as reaction [\[1\]](#) or [\[2\]](#): it is a requirement of this reaction that the potential is held within the passive range. This may be achieved by the cathodic reactant in the solution, such as oxygen, or it may be applied from an external power supply. In the absence of other oxidizing agents, only reaction [\[1\]](#) or [\[2\]](#) can provide and maintain passivity. For more noble metals, reduction of water is not possible, and passivity can be maintained only by reaction [\[1\]](#). These metals are, of course, immune from corrosion (and passivation) in the absence of dissolved oxygen. Base metals such as aluminum, when bared in solution (these metals inevitably carry a prior air-formed oxide film), are rendered passive by reduction of water because the initial potential is so low.<sup>59,60,66</sup> Passivity can then be maintained by reduction of oxygen because the potential rises significantly during passivation. Passivating agents in solution may be divided broadly into two groups. Those providing the cathodic reactant are oxidizing agents and raise the open-circuit potential of the metal into the passive regime, but only in sufficient concentration. The process is shown schematically in [Figure 2](#). In insufficient concentration, such oxidizing agents raise the potential further into the active region, thereby accelerating corrosion. Such behavior is well typified by the long-known reaction between iron and nitric acid. In concentrated

nitric acid, iron is passive, but if the acid is diluted, very powerful corrosion occurs with vigorous evolution of nitrogen oxides. This process was reported earlier by Keir<sup>7</sup> and Faraday.<sup>8</sup> Many oxidizing agents fall into this category, such as chromates, molybdates, oxygen, and hydrogen peroxide acting on steels. Some oxidizing agents become aggressive in reduced form, and cannot be regarded as passivating agents; these include for example, the chlorate anion which is cathodically reduced to chloride on iron. The chloride anion can initiate pitting corrosion, particularly at high potential, and the high potential is itself brought about by the same cathodic reaction.

Other passivating agents, such as phosphates<sup>70–73</sup> and benzoates<sup>74</sup> (for steels) do not fall into this category and they have no oxidizing action. Their role in enhancing passivity is to aid formation of the passive film under the cathode present in solution. In a polarization curve, this would be observed as a decrease in the passive current density, often coupled with a decrease in the potential of the active–passive transition (see [Figure 3](#)). These chemical passivating agents act by forming highly insoluble compounds with the dissolving metal (such as ferric phosphates and benzoates). The salts are precipitated over areas of the metal surface which may become active. Presumably, a passivating oxide is then formed beneath the deposited metal salt, since the metal is no longer capable of rapid dissolution, although this has not been firmly established. The formation of azelaic acid from linseed oil<sup>75,76</sup> allows precipitation of sparingly soluble ferric azelate as a passivating agent in linseed oil-based paints. Again, the metal presumably passivates by oxide film formation beneath the deposited azelate. For these passivating agents to be effective, an oxidizing agent, such as oxygen must be present.

Chromate ions fall into both the categories, namely as both an oxidizing agent and a source of insoluble film.<sup>77,78</sup> Their oxidizing power raises the potential for a number of metal systems into the passive region. The reduced form is Cr(III), either as  $\text{Cr}_2\text{O}_3$  or as a spinel with the metal oxide of the substrate, which is deposited onto the metal surface; this is itself a passivating agent and acts as such for many metals. These prime processes render chromates as effective passivating agents, and are responsible for the use of chromates as inhibitive pigments in metal priming paints (often as zinc chromate).<sup>||</sup>

<sup>8</sup>Editor's note: Resources are now available, both as commercial programs and on the world-wide web<sup>69</sup> that allow calculation of  $E$ –pH diagrams for many metals, taking account of a wide range of dissolved and solid species.

<sup>||</sup>Editor's note: Unfortunately chromate's power as a corrosion inhibitor is matched by its toxicity, and it is now banned for most applications.

Other forms of similar chemical passivating agent act where no oxide is formed. These must be mentioned here, although their action is not truly passivating. Although the dissolution–precipitation mechanism for oxide formation on metals like iron does not generally lead to passivation, some salt films formed by precipitation of dissolved ions from solution may give rise to significant passivity. Thus, silver in acidic chloride solutions forms a very stable insoluble layer of AgCl, which reduces the corrosion rate of the metal substantially. The chloride is formed, only partially, by precipitation from solution. As such the AgCl layer is thick relative to the normally formed oxide film on metals such as aluminum or stainless steel, and results in visible tarnishing of the metal. Although the corrosion rate is thereby rendered low, the metal is not strictly passive, and tarnishing of silver by silver chloride is not only unsightly – it is slowly damaging. The behavior of lead in sulfuric acid is similar because of the low solubility of lead sulfate.

Passivity can also be enhanced by incorporating components that catalyze the cathodic reaction, thereby raising the potential. By alloying titanium with small quantities of platinum or palladium, or by implantation of these elements into the surface, the cathodic hydrogen evolution reaction is thus accelerated, and titanium becomes anodically protected in appropriate environments.<sup>79</sup> Interestingly, this simple form of anodic protection does not involve an external power supply. Platinum and palladium function as good hydrogen catalysts – they raise the exchange current density for hydrogen evolution. A similar mechanism has been proposed for the action of lead-based pigments in priming paints.<sup>75</sup>

### 2.02.7 Passivation in Nonaqueous Liquids

Far less is known of the corrosion and passivation of metals in nonaqueous solvents and solutions,<sup>80</sup> and the topic can be mentioned only briefly here. The prime requirement for passivity of metals in water is the formation of an oxide film by anodic reaction with oxygen obtained from water. This is not always available in organic solvents. Thus, polarization of nickel in methanol containing sulfuric acid<sup>81</sup> shows no passive region in solutions containing less than 2 wt% water, but shows an increasingly large passive potential range, and lower passive current density, as the water content is increased above 2 wt%. Passive oxide formation arises from reaction with the water

component. Reaction of the metal with the methanol component to produce the oxide is clearly not possible. Some metals can react with the methanol component of methanolic solutions, but such reaction produces the nonpassivating methoxide rather than the oxide, and results in corrosion. The effect is seen clearly by the reaction of titanium with alkaline methanol solutions.<sup>65</sup> Generally, the effect of chloride in inducing pitting corrosion and stress corrosion cracking in metals such as titanium is increased substantially as the water content of the methanol solution is reduced, demonstrating the destabilizing effect of the reduced water activity on the stability of the passive state. Both passivation and corrosion can be difficult to predict in nonaqueous liquids in the absence of laboratory tests.

## 2.02.8 Passivity of Alloys

While the same basic mechanism for passivity of pure metals also applies to alloys, the processes involved in the passivation of alloys have an added complexity. In many cases, only one component of the alloy has the property of being passive in a particular environment. Alloys such as stainless steels, which contain highly passive components (chromium in this case), owe their corrosion resistance to the surface enrichment of the passivating component.<sup>82</sup> Thus, stainless steels resist corrosion in many acidic systems (where iron or carbon steel would be poorly passive or not passive at all) by a passivating oxide film containing Cr predominantly as Cr(III). Surface analytical techniques such as Auger electron and X-ray photoelectron spectroscopies reveal substantial enrichment of chromium in the passivating oxide film on these alloys.<sup>32,33,83–87</sup> There are only two ways by which this enrichment can arise. Either the other component (iron in the case of binary iron/chromium stainless steels) is left behind at the metal surface when the chromium oxidizes, or it is dissolved during passivation. In aqueous corrosion, particularly at ambient temperatures, it is undoubtedly dissolution of the iron component that causes chromium enrichment of passive stainless steel surfaces.<sup>64</sup> This contrasts gaseous oxidation of the same class of metals at high temperature, where chromium-rich oxide films are also formed, but iron cannot dissolve in the environment, and diffusion in the metal phase is much more rapid. Classically, a minimum amount of chromium is required in the alloy before chromium enrichment in the oxide film can be achieved: for stainless steels,

this is determined to be around 12–13 wt%. Steels containing less than this amount of chromium are not regarded as stainless. The basis of this is as follows. In environments, corrosive towards iron but passivating towards chromium (such as sulfuric acid), iron dissolves selectively from the surface of the alloy, and so the surface concentration of chromium increases to a level where the basic chromium-rich oxide film can cover the surface completely: the metal is then passive. This film contains significant quantities of Cr(III), but iron ions are also found in its structure, generally decreasing towards the film–electrolyte interface. Steels containing greater than about 12–13% chromium show a dramatic improvement in their passivating properties, in comparison to those of lower chromium content.<sup>88</sup> Analyses of such oxide films are performed using *ex situ* surface analytical techniques, such as Auger electron spectroscopy, X-ray photoelectron spectroscopy, and secondary ion mass spectrometry coupled with some form of depth profiling. Most such analyses performed to date have been carried out on surfaces exposed to the solution for relatively less time (seconds or minutes), despite the fact that steady-state passivity of stainless steels takes much longer to achieve. It is not known whether, after a sufficiently long period of exposure, the oxide film on stainless steel is composed entirely of chromium oxides.

The ease with which stainless steels can passivate increases with the level of chromium within the alloy, and hence, materials with higher chromium content are more passive (i.e., conduct a lower passive current density) and passivate more readily (i.e., the critical current density is lower and the active–passive transition is lower in potential). They are also passive in more aggressive solutions: the pitting potential is higher.

The precise mechanism by which surface enrichment of chromium through dissolution of iron in stainless steels occurs is still under some debate.<sup>64,89–91</sup> For alloys which are single-phase solid solutions, the phenomenon is readily understood if the passivating element is the major component of the alloy. The corrodible element then simply dissolves from the metal surface enriching the surface with the passivating element which then completes its passivating oxide. However, far less than 50% chromium is required to achieve passivity. Examination of the repassivation of stainless steels shows evidence of dissolution of the corrodible components from the film as it grows.<sup>64</sup> Excess iron ions in the film are dissolved and replaced by chromium ions from the metal, progressively enriching the film with chromium until passivity is

reached. However, the process may not be so simple. Recent ideas of percolation through binary alloys involve dissolution of individual and clusters of iron atoms from the alloy surface.<sup>89–91</sup> The residual chromium atoms are able to diffuse over the surface, progressively uncovering iron atoms and iron atom clusters. These are dissolved until there is sufficient chromium on the surface to link up into a continuous passivating network. The threshold concentration of Cr in the alloy ( $\sim 12\%$ ) is then determined as the percolation threshold below which interlinked networks of iron atom clusters exist through the alloy, and it is no longer stainless. Above this threshold composition, continuous percolation clusters do not exist and the alloy is passive and stainless. The attraction of this model is that its concepts can be extended to the nucleation of pitting corrosion of stainless steels<sup>92</sup> (see below). The distinction between the two modes of iron dissolution and associated chromium enrichment is, however, a fine one.

Stainless steels show another interesting feature. At high potentials, passivation by an oxide rich in Cr(III) is lost since the Cr(III) component of the oxide is transpassively dissolved in chromate ions (line FG in [Figure 4](#)). In solutions in which iron oxides are stable at high potential (mildly alkaline) and the metal does not undergo pitting corrosion, the resulting iron oxide can then provide some passivity: the roles of the two components of the alloy are thus reversed. If the nonchromium components of the steel are also not passive at high potentials, the metal corrodes transpassively. Very powerful oxidizing agents can bring about transpassive corrosion of stainless steel. Under normal conditions of use in dilute aqueous solutions, however, these high potentials would not be achieved, and chromium provides the prime passivity of these materials.

For stainless steels to remain passive, the level of chromium defined by the bulk composition must be maintained throughout the entire metal matrix. If local regions exist within the alloy microstructure where the chromium level is depleted, these become susceptible to localized corrosion, and increasingly so as the chromium content is reduced. Ultimately, if the chromium content is reduced locally below  $\sim 12\%$ , this region no longer carries the composition of a stainless steel, and corrodes as a nonstainless steel alloy. However, any reduction in the local chromium concentration of the alloy matrix is deleterious to passivity, since these alloys become progressively less passive as the chromium concentration is decreased. Such conditions are found under sensitizing heat treatments, commonly in or around welds (the heat-affected zone).



In these regions, at the appropriate temperature, chromium carbides precipitate in the grain boundaries depleting the matrix around the carbides of chromium.<sup>88</sup> The grain boundaries may then activate in service under conditions where the grain matrix is passive.

In multiple-phase alloys, the situation is different. The passivity of each phase is of importance, but there can also be a significant synergy between the behavior of adjacent phases. The presence of copper-rich precipitates in aluminum alloys containing the element accelerates the cathodic reaction locally because the exchange current density for the cathodic reaction on the relatively noble precipitate is higher than it is on the surrounding aluminum matrix. In passivating electrolytes and in the absence of pitting agents such as chloride, passivity is thus enhanced because of the increased potential. However, in the presence of chloride, the potential may be raised into the pitting regime, and passivity then becomes degraded. Aluminum alloys containing more noble alloying elements such as copper or iron are generally less resistant to pitting corrosion than pure aluminum.

### 2.02.9 Compositions of Passivating Oxide Films

The composition, structure and even thickness of passivating oxide films on metals are in fact extremely difficult to determine, mainly because these oxide films are so thin, and are 'held together' by the compositions of the interfaces (with the metal and with the electrolyte) as well as by the high electric field they carry. Many methods of determination are *ex situ* techniques, requiring removal of the specimen from the electric field as well as from the electrolyte. These methods include Auger electron spectroscopy (AES), X-ray photoelectron spectroscopy (XPS) and secondary ion mass spectrometry (SIMS), as well as X-ray diffraction (XRD).<sup>32,33</sup> A range of *in situ* methods, such as ellipsometry, frequency response analysis<sup>#</sup> and photocurrent spectroscopy are also used to provide information on the passive film.<sup>32,33</sup> These techniques, however, give more indirect information; they do not present compositional or structural information directly, but probe other properties of the passive interface, from

which more detailed understanding must be inferred. The new techniques of scanning tunneling and atomic force microscopies, which can be used *in situ*, may yield some information in the future.

The thickness of the oxide film is most readily determined by cathodic reduction, provided the film is cathodically reducible and the reduction is 100% current efficient. The cathodic charge involved then determines the film thickness for films of known composition. The method is suitable only for more noble metals, and for most structural metals it is not relevant. Film thicknesses determined by ellipsometry have been used successfully, but assumptions of the refractive index must be made. The passivating film on iron is determined to be  $\text{Fe}_3\text{O}_4$ ,  $\gamma\text{-Fe}_2\text{O}_3$  or  $\text{FeOOH}$ , depending on the conditions under which it is formed.<sup>3,32,33</sup> The thickness of the film formed in borate buffer solutions is up to  $\sim 4\text{--}5$  nm, the value depending on the potential at which it is formed. The thickness is a linear function of potential. There is now significant evidence that the  $\text{Fe(III)}$  film which passivates iron contains some  $\text{Fe(IV)}$ ,<sup>93</sup> a phenomenon which may account for the sometimes necessarily high overpotential required to passivate the metal. Surface analyses of passive films on iron, as well as other metals such as aluminum and stainless steel, show that the outer surfaces are usually hydrated, equivalent to hydroxide ions forming part of the outer structure in place of oxide ions.<sup>94-96</sup> This is, of course, only to be expected from film growth in aqueous solution. The inner regions of the films tend to be less hydrated or not hydrated at all. The passivating oxide on aluminum is reckoned to be amorphous, but crystallizes with increasing thickness during anodizing.

The incorporation of anions from the electrolyte, such as borate and carbonate, into the oxide has also been shown to occur on iron and cobalt,<sup>97</sup> such anions being restricted to the outer layers of the film. Attempts to determine chloride incorporation into passive iron surfaces from chloride-containing electrolytes have met with contradictory results, and it is still not known whether or not chloride incorporation is a precursor step to pitting corrosion.<sup>32,33,98-101</sup> Neither is this mechanistically important, but vexed question have been answered unambiguously for other metals.

The oxide film composition on alloys is inevitably more complex; some discussion of chromium-containing alloys is given above. Generally, and not surprisingly, the components of the alloy are to be found in the passivating oxide film,<sup>101</sup> but the role that these play in determining passivity and its breakdown is far

<sup>#</sup>Editor's note: now generally known as electrochemical impedance spectroscopy (EIS).

more open to question. Stainless steels show the presence of iron, chromium, and nickel in the oxide (and molybdenum for alloys containing the element), with elemental ratios that depend on pH and potential. By various *ex situ* techniques, chromium is found in (III), (IV), and (VI) oxidation states in varying proportions.<sup>32,33,84–87,101</sup> The reasons why changes in the oxide film composition should improve passivity and resistance to breakdown remain speculative.

## 2.02.10 Breakdown of Passivity and Pitting

Probably less surprising than the phenomenon and characteristics of passivity itself, is the breakdown of passivity, and the very high rate of localized corrosion that can ensue. The passivating oxide film is extremely thin, and its existence and stability depend significantly on the composition of the environment and the very high electric field it carries. It is in essence fragile, chemically, electrochemically, and mechanically, but the fragility depends on the metal and the environment as a system. Mechanical breakdown of the oxide film arises when the material is under tensile stress and can give rise to stress-corrosion cracking or corrosion fatigue. Mechanical breakdown can also arise from an erosive or cavitative action from the environment. These processes generate a fresh metal surface, the reaction of which can be twofold. In suitably quiescent environments, the bare metal surface repassivates, and the electrochemical reaction with the environment causes no significant damage, although a continuing erosive action does lead to loss of material through wear. During corrosion fatigue too, the regrowth of the passivating film over the surface can help wedge open an incipient crack during the compressive half-cycle, allowing mechanical crack growth.\*\*

Chemical breakdown of passivity occurs naturally enough if the potential is lowered into the active regime (region AB in Figure 4). This can occur if the cathodic reactant supporting passivity, such as oxygen dissolved in the electrolyte, is depleted, as occurs locally in crevices or occluded regimes of the

structure. Chemical breakdown also arises at high potential in the presence of aggressive ions, usually anions, which interact with the metal enhancing dissolution (region DE in Figure 4). The most common aggressive anion is chloride, aggressive to very many passive metals. In such cases, absence of the aggressive ion would impose passivity at the same potential: the process is, thus, essentially different from crevice corrosion.

Localized corrosion can occur if the passivating element of an alloy is locally depleted from the matrix. This may occur in the sensitized regions of stainless steels for example, as outlined above. Other alloy components too, may be deleterious towards the passivity of alloys. For example, the presence of significant quantities of sulfur as an impurity in ferrous- and nickel-based alloys is generally degrading towards passivity.<sup>23,33,102,103</sup> Sulfur is incorporated into the oxide film or accumulates at the metal–oxide interface; the element retards the formation of the oxide film and catalyses dissolution of iron and nickel, often remaining adsorbed on the dissolving metal surface. In extreme cases, a sulfide film forms on the metal surface, which is nonprotective. Appropriate heat treatment of such alloys allows segregation of the sulfur to the grain boundaries or precipitation of sulfides, both leading to very high local concentrations of sulfur and premature failure of passivity at these sites.

Where the environment is potentially corrosive, however (i.e., contains aggressive ions), even though the overall surface remains passive, corrosion can advance into the bare metal surface. The question is, how can this happen? In stress corrosion cracking attack occurs mainly around the active–passive transition (BC in Figure 4), where oxide film growth still occurs, but the state of passivity is potentially unstable, because of the proximity in potential of the active region (AB in Figure 4). Dissolution occurs simultaneously with repassivation (regrowth of the oxide film). A small ohmic resistance in the electrolyte between the external cathodic area and the anodic incipient crack tip may be sufficient to lower the potential of the crack tip into the active regime. Alternatively, a small increase in acidity developed at the crack tip as a consequence of anodic reaction may enlarge the active loop a little by raising the potential of the active–passive transition locally. Some anodic reactions at the crack tip may cause local brittleness, such as dealloying or the diffusion of cathodically reduced hydrogen in atomic form into the metal ahead of the crack tip. These processes allow repeated rupture at the crack tip, even if it

\*\*Editor's note: This statement is a little misleading. Wedging open of a crack by corrosion product increases the minimum stress intensity factor without affecting the maximum stress intensity factor, thereby reducing  $\Delta K$ , and hence fatigue crack growth rate. This process is known as oxide-induced crack closure. However, wedging by corrosion product can lead to tensile stresses at the crack tip that enhance SCC crack growth rate.

has already repassivated, because of the embrittled local metal matrix. Stress corrosion cracking also occurs near the passive–active transition at higher potential when such a transition is available (near point D in [Figure 4](#)). In this case, chloride undoubtedly enhances the ability of an incipient crack to propagate by enhancing dissolution at the crack tip, even though the pitting potential (the potential of point D) is not necessarily exceeded.

There are many forms of pitting corrosion (the formation of holes by corrosive action). The various forms have been reviewed by Szklarska-Smialowska.<sup>104</sup> Sometimes activation of a steel brought about by lowering the potential from the passive potential regime into the active regime produces etch pits, a form of uneven corrosion associated with different crystal planes within the metal. This process is less sensitive to the type of anion present, and more associated with the pH changes that occur during activation in unbuffered solutions. The pitting process considered here is a process involving the formation of small holes in an otherwise passive surface as a consequence of the aggressive action of a component of the electrolyte. It is a form of localized corrosion which involves loss of passivity locally, but does not require a stress (although it may be enhanced by a stress). It usually occurs at high potential, where one might expect passivity to dominate. In pitting corrosion, passivity is lost or ruptured through the chemical or electrochemical action of a specific component of the environment. The most commonly encountered pitting agent in aqueous electrolytes is chloride, although some other anions may also induce pitting. Notably, these are the other halides. Sulfur oxyanions such as thiosulphate,<sup>23,105</sup> and indeed sulfide ions, are conducive towards pitting corrosion in ferrous materials and nickel-based materials. It is of some consequence that most anions capable of causing pitting in particular metals also induce stress corrosion cracking of the same metals, although the converse is not necessarily true. Many metals undergo pitting corrosion in chloride solutions of sufficient concentration; these include steels and stainless steels, nickel, copper, and aluminum, and their alloys, and many more.<sup>††</sup>

<sup>††</sup>Editor's note: It is a requirement for pitting by the mechanism discussed here that the bulk of the component is passive in order to provide a large cathode area to drive the local anode. Consequently, carbon steels do not suffer from this form of pitting in neutral chloride solutions, since steel is not passive in such solutions. However, steels may suffer from transient localized corrosion in neutral chloride solutions, such as seawater, due to the presence of mill scale and/or the local effects of sulfur derived from sulfide inclusions.

A few metals are resistant to chloride-induced pitting, including chromium, titanium, and tantalum, but they are not necessarily immune to pitting, only that they are resistant. Some other anions may also induce pitting but outside the normally encountered range of corrosion potentials, and are therefore not regarded as specific pitting agents. For example, nitrate ions, which passivates towards aluminum under normal potentials, induce pitting in dilute nitric acid solutions at high potentials. Such potentials are only accessible through application of an external voltage source.

Precisely how these anions nucleate pitting in a passive metal surface is still largely unsolved, although a range of models exists. Pits in chloride solutions are often rare events.<sup>23,106</sup> In stainless steels, pits can be very widely spaced apart, and most of the surface is passive. Pit propagation rates, are however, very fast: a propagation rate equivalent to a current density of 10–100 kA m<sup>-2</sup> is common.<sup>23,106</sup> In chloride solutions, pitting is characterized by a minimum potential, called the pitting potential<sup>104</sup> (point D in [Figure 4](#)). Only above the pitting potential is pitting observed to occur. The metal is in essence passive below this potential, and this is a commonly used design criterion. However, detailed examination of the passive region (i.e., above the passivation potential and below the pitting potential, the region CD in [Figure 4](#)) of steels and stainless steels shows that the passive current is more noisy in chloride solutions than it is in the absence of chloride.<sup>23,106–108</sup> The origin of this noise is the nucleation and propagation of 'metastable' pits (also sometimes called unstable pits). Metastable pits are those which grow for a short period and then die through repassivation.<sup>23,106–111</sup> These are observed both below and above the pitting potential. Although these metastable pits do not generally cause significant damage to the metal, apart from a degree of microscopic surface roughening, they are evidence that passivity is not fully stable in the presence of chloride ions, even below the pitting potential. For these materials at least, the pitting potential (sometimes called the breakdown potential, erroneously, since breakdown of passivity occurs at lower potentials for ferrous materials) is not a pit nucleation potential: it can only be regarded as the minimum potential for stable pitting. Pits which are stable propagate almost indefinitely, either until total penetration of the metal, or until they are large enough to be washed out by the bulk electrolyte. Such noise in the current can be observed throughout the passive range of potential if the experiment is carried out carefully enough.<sup>106</sup>

The pitting potential (point D in [Figure 4](#)) is sometimes treated as a type of equilibrium potential. There are empirical reasons for this. The pitting potential is often observed to decrease linearly with  $\log(\text{Cl}^-)$  (the chloride activity or concentration), giving an apparently Nernstian form.<sup>104</sup> However, observation of metastable pitting at potentials well below the pitting potential probably precludes this notion. In addition, if the potential sweep direction is reversed at point E, the polarization curve shows strong hysteresis. The negatively moving sweep lies at higher currents, and the potential at which the pitting metal repassivates is much lower than point D. (The point where the metal repassivates in the negative sweep is sometimes called the repassivation potential.) It must also be noted that the pitting potential itself depends on the prior surface treatment of the metal, such as the surface roughness.<sup>112</sup> These facts are inconsistent with the pitting potential describing some simple electrochemical equilibrium. The pitting potential is nevertheless an extremely useful engineering parameter.

Pitting corrosion requires an incubation period or induction time to nucleate.<sup>113,114</sup> Even after initial nucleation, further events are sporadic in time. Several possible mechanisms of nucleation have been put forward. Complexing of metal cations on the surface of the film has been proposed to lead to local dissolution of the oxide,<sup>113</sup> the site then receding to the metal surface. Alternatively, chloride migration through the oxide film may lead to its accumulation as the metal chloride at the metal–film interface. This, if it occurs, could well lead to mechanical failure of the film by bursting, since metal chlorides are of greater molar volume than the corresponding oxides. The notion is appealing since it provides for a high local chloride concentration at the metal–film interface once the film is ruptured, providing an immediate pit propagation path. Film rupture could instead be induced by condensation of vacancies at the metal–film interface.<sup>51</sup> The idea of mechanical film rupture carries the added appeal that pitting events on iron microelectrodes observed potentiostatically show an initiating very fast current spike.<sup>107,115</sup> The event is microscopically violent. Recent observations with stainless steel microelectrodes show that pits here are also initiated with a violent current jump.<sup>116,117</sup> The magnitudes of the events are very small, generally up to some hundreds of picoamperes, indicative not of a low reaction rate, but of the microscopic size of the nucleation event. Interestingly, many of these nucleation events show

no propagation stage at all, not even in a metastable pit, but die immediately after nucleation. The implication is that while pit growth may be a rare event over the metal surface, the nucleation event may in fact be rather common. The same nucleation mechanism may not be applicable to all metals which pit in chloride solution, although current fluctuations are observed from aluminum in chloride solutions below the pitting potential. It has also been suggested that passive films may always undergo continuous breakdown/repair events on a microscopic scale, even in solutions which are fully passivating. This interesting idea takes the nucleation event away from the properties of the aggressive chloride anion. Chloride would then serve merely to propagate pits from these nuclei, and prevent their repassivation.

Steels and stainless steels show preferential nucleation of pits at inclusions, most notably sulfide inclusions.<sup>23,118</sup> Other sulfur-rich regions in ferrous and nickel-based alloys may also lead to premature failure. It has been shown that accumulation of sulfur on the surface of these materials retards passivity and enhances dissolution of the metal. These effects occur in any solution in which the metal shows an active region, and are also preferential pitting sites in the presence of chloride. A recent notion<sup>92</sup> for pit nucleation in stainless steels suggests that iron-rich clusters found randomly distributed in the metal structure are active when they become exposed to the electrolyte, since they do not carry sufficient chromium to allow their passivation. These are the pit nucleation sites. They become progressively exposed to the solution through the normal passive dissolution rate. This model cannot be generally applicable to pitting corrosion since it cannot account for pit nucleation in single component metals, such as iron and aluminum. In fact, any site on the metal surface capable of depassivation for any reason, is a potential pit nucleation site. For it to develop into a pit simply requires an anodic reaction capable of procuring a more aggressive anolyte, as outlined below.

The fact that amorphous metals show a higher resistance to pitting corrosion than their polycrystalline counterparts can offer more than one explanation. Such amorphous metals made from iron, chromium, and nickel simulate the stainless steel and show significantly high pitting potentials.<sup>118–121</sup> These alloys are usually made with significant quantities of nonmetallic element additions such as boron in order to retard crystallization during quenching from the melt. Such elements, which are found in the oxide film,<sup>122</sup> may aid

passivity and inhibit pit nucleation by aiding amorphization of the passive film, or by their own specific chemical action. More probably, however, it is the absence of metallurgical defects such as grain boundaries and inclusions which inhibit pit nucleation.

Once nucleated, anodic reaction at the incipient pit then requires a corresponding cathodic reaction on the surrounding passive surface if the metal is pitting in an open circuit, or at the counter electrode if pitting is carried out potentiostatically. Anodic reaction generates cations by dissolution, and  $H^+$  by hydrolysis of the dissolved cations. Acidity is also generated if the metal repassivates. Both the metal cations and  $H^+$  require neutralization, accomplished by ingress of anions. If chloride is the only available anion, its local concentration increases; the locally higher chloride concentration enhances local metal dissolution, and prevents repassivation.<sup>123</sup> The enhanced dissolution then draws more chloride into the now propagating pit, enhancing dissolution even further. Growth of the pit, is in essence, fuelled by its own reaction products: it is a feedback mechanism. The process is sometimes termed autocatalytic. Pit growth is further supported by the lower local pH. The pit anolyte becomes a saturated (or near-saturated) solution of the metal chloride, and is highly acidic. Some 60–70% of saturation of the metal chloride is required to prevent repassivation of stainless steel. It follows from this, that the presence of other anions in solution, in addition to chloride, but which are not aggressive (e.g.,  $SO_4^{2-}$ ) would reduce the ability of the metal to undergo pitting.<sup>\*\*</sup> Both ions are then transportable into the pit anolyte and it is more difficult to build up sufficient chloride to establish propagation: this is found in practice.<sup>124,125</sup>

It is apparent that such a mechanism depends strongly on the transport properties of the electrolyte components into and out of the pit. In stainless steels, pit propagation has been shown to be controlled by diffusion of ions between the pit interior and the external electrolyte.<sup>106,125</sup> The behavior of the pit site depends on its degree of occlusion: pitting is easier on rough surfaces because of the greater occlusion of sites. Surfaces of rougher finish usually display a lower pitting potential. More occluded sites can more readily retain the dissolved cations required to draw chloride into the pit anolyte.

In the early stages of pit propagation on stainless steel in chloride solution, when the pit is small, its depth alone is insufficient to act as a diffusion barrier. Diffusion is then restricted by a perforated cover which exists over the pit mouth; the perforation arises from the initiating event, and the cover exists because of undermining of the surrounding passive film as the pit expands. This perforated cover is critical to survival of the pit through the so-called metastable period of growth. Small ruptures in the cover during the metastable growth period enhance the propagation rate without terminating the pit. However, if this cover is totally lost by rupture before a critical stage in the growth of the pit, the anolyte is washed out (the outward diffusion of cations becomes fast) and the pit repassivates (hence, the term metastable). Pit growth does not then achieve stability. The critical parameter here is the product of the pit growth current density and its radius<sup>106,125</sup>; this pit stability product must reach a value of  $\sim 3 \text{ mA cm}^{-1}$  for pit growth on stainless steel to stabilize. Once the critical pit stability product is achieved, the pit can propagate without its cover. The pit depth alone is then a sufficient diffusion barrier to ensure the appropriate high chloride concentration within the anolyte, and pit growth achieves stability. Corrosion pits in chloride solution, thus pass through three consecutive steps of growth. The nucleation event is followed by metastable pit growth. Growth is metastable because the pit depth alone is an insufficient barrier to diffusion and may terminate at any point by rupture of the sustaining cover, resulting in repassivation. If the pit grows to a stage where the pit depth alone is sufficient to maintain the diffusion barrier, it enters the third stage and its growth becomes stable. Most pits die at the nucleation stage, and show no propagation. A few survive to become metastable; of those propagating metastably, only a few achieve stability.

It is worth mentioning that although pitting corrosion is generally undesirable, the process does in fact have its uses. Aluminum sheet used for the preparation of printers' lithographic sheet is subject to a preliminary treatment involving a highly controlled electrochemically induced pitting process in electrolytes based on either hydrochloric acid or nitric acid.<sup>126</sup> This procedure, termed electrograining, is designed to roughen the surface on a microscopic scale prior to anodizing. Pitting corrosion may also be induced into the nickel anodes used in nickel electroplating baths containing chloride in order to prevent their passivation, and allow continuous replenishment of the nickel ions in the electrolyte as they are removed.

<sup>\*\*</sup>Editor's note: Arguably, sulfate also acts to limit the drop in pH in the pit, since the second  $pK_a$  for sulfate (the pH at which equal concentrations of  $SO_4^{2-}$  and  $HSO_4^-$  will be present) is  $\sim 1.9$ , above the pH needed to achieve stable active dissolution.



## References

- Wagner, C. *Corros. Sci.* **1965**, 5, 751.
- Brusic, V. In *Oxides and Oxide Films*; Diggle, J. W., Ed.; Marcel Dekker: New York, 1972; Vol. 1.
- Pourbaix, M. *Atlas of Electrochemical Equilibria in Aqueous Solutions*; Pergamon/CEBELCOR: Oxford, 1966.
- <http://www.argentumsolutions.com/> viewed on 7 May 2009.
- Staehle, R. W.; Forty, A. J.; van Rooyen, D. Eds. *Fundamental Aspects of Stress Corrosion Cracking*; NACE: Houston, TX, 1969.
- Tomashov, N. D.; Chernova, G. P. *Passivity and Protection of Metals* Plenum Press: New York, 1967; Vol. 9.
- Keir, J. *Philos. Trans. Roy. Soc. Lond.* **1790**, 80, 359.
- Faraday, M. *Experimental Researches in Electricity*; University of London: London, 1844; Vol. 2.
- Evans, U. R. *Ind. Engng. Chem.* **1925**, 17, 363.
- Evans, U. R. *The Corrosion and Oxidation of Metals*; Arnold: London, 1960; Chapter 7.
- Evans, U. R. *The Corrosion and Oxidation of Metals*; Arnold: London, 1968; First Supplementary Volume, Chapter 7.
- Evans, U. R. *The Corrosion and Oxidation of Metals*; Arnold: London, 1976; Second Supplementary Volume, Chapter 7.
- Tafel, J. *Zeit. Physik. Chem.* **1905**, 50A, 641.
- Hoar, T. P. In *Modern Aspects of Electrochemistry*; Bockris, J. O'M., Ed.; Butterworths: London, 1959; Vol. 2, p 262.
- Hoar, T. P.; Mowatt, J. A. S. *Nature* **1950**, 165, 64.
- Hoar, T. P.; Mears, D. C.; Rothwell, G. P. *Corros. Sci.* **1965**, 5, 279.
- Hoar, T. P.; Mears, D. C. *Proc. Roy. Soc. Lond.* **1966**, A294, 486.
- Edeleanu, C.; Gibson, J. G. *Chem. Ind.* **1961**, 301(10), 301–308.
- Turnbull, A. Ed. *Corrosion Chemistry in Pits, Crevices and Cracks*; HMSO: London, 1987.
- Kolotyrkin, J. M. *Corrosion* **1963**, 19, 261t.
- Wranglen, G. *Corros. Sci.* **1974**, 14, 331.
- Staehle, R. W.; Brown, B. F.; Kruger, J.; Agrawal, A. Eds. *Localized Corrosion*; NACE: Houston, TX, 1974.
- Isaacs, H. S.; Bertocci, U.; Kruger, J.; Smialowska, S. Eds. *Advances in Localized Corrosion*; NACE: Houston, TX, 1990.
- Young, L. *Anodic Oxide Films*; Academic Press: London, 1961.
- Hoar, T. P.; Mott, N. F. *J. Phys. Chem. Solids* **1959**, 9, 97.
- Tajima, S. In *Advances in Corrosion Science and Engineering*; Fontana, M. G., Staehle, R. W., Eds.; Plenum: New York, 1970; Vol. 1.
- Wood, G. C. In *Oxides and Oxide Films*; Diggle, J. W., Ed.; Marcel Dekker: New York, 1972; Vol. 2.
- Furneaux, R. C.; Thompson, G. E.; Wood, G. C. *Corros. Sci.* **1978**, 18, 853.
- Shimuzu, K.; Kobayashi, K.; Thompson, G. E.; Wood, G. C. *Philos. Mag. A* **1992**, 66, 643.
- Pedeferrri, P. *Imagination on Titanium*; Cooperativa Libreria Universitaria del Politecnico: Milan, 1987.
- de Gromoboy, T. S.; Shreir, L. L. *Electrochim. Acta* **1966**, 11, 895.
- Froment, M. Ed. *Passivity of Metals and Semiconductors*; Elsevier: Amsterdam, 1983.
- MacDougall, B. R.; Alwitt, R. S.; Ramanarayanan, T. A. Eds. *Oxide Films on Metals and Alloys, The Electrochemical Society Proceedings*, 99–22, Pennington: New Jersey, 1992.
- Kabanov, B.; Burstein, R.; Frumkin, A. *Disc. Farad. Soc.* **1947**, 1, 259.
- Heusler, K. E. *Zeit. Elektrochem.* **1958**, 62, 582.
- Bockris, J. O'M.; Drazic, D.; Despic, A. *Electrochim. Acta* **1961**, 4, 325.
- Weissmantel, C.; Schwabe, K.; Hecht, G. *Werkst Korros.* **1961**, 12, 353.
- Sato, N.; Okamoto, G. *J. Electrochem. Soc.* **1964**, 111, 197.
- Bockris, J. O'M.; Reddy, A. K. N. *Modern Electrochemistry*; Macdonald: London, 1970; Vol. 2.
- Bessone, J.; Karakaya, L.; Lorbeer, P.; Lorenz, W. J. *Electrochim. Acta* **1977**, 22, 1147.
- Burstein, G. T.; Ashley, G. W. *Corrosion* **1983**, 39, 241.
- Misra, R. D. K.; Burstein, G. T. *Corros. Sci.* **1984**, 24, 305.
- Burstein, G. T.; Newman, R. C. *Electrochim. Acta* **1980**, 25, 1009.
- Burstein, G. T.; Newman, R. C. *J. Electrochem. Soc.* **1981**, 128, 2270.
- Verwey, E. J. W. *Physica* **1935**, 2, 1059.
- Cabrera, N.; Mott, N. F. *Rep. Prog. Phys.* **1948/49**, 12, 163.
- Dignam, M. J. In *Oxides and Oxide Films*; Diggle, J. W., Ed.; Marcel Dekker: New York, 1972; Vol. 1, p 91.
- Fromhold, A. T. In *Oxides and Oxide Films*; Diggle, J. W., Vijn, A. K., Eds.; Marcel Dekker: New York, 1976; Vol. 3, pp 1.
- Kirchheim, R. *Electrochim. Acta* **1987**, 32, 1619.
- Davenport, A. J.; Brustein, G. T. *J. Electrochem. Soc.* **1990**, 137, 1496.
- Chao, C. Y.; Lin, L. F.; Macdonald, D. D. *J. Electrochem. Soc.* **1981**, 128, 1187, 1194.
- Ghez, R. *J. Chem. Phys.* **1973**, 56, 1838.
- Burstein, G. T.; Davenport, A. J. *J. Electrochem. Soc.* **1989**, 136, 936.
- Güntherschultze, A.; Betz, H. *Zeit. Phys.* **1934**, 91, 70, 92, 367..
- Dewald, J. F. *J. Phys. Chem Solids* **1957**, 2, 55.
- Sato, N.; Cohen, M. *J. Electrochem. Soc.* **1964**, 111(512), 624.
- Diggle, J. W. In *Oxides and Oxide Films*; Diggle, J. W., Ed.; Marcel Dekker: New York, 1973; Vol. 2, p 280.
- Nii, K. *Corros. Sci.* **1970**, 10, 571.
- Hagyard, T.; Williams, J. R. *Trans. Farad. Soc.* **1961**, 57, 2288.
- Hagyard, T.; Earl, W. B. *J. Electrochem. Soc.* **1967**, 114, 694.
- Beck, T. R. *Corrosion* **1974**, 30, 408.
- Burstein, G. T.; Ashley, G. W. *Corrosion* **1984**, 40, 110.
- Burstein, G. T.; Marshall, P. I. *Corros. Sci.* **1983**, 23, 125.
- Burstein, G. T.; Marshall, P. I. *Corros. Sci.* **1984**, 24, 449.
- Burstein, G. T.; Whillock, G. O. H. *J. Electrochem. Soc.* **1989**, 136(1313), 1320.
- Burstein, G. T.; Cinderey, R. J. *Corros. Sci.* **1991**, 32, 1195.
- Scully, J. C. Ed. *The Theory of Stress Corrosion Cracking in Alloys*; NATO: Brussels, 1971.
- Sato, N.; Kudo, K. *Electrochim. Acta* **1971**, 16, 477.
- Stress Corrosion Cracking and Hydrogen Embrittlement of Iron Base Alloys*; NACE: Houston, TX, 1975.
- Mayne, J. E. O.; Pryor, M. J. *J. Chem. Soc.* **1949**, 1831–1835.
- Cohen, M. J. *Phys. Chem.* **1952**, 56, 415.
- Mellors, G. W.; Cohen, M.; Beck, A. F. *J. Electrochem. Soc.* **1952**, 105, 332.

73. Mayne, J. E. O.; Menter, J. W. *J. Chem. Soc.* **1954**, 103–107.
74. Brasher, D. M.; Mercer, A. D. *Br. Corros. J.* **1968**, 3, 120.
75. Appleby, A. J.; Mayne, J. E. O. *J. Oil Col. Chem. Assoc.* **1967**, 50, 897.
76. Mayne, J. E. O.; Page, C. L. *Br. Corros. J.* **1972**, 7(111), 115.
77. Hoar, T. P.; Evans, U. R. *J. Chem. Soc.* **1932**, 2476–2481.
78. Szklarska-Smialowska, Z.; Staehle, R. W. *J. Electrochem. Soc.* **1974**, 121, 1146.
79. Stern, M.; Wissenberg, H. *J. Electrochem. Soc.* **1959**, 106(755), 759.
80. Heitz, E. In *Advances in Corrosion Science and Technology*; Fontana, M. G., Staehle, R. W., Eds.; Plenum Press: New York, 1974; Vol. 4, pp 149.
81. Mazza, F. *Werkst. Korros.* **1969**, 20, 199.
82. Vernon, W. H. J.; Wormwell, F.; Nurse, T. J. *J. Iron Steel Inst.* **1944**, 150, 81.
83. Cahoon, J. R.; Bandy, R. *Corrosion* **1982**, 38, 299.
84. Olefjord, I. *Mater. Sci. Eng.* **1980**, 42, 161.
85. Olefjord, I.; Elfstrom, B. O. *Corrosion* **1982**, 38, 46.
86. Castle, J. E.; Clayton, C. R. *Corros. Sci.* **1977**, 17, 7.
87. Asami, K.; Hashimoto, K.; Shimodaira, S. *Corros. Sci.* **1976**, 16, 387.
88. Uhlig, H. H. *Corrosion and Corrosion Control*, 2nd edn.; Wiley: New York, 1971; Chapter 5.
89. Sieradzki, K.; Newman, R. C. *J. Electrochem. Soc.* **1986**, 133, 1979.
90. Song, Q.; Newman, R. C.; Cottis, R. A.; Sieradzki, K. *J. Electrochem. Soc.* **1990**, 137, 435.
91. Song, Q.; Newman, R. C.; Cottis, R. A.; Sieradzki, K. *Corros. Sci.* **1990**, 31, 621.
92. Williams, D. E.; Newman, R. C.; Song, Q.; Kelly, R. G. *Nature* **1991**, 350, 216.
93. Chin, Y.-T.; Cahan, B. D. *J. Electrochem. Soc.* **1992**, 139, 2432.
94. Okamoto, G. *Corros. Sci.* **1973**, 13, 471.
95. McBee, C. L.; Kruger, J. *Electrochim. Acta* **1977**, 17, 1337.
96. Bessone, J. B.; Salinas, D. R.; Mayer, C. E.; Ebert, M.; Lorenz, W. J. *Electrochim. Acta* **1992**, 37, 2283.
97. Burstein, G. T.; Davies, D. H. *Corros. Sci.* **1980**, 20, 989; 1143.
98. Goetz, R.; MacDougall, B. J.; Graham, M. J. *Electrochim. Acta* **1986**, 31, 1299.
99. Mitrovic-Stepanovic, V.; MacDougall, B. J.; Graham, M. J. *Corros. Sci.* **1987**, 27, 239.
100. Landolt, D.; Mischler, S.; Vogel, A.; Mathieu, H. J. *Corros. Sci.* **1990**, 31, 431.
101. Mischler, S.; Vogel, A.; Mathieu, H. J.; Landolt, D. *Corros. Sci.* **1991**, 32, 925.
102. Marcus, P. C. *R. Acad. Sci. Paris., Sér II* **1987**, 305, 675.
103. Marcus, P.; Moscatelli, M. *Mém. Etud. Sci. Rev. Métall.* **1988**, 85, 561.
104. Szklarska-Smialowska, Z. *Pitting Corrosion of Metals*; NACE: Houston, TX, 1986.
105. Newman, R. C. *Corrosion* **1985**, 41, 450.
106. Pistorius, P. C.; Burstein, G. T. *Philos. Trans. Roy. Soc. Lond. A* **1992**, 341, 531.
107. Bertocci, U.; Koike, M.; Leigh, S.; Qiu, F.; Yang, G. *J. Electrochem. Soc.* **1986**, 133, 1782.
108. Isaacs, H. S. *Corros. Sci.* **1989**, 29, 313.
109. Forchhammer, P.; Engell, H. J. *Werkst. Korros.* **1969**, 20, 1.
110. Williams, D. E.; Westcott, C.; Fleischmann, M. *J. Electrochem. Soc.* **1985**, 132(1796), 1804.
111. Stockert, L.; Böhnli, H. *Mater. Sci. Forum* **1989**, 44(45), 313.
112. Coates, G. E. *Mater. Perform.* **1990**, 29(8), 61.
113. Hoar, T. P.; Jacob, W. R. *Nature* **1967**, 216, 1299.
114. Heusler, K. E.; Fischer, L. *Werkst. Korros.* **1976**, 27, 551.
115. Bertocci, U.; Yang-Xiang, Y. *J. Electrochem. Soc.* **1984**, 131, 1011.
116. Riley, A. M.; Wells, D. B.; Williams, D. E. *Corros. Sci.* **1991**, 32, 1307.
117. Burstein, G. T.; Mattin, S. P. *Philos. Mag. Lett.* **1992**, 66, 127.
118. Masumoto, T.; Hashimoto, K. *Ann. Rev. Mater. Sci.* **1978**, 8, 215.
119. Hashimoto, K. In *Amorphous Metallic Alloys*; Luborsky, F. E., Ed.; Butterworths: London, 1983; pp 471.
120. Diegle, R. B.; Sorensen, N. R.; Tsuru, T.; Latanision, R. M. In *Treatise on Materials Science and Technology*; Scully, J. C., Ed.; Academic Press: London, 1983; Vol. 23, pp 59.
121. Wislowska, M.; Janik-Czakor, M. *Br. Corros. J.* **1985**, 20, 36.
122. Burstein, G. T. *Corrosion* **1981**, 37, 549.
123. Galvele, J. R. *J. Electrochem. Soc.* **1976**, 123, 464.
124. Leckie, H. P.; Uhlig, H. H. *J. Electrochem. Soc.* **1966**, 115, 1262.
125. Pistorius, P. C.; Burstein, G. T. *Corros. Sci.* **1992**, 33, 1885.
126. Laevers, P.; Terryn, H.; Vereecken, J. *Trans. Inst. Met. Finish.* **1992**, 70, 105.

## 2.03 Crevice Corrosion

### N. Corlett

Lloyd's Register EMEA, Denburn House, 25 Union Terrace, Aberdeen, AB10 1NN, UK

### L. E. Eiselstein

Exponent, Inc., Menlo Park, CA, USA

### N. Budiansky

Exponent, Inc., Natick, MA, USA

© 2010 Elsevier B.V. All rights reserved.

---

2.03.1	Introduction	754
2.03.2	Theories of Crevice Corrosion	754
2.03.2.1	Overview	754
2.03.2.2	Critical Crevice Solution	755
2.03.2.3	IR Drop	756
2.03.2.4	Stabilization of Metastable Pits	757
2.03.2.5	Similarity to Pitting	757
2.03.2.6	Variables Affecting Crevice Corrosion	758
2.03.2.6.1	Crevice geometry	758
2.03.2.6.2	Solution chemistry	758
2.03.2.6.3	Alloying	759
2.03.3	Evaluation of Crevice Corrosion	760
2.03.3.1	Variables Affecting Crevice Corrosion Testing	760
2.03.3.2	Field or <i>In Situ</i> Tests	760
2.03.3.3	Laboratory Tests	760
2.03.3.3.1	ASTM G 48-03, standard test methods for pitting and crevice corrosion resistance of stainless steels and related alloys by use of ferric chloride solution	760
2.03.3.3.2	ASTM G 78-01, standard guide for crevice corrosion testing of iron-base and nickel-base stainless alloys in seawater and other chloride-containing aqueous environments	761
2.03.3.3.3	ASTM F 746-87 (Reapproved 1999), standard test method for pitting or crevice corrosion of metallic surgical implant materials	761
2.03.3.3.4	ASTM F 2129-06, standard test method for conducting cyclic potentiodynamic polarization measurements to determine the corrosion susceptibility of small implant devices	762
2.03.3.3.5	Remote crevice assemblies	762
2.03.4	Practical Design Aspects	762
2.03.5	Industry Specific Examples of Crevice Corrosion	763
2.03.5.1	Medical Devices and Implants	763
2.03.5.1.1	Dental crevice corrosion	766
2.03.5.1.2	Nickel-free alloys	766
2.03.5.2	Chemical and Power Plants	766
2.03.5.2.1	Boiler and steam generators	766
2.03.5.2.2	Heat exchangers and condensers	766
2.03.5.2.3	Pressurized-water reactors (PWR) and boiling-water reactors (BWR)	766
2.03.5.3	Aerospace	767
2.03.5.4	Nuclear Waste Isolation	767
2.03.5.5	Underground Structures	768
References		769

---

**Abbreviations**

<b>BWR</b>	Boiling-water reactor
<b>CCS</b>	Critical crevice solution
<b>CCT</b>	Critical crevice temperature
<b>CPT</b>	Critical pitting temperature
<b>DMC</b>	Dissimilar metal crevice
<b>ELI</b>	Extra low interstitial
<b>IGA</b>	Intergranular attack
<b>MCA</b>	Multiple crevice assembly
<b>MIC</b>	Microbiologically influenced corrosion
<b>PBS</b>	Phosphate-buffered saline
<b>PREN</b>	Pitting resistance equivalence number
<b>PWR</b>	Pressurized-water reactor
<b>SCC</b>	Stress corrosion cracking
<b>TPLO</b>	Tibial plateau leveling osteotomy

**Symbols**

$E_b$	Breakdown potential
$E_{\text{corr}}$	Corrosion potential
$E_{\text{crit}}$	Potential above which localized corrosion may occur
$E_p$	Protection or repassivation potential
$E_r$	Rest potential
$X_{\text{crit}}$	Distance into crevice to achieve the primary pitting potential
$\Delta E$	$E_{\text{crit}} - E_{\text{corr}}$
$\Delta\phi$	IR Drop into crevice

**2.03.1 Introduction**

Crevice corrosion is a form of localized attack that occurs within occluded regions or crevices of metallic components. The attack is caused by a change in the environment of the crevice relative to the bulk solution. Usually, the term crevice corrosion is limited to describing the attack in normally passive metals and alloys (e.g., stainless steels); however, in the broader sense, the corrosion of nonpassive metals and alloys (e.g., carbon steel) by differential aeration may also be regarded as a form of crevice corrosion. Crevices occur in many engineered structures; consequently, crevice corrosion is a common form of corrosion in most, if not all, industries. Crevices can be either man-made by design, such as in washers, pipe flanges, or overlapping fuselage skins on aircraft, or they can occur naturally as a result of biofouling, deposits, and debris. Many similarities exist between crevice corrosion and other forms

of localized attack, such as pitting, intergranular attack, environmentally-assisted cracking, and dealloying.<sup>1,2</sup> In all these instances, the electrochemical and chemical conditions in the shielded surfaces within the crevice, pit, or crack, become altered when compared with the conditions on the boldly exposed surfaces. Crevice corrosion is usually described in two phases: initiation and propagation. The initiation phase may be further divided into three stages: deoxygenation, alteration of the crevice solution chemistry, and depassivation. Many variables affect crevice corrosion, both in terms of the time-to-initiation and the rate and extent of propagation. For a given material, perhaps the most important factors are the geometry of the crevice and the bulk properties of the environment. In this chapter, the emphasis is on the crevice corrosion of passive metals and alloys in aerated chloride environments since this is one of the most common types of crevice corrosion. The mechanisms of crevice corrosion are discussed, together with the effects of the many variables that affect it. Modeling and testing for resistance to crevice corrosion are discussed, as are practical design aspects and methods to minimize attack. Finally, some industry-specific examples of crevice corrosion are provided.

**2.03.2 Theories of Crevice Corrosion****2.03.2.1 Overview**

Crevice corrosion was originally described by Mears and Evans<sup>3</sup> and Uhlig,<sup>4</sup> as resulting from the development of a differential aeration cell. Mears and Evans found that accelerated corrosion occurred when a passive metal surface was in intimate contact with that of an inert material. They proposed that oxygen consumed by a cathodic reaction is replenished more slowly in the occluded region between the metal and the inert object, and that the metal surface within the crevice is deoxygenated and anodic compared to the boldly exposed surfaces outside the crevice. This difference in oxygen concentration in the solution inside the crevice relative to the bulk solution outside the crevice leads to accelerated corrosion within the crevice. Following these early observations and theories, substantial research has focused on developing a more detailed explanation of crevice corrosion.

Three general classes of theories have been used to describe the phenomenon of crevice-corrosion:

- the development of a critical crevice solution (CCS);

- the development of a critical ohmic potential difference (IR drop);
- the stabilization of metastable pits by the crevice geometry.

An ideal crevice may be described as one having a uniform gap, typically between 0.1 and 100  $\mu\text{m}$ , along its entire length or depth, and it is formed between the substrate and another surface that may be metallic or nonmetallic, as shown in **Figure 1**.

Ideal crevice geometries rarely exist even in well controlled laboratory experiments. As the crevice gap gets narrower, crevice corrosion is more likely to occur due to restricted mass transport. In addition, as the gap narrows, the surface finishes on the two materials forming the crevice become increasingly important. Also, the effect of surface finish makes it difficult to accurately characterize the crevice gap as is illustrated in **Figure 2**.

### 2.03.2.2 Critical Crevice Solution

Work on crevice corrosion modeling in the late 1960s and the early 1970s focused on the growth stage of crevice corrosion.<sup>5,6</sup> The work of Crolet and Defranoux<sup>7</sup> in 1973 represents the first attempt to model the initiation stage of crevice corrosion. Crolet and Defranoux modeled the time it takes to develop a critical chemical environment (low pH and high halide concentration) within a crevice as a function of crevice geometry, alloy composition, and bulk

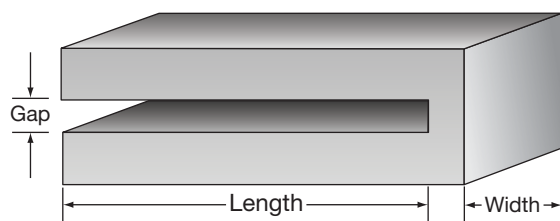


**Figure 1** Schematic of an ideal crevice geometry.

solution chemistry. The development of a CCS chemistry has been used successfully by several researchers to rank alloy performance.<sup>6,8–10</sup>

In 1978, Oldfield and Sutton<sup>5,6</sup> further developed the Crolet and Defranoux model to the point that it could be used to predict crevice corrosion susceptibility. Their model considered the effect of the crevice geometry (i.e., depth and width) on the mass transport of chemical species into and out of the crevice, and then, the manner in which this process led to the formation of a critical crevice solution. Their model consisted of four stages: (1) deoxidization, (2) an increase in salinity and acidity, (3) depassivation, and (4) propagation. In their model, crevice corrosion initiation occurs when a creviced metal or alloy is exposed to an aerated, neutral pH, chloride environment. Initially, corrosion occurs over the entire surface, both within the occluded region and over the boldly exposed surfaces. In order for crevice corrosion to occur, the exposed metal must be passive in the bulk environment. Initially, metal dissolution occurs at the passive current density, which is typically of the order of  $1 \mu\text{A cm}^{-2}$  or less, and both anodic and cathodic reactions occur on all surfaces. As the solution containing dissolved oxygen is consumed at cathodic sites on the noncreviced surfaces, it is replenished from the bulk solution. In occluded regions, however, where mass transport is limited, oxygen becomes depleted and the metal surfaces within the crevice become net anodic, while the boldly exposed surfaces become net cathodic. This difference in the dissolved oxygen concentration sets up an oxygen concentration cell between the passive boldly exposed surfaces and the crevice mouth (cathode), and the occluded region of the crevice (anode). The depletion of dissolved oxygen in the solution contained within the crevice polarizes the metal surfaces in the crevice to lower, more negative potentials.

Although differential aeration is sufficient to induce crevice corrosion in certain metals and alloys, it only provides the initial driving force for crevice

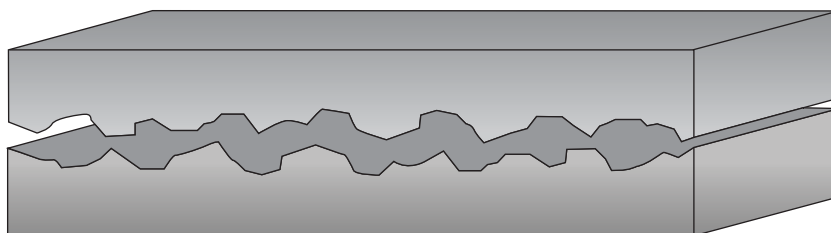


**Figure 2** Schematic of hypothetical crevice geometry.



corrosion in stainless alloys. In chloride containing solutions, the iron and chromium cations, which are oxidized as they diffuse through the passive film, dissolve, and accumulate in the crevice. The limited mass transport of metal ions out of the crevice causes metal-ion accumulation, and to preserve electroneutrality, anions (e.g., chloride ions) diffuse into the crevice through electromigration, leading to an increased metal-chloride concentration. The pH within the crevice drops as a result of the metal-ion hydrolysis.

When the concentration of chlorides is sufficiently high and the pH is sufficiently low, the passive film is no longer able to maintain stability, and active corrosion results. This CCS theory relies on the accumulation of aggressive species within the crevice, and subsequent depassivation followed by active dissolution, as indicated by polarization curve a in **Figure 3**. Meanwhile, the boldly exposed surfaces remain in the passive state, as indicated by polarization curve c shown in **Figure 3**. The CCS theory predicts that the most severe crevice corrosion damage should occur in the deepest regions of the crevice since these would be the first areas to become deoxygenated because of the oxygen mass transport limitations. In some systems, however, crevice corrosion is observed at intermediate distances from the crevice mouth. Another limitation of the CCS model, as noted in the Oldfield and Sutton paper (1973), is that no consideration is given to the effect of the IR drop during the initiation stage.

### 2.03.2.3 IR Drop

The ohmic potential difference or the so-called IR drop theory for describing crevice corrosion was developed by Pickering.<sup>11,12</sup> The IR drop refers to the variation in potential between the crevice interior and the boldly exposed surfaces surrounding the crevice mouth. If the IR drop is sufficiently large, the potential in the crevice can drop below the value required to maintain a stable passive film, thereby initiating crevice corrosion through depassivation. The IR drop increases as the aspect ratio (i.e., length to depth ratio) or tightness of the crevice increases. The IR drop is also affected by other factors such as solution chemistry and conductivity, as well as the presence of other physical objects, such as hydrogen bubbles, solid corrosion products, and salt films that may further block the crevice.<sup>12</sup>

When the metal surfaces within the crevice become net anodic, the local corrosion potential typically becomes more active (i.e., more negative). With the relatively large boldly exposed surfaces supporting the cathodic reactions at more noble (i.e., more positive) potentials, it might be expected that the small surface area within the crevice region would be polarized to higher potentials where it would no longer be active. Due to large IR drops, however, the potential of the crevice region can be hundreds of millivolts lower than that of the boldly exposed surfaces.<sup>11,12</sup>

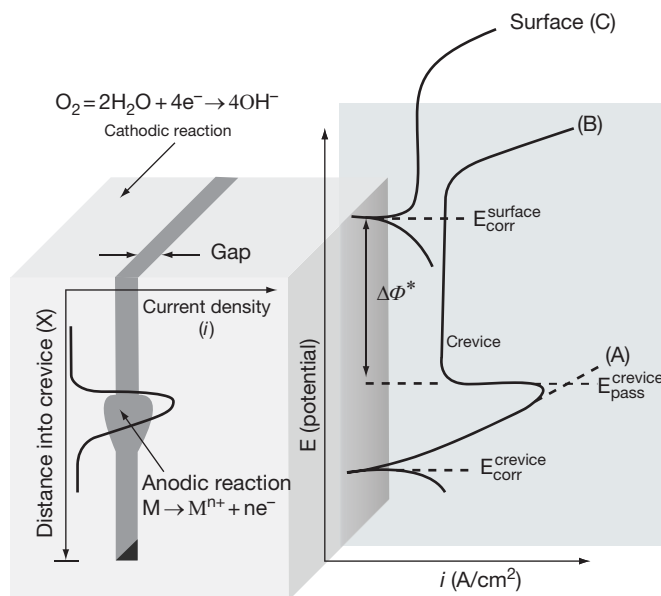


**Figure 3** Schematic of crevice corrosion. Net anodic reactions occur within the crevice environment while the boldly exposed surface is net cathodic. Three possible polarization behaviors are shown: (A) active dissolution within the crevice region, (B) active-passive behavior within the crevice region, and (C) passive behavior on the boldly exposed surface.

In metals and alloys that exhibit an active-to-passive transition in bulk environments, the boldly exposed surfaces are maintained in the passive region in aerated solutions, as indicated by polarization curve B in **Figure 3**. The large IR drop, however, can cause the local potential of the metal surfaces within the crevice to be less than the primary passivation potential, resulting in accelerated metal dissolution. The distance into the crevice where the interfacial potential reaches the primary pitting potential, is referred to as  $X_{\text{crit}}$ , and the critical IR drop to achieve this potential is called  $IR^*$  or  $\Delta\phi^*$ .<sup>11,12</sup> As the distance into the crevice increases, the resistance increases and the current decreases; consequently, the degree of crevice corrosion also decreases. The IR drop theory predicts the intermediate attack that is typically observed in many situations in which the metal or alloy undergoes an active-to-passive transition in the bulk environment, but it does not model the solution concentration process occurring in the crevice.

If the CCS and IR drop theories are combined, the behavior of metals and alloys that do not exhibit an active-to-passive transition in bulk solutions, but do show such behavior in lower pH solutions, can be explained. For instance, by applying both the CCS and the IR drop theories, the crevice corrosion behavior of Inconel 625 can be explained.<sup>13,14</sup>

Indeed, the majority of materials that are susceptible to crevice corrosion are passive in the bulk environment (e.g., stainless steels in aerated chloride environments) and do not normally exhibit an active-to-passive transition. Stewart and Kelly investigated the behavior of 300 series stainless steels taking into consideration the interaction of both the CCS model and the IR drop theory for initiation and propagation.<sup>1,15,16</sup> Their model considered conditions whereby an alloy was passive in the bulk environment, as shown in **Figure 3**, polarization curve c, but where crevice solution concentration and acidification must occur to allow an active-to-passive transition within the crevice, as shown in **Figure 3**, polarization curve b, which, in turn, results in crevice corrosion in the active region. With this approach, the Stewart and Kelly model correctly predicts the intermediate crevice-corrosion damage typically observed on many metals and alloys.

#### 2.03.2.4 Stabilization of Metastable Pits

Crevice corrosion occurs at potentials below the pitting potential in most environments. Similarly, metastable pitting occurs on stainless steel alloys at

potentials less than the pitting potential.<sup>2,17</sup> Stockert and Boehni<sup>18</sup> have suggested that crevice corrosion is initiated on stainless steels as a result of the occluded environment preventing the repassivation of metastable pits. Typically, repassivation of metastable pits occurs as a result of the pit's inability to maintain a critical solution concentration necessary for autocatalytic pit growth. The geometry of the occluded region prevents mass transport of metal-ion hydrolysis products generated from the metastable pitting, out of the crevice, which leads to an alteration of the crevice chemistry in a manner similar to the CCS model first proposed by Crolet and Defranoux<sup>7</sup> and Oldfield and Sutton.<sup>5,6</sup> Oldfield and Sutton observed that random metastable pits formed within the crevice in areas where mass transport was most limited. As exposure time increases, the density of metastable pitting events within the crevice increases; this is followed by pit coalescence as the density of the pits increases further. This coalescence of metastable pits is observed on electrode surfaces prior to crevice corrosion propagation. Other authors support Stockert and Boehni's contention.<sup>19,20</sup> For example, Laycock *et al.* hypothesized that crevice corrosion could be initiated by a random metastable pitting event occurring at a critical location within a crevice, where the metastable pits would then stabilize.

#### 2.03.2.5 Similarity to Pitting

Crevice corrosion and pitting corrosion are similar in many respects. The ranking of metal alloys for crevice corrosion and pitting corrosion are almost identical, and, therefore, it follows that the effect of alloying elements and the environmental effects on crevice corrosion and pitting are also similar.<sup>2</sup> One of the differences, however, between the two mechanisms is the initiation site for corrosion. In pitting corrosion, the initiation sites are, typically, heterogeneities in the metal or alloy surface (e.g., MnS inclusions in stainless steel or second phase particles in aluminum alloys) that are more susceptible than the metal or alloy matrix (e.g., MnS inclusions in stainless steel or second phase particles in aluminum alloys). In contrast, the initiation sites for crevice corrosion are generally defined by occluded regions as discussed previously, although pitting at surface heterogeneities, such as inclusions, has also been observed within crevices. While pitting generally occurs in halide containing solutions, crevice corrosion can also occur in nonhalide solutions, for example, nickel in sulfuric acid environments.<sup>2,17</sup> Also, the initiation mechanism is different for pitting

and crevice corrosion. Pitting is thought to be a random or stochastic process with respect to time and location, with metastable pits forming below the critical pitting potential, whereas crevice corrosion is generally considered a more deterministic process.<sup>2</sup>

Both pitting and crevice corrosion exhibit critical threshold potentials and temperatures. Typically, the critical crevice potential is lower than the critical pitting potential as the solution chemistry can change more rapidly in a crevice due to metal-ion hydrolysis and electromigration than in a pit on a boldly exposed surface. As a consequence, crevice corrosion usually initiates more readily than pitting. The critical crevice temperature (CCT) is usually lower than the critical pitting temperature (CPT) for many alloys for similar reasons.<sup>2</sup>

### **2.03.2.6 Variables Affecting Crevice Corrosion**

#### **2.03.2.6.1 Crevice geometry**

The crevice gap plays a major role in the development of the conditions required for crevice corrosion. Both the gap and the depth of the crevice control the mass transport (solution concentration, acidification, and deoxygenation) and potential gradients that develop within the crevice. In crevices with large gaps the mass transport of oxygen is relatively unaffected compared to bulk solutions, and crevice corrosion is unlikely. Narrow crevice gaps, however, create steep concentration gradients, which are more apt to initiate crevice corrosion closer to the crevice mouth. In addition, in narrow crevices the surface finishes on each side of the crevice become increasingly important. When the crevice surfaces are very close together the minimum crevice gap is dictated by the surface roughness. Large crevice gaps, however, are unaffected by surface roughness.

Various scaling factors are used to describe the effect of the crevice gap and depth on crevice corrosion; as the aspect ratio increases, mass transport gets more difficult and crevice corrosion becomes more likely. Additionally, studies have shown that large aspect ratios lead to crevice corrosion initiation closer to the mouth opening due to IR drop mechanisms.<sup>21</sup> To account for these effects, scaling laws are typically given in terms of the aspect ratio  $L/G$  or  $L^2/G$  where  $L$  is the depth at which crevice corrosion is first observed, and  $G$  is the crevice gap. Such scaling allows corrosion engineers and scientists to extrapolate crevice corrosion test results to other proposed design conditions.

#### **2.03.2.6.2 Solution chemistry**

For a given material, susceptibility to crevice corrosion and the rate at which it occurs are dependent on the environment to which it is exposed. Temperature plays an important role in a material's susceptibility to crevice corrosion. Below a critical temperature, a material is regarded as resistant to crevice corrosion, and corrosion rates are very low. Conversely, above this critical temperature, the corrosion rate increases sharply with increasing temperature. Additionally, one of the main natural crevice corrosion formers is biofilm growth. In specific temperature ranges, biofilms accelerate crevice corrosion by facilitating the cathodic reactions. Biofilms are less active above and below this temperature range leading to a reduced effect on the cathodic reactions, and therefore, lower crevice corrosion rates.

Solution chemistry plays an important role in the susceptibility of metals and alloys to crevice corrosion. Chloride-containing solutions are the most widely investigated and characterized environments in which crevice corrosion occurs on otherwise normally corrosion resistant materials.<sup>22,23</sup> Chloride ions facilitate crevice corrosion initiation and propagation. A critical concentration of chloride ions has been determined for many materials; below this critical concentration, crevice corrosion does not occur. Above this concentration, however, crevice corrosion is strongly dependent on concentration. As the concentration of chloride ions increases, the potential at which crevice corrosion initiates, decreases.<sup>24</sup> One explanation for this is that chloride-ion concentration plays a significant role in the mechanisms of pitting and metastable pitting. As the chloride ion concentration increases, the potential at which metastable pitting occurs decreases, as does the pitting potential. Metastable pits have been found on surfaces within crevices at the onset of crevice corrosion, and pit coalescence, at later stages.

The solution flow rate has been shown to affect the initiation and propagation phases of crevice corrosion differently. The initiation stages are inhibited by solution flow by enhancing the mass transport of oxygen to creviced regions.<sup>22,23</sup> Additionally, solution flow can help reduce the occurrence of crevice corrosion resulting from natural crevice formers by preventing sediment accumulation or attachment (e.g., biofilms or microorganisms).<sup>23</sup> Once crevice corrosion initiates, however, solution flow can increase the rate of crevice corrosion by increasing the rate-limiting cathodic reaction of oxygen reduction on the boldly exposed

surfaces outside the crevice. As the cathodic reaction increases, so the anodic dissolution reaction in the crevice must also increase.

### 2.03.2.6.3 Alloying

The alloy additions that impart resistance to pitting corrosion are for the most part the same as those that make alloys more resistant to crevice corrosion. One of the most widely investigated groups of alloys are the stainless steels. The additions of chromium, molybdenum, nitrogen, and nickel have a significant influence on the crevice corrosion resistance of many alloys. The crevice corrosion rate of austenitic stainless steels has been shown to decrease with increasing chromium additions in seawater.<sup>23</sup> The addition of chromium enhances the passivity of the oxide film, making it more resistant to breakdown. As with resistance to pitting, crevice corrosion resistance is enhanced by the addition of molybdenum. The addition of nickel has been shown to be beneficial to the crevice corrosion resistance of 2.5% Mo austenitic stainless steels, while it has shown very little effect for 6.5% Mo stainless steels. Molybdenum and nitrogen additions have been shown to have a synergistic effect. In alloys that contain molybdenum, nitrogen addition results in significant decreases in the crevice corrosion rate. Similar results are observed for ferritic stainless steels as for austenitic stainless steels.<sup>23</sup> Manganese sulfide inclusions have also been shown to influence the crevice corrosion resistance of austenitic stainless steels; they have been found to destabilize passive films, leading to an increased susceptibility to crevice corrosion.<sup>2,25–30</sup>

The pitting resistance of different stainless steel alloys is generally approximated from the alloy composition by means of the pitting resistance equivalence number (PREN) equation.<sup>23</sup> A typical PREN formula for stainless steels<sup>31</sup> is  $PREN = Cr + 3.3Mo + 30N$ , while, according to Roberge,<sup>32</sup> the most widely used formula for austenitic and duplex stainless steels is  $PREN = Cr + 3.3 (Mo + 0.5W) + xN$ , where  $x = 16$  for duplex stainless steel, and  $x = 30$  for austenitic alloys. This shows that increasing chromium, molybdenum, and nitrogen will increase the pitting and crevice corrosion resistance of a stainless steel. According to Grubb and DeBold,<sup>33</sup> the numerical value of the PREN is approximately equal to the critical crevice temperature (CCT) as measured in degrees Celsius in natural seawater or in ferric chloride solution. This can be seen by comparing the PREN formula with the formula for the CCT in degrees Celsius for stainless

steels, which is given by  $CCT = 2.5Cr + 7.6Mo + 31.9N - 41.0$ .<sup>34</sup> PREN and CCT data are presented for a number of alloys in 30 °C filtered seawater for 30 days in Table 1, which shows the limited equivalence between PREN and CCT.

High performance nickel alloys show improvements in crevice corrosion resistance similar to stainless steels in terms of alloying elements. Alloy C-276, which contains 8% molybdenum, has a relatively higher crevice corrosion resistance, when compared with alloys with lower molybdenum contents.

**Table 1** Crevice corrosion rankings in 30 °C filtered seawater for 30 days, with PREN<sup>a</sup> and CCT<sup>b</sup>

Alloy	UNS designation	Crevice corrosion resistance ranking	PREN	CCT (°C)
Hastalloy C-276	N10276	1	66.7	
Inconel 625	N06625	1	50.4	
AL 29-4	S44700	1	42.8	
AL 29-4-2	S44735	1	42.7	
Monit	–	1	37.8	
Sea-Cure	S44660	2	35.2	
Ferrallium 255	S32550	3	36.8	22.5
Hastelloy G-3	N06985	4	45.9	
Haynes 20 Mod	–	5	38.1	
26-1S	S44626	6	28.3	
20Mo-6	N08026	7	42.4	
E-Brite	S44627	8	29.2	
AL-4X	–	9	34.7	
AL-6X	N08366	10	41.5	
254SMO	S31254	11	46.1	
Hastelloy G	N06007	12	41.3	
904L	N08904	13	36.0	0
AISI 216	S21600	14	38.8	
254 FER	–	15	40.8	
254 SLX	N8904	16	36.6	
Rex 734	S31675	17	42.8	
Type 317LM	S31725	18	34.8	
Nitronic 50	S20910	19	36.5	
JS700	N08700	20	35.2	
Type 316	S31600	21	25.4	–2.5
20Cb-3	N08020	22	26.7	0

<sup>a</sup>Bond, A. P.; Dundas, A. J. *Mater. Perform.* **1984**, 23(7), 39.

<sup>b</sup>Roberge, P. R. *Handbook of Corrosion Engineering*, McGraw-Hill: New York, 1999; p 734.

Similarly, increases in chromium content lower the rate of crevice corrosion.<sup>13</sup>

Titanium and its alloys are, typically, very resistant to crevice corrosion; for instance, pure titanium (Ti-Grade 2) will not generally undergo crevice corrosion below 70 °C, regardless of the solution pH or chloride concentration. When the pH exceeds 10, pure titanium will not undergo crevice corrosion at any temperature.<sup>35</sup> Although titanium and its alloys have high resistance to crevice corrosion, small additions of alloying elements lead to a marked reduction in the rates of crevice corrosion.<sup>31</sup> The addition of noble alloying elements, such as platinum and palladium, as well as copper, significantly decreases the crevice corrosion rate of titanium alloys by providing additional cathodic reaction sites within the crevice. Increasing the number and area of cathodic reaction sites within the crevice allows for the reduction of hydrogen ions, preventing the large scale separation of anodic and cathodic reaction sites.<sup>31</sup>

### 2.03.3 Evaluation of Crevice Corrosion

Numerous tests have been developed to investigate and evaluate the crevice corrosion susceptibilities of metals and alloys. The reviews by Kearns and Kain describe many of the test methods.<sup>9,36–38</sup> In general, testing has been focused primarily on normally passive alloys, and in particular, it has been directed towards the identification and development of more corrosion resistant alloys for marine applications and certain process industries, such as the pulp and paper industry.

Of the many tests that have been developed, several broad classifications can be made based on the type of test, for example, field or *in situ* tests, as opposed to those conducted in the laboratory, and real-time tests versus accelerated tests. Another differentiation can be made between electrochemical and nonelectrochemical (e.g., simple immersion) tests, as well as those tests designed specifically to investigate initiation rather than propagation. Further classifications can be made according to the specific environment, the type of crevice former used, and the geometry of the specimen (e.g., flat sheet, cylindrical, etc.)

As is often the case with testing versus real-life experience, the occurrence or absence of crevice corrosion in a given test is no assurance that it will or will not occur under normal service conditions, either as one moves from the laboratory to the field, or as field process conditions change with time.

#### 2.03.3.1 Variables Affecting Crevice Corrosion Testing

In designing or selecting an appropriate test for evaluating crevice corrosion, a number of variables need to be taken into consideration:

- The metallurgical condition of the metal or alloy, including its composition and surface finish.
- The material used for the crevice former, including its surface finish. The nature of the crevice former can affect the crevice geometry, through relaxation of the crevice gap over time. If a metallic crevice former is used, then dissimilar metal corrosion may be an issue to consider.
- Crevice geometry, including the crevice gap, length or depth, and tightness. The geometry of the crevice can affect the initiation and propagation phases differently, and partly determine the crevice-to-barely-exposed surface area ratio.
- The bulk environment, including solution chemistry, temperature, and flow rate, all of which affect crevice corrosion and can be utilized to accelerate testing.

#### 2.03.3.2 Field or *In Situ* Tests

ASTM International standard G 4-01, Standard Guide for Conducting Corrosion Tests in Field Applications, provides general guidance for such tests, particularly with respect to surface preparation, specimen design, test-rack assembly, and post-test evaluation.<sup>39</sup> The standard mentions crevice corrosion and makes reference to ASTM standard G 78-01. The use of test racks to investigate *in situ* crevice corrosion provides little information regarding initiation and propagation rates.<sup>9,36</sup> However, this approach is effective for screening and ranking different alloys.<sup>40</sup>

#### 2.03.3.3 Laboratory Tests

##### 2.03.3.3.1 ASTM G 48-03, standard test methods for pitting and crevice corrosion resistance of stainless steels and related alloys by use of ferric chloride solution

ASTM standard G 48-03 lists several procedures to determine the pitting and crevice corrosion resistance of stainless steels and other nickel-based corrosion-resistant alloys, when exposed to oxidizing chloride environments.<sup>41</sup> This test describes four procedures, identified as methods A, B, C, and D. Method



A is a ferric chloride pitting test, and Method C is a test developed for determining the critical pitting temperature; therefore, these two methods will not be discussed.

Method B is a ferric chloride test that was developed by Streicher for determining both the pitting and crevice corrosion resistance of iron- and nickel-based alloys.<sup>42</sup> In this test, the crevices are formed by two plastic blocks held against the specimen faces. The maximum depth or mass loss is measured after immersion for a specified time. The recommended temperatures and duration are 23 or 50 °C, and 72 h, respectively.

Method D is used to rank alloys with respect to the minimum critical crevice temperature to cause initiation of crevice corrosion in 72 h, and is similar to the MTI-2 test developed by Treseder.<sup>43</sup> The critical crevice temperature is defined by ASTM G 48 as the minimum temperature to produce crevice attack to a depth of at least 0.025 mm on the surface of the specimen beneath the crevice former in 72 h.

These accelerated test methods (A–D) were designed to minimize corrosion initiation times compared with most natural environments. The rationale for using ferric chloride solutions is that similar solutions are expected to develop within a pit or crevice site.<sup>44</sup> (While this may have been the original rationale, it is not certain why ferric chloride works (rather than any other chloride solution). Rather ferric ion reduction provides a powerful cathodic reaction, leading to a very positive potential that ensures that crevice corrosion will occur if the potential is above the CCT.) The relative performance of alloys in ferric chloride solution tests has been correlated to performance in certain real environments, such as natural seawater at ambient temperature<sup>45</sup> and strongly oxidizing, low pH, chloride-containing environments.<sup>10</sup> Several exceptions to these correlations, however, have been reported.<sup>46,47</sup> This test method notes that surface preparation can significantly influence results. For instance, grinding or pickling of stainless steel surfaces can destroy the passive layer; however, a 24-h air-passivation after grinding or pickling will minimize these differences.

#### **2.03.3.3.2 ASTM G 78-01, standard guide for crevice corrosion testing of iron-base and nickel-base stainless alloys in seawater and other chloride-containing aqueous environments**

ASTM G 78-01 was developed to measure the crevice corrosion resistance of iron- and nickel-based

alloys to chloride containing solutions for a specified time period.<sup>48</sup> This standard recommends a 30-day exposure. The sample surface is occluded with two multiple-gap plastic washers, or so-called multiple crevice assemblies (MCA), that are firmly pressed against both surfaces. This test was developed in the 1970s and is often cited in the literature. Tests are performed on triplicate specimens to allow for statistical analysis, with the crevice formers tightened using a calibrated torque wrench. Crevice initiation and propagation are addressed by the number of sites initiated, and the maximum depth of attack, respectively. Round-robin testing by both NACE T-5H-6 and ASTM G 1.09 task groups report results illustrating the variability of these types of test. The use of multiple-crevice assemblies can be useful for the ranking of alloys, as well as for investigating the effect of other variables; however, multiple-crevice assemblies should not be used for predicting alloy performance in other conditions.

#### **2.03.3.3.3 ASTM F 746-87 (Reapproved 1999), standard test method for pitting or crevice corrosion of metallic surgical implant materials**

ASTM F 746 can be used to evaluate the localized corrosion resistance of alloys for implantable medical devices and surgical instruments.<sup>49</sup> It is a modified version of a test developed by Syrett,<sup>50</sup> and is used as a screening test to rank alloys.

A cylindrical sample of the alloy to be tested is fitted with an inert tapered collar and then immersed in a phosphate-buffered saline (PBS) solution at 37 °C. After stabilization over 1 h, the sample is polarized to a potential much more noble than its rest potential, typically 0.8 V (SCE), in order to stimulate localized corrosion – either pitting or crevice corrosion. The onset of localized corrosion is evident as a rapid increase in the current. If localized corrosion cannot be stimulated, then, after 15 min, the test is terminated. If localized corrosion is stimulated, however, the potential is immediately decreased to the first of several preselected potentials (usually the rest potential plus 0.05 V), and the current is monitored to see whether the sample repassivates, or continues to corrode. If the sample does not repassivate after 15 min, the test is terminated. If the sample does repassivate, the stimulation step is repeated, followed by the next repassivation step. The critical potential for localized corrosion is defined as the most noble preselected potential at which repassivation occurs. Post-test examination of the sample establishes

whether the localized corrosion resulted from pitting of the exposed surface, or from crevice corrosion in the tapered collar.

**2.03.3.3.4 ASTM F 2129-06, standard test method for conducting cyclic potentiodynamic polarization measurements to determine the corrosion susceptibility of small implant devices**

ASTM F 2129 was developed to evaluate the localized corrosion resistance of medical implants in their finished condition.<sup>51</sup> The method can, however, also be used for screening alloys and evaluating component parts of implants. Implants (or alloy components) are immersed in PBS at 37°C for up to 1 h to stabilize at the so-called rest potential ( $E_r$ ) or open circuit potential, after which the potential of the sample is increased slowly (0.167 or 1 mV s<sup>-1</sup>) in a positive (noble) direction. The breakdown potential ( $E_b$ ) at which localized corrosion occurs is evident by a rapid increase in the current and, typically for stainless steels or Nitinol in PBS, can be observed by the appearance of a cloud of corrosion product forming around the breakdown location. If no breakdown occurs before a preset vertex potential is reached, usually 0.8 or 1 V (SCE), then the test can be terminated. If breakdown does occur, and the test is designed to be destructive, then the potential sweep is reversed and monitored for repassivation at the so-called protection or repassivation potential ( $E_p$ ). There remains, however, some controversy among researchers over how to interpret the data obtained from this test. One approach is to consider the gap between the breakdown and rest potentials (i.e.,  $E_b - E_r$ ). This gap provides a measure of the pitting corrosion resistance, whereby, the greater this gap, the greater the resistance to pitting corrosion. Although not universally accepted by researchers, this is a commonly accepted parameter for the ranking of different alloys or material processing.<sup>52–56</sup> Similarly, the parameter  $E_p - E_r$  is sometimes used as a measure of crevice corrosion resistance. This last parameter, however, is very dependent upon the amount of pitting or crevice corrosion that occurs before the potential scan is reversed.<sup>57</sup> An alternative approach for finished devices is to consider the parameter  $E_b - E_r$  as a measure of localized corrosion resistance, together with a posttest microscopic examination to determine whether breakdown occurred because of pitting or crevice corrosion.

ASTM G 61-86, Standard Test Method for Conducting Cyclic Potentiodynamic Polarization Measurements for Localized Corrosion Susceptibility of

Iron-, Nickel-, or Cobalt-Based Alloys, is similar to ASTM F 2129 with the exception that the test is performed at 25°C in 3.5% sodium chloride solution.<sup>58</sup>

**2.03.3.3.5 Remote crevice assemblies**

The use of remote crevice assemblies is an electrochemical approach that allows for the evaluation of both the initiation and propagation phases of crevice corrosion.<sup>8,59–61</sup> This approach entails the physical separation of the anode (crevice) and the cathode (boldly exposed surface) which are electrically connected via a zero-resistance ammeter; this, therefore, permits the measurement of the current flow between the anode and the cathode. Plotting the current versus the time provides information regarding initiation times, as well as propagation rates (based on the total charge passed), and the reproducibility of results is reportedly good.<sup>9</sup>

## **2.03.4 Practical Design Aspects**

As described above, crevice corrosion occurs in both fabricated and natural crevice regions. In both cases, occluded regions formed by the close contact between a metal surface and a nonmetal crevice former or a second metal surface can lead to accelerated corrosion attack in these regions. In order to prevent crevice corrosion from occurring, occluded regions and sharp inside corners should be avoided, wherever possible.<sup>62,63</sup> When materials are joined by rivets, continuous welding, or soldering, sealants should be used to prevent water uptake into occluded regions. When occluded regions cannot be avoided, decreasing the aspect ratio between the crevice depth and crevice gap can lessen the severity of crevice corrosion damage by reducing the steepness of concentration and potential gradients within the crevice. Metal-to-nonmetal crevices (e.g., gaskets) should be avoided because the crevice gap is typically much less than metal-to-metal crevices; this is because the nonmetal crevice former can conform to the metal surface resulting in tighter crevice geometries.<sup>62,63</sup> Metal-to-nonmetal crevices are typically designed to prevent water uptake; however, there is a fine line between being tight enough to prevent water uptake, and tight enough to facilitate capillary action, leading to severe crevice corrosion. Crevice corrosion can also be mitigated by careful material selection or processing. Materials that have a higher crevice corrosion resistance can be used as an overlay

in areas susceptible to crevice corrosion, to minimize damage. Materials with higher critical crevice temperatures or potentials, or generally higher PREN materials, tend to be more resistant to crevice corrosion. The ranking of crevice corrosion resistance for various stainless steels and nickel based alloys in seawater, along with PREN<sup>64</sup> and CCT<sup>32</sup> values, is given in [Table 1](#).

Materials can also be processed to help avoid crevice corrosion. Metal surfaces outside crevice regions can be painted to prevent cathodic reactions taking place, effectively reducing the area ratio between the anode and cathode regions, thus reducing the rate of crevice corrosion attack.

Additionally, processes can be designed to help prevent crevice corrosion. Natural crevices, such as precipitates and deposits, can be avoided by adding filtration systems to industrial process lines early in the process, to prevent deposits in stagnant regions of the process line.

Solution phase inhibitors or supporting electrolytes can also be added to processing lines to either inhibit corrosion directly, or change solution conductivity to minimize ohmic potential effects, or disrupt ion migration into occluded regions.

### 2.03.5 Industry Specific Examples of Crevice Corrosion

Crevice corrosion is a common form of corrosion that affects a wide range of materials used in almost all industries. Metal-to-metal and metal-to-nonmetal crevices can lead to crevice corrosion in a wide variety of typical designs used for consumer and industrial products. Metal-to-metal crevices typically occur between strands in wire rope, around incomplete fusion welds in pipes and plates (see [Figure 4](#)), under o-rings and gaskets, in tube-to-tube sheet connections, in threaded connectors, and in a wide variety of other industrially-used geometries (see [Figure 5](#)).<sup>22</sup> Nonmetal-to-metal crevices can occur as a result of o-ring seals, gasket-to-flange joints, tape-coatings, barnacles on metallic surfaces, valve steam packing, dirt, sand, or mud deposits. This section will review how crevice corrosion affects material selection and mechanical design in a few exemplar industries.

#### 2.03.5.1 Medical Devices and Implants

Implantable medical devices are often used in situations where crevices are likely or unavoidable; for

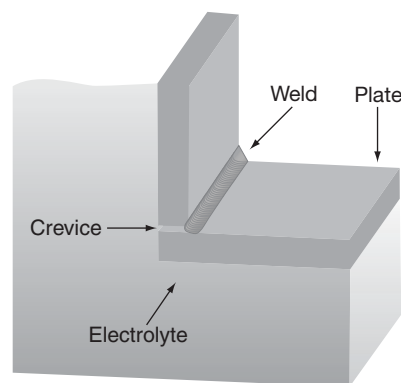


**Figure 4** Example of crevice in welded structure.

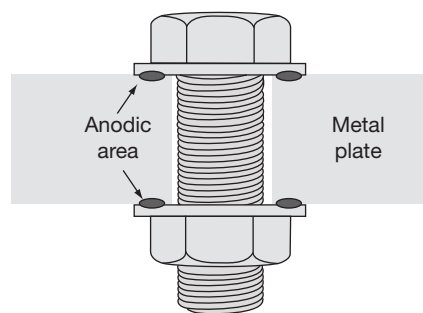


**Figure 5** Example of crevice in welded structure.

instance, where the device is held against tissue or bone, where biofilms develop on the surface, or where two component parts of the device come together, such as screws in bone plates, or the crevice between a tapered stem and ball in a total hip replacement. For this reason, medical devices are required to possess long-term resistance to crevice corrosion during their expected service lifetimes. Common biomedical alloys used for long-term implants are stainless steels, cobalt–chromium–molybdenum alloys (including MP35N and Elgiloy), and titanium alloys. These alloys get their corrosion resistance from the presence of a thin passive film that is generally resistant to uniform corrosion, as well as pitting and crevice corrosion in the warm saline environment of the human body. The pH in the body is maintained at a relatively constant value of 7.4 by phosphate and carbonate buffering, under normal conditions. After surgery, however, the pH at the implant site may range from 5.5 to 9.0, as a result of immunological responses or infections.<sup>65</sup> In the case of a hematoma, the pH can remain at 5.5 for several days.<sup>66</sup> When implant crevice corrosion occurs, the pH may drop to 1 or even lower.<sup>67</sup>

The localized-corrosion resistance of long-term implants is important not only with respect to the maintenance of the mechanical and structural integrity of the implant, but also with respect to the rate at which leachable substances, such as nickel and chromium ions, are released into the body. The release of leachable substances, albeit at very low rates, can elicit an immunological response. This response can vary from person to person and can determine the difference between success and failure of the implant. An example is the corrosion and wear around orthopedic and dental implants that can cause metallosis of the surrounding tissue, and loosening of the implant at the fixation site.<sup>68–71</sup> Although commercial metallic biomaterials are generally corrosion-resistant, there has always been a concern that trace metal ions may be released into the human body because of pitting or crevice corrosion.

Titanium alloys, such as Ti Gr2 and Ti–6Al–4V, are generally ranked as having the greatest resistance to corrosion in saline solutions and are considered resistant to pitting up to the maximum normally-investigated potentials used for testing biomedical implant materials (i.e., 0.8 V SCE).<sup>51</sup> Titanium and its alloys typically show either negative hysteresis or no hysteresis in potentiodynamic polarization tests (i.e., current density falling off as rapidly or more rapidly on the reverse scan than on the forward scan), indicating that passive film growth is enhanced with increasing potential. Consequently, materials exhibiting no hysteresis or negative hysteresis are considered immune to pitting and crevice corrosion.<sup>51,65</sup> Nevertheless, titanium alloys can, under certain *in vivo* conditions such as fretting, show signs of pitting and crevice corrosion as discussed below.<sup>72</sup>

The corrosion resistance of Nitinol (or NiTi), which has an approximately equal nickel and titanium content, is not considered as great as that of titanium or other titanium alloys, such as Ti Gr2 or Ti–6Al–4V. As it exhibits superelastic and shape memory behavior, however, Nitinol is used extensively as an alloy for implantable medical devices, particularly for devices that are deployed endovascularly. There have been some reports that Nitinol will experience *in vivo* breakdown of the passive film, and subsequent localized corrosion. These reports of pitting or crevice corrosion observed on explants,<sup>73–76</sup> however, appear to have been a result of the explants being exposed to decontamination solutions, such as bleach, rather than as a result of actual *in vivo* corrosion.<sup>77–79</sup> Jacobs *et al.* examined Nitinol explants that had been implanted

for over 10 years, and that had not been decontaminated with bleach, and found no significant pitting or crevice corrosion.<sup>80</sup> Guidoin *et al.* examined Nitinol stents (with a radiopaque platinum coil wrapped around the Nitinol wire to make the device more visible during X-ray radiography) which they disinfected with bleach, and found little corrosion, except at the crevice between the coil and the Nitinol wire.<sup>73</sup>

The ASTM F 75 specification cobalt–chromium–molybdenum alloys, such as MP35N and Elgiloy, do not exhibit a hysteresis loop in their cyclic polarization curves and are generally thought to be resistant to pitting and crevice corrosion in physiological environments. These alloys exhibit electrochemical behavior in the passive range that differs from that of other biomedical alloys. In particular, their cyclic potentiodynamic polarization curves typically exhibit an increase in current at potentials of about 0.4 V SCE, and perhaps another at about 0.7 V SCE, but they do not show evidence of localized corrosion.<sup>81</sup> The first increase is thought to be associated with a solid-state oxidation reaction involving the conversion of Co(II) to Co(III). The second increase appears to be associated with transpassive dissolution that results in the release of chromium and nickel ions. The transpassive dissolution observed on cobalt–chromium–molybdenum alloys is a general dissolution type of corrosion and does not generally result in crevice or pitting corrosion. These alloys have exhibited pitting and crevice corrosion under certain *in vivo* conditions, however, and these will be discussed below.

Although 316L and ASTM F 138 (ISO 5832-1) specification stainless steels are alloys used for medical implants, they are susceptible to crevice corrosion in human body fluids.<sup>23</sup> Such crevice corrosion can release metallic ions into the tissues surrounding the implants, causing local irritations or systemic effects. The potential for crevice corrosion of 316L stainless steel *in vivo* is not surprising, since 316L has a CCT below body temperature (see [Table 1](#)).

According to Bai and Gilbert,<sup>65</sup> researchers found that 91% of 316 stainless steel multicomponent explants had undergone visible corrosion, and that crevice corrosion was the primary type of attack.<sup>82</sup> Bai and Gilbert<sup>65</sup> also report the findings of a retrieval study<sup>83</sup> in which it was found that 89% of the plates and 88% of the screws of 250 stainless steel internal fixation devices showed evidence of pitting and crevice corrosion. The environment within the crevices formed between plates and screws of orthopedic devices can be altered from that of the normal *in vivo* environment, such that values ranging from

pH 5 to 7, less than 8–110 mmHg for  $pO_2$ , and less than 10–300 mmHg for  $pCO_2$  can be formed.<sup>84</sup>

Some of this corrosion is a reflection of the quality of the stainless steel used in those pioneering days; it had higher carbon and inclusion content than the medical-grade materials used nowadays. Since that time, there have been significant changes in the composition specified for medical grade 316L (ASTM F 138), which now has a specified minimum PREN of 26.<sup>85–87</sup> The first improvement came with the development of AISI 316L, which is still widely used for plates, screws, and nails in orthopedic surgery. As there were continuing reports of *in vivo* stainless steel corrosion, a new type of stainless steel was introduced in the mid-1980s. This alloy has higher chromium and manganese than 316L, and 0.5% nitrogen is added for increased corrosion resistance.<sup>87</sup>

In 1972, Cohen and Wulff described a cobalt-alloy plate and screws that had been removed from a patient; the persistent pain that the patient experienced appeared to be associated with corrosion.<sup>88</sup> The plates and screws were found to have failed because of crevice corrosion between the plate and bone. The plate composition was similar to Stellite 25 (Co–20Cr–15W–10Ni) and the screw composition was similar to Stellite 21 (Co–27Cr–5.5Mo). Cohen and Wulff noted that the corrosion was associated with the plate and not the screws. Reports of corrosion problems and adverse tissue response with Stellite alloys, however, have been extremely rare.<sup>89</sup>

Brown *et al.* discussed crevice corrosion in stainless steel bone plates and screws<sup>69</sup> and modular hip implants.<sup>68</sup> Crevice corrosion tests with bone plates and screws exposed for up to 1 year showed that crevice corrosion does not occur in isotonic saline solutions (0.9% NaCl) for periods of up to 1 year, but can occur in hypertonic saline solutions (7.2% NaCl). Brown *et al.* also observed corrosion of bone plates and screws that had been fixed to the tibia of sheep, but concluded that this corrosion, as well as the corrosion reported on clinically retrieved implants, was initiated by fretting corrosion, which predisposes the contact area to crevice corrosion attack.

Multiple-component systems used in orthopedic surgery provide flexibility in choosing the optimal implant, but introduce the possibility of crevice corrosion that could limit the implant's longevity, either because of unfavorable tissue response to corrosion products or device failure.<sup>68</sup> Based on their high *in vivo* corrosion resistance, both titanium and cobalt–chromium alloys are often used for total

joint replacements.<sup>90</sup> Because these joints are articulating, the wear resistance of the alloys is also important. Compared with cobalt–chromium alloys, titanium alloys have relatively poor wear properties, and therefore, the cobalt-base alloys are more commonly used for the articulating components of total joint replacements.<sup>90</sup> Since the 1980s, the modular joint, in which the femoral-head component is fabricated from a cobalt-base alloy and the stem from extra-low interstitial (ELI) Ti–6Al–4V alloy, has gained popularity, particularly for the artificial hip. The galvanic couple created by this arrangement was not considered a problem, as both alloys were passive. By the early 1990s, however, there had been reports of corrosion observed on these implants and Brown *et al.*<sup>68–69</sup> attributed these instances to a fretting-assisted crevice-corrosion mechanism.

The work by Brown *et al.*, in 1995 on 79 retrieved tapered modular hip implants indicated similar behavior, that is, the effect of fretting on crevice corrosion initiation. This work suggested that design changes that decreased the propensity for fretting also reduced the chance of crevice corrosion.<sup>68</sup> In addition, Gilbert *et al.* examined 148 total modular hip implants with mixed (Ti–Al–4V)/Co–Cr and Co–Cr/Co–Cr stem and head combinations,<sup>72</sup> and reported that both combinations showed about the same amount of corrosion in the creviced region between the tapered stem and head. They concluded that galvanic effects were not significant, but that crevice corrosion could occur in cobalt–chromium alloys in fretting and wear situations. Cobalt–chromium–molybdenum alloys, therefore, appear to be resistant to pitting and crevice corrosion in the unloaded condition, but are susceptible to deterioration in the presence of mechanical loads. This form of crevice corrosion has been described by Gilbert and Jacobs as mechanically-assisted crevice corrosion.<sup>67</sup>

As reported by Thomas *et al.*, cemented titanium stems in hip arthroplasty have experienced proximal cement–stem debonding, which can result in a crevice, and early failure.<sup>91</sup> This was well publicized with the 3M Capital hip implant failures. Thomas *et al.* discussed their examination of a series of 12 cemented titanium Furlong Straight Stems that required revision at a mean implant time of 78 months, as a result of thigh pain. They reported that the stems were severely corroded in a pattern that was typical of crevice corrosion. Their conclusion was that the combination of a titanium stem and cement appears to facilitate fretting-induced crevice corrosion for an otherwise crevice corrosion resistant material.



Crevice corrosion has also been found on tibial plateau leveling osteotomy (TPLO) plates and associated bone screws that had been implanted in dogs for ~3 years.<sup>92</sup> It was reported that surface irregularities and porosity of TPLO plates from the casting process provided crevice corrosion initiation sites in the occluded region between the plates and screws.

Crevice corrosion has also been seen on spinal surgery hardware. Tezer *et al.* noted that crevice and fretting corrosion can occur at the junctions of rod-screw, rod-hook, transverse-connector rods, and other connector rods in modular spinal implants.<sup>93</sup> They recommended using alloys with better corrosion resistance to inhibit crevice and fretting corrosion. Modular-spine implants are used to aid fusion, but fretting and corrosion can occur between modular components. Kirkpatrick *et al.* examined the corrosion on 47 explanted spinal implants that were manufactured by a variety of companies.<sup>94</sup> They observed that the stainless steel implants exhibited a range of corrosion, from minor to severe damage, that was consistent with previously observed mechanically-assisted crevice corrosion. Titanium-alloy implants, however, showed no significant corrosion. The single cobalt-alloy explant showed no evidence of corrosion.

#### **2.03.5.1.1 Dental crevice corrosion**

With dental implants there is the possibility of microbiologically-influenced corrosion (MIC) affecting crevice corrosion in the creviced region between the dental implant and the gingival epithelium.<sup>71</sup> According to Megremis and Carey, seepage of oral secretions into the crevices created between the restoration and the tooth can lead to microorganism invasion, generation of acidic conditions, the operation of differential aeration cells, and crevice corrosion.<sup>95</sup> The creation of crevice conditions in amalgams can increase acidity to well below a pH of 4. To enhance the crevice corrosion resistance of dental surgical materials, the German Federal Health Department recommended minimum amounts of chromium and molybdenum of 20% and 4%, respectively.<sup>95</sup> In 2006, Wylie *et al.* performed electrochemical testing in artificial saliva at different pHs, on two nickel-based dental casting alloys, before and after porcelain-firing heat treatments.<sup>96</sup> Crevice corrosion was observed on alloys exposed to pH 2.5 saliva. They noted, not surprisingly, that the presence of crevices and lower chromium-content nickel-base alloys could lead to crevice corrosion in dental casting alloys, but this could be avoided by an increase in the chromium content of the alloy.

#### **2.03.5.1.2 Nickel-free alloys**

Many medical implants contain nickel, which has led to concerns regarding nickel toxicology and its effect on the implants' biological performance.<sup>70,97–98</sup> As a result, there have been several recent efforts to develop nickel-free biomedical alloys.<sup>97</sup> Along these lines, Reclaru *et al.* analyzed the crevice corrosion behavior and the cation release of five nominally nickel-free austenitic steels in artificial sweat and bone plasma.<sup>98</sup> Generally, the amount of cation release was substantially higher in the artificial sweat solution than in the bone plasma under creviced conditions.<sup>99</sup>

### **2.03.5.2 Chemical and Power Plants**

#### **2.03.5.2.1 Boiler and steam generators**

It has been estimated that the second most common type of tube failure in fire-tube boilers is concentration-cell corrosion, frequently referred to as crevice corrosion, due to the build-up of iron oxide sediment or scale.<sup>100</sup> On waterside fire-tubes, corrosion occurs beneath deposits that foul the surface and become anodic relative to the periphery of the deposits. According to Esmacher *et al.*,<sup>100</sup> crevice corrosion also occurs at tube-to-tubesheet roll joints, particularly if high thermal stresses cause flexing at the joint, and crack protective oxides or allow water ingress into the crevice.

#### **2.03.5.2.2 Heat exchangers and condensers**

Heat exchangers and condensers are widely used in the power generation and chemical processing industry. Almost all heat exchangers have crevices at the tube-sheet and the tube support-plate locations. For example, in the nuclear power industry, crevice corrosion has resulted in costly tube denting (see [Section 2.03.5.2.3](#)), as well as intergranular attack (IGA), and stress corrosion cracking (SCC) of Inconel 600 (Alloy 600) in tube-sheet and tube support-plate crevices.<sup>101</sup>

Dissimilar metal crevices (DMC) are common features of heat exchangers and condensers. Tube-to-tube sheet joints frequently contain crevices and dissimilar tube and tubesheet materials. Work by Kearns<sup>102</sup> and Maurer<sup>103</sup> on DMC in seawater have shown that the more corrosion resistant materials in a DMC can be made to corrode as a result of the corrosion products from the less resistant alloys.

#### **2.03.5.2.3 Pressurized-water reactors (PWR) and boiling-water reactors (BWR)**

Crevices in oxidizing environments, or boiling at heat-transfer surfaces, can result in a variety of crevice corrosion problems for both BWR and PWR

operations. According to Ford *et al.*, in most BWR designs, the coolant purity approaches that of theoretically pure water (i.e., a room-temperature conductivity of  $0.055 \mu\text{S cm}^{-1}$ ), with dissolved chloride and sulfate ion concentrations below 5 ppb, in order to help prevent the concentration of impurities in crevices.<sup>104</sup>

One of the main differences between the PWR and BWR designs is that a PWR has a steam generator that isolates the primary water (i.e., water heated by the reactor core under pressure) from the secondary water that is boiled to make the steam that runs the turbines. A serious crevice corrosion problem appeared in PWRs during the mid-1970s.<sup>105</sup> The phenomenon became known as denting, and it occurred in Inconel 600 tubing because of corrosion in the crevices between the tubes and the carbon steel support plates or tube sheets. In the crevices between the Inconel 600 steam generator tubes and the steel tube-sheets, tube support-plates, and sludge deposits, where water circulation is restricted by geometry and deposits, boiling can concentrate the very low levels of impurities in the secondary water to very high concentrations. This is known as hideout. The concentration of impurities in crevices, under heat transfer conditions, can be 20 000 times that present in the bulk secondary water.<sup>105,106</sup> Denting can restrict primary water flow and result in SCC and IGA, which may result in primary water leaking into the secondary side. Tube damage from hideout, such as wastage, pitting, and denting has been largely eliminated by appropriate management of secondary water chemistry, which includes reducing condenser impurity in-leakage, reducing air in-leakage, using make-up water of higher purity, using boric acid to inhibit acidic chloride attack, and using condensate polishers to purify the feedwater. Newer steam generator designs have used Inconel 690 (Alloy 690) or Incoloy 800 (Alloy 800) that are more corrosion resistant to the highly concentrated environments that can develop in the tube-sheet and tube support-plate crevices, and under sludge piles.<sup>105</sup>

### 2.03.5.3 Aerospace

Most commercial aircraft utilize aluminum alloys for their airframe structures, which are susceptible to pitting, crevice corrosion, exfoliation, and environment-assisted cracking under normal operating conditions.<sup>107–109</sup> Crevice corrosion on aircraft can occur at unsealed joints or at joints where the fillet seal has broken, on fuselage structures held in intimate contact with wet insulation blankets, and on aluminum and

stainless steel tubing under rubber clamps.<sup>107</sup> As described by Inman *et al.*, crevice corrosion and subsequent fatigue cracking of airframe structures can occur and lead to loss of life. They list a number of examples whereby crevice corrosion along riveted structures, which are difficult to inspect, led to fatigue cracking and subsequent failure of sections of the fuselage.<sup>108</sup> For instance, in 1981, the failure of a large portion of the fuselage of a commercial aircraft in Taiwan was attributed to undetected fuselage-skin corrosion that led to fatigue cracking. Another incident in Hawaii in 1988 revealed that fatigue cracking can occur in corroded fuselage structures.<sup>108</sup> Due to its nature, crevice corrosion in aircraft can be difficult to detect until it exceeds the limits allowed by design. As described by Inman *et al.*, moisture is drawn into crevices during normal service, and pollutant gases can dissolve in the water to form corrosive solutions which attack the protective oxide layer. Aircraft operating in marine environments have to contend with additional chloride ion ingress. Also, routine maintenance and cleaning procedures, such as washing and cleaning, can contribute to crevice corrosion.

According to Sankaran *et al.*, crevice corrosion can lead to severe intergranular and exfoliation corrosion, which, in turn, can lead to increased stress and crack growth rates due to the volumetric increase of corrosion products within creviced regions.<sup>110</sup> Faying-surface sealants, such as polysulfide sealants, have dramatically reduced the crevice corrosion of fuselage lap and similar aircraft joints.<sup>107</sup>

### 2.03.5.4 Nuclear Waste Isolation

High level nuclear waste, such as that resulting from spent nuclear fuel from commercial nuclear reactors used for power generation, needs to be isolated from the environment for 1000–10 000 years or longer.<sup>111,112</sup> Corrosion of the containment materials is considered to be the principal mode of degradation that will limit the lifetime of the waste package.<sup>113</sup> As crevice corrosion is thought to be a part of the limiting lifetime of these containment systems, much of the research on crevice corrosion in the last ten years has been devoted to a better understanding of crevice corrosion mechanisms in this highly engineered containment system.<sup>112</sup> With the proposed repository designs, crevices could be formed between the waste package and the emplacement pallet, by the deposition of mineral precipitates, corrosion products, dust, or by contact with rocks, and the drip shield or ground support materials.<sup>113</sup>

A common approach taken by many nations is to bury the waste underground in corrosion resistant containers. Early work at Yucca Mountain in Nevada, a potential repository site in the United States, initially focused on austenitic stainless steels as the container material<sup>112</sup>; however, this material selection has evolved over the years as the design requirements have increased. Originally, 304 stainless steel was specified as the container material, but as the corrosion resistance requirements increased, first Alloy 825, then Alloy 625, and finally Alloy 22, were selected. Alloy 22, a Ni–22Cr–13Mo–4Fe–3W alloy, was selected in order to have the highest resistance to localized corrosion phenomena, such as stress corrosion cracking, pitting, and crevice corrosion.<sup>112–115</sup> Since 1998, the waste-package design for the high-level waste repository at Yucca Mountain has specified a double-walled cylindrical container with the outer container made from Alloy 22, to resist corrosion, and an inner container made of Type 316 nuclear-grade stainless steel to provide strength and radiation shielding.<sup>112,113</sup> The container will be covered by a Ti Gr7 drip shield to guard against rock fall and prevent contact with water seepage during the first few hundred years.<sup>112</sup> Alloy 22 is extremely resistant to localized corrosion as a result of the formation of a 5–6-nm thick, chromium-rich oxide film. The general corrosion rate of Alloy 22 in acidic to alkaline solutions is expected to be well below  $0.1 \text{ mm year}^{-1}$  ( $0.004 \text{ mil year}^{-1}$ ), and therefore, the life of the containers for Yucca Mountain should not be limited by passive dissolution.<sup>112</sup>

Although the United States is considering burial in unsaturated formations (i.e., above the water table), and will therefore have to consider oxidizing redox potentials, it is unlikely that pitting corrosion will be life limiting, as it is unlikely that in this environment (hot concentrated groundwater), a sufficiently high electrochemical potential would be developed to initiate pits on the exposed surface of Alloy 22.<sup>112</sup>

As described by Rebak and McCright,  $E_{\text{crit}}$  is considered the potential above which localized corrosion could occur. The margin of safety against localized corrosion, therefore, will be the value of  $\Delta E$ , where  $\Delta E$  is the difference between  $E_{\text{crit}}$  and the uniform or passive corrosion rate,  $E_{\text{corr}}$  (i.e.,  $\Delta E = E_{\text{crit}} - E_{\text{corr}}$ ).<sup>112</sup> As the value of  $\Delta E$  increases, so does the margin of safety for localized corrosion.  $E_{\text{corr}}$  and  $E_{\text{crit}}$  both depend on the surface condition of the alloy, the environment, and the ambient temperature. Critical temperatures for pitting and crevice corrosion have been measured, and among the highest are those for nickel alloys.

Reassuringly, He and Dunn's work on crevice corrosion propagation indicate that although crevice corrosion of Alloy 22 is possible under some environmental conditions which may develop on the repository waste containers, the maximum penetration depth of localized attack is significantly less than the outer-container wall thickness, even under the aggressive environmental conditions used in their laboratory tests.<sup>113</sup>

### 2.03.5.5 Underground Structures

Most buried or submerged steel structures, such as pipelines and underground storage tanks, are painted or coated and cathodically protected to protect them from corrosion. If the coating becomes damaged or blistered, crevices can form underneath the protective coating and lead to crevice corrosion.<sup>116–118</sup> To compound the problem, cathodic protection may not be able to penetrate into the crevices formed by disbonded coatings. This so-called shielding is believed to be more severe for certain types of coating (e.g., polyolefin tape) and low conductivity groundwater.<sup>119</sup> Li *et al.*<sup>118</sup> have shown that the steel surface in freshly formed crevices under cathodic protection in dilute chloride environments may not immediately achieve the required protection potential of less than  $-0.850 \text{ V}$  (Cu/CuSO<sub>4</sub>). They have shown, however, that the crevice will become more alkaline as the cathodic reaction consumes the oxygen and forms hydroxide. The hydroxide ions then attract chloride ions into the crevice to maintain charge balance, which, in turn, increases the conductivity within the crevice, allowing protection potentials to be achieved.

It is important to realize that the foregoing description of corrosion within crevices as a result of damaged coatings should not be taken to imply either that carbon steels are susceptible to conventional crevice corrosion in neutral groundwaters or similar near-neutral solutions, or that crevice corrosion can occur on a steel structure that is cathodically protected. Under these conditions, corrosion does not occur by a conventional crevice corrosion mechanism, as the external potential is more negative than the corrosion potential, and therefore, the anodic reaction under the coating cannot be balanced by the external cathodic reaction. Instead, the corrosion derives from the fact that polymeric coatings are much more permeable to oxygen than to ions, and hence oxygen can penetrate the coating while the cathodic protection current cannot. As a result, the steel under the coating corrodes by a localized or general corrosion

mechanism, controlled by the rate of oxygen permeation through the coating. Similarly, a metal-metal crevice in a carbon steel structure will only suffer from crevice corrosion by the conventional mechanism when the external surface is passive, for example, in alkaline solutions. In neutral or acid solutions, such as acidic groundwaters and seawater, where the steel undergoes active corrosion, some iron dissolution will initially occur in the crevice, but this will quickly raise the ferrous ion concentration to such a level that either the  $\text{Fe}/\text{Fe}^{2+}$  reaction reaches equilibrium or the precipitation of ferrous oxides or hydroxides blocks the crevice and stifles the corrosion. When the external surface is subject to cathodic protection this simply reinforces this tendency, and the steel in the crevice will normally passivate.

Fessler *et al.*<sup>117</sup> noted that cathodic protection potentials should not be decreased to compensate for crevices, as potentials that are too low will form hydrogen bubbles in the crevice, which, in turn, will block the protection current. They suggested that the pipe-to-soil potentials should be maintained roughly between  $-0.850$  and  $-1.10$  V ( $\text{Cu}/\text{CuSO}_4$ ) to avoid this problem.

## References

- Kelly, R. G. In *Encyclopedia of Electrochemistry: Corrosion and Oxide Films*; Stratmann, M., Frankel, G. S., Eds.; Wiley-VCH: Weinheim, 2003; Vol. 4, Chapter 4.1, pp 275–307.
- Szklarska-Smialowska, Z. *Pitting and Crevice Corrosion*; NACE International: Houston, TX, 2005.
- Mears, R. B.; Evans, U. R. *Trans. Faraday Soc.* **1934**, 30, 417–423.
- Uhlig, H. H. *Trans. of AIME* **1940**, 140, 387–432.
- Oldfield, J. W.; Sutton, W. H. *Br. Corros. J.* **1978**, 13(1), 13–22.
- Oldfield, J. W.; Sutton, W. H. *Br. Corros. J.* **1978**, 13(3), 104–111.
- Crolet, J. L.; Defranoux, J. M. *Corros. Sci.* **1973**, 13(7), 575–585.
- Kain, R. M. *Mater. Perform.* **1984**, 23(2), 24–30.
- Kain, R. M. In *ASM Handbook; Corrosion* ASM International: Metals Park, OH, 1987; Vol. 13, p 405.
- Oldfield, J. W. *Int. Mater. Rev.* **1987**, 32(3), 153–170.
- Pickering, H. W. In *Corrosion and Corrosion Protection*; Frankenthal, R. P., Mansfeld, F., Eds.; The Electrochemical Society: Pennington, 1981; p 85.
- Pickering, H. W. *Corros. Sci.* **1989**, 29(2/3), 325–341.
- Lillard, R. S.; Jurinski, M. P.; Scully, J. R. *Corrosion* **1994**, 50(4), 251–265.
- Shaw, B. A.; Moran, P. J.; Gartland, P. O. *Corros. Sci.* **1991**, 32(7), 707–719.
- Kelly, R. G. In *Critical Factors and Challenges in Crevice Corrosion*; CORROSION/01 Research Topical Symposium, 2001; Frankel, G. S., Scully, J. R., Eds.; NACE International: Houston, TX, 2001; pp 128–156.
- Kelly, R. G.; Stewart, J. In *Passivity of Metals and Semiconductors*; Ives, M. B., MacDougall, B. R., Bardwell, J. A., Eds.; The Electrochemical Society: Pennington, 1999; Vol. VIII, pp 546–554.
- Szklarska-Smialowska, Z.; Mankowski, J. *Corros. Sci.* **1978**, 18, 953–960.
- Stockert, L.; Boehni, H. *Mater. Sci. Forum* **1989**, 44/45.
- Laycock, N. J.; Stewart, J.; Newman, R. C. *Corros. Sci.* **1997**, 39(10–11), 1791–1809.
- Kehler, B. A.; Ilevbare, G. O.; Scully, J. R. In *Crevice Corrosion Behavior of Ni-Cr-Mo Alloys: Comparison of Alloys 625 and 22*; CORROSION/01 Research Topical Symposium, 2001; Frankel, G. S., Scully, J. R., Eds.; NACE International: Houston, TX, 2001; pp 30–64.
- Abdulsalam, M. I.; Pickering, H. W. In *The Roles of Aspect Ratio and Oxidizing Potential in Crevice Corrosion*; Critical Factors in Localized Corrosion III, 1998; Kelly, R. G., Frankel, G. S., Natishan, P. M., Newman, R. C., Eds.; The Electrochemical Society: Pennington, 1998; pp 395–408.
- Sedriks, A. J. In *Overview of Crevice Corrosion Issues for Chromium-Containing Alloys*, CORROSION/96 Research Topical Symposia, 1996; Ives, M. B., Oldfield, J. W., Eds.; NACE International: Houston, TX, 1996; pp 279–310.
- Sedriks, A. J. *Corrosion of Stainless Steels*, 2nd ed.; Wiley: New York, 1996.
- Combrade, P. In *Corrosion Mechanisms in Theory and Practice*; Marcus, P., Ed.; Marcel Dekker: New York, 2002; pp 349–397.
- Brossia, C. S. In *Effects of MnS Inclusions on Crevice Corrosion of Stainless Steels in Neutral Chloride Solutions*, Critical Factors in Localized Corrosion III; Kelly, R. G., Frankel, G. S., Natishan, P. M., Newman, R. C., Eds.; The Electrochemical Society: Pennington, 1998; pp 326–338.
- Brossia, C. S.; Kelly, R. G. In *On the Role of Alloy Sulfur in the Initiation of Crevice Corrosion in Stainless Steel*, Critical Factors in Localized Corrosion II; Natishan, P. M., Kelly, R. G., Frankel, G. S., Newman, R. C., Eds.; The Electrochemical Society: Pennington, 1995; pp 201–217.
- Brossia, C. S.; Kelly, R. G. *Corros. Sci.* **1998**, 40(11), 1851–1871.
- Brossia, C. S.; Kelly, R. G. *Corrosion* **1998**, 54, 145–154.
- Szklarska-Smialowska, Z. In *Sulfide Inclusions in Steel*; deBarbadillo, J. J., Snape, E., Eds.; ASM International: Metals Park, OH, 1975; p 380.
- Szklarska-Smialowska, Z.; Mankowski, J. *Corros. Sci.* **1978**, 18, 953–960.
- Ijsseling, F. P. *Survey of Literature on Crevice Corrosion (1979–1998)*; European Federation of Corrosion Publications, 2000; p 30.
- Roberge, P. R. *Handbook of Corrosion Engineering*; McGraw-Hill: New York, 1999; p 734.
- Grubb, J. F.; DeBold, T.; Fritz, J. D. In *ASM Handbook; Corrosion: Materials* ASM International: Metals Park, OH, 2005; Vol. 13B, p 54.
- Renner, M.; Heuber, U.; Rockel, M. B.; Wallis, D. *Werkst. Korros.* **1986**, 37, 183.
- Noel, J. J.; Shoesmith, D. W.; Ikeda, B. M. In *Crevice Corrosion of Alpha Titanium Alloys*, CORROSION/01 Research Topical Symposium, 2001; Frankel, G. S., Scully, J. R., Eds.; NACE International: Houston, TX, 2001; pp 65–102.
- Kain, R. M. In *ASM Handbook; Corrosion: Fundamentals, Testing, and Protection* ASM International: Metals Park, OH, 2003; Vol. 13A, p 549.
- Kain, R. M. In *Evaluating Crevice Corrosion Susceptibility*, CORROSION/96 Research Topical Symposium; Ives, M. B., Oldfield, J. W., Eds.; NACE International: Houston, TX, 1996; p 401.

38. Kearns, J. R. In *Corrosion Tests and Standards: Applications and Interpretation*; Baboian, R., Dean, J., S. W., Hack, H. P., Haynes, G. S., Sprowls, D. O., Eds.; ASM International: Metals Park, OH, 1995; Chapter 19, p 175.
39. ASTM, G 4-01: *Standard Guide for Conducting Corrosion Tests in Field Applications*; ASTM International: West Conshohocken, PA, 2001.
40. Tuthill, A. H. *Mater. Perform.* **1985**, 24(9), 43.
41. ASTM, G 48-03: *Standard Test Methods for Pitting and Crevice Corrosion Resistance of Stainless Steels and Related Alloys by Use of Ferric Chloride Solution*; ASTM International: West Conshohocken, PA, 2003.
42. Streicher, M. A. *Corrosion* **1974**, 30(3), 77-91.
43. Treseder, R. S. *Method MTI-2 for Laboratory Testing of Wrought Iron- and Nickel-Base Alloys for Relative Resistance to Crevice Corrosion in a Standard Ferric Chloride Solution*; The Materials Technology Institute of the Chemical Process Industries, 1980; pp 16-27.
44. Turnbull, A. *Corros. Sci.* **1983**, 23(8), 833-870.
45. Garner, A. *Corrosion* **1981**, 37(3), 178.
46. Tsujikawa, S. *A New Test for Predicting Pitting Corrosion Resistance of CRAs in Sour Environments*, CORROSION/88; Paper no. 64; NACE International: St. Louis, MO, 1988.
47. Wensley, A.; Reid, C.; Brown, D.; Christi, D. In *Corrosion of Stainless Alloys in a Chlorine Dioxide Bleached Pulp Washer*; Proceedings of Technical Association of the Pulp and Paper Industry Engineering Conference, 1991 TAPPI Press: Atlanta, GA, 1991; pp 499-503.
48. ASTM, G 78-01: *Standard Guide for Crevice Corrosion Testing of Iron-Base and Nickel-Base Stainless Alloys in Seawater and Other Chloride-Containing Aqueous Environments*; ASTM International: West Conshohocken, PA, 2001.
49. ASTM, F 746-87 (Reapproved 99): *Standard Test Method for Pitting or Crevice Corrosion of Metallic Surgical Implant Materials*; ASTM International: West Conshohocken, PA, 1999.
50. Syrett, B. C. *Corrosion* **1977**, 33(6), 221.
51. ASTM, F 2129-06: *Standard Test Method for Conducting Cyclic Potentiodynamic Polarization Measurements to Determine the Corrosion Susceptibility of Small Implant Devices*; ASTM International: West Conshohocken, PA, 2006.
52. Frankel, G. S. In *ASM Handbook; Corrosion: Fundamentals, Testing, and Protection* ASM International: Metals Park, OH, 2003; Vol. 13A, p 236.
53. Leclerc, M. F. In *Corrosion, Metal/Environment Reactions*; Shreir, L. L., Jarman, R. A., Burstein, G. T., Eds.; Butterworth Heinemann: Oxford, 1994; Vol. 1, p 2:164.
54. Pound, B. G. *J. Biomed. Mater. Res.* **2006**, 77A, 185-191.
55. Silverman, D. C. In *Tutorial on Cyclic Potentiodynamic Polarization Technique*, CORROSION/98; NACE International: San Diego, CA, 1998; Paper no. 299.
56. Wilde, B. E.; Williams, D. E. *Electrochim. Acta* **1971**, 16, 1971-1985.
57. Wilde, B. E. *Corrosion* **1972**, 28(8), 283-291.
58. ASTM G 61-86 (Reapproved 2003): *Standard Test Method for Conducting Cyclic Potentiodynamic Polarization Measurements for Localized Corrosion Susceptibility of Iron-, Nickel-, or Cobalt-Based Alloys*; ASTM International: West Conshohocken, PA, 2003.
59. Kain, R. M.; Klein, P. A. In *Crevice Corrosion Propagation Studies for Alloy N06625: Remote Crevice Assembly Testing in Flowing Natural and Chlorinated Seawater*, NACE Corrosion/90; NACE International: Las Vegas, NV, 1990; Paper no. 158.
60. Lee, T. S. In *Electrochemical Corrosion Testing*, ASTM STP 727; Mansfeld, F., Bertocci, U., Eds.; ASTM International: West Conshohocken, PA, 1981; p 43.
61. Lee, T. S. In *Electrochemical Techniques for Corrosion Engineering*; NACE International: Houston, TX, 1986.
62. Fontana, M. G.; Greene, N. D. *Corrosion Engineering*; McGraw-Hill: New York, 1967.
63. Uhlig, H. H. *Corrosion and Corrosion Control*; John Wiley: New York, 1971.
64. Bond, A. P.; Dundas, A. J. *Mater. Perform.* **1984**, 23(7), 39.
65. Bai, Z.; Gilbert, J. L. In *ASM Handbook; Corrosion: Environments and Industries*, ASM International: Materials Park, OH, 2006; Vol. 13C, pp 837-852.
66. Laing, P. G. In *Corrosion and Degradation of Implant Materials*, ASTM STP 684; ASTM International: West Conshohocken, PA, 1979; pp 199-211.
67. Gilbert, J. L.; Jacobs, J. J. In *Modularity of Orthopedic Implants*, ASTM STP 1301; ASTM International: West Conshohocken, PA, 1997; pp 45-59.
68. Brown, S. A.; Flemming, C. A.; Kawalec, J. S.; Placko, H. E.; Vassaux, C.; Merritt, K.; Payer, J. H.; Kraay, M. J. *J. Appl. Biomater.* **1995**, 6(1), 19-26.
69. Brown, S. A.; Simpson, J. P. *J. Biomed. Mater. Res.* **1981**, 15(1), 867-878.
70. Eiselstein, L. E.; Proctor, D. M.; Flowers, T. C. *Mater. Sci. Forum* **2007**, 539-543, 698-703.
71. Hanawa, T. *Mater. Sci. Forum* **2006**, 512, 243-248.
72. Gilbert, J. L.; Buckley, C. A.; Jacobs, J. J. *J. Biomed. Mater. Res.* **1993**, 27(12), 1533-1544.
73. Guidoin, R.; et al. *J. Endovasc. Ther.* **2000**, 7(2), 105-122.
74. Guidoin, R.; Zhang, Z.; Dionne, G.; Douville, Y.; King, M.; Legrand, A.-P.; Doppelt, P. In *Corrosion of the Nitinol Wire of Endovascular Prostheses: Does Nickel Ion Release Impair the Devices Performance?* Materials and Processes for Medical Devices Conference ASM International: St. Paul, MN, 2005; pp 284-289.
75. Heintz, C.; Riepe, G.; Birken, L.; Kaiser, E.; Chakfé, N.; Morlock, M.; Delling, G.; Imig, H. *J. Endovasc. Ther.* **2001**, 8(3), 248-253.
76. Riepe, G.; Heintz, C.; Kaiser, E.; Chakfé, N.; Morlock, M.; Delling, G.; Imig, H. *Eur. J. Vasc. Endovasc. Surg.* **2002**, 24(2), 117-122.
77. Lasley, C. C.; Mitchell, M. R. In *The Corrosion of Nitinol by Exposure to Decontamination Solutions*, The International Conference on Shape Memory and Superelastic Technologies, 2003; ASM International: Monterey, CA, 2003; pp 375-384.
78. Walak, S. *Analysis of Nitinol Stent-Grafts After Long-Term In-Vivo Exposure*, Materials and Processes for Medical Devices Conference; ASM International: St. Paul, MN, 2005; pp 290-294.
79. Personal communication. Warner, C. P. to Eiselstein, L. E. Menlo Park, CA, 2007.
80. Jacobs, T. S.; Won, J.; Gravereaux, E. C.; Faries, P. L.; Morrissey, N.; Teodorescu, V. J.; Hollier, L. H.; Marin, M. L. *J. Vasc. Surg.* **2003**, 37(1), 16-26.
81. Pound, B. G. In *Electrochemical Behavior of Cobalt-Chromium Alloys*; Materials and Processes for Medical Devices Conference, 2007 ASM International: Desert Springs, CA, 2007.
82. Colangelo, V. J.; Greene, N. D. *J. Biomed. Mater. Res.* **1969**, 3(2), 247-265.
83. Cook, S. D.; Thomas, K. A.; Harding, A. F.; Collins, C. L.; Haddad, R. J., Jr.; Milicic, M.; Fischer, W. L. *Biomaterials* **1987**, 8(3), 177-184.



84. Cahoon, J. R.; Hill, L. D. *J. Biomed. Mater. Res.* **1978**, *12* (6), 805–821.
85. Zardiackas, L. D.; Roach, M.; Williamson, S.; Bogan, J. A. In *Stainless Steels for Medical and Surgical Applications*, ASTM STP 1438; Winters, G. L., Nutt, M. J., Eds.; ASTM International: West Conshohocken, PA, 2003; pp 194–207.
86. Windler, M.; Steger, R. In *Stainless Steels for Medical and Surgical Applications*, ASTM STP 1438; Winters, G. L., Nutt, M. J., Eds.; ASTM International: West Conshohocken, PA, 2003; pp 39–49.
87. Windler, M.; Steger, R.; Winters, G. L. In *Stainless Steels for Medical and Surgical Applications*, ASTM STP 1438; Winters, G. L., Nutt, M. J., Eds.; ASTM International: West Conshohocken, PA, 2003; pp 72–80.
88. Cohen, J.; Wulff, J. *J. Bone Joint Surg. Am.* **1972**, *54*(3), 617–628.
89. John, K. R. In *ASM Handbook; Corrosion: Environments and Industries* ASM International: Materials Park, OH, 2006; Vol. 13C, pp 820–825.
90. Bundy, K. J.; Zardiackas, L. D. In *ASM Handbook; Corrosion: Environments and Industries* ASM International: Materials Park, OH, 2006; Vol. 13C, pp 853–890.
91. Thomas, S. R.; Shukla, D.; Latham, P. D. *J. Bone Joint Surg. Br.* **2004**, *86*(7), 974–978.
92. Charles, A. E.; Ness, M. G. *Vet. Surg.* **2006**, *35*(5), 438–444.
93. Tezer, M.; Kuzgun, U.; Hamzaoglu, A.; Ozturk, C.; Kabukcuoglu, F.; Sirvanci, M. *Arch. Orthop. Trauma Surg.* **2005**, *125*(6), 417–421.
94. Kirkpatrick, J. S.; Venugopalan, R.; Beck, P.; Lemons, J. *J. Spinal Disord. Tech.* **2005**, *18*(3), 247–251.
95. Megremis, S.; Carey, C. M. In *ASM Handbook; Corrosion: Environments and Industries* ASM International: Materials Park, OH, 2006; Vol. 13C, pp 891–921.
96. Wylie, C. M.; Shelton, R. M.; Fleming, G. J.; Davenport, A. *J. Dent. Mater.* **2007**, *23*(6), 714–723.
97. Ossa, C. P.; Rogero, S. O.; Tschiptschin, A. P. *J. Mater. Sci. Mater. Med.* **2006**, *17*(11), 1095–1100.
98. Reclaru, L.; Ziegenhagen, R.; Eschler, P. Y.; Blatter, A.; Lemaitre, J. *Acta Biomater.* **2006**, *2*(4), 433–444.
99. Schutz, R.; Thomas, D. In *Metals Handbook; Corrosion*, 9th ed.; ASM International: Metals Park, OH, 1987; Vol. 13, p 669.
100. Esmacher, M. J.; Gheysen, G.; Rossi, A.; Farraro, J. F.; Sehl, P. In *Firetube Boiler Failures: Review of Case Histories*, CORROSION/05; NACE International: Houston, TX, 2005; Paper no. 433.
101. Cohen, P. Ed. *The ASME Water Handbook on Water Technology For Thermal Power Systems*; AIME: New York, 1989.
102. Kearns, J. R.; Johnson, M. J.; Grubb, J. F. In *Accelerated Corrosion in Dissimilar Metal Crevices*; CORROSION/86; NACE International: Houston, TX, 1986; Paper no. 228.
103. Maurer, J. R. *Mater. Perform.* **1994**, *33*(4), 51–54.
104. Ford, F. P.; Gordon, B. M.; Horn, R. M. In *ASM Handbook; Corrosion: Environments and Industries* ASM International: Materials Park, OH, 2006; Vol. 13C, pp 341–361.
105. Scott, P. M.; Combrade, P. In *ASM Handbook; Corrosion: Environments and Industries* ASM International: Materials Park, OH, 2006; Vol. 13C, pp 362–385.
106. MacDonald, D. D.; Begley, J. A.; Bockris, J. O'M.; Kruger, J.; Mansfeld, J. B.; Rhodes, P. R.; Staehle, R. W. *Mater. Sci. Eng.* **1981**, *50*(1), 19–42.
107. Adjorlolo, A. In *ASM Handbook; Corrosion: Environments and Industries*, ASM International: Materials Park, OH, 2006; Vol. 13C, pp 598–612.
108. Inman, M. E.; Kelly, R. G.; Willard, S. A.; Piascik, R. S. In *Coordinated Metallographic, Chemical, and Electrochemical Analyses of Fuselage Lap Splice Corrosion*, Proceedings of the FAA-NASA Symposium on the Continued Airworthiness of Aircraft Structures, FAA Center of Excellence in Computational Modeling of Aircraft Structures, Atlanta, Georgia, August 28–30, 1997; DOT/FAA/AR-97/2 Office of Aviation Research: Washington, DC, 1997; pp 129–146.
109. Simon, L. B.; Skennerton, G.; Elster, J. L.; Wikswo, J. P.; Kelly, R. G. In *Aging Aircraft 2000*; NASA: St. Louis, 2000.
110. Sankaran, K. K.; Perez, R.; Smith, H. In *ASM Handbook; Corrosion: Environments and Industries*, ASM International: Materials Park, OH, 2006; Vol. 13C, pp 195–204.
111. Kruger, J.; Rhyne, K. *Nucl. Chem. Waste Manage.* **1982**, *3*, 4.
112. Rebak, R. B.; McCright, R. D. In *ASM Handbook; Corrosion: Environments and Industries*; ASM International: Materials Park, OH, 2006; Vol. 13C, p 421.
113. He, X.; Dunn, D. S. *Corrosion* **2007**, *63*, 2.
114. Carranza, R. M. *J. Met.* **2008**, *60*, 1.
115. Carranza, R. M.; Rodríguez, M. A.; Rebak, R. B. *Corrosion* **2007**, *63*, 5.
116. Beavers, J. A.; Thompson, N. G. *Mater. Perform.* **1997**, *36*(4), 13–19.
117. Fessler, R. R.; Markworth, A. J.; Parkins, R. N. *Corrosion* **1983**, *39*(1), 20–25.
118. Li, Z.; Gan, F.; Mao, X. *Corros. Sci.* **2002**, *44*(4), 689–701.
119. Sridhar, N.; Dunn, D. S. In *Application of a General Reactive Transport Model to Predict Environment Under Disbonded Coatings*, CORROSION/00; NACE International: Houston, TX, 2000; Paper no. 366.

## 2.04 Pitting Corrosion

**M. G. Alvarez**

Comisión Nacional de Energía Atómica (CNEA), CAC Dpto. Materiales, Avda. Gral. Paz 1499, (B1650KNA) San Martín, Buenos Aires, Argentina

**J. R. Galvele**

Instituto Sabato, Universidad Nacional de San Martín, Av. Gral Paz 1499, (B1650KNA) San Martín, Buenos Aires, Argentina

© 2010 Elsevier B.V. All rights reserved.

<b>2.04.1</b>	<b>Introduction</b>	773
2.04.1.1	Definition of the Problem	773
2.04.1.2	Anions Producing Pitting in Metals	774
2.04.1.3	Three Types of Pitting	774
<b>2.04.2</b>	<b>Experimental Aspects of Pitting</b>	775
2.04.2.1	Pitting Morphologies	775
2.04.2.2	Characteristic Electrochemical Parameters for Pitting	776
2.04.2.2.1	Pitting potential	777
2.04.2.2.2	Repassivation potential	778
2.04.2.2.3	Inhibition potential	778
<b>2.04.3</b>	<b>Effect of the Bulk Solution Composition</b>	779
2.04.3.1	Aggressive Solutions	779
2.04.3.2	Inhibitors	779
2.04.3.3	pH	780
<b>2.04.4</b>	<b>Composition of the Solution inside Pits</b>	780
2.04.4.1	Electrolyte inside Pits	780
2.04.4.2	Gas Evolution from Pits	781
<b>2.04.5</b>	<b>Effect of Alloying Elements</b>	781
<b>2.04.6</b>	<b>Pitting Nucleation Sites</b>	782
<b>2.04.7</b>	<b>Effect of Temperature</b>	783
<b>2.04.8</b>	<b>Mechanism of Stable Pitting Growth</b>	783
<b>2.04.9</b>	<b>Passive Film Breakdown</b>	792
2.04.9.1	Ion Penetration Mechanisms	792
2.04.9.2	Film Breakdown Mechanisms	792
2.04.9.3	Passive Film Breakdown and Metastable Pits	793
<b>2.04.10</b>	<b>Pitting of Aluminum Alloys</b>	795
2.04.10.1	Pitting and Intergranular Corrosion	795
<b>2.04.11</b>	<b>Pitting of Stainless Steels</b>	795
2.04.11.1	Pitting and Crevice Corrosion	795
2.04.11.2	Critical Pitting Temperature (CPT)	797
<b>References</b>		798

### Glossary

**Adsorption** The surface retention of solid, liquid, or gas molecules, atoms, or ions by a solid or liquid.

**Critical pitting temperature** The lowest temperature at which the growth of stable pits is possible.

**Crystallographic plane** A distinct plane in a crystal lattice.

**Depassivation** Loss of the state of being passive.

**Electropolished** A smooth and polished surface produced by making the specimen the anode in an electrolytic cell.

**Etch** A roughened surface produced by chemical, electrochemical, or mechanical means.

**Hydrolysis** In aqueous solutions of electrolytes, the reactions of cations with water to produce a

weak base or of anions to produce a weak acid.

**Inhibition potential** The potential above which pits repassivate in solutions containing inhibitors.

**Intermetallic compound** A type of phase formed when atoms of two or more metals combine in a fixed ratio to produce a crystal different in structure from the individual metals.

**Protection potential or repassivation potential** Minimum potential below which already existing pits stop growing.

**Vacancy** A site in a crystal unoccupied by an atom.

**Weak acid** An acid that dissociates only partially into hydrogen ions and anions in solution.

## Abbreviations

**CCT** Critical crevice temperature

**CPT** Critical pitting temperature

**ESCA** Electron spectroscopy for chemical analysis

**NMR** Nuclear magnetic resonance

**SCE** Saturated calomel electrode

**SHE** Standard hydrogen electrode

## Symbols

**c.d.** Current density

**$C_i$**  Concentration of component  $i$

**$D_i$**  Diffusion coefficient of component  $i$  ( $\text{cm}^2 \text{s}^{-1}$ )

**$E_c^*$**  Corrosion potential of the metal in the solution inside a pit

**$E_i$**  Inhibition potential

**$E_p$**  Pitting potential

**$E_r$**  Repassivation potential

**$F$**  Faraday constant

**$i$**  Current density ( $\text{A cm}^{-2}$ )

**$j_{\text{pas}}$**  Passive current density

**$j_{\text{pit}}$**  Current density inside a pit

**$J_i$**  Flux of component  $i$

**$K_a$**  Equilibrium constant for the dissociation of an acid

**$*K_1$**  Equilibrium constant for the first step of the hydrolysis reaction

**$K_w$**  Ionic product of water

**$R$**  Gas constant

**$T$**  Temperature ( $^\circ\text{K}$ )

**$x$**  Pit depth (cm)

**$\eta$**  Polarization

**$\phi$**  Electrical potential

## 2.04.1 Introduction

### 2.04.1.1 Definition of the Problem

Numerous metals and alloys, such as aluminum, stainless steel, titanium, zirconium, and so on have a very high practical interest because in many corrosive environments, they remain passive. For example, a 1 mm thick sheet of any of these metals can resist the action of the corrosive environment for several thousands of years. Nevertheless, under certain environmental conditions, the passive surface of these metals can show very localized corrosion points, where the 1 mm sheet can develop a hole in less than 1 h. This process of localized metal degradation is known as pitting corrosion ([Figure 1](#)).

When the possibility of pitting corrosion is suspected, there are several ways by which the problem can be treated. At the design stage of equipment, one possible approach is the selection of alloys that will resist pitting corrosion in the given working environment. If, because of the properties required from the alloy, or because of economical reasons, this solution is not convenient, the other possibility for dealing with the pitting corrosion problem is control of the corrosive

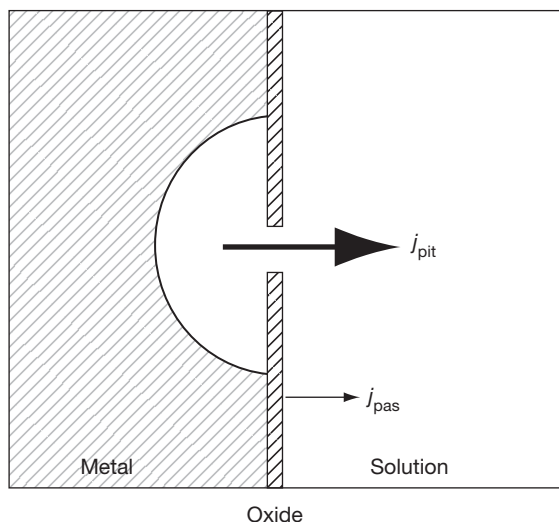


**Figure 1** Pitting corrosion. Numerous metals and alloys, such as aluminum, stainless steel, titanium, zirconium, and so on have a very high practical interest because in many corrosive environments they remain passive, with corrosion current densities of the order of  $j_{\text{pas}} = 10^{-6} \text{ A cm}^{-2}$ . Nevertheless, under certain environmental conditions, the passive surface of those metals could show very localized corrosion points, where the corrosion rate reaches values close to  $j_{\text{pit}} = 1 \text{ A cm}^{-2}$ . This process of localized metal degradation is known as pitting corrosion.

environment. This could be done by controlling the concentration of the pitting-inducing anions, by the use of appropriate inhibitors, by controlling the oxygen content of the corrosive environment, and so on. Most of these subjects will be dealt with in this chapter.

### 2.04.1.2 Anions Producing Pitting in Metals

As shown in [Table 1](#), there is a wide number of anions capable of producing pitting of a variety of metals, in aqueous solutions.<sup>1–37</sup>

It is common to find publications in which some specific properties are attributed to chloride anions that would make them particularly aggressive as

**Table 1** Anions producing pitting in metals

<i>Metal</i>	<i>Aggressive anion</i>	<i>Ref</i>
Aluminum	Cl <sup>−</sup>	1, 2, 3
	Br <sup>−</sup>	1, 2
	I <sup>−</sup>	1, 2
	ClO <sub>4</sub> <sup>−</sup>	1, 4
	NO <sub>3</sub> <sup>−</sup>	1, 5
Cadmium	SCN <sup>−</sup>	6, 7
	Cl <sup>−</sup>	8, 9
	Br <sup>−</sup>	8
	ClO <sub>4</sub> <sup>−</sup>	8
	SO <sub>4</sub> <sup>2−</sup>	8, 9
Iron	Cl <sup>−</sup>	10, 11, 12
	Br <sup>−</sup>	10, 11
	I <sup>−</sup>	10, 13
	ClO <sub>4</sub> <sup>−</sup>	10, 11, 14, 15
	SO <sub>4</sub> <sup>2−</sup>	11, 16, 17
Nickel	Cl <sup>−</sup>	13, 18
	Br <sup>−</sup>	13, 19
	I <sup>−</sup>	13
Stainless steel	Cl <sup>−</sup>	20, 21, 22, 23, 24
	Br <sup>−</sup>	20, 21, 22, 23, 24
	SCN <sup>−</sup>	25
Tin	Cl <sup>−</sup>	26
	ClO <sub>4</sub> <sup>−</sup>	27
	SO <sub>4</sub> <sup>2−</sup>	26
	NO <sub>3</sub> <sup>−</sup>	26
Titanium	Cl <sup>−</sup>	28, 29, 30, 31
	Br <sup>−</sup>	28, 29, 31
	I <sup>−</sup>	29, 32, 33
Zinc	Cl <sup>−</sup>	8, 34
	Br <sup>−</sup>	8, 35
	I <sup>−</sup>	34, 35
	NO <sub>3</sub> <sup>−</sup>	34, 35
	SO <sub>4</sub> <sup>2−</sup>	8, 34, 35
	ClO <sub>4</sub> <sup>−</sup>	35
Zirconium	Cl <sup>−</sup>	29, 32, 33, 36
	Br <sup>−</sup>	29, 32, 33
	I <sup>−</sup>	29, 32, 33
	ClO <sub>4</sub> <sup>−</sup>	37

promoters of pitting corrosion. Nevertheless, this suggestion was dismissed by Hoar<sup>14</sup> as early as in 1947, when discussing the iron pitting mechanism. According to Hoar, the action of the chloride anions should not be related to a strong selective adsorption on the metal, as some authors were suggesting, or to a particularly penetrating power of chlorides into the passive film, as suggested by others. Hoar<sup>14</sup> reported that anions such as ClO<sub>4</sub><sup>−</sup> were as aggressive as Cl<sup>−</sup>. He suggested that the effect of Cl<sup>−</sup>, being a nondepositing ion, had a strong influence on the pH in the electrolyte adjacent to the metal anode. According to Hoar, Cl<sup>−</sup> ions replaced OH<sup>−</sup> ions in the solution close to iron, which was the metal under discussion, thus hindering the process of precipitation of Fe(OH)<sub>2</sub>. On the basis of these ideas, Hoar<sup>27</sup> had been able to show even earlier, in 1937, that tin suffered pitting in NaClO<sub>4</sub> solutions. Comparing anions of similar aggressive power, the reason for finding chloride anions in most of the practical cases of pitting is the extensive distribution of NaCl in nature. In fact, very special care has to be taken to have chloride free environments.

### 2.04.1.3 Three Types of Pitting

When reviewing the literature on pitting, it was found that the mixture of different processes, with similar corrosion shapes, was the source of serious confusion because the same mechanism was attributed to all of them.<sup>38</sup> The review showed that, at least three different types of pitting were being discussed, without any clear distinction among them. They can be identified as:

1. electrochemical depassivation,
2. chemical depassivation,
3. etch pitting.

Electrochemical depassivation is the most common of the three, and from a practical point of view, it is also the most relevant. It is found in neutral and alkaline solutions. It develops on otherwise passive metals, and it is characterized as being associated with a pitting potential. It is observed only above this potential, remaining passive below it. In this chapter, when talking about pitting corrosion, we will be referring to this type of attack.

In certain acid solutions, iron, nickel, and other metals show polarization curves of the type shown in [Figure 2](#). Curves similar to those shown in [Figure 2](#) were reported by Piron *et al.*<sup>39</sup> for nickel and for Inconel alloy, by Nobe and Tobias<sup>40</sup> for iron,

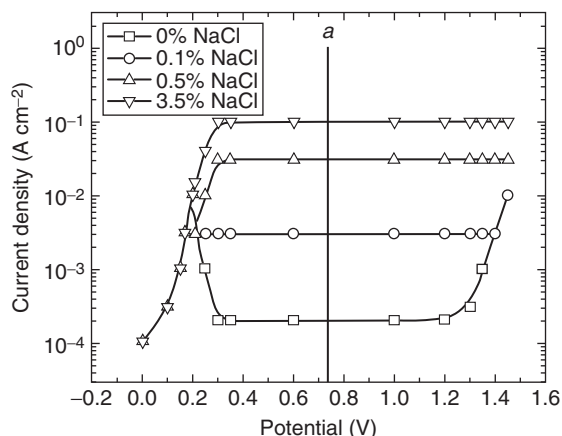


**Figure 2** Typical shapes of the polarization curves for iron, nickel, and their alloys, in aqueous solutions of pure 1 M  $\text{H}_2\text{SO}_4$  and in acid with various contents of NaCl. In pure acid the metal shows an active zone, followed by a passive zone, and finally a current increase because of transpassivity or to oxygen evolution. If the polarization curves are measured in solutions containing various amounts of NaCl, it is observed that the current in the passive zone increases and eventually, at a given NaCl content, passivity fails to appear. If the metal, in pure  $\text{H}_2\text{SO}_4$ , is kept at a potential such as *a*, it becomes passive. If, at this point NaCl is injected into the solution, keeping the potential constant, a current increase will be observed, until the stationary polarization curve for the new solution composition is reached. In the transition from the initial passive state to the new corrosion current, pits are formed on the passive surface, which, in the present chapter, are called chemical depassivation. The potential and the current density values in this figure are arbitrary. The values are in the order of magnitude expected for these metals, but were chosen only for illustration purposes.

by Condit<sup>41</sup> for iron–nickel alloys. Engell and Stolica<sup>42</sup> reported that if iron is passivated in chloride-free sulfuric acid, at a potential somewhere between 0.5 and 1.0 V(SCE), and chloride ions are then injected into the solution, pits are formed on the metal. This type of pitting, resulting from a change in the chemical composition, is classified as chemical depassivation. No pitting potential was found in these experiments, and from Figure 2, it can be concluded that it is the transition from one polarization curve to the curve pertaining to the new solution. From a practical point of view, it is a very uncommon case of corrosion. On the other hand, contrary to the earlier opinion of some authors, there is no evidence that would suggest that the same mechanism is acting both in electrochemical depassivation and chemical depassivation.

A third type of pitting is etch pitting. It is crystallographic in nature, and it was developed mainly as a

technique for metallography. It was described in detail by Ives,<sup>43</sup> and falls outside the scope of this chapter.

This chapter deals with electrochemical depassivation, with some references to chemical depassivation.

## 2.04.2 Experimental Aspects of Pitting

### 2.04.2.1 Pitting Morphologies

In general, when corrosion develops spontaneously, without external currents being applied, pits develop in a very localized way in irregular shapes. Usually, it is observed that once a pit nucleates, no other pits are formed in the surrounding areas. The reason is that while the anodic reaction is concentrated in the pit, the surrounding areas are the location for the cathodic reaction, usually oxygen reduction, which produces local changes in pH, inhibiting the formation of new pits close to the active one.

If, on the other hand, pits are formed by the application of an external current, once they are formed the pits can spread laterally to most of the metal surface. The rate of the spreading of corrosion is controlled by the solubility of the passive film in the acid solution produced inside the pit. For example, pits on cadmium,<sup>9</sup> iron,<sup>12</sup> and zinc<sup>34</sup> were found to spread sideways very easily, while pits on aluminum and stainless steels remained localized, because of the resistance of the passive film to dissolution. In the particular case of stainless steels, pits could remain closed, and the magnitude of corrosion is made visible only after a slight abrasion of the surface film.<sup>44</sup> Closed pits have been reported on stainless steels by Rosenfeld and Danilov,<sup>45</sup> while Yahalom *et al.*<sup>46</sup> observed the initial passive film covering the surface of closed pits. An example of covered pits in stainless steel could be found in the paper by Laycock *et al.*<sup>47</sup> Another example of covered pits, in this case for high purity iron pitted in a sodium chloride solution with a borate buffer, could be found in the paper by Alvarez and Galvele.<sup>48</sup>

When working under controlled electrochemical conditions, it is frequent to find that hemispherical electropolished pits are formed, as shown in Figure 3. These pits were produced on pure aluminum, in a  $\text{NaNO}_3$  solution, at constant potential. Similar pits were reported for iron in chloride and in sulfate solutions, for stainless steels in chloride solutions, and so on. The rounded polished morphology of pitting is the result of the random dissolution of the metal atoms, inside the pit, particularly when such a



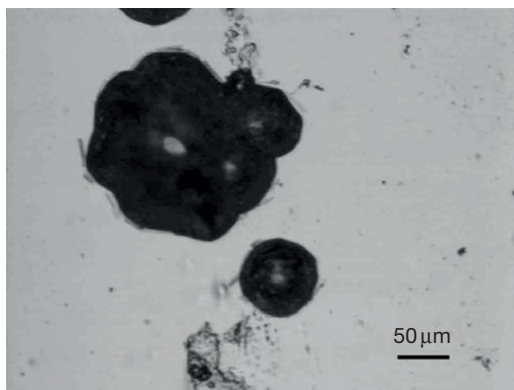


**Figure 3** Hemispherical pits on aluminum 99.999% in 1.0 M  $\text{NaNO}_3$  solution at  $E = 1.84 V_{\text{SHE}}$ . (Courtesy S. Fernández and R. M. Carranza).

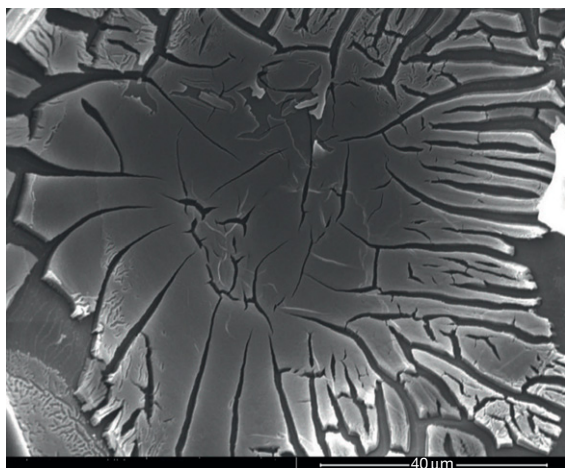


**Figure 4** SEM picture of the interior of a pit of aluminum 99.999% in 1.0 M  $\text{NaNO}_3$  solution at  $E = 1.84 V_{\text{SHE}}$ . The bottom of the pits covered with corrosion products showing a 'dried mud' structure. (Courtesy S. Fernández and R. M. Carranza).

dissolution takes place through a film of corrosion products, as shown in [Figure 4](#). On the other hand, it is also common to observe that pits could grow developing crystallographic planes. An interesting case is that of pitting of aluminum in chloride solutions. In this system, pits grow developing  $\{100\}$  planes, [Figure 5](#). In the particular case of aluminum, this type of attack can lead to the development of deep tunnels, as shown in [Figure 6](#). The production of these tunnels has a practical use, because it is applied to the production of foils for electrolytic condensers.<sup>49</sup> Crystallographic etching, like that shown for aluminum in chloride solutions, was also found for aluminum in bromide, iodide, and perchlorate solutions.<sup>6</sup> Crystallographic planes inside the pits were also reported for iron in

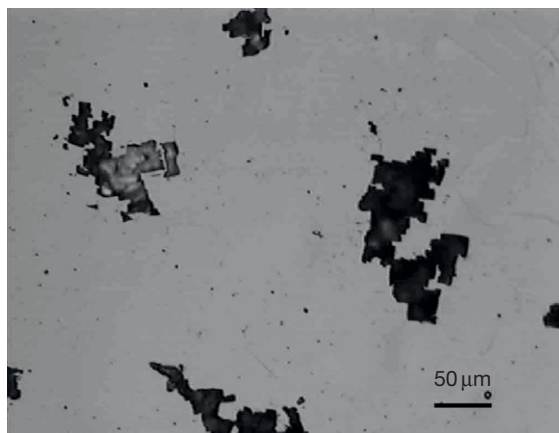


**Figure 5** Pitting of aluminum in chloride solutions. Aluminum 99.999% in 1.0 M  $\text{NaCl}$  solution at  $E = -0.420 V_{\text{SHE}}$ . (Courtesy S. Fernández and R. M. Carranza).

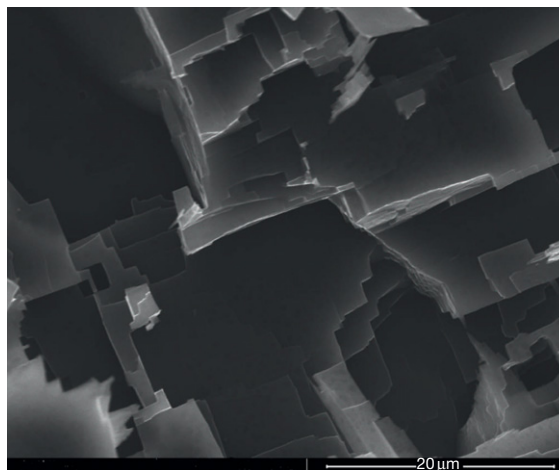


**Figure 6** SEM picture showing the  $\{100\}$  planes developed inside pits of aluminum 99.999% in 1.0 M  $\text{NaCl}$  solution at  $E = -0.420 V_{\text{SHE}}$ . (Courtesy S. Fernández and R. M. Carranza).

perchlorate solutions,<sup>15</sup> for cadmium in chloride solutions,<sup>9</sup> for zinc in chloride solutions,<sup>34</sup> and so on.

#### 2.04.2.2 Characteristic Electrochemical Parameters for Pitting

When the use of electronic instruments, such as potentiostats, was introduced in corrosion studies, several potential values, characteristic of the pitting process, were found. The most relevant ones were: pitting potential, repassivation potential, and inhibition potential.

### 2.04.2.2.1 Pitting potential

It was found that electrochemical depassivation, or pitting, did not appear at any arbitrary potential value, but only above a certain potential called pitting potential ( $E_p$ ). Below this potential, no pitting was observed, no matter how long the metal was exposed to the action of the environment. Above  $E_p$ , on the other hand, pitting would start almost immediately, as it was the case with aluminum in chloride solutions, or after a short induction time, as in the case of stainless steels. This pitting potential is a function of the composition of the environment, the temperature, the composition of the alloy, and so on. Figure 7 shows a typical example of an anodic polarization curve, where the pitting potential of aluminum in a NaCl solution is shown.

Curves like that shown in Figure 7 could be drawn by applying a constant potential, and waiting for the current to reach a stationary value. Then, the potential is increased, in steps of  $\sim 10$  mV, and the new current value is recorded. When the pitting potential is reached the current starts to increase, and pits start to develop on the metal surface. This technique for measuring  $E_p$  is usually called the potentiostatic technique. In the early studies of pitting, some authors had doubts about the validity of the pitting potential, suggesting that if the waiting time at constant potential was extended long enough, pitting would be found at potentials below  $E_p$ . In order to test this possibility a constant potential technique was applied to measure  $E_p$ . In this case, a different sample was used at each potential, the samples were kept for an extended time, the current was measured and after the measurement the samples

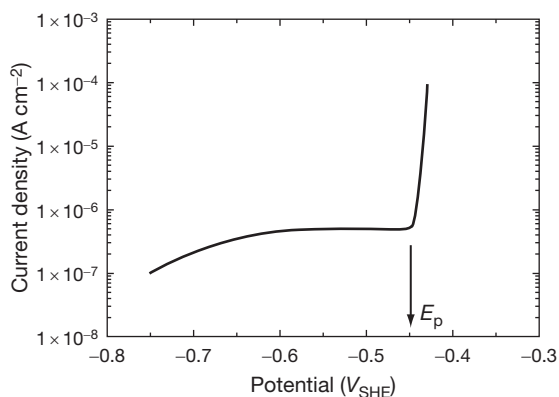


**Figure 7** Pitting potential ( $E_p$ ). Curve based on measurements for aluminum in NaCl solutions. Reprinted from Galvele, J. R.; De Micheli, S. M. de. *Corros. Sci.* **1970**, *10*, 795–807, with permission from Elsevier.<sup>60</sup>

were observed under the microscope. Figure 8 is an example of this technique. The constant potential measurements confirmed the validity of the pitting potential as a transition potential between passivity and localized corrosion.

Horvath and Uhlig,<sup>50</sup> working with stainless steels and related alloys, defined the pitting potential as the lowest potential at which pitting could not be observed after a 10 h or longer period at constant potential. According to these authors, reproducibility was in the order of  $\pm 5$  mV.

Instead of the above-mentioned potentiostatic technique, which tends to be time consuming, another technique frequently used is the potentiokinetic technique, where the electrode potential is changed at a constant scanning rate, while the current is being recorded. One limitation of this technique is that the pitting potential values found can be slightly high, because not enough time is given for the pits to nucleate. Another technique for measuring the pitting potential was introduced by Pessall and Liu.<sup>51</sup> In this technique, the specimen is exposed to the solution, at constant potential, while the metal surface is scratched with a diamond point, or another sharp instrument, to break the passive oxide film. If the potential is lower than the pitting potential, the exposed metal repassivates in a very fast rate. On the other hand, if the potential is above the pitting potential, the repassivation rate is very slow or no repassivation is observed. By measuring the repassivation time, at different potentials, it is possible

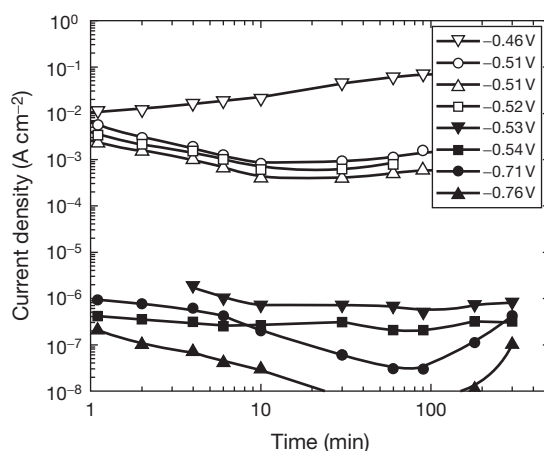


**Figure 8** Constant potential technique for measuring  $E_p$ . Curves based on measurements for aluminum in NaCl solutions. Reprinted from Galvele, J. R.; De Micheli, S. M. de. *Corros. Sci.* **1970**, *10*, 795–807, with permission from Elsevier.

to measure  $E_p$  with dispersion lower than 10 mV. Pessal and Liu developed this technique to solve the problem caused by high dispersion in  $E_p$  found for various metals when using potentiokinetic techniques. For the same reason some authors, when measuring pitting potentials, used various techniques in each system, to make sure that the  $E_p$  values found were reliable.<sup>9,34,48</sup>

#### 2.04.2.2.2 Repassivation potential

Another characteristic potential of the pitting process was described by Pourbaix<sup>52</sup> and it is known as the repassivation potential. Pourbaix reported that pits, which will start to grow at the pitting potential, or above, will keep growing even when the potential is lowered below  $E_p$ , Figure 9. The pits will stop growing only when the potential is lower than a certain value called repassivation potential, or protection potential,  $E_r$ . As found by Suzuki and Kitamura,<sup>53</sup> the value of the repassivation potential is related to the occlusion of the pit. As described later, Wilde and Williams<sup>54</sup> found, for a series of steel alloys, that the bigger the difference between  $E_p$  and  $E_r$ , the more susceptible the alloy was to crevice corrosion.

#### 2.04.2.2.3 Inhibition potential

The third characteristic potential was first described by Schwenk,<sup>24</sup> for stainless steels in chloride solutions containing nitrates. It was reported that in these solutions, when increasing the potential above the pitting potential, the current increased. But eventually a potential was reached above which the pits

were repassivated. This potential was called inhibition potential,  $E_i$ , Figure 10, and it has been reported in numerous systems. Kuzub and Novitskii<sup>55</sup> found that  $E_i$ , for stainless steels in chloride plus nitrate solutions was a function of the chromium content of the steel. At higher chromium contents  $E_i$  was lower, and the inhibition of pitting was easier.

Vetter and Strehblow<sup>11</sup> measured the inhibition potential for iron in perchlorate solutions, for iron and nickel in chloride plus nitrate solutions, and for iron in chloride plus perchlorate solutions. Strehblow and Titze<sup>56</sup> also reported inhibition potentials for iron in bromide plus perchlorate solutions, in iodide plus nitrate solutions, and in iodide plus perchlorate solutions and for nickel in bromide plus nitrate solutions.

While the pitting potential,  $E_p$ , has important practical applications, this does not seem to be the case with the pitting inhibition potential. Keitelman and Galvele<sup>57</sup> studied the anodic behavior of high purity iron in a 0.5 M sodium sulfate solution. They measured the pitting potential of iron in pH 9.0 and pH 10.0 solutions. The pitting potential was found to be very close to the corrosion potential measured in a  $\text{Na}_2\text{SO}_4$ , pH 2.7, pit-like solution. On the other hand, the pitting inhibition potential measured in a 0.5 M  $\text{Na}_2\text{SO}_4$ , pH 10.0, solution was very close to the passivation potential found for the metal in the pit-like solution. The practical use of the pitting inhibition potential was limited, because susceptibility to crevice corrosion was observed at potentials above the pitting inhibition potential. Keitelman and Galvele<sup>57</sup> concluded that the pitting inhibition potential could

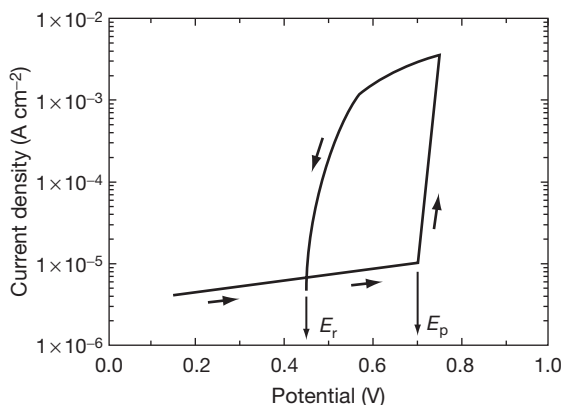


**Figure 9** Typical polarization curve showing  $E_r$ : repassivation potential;  $E_p$ : pitting potential for a metal, like stainless steel, in a chloride solution.<sup>38</sup> Reprinted from Galvele, J. R. *Corros. Sci.* **2005**, 47, 3053–3067, with permission from Elsevier.

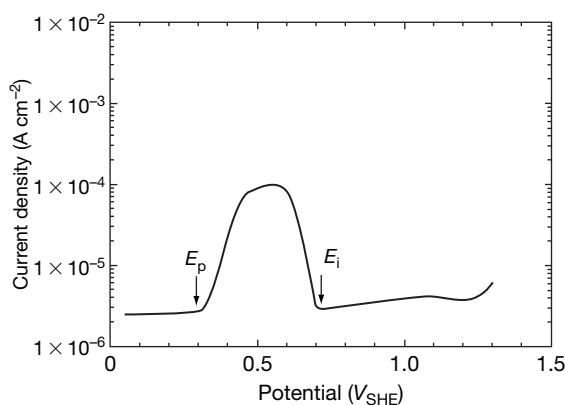


**Figure 10** Typical anodic polarization curve showing the presence of a pitting potential,  $E_p$ , and an inhibition potential,  $E_i$ .<sup>38</sup> Reprinted from Galvele, J. R. *Corros. Sci.* **2005**, 47, 3053–3067, with permission from Elsevier.

not be used to stop pitting corrosion, because in those areas where a high potential drop could be found, like in a crevice, the pitting inhibition potential was not reached and crevice corrosion developed.

It is important to notice that two different forms of crevice corrosion have just been mentioned. The first one is related to the repassivation potential,  $E_r$ , which can be exemplified by the work by Wand and Newman,<sup>58</sup> and the second one, related to the inhibition potential,  $E_i$ , which is exemplified by the work of Al-Zaharani and Pickering.<sup>59</sup> These two types of crevice corrosion were pointed out recently by Galvele.<sup>60</sup>

## 2.04.3 Effect of the Bulk Solution Composition

### 2.04.3.1 Aggressive Solutions

**Table 1** shows the wide variety of ions capable of producing pitting in various metals. What is common to all of them is that none of those ions produce insoluble compounds with the metal under consideration. Another general property is that all the anions involved produce strong acids and they do not interfere with the hydrolysis reaction of the dissolved metal ions with water. The same metal shows different pitting potentials in different environments, and the differences can be substantial, as shown in **Figure 11** for aluminum. The case of titanium is of high practical interest, because Beck<sup>28</sup> reported that

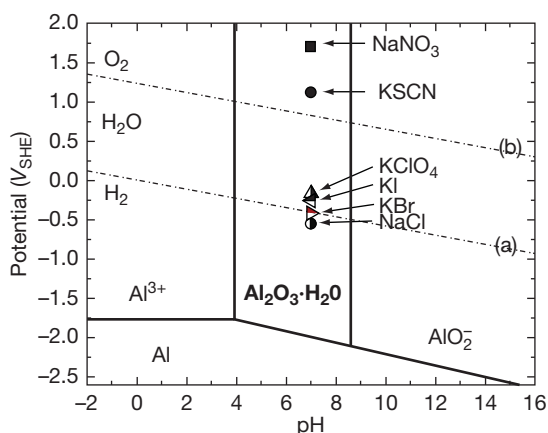


**Figure 11** Pitting potentials reported for aluminum in various solutions. For references purposes, the pitting potential values were superimposed on an Al-H<sub>2</sub>O potential-pH diagram. (a) Equilibrium values for the reaction of hydrogen evolution. (b) Equilibrium values for the reaction of oxygen evolution. From the pits produced near line (a) it is expected the hydrogen will evolve from the pits. On the other hand, from pits produced on aluminum in nitrate solutions the evolution of nitrogen bubbles was detected.

the pitting potential of titanium in chlorides was very high, being  $\sim 10$  V higher than that in other halide solutions. In some cases, the differences in pitting potentials could be small and with specific deviations. For example, for zinc<sup>34</sup> it was reported that the pitting potential was very similar in solutions containing chlorides, iodides, or sulfates, but the pitting potential measured in nitrate solutions was almost 200 mV higher than that in the previously mentioned solutions.

The pitting potential of a metal is also a function of the aggressive anion concentration. It is a general rule that the higher the aggressive anion concentration, the lower the pitting potential. **Figure 12** shows an example of the relation between pitting potential and NaCl concentration for pure aluminum and some of its alloys with copper. In general, relationships of the type

$$E_p = A - B \log C_x$$

are reported,  $A$  and  $B$  being constants,  $E_p$  the pitting potential, and  $C_x$  the concentration in moles of the aggressive anion. A review of the literature<sup>38</sup> shows that the value of  $B$  varies from metal to metal, going from  $\sim 50$  mV up to  $\sim 100$  mV for pure metals. For Fe-Cr alloys, typical values around 200 mV were reported.

### 2.04.3.2 Inhibitors

When the metal is exposed to the action of a mixed electrolyte, different behaviors are observed. If only one of the anions is aggressive and the other anions are inactive from the pitting point of view, the pitting potential will change as if only the aggressive ions

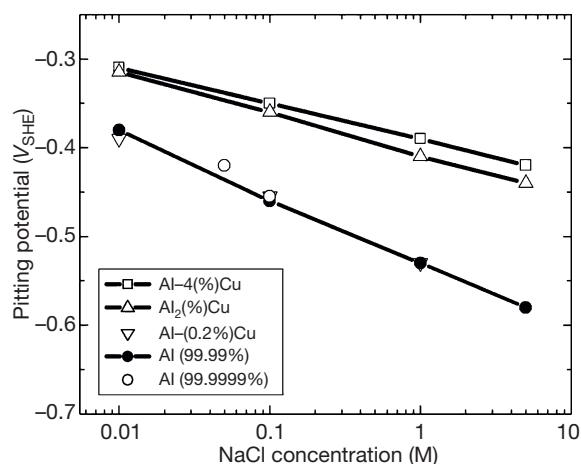
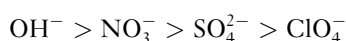


**Figure 12** Effect of NaCl concentration on the pitting potential of aluminum and some of its alloys. Reprinted from Galvele, J. R.; De Micheli, S. M. de. *Corros. Sci.* **1970**, *10*, 795-807, with permission from Elsevier.

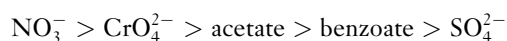
were present. If the content of the aggressive anion is reduced, the pitting potential will decrease. But there is a minimum concentration of aggressive anion, below which no pitting can be produced. This minimum value changes from metal to metal. **Table 2** shows the minimum chloride concentrations found for pitting of various alloys in mixtures of sulfuric acid plus sodium chloride solutions. In this case, only chemical depassivation was considered.

As for electrochemical depassivation, it was observed that a nonaggressive anion could increase the pitting potential value. Leckie and Uhlig<sup>62</sup> as well as Rosenfeld and Danilov<sup>45</sup> studied these effects on austenitic stainless steels. Leckie and Uhlig<sup>62</sup> reported that for chloride ion concentrations higher than 0.1 M, the pitting inhibition efficiency of the studied anions was in the following decreasing order:



Schwenk<sup>24</sup> reported that while  $\text{NO}_3^-$  ion inhibited pitting of stainless steels in chloride-containing solutions, it did not inhibit pitting in bromide containing solutions.

Böhni and Uhlig<sup>63</sup> reported for aluminum similar results to those found for stainless steels in chloride solutions. In the case of aluminum, it was assumed that the metal was immune to pitting when the pitting potential was above  $0.8 V_{\text{SHE}}$ . Böhni and Uhlig<sup>63</sup> found that the inhibition efficiency for aluminum in chloride containing solutions was in the following decreasing order:



De Micheli and Galvele<sup>6</sup> studied the effect of mixtures of anions on the pitting potential of aluminum. They found that in mixtures of chloride plus perchlorate anions, a smooth transition was observed on the pitting potential values. In mixtures of chloride plus

nitrate solutions, a clear inhibition effect of the nitrate ion was observed. Nevertheless, one point of interest is that aluminum, in a 1 M NaCl solution, showed a pitting potential of  $-0.64 V_{\text{SHE}}$ , and the pitting was inhibited by  $\text{NO}_3^-$  ions, but on the other hand, if the potential was above  $+1.84 V_{\text{SHE}}$ , the  $\text{NO}_3^-$  ion itself produced pitting on aluminum.<sup>1,5</sup> In mixtures of sulfate plus chloride anions, the sulfate ion had little effect on the pitting potential of aluminum.<sup>6</sup> The pitting potential values were the same as those found in chloride solutions without sulfate ions. It was only at very low chloride concentrations, less than  $10^{-3}$  M, that sulfate showed some effect on the pitting potential.

The inhibiting effect of sulfate ions in chloride-containing solutions was reported for the pitting of nickel,<sup>64</sup> zirconium,<sup>32</sup> and titanium.<sup>31</sup>

Numerous authors reported that weak acid salts acted as pitting inhibitors for stainless steel and for aluminum in chloride containing solutions. Similar observations were made for other metals. For example, the pitting potential of zinc, in sodium chloride solutions and in sodium perchlorate solutions, was increased by adding borate ions to the solutions.<sup>35</sup> The pitting potential of iron in sodium chloride solutions was also increased by adding borate salts.<sup>48</sup> In numerous applications chromates were found to be very efficient as pitting inhibitors, but the carcinogenic nature of chromate requires the search for alternative solutions.

### 2.04.3.3 pH

According to Kaesche,<sup>65</sup> for aluminum in NaCl aqueous solutions, the pH of the solution had no effect on  $E_p$ , for pH values ranging from pH 2 up to pH 11. For stainless steels, on the other hand, Leckie and Uhlig<sup>62</sup> found that the pitting potential was pH independent up to pH 8, but increased sharply with the pH for higher pH values. Similarly, Alvarez and Galvele<sup>48</sup> found that an increase in pH produced an increase in the pitting potential for iron in NaCl solutions, **Figure 13**. Inhibiting effects due to alkaline solutions were also reported for nickel,<sup>66</sup> cadmium,<sup>9</sup> zinc,<sup>35</sup> and so on.

## 2.04.4 Composition of the Solution inside Pits

### 2.04.4.1 Electrolyte inside Pits

From the earliest studies on pitting it was assumed that the composition of the solution inside the pits

**Table 2** Minimum chloride concentration necessary for chemical depassivation of various metals and alloys in mixtures of  $\text{H}_2\text{SO}_4 + \text{NaCl}$  solutions

Metal	Minimum $\text{Cl}^-$ concentration (N)	Reference
Iron	0.0003	61
Fe-5.6Cr	0.017	61
Fe-20Cr	0.1	61
Fe24.5Cr	1.0	61
Fe-18.6Cr-9.9Ni	0.1	61
Nickel	0.001	18



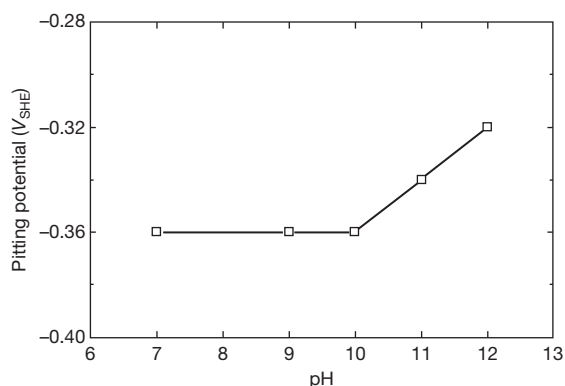


**Figure 13** Pitting potential of high purity iron, in 1.0 M NaCl at various pH values. Reprinted from Alvarez, M. G.; Galvele, J. R. *Corros. Sci.* **1984**, 24, 27–48, with permission from Elsevier.

was different from that outside. A pH decrease in the solution inside aluminum pits was reported by Edeleanu and Evans in 1951.<sup>67</sup> Hagyard and Santhiapillai,<sup>68</sup> prepared very simple artificial pits on an aluminum sample, and reported that, while the pH of the NaCl solution was 6.2, the pH inside the pit was  $\sim 3.5$ . They also found that the chloride concentration inside the pit increased, reaching values about ten times higher than those in the bulk solution. They also found that the concentrated aluminum chloride solution produced inside the pit could flow by gravity outside the pit, activating the metal surface it touched. Wong and Alkire<sup>69</sup> measured the pH of solution inside naturally occurring pits in aluminum, and confirmed that the pH of the solution inside the pits was between 3 and 4. They also found that the solution flowing from the pits, mentioned by Hagyard and Santhiapillai, was not an  $\text{AlCl}_3$  solution, as earlier believed by various authors, but the dominant species was either  $\text{Al(OH)Cl}_2$  or  $\text{Al(OH)}_2\text{Cl}$ . The distinction between the two species was uncertain because their NMR spectra were similar. According to Wong and Alkire,<sup>69</sup> the efficiency of the anodic reaction of metal dissolution inside the aluminum pits was found to be close to 80%, the side reaction being the evolution of hydrogen gas.

Abundant work on actual pits, as well as crevices, has shown beyond any doubt that the solution inside the pits and crevices has a lower pH and a higher ionic concentration than the bulk solution. For copper in sea water, pH 8, the pH found inside the pits was of the order of 5<sup>70</sup> and for iron, the pH measured inside the pits was  $\sim 3.5$ , while the pH of the bulk solution

could have values between 2 and 10.<sup>71,72</sup> For stainless steels exposed to neutral 0.5 M NaCl solutions, the pH inside the pit was found to be lower than 1.0, while the chloride concentration was 6.2 M.<sup>72</sup>

#### 2.04.4.2 Gas Evolution from Pits

The evolution of gas bubbles from pits was reported in the early studies on pitting. Kaesche reported the evolution of hydrogen from pits of aluminum, growing in a NaCl solution.<sup>65</sup> Evolution of hydrogen was also found from aluminum pits produced in perchlorate solutions.<sup>4</sup> Hydrogen evolution was also reported from pits in iron<sup>73</sup> and titanium.<sup>28</sup> Wexler and Galvele<sup>5</sup> reported gas evolution from pits in aluminum in sodium nitrate solutions, but in this case the gas evolving was found to be nitrogen. This observation was confirmed by Barger and Benson.<sup>74</sup>

An evaluation made of the gases evolved from the pits in titanium and in aluminum showed that the hydrogen evolving was equivalent to  $\sim 10\%$  of the total anodic current in the pit.

#### 2.04.5 Effect of Alloying Elements

It was observed that the pitting potential of a metal could be strongly modified with the use of alloying elements. This is an aspect of high technological interest and abundant work has been done on this subject. It is interesting to point out that there are cases in which the aims of the technological application could be pointing to completely opposite directions. For example, for stainless steels, the main interest was to find alloying elements that could lead to the highest possible pitting potential, and thus obtain a very resistant alloy. On the other hand, with aluminum, one of the technological interests was to find an alloy with the lowest possible pitting potential in sea water. The reason was that aluminum was a very attractive metal to be used as sacrificial anode, for cathodic protection. The limitation was that the pitting potential of aluminum, in sea water, was  $\sim 1$  V higher than the equilibrium potential for the  $\text{Al}/\text{Al}^{3+}$  reaction. Consequently, much work was oriented to the search of alloying elements that could lower the pitting potential of aluminum.

The extensive work on the effect of alloying elements on increasing the pitting potential of stainless steels has been reviewed by various authors.<sup>75–79</sup> In general, chromium, vanadium, molybdenum,

tungsten, rhenium, nickel, and nitrogen were found to be beneficial alloying elements, as all of them increased the pitting potential of stainless steel. On the other hand, alloying elements such as manganese or sulfur were found to be detrimental. As pointed out by Horvath and Uhlig,<sup>51</sup> care should be taken when making extrapolations. These authors found that while molybdenum was beneficial for stainless steels in chloride-containing solutions, it was detrimental in bromide-containing solutions.

Some elements, to be effective, need the presence of a third element. This is the case of molybdenum, in ferrous alloys. It requires the presence of chromium to inhibit pitting, and the higher the chromium content the more effective molybdenum would be.<sup>80</sup> It was found, with binary Fe–Mo alloys, that the pitting potential of Fe–5Mo was only slightly higher than that of pure iron.<sup>81</sup>

Nitrogen strongly increases the pitting potential of austenitic stainless steels in chloride solutions. Osozawa *et al.*<sup>77</sup> studied stainless steels containing from 0.02% to 0.2% N. They found that during corrosion all the nitrogen was transformed into ammonium ion, preventing the lowering of pH before the sites could grow as ordinary pits.

Another metal about which abundant information on the effect of alloying elements is available is aluminum. For aluminum alloys with ~5% of the alloying metal, it is known that copper increases the pitting potential of aluminum in chloride solutions, while zinc decreases it, and magnesium has almost no effect, Figure 14.<sup>82,83</sup>

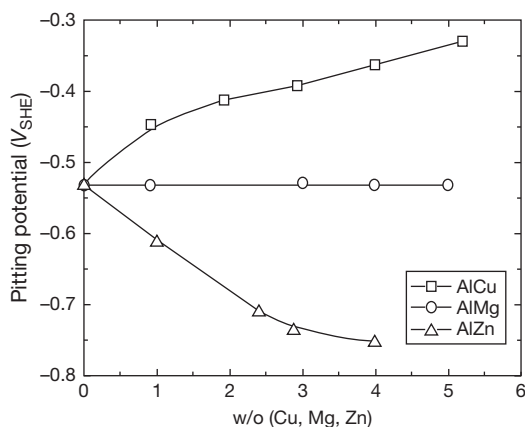


**Figure 14** Pitting potential of binary Al–Cu, Al–Mg and Al–Zn alloys in 1 M NaCl solution. Reprinted from Muller, I. L.; Galvele, J. R. *Corros. Sci.* **1977**, *17*, 179–193, with permission from Elsevier.

Reding and Newport<sup>84</sup> studied ~2500 aluminum alloys in sea water. The alloys were made with practically all the metals of the periodic table. The purpose of their work was to develop aluminum anodes for cathodic protection in sea water. To measure the efficiency of the alloys, the authors circulated a constant anodic current density and measured the potential as function of time. As an old technique for measuring pitting potentials, the galvanostatic technique, consisted in applying a constant current to the sample in the corrosive environment and measuring the potential reached by the sample,<sup>85</sup> Reding and Newport's results could be used to have a rough estimate of the effect of those alloying elements on the pitting potential of aluminum in sea water, as shown in Figure 15. It is only a rough estimate, as in the galvanostatic technique, various anodic currents were applied to make sure that the same potential was reached. Nevertheless Figure 15 gives an initial idea of what the effect of those alloying elements will be on the pitting potential of aluminum in chloride solutions.

## 2.04.6 Pitting Nucleation Sites

The nucleation pit sites have frequently been found to be related to microscopic features on the metal surface. In stainless steels, the pits are usually related to the presence of inclusions. Smialowski *et al.*<sup>86</sup>

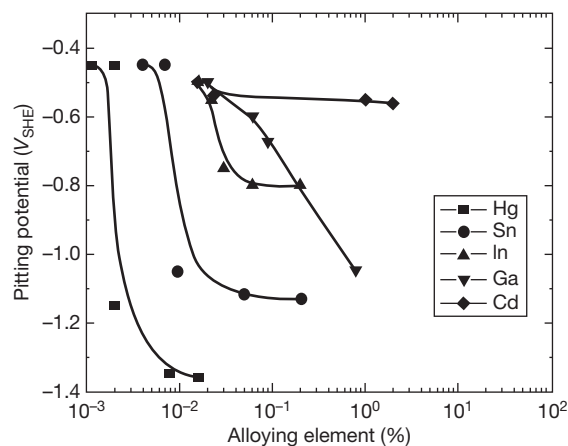


**Figure 15** Estimated pitting potential values for binary aluminum alloys in sea water. The estimation is on the basis of the assumption that the measurements made by Reding and Newport<sup>84</sup> lead to electrode potentials close to those obtained in galvanostatic techniques used for pitting potential measurements.

reported that pits are initiated at nonmetallic inclusions, mixed manganese sulfide inclusions being the most effective ones. According to these authors, in the absence of the sulfide inclusions, chromium oxide particles can nucleate pitting.

For low alloy steels, the preferential sites for nucleation of pits were found to be manganese sulfide particles.<sup>87</sup> For nickel, it was reported that pits nucleated either on surface scratches, on grain boundaries or on nickel sulfide inclusions.<sup>88,89</sup>

Suter *et al.*<sup>90</sup> studied the initiation of individual pits on MnS inclusions on 304 stainless steel, with and without mechanical stress. Working in 1 M NaCl solution, the authors found that in those areas where there were no inclusions, no pitting was nucleated at potentials below oxygen evolution. Specimens with shallow MnS inclusions showed metastable pitting but not stable pitting. Specimens with deep MnS inclusions showed active pitting.

#### 2.04.7 Effect of Temperature

The pitting potentials of stainless steels<sup>53</sup> and of aluminum<sup>91</sup> were found to decrease with an increase in temperature. The case of stainless steels is complicated by various factors. Horvath and Uhlig<sup>50</sup> studied the pitting potentials of Ni, of Cr–Ni, Cr–Fe alloys, and of various stainless steels. When studying the behavior of 15% Cr, 13% Ni stainless steel in 0.1 N NaCl, they reported that the pitting potential measured at 0 °C was 0.5 V higher than that measured at 25 °C. They also found that on adding Mo, the pitting potential at 25 °C increased, and at 0 °C, the pitting potential decreased. Eventually, with near 2.4% Mo a reversion in the pitting potential values was reached, as schematically shown in Figure 16. The authors reported that for 1.3% Mo the pitting potentials at 0 °C and at 25 °C were the same. Another observation made by these authors was that the results obtained in chloride solutions could not be extrapolated to other halide solutions. In 0.1 N NaBr solution, the pitting potential at 25 °C was higher than that at 0 °C, and also the addition of Mo decreased the pitting potential value at both temperatures.

Another example of complex relation between pitting potential and temperature is described by Beck<sup>28</sup> for the pitting of titanium in chloride, bromide, and iodide solutions. According to Beck, in chloride solutions, the pitting potential at room temperature is close to 10 V, and drops to ~1 V at

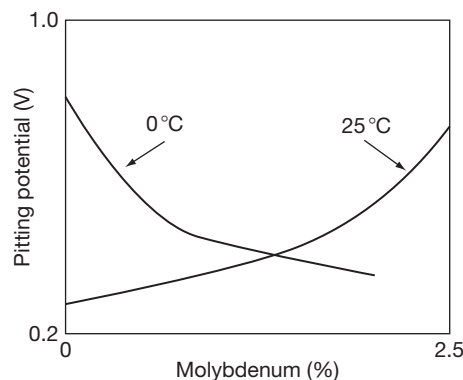


**Figure 16** Schematic view of the effect of Mo and temperature on the pitting potential for 15% Cr, 13% Ni stainless steel, in 0.1 N NaCl solution, as described by Horvath and Uhlig. Reproduced from Horvath, J.; Uhlig, H. H. *J. Electrochem. Soc.* **1968**, *115*, 791–795.

200 °C. On the other hand, in bromide solutions, the pitting potential of Ti starts at 1.7 V at 0 °C, drops to 0.9 V at room temperature, and remains constant up to above 100 °C. Finally, in iodide solutions, the pitting potential of Ti starts at ~1.0 V at 0 °C, increases to a couple of V at 50 °C, and from this temperature to at least 100 °C it remains almost constant at 0.45 V.

It is taken into account that in most of the cases, polyvalent cations are involved, which means that a variety of oxy- and hydroxyl-compounds can be produced, each of them with a different thermal stability. Besides, there are anions in solutions such as iodides that decompose by oxidation, while others such as nitrates decompose by reduction, giving a variety of chemical products. Considering also that most of these reactions will have different behaviors at different temperatures, it seems very improbable that a unique explanation could be found for the effect of temperature in all the cases of pitting. Most probably, each case will require a separate study.

Related to temperature and pitting, a parameter called critical pitting temperature (CPT) has been introduced in recent times, as described below, and is extensively used for grading stainless steels.

#### 2.04.8 Mechanism of Stable Pitting Growth

A mechanism that attempts to explain stable pit growth, should also explain:

1. the nature of the pitting potential, and its properties;
2. the nature of the repassivation potential, and its properties;
3. the nature of the inhibition potential; and so on.

Historically, the development of mechanisms for pitting was simultaneous with the mechanistic studies of passivity. Pitting being a process of failure of passivity, it is natural that the mechanisms suggested for pitting were closely related to the authors' ideas on passivity. Consequently, in the older literature, it is found that those authors who sustained that passivity was the result of adsorption of oxygen atoms on the metal surface, favored the idea that pitting was the result of preferential adsorption of the aggressive anions, displacing the oxygen atoms.<sup>20,50,62,63,92</sup> Hoar,<sup>14,27</sup> as early as in 1937, questioned the mechanism based on competitive adsorption, supported by Kabanov and the concept of high penetrating power of  $\text{Cl}^-$  for the oxide films, supported at that time by Britton and Evans.

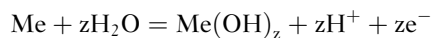
The idea that aggressive anions led to pitting by penetrating the passive film was supported by various authors. But, Vetter and Strehblow<sup>93</sup> pointed out that a migration of polyatomic aggressive anions such as  $\text{SO}_4^{2-}$ ,  $\text{ClO}_4^-$ , or  $\text{SCN}^-$  through a solid layer was not conceivable. Figure 17 illustrates the point made by these authors.

Hoar<sup>14,27</sup> described a different view for the action of the so-called 'aggressive ions.' The new mechanism introduced by Hoar, allowed him to predict new cases of pitting, stating that the only condition required

from the aggressive anion was that it would neither interfere with the process of anodic dissolution of the metal, nor with the hydrolysis reaction of the metal cations with the water molecules. According to Hoar, the  $\text{Cl}^-$  replaced the  $\text{OH}^-$  ions consumed by the metal ions and allowed the pH at the anode to fall to values where no solid products would be formed on the metal surface, but in the bulk of the solution.

Hoar's model of pitting became known as the localized acidification model and received reasonable wide acceptance, because it gave a good explanation of the nature of the aggressive anions, the change in composition inside the pits, and so on. Following Hoar's description, it was perhaps more appropriate to call it the  $\text{OH}^-$  depletion model, but it is just a semantic problem.

The introduction of potentiostats in corrosion studies and the discovery of pitting potentials were causes of concern for the supporters of this model, because it did not predict the existence of a pitting potential. Van Muylder *et al.*<sup>70</sup> were the first to attempt an explanation for the existence of a pitting potential value with an acidification process. They used the E-pH equilibrium diagram for  $\text{Cu-H}_2\text{O}$  to explain pitting of copper in chloride solutions. Figure 18 could be used to explain their ideas. Let us assume that  $\text{pH}_{\text{SOL}}$  is the pH of the bulk solution. Above the potential  $E_1$  the anodic reaction of the metal begins as



leading to localized acidification.

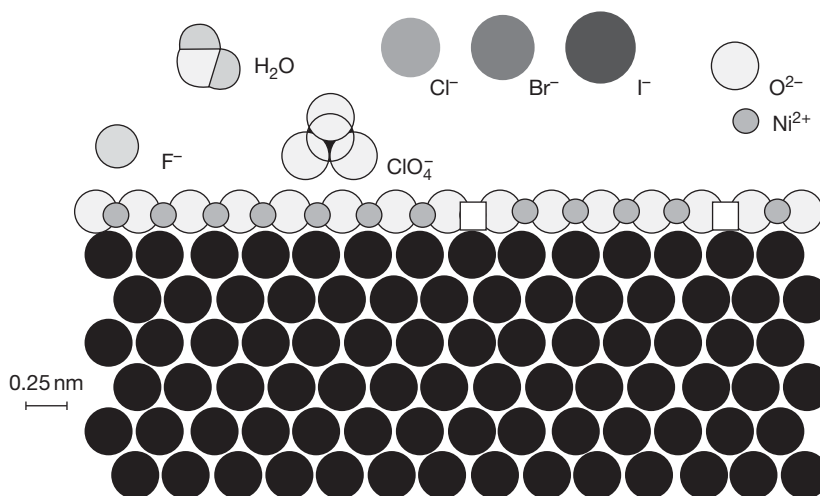


**Figure 17** Relative sizes of metal and ions, for Ni covered with a single layer of  $\text{NiO}$ . Sizes and bond angles from: Linus Pauling, *The Nature of the Chemical Bond*, Cornell University Press, New York, 1960.

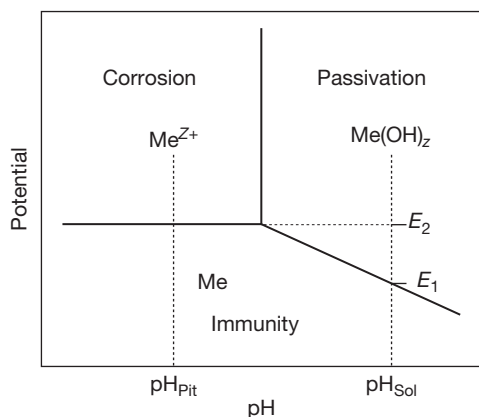
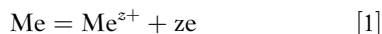
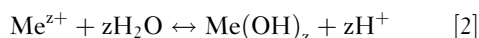


**Figure 18** Explanation of the nature of  $E_p$ , on the basis of the ideas of Van Muylder *et al.*<sup>70</sup> Pits became stable only at potentials above  $E_2$ .

Nevertheless, if the electrode potential is lower than  $E_2$ , the acidification will shift locally the system to the immunity region, see **Figure 18**, and the anodic reaction of metal dissolution will stop. Then, any localized acidification will disperse by diffusion of the protons to the bulk solution. According to Van Muylder *et al.*,<sup>70</sup> it is only when the metal reaches the potential  $E_2$  that the solution at the anodic region could reach the value  $\text{pH}_{\text{PTB}}$  **Figure 18**, and the reaction of anodic dissolution becomes thermodynamically possible:



Soluble products will be produced at the anode, and they will not interfere with the corrosion process. This reaction will be followed by the hydrolysis equilibrium:



which will perpetuate the localized acidification in the anodic region.

According to Van Muylder *et al.*<sup>70</sup> mechanism, passivity of the metal by insoluble hydroxides or oxides becomes thermodynamically unstable at potentials above  $E_2$ . In other words, the pitting potential is a thermodynamically based value and is given by eqn [1]. This mechanism was successfully used to explain the pitting potential of copper in chloride solutions. Nevertheless, it failed when applied for example to aluminum, as can be seen in **Figure 11**. It also failed when applied to iron, zinc, and so on. It was found that it did not work with those metals whose  $\text{Me}/\text{Me}^{z+}$  equilibrium potential was lower than that for hydrogen evolution. The model did

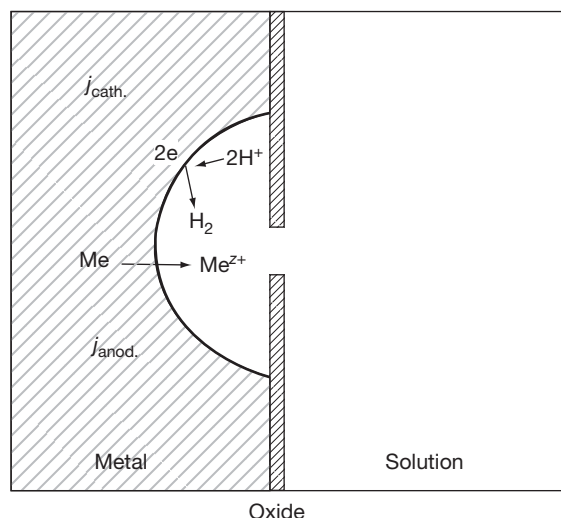
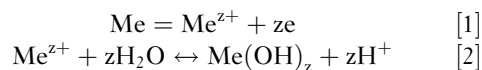


**Figure 19** Anodic and cathodic reactions inside a pit.

not take into account the reactions of proton consumption that could take place inside the pit, as shown in **Figure 19**.

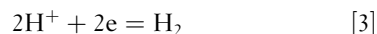
This mechanism was modified by Galvele and co-workers to explain the pitting potentials of such metals as zinc, cadmium, aluminum, or iron and the pitting potentials found in the presence of reducible anions or inhibitors.<sup>5,9,12,34,82,83,94-98</sup> These authors introduced an electrochemical kinetic explanation for the pitting potential.

The key point of the mechanism is that there is a pH drop on the anode surface and that this pH drop is a necessary condition to sustain pitting. The rate at which the protons are produced will be given by eqns [1] plus [2]:

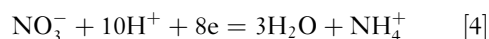


On the other hand, the consumption of protons can take place by various processes:

by direct reduction:



by reaction with reducible anions:



by reaction with weak acid anions ( $\text{L}^-$ ):



or by diffusion of protons from the anode region to the bulk solution. The rates for eqns [1], [3], and [4] are



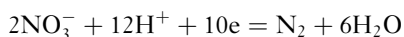
potential dependent, while eqn [5] and diffusion are potential independent.

Assuming that the metal is in an alkaline solution, in absence of reducible anions or buffer ions, but in presence of a strong acid salt, which acts only as a supporting electrolyte, the processes inside the pit can be analyzed. Protons will be produced by reactions [1] and [2], and will be consumed by reaction [3]. Reaction [1] is potential dependent, and the higher the potential, the higher the rate of production of protons. On the other hand, with reaction [3], the lower the potential the higher the rate of consumption of protons. If diffusion of protons from the pit to the bulk solution is ignored, there will be a potential at which the rate of production of protons will be equal to the rate of consumption of protons. This is the potential at which reaction [1] and reaction [3] are equal, and it is the corrosion potential of the metal in the acidified solution inside the pit ( $E_c^*$ ). According to Galvele and co-workers, the corrosion potential of the metal in the pit-like solution is the minimum potential at which pitting can be sustained, so the pitting potential will be

$$E_p \geq E_c^*$$

Actually, to compensate for the protons diffusing from the pit to the bulk solution,  $E_p$  should be slightly higher than  $E_c^*$ .

If reducible anions are present, the pitting potential will have to increase to values at which the anion reduction becomes negligible. For example, the pitting potential for pure Al in 1 M NaCl solutions is  $\sim -0.53 V_{\text{SHE}}$ , while in 1 M  $\text{NaNO}_3$  solutions it is  $+1.70 V_{\text{SHE}}$ . Wexler and Galvele<sup>5</sup> reported that during pitting of Al in nitrate solutions bubbles of  $\text{N}_2$  are evolved from the pits. This indicates that the following reaction is taking place:



This reaction produces a heavy consumption of protons, and as shown by the N- $\text{H}_2\text{O}$  Pourbaix E-pH equilibrium diagrams, a high potential has to be reached for this reaction to become negligible. This is the explanation offered for the high pitting potentials found for Al in nitrate solutions.

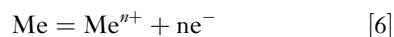
One serious criticism to any acidification mechanism for pitting was raised by Vetter and Strehblow.<sup>99</sup> They studied the pitting of iron in a mixture of chloride plus sulfate solutions with phthalate buffer (pH = 5), and observed the formation of small corrosion pits with a diameter of  $\sim 1\text{--}50 \mu\text{m}$ . The authors

calculated the composition changes taking place in a  $2 \mu\text{m}$  pit. Their calculations showed that the current density inside the pit was  $\sim 9 \text{ A cm}^{-2}$ , the pH change was  $+0.85$ , the potential change was  $-0.018 \text{ V}$ , and the change in iron concentration was  $+0.9 \text{ mol l}^{-1}$ . These authors concluded that no significant changes of pH, or any ion concentration could be expected in very small pits. Consequently, a second mechanism, other than that of localized acidification, should be assumed.

Reviewing Vetter and Strehblow's results, it is observed that, contrary to what experience has shown about the composition inside the pits, their calculations did not show a decrease in the pH, but an increase of it. As mentioned above, for iron the pH measured inside the pits was  $\sim 3.5$ , while the pH of the bulk solution could have values between 2 and 10.<sup>71,72</sup> The reasons were that the authors chose to ignore the hydrolysis of the metal ions and that they were studying a case of chemical depassivation.

Galvele<sup>95,96</sup> made an analysis of the transport processes taking place inside a pit, taking into account the hydrolysis of the metal ions. This ion transport analysis showed that not only significant acidification was possible in very small pits, but also that a quantitative explanation could be found for the effect of pH, inhibitors, aggressive ion concentration, and so on, on the pitting potential.

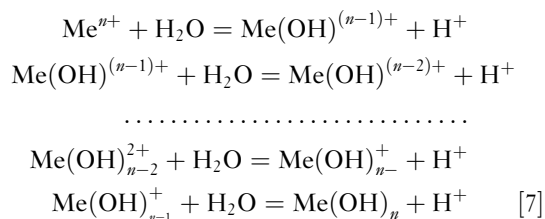
The transport analysis was made in the following way. Let us assume, for the sake of simplicity, that we have a pit like the one in Figure 20. At the bottom of this pit an anodic reaction of the type



will take place. No reaction takes place at the walls of the pit. Thus, a unidirectional pit model is obtained, with considerable simplification in the mathematical treatment that will follow. If pit initiation took place, for example, at the bottom of a crack in the surface oxide film, Figure 20 would be an exact description of the process. For a hemispherical pit, Figure 20 would seem to be a gross oversimplification. But, according to Vetter and Strehblow,<sup>93</sup> the mathematical problem of a hemispherical pit could be transformed into an equivalent plane problem by increasing the diffusion path by a factor of the order of 3. As shown below, when calculating the concentration gradients inside pits, only orders of magnitude are considered, so this correction factor can be ignored.

Reaction [6] is assumed to take place in a sodium or potassium salt of an aggressive but noncomplexing

anion. The pH of the bulk solution, which could have any value, is given as a boundary condition. It is also assumed that reaction [6] is followed by a series of hydrolysis equilibrium reactions of the type:



This equilibrium is known to be very quickly reached,<sup>100</sup> so the reactions in eqn [7] will always be in equilibrium. In the first publication<sup>95</sup> only the first step in reactions in eqn [7] was taken into account. In the second publication<sup>96</sup> all the hydrolysis steps from eqn [7] were considered.

To give an idea of the method used in the calculation, one example of the first publication will be described. The same procedure was used in the other cases. In the first publication<sup>95</sup> only the first step of hydrolysis from eqn [7] was considered. This is a simplified description of the processes taking place inside a pit; but it will give the minimum degree of acidification expected inside the pit.

The flow of ions inside the pit is given by the following equation<sup>101</sup>:

$$\mathcal{F}_i = D_i \frac{dC_i}{dx} + D_i \frac{z_i F}{RT} C_i + \frac{d\phi}{dx} \quad [8]$$

where  $\mathcal{F}_i$  is the flow of ions  $i$ ,  $D_i$  the diffusion coefficient of the same ions,  $C_i$  their concentration,  $x$  the pit depth as shown in Figure 20,  $(d\phi/dx)$  the gradient of potential  $\phi$ ,  $z_i$  the valence of ions  $i$ ,  $F$  the Faraday constant,  $R$  the gas constant, and  $T$  the absolute temperature.

As shown by Vetter and Strehblow,<sup>99</sup> small ionic concentration changes should be expected at pit initiation. So the sodium salt, in the bulk solution, will act as a supporting electrolyte for the species formed in reactions [6] and [7]. This means that the transport of all these species will be due to ion diffusion. The contribution of ion migration can be ignored, which again contributes to a simplification in the mathematical treatment. Consequently, reaction [8] is reduced to:

$$\mathcal{F}_i = D_i \frac{dC_i}{dx} \quad [9]$$

As it is assumed that the bulk solution could have any pH value, the first step in reaction [7] has to be rewritten to account for the contribution of the OH-ions in alkaline solutions:

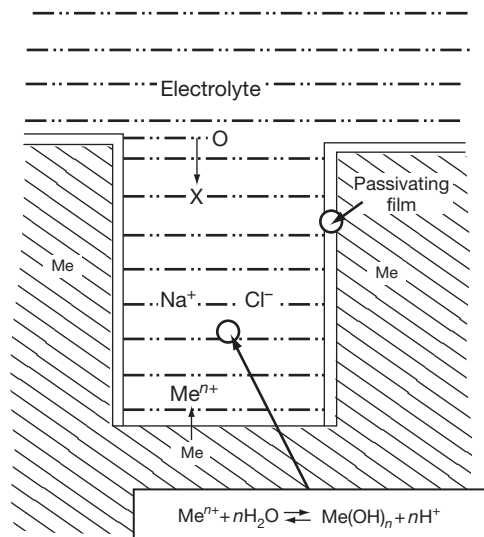
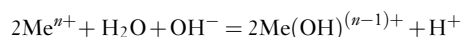


**Figure 20** Unidirectional pit model used for calculation of the corrosion species present inside a pit. Reprinted from Galvele, J. R. *Corros. Sci.* **1981**, 21, 551–579, with permission from Elsevier.



Species S:	1	2	3	4	5
					[10]

From eqn [10] we find that inside the pit there are five species (S1–S5), the concentrations of which should be calculated. The detailed mathematical treatment for a system like this can be found in Vetter's book on Electrochemical Kinetics.<sup>101</sup> The five unknown concentrations are calculated by resolution of the five following equations:

the flow of the species containing Me atoms will be given by

$$D_1 \frac{dC_1}{dx} + D_4 \frac{dC_4}{dx} = \frac{i}{nF} \quad [11]$$

the flow of the species containing O atoms will be given by

$$D_2 \frac{dC_2}{dx} + D_3 \frac{dC_3}{dx} + D_4 \frac{dC_4}{dx} = 0 \quad [12]$$

and the flow of the species containing H atoms will be given by

$$2D_2 \frac{dC_2}{dx} + D_3 \frac{dC_3}{dx} + D_4 \frac{dC_4}{dx} + D_5 \frac{dC_5}{dx} = 0 \quad [13]$$

Finally, the two following equilibrium relations must be considered

$$^*K_1 = \frac{C_4 C_5}{C_1} \quad [14]$$

which is the law of mass action applied to the first step of hydrolysis in eqn [7], and

$$K_w = C_3 C_5 \quad [15]$$

which is the ionic product of water.

The boundary conditions used in the calculations were  $C_1 = C_4 = 0$ , the values for  $C_3$  and  $C_5$  were given by the pH of the bulk solution. As for the ionic diffusion coefficients, since they were very similar in aqueous solutions, they were taken as  $D_1 = D_2 = D_4 = 10^{-5} \text{ cm}^2 \text{ s}^{-1}$ . The only exceptions were  $\text{OH}^-$  ions, for which a value of  $D_3 = 5.3 \times 10^{-5} \text{ cm}^2 \text{ s}^{-1}$  was used, and  $\text{H}^+$  ions for which a value of  $D_5 = 9.3 \times 10^{-5} \text{ cm}^2 \text{ s}^{-1}$  was used. The equilibrium constants for the hydrolysis reactions of eqn [7] were taken from the literature.<sup>102–104</sup>

The concentrations of all the species inside the pit were calculated as a function of the parameter  $x.i$ ,  $x$  being the length of the pit with  $x = 0$  at the opening of the pit and  $i$  the current density of the reaction [6]. Figure 21 shows the results of the calculations for iron, in a pH 10 solution. The concentration of protons, which remains constant at low  $x.i$  values, shows a sharp increase as soon as  $x.i$  reaches a value of  $10^{-6} \text{ A cm}^{-1}$ . The next question is to find out what pH is necessary to start pitting. From the Pourbaix diagrams a pH value is found for the transition between corrosion and passivity. This value is shown as a cross identified as (a). As pits initiate with current densities close to  $1 \text{ A cm}^{-2}$ , if only  $x.i = 10^{-6} \text{ A cm}^{-1}$  is required to reach the necessary acidification, pits as small as  $0.01 \mu\text{m}$  could be initiated by this mechanism.

One criticism that could be made to the calculations in Figure 21 is that the choice of the critical pH is arbitrary. This objection can be disregarded if instead of using the first hydrolysis step, in eqn [7], all the hydrolysis steps are taken into account.<sup>96</sup> Figure 22 shows an example of these calculations. Again the example given is for iron in a pH 10 solution. For the sake of simplicity, only the iron compounds are shown. For low  $x.i$  values the almost exclusive product is solid  $\text{Fe}(\text{OH})_2$ , but above  $x.i \ 10^{-6} \text{ A cm}^{-1}$   $\text{Fe}^{2+}$  becomes the main corrosion product. Another example of the full hydrolysis calculations, in this case for aluminum, can be seen in Figure 23.

These calculations were made for the ionic concentration diagrams of the following systems:  $\text{Zn}/\text{Zn}^{2+}$ ;  $\text{Fe}/\text{Fe}^{2+}$ ;  $\text{Ni}/\text{Ni}^{2+}$ ;  $\text{Al}/\text{Al}^{3+}$ ;  $\text{Cr}/\text{Cr}^{3+}$ ; and  $\text{Co}/\text{Co}^{2+}$ . It has also been shown<sup>95</sup> that these ion concentration diagrams give a quantitative explanation of the influence of solution pH, buffer ions, and inhibitors, on the pitting potential and they also

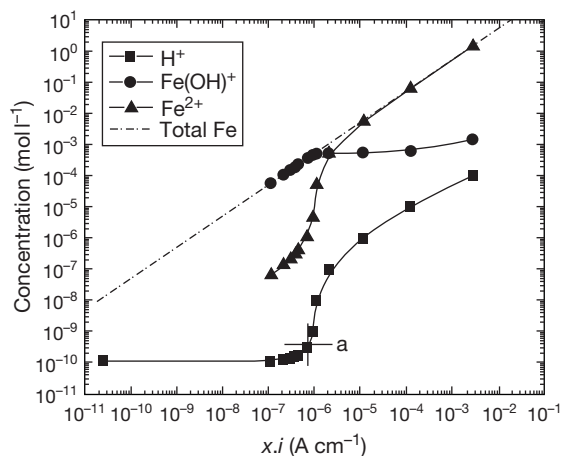


**Figure 21** Unidirectional pit model for Fe, assuming that only the first hydrolysis step is relevant. The critical  $\text{H}^+$  concentration is shown by the cross (a). Reproduced from Galvele, J. R. *J. Electrochem. Soc.* **1976**, 123, 464–474, with permission from the Electrochemical Society.

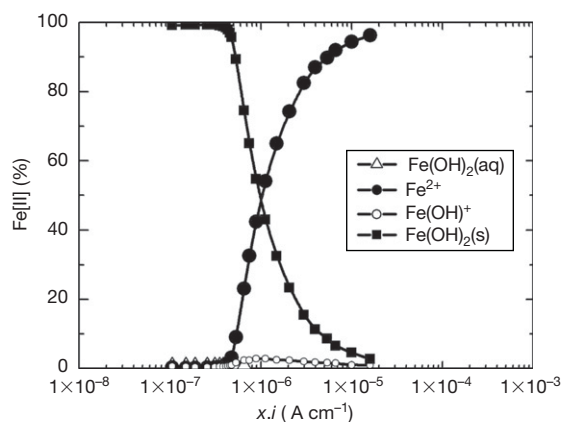


**Figure 22** Percentage of metal compounds inside an Fe pit, according to the full hydrolysis pit model. The critical  $x.i$  value, for pits to start developing, is taken at the point when solid species concentration is equal to soluble species concentration. Reprinted from Galvele, J. R. *Corros. Sci.* **2005**, 47, 3053–3067 and Galvele, J. R. *Corros. Sci.* **1981**, 21, 551–579, with permission from Elsevier.

give an explanation of the existence of a pitting repassivation potential.

By changing the external pH value in the boundary conditions of the above mentioned calculations, it is possible to evaluate the effect of pH on the pitting potential. Figure 24 shows the proton concentrations for unidirectional pits of iron, with external pH values going from 9 to 12. It is observed that by increasing the external pH value, the proton

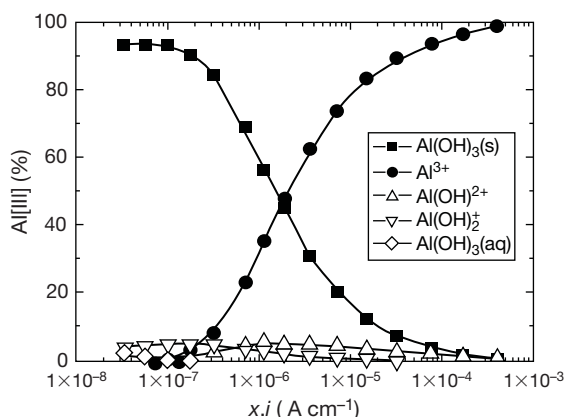


**Figure 23** Percentage of metal compounds inside an Al pit, according to the full hydrolysis pit model. Reprinted from Galvele, J. R. *Corros. Sci.* **2005**, 47, 3053–3067 and Galvele, J. R. *Corros. Sci.* **1981**, 21, 551–579, with permission from Elsevier.

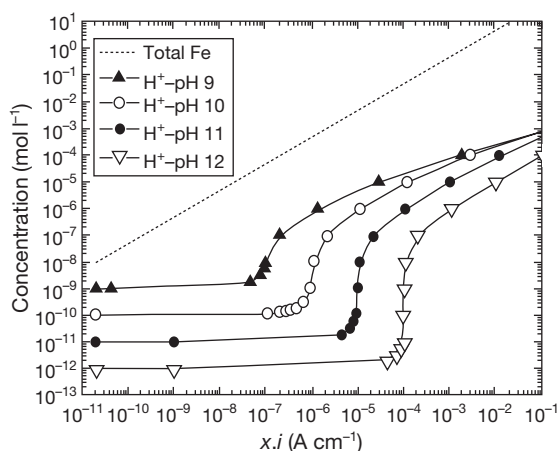


**Figure 24** Effect of the pH of the bulk solution on  $x.i$ . The higher the pH, the more difficult it is to reach the critical  $x.i$  value for pitting. Reproduced from Galvele, J. R. *J. Electrochem. Soc.* **1976**, 123, 464–474, with permission from the Electrochemical Society.

concentration curve is shifted to higher  $x.i$  values. For a given  $x$  value, this means that with higher bulk solution pH values, higher current density values will be required to attain the same acidification. If the current density inside the pit is potential dependent, as it is generally the case, this higher current density requirement will be reflected as higher pitting potential values.

Using the full hydrolysis model the following critical  $x.i$  values were found:<sup>96</sup>

$$\text{pH} = 0; \quad x.i = 5.0 \times 10^{-7} \text{ A cm}^{-1}$$

$$\text{pH} = 11; \quad x.i = 5.0 \times 10^{-6} \text{ A cm}^{-1}$$

$$\text{pH} = 12; \quad x.i = 5.0 \times 10^{-5} \text{ A cm}^{-1}$$

For pH values above 9 it is observed that an increase in one unit in the pH value leads to an increase of one order of magnitude in the  $x.i$  value. If the relation between potential and current density inside the pit follows a logarithmic law, the pitting potential should be expected to follow a law of the type

$$E_p = A + B \cdot \text{pH} \quad [16]$$

where  $B$  is equal to the Tafel slope for the metal in the acid pit-like solution. Such a relation was found for iron in NaCl solutions (Figure 13)<sup>48</sup> and for cadmium in NaCl and in Na<sub>2</sub>SO<sub>4</sub> solutions,<sup>9</sup> both at pH values above 10. In all these cases, the  $B$  value of eqn [16] was very close to the Tafel slope of the metal in the pit-like solution.

In the case of trivalent metals, as it is the case with aluminum, the presence of a further step of hydrolysis slows down the effect of the external pH on the  $x.i$  value. As shown in Figure 23, the transition from passivity to pitting is not as sharp as for divalent metal ions, Figure 22. Consequently, for comparison reasons, the critical  $x.i$  value chosen was the point where the concentrations of solid Al(OH)<sub>3</sub> and soluble Al<sup>3+</sup> were equal, that is, the intersection point of both concentration curves. The results found were<sup>96</sup>:

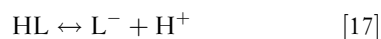
$$\text{pH} = 5; \quad x.i = 1.4 \times 10^{-6} \text{ A cm}^{-1}$$

$$\text{pH} = 8; \quad x.i = 2.0 \times 10^{-6} \text{ A cm}^{-1}$$

$$\text{pH} = 10; \quad x.i = 3.1 \times 10^{-6} \text{ A cm}^{-1}$$

According to the full hydrolysis calculation,<sup>96</sup> for divalent metal ions an increase of only one unit in the pH of the bulk solution produced an increase as big as one order of magnitude in the  $x.i$  value. On the other hand, for aluminum an increase of five pH units produced just a two-fold increase in the  $x.i$  value. The conclusion is that the critical  $x.i$  value, for aluminum, is practically independent of the external pH. This conclusion is in agreement with the experimental observations made by Kaesche,<sup>65</sup> who found that the pitting potential of aluminum was not affected by the solution pH.

The presence of anions of weak acid salts is also very important for the localized acidification at the bottom of the pit. If weak acid salts are present, the anions of those salts will react with the protons, and hinder the localized acidification process. The equilibrium involved will be



where HL is the weak acid and L is the weak acid anion. The equilibrium constant of this reaction will be

$$K_a = \frac{C_{L^-} \cdot C_{H^+}}{C_{HL}} \quad [18]$$

If reaction [17] is introduced as a boundary condition in the ion concentration diagrams, the effect of weak acid salts on the localized acidification can be evaluated. **Figure 25** shows the effect of  $10^{-2}$  M borax on the concentration of the various species in a unidirectional zinc pit. **Figure 26** shows how the concentration of protons is shifted to higher  $x.i$  values when the concentration of borax is increased. The higher the borax concentration, the higher the  $x.i$  values necessary to reach the same acidification. An increase of one order of magnitude in the borax concentration leads to an increase of about one order of magnitude in the  $x.i$  value. If the relationship between the potential and the current density inside the pit follows a logarithmic law, we conclude that the pitting potential of zinc should be related to the borax concentration by an equation of the type

$$E_p = A + B \log C_b \quad [19]$$

$C_b$  being the concentration of the borax. The value of  $B$  should be equal to the Tafel slope of the metal in the pit-like solution. Logarithmic relationships of this type between the pitting potential and the

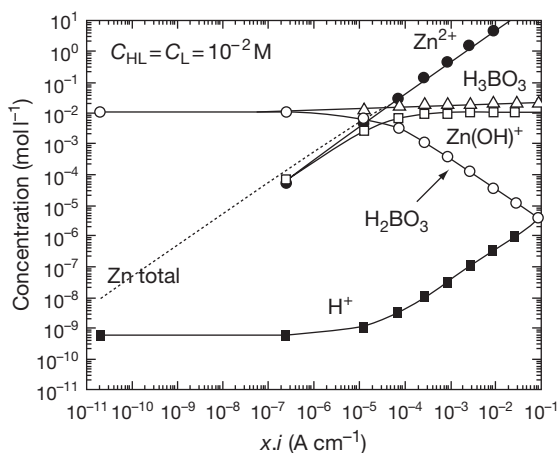


**Figure 25** Effect of a buffer on the proton concentration inside a pit of for Zn. The maximum buffer capacity is found when the concentrations of HL and  $L^-$  are equal. When the concentration of  $L^-$  begins to decrease, the concentration of  $H^+$  increases and the pit becomes stable. Reproduced from Galvele, J. R. *J. Electrochem. Soc.* **1976**, 123, 464–474, with permission from the Electrochemical Society.

buffer concentration for zinc have been reported by Augustynski *et al.*<sup>35</sup> Relationship [19] was also found to work in the case of pitting of high-purity iron in NaCl solutions in the presence of sodium borate as inhibitor.<sup>84</sup>

The efficiency of a weak acid salt as a pitting inhibitor will depend on the way in which the equilibrium of eqn [17] is shifted. The more the equilibrium is shifted to the left in eqn [17] the more efficiently the salt acts as a pitting inhibitor. This is equivalent to saying that the lower the  $K_a$  value, in eqn [18], the more efficient the inhibitor will be.<sup>95</sup>

The ion concentration diagrams can also explain the existence of a pitting repassivation potential, lower than the pitting potential, **Figure 9**. **Figure 27** is a simplified picture of **Figure 21**. As soon as the system reaches a critical  $x.i$  value,  $x.i_1$  in **Figure 27**, the pit will start to grow. If the potential remains constant, the current density will also be constant, but  $x$  will increase with time and so will  $x.i$  ( $x.i_2$  in **Figure 27**). If the potential is then lowered, the current density will drop, but the pit will continue to grow while the  $x.i$  value is higher than  $x.i_1$ . This means that pits will grow at potentials lower than the initiation potential. Finally the pit will stop growing either because the value  $x.i$  is lower than the minimum required for the pit growth to occur, or because the electrode potential is lower than the corrosion potential in the solution inside the pit,  $E_c^*$ . This mechanism explains the observation made by Suzuki and Kitamura<sup>53</sup>: the deeper the pit the lower the repassivation potential.

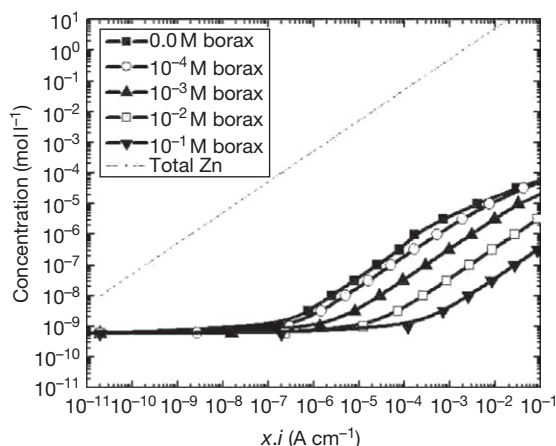


**Figure 26** Effect of buffer concentration on the  $x.i$  for Zn. Reproduced from Galvele, J. R. *J. Electrochem. Soc.* **1976**, 123, 464–474, with permission from the Electrochemical Society.



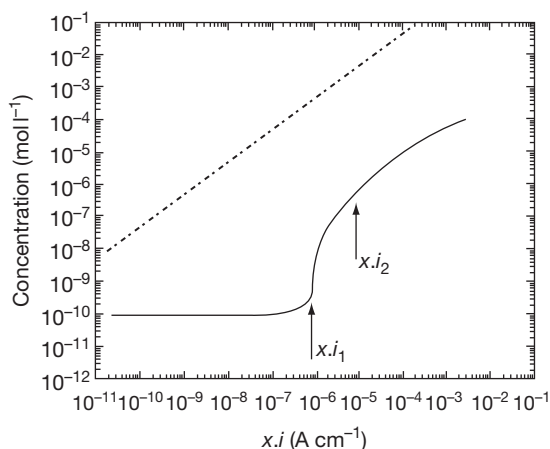


**Figure 27** Origin of the repassivation potential,  $E_r$ . At  $x.i_1$  a pit starts to grow and the potential is  $E_p$ . At constant potential  $i$  remains constant but  $x$  increases, leading the system to  $x.i_2$ . If the potential is lowered, the growth of the pit will not stop until  $x.i_1$  is reached. As the value of  $x$  has increased, the value of  $i$  must be lower, which means a lower  $E$  value. The new  $E$  value at which pitting stops is known as  $E_r$ .

If the concentration of the aggressive anion salt is changed over a wide range of values, the assumption that this salt is acting as a supporting electrolyte, which leads to the use of eqn [9], is not valid. Eqn [8] is to be used, which indicates the presence of an extra electrical potential inside the pit. Figure 28 is a simplified diagram where the appearance of a migration phenomenon at high  $x.i$  values is shown. For the sake of simplicity, the hydrolysis reactions have been ignored. The electrical potential, due to the migration phenomenon, starts to increase as soon as the concentrations of  $\text{Na}^+$  ions and  $\text{Cl}^-$  ions from the NaCl solution start to diverge. The electrical potential values, for different NaCl concentrations, and  $x.i$  values are shown in Figure 29.

An important conclusion from the transport process studies<sup>94–97</sup> was the nature of the pitting potential. It was concluded that the pitting potential had no relation with thermodynamic equilibrium, as suggested by Van Muylder *et al.*,<sup>70</sup> but it was given by the following equation:

$$E_p = E_c^* + \eta + \phi \quad [20]$$

$E_p$  being the pitting potential,  $E_c^*$  the corrosion potential in the pit-like solution,  $\eta$  the polarization needed to reach the critical  $x.i$  value, and  $\phi$  the electrical potential induced by the migration of the aggressive anions to the bottom of the pit. The validity of eqn [20] was tested in numerous

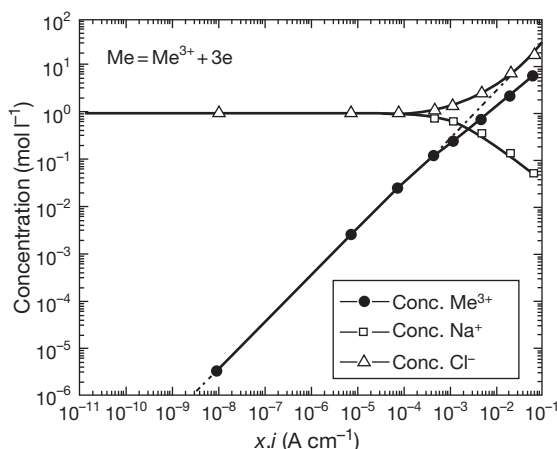


**Figure 28** Migration effect inside a pit in a 1 M NaCl solution. The contribution of migration begins when the concentrations of  $\text{Na}^+$  and  $\text{Cl}^-$  start to diverge. The migration also affects the movement of  $\text{Me}^{3+}$  ions, observed in the deviation of the concentration line at lower  $x.i$  values. Reproduced from Galvele, J. R. *J. Electrochem. Soc.* **1976**, 123, 464–474, with permission from the Electrochemical Society.

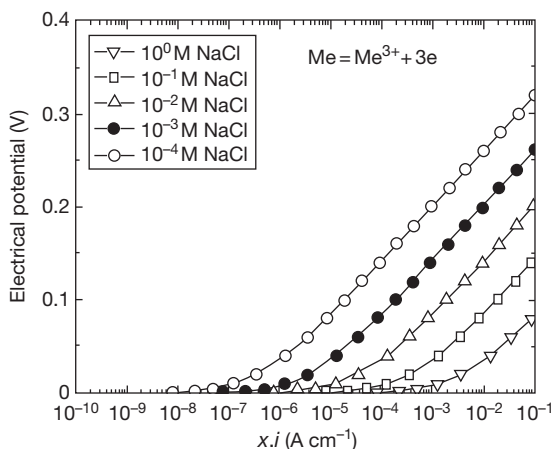


**Figure 29** Effect of the NaCl concentration on the potential  $\phi$  inside the pit because of migration. Reproduced from Galvele, J. R. *J. Electrochem. Soc.* **1976**, 123, 464–474, with permission from the Electrochemical Society.

publications<sup>38,44,82,83,97,98</sup> and some of the results are shown in Table 3. Eqn [20] was also confirmed in an independent work by Newman *et al.*<sup>105</sup> Besides, calculations and measurements made on high purity zinc in NaCl solutions with various concentrations of borate buffer, under conditions where the aggressive solution was not acting as a supporting

electrolyte, and eqn [8] had to be used, also confirmed the validity of eqn [20] for the calculation of the pitting potential.

### 2.04.9 Passive Film Breakdown

In the previous section, the mechanism of propagation of stable pits was discussed. But, a previous step is the passive film breakdown, a problem that was anticipated in Figure 17. The breakdown of the passive film and the very initiation of pits are two of the not clearly understood aspects of the pitting process.<sup>106</sup> One source of confusion was the fact that no distinction was made between the three different types of pitting described at the beginning of this chapter. Thus, very often mechanisms were suggested for all types of pitting only on the basis of experiments either on chemical depassivation or on electrochemical depassivation. Another source of confusion was related to the nature of passivity. As pitting is a process of passivity breakdown, any mechanism of pitting had to be related to some mechanism of passivity. For a long time, there were strong discussions between those who maintained that passivity was due to an adsorbed monolayer of oxygen and those who claimed that passivity was due to the formation of a three-dimensional oxide film on the metal surface. Those supporting the idea of an adsorbed monolayer based their pitting mechanisms on the idea of competitive adsorption between the passivating and the aggressive species on the metal surface.<sup>107,108</sup> Those in favor of a passive three-dimensional oxide film tried to find a way to undermine that film. As it is now known that the oxide films present on passive metals are at least several monolayers thick, in this chapter it will be assumed that the metal is initially covered by a three-dimensional passivating oxide film. Theories of pit initiation have been classified into two main groups: film penetration and film breaking.

#### 2.04.9.1 Ion Penetration Mechanisms

The early literature on passive films assumed that the oxide film was acting as a static barrier that isolated the metal from the solution. In order to initiate pitting under such conditions some reaction had to take place to bring the metal in contact with the aggressive ions of the solution. One possible way to initiate pits was for the aggressive ions to migrate into the passive film, thus contaminating it. Anion

migration would be stimulated by the high electric field in the film. As a result of changes of the properties of the passive film, high currents could start to circulate through the contaminated zones and pitting would start.<sup>109</sup> Nevertheless, Vetter and Strehblow<sup>93</sup> pointed out that the migration of polyatomic aggressive anions such as  $\text{SO}_4^-$ ,  $\text{ClO}_4^-$ , or  $\text{SCN}^-$  through a solid layer was not conceivable.

The contamination of the passive films by aggressive anions has been confirmed in several cases. In others, the results obtained by different techniques are conflicting. Basing his studies on impedance measurements, Pryor<sup>110</sup> suggested that migration of chloride ions took place into anodized aluminum films. McBee and Kruger,<sup>111</sup> by ellipsometric studies on pure iron, and on Fe–Cr and Fe–Cr–Mo alloys, found that the injection of chloride ions in the medium produced changes in the properties of the oxide film, probably by penetration of the film. These changes were reversible and the properties of the oxide film were recovered after removing the chloride ions from the medium. Nevertheless, it could not be confirmed that the observations made by McBee and Kruger were due to migration of chloride ions into the film. Marcus *et al.*<sup>112</sup> found chloride present in passive films on nickel using electron spectroscopy for chemical analysis (ESCA) and *in situ* radiotracer measurements. The establishment of a critical concentration of chloride in the film is a prerequisite for the localized breakdown of the film. On the other hand, other authors<sup>113–115</sup> found no incorporation of aggressive ions into the passive film prior to pitting.

The point-defect model for passive film growth developed by Lin *et al.*<sup>116</sup> has been used to explain pit initiation by assuming that the aggressive anion adsorption at the outer layer of the barrier film results in the formation of cationic vacancies. The excess of vacancies at the metal/film interface will lead to the formation of voids and pitting initiation.

#### 2.04.9.2 Film Breakdown Mechanisms

There are two different film breakdown models. In one of them, pitting is considered to start at flaws always present in the oxide film<sup>117,118</sup> while in the other pit initiation results from a continuous state of breakdown and repair of the passive film.<sup>119,120</sup> In these models the role of the aggressive anions is to prevent repassivation at the local breakdown sites.

There are theoretical reasons to expect the existence of flaws in the passive film. Fromhold<sup>121</sup>

**Table 3** Comparison between experimental pitting potential values, measured in 1 M NaCl solution and theoretical values calculated with Eqn [20]. Potentials in  $V_{SHE}$

Alloy	$E_p$ theoretical	Ref.	$E_p$ experimental	Ref.
Al 99.99%	-0.54	83	-0.53	1
Al-3Cu	-0.43	83	-0.43	82
Al-3 Mg	-0.56	83	-0.53-0.57	83
Al-3Zn	-0.76	83	-0.75	83
Fe-18Cr	0.60	44	0.58-0.62	80
Fe-18Cr-1Mo	0.73	44	0.64-0.70	80
Fe-18Cr-2Mo	0.88	44	0.70-0.82	80
Fe-18Cr-5Mo	1.03	44	1.00-1.04	80

pointed out that the act of forcing an ionic species through a compact passive film to produce additional film growth will seriously affect the compact film itself. He found that the electrochemical potential gradients inside the film give rise to extremely large stress values, high enough to produce the mechanical breakdown of the passive film and to transform the crystalline structure of the film into an amorphous one. On the other hand, Sato<sup>122</sup> found that mechanical stresses resulting from electrostriction and surface tension effects may exceed the breakdown stress of the oxide film. In a later paper, the author predicted<sup>123</sup> that there is a critical potential above which breakthrough pores would be formed in the film. This critical film breakdown potential is lower as the surface tension at the metal-electrolyte interface is smaller, and hence, the anion adsorption is stronger.

#### 2.04.9.3 Passive Film Breakdown and Metastable Pits

If, as suggested by the film breakdown theories, flaws really exist in the passive film, and if for sustained pit growth a critical  $x.i$  value has to be reached, it is reasonable to expect that, below the pitting potential, incipient processes of pit initiation should exist. Indications of passive film breakdown and repassivation events were reported by Galvele *et al.*<sup>124,125</sup> when studying the repassivation rate of various metals and alloys. The current decay, when measuring repassivation rates, could be described by a relation of the type

$$i = A.t^b$$

where,  $i$  is the current density,  $t$  is the time and  $A$  and  $b$  are constants. A value of  $b = -1$  is typical of a high field film formation reaction, and it is usually related to the formation of a compact highly protective

passive film. Galvele *et al.*<sup>124,125</sup> studied the repassivation rate for zirconium in various halide solutions, as well as for brass in pH 12, 1 M NaNO<sub>2</sub> solution. They observed that at potentials well below the pitting potential the value of  $b$  was  $-1$ . Then there was a region of potentials where an initial value of  $b = -0.5$ , typical of a diffusion controlled process, was observed, but after a few seconds the current density decreased and returned to values expected for a repassivation rate of  $b = -1$ . At higher potentials, close to the pitting potential, the value of  $b$  increases above  $b = -0.5$ , reaching eventually positive values, as is typical in pitting processes. The intermediate potential region, in which the initial repassivation rate is not as fast as at lower potentials but after a short time the highly protective oxide film is reformed, was identified by the authors as the region where passivity breakdown takes place. They also concluded that the repassivation rate technique was very convenient for detecting the passivity breakdown. No other references were found in the literature where this line of work was followed.

On the other hand, many investigators have observed that the formation of a stable pit is preceded by electrochemical noise. The noise events took the form of transient fluctuations of potential under galvanostatic control, or of current fluctuations under potentiostatic control. Such transients have been reported for many years in stainless steel,<sup>51,126,127</sup> and Al,<sup>7,118,128</sup> and were originally attributed to passive film breakdown and repassivation events.<sup>51,122,123,129</sup>

Afterwards, it was found that each of these electrochemical noise events originates from the formation, growth, and repassivation of a microscopic pit.<sup>130-134</sup> These short life pits, now referred to as metastable pits, can form at potentials well below the pitting potential (which is associated with onset of stable pit growth) and during the induction time before the initiation of stable pitting at potentials above the pitting potential.

Metastable pit growth is a characteristic feature of the pitting corrosion of stainless steel in chloride solutions,<sup>130-135</sup> although indications of metastable pitting have also been reported for other metals and alloys such as iron-chromium alloys,<sup>136</sup> aluminum,<sup>137</sup> and titanium.<sup>138</sup> Metastable pits grown on stainless steel are covered by a layer that is a remnant of the passive film<sup>130,131</sup>; the rupture of their covers results in dilution of the local pit environment and repassivation of the pits.<sup>45,139</sup>

Metastable pitting transients exhibited by stainless steels in chloride solutions have a characteristic shape

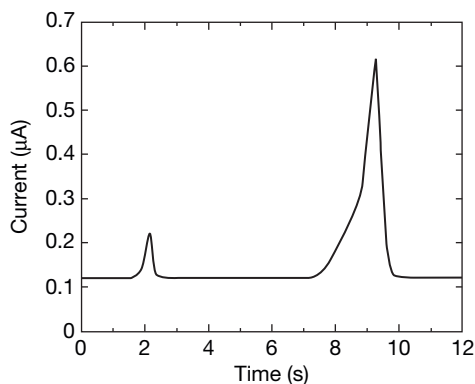


**Figure 30** Current transients typical of pre-pits.

(Figure 30). The current increases above the background passive current as the pit nucleates and begins to grow. After a short growth period, the metastable pit repassivates and the current quickly decreases to the level of the original passive current. At open circuit, metastable pitting events result in potential transients with a typical shape consisting of a rapid potential drop followed by a slow increase.<sup>140</sup>

There appear to be no discernible differences between metastable pit growth and the early growth of a stable pit.<sup>134</sup> Therefore, studies of metastable pits were performed in order to gain knowledge about the critical factors that determine the stable growth of pits. Two main lines of information may be obtained from such investigations: stochastic data such as a relationship between the nucleation frequencies of metastable and stable pits,<sup>133,141,142</sup> and kinetic data deduced from the analysis of individual current transients.<sup>130,131</sup>

Frankel *et al.*<sup>130</sup> showed that during the metastable pit growth the pit current increases approximately with the square of time. Making the assumption that the pits associated with these transients are hemispherical in shape, they concluded that the current density was approximately constant with time during most of the metastable pit growth. The transients showed lifetimes as long as 15 s, but typically less than 5 s, and their magnitude varied from 4  $\mu\text{A}$  to 20  $\mu\text{A}$ . Other authors found a growth-rate distribution of metastable pits at each potential and that the metastable pit current follows a power law relationship  $I \sim t^n$  with  $n$  between 0.5 and 1.5.<sup>133,142–144</sup>

According to Frankel *et al.*,<sup>130</sup> metastable pit growth is controlled by the Ohmic resistance of the porous pit cover. Pits repassivated when their cover ruptured and the Ohmic barrier was lost. On the

other hand, if a salt film is present when the cover breaks, pit stability is maintained.

Pistorius and Burstein<sup>131,145–147</sup> believe that the rate of growth of individual pits is controlled by diffusion of metal cations from the pit interior, the surface of which is covered with a salt film even before the cover is lost. During metastable growth, the pit depth is too small to account for the diffusion barrier but the perforated cover over the pit mouth provides an additional diffusion barrier which enables the concentrated pit solution to be maintained. The transition to stable pit growth occurs when the pit has grown sufficiently for its own depth to act as a diffusion barrier. The critical condition under which this transition occurs is determined by the magnitude of the product of the pit current density,  $i$ , and its depth,  $a$ , called the ‘pit stability product.’ All pits grow initially in the metastable condition, with a pit stability product which increases linearly with time, but below the critical value. Once the critical value of  $ia$  is exceeded, pit growth is stable and the pit propagates in the absence of the cover.

Because of the small anodic currents generated during individual metastable events and to avoid these transients being obscured by the passive current or simultaneous transients, experiments must be performed by exposing a restricted surface area of the specimen tested. Most metastable pitting research has been carried out using embedded wires of less than 1 mm diameter (10–500  $\mu\text{m}$ ).<sup>130,131,134,135,137,145–148</sup> Events of amplitude down to *ca.* 1 pA in amplitude can be detected if the electrode is small enough. Using very low noise systems, some authors<sup>138,149–151</sup> have observed small current transients, which exhibit a shape different from that of typical metastable pits in that the current increased sharply and then decayed relatively slowly to the background. These peaks were attributed to nucleation and subsequent repassivation events.

Williams *et al.* have presented a statistical model relating the probability of forming a large propagating pit to the nucleation, death, and propagation characteristics of metastable pits.<sup>132,139,142</sup> The proposed statistical model states that the probability that a stable pit is formed is equal to the probability of forming a metastable pit times the probability that the metastable pit survives to become a stable pit. Thus, the nucleation frequency for stable pits is expressed in terms of the nucleation frequency for metastable pits and a probability of repassivation.<sup>133,141,142,152</sup> Underlying this approach is the

concept that if metastable pits form then a stable pit is sure-to-happen at some time.

## 2.04.10 Pitting of Aluminum Alloys

### 2.04.10.1 Pitting and Intergranular Corrosion

In spite of having a rather low pitting potential, aluminum and certain aluminum alloys are successfully used in marine environments, the reason being that the passive film on aluminum is not a good electron conductor and the electrochemical reduction of oxygen is hindered. This is not the case if copper is present in the alloy. It has been found that the presence of copper in the alloy facilitates the reduction of oxygen, **Figure 31**. Thus copper becomes a deleterious contaminant in these environments, because through the cathodic reaction of oxygen, the presence of copper causes an increase in the electrode potential, which gets above the pitting potential of the aluminum alloy.

Pitting can also be the cause of other types of localized corrosion in aluminum–copper alloys. For example, it has been shown<sup>1</sup> that the susceptibility to intergranular corrosion of aged Al–4%Cu alloys is related to the difference in pitting potentials between a solute-depleted zone, surrounding the intermetallic precipitates along the grain boundaries, and that of the grain bodies. As shown in **Figure 12**, the pitting potentials of the grains in chloride containing solutions were almost 100 mV higher than those of

the copper-depleted zone at the grain boundaries. **Figure 12** can be divided into three zones. The first one is below the pitting potential of Al–0.2%Cu, which is in equilibrium with the intermetallic  $\text{Al}_2\text{Cu}$ . In this zone, the alloy will remain passive. The second zone in **Figure 12**, is between the pitting potentials of Al–0.2%Cu and Al–4%Cu. In this area of potentials only the copper depleted zone along the grain boundaries will corrode, giving intergranular corrosion. Finally, in the third zone, in the upper part of the figure, all the phases of the alloy will corrode. Intergranular corrosion would not appear in every corrosive medium, but only in those where the aluminum alloys showed pitting, such as  $\text{Br}^-$ ,  $\text{I}^-$ , and  $\text{ClO}_4^-$ , as shown in **Table 4**. The difference in the pitting potentials was a function of the heat treatment of the alloys and for certain heat treatments the difference was so small that the alloys were rendered immune to intergranular corrosion.<sup>82</sup>

## 2.04.11 Pitting of Stainless Steels

### 2.04.11.1 Pitting and Crevice Corrosion

Pitting and crevice corrosion of stainless steels in chloride solutions are frequently found together, the most frequent observation being that stainless steels will fail most frequently by crevice corrosion, rather than by pitting. The prevalence of crevice corrosion, over pitting, has led to the development of a special cell, known as the Avesta cell, where pitting of stainless steels could be measured without the interference of crevice corrosion.<sup>153</sup>

Susceptibility to crevice corrosion was found to be related with  $\eta$  in eqn [20],<sup>38</sup> as shown in **Table 5**. This observation, together with the explanation of the nature of the repassivation potential,  $E_r$ , given in **Figure 27**, helps to explain the empirical relation found by Wilde and Williams between  $E_r$  and the susceptibility to crevice corrosion of stainless steels in sea water.<sup>54</sup>

Wilde and Williams found an empirical relation that related the difference  $E_p - E_r$  and the susceptibility to crevice corrosion in sea water. The anodic reaction inside the pit allows to explain the data in **Table 5**, as well as the empirical relation found by Wilde and Williams. These authors showed that the larger the difference between the pitting potential and the repassivation potential,  $E_p - E_r$ , the more susceptible the alloy was to crevice corrosion. **Figure 32** shows some of their results. It is important to notice that the technique developed by Wilde and Williams

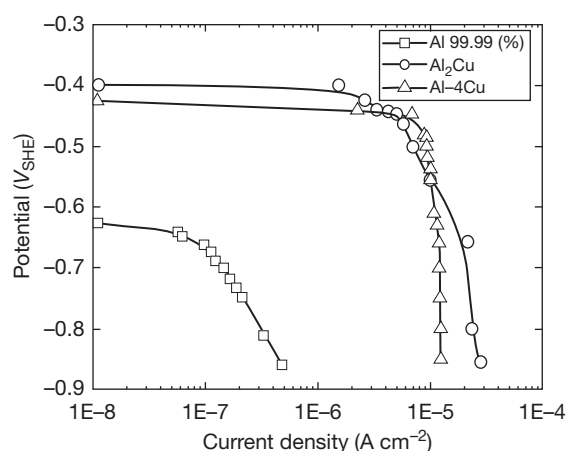


**Figure 31** Cathodic polarization curves in air-saturated 1 M NaCl of pure aluminum, solubilized Al–4%Cu, and intermetallic  $\text{Al}_2\text{Cu}$ . Reprinted from Galvele, J. R.; De Micheli, S. M. de. *Corros. Sci.* **1970**, 10, 795–807, with permission from Elsevier.



**Table 4** Relation between pitting potentials and intergranular corrosion of aged Al-4%Cu alloys in solutions other than NaCl

Electrolyte	Pitting potentials ( $V_{SHE}$ )		Intergranular corrosion <sup>a</sup>
	99.99% Al	Al-4%Cu (solub.)	
			Al-4%Cu (aged)
1 M KBr	-0.42	-0.28	Yes (-0.40)
1 M KI	-0.26	-0.13	Yes (-0.23)
1 M NaClO <sub>4</sub>	-0.17	+0.03	Yes (-0.14)
1 M NaNO <sub>3</sub>	+1.80	+1.85	No (+1.85)
1 M Na <sub>2</sub> SO <sub>4</sub>	>+3.0	>+3.0	No (+3.0)
1 M H <sub>2</sub> SO <sub>4</sub>	>+3.0	>+3.0	No (+3.0)
0.1 M NaIO <sub>3</sub>	>+3.0	>+3.0	No (+3.0)
1 M Ammonium tartrate	>+3.0	>+3.0	No (+3.0)

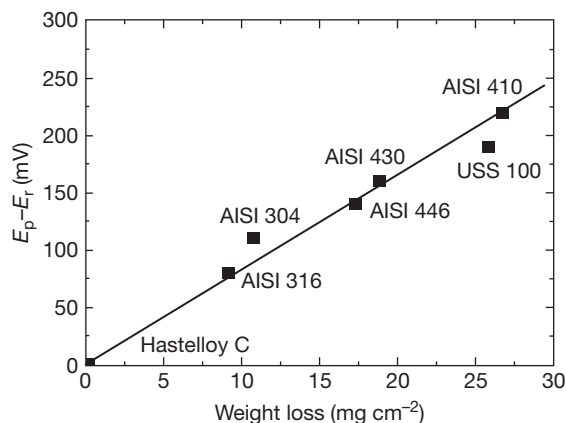
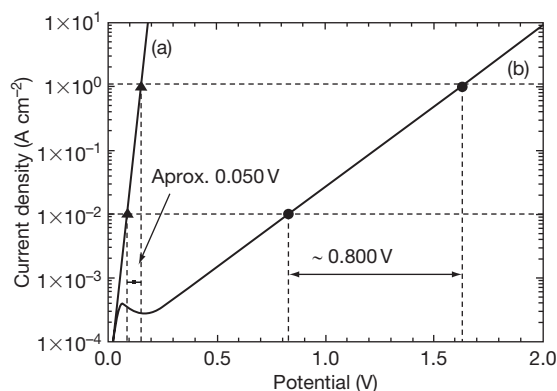
<sup>a</sup>In parentheses, potentials at which the intergranular corrosion susceptibility was tested.  
 Reprinted from Galvele, J. R.; De Micheli, S. M. de. *Corros. Sci.* **1970**, *10*, 795–807, with permission from Elsevier.

**Table 5** Overpotential values,  $\eta$ , from eqn [20], versus crevice corrosion susceptibility for various metals and alloys in NaCl solutions

Metal	$\eta$ mV	Crevice corrosion	Reference
Al-3Zn	10	No	83
Cadmium	~20	No	9
Zinc	~20	No	34
Iron	~30	No	48
Al-3Cu	40	No	82
Al-3Mg	150	No	83
Aluminum	170	No	82
Nickel	470	Yes	154
Fe-18Cr	670	Yes	44
Fe-18Cr-1Mo	740	Yes	44
Fe-18Cr-2Mo	880	Yes	44
Fe-18Cr-5Mo	1000	Yes	44

assumes that the depth of the pits is the same in all the samples under comparison and that this condition is achieved when the current density reaches  $0.2 \text{ A cm}^{-2}$ . Nevertheless, this condition will be true only when the number of pits in all the tested samples is similar.

The explanation for Wilde and Williams's correlation could be found in Figure 33. We will assume that the current density, when pitting starts, is of the order of  $1 \text{ A cm}^{-2}$ . We will also assume that curve (a) shows the Tafel curve for iron in a pit-like solution in NaCl and curve (b) is a pseudo-Tafel curve for stainless steel, this last value being on the basis of

**Figure 32** Comparison between the difference  $E_p - E_r$ , measured potentiokinetically in a NaCl solution, and crevice corrosion measured after long exposures in sea water. Reprinted from Wilde, B. E.; Williams, E. *Electrochim. Acta* **1971**, *16*, 1971–1985, with permission from Elsevier.**Figure 33** Susceptibility to crevice corrosion in NaCl solutions based on the relation inside the pit, for iron (a)<sup>48</sup> and for stainless steel (b)<sup>44</sup> the potential scale is arbitrary, and was chosen for illustrative purposes. In this example the following assumptions are made: critical value  $x \cdot i = 10^{-6} \text{ A cm}^{-1}$ , pit size  $x = 10^{-6} \text{ cm}$ , crevice size  $x = 10^{-4} \text{ cm}$ . In case (a) the difference in potential required to start pitting corrosion from that to start crevice corrosion will be of only 50 mV. In case (b) crevice corrosion will start at a potential 800 mV lower than that required to start pitting.

Galvele *et al.*<sup>44</sup> If the critical  $x \cdot i$  value is of the order of  $x \cdot i = 10^{-6} \text{ A cm}^{-1}$ , pitting could start on any flaw of  $10^{-6} \text{ cm}$ . If the pit is allowed to grow up to  $10^{-4} \text{ cm}$ , to reach again the critical  $x \cdot i$  value the current density will have to drop to  $10^{-2} \text{ A cm}^{-2}$ . In the case of curve (a) the difference  $E_p - E_r$  will be of only 50 mV. On the other hand, the difference  $E_p - E_n$  for curve (b) will be

of 800 mV. If, instead of a pit of  $10^{-4}$  cm, we have a crevice of the same size, in case (a) the difference between pitting and crevice corrosion will be of only 50 mV, a value usually obscured by the corrosion potential oscillations in practical cases, and it could be concluded that metal (a) is not susceptible to crevice corrosion. On the other hand, for metal (b), crevice corrosion will start at a potential 800 mV lower than that required for pitting, and this metal will be more susceptible to crevice corrosion than to pitting.

The relation between pitting and crevice corrosion was supported by Wood *et al.*<sup>118</sup> They studied the evolution of crevice corrosion of AISI type 304 austenitic stainless steel under a 13 mm diameter  $\times$  0.3 mm glass microscope cover slide, at constant potential, in an air saturated 5% NaCl solution of pH 8.0. The development of crevice corrosion was followed with an appropriate optical system. They observed that while at 600 mV<sub>SCE</sub>, pits nucleated on the entire metal surface, at 400 mV<sub>SCE</sub>, pits nucleated only under the glass cover and spread laterally to take the shape of crevice corrosion. According to these authors, their study confirmed the close link between pitting and crevice corrosion in the case of stainless steels, and it strongly suggested that crevice corrosion is really no more than 'lateral pitting' occurring within an occluded area.

### 2.04.11.2 Critical Pitting Temperature (CPT)

Pitting corrosion of stainless steel and nickel base alloys is characterized by the existence of a CPT, which is defined as the lowest temperature at which the growth of stable pits is possible. At temperatures lower than CPT no stable pitting can occur and only transpassive corrosion takes place. Brigham and Tozer<sup>78</sup> introduced the concept of the CPT as a criterion for ranking resistance of different austenitic stainless steels to pitting corrosion: the higher the CPT, the more resistant the alloy is to pitting.

CPT can be determined by exposing steel samples to an oxidized chloride solution such as FeCl<sub>3</sub> and increasing the temperature in a sequence of test periods until pitting is observed.<sup>156</sup>

The CPT can also be determined electrochemically, either by varying the potential at different constant temperatures or by varying the temperature at different constant potentials.<sup>156–159</sup> At temperatures lower than CPT, passivity breakdown is observed at extremely high anodic potentials, corresponding to transpassive dissolution. Just above the CPT, pitting

can occur and breakdown potentials far below those required for transpassivity are measured. The potential independent CPT is then determined as the temperature at which a sudden decrease in breakdown potential from the transpassive range to the pitting range is observed (Figure 34). The CPT of many stainless steels falls in the range of 10–90 °C.<sup>78,159</sup>

If the simultaneous occurrence of crevice corrosion is eliminated, as is the case when the Avesta cell<sup>153</sup> is used, the CPT can be defined with an absolute accuracy of 1–2 °C.<sup>158,159</sup> On the other hand, when crevice corrosion occurs, localized corrosion initiates at a temperature lower than the CPT, which is called critical crevice temperature (CCT) and the transition from high to low breakdown potentials happens over a temperature interval in which intermediate values of the breakdown potential are observed.<sup>160</sup>

The CPT value is virtually independent of pH in the range 1–7,<sup>158</sup> and of chloride concentration in the range 0.01–5 M.<sup>47,158</sup> However, the CPT is affected by the sulfate concentration,<sup>161</sup> and changes appreciably with surface roughness.<sup>162</sup>

Metastable pitting could occur at temperatures below the CPT, but stable pitting was only detected at the conventional CPT value.<sup>135,160,163</sup> This suggested that the CPT transition was related to the ability of a metastable pit to become stable. Assuming that an anodic salt film must be maintained in all stable pits, CPT has been interpreted as a competition between salt film and oxide formation within the pit.<sup>47,163</sup> Below CPT, passivation would prevent pits from achieving the current density necessary to maintain a concentrated local chemistry and the salt

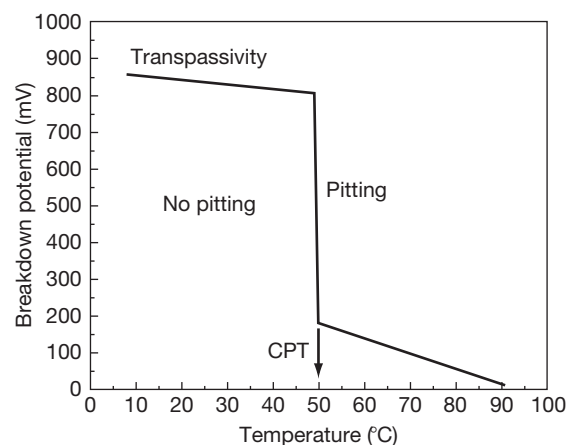


Figure 34 Critical pitting temperature.

layer precipitation is impossible. A slight modification of this model proposed that the CPT is the temperature below which the salt precipitation, rather than stabilizing the anodic process, mediates the oxide passivation in a manner similar to that of the passivation of iron in sulfuric acid.<sup>46</sup> A further refinement of this theory suggests that a stable pit must be able to undercut the surface, thus creating a passivated lacy metal cover that retains the pit contents;<sup>144,164,165</sup> thus the critical event that cannot occur below the CPT is a high rate active film-free dissolution at the undercutting site inside the pit.

## References

- Galvele, J. R.; De Micheli, S. M. *Corros. Sci.* **1970**, *10*, 795–807.
- Dallek, S.; Foley, R. T. *J. Electrochem Soc.* **1976**, *123*, 1775–1779.
- Metzger, M. J. *Phys. (Colloque C4, supplément 10)*. **1975**, *36*, C4–387; C4–393.
- Freiman, L. I.; Kolotyrkin, Ya. M. *Z Metallv* **1966**, *2*, 488–490.
- Wexler, S. B.; de Galvele, J. R. *J. Electrochem. Soc.* **1974**, *121*, 1271–1276.
- De Micheli, S. M.; de Galvele, J. R. *Metalurgia (ABM)* **1971**, *27*, 589–596.
- Galvele, J. R.; De Micheli, S. M.; de Muller, I. L.; Wexler, S. B.; de Alanis, I. L. In *Localized Corrosion*; U. R. Evans Conference on Localized Corrosion, Williamsburg, Virginia, USA, December 6–10, 1974; Staehle, R. W., Brown, B. F., Kruger, J., Agrawal, A., Eds.; National Association of Corrosion Engineers: Houston, Texas, USA, 1971; pp 580–599.
- Augustynski, J. *Corros. Sci.* **1973**, *13*, 955–965.
- Alvarez, M. G.; Galvele, J. R. *J. Electrochem. Soc.* **1980**, *127*, 1235–1241.
- Kolotyrkin, Ya. M.; Freiman, L. I. *Dokl. Akad. Nauk. SSSR* **1965**, *162*, 376–379.
- Vetter, K. J.; Strehblow, H. H. *Ber. Bunsen-Ges. Phys. Chem.* **1970**, *75*, 449–455.
- Semino, C. J.; Galvele, J. R. *Corros. Sci.* **1976**, *16*, 297–306.
- Strehblow, H. H. Abstract 96. *The Electrochemical Society Extended Abstracts*; Fall Meeting, Las Vegas, Nevada, Oct. 17–22, 1976; p 264.
- Hoar, T. P. In *Electrode Processes (Discussions of the Faraday Society, No 1, 1947)*; Reprinted by Butterworths: London, UK, 1961; pp 299–300.
- Freiman, L. I.; Kolotyrkin, Ya. *Corros. Sci.* **1965**, *5*, 199–209.
- Tousek, J. *Corros. Sci.* **1972**, *12*, 15–28.
- Kodama, T. *Proceedings Fifth International Congress Metallic Corrosion*; Tokyo: Japan, May 1972; p 223, National Association of Corrosion Engineers, Houston, Texas, USA, 1974.
- Ammar, I. A.; Darwish, S. *Electrochim. Acta* **1968**, *13*, 781–789.
- Ammar, I. A.; Darwish, S.; Riad, S. *Electrochim. Acta* **1968**, *13*, 1875–1882.
- Böhni, H.; Uhlig, H. H. *Corros. Sci.* **1969**, *9*, 353–355.
- Glazkova, S. A.; Shvarts, G. L.; Freiman, L. I.; Tavadze, F. N. *Z. Metallv* **1974**, *10*, 9–16.
- Hoar, T. P.; Jacob, W. R. *Nature*. **1967**, *216*, 1299–1301.
- Kolotyrkin, Ya. M.; Golovina, G. V.; Florianovich, G. M. *Dokl. Akad. Nauk SSSR* **1963**, *148*, 1106–1109.
- Schwenk, W. *Corrosion* **1964**, *20*, 129t–137t.
- Ijzermans, A. B. *Corros. Sci.* **1970**, *10*, 607–615.
- Brenner, S. *Tech. Publ. Inst. Tin Res. Dev. Council D.* **1935**, No. 2. Quoted by: Hoar, T. P. In *Electrode Processes (Discussions of the Faraday Society, No. 1, 1947)*, pp 299–300; Butterworths: London, UK, 1961.
- Hoar, T. P. *Trans. Faraday Soc.* **1937**, *33*, 1152.
- Beck, T. R. *J. Electrochem. Soc.* **1973**, *120*, 1310–1324.
- Abd Rabbo, M. F.; Boden, P. J. In *Localized Corrosion*; U. R. Evans Conference on Localized Corrosion, Williamsburg, Virginia, USA, December 6–10, 1971; Staehle, R. W., Brown, B. F., Kruger, J., Agrawal, A., Eds.; National Association of Corrosion Engineers: Houston, Texas, USA, 1974; pp 653–660.
- Breiter, M. W. *Electrochim. Acta* **1970**, *15*, 1195–1200.
- Dugdale, I.; Cotton, J. B. *Corros. Sci.* **1964**, *4*, 397–411.
- Kolotyrkin, Ya. M.; Gilman, V. A. *Dokl. Akad. Nauk. SSSR* **1961**, *137*, 642–645.
- Kolotyrkin, Ya. M. In *Proceedings First International Congress Metallic Corrosion*; Butterworths: London, 1962; p 10.
- Alvarez, M. G.; Galvele, J. R. *Corrosion* **1976**, *32*, 285–294.
- Augustynski, J.; Dalard, F.; Sohm, J. C. *Corros. Sci.* **1972**, *12*, 713–724.
- Cragnolino, G.; Galvele, J. R. In *Passivity of Metals*; Proceedings of The Fourth International Symposium on Passivity, Warrenton, Virginia, USA, October 17–21, 1977; Frankenthal, R. P., Kruger, J., Eds.; The Electrochemical Society, Inc.: Princeton, New Jersey, USA, 1978; pp 1053–1057.
- Gilman, V. A.; Kolotyrkin, Ya. M. *Z. Metallv* **1966**, *2*, 360–361.
- Galvele, J. R. In *Passivity of Metals*; Proceedings of The Fourth International Symposium on Passivity, Warrenton, Virginia, USA, October 17–21, 1977; Frankenthal, R. P., Kruger, J., Eds.; The Electrochemical Society, Inc.: Princeton, New Jersey, USA, 1978; pp 285–327.
- Piron, D. L.; Koutsoukos, E. P.; Nobe K. *Corrosion* **1969**, *25*, 151–156.
- Nobe, K.; Tobias, R. F. *Corrosion* **1964**, *20*, 263t–266t.
- Condit, D. O. In *Proceedings Fifth International Congress Metallic Corrosion*; Tokyo, Japan, May 1972; pp 160–163, Published by the National Association of Corrosion Engineers: Houston, Texas, USA, 1974.
- Engell, H. J.; Stolice, N. D. *Arch. Eisenhüttwes* **1959**, *30*, 239–248.
- Ives, M. B. In *Localized Corrosion*; U. R. Evans Conference on Localized Corrosion, Williamsburg, Virginia, USA, December 6–10, 1971; Staehle, R. W., Brown, B. F., Kruger, J., Agrawal, A., Eds.; National Association of Corrosion Engineers: Houston, Texas, USA, 1974; pp 78–103.
- Galvele, J. R.; Lumsden, J. B.; Staehle, R. W. *J. Electrochem. Soc.* **1978**, *125*, 1204–1208.
- Rosenfeld, I. L.; Danilov, I. S. *Corros. Sci.* **1967**, *7*, 129–142.
- Yahalom, J.; Ives, L. K.; Kruger, J. *J. Electrochem. Soc.* **1973**, *120*, 384–386.
- Laycock, N. J.; Moayed, M. H.; Newman, R. C. *J. Electrochem. Soc.* **1998**, *145*, 2622–2628.

48. Alvarez, M. G.; Galvele, J. R. *Corros. Sci.* **1984**, *24*, 27–48.
49. Good, D. J. *Electrochem. Soc.* **1997**, *144*, 1965–1971.
50. Horvath, J.; Uhlig, H. H. *J. Electrochem. Soc.* **1968**, *115*, 791–795.
51. Pessall, N.; Liu, C. *Electrochim. Acta* **1971**, *16*, 1987–2003.
52. Pourbaix, M. *Corrosion* **1970**, *26*, 431–438.
53. Suzuki, T.; Kitamura, Y. *Corrosion* **1972**, *28*, 1–6.
54. Wilde, B. E.; Williams, E. *Electrochim. Acta* **1971**, *16*, 1971–1985.
55. Kuzub, V. S.; Novitskii, V. S. *Z. Metallov.* **1976**, *12*, 177–180.
56. Strehblow, H. H.; Titze, B. *Corros. Sci.* **1977**, *17*, 461–472.
57. Keitelman, A. D.; Galvele, J. R. *Corros. Sci.* **1982**, *22*, 739–751.
58. Wang, S.; Newman, R. C. *Corrosion* **2004**, *60*, 448–454.
59. Al-Zahrani, A. M.; Pickering, H. W. *Electrochim. Acta* **2005**, *50*, 3420–3435.
60. Galvele, J. R. *Corros. Sci.* **2005**, *47*, 3053–3067.
61. Stolica, N. *Corros. Sci.* **1969**, *9*, 455–470.
62. Leckie, H. P.; Uhlig, H. H. *J. Electrochem. Soc.* **1966**, *113*, 1262–1267.
63. Böhni, H.; Uhlig, H. H. *J. Electrochem. Soc.* **1969**, *116*, 906–910.
64. Szklarska-Smialowska, Z. *Corros. Sci.* **1971**, *11*, 209–221.
65. Kaesche, H. Z. *Phys. Chem. NF.* **1962**, *34*, 87–108.
66. Prazhak, M.; Toushek, Ya.; Spanilyi, V. Z. *Metallov.* **1969**, *5*, 371–375.
67. Edeleanu, C.; Evans, U. R. *Trans. Faraday Soc.* **1951**, *47*, 1121–1135.
68. Hagyard, T.; Santhiapillai, J. R. *J. Appl. Chem.* **1959**, *9*, 323–330.
69. Wong, K. P.; Alkire, R. C. *J. Electrochem. Soc.* **1990**, *137*, 3010–3015.
70. Van Muylder, J.; Pourbaix, M.; Van Laer, P. In *Rapport Technique No 127*; CEBELCOR: Brussels, 1965.
71. Smith, J. A.; Peterson, M. H.; Brown, B. F. *Corrosion* **1970**, *26*, 539–542.
72. Suzuki, T.; Yamabe, M.; Kitamura, Y. *Corrosion* **1973**, *29*, 18–22.
73. Pickering, H. W.; Frankenthal, R. P. *J. Electrochem. Soc.* **1972**, *119*, 1297–1304.
74. Barger, C. B.; Benson, R. C. *J. Electrochem. Soc.* **1980**, *127*, 2528–2530.
75. Kolotyrkin, Ya. M. *Corrosion* **1963**, *19*, 261t–268t.
76. Szklarska-Smialowska, Z. *Corrosion* **1971**, *27*, 223–233.
77. Osozawa, K.; Okato, N.; Fukase, Y.; Yokota, K. *Corros. Eng. (Boshoku Gijutsu)*, **1975**, *24*, 1–7.
78. Brigham, R. J.; Tozer, E. W. *Corrosion* **1974**, *30*, 161–166.
79. Szklarska-Smialowska, Z. In *Pitting and Crevice Corrosion*; NACE International: Texas, 2005.
80. Lizlovs, E. A.; Bond, A. P. *J. Electrochem. Soc.* **1975**, *122*, 719–722.
81. Stout, D. A.; Lumsden, J. B.; Staehle, R. W. *Corrosion* **1979**, *35*, 141–146.
82. Muller, I. L.; Galvele, J. R. *Corros. Sci.* **1977**, *17*, 179–193.
83. Muller, I. L.; Galvele, J. R. *Corros. Sci.* **1977**, *17*, 995–1007.
84. Reding, J. T.; Newport, J. J. *Mater. Prot.* **1966**, *5*, 15–18.
85. Smialowska, S.; Czachor, M. In *Localized Corrosion*; U. R. Evans Conference on Localized Corrosion, Williamsburg, Virginia, USA, December 6–10, 1971; Staehle, R. W., Brown, B. F., Kruger, J., Agrawal, A., Eds.; National Association of Corrosion Engineers: Houston, Texas, USA, 1974; pp 353–362.
86. Smialowski, M.; Szklarska-Smialowska, Z.; Rychcik, M.; Szummer, A. *Corros. Sci.* **1969**, *9*, 123–125.
87. Wranglen, G. *Corros. Sci.* **1974**, *14*, 331–349.
88. Tokuda, T.; Ives, M. B. *Corros. Sci.* **1971**, *11*, 297–306.
89. Schatt, W.; Worch, H. *Corros. Sci.* **1971**, *11*, 623–629.
90. Suter, T.; Webb, E. G.; Böhni, H.; Alkire, R. C. *J. Electrochem. Soc.* **2001**, *148*, B174–B185.
91. Weinstein, S. *Tesis*; Universidad Nacional de Rosario: Argentina, 1975.
92. Kabanov, B.; Burstein, R.; Frumkin, A. In *Electrode Processes (Discussions of the Faraday Society, No 1, 1947)*; Reprinted by Butterworths: London, UK, 1961; pp 259–269.
93. Vetter, K. J.; Strehblow, H. H. In *Localized Corrosion*; U. R. Evans Conference on Localized Corrosion, Williamsburg, Virginia, USA, December 6–10, 1971; Staehle, R. W., Brown, B. F., Kruger, J., Agrawal, A., Eds.; National Association of Corrosion Engineers: Houston, Texas, USA, 1974; pp 240–251.
94. Galvele, J. R. In *Passivity and its Breakdown on Iron and Iron Base Alloys*; Staehle, R. W., Okada, H., Eds.; NACE: Houston, TX, 1976; pp 118–120.
95. Galvele, J. R. *J. Electrochem. Soc.* **1976**, *123*, 464–474.
96. Galvele, J. R. *Corros. Sci.* **1981**, *21*, 551–579.
97. Gravano, S. M.; Galvele, J. R. *Corros. Sci.* **1984**, *24*, 517–534.
98. Keitelman, A. D.; Gravano, S. M.; Galvele, J. R. *Corros. Sci.* **1984**, *24*, 535–545.
99. Vetter, K. J.; Strehblow, H. H. *Ber. Bunsen-Ges. Phys. Chem.* **1970**, *74*, 1024–1035.
100. Hunt, J. P. In *Metal Ions in Aqueous Solutions*; Benjamin: New York, 1963; pp 46–48.
101. Vetter, K. J. In *Electrochemical Kinetics*; Academic Press: New York, 1961; p 171.
102. Sillen, L. G.; Martell, A. E. In *Stability Constants of Metal-Ion Complexes, Special Publication No. 17*; The Chemical Society: London, 1964.
103. Sillen, L. G.; Martell, A. E. In *Stability Constants of Metal-Ion Complexes, Special Publication and Supplement 1, Special Publication 25*; The Chemical Society: London, 1964.
104. Smith, R. M.; Martell, A. E. In *Critical Stability Constants*; Plenum Press: New York, 1976; Vol. 4.
105. Newman, R. C.; Ajawi, M. A. A.; Ezuber, H.; Turgoose, S. *Corros. Sci.* **1988**, *28*, 471–477.
106. Frankel, G. S. *J. Electrochem. Soc.* **1998**, *145*, 2186–2198.
107. Uhlig, H. H. *J. Electrochem. Soc.* **1950**, *97*, 215C–220C.
108. Kolotyrkin, Ja. M. *J. Electrochem. Soc.* **1961**, *108*, 209–216.
109. Hoar, T. P.; Mears, D. C.; Rothwell, G. P. *Corros. Sci.* **1965**, *5*, 279–289.
110. Pryor, M. J. In *Localized Corrosion*; U. R. Evans Conference on Localized Corrosion, Williamsburg, Virginia, USA, December 6–10, 1971; Staehle, R. W., Brown, B. F., Kruger, J., Agrawal, A., Eds.; National Association of Corrosion Engineers: Houston, Texas, USA, 1974; pp 2–11.
111. Mc. Bee, C. L.; Kruger, J. In *Passivity and its Breakdown on Iron and Iron Base Alloys*; Staehle, R. W., Okada, H., Eds.; NACE: Houston, TX, 1976; pp 131–132.
112. Marcus, P.; Herbelin, J. M. *Corros. Sci.* **1993**, *34*, 1123–1145.
113. Szklarska-Smialowska, Z.; Viehhaus, H.; Janik-Czachor, M. *Corros. Sci.* **1976**, *16*, 649–652.

114. Janik-Czachor, M.; Kaszczyszyn, S. *Mater. Corros. (Werkst. Korros.)* **1982**, 33, 500–504.
115. Bardwell, J. A.; MacDougall, B.; Sproule, G. I. *J. Electrochem. Soc.* **1989**, 136, 1331–1336.
116. Lin, L. F.; Chao, C. Y.; Macdonald, D. D. *J. Electrochem. Soc.* **1981**, 128, 1194–1198.
117. Hoar, T. P. *Trans. Faraday Soc.* **1949**, 45, 683–693.
118. Wood, G. C.; Richardson, J. A.; Abd Rabbo, M. F.; Mapa, L. B.; Sutton, W. H. In *Passivity of Metals*; Proceedings of The Fourth International Symposium on Passivity, Warrenton, Virginia, USA, October 17–21, 1977; Frankenthal, R. P., Kruger, J., Eds.; The Electrochemical Society, Inc.: Princeton, New Jersey, USA, 1978; pp 973–988.
119. Videm, K. *The electrochemistry of uniform corrosion and pitting of aluminum, Kjeller Report KR-140*; Institut for Atomenergy: Kjeller, Norway, 1974.
120. MacDougall, B. J. *Electrochem. Soc.* **1979**, 126, 919–925.
121. Fromhold, A. T. In *Passivity and its Breakdown on Iron and Iron Base Alloys*; Staehle, R. W.; Okada, H., Eds.; NACE: Houston, TX, 1976; pp 161–164.
122. Sato, N. *Electrochim. Acta.* **1971**, 16, 1683–1692.
123. Sato, N. *J. Electrochem. Soc.* **1982**, 129, 255–260.
124. Galvele, J. R.; Torresi, M.; Carranza, R. M. *Corros. Sci.* **1990**, 31, 563–571.
125. Galvele, J. R. Analysis of the Critical Factors in Pit Initiation and Propagation, In Frankel, G. S., Newman, R. C., Eds.; *Proceedings of the Symposium on Critical Factors in Localized Corrosion*, The Electrochemical Society, Inc.: Pennington, NJ, 1992; pp 94–108.
126. Hisamatsu, Y.; Yoshii, T.; Matsumura, Y. In *Localized Corrosion*; U. R. Evans Conference on Localized Corrosion, Williamsburg, Virginia, USA, December 6–10, 1971; Staehle, R. W., Brown, B. F., Kruger, J., Agrawal, A., Eds.; National Association of Corrosion Engineers: Houston, Texas, USA, 1974; pp 427–436.
127. Forchhammer, P.; Engell, H. J. *Werkst. Korros.* **1969**, 20, 1–12.
128. Wood, G. C.; Sutton, W. H.; Richardson, J. A.; Riley, T. N. K.; Malherbe, A. G. In *Localized Corrosion*; U. R. Evans Conference on Localized Corrosion, Williamsburg, Virginia, USA, December 6–10, 1971; Staehle, R. W., Brown, B. F., Kruger, J., Agrawal, A., Eds.; National Association of Corrosion Engineers: Houston, Texas, USA, 1974; pp 526–546.
129. Okamoto, G.; Tachibana, K.; Nishiyama, S.; Sugita, T. In *Passivity and its Breakdown on Iron and Iron Base Alloys*; Staehle, R. W.; Okada, H., Eds.; NACE: Houston, TX, 1976; pp 106–109.
130. Frankel, G. S.; Stockert, L.; Hunkeler, F.; Boehni, H. *Corrosion* **1987**, 43, 429–436.
131. Pistorius, P. C.; Burstein, G. T. *Phil. Trans. R. Soc. Lond.* **1992**, 341, 531–559.
132. Williams, D. E.; Westcott, C.; Fleischmann, M. J. *Electrochem. Soc.* **1985**, 132, 1804–1811.
133. Williams, D. E.; Stewart, J.; Balkwill, P. H. *Corros. Sci.* **1994**, 36, 1213–1235.
134. Isaacs, H. S. *Corros. Sci.* **1989**, 29, 313–323.
135. Garfias-Mesias, L. F.; Sykes, J. M. *Corros. Sci.* **1999**, 41, 959–987.
136. Bertocci, U.; Koike, M.; Leigh, S.; Qui, F.; Yang, G. *J. Electrochem. Soc.* **1986**, 133, 1782–1786.
137. Pride, S. T.; Scully, J. R.; Hudson, J. L. *J. Electrochem. Soc.* **1994**, 141, 3028–3040.
138. Burstein, G. T.; Souto, R. M. *Electrochim. Acta.* **1995**, 40, 1881–1888.
139. Isaacs, H. S. In *Localized Corrosion*; U. R. Evans Conference on Localized Corrosion, Williamsburg, Virginia, USA, December 6–10, 1971; Staehle, R. W., Brown, B. F., Kruger, J., Agrawal, A., Eds.; National Association of Corrosion Engineers: Houston, Texas, USA, 1974; pp 158–167.
140. Isaacs, H. S.; Ishikawa, Y. *J. Electrochem. Soc.* **1985**, 132, 1288–1293.
141. Williams, D. E.; Westcott, C.; Fleischmann, M. J. *Electrochem. Soc.* **1985**, 132, 1796–1804.
142. Balkwill, P. H.; Wescott, C.; Williams, D. E. *Mater. Sci. Forum* **1989**, 44–45, 299–313.
143. Ezuber, H.; Newman, R. C. Growth Rate Distribution of Metastable Pits. In *Critical Factors in Localized Corrosion*; Frankel, G. S., Newman, R. C., Eds.; The Electrochemical Society Inc.: New Jersey, 1992; pp 120–133.
144. Moayed, M. H.; Newman, R. C. *Corros. Sci.* **2006**, 48, 1004–1018.
145. Pistorius, P. C.; Burstein, G. T. *Corros. Sci.* **1992**, 33, 1885–1897.
146. Burstein, G. T.; Pistorius, P. C.; Mattin, S. P. *Corros. Sci.* **1993**, 35, 57–62.
147. Pistorius, P. C.; Burstein, G. T. *Corros. Sci.* **1994**, 36, 525–538.
148. Laycock, N. J.; Newman, R. C. *Corros. Sci.* **1997**, 39, 1771–1790.
149. Burstein, G. T.; Vines, S. P. *J. Electrochem. Soc.* **2001**, 148, B504–B516.
150. Ilievare, G. O.; Burstein, G. T. *Corros. Sci.* **2001**, 43, 485–513.
151. Burstein, G. T.; Liu, C. *Corros. Sci.* **2007**, 50, 2–7.
152. Stewart, J.; Williams, D. E. *Corros. Sci.* **1992**, 33, 457–463.
153. Qvarfort, R. *Corros. Sci.* **1988**, 28, 135–140.
154. Alvarez, M. G.; Galvele, J. R. In *IV Reunión Latinoamericana de Electroquímica y Corrosión*; Caracas: Venezuela, 1979.
155. Carranza R. M. Rodríguez M. A. Environmental and Geometrical Conditions to Sustain Crevice Corrosion in Alloy 22, NACE 2007, National Association of Corrosion Engineers, October 31–November 3, Las Vegas, Nevada Paper No 08175.
156. Brigham, R. J.; Tozer, E. W. *Corrosion* **1973**, 29, 33–36.
157. ASTM-G150–99. *Standard Test Method for Electrochemical Critical Pitting Temperature Testing of Stainless Steels*; American Society of Testing and Materials, 1999; pp 638–649.
158. Qvarfort, R. *Corros. Sci.* **1989**, 29, 987–993.
159. Arvig, P. E.; Bisgard, A. D. *Paper No 437 presented at Corrosion'96*; National Association of Corrosion Engineers: Houston, Texas, USA, 1996.
160. Jakobsen, P. T.; Maahn, E. *Corros. Sci.* **2001**, 43, 1693–1709.
161. Deng, B.; Jiang, Y.; Liao, J.; Hao, Y.; Zhong, Ch.; Li, J. *Appl. Surf. Sci.* **2007**, 253, 7369–7375.
162. Moayed, M. H.; Laycock, N. J.; Newman, R. C. *Corros. Sci.* **2003**, 45, 1203–1216.
163. Salinas-Bravo, V. M.; Newman, R. C. *Corros. Sci.* **1994**, 36, 67–77.
164. Ernst, P.; Newman, R. C. *Corros. Sci.* **2002**, 44, 927–941.
165. Ernst, P.; Newman, R. C. *Corros. Sci.* **2002**, 44, 943–954.



## 2.05 Dealloying

**R. C. Newman**

University of Toronto, Department of Chemical Engineering and Applied Chemistry, 200 College Street, Toronto, Ontario M5S 3E5, Canada

© 2010 Elsevier B.V. All rights reserved.

2.05.1	Introduction and Background	802
2.05.1.1	Definition of Dealloying	802
2.05.1.2	Use of Dealloying to Make Interesting Nanomaterials	802
2.05.1.3	History of Dealloying	802
2.05.1.4	Dealloying of Industrial Alloys	802
2.05.2	Mechanisms of Dealloying	804
2.05.2.1	Transport of the More Noble Metal	804
2.05.2.2	Potential Dependence of Dealloying and the Critical Potential	804
2.05.2.3	Order and Disorder	806
2.05.2.4	Ternary Element Effects	807
2.05.2.5	Why does Brass Dealloy at 20% Zinc?	807
2.05.3	Dealloying in Stress Corrosion Cracking	807
2.05.4	Summary and Future Prospects	808
References		808

### Glossary

**Critical potential for dealloying** Potential above which nanoporosity is formed and the rate of dealloying levels out with time rather than decaying to a very low value.

**High-density site percolation threshold** A site percolation threshold with the additional requirement that all sites forming a percolation path have at least  $m$  like-neighbors, where  $m > 2$ . Written as  $p_c(m)$ .

**Parting limit** Atom fraction of less-noble element in a binary solid–solution alloy below which dealloying does not occur, irrespective of how oxidizing is the potential. Usually lies in the range 0.5–0.6; can sometimes be *ca.* 0.2, for example in  $\alpha$ -brass.

**Percolation theory** Mathematical theory, applied to more-or-less disordered geometrical systems, that deals with the statistics of interconnection of sites or bonds with a specified property (e.g., for a binary metallic solid solution the relevant property is atom identity and the relevant version of the theory is lattice-site percolation).

**Site percolation threshold** Fractional occupancy of sites, usually on a lattice, by a particular

type of entity (e.g., atom of one kind in a binary solid solution) at which long-range connectivity of such sites appears. Written as  $p_c(\text{site})$ .

### Abbreviations

**NAB** Nickel–aluminum bronze

**SCC** Stress corrosion cracking

### Symbols

***a*** Atom diameter or spacing (m)

***b<sub>a</sub>*** Anodic Tafel coefficient (V)

***D<sub>s</sub>*** Surface diffusion coefficient ( $\text{m}^2 \text{s}^{-1}$ )

***E<sub>0</sub>*** Equilibrium metal–metal ion electrode potential (nonstandard metal ion activity)

***E<sub>c</sub>*** Critical potential for dealloying (V)

***F*** Faraday's constant ( $\text{C mol}^{-1}$ )

***i*** Anodic current density ( $\text{A m}^{-2}$ )

***i<sub>0</sub>*** Exchange current density ( $\text{A m}^{-2}$ )

***j*** Diffusion flux ( $\text{mol m}^{-2} \text{s}^{-1}$ )

***p*** Atom fraction in a solid solution alloy

***p\**** The parting limit, expressed as an atom fraction

***S*** Excess interfacial energy per volume of a nanoscale pit in an alloy surface ( $\text{J m}^{-3}$ )

$\eta_{th}$  Thermodynamic shift in equilibrium electrode potential due to curvature (V)  
 $\gamma$  Solid–liquid interfacial energy ( $\text{J m}^{-2}$ )  
 $\Omega$  Molar volume ( $\text{m}^3$ )  
 $\xi$  Blob size or percolation backbone dimension in percolation theory (m)

## 2.05.1 Introduction and Background

### 2.05.1.1 Definition of Dealloying

Dealloying is the selective electrolytic dissolution of a less-noble element from a metallic solid solution or intermetallic compound. The product of this dissolution, which usually requires an oxidizing acidic solution, is a nanoporous metal consisting mostly of more noble element(s). **Figure 1** show the morphology usually seen in dealloyed noble-metal alloys: an interconnected ligament/pore structure with nearly zero net curvature. The size scale of the porosity in these pictures is typical for silver–gold alloys dealloyed in perchloric acid; the more common nitric acid immersion usually gives a larger pore size.

### 2.05.1.2 Use of Dealloying to Make Interesting Nanomaterials

Recently, there has been a resurgence of interest in dealloying,<sup>1–3</sup> driven by potential technological applications and the remarkable properties of the nanoporous products such as near-theoretical strength in compression,<sup>4</sup> a size-scale-dependent elastic modulus,<sup>5</sup> and under a particular alloy composition and dealloying procedure, the formation of a material with an unusual combination of exceptionally low modulus and relatively good mechanical integrity.<sup>6</sup> Many potential applications of dealloyed materials are under investigation, particularly, in the areas of catalysis<sup>7–9</sup> and sensing.<sup>10,11</sup> Metal foils that are dealloyed, on one side, show potential-dependent bending in electrolytes due to surface stress effects and are thought to have potential as microactuators.<sup>12</sup> This literature is quite different from that which is concerned with dealloying as a corrosion problem.

### 2.05.1.3 History of Dealloying

Dealloying is an ancient technology, and was used by several civilizations to gild the surfaces of objects that

were made mainly of copper and/or silver.<sup>13</sup> Such treatments generally involved the application of heat as well as chemical attack, and the resulting surface would have had a good luster due to some consolidation or coarsening of the nanoporous material – an important factor, because ordinary dealloying performed at room temperature gives a brittle, brownish product. There appears to have been a spectrum of techniques, ranging from true dealloying (with a liquid, but not necessarily very aqueous, environment present on the metal throughout) to a dry-oxidation/ aqueous oxide-dissolution cycle. A closely related use of dealloying was for a more macroscopic separation or ‘parting’ of metals – this was also done by a kind of pack cementation, where, for silver–gold alloys, silver was converted into silver chloride by salt, acid, oxidant, and heat. Later – at an uncertain date, some time in the early 1500s – nitric acid first came into use. But, before that, reagents that contained nitric acid had been invented. There are several different recipes in the *Codex Atlanticus* (ca. 1508) on the use of saltpeter (potassium nitrate) as the source of the nitrate ions (Leonardo da Vinci may have written these recipes himself, but they are not in his usual mirror writing).<sup>13</sup> Since then, nitric acid has been the preferred reagent for dealloying of gold alloys.<sup>14</sup>

The key discovery about the parting of gold alloys was that the less-noble metal or metals had to be present above a certain percentage; otherwise, there was no dealloying. So, if one has, say, an alloy with 40 at.% silver and 60 at.% gold, one has to melt it with more silver so that the silver content exceeds ~60 at.%. This discovery may be very ancient, and the ‘parting limit’ was the most striking feature of dealloying. We will return to the parting limit (or rather limits, because there is another one near 20%) later on.

### 2.05.1.4 Dealloying of Industrial Alloys

Dealloying is also a major corrosion problem in industrial alloys – not so much in itself, as a mechanism of general deterioration, but for its role in stress corrosion cracking (SCC). Dezincification of brass must have been noticed in Roman times; but, the first scientific records date from the early twentieth century, when this was a severe problem affecting  $\alpha$ -brass seawater condenser tubes.<sup>15–17</sup> Bengough and May first systematized the addition of arsenic (in amazingly small amounts, less than 0.05 wt%) for dezincification resistance.<sup>18</sup> Another remedial method, more rarely applied, was to reduce the zinc content to below

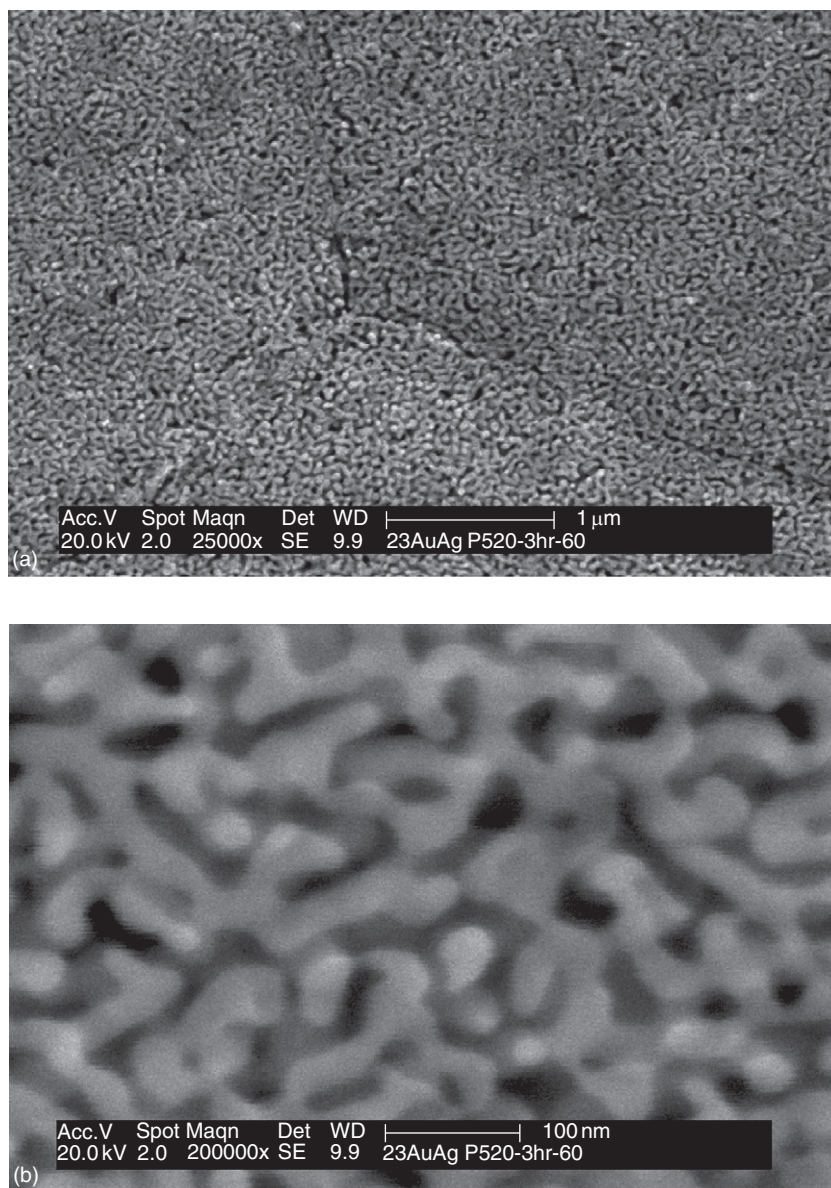


**Figure 1** Morphology of Ag–Au alloys dealloyed in perchloric acid showing an interconnected ligament/pore structure with nearly zero net curvature. (a) Reproduced from Senior, N. A.; Newman, R. C. *Nanotechnology* **2006**, 17, 2311–2316. (b) Reproduced from Senior's PhD thesis (University of Manchester, ca. 2005).

20%; but, this adversely affected other properties including general corrosion resistance.  $\beta$ -Brass is more susceptible than  $\alpha$ -brass, as one would expect given its higher zinc content. More recently, other copper alloys such as nickel–aluminum bronze (NAB) have shown dealloying,<sup>19</sup> but these are more complex systems as they are usually multiphase. Dealloying has occurred, but rarely, in various other commercial solid-solution alloys that satisfy the basic

compositional requirement. Alloys used as thin films for magnetic or other applications could potentially suffer from atmospheric dealloying.

There are analogous phenomena that occur in gaseous environments, or in vacuum where one element is volatile.<sup>20</sup> For the most part, these appear to involve lattice diffusion, which places them apart from normal electrolytic dealloying, where transport is by surface diffusion, as discussed below.

## 2.05.2 Mechanisms of Dealloying

### 2.05.2.1 Transport of the More Noble Metal

Historically, three types of mechanisms have been proposed to explain how two alloying constituents, intermixed on an atomic scale, can be separated so effectively by electrolytic action. Perhaps the most obvious is that the dissolution is not really selective at all, but that both elements dissolve, then one replates. But, while there is some evidence that this may occur – very locally – during dezincification of brass,<sup>21</sup> it is clearly not operating in the more general case. The second mechanism, promoted by Pickering and Wagner, involves divacancy injection and room-temperature lattice diffusion of these vacancies.<sup>20,22,23</sup> This appears to be inconsistent with the rapid kinetics of dealloying, but as Pickering pointed out, it would account for the common observation of a significant residue of less-noble metal in the dealloyed material, whereas (in his opinion at the time) it would appear impossible that any less-noble metal could survive at such high anodic overpotentials. Later, Pickering rationalized this by postulating a large IR potential drop within the porous structure, so that the overpotential was actually small at the corrosion front.<sup>24</sup> Apart from graded solid solution compositions, he also observed intermediate phase formation in dealloyed  $\epsilon$ -brass by X-ray diffraction.<sup>25</sup> (Remarkably, this exact experiment was first reported in 1933!<sup>26</sup>) This strongly impressed Pickering with the necessity of postulating some bulk diffusion mechanism.

Recently, most authors have preferred to appeal to surface diffusion as the operative transport mechanism for the more noble metal (the intermediate-phase problem has not, to our knowledge, been addressed from this standpoint and would make an interesting study). A.J. Forty and his group made transmission electron microscopy (TEM) observations of the early stages of porosity formation in silver–gold alloys immersed in nitric acid, and developed a model for the parting limit based on surface diffusion and filling of incipient pores.<sup>27–33</sup> They were also very interested in the formation of gold oxide during dealloying, something that affects the mobility of the gold. Sieradzki *et al.*<sup>34</sup> carried out atomistic Monte Carlo simulations of dealloying and reproduced several of the main features including parting limits, which were ascribed (not quite accurately in the case of the ‘55%’ threshold) to site percolation thresholds in the lattice. Erlebacher developed a much more sophisticated simulation scheme, focusing mainly on morphology, kinetics, and potential dependence.<sup>35</sup>

There may be a niche for bulk diffusion as a partial explanation of the volume shrinkage (a few percent to almost 30%) that occurs during dealloying of silver–gold alloys, but some kind of plastic contraction is almost certainly involved.<sup>36</sup>

### 2.05.2.2 Potential Dependence of Dealloying and the Critical Potential

Pickering made comprehensive studies of the electrode potential dependence of dealloying, and the *critical potential* for dealloying ( $E_c$ ). These experiments did not give a meaningful  $E_c$  for  $\alpha$ -brass because copper dissolution intervened<sup>25</sup>; but, in binary gold alloys, he observed the now-famous shape of curve shown in **Figure 2**. Up to a certain potential ( $E_c$ ), the current density is low and almost potential independent; then it increases steeply at  $E_c$ .<sup>29</sup> Uniform nanoporosity forms only above  $E_c$ , although Pickering often referred to ‘pitting’ or localized porosity below  $E_c$ .<sup>37</sup> As more gold is added to the alloy,  $E_c$  increases until, at the parting limit, only the flat, ‘passive’ region is observed. Up to a certain gold content, this behavior was reproduced, with good quantitative agreement with experiment, by Erlebacher’s simulations.<sup>35</sup> Then, a small refinement (prohibition of dissolution of atoms with 10 or 11 neighbors) reproduced the experimentally observed ‘55%’ parting limit almost exactly<sup>38</sup> – **Figure 3**. It was shown that this was close, but not identical, to a high-density percolation threshold for the lattice.<sup>39</sup> The effect of varying the surface diffusion kinetics was surprisingly small – a few percent – **Figure 4**.

Recently, there has been much discussion of the true value and meaning of  $E_c$ . In 1993, Sieradzki gave a model for  $E_c$  based on two effects: thermodynamic (necessity of dissolving less-noble metal from very small clusters of atoms, thus creating a gold surface with very high curvature) and kinetic (necessity of dissolving these atoms at a certain *rate* to avoid infilling by surface diffusion of gold).<sup>40</sup> More recently, it is proposed that an intrinsic critical potential can be identified, in simulation and experiment, that corresponds only to the thermodynamic (curvature) effect.<sup>35,41–43</sup>

A simplified version of Sieradzki’s original model can be written down in a few lines. The random arrangement of atoms in the solid solution can be characterized,<sup>44</sup> in the language of percolation theory, as a ‘blob and string’ arrangement – ‘blobs’ are regions where, statistically, one kind of atom (say, Ag in Ag–Au) is densely clustered, while the ‘strings’ are chains of Ag atoms joining the blobs together.



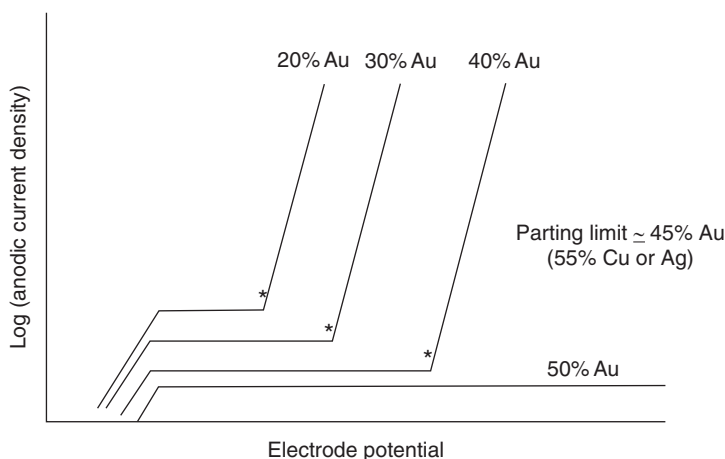


**Figure 2** Schematic anodic dissolution behavior of a silver-gold or copper-gold alloy undergoing dealloying in a nonoxidizing aqueous acid, showing critical potentials for nanoporosity generation (\*) and the inability to form nanoporosity when the silver or copper content falls below the parting limit.

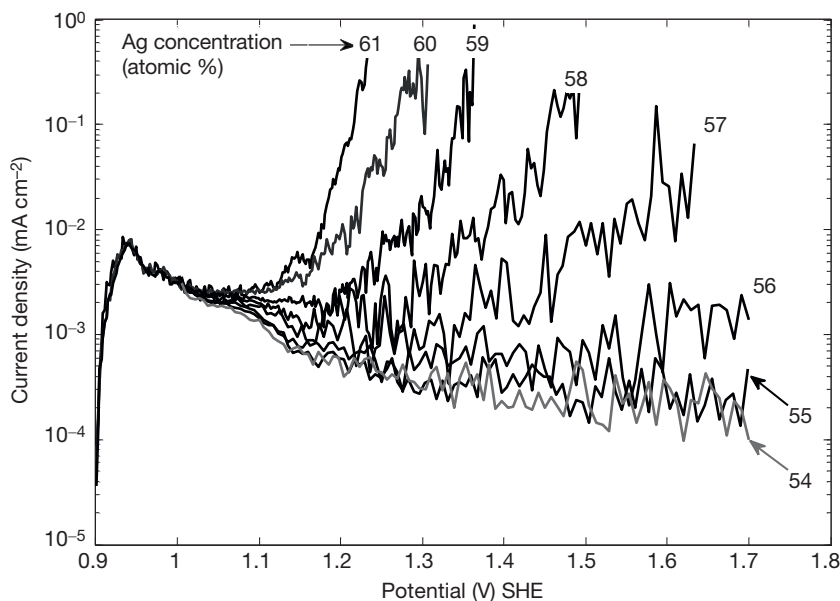


**Figure 3** Dynamic current-voltage curves generated by the modified MESOSIM code for the indicated Ag contents in Ag-Au (at. %). Dissolution from 10- and 11-coordinated sites is prohibited. Potential ramping rate is  $2 \text{ mV s}^{-1}$ . Reproduced from Artymowicz, D. M.; Newman, R. C.; Erlebacher, J. *Philos. Mag.* **2009**, *89*, 1663–1693.

Another name for the ‘blob’ size is the percolation backbone diameter. We call this quantity  $\xi$ . This can be shown to be approximately given by

$$\xi = \frac{1+p}{1-p} \quad [1]$$

in units of atom diameters ( $a$ ), where  $p$  is the atom fraction of the less-noble element (Ag).

So, the initial surface of the alloy can be considered to be intersected by numerous blobs of Ag that,

when dissolved, create tiny pits with highly curved Au surfaces. These surfaces have a solid-liquid interfacial free energy  $\gamma$ . The excess interfacial energy  $S$  per unit volume of a hemispherical pit created by the dissolution of a typical ‘blob’ (diameter  $\xi a$ , radius  $\xi a/2$ ) is

$$S = \frac{2\gamma}{\xi a/2} = \frac{4\gamma}{\xi a} \quad [2]$$

(neglecting the slight difference in  $\gamma$  that must exist between the gold-rich pit and the original alloy



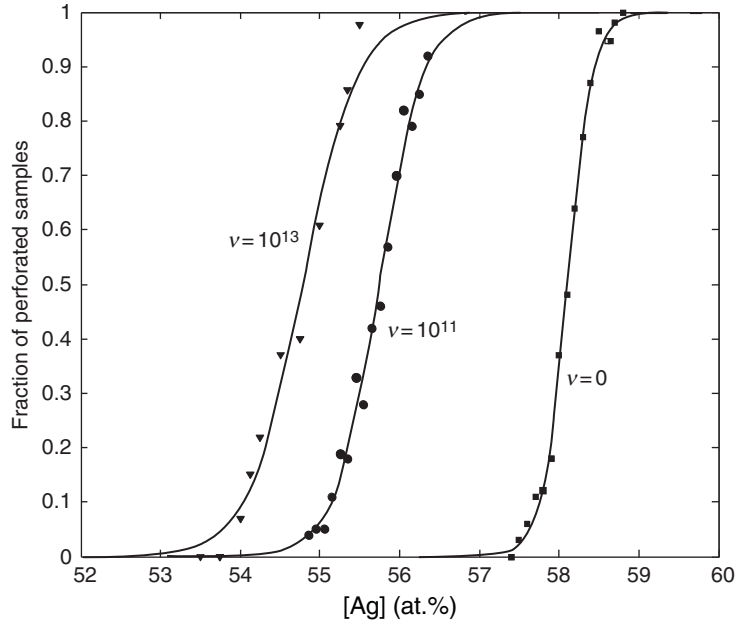


**Figure 4** Fraction of samples perforated by dealloying as a function of the 'Ag' content with dissolution of 10- and 11-coordinated atoms prohibited and surface diffusivity set to high, intermediate and negligible values, by changing  $v$ . Samples were 100 atomic layers thick and simulations run for a maximum time of  $10^5$  s. Perforation was defined as dissolution of the first atom from the bottom layer. Simulations stopped at perforation or when the elapsed time exceeded  $10^5$  s.  $v$  is the value of the pre-exponential constant  $v_{\text{diffusion}}$  in eqn [1]. Reproduced from Artymowicz, D. M.; Newman, R. C.; Erlebach, J. *Philos. Mag.* **2009**, 89, 1663–1693.

surface.) So, if we multiply  $S$  by the molar volume  $\Omega$ , we obtain the energy per mole. Dividing by Faraday's constant gives us a shift in the equilibrium electrode potential,  $\eta_{\text{th}}$ , for the Ag that was in the pit compared with ordinary bulk Ag:

$$\eta_{\text{th}} = \frac{S\Omega}{F} = \frac{4\gamma\Omega}{F\xi a} \quad [3]$$

This shift is positive, so it represents a thermodynamic contribution to the difference between the ordinary Ag equilibrium potential and the critical potential. So, for  $p > p^*$ , where  $p^*$  is the parting limit ( $\approx 0.55$ ),

$$\eta_{\text{th}} = \frac{4\gamma\Omega(1-p)}{Fa(1+p)} \quad [4]$$

This agrees quite well with observation for Au and Pt alloys, provided that the  $E_{\text{crit}}$  value for the former is measured extremely slowly, to give a so-called intrinsic critical potential. To have easy dealloying, though, it is necessary for the *rate* of dissolution of the Ag blob to exceed the rate at which the pit is infilled by surface diffusion of Au. This requires an additional overpotential  $\eta_k$  that can be written as

$$\eta_k = b_a \log \frac{i}{i_0} \quad [5]$$

with  $i$  being equated to the flux of Au diffusing into the pit at the critical potential (Sieradzki used a linearized kinetic expression rather than this Tafel version). This flux  $j$  is given by a Fickian steady-state diffusion flux of the form

$$j = \frac{\alpha D_s}{\Omega \xi a} \quad [6]$$

where  $\alpha$  is a geometrical coefficient and  $D_s$  the surface diffusivity of Au. So  $\eta_k$  is given by

$$\eta_k = b_a \log \frac{\alpha F D_s (1-p)}{\Omega (1+p) a i_0} \quad [7]$$

and the critical potential  $E_c$  is given by

$$E_c = E_0 + \frac{4\gamma\Omega(1-p)}{Fa(1+p)} + b_a \log \frac{\alpha F D_s (1-p)}{\Omega (1+p) a i_0} \quad [8]$$

### 2.05.2.3 Order and Disorder

Most studies of dealloying have used more or less disordered binary alloys, but comparison of ordered and disordered material have been made for the copper–gold system. The finding is that dealloying is more difficult (requires a higher potential) in the

ordered material.<sup>45</sup> This can be explained by considering the connectivity of less-noble metal atoms in the lattice – the disordered alloy has a cluster structure in which less-noble atoms comprising the dissolution path have many like neighbors, facilitating penetration of the electrolyte.

#### 2.05.2.4 Ternary Element Effects

Ternary element effects in dealloying are both intriguing and practically important. A long time ago, it was suggested that the beneficial effect of arsenic in brass was associated with the blocking of step edges, slowing down the surface diffusion of copper<sup>21,46</sup>; this stops macro-dealloying, but can be detrimental for SCC resistance, as explained below – very fine porosity makes for brittle behavior. Lately, Erlebacher has explored the behavior of Ag–Au–Pt alloys, which show a refined porosity compared with Ag–Au, for possible applications.<sup>47</sup>

#### 2.05.2.5 Why does Brass Dealloy at 20% Zinc?

So why do some alloys show dealloying at the fcc site percolation threshold (20 at.%), while others require 55% of less-noble element? The conditions for dezincification of  $\alpha$ -brass are quite specific – corrosion has to proceed for some time (usually in an aerated chloride solution), then dealloying starts under the resulting porous corrosion product – an extremely old observation. Lucey,<sup>48,49</sup> and later Newman *et al.*,<sup>21</sup> gave different variants of the same explanation – there is an enrichment of copper ions (Lucey referred to solid  $\text{CuCl}$ ) under the corrosion product, then the conditions become very close to *equilibrium* for the copper, and the exchange current density somehow enhances the mobility of copper, exposing more zinc for dissolution (but still respecting the site percolation threshold). Newman *et al.*<sup>21</sup> showed that dezincification could be monitored electrochemically at the equilibrium potential of a copper electrode in solutions containing  $\text{CuCl}_2^-$ , which is the dissolution product of Cu in chloride solutions. An example of one of their dezincified samples is shown in **Figure 5** – in industrial parlance this would be called ‘plug’ or localized type dezincification.

### 2.05.3 Dealloying in Stress Corrosion Cracking

The role of dealloying in SCC is an old subject of discussion. For binary gold alloys, the correlation

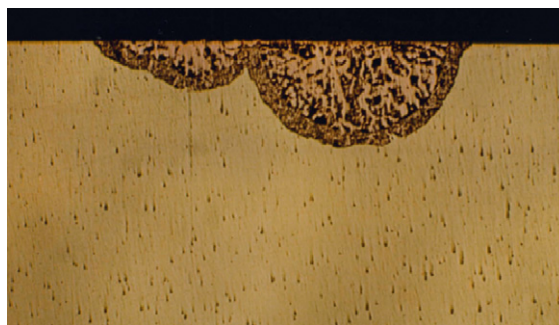


**Figure 5** Plug-type dezincification in  $\alpha$ -brass. Reproduced from Newman, R. C.; Shahrabi, T.; Sieradzki, K. *Corros. Sci.* **1988**, 28, 873–886.

between the two is transparent,<sup>50</sup> but the actual mechanism of crack growth (and this may be different for intergranular and transgranular SCC) remains controversial. According to Sieradzki and Newman,<sup>50</sup> both forms of SCC require only a thin dealloyed layer, which triggers a brittle substrate microcrack; such crack jumps in fcc metals are impossible according to traditional mechanics, but evidence for the phenomenon has mounted – it is especially easy to demonstrate for the intergranular variant in silver–gold alloys,<sup>51–54</sup> but also for brass in ammonia.<sup>55</sup> Even those who prefer another microscopic mechanism admit a very high crack velocity, for example,  $20 \text{ mm s}^{-1}$ , in the case of silver–gold, which cannot be rationalized by any continuous-dissolution type of mechanism.<sup>56</sup>

The important industrial alloys where dealloying has been blamed for SCC are austenitic and duplex stainless steels (in hot chloride, chloride– $\text{H}_2\text{S}$ , or caustic solutions) and copper alloys including  $\alpha$ -brass (traditionally in aqueous ammonia but also in simple solutions like copper sulfate). These are more challenging to study, because there is always some simultaneous oxidation of all the alloy components, and the dealloyed layers are thin.<sup>57</sup> A key finding was that the compositional dependences of dealloying and transgranular SCC in brass, exposed to a solution with which copper is equilibrated, are identical.<sup>58</sup> Research on stainless steels using caustic solutions, where nickel is the ‘noble’ metal,<sup>59</sup> has led to another current thread of study in noble-metal alloys – namely the ability to produce a nanoporous dealloyed layer at very low contents of noble metal. If the anodic overpotential is small enough, dealloying can occur in an alloy with only a percent or two of noble metal, and a nanoporous layer can be produced whose composition is not far removed from that of the original alloy.

## 2.05.4 Summary and Future Prospects

At the time of writing (Spring 2009) we are in the midst of a flood of new literature on dealloying. Over the next few years, practical applications of nanoporous metals (catalysts, sensors, actuators, etc.) will flourish. In turn, long-standing practical corrosion phenomena will be illuminated, especially with regard to the micromechanisms of SCC. We can anticipate that practically every case of SCC in solid-solution alloys will be understood better, and improved preventive measures devised, now that such a wide range of new techniques and concepts is being brought to bear upon the properties and applications of nanoporous metals. Corrosion is just like any other subject – it tends to grow at its interfaces with other disciplines. Also, its standing in the wider scientific community grows with the variety of scientists from remote fields who become interested in corrosion phenomena. Just to give one example, attempts by the author to understand the role of minor alloying elements in dealloying and SCC (arsenic in brass; phosphorus in austenitic stainless steel<sup>46</sup>) were quite primitive at the time, but are now of renewed interest with the discovery of ternary Au–Ag–Pt alloys that show very stable nanoporosity.<sup>47</sup> Also, corrosion scientists can contribute to solving new problems that will come with new technologies. When we start to use nanoporous metals in devices, or alloy nanoparticles as electrocatalysts, a range of new corrosion issues will arise, such as the gradual dissolution of residual less-noble metal that may be essential for the desired function (a Pt–Co alloy is under consideration for hydrogen fuel-cell cathode catalyst formulations, and some candidate alloy electrocatalysts are being made by dealloying).

## References

- Weissmueller, J.; Newman, R. C.; Jin, H. J.; Hodge, A. M.; Kysar, J. W. *MRS Bull.* **2009**, 34, 577–586.
- Schofield, E. *Transact. Inst. Metal Finish.* **2005**, 83, 35–42.
- Newman, R. C.; Corcoran, S. G.; Erlebacher, J.; Aziz, M. J.; Sieradzki, K. *MRS Bull.* **1999**, 24, 24–28.
- Volkert, C. A.; Lilleodden, E. T.; Kramer, D.; Weissmueller, J. *Appl. Phys. Lett.* **2006**, 89, 061920.
- Mathur, A.; Erlebacher, J. *Appl. Phys. Lett.* **2007**, 90, 061910.
- Senior, N. A.; Newman, R. C. *Nanotechnology* **2006**, 17, 2311–2316.
- Xu, C. X.; Su, J. X.; Xu, X. H.; Liu, P. P.; Zhao, H. J.; Tian, F.; Ding, Y. *J. Am. Chem. Soc.* **2007**, 129, 42–43.
- Zeis, R.; Mathur, A.; Fritz, G.; Lee, J.; Erlebacher, J. *J. Power Sources* **2007**, 165, 65–72.
- Zeis, R.; Lei, T.; Sieradzki, K.; Snyder, J.; Erlebacher, J. *J. Catal.* **2008**, 253, 132–138.
- Qian, L. H.; Yan, X. Q.; Fujita, T.; Inoue, A.; Chen, M. W. *Appl. Phys. Lett.* **2007**, 90, 153120.
- Yu, F.; Ahl, S.; Caminade, A. M.; Majoral, J. P.; Knoll, W.; Erlebacher, J. *Analyt. Chem.* **2006**, 78, 7346–7350.
- Kramer, D.; Viswanath, R. N.; Weissmueller, J. *Nano Lett.* **2004**, 4, 793–796.
- Reti, L. *Isis* **1965**, 56, 307–319.
- Seath, J.; Beamish, F. E. *Ind. Eng. Chem. Analyt. Ed* **1938**, 10, 639–641.
- Bengough, G. D. *J. Inst. Met.* **1922**, 27, 51–72.
- Bengough, G. D.; Jones, R. M. *J. Inst. Met.* **1913**, 10, 13–118.
- Gibbs, W. E. *Transact. Faraday Soc.* **1916**, 11, 2–3.
- Bengough, G. D.; May, R. J. *Inst. Met.* **1924**, 32, 81–269.
- Lenard, D. R.; Bayley, C. J.; Noren, B. A. *Corrosion* **2008**, 64, 764–772.
- Pickering, H. W.; Kim, Y. S. *Corros. Sci.* **1982**, 22, 621–635.
- Newman, R. C.; Shahrabi, T.; Sieradzki, K. *Corros. Sci.* **1988**, 28, 873–886.
- Pickering, H. W. *J. Electrochem. Soc.* **1968**, 115, 143–147.
- Pickering, H. W.; Wagner, C. J. *Electrochem. Soc.* **1967**, 114, 698–706.
- Pickering, H. W. *Mater. Sci. Eng. A* **1995**, 198, 213–223.
- Pickering, H. W. *J. Electrochem. Soc.* **1970**, 117, 8–15.
- Stillwell, C. W.; Turnipseed, E. S. *Phys. A. J. Gen. Appl. Phys.* **1933**, 4, 263.
- Forty, A. J.; Durkin, P. *Philos. Mag. A* **1980**, 42, 295–318.
- Forty, A. J. *Nature* **1979**, 282, 597–598.
- Forty, A. J. *Philos. Mag. A* **1982**, 46, 521–530.
- Forty, A. J. *Gold Bull.* **1981**, 14(1), 25–35.
- Forty, A. J.; Rowlands, G. *Philos. Mag. A* **1981**, 43, 171–188.
- Durkin, P.; Forty, A. J. *Philos. Mag. A* **1982**, 45, 95–105.
- Smith, D. J.; et al. *Inst. Phys. Conf. Series* **1982**, 61, 483–486.
- Sieradzki, K.; Corderman, R. R.; Shukla, K.; Newman, R. C. *Philos. Mag. A* **1989**, 59, 713–746.
- Erlebacher, J. *J. Electrochem. Soc.* **2004**, 151, C614–C626.
- Parida, S.; Kramer, D.; Volkert, C. A.; Rosner, H.; Erlebacher, J.; Weissmueller, J. *Phys. Rev. Lett.* **2006**, 97, 035504.
- Fritz, J. D.; Pickering, H. W. *J. Electrochem. Soc.* **1991**, 138, 3209–3218.
- Artymowicz, D. M.; Newman, R. C.; Erlebacher, J. *Electrochem. Soc. Transact.* **2006**, 3(31), 499–506.
- Artymowicz, D. M.; Newman, R. C.; Erlebacher, J. *Philos. Mag.* **2009**, 89, 1663–1693.
- Sieradzki, K. *J. Electrochem. Soc.* **1993**, 140, 2868–2872.
- Rugolo, J.; Erlebacher, J.; Sieradzki, K. *Nat. Mater.* **2006**, 5, 946–949.
- Dursun, A.; Pugh, D. V.; Corcoran, S. G. *J. Electrochem. Soc.* **2005**, 152, B65–B72.
- Dursun, A.; Pugh, D. V.; Corcoran, S. G. *Electrochem. Solid State Lett.* **2003**, 6, B32–B34.
- Erlebacher, J.; Aziz, M. J.; Karma, A.; Dimitrov, N.; Sieradzki, K. *Nature* **2001**, 410, 450–453.
- Parks, B. W., Jr; Fritz, J. D.; Pickering, H. W. *Scr. Metall.* **1989**, 23, 951–956.
- Newman, R. C. *Corros. Sci.* **1992**, 33, 1653–1657.
- Snyder, J.; Asanithi, P.; Dalton, A. B.; Erlebacher, J. *Adv. Mater.* **2008**, 20, 4883–4886.
- Lucey, V. F. *Br. Corros. J.* **1965**, 1(2), 53–59.
- Lucey, V. F. *Br. Corros. J.* **1965**, 1(1), 9–14.
- Sieradzki, K.; Newman, R. C. *J. Phys. Chem. Solids* **1987**, 48, 1101–1113.

- 
51. Kelly, R. G.; Frost, A. J.; Shahrabi, T.; Newman, R. C. *Metall. Trans. A* **1991**, 22A, 531–541.
  52. Saito, M.; Smith, G. S.; Newman, R. C. *Corros. Sci.* **1993**, 35, 411–416.
  53. Friedersdorf, F.; Sieradzki, K. *Corrosion* **1996**, 52, 331–336.
  54. Barnes, A.; Senior, N. A.; Newman, R. C. *Metall. Trans. A* **2009**, 40, 58–68.
  55. Newman, R. C.; Shahrabi, T.; Sieradzki, K. *Scr. Metall.* **1989**, 23, 71–74.
  56. Serebrinsky, S. A.; Galvele, J. R. *Corros. Sci.* **2004**, 46, 591–612.
  57. Newman, R. C.; Corderman, R. R.; Sieradzki, K. *Br. Corros. J.* **1989**, 24, 143–148.
  58. Sieradzki, K.; Kim, J. S.; Cole, A. T.; Newman, R. C. *J. Electrochem. Soc.* **1987**, 134, 1635–1639.
  59. Deakin, J.; Dong, Z. H.; Lynch, B.; Newman, R. C. *Corros. Sci.* **2004**, 46, 2117–2133.

## 2.06 Intergranular Corrosion

**D. L. Engelberg**

Materials Performance Centre, The Mill/A11, School of Materials, University of Manchester, P.O. Box 88, Sackville Street, Manchester M60 1QD, UK

© 2010 Elsevier B.V. All rights reserved.

<b>2.06.1</b>	<b>Nature of Intergranular Corrosion</b>	810
2.06.1.1	Theories of Intergranular Corrosion	811
2.06.1.2	Metallurgical Aspects	812
2.06.1.3	Grain Boundary Structure and Networks	812
2.06.1.4	Grain Boundary Susceptibility	813
<b>2.06.2</b>	<b>Intergranular Corrosion of Metals and Alloys</b>	814
2.06.2.1	Aluminum Alloys	814
2.06.2.2	Stainless Steels	815
2.06.2.2.1	Sensitization of austenitic stainless steel	815
2.06.2.2.2	Prevention of sensitization	817
2.06.2.2.3	Weld decay and knife line attack	818
2.06.2.2.4	Ferritic, martensitic, duplex, and precipitation hardening stainless steels	818
2.06.2.3	Nickel and Nickel Alloys	819
2.06.2.4	Other Metals and Alloys	820
<b>2.06.3</b>	<b>Intergranular Corrosion Testing</b>	820
2.06.3.1	Standard Practices and Test Methods	820
2.06.3.2	Microstructure Screening	823
2.06.3.3	Degree of Sensitization Testing	823
<b>References</b>		826

### Abbreviations

**CSL** Coincidence site lattice  
**DOF** Degree of freedom  
**FCC** Face centered cubic  
**GB** Grain boundary  
**HAZ** Heat affected zone  
**IGA** Intergranular attack  
**IGC** Intergranular corrosion  
**NHE** Normal hydrogen electrode  
**SCE** Saturated calomel electrode  
**TTP** Time–temperature–precipitation  
**UVW** Miller indices

### Symbols

***E*** Potential (V)  
***i*** Current density ( $\text{A cm}^{-2}$ )  
***t*** Time (s)  
***O*** Charge density ( $\text{C cm}^{-2}$ )  
 **$\theta$**  Rotation angle ( $^{\circ}$ )

### 2.06.1 Nature of Intergranular Corrosion

Intergranular corrosion (IGC) is a form of localized corrosion that proceeds along grain boundaries, synonymously referred to as intergranular attack (IGA). Localized corrosion at grain boundaries is caused by the anodic dissolution of (i) regions depleted of alloying elements, (ii) second phase precipitates, or (iii) regions with segregated alloying or impurity elements. The remaining part of the exposed surface typically functions as the cathode, and large cathodic areas support the anodic dissolution process. The ratio between cathode and anode is generally in excess of unity, and is dependent on factors such as the volume fraction and distribution of electrochemically active phases, the distribution of deleterious alloying and impurity elements, as well as grain size, particularly in nanocrystalline materials. The corrosion rate is dependent on the prevailing corrosion mechanism, and factors such as the diffusion of species to or from the anodic front can govern the dissolution kinetics.



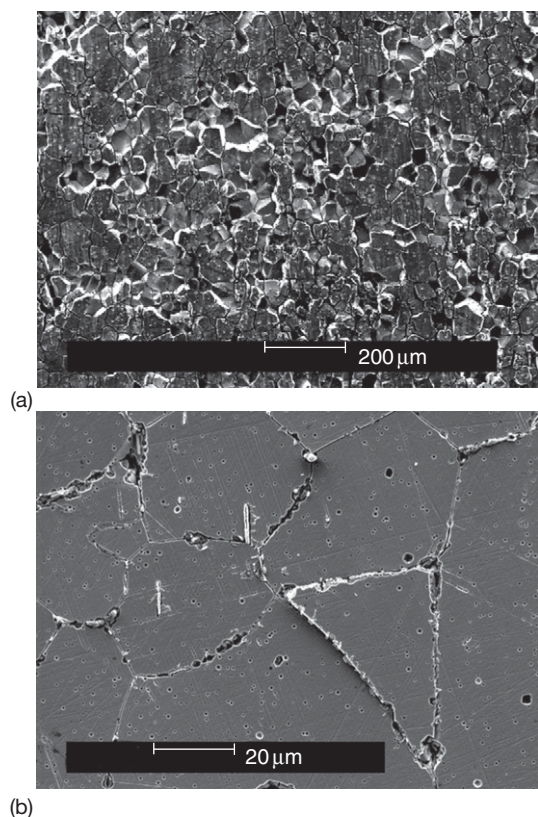


**Figure 1** Scanning electron micrographs of sensitized austenitic stainless steels with (a) a severely attacked surface after grain dropping, and (b) a dislodged grain on an attacked surface.

IGC occurs in pure metals as well as engineering alloys, and the term sensitization is frequently used to describe microstructure sensitivities to intergranular attack. In stainless steels, for example, sensitization can be caused through the precipitation of chromium-rich carbides at grain boundaries ([Section 2.06.2.2.1](#)). A major characteristic of IGC is the development of a relatively homogenous and uniform depth of attack. The dissolution of grain boundaries causes the dislodgement of grains, often referred to as grain dropping. Grain dropping is responsible for most of the weight loss observed after IGC exposure, and corrosion rates can therefore be several orders of magnitude higher than during general corrosion. The nature of intergranular attack with grain dropping events is shown in [Figure 1](#). A metallographic section with a uniform depth of attack is shown in [Figure 2](#). Nonuniform IGC attack can also occur, and is typically related to microstructure heterogeneities, as well as factors that locally impair the corrosion process. The latter may include, for instance, the coverage of part of an exposed surface with an electrochemically nonactive deposit, or local differences in solution chemistry.

### 2.06.1.1 Theories of Intergranular Corrosion

Three main theories summarize the occurrence of IGC, comprising (i) the element depletion theory, (ii) the microcell or electrochemical theory, and (iii)

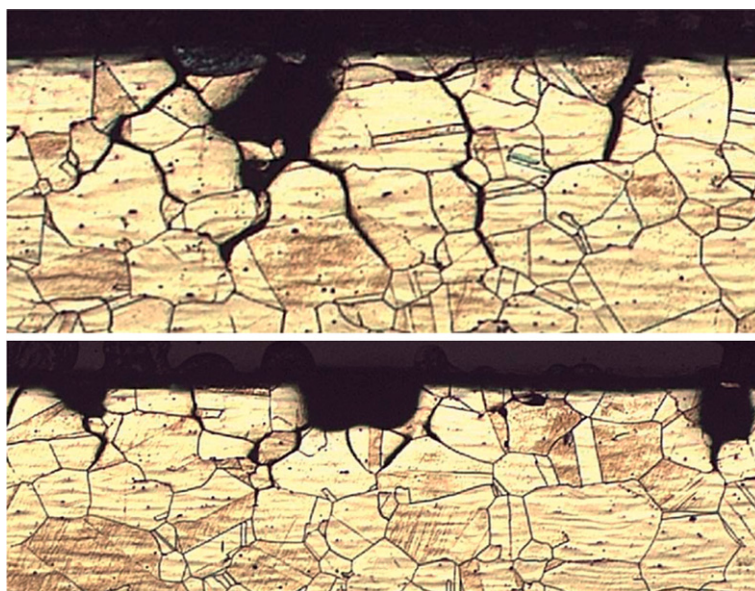


**Figure 2** Optical micrographs of two metallographic sections after IGC testing of sensitized austenitic stainless steel. The images highlight the intergranular nature of attack with grain dropping events close to the specimen surface. After IGC testing the sample was etched in 10% oxalic acid to reveal the intergranular nature of attack.

the segregation theory.<sup>1,2</sup> The depletion theory is based on the local impoverishment of an alloy element, such as chromium in the vicinity of chromium-rich carbides. This results in the breakdown of the passive film in the vicinity of these carbides, producing preferred sites for anodic dissolution. The microcell or electrochemical theory is based on the formation of a local electrochemical cell between precipitate and matrix, followed by dissolution of the less noble element or phase. A typical example is the anodic dissolution of second phase precipitates, such as  $\text{Al}_3\text{Mg}_2$  in the 5XXX series aluminum alloys. The segregation theory is based on the presence of an increased concentration of alloying or impurity elements at or in the vicinity of the grain boundary, such as sulfur or phosphorus in stainless steels. Dissolution of these regions is related to the adsorption of these elements at the grain boundary, ultimately changing the chemical and electrochemical activity.<sup>3</sup>

Another theory of IGC also considers local stresses at boundaries, introduced through the nucleation of second phase precipitates.<sup>1,4</sup> Preferred local attack then takes place at these distorted lattices, close to the second phase precipitate. It is also hypothesized that stresses and strains may lead to a higher degree of atomic disorder of the boundary, resulting in a higher driving force for anodic dissolution. Microscopic stresses or strains at grain boundaries possibly play a secondary role in IGC, for example, they may be responsible for enhanced diffusion pathways.

### 2.06.1.2 Metallurgical Aspects

The material composition and associated crystallographic structure have a large effect on the IGC behavior including, (i) the type of alloying and impurity element, (ii) the associated concentrations, (iii) their spatial distributions, and (iv) individual electrochemical activities. The type and concentration of alloying or impurity elements generally determines the crystallographic equilibrium structure of a material, and possible phase transformations change element solubilities and associated diffusivities. For example, increasing the concentration of carbon or the concentration of chromium in austenitic stainless steels, respectively, decreases and increases the time to form chromium depleted zones in the vicinity of chromium-rich carbide precipitates.<sup>4</sup> The spatial distribution and connectivity of susceptible microstructure constituents is also important, since IGC cannot be sustained without an inter-connected network of susceptible entities. Large distances between susceptible constituents

impede or even prevent the formation of a connected intergranular pathway throughout the microstructure. The electro-chemical activity determines the tendency to dissolve individual elements, even if present only in solid solution or bound to complex intermetallic phases. For example, in the 2XXX series aluminum-copper alloys the presence of copper in solid solution raises the electrochemical potential of the matrix phase, and therefore reduces the electrochemical potential difference to copper-rich precipitates.<sup>5</sup>

The IGC behavior is a strong function of cold work and grain size.<sup>1,4,6</sup> Cold work introduces strain energy into the material, producing changes in the microstructure, such as the occurrence of slip bands, microcell arrays, or phase transformations. These changes are strongly dependent on the crystallographic structure and material composition. For instance, in leaner grade austenitic stainless steels (i.e., Type 304), a considerable volume fraction of deformation induced martensite can develop with the introduction of medium to large amounts of cold work (i.e., >20%). The susceptibility to IGC is then governed by the stability and sensitization propensity of the phases present. The application of small amounts of cold work ( $\leq 20\%$ ) prior to sensitization enhances the diffusion of elements along slip lines, and promotes precipitation at grain boundaries. Subsequent sensitization heat treatments have a strong influence on the precipitation kinetics, and the choice of sensitization temperature can change the location for precipitation, from predominantly at grain boundaries to precipitation at slip bands. The application of higher sensitization temperatures can even induce recrystallization. The effect of grain size on the IGC behavior is dependent on the investigated corrosion system,<sup>4</sup> and differing IGC behaviors with grain size have been observed, for example, with exposures to mildly or strongly oxidizing media.<sup>1</sup> In stainless steels, the sensitization propensity has been reported to increase with decreasing grain size, associated with greater amounts of chromium that can enter the grain boundary region and form chromium-rich precipitates in a given time interval.<sup>6</sup> Contrarily, decreasing sensitization propensities with decreasing grain sizes have also been found, attributed to larger grain boundary surface areas and the formation of a less continuous network of precipitates.<sup>1,4</sup>

### 2.06.1.3 Grain Boundary Structure and Networks

Grain boundaries are in a higher state of disorder than the crystal lattice, that is, they represent 2-dimensional

lattice imperfections, with increased surface energies compared to the grain interior. This explains why grain boundaries are more active than the adjacent matrix phase, and can therefore easily be revealed with metallographic etching techniques. A simplified geometric description of a grain boundary crystallographic structure uses five macroscopic degrees of freedom (DOF).<sup>7,8</sup> These include three DOF for the relative misorientation between the crystal lattices of two neighboring grains, and the remaining two DOF for referencing the grain boundary plane to the grain orientations. The relative misorientation is described with a rotation axis (UVW) common to both adjoining grains, accounting for two DOF, and a rotation angle ( $\theta$ ) around this axis, defining the third DOF. Grain orientation relationships (misorientations) can be obtained from 2-dimensional assessments (i.e., a plain metallographic section), but information about the grain boundary plane typically involves 3-dimensional material characterization.<sup>7</sup>

The grain boundary network is heterogeneous, and consists of an assembly of different grain boundary crystallographic structures, with inherently different grain boundary free energies. These energy variations have a large influence on material properties, such as segregation, precipitation, diffusion, and migration behavior. Different grain boundary crystallographic structures therefore have different susceptibilities to IGC, and their resistance can vary as a function of exposure condition. In austenitic stainless steels, for example, the application of an electrolytic nitric acid etch (ASTM E 112),<sup>9</sup> to determine the ASTM grain size, outlines the grain boundary network, without attacking coherent annealing twin boundaries. The coherent twin boundaries have more than one order of magnitude lower surface energy ( $\approx 0.02 \text{ J m}^{-2}$ ) than general high angle grain boundaries ( $\approx 1 \text{ J m}^{-2}$ ), and are therefore more resistant to attack. The application of an electrolytic oxalic acid etch,<sup>10</sup> in contrast, outlines the complete grain boundary network, including coherent twins. This behavior highlights the relationship between exposure condition and grain boundary free energy on material susceptibility.

The connectivity of grain boundaries also plays an important part. Crystallographic constraints, in the form of clustering of crystallographically related boundaries, can create large regions with corrosion resistant or susceptible grain boundary clusters. This is often observed in low- to medium stacking fault energy face centered cubic (FCC) materials, such as copper or austenitic stainless steels. Large regions with clusters of low energy boundaries, such as twins, can

impede the growth of IGC. Further information about grain boundary structure, surface energy and physical property relationships,<sup>11,12</sup> as well as the influence of grain boundary connectivity,<sup>7</sup> can be found elsewhere in the literature.

#### 2.06.1.4 Grain Boundary Susceptibility

Localized attack at grain boundaries is a function of the 3-dimensional grain boundary structure (5 DOF), and reduced susceptibilities to intergranular corrosion are associated with low energy grain boundaries. The group of low energy grain boundaries comprises low angle grain boundaries, as well as certain high angle grain boundary configurations, such as twin boundaries. Low angle grain boundaries, with misorientations below  $15^\circ$ , are typically less susceptible to attack than high angle grain boundaries. The resistance of low angle grain boundaries increases with decreasing misorientation, and threshold angles for grain boundary resistance have also been reported.<sup>13</sup> The presence of a significantly increased fraction of low angle grain boundaries after plastic deformation, however, is responsible for enhanced diffusion pathways and increased IGC propensities.

High angle grain boundaries, with misorientations in excess of  $15^\circ$ , also possess certain low energy configurations which are more resistant to IGC. **Figure 3** shows a grain boundary network of a sensitized austenitic stainless steel with a mixture of attacked and resistant high-angle grain boundaries. Low energy grain boundaries, such as twin boundaries,

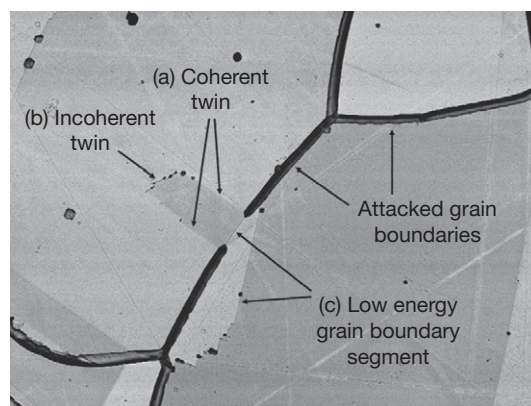


**Figure 3** Backscattered scanning electron micrograph of a grain boundary network in a sensitized austenitic stainless steel, with susceptible and immune grain boundaries. (a) Coherent and (b) incoherent twin grain boundaries, as well as some (c) low energy grain boundary segments show full or partial immunity to attack.



generally show a high resistance to IGC. To characterize different grain boundary structures numerous geometric models are available. For microstructure-property investigations, in particular corrosion studies in cubic crystal systems, the coincidence site lattice (CSL) model has frequently been used. This model is based on three macroscopic DOF ( $(\theta)/(UVW)$ ), and does not take the grain boundary plane into consideration. In the CSL model, grain boundaries are defined with the inverse volume density of coinciding lattice atom sites ( $\Sigma$ ), that is, a high density of coinciding atoms is associated with low  $\Sigma$  boundaries. Grain boundaries up to  $\Sigma 29$  are typically considered to be resistant, but large variations in IGC susceptibilities of different grain boundary types have been observed. The misorientation is only an indicator for grain boundary resistance. Increased microstructure resistance is frequently associated with the presence of twin ( $\Sigma 3$ ) grain boundaries, which are usually the most prominent group in the low  $\Sigma$  boundary population.<sup>7</sup>

The most resistant grain boundary is the coherent twin boundary, defined as  $\Sigma 3$  in the CSL model. Coherent twins can be expressed as a symmetrical tilt grain boundary with low-index  $\{111\}$  grain boundary planes. These boundaries therefore have a high density of coinciding atom sites, and a low energy grain boundary plane configuration. Other  $\Sigma 3$  grain boundaries, such as the incoherent twin, are more susceptible to IGC than coherent  $\Sigma 3$  twins. Incoherent twin boundaries are frequently associated with symmetrical tilt boundaries on  $\{112\}$  planes, and have a higher free energy ( $\approx 0.5 \text{ J m}^{-2}$ ) than their coherent counterpart ( $\approx 0.02 \text{ J m}^{-2}$ ). **Figure 3** highlights the difference in twin boundary susceptibility and also gives examples of other resistant low-energy grain boundary segments. Certain low  $\Sigma$  grain boundaries as well as some general high angle grain boundary configurations can also possess low index habit planes, leading to an increased IGC resistance. Additional factors, such as (i) the deviation from exact reference misorientation, (ii) the deviation from low index grain boundary plane configuration (i.e., curved boundary plane), or (iii) grain boundary faceting, can also influence the IGC resistance.

## 2.06.2 Intergranular Corrosion of Metals and Alloys

Aluminum alloys, stainless steels, and nickel alloys are the most common material systems associated

with intergranular corrosion. This section gives a brief review of IGC in common alloy systems, with strategies to mitigate these problems.

### 2.06.2.1 Aluminum Alloys

The occurrence of IGC in aluminum alloys is a function of the material composition, and certain alloying elements are responsible for the prevailing corrosion mechanism. The IGC susceptibility of heat treatable aluminum alloys is mainly related to the quenching and ageing treatment after solution annealing and small changes in these routines can cause significant changes in material resistance.<sup>14</sup> Another important factor for the IGC behavior is also the thermomechanical process history. Alloy groups that have been generally associated with IGC include, precipitation hardenable 2XXX series Al–Cu alloys, work hardenable 5XXX series Al–Mg alloys, and precipitation hardenable 7XXX Al–Zn–Mg alloys. The 6XXX precipitation hardenable Al–Mg–Si series has also shown IGC, but to a far smaller extent than the other alloy groups. The above-mentioned aluminum alloys are also associated with exfoliation corrosion, which is a type of intergranular corrosion which proceeds parallel to the specimen surface. Exfoliation corrosion is related to the development of excessive corrosion products at grain boundaries, indicating a layer-wise spallation of plate-like grain segments. This type of attack occurs in highly orientated microstructures of wrought aluminum alloys. IGC and exfoliation corrosion proceed in a similar manner, but exfoliation has also been found in materials which were not susceptible to IGC.

In 2XXX series Al–Cu alloys, including Al–Cu–Mg and Al–Cu–Li alloys, IGC behavior is primarily influenced by the copper concentration.<sup>5,14,15</sup> Copper in solid solution increases the corrosion potential of the matrix phase, and copper segregation or depletion can cause local variations in the electrochemical potential. Copper-depleted regions are less noble and susceptible to anodic dissolution in particular, if adjacent to copper-rich intermetallic phases such as  $\text{Al}_2\text{Cu}$ ,  $\text{Al}_2\text{CuMg}$ , or  $\text{Al}_2\text{CuLi}$ . Dissolution takes place in narrow regions close to precipitated phases at the grain boundary. Dealloying of copper-containing intermetallic phases, and copper re-precipitation has also been reported to support local dissolution reactions.<sup>5</sup> To reduce IGC susceptibilities, specifically designed heat and quenching treatments can be employed, which produce a uniform distribution of precipitates.<sup>15</sup> In the 5XXX series Al–Mg alloys with more than 3% Mg, the susceptibility to IGC

is typically based on the dissolution of the intergranularly precipitated  $\beta$ - $\text{Al}_3\text{Mg}_2$  phase.<sup>5,15</sup> This phase predominantly precipitates in the temperature range between 50 and 200 °C, due to a rejection of magnesium out of solid solution. Mg-depleted regions have also been found in the vicinity of the  $\beta$ -phase. Electrochemical measurements on bulk  $\beta$ - $\text{Al}_3\text{Mg}_2$  in NaCl solution indicated more electro-negative corrosion and passivity breakdown potentials than the aluminum matrix phase. These potential differences are responsible for the anodic dissolution of the  $\beta$ - $\text{Al}_3\text{Mg}_2$  phase.<sup>5</sup> Microalloying with zinc produces a stable Al-Mg-Zn phase ( $\tau$ -phase) and precludes the precipitation of  $\beta$ - $\text{Al}_3\text{Mg}_2$  in the 5XXX series alloys. In the 7XXX series Al-Zn-Mg alloys, IGC has frequently been attributed to the presence of Mg-rich grain boundary precipitates, as well as intergranular enrichments of Mg and Zn. Copper bearing 7XXX series Al-Zn-Mg-Cu alloys have been reported to contain copper depleted regions at grain boundaries, with an IGC mechanism similar to the 2XXX series Al-Cu alloys.<sup>15</sup> The application of over-aging heat treatments, and the resultant uniform distribution of precipitates can prevent IGC.<sup>15</sup> In the 6XXX series, Al-Mg-Si alloys IGC has been attributed to the anodic dissolution of the hardening phase  $\text{Mg}_2\text{Si}$ .<sup>15</sup>

### 2.06.2.2 Stainless Steels

Stainless steels can broadly be divided into five groups, comprising (i) ferritic, (ii) austenitic, (iii) martensitic, (iv) duplex (austenitic-ferritic), and (v) precipitation

hardenable materials. Different crystallographic structures have different corrosion behavior, often related to variations in diffusivity and solubility. Chromium depletion is the most common cause for IGC in these alloys, and degradation at grain boundaries is normally referred to as sensitization.<sup>1,4,6</sup> Sensitization is brought about by the presence of chromium-rich phases at grain boundaries, such as carbides, nitrides or intermetallic phases.<sup>16</sup> Exposure of sensitized stainless steel to oxidizing media produces intergranular attack at these chromium depleted regions.<sup>1,4</sup> In highly oxidizing media, such as boiling nitric acid, IGC can also occur in annealed stainless steel. This form of attack is generally related to the segregation and preferred dissolution of impurity elements at grain boundaries.<sup>2</sup>

#### 2.06.2.2.1 Sensitization of austenitic stainless steel

Sensitization is caused by thermal or thermomechanical process treatments, such as annealing, welding, or hot working. Exposure of austenitic stainless steels to temperatures between 450 and 850 °C can induce sensitization, due to the precipitation of chromium-rich carbides.<sup>6,16</sup> Figure 4(a) schematically shows sensitized grain boundaries decorated with chromium carbide precipitates and associated chromium depleted zones. Adverse service conditions, in the form of exposure to neutron irradiation in nuclear plant, can also cause sensitization, but without the nucleation of carbides. The amount of depletion typically varies between different boundary types, due to different grain boundary crystallographic structures.

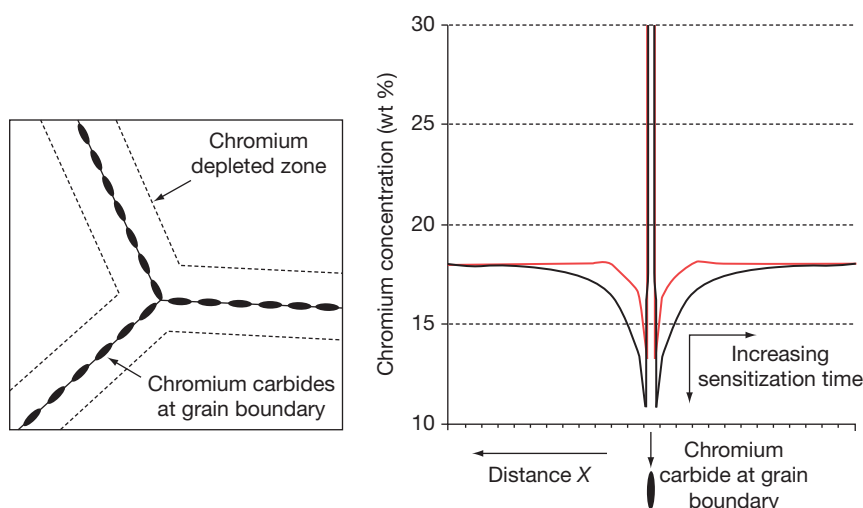


**Figure 4** Schematic illustration of a sensitized grain boundary with chromium carbide precipitates and typical chromium depletion profiles. Longer sensitization treatments increase both the width and depth of the chromium depletion profiles, until chromium replenishment takes place.



The depletion profiles in **Figure 4(b)** show a chromium composition gradient in the direction perpendicular to the boundary, with the shape and depth dependent on applied heat treatment parameters. The depletion is caused by the slow diffusivity of chromium, compared to carbon, producing regions with local chromium impoverishment, followed by a breakdown of the passive film at these regions. In **Figure 4**, the high concentration of chromium at the grain boundary is associated with the presence of chromium-rich carbide precipitates. The influence of reduced chromium concentrations on the anodic behavior of these regions, for example, if exposed to oxidizing environments, is shown in **Figure 5**. Lower chromium concentrations show increased current densities in the active as well as passive regions of the anodic polarization curve.

A major factor for the development of chromium depleted regions is the chromium and carbon content, as well as the solubility of carbon in the matrix phase. Nucleation of carbides is caused by a decreasing solubility of carbon in the austenitic matrix phase with decreasing temperature, for instance on cooling through the sensitization temperature regime.<sup>16</sup> The dominant carbide in austenitic stainless steels is  $\text{Cr}_{23}\text{C}_6$ , but impurity elements, such as nitrogen and boron, as well as alloying elements usually alter this composition. The presence of high nitrogen contents, for example, may cause sensitization through the

nucleation of  $\text{Cr}_2\text{N}$ . The addition of alloying elements, such as molybdenum in higher alloyed stainless steels (i.e., type 316), may also promote the nucleation of intermetallic phases, such as  $\sigma$ -phase  $(\text{FeNi})_x(\text{CrMo})_y$ <sup>16</sup> or  $\chi$ -phase  $(\text{Fe}_{36}\text{Cr}_{12}\text{Mo}_{10})$ .<sup>16</sup>

A typical method to illustrate the sensitization behavior is the time–temperature–precipitation (TTP) diagram, shown in **Figure 6**. TTP diagrams give an indication of the influence of material parameters on the sensitization propensity. **Figure 6(a)** shows the influence of carbon content, and **Figure 6(b)** the influence of grain boundary structure on sensitization. Increasing the carbon content increases the propensity to sensitization at shorter exposure times. The same is observed with different grain boundary structures. Precipitation occurs in the order of decreasing grain boundary energy, starting with a rapid decoration of  $\delta$ -ferrite–austenite interfaces, followed by precipitation at general high-angle, then incoherent twin and finally coherent twin boundaries. Heat treatments in the lower temperature regime, that is, below  $450^\circ\text{C}$ , usually have no significant effect on sensitization due to markedly reduced diffusivities. In the presence of preexisting carbide nuclei, however, sensitization has been reported below  $450^\circ\text{C}$  after prolonged exposure. This is referred to as low-temperature sensitization, and the occurrence may take years before it becomes significant.<sup>6</sup>

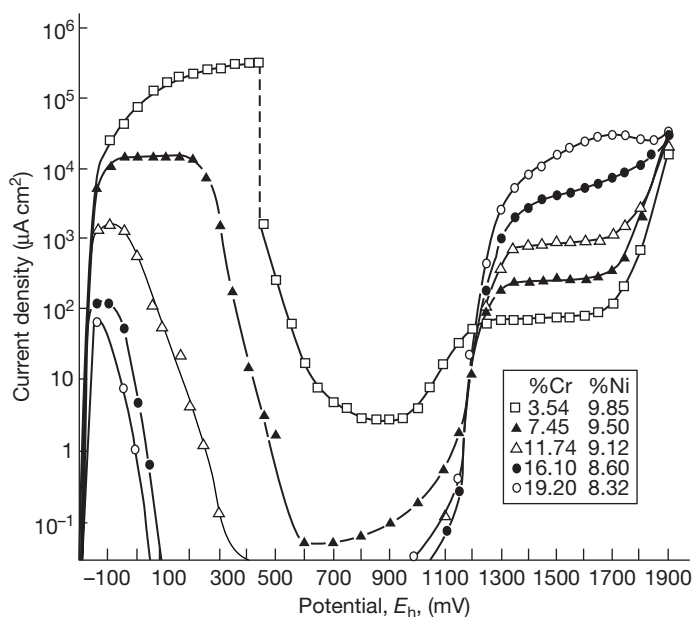


**Figure 5** Anodic polarization curves of Fe–9% Ni–x% Cr alloys in deaerated 2 N  $\text{H}_2\text{SO}_4$  solution at  $25^\circ\text{C}$ . Potentials are given versus normal hydrogen electrode (NHE,  $E_h$ ). Reproduced from Osozawa, K.; Engell, H.-J. *Corros. Sci.* **1966**, 6, 389–393.

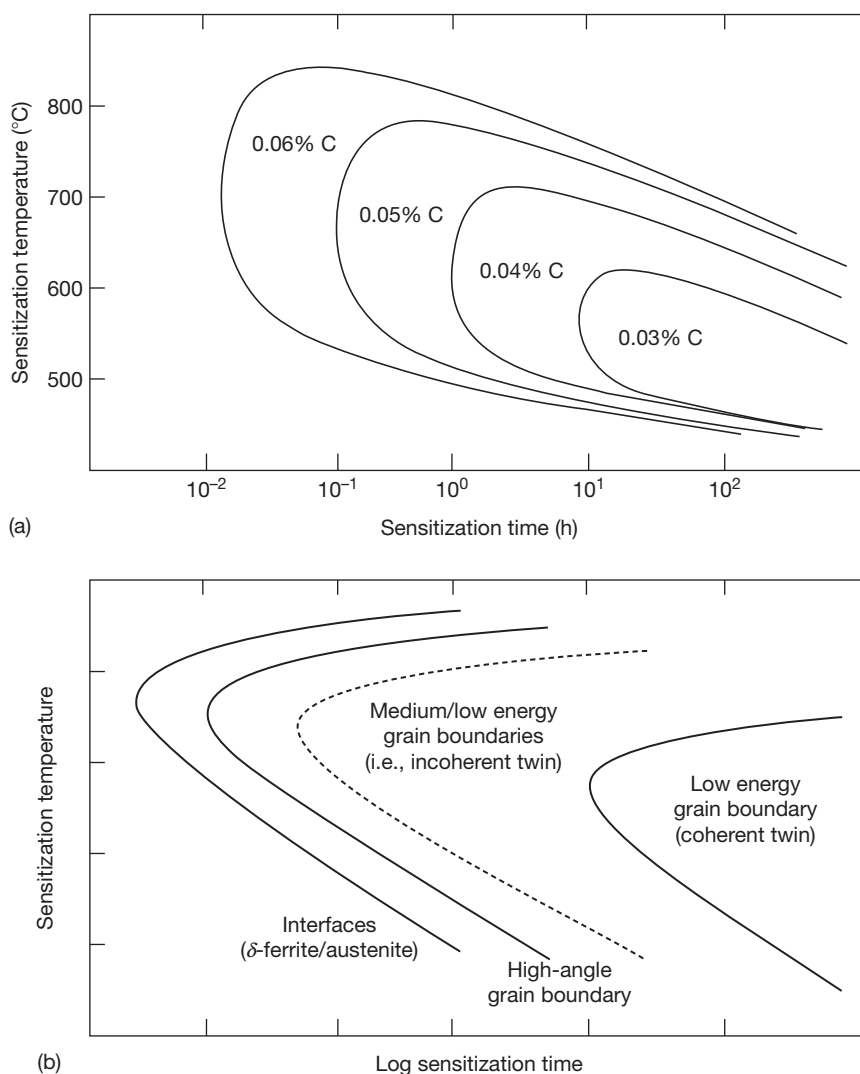


**Figure 6** Schematic time–temperature–precipitation (TTP) diagram of austenitic stainless steels with the influence of (a) different carbon contents (based on data from Trillo *et al.*<sup>48</sup>), and (b) different grain boundary structures (based on data from Marshall<sup>16</sup> and Bruemmer and Was<sup>49</sup>).

#### 2.06.2.2.2 Prevention of sensitization

For the prevention of sensitization in austenitic stainless steels, numerous possible mitigation strategies are available. (i) A reduction of the carbon content to concentrations below 0.03% (L-grade) usually prevents sensitization, but prolonged exposures in the sensitization temperature regime may still cause chromium depletion. (ii) The addition of stabilizing elements, such as titanium or niobium (stabilized grades, i.e., Type 321, Type 347), bind carbon into MC-type carbides. This reduces the available carbon in solid solution, and prevents the nucleation of intergranular  $M_{23}C_6$  carbides. Stabilizing heat treatments at temperature in the region of 800–900 °C are

typically applied to precipitate intragranular MC-type carbides. (iii) The application of a solution annealing treatment dissolves existing carbides, and fast cooling/quenching through the sensitization temperature regime prevents carbide nucleation. Typical solution annealing heat treatments for stainless steels are carried out between 1000 and 1150 °C. Sensitization can occur if the material is afterwards heated into the sensitization temperature regime. (iv) Prolonged exposure periods within the sensitization temperature regime can replenish chromium depleted regions with chromium from the grain interior. This is referred to as desensitization treatment. (v) Metallurgical alterations, such as alloying with higher chromium

contents, or the addition of molybdenum, as well as (vi) changes of manufacture or service conditions, such as the reduction of critical exposure temperatures, are possible measures to prevent sensitization.

### 2.06.2.2.3 Weld decay and knife line attack

During welding, in particular fusion-based welding processes, material situated in the fusion zone is locally exposed to temperatures close to the melting point. This induces a temperature gradient with distance from the fusion zone, referred to as the heat affected zone (HAZ), and material within the HAZ can be exposed to temperatures that cause sensitization. On exposure to IGC promoting environments, attack usually takes place in a band parallel to the fusion line. This process is known as weld decay. **Figure 7** shows a typical appearance and location of

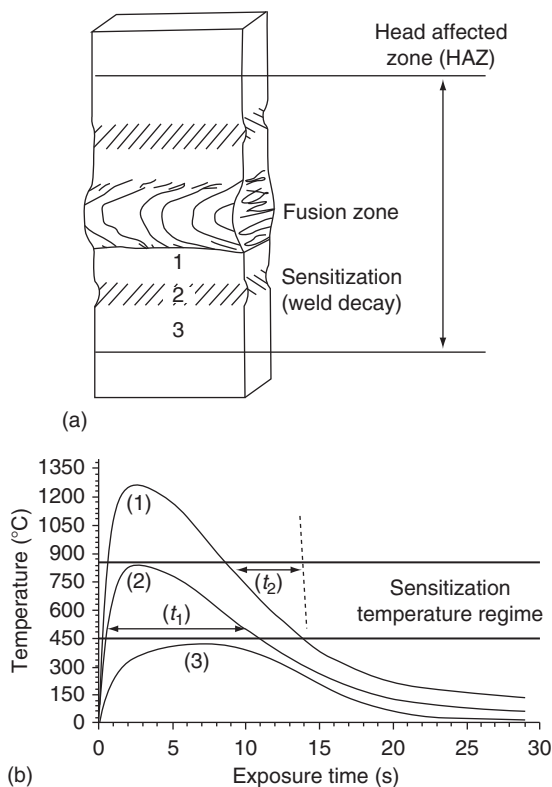


**Figure 7** Schematic drawing of the occurrence of weld decay. (a) Weld line with fusion zone, heat affected zone (HAZ) and sensitized region. (b) Typical temperature-time profiles at points 1, 2, and 3 highlight different exposure times within the sensitization temperature regime ( $t_1 > t_2$ ). Reproduced from Procter, R. P. M. Section 1.3 – Effects of Metallurgical/structure on Corrosion. In *Shreir's Corrosion Handbook*, 3rd ed. Metal/Environment Reactions; Shreir, L. L., Jarman, R. A., Burstein, G. T., Eds.; 2000; pp 1–44.

weld decay, and gives three typical temperature profiles (1, 2, 3) with distance from the fusion zone. The time ( $t$ ) at elevated temperature, specimen dimensions, welding process, and associated welding parameters are crucial factors for the occurrence of weld decay.

Knife line attack is associated with IGC in weldments of stabilized stainless steels. This phenomenon occurs after exposing stabilized materials, containing intragranular TiC or NbC precipitates, to temperatures that dissolve these stabilizing MC-type carbides. The required temperature range is typically in excess of 1150 °C, and can occur during fusion-based welding processes. On rapid cooling, neither the MC-type carbides, nor the  $M_{23}C_6$  are precipitated and the carbon remains in solid solution. MC-type carbides are preferentially nucleated at temperatures between 800 and 900 °C, whereas intergranular  $M_{23}C_6$ -type carbides have a stronger driving force for nucleation at lower temperatures. Re-heating to temperatures within the sensitization regime, that is, 450–750 °C, then preferentially precipitates intergranular  $M_{23}C_6$ -type carbides in the HAZ, rendering the microstructure susceptible to IGC. Knife line attack occurs close to the weld bead, since high temperatures are required for the dissolution of the MC-type carbides.

### 2.06.2.2.4 Ferritic, martensitic, duplex, and precipitation hardening stainless steels

Sensitization in ferritic stainless steels is usually caused by the formation of intergranular chromium-rich carbides ( $M_{23}C_6$ ) and nitrides ( $M_2N$ ).<sup>17</sup> Similarly to austenitic stainless steels, chromium depletion is the cause for IGC in mildly oxidizing solutions, and the dissolution of intergranular carbides or segregated elements causes IGC in solutions with a high oxidizing power.<sup>17,18</sup> Rapid precipitation of intergranular carbides has been reported to occur in the sensitization temperature regime between 430 and 930 °C,<sup>17</sup> but annealing in excess of 930 °C, followed by rapid cooling, cannot prevent sensitization. This occurs due to significantly faster diffusivities of chromium, carbon, and nitrogen in ferrite compared to austenite.<sup>17,19</sup> For IGC resistance, desensitization treatments between 700 and 800 °C can be used to replenish the chromium depleted regions.<sup>17</sup> The addition of stabilizing elements, in the form of titanium or niobium, is also common practice to prevent IGC in these materials.

The susceptibility of martensitic stainless steels to IGC is a strong function of the microstructure

condition, and is dependent on the preceding thermal history. Peak hardened microstructures after quenching have an increased resistance to IGC. An increased sensitivity to IGC has been reported after temper annealing at temperatures between 450 and 650 °C, due to the precipitation of intergranular carbides.<sup>1,19,20</sup>

Exposure of martensitic stainless steels to temperatures in excess of 700 °C equilibrates local differences in the chromium content, leading to desensitization.<sup>1</sup>

Austenitic–ferritic (duplex) stainless steels contain ~50% ferrite and ~50% austenite and usually have a good resistance to IGC. These alloys possess higher chromium contents (above 20%), with carbon concentrations far below 0.03%, and modern duplex stainless steels have insufficient carbon for sensitization. Susceptibility of duplex stainless steels is frequently associated with the presence of a critical fraction of austenite–ferrite interfaces.<sup>21,22</sup> In the presence of sufficient carbon, these interfaces are prone to carbide precipitation after short exposure times, due to rapid diffusion of carbon and chromium in ferrite. Narrow chromium depletion regions form at the austenitic side of the interface, due to the slower diffusion kinetics of chromium in austenite.<sup>21,22</sup> Sensitization is not confined to ferrite–austenite interfaces, and chromium depletion also occurs at austenite–austenite boundaries. Desensitization proceeds faster than in austenitic stainless steel, and duplex stainless steels can undergo rapid healing of chromium depleted regions. Generally, intergranular carbide precipitation occurs at temperatures between 450 and 850 °C,<sup>4</sup> with solution annealing usually carried out at temperatures in excess of 1000 °C. Duplex stainless steels also undergo complex precipitation and decomposition reactions, with the formation of intermetallic phases such as  $\sigma$ -phase and  $\chi$ -phase.<sup>16,20</sup> These intermetallic phases are rich in chromium and molybdenum, usually nucleate at grain boundaries, and can cause local element depletions, rendering duplex stainless steels susceptible to IGC.

Precipitation hardenable stainless steels, such as the martensitic 17-4 PH grade (17%Cr/4%Ni/4%Cu) derive their strength from the nucleation of intermetallic strengthening phases on ageing. These strengthening phases are typically soluble in austenite, and precipitate on the formation of martensite. Fully austenitic alloys are also available, which are strengthened by intermetallic precipitates, such as Ni<sub>3</sub>Ti. Sensitization in these materials typically occurs on heat treating and reversion of martensite into austenite, often associated with the HAZ after

welding.<sup>1</sup> Precipitation hardenable stainless steels are susceptible to sensitization similar to their austenitic counterparts, with temperatures up to  $\approx$ 850 °C.

### 2.06.2.3 Nickel and Nickel Alloys

Structural nickel alloys can broadly be grouped according to their main compositional constituents, comprising nickel–chromium–iron alloys (Ni–Cr–Fe), nickel–chromium–molybdenum alloys (Ni–Cr–Mo), and nickel–molybdenum alloys (Ni–Mo).<sup>1,3,4</sup> These alloy systems behave similarly to austenitic stainless steels, and the main alloying elements for improved IGC resistance are chromium and molybdenum. Chromium gives resistance in oxidizing media, whereas molybdenum increases the resistance in reducing media. Nickel has a low solubility of carbon, and even concentrations below 0.03% can cause sensitization due to the precipitation of chromium-rich carbides. Chromium nitrides and the presence of certain intermetallic phases can also cause sensitization, as well as segregated elements, such as sulfur or phosphor. For instance, IGC in pure nickel can occur through the presence of sulfur segregation at grain boundaries, with the extent dependent on the grain boundary crystallographic structure and the exposed environmental condition.<sup>23</sup>

Ni–Cr–Fe<sup>1,3,4</sup> alloys are the largest group of nickel-based alloys. The chromium content typically varies from 15% in the basic grades, for example, alloy 600, to far in excess of 30% in the higher-alloyed materials, such as alloy 690. For increasing the corrosion and pitting resistance, 2–3% molybdenum and copper are frequently added. Molybdenum bearing alloys, however, can develop complex carbides and intermetallic phases. Depending on the carbon content, Ni–Cr–Fe alloys are susceptible to sensitization in the temperature range between 450 and 850 °C, forming carbides of type M<sub>23</sub>C<sub>6</sub> and M<sub>7</sub>C<sub>3</sub>. Solution annealing with fast quenching routines can be used to prevent sensitization.

Ni–Cr–Mo<sup>1,3,4</sup> alloys have a higher resistance to localized corrosion, due to the presence of increased concentrations of molybdenum, typically between 10% and 20%, such as alloy 22. The combination of high chromium and increased molybdenum contents make these alloys highly resistant to a broad spectrum of oxidizing and reducing environments. In contrast, the presence of molybdenum creates more complex carbides and intermetallic phases. Sensitization depends on the carbon content, but can occur between 600 and 1150 °C. The microstructure

nucleates carbides of type  $M_6C$ ,  $M_{23}C_6$ , and  $M_2C$ , producing regions depleted in chromium and molybdenum. Solution annealing only becomes effective at temperatures in excess of 1220 °C.<sup>4</sup> Additional elements such as copper, tantalum, and tungsten are often incorporated to improve the corrosion resistance.

Ni–Mo<sup>3</sup> alloys typically contain 25–30% molybdenum, and can form ordered intermetallic phases of the types  $Ni_4Mo$  and  $Ni_3Mo$ . These alloys have an excellent resistance to reducing media, and IGC occurs in regions depleted of molybdenum. Intergranular carbides, such as  $M_2C$ ,  $M_6C$ ,  $M_{12}C$ , can also form. To prevent sensitization, materials with carbon contents below 0.005% are utilized. Knife-line attack can occur if these alloys are heated in excess of 1250 °C.<sup>3</sup>

#### 2.06.2.4 Other Metals and Alloys

Most metals and alloy systems are susceptible to IGC, and a few examples of different alloy systems are briefly summarized. Copper is susceptible to IGC with exposure to certain etching solutions, such as mixtures of hydrochloric and acetic acid, as well as in solutions containing high concentrations of ammonia.<sup>24</sup> Brass is intergranularly attacked by ferric sulfate and cobalt sulfate,<sup>24</sup> and iron is susceptible to IGC in ammonium nitrate solutions.<sup>25</sup> Pure zinc,<sup>26</sup> containing small amounts of lead, tin, aluminum, or other impurity elements, shows a strong sensitivity to IGC when exposed to hot water or steam environments. Zinc alloys with 4% and 12% aluminum also suffer from IGC in concrete, which is mostly attributed to the segregation of impurity elements and the formation of aluminum rich grain boundary phases.<sup>26</sup> Zirconium shows IGC after immersion in high concentrations of hydrochloric acid containing small amounts of oxidizers, such as ferric- or cupric-ions.<sup>27</sup> More examples of localized attack can be found in the individual material sections of this book.

### 2.06.3 Intergranular Corrosion Testing

Intergranular corrosion testing is carried out either under real service conditions, in simulated service environments, or in accelerated test environments. Accelerated tests are required to rank exposed materials in a similar order as exposure to real service environments. However, the rates of degradation in these tests may not have any relation to the actual

service environment. For accelerated IGC testing, numerous standard practices and test methods are available, but IGC testing can also be carried out in nonstandardized environments. Calculated corrosion rates after IGC exposures are based on the same principles as for general corrosion, implying a homogeneous dissolution. Localized attack must be reported separately.

#### 2.06.3.1 Standard Practices and Test Methods

A range of standard practices and test methods for the assessment and ranking of IGC behaviors are available, and have been published under the auspice of different organizations and institutions. These include the International Standard Organization (ISO),<sup>28–33</sup> the National Association of Corrosion Engineers (NACE) and the American Society for Testing Materials (ASTM).<sup>10,34–41</sup> A large number of national standards are also available. In this section, ASTM and ISO standards for assessing the IGC behavior of aluminum alloys, stainless steels, and nickel alloys are summarized. **Table 1** gives the standard practices for IGC of aluminum alloys, **Table 2** for IGC testing of stainless steels and **Table 3** for nickel alloys. Exfoliation tests for aluminum alloys are also included in **Table 1**.

IGC tests in **Table 1** dissolve specific material constituents that are characteristic of individual aluminum alloys. The tested specimens are either assessed with weight loss measurements, in the case of exposure to nitric acid (ASTM G 67),<sup>38</sup> or using metallographic sectioning methods. Both exfoliation tests in **Table 1** are assessed by visual examination of the exposed surfaces. IGC tests in chloride containing solutions (ISO 11846, ISO 15329)<sup>32,33</sup> produce, with anodic polarization, a localized breakdown of the passive film, which results in either intergranular or intragranular pit initiation sites. The location of these initiation events is then used for material discrimination, with intergranular sites identifying IGC susceptible materials. Further analysis may also comprise an assessment of the extent of intergranular attack, in order to categorize the material with susceptibility ratings. Information about the influence of individual alloying elements, changes in electrolyte concentrations, or the influence of exposure parameters can be found in the literature, including the ASSET<sup>42</sup> (ASTM G 66),<sup>41</sup> EXCO<sup>42</sup> (ASTM G 34),<sup>34</sup> nitric acid<sup>43</sup> (ASTM G67),<sup>38</sup> and chloride/peroxide<sup>14</sup> (ASTM G 110/ISO 11846)<sup>33,36</sup> test.



**Table 1** ASTM and ISO practices for IGC and exfoliation testing of aluminum alloys

<i>Standard</i>	<i>Test solution</i>	<i>Materials</i>	<i>Nature of attack</i>	<i>Duration / temperature</i>
ASTM G 34 (2001)	Sodium chloride, potassium nitrate, nitric acid -EXCO-	Wrought; AA2XXX, AA7XXX	Exfoliation	≤48–96 h/25 °C
ASTM G 66 (1999)	Ammonium chloride, ammonium nitrate, ammonium tartrate, hydrogen peroxide -ASSET-	Wrought, AA5XXX (>2% Mg)	Exfoliation	24 h/65 °C
ASTM G 67 (2004)	Nitric acid -NAMLT-	Wrought, AA5XXX (Al–Mg; Al–Mg–Mn)	GB precipitation (Al <sub>3</sub> Mg <sub>2</sub> )	24 h/30 °C
ASTM G 110 (2003)	Sodium chloride, hydrogen peroxide	Wrought + cast; AA2XXX, AA6XXX, AA7XXX	GB precipitation	>6 h/30 °C
ISO 11846 (2008)	(Method A) sodium chloride, hydrogen peroxide	Wrought + cast; AA2XXX, AA6XXX, AA7XXX	(Method A–C) GB precipitation	>6 h/30 °C
	(Method B) sodium chloride, hydrochloric acid	Wrought + cast; Solution heat-treatable Aluminum alloys		24 h/RT
	(Method C) anodic polarization in sodium chloride	Aluminum–lithium alloys		Polarization/RT
ISO 15329 (2008)	Sodium chloride	Wrought + cast; Solution heat-treatable AA2XXX, AA6XXX, AA7XXX, AA8XXX	GB precipitation	Polarization/RT

RT = Room temperature, GB = Grain boundary.

IGC tests for austenitic, ferritic, and duplex stainless steels are summarized in **Table 2**. Two different test methods are typically distinguished, on the basis of either material quality testing or sensitization propensity testing. The later assessment involves the exposure of materials to short sensitization heat treatments before IGC testing, with the aim to provide information about the propensity of the material to develop a sensitized grain boundary network. Material quality testing is typically carried out without any additional heat treatment. The IGC tests in **Table 2** are assessed either with weight loss measurements (ASTM A 262 – Method B, C, F and ISO 3651-1),<sup>10,29</sup> or by visual inspection of the exposed specimen surface after bending (ASTM A 262 – Method E and ISO 3651-2).<sup>10,30</sup> Bending tests only provide a qualitative measure of the IGC susceptibility, and these test environments are typically less aggressive. Metallographic sectioning can also be used for further susceptibility discrimination. Tests summarized in **Table 2** are all sensitive to intergranular chromium depletion, but individual tests also show sensitivities to chromium-rich phases, molybdenum-depletion around  $\sigma$ -phase, or other microstructural constituents, such as end-grains.

The oxalic acid test in **Table 2** is an electrolytic screening test, and is used for rapid assessment of cast and wrought austenitic (ASTM A262 – Method A)<sup>10</sup>

and ferritic (ASTM A763 – Method W)<sup>39</sup> stainless steels. The recommended current density and exposure time severely over-etch the microstructure, in order to facilitate a simple microstructure susceptibility classification.<sup>17</sup> The test reveals chromium depleted regions in the vicinity of sensitized boundaries or intermetallic phases.<sup>17</sup> Experiments with pure chromium have also indicated an attack of chromium rich phases,<sup>22</sup> making the oxalic acid test suitable for accepting resistant materials, but not for the rejection of susceptible material heats.<sup>17</sup> The oxalic acid test discriminates three different microstructure conditions comprising, (i) an IGC resistant step-like microstructure, (ii) a dual microstructure, containing a mixture of stepped and ditched grain boundaries, and (iii) a ditched structure, associated with deep, grain-surrounding etch trenches. **Figure 8** compares these classifications for a wrought austenitic stainless steel plate. The standard oxalic acid test yields only qualitative information, but quantitative information about the attacked grain boundary network can also be extracted. The extent of susceptible grain boundaries can be determined, for instance, by using the oxalic acid test in conjunction with image analysis methods, or with mean linear intercept procedures. These assessments can provide valuable information to quantify material susceptibilities.

**Table 2** ASTM and ISO practices for IGC testing of stainless steels<sup>10,29,30,39</sup>

<i>Standard</i>	<i>Test solution</i>	<i>Materials</i>	<i>Nature of attack</i>	<i>Duration/ temperature</i>
ASTM A 262 (2008)	(Method A) 10% Oxalic acid or ammonium persulfate	(Methods A–C, E) Wrought + cast; austenitic SS	(A) Chromium depletion end grains	Polarization/ RT
	(Method B) Ferric sulfate, 50% sulfuric acid		(B) Chromium depletion $\sigma$ -phase in Ti + Nb stabilized and Cr–Ni–Mo containing SS	120 h/boiling
	-STREICHER-		(C) Chromium depletion $\sigma$ -phase in Cr–Ni–Mo containing SS, end-grains	240 h/boiling
	(Method C) 65% Nitric acid			
	-HUEY-			
	(Method E) Copper, copper sulfate, 16% sulfuric acid	(E) Weldments	(E) Chromium depletion	24 h/boiling
ASTM A 763 (2004)	-STRAUSS-			
	(Method F) Copper, copper sulfate, 50% sulfuric acid	(F) Cast austenitic SS	(F) Chromium depletion in Cr–Ni–Mo containing castings	120 h/boiling
	[*(Method D) 10% Nitric acid, 3% hydrofluoric acid]	(D) Type 316, 316L, 317, 317L	(D) Chromium depletion	4 h/70 °C
	-WARREN-			
ASTM A 763 (2004)	(Method W) 10% Oxalic acid	(Methods W–Z) Ferritic SS	(Methods W–Z) Chromium depletion	Polarization/ RT
	(Method X) Ferric sulfate, 50% sulfuric acid		(X) Intermetallic phases in Ti/Nb stabilized SS	24–120 h/ boiling
	(Method Y) Copper, copper sulfate, 50% sulfuric acid			96–120 h/ boiling
	(Method Z) Copper, copper sulfate, 16% sulfuric acid	(Z) Weldments		24 h/boiling
ISO 3651-1 (1998)	65% Nitric acid	Wrought + cast; austenitic and duplex SS	Chromium depletion	240 h/boiling
ISO 3651-2 (1998)	-HUEY-			
	(Method A) Copper, copper sulfate, 16% sulfuric acid	(Methods A–C) Wrought + cast + weldments; (A) Austenitic, ferritic, duplex SS #	(Methods A–C) Chromium depletion	20 $\pm$ 5 h/ boiling
	-STRAUSS-			
ISO 3651-2 (1998)	(Method B) Copper, copper sulfate, 35% sulfuric acid	(B) Austenitic, duplex SS #		20 $\pm$ 5 h/ boiling
	(Method C) Ferric sulfate, 40% sulfuric acid	(C) Austenitic, ferritic, duplex SS #		20 $\pm$ 5 h/ boiling

\*Excluded from ASTM A262, # Material range defined in standards, SS = Stainless steel.

The ferric sulfate–sulfuric acid test is manifest in a broad range of standard procedures (such as ASTM A262 – Method B), and can be used to detect chromium depletion in austenitic, ferritic and duplex stainless steels (Table 2), as well as in nickel–chromium and nickel–chromium–molybdenum based alloys (Table 3). Generally, an increase in the sulfuric acid concentration from 10% to 60% significantly increases the corrosion rate in this test,<sup>17</sup> whereas the ferric sulfate functions as an inhibitor for stainless steel corrosion.<sup>17</sup> It is therefore recommended to regularly

replenish ferric sulfate, to maintain passive conditions and avoid excessive general corrosion.<sup>17</sup>

Nitric acid IGC tests, such as ASTM A 262 – Method C (Huey),<sup>10</sup> are highly oxidizing and attack chromium depleted regions, regions with segregated impurity or alloying elements, as well as exposed end grains. After deformation, attack at slip bands has also been reported.<sup>1</sup> Experiments with pure chromium also indicated that the nitric acid test readily attacks chromium rich phases.<sup>22</sup> The accumulation of hexavalent chromium ions, typically brought about by leaching out

**Table 3** ASTM and ISO practices for IGC testing of nickel-based alloys. (GB = Grain boundary/# Material range defined in standards)<sup>28,35</sup>

Standard	Test solution	Materials	Nature of attack	Duration/ temperature
ASTM G 28 (2008)	(Method A) Ferric sulfate, 50% sulfuric acid	Wrought + weldments; Ni-based, Cr-bearing alloys #	GB precipitates	24–120 h/ boiling
	(Method B) Sulfuric acid, hydrochloric acid, ferric chloride, cupric chloride	Wrought; Ni-base, Cr-bearing alloys #	GB precipitates	24 h/boiling
ISO 9400 (1996)	Method (A) Ferric sulfate, 50% sulfuric acid	Ni-based, Cr-based alloys #	GB precipitates	24–120 h/ boiling
ISO 9400 (1996)	Method (B) Copper, copper sulfate, sulfuric acid	Wrought + weldments; Ni-based, Cr-bearing alloys #	GB precipitates, excluding $\chi$ -, $\sigma$ -phase, TiC + TiN	$\geq 24$ h/boiling
	Method (C) Hydrochloric acid	High Mo-containing Ni and Ni–Cr base alloys #	GB Precipitates, Mo depletion	168 h/boiling
	Method (D) Nitric acid	Wrought; Ni-based, Cr-bearing alloys #	GB Precipitates, $\chi$ -, $\sigma$ -phase, TiC + TiN	$\geq 48$ h/boiling

from dissolved second phases, significantly increases the corrosion rate in this solution.<sup>17,22</sup>

The copper sulfate–16% sulfuric acid IGC test (Strauss) was initially recommended for the assessment of stainless steels with test durations of several hundreds of hours.<sup>17</sup> For accelerated testing, either metallic copper, or an increased concentration of sulfuric acid can be utilized.<sup>17</sup> Synergistic effects of the addition of higher concentrations of sulfuric acid and the contact to copper are utilized for IGC testing of cast stainless steels, such as ASTM A262 – Method F.<sup>10</sup> In sulfuric acid, cupric ions function as an inhibitor.<sup>17</sup>

The IGC resistance of stainless steels in mildly oxidizing solutions is a function of the chromium content, as shown in Figure 5.<sup>44</sup> An increase in the chromium content reduces the active–passive transition current density and enlarges the passive regions which makes passivation easier. In highly oxidizing solutions, such as boiling nitric acid, the presence of intermetallic phases and the segregation of solute atoms at grain boundaries also play a very important role. Annealed, nonsensitized stainless steels,<sup>2,45</sup> as well as pure nickel<sup>23</sup> and nickel alloys<sup>3</sup> have been found to undergo IGC in these highly oxidizing environments. Figure 9 gives a schematic summary of an anodic polarization curve for austenitic stainless steel in sulfuric acid with superimposed potential regions of the ASTM A 262<sup>10</sup> tests. The oxalic acid test is not shown, and would be located at a potential higher than the Huey test.

IGC tests for nickel alloys are summarized in Table 3. These tests are restricted to a range of alloy groups comprising alloy 600, alloy 625, alloy

800, alloy 825, and alloy C-276. A list of susceptible materials is given in the corresponding standard practices. Evaluation of the IGC susceptibility is carried out by visual examination after bending (ISO 9400 – Method B),<sup>28</sup> or with weight loss measurements. Additional metallographic examinations are generally recommended. It is also recommended to compare differences in the measurements of weight loss to material reference conditions, since variations in composition and thermomechanical process history may exert a large effect on determined corrosion rates. This is also reflected in differences in the recommended exposure durations, which vary with alloy composition (ASTM G 28).<sup>35</sup>

### 2.06.3.2 Microstructure Screening

Metallographic etching procedures can be used for rapid first principle assessments of IGC susceptibilities. This requires knowledge of individual microstructure constituents attacked by the metallographic etching procedure and, more importantly, whether there exists a relationship between these constituents and the real IGC behavior. For instance, a typical test for aluminum–magnesium alloys (5XXX) is the orthophosphoric acid etch. This etch highlights intermetallic  $\beta$ -phase ( $\text{Al}_3\text{Mg}_2$ ) precipitates, and has been used to gain information for exfoliation testing.<sup>42</sup>

### 2.06.3.3 Degree of Sensitization Testing

For characterizing the degree of sensitization, (i) the length of grain boundaries with chromium depletion, (ii) the width of the depleted zone, and (iii) the

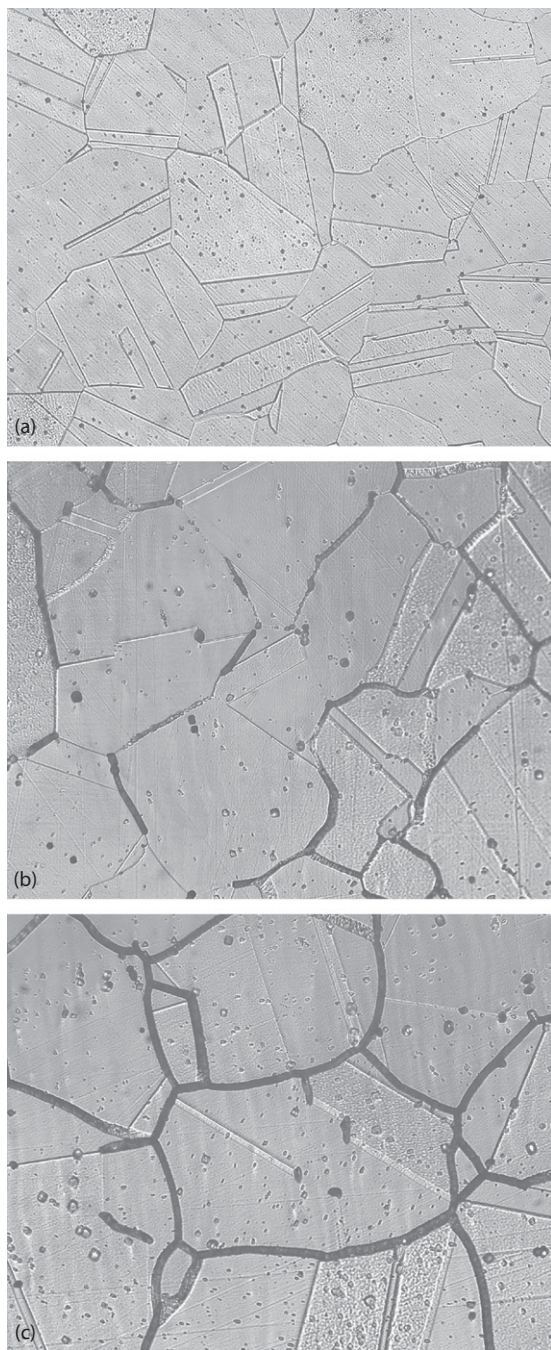


**Figure 8** Optical micrographs of a Type 304 austenitic stainless steel after IGC screening in 10 wt% oxalic acid. Micrograph (a) shows a stepped, (b) a dual, and (c) a ditched microstructure.

minimum chromium concentration should be taken into consideration. For this purpose, a number of electrochemical test methods to quantify the degree of sensitization in stainless steels and nickel-base

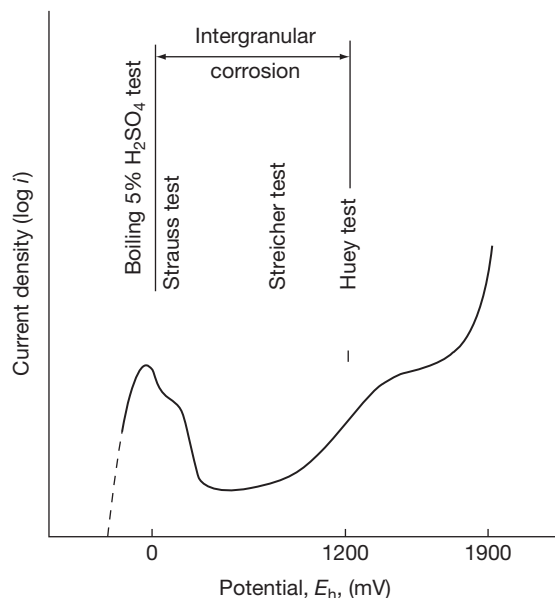


**Figure 9** Schematic polarization curve of an austenitic stainless steel in deaerated sulfuric acid with superimposed potential regimes for the ASTM A 262 test methods. Potentials are given versus the normal hydrogen electrode (NHE,  $E_h$ ). Reproduced from Osozawa, K.; Bohnenkamp, K.; Engell, H.-J. *Corros. Sci.* **1966**, 6, 421–433.

alloys are available.<sup>20</sup> Electrochemical tests are typically considered to be more sensitive for measuring the whole spectrum of sensitization, including lightly to severely sensitized materials. A saturation of the discriminating power, however, has been reported at high degrees of sensitization.<sup>46</sup> IGC tests based on weight loss or surface fracture measurements (i.e., [Tables 2 and 3](#)) are more sensitive to medium and high degrees of sensitization, but can generally not discriminate low to medium degrees of sensitization.

Three electrochemical test methods are typically used for the assessments of the degree of sensitization, as summarized in [Table 4](#). These test comprise (i) the electrochemical reactivation (EPR)<sup>37</sup> test, (ii) the double-loop electrochemical potentiokinetic reactivation (DL-EPR)<sup>47</sup> test, and (iii) Cihal's DL-EPR<sup>31</sup> test. All tests are based on similar principles, but differ in the way the data are analyzed. [Figure 10\(a\)](#) shows EPR curves for a sensitized and non-sensitized stainless steel and [Figure 10\(b\)](#) shows a DL-EPR curve for a sensitized stainless steel with characteristic parameters. All three methods for quantifying the degree of sensitization are based on measuring the reactivation current density ( $i_{\text{reactivation}}$ ) in a solution of sulfuric acid and thiocyanate. The thiocyanate functions as a

**Table 4** Methods for detecting and quantifying the degree of sensitization in stainless steels and nickel alloys<sup>31,37,47</sup>

Method	Test solution	Materials	Assessments
ASTM G 108 (2004)	0.5 M Sulfuric acid + 0.01 M KSCN	Type 304/Type 304L	$Q_{\text{reactivation}}$ and $i_{\text{reactivation}}$ ( $Q_{\text{reactivation}}/\text{GB area}$ )
-EPR Test-			
ISO 12732 (2006)	0.5–2.5 M Sulfuric acid + 0.001–	Stainless steels	Ratio = ( $i_{\text{reactivation}}/i_{\text{anodic}}$ )
-Cihal's DL-EPR Method-	0.05 M KSCN	Nickel alloys	Ratio = ( $i_{\text{reactivation}}/\text{GB area}$ )/ ( $i_{\text{anodic}}/\text{Specimen area}$ )
			Ratio = ( $Q_{\text{reactivation}}/\text{GB area}$ )/ ( $Q_{\text{anodic}}/\text{Specimen area}$ )
DL-EPR	0.5 M Sulfuric acid + 0.01 M KSCN	Type 304	Ratio = ( $i_{\text{reactivation}}/i_{\text{anodic}}$ )

GB = Grain boundary,  $i_{\text{reactivation}}$  = Maximum reactivation current density,  $Q_{\text{reactivation}}$  = Reactivation charge density,  $Q_{\text{anodic}}$  = Anodic charge density.

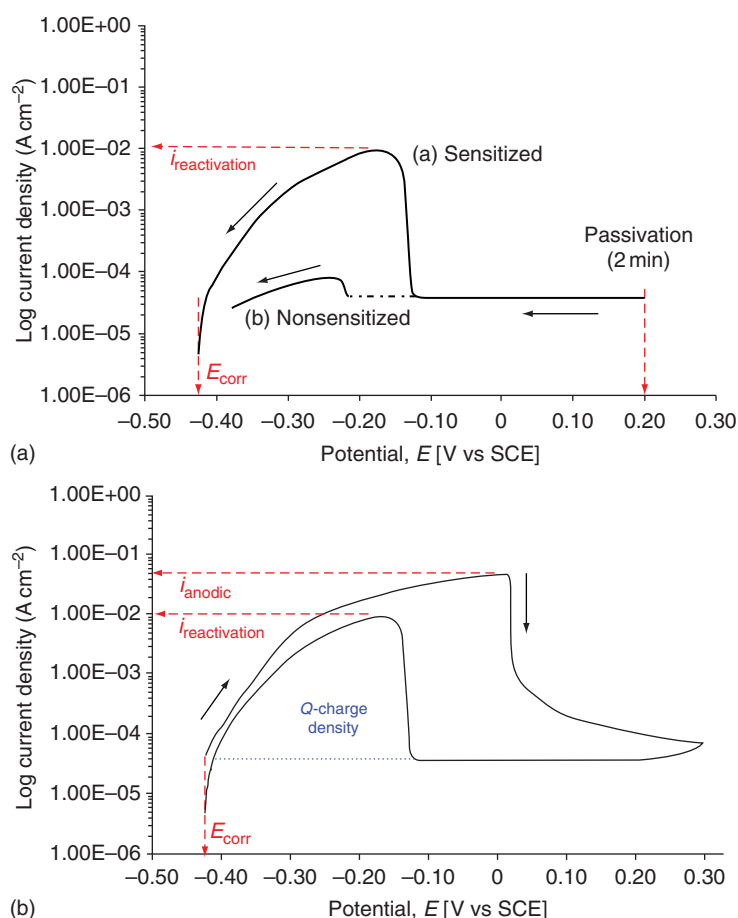


**Figure 10** (a) Schematic diagram of an EPR test for sensitized (curve a) and non-sensitized (curve b) stainless steel. (b) Schematic diagram of a DL-EPR test with characteristic parameters. ( $E_{\text{Corr}}$  = corrosion potential,  $i_{\text{anodic}}$  = maximum anodic current density,  $i_{\text{reactivation}}$  = reactivation current density,  $Q$  = charge density.)

depassivator, and increases the anodic dissolution during the anodic sweep, as well as the grain boundary attack during the reactivation sweep.<sup>47</sup> On sensitized material, the breakdown of the passive film on chromium depleted areas leads to the reactivation peak, but on nonsensitized material, the passive film remains

virtually intact, and either no or only a small increase in reactivation current density is observed. The maximum height ( $i_{\text{reactivation}}$  – current density) and area ( $Q$  – charge density) under the reactivation curve is a quantitative measure of the degree of sensitization (Figure 10).



The EPR test is a standard test method (ASTM G 108),<sup>37</sup> often referred to as the single-loop EPR test (SL-EPR). Evaluation of the degree of sensitization is carried out after an initial passivation treatment (+0.2 V<sub>SCE</sub> for 2 min), by measuring the maximum reactivation current ( $i_{\text{reactivation}}$ ) or charge density ( $Q$ ). The reactivation charge density can also be normalized to the grain size, and gives a measure of attacked grain boundary area. After testing, the specimen has to be examined under an optical microscope, to determine whether the measured reactivation current is derived from chromium depleted regions at the grain boundaries, and not from intragranular pitting. A major drawback of this test is its sensitivity to material composition, thermomechanical process history, surface finish, and nonmetallic inclusions.<sup>37</sup>

An advanced version of the EPR tests is the double-loop technique (DL-EPR)<sup>47</sup> for Type 304 stainless steels. This test has frequently been used due to its ease of application. The degree of sensitization is determined with the maximum reactivation current density ( $i_{\text{reactivation}}$ ) divided by the maximum anodic current density ( $i_{\text{anodic}}$ ), without assessment of the grain boundary area. For an improved correlation between results derived from the DL-EPR and the EPR test, however, it is recommended to normalize the reactivation current density by the grain boundary area.<sup>47</sup> The DL-EPR test is not sensitive to the surface finish of the specimen, since the anodic sweep causes a general dissolution of the test surface.

A modified version of the DL-EPR test, based on Cihal's method, has been incorporated as a standard test method (ISO 12732).<sup>31</sup> This test is applicable for a broad range of stainless steels, including supergrades, as well as for certain nickel-base alloys. For this purpose, the sulfuric acid and thiocyanate concentrations can be tailored (Table 4). The assessment of Type 304 stainless steel is carried out with the same test parameters and solution concentrations as used for the EPR and DL-EPR tests. Cihal's test is assessed with the ratio of the reactivation current density, divided by the grain boundary area, and the maximum anodic current density, divided by specimen area. This accounts for a general dissolution of the surface during the anodic sweep, in relation to the dissolution of the sensitized grain boundary area during the reactivation sweep. The same assessment can also be carried out by using the charge densities instead of current densities. For comparing sensitized materials with similar grain sizes, the ratio between the maximum reactivation current density ( $i_{\text{reactivation}}$ ) and the maximum

anodic current density ( $i_{\text{anodic}}$ ) can also be employed, similar to the DL-EPR test.<sup>47</sup> A comparison of typical values for the EPR, DL-EPR, and Cihal's test is given in corresponding literature sources.<sup>31,47</sup>

## Acknowledgments

The author would like to thank Dr. T.J. Marrow, Dr. P.M. Wood and Prof. S.B. Lyon for their support and valuable feedback during the preparation of this manuscript.

## References

1. Cihal, V. *Intergranular Corrosion of Steels and Alloys*; Elsevier, 1984.
2. Joshi, A.; Stein, D. F. *Corrosion* **1972**, 28(9), 321–330.
3. Kasparova, O. V. *Protect. Met.* **2000**, 36(6), 524–532.
4. Henthorne, M. *STP 516: Localized Corrosion – Cause of Metal Failure*; ASTM, 1972; pp 66–119.
5. Buchheit, R. G.; Boger, R. K.; Carroll, M. C.; Leard, R. M.; Paglia, C.; Searls, J. L. *J. Miner. Met. Mater. Soc.* **2001**, 53(7), 29–36.
6. Dayal, R. K.; Parvathavarthini, N.; Raj, B. *Int. Mater. Rev.* **2005**, 50(3), 129–155.
7. Randle, V. *Acta Metall. Mater.* **1994**, 42(6), 1769–1784.
8. Wolf, D. In *Materials Interfaces – Atomic-Level Structure and Properties*; Wolf, D., Yip, S., Eds.; Chapman & Hall, 1992; pp 1–57.
9. ASTM E 112: Standard Test Method for Determining Average Grain Size; 1996.
10. ASTM A 262: Standard Practices for Detecting Susceptibility to Intergranular Attack in Austenitic Stainless Steel; 2001.
11. Sutton, A. P.; Balluffi, R. W. *Interfaces in Crystalline Materials*; Oxford University Press, 1995.
12. Wolf, D.; Merkle, K. L. In *Materials Interfaces: Atomic-Level Structure and Properties*; Wolf, D., Yip, S., Eds.; Chapman & Hall, 1992; pp 87–150.
13. Bennet, B. W.; Pickering, H. W. *Metall. Trans. A* **1985**, 18, 1117–1124.
14. Lifka, B. W.; Sprowls, D. O. *ASTM STP 516: Localized Corrosion – Cause of Metal Failure*; ASTM, 1972; pp 120–144.
15. Davis, J. R. *Corrosion of Aluminum and Aluminum Alloys*; ASM International, 1999.
16. Marshall, P. *Austenitic Stainless Steels – Microstructure and Mechanical Properties*; Elsevier, 1984.
17. Streicher, M. A. In *ASTM STP 656: Intergranular Corrosion of Stainless Alloys*; Steigerwald, R. F., Ed.; ASTM, 1978; pp 3–84.
18. Frankenthal, R. P.; Pickering, H. W. *J. Electrochem. Soc.* **1973**, 120(1), 23–26.
19. Lula, R. A.; Davis, J. A. *ASTM STP 656: Intergranular Corrosion of Stainless Alloys*; ASTM, 1978; pp 233–247.
20. Cihal, V.; Stefec, R. *Electrochim. Acta* **2001**, 46, 3867–3877.
21. Devine, T. M. *Acta Metall.* **1988**, 36(6), 1491–1501.
22. Devine, T. M.; Drummond, B. J. *Corrosion* **1981**, 37(2), 104–115.
23. Palumbo, G.; Aust, K. T. *Acta Metall. Mater.* **1990**, 38(11), 2343–2352.

24. Uhlig, H. H.; Duquette, D. J. *Corros. Sci.* **1969**, *9*, 557–560.
25. Mieluch, J.; Smialowski, M. *Corros. Sci.* **1964**, *4*, 237–243.
26. Zhang, X. G. *Corrosion and Electrochemistry of Zinc*; Springer, 1996.
27. Nielsen, R. In *Ullmann's Encyclopedia of Industrial Chemistry*, 5th ed.; Elvers, B., Hawkins, S., Eds.; VCH, 1996; Vol. 28A.
28. ISO 9400: Nickel-Based Alloys-Resistance to Intergranular Corrosion 1996.
29. ISO 3651-1: Determination of Resistance to Intergranular Corrosion of Stainless Steels: Part 1: Austenitic and Ferritic–Austenitic (Duplex) Stainless Steels – Corrosion Test in Nitric Acid Medium by Measurement of Loss in Mass (Huey Test) 1998.
30. ISO 3651-2: Determination of Resistance to Intergranular Corrosion of Stainless Steels: Part 2: Ferritic, Austenitic, and Ferritic–Austenitic (Duplex) Stainless Steels – Corrosion Test in Media Containing Sulfuric Acid 1998.
31. ISO 12732: Corrosion of Metals and Alloys – Electrochemical Potentiokinetic Reactivation Measurement using the Double Loop Method (based on Cihal's Method) 2006.
32. ISO 15329: Corrosion of Metals and Alloys – Anodic Test for Evaluation of Intergranular Corrosion Susceptibility of Heat-Treatable Aluminum Alloys 2008.
33. ISO 11846: Corrosion of Metals and Alloys – Determination of Resistance to Intergranular Corrosion of Solution Heat-Treatable Aluminum Alloys 2008.
34. ASTM G 34: Standard Test Method for Exfoliation Corrosion Susceptibility in 2XXX and 7XXX Series Aluminum Alloys (Exco Test) 2001.
35. ASTM G 28: Standard Test Methods of Detecting Susceptibility to Intergranular Corrosion in Wrought, Nickel Rich, Chromium-Bearing Alloys 2002.
36. ASTM G 110: Standard Practice for Evaluating Intergranular Corrosion Resistance of Heat Treatable Aluminum Alloys by Immersion in Sodium Chloride + Hydrogen Peroxide Solution 2003.
37. ASTM G 108: Standard Test Method for Electrochemical Reactivation (EPR) for Detecting Sensitization of AISI 304 and 304L Stainless Steel 2004.
38. ASTM G 67: Standard Test Method for Determining the Susceptibility to Intergranular Corrosion of 5XXX Series Aluminum Alloys by Mass Loss After Exposure to Nitric Acid (NAML Test) 2004.
39. ASTM A 763: Standard Practice for Detecting Susceptibility to Intergranular Attack in Ferritic Stainless Steel 2004.
40. ASTM G 31: Standard Practice for Laboratory Immersion Corrosion Testing of Metals 2004.
41. ASTM G 66: Standard Test Method for Visual Examination of Exfoliation Corrosion Susceptibility of 5XXX Series Aluminum Alloys (ASSET Test) 2005.
42. Sprowls, D. O.; Walsh, J. D.; Shumaker, M. B. *ASTM STP 516: Localized Corrosion – Cause of Metal Failure*; ASTM, 1972; pp 38–65.
43. Craig, H. L., Jr. *ASTM STP 516: Localized Corrosion-Cause of Metal Failure*; ASTM, 1972; pp 17–37.
44. Osozawa, K.; Engell, H.-J. *Corros. Sci.* **1966**, *6*, 389–393.
45. Osozawa, K.; Bohnenkamp, K.; Engell, H.-J. *Corros. Sci.* **1966**, *6*, 421–433.
46. Clarke, W. L.; Cowan, R. L.; Walker, W. L. In *ASTM STP 656: Intergranular Corrosion of Stainless Alloys*; Steigerwald, R. F., Ed.; ASTM, 1978; pp 99–132.
47. Majidi, A. P.; Streicher, M. A. *Corrosion* **1984**, *40*(11), 584–593.
48. Trillo, E. A.; Beltran, R.; Maldonado, J. G.; Romero, R. J.; Murr, L. E.; Fisher, W. W.; Advani, A. H. *Mater. Char.* **1995**, *35*, 99–112.
49. Bruemmer, S. M.; Was, G. S. *J. Nucl. Mater.* **1994**, *216*, 348–363.

## 2.07 Galvanic Corrosion

**H. P. Hack**

176 Via Dante, Arnold, MD 21012, USA

© 2010 Elsevier B.V. All rights reserved.

2.07.1	Introduction	829
2.07.2	Electrochemical Theory	829
2.07.3	Examples of Galvanic Corrosion	836
2.07.4	Benefits of Galvanic Corrosion	837
2.07.5	Recognizing Galvanic Corrosion	838
2.07.6	Predicting Galvanic Corrosion	838
2.07.6.1	Experience	839
2.07.6.2	Exposure Data	839
2.07.6.3	Laboratory Data	839
2.07.6.4	Computer Modeling	839
2.07.6.5	Physical Scale Modeling	840
2.07.6.6	Wagner Number	840
2.07.7	Prevention	841
2.07.8	Testing	844
2.07.8.1	General Principles	844
2.07.8.2	Testing Hardware	844
2.07.8.3	Making a Galvanic Series	844
2.07.8.4	Determining Polarization	845
2.07.8.5	Determining $IR$ Drop	845
2.07.8.6	Determining Corrosion Rate	846
2.07.8.7	Accelerated Tests	847
2.07.8.8	Atmospheric Testing	847
2.07.9	Standards	850
2.07.10	Useful Galvanic Corrosion Data	850
2.07.10.1	Atmospheric Corrosion	850
2.07.10.2	Seawater Immersion	851
2.07.10.3	Other Environments	853
References		855

### Abbreviations

**C.D.** Current density

**FS** Full scale

**IR** Potential drop due to a current across a resistance

**LCS** Low carbon steel

**MRE** Meals ready to eat

**SS** Stainless steel

### Symbols

**A** Cross-sectional area

**$B_a$**  Anodic Tafel slope

**$B_c$**  Cathodic Tafel slope

**$dE/di$**  Local slope of the polarization curve

**$E_A$**  Potential of material A

**$E_{AB}$**  Coupled potential of materials A and B

**$E_B$**  Potential of material B

**$E$**  Potential

**$E_{corr}$**  Corrosion potential

**$E_{couple}$**  Coupled potential

**$E(H^+/H_2)$**  Potential of the reaction between hydrogen ions and hydrogen gas

**$E(M/M^+)$**  Potential of the reaction between metal M with its ions

**$E(N/N^+)$**  Potential of the reaction between metal N with its ions

**$E_{pp}$**  Primary passivation potential

**$i$**  Current density

$i_0$ ( $\text{H}_2/\text{M}$ )	Exchange current density for the reaction of hydrogen gas on metal M
$i_0$ ( $\text{H}_2/\text{N}$ )	Exchange current density for the reaction of hydrogen gas on metal N
$i_0$ ( $\text{M}$ )	Exchange current density for the reaction of metal M with its ions
$i_0$ ( $\text{N}$ )	Exchange current density for the reaction of metal N with its ions
$i_{\text{cc}}$	Critical current density
$i_{\text{corr}}$ (couple)	Current exchanged between all anode and cathode reactions
$i_{\text{corr}}$ ( $\text{M}$ )	Corrosion rate per unit area of metal M
$i_{\text{corr}}$ ( $\text{N}$ )	Corrosion rate per unit area of metal N
$i_{\text{corr}}$	Corrosion current density
$I_{\text{corr}}$	Total corrosion current
$I_{\text{measured}}$	Measured galvanic current
$i_p$	Passive current density
$I$	Current
$I_{\text{AB}}$	Coupled current between materials A and B
$I_{\text{anodic}}$	Total anodic current
$I_{\text{applied}}$	Total applied current
$I_{\text{cathodic}}$	Total cathodic current
$I_{\text{total}}$	Total current
$L$	Length
$n$	Number of electrons exchanged in a reaction
$R$	Resistance
$W$	Wagner number
$\rho$	Resistivity

## 2.07.1 Introduction

Galvanic corrosion, also known as bimetallic corrosion, is a common mode of corrosion failure that is, for the most part, entirely preventable by proper corrosion design. It is the aim of this chapter to provide the reader with the knowledge and data to aid in recognizing this form of corrosion when it occurs and making the right design decisions to prevent it.

The ASTM International Committee G01 on Corrosion of Metals defines galvanic corrosion as “accelerated corrosion of a metal because of an electrical contact with a more noble metal or nonmetallic conductor in a corrosive environment.”<sup>1</sup> NACE International defines galvanic corrosion as “corrosion associated with the current resulting from an electrical coupling of dissimilar electrodes in an electrolyte.”<sup>2</sup> International Organization for Standards (ISO) defines galvanic corrosion as “Corrosion due to the action of a corrosion cell [a short-circuited combination of different electrodes connected in

series with an ionic conductor].”<sup>3</sup> Other organizations that have definitions for galvanic corrosion include The Electrochemical Society, the American Water Works Association, The American Chemical Society, and others. What these definitions all have in common is that galvanic corrosion involves the electrical interaction of at least two different metals or nonmetallic conductors in an environment that accelerates the corrosion of at least one of them. The common factors are dissimilar metals, electrical contact, and a conductive electrolyte in contact with them. If any of these factors is absent, galvanic corrosion cannot occur.

Galvanic corrosion accelerates the normal corrosion of a metal in an electrolyte. Even without galvanic corrosion, metals may suffer from uniform corrosion, crevice corrosion, pitting, or other forms of corrosion. Galvanic corrosion has an accelerating effect on these other forms of corrosion and, in some cases, causes a form of corrosion to occur that would otherwise not be seen.

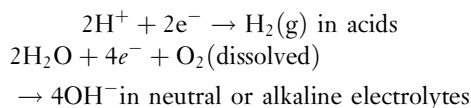
## 2.07.2 Electrochemical Theory

When a metal or nonmetallic conductor is immersed in a conductive solution, or an electrolyte, a series of reactions takes place that can cause corrosion. The corrosion reaction itself involves a change in the charge of the metal atoms from zero in the metal to a positive value for metal ions in the solution. Because this is a positive change in charge the reaction is called an anodic reaction and can be written as:



where M = some metal atom or ion, and  $n$  is a number typically between 1 and 3 depending on the metal and electrolyte.

Since this reaction generates free electrons and since charge neutrality must be maintained, these electrons must be used up in one or more other reactions where charge is reduced in order for corrosion to proceed. These are called cathodic reactions, and the most common ones found in aqueous environments are:



The progression of the anodic and cathodic reactions, the flow of electrons, and the ionic motion in the electrolyte needed to complete the current flow are

shown in **Figure 1** for a piece of iron corroding in neutral water.

Corrosion cannot proceed unless all of the electrons generated by the anodic reaction are used up by a cathodic reaction. The balance between these two reactions leads to each metal, alloy, or nonmetallic conductor equilibrating at an electrochemical potential that is unique to that material and electrolyte, called the corrosion potential. For a given electrolyte, the corrosion potential of a number of materials can be listed together. Such a listing, where the materials are arranged according to ascending or descending corrosion potential, is called a galvanic series. If two materials with different corrosion potentials are immersed in that electrolyte and electrically coupled, there is a driving force for a current, called the galvanic current, to flow between them. It is this flow of current that increases corrosion of the material with the more negative potential, called the anode, while suppressing the corrosion of the more positive material, called the cathode.

The most common galvanic series is the one shown in **Figure 2** for metals in seawater. Metals

with more negative corrosion potentials are said to be anodic compared to metals with more positive, or cathodic, potentials in a galvanic series.

In this case, the corrosion potentials are given as ranges, since seawater composition can vary and since corrosion potentials can be influenced by the presence of corrosion products on the surface of the corroding metal. Some metals show two bands of corrosion potentials, one in white and the other in black. These are metals that can exist in two different states in seawater, a passive state during which they are not corroding and an active state when they are corroding. Each state is associated with a different range of corrosion potentials. This galvanic series is only applicable in seawater at a specific temperature range and flow rate, and should not be applied to other environments.

Galvanic series are useful to predict which metal in a pair of electrically connected materials in an electrolyte, called a galvanic couple, will tend to have its corrosion rate accelerated by the electrical contact. The fact that there is a driving force for current to flow between the dissimilar materials and

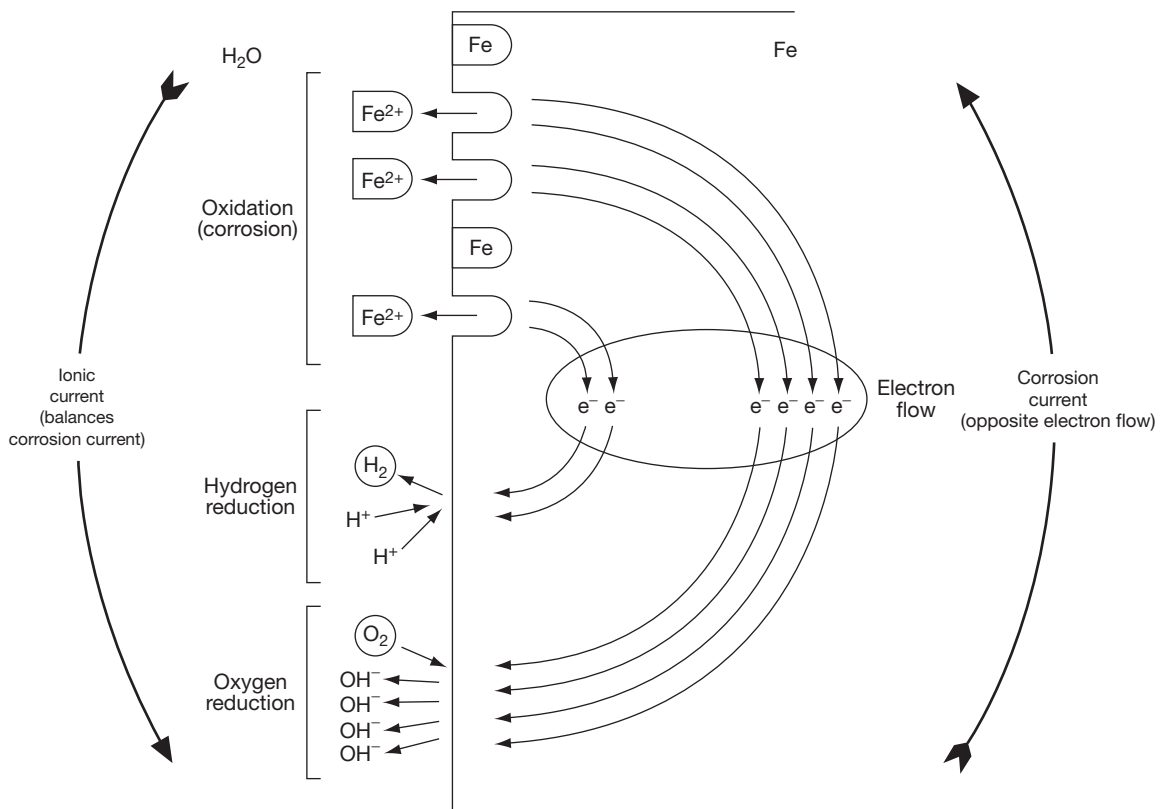


**Figure 1** Iron corroding in water. Reproduced from Hack, H. P. *Corrosion Testing Made Easy*; NACE International: Houston, TX, 1993; Volume 2.



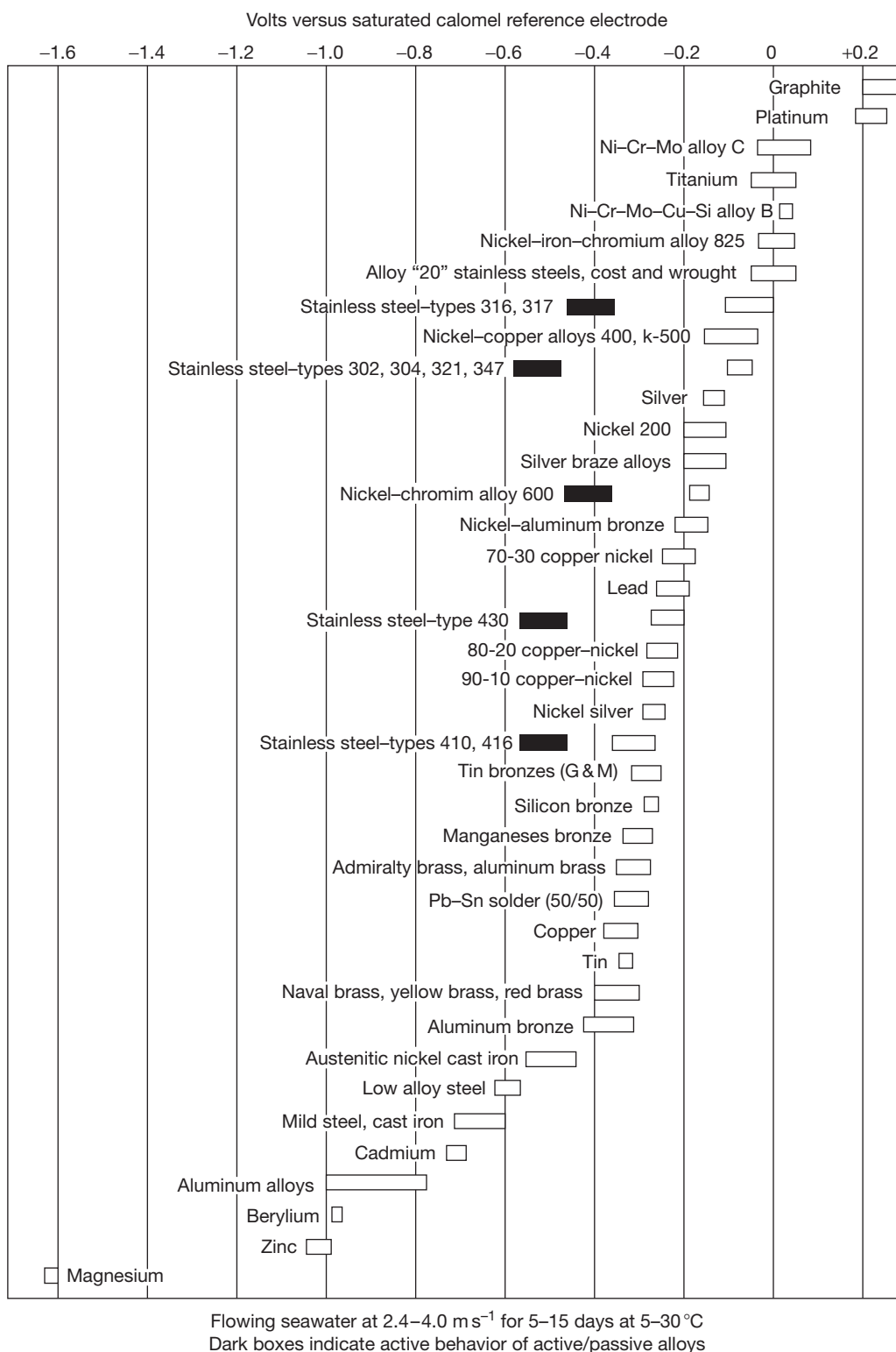


**Figure 2** Galvanic series for metals in seawater with moderate flow. Reproduced from Standard G82: Guide for Development and Use of a Galvanic Series for Predicting Galvanic Corrosion Performance, *ASTM Book of Standards*; ASTM International: West Conshohocken, PA, 2006.

for the corrosion of the anode in the couple to increase does not mean, however, that the magnitude of this current and resulting corrosion will be significant.

When two dissimilar materials with dissimilar corrosion potentials are coupled in an electrolyte, they will each be forced to a common potential somewhere between the two individual corrosion potentials. When coupled, materials with similar corrosion potentials have no driving force for causing galvanic corrosion. However, materials far apart in potential will not necessarily result in higher galvanic corrosion rates than materials close together in potential. The magnitude of current flow and the increase in corrosion rate due to this coupling are determined by the tendency of each of the materials in the couples to deliver current when its potential is forced to change, called polarization. If a material delivers little current for a large change in potential, it is said to have a large polarization resistance, while if it can deliver a large current for a small enforced potential change, it is said to have a small polarization resistance. This is illustrated by plotting the current produced as a function of applied potential, called a polarization curve. Examples of polarization curves for metals with high and low polarization resistances are shown in Figure 3. In this figure, when the cathode has low polarization resistance and the anode has high resistance, the couple is said to be under cathodic control. When the reverse is the case, the couple is said to be under anodic control, and when the polarization resistances of the anode and cathode reactions are similar the couple is said to be under mixed control.

When two materials are coupled in an electrolyte, the galvanic current flowing between them is determined by a superposition of the cathodic polarization curve of the anodic metal with the anodic polarization curve of the cathodic material, shown in Figure 4. In this figure,  $I_{\text{measured}}$  is the galvanic current that flows through the metallic path between the two metals, in this case copper and iron.

The magnitude of the galvanic current flowing in a galvanic couple gives a qualitative feel for the amount of increased corrosion of the anode, but it is not a good quantitative measure. To understand why this is so, it is necessary to look at the magnitude of the anodic and cathodic reactions that are occurring on each metal in the couple, both before the metals are electrically connected and afterwards. To understand corrosion rates in a galvanic couple, it is necessary to look at a plot of individual reaction

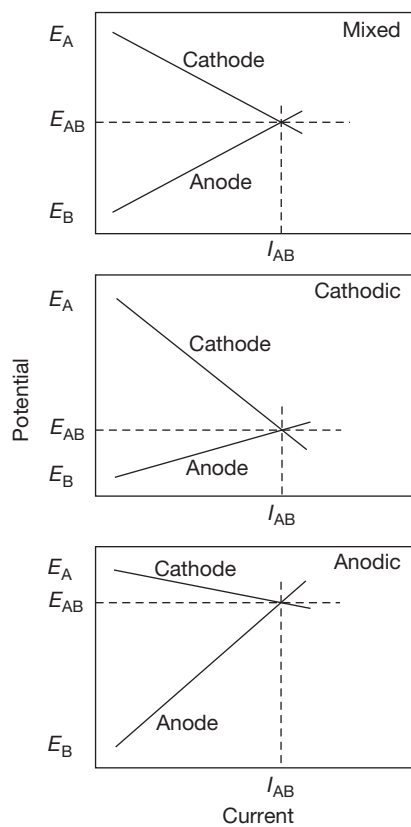


**Figure 3** Effect of polarization resistance on anode and cathode reactions. Reproduced from Standard G82: Guide for Development and Use of a Galvanic Series for Predicting Galvanic Corrosion Performance, *ASTM Book of Standards*; ASTM International: West Conshohocken, PA, 2006.

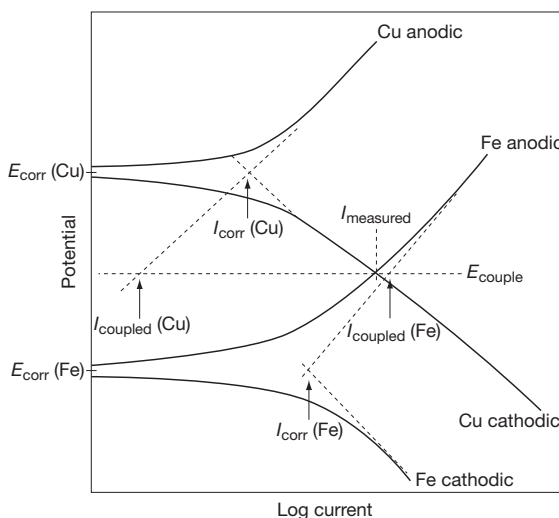


**Figure 4** Superposition of polarization curves to determine galvanic current. Reproduced from Hack, H. P. *Corrosion Testing Made Easy*; NACE International: Houston, TX, 1993; Volume 2.

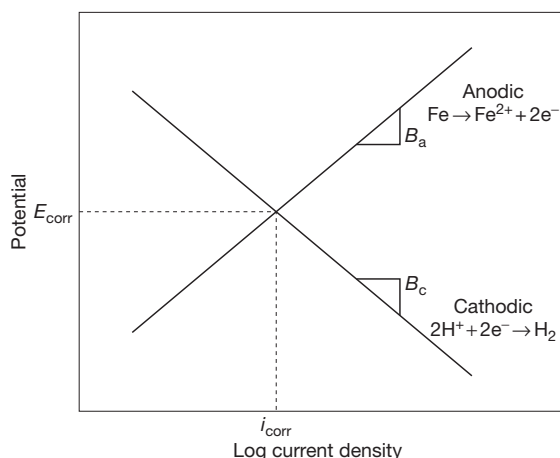


**Figure 5** Evans diagram for a corroding metal. Reproduced from Hack, H. P. *Corrosion Testing Made Easy*; NACE International: Houston, TX, 1993; Volume 2.

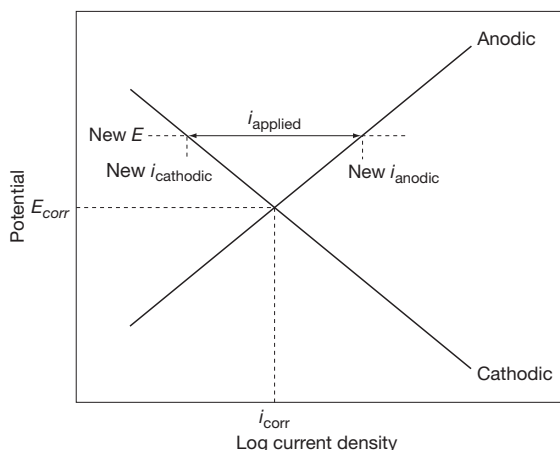


**Figure 6** Relationship between a forced potential shift and applied current. Reproduced from Hack, H. P. *Corrosion Testing Made Easy*; NACE International: Houston, TX, 1993; Volume 2.

rates as a function of potential, called an Evans diagram, for each of the materials in the couple before they are coupled (Figure 5). This figure shows the cathodic reaction to be hydrogen production, but any cathodic reaction, such as oxygen reduction, would behave similarly. The corrosion rate for iron in this diagram is  $i_{\text{corr}}$  and the corrosion potential is  $E_{\text{corr}}$ .

The rate of the anodic reaction increases as the potential becomes more positive, while the rate of the cathodic reaction increases as the potential becomes more negative. The net current flowing to or from the metal is the difference between these two

currents, or zero at the point where the two curves cross. Applying a current will force a potential shift to occur, as shown in the Evans diagram in Figure 6.

When two materials are coupled, the Evans diagrams for them are shown in Figure 7.

For two materials in electrical contact, the sum of all anodic reactions must equal the sum of all cathodic reactions. Where the anodic sum crosses the cathodic sum determines the potential of the galvanic couple, called the coupled potential. Once this potential is known, the rates of all reactions on both materials are read from the Evans diagram for each reaction at that coupled potential. This coupled potential can also be obtained from polarization curves, as shown in Figure 4. Figure 8 shows the polarization curves on an Evans diagram so that the relationship can be seen. The galvanic current from the polarization curves is the actual measurable current that flows between the two materials, but is not necessarily directly related to the corrosion rate of the anode.

In practice, it is difficult to determine the exact position of all reaction curves on all materials, particularly in complex environments like seawater. For this reason, it is more common to determine corrosion rates for galvanic corrosion by first determining the coupled potential using polarization curves, and then testing the anode material by holding it at that potential and measuring the actual corrosion rate experienced.

All the Evans diagrams and polarization curves for galvanic couples shown above have used either current density or total current on the horizontal axis, assuming that the exposed surface areas of the anode and cathode metals are the same. The effect of different exposed surface areas of the anode and cathode materials can be examined by realizing that the total current is just the current density multiplied by the exposed surface area. Larger exposed areas will shift the polarization curves to the right for that material. The effect of this on coupled potential and galvanic current is shown in Figure 9.

This leads to the conclusion that to minimize galvanic corrosion small cathode–anode area ratios are required, or conversely the larger this ratio, the larger is the galvanic corrosion. This is sometimes called the catchment area principle. For this reason, to control galvanic corrosion it is best to paint the noncorroding cathode, not the corroding anode, contrary to what might be inferred at first glance.

Polarization does not always take the form of straight lines on Evans diagrams. Real polarization

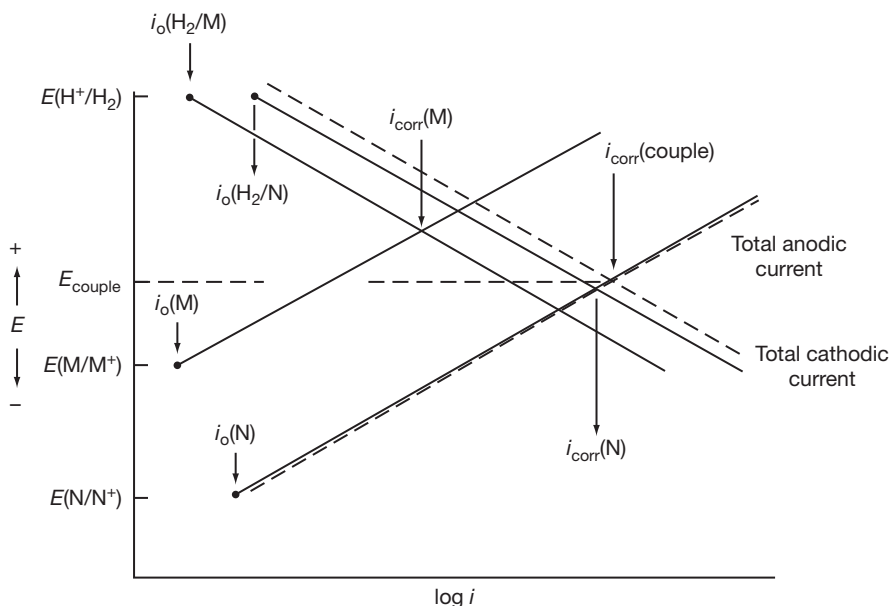


**Figure 7** Evans diagram for two materials in electrical contact. Reproduced from Standard G82: Guide for Development and Use of a Galvanic Series for Predicting Galvanic Corrosion Performance, *ASTM Book of Standards*; ASTM International: West Conshohocken, PA, 2006.

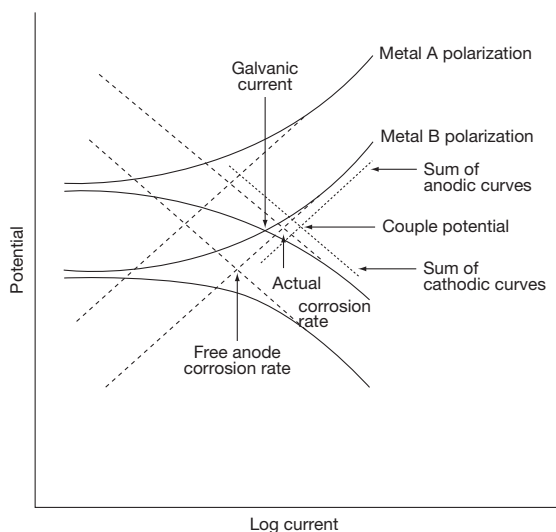


**Figure 8** Polarization curves on an Evans diagram. Reproduced from Hack, H. P. *Corrosion Testing Made Easy*; NACE International: Houston, TX, 1993; Volume 2.

curves are affected by the formation of corrosion products and the ability of reactants and reaction products to move to and from the surface where the reactions take place. This leads to various polarization curve shapes, including some that curve back on themselves, as shown in [Figure 10](#).

Galvanic reactions with materials having these types of curves can lead to some unusual corrosion

consequences, including having several different stable corrosion potentials for a given galvanic couple, as seen in [Figure 11](#).

If more than two materials with different corrosion potentials are electrically connected, they can be analyzed using the same principles as when two materials are analyzed, that is, using Evans diagrams. The anode and cathode reaction curves for all three materials are normalized to the proper surface areas and then put on the same diagram, together with the total anodic and total cathodic curves. Then the intersection point of latter curves defines the coupled potential. From this coupled potential the corrosion rate of all three materials can be determined.

Galvanic corrosion can also be affected by electrical or ionic resistances between the two coupled materials. Electrical resistance can come about if one of the materials is a poor electrical conductor or if the contact between them is not made properly. Ionic resistance occurs because electrolytes are not perfect conductors, so that high electrolyte resistivity coupled with a large distance between the anode and cathode materials can lead to significant resistance between the anode and cathode. Electrical and ionic resistance are treated the same when determining their effect on a galvanic couple. The total circuit resistance is the product of the galvanic current and the various resistances, frequently called *IR* drop. The effect of *IR* drop is seen in [Figure 12](#).

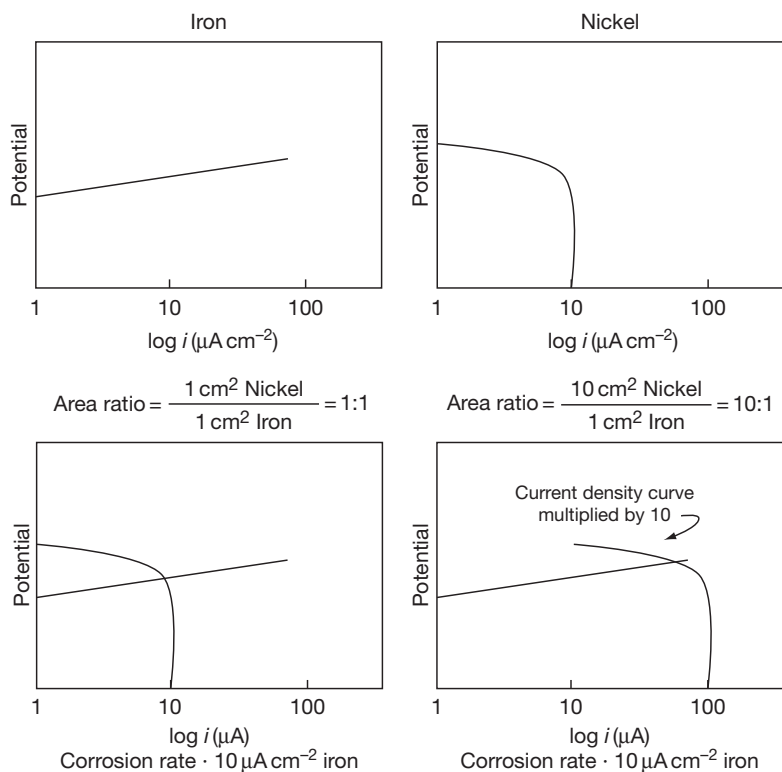


**Figure 9** Effect of area ratio on superimposed polarization curves. Reproduced from Hack, H. P. *Corrosion Testing Made Easy*; NACE International: Houston, TX, 1993; Volume 2.

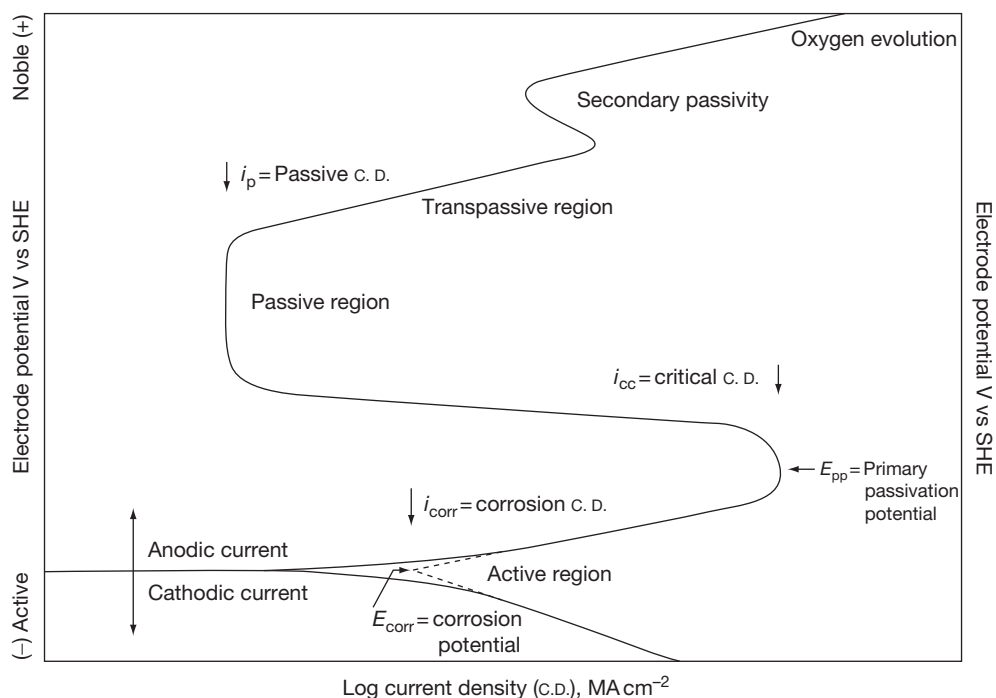


**Figure 10** Polarization curve for passive-film-forming metal such as 430 stainless steel in sulfuric acid. Standard G3: Practice for Conventions Applicable to Electrochemical Measurements in Corrosion Testing, *ASTM Book of Standards*; ASTM International: West Conshohocken, PA, 2006.



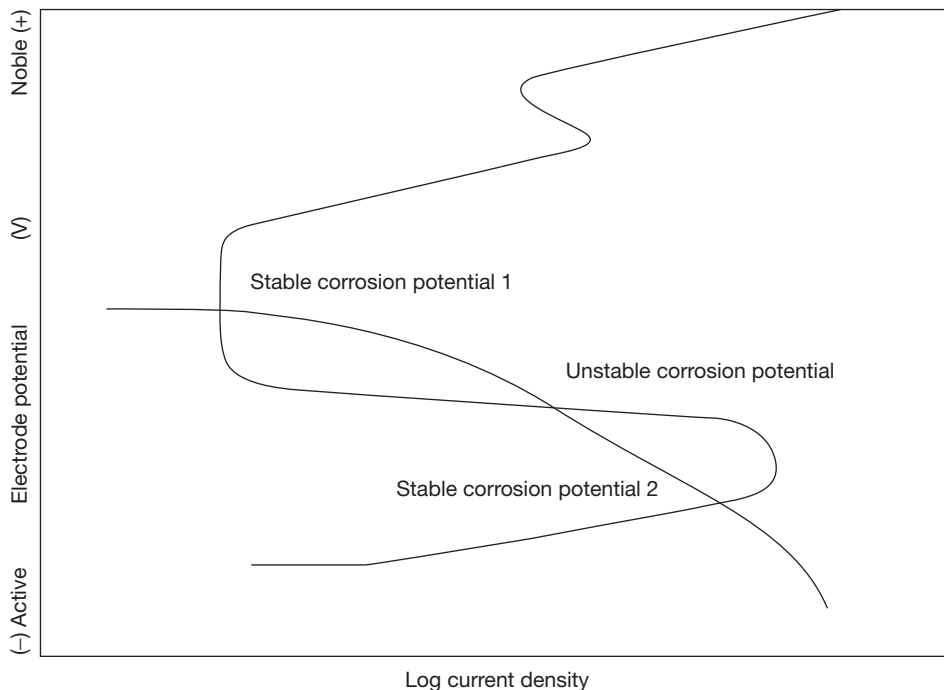


**Figure 11** Triple crossing of anodic and cathodic polarization curves leading to two stable corrosion potentials.

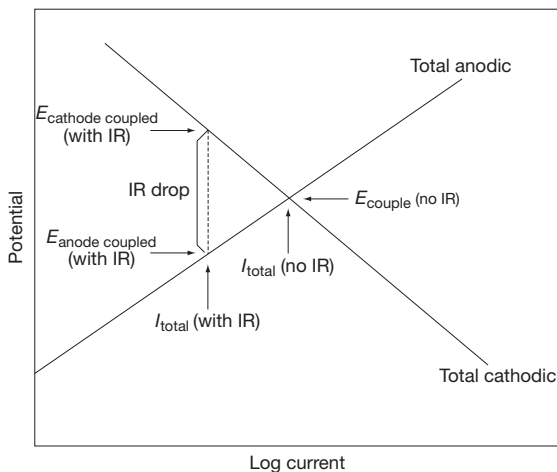


**Figure 12**  $IR$  drop leading to anode and cathode being at different potentials. Reproduced from Hack, H. P. *Corrosion Testing Made Easy*; NACE International: Houston, TX, 1993; Volume 2.

$IR$  drop leads to the anodic and cathodic materials being at different potentials, with the associated lowering of corrosion rate of the anode from the value if there were no resistance. Low galvanic currents lead to low  $IR$  drop, so this effect is more pronounced on large structures. Also, larger distances between anode and cathode lead to larger  $IR$  drops, and therefore

lower galvanic corrosion rates. For this reason, in galvanic couples that are large or where electrolyte resistance is high, galvanic corrosion rates are highest on the anode closest to the cathode and drop off as distance between anode and cathode increases. This falloff in corrosion rate with distance is one good method for identifying galvanic corrosion, although if conductivity is high or distances are small this dropoff effect may not be observed. This can be seen in [Figure 13](#).

### 2.07.3 Examples of Galvanic Corrosion

One typical example of galvanic corrosion is the use of dissimilar metal fasteners. When the fastener is anodic compared to the structure that it is fastening, the anode-to-cathode ratio is large and the fasteners will corrode quickly. When the fastener is cathodic compared to the structure the anode-to-cathode ratio is small and the corrosion acceleration of the structure around the fasteners is present but minimal as long as the electrolyte conductivity is high, as seen in [Figure 14](#).

Galvanic corrosion also commonly occurs in the attachment of dissimilar metal piping. Here,

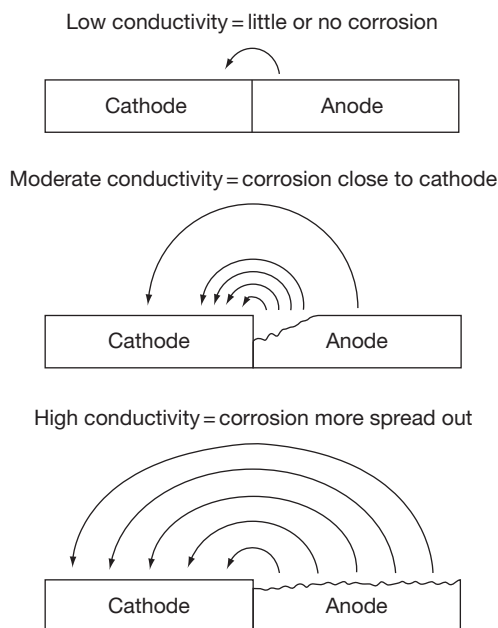


**Figure 13** Concentration of corrosion near cathode as a function of conductivity. Reproduced from Hack, H. P. *Corrosion Testing Made Easy*; NACE International: Houston, TX, 1993; Volume 2.

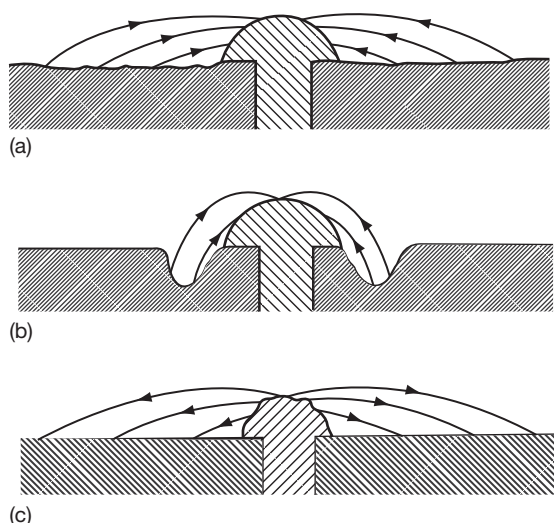


**Figure 14** Corrosion of fasteners and base plate in relation to the anode.<sup>6</sup> (a) Base plate is the anode in high-conductivity water; (b) base plate is the anode in low-conductivity water; (c) fastener is the anode.

corrosion of the more anodic pipe will be concentrated at the junction with the cathode.

Structures made from dissimilar metals are sometimes joined in soils. This can be inadvertent, such as when a section of pipe is replaced with a new piece of

pipe, not realizing that the new pipe is frequently cathodic to the old pipe. The new pipe will therefore cause the old pipe to corrode faster.

Sometimes in a mixed-metal structure one part that corrodes quickly will be 'upgraded' to a more corrosion-resistant material. Steel may be replaced with stainless steel, stainless steel with nickel alloys, etc. The more corrosion-resistant material is frequently cathodic to the other materials in the structure, causing galvanic corrosion of the structure close to the parts that were replaced. This makes it look like the corrosion problem is moving around the structure, while it is in fact due to lack of attention to galvanic corrosion in design of the replacement material.

Tube-tubesheet heat exchangers frequently use different materials for the tubes than for the tube-sheet, support structure, or shell. This can lead to galvanic corrosion of any of these parts, depending on the particular material combinations chosen.

## 2.07.4 Benefits of Galvanic Corrosion

Galvanic corrosion can be beneficial. The potential and current between dissimilar metals is used in a sensor for time of wetness in atmospheric corrosion testing.<sup>7</sup> When rainwater or dew is present on the sensor, a galvanic couple exists, whereas when the moisture is not present the galvanic couple is not active. Similar sensors can be buried inside lap joints or other hard-to-access areas and can be used to determine whether sufficient moisture is present for corrosion to occur where it cannot be seen.

Special materials that can generate high galvanic corrosion currents have been prepared in powder form. When wetted, these powders result in galvanic corrosion rates that are so high that significant heat is generated. This is how meals for the U.S. Armed Forces, called MREs (meals ready to eat), are heated in the field: just add water to get a hot meal.

There are other benefits to high galvanic corrosion rates. Special corrodible pins, consisting of a hollow anode with a cathode on the inside, have been produced in a way that the failure time for the pin is well characterized. Such pins are used in seawater to keep crab and lobster pot buoys submerged to prevent poaching for a given time period, after which the buoys are released by corrosion of the pin and the pots can be retrieved by their owners. A similar system is used to cause military sonobuoys,

used to detect enemy submarines, to sink after their useful lifetime is exhausted. A corrodible plug is used for this purpose to allow flooding of the buoy after a known period of time.

Galvanic corrosion is the basis for the operation of most batteries. The galvanic current produced by the couple is put to good use in our toys, cell phones, and other electronic hardware.

Finally, the cathode in a galvanic couple frequently has its corrosion rate decreased as a result of the couple. This is the basis for sacrificial anode cathodic protection used widely in seawater and soils to protect steel structures. By coupling the steel to a piece of anodic material such as zinc, aluminum, or magnesium, the accelerated corrosion of the anode causes corrosion of the steel to be reduced. The anode sacrifices itself to prevent corrosion of the steel and is periodically replaced as it is consumed.

### 2.07.5 Recognizing Galvanic Corrosion

There is no absolutely certain method of determining that corrosion seen on a structure is actually galvanic corrosion, since the action of galvanic corrosion is usually to accelerate the type of corrosion normally experienced by the anode material. There are clues, however, that can help to make the determination. Galvanic corrosion always involves two materials with different corrosion potentials electrically connected in a common electrolyte. Therefore, if two materials with different corrosion potentials are present in the system and they are electrically connected in a common electrolyte, this is a strong clue that the corrosion that is observed is galvanically accelerated. This is particularly true if the anodic material has a small surface area compared to the cathodic material and the two different materials are close together. If both materials are corroding, then this corrosion is unlikely to be galvanically accelerated.

There is one good indicator for galvanic corrosion, however. If the anodic material corrodes the fastest near the cathodic material, and if the amount of corrosion lessens as distance increases from the cathode, galvanic corrosion is the likely cause. For example, if a flange connects two dissimilar metal pipes and the metal with the more negative corrosion potential is corroding a lot near the flange and less far away from the flange, galvanic corrosion is indicated. Thickness loss of the anodic metal near

dissimilar metal lap joints or fasteners is likely to be due to galvanic corrosion. Some examples of galvanic corrosion are shown in [Figures 15–18](#).

### 2.07.6 Predicting Galvanic Corrosion

When designing a structure it is important to take into account galvanic corrosion either by preventing it or by predicting where it will occur and how much metal will be lost over time so that structure lifetime can be determined and maintenance activities can be planned accordingly. The methods used to predict galvanic corrosion include experience with similar materials and geometries in similar environments, use of exposure data in similar environments, use of laboratory test data, computer modeling, physical scale

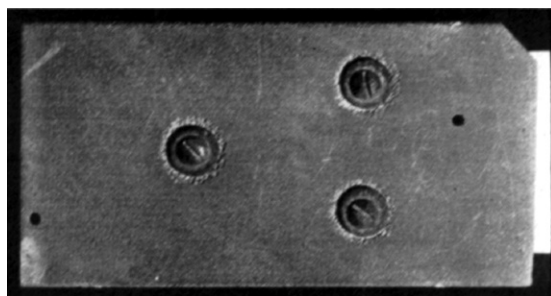


**Figure 15** Corrosion of an anodic plate due to cathodic screws. Reproduced from Copson, H. R. In *Corrosion Resistance of Metals and Alloys*, 2nd ed.; LaQue, F. L., Copson, H. R., Eds.; Reinhold Publishing: New York, NY, 1963; p 36, Chapter 1.

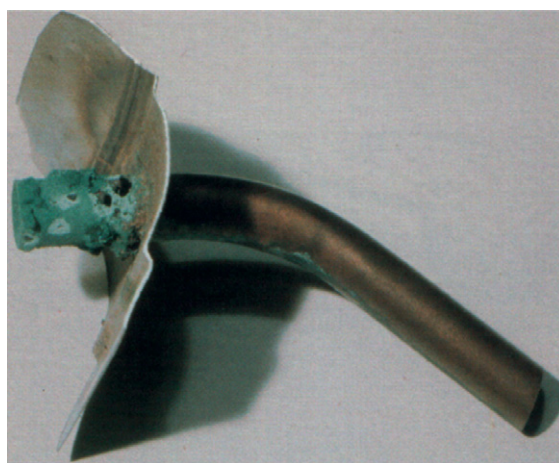


**Figure 16** Corrosion of copper pipe in a stainless-steel hot water cylinder. Reproduced from Francis, R. *Galvanic Corrosion: A Practical Guide for Engineers*; NACE: Houston, TX, 2001.



**Figure 17** Corrosion of a carbon steel weld in piping carrying partially deaerated seawater. Reproduced from Francis, R. *Galvanic Corrosion: A Practical Guide for Engineers*; NACE: Houston, TX, 2001.

modeling, and numerical calculations such as Wagner number. Each of these will be discussed below.

### 2.07.6.1 Experience

The best way to predict galvanic corrosion is to rely on experience with similar materials in similar geometries under similar environmental conditions to those of the structure being predicted. If you are designing a power plant condenser, experience with other power plant condensers is most useful, whereas if you are designing a metal roof system for a building, experience with similar roofing systems is the most valuable information to use. Locating data for the exact materials, the exact geometry, and the same environment can be difficult or impossible, in which case prediction must be based on another method.

### 2.07.6.2 Exposure Data

When the exact geometry cannot be found, exposure data from similar materials in a similar environment to that of interest can be used instead. The geometrical effects of area ratio and proximity of dissimilar materials can usually be accounted for in a qualitative fashion, while computer modeling can sometimes be used to get more quantitative predictions. Besides

selecting data from the same materials as those of interest, the most important test variable to consider is the environment. Galvanic corrosion can be very different in atmospheric environments, immersion in seawater or other chemicals, soils, inside concrete (such as reinforcing bar), etc. Even for atmospheric exposure, many variables can affect corrosion such as industrial versus rural, proximity to the sea, rainfall, humidity, amount of sunshine, and geometrical effects such as angle of exposure and shielding by neighboring structures.

### 2.07.6.3 Laboratory Data

Small-scale exposures of specimens in the laboratory can sometimes yield valuable information needed to predict galvanic corrosion. Laboratory tests can generate data on corrosion potentials, polarization behavior, and galvanic currents for specific geometries. Information regarding how to measure corrosion potentials and generate a galvanic series in a specific environment is given in a standard guide from ASTM International.<sup>5</sup> There are probably as many ways to generate polarization curves as there are investigators, but a good place to start is by generating either a potentiodynamic scan or a series of potentiostatic tests. Potentiostatic tests can also give a measure of the amount of corrosion of a metal as a function of its potential. Methods for conducting these tests are beyond the scope of this chapter.

Once corrosion potentials are known for the materials of interest in the environment of interest, classification of the material as an anode or a cathode can be made. Superposition of a cathodic polarization curve of the anode metal with an anodic polarization curve of the cathode material, with suitable scaling for relative surface areas, can generate information on the potential of the couple. Assuming no  $IR$  drop, this potential is the potential of both of the materials in the couple. Using potentiostatic corrosion rate data at this potential, the corrosion rate of the anode can be determined. This process of predicting galvanic corrosion rate from laboratory data is shown in [Figure 18](#).

### 2.07.6.4 Computer Modeling

Computer modeling, specifically boundary element modeling and to a lesser extent finite element modeling, can be used to predict the amount and distribution of galvanic corrosion on a complex structure. The computer requires input of a detailed geometrical

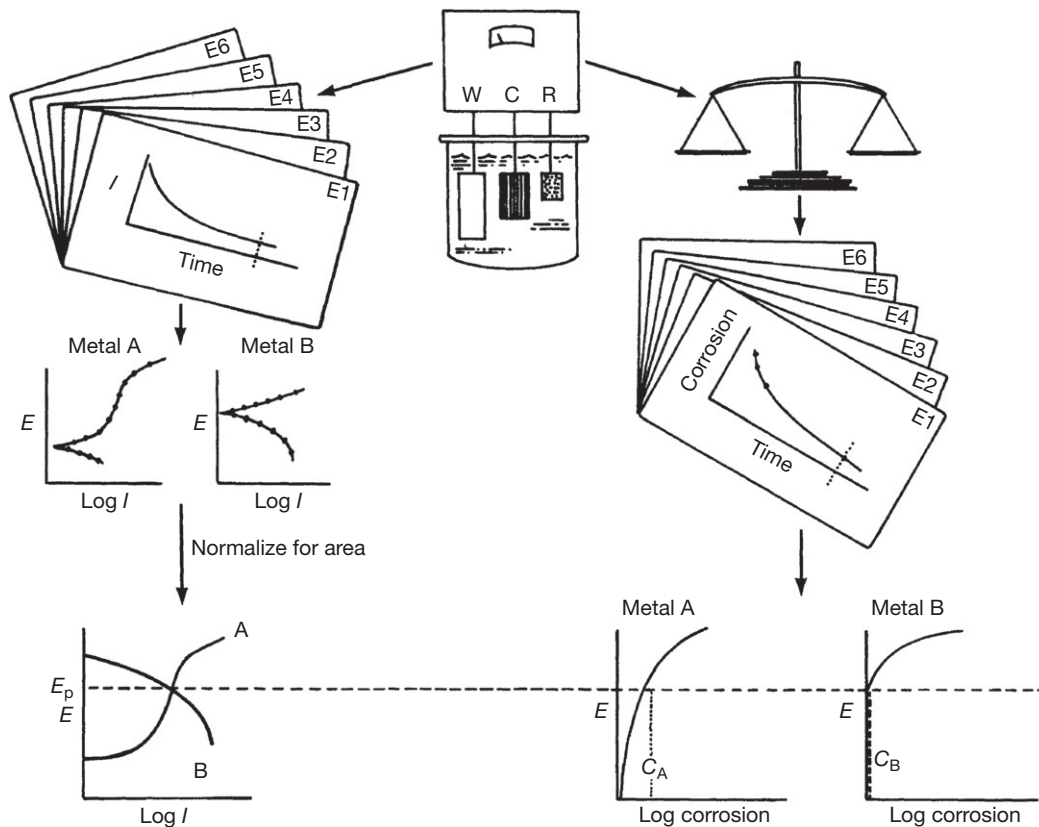


**Figure 18** Predicting galvanic corrosion rate from potentiostatic data. Reproduced from Hack, H. P. *Corrosion Testing Made Easy*; NACE International: Houston, TX, 1993; Volume 2.

model of all surfaces exposed to the environment, the ionic conductivity of the environment, and the polarization curves for all of the materials involved. The latter is the most difficult data to obtain, since in many real situations polarization curves vary as a function of time and potential. Nevertheless, some excellent modeling has been conducted for large structures in seawater, mostly related to sacrificial anode cathodic protection (the opposite of galvanic corrosion) but to a lesser extent to galvanic corrosion.<sup>8-21</sup> Examples are shown in [Figures 19 and 20](#).

### 2.07.6.5 Physical Scale Modeling

Physical scale modeling of complex structures has also been used to predict the amount and distribution of galvanic corrosion and cathodic protection.<sup>22-25</sup> Known by some investigators as dimension and conductivity scaling (DACS), proper scale modeling of corrosion processes involves increasing the resistivity of the environment by a factor equal to the dimensional scale factor. For example, a 1:10 scale model

must be tested in an environment that has 10 times the resistivity of the full-scale environment, as seen in [Figure 21](#).

### 2.07.6.6 Wagner Number

The Wagner number is the ratio of the polarization resistance of the materials of interest to the resistivity of the environment, expressed as the slope of a polarization curve.<sup>12,26,27</sup> It can be expressed as

$$W = (dE/di)/R \quad [1]$$

where  $dE/di$  is the local slope of the polarization curve of the metal of interest and  $R$  is the resistivity of the electrolyte.

If the Wagner number is large, galvanic current will flow far from the interface between anode and cathode, whereas if the Wagner number is small galvanic current will be more localized near the joint. Thus, large Wagner numbers are indicative of uniform distribution of galvanic corrosion, while



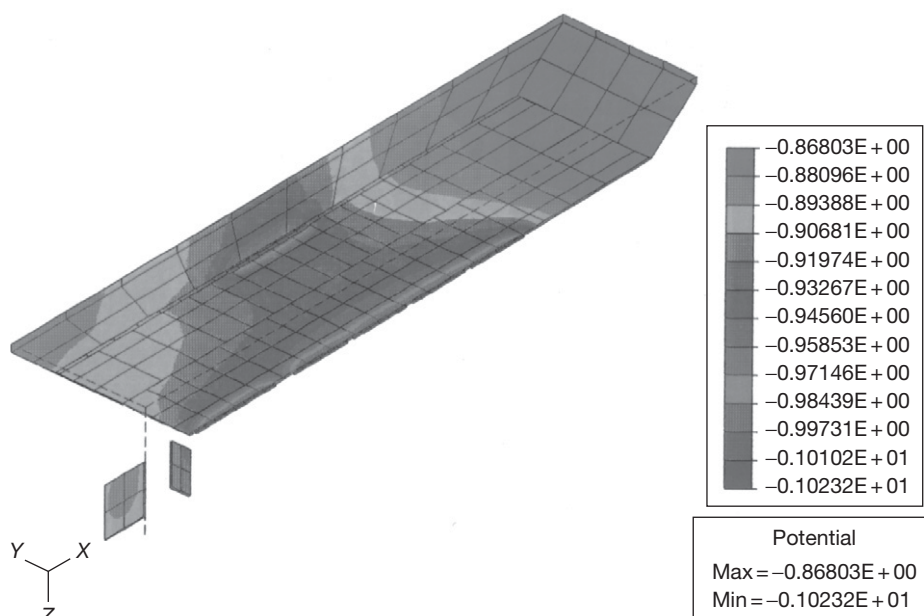


**Figure 19** Computer-predicted potential distribution on a 48-ft barge with sacrificial anodes (half model). Reproduced from Hack, H. P.; Janeczko, R. M. Verification of the boundary element modelling technique for cathodic protection of large ship structures, CARDIVNSWC-TR-61-93/02, Naval Surface Warfare Center Carderock Division, Bethesda, MD, December 1993.

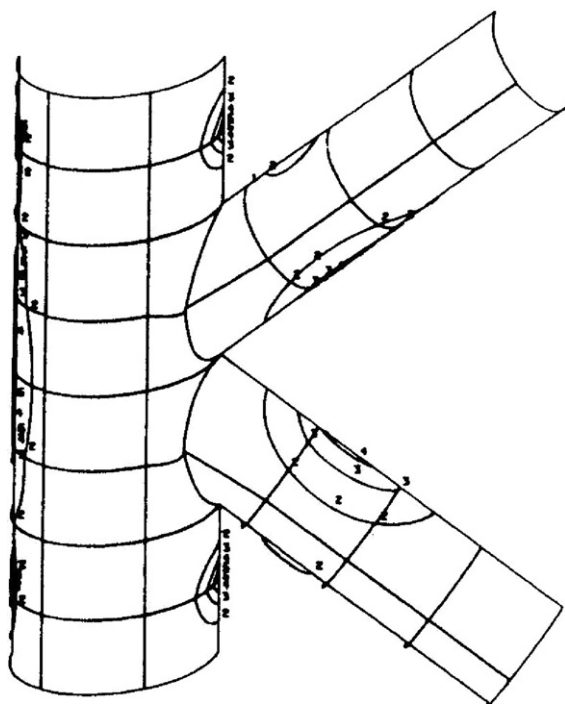


**Figure 20** Computer prediction of potential profiles on cathodically protected K joint on offshore oil platform. Reproduced from Adey, R. A.; Niku, S. M. In *Galvanic Corrosion*; Hack, H. P. Ed.; ASTM International: West Conshohocken, PA, 1988; ASTM STP 978, pp 96-117.

small Wagner numbers indicate localized galvanic corrosion. The effect of Wagner number is shown in [Figure 22](#).

### 2.07.7 Prevention

There are several ways to minimize or prevent galvanic corrosion. These include design changes, electrical isolation, electrical insulation, exclusion of the environment, increasing  $IR$  drop, anode-to-cathode area ratio control, corrosion inhibitors, cathodic protection, and counter-current devices. Each of these corrosion control methods seeks to reduce or eliminate one of the requirements for galvanic corrosion to occur: materials with dissimilar corrosion potentials, metallic pathway, and ionic pathway.

Design changes can be made to minimize or eliminate contact of dissimilar metals. One such change is the use of a galvanic strip, shown in [Figure 23](#). Use of this strip forces the dissimilar metal contact to occur in a metallurgically bonded transition material where water has limited access.

Electrical isolation eliminates galvanic corrosion by removing the metallic pathway between the dissimilar materials. This is usually accomplished with nonconductive spacers, gaskets, washers, and sleeves.

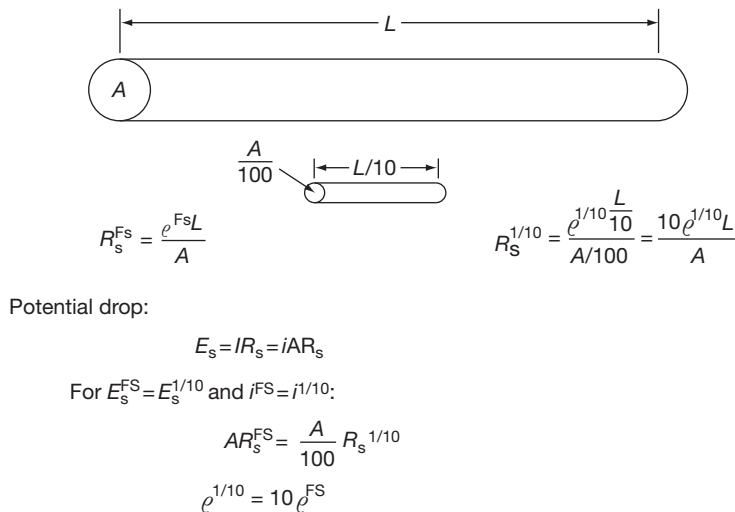


**Figure 21** Calculations to scale dimensions and conductivity for a galvanic couple.

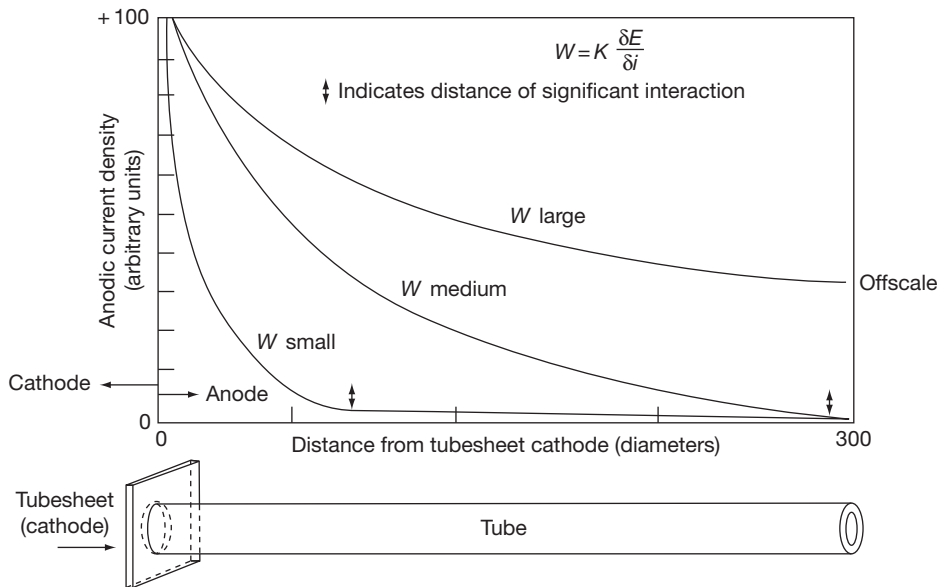


**Figure 22** Effect of Wagner number on galvanic current distribution down an anodic tube. Reproduced from Scully, J. R.; Hack, H. P. In *Galvanic Corrosion*; Hack, H. P., ED., ASTM International: West Conshohocken, PA, 1988; ASTM STP 978, pp 136–157.

Typical methods for providing electrical isolation in a bolted joint are illustrated in [Figure 24](#).

Commercial isolation devices are also available for pipelines from several manufacturers. The material that is used for isolation must be electrically nonconductive, so carbon-bearing rubbers cannot be used. It does not matter whether the isolation material absorbs electrolyte, so it can be porous. Typical isolation materials include Acetal, glass-reinforced plastic, Mylar, and polyethylene. Many nonmetallic bearing materials provide electrical isolation automatically

for rotating equipment. Providing electrical isolation for complex structures is extremely difficult. Many isolator pieces are usually used, and unintentional shorts are difficult to control. Such unintentional shorts include pipe hangers, ground wires for electrical equipment, machining burrs, and inadvertent movable equipment like screwdrivers or steel wool pads. When providing electrical isolation it is imperative to check that electrical conductivity has been eliminated after assembly and periodically thereafter. Such checks must be done with the equipment dry.

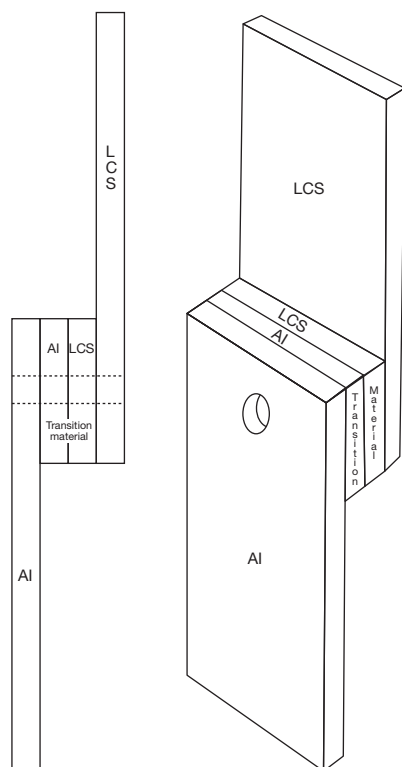


**Figure 23** Use of a bimetallic transition material to minimize galvanic corrosion between low carbon steel (LCS) and aluminum. Reproduced from Baboian, R.; Haynes, G.; Turcotte, R. In *Galvanic Corrosion*; Hack, H. P., Ed.; ASTM International: West Conshohocken, PA, 1988; ASTM STP 978, pp 249–259.

Insulation is different in that the intent is not to remove the metallic pathway but instead to provide spacing between the anode and cathode to increase the resistance of the ionic pathway. This is commonly used in high-resistivity environments such as atmospheric exposure, where a small increase in spacing will have a large effect on ionic resistance. For this reason, plastic spacers are frequently used between stainless steel fasteners and aluminum siding material. Another application of this principle is the use of nonmetallic spool pieces to separate dissimilar metals in piping systems. Although the dissimilar metals may still be in metallic contact through supporting structure, the spool piece provides ionic resistance which lowers the amount of galvanic corrosion, and also causes the corrosion to be less localized on the anode pipe near the cathode.<sup>28</sup>

Galvanic corrosion can also be stopped by excluding the environment from the anode, the cathode, or both. This has sometimes been done successfully with the use of paint; however, paint systems will

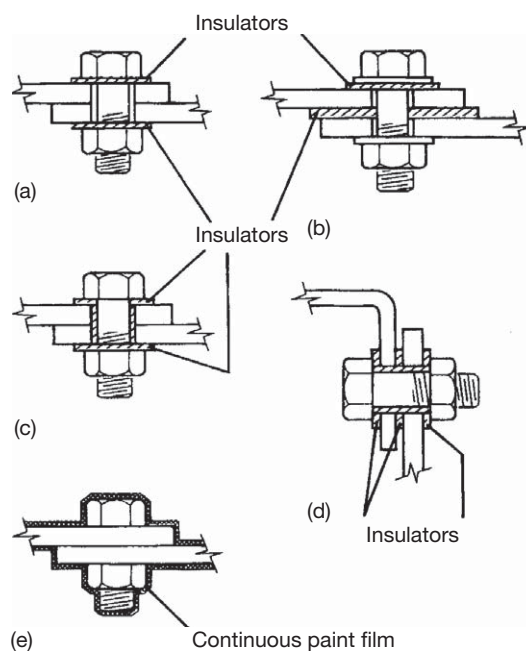


**Figure 24** Designs for insulating joints to avoid corrosion likely if the fastener is anodic to the plate<sup>1</sup>: (a) bolt and plates are of different alloys (not ideal; see text); (b) the bolt is the same alloy as the lower plate; (c) same as (a) with insulating sleeve on bolt shank; (d) bolt and plates are all of different alloys; (e) suitable only for atmospheric or occasionally wetted surface. Courtesy of HMSO. Reproduced from Francis, R. *Galvanic Corrosion: A Practical Guide for Engineers*; NACE: Houston, TX, 2001.

develop defects over time which must be accounted for. Water-excluding greases, silicone sealants, and heavy nonmetallic linings will work for various periods of time, until they wash out or deteriorate enough to absorb electrolyte. It is safest to exclude the environment from the cathode, since this will eliminate the driving force for the galvanic corrosion.

Anything that increases the resistance of the ionic path between anode and cathode will reduce the rate of galvanic corrosion. Reducing electrolyte conductivity, increasing anode-to-cathode spacing, and providing nonmetallic barriers in the electrolyte between the anode and cathode are effective corrosion control methods.

Since the magnitude of galvanic corrosion is a function of the ratio of the wetted surface areas of the cathode to the anode, reducing this ratio will reduce galvanic corrosion. Masking of the cathode with paint can be highly effective, whereas painting of the anode alone must never be done. Area ratio control is most effectively done during the design phase of a structure. For example, fasteners should

be cathodic to the materials they fasten. When putting stainless steel fasteners through aluminum for seawater use, there are surface treatments that will make even this small area of noble material appear even smaller by masking the corrosion potential of the fastener. Such treatments include galvanizing, cadmium plating, and the use of a proprietary fastener treatment called Alumizite.

Corrosion inhibitors can control galvanic corrosion either by acting directly to prevent corrosion of the anode, called anodic inhibitors, or by increasing the polarizability of the cathode to lower its driving force on the anode, called cathodic inhibitors. Inhibitors that do both are called mixed inhibitors. If an anodic inhibitor is used, the coupled potential will shift in the cathodic direction, whereas a cathodic inhibitor will cause the coupled potential to shift in the anodic direction. Automobile cooling systems contain a variety of materials, including steel, copper alloys, and aluminum, all in direct metallic contact in a common electrolyte, the antifreeze/coolant. For this reason, companies that produce antifreeze/coolants have developed a suite of corrosion inhibitors that are highly effective at controlling galvanic corrosion in automobile engines, provided they are changed out every few years to replenish the inhibitors.

Cathodic protection of a structure will eliminate galvanic corrosion since it provides electrodes that are anodic to both materials in the galvanic couple. This is true for both sacrificial and impressed current cathodic protection systems. The one caution regarding this is that the normal corrosion of aluminum in seawater cannot be prevented by cathodic protection, and over-protection will cause considerable damage to the aluminum. Therefore, when trying to prevent galvanic corrosion of aluminum caused by contact with other materials, just enough cathodic protection should be used to polarize the other materials to the corrosion potential of the aluminum. The cathodic protection system must have an ionic path to all cathodes in the galvanic couple to be effective. Since cathodic protection cannot reach into faying surfaces, it is usually good practice to use nonconductive, nonporous spacers between dissimilar metals so protected, not to provide isolation but to force any potential galvanic currents to travel outside of the faying surface area where they can be mitigated by the cathodic protection system. A typical insulation scheme for faying surfaces uses two layers of MIL-I-24391 tape<sup>29</sup> with a total thickness of 0.43 mm (0.017 in.).

Counter-current devices are relatively new to the field of galvanic corrosion control. Their principle is

that they generate an *IR* drop in the electrolyte counter to the *IR* drop generated between the anode and cathode in a galvanic couple. This effectively prevents current from flowing in the electrolyte, stopping the galvanic corrosion. To date, one such device, called a bielectrode, has been the subject of research<sup>30–33</sup> and patents.<sup>34</sup> The galvanic couple geometry that can be controlled with this technology must be well controlled, and control of the counter current is the most difficult part of designing such a system. The principle of a counter-current device is shown in [Figure 25](#).

### 2.07.8 Testing

Galvanic corrosion testing is a complex subject that is discussed in detail elsewhere.<sup>4,35–39</sup> This chapter provides only a summary.

#### 2.07.8.1 General Principles

In general, when conducting tests for galvanic corrosion, the closer the test comes to the actual situation, the more accurate will be the results. The environment must be accurately modeled, with the amount of any constituents that might affect the reactions accurately reproduced and the amount of fluid flow reproduced as well. The materials tested should accurately reflect the materials of interest in composition, thermal processing, and surface films or treatments. If materials are to be tested as a couple, the geometry should reflect as closely as possible that being studied. Finally, galvanic corrosion, like any other form of corrosion, can be strongly time-dependent. Tests must be conducted over sufficient duration to ensure that the results can accurately predict corrosion behavior over the service life anticipated.

#### 2.07.8.2 Testing Hardware

The most accurate test is one in which the actual hardware is exposed in the actual environment for the anticipated service life. In practice this seldom can be done, so that approximations may be required. The considerations for hardware testing are discussed elsewhere.<sup>35</sup>

#### 2.07.8.3 Making a Galvanic Series

If a galvanic series is to be constructed, it is important that the materials and environment accurately reflect those of interest. In many environments, corrosion

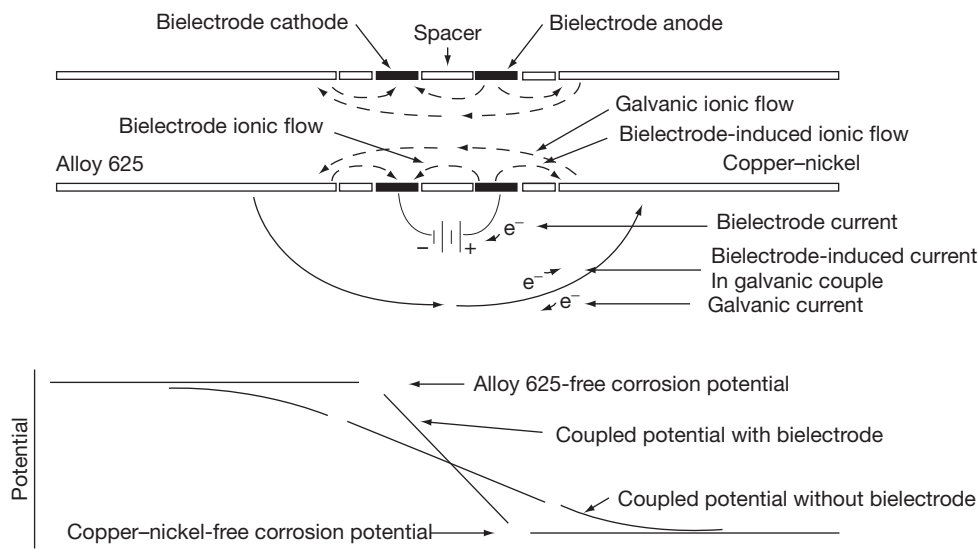


**Figure 25** Principle of operation of counter-current device. Reproduced from Shifler, D. A. Advanced measures to control galvanic corrosion in piping systems, CARDIVNSWC-TR-61-99-18 Naval Surface Warfare Center Carderock Division, Bethesda, MD, September 1999.

potential varies with time, so that the length of time of the measurement must be long enough to allow measurement of the full range of potentials. These, and other considerations for developing a galvanic series, are discussed in more detail elsewhere.<sup>5</sup>

#### 2.07.8.4 Determining Polarization

Polarization curves may be developed in a variety of ways, depending on the corrosion system being modeled. Potentiodynamic polarization curves are generated by holding a specimen at a given potential and gradually sweeping the potential in one direction while measuring the current required. If the starting potential is the corrosion potential, then an anodic polarization curve is generated by sweeping in the positive direction, while a cathodic polarization curve is generated by sweeping in the negative direction. Sometimes scans are started at a cathodic potential and swept in the positive direction, generating both anodic and cathodic branches of the polarization curve in a single scan. Sometimes the specimens may be pre-exposed before starting the scan either freely corroding or at a potential indicative of the likely coupled potential. The speed of the potential scan is important, with slower usually giving better results. Details of generating polarization curves are discussed elsewhere.<sup>4,37,40-44</sup>

Polarization curves can also be generated potentiostatically by taking a series of specimens and

holding each at a different constant potential while measuring current as a function of time. This better approximates the potential behavior of a galvanic couple than a potentiodynamic scan, and current stability over time is easily obtained, but the technique is very labor and time intensive and is seldom used in practice. Details of how to perform this type of testing are discussed elsewhere.<sup>4,42,45,46</sup>

Actual galvanic couples of the materials of interest may be exposed in the proper environment while the coupled potential and galvanic current are measured as a function of time. Although the exact geometry is usually not modeled in this type of test, typically the anode-to-cathode area ratio is modeled by adjusting specimen size. This type of testing yields galvanic current information which may not be directly related to the magnitude of galvanic corrosion, but if the anode and cathode corrosion potentials are more than 120 mV apart, the anodic reactions on the coupled cathode are almost completely suppressed and the cathodic reactions on the anode are almost completely suppressed, so that the galvanic current will give a rough measure of the anode corrosion rate.<sup>4</sup> Exposure testing of coupled specimens is discussed elsewhere.<sup>4,35</sup>

#### 2.07.8.5 Determining *IR* Drop

The above testing usually does not take into account *IR* drop. *IR* drop can be measured during an exposure of galvanic couples either by using a small



reference electrode or Luggin–Haber capillary and moving it near the various surfaces, or by rapid interruption of the galvanic current if this current travels through an external wire followed by immediate measurement of potential. Typical interruption times are on the order of milliseconds. The various methods of measuring  $IR$  drop are described elsewhere.<sup>47</sup>

### 2.07.8.6 Determining Corrosion Rate

Once corrosion current is known, corrosion rate can be calculated using Faraday's law.<sup>48</sup> If the anode and cathode corrosion potentials are more than 120 mV

apart, the current that can be used in Faraday's law calculations is the galvanic current. If not, Evans diagrams must be used to determine reaction currents that can be put into Faraday's law to get corrosion rates of the anode and cathode materials.

An easier method for obtaining corrosion rates is to determine specimen mass of the anode metal before and after an exposure in a galvanic couple or at a potential indicative of the coupled potential. This corrosion rate should be compared to that of a freely corroding specimen of the anode metal to determine the amount of acceleration due to the presence of the couple.

Some highly localized corrosion phenomena, such as pitting and crevice corrosion, cannot be easily quantified by mass loss measurements. In those cases, other methods besides corrosion rate must be used to determine the amount of acceleration of the corrosion by the galvanic couple.<sup>49</sup>

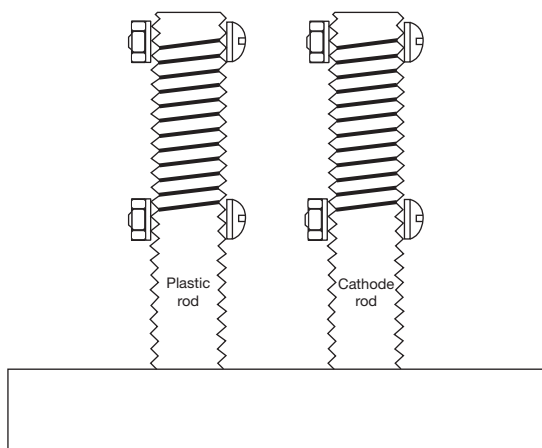


**Figure 26** Wire-on-bolt or CLIMAT test specimens. Reproduced from Standard G116: Practice for Conducting Wire-on-Bolt Test for Atmospheric Galvanic Corrosion, *ASTM Book of Standards*; ASTM International: West Conshohocken, PA, 2006.

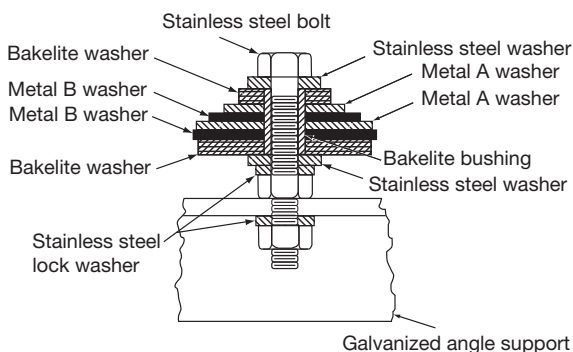


**Figure 27** Washer atmospheric test specimen. Reproduced from Standard G149 (withdrawn 2004): Practice for Conducting the Washer Test for Atmospheric Galvanic Corrosion, *ASTM Book of Standards*; ASTM International: West Conshohocken, PA, 2006.

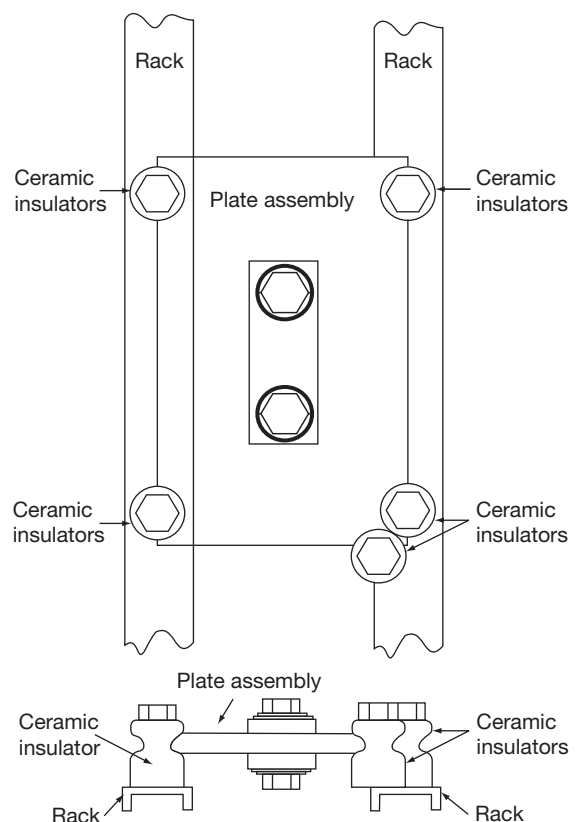


**Figure 28** ISO atmospheric corrosion test using plate material. Reproduced from Hack, H. P. *Corrosion Testing Made Easy*; NACE International: Houston, TX, 1993; Volume 2.

### 2.07.8.7 Accelerated Tests

Accelerated testing to predict galvanic corrosion is not normally productive. Any attempt at accelerating the corrosion has a significant chance of changing the corrosion mechanism, invalidating the data that is collected. It is far more productive to allow the galvanic corrosion to proceed at its normal pace and use accurate current and mass loss measuring techniques to get data in a shorter time period.

### 2.07.8.8 Atmospheric Testing

There are several standard tests for galvanic corrosion in the atmosphere. The most popular of these is called the wire-on-bolt, or CLIMAT, test<sup>50,51</sup> (Figure 26). This test consists of wrapping a wire

made from the anode material around a threaded rod made from the cathode material. If the anode and cathode are not known beforehand, two tests are run with the materials reversed. A control is usually run consisting of the anode wire wrapped around a nonconductive rod so that the non-galvanically accelerated corrosion of the anode material can be compared with its corrosion in the galvanic couple. This test is fast, typically taking 30 days, and sensitive, and only has the disadvantage that the materials must be available in the appropriate wire or threaded rod forms.

For materials that cannot be made into the right form for the wire-on-bolt test, another test using stacked washers of the anode and cathode material alternating can be used.<sup>52</sup> Although this test is not as sensitive and usually requires longer exposures, it is

Fastener selection-above water

Fastener	C steel <sup>a</sup>	Aluminum <sup>a</sup>	Copper-based alloy <sup>a</sup>	Stainless-steel alloy <sup>a</sup>	Alloy 400 <sup>a</sup>
Steel, Zn/Cd	G	R	R	R	R
Aluminum	Y	Y	R	R	R
Copper alloy	G	R <sup>b</sup>	Y	R	R
Type 316 SS	G	Y <sup>b</sup>	Y	Y	Y
Alloy 400	G	R <sup>b</sup>	G	G	G
Ni-Cr-Mo	G	Y <sup>b</sup>	G	G	G
MP35N	G	Y <sup>b</sup>	G	G	G
Titanium	G	Y <sup>b</sup>	G	G	G

<sup>a</sup>Material to be fastened.

<sup>b</sup>Loss of aluminum around fastener has caused structural failure in coastal buildings, but stainless-steel fasteners are widely used.

G = generally satisfactory. Y = may be satisfactory; detailed information needed. R = avoid.

(a)

Fastener	Graphite composite <sup>a</sup>	Wood <sup>a</sup>	Concrete <sup>a</sup>	FRP <sup>a</sup>	Rubber <sup>a</sup>
Steel, Zn/Cd	R	Y	G	Y	Y
Aluminum	R	Y	Y	Y	Y
Copper alloy	R	G	G	G	G
Type 316 SS	R	Y	G	G	G
Alloy 400	R	G	G	G	G
Ni-Cr-Mo	?	G	G	G	G
MP35N	?	G	G	G	G
Titanium	?	G	G	G	G

<sup>a</sup>Material to be fastened.

G = generally satisfactory. Y = may be satisfactory; detailed information needed. R = avoid.

? = very limited information available; suggest caution.

(b)

**Figure 29** Fastener selection – above water. Reproduced from Ross, R. W., Jr.; Tuthil, A. H. *Master. Perform* 1990, 29(4), 65–69.

Corroding metal	Coupled metal									
	Aluminum	Anodized Al	Zinc	Carbon steel	Weathering steel	Tin	Lead	Copper	Nickel	Stainless steel
Magnesium										
Aluminum										
Anodized aluminum										
Zinc										
Carbon steel										
Weathering steel										
Tin										
Lead										
Copper										
Nickel										
Stainless steel										

■, no risk of galvanic corrosion; ■, some increase in corrosion; ■, large increase in corrosion; □, no data.

(a)

Corroding metal	Coupled metal									
	Aluminum	Anodized Al	Zinc	Carbon steel	Weathering steel	Tin	Lead	Copper	Nickel	Stainless steel
Magnesium										
Aluminum										
Anodized aluminum										
Zinc										
Carbon steel										
Weathering steel										
Tin										
Lead										
Copper										
Nickel										
Stainless steel										

■, no risk of galvanic corrosion; ■, some increase in corrosion; ■, large increase in corrosion; □, no data.

(b)

Corroding metal	Coupled metal									
	Aluminum	Anodized Al	Zinc	Carbon steel	Weathering steel	Tin	Lead	Copper	Nickel	Stainless steel
Magnesium										
Aluminum										
Anodized aluminum										
Zinc										
Carbon steel										
Weathering steel										
Tin										
Lead										
Copper										
Nickel										
Stainless steel										

■, no risk of galvanic corrosion; ■, some increase in corrosion; ■, large increase in corrosion; □, no data.

(c)

**Figure 30** Risk of galvanic corrosion in an (a) urban atmosphere, (b) rural atmosphere and (c) marine atmosphere for some common metals. Reproduced from Francis, R. *Galvanic Corrosion: A Practical Guide for Engineers*; NACE: Houston, TX, 2001.

Fastener	C steel <sup>a</sup>	Aluminum <sup>a</sup>	Copper-based alloy <sup>a</sup>	Stainless-steel alloy <sup>a</sup>	Alloy 400 <sup>a</sup>
Steel, Zn/Cd	Y	R <sup>b</sup>	R	R	R
Aluminum	R	Y	R	R	R
Copper alloy	G	R	Y	R	R
Type 316 SS	G	R <sup>b</sup>	Y	R	R
Alloy 400	G	R <sup>b</sup>	G	Y	Y
Ni-Cr-Mo	G	R <sup>b</sup>	G	G	Y
MP35N	G	R <sup>b</sup>	G	G	G
Titanium	G	R <sup>b</sup>	G	G	G

<sup>a</sup>Material to be fastened.

<sup>b</sup>Loss of aluminum around fastener is as serious as loss of fastener.

G = generally satisfactory. Y = may be satisfactory; detailed information needed. R = avoid

Fastener	Graphite composite <sup>a</sup>	Wood <sup>a</sup>	Concrete <sup>a</sup>	FRP <sup>a</sup>	Rubber <sup>a</sup>
Steel, Zn/Cd	R	R	Y	Y	Y
Aluminum	R	Y	R	R	R
Copper alloy	R	G	G	G	G
Type 316 SS	R	R	Y <sup>b</sup>	R <sup>c</sup>	R
Alloy 400	R	G	G	G	G
Ni-Cr-Mo	?	G	G	G	G
MP35N	?	G	G	G	G
Titanium	?	G	G	G	G

<sup>a</sup>Material to be fastened.

<sup>b</sup>The alkalinity of concrete provides protection for small areas of type 316 extending beyond the concrete.

<sup>c</sup>Some small boat manufacturers report good performance for type 316 bolting in FRP hulls below waterline when bolts are packed with water-repellent lubricant and recessed in FRP.

G = generally satisfactory. Y = may be satisfactory, detailed information needed. R = avoid.

? = very limited information available; suggest caution.

**Figure 31** Fastener selection – below water. Reproduced from Ross, R. W., Jr.; Tuthill, A. H. *Master. Perform* **1990**, 29(4), 65–69.

Valve trim alloy \ Valve body alloy	Managanes bronze	NAB	Alloy K-500	316L	22% Cr duplex	Super duplex	6% Mo aust.	Alloy 625	Alloy C-276
Cast iron/steel (bare)	Acceleration of corrosion probable	Acceleration of corrosion unlikely	Acceleration of corrosion unlikely	Acceleration of corrosion unlikely	Acceleration of corrosion unlikely	Acceleration of corrosion unlikely	Acceleration of corrosion unlikely	Acceleration of corrosion unlikely	Acceleration of corrosion unlikely
Cast iron/steel (coated)	Acceleration of corrosion unlikely	Acceleration of corrosion unlikely	Acceleration of corrosion unlikely	Acceleration of corrosion unlikely	Acceleration of corrosion unlikely	Acceleration of corrosion unlikely	Acceleration of corrosion unlikely	Acceleration of corrosion unlikely	Acceleration of corrosion unlikely
Aust. cast iron	Acceleration of corrosion unlikely	Acceleration of corrosion unlikely	Acceleration of corrosion unlikely	Acceleration of corrosion unlikely	Acceleration of corrosion unlikely	Acceleration of corrosion unlikely	Acceleration of corrosion unlikely	Acceleration of corrosion unlikely	Acceleration of corrosion unlikely
Gunmetal	Acceleration of corrosion unlikely	Acceleration of corrosion unlikely	Acceleration of corrosion unlikely	Acceleration of corrosion unlikely	Acceleration of corrosion unlikely	Acceleration of corrosion unlikely	Acceleration of corrosion unlikely	Acceleration of corrosion unlikely	Acceleration of corrosion unlikely
NAB	Acceleration of corrosion unlikely	Acceleration of corrosion unlikely	Acceleration of corrosion unlikely	Acceleration of corrosion unlikely	Acceleration of corrosion unlikely	Acceleration of corrosion unlikely	Acceleration of corrosion unlikely	Acceleration of corrosion unlikely	Acceleration of corrosion unlikely
Super duplex	Acceleration of corrosion unlikely	Acceleration of corrosion unlikely	Acceleration of corrosion unlikely	Acceleration of corrosion unlikely	Acceleration of corrosion unlikely	Acceleration of corrosion unlikely	Acceleration of corrosion unlikely	Acceleration of corrosion unlikely	Acceleration of corrosion unlikely
6% Mo aust.	Acceleration of corrosion unlikely	Acceleration of corrosion unlikely	Acceleration of corrosion unlikely	Acceleration of corrosion unlikely	Acceleration of corrosion unlikely	Acceleration of corrosion unlikely	Acceleration of corrosion unlikely	Acceleration of corrosion unlikely	Acceleration of corrosion unlikely
Alloy 625	Acceleration of corrosion unlikely	Acceleration of corrosion unlikely	Acceleration of corrosion unlikely	Acceleration of corrosion unlikely	Acceleration of corrosion unlikely	Acceleration of corrosion unlikely	Acceleration of corrosion unlikely	Acceleration of corrosion unlikely	Acceleration of corrosion unlikely
Alloy C-276	Acceleration of corrosion unlikely	Acceleration of corrosion unlikely	Acceleration of corrosion unlikely	Acceleration of corrosion unlikely	Acceleration of corrosion unlikely	Acceleration of corrosion unlikely	Acceleration of corrosion unlikely	Acceleration of corrosion unlikely	Acceleration of corrosion unlikely

Acceleration of corrosion unlikely;      Acceleration of corrosion possible;  
 Acceleration of corrosion probable.

**Figure 32** Alloys suitable for valve trim in ambient temperature seawater. Reproduced from Francis, R. *Galvanic Corrosion: A Practical Guide for Engineers*; NACE: Houston, TX, 2001.

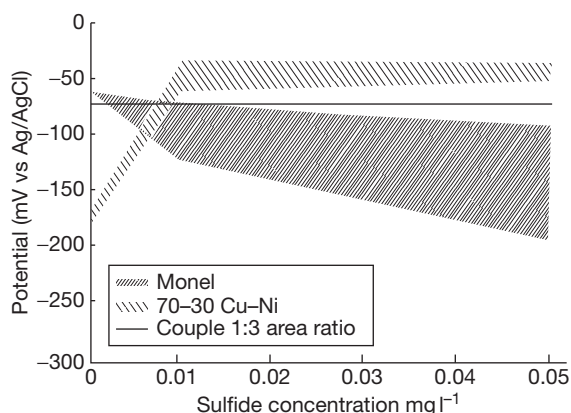


**Figure 33** Potential reversal of copper-nickel piping alloys due to sulfide pollution.

**Table 1** Weight loss of iron for Fe/M bimetallic couples in 1% NaCl<sup>a 58</sup>

<i>M</i>	Weight loss of iron (mg)	Weight loss of <i>M</i> (mg)	Difference in standard electrode potentials (V) <sup>b</sup>
Copper	183.1	0.0	+0.785
Nickel	181.1	0.7	+0.19
Tin	171.1	2.5	+0.30
Lead	183.2	3.6	+0.31
Aluminum	9.8	105.9	-1.23
Cadmium	0.4	307.9	+0.04
Zinc	0.4	688.0	-0.32
Magnesium	0.0	3104.0	-1.90

<sup>a</sup>Weight loss data after Bauer and Vogel.<sup>5</sup>

<sup>b</sup>The + sign indicates that iron has a more negative standard electrode potential than the second metal.

not necessary to know before hand which material is the anode. Although it has many advantages, this test is no longer covered by a current standard in ASTM. The test specimen is shown in [Figure 27](#).

Sometimes deterioration in properties such as tensile strength or modulus due to galvanic corrosion is needed. For this, a plate test was designed and standardized by ISO.<sup>53</sup> In this test, a plate of the anode material has a strip of the cathode material affixed to it. After exposure, the anode plate can be cut into tensile specimens to test for deterioration of physical properties. Like the wire-on-bolt test, if the anode is not known beforehand, two tests are run with the materials reversed. Like the washer test, longer exposures are required but the plate form of the material is usually easier to get ([Figure 28](#)).

When performing atmospheric testing there are variables that must be considered. The amount of galvanic corrosion will be a function of the atmosphere, its rainfall acidity, chloride content, and time of wetness, which is a function of rainfall, amount of sunshine, prevailing winds, and other variables. Corrosion can be affected by the angle of exposure of specimens, sheltering from wind and sunlight, and height above ground, among others. Corrosion in the atmosphere is also a function of season; so long tests, or multiple short tests over at least a year, are required to get a proper indication of corrosion performance.<sup>54</sup>

## 2.07.9 Standards

There are many standards used in evaluating and preventing galvanic corrosion. A good reference for these is published by ASTM International,<sup>38</sup> and only a summary is given here. Standards fall into a variety of categories: those that relate to corrosion testing in general such as standards on how to clean specimens after test, general galvanic corrosion test guidelines, specific galvanic corrosion tests such as the CLIMAT test, electrochemical test standards whose results can be used in galvanic corrosion studies such as potentiodynamic polarization tests, and standards for protection methods which can be applied to galvanic corrosion such as cathodic protection standards. These standards have been developed by ASTM International, NACE International, the ISO, the European standards agency (CEN), and numerous countries' standards organizations. Listing of these standards and what they can be used for is beyond the scope of this chapter, and the reader is directed to ASTM International.<sup>38</sup>

## 2.07.10 Useful Galvanic Corrosion Data

The following data may prove useful for estimating rates of galvanic corrosion.

### 2.07.10.1 Atmospheric Corrosion

[Figure 29](#) contains useful data showing galvanic corrosion performance of fasteners in the atmosphere. [Figure 30](#) shows galvanic corrosion performance of a large number of material combinations in urban, rural, and marine atmospheres.



**Table 2** Degree of corrosion at bimetallic contacts<sup>a 59</sup>

Metal considered	Contact metal						
	1	2	3	4	5	6	7
	Gold, platinum, rhodium, silver	Monel, Inconel, nickel-molybdenum alloys	Cupronickels silver solder, aluminum bronzes, tin bronzes, gunmetals	Copper brasses, 'nickel silvers'	Nickel	Lead, tin and soft solders	Steel and cast Iron
1. Gold, platinum, rhodium, silver	–	A	A	A	A	A	A
2. Monel, Inconel, nickel-molybdenum alloys	B	–	A	A	A	A	A
3. Cupronickels, silver solder, aluminum bronzes, tin bronzes, gun metals	C(k)	B or C	–	A	A	A	A
4. Copper, brasses, 'nickel silvers'	C(k)	B or C	B or C(g)	–	B or C	B or C (p)	A
5. Nickel	C	B	A	A	–	A	A
6. Lead, tin and soft solders	C	B or C(t)	B or C(q)	B or C(q)	B	–	A or C(r)
7. Steel and cast Iron (a) (f) (w)	C	C	C	C	C(k)	C(k)	–
8. Cadmium (u)	C	C	C	C	C	B	C
9. Zinc (u)	C	C	C	C	C	B	C
10. Magnesium and magnesium alloys (chromated) (b) (a)	D	D	D	D	D	C	D
11. Austenitic Fe-18Cr-8Ni	A	A	A	A	A	A	A
12. Stainless steel Fe-18Cr-2Ni	C	A or C(s)	A or C(s)	A or C(s)	A	A	
13. 13% Cr	C	C	C	C	B or C	A	A
14. Chromium	A	A	A	A	A	A	A
15. Titanium	A	A	A	A	A	A	A
16. Aluminum and aluminum alloys (n) (a) (w)	D	C	D(e)	D(e)	C(k)	B or C	B or C

<sup>a</sup>Based on data provided by members of the I.S.M.R.C. Corrosion and Electrodeposition Committee and others, and arranged by Mrs. V. E. Rance.

A. The corrosion of the 'metal considered' is not increased by the 'contact metal.'

B. The corrosion of the 'metal considered' may be slightly increased by the 'contact metal.'

C. The corrosion of the 'metal considered' may be markedly increased by the 'contact metal.' (Acceleration is likely to occur only when the metal becomes wet by moisture containing an electrolyte, e.g., salt, acid, combination products. In ships, acceleration may be expected to occur under in-board conditions, since salinity and condensation are frequently present. Under less severe conditions the acceleration may be slight or negligible.)

D. When moisture is present, this combination is inadvisable, even in mild conditions, without adequate protective measures.

### 2.07.10.2 Seawater Immersion

**Figure 31** contains data showing galvanic corrosion performance of fasteners underwater. **Figure 32** shows galvanic corrosion performance of a number of alloys used for valve trim in seawater. **Figure 33**

shows how small variations in composition of seawater caused by pollution can actually reverse the relative galvanic corrosion performance of certain alloys, reversing the anode and the cathode in a galvanic couple.

**Table 3** Degree of corrosion at bimetallic contacts<sup>63</sup> (Continued)

8	9	10	11	12	13	14	15	16
Cadmium	Zinc	Magnesium and magnesium alloys (chromated)	Stainless Austenitic Fe-18Cr-2Ni	Fe-18Cr-2Ni	13% Cr	Chromium	Titanium	Aluminum and aluminum alloys
A	A	A	A	A	A	A	A	A
A	A	A	A	A	A	A	A(x)	A
A	A	A	B or C	B	A	B or C	B or C	A(e)
A	A	A	B or C	B or C	A	B or C	B or C	A(e)
A	A	A	B or C	B or C	A	B or C	B or C	A
A	A or C(r)	A	B or C	B or C	B or C	B or C	B or C	A
A(m)	A(m) (l)	A	C	C	C	C(k)	C	A(m)
—	A	A	C	C	C	C	C	B
B	—	A	C	C	C	C	C	C(i)
B or C	B or C	—	C	C	C	C	C	B or C(c)
A	A	A	(v)	A	A	A	A	A
A	A	A	A	(v)	A	A	(o)	A
A	A	A	C	C	(v)	C	C	A
A	A	A	A	A	A	—	A	A
A	A	A	A	A	A	A	—	A
A	A	A(c) (h)	B or C	B or C	B or C	B or C(d)	C	(v)

**Table 4** Total corrosion rate acceleration factors due to dissimilar metal coupling at 1:1 area ratio in flowing seawater (mean flow rate about 1–2 m s<sup>-1</sup>)<sup>59</sup>

Coupled metal (wrought form)	Uncoupled corrosion rate <sup>a</sup>	Acceleration factor <sup>b</sup> due to dissimilar metal coupling with:	
		Titanium	Mild steel
Zinc	0.05	4	10
SIC aluminum	0.008	30	60
Mild steel.	0.15	2	1
Lead	0.01	3	3 MS
2% aluminum brass	0.01	3	3 MS
10% aluminum bronze	0.02	3	3 MS
Nickel aluminum bronze	0.015	1	3 MS
Copper	0.03	6	3 MS
90/10 cupro-nickel (1% Fe)	0.02	3	3 MS
Monel 400	0.005	2	3 MS
Stainless steel type 316	0.005	2	3 MS

<sup>a</sup>Corrosion rates relate to general corrosion only and are average rates obtained over about one year's exposure.<sup>b</sup>Acceleration factors quoted for coupled metal corroding unless indicated by suffix (MS) for mild steel corroding.

Quantitative data is presented in, [Table 1–9](#), [Table 1](#) shows weight loss data for iron in saltwater when coupled to various alloys. [Table 2](#) is an extensive list showing how various alloys perform when

galvanically coupled to each other in various environments. [Table 3](#) is a continuation of [Table 2](#) with more alloy combinations. [Table 4](#) gives the amount of galvanic corrosion of various alloys when they are

coupled to titanium or mild steel. **Table 5–7** can help to predict galvanic corrosion performance in seawater heat exchangers. **Table 5** shows galvanically accelerated crevice corrosion when Monel K-500 is

**Table 5** Maximum depth of crevice attack for couples of alloy K-500 and super duplex stainless steel<sup>60</sup>

Couple	Alloy	Maximum pit depth (mm)	
		Washer/plate	Plate/plate
1	K-500	0.26	0.33
	K-500	0.12	0.30
2	Super duplex	0.00	0.00
	Super duplex	0.00	0.00
3	Super duplex	0.00	0.00
	K-500	0.32	0.35
4	Super duplex	0.00	0.00
	K-500	0.42	0.44
5	Super duplex	0.00	0.00
	K-500	0.52	0.50

Couples were at a 1:1 area ratio and exposed to natural sea-water at ambient temperature for 84 days.

**Table 6** Corrosion rate of Muntz metal coupled to various condenser tube alloys<sup>60</sup>

Tube alloy	Corrosion rate (mm year <sup>-1</sup> )	
	Inlet end	Outlet end
None	0.225	0.225
90/10 Cu-Ni	0.846	0.279
6% Mo austenitic	2.80	2.31
Titanium	6.96	6.99

This information is taken from Fu and Chow.<sup>16</sup>

coupled to a super duplex stainless steel. **Table 6** presents galvanic corrosion information for Muntz metal when coupled to other seawater heat exchanger alloys. **Table 7** shows the amount of galvanic corrosion that can occur in heat exchangers when aluminum bronze tubesheets are coupled to stainless steel or titanium tubes. Other useful data for predicting galvanic corrosion of Naval seawater valve materials can be found in Hack.<sup>56</sup> **Table 8** is useful for comparing galvanic corrosion performance of a variety of different alloys used in seawater when galvanically coupled to each other. Finally, **Table 9** shows the effect of galvanically coupling a large variety of different materials to a titanium alloy at various area ratios and flow rates in seawater.

Data given in Hack<sup>57</sup> contain extensive polarization data in seawater at various flow rates that can be used for predicting galvanic corrosion between some common materials used in seawater at any area ratio. This information is also useful as boundary conditions for computerized boundary element analysis for prediction of the amount and spatial distribution of galvanic corrosion and cathodic protection.

### 2.07.10.3 Other Environments

Finding existing galvanic corrosion data in environments other than the atmosphere or seawater can be challenging, and frequently such data do not exist and must be created by running tests. **Figures 34 and 35** show galvanic series generated in carbon dioxide or hydrogen sulfide environments. Scattered data are also contained in some of the general corrosion texts or guides.<sup>59,63–66</sup>

**Table 7** Effect of temperature on the galvanic corrosion of aluminum bronze (alloy D) coupled to 6% Mo austenitic stainless steel or titanium heat exchanger tubes<sup>60</sup>

Alloy	Tube end	Corrosion rate (mm year <sup>-1</sup> )			
		Seawater at 22 °C	Brackish water at 22 °C	Seawater at 6 °C	Brackish water at 11 °C
6% Mo austenitic	Inlet	0.633	0.117	0.048	0.097
	Outlet	0.634	0.150	0.087	0.224
Titanium	Inlet	1.86	0.201	0.059	0.201
	Outlet	3.03	0.373	0.049	0.226

This information is taken from Ref. 16.

**Table 8** Galvanic corrosion in seawater at 1:1 area ratio

Alloy Inducing galvanic effect	Seawater Velocity, ft/s	Corrosion rate (mpy) measured on sample of					
		Ti-6-4	Inconel 625	Monel	70/30 Cu-Ni	Ni-Al Bronze	G Bronze
None (Freely Corroding)	3	0.2	0.1	3.5	1.4	3.7	6.3
	13	0.1	0.1	0.6	6.0	7.0	9.3
Ti-6-4	3		0.1	3.2	3.8	11.3	21.4
	13		0.1	0.6	3.0	10.0	12.9
Inconel 625	3	0.2		3.5	19.6	32.4	37.8
	13	0.1		0.7	4.6	10.5	15.1
Monel	3	NIL	0.1		8.1	20.4	26.9
	13	0.1	NIL		4.1	11.7	12.2
70/30 Cu-Ni	3	0.2	NIL	1.5		4.1	4.9
	13	NIL	NIL	0.6		5.6	12.4
Ni-Al Bronze	3	0.1	NIL	0.9	1.3		4.4
	13	0.1	0.1	0.5	1.9		17.5
G Bronze	3	NIL	NIL	0.5	1.4	2.7	
	13	0.2	0.2	0.4	1.9	3.3	

**Table 9** Summary of corrosion performance of materials coupled to Ti-6211<sup>66</sup>

Alloy	Acceleration factors							
	$<0.01 \text{ m s}^{-1}$				$0.5 \text{ m s}^{-1}$			
	1:1		10:1		1:1		10:1	
	General	Pitting	General	Pitting	General	Pitting	General	Pitting
Ni-Al bronze	2.3	1.1	10.0	1.4	0.9*	2.6	0.9	4.9+
Gun metal	7.1	1.6	38.1	3.8	3.4	1.2	6.8	1.4
Superston 40	2.9	1.0	10.0	1.0	3.4	1.0	6.0	—
CA706	17.0	—	34.7	—	6.0	—	11.2	—
CA715	3.3	45.7+	13.5	12.1	1.5	1.8	3.7	3.8
CA719	3.5	0.8	18.2	3.0	0.9	1.3	1.1	1.6
Inconel 625	1.0	1.0	1.0	1.0	1.0	1.0	1.0	1.0
Hastelloy C	1.0	1.0	1.0	1.0	1.0	1.0	1.0	1.0
Monel 400	0.9	3.6+	3.2	3.6+	0.8	0.9	1.0	10.0+
Monel K-500	1.3	1.6	3.6	2.6	0.7	0.5	2.1	2.2
Mild steel	1.7	2.7	5.1	5.7	1.8	0.7	23.5	23.2+
HY-80	1.9	4.2	5.7	6.4	2.0	1.2	13.0	14.6+
HY-130	1.8	2.8	5.6	17.3	1.8	2.4	21.1	42.1+
Ni-resist 1B	2.1	—	10.0	—	3.3	—	27.6	—
Stainless steel 304	2.2	0.3	6.0	0.2	0.9	1.5	0.5	1.8
Stainless steel 316	1.0	0.0	1.0	1.2	0.4	0.3	0.0	0.1
17-4 PH	29.7	6.5+	100.0	8.8+	0.8	1.1	16.3	1.9+
Carpenter 20 Cb-3	1.0	—	1.0	—	0.0	0.0	0.0	0.4
Nitronic 50	1.0	1.0	1.0	1.0	1.0	**	1.0	0.0
Nitronic 60	1.0	0.5	—	9.7	1.0	0.3	0.4	0.5
Aluminum 5456-H117	3.3	1.9	17.4	2.0	12.7	8.3	254.3	35.0+
Stellite	1.0	1.0	—	—	1.0	—	1.0	—
Ti-40	1.0	1.0	1.0	1.0	1.0	1.0	1.0	1.0
Ti-3Al-2.5V	1.0	1.0	1.0	1.0	1.0	1.0	1.0	1.0
Ti-6Al-4V	1.0	1.0	1.0	1.0	1.0	1.0	1.0	1.0

\*Factors less than 1.0 are the result of variability in behavior and do not represent sacrificial cathodic protection by the Ti-6211.

\*\*No data.

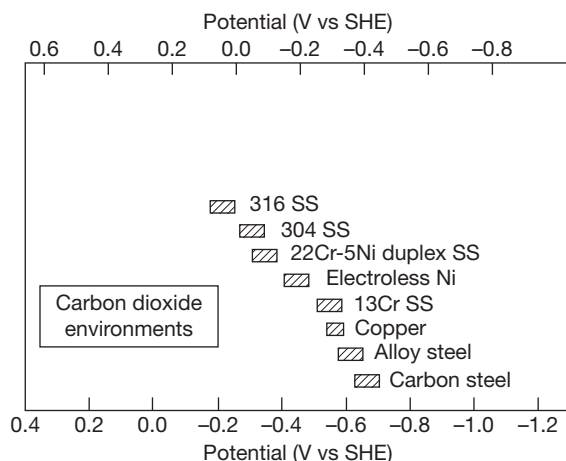


**Figure 34** Corrosion potential chart for metals and alloys in carbon dioxide environments giving the relationship of their free corrosion potentials.  $\text{CO}_2$  partial pressure = 10–100 kPa, chloride =  $0.5\text{--}20\text{ g l}^{-1}$ , and temperature =  $20\text{--}30^\circ\text{C}$ . Reproduced from Efrid, K. D. In *Galvanic Corrosion*; Hack, H. P., Ed.; ASTM International: West Conshohocken, PA, 1988; ASTM STP 978, pp 260–282.

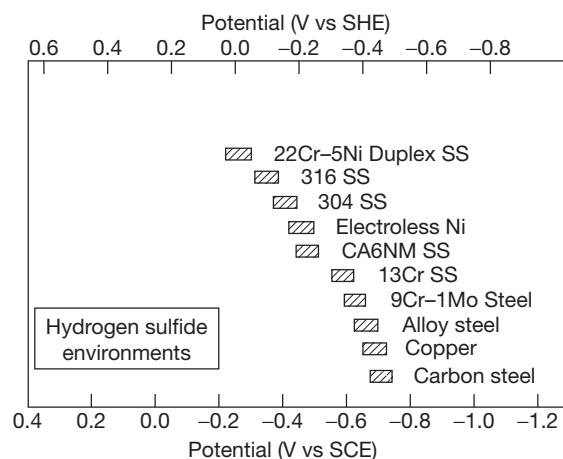


**Figure 35** Corrosion potential chart of metals and alloys in hydrogen sulfide environments giving the relationships of their free corrosion potentials.  $\text{H}_2\text{S}$  partial pressure = 1 atm, 5% NaCl + 0.5%  $\text{CH}_3\text{COOH}$ , and temperature =  $20\text{--}60^\circ\text{C}$ . Reproduced from Efrid, K. D. In *Galvanic Corrosion*; Hack, H. P., Ed.; ASTM International: West Conshohocken, PA, 1988; ASTM STP 978, pp 260–282.

## References

1. Standard G15: Terminology Relating to Corrosion and Corrosion Testing *ASTM Book of Standards*; ASTM International: West Conshohocken, PA, 2006.
2. *Standard Terminology for Corrosion*, NACE Publications Style Manual, 2nd ed., NACE International: Houston, TX, 1989.

3. ISO 8044: Corrosion of Metals and Alloys – Vocabulary The International Organization for Standardization: Geneva, 1989.
4. Hack, H. P. *Corrosion Testing Made Easy*; NACE International: Houston, TX, 1993; Volume 2.
5. Standard G82: Guide for Development and Use of a Galvanic Series for Predicting Galvanic Corrosion Performance, *ASTM Book of Standards*; ASTM International: West Conshohocken, PA, 2006.
6. Francis, R. *Galvanic Corrosion: A Practical Guide for Engineers*; NACE: Houston, TX, 2001.
7. Standard G84: Practice for Measuring Time-of-Wetness on Surfaces Exposed to Wetting Conditions as in Atmospheric Corrosion Testing, *ASTM Book of Standards*; ASTM International: West Conshohocken, PA, 2006.
8. Astley, D. J. In *Galvanic Corrosion*; Hack, H. P., Ed.; ASTM International: West Conshohocken, PA, 1988; ASTM STP 978; pp 53–78.
9. Fu, J. W. In *Galvanic Corrosion*; Hack, H. P., Ed.; ASTM International: West Conshohocken, PA, 1988; ASTM STP 978; pp 79–85.
10. Adey, R. A.; Niku, S. M. In *Galvanic Corrosion*; Hack, H. P., Ed.; ASTM International: West Conshohocken, PA, 1988; ASTM STP 978, pp 96–117.
11. Kasper, R. G.; Crowe, C. R. In *Galvanic Corrosion*; Hack, H. P., Ed.; ASTM International: West Conshohocken, PA, 1988; ASTM STP 978, pp 118–135.
12. Scully, J. R.; Hack, H. P. In *Galvanic Corrosion*; Hack, H. P., Ed.; ASTM International: West Conshohocken, PA, 1988; ASTM STP 978, pp 136–157.
13. Hack, H. P.; Janeczko, R. M. Verification of the boundary element modelling technique for cathodic protection of large ship structures, CARDIVNSWC-TR-61-93/02, Naval Surface Warfare Center Carderock Division, Bethesda, MD, December 1993.
14. Fu, J. W. *Corrosion* **1982**, 38(5), 295.
15. Fu, J. W. A finite element analysis of corrosion cells with mathematical as well as experimental verifications, Scientific Paper 80-IDZ-MEEIC-P1, Westinghouse Corp., Pittsburgh, PA.
16. Fu, J. W.; Chow, J. D. K. *Mater. Perform.* **1982**, 21, 9.
17. Kasper, R. G.; April, M. G. *Corrosion* **1983**, 39(5), 181.
18. Strommen, R.; Rodland, A. *Mater. Perform.* **1981**, 20, 15.
19. Munn, R. S. *Mater. Perform.* **1982**, 21, 29.
20. Decarlo, E. A. In *Corrosion/82*; NACE International: Houston, TX, 1982; Paper no. 165.
21. Doig, P.; Flewitt, P. E. J. *J. Electrochem. Soc.* **1979**, 2057.
22. Clerbois, L. E.; Heintz, F.; Ijselling, F.; Rowlands, J.; Simpson, J. *Br. Corros. J.* **1985**, 20(3), 107–116.
23. Decarlo, E. Computer techniques for offshore corrosion protection, *Sea Technology*; Sep. 1981.
24. Hack, H. P. *Corrosion* **1989**, 45(7), 601–606.
25. Tighe-Ford, D. J.; McGrath, J. N.; Hodgkiss, L. *Corros. Prevent. Control* **1985**, 32(5), 89–91.
26. Wagner, C. J. *Electrochem. Soc.* **1951**, 98, 116.
27. Wagner, C.; Traud, W. *Z. Electrochemie Bc-Bunsenges Phys. Chem.* **1938**, 44.
28. Hack, H. P.; Wheatfall, W. L. In *Corrosion/95*; NACE International: Houston, TX, 1995; Paper no. 272.
29. Military Specification – Insulation Tape, Electrical, Plastic Pressure-Sensitive, MIL-I-24391C Amendment 1, U.S. Government Printing Office, August 1991.
30. Shifler, D. A.; Hack, H. P.; Melton, D. In *Corrosion/98*; NACE International: Houston, TX, 1999; Paper no. 706.
31. Shifler, D. A.; Melton, D.; Hack, H. P. Proceedings of the 1997 Tri-Service Conference on Corrosion, Wrightsville Beach, NC, November 1997.



32. Tossey, B. M.; Beavers, J. A. In *Corrosion/2007*; NACE International: Houston, TX, 2007; Paper no. 07244.
33. Garrity, K. Galvanic corrosion inhibiting coupling interposed between two dissimilar pipes, US Patent No. 5,739,424, 1998.
34. Control for galvanic corrosion inhibiting coupling, US Patent Application No. 11/510,394, 2006.
35. Standard G71: Guide for Conducting and Evaluating Galvanic Corrosion Tests in Electrolytes, *ASTM Book of Standards*; ASTM International: West Conshohocken, PA, 2006.
36. Hack, H. P. In *Metals Handbook – Corrosion: Fundamentals, Testing, and Protection*; ASM International: Metals Park, OH, 2003; Vol. 13A.
37. Baboian, R. In *Electrochemical Techniques for Corrosion Engineering*; Baboian, R., Ed.; NACE International: Houston, TX, 1986.
38. Baboian, R. Ed. *Corrosion Tests and Standards – Application and Interpretation*, 2nd ed.; ASTM International: West Conshohocken, PA, 2005; MNL 20.
39. Champion, F. A. *Corrosion Testing Procedures*; Chapman and Hall: London, UK, 1952.
40. Standard G 5: Standard Reference Test Method for Making Potentiostatic and Potentiodynamic Anodic Polarization Measurements; ASTM International: West Conshohocken, PA, 2006.
41. Dean, S., Jr. In *Electrochemical Techniques for Corrosion Engineering*; Baboian, R., Ed.; NACE International: Houston, TX, 1986.
42. Hack, H. P. In *Electrochemical Techniques for Corrosion Engineering*; Baboian, R., Ed.; NACE International: Houston, TX, 1986.
43. Scully, J. R. In *Electrochemical Techniques for Corrosion Engineering*; Baboian, R., Ed.; NACE International: Houston, TX, 1986.
44. Siebert, O. W. In *Electrochemical Techniques for Corrosion Engineering*; Baboian, R., Ed.; NACE International: Houston, TX, 1986.
45. Hack, H. P. In *Corrosion/83*; NACE International: Houston, TX, 1983; Paper no. 73.
46. Hack, H. P.; Scully, J. R. *Corrosion* **1986**, 42(2), 79–90.
47. Hack, H. P.; Moran, P. J.; Scully, J. R. In *The Measurement and Correction of Electrolyte Resistance in Electrochemical Tests*; Scribner, L. L., Taylor, S. R., Eds.; ASTM International: West Conshohocken, PA, 1990; STP 1056, pp 5–26.
48. Standard G102: Standard Practice for Calculation of Corrosion Rates and Related Information from Electrochemical Measurements; ASTM International: West Conshohocken, PA; Standard G46: Guide for Examination and Evaluation of Pitting Corrosion, *ASTM Book of Standards*; ASTM International, West Conshohocken, PA, 2006.
49. Compton, K. G.; Mendizza, A. In *Symposium on Atmospheric Corrosion of Non-Ferrous Metals*; ASTM International: West Conshohocken, PA, 1955; STP 175, pp 116–125.
50. Doyle, D. P.; Goddard, H. G. *Nature* **1963**, 200(4912), 1167–1168.
51. Standard G116: Practice for Conducting Wire-on-Bolt Test for Atmospheric Galvanic Corrosion, *ASTM Book of Standards*; ASTM International: West Conshohocken, PA, 2006.
52. Standard G149 (withdrawn 2004): Practice for Conducting the Washer Test for Atmospheric Galvanic Corrosion, *ASTM Book of Standards*; ASTM International: West Conshohocken, PA, 2006.
53. ISO 7441: Corrosion of Metals and Alloys – Determination of bimetallic corrosion in outdoor exposure corrosion tests, The International Organization for Standardization: Geneva, 1984.
54. Standard G50: Conducting Atmospheric Corrosion Tests on Metals, *ASTM Book of Standards*; ASTM International: West Conshohocken, PA, 2006.
55. Hack, H. P. *J. Testing Eval* **1980**, 8(2), 74–79.
56. Aylor, D. M.; Hays, R. A.; Marshall, L. S. In *Corrosion 2000*; NACE International: Houston, TX, 2000; paper 00640.
57. Hack, H. P. Atlas of polarization diagrams for naval materials in seawater, Report CDNSRDC-TR-61–94/44, Naval Surface Warfare Center Carderock Division, Bethesda, MD, April 1995.
58. Bauer, O.; Vogel, O. *Mitt. MatPrufAmt. Inst. Metallforsch. Berl.* **1918**, 36, 114.
59. Shrier, L. L. Ed. *Corrosion*; Newnes-Butterworth: London, UK, 1976; Vol. 1, Chapter 1.7.
60. Gehring, G. A.; Kyle, R. J. In *Corrosion/82*; NACE International: Houston, TX, 1982; Paper no. 60.
61. Niederberger, R. B.; Gudas, J. P. The effect of seawater velocity on galvanic interactions of piping system alloys, Unpublished data, Naval Surface Warfare Center Carderock Division, Bethesda, MD, February 1979.
62. Caplan, I. L.; Hack, H. P. The galvanic effects of titanium coupled to various marine alloys in seawater, Report CDNSRDC-SME-80/54, Naval Surface Warfare Center Carderock Division, Bethesda, MD, October 1980.
63. *Guide for Engineers*; NACE International: Houston, TX, 2001.
64. Fontana, M. G. *Corrosion Engineering*; McGraw-Hill: New York, NY, 1986.
65. Uhlig, H. H. *Corrosion and Corrosion Control*; Wiley: New York, NY, 1971.
66. *Bimetallic Corrosion*; National Corrosion Service, Department of Industry, Colibri Press: England, 1982; Publication No. 14.

## 2.08 Environmentally Assisted Cracking Overview

**R. C. Newman**

Department of Chemical Engineering and Applied Chemistry, University of Toronto, Canada

© 2010 Elsevier B.V. All rights reserved.

2.08.1	Introduction	857
2.08.2	Appearance of EAC	858
2.08.3	Stress and Strain in EAC	859
2.08.4	Test Methods for EAC	861
2.08.5	Mechanisms of the Environmental Enhancement in EAC	862
2.08.5.1	Occurrence of EAC in Pure Metals	863
2.08.6	Emerging Environments and Future Outlook	863
References		863

### Abbreviations

**CF** Corrosion fatigue  
**CGR** Crack growth rate  
**EAC** Environment-assisted cracking  
**HE** Hydrogen embrittlement  
**HIC** Hydrogen-induced cracking  
**LME** Liquid metal embrittlement  
**SCC** Stress corrosion cracking  
**SICC** Strain-induced corrosion cracking  
**SSCC** Sulfide stress corrosion cracking

### Symbols

**a** Crack length  
**K** Stress intensity factor (strictly  $K_I$  for crack-opening load)  
 **$K_c$**  Critical stress intensity factor  
 **$K_{max}$**  Maximum stress intensity factor (in fatigue)  
 **$K_{th}$**  Threshold stress intensity for EAC (also called  $K_{ISCC}$ )  
**N** Number of cycles (in fatigue)  
 **$N_f$**  Number of cycles to failure (in fatigue)  
**R** Minimum load divided by maximum load (in fatigue)  
 **$v$**  Crack velocity ( $= da/dt$ )  
 **$\Delta K$**  Stress intensity range (in fatigue)  
 **$\Delta\sigma$**  Stress range (in fatigue)  
 **$\varepsilon$**  Tensile strain  
 **$\sigma$**  Tensile stress  
 **$\sigma_y$**  Yield stress

### 2.08.1 Introduction

Environment-assisted cracking (EAC) is the gradual growth of cracks under the combined – usually simultaneous – influence of stress and environment. The stress may be applied or internal (residual). The environment may be an aqueous solution or moist atmosphere, a nonaqueous liquid such as ammonia, a gas, a liquid metal, or a solid metal at a high homologous temperature. Whenever the environment is an electrolyte, the EAC process must have a partly electrochemical (i.e., corrosion) character. This may be the dominant factor or a secondary one, depending on the details of the particular system. A simple electrochemical effect is the discharge of hydrogen ions during corrosion of steel in water; the resulting hydrogen atoms may diffuse into the steel and cause embrittlement.

When the stress is more or less static, or varies over a small range, EAC is called as stress corrosion cracking (SCC), hydrogen embrittlement (HE), or liquid metal embrittlement (LME). When a blatantly cyclic stress is present, EAC is usually called corrosion fatigue (CF), hydrogen-assisted fatigue, and so on, although some specialists argue that within this category there are separate phenomena called ‘true corrosion fatigue’ and ‘stress corrosion fatigue’ (discussed later). **Figure 1**, from Andresen, shows the extremes that are easily categorized as ‘static’ or ‘fatigue’ loading, and some of the possibilities in between.

Even if we are sure that a cracking phenomenon is caused by hydrogen (as in the SCC of high-strength steels), we still call it SCC if it occurs under natural

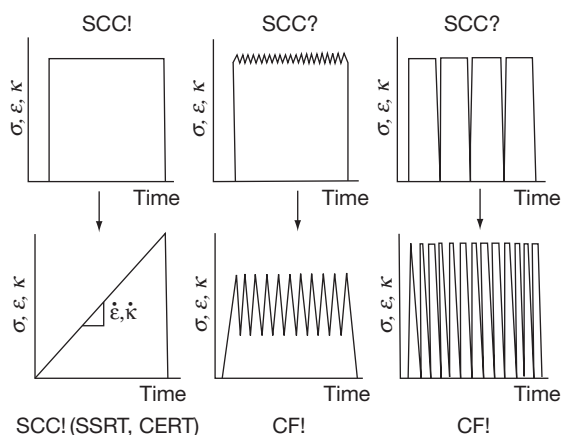


**Figure 1** Illustration of the loading patterns that may occur in a component at risk of EAC, and the appropriate nomenclature. Courtesy of P.L. Andresen.

corrosion conditions. Where the distinction becomes blurred is when the steel is coated with a mildly sacrificial metal such as cadmium, and hydrogen may be absorbed through this galvanic action and not by corrosion of the steel substrate. Under full-scale cathodic protection, we would not refer to SCC, but to HE.

In principle, any EAC problem can be mitigated in one of three ways – modify the stress, modify the material, or modify the environment (which would include changing the electrode potential, either by galvanic contact or by imposing a potential). Thus, EAC presents a large number of possible variables, but also a large number of possible countermeasures. A major variable is yield strength – strong alloys are generally more susceptible to EAC, especially where hydrogen absorption is involved, and this limits their application in practice.

Many international conferences on EAC have been held since the 1940s, but a particular landmark was the Ohio State University conference in 1967.<sup>1</sup> This dealt mainly with SCC, but specialist proceedings are also available on CF<sup>2</sup> and LME,<sup>3</sup> recently called ‘metal-induced fracture’ in view of cracking observed with solid metal contact. A regular conference series on hydrogen effects in materials is held in Jackson Hole, Wyoming and has recently joined with a series pioneered in France called ‘Corrosion–Deformation Interactions.’<sup>4</sup> The most recent conference that attempted to cover the entire field of EAC was held in Banff, Canada, in 2004,<sup>5</sup> and was a sequel to a 1987 conference that had a similar ambitious scope.<sup>6</sup> There is a vast journal literature on EAC.

The crack growth rates (CGRs) in EAC vary quite widely, and the lower limit of CGR, if there is one, has probably not been observed yet. At some point, especially at elevated temperatures, the CGR will become equal to a creep crack growth rate, at which point it may not be appropriate to talk about EAC. Creep, though, can also be affected by the environment. There is a whole area of research called creep–fatigue–oxidation interaction, and a related phenomenon that occurs under static loading, called oxygen embrittlement.<sup>7</sup> These phenomena are usually studied in the context of gas turbine materials, but there may be a link with SCC in hot water or steam systems.

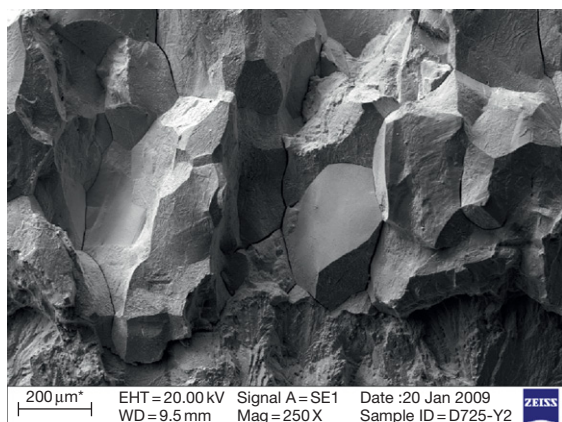
For SCC, the CGRs tend to range from about  $10^{-12} \text{ m s}^{-1}$  ( $30 \mu\text{m year}^{-1}$ ) to  $10^{-7} \text{ m s}^{-1}$  ( $9 \text{ mm day}^{-1}$ ). In the laboratory, faster rates are possible. From an industrial perspective, the lower range of rates is manageable by appropriate inspection; the highest rates are not, but they occur in certain well-known high-risk situations, such as contact of austenitic stainless steel with strong, hot chloride solutions, or contact of a susceptible alloy with mercury. Usually something has gone badly wrong when such rates occur. The fastest form of EAC is LME, which can appear almost instantaneously in certain combinations such as mercury (or liquid gallium) and a high-strength aluminum alloy.

## 2.08.2 Appearance of EAC

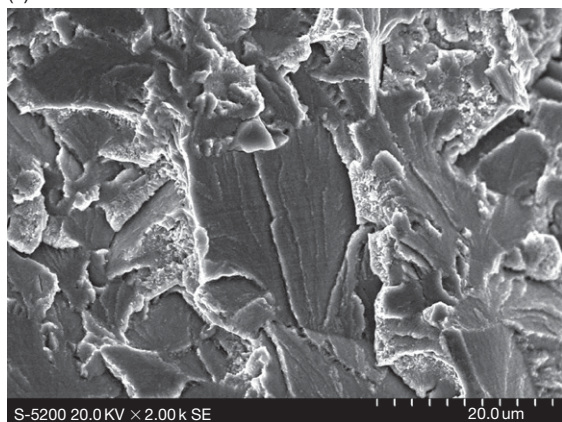
There are three common types of crack morphology in EAC: intergranular, transgranular (cleavage-like), and transgranular (fatigue-like) (Figure 2). When a CF surface shows ‘brittle striations,’ there is not much distinction from a cleavage-like SCC fracture surface, which might be obtained in the same environment by monotonic dynamic straining. There are also some cases of HE (in lower strength steels and some aluminum alloys) in which the fracture surface is dimpled, but the dimples are smaller than those that occur in a normal ductile fracture performed in air.

Classical cases of SCC (brass in aqueous ammonia; carbon steel in hot caustic or nitrate solution) were usually intergranular, but later the transgranular form became more common as new materials and technologies were developed, chiefly process industries that exposed austenitic stainless steels to the risk of SCC due to hot aqueous chloride. CF is usually transgranular, but can be intergranular at low cyclic stress (intensity) amplitudes, or in alloys with sensitive grain boundaries, such as sensitized stainless steel or

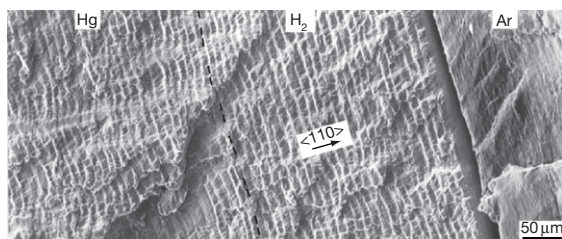
high-strength aluminum alloys. LME is usually intergranular in practice, but occurs in monocrystals of many metals (Al, Ni, etc.) in the laboratory. Hydrogen affects both intergranular and transgranular fracture. A recent review by Lynch discusses many fractographic details seen in EAC, and proposes that



(a)



(b)



(c)

**Figure 2** Fracture appearance in EAC: (a) Mainly intergranular SCC of Alloy 600, courtesy Bob Cottis, School of Materials, University of Manchester; (b) Transgranular cleavage-like SCC of Alloy 800 in 50% NaOH at 280 °C; (c) Fatigue of a nickel monocrystal showing successive regions of fracture in mercury (brittle striations), hydrogen (brittle striations), and argon (ductile striations). Reproduced from Lynch, S. P. *Acta Metall.* **1988**, 36, 2639–2661.

many EAC phenomena might be unified under an adsorption-induced plastic microfracture type of mechanism.<sup>8</sup>

The phenomenon of hydrogen-induced cracking of steel (HIC) occurs in pipes carrying sour oil or gas. It is not driven by preexisting external or internal stress, but by the pressure of hydrogen that is discharged as part of a corrosion reaction, enters the metal at a huge effective activity in accordance with the Nernst equation, then recombines to form high-pressure gas at defects inside the metal. It is only barely to be considered a case of EAC, and is not discussed further in this article. Importantly, though, when we increase the strength of steel used to make such pipes, we risk a transition from HIC to SSCC (sulfide stress corrosion cracking) which is a true SCC phenomenon, also caused by hydrogen, but under the influence of the stress in the pipe (**Figure 3**).

One difference that usually helps to distinguish SCC and CF is the multiplicity of cracks. CF, like ordinary fatigue, usually shows few and relatively flat cracks, whereas SCC often shows complex branched and intertwined cracks (**Figure 4**). An important factor in creating such crack patterns is the amount of local driving force (loosely, the local stress intensity factor  $K$ ) that is needed to propagate the crack. If this is low, then the presence of many parallel or overlapping cracks (which reduces the  $K$  value at each crack tip) is not a hindrance to the propagation of each one.

Cracking of welded or cast components cannot always be classified as ‘intergranular’ or ‘transgranular,’ and the morphologies are often complex.

### 2.08.3 Stress and Strain in EAC

Strong alloys are used because they need to resist stresses in service, so for these materials the main source of stress is often an externally applied load, such as

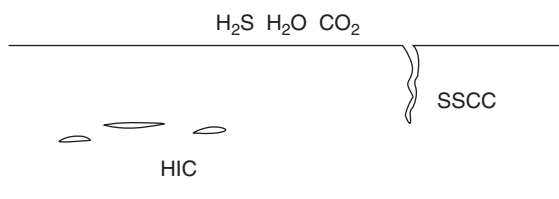


**Figure 3** Distinction between HIC (hydrogen-induced cracking) and SSCC (sulfide stress corrosion cracking) as made in the oil and gas industry. HIC is not caused by the stresses present in the pipe or vessel, but by the pressure of internal hydrogen gas.





**Figure 4** Illustration of the meandering path taken by typical stress corrosion cracks, indicative of a low local driving force required for crack advance (transgranular SCC of AISI type 316 stainless steel in 4 M NaOH at 280 °C).

internal pressure in a pipe. Ductile alloys such as austenitic stainless steel are not much used for major load-bearing structure, so they usually crack under the influence of internal residual stresses (e.g., at welds). Cyclic stresses, if present, can arise from rotation, vibration, thermal fluctuation, intermittent operation, and so on. Superimposition of static and cyclic stresses is a major topic in fatigue, and thus also in corrosion fatigue.

A distinction between EAC and ordinary fatigue is that hardening is generally detrimental for EAC, whereas it is one of the ways to improve fatigue resistance.

Low-frequency, low-amplitude cycling can cause major enhancement of SCC under conditions where it would not be appropriate to refer to fatigue – such as one cycle per startup of a nuclear reactor, or one cycle per spring thaw for a pipeline crossing a riverbed. This reflects a general truth about SCC, which is that for the most part it is a plastic-strain-driven phenomenon (at least that is the prevailing opinion – this may change). If the load is completely static, cracking is less likely because any transient creep strain becomes exhausted, and there is nothing to drive processes such as oxide film rupture. R.N. Parkins is credited for much of the modern understanding of this issue, and for the idea that there exists a continuum of EAC from SCC through intermediate cases to true CF.<sup>9</sup> Figure 5 illustrates, schematically, the effect of low-amplitude cycling on the two kinds of external pipeline cracking studied by Parkins – ‘near-neutral pH’ and ‘carbonate–bicarbonate.’

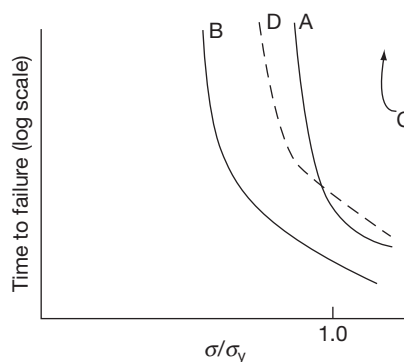


**Figure 5** Schematic behavior of carbon steel pipeline material subject to external SCC with and without low-amplitude cyclic loading. In high-pH carbonate–bicarbonate, the time to failure decreases from line A to line B upon cycling. In near-neutral pH bicarbonate–CO<sub>2</sub>, there is scarcely any cracking without cycling (line C) but cracking occurs with cycling (line D).

EAC of pressurized or otherwise actively loaded equipment made of high-strength materials causes particular concern because it can lead to catastrophic failure. A crack initiates, grows at an increasing rate, then fast fracture occurs when  $K$  (or  $K_{\max}$  in the case of CF) reaches  $K_c$ . On the other hand, in something like a stainless steel pipe carrying a corrodent under low pressure, where there is no meaningful  $K_c$ , the outcome of EAC is usually a leak. This can be serious, but it is usually more manageable than a fast rupture. Naturally, there are cases that fall somewhere in between, and here there may be uncertainty as to the structural outcome of an EAC incident; modeling and simulation can provide some of the answers, but some kind of full-scale component test may be required.

When fracture mechanics methods are applied to SCC, HE, or LME, a flat or ‘plateau’ region is observed at intermediate  $K$  values – Figure 6. (The author’s Ph.D. advisor, G.T. Burstein, used to insist that such features should be called ‘ledges,’ not ‘plateaux.’) This shows that a limiting condition has been reached where something other than the mechanics controls the crack growth rate. This ‘chemical’ rate control is generally due to a rate-limiting dissolution, diffusion, or adsorption process. Also, the critical stress intensity factor  $K_c$  may be reduced, in effect, by hydrogen-producing environments; the implications of this are both serious and poorly understood. (‘In effect,’ because  $K$  is a static quantity and the reduction in apparent  $K_c$  value may be due to dynamics associated with the overload of the crack – that is,



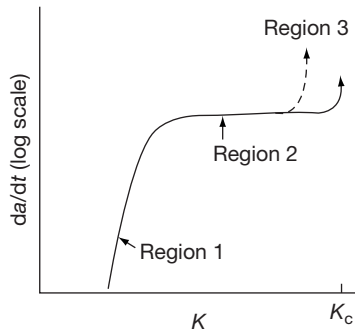


**Figure 6** Schematic crack velocity versus stress intensity curve for EAC (without cyclic loading) showing the ‘plateau’ region at intermediate  $K$  values. Such curves are often drawn as though there is no reduction in  $K_c$  due to the environment, but in reality such reductions (dashed line) can occur and are troublesome in certain safety-related prediction procedures.

there is a strain rate sensitivity of the apparent reduction in  $K_c$ .)

Stress in a real component is always multiaxial to some extent, but most SCC behavior is referred to the principal tensile stress, whether residual or applied. The stress *state* is important, though, in hydrogen-affected EAC. This is because three-dimensional (3D) lattice dilation can increase the solubility of hydrogen in the metal and thus, potentially, the susceptibility to cracking. A number of authors have shown easier cracking in mode I (tension) loading than in mode III (torsion) in certain systems believed to involve hydrogen entry into the metal.<sup>10</sup>

In components subject to fatigue, the mean stress is rarely zero. Certain effects of the  $R$  parameter (minimum load/maximum load) are known in ordinary fatigue, but in CF these are magnified. To some extent, this can be dismissed as the superimposition of SCC (due to the mean load) on CF (due to the cyclic load), but as CF occurs in environments where SCC does not, it is an important consideration. **Figure 7** indicates the distinction between ‘true corrosion fatigue’ and ‘stress corrosion fatigue’ that is made by some authors. The hump or plateau feature at intermediate  $\Delta K$  values is due to SCC-like crack growth, and thus becomes more noticeable with increasing mean stress. Cyclic loading frequency is a key variable affecting crack growth in CF, in contrast to ordinary fatigue, because the corrosion process (this also applies to hydrogen-assisted fatigue) needs time to do its work on each cycle, and if the frequency is too high, the cracking behavior may revert to that seen in an inert environment. It is easy to see that all this is amenable to a mathematical modeling approach based on superposition of a time-dependent

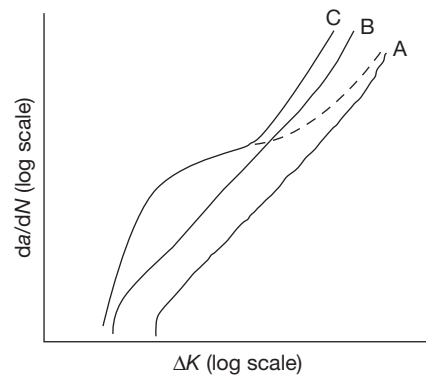


**Figure 7** Fatigue crack growth curves showing some different possible effects of an environment. Line A is for an inert environment. Then, the distinction is made between ‘true corrosion fatigue’ (line B) and ‘stress corrosion fatigue’ (line C; alternatively the dashed line), which shows a plateau-like feature at intermediate  $\Delta K$  values. Most corrosion engineers do not make this distinction, and most corrosion fatigue is of type C.

‘monotonic’ or ‘SCC’-like element of crack advance and a ‘cyclic’ contribution.

One type of SCC has its own special name. SICC (strain-induced corrosion cracking)<sup>11</sup> occurs in steel exposed to hot water when sufficiently large strains arise to fracture the magnetite film on the surface. This is not much different from any other case of SCC where dynamic strain is mandatory, and, indeed, CF occurs quite readily under such conditions, at least in the laboratory.

## 2.08.4 Test Methods for EAC

An excellent manual on SCC testing is available, written by Sedriks.<sup>12</sup> Testing for CF is no different from ordinary fatigue testing, except that the environment has to be contained around the sample – this of course presents a challenge when the environment is a gas or a hot, pressurized aqueous solution. Electrochemistry adds another level of complexity, especially in an autoclave.

Regarding specimen design, all EAC testing can be classified as (a) smooth-specimen testing, or (b) defected (e.g., precracked) specimen testing, and for SCC these can be further subdivided into selfloaded (e.g., bolt-loaded) and machine-loaded designs (fatigue, unless purely thermal, generally requires a testing machine). The advantage of using a machine, despite the extra complexity, is that the loading can be active; this is especially important in view of the proven role of low-level dynamic strains in SCC. Also, one can use a

test machine to do a slow strain rate test – an important accelerated method for mapping out SCC susceptibility rapidly and economically.

For SCC, HE, LME, etc. one can use precracked specimen testing to obtain the CGR, or crack velocity ( $v$ , or  $da/dt$ ) as a function of the stress intensity factor  $K$  as shown in **Figure 6** – although only up to a point for ductile alloys, which undergo large-scale yielding that puts a limit on  $K$  values that can be validly quoted. This does not affect the study of crack growth at relatively low  $K$  values near the threshold ( $K_{th}$  or  $K_{ISCC}$ ) below which crack growth stops altogether (it should be noted that not all authors agree with the existence of a true  $K_{th}$  for SCC). In some types of SCC, copious multibranched cracking makes  $K$  a questionable parameter, but this can be handled to some extent by machining side grooves on the specimen to keep the crack straight. The determination of  $da/dt$  is a big subject in itself – the most sophisticated laboratories generally use sensitive and stable electrical resistance (DC potential drop) methods.

Similarly, we can use precracked specimens to obtain  $da/dN$  versus  $\Delta K$  curves in an environment. This is one of the most difficult of all corrosion experiments, especially if done in an autoclave.

For the most difficult types of EAC – such as the SCC of annealed stainless steels in reducing high temperature water, or the SCC of pipeline steels in near-neutral pH solutions, or HE of ordinary carbon steels in general, the occurrence of truly stable crack growth at constant  $K$  is questionable. In that case, some dynamic loading, such as fatigue loading or periodic unloading, is mandatory for stable cracking to occur. Clearly, this might represent a nomenclature problem – but generally we prefer to stay with ‘SCC’ (see **Figure 1**) so long as the mean stress dominates the cracking behavior. Slow strain rate testing especially exaggerates the propensity of such systems to show SCC in practice. If we believe the results of slow strain rate tests, we would never cathodically protect steel.

Data presentation is straightforward for precracked specimen testing:  $da/dt$  (crack velocity) versus  $K$ , or  $da/dN$  versus  $\Delta K$ . For smooth-specimen testing, there is a multitude of types of data that can be gleaned from a test – for fatigue, the presentation is generally in the form of  $\Delta\sigma$  (cyclic stress range) versus  $N_f$  (number of cycles to failure), and the effect of an environment is often to remove the ‘fatigue limit’ at low  $\Delta\sigma$  – **Figure 8** (incidentally, such testing is normally done at quite a high frequency, so crack growth may not be much affected by corrosion – the main effect is to assist crack initiation). For SCC,

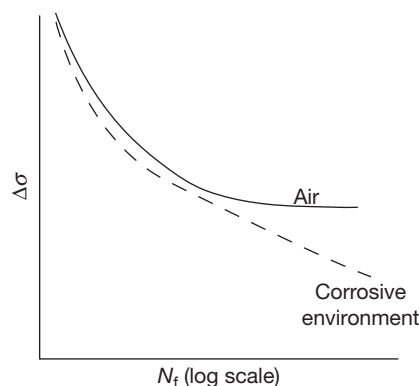


**Figure 8** Disappearance of the fatigue limit in corrosion fatigue tests conducted on smooth specimens.

smooth self-loaded samples can be examined for cracks after a fixed period of time, or examined periodically and reimmersed each time (this seems dubious, but has been done, especially for long tests in hot, pressurized water), or monitored continuously by optical microscopy or acoustic emission. Multiple samples may be tested at the same condition. Ideally, the output should be a plot of time to failure against stress. Machine-loaded samples, and especially slow strain rate tests, enable a better distinction of crack initiation and crack growth – for slow strain rate, one can obtain a variety of quantities as discussed by Sedriks – strain to failure (normalized to air), reduction in area at fracture, maximum stress, and so on. Low-amplitude cyclic strains (not enough to be called fatigue) often enhance SCC susceptibility, as discussed earlier, and can be applied automatically with some modern slow strain rate machines.

### 2.08.5 Mechanisms of the Environmental Enhancement in EAC

A detailed discussion of crack-tip mechanisms is deferred to the SCC chapter. Broadly, the proposed mechanisms fall into several categories, which still excite controversy.

- Decohesion or enhanced plastic rupture caused by hydrogen or liquid metal adsorption or absorption.
- Slip-dissolution or slip-oxidation – that is, crack growth by a highly localized corrosion process, exacerbated by local plastic deformation.
- Film-induced substrate fracture (film-induced cleavage).
- Creep-like mechanisms, for example, ‘surface mobility,’ vacancy injection.

Many reviews are available – including the one by the author.<sup>13</sup>

In CF the possibilities are expanded, and simple anodic dissolution (without any apparent surface film) or simple passive film formation can cause an enhancement in crack initiation and  $da/dN$ . Generally CF can be seen with more subtle environmental effects than SCC.

Not much discussion has occurred lately on mechanisms of LME, but there was an intriguing study showing that in one well-known system (Ga on Al) first-principles quantum calculations could show that surface alloying (intermixing of Ga and Al in the first atomic layer) should occur.<sup>14</sup> This might be a general mechanism of, or rather first step in, LME. In any event, whatever the interaction is, it is extremely shallow, yet causes the fastest of all EAC phenomena. Quantum calculations are also giving insight into hydrogen effects in metals.

#### 2.08.5.1 Occurrence of EAC in Pure Metals

CF and LME are well known to occur in pure metals, but SCC of pure metals was controversial until recently. Extremely pure iron does not crack in nitrate or caustic (and presumably other intergranular cracking environments), and intergranular SCC of pure copper could be dismissed as some kind of grain-boundary segregation effect, but in fact it should have been obvious from the earliest observations of transgranular SCC in carbon steel that pure iron would also crack transgranularly in the same (peculiar) environments – CO–CO<sub>2</sub>–H<sub>2</sub>O, and anhydrous liquid ammonia. The issue was laid to rest by the observation of transgranular SCC in pure copper, which has occurred now and again in practice. This is discussed further in the Chapter 2.09, Stress Corrosion Cracking.

#### 2.08.6 Emerging Environments and Future Outlook

Until the advent of the slow strain rate test in the 1970s, most EAC phenomena were discovered in the field, not in the lab. Even now we can be caught out by a new environmental effect. So, as technologies develop, we need to anticipate possible EAC problems. For example, the prospects for supercritical water-cooled nuclear power plants are critically dependent on the development of new materials that are resistant to EAC in such extreme environments

(and with neutron irradiation, radiolysis, etc.). Other new energy technologies such as thermochemical–electrochemical hydrogen production have unusual environments that could cause unexpected EAC problems. Finally, even the ‘pure water’ problem is not solved yet, because next-generation nuclear plants will have to operate for 60–100 years, and late-onset EAC is possible in the presently used materials.

We need to develop multiscale understanding of EAC, from the quantum level to the component level, before we can truly have a predictive capability. We know already that EAC can be *controlled* at all these scales – one can add some element that interacts chemically with hydrogen and mitigates its embrittlement effect, or one can induce a surface residual stress in a whole component that prevents crack initiation. In between, one can control intergranular EAC at the granular level, by inducing the formation of a high fraction of geometrically special, nonsusceptible grain boundaries – so-called grain boundary engineering. So, despite the formidable challenges presented by EAC, we have a wide range of countermeasures at many length scales.

#### References

1. Staehle, R. W.; Forty, A. J.; van Rooyen, D., Eds. *Fundamental Aspects of Stress-Corrosion Cracking*; NACE: Houston, TX, 1969.
2. Crooker, T. W.; Leis, B. N. *Corrosion Fatigue – Mechanics, Metallurgy, Electrochemistry and Engineering*, ASTM STP 801; ASTM: Philadelphia, 1983.
3. Kamdar, M. H., Ed. *Embrittlement by Liquid and Solid Metals*; TMS-AIME: Warrendale, PA, 1984.
4. Thompson, A. W.; Moody, N. R.; Ricker, R. E.; Was, G. S.; Jones, R. H., Eds. *Hydrogen Effects on Material Behavior and Corrosion-Deformation Interactions*; TMS-AIME: Warrendale, PA, 2003.
5. Shipilov, S. A.; Jones, R. H.; Olive, J.-M.; Rebak, R., Eds. *Environment-Induced Cracking of Materials*; Elsevier, 2008.
6. Gangloff, R. P.; Ives, M. B., Eds. *Environmental-Induced Cracking of Metals*; NACE: Houston, TX, 1990.
7. Woodford, D. A. *Energy Mater.* **2006**, 1(1), 59–79.
8. Lynch, S. P. In *Corrosion/2007*; NACE: Houston, TX, 2007; Paper no. 489.
9. Parkins, R. N.; Belhimer, E.; Blanchard, W. K., Jr. *Corrosion* **1993**, 49, 951–966.
10. Pickens, J. R.; Gordon, J. R.; Green, J. A. S. *Metall. Trans A.* **1983**, 14A, 925–930.
11. Seifert, H. P.; Ritter, S. J. *Nucl. Mater.* **2008**, 378, 312–326.
12. Sedriks, A. J. *Stress Corrosion Cracking Test Methods*; NACE: Houston, TX, 1989.
13. Newman, R. C. In *Stress Corrosion Cracking Mechanisms. Corrosion Mechanisms in Theory and Practice*, 2nd ed.; Marcus, P., Oudar, J., Eds. Marcel Dekker: New York, 2002; pp 399–450.
14. Stumpf, R.; Feibelman, P. J. *Phys. Rev. B* **1996**, 54, 5145–5150.

## 2.10 Hydrogen Embrittlement

**R. A. Cottis**

Corrosion and Protection Centre, School of Materials, University of Manchester, Manchester M60 1QD, UK

© 2010 Elsevier B.V. All rights reserved.

2.10.1	Introduction	903
2.10.2	Terminology	903
2.10.3	Entry of Hydrogen into Metals	903
2.10.3.1	Entry from the Gas Phase	903
2.10.3.2	Entry from the Aqueous Phase	904
2.10.4	Location of Hydrogen in Steel	905
2.10.5	Transport of Hydrogen in Iron and Steel	906
2.10.6	Sources of Hydrogen	907
2.10.7	Effect of Hydrogen on Mechanical Properties	911
2.10.7.1	Elastic Constants	911
2.10.7.2	Yield Stress	911
2.10.7.3	Plastic Behavior	911
2.10.8	Hydrogen Embrittlement of Steels	912
2.10.9	Hydrogen Embrittlement of Other Alloys	913
2.10.10	The Influence of Microstructure and Composition	913
2.10.11	Theories of Hydrogen Embrittlement	914
2.10.11.1	The Pressure Theory	914
2.10.11.2	Decohesion Theories	915
2.10.11.3	Surface Energy Theories	915
2.10.11.4	Hydride Formation	915
2.10.11.5	Local Plasticity Theories	915
2.10.12	Hydrogen Embrittlement Tests	915
2.10.12.1	Constant Stress Tests	916
2.10.12.2	Controlled Strain-Rate Tests	916
2.10.12.3	Fracture Mechanics Tests	917
2.10.13	Controlling Hydrogen Embrittlement in Service	918
2.10.13.1	Reduction of Hydrogen Content	919
2.10.13.2	Increasing Resistance of Steel	920
2.10.13.3	Prediction of Behavior	921
2.10.14	Modeling of Hydrogen Embrittlement	921
References		921

### Abbreviations

**AIDE** Adsorption-induced dislocation emission

**bcc** Body centered cubic

**CTOD** Crack tip opening displacement

**fcc** Face centered cubic

**hcp** Hexagonal close packed

**HELP** Hydrogen-induced localized plasticity

**HEDE** Hydrogen-enhanced decohesion

**HIC** Hydrogen-induced cracking

**HISC** Hydrogen-induced stress cracking

**SCC** Stress corrosion cracking

**SCE** Saturated calomel electrode

**SOHIC** Stress-oriented hydrogen-induced cracking

**SSC** Sulfide stress cracking

### Symbols

***a*** Crack length

***K*** Stress intensity factor

***K<sub>IC</sub>*** Critical stress intensity factor for fast fracture

***K<sub>ISCC</sub>*** Critical stress intensity factor for SCC

***r*** Distance ahead of crack tip

***σ<sub>th</sub>*** Threshold stress for SCC

## 2.10.1 Introduction

There are many applications in which the yield strength of the material of construction is a limiting factor in the design. For example, a large proportion of the weight of an offshore oil production platform consists of the structure required to resist wave forces, with a relatively small proportion being the 'topside' equipment that actually does the work. If the strength of the material of the structure could be increased, this would allow the structure itself to be made lighter, with the consequence that the weight of the topside equipment could be increased. Thus, materials offering high strength-to-weight or strength-to-volume ratio are in high demand in many fields of engineering. Steels can be produced with yield strengths above 2000 MPa, and at first sight, one might expect these to have widespread application. Unfortunately, things are not that simple, and as the yield strength of materials is increased, other mechanical properties tend to decrease. In particular, the materials become more susceptible to brittle fracture, especially when assisted by environmental factors, such as hydrogen embrittlement, stress corrosion cracking, or corrosion fatigue. The related problem of hydrogen-induced blister formation or hydrogen-induced cracking tends to be more of a problem in lower-strength steels used for crude oil transmission pipelines.

It is now well established that high-strength steels are susceptible to embrittlement by dissolved hydrogen, and the majority of stress corrosion cracking (SCC) failures of these materials are attributed to hydrogen embrittlement. This should not be taken to imply that other mechanisms of SCC do not occur. However, the ease with which hydrogen can be picked up from aqueous environments is such that other SCC processes are rarely a practical problem for high-strength steels.

This document is based on a Chapter on SCC of High Strength Steels that was produced for the 3rd Edition in about 1989. It has been revised for the 4th Edition to incorporate some updated references, particularly in respect of mechanistic aspects of hydrogen embrittlement, and to provide some information on hydrogen embrittlement of materials other than carbon and low-alloy steels. Hydrogen embrittlement continues to be a major area of research, with nearly 9000 publications in the period from 1980 to Spring 2009. A number of reviews of the aspects of hydrogen embrittlement have been published in the last 25 years<sup>1-3</sup> to which the reader is referred for further information.

## 2.10.2 Terminology

As with several aspects of corrosion technology, the terminology of the effects of hydrogen on metals is somewhat confused. We can identify two general classes of hydrogen effect:

- quasi-brittle fracture of higher strength materials that can occur with relatively low concentrations of hydrogen; we term this hydrogen embrittlement, although some processes that almost certainly occur by this mechanism are also termed SCC, such as the SCC of high-strength aluminum alloys in water or water vapor; and
- surface blistering and internal cracking at sulfide and other inclusions in lower-strength materials (primarily carbon steels) due to very high internal hydrogen fugacities, leading to hydrogen pressure-induced cracking, commonly termed hydrogen-induced cracking (HIC) (it is unfortunate that the term 'hydrogen-induced cracking' has also been used as a generic term for any cracking due to hydrogen); processes in this class are discussed separately in the subsequent **Chapter 2.11, Cracking Stimulated by Hydrogen**.

However, as is often the case in corrosion, things are not really that simple, and there is a spectrum of behaviors between these two extremes, including processes such as stress-oriented hydrogen-induced cracking (SOHIC), sulfide stress cracking (SSC) of pipeline steels, and hydrogen-induced stress cracking (HISC) of duplex stainless steels. Just to complicate the terminology further, there is the phenomenon of hydrogen cracking that is experienced at higher temperatures as a result of internal methane production by reaction between dissolved hydrogen and carbon.

## 2.10.3 Entry of Hydrogen into Metals

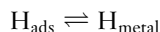
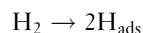
Hydrogen can enter metals, either from the gas phase, or by way of the electrochemical reduction of hydrogen-containing species, from the aqueous phase. This section is largely based on work on carbon and low-alloy steels.

### 2.10.3.1 Entry from the Gas Phase

Several models have been proposed for the entry of hydrogen from the gas phase, and the details of the process remain somewhat uncertain. In general terms however, the reactions involved are the adsorption of



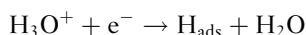
molecular hydrogen (other gases such as hydrogen sulfide can also act as a source of hydrogen, but they will typically require water to facilitate the reactions involved and are arguably aqueous phase reactions), the dissociation of the hydrogen molecule to produce hydrogen atoms adsorbed onto the surface, and the subsequent diffusion of the adsorbed hydrogen atoms into the metal lattice:



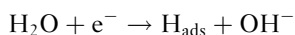
For perfectly clean and film-free iron surfaces, the rate-controlling step in this process may be the dissociation step.<sup>4</sup> This will be proportional to the partial pressure of hydrogen, and consequently so will the rate of hydrogen entry into the metal. In more realistic situations, surface films such as passive or air-formed oxide films, or the presence of gases, such as oxygen, which adsorb competitively with hydrogen, may play an important role.

### 2.10.3.2 Entry from the Aqueous Phase

The mechanism of electrochemical production of hydrogen on steel in aqueous solution has received much attention. It is accepted that the reaction occurs in two main stages. The first of these is the initial charge transfer step to produce an adsorbed hydrogen atom, known as the Volmer reaction. In acid solution, this involves the reduction of a hydrogen ion.



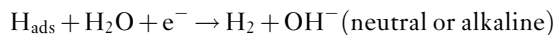
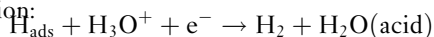
In neutral and alkaline solution, where the concentration of hydrogen ions is very low, the reaction switches to the reduction of water molecules:



The second stage of the reaction to produce molecular hydrogen may occur through either of two mechanisms. In the first of these, known as chemical desorption, chemical recombination, or the Tafel reaction, two adsorbed hydrogen atoms combine to produce a hydrogen molecule:

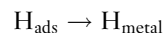


Alternatively, the adsorbed hydrogen atom may participate in a second electrochemical reaction, known as electrochemical desorption, or the Heyrovsky reaction:



For iron, it is reasonably well established that the reaction goes by way of chemical recombination under most circumstances, although there is some evidence that electrochemical desorption may take over in very alkaline solutions or at large overpotentials.

A third reaction, which goes in parallel with the desorption reaction, is the entry of atomic hydrogen into the steel from the surface adsorbed state:



In most circumstances, the kinetics of this reaction are controlled by the rate at which the hydrogen can diffuse into the underlying steel, and this reaction is essentially in equilibrium. Consequently, it is difficult to study the kinetics of this reaction. A particular situation in which this may be very important relates to the conditions at crack tips, where the hydrogen may be transported into the bulk by dislocation motion, giving rise to very high rates of hydrogen entry.

As the hydrogen entry reaction is generally in equilibrium, the hydrogen concentration just below the entry surface is directly related to the surface concentration or coverage. Consequently, the rate of entry of hydrogen into the steel is controlled by the balance between the first and second stages of the hydrogen evolution reaction, since these control the coverage of adsorbed hydrogen. In the case of chemical recombination as the second stage in the reaction, the rate of hydrogen evolution is proportional to  $(\text{H}_{\text{ads}})^2$  (since two adsorbed hydrogen atoms are involved in the reaction), while the rate of hydrogen entry (or the equilibrium concentration just below the surface, which is usually the controlling factor) is proportional to  $(\text{H}_{\text{ads}})$ . Thus, as the cathodic current increases so the subsurface hydrogen concentration (and hence, the rate of hydrogen diffusion through a membrane) increases as the square root of the cathodic current (assuming that the current due to hydrogen entering the steel is small compared to that due to hydrogen evolution, as is usually the case).

However, when the second stage in the hydrogen evolution reaction is electrochemical desorption, the rate of this reaction is increased as the potential becomes more negative, and the adsorbed hydrogen concentration may remain constant or fall, according to the detailed electrochemistry. This results in curves such as that shown in **Figure 1** for steel in seawater.

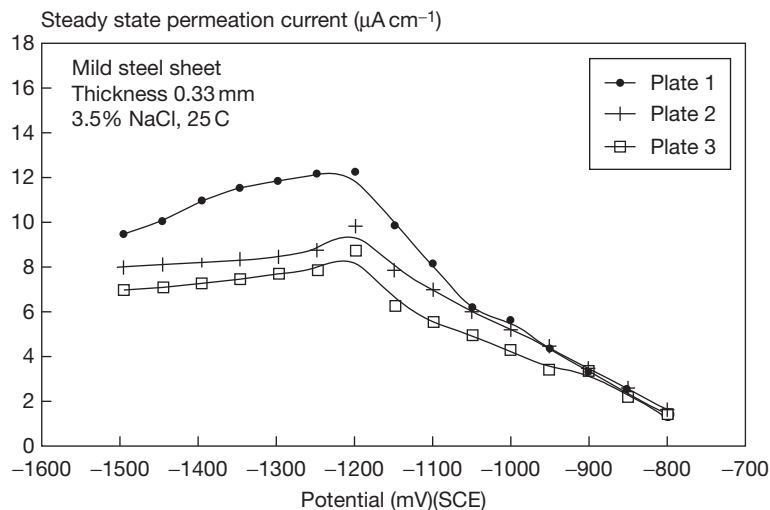


**Figure 1** Hydrogen permeation current as a function of applied potential, showing effect of change in reaction mechanism below  $-1200$  mV (SCE). Reproduced from Obuzor, U. W. PhD Thesis, UMIST, Manchester 1989.

Whether the adsorbed hydrogen is produced from the gas phase or from aqueous solution, it appears that the presence of hydrogen atoms distorts the crystal structure of the metal surface<sup>5</sup> and this results in a surface solubility that is higher than that of the bulk. The depth of this distortion is not clear, but it seems possible that this distorted zone may play an important part in initiating brittle fracture processes.

#### 2.10.4 Location of Hydrogen in Steel

Hydrogen exists in metals in the monatomic form, and is commonly described as atomic hydrogen. In practice, the state of charge of the hydrogen atom is not known with any certainty, but it seems probable that it tends to acquire a slight negative charge by attracting electrons from the valence orbitals of the metal lattice. It has been suggested that this results in a weakening of the metal-metal bond which is responsible for hydrogen embrittlement.<sup>6</sup>

Hydrogen has a very low solubility in the iron lattice, which makes direct observation of the location of the hydrogen atom in the lattice very difficult. The hydrogen definitely occupies an interstitial site in the *bcc* iron lattice. Two such sites are normally associated with interstitial solutes in *bcc* structures, the tetrahedral and the octahedral sites (see Figure 2). Indirect evidence<sup>7</sup> suggests that hydrogen occupies the tetrahedral site.

In addition to interstitial sites in the lattice, hydrogen atoms are also strongly attracted to defect sites in

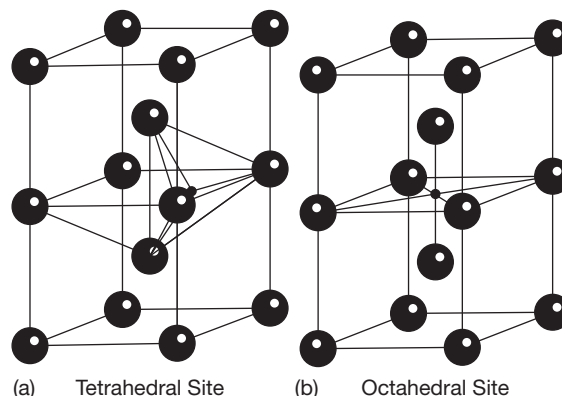


**Figure 2** Octahedral and tetrahedral sites in the *bcc* lattice.

the metal, and these are referred to as 'traps.' Trap sites include vacancies, solute atoms, dislocations, grain boundaries, voids, and nonmetallic inclusions. Of the various trap types in iron and steel, vacancies are relatively unimportant at ambient temperatures, simply because of their low concentration. Somewhat surprisingly, it appears that grain boundaries in pure iron also trap very little hydrogen, although segregation of carbon and other impurity atoms to the grain boundary can increase the tendency for trapping.<sup>8</sup> The more important trap sites in iron and steel appear to be phase boundaries, dislocations, voids, and inclusions.<sup>9</sup> Trap types may be classified in various ways, two of the more important being related to the number of hydrogen atoms which can be

accommodated in the trap and to the binding energy of the trap. These are summarized in [Table 1](#).

It should be noted that the terms saturable and reversible are rather loosely defined in relation to hydrogen trapping. Thus, some workers take the view that reversible and nonsaturable traps are the same (since the equilibrium hydrogen content of the trap will vary with the fugacity). Similarly, the term reversible is given a slightly different meaning from that in electrochemical reaction kinetics, where it relates to the activation energy of a reaction, rather than the overall free energy change.

There are many ways in which trapping can be studied, but the wide range of trap types and geometries make it difficult to determine the properties of specific trap sites.

Hydrogen trapped in voids consists of adsorbed hydrogen on the walls of the void, together with molecular hydrogen in the void itself. With high fugacities of hydrogen in the steel, such as can be developed in steels in contact with acidic solutions containing hydrogen sulfide, very high pressures may be developed in the void. When combined with the hydrogen embrittlement of the steel around the void, this can lead to the growth of cracks around the void. Such cracks typically develop around nonmetallic inclusions which have been flattened by rolling, giving characteristic blisters lying parallel to the rolling direction. This phenomenon is known as hydrogen-induced cracking.

### 2.10.5 Transport of Hydrogen in Iron and Steel

As a small interstitial atom, hydrogen diffuses rapidly in iron, the diffusion rate being of a similar order to that of solutes in aqueous solution.

**Table 1**     Classification of trap types

<i>Classification</i>	<i>Description</i>
Saturable	The number of sites for hydrogen atoms is fixed (e.g., grain boundaries, dislocations)
Nonsaturable	The number of sites for hydrogen atoms in the trap varies according to the fugacity (e.g., voids)
Reversible	The trap binding energy is relatively small, and hydrogen may escape from the trap as well as enter it
Irreversible	The trap binding energy is large, and hydrogen will not leave the trap at ambient temperature

The study of the transport of hydrogen in steel is commonly undertaken by hydrogen permeation measurements. This involves the permeation of hydrogen through a thin steel membrane (typically less than 1 mm thick). Hydrogen entry may be from the gas phase or from solution, while the flux of hydrogen through the membrane may be determined either by vacuum extraction of the gas to a suitable detector, or, somewhat more simply, by electrochemical oxidation of the hydrogen to hydrogen ions. The latter method forms the basis of the electrochemical hydrogen permeation cell developed originally by Devanathan and Stackurski<sup>10</sup> and illustrated in [Figure 3](#). This has subsequently been developed into a monitoring technique by Berman *et al.*,<sup>11</sup> while Arup<sup>12</sup> has developed a small self-contained sensor using battery technology, shown in [Figure 4](#).

In permeation measurements, the first signs of hydrogen diffusing through 1-mm steel membranes can be observed in a few minutes. The practical measurement of diffusion parameters tends to be rather unreproducible, because of the role of the various forms of trap, which tend to increase the solubility of hydrogen in the steel and thereby decrease the apparent diffusion coefficient. For pure iron at temperatures above  $\sim 350$  K, the activation energy for diffusion is  $\sim 7.6$  kJ mol<sup>-1</sup>, with  $D_0$  being in the region of  $1\text{--}2.5 \times 10^{-7}$  m<sup>2</sup> s<sup>-1</sup>. At ambient temperatures, the activation energy ranges from  $\sim 4$  to 7 kJ mol<sup>-1</sup>, with  $D_0$  ranging from  $\sim 0.5$  to  $1.2 \times 10^{-7}$  m<sup>2</sup> s<sup>-1</sup>. Diffusion coefficients at 298 K are thus  $\sim 7 \times 10^{-9}$  m<sup>2</sup> s<sup>-1</sup>.

The above data relate to very pure iron samples with low dislocation densities. In real steels, the trapping effects result in much lower apparent diffusivities, which are dependent on the metallurgical state of the steel as well as its chemical composition. Typical values for the apparent diffusion coefficient of hydrogen in high strength alloy steel at room temperature are in the region of  $10^{-11}$  m<sup>2</sup> s<sup>-1</sup>.

In the context of hydrogen embrittlement, an important aspect of transport processes is the influence of plastic strain on the behavior of hydrogen in a metal. Brass and Chene<sup>13</sup> reviewed these effects, and concluded:

“The nature of hydrogen-deformation interactions may be complex and opposite effects can be observed during the exposure of iron or nickel base alloys to a hydrogen source:

- (a) Strain may enhance hydrogen ingress in b.c.c. alloys as a consequence of a local destruction of the oxide films, while strain-induced defects favor hydrogen trapping;

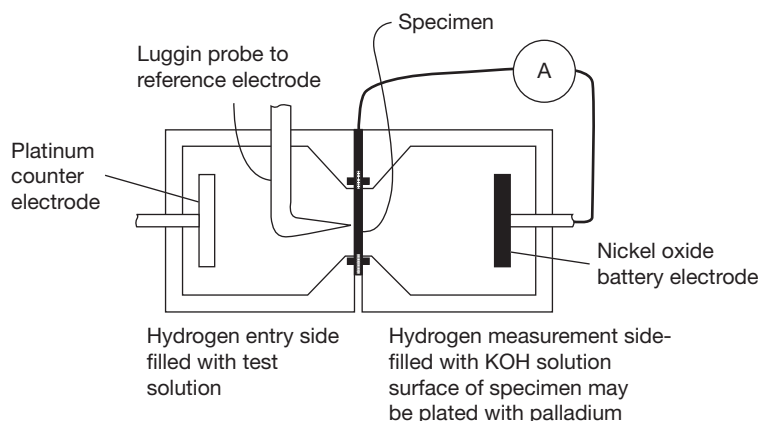


**Figure 3** Hydrogen permeation cell (schematic).

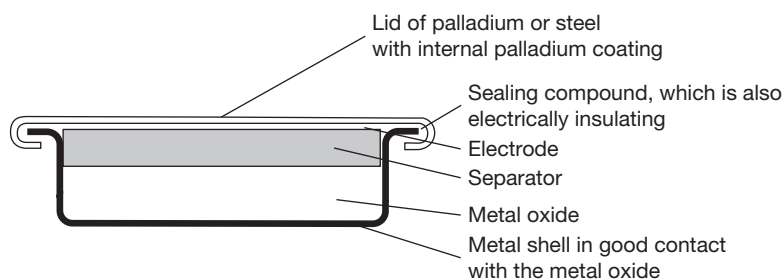


**Figure 4** Permeation cell using battery technology. Reproduced from Arup, H. Proceedings of the 9th Scandinavian Corrosion Congress, 1984; p 825.

- (b) Pipe diffusion may occur in the dislocation network of predeformed samples, whereas hydrogen accelerated transport by mobile dislocations is expected during plastic deformation in f.c.c. structures;
- (c) Both the local plasticity and the embrittlement of these alloys are increased by hydrogen."

Using *in situ* observations in an environmental TEM, Robertson<sup>14</sup> has obtained further experimental confirmation of the influence of hydrogen on dislocation dynamics, and confirmed that hydrogen enhanced dislocation mobility.

### 2.10.6 Sources of Hydrogen

The thermodynamics of the reaction of iron with water are such that iron is always thermodynamically capable of displacing hydrogen from water, although the driving force is small at ambient temperatures, except in reasonably strong acids. Thus, iron does not suffer from serious corrosion in oxygen-free neutral

or alkaline solutions. However, rates of hydrogen evolution which are insufficient to cause significant corrosion may still produce enough hydrogen to create a serious embrittlement problem for high strength steels. The hydrogen which is produced dissolves readily in the steel, and remarkably small concentrations of hydrogen (less than 1 ppm) can cause embrittlement. In addition to corrosion itself, many of the standard chemical and electrochemical treatments employed to protect steel against corrosion also tend to drive hydrogen into the steel. Some of the major sources of hydrogen are:

- **Welding** Hydrogen introduced into welds produces a particularly acute problem, as the weld and the heat-affected zone are inevitably regions of high residual stresses, contain inherent defects, and are frequently intrinsically more brittle than the parent material. Thus, it is important to minimize the introduction of hydrogen into welds, even for lower strength steels. Gas welding of steels using an oxyacetylene flame will inevitably introduce hydrogen as a result of the hydrogen-containing gases in the flame. In theory, electric arc welding,

particularly if the arc is protected from atmospheric moisture by inert gas shielding, will not introduce hydrogen. However, with normal manual metal arc welding using flux coated electrodes, it is possible for the flux coating to absorb moisture from the atmosphere, and this will react with the molten steel to produce hydrogen. For this reason, it is good practice to store coated welding electrodes in an oven in order to drive off any moisture.

- *Acid Pickling* This process is widely used for removing rust and mill scale from steel, or for removing internal scales from boilers. The objective of the process is the dissolution of iron oxides or hydroxides, or hardness scales, but at the same time, the iron will also tend to corrode in the acid, with hydrogen evolution as the cathodic reaction. This leads to hydrogen entry into the steel which may lead to hydrogen embrittlement or blister formation due to HIC.

As dissolution of the steel is normally an undesirable side-effect of the pickling process, resulting in loss of metal and wasteful consumption of acid, it is normal practice to add inhibitors (usually referred to as 'pickling restrainers') to the acid. Unfortunately, many of these work by interfering with the hydrogen recombination reaction, rather than the initial production of adsorbed hydrogen atoms. This has the effect of increasing the surface coverage by adsorbed hydrogen atoms, and consequently, the rate of entry of hydrogen into the steel is increased, even though the overall rate of hydrogen production is reduced. For this reason, it is most important that pickling restrainers for use with high strength steels should be tested for their effects on the uptake of hydrogen as well as their efficiency as inhibitors.

- *Degreasing and Cleaning* Various processes can be applied for the removal of grease and other contaminants prior to painting, electroplating, or other surface treatments. Degreasing in organic solvents (e.g., vapor degreasing) is unlikely to generate significant quantities of hydrogen unless the fluid is contaminated with water or other species, such as hydrogen chloride, capable of liberating protons. Cleaning in aqueous alkali without applied polarization is also unlikely to introduce much hydrogen, although any tendency for pitting corrosion due to chloride contamination could give rise to local problems. Cathodic cleaning, in which hydrogen is deliberately evolved on the steel is clearly undesirable.

- *Electroplating* Electroplated metal coatings provide a convenient and effective means of protecting steel against atmospheric corrosion, with zinc and cadmium being particularly useful because of their ability to provide sacrificial protection to the steel substrate at breaks in the coating. Unfortunately, all metal deposition processes require the application of potentials at which hydrogen evolution is possible (in theory it would be possible to deposit copper and more noble metals above the hydrogen evolution potential, but as this would also be a potential at which iron would dissolve anodically, this would not produce good deposits). Thus, the electrodeposition of coatings almost inevitably introduces hydrogen into the metal. The majority of electrodeposited coatings on iron are much less permeable to hydrogen than iron, the major exceptions to this being other *bcc* metals, with chromium being the only example in widespread use (although even here chromium is generally used with an undercoat of nickel or copper, which will act as a barrier). Consequently, most of the hydrogen uptake occurs in the early stages of the deposition process, before a complete coverage of the coating metal has been achieved, and the start of the deposition process is particularly critical in determining the amount of hydrogen absorbed. Clearly, the highest possible ratio of metal deposition rate to hydrogen generation rate is required in this period, and this tends to be favored by high current densities. For this reason (among others), a high current density 'flash' deposit of metal is often used as the first stage of a two-stage plating scheme. Bath composition is also important in controlling the entry of hydrogen into the steel.

Once high-strength steel components have been electroplated, it is possible (and often mandatory) to reduce the damaging effects of the hydrogen by baking at  $\sim 200^\circ\text{C}$ . In part, this serves to allow hydrogen to diffuse through the coating and out to the atmosphere, but the redistribution of the remaining hydrogen within the steel, reducing damaging local high concentrations, is probably also an important part of this de-embrittlement treatment.

A very important area of use for electroplated high-strength steels is fasteners and other high stress components in aircraft. These are generally protected by cadmium plating, although the toxicity of cadmium and its compounds is giving rise to a search for alternatives. In this application, the avoidance of hydrogen embrittlement is clearly essential, and as a result, a



wide range of standard procedures and tests for cadmium plating of high-strength steels are available as civil or military specifications and codes of practice.<sup>15</sup>

- **Phosphating** Phosphating, which is widely used as a pretreatment for steel prior to painting, involves the controlled corrosion of the steel in acid solution, and inevitably leads to the uptake of hydrogen. By limiting the free acid in the phosphating bath, and by introducing oxidizing agents to raise the working potential, the uptake of hydrogen may be reduced.
- **Painting** Conventional paints are normally innocuous, but it seems possible that some modern water-based paints, particularly those applied by cathodic electrophoresis, may introduce significant quantities of hydrogen into the steel. Fortunately, these paints are generally stoved after application, and this is effective in removing the hydrogen, which permeates very easily through the paint film.<sup>16</sup> Additionally, these paints are applied primarily to lower-strength steels in motor vehicle bodies and similar applications, and as far as the author is aware, no problems have been experienced in service. However, suitable tests would be advisable if it is intended to use these processes with high-strength steels.

Paint strippers may give rise to hydrogen entry into steel, and in critical applications, such as the treatment of aircraft components, commercial paint strippers should be tested before use.

- **Corrosion in Service** Most of the modes of hydrogen entry discussed above involve a single brief charging period, and as a result are treatable, in that the hydrogen can be removed by a suitable de-embrittlement treatment (provided the embrittlement is not so severe that cracks are formed before the de-embrittlement treatment can be applied). In contrast, the entry of hydrogen due to corrosion in service is generally continuous. Thus, de-embrittlement is not feasible, and the control of hydrogen embrittlement of high strength steels presents a much more difficult problem.

In general, hydrogen will enter steel during any corrosion process involving hydrogen ion or water reduction as one of the cathodic reactions. It is frequently implied that the applied potential must be below the equilibrium potential for hydrogen evolution before hydrogen entry into steel is possible. However, for two related reasons this is not true. Firstly, the

equilibrium potential for hydrogen evolution at a given pH is that potential at which protons or water molecules at the metal–solution interface are in equilibrium with molecular hydrogen at a partial pressure of one atmosphere. As the partial pressure of hydrogen is reduced, so the equilibrium potential will increase, in accordance with the Nernst equation, and even at potentials of 200 mV above the 1-atm equilibrium potential, there will be a significant concentration of hydrogen at the metal surface. Secondly, for high-strength steels, the matrix concentration of hydrogen required to cause embrittlement is very small, as the hydrogen tends to concentrate at phase boundaries and other trap sites. Thus, hydrogen embrittlement has been observed in high-strength steel in contact with gaseous hydrogen at pressures below one thousandth of an atmosphere.

A second difficulty in predicting the effect of particular corrosion conditions on the rate of hydrogen uptake by steel is the strong influence of local conditions. For passive steel, where the corrosion potential is several hundred mV above the 1-atm hydrogen equilibrium potential, one would not expect problems of hydrogen embrittlement, and this is frequently used as an argument against a hydrogen embrittlement mechanism of SCC in environments such as phosphates and carbonate/bicarbonate. However, the local environment in pits, cracks, or crevices may be very different from conditions at the free surface. In particular, acidification may occur due to metal–ion hydrolysis (especially for chromium-containing steels), and the potential in the localized corrosion cavity may be considerably more negative than that measured at the free surface. The net result is that the conditions within the cavity may be favorable for hydrogen evolution, even though the free surface conditions imply that hydrogen embrittlement is very unlikely.

In neutral saline environments, such as seawater, the rate of hydrogen entry is controlled by (among other things) the applied potential. In this case (and probably many others) the response observed, even at a smooth surface, is not as simple as might be expected, largely because of changes in the chemistry of the liquid in immediate contact with the steel. This is indicated in **Figure 5** due to Barth *et al.*,<sup>17</sup> which shows the rate at which hydrogen permeates through a steel membrane in response to a range of applied potentials. Note that hydrogen enters steel in aerated solution when it is anodically polarized to well above the nominal equilibrium potential for hydrogen ( $\sim -650$  mV versus SCE for this near-neutral

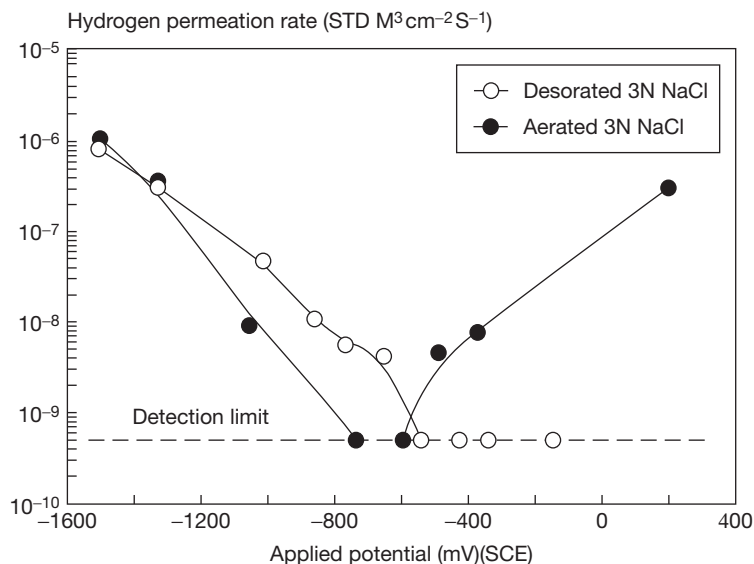


**Figure 5** Hydrogen permeation current as a function of applied potential, showing effect of oxygen concentration and applied potential. Reproduced from Barth, C. F.; Troiano, A. R. *Corrosion* 1972, 28(7), 259–263.

solution). Similar behavior has been observed in work that has taken account of the shielding effect of a crack or crevice<sup>18</sup> and this has shown that the effects of applied potential can be explained on the basis of the local potential and pH in relation to the hydrogen equilibrium potential. Figure 6 shows typical results obtained in this work, and it can be seen that the hydrogen overpotential and the rate of hydrogen entry into the steel increase with both anodic and cathodic polarization. Detailed prediction of the effect of applied potentials on the rate of hydrogen entry require very careful consideration of many factors, including the exact composition of the solution (especially with respect to the oxygen concentration), the geometry of the component (especially the presence of any cracks or crevices), and the mass transport conditions. In general terms however, when considering the performance of steel in seawater, it seems probable that slight cathodic polarization to  $\sim -750$  or  $-800$  mV (SCE) may reduce the rate of hydrogen entry compared to free corrosion conditions, because the increased pH obtained as a result of the cathodic polarization outweighs the lowered potential. Further decrease in potential increases the rate of hydrogen entry down to  $\sim -1200$  mV (SCE), when electrochemical desorption takes over as the second stage of the hydrogen evolution reaction, and at potentials that are more negative, the rate of hydrogen entry remains roughly constant.

In deaerated neutral salt solutions, anodic polarization of chromium-free steel tends to lower the rate of hydrogen entry, as the fall in pH due to ferrous ion hydrolysis is relatively limited, and cannot compensate for the more positive potential. However, in aerated solution, the ferrous ion can be oxidized to ferric in solution by dissolved oxygen, and as ferric hydroxide is much less soluble than ferrous hydroxide, the pH can fall much lower. (This reaction is a serious problem when trying to measure the solution pH in cracks and crevices, and much of the early work which shows very acid pH values in cracks in carbon steels is now known to be incorrect because this reaction was allowed to occur between extracting the crack solution and measuring its pH). In addition to lowering the surface pH, it seems possible that the precipitated film of ferric hydroxide/oxide also presents an ohmic resistance, and may thereby allow the surface potential to become lower than that measured in the bulk solution. It seems probable that the combination of these two effects was responsible for the increase in permeation current observed for anodic polarization by Barth *et al.*<sup>18</sup> Many steels contain small, but significant concentrations of chromium, and it should be appreciated that chromium concentrations of  $\sim 1\%$  can markedly increase the tendency for local acidification, owing to the much stronger tendency for chromium ion hydrolysis.

As considerations such as those discussed above have become more widely appreciated, it has become

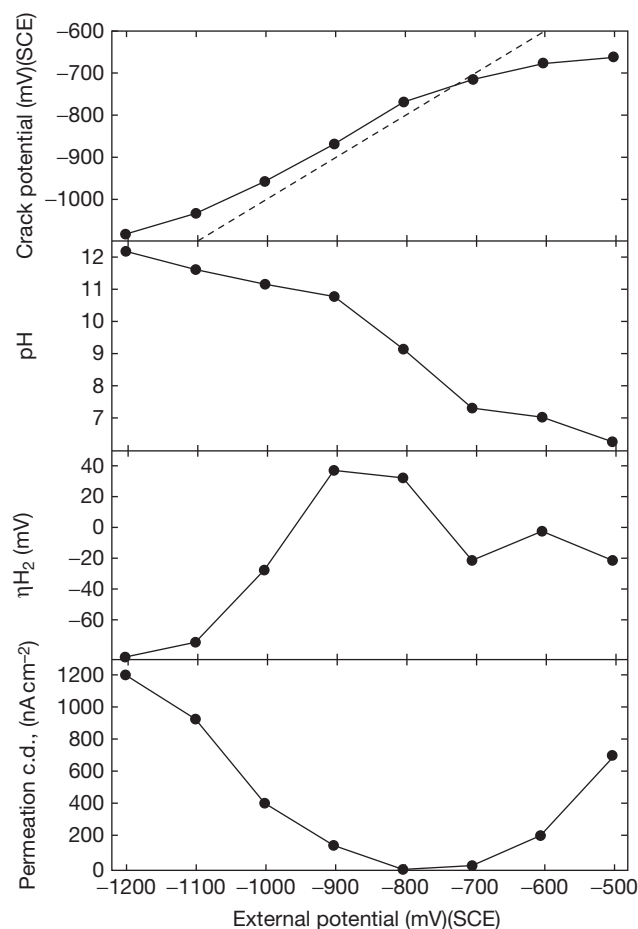


**Figure 6** Potential and pH in a simulated crevice, and effect on hydrogen permeation current. Reproduced from Taqi, E. A.; Cottis, R. A. *Corrosion Chemistry within Pits, Cracks and Crevices*; Turnbull, A.; NPL: London, 1987; 483–494.

clear that it is quite difficult to specify aqueous environments in which hydrogen entry into steel will occur at a sufficiently low rate that the possibility of hydrogen embrittlement can be discounted. The main candidates for such an environment are strong alkalis and highly oxidizing environments, such as nitric acid or nitrates, which are free of species, such as chloride, which predispose to pitting or crevice corrosion, and high temperature environments, such as water at 250 °C (since the deleterious effects of dissolved hydrogen decrease at high temperatures).

## 2.10.7 Effect of Hydrogen on Mechanical Properties

### 2.10.7.1 Elastic Constants

While there is some evidence of small changes in the elastic properties of steel as a result of dissolved

hydrogen<sup>19</sup> these changes are small, and of little practical consequence. This is perhaps to be expected in view of the very low solubility of hydrogen in the iron lattice and the small effect on the metal–metal bond strength.

### 2.10.7.2 Yield Stress

The effect of hydrogen on the yield stress of iron and steels is unpredictable. For very pure iron single crystals and polycrystals, the yield stress is frequently found to be decreased by hydrogen, but it may increase or stay the same, depending on the dislocation structure, crystal orientation, and purity of the iron.<sup>20</sup> Little information is available for steels.

### 2.10.7.3 Plastic Behavior

The effect of hydrogen on the plastic behavior of iron and steel is somewhat complex, as hydrogen may

harden or soften the material, according to its structure and the mode of slip. On the basis of work on single crystals of pure iron, Lunarska<sup>20</sup> has concluded that segregation of hydrogen around dislocations decreases their elastic stress fields. At room temperature (where the rate of diffusion of hydrogen is sufficiently high that it can keep up with a moving dislocation), this leads to a softening of single crystals when only one slip system is operative. The hydrogen also suppresses cross-slip of screw dislocations, and this results in increased work hardening when multiple slip systems are active. Lunarska also notes that “the presence of residuals (even at very low concentration) can drastically change all of these effects.”

It is partly because of the variable effect of hydrogen (giving both softening and hardening, according to the nature of the slip) that the extrapolation of model experiments on very pure iron to predict the behavior of commercial materials is so difficult. It is further hindered by the ability of dissolved hydrogen to modify the dislocation structure of a straining material.

### 2.10.8 Hydrogen Embrittlement of Steels

By far the most important impact of dissolved hydrogen on the mechanical properties of steels and particularly high-strength steels is the production of apparently brittle fracture where the steel would normally behave in a ductile fashion. If a steel contains dissolved hydrogen, this can result in immediate

fracture at stresses approaching the fracture stress in the absence of hydrogen, or it may result in delayed failure at lower stresses (Figure 7). The latter behavior is most pronounced for tensile tests on notched or precracked specimens, as the stress field around the notch or crack creates a high triaxial stress which dilates the metal lattice and tends to attract hydrogen from other parts of the specimen.

Some typical properties of common steels when exposed to environments supplying hydrogen are presented in Table 2. This table is presented to illustrate the order of magnitude of hydrogen embrittlement effects, and it is important to appreciate that the heat treatment and mechanical processing of a particular material, as well as the exposure conditions, can markedly affect its resistance to hydrogen embrittlement. Many of the data presented in this table have been extracted from the reviews of Sandoz<sup>21</sup> and McIntyre.<sup>22</sup> One useful fact that is indicated by the data in Table 2 is the good hydrogen embrittlement resistance of maraging steels when used somewhat below their ultimate capability. These data also illustrate the general result that a given steel will usually have a greater susceptibility to hydrogen embrittlement as it is tempered to a higher strength.

The effect of strength of the embrittlement can be rationalized by considering the changes in the size of the plastic zone at the crack tip as a function of the yield strength. The stress ahead of a perfectly sharp crack is proportional to  $1/r$ , where  $r$  is the distance from the crack tip. This goes to infinity as  $r \rightarrow 0$ , so there must be a plastic zone ahead of the crack that has yielded. The size of this plastic zone will be

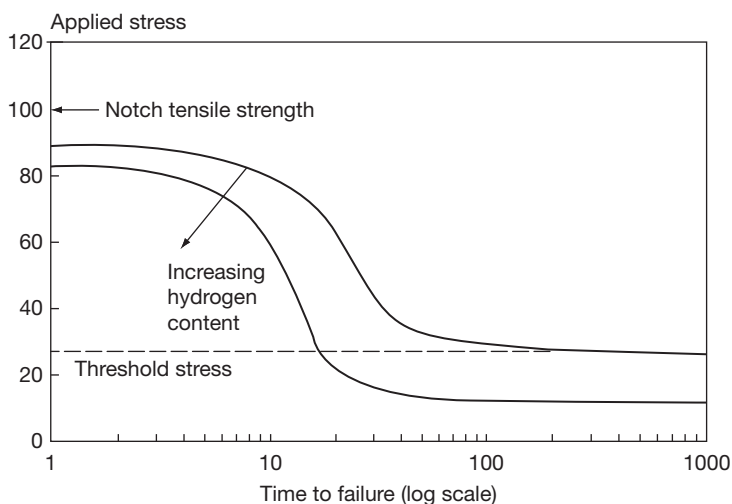


**Figure 7** Typical results of static load tests on notched specimens.

**Table 2** Typical properties of common high-strength steels in salt solutions

Material	Yield stress (MPa)	Failure time <sup>a</sup> (h)	$K_{Ic}$ (MPa√m)	$K_{ISCC}$ (MPa√m)	Plateau velocity (m s <sup>-1</sup> )
HY130	900	NF	130–170	60–140	$5 \times 10^{-8}$
300M	1600	40–150	—	115	$10^{-8}$
4340	1400–1800	—	—	20	$10^{-5} - 10^{-2}$
4340	<1400	—	—	30–80	
4130	1300	—	—	30	$10^{-6} - 10^{-4}$
4130	1050	—	—	120	
18Ni MS	1900	400	40–100	5–35	
18Ni MS	1500	10,000	180	40–100	
18Ni MS	1200	NF	160	120	$10^{-5}$

<sup>a</sup>The failure time presented is the approximate time to failure at an applied stress of 75% of the yield stress of the material.  
MS = Maraging Steel.

approximately inversely proportional to the yield stress, and the peak stress will be equal to the yield stress. This discussion oversimplifies the stress state ahead of the crack tip, which is three dimensional and rather complex. However, the general conclusion is accurate. Thus, a higher strength material will have a smaller plastic zone with a larger stress in it, both the factors tend to increase the tendency for hydrogen to concentrate in this region and to cause fracture.

### 2.10.9 Hydrogen Embrittlement of Other Alloys

While the majority of work on hydrogen embrittlement is concerned with high strength steels, many other alloys have been shown to suffer embrittlement by hydrogen. We can list a few general factors that have a strong influence on typical susceptibility to hydrogen (though, like most generalizations, there will be exceptions):

- Susceptibility increases as the yield strength increases. This is an almost inevitable consequence of the reduction in the volume of the crack tip plastic zone and the increase in stress within that zone as the yield strength increases.
- Face-centered cubic (*fcc*) alloys are less susceptible than body-centered cubic (*bcc*) alloys. There are several reasons for this, (1) the greater inherent ductility of *fcc* alloys; (2) the much lower diffusion coefficient for hydrogen in *fcc* structures; and (3) the much greater solubility of hydrogen in *fcc*.
- Hexagonal close-packed (*hcp*) alloys might be expected to have an intermediate susceptibility between *fcc* and *bcc*, having lower inherent ductility than *fcc* but comparable hydrogen solubility and diffusion coefficient. However, many of the common

*hcp* alloys (Ti, Mg, Zr among others) form stable hydrides, and are therefore susceptible to hydrogen embrittlement by a hydride cracking mechanism.

It is sometimes stated that *fcc* alloys (such as austenitic stainless steels) are immune from hydrogen embrittlement. However, this is an overstatement; it is more accurate to say that they are more resistant, which typically means that more hydrogen, and/or a longer time are necessary for fracture to occur. Thus, hydrogen embrittlement has been observed in nickel sheet (used in the author's laboratory as a cathode in an electrochemical machining cell), high strength aluminum alloys,<sup>23</sup> and austenitic<sup>24</sup> and duplex<sup>25</sup> stainless steels. There are relatively few reports of hydrogen embrittlement of copper or copper-based alloys, but this is probably due to the noble character of copper, which means that hydrogen cannot be produced at a significant concentration by corrosion of copper, rather than to any inherent immunity from embrittlement.

### 2.10.10 The Influence of Microstructure and Composition

The influence of the composition and metallurgical structure of steels on their susceptibility to hydrogen embrittlement have been discussed from a theoretical basis by Bernstein and Pressouyre.<sup>6</sup> They considered the nature of the various trap sites in the steel, both with respect to their tendency to accumulate hydrogen, and their sensitivity to fracture in the presence of hydrogen. This approach seems to offer considerable potential in respect of designing alloys for hydrogen resistance without sacrificing other properties, although with our current knowledge the methods are probably more relevant for the rationalization of results.



As a general rule, the damage due to dissolved hydrogen tends to become more severe as the strength of the steel increases. In part, this may be associated with the greater resistance of the stronger material to plastic deformation, which facilitates the transition to brittle behavior. In addition, the size of the crack tip plastic zone, which defines the size of the region to which hydrogen is attracted, is inversely proportional to the yield strength of the material. Hence, for the stronger steels, a given amount of dissolved hydrogen will be concentrated into a smaller region, and will, therefore, have a more damaging effect. However, this general effect of strength level does not explain all aspects of hydrogen embrittlement of high strength steel, and steels with the same mechanical properties may be affected by hydrogen in quite different ways as a result of their different microstructures.

A particularly important aspect of the microstructural state of the steel is the condition of the grain boundary. As noted in [Section 2.10.4](#) above, 'pure' grain boundaries do not act as major sites for the trapping of hydrogen, but it is clear that impurity segregation and carbide precipitation at the grain boundary may significantly modify its behavior. Thus, it is now widely recognized that there is a strong link between various forms of temper embrittlement and hydrogen embrittlement, and quite small changes in tempering treatment can give large variations in hydrogen embrittlement resistance.<sup>26,27</sup>

On a more positive note, it seems clear that steels can be made more resistant to the effects of hydrogen by incorporating as many strong, finely dispersed traps in the microstructure as is possible, while ensuring that there are no continuous trap sites (such as embrittled grain boundaries). This may explain the better resistance of steels hardened by cold-working compared to quenched and tempered steels.<sup>28</sup> Whatever the reason, this effect is particularly fortunate in the production of prestressed concrete, where cold-drawn pearlitic (or 'patented') wires give high strength levels (~1700 MPa) with good (though not complete) resistance to hydrogen embrittlement. In this particular case, it is probably also important that most of the phase boundaries in the structure lie parallel to the tensile axis, allowing them to collect large quantities of hydrogen without serious detriment to the performance of the wire. When such wires do suffer from hydrogen embrittlement, they exhibit a characteristic elongated 'green-stick' fracture.

Similarly, it seems that retained austenite may be beneficial in certain circumstances<sup>29</sup> probably because the austenite acts as a barrier to the diffusion

of hydrogen, although in high concentrations (such as are obtained in duplex stainless steels) the austenite can also act as a crack-stopper (i.e., a ductile region in the microstructure which blunts and stops the brittle crack).

### **2.10.11 Theories of Hydrogen Embrittlement**

Despite the major technical importance of hydrogen embrittlement, and the wealth of research work on the subject, the mechanism (or perhaps mechanisms) of hydrogen embrittlement remains uncertain. Much of the book edited by Oriani, Hirth, and Smialowski is concerned with mechanistic aspects of hydrogen embrittlement, and the reader is referred in particular to the summary by Thomson and Lin.<sup>30</sup>

In considering hydrogen embrittlement mechanisms, it is important to keep in mind the concentration of hydrogen in the steel, as matrix concentrations are very low, typically of the order of one atom of hydrogen for every  $10^6$  iron atoms. It is very difficult to see how such small amounts of hydrogen can modify fracture properties so markedly, and it must be supposed that hydrogen present in traps or possibly in surface layers (where the solubility may be markedly increased)<sup>6</sup> is the main cause of embrittlement. Thus, realistic mechanisms of hydrogen embrittlement will be based on the effect of hydrogen on dislocation behavior, on the effect of hydrogen at phase boundaries or grain boundaries or on the effect of hydrogen at the metal surface. These factors will be assisted by the concentration of hydrogen to the region of triaxial tensile stress ahead of the crack.

In considering the various theories, it is also apparent that many of them may be considered as alternative descriptions of essentially the same physical process, or as descriptions of parallel processes which collaborate in the failure. Thus, a complete description of hydrogen embrittlement in a given situation will almost inevitably incorporate aspects of several of the following theories.

#### **2.10.11.1 The Pressure Theory**

The earliest theory of hydrogen embrittlement was probably the planar pressure theory advanced by Zappfe<sup>31</sup> in 1941. This essentially proposes that the effect of hydrogen is to create very high pressures of hydrogen gas in voids and other defects within the metal thereby assisting in the fracture of the steel.

While this is an important aspect of the blistering of steel by HIC, it cannot by itself explain the hydrogen embrittlement of high strength steels, where fracture may occur in steel in equilibrium with hydrogen at very low pressures.<sup>32</sup> Some concentration of hydrogen may occur as a result of dislocation transport, but it is difficult to see how significant internal pressures can be generated by hydrogen entering from an external pressure of one thousandth of an atmosphere, yet this can cause hydrogen embrittlement.

### 2.10.11.2 Decohesion Theories

The decohesion models proposed by Troiano, Oriani, and others<sup>33–35</sup> suggest that the role of hydrogen is to weaken the interatomic bonds in the steel, thereby facilitating grain boundary separation or cleavage crack growth. In view of the very low hydrogen concentration in the matrix, it is necessary for some method to exist by which the hydrogen can be concentrated at the site of the fracture. For cracking along phase or grain boundaries, this can be explained in terms of the trapping of hydrogen at the phase boundary. It is a little more difficult to see how transgranular cracking can be explained; processes which have been invoked include the concentration of hydrogen at the region of triaxial tensile stress at the crack tip and local high concentrations of hydrogen being generated by reaction or adsorption at the crack tip.

### 2.10.11.3 Surface Energy Theories

Surface energy theories were first proposed by Petch and Stables.<sup>36</sup> By lowering the surface energy of the newly formed crack, the hydrogen reduces the stress intensity required for brittle fracture. As with the decohesion models, surface energy models only seem reasonable for the case of hydrogen derived from surface layers or grain boundaries, since the hydrogen adsorption must occur at the same time as the fracture event in order for the reduction in surface energy to be effective in lowering the energy required for fracture.

### 2.10.11.4 Hydride Formation

In some systems, notably titanium alloys, hydrogen embrittlement has been attributed to the formation and subsequent fracture of brittle hydride phases at the crack tip. This has been postulated by Gahr *et al.*<sup>37</sup> as a mechanism of hydrogen embrittlement of niobium. While there is little evidence for hydride

formation in steels, it can be argued that hydrides would be unstable and would dissolve as soon as the crack has propagated through them. In view of recent evidence of significant structural rearrangement of steel surface containing chemisorbed hydrogen,<sup>6</sup> the possibility should also be considered of the induction of cleavage by a brittle surface film, similar to the film-induced cleavage model of stress corrosion cracking.<sup>38</sup>

### 2.10.11.5 Local Plasticity Theories

Various workers have suggested that hydrogen acts by reducing the stress required for dislocation motion. This follows observations by several workers (summarized by Morgan and McMahon<sup>39</sup>) of enhanced dislocation motion in thin films exposed to hydrogen. Similarly, Lynch<sup>40</sup> found very similar fractography for liquid metal embrittlement and hydrogen embrittlement, and proposed that both processes involve the facilitation of dislocation emission at the crack tip. Lynch,<sup>3</sup> echoing the earlier review of Birnbaum *et al.*,<sup>2</sup> describes the three currently favored mechanisms:

- hydrogen-enhanced localized plasticity (HELP);
- hydrogen enhanced decohesion (HEDE); and
- adsorption-induced dislocation emission (AIDE).

In the HELP mechanism, crack propagation occurs by highly localized slip due to local softening by hydrogen at the crack tip. HEDE is due to weakening of the metal-metal bond allowing brittle fracture rather than plastic deformation (essentially this is the decohesion model described above). AIDE is described by Lynch as "... based on hydrogen induced weakening of interatomic bonds (as for HEDE) but with crack growth occurring by localized slip (as for HELP)." The corrosion-enhanced plasticity model proposed by Delafoss and Magnin<sup>41</sup> is rather more general description of an essentially similar model to HELP, in that the enhanced plasticity may be due to corrosion, as well as hydrogen, effects.

### 2.10.12 Hydrogen Embrittlement Tests

There are several classes of test for hydrogen embrittlement, according to the application. Three general types of mechanical test can be identified, together with chemical and electrochemical tests intended to determine the hydrogen content of steels or the rate of entry of hydrogen from an environment.

### 2.10.12.1 Constant Stress Tests

The simplest test for hydrogen embrittlement involves applying a constant stress to a specimen. This can be applied both to the testing of samples which already contain hydrogen (e.g., as a result of electroplating) and to the testing of samples in environments causing hydrogen entry. The specimen may take various forms but is commonly a tensile specimen. Particularly where the test is being used to examine the effect of dissolved hydrogen which is already present in the steel, the specimen may be notched, in order to develop a region of triaxial stress at the tip of the notch that will tend to concentrate hydrogen.

When a constant stress test of a notched specimen is being used for the evaluation of samples containing hydrogen, it is commonly referred to as a sustained load test, although the terms stress rupture and static fatigue are also used in the older literature. The results of a typical sustained load test are shown in **Figure 7**. At a stress which is frequently (though not necessarily) below the notch tensile strength for hydrogen-free material, the specimen will fail instantaneously as a result of the damaging effect of the uniform hydrogen concentration in the steel. At lower stresses, delayed failure occurs as hydrogen diffuses to the region of triaxial stress at the tip of the notch. Eventually, as the stress is reduced, the quantity of hydrogen in the neighborhood of the notch is insufficient to cause failure, and a critical or threshold stress is reached. The behavior of a steel sample in this test is a function of both the material and the hydrogen concentration, with an increase in hydrogen concentration giving instantaneous failure at lower stresses, shorter times to failure, and a lower critical stress. Testing at lower temperatures will give longer failure times, since the rate-controlling process is hydrogen diffusion, but the critical stress will go down, as the intrinsic tendency of the steel to brittle rather than ductile failure is increased. At elevated temperatures, hydrogen may be lost by degassing and by trapping, and in this case, the critical stress will increase. The failure stress is also strongly influenced by the notch tip radius, with a smaller radius giving shorter times to failure and failure at lower stresses. This can be explained in terms of the size and intensity of the region of triaxial stress at the notch tip, with a sharper notch giving a smaller triaxial region, which can develop a higher hydrogen concentration in a given time. Because of the difficulty of obtaining a reproducible notch tip geometry, the sustained load test tends to give rather scattered results. Smooth specimens can be used for sustained

load testing, but in this case, the defects responsible for local hydrogen concentration will typically be surface or near-surface nonmetallic inclusions, and the chance organization of these will give highly scattered results. Smooth specimen results will also tend to be nonconservative, as the majority of real components are liable to contain stress concentrators of one form or another.

In addition to testing for the effects of preexisting hydrogen in the steel, sustained load tests can also be used to test for the effect of hydrogen entering from the environment. Both smooth and notched specimens can be used. At short times, the results obtained will differ from those for steels containing dissolved hydrogen, since time will be required for the hydrogen to enter the steel. However, this time can be very short, since hydrogen can diffuse  $\sim 10\text{ }\mu\text{m}$  in 1 s, and failure times of the order of seconds can be obtained for severe environments and loading conditions. For tests at ambient temperature, it is found that the critical stress is reached fairly quickly, and it is generally found that failures will occur within a month of exposure of the samples. This provides something of a problem in relating service behavior to laboratory tests, since service failures are often observed after much longer exposure times. This may be a result of variations in exposure conditions in service or it may be associated with the need to develop initiating defects by pitting corrosion or similar processes. Whatever the cause, it does lead to the conclusion that sustained load tests cannot be used to predict service life with any accuracy.

### 2.10.12.2 Controlled Strain-Rate Tests

Controlled strain-rate tests were first developed by Parkins<sup>42</sup> for the study of stress-corrosion cracking. These took the form of constant strain-rate tests (also known, perhaps more accurately, as constant extension rate tests). Since then alternative forms of test have been developed to modify the conditions under which the specimen is exposed.

The slow strain-rate test is based on the principle that stress corrosion cracking processes are normally dependent on plastic strain in the material. By extending the specimen very slowly, any stress corrosion cracking phenomena are given every possible opportunity to occur, hence, the slow strain-rate test can quickly reveal any tendency to cracking in a given metal–environment combination. A particular advantage of the slow strain-rate test is that failure of the specimen will always occur in a reasonable time, if

only by normal ductile fracture processes. Test durations clearly depend on the strain-rate and the ductility of the metal, but typical test durations for steels in hydrogen embrittling environments are  $\sim 1$  week. In addition to providing a rapid indication of the possibility of SCC in a particular system, the slow strain-rate test can also be used to study the effect of material and environmental factors on the susceptibility. For example, **Figure 8** shows the effect of environment composition and tempering temperature on the reduction in area obtained for tests on a quenched and tempered steel in various aqueous solutions. The minimum in the reduction in area which can be seen for tempering temperatures of  $350^\circ\text{C}$  provides evidence of the interaction between hydrogen embrittlement and temper embrittlement.

While the conventional slow strain-rate test offers many benefits, it does suffer from a tendency to overstate the susceptibility of materials to hydrogen embrittlement. Thus, structural steels of modest strength will fail even under conditions giving relatively low rates of hydrogen entry. This is because the enforced plastic deformation provides a very severe test condition, which may not be reproduced in service when

relatively low stresses are applied to components. This problem is partly addressed by the sustained load test, but this may be unduly mild, as there will be no plastic strain in the specimen once the initial creep strain has died away. In order to provide a test with intermediate severity, Erlings and his co-workers<sup>43</sup> developed a test which exposes the specimen to a quasi-constant strain-rate, but at the same time keeps the specimen within the elastic range. This involves prestraining a slow strain-rate specimen up to the yield stress. Then the specimen is exposed to a regular cycle, the stress being reduced (typically) to 90% of the yield stress, slowly strained to 95% of the yield stress, then dropping back to 90%. This test is proposed as a part of a sequence of tests, starting with the low-cost slow strain-rate test, for the qualification of materials for service, as indicated in **Figure 9**.

Another modification to the slow strain-rate test involves the superimposition of a low amplitude sine wave ripple on the slow uniform extension (**Figure 10**). In effect, this produces higher strain-rates (which appear to be more damaging for hydrogen embrittlement), while still giving a long test duration, with adequate time for the accumulation of hydrogen in the steel.<sup>44</sup>

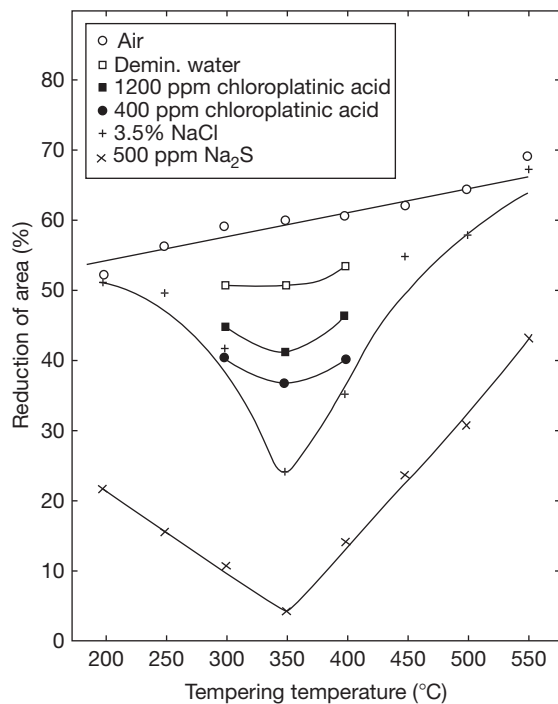


**Figure 8** Variation of reduction in area as a function of tempering temperature. Reproduced from Johnston, J. W.; Cottis, R. A.; Procter, R. P. M. *Electrochem. Soc. Extended Abstracts* 1987, 87(2), 454–455.

### 2.10.12.3 Fracture Mechanics Tests

One problem of both sustained load and slow strain-rate tests is that they do not provide a means of predicting the behavior of components containing defects (other than the inherent defect associated with the notch in a sustained load test). Fracture mechanics provide a basis for such tests, and measurements of crack velocity as a function of stress intensity factor,  $K$ , are widely used. A typical graph of crack velocity as a function of  $K$  is shown in **Figure 11**. Several regions may be seen on this curve. At low stress intensity factors, no crack growth is observed until a threshold stress intensity factor,  $K_{\text{ISCC}}$  is reached. Typically,  $K_{\text{ISCC}}$  is fairly insensitive to the rate of hydrogen entry into the steel (as the crack is not growing at a significant rate, hydrogen will eventually accumulate at a sufficient concentration at the crack tip, whatever the rate of entry). As the stress intensity factor increases above  $K_{\text{ISCC}}$  the crack growth rate increases rapidly, until a plateau crack velocity is attained. The plateau velocity is a function of the rate of hydrogen entry, and the plateau is usually attributed to the availability of hydrogen at the crack tip being the rate-limiting factor. Finally, the crack velocity increases again as the stress intensity factor approaches the critical stress intensity factor for fast fracture,  $K_{\text{IC}}$ .

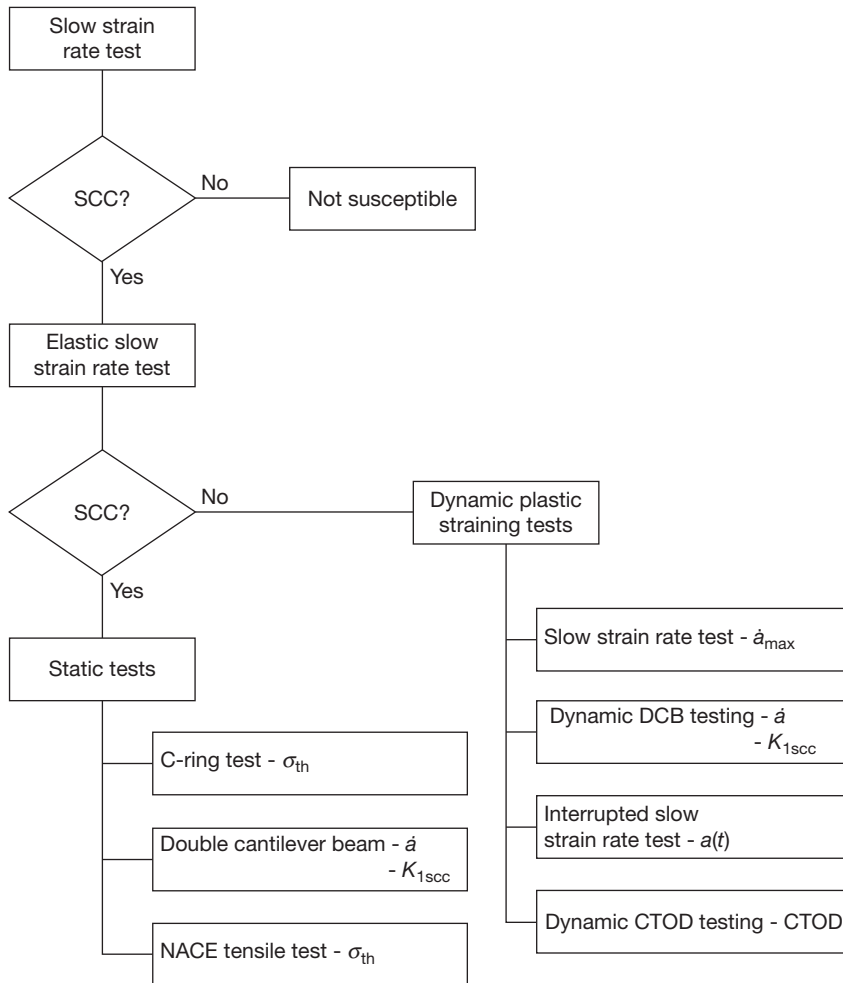


**Figure 9** 'Elastic' slow strain-rate test. Reproduced from Crooker, T. W.; Hauser, J. A. H A Literature Review on the Influence of Small-Amplitude Cyclic Loading on Stress Corrosion Crack Growth in Alloys, NRL Memorandum Report 5763, Naval Research Laboratory, Washington DC, April 3, 1988.

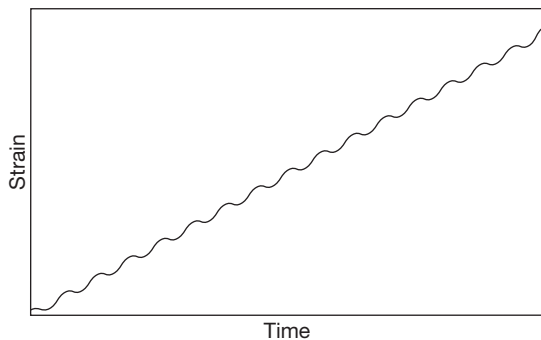


**Figure 10** Strain-time history for 'Ripple' test (schematic).

In this region, the fracture consists partly of ductile tearing and partly of hydrogen embrittlement, with the hydrogen assisting the fracture of the tougher areas in the metal. The above discussion has assumed that the

crack is loaded in Mode I (the crack opening mode, with a tensile stress normal to the plane of the crack). Hydrogen has relatively little effect in Modes II or III, as these generate shear stresses at the crack tip, rather than tensile stresses, and the shear behavior of steels is relatively little affected by hydrogen, presumably because dilation of the lattice at the crack tip (which does not occur in Modes II and III) is required for hydrogen accumulation.

### 2.10.13 Controlling Hydrogen Embrittlement in Service

Clearly there are two major ways in which hydrogen embrittlement can be controlled in service – either the hydrogen content of the steel can be reduced



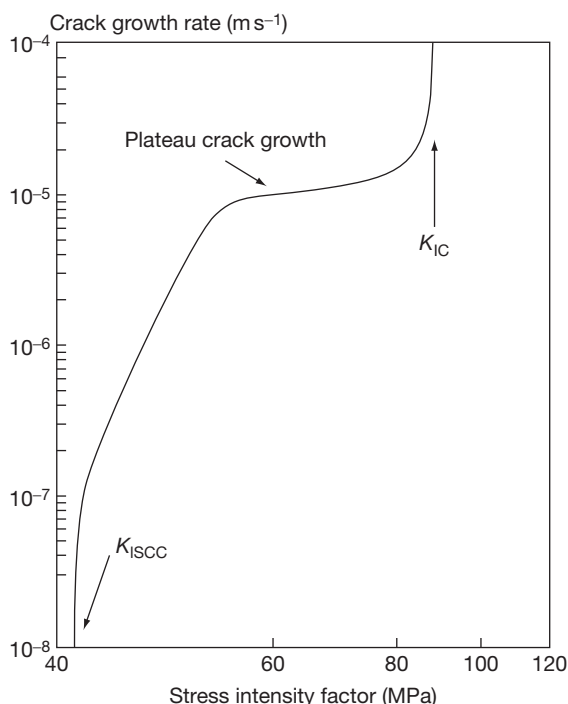


**Figure 11** Stress-corrosion crack velocity as a function of applied stress intensity factor.

(by limiting the rate of entry or by baking to remove existing hydrogen), or the steel can be made more resistant to hydrogen.

### 2.10.13.1 Reduction of Hydrogen Content

Preexisting hydrogen in steel, introduced by electroplating or other processing, can be reduced by a suitable de-embrittlement treatment, as discussed above. A more difficult problem is the limitation of hydrogen entry in service. The feasibility of controlling hydrogen embrittlement in this way will clearly depend on the application, and in particular on the source from which the hydrogen is entering the steel. Thus, hydrogen pickup from acid pickling can be reduced by the use of appropriate inhibitors, and de-embrittlement treatments can be used after pickling. In contrast, hydrogen entry into components in an electrical generator using hydrogen as the cooling gas cannot easily be modified.

In general preventing the entry of hydrogen from the gas phase is liable to be difficult. Inhibition is possible, for example, small quantities of oxygen can markedly reduce the rate of hydrogen uptake, presumably as a result of blocking active sites on the metal

surface. Similarly, ethylene gas will react with adsorbed hydrogen atoms, thereby preventing them from diffusing into the steel. However, there will be few cases in which it is permissible to modify the environment in this way (adding oxygen to hydrogen will certainly cause some concern). Organic coatings will not generally be very effective in reducing hydrogen entry, since these are usually rather permeable to hydrogen. Furthermore, such coatings are usually susceptible to local damage. Metal coatings may offer some reductions in hydrogen entry, as most close-packed metals have a significantly lower diffusion coefficient for hydrogen than iron, although this is partially compensated for by a higher solubility.

In aqueous solutions, it becomes somewhat more feasible to modify the entry of hydrogen into the steel. This can be achieved by the addition of inhibitors to the solution, by control of the electrochemical potential of the metal and by coatings.

In situations such as the acid pickling of steel or the use of steel pipes to handle sour oil streams, the use of suitable inhibitors can give a significant reduction in hydrogen entry. In this context, it is important to emphasize that the efficiency of an inhibitor in reducing hydrogen entry is not the same as its efficiency in reducing corrosion. Thus, arsenic and antimony compounds are effective inhibitors of corrosion of steel in acid, but they achieve this by inhibiting the hydrogen recombination reaction, thereby increasing the rate of hydrogen entry into the steel. In contrast, the addition of chloroplatinic acid to a solution will increase the corrosion rate by accelerating the hydrogen evolution reaction. However, a part of this acceleration arises because the hydrogen recombination reaction is catalyzed by the particles of platinum which are deposited on the surface by an exchange reaction. As a result, chloroplatinic acid acts as an inhibitor of hydrogen entry. This can be seen in [Figure 8](#), where the addition of chloroplatinic acid to 3.5% sodium chloride solution has increased the reduction in area for a given heat treatment. Clearly, this is impractical for service use, but several organic inhibitors are available which are effective in reducing both corrosion and hydrogen entry into the steel.

The electrochemical potential has a direct influence on the entry of hydrogen into steel from aqueous solutions, and control of potential represents an obvious way to control hydrogen uptake. Unfortunately, the effect of potential on hydrogen entry is complex, and is strongly dependent on solution composition. For example, as has been discussed above, it has been shown<sup>18</sup> that anodic polarization of steel in salt

solution will give an increased rate of hydrogen entry in aerated solution, but negligible entry in deaerated solution. The situation becomes even more complex in passivating environments, especially where pitting or crevice corrosion can occur. As a generalization, for aerated neutral salt solutions the optimum potential for minimum hydrogen uptake appears to be slightly below typical free corrosion potentials, a typical value for seawater being  $\sim -750$  to  $-800$  mV (SCE). This potential is also sufficient to reduce corrosion rates, but it gives very little margin for potential differences over the structure being protected. Potentials much below  $-900$  mV will undoubtedly increase the rates of hydrogen entry, and in view of the hazards involved in overprotection, the deliberate application of cathodic protection to high strength steel structures is probably best avoided.

As in gaseous environments, metal coatings can reduce the rate of hydrogen entry by acting as a low permeability barrier. In addition, the coating metal may also modify the electrochemical properties at the metal–solution interface, as in the case of traces of platinum derived from chloroplatinic acid. For application in seawater and other neutral salt solutions, zinc, and cadmium probably offer the best combinations of properties, having low exchange current densities for hydrogen evolution and relatively low hydrogen permeabilities. In the event that part of the steel substrate is exposed by mechanical damage, a zinc coating has a rather low corrosion potential in seawater, and may be expected to give rapid hydrogen entry. However, cadmium gives a potential which is around that at which the minimum rate of hydrogen entry is observed, and is highly recommended as a coating material for high strength steels. Unfortunately, the toxicity of cadmium compounds precludes its use in most applications. Proposed schemes for ‘cadmium replacement’ should be examined carefully for their effect on hydrogen embrittlement as well as their corrosion performance.

Organic coatings such as paints are also effective in reducing the corrosion of steel, but as with inhibitors, it is not certain that this will also mean that the rate of hydrogen entry is reduced. Organic coatings are typically rather permeable to water, and it is possible for this to be reduced to hydrogen. Whether this hydrogen subsequently enters the steel will depend on the characteristics of the coating–steel interface, and little is known about this. It is recommended that suitable tests should be performed before using organic coatings for protection of high strength steels.

### 2.10.13.2 Increasing Resistance of Steel

For a given steel, the hardness will play a major part in determining its resistance to hydrogen embrittlement, but other factors are also significant. Thus, it is particularly important to obtain an appropriate microstructure, without any temper embrittlement or other deleterious features (see above). Where possible the use of work-hardened ferritic–pearlitic structures will probably give better performance than quenching and tempering, providing the stress is applied parallel to the working direction.

In particularly severe conditions, it may be found necessary to use austenitic steels, such as stainless steels from the 300 series. The *fcc* structure of austenite is inherently more ductile than *bcc* ferrite, and it is therefore less liable to switch to brittle modes of fracture in the presence of hydrogen. Additionally the permeability of austenitic steels is less than that of ferritic. The common commercial grades of austenitic stainless steel tend to be rather marginal in respect of the stability of the austenite phase, and they are therefore susceptible to the formation of martensite by strain-induced transformation. This martensite is susceptible to hydrogen embrittlement, and it is therefore important to ensure that steels used for hydrogen service have sufficient austenite stabilizing elements, primarily nickel. This is illustrated in Figure 12, where the effect of nickel content on the residual ductility in hydrogen is presented.<sup>45</sup> Below  $\sim 10\%$  Ni there is a strong tendency to strain-induced martensite

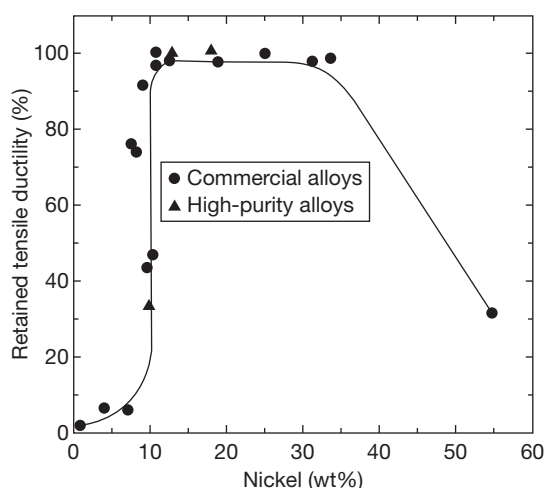


**Figure 12** Effect of nickel content on residual ductility of austenitic stainless steels. Reproduced from Caskey, G. R. Third International Congress on Hydrogen and Materials, Paris, 1982; p 611–616.

formation, and low residual ductilities are observed. Once the austenite becomes fully stable however, there is hardly any loss in ductility due to hydrogen.

### 2.10.13.3 Prediction of Behavior

An important aspect of the use of materials in aggressive environments is the prediction of service life, such that planned maintenance procedures can be used. A typical approach that might be suggested for steels in conditions where hydrogen embrittlement can occur is to assume a maximum possible defect in the structure, usually based on the expected capabilities of the inspection system. Using a suitable relationship for the crack velocity as a function of stress intensity factor, the time to failure is calculated by integrating from the initial defect size up to that necessary for fast fracture. While this method is attractive in theory, in practice it is liable to be rather unproductive for high strength steels. The reason for this is that typical plateau crack velocities for hydrogen embrittlement are very high (between  $10^{-6}$  and  $10^{-2} \text{ m s}^{-1}$ ), and the transition from  $K_{\text{ISCC}}$  to the plateau occurs over a rather small range of stress intensity factor. Thus, unless the initial defect happens to give a stress intensity factor fractionally above  $K_{\text{ISCC}}$ , this calculation will predict either no failure or a very short life (even  $10^{-6} \text{ m s}^{-1}$  corresponds to a crack velocity of  $3.6 \text{ mm h}^{-1}$ ). Currently, the understanding of the failure of components by hydrogen embrittlement after long periods in service remains somewhat limited, but in many cases, it seems probable that pitting corrosion plays an important part in the slow crack initiation process. Thus, prediction of life in hydrogen embrittlement conditions should be concerned with initiation processes in addition to the crack growth above  $K_{\text{ISCC}}$ , although there is not yet a sufficiently clear understanding of the initiation processes for this to be a productive exercise.

### 2.10.14 Modeling of Hydrogen Embrittlement

At a fundamental level, improvements in techniques for *ab initio* modeling at the atomic level, coupled with the continuing rapid increase in the power of high performance computers, has led to a significant improvement in our understanding of the behavior of hydrogen in metals, including aspects such as the binding energy of hydrogen to dislocations<sup>46</sup> and the segregation of hydrogen to grain boundaries.<sup>47</sup>

While it is not currently feasible to construct a completely reliable *ab initio* model of hydrogen embrittlement initiation or propagation, some moves have been made in that direction. Serebrinsky *et al.*<sup>48</sup> have developed a model of intergranular hydrogen embrittlement “based upon: (1) a cohesive law dependent on impurity coverage that is calculated from first principles; (2) a stress-assisted diffusion equation with appropriate boundary conditions accounting for the environment; (3) a static continuum analysis of crack growth including plasticity; and (4) the Langmuir relation determining the impurity coverage from its bulk concentration.” They concluded that “The calculations reproduce the following experimental trends: (1) time to initiation and its dependence on yield strength and stress intensity factor; (2) finite crack jump at initiation; (3) intermittent crack growth; (4) stages I and II of crack growth and their dependence on yield strength; (5) the effect of the environmental impurity concentration on the threshold stress intensity factor; and (6) the effect of temperature on stage II crack velocity in the low-temperature range.”

## References

1. *Hydrogen Degradation of Ferrous Alloys*; Oriani, R. A., Hirth, J. P., Smialowski, M., Eds.; Noyes Publications: Park Ridge, New Jersey, 1984.
2. Birnbaum, H. K.; Robertson, I. M.; Sofronis, P.; Teter, D. 2nd International Conference on Corrosion-Deformation Interactions, CDI '96, Nice, France, 24–26 Sept 1996, pp 172–195, 1997.
3. Lynch, S. In *Corrosion/2007*; NACE International: Houston, Tx, p 55 2007; Paper 07493.
4. Pasco, R. W.; Ficalora, P. J. *Hydrogen Degradation of Ferrous Alloys*; Oriani, R. A., Hirth, J. P., Smialowski, M., Eds.; Noyes Publications: Park Ridge, New Jersey, 1984; pp 199–214.
5. Imbuhl, R.; Behm, R. J.; Christmann, K.; Ertl, G.; Matsushima, T. *Surf. Sci.* **1982**, *117*, 257.
6. Bernstein, I. M.; Pressouyre, G. M. *Hydrogen Degradation of Ferrous Alloys*; Oriani, R. A., Hirth, J. P., Smialowski, M., Eds.; Noyes Publications: Park Ridge, New Jersey, 1984; pp 641–685.
7. Puls, M. P. *Hydrogen Degradation of Ferrous Alloys*; Oriani, R. A., Hirth, J. P., Smialowski, M., Eds.; Noyes Publications: Park Ridge, New Jersey, 1984; pp 114–130.
8. Asaoka, T.; Lapasset, G.; Aucouturier, M.; Lacombe, P. *Corrosion* **1978**, *34*, 39.
9. Kedzierzawski, P. *Hydrogen Degradation of Ferrous Alloys*; Oriani, R. A., Hirth, J. P., Smialowski, M., Eds.; Noyes Publications: Park Ridge, New Jersey, 1984; pp 271–288.
10. Devanathan, M. A. V.; Stackurski, Z. J. *Electrochem. Soc.* **1964**, *111*(5), 619.
11. Berman, D. A.; Beck, W.; Deluccia, J. J. *Hydrogen in Metals*; Bernstein, L. M., Thompson, A. W., Eds.; ASM, 1974; pp 575–607.
12. Arup, H. *Proceedings of the 9th Scandinavian Corrosion Congress* 1984, p 825.

13. Brass, A. M.; Chene, J. *Mater. Sci. Eng. A* **1998**, A242, 210–221.
14. Robertson, I. M. *Eng. Fract. Mech.* **2001**, 68, 671–692.
15. See, for example, AMS 2401C, ASTM A165, ISO 2082, BS1706 and BS3382.
16. Echizen, Y.; Takada, K. *Kinsoku Hyomen Gijutsu* **1987**, 38(3), 113–115.
17. Barth, C. F.; Troiano, A. R. *Corrosion* **1972**, 28(7), 259–263.
18. Taqi, E. A.; Cottis, R. A. *Corrosion Chemistry within Pits, Cracks and Crevices*; Turnbull, A., Ed.; NPL: London, 1987; pp 483–494.
19. Lunarska, E.; Zielinski, A.; Smialowski, M. *Acta Met.* **1977**, 25, 305–308.
20. Lunarska, E. *Hydrogen Degradation of Ferrous Alloys*; Oriani, R. A., Hirth, J. P., Smialowski, M., Eds.; Noyes Publications: Park Ridge, New Jersey, 1984; pp 321–352.
21. Sandoz, G. In *Stress Corrosion Cracking in High Strength Steels and in Titanium and Aluminium Alloys*; Brown, B. F., Ed.; Naval Research Laboratory: Washington, 1972; pp 79–145.
22. McIntyre, P. *Hydrogen Degradation of Ferrous Alloys*; Oriani, R. A., Hirth, J. P., Smialowski, M., Eds.; Noyes Publications: Park Ridge, New Jersey, 1984; pp 763–798.
23. Magnin, T. *Mater. Sci. Forum* **1996**, 217–222, 83–94.
24. Shivanyuk1, V.; Gavriljuk, V.; Foct, J. *Mater. Sci. Forum* **2007**, 539–543, 4249–4254.
25. Cassagne, T.; Busschaert, F. In *Corrosion/2005*; NACE International: Houston, Tx, 2005; p 26; Paper No 05098.
26. Hipsley, C. A. *Mater. Sci. Technol.* **1987**, 3(11), 912–922.
27. Johnston, J. W.; Cottis, R. A.; Procter, R. P. M. *Electrochem. Soc. Extended Abstracts* **1987**, 87(2), 454–455.
28. Ryder, D. A.; Davies, T. J.; Strecker, E. 2nd International Congress on Hydrogen in Metals; 1977; Vol. 3; Pergamon Press; Paper 3B2.
29. Kerr, R.; Guiterrez-Solana, F.; Bernstein, I. M.; Thompson, A. W. *Met. Trans. A* **1987**, 18A, 1011–1022.
30. Thompson, R.; Lin, I. H. *Hydrogen Degradation of Ferrous Alloys*; Oriani, R. A., Hirth, J. P., Smialowski, M.; Noyes Publications: Park Ridge, New Jersey, 1984; pp 454–511.
31. Zappfe, C.; Sims, C. *Trans. AIME* **1941**, 145, 225.
32. Oriani, R. A.; Josephic, P. H. *Acta Metall.* **1974**, 22, 1065.
33. Troiano, A. R. *Trans. ASM* **1960**, 52, 54.
34. Morlet, J. G.; Johnson, H. H.; Troiano, A. R. *J. Iron Steel Inst.* **1958**, 189, 37.
35. Oriani, A. *Stress Corrosion Cracking and Hydrogen Embrittlement of Iron Base Alloys*; NACE: Houston, TX, 1973; Vol. 5, pp 351–358.
36. Petch, N. J.; Stables, P. *Nature* **1952**, 169, 842.
37. Gahr, S.; Grossbeck, M. L.; Birnbaum, H. *Acta Met.* **1977**, 25, 125.
38. Sieradzki, K.; Newman, R. C. *Phil. Mag. A* **1985**, 51, 95.
39. Morgan, M. J.; McMahon, C. J., Jr. *Hydrogen Degradation of Ferrous Alloys*; Oriani, R. A., Hirth, J. P., Smialowski, M., Eds.; Noyes Publications: Park Ridge, New Jersey, 1984; pp 608–640.
40. Lynch, S. *Scripta Met.* **1979**, 13, 1051.
41. Delafoss, D.; Magnin, T. *Eng. Fract. Mech.* **2001**, 68, 693–729.
42. Ugiansky, G. M.; Payer, J. H. Eds. *Stress Corrosion Cracking—The Slow Strain Rate Technique*; ASTM STP, 1979; p 665.
43. Erlings, J. G.; de Groot, H. W.; Nauta, J. *Corros. Sci.* **1987**, 27(10/11), 1153–1167.
44. Crooker, T. W.; Hauser, J. A. H. A Literature Review on the Influence of Small-Amplitude Cyclic Loading on Stress Corrosion Crack Growth in Alloys, NRL Memorandum Report 5763, Naval Research Laboratory, Washington DC, April 3, 1988.
45. Caskey, G. R. Third International Congress on Hydrogen and Materials Paris, 1982, pp 611–616.
46. Gesari, S. B.; Irigoyen, B. L.; Juan, A. *Surf. Rev. Lett.* **2005**, 12(2), 227–232.
47. Gesari, S. B.; Pronsato, M. E.; Juan, A. *Surf. Rev. Lett.* **2002**, 9(3 & 4), 1437–1442.
48. Serebrinsky, S.; Carter, E. A.; Ortiz, M. *J. Mech. Phys. Solids* **2004**, 52, 2403–2430.

## 2.11 Cracking Stimulated by Hydrogen

**C. M. Fowler**

Exova Corrosion Centre, 182 Halesowen Road, Netherton, Dudley, West Midlands DY2 9PL, UK

© 2010 Elsevier B.V. All rights reserved.

2.11.1	Introduction	923
2.11.2	Sources of Hydrogen	923
2.11.3	Hydrogen Pressure Induced Cracking (HPIC)	924
2.11.4	Hydrogen Embrittlement	925
2.11.5	Stress Oriented Hydrogen Induced Cracking (SOHIC)	925
2.11.5.1	SOHIC Mechanism	925
2.11.6	Testing Methods for Hydrogen Cracking	926
2.11.6.1	Hydrogen Pressure Induced Cracking	926
2.11.6.2	Hydrogen Embrittlement	926
2.11.6.3	Testing for SOHIC	927
References		927

### Abbreviations

<b>EFC</b>	European Federation of Corrosion
<b>HIC</b>	Hydrogen induced cracking
<b>HPIC</b>	Hydrogen pressure induced cracking
<b>SOHIC</b>	Stress orientated hydrogen induced cracking
<b>SSCC</b>	Sulfide stress corrosion cracking

### Symbols

<b>HAZ</b>	Heat affected zone
<b>HV10</b>	Vickers hardness 10 Kg load
<b>H<sub>2</sub>S</b>	Hydrogen sulfide
<b>MPa</b>	Mega pascals

### 2.11.1 Introduction

There are several forms of environmental cracking that are either stimulated or produced by hydrogen.

Over the past decade and in previous decades, there have been a significant number of pipeline failures attributed to such mechanisms. The types of cracking and compatibility of materials will be described in this chapter.

In an ideal world, high strength steels would be fully utilized in, for example, pipelines and offshore structures, the weight advantage being very attractive. However, in general terms, as the strength of steel increases

so does the susceptibility to hydrogen embrittlement. This has been treated in the previous chapter, and only one variant of this process, which is experienced in harder welds in pipeline steels, will be discussed here.

In addition to the hydrogen embrittlement of harder steels, there are also hydrogen cracking mechanisms that occur in softer steels, such as hydrogen pressure induced cracking (HPIC), and these processes are the focus of this chapter.

Hydrogen embrittlement is clearly a function of dissolved atomic hydrogen, while HPIC clearly depends on the formation of molecular hydrogen within the steel (and hence depends on the presence of very high hydrogen fugacity). However, a crack morphology now recognized and termed stress orientated hydrogen induced cracking (SOHIC) has been defined, and modern thinking suggests that the crack mechanism is driven by a combination of atomic and molecular hydrogen. This latter crack mechanism has been and is still the subject of much research.

The three types of cracking described above have all been responsible for a significant number of pipeline and pressure vessel failures.

In an effort to provide a clear picture, the three crack mechanisms will be dealt with separately.

### 2.11.2 Sources of Hydrogen

The general sources of hydrogen have been described in the previous chapter; here we concentrate on the



production of the very high hydrogen fugacities that are necessary for HPIC and SOHIC. In order to achieve these high fugacities, it is necessary to generate hydrogen at the metal surface at an activity that would be in equilibrium with a very high partial pressure of hydrogen (far above atmospheric pressure). The only common way in which this can be achieved is by corrosion in the presence of hydrogen sulfide ( $\text{H}_2\text{S}$ ). The hydrogen sulfide may be naturally-occurring in oil and gas reservoirs (produced fluids may contain more  $\text{H}_2\text{S}$  than oil, with the highest reported  $\text{H}_2\text{S}$  content being 87%<sup>1</sup>) or from reservoir souring as a result of infection by sulfate reducing bacteria introduced during water injection.

**Figure 1** illustrates the processes that are involved in the production of hydrogen gas at the steel surface. In most environments, the vast majority of the hydrogen is evolved as gas and the amount entering the steel is very small (typically less than 1%).

The mechanism whereby the atomic hydrogen enters the steel in great quantities depends on the poisoning of the recombination reaction in which two adsorbed hydrogen atoms combine to form a hydrogen molecule that then disperses as dissolved hydrogen or as bubbles of gas. This causes the adsorbed hydrogen concentration to increase and consequently, more hydrogen enters the steel.

While several species act as poisons for hydrogen recombination,  $\text{H}_2\text{S}$  is by far the most common source of problems, largely because of its presence in oil and gas production. It is considered that the presence of the  $\text{HS}^-$  from disassociated hydrogen sulfide is the primary poison. Thus, in the presence of hydrogen sulfide, it has been estimated that more than 90% of the atomic hydrogen produced can enter the steel substrate.

It has also been suggested that the  $\text{HS}^-$  ion acts as a catalyst for hydrogen entry, and details of the mode of action of  $\text{H}_2\text{S}$  remain to be clarified. However, the facts are that in the presence of hydrogen sulfide or other

particular compounds such as cyanides, atomic hydrogen can enter steel in vast quantities, whereas under highly corrosive conditions such as corrosion in hydrochloric acid, where copious quantities of gaseous hydrogen is produced, hydrogen atoms do not enter the steel anywhere near such amounts.

### 2.11.3 Hydrogen Pressure Induced Cracking (HPIC)

This phenomenon is also called blister cracking, stepwise cracking, or simply hydrogen induced cracking (HIC). HPIC is far more descriptive as it is the pressure of hydrogen that causes the cracking as described later.

Atomic hydrogen enters the steel substrate and will continue in theory to the other side; however, the atoms collect at sites such as metal-inclusion interfaces, voids, and other crystal defects. While hydrogen is essentially insoluble in metals in a molecular form, hydrogen molecules can form at metal-inclusion interfaces, leading to the development of internal pockets of hydrogen. Further, atoms are attracted to this site, form more hydrogen molecules, and a gas pressure builds up. This pressure can reach many MPa, and eventually, the yield strength of the steel is exceeded and cracks are initiated. As more hydrogen enters the steel and further small cracks initiate, some of the cracks join together in a shear mode. These often look like steps, hence, the name stepwise cracking, see **Figures 2 and 3**.

Generation of hydrogen by corrosion processes

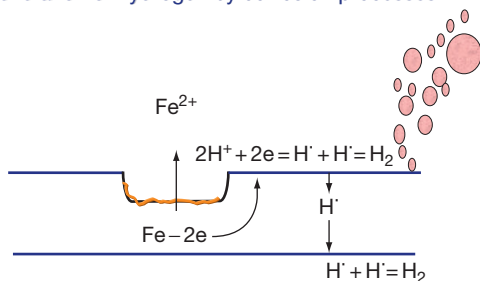


**Figure 1** The corrosion process.

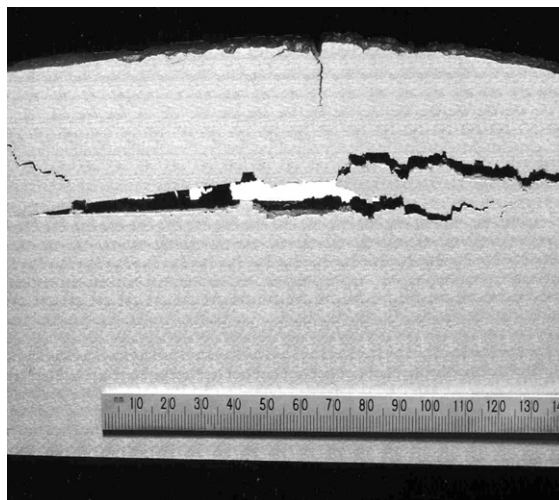


**Figure 2** Example of HPIC in Plate Steel (courtesy Hay, M. Shell Canada).

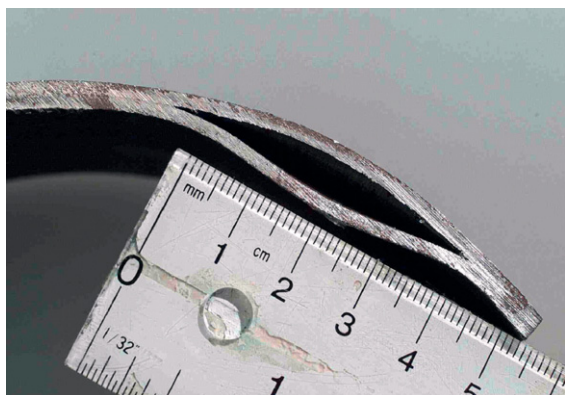


**Figure 3** HPIC in pipeline steel (courtesy Hay, M. Shell Canada).

During the era of ‘controlled rolled plate,’ such features were not uncommon and a number of failures occurred.

Steels have now been developed with improved microstructure, achieved using calcium treatment which minimizes the inclusions and banded microstructure that are the sites for HPIC initiation. Having said that, HPIC failures are still occurring when high levels of  $H_2S$  are encountered, thus, steels for use in sour environments should be tested – see [Section 2.11.6](#).

HPIC can occur in low strength steels with hardness levels well-below the recognized level needed for hydrogen embrittlement to occur.

#### 2.11.4 Hydrogen Embrittlement

The first distinction to be made is that hydrogen embrittlement is an atomic hydrogen mechanism not a molecular hydrogen mechanism. Hydrogen embrittlement is a particular problem in the oil and gas industry in the context of welds, where higher hardness than the parent plate can be obtained, together with high residual stresses. Owing to the high hydrogen levels that can be achieved by the action of  $H_2S$ , failure can occur at somewhat lower levels than is normally found for hydrogen embrittlement. When it occurs in the presence of  $H_2S$ , the phenomenon is known as sulfide stress corrosion cracking (SSCC) or sulfide stress cracking (SSC).

In general terms, the higher the strength and hardness of a steel the higher the susceptibility to this form of cracking. The industry recognized upper hardness limit as Vickers  $HV_{10}$  248 or Rockwell ‘C’ scale 22, see [Figure 4](#).<sup>2</sup>

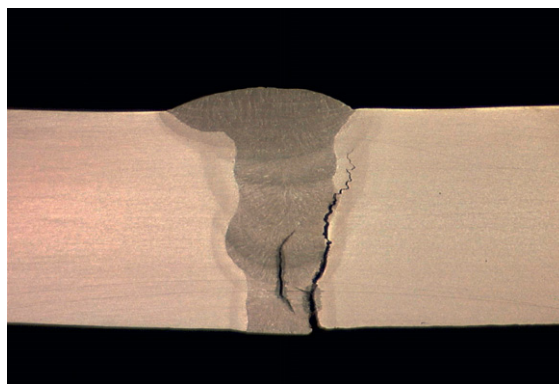


**Figure 4** Hydrogen embrittlement (SSCC) of Pipeline weld.

#### 2.11.5 Stress Oriented Hydrogen Induced Cracking (SOHIC)

The morphology of this type of crack is illustrated in [Figure 5](#).

This type of cracking has also been termed ladder cracking or stacked array cracking.

Pargeter has presented a documentary history of SOHIC failures<sup>3</sup>; the evidence strongly suggests that a complex or tri-axial stress condition is required to generate such cracking, in combination with a high flux of hydrogen. It is important to note that the stress can be residual rather than applied.

The first SOHIC failures occurred in spirally welded line-pipe ([Figure 6](#)). There have been a number of catastrophic bursts.

By virtue, its manufacturing process, spirally welded pipe has a high residual stress adjacent to the weld. SOHIC cracks are often positioned adjacent to the heat-affected zone (HAZ) of the weld.

SOHIC has also been identified in failures in pressure vessels, and in one case a seamless pipeline.

##### 2.11.5.1 SOHIC Mechanism

At the time of writing, there are a number of ongoing research programs to try to fully identify the SOHIC mechanism, and one to develop an acceptable test method.

It is generally considered that the following events occur: the steel is flooded with hydrogen from the corrosion process, there is a tri-axial stress, voids are generated, and small internal blister type cracks initiate by the HIC mechanism of molecular hydrogen being formed and trapped. These small cracks themselves generate internal stress fields which further attract atomic hydrogen, further small

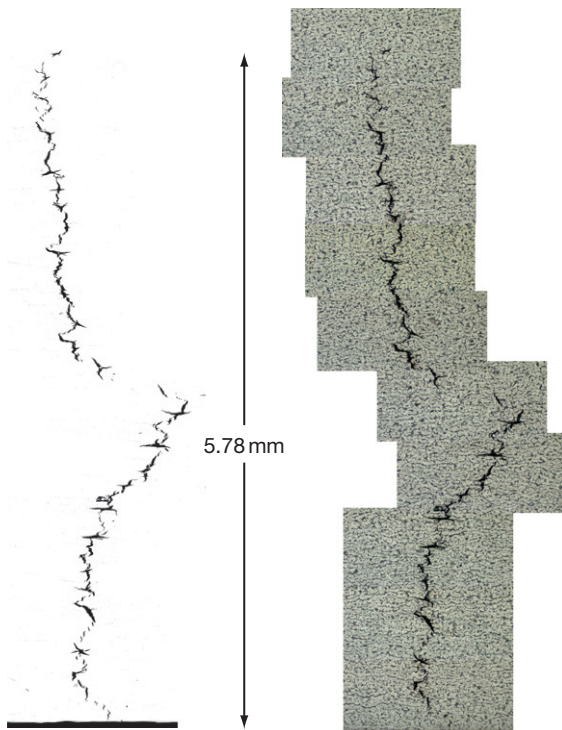


**Figure 5** Stress-oriented hydrogen induced cracking (SOHIC).



**Figure 6** Spirally welded pipe – SOHIC failure (courtesy Shell Canada).

cracks initiate in the through thickness direction, which heightens the stress level, atomic hydrogen then leads to cracking by processes similar to those involved in hydrogen embrittlement, the resultant cracks joining up the small HIC cracks. The eventual failure is by coalescence of the through wall features.

Some workers in the field are also of the opinion that the initial cracks could be formed around small spherical inclusions. In some instances, these have been found in the center of the crack. The definitive mechanism whereby the cracks form in a vertical array is yet to be discovered.

Current research has identified the overall importance of a tri-axial stress, and a test method that applies a complex stress field to the sample is in the late stages of refinement.

It should be noted that SOHIC is not limited to line-pipe, it has been observed in plates and fittings. Interestingly, the materials in question had hardness significantly below the level accepted for SSCC/hydrogen embrittlement resistance.

## **2.11.6 Testing Methods for Hydrogen Cracking**

### **2.11.6.1 Hydrogen Pressure Induced Cracking**

An industry accepted test method has been developed and used for many years, namely NACE TM0284.<sup>4</sup> The method is quoted in many standards such as ISO 15156<sup>2</sup> and EFC publication No. 16.<sup>5</sup>

It is important to note that ISO 15156, the industry standard for sour oil and gas production, notes that all tests should be undertaken on samples representative of the final product form.

Although stress is thought not to influence HPIC, it has been noted several times by various workers that residual strain can be detrimental, as such tests on plate have shown no failure, whereas tests in pipe made from the plate have exhibited failure when the outer strain level reached 2% or more.

The test is a simple immersion test of unstressed coupons which are exposed to H<sub>2</sub>S saturated brine. After a set exposure time, the samples are metallographically examined for cracks.

### **2.11.6.2 Hydrogen Embrittlement**

Considerable further work has been undertaken since Erlings' work described in the previous chapter,<sup>6</sup> and there are now several variations in loading technique, such as interrupted slow strain and step loading slow strain rate testing.

One of the more common loading schemes is illustrated in **Figure 7**:

Further information on this type of testing can be found in ASTM F 1624-06.<sup>7</sup>

Other published test methods include:

NACE TM0177<sup>8</sup> methods A, B, C, and D; method 'A' smooth tensile, method 'B' three point bend (now largely superseded by other configurations), method 'C' ring, method 'D' double cantilever bend.

EFC 16<sup>5</sup> Four Point Bend (ASTM G39)\_Mostly applicable to Weld qualification.

NACE TM0198<sup>9</sup> Slow Strain Rate

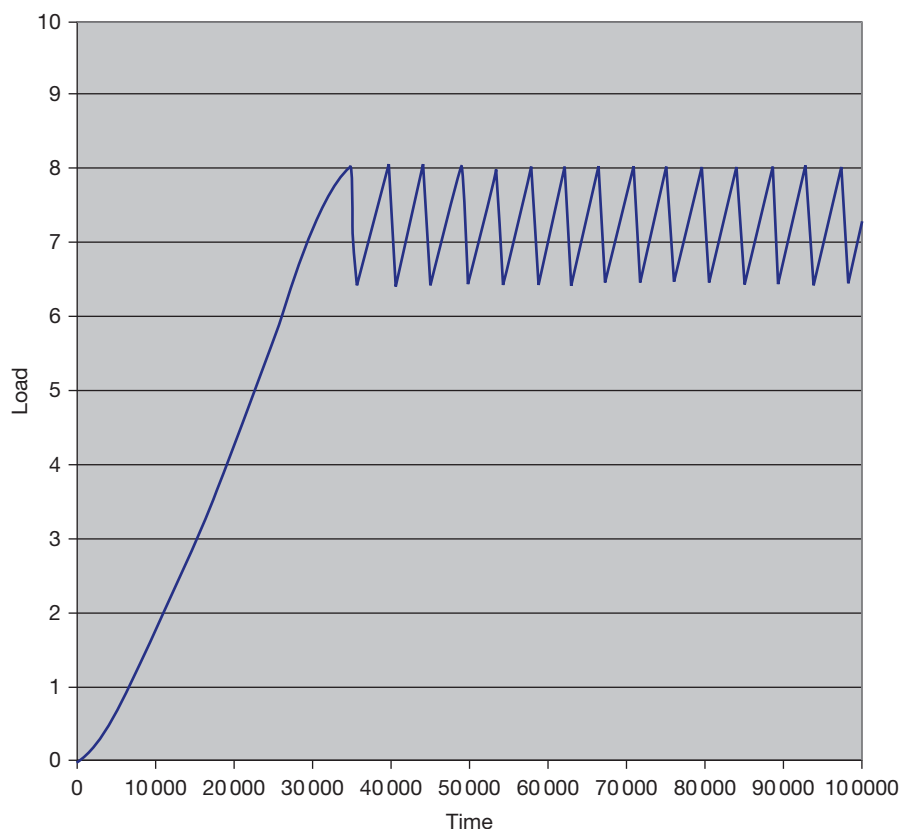


**Figure 7** Load-time history for a cyclic slow strain rate test.

### 2.11.6.3 Testing for SOHIC

At the time of writing, there is currently no universally accepted test for SOHIC. There are two published methods, one for pressure vessel plate (NACE TM0103<sup>10</sup> the double beam test, not to be confused with the double cantilever beam test; under review for withdrawal) and one for line-pipe (HSE Publication OTI 95 635<sup>11</sup> the full ring test).

## References

1. Kutney, G. *Sulfur: History, Technology, Applications and Industry*; ChemTec Publishing, 2007; p 146, ISBN 1895198372, 9781895198379.
2. ISO 15156/MR0175; NACE International: Houston, TX.
3. Pargeter, R. J. In *Corrosion 2007*; NACE International: Houston, TX, 1975; Paper 07115.
4. NACE TM0284; NACE International: Houston, TX.
5. *Materials Requirements for Carbon and Low Alloy Steels for H<sub>2</sub>S-Containing Environments in Oil and Gas Production EFC 16*, 2nd ed., 2002; pp 64; Maney Publishing: London, ISBN 1 90265 354 8.
6. Erlings, J. G.; de Groot, H. W.; Nauta, J. *Corros. Sci.* **1987**, 27(10/11), 1153–1167.
7. ASTM F1624–06 *Standard Test Method for Measurement of Hydrogen Embrittlement Threshold in Steel by the Incremental Step Loading Technique*; ASTM International: Philadelphia, 2006.
8. NACE TM0177; NACE International: Houston, TX.
9. NACE TM0198; NACE International: Houston, TX.
10. NACE TM0103; NACE International: Houston, TX.
11. HSE OTI 95–635 *The Full Ring Test*; UK Health and Safety Executive – Books.

## 2.09 Stress Corrosion Cracking

**R. C. Newman**

Department of Chemical Engineering and Applied Chemistry, University of Toronto, Canada

© 2010 Elsevier B.V. All rights reserved.

2.09.1	Introduction and Definitions	865
2.09.2	Metal–Environment Combinations Showing SCC; the Issue of Mechanical Difficulty	866
2.09.3	Role of Metallurgy in SCC	870
2.09.3.1	Summary of Metallurgical Factors in SCC	870
2.09.3.2	Solid Solution Composition	871
2.09.3.3	Grain Boundaries, without Precipitation	873
2.09.3.4	Grain Boundary Precipitation	875
2.09.3.5	Yield Strength, Including Cold Work Effects	876
2.09.4	Crack Nucleation, Crack Coalescence, 3D Crack Morphology, Effect of Distributed Grain Boundary Character	880
2.09.5	Crack Chemistry in SCC	882
2.09.6	Role of the Environment in SCC	885
2.09.7	Anodic SCC Models	886
2.09.7.1	Interlude – Ultra-Sharp Cracks	890
2.09.8	Chemistry Considerations for SCC by Slip-Dissolution	890
2.09.9	More Comments on Hydrogen Embrittlement as a Mechanism of SCC	890
2.09.10	Film-Induced Substrate Fracture ('Film-Induced Cleavage')	892
2.09.11	Surface Mobility, Vacancy Based Models, and Others	895
2.09.11.1	Vacancy Injection Models for Low-Temperature SCC	896
2.09.11.2	Adsorption-Induced Dislocation Emission	896
References		898

### Abbreviations

**AIDE** Adsorption-induced dislocation emission  
**BWR** Boiling water reactor  
**C steel** Carbon steel  
**CI-SCC** Chloride-induced SCC (of stainless steel)  
**EAC** Environmentally assisted cracking  
**EBSD** Electron backscattered diffraction  
**EDS** Energy dispersive analysis of X-rays  
**FIB** Focused ion beam  
**GB** Grain boundary  
**HEDE** Hydrogen-enhanced dislocation emission  
**HELP** Hydrogen-enhanced local plasticity  
**HS** High strength (steel)  
**HSLA** High strength low alloy (steel)  
**HT** High temperature (water)  
**HWC** Hydrogen water chemistry (in BWR)  
**IASCC** Irradiation-assisted SCC  
**IG** Intergranular  
**IGA** Intergranular attack  
**LA** Low alloy (steel)  
**LME** Liquid metal embrittlement

**LT** Low temperature (water)  
**MS** Medium strength (steel)  
**PWR** Pressurized water reactor  
**Q&T** Quenched and tempered (steel)  
**RIS** Radiation-induced segregation  
**SCC** Stress corrosion cracking  
**SDM** Slip dissolution model (for SCC)  
**SMM** Surface mobility model  
**SS** Stainless steel  
**SSRT** Slow strain rate test  
**TEM** Transmission electron microscope (or microscopy)  
**TG** Transgranular

### Symbols

***a*** Atom diameter (in the SMM)  
***a<sub>c</sub>*** Critical depth of pit or crack  
***A*** Atom fraction of less-noble metal atoms in an alloy  
***D<sub>s</sub>*** Surface diffusion coefficient (in the SMM)



$E$	Electrode potential, Young's modulus
$E_m$	Mixed potential
$E_R$	Repasivation potential
$f$	Oxide-film fracture strain
$F$	Faraday's constant
$i$	Current density
$\bar{i}$	Mean anodic current density flowing during a time interval
$i_0$	Exchange current density
$i_{\max}$	Maximum anodic current density flowing on a bare metal surface
$i_{\text{net}}$	Net current density
$K_{(I)}$	(Mode I) Stress intensity factor
$K_{Ic}$	Critical stress intensity factor
$K_{Isc}$	Threshold stress intensity factor for SCC
$L$	Diffusion distance along the crack flank (in the SMM)
$L$	Distance ahead of the crack tip where the crack-tip strain rate is evaluated
$n$	Number of electrons transferred per atom oxidized; inverse strain hardening coefficient
$N_A$	Avogadro's number
$Q^{-1}, f$	Quantities of interest in internal friction measurement
$s$	Crack-tip strain rate
$v$	Velocity of SCC or corrosion (or $V_{sc}$ , $V_{crack}$ , $V_{corrosion}$ , etc.)
$\delta$	Crack-tip opening displacement according to ordinary fracture mechanics
$\epsilon_p$	Plastic strain
$\epsilon(r)$	Plastic strain distribution ahead of a crack tip
$\Omega$	Molar volume of metal
$\sigma$	Stress
$\sigma_y$	Yield stress
$\tau$	Interval between film rupture events at a crack tip

## 2.09.1 Introduction and Definitions

Stress corrosion cracking (SCC) is the gradual growth of cracks under the simultaneous influence of a nominally static stress and a chemically reactive environment. The meaning of 'nominally static' is discussed in **Chapter 2.08, Environmentally Assisted Cracking Overview** – this does not exclude slow or low-amplitude dynamic loading, or periodic unloading. It is convenient to refer to SCC as occurring under 'tensile' stress, although shear stresses certainly play a major role microscopically, and some SCC testing is done under mode III loading (antiplane shear; torsion), to confirm whether or not hydrogen is playing a

role in the cracking – hydrogen is supposed to be less aggressive under torsion because there is, nominally, no lattice dilation to increase the solubility of hydrogen. In this chapter, we restrict ourselves to metals, although interesting SCC phenomena occur in glasses and hot rocks, and are thought to be involved in major geologic upheavals.<sup>1</sup> Actually, fracture of brittle solids can be more amenable to first-principles calculations than the more complex phenomena that occur in metals, so in some ways nonmetals are at the leading edge of the subject.<sup>2</sup> Polymers and polymer–matrix composites also show environmentally assisted cracking (EAC) phenomena that some people would call SCC.

In metals, SCC cracks are normally multiple, branched, and either intergranular, or transgranular and cleavage-like (see **Chapter 2.08, Environmentally Assisted Cracking Overview**, for examples). Sometimes the two modes coexist, or transgranular SCC occurs simultaneously with intergranular corrosion – **Figure 1**. This fractography, when examined in sufficient detail, continues to provide important clues to the cracking mechanism, whether in the laboratory or in the field.<sup>3,4</sup> In particular, transgranular SCC facets are close to a particular fracture plane, for example, {110} in  $\alpha$ -brass, but have ultrafine detail indicative of the operation of plastic processes on the nanometer scale.

SCC can be considered a 'brittle' mode of failure, in that the material fails to manifest its usual tensile strength and ductility. But SCC is always accompanied by microscopic plastic strain, and many believe that such strains, occurring dynamically at the crack tip, are a causal factor of crack growth.

It is easier to pose the question – what kinds of EAC are not SCC – than to list pedantically what is SCC. So, hydrogen-induced cracking of a high-strength steel due to gaseous hydrogen, or to excessive cathodic protection, is not SCC. But cracking of the same material in saltwater under free corrosion conditions is SCC, even if we are 100% sure it is due to hydrogen released by the corrosion process. Liquid metal embrittlement (LME) is not SCC. Cracking of high-strength steel in dry gaseous chlorine<sup>5</sup> is SCC, but cracking in dry gaseous  $H_2S$  might be too obviously a hydrogen effect to be SCC. Cracking of carbon steel in anhydrous liquid ammonia is certainly SCC. Cracking of alloys in air at very high temperatures where dry oxidation and creep are both possible could, arguably, be called SCC,<sup>6</sup> although such phenomena have other names such as oxygen embrittlement. But despite these nonaqueous

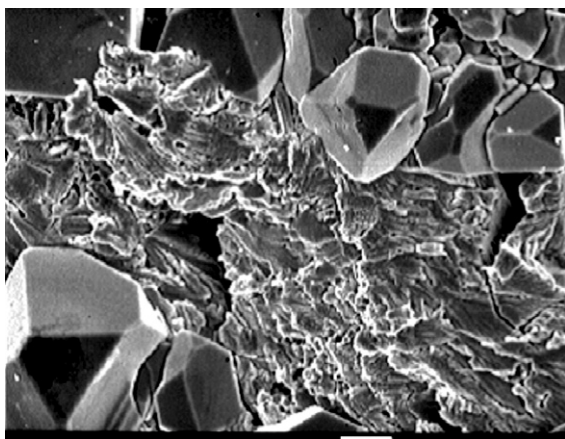


**Figure 1** SCC of Monel 400 in copper sulfate solution, showing intergranular corrosion/SCC and transgranular SCC. Reproduced from Barnes, A.; Deakin, J.; Newman, R. C. *Corrosion* **2007**, 63, 416–418.

examples, the vast majority of SCC is caused by some combination of water, oxidant, and ions or soluble molecules. And like other forms of corrosion, most SCC can be retarded or prevented by removing oxygen.

The velocity of SCC (crack growth rate) can be as high as  $10^{-5} \text{ m s}^{-1}$  or as low as  $10^{-12} \text{ m s}^{-1}$ . Common practical rates are in the range  $10^{-11}$ – $10^{-8} \text{ m s}^{-1}$  – roughly, 1  $\mu\text{m}$  to 1 mm per day. In real components, cracking is often intermittent, occurring during start-ups or other plant transients, which can make the apparent or average crack velocity very low indeed.

The consequences of SCC are quite different in low-strength and high-strength alloys. In a high-strength material, stresses are usually externally imposed, and growth of a stress corrosion crack can lead to catastrophic rupture when the fracture toughness is exceeded, whereas in low-strength materials, the dominant stresses are often internal (residual), and SCC causes leakage or gradual plastic tearing.

The history of SCC has often been told, and will be mentioned quite briefly. In this chapter, we focus on modern understanding of the various phenomena that are classified as SCC and their practical significance.

### 2.09.2 Metal–Environment Combinations Showing SCC; the Issue of Mechanical Difficulty

The major difference between different SCC phenomena is the severity of the mechanical conditions

that are required (e.g., value of stress normalized to the yield stress or necessity of time variation in stress). Such considerations, and the notion of a spectrum of phenomena from SCC through corrosion fatigue, depending on the importance of dynamic straining, were introduced in **Chapter 2.08, Environmentally Assisted Cracking Overview**.

**Table 1** gives a summary of the known SCC systems with one new feature – we try to categorize them according to the difficulty of cracking in a real component, on a scale of 1–5. So, 1 means SCC that requires only a low and not particularly dynamic tensile stress, while 5 means SCC that has only been observed under laboratory conditions and requires dynamic tensile loading (slow strain rate testing), or major cyclic loading, or alternatively an improbably oxidizing potential. Of course, there is always a first time for a phenomenon to occur in the field, but at least we can be sure that a 4 or a 5 would require unusually severe conditions, and might be classified as corrosion fatigue in any case.

An explosion in the number of known SCC combinations (material ... metallurgical condition ... environment) occurred when the slow strain rate test (SSRT) was introduced in the 1970s.<sup>7</sup> This test exposes a smooth tensile sample to the environment, often with electrochemical potential control, and the sample is slowly strained to failure at an engineering strain rate of typically  $10^{-7}$ – $10^{-5} \text{ s}^{-1}$ .<sup>8</sup> The use of the SSRT revealed, almost for the first time, SCC processes that had not yet occurred in the field, such as the cracking of pure copper in sodium nitrite solution.<sup>9</sup> Some of these subsequently did occur in the field; others never have. To call the SSRT ‘too severe’ misses the point – it is a tool for predicting and understanding SCC. No one thinks that all SCC observed in SSRT can or will occur under realistic component loading. Sometimes, especially for hydrogen-related SCC, one can rationalize this neatly in terms of when, during a SSRT, cracks initiate and cause the load-extension curve to deviate from that measured in an inert environment – **Figure 2**.

Some cases of SCC are hard to predict and control because the environment that causes cracking is not well-characterized, or exists only transiently. This is the case for nuclear steam generators, where impurities present at parts per billion or trillion in the feedwater (Pb ... S) concentrate on heat-transfer surfaces under deposits<sup>10</sup> – **Figure 3**. Sometimes these cause SCC during operation, but it is increasingly thought that cracking may occur during plant

start-up, or even during plant shut-down, when oxygen is more available. Test methods that incorporate heat transfer into the test specimen are useful for the clarification of such mechanisms.<sup>11</sup>

The more usual test methods for SCC have been very well discussed by Sedriks, and are not given their own special section in this chapter; miscellaneous comments on test methods are inserted into

**Table 1** Summary of metal–environment combinations that are susceptible to SCC

<i>Material</i>	<i>Environment</i>	<i>Exacerbating or inhibiting factors</i>	<i>Severity (scale 1–5) 1 highest</i>	<i>Other notes</i>
Carbon steel	Hot conc aq caustic O <sub>2</sub>	GB precipitation, segregation C, P ...	2	IG
Carbon steel	Active–passive transition Warm-hot conc aq nitrate Nitrate can be the oxidant 'Transpassive' state	Evap cond's GB precipitation, segregation C, P ...	1	IG
Carbon steel	Warm aq carbonate– bicarbonate O <sub>2</sub>	GB precipitation, segregation C, P ...	3	IG
Carbon steel	Active–passive transition Anhydrous NH <sub>3</sub> with O <sub>2</sub> Ambient <i>T</i> Also NH <sub>3</sub> /CH <sub>3</sub> OH	<b>H<sub>2</sub>O</b>	3	TG Also pure Fe
Carbon steel	Aq CO–CO <sub>2</sub> Ambient <i>T</i> O <sub>2</sub> not required?		3	TG Also pure Fe
Carbon steel	Aq CO <sub>2</sub> –HCO <sub>3</sub> <sup>–</sup> near-neutral Ambient <i>T</i>	Higher strength <b>Dynamic strain required in, e.g., X65 grades</b>	4	TG H effect
Carbon steel	O <sub>2</sub> not required? Methanol [ethanol] O <sub>2</sub> Ambient <i>T</i>	?	3 [ethanol 4]	IG TG with Cl <sup>–</sup>
Carbon steel	Warm aq amine containing mixtures (NH <sub>3</sub> ?) O <sub>2</sub> not required?	CO <sub>2</sub>	3	IG/TG
Carbon steel	HT water (> 150 °C) O <sub>2</sub>	Ionic impurities Cu deposition MnS inclusions	3	H effect in HS TG
Q&T LA steels MS	Hot water, steam Some O <sub>2</sub>	GB segregation, e.g., P Ionic impurities	2–4	IG
Carbon steel Q&T LA steels MS	Aq CO <sub>2</sub> –H <sub>2</sub> S No O <sub>2</sub>	Higher strength <b>Fewer large carbides T &gt; 60 °C</b>	1–4	TG/IG H effect
HS C steel HSLA steels	Moist air...Water...Saltwater O <sub>2</sub>	Higher strength <b>T &gt; 60 °C Various metallurgy Only in ultra-HS</b>	1–3	IG/TG H effect
HSLA steels HSLA steels	Dry Cl <sub>2</sub> Dry H <sub>2</sub> S	O <sub>2</sub>	3 2	IG IG/TG H effect
HS carbon steel (prestressing wire)	Water O <sub>2</sub>	Salts Lack of high pH <b>Elongated microstructure favorable</b>	3	IG/TG
Strong SS Martensitic, etc.	Salt water O <sub>2</sub> Ambient <i>T</i>	H <sub>2</sub> S Other reduced sulfur Crevice, deposits Higher strength <b>T &gt; ?</b>	2	TG/IG H effect Requires loc corr

Continued

**Table 1** Continued

<i>Material</i>	<i>Environment</i>	<i>Exacerbating or inhibiting factors</i>	<i>Severity (scale 1–5) 1 highest</i>	<i>Other notes</i>
Austenitic SS	Warm-hot aq $\text{Cl}^-$ (duplex requires higher $T$ )	$\text{H}_2\text{S}$	1	TG
Duplex SS	$\text{O}_2$ (trace)	Other reduced sulfur Evap cond's Crevices, deposits Mg, Ca (evap cond's) Cold work (lower Ts) Intermetallics (duplex or high austenitic) <b>Ni &gt; 12% (absolute resistance for Ni &gt; 40%)</b> <b>Silicate or other inhibitors</b> <b>Low free P (not commercial)</b>		Requires loc corr
Austenitic SS Duplex SS	Hot aq caustic (needs hotter than $\text{Cl}^-$ ) Occurs without $\text{O}_2$ in lab Duplex less sensitive	Evap cond's	1	TG
Austenitic SS	HT water with $\text{O}_2$ e.g., 290 °C	Cold work Neutron irradiation Ionic impurities Crevices	2–4	IG/TG
Austenitic SS	HT water without $\text{O}_2$ e.g., 290 °C	Cold work Neutron irradiation Ionic impurities?	3–5	IG/TG
Austenitic SS Sensitized	HT water with $\text{O}_2$ e.g., 290 °C Occurs as low as 80 °C	Cold work Neutron irradiation Ionic impurities Crevices	1	IG
Austenitic SS Sensitized	HT water without $\text{O}_2$ e.g., 290 °C	Cold work Neutron irradiation Ionic impurities?	3–5	IG
Austenitic SS Sensitized (also Alloy 600 sensitized)	Aq solutions of reduced sulfur species – $\text{S}_2\text{O}_3^{2-}$ , $\text{S}_4\text{O}_6^{2-}$ , $\text{FeS}/\text{O}_2/\text{H}_2\text{O}$ (others?) Ambient $T$	<b>Excess strong-acid anions → IGA/pitting</b>  <b>Alloyed Mo strongly beneficial</b>	1	IG
Austenitic or duplex weld metal	All the above	Complex; generally more resistant than annealed material; can be similar to duplex	3–5	Complex
Ni base alloys e.g., Alloy 600	HT water without $\text{O}_2$ e.g., 310 °C	$\text{H}_2$ in certain range near Ni/NiO equilibrium Cold work <b>Grain boundary carbides</b> <b>Switch to Alloy 800 or 690</b>	2	IG
Ni base alloys e.g., Alloy 600	HT water with $\text{O}_2$ e.g., 310 °C	Cold work Neutron irradiation Ionic impurities Crevices	2	IG
Ni base alloys e.g., Alloy 600	Complex HT environments (nuclear SG crevices, etc.)	$\text{O}_2$ or other nonreducing condition during start-up Deposits Boiling Pb, reduced S from sulfate reduction	2	IG

Continued

**Table 1** Continued

<i>Material</i>	<i>Environment</i>	<i>Exacerbating or inhibiting factors</i>	<i>Severity (scale 1–5) 1 highest</i>	<i>Other notes</i>
<b>Switch to Alloy 800 or 690</b> <b>Clean deposits</b> <b>Design out heat-transfer crevices</b> <b>Extreme conditions only</b>				
Corrosion resistant Ni base alloys e.g., 625	Cl <sup>-</sup> /H <sub>2</sub> S [S] HT e.g., 200 °C No O <sub>2</sub>		3	IG
Strong Ni base alloys (γ')	HT water LT aq solutions	Highest strength normally most susceptible.	2–3	IG/TG H effect at low T
Monel 400 (70Ni–30Cu)	Hot water, or aq sulfate esp with Cu <sup>++</sup>	Coldwork	3–4	IG/TG
Monel 500 (high strength)	Sulfide containing seawater	Highest strength normally most susceptible.	3–4	IG
Pure or nearly pure Cu	Aq ammonia Ambient T	Thin-layer exposure High P content Cold work	3–4	IG
Pure Cu	Aq nitrite O <sub>2</sub> (possibly not essential) Ambient T	<b>Needs dynamic strain</b> (?always)	3–4	TG
Pure Cu	Aq acetate and others inc complex industrial Ambient T	Cold work	4–5	IG [TG]
Pure Cu	O <sub>2</sub> Warm aq sulfide	?	5	IG
Pure Cu	No O <sub>2</sub> Hot (e.g., 300 °C) dry halogens	<b>Only one report</b> <b>Only shown in dynamic-load testing</b>	4	IG
α Brass	Aq ammonia O <sub>2</sub> Ambient T Also amines	Thin-layer exposure pH ~ 7 or ~ 11 Cold work	1	IG/TG
α Brass	Aq nitrite Ambient T O <sub>2</sub> (possibly not essential)	Synergistic effect of other anions e.g., MoO <sub>4</sub> <sup>-</sup> <b>Difficult without dynamic strain?</b>	2–3	TG
α Brass	Aq sulfate, nitrate (CuSO <sub>4</sub> , Cu(NO <sub>3</sub> ) <sub>2</sub> ) Ambient T		3	TG
α Brass	Other aq – acetate, chlorate	<b>Difficult without dynamic strain</b>	4	IG/TG
Al bronze	Aq ammonia O <sub>2</sub> Ambient T	<b>Borderline Al content for SCC</b>	3	IG/TG
β Brass 'Mn bronze'	Water, aq solutions Ambient T		3	TG
Other Cu base inc strong alloys (Cu–Ti, Cu–Be)	Aq ammonia O <sub>2</sub> Ambient T		3	IG/TG
Strong Ti alloys	Salt water O <sub>2</sub> Ambient T (separate phenomena at HT)	Sharp preexisting flaws	2–4	TG
Ti and simple alloys	Acids, methanol Ambient T	<b>H<sub>2</sub>O (for methanol)</b> <b>In acids, etc. requires severe mechanics</b>	2–4	TG H effect (probably)

Continued



**Table 1** Continued

<i>Material</i>	<i>Environment</i>	<i>Exacerbating or inhibiting factors</i>	<i>Severity (scale 1–5) 1 highest</i>	<i>Other notes</i>
Ti, Zr and alloys	Fuming or v hot HNO <sub>3</sub> Liq N <sub>2</sub> O <sub>4</sub>		3–4	TG
Ti, Zr and alloys	Dry halogens	<b>Severe mechanics required</b>	3–4	TG
Ti, Zr and alloys	HT water Cooling after hydrogen absorption at temperature	High pH aggressive for Zr H absorption	3–4	TG Hydride cracking
Strong Al alloys 7000, 2000, 8000	Aq chloride (water only in extreme cases) Ambient <i>T</i> O <sub>2</sub>	Under- or peak ageing Cu alloying generally <b>Overageing</b> <b>Flat grain structure in sheet</b>	2	IG
Medium strength 7000Al (weldable)	Aq chloride Ambient <i>T</i> O <sub>2</sub>	Weld toe cracking	3	IG
Medium strength 5000Al	Aq chloride Ambient <i>T</i> O <sub>2</sub>	GB intermetallic precipitation	3–4	IG
Various Al	Organics e.g., chlorinated	Poorly understood – also other reactive metals	3–4	IG
MgAl alloys	Aq chloride Ambient <i>T</i>	<b>Requires fairly severe mechanics</b>	3–4	TG
Au alloys – AuCu, AuAg – also Pt alloys	Aq acids (also some neutral solutions) Strong oxidant or complexant required for AuAg	<b>Requires dealloying – stops at parting limit</b>	1	IG  TG in single crystals

C steel, Carbon steel; GB, Grain boundary; HS, High strength (steel); HSLA, High strength low alloy (steel); HT, High temperature (water); IG, Intergranular; IGA, Intergranular attack; LA, Low alloy (steel); LT, Low temperature (water); MS, Medium strength (steel); Q&T, Quenched and tempered (steel); SCC, Stress corrosion cracking; SS, Stainless steel; TG, Transgranular.

the text as appropriate. For completeness, we note that test methods can be roughly classified as follows:

- Type of specimen  
Smooth ... defected (notch ... precrack).
- Severity of loading  
Static (constant load ... constant deflection) ...  
Dynamic (monotonic ... slow cyclic).
- Loading mode  
Tension ... bending ... torsion ... multiaxial.
- Environment exposure  
Simple immersion ... electrochemical control ...  
thin layer/evaporating/heat transfer ... gaseous environment.

## 2.09.3 Role of Metallurgy in SCC

### 2.09.3.1 Summary of Metallurgical Factors in SCC

Not all SCC requires a special metallurgical condition – the transgranular cracking of pure copper in sodium nitrite solution, of pure iron in anhydrous

liquid ammonia or CO–CO<sub>2</sub>–H<sub>2</sub>O, or of pure zirconium in hot fuming nitric acid, is a property of the pure metal lattice. But generally, there is some exacerbating metallurgical factor, such as:

- Unfavorable solid solution composition, allowing selective dissolution of one or more less-noble alloy components (dealloying – see **Chapter 2.05, Dealloying**).
- Presence of grain boundaries, especially those with grain-boundary segregation of solutes or impurities.
- Presence of reactive phases at grain boundaries.
- Presence of solute-depleted regions adjacent to grain boundaries.
- Cold work and hardening in general.
- Features tending to localize strain – dynamic strain ageing, intense deformation bands, dislocation ‘channeling’ in neutron-irradiated materials.

Conversely, metallurgy may mitigate the possibility of SCC, as in duplex stainless steels, where the different electrochemical properties of the ferrite and austenite phases dictate different potential dependences of SCC

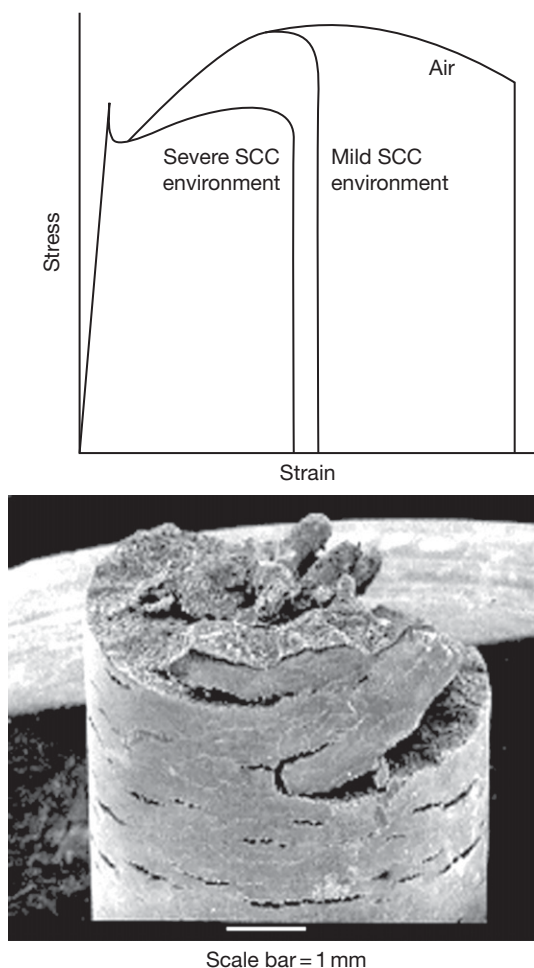


**Figure 2** Schematic stress–strain curves obtained on carbon steel using the slow strain rate test: in air, in an environment causing severe SCC (e.g., anhydrous ammonia–methanol – see micrograph, courtesy W. Zheng), in an environment where cracking requires severe straining of the sample, to the point that necking has begun before cracks appear (e.g., aqueous  $\text{CO}_2$  solution).

for each phase – and since the alloy can only have one corrosion potential, this is not (usually) a value where both phases can crack rapidly – [Figure 4](#). This topic was discussed in some detail in another review,<sup>12</sup> so will not be elaborated here. Instead, we focus on a more recent development of SCC mitigation by so-called grain boundary engineering.

### 2.09.3.2 Solid Solution Composition

There is persuasive evidence that SCC of many solid-solution alloys involves dealloying (see [Chapter 2.05, Dealloying](#)). In the 1950s, H.R. Copson produced his famous ‘Copson curve’ for time to failure as a function

of nickel content in chloride-induced SCC (Cl-SCC) of austenitic stainless steels, or duplex at the lowest Ni contents.<sup>13</sup> Around the same time, L. Graf produced very similar composition dependences for noble-metal alloys (CuAu, AgAu) where gold played (on a dealloying hypothesis) the same role as nickel.<sup>14</sup> SCC vanishes near the parting limit for dealloying, which is  $\sim 45$  at.% of more-noble metal. The similarity was noticed by Latanision and Staehle,<sup>15</sup> who proposed that nickel was enriched on the crack walls and protected them in lieu of a passive film, along the same lines as Graf (nowadays, we would suggest a more direct causal role of dealloying at the crack tip – see [Section 2.09.10](#)). This very attractive hypothesis was later abandoned, apparently because the new surface analytical technique of Auger electron spectroscopy failed to detect nickel enrichment on fracture surfaces (Staehle, private communication). In fact, there is nickel enrichment, but it is subtle, and there is simultaneous dissolution of the alloy components.<sup>16</sup> Importantly, the state of the crack walls in Cl-SCC is precisely that of active crevice corrosion, so one need not be distracted by considerations of passive films.<sup>17</sup> There is some evidence, from cross-sectional TEM examination, for dealloying at the crack tip.<sup>18</sup>

The Copson and Graf curves are compared in [Figure 5](#), adapted from Newman.

In strong, hot caustic solutions, dealloying of stainless steel is much more blatant than in chloride.<sup>19</sup> A dealloyed layer formed in a caustic environment that induces SCC is shown in [Figure 6](#). Also, the dependence of caustic SCC on nickel content is similar to that of Cl-SCC – for example, SCC occurs readily in type 310 stainless steel (20% Ni), but requires more extreme conditions in Alloy 800 (33% Ni) – but when it does occur, it is spectacular – see [Figure 2b](#) in [Chapter 2.08, Environmentally Assisted Cracking Overview](#). The dealloying of 310SS and its ability to inject a crack into the ductile substrate are shown in [Figure 7](#).

Latanision and Staehle<sup>15</sup> noted that only a small Ni content, ca. 1%, was required for SCC, and at first sight this seems to favor the Graf type of mechanism, rather than one requiring an actual dealloyed layer of definable mechanical properties. But alloys with low contents of more-noble metal can form discrete, nanoporous dealloyed layers at low dealloying overpotentials, because the layer is not pure more-noble metal – it is an alloy. This was clearly shown in [Figure 6](#).<sup>19</sup> Type 316 stainless steel (12% Ni) formed a dealloyed layer with about equal amounts of Ni and residual Fe. [Figure 8](#) shows a better example of

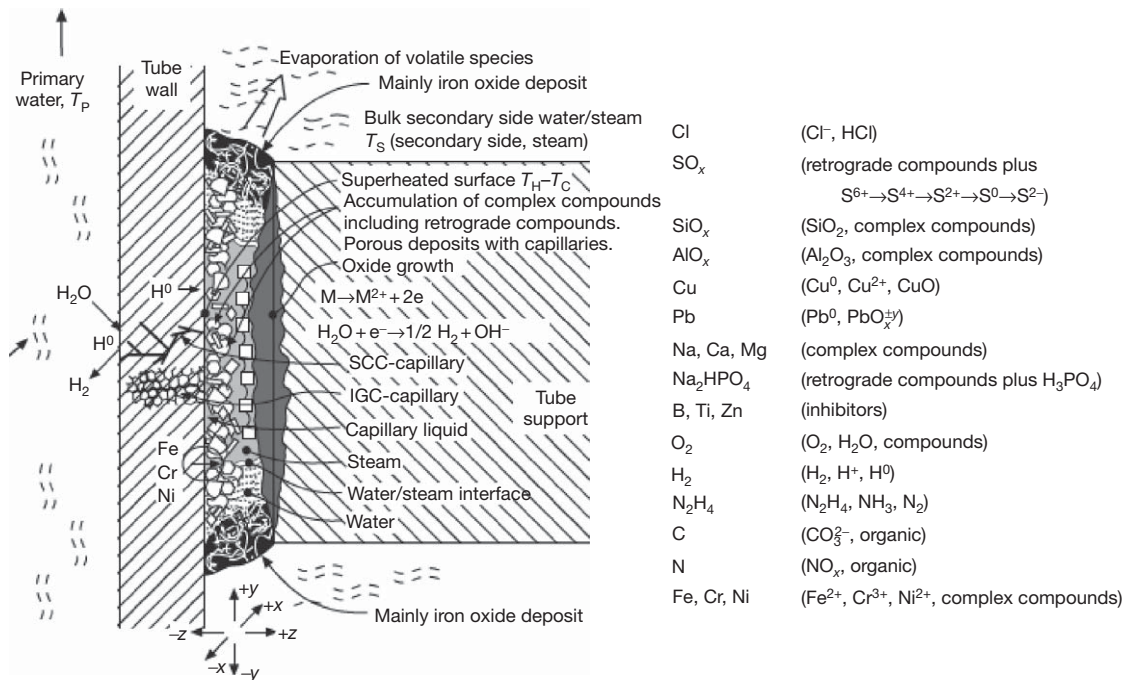


**Figure 3** Complex chemistry of a nuclear steam generator and location of corrosion phenomena. Adapted from Staehle, R. W.; Gorman, J. A. *Corrosion* **2003**, 59, 931–994; 60, 5–63; **2004**, 60, 115–180.

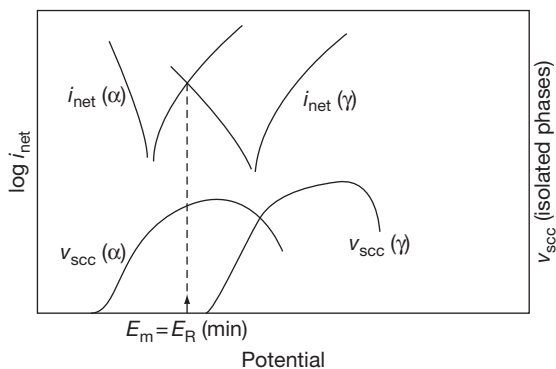


**Figure 4** Reason for the greater resistance of duplex than austenitic stainless steel to chloride-induced SCC – both phases cannot (usually) be at their optimal cracking potential simultaneously, and under mild conditions, there can only be one mixed potential ( $E_m$ ), and one phase is commonly below the minimum possible value of its repassivation potential ( $E_R$ ) by Tsujikawa's criterion. The case illustrated would give very restrained SCC because the  $\gamma$  phase does not crack at all. Reproduced from Newman, R. C. *Stress Corrosion Cracking Mechanisms*. In *Corrosion Mechanisms in Theory and Practice*, 2nd ed; Marcus, P., Oudar, J., Eds.; Marcel Dekker: New York, 2002; pp 399–450.

95Ag–5Au (at.%) alloy. So, one cannot rule out a causal role of an actual dealloyed layer, even at 1% of noble metal, despite assertions to the contrary that appear now and again in the literature.<sup>20,21</sup>

As mentioned in **Chapter 2.05, Dealloying**, not all binary alloy systems show the parting limit (55 at.% less-noble element) seen in binary gold alloys – SCC and superficial dealloying of CuZn or CuAl alloy monocrystals in cuprous ammonia solutions starts at 20 at.% less-noble element, or even a little lower for the CuAl system – **Figure 9**. This has been identified as being at, or close to, a site percolation threshold for the fcc lattice.<sup>22</sup> Departures from this threshold could be due to like-with-like atomic clustering in the solid solution. Intergranular SCC in ordinary polycrystals persists at lower Zn contents, but transgranular SCC vanishes.<sup>23</sup> Evidently, the intergranular variant does not require an actual dealloyed layer, which is reasonable, as pure copper also shows intergranular SCC in ammonia solutions.

Other alloy systems where dealloying should be considered as a cause of, or contributing factor to, SCC include Monel (70Ni–30Cu)<sup>24</sup> and cupronickel. It is likely, though unproven, that some systems may switch from the '55%' to the '20%' threshold at high temperatures such as 300 °C. As a topical example, there is some evidence that Alloy 690 (Ni–29Cr–8Fe) shows dealloying in hot caustic environments, despite the sum of the Cr and Fe contents being well below 55%.<sup>25</sup>

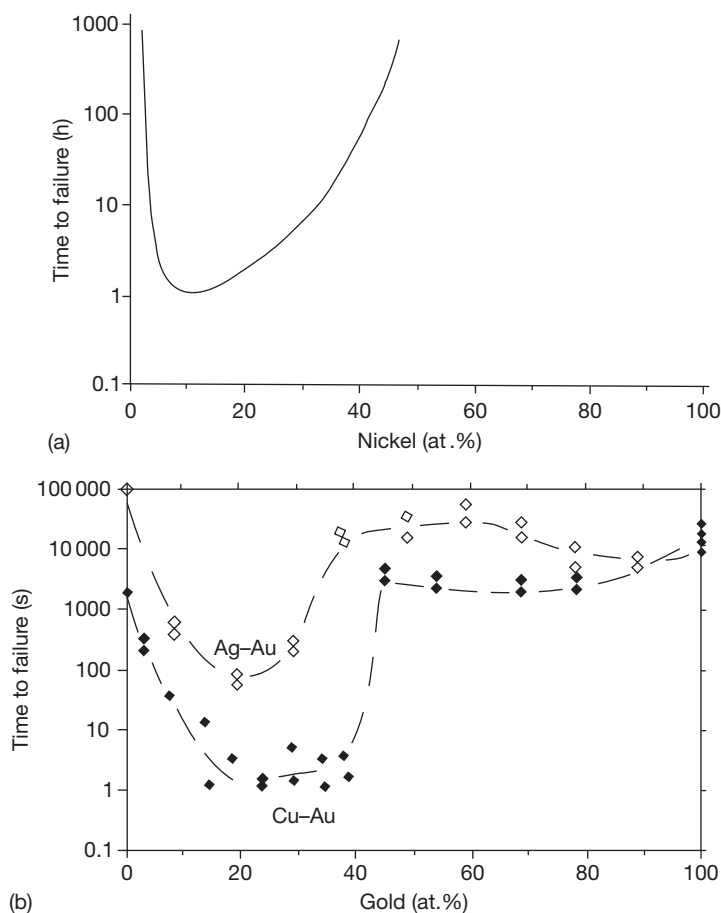


**Figure 5** (a) The 'Copson curve'<sup>13</sup> for chloride-induced SCC of stainless steels; (b) the corresponding behavior of noble metal alloys in aqua regia, Reproduced from Newman, R. C. *Stress Corrosion Cracking Mechanisms*. In *Corrosion Mechanisms in Theory and Practice*, 2nd ed; Marcus, P., Oudar, J., Eds.; Marcel Dekker: New York, 2002; pp 399–450.

### 2.09.3.3 Grain Boundaries, without Precipitation

Since the advent of modern analytical TEM and sample preparation techniques such as focused ion beam (FIB), few have gone back to the classical SCC systems and questioned what is at the grain boundaries, and whether SCC is dependent on a second phase at the boundary, or on some more subtle chemical effect such as equilibrium segregation of alloying elements or impurities. Regarding the case of carbon steel in hot caustic or nitrate solutions, it has been known from the time of H.H. Uhlig<sup>26</sup> that SCC does not occur, or anyway is much more difficult, in 'pure' iron. But it is not clear whether carbide precipitation, or merely monolayer segregation of carbon or some element, is required for SCC. Modern techniques, including atom-probe field ion microscopy provide

some answers, but also raise questions.<sup>27</sup> Most likely, in the case of carbon as the only impurity, fine carbides are required, but we do know that phosphorus and even molybdenum can induce SCC by pure segregation, without carbides (although carbides make matters worse).<sup>28</sup> In a related study, it was shown that an amorphous Fe–P alloy, simulating the grain boundary composition of a segregated alloy, showed enhanced anodic activity in the right potential range to explain the SCC observations.<sup>29</sup> This research was inspired by a classic study on steam-turbine rotor steel by J. F. Newman.<sup>30</sup>

The literature on grain boundary segregation and SCC has become quite large. For example, sulfur is a strong grain boundary segregant in nickel, and causes intergranular corrosion and/or SCC, depending on the conditions.<sup>31</sup> Magnesium segregation has been

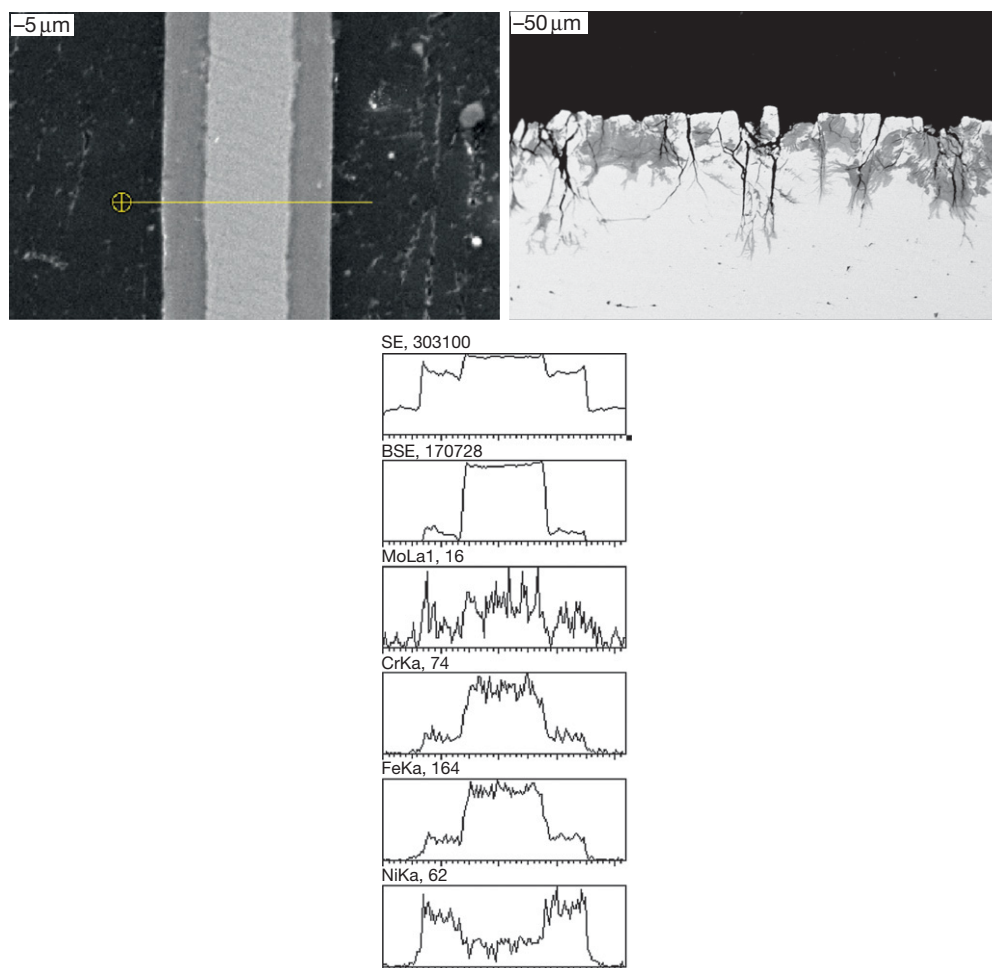


**Figure 6** Secondary electron image and matching line profile across a 316SS foil exposed to 50% NaOH at 140 °C for 20 h, and SCC occurring in the same condition. Reproduced from Deakin, J.; Dong, Z.; Lynch, B.; Newman, R. C. *Corros. Sci.* **2004**, 46, 2117–2133.

implicated in SCC of Al–Mg and Al–Mg–Zn alloys.<sup>32</sup> But it would not be sensible to conclude that all intergranular cracking (in the absence of precipitation) is caused by segregation. For example, there is no evidence that this is the case in solid-solution alloys like brass (in aqueous ammonia) or AuCu, AuAg, etc. – in these dealloying systems, it is more likely that the dealloyed layer is simply weaker at the grain boundary – not surprisingly, because it is known that in dealloying, individual grains retain their gross orientation, so a grain boundary is an awkward site for the nanoporosity-formation process to negotiate, leaving inevitable weakness (lack of connection of nano-ligaments across the grain boundary)<sup>33</sup> – **Figure 10**.

Once we consider temperatures in the 300–330 °C range, as in nuclear power plants, intergranular SCC

may start to merge with low-temperature creep fracture, and clean boundaries may actually be more susceptible than those with precipitation. Hydrogen from corrosion may be facilitating such fractures. Arioka *et al.*<sup>34</sup> claimed common evidence for creep-like phenomena including cavities and grain-boundary nickel enrichment in tests of types 304 and 316 steels in both air (at 450–550 °C) and simulated pressurized water reactor (PWR) water (at 360 °C). We await conclusive evidence on the latter, but this is potentially a very important advance. Recently, the same group has argued that intergranular SCC of carbon steel can occur by a hydrogen-assisted creep-like mechanism near reactor operating temperatures,<sup>35</sup> a phenomenon of interest to operators of Canadian CANDU plants, which have carbon-steel feeder pipes. It has also been shown that creep



occurs in Alloy 600 (Ni–16Cr–9Fe) at 360 °C and can be enhanced by hydrogen absorbed from the environment,<sup>36</sup> although a definite role of such creep in SCC has not been established. Again, carbide precipitation at grain boundaries is beneficial. Ingress of oxygen into grain boundaries is probably the key factor in this case, and is discussed later.

Under neutron irradiation at water reactor operating temperatures, stainless steels and nickel base alloys become harder owing to atom displacement and the formation of dislocation loops, and eventually, can suffer from irradiation-assisted SCC (IASCC).<sup>37</sup> Not only the increased hardness, but also

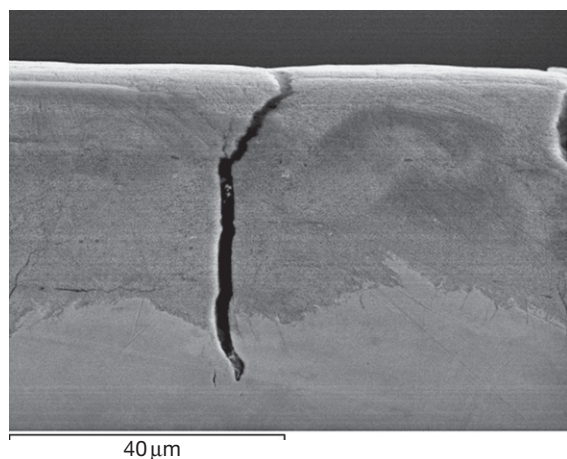


**Figure 7** Dealloying of type 310 stainless steel in 50% NaOH at 280 °C with hydrogen overpressure, showing possible crack injection into the unattacked substrate upon subsequent bending in air. Courtesy of Z.L. Coull, University of Toronto.

radiation-induced segregation (RIS) of alloying elements might contribute to the increased susceptibility to SCC. Vacancies created by irradiation migrate to grain boundaries, and the atomic mobilities are such that Ni is enriched and Cr depleted near these boundaries.<sup>38</sup> This is distinct from ordinary equilibrium segregation and is much wider than a single monolayer. Such phenomena are conveniently studied using proton irradiation, which induces less radioactivity than neutrons, and enables SCC testing to be done in an ordinary laboratory with comparable material properties to neutron-irradiated material.<sup>39</sup> Using such methods, it was shown that light annealing removed some small defects and suppressed SCC without changing significantly the hardness or the RIS.<sup>40</sup> The likely reason is that the small defects were promoting intense strain localization at grain boundaries by a process called dislocation channeling, and suggests that this – not segregation or hardness *per se* – was the primary cause of SCC.<sup>41</sup> Nevertheless, by adding oversized solutes such as Zr, RIS could be reduced, and this did reduce the susceptibility to SCC.<sup>42</sup>

The strain localization induced by neutron irradiation is the most extreme example of a general principle that SCC is more likely – and will occur under milder loading conditions – the more localized is the deformation at the crack tip. This can be illustrated as shown in [Figure 11](#).

#### 2.09.3.4 Grain Boundary Precipitation

The most notorious example of SCC due to grain boundary precipitation is that of weld-sensitized

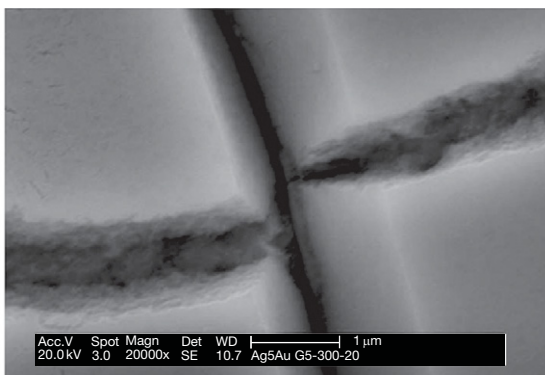
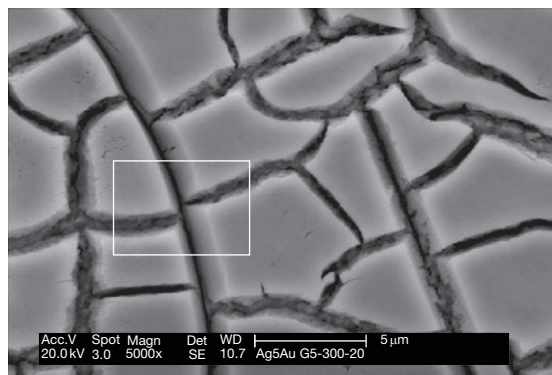


**Figure 8** Dealloyed layer formed on an unstressed 95Ag–5Au (a/o) alloy in 0.77 M HClO<sub>4</sub> at 20 °C. The layer was grown by applying an anodic current density of 5 mA cm<sup>−2</sup> for 300 s. We can see that a well-defined nanoporous metal layer is formed, even at this low Au content, and obviously must have a very high residual Ag content. The propensity of dealloying to induce tensile stress by lattice shrinkage is also evident – this is part of the reason why alloys crack under such mild mechanical conditions compared with pure metals. Courtesy of N.A. Senior, PhD thesis, University of Manchester, 2004.

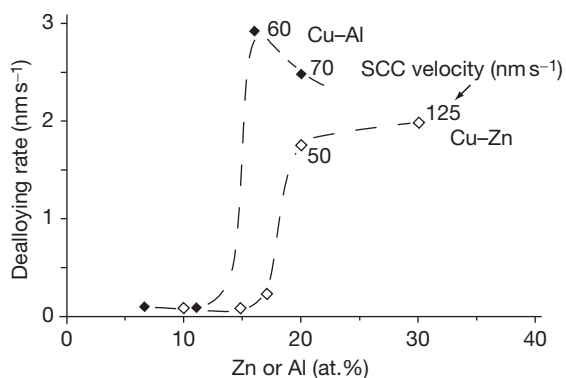


**Figure 9** SCC and dealloying of Cu–Zn and Cu–Al monocrystals in cuprous ammonia solution as a function of solute content. Reproduced from Newman, R. C. *Stress Corrosion Cracking Mechanisms*. In *Corrosion Mechanisms in Theory and Practice*, 2nd ed; Marcus, P., Oudar, J., Eds.; Marcel Dekker: New York, 2002; pp 399–450.

austenitic stainless steel (type 304SS) in slightly oxidizing hot water in boiling water reactor (BWR) nuclear power plants.<sup>43,44</sup> The cost of this cracking to the industry, in terms of plant availability, was massive through the 1970s and 1980s (it is interesting to recall that even this cracking was not detected in the laboratory until the introduction of slow strain rate testing). Chromium depletion adjacent to the grain boundary carbides (generally  $\text{Cr}_{23}\text{C}_6$ ) localizes corrosion and causes the cracking. This topic has probably been studied ‘to death,’ and cracking is well under control in those plants that still have 304SS – hydrogen is added to the water in stoichiometric excess compared with oxygen (and other oxidants produced by radiation, principally hydrogen peroxide), and noble metals are plated out on the plant surfaces to catalyze the hydrogen oxidation half-reaction and, thus, ensure that the conditions remain net-reducing.<sup>45</sup>

Although sensitized stainless steel is rather ‘old hat,’ and scarcely exists in modern plants that use low-carbon or stabilized austenitic steels, new insights are still being produced in studies that use low-temperature SCC of sensitized material as a model system to explore fundamental geometric features of SCC.<sup>46</sup> This kind of SCC, which generally occurs in solutions of partially reduced sulfur species (between sulfate and sulfide in oxidation state), is easy to study and amenable to incorporation into advanced tools such as synchrotron light sources. Originally, it was called ‘polythionic acid SCC’<sup>47</sup> because such acids (chiefly tetrathionic acid,  $\text{H}_2\text{S}_4\text{O}_6$ ) were believed to be produced in refinery

equipment by the reaction of iron sulfide scales with oxygen and water. Later both 304SS<sup>48</sup> and Alloy 600 (Ni–16Cr–9Fe)<sup>49,50</sup> were shown to be susceptible to SCC in dilute, aerated thiosulfate ( $\text{S}_2\text{O}_3^{2-}$ ) solutions. Thiosulfate was also the only soluble aggressive species detected in one study of the reaction of FeS with aerated water.<sup>51</sup>

Apart from sensitized stainless steels, the main materials where grain-boundary precipitation is implicated in SCC are aluminum alloys, and especially those of high strength (2000 series, 7000 series, 8000 (Al–Li) series) used in aircraft. SCC can occur in lower-strength 5000 series (Al–Mg–X) alloys<sup>52</sup> when reactive precipitates are present at grain boundaries, such as  $\text{Al}_3\text{Mg}_2$ , the  $\beta$  phase in the binary Al–Mg system, and in other conditions when the stresses are severe. So this is different from SCC of sensitized stainless steel, where it is the solute-depleted zone, not the particle, that is sensitive to corrosion. At the other extreme is the SCC of binary Al–Cu alloys aged to produce Cu-depleted zones adjacent to grain boundaries,<sup>53</sup> where the Cu-depleted material dissolves faster, at a given potential, than the matrix (there are doubts as to whether this should really be called SCC, as nearly all grain boundaries are attacked – it is more like a strain-accelerated intergranular corrosion). Regarding the highest-strength Al–Zn–Mg–Cu (7000 series) alloys, the roles of reactive particles and solute-depleted zones have been controversial, but it appears – currently – that the reactive  $\text{MgZn}_2$  particles are implicated. Such an explanation provides a neat rationalization of the protective effect against SCC of overaging such alloys, as is done for all aircraft construction (the so-called T7 temper). More copper enters the precipitates with overaging, and reduces their excess reactivity compared with the matrix<sup>54</sup> – **Figure 12**.

Recently discovered examples of precipitation effects include the presence of boron, presumably as nickel boride, at the grain boundaries of Monel 400, leading to intergranular corrosion and SCC.<sup>55</sup> However, it is doubtful that such precipitates are necessary in the general case of intergranular corrosion of Monel<sup>24</sup> – they merely accelerate it by providing a nickel-rich path.

### 2.09.3.5 Yield Strength, Including Cold Work Effects

Most SCC is exacerbated by high yield strength, and there must be more than one reason for this behavior – perhaps four or five – depending on the alloy

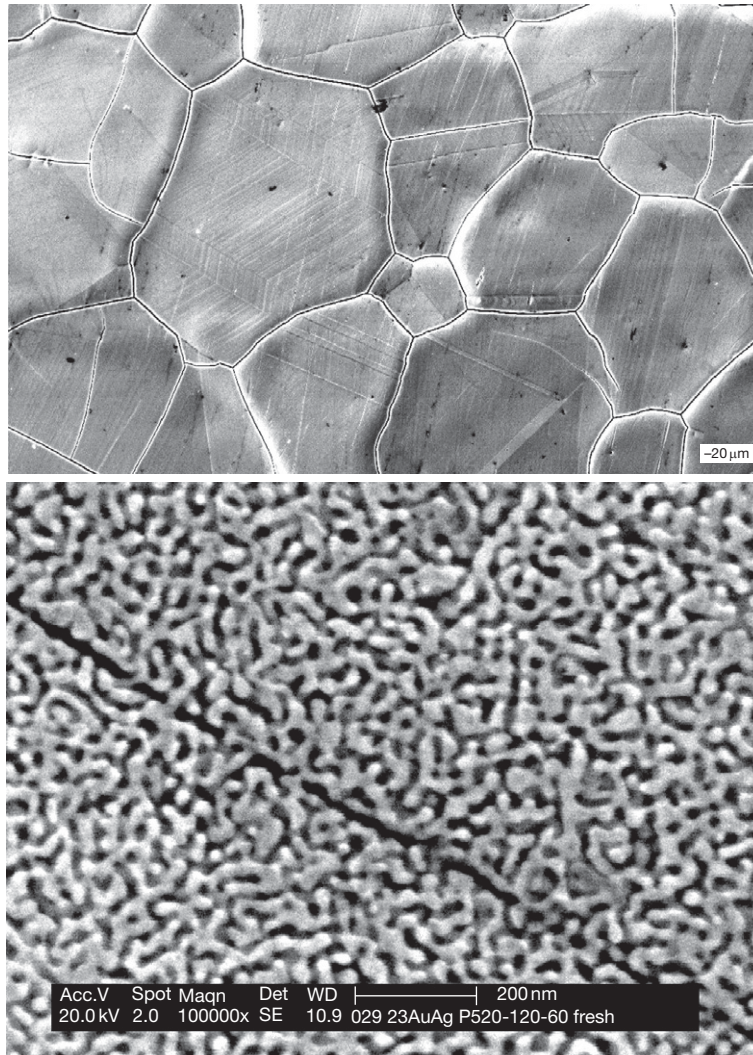


**Figure 10** Spontaneous intergranular fracture of dealloyed AuAg, and the explanation in terms of limited connection of nano-ligaments across grain boundaries. Reproduced from Senior, N. A.; Newman, R. C. *Nanotechnology* **2006**, *17*, 2311–2316.

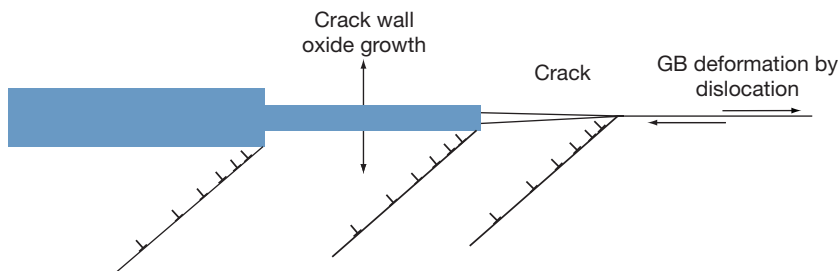


**Figure 11** Enhancement of intergranular SCC by strong shear band intersection with grain boundaries, as seen in cold worked and especially neutron-irradiated austenitic steels. Adapted from Was, G. S. Proceedings of the 11th International Conference on Environmental Degradation of Materials in Nuclear Power Systems – Water Reactors, American Nuclear Society, La Grange Park, IL, 2004; pp 965–985.



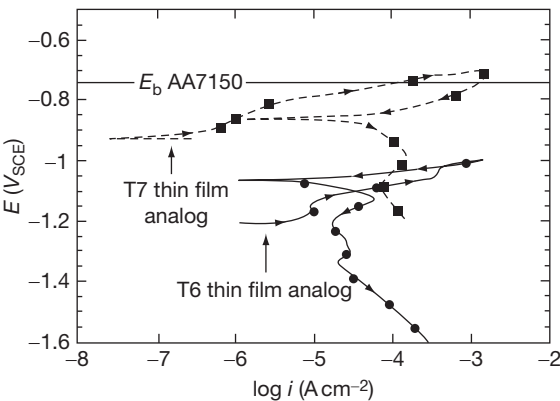


**Table 3**

Composition of AA7150-T6 constituents measured by analytical TEM (five replicate measurements were made on a single sample)

Element	Matrix	SDZ	Precipitate
Al	92	95	74
Mg	4.6	3.8	11
Zn	2.5	0.8	12
Cu	0.9	0.4	3.3

**Table 4**

Composition of AA7150-T7 constituents measured by analytical TEM (five replicate measurements were made on a single sample)

Element	Matrix	SDZ	Precipitate
Al	94.5	96	52
Mg	3.1	2.6	17
Zn	1.3	0.8	1.5
Cu	1.1	0.3	30

**Figure 12** Demonstration that the reduced anodic activity and (probably) SCC susceptibility of grain boundaries in overaged high-strength aluminum alloy 7150 is due to more copper entering the  $Mg_2Zn$  precipitates. Reproduced from Ramgopal, T.; Gouma, P. I.; Frankel, G. S. *Corrosion* **2002**, 58, 687–697.

system. However, we can make certain generalizations. In very strong steels, exposed to ambient-temperature water (with or without salts), there is no doubt whatever that SCC is due to absorbed hydrogen. The crack path is commonly intergranular, along prior austenite grain boundaries, in tempered-martensite microstructures, but can also be transgranular, cleavage-like in these and in other, more exotic steels such as precipitation strengthened alloys.<sup>56</sup> If we add hydrogen sulfide to the environment, as in sour gas systems, lower-strength steels become susceptible, although ordinary carbon steel remains essentially immune to SCC (it may suffer from hydrogen pressure-induced cracking – see **Chapter 2.08**,

**Environmentally Assisted Cracking Overview**). A theme in recent oil-and-gas material development has been the gradual (very gradual) increase in the yield strength of low-alloy steel that can be employed in sour-gas applications.<sup>57</sup> Stainless steels based on Fe–13Cr (–Ni...–Mo...) have also been developed for mildly sour systems.

There is a class of SCC problem in carbon steels that involves apparently innocuous near-neutral-pH water, yet occurs with alarming frequency on the external surfaces of high-pressure gas transmission pipelines.<sup>58–60</sup> Usually the problem can be traced to some dynamic loading, such as freezing and thawing, and it is thought that SCC cannot occur under perfectly static loading, consistent with a hydrogen effect in low-strength steel, but stronger steels than the usual X-65 grade, such as X-80, seem not to require this ‘fatigue’ component; if such steels are installed in the field, the risk of SCC may be increased (but there is much we still do not understand about this phenomenon).

Since we know that  $H_2S$  increases the percentage of discharged hydrogen that enters the steel, its special severity clearly reflects a correlation between SCC and the concentration of atomic hydrogen that develops at some special site near the crack tip. Exactly what this site is, and what the hydrogen does when it gets there, are still under debate, but the general correlation is secure; we give a recent example of such reasoning.<sup>61</sup> *Ab initio* quantum-chemistry modeling is starting to illuminate some old questions such as – how does hydrogen interact with dislocations?<sup>62</sup> The current view seems to be that hydrogen can either promote or hinder dislocation motion, depending on factors such as strain rate and presence of other interstitials, as well as the crystal structure of the material, presence of interfaces, etc. Spectacular studies of hydrogen-dislocation interactions have been done using *in situ* transmission electron microscopy.<sup>63</sup> Also the growing interest in metals as storage media in hydrogen technology has provided complementary information.<sup>64</sup>

To quantify the SCC of high-strength steels, fracture mechanics techniques are indispensable. Generally speaking,  $K_{Ic}$  falls gradually with increasing yield strength, while  $K_{Isc}$  falls steeply above a certain yield strength value – **Figure 13**.

High-strength steel wire (prestressing steel) is more resistant to SCC than other material forms because it has a highly elongated grain structure, and an intergranular crack has to take a tortuous path to cross the wire.<sup>65</sup> However, failures have occurred in such

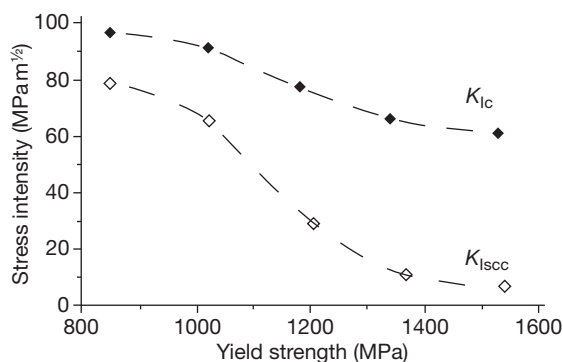


**Figure 13** Classical dependence of fracture toughness ( $K_{Ic}$ ) and SCC threshold in seawater ( $K_{Isc}$ ) on yield strength, for old-fashioned ultra-high strength AISI 4340 steel. Reproduced from Newman, R. C. *Stress Corrosion Cracking Mechanisms*. In *Corrosion Mechanisms in Theory and Practice*, 2nd ed; Marcus, P., Oudar, J., Eds.; Marcel Dekker: New York, 2002; pp 399–450.

material. A similar effect protects sheet made from high-strength 2000-series (Al–Cu) alloys.

The effects of yield strength on SCC become murky when we depart from high-strength steels. For aluminum alloys, maximum sensitivity to SCC is commonly seen in the underaged or peak-aged condition, and the beneficial effect of overaging (in the most sensitive AlZnMgCu systems) is thought to involve alloying of Cu into the  $MgZn_2$  precipitates at the grain boundaries. So, the root cause of the beneficial effect is related to the corrosion resistance – that is, anodic kinetics – of the grain-boundary phase, but hydrogen may be the actual cracking agent. Often *preexposure embrittlement* is observed – the material will crack in air or an inert environment after precorrosion<sup>66</sup> – **Figure 14**. Usually this is due to hydrogen, but a further complication is that cracking can even occur without water exposure (especially at slightly elevated temperature) by a creep-like mechanism<sup>67</sup> which sometimes involves a solid-metal-embrittlement type of action of internal lead particles.<sup>68</sup> Generally speaking, in these materials, the effect of yield strength is subordinate to microstructural considerations.<sup>69</sup> A similar picture presents itself when we consider  $\beta$ -titanium (bcc-titanium) alloys<sup>70–72</sup> – there is no doubt that hydrogen can embrittle the material, but the corrosion reaction has to be considered as well and the effect of yield strength *per se* cannot be divorced from microstructure. Incidentally, the SCC of titanium alloys has an exciting history – in the 1960s and early 1970s a high-strength  $\alpha$ – $\beta$  alloy was under consideration for the US supersonic passenger airliner project,

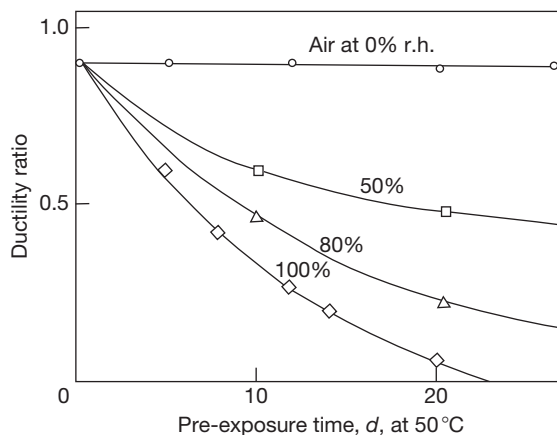


**Figure 14** The preexposure embrittlement phenomenon in AlZnMg alloys. Reproduced from Scamans, G. M.; Alani, R.; Swann, P. R. *Corros. Sci.* **1976**, *16*, 443–459.

but the project was abandoned – partly because of an energy crisis, and partly because of unanticipated SCC of the alloy when precracked.<sup>73</sup> The Apollo program was also plagued by SCC incidents, one involving methanol, which was one of a number of exotic environments found to cause SCC during that period.<sup>74</sup> The history of SCC from 1965 to 1990, including such practical experience, was reviewed by Procter and Newman.<sup>75</sup>

Solid-solution alloys that are not known to be susceptible to hydrogen also show deleterious effects of higher yield strength, and in particular cold work, on SCC. This is highly topical in the nuclear power industry, not only because certain components are inherently coldworked during manufacture (e.g., steam-generator tubes are straightened) but also because surface damage and surface condition generally are known to influence, critically, the initiation of SCC. So, whereas early failures of 304SS piping in BWR systems were confined to weld-sensitized material, nonsensitized but coldworked material began to show failures later on; such cracking will even occur in reducing conditions with hydrogen overpressure,<sup>76</sup> where it is associated with intense strain localization at grain boundaries as revealed by cross-sectional TEM.<sup>77</sup> Such localization, which we discussed earlier in the context of neutron irradiation, is probably fundamental to SCC and to the effect of yield strength, so we may formulate a rule along the following lines – *other things being equal, SCC will occur under milder loading conditions, the more localized is the plasticity near the crack tip*.

Using advanced nanoscale analytical techniques, it has been shown (Lozano Perez, unpublished) that



cold worked austenitic stainless steel exposed to PWR primary water undergoes a kind of internal grain boundary Cr oxidation and elemental Ni enrichment quite similar to what occurs in Alloy 600 in the annealed condition. Apparently the shear bands or twin deformation bands intersecting the grain boundary enhance oxidation along the grain boundary as well as along themselves. So, one could speculate that cold work removes the Fe-induced barrier to internal oxidation of Cr, unifying the mechanism of low-potential SCC in the Ni- and Fe-rich materials.

It should be mentioned that there is a related but different interpretation of the effect of cold work, or of yield strength generally<sup>76,78</sup> – this can only be understood by referring to details of the slip-dissolution model (SDM) for SCC, so we defer the discussion to that section.

Reverting to higher-strength steels for a moment, a problematic phenomenon in power generation is the SCC of turbine components made of quenched and tempered low-alloy steels. This does occur more easily in stronger material, but does not seem to be a hydrogen effect, and occurs at elevated temperatures where hydrogen does not affect the properties of steel because it cannot be localized for long enough near the crack tip.<sup>79</sup>

#### **2.09.4 Crack Nucleation, Crack Coalescence, 3D Crack Morphology, Effect of Distributed Grain Boundary Character**

It is fundamental to SCC that multiple cracks, or at least branched cracks, always occur. Whenever that happens, the nearby crack segments mutually shield each other from the local stress, so that we can say each crack has an effective  $K_I$  value that is less than the nominal one. An important stage in the life of a crack is the point where it becomes connected along the free surface for a distance similar to the specimen or component thickness. This process of crack coalescence was studied by Parkins using mainly intergranular carbonate–bicarbonate SCC of steel<sup>80,81</sup> – **Figure 15** – and is also of key importance in the other type of external pipeline cracking – so-called ‘near-neutral pH,’ transgranular SCC<sup>82</sup> – **Figure 16**. Akashi and others have created detailed conceptual models, suitable for statistical treatment, in which there is a long delay in the formation of a free-running crack<sup>83</sup> – **Figure 17**.

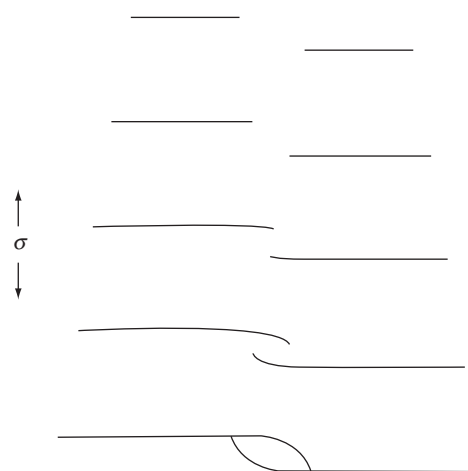


**Figure 15** Coalescence of SCC on a surface (increasing time from top to bottom). Adapted from Parkins, R. N.; Singh, P. M. *Corrosion* **1990**, *46*, 485–499.

The crack coalescence phenomenon does not in itself imply anything distributed about the grain boundary properties – simply that only so many cracks per unit area can nucleate and grow for any distance. But recently the idea of grain boundary engineering has become a popular way to try to suppress, or at least understand, the progress of SCC in industrial alloys.<sup>46,84–87</sup> The development of software for automatic indexing of backscattered electron diffraction (EBSD) patterns was the key technical advance that made this possible. Recently this has been combined with 3D tomographic X-ray imaging in a synchrotron light source – **Figures 18 and 19**. The idea of grain boundary engineering is to create as many ‘special’ grain boundaries as possible within the microstructure by thermomechanical treatment. Annealing twins have special boundaries, but do not in themselves obstruct crack growth to any great extent; the crack easily bypasses the long boundaries. The boundaries that are most important are those that have a particular periodicity of registry between the lattices on either side, not only twin boundaries but also those of higher-order periodicity.<sup>88</sup> Such boundaries are less likely to have segregation of impurities, or detrimental forms of precipitation, and form ductile bridges that are believed – in one theory<sup>46</sup> – to shield the crack tip from part of the applied nominal stress intensity. Under sensitization treatment, they have delayed chromium carbide precipitation. Ordinary industrial alloys already contain special grain boundaries, often in highly variable fractions, and the challenge is to

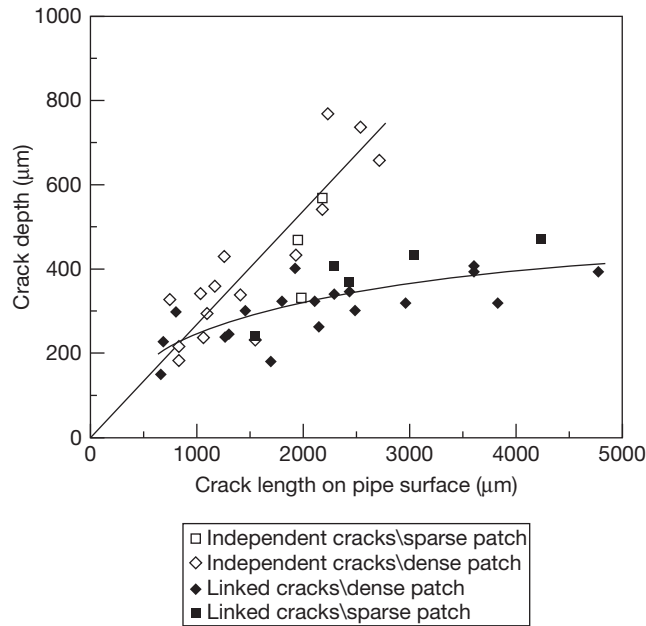


**Figure 16** Behavior of crack colonies on a pipeline subject to near-neutral-pH SCC. Reproduced from Chen, W.; King, F.; Vokes, E. *Corrosion* **2002**, 58, 267–275.

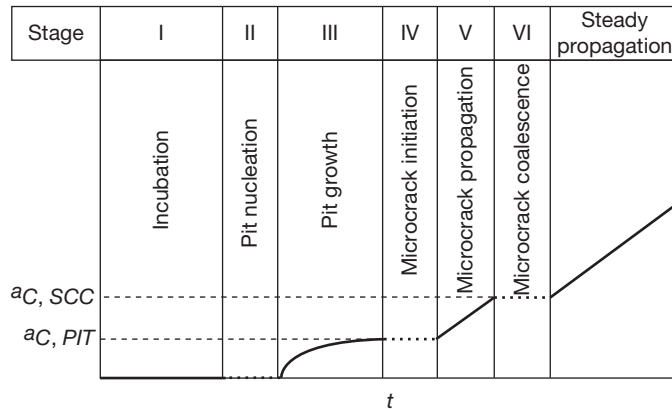


**Figure 17** Life history of SCC, according to Akashi and Nakayama. Reproduced from Akashi, M.; Nakayama, G. *Effects of the Environment on the Initiation of Crack Growth*; ASTM STP 1298, Philadelphia, PA, 1997; pp 150–164.

increase this fraction whilst maintaining a reproducible, flexible, and economical processing route. A drawback is sometimes that the thermal treatments required to obtain high fractions of special boundaries have to be done at lower than normal temperature, which carries certain hazards such as deleterious precipitation reactions.

EBSD is not only able to index a microstructure – it also gives information on plastic strains and their localization.<sup>89</sup> An important result is that ‘special’ grain boundaries are soft – they do not sustain

dislocation pile-ups. This is a further reason why they are resistant to SCC, which is greatly exacerbated by strain localization as we already discussed.

When SCC occurs in a microstructure with distributed grain boundary properties, the crack initially develops a ramified 3D morphology with uncracked ligaments. There are slightly different ways to approach the problem of cracking resistance in such a geometry. The simplest approach is based on percolation theory<sup>90</sup>; under slow strain rate conditions, where ductile ligaments will always be torn

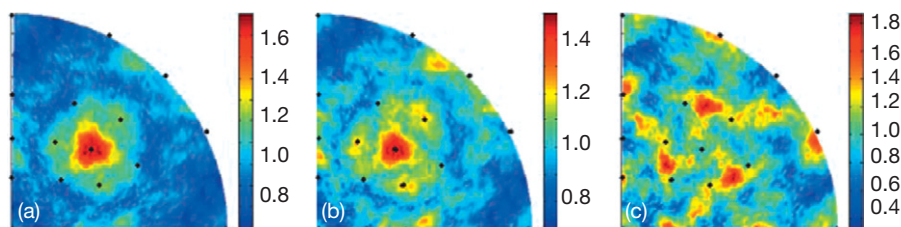


**Figure 18** Capability of EBSD and tomographic imaging to identify the crack path in 3D for intergranular SCC and identify the boundaries that do, or do not, crack. Reproduced from King, A.; Johnson, G.; Engelberg, D.; Ludwig, W.; Marrow, J. *Science* **2008**, 321, 382–385.

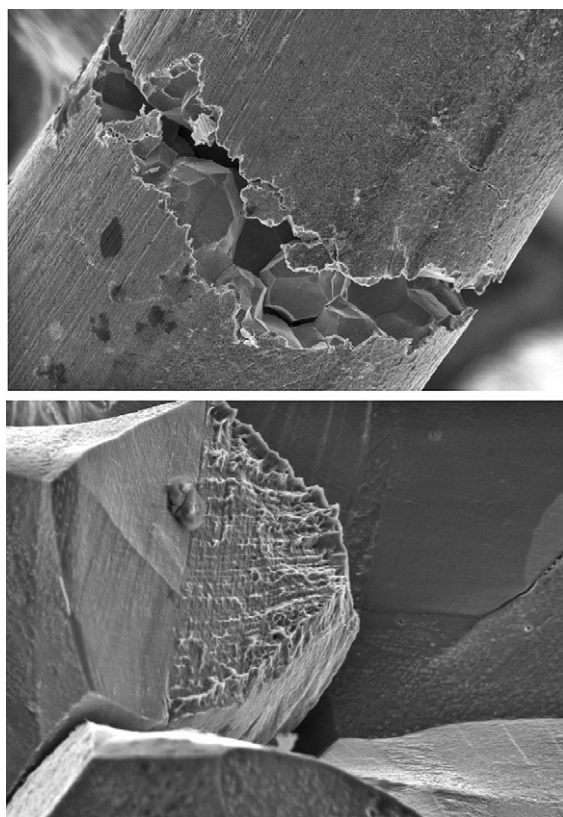


**Figure 19** Appearance of the cracked sample for the kind of experiment shown in [Figure 18](#), and illustration of the presence of ductile ligaments on the fracture surface. Courtesy of D.L. Engelberg.

apart, macroscopic SCC starts to occur when a certain fraction of grain boundary segments are susceptible and can form a connected 3D network (where connection is allowed at edges as well as faces). This percolation threshold is only  $\sim 23\%$ , and such a microstructure would never develop a macroscopic crack under constant load conditions. The same authors noted that for fractions of susceptible boundaries greater than  $89\%$ , no ligaments should form and

SCC should become ‘completely brittle.’ Later the actual grain-boundary Cr contents were taken into account in such an approach.<sup>91</sup> A more sophisticated approach entails restricting the definition of ‘connection’ to grain faces, and incorporating stress via the inability of the crack to propagate in unfavorable directions<sup>84,92</sup> – [Figure 20](#) – but is still essentially a modified percolation concept. In contrast, the model developed in Manchester<sup>93–96</sup> has elements of percolation, but places great emphasis on the shielding effect of uncracked ligaments, by actually calculating the magnitude of such shielding.

Of course, the physics of granular networks can be taken further than this – such networks and their behavior under fracture, dielectric breakdown, etc. have been a favorite topic in statistical physics.<sup>97</sup>

### 2.09.5 Crack Chemistry in SCC

A crack is, literally, a crevice, so we do not need to reiterate concepts that can be found in [Chapter 2.03, Crevice Corrosion](#). Reviews of crack chemistry are available,<sup>98</sup> and a second conference ‘CCPCC2’ was held in 2009 to mark the twenty-fifth anniversary of a landmark conference at the National Physical Laboratory in 1984.<sup>99</sup>

An important aspect of SCC that relates to local chemistry is the evolution of cracks from pits or other localized corrosion sites. There is a mechanics aspect, in that a pit creates a stress concentration, but often the local solution chemistry is the dominant factor. For low-alloy steels, a recent review addressed both the chemistry and mechanics aspects,<sup>100</sup> but the premier example of such a sequence occurs in the chloride-induced SCC (Cl-SCC) of austenitic or duplex stainless steels. This is less well-known than it might be, because much of the published discussion is in obscure sources. [Figure 21](#) shows the early stage of Cl-SCC from a site of crevice corrosion.

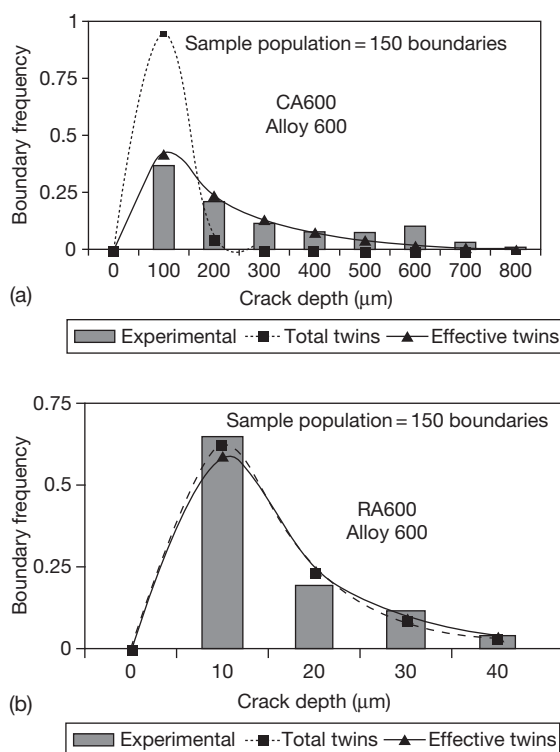


**Figure 20** Grain boundary engineering of Alloy 600 against SCC, compared with a model based on connectivity of grain faces (CA – normal; RA – engineered). Reproduced from Lehockey, E. M.; Brennenstuhl, A. M.; Thompson, I. *Corros. Sci.* **2004**, 46, 2383–2404.

Whenever SCC occurs in stainless steel in an aqueous halide environment, the local condition in the crack is similar to that in an active, strongly acidified, but slowly dissolving (because very tight) crevice. This was stated most clearly by Tsujikawa,<sup>18,101</sup> who first argued that the lower critical potential for chloride-induced SCC (CI-SCC) of austenitic stainless steel was simply the repassivation potential (sometimes called protection potential) for crevice corrosion. This immediately replaced fanciful notions such as the critical potential being due to the onset of adsorption of some special species at the crack tip,<sup>102</sup> which are still taken seriously in some textbooks. Given that the propagation rate or velocity ( $v_{\text{corrosion}}$ ) of localized corrosion varies with the geometry and potential because of diffusional or ohmic control of the dissolution rate, we can readily imagine that certain conditions would favor localized corrosion over SCC, or vice versa, even at a given temperature. Then when we factor in temperature, the apparent activation energy that applies to the crack velocity

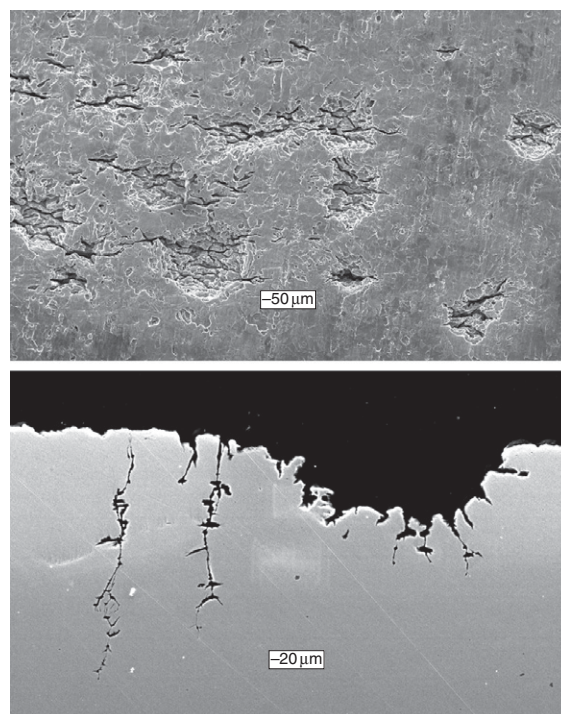


**Figure 21** Early stages of CI-SCC of austenitic stainless steel at low temperature (80 °C), starting from a corroding crevice. Courtesy of S. Wang, PhD thesis, UMIST, 2002.

( $v_{\text{crack}}$ ) is higher than that for  $v_{\text{corrosion}}$ . Obviously, SCC can only occur if  $v_{\text{crack}}(T, \text{alloy}) > v_{\text{corrosion}}(T, \text{alloy}, \text{potential})$  – **Figure 22**.

Such a framework can explain the commonly observed critical temperature for CI-SCC of basic austenitic grades (304[L], 316[L]), as indicated in **Figure 23**. For all but the most extremely slow (i.e., blocked or stifled) localized corrosion, the slowest sustained rates of penetration tend to lie in the range of a few to 10 mm year<sup>-1</sup>. This is also the order of magnitude of  $v_{\text{crack}}$  at 50 or 60 °C. But in order for a crack to initiate from a small pit that is growing at 100 or even 1000 mm year<sup>-1</sup>, the temperature must be much higher, so that the condition  $v_{\text{crack}} > v_{\text{corrosion}}$  is maintained. Thus, when CI-SCC occurs at very high temperatures, it generally initiates from small pits, but at the lowest temperatures, it initiates from underdeposit corrosion sites – or sometimes in tight metal–metal or metal–polymer crevices. SCC of 304SS or 316SS can even be made to occur at room temperature by depositing MgCl<sub>2</sub> (or sea salt, which amounts to the same thing) on the steel, and controlling the relative humidity at a



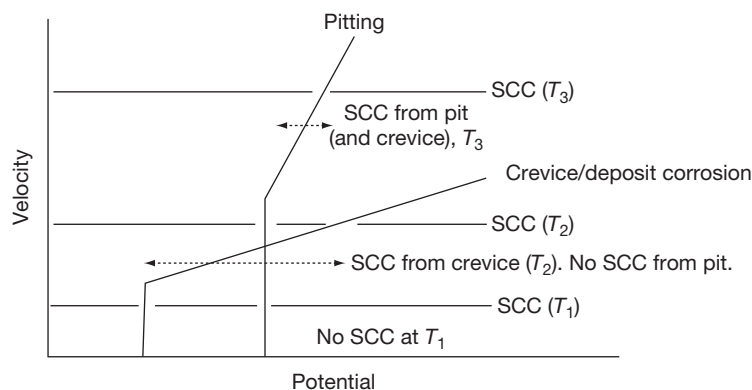


**Figure 22** Potential dependence of SCC and localized corrosion in austenitic stainless steel, based on the work of Tsujikawa.

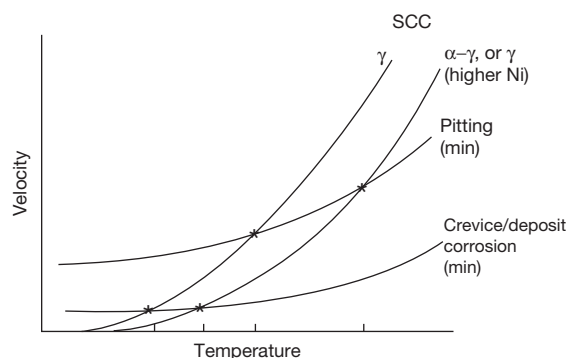


**Figure 23** Origin of the 'critical' temperature for Cl-SCC of austenitic or duplex stainless steel, based on the work of Tsujikawa.

value in the 30–35% range where the surface remains wetted by nearly-saturated  $\text{MgCl}_2$  solution.<sup>103,104</sup> Recently authors have rediscovered this kind of effect<sup>105</sup> – and the role of  $\text{MgCl}_2$  (for the sea salt case) has become mildly controversial.<sup>106,107</sup> But the Japanese data from the 1980s were so convincing that there does not appear to be much room for doubt as to the role of Mg. The true application limits of duplex stainless steels are made apparent when such testing is used – a temperature limit of 100–110 °C seems to emerge,<sup>106</sup> contrary to the optimistic assessments made by alloy manufacturers when testing was only being done in NaCl solutions. In further work on this issue, the role of carnotite ( $\text{KMgCl}_3$ ) would repay investigation. It is unlikely that the cases of easy SCC at low temperatures are associated with some Na-rich solution; more likely is that

evaporation experiments done to date have not gone to a high enough level of concentration (80 times at least). But it is also possible that the solids precipitated from seawater have a crevice effect, exacerbating SCC, that is absent when one starts from a binary mixture of NaCl and  $\text{MgCl}_2$ .

Tsujikawa's analysis shows very clearly that the atomistic mechanism of Cl-SCC is not slip-dissolution, but some kind of embrittlement – most likely film-induced cleavage.

The SCC velocity  $v_{\text{crack}}$  is affected strongly by nickel alloying, which lowers  $v_{\text{crack}}$  while leaving  $v_{\text{corrosion}}$  relatively unaffected – thus, as we move from types 304 or 316 stainless steel to type 310 (20% Ni) and eventually Alloy 800 (33% Ni), a higher and higher temperature is required for SCC. Eventually, somewhere above the nickel content of Alloy 800, SCC ceases altogether. This is envisaged – in Toronto anyway – as a parting limit for dealloying (see **Chapter 2.05, Dealloying**).

The situation in aluminum alloys is more complex, because the more susceptible grades are not solid solutions, and some phases are exceptionally reactive ( $\text{Al}_2\text{LiMg}$ ,  $\text{MgZn}_2$ ,  $\text{Mg}_3\text{Al}_2$ ). Even pure water or water vapor can attack such phases,<sup>66</sup> and does so in a peak-aged, high-strength  $\text{AlZnMgCu}$  alloy such as the 7075 grade, although salt water does so more rapidly, and causes more rapid SCC. As mentioned previously, the beneficial effect of overaging on SCC resistance of  $\text{AlZnMgCu}$  alloys is thought to be due to more copper being incorporated into  $\text{MgZn}_2$  precipitates, thus ennobling them. In underaged  $\text{AlCu}$  alloys, localized corrosion attacks Cu-depleted regions adjacent to the grain boundaries

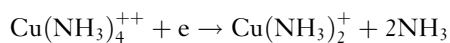


(this is hardly SCC at all, more like intergranular corrosion). So the generalization that SCC is associated with localized corrosion, for passive alloys in halide solutions, remains intact, but has exceptions.

A key question that always arises when considering crack chemistry is – does the crack tip ‘feel’ the externally applied or naturally established electrode potential? Much ink has been spilled on this topic! Clearly, when the crack walls are quite active, it is difficult for the external potential to be thrown down the crack. But for relatively passive systems, such as titanium alloys, external polarization of the crack tip is possible. Importantly, even if there is a large IR potential drop down the crack, and the crack-tip potential is only slightly elevated from its local mixed or corrosion potential, there is a change in crack chemistry in accordance with the diffusion-migration balance for the nonreacting ions such as  $\text{Cl}^-$ . At room temperature, this is one order enrichment of  $\text{Cl}^-$  for every 59 mV ( $2.3RT/F$ ) of potential drop down the crack.<sup>108</sup> For sulfate, it should be one order for every 29.5 mV. This must be a major factor in the SCC of turbine disk steels in dilute condensate.<sup>79</sup> Similarly, crack chemistry also plays a role in the numerous SCC phenomena that occur in high temperature water, especially in the somewhat oxygenated water that is present in a BWR water circuit.<sup>44</sup> If the environment inside the crack were truly pure water, practically no ‘local cell’ action could develop between the inside and outside of the crack, even if oxygen is present outside. In practice, there can be traces of sulfate derived from ion-exchange resin beads, and possibly dissolution of sulfide inclusions in the metal. The crack concentrates these anions by an electromigration process as described above, to the extent that metal cations from the alloy are soluble under the given crack conditions to balance their charge. The electrode potential at the crack tip may be only slightly shifted positive of its open-circuit value, but the open-circuit potential difference between the inside and outside drives the anion accumulation. When oxygen is removed, the potentials inside and outside the crack approach each other and the anion accumulation is less.

A specialized type of crack chemistry consideration occurs in ammonia-SCC of brass.<sup>109</sup> If we immerse a stressed brass sample in dilute – say 1 M – aqueous ammonia in a beaker open to the air, and wait, after a while we see the solution turning blue – this is the cuprammonium II complex ion,  $\text{Cu}(\text{NH}_3)_4^{2+}$ . Shortly after that, the sample starts to crack. The cathodic reaction is the reduction of the

Cu II ammonia complex to the Cu I complex:



which may, depending on the conditions, reprecipitate as a black tarnish film consisting mainly of  $\text{Cu}_2\text{O}$  with some oxidized zinc.

Deep inside the crack, there are no Cu II ions – the crack walls efficiently scavenge these and reduce them to Cu I (so the old notion that adsorption of these ions causes cracking<sup>102</sup> is untenable). The environment at the crack tip is really an ammoniacal Cu I solution (containing zinc), and is very nearly in equilibrium with the copper in the brass. Indeed, SCC occurs in a simulation of such a solution,<sup>110,111</sup> dealloying can be demonstrated electrochemically, and a convincing correlation between such dealloying and SCC was obtained for monocrystals of different zinc contents.<sup>22</sup> Both dealloying and SCC ceased below 20% Zn (intergranular SCC may persist to lower Zn contents) – see **Chapter 2.05, Dealloying**.

## 2.09.6 Role of the Environment in SCC

An important clue to the role of the environment came as soon as fracture mechanics techniques started to be used for SCC investigations: nearly all SCC shows a ‘plateau’ crack velocity at intermediate  $K_I$  values – see **Chapter 2.08, Environmentally Assisted Cracking Overview**. We have to take care that the extent of this region is not exaggerated in studies of ductile alloys,<sup>112</sup> where  $K_I$  becomes invalid because of large-scale yielding at the crack tip, but it is definitely a real phenomenon. So what does that tell us? It tells us that the mechanics are not controlling the crack velocity. So if the rate controlling process is not the mechanics, it must be something ‘chemical.’ The crack velocity could be controlled by:

- The rate of oxidation or dissolution at the crack tip (which in turn can be controlled by the local environment in the crack and the local – not free-surface – potential).
- The rate of hydrogen adsorption or diffusion.
- The rate of some surface diffusion process of metal atoms or ions, and possibly others.

For SCC that occurs in an electrolyte, electrochemical considerations dominate our thinking. There are about six distinct electrochemical circumstances where SCC occurs – **Figure 24**. They are:

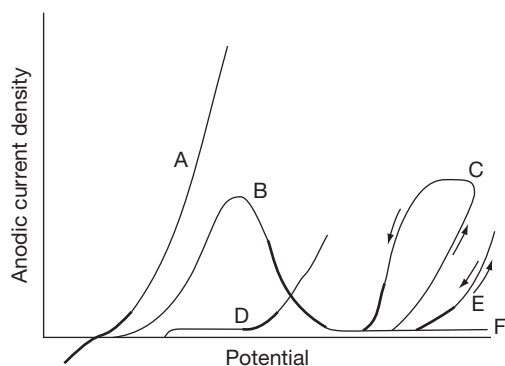


**Figure 24** Regions of potential (bold lines) where SCC is likely in given electrochemical circumstances – (A) Active system, near the corrosion potential (strong alloy, hydrogen effect). (B) Active–passive transition. (C) Localized corrosion system near the repassivation potential. (D) Dealloying system near the critical potential. (E) Mild transpassivity. (F) No special reactivity, but high temperature or other exacerbating factor on film growth.

- A more-or-less actively corroding state, where SCC is entirely or predominantly due to hydrogen absorption – for example, high-strength steel in salt water.
- A compromised or borderline passive state, where SCC seems to be due to some anodic process at the crack tip – for example, carbon steel in hot caustic, nitrate, or carbonate–bicarbonate.<sup>113</sup>
- A state of slow localized corrosion (slow because otherwise it would be faster than the cracking) in a halide solution – for example, austenitic stainless steel in hot chloride.<sup>16</sup>
- A state of dealloying (see **Chapter 2.05, Dealloying**) – for example, brass in ammonia solution.<sup>22</sup> This does not exclude a role of dealloying in some of the other categories.
- A state of mild transpassivity, for example, due to Cr VI dissolution in a stainless alloy.
- A stable filmed state, but where the film growth kinetics, especially at deformation features, are such as to allow a certain rate of cracking despite little or no dissolution – for example, cold-worked austenitic stainless steel in hot water.<sup>76</sup>

Also we have to consider various hard-to-classify systems where SCC occurs, but not much seems to happen electrochemically – for example, transgranular cracking of carbon steel in anhydrous liquid ammonia or ammonia–methanol,<sup>114,115</sup> or intergranular cracking of nickel alloy 600 in reducing hot water.<sup>116</sup> These are probably exotic forms of embrittlement, caused by nitrogen<sup>115</sup> and oxygen<sup>117–119</sup> respectively, rather than hydrogen. It was also

suggested, more speculatively, that transgranular SCC of carbon steel in  $\text{CO-CO}_2\text{-H}_2\text{O}$ <sup>120</sup> could be due to carbon embrittlement,<sup>121</sup> and that CO might be involved in SCC of carbon steel in oxygenated alcohols.<sup>122</sup>

Most, though not all, of these SCC schemes can be summarized as follows – SCC may occur, given the right metallurgy and stress, when the metal is passive, but not too passive. Most SCC requires some interaction between the environment and bare metal, and a passive film that forms almost instantaneously screens that interaction. Whether the actual crack growth occurs by purely anodic means, by hydrogen embrittlement, or by some other mechanism, is not always clear; Parkins' concept of the 'stress corrosion spectrum' – hydrogen effects at one end, dissolution at the other, remains valid today.<sup>123,124</sup> As a prelude to the next sections, we show '1980s' and '2000s' SCC spectra in **Figure 25**.

## 2.09.7 Anodic SCC Models

Since the 1940s, a popular scheme for the growth of SCC has been the accumulation of small dissolution or oxidation events at the crack tip, each caused by the rupture of some partially protective surface film – **Figure 26**. A popular term, probably coined by R.W. Staehle, is 'slip-dissolution,' recognizing that not all (or perhaps not any) of the oxidized metal remains actually dissolved in the small volume of solution inside the crack.

In the SDM, the plateau crack velocity is explained by postulating that above a certain  $K_I$  value, the crack tip is essentially bare the whole time, and dissolves or oxidizes at a limiting rate that is set by the local chemistry and potential in the crack. The actual value of the plateau velocity is then given by:

$$v = \frac{i_{\max} \Omega}{nF} \quad [1]$$

where  $v$  is the crack velocity,  $i_{\max}$  the maximum anodic current density flowing on the bare metal surface,  $\Omega$  the molar volume of the metal,  $F$  is Faraday's constant, and  $n$  is the number of electrons transferred per metal atom dissolved or oxidized.

In the 1970s and 1980s, many publications showed agreement of plateau velocities with eqn [1], where  $i_{\max}$  was determined by various transient electrochemical methods, including rapid tensile straining,<sup>125</sup> scratching,<sup>126</sup> potential stepping,<sup>127</sup> or rapid potential scanning.<sup>113</sup> Parkins played a great role in

The 1980s SCC spectrum									
Anodic	CS	Brass	$\gamma$ SS	Al alloy	CS	Ti alloy	Mg alloy	HSS	Hydrogen
	$\text{NO}_3^-$	$\text{NH}_3$	$\text{Cl}^-$	Salt	$\text{CO}_2/\text{HCO}_3^-$	$\text{Salt}$			
	$\text{OH}^-$	(etc.)	$\text{OH}^-$	water		water			
	$\text{HCO}_3^-/\text{CO}_3^{--}$		HT water						
-----									
An alternative spectrum									
Anodic direct (ductile)	Slip-dissolution/oxidation		Internal oxidation		?hybrid	Film-induced cleavage		Anodic indirect (brittle)	
	$\text{CS}/\text{NO}_3^-$ , $\text{OH}^-$ ..		Alloy 600		$\text{CS}/\text{hot water}$	Brass, Au alloys			
	$\gamma\text{SS}/\text{hot water}$ (..?LP)		hot water/ $\text{H}_2$		(transgranular)	$\gamma\text{SS}/\text{Cl}^-$ , $\text{OH}^-$			
	Sensitized SS				Pure Cu/nitrite	$\text{CS}/\text{liq NH}_3$ , $\text{CO}-\text{CO}_2$			
Hydrogen direct	Pure Cu/ $\text{NH}_3$								Hydrogen indirect
	High strength steel type		Strong role of corrosion		H assisted creep				
	HS steels (ambient)		CS		Al alloys		$\text{CS}/\text{hot water}$		
	Ti alloys (ambient)		$\text{CO}_2/\text{HCO}_3^-$				(intergranular)		
									Other hot water?

Figure 25 Old and new SCC 'spectra.'

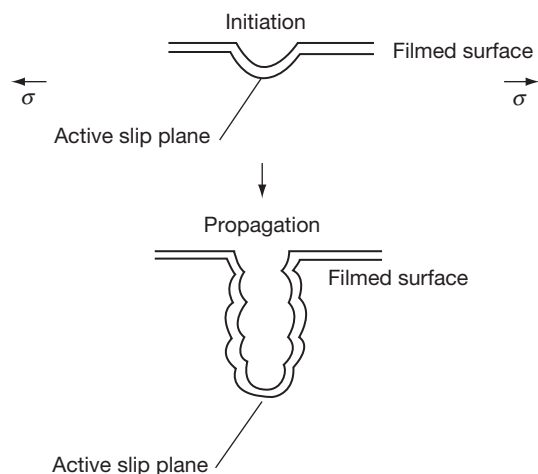


Figure 26 The slip-dissolution (or oxidation) model, after Staehle.

evaluating and comparing these techniques in carbon steel systems – Figures 27 and 28. But throughout, there were concerns that the model was being over-stretched beyond carbon steel, with such views emanating especially from specialists in hydrogen embrittlement. Application of the SDM to SCC of Al–Mg alloys was certainly controversial.<sup>128</sup> Currently, it appears that the SDM may be valid for intergranular SCC of carbon steel in caustic, nitrate, or carbonate–bicarbonate solutions, and for a number of stainless alloys in hot water. Transgranular SCC in general does not seem to fit well with the SDM – according to Sieradzki, growth of a sharp transgranular crack is not possible under static loading,<sup>129</sup> and there are kinetic difficulties in many systems, such as

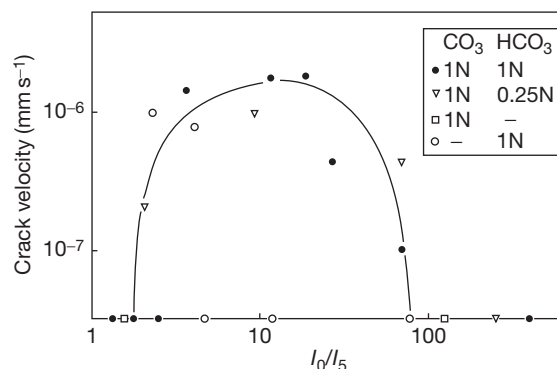
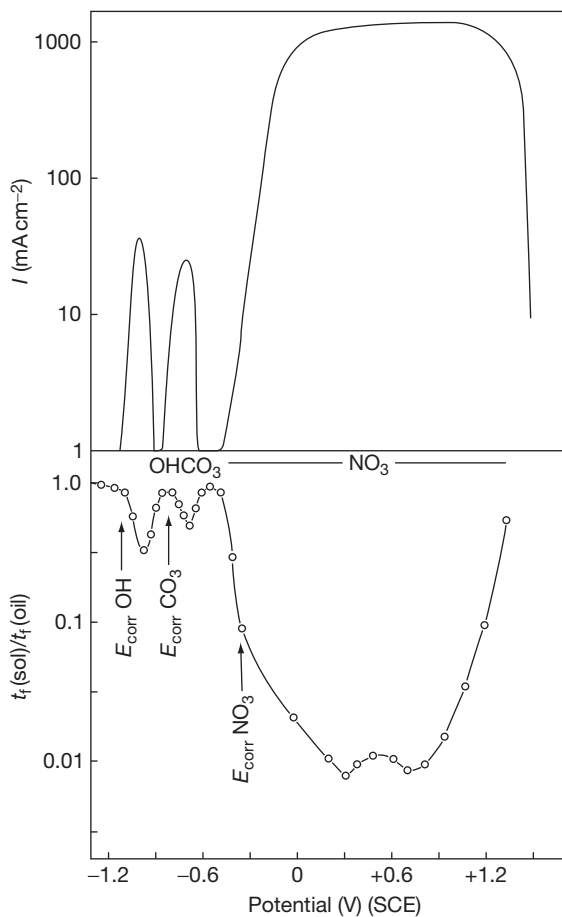


Figure 27 Analysis of current decays after potential stepping from a reducing potential to the given potential, for carbon steel in aqueous carbonate–bicarbonate, showing correlation with SCC velocity ( $I_0$  = peak current;  $I_5$  = current after 5 s). Modified from Parkins, R. N. *Corros. Sci.* **1980**, 20, 147–166.

brass in nitrite solution.<sup>130</sup> In general, it is probably safe to say that the SDM may apply to a number of cases of intergranular SCC in passivating environments without chloride-induced localized corrosion. It certainly does not apply to – say – chloride-induced SCC (Cl-SCC) of austenitic stainless steel, where the condition of the crack walls and tip is precisely that of an actively corroding crevice with a low pH and no possibility of very high local anodic current densities.<sup>16,131</sup> Recent pronouncements to the effect that the SDM does explain Cl-SCC<sup>132</sup> did not take into account the crack chemistry or realistic current densities that could flow at the crack tip when the metal is already in the active state.



**Figure 28** Similar correlation to **Figure 27**, but using the difference between the current densities measured in fast and slow potential scans. Modified from Parkins, R. N. *Corros. Sci.* **1980**, 20, 147–166.

Below the plateau crack velocity, the SDM postulates that partial repassivation of the metal occurs between film rupture events at the crack tip – **Figure 29**. So instead of  $i_{\max}$ , we write  $\bar{i}$  as the mean anodic current density at the crack tip; this is given by:

$$\bar{i} = \frac{1}{\tau} \int_0^{\tau} i(t) dt \quad [2]$$

where  $i(t)$  is the anodic current density transient on the bare metal surface, and  $\tau$  is the interval between film rupture events. The crack velocity is now:

$$v = \frac{\bar{i}\Omega}{nF} = \frac{\Omega}{nF\tau} \int_0^{\tau} i(t) dt \quad [3]$$

If we write the crack-tip strain rate as  $s$  (for the moment we suppose this is applied externally), and the strain

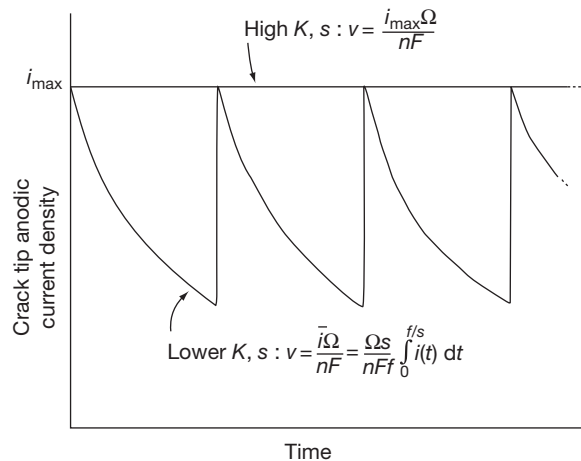


**Figure 29** The variation of anodic current density at the crack tip with time, as envisaged by the slip-dissolution model.

to failure of the oxide film as  $f$ , then  $\tau = f/s$ , and

$$v = \frac{\Omega s}{nFf} \int_0^{f/s} i(t) dt \quad [4]$$

This treatment begs a number of questions, including – is the process really stepwise like this, or can it be considered as a more continuous process of stretching of a partially formed, perhaps gel-like film? Probably it is stepwise locally, but along the crack front at any given moment, there will be elements of surface that are at all possible stages of the cycle.

It is fundamental to the SDM that dynamic plasticity is occurring at the crack tip. Sometimes this is supplied by external means, such as thermal stresses that accumulate during the start-up of a BWR. But what about purely static loading – where does the dynamic strain come from in that case? In part, this can be due to low-temperature creep, but most authors have appealed to the crack growth itself as the source of the dynamic strain. Ahead of a crack, there is a plastic strain distribution  $\varepsilon(r)$  where  $r$  is distance from the crack tip – **Figure 30**. Since  $\varepsilon$  falls off with increasing  $r$ , any corrosion or oxidation process that extends the crack must cause the whole strain distribution to move in the direction of crack growth, and this causes a strain transient ahead of the crack. This scheme was first clearly described by Vermilyea<sup>133</sup> and has been developed recently by Shoji<sup>134</sup> using a more modern strain distribution that had performed well in direct experimental tests on a ferritic material<sup>135</sup> – **Figure 31**. This possible, successful, though much-criticized, form is due to

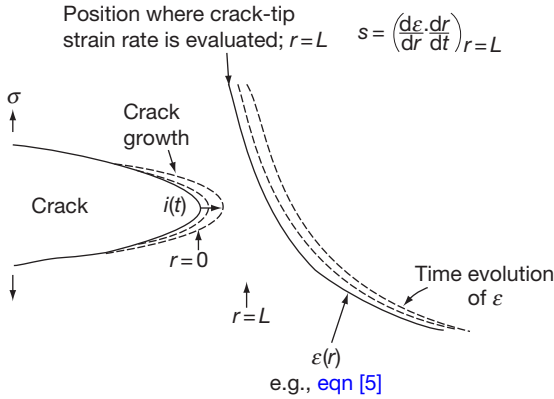


**Figure 30** Basis for growth of SCC by slip-dissolution under static load – the crack growth itself provides dynamic plastic strain.

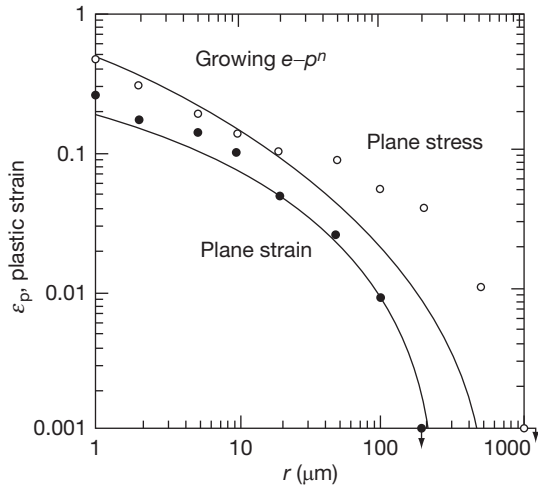


**Figure 31** Comparison of experimental plastic strain distributions ahead of a growing crack with two reasonable models (for FeSi monocrystal samples). Reproduced from Gerberich, W. W.; Davidson, D. L.; Kaczorowski, M. J. *Mech. Phys. Solids* **1990**, 38, 87–113.

Gao and Kwang<sup>136</sup> – they gave the strain ahead of the crack tip as:

$$\varepsilon_{ct} = \beta \left( \frac{\sigma_y}{E} \right) \left\{ \ln \left[ \left( \frac{\lambda}{r} \right) \left( \frac{K}{\sigma_y} \right)^2 \right] \right\}^{n/(n-1)} \quad [5]$$

where  $r$  is distance ahead of the crack, and  $n$  is the inverse strain hardening coefficient;  $\beta$  and  $\lambda$  are dimensionless.

Recently this picture has been challenged in some of its details, and its status remains unclear. According to Sieradzki,<sup>129</sup> it can only work if the corrosion is

strongly directional, leading to the idea that it is – perhaps – only valid for intergranular SCC where there is an active path of some kind. M.M. Hall also criticizes the Vermilyea–Andresen–Shoji approach in many respects and has used a modified creep cracking approach to develop a different type of ‘SDM’.<sup>137–139</sup> Generally, Shoji’s variant of the SDM is very attractive and makes a good playing field to explore the dependence of SCC on various parameters, but the last word has not been said on this subject using such continuum approaches.

When we discussed cold work effects in SCC, discussion of the approach taken in the SDM was deferred to this section. Essentially, the SDM proposes that a stronger material has a sharper crack. Now this has become a controversial issue, not least because stress corrosion cracks are much sharper than one would naively expect from the equations of ordinary elastic–plastic fracture mechanics, such as the one that gives the crack-tip opening displacement ( $\delta$ ) as a function of stress intensity factor, modulus, and flow stress:

$$\delta = \frac{K_I^2}{E\sigma_0} \quad [6]$$

which gives values for  $\delta$  on the order of microns rather than the experimentally observed nanometers.<sup>140</sup>

But, allowing the basic assumption of the sharper crack, the SDM postulates, following Vermilyea, that the average dissolution (oxidation) rate at the crack tip (allowing for film rupture and partial repassivation) and the time-averaged plastic strain rate at and ahead of the crack tip mutually cause and determine each other. Some might call this a ‘circular’ argument, but it is not, in principle. So, we develop two equations – one giving the strain transient that results from a particular corrosion transient, and the other being the converse. Solving these simultaneous equations gives the crack velocity as a function of the stress intensity factor  $K_I$ , with one major adjustable parameter – the cutoff distance ahead of the crack tip at which we calculate the plastic strain rate for the purposes of the calculation (the applicable strain distribution does not allow for calculation of the strain or strain rate exactly at the crack tip). Now, we can see that if the material is stronger, and the crack sharper, the corrosion transient at the crack tip does not have to penetrate the material so deeply to create a given strain rate (other things being equal), so when we solve the equations we get a faster crack velocity. The present author developed Shoji’s equations, identified some critical issues, and made



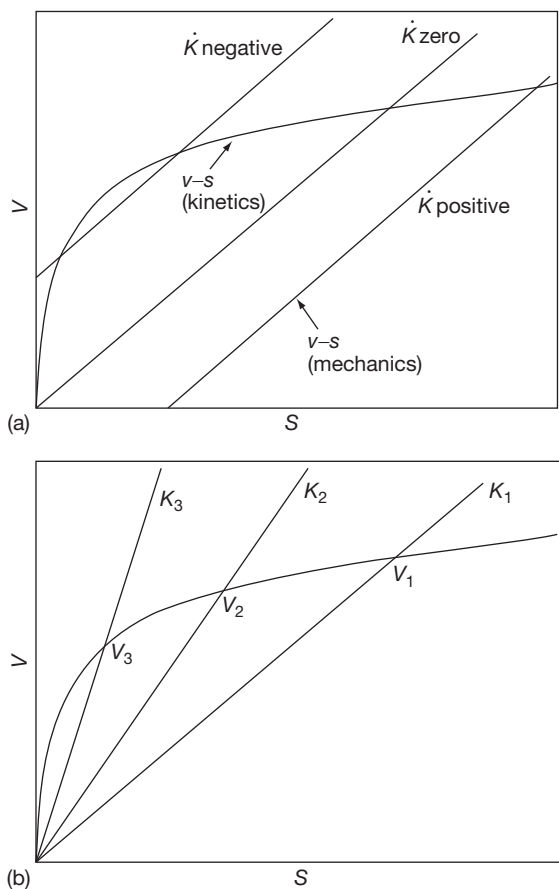


**Figure 32** (a) Graphical depiction of how solutions to the equations of the slip-dissolution model lie at the intersection of two relationships between crack velocity and crack-tip strain rate. The possibility of two crack velocities satisfying the equations for negative loading rate is illustrated. (b) Illustration of how this graphical formulation of the slip-dissolution model leads to the creation of a  $V$ - $K$  curve. Reproduced from Newman, R. C.; Healey, C. *Corros. Sci.* **2007**, 49, 4040–4050.

some new predictions such as the existence of dual steady states under certain loading conditions<sup>141</sup> – [Figure 32](#).

### 2.09.7.1 Interlude – Ultra-Sharp Cracks

Spectacular work has been done on the geometry, micromechanics, and microchemistry of SCC by Bruemmer and Thomas at the Pacific Northwest National Laboratory, which directly addresses this issue of crack sharpness as well as many other microscopic mechanistic issues, including strain localization by shear bands, alloy enrichment and depletion ahead of the crack, oxygen penetration, and porosity development ahead of the crack, as well as issues connected

with neutron irradiation and impurity concentration (Pb...S).

Several figures are reproduced from these authors' recent work with their original captions in [Figures 33–36](#).

### 2.09.8 Chemistry Considerations for SCC by Slip-Dissolution

When unalloyed carbon steel cracks in nitrate, caustic, or carbonate–bicarbonate solution, the conditions are always such as to promote the formation – perhaps fleetingly – of soluble complexes. In caustic solutions, the soluble species is  $\text{Fe}(\text{OH})_4^{2-}$ ; in carbonate–bicarbonate, it is  $\text{Fe}(\text{CO}_3)_2^{2-}$ <sup>142</sup> (or similar bicarbonate complex<sup>143</sup>), and in nitrate it is probably an unknown complex that forms with some reduction product of nitrate. The present author used to believe that nitrate SCC was happening near the active–passive transition, like caustic or carbonate–bicarbonate SCC, but actually, the potentials are very oxidizing, in what could be called a transpassive region<sup>113</sup> – at least when the solution is hot and concentrated. But iron does not normally suffer from transpassive dissolution. What must be happening is that normally, nitrate contacting an iron surface is reduced so far (e.g., to  $\text{N}_2$  or  $\text{NH}_4^+$ ) that it becomes harmless, but that in a certain range of potentials, it is reduced to something that forms a soluble complex with iron. We do not know what that is – it could be an NO species. ‘Transpassive’ corrosion also occurs in zirconium in strong nitric acid, and must be due to a similar complexation effect.<sup>144</sup>

As Parkins has often shown, intergranular SCC of carbon steel is preceded by mild intergranular corrosion, and to the extent that fine carbides are to blame, this can be rationalized by their diminished passivation ability.<sup>145</sup> Similarly, where phosphorus segregation is involved, insights can be obtained by studying an amorphous iron phosphorus alloy<sup>29</sup> or simply an iron phosphide, as a rough simulation of the reacting material at the grain boundary. In the case of sensitized stainless steels or nickel base alloys, a range of alloys with reduced Cr contents can be prepared for transient electrochemical experiments.<sup>126</sup>

### 2.09.9 More Comments on Hydrogen Embrittlement as a Mechanism of SCC

Some of the oldest controversies in SCC research concern the role of hydrogen embrittlement. R.N.

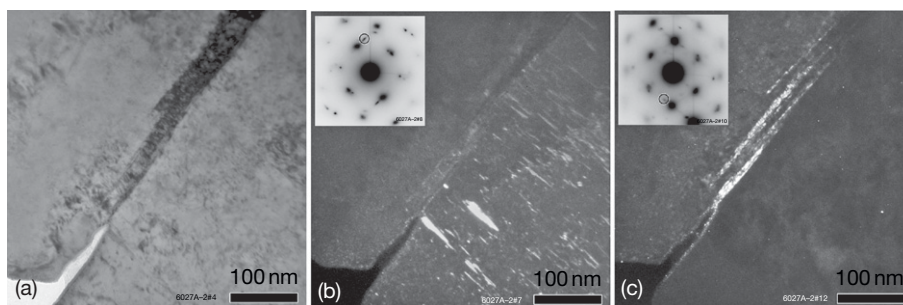


**Figure 33** Crack tip region in CW316LSS sample tested in BWR HWC: (a) TEM brightfield image showing shear bands at tip. (b)  $\langle 111 \rangle$  Relrod darkfield image highlighting faults (one of four variants) in grain at right. (c) Relrod darkfield image highlighting faults along grain boundary in grain at left. Inset diffraction patterns show relrod reflections used for imaging. Commentary – these images show extraordinary martensite-like shear transformations ahead of cracks in cold-worked stainless steel, and vividly illustrate the strain localization that is responsible for much of the severity of SCC in cold worked material. Adapted from Toloczko, M. B.; Andresen, P. L.; Bruemmer, S. M. SCC Crack Growth of Cold-Worked 316LSS in BWR Oxidizing and Hydrogen Water Chemistry Conditions, Proceedings of the 13th International Conference Environmental Degradation of Materials in Nuclear Power Systems – Water Reactors, Canadian Nuclear Society, 2007; Paper 141.

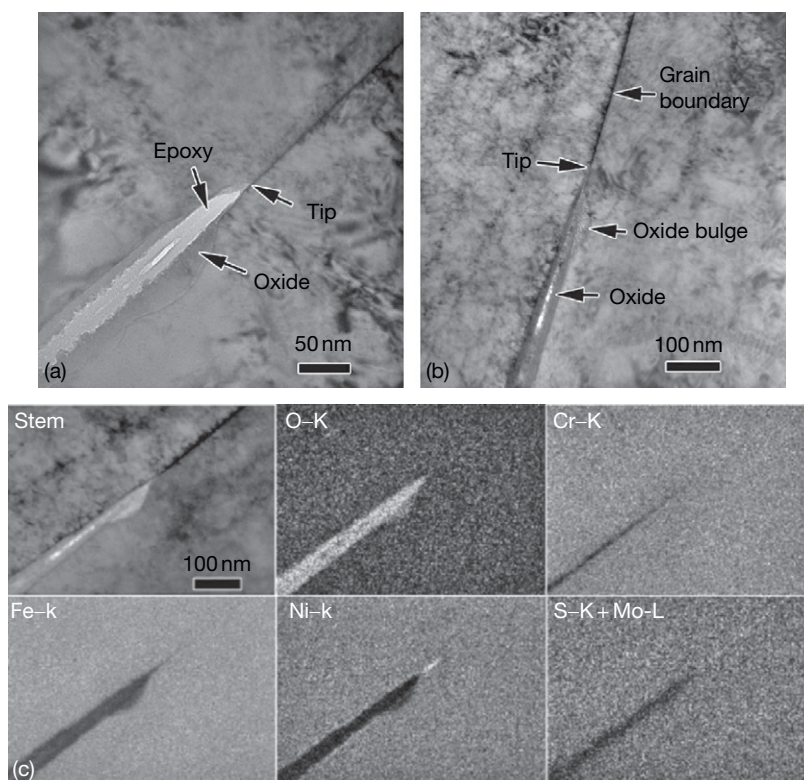


**Figure 34** Open (a) and oxide-filled (b) crack tips in a BWR core shroud sample. EDS x-ray maps of oxide-filled tip (c) show Fe/Ni loss in oxide, Ni concentrated ahead of tip, and Mo segregation along the leading grain boundary. Commentary – this is neutron-irradiated material from plant, so there could be complex processes at play, including atomic mobility that leads to Ni enrichment ahead of the crack, and Mo segregation. Adapted from Thomas, L. E.; Edwards, D. J.; Asano, K.; Ooki, S.; Bruemmer, S. M. Crack-Tip Characteristics in BWR Service Components, Proceedings of the 13th International Conference Environmental Degradation of Materials in Nuclear Power Systems – Water Reactors, Canadian Nuclear Society, 2007; Paper 143.

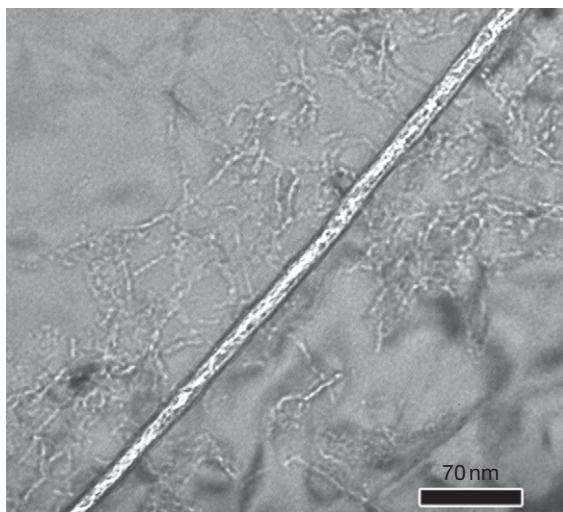


**Figure 35** TEM underfocus image showing oxide-filled IG crack and adjacent tunnel-like structure along walls in Ringhals-4 alloy 182 sample. Commentary – the striking feature is the apparent oxidation along dislocation lines either side of the crack. Adapted from Thomas, L. E.; Bruemmer, S. M. *High-Resolution Analytical Microscopy of Environmental Cracks in Alloy 182 Weldments*, 11th International Conference on Environmental Degradation of Materials in Nuclear Power Systems – Water Reactors, American Nuclear Society, 2003; p 1212.

Parkins used to refer to a stress corrosion ‘spectrum’ that had SCC of high-strength steel at one end and SCC of ordinary carbon steel at the other, with various aluminum and titanium systems near the middle.<sup>123</sup> Recently titanium alloys seem to have arrived firmly somewhere near the hydrogen (high-strength steel) end,<sup>70</sup> although clearly the discharge of hydrogen ions depends on electrochemical factors like the repassivation rate of the metal at the crack tip. Nowadays, no one seems to believe in Theodore Beck’s ‘electrochemical knife’ (SDM) that he proposed in the 1960s and early 1970s.<sup>146</sup> A general difficulty with aluminum and titanium alloys is that hydrogen is always generated in copious quantities at the crack tip, but this does not mean it always plays an important role in cracking. Probably these mechanisms will continue to be considered somewhat hybrid in nature. A similar comment could be made about martensitic stainless steels in ambient chloride solutions, or carbon steel in near-neutral-pH bicarbonate solutions.<sup>147</sup>

It was once thought that high-strength low-alloy steels immersed in salt water had an acidic crack chemistry, and that this assisted hydrogen discharge in the crack,<sup>148</sup> but later it appeared that this was

mistaken, at least for steels without chromium.<sup>149,150</sup> The original experiments suffered from air-oxidation of Fe (II) to Fe (III), causing acidification. But crack depth also affects the crack chemistry (deep cracks tend to self-corrode and thus have less or no tendency to acidify, even with Cr alloying), and it was sometimes reported in the 1980s that short cracks grew faster than long ones.<sup>151</sup> The pH changes in such short cracks depend very sensitively on the external corrosion potential (which depends on alloying content), and no generality of the ‘chemical short crack effect’ was ever established. Essentially, we know that acidification occurs, with Cr alloying, if we anodically polarize the material from its natural corrosion potential. So under free corrosion conditions, there has to be both Cr alloying and some other element (Mo, Ni for example) that ennobles the anodic reaction on the free surface – then, if we are (un)lucky, we can see the chemical short crack effect. Maraging steels, which contain large amounts of Ni, are good candidates for such behavior.

There is no space here for a detailed discussion of hydrogen embrittlement mechanisms, but the subject has been very well-documented, not only in journal literature but in a series of conferences.<sup>152</sup> To the nonspecialist, theories of hydrogen effects seem very confusing and mutually contradictory – some theories postulate a kind of hardening, leading to decohesion of the lattice or of a grain boundary,<sup>153</sup> while others postulate a local softening leading to highly localized plastic rupture.<sup>154,155</sup> Strain rate affects the predominant mechanism. Quantum mechanics modeling gives insights into the interaction of hydrogen with other solutes,<sup>62</sup> with dislocations, and with grain boundaries. Two types of softening effect are proposed in the literature – Lynch<sup>152</sup> sees this as a surface or very near-surface effect attributed to a lifting of a compressive surface stress by hydrogen adsorption (or very local absorption), while the ‘HELP’ (hydrogen enhanced local plasticity) mechanism<sup>63</sup> postulates that internal hydrogen reduces the repulsion between dislocations in their slip plane – **Figure 37**.

### **2.09.10 Film-Induced Substrate Fracture (‘Film-Induced Cleavage’)**

It is recognized that certain cases of SCC are too rapid to be due to any version of the SDM, and that some of them occur under conditions where hydrogen absorption can be ruled out. Many of these have in common that they occur in relatively concentrated solid



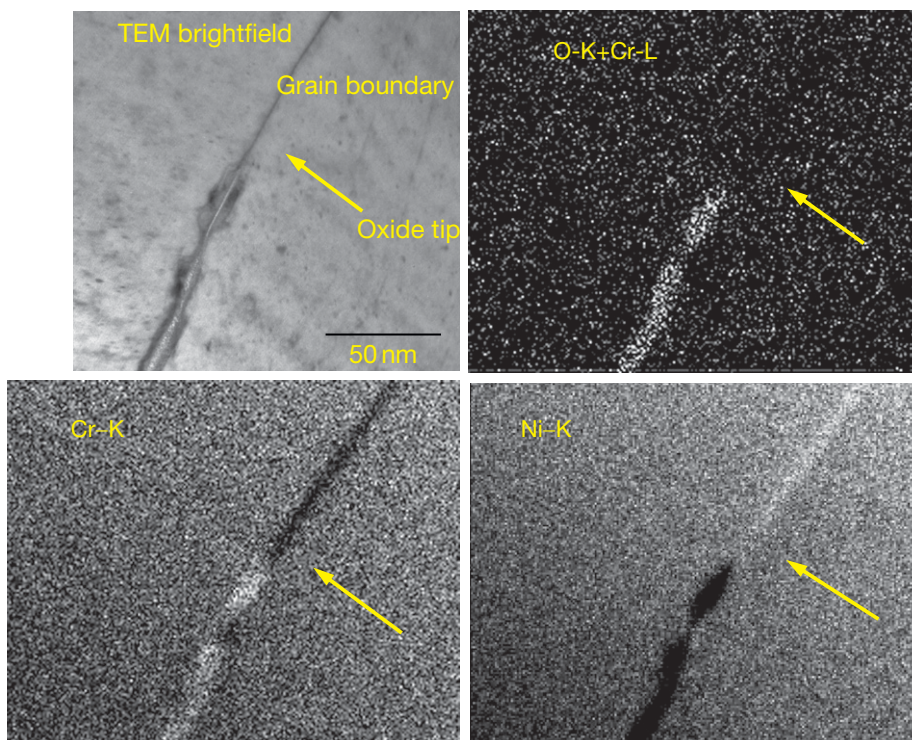


**Figure 36** EDS maps showing the leading edge of IG attack ahead of primary-side IGSCC in an Alloy 600 steam generator tube are presented. Cr is highly enriched in the tip oxide and Ni is enriched along the grain boundary ahead of the tip. Commentary – these depletions and enrichments need to be studied in the context of internal oxidation and other models. Adapted from Bruemmer, S. M.; Thomas, L. E. Crack-Tip Examinations of Primary-Water Stress Corrosion Cracking in Alloy 600, Proceedings of Fontevraud 6 International Symposium on Contributions of Materials Investigations to Improve the Safety and Performance of Light-Water Reactors, French Nuclear Energy Society, 2006; p 603.

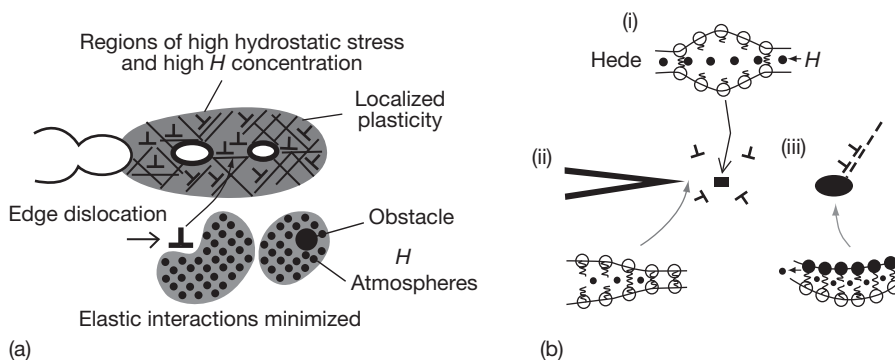


**Figure 37** Plastic hydrogen fracture mechanisms, according to Lynch. Reproduced from Lynch, S. P. In *Corrosion/2007*; NACE: Houston, TX, 2007; Paper No 489.

solutions – brass, copper–gold or silver–gold alloys, austenitic stainless steel.<sup>18</sup> A natural idea is that such rapid cracking could be due to dealloying (see **Chapter 2.05, Dealloying**), but not just to a repetitive process of formation and fracture of a dealloyed layer – the rapid cracking requires that the fracture

of the dealloyed layer injects a brittle microcrack, even into a fcc substrate that is normally considered unconditionally immune to brittle fracture<sup>156</sup> – **Figure 38**. The original source for this concept was a remarkable study on brass by Edeleanu and Forty in the late 1950s.<sup>157</sup> Optical microscopy of the side

surface of an  $\alpha$ -brass crystal immersed under stress in ammonia solution showed what appeared to be regular brittle crack jumps of a few microns, each starting and ending at a slip trace. The authors stopped short of stating that the fcc lattice was undergoing a true cleavage process, as this was considered impossible even then. They proposed that the material between slip bands was embrittled by short-range order, and that corrosion – perhaps selective – at the slip band was required to reveal this intrinsic brittleness in the material. Their observations were confirmed by the group of E.N. Pugh.<sup>158</sup> Pugh introduced a clever method to detect discontinuities in crack growth, based on the use of periodic load pulsing to mark the fracture surfaces, and deduced that indeed the cracks were proceeding by a series of jumps. Acoustic emission was used as supporting evidence. Pugh did not adopt the short-range order suggestion, but did consider for some time that hydrogen might be causing the effect; he later rejected this, paving the way for the acceptance of a cleavage process initiated by dealloying.<sup>159</sup> Sieradzki and Newman presented arguments based on dislocation dynamics that went some way toward establishing a feasible framework for such effects.<sup>160,161</sup> This was considered a bizarre suggestion by many, but recent insights into the extraordinary mechanical properties of dealloyed layers (near-theoretical strength in compression,<sup>162</sup> size-scale-dependent elastic modulus,<sup>163</sup> surface stress-driven bending<sup>164</sup>) are reawakening interest in the possibility that such crack injection can occur.<sup>165</sup> Pugh considered that intergranular cracking in brass was a continuous process, but actually the strongest evidence for the film-induced fracture hypothesis comes from studies of intergranular SCC in noble-metal

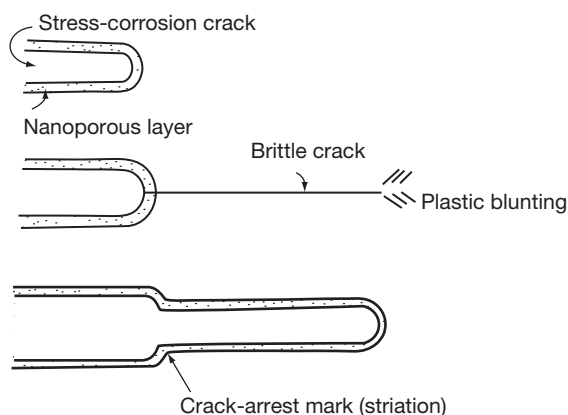


**Figure 38** The film-induced cleavage concept, for a system showing dealloying.

alloys<sup>166–168</sup> – **Figure 39**. Crack jumps into a silver–gold substrate of 50–100  $\mu\text{m}$  can easily be obtained from preformed dealloyed layers. A key experiment is to dealloy under an applied potential, then step the potential to a value where little or no further

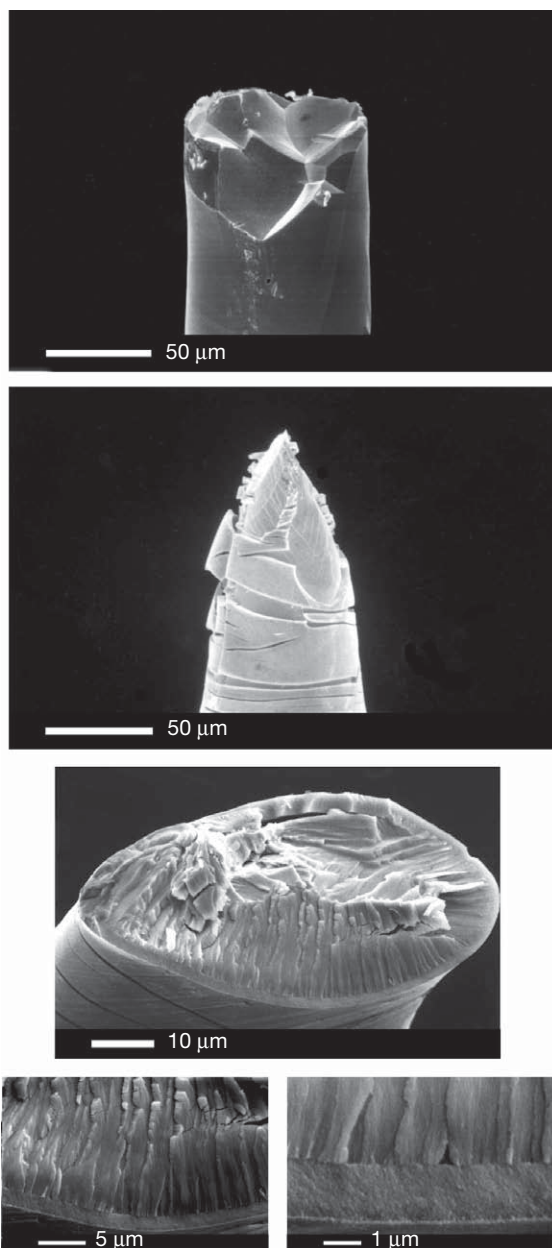


**Figure 39** Brittle fracture of AuAg – intergranular or transgranular – obtained after surface dealloying; the middle picture illustrates the effect of ageing the dealloyed layer, which destroys its ability to inject a brittle crack by coarsening its nanoporosity. Reproduced from Barnes, A.; Senior, N. A.; Newman, R. C. *Metall. Trans. A* **2009**, *40*, 58–68.



faradaic reaction can occur, then load the sample to failure. This also showed good promise for transgranular fracture,<sup>166</sup> although more work remains to be done in that area. In both cases, ageing of the dealloyed layers destroys their ability to inject a crack – probably owing to coarsening of their porosity by surface diffusion.

Clearly, the crack injection phenomenon relies on the special properties of dealloyed layers, including their intrinsic brittleness. A key aspect is the absence of a crystallographic interface – dealloyed layers retain the same lattice orientation that they had before dealloying, so the crack can cross into the substrate without meeting any dislocation structures. Provided it is injected at a velocity close to the velocity of sound in the crystal, it can continue to grow for some distance even in a fcc material, as discussed by Sieradzki and Newman.<sup>158</sup>

### 2.09.11 Surface Mobility, Vacancy Based Models, and Others

A large amount of research has been done by the group of J.R. Galvele, based around a surface mobility model (SMM) that he proposed in 1987.<sup>169</sup> This is a kind of creep crack growth model in which crack extension occurs by surface diffusion of metal atoms (perhaps partially oxidized or chelated – this is not always clear) away from the crack tip. The basic crack growth equation is – using Galvele's own notation:

$$\text{cpr} = \frac{D_s}{L} \left[ \exp\left(\frac{\sigma \cdot a^3}{kT}\right) - 1 \right] \quad [7]$$

where cpr means crack propagation rate,  $D_s$  is the applicable surface (self) diffusivity,  $L$  is a diffusion length along the crack flank (Galvele always uses  $10^{-8}$  m for this),  $\sigma$  is the opening stress at the crack tip, and  $a^3$  is the atomic size (approximate volume of a vacancy). The crack velocity is considered to correlate with the melting point of a surface compound (which in turn correlates with surface diffusivity on a contaminated surface), or in some cases with a kind of enhanced exchange of metal atoms at the crack surface (exchange current), for which a different equation was developed<sup>170</sup>:

$$D_s = \frac{i_0 N_A A n^2 a^4}{6F} \quad [8]$$

where  $i_0$  is the exchange current density,  $N_A$  is Avogadro's number,  $A$  is the atom fraction of base (reactive) metal atoms in the alloy (this was called

$AF$  in the original paper),  $n$  is a kind of dimensionless distance or average hop size,  $a$  is the atom size,  $F$  is Faraday's constant, and the 6 arises because this is the number of neighboring sites of an atom in a close-packed plane.

The SMM does have the attractive feature that (with an atomically sharp crack, and allowing for some adjustable parameters such as stress at the crack tip) it seems to rationalize literature data on SCC velocities. Not enough independent research has been done on the concept to give a final answer as to its merits.

The chemical potential gradients could be in the right direction for crack growth in the SMM, but – according to Friedersdorf and Sieradzki<sup>171</sup> – only if one neglects capillary effects – tight cracks would close up, and the SMM can only work with a relatively blunt crack (as in the creep analogues that can be found in the literature). Friedersdorf and Sieradzki also stated that the change in vacancy formation energy due to stress ( $\sigma a^3$ ) had been wrongly assigned because this quantity is appropriate for the interior of the solid, not the crack-tip surface. They also argued that chemical potentials should be used, not concentrations. The crack velocities estimated by Friedersdorf and Sieradzki are many orders of magnitude lower than those suggested by Galvele, although their amended model does have the drawback that it assumes equilibrium vacancy concentrations, as pointed out by Galvele himself.<sup>172</sup>

One source of confusion in the published discussions of the Galvele model is that between 1987 and 1994, he shifted the location of the site where the stress was assumed to act from the crack tip surface to somewhere just ahead of the crack, thus – perhaps – justifying the use of  $\sigma a^3$ . This is an unsatisfactory aspect of the SMM, as it introduces an arbitrary additional vacancy transport process that must occur within the solid – this is simply assumed to be rapid compared with transport along the crack flank. Friedersdorf and Sieradzki were analyzing a version of the SMM that had been changed a few months before they published their analysis, to deal with the  $\sigma a^3$  problem.

Our summary of the current state of the SMM is shown in **Figure 40**.

Intriguing intergranular SCC phenomena were demonstrated by the Galvele group for copper and silver, and silver alloys, in hot, dry halogen atmospheres.<sup>173–175</sup> The lowest temperature where cracking was studied was 200 °C. These observations were considered to be a cornerstone of the SMM, as they related directly to classic studies of enhanced surface

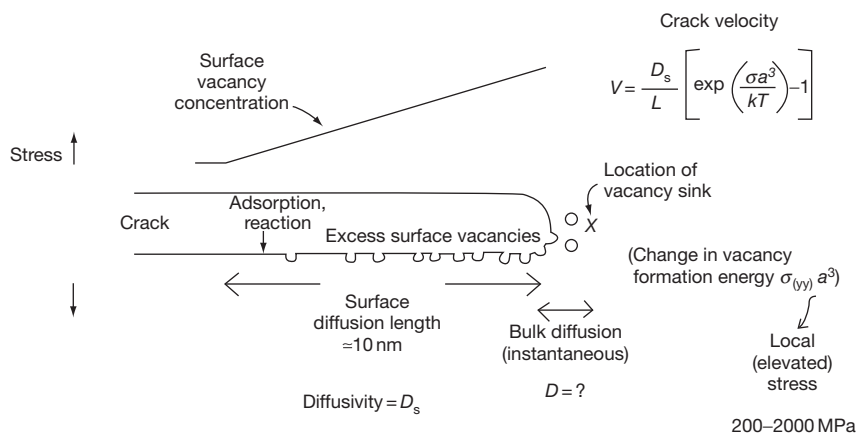


**Figure 40** Current state of the Surface Mobility Model, as envisaged by the author.

mobility due to halogen adsorption.<sup>176</sup> Other explanations are possible, of course. Ion mobility in copper and silver halides could be high.

#### 2.09.11.1 Vacancy Injection Models for Low-Temperature SCC

It is interesting that the moving of the vacancy sink ahead of the crack turns the SMM into a *vacancy injection* model, qualitatively similar to those proposed by other authors, including E.I. Meletis<sup>177</sup> and the late Denny Jones<sup>178</sup> who believed that he had detected interdiffusion in metallic bilayers subjected to anodic dissolution. In those models, the enhancement by stress of equilibrium vacancy concentration inside the solid was not taken into account – at least not explicitly – although it was probably part of the thought process.

One of several ‘orphan’ SCC models is that of Aaltonen and others in Finland, based on internal friction studies<sup>179,180</sup> – **Figure 41**. These results are so surprising (much more so, we would submit, than film-induced cleavage) that no other author has seriously addressed them. Essentially, these authors showed that anodic polarization of copper wires at 80 °C in a sodium nitrite solution, under conditions promoting duplex Cu(I)–Cu(II) oxide formation, produced defects that behaved like vacancies under the standard protocols used for internal friction measurement. They even claimed a reduction in shear modulus of the whole wire specimen. Later they reported an increase in creep rate under similar conditions.<sup>181</sup> One’s immediate reaction is that even if such vacancies were to be produced, they must be confined within nanometers of the metal–film

interface, so how is it possible for this nm-thick layer to dominate the internal friction response, or sample modulus, when the smallest sample dimension is 0.5 mm? Yet the results are quite striking, showing Hasiguti peaks in the anodically treated samples. One possibility (acting as devil’s advocate) is that there is an autoreduction or disproportionation of a thick oxide, which produces metallic copper with a high defect density. Yet even in that case, the defected metallic layer should be a tiny fraction of the total sample dimension. But we should certainly not dismiss such observations. Metals like copper and silver may have high mobility for certain substitutional elements.

Very recently (Hanninen *et al.*, unpublished) a variety of techniques have been used to support the proposed vacancy injection model. Dislocation structures are altered near the surface during anodic polarization in the range of potentials that cause SCC of copper in nitrite. This does not mean that vacancies are penetrating the material to the entire depth to which altered behavior is observed – as shown many years ago, a near-surface effect can alter bulk mechanical properties, at least in fairly thin wire or sheet. So the relevance of vacancy injection to crack propagation may lie in the inducement of more intense localized plasticity, rather than some kind of embrittlement by the vacancies themselves.

Of course, vacancies can be involved in creep-like SCC phenomena when the temperature exceeds 300 °C, as discussed earlier.<sup>34</sup>

#### 2.09.11.2 Adsorption-Induced Dislocation Emission

According to Lynch (private communication), ‘surface mobility’ can be harmonized with a mechanism of

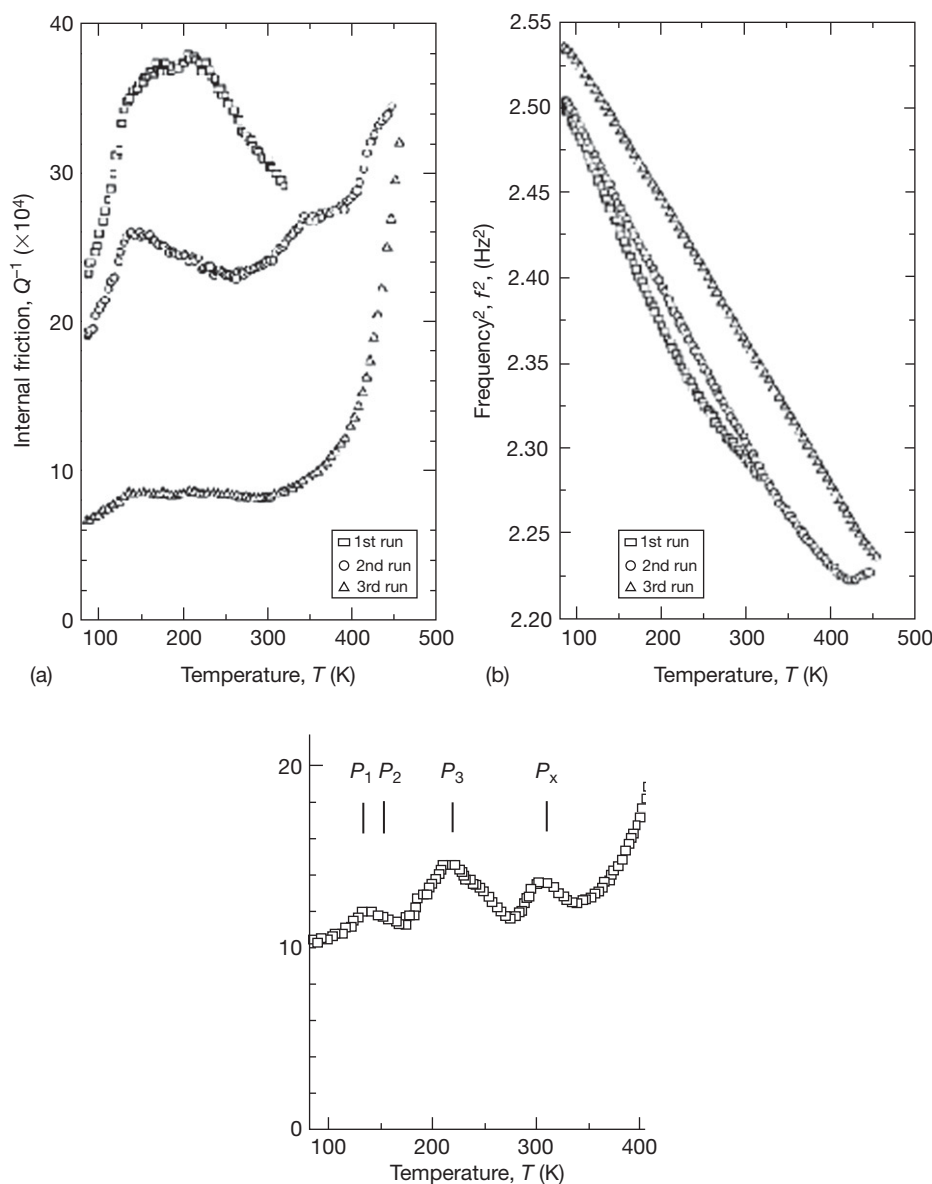


**Figure 41** Upper: Temperature dependence of internal friction  $Q^{-1}$  (a) and oscillation frequency  $f^2$  (b) for copper polarised in 0.3 M  $\text{NaNO}_2$  solution for 2 h at  $-150 \text{ mV}_{\text{SCE}}$  and subsequently for 10 h at  $+100 \text{ mV}_{\text{SEC}}$  at 353 K ( $80^\circ\text{C}$ ). During first run heating was performed up to 320 K, and during second and third runs up to 450 K. Lower: Location of the usual Hasiguti peaks for copper. Reproduced from Aaltonen, P.; Jagodzinski, Y.; Tarasenko, A.; Smouk, S.; Hanninen, H. *Corros. Sci.* **1998**, *40*, 903–908.

crack growth wherein adsorption of species from the environment, including hydrogen, facilitates dislocation emission from the crack tip, leading to a highly localized plastic fracture.<sup>152</sup> As he points out, both mechanisms involve the weakening of bonds between metal atoms, and some proportionality between the resulting crack growth rates might be expected. A strength of Lynch's proposal is that it easily encompasses liquid metal and hydrogen embrittlement,

whereas these are treated a little vaguely in the SMM. Like Galvele, Lynch cites particular experiments showing very high crack velocities, to argue against dissolution or other bulk effects, but with more justification, in that the cracking of nickel monocrystals in mercury or hydrogen does seem to be a continuous process without crack jumps, whereas Galvele's studies of SCC in noble-metal alloys<sup>182</sup> claim continuous crack velocities of up to  $20 \text{ mm s}^{-1}$ , but are

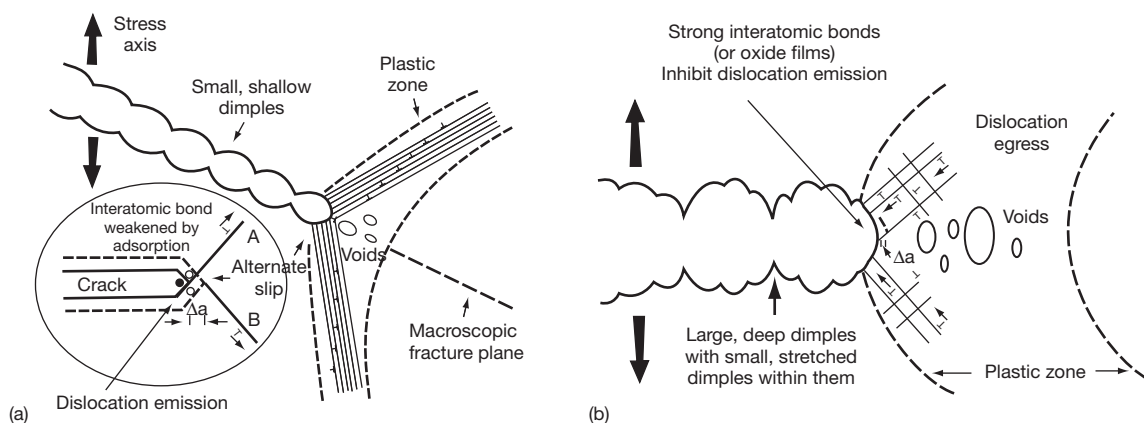


**Figure 42** The AIDE mechanism. Reproduced from Lynch, S. P. In *Corrosion/2007*; NACE: Houston, TX, 2007; Paper No 489.

contradicted by the experimental evidence for large brittle crack jumps in such systems.<sup>166</sup>

From an energetic point of view, the Lynch mechanism, or adsorption induced dislocation emission (AIDE) relies on the occurrence of intense plasticity within a very small volume at the crack tip. This can lower the total energy of fracture, which is integrated over the whole deformed volume around the crack. The proposed micromechanism is shown in Figure 42.

A possible weakness of the AIDE mechanism used to be the insistence on a truly 2D interaction rather than any 3D reaction mechanism. Nowadays, Lynch tends to accommodate a near-surface process zone, although in the case of LME in immiscible systems, this must be very shallow. An intriguing suggestion, based on first-principles calculations for Ga on Al, is that LME systems, bulk-miscible or not, are those in which there is facile alloying of the liquid metal into the first one or two atomic layers of the substrate.<sup>183</sup> Since surface alloying is also known in vacuum deposition and in underpotential deposition of metals on copper and other substrates,<sup>184,185</sup> this raises the interesting possibility that – for example – Pb ions could cause cracking of copper or other metals by an underpotential displacement reaction followed by a LME-type cracking.

Other local softening models exist, such as that of T. Magnin, which although mainly developed for hydrogen effects<sup>153</sup> has also been applied to ‘anodic’ SCC.<sup>186</sup> Such softening may very well occur – the question is whether, in a given instance, it is essential for cracking. In corrosion fatigue, it is well-established that ordinary active dissolution in noble metals like copper can promote cracking,<sup>187</sup> and so the dissolution must be enhancing plasticity, since

fatigue is essentially a plastic fracture (no evidence of brittleness is seen on such fractures). So it is not at all unreasonable to propose a similar effect in SCC, at least where dynamic straining is applied externally, as in a SSRT.

## References

1. Kilburn, C. R. J.; Petley, D. N. *Geomorphology* **2003**, 54, 21–32.
2. Ogata, S.; Shimojo, F.; Kalia, R. K.; Nakano, A.; Vashishta, P. *J. Appl. Phys.* **2004**, 95, 5316–5323.
3. Lynch, S. P.; Moutsos, S. *J. Failure Anal. Preven.* **2006**, 6, 54–69.
4. Lynch, S. P. *Mater. Sci. Eng. A: Struct. Mater.: Prop., Microstruct. Process.* **2007**, 468–470, 74–80.
5. Kerns, G. E.; Staehle, R. W. *Scr. Metall.* **1972**, 6, 1189–1194.
6. Le Calvar, M.; Scott, P. M.; Magnin, T.; Rieux, P. *Corrosion* **1998**, 54, 101–105.
7. *Stress-Corrosion Cracking – The Slow Strain Rate Technique*; Ugiansky, G. M.; Payer, J. H. Eds. ASTM STP 665, ASTM: Philadelphia, 1977.
8. Sedriks, A. J. *Stress Corrosion Cracking Test Methods*; NACE: Houston, TX, 1989.
9. Pednekar, S. P.; Agrawal, A. K.; Chaung, H. E.; Staehle, R. W. *J. Electrochem. Soc.* **1979**, 126, 701–702.
10. Staehle, R. W.; Gorman, J. A. *Corrosion* **2003**, 59, 931–994; **2004**, 60, 115–180.
11. Poulson, B. *Corros. Sci.* **2004**, 46, 729–753.
12. Newman, R. C. *Stress Corrosion Cracking Mechanisms*. In *Corrosion Mechanisms in Theory and Practice*, 2nd ed; Marcus, P., Oudar, J., Eds.; Marcel Dekker: New York, 2002; pp 399–450.
13. Copson, H. R. Effect of Composition on Stress Corrosion Cracking of Some Alloys Containing Nickel. In *Physical Metallurgy of Stress Corrosion Fracture*; Rhodin, T. N., Ed.; Interscience: New York, 1959; pp 247–269.
14. Graf, L. Stress-Corrosion Cracking in Homogeneous, Nonsupersaturated Alloys Containing Noble or No Noble Metals. In *Fundamental Aspects of Stress-Corrosion Cracking*; Staehle, R. W., Forty, A. J., van Rooyen, D., Eds.; NACE: Houston, TX, 1969; pp 187–201.

15. Latanision, R. M.; Staehle, R. W. Stress-Corrosion Cracking of Iron-Nickel-Chromium Alloys. In *Fundamental Aspects of Stress-Corrosion Cracking*; Staehle, R. W., Forty, A. J., van Rooyen, D., Eds.; NACE: Houston, TX, 1969; pp 214–307.
16. Newman, R. C.; Corderman, R. R.; Sieradzki, K. *Br. Corros. J.* **1989**, *24*, 143–148.
17. Tamaki, K.; Tsujikawa, S.; Hisamatsu, Y. Development of a New Test Method for Chloride Stress Corrosion Cracking of Stainless Steels in Dilute NaCl Solutions. In *Advances in Localized Corrosion*; Isaacs, H. S., Bertocci, U., Kruger, J., Smialowska, S., Eds.; NACE: Houston, TX, 1991; pp 207–214.
18. Nisbet, W. J.; Lorimer, G. W.; Newman, R. C. *Corros. Sci.* **1993**, *35*, 457–469.
19. Deakin, J.; Dong, Z.; Lynch, B.; Newman, R. C. *Corros. Sci.* **2004**, *46*, 2117–2133.
20. Maier, A.; Fernandez, J. S.; Galvele, J. R. *Corros. Sci.* **1995**, *37*, 1–16.
21. Serebrinsky, S. A.; Galvele, J. R. *Corros. Sci.* **2004**, *46*, 591–612.
22. Sieradzki, K.; Kim, J. S.; Cole, A. T.; Newman, R. C. *J. Electrochem. Soc.* **1987**, *134*, 1635–1639.
23. Pugh, E. N.; Craig, J. V.; Sedriks, A. J. Stress-Corrosion Cracking of Copper, Silver and Gold Alloys. In *Fundamental Aspects of Stress-Corrosion Cracking*; Staehle, R. W., Forty, A. J., van Rooyen, D., Eds.; NACE: Houston, TX, 1969; pp 118–158.
24. Barnes, A.; Deakin, J.; Newman, R. C. *Corrosion* **2007**, *63*, 416–418.
25. Staehle, R. W. Private communication.
26. Uhlig, H. H. Evaluation of Stress-Corrosion Cracking Mechanisms. In *Fundamental Aspects of Stress-Corrosion Cracking*; Staehle, R. W., Forty, A. J., van Rooyen, D., Eds.; NACE: Houston, TX, 1969; pp 86–97.
27. Atrens, A.; Wang, J. Q.; Stiller, K.; Andren, H. O. *Corros. Sci.* **2006**, *48*, 79–92.
28. Bandyopadhyay, N.; Briant, C. L. *Corrosion* **1985**, *41*, 274–280.
29. Bandyopadhyay, N.; Newman, R. C.; Sieradzki, K. Caustic SCC of an Fe–3Ni alloy, effects of alloying additions or impurities; Proceedings of the 9th International Congress on Metallic Corrosion, Toronto, 1984; Vol. 2, pp 210–215, NRC: Ottawa.
30. Harrison, R. P.; de G Jones, D.; Newman, J. F. Caustic Cracking of Temper Embrittled Steels. In *Stress-Corrosion Cracking and Hydrogen Embrittlement of Iron-Base Alloys*; Staehle, R. W., Hochmann, J., McCright, R. D., Slater, J. E., Eds.; NACE: Houston, TX, 1977; pp 659–662.
31. Danielson, M. J.; Oster, C. A.; Jones, R. H. *Corros. Sci.* **1991**, *32*, 1–21.
32. Scamans, G. M.; Holroyd, N. J. H.; Tuck, C. D. S. *Corros. Sci.* **1987**, *27*, 329–347.
33. Senior, N. A.; Newman, R. C. *Nanotechnology* **2006**, *17*, 2311–2316.
34. Arioka, K.; Yamada, T.; Terachi, T.; Miyamoto, T. *Corrosion* **2008**, *64*, 691–706.
35. Staehle, R. W. Private communication.
36. Paraventi, D. J.; Angelii, T. M.; Was, G. S. *Corrosion* **2002**, *58*, 675–686.
37. Was, G. S. *Fundamentals of Radiation Materials Science, Metals and Alloys*; Springer: New York, 2007.
38. Faulkner, R. G. *J. Nucl. Mater.* **1997**, *251*, 270–276.
39. Was, G. S.; Busby, J. T.; Allen, T.; Kenik, E. A.; Jensson, A.; Bruemmer, S. M.; Gan, J.; Edwards, A. D.; Scott, P. M.; Anderson, P. L. *J. Nucl. Mater.* **2002**, *300*, 198–216.
40. Busby, J. T.; Sowa, M. M.; Was, G. S.; Kenik, E. A. *J. ASTM Int.*; 2004, 1.
41. Jiao, Z.; Busby, J. T.; Was, G. S. *J. Nucl. Mater.* **2007**, *361*, 218–227.
42. Hackett, M. J.; Busby, J. T.; Was, G. S. *Metall. Mater. Trans. A* **2008**, *39*, 218–224.
43. Andresen, P. L.; Ford, F. P. *Mater. Sci. Eng. A* **1988**, *A103*, 167–184.
44. Andresen, P. L. *Corrosion* **2008**, *64*, 439–464.
45. Kim, Y.-J.; Niedrach, L. W.; Andresen, P. L. *Corrosion* **1996**, *52*, 738–743.
46. King, A.; Johnson, G.; Engelberg, D.; Ludwig, W.; Marrow, J. *Science* **2008**, *321*, 382–385.
47. Samans, C. H. *Corrosion* **1964**, *20*, 256t–262t.
48. Isaacs, H. S.; Vyas, B.; Kendig, M. W. *Corrosion* **1982**, *38*, 130–136.
49. Newman, R. C.; Roberge, R.; Bandy, R. *Corrosion* **1983**, *39*, 386–390.
50. Newman, R. C.; Bandy, R.; Roberge, R. *Environmental Degradation of Materials in Nuclear Power Systems – Water Reactors*; NACE: Houston, TX, 1984; pp 636–647.
51. Horowitz, H. H. *Corros. Sci.* **1983**, *23*, 353–362.
52. Jones, R. H.; Gertsman, V. Y.; Vetrano, J. S.; Windisch, C. F. *Scr. Mater.* **2004**, *50*, 1355–1359.
53. deWexler, S. B.; Galvele, J. R. *J. Electrochem. Soc.* **1974**, *121*, 1271–1276.
54. Ramgopal, T.; Gouma, P. I.; Frankel, G. S. *Corrosion* **2002**, *58*, 687–697.
55. Brennenstuhl, A. unpublished research.
56. Lee, Y.; Gangloff, R. P. *Metall. Mater. Trans. A* **2007**, *38*, 2174–2190.
57. Asahi, H.; Yagi, A.; Ueno, M. *ISIJ Int.* **1993**, *33*, 1190–1195; **1993**, *33*, 1275–1280; **1994**, *34*, 290–294; *Corrosion* **1994**, *50*, 537–545.
58. Chu, R.; Chen, W.; Wang, S.-H.; King, F.; Jack, T. R.; Fessler, R. R. *Corrosion* **2004**, *60*, 275–283.
59. Parkins, R. N.; Blanchard, W. K., Jr.; Delanty, B. S. *Corrosion* **1994**, *50*, 394–408.
60. Parkins, R. N.; Zhou, S. *Corros. Sci.* **1997**, *39*, 159–173.
61. Kehler, B. A.; Scully, J. R. *Corrosion* **2008**, *64*, 465–477.
62. Gavriljuk, V. G.; Shivanyuk, V. N.; Shanina, B. D. *Acta Mater.* **2005**, *53*, 5017–5024.
63. Robertson, I. M. *Eng. Fract. Mech.* **2001**, *68*, 671–692.
64. Pundt, A.; Kirchheim, R. *Annu. Rev. Mater. Res.* **2006**, *36*, 555–608.
65. Toribio, J. *Eng. Fract. Mech.* **2008**, *75*, 2683–2694.
66. Scamans, G. M.; Alani, R.; Swann, P. R. *Corros. Sci.* **1976**, *16*, 443–459.
67. Behnood, N.; Cai, H.; Evans, J. T.; Holroyd, N. J. H. *Mater. Sci. Eng. A* **1989**, *A119*, 23–32.
68. Singh, P. M.; Lewandowski, J. J.; Holroyd, N. J. H.; Evans, J. T. *Proceedings of Parkins Symposium on Fundamental Aspects of Stress Corrosion Cracking*; Meletis, E. I., Parkins, R. N., Eds.; TMS, Warrendale, PA, 1992; pp 567–583.
69. Holroyd, N. J. H.; Vasudevan, A. K.; Christodoulou, L. *Aluminum Alloys – Contemporary Research and Applications*; Academic Press, Inc.: London, 1989; pp 463–483.
70. Gaudett, M. A.; Scully, J. R. *Metall. Mater. Trans. A* **1999**, *30A*, 65–79A.
71. Gaudett, M. A.; Scully, J. R. *Metall. Mater. Trans. A* **2000**, *31A*, 81A–92A.
72. Teter, D. F.; Robertson, I. M.; Birnbaum, H. K. *Acta Mater.* **2001**, *49*, 4313–4323.
73. Peterson, M. H.; Brown, B. F.; Newbegin, R. L.; Groover, R. E. *Corrosion* **1967**, *23*, 142–148.
74. Meyn, D. A. *Corros. Sci.* **1967**, *7*, 721–723.



75. Newman, R. C.; Procter, R. P. M. *Br. Corros. J.* **1990**, 25, 259–269.
76. Andresen, P. L.; Morra, M. M. *J. Nucl. Mater.* **2008**, 383, 97–111.
77. Lozano-Perez, S.; English, C. A.; Terachi, T. In *Corrosion/2008*; NACE: Houston, TX, 2008; Paper No. 495.
78. Peng, Q. J.; Kwon, J.; Shoji, T. *J. Nucl. Mater.* **2004**, 324, 52–61.
79. Turnbull, A. *Corrosion* **2008**, 64, 420–438.
80. Parkins, R. N.; Singh, P. M. *Corrosion* **1990**, 46, 485–499.
81. Parkins, R. N.; Belhimer, E.; Blanchard, W. K., Jr. *Corrosion* **1993**, 49, 951–966.
82. Chen, W.; King, F.; Vokes, E. *Corrosion* **2002**, 58, 267–275.
83. Akashi, M.; Nakayama, G. *Effects of the Environment on the Initiation of Crack Growth*; ASTM STP 1298, Philadelphia, PA, 1997; pp 150–164.
84. Cheung, C.; Erb, U.; Palumbo, G. *Mater. Sci. Eng. A.* **1994**, 185, 39–43.
85. Schuh, C. A.; Kumar, M.; King, W. E. *Acta Mater.* **2003**, 51, 687–700.
86. Engelberg, D. L.; Humphreys, F. J.; Marrow, T. J. *J. Microsc.* **2008**, 230, 435–444.
87. Reed, B. W.; Kumar, M.; Minich, R. W.; Rudd, R. E. *Acta Mater.* **2008**, 56, 3278–3289.
88. Palumbo, G.; Aust, K. T.; Lehockey, E. M.; Erb, U.; Lin, P. *Scr. Mater.* **1998**, 38, 1685–1690.
89. Zaefferer, S.; Wright, S. I.; Raabe, D. *Metall. Mater. Trans. A.* **2008**, 39, 374–389.
90. Wells, D. B.; Stewart, J.; Herbert, A. W.; Scott, P. M.; Williams, D. E. *Corrosion* **1989**, 45, 649–660.
91. Gaudett, M. A.; Scully, J. R. *Metall. Trans. A.* **1994**, 25A, 775–787.
92. Lehockey, E. M.; Brennenstuhl, A. M.; Thompson, I. *Corros. Sci.* **2004**, 46, 2383–2404.
93. Marrow, T. J.; Babout, L.; Jivkov, A. P.; Wood, P.; Engelberg, D.; Stevens, N.; Withers, P. J.; Newman, R. C. *J. Nucl. Mater.* **2006**, 352, 62–74.
94. Babout, L.; Marrow, T. J.; Engelberg, D.; Withers, P. J. *Mater. Sci. Technol.* **2006**, 22, 1068–1075.
95. Jivkov, A. P.; Marrow, T. J. *Theor. Appl. Fract. Mech.* **2007**, 48, 187–202.
96. Jivkov, A. P.; Stevens, N. P. C.; Marrow, T. J. *J. Pressure Vessel Technol.-Trans. ASME*; 2008, 130.
97. Duxbury, P. M.; McGarrity, E. S.; Holm, E. A. *Mech. Mater.* **2006**, 38, 757–771.
98. Turnbull, A. *Corrosion* **2001**, 57, 175–189.
99. *Corrosion Chemistry within Pits, Crevices and Cracks*; Turnbull, A. Ed. HMSO: London, 1987.
100. Turnbull, A.; Horner, D. A.; Connolly, B. J. *Eng. Fract. Mech.* **2009**, 76, 633–640.
101. Shinohara, T.; Tsujikawa, S.; Hisamatsu, Y. *Boshoku Gijutsu (Corros. Eng.)* **1985**, 34, 283–290.
102. Uhlig, H. H. In *Stress-Corrosion Cracking and Hydrogen Embrittlement of Iron-Base Alloys*; Staehle, R. W., Hochmann, J., McCright, R. D., Slater, J. E., Eds.; NACE: Houston, TX, 1977; pp 174–179.
103. Shoji, S.; Ohnaka, N.; Furutani, Y.; Saito, T. *Boshoku Gijutsu (Corros. Eng.)* **1986**, 35, 559–565.
104. Shoji, S.; Ohnaka, N. *Corros. Eng.* **1989**, 38, 111–120.
105. Drugli, J. M.; Steinsmo, U. *ACOM (Sweden)* **1998**, 4, 7.
106. Hinds, G.; Turnbull, A. *Corros. J.* **2008**, 64, 101–106.
107. Turnbull, A.; Zhou, S.; Nicholson, P.; Hinds, G. *Corros. J.* **2008**, 64, 325–333.
108. Galvele, J. R. *J. Electrochem. Soc.* **1976**, 123, 464–474.
109. Bertocci, U.; Pugh, E. N. In *Corrosion Chemistry Within Pits, Crevices and Cracks*; Turnbull, A., Ed.; HMSO: London, 1987; pp 187–198.
110. Bertocci, U.; Thomas, F. I.; Pugh, E. N. *Corrosion* **1984**, 40, 439–440.
111. Shahrabi, T.; Newman, R. C.; Sieradzki, K. *J. Electrochem. Soc.* **1993**, 140, 348–352.
112. Speidel, M. O. *Corrosion* **1977**, 33, 199–203.
113. Parkins, R. N. *Corros. Sci.* **1980**, 20, 147–166.
114. Procter, R. P. M.; Omidéy, M. V. E.; Newman, R. C.; Zheng, W. *Corros. Sci.* **1992**, 33, 1009–1031.
115. Newman, R. C.; Zheng, W.; Procter, R. P. M. *Corros. Sci.* **1992**, 33, 1033–1051.
116. Scott, P. M.; Combrade, P. In *ASM Handbook, Vol. 13C. Corrosion: Environments and Industries* 2006; Vol. 13C, pp 362–385.
117. Scott, P. M.; Le Calvar, M. In *Proceedings of the Sixth International Symposium on Environmental Degradation of Materials in Nuclear Power Systems – Water Reactors* 1993; pp 657–667.
118. Newman, R. C.; Gendron, T. S.; Scott, P. M. *Proceedings of the Ninth International Symposium on Environmental Degradation of Materials in Nuclear Power Systems – Water Reactors*, TMS-AIME, Warrendale, PA, 2000; pp 79–93.
119. Scenini, F.; Newman, R. C.; Cottis, R. A.; Jacko, R. J. *Corrosion* **2008**, 64, 824–835.
120. Brown, A.; Harrison, J. T.; Wilkins, R. *Electrochemical Investigations of Stress Corrosion Cracking of Plain Carbon Steel in Carbon Dioxide–Carbon Monoxide–Water System*. In *Stress-Corrosion Cracking and Hydrogen Embrittlement of Iron-Base Alloys*; Staehle, R. W., Hochmann, J., McCright, R. D., Slater, J. E., Eds.; NACE: Houston, TX, 1977; pp 686–695.
121. Hannah, I. M.; Newman, R. C.; Procter, R. P. M. *Environmental Cracking of C–Mn Steel in CO/CO<sub>2</sub>/H<sub>2</sub>O Solutions*. In *Hydrogen Effects on Materials Behaviour*; Moody, N. R., Thompson, A. W., Eds.; TMS: Warrendale, PA, 1990; pp 965–974.
122. Newman, R. C. *Corrosion* **2008**, 64, 819–823.
123. Parkins, R. N. *Br. Corros. J.* **1972**, 7, 15–28.
124. Parkins, R. N. *JOM* **1992**, 44, 12–19.
125. Diegle, R. B.; Vermilyea, D. A. *J. Electrochem. Soc.* **1975**, 122, 180–188.
126. Newman, R. C.; Sieradzki, K. *Corros. Sci.* **1983**, 23, 363–378.
127. Smart, N. R.; Scott, P. M.; Procter, R. P. M. *Corros. Sci.* **1990**, 30, 877–901.
128. Ford, F. P.; Burstein, G. T.; Hoar, T. P. *J. Electrochem. Soc.* **1980**, 127, 1325–1331.
129. Sieradzki, K. *Atomistic and Micromechanical Modeling Aspects of Environment-Induced Cracking of Metals*. In *Environment-Induced Cracking of Metals*; Gangloff, R. P., Ives, M. B., Eds.; NACE: Houston, TX, 1990; pp 125–137.
130. Cole, A. T.; Newman, R. C.; Sieradzki, K. *Corros. Sci.* **1988**, 28, 109–118.
131. Newman, R. C.; Mehta, A. In *Stress-corrosion Cracking of Austenitic Alloys, Environment-Induced Cracking of Metals*; Gangloff, R. P., Ives, M. B., Eds.; NACE: Houston, TX, 1990; pp 489–510.
132. Holzleitner, S.; Kranister, W.; Mori, G.; Schmuki, P. In *Corrosion/2008*; NACE: Houston, TX, 2008; Paper No. 486.
133. Vermilyea, D. A. *A Film Rupture Model for Stress Corrosion Cracking*. In *Stress-Corrosion Cracking and Hydrogen Embrittlement of Iron-Base Alloys*; Staehle, R. W., Hochmann, J., McCright, R. D., Slater, J. E., Eds.; NACE: Houston, TX, 1977; pp 208–217.

134. Lu, Z.; Shoji, T. *J. Pressure Vessel Technol. (Trans. ASME)* **2006**, *128*, 318–327.
135. Gerberich, W. W.; Davidson, D. L.; Kaczorowski, M. *J. Mech. Phys. Solids* **1990**, *38*, 87–113.
136. Gao, Y. C.; Kwang, K. C. Elastic-plastic fields in steady crack growth in a strain-hardening material. In Proceedings of the 5th International Conference on Fracture, Cannes, March/April 1981, vol. 2, pp 669–682 (1981).
137. Hall, M. M., Jr. Crack Tip Strain Rate Equation with Applications to Hydrogen Embrittlement and Active Path Dissolution Models of Stress Corrosion Cracking. In *Environment-Induced Cracking of Materials*; Shipilov, S., Jones, R. H., Olive, J. M., Rebak, R. B., Eds.; Elsevier: Amsterdam, 2008; pp 59–68.
138. Hall, M. M., Jr. *Corros. Sci.* **2008**, *50*, 2902–2905.
139. Hall, M. M., Jr. *Corros. Sci.* **2009**, *51*, 225–233.
140. Bruemmer, S. M.; Thomas, L. E. *Surf. Interface Anal.* **2001**, *31*, 571–581.
141. Newman, R. C.; Healey, C. *Corros. Sci.* **2007**, *49*, 4040–4050.
142. Davies, D. H.; Burstein, G. T. *Corrosion* **1980**, *36*, 416–422.
143. Zhou, S.; Stack, M. M.; Newman, R. C. *Corros. Sci.* **1996**, *38*, 1071–1084.
144. Nagano, H.; Kajimura, H. *Corros. Sci.* **1996**, *38*, 781–791.
145. Green, J. A. S.; Parkins, R. N. *Corrosion* **1968**, *24*, 66–69.
146. Beck, T. R.; Grens, E. A., Jr. *J. Electrochem. Soc.* **1969**, *116*, 177–184.
147. Parkins, R. N.; Beavers, J. A. *Corrosion* **2003**, *59*, 258–273.
148. Brown, B. F.; Fujii, C. T.; Dahlberg, E. P. *J. Electrochem. Soc.* **1969**, *116*, 218–219.
149. Cottis, R. A.; Alavi, A.; Taqi, E. A. Chemical Conditions and Hydrogen Generation Within Crevices in Carbon-Manganese Steels. In *Advances in Localized Corrosion*; Isaacs, H. S., Ed.; NACE-9: Houston, TX, 1990; pp 403–406.
150. Turnbull, A.; Ferriss, D. H. *Corros. Sci.* **1987**, *27*, 1323–1350.
151. Gangloff, R. P. *Metall. Trans. A* **1985**, *16A*, 953–969.
152. Now joined with another series called Corrosion Deformation Interactions – International Conference on Hydrogen Effects on Materials Behavior and Corrosion Deformation Interactions; Moran, WY; USA; Sept. 2002; pp 22–26.
153. Katz, Y.; Tymiak, N.; Gerberich, W. W. *Eng. Fract. Mech.* **2001**, *68*, 619–646.
154. Lynch, S. P. In *Corrosion/2007*; NACE: Houston, TX, 2007; Paper No 489.
155. Delafosse, D.; Magnin, T. *Eng. Fract. Mech.* **2001**, *68*, 693–729.
156. Rice, J. R.; Thomson, R. *Phil. Mag.* **1974**, *29*, 73–97.
157. Edeleanu, C.; Forty, A. J. *Phil. Mag.* **1960**, *58*, 1029–1040.
158. Beavers, J. A.; Pugh, E. N. *Metall. Trans. A* **1980**, *11A*, 809–820.
159. Pugh, E. N. *Corrosion* **1985**, *41*, 517–526.
160. Sieradzki, K.; Newman, R. C. *Philos. Mag. A* **1985**, *51*, 95–132.
161. Sieradzki, K.; Newman, R. C. *J. Phys. Chem. Solids* **1987**, *48*, 1101–1113.
162. Volkert, C. A.; Lilleodden, E. T.; Kramer, D.; Weissmüller, J. *Appl. Phys. Lett.* **2006**, *89*, 061920.
163. Mathur, A.; Erlebacher, J. *Appl. Phys. Lett.* **2007**, *90*, 061910.
164. Kramer, D.; Viswanath, R. N.; Weissmüller, J. *Nano Lett.* **2004**, *4*, 793–796.
165. Weissmüller, J.; Newman, R. C.; Jin, H. J.; Hodge, A. M.; Kysar, J. W. *MRS Bull.* **2009**, *34*, 577–586. Special issue.
166. Kelly, R. G.; Shahrabi, T.; Frost, A. J.; Newman, R. C. *Metall. Trans. A* **1991**, *22A*, 191–197.
167. Saito, M.; Smith, G. S.; Newman, R. C. *Corros. Sci.* **1993**, *35*, 411.
168. Barnes, A.; Senior, N. A.; Newman, R. C. *Metall. Trans. A* **2009**, *40*, 58–68.
169. Galvele, J. R. *Corros. Sci.* **1987**, *27*, 1–33.
170. Galvele, J. R. *Acta* **2000**, *45*, 3537–3541.
171. Sieradzki, K.; Friedersdorf, F. J. *Corros. Sci.* **1994**, *36*, 669–675.
172. Galvele, J. R. *Corros. Sci.* **1994**, *36*, 901–910.
173. Bianchi, G. L.; Galvele, J. R. *Corros. Sci.* **1987**, *27*, 631–635.
174. Bianchi, G. L.; Galvele, J. R. *Corros. Sci.* **1993**, *34*, 1411–1422.
175. Bianchi, G. L.; Galvele, J. R. *Corros. Sci.* **1994**, *36*, 611–619.
176. Delamare, F.; Rhead, G. E. *Surf. Sci.* **1971**, *28*, 267–284.
177. Meletis, E. I.; Lian, K. J. *Mech. Behav. Mater.* **1995**, *6*, 69–84.
178. Jones, D. A.; Jankowski, A. F.; Davidson, G. A. *Metall. Mater. Trans. A* **1997**, *28A*, 843–850.
179. Aaltonen, P.; Jagodzinski, Y.; Tarasenko, A.; Smouk, S.; Hanninen, H. *Corros. Sci.* **1998**, *40*, 903–908.
180. Jagodzinski, Y.; Aaltonen, P.; Smouk, S.; Tarasenko, A.; Hanninen, H. *J. Alloys Compd.* **2000**, *310*, 256–260.
181. Aaltonen, P.; Jagodzinski, Y.; Hanninen, H. Vacancy Generation in Electrochemical Oxidation/Dissolution of Copper in NaNO<sub>2</sub> Solution and its Role in SCC Mechanism. In Proceedings of International Conference on Hydrogen Effects on Materials Behavior and Corrosion Deformation Interactions, Moran, WY, USA, 22–26 Sept. 2002, pp 597–606; TMS-AIME, 2003.
182. Serebrinsky, S. A.; Galvele, J. R. *Corros. Sci.* **2004**, *46*, 591–612.
183. Stumpf, R.; Feibelman, P. J. *Phys. Rev. B* **1996**, *54*, 5145–5150.
184. Tersoff, J. *Phys. Rev. Lett.* **1995**, *74*, 434–437.
185. Robert, S.; Gauthier, S.; Bocquet, F.; Rousset, S.; Duvault, J. L.; Klein, J. *Surf. Sci.* **1996**, *350*, 136–144.
186. Magnin, T.; Chambreuil, A.; Chateau, J. P. *Int. J. Fract.* **1996**, *79*, 147–163.
187. Yan, B.; Farrington, G. C.; Laird, C. *Acta Metall.* **1985**, *33*, 1533–1545.

## 2.12 Corrosion Fatigue

**R. Akid**

Materials & Engineering Research Institute, Sheffield Hallam University, Howard Street, Sheffield S1 1WB, UK

© 2010 Elsevier B.V. All rights reserved.

2.12.1	Introduction and Historical Perspective	929
2.12.2	Fundamentals of Fatigue Failure	930
2.12.3	Corrosion Fatigue Regimes, Mechanisms, and Modeling	932
2.12.3.1	Initiation and Short Crack Growth	932
2.12.3.1.1	Passive film breakdown and pitting	933
2.12.3.1.2	Pitting corrosion fatigue models	938
2.12.3.2	Long Crack Growth	938
2.12.3.2.1	LEFM-based corrosion fatigue models	940
2.12.4	Variables Affecting Corrosion Fatigue	940
2.12.4.1	Microstructure	941
2.12.4.2	Loading Frequency	941
2.12.4.3	Solution/Electrochemical Conditions	942
2.12.4.4	Surface Condition	942
2.12.4.5	Stress State	944
2.12.5	Corrosion Fatigue of Specific Alloys	944
2.12.5.1	Ferrous Alloys	944
2.12.5.2	Stainless Steels	946
2.12.5.3	Aluminum Alloys	947
2.12.5.4	Titanium Alloys	948
2.12.6	Prevention of Corrosion Fatigue	949
2.12.6.1	Prevention by Barrier Coatings and Surface Treatments	949
2.12.6.2	Prevention by Cathodic Protection	950
2.12.7	Summary	950
References		951

### Abbreviations

**AA2024** Aluminum Alloy 2024  
**ASME** American Society of Mechanical Engineers  
**ASTM** ASTM International  
**BWR** Boiler water reactor  
**c.p.** Commercially pure  
**CF** Corrosion fatigue  
**CGRs** Crack growth rates  
**CP** Cathodic protection  
**DA** Damage accumulation  
**EAC** Environmentally assisted cracking  
**HSLA** High-strength low-alloy  
**LEFM** Linear elastic fracture mechanics  
**MSC** Microstructurally short crack  
**OCP** Open circuit potential

**PSBs** Persistent slip bands

**PSC** Physically short crack

**RTP** Roller quench temper

**S-N** Stress vs number of fatigue cycles

### Symbols

**a** Defect size

**B, x, and  $\beta$**  Constants

**C** Pit radius

**d** A microstructural dimension

**D** LEFM threshold crack growth rate

**f** Frequency

**F** Geometry factor

**K<sub>max</sub>** Maximum stress intensity

\*It is the intention in this chapter to discuss some of the more recent developments in the field of corrosion fatigue. Given the previous edition's emphasis on long crack growth, much of this chapter is devoted to an understanding of the early stages of corrosion fatigue, often termed the 'initiation' stage.

$K_{\min}$	Minimum stress intensity
$K_t$	Stress concentration factor
$m$	Constant
$m1, m2, A, \text{ and } x$	Experimentally determined constants
$N$	Number of cycles
$N_f$	Number of cycles to failure
$Q$	Function based on crack shape
$R$	Stress ratio
$r_p$	Size of the plastic zone
$t$	Time
$t_{p/c}$	Time to pit/crack transition
$\gamma$	Shear strain
$\gamma_{eq}$	Equivalent strain
$\Delta K$	Crack tip stress intensity factor range
$\Delta K_{th}$	Threshold stress intensity factor
$\sigma$	Stress
$\sigma_a$	Stress amplitude
$\sigma_y$	Yield strength

### 2.12.1 Introduction and Historical Perspective

The term *fatigue* was coined in the latter half of the nineteenth century, although this type of failure had previously been recognized in the early 1800s as a different type of fracture occurring in the axles of the railway locomotives and carriages. In 1843, Rankine<sup>1</sup> attributed this behavior to a gradual deterioration of the material during its service life. Other views held at the time were that the metal had become tired, lost its nature, or crystallized.

Fatigue cracking<sup>2</sup> is a consequence of highly localized plastic deformation, where the vast majority of cracks start at a free surface. However, it is not necessary for the bulk of the grains in a piece of metal to deform plastically for it to fail by fatigue, and continued cyclic plastic deformation in one localized surface region is sufficient for fatigue failure to occur. This aspect distinguishes the problem from any other form of mechanical failure, the basic features of fatigue failure being the ‘initiation’ of surface microcracks and their subsequent propagation through the bulk of the material.

*Corrosion fatigue* is a term used to describe cracking (including both initiation and growth) in materials subject to the combined actions of a fluctuating (cyclic) stress and corrosion. Electrochemical reactions taking place at the metal–environment interface govern whether the mechanism of failure is controlled

by anodic dissolution or hydrogen embrittlement. Unlike the phenomenon ‘*stress corrosion cracking*’ where cracking is often controlled by specific combinations of material–environment, for example, brass in ammonia-containing environments, this specificity rarely applies in this type of cracking process. In fact, environments as innocuous as moist air can lead to severe reductions in the fatigue resistance of high-strength engineering alloys.<sup>3</sup>

Haigh<sup>4</sup> published possibly the earliest recorded paper on corrosion fatigue while seeking to explain the failure of towing ropes that were kept in a state of frequent vibration when exposed to sea water. Later work by McAdam<sup>5</sup> and Gough<sup>6</sup> laid the foundations for work on the subject of corrosion fatigue. McAdam’s work showed the danger of adopting higher-strength alloy steels in preference to ordinary steels. It is now established that an increase in tensile strength of low corrosion-resistance alloys is associated with a decreased resistance to corrosion fatigue. McAdam’s work also included the connection between pitting and cracking and showed the time-dependency effects due to corrosion by studying the effects of frequency of loading on fatigue lifetime. The influence of the environment on fatigue is assessed by plotting the relationship of stress to number of cycles to failure, the so-called ( $S$ – $N$ ) curve. Figure 1 shows the results of  $S$ – $N$  tests on different substrates in a 3.5% NaCl solution at open-circuit potential and open to the atmosphere. Here, it can be seen that the most significant impact of the environment is seen at stress levels close and below the in-air fatigue limit, a region that might historically have been deemed the ‘crack initiation’ region. As will be discussed later, it is now known that the environment has a major effect on the early stages of crack growth in the microstructural fracture mechanics regime.<sup>7</sup>

The electrochemical aspects of corrosion fatigue were clearly demonstrated in the studies of Evans and Simnad.<sup>8,9</sup> An important aspect of this work included observations showing an increase in corrosion rate with increase in applied stress (see Section 2.12.3). These results highlighted an increase in metal dissolution when the degree of plasticity increased. Furthermore, it was noted that when the material was subject to stresses within the elastic range, the rate of corrosion hardly differed from when the material was unstressed.

Another feature of this work included the effects of an applied cathodic current. In this case, it was found that fatigue lives were enhanced in neutral salt solutions, in which the rate of metal dissolution at potentials below the open-circuit potential was

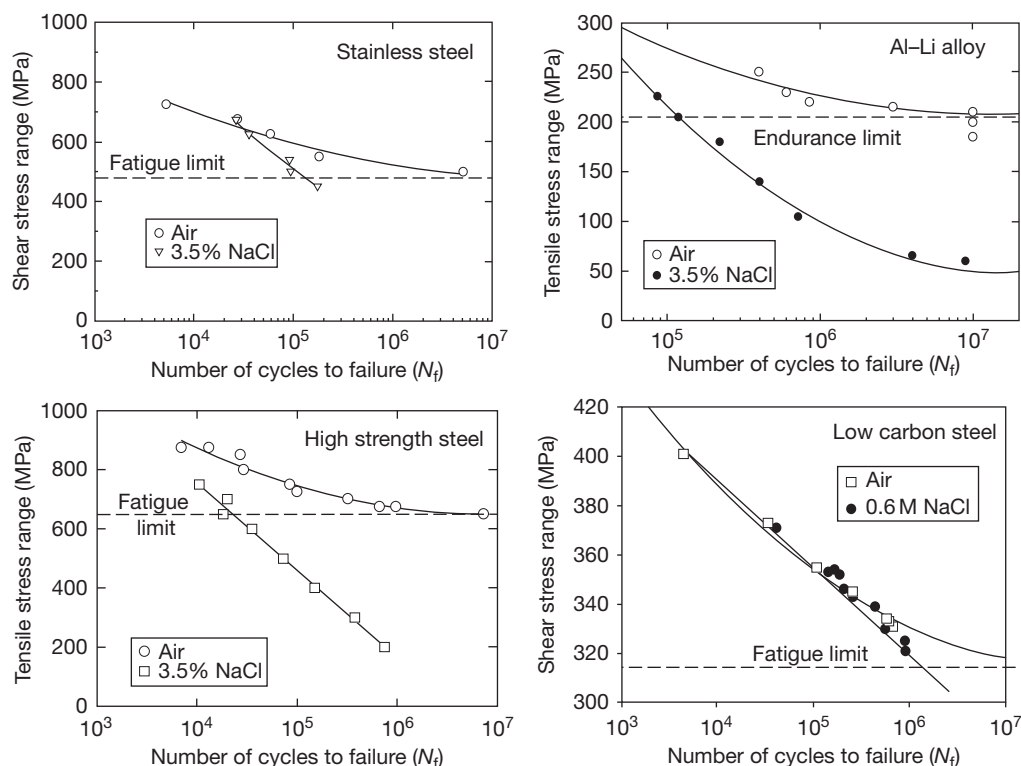


**Figure 1** S-N curves for various alloys in 3.5% (0.6M) NaCl. Reproduced from Miller, K. J.; Akid, R. *Proc. R. Soc. Lond. A* **1996**, 452, 1411–1432.

negligible. For acidic solutions, a greater applied cathodic current was required for protection before an equivalent improvement in fatigue life was observed. The conclusion given was that ‘while elastic deformation does not affect the chemical or electrochemical properties of the iron, deformation beyond the elastic limit (which may occur if pits produce stress intensification) alters these properties, making the iron behave like a more reactive metal. This behavior was later confirmed by measuring the growth rates of pits under different values of stress (see [Section 2.12.3.1.2](#)).

The following sections of this chapter will address the mechanisms and factors affecting the fatigue life of various engineering alloys operating within corrosive environments.

## 2.12.2 Fundamentals of Fatigue Failure

Before going on to discuss corrosion fatigue in detail, it is worthwhile briefly outlining the basic fundamentals of fatigue in the absence of an environment. Given this

understanding, it is considered that the reader will better appreciate the role of the environment in the corrosion fatigue process.

Fatigue damage is responsible for around 70–80% of the rupture cases of mechanical engineering components and structures in the world; therefore, an understanding of how cracks initiate and propagate would be useful when designing these structures.

It is generally accepted that purely elastic deformations are totally reversible and do not induce damage. Furthermore, it is accepted that fatigue rupture is related to the localization of plastic deformation,<sup>10</sup> and during cyclic loading, the following occurs<sup>11</sup>:

- cyclic softening or hardening: at constant strain amplitude, the stress amplitude decreases or increases respectively,
- crack development via surface intrusion and extrusions,
- crack propagation.

The main site for crack initiation is generally the material surface, as the surface grains may deform plastically and crack more easily than other grains,



because not only are they in contact with the environment, which has a great role in fatigue damage, but they are also the only ones not totally surrounded by other grains, that is, unconstrained.

Initiation sites most frequently encountered include the material surface defects – stress concentrations near notches, corners, holes, etc. In the case of smooth specimens, without any macroscopic defects, slip bands form at the surface on activated slip systems in grains favorably oriented. These slip bands are associated with intrusions/extrusions, see **Figure 2**, which may act as crack initiation sites.

For some materials, such as body-centered cubic (bcc) alloys, initiation may be intergranular owing to shape changes of the near surface; this leads to deformation incompatibility which in turn contributes to localized deformation irreversibility at the grain boundaries. This effect has been attributed to the, thermally activated, so-called asymmetric glide of the screw dislocations in tension and compression.<sup>10,13</sup> Also, crack initiation very often takes place at interfaces such as inclusion/matrix or second phase/matrix.

There appears to be no real distinction between crack initiation and crack propagation, just as it is difficult to know when a slip band becomes a crack. **Figure 3** presents a schematic of the development of a crack from a free surface, while **Figure 4** relates the crack growth rate with the crack size and the relevant crack growth regime.

**Figure 3** shows that a crack initiates from the free surface, usually in the largest grain along a shear slip plane at  $45^\circ$  to the loading axis. Plasticity induced in the grain drives the crack until a dislocation build-up occurs as the crack tip approaches the grain boundary between grains 1 and 2. As the crack tip approaches the first grain boundary ( $d_1$ ), in **Figure 4**, the growth rate of the crack decreases. There are now two possible outcomes depending upon the level of the applied stress; if the stress is below the fatigue limit, the crack decelerates and may arrest, and if the stress level is above the fatigue limit, the crack grows into the next grain and can continue to propagate throughout the structure. A revised definition of the fatigue limit might be ‘the stress level where a crack does not propagate beyond a defining microstructural dimension.’ This dimension being one or several grains or a value related to the microstructure, for example, martensite lath size or prior austenite grain boundary size. At and around the fatigue limit, the ‘short’ crack growth behavior is very nonlinear. This nonlinear

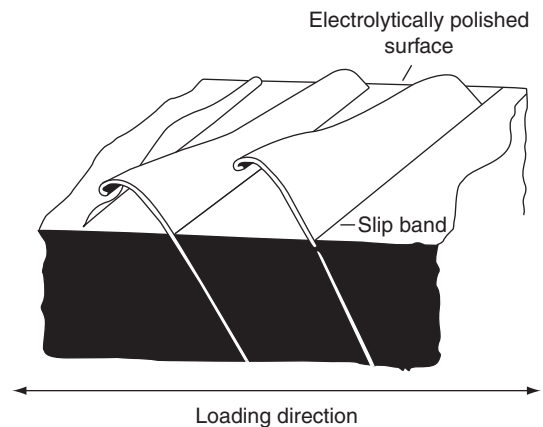


**Figure 2** Formation of intrusions and extrusions at persistent slip bands (PSBs) during fatigue loading. Reproduced from Forsyth, P. J. E. *J. Inst. Metals* **1951/2**, 80, 181.

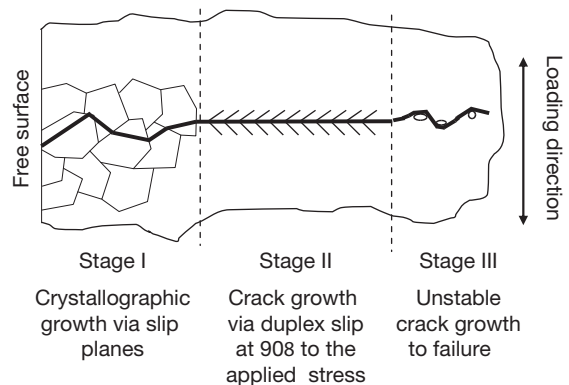


**Figure 3** Schematic illustrating different fatigue crack growth stages.

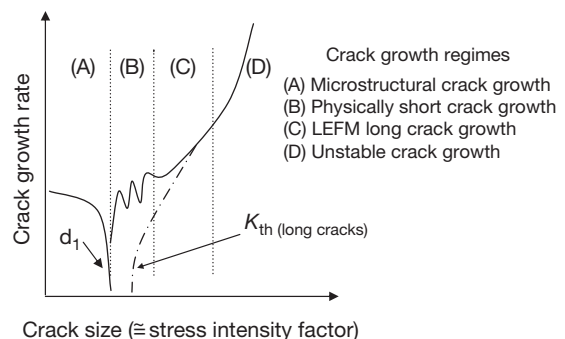


**Figure 4** Fatigue crack growth rate as a function of crack size.

'short crack' growth behavior continues as the crack propagates through the microstructure. However, as the crack tip stress intensity increases with crack length, the effective barrier resistance of the grain structure diminishes until the crack growth is unaffected by the microstructure. At this point, the ratio of the crack tip plastic zone size to crack length is around 0.02, and the crack may be considered to fall within the linear elastic fracture mechanics (LEFM) regime and is described as a 'long crack' (see Section 2.12.4.2).

The first two crack growth stages (A and B) shown in Figure 4 have 'historically' been considered as the *initiation* stage, while the third regime (C) is the representative of the *propagation* stage. The variables affecting each of these stages are further discussed in Section 2.12.4.

### 2.12.3 Corrosion Fatigue Regimes, Mechanisms, and Modeling

The following section is aimed at addressing the different regimes that contribute to the damage processes of pit and crack development and subsequent growth of corrosion fatigue cracks. The section is divided into the growth of defects (pits and cracks) from smooth surfaces and the growth of preexisting long cracks. The examples given in this section relate predominantly to steels actively corroding within chloride environments; however, where appropriate, work illustrating other metal/environment systems is also discussed.

#### 2.12.3.1 Initiation and Short Crack Growth

It has recently been recognized that cracks develop very early in the lifetime of a component and that the fatigue crack initiation period is considered to be a negligible phase in the fatigue failure process.<sup>14,15</sup> The premise is that fatigue cracks initiate below the fatigue limit but the rate of propagation is controlled by numerous factors and under some cases this rate is sufficiently small to be considered negligible, leading to infinite fatigue life. An important point here is that if the conditions change, for example, a fatigue load excursion above the fatigue limit stress, the propagation rate may change causing the crack to grow beyond a critical threshold size.

The corrosion fatigue process may be considered analogous to that of air fatigue, notably because damage occurs very early in life and the defect, pit or

crack propagates at a rate governed by the loading/environmental conditions. As will be discussed later, processes such as passive film breakdown and pitting play an important role in contributing to the early stages of damage, Figure 5.

Figure 5 shows the typical development stages for air and corrosion fatigue cracking. In air, a crack develops on the surface at some defined size,  $a_0$ , often related to the surface roughness or a metallurgical feature such as an inclusion, and then grows up to the major microstructural barrier. If the stress level is not above the fatigue limit, crack arrest occurs and a nonfailure condition exists. If the stress level is just above the fatigue limit, the crack can grow beyond the major microstructural barrier and a failure condition exists. Under corrosion fatigue conditions, surface film breakdown or local microgalvanic activity occurs leading to localization of corrosion (pitting). Subject to the nature of the environment, pit growth continues until a transition to cracking occurs. Environment-assisted crack growth then ensues until failure occurs.

In terms of fatigue life, the most important regimes are (a) in air, the stage I (shear) to stage II (tensile) crack transition; Figure 3 and (b) in corrosion fatigue, the pit-crack transition. These regions are highlighted in Figure 5. At this point, the crack is propagating at its lowest rate. A similar feature is observed for corrosion fatigue loading.<sup>7</sup> In the case of air fatigue, the microstructural barriers impede crack growth; in corrosion fatigue, pit growth rate

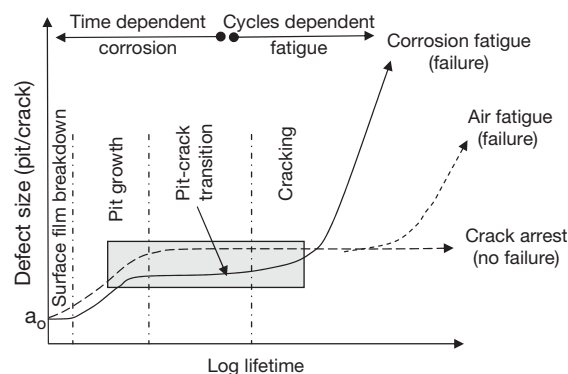


**Figure 5** Schematic showing the behavior of fatigue cracks under air and corrosion fatigue conditions. Note that the stress level for the corrosion fatigue curve is less than the in-air fatigue limit of the material. Individual annotated regimes are for corrosion fatigue only. Reproduced from Akid, R. In *Effects of Environment on the Initiation of Crack Growth*; Van der Sluys, W. A., Piascik, R. S., Zawiercha, R., Eds.; ASTM STP 1298, 1997, pp 1–17.

decreases (see Figure 8) as it is governed largely by solution chemistry and electrochemistry, which change as the pit size increases. Akid<sup>16</sup> undertook a comparison of these transition regimes in a high-strength steel for fatigue in air and in 0.6 M NaCl (see Figure 6). The following main conclusion can be drawn: the stage I to stage II transition in air takes place at a greater fraction of lifetime and at defect sizes larger than that of the pit/stage II transition (see shaded regions). The implication of this result is that stage II tensile cracking can be promoted by the presence of a pit and occurs earlier in the lifetime of a component subject to corrosion fatigue when compared to identical loading conditions in the absence of the environment, that is, air fatigue loading.

The term ‘crack initiation’ has generally been considered as that period prior to the observation of a crack. This leads to a problem, notably, ‘when is a crack observable?’; hence quantification of the period of initiation becomes subjective and dependent upon the equipment being used to monitor the surface. This problem was recognized by Ford<sup>17</sup> who proposed that initiation, under environment-assisted cracking conditions, comprises only the time required to form a localized environment and as all surfaces contain geometrical discontinuities, this period, relative to the total lifetime, will comprise only a few percent. This is in keeping with the premise that propagation dominates the damage process.

### 2.12.3.1.1 Passive film breakdown and pitting

Many commercial alloys contain inclusions, and these can provide the sites for crack initiation in both air and corrosion fatigue. Inclusions are chemically

different to the matrix in which they are contained and therefore will have a different electrochemical behavior to that of the matrix. Furthermore, the passive film developed over the site of an inclusion will differ primarily in its chemistry and thickness from the passive film formed on the matrix. The consequence of this is that these sites are preferentially attacked in the presence of depassivating agents such as chloride ions; for example, AlCu-type inclusions in AA2024 alloys suffer preferential chemical attack and can promote pitting.<sup>18</sup>

The effect of pitting on a component's fatigue life was demonstrated in the early work of McAdam,<sup>5</sup> and Evans and Simnad<sup>8,9</sup> in which it was shown that pre-pitting a specimen prior to air fatigue testing results in pits acting like notches, thereby lowering the fatigue limit. However, pre-pitting tests differ significantly from full immersion or cyclic immersion corrosion fatigue tests, which will be discussed later. Jack and Paterson<sup>19</sup> concluded, in their work on three turbine rotor shafts (2% Cr/Ni/Mo/V steel), that cracks initiated at corrosion pits and grew by high cycle fatigue. Metallographic examination of the rotor shafts showed that pits were widely distributed and some pits were present without cracks while all the cracks had initiated at pits. This would seem to imply that in these materials, cracking occurs after the onset of pitting and not the reverse.

Conversely, Duquette and Uhlig<sup>20</sup> argued that initial pit formation is not a requirement for corrosion fatigue. Evidence from their research suggested that the applied stress level determines whether cracks develop from pits or from slip bands. At high-stress levels, slip bands form quickly with insufficient time for pit formation to take place; hence slip-band

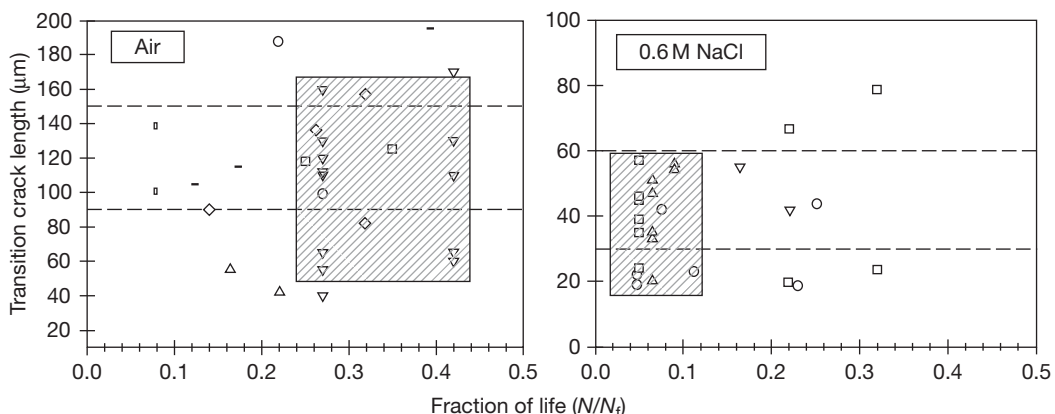


**Figure 6** Comparison of stage I crack/stage II crack and pit/stage II crack transition for a high-strength carbon steel ( $\sigma_y$ : 1440 MPa) in air and 0.6 M NaCl. Fully reversed torsion. Reproduced from Akid, R. In *Effects of Environment on the Initiation of Crack Growth*; Van der Sluys, W. A., Piascik, R. S., Zawiercha, R., Eds.; ASTM STP 1298, 1997, pp 1–17.

cracking dominates. It should be clarified that the above study relates to the work carried out on 0.18% C steel at pH values of 2–4. However, the development of pits or slip-band dissolution was observed to be dependent upon solution conditions as shown by Akid<sup>21</sup> who, using a similar steel, showed that pitting was the preferred corrosion mechanism at near-neutral pH values, while at pH 2, slip-band dissolution was the dominant process.

Magnin<sup>22</sup> described the effects of the stress–environment interaction on dislocations, illustrating that such interactions increase the dislocation density at the crack tip causing a more localized form of damage than would occur in the absence of the environment.

From the above discussion, it is therefore clear that substantial evidence exists for pitting to be one of the principal mechanisms for the initiation of corrosion fatigue cracks. Leis *et al.*<sup>23</sup> summarized some of the effects that are attributable to pitting, suggesting that pitting may accelerate the initiation process through a mechanical notch effect; pits may concentrate aggressive chemical species in the environment and that pits may serve to raise locally the stress above yield in a nominally elastically loaded material. The following section provides a summary of the influence of different variables on the development and growth of short cracks. From the results of numerous tests conducted under a wide range of conditions, a model is proposed for predicting corrosion fatigue lifetime.

### **Surface films and film breakdown**

With the exception of some of the noble metals, the majority of engineering metals and alloys exist with a surface film that offers corrosion protection to a greater or lesser degree. Classically, this is seen in the range of alloys known as the *stainless steels*. Stainless steels contain greater than 12% Cr which, along with other alloying elements, gives rise to a mixed oxide surface film having a thickness of the order of tens of nanometers. Similarly, the corrosion resistance of Al and Al alloys is attributed to the presence of a thin aluminum oxide film.

As previously discussed, fatigue and corrosion are both highly localized surface phenomena. The nature of the metal surface, in conjunction with the chemistry of the electrolyte, therefore plays a significant role in establishing the type and degree of damage arising during corrosion fatigue. As discussed above, the inherent resistance of a material to corrosion is

based upon the properties of the surface film. Breakdown of this film leads to the separation of anode and cathode sites and to the development of localized corrosion, for example, pitting. The ability to overcome this resistance to surface damage might therefore be seen as a ‘primary threshold’ with pit growth occurring above this threshold. A value for this threshold would be dependent upon the nature of the oxide film, notably its mechanical and chemical properties and thickness,<sup>24</sup> the nature of the electrolyte,<sup>25,26</sup> and the magnitude of applied stress to which the film is subjected.<sup>26</sup>

### **Pitting**

The association of pits as precursors to crack initiation was demonstrated over 70 years ago by McAdam.<sup>5</sup> Recent corrosion fatigue studies<sup>27–29</sup> have shown that pitting is often associated with inclusions or constituent particles lying within the matrix of the alloy, for example, manganese sulfide in steel. The chemical nature, size, and distribution of such particles play an important role in the early stages of corrosion fatigue damage.

Muller<sup>30</sup> considered the influence of early fatigue crack growth based on crack initiation as the failure criteria. A model was proposed based on corrosion kinetics and fracture mechanics featuring three different corrosion conditions: general, pitting, and passive corrosion. In the case of pitting corrosion, the lifetime is determined by a critical pit depth from which a fatigue crack can develop. In passive corrosion conditions, the lifetime is determined by slip characteristics and repassivation kinetics leading to a critical corrosion current below which no corrosion fatigue cracks can initiate. Experimental results from crack initiation tests on chromium–nickel steels showed good correlation with the theoretical models. The model further proposed that all the three modes of corrosion are dependent upon the applied stress.

An extended discussion of the influence of stress on pitting and pit growth rates can be found from Akid.<sup>16</sup> In summary, it is suggested that pit growth rate is influenced by the degree of plasticity within the grains surrounding the pit and that boundary conditions exist for the effects of stress on pit growth rate, these being the onset and saturation of plastic deformation (see **Figure 7**). The pit growth rate coefficient is based upon measurements of pit size prior to the pit–crack transition. This influence of stress on pit development/growth is supported by

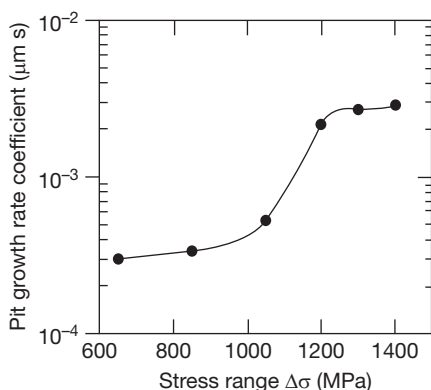


**Figure 7** Influence of stress on pit growth rate coefficient. Q2N steel (0.12%C),  $\sigma_y = 790$  MPa; 3 pt bend testing,  $R = 0.01$ ; in artificial seawater. Derived from experimental data from reference. Reproduced from Wu, X. J. Ph.D. Thesis, University of Sheffield, 1995.

work recently conducted concerning the electrochemistry of deformed smooth surfaces.<sup>32</sup>

#### Pit/crack transition

It has been demonstrated above that pits act as sites for crack initiation and that pit growth rate is a function of material, environment, and loading conditions. The transitional stage from a pitting (time-dependent) dominated regime to that of a mechanical (cycles-dependent) regime is a critical stage in the corrosion fatigue process. Recent results<sup>33</sup> have shown that, not surprisingly, this transition stage is dependent upon local solution chemistry, stress, and time. Interestingly, during this study, which concerned the corrosion fatigue of two thermo mechanically processed steels, one containing Mo/V additions and one without, the transition times and dependencies on stress were different; however, the lifetimes were similar. This arose because the pit size at which the transition occurred differed between the two steels. Unfortunately this makes modeling of corrosion fatigue slightly more complex than would ideally be desired. However, given sufficient statistical confidence, it would be possible to develop a model based upon a 'process-competition' approach in which stages were assigned depending upon the dominant process, that is, stress-assisted pitting and dissolution-assisted cracking. Such an approach is described in Akid.<sup>16</sup>

An example of the pit-to-crack transition from the study by Ebera<sup>34</sup> is given in **Figure 8**. Here, it can be seen that a significant number of cycles elapses before a crack initiates from the pit. Ebera found that the

maximum depth of the corrosion pit at the crack initiation stage is  $23.5 \mu\text{m}$  in plane bending at a stress of 228 MPa ( $N/N_f = 0.968$ ) and  $17.8 \mu\text{m}$  in plane bending at a stress of 280 MPa ( $N/N_f = 0.645$ ). However, it should be noted that the test frequency used in this study was 60 Hz which gives times for the pit-to-crack transition of 23 and 9 h, respectively for stress levels of 228 and 280 MPa.

The relationship between stress and time to the pit-crack transition for Ebera follows the trend observed by Akid<sup>31</sup> who correlated data for a range of steels tested in chloride environments under different loading conditions (see below) and found the following trend:

$$t_{p/c} = (A/\sigma)^C$$

where  $t_{p/c}$  is the time to pit-crack transition in seconds,  $\sigma$  is the applied stress in MPa, and  $A$  and  $C$  are constants dependent upon material, environment, loading mode, and test frequency.

**Figure 9** presents the analysis of nine different studies where the corrosion fatigue mechanism involved a pit-crack transition. The numbers in square brackets given in the figure refer to references cited in Akid.<sup>16</sup> These data represent steels tested under torsion, uniaxial, rotating bending and 3 pt bend loading at different frequencies within chloride environments.

#### Physically short crack/long crack interface

It is well established for both air and CF cracking that short cracks grow at rates many times that of 'ΔK equivalent' long cracks.<sup>35</sup> Subject to the limitations of calculating ΔK values for small defect sizes, **Figure 10** shows that conventional LEFM analyses are not appropriate for predicting the transition from pitting to cracking. At longer crack lengths, there is a good correlation between smooth specimen tests and LEFM test data. The data in **Figure 10** suggest that there is a greater correlation between physically short cracks and long cracks close to  $\Delta K_{th}$  and that the pit-to-crack transition may be independent of the stress intensity factor. This degree of correlation between short and long crack growth rates shows the value of conducting short crack corrosion fatigue tests, notably that information on both microstructural short crack behavior and 'long crack' thresholds can be obtained using short crack test methods.

As discussed previously, in particular for passive metals/alloys, the early stages of corrosion fatigue often involve local breakdown of the passive film



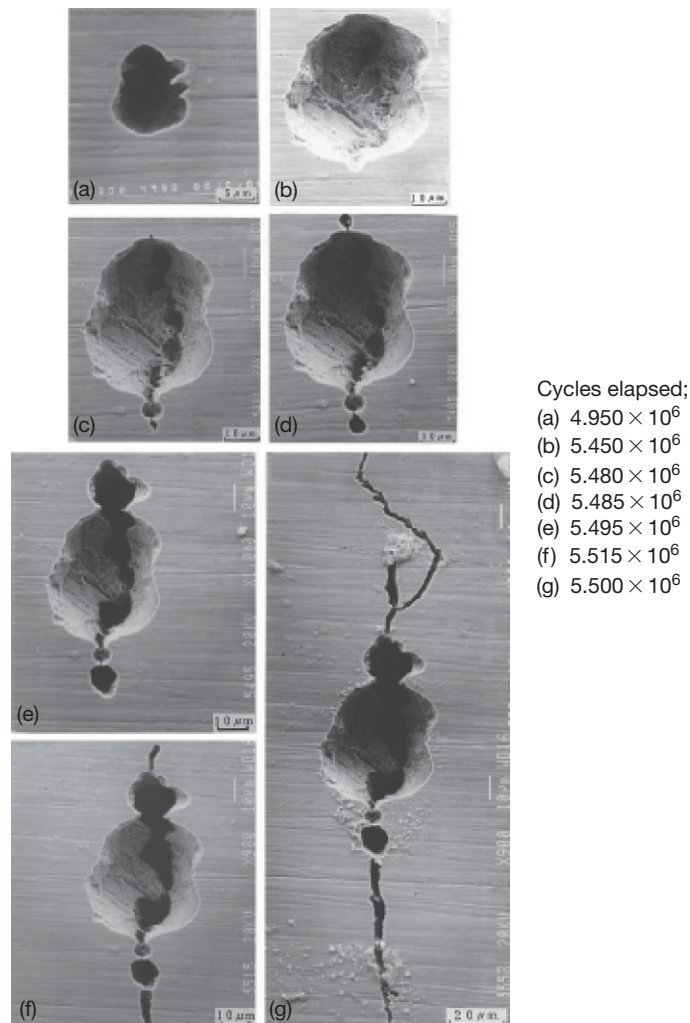


**Figure 8** CF crack development of a pit: 12% Cr stainless steel; 3.5% NaCl; stress level 228 MPa (after 34); cycles elapsed, (a)  $4.950 \times 10^6$  (b)  $5.450 \times 10^6$  (c)  $5.480 \times 10^6$  (d)  $5.485 \times 10^6$  (e)  $5.495 \times 10^6$  (f)  $5.515 \times 10^6$  (g)  $5.500 \times 10^6$ .

followed by active corrosion, that is, pitting. This time dependent corrosion phase eventually gives way to crack formation and a transfer into a 'predominantly' mechanical, fatigue-cycles dominated regime. The characterization of these features, summarized in **Table 1**, is based upon numerous studies during which damage is monitored via a plastic replication technique.<sup>28,33,36–40</sup>

An alternative model, appropriate for slip-band cracking is given in **eqn [3]**.

On the basis of these studies and equivalent tests conducted in an air environment, the following simple models have been proposed<sup>37,42</sup> which account for the individual stages identified in **Table 1**. These models are either based upon a modified in-air short crack growth model<sup>37</sup> or on the degree of plasticity at the

crack tip,<sup>42</sup> see **eqns [1], [2], and [3]**, respectively.

$$\frac{da}{dN} = A\gamma^\alpha (d - a) \text{ MSC} \quad [1]$$

$$\frac{da}{dN} = B\gamma^\beta a - D \text{ PSC} \quad [2]$$

where MSC and PSC represent the microstructural short crack and physical short crack regimes, respectively.  $A$ ,  $B$ ,  $\alpha$ , and  $\beta$  are constants depending upon material and environment;  $\gamma$  is the shear strain, and  $d$  is a microstructural dimension, for example, grain size,  $a$  is the defect size, that is, pit size or crack length, and  $D$  is the LEFM threshold crack growth rate.

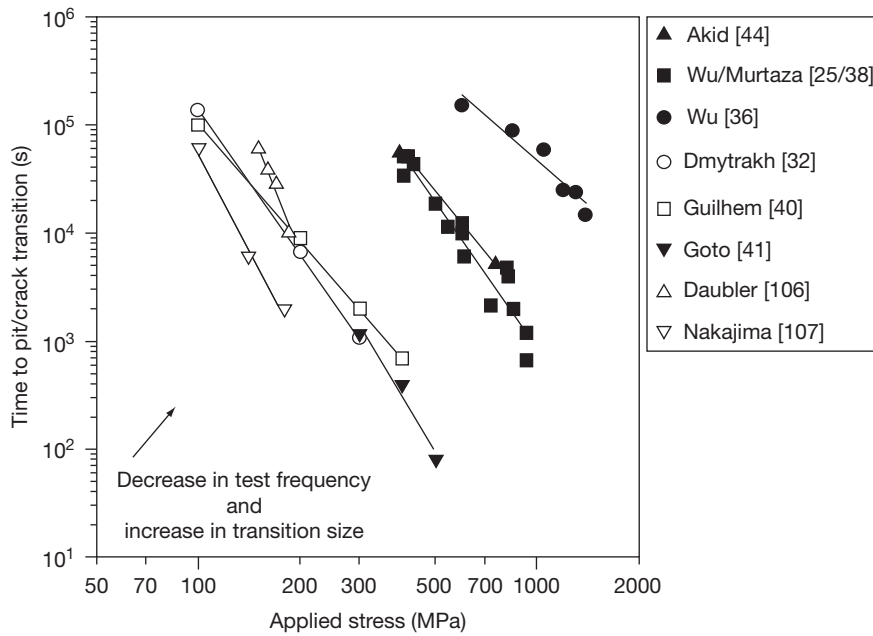


**Figure 9** Relationship between time to pit-crack transition and applied stress for various steels. Reproduced from Akid, R. In *Effects of Environment on the initiation of Crack Growth*; Van der Sluys, W. A. Piascik, R. S., Zawiercha, R., Eds.; ASTM STP 1298, 1997, pp 1–17.

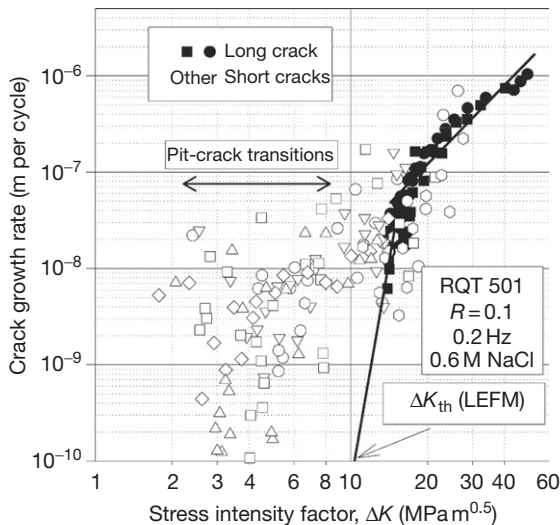


**Figure 10** Comparison of short and long corrosion fatigue crack growth rates for a C-steel ( $\sigma_y = 500$  MPa). Conditions: artificial seawater at OCP and uniaxial loading at a stress ratio,  $R = 0.1$ . Note open symbols represent data from smooth specimen short crack tests and solid symbols represent data from pre-cracked specimens.  $\Delta K$  values for short cracks are based upon an average crack shape aspect ratio and geometry factor of 0.65–0.7 depending upon crack size. Reproduced from Akid, R. In *Effects of Environment on the initiation of Crack Growth*; Van der Sluys, W. A. Piascik, R. S., Zawiercha, R., Eds.; ASTM STP 1298, 1997, pp 1–17.

**Table 1** Designated damage regimes relating to the early stages of corrosion fatigue

Damage regime	Process	Influential factors
1	Pitting	Solution composition, pH, applied stress
2	Pit/crack transition	Pit shape/local pit environment, applied stress state
3	Environment-assisted short fatigue crack growth	Local crack tip chemistry, applied stress state
4	Physically short crack growth	Applied stress state ( $\Delta K$ )

$$\frac{da}{dN} = C(r_p)^m \quad [3]$$

Here,  $C$  and  $m$  are constants depending upon material and environment, and  $r_p$  is the size of the plastic zone.<sup>31</sup>

Where the applied stress state differs from a uniaxial loading condition, for example, fully reversed torsion or tension, a modification is made to eqns [1], [2], and [3] in which  $\gamma$  is replaced by  $\gamma_{eq}$ , an equivalent strain based upon the multiaxial loading condition in which both the principal strain and the strain normal to the shear plane are taken into account.<sup>43,44</sup>

While this approach offers a number of advantages in terms of the application of LEFM analyses, it does not recognize that pit growth is influenced by the microstructural state and that the transition from a pit to a crack is influenced by plasticity. This latter effect has significant implications for the application of LEFM to such small defects. This can be seen in **Figure 10** which shows pit–crack transitions occurring well below the LEFM threshold.

Modeling corrosion fatigue behavior, like modeling air fatigue, has fallen into two main categories based upon the existence or otherwise on a defect. Typically, the models address either the development and growth of defects (initiation) or the propagation of defects which fall under the boundary conditions of LEFM.

### 2.12.3.1.2 Pitting corrosion fatigue models

As discussed in the previous section, initiation is commonly referred to as the ‘nucleation stage,’ that is, the beginning of defect development. Unfortunately, this can cause uncertainty with the accuracy in prediction of lifetime, as nucleation is somewhat dependent upon the first observation of a defect (crack or pit). Initiation might also be defined as ‘life to a certain detectable defect size.’ This subtle distinction requires that designers carefully consider the ‘inspectability’ or ‘detectability’ of a component or structure. A number of researchers have also suggested that stress intensity factor can be used to define specific stages of the CF process.<sup>45, 46</sup> Given that pitting corrosion is often a precursor to fatigue crack development, this section will provide details on pitting corrosion fatigue models developed to predict CF lifetime. These models are based upon the damage mechanism that consists of the formation of a pit and eventual

development of a crack from the pit site. A more detailed review of this subject is given by Hagn.<sup>47</sup>

The models of Hoepfner,<sup>45</sup> Lindley,<sup>48</sup> Kawai,<sup>49</sup> Kondo,<sup>50</sup> and Chen<sup>51</sup> rely on a transition from pitting to cracking defined by a stress intensity threshold value ( $\Delta K_{th}$ ) or that the stress intensity associated with a pit can be defined based upon its geometry, often assuming the pit is hemispherical. **Table 2** summarizes the approaches adopted by these authors.

One major problem that has not been addressed when applying a fracture mechanics approach to corrosion fatigue lifetime prediction of nondefective surfaces is the important point that LEFM analyses tend to assume that cracks do not propagate below the  $\Delta K_{th}$  value. Yet it is known that cracks do initiate at pit sites below the threshold value (calculated using the dimensions of the pit), as illustrated in **Figure 10** above. In considering the results shown in **Figure 10**, the role of crack closure should be considered. Corrosion may affect crack closure in two ways, notably: corrosion can lead to oxide film formation on the crack walls, leading to an increase in closure, or corrosion can remove material by dissolution, leading to a reduction in crack closure. Crack closure is associated more with long cracks than with short cracks because of the limited crack opening displacement of small defects.

### 2.12.3.2 Long Crack Growth

Differentiation of ‘short’ and ‘long’ crack growth is normally made based upon the degree of yielding or plasticity occurring at the crack tip. Knott<sup>52</sup> has shown that LEFM analysis is applicable when the plastic zone size ( $r_p$ ) is less than one-fiftieth (1/50) of the crack length.

**Table 2** Summary of pitting corrosion fatigue models

Author	Model	Comments
Hoepfner <sup>45</sup>	$K = 1.1\sigma\sqrt{\pi\frac{a}{Q}}$ and $t = \left(\frac{d}{c}\right)^3$	$\sigma$ = applied stress, $a$ is pit length, $Q$ is a function based on crack shape, $t$ is time to attain pit depth for corresponding threshold value, $d$ is pit depth, and $c$ is a constant dependent upon material and environment
Lindley <sup>48</sup>	$K_{th} = \frac{\Delta\sigma\sqrt{(\pi a)[1.13 - 0.07(a/c)^{0.5}]}}{[1 + 1.47(a/c)^{1.64}]^{0.5}}$	Pits considered as semielliptical cracks. $a$ is a minor and $c$ is a major axis of semielliptical crack
Kawai <sup>49</sup>	$\Delta\sigma = \frac{\Delta K_{all}}{F\sqrt{\pi h_{max}}}$	$\Delta K_{all}$ determined from $da/dN$ vs. $\Delta K$ plot. $F$ is a geometry factor and $h$ is maximum pit depth
Kondo <sup>50</sup>	$\Delta K_p = 2.24\sigma_a\sqrt{\pi c\alpha/Q}$ and $c = C_p(N/f)^{1/3}$	Assumes pit as a crack, $\sigma_a$ is stress amplitude, $a$ is aspect ratio (assumed constant) and $Q$ is a shape factor. $C$ is pit radius, $N$ , number of fatigue cycles, and $f$ is cyclic frequency
Chen <sup>51</sup>	$\Delta K_{tr} = (1.12K_t\Delta\sigma\sqrt{\pi c_{tr}})/\Phi = \Delta K_{th}$	$K_t$ is a stress concentration factor, $c$ is half-pit diameter and $\Phi$ is a shape factor determined by the pit diameter and depth

For uniaxial loading, the size of the plastic zone is given by eqn [4].

$$r_p = \frac{1}{2\pi} \left[ \frac{\Delta K_I}{2\sigma_y} \right] \quad [4]$$

where  $K_I$  is the stress intensity factor ( $\text{MPa} \sqrt{\text{m}}$ ) and  $\sigma_y$  is the yield strength (MPa).

A bounding condition for LEFM applicability is therefore the relationship between  $r_p$  and the crack length, as previously described.

Unlike the  $S$ - $N$  tests, which use smooth ‘defect-free’ specimens, LEFM test methods use a precracked specimen, which is subject to fatigue cycling within the desired environment. Measurements of crack length are taken at selected intervals at a specified stress ratio (minimum/maximum load). The results of this type of test are presented in a fatigue crack growth rate curve as shown in Figure 11. Here, LEFM long crack growth is associated with the stage II regime of the crack growth rate diagram and is often called the ‘Paris’ region.<sup>53</sup> This region is defined by the empirical relationship given in eqn [5];

$$\frac{da}{dN} = C(\Delta K)^m \quad [5]$$

where  $\Delta K = K_{\max} - K_{\min}$ , and  $A$  and  $m$  are material-, temperature-, microstructure- and stress-ratio-dependent constants. Values of  $m$  that have been reported in the literature lie typically in the ranges of values  $2 \leq m \leq 5$ . This equation is widely used in its integrated form to evaluate the lifetime of cracked structures knowing the stress field, the threshold and critical values of  $K$  and the constants  $A$  and  $m$ .

This empirical relation given in eqn [5] contains the self-similarity of the fatigue crack growth process. However, it is only valid within a so-called intermediate, medium-amplitude part of the fatigue kinetic diagram (stage II), as shown in Figure 11.

A threshold effect is observed,  $\Delta K_0$  (or  $\Delta K_{th}$ ), which occurs when the crack growth rate equals a value of approximately the order of one atomic spacing per cycle. Hence the plot is generally divided into three regions. When the maximum stress intensity factor becomes higher, the crack growth curve deviates from linearity (the ‘Paris’ region), and crack instability and rapid acceleration can occur terminating in failure (stage III).

In stage I, the crack growth rate is very low, and experimental data have shown that the crack growth in this region is greatly affected by microstructure, environment, and stress ratio.<sup>54–57</sup>

The self-similitude concept postulates that cracks of different lengths will have the same stress and strain fields, and hence the same crack growth rate if they are subject to the same applied  $\Delta K$ . This means that cracks in specimens and structures can be directly compared. However, small-scale yielding (SYY) conditions are assumed to prevail, where SYY is dependent upon crack opening displacement and a nonhardening material. This leads to the condition that the limiting stress amplitude is less than one-third of the yield stress. More generally, for this concept to hold, low applied stress levels are required.

Substantial work on the relationship between  $\Delta K$  and the crack growth rate followed on from the work of Paris and Erdogan, although it was not until the

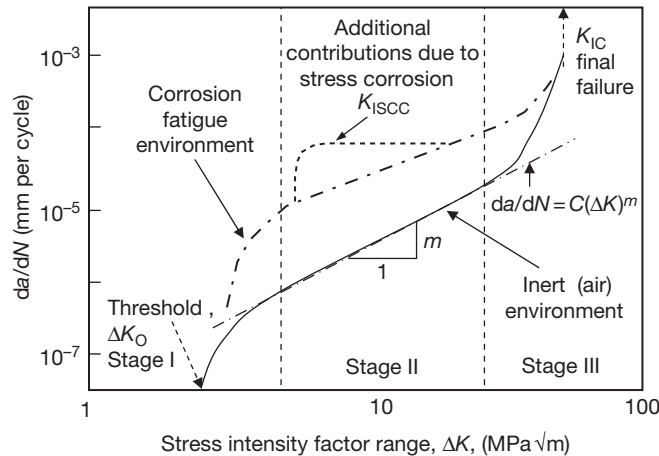


**Figure 11** LEFM fatigue crack growth curves showing behaviour for air, corrosion fatigue and corrosion fatigue plus stress–corrosion interactions.

early 1970s that an international conference was held<sup>58</sup> to review the subject of corrosion fatigue.

As can be seen from the schematic in Figure 11, the environment generally causes an increase in the crack propagation rate for a given  $\Delta K$  value. Furthermore, crack growth rate can be further augmented if the material is also susceptible to stress corrosion cracking within the test environment.

### 2.12.3.2.1 LEFM-based corrosion fatigue models

There are numerous models cited in the literature that attempt to quantify the contribution from both electrochemistry and the mechanical loading condition. These models may be characterized under the following categories: process superposition, process competition, and process interaction.

Wei and Landes<sup>59</sup> first proposed a *process superposition model*, which summed the stress corrosion component of crack growth with that of air fatigue crack growth. The model can be expressed as eqn [6].

$$(da/dN)_{cf} = (da/dN)_r + \int da/dt K(t) dt \quad [6]$$

where  $(da/dN)_{cf}$  is the rate of fatigue crack growth in an aggressive environment,  $(da/dN)_r$  is the rate of fatigue crack growth in an inert environment, and the integral term is the environmental contribution obtained from sustained load crack growth in the same environment. This model takes no account of any synergistic interactions between corrosion and fatigue. Later refinements of this approach were predicated on the recognition that environmentally assisted crack growth is the result of sequential processes and is controlled by the slowest process in the sequence.<sup>60</sup>

Austen and Walker<sup>61</sup> proposed the *process competition model* on the basis that stress corrosion and fatigue (or true corrosion fatigue) are mutually competitive and not additive as postulated by Wei and Landes. It is assumed that the crack will propagate by the fastest available mechanism at the stress intensity operative for a given crack length. The model is given in eqn [7].

$$(da/dN)_{cf} = (da/dN)_r + (da/dt) \times 1/f \quad [7]$$

where the first two terms are as in eqn [6] and  $(da/dt) 1/f$  accounts for the stress corrosion contribution.

The *process interaction model* was developed to allow interactions to occur, particularly in those systems that exhibit a degree of susceptibility to SCC.<sup>62</sup>

This model has been used to predict corrosion fatigue data for steel and aluminum in air and saline environments. The model is given in eqn [8].

$$\left(\frac{da}{dN}\right)_e = m_1 (\Delta K_{eff})^{m_2} + \int_0^{1/f} A v K_{eff}^\alpha dt \quad [8]$$

Here,  $\Delta K_{eff}$  is the effective stress intensity factor, adjusted for blunting and crack branching,  $v$  accounts for the influence of load cycle on stress corrosion rate,  $f$  is the frequency, and  $m_1$ ,  $m_2$ ,  $A$ , and  $\alpha$  are experimentally determined constants.

The ability to predict fatigue lifetime relies upon accurate information on defect size (cracks or pits), shape, and orientation with respect to the applied stress and local crack tip chemistry. Panasyuk *et al.*<sup>63</sup> proposed the use of ‘invariant diagrams’ in order to account simultaneously for the stress–strain state and the electrochemical conditions at the crack tip. They showed that for a range of alloys, including steel, Al and Ti, the pH at the crack tip differed from that of the bulk solution (NaCl, pH 6.5) by up to 5 pH points, ranging from 0.8 to 3.5. Similar studies have also been conducted by other researchers.<sup>64</sup> In contrast to measurements made at the open circuit potential, Turnbull assessed the crack tip pH and potential changes when steel was subjected to cathodic overpolarization of  $-1100$  mV (SCE). He found that the pH increased up to pH 13 and the potential moved 120 mV in the positive direction (i.e., towards the free corrosion potential). Furthermore, knowledge of the local stress–strain conditions at the crack tip is critical. Novel techniques are now being developed to obtain the geometrical shape of cracks and pits, for example, 3-D synchrotron X-ray imaging<sup>65</sup> and light-interference microscopy.<sup>66</sup> It should be noted that some of the early studies which used crack tip solution chemistry as a means to elucidate the crack tip mechanisms suffered from the fact that solutions oxidized before analysis could take place.

### 2.12.4 Variables Affecting Corrosion Fatigue

The significance of environmental effects on corrosion fatigue life has been reported by various workers. Evans and Simnad<sup>8,9</sup> in their two stage tests showed how removing the environment after a certain percentage of the expected life did not substantially increase the fatigue life. Rollins *et al.*<sup>67</sup> also concluded that the action of the corrosive environment is of



primary importance in the crack initiation stage. Duquette and Uhlig<sup>20</sup> suggested that a delay in crack initiation or early propagation, attributed to a reduction in dissolution by adopting a higher corrosion-resistant material, would lead to an improvement in the fatigue life. However, many of the earlier studies were devoted to assessing lifetime rather than quantifying crack growth. In this respect, relatively little attention has been paid to the anomalous crack growth rates of short cracks in corrosion fatigue even though they have been observed and known to exist for some time.<sup>37,68</sup> Such studies are expected to increase as environment-assisted growth of small fatigue cracks becomes increasingly recognized as an important failure mode, often dominating total life.<sup>69</sup> As discussed, most corrosion fatigue life prediction methods are dominated by the application and analysis of long crack data.<sup>70</sup> However, where defects develop from smooth 'engineering' surfaces, the application of linear elastic fracture mechanics (LEFM) becomes limited. It is therefore necessary to develop models that account for the development and growth of pits and short cracks. Furthermore, before such models can be applied, it is further necessary to consider the factors which affect the development of such small defects during the early stages.

Consideration of some of these factors is given below.

#### 2.12.4.1 Microstructure

It is widely recognized that the 'in-air' fatigue performance of a material can be significantly influenced by varying the grain size. The principal effect of grain size on short, stage I – shear, crack growth is the introduction, ahead of the crack, of physical barriers whereby the grain boundary acts as a demarcation between two grains having different slip orientations. Therefore, by introducing a large number of barriers into the system, that is, reducing the grain size, cracks are required to orientate themselves along many different planes. The effect of this is one of crack speed deceleration, and, where the stress level is below that of the fatigue limit, crack arrest.

With respect to corrosion fatigue, there is currently no direct evidence to suggest a relationship between grain size and corrosion performance, and hence corrosion fatigue resistance. However, since the environment can influence the ability of a crack to surmount the microstructural barrier, it would not be unreasonable to suggest that corrosion moderates the influence of grain size on fatigue strength.

Furthermore, given that most engineering materials contain metallurgical heterogeneities such as intermetallic particles (IMPs) and second phase precipitates, which can give rise to sites for preferential dissolution and pitting, it might sensibly be expected that a change in corrosion fatigue response will occur with changes in alloy chemistry. IMPs are particularly influential on corrosion fatigue lifetime as they lead to multisite damage and crack initiation. Furthermore, IMP can bridge individual grains, thereby reducing the influence of microstructure on crack growth. Murtaza and Akid<sup>38</sup> conducted intermittent air fatigue–corrosion fatigue loading tests and showed that the dominant microstructural feature in the corrosion fatigue behavior of a high-strength spring steel was the prior austenite grain size. Individual microstructural phases can also influence the initiation behavior, for example, duplex stainless steel consists of almost equal fractions of ferrite and austenite. However, the pitting behavior of these two phases is different with pitting being preferred in the ferrite phase.<sup>26</sup>

#### 2.12.4.2 Loading Frequency

The influence of loading frequency on 'long-crack' corrosion fatigue resistance is well documented, being attributed to time-dependent effects of corrosion which are ascribed to mass transport and electrochemical reaction rate limitations.<sup>71–73</sup>

The role of frequency on the development and growth of short fatigue cracks is, however, less well documented. Studies on smooth specimen fatigue tests<sup>42</sup> have shown that frequency influences short fatigue crack growth rates (see [Figure 12](#)). The most striking feature of this figure is that crack growth rates are enhanced at a point where the mechanical driving force is at a minimum, that is, when a crack is small and below a critical size–aspect ratio for the transfer from the stage I – shear to stage II – tensile plane. This is not an unreasonable observation as the damage process moves from a 'predominantly' time-dependent corrosion process to a mechanical, cycles-dependent fatigue mechanism. [Figure 12](#) shows that the differences in lifetime for tests at 10 and 0.01 Hz, which account for a reduction in life of 70%, occur during the growth of a defect below a size of 200  $\mu\text{m}$ . Here, it can be seen that crack growth rates, based on measurements of surface defect size with increasing number of fatigue cycles, for 0.01 Hz are around an order of magnitude higher than at 10 Hz for the same loading conditions.

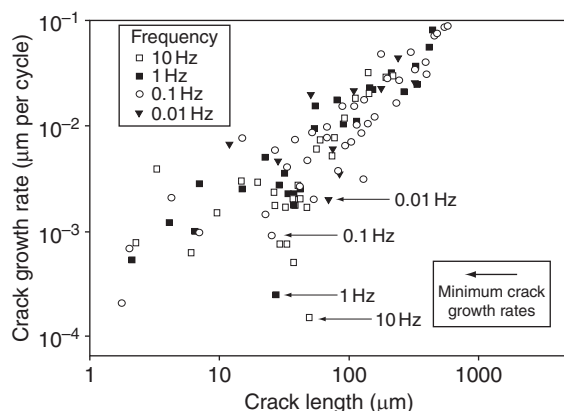


**Figure 12** Influence of loading frequency on short corrosion fatigue crack growth of a low-alloy structural carbon steel in artificial seawater. Grain size approximately 10 µm. 3 Pt bend tests, stress ratio = 0.1. Reproduced from Akid, R., Wu, X. J. *Structural Materials in Marine Environments*. The Royal Society, London, UK. The Institute of Materials; 1994; pp 330–345, ISBN 1 86125 0029.

This accelerated growth at low frequency results in fatigue lifetimes of 5000 and 20 000 cycles for 0.01 and 10 Hz, respectively.

#### 2.12.4.3 Solution/Electrochemical Conditions

The corrosion resistance of a metal or alloy is normally derived from its ability or inability to form a stable passive film. The majority of passive films are based upon the formation of an oxide film and therefore the nature of the environment, that is, oxidizing or reducing, has a marked affect on film formation.

Corrosion fatigue studies<sup>7</sup> on polished carbon steel BS4360 50D showed that neutral pH chloride solutions promoted pitting, while low pH, acidic chloride solutions promoted slip-band dissolution. These differences were attributed, respectively, to local weaknesses in the surface oxide film around inclusions, hence pitting, and total dissolution of the oxide film at low pH levels, allowing access to slip bands within the grain and accelerated corrosion at these sites. The effect of these differences, in terms of fatigue behavior, is such that multiple site damage (cracking) occurred in an acidic solution, followed by coalescence of cracks and a subsequent reduction in fatigue lifetime when compared to near-neutral solution conditions.

Where solution conditions were modified to increase the thickness of the passive film,<sup>24</sup> the time

to pit formation was increased. A decrease in the propensity for local corrosion (pitting) can also be affected by modifying the solution conditions, that is, by using inhibitors. Such effects have been observed under corrosion fatigue conditions<sup>25</sup>; here, corrosion fatigue lifetimes increase on the addition of an oxidizing inhibitor, sodium nitrite ( $\text{NaNO}_2$ ). The improved CF performance is attributed to a delay in pitting and therefore an increase in time prior to crack formation.

Where electrochemical conditions are controlled to eliminate the effects of anodic dissolution, that is, cathodic polarization (CP), it is observed that the corrosion fatigue resistance is restored towards that observed for identical tests in air. It should be noted that CP may not be effective where a component or structure contains cracks that can propagate under LEFM conditions. For 'smooth' surfaces, a nonfailure condition was observed for fatigue tests carried out below the in-air fatigue limit in NaCl with CP, compared to very early failure in the absence of CP (see [Figure 13](#)).<sup>73</sup> The effect of polarization on crack growth rate requires an understanding of the crack tip electrochemistry as this controls the dissolution, repassivation, and hydrogen evolution kinetics. The trends are also subject to the nature of the material tested, and suppression of the metal dissolution reaction through the application of a negative potential is not effective for all metals. For example, applying a negative potential to Al and its alloys can lead to corrosion because the cathodic reaction promotes the formation of a high-pH solution, and as aluminum is amphoteric it can undergo dissolution at both high- and low-pH values.

#### 2.12.4.4 Surface Condition

As previously discussed, fatigue is the consequence of an extremely localized surface phenomenon. It is therefore not unreasonable that changes in the surface condition of a material have a marked effect on fatigue performance. Furthermore, it is well documented that fatigue lifetime decreases on increasing the surface roughness.<sup>74</sup> This reduction in lifetime is attributed to the presence of 'micronotches' associated with the peaks and troughs of the surface profile.

Changing the nature of the surface condition, notably stress state and microstructural condition, through the application of shot peening is a method adopted to improve fatigue performance. Here, the surface is deformed by impingement of glass or metal

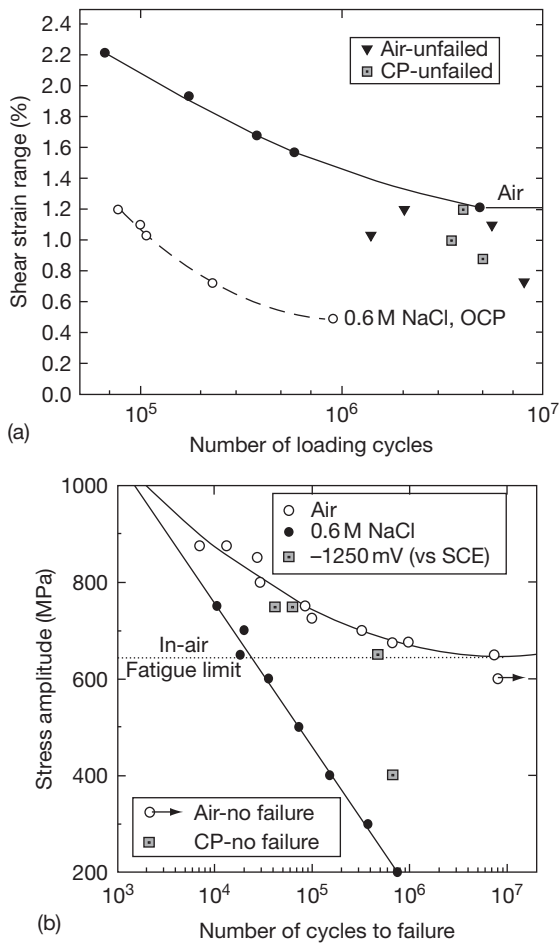


**Figure 13** Influence of environment and electrochemical potential on fatigue strength; (a) fully reversed torsion loading (b) fully reversed axial loading; High-strength carbon steel ( $\sigma_y = 1100$  MPa). Reproduced from Akid, R. In *Hydrocarbon Transport and Cracking of Metals*; Turnbull, A., Ed.; The Institute of Materials, 1995; pp 50–61. Note that shear loading, as occurs in a torsion test, tends to be insensitive to hydrogen, while axial loading is more sensitive.

beads which impart a compressive residual stress in the surface layers of the metal. The interpretation of increased lifetime has, previously, been attributed solely to residual stress effects. However, it has been shown<sup>7</sup> that the resulting distortion of the microstructure also has a significant effect on the short fatigue crack growth. Figure 14 provides an example of the reduction in fatigue crack growth rate (FCGR) that occurs on the application of shot peening. Here, the FCGR under peened conditions is compared with predicted FCGR data derived from

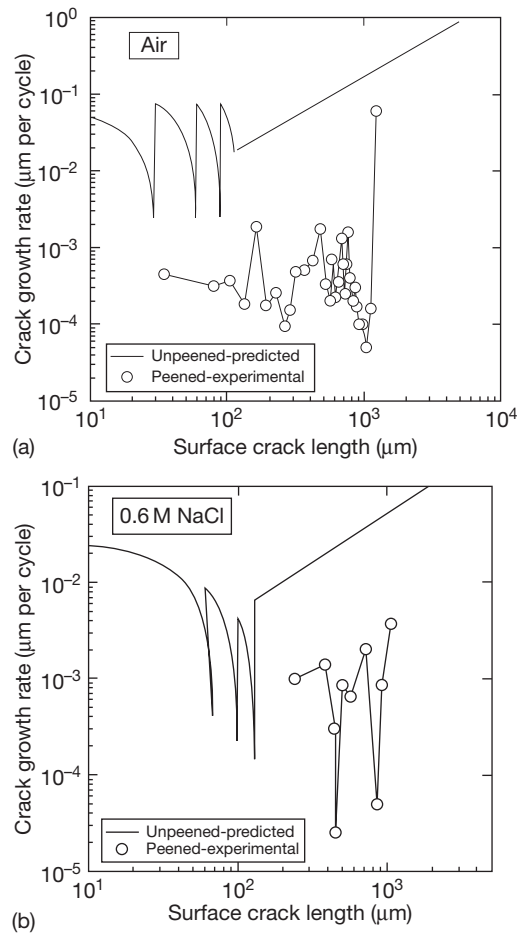


**Figure 14** Influence of shot peening on short fatigue crack growth. (a) Air;  $\Delta\tau = 1050$  MPa,  $N_f$  (peened)  $1.4 \times 10^6$  cycles,  $N_f$  (unpeened) 114 000 cycles. (b) 0.6 M NaCl;  $\Delta\tau = 820$  MPa,  $N_f$  (peened) 270 000 cycles,  $N_f$  (unpeened) 107 000 cycles. Note solid lines represent predicted growth rates based upon a crack growth model.  $\Delta\tau_{fl} = 920$  MPa.

air tests conducted on unpeened samples at the same stress level.

Figure 14 further shows that FCG rates are decreased by an average of two orders of magnitude for both air and corrosion fatigue tests, respectively, and that despite testing in 0.6 M NaCl the fatigue crack growth rates of peened specimens are significantly lower than the predicted in-air growth rates of specimens peened to the same Almen intensity. Comparison of the fatigue lives, as given in the caption of Figure 14, shows that shot peening gives an improvement in fatigue lifetime of 13 and  $2.5\times$  for air and corrosion fatigue, respectively.

### 2.12.4.5 Stress State

Many studies have been devoted to assessing the fatigue performance of materials through the application of simple stress-life ( $S-N$ ) type testing. Such an experimental approach often adopts a simple (uniaxial) loading condition and an 'inert' (air) environment. However, engineering structures and components are often subjected to nonuniform, asymmetrical loading within environments of varying aggressivity.

The implication of adopting a simple uniaxial constant-load test condition is that a crack may propagate, in shear, and fail to transfer to a fatal mode I, tensile crack. Where a multiaxial loading condition applies, both the maximum shear strain and strain normal to the maximum shear plane govern whether or not a crack will arrest (nonpropagating crack) or grow to failure.<sup>75</sup>

Recent multiaxial 'in-air' fatigue tests<sup>75</sup> have shown that, for mixed tension-torsion testing, the application of a static tensile stress, superimposed on a cyclic torsional load, significantly reduces the fatigue lifetime. Conversely, a compressive stress increases the lifetime, such effects being attributed to the relationship of the orientation of crack and stress state, and its relationship to the microstructure. Corrosion fatigue tests conducted under identical conditions<sup>75</sup> showed that the environment eliminates the effects of the stress state and the early stages of damage (see Figure 15(a)), are controlled by the environment, via a pitting mechanism, with fatigue lifetime becoming independent of biaxial stress state (see Figure 15(b)). As the crack size increases, environmental effects are more dominant for negative biaxial stress states; while at positive biaxial stress states, the mechanics dominate crack growth.

Additional corrosion fatigue studies concerned with block loading sequences, that is, damage accumulation (DA) loading<sup>76</sup> have also shown that corrosion fatigue lifetime is primarily governed by the ability to develop a small defect, that is, a pit, which transforms to a stage I, tensile crack. In this respect, there are two distinct regimes of damage; notably, a time-dependent corrosion regime, governed principally by solution chemistry, followed by a cycle dependent fatigue regime, governed by the magnitude of stress and mode of loading. Where appropriate conditions apply, that is, crack size and stress state,<sup>73</sup> the ability to generate hydrogen capable of being adsorbed into the metal matrix ahead of the

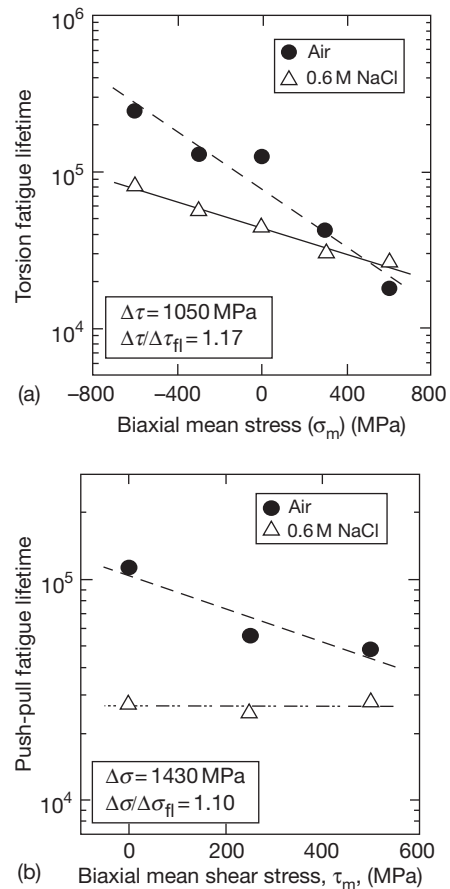


**Figure 15** Influence of biaxial stress state on corrosion fatigue lifetime, (a) fully reversed torsion with tensile and compression loading, (b) fully reversed axial loading with static torsion loading. High-strength spring steel, loading frequency of 5 Hz. Reproduced from Akid, R.; Zhang, W. In *Engineering Against Fatigue*; Beynon, J. H., Brown, M. W., Lindley, T. C., Smith, R. A., Tompkins, B., Eds.; A. A. Balkema: Rotterdam, Brookfield, 1999.

crack tip will also play a part in controlling damage and hence lifetime.

## 2.12.5 Corrosion Fatigue of Specific Alloys

### 2.12.5.1 Ferrous Alloys

Carbon steel is the highest tonnage alloy used within the engineering sector. It is, however, an alloy with limited corrosion resistance and therefore its application where both stress and corrosion may operate in combination needs careful consideration. In an attempt to extend the service life of steel

structures, carbon steels are often subjected to cathodic protection (CP), for example, in oil and gas exploration applications. In some cases, these materials are also painted to reduce the current demand from the CP system. CP reduces the operating electrode potential of the steel to typically more negative than  $-850$  mV (vs. Ag/AgCl), that is, below its natural open circuit potential. Where CP is used, careful material selection is required in order to prevent any possible hydrogen embrittlement (HE) problems. Typically, steels having yield strengths of less than about 700 MPa are considered to be immune from HE, although this is affected by the loading conditions and hydrogen concentration.

Given that chloride is very aggressive towards ferrous based materials and that many structures are located either offshore or in coastal regions, it is not surprising that many studies have been devoted to the corrosion fatigue behavior of steels in seawater or artificial seawater environments.

The 1970 and early 1980s saw significant research activity devoted to the corrosion fatigue resistance of offshore structural steels and pressure vessel steels<sup>55,57,61,77</sup> and more latterly to steels having refined microstructures such as roller quench temper (RTP) grades.<sup>33,42</sup>

Barsom<sup>78,79</sup> demonstrated the effects of frequency and cyclic waveform, identifying crack growth regimes above and below the threshold stress intensity factor for stress corrosion cracking. He observed that low loading rates (negative sawtooth) were more detrimental than high loading rates (positive sawtooth) and attributed this to the time available for corrosion and crack extension during the loading part of the cycle. Scott<sup>80</sup> in a separate study illustrated the effects of stress ratio on crack growth rate and cathodic protection on the evolution of a SCC plateau region. The plateau region exhibits an independence of crack growth on the stress intensity value, suggesting that a rate-limiting process is operative. In this case, the rate determining step was attributed to hydrogen evolution and transport at the crack tip.

The specific mechanism(s) leading to corrosion fatigue remain(s) in debate. Gangloff<sup>81</sup> summarized the possible processes that lead to enhanced fatigue crack growth under CF loading suggesting the following mechanisms may be involved: hydrogen embrittlement, film rupture, dissolution, and repassivation; enhanced localized plasticity and interactions of dislocations with surface dissolution, films, or adsorbed atoms.

The dominant mechanism is controlled by both the nature of the materials and the electrochemical conditions at the crack tip. Metals with high yield strength are susceptible to HE unless the local crack tip pH values are alkaline which then lead to charge transfer controlled dissolution process governing crack growth. Wei<sup>82</sup> showed, for an X-70 pipeline steel in a carbonate–bicarbonate solution at pH = 9, that changing cyclic frequency and temperature led to changes in fatigue crack growth rate, indicating the important role of dissolution kinetics.

Environment also has a role to play in the cracking of a high-strength low-alloy (HSLA) steel. Recent work has been conducted by Ritter<sup>83</sup> who studied the CF crack growth behavior of different RPV steels over a wide range of environmental (temperature, electrochemical potential, dissolved oxygen,  $\text{SO}_4^{2-}$ ,  $\text{Cl}^-$ ), loading ( $\Delta K$ ,  $R$ ) and material (S, MnS, microstructure) parameters in oxygenated or hydrogenated high temperature water, applying cyclic load tests with precracked fracture mechanics specimens. The application of hydrogenated water was always found to result in a reduction of low-frequency CF crack growth rates (CGRs) by at least one order of magnitude with respect to oxygenated conditions. A few hours after changing from oxidizing to reducing conditions, the CGRs dropped below the corresponding ASME crack growth curves.

Ford also showed the importance of passive film rupture and transient anodic dissolution for pressure vessel steels for high temperature pure-water environments.<sup>84</sup> Faraday's law was employed to determine the metal loss during active dissolution, the total metal loss being an integral of the current–time transient response of the metal. The contribution from anodic dissolution was shown to be strain rate and cyclic frequency dependent.

The microstructure of the material has also been shown to play an important role in the resistance to CF cracking. Using a superposition model for a high-purity FeCrNi alloy, Gao<sup>85</sup> assessed the role of microstructure in hydrogen-assisted corrosion fatigue crack growth. He concluded that the environmentally assisted crack growth rate in  $\alpha$ -martensite was only twice as high as that in vacuum, while the rate through the austenite grain and twin boundaries is more than one order of magnitude faster. He suggested that the results indicated that strain-induced  $\alpha$ -martensite formation is not a principal contributor to the environmental enhancement of corrosion fatigue crack growth and is not necessary for hydrogen embrittlement.



Mechanical factors also influence the nature of the cracking mechanism. Wu<sup>86</sup> studied the influence of strain rate on the low-cycle fatigue resistance of ASTM A 533B low-alloy pressure vessel steel in simulated BWR water. At strain rates above  $0.001\% \text{ s}^{-1}$ , the fatigue life decreased almost linearly with decrease in the strain rate on a log–log plot with environmental effects tended to become saturated at strain rates below  $0.001\% \text{ s}^{-1}$ . It was suggested that the change in strain rate leads to a change in the environment-assisted cracking (EAC) mechanism from hydrogen-induced cracking to a film-rupture-slip-dissolution-controlled process, mainly influencing the rupture rate of oxide film at the crack tip, and mass transfer and local electrochemistry processes in the system. It was also proposed that MnS inclusions play an important role in fatigue crack initiation and propagation where dissolution of the inclusions in the high temperature water environment results in  $\text{H}_2\text{S}$  formation which may enhance the hydrogen-induced cracking process.

While there is general agreement on the role of hydrogen in EAC for high- and low-strength steels in aqueous low temperature environments, it remains debated as to the exact mechanisms operative at high temperatures.

### 2.12.5.2 Stainless Steels

The susceptibility of stainless steels to CF is dependent upon the steel grade, notably ferritic, martensitic, austenitic, or duplex, the strength level, and environmental conditions.

Stainless steels are renowned for their superior corrosion resistance when compared to low-alloy carbon steels. However, where the prevailing environmental conditions lead to pitting corrosion the fatigue strength of the stainless steel grades is often not appreciably greater than the nonalloyed steel counterparts, assuming equivalent mechanical strength levels.

An example of the reductions in fatigue strength of a range of stainless steel grades is given in Table 3. The data represent rotating bending test results (stress ratio equal to  $-1$ ) in air and for samples moistened in 3% NaCl solution.

It can be seen from Table 3 that there is a significant reduction in endurance limit of the ferritic and martensitic grades, being some 30–50% of the in-air limit. Increasing the corrosion resistance to an austenitic grade improves the CF resistance, while a combination of high mechanical strength and good

**Table 3** Rotating bending fatigue test results for different stainless steel grades

Steel grade	Yield strength (0.2%, MPa)	Air fatigue limit (MPa)	CF endurance limit (MPa)
410 (martensitic)	440	340	130
12% Cr Mo (ferritic)	55	415	140
Precipitation-hardened martensitic	1060	550	230
304 (austenitic)	326	260	230
316 (austenitic)	223	270	260
Duplex	475	450	355

Reproduced from Shrier, 3rd ed.

corrosion resistance can be obtained by moving to a duplex grade.

The nature of the CF mechanism operative in stainless steels remains in debate. While it is recognized that active dissolution takes place when the passive film is broken, it is not entirely clear whether hydrogen, generated as a result of metal ion hydrolysis, further contributes to the crack propagation rate.

Using long focal length video optical microscopy to measure hydrogen bubble diameters at the crack mouth, Olive<sup>87</sup> conducted *in situ* monitoring of natural cracks. A boundary condition of the hydrogen evolution inside a crack was obtained and, by considering the electrochemical reactions occurring inside a crack, a minimum volume of metal dissolved per cycle at the crack tip was proposed. No comment was made as to any synergistic effect of hydrogen adsorption and any consequential changes in embrittlement ahead of the crack tip.

Magnin<sup>88</sup> studied the corrosion fatigue damage mechanisms leading to crack initiation in high-purity ferritic stainless steels (Fe–26Cr–1Mo wt%) in a 3.5% NaCl solution at 300 K and an imposed anodic corrosion potential. Particular attention was paid to the influence of strain rate on both the plastic deformation mechanisms and dissolution characteristics, which govern the crack initiation process. In summary, it was found that:

- At high strain rates (about  $10^{-2} \text{ s}^{-1}$ ), pencil glide induces strain localization at grain boundaries; dissolution is localized at grain boundaries; crack initiation is intergranular, and lifetimes are reduced in comparison with those in air.

- At intermediate strain rates (about  $10^{-3} \text{ s}^{-1}$ ), dissolution is entirely localized at grain boundaries because of pencil glide; crack initiation is intergranular, and fatigue lifetimes are shorter than at high strain rates.
- At low strain rates (less than  $10^{-4} \text{ s}^{-1}$ ), the amount of dissolution is lower than the critical value for corrosion fatigue damage; crack initiation is transgranular, and fatigue lifetimes are similar in air and in the corrosive solution.

Nyström<sup>89</sup> presented a study showing the effects of heat treatment and resulting changes in microstructural condition on the low-cycle CF resistance of 25% ferrite and 75% austenite duplex stainless steel. He and his coworker pointed out a major drawback of duplex stainless steel, being that of the susceptibility of the ferritic phase to 475 °C embrittlement; potentially limiting the use of duplex stainless steel to temperatures below 250 °C. The mechanical properties of duplex stainless steel were compared to those of an austenitic stainless steel. The results indicate that the fatigue properties of the duplex grade are little affected by annealing at 475 °C for 100 h. In addition, after annealing, the impact toughness remained high at 130 J. The austenitic grade has the same nominal fatigue crack growth threshold as the duplex grade; however, the effective crack growth threshold, related to the (intrinsic) internal resistance of the material to crack extension and the (extrinsic) level of crack closure, of the duplex grade is higher than that of the austenitic grade.

### 2.12.5.3 Aluminum Alloys

Aluminum alloys may be classed as either heat-treatable or nonheat-treatable, providing a range of alloys with different properties. The main industrial alloys include the Al–Cu; 2xxx series, Al–Zn–Mg 5xxx series, and Al–Mg–Zn 7xxx series. Heat treatment of these alloys produces precipitation hardening which can be controlled to alter the tensile and yield strength. This in turn affects the sensitivity of the alloys to environment sensitive cracking and localized corrosion. Like the high-strength steels, the high-strength 2xxx and 7xxx series have reduced resistance to stress corrosion cracking, hydrogen embrittlement, and corrosion fatigue. Furthermore, it has been shown that small fatigue cracks grow faster than, and below the thresholds of, long cracks in both active (air at 60% relative humidity) and inert (vacuum and dry nitrogen) environments.<sup>90</sup>

Of major interest to the aerospace industry is the role of intermetallic precipitates in the development of pitting and subsequent crack initiation. Inclusions may be either anodic or cathodic with respect to the surrounding matrix. In either case, a microgalvanic cell is established which leads to local corrosion. Pit-like features act as stress concentration sites where crack initiation can take place. Metal ion hydrolysis leads to the formation of a low-pH solution within the pit. In turn, this can lead to hydrogen embrittlement or advancement of the crack via metal dissolution. The heat-treatable alloys tend to be more susceptible to EAC because the heat-treatment ageing process has a marked influence on the resulting microstructure of the material. Kumai *et al.*<sup>91</sup> showed that ageing of the Al–Li and Al–Li–Cu alloys can lead to precipitate free zones along the grain boundaries, affecting the corrosion resistance of the alloys. In another study, it was shown that where the addition of Li promotes the formation of a passive film, the corrosion resistance of the alloy was increased.<sup>92</sup>

Ro *et al.*<sup>93</sup> showed that the LEFM-regime fatigue crack growth kinetics for an Al–Cu–Mg/Li alloy were dependent not only on  $\Delta K$  and stress ratio,  $R$  but also on the factor  $P_{\text{H}_2\text{O}}/f$ , namely, the ratio of water vapor pressure to cyclic frequency. It was observed that the water vapor exposure dependence of  $da/dN$  exhibits four regimes of behavior and that there is no exposure effect below a threshold  $P_{\text{H}_2\text{O}}/f$  of 0.01 Pa s. At moderate water vapor exposures (0.02–2 Pa s), impeded molecular flow governs  $da/dN$ , whereas hydrogen diffusion rate limitation and surface reaction saturation intervene to reduce the  $da/dN$  dependence on  $P_{\text{H}_2\text{O}}/f$  at higher exposures. A plateau growth rate response was observed above 100–1000 Pa s.

The importance of mechanical loading effects on AA7075–T651, notably periodic overloads, was shown by Chlistovsky *et al.*<sup>94</sup> for smooth specimens. They concluded that the effect of periodic overloads was limited at high-cyclic amplitude loads ( $\Delta S$  values) between 100 and 450 MPa, but below this value fatigue life was significantly reduced (see Figure 16).

It was concluded that the reduction was due to premature crack initiation from surface pitting.

Further clarification of the role of overloads may be gained by considering their role in the development of short fatigue crack growth. Akid's study on damage accumulation under corrosion fatigue conditions<sup>76</sup> showed that cracks grow faster when subject to a low–high stress sequence in comparison

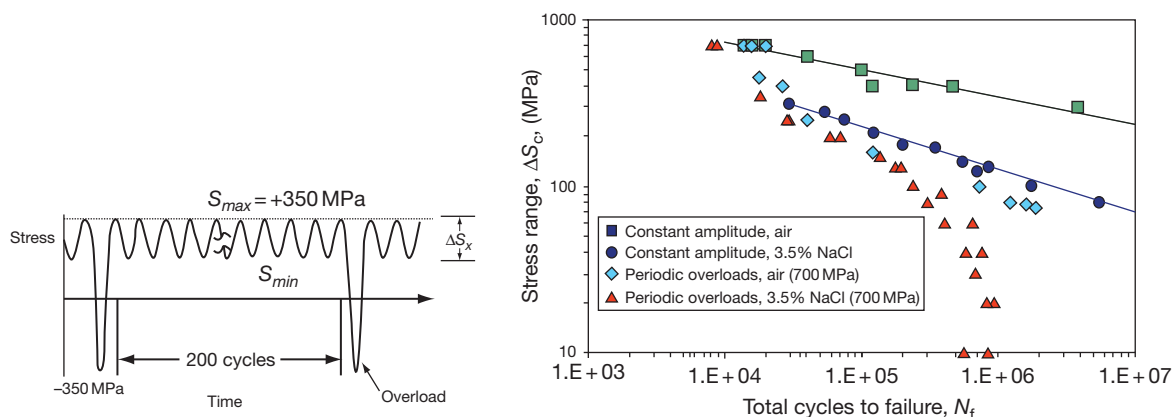


**Figure 16** Periodic overload sequence and fatigue life data for 7075-T651 aluminum alloy in air, and simulated seawater. Reproduced from Chlistovsky, R. M.; Heffernan, P. J.; DuQuesnay, D. L. *Int. J. Fatigue* **2007**, 29, 1941–1949.

to that of a high–low stress sequence. This observation was rationalized on the basis that during low stress cycling (below the in-air fatigue limit), the corrosion component is more damaging than the fatigue component. Where tests are conducted at an initial high stress (above the in-air fatigue limit), the contribution from corrosion is small compared to that from fatigue. In the case of Chlistovsky's study, the maximum effect of overloads was seen for corrosion fatigue below the in-air fatigue limit. Here, corrosion can progress the defect up to the microstructural barrier where, in principle, a single overload can propagate the defect beyond the barrier. When the stress level is restored to below the in-air fatigue limit, the crack progresses assisted by corrosion up to the next major microstructural barrier.

The presence of preexisting corrosion pits on the fatigue behavior of notched 7075-T7351 was studied by Pao *et al.*<sup>95</sup> Corrosion damage was produced by immersion in 3.5 wt% NaCl solution for 336 h. They observed that pitting shortens the fatigue crack initiation life in air by a factor of two to three and decreases the fatigue crack initiation threshold,  $(\Delta K/\sqrt{\rho})_{th}$ , by about 50%, where  $\rho$  is the notch root radius. Fatigue cracks in polished blunt-notched specimens often initiated from large constituent particles.

#### 2.12.5.4 Titanium Alloys

Titanium has found important uses in a range of sectors, including aerospace, offshore and biomedical because of its good fatigue strength, low specific weight, and good corrosion resistance. Its high corrosion resistance is attributed to the instantaneous

formation of an inert Ti oxide surface layer. However, low wear resistance and the poor tribological properties of titanium and its alloys are of concern. This is of particular importance in the case of metal release within the body and potential poor performance where there is a combination of fretting, fatigue, and a corrosive environment that is not conducive to the repassivation of the alloy.

Titanium alloys can be classified into three main groups depending upon the microstructural condition of the alloy, namely,  $\alpha$ ,  $\alpha/\beta$ , or metastable  $\beta$ . The microstructural condition and state of alloying provide Ti alloys with a wide range of mechanical properties, notably yield strengths up to 1400 MPa. This in turn gives a range of fatigue strength for these alloys.

Ti alloys have been shown to be susceptible to both corrosion fatigue and stress corrosion cracking.<sup>96</sup> As with other alloys that show this combination, there can be a marked increase in crack growth rates when the loading–defect size combination leads to stress intensity values above  $K_{ISCC}$ . These were obtained using precracked specimens, and the increase in crack growth rate has been attributed to hydrogen embrittlement. Shipilov<sup>97</sup> reported that, depending upon the nature of the environment used, cathodic and anodic polarization excursions may or may not accelerate or retard crack growth in VT20 and TS6 alloys. It is of interest to note that the effects of cathodic polarization, notably retardation in crack growth, can depend upon the nature of the material and the size of the crack; for these Ti alloys, crack growth is retarded, while for high strength steel, as shown in Figure 13, the development of pits and subsequent short fatigue cracks was retarded.

Goa showed that the fatigue response of Ti alloys in water vapor is identical to that of Al alloys<sup>98</sup> where crack growth rates increased with increasing water vapor pressure up to the saturation pressure. Frequency effects were also studied, and it was observed that crack growth rates increased with decreasing frequency and reached a maximum that depended upon  $\Delta K$  after which growth rates decreased to those comparable with rates observed in vacuum or other inert environments.

With the recent increase in the use of Ti alloys for prosthetic devices, there has been a significant amount of research on the fatigue and corrosion behavior of alloys, such as Ti4V6Al, in actual and simulated body environments. Leinebach *et al.*<sup>99</sup> investigated the cyclic deformation behavior of the binary titanium alloys Ti-6Al-4V and Ti-6Al-7Nb under axial stress-controlled constant amplitude and increasing load tests as well as in loading sequences based on gait patterns from human walking. They concluded that slight differences in the materials' microstructures result in differences of the fatigue and cyclic deformation behavior. In comparison to the results of constant loading rate tests, the standard walking gait pattern tests revealed shorter lifetimes for identical maximum stresses. It was also noted that the fatigue strength was also decreased by corundum grit blasting, that is, increase in surface roughness.

Papakyriacou *et al.* similarly conducted long-term corrosion fatigue tests comparing potential skeletal implant materials, namely cold-worked c.p. niobium and commercially pure (c.p.) tantalum with titanium and Ti-6Al-7Nb alloy.<sup>100</sup> Constant amplitude fatigue experiments (*S-N* curves) were performed at an ultrasonic frequency of 20 kHz with two different surface structures (ground surface and blasted and shot-peened surface) in ambient air and in a corrosive fluid similar to the body fluid in the oral cavity. They recorded a decrease in fatigue limit of 5–20% at 20 million cycles and a detrimental effect of surface finish on the Ti alloys compared to the Nb and Ta candidate materials. However, while this study shows that the Ti alloys can suffer from corrosion fatigue, it should be noted that the extreme high-cyclic test frequency used is not representative of typical implant loading conditions. Given that CF is more pronounced at low test frequencies, the results obtained in this study are likely to be conservative.

Titanium alloys are also gaining increased use in aerospace applications and are used in aircraft gas turbine engine blades and discs as well as in highly stressed components such as forged wing structures

and landing gear components. In this type of application, there is also the possibility that an additional damage mechanism may be operative, notably that of fretting. Fretting is the surface damage that occurs when contacting surfaces between mating bodies experience an oscillatory motion of small amplitude. The combination of this motion between two surfaces that are subject to loading is termed 'fretting fatigue.' Fretting fatigue increases the tensile and shear stresses at the contact surface producing surface defects which can act as stress concentration sites. Lietch *et al.*<sup>101</sup> investigated the fretting fatigue behavior of Ti-6Al-4V in ambient laboratory air and under a controlled environment consisting of synthetic seawater. Tests were performed over a wide range of the maximum axial stresses, ranging from 380 to 760 MPa, to examine both low- and high-cycle fatigue regimes. They concluded that seawater had a deleterious effect on fretting fatigue life in the low-cycle fatigue regime but improved the life in the high-cycle fatigue regime. *S-N* data showed marginal differences between the fatigue limit in air and in seawater, although there were limited data points and a high degree of scatter. The results of Leitch (Ti alloy) differ from those obtained by Shaluf,<sup>102</sup> working on a high-strength steel, in which Shaluf showed that fretting under corrosion fatigue conditions reduced the fatigue life at all stress levels.

## 2.12.6 Prevention of Corrosion Fatigue

Prevention of corrosion fatigue relies upon simple strategies such as lowering the fatigue stress level, adopting more corrosion-resistant alloys or eliminating the corrosion activity, in this case, by either forming a barrier on the surface of the substrate or by applying a negative electrode potential to suppress the anodic dissolution reaction. The former of these strategies, notably reducing the stress, is by far the easiest approach; however, this will reduce the operating loads that can be applied to a given component or structure. Consequently, this approach is rarely used.

### 2.12.6.1 Prevention by Barrier Coatings and Surface Treatments

Historically, barrier coatings have been used to protect substrates from reacting with the environment. Metallic and nonmetallic coatings, for example, hot-

dip galvanizing and paints offer differing benefits such as cost and ease of applicability, wear resistance, increased corrosion resistance, etc. However, there have been mixed benefits of applying coatings with respect to the enhancement of fatigue lifetime. The principle philosophy behind this approach is that the coating system will prevent contact of the corrosive media, and hence the material will essentially act as if it was under stress within a benign environment. This does, however, rely on the barrier remaining intact and not suffering failure from fatigue itself. Where coating breakdown does occur, there are several possible outcomes. With nonmetallic coatings, localized corrosion may take place at the coating failure site, thereby leading to a local stress concentration. In the case of a metallic coating, it is possible that the coating acts in a sacrificial manner and protects the underlying substrate, for example, Zn and Al coatings on steel. However, it should be pointed out that when the electrochemical potential of a coating is significantly lower than that of the substrate these types of coatings can liberate hydrogen during the dissolution process. This in turn can be adsorbed into the metal and, subject to the nature of the substrate, lead to hydrogen embrittlement. Alternatively, where a metallic coating is noble to the underlying substrate, failure of the coating can lead to accelerated localized corrosion due to galvanic action between the two dissimilar metals and subsequent crack initiation. A further consideration is that of crack initiation in the coating. This is particularly relevant for hard coatings that lack ductility, for example, chromium and nickel. The effects on fatigue life of crack initiation can be compounded if the coating is noble to the substrate, for example, Ni on steel. The initiation of a crack can lead to solution ingress to the substrate and the formation of a local galvanic cell whereby the underlying steel substrate is attacked locally leading to pitting and the formation of a stress concentrating feature.

As previously discussed, both shot peening and surface coatings can influence the fatigue performance of a material. Asquith *et al.*<sup>103</sup> assessed the combination of shot peening and a plasma electrolytic oxidation (PEO) treatment on the corrosion performance of a 2024 aluminum alloy. Shot peening was found to decrease the corrosion resistance, as assessed by electrochemical impedance spectroscopy, while shot peening followed by PEO improved the corrosion resistance. Marin de Camargo *et al.*<sup>104</sup> assessed the effects of coating residual stresses on the fatigue performance of a 7070 Al alloy. They

concluded that a 17% Co thermally sprayed coating improved the axial fatigue resistance, while different anodizing treatments decreased fatigue resistance. Shot peening of anodized layers improved the fatigue life over that of nonshot-peened surfaces.

Alternative surface treatments that influence the surface metallurgy, and hence the localized corrosion performance have also been investigated. Wu *et al.*<sup>105</sup> evaluated the effects of laser surface melting (in air and in N<sub>2</sub>), using an excimer laser, to improve the resistance to fatigue cracking of aluminum alloy 6013 induced by pitting corrosion. Analysis of the electrochemical impedance measurements showed that the laser-formed AlN and/or Al<sub>2</sub>O<sub>3</sub> layer can greatly reduce the rate of electrochemical reaction. The corrosion fatigue lives of the air-treated and the N<sub>2</sub>-treated specimens were found to increase by two and four times compared to the untreated specimens. Furthermore, the corrosion current for the laser-treated specimens (measured during the fatigue test) was considerably lower than that for the untreated specimens, the improvement in lifetime being considered to be due to the excellent initiation resistance to pitting corrosion of the laser-treated specimens.

### **2.12.6.2 Prevention by Cathodic Protection**

Cathodic protection operates on the principle of lowering the potential of the metal to a value below its normal open-circuit potential. This topic is covered elsewhere in this book and therefore will not be discussed in detail. However, its relevance to corrosion fatigue is that the cathodic partial reaction can lead to the generation of atomic hydrogen which in turn can give rise to hydrogen embrittlement of high-strength alloys. A typical rule of thumb when protecting steel is to prevent the potential becoming more negative than  $-900\text{ mV (Ag/AgCl)}$  and use alloys that have a yield strength less than 700 MPa.

## **2.12.7 Summary**

This chapter has considered the role of corrosion on the fatigue performance of a range of engineering materials. Specific attention has been given to discussing the early stages of corrosion fatigue for damage emanating at nominally ‘defect’ free surfaces. This stage has traditionally been referred to as ‘initiation.’



Corrosion fatigue damage of alloys in aggressive solutions progresses through several stages including surface film breakdown, localized dissolution/pitting at slip bands or nonmetallic inclusion, transfer from corrosion-dominated growth to fatigue cycles-dependent cracking and subsequent transfer to, environmentally-assisted microstructurally independent cracking in a 'continuum mechanics' growth regime.

A number of factors have been shown to influence individual stages of the corrosion fatigue process; including atmospheric or solution conditions, electrochemical potential, applied stress state, loading frequency, surface stress state and microstructural condition.

The 'free corrosion' fatigue lifetime of 'smooth' specimens is considered to be dominated by the ability to grow a defect, that is, a pit or crack, beyond crack-arresting microstructural barriers inherent within the material. Given the appropriate solution and loading conditions, this early dissolution dominated regime, along with the transition of a pit to a crack, has a major effect on the fatigue lifetime of a material. The major factors, which are known to control smooth specimen lifetime under in-air fatigue loading, notably microstructure, loading mode and biaxial stress state, play a less significant role under corrosion fatigue conditions. Test frequency, however, is a dominant factor in controlling smooth specimen corrosion fatigue lifetime. Overall it is considered that the environment, in particular, anodic dissolution plays a major part in controlling fatigue lifetime for stress levels below the in-air fatigue limit.

In the case of corrosion fatigue of structures containing preexisting defects, the most important factors include solution chemistry, test frequency, load ratio, and crack tip stress intensity. Of particular concern for cracked components is hydrogen embrittlement, especially when high-strength alloys are employed in conjunction with cathodic protection. A similar problem can arise if these materials are cleaned in acidic solutions or electroplated.

The nature of the surface is especially important, as corrosion fatigue is predominantly a surface phenomenon. Controlling the surface residual stress state, surface roughness, electrode potential and applying coatings have a marked effect on performance. Coatings, in particular, can be a low-cost strategy to exclude contact between the substrate and the environment and, in effect, simulate an inert environment for the material. Caution is required where the coating is brittle and noble to the substrate as this may accelerate damage and decrease fatigue lifetime.

## References

- Rankine, W. *Proc. Inst. Civil Eng.* **1843**, 2, 105–108.
- Frost, N. E.; Marsh, K. J.; Pook, L. P. *Metal Fatigue*; Oxford: Clarendon Press, 1974; p 26.
- Lisagore, W. B. Crooker, T. W.; Leis, B. N.; Eds. *Environmentally Assisted Cracking: Science and Engineering*, ASTM STP 1049, 1990.
- Haigh, B. P. *J. Inst. Metals* **1917**, 18, 55–77.
- McAdam, D. J. *Proc. ASTM* **1926**, 26, 224–254.
- Gough, H. J. *J. Inst. Metals* **1932**, 49, 17–92.
- Miller, K. J.; Akid, R. *Proc. R. Soc. Lond. A* **1996**, 452, 1411–1432.
- Evans, U. R.; Simnad, M. T. *Proc. Roy. Soc. A* **1947**, 188A, 372–392.
- Simnad, M. T.; Evans, U. R. *J.I.S.I.* **1947**, 156, 531–539.
- Mughrabi, H. *Scr. Metall.* **1992**, 26, 1499–1504.
- Klesnil, M.; Lukas, P. *Fatigue of Metallic Materials*; Elsevier Scientific, 1980.
- Forsyth, P. J. E. *J. Inst. Metals* **1951/2**, 80, 181.
- Magnin, T.; Driver, J.; Lepinoux, J.; Kubin, L. P. *Rev. Phys. Appl.* **1984**, 19, 483–502.
- Suresh, S.; Ritchie, R. O. *Int. Metals Rev.* **1984**, 29, 445–476.
- Miller, K. J. *Fatigue Fract. Eng. Mater. Struct.* **1993**, 16(9), 931–940.
- Akid, R. In *Effects of Environment on the Initiation of Crack Growth*; Van der Sluys, W. A., Piascik, R. S., Zawiercha, R., Eds.; ASTM STP 1298, **1997**, pp 1–17.
- Ford, F. P. In *Environment-Sensitive Fracture*; Dean, S. W., Pugh, E. N., Ugiansky, G. M., Eds.; ASTM STP 821, **1984**, pp 32–51.
- Frankel, G. S. *J. Electrochem. Soc.* **1998**, 145(6), 2186–2198.
- Jack, A. R.; Paterson, A. N. In *Conference of Institute of Mechanical Engineers*, London, UK **1977**; pp 75–83.
- Duquette, D. J.; Uhlig, H. H. *Trans. ASM* **1969**, 62, 839–845.
- Akid, R.; Miller, K. J. *Fatigue Fract. Eng. Mater. Struct.* **1991**, 14, 637–649.
- Magnin, T.; Landon, J. M. *Mater. Sci. Eng.* **1995**, 76, L7–L10.
- Leis, B. N.; et al. *Corrosion Fatigue Crack Initiation in an Iron-Caustic System* ASTM STP 801, **1983**, pp 197–228.
- Isaacs, H. S.; Kissel, G. J. *Elect. Soc.* **1972**, 119, 1628–1631.
- Wu, X. D. Ph.D. Thesis, University of Sheffield, 1995.
- Vignal, V.; Mary, N.; Valot, C.; Oltra, R.; Coudreuse, L. *Electrochem. Solid State Lett.* **2004**, 7(4), 1–11.
- Cottis, R. A.; Markfield, A.; Haritopoulos, P. In *Environment Assisted Fatigue*; EGF 7 Scott, P., Ed.; Mechanical Engineering Publications: London, 1990; pp 381–393.
- Wang, Y.; Akid, R. *Corros. J. Sci. Eng.* **1996**, 52(2), 92–102.
- Boukerrou, A.; Cottis, R. A. *Corros. Sci.* **1993**, 35(1–4), 577–585.
- Muller, M. *Met. Trans. A* **1982**, 13, 649–655.
- Wu, X. J. Ph.D. Thesis, University of Sheffield, 1995.
- Dmytrakh, I. M.; Akid, R.; Miller, K. J. *Br. Corros. J.* **1997**, 32(2), 1–7.
- Hu, H. Ph.D. Thesis, University of Sheffield, 1997.
- Ebera, R. *Eng. Failure Anal.* **2006**, 13, 516–525.
- Gangloff, R. P.; Wei, R. P. In *Proceedings of the Second Engineering Foundation International Conference – Small Fatigue Cracks*, 1986; pp 239–264.
- Wu, X. D. Ph.D. Thesis, University of Sheffield, 1995.

37. Akid, R.; Miller, K. J. *Fatigue Fract. Eng. Mater. Struct.* **1991**, *14*, 637–649.
38. Murtaza, G.; Akid, R. *Int. J. Fatigue* **1996**, *18*(8), 557–566.
39. Zhang, W.; Akid, R. *Fatigue Fract. Eng. Mater. Struct.* **1997**, *20*(4), 547–557.
40. Guillem, F. M.Phil. Thesis, University of Sheffield, 1998.
41. Goto, M.; Nisitani, H. *Fatigue Fract. Eng. Mater. Struct.* **1992**, *15*(4), 335–363.
42. Akid, R., Wu, X. J. *Structural Materials in Marine Environments*. The Royal Society, London, UK. The Institute of Materials; 1994; pp 330–345, ISBN 1 86125 0029.
43. Zhang, W.; Akid, R. *Fatigue Fract. Eng. Mater. Struct.* **1997**, *20*(4), 547–557.
44. Akid, R.; Wang, Y. Z.; Fernando, U. In *Corrosion-Deformation Interactions*; Magnin, T., Gras, J. M., Eds.; Les Editions de Physique Les Ulis, 1993; pp 659–670.
45. Hoepfner, D. W. In *Fatigue Mechanisms*; STP 675. Fong, J. T., Ed.; ASTM: Philadelphia, PA, 1979; p 841.
46. Wei, R. P.; Gangloff, R. P. In *Fracture Mechanics: Perspectives and Directions*; ASTM STP 1020; Wei, R. P., Gangloff, R. P., Eds.; ASTM: Philadelphia, PA, 1989; pp 233–264.
47. Hagn, L. *Mater. Sci. Eng. A* **1998**, *103*, 193.
48. Lindley, T. C.; McIntyre, P.; Trant, P. J. *Metal. Technol.* **1982**, *9*, 135.
49. Kawai, S.; Kasai, K. *Fract. Eng. Mater. Struct.* **1985**, *8*, 115–127.
50. Kondo, Y. *Corros. Sci.* **1985**, *45*, 1.
51. Chen, G. S.; et al. *Mater. Sci. Eng. A* **1996**, *219*, 126.
52. Knott, J. F. *Fundamentals of Fracture Mechanics*; Butterworths, 1973; p 134.
53. Paris, P.; Erdogan, F. *Trans. ASME, J. Basic Eng.* **1963**, *85*, 528–534.
54. Taylor, D.; Knott, J. F. *Fatigue Eng. Mater. Struct.* **1981**, *4*, 147–155.
55. Craig, H. L., Jr. Crooker, T. W.; Hoepfner, D. W. Eds. *Corrosion Fatigue Technology*, ASTM STP 642, 1978.
56. Congelton, J.; Craig, I. H.; Olieh, R. A.; Parkins, R. N. In *Corrosion Fatigue: Mechanics, Metallurgy, Electrochemistry and Engineering*, ASTM 801; Crooker, T. W., Leis, B. N., Eds.; 1984, pp 367–389.
57. Austen, I. M.; Walker, E. F. In *Influence of Environment on Fatigue*; IMech E Conference Publications 1977–4. The Institution of Mechanical Engineers, 1977; pp 1–10.
58. Devereux, O. F.; McEvily, A. J.; Staehle, R. W. Eds. *Corrosion Fatigue: Chemistry, Mechanics and Microstructure*; NACE-2, National Association of Corrosion Engineers, 1972.
59. Wei, R. P.; Landes, J. D. *Materials. Res. Stds.* **1969**, *9*, 25.
60. Gangloff, R. P.; Wei, R. P. *Metall. Trans. A* **1977**, *8*, 1043–1053.
61. Austen, I. M.; Walker, E. F. *Fatigue* **1984**, *84*, 1457–1469.
62. Rhodes, D.; Musuva, J. K.; Radon, J. C. *Eng. Fract. Mech.* **1981**, *15*(3–4), 407–419.
63. Panasyuk, V. V.; Ratch, L. V.; Dmytrakh, I. N. *Fatigue Eng. Mater. Struct.* **1984**, *7*(1), 1–11.
64. Turnbull, A. Ed. *Corrosion Chemistry in Pits, Crevices and Cracks*; HMSO: London, 1987.
65. Nakayama, T.; Yuse, F.; Tsubokawa, Y. *Corros. Sci.* **2007**, *49*, 130–138.
66. Frantzikonis, G. N.; et al. *Eur. J. Mech. A: Solids* **2000**, *19*(2), 309–318.
67. Rollins, V.; et al. *Br. Corros. J.* **1970**, *5*, 33–40.
68. Gangloff, R. P. *Res. Mech. Lett.* **1981**, *1*, 299–306.
69. Akid, R.; Miller, K. J. In *Environmental Assisted Fatigue*; EGF 7; Scott, P., Ed.; Mechanical Engineering Publications: London, 1990; pp 415–434.
70. Craig, H. L., Jr. Crooker, T. W.; Hoepfner, D. W. Eds. *Corrosion Fatigue Technology*, ASTM STP 642, 1978.
71. Congelton, J.; Craig, I. H.; Olieh, R. A.; Parkins, R. N. In *Corrosion Fatigue: Mechanics, Metallurgy, Electrochemistry and Engineering*; Crooker, T. W., Leis, B. N., Eds.; ASTM 801, 1984, pp 367–389.
72. Wei, R. P.; Gangloff, R. P. In *Fracture Mechanics: Perspectives and Directions*; ASTM STP 1020; Wei, R. P., Gangloff, R. P., Eds.; American Society for Testing and Materials: Philadelphia, PA, 1989; pp 233–264.
73. Akid, R. In *Hydrogen Transport and Cracking of Metals*; Turnbull, A., Ed.; The Institute of Materials, 1995; pp 50–61.
74. Taylor, D.; Clancey, M. *Fatigue Fract. Eng. Mater. Struct.* **1991**, *14*(2/3), 329–336.
75. Akid, R.; Zhang, W. In *Engineering Against Fatigue*; Beynon, J. H., Brown, M. W., Lindley, T. C., Smith, R. A., Tompkins, B., Eds.; A.A.Balkema: Rotterdam, Brrokfield, 1999.
76. Akid, R. *Fatigue Fract. Eng. Mater. Struct.* **1996**, *19*(2/3), 277–285.
77. Ford, F. P. In *Environment-Sensitive Fracture*, ASTM STP 821, Dean, S. W., Pugh, E. N., Ugiansky, G. M., Eds.; 1984, pp 32–51.
78. Barsom, J. M. *Eng. Fracture Mech.* **1971**, *3*, 15–25.
79. Barsom, J. M. In *NACE-2*, 1972; pp 424–436.
80. Scott, P. M. In *Advances in Fracture Mechanics*; Chell, G., Ed.; Applied Science Publishers, 1981.
81. Gangloff, R. P. In *Corrosion Tests and Standards Manual: Application and Interpretation*; Baboian, R., Ed.; American Society for Testing and Materials: Philadelphia, PA, 1995.
82. Wei, R. P.; Chiou, S. *Eng. Fracture Mech.* **1992**, *41*(4), 463–473.
83. Ritter, S.; Seifert, H. P. *J. Nucl. Mater.* **2007**, *360*(2), 170–176.
84. Ford, F. P.; Hudak, S. J., Jr. In *Small Fatigue Cracks*. Ritchie & Langford Ritchie, R. O., Lankford, J., Eds.; 1986.
85. Goa, M.; Wei, R. P. *Scr. Metall. Mater.* **1993**, *28*(7), 853–856.
86. Wu, X.; Katada, Y. *Corros. Sci.* **2005**, *47*(6), 1415–1428.
87. Olive, J. M.; Cwiek, J.; Desjardins, D. *Corros. Sci.* **1999**, *41*, 1067–1078.
88. Magnin, T.; Coudreuse, L. *Mater. Sci. Eng.* **1985**, *72*, 125–134.
89. Nyström, M.; Karlsson, B. *Mater. Sci. Eng. A* **1996**, *215*, 26–38.
90. Lankford, J. *Fatigue Fract. Eng. Mater. Struct.* **1983**, *6*, 15–31.
91. Kumai, C.; et al. *Corrosion (NACE)* **1989**, *45*(4), 294–303.
92. Gui, J.; Devine, T. M. *Scr. Metall.* **1987**, *21*, 853–857.
93. Ro, Y. J.; Agnew, S. R.; Bray, G. H.; Gangloff, R. P. *Mater. Sci. Eng. A* **2007**, *468–470*, 88–97.
94. Chlistovsky, R. M.; Heffernan, P. J.; DuQuesnay, D. L. *Int. J. Fatigue* **2007**, *29*, 1941–1949.
95. Pao, P. S.; Gill, S. J.; Feng, C. R. *Scr. Mater.* **2000**, *43*, 391–396.
96. Pelloux, R. M. *Proceedings of Fatigue of Materials and Structures Sherbrooke: Canada*, July 1978; pp 8–26.
97. Shipilov, S. A. *Fatigue Fract. Eng. Mater. Struct.* **2001**, *25*(9), 243–259.
98. Gao, S. J.; Wei, R. P. *Mater. Sci. Eng.* **1984**, *62*, 65–78.
99. Leinenbach, C.; Schwilling, B.; Eifler, D. *Mater. Sci. Eng C* **2005**, *25*(3), 321–329.
100. Papakriacou, M.; Mayera, H.; Pypenb, C.; Plenk, H., Jr.; Stanzl-Tschegga, S. *Int. J. Fatigue* **2000**, *22*(10), 873–886.
101. Lietch, L. C.; Lee, H.; Mall, S. *Environ. Mater. Sci. Eng. A* **2005**, *403*(1–2), 281–289.
102. Shaluf, I. M. M.Sc. Thesis, University of Sheffield, 1993.

- 
103. Asquith, D. T.; *et al.* *Thin Solid Films* **2007**, 516(2–4), 417–421.
  104. Marin de Camargo, J. A.; *et al.* *Surf. Coat. Technol.* **2007**, 201, 9448–9455.
  105. Xu, W. L.; Yue, T. M.; Man, H. C.; Chan, C. P. *Surf. Coat. Technol.* **2006**, 200, 5077–5086.
  106. Daeubler, M. A.; Thompson, A. W.; Bernstein, I. M. *Metall Trans* **1991**, 22A, 513–519.
  107. Nakajima, N.; Tokaji, K. *Fatigue Fract. Eng. Mater. Struct.* **1995**, 18, 345–351.

## 2.14 Under Film/Coating Corrosion

**H. N. McMurray and G. Williams**

Materials Research Centre, School of Engineering, Swansea University, Singleton Park, Swansea, SA2 8PP, UK

© 2010 Elsevier B.V. All rights reserved.

2.14.1	Introduction	988
2.14.2	Cathodic Delamination	989
2.14.2.1	Disbondment Mechanism	991
2.14.2.2	Preventing Cathodic Delamination	992
2.14.2.3	Modifying Metal Composition	995
2.14.3	Filiform Corrosion	996
2.14.3.1	General FFC Characteristics	996
2.14.3.2	FFC on Aluminum Surfaces	997
2.14.3.3	Surface-Active FFC on Aluminum	999
2.14.3.4	FFC on Iron (Steel) Surfaces	1000
References		1003

### Abbreviations

<b>EB</b>	Emeraldine base
<b>EPMA</b>	Electron micro-probe analysis
<b>ES</b>	Emeraldine salt
<b>FFC</b>	Filiform corrosion
<b>H-CS</b>	Camphor sulfonic acid
<b>H<sub>2</sub>-PP</b>	Phenyl phosphonic acid
<b>H-pTS</b>	<i>para</i> -Toluene sulfonic acid
<b>HDG</b>	Hot-dip galvanized steel
<b>ICP</b>	Intrinsically conducting polymer
<b>LB</b>	Leucoemeraldine base
<b>PVB</b>	Polyvinyl butyral
<b>PAni</b>	Polyaniline
<b>SHE</b>	Standard hydrogen electrode
<b>SIMS</b>	Secondary ion mass spectrometry
<b>SKP</b>	Scanning kelvin probe
<b>SKPFM</b>	Scanning kelvin probe force microscope
<b>XPS</b>	X-ray photoelectron spectroscopy

### Symbols

$E_{\text{corr}}$	Free corrosion potential (V)
$E_{\text{intact}}$	Free corrosion potential of an intact polymer coated metal (V)
$pK_a$	Acid dissociation constant
$x_{\text{del}}$	Delamination distance ( $\mu\text{m}$ )
$t_{\text{del}}$	Delamination time since electrolyte contact (min)
$t_i$	Delamination initiation period (min)
$\phi_{\text{sc}}$	Strontium chromate pigment volume fraction
$\phi_{\text{pa}}$	Polyaniline pigment volume fraction

### 2.14.1 Introduction

Corrosion-driven organic coating delamination, in which the more-or-less intact coating becomes physically separated from the underlying substrate, is a key failure process affecting painted, lacquered and otherwise organically coated metal products, and the subject has been reviewed elsewhere.<sup>1–6</sup> Here, we will attempt a brief overview and update of the topic. In so doing, we will concentrate on two processes of corrosion-driven coating delamination, which have been extensively characterized and have reasonably well-defined mechanisms, namely *cathodic delamination* and *filiform corrosion* (FFC). Both of these phenomena tend to propagate from preexisting breaks or penetrative defects in the organic coating, which act to admit species from an external electrolyte. In the case of cathodic delamination, separation of the organic coating is linked to the cathodic reaction in a localized corrosion cell. In the case of FFC, separation of the organic coating is frequently linked to the anodic reaction. As such, cathodic delamination and FFC are closely related to the phenomena of cathodic blistering and anodic blistering.<sup>7–10</sup> It is not our intention to further describe or discuss blistering as a separate phenomenon. Neither is it our intention to describe or discuss the processes by which ions from an external electrolyte diffuse or migrate through a nominally intact organic coating.<sup>11–13</sup> We will restrict our comments to situations in which electrolyte species have penetrated through a penetrating defect and describe the

corrosion processes that then ensue at the defect and beneath the organic coating.

### 2.14.2 Cathodic Delamination

One of the most common and therefore economically important mechanisms of coating delamination on iron (mild steel) and zinc (galvanized) surfaces involves so-called cathodic delamination.<sup>1,3,4,14–24</sup> This process can occur wherever the metallic substrate becomes exposed to scratches or cut edges during manufacturing or through in-service damage. Numerous studies have indicated that when iron or zinc substrates are exposed to aqueous electrolyte through penetrative defects in an organic coating, a *cathodic delamination cell* may become established. In this cell, a thin layer of electrolyte, which penetrates beneath a region of already delaminated coating, acts to couple anodic metal dissolution occurring at the coating defect to cathodic oxygen reduction occurring at the site of coating disbondment. An alkaline environment forms at the cathode, and suggested mechanisms of coating disbondment include the dissolution of an amphoteric metal oxide film at the metal–coating interface (in the case of zinc), base-catalyzed polymer degradation, base-catalyzed hydrolysis of interfacial bonds, and attack on the polymer by hydrogen peroxide and other reactive intermediates in cathodic oxygen reduction.

Koehler showed that cathodic delamination (which he called halo detachment) occurred only when group I (alkali metal) cations were available to act as counter ions to cathodically generated  $\text{OH}^-$ .<sup>14</sup> This is because only group I cations possess the hydrolytic stability and solubility at high pH necessary to support a strongly alkaline electrolyte. Ammonium salts do not produce cathodic delamination because the ammonium cation ( $\text{NH}_4^+$ ,  $\text{p}K_a$  9.3) decomposes to ammonia ( $\text{NH}_3$ ) at high pH.<sup>14,21</sup> Group II (alkaline earth) salts do not produce cathodic delamination because of the limited solubility of group II hydroxides.<sup>14,21,25</sup> When group I cations are present, a very high local pH can be produced. In a work involving cellulose nitrate coatings on iron, Ritter and Kruger measured a pH approaching 14 beneath the delaminated coating for a natural corrosion situation with 0.05 M NaCl.<sup>26</sup> However, from their accompanying ellipsometric measurements, it seems most likely that actual delamination took place when the pH was  $\sim 11$ .

Two possible routes exist for species undergoing transport to the cathodic site, (vertically) through the coating or (horizontally) along the polymer–substrate interface. Leidheiser *et al.* showed that water transport occurs through the coating.<sup>1,18</sup> They also showed that oxygen transport occurs predominantly through the coating in nonpigmented coatings, with a minor contribution from interfacial transport. Water and oxygen transport are not usually the rate controlling processes in cathodic delamination.<sup>1,18</sup> However, in pigmented coatings, where the pigment hinders through-coating diffusion, interfacial oxygen transport can become important and rate limiting.<sup>21</sup> Leidheiser identified a linear relationship between cation diffusion coefficient in aqueous solution and cathodic delamination rate for a range of group I chloride salts. This suggested that cation transport occurred principally through migration along the interface. However, because delamination rates also showed a strong dependence on film thickness, through-coating transport could not be ruled out.<sup>27</sup> The notion of interfacial cation migration was further supported by the work of Castle and Watts.<sup>28</sup> They used electron probe micro-analysis (EPMA) to show that  $\text{Na}^+$  cations superficially penetrated the delaminated coating from both bulk solution and the interface, but detected no  $\text{Na}^+$  within the interior of the coating, thus ruling out the possibility of through-coating transport. They also found that delamination rate decreased with increasing substrate surface roughness and, therefore, increasing tortuosity of the coating–substrate interface. This finding is also consistent with the notion of interfacial cation migration as the rate controlling step.

Probably the most systematic recent work on the cathodic delamination of organic coatings from iron<sup>29–31</sup> and the zinc surface of electrogalvanized steel<sup>32–34</sup> was carried out by Stratmann *et al.* in a series of experiments designed to preclude the possibility of through-coating cation transport. They prepared their samples and used a scanning Kelvin probe (SKP) apparatus in a configuration similar to that shown in Figure 1. Under these circumstances, a cathodic delamination cell becomes established, and a thin layer of electrolyte ingresses beneath the delaminated coating in the manner shown schematically in the lower part of Figure 2. The SKP is calibrated to record the local free corrosion potential ( $E_{\text{corr}}$ ) as a function of distance ( $x$ ) from the edge of the organic coating defect. As delamination proceeds,  $E_{\text{corr}}(x)$  profiles develop as shown schematically in the upper part of Figure 2. These may be approximately resolved into four characteristic regions as follows:



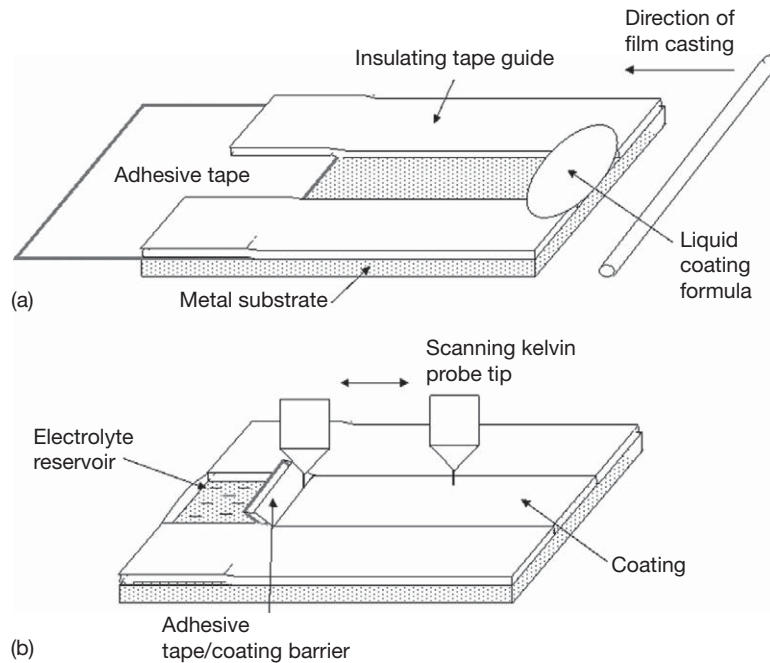


**Figure 1** Schematic diagram showing (a) sample preparation and (b) experimental procedure for a typical delamination experiment.

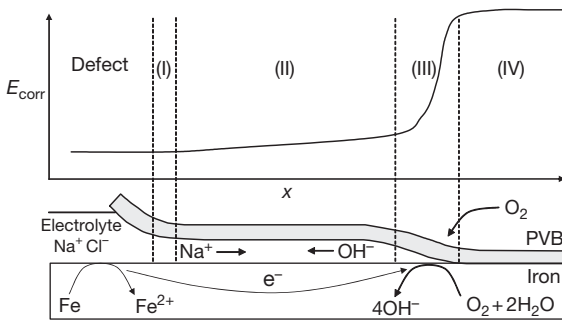


**Figure 2** Schematic representation of the corrosion-driven delamination cell showing correspondence with various regions of the time-dependent  $E_{\text{corr}}(x)$  profile.

1. The region immediately next to the defect where  $E_{\text{corr}}$  is low and ultimately becomes similar to that of the freely corroding metal.
2. A region of  $E_{\text{corr}}$  gradient linking region (I) with region (III) below and resulting, at least in part, from ohmic resistance to ionic current flow in the thin under-coating electrolyte layer.
3. A region of sharp transition in  $E_{\text{corr}}$  corresponding to the cathodic delamination front where coating disbondment takes place.
4. A region of as yet undelaminated polymer where oxygen can diffuse to the metal surface but electrolyte is not present and metal cannot

corrode. Here,  $E_{\text{corr}}$  (or the intact potential  $E_{\text{intact}}$ ) is high.

Stratmann's technique is robust and reproducible. Figure 3 shows SKP derived  $E_{\text{corr}}(x)$  profiles obtained, by ourselves, from unpigmented 30  $\mu\text{m}$  polyvinyl butyral (PVB) coatings on the zinc surface of (hot dip) galvanized steel (HDG), undergoing cathodic delamination with 5% aqueous NaCl in contact with the coating defect. The location of the delamination front can be determined from the point of maximum  $dE_{\text{corr}}(x)/dx$  gradient.<sup>30</sup> The distance ( $x_{\text{del}}$ ) over which delamination has occurred is related to the time since electrolyte contact ( $t_{\text{del}}$ ) by,

$$x_{\text{del}} = k_d(t_{\text{del}} - t_i)^{1/2} \quad [1]$$

where  $k_d$  is a parabolic rate constant and  $t_i$  is the initiation period – that is the time delay between electrolyte contact and the onset of cathodic delamination. Initially, the substrate–coating interface is intact, and anions and cation ingress simultaneously by diffusion. Because the coating is fully hydrated at the time of electrolyte contact,  $t_i$  was taken to be the time required for interfacial ionic concentration to rise to a level capable of supporting cathodic  $\text{O}_2$  reduction.<sup>30</sup> Below a concentration threshold of 0.05 M inside the defect, delamination was not observed, implying that a minimum interfacial ionic

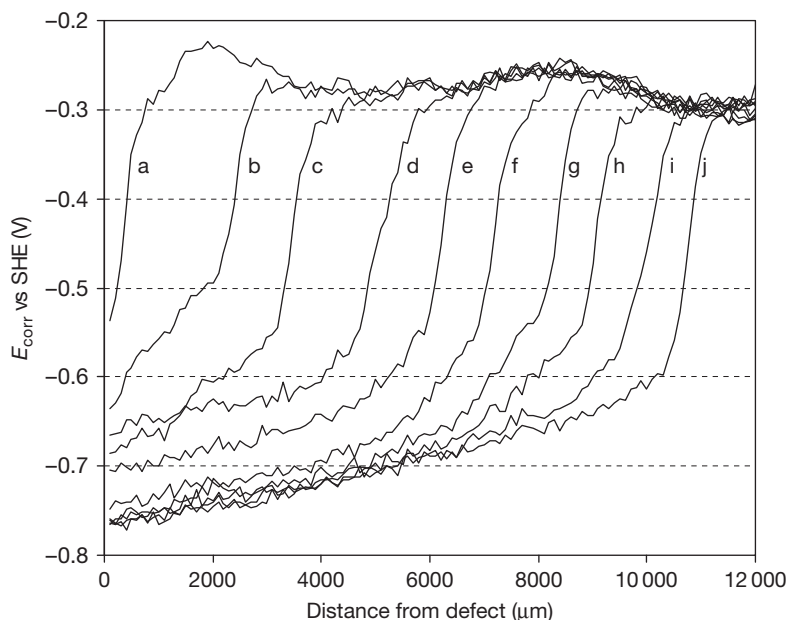


**Figure 3** Time-dependent  $E_{\text{corr}}$  (versus standard hydrogen electrode, SHE) as a function of distance ( $x$ ) from the defect edge profiles recorded for unpigmented 30  $\mu\text{m}$  polyvinyl butyral (PVB) coatings on HDG zinc substrate. Electrolyte in contact with the defect is  $0.86 \text{ mol dm}^{-3}$  NaCl: curve (a) = 120 min, (b) = 240 min, (c–e) at 120 min intervals.

concentration is required. Once interfacial  $\text{O}_2$  reduction begins, cations migrate towards the underfilm cathode, and anions migrate towards the defect anode, that is, anions from the experimental electrolyte are excluded from the electrolyte layer forming beneath the delaminated coating.<sup>30</sup>

In agreement with the earlier findings of Leidheiser<sup>1,27</sup> the value of  $k_d$  in eqn [1] was found to increase with the aqueous diffusion coefficient of the group I cation used in the experimental electrolyte, that is, in the order  $\text{Li}^+ < \text{Na}^+ < \text{K}^+ < \text{Cs}^+$ . The identity of the counter anion ( $\text{Br}^-$ ,  $\text{F}^-$ ,  $\text{Cl}^-$ ,  $\text{ClO}_4^-$ ) was found to have no influence on  $k_d$ , and the absence of anions in the under-film region was confirmed by Auger analysis.<sup>30</sup> The electrolyte layer forming beneath the delaminated coating was found to be 2–3  $\mu\text{m}$  thick. However, the diffusion coefficients calculated for cations migrating in this layer were calculated to be more than 10 times smaller than in aqueous solution. It was therefore proposed that the electrolyte layer takes the form of a gel comprising highly oxidized polymer in water.<sup>30</sup>

On the basis of the above, it would seem clear that the rate determining step in cathodic delamination is typically the transport of cations from the external electrolyte along the interface between the organic coating and the metal substrate. However, this notion should be regarded with caution because the coated

metal systems used to study the intrinsic kinetics of cathodic delamination have largely been ‘model’ systems comprising unpigmented polymer films coated onto metals which are good electrocatalysts for cathodic  $\text{O}_2$  reduction, and with no prior application of any chemical ‘pretreatment’ or ‘conversion coating’ to influence adhesion and/or rates of interfacial electron transfer. The rate determining step in any complex process is always the slowest step. In practical coated systems pigments capable of inhibiting cathodic oxygen reduction may be added to the organic coating, an inhibitory pretreatment applied to the metal substrate, or the elemental composition of the metal surface modified to reduce activity for oxygen reduction. Under these circumstances, the rates of cathodic delamination may be greatly diminished without any obvious influence on the facility of interfacial cation transport – as will be discussed further under *preventing cathodic delamination* given below.

#### 2.14.2.1 Disbondment Mechanism

A question arises as to exactly how the presence of cathodic  $\text{O}_2$  reduction and an alkaline environment produces disbondment of an organic coating from the underlying substrate. We should say immediately that it is very unlikely that any single, unique and universal disbondment mechanism exists. More

probably, there are a number of possible mechanisms that may occur alone or in combination depending on the nature of the coated metal system under consideration. In any particular system, the relevant mechanism will be that which proceeds at the fastest rate. Modifying the system to inhibit a particular mechanism may reduce the rate of cathodic delamination, but not prevent it completely if another mechanism is available.

The first possible mechanism is the alkaline dissolution of a preexisting (air-formed) oxide layer at the substrate–coating interface. In the case of metals such as zinc with strongly amphoteric oxides, which dissolve at moderately high pH, this would seem a reasonable hypothesis. Stratmann *et al.* have shown that the oxide layer on zinc actually thickens in the delaminated zone, but that this occurs via a dissolution–reprecipitation mechanism.<sup>32</sup> However, iron III oxides are only weakly amphoteric and dissolve only at very high pH (approaching 14). Consequently, the iron surface tends to remain passive in the delaminated zone.<sup>29</sup> Reduction of iron III to a more soluble iron II oxide is possible as potentials decrease.<sup>35</sup> However, Castle and Watts used X-ray photoelectron spectroscopy (XPS) to show that iron oxide within the delaminated region only became reduced in localized patches and that the delaminated region extended well beyond these.<sup>36</sup> They concluded that oxide dissolution is not a significant factor in cathodic delamination on iron.

The second possibility is that alkaline electrolyte physically displaces the coating at the substrate–coating interface.<sup>14</sup> Aqueous displacement was first suggested by Evans in terms of the ability of alkaline solution to creep over the metal surface.<sup>37</sup> The ‘wetability’ of an electrode surface increases with decreasing (electrolyte–electrode) interfacial energy and latter reaches a maximum at the potential of zero charge.<sup>38,39</sup> On this basis it has been pointed out that the affinity for water of an oxide covered metal surface will tend to increase as the pH becomes increasingly removed from the isoelectric point (pH point of zero charge) of that oxide.<sup>40</sup> If it is assumed that the isoelectric point lies near or below neutral pH, a competitive displacement of the coating by water will be promoted as pH, and therefore water affinity is increased. It has also been argued that competitive displacement may occur when oxide–polymer acid–base interactions make a significant contribution to coating adhesion.<sup>41</sup>

The third possibility is that alkaline electrolyte reacts directly with the coating polymer in such a way as to break covalent chemical bonds existing

within the coating or between the substrate and the coating. Carboxylic esters are known to undergo alkaline hydrolysis (saponification), and this process has long been thought of as important in cathodic delamination.<sup>36</sup> Many polyesters, epoxy esters, alkyd resins and other polymers bearing ester functionality are susceptible to hydrolysis; and so are polymers bearing urethane and urea linkages. It has been shown using XPS that coatings based on melamine–formaldehyde and urea–formaldehyde coatings cross linked with epoxy resin oligomers cathodically delaminating from steel in 5% aqueous NaCl showed chemical change consistent with hydrolysis of ester, urethane, and/or urea linkages.<sup>42,43</sup> The same studies also showed that the delaminated steel surface was covered with an organic residue indicative of cohesive failure within the coating. Conversely, for cross linked polybutadiene coatings, which develop only very limited quantities of carboxylic and ester functionality during oxidative curing, evidence of hydrolysis damage is limited to a layer of more highly oxidized polymer immediately adjacent to the substrate surface.<sup>44</sup> Castle and Watts concluded that, whilst there is no universally applicable mechanism of cathodic disbondment, the more resistant the coating polymer is to alkaline hydrolysis the more likely is an interfacial separation rather than a cohesive failure due to coating degradation.<sup>45</sup>

Stratmann *et al.* have pointed out that  $\text{OH}^-$  is not the only cathodically produced species capable of destroying iron–oxygen–polymer bonds such as  $\text{Fe-O-CO-R}$  (where  $\text{R} = \text{organic}$ ).<sup>31</sup> Many short lived intermediates of  $\text{O}_2$  reduction, such as  $\text{O}_2^{\cdot-}$ ,  $\text{HO}_2^{\cdot}$ ,  $\text{HO}_2^-$ ,  $\text{H}_2\text{O}_2$ , and  $\text{HO}^{\cdot}$  may be more reactive than  $\text{OH}^-$  itself. The same authors go on to show that an epoxy coated iron exposed to 1 M aqueous NaOH through a coating defect delaminates six times more slowly than the same system exposed to 1 M aqueous NaCl and held in the presence of air.<sup>31</sup> The intermediates of cathodic  $\text{O}_2$  reduction are capable of reacting with a wide range of organic functionalities (particularly in the case of  $\text{HO}^{\cdot}$ ). Consequently, in their presence, carboxylic ester functionality and/or other functionalities susceptible to alkaline hydrolysis are not required for polymer degradation or disbondment to occur.

### 2.14.2.2 Preventing Cathodic Delamination

Under circumstances where disbondment occurs through physical displacement of the coating it might reasonably be assumed that disbondment could be discouraged by promoting coating adhesion. Funke has

described adhesion as the most important and decisive property of a coating.<sup>46–48</sup> Functionalized silanes have been widely used as reactive coupling agents for improving the adhesion of organic coatings to steel. Examples include vinyl silanes for improving wet adhesion of alkyd coatings,<sup>49</sup> amino and epoxy silanes for epoxy/polyamide and polyurethane coatings,<sup>48</sup> and various other silanes for improving adhesion of automotive electrocoats.<sup>50</sup> Marsh *et al.* treated steel substrates with prehydrolyzed allyltriethoxysilane prior to coating with unpigmented alkyd resin.<sup>51</sup> They found that silanization improved both wet and dry adhesion but subsequently found no relationship between adhesion and rates of cathodic delamination. Leidheiser did find that treating an iron surface with silane prior to coating with polybutadiene resulted in significantly reduced rates of cathodic delamination.<sup>1</sup> However, it is not clear that this effect had anything to do with adhesion because impedance measurements on silane treated iron also showed large increases in charge transfer resistance and, therefore, decreased electrochemical activity for cathodic oxygen reduction.<sup>1</sup> Overall, it would seem that improving coating adhesion alone may not improve resistance to cathodic delamination if an alternative disbondment mechanism, such as hydrolysis of the coating polymer, is available.<sup>52</sup>

Inorganic pretreatments or conversion coatings are frequently applied to metal substrates prior to coating with paint or lacquer as a means of both promoting adhesion and chemically inhibiting corrosion.<sup>53</sup> Pretreatments based on phosphoric or chromic acids react electrochemically with the metal and substantially replace the air-formed oxide film with a layer of metal phosphate or mixed chromium oxide.<sup>53</sup> Such a layer may disfavor cathodic delamination if it is more resistant to alkaline dissolution than the original oxide layer, and/or if it inhibits cathodic O<sub>2</sub> reduction. It has long been proposed that resistance to alkaline dissolution determines resistance to cathodic delamination in the case of metal phosphate pretreatment layers.<sup>54,55</sup> A recent study has similarly concluded that interfacial stability is strongly influenced by the chemical stability of conversion layers to hydroxide generated by cathodic O<sub>2</sub> reduction.<sup>56</sup> However, SKP studies of thin phosphate-based conversion coatings on zinc (galvanized steel) have shown that these also inhibit cathodic O<sub>2</sub> reduction and produce a corresponding cathodic (negative) shift in the potential of the polymer coated surface.<sup>57</sup> This effect is attributed to the replacement of n-semiconducting zinc oxide with an electrically insulating zinc phosphate layer that obviously reduces the driving force for cathodic

delamination. Similarly, SKP studies of chromate conversion coatings on galvanized steel have shown a cathodic potential shift relative to the unmodified zinc surface.<sup>58</sup> This finding might seem paradoxical at first given the oxidizing nature of chromium VI species. However, cathodic inhibition by chromate has been reported by a number of authors.<sup>59–61</sup>

Corrosion inhibitor pigments based on sparingly soluble salts or ion-exchange solids are often dispersed in paint coatings with the aim of preventing or retarding corrosion-driven coating failure. The SKP technique has been used to study the influence of strontium chromate (SrCrO<sub>4</sub>) pigment on the kinetics of cathodic delamination affecting polyvinylbutyral coatings adherent to the intact zinc surface of hot dip galvanized steel.<sup>62</sup> When the defective electrolyte was saturated with SrCrO<sub>4</sub>, CrO<sub>4</sub><sup>2−</sup> anions were excluded from the under-film electrolyte layer by the delamination cell electric field, and delamination rates were reduced by less than 25%. In contrast, dispersions of SrCrO<sub>4</sub> pigment in the PVB coating allowed CrO<sub>4</sub><sup>2−</sup> diffusion directly into the under-film electrolyte layer. Figure 4(a) shows a series of  $x_{\text{del}}$  versus  $(t_{\text{del}} - t_i)^{1/2}$  plots for various values of pigment volume fraction ( $\phi_{\text{SC}}$ ). The slopes of these plots decrease as  $\phi_{\text{SC}}$  increases and deviations from linearity consistent with departure from pure cation migration control occur for  $\phi_{\text{SC}} \geq 0.049$ . The dependence of  $k_d$  values, obtained from initial  $x_{\text{del}}$  versus  $(t_{\text{del}} - t_i)^{1/2}$  slopes, on  $\phi_{\text{SC}}$  is given in Figure 4(b), which shows that  $k_d$  tends to zero for  $\phi_{\text{SC}} = 0.064$ . On the basis of these findings, it was proposed that replacement of under-film O<sub>2</sub> reduction by a self-limiting reduction of CrO<sub>4</sub><sup>2−</sup> to insoluble Cr(III) (hydr)oxide is the most significant factor in decreasing delamination rates.<sup>62</sup>

When the same SKP approach was used to study dispersions of silica and bentonite based rare earth (Ce<sup>3+</sup>), cation-exchange pigments in a PVB coating on zinc (galvanized steel) Ce<sub>(aq)</sub><sup>3+</sup> was found to exchange directly into the under-film electrolyte and significantly retard coating delamination.<sup>63</sup> On a nonpretreated zinc surface, delamination was not halted completely because the under-film exchange of Na<sup>+</sup> by Ce<sup>3+</sup> was itself incomplete. The resulting precipitation of Ce(OH)<sub>3</sub> increased the under-film electrolyte layer resistivity, but, unlike the Cr(III) (hydr)oxide described above, Ce(OH)<sub>3</sub> did not form a coherent surface film capable of stifling O<sub>2</sub> reduction at the cathodic delamination front.<sup>27</sup> However, when the same cation-exchange pigments were used in conjunction with a chromate based pretreatment this appeared to influence the surface nucleation of Ce(OH)<sub>3</sub> to

produce a coherent film, stifling  $O_2$  reduction and producing a profound inhibition of cathodic delamination.<sup>64</sup> Lyon *et al.* have reported a similar synergistic activity between zinc–phosphate and commercial  $Ca^{2+}$  cation-exchanged silica (Shieldex™).<sup>65</sup>

There has been recent interest in the use of intrinsically conducting polymers (ICPs) for corrosion control and the topic has been subject to review.<sup>66,67</sup> Many studies have focused on polyaniline (PAni).<sup>68–70</sup> PAni exists in various states interrelated by the redox and acid–base equilibria<sup>71,72</sup> but it is the emeraldine

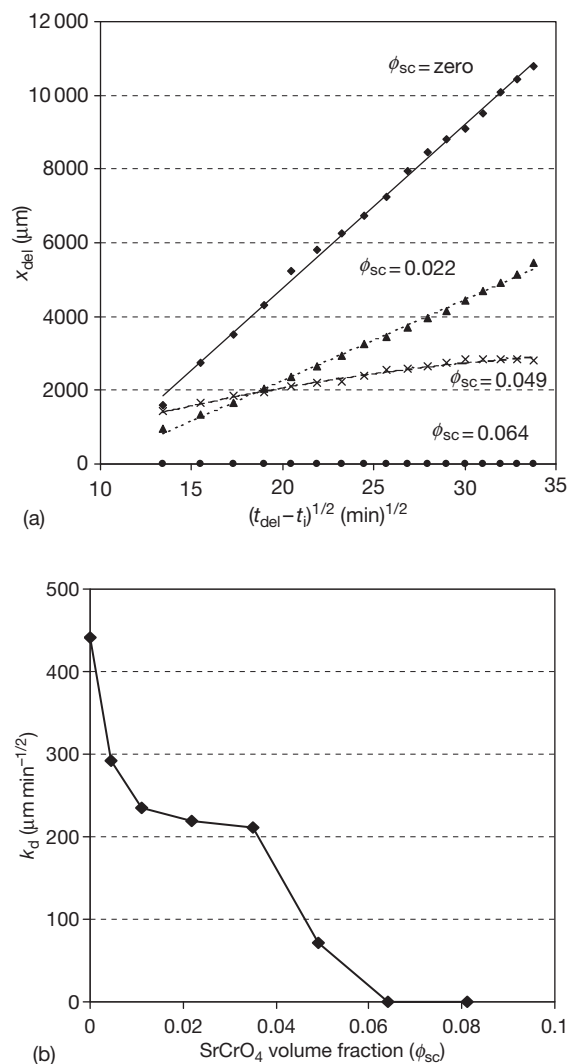


**Figure 4** Delamination kinetics for  $SrCrO_4$  pigmented  $30 \mu m$  PVB coatings on HDG zinc substrate. Electrolyte in contact with the defect is uninhibited  $0.86 \text{ mol dm}^{-3}$  NaCl. (a) Plots of  $x_{del}$  versus  $(t_{del} - t_i)^{1/2}$  for varying  $SrCrO_4$  volume fraction ( $\phi_{sc}$ ). (b) Plot of the initial  $x_{del}$  versus  $(t_{del} - t_i)^{1/2}$  slope ( $k_d$ ) as a function of ( $\phi_{sc}$ ).

salt (ES) which is electronically conductive and most widely used for corrosion control. The ES is produced by protonating or ‘doping’ the partially oxidized PAni emeraldine base (EB) using Bronsted acids.<sup>73–76</sup> PAni ES may be applied to metal surfaces directly by electrodeposition<sup>77,78</sup> or deposition of water-borne dispersions.<sup>79</sup> However, PAni ES particles may also be dispersed in a conventional polymer binder.<sup>80,81</sup> The protection of carbon steel by PAni ES has been variously ascribed to substrate ennoblement, the formation of a passive oxide film and anodic inhibition through precipitation of an insoluble metal salt of the dopant anion.<sup>66,67</sup> The ES/LB (leuco base) redox couple is generally regarded as being responsible for establishing substrate potentials in the passive regime.<sup>67,69,72,82</sup> Furthermore, it has been suggested that PAni ES becoming reduced to LB is cyclically reoxidized by the atmospheric  $O_2$ , thus extending the period of ennoblement.<sup>67,69,71,72,83,84</sup> It has also been proposed that the displacement of cathodic oxygen reduction away from the metal–coating interface acts to suppress cathodic delamination.<sup>66,82,85</sup>

This last notion has been investigated using coatings comprising various volume fractions of particulate polyaniline (PAni) dispersed in a polyvinylbutyral binder applied to iron substrates.<sup>86,87</sup> SKP was used to measure substrate potentials in air and follow corrosion-driven cathodic delamination when 5% (w/v) (0.86 M) aqueous NaCl was brought into contact with a coating defect. PAni EB was found to have no effect on either substrate potential or delamination kinetics. **Figure 5** shows delamination kinetics for various

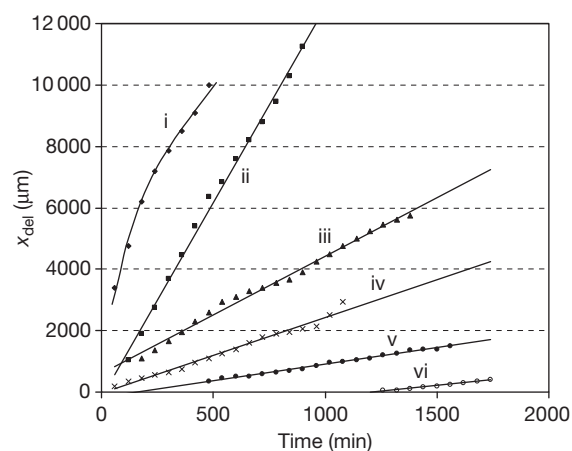


**Figure 5** Plots of  $x_{del}$  versus time for  $30 \mu m$  PVB/PAni-pTS coatings on iron with various PAni-pTS pigment volume fractions ( $\phi_{pa}$ ). In each case, the electrolyte in contact with the defect is  $0.86 \text{ mol dm}^{-3}$  NaCl (aq).  $\phi_{pa}$  key: (i) 0, (ii) 0.05 (iii) 0.1 (iv) 0.15 (v) 0.2, and (vi) 0.25.



volume fractions ( $\phi_{pa}$ ) of *p*-toluene sulfonic acid doped Pani ES (Pani-pTS). It may be seen that when  $\phi_{pa} \geq 0.05$  the  $x_{del}$  increases linearly with  $t_{del}$  and not parabolically according to eqn [1]. Delamination rate ( $dx_{del}/dt_{del}$ ) decreases monotonically from 12.8 to  $0.83 \mu\text{m min}^{-1}$  as  $\phi_{pa}$  is increased from 0.05 to 0.25, a finding summarized in curve (ii) of Figure 6. Curve (i) of Figure 6 shows the mean  $E_{intact}$  (potential of undelaminated surface) values plotted versus  $\phi_{pa}$ . The critical volume fraction required for long-range electrical conduction in a percolating network is  $\sim 0.17^{88}$  and  $E_{intact}$  appears to become constant and determined by the PANi ES/EB couple for  $\phi_{pa} \geq 0.2$ .

PAni ES doped using *p*-toluenesulfonic (H-pTS), camphorsulfonic (H-CS), phosphoric ( $\text{H}_3\text{PO}_4$ ) and phenylphosphonic ( $\text{H}_2\text{-PP}$ ) acids increased substrate potentials by up to 0.36 V and inhibited cathodic delamination, with the efficiency order  $\text{H-pTS} < \text{H-CS} < \text{H}_3\text{PO}_4 = \text{H}_2\text{-PP}$ .<sup>87</sup> Conversely, dopant sodium salts added to the corrosive electrolyte when the coating did not contain PANi were not found to inhibit delamination. On this basis, it is concluded that, on iron, the inhibition of cathodic delamination by polyaniline did arise primarily from cathodic  $\text{O}_2$  reduction becoming relocated from the ennobled substrate onto the coating ES. However,  $\text{Fe}_3(\text{PO}_4)_2$  and FePP salt films formed through redox reactions at the ES–substrate interface also contributed by hindering electron transfer at the substrate surface. Without these ‘chemical’ contributions to inhibition, ES could

only slow up cathodic delamination on iron and not prevent it.<sup>86,87</sup> It should also be noted that the reoxidation of LB to ES is only likely to occur at significant rates when the coating is in contact with air, that is under nonimmersion conditions. PANi is therefore unlikely to be of significant benefit when a coated metal is immersed in aqueous electrolyte.

### 2.14.2.3 Modifying Metal Composition

Metals differ considerably in their electrocatalytic activity for cathodic oxygen reduction. Pure aluminum, for example, is virtually inactive as an oxygen cathode.<sup>89</sup> This inert behavior probably reflects the electronic properties of the surface aluminum oxide that, as an electrical insulator with a wide band gap, disfavors interfacial electron transfer. Ion implantation of aluminum or titanium into iron has been shown to reduce both surface activity and rates of cathodic delamination.<sup>1,90</sup> Hydrated oxide or hydroxide layers produced through the interaction of group II (alkaline earth) metal cations with hydroxide anions are similarly known to act as effective blockers of cathodic  $\text{O}_2$  reduction.<sup>91</sup> On this basis, alloying with aluminum and/or group II elements might reasonably be expected to reduce the susceptibility of a given metal to cathodic delamination. In structural metals, the scope for alloy development is limited by the need to preserve the mechanical properties. In metallic coatings, there is greater freedom, and significant advances have been seen in the field of zinc-based (galvanized) coatings for steel.<sup>92</sup>

Souto and Scantlebury have shown that hot dip galvanized steels in which the zinc layer is alloyed with 5% aluminum (Galfan) and 55% aluminum (Aluzinc) exhibit a much increased resistance to cathodic delamination relative to a conventional (zinc only) system.<sup>93</sup> Paradoxically, when the same Zn and Zn–Al alloy coatings were studied using a rotating disc electrode all three were found to be highly active  $\text{O}_2$  cathodes.<sup>21</sup> This suggests that the improved delamination resistance exhibited by the Zn–Al alloy coatings results from a fragmentation of cathodic sites rather than general surface deactivation. That is to say the heterogeneous microstructure of the Zn–Al alloy coatings, consisting as it does of interlocking zinc-rich and aluminum-rich phases, is reflected in local composition of the interfacial oxide layer. Blocking of electron transfer over aluminum-rich oxide regions would then disfavor the formation of a continuous delamination front and prevent the front from advancing from one zinc-rich region to the next.

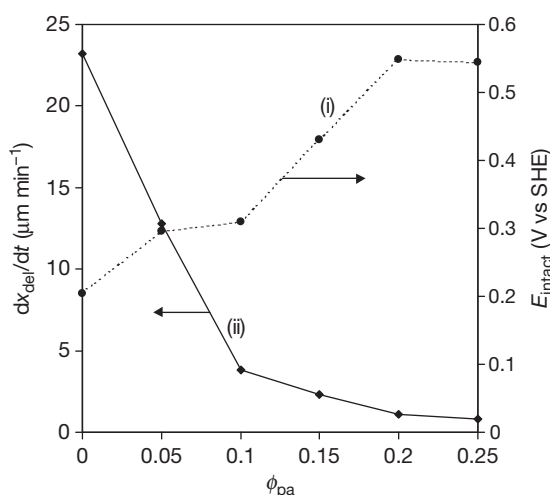


**Figure 6** Summary plot (a)  $E_{intact}$  and (b) delamination rate ( $dx_{del}/dt$ ) as a function of  $\phi_{pa}$  for  $30 \mu\text{m}$  PVB/PAni-pTS. Initial  $dx_{del}/dt_{del}$  is plotted in the case of the PVB ( $\phi_{pa} = 0$ ) coating.

Stratmann *et al.* used SKP to show that cathodic delamination occurred rapidly on zinc (electrogalvanized steel) but not on the zinc-rich intermetallic phase  $\text{MgZn}_2$ , which frequently forms in Zn–Mg alloy coatings.<sup>94</sup> The potential of the intact  $\text{MgZn}_2$ –oxide–polymer interface was found to be  $\sim 0.7$  V more negative than the corresponding Zn–oxide–polymer interface. This increase in cathodic polarization was attributed to a large band gap in the  $\text{MgZn}_2$  interfacial oxide, resembling that of  $\text{MgO}$ . Dissolution of magnesium oxide under cathodic conditions is unlikely because group II oxides are basic and become more insoluble as pH increases. However,  $\text{MgZn}_2$  exposed to neutral aqueous NaCl at an organic coating defect was found to become rapidly dealloyed through Mg dissolution. In so doing, the defect potential rose to resemble freely corroding zinc ( $-0.7$  V vs SHE). Potentials in the defect were actually higher than those in the intact coated area and no driving force existed for cathodic delamination.<sup>94</sup>

### 2.14.3 Filiform Corrosion

An underfilm corrosion phenomenon, producing ‘hair-like’ corrosion tracks on lacquer-coated steel, was first reported in the scientific literature by Sharman in 1944,<sup>95</sup> who used the phrase FFC to describe these features. FFC is regarded as a type of atmospheric corrosion, principally affecting organic-coated iron (steel) and aluminum surfaces, initiating at penetrative coating defects and producing characteristic thread-like under-film deposits of corrosion product. An example of the typical appearance of corrosion filaments on organic coated aerospace aluminum alloy is given in [Figure 7](#). Although FFC attack is largely considered to be superficial in nature, it is aesthetically unpleasant and hence undesirable in modern organic-coated metal products.

Much of the research carried out in FFC prior to 1995 has been comprehensively reviewed elsewhere.<sup>5,6</sup>

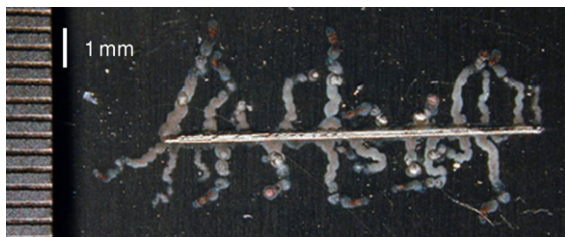


**Figure 7** Filiform corrosion observed on aluminum alloy AA2024-T3 coated with a clear film of PVB.

It is not our intention to recover the same ground, but rather to give a general overview of FFC and a subsequent outline of recent developments in the field.

#### 2.14.3.1 General FFC Characteristics

It is generally accepted that FFC initiates when aggressive species, such as chloride ions, permeate through an organic coating, usually at a defect or weakness in the coating and accumulate at the metal–coating interface. FFC only occurs in the presence of atmospheric oxygen and high humidity, although the humidity range over which corrosion is observed is dependent upon the metal studied. Slabaugh *et al.*<sup>96</sup> observed FFC occurrence over a 30–95% relative humidity range for common aerospace aluminum alloys coated with a range of organic coating types, while FFC activity on iron (steel) samples is reported to cease at humidity levels below 60%.<sup>5</sup> The motion of individual corrosion filaments is largely directionally stable, propagating in relatively straight lines for appreciable distances. It has also been reported that filaments growing on aluminum alloy surfaces do so preferentially along the rolling or extrusion axis.<sup>6,97</sup> Such behavior is thought to arise from corrosion filaments following a ‘path of least resistance’ formed by lines of intermetallic precipitates present at the elongated grain boundaries of the rolled/extruded alloy microstructure. Corrosion filaments do not generally cross each other, nor do they propagate through a break in the surface coating.<sup>5</sup>

Corrosion filaments consist of a mobile, electrolyte-filled head, containing metal cations and aggressive anions (such as  $\text{Cl}^-$ ), and a tail of dry, porous corrosion product. FFC head regions typically exhibit a low pH towards their leading edge (as low as pH 1) as a consequence of cation hydrolysis. The primary driving force for filament advancement is thought to be differential aeration, arising from facile mass transport of gaseous  $\text{O}_2$  through the filament-tail. The oxygen concentration cell formed directs anodic metal dissolution towards the leading-edge of the filament-head, while the principal site of cathodic oxygen reduction lies towards the trailing-edge of the active head. Aggressive anions ( $\text{Cl}^-$ ) and water are conserved in the filament head electrolyte and corrosion filaments are reported to continue propagating for long periods of time (months or years). Although these general principles are considered to hold true for FFC on both aluminum and iron surfaces, there are notable mechanistic differences,

and these will be discussed separately for each type of surface in the following sections.

It should also be noted that there are several anecdotal reports of FFC observed on coated magnesium surfaces.<sup>5,6,98,99</sup> However, magnesium underfilm corrosion has received relatively little in the way of scientific study and a description of FFC remains limited to observations of vigorous  $H_2$  evolution and a low pH (2–3) within electrolyte filled head regions.<sup>99</sup> In fact, there seems to be a degree of confusion regarding magnesium FFC, as the term is commonly used to describe a type of localized corrosion observed when magnesium and its alloys are immersed in bulk chloride-containing electrolyte.<sup>100,101</sup>

### 2.14.3.2 FFC on Aluminum Surfaces

Filiform activity on aluminum has been shown to initiate at a range of different coating discontinuity sites such as cut edges,<sup>5,96</sup> scratches<sup>6,96–98,102</sup> and rivet heads.<sup>6,99</sup> At such defects, the presence of contaminating salts, such as chlorides will have resulted in production of  $AlCl_3$  and  $Al(III)$  oxychloride salts ( $Al(OH)_2Cl$  and  $Al(OH)Cl_2$ ) at the exposed aluminum surface. The dissolution of these salts in the adsorbed humidity film present at high humidity subsequently produces an aqueous electrolyte capable of supporting corrosion. Chloride is known to disrupt the passivity of aluminum by reacting with the protective aluminum (hydr)oxide film to produce water soluble aluminum (III) oxychloride complexes. The passive layer breakdown is usually local in nature, resulting in the initiation of highly localized sites of anodic metal dissolution and producing pit-like excavations of the aluminum surface. The generation of the active heads of propagating FFC filaments probably results from the migration of such sites beneath coated regions adjacent to a penetrative defect. **Figure 8(a)** shows a possible mechanism by which corrosion filaments may become initiated through the presence of differential aeration. In this scheme, it is assumed that oxygen transport to the metal surface through the thin adsorbed electrolyte film at the exposed aluminum surface is significantly easier than through a relatively thick organic coating. Hence cathodic oxygen reduction is favored on the bare metal while anodic aluminum dissolution will tend to become concentrated at the  $O_2$ -deficient metal–electrolyte–coating interface. Correspondingly, the coating will become undercut while  $Cl^-$  ions will migrate beneath the delaminated coating to preserve

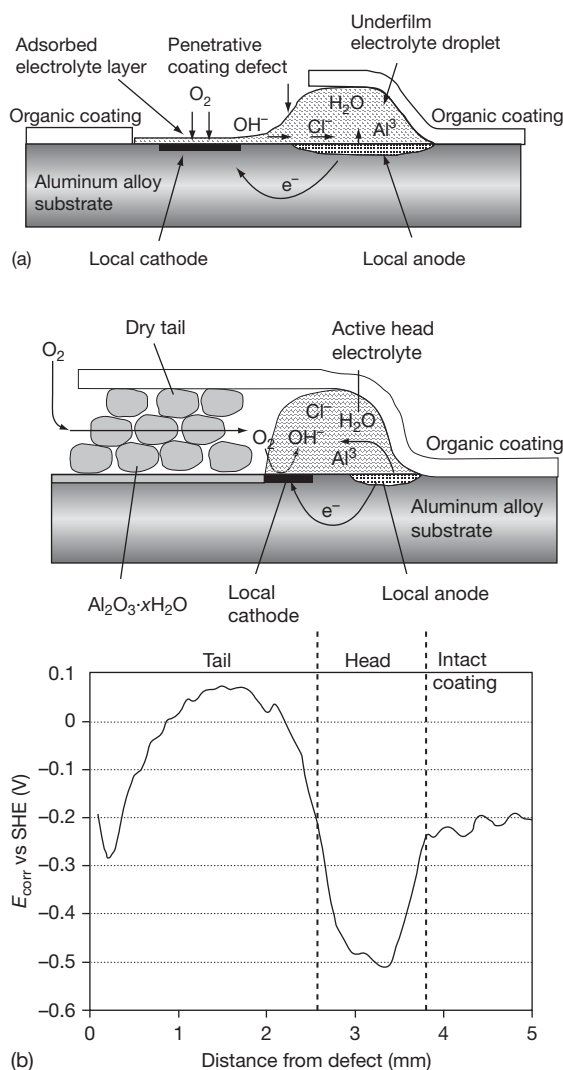


**Figure 8** Schematic diagram showing the processes involved during (a) initiation and (b) propagation of a corrosion filament. A SKP-derived free corrosion potential distribution, measured along the length of a propagating filament on organic-coated AA2024-T3, showing typical  $E_{corr}$  values in each separate region is also given in (b).

electroneutrality and water will be drawn in by osmosis to produce an electrolyte droplet.

Once initiated, corrosion filaments propagate away from the coating defect, under the influence of an  $O_2$  concentration cell of the type represented schematically in **Figure 8(b)**. Aluminum (III) cations produced by anodic dissolution at the leading edge of the filament head migrate towards a cathodic region at the trailing edge of the active head and combine with  $OH^-$  anions generated by cathodic oxygen reduction. Stepwise hydrolysis of  $Al^{3+}$  (or more

correctly  $[\text{Al}(\text{H}_2\text{O})_6]^{3+}$  cations eventually leads to the precipitation of the water insoluble corrosion product  $\text{Al}(\text{OH})_3$ . **Figure 8(b)** also includes an empirically-derived free corrosion potential ( $E_{\text{corr}}$ ) profile, obtained along the length of a propagating filament on aluminum by SKP potentiometry.<sup>103</sup> The profile shows that  $E_{\text{corr}}$  values tend to be lower towards the leading edge of the FFC active head and higher towards the trailing edge. This is consistent with the extent of anodic depolarization, and hence anodic dissolution, being greatest at the leading edge.

Constant migration of  $\text{Cl}^-$  anions toward the anodic leading edge results in the retention of all water-soluble ions and, through osmosis, all liquid water within the FFC active head. Several authors have used surface analysis techniques such as secondary ion mass spectrometry (SIMS)<sup>103</sup> and X-ray emission<sup>104</sup> to demonstrate that  $\text{Cl}^-$  ions applied at a penetrative defect are conserved within the filament head, with little evidence of entrapment in defect or tail regions of the FFC-affected surface. The high  $E_{\text{corr}}$  values observed in the tail region of the FFC filament represented in **Figure 2(b)** is due to the deposition of a thick, substantially dry, hydrated aluminum (III) oxide ( $\text{Al}_2\text{O}_3 \cdot x\text{H}_2\text{O}$ ) layer, formed as an  $\text{Al}(\text{OH})_3$  corrosion product left behind in the wake of the advancing filament head slowly losing water. Relatively easy  $\text{O}_2$  diffusion through the porous  $\text{Al}_2\text{O}_3 \cdot x\text{H}_2\text{O}$  deposit allows the FFC differential aeration cell, and hence filament propagation, to be maintained over significant distances. The high  $E_{\text{corr}}$  values observed in the FFC tail imply increased passivity in these regions, which may help to explain empirical observations that individual corrosion filaments generally avoid intersecting others.<sup>6</sup> Such highly passive areas would tend to disfavor further anodic activity, and an encroaching FFC head region would be forced to redirect onto adjacent uncorroded areas.

Several authors have observed the formation of hydrogen gas bubbles within filament heads produced on aluminum surfaces.<sup>6,96,105</sup> Hoch employed pH indicator dyes incorporated within organic coatings to determine pH values of 2–3 at leading edges of aluminum filament head.<sup>99</sup> Such levels of acidity will tend to maintain active aluminum dissolution in these regions. A combination of low pH, caused by proton release via partial hydrolysis of  $[\text{Al}(\text{H}_2\text{O})_6]^{3+}$  cations, negative  $E_{\text{corr}}$  values of  $\sim -0.5$  V versus SHE,<sup>103</sup> along with oxygen deficiency at the leading edge of the filament head are thought to result in a secondary cathodic reaction involving hydrogen evolution.

Experimental support for an anodic disbondment mechanism of FFC on aluminum is principally derived from the observations of FFC behavior under different  $\text{O}_2$  transport regimes. Ruggieri and Beck<sup>5</sup> showed that FFC advancement ceased when filament tails were sealed in such a way as to halt the ingress of air. They also demonstrated that stationary filaments became reactivated when organic coatings above tail regions were cut open. Lenderink<sup>102</sup> provided further support for the importance of through-tail  $\text{O}_2$  diffusion by reporting that FFC propagation rates remained unaffected on samples where a metal foil had been deposited over the organic coating to obstruct through-coating  $\text{O}_2$  transport.

The use of conventional electrochemical techniques to study FFC has routinely been limited by the absence of bulk electrolyte, the presence of highly resistive organic coatings and the small size of the local corrosion cell. However, in the last decade, significant developments in the SKP have greatly facilitated the quantitative electrochemical investigation of FFC. It has been shown that SKP is capable of visualizing the free corrosion potential ( $E_{\text{corr}}$ ) distributions associated with individual corrosion filaments.<sup>106–108</sup> *In situ*, SKP scanning has also been used to generate a series of time-dependent  $E_{\text{corr}}$  distribution patterns that provide information on filament initiation, propagation, and termination rates within a filament population.<sup>97,103</sup> FFC propagation rates on AA2024-T3, quantified by SKP,<sup>103</sup> are shown to be strongly dependent on the quantity of the initiating chloride, confirming that the ability to control the quantity of chloride ion entering a filament-head population is critical to the reproducibility of any quantitative FFC test procedure. Other *in situ* techniques, such as Fourier transform infrared (FTIR) microspectroscopy, have also been used in conjunction with SKP scanning to give additional information regarding the constituent salts present within propagating electrolyte-filled FFC heads.<sup>109</sup>

The same *in situ* techniques have also been employed to study inhibition of FFC by in-coating pigments based on both conventional Cr(VI) chemistry<sup>110</sup> and novel anion-exchange hydrotalcite minerals.<sup>111–113</sup> Previous *ex situ* studies, using a combination of electron microscopy and X-ray and SIMS techniques, showed that Cr(VI) species inhibit FFC on copper-containing AA2024 primarily by stifling S-phase particle dealloying and subsequent cathodic  $\text{O}_2$  reduction. *In situ* SKP studies confirmed this finding, but in addition demonstrated that a significant depression in  $E_{\text{corr}}$  of the intact coated metal



surface resulted from a reversible, nonfaradaic adsorption of Cr(VI) species, which also contributed to FFC inhibition.<sup>110</sup>

### 2.14.3.3 Surface-Active FFC on Aluminum

Within the last decade it has been established that thermo-mechanical processing and/or shear deformation of aluminum alloys can produce a surface microstructure which differs considerably from the bulk.<sup>114–123</sup> Deformed aluminum alloy surface layers are typically up to a few micrometers thick, consisting of fine, submicron grain sizes where the presence of second phase particles stabilize grain boundaries and prevent recrystallization. Many researchers have so far demonstrated that a strong correlation exists between the presence of a deformed surface layer and susceptibility of painted alloy samples to FFC.<sup>114–123</sup> In several cases, the severity of FFC attack is increased by heat treatment, and attributed to thermally-promoted precipitation of intermetallic particles in the surface layer. The morphology of FFC on surface-activated samples is considered to differ from that discussed in the previous section and shown in Figure 7. FFC attack on samples comprising a deformed surface layer proceeds rapidly and is highly cosmetic and superficial in nature, limited only to the depth of the surface layer itself. Frequently FFC takes the form of numerous narrow filaments, propagating on a parallel course and separated laterally by only small distances, giving the impression of a single coalesced corrosion front. Figure 9 shows this type of cosmetic FFC affecting automotive alloy AA6016-T4 coated with a clear

organic film, where corrosion was initiated by controlled application of aqueous hydrochloric acid to a penetrative coating defect.

Surface-active FFC has been reported on a wide range of alloys, ranging from model Al-Fe-Mg-Si<sup>123</sup> and binary Al-X (X = Fe, Cu, Mn and Mg)<sup>120</sup> systems through to automotive and architectural 5000<sup>118,122</sup> and 8000<sup>114–116</sup> series alloys. However, the majority of research in this area has concentrated on 3000 (Al-Mn)<sup>114–119,121</sup> and 6000 (Al-Mg-Si)<sup>124–128</sup> series alloys designed for automotive panel applications. The increased FFC susceptibility of AA3005 samples comprising damaged surface layers is thought to derive from preferential precipitation of noble Mn and Fe rich intermetallics,<sup>119</sup> leading to a cathodic activation of the surface layer with respect to the bulk alloy. Several authors have confirmed that when the surface layer is removed, the extent of FFC is considerably reduced and the type of attack is restricted to a much slower ‘deep pitting’ mode of corrosion,<sup>117,122</sup> more closely resembling the type of features shown in Figure 6.

*In situ* SKP potentiometry has recently been used to follow the kinetics of FFC propagation and measure underfilm corrosion potentials associated with head and tail regions of surface-active FFC affecting organic-coated AA6016.<sup>125</sup> The authors report that for this alloy, surface abrasion and subsequent heat-treatment produces a significant depression in surface potential compared with the bulk material and this forms an additional thermodynamic driving force for rapid ‘surface-active’ corrosion. They conclude that although differential aeration remains a major driving force for FFC propagation, the filament cell potential will also contain a contribution arising from the dissimilar electrochemical characteristics of the surface deformed layer present at the leading edge of the FFC head and bulk alloy exposed by layer dissolution. A schematic representation of the mechanism of ‘surface-active’ FFC, where the deformed layer reacts as a sacrificial anode with respect to bulk AA6016, is given in Figure 10. Also included is a representation of the expected relationship of corrosion potential with distance across the FFC cell, confirmed empirically by *in situ* SKP measurements.<sup>125</sup>

Several authors have shown that problems of increased FFC susceptibility, through the introduction of a damaged layer by thermomechanical alloy processing, can be controlled by etching the surface using acid or alkali cleaner prior to coating.<sup>117,122,125</sup> However, automotive manufacturers frequently rectify surface defects in formed panels by mechanical

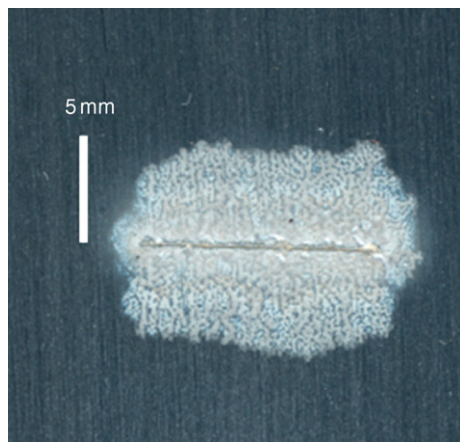


**Figure 9** Filiform corrosion observed on aluminum alloy AA6016-T4 overcoated using PVB. Courtesy of A. Coleman.



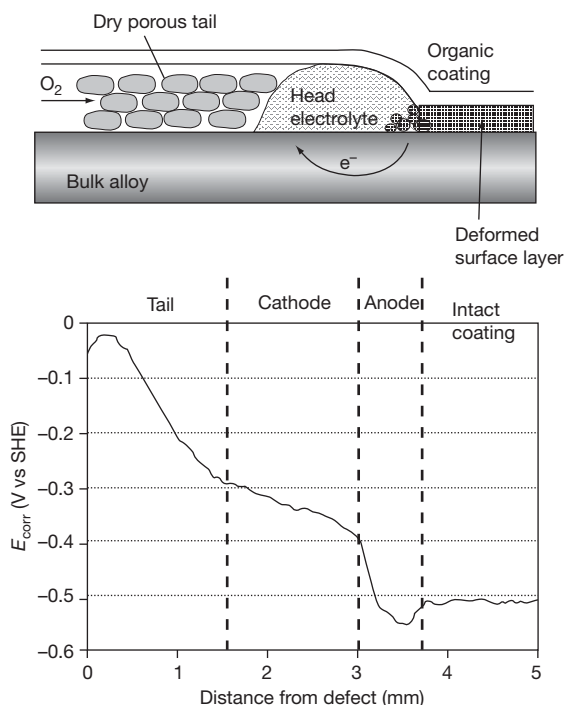


**Figure 10** Schematic representation of the physical regions within a surface active FFC corrosion cell and proposed relationship with SKP-derived corrosion potential versus distance profiles.

grinding immediately prior to pretreatment and painting. This procedure reintroduces a deformed layer, subsequently reactivating the surface with respect to FFC and is liable to serious underfilm cosmetic failure. To avoid the introduction of a costly postgrinding etch or cleaning process, researchers are investigating new coating and/or pretreatment technologies which are capable of inhibiting FFC attack on surface-damaged alloys. To date, coatings based on phenylphosphonic acid dissolved in a polyvinylbutyral matrix are among the most promising candidates, demonstrating profound inhibition of FFC on AA6111-T4 automotive alloy samples comprising shear-deformed surface active layers.<sup>126</sup>

#### 2.14.3.4 FFC on Iron (Steel) Surfaces

The general consensus regarding the mechanism of FFC on iron is that filament advance remains driven by differential aeration,<sup>5,6</sup> arising from facile mass transport of atmospheric  $O_2$  through the filament-tail. As in the case of aluminum, cathodic oxygen reduction is considered to be localized at the droplet trailing-edge and anodic metal dissolution located at

the leading-edge of the electrolyte filled head. However, although this anodic disbondment mechanism is largely accepted for FFC on aluminum, there persists some controversy regarding the location of the anodic and cathodic sites for corrosion filaments propagating on a coated iron surface. Since, as discussed in the preceding section, organic-coated iron surfaces are well known to undergo corrosion-driven delamination via a cathodic disbondment route, several authors have suggested that a similar process plays a major role in the mechanism of FFC on iron. In this alternative mechanism, cathodic activity is proposed to occur in a narrow area in the front part of the filament head,<sup>6,102,129</sup> although it has also been suggested that a site of cathodic activity exists a small distance in front of the filament leading edge.<sup>130,131</sup> Drawing on observations previously noted for blister formation on steel, Funke<sup>130,131</sup> proposes a mechanism whereby FFC is characterized by the development of an underfilm cathode, which precedes the head electrolyte droplet. This cathodic region appears at some distance from the front of the head and grows due to the generation of underfilm hydroxyl ions, up to a point where the trailing filiform head draws near and the two regions merge. At this point  $OH^-$  ions migrate towards the anode while metal cations present within the head electrolyte migrate forward in the direction of the preceding cathode. This results in a polarity reversal where the previously cathodic front region is transformed to become the anodic leading edge of the filiform head. The whole process is then repeated and is considered to be consistent with both the observed saltatory (jumping) movement of FFC on iron and the segmented appearance of corrosion tracks. A schematic representation of this theory is shown in Figure 11.

Ruggieri and Beck<sup>5</sup> dispute this hypothesis, pointing out that the model is inconsistent with asymmetric separation of the cathodic and anodic zones in the corrosion cell, and that previous studies had shown no experimental evidence of cathodic detachment in the vicinity of the propagating filaments. In addition, since the preceding cathode directs the FFC, it is implicit that ionic current must flow from the anode through the coating. The size of the cathode would thus be limited by the high resistance of an adherent metal-coating interface. It could however be argued that diffusion of ions from the preceding cathodic area to the head might occur through a layer of adsorbed water existing at the coating-metal interface. Ruggieri and Beck calculate that the thickness of the aqueous layer required would be  $3.5 \times 10^{-5}$  mm,<sup>5</sup>

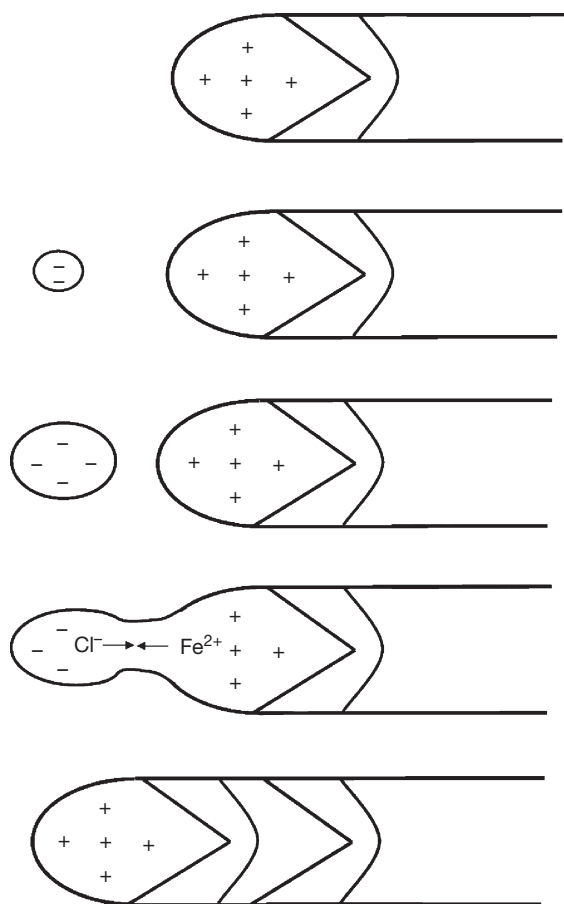


**Figure 11** Filiform corrosion via a cathodic disbondment mechanism as proposed by Funke<sup>130,131</sup> for a protective organic coating on iron (steel).

which would tend to indicate a region of coating disbondment. As mentioned previously, the lack of empirical observation of the regions of coating disbondment preceding a propagating filiform head is taken as a further argument for rejecting the cathodic disbondment FFC mechanism.

Another point of debate concerns the role of the cation associated with the initiating anion (usually chloride). Several authors argue that although initiating anions are conserved in the filament head electrolyte, the corresponding cations present consist solely of  $\text{Fe}^{2+}$  and  $\text{Fe}^{3+}$  produced by the metallic corrosion process.<sup>132,133</sup> X-ray spectroscopic and SIMS evidence are presented showing that filament heads do not contain the cation of the initiating salt. Therefore, if corrosion is initiated by applying a salt such as a group (I) chloride to a penetrative coating defect, then a question mark arises as to the eventual fate of the group (I) cations.

To address this issue Williams and McMurray<sup>133</sup> used a combination of *in situ* SKP and *ex situ* imaging SIMS measurements to elucidate the role of group (I) cations in the initiation of FFC on iron by aqueous group (I) chloride salts and to additionally determine the contribution of cathodic disbondment processes in filament propagation. It was demonstrated that group (I) chloride – initiated FFC proceeded via a two stage mechanism. Phase 1 of the underfilm corrosion process comprised the radial growth of a depassivated, roughly circular area surrounding the penetrative defect onto which a controlled quantity of initiating group (I) chloride was originally applied, indicating localized anodic iron dissolution at the defect site coupled to cathodic delamination of the surrounding coating. Imaging SIMS confirmed that the area was abundant in the group (I) cation associated with the initiating salt, showing that phase 1 consisted of group (I) cation migration beneath the delaminating coating to form an alkaline under-film electrolyte layer. As phase 1 continued, group (I) cations became progressively replaced in the vicinity of the defect site by  $\text{Fe}^{2+}$  cations, which in turn were prevented from entering the alkaline under-film layer due to the insolubility of  $\text{Fe(II)}$  hydroxide. Once group (I) cations were exhausted in the defect region, phase 1 cathodic delamination ceased and phase II commenced, where a polarity reversal occurred in which anodic activity was driven beneath the delaminated coating. Underfilm anodic fragments formed corrosion filament heads which propagated across the well-defined circular zone of cathodically delaminated coating left by phase 1 at a constant speed of  $\sim 0.3 \mu\text{m min}^{-1}$ . Filaments were also shown to propagate beyond this zone with only a minimal decrease in velocity. For these filaments no evidence of cathodic activity preceding the head region was observed. The entire process is exemplified by the selection of  $E_{\text{corr}}$  distribution maps, obtained by *in situ* SKP scanning of a PVB-coated iron sample after initiation of under-film corrosion using a controlled quantity of NaCl, given in Figure 12. When  $\text{FeCl}_2$  was substituted for NaCl as the initiating salt, a cathodic delamination phase was not observed, although FFC occurred as before and propagation rates similar to those initiated with group (I) chlorides were measured. Because filament velocities were similar beneath cathodically delaminated and intact coatings, it was concluded that cathodic delamination cannot be a rate determining step in the propagation of FFC on organic-coated iron.<sup>133</sup>

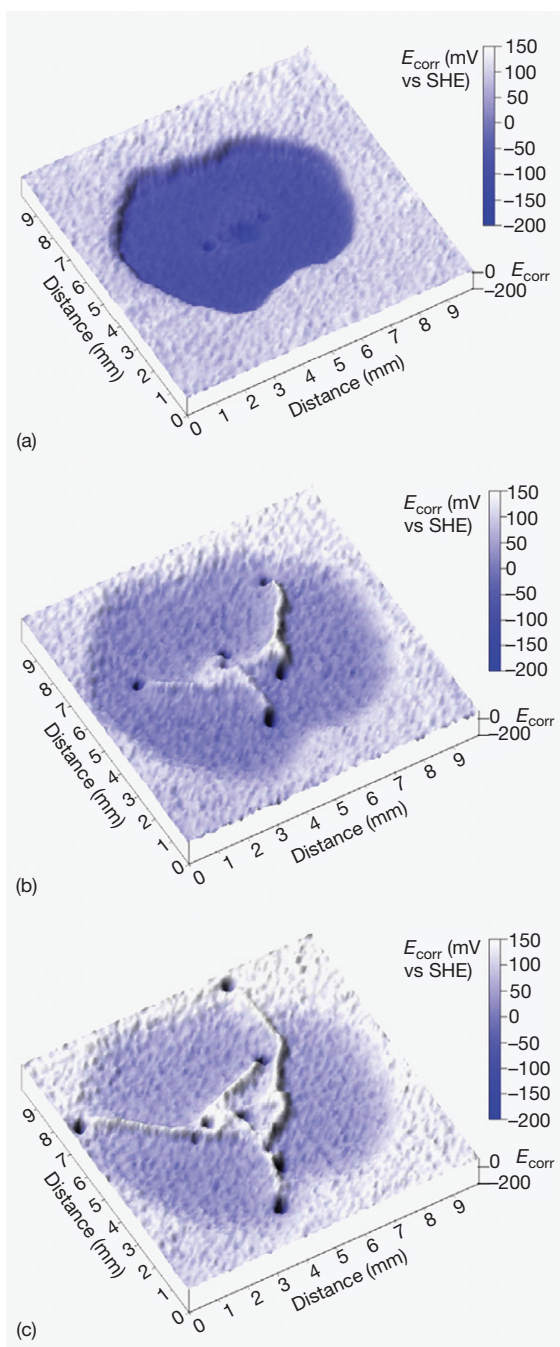


**Figure 12** Surface maps showing  $E_{\text{corr}}$  distributions measured over a PVB coated iron surface at  $t =$  (a) 16, (b) 130, and (c) 240 h, following initiation of underfilm corrosion at a penetrative coating defect using  $2 \mu\text{l}$  of  $10^{-3} \text{ mol dm}^{-3}$  NaCl (aq). (a) shows an initial cathodic disbondment process (phase 1), while (b) and (c) respectively demonstrate the propagation of corrosion filaments both within and beyond the boundary of the well defined, cathodically delaminated zone (phase II).

The findings of this work imply that the hydrolytic instability of ferrous ions, generated by underfilm anodic activity, precludes  $\text{Fe}^{2+}$  cations from coupling with remote cathode sites in both phases of the corrosion process. However, the possibility of short range coupling over distances of  $<0.1 \text{ mm}$ , that is, less than the lateral resolution of the SKP used in this study, cannot be ruled out. Indeed a subsequent higher resolution scanning Kelvin probe force microscope (SKPFM) investigation of iron FFC identified a possible cathodic area  $\sim 10\text{--}20 \mu\text{m}$  in front of the principally anodic leading edge of the head electrolyte. A recent time-lapse photographic investigation of individual corrosion filaments propagating on iron has shown that dark rings of a similar dimension form at the anterior of electrolyte filled heads,<sup>134</sup> and are associated with the saltatory motion of FFC. A photographic image showing this phenomenon, recorded using an optical microscope under reflective illumination, is given in Figure 13. It is considered that an increase in local pH at the head perimeter, caused by facile through-coating oxygen ingress at this point is responsible for the ring formation. When oxygen was excluded from the environment in contact with the filament head, but allowed to ingress through the porous tail, filaments continued to propagate at the same rate measured in air. However, under these conditions, neither ring formation nor filament saltation was observed and the filament advancement was steady in nature. The authors conclude that this apparent anterior cathodic activity is not a rate determining process in FFC on iron, but is an important factor in constraining the lateral spread of filament head electrolyte.<sup>134</sup>

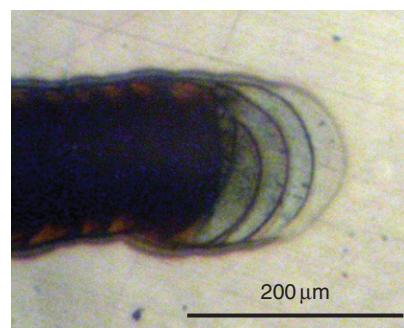


**Figure 13** Magnified optical image of the head region of a corrosion filament propagating on a coated iron substrate in humid air, showing the formation of 'cathodic' corrosion product rings. Courtesy of T. Watson.

## Acknowledgments

The authors would like to thank Drs. Trystan Watson and Andrew Coleman for supplying some of the diagrams shown in this work.

## References

- Leidheiser, H. J. *Adhes. Sci. Technol.* **1987**, 1, 79.
- Greenfield, D.; Scantlebury, D. J. *J. Corros. Sci. Eng.* **2000**, 2(26). ISSN 1466-8858.
- Grundmeyer, G.; Simoes, A. In *Encyclopedia of Electrochemistry*; Bard, A. J., Stratmann, M., Frankel, J., Eds.; Wiley-VCH: New York, 2003; Vol. 5, pp 500-566.
- Ogle, K.; Simoes, A. In *Encyclopedia of Electrochemistry*; Bard, A. J., Stratmann, M., Frankel, J., Eds.; Wiley-VCH: New York, 2003; Vol. 4, pp 460-499.
- Ruggieri, R. T.; Beck, T. R. *Corrosion* **1983**, 39, 452.
- Bauista, A. *Prog. Org. Coat.* **1996**, 28, 49.
- Mayne, J. E. O. *J. Oil Colour Chem. Assoc.* **1950**, 31, 538.
- Funke, W. In *Corrosion Control by Organic Coatings*; Leidheiser, H., Ed.; NACE: Houston, 1981; pp 97-102.
- Gowers, K. R.; Scantlebury, J. D. *Corros. Sci.* **1983**, 23, 935.
- Nguyen, T.; Hubbard, J. B.; McFadden, G. B. *J. Coat. Technol.* **1991**, 63, 43.
- Mayne, J. E. O. *J. Oil Colour Chem. Assoc.* **1949**, 32, 481.
- Skoulikidis, T.; Ragoussis, A. *Corrosion* **1992**, 48, 666.
- Leidheiser, H.; Granata, R. D. *IBM J. Res. Dev.* **1988**, 32, 582.
- Koehler, E. L. *Corrosion* **1977**, 33, 209.
- Leidheiser, H.; Kendig, M. W. *Corrosion* **1979**, 32, 69.
- Leidheiser, H.; Wang, W. *J. Coat. Technol.* **1981**, 53, 77; *Proc. Electrochem. Soc.* **1984**, 84, 239.
- Ritter, J. J. *J. Coat. Technol.* **1982**, 54, 51.
- Leidheiser, H.; Igetoft, L.; Wang, W. *Prog. Org. Coat.* **1983**, 11, 19.
- Koehler, E. L. *Corrosion* **1984**, 40, 5.
- Stratmann, M.; Streckel, H.; Feser, R. *Corros. Sci.* **1991**, 32, 467.
- Sharman, J. D. B.; Sykes, J. M.; Handyside, T. *Corros. Sci.* **1993**, 35, 1375.
- Stratmann, M.; Feser, R.; Leng, A. *Electrochim. Acta* **1994**, 39, 1207-1214.
- Furbeth, W.; Stratmann, M. *Fresenius J. Anal. Chem.* **1995**, 353, 337.
- Furbeth, W.; Stratmann, M. *Prog. Org. Coat.* **2000**, 39, 23.
- Lorimer, J. W., Ed. *Solubility Data Series. Alkaline Earth Hydroxides in Water and Aqueous Solutions*; IUPAC, Pergamon Press: Oxford, 1992; Vol. 52.
- Ritter, J. J.; Kruger, J. In *Corrosion Control by Organic Coatings*; Leidheiser, H., Ed.; NACE: Houston, 1981; p 28.
- Leidheiser, H.; Wang, W. *J. Coat. Technol.* **1981**, 53, 77.
- Watts, J. F.; Castle, J. E. *J. Mater. Sci.* **1984**, 19, 2259.
- Leng, A.; Streckel, H.; Stratmann, M. *Corros. Sci.* **1999**, 41, 547.
- Leng, A.; Streckel, H.; Stratmann, M. *Corros. Sci.* **1999**, 41, 579.
- Leng, A.; Streckel, H.; Stratmann, M. *Corros. Sci.* **1999**, 41, 599.
- Furbeth, W.; Stratmann, M. *Corros. Sci.* **1999**, 43, 207.
- Furbeth, W.; Stratmann, M. *Corros. Sci.* **1999**, 43, 228.
- Furbeth, W.; Stratmann, M. *Corros. Sci.* **1999**, 43, 243.
- Koehler, E. L. *J. Electrochem. Soc.* **1985**, 132, 1005.
- Castle, J. E.; Watts, J. F. In *Corrosion Control by Organic Coatings*; Leidheiser, H., Ed.; NACE: Houston, 1981; p 78.
- Evans, U. R. *The Corrosion and Oxidation of Metals*; St Martins Press: NY, 1960.
- Bard, A. J.; Faulkner, L. R. *Electrochemical Methods - Fundamentals and Applications*; Wiley: NY, 1980; pp 494-496.
- Delahay, P. *Double Layer and Electrode Kinetics*; Interscience, 1966; pp 17-32.
- Bolger, J. C.; Michaels, A. S. In *Interface Corrosion for Polymer Coatings*; Weiss, P., Cheever, G. D., Eds.; Elsevier: NY, 1968; p 3.
- Fowkes, F. M. *Ind. Eng. Chem. Prod. Res. Dev.* **1978**, 17, 3.
- Hammond, J. S.; Holubka, J. W.; Dickie, R. A. *J. Coat. Technol.* **1979**, 51, 45.
- Hammond, J. S.; Holubka, J. W.; Dickie, R. A. *Corros. Sci.* **1981**, 21, 239.
- Dickie, R. A.; Hammond, J. S.; Holubka, J. W. *Ind. Eng. Chem. Prod. Res. Dev.* **1981**, 20, 339.
- Castle, J. E.; Watts, J. F. *Ind. Eng. Chem. Prod. Res. Dev.* **1985**, 24, 361.
- Funke, W. *J. Oil Colour Chem. Assoc.* **1979**, 62, 63.
- Funke, W. *J. Oil Colour Chem. Assoc.* **1985**, 68, 229.
- Funke, W.; Leidheiser, H. *J. Oil Colour Chem. Assoc.* **1987**, 70, 121.
- Marsh, J.; Scantlebury, J. D.; Lyon, S. B. In *Surface Engineering: Fundamentals of Coatings*; Datta, P. K., Gray, J. S., Eds.; Royal Society of Chemistry: Cambridge, 1993; Vol. 1, p 568. Publication no. 126.
- Sabata, A.; Van Ooij, W. J.; Koch, R. J. *J. Adhes. Sci. Technol.* **1993**, 7, 1153.
- Marsh, J.; Scantlebury, J. D.; Lyon, S. B. *Corros. Sci.* **2001**, 43, 829.
- Harun, M. K.; Marsh, J.; Lyon, S. B. *Prog. Org. Coat.* **2005**, 54, 317.
- Suzuki, I. *Corrosion Resistant Coatings Technology*; Marcel Dekker: New York, 1989; pp 167-205.
- Wiggle, R. R.; Smith, A. G.; Petrocelli, J. V. *J. Paint Technol.* **1968**, 40, 174.
- Sommer, A. J.; Leidheiser, H. *Corrosion* **1987**, 43, 661.
- Ogle, K.; Morel, S.; Meddahi, N. *Corros. Sci.* **2005**, 47, 2034.
- Klimow, G.; Fink, N.; Grundmeier, G. *Electrochim. Acta* **2007**, 53, 1290.
- Forget, L.; Delhalle, J.; Mekalif, Z. *Mater. Corros.* **2001**, 52, 181.
- Kuznetsov, Yu. I.; Rosenfeld, I. L.; Agalarova, T. A. *Prot. Met.* **1982**, 18, 438.
- Rosenfeld, I. L. *Corrosion Inhibitors*; McGraw Hill: New York, 1981; p 145.
- Zhao, J.; Frankel, G.; McCreery, R. L. *J. Electrochem. Soc.* **1998**, 145, 2258.
- Williams, G.; McMurray, H. N. *J. Electrochem. Soc.* **2001**, 148, B377.
- McMurray, H. N.; Williams, G.; Worsley, D. A. *J. Electrochem. Soc.* **2002**, 149, B154.
- McMurray, H. N.; Williams, G.; Worsley, D. A. *Corros. Eng. Sci. Technol.* **2003**, 38, 112.
- Zin, I. M.; Pokhmurski, V. I.; Scantlebury, J. D.; Lyon, S. B. *J. Electrochem. Soc.* **2001**, 148, B293.
- Tallman, D. E.; Spinks, G. M.; Dominis, A. J.; Wallace, G. G. *J. Solid State Electrochem.* **2002**, 6, 73.
- Spinks, G. M.; Dominis, A. J.; Wallace, G. G.; Tallman, D. E. *J. Solid State Electrochem.* **2002**, 6, 85.
- Wessling, B. *Adv. Mater.* **1994**, 6, 226.
- Wessling, B. *Synth. Met.* **1997**, 85, 1313.

70. Kinlen, P. J.; Ding, Y.; Silverman, D. C. *Synth. Met.* **1997**, *85*, 1327.
71. Bernard, M. C.; Joiret, S.; Goff, A. H.-Le.; Phong, P. V. *J. Electrochem. Soc.* **2001**, *148*, B12.
72. Kinlen, P. J.; Menon, V.; Ding, Y. *J. Electrochem. Soc.* **1999**, *146*, 3690.
73. Lu, X.; Ng, H. Y.; Xu, J.; He, C. *Synth. Met.* **2002**, *128*, 167.
74. Lu, W.; Eisenbaumer, R. L.; Wessling, B. *Synth. Met.* **1995**, *71*, 2163.
75. Wessling, B. *Synth. Met.* **1999**, *102*, 1396.
76. Tawde, S.; Mukesh, D.; Yakhmi, J. V. *Synth. Met.* **2002**, *125*, 401.
77. Bernard, M. C.; Hugot-Le Goff, A.; Joiret, S.; Ginih, N. N.; Toan, N. N. *J. Electrochem. Soc.* **1999**, *146*, 995.
78. Galkowski, M.; Malik, M. A.; Kulesza, P. J.; Bala, H.; Miecznikowski, K.; Włodarczyk, R.; Adamczyk, L.; Chojak, M. *J. Electrochem. Soc.* **2003**, *150*, B249.
79. Posdorfer, J.; Wessling, B. *Synth. Met.* **2001**, *119*, 363.
80. Talo, A.; Forsén, O.; Yläsaari, S. *Synth. Met.* **1999**, *102*, 1394.
81. Kaiser, A. B.; Liu, C.-J.; Gilberd, P. W.; Chapman, B.; Kemp, N. T.; Wessling, B.; Partidge, A. C.; Smith, W. T.; Shapiro, J. S. *Synth. Met.* **1997**, *84*, 699.
82. Schauer, T.; Joos, A.; Dulog, L.; Eisenbach, C. D. *Prog. Org. Coat.* **1998**, *33*, 20.
83. Tallman, D. E.; Pae, Y.; Biervagan, G. P. *Corrosion* **1999**, *55*, 779.
84. Gašparac, R.; Martin, R. C. *J. Electrochem. Soc.* **2001**, *148*, B138.
85. Wessling, B.; Posdorfer, J. *Synth. Met.* **1999**, *102*, 1400.
86. Holness, R. J.; Williams, G.; Worsley, D. A.; McMurray, H. N. *J. Electrochem. Soc.* **2005**, *152*, B73.
87. Williams, G.; Gabriel, A.; Cook, A.; McMurray, H. N. *J. Electrochem. Soc.* **2006**, *153*, B425.
88. Sahimi, M. *Applications of Percolation Theory*; Taylor and Francis Ltd: London, 1994; pp 201–207.
89. Dafydd, H.; Worsley, D. A.; McMurray, H. N. *Corros. Sci.* **2005**, *47*, 3006.
90. Granata, R. D.; De Crosta, M. A.; Leidheiser, H. *Proc. Int. Cong. Met. Corros.* **1984**, 264–268.
91. Davies, J. R. *Corrosion: Understanding the Basics*; ASTM International, 2000; p 403.
92. Suzuki, I. *Corrosion Resistant Coatings Technology*; Marcel Dekker: New York, 1989; pp 21–108.
93. Souto, R. M.; Scantlebury, D. J. *Prog. Org. Coat.* **2005**, *53*, 63.
94. Hausbrand, R.; Stratman, M.; Rohwerder, M. *Steel Res.* **2003**, *74*, 253.
95. Sharman, C. F. *Nature* **1944**, *153*, 621.
96. Slabaugh, W. H.; Dejager, W.; Hoover, S. E.; Hutchinson, L. L. *J. Paint Technol.* **1972**, *44*, 76.
97. Williams, G.; McMurray, H. N.; Hayman, D.; Morgan, P. C. *Phys. Chem. Comm.* **2001**, *6*, 26–31.
98. Van Loo, M.; Laiderman, D. D.; Bruhn, R. R. *Corrosion* **1953**, *9*, 277.
99. Hoch, G. M. A Review of Filiform Corrosion. In *Localised Corrosion*; Staehle, R. S., Brown, B. F., Kruger, J., Agrawal, A., Eds.; NACE: Houston, 1974; p 134.
100. Lunder, O.; Lein, J. E.; Hesjevik, S. M.; Aune, T. K.; Nisancioglu, K. *Werkst. Korros.* **1994**, *45*, 331.
101. Schmutz, P.; Guillaumin, V.; Lillard, R. S.; Lillard, J. A.; Frankel, G. S. *J. Electrochem. Soc.* **2003**, *150*, B99.
102. Lenderink, H.J.W. PhD thesis, Technical University of Delft, 1995.
103. Williams, G.; McMurray, H. N. *J. Electrochem. Soc.* **2003**, *150*, B380.
104. Szymanski, R.; Jamieson, D. N.; Hughes, A. E.; Mol, A.; Van der Zwaag, S.; Ryan, C. G. *Nucl. Instrum. Methods. Phys. Res., Sect. B* **2002**, *190*, 365.
105. Mol, J. M. C.; Hinton, B. R. W.; Van der Weijde, D. H.; De Wit, J. H. W.; Van der Zwaag, S. *J. Mater. Sci.* **2000**, *35*, 1629.
106. Schmidt, W.; Stratmann, M. *Corros. Sci.* **1998**, *40*, 1441.
107. Grundmeier, G.; Schmidt, W.; Stratmann, M. *Electrochim. Acta* **2000**, *45*, 2515.
108. Le Bozec, N.; Persson, D.; Nazarov, A.; Thierry, D. *J. Electrochem. Soc.* **2002**, *149*, B403.
109. LeBozec, N.; Persson, D.; Thierry, D. *J. Electrochem. Soc.* **2004**, *151*, B440.
110. McMurray, H. N.; Williams, G.; O'Driscoll, S. J. *Electrochem. Soc.* **2004**, *151*, B406.
111. Williams, G.; McMurray, H. N. *Electrochem. Solid-State Lett.* **2003**, *6*, B9.
112. Williams, G.; McMurray, H. N. *Electrochem. Solid State Lett.* **2004**, *7*, B13.
113. McMurray, H. N.; Williams, G. *Corrosion* **2004**, *60*, 219.
114. Leth-Olsen, H.; Nisancioglu, K. *Corros. Sci.* **1998**, *40*, 1179.
115. Leth-Olsen, H.; Afseth, A.; Nisancioglu, K. *Corros. Sci.* **1998**, *40*, 1195.
116. Leth-Olsen, H.; Nordlien, J. H.; Nisancioglu, K. *Corros. Sci.* **1998**, *40*, 2051.
117. Afseth, A.; Nordlien, J. H.; Scamans, G. M.; Nisancioglu, K. *Corros. Sci.* **2001**, *43*, 2093.
118. Afseth, A.; Nordlien, J. H.; Scamans, G. M.; Nisancioglu, K. *Corros. Sci.* **2001**, *43*, 2359.
119. Afseth, A.; Nordlien, J. H.; Scamans, G. M.; Nisancioglu, K. *Corros. Sci.* **2002**, *44*, 2491.
120. Afseth, A.; Nordlien, J. H.; Scamans, G. M.; Nisancioglu, K. *Corros. Sci.* **2002**, *44*, 2529.
121. Afseth, A.; Nordlien, J. H.; Scamans, G. M.; Nisancioglu, K. *Corros. Sci.* **2002**, *44*, 2543.
122. Zhou, X.; Thompson, G. E.; Scamans, G. M. *Corros. Sci.* **2003**, *45*, 1767.
123. Ambat, R.; Davenport, A. J.; Afseth, A.; Scamans, G. *J. Electrochem. Soc.* **2004**, *151*, B53.
124. Liu, Y.; Zhou, X.; Thompson, G. E.; Hashimoto, T.; Scamans, G. M.; Afseth, A. *Acta Mater.* **2007**, *55*, 353.
125. McMurray, H. N.; Coleman, A. J.; Williams, G.; Afseth, A.; Scamans, G. M. *J. Electrochem. Soc.* **2007**, *154*, C339.
126. Coleman, A. J.; McMurray, H. N.; Williams, G.; Afseth, A.; Scamans, G. M. *Electrochem. Solid-State Lett.* **2007**, *10*, C35.
127. Scamans, G. M.; Afseth, A.; Thompson, G. E.; Liu, Y.; Zhou, X. *Mater. Sci. Forum* **2006**, *519–521*, 647.
128. Svenningsen, G.; Larsen, M. H.; Lein, J. E.; Nordlien, J. H.; Nisancioglu, K. In Proceedings of the 9th International Conference on Aluminium Alloys (ICAA9); Nie, J. F., Morton, A. J., Muddle, B. C., Eds.; Institute of Material Engineering Australasia Ltd.: Melbourne, Australia, 2004; p 818.
129. Leblanc, P. P.; Frankel, G. S. *J. Electrochem. Soc.* **2004**, *151*, B105.
130. Funke, W. *Prog. Org. Coat.* **1981**, *9*, 29.
131. Funke, W. *Ind. Eng. Chem. Prod. Res. Dev.* **1985**, *24*, 343.
132. Koehler, E. L. *Corrosion* **1977**, *33*, 209.
133. Williams, G.; McMurray, H. N. *Electrochem. Commun.* **2003**, *5*, 871.
134. Watson, T. M.; McMurray, H. N.; Williams, G.; Coleman, A. C. In *Corrosion in Marine and Saltwater Environments II*; Proceedings of the 206th Electrochemical Society Meeting., Honolulu, Hawaii, USA, October 2004; Shifler, D. A., Tsuru, T., Natishan, P. M., Ito, Y., Eds.; ECS, 2005; p 321.



## 2.13 Flow Assisted Corrosion

**H. G. Schmitt and M. Bakalli**

Iserlohn University of Applied Sciences, Frauenstuhlgeweg 31, D-58644 Iserlohn, Germany

© 2010 Elsevier B.V. All rights reserved.

<b>2.13.1</b>	<b>Introduction</b>	955
<b>2.13.2</b>	<b>Flow Dynamic Basics</b>	955
2.13.2.1	Laminar and Turbulent Flow	955
2.13.2.2	The Boundary Layer	957
2.13.2.3	Flow Patterns	959
<b>2.13.3</b>	<b>Corrosion Aspects</b>	960
2.13.3.1	Scale-free Surfaces	960
2.13.3.2	Scale-Covered Surfaces	962
2.13.3.2.1	Scale destruction	964
2.13.3.2.2	Corrosion intensity after scale destruction	969
2.13.3.3	Tools for Investigating Flow-Assisted Corrosion	970
2.13.3.3.1	Rotating disc electrode	971
2.13.3.3.2	Rotating cylinder electrode	972
2.13.3.3.3	Rotating cage	972
2.13.3.3.4	Pipe and channel flow	973
2.13.3.3.5	Impinging jet	973
2.13.3.3.6	Maximum local flow intensities	973
2.13.3.4	Erosion Corrosion and Cavitation Corrosion	977
2.13.3.4.1	Solid particle impingement	978
2.13.3.4.2	Liquid droplet impingement	979
2.13.3.4.3	Gas bubble impingement	979
2.13.3.4.4	Cavitation	979
2.13.3.5	Corrosion Control	979
2.13.3.5.1	Fluid mechanics and design	979
2.13.3.5.2	Materials selection	980
2.13.3.5.3	Environment control	980
2.13.3.5.4	Cathodic protection	983
2.13.3.5.5	Control of solid particle impingement attack	984
2.13.3.5.6	Control of liquid droplet impingement attack and cavitation	985
2.13.3.5.7	Predictive modelling	985
<b>References</b>		985

### Abbreviations

**DRA**s Drag-reducing agents  
**FEC** Flow enhanced corrosion  
**FED** Frek energy density  
**FILC** Flow-induced localized corrosion

### Symbols

**a** Exponent (constant)  
**A** Amplitude of the noise current density from the polynomial fitting ( $A m^2$ )

**b** Microelectrode width (m)  
**c<sub>0</sub>, c\*** Solution concentration at the electrode surface ( $mol m^{-3}$ )  
**c<sub>bulk</sub>** Bulk solution concentration ( $mol m^{-3}$ )  
**c<sub>S</sub>** Concentration at the entrance of the pores ( $mol m^{-3}$ )  
**d** Diameter of the pipe/characteristic diameter/thickness layer (m)  
**d<sub>N</sub>** Nernst diffusion layer thickness (m)  
**D** Diffusion coefficient ( $m^2 s^{-1}$ )  
**D<sub>Pr</sub>** Diffusion coefficient in the Prandtl layer ( $m^2 s^{-1}$ )

**$D_S$**  Diffusion coefficient in the pores of the scale ( $\text{m}^2 \text{s}^{-1}$ )

**$E_D$**  Hydrodynamic energy density (Pa)

**$E_D^F$**  Freak energy density (Pa)

**$F$**  Faraday constant (96 485) ( $\text{C mol}^{-1}$ )

**$Fr$**  Froude number

**$g$**  Acceleration due to gravity ( $\text{m s}^{-2}$ )

**$h_{\text{eff}}$**  Effective height of the liquid film (m)

**$j_c$**  Corrosion current density ( $\text{A m}^{-2}$ )

**$j_D$**  Diffusion controlled current density ( $\text{A m}^{-2}$ )

**$k$**  Mass transport coefficient ( $\text{m s}^{-1}$ )

**$k$**  Constant on the L  veque equation ( $\text{N m}^4 \text{A}^{-3}$ )

**$k_1, k_2, k_3$**  Constants

**$K$**  Average height of all roughness peaks

**$l$**  Tube or channel length/microelectrode length (m)

**$L$**  Characteristic length (m)

**$m_{Pr}$**  Mass transport rate in the Prandtl's boundary layer ( $\text{mol m}^{-2} \text{s}^{-1}$ )

**$m_S$**  Mass transport rate in the pores of the scale ( $\text{mol m}^{-2} \text{s}^{-1}$ )

**$n$**  Exponent (depends on  $Re$ )

**$Pe$**  Dimensionless Peclet number

**$R$**  Inner radius of the pipe (m)

**$r_{RC}$**  Radius of the rotated cage (m)

**$Re$**  Dimensionless Reynolds number

**$Re_{RC}$**  Dimensionless Reynolds number in rotated cage

**$Sc$**  Dimensionless Schmidt number

**$Sh$**  Dimensionless Sherwood number

**$Ta$**  Dimensionless Taylor number

**$u^+$**  Normalized (dimensionless) flow velocity

**$u_b$**  Bulk flow velocity ( $\text{m s}^{-1}$ )

**$u_c$**  Velocity at the pipe centreline ( $\text{m s}^{-1}$ )

**$u_{\text{crit}}$**  Critical flow velocity ( $\text{m s}^{-1}$ )

**$u_p$**  Particle velocity ( $\text{m s}^{-1}$ )

**$u_r$**  Axial velocity ( $\text{m s}^{-1}$ )

**$u_{SL}$**  Superficial liquid velocity ( $\text{m s}^{-1}$ )

**$u_{SG}$**  Superficial gas velocity ( $\text{m s}^{-1}$ )

**$u_t$**  Translational velocity of the slug front ( $\text{m s}^{-1}$ )

**$u_f$**  Average velocity of the liquid film ( $\text{m s}^{-1}$ )

**$u_x$**  Shear velocity ( $\text{m s}^{-1}$ )

**$U$**  Average fluid velocity in the pipe ( $\text{m s}^{-1}$ )

**$U_0$**  Flow velocity at the boundary layer ( $\text{m s}^{-1}$ )

**$v$**  Corrosion rate ( $\text{g m}^{-2} \text{h}$ )

**$w$**  Energy density/mass transport rate/corrosion rate ( $\text{Pa/mol m}^{-2} \text{s}^{-1}/\text{g m}^{-2} \text{h}$ )

**$w_{er}$**  Mass loss rate in erosion corrosion ( $\text{g m}^{-2} \text{h}$ )

**$Y$**  Axial position/distance from the wall (m)

**$y^+$**  Normalized (dimensionless) wall distance

**$Z$**  Number of charges

**$\delta_{Pr}$**  Prandtl's boundary layer thickness

**$\Delta c$**  Concentration gradient ( $\text{mol m}^{-3}$ )

**$\Delta p, \Delta P$**  Pressure loss (Pa)

**$\epsilon$**  Relative roughness

**$\lambda$**  Tube friction factor

**$\mu$**  Hydrodynamic viscosity (Pa s)

**$\nu$**  Kinematic viscosity of flowing fluid ( $\text{m}^2 \text{s}^{-1}$ )

**$\omega$**  Wave frequency/rotational speed ( $\text{s}^{-1}$ )

**$\Phi_{\text{destruct}}$**  Rate of scale destruction

**$\Phi_{\text{scale}}$**  Rate of scale formation

**$\rho$**  Density ( $\text{kg m}^{-3}$ )

**$\sigma_B$**  Fracture stress of the scales (Pa)

**$\tau_{RC}$**  Wall shear stress in rotated cage (Pa,  $\text{N m}^{-2}$ )

**$\tau_w$**  Wall shear stress (Pa,  $\text{N m}^{-2}$ )

## 2.13.1 Introduction

Flowing media are encountered in nearly all technical systems, for example, in heat exchangers, pumps, hydraulic machines, steam generators, different components of power stations, chemical plants, and the oil and gas industry, and in many cases, corrosion failures occurred due to flow effects. Understanding the mechanisms involved needs a detailed knowledge of both corrosion (specifically electrochemical corrosion) and fluid dynamics.

On the corrosion side, the type of material and the status of its surface (scale-free or scale-covered) are decisive. On the fluid dynamics side, the type of flow regime must be considered (developed laminar and turbulent flow; disturbed flow; one-phase, two-phase, multiphase flow without and with solid particles; and in the case of multiphase flow, horizontal, inclined, and vertical flow).<sup>1–11</sup>

## 2.13.2 Flow Dynamic Basics

### 2.13.2.1 Laminar and Turbulent Flow

The intensity of flow can be characterized as either laminar or turbulent. In laminar pipe flow, the profile of the local flow velocity,  $u_r$ , is parabolic (Figure 1(a)) and can be calculated according to eqn [1].<sup>12</sup>

$$u_r = u_c [1 - (y/R)^2] \quad [1]$$

where  $u_r$  is the axial velocity,  $u_c$  is the velocity at the pipe centerline,  $y$  is the axial position, and  $R$  is the inner radius of the pipe. Equation [1] is an analytical solution of the Navier–Stokes equation and the continuity equations of the fluid flow.

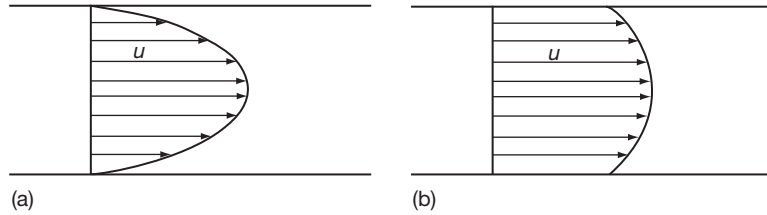


**Figure 1** Velocity profile in (a) laminar flow and (b) turbulent flow.

In turbulent pipe flow, the profile of the local flow velocity,  $u_r$ , is logarithmic (**Figure 1(b)**) and can be calculated according to **eqn [2]**.<sup>12</sup>

$$u_r = u_c [1 - (y/R)]^{1/n} \quad [2]$$

where  $n$  depends on the Reynolds number ( $Re$ ). **Equation [2]** is based on extensive experimental analysis, because no exact solution of the Navier–Stokes equation can be given for turbulent pipe flow.

The dimensionless  $Re$  is commonly used to characterize the nature of fluid flow. For liquid flow through pipes,  $Re$  is defined according to **eqn [3]**.<sup>12</sup>

$$Re = \frac{uL}{\nu} = \frac{u\rho L}{\mu} \quad [3]$$

where  $u$  is the average fluid velocity in the pipe ( $\text{m s}^{-1}$ ),  $L$ , the characteristic length (for pipe flow the diameter,  $d$ , of the pipe) (m), and  $\nu$ , the kinematic viscosity of flowing fluid ( $\text{m}^2 \text{s}^{-1}$ ), which can be expressed as the ratio of the hydrodynamic viscosity  $\mu$  (Pa s) and the density  $\rho$  ( $\text{kg m}^{-3}$ ).

From the  $Re$ , the flow regime can be derived. For Newtonian liquids, pipe flow is in the:

- developed laminar flow regime, if  $Re < 2300$ ;
- transition (buffer) flow regime, if  $2300 < Re < 4000$ ;
- turbulent flow regime, if  $Re > 4000$ .

In flow systems with real liquids, energy losses occur as a result of friction at the solid wall and due to eddies (vortices) in the near-wall region. In the laminar flow regime, the pressure loss in a pipe or channel is proportional to the average flow velocity,  $u$ , and can be quantified according to the Hagen–Poiseuille equation (**eqn [4]**).<sup>13</sup>

$$\frac{\Delta p}{l} = 32\mu u \frac{1}{d^2} \quad [4]$$

where  $\Delta p$  is the pressure loss,  $l$  is the tube or channel length, and  $d$  is the characteristic diameter. However, in technical systems, the surface roughness has to be considered with a tube friction factor  $\lambda$  (**eqn [5]**),

which depends on both the surface roughness and the flow regime ( $Re$ ).<sup>13</sup>

$$\Delta p = \lambda \frac{l}{d} \frac{u^2}{2} \rho \quad [5]$$

For laminar flow ( $Re < 2300$ ), the friction factor is a direct function of the  $Re$  (**eqn [6]**):

$$\lambda = \frac{64}{Re} \quad [6]$$

In the case of turbulent flow, the friction factor is strongly dependent on the  $Re$ , and  $\Delta p$  will increase proportional to  $u^2$ . For  $2300 \leq Re \leq 10^5$ , the following relationship was found by Blasius for smooth surfaces (**eqn [7]**):

$$\lambda = \frac{0.3164}{Re^{1/4}} \quad [7]$$

In the case of small  $Re$ , the thickness of the boundary layer may be sufficient to cover all roughness peaks. The pressure loss will be slightly greater than in the case of smooth walls. However, it occurs according to the same physical laws relevant to the laminar region. With increasing  $Re$ , the boundary layer becomes thinner and thinner, and the roughness elements penetrate through the boundary layer into the main flow stream resulting in considerable drag and pressure loss. Thus, with increasing flow velocity, the pressure loss becomes more dependent on the surface roughness. At high roughness, the viscous forces in the near-wall boundary layer become negligible.

Regardless of the multitude of roughness forms and their distribution, a relative roughness,  $\varepsilon$ , is defined according to **eqn [8]**:

$$\varepsilon = \frac{K}{d} \quad [8]$$

where  $K$  is the average height of all roughness peaks. **Equation [8]** also indicates that wall effects decrease with increasing pipe diameter. In the case of fully developed flow, the friction factor  $\lambda$  becomes

independent of the  $Re$  and can be calculated according to eqn [9] (Prandtl, Karman).<sup>14</sup>

$$\lambda^{-1/2} = 2 \log \frac{d}{K} + 1.14 \quad [9]$$

These equations are empirical in nature. However, they clearly indicate that pressure losses in pipes strongly depend on the flow velocity (more general: the  $Re$ ) and on fluid–wall interactions, which depend on the surface roughness on the solid side and on the nature of the boundary layer on the fluid side. In the following section, the nature of the boundary layer is looked at in more detail.

### 2.13.2.2 The Boundary Layer

The boundary layer is a near-wall region with non-uniform flow in a small layer between the bulk flow and the solid wall. This small layer is not constant over a greater length, but develops gradually in the flow direction. All friction effects occur within this layer, while in the bulk region, the flow is friction-free in the ideal case.

The development of the boundary layer is shown schematically in Figure 2. A thin plate is hit by a free flow with the velocity  $U_0$ . A boundary layer starts forming at the plate surface. The gradient of flow

velocity,  $u(y)$  – with  $y$  giving the distance from the plate surface – changes over the length of the plate. The thickness of the boundary layer increases with the distance,  $x$ , from the front of the plate. The Prandtl's boundary layer,  $\delta_{Pr}$ , is defined as the distance  $y$  where the local flow velocity is only 1% smaller than the bulk velocity (eqn [10]).<sup>15</sup>

$$\delta_{Pr} = \mathcal{N}(U_{y=0.99U_0}) \quad [10]$$

The flow in the boundary layer can be laminar or turbulent. In a small region after the leading edge of the plate where the boundary layer thickness is still small, the flow regime is laminar. With increasing thickness of the boundary layer along the plate, the boundary layer becomes increasingly unstable and turbulences are formed. The region where laminar flow changes to turbulent flow is called the transition region. The thickness of the boundary layer increases step-like along the plate. The time-averaged velocity profiles are shown in Figure 2. In the laminar region, the wall shear stresses,  $\tau_w$ , decrease up to the transition region. There wall shear stresses  $\tau_w$  increase spontaneously because the ratio between the change of flow velocity,  $du$ , and the distance,  $dy$ , from the plate increases spontaneously. However,  $\tau_w$  decreases gradually along the plate length,  $x$ .

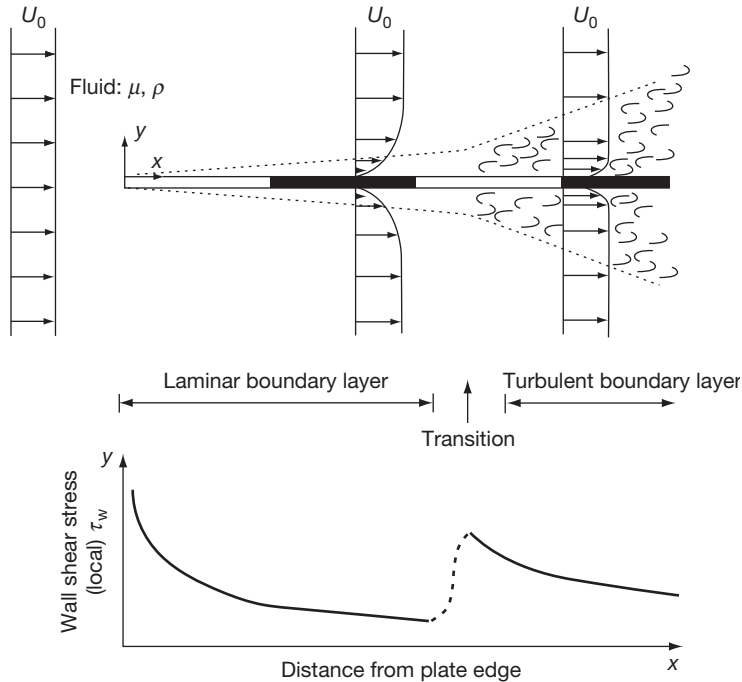


**Figure 2** Boundary layer along a thin plate.

The properties of the boundary layer can be characterized by local  $Re$ , which are related either to the layer thickness,  $\delta_{Pr}$ , or to the distance,  $x$ , from the front of the plate (eqns [11] and [12]).<sup>15</sup>

$$Re_{\delta_{Pr}} = \frac{U_0 \delta_{Pr}}{\mu} \quad [11]$$

$$Re_x = \frac{U_0 x}{\mu} \quad [12]$$

*Laminar boundary layer:* The layer thickness,  $\delta_{Pr}$ , increases with the distance from the leading edge of the plate and decreases with the flow velocity,  $U_0$ . This can be expressed by the Blasius equation (eqn [13]).<sup>15</sup>

$$\delta_{Pr} = 5.0 \sqrt{\frac{\nu x}{U_0}} = \frac{5.0x}{\sqrt{Re_x}} \quad [13]$$

The wall shear stress,  $\tau_w$ , is directly related to the gradient of the flow velocity (eqn [14]).

$$\tau_w = \mu \left( \frac{dU}{dy} \right)_{y=0} = 0.332 \mu \frac{U_0}{x} \sqrt{Re_x} \quad [14]$$

where  $\mu$  is the hydrodynamic viscosity (Pa s).

*Turbulent boundary layer:* The turbulent boundary layer exhibits a much more complex structure than the laminar boundary layer. The major part of the boundary layer consists of the turbulent zone (Figure 3) with a chaotic turbulence activity and permanently changing flow pattern. The turbulent zone is again divided into an outer zone and an inner zone (often called buffer zone). Only in the inner zone are viscous effects encountered.<sup>16,17</sup>

Close to the wall, in the inner zone (Figure 3), the fluctuations are damped, resulting in a viscous sublayer with laminar flow profile. In general, the flow pattern in the viscous sublayer is taken as quasi-static. However, it has been shown experimentally that turbulences in the outer and, specifically, in the buffer zone can affect the flow situation in the viscous sublayer, causing fluctuations of the thickness and the flow pattern in the viscous sublayer.<sup>18–20</sup>

The three regions of the turbulent boundary layer can be mathematically resolved using the normalized (dimensionless) flow velocity,  $u^+$  (eqn [15]), and the normalized (dimensionless) wall distance,  $y^+$  (eqn [16]).

$$u^+ = \frac{u}{u_x} \quad [15]$$

$u$  is mean velocity in turbulent boundary layer ( $\text{m s}^{-1}$ )

$$y^+ = \frac{y u_x}{\nu} \quad [16]$$

where  $y$  is distance from the wall (m),  $u_x = \sqrt{(\tau_w/\rho)}$  is shear velocity ( $\text{m s}^{-1}$ ),  $\nu$ , the kinematic viscosity ( $\text{m}^2 \text{s}^{-1}$ ),  $\tau_w$ , the wall shear stress ( $\text{N m}^{-2}$  or Pa), and  $\rho$ , the fluid density ( $\text{kg m}^{-3}$ ).

The velocity distribution in the viscous sublayer ( $y^+ < 5$ ), in the buffer region ( $5 < y^+ < 30-40$ ), and the outer turbulent zone ( $30-40 < y^+ < 100$ ) can be calculated according to the equations given in the semilogarithmic plot in Figure 4.<sup>18</sup>

The local flow velocity in the viscous sublayer can be calculated according to eqn [17]:

$$u = \frac{\tau_w}{\mu} y \quad [17]$$

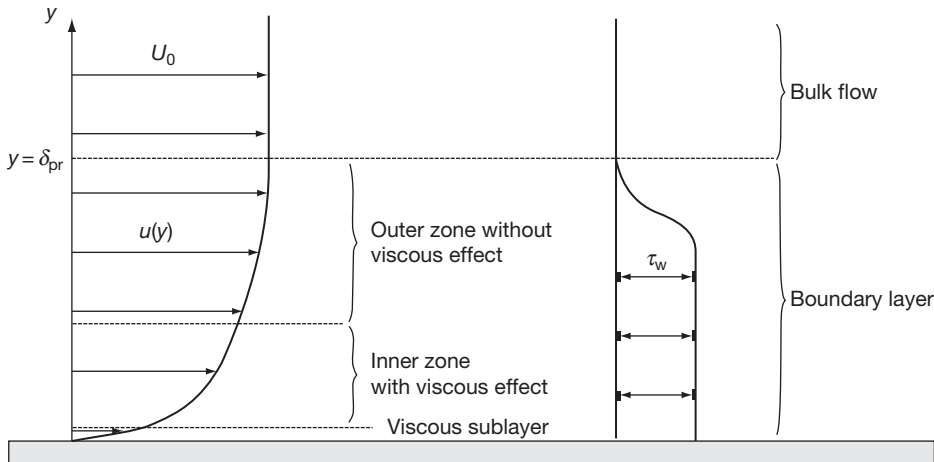
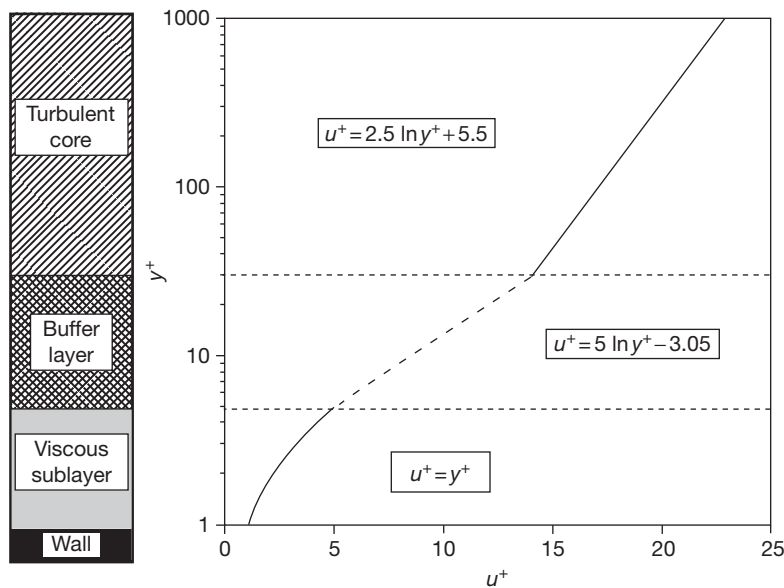


Figure 3 Turbulent boundary layer.





**Figure 4** Structure of the turbulent boundary layer and distance-related velocity distribution. Reproduced from Davies, J. T. In *Turbulence Phenomena*; Academic Press: New York, 1972; Chapter 2, pp 121–143.

### 2.13.2.3 Flow Patterns

The interaction intensity between flowing media and solid walls depends on the number of phases and on the magnitude and relative ratio of the superficial velocities of each phase involved. (The superficial velocity is calculated separately for each phase assuming that no other phase is present). The easiest-to-describe flow pattern is the undisturbed, developed single phase flow. Much more complicated and more dangerous, with respect to flow-induced localized corrosion, (FILC) is the disturbed single phase flow as encountered downstream of weld beads, pipe fittings, valves, orifice plates, at pipe joints, upsets, bends, tees, elbows, or tube inlets of heat exchangers. The hydrodynamic description becomes even more challenging in the case of two-phase flow (liquid–liquid, liquid–gas, liquid–solid) and multiphase flow (liquid–liquid–gas, liquid–liquid–solid, liquid–gas–solid, liquid–liquid–gas–solid) in horizontal, inclined, or vertical flow systems, not to mention additional conditions of surface or flow directional disturbances. **Figures 5–7** give examples of mixed phase flow patterns.<sup>9,21,22</sup>

What makes exact hydrodynamic descriptions so difficult is the fact that a multitude of fluid–wall interactions can take place, including mass transfer, heat transfer, fluctuating shear stresses parallel to the surface, fluctuating energy densities (fluctuating pressures) perpendicular to the surface, particle impact (erosion), and near-wall gas bubble collapse

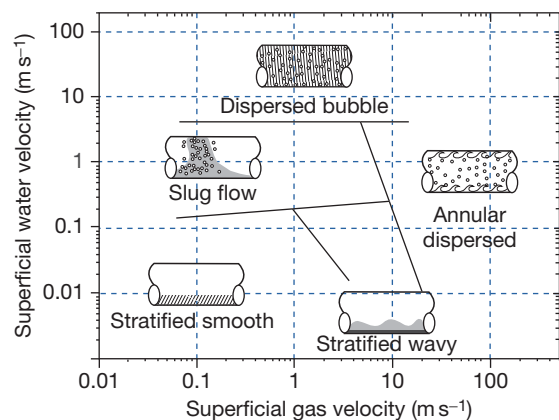


**Figure 5** Flow patterns in horizontal liquid–gas pipe flow. Adapted from Lotz, U. *Velocity Effects in Flow Induced Corrosion*, Corrosion'90; NACE International: Houston, TX, 1990; Paper no. 27; Weisman, J. In *Handbook of Fluids in Motion*; Cheremisinoff, N. P., Gupta, R., Eds.; Ann Arbor Science Publishers: Ann Arbor, MI, 1983; pp 409–424; Govier, G. W.; Aziz, K. *The Flow of Complex Mixtures in Pipes*; Van Nostrand Reinhold: New York, 1972; pp 324, 326, 506.

(cavitation) (**Figure 8**). Besides these kinds of interactions, the nature of the wall (surface roughness, hardness, ductility, and fracture toughness, presence of protective layers like films, coatings, or scales) plays a significant role. This is the reason why predictive mathematical models in flow-assisted corrosion are available only for relatively simple flow systems.

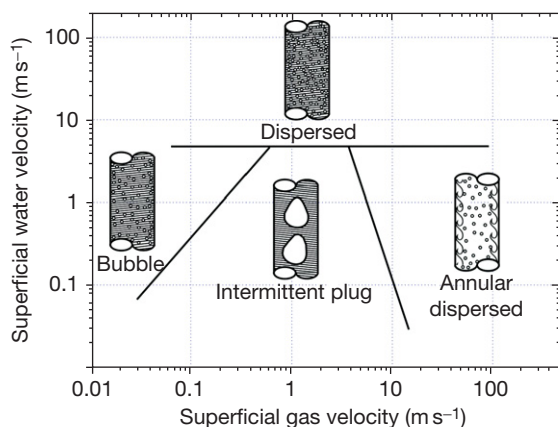


**Figure 6** Flow patterns in vertical liquid–gas pipe flow. Adapted from Lotz, U. *Velocity Effects in Flow Induced Corrosion*, Corrosion'90; NACE International: Houston, TX, 1990; Paper no. 27; Weisman, J. In *Handbook of Fluids in Motion*; Cheremisinoff, N. P., Gupta, R., Eds.; Ann Arbor Science Publishers: Ann Arbor, MI, 1983; pp 409–424; Govier, G. W.; Aziz, K. *The Flow of Complex Mixtures in Pipes*; Van Nostrand Reinhold: New York, 1972; pp 324, 326, 506.

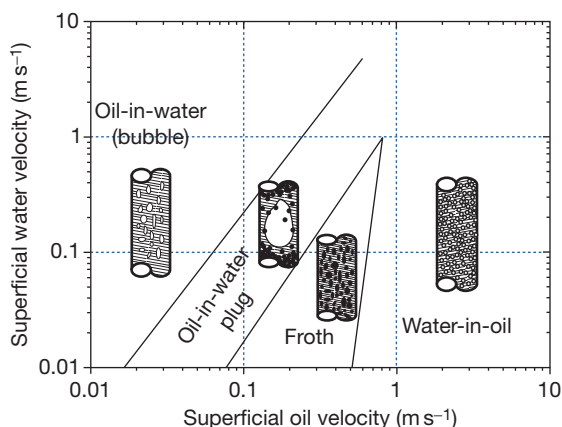


**Figure 7** Flow patterns in vertical liquid–liquid (oil–water) pipe flow. Adapted from Lotz, U. *Velocity Effects in Flow Induced Corrosion*, Corrosion'90; NACE International: Houston, TX, 1990; Paper no. 27; Weisman, J. In *Handbook of Fluids in Motion*; Cheremisinoff, N. P., Gupta, R., Eds.; Ann Arbor Science Publishers: Ann Arbor, MI, 1983; pp 409–424; Govier, G. W.; Aziz, K. *The Flow of Complex Mixtures in Pipes*; Van Nostrand Reinhold: New York, 1972; pp 324, 326, 506.

### 2.13.3 Corrosion Aspects

Flow can enhance uniform corrosion or initiate and propagate localized corrosion. The first case is mostly encountered when the material's surface is bare

(i.e., scale free) or is covered with a very porous and thus nonprotective scale. This case will be described as flow-enhanced corrosion (FEC). In contrast the acronym FILC will be used to describe flow-induced localized corrosion generally found under corrosion conditions when more or less protective scales cover the material's surface and are destructed by flow effects.<sup>23–26</sup>

#### 2.13.3.1 Scale-free Surfaces

Under free corrosion conditions, the corrosion rate is flow dependent when the rest potential,  $U_R$ , is in the potential range of the mass transport (diffusion)-controlled region of the cathodic partial current density–potential curve  $j^-$  (Figure 9).  $U_{(Me)}^*$  and  $U_{(CA)}^*$  are the equilibrium potential of the metal–metal ion redox reaction and the cathodic redox reaction, respectively. The corrosion current density,  $j_c$ , is then equal to the diffusion current density,  $j_D$ , of the cathodic partial current density–potential curve  $j^-$ , and  $j_D$  depends on the flow, according to the Fick's law (eqn [18]).<sup>27</sup>

$$j_D = \frac{zFD\Delta c}{d_N} \quad [18]$$

where  $D$  is the diffusion coefficient of the cathodically active species ( $\text{m}^2 \text{s}^{-1}$ ),  $z$ , the number of charges exchanged in the cathodic reaction,  $F$ , Faraday's constant ( $96\,485 \text{ C mol}^{-1}$ ),  $d_N$ , the Nernst diffusion layer thickness (m), and  $\Delta c$ , the concentration gradient of the cathodically active species between the bulk solution ( $c_{\text{bulk}}$ ) and the electrode surface ( $c^*$ ). Under diffusion controlled conditions,  $c^*$  is equal to zero (Figure 10).

In laminar flow regimes,  $d_N$  ranges between 1 and  $100 \mu\text{m}$  and depends on the bulk flow velocity,  $u_0$ , according to eqn [19], where  $n$  can take values between 0.5 and 1.<sup>17</sup>

$$d_N = \frac{1}{u_0^n} \quad [19]$$

The hydrodynamic layers next to the metal surface will exhibit a transition from pure diffusion and migration immediately next to the surface to a convection-dominated region further away from the surface. It is mathematically convenient to consider a simplified model of the interface that consists of a layer in which only diffusion and migration occur, known as the Nernst diffusion layer, in direct contact with bulk solution, which has a constant composition. The thickness,  $d_N$ , of the Nernst diffusion layer is

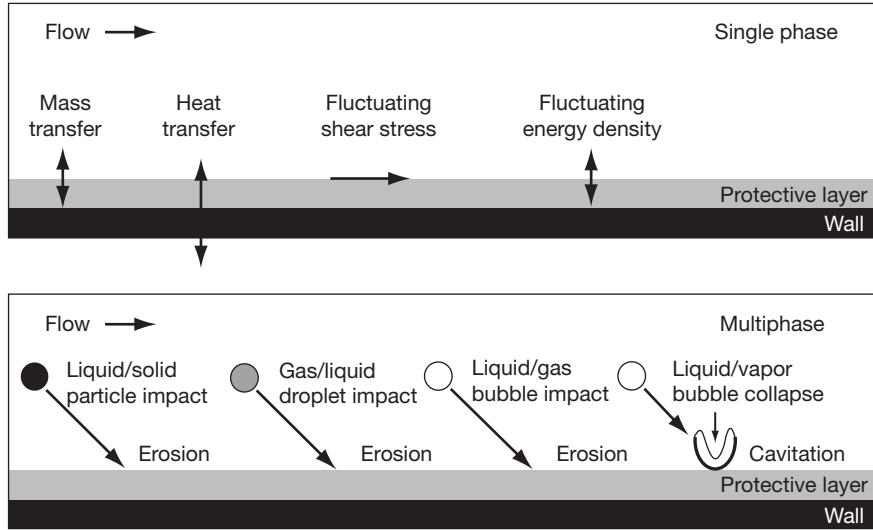


**Figure 8** Fluid-wall interactions in flow systems. Reproduced from Heitz, E. In *Flow-Induced Corrosion: Fundamental Studies and Industry Experience*; Kennelley, K. J., Hausler, R. H., Silverman, D. C., Eds.; NACE International: Houston, TX, 1991; pp 1:1–1:29.

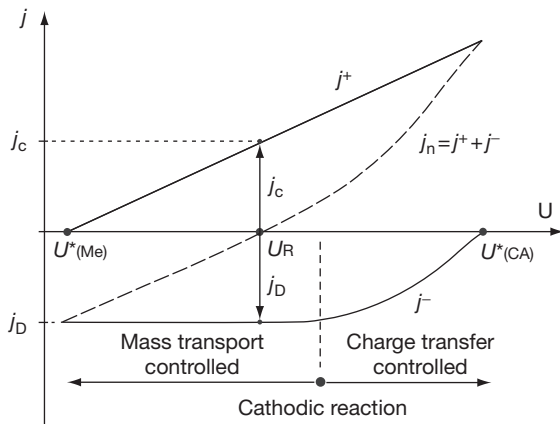


**Figure 9** Current density–potential plot for diffusion controlled metal corrosion.

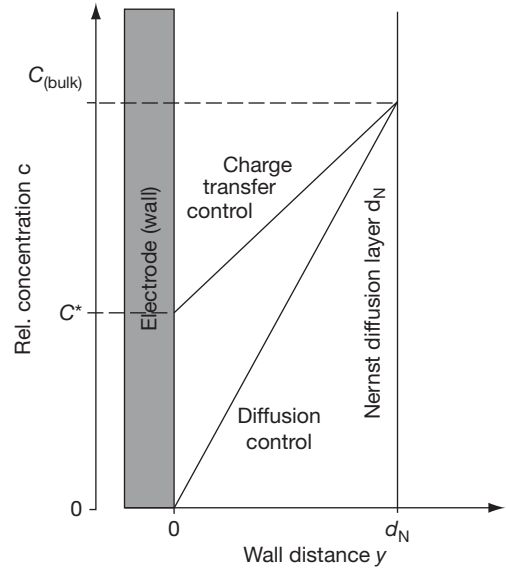


**Figure 10** Concentration gradients in Nernst diffusion layer.

proportional to the thickness of the Prandtl boundary layer,  $\delta_{Pr}$  (eqn [20]).

$$d_N \sim \left(\frac{D}{\nu}\right)^{1/3} \delta_{Pr} \quad [20]$$

For aqueous solutions with kinematic viscosities,  $\nu$ , in the order of  $10^{-2} \text{ cm}^2 \text{ s}^{-1}$  and diffusion coefficients in the order of  $10^{-5} \text{ cm}^2 \text{ s}^{-1}$ ,  $d_N$  ranges in the order of 10% of the Prandtl boundary layer.

The ratio between the kinematic viscosity and the diffusion coefficient is also called Schmidt number,  $Sc$  (eqn [21]).<sup>17</sup>

$$Sc = \frac{\nu}{D} = \left(\frac{u_0 l}{D}\right) / \left(\frac{u_0 l}{\nu}\right) = \frac{Pe}{Re} \quad [21]$$

$Pe$  is the Peclet number ( $=u_0 l/D$ ). When the flow becomes turbulent (high  $Re$ , rough surfaces), the transport conditions become more complicated and can be expressed only semiquantitatively. For  $Sc$  in the order of  $10^3$ , the diffusion boundary layer thickness is of the order of 1/6 of the thickness of the viscous sublayer. Thus, the diffusion boundary layer reacts directly to changes in the thickness of the viscous sublayer.

For turbulent flow, a general equation exists for mass transport correlations at different flow patterns, based on the dimensionless parameters  $Re$ ,  $Sc$ , and  $Sh$  (eqn [22]).<sup>28</sup>

$$Sh = aSc^b Re^c \quad [22]$$

The Sherwood number,  $Sh$ , describes the ratio of total mass transport to mass transport by molecular diffusion (eqn [23]).<sup>29</sup>

$$Sh = \frac{kL}{D} \quad [23]$$

where  $k = D/d_N$  is the mass transport coefficient ( $\text{m s}^{-1}$ ), and  $L$ , the characteristic length (m). The constants  $a$ ,  $b$  and  $c$  in eqn [22] are given in Table 1 for different flow devices.

### 2.13.3.2 Scale-Covered Surfaces

At scale-covered metal surfaces, molecular pore diffusion becomes the rate-determining step (Figure 11). This depends, of course, on the pore size and density.

In general, the corrosion rate becomes nearly independent of flow under the assumption that the thickness or the existence of the scale is not influenced by the flowing medium, for example, due to enhanced dissolution or cracking and subsequent spalling. The major concentration gradient of electro-active species (transported to or from the metal surface at the bottom of the pores) occurs in the pores.<sup>9,30</sup> The flow intensity at the scale-covered surface will influence only the convective diffusion of electro-active species in the Prandtl boundary layer to the entrance of the pores, which generally results in only a small concentration gradient (Figure 11).

The mass transport in the laminar Prandtl boundary layer,  $d_{Pr}$ , and in the pores of the scale can be described by Fick's law (eqns [24] and [25]):

$$m_{Pr} = D_{Pr} \frac{c_{bulk} - c_s}{d_{Pr}} \quad (\text{Diffusion in Prandtl layer}) \quad [24]$$

$$m_s = D_s \frac{c_s - c_0}{d_s} \quad (\text{Pore diffusion}) \quad [25]$$

**Table 1** Mass transport relationships for important flow systems

Flow system	Power law $Sh = aSc^b Re^c$	Range of validity	Characteristic length and $Re$
Free rotated disc			
Laminar flow	$0.60Sc^{1/3}Re^{1/2}$	$10^2 < Re < 10^5$	$L = r, Re = \frac{\omega r^2}{\nu}$
Turbulent flow	$0.011Sc^{1/3}Re^{0.87}$	$Re > 10^6$	
Rotated disc in front of wall			
Laminar flow	$17.3Sc^{1/3}Re^{0.34}$	$9 \times 10^4 < Re < 6 \times 10^5$	$L = r, Re = \frac{\omega r^2}{\nu}$
Turbulent flow	$0.05Sc^{1/3}Re^{0.78}$	$Re > 6 \times 10^5$	
Free rotated cylinder			
Turbulent flow	$0.079Sc^{0.35}Re^{0.7}$	$10^2 << Re < 4 \times 10^5$	$L = r, Re = \frac{\omega r^2}{\nu}$
Coaxial cylinder	$0.0027Sc^{1/3}Re$	$Re < 2.7 \times 10^5$	$L = r, Re = \frac{\omega r^2}{\nu}$
Flat plate in channel and tube flow			
Laminar flow	$2.54Sc^{1/3}Re(d_e/l)^{1/3}$	$Re < 2300$	$L = d_e, Re = \frac{d_e u}{\nu}$
Turbulent flow	$0.079Sc^{0.35}Re^{0.7}$	$Re < 2300$	$d_e = \frac{4 \times \text{cross section area}}{\text{perimeter}}$
Flat plate in free area			
Laminar flow	$0.34Sc^{1/3}Re^{1/2}$	$Re < 5 \times 10^5$	$L = l, Re = \frac{lu}{\nu}$
Rotated cage			
Turbulent	NA	NA	$Re_{RC} = \frac{\omega r_{RC}^2}{\nu}$
Impinging Jet			
Region A (laminar)	$1.51Re^{0.5}Sc^{0.33} \left(\frac{H}{d}\right)^{-0.054}$	$Re < 2000$	$L = d, Re = \frac{du}{\nu}$
Region B (transition)	$1.12Re^{0.5}Sc^{0.33} \left(\frac{H}{d}\right)^{-0.054}$	$4000 < Re < 16\,000$	$d$ : nozzle diameter $u$ : flow velocity in nozzle

Source: DIN 50920, Corrosion of Metals, Part I. *Corrosion Testing in Flowing Liquids; General*, (in German); Beuth Verlag: Berlin, Germany, 1985; Papavinasam, S.; Revie, R.W.; Attard, M.; Demoz, A.; Sun, H.; Donini, J.C.; Michaelian, K. In *Inhibitor Selection for Internal Corrosion Control of Pipelines: 1. Laboratory Methodologies*, Corrosion'99; NACE International: Houston, TX, 1999; Paper no. 1; Poulson, B. *Corros. Sci.* **1983**, 23(4), 391–430; Poulson, B.; Robinson, R. *Corros. Sci.* **1986**, 26(4), 265–280.

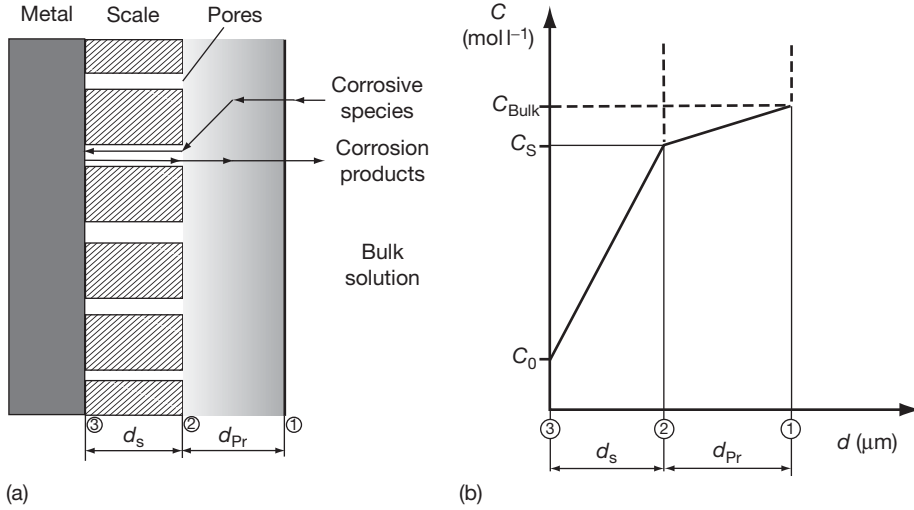


**Figure 11** (a) Corrosion process on scale-covered metal surfaces and (b) concentration gradient of electro-active species from the bulk solution to the metal surface.

where  $m_{Pr}$  is the mass transport rate in the Prandtl boundary layer ( $\text{mol m}^{-2} \text{s}^{-1}$ );  $m_s$  is the mass transport rate in the pores ( $\text{mol m}^{-2} \text{s}^{-1}$ );  $D$  is the diffusion coefficient of the electro-active species (i) under convective diffusion in the Prandtl layer ( $D_{Pr}$ ) and (ii) in the pores of the scale ( $D_s$ );  $c$ , the concentration ( $\text{mol m}^{-3}$ ) of the electro-active species (i) in the bulk ( $c_{\text{bulk}}$ ), (ii) at the entrance of the pores ( $c_s$ ), and (iii) at the metal surface ( $c_0$ ); and  $d_s$  is the thickness of the layer (m).

The kinetics of corrosion processes at scale-covered materials results from a combination of the following simplified partial processes:

1. Transport of corrosive species to the scale (eqn [26])<sup>9</sup>:

$$v_1 = k_1(c_{\text{bulk}} - c_s) \quad [26]$$

This process is controlled by the combination of convection and diffusion. The coefficient  $k_1$  is flow-dependent.

2. Transport of electro-active species through the pores of the scale (eqn [27]):

$$v_2 = k_2(c_{\text{bulk}} - c_s) \quad [27]$$

This process is mainly controlled by diffusion. The coefficient  $k_2$  is strongly dependent on the pore structure of the scale but is not flow-dependent.

3. Interface reaction (eqn [28]):

$$v_3 = k_3 c_0 \quad [28]$$

The coefficient  $k_3$  is potential-dependent, but not flow-dependent. Under conditions of stationary mass transport rate, the following equations are valid (eqns [29] and [30]):

$$c_{\text{bulk}} = (c_{\text{bulk}} - c_s) + (c_s - c_0) + c_0 \quad [29]$$

or

$$v = v_1 + v_2 + v_3 \quad [30]$$

Regarding eqns [26]–[28] and the assumptions in eqns [29] and [30], the following relationships will result (eqns [31] and [32]):

$$c_{\text{bulk}} = \frac{v}{k_1} + \frac{v}{k_2} + \frac{v}{k_3} \quad [31]$$

with

$$v = v_1 + v_2 + v_3 = \frac{c_{\text{bulk}}}{(1/k_1) + (1/k_2) + (1/k_3)} \quad [32]$$

where  $v$  is the corrosion rate ( $\text{g m}^{-2} \text{h}$ );  $k_1$ ,  $k_2$ ,  $k_3$  are coefficients, where only  $k_1$  is flow-dependent.  $k_2$  and  $k_3$  depend on the pore structure (size, density). As the scale is growing and the porosity is decreasing, that is,  $k_2 \rightarrow 0$ , the flow velocity effect will decrease.

The rate of scale formation,  $\Phi_{\text{scale}}$ , is proportional to the mass conversion rate (corrosion rate) according to eqn [33]:

$$\Phi_{\text{scale}} = K_1 v \quad [33]$$

The rate of scale destruction is influenced by the flow intensity, which is expressed mostly in terms of wall shear stress,  $\tau_w$  (eqn [34]):



$$\Phi_{\text{destruct}} = K_2 \tau_w^a \quad [34]$$

The proportionality factor,  $K_2$ , is mainly influenced by the binding forces between the particles (e.g., crystallites) forming the scale and the adhesion between scale and base material. The exponent,  $a$ , relates to the flow pattern and the contribution of erosion and cavitation. For a dynamic equilibrium ( $\Phi_{\text{scale}} = \Phi_{\text{destruct}}$ ), it follows that

$$K_1 v = K_2 \tau_w^a \quad [35]$$

$$v = \frac{K_2}{K_1} \tau_w^a = K_3 \tau_w^a \quad [36]$$

These equations (eqns [35] and [36]) describe the relation between the mass conversion rate (corrosion rate) and the flow intensity, expressed in terms of wall shear stress,  $\tau_w$ . The proportionality factor,  $K_3$ , describes the density of the scale, its porosity, the binding forces between the particles forming the scale, and finally its fracture stress.<sup>30–32</sup>

### 2.13.3.2.1 Scale destruction

For each corrosion system, a critical flow intensity  $I_{\text{crit}}$  can be identified above which the scale is destroyed and its protectiveness is lost (Figure 12). The corrosion rate increases abruptly and finally becomes purely mass transport controlled according to the boundary conditions of a scale-free system.<sup>25,30</sup>

The classic mechanism of scale destruction above the critical flow intensity is sketched in Figure 13. It is assumed that near-wall microturbulences cause local thinning of the scale, which locally becomes porous and finally is completely carried away by the flow. Once a scale-free, unprotected local surface area has formed, the local flow intensity prevents the

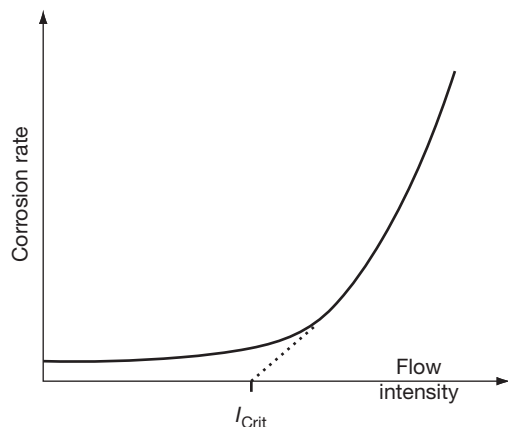


**Figure 12** Dependence of corrosion rate on flow intensity.

reformation of the protective scale, and local penetrations start producing the characteristic pattern of FILC. While it is possible that the scale is destroyed particle by particle and crystal by crystal during interaction with the flowing media, more recent observations revealed that scales of oxides, carbonates, phosphates, and sulfides rather crack and spall.<sup>33,34</sup> Figures 14 and 15 give examples of iron carbonate and iron sulfide scales from which parts of the scales experienced cracking and spalling. The fracture stresses of such scales have been measured<sup>33–35</sup> and range in the order of 75–720 MPa for iron carbonate scale from CO<sub>2</sub> corrosion of steel and 50–150 MPa for iron sulfides from H<sub>2</sub>S corrosion of steel. The fracture stresses are influenced by the porosity and thickness of the scale and increase dramatically when formed in the presence of effective corrosion inhibitors.<sup>36,37</sup> Figure 16 shows the failure mode diagram of corrosion-produced iron carbonate scales in the absence and presence of corrosion inhibitor. The corrosion inhibitor decreases the scale thickness, and hence, increases the critical fracture strain. The data were used to evaluate the surface fracture stress of iron carbonates (Figure 17).<sup>34,38</sup>

In view of the magnitude of the fracture stresses and adhesion strengths measured for corrosion product scales,<sup>34,35,38</sup> which number in the MPa range (Table 2), it appears difficult to understand that wall shear stresses in the range of 10–100 Pa (technical systems) or at maximum up to 10<sup>3</sup>–10<sup>4</sup> Pa (extreme local flow intensities) can cause cracking and spalling of scales.

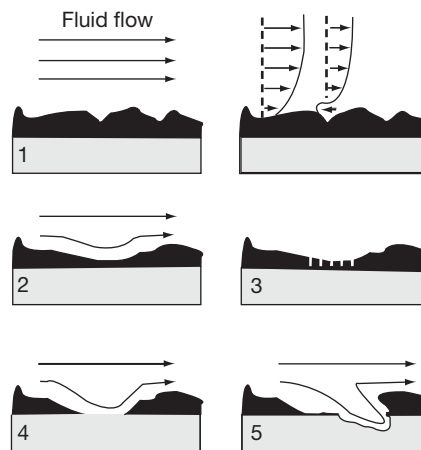
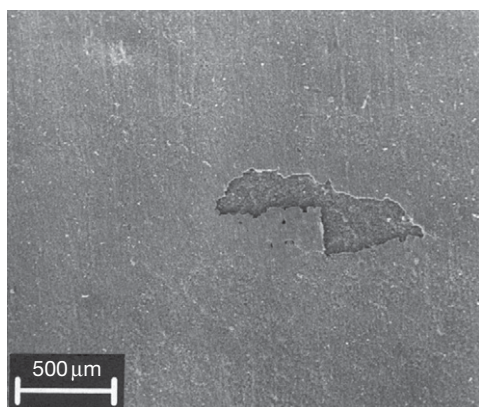
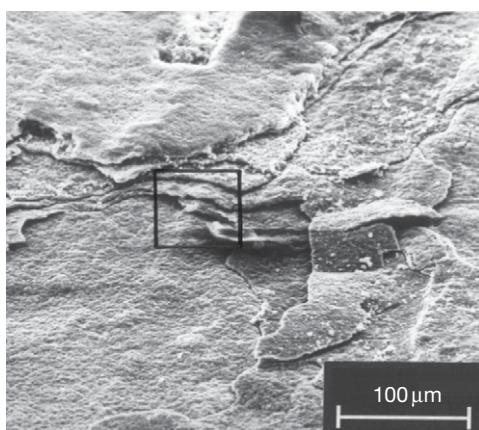


**Figure 13** Classic mechanism for initiation of FILC. Reproduced from Pini, G.; Weber, J. *Technische Rundschau Sulzer* (in German) **1979**, 2, 69.



Carbonate scale

**Figure 14** Cracking and spalling of iron carbonate scale during flow experiments. Reproduced from Schmitt, G.; Mueller, M.; Papenfuss, M.; Strobel-Effertz, E. In *Understanding Localized CO<sub>2</sub> Corrosion of Carbon Steel from Physical Properties of Iron Carbonate Scales*, Corrosion'99; NACE International: Houston, TX, 1999; Paper no. 38.



Sulfide scale

**Figure 15** Cracking and spalling of iron sulfide scale during flow experiments. Reproduced from Schmitt, G.; Bosch, C.; Pankoke, U.; Bruckhoff, W.; Siegmund, G. In *Evaluation of Critical Flow Intensities for FILC in Sour Gas Production*, Corrosion'98, NACE International: Houston, TX, 1998; Paper no. 46.

As it is clearly proven that flow-induced fluid dynamic forces can destroy protective layers, it is necessary to define such forces, which obviously act not parallel to the surface (as the wall shear stress) but rather perpendicular to the surface (Figure 18). This hydrodynamic force perpendicular to the wall shall be called hydrodynamic energy density,  $E_D$  (Pa). For the initiation of FILC, the hydrodynamic energy density

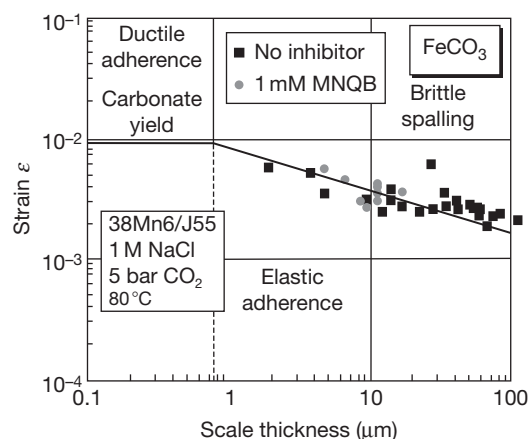


**Figure 16** Failure mode diagram of FeCO<sub>3</sub> (data from 4-point-bent-tests). Reproduced from Schmitt, G.; Mueller, M.; Papenfuss, M.; Strobel-Effertz, E. In *Understanding Localized CO<sub>2</sub> Corrosion of Carbon Steel from Physical Properties of Iron Carbonate Scales*, Corrosion'99; NACE International: Houston, TX, 1999; Paper no. 38.

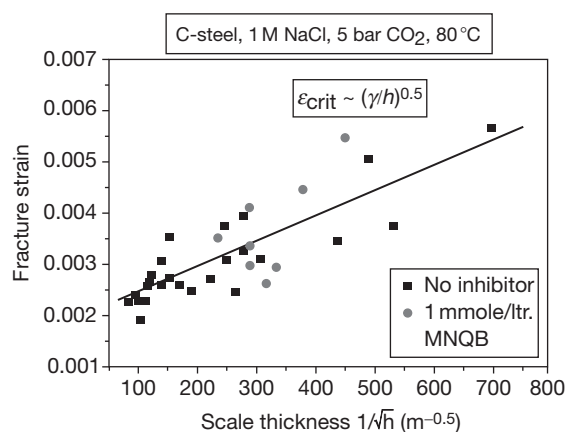


**Figure 17** Evaluation of surface fracture energy  $\gamma$  of iron carbonate scales from fracture strain measurements. Reproduced from Schmitt, G.; Bosch, C.; Mueller, M.; Siegmund, G. In *A Probabilistic Model for Flow Induced Localized Corrosion*, Corrosion'2000; NACE International: Houston, TX, 2000; Paper no. 49.

must be, at least locally, equal or greater than the fracture stress of the scales,  $\sigma_B$  (Pa) (eqn [37]).

$$E_D \geq \sigma_B \quad [37]$$

While the wall shear stress,  $\tau_w$  (Pa), has been clearly defined (eqn [14]) and measured for a long time, the hydrodynamic energy density,  $E_D$  (Pa), has been defined only recently<sup>39,40</sup> during investigations,

aiming at identifying the interaction energy of singly near-wall turbulence elements via microelectrochemical flow measurements.

This approach used the L  veque equation<sup>41</sup>(eqn [38]), which correlates the wall shear stress with the diffusion current density of a tracer redox system at a microelectrode (diameter 15–200   m) under defined flow conditions.

$$\tau_w = k[j_D]^3 \quad [38]$$

**Table 2** Comparison of system forces

Forces	Magnitude (Pa)
<i>Wall shear stress</i>	
Technical systems	10 <sup>0</sup> –10 <sup>2</sup>
Extreme flow intensities	10 <sup>3</sup> –10 <sup>4</sup>
Adherence of scales	10 <sup>6</sup> –10 <sup>7</sup>
<i>Fracture stress of scales</i>	
High porosity	10 <sup>7</sup> –10 <sup>8</sup>
Low porosity	10 <sup>8</sup> –10 <sup>9</sup>

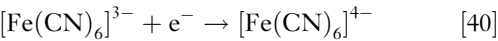
Source: Schmitt, G.; Mueller, M.; Papenfuss, M.; Strobel-Effertz, E. In *Understanding Localized CO<sub>2</sub> Corrosion of Carbon Steel from Physical Properties of Iron Carbonate Scales*, Corrosion'99; NACE International: Houston, TX, 1999; Paper no. 38; Schmitt, G.; Bosch, C.; Pankoke, U.; Bruckhoff, W.; Siegmund, G. In *Evaluation of Critical Flow Intensities for FILC in Sour Gas Production*, Corrosion'98; NACE International: Houston, TX, 1998; Paper no. 46; Schmitt, G.; Bosch, C.; Mueller, M.; Siegmund, G. In *A Probabilistic Model for Flow Induced Localized Corrosion*, Corrosion'2000; NACE International: Houston, TX, 2000; Paper no. 49; Schmitt, G.; Mueller, M. In *Critical Wall Shear Stresses in CO<sub>2</sub> Corrosion of Carbon Steel*, Corrosion'99; NACE International: Houston, TX, 1999; Paper no. 44.

with

$$k = \frac{\mu}{0.81^3 z^3 c_0 l^2 b^3 D^2} \quad [39]$$

where  $k$  is a constant depending on the dynamic viscosity,  $\mu$  (Pa s), of the electro-active species, the number  $z$  of electrons exchanged in the tracer redox system, the concentration,  $c_0$  (mol m<sup>−3</sup>), and diffusion coefficient,  $D$  (m<sup>2</sup> s<sup>−1</sup>), of the redox system, and the geometry of the microelectrode: the length,  $l$  (m), and the width,  $b$  (m).

The measured flow dependent parameter is  $j_D$  (A m<sup>−2</sup>), the diffusion current density of the mass transport-controlled redox reaction. Most commonly, the hexacyano-ferrate(II/III) redox system (eqn [40]) is used as tracer redox system in such measurements, because of its simple one-electron transfer and known system parameters.



Under turbulent flow conditions, the diffusion-controlled current densities,  $j_D(t)$ , measured at microelectrodes are fluctuating with time (Figure 19) due to fluctuations in the Nernst diffusion layer, which is caused by turbulence elements disturbing the viscous sublayer of the turbulent boundary layer. In order to evaluate the information contained in the noise of the diffusion current densities, the noise data (after subtraction of the DC part) have been subjected to a Wavelet transform, which yields the signal amplitudes in the frequency and time domain (Figure 20).

For each time resolution, an amplitude/frequency spectrum is obtained. It appears that at different times

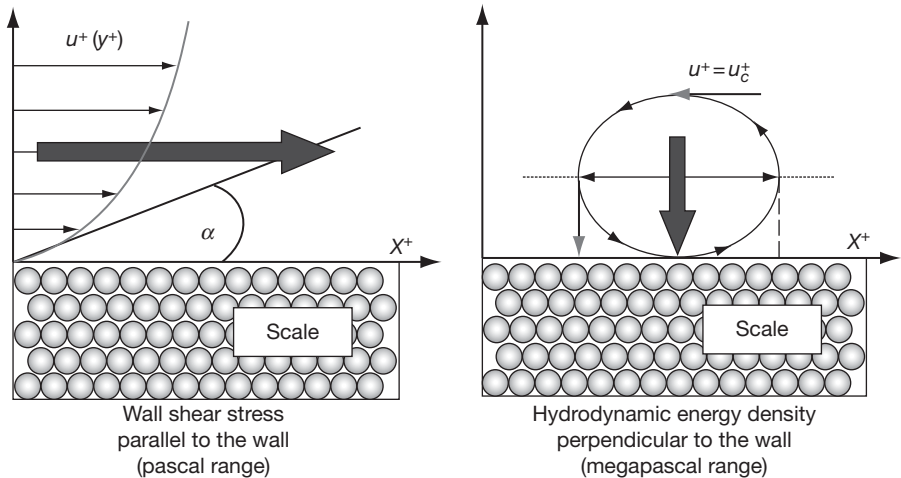


**Figure 18** Interaction of hydrodynamic forces with scales.

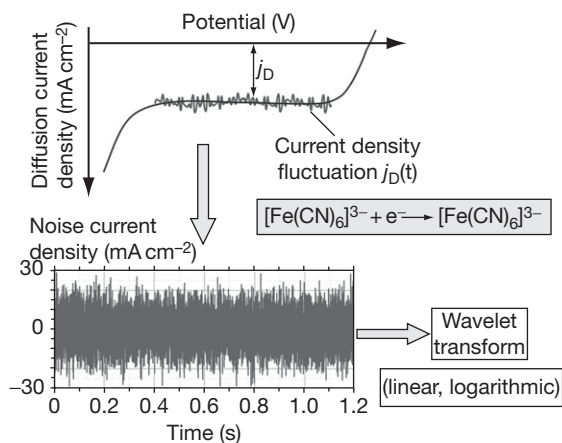


**Figure 19** Evaluation of diffusion controlled current density noises.

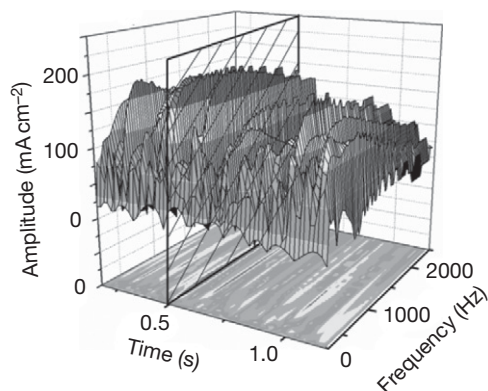


**Figure 20** Linear wavelet transform of current noise signal.

different amplitude fluctuations are encountered. Furthermore, no discrete frequency spectra are observed even at very high time resolution. Based on this, broad frequency range simulations have been performed with the aim of investigating whether the frequency spectra obtained can provoke high-intensity singularities, which significantly exceed the general noise level. The simulation was performed according to the algorithm expressed in eqn [41].<sup>39,40</sup>

$$j_D(t) = \sum_{\omega} A(\omega) \sin(\omega t)_{t_0} \quad [41]$$

At an arbitrarily chosen time (e.g., at the time 0.5 s, Figure 20), the corresponding amplitude/frequency spectrum is obtained (Figure 21). If all amplitudes at all frequencies in the selected frequency range are added for this specific time according to eqn [41], a singularity arises that represents the same singular

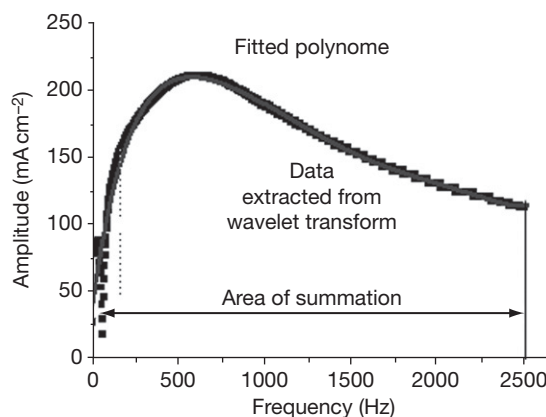


**Figure 21** Polynomial fitting (fourth grade) for time cut in Wavelet data.

situation when oceanic ‘freak waves’ (Rogue Waves)<sup>42,43</sup> are formed. In this case, a group of surface waves with different wave heights (amplitudes) travels in the same direction, but with different velocities. When all waves of this group are phased in for a single moment, that is, when they meet at the same time, a single wave is formed that piles up orders of magnitude higher than the average height of the group of waves. This singularity contains the power of all waves included, and the volume elements of this singular wave contain the highest energy density possible under these conditions.

In order to apply the same algorithm on the amplitude/frequency profile chosen in the example according to Figure 21, the amplitude/frequency function is fitted with a polynomial equation, which is inserted in eqn [41] for the amplitude  $A$ . The summing-up range shall include the relevant frequency range (e.g., 1–2500 Hz; see Figure 21). Within a unit time of 1 s, the summing-up procedure will be repeated in very small time steps, for example,  $1/250\,000$  s.<sup>39,40</sup>

The results of this calculation are presented in Figure 22. A singularity is found in the time range close to  $t = 1$  s, the amplitude of which exceeds the general noise level by orders of magnitude. Taking into account that the amplitudes represent diffusion current densities, the maximum in Figure 22 represents a fictive maximum diffusion current density in the order of  $500.000 \text{ mA cm}^{-2}$ . This phenomenon repeats at all unit time intervals.

The physical meaning of this maximum current density (called ‘freak current density’) is that, at the time of this ‘freak’ event, volume elements of the ‘freak wave’ in a near-wall turbulence element close



to the viscous sublayer is accelerated perpendicular toward the solid surface (Figure 23), reaching through the viscous sublayer down to the solid. If a microelectrode is present on the surface, the viscous sublayer, and hence, the Nernst diffusion layer is deformed for a very short time (in the range of milliseconds) to thicknesses that allow extreme high mass transport rates.

The energy density,  $E_D$ , of a freak wave volume element accelerated toward the surface can be

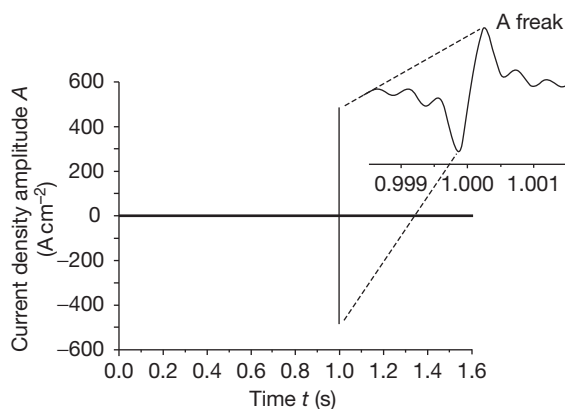


**Figure 22** Simulation of the noise current density based on Wavelet transform data. Phasing-in of amplitudes in the unit time region. Reproduced from Schmitt, G.; Werner, C.; Bakalli, M. In *Evaluation of Local Energy Densities in Disturbed Flow: A New Approach to Characterize Inhibitor Efficiencies to Mitigate Erosion Corrosion*, Proceedings of European Conference, EUROCORR'2004, Nice, France, Sept 12–16, 2004; European Federation of Corrosion, The Institute of Materials, London, 2004.

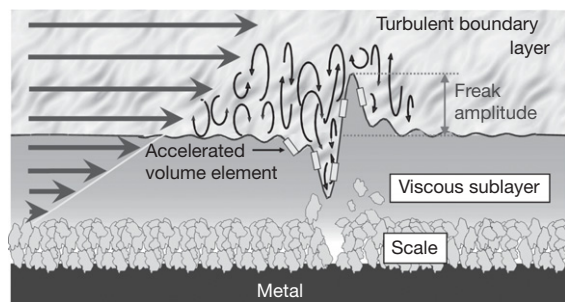


**Figure 23** Model of freak wave impact on protective scales. Reproduced from Schmitt, G.; Werner, C.; Bakalli, M. In *Evaluation of Local Energy Densities in Disturbed Flow: A New Approach to Characterize Inhibitor Efficiencies to Mitigate Erosion Corrosion*, Proceedings of European Conference, EUROCORR'2004, Nice, France, Sept 12–16, 2004; European Federation of Corrosion, The Institute of Materials, London, 2004.

expressed according to classic wave dynamics with eqn [42].<sup>44</sup>

$$w = \frac{dE}{dV} = \frac{1}{2} \rho A^2 \omega^2 \quad [42]$$

where  $w$  is energy density (Pa),  $\rho$  is density ( $\text{kg m}^{-3}$ ),  $A$  is wave amplitude (m), and  $\omega$  is wave frequency ( $\text{s}^{-1}$ ). Both energy density and wall shear stress have the unit Pascal. It is, therefore, assumed that the same relation used in the L  veque equation can be used to calculate the 'freak' energy density,  $E_D^F$ , from the freak current density,  $j_D^F$  (eqn [43]):

$$w_F = \tau_F = E_D^F = k_{\text{red/ox}} [j_D^F(t)]^3 \quad [43]$$

or by using eqn [41]:

$$\tau_F = E_D^F = k_{\text{red/ox}} \left( \sum_{\omega} A(\omega) \sin(\omega t_F) \right)^3 \quad [44]$$

$k_{\text{red/ox}}$  is a calibration factor which relates to the redox system used for measuring the diffusion-controlled current noise fluctuations. For the hexacyanoferrate redox system, this calibration factor has been evaluated to<sup>45</sup>:

$$k_{\text{red/ox}} = 2.14 \times 10^{-8} \quad (\text{Nm}^4 \text{A}^{-3}) \quad [45]$$

A freak amplitude of  $500\,000 \text{ mA cm}^{-2}$  (Figure 22) would then amount to a freak energy density (FED) of  $\sim 3 \text{ GPa}$ , which is by far enough to crack any protective scale. For comparison, the fracture stress of iron carbonate single crystals have been estimated to range in the order of  $1.4 \text{ GPa}$ , while fracture stresses of iron carbonate layers from  $\text{CO}_2$  corrosion of steel have been measured to range in the order of  $0.075\text{--}0.72 \text{ GPa}$ .<sup>34</sup>

Thus, the critical flow intensity, which can cause cracking and subsequent spalling of protective scales, and therefore, will initiate FILC that can be determined with eqn [43] using mass transfer-controlled current density noise data from flush-mounted microelectrodes with subsequent Wavelet transform treatment.

Based on this FED model, the effect of additives (inhibitors, drag reducers/flow improvers) on the prevention of FILC can easily be understood. Assuming that the critical fracture stress of an iron carbonate scale is  $200 \text{ MPa}$  (Figure 24), a FED of about  $3000 \text{ MPa}$  encountered under given flow conditions in a  $\text{CO}_2$  corrosion system is by far enough to crack the scale. Addition of  $1 \text{ mM C12-quat(PEGmod)}$  (polyethylenglycol-modified C12-quaternary alkyl-ammonium halide) reduces the FED significantly



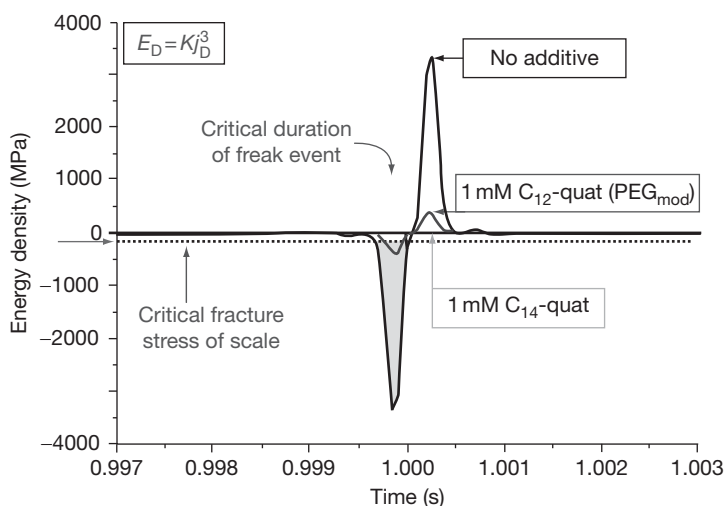


**Figure 24** Effect of additives on freak energy densities. Reproduced from Schmitt, G.; Werner, C.; Bakalli, M. In *Fluid Mechanical Interactions of Turbulent Flowing Liquids with the Wall – Revisited with a New Electrochemical Tool*, Corrosion'2005; NACE International: Houston, TX, 2005; Paper no. 344.

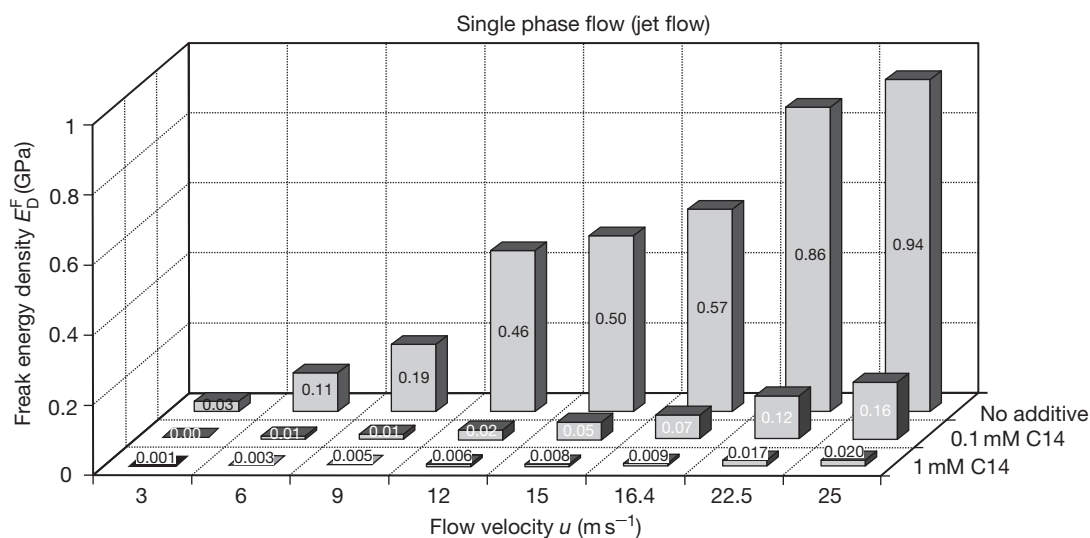


**Figure 25** Effect of flow velocity and C14-Quat concentration on maximum (freak) energy density in single phase flow. Reproduced from Schmitt, G.; Bakalli, M. In *Quantification of Maximum Energy Densities Between Flowing Liquids and Solid Walls – Effect of Flow Improving Additives*, Proceedings of European Conference, EUROCORR'2006, Maastricht, The Netherlands, Sept. 24–28, 2006; European Federation of Corrosion, The Institute of Materials: London, 2006.

under otherwise constant conditions, and cannot, however, reduce it below the fracture stress of the scale. Only with 1 mM C14-quat (tetradecyltrimethylammonium bromide) could the freak energy density be reduced significantly below the fracture stresses of the scale, and thus, the onset of FILC be prevented.<sup>39,40</sup>

The effect of C14-Quat concentrations at different jet nozzle velocities on the maximum (freak)

energy densities encountered in aqueous liquids with kinematic viscosities in the order of 1 mPa s is very significant and consistent and supports the FED approach.

#### 2.13.3.2.2 Corrosion intensity after scale destruction

After flow-induced local destruction of protective scales, layers, or films, the surface of the base material

is attacked like a bare metal surface, depending on the environmental conditions, that is, depending on the relative contributions of the corrosion and the erosion part to the rate of materials loss. These contributions can be estimated from the exponent  $a$  in eqn [46], which aims to relate the mass loss rate,  $w_{\text{er}}$ , in erosion corrosion to the bulk flow velocity,  $u_b$ .<sup>4</sup>

$$w_{\text{er}} \propto u_b^a \quad [46]$$

For mass control of the corrosion reaction, the exponent  $a$  is 0.33 for laminar flow and 0.8–1.0 for developed turbulent flow. It is zero for charge transfer (activation) control and somewhere between 0 and 1 under mixed control. The exponent  $a$  is 1 also for materials with passive films under activation/repassivation control. If erosive effects are contributing,  $a$  is  $>1$ , for example, 2–3 in the case of solid particle impingement or even 5–8 in the case of cavitation attack or liquid droplet impingement in high-speed gas flow.

While the bulk flow velocity in full bore flow or superficial flow velocities of the phases in question are readily measured and controlled, it is appreciated that, specifically, in disturbed flow, the flow characteristics in the direct vicinity of the wall are much more important than the bulk flow situation. Therefore, the trend is increasing to evaluate at least the existing wall shear stresses. However, bulk parameters are still used to characterize a given flow system.

### 2.13.3.3 Tools for Investigating Flow-Assisted Corrosion

A great variety of laboratory tools is available for investigating flow-assisted corrosion.<sup>46</sup> Lab tools used include (Figures 26–28)<sup>28,47–50</sup>:

- rotated probes;
- pipes and channels; and
- jet impingement.

Rotated probes with axial symmetry include the free-rotated disc, the disc in front of a wall, the free-rotated cylinder, and the coaxial cylinder (Figure 26).<sup>28</sup> Another set-up of rotated probes is the rotated cage (Figure 27), which contains coupons arranged between holders in such a way that the outer surface of the coupons forms parts of the surfaces of a rotating cylinder.<sup>48</sup>

The industrially prevalent type of flow exists in pipes. Therefore, flow studies with tubes/pipes and channels (Figure 26) are performed in those cases where a direct correlation with real flow situations in pipes is needed.

A very powerful tool is the impinging jet (Figure 28), which is specifically suitable to investigate susceptibilities of materials to FILC under severe flow intensities and to study the efficiency of corrosion mitigation, for example, the application of corrosion inhibitors under such conditions. A newly

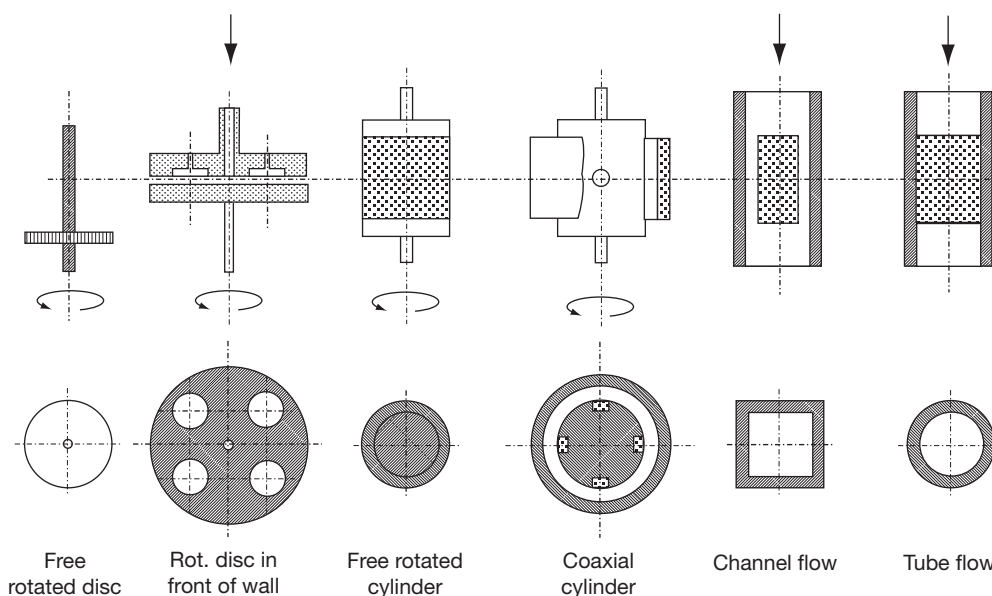


**Figure 26** Standardized tools to investigate flow-assisted corrosion. Reproduced from DIN 50920, Corrosion of Metals, Part I; In *Corrosion Testing in Flowing Liquids; General* (in German); Beuth Verlag: Berlin, Germany, 1985.

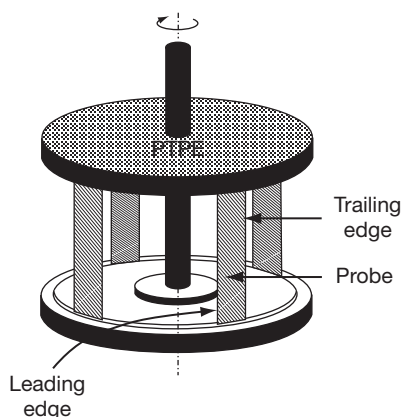


**Figure 27** Rotated cage arrangement. Reproduced from Schmitt, G.; Bruckhoff, W. In *Relevance of Laboratory Experiments for Investigation and Mitigation of Flow Induced Corrosion in Gas Production*, Corrosion'88; NACE International: Houston, TX, 1988; Paper no. 357.

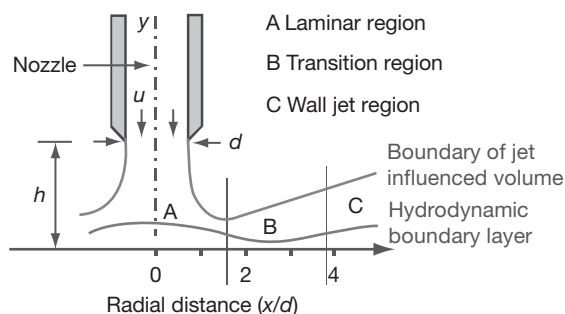


**Figure 28** Hydrodynamic flow pattern at the submerged impinging jet. Reproduced from Dawson, J. L.; Shih, C. C. In *Corrosion'90*; NACE International: Houston, TX, 1990; Paper no. 21.

developed modification is the gas-pulsed impinging jet (Figure 29), which can simulate the damaging effect of slug flow without using a slug flow loop.<sup>46</sup>

Mass transport relationships available for the different experimental tools are listed in Table 1. The merits and limitations of each tool are discussed in the literature.<sup>46</sup> Here, the authors clearly differentiate between corrosion experiments (where corrosion rates are directly calculated from time and surface related mass loss measurements and where localized corrosion can be observed by visual inspection of the corroded specimens) and electrochemical experiments, which may give information on corrosion rates as well, but should rather be used for mechanistic investigations, specifically to determine the nature of rate-determining steps in corrosion mechanisms.

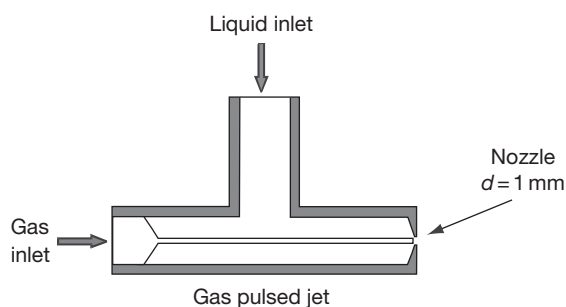


**Figure 29** Gas-pulsed impinging jet. Reproduced from Schmitt, G.; Bakalli, M. In *A Critical Review of Measuring Techniques for Corrosion Rates under Flow Conditions*, Corrosion'2006; NACE International: Houston, TX, 2006; Paper no. 593.

### 2.13.3.3.1 Rotating disc electrode

The rotating disc electrode (RDE) is preferentially used to investigate mass transport phenomena in laminar flow conditions. According to the Levich equation (eqn [47]),<sup>51</sup> the mass transport rate,  $w$ , in a mass transport-controlled system is constant over the disk surface and proportional to the square root of the angular velocity,  $\omega$ , of the disc:

$$w = k\sqrt{\omega} \quad [47]$$

where  $w$  is the mass transport rate, for example, expressed in terms of mass loss rates ( $\text{g m}^{-2} \text{h}^{-1}$ ),  $\omega$  is the angular velocity in radian per second, and  $k$  is the constant, containing the diffusion coefficient,  $D$ , of the rate-determining diffusing species ( $\text{m}^2 \text{s}^{-1}$ ), its concentration,  $C_{\text{bulk}}$ , in the bulk solution ( $\text{mol m}^{-3}$ ), and the kinematic viscosity,  $\nu$ , of the solution investigated ( $\text{m}^2 \text{s}^{-1}$ ) (eqn [48]).

$$k = 0.6205 D^{2/3} \nu^{-1/6} C_{\text{bulk}} \quad [48]$$

The mass transport rate can also be studied electrochemically. In the case of mass transport control, the diffusion-limited current density measured at a rotated disc electrode is proportional to the square root of the angular velocity,  $\omega$  (eqn [49]):

$$j_D = 0.6205 n F D^{0.66} \nu^{-0.167} \omega^{0.5} C_{\text{bulk}} \quad [49]$$

with the number of electrons  $n$  exchanged in the specific electrode reaction,  $F$  ( $96485 \text{ C mol}^{-1}$ ), and the other parameters as defined earlier.

A graph of  $j_D$  versus  $\sqrt{\omega}$  or  $w$  versus  $\sqrt{\omega}$  (Figure 30) should give a straight line going through the origin if the electrode reaction in question is purely

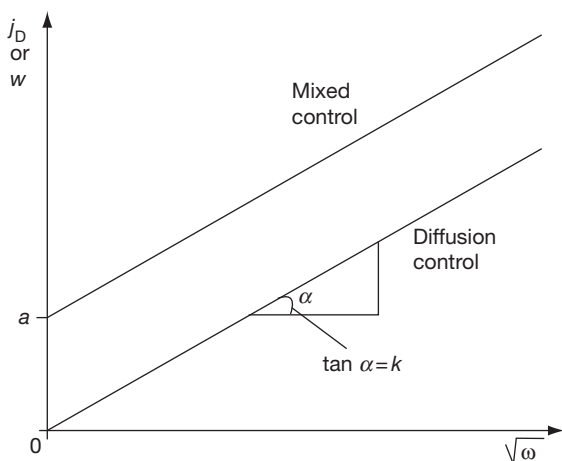


**Figure 30** Levich plot for diffusion controlled and mixed controlled corrosion rate at rotated disc.

diffusion controlled. If the straight line cuts the ordinate according to the equation  $w = a + k\sqrt{\omega}$ , there are either experimental problems (e.g., shaft wobbling, formation of vortices, entrainment of gas bubbles, etc.) or there is an additional electrode reaction involved that is not diffusion limited. From the slope of the straight line in the  $j_D$  versus  $\sqrt{\omega}$  diagram, the diffusion coefficient of the species determining the electrode reaction can be measured very accurately (eqn [49]). The flow pattern at the surface of the rotated disc can be described in terms of dimensionless parameters (Table 1).

#### 2.13.3.3.2 Rotating cylinder electrode

The rotating cylinder electrode (RCE) has the advantage that the complete flow regime from laminar to turbulent can be tested in the same arrangement. Three flow regimes can be differentiated<sup>52,53</sup>:

1. Laminar flow at low rotational speeds of the cylinder (the velocity profile is tangential).
2. Laminar flow superimposed with some turbulent vortices in radial and axial motion above a critical Taylor number ( $Ta = Re[(r_o - r_i)/r_i]$ , where  $Ta$  is dimensionless Taylor number,  $Re$  is Reynolds number,  $r_o$  is outer cylinder radius (static),  $r_i$  is inner cylinder radius (rotating)).
3. Fully turbulent flow above critical  $Re$ .

The transition from laminar to turbulent flow is  $\sim 200$ . Below this critical  $Re$ , the  $Sb$  is constant ( $Sb = 37$ ) and independent of  $Re$ .<sup>54</sup> At  $Re > 200$ , that is, in the turbulent region, the following dimensionless

equation can be used for the system rotating inner cylinder/static outer cylinder (eqn [50])<sup>55</sup>:

$$Sb = 0.00791 Re^{0.7} Sc^{0.356} \quad [50]$$

This equation correlates with data from mass transfer, heat transfer, and friction measurements at cylinders rotating in liquids. The flow intensity at the cylinder wall can be calculated from eqn [51]<sup>56</sup>:

$$\tau_w = 0.0791 Re^{-0.3} \rho r^2 \omega^2 \quad [51]$$

where  $\tau_w$  is the wall shear stress (Pa),  $\rho$  is the solution density ( $\text{kg m}^{-3}$ ),  $r$  is the cylinder radius (m), and  $\omega$  is the rotational speed ( $\text{s}^{-1}$ ).

Corrosion rate at a rotating cylinder is correlated with wall shear stresses using eqn [52].

$$w = a\tau^b \quad [52]$$

where  $w$  is the corrosion rate ( $\text{mm a}^{-1}$ ),  $\tau$  is the wall shear stress (Pa), and  $a$  and  $b$  are constants depending on solution parameters, chemistry, and corrosion product film and require definition.

#### 2.13.3.3.3 Rotating cage

The rotating cage (Figure 27) is commonly used to screen the susceptibility of materials to FILC and to evaluate corrosion inhibitors for their efficiency to prevent initiation of FILC. Due to the many experimental advantages and the successful use of rotated cage data in service, attempts have been made to quantify the flow intensities encountered at coupons rotated in the rotated cage. Equation [53] was developed as an approximation to estimate the wall shear stress at coupons in the rotated cage<sup>57,58</sup>:

$$\tau_{RC} = 0.0791 Re_{RC}^{-0.3} \rho r_{RC}^2 \omega^{2.3} \quad [53]$$

where  $\tau_{RC}$  is the wall shear stress in rotated cage (Pa),  $Re_{RC}$  is the Reynolds number of rotated cage ( $Re_{RC} = \omega r_{RC}^2 / \nu$ ),  $r_{RC}$  is the radius of the rotated cage (m),  $\rho$  is the solution density ( $\text{kg m}^{-3}$ ), and  $\omega$  is the rotational speed ( $\text{s}^{-1}$ ).

This equation is valid only for a certain geometry of the rotated cage with a certain number of coupons in a certain position. Comparison of critical wall shear stresses obtained from both rotated cage and impinging jet experiments for initiation of FILC in different corrosion systems revealed that the critical wall shear stresses calculated according to eqn [53] are about a factor of 2 higher than the values received via eqn [56] for the impinging jet.<sup>59</sup>

### 2.13.3.3.4 Pipe and channel flow

Flow experiments in tubes (pipes) or channels are rated as most service-related and most predictive, because the flow pattern in pipes and channels is encountered in technical plants and is well defined by equations for mass, heat, and momentum transfer. In the lab, pipe and channel flow experiments are generally performed in flow loops. The corrosion-relevant flow intensity at pipe or channel walls is best defined by the wall shear stress,  $\tau_w$ , which can be measured as a pressure drop  $\Delta P$  along a given length  $\Delta L$  of the pipe with a diameter  $d$  (eqn [54])<sup>13,15</sup>:

$$\tau_w = \left( \frac{\Delta P}{\Delta L} \right) \left( \frac{d}{4} \right) \quad [54]$$

The wall shear stress can also be measured electrochemically at microelectrodes flush mounted in pipe walls using the Léveque Equation (eqn [38]).<sup>41</sup>

For a microelectrode with disc-shaped electrode surface (diameter 15–60  $\mu\text{m}$ ) located in the region of highest turbulence of an impinging jet with a hexacyanoferrate (II/III) solution, a factor  $k = 3 \times 10^{-8} \text{ N m}^4 \text{ A}^{-3}$  (eqn [38]) was obtained.<sup>39,40</sup> This value is given here for orientation on its range of magnitude. The microelectrode approach offers the advantage of measuring local wall shear stresses also at sites of disturbed flow (at obstacles, steps, grooves, etc.). Microelectrodes with diameters in the range of the size of microturbulence elements (e.g.,  $\ll 100 \mu\text{m}$ ) allow the mapping of local wall shear stresses at surfaces with high lateral resolution.

The microelectrode approach was successfully used to quantify local and maximum fluid–wall interactions under slug flow intensities<sup>40,60</sup> expressed in terms of Froude numbers. The Froude number ( $Fr$ ) is defined according to eqn [55].<sup>61</sup>

$$Fr = \frac{u_t - u_f}{\sqrt{g \cdot h_{\text{eff}}}} \quad [55]$$

where  $u_t$  is the translational velocity of the slug front ( $\text{m s}^{-1}$ ),  $u_f$  is the average velocity of the liquid film ( $\text{m s}^{-1}$ ),  $g$  is the acceleration due to gravity ( $\text{m s}^{-2}$ ), and  $h_{\text{eff}}$  is the effective height of the liquid film (m). The higher the  $Fr$ , the higher the slug flow intensity.

### 2.13.3.3.5 Impinging jet

The impinging jet, specifically, the submerged impinging single phase jet (Figure 28), has proved its usefulness to investigate flow effects in corrosion systems, specifically, the initiation of FILC. The flow pattern at

the impinging surface has been extensively studied and several detailed mathematical expressions of the hydrodynamics are available.<sup>62,63</sup> On the impinging surface, three hydrodynamic regions can be differentiated (Figure 28): the stagnation region (region A), a region with high turbulence intensities (region B), and the wall jet region (region C). For region B, the wall shear stress can be calculated according to eqn [56]<sup>47,63</sup>:

$$\tau_w = 0.0447 \cdot \rho \cdot u_0^2 \cdot Re^{-0.182} \left( \frac{x}{d} \right)^{-2} \quad [56]$$

where  $\tau_w$  is the wall shear stress (Pa),  $\rho$  is the fluid density ( $\text{kg m}^{-3}$ ),  $d$  is the inner diameter of the jet nozzle (m),  $u_0$  is the fluid velocity at the front of the jet nozzle ( $\text{m s}^{-1}$ ),  $x$  is the radial distance from the jet nozzle center line (m),  $Re$  is based on the dimensions of the jet ( $Re = u_0 d / \nu$ ), and  $\nu$  is the kinematic viscosity ( $\text{m}^2 \text{ s}^{-1}$ ). With microelectrodes flush mounted into the impinging surface, local wall shear stresses can be measured using the Léveque equation (eqn [38]). The impinging jet is commonly used to test the efficiencies of additives (inhibitors, flow improvers) for preventing FILC.

A modification of the impinging single phase jet is the gas-pulsed jet, which has been developed to test under flow intensities exceeding slug flow conditions. Figure 31 shows the wavelet transform plots of the time-related frequency/amplitude distributions obtained at microelectrodes impinging with a gas pulsed jet (Figure 29)<sup>50,64</sup> at a constant superficial liquid velocity,  $v_{\text{SL}}$ , of  $12 \text{ m s}^{-1}$  (at the jet nozzle) and two different superficial gas velocities,  $v_{\text{SG}}$  (Figure 31(a):  $16 \text{ m s}^{-1}$  and Figure 31(b):  $22.3 \text{ m s}^{-1}$ ) at 1 gas pulse per second with a duration of 50 ms. The gas-pulsed impingement under conditions according to Figure 31(b) yielded responses with considerable intensities in a frequency range ( $>1000 \text{ Hz}$ ) clearly exceeding the typical range encountered in a moving slug flow at  $Fr = 13$  (Figure 31(c)). The gas-pulsed impinging jet is a new versatile and small-scale experimental device to test flow-improving additives and the efficiency of corrosion inhibitors under slug flow conditions.

Equations for determining wall shear stresses and limiting current densities in different experimental set-ups are collected in Table 3.

### 2.13.3.3.6 Maximum local flow intensities

In most technical corrosion systems, the materials applied are exposed to the flowing media with a scale-covered surface. This makes scale cracking



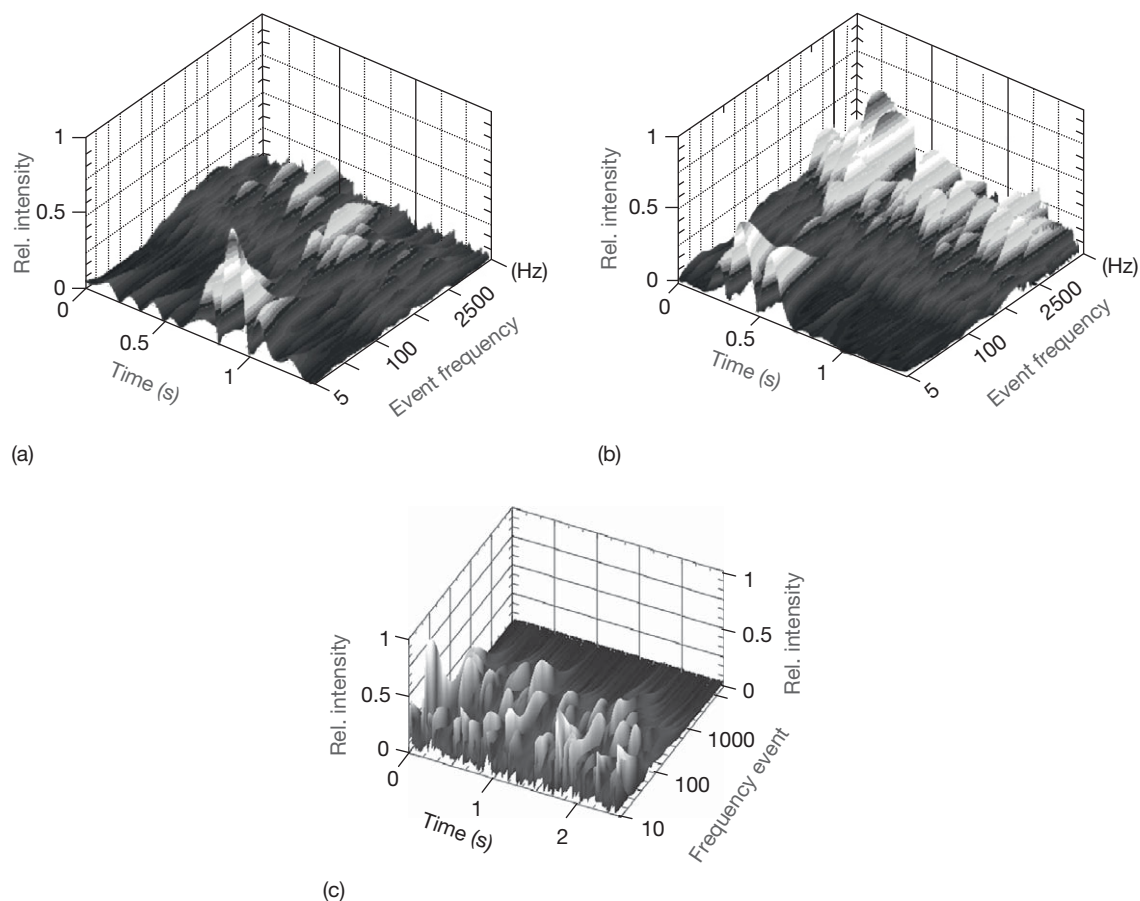


**Figure 31** Flow intensities at surface impinged with the gas-pulsed jet (a, b) and treated with a moving horizontal slug (c). Reproduced from Schmitt, G.; Al-Janabi, Y. T.; Plagemann, P.; Bakalli, M. *Can the Gas-Pulsed Impinging Jet Simulate Slug Flow?*, Proceedings of European Conference, EUROCORR'2003, Budapest, Hungary, Sept 28–Oct 2, 2003; European Federation of Corrosion, The Institute of Materials: London, 2003.

and spalling the prevailing mechanism of FILC initiation. The evaluation of critical flow intensities, therefore, needs the selection of the appropriate experimental tools, which at acceptable experimental flow conditions can produce maximum (local) flow energy densities high enough to overcome the fracture stresses of the scales involved. (Editor's note: The theory presented here is based on a hypothesis to explain the creation of mechanical forces that are sufficient to fracture and remove protective layers and scales. While the hypothesis is plausible and provides an explanation for a number of experimental flow results, further work is needed to confirm this hypothesis and to understand fully the mechanism of scale removal.)

The maximum (freak) energy densities encountered in different flow systems have been quantified by microelectrochemical current noise measurements

and subsequent Wavelet transform analysis using the algorithm outlined elsewhere in this volume. The maximum local flow intensities achieved with different experimental flow devices under single-phase and two-phase flow conditions are compared in [Figure 32](#) with a logarithmic scale for liquids with viscosities in the range of 0.8–1.1 mPa s (e.g., aqueous solutions with moderate concentrations of dissolved solids).<sup>39,40,45,67</sup>

The maximum energy densities encountered under slug flow conditions range from 3 MPa (Froude number 5:  $u_{SL} = 0.5 \text{ m s}^{-1}$ ;  $u_{SG} = 2.0 \text{ m s}^{-1}$ ) to 30 MPa (Froude number 13:  $u_{SL} = 1.5 \text{ m s}^{-1}$ ;  $u_{SG} = 6.0 \text{ m s}^{-1}$ ).<sup>39,40</sup> With the gas-pulsed impinging jet energy densities can easily be achieved, which are 60–110 times higher than under severe moving slug flow conditions ( $Fr = 13$ ).<sup>67</sup> It appears that the superficial liquid velocity ( $u_{SL}$ ) is more important for achieving high maximum (freak) energy densities than the superficial gas

**Table 3** Equations for determining wall shear stresses and limiting current densities with different lab tools for investigation of flow-assisted corrosion

Exp. tool	Method		Wall shear stress	Reference	Limiting current density	Reference
	Mass loss	Electrochemical				
Rotating disk	+	+	$\tau = 6.302 \nu \rho \omega \sqrt{Re}$	66	$j_D = 0.6205 nFD^{0.66} \nu^{-0.167} \omega^{0.5} C_{\text{bulk}}$	55
Rotating cylinder	+	+	$\tau_{\text{RCE}} = 0.0791 Re_c^{-0.3} \rho r_c^2 \omega^2$	58	$j_D = 0.0791 nFC_{\text{bulk}} (\omega r)^{0.7} (r/\nu)^{-0.3} (\nu/D)^{-0.644}$	17
Rotating cage	+	–	$\tau_{\text{RC}} = 0.0791 Re_{\text{RC}}^{-0.3} \rho r_{\text{RC}}^2 \omega^{2.3}$	30	$j_D^3 - k\tau$ , Léveque equation at microelectrodes under stationary condition	45, 70
			$\tau = \eta k (j^3 + 2k_c^2 dj/dt)$ (electrochemically)	67		
Flow loop	+	+	$\tau_w = (\Delta P/\Delta L)(d/4)$	13, 15	(a) Tube: $j_D = 0.320 nFD^{2/3} \nu^{-1/6} l^{-1/3} r^{-1/3} u^{0.33} C_{\text{bulk}}$ $l, r$ – tube electrode length and diameter, respectively	17, 71 17
					(b) Channel: $j_D = 0.81 nFD^{2/3} \nu^{-1/6} u^{1/2} C_{\text{bulk}}$	
Impinging jet	+	+	$\tau_w = 0.0447 \rho u_0^2 Re^{-0/182} x/d^{-2}$	65, 66	$j_D = knFC_{\text{bulk}} D^{2/3} \nu^{-1/6} (0/637u/r)^{1/2}$ $r$ : electrode radius	71
					$j_D^3 = k\tau$ , Levêque equation, stationary condition	70

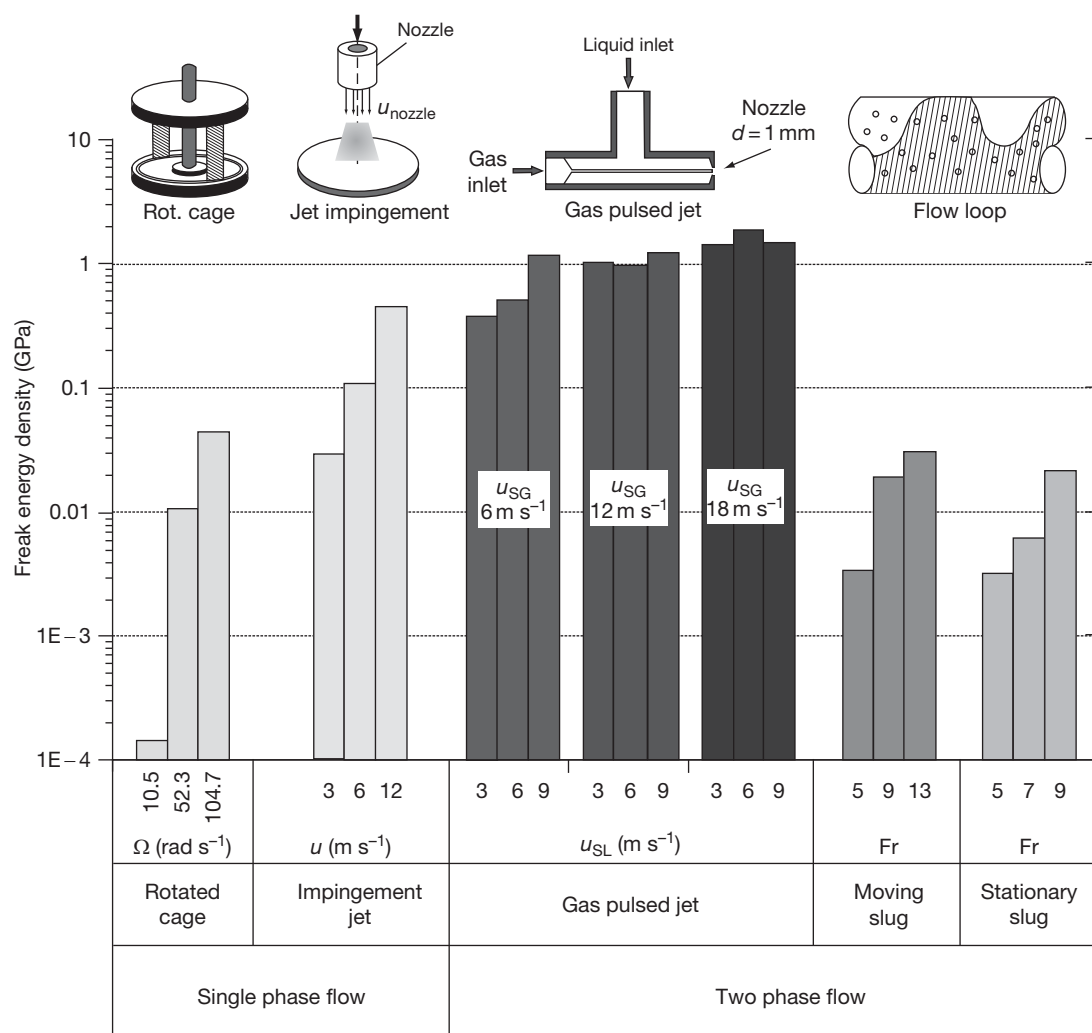


**Figure 32** Maximum (freak) flow intensities in different flow systems. Adapted from Schmitt, G.; Werner, C.; Bakalli, M. In *Evaluation of Local Energy Densities in Disturbed Flow: A New Approach to Characterize Inhibitor Efficiencies to Mitigate Erosion Corrosion*, Proceedings of European Conference, EUROCORR'2004, Nice, France, Sept 12–16, 2004, European Federation of Corrosion, The Institute of Materials: London, 2004; Schmitt, G.; Werner, C.; Bakalli, M. In *Fluid Mechanical Interactions of Turbulent Flowing Liquids with the Wall – Revisited with a New Electrochemical Tool*, Corrosion'2005; NACE International: Houston, TX, 2005; Paper no. 344; Schmitt, G.; Bakalli, M. In *Quantification of Maximum Energy Densities Between Flowing Liquids and Solid Walls – Effect of Flow Improving Additives*, Proceedings of European Conference, EUROCORR'2006, Maastricht, The Netherlands, Sept. 24–28, 2006, European Federation of Corrosion, The Institute of Materials: London, 2006; Nakoryakov, V. E.; Kashinsky, O. N.; Kozmenko, B. K. In *Measuring Techniques in Gas-Liquid Flows*; Delhay, J. M., Cognet, C., Eds.; Springer: Heidelberg, 1984; pp 695–721.

velocity. In the gas-pulsed jet approach, the gas pulse was injected once per second with duration of 50 ms. This indicates that the gas pulsed impinging jet can be used as an alternative experimental tool to the space-, time-, and cost-consuming slug flow loop, at least for screening purposes.

In single phase flow, the jet impingement allows the coverage of a wide range of maximum energy

densities under easily achieved flow conditions. Thus, with the usual jet cell geometries, jet nozzle velocities of 3 or 12 m s<sup>-1</sup> create maximum energy densities of about 28 and 940 MPa, respectively.<sup>45</sup> The flow intensities produced in the rotating cage are comparatively smaller. At angular velocities as low as 10.5 rad s<sup>-1</sup> (equivalent to 100 rpm), the maximum energy density reaches only 0.14 MPa. However, even at 100.5 rad s<sup>-1</sup>

(equivalent to 1000 rpm), the maximum local flow intensities amount only to 44 MPa. In view of the fracture stresses and adherence forces generally encountered for scales formed under corrosion conditions (Figure 33), the rotating cage finds its application for the quantification of critical flow conditions in the moderate range of flow intensities. The impinging jet and, even more, the gas-pulsed impinging jet can be used up to extreme fracture stresses of scales. Figure 33 demonstrates once more the importance of the FED approach for the understanding of the initiation step of FILC.

### 2.13.3.4 Erosion Corrosion and Cavitation Corrosion

Although FILC can occur already in single phase liquid flow, localized material attack very often is encountered in two-phase and multiphase flow. Thus, solid particle impact in a liquid or gas phase, liquid droplet impact in a gas phase, gas bubble impact in a liquid phase, and near-wall vapor bubble collapse in a liquid phase (Figure 8) can damage material surfaces with a mechanical and a corrosive contribution. While the material attack

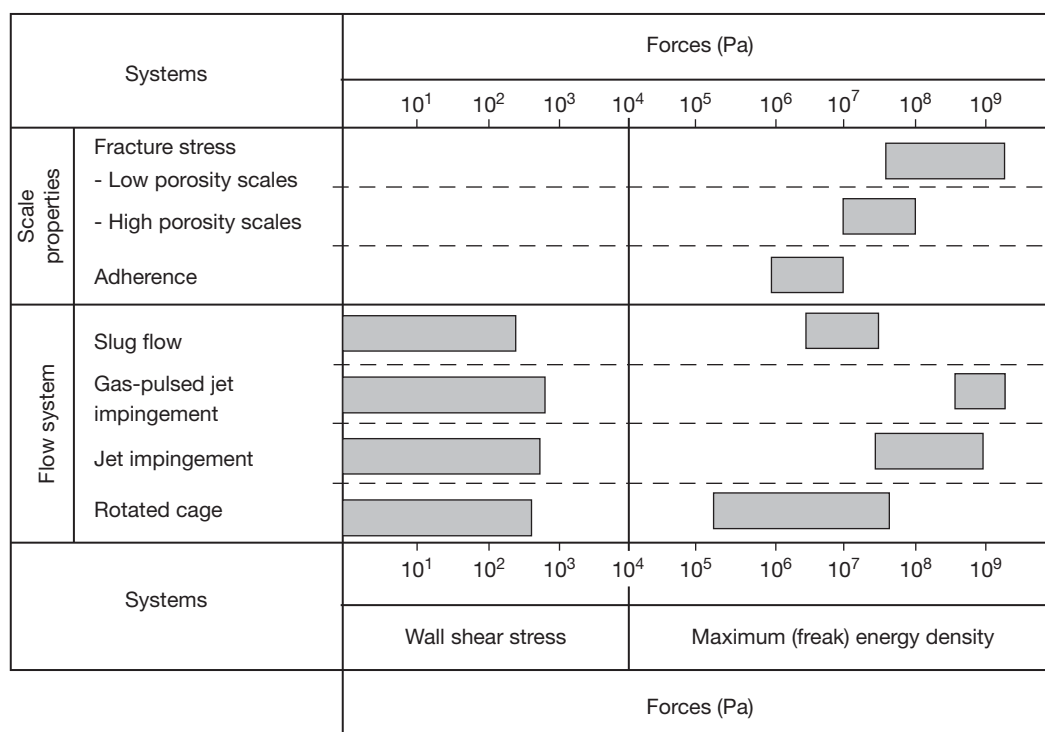


**Figure 33** Comparison of mechanical and hydrodynamic forces. Adapted from Schmitt, G.; Mueller, M.; Papenfuss, M.; Strobel-Effertz, E. In *Understanding Localized CO<sub>2</sub> Corrosion of Carbon Steel from Physical Properties of Iron Carbonate Scales*, Corrosion'99; NACE International: Houston, TX, 1999; Paper no. 38; Schmitt, G.; Bosch, C.; Pankoke, U.; Bruckhoff, W.; Siegmund, G. In *Evaluation of Critical Flow Intensities for FILC in Sour Gas Production*, Corrosion'98; NACE International: Houston, TX, 1998; Paper no. 46; Schmitt, G.; Bosch, C.; Mueller, M.; Siegmund, G. In *A Probabilistic Model for Flow Induced Localized Corrosion*, Corrosion'2000; NACE International: Houston, TX, 2000; Paper no. 49; Schmitt, G.; Mueller, M. In *Critical Wall Shear Stresses in CO<sub>2</sub> Corrosion of Carbon Steel*, Corrosion'99; NACE International: Houston, TX, 1999; Paper no. 44; Schmitt, G.; Werner, C.; Bakalli, M. In *Evaluation of Local Energy Densities in Disturbed Flow: A New Approach to Characterize Inhibitor Efficiencies to Mitigate Erosion Corrosion*, Proceedings of European Conference, EUROCORR'2004, Nice, France, Sept 12–16, 2004, European Federation of Corrosion, The Institute of Materials: London, 2004; Schmitt, G.; Werner, C.; Bakalli, M. In *Fluid Mechanical Interactions of Turbulent Flowing Liquids with the Wall – Revisited with a New Electrochemical Tool*, Corrosion'2005; NACE International: Houston, TX, 2005; Paper no. 344; Schmitt, G.; Bakalli, M. In *Quantification of Maximum Energy Densities Between Flowing Liquids and Solid Walls – Effect of Flow Improving Additives*, Proceedings of European Conference, EUROCORR'2006, Maastricht, The Netherlands, Sept. 24–28, 2006, European Federation of Corrosion, The Institute of Materials: London, 2006; Nakoryakov, V. E.; Kashinsky, O. N.; Kozmenko, B. K. In *Measuring Techniques in Gas–Liquid Flows*; Delhay, J. M., Cagnet, C., Eds.; Springer: Heidelberg, 1984; pp 695–721.

produced by the first three cases of impingement is generally termed erosion or – in the case of corrosive contributions – erosion corrosion, the material damage by near-wall vapor bubble collapse is called cavitation or – in the case of corrosive contributions – cavitation corrosion. Typical examples of erosion corrosion and cavitation corrosion are given in [Figures 34–36](#).

#### 2.13.3.4.1 Solid particle impingement

Solid particles entrained in a flowing liquid can damage a material surface if they impact with a kinetic energy above critical values, which are material specific and relate to the nature and properties of scales, layers, or films, and the base material. The effective kinetic impact energy of the particle depends on the impact velocity,  $u_p$ , the impact angle, and the particle density, size, shape, relative hardness, and micro-roughness. At low effective impact energies, the particle impact destroys only the scales, layers, or films and activates the surface for corrosion. In this case, the kinetics of reformation of the scales, layers, or films ('repassivation') play an essential role for the final corrosion rate. At higher impact energies, the particles may penetrate into the surface of the material and can even cut out solid particles.



**Figure 34** Erosion corrosion and cavitation corrosion at pump impeller (cast duplex stainless steel).

The rate of erosion corrosion,  $w_{er}$ , is, therefore, proportional to the kinetic energy of the impinging particle, that is, proportional to  $u_p^2$ , and the frequency of impacts, that is, proportional to  $u_p$ . Thus, in a first approximation, the rate of erosion corrosion correlates with the particle velocity in a cubic relationship (eqn [57])<sup>68</sup>:

$$W_{er} \propto u_p^3 \quad [57]$$

Under conditions where the effective particle impact energy is above the critical value for scale, layer, or film destruction, but below the critical value for eroding the base material, the rate of erosion corrosion, is generally, directly proportional to the particle velocity and its concentration.<sup>68</sup> Velocity exponents up to 3 are encountered under conditions of base material erosion.

Impact angle of particles in nondisturbed turbulent pipe flow are generally below  $5^\circ$ . However, under

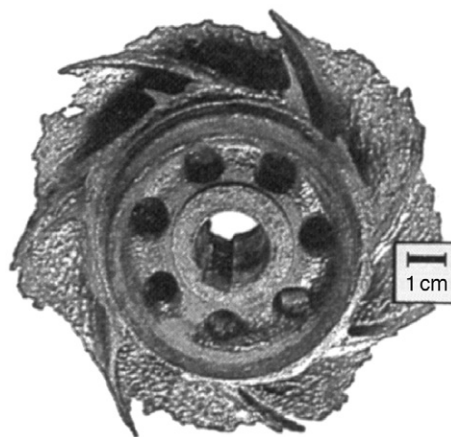


**Figure 35** Erosion corrosion and cavitation corrosion at pump impeller (cast carbon steel).

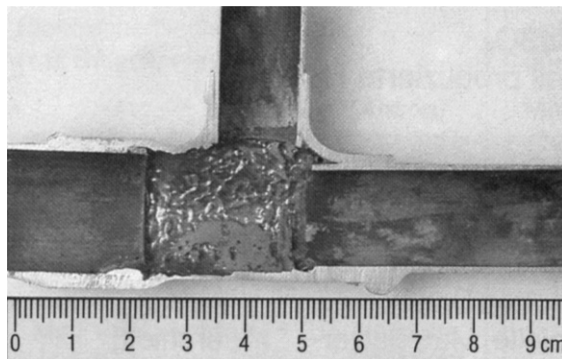


**Figure 36** Erosion corrosion at flow disturbance in copper pipe for cold tap water.



conditions of disturbed flow, a wide range of impact angle will be encountered. Erosion corrosion of brittle materials by slurries increases, with the particle impact angle reaching a maximum at an angle of  $90^\circ$ . Ductile materials develop erosion corrosion maxima at angles in the range of  $15^\circ$ – $50^\circ$ .<sup>23</sup> Erosive attack drops dramatically when the impacting particles are softer than the base material.

#### 2.13.3.4.2 Liquid droplet impingement

Liquid droplets entrained with fast-flowing gases or vapors can impinge on the surface with energy densities far higher than single phase or multiphase liquid flows. The result is the destruction of scales, layers, or films and, in severe cases, also the deformation of the surface to form discrete sharp-edged pits, which are gradually deepened by continued droplet impacts. Under such conditions, the mechanical part of erosion corrosion dominates, as in cavitation corrosion. However, the overall mass loss is still influenced by the kinetics of repassivation processes, which can be enhanced by appropriate alloying (e.g., increase of Mo content in stainless steels) or by the addition of powerful corrosion inhibitors. Liquid droplet impingement is encountered in low-pressure steam turbine blades operated with wet steam or in aircraft and helicopter rotors frequently operated in rain.

#### 2.13.3.4.3 Gas bubble impingement

Gas bubbles entrained with fast-flowing fluids can damage protective scales, layers, or films locally when the impact energy is high enough. This may happen specifically at sites of disturbed flow, for example, at the inlets of heat exchanger tubes where air bubbles can develop a substantial radial velocity component. The morphology of the damage starts with isolated ‘horseshoes,’ which grow together and finally cause considerable roughening of the surface.

#### 2.13.3.4.4 Cavitation

When gas bubbles implode in very close vicinity to the surface, they form very small liquid ‘microjets,’ which impact on the surface with flow velocities of up to  $100 \text{ m s}^{-1}$  (Figure 37). This is enough to destroy protective layers and deform the material in a way that particles of the base material are loosened and carried away. Cavitation bubbles with diameters  $<1 \text{ mm}$  can form at sites where, due to local turbulence conditions (e.g., at sharp diameter changes in pipes, edges of propellers, turbine blades or pump impellers), the hydrostatic pressure decreases for a

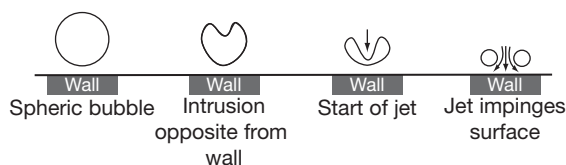


**Figure 37** Collapse (implosion) of cavitation bubble with jet formation.

very short time below the saturation vapor pressure of the liquid. The collapse occurs downstream in higher pressure regions. Vibrating solid surfaces, for example, the cooling water side of diesel engine cylinder liners or the shell-side of heat exchanger tubing, may also experience cavitation attack.

In cavitation corrosion, the mechanical contribution is by far dominating. However, the corrosion contribution should not be neglected, because it can be influenced significantly by enhancing the repassivation kinetics and by using appropriate corrosion inhibitors. Even the mechanical impact can be reduced by flow improving additives.

#### 2.13.3.5 Corrosion Control

The basic methods for controlling flow-assisted corrosion and/or FILC include design modifications, changing of flow regime, and the improvement of the fluid mechanical properties of the flowing medium.

##### 2.13.3.5.1 Fluid mechanics and design

The majority of failures by flow-assisted corrosion or FILC are based on poor design and ignorance of fluid mechanical principles. Therefore, flow related design is the most important corrosion control method. The design should primarily aim at reducing the flow velocity. The importance of this measure can be derived from eqn [46], which relates the corrosion rate to the flow velocity. For mass-controlled corrosion reactions, the exponent of the velocity term is 0.33 for laminar, but up to 1 for turbulent flow. For flow conditions causing destruction of protective scales, the exponent can reach values up to 3 and amount to 8 for cavitation conditions.

Rules of thumb have been empirically developed in different industries to estimate critical flow velocities, which should not be exceeded. One rule that was originally established in power generation for preventing FILC in pipes for wet steam has been adapted by the oil and gas industry as API-RP 14E,<sup>69,70</sup> where the critical flow velocity is inversely

proportional to the square root of the medium density (eqn [58]):

$$u_{\text{crit}} = C(\text{Density})^{-1/2} \quad [58]$$

With a proportionality factor  $C$  of 7.6 and the density given in ( $\text{kg m}^{-3}$ ), the critical flow velocity is obtained in ( $\text{m s}^{-1}$ ). The proportionality factor is 100 (for inhibited systems 150–200) if the density is given in  $\text{lbs ft}^{-3}$ . The critical velocity is then obtained in  $\text{ft s}^{-1}$ . For liquid flows, the proportionality factor of 100 is very conservative; for gas flows, it underestimates the potential for erosion. This holds also for information contained in BS EN ISO 13703:2001 developed for offshore applications.<sup>71</sup>

For plumbing systems in tap water distribution, critical flow velocities are given, for example, for steel ( $4 \text{ m s}^{-1}$ ) and copper ( $2 \text{ m s}^{-1}$ ). Many critical parameters have been worked out for materials in seawater application. Maximum design velocities for CuNi10 (UNS C70600) piping for seawater have been related to pipe diameters based on measurements of critical wall shear stresses (Figure 38).<sup>72</sup> For CuNi30 (UNS C71500)  $4.5 \text{ m s}^{-1}$  and CuNi10 (UNS C70600)  $3.6 \text{ m s}^{-1}$  have been accepted industrially as critical flow velocities in large piping for unpolluted seawater.<sup>72</sup> Critical flow parameters for copper alloy tubing are collected in Table 4.<sup>7,10</sup> In the chemical industry, the general (conservative) design rule is to prevent flow velocities above  $1.5 \text{ m s}^{-1}$ .

Proper design should also avoid abrupt changes in the flow system geometry, for example, steps, grooves, solder beads, rectangular elbows, tees, etc. Experience shows that flow disturbances as small as corrosion pits (even smaller than 1 mm) or burrings

on cut ends of tubing may create sufficient turbulence to destroy protective layers and initiate FILC. Erosion corrosion at heat exchanger tube-inlets can be solved by plastic inserts.

### 2.13.3.5.2 Materials selection

Selection of materials with higher resistance to flow-assisted corrosion is another option for corrosion control by design. Flow resistance is often related to the hardness of the material. Figure 39 gives an example for copper and copper alloys in tap water.<sup>73</sup> The erosion corrosion performance of valve materials in seawater is compared in Figure 40.<sup>74</sup> Material selection is also helpful for mitigating cavitation corrosion. Figure 41 presents different materials with respect to the relative material loss by cavitation.<sup>75</sup>

The variety of materials is great for application in fast-flowing media, for example, ferritic, ferritic-austenitic (duplex) and austenitic steels, NiCr alloys and titanium and its alloys (Figure 42).<sup>6</sup> To combat erosion corrosion by fluids containing solid particles, successful developments have been made with cast alloys and duplex steels. However, materials should not be selected only by their flow resistance, but also with consideration of susceptibility to localized corrosion such as pitting, which is a common problem with stainless steels and also nickel-base alloys, specifically in slow-flowing and stagnant media and under deposits. In these cases, decreasing the flow rate may not be the appropriate remedy for corrosion control.

In special applications, surface protection by metallic, organic, or ceramic coatings can be a solution to prevent FILC. The adhesion and mechanical stability of such protective layers is important.

### 2.13.3.5.3 Environment control

Environment control includes influencing the fluid chemistry and the fluid hydrodynamics (flow improvement).

Reducing the corrosivity of the flow system by removal or exclusion of corrosive components is surely an efficient step to control flow-assisted corrosion. An example would be the removal of oxygen from seawater or adjustment of pH. However, this is often not possible or not feasible. In these cases, the selection of appropriate additives can be very effective. Corrosion inhibitors are known to foster the formation of more flow-resistant protective scales with higher fracture stress, and hence, improve the resistance to FILC.

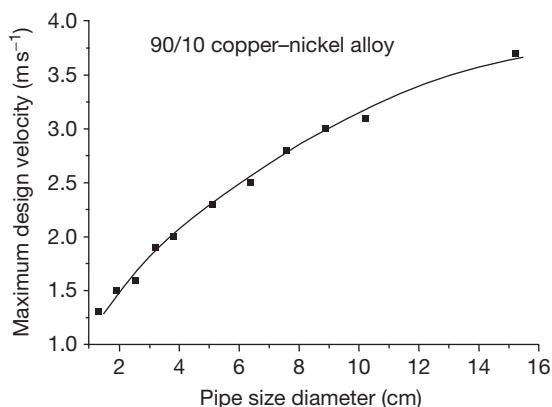


**Figure 38** Maximum design velocities of piping for seawater. Reproduced from Efrid, K. D. *Corrosion* **1973**, 33(1), 3–8.

**Table 4** Critical flow parameters for copper alloy tubing in seawater

Alloy	Critical shear stress ( $\text{N m}^{-2}$ )	Critical velocity in 25-mm tube ( $\text{m s}^{-1}$ )	Design velocity ( $\text{m s}^{-1}$ ) <sup>a</sup>	Maximum tubular design velocity ( $\text{m s}^{-1}$ )
Cupronickel with Cr	297	12.6	8.6	9
CuNi30	48	4.6	3.1	4.5–4.6
CuNi10	43	4.3	2.9	3–3.6
Al Bronze			2.7	
Arsenical A1 Brass	19	2.7	1.9	2.4
Inhibitory Admiralty				1.2–1.8
Low Si Bronze				0.9
P-deoxidized Copper	9.6	1.9	1.3	0.6–0.9

<sup>a</sup>Based on 50% critical shear stress.

Source: Roberge, P. In *Corrosion Testing Made Easy*; Syrett, B. C., Series, Eds.; NACE International: Houston, TX, 2004; Postlethwaite, J.; Nesic, S. In *Uhlig's Corrosion Handbook*, 2nd ed.; Winston Revie, R., Ed.; Wiley: New York, 2000; Chapter 15, pp 249–272; Smart, J.S., III *A Review of Erosion Corrosion in Oil and Gas Production*, Corrosion'90; NACE International: Houston, TX, 1990; Paper no. 10.

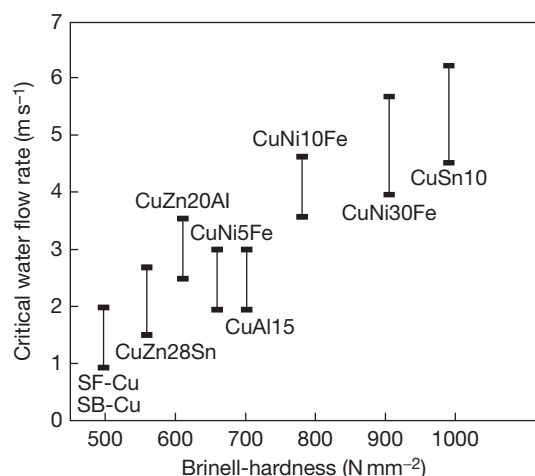


**Figure 39** Maximum allowable flow velocity for water in copper and copper alloy piping. Reproduced from Sick, H. *Werks. Korros.* **1972**, 23, 12.

The efficiency of corrosion inhibitors in flowing media depends on local flow intensities (**Figure 43(a)**). Above critical flow intensities, inhibitors lose their efficiency. Under these conditions, the material surface is subject to FILC. Critical flow intensities for FILC initiation can also depend on the inhibitor concentration (**Figure 43(b)**). This depends on the chemical structure of the active inhibitor compounds and the formulation of inhibitor packages.<sup>76</sup> Economical inhibition of corrosion under turbulent flow conditions needs functional additives that inhibit under high critical flow intensities at low concentrations.

In any case, the inhibitor concentration should be adjusted to the flow intensity and to a given target corrosion rate. With increasing flow intensity, an increase of the inhibitor concentration is likely to be necessary to reduce the corrosion rate below the target value. Failure prevention must be the primary goal for the selection of the type and the concentration of a functional additive.

However, reduction of the corrosion rate is not the only effect of corrosion inhibitors. They may also influence the flow dynamic property of the fluid, that is, by acting as a drag reducer, or in other words, as a flow improver.<sup>37</sup> There is literally no flow process that cannot be influenced by adding such 'drag-reducing agents' (DRA): frictional resistance of turbulent pipe and boundary layer flow is diminished; local energy losses at flow obstacles are reduced; the periodic formation of vortices in the flow field behind a cylinder experiences a shift to lower frequencies; resistance to laminar flow in porous media is increased; sedimentation and flocculation processes become accelerated; the efficiency of hydraulic transport of solids rises; the onset of cavitation starts at higher flow velocities and causes less damage to materials; flow noise becomes less intense. DRA have been suggested in various technical fields, for example, in industrial water distribution systems to reduce the pumping energy, in oil and gas transport as well as in hydraulic transport of solids (e.g., coal), to increase (e.g., double) the capacity of pipelines, in waste water pipe networks to reduce the residence time of waste water in sewers at peak loads, in ship technology to reduce the flow friction in order to increase the speed of ships (e.g., cut in half the

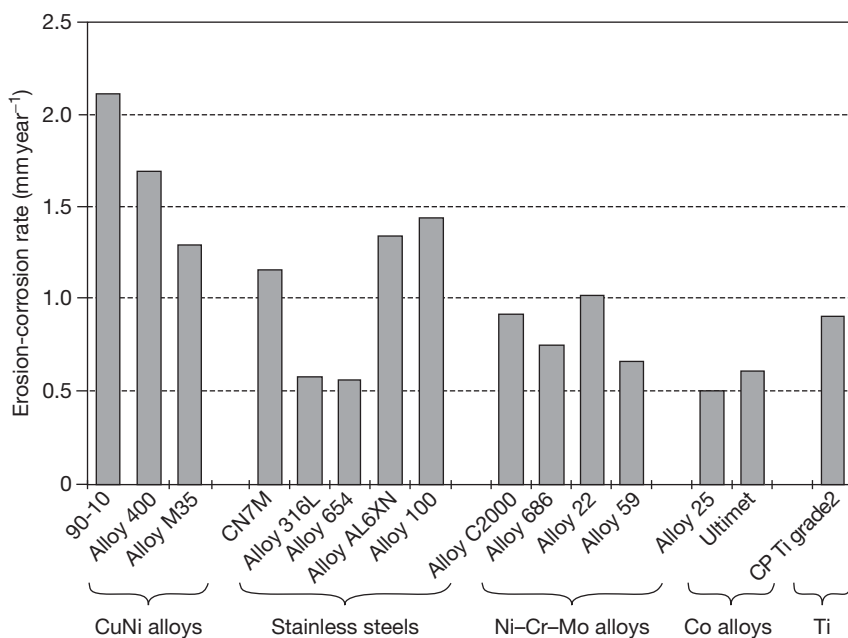


**Figure 40** Valve materials in seawater. Reproduced from Ruedisueli, R. L.; Aylor, D. M. In *Erosion Resistance Testing for Candidate Seawater Valve Materials*, Corrosion'2001; NACE International: Houston, TX, 2001; Paper no. 468.

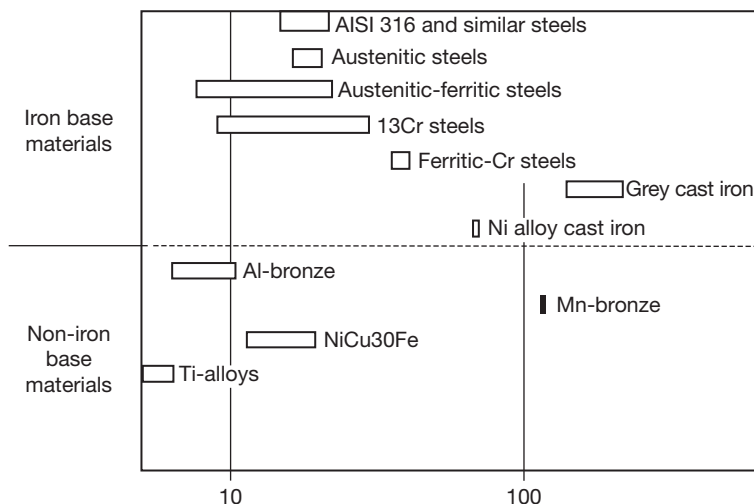


**Figure 41** Cavitation resistance of different pump materials. Reproduced from Weber, J. VDI-Report No. 365, 1980, pp 73.

drag of a super-tanker), in fire fighting technology to reduce the jet spray and increase the throwing distance of the water jet from the fire-hose nozzle (e.g. by a factor of 5).

DRAs include polymers like polyethylenoxides, polyacrylamides, guar gum, sodium carboxymethylcelluloses, and other polymers, which are, however, only effective at mole masses  $>10^6$  Da. Besides polymers, complex detergent mixtures, for example, an

equimolar mixture of cetyltrimethylammonium bromide (CTAB) and 1-naphthole, and other quaternary ammonium salts can exhibit drag-reducing activity.<sup>8,37,77</sup> However, these compounds become DRAs only above the critical micelle concentration (cmc). It is assumed that near-wall turbulence elements interact with the DRA under energy dissipation into internal energy by viscous actions. For polymers, this implies shear-induced

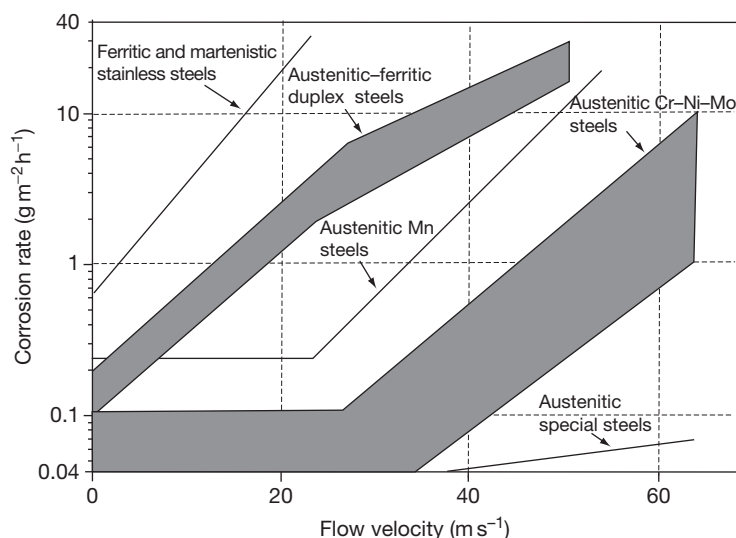


**Figure 42** Materials performance in media with high levels of hydrogen sulfide and low pH. Reproduced from Weber, J. *Br. Corros. J.* **1992**, 27(3), 193–199.

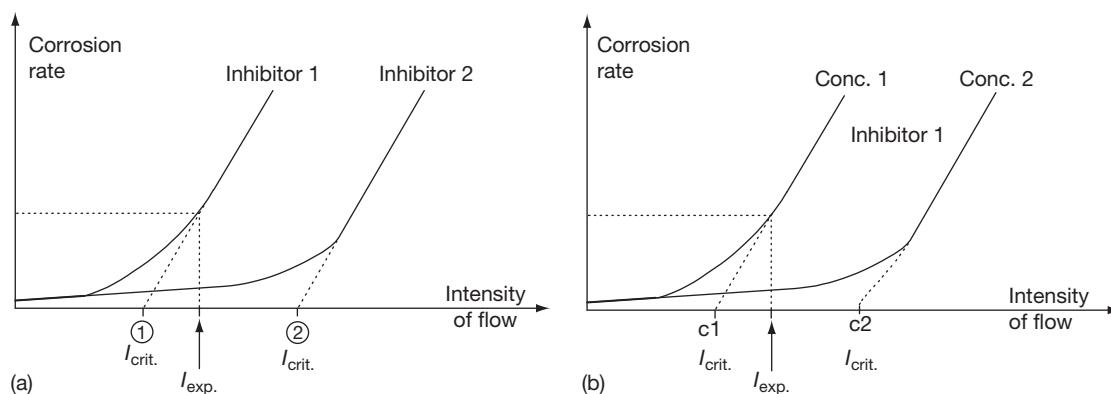


**Figure 43** Effect of flow intensity on corrosion inhibitor performance.

coil-stretch actions, for surface active compounds, shear-induced deformation of supramolecular micelle structures.

The effect of additives in two-phase flow systems was observed, for example, in brine/hydrocarbon mixtures under annular mist flow conditions with a superficial gas velocity of  $18.4 \text{ m s}^{-1}$  and a superficial liquid velocity of  $0.015 \text{ m s}^{-1}$  at  $80^\circ\text{C}$ , and  $\text{CO}_2$  partial pressures of up to 25 bar (Figure 44).<sup>8</sup> In the presence of  $1 \text{ mmol l}^{-1}$  additive, the relationship between wall shear stress and gas density ( $\text{CO}_2$  gas pressure) significantly deviated from the linear relationship measured in the absence of additives. The highest effect was measured at higher  $\text{CO}_2$  pressures

in the presence of higher molecular alkylamines. The wall shear stress could be reduced by a factor of 5, thus reducing the risk of FILC.<sup>8</sup>

The drag-reducing efficiency of C14-quat (tetradecyl-trimethylammonium bromide) in single phase flow and under slug flow conditions is exemplified in Figure 25 and Figure 45, respectively. The interaction intensity between aqueous liquids and the solid wall is, here, characterized by the maximum (freak) energy density of the flow system.

#### 2.13.3.5.4 Cathodic protection

Cathodic protection could also be used for corrosion control in flow systems. The application is, however,



limited because it is technically often difficult to provide the appropriate protection current inside pipes, valves, or pumps, by auxiliary anodes due to difficult geometries. Furthermore, evolution of hydrogen might be a problem, for example, in the case of titanium and other materials that could experience hydrogen embrittlement.

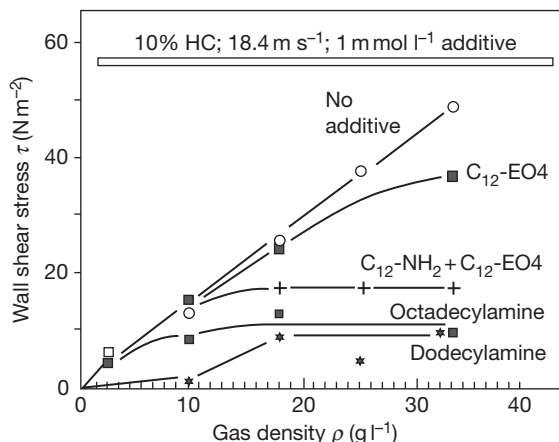


**Figure 44** Flow improving effect of additives in annular mist flow loop under CO<sub>2</sub> corrosion conditions. Reproduced from Schmitt, G.; Bücken, W. In *Effect of Corrosion Inhibitors and Surfactants on the Fluid Dynamic Properties of Multiphase Annular Mist Flow in CO<sub>2</sub> Corrosion Systems*, Corrosion'92; NACE International: Houston, TX, 1992; Paper no. 6.

### 2.13.3.5.5 Control of solid particle impingement attack

Control measures can include appropriate material selection, application of functional additives, and flow adjustment. Material selection often ends up with carbon steel because of its relatively low price. Erosive metal loss is then generally compensated by higher wall thicknesses. Stainless iron-base alloys exhibit satisfactory erosion corrosion resistance due to fast healing passive layers, but are more costly. The materials listed in Figure 40 in terms of corrosion resistance for valve applications also exhibit good resistance to erosion corrosion. However, material selection has to account also for the concentration and the nature (hardness) of the suspended solids. Criteria are different for flow systems with low concentrations of suspended particles and for slurries with high concentration of solids. High-Cr-Mo alloys with high carbon content (e.g., 20–28% Cr, 2% Mo, 2–2.5% C) have been successfully used for slurries with pH values down to 4. For more corrosive environments, the carbon content should be reduced. For sand and gravel pumps, Ni-hard alloys (4% Ni, 2% Cr) found successful application in the case of mildly corrosive conditions. Also rubber-lined pumps are an option for abrasive slurries (particle size >3 mm).

The literature reports on the excellent performance of Stellite (cast Co alloy) and silicon carbide during the handling of slurries with pumps. Figure 46

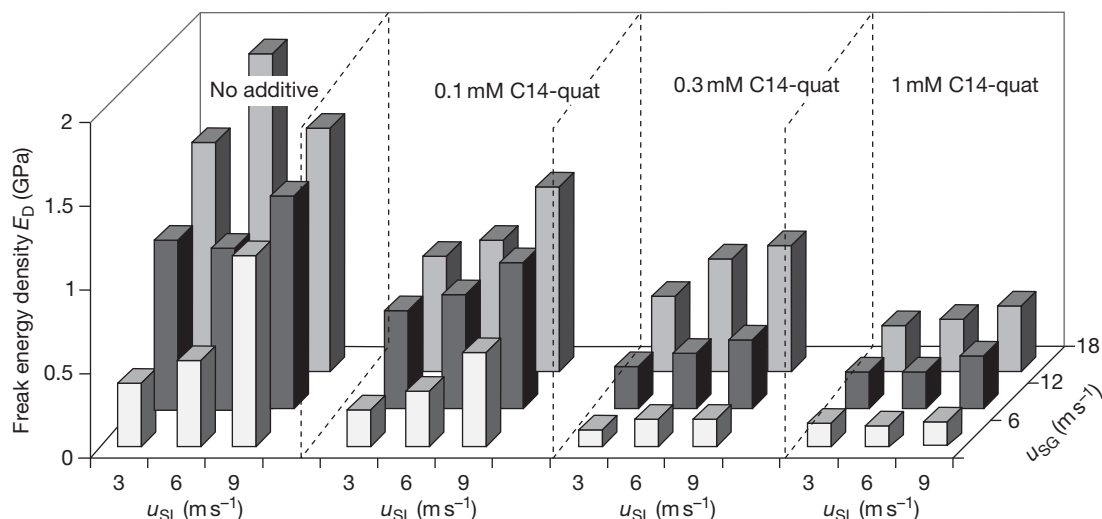


**Figure 45** Effect of flow velocity and C14-Quat concentration on the maximum (freak) energy density under slug flow conditions simulated via gas-pulsed impinging jet. Reproduced from Schmitt, G.; Bakalli, M.; Hoerstermeier, M. In *Contribution of Drag Reduction to the Performance of Corrosion Inhibitors in One- and Two-Phase Flow*, Corrosion'2007; NACE International: Houston, TX, 2007; Paper no. 615.

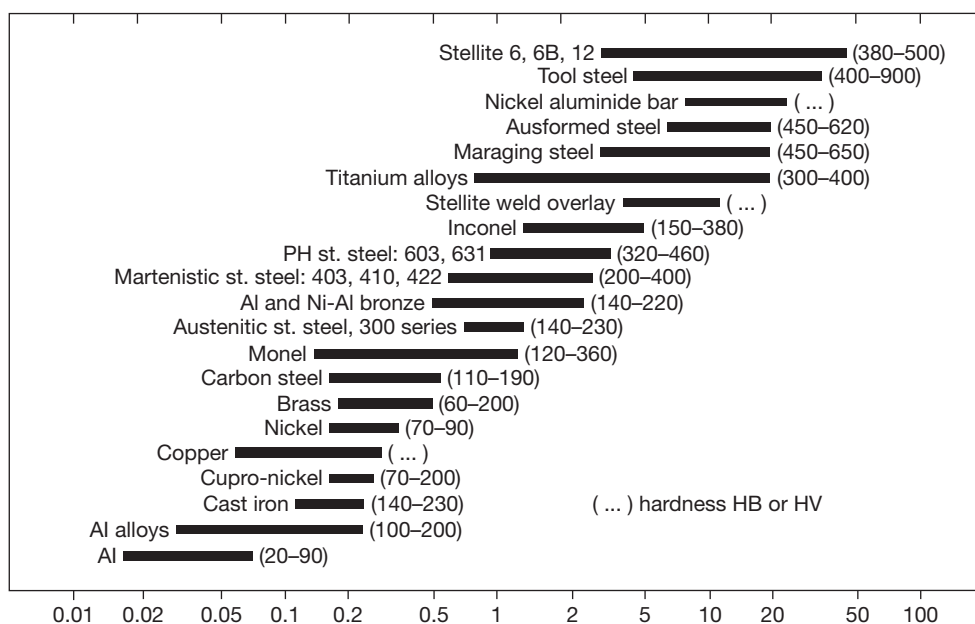


**Figure 46** Normalized erosion resistance of materials relative to 316 SS (HV 170). Reproduced from Heymann, F. J. In *ASM Metals Handbook: Friction, Wear and Lubrication Technology*, Vol. 18; ASM: Metals Park, OH, 1992; pp 221–232.

gives an overview of the erosion resistance of various materials, normalized relative to 316 austenitic stainless steel with a hardness of HV 170.<sup>78</sup> These data relate mainly to impingement and cavitation test results and fit together, because the mechanical part dominates in both failure mechanisms. However, these data should be taken only as a first orientation.

#### 2.13.3.5.6 Control of liquid droplet impingement attack and cavitation

Due to similar effects, failure prevention under conditions of liquid droplet impingement and cavitation can use similar options in material selection and flow control by design. **Figures 41 and 46** show a good orientation for material selection. However, polymeric materials, for example, high-density polyethylene (HDPE) or rubber, could also provide a solution. Flow control of droplet impingement should consider the droplet density (amount of impacting liquid), droplet size, and angle of droplet impact. Design options depend on the technical situation. If feasible, droplets should be removed, for example, by cyclones, or deflected with impingement plates. Guidelines for avoiding cavitation by proper design of pumps, orifices, valves, and elbows, are given in the literature.<sup>79</sup> They primarily aim at changing the hydraulic conditions. For centrifugal pumps, the major design parameter is the pressure difference between the total absolute pressure and the vapor

pressure at the pump suction. Corrosion inhibitors have been successful in reducing cavitation attack in cooling systems of diesel engines. Another option is to use flow-improving additives (superhigh molecular polymers, micellar aggregates).

#### 2.13.3.5.7 Predictive modelling

Computational fluid dynamics (CFD) methods have been successfully applied to predict flow fields and mass transfer rates for various system geometries in single phase and multiphase flow.<sup>80,81</sup> For fluids with entrained solid particles, the CFD procedure includes flow simulation, calculation of particle tracking, and assessment of erosion rates.<sup>81–87</sup> A comparison of results from different CFD approaches with experimental data indicates that CFD is a powerful tool in predicting erosion and erosion corrosion.<sup>86</sup>

## References

1. Heitz, E.; Weber, S.; Liebe, R. In *Erosion Corrosion and Erosion of Various Materials in High Velocity Flows Containing Particles*, Proceedings of Symposium on Flow-Induced Corrosion; Fundamental Studies and Industry Experience; Kennelley, K. J., Hausler, R. H., Silverman, D. C., Eds.; NACE: Houston, TX, 1991; pp 5:1–5:15.
2. Hausler, R. H.; Schmitt, G. *Hydrodynamic Flow Effects on Corrosion Inhibition*, Corrosion'2004; NACE International: Houston, TX, 2004; Paper no. 402.

3. Schmitt, G.; Gudde, T. *Local Mass Transport Coefficients and Local Wall Shear Stresses at Flow Disturbances*, Corrosion'95; NACE International: Houston, TX, 1995; Paper no. 102.
4. Schmitt, G. In *Flow Induced Localized Corrosion – A Challenge for Corrosion Inhibition in Oil and Gas Production*, Proceedings of the 15th Annual Conference Corrosion Problems in Industry, Alexandria, Egypt, Oct. 9–10, 1996; pp 1–15.
5. Schmitt, G.; Pankoke, U.; Bosch, C.; Gudde, T.; Strobel-Effertz, E.; Papenfuß, V.; Bruckhoff, W. In *Initiation of Flow Induced Localized Corrosion in Oil and Gas Production. Hydrodynamic Forces vs. Mechanical Properties of Corrosion Product Scales*, Proceedings of the 13th International Corrosion Congress, Melbourne, Australien, Nov. 25–29, 1996; Vol. 2, Paper no. 150.
6. Weber, J. *Br. Corros. J.* **1992**, 27(3), 193–199.
7. Roberge, P. In *Corrosion Testing Made Easy*; Syrett, B. C., Series, Eds.; NACE International: Houston, TX, 2004.
8. Schmitt, G.; Bücken, W. In *Effect of Corrosion Inhibitors and Surfactants on the Fluid Dynamic Properties of Multiphase Annular Mist Flow in CO<sub>2</sub> Corrosion Systems*, Corrosion'92; NACE International: Houston, TX, 1992; Paper no. 6.
9. Lotz, U. *Velocity Effects in Flow Induced Corrosion*, Corrosion'90; NACE International: Houston, TX, 1990; Paper no. 27.
10. Postlethwaite, J.; Nesic, S. In *Uhlig's Corrosion Handbook*, 2nd ed.; Winston Revie, R., Ed.; Wiley: New York, 2000; Chapter 15, pp 249–272.
11. Efid, K. D. In *Uhlig's Corrosion Handbook*, 2nd ed.; Winston Revie, R., Ed.; Wiley: New York, 2000; Chapter 14, pp 233–248.
12. Munson, B.; Young, D. F.; Okiishi, T. H. *Fundamentals of Fluid Mechanics*, 3rd ed.; Wiley: New York, 1988; Chapter 8, pp 459–549.
13. Oertel, H. *Prandtl-Führer durch die Strömungslehre*, (in German), 10th ed.; Carl Hanser: München Wien, 1990.
14. VDI-Wärmeatlas. Druckverlust bei der Strömung durch Rohre (in German) 8th ed.; VDI: Düsseldorf, Germany, 1997.
15. Schlichting, H.; Gersten, K. *Boundary Layer Theory*, 8th ed.; Springer-Verlag: Berlin, 2003.
16. Rathnasingham, R.; Breuer, K. S. *Phys. Fluids* **1997**, 9, 1867.
17. Štulík, K.; Pacakova, V. *Electroanalytical Measurements in Flowing Liquids*; Ellis Horwood: Chichester, 1986.
18. Davies, J. T. *Turbulence Phenomena*; Academic Press: New York, 1972; Chapter 2, pp 121–143.
19. Durst, F.; Jovanovic, J.; Sender, J. J. *Fluid Mech.* **1995**, 295, 305–335.
20. Nepomuceno, H. G.; Lueptow, R. M. *Phys. Fluids* **1997**, 9, 2732–2739.
21. Weisman, J. In *Handbook of Fluids in Motion*; Cheremisinoff, N. P., Gupta, R., Eds.; Ann Arbor Science Publishers: Ann Arbor, MI, 1983; pp 409–424.
22. Govier, G. W.; Aziz, K. *The Flow of Complex Mixtures in Pipes*; Van Nostrand Reinhold: New York, 1972; pp 324, 326, 506.
23. Heitz, E. In *Flow-Induced Corrosion: Fundamental Studies and Industry Experience*; Kennelley, K. J., Hausler, R. H., Silverman, D. C., Eds.; NACE International: Houston, TX, 1991; pp 1:1–1:29.
24. Schmitt, G.; Bruckhoff, W.; Faessler, K.; Blummel, G. In *Flow Loop versus Rotating Probes – Correlations Between Experimental Results and Service Applications*, Corrosion'90; NACE International: Houston, TX, 1990; Paper no. 23.
25. Lotz, U.; Heitz, E. *Werkst. Korros.* **1983**, 34, 454–461.
26. Deslouis, C. *Elec. Chim. Acta* **2003**, 48, 3279–3288.
27. Heinze, J. *Ber. Bunsengesellsch. Phys. Chem.* **1980**, 84, 785.
28. DIN 50920, Corrosion of Metals, Part I. *Corrosion Testing in Flowing Liquids; General*, (in German); Beuth Verlag: Berlin, Germany, 1985.
29. Newman, J. S. *Electrochemical Systems*; Prentice Hall: Englewood Cliffs, NJ, 1971.
30. Pini, G.; Weber, J. *Technische Rundschau Sulzer*, (in German) **1979**, 2, 69.
31. Epstein, N. In *Fouling in Heat Exchangers*; Proceedings of the 6th International Heat Transfer Conference, Toronto: Canada, 1978; p 235.
32. Schmitt, G.; Buecken, W.; Fanebust, R. *Corrosion* **1992**, 48(5), 431–440.
33. Schmitt, G.; Gudde, T.; Strobel-Effertz, E. In *Fracture Mechanical Properties of CO<sub>2</sub> Corrosion Product Scales and Their Relation to Localized Corrosion*, Corrosion'96; NACE International: Houston, TX, 1996; Paper no. 9.
34. Schmitt, G.; Mueller, M.; Papenfuss, M.; Strobel-Effertz, E. In *Understanding Localized CO<sub>2</sub> Corrosion of Carbon Steel from Physical Properties of Iron Carbonate Scales*, Corrosion'99; NACE International: Houston, TX, 1999; Paper no. 38.
35. Schmitt, G.; Bosch, C.; Pankoke, U.; Bruckhoff, W.; Siegmund, G. In *Evaluation of Critical Flow Intensities for FILC in Sour Gas Production*, Corrosion'98; NACE International: Houston, TX, 1998; Paper no. 46.
36. Schmitt, G.; Bosch, C.; Bauer, H.; Mueller, M. In *Modelling the Drag Reduction Effect of CO<sub>2</sub> Corrosion Inhibitors*, Corrosion'2000; NACE International: Houston, TX, 2000; Paper no. 2.
37. Schmitt, G. In *Drag Reduction – A Widely Neglected Property of Corrosion Inhibitors*, Proceedings of the 9th European Symposium Corrosion Inhibitors (9 SEIC), Ferrara/Italy, Ann. Univ. Ferrara, N.S., Sez. V, Suppl. no. 11, 2000; pp 1089–1122.
38. Schmitt, G.; Bosch, C.; Mueller, M.; Siegmund, G. In *A Probabilistic Model for Flow Induced Localized Corrosion*, Corrosion'2000; NACE International: Houston, TX, 2000; Paper no. 49.
39. Schmitt, G.; Werner, C.; Bakalli, M. In *Evaluation of Local Energy Densities in Disturbed Flow: A New Approach to Characterize Inhibitor Efficiencies to Mitigate Erosion Corrosion*, Proceedings of European Conference, EUROCORR'2004, Nice, France, Sept 12–16, 2004, European Federation of Corrosion, The Institute of Materials: London, 2004.
40. Schmitt, G.; Werner, C.; Bakalli, M. In *Fluid Mechanical Interactions of Turbulent Flowing Liquids with the Wall – Revisited with a New Electrochemical Tool*, Corrosion'2005; NACE International: Houston, TX, 2005; Paper no. 344.
41. Deslouis, C.; Tribollet, B.; Cromolet, R.; Vlachos, G. *La Houille Blanche*, (in French), **1987**, 6, 459–467.
42. Onorato, M.; Osborne, A. R.; Serio, M.; Bertone, S. *Phys. Rev. Lett.* **2001**, 25, 5831–5834.
43. Osborne, A. R.; Onorato, M.; Serio, M. *Phys. Lett. A* **2000**, 275, 386–393.
44. Hering, E.; Martin, R.; Stohrer, M. *Physic for Engineers*, 8th ed.; Springer-Verlag: Berlin, 2002; Chapter 5, pp 386–390.
45. Schmitt, G.; Bakalli, M. In *Quantification of Maximum Energy Densities Between Flowing Liquids and Solid Walls – Effect of Flow Improving Additives*, Proceedings of European Conference, EUROCORR'2006, Maastricht, The Netherlands, Sept. 24–28, 2006, European Federation of Corrosion, The Institute of Materials: London, 2006.
46. Schmitt, G.; Bakalli, M. In *A Critical Review of Measuring Techniques for Corrosion Rates under Flow Conditions*, Corrosion'2006; NACE International: Houston, TX, 2006; Paper no. 593.

47. Dawson, J. L.; Shih, C. C. *Corrosion*'90; NACE International: Houston, TX, 1990; Paper no. 21.
48. Schmitt, G.; Bruckhoff, W. In *Relevance of Laboratory Experiments for Investigation and Mitigation of Flow Induced Corrosion in Gas Production*, Corrosion'88; NACE International: Houston, TX, 1988; Paper no. 357.
49. Matsumura, M.; Oka, Y.; Okumoto, S.; Furaya, H. In *Jet-in-slit Test for Studing Erosion Corrosion, Laboratory Corrosion Tests and Standards*, ASTM STP 866; American Society for Testing and Materials: Philadelphia, PA, 1985; pp 358–372.
50. Schmitt, G.; Al-Janabi, Y. T.; Plagemann, P.; Bakalli, M. *Can the Gas-Pulsed Impinging Jet Simulate Slug Flow?* Proceedings of European Conference, EUROCORR'2003, Budapest, Hungary, Sept 28–Oct 2, 2003, European Federation of Corrosion, The Institute of Materials: London, 2003.
51. Levich, V. G. *Physicochemical Hydrodynamics*, Prentice-Hall: Englewood Cliffs, NJ, 1962.
52. Newman, J. S. *Electrochemical Systems*, Prentice Hall: Englewood Cliffs, NJ, 1973.
53. Mizushima, T. In *Advances in Heat Transfer*, Vol. 7; Irvine, T. F., Hartnett, J. P., Eds.; Academic Press: New York, 1971, pp 87–161.
54. Gabe, D. R. J. *Appl. Electrochem.* **1974**, *4*, 91–108.
55. Eisenberg, E.; Tobias, C. W.; Wilke, C. R. *J. Electrochem. Soc.* **1954**, *101*(6), 306–319.
56. Silverman, D. C. *Corrosion* **1984**, *40*(5), 220–226.
57. Papavinasam, S.; Revie, R. W.; Attard, M.; Demoz, A.; Sun, H.; Donini, J. C.; Michaelian, K. In *Inhibitor Selection for Internal Corrosion Control of Pipelines: 1. Laboratory Methodologies*, Corrosion'99; NACE International: Houston, TX, 1999; Paper no. 1.
58. ASTM G184, *Standard Practice for Evaluating and Qualifying Oilfield and Refinery Corrosion Inhibitors using the Rotating Cage*; ASTM: West Conshohocken, PA, 2005.
59. Schleich, W.; Feser, R.; Schmitt, G.; Haarmann, S.; Schnier, K. In *Effect of Seawater Chlorination on the Erosion Behaviour of CuNi 90/10*, Proceedings of European Conference, EUROCORR'2007, Freiburg, Germany, Sept 9–13, 2007, European Federation of Corrosion, The Institute of Materials: London, 2007.
60. Schmitt, G.; Bosch, C.; Plagemann, P.; Moeller, K. In *Local Wall Shear Stress Gradients in the Slug Flow regime – Effect of Hydrocarbon and Corrosion Inhibitor*, Corrosion'2002; NACE International: Houston, TX, 2002; Paper no. 224.
61. Jepson, W. P.; Zhou, S. In *Experimental Study of Multiphase Slug Flow Characteristics and their Effect on Corrosion in Pipelines*, Corrosion'92; NACE International: Houston, TX, 1992; Paper no. 81.
62. Giralt, F.; Trass, O. *Can. J. Chem. Eng.* **1975**, *53*, 505–511.
63. Giralt, F.; Trass, O. *Can. J. Chem. Eng.* **1976**, *54*, 148–155.
64. Schmitt, G.; Möller, K.; Werner, C.; Plagemann, P.; Deslouis, C.; Bosch, C.; Schöning, M. J.; Janabi, Y. T.; Belghazi, A. In *Microturbulence Intensities in Disturbed Flow Regimes Quantified by Micro-electrochemical Measurements*, Proceedings of the 53th Annual Meeting on International Society of Electrochemistry (ISE), Electrochemistry in Molecular and Microscopy Dimensions; Düsseldorf, Germany, Sept. 15–20, 2002.
65. Nakoryakov, V. E.; Kashinsky, O. N.; Kozmenko, B. K. In *Measuring Techniques in Gas–Liquid Flows*; Delhay, J. M., Cognet, C., Eds.; Springer: Heidelberg, 1984; pp 695–721.
66. Toth, K.; Štulík, K.; Kutner, W.; Feher, Z.; Lindner, A. *Pure Appl. Chem.* **2004**, *76*(6), 1119–1138.
67. Schmitt, G.; Bakalli, M.; Hoerstemeier, M. In *Contribution of Drag Reduction to the Performance of Corrosion Inhibitors in One- and Two-Phase Flow*, Corrosion'2007; NACE International: Houston, TX, 2007; Paper no. 615.
68. Lotz, U.; Postlethwaite, J. *Corros. Sci.* **1990**, *30*, 95.
69. API-RP 14E. *Recommended Practice for Design and Installation of Offshore Production Platform Piping Systems*, 5th revised ed.; American Petroleum Institute: Washington, DC, 2000.
70. Smart, J. S., III *A Review of Erosion Corrosion in Oil and Gas Production*, Corrosion'90; NACE International: Houston, TX, 1990; Paper no. 10.
71. BS EN ISO 13703. *Petroleum and Natural Gas Industries – Design and Installation of Piping Systems on Offshore Production Platforms*; 2001.
72. Efrid, K. D. *Corrosion* **1973**, *33*(1), 3–8.
73. Sick, H. *Werks. Korros.* **1972**, *23*, 12.
74. Ruedisueli, R. L.; Aylor, D. M. *Erosion Resistance Testing for Candidate Seawater Valve Materials*, Corrosion'2001; NACE International: Houston, TX, 2001; Paper no. 468.
75. Weber, J. VDI-Report No. 365.1980, 73.
76. Schmitt, G. In *Hydrodynamic Limitations of Corrosion Inhibitor Performance*, Proceedings of the 8th European Symposium on Corrosion Inhibitors (8 SEIC); Ferrara/Italy; Ann. Univ. Ferrara, N.S., Sez. V, Suppl. N.10., 1995; pp 1075–1099.
77. Schmitt, G. In *Corrosion Inhibitors in the Mirror of the Ferrara Conferences*, Proceedings of the 10th European Symposium on Corrosion Inhibitors (10 SEIC); Ferrara/Italy; Ann. Univ. Ferrara, N.S., Sez. V, Suppl. N.12, 2005.
78. Heymann, F. J. In *ASM Metals Handbook: Friction, Wear and Lubrication Technology*, Vol. 18; ASM: Metals Park, OH, 1992, pp 221–232.
79. Tullis, J. *Hydraulics of Pipelines: Pumps, Valves, Cavitation, Transients*; Wiley: New York, 1989; pp 59, 78.
80. Postlethwaite, J.; Nescic, S.; Adamopoulos, G.; Bergstrom, D. *J. Corros. Sci.* **1993**, *35*, 627.
81. Zeisel, H.; Durst, F. In *Computation of Erosion-Corrosion Processes in Separated Two-Phase Flows*, Proceedings of Symposium on Flow-induced Corrosion, Fundamental Studies and Industry Experience; Kennelley, K. J., Hausler, R. H., Silverman, D. C., Eds.; NACE International: Houston, TX, 1991; pp 9:1–9:21.
82. Wallace, M. S.; Peters, J. S.; Scanlon, T. J.; Dempster, W. M.; McCulloch, S.; Ogilvie, J. B. In *CFD-based Erosion Modelling of Multi-orifice Choke Valves*, Proceedings of 2000 ASME Fluids Engineering Summer Meeting; Boston, MA, 11–15 June, 2000; Paper No. FEDSM2000-11244.
83. Wallace, M. S. Ph.D. Thesis, University of Strathclyde, Glasgow, 2001.
84. Edwards, J. K. Ph.D. Thesis, The University of Tulsa, 2000.
85. Chen, X.; McLaury, B. S.; Shirazi, S. A. *Comput. Fluids* **2004**, *33*(10), 1251–1272.
86. Barton, N. A. Erosion in elbows in hydrocarbon production systems: Review document, HSE Report 15; TÜV NEL Ltd, Scotisch Enterprise Technology Park, East Kilbride, Glasgow, 2003.
87. Mazumder, Q. H.; Shirazi, S. A.; McLaury, B. S. In *A Mechanistic Model to Predict Sand Erosion in Multiphase Flow in Elbows Downstream of Vertical Pipes*, Corrosion'2004; NACE International: Houston, TX, 2004; Paper no. 662.

## 2.15 Tribocorrosion

**R. J. K. Wood**

School of Engineering Sciences, Lanchester Building, University of Southampton, Southampton SO17 1BJ, UK

© 2010 Elsevier B.V. All rights reserved.

<b>2.15.1</b>	<b>Introduction and Definitions</b>	1007
<b>2.15.2</b>	<b>Tribocorrosion Fundamentals</b>	1010
<b>2.15.2.1</b>	<b>Factors Affecting Tribocorrosion</b>	1010
2.15.2.1.1	Material parameters and composition	1010
2.15.2.1.2	Environment factors	1011
2.15.2.1.3	Friction	1014
<b>2.15.2.2</b>	<b>Corrosion and Associated Electrochemical Reactions</b>	1014
2.15.2.2.1	Tribofilms	1015
2.15.2.2.2	Depassivation and repassivation kinetics	1016
2.15.2.2.3	Critical velocity concept	1017
2.15.2.2.4	Flow corrosion	1019
<b>2.15.2.3</b>	<b>Wear Fundamentals</b>	1021
2.15.2.3.1	Solid particle erosion	1021
2.15.2.3.2	Cavitation erosion	1025
2.15.2.3.3	Abrasion	1028
<b>2.15.2.4</b>	<b>Experimental Techniques</b>	1028
<b>2.15.3</b>	<b>Tribocorrosion Mechanisms</b>	1028
<b>2.15.3.1</b>	<b>Mechanical–Electrochemical Interactions</b>	1029
2.15.3.1.1	Erosion-corrosion	1029
2.15.3.1.2	Abrasion-corrosion	1031
2.15.3.1.3	Sliding wear-corrosion	1033
<b>2.15.3.2</b>	<b>Wear-Corrosion Interactions</b>	1034
2.15.3.2.1	Mechanisms of enhanced surface degradation	1034
2.15.3.2.2	Erosion-corrosion models	1038
<b>2.15.4</b>	<b>Present and Future Applications of Tribocorrosion</b>	1043
<b>2.15.4.1</b>	<b>Chemical Mechanical Polishing (CMP)</b>	1043
<b>2.15.4.2</b>	<b>Erosion-Corrosion</b>	1044
<b>2.15.4.3</b>	<b>Biotribocorrosion</b>	1045
2.15.4.3.1	Dentistry	1045
2.15.4.3.2	Replacement joints	1046
<b>2.15.5</b>	<b>Conclusions</b>	1048
<b>References</b>		1048

### Abbreviations

**AISI** American Iron and Steel Institute  
**ASTM** American Society for Testing and Materials  
**BS** Bovine serum  
**CMP** Chemical mechanical polishing  
**CRA** Corrosion resistant alloy  
**CS** Carbon steel  
**DLC** Diamond-like carbon  
**ECN** Electrochemical noise  
**HVOF** High velocity oxy-fuel

**KE** Kinetic energy  
**NAB** Nickel aluminum bronze  
**OCP** Open circuit potential  
**PBS** Phosphate buffer solution  
**RCE** Rotating cylinder electrode  
**RDE** Rotating disc electrode  
**SEM** Scanning electron microscope  
**SF** Synovial fluid  
**SWR** Specific wear rate  
**UNS** Unified Numbering System  
**WJE** Wall jet electrode



**Symbols**

**a** Scaling constant  
**a<sub>j</sub>** Jump distance (m)  
**a<sub>r</sub>** Asperity radius (m)  
**A** Apparent area of contact (m<sup>2</sup>)  
**A<sub>a</sub>** Affected area (m<sup>2</sup>)  
**A<sub>crater</sub>** Crater area (m<sup>2</sup>)  
 **$\dot{A}_e$**  Normalized rate of active surface area (m<sup>2</sup>)  
**A<sub>r</sub>** Real contact area (m<sup>2</sup>)  
**A<sub>s</sub>** Surface area of electrode (m<sup>2</sup>)  
**A<sub>atom</sub>** Atomic weight of the dissolving metal during electrochemical corrosion  
**b<sub>a</sub>** Anodic Tafel slope (m V decade<sup>-1</sup>)  
**B** Migration kinetic constant ( $\alpha z F a_j / RT$ )  
**C** Pure static corrosion (mg s<sup>-1</sup>)  
**C<sub>b</sub>** Bulk concentration of species (M, mM, mol cm<sup>-3</sup>)  
**C<sub>eq</sub>** Concentration of soluble ferrous ions at equilibrium (M, mM, mol cm<sup>-3</sup>)  
**C<sub>k</sub>** Cutting characteristic velocity (m s<sup>-1</sup>)  
**C<sub>p</sub>** Weight of solids per unit volume (kg m<sup>-1</sup>)  
**C<sub>s</sub>** System constant  
**C<sub>v</sub>** Solids volume fraction  
**C'** Solid free corrosion rate (mg s<sup>-1</sup>)  
**C''** Corrosion rate under wear-corrosion (mg s<sup>-1</sup>)  
**C<sub>0</sub>** Concentration of species at electrode surface (M, mM, mol cm<sup>-3</sup>)  
**C<sub>1</sub>** Constant  
**C<sub>∞</sub>** Concentration of soluble ferrous ions in the bulk solution (M, mM, mol cm<sup>-3</sup>)  
**d** Particle diameter (m)  
**da/dn** Crack growth rate  
**D** Diffusion coefficient (cm<sup>2</sup> s<sup>-1</sup>) or average diameter of wear particle (m)  
**E** Pure erosion (mg s<sup>-1</sup>)  
**E<sub>applied</sub>** Applied potential (V)  
**E<sub>k</sub>** Kinetic energy of impacting particle (J)  
**E<sub>r</sub>** Erosion rate (mg kg<sup>-1</sup>)  
**f** Contact frequency between interacting surfaces  
**f<sub>a</sub>** Stripping coefficient  
**F** Faraday's constant (C or A s mol<sup>-1</sup>)  
**F<sub>f</sub>** Friction force (N)  
**g<sub>cfs</sub> ≡ (da/dn)<sub>cfs</sub>** Maximum attainable crack growth rate under given corrosion fatigue conditions  
**g<sub>r</sub> ≡ (da/dn)<sub>r</sub>** Average crack growth rate during the generation of a wear debris particle in the reference environment  
**g<sub>s</sub> ≡ (da/dn)<sub>s</sub>** Crack growth rate in the corrosive environment under sustained stresses  
**G** Constant  
**h** Wear depth (m)  
**H** Hardness (Vickers number)

**H\*** Hardness with anodic dissolution (Vickers number)  
**i** Current density (A m<sup>-2</sup>)  
**i<sub>a</sub>** Activation-controlled current density or anodic current density passing through apparent area (A m<sup>-2</sup>)  
**i<sub>act</sub>** Activated current density (A m<sup>-2</sup>)  
**i<sub>corr</sub>** Corrosion current density (A m<sup>-2</sup>)  
**i<sub>d</sub>** Diffusion-controlled current density (A m<sup>-2</sup>)  
**i<sub>r</sub>** Average anodic current density passing through the real area of contact (A m<sup>-2</sup>)  
**i<sub>p</sub>** Passive current density (A m<sup>-2</sup>)  
**i<sub>peak</sub>** Peak current density (A m<sup>-2</sup>)  
**i<sub>s</sub>** Anodic current density for steady state corrosion on the passivated metal surface (A m<sup>-2</sup>)  
**i<sub>th</sub>** Threshold current density to induce synergy (A m<sup>-2</sup>)  
**i<sub>u</sub>** Unaffected current density (A m<sup>-2</sup>)  
**I** Anodic or cathodic current (A)  
**I<sub>a</sub>** Anodic current (A)  
**I<sub>ac</sub>** Activated current (A)  
**I<sub>a,w</sub>** Anodic current under sliding wear (A)  
**I<sub>p</sub>** Passive current (A)  
**I<sub>peak</sub>** Peak current about I<sub>p</sub> (A)  
**I<sub>lim</sub>** Limiting current (A)  
**i<sub>0</sub>** Maximum current density on fresh metal surface at the start of repassivation (A m<sup>-2</sup>)  
**J** Flux of species (mol s<sup>-1</sup> cm<sup>-2</sup>)  
**k** Dimensionless wear coefficient  
**k<sub>a</sub>** Anodic rate constant  
**k<sub>B</sub>** Rate constant  
**k<sub>d</sub>** Generation rate of wear particles  
**k<sub>1</sub>** Forward reaction rate  
**k<sub>-1</sub>** Backward reaction rate  
**k<sub>m</sub>** Mass-transport coefficient (cm s<sup>-1</sup>)  
**K** Constant  
**K<sub>a</sub>** Proportionality constant  
**K<sub>w</sub>** Proportionality constant  
**K<sub>1</sub>** Constant  
**l** Length of wear track (m)  
**L** Characteristic length or sliding distance (m)  
**L<sub>ox</sub>** Oxide layer thickness (m)  
**m** Mass of oxide removal (kg) or energy exponent  
**M<sub>ox</sub>** Mass of oxide (kg)  
**M<sub>p</sub>** Mass of sand impacting the surface per unit time (kg s<sup>-1</sup>)  
**M<sub>R</sub>** Metal dissolution rate (mol cm<sup>-2</sup> s<sup>-1</sup>)  
**M<sub>w</sub>** Oxide molar mass (g mol<sup>-1</sup>)  
**n** Velocity ratio exponent or bulk concentration exponent or number of contact cycles at a given crack site  
**n<sub>r</sub>** Scratch overpotential (V)

**$N_c$**  Number of critical microcracks on a unit area of the wear surface that are ready to propagate

**$N_r$**  Number of critical microcracks that are ready to propagate to generate wear debris in a reference environment

**$\Delta N_c$**  Increment of the number of critical microcracks due to the presence of corrosion

**$N$**  Number of erodent impacts

**$N_{o,u}$**  Total number of surface sites available

**$N_u$**  Number of moles of oxide formed (mol)

**$p$**  Pressure (Pa)

**$q$**  Charge passed =  $\int I dt$  (C)

**$Q$**  Wear volume loss ( $m^3$ )

**$r_p$**  Particle radius (m)

**$R$**  Universal molar gas constant (= 8.31451  $J K^{-1} mol^{-1}$ )

**$Re$**  Reynolds number

**$R_f$**  Roundness factor for particle (value 0–1)

**$s$**  Total sliding distance (m)

**$S$**  Synergy (mg or  $mg s^{-1}$ )

**$Sc$**  Schmidt number

**$Sh$**  Sherwood number

**$t$**  Time (s)

**$t_c$**  Critical time for crack to propagate a length  $D$  (s)

**$t_0$**  Time to produce a scratch (s)

**$T$**  total wear or erosion loss ( $mg s^{-1}$ )

**$T_s$**  Temperature of the surface ( $^{\circ}C$ )

**$U$**  Free stream velocity or relative sliding velocity ( $m s^{-1}$ )

**$U_{cr}$**  Critical velocity for plastic deformation ( $m s^{-1}$ )

**$U_f$**  Velocity component normal to surface ( $m s^{-1}$ )

**$U_p$**  Particle velocity ( $m s^{-1}$ )

**$\nu^*$**  Friction velocity ( $=\sqrt{(\tau_w/\rho)}$ ) ( $m s^{-1}$ )

**$\nu_e$**  Sliding velocity ( $m s^{-1}$ )

**$V$**  Volume loss ( $m^3$ )

**$V_p$**  Particle volume ( $m^3$ )

**$V_u$**  Erosion rate ( $\mu m^3$  per impact)

**$V_c$**  Material loss due to ‘pure’ corrosion without the effect of mechanical wear ( $m^3$ )

**$V_{cw}$**  Total material loss during corrosion wear due to both corrosion and wear ( $m^3$ )

**$V_w$**  Pure wear loss in otherwise the same environment as in the corrosion wear process but without corrosion ( $m^3$ )

**$V_{wc}$**  Material loss due to wear during corrosion wear ( $m^3$ )

**$W$**  Normal load (N)

**$y$**  Vertical height (m)

**$y^+$**  Dimensionless scale

**$z$**  Number of electrons, average valance, charge on migrating species

**$\alpha$**  Angle of impact ( $^{\circ}$ )

**$\alpha_1$**  Symmetry constant

**$\delta$**  Boundary layer thickness or repassivated oxide thickness (m)

**$\Delta C$**  Change in concentration of species ( $= (C_b - C_0)$ ) (M, mM,  $mol cm^{-3}$ )

**$\Delta C$**  Enhancement of  $C$  due to the presence of erosion ( $mg$  or  $mg s^{-1}$ )

**$\Delta E$**  Synergistic effect or enhanced erosion rate due to corrosion ( $mg$  or  $mg s^{-1}$ )

**$\Delta H$**  Change in hardness (Hv or Pa)

**$\Delta V_c$**  Wear-induced corrosion ( $m^3$ )

**$\Delta V_s$**  Synergistic effect ( $m^3$ )

**$\Delta V_w$**  Corrosion-induced wear ( $m^3$ )

**$\Delta \varphi$**  Potential difference across oxide (V)

**$\epsilon_c$**  Critical plastic strain ( $\mu m m^{-1}$ )

**$\eta$**  Turbulent eddy viscosity (Pa s)

**$\theta$**  Surface coverage fraction

**$\kappa$**  Specific wear rate ( $mm^3 N^{-1} m^{-1}$ )

**$\rho_f$**  Density of fluid ( $kg m^{-3}$ )

**$\rho_{ox}$**  Density of oxide ( $kg m^{-3}$ )

**$\rho_p$**  Density of particle ( $kg m^{-3}$ )

**$\rho_T$**  Density of target material ( $kg m^{-3}$ )

**$\sigma$**  Dynamic plastic flow stress for target ( $N m^{-2}$ )

**$\tau$**  Passive film recovery time (s)

**$\tau_w$**  Wall shear stress ( $N m^{-2}$ )

**$\tau_0$**  Characteristic passivation time of a metal during repassivation from a fresh surface (s)

**$\tau_i$**  Characteristic reaction time for the reaction controlling a corrosion fatigue process (s)

**$\nu$**  Kinematic viscosity ( $m^2 s^{-1}$ )

**$\mu$**  Dynamic viscosity (Pa s) or coefficient of friction

### 2.15.1 Introduction and Definitions

The term ‘tribo’ has origins in the Greek word ‘tribos’ (rubbing), which led to the sciences of lubrication, friction, and wear being called ‘Tribology,’ while the term corrosion has its origins in the medieval Latin word ‘corrodere,’ which means to gnaw through with ‘cor’ meaning intensive force and ‘rodere’ to gnaw.<sup>1</sup> For this chapter, corrosion will be used to relate to surface degradation involving electrochemical and chemical processes. Therefore, the term tribocorrosion refers to the surface degradation mechanisms when mechanical wear and chemical/electrochemical processes interact with each other. Many of the mechano–electrochemical interactions involved in tribocorrosion are time dependent and nonlinear. Recent activity in tribocorrosion research aims at addressing

the need to select or design new surfaces for future equipment as well as minimize the operating costs and extend the life of existing machinery and medical devices. The subject therefore includes the interaction of corrosion and erosion (solids, liquid flow, and droplet impingements or cavitation bubbles), abrasion, adhesion, fretting, and fatigue wear processes. Tribocorrosion is often linked to the synergy or antagonism resulting from the coupling of mechanical and environmental effects. For example, during friction the adhesive dissipation of energy is often influenced by chemical effects.<sup>2</sup> Similarly, stainless steels rely on a 1–10 nm thick passive film for their protection from aggressive and corrosive environments. This film forms essentially instantaneously by reaction with the environment but abrasion can lead to a local rupture or complete removal of the film and permanent deformation of the substrate. This can lead to areas of the substrate being exposed to the aggressive environment and unless repassivation (repair or self-healing) mechanisms reform the passive film to inhibit corrosion processes, accelerated anodic dissolution will occur within these sites.

The subject area does, however, suffer from rather loosely defined terms that sometimes relate to the same processes. Thus, to help readers, the terms used in this chapter and their definitions are given in the following paragraphs, but some overlap between these terms is inevitable.

The term flow-corrosion (sometimes referred to as flow-enhanced corrosion, flow-induced corrosion, or flow-accelerated corrosion (FAC) in some texts) will be used to describe corrosion that occurs on surfaces exposed to laminar or turbulent flow but is unable to disrupt passive surface films or corrosion layers.

Erosion-corrosion will be used where mechanical processes as well as flow effects are acting on the surface. This covers solid particle, liquid droplet, cavitation impingement, and some highly turbulent flows where energetic jetting or impingement flows onto the surface occur and can disrupt surface films or layers. Surface film disruption is by mechanical processes associated with contact stresses, stress wave reinforcement, surface shear stresses or pressure fluctuations generated on the surface through water hammer, dynamic fluid pressures, transverse momentum transfer, etc. These mechanical processes can lead to increased corrosion through electrochemical and chemical processes. Reference is normally made to the critical flow velocity above which erosion-corrosion occurs for specific flow geometries and materials.

Tribocorrosion will be used to cover the much broader area or all wear and corrosion interactions. This will cover, for example, abrasion-corrosion and sliding wear-corrosion. Wear is the term used to cover abrasive, adhesive, oxidative, fretting, fatigue-based processes that are part of mechanically induced surface degradation and material loss mechanisms.

Understanding tribocorrosion processes is important if costs associated with material losses are to be minimized. For example, modern fluid handling and propulsion systems face increasing demands for higher flow rates with the inherent risk of flow-corrosion, and if solids are entrained and impinge on the surface or cavitation occurs near the surface, erosion-corrosion can result and accelerate material loss significantly. This is especially true for industries that transport slurries and other particle-laden fluids in pipes or seawater propulsion systems such as offshore and marine technologies. These industries expend the equivalent of millions of pounds every year to repair erosion-corrosion damage caused by solid particle impingement and cavitation. Typical examples of this kind of material destruction are erosion-corrosion damage to pump impellers (see [Figure 1](#)), propellers, valves, heat exchanger tubes, pneumatic and hydro-transport systems, fluidized bed combustors, and many other types of fluid-handling equipment. The erosion-corrosion data and models published in the open literature aspire to allow informed surface selection for combined erosion and corrosion resistance. They are rarely based on substantive physical understanding and some approaches are simply designed to make numerical modeling easier. The erosion-corrosion data are very patchy and incomplete, and therefore hamper any improvement in the performance of machines in aggressive environments.



**Figure 1** Cavitation-corrosion of a 150 mm diameter bronze centrifugal pump impeller from a swimming pool pump.

Tribocorrosion is also critical to long-term human health and patient mobility. The correct understanding of biotribocorrosion and joint design can offer huge savings for health services and impact on the quality of life. For example, current predictions suggest 268 000 total knee arthroplasty revisions will be required per annum in the United States by 2030 as against 38 000 now.<sup>3</sup> Estimating a cost of \$30k per revision, this implies an additional annual cost of \$6.9 billion at today's costs. Extending joint life through improved tribological design would therefore allow enormous savings in surgery costs besides allowing patients to remain active and in employment. Hence, there is growing need to understand the human cellular and biological reactions to metal ion release generated by tribocorrosion processes as well as surface biotribology performance of these joint implants.

On the positive side, tribocorrosion phenomena can be used as a manufacturing process such as in the chemical–mechanical polishing of silicon wafers. The coupling of mechanical and environmental effects can also create surfaces of specific reaction layers on materials that could inhibit corrosion and/or wear. Examples of this are self-lubricating and/or self-healing surface layers.<sup>4</sup>

The presence of well-adhered oxide surface films or loosely adhered layers of corrosion products and the ability to reform these films and layers are also critical in many engineering applications where control of friction and wear are important in sliding contacts. These contacts involve contact between the high spots on the interacting surfaces due to their roughness after machining or finishing. Therefore, the load on a contact is rarely distributed evenly over the apparent contact area but is rather distributed among high-spot (asperity) contacts between surfaces, often referred to as junctions. The actual contact area between surfaces is therefore the sum of the individual areas of junctions and will likely be proportional to the normal load. Friction and wear generally are developed by interactions between these asperities, which can be

subjected to severe contact stresses that often result in temporary flattening (elastically) or, if yield stresses are exceeded, permanent plastic flow and deformation of the surface. The friction forces are typically lowered when oxide layers are present on asperities compared with asperity contacts between bare metal. For some systems, the friction forces can be modeled by summing the forces associated with adhesive and deformation processes relating to these asperities. Adhesive forces are often related to the shear strength of junctions made between contacting asperities of surfaces in relative motion and relate to the frictional work. The presence of oxide films or corrosion products on these asperities will alter the level of frictional work and the resulting surface temperatures. **Figure 2** illustrates how oxide-filmed asperities may interact during sliding, assuming that the oxides deform with the asperity. The asperities on the two interacting surfaces are represented as idealized cylindrical protrusions (i.e., flattened protrusions), thereby allowing a flat circular contact of radius ' $a_n$ ' in plan view, to visualize the actual contact area evolution as asperities slide over each other.

Unpredictable interactions can result between wear and corrosion when the surfaces in contact have complex, multiple-phase microstructures that can lead to microgalvanic activity and selective phase corrosion (localized attack) as well as wear modes involving wear debris or corrosion products along with the interacting surfaces that can roll or slide within the contact. Examples of such surfaces include composites or surfaces that undergo compositional changes induced by tribological interactions. For instance, the presence of carbides in a metallic surface, typically formed for improved wear resistance, establishes a microcorrosion cell as the carbide is likely to be cathodic with respect to the surrounding metallic matrix. This can result in the preferential anodic dissolution of the metallic matrix close to or at the matrix–carbide interface and thereby accelerate carbide removal from surfaces and reduce the antiwear properties of the surface.

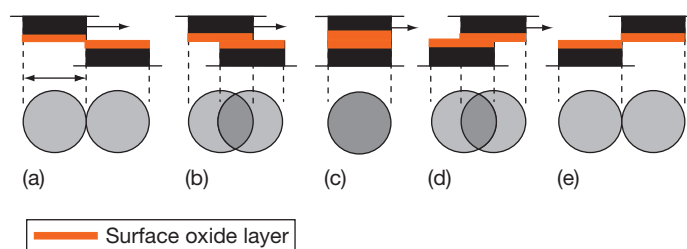


**Figure 2** Schematic of asperity–asperity interactions of a passivated surface.

## 2.15.2 Tribocorrosion Fundamentals

### 2.15.2.1 Factors Affecting Tribocorrosion

The corrosion dependence on material properties is complex within tribocontacts. Reference to the galvanic series (see **Chapter 2.07, Galvanic Corrosion**) is useful to understand the potential differences possible when a depassivated metal is electrically coupled to a passive metal. This potential difference will drive charge transfer within the contact. This charge transfer is likely to be a function of the magnitude of surface degradation by mechanical processes and how this is affected by the material chemistry, the environmental chemistry, the microstructure, mass transport, and the rate and extent of depassivation, should the surface be passivated. The influence of material parameters on wear is discussed in the following section.

#### 2.15.2.1.1 Material parameters and composition

A review of available wear models such as those used in solid particle erosion shows the diversity of material properties that have been included in published predictive wear equations. Meng and Ludema,<sup>5</sup> for example, have reviewed 28 erosion models and found that on average only five parameters are used per equation but in total 33 different parameters, not all material properties, are quoted. These are tabulated in **Table 1**.

Simpler approaches based on a few parameters are still in use and are shown to have wide applicability

and therefore are useful. For example, the main theory for sliding wear of metals is based on the assumption that contact between two surfaces occurs where asperities contact and the local deformation is plastic (see **Figure 2**). The Figure shows the interaction between sliding asperities as one slides over the other; see **Figures 2(a)–2(e)**. The true contact area is therefore given by the summation of individual asperity contact areas and is proportional to the normal load.

The overall wear volume loss,  $Q$ , per unit sliding distance is associated with the detachment of material from the asperity contacts and the volume of each particle of wear debris will relate to the size of the individual asperity contact. Assuming that the debris volume,  $\delta V$ , is proportional to  $a_r^3$  gives the well-known Archard wear law<sup>6</sup>:

$$Q = \frac{kW}{H} \quad [1]$$

The Archard wear law suggests, for a system with constant  $k$ , that the wear rate is directly proportional to load on the contact but inversely proportional to the surface hardness,  $H$ , of the wearing material. It can be written:

$$\kappa = \frac{V}{WL} = \frac{k}{H} \quad [2]$$

where  $\kappa$  is the dimensional specific wear rate (SWR) (typically quoted as  $\text{mm}^3 \text{Nm}^{-1}$  or  $\text{m}^2 \text{N}^{-1}$ ),  $V$  the volume loss,  $W$  the applied load, and  $L$  the sliding distance.

A similar wear equation to the adhesive Archard wear law (eqn [2]) can be derived for abrasion.<sup>7</sup> It is

**Table 1** Parameters selected in wear models<sup>5</sup>

<i>Erodent/abradent</i>	<i>Target</i>	<i>Fluid flow</i>
Density	Density	Impact angle
Hardness	Hardness	Impact angle max. wear
Moment of inertia	Flow stress	Kinetic energy (KE) transfer between particle and target
Roundness	Young's modulus	Temperature
Single mass	Fracture toughness	Corrosivity
Size	Critical plastic strain	
Velocity	Depth of deformation	
Rebound velocity	Incremental strain per impact	
KE of particle	Thermal conductivity	
	Melting temperature	
	Enthalpy of melting	
	Cutting energy	
	Deformation energy	
	Heat capacity	
	Weibull flaw parameter	
	Lamé constant	
	Grain diameter	



also interesting to note that models developed for predicting current from depassivated surfaces show a  $(W/H)^{1/2}$  dependence, as discussed later in [Section 2.15.3.1.3](#).

Turning now to solid particle erosion, it is tempting to assume that solid particle erosion rates would also be inversely dependent on the surface hardness,  $H$ , as predicted by simple plastic deformation erosion models, [eqn \[3\]](#), where  $\alpha$  is the erodent impact angle. A more complex model, also given by Hutchings,<sup>8</sup> includes the critical strain concept, [eqn \[4\]](#) and this predicts the erosion should be dependent on  $H^{3/2}$ . However, these relationships rarely hold in practice for engineering materials.

Erosion models

$$E_r = \frac{K \rho_T U_p^n}{H} f(\alpha) \quad [3]$$

$$E_r = \frac{K_1 \rho_T \rho_P^{1/2} U_p^3}{\epsilon_c^2 H^{3/2}} \quad [4]$$

where:  $K$  is a constant,  $\rho_T$  is the density of the target,  $\rho_P$  is the density of the particle,  $U_p$  is the particle velocity, and  $\epsilon_c$  is the critical plastic strain.

Corrosion resistant alloys (CRAs) are widely used to resist flow corrosion. For example, chromium is added to improve the resistance to flow corrosion of carbon steel (CS), see Poulson.<sup>9</sup> [Figure 3](#) shows the trend for such a passive system (where passive means that the surface has a propensity to form a protective surface film or layer with high impedance and thus suppresses charge transfer at the metal–

liquid interface) as a function of flow velocity and its vulnerability to mechanical processes, which accelerate corrosion loss rates. In general, corrosion-resistant alloys do not resist erosion well and the interactions that exist between corrosion and erosion are not well understood. These interactions are sometimes referred to as synergistic or antagonistic. These terms refer to the possibility that simple summing of the mechanically induced material loss without a corrosive contribution and the electrochemical (corrosion) material loss without mechanical stimulus does not give an accurate material loss for tribocorrosion conditions. Some surface–environment conditions suffer accelerated material loss where the actual loss rates are higher than the simple summation of the pure mechanical and electrochemical levels. This case is termed ‘synergistic,’ while combinations of surface/environment that result in reduced material loss and are below the levels of the simple summation are termed ‘antagonistic’ (negative synergy). This presents a dilemma for those seeking erosion–corrosion-resistant surface selections. Also, cost reduction considerations favor replacing expensive solid alloy components with coatings on CS substrates, and hence, considerable effort is now being made to research coating performance under erosion–corrosion.

#### 2.15.2.1.2 Environment factors

Corrosion is a reaction process on metallic surfaces that occurs as a result of interaction with the environment. The rates and modes of corrosion attack are

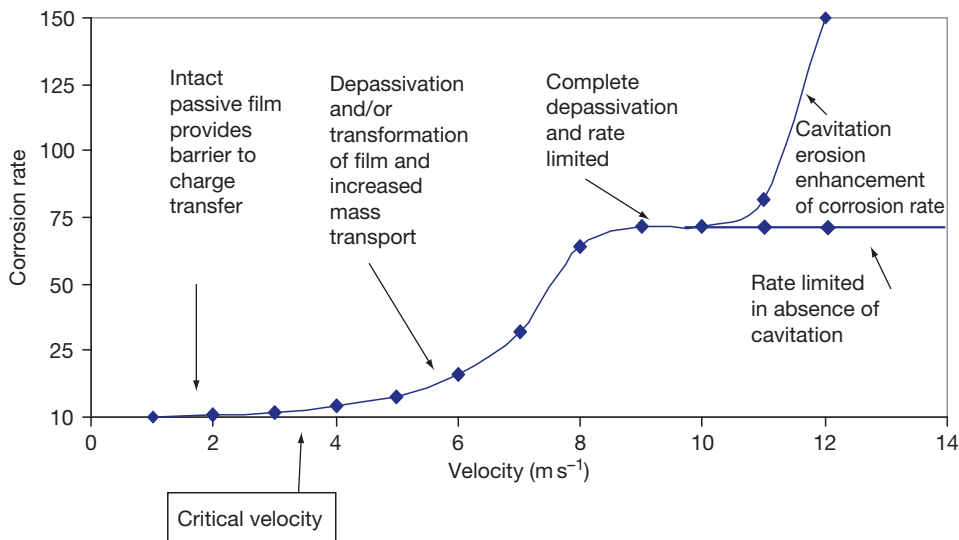


**Figure 3** Arbitrary flow corrosion rates versus flow velocity.

related to the environmental conditions such as pH, dissolved oxygen, salinity, temperature, flow structure, and whether biofouling occurs. The latter point is often ignored but can have dramatic effects.

The influence of environmental factors on erosion-corrosion is likely to be very system dependent. However, the sensitivity of wall wastage rates to such environmental parameters can be found in the literature. Kim *et al.*<sup>10</sup> report how these parameters effect the galvanic corrosion of CS in alkaline-chloride solutions. They studied the aqueous corrosion characteristics of a CS coupled to type-304 (UNS S30400) stainless steel in deaerated solutions as a function of velocity, pH, and temperature. They found that the galvanic corrosion between CS and type-304 stainless steel was effected by the presence of an oxide layer formed on the CS. The galvanic current density increased with increasing flow velocity (between 0 and  $0.6 \text{ m s}^{-1}$ ) and temperature (between 25 and  $75^\circ\text{C}$ ), but decreased with increasing pH from 8 to 10. Flow velocity effects were only significant at 50 and  $75^\circ\text{C}$ . This effect can be explained by the increased solubility of magnetite (corrosion oxidation product) at the higher temperatures. The importance of passive films and their stability will be addressed in more detail later in this chapter.

Proteinaceous material present in natural joint lubricants can play an important influence within biomedical implants, particularly on metallic joint surfaces. Research has shown that proteins have different affinities for different metals, probably as a result of various ligands in their molecular structure that have different bonding energies and therefore different affinities for specific cations.<sup>11</sup> The effect of albumin (a protein found in serum) on the corrosion rate of biometallic materials is varied with Al and Ti being unaffected, Cr and Ni showing a slight increase, while Co and Cu dissolve at a much greater rate.<sup>12</sup> Williams *et al.*<sup>13</sup> found that the corrosion rate of stainless steel and commercially pure titanium increased when exposed to proteins in a static environment, while under fretting contact conditions, proteins were found to decrease the corrosion rate of the stainless steel but had little appreciable effect on titanium alloys. In a recent study on the effect of synovial fluid (SF) on corrosion properties of CoCrMo alloys,<sup>14</sup> proteins were found to be absorbed on the surface. It was hypothesized that protein (normally negatively charged) adsorbs to generate a film that reduces the corrosion rate by acting as a negatively charged barrier preventing corrosive anions (e.g.,  $\text{Cl}^-$ ) approaching the CoCrMo interface. Contu *et al.*,<sup>15</sup>

on the other hand, attributed the reduction in corrosion rate of CoCrMo in bovine serum (BS) to the anodic dissolution process being under diffusion control resulting in positive shifts in surface potentials compared with inorganic solutions at the same pH. Goldberg *et al.*<sup>16</sup> carried out a series of scratch tests on CoCrMo (ASTM F75) samples and found a decrease in peak currents (decrease in corrosion rate). The authors attributed this to the barrier effects of the adsorbed protein preventing water from reaching the sample surface, or lubrication resulting in less material removed from the surface during scratching.

A guide to system performance for solutions with different pH can be found by reference to the relevant potential–pH (Pourbaix) diagram. This approach has been illustrated by Stack<sup>17</sup> in a regime mapping approach to erosion-corrosion and by Celis<sup>18</sup> for sliding wear-corrosion contacts.

The influence of the bulk oxygen concentration,  $C_b\text{O}_2$ , in aqueous environments on the corrosion rate depends on the controlling corrosion mechanisms, which will be discussed in greater detail later in the chapter. The dramatic influence of oxygen levels on fretting wear-corrosion rates of a type-304L stainless steel sleeve fretting against a 304L tube in simulated nuclear plant conditions using boric acid with Lithine (an inhibitor) at a pH of 8.7 is illustrated in Figure 4 from Deforge *et al.*<sup>19</sup> It is also interesting to see that most tribocorrosion occurs on the sleeve for systems

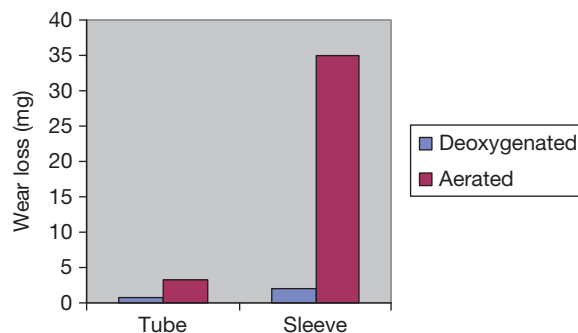


**Figure 4** Fretting wear loss of stainless steel type-304L tubes in contact with a stainless steel type-304L sleeve after 1 week in boric acid + lithine, pH = 8.7 at room temperature. The OCPs for the deaerated (overpressure of hydrogen) and aerated conditions were  $-0.630$  and  $-0.030 \text{ V}$  versus SHE, respectively. Reproduced from Deforge, D.; Wenger, F.; Ponthiaux, P.; Lina, A.; Ambard, A. Tribocorrosion of AISI 304L stainless steel sliding against AISI 304L stainless steel in nuclear environment, 207th Electrochemical Society Meeting, Quebec City, Canada May 2005, session E1 on Chemical, Electrochemical, and Mechanical Effects on CMP, Tribocorrosion, and Biotribocorrosion, abstract #313.

exposed to flow, and under mass transport control, the corrosion rate can be found to be directly proportional to  $C_bO_2$ , or  $C_bO_2^n$ , where  $n$  is flow and system dependent.

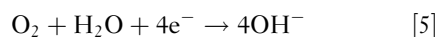
Temperature of the surfaces is an important variable which can influence wear-corrosion rates and hence the temperature of the environment, be it air or lubricant, must be taken into account. In addition, many contacts between surfaces in relative motion result in an increased heating of the contact zones due to friction. In aqueous solutions, temperature not only influences the pH, solubility of gases (i.e., oxygen and carbon dioxide), and ionic species as well as diffusion rates of reactant species but can also affect the kinetics of oxidation reaction at the oxide-metal interface and the dissolution of oxides at the oxide-water interface. Added complications can occur when elevated temperatures increase hydrogen diffusion rates, and if this effect is coupled with a surface susceptibility to hydrogen embrittlement, then increased wall loss can result.

In nuclear power plant, the effect of water chemistry has been shown to strongly influence the wear rates of 304L stainless steel in pressurized high temperature water. The high temperature of the water promotes thicker oxide layers that are harder due to the formation of micron-sized magnetite crystallites. If these layers are detached and stay within the contact, they can create very abrasive (rolling abrasion where entrained oxide particles roll and indent the contact surfaces) wear conditions. For low-pH waters between 5 and 7, Kaczorowski<sup>20</sup> reports dramatic increases in material loss by the promotion of such three-body mechanisms and by decreasing the electrochemical potential in the electronegative direction.

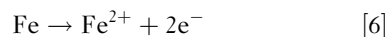
Another major environmental factor with significant influence on erosion-corrosion rates is that of flow (see **Chapter 2.13, Flow Assisted Corrosion**), but care needs to be taken to use appropriate flow characterization parameters. For example, a single value of flow velocity referred to as the critical velocity is often quoted to represent a transition from flow corrosion to enhanced mechanical-corrosion interactive erosion-corrosion processes. It is also used to indicate the resistance of the passive and protective films to mechanical breakdown.<sup>21</sup> However, it should be remembered that a single value of free stream velocity can result in widely different flow field structures that are dependent on the Reynolds number of the flow geometry and type and thickness of boundary layer induced at the liquid-solid interface. These factors will directly affect the velocity profiles and

transverse momentum transfer close to the solid-liquid interface, which will be shown later to influence the thickness of the boundary and subviscous layers and thereby dictate wall shear stress levels and mass transport efficiencies. Therefore, critical velocity values are very geometry or test rig specific and can not be readily applied to predict component service life in generic flow systems.

Poulson<sup>9</sup> has investigated the effects of flow on corrosion of CS and the effects of depassivation of the surface (see **Figure 5**). The corrosion of CS in neutral solutions is governed by the reduction of dissolved oxygen as shown in eqn [5].



This cathodic electrochemical reaction drives the anodic dissolution of iron, in eqn [6].



Poulson reported that the flow corrosion rate was closely related to the mass-transport coefficient. However, under detached/separated flow conditions (such as flows through sudden expansion pipe work), the rate can be independent of flow.

Al-Hosani *et al.*<sup>22</sup> have studied the galvanic corrosion induced by the coupling of copper-based alloys to Mo-stainless steels in static Arabian Gulf seawater under a variety of conditions including temperatures, cathode-anode area ratios and stirring. For static conditions, the corrosion rates were found to be proportional to the cathode-anode area ratio. This can be attributed to the fact that the cathodic reaction (the reduction of oxygen) controls the overall corrosion process, and this is diffusion controlled. However, the galvanic corrosion rate of the couples increased nonlinearly with a rise in temperature to reach a maximum at 50 °C, decreasing sharply at higher temperatures due to the decreased solubility of  $O_2$  in solution at this temperature. The effect of stirring the electrolyte shifted the open circuit

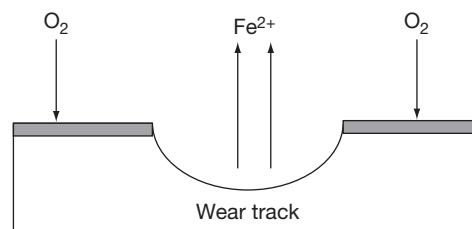


**Figure 5** Corrosion of carbon steel (CS) activated by wear that depassivates surface in the wear track.

potential (OCP) of the stainless steel to a more electro-negative value. Thus, the corrosion rates in the stirred solutions were found to be 1.33–3.0 times above those measured in stagnant solutions.

Erosion-corrosion conditions can themselves develop local microgalvanic cells between eroded and uneroded surface areas. Such microgalvanic cells have been reported between erosion-affected regions (depassivated) of a surface and noneroded regions (passive). For example, enhanced material loss rates due to such galvanic cells are reported by Hodgkiess.<sup>23</sup>

The environment can change the wear mechanism and thereby the wear rate and life of surfaces. This is illustrated by the tribological properties of plasma-sprayed Cr<sub>2</sub>O<sub>3</sub> coatings, studied by Wei,<sup>24</sup> at room temperature, using distilled water, water-ethanol, *n*-monohydric alcohols, and polyhydric alcohols as lubricants. Testing indicated that both friction and wear were much higher (approximately twice) in water than in the *n*-monohydric alcohols. Analysis of the morphology and composition of the worn surfaces indicated that the wear of Cr<sub>2</sub>O<sub>3</sub> coating was controlled by the combination of microfracture and tribochemical wear in water and was only controlled by microfracture in ethanol.

### 2.15.2.1.3 Friction

Friction is the resistance force encountered when surfaces in contact move relative to each other. A popular way to express this force in terms of a loaded sliding contact is by using the dynamic coefficient of friction,  $\mu$ , defined as the frictional force,  $F_f$ , divided by the normal load,  $W$ , on the contact when the contact is sliding.

$$\mu = \frac{F_f}{W} \quad [7]$$

For lubricated contacts in relative motion separated by a film of lubricant, the dynamic coefficient of friction,  $\mu$ , is typically very low ( $<0.1$ ) and can be as low as 0.1, even when the lubricant film is only a few nanometers thick. These values compare with values of  $\sim 1.0$  for unlubricated dry sliding. Friction between contacting surfaces in relative motion results primarily from forces acting perpendicular to the applied load. As the fluid film thins, the interaction of surface asperities can cause increases in friction. Water, however, is regarded as a poor lubricant, as it does not form a fluid film readily or support loads due to a minimal pressure–viscosity interaction. However,

water-lubricated contacts reduce the contact temperature compared with dry contacts and aqueous lubricants are being considered as an environmentally acceptable alternative to hydrocarbon-based oils. It should be noted that the friction force required to be overcome to induce relative motion in a contact can be used in eqn [7] and  $\mu$  is then termed the static coefficient of friction and is typically higher than the dynamic values.

Bowden and Tabor<sup>25</sup> proposed a model, which in its simplest form assumes that frictional forces arise from adhesive forces and deformation forces induced by the abrasive ploughing nature of the harder asperities interacting with the softer ones of the counter surface. The adhesive force is linked to the asperity–asperity contact, which makes up the real area of contact between surfaces and the junctions between them. The shear strength of these junctions influences the level of friction. Adhesive effects are thought to be due to the summation of interfacial intermolecular interactions that operate at the asperity contacts. There are also likely to be some chemical processes activated within the contact, such as oxidation, which can form coherent films and their composition can influence friction levels. The presence of oxide layers and adsorbed films on metal surfaces generally weakens the shear strength of the asperity junctions and thus lower adhesive forces resist motion resulting in lower friction. For example, a multilayered film can be formed on ferrous surfaces under dry sliding, typically with FeO close to the surface, which is covered by a layer of Fe<sub>3</sub>O<sub>4</sub>, which in turn is covered by Fe<sub>2</sub>O<sub>3</sub>. The Fe<sub>2</sub>O<sub>3</sub> layer is associated with high friction ( $\mu = 1.1$ ), but if this layer is penetrated exposing the sublayers, then lower friction ( $\mu = 0.5$ ) can result.<sup>26</sup> However, for soft ductile metals, and where the oxide layers or adsorbed films are partially removed, appreciable adhesion between nascent (freshly formed or exposed material) surfaces can result. Adhesion can also be enhanced if similar surfaces are in contact, that is, stainless steel pairs.

### 2.15.2.2 Corrosion and Associated Electrochemical Reactions

This section reviews the relevant corrosion reactions related to tribocorrosion and the important role of the surface films formed under tribocorrosion conditions called tribofilms.

### 2.15.2.2.1 Tribofilms

Published research has tried to deal with the synergistic and antagonistic effects between erosion and corrosion processes, which result in accelerated material loss (synergism) or in some cases actually decelerate material loss (antagonism, sometimes called negative synergism).<sup>27–31</sup> A wide range of corrosion-resistant materials relies on a relatively thin surface film to provide a barrier (of high impedance) to charge transfer (and thus corrosion) between the relatively active bulk material and the corrosive environment. The thickness of such films is dependent on time, temperature, interfacial potential, pH, and the environment (i.e., species concentration and type). The films range from being tens of Angstroms to hundreds of Angstroms thick and are formed in relatively short times, typically <1 s. These films render the surface passive, but for fluid machinery handling flows where solid particles have been entrained or cavitation is induced, the passive film can be removed by mechanical wear or bubble collapse/microjet/shockwave impingement processes. Where the film is mechanically removed, charge transfer can occur at the interface without retardation from the barrier film.<sup>32</sup> The stability of these surface films will depend on their adherence to the parent bulk material and their cohesive strength when subjected to contact stresses. The solubility of the surface films within the changing environment of tribocontacts will also influence the stability and could instigate compositional changes in the surface film. Clearly, density and hardness of the surface films will influence the micro-contact mechanics of tribological processes of wear and friction.

Similar mechano–electrochemical processes occur in sliding contacts where tribochemical wear occurs by detrimental chemical reactions within the contact, induced by the local environment, and in combination with the mechanical contact mechanisms and induced stress fields. Contact between the sliding surfaces can accelerate chemical and electrochemical reactions and material removal. Sliding contact results in increased surface temperatures and can induce surface cracks and the generation of nascent surfaces, which are highly reactive with their environment. However, the chemical formation of surface films can be advantageous, as they can have low friction properties and also promote material transfer to change the contact from base–base material to chemical film–chemical film and thus change the contact conditions.

The interaction between the tribofilms formed on interacting surfaces often results in nanometer-thick

mechanically mixed layers that are formed in the shear zone between the contacting surfaces. These layers are often a mixture of components from both surfaces generated by material transfer but also contain corrosion products, wear debris, and remnants of any passive film, if the surfaces are passive metallic systems. This layer is often referred to as the tribofilm and its composition and thickness will control the level of tribocorrosion at the contact when sliding wear occurs in a corrosive environment. The environment clearly has an influence on the composition of the film. For example, the environment will determine whether oxides or sulfides can form or whether calcium carbonate (chalk)-based films can form.

Mischler *et al.*<sup>33</sup> show the importance of the passive film in controlling wear rates and friction when testing CS in borate solution (pH 8.4). They reported two concurrent mechanisms: (1) oxidative wear involving the detachment of passive film followed by repassivation; and (2) surface disruption by abrasion, subsurface deformation, and cracking. Interestingly, when held at cathodic potentials, there was no film present and asperity interaction resulted in debris being smeared over the wear track, subsequently decreasing the wear rate.

A mechanistic view given by Staehle<sup>34</sup> looks at the initial interaction of dislocations in the metal substrate with surface films in terms of single and cross-slip and conditions for perforating these films. This approach suggests that the significant properties of initial films in terms of interaction with dislocations are plasticity, strength, stacking fault energy, and epitaxy. Other factors to consider are the duration in which the surface is totally or partially film-free, the kinetics of film-free and repassivation regions, and the dependence of these film-free and repassivation regions on pH, potential, environment, alloy composition, temperature, mass-transport, and contact-induced stress. Staehle shows that film-free areas only represent 10% of the surface area affected, as repassivation occurs very quickly under high-speed/strain elongation tests. It was also found that the reaction rates on the mechanically affected surface areas were one to two orders of magnitude higher than nonaffected areas. This emphasizes the importance of film integrity in minimizing corrosion rates. Staehle concludes that increasing the chromium content or the presence of a Molybdate inhibitor increased the rate of repassivation of steels. However, increasing the concentration of sulphates and the presence chlorides reduced the rate of repassivation.



### 2.15.2.2.2 Depassivation and repassivation kinetics

#### Depassivation

Depassivation in tribocontacts involves the rapid removal of the surface layers and sometimes the underlying bulk material by mechanical action such as surface abrasion, adhesion, plastic deformation, cutting, thermal cycling, fatigue and particle erosion, cavitation bubble, or liquid droplet impact mechanisms. For example, Figure 6 illustrates the level of damage to passive films as a function of solid particle impingement angle. Mechanical removal and/or rupture of the passive layer enables charge transfer to proceed at varying rates and parent metal dissolution is likely. 'Recovery' or repassivation aspects of the passive film are therefore important. Figure 7 shows the current response over time for individual solid particle impacts on the naturally passivating system of stainless steel in a NaCl solution. Some impacts will only result in partial passive layer removal or cracking, which will influence repassivation kinetics and possibly the composition of the regrown layer.

Mechanical deformation that disrupts and perforates passive films takes place by dislocation movement. Dislocation interaction with the passive film

can lead to rupture and/or perforation that results in a transient exposure of highly reactive parent material. This process is sometimes referred to as 'slip dissolution.' The degree of disruption to the passive film depends on whether the slip is concentrated on a single plane or is diffuse on multiple planes as with cross-slip. An illustration of a passive film disruption by slip in a single plane is shown in Figure 8. As Figure 8 (b) shows, if the displacement is great enough, corrosion occurs under the passive film, which will further compromise the integrity of the film if subjected to further deformation in a tribocontact.

#### Repassivation

Surface coverage models for passive film growth/recovery typically relate to steady state film formation and are not applicable to transient events of  $<1$  s duration, which are often found in tribocorrosion. However, these models are useful and they consider the number of moles of oxide formed  $N_u$  as a ratio of the total number of surface sites available,  $N_{o,u}$ , in units of  $\text{mol cm}^{-2}$  (from Jemmely *et al.*<sup>35</sup>):

$$\theta = \frac{N_u}{N_{o,u}} \quad [8]$$

The rate of lateral surface coverage during early stages of repassivation of nascent surfaces, assuming complete oxidation of the parent metal to oxide, can be given by

$$\frac{d\theta}{dt} = i \left( \frac{M_{ox}}{L_{ox} \rho_{ox} z F} \right) \quad [9]$$

where  $i$  is the anodic current density,  $z$  is the charge number,  $L_{ox}$  is the oxide film thickness,  $\rho_{ox}$  is the oxide density, and  $M_{ox}$  is the molar mass of the oxide.

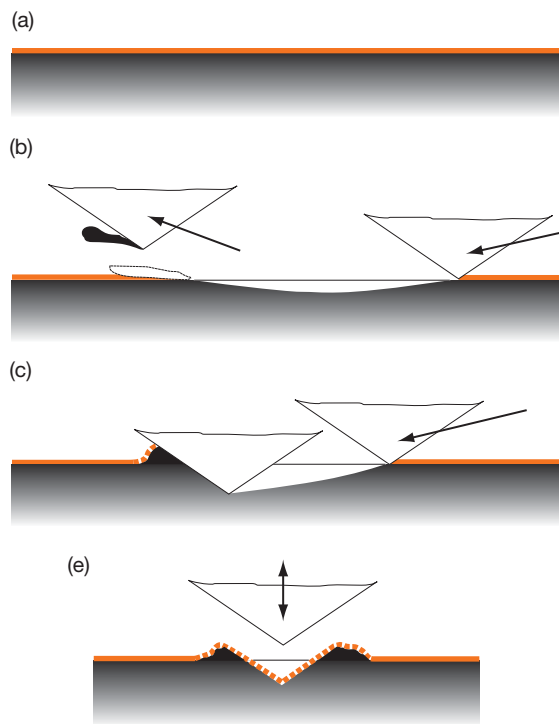


**Figure 6** Schematic showing that the level of passive layer damage is dependent on particle impact angle.

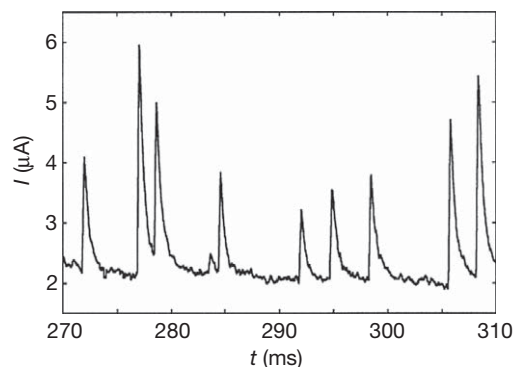


**Figure 7** Current transients in erosion–corrosion due to depassivation/repassivation. Reproduced from Sasaki, K.; Burstein, G. T. *Philos. Mag. Lett.* **2000**, *80*(7), 489–493.

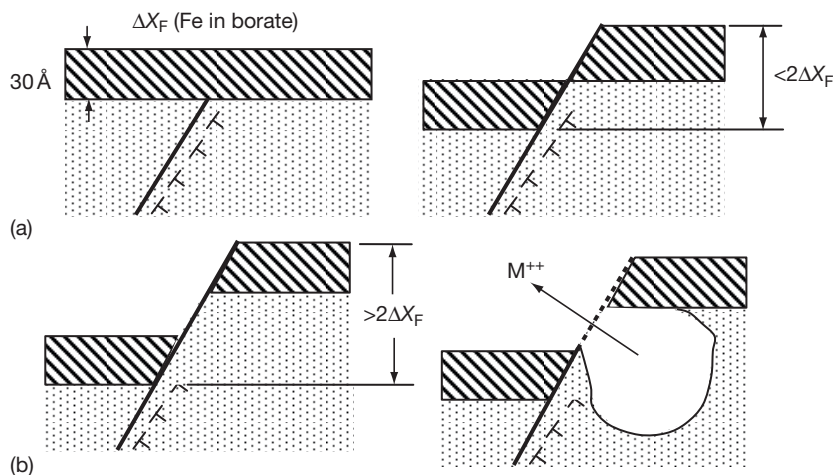


**Figure 8** (a) Dislocation on a single slip plane with the surface covered by a thin passive film (b) dislocation is more extensive and film is perforated and corrosion occurs under passive film. Reproduced from Staehle, R. W. *Corros. Sci.* **2007**, 49, 7–19.

If Tafel kinetics applies then the anodic current density  $i$  can be given by

$$i = k_a(1 - \theta)\exp\left(\frac{E_{\text{applied}}}{b_a}\right) \quad [10]$$

where  $k_a$  is the rate constant and  $b_a$  is the Tafel slope ( $=dE/d\ln i$ ). This assumes that oxidation occurs exclusively on bare parent metal.

Film growth models may then be used to explain the thickening of oxide layers. These models assume growth occurs by high field conduction which is thought to apply over the longer term and are therefore not applicable in the early stages of repassivation of nascent surface sites.

$$i = k_B \exp\left(\frac{B\Delta\varphi}{L_{\text{ox}}}\right) \quad [11]$$

where  $k_B$  is the rate constant and the migration kinetic constant for a single ionic species  $B = \alpha_1 z F a_j / RT_s$ . Here  $\alpha_1$  is a symmetry constant,  $z$  is the charge on the migrating ionic species, and  $a_j$  is the jump distance. The term  $\Delta\varphi$  is the potential difference across the oxide layer and taken to be the difference between the electrode potential and the minimum potential for the initiation of film growth. The other term in the equation is the oxide layer thickness,  $L_{\text{ox}}$ .

This can be linked to the current–time transients by setting:

$$L_{\text{ox}} = \frac{M_{\text{ox}} q}{z F \rho_{\text{ox}}} \quad [12]$$

Where  $q$  is the charge passed or  $\int i dt$ .

The use of such models to predict wall loss rates under depassivation–repassivation conditions depends

on the assumptions mentioned earlier and knowing the oxidation process and the associated charge number as well as the area of depassivation due to the wear processes. Some of the possible environmental factors that effect depassivation and repassivation are summarized for erosion–corrosion in [Table 2](#).

Thus, if the contact conditions allow, the rupture of the passive film can be repaired as shown schematically in [Figures 9–11](#). This is an ideal case where accelerated dissolution of the substrate is minimal. Obviously, more severe abrasion would result in accelerated corrosion by inhibiting effective repassivation.

#### 2.15.2.2.3 Critical velocity concept

The velocity profile established between flowing electrolyte and a solid surface, see [Figure 12](#), generates a maximum shear stress at the wall–liquid interface.

The wall shear stresses can be calculated from [eqn \[13\]](#).

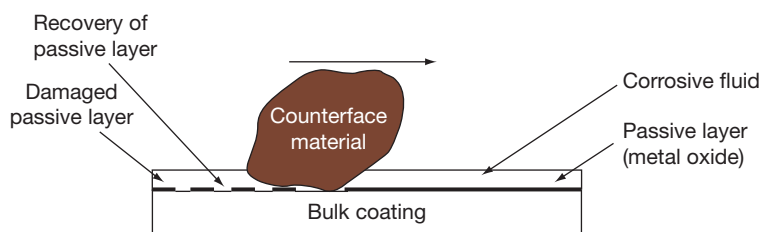
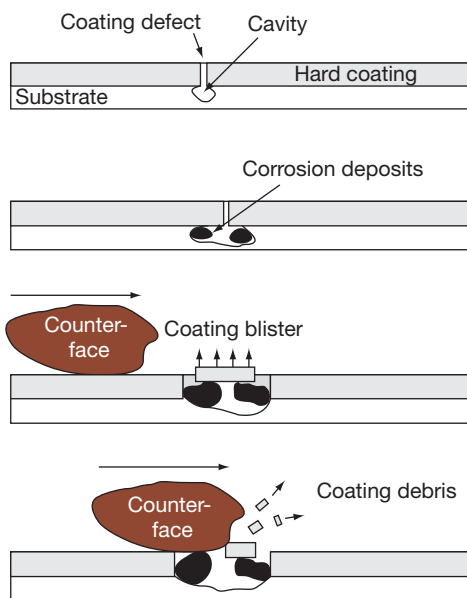
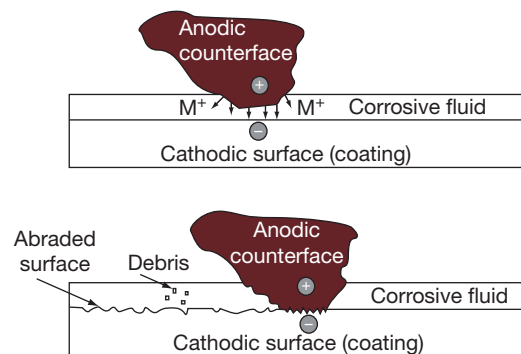
$$\tau_w = (\mu + \eta) \frac{dU}{dy} \quad [13]$$

where  $\mu$  is the dynamic viscosity of fluid,  $\eta$  is the turbulent eddy viscosity, and  $dU/dy$  is the velocity gradient at the wall. For laminar flows, the turbulent eddy viscosity can be set to zero.

These are stresses that could be applied to loosely adherent surface deposits/layers or passive films and change mass-transport conditions thereby influencing flow corrosion and erosion–corrosion. However, it is now thought that passive film removal and its associated critical velocity is related to mass-transport-induced

**Table 2** Possible influences on the depassivation and repassivation kinetics, adapted from Wood<sup>27</sup>

<i>Environmental Factor</i>	<i>Depassivation processes that cause passive film removal or disruption</i>	<i>Repassivation processes that encourage regrowth (repair) of the passive film</i>
Solid particle impact	Plastic deformation or cutting	Enhanced repassivation on plastically extruded regions
Surface/liquid interface	High velocities/wall shear stresses	Film growth kinetics(monolayer coverage plus lateral film growth)
Occluded geometries/pits	Local environment changes such as low pH	Metastable pits
Contact stress/shear stress/thermal pulse by frictional heat	Destabilises and delaminates passive film	Thermal pulse enhances film regrowth
Temperature	Local temperature	Local temperature
Turbulence bulk flow structure	Turbulent flow features shear the film from surface	Rougher/larger surface area

**Figure 9** Wear-corrosion of hard coatings on metallic substrates where damage to the passive film results in repassivation and healing of the passive film on the coating. Reproduced from Wood, R. J. K. *J. Phys. D: Appl. Phys.* **2007**, 40, 5502–5521. After Dearnley, P. A.; Aldrich-Smith, G. *Wear* **2004**, 256, 491–499.**Figure 10** Corrosion-wear of hard coated metallic alloy. Pitting/blistering of the hard coating culminates in mechanical fragmentation and removal of the coating. Reproduced from Wood, R. J. K. *J. Phys. D: Appl. Phys.* **2007**, 40, 5502–5521. After Dearnley, P. A.; Aldrich-Smith, G. *Wear* **2004**, 256, 491–499.**Figure 11** Wear-corrosion leading to increased coating material loss due to anodic roughening of the counterface. Reproduced from Wood, R. J. K. *J. Phys. D: Appl. Phys.* **2007**, 40, 5502–5521. After Dearnley, P. A.; Aldrich-Smith, G. *Wear* **2004**, 256, 491–499.

mechanisms (surface dissolution and polarization) and not wall shear stress,  $\tau_w$  (see eqn [13]), as previously assumed.

For single-phase turbulent flows in pipes, a ‘break-away’ or ‘critical velocity’ above which damage occurs to pipe surfaces has been reported based on

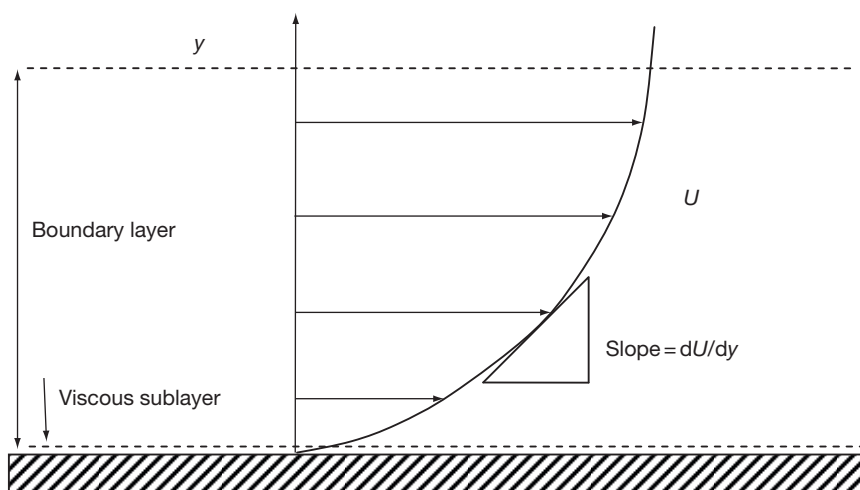


**Figure 12** Near-wall velocity profile.

**Table 3** Critical flow parameters for copper alloy tubing in seawater, after Roberge<sup>36</sup>

<i>Alloy</i>	<i>Critical shear stress (<math>\text{Nm}^{-2}</math>)</i>	<i>Critical velocity in 25 mm diameter pipe (<math>\text{m s}^{-1}</math>)</i>	<i>Design velocity based on 50% critical shear stress (<math>\text{m s}^{-1}</math>)</i>	<i>Maximum tubular design velocity (<math>\text{m s}^{-1}</math>)</i>
Cupro-nickel with Cr	297	12.6	8.6	9.0
70–30 Cupro-nickel	48	4.6	3.1	4.5–4.6
90–10 Cupro-nickel	43	4.3	2.9	3.0–3.6
Aluminum bronzes			2.7	
Arsenical A1 brass	19	2.7	1.9	2.4
Inhib. admiralty				1.2–1.8
Low Si bronze				0.9
P-deoxidized copper	9.6	1.9	1.3	0.6–0.9

the principles of the critical wall shear stress required to strip the passive film off the pipe surface. **Table 3** lists typical values for various copper alloys in pipe geometries handling seawater.

#### 2.15.2.2.4 Flow corrosion

Flow corrosion is defined as the corrosion resulting from the effect of flow of a fluid that does not contain solid particles in sufficient concentration and/or size to impinge on the metal surface.<sup>37</sup> The reactants are transported to a metal surface by diffusion or convection, while the products must be removed by the same mass transport mechanisms or accumulate as scales.<sup>38</sup>

Corrosion models have been developed over the years that have attempted to establish the relationship between fluid dynamics, mass transport, and ultimately the chemical and electrochemical reactions that occur on the surface of a metal. These

models have recently been discussed in a series of papers by Nesic *et al.*<sup>39</sup> The models describe the formation of protective scales and assess quantitatively the conditions (chemical and hydrodynamic) under which scales form, and only consider the dissolution of such scales. These models tend to neglect the lateral momentum transfer associated with turbulence, which are now considered important in understanding flow corrosion.

Mass transfer of reactants to and from the electrode surfaces plays an important role during flow corrosion where the dissolved oxygen or the dissolved metal ions have to diffuse from the solution to the metal or from the metal to the solution, respectively.<sup>40</sup> Mass-transport has been studied by several authors in different hydrodynamic systems that use convection to enhance the rate of mass transfer to the electrode. Such devices include free and submerged

jet impingement geometries, rotating disc electrodes (RDE), and rotating cylinder electrodes (RCE). However, recently, the microwall jet electrode (WJE) has been deployed to investigate the quantitative electrochemistry during process flows.

The standard model used to describe flow corrosion current densities for mixed controlled reactions (where activation and diffusion processes are present) is the modified Koutecky–Levich model<sup>41</sup> given in eqn [14], where  $k_m$  (the mass transport coefficient) can be derived from eqns [29]–[31], will need correcting. Equation [14] is the summation of activation current density,  $i_a$ , which is controlled by the charge transfer kinetics and the diffusion controlled current density,  $i_d$ , which is related to the mass transport of species to and from the reacting surface.

$$\frac{1}{i} = \frac{1}{i_a} + \frac{1}{i_d} = \frac{1}{zFk_1} + \frac{k_{-1}}{k_1 zFk_m} \quad [14]$$

where  $i$  is the corrosion current density,  $n$  is the number of electrons,  $F$  is the Faraday's constant,  $k_1$  is the forward reaction rate, and  $k_{-1}$  is the backward reaction rate.

The values of  $k_m$  are normally obtained from non-dimensional correlations between the Sherwood number  $Sb = (k_m L/D)$ , the Schmidt number  $Sc = (\nu/D)$ , and the Reynolds number  $Re = (UL/\nu)$ .

$$Sb = aRe^x Sc^y \quad [15]$$

Giving

$$k_m = aD^{1-y} L^{x-1} \nu^{y-x} U^x \quad [16]$$

Taking typical values for the exponents as  $x=0.6$  and  $y=0.33$  for turbulent pipe flows where  $2000 < Re < 5000$ <sup>9</sup> gives

$$k_m = aU^{0.6} \left( \frac{D^{0.66}}{\nu^{0.27} L^{0.4}} \right) \quad [17]$$

where  $D$  is the diffusion coefficient,  $U$  is the flow velocity,  $\nu$  is the kinematic viscosity,  $L$  is the characteristic length, and  $a$  is the scaling constant.

Flow corrosion rates induced by solids-free flows, as suggested by eqn [14], have been shown to depend on  $k_m^n$  where  $n$  varies depending on the surface–environment combinations and the controlling corrosion mechanism. For example, corrosion rates for copper alloys in seawater under partial activation or mixed control are shown to have  $n < 1$ . Steels in sulfuric acid and under simple mass transfer control have  $n = 1$ ; while for steels in water where flow modifies the corrosion potential and also influences the solubility of the oxide,  $n$  lies between 1 and 3, see Poulson.<sup>9</sup> The rates of

mass-transport processes also increase with increasing surface roughness. For pipes, different relationships apply depending on the surface finish. When surface roughness is developed on a pipe wall, the rate of mass transfer is proportional to the flow turbulence or the velocity distribution in the laminar sublayer.<sup>36</sup> For a fully eroded pipe with so-called scalloped surfaces where erosion scars resemble inverted scallop shells

$$Sb = 0.005 Re Sc^{0.33} \quad [18]$$

For a previously roughened pipe

$$Sb = 0.007 Re^{0.96} Sc^{0.33} \quad [19]$$

The upper bound value is reached for extremely rough surfaces and given by

$$Sb = 0.01 Re Sc^{0.33} \quad [20]$$

However, a power-law relationship between erosion-corrosion rate and  $k_m$  is not always seen as in the case of steel where surface films are removed above a critical  $k_m$  resulting in a sudden increase in erosion-corrosion rate.

It has also been proposed that corrosion films/coatings can also be damaged and/or completely removed by mechanical forces resulting from the impact of either small fluid packages contained in eddies and/or bubbles created by highly turbulent flows.<sup>42</sup> Attempts to quantify the effective hydrodynamic forces in terms of wall shear stresses have been confronted with the problem that the measured wall shear stresses in flow corrosion susceptible systems are orders of magnitude too small,<sup>43,44</sup> even under highly disturbed flow conditions, to overcome the fracture mechanics of the surface scales. It has been calculated that the destruction of such layers would require shear forces of the order of 1 MPa, while measurable wall shear stresses, even in highly turbulent flow, are only of the order of 1 Pa,<sup>45</sup> and thus are too small to be the right parameter to quantify hydrodynamic forces responsible for the initiation of flow corrosion. Nevertheless, critical flow intensities are undoubtedly identified in terms of critical wall shear stresses above which corrosion products are hydrodynamically damaged. This leads to the significance of lateral momentum transfer by the near-wall turbulence structures in the hydrodynamic boundary layer that disturb scales and/or protective films.<sup>42–45</sup>

The near-wall region can be divided into three distinct regions: (1) the viscous sublayer, (2) the buffer layer, and (3) the fully turbulent region. Turbulent features are often reported with reference to the dimensionless scale  $y^+ = v^* y/\nu$ , where  $v^*$  is the



friction velocity ( $=\tau_w/\rho$  or wall shear stress over fluid density),  $y$  is the vertical height above a horizontal surface, and  $\nu$  is the kinematic viscosity of the fluid. The viscous sublayer extends from the wall out to  $y^+ = 5-8$ . In this region, the mean velocity profile is linear and it is assumed that this region is devoid of turbulence. However, flow visualization has revealed slow-moving oscillations known as near-wall or sub-layer streaks.<sup>46,47</sup> These streaks are  $\sim 100y^+$  units across and  $1000y^+$  units long and are believed to occur as a result of elongated regions of alternating low- and high-speed fluid produced by streamwise vortices close to the wall. The near-wall streaks slowly lift up into the buffer region, where they undergo a distinct oscillation and finally break up violently  $\sim y^+ = 40$  (see **Figure 13**).<sup>48,49</sup> The majority of the turbulence production occurs in the buffer region from  $y^+ = 8$  to 30 to 50 during violent outward ejections of low-speed fluid and for continuity considerations, the ejections are followed by a sweeping inrush of high-speed fluid at a shallow angle toward the wall. An ejection transports low-momentum fluid from the wall region into the main flow. Conversely, sweep events transport high-momentum fluid from the main flow toward the wall (**Figure 13**) at velocities close to  $0.9U$ , where  $U$  is the free stream velocity. The result of these flows is fluctuating wall shear stresses, see **eqn [13]**, and pressures which will influence erosion-corrosion rates and mechanisms locally.

### 2.15.2.3 Wear Fundamentals

#### 2.15.2.3.1 Solid particle erosion

To understand erosion-corrosion, it is desirable to first understand the erosion mechanisms. Solid particle erosion in liquid systems is a process by which

discrete small solid particles that are suspended in the flow, with inertia, strike the surface of a material causing damage or material loss to its surface. Erosion can be a problem for components such as gas and hydraulic turbine blades, propulsors, pipelines, valves and fluidized bed combustion systems. An example of the surface features erosion can develop in flow through a valve is shown in **Figure 14**. Erosion does have its beneficial applications, notably for cleaning and preparation of surfaces for subsequent coating/painting, descaling/dewaxing of production risers in the oil and gas industries, oil sand transportation, hydrotransport systems and quarrying rocks using abrasive cutting jets, or subsea steel oil structures using submerged abrasive water jets.

The flow conditions along with the properties of the target material or any film, if present, as well as the fluid and erodent properties will influence the contact mechanics of the erodent to component surface interactions. The main important target material properties are hardness, fracture toughness, coefficient of restitution elasticity, and the degree of surface roughness. The general expression for erosion rate,  $E$ , has been established empirically and can take the form

$$E = M_p K f(\alpha) U_p^n \quad [21]$$

where  $M_p$  is the mass of particles impacting on the surface,  $U_p$  is the particle velocity on impact,  $\alpha$  is the particle impact angle,  $K$  and  $n$  (typically between 2 and 3)<sup>50</sup> are constants assumed to be dependent on the characteristics of the erodent/target materials involved, and  $f(\alpha)$  is a functional relationship for the dependence of the erosion rate on the impact angle.<sup>51</sup>

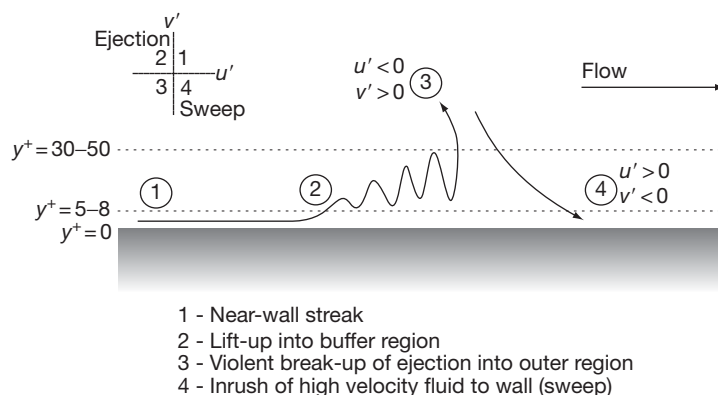


**Figure 13** Schematic showing the near-wall turbulence structures within the viscous sublayer, buffer layer, and fully turbulent region.



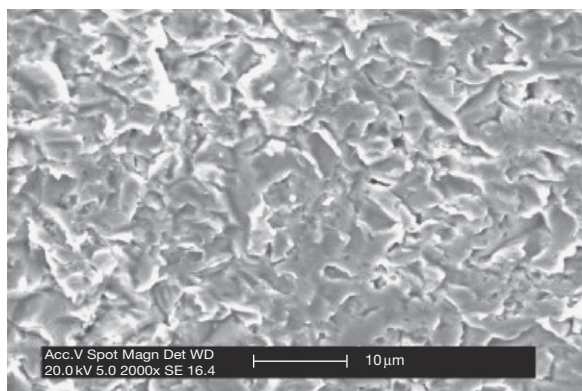
**Figure 14** Sand erosion patterns of a Stellite tapered flow passage located downstream of a choke valve that induced swirl flow. Large bore is 75 mm in diameter.

This can be rewritten for the unit volume loss per impact,  $V_u$ , as

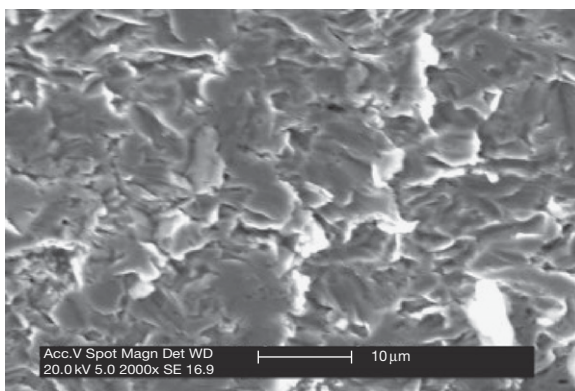
$$V_u = E_k^m f(\alpha) C_v G \quad [22]$$

where  $V_u$  is the volume loss per impact in units of  $\text{m}^3$  per impact,  $E_k$  is the particle kinetic energy (KE),  $m$  is the energy exponent with  $m = 0.5n$  assuming  $E \propto d^3$  where  $d$  is the particle diameter,  $C_v$  is the volume fraction,  $G$  is a constant, and  $f(\alpha)$  is as before. From eqn [21] or [22], it can be seen that the erosion rate will be strongly dependent on the KE of the impacting particles, the number of impacting particles, and the impact angle. All three of these factors vary for most industrial components exposed to solid particle-laden flows, and therefore, to sustain long service life, the internal surfaces must perform over a wide range of solid impact conditions. The sand-to-wall impact conditions are likely to depend on the flow regime present, the orientation and/or geometry of the component, the ability of the flow to keep the particles in suspension<sup>52</sup> and the relative size of erodents with respect to boundary layer thickness (small particles can form protective clouds within subviscous layers). For suspended solids traveling in a horizontal liquid flow, both the solid particle impact velocities ( $< 3.0 \text{ m s}^{-1}$ ) and angles are relatively low for most practical purposes.<sup>53</sup> Typical impact erosion craters are shown in Figure 15.<sup>54</sup>

Plots of  $V_u$  against KE of impact,  $E_k$  can be used to map the erosion performance of surfaces. These maps enable comparisons to be made between materials



(a)



(b)

**Figure 15** SEM micrographs of 0.2% CS (a)  $7 \text{ m s}^{-1}$  and (b)  $12 \text{ m s}^{-1}$ , 1 wt.% silica ( $296 \mu\text{m}$ ) sand in 0.1 M NaOH at  $40^\circ\text{C}$ , test time = 30 min. The eroded region observed was located approximately normal to the flow and in the center of the sample. Reproduced from Harvey, T. J.; Wharton, J. A.; Wood, R. J. K. *Tribology – Mater. Surf. Interfaces* 2007, 1(1), 33–47.

at a wide range of impact energies covering various particle sizes and velocities. However, it can be concluded that this plot format is not well suited to accommodating high levels of uniform corrosion in the presence of low energy and low concentrations of solid impacts. The approach assumes that all mass loss (mechanical and electrochemical) is generated by the impacting particle, and hence, all the erosion-corrosion ( $T$ ) data lie well above the  $E$  power law fit (straight line on **Figure 16**). As erosion becomes more influential (i.e., higher KE or higher sand concentrations), the data begin to approach the  $E$  power law fit, that is, the data move from left to right for increasing KE and vertically down for increasing sand concentration.  $E_k$  is defined as

$$E_k = 2/3\pi r_p^3 \rho_p U_p^2 \quad [23]$$

where  $r_p$  is the particle radius,  $\rho_p$  the erodent particle density, and  $U_p$  the impact velocity. Care should be taken as experimental evidence shows that erosion rates can be dependent on  $U_p^n d^y$  where  $U_p$  is the particle velocity and  $d$  is the particle diameter, and  $n$  and  $y$  are far removed from 2 to 3 assumed in the simple energy approach seen earlier.<sup>55</sup>

The main parameters of concern for erosion relate to the solid particle–target interactions and hence the number of particles impinging, individual particle

energies, particle impingement angles, particle-to-target hardness ratios, and the shape of the particles. Near wall particle–particle interactions can also severely influence erosion rates when the volume concentration of solid particles present is high.

Finnie<sup>56</sup> developed an erosion model based on cutting wear mechanisms of the form:

$$V_u = C_1 \frac{M_p U_p^2}{4\sigma} f(\alpha) \quad [24]$$

where  $C_1$  is an arbitrary constant denoting the proportion of particles that cut the surface. Gane and Murray<sup>57</sup> found a value of  $C_1 = 0.5$  and gave reasonable predictions. Keating and Nesic,<sup>58</sup> in numerically predicting erosion-corrosion in bends and sudden expansions by two-phase flows (liquid–solid), used a modified Finnie approach based on earlier work by Bergevin.<sup>59</sup> This approach incorporated the concept of a critical velocity for plastic deformation,  $U_{cr}$ . They substituted  $(U_p \sin \alpha - U_{cr})$  for the impact velocity in eqn [24] to give

For low angles ( $\alpha \leq 18.5^\circ$ )

$$V_u = \frac{M_p (U_p \sin \alpha - U_{cr})}{2\sigma} \times \left[ U_p \cos \alpha - \frac{3}{2} (U_p \sin \alpha - U_{cr}) \right] \quad [25]$$

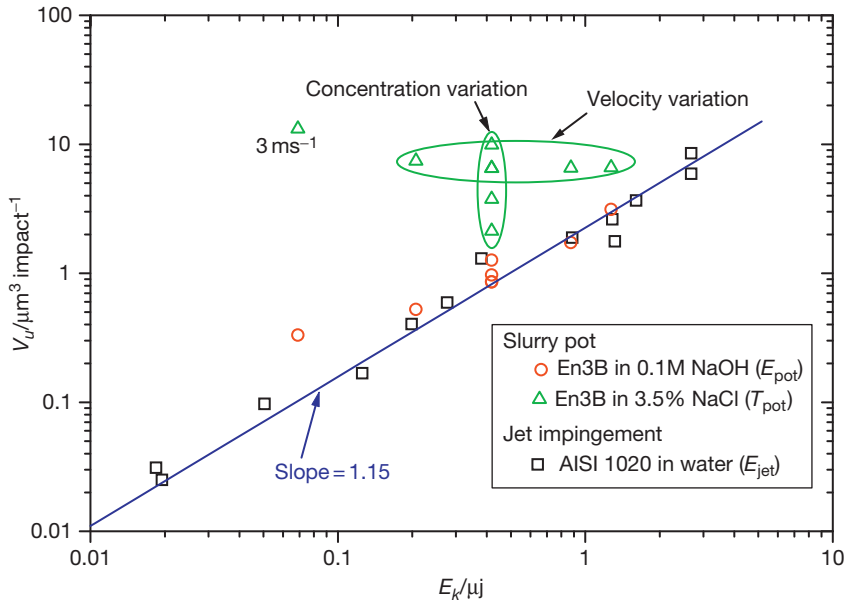


**Figure 16** Comparison of volume loss per impact against particle impact KE (slurry pot)<sup>54</sup> and jet impingement studies.<sup>31</sup> The  $\Delta$  indicates erosion–corrosion data, displaying the two sets of data (concentration and velocity) presented in previous plots.  $E_{pot}$  and  $E_{jet}$  are taken as mechanically nominated erosion from the slurry pot and jet impingement rigs respectively and  $T_{pot}$  is the erosion–corrosion data from the slurry pot.

For higher angles of impingement

$$V_u = \frac{M_p (U_p \sin \alpha - U_{cr})^2 \cos^2 \alpha}{12\sigma \sin^2 \alpha} \quad [26]$$

Bitter<sup>60</sup> quotes a value of  $U_{cr} = 0.668 \text{ m s}^{-1}$  for steel. Keating and Nesic used this value to successfully predict erosion rates in a sudden expansion and found the original Finnie model not to be so accurate. However, they modeled erosion-corrosion damage in a U-bend, using the original Finnie model as the modified version yielded no erosion due to the low particle velocities involved. Keating and Nesic concluded that their modeling needs more experimental validation before further refinements can be made.

Erosion models typically recognize that two erosion mechanisms act, cutting and deformation erosion, with discrete models representing each, such as the Neilson and Gilchrist erosion model used for rocket motor nozzles.<sup>61</sup> Such models have been successfully used by Forder<sup>62</sup> and Wood and Jones<sup>63–67</sup> to predict erosion of internal components within choke valves and slurry ducts. The cutting erosion model for low impact angles was first proposed by Finnie<sup>56</sup> and later modified by Hashish.<sup>55</sup> The deformation model was proposed by Bitter<sup>60</sup> and is thought to be applicable at higher impact angles ( $30^\circ$ – $90^\circ$ ). Particle shape and material properties for both particle and target have been included, which earlier simpler models have not considered. As the particle impingement angles are predicted to be below  $10^\circ$ , for critical components such as straights and bends, see Wood and Jones,<sup>63–67</sup> the contribution to the overall wear rate from deformation mechanisms can be ignored, and hence, the

volumetric erosion per impact can be given by the modified Hashish model only

$$V_u = \left\{ \frac{100}{2\sqrt{29}} r_p^3 \left( \frac{U_p}{C_k} \right)^n \sin 2\alpha \sqrt{\sin \alpha} \right\} \quad [27]$$

where  $n = 2.54$  and

$$C_k = \sqrt{\frac{3\sigma R_f^{0.6}}{\rho_p}} \quad [28]$$

Experimental studies on pipe systems show variation of the erosion mechanism and location with flow regimes. Wood and Jones<sup>63–67</sup> show erosion damage of AISI 304L stainless steel pipe components with a nominal wall thickness of 5 mm from a horizontal pipe loop tests. The pipes were of 80 mm nominal bore, although the actual mean of a series of measurements was 77.8 mm. The erosion of the bend with the greatest curvature of the whole loop ( $R_c/D = 1.2$ ) was analyzed along with its upstream straight.

Figure 17 shows the top internal surfaces (12 o'clock position) of the straight pipe after 210 h of slurry testing at  $3 \text{ m s}^{-1}$  with an asymmetric slurry flow of 10% (w/w) sand of 500–1400  $\mu\text{m}$  in size in water. Figure 18 shows the overall component details for the straight and bend investigated. The damage in Figure 17 is consistent with that of the as-manufactured (scaled) surface finish. There appears to be no significant erosion impact damage, although a few individual impact craters are seen due to impacts from the relatively few sand particles that are entrained into the energetic upper fluid flow. The lack of damage seen in Figure 17 is in contrast with the damage seen at the bottom of the straight pipe section as shown in Figure 19. This reflects

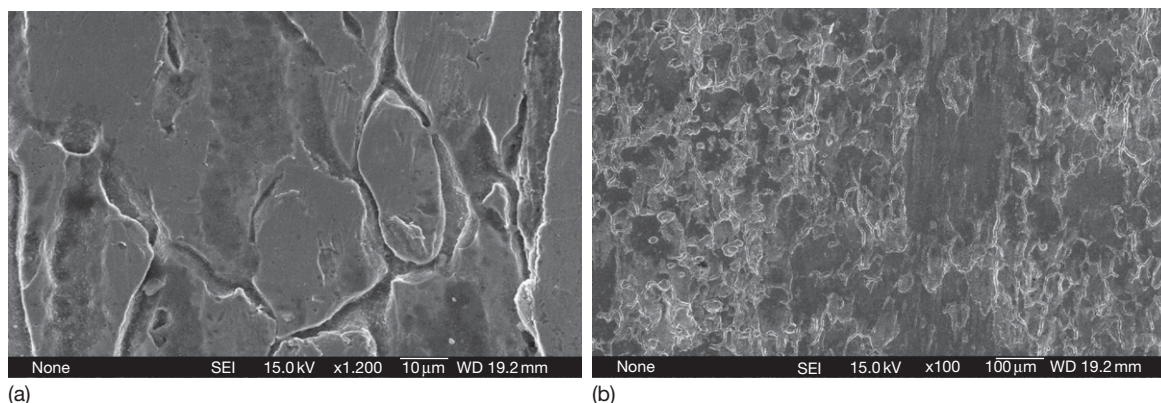


**Figure 17** SEM micrographs at (a) high and (b) low magnifications showing surface morphology of straight position (top A position) (after 210 h).



the asymmetry of sand burden in the flow with the majority of sand particles traveling in the bottom half of the pipe and only a few energetic particles saltating into the flow streams in the top half of the pipe.

In **Figure 19**, the impact features reveal that the erosion processes occurred by a simultaneous plastic deformation and microcutting of the stainless steel pipe surface, similar to type II cutting mentioned by Hutchings when the erodent rotates backwards on impact and efficiently machines the surface.<sup>8</sup>

Erosion of the bend outer wall at section two (shown in **Figure 18**) is even more intense as shown in **Figure 20**. The surface of the bend at position C (3 o'clock) has clearly been eroded with evidence of low-angle impingements with extensive plastic deformation and cutting (type II) resulting in the removal of the as-manufactured surface morphology. This level of damage is a result of impingement

by the larger and energetic sand particles with the bend wall and reflects the repositioning of the particle burden due to the bend geometry and resulting change in flow direction. Erosion-corrosion models should concentrate on such impact scars and their repassivation.

#### 2.15.2.3.2 Cavitation erosion

Cavitation bubble collapse close to a solid surface can damage the surface by two mechanisms: shock wave impingement and high-speed liquid microjet impingement. Shock waves are formed by the rapid collapse of the bubble, which generates very high internal temperatures and pressures that are relieved by shock wave propagation. The presence of the solid surface generates asymmetric bubble collapse and the formation of a microjet with a diameter of 10–50  $\mu\text{m}$  that impinges onto the surface at normal incidence

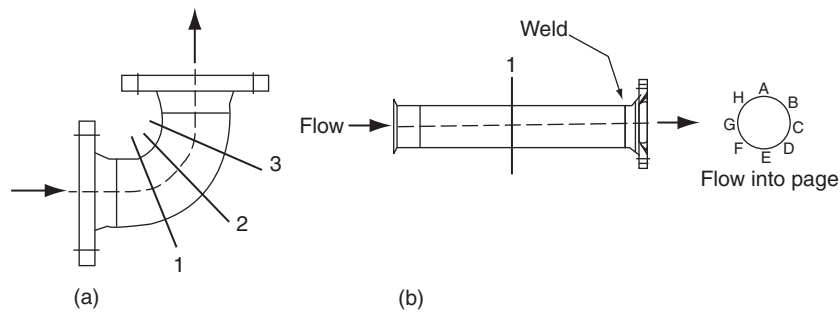


**Figure 18** Drawings of bend and straight sections which were mounted horizontally and subjected to asymmetric slurry flow for 210 h.

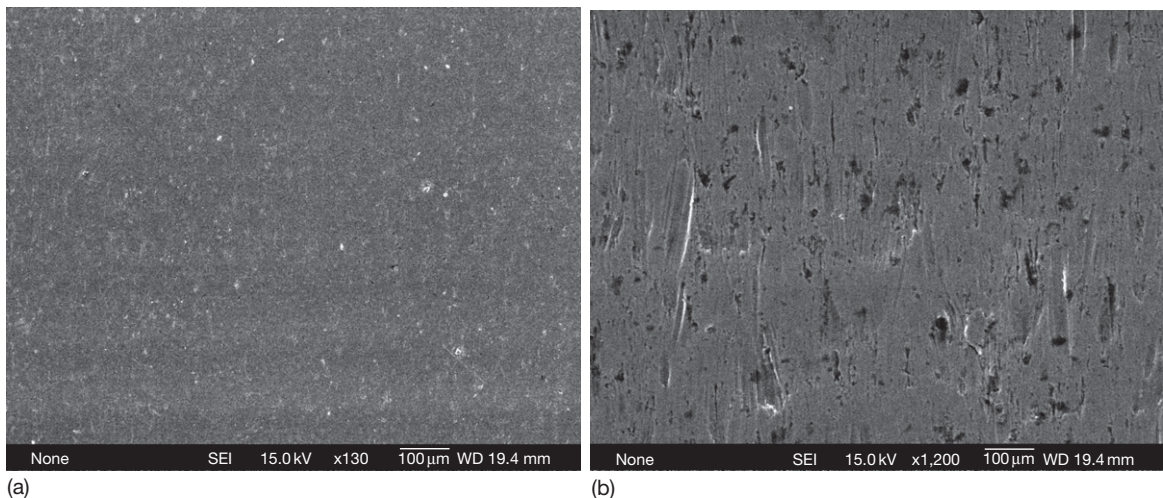


**Figure 19** SEM micrographs showing the surface morphology of the straight pipe at the bottom (position E) after 210 h. (b) shows individual impact scars from sand microcutting at low angle impingements with the pipe surface.



at  $\sim 250\text{--}300\text{ m s}^{-1}$ . Both of these processes produce localized temperature rise, high intensity turbulence, and transient high pressures of the order of  $\rho cV$ . These pressures are large enough to cause plastic deformation in most engineering surfaces. These pressures and temperatures enhance mass transport and electrochemical reactions and thereby also accelerate corrosion rates of metallic surfaces. The erosion produced by such near-wall bubble collapse is thought to be dominated by a fatigue process and thus cavitation erosion resistant surfaces tend to have high fatigue resistance.

The overall damage induced by cavitation and corrosion therefore involves the interaction of

hydrodynamic, mechanical, metallurgical, and chemical factors. The presence of oxygen and aggressive ions in the electrolyte is thought to be important parameters in controlling cavitation-corrosion rates. Liu *et al.*<sup>68</sup> show that cavitation-corrosion of CS in NaCl solutions is mainly controlled by the diffusion of oxygen to the surface and is sensitive to temperature and NaCl concentrations, see [Figures 21 and 22](#). The erosion process promotes anodic dissolution reactions, which are charge transfer (activation) controlled. The impingement of the microjets is also likely to contribute to surface activation by damaging the surface layer of CS corrosion products. They also

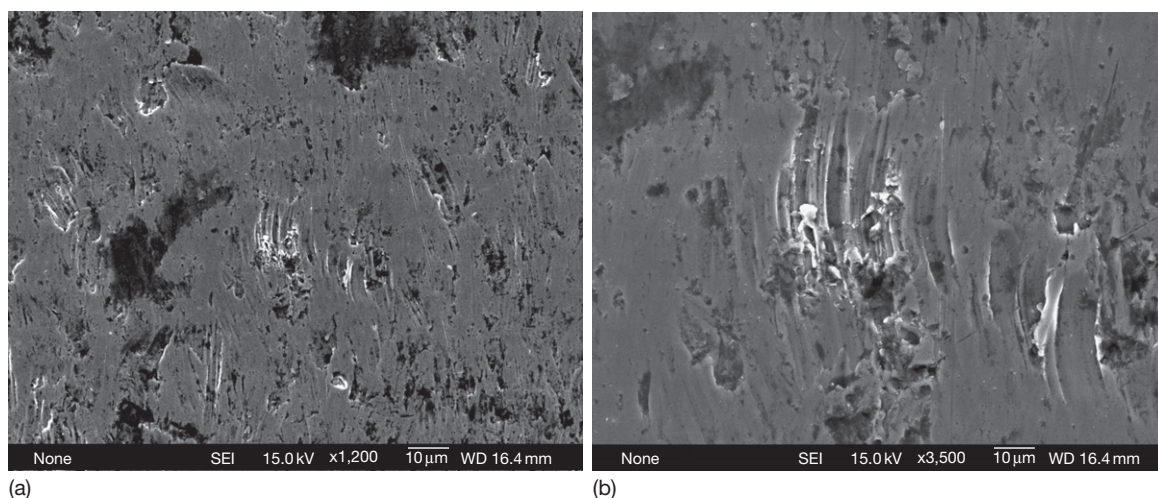


**Figure 20** Micrographs showing the surface morphology of bend erosion outer wall at section two and position C. Both images show impact craters with extensive plastic deformation and cutting damage.

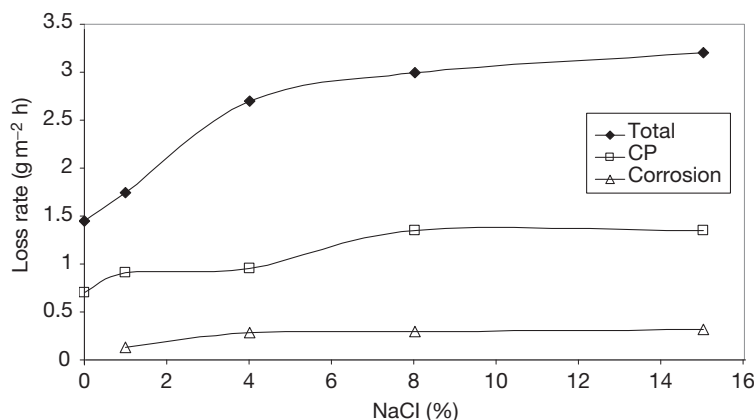


**Figure 21** Effect of cathodic protection on cavitation-corrosion of CS. Total = cavitation-corrosion loss rate, CP = loss rate under cathodic protection (Cathodic overpotential of 450 mV), Corrosion = corrosion rate from *in situ* electrochemical measurements. Reworked data from Lui, J.; Lin, Y.; Yong, X.; Li, X. *Corrosion* **2005**, 61(11), 1061–1069.

show that the application of cathodic protection dramatically reduced the surface wastage rates.

Little systematic research appears to have been conducted on cavitation-corrosion. However, surfaces that combine high fracture toughness and corrosion resistance have typically been studied. A cathodic arc plasma ion plated Ni–Al film on AISI 1045 CS has been reported by Chang *et al.*<sup>69</sup> to show good cavitation erosion-corrosion resistance. Three coating compositions were studied, Ni–48Al, Ni–40Al, and Ni–30Al, and all increased the cavitation erosion resistance of the substrate 10 times and the erosion-corrosion resistance to 3.5% NaCl solutions two times and to 3.5% HCl solutions three times. The potentiodynamic polarization data of the coated specimens in these two electrolytes indicated that the coated specimens exhibited a more electropositive corrosion potential and a lower corrosion current density than did the bare substrate material. However, cavitation erosion

induced pitting corrosion of the substrate and this accelerated the mass loss rate of specimens (see **Figure 23**).

Chernega *et al.*<sup>70</sup> found that cyclic cavitation erosion-corrosion interactions increased the material loss of complex carbide coatings 1.5–2 times the continuous cavitation rates. They found that cyclic cavitation-corrosion wear processes on high velocity oxy-fuel (HVOF) carbide coatings based on Cr, Cr–Zr, Cr–Nb, Cr–Si, and Nb were enhanced by 10–20% in NaCl solutions compared with pure water. The cyclic cavitation-corrosion treatment enhanced the average corrosion processes over time by factors of between 2 and 4 compared with a continuous cavitation corrosion influence. This enhancement was related to the destruction of the protective surface oxide films, the removal of corrosion products, and the increase in microcracks in the diffusion coating as a result of microshocks produced by near-surface cavitation bubble collapse.

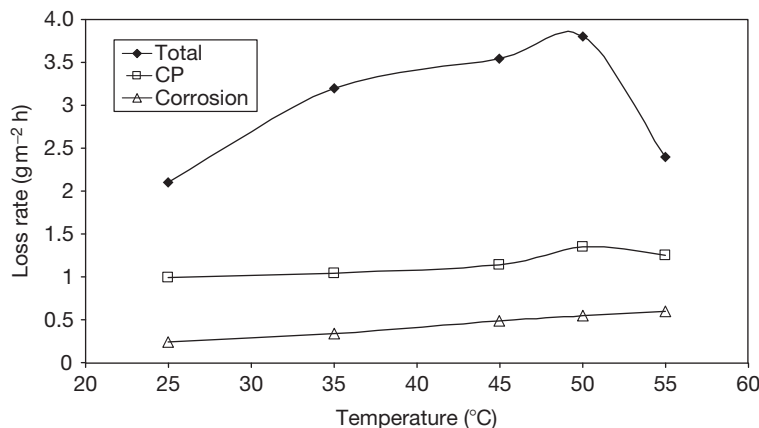


**Figure 22** Effect of cathodic protection on cavitation-corrosion of CS. Total = cavitation-corrosion loss rate, CP = loss rate under cathodic protection (Cathodic overpotential of 450 mV), Corrosion = corrosion rate from *in situ* electrochemical measurements. Reworked data from Lui, J.; Lin, Y.; Yong, X.; Li, X. *Corrosion* **2005**, 61(11), 1061–1069.

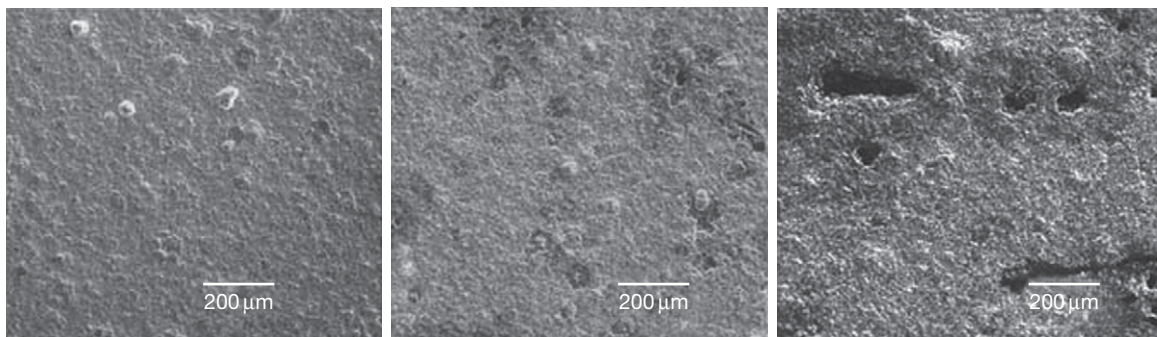


**Figure 23** Surface morphology of a Ni–48Al intermetallic coating (a) untested, (b) tested for 30 min, and (c) for 60 min in 3.5% NaCl electrolyte at ASTM G32–98 ultrasonic cavitation test conditions. Reproduced from Chang, J. T.; Yeh, C. H.; He, J. L.; Chen, K. C. *Wear* **2003**, 255, 162–169, Part 1 AUG–SEP 2003.

**2.15.2.3.3 Abrasion**

There are two types of abrasion: two-body or grooving abrasion as shown in **Figure 24(a)**, while three-body or rolling abrasion is illustrated in **Figure 24(b)**. There are various important parameters that control abrasion rates such as the hardness ratio between abrasant and target, the load per particle, the role of the fluid film and if it supports the contact load, particle entrainment, size and shape, and friability. Wear rates of rolling abrasion are generally lower than those generated by grooving abrasion. Industrial surveys place abrasion as the most common wear mechanism with over 50% of wear problems being associated with both types of abrasion.<sup>71</sup> In abrasive wear, material is removed or displaced from a surface by hard particles, or sometimes by hard protuberances or asperities on a counterface, forced against and sliding along the surface. The sources of the hard particles, which can be entrained into the sliding contact, include contaminants from the outside environment, wear debris, and oxidation products formed with the tribocontact or other chemical processes.

**Figure 24(c)** is a schematic of three-body rolling abrasion of a passive surface showing a wear rate that strips the passive film completely.

**2.15.2.4 Experimental Techniques**

**Table 4** lists the variety of experimental techniques used to study wear-corrosion interactions or aspects of these interactions. Most are either corrosion cells attached to wear testers or attempts to modify corrosion cells to induce some tribological contact (i.e., scratch test or adding slurry in a rotating disc/cylinder electrode). This is not ideal as experimental setups should reflect the best approach for wear and corrosion measurements and should be designed specifically and should not be just a modified existing tribotester.

**2.15.3 Tribocorrosion Mechanisms**

The interaction between tribological and electrochemical corrosive effects causes materials to corrode

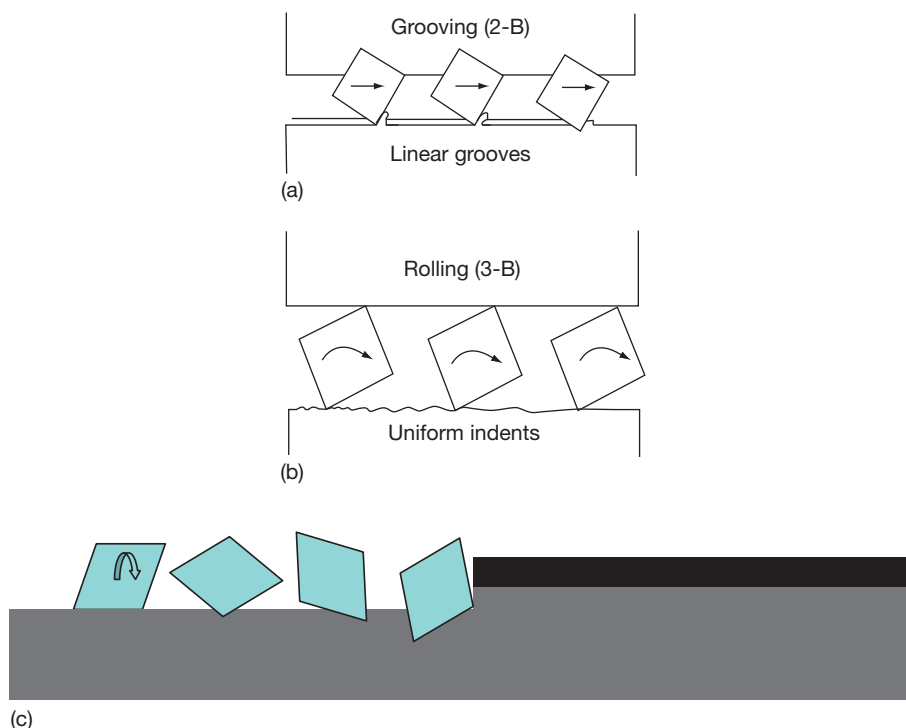


**Figure 24** (a) and (b): Schematics of two-body grooving and three-body rolling abrasion, (c). Depassivation of a passive surface by three-body rolling abrasion removes the passive layer and some substrate material revealing bare metal surface.

**Table 4** Experimental techniques used to study wear-corrosion interactions or aspects of these interactions

	<i>Technique</i>	<i>Parameters evaluated</i>	<i>Comment</i>
Engineering-based rig with added electrochemical cell	Pin-on-disc, block on cylinder	Friction, linear wear, temperature, wear scar, electrochemical parameters, current/potential versus time, polarization, <i>in situ</i> AC techniques (EIS)	Can generate complex electrochemical outputs and functionality of electrochemical cells – needs careful scrutiny
	Reciprocating pin on plate		
Electrochemical rig with mechanical elements added	Abrasion and microabrasion		
	Continuous grinding		
	Instantaneous fracture <sup>72</sup>		
	Scratch tester <sup>73</sup>		
	Rapid strain <sup>74,75</sup>		
	Guillotine cutting <sup>76</sup>		
	Triboellipsometry <sup>77</sup>		
	Cavitation hydrodynamic and vibrating horn)		Vibrating horn not representative of hydrodynamic cavitation erosion
	Impinging fluid jet/slurry jet	Peak current densities (passive and nascent), surface potential, repassivation rates, wear rate, volume loss per impact, friction, surface temperature	Uniform current distribution but shear rate varies with radius
	Pipe flow		Nonuniform flow/mass transfer distribution, rough surfaces, nonuniform current distribution
	Rotating disc (laminar)		Nonuniform current distribution, shear rate varies with radius of disc
	Rotating cylinder (turbulent)		Uniform current distribution but smooth electrode surface

at a substantially higher rate than those experienced under static or quiescent conditions.

### 2.15.3.1 Mechanical–Electrochemical Interactions

This section focuses on erosion-corrosion, abrasion-corrosion, and sliding wear-corrosion interactions as there is published work in these areas. The effects of the environment on the wear-induced fatigue life are not well researched and thus are not well understood and will not be reviewed further but the readers are referred to Sethuramiah<sup>78</sup> for a review of related work.

#### 2.15.3.1.1 Erosion-corrosion

There are several possible regions of erosion-corrosion interaction between different flow regimes and corrosion. The most significant erosion-corrosion regions are where turbulent slurry flow and corrosion overlap and where cavitation interacts with corrosion, although it is possible that solids entrained into laminar flows could induce erosion-corrosion if their impact energy is sufficient to cause plastic deformation of the surface or puncture the tribofilm.

Figure 25 shows the mass loss rates for various sand concentrations for CS in 0.1 M NaOH solution for erosion rates and in 3.5% NaCl solution for erosion-corrosion rates.<sup>54</sup> These results were

obtained at  $7 \text{ m s}^{-1}$  fluid stream velocity and at  $40^\circ\text{C}$ . The erosion rates  $E$  (0.1 M NaOH solution results) show a nonlinear increase with increasing velocity. The static corrosion rate  $C$  is shown on the far left and this plus the erosion rates at the various velocities should equate to the erosion-corrosion rates  $T$  at the various velocities if no synergistic effects are present. However, as seen, the synergy terms goes negative and the interactions between  $E$  and  $C$  are, therefore, antagonistic at 0.5 w/w% sand concentration ( $T < (E+C)$ ), while a synergy is present for higher concentrations ( $T > (E+C)$ ).

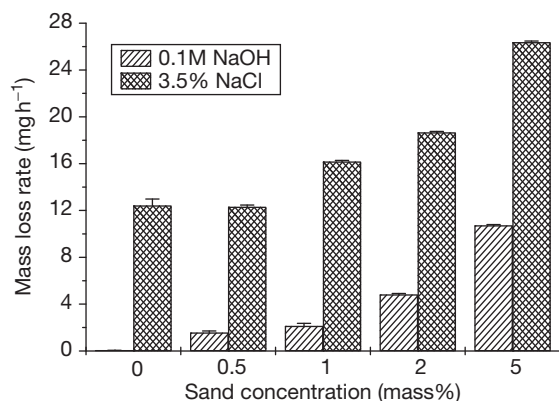


**Figure 25** Experimental results for sand concentration variation at  $7 \text{ m s}^{-1}$  (294  $\mu\text{m}$  silica sand at  $40^\circ\text{C}$ ). The exposed surface area of the sample to erosion was  $3.4 \text{ cm}^2$ . Reproduced from Harvey, T. J.; Wharton, J. A.; Wood, R. J. K. *Tribology – Mater. Surf. Interfaces* **2007**, 1(1), 33–47.

**Figure 26** shows results for the same material as **Figure 25** at 0% and 1% (w/w) sand concentrations for a variety of velocities at  $40^\circ\text{C}$ .<sup>54</sup> This shows that erosion rate  $E$  is dependent on  $V^2$  but that the erosion-corrosion rate  $T$  is not linearly dependent on either  $V$  or  $V^2$ . At  $3 \text{ m s}^{-1}$  there is an antagonism, while at higher velocities a synergy is seen due to the presence of surface residual stresses and scales (layers) generated by the drawing processes used to manufacture these cylindrical samples.

When corrosion rate is partially or wholly controlled by mass transfer of reactant or product from the surface, then local conditions under erosion may well influence the mass transfer kinetics (measured by the mass transfer coefficient  $k_m$ ). Under such conditions the corrosion will be controlled by the mass transfer (typically diffusion processes) and the driving concentration gradient (relative concentrations of active species near surface compared with free stream concentrations).<sup>79</sup> Both the mass transfer and concentration gradient will be affected by solid particle impingement that influences the local fluid flow field and increases surface roughness. Erosion will also increase the surface area wetted by the corrosive electrolyte and could establish microgalvanic cells on the surface with damaged areas being anodic to the passive and (cathodic) unaffected areas.

The relationships between fluid mechanics and induced flow patterns for both open and closed fluid systems are covered elsewhere.<sup>80</sup> It is important to

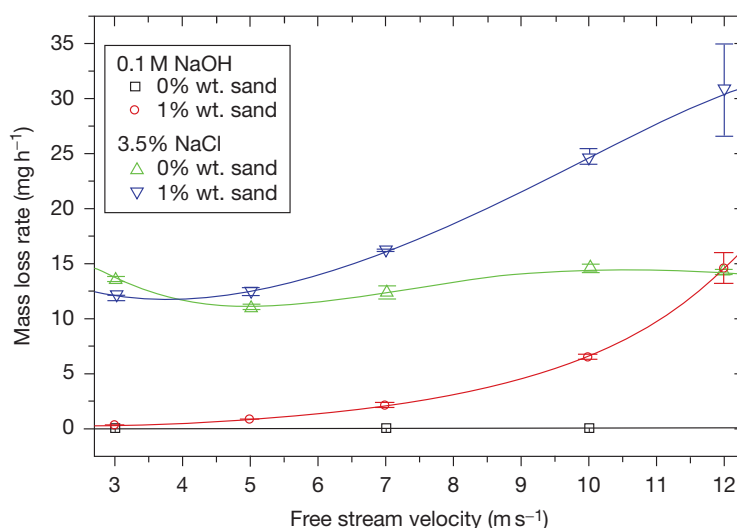


**Figure 26** Experimental results for free stream velocity variation at 0% and 1% by weight sand concentration (294  $\mu\text{m}$  silica sand at  $40^\circ\text{C}$ ). Reproduced from Harvey, T. J.; Wharton, J. A.; Wood, R. J. K. *Tribology – Mater. Surf. Interfaces* **2007**, 1(1), 33–47.



understand the near-wall flow conditions if erosion-corrosion rates and locations are to be accurately quantified for engineering components. In particular, the development of eddy structures in turbulent flows through lateral momentum transfer between fluid elements, which in turn disrupt the turbulent boundary layers that are developed within near-wall flows,<sup>81–83</sup> requires particular attention as such eddies can develop localized damage patterns on solid surfaces that can lead to an accelerated loss of fluid containment and thus considerably decrease component life. An example is given in the following section, namely rippling in pipe flows

#### **Rippling of pipe surfaces by erosion-corrosion induced by near-wall turbulence**

For multiphase flows (solid–liquid), it is assumed that initially the turbulent eddy pattern in the flow is determined by the surface roughness generated by the finishing of the pipe (see **Figure 27(a)**). The ability of the sand particles to erode is largely determined by the bulk flow but will result in the modification of the surface roughness. The initial surface roughness is thus replaced by the roughness resulting from individual erosion events. In ductile materials, such as stainless steels, this roughness will be in proportion to the impact scar dimensions (**Figure 27(b)**). These in turn give rise to a new eddy pattern in the near-wall flow. During the erosion process, the sand particles have to pass through these eddies and are thereby deflected. The eddy pattern determines the angle of impact and areas of increased sand particle impact and also the corrosion rates over the surface. The concentration of damage at specific points results in the establishment of a ripple pattern, reflecting the turbulence pattern. The surface waviness increases

until a steady state is reached, at which point the surface continues to wear but the wavelength and shape remain constant (**Figure 27(c)**). The final waviness is thus a reflection of the conditions to which the material is exposed. The more severe the condition, the greater the turbulence in the boundary layer and hence the larger the wavelengths and amplitudes of surface waviness.

#### **2.15.3.1.2 Abrasion-corrosion**

The interactions between two sliding metallic surfaces that entrain abrasives between them in a corrosive environment are often complex. **Figure 28** is an attempt to schematically represent some of the possible processes involved when abrasive (body 3) enters a sliding contact between bodies 1 and 2. The abrasive can depassivate the surface by penetrating or removing the oxide layer thereby enhancing corrosion at these sites. Abrasive wear particles can be formed from either or both surfaces and can be transferred and deposited on the opposite surface (4 and 5) resulting in galvanic coupling and accelerated corrosion. The ploughing and indentation action of the abrasives on the surfaces will also induce residual stresses (tensile and compressive) and induce strains that could result in microgalvanic cells being established between affected and unaffected surface areas. Abrasion of the original oxide layer could also result in better corrosion-resistant films by producing new surfaces of different composition. For example, the good abrasive corrosion behavior of plasma-nitrided 4140 low-alloy steel reported by Lee *et al.*<sup>84</sup> was linked to the presence of the nitrided layer with a homogeneous structure of  $\epsilon$  and  $\gamma'$  phases enriched with Cr and N atoms. Under abrasion-corrosion, this layer produced a thick and dense protective layer that

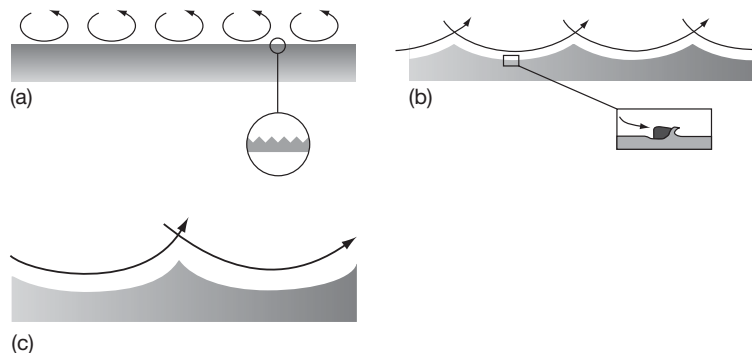


**Figure 27** Ripple formation due to turbulence eddies and the influence between microroughness and eddy size: (a) initial stage with turbulence boundary layer, microroughness determined by prior machining operations; (b) intermediate stage with larger eddies due to changing surface roughness; microroughness determined by the individual erosion event; (c) final stage with steady ripple pattern, after. Reproduced from Karimi, A.; Schmid, R. K. *Wear* **1992**, 156, 33–47.

resulted in a significant decrease in corrosion current in chloride solutions.

**Figure 29** shows results from microabrasion and abrasion-corrosion tests showing a synergy for all but very low concentrations of abrasive. The lowest concentration shows a slight antagonism and under these conditions, two-body grooving abrasion dominates while at concentrations above 0.05 volume fraction the mechanism is three-body rolling abrasion. This shows that the type of abrasion can lead to different wear-corrosion interactions.

More complex and sometimes negative (antagonistic) interactions between abrasion and corrosion occur on composite surfaces.<sup>85</sup> Here, preferential corrosion at the carbide–binder interface resulted in

a 20% reduction in abrasion-corrosion wear rate compared with purely abrasive conditions. The physical mechanism of this antagonism is thought to relate to the preferential corrosion of metallic tungsten at the carbide–binder interface resulting in loose and flexible carbides and a lowering contact stresses under abrasion conditions that in turn reduces material loss, see **Figures 30 and 31**.

*In situ* electrochemical measurements made during abrasion-corrosion tests are useful as they record the kinetics of the reactions occurring and as well inform on the degree of depassivation and repassivation. **Figure 32** is a typical example of such measurements. It shows the OCP and current recorded during separate microabrasion-corrosion tests at pH 11 on a thermally

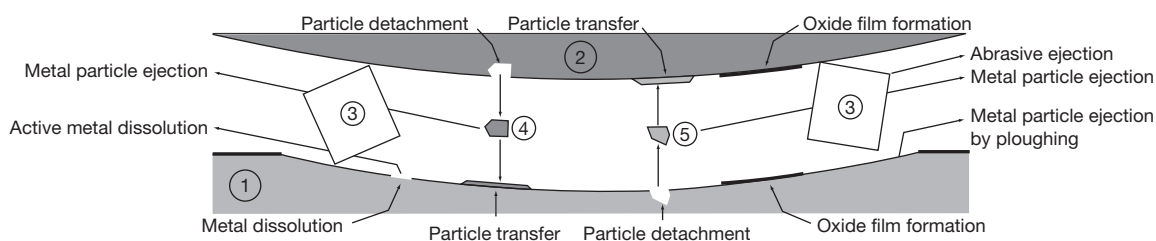


**Figure 28** Schematic illustration of the tribocorrosion contact involving two metallic samples (first body and second body) and abrasive particles (third body). Wear particles originating from the first and second bodies (4 and 5) form additional contact components. The corresponding material fluxes are also indicated.

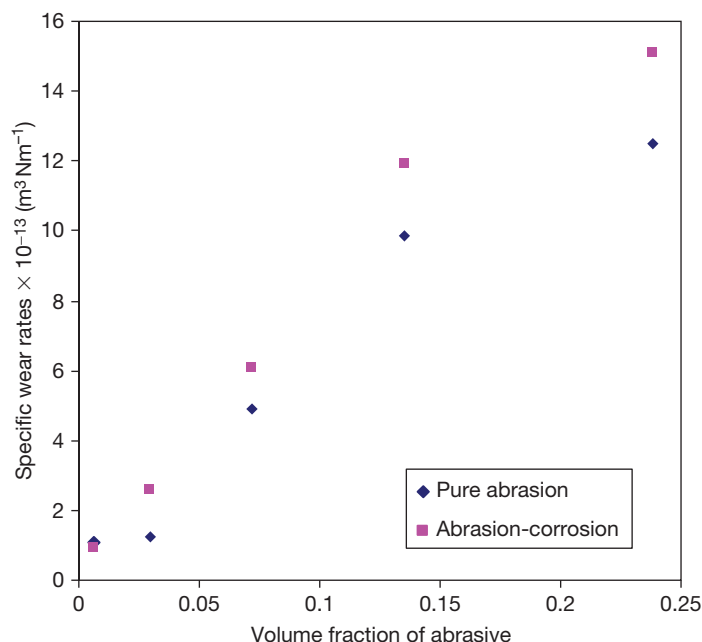


**Figure 29** Microabrasion and abrasion-corrosion expressed as specific wear rates (SWR) of type-316 stainless steel as a function of abrasive concentration. The load was 5 N and the electrolyte was distilled water for the abrasion tests and 3.5% NaCl solution for abrasion-corrosion. The abrasive used was 4  $\mu$ m SiC.

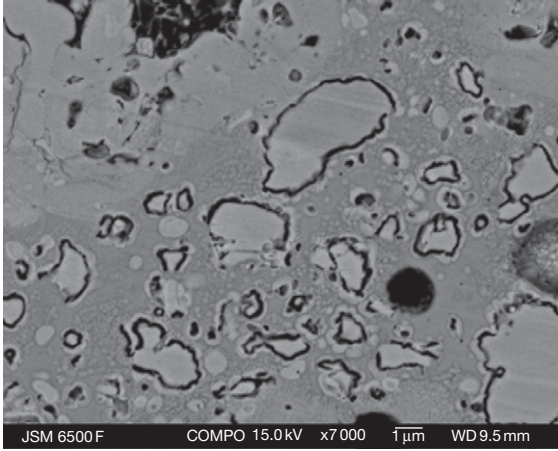


**Figure 30** Selective corrosion of W and  $W_2C$  phases (which are formed due to decarburization of WC) around the periphery of the carbide grains in a HVOF sprayed WC-10Co-4Cr coating when exposed to an alkaline environment of pH 11 for 168 h.

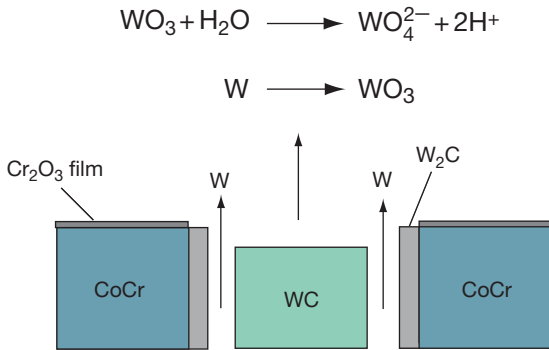


**Figure 31** Schematic showing the selective corrosion of W and  $W_2C$  phases in a WC-10Co-4Cr coating.

sprayed tungsten carbide coating. The potential drops by  $\sim 60$  mV over a 250 s period once ball rotation and abrasion commences, while the current instantly increases from low freely corroding levels to  $2 \mu\text{A}$ . Both these trends show that depassivation is occurring in the wear scar area. On stopping the rotation of the ball, and thus abrasion, at 2200 s, the potential recovers in the electropositive direction and the current decreases toward the initial freely corroding levels, indicating repassivation of the wear scar.

### 2.15.3.1.3 Sliding wear-corrosion

As discussed earlier, typically passive oxide films are responsible for the corrosion resistance of metallic surfaces. However, these oxides are vulnerable when subjected to tribological contact conditions where

mechanical effects can damage or completely remove these films. This typically leads to accelerated corrosion in regions of damaged or removed oxide films.<sup>86</sup>

Ponthiaux<sup>87</sup> suggests that it is important to understand the galvanic activity resulting from worn areas surrounded by unworn areas in order to predict the performance of tribocorrosion contacts. Garcia<sup>88</sup> developed a model for the current  $I$  that flows through an electrode of area  $A$  at a given anodic potential when subjected to a reciprocating wearing contact with a frequency of  $f$  as

$$I = fA_a \int_0^{1/f} i_a(t) dt + f(A_s - A_a) \int_0^{1/f} i_p(t) dt \dots \quad [29]$$

where  $A_a$  is the worn area,  $A_s - A_a$  is the passive area,  $i_a(t)$  is the repassivation current density, and  $i_p(t)$  is the passive current density at a given anodic potential.

A model that incorporates a time constant for repassivation has been developed by Goldberg<sup>89</sup> for currents generated by scratching passive surfaces. It has the form

$$I(t) = I_{\text{peak}} \exp\left(\frac{-(t - t_0)}{\tau}\right) + I_p \dots \quad [30]$$

If Tafel behavior is applicable, then

$$I_{\text{peak}} = i_p A_r e^{[n_f/b_a]} + \frac{\delta \rho_{\text{ox}} z F A_r}{M_w \tau} \dots \quad [31]$$

where  $I_{\text{peak}}$  is the peak current ( $I_{\text{peak}} = I_{\text{max}} - I_p$ ),  $I_{\text{max}}$  is the maximum recorded current,  $\tau$  is the time constant for repassivation,  $t_0$  is the time to produce the scratch,  $I_p$  is the passive current at  $t = \infty$ ,  $i_p$  is the current density for passivation,  $A_r$  is the scratch area,  $n_f$  is the scratch overpotential,  $b_a$  is the Tafel slope,  $\delta$  is the repassivated oxide thickness,  $\rho_{\text{ox}}$  is the oxide density,  $z$  is the charge on the cation,  $F$  is Faraday's constant, and  $M_w$  is the oxide molar mass.

Mischler<sup>90</sup> developed a model for reciprocating contacts that includes the effects of load and material hardness. He modeled the anodic current  $I_{a,w}$  generated by wear induced by a hard insulating counter body.

$$I_{a,w} = K_w l f \left(\frac{W}{H}\right)^{\frac{1}{2}} \int_0^{1/f} i dt \dots \quad [32]$$

where  $K_w$  is the proportionality factor,  $l$  is the length of wear track,  $W$  is the normal load,  $H$  is the hardness of metal,  $t$  is the instant time,  $f$  is the frequency of reciprocation of contact or rotation rate if for pin-on-disc, and  $i$  is the instantaneous current density.

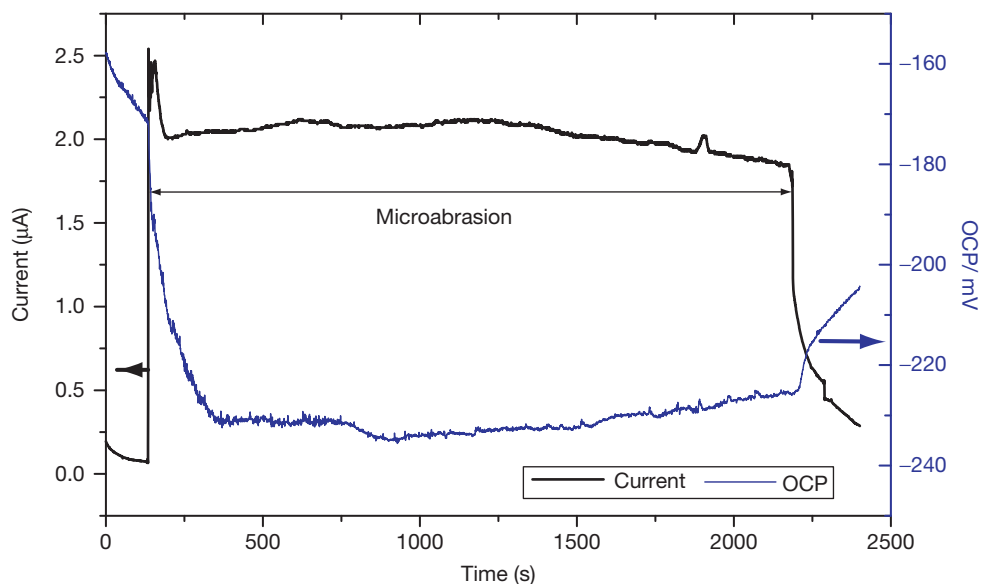


**Figure 32** OCP and current as a function of time during microabrasion of a 250  $\mu\text{m}$  thick D-Gun WC-10Co-4Cr coating on stainless steel 316 for a sliding distance of 90 m using 0.16 volume fraction slurry of 4.5  $\mu\text{m}$  SiC abrasives suspended in NaOH solution of pH 11. The applied load was 0.2 N and a Zirconia ball of 25.5 mm dia was rotated to give a sliding velocity of 0.05  $\text{m s}^{-1}$ . Reproduced from Wood, R. J. K. *J. Phys. D: Appl. Phys.* **2007**, 40, 5502–5521.

These three models are essentially based on the same principle but involve different contact parameters. Their validity may be limited to the specific test conditions/rig geometry used in their development. More complex models are being developed for tribocorrosion interactions in aqueous sliding contacts,<sup>91</sup> and these will be explored in the following section. However, it is extremely important to recognize the roles of reactive species in the tribological processes. Jiang and Stack<sup>92</sup> discuss the mechanisms of wear debris generation and the roles of reactive species in the generation of wear debris during sliding wear in gaseous or aqueous environments. Low cycle fatigue was taken as an important mechanism for the generation of wear debris particles during sliding wear of metals. The generation of wear debris particles was described as a process of microcrack initiation and propagation. The presence of reactive species in the environment was taken to chemically activate reaction(s) at the crack tip that weaken(s) the bonding of atoms at the tip, increasing the rate of generation of wear debris particles. The ratio between the contact frequency and the corrosion passivation rate was found to be a very important factor in determining the dominant material loss regime for a given tribosystem. At low values, wear-induced corrosion tends to be more significant in causing the overall material loss.

However, corrosion-induced wear tends to be the dominant regime for material loss at high values.

### 2.15.3.2 Wear-Corrosion Interactions

#### 2.15.3.2.1 Mechanisms of enhanced surface degradation

These interactions can be defined as follows. The total damage under wear-corrosion,  $T$ , can be represented as

$$T = E + C + S \quad [33]$$

where  $E$  is the pure wear material loss and  $C$  is the pure corrosion rate. The synergistic effect (interactive term),  $S$ , is referred to as  $\Delta E$  or  $(\Delta C + \Delta E)$  depending on the literature source, where  $\Delta E$  is the enhanced wear loss due to corrosion and  $\Delta C$  is the enhanced corrosion due to wear.

Synergy is defined as ‘the difference between wear-corrosion and the summation of its two parts’ and can be expressed by eqns [34] and [35].

$$\Delta E = T - (E + C + \Delta C) \quad [34]$$

or

$$S = \Delta E + \Delta C = T - (E + C) \quad [35]$$

where  $T$ ,  $C$ , and  $E$  are typically gravimetric terms relating to wear-corrosion, electrochemical corrosion (*in situ*), and mechanical wear mechanisms respectively.  $C$  can be taken as the corrosion current under static conditions and  $\Delta C$  measured *in situ* when wear processes are occurring. Under erosion, more confusion exists in the literature as static  $C$  or flow only corrosion rates  $C'$  are used leading to very different values of  $S$  as shown in eqns [36]–[38].

$$T = E + C + \Delta E + \Delta C \quad [36]$$

$$T = E + C' + \Delta E + \Delta C' \quad [37]$$

$$T = E + C'' + \Delta E \quad [38]$$

where  $C'$  is the solids free flow corrosion rate and  $C''$  is the corrosion rate under wear-corrosion conditions. The ASTM G 119-93 standard is a useful guide for researchers wishing to evaluate synergy.<sup>93</sup> It should be noted that researchers working in the field of tribo-corrosion are now moving away from evaluation of and using the terms synergy and antagonism in favor of quantifying the rates of electrochemical–mechanical interactions and identifying their mechanisms and physical meaning.

Wear can mechanically strip the protective corrosion film creating fresh reactive corrosion sites and produce  $\Delta C$ ,<sup>94</sup> depending on the rate of repassivation and the integrity of the film formed. Other possible wear-enhanced corrosion mechanisms include (1) local acidification at wear sites, accelerating corrosion rates, and prohibiting film formation; (2) increased mass transport by high turbulence levels; (3) lowering the fatigue strength of a metal by corrosion; (4) anodic wear scars can cathodically polarize the surrounding unworn surfaces and destabilize passive films in these regions enhancing corrosion<sup>95</sup>; and (5) surface roughening of the specimen during wear-enhanced mass transfer effects increasing the corrosion rate.<sup>95</sup> Corrosion-enhanced wear mechanisms are also possible ( $\Delta E$ ). The  $\Delta E$  wear rate could be due to (6) the removal of work-hardened surfaces by corrosion processes, which expose the underlying base metal to erosion mechanisms<sup>96</sup>; (7) preferential corrosive attack at grain boundaries resulting in grain loosening and eventual removal<sup>97</sup>; (8) the increase in the number of stress concentration defects resulting from micropitting; and (9) detachment of plastically deformed flakes on the metal surface due to stress corrosion cracking. Corrosion can increase surface roughness, which in turn can increase wear processes. This is not a synergistic interaction.

Most of these mechanisms, if dominant, would be expected to lead to positive synergy (i.e., detrimental and an acceleration of wear-corrosion). However, in some instances, an antagonism can occur. Possible mechanisms that reduce wear rates ( $-\Delta E$ ) are (10) microgalvanic (work-function difference) effect-induced inhomogeneous shot-peening<sup>98</sup> by high-velocity sand particle impacts or; (11) the presence of a soft or loosely adherent corrosion film or; (12) the blunting of the crack tips by lateral dissolution retarding the speed of crack propagation. The reduction in corrosion rates ( $-\Delta C$ ) could result from (13) a rapid corrosion film growth, scaling, or the formation of a passive film reducing corrosion rates dramatically or; (14) the generation of thermally affected film.

Malka *et al.*<sup>99</sup> give an example of where positive synergies are dominant and have looked at whether erosion enhances corrosion and/or corrosion enhances erosion in pipe loop experiments on uncoated AISI 1018 CS. The tests solutions contained 1 wt% NaCl solutions purged with CO<sub>2</sub> (partial pressure of 1.2 bar) and 2 wt% silica sand (275  $\mu\text{m}$  in size). They found that erosion enhances corrosion and corrosion enhances erosion but the dominant synergistic effect was that of corrosion on erosion, that is,  $\Delta E$ . For roughly equal corrosion ( $C'$ ) and erosion rates ( $E$ ), the total mass loss ( $T$ ) was equal to two to three times the simple summation of  $E$  and  $C'$ , ( $E+C'$ ), showing significant synergy under 2 m s<sup>-1</sup> flow velocities.

It has also been shown that for a variety of engineering materials the synergistic effects, which result in the damage due to separate corrosion and erosion processes, are normally greater than the sum of the individual damage processes and can accelerate material removal significantly 50 times in some cases (i.e.,  $T = 50 \times (C' + E)$ ), see Wood and Hutton.<sup>31</sup> Thus, the levels of  $S$  can be as high as 50 times the expected mass loss rate and would comprise most safety margins used in the design of fluid machinery and pipe systems.

An example of antagonism was seen in erosion-corrosion testing of naval grade cast nickel aluminum bronze (NAB) under jet impingement conditions with a 2.5% (w/w) sand/3.5% NaCl solution slurry. Figure 33 shows the rig used and Figure 34 shows the results from combined erosion-corrosion ( $T$ ), erosion ( $E$ ), and flow corrosion ( $C'$ ) tests for different sand particle kinetic energies generated under the conditions detailed in Table 5. As can be seen, the  $T$  values are less than  $E+C'$  values.



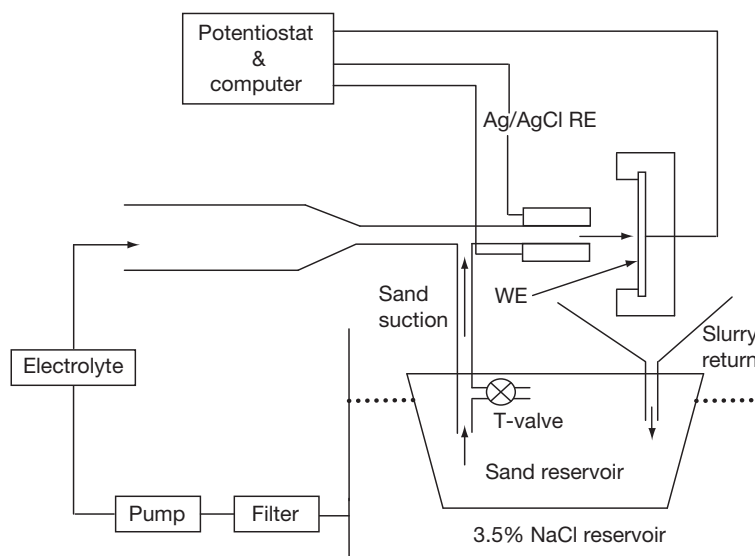


**Figure 33** Modified jet impingement slurry rig used for electrochemical measurement under flow corrosion and erosion-corrosion.

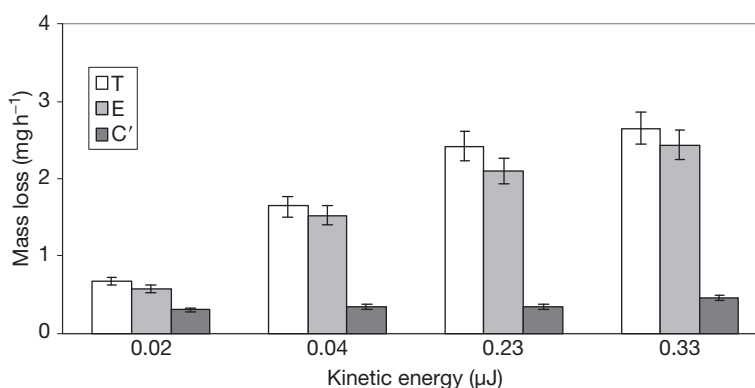


**Figure 34** Mass loss rates for cast nickel aluminum bronze (NAB) at different kinetic energies. Conditions: 2.5–3.0 w/w% silica sand concentration, 3.5% NaCl solution.

The reason for this antagonistic effect was determined by profiling the microhardness of uneroded and eroded areas to reveal an increase in surface hardness in eroded areas as shown in [Figure 35](#). Within the erosion scar, the hardness was doubled by hardening processes by the  $10^5$ – $10^6$  strain rates induced by the sand impacts. Transverse sections revealed a work-hardened layer some 125 nm thick, while for erosion-corrosion the layer was 250 nm thick and the erosion mechanisms were subtly different. How corrosion influences the depth of work-hardening is not clear but it is likely that work-hardening will change the surface potential and thereby will decrease the

corrosion reaction rate of the eroded surface as well as reduce erosion rates.

It is difficult to represent the interactive terms between wear and corrosion graphically to allow instant insight for designers and equipment operators. But some attempts at mapping are useful, particularly where quantitative terms are used for material loss rates. Such maps can also indicate the tribocorrosion regimes or dominant loss mechanism. This can be used to select more resistant surfaces or compositions. An example of such a plot for erosion-corrosion is given in [Figure 36](#). Here the corrosion loss rates ( $C'$ ) have been plotted against the mechanical loss rates given by  $(T - C')$ . This assumes that  $\Delta C'$  is negligible

**Table 5** Conditions used for the erosion and erosion–corrosion experiments (CP = cathodic protection)

Experiments	Jet velocity ( $\text{m s}^{-1}$ )	Sand diameter ( $\mu\text{m}$ )	Test solution	Re jet
Corrosion (C')	3.1–6	—	3.5% NaCl	
Erosion (E)	3.1–6	135 and 235 (mean diameter)	3.5% NaCl with CP	18415–29702
Erosion–corrosion (T)	3.1–6	135 and 235 (mean diameter)	3.5% NaCl	

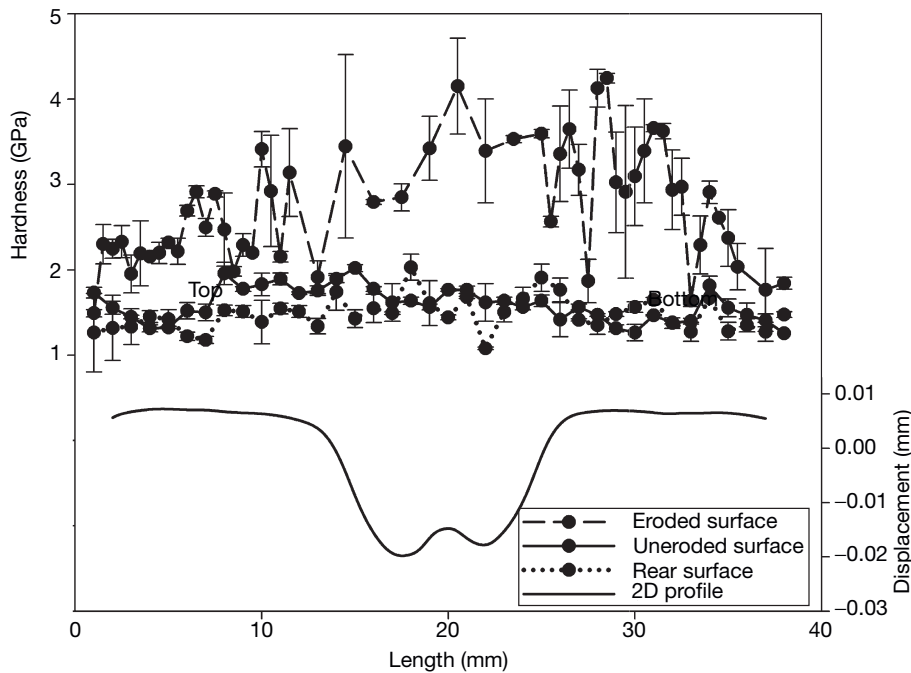


**Figure 35** Hardness measurement for NAB on eroded and uneroded and back surface tested at  $6 \text{ m s}^{-1}$  with its 2D-profile. Positions (1) and (3) represent hardness measurements through the center of the erosion scar and far away from the scar respectively. Reproduced from Barik, R. C. Environmental factors affecting the marine corrosion performance of nickel aluminium bronze, PhD thesis, School of Engineering Sciences, University of Southampton, 2006.

and can be ignored. Results for CS, cast nickel aluminium bronze, and a sprayed nickel aluminium bronze coating are shown. The regimes are also shown defined by the ratio  $(T - C')/C'$ , where low values show electrochemical processes to be dominant, values between 0.1 and 1 are in the corrosion-erosion regime, while values between 1 and 10 are in the erosion-corrosion regime and values over 10 are in the mechanically dominated regime.

For abrasion-corrosion, a variation in synergy levels has been linked to the abrasion mechanism present in the contact. Figure 37 shows results from microabrasion-corrosion tests on types 304 and 316 stainless steel (UNS S30403 and S31603) and super duplex stainless steel (UNS 32760).<sup>100</sup> The levels of synergy are represented as a percentage calculated

by eqn [39] where  $C$  (passive corrosion rates) are assumed negligible.

$$\frac{S}{T} \times 100 = \frac{T - E}{T} \times 100 \quad [39]$$

The synergy levels ( $S/T \times 100$ ) are plotted against volume fraction of abrasive. The abrasive used was  $4.5 \mu\text{m}$  SiC particles. The abrasive mode is dependent on the abrasive concentration. For low concentrations of abrasive, a two-body grooving abrasion process dominates, while for higher concentrations three-body rolling abrasion processes dominate. It can be seen from Figure 37 that the synergy resulting from a two-body wear mode was highly variable as evidenced by the large degree of scatter. Both S31603 and S32760 stainless steels produced negative values

of  $S$  under this wear condition, while  $S$  was positive for S30403. The large antagonisms produced by the two-body wear mechanism may be a reflection of the differences in repassivation kinetics and/or composition of the passive films reducing the overall level of two-body abrasion.<sup>100</sup> However, the mixed-mode region shows a significant reduction in scatter for each stainless steel. Likewise all the three stainless steel types within the three-body region showed an improved reproducibility with increasing volume fraction of abrasive. Rabinowicz *et al.*<sup>101</sup> in their

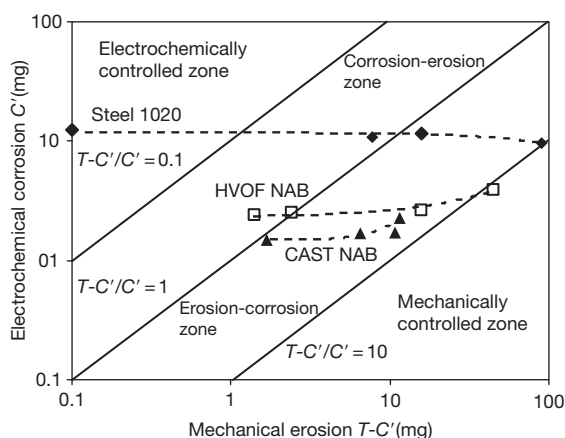


**Figure 36** Erosion-corrosion regime map with electrochemical material loss versus mechanical material loss for erosion-corrosion of CS AISI 1020, HVOF Nickel Aluminum Bronze coating and cast Nickel Aluminum Bronze under jet impingement conditions with 2% (w/w) sand in seawater. Reproduced from Wood, R. J. K. *Erosion-Corrosion, Comprehensive Structural Integrity*; Elsevier: Oxford, UK, 2007.

study of abrasive wear under a three-body regime reported that three-body abrasion leads to more reproducible test results compared with two-body. Batchelor and Stachowiak<sup>102</sup> have also suggested that three-body abrasion is more effective in removing the corrosion products, and by implication any passive film present, during abrasion-corrosion. **Figure 37** also shows that under three-body wear,  $S$  generally converges with increasing slurry concentration to a uniform positive synergy of 18% for the three stainless steels.

### 2.15.3.2.2 Erosion-corrosion models

Ferng *et al.*<sup>103,104</sup> modeled erosion-corrosion in pipe flow by adding the erosion and corrosion contributions together. The erosion model was based on droplet impingement but used an oxide removal based on eqn [40] for predicting the mass of oxide removed,  $m$ ,

$$m = C_s N f(\alpha) \frac{\rho_f U_f^2}{H} \quad [40]$$

where  $C_s$  is a system constant,  $N$  is the frequency of impingement,  $f$  is a characteristic function,  $\alpha$  is the impact angle,  $\rho_f$  the fluid density,  $U_f$  is the normal velocity, and  $H$  is the pipe wall hardness.

The metal loss rate,  $M_R$ , in  $\text{mol cm}^{-2}\text{s}^{-1}$  model is based on a mixed control corrosion process of dissolution of magnetite and the mass transfer of ferrous ions  $\text{Fe}^{2+}$  giving

$$M_R = \frac{C_{eq} - C_{\infty}}{(1/2k_1) + (1/k_m)} \quad [41]$$

where  $k_1$  is the reaction rate constant,  $C_{eq}$  is the

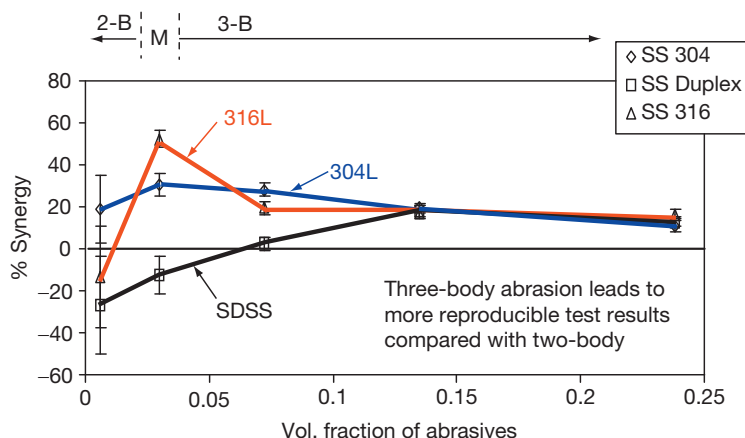


**Figure 37** Synergy % ( $[S/T] \times 100$ ) versus volume fraction of the abrasives for UNS S30403, S31603 and S32760. Low volume fraction of abrasive gives two-body grooving abrasion while higher concentration generate three-body rolling abrasion. Intermediate concentrations caused a mixed two- and three-body mode (M on figure).

soluble ferrous ion concentration in equilibrium with magnetite,  $C_\infty$  is the soluble ferrous ion concentration in the bulk solution, and  $k_m$  is the mass transfer coefficient. The combination of eqns [40] and [41] with 3-D fluid modeling has been successfully used to predict erosion-corrosion rates of pipes and fittings and the location of erosion-corrosion attack.

Erosion damage by solid particle impact or cavitation bubble collapse to an oxide or passive film will reveal the underlying nascent surface inducing a higher activity (higher corrosion current), for a limited duration, than for the intact oxide surface. Bozzini *et al.*<sup>105</sup> employed a simple approximate model using a 'recovering target' concept similar to those used in Section 2.15.3.1.3 for sliding wear-corrosion. This erosion-corrosion model has the advantage that it can be applied to both passivating and actively corroding conditions. The impacting particles are modeled with rigid spheres of uniform radius  $r_p$ . Particle impact is assumed to be a Poisson process with parameter  $\lambda$  (impacts  $\text{m}^{-2} \text{s}^{-1}$ ). It is assumed that each impact gives rise to an alteration of the corrosion rate through a localized change in corrosion current density for a period of time, relating to a recovery to its initial state. The effective corrosion current density,  $i_{\text{corr}}$  ( $\text{nA cm}^{-2}$ ), at a given electrode potential (typically the corrosion potential) can be related to the mechanically influenced corrosion component of the synergistic damage through a coefficient  $f_a$ , (such that  $0 \leq f_a \leq 1$ ) expressing the fraction of the corroding surface, which is affected by the erosive action of impinging particles, by eqn [42]

$$i_{\text{corr}} = f_a i_{\text{act}} + (1 - f_a) i_u \quad [42]$$

where the subscripts 'act' and 'u' relate to 'activated' and 'unaffected' respectively. The current densities  $i_{\text{act}}$  and  $i_u$  are characteristic of the corroding material in the absence and in the presence of the erosive action and can be measured separately by means of suitable experiments. In general, the coefficient  $f_a$  can be defined in eqn [43]:

$$f_a = \left( \frac{\text{No. of impacts}}{\text{Control area}} \right) \times \left( \frac{\text{Damaged area}}{\text{Impact}} \right) \times \text{Recovery time} = \lambda A_a \tau \quad [43]$$

where  $A_a$  is the affected surface area and  $\tau$  is the passive recovery time.

Equation [42] indicates an accelerating element to corrosion caused by film damage or removal and is one element of the complex interactions between erosion and corrosion that needs to be understood. A similar approach that includes particle

impingement angle and assumes an exponential repassivation reaction has been developed by Lu.<sup>106</sup>

$$i_{\text{corr}} = i_s + i_{\text{peak}} \frac{\tau \dot{A}_e}{1 + \tau \dot{A}_e} \quad [44]$$

where  $\dot{A}_e$  is the normalized rate of active surface area generated

$$\dot{A}_e = \left( \frac{C_p U \sin \theta}{\rho_p V_p} \right) A_{\text{crater}} \quad [45]$$

where  $i_s$  is the stable passive current density,  $i_{\text{peak}}$  is the peak response in local current density due to impingement,  $\tau$  is the exponential decay constant,  $C_p$  is the mass of solids per unit volume,  $U$  is the impact velocity,  $\theta$  is the impact angle,  $\rho_p$  is the particle density,  $V_p$  is the particle volume, and  $A_{\text{crater}}$  is the crater area.

More recent erosion-corrosion models incorporate dynamic Hertzian impact area models and squeeze film effects in an attempt to evaluate more accurately actual areas of depassivation and actual particle impact velocities, Harvey.<sup>54</sup>

As mentioned earlier, the synergistic term  $S$  can be positive or negative (antagonistic). Bozzini *et al.*<sup>105</sup> showed that annealed CS had a more active corrosion potential before it was work hardened, resulting in  $i_u > i_a$  and by using eqn [42] showed a reduction (i.e., an antagonism) in overall corrosion rate with erosion present.

The Bozzoni model or ones of that type go some way to explain experimental trends. For example, Neville *et al.*<sup>107</sup> have shown that the corrosion current density increases with increasing solid loading (200, 400 and 600  $\text{mg l}^{-1}$ ) for UNS S31603 under an impinging jet of 3.5% NaCl at 17  $\text{m s}^{-1}$ . Synergistic effects have also been shown to be a function of impinging solid particle energy for various stainless steels (UNS S31603, S32100, S32250, and S32760).<sup>108</sup> Such results indicate that synergy is more pronounced at lower particle energies. For example, under an erosion energy of 0.02  $\mu\text{J}$  per impact, the volume loss under erosion-corrosion for UNS S32250 is ten times that for erosion alone. However, at higher energies,  $\sim 7.5 \mu\text{J}$ , the erosion-corrosion rate is only 1.4 times that for erosion alone. Under very low energy impacts, little differences between erosion and erosion-corrosion rates are recorded for passive steels suggesting that impact energies above a critical value maybe required to initiate depassivation.

There are data reported in the literature that certain erosion-corrosion test conditions producing an antagonism, while others produce a positive synergy. The author in Wood<sup>28</sup> reports antagonisms for a superduplex steel UNS S32750 in 3.5% NaCl solutions at  $E_k = 0.05 \mu\text{J}$  and  $90^\circ$  impingement angle. However, Neville and Hu observed a positive synergy on two superaustenitic stainless steels (UNS S31254 and S32654) and a superduplex steel UNS S32750, but these tests were conducted at a higher  $E_k$  of  $4 \mu\text{J}$ .<sup>29</sup> This suggests a complex relationship with synergy as a function of erosion conditions (energy) and repassivation tendency as this effects the crater size, crater shape, levels of strain rate, and passive film or oxide layer recovery time. Table 6 shows some typical values for  $E_k$  that may be generated in pipes, valves, pumps, and propulsors. It assumes average sand particles of  $100 \mu\text{m}$  in diameter and that these have velocities comparable to the average fluid velocities of the systems. Therefore, erosion-corrosion data are required at these energies if correct material selection is to be made.

Erosion-corrosion conditions can themselves develop local microgalvanic cells between eroded and uneroded surface areas. Such microgalvanic cells have been reported between erosion affected regions (depassivated) of a surface and noneroded regions (passive). For example, enhanced material loss rates due to such cells are reported by Hodgkiess.<sup>23</sup>

To summarize, Table 7 is an attempt to list the mechanisms that may influence the sign of the interactive terms namely the  $\Delta C$  and  $\Delta E$  components.

Another possible synergy mechanism for  $\Delta E$  has been suggested by Guo *et al.*,<sup>110</sup> who studied near-surface hardness changes induced by erosion strain hardening and corrosion softening on AISI 1045 CS and observed that the relative hardness degradation,  $\Delta H_v/H_v$ , could be correlated approximately with the anodic current density,  $i_a$ , as expressed in eqn [46]:

$$\frac{\Delta H_v}{H_v} = -B \log \left[ \frac{i_a}{i_{th}} \right] \quad [46]$$

**Table 6** Potential particle kinetic energies and flow velocities for marine components

	Marine component			
	Pipe	Valve	Pump	Propulsor
Velocity ( $\text{m s}^{-1}$ )	0–3	5	10	25
Particle diameter ( $\mu\text{m}$ )	100	100	100	100
Particle KE ( $\mu\text{J}$ )	0–0.007	0.02	0.07	0.44

where  $\Delta H_v = H_v^* - H_v$  and is the change of hardness due to anodic dissolution at the surface,  $H_v$  and  $H_v^*$  the hardness without and with anodic current present at the electrode surface respectively,  $B (>0)$  is an experimental constant, and  $i_{th}$  is the threshold anodic current density to induce the synergistic electrochemical-mechanical effect, that is, when  $i_a \leq i_{th}$ ,  $\Delta H_v = 0$ . However, relatively large anodic currents were employed to achieve relatively minor changes in hardness (typically 0.1%). This could be an artifact of the experimental equipment employed as a microhardness tested was performed. Thus, surface layer properties were affected by the substrate as more than 10% of the coating thickness was penetrated during measurement.

### Empirically based models of synergy

Wood and Hutton,<sup>31</sup> summarizing experimental data published on erosion wear over a wide range of solid particle and cavitation erosion experiments, found that the data fell within two groups: the medium- and high-synergy systems. The erosion-corrosion enhancement,  $S$ , was found to be closely linked to the pure erosion component  $E$ . Two expressions were derived by plotting  $S/C'$  against  $E/C'$  ratios to obtain the following expressions: For the medium-synergy group

$$\begin{aligned} 1 \frac{S}{C'} &= \exp \left[ 1.277 \ln \left( \frac{E}{C'} \right) - 1.9125 \right] \\ &= 0.1477 \left( \frac{E}{C'} \right)^{1.277} \end{aligned} \quad [47]$$

For the high-synergy group

$$\begin{aligned} 2 \frac{S}{C'} &= \exp \left[ 0.755 \ln \left( \frac{E}{C'} \right) + 1.222 \right] \\ &= 3.3940 \left( \frac{E}{C'} \right)^{0.755} \end{aligned} \quad [48]$$

### Sliding wear models

A sliding wear model proposed by Jiang *et al.*<sup>91</sup> defined the total wear-corrosion loss  $V_{cw}$  as

$$V_{cw} = (V_w + \Delta V_w) + (V_c + \Delta V_c) \quad [49]$$

where  $V_c$  is the pure corrosion loss,  $V_w$  is the material loss due to wear,  $\Delta V_c$  is the wear-induced corrosion, and  $\Delta V_w$  is the corrosion-induced wear.

They looked at material loss due to corrosion,  $V_c$ , during sliding in a corrosive environment and related this to the anodic corrosion current under the influence of wear by Faraday's law. For metals that can



**Table 7** 'Synergy' overview of processes that could lead to positive and negative interactive effects between mechanical and electrochemical processes present under erosion-corrosion conditions

Factor	Positive interaction	Negative interaction
Critical impact energy	Above critical impact energy to penetrate/damage passive/product film/coverage. Results in increased charge transfer at the liquid/metal interface	Below critical impact energy. Results in reduced charge transfer at the liquid/metal interface as film composition could be influenced by impact
Surface roughness, $R_a$	Roughening effects on mass transfer coefficients unknown but $k_m$ is likely to increase with increasing $R_a$ . The Silverman review <sup>109</sup> suggests that the mass-transfer dependence on Reynolds number is affected by surface roughness as $k_m \propto Re^{0.9}$ with solids eroding the surface compared to $k_m \propto Re^{0.65}$ for solids-free flows for rotating cylinder work due to roughening effects on the surface. Roughness may promote microturbulence, affecting the local double layer. Roughness could also promote local microelectrode behavior (potential field distortion) at the tips of impact craters	Roughness influences the contact mechanics of angular solid particle impingement. Increased roughness could reduce contact stresses and thereby the near and far field stress distributions
Plastic deformation/strain	Plastically deformed and stressed surfaces enhance corrosion processes. Corrosion causes premature detachment of plastically deformed or strain hardened impact crater lips	
Increased or unsteady hydrodynamics or turbulence	Unsteady hydrodynamics leads to instability of the double layers (nonsteady state) and unsteady driving concentration gradients of active species	High concentrations of solid particles could block the surface from incoming particles. Particle-particle interaction alters impact conditions
Contact temperature	Local surface (flash) temperatures could be significantly higher around and within impact craters which could accelerate corrosion rates	Local surface (flash) temperatures could influence oxide film composition and microstructure and thus could produce more erosion resistant films
Localized corrosion	Pitting and microgalvanic corrosion cells due to localized defects in the passive layers induced by erosion or exposure of inclusions or voids. Crack systems would also be vulnerable to crevice corrosion attack and accelerated crack propagation. Microgalvanic corrosion cells could be formed between erosion craters and surrounding unaffected areas	Strain-induced shift in surface potential in the electropositive direction
Multiphase surfaces	Corrosion of interface – potential to lose bond integrity between hard and binder phases, binder recession due to corrosion leaves hard phase loose to be removed by mechanical action. These interactions could also apply to splat boundaries which exist after spraying	Substrate corrosion products can eject via interconnecting pores onto the coating surface, reducing erosion rate
Passive film state	Depassivation: removal of air-borne oxides or oxide layers produced by passivation. Oxide layer could increase friction between impacting solid particle and the bulk substrate material	The overall recovery times for repassivation and adherent oxide layers formed by passivation are important relative to depassivation events. Oxide layers could also decrease the friction between impacting solid particle and the bulk substrate material. Alternatively denser oxide could be formed that reduces corrosion or erosion or both

Source: Partly taken from reviews by Wood<sup>31</sup> and Wang.<sup>30</sup>

passivate in the corrosion environment, the anodic corrosion current is composed of two components: (1) the repassivation anodic current density of  $i_a$  passing through the area,  $A_r$ , where the passive film

has been removed/damaged by the mechanical wear action; and (2) the passive current density of  $i_p$  passing through the rest of the apparent area of contact,  $A - A_r$ , where the passive film has been fully

developed.  $A$  is equal to the apparent area of contact, assuming that the area surrounding the wear track is insulated from electrochemical reactions. For nonpassive metals, the current density can be taken as  $i_p$ . It was assumed that a depassivation–repassivation event occurs in between two successive contact events during corrosion–wear sliding tests and that the removal of the passive films during sliding corrosion–wear occurs on the real area of contact,  $A_r$ , which depends on the mechanical properties of the material and the contact surface topographies. For sliding between two ductile rough bodies or a hard rough body sliding on a smooth ductile, the real contact area  $A_r$  is proportional to  $l(W/H)^{1/2}$ , where  $l$  is the width of the wear track.

Thus,

$$V_c + \Delta V_c = I_{ac} t A_{atom} / (zF\rho_t) \quad [50]$$

where

$$I_{ac} = A_r i_r + (A - A_r) i_a \quad [51]$$

Using eqn [32] due to Mischler

$$A_r i_r = I_{a,w} = K_w l f \left( \frac{W}{H} \right)^{1/2} \int_0^{1/f} i \, dt \quad [52]$$

where

$$i = (i_0 - i_a) \exp(-t/\tau_0) + i_a \quad [53]$$

The characteristic passivation time,  $\tau_0$ , reflects how easily the metal surface passivates. The lower the value of  $\tau_0$ , the more easily the metal tends to passivate. For nonpassive materials,  $i_0 = i_a$ , and the anodic dissolution current,  $i = i_a$ , is constant. This gives

$$V_c + \Delta V_c = [A_{atom} s / (zF\rho_t v_e)] \left\{ A_a i_a + K_a l (W/H)^{1/2} (i_0 - i_a) f \tau_0 [1 - \exp(-1/f\tau_0)] \right\} \quad [54]$$

where  $s$  is the total sliding distance,  $v_e$  is the sliding velocity,  $K_a$  is a proportionality constant, and  $f$  is the contact frequency between interacting surfaces.

This approach is coupled to the concept of micro-fatigue crack propagation where a critical time,  $t_c$ , is required for an existing microcrack nucleus to propagate a length,  $D_a$ , taken as the diameter of a wear debris particle and is then related to the microcrack growth rate,  $da/dn$ . There are various scenarios of how corrosion affects crack propagation. First, corrosion can increase the number of potential microcrack initiation sites,  $N_c$ . Second, reactive or corrosive species at the crack tip can promote the

propagation of the crack, increasing the generation rate of wear debris particles by reducing  $t_c$ . Third, the corrosive environment may also affect the average wear debris particle diameter,  $D_a$ , although it is difficult to predict how this factor will vary with the corrosion conditions. Finally, it is possible under certain conditions that wear is reduced as a result of crack-tip blunting or the formation of some wear-protective load-bearing areas from the corrosion products. However, Jiang *et al.*<sup>91</sup> considered the corrosion-enhanced microcrack propagation only.

The wear volume of a specimen is equal to the product of the average volume of a single particle and the total number of wear debris particles generated within a sliding time,  $t$ , which can be expressed by

$$V = \frac{\pi D_a^3}{6} k_d A_a t = \frac{\pi D_a^3 s}{6 v_e} k_d A_a \quad [55]$$

where  $k_d$  is the particle generation rate.

They assumed that during sliding wear, a microcrack is initiated on the wear surface and will propagate for a certain distance after each contact with an asperity from the counter surface. A wear debris particle is generated after a certain number of cycles of contact at the same spot with the encountering surface.

The critical time,  $t_c$ , for generating a wear debris particle with an average size,  $D_a$ , from an existing microcrack nucleus is related to the microcrack growth rate,  $da/dn$ , by

$$D_a = \int_0^{t_c} \frac{da}{d\tau} d\tau = \int_0^{t_c} \frac{da}{dn} f d\tau \quad [56]$$

If  $N_c$  active microcrack sites are present on a unit area of the wear surface that are ready to propagate, then the generation rate,  $k_d$ , of wear debris particles can be calculated by

$$k_d = N_c / t_c \quad [57]$$

Several factors are considered: the number of cracks that are above a critical size and thus propagate; the influence of stresses induced during the wear process; as well as corrosion fatigue processes. This process considers mechanical aspects in a reference environment, interactions of cyclic mechanical loading and the attack by the environment and sustained load crack growth; the following terms were developed:

$$k_d = (N_r + \Delta N_c) \{ g_r + g_{cfs} [1 - \exp(-1/f\tau_i)] + g_s \} f D_a^{-1} \quad [58]$$

where  $N_r$  is the number of critical microcracks that are ready to propagate to generate wear debris

in a reference environment,  $\Delta N_c$  is increment of the number of critical microcracks due to the presence of corrosion, and  $\tau_i$  is the characteristic reaction time for the reaction controlling a corrosion fatigue process.

Substituting this expression into eqn [57] gives the wear contribution  $V_{wc} = V_w + \Delta V_w$ :

$$V_{wc} = \frac{\pi D_a^2 A_a s}{6l} [N_r g_r + \Delta N_c g_r + (N_r + \Delta N_c) \times \{g_{cfs}[1 - \exp(-1/f\tau_i)] + g_s\}] \quad [59]$$

Thereby the total wear-corrosion loss, given by eqn [49], can be predicted by summing eqns [54] and [59].

## 2.15.4 Present and Future Applications of Tribocorrosion

Previous sections have focused on ‘heavy’ engineering applications and solution and models appropriate to these conditions. This knowledge and understanding have matured over the past 20 years or so. However, it may be the more subtle tribocorrosion problems that will drive further development and understanding. For example, corrosion–wear interactions can be used to control material loss for manufacturing of silicon wafers. This process is called chemical–mechanical planarization (CMP) and is an important process for building multilevel interconnections for electronic devices. CMP techniques have been developed for machining tungsten, aluminum, and copper. The fundamentals of these processes are not well understood

and are an active area of research at present. The supporting electrolyte used in manufacturing is acidic and oxidizing leading to material removal by a cyclic process of passivation–film abrasion followed by repassivation and then passivation–film abrasion and so on. These are similar to wear–corrosion processes discussed earlier in the chapter.

### 2.15.4.1 Chemical Mechanical Polishing (CMP)

Figure 38 illustrates the general process with the silicon wafer typically being loaded horizontally and pressed onto a rotating conditioning pad with the contact between the wafer and pad being lubricated by a slurry. The wafer holder is itself rotated as well.

The roles of mechanical abrasion and electrochemical dissolution during CMP of aluminum have been studied by Tsai and Huang.<sup>111</sup> They found, as expected, that the total metal removal rate and the electrochemical dissolution rate of aluminum in 5 vol% phosphoric acid + 0.5 M citric acid solution (pH 4) increased with increasing contact pressure and specimen rotation speed. However, the contribution of electrochemical dissolution to the total removal rate of aluminum was less than that produced by mechanical abrasion. They also detected metallic aluminum in the solution, indicating that the passive film was not the sole material removed under the chemical–mechanical abrasion condition but some wear of the parent material had occurred.

The influence of the type of conditioning pad used has been studied by Tan *et al.*<sup>112</sup> They studied three

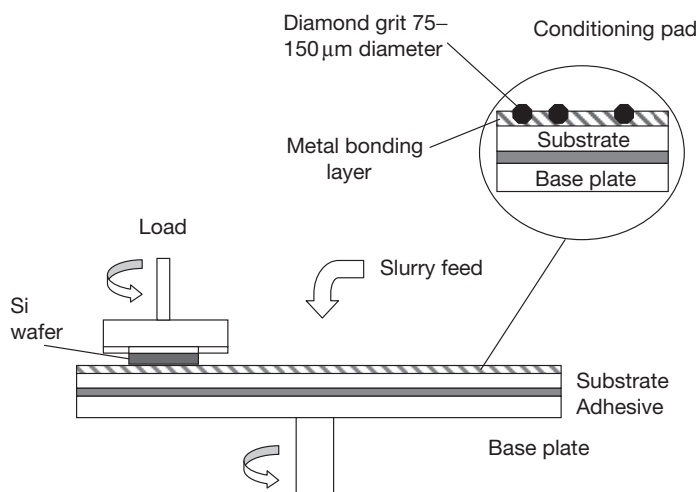


**Figure 38** Schematic of a CMP set-up with a rotating wafer loaded against a rotating conditioner pad supported by a base plate.

types of conditioners: (1) bonded by electroplating nickel; (2) brazing Ni–Cr alloy; and (3) diamond-like carbon (DLC) film deposition on a brazed conditioner. They found that after wear-corrosion testing, the DLC film deposited on the conditioner surface of brazed Ni–Cr alloy exhibited better overall performance in terms of a higher removal rate. The pad suffered a lower wear loss and a better corrosion resistance compared with the other two conditioners.

Ziomek-Moroz *et al.*<sup>113</sup> researched into CMP of different metallic thin films, such as tungsten and copper in aqueous media. They emphasize the importance of constructing wear-corrosion maps for these complicated tribocorrosion-metallic thin film systems. The wear component followed the Preston wear equation,<sup>114</sup> namely

$$b = \int_{t_1}^{t_2} kpU dt \quad [60]$$

where  $b$  is the wear depth developed between time  $t_1$  and  $t_2$ ,  $k$  is a wear factor,  $p$  is pressure, and  $U$  is the relative velocity of the workpiece contact point with respect to the tool contact point. Equation [60] can be rearranged in terms of volume loss ( $V$ ), normal applied load ( $W$ ), and sliding distance ( $L$ ), as shown in eqn [61].

$$k = \frac{b}{\int pU dt} = \frac{b}{pL} = \frac{bA}{WL} = \frac{V}{WL} \quad [61]$$

Ziomek-Moroz *et al.* found that the synergism between corrosion and erosion during CMP of thin metallic films is a key factor in controlling the polish rate and makes this process very complex. For the CMP of tungsten and copper, the presence of a passive protective film on the metal surface plays a critical role in successful planarization. Therefore, understanding the corrosion mechanisms that control both the polish rate and the passivation behavior of the thin films are critical in controlling CMP.

The direct planarizing of tungsten by wear processes is difficult because of its high hardness. Therefore, an effective approach has been developed to facilitate planarizing of a tungsten surface by removing a continuously growing passive film on tungsten when exposed to a low-pH potassium ferricyanide slurry. Since the passive film is softer than tungsten, this chemical mechanical planarization process is effective. Akonko *et al.*<sup>115</sup> have investigated the corrosion, wear, and corrosive wear behavior of tungsten in  $K_3[Fe(CN)_6]$  slurries. The tungsten removal rate increased with increasing slurry pH and surface potential.

## 2.15.4.2 Erosion-Corrosion

In order to gain further understanding of the effects of erosion-enhanced corrosion,  $\Delta E$ , electrochemical noise techniques are being used.<sup>116</sup> These measurements allow current and/or potential perturbations about the mean corrosion current to be analyzed without grossly polarizing the surfaces. These perturbations are thought to provide valuable information on the extent of passive film rupture and repassivation during flow-enhanced corrosion and erosion-corrosion. Although individual impacts or pitting events are difficult to resolve, the result of multiple impacts or pits as over time is useful as a diagnostic tool to detect possible surface degradation mechanisms.

Figure 39 shows a corrosion flow cell designed for electrochemical noise analysis for pipe flow with no solids present in the fluid. Typically, two ‘nominally identical’ working electrodes are used and their potential noise recorded relative to a reference electrode, together with the current noise between the two working electrodes. Figure 40 shows typical potential and current responses at a pipe Reynolds number of 2000 (just around the transition from laminar to turbulent flow) on type-304 stainless steel in 3.5% NaCl solution.

Sasaki and Burstein observed current transients for single-particle impacts<sup>117</sup> on passive stainless steels, illustrating that monitoring such transients can provide direct information on the erosion-corrosion processes. A simple way to analyze such data is to take the standard deviation of the current traces under flow corrosion,  $\sigma_c$ , and under erosion-corrosion,

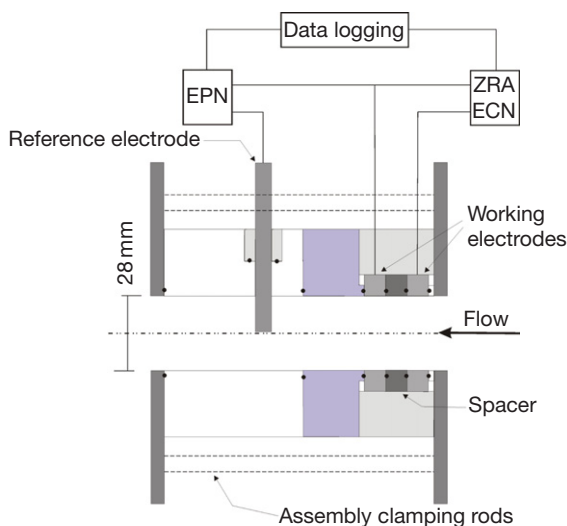


**Figure 39** Schematic of electrochemical flow cell and measurement set-up.

$\sigma_T$ . Attempts are currently being made to link the standard deviation ratio  $\sigma_c/\sigma_T$  to synergy, see [Figure 41](#).

Caution should be applied to any electrochemical measurement under erosion-corrosion conditions. Other issues make electrochemical analysis and its comparison to synergy difficult. These include the possibility of local film currents between anodes/cathodes,<sup>118</sup> which will not be seen by ECN measurements or by potentiostats and the effects of charging/recharging double-layer currents due to fluctuating local events.

### 2.15.4.3 Biotribocorrosion

#### 2.15.4.3.1 Dentistry

The use of artificial materials to replace natural dental tissue is common in dentistry. Due to health

aspects, there is concern about the risks that the corrosion and wear of these materials may induce. Linear wear and the release of wear particles are especially of interest. The insight into wear-corrosion processes in dentistry is, however, still in its infancy. Lambrechts *et al.*<sup>119</sup> give an overview of the degradation processes that occur on artificial materials used in dentistry, especially in restorative dentistry. Light-cured composite resins of inorganic silica fillers in organic (polymer) resins are currently seen as viable alternatives to amalgam. Wear of dental composite resins involves adhesion, abrasion, attrition, chemical degradation, and fatigue, see [Table 8](#). These mechanisms often act simultaneously and/or sequentially and interact with each other in a complex form, making the prediction of loss rates difficult.

Wear in the filled composites occurs by a complex set of processes involving tribochemical reactions between the filler particles and water, formation of surface films containing a mixture of filler fragments and reaction products, and film delamination, as well as dissolution of the reaction products.<sup>120</sup>

The wear behavior of a dental ceramic composite containing 92 wt% silica glass and alumina filler particles in a polymeric resin matrix has been examined by Nagarajan *et al.*<sup>121</sup> Wear tests confirmed the presence of Al and other elemental constituents of the filler particles. It is proposed that three simultaneous processes occur at the sliding contact: tribochemical reactions and film formation, dissolution of the reacted products, and mechanical removal of the film by microfracture. At low loads, wear occurs primarily by a tribochemical mechanism, that is, formation and dissolution of the reaction products.

Lewis and Dwyer-Joyce<sup>122</sup> have reviewed the current understanding of wear of enamel and dentine in teeth and highlight the major influencing factors. They looked at various tribological conditions to which teeth are exposed. These include noncontact between opposing teeth, contact but no sliding, and contact with sliding between opposing teeth. They emphasize that the largest single influencing factor is that of the chemical environment and this interacts with a synergistic effect with all wear mechanisms to enhance material loss rates. Research has shown that increasing acidity reduces both hardness and elastic modulus of enamel in an appropriate linear relationship without load or sliding between teeth. Material loss for both enamel and dentine increases with decreasing pH generated by acids found in soft drinks. Citric acid adjusted by NaOH (to the required pH range between 2 and 6.5) and citric acid with titratable

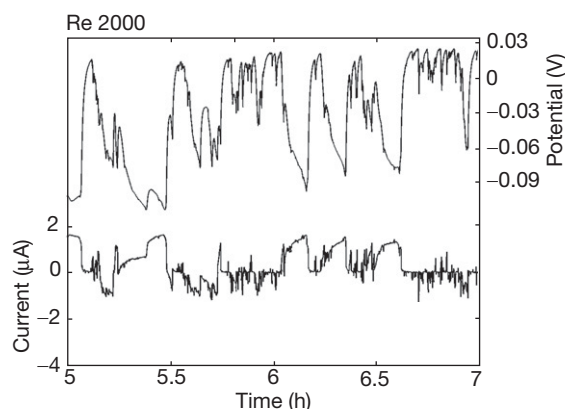


**Figure 40** Electrochemical current and potential noise for AISI 304L in 3.5 wt.% NaCl solution.

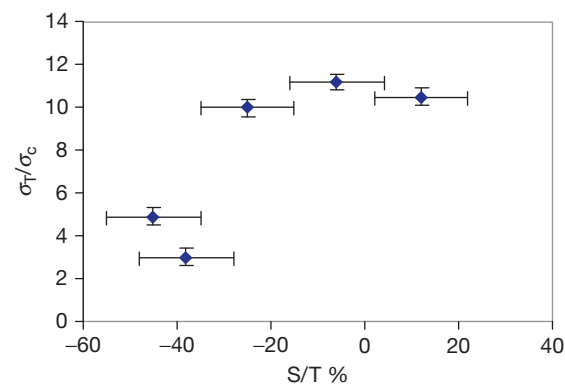


**Figure 41** Standard deviation of erosion-corrosion current noise divided by the standard deviation of corrosion current noise as a function of the synergy as presented by gravimetric S/T%. Data from erosion-corrosion jet impingement tests on HVOF nickel aluminum bronze and aluminum alloy coatings in sand/3.5% NaCl slurries.



**Table 8** Dental wear and wear-corrosion processes

<i>Wear mechanism</i>	<i>Effect</i>	<i>Driving mechanism</i>	<i>Cause</i>
Abrasion	Occlusal material wear	Frictional surface interactions three-body abrasion	Toothbrush/paste food bolus
Attrition	Changes surface texture	Sharp asperities two-body abrasion	Antagonistic surface 50% harder than the wearing surface
Chemical wear	Degrades silane couplings in composites	Wetting	Food or saliva
Surface fatigue	Surface layer delamination and severe roughening	Rolling contacts and cyclic loads	Subsurface stress concentrations
Adhesive	Platelet-shaped wear transferred to antagonistic surface which can either reduce or enhance wear rates	Asperity–asperity interaction	Shear stresses

acidity give the highest loss rates. In the contact without sliding between teeth, the enamel loss increases with increasing load or cyclic load. For contacts with sliding, a nonlinear relationship is seen, with wear rates decreasing as the pH drops from 7 to 3 but increasing when the pH is further decreased to 1. Until now, these synergistic and antagonistic effects between the chemical and mechanical tooth wear have not been properly investigated.

Dental implants, on the other hand, are used to replace teeth lost due to decay, trauma, or periodontal diseases. These implants are subject to micromovements at the implant–bone interface or implant–porcelain interface due to the transmitted mastication loads and also subject to the aggressive oral environment. Such implants are thereby subject to tribocorrosion that can lead to implant failure. Vieira *et al.*<sup>123</sup> studied titanium grade 2 in contact with low-pH artificial saliva under fretting conditions and with different inhibitors. They found that the addition of citric acid or anodic inhibitor to artificial saliva resulted in a slight improvement in the tribocorrosion behavior of Ti. No significant differences were observed in the wear rate per dissipated energy, but a lower wear volume loss was obtained that can be attributed to the slightly lower corrosion rate observed in these solutions during the fretting tests. This increased protection was attributed to the oxidation and reduction reactions occurring in the contact area during fretting. They noted that the tribolayers formed in the contact became more stable after ~7000 cycles in solutions containing citric acid or anodic inhibitor, and resulted in lower coefficient of friction and a lower corrosion current. The addition of a cathodic or an organic inhibitor to the artificial saliva resulted in a

**Figure 42** Total hip replacement joint in CoCrMo.

deteriorating performance of the titanium. Both an increase in the wear volume loss per unit-dissipated energy and a significantly higher corrosion rate during fretting tests were observed in these solutions.

The tribocorrosion of orthodontic archwires is also a growing research area and various stainless steel archwires have been investigated by Berradja.<sup>124</sup> They found the fluctuations in potential and current during fretting–corrosion are more pronounced at increased sliding frequency than at increased applied normal loads.

#### 2.15.4.3.2 Replacement joints

Researchers are becoming increasingly interested in metal-on-metal (MoM) joint implants, see [Figure 42](#), with studies being focused on their wear and corrosion (ion release) behavior. The corrosion, wear, and wear-corrosion behavior for three materials (high-carbon CoCrMo, low-carbon CoCrMo, and UNS S31603) have been discussed by Yan *et al.*<sup>125</sup> In the steady state regime, 20–30% of the material

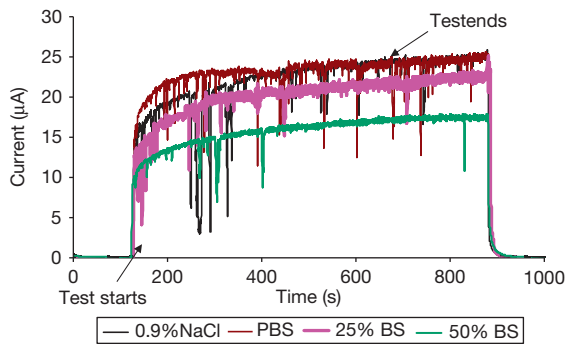


**Figure 43** Electrochemical current noise obtained in microabrasion-corrosion test on as-cast CoCrCo ( $1.0 \text{ g cm}^{-3}$  SiC) in 0.9% NaCl, phosphate buffered saline (PBS) solutions, 25% and 50% bovine serum (BS) at  $37^\circ\text{C}$ . Reproduced from Sun, D. Wharton, J. A.; Wood, R. J. K.; Ma, L.; Raithforth, W. M. Microabrasion-corrosion of cast CoCrMo alloy in simulated body fluids, presented Leeds-Lyon 2007, Tribol. Int. submitted for publication.

degradation was attributed to corrosion-related damage. High-carbon CoCrMo showed excellent corrosion, wear, and corrosion-wear resistance and therefore delivered the best overall performance in terms of a lower wear rate, a lower friction coefficient, and a higher resistance to corrosion. Proteins in the joint fluids are thought to play a key role but this mechanism is not well understood.

Sinnett-Jones *et al.*<sup>126</sup> investigated the synergistic effects of corrosion and wear of surgical grade cast F-75 cobalt–chromium–molybdenum (CoCrMo) alloy. Microabrasion-corrosion identified depassivation and repassivation processes and showed strong synergistic effects ranging from negative to positive. The synergistic levels appear to be dependent on the integrity of the passive films and the repassivation kinetics.

The role of protein in the tribocorrosion of metal implants is not well understood but initial studies

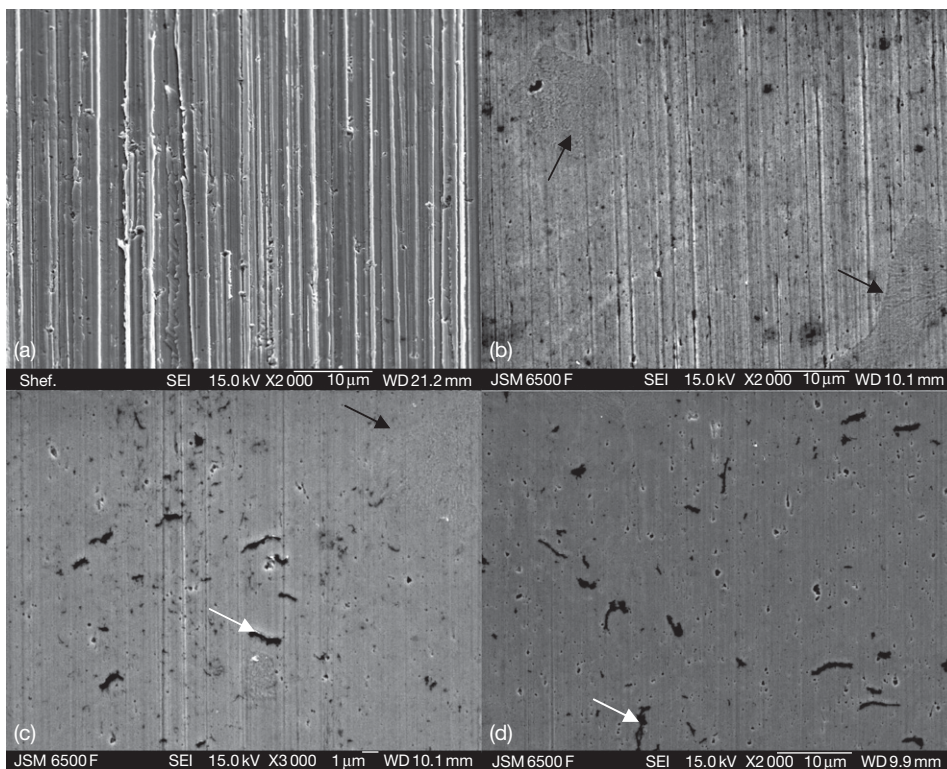


**Figure 44** SEM micrographs of wear scars on as-cast CoCrMo under pure sliding conditions in (a) 0.9% NaCl, (b) PBS, (c) 25% BS, (d) 50% BS at  $37^\circ\text{C}$ . Black arrows show a carbide standing proud of the surface. The white arrows show possible protein and wear debris on the worn surfaces. Polished wear scars, as opposed to two-body abrasion seen in (a) and (b), were produced in proteinaceous solutions indicating proteins form a lubrication film which protect the surface. Reproduced from Sun, D. Wharton, J. A.; Wood, R. J. K.; Ma, L.; Raithforth, W. M. Microabrasion-corrosion of cast CoCrMo alloy in simulated body fluids, presented Leeds-Lyon 2007, Tribol. Int. submitted for publication.

show conflicting trends with corrosion being either enhanced or reduced when protein is present and adsorbed onto the articulating surfaces. Sun<sup>127</sup> has studied abrasion-corrosion of cast CoCrMo in saline (0.9% NaCl and phosphate buffer solution (PBS)) and protein containing solutions of BS. *In situ* current noise results, see **Figure 43**, show reduced current levels when proteins are present.

Using the same test geometry, but removing the abrasives, so that the alumina ball abrades the CoCrMo surface under sliding wear mode, again shows that the presence of protein alters and reduces the wear mechanism and rate as seen in **Figure 44**.

### 2.15.5 Conclusions

Tribocorrosion has only recently been recognized as an important underpinning area of corrosion and therefore is in its infancy. This chapter has defined tribocorrosion and presented the fundamental principles behind wear, flow corrosion, erosion-corrosion, cavitation erosion-corrosion, sliding wear-corrosion, and abrasion-corrosion interactions. It has shown the key material and environmental parameters that influence tribocorrosion and used examples to illustrate the performance of materials under a variety of tribocorrosion conditions. It has outlined the conditions under which tribocorrosion occurs in aqueous solutions and shown that the depassivation and repassivation kinetics within tribocorrosion conditions need to be understood or controlled if accelerated damage is to be avoided. It has discussed the motivation behind current research and presented some examples of where tribocorrosion research will play a major role in the future, such as in biotribocorrosion, manufacturing, and erosion-corrosion detection to aid condition monitoring of fluid machinery and chemical processes.

The influence of the corrosive environment is shown to be important in controlling wear and friction and the evolution of near-surface triboinduced layers, which are critical in both erosion-corrosion and wear-corrosion situations. The chapter has identified the key interactions between wear and corrosion mechanisms that occur along with some models and mapping techniques that aim at informing material selection and predict performance. However, these need major development before robust predictions can be made as our understanding of the mechano-electrochemical interactions in tribocorrosion are incomplete.

### Acknowledgments

I thank all those in my research group who helped with this chapter and particularly Dr Julian Wharton for various figures and material and his constant encouragement. I also thank Drs Terry Harvey and Mandar Thakare as well as Dan Sun (PhD student) for their help with figures.

### References

1. *Oxford Dictionary of English*, 2nd ed.; Oxford University Press, 2005.
2. Fischer, A.; Mischler, S. J. *Phys. D; Appl. Phys.*; **2006**, 39(15); doi: 10.1088/0022-3727/39/15/E01.
3. Kurtz, S.; Ong, K.; Lau, E.; Mowat, F.; Halpern, M. *J Bone Joint Surg. Am.* **2007**, 89, 780–785.
4. Celis, J.-P.; Ponthiaux, P. *WEAR* **2006**, 261(9), 937–938.
5. Meng, H. C.; Ludema, K. C. *Wear* **1995**, 181–183, 443–457.
6. Archard, J. F. *J. Appl. Phys.* **1953**, 24, 981–988.
7. Archard, J. F. *Wear Theory and Mechanisms*. In *Wear Control Handbook*; Peterson, M. B., Winer, W. O., Eds.; ASME: New York, 1980; pp 35–80.
8. Hutchings, I. M. *Tribology – Friction and Wear of Engineering Materials*; Arnold: London, 1992.
9. Poulson, B. *Wear* **1999**, 233–235, 497–504.
10. Kim, J. G.; Choi, Y. S.; Lee, H. D.; Chung, W. S. *Corrosion* **2003**, 59(2), 121–129.
11. Jacobs, J. J.; Hallab, N. J.; Skipor, A. K.; Urban, R. M. *Clin. Orthop.* **2003**, 417, 139–147.
12. Williams, D. F.; Clark, G. C. F. *J. Mater. Sci.* **1982**, 17(6), 1675–1682.
13. Williams, R. L.; Brown, S. A.; Merritt, K. *Biomaterials* **1988**, 9, 181–186.
14. Lewis, A. C.; Kilburn, M. R.; Papageorgiou, I.; Allen, G. C.; Case, C. P. *J. Biomed. Mater. Res. A* **2005**, 73(4), 456–467.
15. Contu, F.; Elsener, B.; Bohni, H. *Corros. Sci.* **2005**, 47, 1863–1875.
16. Goldberg, J. R.; Gilbert, J. L. *J. Biomed. Mater. Res.* **1997**, 37(3), 421–431.
17. Stack, M. M.; Jana, B. D. *Tribol int* **2005**, 38(11–12), 995–1006.
18. Celis, J.-P.; Ponthiaux, P.; Wenger, F. *Wear* **2006**, 261(9), 939–946.
19. Deforge, D.; Wenger, F.; Ponthiaux, P.; Lina, A.; Ambard, A. Tribocorrosion of AISI 304L stainless steel sliding against AISI 304L stainless steel in nuclear environment, 207th Electrochemical Society Meeting, Quebec City, Canada May 2005, session E1 on Chemical, Electrochemical, and Mechanical Effects on CMP, Tribocorrosion, and Biotribocorrosion, abstract #313.
20. Kaczorowski, D.; Combrade, P.; Vernot, J. Ph.; Beaudouin, A.; Crenn, C. *Tribol Int.* **2006**, 39, 1503–1508.
21. Hu, X.; Neville, A. *Wear* **2005**, 258(1–4), 641–648.
22. Al-Hosani, H. I.; Saber, T. M. H.; Mohammed, R. A.; Shams El Din, A. M. *Desalination* **1997**, 109, 25–37.
23. Hodgkiess, T.; Neville, A.; Shrestha, S. *Wear* **1999**, 235, 623–634.
24. Wei, J. J.; Xue, Q. J.; Wang, H. Q. *Lubr. Eng.* **1993**, 49(12), 948–953.

25. Bowden, F. P.; Tabor, D. *The Friction and Lubrication of Solids*; Clarendon Press: Oxford, Part I, 1950; Part II, 1964.
26. Morris, S.; Wood, R. J. K.; Harvey, T. J.; Powrie, H. E. G. *Wear* **2003**, 255, 430–443.
27. Wood, R. J. K. Challenges of living with erosion-corrosion, *Advanced materials for fluid machinery*, IMechE Conference Transactions; PEP London: UK **2004**; pp 113–132.
28. Wood, R. J. K. *La Houille Blanche* **1992**, 7–8, 605–610.
29. Neville, A.; Hu, X. *Wear* **2001**, 251, 1284–1294.
30. Wang, H. W.; Stack, M. M. *J. Mater. Sci.* **2000**, 35, 5263–5273.
31. Wood, R. J. K.; Hutton, S. P. *Wear* **1990**, 140, 387–394.
32. Stemp, M.; Mischler, S.; Landolt, D. *Wear* **2003**, 255(1–6), 466–475.
33. Mischler, S.; Spiegel, A.; Landolt, D. *Wear* **1999**, 225–229, 1078–1087.
34. Staehle, R. W. *Corros. Sci.* **2007**, 49, 7–19.
35. Jemmely, P.; Mischler, S.; Landolt, D. *Wear* **2000**, 237, 63–76.
36. Roberge, P. *Erosion-Corrosion, Corrosion Testing Made Easy Series*; NACE International: Houston, USA, 2004.
37. Efrid, D.; Wright, E. J.; Boros, J. A.; Hailey, T. G. *Corrosion* **1993**, 49, 992–1003.
38. Kennelly, K. J.; Hausler, R. H.; Silverman, D. C. NACE Corrosion/1990; 1990.
39. Nesic, S.; Nyborg, R.; Stangeland, A. *Corrosion* **2003**, 59, 443–456.
40. Sedamed, G. H.; Abdo, M. S. E.; Amder, M.; El-Latif, G. A. *Int. Comm. Heat mass Transfer* **1998**, 25(3), 443–451.
41. Wood, R. J. K.; Hutton, S. P.; Schiffrin, D. J. *Corros. Sci. J.* **1990**, 30(12), 1177–1201.
42. Schmitt, G.; Bosch, C.; Plagemann, P.; Moeller, K. Local wall shear stress gradients in the slug flow regime – Effects of hydrocarbon and corrosion inhibitor, NACE CORROSION/2002; 2002, Paper No. 02244.
43. Schmitt, G.; Gudde, T. Local mass transport coefficients and local wall shear stresses at flow disturbances, NACE CORROSION/1995, 1995, Paper No. 102.
44. Schmitt, G.; Gudde, T.; Strobel-Effertz, E. Fracture mechanical properties of CO<sub>2</sub> corrosion product scales and their relation to localised corrosion, NACE CORROSION/1996, 1996, Paper No. 9.
45. Wharton, J. A.; Wood, R. J. K. *Wear* **2004**, 256, 525–536.
46. Donohue, G. L.; Tiedermann, W. G.; Reischman, M. M. *J. Fluid Mech.* **1972**, 56, 559–575.
47. Kline, S. J.; Reynolds, W. C.; Schraub, F. A.; Rundstrander, P. J. *Fluid Mech.* **1967**, 30, 741–773.
48. Kim, H. T.; Kline, S. J.; Reynolds, W. C. *J. Fluid Mech.* **1971**, 50, 133–160.
49. Blackwelder, R. F. Some ideas on the control of near-wall eddies, AIAA; 1989, Paper 89–1009.
50. Faddick, R. R. Wear in pipes, Short course on slurry pipelining technology, Camborne School of Mines, 1982, pp 1–15.
51. Haugen, K.; Kvernfold, O.; Ronald, A.; Sandberg, R. *Wear* **1995**, 186–187, 179–188.
52. Turchaninov, S. P. *The Life of Hydrotransport Pipelines*; Nedra Press: Moscow, Russia, 1973.
53. Shimoda, K.; Yukawa, T. Erosion of pipe bend in pneumatic conveyer, Proceedings of the 6th International Conference On Erosion by Liquid and Solid Impact, University of Cambridge, 1983, Paper 59.
54. Harvey, T. J.; Wharton, J. A.; Wood, R. J. K. *Tribology – Mater. Surf. Interf.* **2007**, 1(1), 33–47.
55. Hashish, M. An improved model of erosion by solid particles, Proceedings of the 7th International Conference on erosion by liquid and solid impact, 1998, Paper 66, published by Cavendish Laboratory.
56. Finnie, I. *Wear* **1972**, 19, 81–90.
57. Gane, N.; Murray, M. S. The transition from ploughing to cutting in erosive wear, Proceedings of the 5th International Conference on Erosion by Solid and Liquid Impact (Cambridge, UK, 1979), paper 40, pp 1–8.
58. Keating, A.; Nesic, S. *Corrosion* **2001**, 57(7), 621–633.
59. Bergevin, K. Effect of slurry velocity on the mechanical and electrochemical components of erosion-corrosion in vertical pipes, Master's thesis, University of Saskatchewan, 1984.
60. Bitter, J. G. A. *Wear* **1963**, 6, 5–21.
61. Neilson, J. H.; Gilchrist, A. *Wear* **1968**, 11, 123–143.
62. Forder, A.; Thew, M. T.; Harrison, D. *Wear* **1998**, 216, 184–193.
63. Wood, R. J. K.; Jones, T. F.; Miles, N. J.; Ganeshalingam, J. *Wear* **2001**, 250(1–12), 771–779.
64. Wood, R. J. K.; Jones, T. F.; Ganeshalingam, J.; Wang, M. Erosion modelling of swirling and non-swirling slurries in pipes, Hydrotransport 15, Banff, Canada, BHR Group, 3–5 June 2002, 497.
65. Wood, R. J. K.; Jones, T. F.; Ganeshalingam, J. Erosion in swirl inducing pipes, ASME Fluids Engineering Division Summer Meeting, Montreal, Canada, July 2002, paper FEDSM2002-31287, ASME International.
66. Wood, R. J. K.; Jones, T. F.; Ganeshalingam, J.; Miles, N. J. *Wear* **2004**, 256(9–10), 937–947.
67. Wood, R. J. K.; Jones, T. F. *Wear* **2003**, 255, 206–218.
68. Lui, J.; Lin, Y.; Yong, X.; Li, X. *Corrosion* **2005**, 61(11), 1061–1069.
69. Chang, J. T.; Yeh, C. H.; He, J. L.; Chen, K. C. *Wear* **2003**, 255, 162–169, Part 1 AUG–SEP 2003.
70. Chernega, S. M.; Loskutova, T. V.; Yantsevych, K. V. *Metallofiz. Noveish. Tekhnol* **2003**, 25, 519–532.
71. Neale, M.; Gee, M. G. *Guide to Wear Problems and Testing for Industry, Tribology in Practice Series*; PEP Ltd.: London, 2000.
72. Beck, T. R. Electrochemical Models for SCC of Titanium. In *Theory of Stress Corrosion Cracking in Alloys*; Scully, J. C., Ed.; NATO: Brussels, 1971; pp 64–85.
73. Cho, E.; Kwon, H. *Corros. Sci. Technol.* **2002**, 31, 448–453.
74. Shibata, T.; Staehle, R. W. Application of high speed elongation technique to stress corrosion cracking of Fe-Cr-Ni Alloys Proceedings of the Fifth International Congress on Metallic Corrosion 1975; pp 487–492.
75. Hoar, T. P.; Scully, J. C. *J. Electrochem. Soc.* **1964**, 348–352.
76. Burstein, G. T.; Sasaki, K. *J. Electrochem. Soc.* **2001**, B282–B287.
77. Ambrose, J. R.; Kruger, J. *Corrosion* **1972**, 28, 30–35.
78. Sethuramiah, A. *Lubricated Wear: Science and Technology, Tribology Series 42*; Elsevier: Amsterdam, 2003.
79. Silverman, D. C. *Corrosion* **2004**, 60(11), 1003–1023.
80. Douglas, J. F.; Gasiorek, J. M.; Swaffield, J. A.; Jack, L. B. *Fluid Mechanics*, 5th ed.; Pearson: Harlow, UK, 2005, ISBN 0–13–129293–5.
81. Cantwell, B. J. *Annu. Rev. Fluid Mech.* **1981**, 13, 457–515.
82. Robinson, S. K. *Annu. Rev. Fluid Motion* **1991**, 23, 601–639.
83. Panton, R. L. *Incompressible Flows*; Wiley/Interscience: New York, 1984, pp 717.

84. Lee, C. K.; Shih, H. C. *J. Mater. Sci.* **2000**, 35(9), 2361–2369.
85. Thakare, M. R.; Wharton, J. A.; Wood, R. J. K.; Menger, C. *Tribol. Int.* **2008**, 41(7), 629–639.
86. Mischler, S.; Spiegel, A.; Landolt, D. *Wear* **1999**, 229, 1078–1087, Part 2.
87. Ponthiaux, P.; Wenger, F.; Drees, D.; Celis, J. P. *Wear* **2004**, 256, 459–468.
88. Garcia, I.; Drees, D.; Celis, J. P. *Wear* **2001**, 249, 452–460.
89. Goldberg, J. R.; Gilbert, J. L. *J. Biomed. Mater. Res.* **1997**, 37(3), 421–431.
90. Mischler, S.; Debaud, S.; Landolt, D. *J. Electrochem. Soc.* **1998**, 145(3), 750–758.
91. Jiang, J.; Stack, M. M.; Neville, A. *Tribol. Int.* **2002**, 35(10), 669–679.
92. Jiaren Jiang; Stack, M. M. *Wear* **2006**, 261(9), 954–965.
93. ASTM Standard G 119–93, Standard Guide for Determining Synergism between Wear and Corrosion; 1993.
94. Zeisel, H.; Durst, F. Computations of erosion-corrosion processes in separated two-phase flows, *NACE Corrosion*, NACE, 1990, Paper No. 29.
95. Vignal, V.; Mary, N.; Ponthiaux, P.; Wenger, F. *Wear* **2006**, 261, 947–953.
96. Zhou, S.; Stack, M. M.; Newman, R. C. *Corrosion* **1996**, 52, 934–946.
97. Matsumura, M. *Corros. Rev.* **1994**, 12, 321–340.
98. Neville, A.; Hodgkiss, T.; Xu, H. *Wear* **1999**, 235, 523–534.
99. Malka, R.; Nešić, S.; Gulino, D. A. *Wear* **2007**, 262(7–8), 791–799.
100. Bello, J. O.; Wood, R. J. K.; Wharton, J. A. *Wear* **2007**, 263, 149–159.
101. Rabinowicz, E.; Dunn, L. A.; Russell, P. G. *Wear* **1961**, 4, 345–355.
102. Batchelor, A. W.; Stachowiak, G. W. *Wear* **1998**, 123, 281–291.
103. Ferng, Y. M.; Ma, Y. P.; Ma, K. T.; Chung, N. M. *Corrosion* **1999**, 55(4), 332–342.
104. Ferng, Y. M.; Ma, Y. P.; Chung, N. M. *Corrosion* **2000**, 56(2), 116–126.
105. Bozzini, B.; Ricotti, M. E.; Boniardi, M.; Mele, C. *Wear* **2003**, 255, 237–245.
106. Lu, B. T.; Luo, J. L.; Ma, H. Y. *J. Electrochem. Soc.* **2007**, 154(3), C159–C168.
107. Neville, A.; Reyes, M.; Xu, H. *Tribol. Int.* **2002**, 35(10), 643–650.
108. Wood, R. J. K. *Wear* **2006**, 261(9), 1012–1023.
109. Nesic, S.; Bienkowski, J.; Bremhorst, K.; Yang, K. S. *Corrosion* **2000**, 56(10), 1005–1014.
110. Guo, H. X.; Lu, B. T.; Luo, J. L. *Electrochim. ACTA* **2005**, 51(2), 315–323.
111. Tsai, W. T.; Huang, T. M. *Thin Solid Films* **2000**, 379(1–2), 107–113.
112. Tan, A. H.; Cheng, Y. C. *Wear* **2007**, 262(5–6), 693–698.
113. Ziomek-Moroz, M.; Miller, A.; Hawk, J.; Cadien, K.; Li, D. Y. *Wear* **2003**, 255, 869–874, Part 2.
114. Preston, F. J. *Soc. Glass Technol.* **1927**, 9, 214–256.
115. Akonko, S. B.; Li, D. Y.; Ziomek-Moroz, M.; Hawk, J.; Miller, A.; Cadien, K. *Wear* **2005**, 259, 1299–1307, Part 2.
116. Wood, R. J. K.; Wharton, J. A.; Speyer, A. J.; Tan, K. S. *Tribol. Int.* **2002**, 35(10), 631–641.
117. Sasaki, K.; Burstein, G. T. *Phil. Mag. Lett.* **2000**, 80(7), 489–493.
118. Oltra, R.; Chapey, B.; Renuad, L. *Wear* **1995**, 186–187, 533–541.
119. Lambrechts, P.; Goovaerts, K.; Bharadwaj, D.; De Munck, J.; Bergmans, L.; Peumans, M.; Van Meerbeek, B. *Wear* **2006**, 261(9), 980–986.
120. Nagarajan, V. S.; Jahanmir, S.; Thompson, V. P. *Dent. Mater.* **2004**, 20(1), 63–71.
121. Nagarajan, V. S.; Hockey, B. J.; Jahanmir, S.; Thompson, V. P. *J. Mater. Sci.* **2000**, 35(2), 487–496.
122. Lewis, R.; Dwyer-Joyce, R. S. *P I MECH. ENG. J.-J. Eng* **2005**, 219(J1), 1–18.
123. Vieira, A. C.; Ribeiro, A. R.; Rocha, L. A.; Celis, J. P. *Wear* **2006**, 261(9), 994–1001.
124. Berradja, A.; Bratu, F.; Benea, L.; Willems, G.; Celis, J.-P. *Wear* **2006**, 261(9), 987–993.
125. Yan, Y.; Neville, A.; Dowson, D.; *J. Phys. D: Appl. Phys.* **2006**, 39(15), 3200–3205.
126. Sinnett-Jones, P. E.; Wharton, J. A.; Wood, R. J. K. *Wear* **2005**, 259(2), 898–909.
127. Sun, D. Wharton, J. A.; Wood, R. J. K.; Ma, L.; Raithforth, W. M. *Tribol. Int.* **2009**, 42(1), 99–110.

## Further Reading

Flow-induced corrosion: Fundamental studies and industrial experience, NACE, symposium proceedings, Corrosion 1990, Houston, USA.

*Engineering Tribology*, John Williams; Cambridge University Press: Cambridge UK.

Ludema, K. C. *Friction, Wear, Lubrication: a Textbook in Tribology*; CRC Press: Boca Raton, FL, 1996; p 45.

Hutchings, I. M. *Tribology: Friction and Wear of Engineering Materials*; Edward Arnold: UK, 1992; co-published by CRC Press, Boca Raton, USA.

*Engineering Tribology*, Stachowiak, G.; Batchelor, A. W.; Elsevier, 2005.



## 2.17 Corrosion in Natural Waters

**S. B. Lyon**

Corrosion and Protection Centre, School of Materials, University of Manchester, Oxford Road, Manchester M13 9PL, UK

This article is a revision of the Third Edition article 2.3 by C.W. Drane and R.J. Oliphant, volume 1, pp 2:43–2:59,

© 2010 Elsevier B.V.

<b>2.17.1</b>	<b>Introduction</b>	1095
<b>2.17.2</b>	<b>Constituents or Impurities in Water</b>	1095
2.17.2.1	Dissolved Gases	1096
2.17.2.2	Oxygen	1096
2.17.2.3	Carbon Dioxide	1097
2.17.2.4	Water Hardness (Carbonate Species)	1097
2.17.2.5	Other Inorganic Species	1098
2.17.2.6	Organic Species	1099
<b>2.17.3</b>	<b>Scaling in Natural Waters</b>	1099
2.17.3.1	Controlling Factors in Scale Formation	1099
2.17.3.2	Calcium Carbonate Scales	1100
2.17.3.3	Other Inorganic Scales	1102
2.17.3.3.1	Silica	1102
2.17.3.3.2	Magnesium hydroxide and silicate	1102
2.17.3.3.3	Calcium sulfate	1102
2.17.3.3.4	Calcium phosphate	1102
2.17.3.3.5	Iron and manganese oxides and hydroxides	1102
2.17.3.4	<b>Fouling Deposits</b>	1103
2.17.3.4.1	Corrosion	1103
2.17.3.4.2	Biofilms	1103
2.17.3.5	<b>Water Treatment</b>	1103
2.17.3.5.1	Water softening and water hardening	1103
2.17.3.5.2	Treatment with acid	1103
2.17.3.5.3	Scale inhibitors and dispersants	1104
2.17.3.5.4	Surfactants	1104
2.17.3.5.5	Corrosion inhibition in potable water systems	1104
<b>2.17.4</b>	<b>Corrosivity of Natural Waters</b>	1104
2.17.4.1	pH	1104
2.17.4.2	Physical Processes	1105
2.17.4.3	Water Chemistry	1105
2.17.4.4	Bacteriological Effects	1105
<b>References</b>		1105

### Glossary

**Calcite** Calcium carbonate.

**Gypsum** Calcium sulfate.

**Permanent hardness** Water hardness that cannot be removed by boiling; for example, the precipitation of calcium sulfate.

**ppm** Strictly parts per million by mass; equivalent to 1 mg of solute per kg of solvent. In dilute solutions and for practical usage, it is equivalent to 1 mg of solute per litre ( $\text{dm}^3$ ) of solvent.

**Temporary hardness** Water hardness that can be removed by boiling causing the loss of dissolved  $\text{CO}_2$ ; for example, the precipitation of calcium carbonate.

**Water hardness** A measure of the tendency of water to precipitate a solid scale; generally related to the concentration of dissolved cations (in particular calcium and magnesium) with respect to dissolved anions (in particular bicarbonate and sulfate).

## Abbreviations

**HVAC** Heating, ventilation and air conditioning

**LSI** Langelier saturation index

**PSI** Puckorius scaling index

**RSI** Ryznar stability index

**TDS** Total dissolved solids

## Symbols

**$K_{sp}$**  Solubility product

**$\Delta G$**  Free energy change

**[x]** The concentration of species 'x' is conventionally denoted by placing it in square brackets

### 2.17.1 Introduction

Metals immersed or partly immersed in water tend to corrode because of their thermodynamic instability. Natural waters may contain some or all impurities such as dissolved solids and gases, colloidal or suspended matter, and biological materials (microbes, algae). All these may affect the corrosive properties of the water in relation to the metals with which it is in contact. The effect may be either of stimulation or of suppression of either the cathodic or the anodic reaction. Thus, some metals may form a natural protective film in a specific water composition and the corrosiveness of the water to these metals depends on whether or not the dissolved species that it contains assist in the maintenance of a self-healing film (i.e., whether they are inhibiting or not).

The metals most commonly used for water systems are iron and steel. These metals often have some sort of applied protective coating; galvanized steel, for example, relies on a thin layer of zinc, which is anodic to the steel except at high temperatures. Many systems, however, contain a wide variety of other materials and the effect of various water constituents on these must be considered. Although there is increasing use of polymeric materials in water systems, metallic components are still very common and include copper, brasses, bronzes, lead, aluminum, stainless steel, and solder.

The passage of natural water through a pipe may modify the composition of the water and hence its corrosive properties. For example, dissolved oxygen or carbon dioxide may be removed partially or wholly by reaction with metals or organisms. Dissolution of a metal into water may, on the other hand, make it more

corrosive. An example of this is the attack of some waters on copper and the subsequent increased pitting corrosion of less noble metals such as iron, galvanized steel, and aluminum. This enhanced pitting is caused by the deposition of minute quantities of copper on the less noble metal, thereby setting up numerous local bimetallic corrosion cells.

Failure of the metal can be the most important effect of corrosive water, but other effects may arise from low concentrations of metallic ions produced by corrosion. Water passed through a lead pipe may contain a toxic concentration of that metal; with copper there is a greater tolerance from the toxicity point of view but staining of fabrics and sanitary fittings may be objectionable. With iron, similarly, discoloration of the water may be unpleasant and may cause damage to materials being processed. The effects of dissolved zinc in the environment have also recently become a concern.

The concentrations of various substances in drinking water or in industrial process waters in the dissolved, colloidal, or suspended form are relatively low but vary considerably. For example, a hardness of 300–400 ppm (as  $\text{CaCO}_3$ ) is sometimes tolerated in potable (drinking) public water supplies, whereas dissolved iron to the extent of  $1 \text{ mg dm}^{-3}$  would be unacceptable. On the other hand, saline waters, including seawater, estuarine water, and brines from boreholes can contain very large quantities of dissolved species; however, these last mentioned types of water are not considered in this section.

### 2.17.2 Constituents or Impurities in Water

The important constituents in natural water can be classified as follows:

1. dissolved gases (e.g., oxygen, nitrogen, carbon dioxide, ammonia, sulfurous gases);
2. mineral constituents, including hardness salts (e.g., calcium, magnesium, carbonate/bicarbonate, etc), sodium salts (e.g., chloride, sulfate, nitrate, etc.), other salts, and dissolved silica;
3. organic matter, including that of both animal and vegetable origin, oil, trade waste (including agricultural) constituents and synthetic detergents;
4. microbiological forms, including various types of algae and slime-forming bacteria.

In water analysis, determinations (except occasionally for dissolved gases) are made on the basis of mass

**Table 1** Typical water analyses (values in  $\text{mg dm}^{-3}$ )

	<i>Very soft water</i>	<i>Moderately soft water</i>	<i>Slightly hard water</i>	<i>Moderately hard water</i>	<i>Hard borehole water</i>	<i>Very hard borehole water</i>
pH	6.3	6.8	7.4	7.5	7.1	7.1
Alkalinity due to	2	38	90	180	250	470
Calcium	10	53	120	230	340	559
Total hardness	5	36	85	210	298	451
Calcium hardness	6	20	39	50	17	463
Sulfate	5	11	24	21	4	149
Chloride	Trace	0.3	3	4	7	6
Silica	33	88	185	332	400	1670
Total dissolved solids						

Source: Drane, C. W.; Oliphant, R. J. *Natural Waters*. In Corrosion, 3rd ed.; Shreir, L. L., Jarman, R. A., Burstein, G. T., Eds., 1994; chapter 2.3.

of solute to volume of solvent ( $\text{mg dm}^{-3}$ ). More strictly, parts per million (ppm) refers to mass of solute to mass of solvent but in dilute solutions, and to all practical purposes, the two units are interchangeable. In treated water for high-pressure boilers, impurities are in much lower concentrations and are measured in parts per billion (ppb, equivalent to  $1 \mu\text{g dm}^{-3}$ ).

Water analysis for drinking-water supplies is concerned mainly with pollution and bacteriological tests. For industrial supplies, a mineral analysis is of more interest. **Table 1** includes a typical selection and gives some indication of the wide range of impurities that can be found.

### 2.17.2.1 Dissolved Gases

Of the dissolved gases occurring in water, oxygen occupies a special position as it is the main cathodic reactant and can control the corrosion reaction rate if mass transport limits the arrival of oxygen to the cathode. Carbon dioxide is scarcely less important as it dissolves in water to giving rise to equilibria with carbonic acid, bicarbonate and carbonate in solution, which are important in the control of solution pH and the solubility of calcium carbonate and, hence, the calcium hardness of the water. Therefore, the quantity of dissolved carbon dioxide in solution controls the solubility of the carbonate rocks that frequently comprise the geology close to boreholes.

Nitrogen is also generally present with oxygen although, as it is significantly less soluble, the mass ratio of dissolved nitrogen to oxygen in water is not the same as in air (it is about 4:3). It has little importance in connection with corrosion, but can be a nuisance if changes in physical conditions (e.g., reduction in local pressure) bring about its release from solution.

Other gases which are occasionally present in natural water usually arise from pollution. Ammonia,

which in various forms may be present in waste waters, attacks copper and copper alloys; its presence in estuarine waters is one of the causes of corrosion of copper-based steam condenser tubes. Hydrogen sulfide may also be the result of pollution but often bacterial action (e.g., by sulfate reducing bacteria) is the main contributor. Both gases initiate and/or accelerate the corrosion of most metals.

### 2.17.2.2 Oxygen

Although other oxidants can occur in natural waters (in particular sulfur species) dissolved oxygen is probably the most significant constituent affecting corrosion; its importance lies in the fact that it is the most important cathodic reactant in neutral solutions. In surface waters, the oxygen concentration is in equilibrium with the atmosphere and, hence, approximates to saturation. Underground waters are more variable in oxygen content and some waters may be effectively oxygen-free. Contact with air, however, usually gives rise to an oxygen concentration similar to the figures in **Table 2**. The solubility is slightly less in the presence of solutes, but this effect is not very significant in natural waters containing less than 1000 ppm dissolved solids.

For many applications, notably feed-water for boilers, removal of oxygen is essential and is accomplished by physical or chemical de-aeration. For many other purposes (e.g., once-through systems, heating, cooling and ventilation, i.e., HVAC systems), however, full de-aeration is not applicable, as the water used is in continuous contact with air, from which it would rapidly take up more oxygen. In these circumstances, chemical treatment, with corrosion inhibitors for example, is necessary to restrict corrosion.

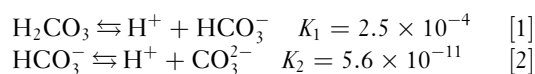
A major difficulty in chemical water treatment is that the oxygen content of the water may not be the same at all points. For example, in a thin layer of water,

between a deposit, crevice or other surface occlusion and the metal on which it is present, the oxygen can be depleted; the difference in oxygen content between the body of water and the stagnant water will then set up a corrosion current which is difficult to suppress.<sup>1,2</sup> Rather, similar conditions occur at the water line of a vessel containing water with air above it. Even if the water is conditioned to inhibit corrosion under submerged conditions, it is difficult to extend the protection to above the water line. Fluctuation in water level extends the area of localized attack.

### 2.17.2.3 Carbon Dioxide

The effect of dissolved carbon dioxide on corrosion is closely linked with the bicarbonate content of the water. In many waters divalent cations (such as calcium and magnesium) are present at significant concentration and, depending on the water chemistry and temperature may precipitate a scale onto surfaces (i.e., hard waters). The stability, or otherwise, of calcium and magnesium in solution depends on a number of factors, the most important of which are pH, dissolved total carbonate concentration (and its speciation as dissolved CO<sub>2</sub>, carbonic acid and bicarbonate) and the concentration of Ca<sup>2+</sup> and Mg<sup>2+</sup>. Any external phenomenon that reduces the solubility of the divalent cations will result in their precipitation, typically as a scale containing either calcium carbonate or magnesium hydroxide (or both).

Calcium bicarbonate requires excess carbon dioxide in solution to stabilize it; the necessary concentration depends on the other constituents of the water and the temperature. Carbon dioxide dissolves in water to give carbonic acid in the following equilibria, with the equilibrium constants ( $K_x$ ) indicated<sup>3</sup>:



However, although carbonic acid is a stronger acid than acetic acid, its concentration in solution in equilibrium with atmospheric carbon dioxide ( $\approx 385$  ppm) is relatively low and, therefore, its effect is considerably less. In the absence of dissolved carbonate species from other sources, the solution pH is therefore determined by the partial pressure of CO<sub>2</sub>:



The speciation among carbonic acid, bicarbonate ion and carbonate ion depends on the above equilibria and, hence, the pH. **Figure 1** shows calculated mole fractions of carbonic acid, bicarbonate ion, and carbonate ion as a function of pH for a fixed total carbonate concentration.

### 2.17.2.4 Water Hardness (Carbonate Species)

The usual classification of water by hardness (**Table 3**) is as follows.

The hardness figures for natural water are very varied but most natural drinking water supplies fall into two well-defined groups:

1. Upland waters of low hardness commonly retained in storage reservoirs. In the United Kingdom, these are supplied to most localities in Scotland, Wales, and the North of England.

**Table 2** Solubility of oxygen in distilled water

Temperature (°C)	Oxygen content of saturated, distilled water	
	mg dm <sup>-3</sup>	ml dm <sup>-3</sup>
0	14.16	9.90
5	12.37	8.65
10	10.92	7.64
15	9.76	6.83
20	8.84	6.18
25	8.11	5.67

Source: Sherwood, J. E.; Stagnitti, F.; Kokkinn, M. J.; Williams, W. D. *Int. J. Salt Lake Res.* **1992**, 1, 1–6.  
Groisman, A. Sh.; Khomutov, N. E. *Russ. Chem. Rev.* **1990**, 59, 1217–1250.

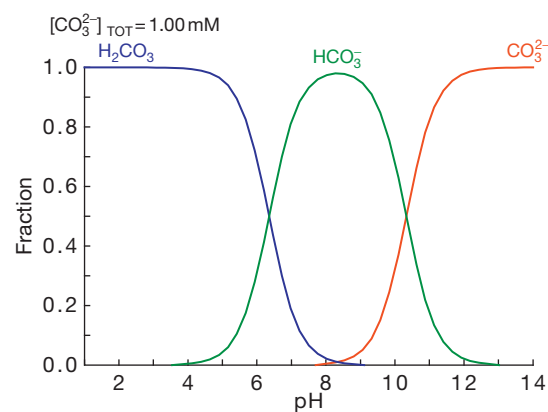


**Figure 1** Calculated mole fractions of carbonic acid, bicarbonate ion, and carbonate ion as a function of pH at a total carbonate species concentration of 1 mM. Calculated with Puigdomenach, I.; *Hydrochemical Equilibrium Constant Database (HYDRA/MEDUSA)*; Royal Institute of Technology: Stockholm. Available at [www.kemi.kth.se/medusa](http://www.kemi.kth.se/medusa).

2. Underground waters of high hardness, usually derived from aquifers in chalk, sandstone or limestone strata. In the United Kingdom, these are found mainly in the East and South of England.

A few sources, most of which are derived from rivers and vary according to season, are intermediate in composition between these.

The corrosive properties of natural waters are governed by many factors and cannot be related to hardness alone, but the following trends are apparent:

1. Soft upland waters are commonly corrosive to most metals, their behavior depending to some extent on pH. They are inevitably unsaturated with respect to calcium carbonate and it is not usually practicable to modify the carbonate equilibrium to make them nonaggressive.
2. Very hard waters are usually not very aggressive provided that they are supersaturated in calcium carbonate. Underground waters with a low pH

**Table 3** Range of calcium hardness for various natural waters

<i>Calcium concentration</i>	<i>Hardness classification</i>
<50 ppm CaCO <sub>3</sub>	Soft
50–100 ppm CaCO <sub>3</sub>	Moderately soft
100–150 ppm CaCO <sub>3</sub>	Slightly hard
150–250 ppm CaCO <sub>3</sub>	Moderately hard
250–350 ppm CaCO <sub>3</sub>	Hard
>350 ppm CaCO <sub>3</sub>	Very hard

Thresh, J. C.; Beale, J. F.; Suckling, E. V. *The Examination of Waters and Water Supplies*, 7th ed.; Taylor, E. W.; Churchill Livingston: London, 1958.

**Table 4** Limits for inorganic species in UK drinking water

<i>Measured parameter</i>	<i>Maximum permitted value</i>	<i>Units of measurement</i>	<i>Point of monitoring</i>
Conductivity	2500	μS cm <sup>-1</sup> at 20 °C	Supply point
pH	6.5–10		Customers' taps
Chloride	250	mg (Cl) dm <sup>-3</sup>	Supply point
Sulfate	200	mg (SO <sub>4</sub> ) dm <sup>-3</sup>	Supply point
Sodium	200	mg (Na) dm <sup>-3</sup>	Customers' taps
Fluoride	1.5	mg (F) dm <sup>-3</sup>	Customers' taps
Ammonium	0.5	mg (NH <sub>4</sub> ) dm <sup>-3</sup>	Customers' taps
Nitrate	50	mg (NO <sub>3</sub> ) dm <sup>-3</sup>	Customers' taps
Nitrite	0.5	mg (NO <sub>2</sub> ) dm <sup>-3</sup>	Customers' taps
Copper	2	mg (Cu) dm <sup>-3</sup>	Customers' taps
Iron	200	μg (Fe) dm <sup>-3</sup>	Customers' taps
Manganese	50	μg (Mn) dm <sup>-3</sup>	Customers' taps
Aluminum	200	μg (Al) dm <sup>-3</sup>	Customers' taps
Lead (now)	25	μg (Pb) dm <sup>-3</sup>	Customers' taps
Lead (after 2013)	10	μg (Pb) dm <sup>-3</sup>	Customers' taps

Source: The Water Supply (Water Quality) Regulations 2000 (and as subsequently amended), UK Government, HMSO.

value caused by excess carbon dioxide content are, however, aggressive unless corrective treatment is applied.

3. Waters of intermediate hardness frequently contain significant amounts of other constituents and there is often a tendency for the scale formed to be loosely attached to the metal surface, permitting corrosion to occur irregularly underneath. In most waters the bicarbonate content is less than the hardness, but a few natural waters are known where the reverse is the case.

### 2.17.2.5 Other Inorganic Species

The principal ions found in natural water supplies include calcium, magnesium, sodium, bicarbonate, sulfate, chloride, and nitrate; also a few parts per million of iron or manganese may sometimes be present. From the corrosion point of view the small quantities of other anions present, for example, nitrite, phosphate, iodide, bromide and fluoride, have little significance. Although larger concentrations of some of these ions, notably nitrite and phosphate, may act as corrosion inhibitors, the small quantities present in natural waters will have little effect. Some of the minor constituents have other beneficial or harmful effects, for example, there is an optimum concentration of fluoride for control of dental caries and very low iodide or high nitrate/nitrite concentrations are objectionable on medical grounds (**Table 4**).

Dissolved ionic species will increase the ionic conductivity of water and, hence, tend to increase metallic corrosion by reducing the ohmic voltage loss between local anodes and cathodes. At low



concentration the effect on ionic conductivity dominates, although chloride will always tend to promote pitting corrosion on passive materials (e.g., stainless steel) that are protected by a thin protective scale. In the latter case, the ratio of chloride to hydroxide (or bicarbonate) can be important.<sup>4</sup> Sulfate in general appears to behave very similarly; Hatch and Rice have shown that small concentrations in distilled water increase corrosion more than similar concentrations of chloride.<sup>5</sup> In practice, high-sulfate waters may attack concrete and the performance of some inhibitors appears to be adversely affected by the presence of sulfate. Sulfates have also a special role in bacterial corrosion under anaerobic conditions.

Regarding iron- and manganese-bearing waters, the small amount of deposit formed is not likely to have much effect on corrosion. However, most iron-bearing waters contain substantial amounts of carbon dioxide which may be troublesome. Manganese-bearing waters may be of a similar type but they sometimes contain complex organic compounds of manganese for which special treatment may be needed. Substantial iron and manganese content in water will tend to promote pitting corrosion of materials such as aluminum, stainless steel and copper. Another mineral constituent of water is silica, present both as a colloidal suspension and as a dissolved species.

### 2.17.2.6 Organic Species

The types of organic matter in water supplies are very diverse; they may be present in suspension, or in colloidal or true solution and may include micro-organisms. The materials are largely derived from decaying vegetable matter but there are many other possible sources including run-off from fields and domestic and industrial wastes. Some of the worst corrosive effects ascribed to natural soft waters are attributed to a rather wide group of organic acids abstracted from peat and mosses, sometimes called humic acids.<sup>6</sup> Such waters have low pH values and are often discolored. They affect ferrous metals appreciably and also attack lead and copper. Corrosion control, either of steel or of copper, is rarely achieved solely by pH correction of such waters.

## 2.17.3 Scaling in Natural Waters

### 2.17.3.1 Controlling Factors in Scale Formation

The deposition of a scale from solution involves the nucleation, crystallization and growth of a new solid

phase. Nucleation of deposits may take place either in solution (homogeneous nucleation) or on a suitable substrate where the *local* (i.e., adjacent to the substrate) chemistry may be particularly conducive to scaling (heterogeneous nucleation). Nucleation is a thermodynamically driven process and the elementary theory predicts that nucleation requires a driving force to overcome the new phase boundary (i.e., surface) created. Thus, the formation of a new phase in a solution *reduces* the overall free energy of the system by precipitating out a supersaturated species; however, it *increases* the local free energy by formation of a new surface. Both of these processes can be modeled (for homogeneous nucleation in solution) as follows<sup>7</sup>:

$$\Delta G_{\text{tot}} = 4/3\pi r^3 \Delta G_{\text{volume}} + 4\pi r^2 \Delta G_{\text{surface}} \quad [4]$$

where  $\Delta G_{\text{tot}}$  is the overall Gibbs free energy change during nucleation;  $\Delta G_{\text{volume}}$  is the free energy change per unit volume of new species formed (which will be negative and favorable);  $\Delta G_{\text{surface}}$  is the free energy per unit surface area of the nucleus (which will be positive and unfavorable). The above equation is easily altered for heterogeneous nucleation (i.e., on a surface). Nucleation theory predicts that nuclei do not grow below a specific, critical dimension, which can be seen clearly in Figure 2.

The above thermodynamic treatment can say nothing about the kinetics of the nucleation process except that at higher supersaturation, the driving force for nucleation is greater. Once nuclei have formed, their subsequent growth is determined by a number of interacting processes, particularly the diffusion of species in solution.

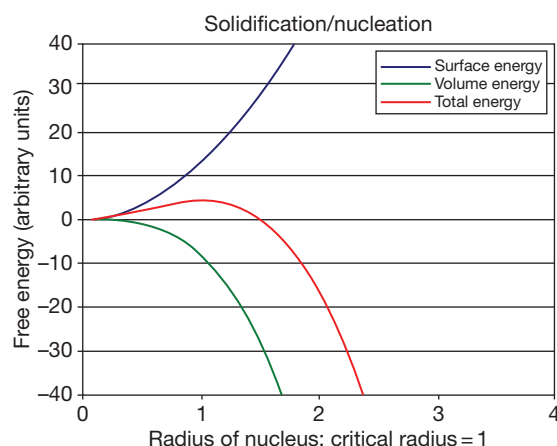


**Figure 2** Variation of surface and volume free energy with nucleus size showing that a critical size is required before stable nucleation is possible.

The solubility of most scale-forming minerals decreases as the temperature increases. Therefore, such solutions will precipitate a scale directly on the heat-transfer surface because of their lower equilibrium solubility at these locations (carbonate scales that form from hard water in domestic kettles being the obvious example). Other soluble species may be scale-forming as a result of changes in pH, pressure, flow, etc. Generally, the crystallization of a scale-forming material from solution is influenced by several factors including the following<sup>8</sup>:

- Local and general supersaturation of the soluble species in solution.
- Solution temperature and particularly temperature differentials especially at surfaces where heat transfer is occurring.
- Solution pH and particularly local changes in pH at cathodic surfaces.
- Pressure, especially where the speciation is controlled by a soluble gas such as CO<sub>2</sub>.
- Flow rate, as this influences local solution temperatures and concentrations, as well as transport of reacting species to the scaling surface.
- Scale nucleation and particularly scale growth are time-dependent processes.
- Surface condition: in particular particles of dirt and rough surfaces will encourage scale nucleation and adherence.

### 2.17.3.2 Calcium Carbonate Scales

The mathematical relationship between carbon dioxide, calcium bicarbonate and calcium carbonate was historically studied by several workers, including Langelier.<sup>9,10</sup> The simpler form of his original equation is (at constant temperature)

$$pH_s = pCa + pAlk + (pK_2 - pK_s) \quad [5]$$

where  $pH_s$  is the pH at which calcium carbonate precipitates,  $pCa$  is the negative logarithm of the calcium concentration expressed as parts per million of CaCO<sub>3</sub>,  $pAlk$  is the negative logarithm of the alkalinity to methyl orange expressed in parts per million of equivalent CaCO<sub>3</sub>,  $pK_2$  is the ionization constant of HCO<sub>3</sub><sup>-</sup>, and  $pK_s$  is the solubility product of CaCO<sub>3</sub>.

This formula does not apply to pH values over 9. Also, as the term  $(pK_2 - pK_s)$  is a function of temperature and ionic strength (dissolved solids), high salinities will affect its accuracy. However, for the analysis of water at constant temperature much useful

information can be obtained from the basic thermodynamic treatment of Langelier. In order to determine whether water is supersaturated with respect to calcium ions, the Langelier saturation index of water (LSI) is defined as

$$LSI = pH - pH_s \quad [6]$$

where pH is the actual pH of the water and  $pH_s$  is the pH of saturation of calcium carbonate. If the LSI is positive the water will be supersaturated with calcium carbonate, which will, therefore, tend to precipitate as a scale. Conversely if the LSI is negative the water tends to dissolve calcium carbonate and is thus nonscaling. Nonscaling waters are expected to be corrosive while waters that scale are expected to be relatively less corrosive.

The LSI is not wholly satisfactory for practical prediction of the scaling and corrosion tendency. This is because it is possible for waters of varying hardness (and hence corrosivity) to have the same LSI value. The Ryznar stability index (RSI) is a modification of the LSI that overcomes this problem<sup>11</sup>:

$$RSI = 2pH_s - pH \quad [7]$$

In this scheme, an index between 6 and 7 is effectively balanced with little tendency to scale. If  $RSI < 6$ , scaling is likely (and corrosion less likely) with the scaling tendency increasing as the index decreases. For  $RSI > 7$  calcium carbonate formation probably does not lead to a protective corrosion inhibitor film and for  $RSI > 8$  mild steel corrosion is likely to become an increasing problem.

Neither the LSI nor the RSI can account for the buffering capacity of the solution. Thus, water that is high in calcium ions, but low in alkalinity and buffering capacity can have a high saturation value for calcium carbonate. Typically, the water has a large thermodynamic driving force for scale precipitation, but does not have much scaling capacity because of the low quantity of carbonate ions present. To account for these effects an alternative index was devised<sup>12</sup> that is tied to the calculated equilibrium pH rather than the measured value. The PSI index is calculated in a manner similar to the Ryznar stability index. Thus:

$$PSI = 2pH_{eq} - pH_s \quad [8]$$

where  $pH_s$  is as defined above;  $pH_{eq} = 1.465 \times \log_{10}[\text{Alkalinity}] + 4.54$ ; and  $[\text{Alkalinity}] = [\text{HCO}_3^-] + 2[\text{CO}_3^{2-}] + [\text{OH}^-]$ . The index is interpreted in a similar manner to the RSI.

It is important to note that the above indices assume relatively dilute solutions and unit activity coefficients for dissolved species. None of the above indices can satisfactorily predict the scaling tendency of water that has significant quantities of other ions in solution, especially if they are present at high concentration. Other indices<sup>13</sup> have therefore been developed for such conditions encountered, for example, in the oil and gas industry.

There are many modern computational tools now available to determine solution speciation in a wide range of conditions. For example, **Figure 3** shows the effects of varying the calcium ion concentration, at constant total carbonate concentration, on the pH of precipitation of a calcium carbonate scale. Thus, as the water hardness (as calcium ion concentration) increases from 0.5 to 4 mM at a total carbonate of 1 mM, the pH for scale precipitation changes from

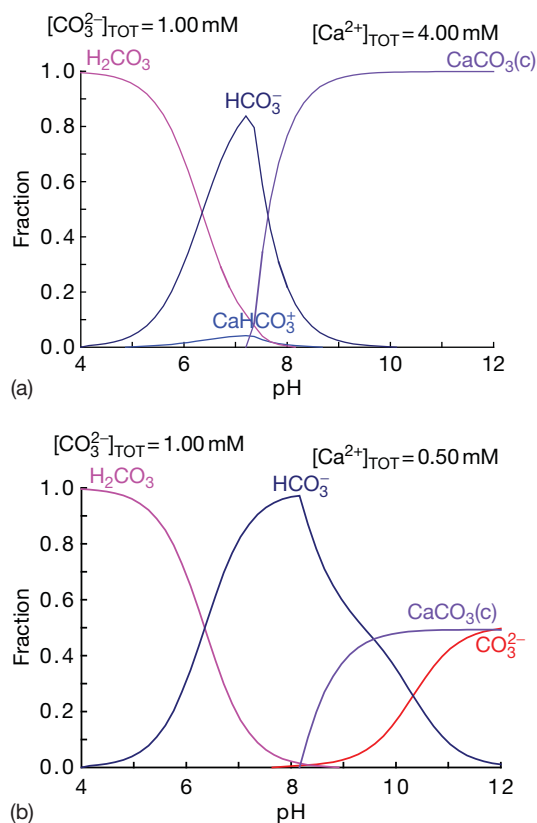


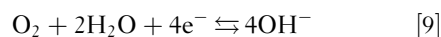
**Figure 3** Mole fraction of stable species as a function of pH for (a) 4 mM and (b) 0.5 mM  $\text{Ca}^{2+}$  concentrations at a constant total carbonate concentration of 1 mM at 298 K. Calculated with Puigdomenach, I.; Hydrochemical Equilibrium Constant Database (HYDRA/MEDUSA); Royal Institute of Technology; Stockholm. Available at [www.kemi.kth.se/medusa](http://www.kemi.kth.se/medusa).

about 8.5 to about 7.5. The domains of pH in which carbonic acid and bicarbonate ion dominate are also clearly evident.

Depending on the circumstances, calcium carbonate scale formation may be detrimental or beneficial. The detrimental effects are summarized below:

- loss of heat transfer efficiency (calcium carbonate has a low thermal conductivity), including reduced life of heat transfer surfaces because of overheating (**Figure 4**);
- loss of pipe diameter leading to reduced flow capacity or an increased pressure requirement to achieve the same flow rate;
- blockage of valves, etc.;
- reduced efficiency of detergents and soaps for washing; and
- deposits left after evaporation of water, which spoils the appearance.

Conversely divalent metal cations can act beneficially, particularly as cathodic inhibitors, for corrosion. This is because of the alkalinity at the cathode caused by oxygen or water reduction:



Thus, the local increase in hydroxide ion concentration will therefore tend to precipitate a scale, even in systems that are not intrinsically scale-forming; as is evidently shown in **Figure 3**. If the scale is sufficiently dense and nonporous, it will provide significant



**Figure 4** Carbonate scale: dense generally protective scale on a steel water pipe with some corrosion evident as general thinning: Photo courtesy of the author.

corrosion protection and, hence, the calcium ions act effectively as inhibitors. The degree of protection afforded by calcium carbonate has been studied by McCauley.<sup>14</sup> The significance of carbon dioxide in corrosion is also discussed in some detail by Simmonds.<sup>15</sup>

### 2.17.3.3 Other Inorganic Scales

Calcium carbonate is by far the most common scaling substance in natural water systems but it is by no means the only one. Thus, all dissolved species will tend to form a scale when their solubility limit is exceeded. Also, although  $\text{CaCO}_3$  is usually dominant in scales formed in potable water, waters used for other industrial purposes (e.g., heating and cooling) may form other deposits depending on the water chemistry. Indeed, many such scales comprise deposits of a range of compounds. Scales may also act to secure (adhere) other forms of fouling deposit (such as mud, silts, etc.) to a substrate.

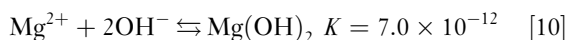
#### 2.17.3.3.1 Silica

Silica is present in many waters; in supplied waters it can be derived from clay and similar soil types. The solubility of silica is relatively high, at least 100 ppm below pH 7, increasing to above 300 ppm at pH 10; therefore, it rarely forms a scale on its own. However, the presence of dissolved silica can promote the precipitation of silicate species, particularly magnesium silicates.<sup>16</sup>

In some more extreme conditions, for example where the supply waters are relatively high in silica, the water requires treatment to prevent scale formation. For example, fouling of heat transfer surfaces and osmosis membranes in desalination plant is problematic<sup>17</sup> and geothermal water and power supply systems tend to readily form silica scales.<sup>18</sup>

#### 2.17.3.3.2 Magnesium hydroxide and silicate

In the presence of significant dissolved magnesium ions and at high pH (typically greater than about 9–10) magnesium hydroxide may precipitate with, and participate in, overall carbonate scale formation<sup>19</sup>:



This is certainly an issue in the formation of scales from brines and marine sources, especially under cathodic protection (and is dealt with elsewhere). However, in the presence of significant dissolved

silica, which may occur in re-circulating evaporative cooling systems for example, formation of magnesium silicate may occur either directly, or by transformation of prior magnesium hydroxide.<sup>20</sup> Deposition of magnesium silicate can generally be prevented by keeping the pH less than about 8 and, more generally, by ensuring that the dissolved silica levels do not exceed 200 ppm.

#### 2.17.3.3.3 Calcium sulfate

Water containing relatively lower quantities of carbonate but a higher concentration of sulfate will tend to form a scale of calcium sulfate (gypsum:  $\text{CaSO}_4 \cdot 2\text{H}_2\text{O}$ ;  $K_{\text{sp}} = 1.95 \times 10^{-4}$ ).<sup>21</sup> Such a water composition may occur naturally but are more commonly found in cooling towers, where acidification with sulfuric acid (to prevent calcite deposition) is used as part of the water treatment system.

In order to avoid precipitation of gypsum on heat transfer surfaces in evaporative cooling systems when using acid treatment, alternative acids could be considered (although these are more corrosive and more expensive). Alternatively, proper blow-down procedures should be used, which involve removal of part of the water from the cooling circuit with replacement with fresh make-up water. Under the correct conditions, calcium sulfate scale formation should not be a problem.

#### 2.17.3.3.4 Calcium phosphate

Phosphoric acid (or more commonly polyphosphate) is commonly added to heating and cooling waters to prevent calcium carbonate scale formation. Generally this functions not necessarily by prevention of precipitation, but by changing the nature of the precipitate such that it does not form as an adherent scale. However, scaling by calcium phosphate (which is less soluble than calcium carbonate) can occur if tricalcium phosphate ( $\text{Ca}_3(\text{PO}_4)_2$ ) is formed as its solubility product is smaller than that of calcium carbonate.<sup>22</sup>

#### 2.17.3.3.5 Iron and manganese oxides and hydroxides

Many scaling deposits may contain small quantities of dissolved iron or manganese. While the levels of these species are usually well below 200 ppb in most water supplies, occasionally higher levels may reach the customer due to corrosion and biological activity in the water supply system from iron and manganese oxidizing bacteria, giving rise to 'red' or 'black' water

quality problems.<sup>23,24</sup> However, in circulating heating and cooling systems, the iron plus manganese concentrations may reach several part per million; unless controlled, iron and manganese oxides are extremely likely to deposit within the system.

The other source of iron in heating and cooling systems is corrosion of the ferrous materials within the system. Indeed, a high level of dissolved iron is a good indicator of an ineffective inhibitor system. The most common scale in hot water systems is magnetite ( $\text{Fe}_3\text{O}_4$ ) while haematite ( $\text{Fe}_2\text{O}_3$ ) is more commonly found in cooling systems.

### 2.17.3.4 Fouling Deposits

The origins of fouling deposits are generally different in origin from scale deposits. The best way to differentiate them is that a scale deposit is a specific and important form of fouling deposit that can, to a large extent, be predicted from the water chemistry.<sup>25</sup> On the other hand, fouling is a general description of any kind of deposit that can form. It includes deposits that arise from inorganic or organic (biological) origins. Thus, in addition to scales, fouling deposits include the following:

- Sediments carried into the system with the make up water, such as silt.
- Products of reactions between the water and chemical additives.
- Insoluble corrosion products.
- Biofilms, including slimes, from bacterial, algal and other origins.

#### 2.17.3.4.1 Corrosion

Corrosion of a metal, giving rise to an insoluble corrosion product on the metal is one of the most common forms of fouling deposit. One of the main purposes of water treatment is to limit the formation of such deposits by controlling or inhibiting the corrosion process. Corrosion (i.e., anodic dissolution) can occur by any of the normal processes and therefore requires a cathodic reactant (oxidizing agent). In open water systems the cathodic reactant is dissolved oxygen while in closed systems hydrogen generation from water reduction can occur. The amount of fouling due to corrosion product formation often increases on (hot) heat transfer surfaces in response to the general increase of corrosion rate with temperature.

#### 2.17.3.4.2 Biofilms

Although natural waters are disinfected for potable (drinking) purposes, the amount of biocide (e.g.,

dissolved chlorine) present may decrease or be eliminated during service (e.g., by heating). Also, water exposed to open air will rapidly pick up all kinds of active biological material (e.g., bacteria, algae, etc.) that may have a direct or indirect effect on corrosion.<sup>26</sup>

The most common consequence of biological activity is the development of a biofilm on the metal substrate. Corrosion in the crevice formed effectively by the biofilm is possible generally by differential aeration or concentration cell mechanisms. Organisms that prefer anaerobic conditions (e.g., sulfate reducing bacteria) may preferentially colonize beneath bio-films, or other deposits, and generate local environments that are conducive to corrosion (e.g., containing sulfide species). Other bacterial organisms (acidophiles) may produce organic or inorganic (sulfuric) acids while yet other organism (e.g., algae) may respire consuming dissolved carbon dioxide and producing oxygen. If none of these issues is significant, the mere presence of an adherent biofilm will reduce heat transfer efficiency and, if it is removed by cleaning, may block valves, etc. Therefore, effective biocidal treatment is essential in both domestic and industrial settings.

### 2.17.3.5 Water Treatment

It is beyond the scope of this section to provide a detailed discussion of water treatment, however, for completeness brief comments are given below.<sup>27</sup>

#### 2.17.3.5.1 Water softening and water hardening

For many applications, calcium carbonate scaling from hard waters may be effectively inhibited by partial exchange of calcium ions with sodium ions, which is the process of cation exchange (water softening). It is important to note that softening, by reducing the scaling tendency of water and by increasing its ionic conductivity, will generally increase the corrosivity of the water. Conversely, where supply waters are extremely soft, mild water hardening is applied by use of lime (calcium hydroxide) treatment. This is especially effective for reducing the general solubility of metals in soft water supplies for domestic purposes.

#### 2.17.3.5.2 Treatment with acid

The traditional method used to control the formation of calcium carbonate scale, especially on heat transfer surfaces in evaporative cooling systems, is to add sufficient acid to create nonscaling conditions. The



carbonic acid–bicarbonate equilibrium is thereby moved in the direction of carbonic acid, which encourages loss of carbonate (as  $\text{CO}_2$ ) from the water. The most commonly used addition is that of sulfuric acid and although calcium sulfate is more soluble than calcium carbonate, as noted above, scaling of gypsum can occur. In such circumstances other acids, such as phosphoric, may be used.

#### **2.17.3.5.3 Scale inhibitors and dispersants**

Scale inhibitors/dispersants function by modifying the kinetics of nucleation and growth of the scale, although the precise mechanisms of action are still a subject of research. The most cost-effective scale inhibitors are inorganic polyphosphates (e.g., sodium hexametaphosphate); however, at higher temperatures these are subject to reversion back to orthophosphate, which is ineffective.<sup>28</sup> Organic phosphonates are also effective and more stable at higher temperatures; however, they are more costly. Organic polymers are also often very effective at inhibition of scaling by limiting nucleation and growth of the precipitated material.

#### **2.17.3.5.4 Surfactants**

Conventional cationic or anionic detergents tend to be used in heating and cooling systems in order to limit the scope of contamination of heat transfer surfaces by oils or greases and function by emulsifying the hydrocarbon contaminants. In addition, non-ionic surfactants are also useful for changing the wetting characteristics of surfaces. This can effectively reduce the tendency for fouling-type materials (silts, biomass) to deposit on surfaces.

#### **2.17.3.5.5 Corrosion inhibition in potable water systems**

Polyphosphates and silicates are suitable, at low concentrations, for use in drinking (potable) water systems for corrosion and/or scale control; they can also, in many cases limit deposition and staining from dissolved iron and manganese. Polyphosphates, used at levels from 2 to 10 ppm are particularly effective at ambient temperatures and at pH of less than 7.5 can effectively inhibit calcium scale growth. For effective corrosion control, some calcium ions in solution are required to assist in the deposition of a calcium phosphate film that limits corrosion of copper, iron and lead. Sodium silicate is less effective on its own but may be used in synergy with sodium hexametaphosphate at an optimum ratio of 4:3.<sup>29</sup>

### **2.17.4 Corrosivity of Natural Waters**

The extent to which water is corrosive (its 'corrosivity') is a function of a considerable number of interacting variables (i.e., oxygen concentration, flow rate, quantity of dissolved species, scaling tendency, etc.).<sup>30–32</sup> In view of this, it is not possible to determine the corrosivity of water for an arbitrary water composition, although it remains a future goal.

#### **2.17.4.1 pH**

The pH of natural waters is rarely outside the fairly narrow range of 4.5–8.5. Within this range, steel corrodes at approximately constant rate. The form which the corrosion takes is, however, affected by the pH. At values between 7.5 and 9.0, there is a tendency for the corrosion products to adhere as a hard crusty deposit.<sup>33,34</sup> Sometimes there are separate 'tubercles,' but these are more usually joined up to form a more or less continuous layer. Attack under the deposit is, however, usually irregular. At lower pH values, adherent corrosion products are not so evident although a very hard form of deposit is sometimes seen in pipes which have been in service for some years. Loss of pressure (due to a reduction in pipe cross section because of the development of internal corrosion product and other scales) is more commonly found in the higher pH range. In the lower pH range corrosion products may stay in suspension giving rise to 'red water' complaints. Water treatment may reduce the amount of corrosion, but if inhibition is not complete or possible, the type of attack is unaltered. For this reason, it is difficult to prevent corrosion in the pH range (4.5–8.5), as even a low degree of attack produces an adherent corrosion product which puts a barrier between the inhibitor and the metal. Grey cast iron behaves in a manner similar to steel at alkaline pH values but at low pH values it is subject to graphitization, which is the preferential dissolution of the ferrous component (graphite being an effective cathode).

Copper is affected to a marked extent by pH. In acid waters, slight corrosion occurs and the small amount of copper in solution may cause green staining of fabrics and sanitary ware. In addition deposition of copper onto aluminum or galvanized surfaces results in pitting of these metals. In most waters the critical pH is about 7.0 but in soft water containing organic acids it may be higher.<sup>35</sup> Localized pitting corrosion of copper occurs as follows: (Type I) in cold water systems where a residual carbon film is present

from the metal drawing process; (Type II) in hot water systems generally where the bicarbonate to sulfate ratio is less than one; (Type III) in cold water systems but associated with an unfavorable bicarbonate to sulfate ratio as in Type II.<sup>36</sup>

Lead is affected by carbonate content, pH value and mineral constituents.<sup>37</sup> With soft waters the simplest method of corrosion control is usually to increase the pH value by adding lime to the water. Zinc coatings on steel (galvanized) are attacked in the same way as iron, but usually more slowly.<sup>38</sup> Very alkaline waters are usually aggressive to zinc and will often remove galvanized coatings; the corrosion products consist of basic zinc carbonate or other basic compounds and may take the form of a thick creamy deposit or hard abrasive particles.

#### 2.17.4.2 Physical Processes

The effects of temperature and fluid flow are complex. The more general factors may, however, be summarized as follows<sup>39,40</sup>: (a) the velocity of corrosion reactions is greater at increased temperatures, (b) temperature changes may affect solubility of corrosion products or shift the position of such equilibria as that existing between calcium carbonate and carbon dioxide, (c) gases are less soluble at increased temperature, an effect which is, however, partly offset by greater diffusion rates and (d) modification of pH value. The overall effect is that corrosion is usually more rapid at higher temperatures, the corrosion products being often more objectionable in nature.

#### 2.17.4.3 Water Chemistry

It is of considerable interest to the water supply industry to be able to predict with certainty the corrosion rate and condition of its assets from the corrosion tendency (corrosivity) of the water. Although the Langelier index is probably the most frequently quoted measure for the corrosivity of water, it is not a very reliable guide. All that the index can do (and all that its author claimed) is to provide an indication of the thermodynamic tendency to precipitate calcium carbonate. It cannot indicate if sufficient material will be deposited to completely cover all exposed metal surfaces; consequently a very soft water can have a strongly positive index but still be corrosive. Similarly the index does not account for the physical form of the precipitate: that is, a semiamorphous 'egg-shell' like deposit can spread uniformly over all the exposed surfaces rather

than forming isolated crystals at a limited number of nucleation sites. Egg-shell type deposits have been shown to be associated with the presence of organic material which affects the growth mechanism of the calcium carbonate crystals.<sup>41</sup> Where a substantial and stable deposit is produced on a metal surface, this can be an effective anticorrosion barrier.

As well as the conventional chemical parameters generally useful in gauging the corrosivity of water, for example, pH, chloride, sulfate etc., various ratios of ions have been found to be significant for particular problems. Thus an increase in the corrosion rate of iron occurs when the chloride-to-carbonate ratio exceeds 3:1<sup>42</sup> and attack of the dezincification prone brasses arises when the chloride to carbonate hardness ratio exceeds 1:3.<sup>43</sup> More usually only very limited correlations can be made between water composition and corrosivity, and even where no multiple ion effects are involved, the response to a change in one parameter may be difficult to model mathematically, for example, the corrosion of iron which passes through a maximum between pH 7.5–8 in some natural waters.<sup>44</sup>

#### 2.17.4.4 Bacteriological Effects

The traditional understanding of the effect of biological activity is outlined in the previous section and focuses on either (a) classical differential aeration or concentration cell effects caused by a biofilmed surface, or (b) biological activity that produces a species that influences adversely the corrosion process.<sup>45</sup> The classical example is *thiobacillus ferrooxidans*, which (in the absence of oxygen) promotes solution phase oxidation of  $\text{Fe}^{2+}$  to  $\text{Fe}^{3+}$  and consequent deposition of iron (III) oxide throughout the water system.

Recently, however, a further adverse effect of such microbial activity has been increasingly recognized. Thus, the oxidation of dissolved reduced species of iron, manganese, copper, etc., to their higher oxidation states will tend to promote pitting corrosion, particularly on passive materials such as stainless steels.<sup>46,47</sup>

## References

1. Evans, U. R. *The Corrosion of Metals*; Arnold: London, 1926; p 93.
2. Martins, J. I.; Nunes, M. C. *Electrochim. Acta* **2006**, *52*, 552–559.
3. Harned, H. S.; Davis, R. D. *J. Am. Chem. Soc.* **1943**, *65*, 2030–2037.

4. Turner, M. E. D. *Proc. Soc. Water Treat. Exam.* **1961**, 10(2), 162; **1965**, 14(2), 81.
5. Hatch, G. B.; Rice, O. J. *Am. Water Works Assoc.* **1959**, 51, 719–727.
6. Eberle, S. H.; Feuerstein, W. *Naturwissenschaften* **1979**, 66(11), 572–573.
7. Fletcher, N. H. *Eur. J. Phys.* **1993**, 14, 29–35.
8. Gabrielli, C. C.; Maurin, G.; Poindessous, G.; Rosset, R. *J. Crystal Growth* **1999**, 200(1–2), 236–250.
9. Langelier, W. F. J. *Am. Water Works Assoc.* **1936**, 28, 1500–1521.
10. Langelier, W. F. J. *Am. Water Works Assoc.* **1946**, 38, 169–178.
11. Ryznar, J. W. J. *Am. Water Works Assoc.* **1944**, 36, 472–486.
12. Puckorius, P. *Power* **1983**, 127(9), 79–81.
13. Stiff, H. A., Jr.; Davis, L. E. *Petroleum Trans. AIME* **1952**, 195, 213.
14. McCauley, R. F.; Abdullah, M. O. J. *Am. Water Works Assoc.* **1958**, 50, 1419.
15. Simmonds, M. A. *Proc. Soc. Water Treat. Exam* **1963**, 12(4), 197; **1964**, 13(1), 40.
16. Gill, J. S. *Colloids Surf. A* **1993**, 74, 101–106.
17. Sheikholeslami, R.; Tan, S. *Desalination* **1999**, 126, 267–280.
18. Gunnarsson, I.; Arnórsson, S. *Geothermics* **2005**, 34, 320–329.
19. Dabir, B.; Peters, R. W.; Stevens, J. D. *Ind. Eng. Chem. Fund.* **1992**, 21(3), 298–305.
20. Gunnlaugsson, E.; Einarsson, A. *Geothermics* **1989**, 18(1–2), 113–120.
21. Hoang, T. A.; Ang, H. M.; Rohi, A. L. *Powder Technol.* **2007**, 179, 31–37.
22. Gill, J. S. In *Calcium Phosphates in Biological and Industrial Systems*; Amjad, Z., Ed.; Kluwer Academic, 1998; Chapter 18.
23. Seth, A.; Bachmann, R. T.; Boxall, J. B.; Saul, A. J.; Edyvean, R. *Water Sci. Technol.* **2004**, 49(2), 27–32.
24. Geldreich, E. G. *Microbial Quality of Water Supply in Distribution Systems*; CRC Press, 1996; pp 82–83.
25. Melo, L. F. Bott, T. R.; Bernardo, C. A. Eds. *NATO ASI Series 3: Applied Science* Springer, 1988; Vol. 145.
26. Videla, H. *Manual of Biocorrosion*; CRC Press, 1996.
27. Faust, S. O.; Alym, O. M. Eds. *Chemistry of Water Treatment*, 2nd ed.; CRC Press: Boca Raton, FL, 1998.
28. Hatch, G. B.; Rice, O. *Ind. Eng. Chem.* **1945**, 37, 710–715.
29. Mehr, M. E.; Shahrabi, T.; Hosseini, M. G. *Anti-Corros. Meth. Mater.* **2004**, 51, 399–405.
30. Geld, I.; McCaul, C. J. *Am. Water Works Assoc.* **1975**, 67(10), 549–552.
31. *Internal Corrosion of Water Distribution Systems*, 2nd ed.; American Water Works Association, 1996.
32. Goddard, H. P. *Water Perform.* **1979**, 18(5), 21–27.
33. Larson, T. E.; Skold, R. V. J. *Am. Water Works Assoc.* **1957**, 49, 1294–1301.
34. Sarin, P.; Snoeyink, V. L.; Bebee, J.; Kriven, W. M.; Clement, J. A. *Water Res.* **2001**, 35, 2961–2969.
35. Gilbert, P. T. *Proc. Soc. Water Treat. Exam.* **1966**, 15, 165.
36. Mattson, E. *Werkst. Korros.* **1988**, 39, 499–503.
37. Cassibba, R. O.; Fernandez, S. J. *Nucl. Mater.* **1989**, 161, 93–101.
38. Pistofidis, N.; Vourlias, G.; Stergioudis, G. J. *Mater. Sci.* **2007**, 42, 2878–2885.
39. Hackerman, N. *Ind. Eng. Chem.* **1952**, 44, 1752–1755.
40. Mahato, B. K.; Voora, S. K.; Shemilt, L. W. *Corros. Sci.* **1968**, 8, 173–180, 737–749.
41. Campbell, H. S.; Turner, M. E. D. J. *Inst. Water Engineers Scientists* **1983**, 37(1), 55.
42. Lawson, T. E. Corrosion by domestic water, Illinois State Water Survey Bulletin #59; Urbana, IL, 1975.
43. Turner, M. E. D. *Proc. Soc. Water Treat. Exam.* **1961**, 10(2), 162.
44. Larson, T. E.; Skold, R. V. *Corrosion* **1958**, 14(6), 43.
45. Coetser, S. E.; Cloete, T. E. *Crit. Rev. Microbiol.* **2005**, 31(4), 213–232.
46. Chamritski, I. G.; Burns, G. R.; Webster, B. J.; Laycock, N. J. *Corrosion* **2004**, 60(7), 658–669.
47. Shi, X.; Acvi, R.; Lewandowski, Z. *Corrosion* **2002**, 58(10), 728–738.

## Further Reading

Thresh, J. C.; Beale, J. F.; Suckling, E. V. *The Examination of Water and Water Supplies*, 6th ed.; J. & A. Churchill: London, 1944.

Faust, S. O.; Alym, O. M. Eds. *Chemistry of Water Treatment*, 2nd ed.; CRC Press, 1998.

Stumm, W.; Morgan, J. J. *Aquatic Chemistry – Chemical Equilibria and Rates in Natural Waters*; Wiley, 1995.

*Internal Corrosion of Water Distribution Systems*, 2nd ed.; American Water Works Association, 1996.

PHREEQC: A Computer Program for Speciation, Batch-Reaction, One-Dimensional Transport, and Inverse Geochemical Calculations, US Geological Service. Available at [water.usgs.gov/software/](http://water.usgs.gov/software/).

## 2.16 Atmospheric Corrosion

**I. S. Cole**

CSIRO Materials Science and Engineering, P.O. Box 56, 37 Graham Road, Highett, Victoria, 3190, Australia

© 2010 Elsevier B.V. All rights reserved.

<b>2.16.1</b>	<b>Typical Atmospheric Conditions</b>	1052
2.16.1.1	Atmospheric Gases	1053
2.16.1.2	Specific Atmospheric Gases	1054
2.16.1.2.1	Sulfur-containing compounds	1054
2.16.1.2.2	Nitrogen-containing compounds	1054
2.16.1.2.3	Strong oxidants, ozone, and hydrogen peroxide	1055
2.16.1.2.4	Organic acids	1055
2.16.1.3	Aqueous Phase Reactions	1055
2.16.1.3.1	Absorption and immediate reaction	1055
2.16.1.3.2	Secondary reactions	1056
2.16.1.3.3	Absorption of other gases	1056
2.16.1.3.4	Oxidation of reduced species	1056
2.16.1.3.5	Ionic reactions in the liquid phase	1057
2.16.1.4	Analysis of Typical Systems	1057
2.16.1.4.1	Sulfuric acid–ammonia–water systems	1057
2.16.1.4.2	Ammonia–nitric acid–water systems	1058
2.16.1.4.3	Ammonia–nitric acid–sulfuric acid–water systems	1058
2.16.1.5	Reactions in Salt Aerosols	1059
2.16.1.6	Aerosols	1059
2.16.1.6.1	Marine aerosol production	1061
2.16.1.6.2	Types of aerosol	1061
2.16.1.7	Cloud Nucleation and Rain Chemistry	1062
2.16.1.8	Redox Potential and pH Diagrams	1065
<b>2.16.2</b>	<b>Transport of Gases and Aerosols</b>	1065
2.16.2.1	General Scale of Movement of Gases and Particles	1065
2.16.2.2	Transportation Processes	1067
2.16.2.2.1	Analytical approach to gas transport	1067
2.16.2.2.2	Aerosol transport	1067
<b>2.16.3</b>	<b>Deposition</b>	1069
2.16.3.1	Forms of Deposition	1069
2.16.3.1.1	Rain	1069
2.16.3.1.2	Gas and particle deposition	1070
2.16.3.1.3	Deposition of gases onto wet and dry surfaces	1073
2.16.3.2	Comparison of Deposition Modes	1074
<b>2.16.4</b>	<b>Role of Rain and Wind in Surface Cleaning</b>	1075
2.16.4.1	Role of Rain in Surface Cleaning	1075
2.16.4.2	Removal of Salts by Wind	1076
2.16.4.3	Transfer of Pollutants in Raindrops to a Surface	1077
<b>2.16.5</b>	<b>Forms of Moisture on Surfaces</b>	1077
2.16.5.1	Effect of RH on Clean Surfaces	1077
2.16.5.2	Effect of Aerosols/Raindrops	1077
2.16.5.3	Rewetting of Surfaces and Condensation	1078
2.16.5.4	Evaporation	1078
2.16.5.4.1	Surface temperature of plates	1078
2.16.5.4.2	Evaporation rate	1079
2.16.5.4.3	Evaporation and condensation on a porous surface	1081

<b>2.16.6</b>	<b>Summary of Environmental Conditions</b>	1082
<b>2.16.7</b>	<b>Surface Reactions</b>	1082
2.16.7.1	Equilibrium Considerations	1082
2.16.7.2	Influence of Electrochemical Processes on Moisture Film Stability and Chemistry	1084
2.16.7.2.1	Oxide precipitation and stability	1086
2.16.7.2.2	Specific features of the atmospheric corrosion of steel	1088
<b>2.16.8</b>	<b>Conclusion</b>	1090
<b>References</b>		1091

## Abbreviations

<b>DRH</b>	Deliquescent relative humidity
<b>ppt</b>	Part per trillion
<b>ppm</b>	Part per million
<b>RH</b>	Relative humidity
<b>TCD</b>	Time of condensation
<b>TCON</b>	Tendency to condensation

## Symbols

<b>C</b>	Concentration of aerosol particles in the atmosphere
<b>C<sub>C</sub></b>	Cunningham correction factor
<b>C<sub>i</sub></b>	Molar concentration of <i>i</i> (species)
<b>C<sub>s</sub></b>	A shape factor of an object
<b>D</b>	Deposition rate (per surface area) of aerosols
<b>D<sub>p</sub></b>	Particle (or aerosol) diameter
<b>H<sub>a</sub></b>	Henry's law constant for gaseous absorption
<b>I</b>	Air turbulence
<b>M</b>	Mass of droplet
<b>M<sub>i</sub></b>	Molar weight of <i>i</i> (species)
<b>p</b>	Air pressure
<b>p<sub>1</sub></b>	Pressure within a drop (on a surface) at the front extremity
<b>p<sub>2</sub></b>	Pressure within a drop (on a surface) at the back extremity
<b>r</b>	Droplet radius (on a surface)
<b>R</b>	The gas constant
<b>R<sub>a</sub></b>	A parameter that characterizes the resistance to deposition across boundary layers
<b>R<sub>c</sub></b>	Critical amount of rain required to guarantee run off
<b>R<sub>i</sub></b>	The amount of rain in a given rain event
<b>R<sub>t</sub></b>	Terrain roughness
<b>r<sub>1</sub></b>	Radius of curvature near the front of a drop
<b>r<sub>2</sub></b>	Radius of curvature near the back of a drop
<b>R<sub>s</sub></b>	The reactivity of a surface
<b>RH<sub>c</sub></b>	Relative humidity at which a surface wets
<b>T</b>	Air temperature (°K)

<b>T<sub>s</sub></b>	Temperature of the (metal) surface
<b>S<sub>i</sub></b>	Initial pollutant load
<b>S<sub>f</sub></b>	Final 'soluble' pollutant load
<b>U<sub>0</sub></b>	The approach velocity (of the air stream) at a distance <i>x</i> <sub>0</sub> , from an object
<b>u*</b>	Average friction velocity in the local boundary layer
<b>V<sub>a</sub></b>	Vapor concentration of the air
<b>V<sub>d</sub></b>	The deposition velocity of aerosols
<b>V<sub>s</sub></b>	Saturation vapor concentration
<b>β</b>	A constant used in calculating deposition efficiency
<b>ξ</b>	Mixing ratio
<b>η</b>	The capture efficiency (of aerosols) of an object
<b>θ</b>	Plate or object angle (from the horizontal)
<b>ρ<sub>p</sub></b>	The density of an aerosol (or particle) droplet
<b>μ</b>	The viscosity of air
<b>σ</b>	Surface tension (between metal surface and droplet)
<b>φ</b>	The difference in contact angle between the front and back of a drop

## 2.16.1 Typical Atmospheric Conditions

The atmosphere is the layer of gases that surround our planet Earth and that are retained by gravity. The atmosphere is not a single entity and may be divided into several regions that are subject to varying physical and chemical conditions. The lowest layer, in which 'weather' occurs, is named the troposphere and is the subject of this chapter. Above this layer, there come, in sequence, the stratosphere, the mesosphere, the thermosphere, the ionosphere, and finally the exosphere. It is the events within the troposphere that are the subject of this chapter. In this section, the typical conditions that control the formation and chemistry of gases, particulate aerosols, or rain within the atmosphere (troposphere) are outlined.



### 2.16.1.1 Atmospheric Gases

The average composition of the atmosphere and the nature of atmospheric cycles for each gaseous constituent are given in **Table 1** (from Seinfeld and Pandis<sup>1</sup>). The atmosphere is a dynamic system with its gaseous constituents being constantly exchanged by vegetation, the oceans, biological organisms, volcanic action, weathering, and human influences. For example, ozone levels are controlled by chemical processes in the upper and lower atmosphere. Methane, nitrous oxide, and carbon monoxide levels are also controlled by biological processes.

When in the atmosphere, a chemical substance may be altered either as a result of sunlight promoting the decomposition of molecules (photochemical reaction) or by chemical reactions with other substances, which can occur either homogeneously or heterogeneously. Such reactions may transform the state of a substance (gas to aerosol), allowing the substance to be removed from the atmosphere more effectively. As will be discussed later, heterogeneous reactions of ammonia and sulfur dioxide gases can lead to the formation of a range of ammonium sulfate particulates that deposit at a significantly faster rate than their gaseous precursors, dramatically affecting the course of atmospheric corrosion.

As evident in **Table 1**, the major constituents of the atmosphere are gases that are relatively inert such

as N<sub>2</sub> and O<sub>2</sub>; however, the atmosphere is an effective oxidizing medium. This is partially due to the presence of free radicals (e.g., the hydroxyl (OH) radical) and partially due to such oxidizing species as ozone (O<sub>3</sub>). Thus, many species are converted into higher chemical oxidation states, which also have an increased polarity and solubility. For example, the partially soluble SO<sub>2</sub> may be converted into SO<sub>3</sub> and then to sulfuric acid, which acidifies rainwater, particulates, and moisture films, with significant consequences for atmospheric corrosion.

The average mixing ratio referred to in **Table 1** is the average ratio of the amount (or mass) of a substance in a given volume to the total amount (or mass) of all constituents in that volume. Thus, for a particular species *i*, the volume mixing ratio is given by

$$\xi_i = C_i / C_{\text{total}} \quad [1]$$

where *C<sub>i</sub>* is the molar concentration of *i* and *C<sub>total</sub>* is the total molar concentration of air.

The mixing ratio can be readily converted to mass concentration by the following equation:

$$\text{Concentration in } \mu\text{g m}^{-3} = \xi_i \times pM_i / RT \quad [2]$$

where *M<sub>i</sub>* is the molecular weight, *p* is air pressure, *R* is the gas constant (8.314 J mol<sup>-1</sup> K<sup>-1</sup>), and *T* is temperature.

**Table 1** Atmospheric gases

Gas	Molecular weight (g)	Average mixing ratio (ppm)	Cycle
Ar	39.948	9340	No cycle
Ne	20.179	18	No cycle
Kr	83.80	1.1	No cycle
Xe	131.30	0.09	No cycle
N <sub>2</sub>	28.013	780 840	Biological, microbiological
O <sub>2</sub>	32	209 460	Biological, microbiological
CH <sub>4</sub>	16.043	1.72	Biogenic, chemical
CO <sub>2</sub>	44.010	355	Anthropogenic, biogenic
CO	28.010	0.12 (NH); 0.06 (SH)	Anthropogenic, chemical
H <sub>2</sub>	2.016	0.58	Biogenic, chemical
N <sub>2</sub> O	44.012	0.311	Biogenic, chemical
SO <sub>2</sub>	64.06	10 <sup>-5</sup> –10 <sup>-4</sup>	Anthropogenic, biogenic, chemical
NH <sub>3</sub>	17	10 <sup>-4</sup> –10 <sup>-3</sup>	Biogenic, chemical
NO	30.007	10 <sup>-6</sup> –10 <sup>-2</sup>	Anthropogenic, biogenic, chemical
NO <sub>2</sub>	46.007		
O <sub>3</sub>	48	10 <sup>-2</sup> –10 <sup>-1</sup>	Chemical
H <sub>2</sub> O	18.015	Variable	Physicochemical
He	4.003	5.2	Physicochemical

Source: Reproduced from Seinfeld, J.; Pandis, S. *Atmospheric Chemistry and Physics: From Air Pollution to Climate Change*; Wiley Interscience: New York, 1997.

### 2.16.1.2 Specific Atmospheric Gases

Our prime concern is with atmospheric gases that determine the interaction of moisture layers with the underlying metals through the following steps:

- Promoting the formation of moisture layers through the formation of hygroscopic particulates.
- Controlling the pH of moisture layers.
- Controlling the dissolution of oxide layers and promoting ligand exchange.

For these reasons, the key compounds are the following:

- Sulfur-containing compounds.
- Nitrogen-containing compounds.
- Strong oxidants (ozone and hydrogen peroxide).
- Organic acids.

#### 2.16.1.2.1 Sulfur-containing compounds

The principal sulfur-containing compounds in the atmosphere are  $\text{H}_2\text{S}$ , dimethyl sulfide (DMS or  $\text{CH}_3\text{SCH}_3$ ),  $\text{CS}_2$ , carbonyl sulfide (OCS), and  $\text{SO}_2$ ,<sup>2</sup> and their mixing ratios (in parts per trillion) are given in Table 2 (modified from Berresheim *et al.*<sup>2</sup>).

The primary sources of hydrogen sulfide are wetlands, plants and soils, and volcanoes. DMS is produced in oceanic waters by benthic and planktonic organisms, probably from the decomposition of dimethyl-sulfiniopropionate.<sup>3</sup> The oxidation of DMS (by OH and nitrate radicals) is a source of methane sulfonic acid and  $\text{SO}_2$  in marine atmospheres. DMS is also the prime source of sulfate cloud condensation nuclei (CCN) in marine atmospheres<sup>4</sup> and is, therefore, a direct contributor to acidified rain.  $\text{CS}_2$  is produced in oceans, wetlands, and plants and soils.<sup>2</sup>

OCS has a low reactivity and a long residence time of  $\sim 7$  years, and 7–8% of it is transported through the troposphere and into the stratosphere.<sup>5</sup> This is important, as the photolysis of OCS or reaction with O atoms leads to the widespread production of  $\text{SO}_2$  in the stratosphere that may reenter the troposphere across broad geographical zones. OCS has a number of sources including  $\text{CS}_2$  oxidation, ocean emission, and biomass burning. While the transformation of OCS to  $\text{SO}_2$  may give rise to a widespread but low level of tropospheric  $\text{SO}_2$ , the prime source of  $\text{SO}_2$  is due to industrial activity.<sup>2</sup>

The oxidation state of OCS, DMS,  $\text{CS}_2$ , and  $\text{H}_2\text{S}$  is 2, that of  $\text{SO}_4$  (and sulfate species) is 6, and that of  $\text{SO}_3$  (and sulfate species) is 6. DMS,  $\text{CS}_2$ , and  $\text{H}_2\text{S}$  are rapidly oxidized (first to sulfur dioxide and then to sulfates) and, thus, have lifetimes of a few days or

**Table 2** Average mixing ratio of a number of gases

Compound	Location	Average mixing ratio (ppt)
$\text{H}_2\text{S}$	Marine surface layer	3.6–7.5
	Coastal regions	65
	Forests	35–60
	Wetlands	450–840
	Urban areas	365
$\text{CH}_3\text{SCH}_3$	Marine surface layer	80–110
	Continental surface layer	8–60
$\text{CS}_2$	Marine surface layer	2–18
	Continental surface layer	35–120
OCS	Marine surface layer	500
	Continental surface layer	500
$\text{SO}_2$	Marine surface layer	20
	North American – clean continental	160
	Coastal Europe	260
	Polluted continental air	1500
	Urban–suburban	10–1
$\text{NO}_x$	Rural	0.2–10
	Remote tropical forest	0.02–0.08
	Remote marine	0.02–0.04
$\text{O}_3$	Urban–suburban	100–400
	Rural	50–120
	Remote tropical forest	20–40
	Remote marine	20–40

Source: Reproduced from Berresheim, H.; Wine, P. H.; Davis, D. D. Sulfur in the Atmosphere. In *Composition, Chemistry and Climate of the Atmosphere*; Singh, H. B., Ed.; Van Nostrand Reinhold: New York, 1995; pp 251–307.

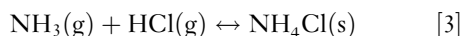
less, while oxidized compounds are stable and their residence times in the atmosphere depend on the deposition rates of the liquid entities (aerosols and raindrops) in which they reside. Thus, while in terms of atmospheric corrosion the critical compounds are sulfur dioxide and sulfates, the transport and reaction of reduced sulfur compounds need to be considered. For example, DMS and OCS may be transported significant distances through the troposphere where they may be oxidized to sulfur dioxide (and other compounds) and, thus, can give rise to low but significant  $\text{SO}_2$  levels, even in isolated nonindustrial areas. Noller *et al.*<sup>6</sup> for example, found that rainwater in the Northern Territory of Australia (an isolated, non-industrial zone) was acidic at least in part because of the oxidation of DMS.

#### 2.16.1.2.2 Nitrogen-containing compounds

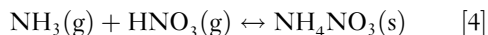
Key nitrogen-containing species in the atmosphere are nitrous oxide ( $\text{N}_2\text{O}$ ), nitric oxide (NO), nitrogen dioxide ( $\text{NO}_2$ ), nitric acid ( $\text{HNO}_3$ ), and ammonia

(NH<sub>3</sub>).<sup>7</sup> N<sub>2</sub>O is emitted from biological sources in soils and waters<sup>8</sup> and has a residence time of more than 50 years. It may be transformed in the stratosphere to NO, which may then transform to nitrogen dioxide, which in turn may transform to nitric acid and reenter the troposphere. Thus, both nitrogen dioxide and nitric acid can be found at significant distances from nitrogen sources. The major sources of nitrogen oxides NO<sub>x</sub> (NO + NO<sub>2</sub>) are fossil fuel combustion, soil release, and biomass burning.<sup>8</sup> **Table 2** indicates that NO<sub>x</sub> concentrations fall away dramatically from urban sources.

NH<sub>3</sub> is the primary basic gas in the atmosphere, with its major sources being animal waste, NH<sub>3</sub>-based fertilizers, and emissions from soils.<sup>9</sup> NH<sub>3</sub> is readily absorbed by surfaces (including water droplets) and therefore, its residence time is short. The concentration is highly variable (from 0.1 to 10 ppb), depending on the distance from the source. Further, ammonia may react directly with gaseous acids, as in the following equations:



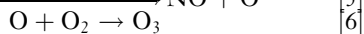
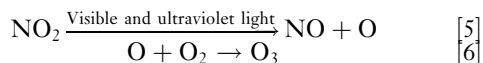
or



where, the equilibrium constant is  $1 \times 10^{16} \text{ atm}^2$  and  $3.35 \times 10^{19} \text{ atm}^2$  for the formation of ammonium chloride and ammonium nitrate, respectively. Thus, as NH<sub>3</sub> is rapidly absorbed in wetted aerosols, and its product NH<sub>4</sub><sup>+</sup> readily reacts to form solids, ammonia salts are a major aerosol component.

### 2.16.1.2.3 Strong oxidants, ozone, and hydrogen peroxide

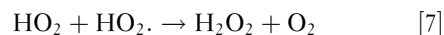
Ozone plays a major role in catalyzing the oxidation of compounds, both in the atmosphere and on surfaces. Most of the Earth's ozone is in the stratosphere; however, it may be transported into the troposphere by so-called tropopause folding events.<sup>10</sup> Ozone may also be produced by industrial activity and from the burning of fuels. As it is highly reactive, its mixing ratio can vary greatly geographically and because of diurnal cycles. Indeed, ozone may be produced by the photolysis of nitrogen dioxide during daylight hours via the following steps:



Ozone will also react with NO at night, so there is commonly a very strong diurnal cycle in ozone concentration levels. Base levels of ozone are ~20–25 ppb,

but they may rise as high as 200–400 ppb close to NO<sub>x</sub> sources.<sup>1</sup>

Hydrogen peroxide concentration is closely related to photochemical activity and has mixing ratios that range from 0.2 to 37 ppb but are centered ~2–4 ppb.<sup>11,12</sup> Hydrogen peroxide commonly forms from radical–radical reactions such as<sup>13</sup>



These radicals commonly form by oxidation of hydrocarbons; however, the radicals may also react with NO<sub>x</sub> compounds so that hydrogen peroxide levels decrease in high NO<sub>x</sub> environments.<sup>12</sup> In the gas phase, hydrogen peroxide may be destroyed by its reaction with the OH radical or by its photolysis, while in the aqueous phase it reacts with SO<sub>2</sub> (eqn [20]). Nevertheless, hydrogen peroxide is the main oxidant found in clouds, fogs, or rain.<sup>1</sup> Other oxidants that are of importance are OH<sup>•</sup> and HO<sub>2</sub><sup>•</sup>, which may be formed by oxidation of hydrocarbons.

### 2.16.1.2.4 Organic acids

The main organic acids of concern are formic acid (HCOOH) and acetic acid (CH<sub>3</sub>COOH). Such acids come from a variety of sources, including industrial activity, biogenic activity in soils, and volcanoes, but the most common source appears to be incomplete combustion. Organic acid concentrations are commonly in the 1–10 ppb range.<sup>14</sup>

### 2.16.1.3 Aqueous Phase Reactions

Prior to discussing particulate deposition and wet deposition, an understanding of aqueous phase reactions is required, as these control the chemistry and, to some extent, the formation of cloud and rain droplets, and aerosols, as well as the absorption of gases onto wet metal surfaces. The reaction of a gas with the liquid phase is controlled both by absorption and the immediate reaction of the absorbed phase, and subsequent reactions that may change the concentration of reaction products.

#### 2.16.1.3.1 Absorption and immediate reaction

It is well established that the concentration of an absorbed gas may be related to the partial pressure of the gas according to the following relationship:

$$A(\text{g}) \leftrightarrow A(\text{aq}) \quad [8]$$

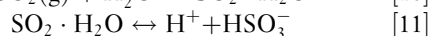
$$[A(\text{aq})] = H_A p_A \quad [9]$$

where  $[A(\text{aq})]$  is the aqueous phase concentration (in

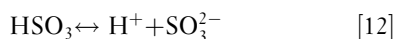
$\text{mol l}^{-1}$ ),  $p_A$  is the partial pressure in the gas phase (in atm.), and  $H_A$  is the Henry's law coefficient for species  $A$ , which is a function of temperature, as defined by Pandis and Seinfeld.<sup>15</sup> According to Seinfeld and Pandis,<sup>1</sup> species with  $H_A < 1000$  will exist mainly in the gas phase, species with coefficients between 1000 and 10 000 are considered moderately soluble in water, and those above 10 000 are considered very soluble. Henry's law coefficients for common gases are set out in Table 3 for a temperature of 298 K. While it is evident from Table 3 that many common gases would be regarded as relatively insoluble (e.g.,  $\text{SO}_2$ ,  $\text{CO}_2$ ), the absorption of these gases may be significantly increased by secondary reactions.

### 2.16.1.3.2 Secondary reactions

Dissociation and other reactions (e.g., oxidation) can decrease the concentration of dissolved species allowing further absorption. For example, absorbed  $\text{SO}_2$  may dissociate as set out below:



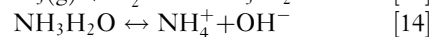
while:



The balance of  $\text{HSO}_3^-$  versus  $\text{SO}_3^{2-}$  depends on pH, with the former dominating at pH values of 2–7 and the latter above this. These dissociation reactions may be taken into account by defining an effective Henry's law coefficient that represents the equilibrium dissolved species when subsequent aqueous reactions are considered. The effective Henry's law coefficient for  $\text{SO}_2$  goes from  $1.23 \text{ M atm}^{-1}$  at a pH of 1 to in excess of  $10^7 \text{ M atm}^{-1}$  at a pH of 8. This has a dramatic effect on S(IV) concentrations in solution, which for a mixing

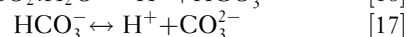
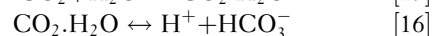
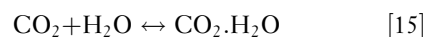
ratio of 200 ppb of  $\text{SO}_2$  at 298 K would increase from  $3 \times 10^{-7}$  to  $3 \times 10^{-3} \text{ M}$  as pH is increased from 0 to 6.<sup>1</sup>

In the case of  $\text{NH}_3$ , the Henry's law coefficient is  $62 \text{ M atm}^{-1}$  and, therefore, the gaseous species is absorbed more readily than  $\text{SO}_2$ , which then dissociates according to the following reactions:



The equilibrium constant ( $K_{\text{eq}}$ ) value for the dissociation of  $\text{NH}_3 \cdot \text{H}_2\text{O}$  is  $1.7 \times 10^{-5}$  and, thus, in solutions with  $\text{pH} < 8$ , the dissolved  $\text{NH}_3$  is predominantly in the form of ammonium ion; for  $\text{pH} < 5$  practically all the available  $\text{NH}_3$  will be dissolved in the aqueous phase. This high solubility of ammonia makes it a dominant species in industrial aerosols.

The Henry's law coefficient for  $\text{CO}_2$  absorption is  $3.4 \times 10^{-2} \text{ M atm}^{-1}$  and, therefore, its absorption would be expected to be quite low; it is indeed so under acidic conditions. The reactions are



The  $K_{\text{eq}}$  value for eqns [16] and [17] are  $4.3 \times 10^{-7}$  and  $4.7 \times 10^{-11}$  respectively, and so in basic conditions  $\text{CO}_2 \cdot \text{H}_2\text{O}$  readily dissociates to bicarbonate and hydrogen ions, allowing continued absorption of  $\text{CO}_2$ . For absorption of  $\text{CO}_2$  (at a mixing ratio of 330 ppm), the effective Henry's law coefficient rises from a value of  $3.4 \times 10^{-2} \text{ M atm}^{-1}$  at a pH of 4–1.5  $\text{M atm}^{-1}$  at a pH of 8.

### 2.16.1.3.3 Absorption of other gases

Nitric acid is extremely water soluble and would be expected to be fully dissolved in solution at all  $\text{pH} > 1$ . Although formic acid has a relatively high Henry's law coefficient, the percent dissolved in the aqueous phase will depend heavily on pH, so that for  $\text{pH} < 4$  only ~10% will be dissolved in solution, while for  $\text{pH} > 7$  almost all formic acid will be dissolved. Ozone is practically insoluble, as indicated by its very low Henry's law coefficient.

### 2.16.1.3.4 Oxidation of reduced species

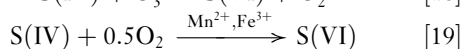
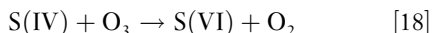
In order to determine the balance between the gas phase and the absorbed phase for a number of compounds, oxidation reactions also need to be included (as noted earlier, the atmosphere is in general strongly oxidizing). A prime and important example is the absorption of  $\text{SO}_2$ , where the oxidation of  $\text{SO}_3^{2-}$  or other forms of S(IV) to  $\text{SO}_4^{2-}$  or other forms of

**Table 3** Henry's law coefficients for common gases

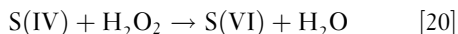
Species	$H \text{ (M atm}^{-1}) \text{ at 298 K}$
$\text{O}_2$	$1.3 \times 10^{-3}$
$\text{O}_3$	$1.1 \times 10^{-2}$
$\text{NO}_2$	$1.0 \times 10^{-2}$
$\text{CO}_2$	$3.4 \times 10^{-2}$
$\text{SO}_2$	1.23
$\text{NH}_3$	62
$\text{OH}$	25
$\text{HCl}$	727
$\text{HCOOH}$	$3.6 \times 10^3$
$\text{CH}_3\text{COOH}$	$8.8 \times 10^3$
$\text{NO}_3$	$2.1 \times 10^5$
$\text{HNO}_3$	$2.1 \times 10^5$

S(VI) is critical, as it allows the continued absorption of SO<sub>2</sub>, according to eqns [11] and [12].

This oxidation may occur via a variety of mechanisms, including reactions with O<sub>3</sub>, H<sub>2</sub>O<sub>2</sub>, and O<sub>2</sub> (catalyzed by Mn (II), Fe (III), and NO<sub>2</sub>), for example:



or

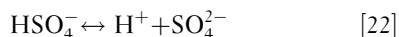


where S(IV) may be HSO<sub>3</sub><sup>-</sup> or SO<sub>3</sub><sup>2-</sup>, and S(VI) is HSO<sub>4</sub><sup>-</sup> or SO<sub>4</sub><sup>2-</sup>.

According to Hoffman and Calvert,<sup>16</sup> the reaction rate for eqn [19] is given by

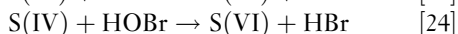
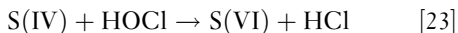
$$1.2 \times 10^6 [\text{Fe(III)}][\text{S(IV)}] \quad [21]$$

The sulfate that forms from the oxidation of S(IV) may exist as SO<sub>4</sub><sup>2-</sup> or HSO<sub>4</sub><sup>-</sup> (H<sub>2</sub>SO<sub>4</sub> dissociates to HSO<sub>4</sub><sup>-</sup> under pH ranges likely for droplets in the atmosphere or on surfaces). The balance is governed by



The  $K_{\text{eq}}$  value for eqn [22] is  $1 \times 10^{-2}$  and thus the concentration of HSO<sub>4</sub><sup>-</sup> will increase with acidity.

Hypochlorous acid (HOCl) and hypobromous acid (HOBr) may also lead to rapid sulfur oxidation:<sup>17</sup>

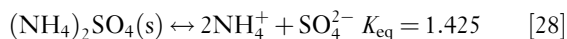
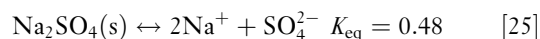


The observation by a number of atmospheric corrosion scientists<sup>18–20</sup> that there is a synergistic effect among SO<sub>2</sub>, NO<sub>2</sub>, and O<sub>3</sub> gases in determining the extent of corrosion, is likely to arise, at least in part, from the role of NO<sub>2</sub> and O<sub>3</sub> in promoting the oxidation to S(VI) and, therefore, the continued absorption of SO<sub>2</sub> gas into moisture layers (be they surface moisture, rain water, or wet aerosols), as well as the acidification of these moisture layers.

### 2.16.1.3.5 Ionic reactions in the liquid phase

The ionic species formed by gaseous absorption (and subsequent oxidation reactions) may combine to form ionic solids that can act as nuclei for cloud drops or aerosol particles. Further, ammonium chloride and ammonium nitrate may form as a direct consequence of gaseous reactions, as detailed in eqns [3] and [4]. The stability of the different solids will depend on the liquid concentration of the various species and pH. Typical reactions and their equilibrium constants

are given below:



### 2.16.1.4 Analysis of Typical Systems

While some of the basic reactions governing gas/aqueous phase interactions are set out in eqns [25]–[28], a rigorous analysis requires the evaluation of the chemical potentials of the gas, liquid, and solid phases as a function of concentration, temperature, and pressure, and the effect of droplet geometry on these factors. This level of detail is outside the scope of this chapter and therefore, the results from detailed analyses of three systems representing industrial and urban environments particularly relevant to atmospheric corrosion are presented, as follows:

- Industrial environment containing H<sub>2</sub>SO<sub>4</sub>, NH<sub>3</sub>, and water vapor
- Urban environment containing HNO<sub>3</sub>, NH<sub>3</sub>, and water vapor
- A mixed industrial/urban environment containing H<sub>2</sub>SO<sub>4</sub>, NH<sub>3</sub>, HNO<sub>3</sub>, and water vapor.

#### 2.16.1.4.1 Sulfuric acid–ammonia–water systems

In this section, we follow the approach of Seinfeld *et al.*<sup>1,21</sup> and consider a system containing gaseous H<sub>2</sub>SO<sub>4</sub>, NH<sub>3</sub>, and water. Aerosols will nucleate homogeneously or heterogeneously and, because of their high solubility, both H<sub>2</sub>SO<sub>4</sub> and NH<sub>3</sub> will be readily absorbed; they will react according to eqns [13], [14], and [28] to form a series of solid and dissolved species, including ((NH<sub>4</sub>)<sub>3</sub>H(SO<sub>4</sub>)<sub>2</sub>), (NH<sub>4</sub>)<sub>2</sub>SO<sub>4</sub>, NH<sub>4</sub>HSO<sub>4</sub>, NH<sub>4</sub><sup>+</sup>, SO<sub>4</sub><sup>2-</sup>, HSO<sub>4</sub><sup>-</sup>, and NH<sub>3</sub>(aq). This system is of prime importance in determining the chemistry of aerosols in industrial locations. Figure 1 (from Seinfeld and Pandis<sup>21</sup>) illustrates this behavior at low RH (30%) and at a H<sub>2</sub>SO<sub>4</sub> concentration of 10 μg m<sup>-3</sup>.

At low ammonia levels, the aerosols consist primarily of H<sub>2</sub>SO<sub>4</sub>, with some NH<sub>4</sub>HSO<sub>4</sub>(s) and significant water (H<sub>2</sub>SO<sub>4</sub> attracts a significant amount of water even at low RH).<sup>21</sup> When the ammonia/sulfuric acid ratio increases above a molar ratio of



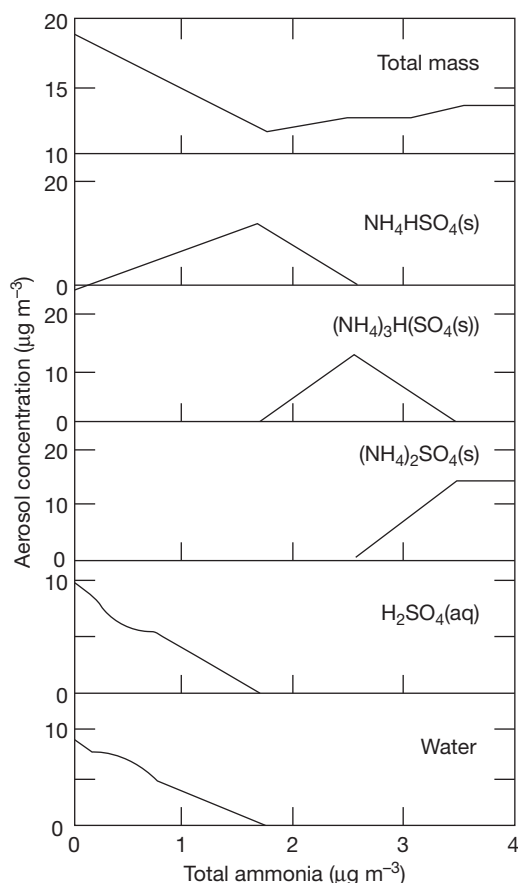


**Figure 1** Aerosol composition for a system containing  $10 \mu\text{g m}^{-3}$   $\text{H}_2\text{SO}_4$  at 30% RH and  $T = 298 \text{ K}$  as a function of the total (gas plus aerosol) concentration. Reproduced from Seinfeld, J.; Pandis, S. *Atmospheric Chemistry and Physics: From Air Pollution to Climate Change*; Wiley Interscience: New York, 1997.

0.5,  $\text{NH}_4\text{HSO}_4(\text{s})$  becomes the dominant species, and  $\text{H}_2\text{SO}_4$  and associated water levels fall to zero.<sup>21</sup> As the molar ratio approaches 1, the salt letovicite  $(\text{NH}_4)_3\text{H}(\text{SO}_4)_2(\text{s})$  forms and gradually replaces  $\text{NH}_4\text{HSO}_4(\text{s})$ . At a molar ratio of 1.25–1.5,  $(\text{NH}_4)_3\text{H}(\text{SO}_4)_2(\text{s})$  goes from being the dominant to the sole species and at molar ratios from 1.5 to 2 ammonium sulfate salts form. At molar ratios of 2 or greater, ammonium sulfate salt is the sole species.<sup>15</sup>

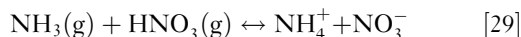
At 75% RH, the results are very different; the system is affected by the deliquescence of  $\text{NH}_4\text{HSO}_4$  (which has a deliquescent relative humidity (DRH) of 40%) and  $(\text{NH}_4)_3\text{H}(\text{SO}_4)_2$  (DRH = 69%), and so is in general a solution of  $\text{NH}_4^+$  and a sulfate species (whose form depends on ammonia levels). Thus, the aerosol is a liquid solution of  $\text{H}_2\text{SO}_4$  at low ammonia levels,  $\text{HSO}_4^-$  at moderate ammonia levels, and  $\text{SO}_4^{2-}$  at

ammonia/sulfate ratios above 1.5, while the solid  $(\text{NH}_4)_2\text{SO}_4$  forms at ratios above 2 when there is sufficient ammonia to completely neutralize the sulfate.<sup>21</sup>

It is evident from the above discussion that the composition and hydrogen ion concentration within a wet aerosol will depend critically on the relative balance of  $\text{H}_2\text{SO}_4$  and  $\text{NH}_3$  in the atmosphere. The hydrogen ion concentration will determine the extent of oxide dissolution promoted by the deposition of the aerosol and thus the extent of corrosion. This result can be generalized to environmental systems containing a range of S-containing gases and ammonia, and it emphasizes the need for an understanding of both acid and alkali precursors in understanding the corrosiveness of an environment.

#### 2.16.1.4.2 Ammonia–nitric acid–water systems

According to Seinfeld and Pandis,<sup>1</sup> ammonia and nitric acid readily react in the atmosphere to form  $\text{NH}_4\text{NO}_3$  (eqn [4]). This may either occur homogeneously or, if the ambient RH is lower than the DRH of  $\text{NH}_4\text{NO}_3$  (62%), it may occur heterogeneously, with  $\text{HNO}_3$  being readily absorbed in wet aerosols ( $H_A = 2.1 \times 10^5 \text{ M atm}^{-1}$ ). If the RH is above the DRH of  $\text{NH}_4\text{NO}_3$ , the compound may dissociate:



However, the equilibrium dissociation constant of  $\text{NH}_4\text{NO}_3$  is highly dependant on temperature and so, for typical atmospheric levels of ammonia and nitrate, almost all of the species will be in the gas phase above  $30^\circ\text{C}$ , while at temperatures approaching  $0^\circ\text{C}$  most of the available species will be solid (below the DRH).<sup>1</sup> Therefore, in urban atmospheres that are low in sulfates but high in acid solutions, ammonium nitrate particulate will readily form.

#### 2.16.1.4.3 Ammonia–nitric acid–sulfuric acid–water systems

This type of environment reflects a typical industrial/urban atmosphere that contains  $\text{NH}_3$ ,  $\text{HNO}_3$ ,  $\text{H}_2\text{SO}_4$ , and water vapor. According to Seinfeld and Pandis<sup>1</sup> a range of solid phases ( $(\text{NH}_4)_2\text{SO}_4$ ,  $\text{NH}_4\text{HSO}_4$ ,  $(\text{NH}_4)_3\text{H}(\text{SO}_4)_2$ ,  $\text{NH}_4\text{NO}_3$ ) and aqueous phases ( $\text{NH}_4^+$ ,  $\text{H}^+$ ,  $\text{HSO}_4^-$ ,  $\text{SO}_4^{2-}$ ,  $\text{NO}_3^-$ ) can exist.

In situations where there is insufficient ammonia to neutralize the sulfate, the sulfate will tend to drive the nitrate to the gas phase and will tend to exist as bisulfate (or  $\text{NH}_4\text{HSO}_4$  if ambient RH is below the DRH of this salt).<sup>1</sup> In ammonia-rich solutions there is competition between sulfate and nitrate for the

available ammonia, which results in a reduction in the formation of ammonia sulfate aerosol compared to systems free of nitric acid.<sup>1</sup>

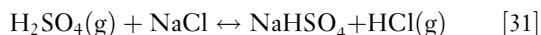
The three cases discussed above highlight under what conditions different compounds in aerosols will form and what aqueous species will exist; they highlight, in particular, the roles of ammonia in neutralizing acid aerosols and nitrates in replacing sulfate aerosol formation. The same factors will also determine the chemistry of cloud nuclei and raindrops. It is apparent that to obtain an accurate understanding of aerosol (or raindrops) formation and chemistry, a full knowledge of gas species is required. From the 1980s onward, a significant body of experimental work<sup>18–20</sup> was carried out on defining the effects of various gas dosages on atmospheric corrosion. Most of these dose functions were on the basis of SO<sub>2</sub> levels, although some<sup>19,20</sup> incorporated the effects of oxidants (such as O<sub>3</sub>). Unfortunately, no consensus was reached as to the appropriate dose function to use, possibly because the exposure regimes incorporated different levels of other gases (e.g., nitrates, ammonia). These earlier studies might have been of more value if the gas regimes at each exposure site had been studied in more depth and a refined characterization scheme developed.

### 2.16.1.5 Reactions in Salt Aerosols

Marine aerosols may react with a range of gaseous species to form products such as ammonium chloride, sodium nitrate, sodium sulfate, and sodium bisulfate; for example, H<sub>2</sub>SO<sub>4</sub>(g) may be absorbed into an aerosol, and it may react with NaCl. This reaction may permit H<sub>2</sub>SO<sub>4</sub> (or other strong acids such as HNO<sub>3</sub> that have lower vapor pressures relative to HCl) to accumulate in the aerosol, increasing acidity, and causing HCl to volatilize<sup>22</sup>:



or

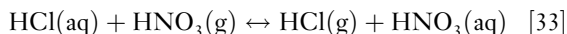


Alternatively, in urban environments HNO<sub>3</sub>(g) may react with marine aerosols:



Thus, gaseous HCl may enter the atmosphere through the dechlorination of airborne sea salt particles; however, as HCl is relatively soluble ( $H_A = 727$ ), it is

readily reabsorbed into atmospheric water droplets. In turn, these HCl-rich droplets may then react with and promote the absorption of other strong acids:



Such cycling of HCl can thus lead to significant acidification of both aerosols and rain or cloud droplets in marine locations<sup>23</sup> with significant contamination by industrial or urban pollutants. The extent of chloride depletion is evident in the work of Keene *et al.*<sup>24</sup> who looked at the Na/Cl ratio of rainwater (the majority of Na and Cl in rain water will be derived from the scavenging of marine aerosol) as a function of distance from the nearest coast in Australia. They found that the ratio moved from close to 0.8 (the expected ratio of seawater) to up to 1.3, at 500 km from the coast, which implies that chloride loss in marine aerosols may be up to 40%.

### 2.16.1.6 Aerosols

Aerosols or particles in the atmosphere may either be emitted from a source directly as particles (primary aerosol) or be formed in the atmosphere by gas-to-particle conversion processes.<sup>1</sup> Primary aerosols may arise from natural sources such as soil dust, sea salt, biological debris, and volcanic dust, or from anthropogenic sources such as industrial dust and soot from fuels or biomass combustion.<sup>8</sup> Of these, soil dust and sea salt are the major sources. Aerosols range in size from tens of angstroms to several hundred micrometers and, as shown in Figure 2,<sup>25</sup> can be divided into two classes: fine particles (<2.5 μm) and coarse particles (>2.5 μm). In general, coarse particles other than water droplets correspond to the primary aerosols and fine particles correspond to the secondary aerosols. Coarse and fine particles are transformed and removed from the atmosphere separately and so they can be treated independently.

As evident in Figure 2, fine particles are divided into two modes – nuclei mode and accumulation mode – the nuclei mode of particles, being from the condensation of gases, grow by coagulation, while the accumulation range of particles largely form from coagulation of the nuclei mode and by condensation of vapors onto existing particles. Typically, the accumulation particles outnumber the coarse particles by three orders of magnitude or more and have up to ten times the surface area.<sup>26</sup> However, the deposition rate of the accumulation particles is two orders of

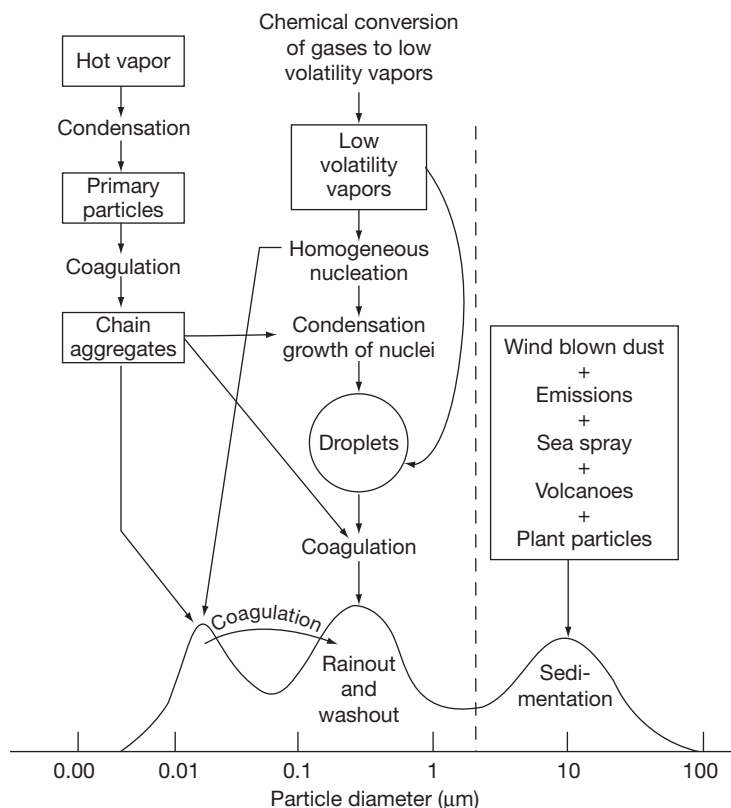


**Figure 2** Idealized schematic of the distribution of aerosol size ranges and sources. Reproduced from Whitby, K. T.; Cantrell, B. Fine Particles. In Proceedings of the International Conference on Environmental Sensing and Assessment, Las Vegas, NV, 1976; Institute of Electrical and Electronic Engineers.

magnitude less than that of coarse particles; therefore, they would be expected to deposit on surfaces at similar rates (see [Section 2.16.3.1.2](#)).

The compositions of fine and coarse aerosols are reasonably distinct, reflecting their diverse origins. Fine aerosols commonly contain sulfate, ammonia, and organic and elemental carbon, while coarse aerosols contain sea salt, dust (silicon, calcium, magnesium, aluminum, and iron), and biogenic organic particles (pollen spores and plant fragments).<sup>27</sup> Nitric acid reacts with both aerosol fractions (according to eqns [4] and [32]) and thus nitrates are found in both size fractions.<sup>27</sup> Thus, the chemistry of the accumulation mode is influenced by the sulfuric acid and ammonia systems described above, while the coarse mode is influenced by the absorption of sulfuric and nitric acids into the marine aerosol.

Both coarse and fine aerosols may be hygroscopic and can absorb water from the atmosphere. The DRH values for common aerosol constituents are given in [Table 4](#).<sup>28,29</sup> The DRH is the RH at which a solid aerosol will absorb enough water to become a

saturated aqueous solution. Further increasing the RH will lead to additional condensation of water into the aerosol. DRH is dependent on temperature and for aerosols with more than one component, it is in general significantly less than that of the more wettable salt. Considering some marine and industrial aerosols, the DRH of a mixture of  $\text{NaNO}_3$  and  $\text{NaCl}$  (which may occur if  $\text{HNO}_3$  is absorbed into a marine aerosol) is 71.3%, while that of a mixture of  $\text{NH}_4\text{NO}_3$  and  $(\text{NH}_4)_2\text{SO}_4$  is 52.3%.<sup>30</sup> When wetted salts are dried, there is often a very strong hysteresis in recrystallization, so that recrystallization may occur at RH levels significantly below the DRH.

Wetted aerosols may also absorb organic molecules, with some studies<sup>31</sup> indicating that these may form an outer surface layer (with the polar part of the molecule in the aqueous solution and the nonpolar in air). The formation of such coatings may dramatically restrict evaporation from the aerosols.

**Table 4** DRH of common aerosols (at 20 °C)

Salt	DRH (%)
Na <sub>2</sub> SO <sub>4</sub>	84.2
NH <sub>4</sub> Cl	80.0
(NH <sub>4</sub> ) <sub>2</sub> SO <sub>4</sub>	79.9
NaCl	75.3
NaNO <sub>3</sub>	74.3
(NH <sub>4</sub> ) <sub>3</sub> H(SO <sub>4</sub> ) <sub>2</sub>	69.0
NH <sub>4</sub> NO <sub>3</sub>	61.8
NaHSO <sub>4</sub>	52.0
(NH <sub>4</sub> )HSO <sub>4</sub>	40.0
MgCl <sub>2</sub>	35.0

Source: Tang, I. N. *Atmos. Environ.* **1980**, *14*, 819–828.  
Tang, I. N.; Munkelwitz, H. R. *Atmos. Environ.* **1993**, *27A*,  
467–473.

### 2.16.1.6.1 Marine aerosol production

Salt aerosols may be generated either by the ocean or from surf, via bursting bubbles generated by ocean whitecaps (breaking waves that generate white foam).<sup>32</sup> particles torn from the crests of ocean whitecaps,<sup>33</sup> or breakers on the shore.<sup>34</sup> Surf waves tend to produce coarse aerosols, while ocean activity produces medium sized aerosols.<sup>35</sup> Thus, the magnitude of aerosol production from the ocean largely depends on the extent of whitecap coverage, which is related to latitude. Equatorial regions have low whitecap coverage and regions at high latitudes have high whitecap coverage.<sup>33</sup> Salt production from surf is dependant on local winds,<sup>34</sup> but may also depend on the seabed profile close to the shore (with steep slopes and mud flats reducing aerosol production).<sup>36</sup> An additional factor that may affect both ocean and surf wave heights (and thus aerosol production) is 'fetch.' To reach their maximum height, waves require a significant length of water where wind can blow across them. This length is defined as the fetch, and if fetch is below a critical value, waves will not reach their maximum height<sup>37</sup> and salt production will be reduced. Along a coast, islands, capes, and other features may reduce the fetch distance.

The implications of these aerosol production dynamics are significant. First, salt production and, thereby, salt deposition and marine aerosol-induced corrosion would be expected to be lower in tropical compared to temperate latitudes. Second, salt production from shallow or relatively narrow bays (<300 km) will be reduced and so will salt deposition and marine aerosol-induced corrosion. Experimental studies by Cole *et al.*<sup>38,39</sup> have demonstrated both the latitude and bay effects on salt production.

### 2.16.1.6.2 Types of aerosol

The nature of aerosols clearly depends on location. In marine and industrial locations, aerosols occur in both the coarse and the fine modes, with the fine mode being dominant adjacent to particular sources (e.g., highways) but falling rapidly with distance from the source.<sup>1</sup> The fine mode is dominated by sulfates, nitrates, and ammonia with the exact chemistry controlled by the processes outlined in **Sections 2.16.2.4.1–2.16.2.4.3**. The coarse mode consists of particles of soil dust, sea salt, fly ash, and particles generated by mechanical wear such as tire wear particles. Aerosol fractions are often derived from particles of less than 1 µm (PM<sub>1</sub>) or 10 µm (PM<sub>10</sub>) in diameter. Typical mass values<sup>1</sup> of PM<sub>1</sub> and PM<sub>10</sub> are 30–150 and 100–300 µg m<sup>−3</sup> for urban locations.

The definition of the acidity of aerosol is quite complex. Three measures are often used, the pH of the aerosols (sometimes referred to as the *in situ* free acidity in aqueous aerosols), strong acidity and free acidity. Strong acidity is the total [H<sup>+</sup>] derived when the collected aerosol is dissolved in an excess of water (nmol H<sup>+</sup> per m<sup>3</sup> of air) while free acidity is the [H<sup>+</sup>] concentration of collected aerosols (without dissolution in water). The pH of aerosols depends heavily on the RH as it controls the aqueous content of the aerosol and, thereby, the concentration of ions. In sulfate containing aerosols, the strong acidity includes H<sup>+</sup> released by bisulfate dissociation which is not included in free acidity. The immediate reaction of an aerosol with a surface would be most affected by the pH of the aerosol; however, the overall impact of the environment on the surface as a whole would be affected by the strong acidity.

Pathak *et al.*<sup>40</sup> looked at the acidity of aerosols in the PM<sub>2.5</sub> range collected in Hong Kong. These aerosols were rich in ammonia and sulfate with their composition controlled by the NH<sub>4</sub><sup>+</sup>:SO<sub>4</sub><sup>2−</sup> ratio which controls the neutralization of acid sulfate (as outlined in **Section 2.16.2.4.1**). A differentiation was made between samples collected when the wind blew off the ocean and that when it blew off the land. Land derived aerosols were ammonia-rich and marine derived aerosols were ammonia poor. Thus, the continental aerosol had a higher strong acidity than the marine derived aerosol (62 vs. 35 nmol H<sup>+</sup> per m<sup>3</sup> of air). However, the free acidity was higher for the marine aerosol (because of the higher water fraction in the marine aerosol). There was a very wide range in pH from −0.62 to 2.35 for all aerosols, with the pH

increasing as the RH and the ammonia: sulfate ratio increased.

Other studies have shown similar low pH values in urban locations. Yao *et al.*<sup>41</sup> found that in Hong Kong the fine aerosol primarily consisted of  $\text{NH}_4^+$  and  $\text{SO}_4^{2-}$  in a ratio of 0.7 which is consistent with letovicite ( $(\text{NH}_4)_3\text{H}(\text{SO}_4)_2$ ) and had an estimated pH from  $-1$  to  $1.5$ . Takeuchi *et al.*<sup>42</sup> sampled aerosol from an urban site in Yokohama, Japan and found that the major constituents of the aerosol were  $\text{NH}_4^+$ ,  $\text{SO}_4^{2-}$ , and  $\text{NO}_3^-$ , with some  $\text{Na}^+$  and  $\text{Cl}^-$ , while the average aerosol pH was estimated to be between  $2$  and  $2.2$ . Some chemical and pH differentiation occurred as a function of size, with the  $\text{PM}_{10}$  aerosol having a slightly lower pH ( $1.9$ – $2.1$ ) and higher concentration of sulfate relative to the  $\text{PM}_2$  fraction (pH  $2$ – $3$ ).  $\text{NH}_4\text{Cl}$  and  $\text{NH}_4\text{NO}_3$  are the major ammonia species reflecting processes that occur in a  $\text{NO}_2$  rich environment (see Section 2.16.2.4.3).

In a marine location, the coarse fraction dominates (typical  $\text{PM}_{10}$  and  $\text{PM}_{2.5}$  ranges are  $1$ – $4$  and  $10$   $\mu\text{g m}^{-3}$ , respectively) and is associated with marine aerosols. Keene *et al.*<sup>23</sup> found that in the air over the ocean, in addition to the coarse fraction, there were also submicron sulfur-containing aerosols. Freshly ejected aerosol will have a pH similar to that of seawater ( $\sim 8$ ), which will rise as the aerosol evaporates and equilibrates with the environment, increasing the ionic concentration. In fact according to Sander and Crutzen<sup>43</sup> the concentration of ions in seawater and marine aerosol (at a RH of  $76.2\%$ ) are respectively  $[\text{Cl}^-]$ ,  $0.55$  and  $5.4$  M,  $[\text{HCO}_3^-]$ ,  $2.3 \times 10^{-3}$  and  $2.7 \times 10^{-2}$  M, for seawater pH of  $8.7$  and an aerosol pH of  $9.5$ . The aerosol pH was calculated for a RH of  $76.2\%$  assuming the solution was saturated with chloride and  $\text{HCO}_3^-$  was in equilibrium with the gas phase. Subsequently, the pH may change as a result of aqueous phase reactions (particularly the absorption of  $\text{H}_2\text{SO}_4$ ) and volatilization of the products of these reactions (e.g.,  $\text{HCl}$ ).<sup>44</sup> Models developed by Chameides and Stelson<sup>45</sup> indicate that the original alkaline pH may be reduced to below  $5$  within  $15$  min. The submicron S-containing aerosols will be primarily formed by the condensation of  $\text{H}_2\text{SO}_4$  in clean environments, or by the absorption of  $\text{H}_2\text{SO}_4$  by fine particulates in polluted environments. Subsequently, these wet aerosols may absorb other gases, including ammonia, which will lead to particle neutralization, so that submicron aerosols in marine locations will have a mixture of  $\text{H}_2\text{SO}_4$ ,  $\text{NH}_4\text{HSO}_4$ ,  $(\text{NH}_4)_2\text{SO}_4$ , and  $\text{NH}_4\text{NO}_3$ .<sup>46</sup>

Historically, there has been considerable variation in the estimated pH of marine aerosols. Recent

work by Keene *et al.*<sup>47</sup> measured the pH of the larger sea-salt fractions (geometric mean diameter (GMD)  $\geq 2.9$   $\mu\text{m}$ ) and found that the median pH ranged from  $3.1$  to  $3.4$ , while the median pH for submicron fractions was  $\leq 1.6$ . This was supported by previous work<sup>48</sup> on marine aerosols off Bermuda, where pH values of aerosols were found to vary from  $0$  to  $4$ – $5$  ( $1.3$   $\mu\text{m}$  aerosols had a pH of  $2$ ,  $2.4$   $\mu\text{m}$   $\sim 3$ , and  $11$   $\mu\text{m}$   $\sim 4.6$ ). It is notable that the pH of these aerosols was strongly buffered by bisulfate. Similar results were found for aerosols measured off New England, although even the coarsest aerosols (GMD  $\geq 10$   $\mu\text{m}$ ) exhibited pH values less than  $4$ . Acidified marine aerosols may be particularly corrosive as the acid component may promote oxide dissolution, while the chloride will attack a metal surface.

Ocean-produced aerosols will have residence times of hours to days and, therefore, could be rendered acidic by gaseous reactions. In contrast, most surf-produced aerosols (see Section 2.16.2) will be deposited within the first few hundred meters of a coast and within minutes of their production, and therefore, there may be insufficient time for enough gaseous absorption to render them acidic.

In rural locations, the coarse aerosol fraction is dominant (typically  $\text{PM}_{10}$  varies from  $2.5$  to  $8$  and  $\text{PM}_{2.5}$  from  $10$  to  $40$ ) and aerosols are of natural sources but with a small anthropogenic source.<sup>49</sup> In remote continental<sup>50</sup> locations, the coarse fraction dominates (typically  $\text{PM}_{10}$  varies from  $0.5$  to  $2.5$  and  $\text{PM}_{2.5}$  from  $2$  to  $10$ ) with source of particles being natural sources such as dust, pollen, plant waxes, or the products of atmospheric oxidation processes outlined in Section 2.16.1.3.

### 2.16.1.7 Cloud Nucleation and Rain Chemistry

Cloud nucleation occurs when aerosols undergo rapid growth in the presence of a supersaturation of water vapor. These aerosols are called CCN. The supersaturation of water arises because of the steady decrease in temperature with distance from the ground, so that when a hot mass of air rises, the RH of the air steadily increases (or alternatively the saturation vapor pressure decreases). CCN will tend to be the larger sized aerosols (from coarse aerosols into the accumulation mode). Once cloud droplets have formed, they may continue to grow by scavenging the remaining aerosols in the clouds or by coalescence. Once a cloud droplet reaches a critical size and falls as rain, it may continue to scavenge aerosols or absorb



gases (as detailed in previous sections) until it reaches the ground.

Because of the processes detailed previously, considerable concentrations of ionic species can build up in rainwater. Typically observed concentrations of the major species are given in Figure 3.<sup>14</sup> However, the formation and deposition of rain drops occur over significant time and spatial scales so that the composition of rainwater will reflect pollutant levels in a general area and not only at the point of deposition. Fog arises when CCN form and grow close to the ground. A number of studies have identified the problem of acid fog, both within cities and in rural and forested areas in their vicinity. North American studies of fog water have indicated pH levels from 2.9<sup>51</sup> to 3.6<sup>52</sup> with high nitrate, ammonia, and sulfate levels.

The variation of chloride concentration in rainwater, shown diametrically in Figure 3 shows a strong dependence on the distance from the location where the rainwater was sampled. Keywood *et al.*<sup>24</sup> have

shown that chloride concentration falls in an approximately exponential fashion, with peak values between 500 and 1000  $\mu\text{eq l}^{-1}$  at the coast,  $\sim 10 \mu\text{eq l}^{-1}$  at 500 km from the coast, and less than  $1 \mu\text{eq l}^{-1}$  in the center of the Australian continent. Given that the prime source of chloride in rainwater is the scavenging of marine aerosols, it is not surprising that they found that the factors that control aerosol concentration (sea state, rainfall) also influenced chloride concentration in rain water.

In Table 5, typical rainwater chemistry and pH values from locations around the globe are given. While there is a tendency for rainwater in or near industrial or urban areas to have low pH values, some industrial sites have relatively high pH values. In the mid-1980s<sup>66</sup> lower pH values were reported (pH of 4.2–4.7) close to the industrial belt in central and eastern Europe. The relatively moderate pH values reported in such industrial centers as Nanjing (China), Dhanbad (India) or Mugla (Turkey) are

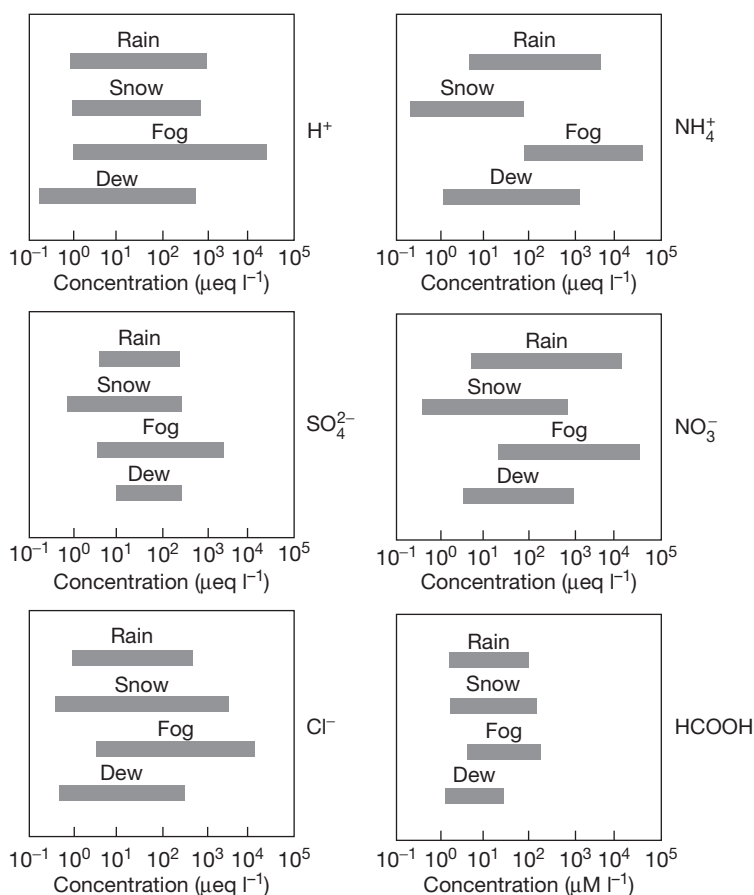


**Figure 3** Concentration ranges of ionic and molecular constituents of different types of atmospheric water. Reproduced from Leygraf, C.; Graedel, T. *Atmospheric Corrosion*; Wiley and Sons: New York, 2000.

**Table 5** Selected rain water compositions (concentration in  $\mu\text{eq l}^{-1}$ )

			<i>pH</i> <i>mean</i>	<i>pH</i> <i>range</i>	$\text{Cl}^-$	$\text{NO}_3^-$	$\text{SO}_4^{2-}$	<i>Na</i>	$\text{NH}_4$	<i>K</i>	<i>Mg</i>	<i>Ca</i>	<i>formate</i>	<i>Ac</i>	<i>Ref</i>
Mt.Rokko	Urban	Japan		4.5–5.1	25	13	12	21	10	0.8	1.8	1.6			53
Mt Awaga	Rural	Japan		4.5–5.3	25	9.5	12	28	11	3.7	3.1	2.6			53
Nanjiing	Urban/Industrial	China	5.15	4.9–5.4	142	39	241	23	193	12	32	295			54
Londrina	Urban/Industrial	Brazil	5.8	5.5–6.1	66	137	92	0	32	0.1	–	–			55
Mugla	Urban/Industrial near power station	Turkey	6.9	4.5–7.7	–	23	124	17	30	3.5	–	–			56
Mexico City	Urban/Industrial	Mexico	4.9	4.7–5.3	9	43	77	5	95	2	4	35			57
Amerfoort	Rural but nearby Urban/Industrial	S. Africa	4.4		10	25	59	9	22	5	7	19	8	6	58
Bangalore	Urban/Industrial	India	4.8		59	27	89	55	29	15	13	89			59
Dhanbad	Industrial-coal	India		4.4–6.9	27	10	63	18	35	13	16	70			60
Louis Trichardt	Rural	S. Africa	4.9		10	8	15	9	10	4	4	12	13	8	58
Jabiru	Rural	Australia		3.6–5.2	7.5	3.2	2.6	3.8	1.7	0.7	0.6	0.3	6.3		61
Katherine	Rural	Australia	4.8		11.8	4.3	3.2	7.0	2.0	0.9	1.0	1.3			61
Dorrigo	Rural	Australia	5.5		65	9.7	15	54	3.3	1.9	11	8.2	4.6	3.8	62
Barrington	Rural	Australia	5.8		24	7.3	8.8	19	7.1	2.2	6.1	11	6.8	5.7	62
Latrobe Valley	Industrial-coal power stations	Australia	5.8		137	11	35	116	–	1	34	26			63
Cape Grim	Isolated-Tasmania	Australia	6.0		1372	2.7	152	1167	1.6	16	247	78			64
Lithgow	Inland – coal power station	Australia	4.8		6.8	7.9	7.8	5.3	11.7	0.9	1.2	2.0	6.9	6.3	65

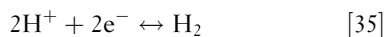
associated with the neutralizing role of ammonia and the alkali metals (particularly  $\text{Ca}^+$ ), despite the high sulfate and nitrate contents of rain water. In urban areas, such as Mt Rokko in Japan, ammonia may play a significant neutralizing role, while nitrate levels tend to be equal in importance to sulfates.

Surprisingly, acid rainwater and cloud droplets have been found in areas remote from any industrial activity. Charlson *et al.*<sup>67</sup> proposed that the concentration of CCN may be controlled by DMS emissions from phytoplankton. Gillet and Ayers<sup>61</sup> found that DMS may indeed promote the formation of acid CCN (pH 4.8–5.8) in Tasmania, a largely rural island off the south-east coast of Australia. The same workers<sup>64</sup> also found acidic cloud droplets (average pH 3.8) and rainwater (average pH 4.9) in a number of inland sites in the remote Northern Territory of Australia. This acidity could be attributed to sulfates from DMS decomposition (the decomposition of DMS is complex, but may be triggered by OH radicals or NO) and to formate and acetate in cloud water and rainwater. Rainwater chemistry in rural and remote areas may also be influenced by the transport of particulate and gaseous matter. Work by Schwartz<sup>68</sup> indicates that industry-produced acids may be deposited up to 1000 km from their source. This is confirmed by Poste *et al.*,<sup>62</sup> who studied rainwater and fog acidity at two locations in northern New South Wales ~200 and 500 km from any industrial location, and ~40 and 60 km from the coast, respectively. Both sites exhibited high levels of salts of marine origin and significant sulfates from anthropogenic sources. Rainwater and fog water had similar compositions, but fog water was more concentrated (by a factor of 3).

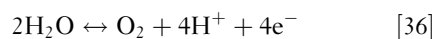
### 2.16.1.8 Redox Potential and pH Diagrams

Graedel and Frankenthal,<sup>69</sup> on the basis of the evidence of Graedel<sup>70</sup> and Garrels,<sup>71</sup> have proposed distribution of potential and pH for dew rain water and fog. Garrels also proposed redox–pH ranges for ‘environments in contact with the atmosphere.’ Graedels and Frankenthals<sup>69</sup> and Garrels<sup>71</sup> distributions along with the potential–pH variations for the redox couples representing the stability of water, hydrogen peroxide, and the reduction of oxygen and ozone are given in [Figure 4](#).

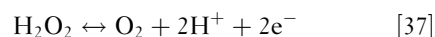
Line A and line B enclose the stability region of water; line A representing



and line B representing



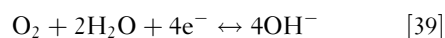
Line C and line D enclose the stability region of hydrogen peroxide; line C representing



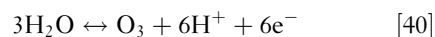
and line D representing



Line E is the variation in potential for the reduction of oxygen



and line F is the variation in potential for the reduction of ozone



The similarity of Garrels<sup>71</sup> and Graedel<sup>70</sup> analyses with the  $\text{H}_2\text{O}_2$  stability boundary (eqn [37]) implies that natural waters behave as if they contain a small amount of dissolved oxygen. It is notable that ‘waters’ not in contact with oxygen such as ground water lose their oxidizing potential.<sup>71</sup> If the redox potential of dew/rain/aerosols is primarily controlled by the oxidizing species present, those with high ozone content would be expected to have higher potentials than predicted by Graedel and Frankenthal.<sup>69</sup>

## 2.16.2 Transport of Gases and Aerosols

### 2.16.2.1 General Scale of Movement of Gases and Particles

In the atmosphere, a series of processes occur in parallel – gaseous species, aerosols, and drops are constantly reacting, while the air is in constant motion on scales of a centimeter or less (tiny eddies) to continental dimensions. At the same time, species are entering the atmosphere from a variety of natural and man-made sources, or are leaving the atmosphere through scavenging by raindrops or by impact with the ground or ground-based objects. The period during which a species stays in the atmosphere is referred to as its residence time (which is closely related to the reactivity of the species) and residence time is closely related to the distance the species may travel from its source. In [Figure 5](#), the temporal scales (residence times) and spatial scales are plotted for a range of chemical species.<sup>1</sup> As the OH radical (formed by photolysis of  $\text{O}_3$  and  $\text{H}_2\text{O}_2$ ) is highly

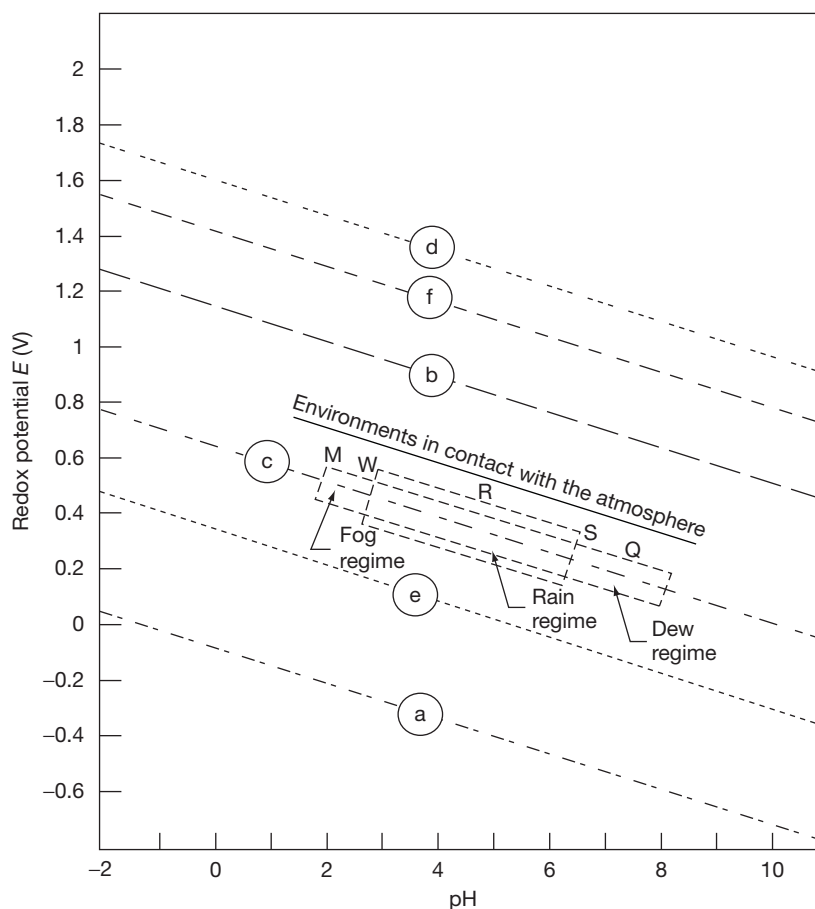


**Figure 4** Redox diagram. Adopted from Pourbaix, M. *Atlas of Electrochemical Equilibria in Aqueous Solutions*, 2nd English Edition; National Association of Corrosion Engineers: 1440 South Creek Drive, Houston Texas 7704, 1974; Graedel, T. E.; Frankenthal, R. P. *J. Electrochem. Soc.* **1990**, 137, 2385–2394.; Garrels, R. M. *Mineral Equilibria at Low Temperature and Pressure*; Harper: New York, 1960. MW represents mine waters, R represents rain waters, S represents streams, and Q represents normal ocean water.

reactive, it has a residence time of less than 0.01 s, and it will travel not more than centimeters from its source. In contrast,  $\text{N}_2\text{O}$  has lifetimes in tens of years, and it will be mixed throughout the global atmosphere (the major pathway for  $\text{N}_2\text{O}$  loss is photodissociation in the stratosphere).

The spatial impact of a species may be increased by its reaction with other species. For example, DMS has a residence time of a few hours and would not be expected to move more than several hundreds of meters from its source, yet as outlined earlier<sup>64</sup> the acidification of cloud droplets and raindrops at inland locations was attributed in part to DMS. As indicated earlier, the decomposition of DMS may produce both  $\text{SO}_2$  and  $\text{H}_2\text{SO}_4$ . The residence time of  $\text{SO}_2$  is significantly greater (days rather than hours) and subsequently its dispersal from source will be greater

(kilometers rather than hundreds of meters). Finally, both gaseous  $\text{SO}_2$  and  $\text{H}_2\text{SO}_4$  are readily absorbed in aerosols that may have residence times of months and which can be dispersed distances ranging from tens to hundreds of kilometers from their source, depending on size. Such aerosols can then either form CCN or be scavenged by either these nuclei or by raindrops and thus acidification of cloud droplets or rain may occur at a significant distance from the original source of DMS.

Figure 5, therefore, has significant implications for atmospheric corrosion, as it highlights that highly reactive species such as hydroxide radicals will travel extremely short distances, oxidants such as  $\text{NO}_x$  and  $\text{H}_2\text{O}_2$  limited distance (although tropospheric  $\text{O}_3$  may travel further), gaseous  $\text{SO}_2$  short distances, and aerosols will travel moderate distances from

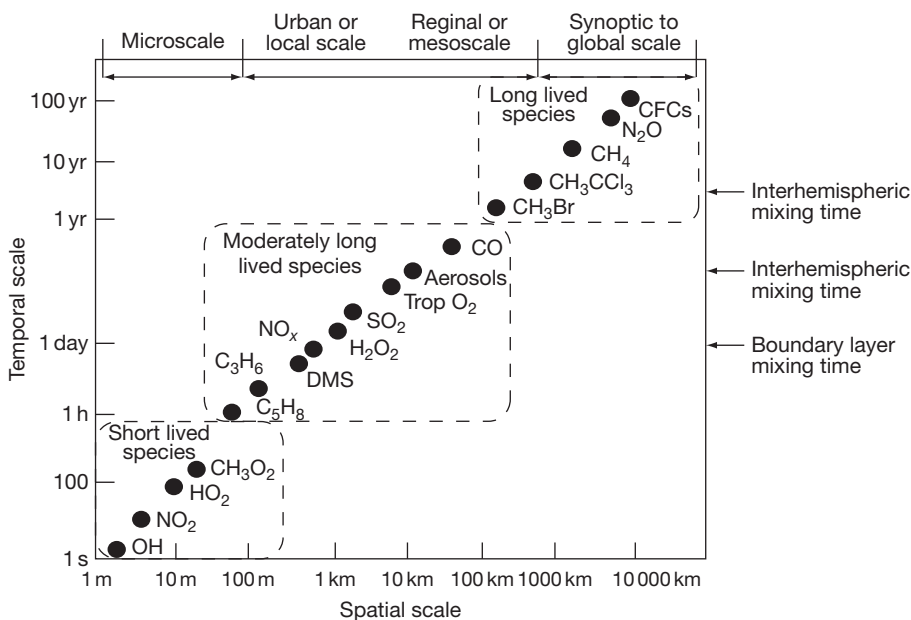


**Figure 5** Spatial and temporal scales of variability for atmospheric constituents. Reproduced from Seinfeld, J.; Pandis, S. *Atmospheric Chemistry and Physics: From Air Pollution to Climate Change*; Wiley Interscience: New York, 1997.

their source. Thus, direct impacts of gaseous species on metallic corrosion will be limited to tens of kilometers from source, while indirect effects via aerosols or rain deposition may be at appreciable distances from source.

### 2.16.2.2 Transportation Processes

More detailed studies of transport have been undertaken either by using an analytical approach (Eulerian or Lagrangian) or by a numerical approach (using computational fluid dynamics (CFD)). In this section, the movement of gaseous species will be illustrated using the analytical approach and that of aerosols using the numerical approach.

#### 2.16.2.2.1 Analytical approach to gas transport

The transport of gases in a turbulent fluid can be modeled<sup>1</sup> using a Gaussian distribution, with the plume equation having the form below when evaluated along the centerline ( $y=0$ ) and at ground ( $z=0$ ).

$$\langle c(x, 0, 0) \rangle = q / (\pi u \sigma_y \sigma_z) \times \exp(-b^2 / 2\sigma_z^2) \quad [41]$$

where  $q$  is the mean concentration from a point source,  $u$  is the wind speed,  $x$  is distance from the source,  $b$  is the effective source height, and  $\sigma_y^2, \sigma_z^2$  are the Gaussian variances.

This equation has a maximum value for some intermediate value of  $x$  and of wind speed. The position of this maximum depends on the stability class of the plume, that is, A (extremely unstable), B (moderately unstable), C (slightly unstable), D (neutral), E (slightly stable), and F (moderately stable). Also, two case scenarios exist – that when the plume has not reached its maximum height and that when it has.<sup>1</sup>

The critical downward distance at which the surface concentration is at a maximum is given in **Figures 6 and 7** (from Seinfeld and Pandis<sup>1</sup>) as a function of source height and plume stability.

It is evident from **Figures 6 and 7** that for low-height sources ( $<10$  m) such as short stacks, the maximum pollutant levels will occur at 100–500 m of the source, while for plumes emitted from sources at a height of 100 m the maxima may occur up to 10 km from the source.

Thus, gaseous pollutants may directly impact on metal structures for distances up to tens of kilometers from their source. However, they may also be absorbed in aerosols and transported significantly greater distances.

#### 2.16.2.2.2 Aerosol transport

The corrosion science literature has concentrated on the transport of marine aerosols and within corrosion science there has been little work on the deposition of



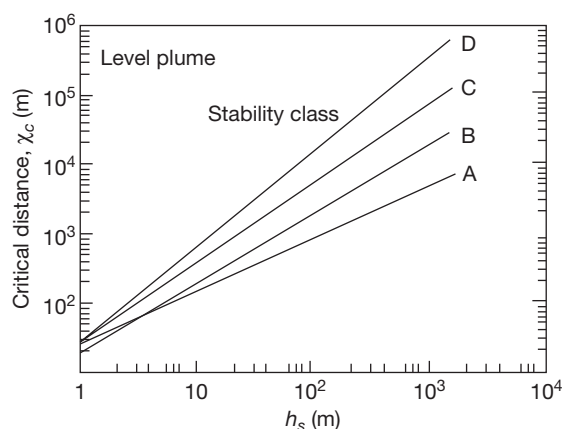


**Figure 6** Critical downwind distance  $x_c$  as a function of source height  $h_s$ , and stability class for a plume that has reached its final height. Reproduced from Seinfeld, J.; Pandis, S. *Atmospheric Chemistry and Physics: From Air Pollution to Climate Change*; Wiley Interscience: New York, 1997.

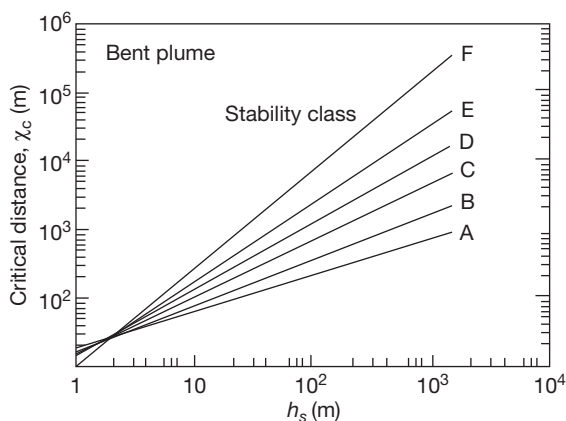


**Figure 7** Critical downwind distance  $x_c$  as a function of source height  $h_s$ , and stability class for a plume that has not yet reached its final height. Seinfeld, J.; Pandis, S. *Atmospheric Chemistry and Physics: From Air Pollution to Climate Change*; Wiley Interscience: New York, 1997.

industrial aerosols, which, as outlined previously, are significantly finer (generally  $<2.5 \mu\text{m}$  diameter). The factors influencing the transport of marine aerosols will also influence industrial aerosols, but industrial aerosols would be less affected by the various deposition processes and would, therefore, have significantly larger residence times, and would be transported longer distances.

Ohba *et al.*<sup>72</sup> proposed that aerosols should be divided into categories: salt produced on the shoreline, which is relatively coarse and whose

concentration showed an exponential decrease with distance from the coast; and salt produced at sea, which is finer and whose concentration showed a slower decrease tending towards an asymptotic value that is relatively constant. Other works<sup>73–79</sup> have confirmed this double dependence of aerosol concentration on distance from the coast and have also shown that aerosol concentration depends on wind strength and direction and, in particular, on the strength and frequency of winds arising over oceans.

Cole *et al.*<sup>80</sup> developed a CFD model of marine aerosol transport. Aerosols are convected by wind, lifted by diffusion, and dragged down by gravity. Gravity depends on aerosol mass and, therefore, diameter, with the wet particle diameter being critically dependant on local RH for salt produced by the sea, but not for salt generated at the shoreline which has had insufficient evaporation time to reach equilibrium with the local RH. Salt is removed from the atmosphere by both wet (rainout and washout) and dry deposition. In rainout, salt aerosols become the nuclei of raindrops that agglomerate and fall to earth (thus, there is insignificant aerosol above the cloud layer). Washout refers to the scavenging of salt aerosols by raindrops and its effectiveness depends on the radius of the aerosol droplet. Dry deposition includes deposition on sloping as well as horizontal surfaces. Trees are particularly effective at scavenging salt from the atmosphere, as too are man-made structures. While medium to large aerosols will be readily trapped, small salt aerosols will follow the air-streams around tree leaves and man-made structures. Therefore, separate models are run for the coarse surf-produced aerosols and the relatively fine ocean-produced aerosols.

**Figure 8** (from Cole *et al.*<sup>80</sup>) shows the effect of wind speed on the salt concentration ( $\% \text{ volume} \times 10^{10}$ ) with distance from the coast for surf-produced aerosols (ground roughness 0.5 m) at a height of 2.0 m above ground level. **Figure 9** (from Cole *et al.*<sup>80</sup>) shows the effect of wind speed on the transport of salt produced in the open ocean over a distance of 50 km from the coast at a height of 2.0 m above ground level (ground roughness 0.5 m, ground RH 70%, rainfall  $1200 \text{ mm year}^{-1}$ ). **Figure 10** (from Cole *et al.*<sup>80</sup>) shows the effect of ground roughness on the salt concentration of surf-produced aerosols (ground roughness does not appear to have a significant effect on the transport of ocean-produced aerosols). **Table 6** gives some typical roughness values of various terrain types (from AS/NZ 1170).

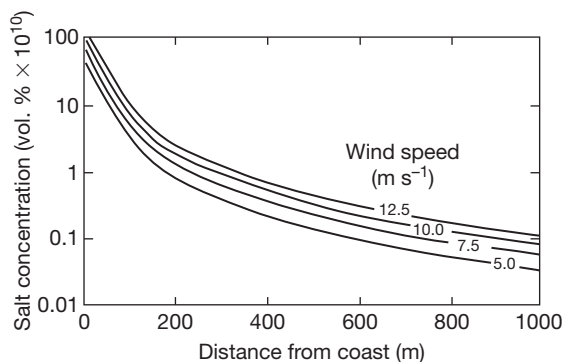


**Figure 8** Effect of wind speed on salt concentration with distance from coast of surf-produced aerosols. Note that this excludes ocean-produced aerosols. Cole, I. S.; Chan, W. Y.; Trinidad, G. S.; Paterson, D. A. *Corros. Eng. Sci. Technol.* **2004**, 39(1), 89–96.

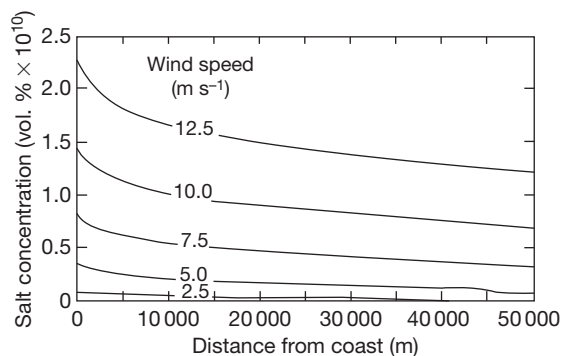


**Figure 9** Effect of wind speed on salt concentration with distance from coast for ocean-produced salt. Reproduced from Cole, I. S.; Chan, W. Y.; Trinidad, G. S.; Paterson, D. A. *Corros. Eng. Sci. Technol.* **2004**, 39(1), 89–96.

Rainfall also has a significant influence on the transport of ocean-produced aerosols. For example, given a wind speed of  $7.5 \text{ m s}^{-1}$ , a ground roughness of  $0.5 \text{ m}$  and  $70\% \text{ RH}$  at a distance of  $200 \text{ km}$  from the coast, uniform rainfalls of  $200$  and  $1600 \text{ mm year}^{-1}$  will reduce aerosol concentrations by  $3\%$  and  $23\%$  respectively, relative to the case of no rain. The effect of  $\text{RH}$  is even more marked. This can be illustrated from the ratios of the aerosol concentration when the surface  $\text{RH}$  is  $20\%$ ,  $70\%$ , and  $90\%$  to that when it is  $50\%$ , which are  $1.4$ ,  $0.5$ , and  $0.2$  respectively (under the same conditions as above).

The strong effect of humidity on salt concentration is related to two effects. The first arises as the model assumes (following Seinfeld and Pandis)<sup>1</sup> that there is a linear decrease in temperature with height and thus a corresponding increase in  $\text{RH}$ ; therefore,

the surface  $\text{RH}$  controls the cloud height. The cloud height is the upper limit for salt aerosol dispersion (aerosols act as scavengers or are scavenged by CCN); therefore, the higher the cloud level, the greater the vertical dispersion of salt and the greater the residence time and transport of the average aerosol. The second effect is on the particle size (or mass). The main constituents of marine aerosols are  $\text{NaCl}$  and  $\text{MgCl}_2$ , with each salt wetting at  $75\%$  and  $35\% \text{ RH}$  (at  $20^\circ\text{C}$ ) respectively, so that above these humidities the aerosol increases its mass, leading to a higher terminal velocity and a greater sink effect of gravity. As the major mass change occurs after the wetting of the  $\text{NaCl}$  constituent, a significant decrease in transport is observed when the surface  $\text{RH}$  is increased from  $50$  to  $70\%$  (recall that the  $\text{RH}$  at a height will be greater than that at the surface). This model has been validated by experimental studies of aerosol deposition across Australia.<sup>38</sup> Experimental and numerical studies indicate that while coarse surf-produced aerosols are deposited close to the coast, those ocean-produced aerosols that have a diameter less than  $2.5 \mu\text{m}$  can be transported significant distances (hundreds of kilometers) from the coast. As industrial aerosols tend to be finer than marine aerosols, it is probable that these too will be transported significant distances from their sources.

## 2.16.3 Deposition

### 2.16.3.1 Forms of Deposition

Traditionally, deposition onto surfaces has been classified as wet or dry deposition, with deposition by rain and snow being defined as wet deposition, and deposition by particulates and aerosols (even when these are wet) being defined as dry. Deposition modes can also be defined as follows:

- Deposition of snow, rain, or fog.
- Deposition of particulates or aerosols.
- Deposition of gases into wet surfaces.
- Depositions of gases onto dry surfaces.

#### 2.16.3.1.1 Rain

Raindrops are generally assumed to have a  $100\%$  efficiency of deposition onto a surface. However, once a raindrop falls onto a surface, it may splash off the surface and break into smaller drops, which could reenter the airflow and not redeposit. Analyses by Cole and Paterson<sup>81</sup> indicated that although splash does occur, it does not lead to significant loss

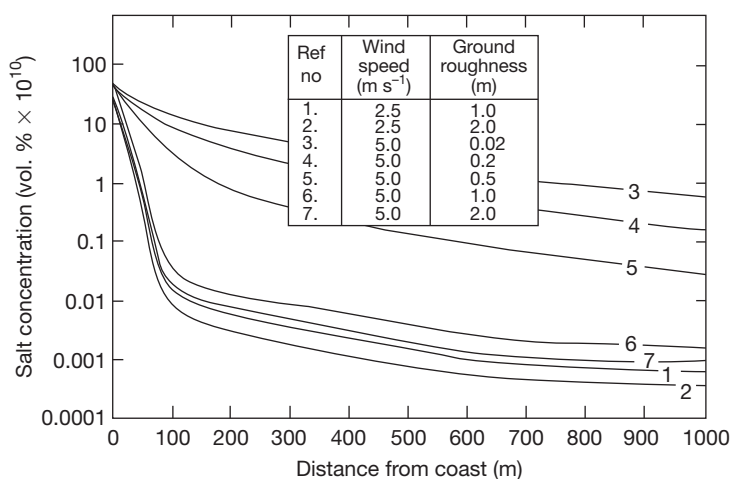


**Figure 10** Effect of ground roughness on salt concentration for surf-produced aerosols. Cole, I. S.; Chan, W. Y.; Trinidad, G. S.; Paterson, D. A. *Corros. Eng. Sci. Technol.* **2004**, 39(1), 89–96.

**Table 6** Typical roughness values (from AS/NZ 1170)

Roughness (m)	Terrain	Roughness (m)	Terrain
2	City buildings (10–30 m)	0.2	Level wooded country; suburban buildings
1	Forests	0.06	Isolated trees, long grass
0.8	High-density metropolitan	0.02	Uncut grass, airfields
0.4	Center of small towns	0.008	Cut grass

of deposition efficiency for rain falling onto stationary objects. However, it can be quite significant for fast-moving objects (e.g., airplanes in flight).

### 2.16.3.1.2 Gas and particle deposition

Similar principles can be applied to both the dry deposition of gases and to the deposition of particles. A generic formulation, common in atmospheric physics, but pioneered in corrosion studies by Haynie,<sup>82,83</sup> and developed by Spence *et al.*,<sup>84</sup> is given by

$$D = CV_d \quad [42]$$

where  $V_d$  is the deposition velocity, and  $C$  is the upstream concentration of depositing species. If  $C$  is measured in  $\text{kg m}^{-3}$ ,  $D$  is measured in  $\text{kg m}^{-2} \text{s}^{-1}$ , and therefore,  $D$  is multiplied by the surface area to get the total deposition.

There are a number of approaches to defining the deposition velocity. One approach, developed for atmospheric corrosion by Spence *et al.*,<sup>84</sup> is the resistance factor approach, where the deposition velocity can be expressed as follows:

$$V_d = 1/(R_a + R_s) \quad [43]$$

where  $R_a$  characterizes the deposition across boundary layers to the surface, and  $R_s$  characterizes the reactivity of the surfaces. If  $R_s$  is low, the value of  $R_a$  determines  $V_d$ .  $V_d$  is determined from an analogy with momentum transport, which gives

$$V_d = u_*^2/U \quad [44]$$

where  $U$  is the upstream velocity, and  $u$  is the average ‘friction velocity’ in the local boundary layer.  $u_*^2$  is proportional to the local turbulent kinetic energy in the boundary layer and thus depends on the size of the obstacle. This approach recognizes the importance of air turbulence, but assumes that the turbulence is generated solely by flow over the obstacle, ignoring the effect of turbulence in the air upstream of the obstacle. Given that  $R_s$  is taken as zero, the work of Spence *et al.*,<sup>84</sup> and Haynie<sup>83</sup> leads to a dependence of deposition velocity on wind speed, where

$$V_d \propto U^n \quad [45]$$

Here the value of the exponent  $n$  varies from 0.6 to 0.7 for sheets and 0.5 for panels and wire.

A more recent approach is that of Klassen and Roberge<sup>85</sup> who considered the effect of inertial

impaction and turbulent diffusion and introduced the following equation for application to CLIMAT units and salt candles:

$$D = CU\eta \quad [46]$$

where  $\eta$  is the capture efficiency of the target. This is multiplied by the projected target area to get the total deposition. This approach implicitly includes turbulence due to the target, but also assumes that there is no upstream turbulence.

In summary, all approaches presented above assume smooth flow upstream of the objects, which effectively mean that they are treating objects isolated from the surrounding environment. In the real environment, upstream turbulence due to ground roughness will vary significantly and may have a major impact on deposition onto salt candles, plates, or buildings.

A variation to the resistance approach is that of Cole *et al.*,<sup>86</sup> in which the overall deposition velocity  $v$  can be calculated from the deposition velocities for the individual deposition mechanisms. A mechanism may act in parallel or in series and when the mechanisms occur together or in parallel (at the same distance from the surface), the deposition velocities can simply be added together:

$$v = \sum_i v_i \quad [47]$$

If the deposition mechanisms occur in different layers and the depositing aerosol must pass through all layers (act in series), deposition velocities must match between layers:

$$v_i = v_j \quad [48]$$

The main deposition mechanisms for aerosol particles are the following:

- Gravitational settling.
- Turbulent diffusion.
- Laminar diffusion (also called Brownian deposition and diffusiophoresis).
- Thermophoresis (migration from high temperatures to low).
- Electrostatic attraction.
- Momentum-dominated impact.
- Vortex shedding (transport by transient laminar flows).
- Filtering (flow past or through raised fabrics).
- Photophoresis (motion generated by an intense beam of light).

However, while all these mechanisms can be important in interior spaces, in open spaces the prime mechanisms

are gravity, momentum-dominated impact, and turbulent diffusion. **Figure 11** compares the efficiency of deposition of particles of increasing sizes onto a cylinder (typical of a salt candle, as described in ISO 9205) via momentum-dominated impact and turbulent diffusion. Efficiency is defined as the percentage of aerosol flux that would pass through the air space in the absence of an object. For very small particles, smaller than 0.1 or 0.01  $\mu\text{m}$  in diameter, electrostatic attraction and laminar diffusion play a significant role in deposition. For small particles with a diameter of  $\sim 1 \mu\text{m}$ , turbulent diffusion dominates, while for larger particles with a diameter of  $\sim 5 \mu\text{m}$  momentum-dominated impact dominates. For particles with a diameter above 20  $\mu\text{m}$  gravitational settling becomes the prime deposition mechanism. As the particle diameter increases past 2.5  $\mu\text{m}$  the deposition efficiency increases dramatically.

An approximate equation for the deposition velocity for momentum dominated impact is<sup>86</sup> as follows:

$$v_i = -x_0/\tau + \sqrt{(x_0/\tau)^2 + U_0^2} \quad [49]$$

where  $U_0$  is the approach velocity at distance  $x_0$  from the object. If  $U_0$  is the upstream velocity,  $x_0$  is of similar

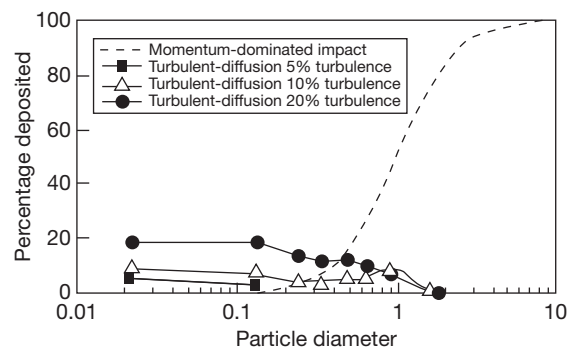


**Figure 11** Influences of momentum-dominated impact and turbulent diffusion on the deposition of aerosols onto a cylinder of arbitrary diameter at arbitrary wind speed, as a percentage of the aerosol flux that would pass through in the absence of the cylinder. The percent turbulence is the turbulence intensity (rms velocity/mean velocity) upstream. The reference diameter is the particle diameter for which 50% of particles are deposited by momentum-dominated impact. For a salt candle the reference diameter is 40 microns. Reproduced from Cole, I. S.; Paterson, D. A.; Lau, D. Holistic Modeling of Gas and Aerosol Deposition and The Degradation of Cultural Objects. In *Physical Techniques in the Study of Art, Archaeology and Cultural Heritage*, to be published by Elsevier, 2007.

size to the object diameter. The relaxation time  $\tau$  is given by

$$\tau = \frac{D_p^2 \rho_p C_c}{18\mu} \quad [50]$$

with particle diameter  $D_p$ , density  $\rho_p$ , air viscosity  $\mu$ , and Cunningham slip correction factor  $C_c$ .

In fact, Cole *et al.*<sup>87</sup> found that if the deposition modes are combined, the deposition onto common objects (plates, salt candles) in the open environment can be estimated by a formula analogous to that of Klassen and Roberge<sup>85</sup>:

$$D = CVA\eta \quad [51]$$

where

$$\eta = 100 \times I^\beta \times C_s \quad [52]$$

and  $I$  is turbulence;  $\beta$  is a constant (determined numerically to be 0.38), and  $C_s$  is the shape factor.

The shape factor, as well as the deposition efficiency, is reasonably robust, being reasonably independent of wind speed; however, it does show a dependency on particle size. In **Table 7** (from Cole *et al.*<sup>87</sup>), deposition efficiencies are given for particles in the size range 1–229  $\mu\text{m}$  for salt candles and exposure plates (at 45° to the airflow). It is apparent that deposition onto salt candles is less efficient than onto exposure plates for small and medium size particles (<21  $\mu\text{m}$  diameter). For large particles (>21  $\mu\text{m}$  diameter), the efficiency of deposition onto salt candles is marginally higher than that onto exposure plates.

In practical terms, this implies that in severe marine locations where large aerosols will make up a large fraction of the aerosol distribution, it is reasonable to assume that the deposition onto an exposure plate will be approximately the same as that onto a salt candle. However, in milder locations the aerosol distribution will be dominated by aerosols of less than 15  $\mu\text{m}$  and so the salt candle measurements of deposition will be ~71% of that on exposure plates.

The average shape factors for particles (assuming the particle distribution given by Fitzgerald<sup>35</sup> of <20  $\mu\text{m}$  for plates and salt candles are given in **Table 8** (from Cole *et al.*<sup>87</sup>). These factors can be used in conjunction with eqn [48] to calculate deposition efficiencies and thus deposition rates. Deposition also depends on turbulence, which in turn depends on the upstream roughness of the terrain. However, the latter dependence is relatively weak

**Table 7** Comparison of salt deposition efficiency on plate and salt candle

Particle diameter ( $\mu\text{m}$ )	Percentage deposition (%)		
	Salt candle	Plate	Ratio
1	9.2	12.2	1.33
6	7.6	12.2	1.61
11	7.2	12.7	1.76
15	9.8	14.4	1.47
21	18.6	16.7	0.90
29	31.0	19.0	0.61
39	50.4	33.2	0.66
72	77.0	66.8	0.87
134	91.8	88.8	0.97
249	96.4	94.4	0.98

Source: Reproduced from Cole, I. S.; Lau, D.; Chan, F.; Paterson, D. A. *Corros. Eng. Sci. Technol.* **2004**, 39(4), 333–338.

**Table 8** Summary of shape coefficients

Object	$C_s$
Salt candle	0.85
Exposure plate at 45° to airflow	1.2
Plate perpendicular to airflow	0.5
Plate parallel to flow	1.67

Source: Reproduced from Cole, I. S.; Lau, D.; Chan, F.; Paterson, D. A. *Corros. Eng. Sci. Technol.* **2004**, 39(4), 333–338.

and can be approximated by

$$I = 0.069 + 0.5R_t \quad [53]$$

where  $R_t$  is terrain roughness.

Thus, as roughness increases from 0.06 to 0.4 m, the deposition efficiency onto a salt candle of aerosols of 20  $\mu\text{m}$  diameter increases from 20% to 30%. Typical values of terrain roughness are 0.06 m for isolated trees and long grass, and 0.4 m for the center of small towns.

This model of deposition onto simple objects can be extended to more complex objects such as buildings or rows of buildings. The deposition onto an isolated building (10 m high and 20 × 20 m in plan) was computed using CFD and the result is given in **Figure 12** (from Cole *et al.*<sup>87</sup>). The randomness in **Figure 12** is caused by the stochastic nature of the simulation. The aerosol deposition rate is lowest near the ground, high near the upper edge of the front face and on the sides, and is highest on the upper corners and upper sides. The deposition rate is highly influenced by local wind turbulence, which is highest on corners and sides. **Table 9** (from Cole *et al.*<sup>87</sup>) gives the average deposition rates for particles of varying diameter onto a building compared to deposition of



the same sized particles onto a salt candle. It is apparent that the average deposition rate onto a building face is less than half that on a salt candle, although deposition onto the edges of a building could be up to twice that on a salt candle.

In **Figure 13** (from Cole *et al.*<sup>87</sup>), the calculated deposition onto a row of 2D buildings is shown (the buildings were 3.32 m high, 12.5 m wide and were spaced 30 m apart). The plot demonstrates the rapid fall-off in deposition with increasing number of houses. Such a fall-off was observed experimentally and is reported in Cole *et al.*<sup>39</sup> The data presented in **Figure 13** has been transformed to derive a theoretical urban facade factor, so that the deposition onto the facade of a dwelling close to the coast in an urban (low-rise) setting would be only 23% of the deposition onto an equivalent facade of a dwelling where there were no dwellings between this dwelling and the coast.

The above examples have been calculated for marine aerosols; however, similar effects would also occur for industrial aerosols, although the exact magnitude of the effects would be dependent on particle size.

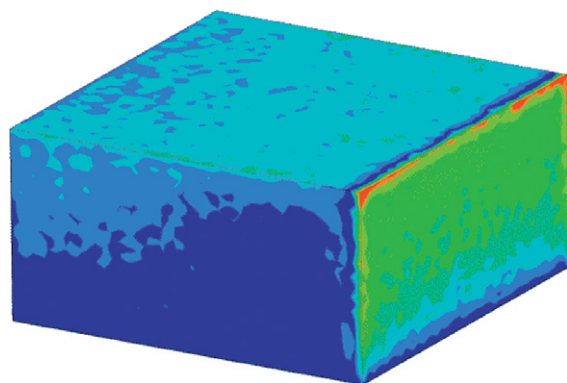


**Figure 12** Aerosol deposition on a building 10 m high and 20 × 20 m in plan. The flow is from right to left. Blue is low concentration and red is high concentration. Reproduced from Cole, I. S.; Lau, D.; Chan, F.; Paterson, D. A. *Corros. Eng. Sci. Technol.* **2004**, 39(4), 333–338.

**Table 9** Deposition ratio on a building relative to an isolated salt candle

Face	Deposition ratio ( $\text{mg m}^{-2}$ )
Front	0.42
Side	0.35
Top	0.49
Back	0.08

Source: Reproduced from Cole, I. S.; Lau, D.; Chan, F.; Paterson, D. A. *Corros. Eng. Sci. Technol.* **2004**, 39(4), 333–338.

### 2.16.3.1.3 Deposition of gases onto wet and dry surfaces

In estimating both the wet and dry deposition of gases onto surfaces, it can be assumed that the gas concentration near the surface approximates the local composition and that any absorbed gas is readily replaced. The absorption of gases into moisture layers on metal surfaces is governed by the same factors that control absorption of gases into aerosols (outlined in **Section 2.16.1.3**) and will in part be controlled by the Henry's law coefficient. In contrast, the surface absorption of gaseous species onto dry surfaces is controlled by normalized reactivity. **Table 10** (from Seinfeld and Pandis<sup>1</sup>) presents the effective  $H_a$  and the normalized reactivity values for various gas species.

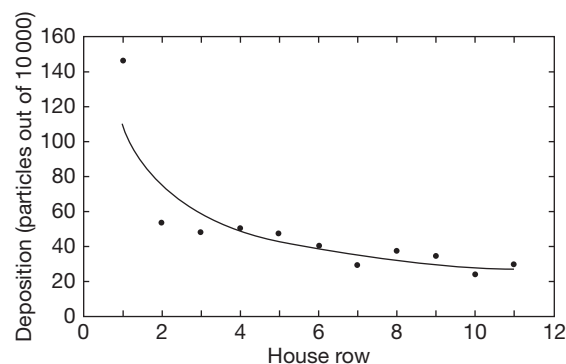


**Figure 13** Results from CFD modeling of deposition onto a row of houses. Reproduced from Cole, I. S.; Lau, D.; Chan, F.; Paterson, D. A. *Corros. Eng. Sci. Technol.* **2004**, 39d(4), 333–338.

**Table 10** Relevant properties of gases for dry deposition calculations

Species	$H_a^a$ ( $\text{Matm}^{-1}$ ) at 298 K	Normalized reactivity
Nitric oxide	$2 \times 10^{-3}$	0
Ozone	$1 \times 10^{-2}$	1
Nitrogen dioxide	$1 \times 10^{-2}$	0.1
Hydrogen sulfide	0.12	–
Ammonia	$2 \times 10^4$	0
Nitrous acid	$1 \times 10^5$	0.1
Sulfur dioxide	$1 \times 10^5$	0
Hydrogen peroxide	$1 \times 10^5$	1
Formic acid	$4 \times 10^6$	0
Acetic Acid	$4 \times 10^6$	0
Hydrochloric acid	$2.05 \times 10^6$	0
Nitric acid	$1 \times 10^{14}$	0

<sup>a</sup>Effective  $H_a$  assuming a pH of 6.5.

Source: Reproduced from Seinfeld, J.; Pandis, S. *Atmospheric Chemistry and Physics: From Air Pollution to Climate Change*; Wiley Interscience: New York, 1997.

The effective  $H_a$  in Table 10 takes into account reactions of the aqueous species. When  $H_a$  is high and the normalized reactivity is low (e.g., sulfur dioxide), deposition will be primarily through absorption into a moisture droplet (be it a wet aerosol or a surface moisture film). When  $H_a$  is low and the normalized reactivity is high (ozone), direct gaseous absorption onto dry surfaces will dominate. Table 10 indicates that those species of prime importance to atmospheric corrosion (ammonia, sulfur dioxide, formic acid, and acetic acid) will all primarily be absorbed through the moisture layer. Of the nitrogen species, nitric acid will be readily absorbed into the moisture layer, while nitrogen dioxide will undergo limited interactions with both a dry and a wet surface. While the oxidizing catalyst  $O_3$  and hydrogen peroxide will be readily absorbed on a dry surface their residence times in the atmosphere are extremely short and, therefore, the source would have to be very close to the metal surface for the concentrations of these gases to be significant. Thus for practical purposes, gaseous deposition onto a dry surface is of marginal importance to atmospheric corrosion.

### 2.16.3.2 Comparison of Deposition Modes

The relative significance of particulate deposition and gaseous deposition in an industrial environment clearly depends on the particulate and gas concentrations (aerosol deposition will dominate in marine environments). However, a comparison of deposition modes in given typical compositions is useful. Consider the deposition onto a plate exposed at an angle of  $45^\circ$  in an exterior environment where the total concentration of particulates is  $20 \mu\text{g m}^{-3}$  (dry weight), which may be ammonium sulfate, ammonium bisulfate, or hydrogen sulfate, while the wind speed is  $3 \text{ m s}^{-1}$  and gaseous concentrations are  $\text{CO}_2$  at 400 ppm,  $\text{SO}_2$  at 75 ppb,  $\text{NH}_3$  at 20 ppb,  $\text{O}_3$  at 200 ppb, and  $\text{H}_2\text{O}_2$  at 10 ppb.

Work by Sehmel<sup>88</sup> indicates that ammonium sulfate particles typically have a bimodal size distribution with peaks at  $\sim 0.7$  and  $3 \mu\text{m}$ , with the smaller particles having three times the concentration (by volume) of the coarse particles. For this exercise, let us simplify the distribution and assume that the mass of fine particles ( $0.7 \mu\text{m}$  diameter) is  $15 \mu\text{g m}^{-3}$  and the mass of coarse particles ( $3 \mu\text{m}$  diameter) is  $5 \mu\text{g m}^{-3}$ .

Deposition of particles traveling horizontally will be dominant and will be defined by eqn [46]. Sehmel<sup>88</sup> indicates that typical efficiencies for 0.7 and  $3 \mu\text{m}$  particles would be  $\sim 0.26\%$  and  $18\%$ , and thus the flux at a typical wind speed of  $3 \text{ m s}^{-1}$  will be  $0.12$  and  $2.7 \mu\text{g m}^{-2} \text{ s}^{-1}$  for the fine and coarse particles, respectively. This then gives a deposition rate per hour of  $10$  to  $150 \mu\text{g m}^{-2}$  or  $108 \mu\text{g/dry weight per hour}$  onto a plate of size  $100 \times 150 \text{ mm}$  at an angle of  $45^\circ$  to the vertical.

If this amount of particulate were to deposit into a moisture film, it would then change the composition of that film to an extent that depends on the particulate composition and thickness of the moisture film. The change in  $[\text{H}^+]$  and  $[\text{SO}_4^{2-}]$  in  $\text{M l}^{-1}$  per hour is given in Table 11.

Modeling by Cole *et al.*<sup>89</sup> estimated that for the gaseous compositions given above, the aqueous phase concentrations will be  $1.7 \times 10^{-6} \text{ M}$  of  $[\text{H}^+]$  and  $1.2 \times 10^{-4} \text{ M}$  of  $[\text{SO}_4^{2-}]$ , or  $0.63 \times 10^{-4} \text{ M}$  of  $[\text{H}^+]$  and  $0.34 \times 10^{-4} \text{ M}$  of  $[\text{SO}_4^{2-}]$  in the absence of  $\text{NH}_3$ . Thus, the deposition of particulate onto a moisture film will substantially increase the ionic content and acidity of the film. If the moisture film persists for a number of hours, particulate deposition is likely to dominate over gaseous absorption.

A second comparison can be made between the hydrogen ion flux to the surface of a similar metal sample from acidified rain and from particulates. In Figure 14, the 'free' hydrogen ion flux per day onto a metal surface is estimated from  $(\text{NH}_4)_3\text{H}$

**Table 11** Effect of particulates on moisture film composition

Particulate concentration ( $\mu\text{g m}^{-3}$ dry weight)	Particulate type	Moisture film thickness ( $\mu\text{m}$ )	$[\text{H}^+]$ (M)	$[\text{SO}_4^{2-}]$ (M)
20	$(\text{NH}_4)_2\text{SO}_4$	100	—	$7.5 \times 10^{-4}$
20	$(\text{NH}_4)_3\text{H}(\text{SO}_4)_2$	100	$4 \times 10^{-4}$	$8 \times 10^{-4}$
20	$\text{NH}_4\text{HSO}_4$	100	$8.5 \times 10^{-4}$	$8.5 \times 10^{-4}$
20	$\text{H}_2\text{SO}_4$	100	$20 \times 10^{-4}$	$10 \times 10^{-4}$
20	$(\text{NH}_4)_2\text{SO}_4$	500	—	$1.5 \times 10^{-4}$
20	$(\text{NH}_4)_3\text{H}(\text{SO}_4)_2$	500	$0.8 \times 10^{-4}$	$1.6 \times 10^{-4}$
20	$\text{NH}_4\text{HSO}_4$	500	$1.7 \times 10^{-4}$	$1.7 \times 10^{-4}$
20	$\text{H}_2\text{SO}_4$	500	$4.0 \times 10^{-4}$	$2.0 \times 10^{-4}$
5	$\text{H}_2\text{SO}_4$	500	$1 \times 10^{-4}$	$0.4 \times 10^{-4}$

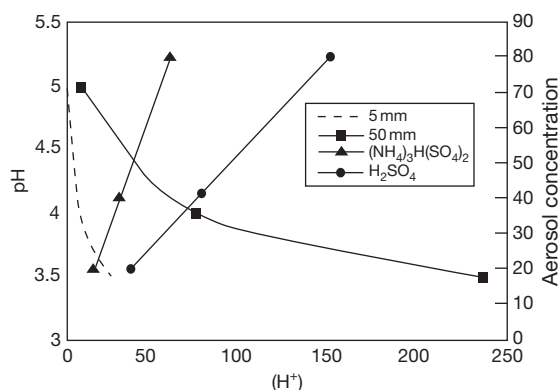


**Figure 14** Hydrogen flux onto a metal surface by particle deposition and rain deposition.

( $\text{SO}_4$ )<sub>2</sub> and  $\text{H}_2\text{SO}_4$ , assuming that the particulate dissociates on the surface in accordance with standard equilibrium constants. This is compared to the free hydrogen ion flux from rain water, assuming an unbuffered solution for a daily rainfall of 5 and 50 mm. It is apparent that fluxes are of similar orders of magnitude, but acidified rain is the major source of  $\text{H}^+$  if the rain water pH is low and rainfall high, while particulate deposition is of prime importance if the rainfall is low and the concentration of acidified particulates is high.

The analysis indicates that while dry deposition of gases onto metal surfaces is likely to be of marginal importance, rain deposition, particulate deposition, and gaseous absorption into moisture films are all likely to be significant sources of both acidity and ion concentration in moisture on metal surfaces in industrial environments. The evaporation of moisture layers formed and enriched by the processes above will lead to the precipitation of a range of ionic compounds (many of which are listed in Table 4). Being hygroscopic, these compounds will promote further wetting if they remain on the surface. The next two sections discuss the cleaning, retention, and wetting of these salts on metal surfaces.

## 2.16.4 Role of Rain and Wind in Surface Cleaning

The products that accumulate on a surface control future hygroscopic wetting and the nature of the moisture films that develop. Surfaces may be cleaned by either rain or wind; however, the effectiveness of these processes is highly dependent on both the characteristics of the wind and rain, and the state of the surface, as discussed below.

### 2.16.4.1 Role of Rain in Surface Cleaning

In this section, a simple model for the movement of raindrops, and thus their ability to clean a 'fresh' surface, is developed. In this context, a fresh surface refers to a surface that remains relatively impervious to moisture (i.e., not a porous surface that absorbs moisture). According to Cole *et al.*,<sup>81</sup> during rain, drops will grow on the surface as they coalesce and absorb impacting droplets until they reach a critical size, above which they begin to move. At the critical size, the gravitational force directed along the plate ( $gM \sin \theta$ ) is balanced by the shear force at the base of the drop ( $\tau A$ ) and a force due to surface tension. The shear force tends to zero when the drop is not moving. For the force due to surface tension, let  $2\phi$  be the difference in interfacial contact angle between the front and the back of the drop. Then, for a drop of radius  $r$ , the radii of curvature near the front and back of the drop ( $r_1$  and  $r_2$  respectively) are roughly given by  $r_1/r = r/r_2 = 1 - \tan \phi$ . The difference in pressure within the drop between the front and back extremities of a drop is then

$$p_1 - p_2 = \sigma/r_1 - \sigma/r_2 \quad [54]$$

If the drop is not moving and the gravitational force is balanced by the surface tension, this pressure difference is hydrostatic and is given as follows:

$$p_1 - p_2 = 2\rho g r \sin \theta \quad [55]$$

By combining eqn [54] and [55], a relationship can be derived for the maximum radius of a stationary drop in terms of the plate angle and the difference in interfacial angle:

$$r^2 = \frac{\sigma}{2\rho g \sin \theta} \left[ \frac{1}{1 - \tan \phi} - (1 - \tan \phi) \right] \quad [56]$$

For air and water  $g = 9.81 \text{ m s}^{-2}$ ,  $\rho = 1000 \text{ kg m}^{-3}$ , and  $\sigma = 0.07275 \text{ Pa m}$ .

A diagram of the maximum drop radius as a function of plate angle and difference in interfacial contact angle is given in Figure 15 (from Cole *et al.*<sup>81</sup>). It is apparent that both the plate angle and the difference in interfacial angle are of prime importance in determining the critical size. In particular, it is notable that the stable drop size increases dramatically as  $\phi$  approaches  $45^\circ$ .

The concept of single-drop movement has been embedded in a more complex model of drop movement, created using a fluid dynamics passage in which 71 million droplets were deposited as simulated rain

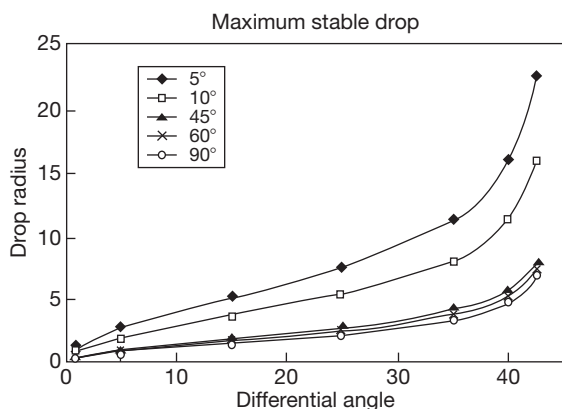


**Figure 15** Variation of maximum stable drop size with  $\phi$ , where  $2\phi$  is the difference in interfacial contact angle between the front and the back of the drop; at five plate orientations ( $\theta = 5^\circ$  to  $90^\circ$ ). Reproduced from Cole, I. S.; Paterson, D. A. *Corros. Eng.. Sci. Technol.* **2007**, 42(2), 91–104.

onto a  $2 \times 2$  m surface and their subsequent movement down the surface was studied.<sup>44</sup>

During the studies,<sup>81</sup> drops on the surface grew by absorbing raindrops impacting on them and by merging with other drops. When drops rolled off the surface, the water they left behind was more than made up for by the collection of smaller drops on the way down. As each drop grew, it rolled faster and so it is reasonable to assume that once a drop reaches a critical size it will remove itself from a surface. Overall, it was observed that over time, the amount of water on the surface built up to a peak and then tended to release at once, giving periods of almost no runoff followed by periods of strong runoff. This is shown in the stepped shape of the pollution level curve in **Figure 16** (from Cole *et al.*<sup>81</sup>). In the experiments,<sup>81</sup> 0.0157 mm of water was deposited per timestep and therefore, the duration of a timestep depended on the simulated rain intensity. Loss of water through evaporation and substrate porosity was not included. The pollutant was assumed to have the solubility of sea salt.

The significance of **Figure 16** can be illustrated with regard to ‘average’ rainstorms in the Australian cities of Adelaide and Darwin, which are chosen as they span the rain intensity variation across mainland Australia, having 4.6 and 28.8 mm h<sup>-1</sup> respectively as average rainfall intensities for a one-hour rain shower with a one-month recurrence interval. Therefore, the average shower timesteps in Adelaide and Darwin would be 13 and 2 s respectively. As shown in **Figure 16**, there is a factor of 10 decrease in soluble pollutant levels on the surface between timesteps 80 and 120. By timestep

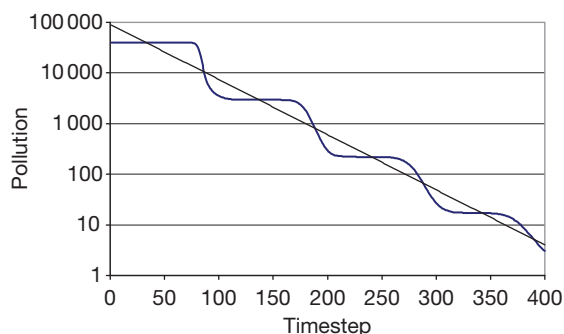


**Figure 16** Pollution levels on the rain-washed part of the surface, together with a fitted exponential decay rate based on simulations of 71 million droplets depositing on a  $2 \times 2$  m surface. Each timestep represents the deposition of 0.0157 mm of water. Reproduced from Cole, I. S.; Paterson, D. A. *Corros. Eng.. Sci. Technol.* **2007**, 42(2), 91–104.

200 (representing 43 min in Adelaide and 6.7 min in Darwin), the amount of pollution left was <1% of the initial value.<sup>81</sup> This only applies to soluble pollutants.

To the first order, the effect of rain on cleaning a fresh plate can be approximated by<sup>81</sup>

$$S_f = S_i \times e^{-\alpha R} \text{ if } R_i - R_c > 0 \quad [57]$$

or

$$S_f = S_i \text{ if } R_i - R_c < 0 \quad [58]$$

where  $S_f$  and  $S_i$  are the final and initial ‘soluble’ pollutant load, respectively,  $R_i$  is the amount of rain (in mm) in a particular rain shower or event, and  $R_c$  is the critical amount of rain required to guarantee runoff and thus cleaning. The value of  $R_c$  depends on drop size, surface parameters (e.g., surface energy), and plate slope, and can be estimated from an analysis such as that presented in **Figure 16**; for conditions relevant to the data set defined above, it can be approximated by  $r/2$  (where  $r$  is the maximum radius of a stationary drop). Experimental studies<sup>87</sup> have verified this formulation and value of  $R_c$ .

#### 2.16.4.2 Removal of Salts by Wind

While in theory the removal of salts by wind could be significant, in practice it is only significant in climates where rain is very limited or when the wind carries abrasive material. In wind tunnel tests, Muster and Cole<sup>90</sup> found that significant amounts of salt were removed only when wind speeds were  $\geq 9$  m s<sup>-1</sup> and RH was  $\leq 40\%$ . These wind speeds represent <10% of the year in Australian cities. Work by Cole *et al.*<sup>87</sup> is in agreement with these results in the case where salts

were dry when deposited, but demonstrated that if salts were wet when deposited, wind speeds of up to  $14 \text{ m s}^{-1}$  did not remove such salt particles. In the case where salt is deposited as a wet aerosol onto reactive surfaces (steel, zinc, aluminum–zinc), the aerosol reacts with the surface as it evaporates and forms a reaction product that binds the crystallized salt to the surface.

#### 2.16.4.3 Transfer of Pollutants in Raindrops to a Surface

This section is concerned with defining the conditions where raindrops will evaporate on a metal surface, leaving precipitated pollutants. In tests where stainless steel, galvanized steel, and zinc plates were exposed to marine environments for periods of 2–24 h, Cole *et al.*<sup>91</sup> observed fine-scale crystals with compositions indicative of marine origin and with geometries consistent with deposition in raindrops. If raindrops are to evaporate, they must not be removed either by the motion of other drops (total rainfall must be less than  $R_c$  defined previously) or by their own motion. If the drop radius is less than that given by eqn [56], stationary drops will not begin to move; however, raindrops will maintain some of their preimpact velocity after contacting the metal surface. For such moving drops, the critical factor is whether they will evaporate before they roll off the metal surface. Work by Cole *et al.*<sup>87</sup> indicates that this is a function of the hydrophilic or hydrophobic nature of the surface and of course the distance they have to travel to roll off the plate. For strongly hydrophilic and strongly hydrophobic surfaces, the difference in interfacial angle ( $2\phi$ ) is small and so drops will tend to roll off in both cases. The presence of corrosion products on a surface can increase  $\phi$ . For example, all but the finest drops ( $<10 \mu\text{l}$ ) will run off an exposure plate (typical dimensions  $150 \times 150 \text{ mm}$  at an angle of  $45^\circ$ ), while quite large drops (up to  $36 \mu\text{l}$ ) may evaporate on an exposed roof (dimensions  $3 \times 3 \text{ m}$ ,  $30^\circ$  angle) on a summer day. This again indicates the difference between exposure plates and actual structures. The residue of raindrops observed by Cole *et al.*<sup>91</sup> might be associated with light rain and fine raindrops.

These studies, on the effectiveness of rain in cleaning surfaces and the nature of rain that can evaporate on a surface, highlight the fact that rain-drop size and rainfall intensity are critical factors in determining the impact of rain on pollutant levels on metal surfaces. In general, locations closer to the

equator will have more intense rain with larger raindrops, which will be more effective in cleaning surfaces, while locations at high or low latitudes will have less intense rain with smaller raindrops, which will be less effective in cleaning surfaces and may in fact evaporate on metal surfaces, thereby increasing the pollutant concentration on such surfaces.

### 2.16.5 Forms of Moisture on Surfaces

This section will discuss how moisture may form as a result of the atmospheric conditions previously discussed. Moisture may form on a surface because of the local RH, via the deposition of rain, fog, and wet aerosols, or because of wetting of hygroscopic salts on the surface.

#### 2.16.5.1 Effect of RH on Clean Surfaces

A surface exposed to ‘humid’ air will adsorb moisture and build up monolayers on the surface. Immediately upon exposure, OH layers will develop on the surface.<sup>14</sup> With further exposure, additional water layers are adsorbed, with the number of layers being dependent on the hydrophobic or hydrophilic nature of the surface, the density of defects on the surface, and the RH of the air. Estimates of the number of monolayers vary from 1 to 2 layers at 40% RH, 2–5 at 60% RH, to 6–10 at 100% RH.<sup>92</sup> It is generally accepted that below 60% RH the monolayers are too thin to sustain the electrochemical corrosion process.

#### 2.16.5.2 Effect of Aerosols/Raindrops

Aerosols show a significant variation in size range depending on the RH of the air and the history of the aerosol. Wet aerosols of marine origin<sup>91</sup> will have a size range of  $5\text{--}120 \mu\text{m}$  and after impact on the surface they will reform into roughly spherical-cap shaped droplets (with the contact angle defined by the surface energy). In general, aerosol droplets falling onto a surface will only cover a fraction of the surface and will, therefore, remain isolated with significant areas of ‘dry’ metal separating the droplets. In contrast, when rain impacts a surface, a high fraction of the surface will become covered by drops, which will undergo coalescence until they reach the critical size for drop movement, or they may be scavenged by a moving drop.



### 2.16.5.3 Rewetting of Surfaces and Condensation

On a clean surface, condensation will occur when the air close to the surface is at 100% RH. The temperature of the surface may vary from that of the ambient air and, therefore, the RH close to the surface may be different from that of the ambient air.

The evaporation of aerosols or rain on surfaces may leave crystallized salts, many of which may be hygroscopic. These salts will wet when the surface RH is greater than the DRH of the contaminant salts. The DRH of a number of common pollutants is given in [Table 4](#). A study by Cole *et al.*<sup>93</sup> compared the nature of surface contaminants with the wetting behavior of wetness sensors attached to metal plates and found that there was a high correlation between the DRH of the salts present and the wetting point of the sensor. Further, the nature of the salts present (and hence the wetting point of the sensor) was highly dependent on location, with severe marine sites contaminated with  $\text{MgCl}_2$  and  $\text{NaCl}$ , marine sites contaminated with  $\text{NaCl}$ , severe industrial sites contaminated with  $(\text{NH}_4)\text{HSO}_4$ , and moderate industrial sites with a marine influence contaminated with  $(\text{NH}_4)_3\text{H}(\text{SO}_4)_2$ ,  $(\text{NH}_4)_2\text{SO}_4$ ,  $\text{NaHSO}_4$ , and  $\text{NH}_4\text{NO}_3$ .

The wetting of such crystalline salts will occur when

$$\text{RH}_s > \text{DRH of any contaminating salt} \quad [59]$$

where  $\text{RH}_s$  is the RH at the metal surface.

An alternative but equivalent expression can be expressed in terms of time of condensation (TCD), tendency to condensation (TCON), and vapor pressure, so that TCD is defined as

$$\text{TCD} = \text{time when TCON} > 0 \quad [60]$$

TCON is simply the difference between the vapor concentration of the air ( $V_a$ ) and the saturation vapor concentration at the metal surface ( $V_s$ ) required for condensation (vapor pressure is in Pascals):

$$\text{TCON} = V_a - V_s \quad [61]$$

and

$$V_s = (\text{RH}_c/100)$$

$$\exp(22.565 - 2377.1 T_s^{-1} - 33623 T_s^{-1.5}) \quad [62]$$

where  $T_s$  is the surface temperature (K) and  $\text{RH}_c$  accounts for the hygroscopicity of contaminating salts, which can be approximated by the DRH of any contaminating salt:

$$V_a = V_{as} \times \text{RH}/100 \quad [63]$$

where  $V_{as}$  is the saturation vapor pressure of the adjacent air, which is given by the following equation:

$$V_{as} = \exp(22.565 - 2377.1 T_a^{-1} - 33623 T_a^{-1.5}) \quad [64]$$

where  $T_a$  is the air temperature.

### 2.16.5.4 Evaporation

Evaporation of moisture from a surface covered with hygroscopic salts can be understood using either the surface RH concept or partial vapor pressure concept. Thus, wetted salts will begin to dry when the surface RH is less than the DRH of the contaminating salt or when the TCON is negative. However, to determine either of these parameters it is necessary to know the temperature of the metal surface.

#### 2.16.5.4.1 Surface temperature of plates

Metal surfaces exposed to the environment will undergo a diurnal cycle, heating up during the day (due to solar heating) and cooling down at night (because of the emission of radiation to the night sky), with both processes modulated by convective interaction with air. The extent of both heating and cooling will depend on a range of environmental factors, including cloud cover, wind speed, and the state of the surface.<sup>94,95</sup>

Condensation and evaporation will tend to reduce this diurnal cycle – condensation will release latent heat restricting further undercooling, while evaporation of moisture films after sunrise will cool surfaces, reducing solar heating. As a result, it may take significant time for metal surfaces to dry after sunrise. Predicted undercooling of a zinc plate openly exposed to the night sky is presented in [Figure 17](#) as a function of temperature. It is apparent that undercooling does not exceed 2.5 °C (still air, clear sky, 50% RH). The RH affects the extent of condensation and the latent heat released during condensation, so that on a clear night with 75% RH, a plate would undercool less than on a clear night with 50% RH. A breeze of 1 m s<sup>-1</sup> significantly reduces undercooling, as does cloud cover.

The rate at which zinc plates heat up after sunrise is presented (for dry plates) in [Figure 18](#) as a function of incident solar radiation which in turn is a function of the time of day. Thermal equilibrium is assumed. [Figure 18](#) can be matched with the solar radiation level for a given location. For example, measured data for Melbourne (latitude 38° S), Australia, indicates that on a clear day close to the September solar equinox (spring), the solar radiation

levels will be 171, 376, and  $696 \text{ W m}^{-2}$  at 1, 2, and 4 h respectively after sunrise, while on a cloudy day they will be 28, 68, and  $222 \text{ W m}^{-2}$  at 1, 2, and 4 h respectively after sunrise. From Figure 18, it is clear that, as a function of solar radiation, the increase in temperature on a cloudy and sunny day is the same. Of course, much less radiation reaches the surfaces on a cloudy day, so the temperature rise on a plate is much lower. Wind dramatically decreases the temperature rise because of forced thermal convection, with a wind speed of  $5 \text{ m s}^{-1}$  more than halving the rise. Figure 19 (from Cole *et al.*<sup>96</sup>) compares the temperature rise of a dry plate with that of a wet plate. The cooling effect of evaporation dramatically

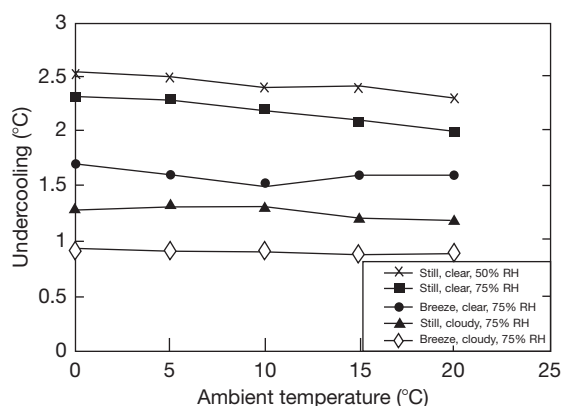


**Figure 17** Predicted undercooling of a metal plate at different RHs. The breeze is  $1 \text{ m s}^{-1}$ . Reproduced from Cole, I. S.; Paterson, D. A. *Corros. Eng. Sci. Technol.* **2006**, 41(1), 67–76.

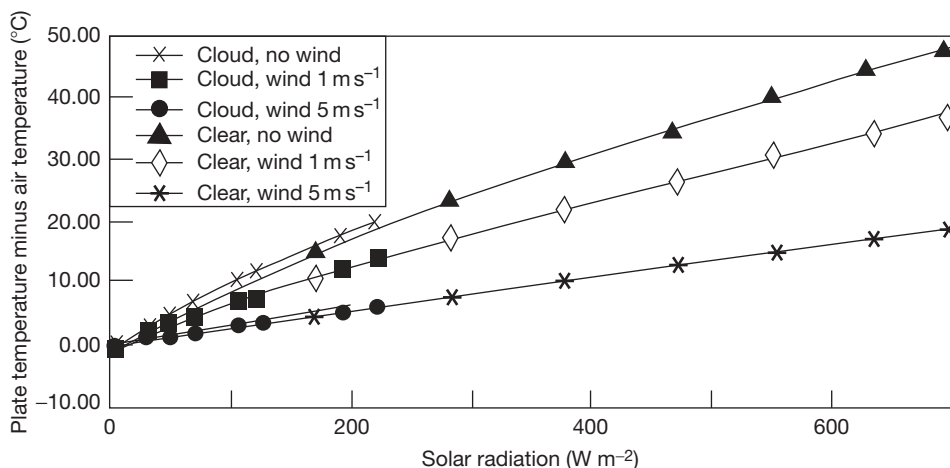


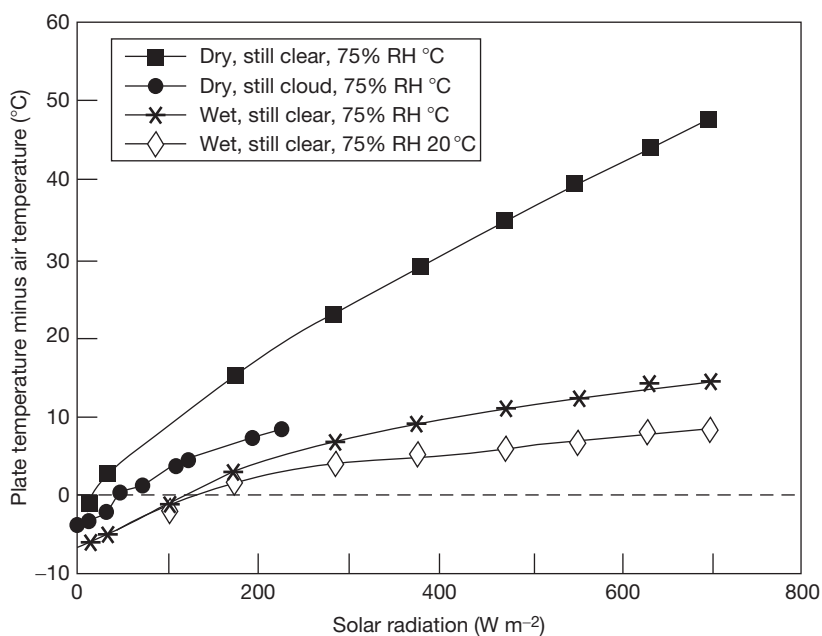
**Figure 18** Predicted heating rate as a function of solar radiation for dry plates. Thermal equilibrium is assumed and the solar radiation is a function of time of day. Reproduced from Cole, I. S.; Paterson, D. A. *Corros. Eng. Sci. Technol.* **2006**, 41(1), 67–76.

reduces surface heating. This reduction is closely tied to the ambient conditions (temperature and RH) that control evaporation.

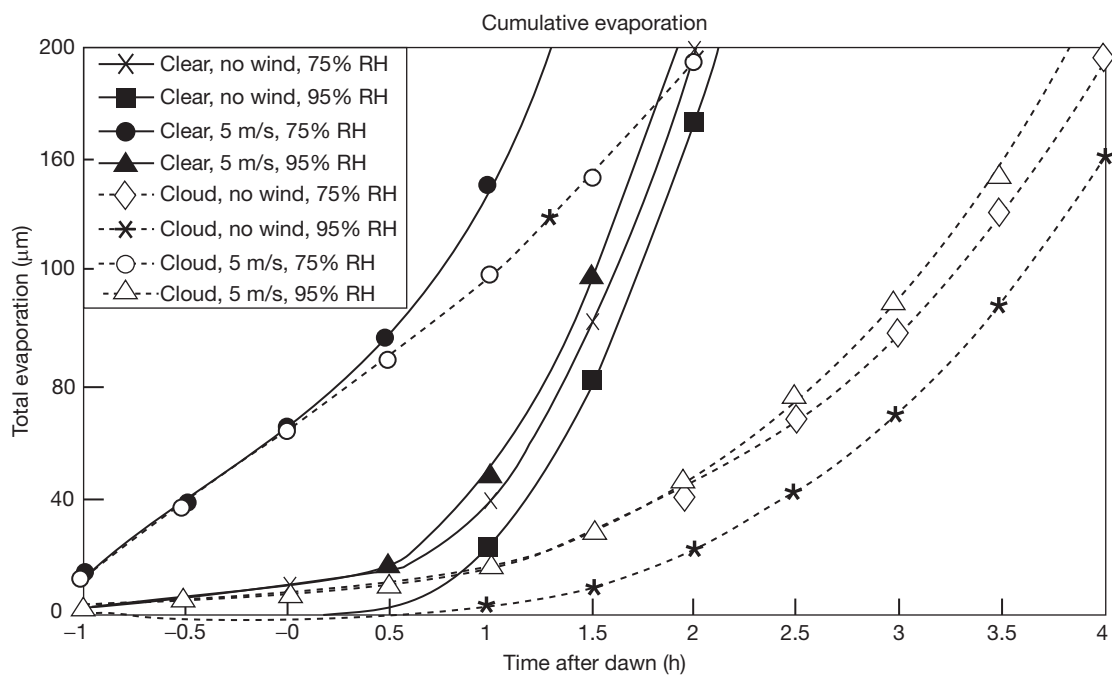
#### 2.16.5.4.2 Evaporation rate

Figure 20 (from Cole *et al.*<sup>96</sup>) shows the evaporation rates on a metal surface (assuming a continuous film) for a variety of environmental conditions as a function of time after sunrise. The rate of evaporation is clearly influenced by surface temperature, as discussed above. With clear skies, a modest wind ( $5 \text{ m s}^{-1}$ ) and not excessive humidity (75%), a moisture film of  $200 \mu\text{m}$  will have evaporated an hour after sunrise. Evaporation actually starts before sunrise as the minimum temperatures (under these conditions) generally occur an hour before sunrise. In contrast, on a cloudy, still day of high humidity (95%), the same moisture film will still not have fully evaporated 4 h after sunrise.

A more precise understanding of the relevance of these effects to corrosion can be obtained if we calculate the time for evaporation of common aerosols. Using the data of Fitzgerald,<sup>35</sup> it can be estimated that a wetted aerosol on the metal surface will have a size range of  $2\text{--}120 \mu\text{m}$  with a median of  $12 \mu\text{m}$  and that a nonequilibrium aerosol (with a solids concentration equal to that of seawater) will have a size range of  $5\text{--}230 \mu\text{m}$  with a median of  $23 \mu\text{m}$ . The time for aerosols with median and extreme dimensions to evaporate is given in Table 12 (from Cole *et al.*<sup>96</sup>). It is apparent that, at least for some aerosols,



**Figure 19** Comparison of temperature rise on a dry plate with that of a wet plate. Reproduced from Cole, I. S.; Paterson, D. A. *Corros. Eng. Sci. Technol.* **2006**, 41(1), 67–76.



**Figure 20** Evaporation rates on a metal surface assuming a continuous film of water. The assumed solar radiation 4 h after dawn is  $696 \text{ W m}^{-2}$  on a clear day and  $222 \text{ W m}^{-2}$  on a cloudy day. Reproduced from Cole, I. S.; Paterson, D. A. *Corros. Eng. Sci. Technol.* **2006**, 41(1), 67–76.

**Table 12** Time to dry (hours) for aerosols of given surface radii

Conditions	Surface radius ( $\mu\text{m}$ )			
	12	23	120	230
Cloud, no wind, 75% RH	Just after dawn	1	3	4
Clear, no wind, 75% RH	Just after dawn	0.6	1.5	2
Cloud, $5\text{ m s}^{-1}$ , 95% RH	Just after dawn	1.1	2.8	3.7
Cloud, $5\text{ m s}^{-1}$ , 75% RH	Prior to dawn	Prior to dawn	0.6	1.7

Source: Reproduced from Cole, I. S.; Paterson, D. A. *Corros. Eng. Sci. Technol.* 2006, 41(1), 67–76.

evaporation will take several hours. Many workers suggest that a peak in corrosion rate occurs during the evaporation phase, as salt concentrates and oxygen diffusion paths shorten.

Cole *et al.*<sup>65</sup> have documented experimentally the duration of periods of wetness that occur on wetness sensors attached to zinc plates that are openly exposed to the atmosphere in a range of locations around Australia.<sup>97</sup> They found that periods of wetness could be divided in three modes which they labeled Mode A, Mode B and Mode C. Mode A are short daytime wetness events with an average duration of  $\sim 2\text{ h}$  (they result from either hygroscopic wetting of deposited salts or rainfall but are of short duration as daytime evaporation is rapid). Mode B are nighttime wetness events that occur when condensation occurs in the evening and evaporation the next morning. The duration of the wetness period varies depending on the severity of the location (and thus the nature of deposited salts) from an average of 10 h in benign (inland) sites to 20 h in severe marine locations. Mode C is wetness periods that last more than 1 day; they are generally associated with the deposition of salts with low DRH (e.g.,  $\text{MgCl}$ ) so that surface RH may not dry out the wetted salts on some days. Again, the duration depends on the severity of the site raging from an average of 72–120 h in marine and severe marine sites.

#### 2.16.5.4.3 Evaporation and condensation on a porous surface

The above analysis refers to clean surfaces; however, on a corroded surface the situation may be more complex. First, many oxides are themselves hygroscopic, and second many oxides are porous and, therefore, when aerosols or raindrops are deposited onto such porous oxides, some of the solution will be absorbed into the pores and will subsequently evaporate, leaving contaminants within the pore structure. In these circumstances, capillary forces may alter the conditions for evaporation and condensation in the

**Table 13** Effect of pore size on tendency to condensate formation

Pore size ( $\text{\AA}$ )	RH for condensation (%)	%TCD (100)	%TCD (75)
Flat surface	100	4.6	43.5
360	98	7.5	45.3
94	90	19.8	52.1

% TCD (100) is the % time the tendency to condensation (TCO) is positive when the surface wetting occurs at 100% RH while % TCD (75) is the % time the TCO is positive when the surface wetting occurs at 75% RH.

pores, making it possible for condensation to occur in an atmosphere of less than 100% RH. These effects are best explored using the differential vapor pressure approach, where the relative lowering of the saturated vapor pressure in pores is given by Thomson's equation.<sup>98</sup>

$$p = p_o e^{-2\sigma M / \rho R T r} \quad [65]$$

where  $p$  and  $p_o$  are the saturated vapor pressures above a concave meniscus of radius  $r$  and a plane surface, respectively,  $\sigma$  is the surface tension of the liquid at absolute temperature  $T$ ,  $\rho$  is its density and  $M$  is its molecular weight of the condensing gas, and  $R$  is the gas constant. It can be estimated that capillary radii of 360, 94, and  $30\text{ \AA}$  will reduce the RH for condensation to 98, 90, and 70% respectively. It has been argued<sup>99</sup> that this effect may explain the observation that steel still corrodes at  $\sim 70\%$  RH, as ferric oxide gel has pore sizes  $\sim 30\text{ \AA}$ ,<sup>100</sup> and therefore, pore condensation may occur. Correspondingly, the period that moisture remains in pores may be considerably greater than that when it is free on the surface. The percent time that the tendency for condensation both on a clean surface and on a contaminated surface is greater than zero is given in Table 13, and compared to that for a clean pore and one contaminated with NaCl when both surfaces are exposed for a year in Canberra. It is apparent that even coarse pores significantly increase

the time when condensation is favored, both with and without chloride contamination, although the effect is more marked in the absence of chloride. Pore condensation and delayed evaporation may be relevant for metals with porous oxide, such as zinc, and could significantly change the wetness periods for these materials.

### 2.16.6 Summary of Environmental Conditions

The analysis in [Section 2.16.3.1](#) indicated that pollutant deposition onto a surface may occur by gaseous absorption into a moisture film, or by deposition of aerosol or of rain. As outlined in [Section 2.16.1.3](#), the composition of gases, aerosol, and rain drops will be affected as they are transported by atmospheric processes. However, the scale of these transport processes is likely to be quite different. Gases, particularly reactive gases, will not be transported far from their sources; aerosols may form relatively close to the pollutant source but may be transported significant distances, while the processes of rain drop formation are complex and will not bear a direct relation to pollutant sources. Thus, it is to be expected that the concentration of atmospheric gases will be highly influenced by local pollutant sources, and aerosol

concentration will also be influenced by local sources but concentrations will spread significantly from these sources, while rain water chemistry will be affected more by the pollutants in a region rather than in one locality.

In [Table 14](#) some key parameters defining gaseous concentrations, aerosols, and rain water chemistry are given for marine, industrial, urban, rural, and remote locations from data presented in this chapter. The table should only be taken as indicative and does not attempt to define the effect of particular local sources on pollutant levels.

### 2.16.7 Surface Reactions

#### 2.16.7.1 Equilibrium Considerations

The conditions within the rain droplet or aerosol may determine the stability of both common metal oxides and the underlying metal. Consider zinc, which in dry environments is covered with a zincite ( $\text{ZnO}$ ) film and which rapidly transforms to zinc hydroxide in the presence of moisture films. The potential–pH diagram of zinc– $\text{CO}_2$ – $\text{H}_2\text{O}$  system<sup>101</sup> (at 25 °C) with Graedel's<sup>101</sup> regimes for dew, rain, and fog and the stability lines for  $\text{H}_2\text{O}$ ,  $\text{H}_2\text{O}_2$ , and  $\text{O}_3$  is presented in [Figure 21](#) (modified with the original from Graedel<sup>101</sup>). At the typical rain regime or fog regime

**Table 14** Summary of gaseous concentration, aerosol type and rain water composition ( $\mu\text{eq l}^{-1}$ ) for marine, industrial, urban, rural, and remote locations

Location type	Marine	Industrial	Urban	Rural	Remote
Gaseous (mixing ratio)					
$\text{SO}_2$ (ppt)	260	1500	160–1500	160	20
$\text{H}_2\text{S}$ (ppt)	65	365	365	35–60	3.6–7.5
$\text{NO}_x$ (ppb)	0.2–1000	10–1000	10–1000	0.2–10	0.02–0.08
$\text{O}_3$ (ppb)	20–40	100–400	100–400	20–40	20–40
Aerosols					
pH	0–9.5	–1–2.4	1.9–3		
Major species	$\text{NaCl}$ , $\text{MgCl}$	$\text{H}_2\text{SO}_4$ , $(\text{NH}_4)_3\text{H}(\text{SO}_4)_2$ , $(\text{NH}_4)_2\text{SO}_4$ , $\text{NH}_4\text{HSO}_4$	$\text{NH}_4\text{NO}_3$ , $\text{NH}_4\text{Cl}$ , $(\text{NH}_4)_2\text{SO}_4$		Dust, pollen plant waxes
Secondary species	$\text{Na}_2\text{SO}_4$ , $\text{H}_2\text{SO}_4$ , $\text{NH}_4\text{HSO}_4$ , $(\text{NH}_4)_2\text{SO}_4$ and $\text{NH}_4\text{NO}_3$ . $\text{NaHSO}_4$		$\text{NaNO}_3$		
Rain water					
pH	4–5.6	4.2–7.3	4.4–6.1	3.6–5.8	5.6–6
$\text{Cl}^-$	100–1300	9–142	10–27	3–25	1–1300
$\text{NO}_3^-$	3–10	40–140	13–140	3–25	3–10
$\text{SO}_4^{2-}$	3–10	70–240	12–60	4–60	3–10
$\text{Na}^+$	100–1200	5–60	20–60	3–30	100–1200
$\text{NH}_4^+$	2–10	30–200	10–30	2–20	2–10
$\text{Ca}^{2+}$		20–300	2–35	2–20	80



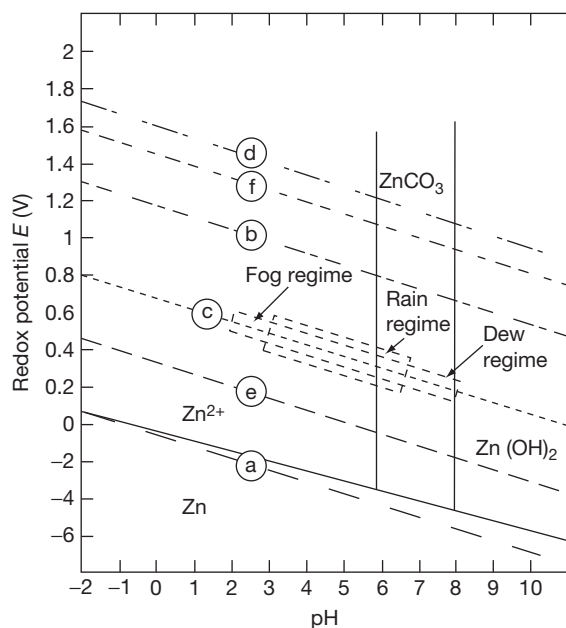
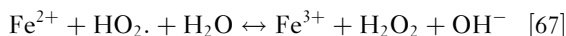
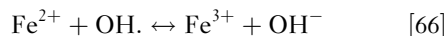


**Figure 21** Potential-pH diagram for the system Zn-CO<sub>2</sub>-H<sub>2</sub>O at 25 °C for a concentration of zinc ions of 0.1 M and a concentration of H<sub>2</sub>CO<sub>3</sub> of 1 \*10<sup>-5</sup> (this is the concentration in equilibrium with gaseous concentration of CO<sub>2</sub> of 340 ppmv). Modified from Graedel, T. E. *J. Electrochem. Soc.* **1989**, 136, 19C-2003C.

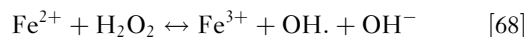
the surface Zn(OH)<sub>2</sub> film and the underlying Zn metal are not the stable phases, and rather Zn<sup>2+</sup> is the stable form. Therefore, dissolution of the zinc hydroxide is expected with the enrichment of the zinc ion concentration in solution. Stable oxide growth would not be expected. This enrichment of zinc ions in solution would then lead to precipitation of solid species.

A more complex situation occurs in the corrosion of iron. In [Figure 22](#), a potential-pH diagram<sup>69</sup> is given for the Fe-H<sub>2</sub>O system (at 25 °C) with the addition of the stability lines for H<sub>2</sub>O, H<sub>2</sub>O<sub>2</sub>, and O<sub>3</sub>. The diagram indicates that in many of the conditions commonly observed in dew rain and fog, the stable phase is either FeOOH or Fe<sup>2+</sup> at low pH values. These low pH values could occur either in fog or during the evaporation phase of dew or rain. However although the initial corrosion product may be Fe<sup>2+</sup>, the intermediate corrosion products are mixed Fe(II) and Fe(III) oxides and the final products contain only Fe(III).<sup>102</sup> The development of these oxides can in part be attributed to the reactive oxidants, hydrogen peroxide (H<sub>2</sub>O<sub>2</sub>), the OH<sub>2</sub> and the hydroperoxyl radical (HO<sub>2</sub>). It will be recalled that the work of Graedel and Goldberg<sup>103</sup> demonstrated

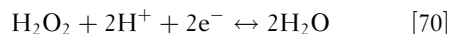
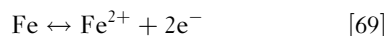
that small but significant concentrations of these oxidants could develop in rain droplets. The free radical and the peroxide reaction are likely to be<sup>103</sup>



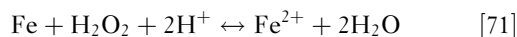
and



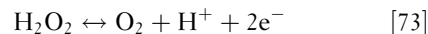
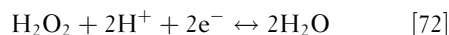
If solutions contain oxidants, the redox potential of the solutions will be influenced by the reduction/oxidation of these oxidants which may influence the stability of oxides and the passivation of metal surfaces. For example, according to Pourbaix<sup>102</sup> in a dilute solution of hydrogen peroxide the iron may be in the domain of the corrosion of iron (formation of Fe<sup>2+</sup>) and the reduction of hydrogen peroxide (point A on [Figure 22](#) at  $E = -0.200$  V and pH = 5.7), so that the following reactions could occur:



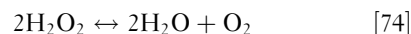
The overall reaction will be



In contrast with a concentrated solution of hydrogen peroxide, iron would be in a passive domain with stable oxides (point B on [Figure 22](#)) and hydrogen peroxide is in its domain of double instability. In this region (below line c and above line d in [Figure 22](#)), hydrogen peroxide may decompose into both water and oxygen according to the following equations:



The overall reaction will be



Thus, the metal surface may facilitate the decomposition of hydrogen peroxide and the evolution of gaseous oxygen, but the iron will remain in the passive state.

However, hydrogen peroxide can act to oxidize sulfite to sulfates as outlined in [eqn \[19\]](#). This will decrease the pH and the H<sub>2</sub>O<sub>2</sub> concentration so that the critical parameter in determining if the peroxide concentration is such that Fe is in a passive or active region of the potential-pH space is the relative concentrations of sulfite and peroxide. Thus, if [H<sub>2</sub>O<sub>2</sub>] > [HSO<sub>3</sub><sup>-</sup>], H<sub>2</sub>O<sub>2</sub> will not be completely

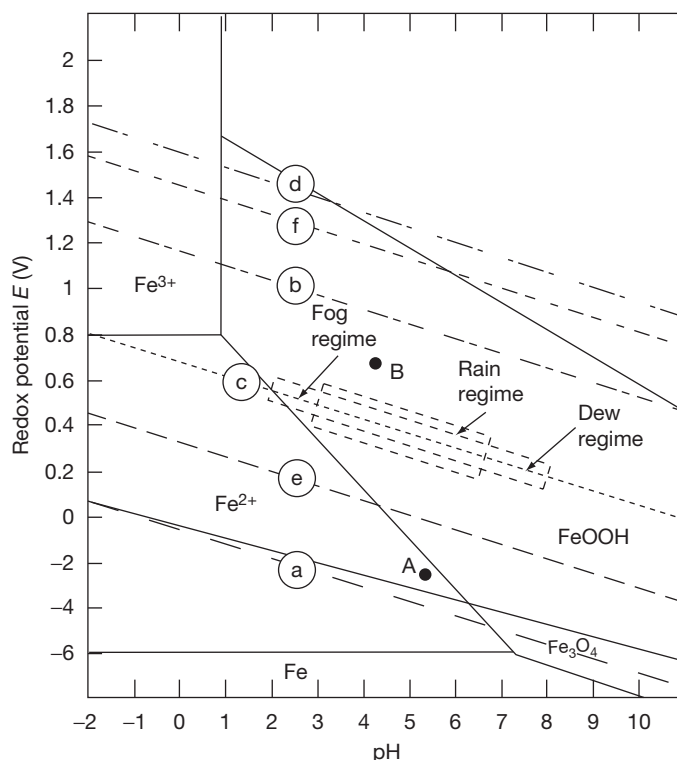


**Figure 22** Potential-pH diagram for the system Fe-H<sub>2</sub>O at 25 °C. Derived from Pourbaix, M. *Atlas of Electrochemical Equilibria in Aqueous Solutions*, 2nd English Edition; National Association of Corrosion Engineers: 1440 South Creek Drive, Houston Texas 7704, 1974; the approximate regimes for fog, rain, and dew are derived from Graedel, T. E.; Frankenthal, R. P. *J. Electrochem. Soc.* **1990**, *137*, 2385-2394.

depleted and hence may be available to passivate the metal surface.<sup>69</sup>

In contrast with the marked changes with the stability of the Fe phases because of the action of the oxidants, they have little effect on the equilibrium condition for the zinc system. On [Figure 21](#), the potentials for reduction of ozone or hydrogen peroxide (at pH values likely to occur in rain water or aerosols) fall in the stability range for Zn<sup>2+</sup>. Hence, the presence of these oxidants will further promote the corrosion of zinc.

Although the *E*-pH diagrams are useful, they only define the equilibrium conditions for relatively simple systems. In reality the kinetics of the corrosion processes are critical in determining the corrosion rate and the corrosion product while both rain drops and aerosols are multicomponent systems involving a wide range of aqueous species (chlorides, sulfates, carbonates, oxidants) and continuous gaseous absorption from the environment. Part of the dynamic nature of this system comes from the electrochemical processes themselves which can induce

separation of anodic and cathodic areas, differential pH at these zones and ion migration driven by local potentials.

#### 2.16.7.2 Influence of Electrochemical Processes on Moisture Film Stability and Chemistry

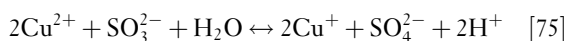
The establishment of separated anodic and cathodic areas may have significant impact on the distribution of species within a droplet. Two examples will illustrate this effect: the first, secondary spreading on zinc is a relatively long range effect, while the second, the development of anodic and cathodic zones associated with particular intermetallic zones containing aluminum 2000 and 7000 series is more local. Neufeld *et al.*<sup>104</sup> studied the effect of wetting fine NaCl crystals on zinc surfaces. It was found that in high humidities (>75% RH) deposited salt crystals rapidly wet forming roughly hemispherical moisture droplets. After a relatively short period, a fine moisture film spreads out from a central droplet. Scanning Kelvin

probe studies indicated an electrochemical cell developed, with the central drop becoming anodic and the secondary spread region cathodic. High pH developed in the secondary spread region and slightly acidic pH values in the central droplet. Neufeld *et al.*<sup>104</sup> demonstrated that significant ion migration occurred with cations (particularly  $\text{Na}^+$ ) migrating into the secondary spread region and anions into the central anodic zone. Correspondingly, after the drop had dried out at the completion of the experiment, quite different corrosion products were found in the two zones with the main product in the secondary spread zone being zinc hydroxycarbonate and the main products in the inner anodic region being zinc hydroxychloride (simonkolleite) and sodium zinc hydroxysulfate chloride (gordite).<sup>91</sup>

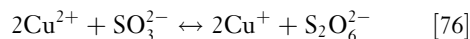
Secondary spreading is significant for a number of reasons. Primarily, the establishment of a very large cathodic zone removes any possibility of cathodic limitations for the corrosion process and thus may increase the initial corrosion processes. However, the high pH in the secondary spread area provides ideal conditions for the absorption of carbon dioxide (via eqns [15]–[17]). At pH 9 the carbonate ion concentration in solution is  $10^6$  times that at a pH of 6. High carbonate concentrations will lead to the precipitation of zinc hydroxy carbonate. Of course, the absorption of carbon dioxide will also tend to neutralize the alkaline pH. The development of significant coverage of the zinc surface by zinc-hydroxy carbonate will limit corrosion in subsequent wetting cycles. Muster *et al.*<sup>105</sup> have demonstrated that the carbonate blocked chloride penetration to anodic sites on the metal surface to a much greater extent than zinc hydroxycarbonate.

Such secondary spreading has also been observed in steel<sup>106</sup> and copper.<sup>107</sup> However, the phenomenon was not observed on aluminum when exposed to the identical condition.<sup>108</sup> The work on copper also shows interesting synergies between secondary spreading and the absorption of gaseous species in an analogous manner to that observed for zinc. Chen *et al.*<sup>108</sup> wetted a NaCl crystal on a copper plate in an atmosphere containing 150 ppb  $\text{SO}_2$  and two different levels of  $\text{CO}_2$  (<5 ppb and ambient 350 ppb). They observed that a narrow band of secondary spreading occurred with an alkaline pH occurring in the spread area, with sulfate and dithionate ( $\text{S}_2\text{O}_6^{2-}$ ) species observed in the secondary spread zone, and the corrosion products nanotokite ( $\text{CuCl}$ ) and pantacamite ( $\text{Cu}_2(\text{OH})_3\text{Cl}$ ) observed in the central droplet region. It is known that  $\text{Cu}^{2+}$  may catalyze the oxidation of S(IV) to S(VI) in an analogous manner to that of the other

transition metal ions  $\text{Mn}^{2+}$  or  $\text{Fe}^{2+}$  (refer to eqn [16]). Thus, the absorption of  $\text{SO}_2$  and its dissociation via eqns [11] and [12] are promoted by the high pH in the secondary spread zone.  $\text{Cu}^{2+}$  catalyzed oxidation of the sulfite may occur by one of the following reactions<sup>76</sup>:



or



The absorption of  $\text{SO}_2$  and the formation of sulfate will lower the pH in the secondary spread area and secondary spreading will cease. The separation of the droplet into cathodic zones and anodic zones in the central area will lead to a higher level of  $[\text{H}^+]$  in the anodic zone which will encourage copper dissolution and the precipitation of nanotokite and pantacamite (rather than NaCl).<sup>108</sup>

Thus, secondary spreading can lead to significant variation in pH and species concentration (both by variations in gaseous absorption and by migration), and so it can lead to the formation of different oxides with the consequence of further corrosion.

Dynamic interactions also occur involving solution chemistry, local pH, corrosion product formation, and electrochemistry at a finer scale. The trenching observed around cathodic intermetallics in aluminum AA2xxx and AA7xxx series alloys can illustrate these effects (this chapter will not attempt to cover the interesting and involved interactions of intermetallics and electrochemistry of these alloys will be discussed elsewhere<sup>109</sup>). To achieve the required strength, the formation of intermetallics is required in these structural aluminum grades. Some of these intermetallics – notably the Al–Cu–Fe–Mn group,<sup>110,111</sup> including  $\text{Al}_6(\text{CuFeMn})$ ,  $\text{Al}_2\text{Cu}$ ,  $\text{Al}_7\text{Cu}_2\text{Fe}$ , and  $\text{Al}_{20}\text{Cu}_2(\text{FeMn})_3$  – have a very strong ability to sustain a cathodic current. Birbilis and Bucheit<sup>110</sup> found that at the corrosion potential of AA7075–T651 in NaCl (i.e.,  $-965 \text{ mV}_{\text{SCE}}$ )  $\text{Al}_7\text{Cu}_2\text{Fe}$  and  $\text{Al}_2\text{Cu}$  could support cathodic currents in excess of 310 and  $470 \mu\text{A cm}^{-2}$ , respectively while Schneider *et al.*<sup>111</sup> showed the cathodic current on  $\text{Al}_{20}\text{Cu}_2(\text{FeMn})_3$  to be ten times greater than that measured on AA2024–T3 alloy surfaces. The high cathodic current sustained by these intermetallics can lead to localized pitting corrosion and to trenching around Al–Cu–Fe–Mn phases.<sup>112–116</sup> The exact mechanism of trenching is still subject to debate with some researchers<sup>112</sup> suggesting that it may be interpreted as galvanic corrosion between the particle and the matrix, and others<sup>113,114</sup> indicating that it is a form of

etching under the high pH conditions occurring at the cathodic intermetallics. In fact Park *et al.*<sup>113</sup> have found pH values  $\sim 9.5$  at around these particles. Under these high pH conditions, it is suggested<sup>114</sup> that the aluminum matrix undergoes cathodic corrosion, together with dissolution of the oxide film producing aluminate ions and hydrogen gas according to the equation



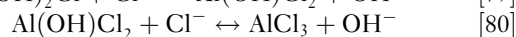
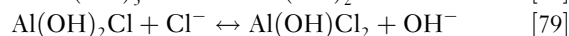
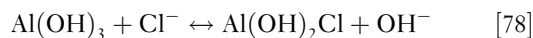
The rate of eqn [77] is highly pH dependent. In fact, Park *et al.*<sup>113</sup> and Vukmirovic *et al.*<sup>115</sup> have found that increased buffering of the solution decreases the rate of pitting around the intermetallic particles which they attribute to the inability to sustain high localized pH values in a buffered solution. As highlighted previously in atmospheric conditions, highly buffered solutions can arise from various acid/salt couples such as the bisulfite/sulfite reactions (eqn [12]). The formation of colloidal alumina gels have been observed<sup>113,116</sup> between anodic and cathodic regions on the surface and these may help maintain both potential and pH differences between these regions. In fact Ilevbare *et al.*<sup>116</sup> have reported that as high pH develops at cathodic sites and low pH at anodic sites, increased galvanic potential differences are created.<sup>116</sup> Thus, under atmospheric conditions, an interplay between local electrochemical activity and local pH may arise, with corrosion product or gel formation controlled by the general chemistry of the droplet solution.

#### 2.16.7.2.1 Oxide precipitation and stability

The fact that a surface is corroding implies that there is metal ion formation, as well as diffusion or migration through the oxide layer, and in many cases, these processes are highly influenced by oxide stability, dissolution, and growth. Oxide stability in its turn is affected by the local pH and ion concentration, which as discussed above, are influenced not only by the original pH of the deposited moisture and subsequent aqueous reaction but also by the establishment of local anodes and cathodes. These interactions will be discussed in relation to the aluminum and zinc systems.

The typical form of an oxide film on aluminum exposed to water or water vapor consists of a thin layer of  $\gamma\text{-Al}_2\text{O}_3$  covered with a thin layer of boehmite ( $\gamma\text{-AlOOH}$ ) which in turn is covered with bayerite ( $\text{Al}(\text{OH})_3$  which can be written as  $\text{Al}_2\text{O}_3 \cdot 3\text{H}_2\text{O}$ ).<sup>117</sup> The stability data of boehmite and bayerite, along with that of CuO and hydrated copper

oxide ( $\text{Cu}(\text{OH})_2$ ) are presented in Figure 22 from the data of Pourbaix.<sup>102</sup> It is evident that very low pH values are required for aluminum oxides to show significant solubility (less than 2.4 for boehmite). In fact only in acidic fogs and very acidic aerosols (for example, referring to Figure 1, the aerosols in the  $\text{NH}_3\text{-SO}_4$  system, where the ammonia/sulfur dioxide ratio is less than 0.5 so that  $\text{H}_2\text{SO}_4$  is the dominant and  $\text{NH}_4\text{HSO}_4$  the secondary species) will boehmite dissolve directly. However, these low pH values may occur in the evaporation phase of rain drops or condensate (i.e., dew) or if localized pH changes occur in association with pitting corrosion or oxygen differentials. However, at a pH of 4 some dissolution of the oxide may occur, particularly in association with defects or cracks in the oxide film. Thus when acid fogs, acidified rain, or acid aerosols (either industrial or marine – but affected by absorption of acids) fall on an aluminum surface some dissolution of the oxide layer is expected, with the electrolyte solution and the underlying metal substrate being in contact through cracks and pores in the surface. Aluminum ions may diffuse through the pores and in sulfate rich environments may form amorphous aluminum sulfate hydrate –  $\text{Al}_x(\text{SO}_4)_y(\text{H}_2\text{O})_z$ , which will gradually transform into aluminate,  $\text{Al}_2(\text{SO}_4)(\text{OH})_4 \cdot 7(\text{H}_2\text{O})_2$ . The pitting may commence beneath defects in the oxide and the progression of the pitting (and further dissolution of the oxide) may be supported by the autocatalytic nature of the pitting process, when anodic regions occur at the bottom of the pit and because of the strong oxygen differential between the bottom and the top or exterior of the pit, cathodic zones also occur in these regions. The formation of gel structures by aluminum sulfate hydrate or other amorphous materials will tend to occur at the mouth of the pit (where the pH is higher) stabilizing the pH and oxygen differentials. In the chloride rich solutions generated by marine aerosols, chloride ions may complex with  $\text{Al}^{3+}$  ions at anodic sites and, thereby, prevent the formation of aluminum hydroxides. Further, aluminum hydroxide chlorides may form either by chlorination of the surface  $\text{Al}(\text{OH})_3$  or in solution. Further reactions with chloride ions can lead to the formation of Cadwaladerite  $\text{AlCl}(\text{OH})_2 \cdot 4\text{H}_2\text{O}$  and then aluminum chloride  $\text{AlCl}_3$ .



Clearly, this reaction is favored in acidic and chloride

rich environments. The dissolution of the boehmite layer will then permit further access of the solution to the substrate and thus enhanced corrosion.

The situation above is very similar for structural alloys with a large range of intermetallics. First, the oxide layers above the intermetallics tend to be thinner with more defects, so that the electrolyte can more easily move through to the substrate. Second, as discussed in a previous section, certain intermetallics may establish large cathodic currents which can reinforce a strong pH difference between the cathodic intermetallic and the anodic matrix, increasing the corrosion rate and promoting more aggressive pitting in the matrix. These potential and pH differences can be supported by the formation of gels as highlighted above.

A second aspect is illustrated by the role of Cu in the corrosion of aluminum alloys. Copper is a more noble metal than aluminum and, therefore, during the corrosion processes will accumulate at the metal oxide boundary; it then migrates through the oxide to the surface where it may form clusters and act as cathodic sites. Copper that has entered into solution or any original copper in solution may be subsequently reduced back to copper metal on cathodic copper containing intermetallics. In the presence of  $\text{Cl}^-$  ions the formation of  $\text{CuCl}^+$  will lower the energy barrier for the deposition of copper onto aluminum that leads to secondary pitting. Thus, copper plating and secondary pitting may be promoted in solutions with moderate pH and high chloride content such as acidified marine aerosols, **Figure 23**.

In the zinc systems, it is meaningful to discuss corrosion that occurs as a result of secondary spreading and that occurs when conditions are not suitable for secondary spreading. If secondary spreading occurs, there is a wide separation of anodic and cathodic zones. In the cathodic regions, alkaline pH values develop and zinc hydroxycarbonate is observed to form both in the laboratory conditions and in the field. **Figure 24** from Graedel<sup>118</sup> gives the zinc carbonate stability diagram with the regime for marine aerosol added. It is evident that under typical conditions of rain, dew, or marine aerosol, zinc carbonate would not be expected to form. Therefore, the high pH and carbonate levels (up to  $10^3$ – $10^4$   $\mu\text{M}$ ) in secondary spreading zones favor the formation of the carbonate whereas it would not form in a 'stable' drop.

In the central anodic zone of the droplet, slightly acidic pH values develop and common corrosion products are gordiate, zinc hydroxy chloride, and

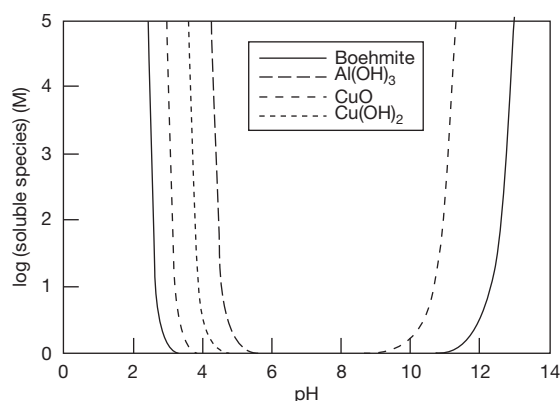


**Figure 23** Stability of boehmite, bayerite and  $\text{CuO}$  and  $\text{Cu(OH)}_2$ . Reproduced from Pourbaix, M. *Atlas of Electrochemical Equilibria in Aqueous Solutions*, 2nd English Edition; National Association of Corrosion Engineers: 1440 South Creek Drive, Houston, Texas 7704, 1974.

zinc hydroxy sulfate. Stability diagrams from Graedel indicated that both the hydroxy sulfate and hydroxy chloride have relatively limited stability regions that require sulfate and chloride concentrations in excess of  $10^2$  and  $10^3$   $\mu\text{eq l}^{-1}$  respectively and zinc ion levels greater than 0.1 M; both these are centered around a pH of 6.2. However, as the anion concentration increases, the pH stability range also increases so that at concentrations of  $10^5$   $\mu\text{eq l}^{-1}$  the hydroxy anions are stable from a pH of just below 6 to nearly 8. On metal surfaces exposed to a marine environment, the concentration of chloride and sulfate in deposited aerosols will range from 0.55 to 5.4 M, that is, from the concentration in seawater (in a freshly formed aerosol that has not yet equilibrated to the atmospheric conditions) to that at saturation point, when the RH is just above the deliquescent RH of the constituents of seawater. Thus, in the solutions formed by the deposition of wetted aerosols, although there will be sufficient chloride to promote the formation of zinc hydroxide chloride, there will not initially be sufficient zinc ions in solution. This may allow the formation of mixed cation OH anions and in fact Cole *et al.*<sup>91</sup> have observed the formation of gordiate after short periods of exposure. Thus, within the central zone of an aerosol droplet, subject to secondary spreading, gordiate and zinc hydroxy-chloride will form. As the droplet evaporates, the concentration of both anions and actions will increase allowing the formation of a wider range of salts such as zinc hydroxysulfate. In droplets that do not undergo secondary spreading similar processes will



occur in the central droplet; however, Cole *et al.*<sup>91</sup> found no evidence of the formation of zinc hydroxycarbonates. Traditional theories to explain how zinc hydroxycarbonate may form in marine chloride rich environments have suggested that zinc hydroxychloride may transform to the hydroxycarbonate with time; however, because of the high pH and carbonate concentration that occur in secondary spreading, the zinc hydroxycarbonate phase may form directly.

However, the zinc OH anions and particularly the hydroxychlorides are not stable under the common pH and chloride concentrations that occur in dew, rain, or fog (see Figure 24). Thus, it is quite possible that zinc hydroxychloride may dissolve under these types of moisture. In Figure 25, the concentrations of chloride and zinc ions that occur when zinc hydroxychloride powder (mass of 1.78 g) is placed in 1 l of a dilute solution of nitric acid with a pH of 4.5 and 6.5 are presented. It is evident that over a period of 500–1500 min (or ~8–24 h) significant chloride levels will build up in solution. Work by Cole *et al.*<sup>119</sup> indicated that moisture layers or droplets might exist on corroded surfaces for equivalent periods (dew may form early in the evening and last until after sunrise; likewise rain that falls in the late evening may not evaporate until the following sunrise) and, therefore, significant chloride concentration could build up

from the dissolution of these oxide layers, enhancing corrosion.

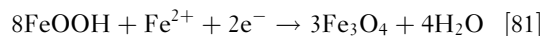
Both these examples indicate that there is a very strong interaction between the atmospheric conditions, forms of deposition, and electrochemical and surface reactions controlling corrosion. This is of course controlled by the pH and chemical composition of the deposited moisture layers, but it is also influenced by drop size and residency time of the drop.

#### 2.16.7.2.2 Specific features of the atmospheric corrosion of steel

While the interactions between the environment and steel are similar to those discussed for aluminum and zinc, the atmospheric corrosion of steel has a number of specific features associated with the following:

- The additional reduction and oxidation pathways provided by the existence and ready transformation between Fe(II) and Fe(III) oxides.
- The high porous and often quite thick physical nature of 'rust' on ferrous surfaces.
- The interactions of Fe with sulfur dioxide and its oxidation products, where  $\text{Fe}^{2+}$  may catalyze the reduction of sulfite to sulfate, while the sulfate ion may characterize the dissolution of iron.

The standard reactions that occur during the atmospheric corrosion of steel are the anodic partial reaction<sup>97</sup> of iron (eqn [69]) and a number of possible cathodic reactions,<sup>120</sup> including oxygen reduction (eqn [39]) and hydrogen reduction (eqn [35]). Hydrogen reduction should dominate over oxygen reduction at pH values less than 4; however, because of the dissolution of iron oxides the electrolyte on top of iron-based metals is well buffered<sup>121</sup> so that  $\text{H}^+$  reduction is negligible. However, a third cathodic reaction is the reduction of  $\text{Fe}^{3+}$  ions within the oxide scale, as first proposed by Evans<sup>122</sup>:



Stratmann<sup>123</sup> suggested that this reaction is critical in controlling and accelerating (relative to the corrosion rate without the redox reaction) the corrosion rate of ferrous alloys during wet and dry cycles. During the wetting of an existing oxide layer, Stratmann observed a corrosion rate much greater than that would be expected by oxygen reduction alone and therefore, proposed that the increased corrosion rate was due to the reduction of  $\text{Fe}^{3+}$  ions. He indeed demonstrated the phenomenon using *in situ* spectroscopy (showing that  $\gamma\text{-FeOOH}$  had in part transformed to

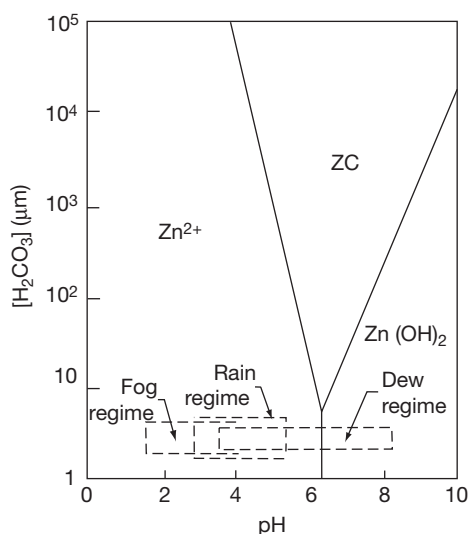


**Figure 24** Stability diagram for zinc carbonate (ZC) in aerated aqueous solutions with varying  $\text{H}_2\text{CO}_3$  content and pH at 25 °C and with zinc ion concentration of 0.1M. Reproduced from Graedel, T. E. *J. Electrochem. Soc.* **1989**, 136, C193–C203.

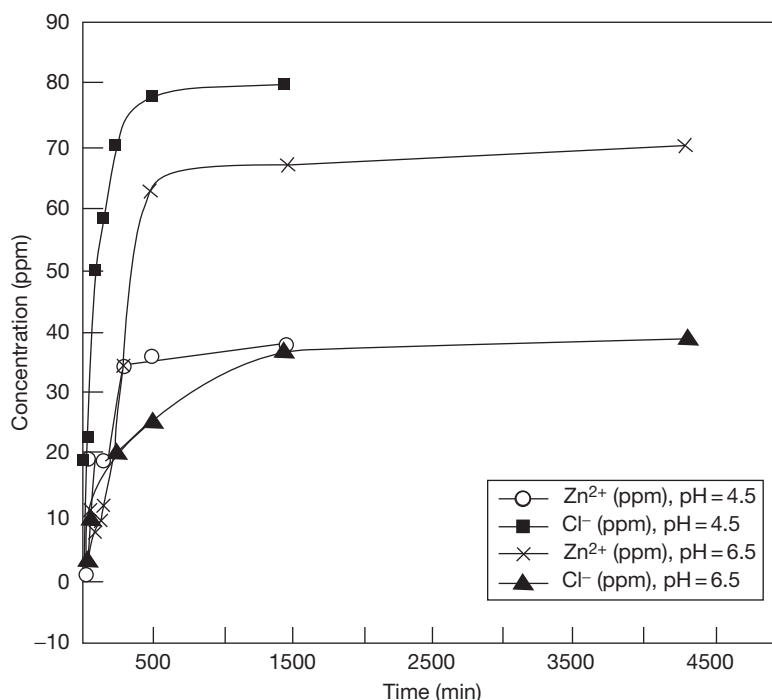


**Figure 25** Concentration in solution of  $\text{Zn}^{2+}$  and  $\text{Cl}^-$  ions due to the dissolution of a zinc hydroxychloride table (1.78 g) in a aqueous solution (1 l) with nitric acid added to give a pH of 4.5 and 6.5.

an  $\text{Fe}(\text{OH})_2$  phase).<sup>123</sup> Further, the oxide scale has a very large area and the formation of  $\text{Fe}^{2+}$  states within the  $\text{FeOOH}$  lattice will control the potential and can dramatically increase the rate of electron transfer reactions, notably oxide reduction, both during the later stages of wetting and during the drying cycle (the reduction of  $\text{Fe}^{3+}$  to  $\text{Fe}^{2+}$  being constrained to the initial wetting period). During the drying cycle, the corrosion rate shows a marked peak while the corrosion potential shifts to more anodic values. The increased corrosion current is associated with the increased availability of oxygen as the pathway from the atmosphere to the oxide layer shortens dramatically as the moisture layer thins down, while Stratmann proposed that the anodic shift is due to the precipitation of corrosion products in the concentrated thin moisture films, which block anodic metal dissolution and eventually dramatically slow the corrosion rate. Further, the  $\text{Fe}^{2+}$  states within the oxide are oxidized during the drying cycle, which reduces the rate of oxygen reduction (reversing the previous effect), and it is only when the oxide is rewetted and new  $\text{Fe}^{2+}$  states are created that electron transfer is again enhanced.

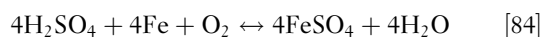
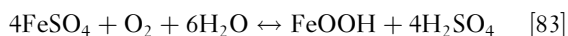
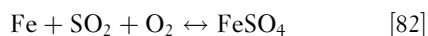
Therefore, in atmospheric corrosion it would be expected that the nature of the climatic cycle and the

nature of oxide layers would have a very pronounced effect on the corrosion rate. At a gross level, atmospheric sequences with a high number of wet/dry cycles are likely to promote a higher corrosion rate than more constant conditions. However, the duration of wet/dry cycles is also important, as Stratmann's work indicates that the extent of  $\text{Fe}^{3+}$  to  $\text{Fe}^{2+}$  reduction in the wetting stage will control the extent of corrosion during the drying stage. Precise details of the kinetics of this transformation are not available in the literature; however, it is possible that during short wet/dry cycles, such as those attributed to wetting or aerosol/rain deposition and subsequent drying during the day (referred to as Mode A wetting in [Section 2.16.5.4](#)), a lesser quantity of  $\text{Fe}^{3+}$  is reduced and thus the corrosion rate is decreased relative to longer wet/dry cycles (overnight and multi-day wetting events, as detailed in [Section 2.16.5.4](#)).

The volume and porosity of the oxide layers will also be critical in controlling the corrosion rate. In this regard, there are two prime effects. First, as outlined in [Section 2.16.5.4.3](#), fine pores will increase the duration of wetness by reducing the RH level at which condensation will occur and also lowering the RH level at which evaporation will occur. Further, increasing the porosity of the oxide will also increase

the cathodic surface area that develops during a wet/dry cycle, thus increasing the corrosion rate. Therefore, it is probable that processes that increase the porosity of the rust layer (such as localized dissolution under acid aerosols) will also increase the overall corrosion rate. However, again there are no systematic studies of this currently reported in the literature.

The last significantly different effect (relative to aluminum and zinc) is the impact of gaseous SO<sub>2</sub> and sulfate compounds on the corrosion of ferrous metals. As outlined in Section 2.16.1.3.4, Fe(III) states may catalyze the oxidation of S(IV) compounds (e.g., HSO<sub>3</sub><sup>-</sup> or SO<sub>3</sub><sup>2-</sup>) to SO<sub>4</sub><sup>2-</sup> or other forms of S(VI). This in turn will promote greater absorption of SO<sub>2</sub> and further acidification of moisture layers. Within moisture layers containing sulfate compounds, sulfur is not consumed in the corrosion reactions, but may act as a catalyst according to the following reactions<sup>124,125</sup>:



Typically, one SO<sub>4</sub><sup>2-</sup> ion can catalyze the dissolution of more than 100 atoms of iron before it is removed by leaching, spalling of rust, or the formation of basic sulfate.<sup>125</sup> The combined effect of the enhanced absorption of SO<sub>2</sub> and the catalytic role of SO<sub>4</sub><sup>2-</sup> ion may be responsible for the very high dependence and rate of ferrous corrosion in industrial environments.<sup>126,127</sup>

There is extensive literature on the nature of ferrous rust products and it is beyond the scope of this review to detail this. A key point, however, is that as the redox reaction from Fe(III) to Fe(II) has a pronounced effect on cyclic corrosion, the development of Fe(III) compounds of greater stability should result in a decrease in the corrosion rate, while compounds of lower stability should result in higher corrosion rates. Partially for this reason, there has been great interest in the development of green rusts (GRs), which were initially identified by Stampfl.<sup>128</sup> A typical carbonate-based GR<sup>129</sup> is Fe<sub>4</sub><sup>2+</sup>Fe<sub>2</sub><sup>3+</sup>(OH)<sub>12</sub>CO<sub>3</sub>·2H<sub>2</sub>O. Reffass *et al.*<sup>130</sup> mapped the sequence of corrosion products that formed when carbon steel corroded in NaHCO<sub>3</sub>/NaCl electrolytes and found that pitting corrosion induced by anodic polarization of the surface in NaHCO<sub>3</sub> led to the initial precipitation of FeCO<sub>3</sub>, and that this FeCO<sub>3</sub> was then transformed to a species identified as a carbonate-based GR, which

later transformed to α-FeOOH. Further, in a study of the oxidation of Fe(II) compounds formed by mixing FeCl<sub>2</sub>·4H<sub>2</sub>O, NaOH and NaHCO<sub>3</sub> in solution, Reffass *et al.*<sup>130</sup> found that three redox couples developed: FeCO<sub>3</sub>/GR(CO<sub>3</sub><sup>2-</sup>), GR(CO<sub>3</sub><sup>2-</sup>)/α-FeOOH, and FeCO<sub>3</sub>/α-FeOOH. If such reaction sequences are reproduced in atmospheric corrosion, then the above redox reactions may have a major role in driving the corrosion rate in an analogous way to that discussed for the Fe(II)/Fe(III) redox couples.

## 2.16.8 Conclusion

An understanding of atmospheric corrosion requires a wide understanding of the transfer of pollutants and moisture to metal surfaces and the form and residence time of the pollutants and moisture on the surface.

Despite the enormous range of the species in the atmosphere, surprisingly few species play an active role in atmospheric corrosion. For a chemical species to promote corrosion, it must be transported and deposited onto the metal surface and it must also be reactive to the surface. These conditions are somewhat contradictory as species that are reactive will readily react in the atmosphere and, therefore, will not be available for surface reactions. Gaseous deposition into surface moisture layers, aerosol deposition, and rain deposition are the prime processes for pollutant deposition onto surfaces. Deposition of reactive gases will only be important close to the gas source, while aerosols will be of higher concentration close to the source but may also be transported significant distances from the source. The formation of rain and absorption of gases or aerosols into rain drops require a complex process including the formation of an aerosol, transformation of the aerosol into CCN, growth of the CCN to form a cloud droplet, and the falling of the rain drop and scavenging of gaseous and aerosol species during the fall. Thus, rain drop chemistry will reflect the regional level of pollutants rather than just the local level. Species such as ammonia, sulfates, chlorides, and (to a lesser extent) nitrates, that are readily absorbed into forms of atmospheric moisture such as aerosols or rain drops will be readily transported and deposited on surfaces. Oxidants such as ozone or hydrogen peroxide are of critical importance as they will both facilitate the oxidation of reduced species (such as sulfites), and thus promote further absorption, as well as controlling the redox potential of the deposited solutions. The pH of aqueous phases in the atmosphere will depend critically on the

balance between acidic (primarily oxides of sulfur and nitrogen) and alkali precursors (predominately the alkali metals and ammonia) and, therefore, can be very variable. Although relatively acidic aerosols may develop, rainwater solutions tend to be highly buffered and, hence, extremes in pH are rare.

Once deposited, pollutants, aerosols, and rainwater may have a number of effects which are mitigated by local micro climatic effects. The microclimate of exposed metal components is in general subject to strong diurnal cycles which are amplified by radiative effects (heating during the day and cooling at night by the emission of radiation of the surface to the night sky) so that low surface RH may occur during daylight hours and high RH at night. Many of the salts deposited in aerosols or rainwater are hygroscopic and so deliquescence of such salts can lead to a cyclic pattern of localized wetting and drying. Although rain can promote the deposition of pollutants and transfer of acidity to the surface, it may also remove pollutants from the surface. The effectiveness of pollutant removal is controlled by the rain intensity and the nature of the surface. Electrochemical and surface reactions may influence the form and chemistry of droplets on a surface. Perhaps the most dramatic example of surface processes inducing droplet instability is secondary spreading. In secondary spreading, a fine moisture film spreads out from the centralized drop, with the central drop forming the anode and the secondary spread region the cathode of an extended electrochemical cell. Alkaline pH develops in the secondary spread region which may promote particular gaseous absorption reactions. For example, in secondary spreading on zinc, the absorption of carbon dioxide and the enrichment of the secondary spread region in carbonate occur and the subsequent precipitation of zinc hydroxycarbonate is promoted. However, pH variations and local electrochemical cells may occur on a much finer scale. In aluminum alloys, copper-containing intermetallics may be preferred sites for cathodic reactions, with high pH in the vicinity of the intermetallics promoting the dissolution of the aluminum matrix. However, the ability of the solutions to sustain such local variations in pH is heavily influenced by their buffering capacity (highly buffered solutions will not support these local variations) which in turn is determined by the history of aqueous and gaseous reactions prior to deposition.

The solution chemistry will be controlled by the precipitation of new oxides and the stability of existing oxides. There can be sharp 'cycles' in ion concentration and pH of deposited moisture. For example in the zinc

system, the zinc hydroxy anions are stable at near neutral pH values and appreciable anion concentrations. These conditions can readily occur during the evaporation of aerosol or rain droplets and, therefore, precipitation of such zinc OH anions is readily observed under these conditions. However, when an aerosol or rain drop is first deposited, it will commonly be acidic with relatively low anion concentrations. Under these conditions, some of the existing surface precipitates are not stable and may dissolve.

Thus, atmospheric corrosion is influenced by a wide range of linked processes, both within the atmosphere and on the surface. However, as in general these processes relate to a relatively narrow band of chemical species, an adequate knowledge of the dynamics of atmospheric corrosion can be constructed.

## References

1. Seinfeld, J.; Pandis, S. *Atmospheric Chemistry and Physics: From Air Pollution to Climate Change*; Wiley Interscience: New York, 1997.
2. Berresheim, H.; Wine, P. H.; Davis, D. D. Sulfur in the Atmosphere. In *Composition, Chemistry and Climate of the Atmosphere*; Singh, H. B., Ed.; Van Nostrand Reinhold: New York, 1995; pp 251–307.
3. Dacey, J. W. H.; Wakeham, S. G. *Science* **1986**, *233*, 1314–1316.
4. Bates, T. S.; Charlson, R. J.; Gammon, R. H. *Nature* **1987**, *329*, 319–321.
5. Chin, M.; Davis, D. D. *J. Geophys. Res.* **1995**, *100*, 8993–9005.
6. Noller, B. N.; Currey, N. A.; Ayers, G. P.; Gillett, R. W. *Sci. Total Environ.* **1990**, *91*, 23–48.
7. National Research Council *Rethinking the Ozone Problem in Urban and Regional Air Pollution*; National Academy Press: Washington, DC, 1991.
8. Intergovernmental Panel on Climate Change (IPCC) *Climate Change 1994: Radiative Forcing of Climate Change and an Evaluation of the IPCC IS92 Emission Scenarios*; Cambridge University Press: Cambridge, UK, 1995.
9. Dentener, F. J.; Crutzen, P. J. *J. Atmos. Chem.* **1994**, *19*, 331–369.
10. Danielson, E. F. *J. Atmos. Sci.* **1968**, *25*, 502–518.
11. Van Valin, C. C.; Luria, M.; Ray, J. D.; Boatman, J. F. *J. Geophys. Res.* **1990**, *95*, 5689–5695.
12. Kleinman, L. J. *J. Geophys. Res.* **1991**, *96*, 20721–20733.
13. Stockwell, W. R. *J. Geophys. Res.* **1995**, *100*, 11695–11698.
14. Leygraf, C.; Graedel, T. *Atmospheric Corrosion*; Wiley and Sons: New York, 2000.
15. Pandis, S. N.; Seinfeld, J. H. *J. Geophys. Res.* **1989**, *94*, 1105–1126.
16. Hoffman, M. R.; Calvert, J. G. *Chemical Transformation Modules for Eulerian Acid Deposition Models: Vol. 2 – The Aqueous-Phase Chemistry*; EPA/600/3–85/017, US Environmental Protection Agency: Research Triangle Park, NC, 1985.
17. Troy, R. C.; Margerum, D. W. *Inorg. Chem.* **1991**, *30*(18), 3538–3543.

18. Chen, Z. Y.; Zakipour, S.; Persson, D.; Leygraf, C. *Corrosion* **2005**, 61(11), 1022–1034.
19. Zakipour, S.; Tidbald, J.; Leygraf, J. J. *Electrochem. Soc.* **1995**, 142(3), 757–764.
20. Svensson, J. E.; Johansson, L. G. J. *Electrochem. Soc.* **1993**, 140(8), 2210–2218.
21. Pilinis, C.; Seinfeld, J. H. *Atmos. Environ.* **1987**, 21, 2453–2466.
22. Clegg, S. L.; Brimblecombe, P.; Wexler, A. S. *J. Phys. Chem. A* **1998**, 102(12), 2137–2154.
23. Keene, W. C.; Sander, R.; Pszenny, A. P.; Vogt, R.; Crutzen, P. J.; Galloway, J. N. *J. Aerosol Sci.* **1998**, 29(3), 339–356.
24. Keywood, M. D.; Chivas, A. R.; Fifield, L. K.; Creswell, R. G.; Ayers, G. P. *Aust. J. Soil Res.* **1997**, 35, 1177–1189.
25. Whitby, K. T.; Cantrell, B. Fine Particles. In Proceedings of the International Conference on Environmental Sensing and Assessment Institute of Electrical and Electronic Engineers: Las Vegas, NV, 1976.
26. Schutz, L.; Kramer, M. J. *Atmos. Chem.* **1987**, 5, 173–184.
27. Wall, S. M.; John, W.; Ondo, J. L. *Atmos. Environ.* **1988**, 22, 1649–1656.
28. Tang, I. N. *Atmos. Environ.* **1980**, 14, 819–828.
29. Tang, I. N.; Munkelwitz, H. R. *Atmos. Environ.* **1993**, 27A, 467–473.
30. Wexler, A. S.; Seinfeld, J. H. *Atmos. Environ.* **1991**, 25A, 2731–2748.
31. Murphy, D. M.; Thomson, D. S.; Middlebrook, A. M.; Shein, M. E. *J. Geophys. Res. Atmos.* **1998**, 103(D13), 16485–16491.
32. Spillane, M. C.; Monahan, E. C.; Bowyes, P. A.; Doyule, D. M.; Staben, P. J. In *Oceanic Whitecaps and Their Role in Air-Sea Exchange Processes*; Monahan, E. C., Macniocail, G., Eds.; D. Reidel Publishing Company: Dordrecht, Holland, 1986; pp 209–218.
33. Monahan, E. C.; Davidson, K. L.; Spiel, D. E. *J. Geophys. Res.* **1982**, 87, 8898–8904.
34. McKay, W. A.; Garland, J. A.; Livesley, D.; Halliwell, C. M.; Walker, M. I. *Atmos. Environ.* **1994**, 28, 3299–3309.
35. Fitzgerald, J. W. *Atmos. Environ.* **1991**, 25A, 533–545.
36. Cole, I. S.; Muster, T.; Paterson, D.; Furman, S.; Trinidad, G. S.; Wright, N. A holistic model of atmospheric corrosion: Extending a microclimate model into a true corrosion model. Paper 12-9-2004. Eurocorr 2004: Long Term Prediction and Modelling of Corrosion, 12–16 Nice: France, September 2004.
37. Bretschneider, C. L. Beach Erosion Board Technical Memorandum No. 118, US Army Corps of Engineers: Washington, DC, 1959.
38. Cole, I. S.; Ganther, W. D.; Paterson, D. A.; King, G. A.; Furman, S. A.; Lau, D. *Corros. Eng. Sci. Technol.* **2003**, 38(4), 259–266.
39. Cole, I. S.; Paterson, D. A.; Ganther, W. D.; Neufeld, A.; Hinton, B.; McAdam, G.; McGeachie, M.; Jeffery, R.; Chotimongkol, L.; et al. *Corros. Eng. Sci. Technol.* **2003**, 38(4), 267–274.
40. Pathak, R. K.; Louie, P. K.; Chan, C. K. *Atmos. Environ.* **2004**, 38(19), 2965–2974.
41. Yao, X.; Ling, T. Y.; Fang, M.; Chang, C. K. *Atmos. Environ.* **2007**, 41(2), 382–393.
42. Takeuchi, M.; Okochi, H.; Igawa, M. *Atmos. Environ.* **2004**, 38(28), 4701–4708.
43. Sander, R.; Crutzen, P. J. *J. Geophys. Res.-Atmos.* **1996**, 101(D4), 9121–9138.
44. Vogt, R.; Crutzen, P. J.; Sander, R. *Nature* **1996**, 383, 327–330.
45. Chameides, W. L.; Stelson, A. W. *J. Geophys. Res.* **1992**, 97(20), 565–580.
46. Yamamoto, N.; Fujii, M.; Endo, O.; Kumagai, K.; Yanagisawa, Y. *Aerosol Sci.* **2002**, 33, 1667–1679.
47. Keene, W. C.; Stutz, J.; Pszenny, A. A. P.; Maben, J. R.; Fischer, E. V.; Smith, A. M.; von Glasow, R.; Pechtl, S.; Sive, B. C.; Varner, R. K. Inorganic chlorine and bromine in coastal New England air during summer *J. Geophys. Res.* **2007**, 112, D10S12; doi:10.1029/2006JD007689.
48. Keene, W. C.; Pszenny, A. P.; Maben, J. R.; Sander, R. *Geophys. Res. Lett.* **2002**, 29, 1101.
49. Hobbs, P. V.; Bowdle, D. A.; Radke, L. F. *J. Climate Appl. Meteorol.* **1985**, 24, 1344–1356.
50. Deepak, A.; Gali, G. *The International Global Aerosol Program (IGAP)*; Deepak Publishing: Hampton, VA, 1991.
51. Jacob, D. J.; Waldman, J. M.; Munger, J. W.; Hoffman, M. R. *Environ. Sci. Technol.* **1985**, 19, 730–736.
52. Isaac, G. A.; Daum, P. H. *Atmos. Environ.* **1987**, 21, 1587–1600.
53. Aikawa, M.; Hiraki, T.; Tamaki, M. *Sci. Total Environ.* **2006**, 366, 275–285.
54. Tu, J.; Wang, H. S.; Zhang, Z. F.; Jin, X.; Li, W. Q. *Atmos. Res.* **2005**, 73(3–4), 283–298.
55. Pelicho, A. F.; Martins, L. D.; Nomi, S. N.; Solci, M. C. *Atmos. Environ.* **2006**, 40(35), 6827–6835.
56. Demirak, A.; Balci, A.; Karaoglu, H.; Tosmur, B. *Environ. Monit. Assess.* **2006**, 123(1–3), 271–283.
57. Baez, A. P.; Belmont, R. D.; Garcia, R. M.; Torres, M.; Padilla, H. *Atmos. Res.* **2006**, 80(1), 67–85.
58. Mpepya, J. N.; Pienaar, J. J.; Galy-Lacaux, C.; Held, G.; Turner, C. R. *J. Atmos. Chem.* **2004**, 47(1), 1–24.
59. Shivashankara, G. P.; Ranga, K.; Ramalingaiah, M. *Indian J. Environ. Health* **1999**, 41, 229–238.
60. Singh, A. K.; Mondal, G. C.; Kumar, S.; Singh, K. K.; Kamal, K. P.; Sinha, A. *Environ. Monit. Assess.* **2007**, 125 (1–3), 99–110.
61. Gillet, R. W.; Ayers, G. P. *Clean Air* **1989**, 23(3), 106–109.
62. Poste, D.; Bridgman, H. A. *J. Atmos. Chem.* **1991**, 13, 83–95.
63. Fitzgerald, W. R. The measurement of acidity in the Latrobe Valley, Victoria In Proceedings of the 7th World Clean Air Congress; Hartmann, H., Ed.; Clean Air Society of Australia and New Zealand: Sydney, 1986; pp 236–244.
64. Ayers, G. P.; Gillett, R. W. *Clean Air* **1988**, 22(2), 53–57.
65. Cole, I. S.; Ganther, W. D. *Corros. Eng. Sci. Technol.* **2006**, 41(2), 161–167.
66. Schaug, J.; Hanssen, J. E.; Nodop, K.; Ottar, B.; Pacyna, J. M. Co-operative program for the Monitoring and Evaluation of the long range transmission of air pollutants in Europe (EMEP) EMEP-CCC-Report 3/87 Norwegian Institute for air Research Lillestrom: Norway, 1987.
67. Charlson, R. J.; Lovelock, J. E.; Andrease, M. O.; Warren, S. G. *Nature* **1987**, 326, 665–661.
68. Schwartz, S. E. *Science* **1989**, 243, 753–763.
69. Graedel, T. E.; Frankenthal, R. P. *J. Electrochem. Soc.* **1990**, 137, 2385–2394.
70. Graedel, T. E. *J. Electrochem. Soc.* **1986**, 133, 2476.
71. Garrels, R. M. *Mineral Equilibria at Low Temperature and Pressure*; Harper: New York, 1960.
72. Ohba, R.; Okabayashi, K.; Yamamoto, M.; Tsuru, M. *Atmos. Environ.* **1990**, 24A(6), 925–935.
73. Gustafsson, M. E. R.; Franzen, L. G. *Atmos. Environ.* **1996**, 30(6), 977–989.
74. Johnson, K. E.; Stanners, J. F. *The Characteristics of Corrosion Test Sites in the Community*; Report EUR 7433; Commission of The European Communities: Luxembourg, 1981.
75. Strekalov, P. V.; Panchenko, Y. *Prot. Met.* **1994**, 30, 254.



76. Corvo, F.; Betancourt, N.; Mendoza, A. *Corros. Sci.* **1995**, 37(12), 1889–1901.
77. Corvo, F.; Hayes, C.; Betancourt, N.; Maldonado, L.; Veleza, L.; Echeverria, M.; De Rincon, O.; Rincon, A. *Corros. Sci.* **1997**, 39(5), 823–833.
78. Morcillo, M.; Chico, B.; Otero, E.; Mariaca, L. *Mater. Perf.* **1999**, 38(4), 72–77.
79. Morcillo, M.; Chico, B.; Mariaca, L.; Otero, E. *Corros. Sci.* **2000**, 42(1), 91–104.
80. Cole, I. S.; Chan, W. Y.; Trinidad, G. S.; Paterson, D. A. *Corros. Eng. Sci. Technol.* **2004**, 39(1), 89–96.
81. Cole, I. S.; Paterson, D. A. *Corros. Eng. Sci. Technol.* **2007**, 42(2), 91–104.
82. Haynie, F. H. In *Atmospheric Corrosion of Metals*; Dean, S. W., Rhea, E. C., Eds.; ASTM STP 767; American Society for Testing and Materials: Philadelphia, PA, 1982; pp 286–308.
83. Haynie, F. H. In *The Degradation of Metals in the Atmosphere*; Dean, S., Lee, T. S., Eds.; ASTM STP 965; American Society for Testing and Materials: Philadelphia, PA, 1988; pp 282–289.
84. Spence, J. W.; Haynie, F. H.; Lipfert, F. W.; Cramer, S. D.; McDonald, L. G. *Corrosion* **1992**, 48(12), 1009–1019.
85. Klassen, R. D.; Roberge, P. R. In Proceedings of NACE 2000 Conference Orlando, Florida, 2000; Paper No. 272.
86. Cole, I. S.; Paterson, D. A.; Lau, D. Holistic Modeling of Gas and Aerosol Deposition and the Degradation of Cultural Objects. In *Physical Techniques in the Study of Art, Archaeology and Cultural Heritage*; Creagh, D., Bradley, D., Eds.; Elsevier: Amsterdam, The Netherlands, 2007; Vol. 2; ISBN-13: 978-0-444-52856-8, ISSN 1871–1731.
87. Cole, I. S.; Lau, D.; Chan, F.; Paterson, D. A. *Corros. Eng. Sci. Technol.* **2004**, 39(4), 333–338.
88. Sehmel, G. A. *Atmos. Environ.* **1980**, 14, 983–1011.
89. Cole, I. S. Mechanism of Atmospheric Corrosion in Tropical Environments In *Marine Corrosion in Tropical Environments*; Dean, S. W., Delgadillo, G. H. – D., Bushman, J. B., Eds.; ASTM STP 1399; American Society for Testing and Materials: West Conshohocken, PA, 2000; pp 33–47.
90. Muster, T. H.; Cole, I. S. *J. Electrochem. Soc.* **2005**, 152(3), B125–B131.
91. Cole, I. S.; Lau, D.; Paterson, D. A. *Corros. Eng. Sci. Technol.* **2004**, 39(3), 209–218.
92. Nagano, H.; Doi, T.; Yamashita, M. *Mater. Sci. Forum* **1998**, 289, 127–134.
93. Cole, I. S.; Ganther, W. D.; Sinclair, J. D.; Lau, D.; Paterson, D. A. *J. Electrochem. Soc.* **2004**, 151(12), B627–B635.
94. Dean, S. W.; Reiser, D. B. Time of Wetness and Dew Formation: A Model of Atmospheric Heat Transfer. In *Atmospheric Corrosion*; Kirk, W. W., Lawson, H. H., Eds.; ASTM STP 1239; American Society for Testing and Materials: West Conshohocken, PA, 1995; pp 3–10.
95. Cole, I. S.; Ganther, W. D.; Paterson, D. A.; Bradbury, A. *Corros. Eng. Sci. Technol.* **2005**, 40(4), 328–336.
96. Cole, I. S.; Paterson, D. A. *Corros. Eng. Sci. Technol.* **2006**, 41(1), 67–76.
97. Dwyer, D. J.; Keleman, S. R.; Kaider, A. *J. Chem. Phys.* **1982**, 76, 1832.
98. Thomson, W. Proceedings of the Royal Society Edinburgh 1928.
99. Skorchellanti, V. V.; Tukachinsky, S. E. *J. Appl. Chem. (USSR)* **1955**, 28, 615.
100. Broad, D. W.; Foster, A. G. *J. Chem. Soc.*; 1946, 446.
101. Graedel, T. E. *J. Electrochem. Soc.* **1989**, 136, 19C–2003C.
102. Pourbaix, M. *Atlas of Electrochemical Equilibria in Aqueous Solutions*; National Association of Corrosion Engineers: 1440 South Creek Drive, Houston Texas 7704, 1974.
103. Graedel, T. E.; Goldberg, K. I. *J. Geophys. Res.* **1983**, 88(C15), 10865–10882.
104. Neufeld, A. K.; Cole, I. S.; Bond, A. M. *Corros. Sci.* **2002**, 44(3), 555–572.
105. Muster, T. H.; Cole, I. S. *Corros. Sci.* **2004**, 46(9), 2319–2335.
106. Tsuru, T.; Tamiya, K. I.; Nishikata, A. *Electrochimica Acta* **2004**, 49(17–18), 2709–2715.
107. Chen, Z. Y.; Persson, D.; Samie, F.; Zakipour, S.; Leygraf, C. *J. Electrochem. Soc.* **2005**, 152(12), B502–B511.
108. Nazarov, A.; Thierry, D. *Electrochimica Acta* **2004**, 49(17–18), 2717–2724.
109. Muster, T.; Hughes, A. E.; Thompson, G. E. Copper in Al alloys. In *Corrosion Research Frontiers*; Nova Publishing: Hauppauge NY, USA, 2009; ISBN-978-1-60741-201-4.
110. Birbilis, N.; Buchheit, R. G. *J. Electrochem. Soc.* **2005**, 152(4), B140–B151.
111. Schneider, O.; Ilevbare, G. O.; Scully, J. R.; Kelly, R. G. *J. Electrochem. Soc.* **2004**, 151(8), B465–B472.
112. Buchheit, R. G.; Grant, R. P.; Hlava, P. F.; McKenzie, B.; Zender, G. L. *J. Electrochem. Soc.* **1997**, 144(8), 2621–2628.
113. Park, J. O.; Apik, C. H.; Huang, Y. H.; Alkire, R. C. *J. Electrochem. Soc.* **1999**, 146, 517–523.
114. Moon, S. M.; Pyun, S. I. *Electrochim. Acta* **1999**, 44, 2445–2454.
115. Vukmirovic, M. B.; Dimitrov, N.; Sieradzki, K. J. *J. Electrochem. Soc.* **2002**, 149(9), B428–B439.
116. Ilevbre, G. O.; Schneider, O.; Scully, J. R.; Kelly, R. G. *J. Electrochem. Soc.* **2004**, 151(8), B453–B464.
117. Graedel, T. E. *J. Electrochem. Soc.* **1989**, 136, C204–C212.
118. Graedel, T. E. *J. Electrochem. Soc.* **1989**, 136, C193–C203.
119. Cole, I. S.; Ganther, W. D.; Lau, D. *Corros. Eng. Sci. Technol.* **2006**, 41(4), 310–320.
120. Schikorr, G. *Werkst. Korros* **1963**, 14, 69.
121. Cermakova-Knotkova, D.; Vlickova, J. *Werkst. Korros* **1970**, 21, 16.
122. Evans, U. R. *Trans. Inst. Met. Finish.* **1960**, 37, 1.
123. Stratmann, M. *Ber. Bunsenges. Phys. Chem.* **1990**, 94, 626–639.
124. Schikorr, G. *Werk. Korr.* **1964**, 15, 457.
125. Schikorr, G. *Werk. Korr.* **1963**, 14, 69.
126. Oesch, S.; Faller, M. *Corros. Sci.* **1997**, 39(9), 1505–1530.
127. Butlin, R. N.; Coote, A. T.; Devenish, M. *Atmos. Environ. B – Urban Environ.* **1992**, 26(2), 199–206.
128. Stampfl, P. P. *Corros. Sci.* **1969**, 9, 185.
129. Hansen, H. C. B. *Caly Miner.* **1989**, 24, 663.
130. Reffass, M.; Sabot, R.; Savall, C.; Jeanin, M.; Creus, J.; Refait, P. *Corros. Sci.* **2006**, 48, 709–726.

## 2.18 Marine Corrosion

**B. Phull**

308 Humphrey Drive, Wilmington, NC 28411, USA

© 2010 Elsevier B.V. All rights reserved.

2.18.1	Introduction	1108
2.18.2	Environment Characteristics	1108
2.18.2.1	Seawater Constituents	1108
2.18.2.2	Dissolved Gases	1110
2.18.2.3	Seawater pH	1110
2.18.2.4	Calcareous Deposits	1111
2.18.2.5	Temperature	1111
2.18.2.6	Effect of Depth	1111
2.18.2.7	Fouling, Macro- and Microorganisms	1111
2.18.2.8	Effect of Velocity	1111
2.18.2.9	Seawater Resistivity	1113
2.18.3	Corrosion and Protection Mechanisms	1113
2.18.3.1	Galvanic Corrosion	1118
2.18.4	Carbon Steels	1120
2.18.5	Cast Irons	1125
2.18.6	Stainless Steels	1125
2.18.7	Copper Alloys	1131
2.18.8	Nickel-Based Alloys	1135
2.18.9	Titanium Alloys	1137
2.18.10	Aluminum Alloys	1138
2.18.11	Magnesium	1142
2.18.12	Zinc	1142
2.18.13	Nonmetallic Materials	1142
2.18.14	Corrosion Protection Methods	1143
2.18.15	Test Methods	1146
	References	1146

### Abbreviations

**ALWC** Accelerated low water corrosion

**BOD** Biological oxygen demand

**CCT** Critical crevice temperature

**CP** Cathodic protection

**CP** Commercial purity (of titanium)

**CPT** Critical pitting temperature

**DO** Dissolved oxygen

**H** Heat treatment term in aluminum alloys (aged condition)

**HE** Hydrogen embrittlement

**IGC** Intergranular corrosion

**L** Low carbon

**Max.** Maximum

**MCA** Multiple crevice assembly

**MSF** Multistage flash (distillation)

**O** Heat treatment term in aluminum alloys (annealed condition)

**P** Perforation

**PH** Precipitation hardening

**PREN** Pitting resistance equivalent number

**PTFE** Poly tetra fluoro ethylene

**RH** Heat treatment term in PH stainless steels

**SCC** Stress corrosion cracking

**SCE** Saturated calomel electrode

**SEM** Scanning electron microscope

**SRB** Sulfate reducing bacteria

**T** Temper heat treatment term in aluminum alloys

**T** Temperature

**TDS** Total dissolved solids

**YS** Yield strength

**Symbols****C<sub>0</sub>** Bulk concentration of oxygen  
(moles cm<sup>-3</sup>)**d** Diameter**D** Diffusion constant**Pr** Prandtl number**U<sub>0</sub>** Bulk flow rate (cm s<sup>-1</sup>)**α** Alpha phase**β** Beta phase**ν** Kinematic viscosity**v** Velocity**2.18.1 Introduction**

This chapter focuses on corrosion and behavior of important engineering materials in seawater. As entire textbooks have been devoted to seawater and marine corrosion, it is clearly not possible to cover this subject in great detail in this chapter.

It is customary to define marine environments in terms of ‘zones’ in which materials might be exposed, *viz.*, atmospheric, splash and spray, tidal, immersion or submerged, and bottom-mud or sediment. This chapter addresses corrosion issues primarily pertaining to the immersion, tidal, and splash zones. Corrosion in marine atmospheres and bottom-mud is covered elsewhere in this book.

Materials are subjected to seawater conditions in numerous applications, for example, ships, pleasure boats, submarines, offshore platforms, subsea pipelines and telecommunications cables, wharfs, seawater-cooled power and chemical plants, desalination plants, fishing gear, and so on. Seawater is a critical resource for food (primarily fish), table salt, and conversion to freshwater (desalination). It is also the primary source for extraction of magnesium and subsequent production of its alloys.

As in so many other environments there is a multitude of factors, which can affect corrosion of materials in seawater. Many of these factors are interrelated, resulting in complicated behavior of materials in specific applications. The important influencing factors are reviewed first, followed by an analysis of the corrosion mechanisms and the behavior of common engineering materials in seawater. Finally, test methods in seawater environments are discussed briefly.

**2.18.2 Environment Characteristics**

Seawater covers ~70% of the earth’s surface. It is a highly complex medium that contains almost every element in the periodic table and a multifarious plethora of living organisms. Hence, it is sometimes described as a ‘living’ medium and considered to be the most corrosive of the natural environments.

**2.18.2.1 Seawater Constituents**

Conventional wisdom is that the corrosivity of seawater is because of its salt (primarily NaCl) content. However, as discussed later in this section, it is not the salt *per se*, but other constituents – especially the dissolved oxygen (DO) and pollutants such as sulfides that often play critical roles. The total salt content is typically expressed in terms of salinity and/or chlorinity. Salinity is the total solid matter (grams) in one kilogram of seawater (after all the organic matter has been oxidized, carbonate converted to oxide, and bromine and iodine replaced by chlorine). From an analytical viewpoint, it is easier to determine the chlorine content, which is expressed as chlorinity – the total amount of chlorine (grams), plus equivalent chlorine assumed to replace bromine and iodine, in 1 kg of seawater. Salinity is related to chlorinity by the following empirical expression:

$$\text{Salinity} = (1.80655 \times \text{Chlorinity}) + 0.03$$

Salinity and chlorinity are usually expressed as grams per kilogram or parts per thousand (g kg<sup>-1</sup>, ppt or ‰). Multiplying by 1000 converts g kg<sup>-1</sup> or ppt to parts per million (ppm). Salinity can also be considered as total dissolved solids (TDS), stated as mg l<sup>-1</sup> (ppm). The properties of seawater can vary considerably by geographical location, seasons, and water depth. **Table 1** shows a comparison of the relative approximate salinities of a number of seas and oceans in the world. River outflows, evaporation, rainfall, melting ice, wind, and wave action – all can exert a strong influence on salinity. Littoral waters are often rendered brackish (*i.e.*, less salty) due to significant river outflow and may contain considerable sediments and pollutants.

The ‘average’ salinity of open ocean waters (*i.e.*, well away from land) is in the range ~32–36 ppt, and the corresponding average chlorinity in the ~18–20 ppt range. The salinity of the landlocked Dead Sea is an order of magnitude higher. **Table 2**

shows the 'average' concentrations of ionic constituents in open seawater of 35‰ salinity. From a corrosion viewpoint, all the ocean waters can be considered as sufficiently corrosive toward carbon steel, typically the most commonly used constructional material, such that corrosion control in some form or another is essential for extended structure and component life and functionality in most cases.

In terms of salt content, the 'average' seawater composition corresponds to ~3.5% NaCl solution. Thus, many researchers who do not have easy access to natural seawater often use this composition as a synthetic substitute. Others use artificial seawater solutions<sup>2</sup> that attempt to more closely mimic real seawater, at least in terms of dissolved salts. The chloride ( $\text{Cl}^-$ ) ion is considered to be the most aggressive specie in seawater, particularly for localized corrosion. Sulfate ( $\text{SO}_4^{2-}$ ) ions play an important

role in the activity of sulfate-reducing bacteria (SRB) which proliferate under anaerobic conditions, and can cause serious corrosion problems for certain materials and applications as discussed later in this section.

Calcium ( $\text{Ca}^{2+}$ ) and bicarbonate ( $\text{HCO}_3^-$ ) ions in seawater contribute toward calcium carbonate ( $\text{CaCO}_3$ ) scale formation, which is especially enhanced on heat transfer surfaces because of the inverse solubility of  $\text{CaCO}_3$  with temperature. Such scales can impede transport of DO to the metal surface, and hence, reduce general corrosion of active metals and the effects of seawater velocity so long as the scale is not dislodged. However, the scale reduces heat transfer, and can significantly increase the probability of localized (under-deposit) corrosion attack, particularly on materials with passive films that are susceptible to such conditions (e.g., 300-series stainless steels, aluminum alloys, nickel-copper alloys, etc.) in aerated seawater. Of course,  $\text{Ca}^{2+}$  and  $\text{HCO}_3^-$  are also critical species in the formation of undersea corals and protective shells by numerous marine organisms such as clams, oysters, barnacles, crabs, lobsters, star fish, urchins, and so on.

Organic matter necessary for biological processes contains carbon, oxygen, hydrogen, nitrogen, and phosphorus. Carbon, oxygen, and hydrogen (e.g., as polysaccharides and lipids) are available in abundance, but usable nitrogen and phosphorus compounds (primarily nitrates and phosphates) are generally limiting nutrients. The main sources of these latter nutrients include, river runoff into the sea, decaying organic matter, and upward water flow from deeper ocean areas. In littoral waters, these nutrients can reach very high concentrations where water runoff from land (e.g., in rivers) discharges large amounts of sewage and fertilizers from anthropogenic sources. Nutrient-rich waters encourage excessive plant growth, which depletes oxygen and kills animal life – a process known as eutrophication. An example of this is 'red tides,' which are associated with phytoplankton (algae) blooms.

Industrial waste from anthropogenic sources that is discharged into any body of water is technically a source of pollutants, which can consist of, for example, heavy metals and inorganic and organic compounds. The introduction of high levels of pollutants can alter the corrosivity of seawater toward certain materials, for example, copper-ion effects on aluminum alloys, sulfides and ammonia on copper alloys, sulfur compounds on steels, and so forth.

**Table 1** Salinity of various ocean waters expressed as approximate total dissolved solids ( $\text{mg l}^{-1}$  or ppm)

Seawater	Approximate TDS (ppm)
Arabian Gulf	47 000
Red Sea	43 000
Mediterranean Sea	41 000
Atlantic Ocean	36 000
Indian Ocean	35 000
Pacific Ocean	34 000
North Sea	33 000
Bering Sea	32 000
Black Sea	22 000
Caspian Sea	13 000
Baltic Sea	8 000
Dead Sea	322 000

**Table 2** Major ionic constituents in seawater of 35‰ salinity (35 000 ppm TDS)<sup>1</sup>

Ion	Concentration (ppm)
Chloride, $\text{Cl}^-$	19 353
Sodium, $\text{Na}^+$	10 760
Sulfate, $\text{SO}_4^{2-}$	2 712
Magnesium, $\text{Mg}^{2+}$	1 294
Calcium, $\text{Ca}^{2+}$	413
Potassium, $\text{K}^+$	387
Bicarbonate, $\text{HCO}_3^-$	142
Bromide, $\text{Br}^-$	67
Strontium, $\text{Sr}^{2+}$	8
Borate, $\text{B}_4\text{O}_7^{2-}$	4
Fluoride, $\text{F}^-$	1

### 2.18.2.2 Dissolved Gases

DO represents the most important species that controls the corrosion behavior of many materials in seawater, even more so than chloride. DO concentration is reported either as  $\text{ml l}^{-1}$  or  $\text{mg l}^{-1}$  ( $\text{ml l}^{-1} \times 1.429 = \text{mg l}^{-1}$ ). The primary factors that control DO content of seawater include temperature, salinity, biological activity, and mixing (flow). The inverse solubility of dissolved oxygen versus temperature and dissolved oxygen versus salinity is depicted in **Figures 1 and 2**, respectively. The DO concentration of the Dead Sea, which has a salinity of  $\sim 322$  ppt, is apparently  $\sim 0.1 \text{ mg l}^{-1}$ .

Oxygen dissolves in seawater either from the atmosphere and/or from plant photosynthesis, which is most prevalent over a depth  $\sim 100$  m. Thus, surface waters at normal atmospheric pressures tend to be saturated or supersaturated in oxygen, including the thin liquid environment in the splash zone. However,

quiescent flow conditions that favor algal growth and proliferation of decaying matter can reduce DO content markedly because of biological oxygen demand (BOD).

The principle reaction in seawater that controls corrosion is oxygen reduction. For any given DO concentration, the corrosion process is often strongly influenced by seawater velocity. This is discussed under corrosion mechanisms later in this chapter. The role of carbon dioxide is discussed in the following section. Other gases such as hydrogen sulfide and ammonia can be generated by bacteria from decaying matter and can influence corrosion of certain materials as discussed later.

### 2.18.2.3 Seawater pH

Clean surface seawater is typically slightly alkaline. This is related to the carbon dioxide ( $\text{CO}_2$ ) equilibrium with the atmosphere. Seawater contains bicarbonate

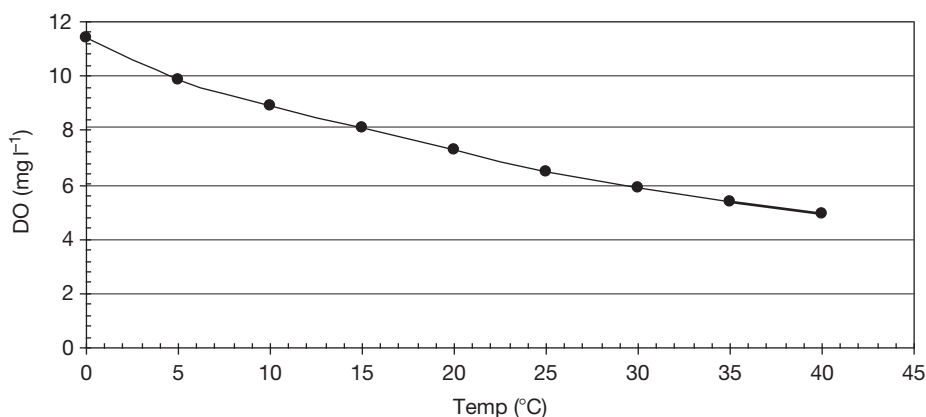


**Figure 1** Dissolved oxygen (DO) versus temperature in natural seawater of 35‰ salinity at 1 atm pressure.

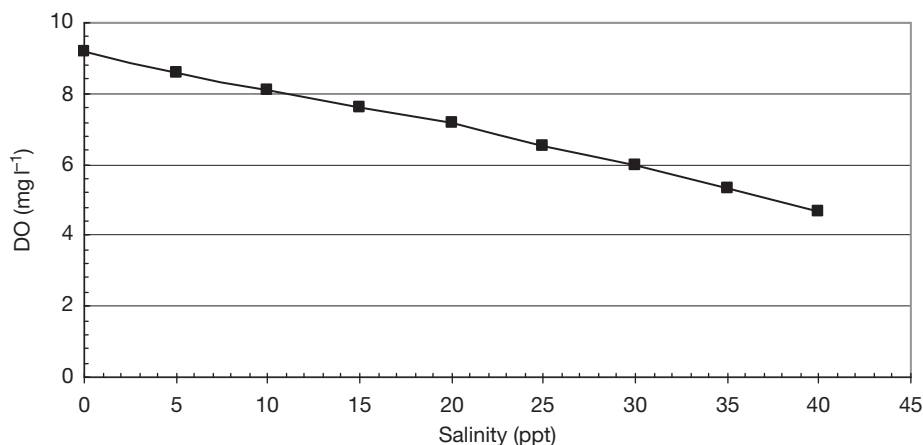


**Figure 2** DO versus salinity in synthetic seawater at 20°C and 1 atm pressure.



( $\text{HCO}_3^-$ ) ions, carbonate ( $\text{CO}_3^{2-}$ ) ions, undissociated carbonic acid ( $\text{H}_2\text{CO}_3$ ), and dissolved  $\text{CO}_2$ . The pH is influenced by temperature,  $\text{CO}_2$  partial pressure (which affects carbonate in solution), photosynthesis, and to a lesser extent by boric acid. These factors interact to maintain the pH in a surprisingly alkaline range (8.1–8.3), and hence, seawater is said to be highly buffered. Hydrogen sulfide, for example, from sulfate-reducing bacterial (SRB) activity, can lower the pH considerably and affect the performance of certain materials.

#### 2.18.2.4 Calcareous Deposits

Calcium, bicarbonate, and magnesium in seawater are important constituents that can result in the formation of calcareous deposits on metal surfaces. Calcareous deposits form on cathodic surfaces and can slow down the corrosion process by inhibiting diffusion of DO and, consequently, its reduction at the metal surface. Calcareous deposit formation is particularly important when large, bare structures (e.g., steel offshore platforms) are cathodically protected in seawater. Without calcareous deposits, current demand for cathodic protection would remain at a high level, consequently, sacrificial anode life would be considerably reduced and the structure may not polarize to adequate protection levels. Calcareous deposit morphology and thickness are affected by current density at the cathode, seawater composition, temperature, and velocity.

#### 2.18.2.5 Temperature

Seawater temperature is also influenced by many geographical factors. Temperature generally decreases with depth. It also varies seasonally at the surface, ranging from  $\sim 35^\circ\text{C}$  at the equator to  $\sim -2^\circ\text{C}$  at the poles. Increasing temperature lowers solubility of dissolved gases and scale-forming calcium compounds such as calcium carbonate, but generally increases biofouling. All these factors can have a complex effect on corrosion behavior as discussed later in this chapter.

#### 2.18.2.6 Effect of Depth

Figures 3 and 4 illustrate how various parameters can vary with depth<sup>2</sup> and geographic location.<sup>3</sup> Generally, DO, temperature, and pH decrease steeply with depth over the first several hundred meters while salinity increases. Hydrostatic pressure increases with depth

while light penetration decreases. It has been postulated that the increase in DO at several 1000 m in the Atlantic Ocean is due to the flow of cold seawater through the ‘funnel’ in the north; but in the Pacific Ocean, this effect is prevented because of a minor flow through the Bering Strait.<sup>4</sup> It is important to recognize that the data shown in Figures 3 and 4, for example, are very site specific. Thus, quite wide variations in parameters can occur from one location to another, which can only be determined from actual measurements. Consequently, these variations can influence corrosion behavior of certain materials.

#### 2.18.2.7 Fouling, Macro- and Microorganisms

Fouling constitutes the attachment of macro- and microorganisms, most prevalent on stationary surfaces. Biofilms apparently start forming on all metallic and nonmetallic surfaces within hours of exposure to seawater.<sup>5</sup> Biofilms which are associated with organic matter and molecules (exopolymers) in seawater are colonized by various bacterial microorganisms. As the films become established, heavier slime formation is followed by attachment of macro species,<sup>6</sup> for example, barnacles, oysters, clams, sea squirts, and vegetable species such as seaweed, bryozoa, hydroids, and codium. The macrofouling species predominate in the tidal zone and can slow down diffusion of dissolved gases, and hence overall corrosion of certain materials. However, shielding of the surface can lead to local anaerobic conditions, anaerobic bacterial activity, and subsequently, localized attack. Some materials (e.g., copper-rich alloys) are more resistant but not entirely immune to macro fouling compared with other materials that foul copiously (e.g., carbon steel, stainless steel, titanium, and even nonmetallics).

#### 2.18.2.8 Effect of Velocity

Velocity can influence corrosion behavior in seawater in multiple ways. If the velocity is too low (quiescent conditions), solids may settle out, subsequently leading to under-deposit attack (e.g., on susceptible grades of stainless steel such as Type 410, 430, 304, 316, etc.). At intermediate velocities, such deposits may be suspended in the flow (once deposits have formed, much higher flow rates may be necessary for their removal than preventing settlement in the first place). As velocity continues to increase, biofilm and calcareous deposit formation diminishes. However,

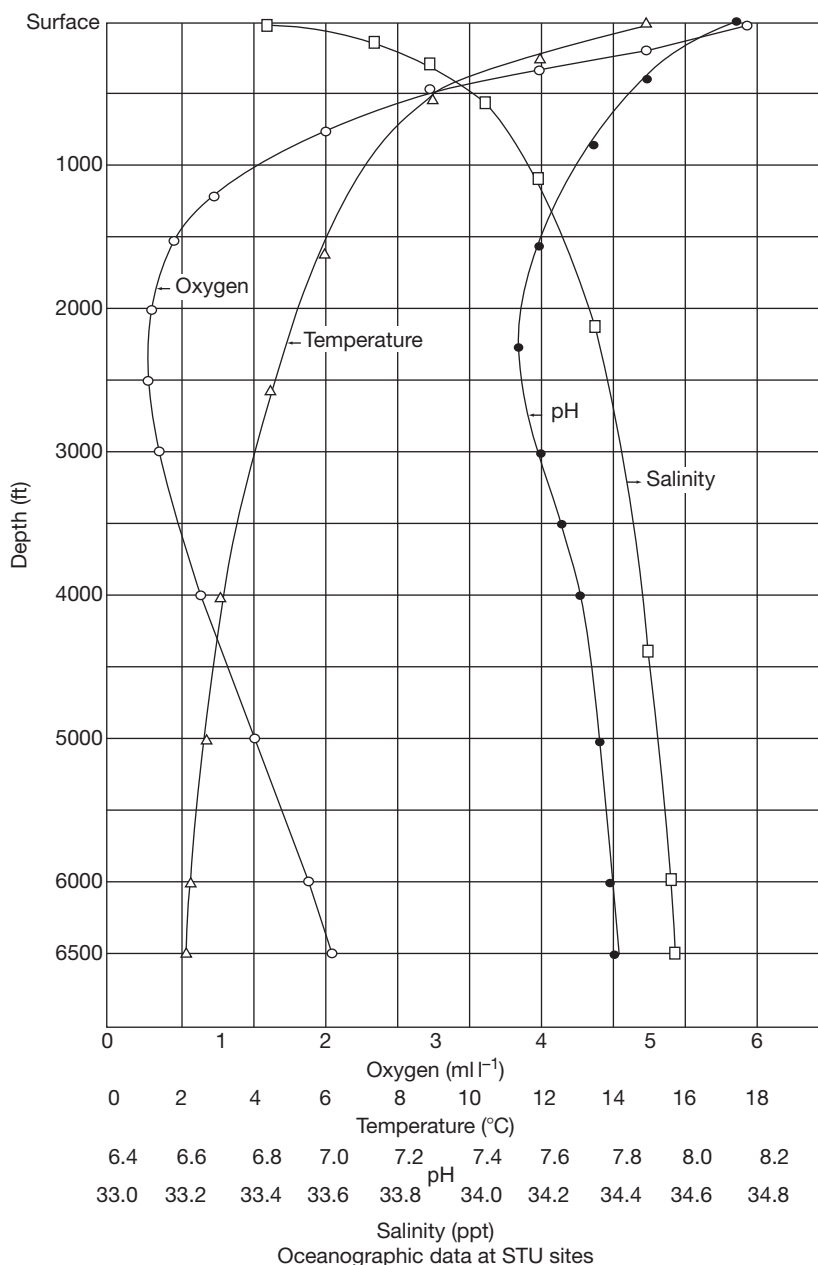


**Figure 3** Variations in DO, temperature, pH, and salinity at a specific Pacific Ocean corrosion test site. Reproduced from Dexter, S.C.; Culberson, C. *Meter. Perform.* **1980**, 19(9), 23.

increased wall shear stress, turbulence, and impingement create conditions conducive for the removal of protective films on solid surfaces – thus, increasing the risk of erosion–corrosion of susceptible materials (e.g., carbon steel, copper-base alloys, aluminum-base alloys). At extreme velocities, even otherwise highly corrosion-resistant materials become increasingly susceptible to cavitation damage. Generally, for active

materials, increasing the velocity increases corrosion rate as more DO is transported to the metal surface. For passive materials, the enhanced diffusion of DO due to higher velocities is usually beneficial as long as the attack (e.g., crevice corrosion) has not been already initiated. Macroorganisms, calcareous deposits, and coatings generally reduce velocity effects, partly by slowing diffusion of oxygen to the metal surface.

However, at higher velocities these protective mechanisms may be negated as discussed earlier.

### 2.18.2.9 Seawater Resistivity

Seawater typically has low electrolytic resistivity (resistivity is reciprocal of conductivity) due to its significant dissolved salt content. Low resistivity generally corresponds to greater local cell action, larger anode–cathode interaction distances, and consequently, higher corrosion rates (particularly for active materials such as carbon steel), higher galvanic corrosion rates, and higher current output from cathodic protection anodes. Table 3 shows that resistivity decreases with increasing salinity and temperature; the resistivity values shown in Table 3 were converted from the conductivity data.<sup>7</sup> Thus, higher resistivities can be expected for seawater affected by fresh water outflows, for example, in coastal areas and for colder waters.

### 2.18.3 Corrosion and Protection Mechanisms

From a corrosion standpoint, chloride ions are considered to be the most aggressive constituent in seawater. The precise role of chloride in the corrosion

process is still not fully understood. For instance, chloride contributes to increased electrolytic conductivity by ion transport. Higher conductivity means that current between anodic and cathodic areas can flow over larger distances, for example, in galvanic couples; the magnitude of local cell currents can also be higher. Thus, the overall effect is typically higher general and/or localized corrosion rates. Corrosion attack at anodic areas is supported by reduction reaction(s) at cathodic sites – typically oxygen reduction in aerated seawater.

Corrosion products can provide some degree of protection if they impede oxygen diffusion to cathodic sites. Reduction in general corrosion rate of steel in seawater due to formation of corrosion products and macrofouling is illustrated in Figure 5.

Oxygen reduction is obviously a critical reaction for metallic corrosion in seawater. Deoxygenation of seawater is a recognized method of corrosion control for carbon steel, for example, in multistage flash distillation plants and water injection in offshore oil/gas production during secondary recovery. Thus, chloride ions are rendered relatively harmless in the complete absence of oxygen. Typical polarization curves for steel in aerated and deoxygenated seawater are shown in Figure 6. It is apparent that although the corrosion potential is nearly 400 mV more ‘active’ in the absence of oxygen, the corrosion rate is significantly lower when compared with aerated seawater.

Differences in oxygen levels between local areas produce potential differences that give rise to concentration cells – commonly referred to as differential oxygenation or differential aeration cells. The low oxygen or anoxic (oxygen-free) area becomes anodic because of its more active (electronegative) potential; conversely, the area of higher oxygen becomes

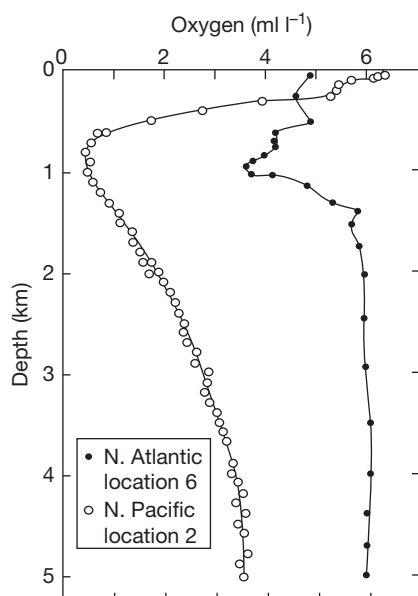


**Figure 4** DO-depth profiles at two specific open ocean test sites. Reproduced from Compton, K.G., *Corrosion* 1970, 26, 448.

**Table 3** Resistivity ( $\Omega\text{cm}$ ) as function of salinity and temperature

Salinity (%)	0°C	5°C	15°C	20°C	25°C	30°C
10	107.1	92.5	80.9	71.6	64	57.7
20	57.3	49.6	43.5	38.5	34.5	31.1
30	39.6	34.4	30.2	26.8	24	21.6
31	38.5	33.4	29.3	26	23.3	21
32	37.4	32.4	28.5	25.3	22.6	20.4
33	36.3	31.5	27.7	24.6	22	19.9
34	35.3	30.7	27	23.9	21.4	19.4
35	34.4	29.9	26.3	23.3	20.9	18.9

Source: Whitfield, M., Jagner, D., Eds. *Marine Electrochemistry, A Practical Introduction*; Wiley, 1981; p 513.

cathodic because of its less active (more electropositive) potential. This is usually demonstrated in the laboratory by setting up a partitioned cell in which one-half is aerated and the other half is deaerated with a steel electrode immersed in each half. The measured open-circuit potentials and couple current flow direction indicates the afore-mentioned anode/cathode relationship. However, as noted by Tomashov,<sup>8</sup> actual corrosion rate of the steel electrode in the aerated half of the cell is greater in chloride solutions, despite being the cathode in the differential-aeration macrocell, than in the deaerated half. This apparent contradiction is due to enhanced microcell action in solutions containing chloride that prevents anodic passivation of the steel. Lower corrosion rates of steel piles in the mud

zone (low oxygen environment) relative to the submerged zone above it (aerated environment) were cited as a practical manifestation of this apparently anomalous behavior. In other words, in seawater, chloride ions and associated high conductivity generates microcell activity that overrides the differential-aeration macrocell. In environments where steel can 'passivate,' for example, chloride-free waters or soils, the classical differential-aeration mechanism is operative.

In anaerobic seawater environments, the oxygen reduction reaction is negated. However, high corrosion rates observed under anoxic conditions have been attributed to microbiological activity, in particular, sulfate-reducing bacteria (SRB, e.g., *Desulfovibrio*

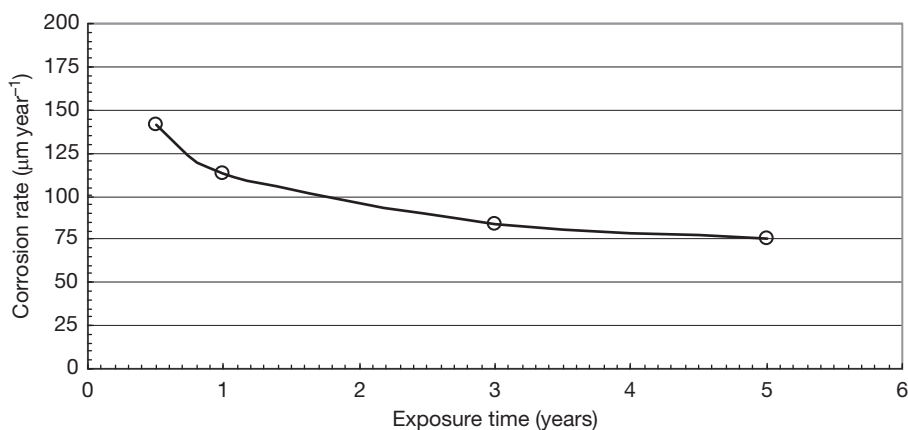


**Figure 5** Decrease in general corrosion rate of carbon steel in quiescent seawater associated with development of corrosion products and macrofouling.

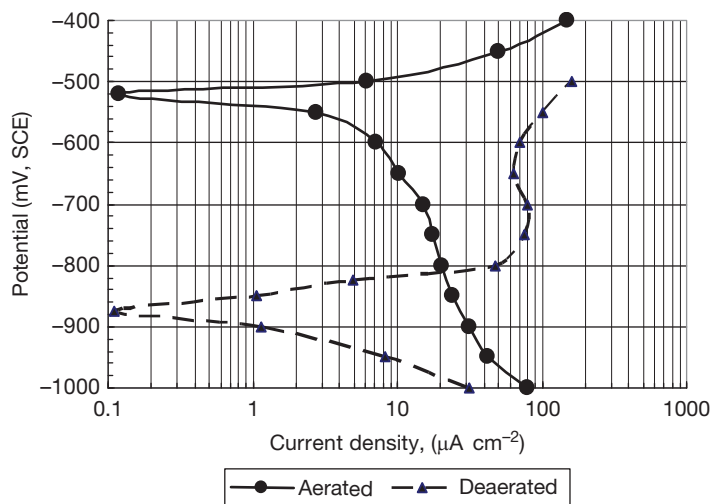


**Figure 6** Polarization curves for carbon steel in aerated versus deaerated seawater.

*desulfuricans*). These bacteria reduce sulfate to sulfide under favorable conditions.<sup>9–11</sup>

While SRB can influence corrosion in anaerobic environments, propagation of corrosion attack is generally most prevalent under conditions of alternate exposure to anaerobic and aerobic environments. In principle, an impervious sulfide film covering the entire metal surface may be protective. However, in practice, such films are rarely impervious and/or continuous. Thus, corrosion at small exposed areas of the substrate is accelerated as the sulfide film serves as a large cathodic surface. The adverse effect of sulfide on corrosion of copper heat exchanger alloys is well known and discussed later in this chapter. Bacteria other than SRB can also influence corrosion behavior in seawater.

As discussed earlier, calcareous deposits form on cathodic surfaces. Although enhanced under cathodic protection conditions, such deposits can also form at cathodic areas associated with corroding surfaces. Hydroxyl ion generation by the oxygen reduction reaction at the cathodes increases the pH at the metal surface. The increase in pH alters the equilibrium, which can result in precipitation of calcium carbonate scale.



Under cathodic overprotection conditions, formation of magnesium hydroxide is favored.



Adherent calcareous deposits slow the diffusion of oxygen to the metal surface. For immersed surfaces, this implies polarization of the oxygen reduction reaction, and hence a decrease in cathodic protection

current demand or a decrease in general corrosion rate when there is no cathodic protection.

Calcareous deposits play a critical role in cathodic protection of bare metal structures in seawater. Early pioneering work by Cox generated several patents, which described the ‘best’ current density ranges to produce the most protective calcareous deposits<sup>12,13</sup> that were referred to as ‘electrocoating.’ Over the years, many research efforts have been pursued for a better understanding and optimization of calcareous deposits.<sup>14–24</sup> It has been shown that the deposits are affected by many variables that include current density, potential, seawater velocity, temperature, and chemistry.

For example, **Figure 7** shows current densities associated with calcareous deposits formed in synthetic seawater at several potentiostatically-controlled protection potentials in 50 h. Variation of deposit morphology with protection potential is illustrated in the SEM photomicrographs in **Figure 8**. At  $-1100$  mV (SCE), the deposits consisted predominately of  $\text{CaCO}_3$  (aragonite) and a trace of  $\text{Mg}(\text{OH})_2$  (brucite). Although the deposits were thick, they were poorly adherent and not very protective since the current density did not decrease significantly. More adherent and protective deposits, composed primarily of  $\text{CaCO}_3$  (aragonite), were formed at  $-800$ ,  $-900$ , and  $-1000$  mV (SCE). At  $-750$  mV (SCE), complete cathodic protection was not attained, and the deposits comprised a mixture of  $\text{CaCO}_3$  and iron corrosion products ( $\text{Fe}_2\text{O}_3$  and  $\text{Fe}_3\text{O}_4$ ). Data are not included in **Figures 7 and 8** for deposits formed at  $-1200$  mV (SCE); however, the current density was  $>10^4$  mA m<sup>-2</sup>, the deposits were thick, gelatinous, mainly  $\text{Mg}(\text{OH})_2$ , and nonprotective. In practice,

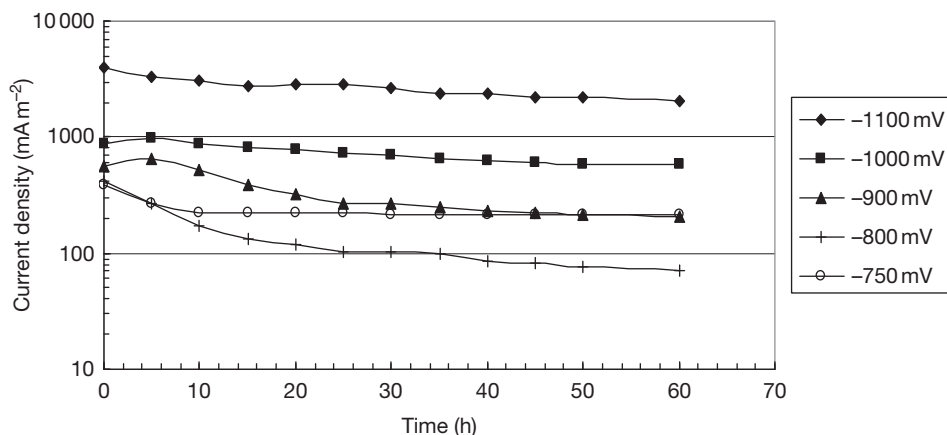


**Figure 7** Current density versus time for clean steel at various protection potentials versus SCE.



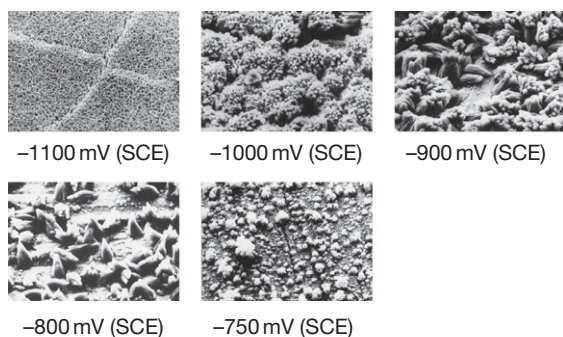


**Figure 8** Morphology of calcareous deposits formed at various potentials in synthetic seawater in 50 h.

many impressed current cathodic protection systems operate at constant current. As calcareous deposits form under constant current conditions, the current density increases at local areas, the potential of the protected metals shifts in the negative direction, and the morphology of the calcareous deposits changes. From a research viewpoint, it is easier to study the formation of, and protection afforded by, calcareous deposits under potentiostatic conditions rather than constant current conditions. Moreover, cathodic protection from well-designed sacrificial-anode systems, which are more common in seawater applications, approximates potentiostatic conditions, that is, anode output decreases as calcareous deposits are formed. However, Humble<sup>14</sup> has shown that the Ca/Mg ratio in calcareous deposits decreases with increasing current density as illustrated in Figure 9. Surprisingly, it has been found that  $\text{Mg}^{2+}$  ions in seawater inhibit  $\text{CaCO}_3$  crystal nucleation and precipitation.<sup>25</sup> However, the greater concentration of  $\text{Mg}^{2+}$  in open seawater compared to  $\text{Ca}^{2+}$  assures that  $\text{CaCO}_3$  will precipitate as aragonite.<sup>26</sup> In other natural waters, precipitation of  $\text{CaCO}_3$  as calcite is favored because the concentration of  $\text{Ca}^{2+}$  is usually much greater than that of  $\text{Mg}^{2+}$ .

Table 4 provides some quantitative and qualitative data on calcareous deposit properties relative to cathodic protection current densities. The solubility of  $\text{CaCO}_3$  decreases with increasing temperature, while that of  $\text{Mg}(\text{OH})_2$  increases. Thus, precipitation of  $\text{CaCO}_3$  is favored in warm seawater, and that of  $\text{Mg}(\text{OH})_2$  in colder seawater. This has been postulated as one possible explanation of higher current density requirements for cathode protection of steel structures in colder seawater. It is apparent that calcareous deposit formation involves complex phenomena; thus, ideally, characterization and optimization of

calcareous deposits for specific applications are best performed locally, *in situ*.

It is generally accepted that protection for materials such as aluminum alloys, titanium alloys, stainless steels, and nickel alloys is conferred by surface passive oxide films. In other words, these materials possess active-passive characteristics. In seawater, active corrosion is suppressed if the material exhibits passive behavior. The air-formed oxide films are thin (typically  $<10$  nm). The composition of the base metal, heat treatment, surface cleaning, surface finish, and the exposure environment are among the primary factors that determine the stability of the passive film. There is some evidence that adsorbed species from the exposure environment, for example, oxygen, contribute to the properties of the passive film.<sup>28</sup>

The most deleterious species toward passive films in seawater is chloride. Film breakdown and rehealing is a dynamic process. However, under certain conditions rehealing may not occur after corrosion has initiated at local areas. This can lead to propagation of attack and high rates of localized corrosion. A classical case of this is crevice corrosion of susceptible stainless steels, for example, under gaskets, under O-rings, at threaded joints, under silt and macrofouling deposits, and so on. Previously, this type of attack was ascribed to oxygen concentration cells, that is, absence of oxygen in the crevice and plentiful supply outside the crevice. However, the modern view is a little more complex. Crevice corrosion has been modeled mathematically and experimentally in a number of ways.<sup>29–33</sup> Deeper and tighter crevices are more susceptible to both the initiation and propagation of crevice corrosion. Metal-to-nonmetal crevices are generally tighter than metal-to-metal crevices because of the easier deformation of the nonmetal. However, metal-to-metal crevices, although less tight, may be equally susceptible to attack because both metal surfaces can contribute metal ions for hydrolysis. In dissimilar alloys, crevice attack on the more susceptible metal occurs first. As the crevice electrolyte becomes more aggressive by the autocatalytic process, crevice corrosion can initiate subsequently on the more resistant alloy.<sup>34</sup>

Electrochemical measurements have been used to demonstrate potential ennoblement and increased cathodic kinetics on passive surfaces covered by biofilms in seawater.<sup>35,36</sup> It has also been shown that biofilms are more prevalent in warm seawater, and hence decrease crevice corrosion initiation time compared to cold seawater. Above a threshold temperature

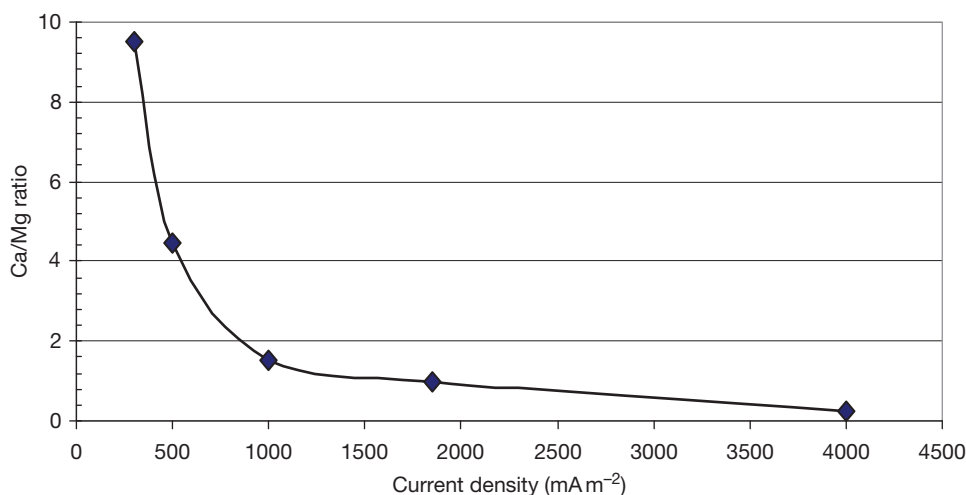


**Figure 9** Ca/Mg ratio in calcareous deposits formed in seawater at various cathodic protection current densities over 3 months. Reproduced from Humble, H. A. *Corrosion* **1948**, 4(7), 358–370.

**Table 4** Calcareous deposits properties relative to cathodic protection current densities

Initial current density (mA m <sup>-2</sup> )	Duration (days)	Calcareous film formed	Current density for continued protection (mA m <sup>-2</sup> )
2000	1	Soft with high Mg content	20–30
1000	2–3	Fairly hard	20–30
500	5–6	Hard, mainly calcareous	20–30
200	20–30	Medium thickness, hard	30–40
100	60–90	Medium thickness, hard	40
60	180	Light, hard	40–50

Source: Doremus, E. P.; Doremus, G. L. *Corrosion* **1950**, 6(7), 216–224.

of  $\sim 50^\circ\text{C}$ , crevice corrosion susceptibility in natural seawater apparently decreases.<sup>32</sup> It has been hypothesized that this behavior is due to reduced microbial activity in biofilms above such temperatures. This is analogous to reduction in crevice corrosion propensity in seawater treated with biocide, for example, 2 ppm residual chlorine, which inhibits biofilms and microbial activity. Crevice corrosion observed at elevated temperatures where biofilms are absent and microbial activity diminished must be explained by other mechanisms. For example,

crevice corrosion of titanium is considered to occur at temperatures  $>70^\circ\text{C}$ .

Empirical data and experience indicate that some alloys are clearly much more resistant to crevice corrosion than others under the same crevice geometry and seawater conditions. It has been postulated that this is due to more stable passive films formed as a result of certain minimum combinations of alloying additions, primarily Cr, Mo, and N. Interestingly, it has been shown that hydrolysis of  $\text{Cr}^{3+}$  and  $\text{Mo}^{3+}$  produces the lowest pH values for the crevice electrolyte.<sup>37</sup> This appears to be the case when insufficient Cr and Mo (and possibly other synergistic elements) are present on the alloy surface to produce a passive film that prevents hydrolysis, acidification, and anodic dissolution. It has been suggested that addition of N to stainless steels can produce ammonium ( $\text{NH}_4^+$ ) ions that raise the pH and effectively neutralize any acidification due to hydrolysis in the crevice.<sup>38</sup>

It is often stated that increasing oxygenation of seawater (e.g., by increasing flow rate) alleviates crevice corrosion. This is based on the widely held view that higher flow rates minimize biofilm attachment and allow easy access of oxygen which is necessary to maintain passivity. That would be the case if oxygen was able to reach all areas of the metal (including the crevice) quickly. In fact, increasing oxygen supply worsens the situation because the oxygen-reduction cathodic reaction is enhanced by depolarization on surfaces outside the crevice, while oxygen diffusion

into the crevice and neutralization of the acidic conditions within the crevice, both necessary for repassivation, remain severely restricted by the crevice geometry. In other words, the trapped acidic electrolyte in the crevice and lack of oxygen ingress keeps the crevice very active, while the area outside the crevice serves as an efficient cathode. Moreover, the rate of attack within the crevice can be very severe since the ratio of the cathode (area outside the crevice) to anode (area inside the crevice) is often quite large in many components in seawater immersion applications. This is illustrated by the example in [Figure 10](#).<sup>39</sup>

Another poorly appreciated fact is the behavior of active-passive metals in deaerated solutions. As stated previously, materials such as stainless steels depend on the formation and maintenance of a passive film on the alloy surface exposed to seawater. A widely held but mistaken view is that deaerated seawater is detrimental because oxygen is unavailable to sustain passivity. However, the fact of the matter is that removal of oxygen from seawater is not normally deleterious toward such alloys because oxygen reduction is the primary cathodic reaction that controls the propagation of pits and/or crevice attack. This has been demonstrated experimentally. Since the seawater pH is near-neutral, the alternative hydrogen-discharge cathodic reaction is negligible. Thus, even if oxygen is unavailable to maintain passivity, corrosion of active-passive alloys in seawater will be imperceptible unless some other cathodic reaction is viable. Even with anaerobic bacteria active under anoxic conditions, corrosion damage occurs predominately when subsequent exposure to aerated conditions occurs.

### 2.18.3.1 Galvanic Corrosion

[Figure 11](#) is a depiction of the typical galvanic series of metals and alloys in seawater that is widely available to engineers. Unfortunately, the severe limitations of adequately predicting galvanic corrosion from such a series alone are commonly underestimated. The series basically represents a ranking of metals and alloys according to their free corrosion potentials in a given environment (in this case, flowing natural seawater at ambient temperature). For a given metal or alloy, the ranking can be influenced by a number of variables, for example, temperature, flow rate, fouling, chlorination, crevices, oxygen content, and so forth. The series provides only qualitative information on likely galvanic corrosion if two dissimilar materials in the series are electrically coupled in the environment. Corrosion of the anodic material (i.e., one with a relatively more electronegative corrosion potential) is likely to be accelerated, and corrosion of the cathodic (i.e., one with a relatively more electropositive corrosion potential) material is slowed or stopped. However, the degree of galvanic interaction cannot be determined quantitatively from the series alone. If Ohm's law applied, then the amount of galvanic attack would be a function of the potential difference between the two dissimilar materials and the total circuit resistance. However, polarization behavior of the materials and their relative area ratios have been found to be much more significant than the potential difference. The example [Figure 12](#) shows that the potential difference between titanium and steel in seawater is nearly double that of copper versus

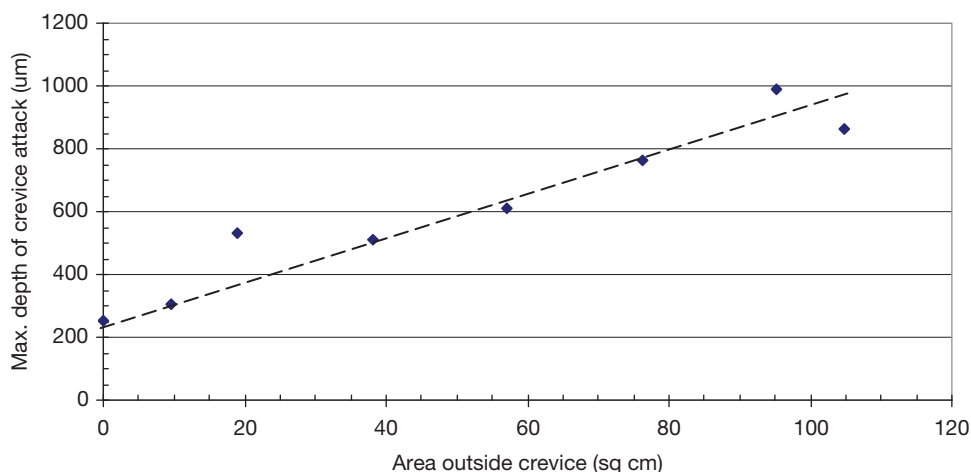


**Figure 10** Maximum depth of crevice attack on 17-Cr stainless steel in seawater versus exposed cathodic (passive) surface area outside crevice. Adapted from Ellis, O. B.; LaQue, F. L. *Corrosion* **1951**, 7(11), 362.

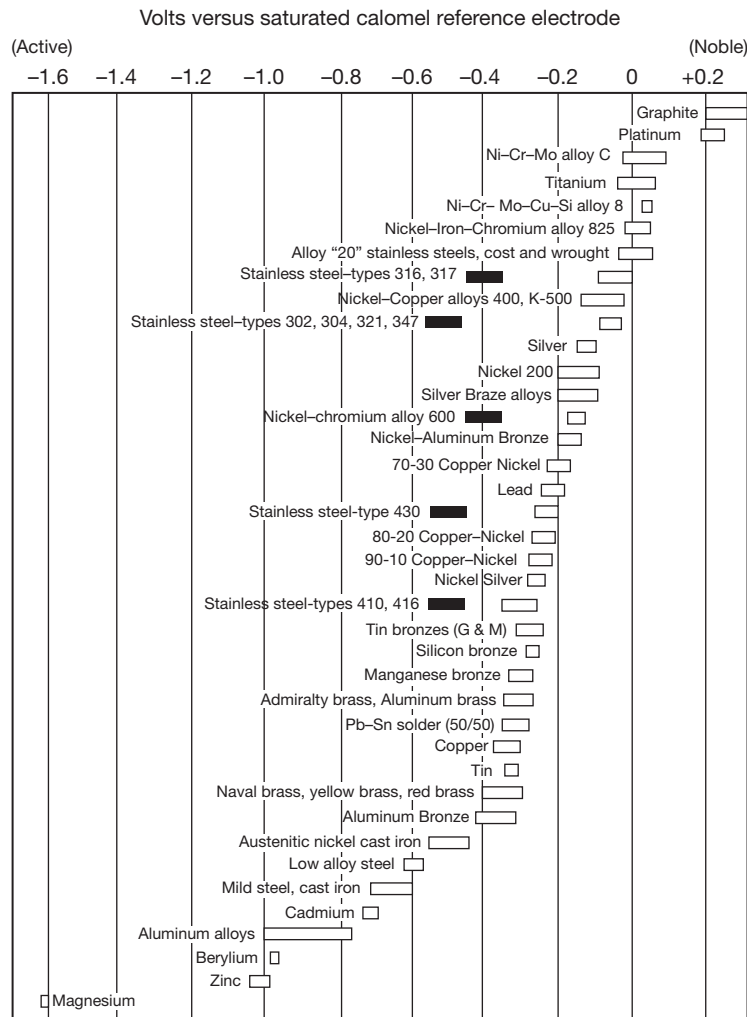


**Figure 11** Typical galvanic series of metals and alloys in flowing natural seawater. Solid bars represent active corrosion potentials for otherwise passive alloys.

steel. However, for the same anode/cathode area ratio, the galvanic current density for the titanium/steel couple (and hence expected corrosion rate of steel) is nearly nine times lower compared to the copper/steel couple. This behavior is due to the polarization of the cathode, for example, oxygen reduction on titanium is less efficient than on copper. Polarization is influenced by surface films. For example, biofilms on metal surfaces generally enhance reduction reactions and hence galvanic corrosion in certain couples.<sup>41</sup> Although chlorination is used for biofouling control (e.g., to maintain heat transfer), low levels have also been found to reduce galvanic corrosion, for example, of copper alloys coupled to more noble alloys, because reduction reactions are polarized appreciably.<sup>42,43</sup> If

calcareous deposits form on cathodic surfaces, they hinder oxygen diffusion, and hence can reduce galvanic corrosion effects.

It is generally accepted that galvanic attack on the anodic member in a dissimilar metal couple intensifies as the cathode/anode area ratio increases. However, geometry and spatial disposition of the anode and cathode can also play an important role. For example, in a retubed seawater heat exchanger, titanium tubes represent a large surface area with respect to the original copper-nickel tube sheet. This generally results in high galvanic corrosion rate of the latter. In a plate-type heat exchanger, the surface area of the titanium plates is very large compared to say the adjoining copper-nickel piping. However, galvanic corrosion of the latter is not usually

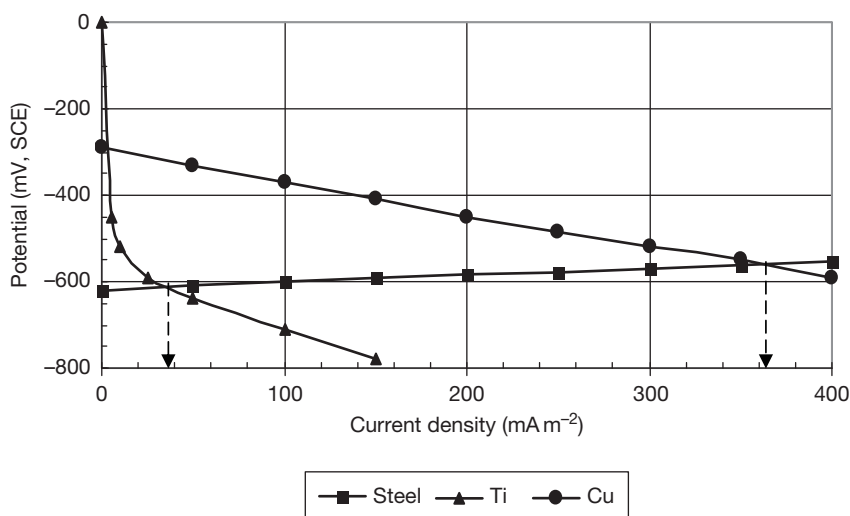


**Figure 12** Polarization curves for carbon steel (anode) versus copper (cathode) and titanium (cathode), illustrating galvanic current density depends on polarization behavior rather than galvanic couple potential difference. Adapted from LaQue, F. L. *Marine Corrosion: Causes and Prevention*; Wiley, 1975; p 195.

significant because the tortuous pathways between the titanium plates represent a high electrolytic resistance.

The galvanic series only relates to consideration of two materials at a time in a galvanic couple. In many practical applications, multiple metals may be involved. For example, if aluminum, steel, copper, and titanium components are all coupled in a system, the galvanic series only indicates that titanium would be cathodic and aluminum would be anodic with respect to each other. The galvanic series would not indicate whether steel and copper would behave anodically or cathodically in the overall system. This could only be determined after measuring the mixed potential (when all the subject metals are electrically coupled).

Another widely misunderstood aspect of galvanic corrosion is the interaction of graphite with other metals. Because of its typically most noble position in the galvanic series, it is often misstated that graphite forms adverse galvanic couples with all metals. Graphite (and graphite-containing materials) can certainly accelerate corrosion of metals such as copper, steel, and aluminum, especially for large cathode/anode area ratios. However, graphite is galvanically compatible with titanium, most Ni–Cr–Mo alloys, and many stainless steels. For example, attack observed on stainless steels in contact with graphite gaskets is often incorrectly attributed to galvanic corrosion. However, practical experience indicates that such attack (and of similar magnitude) is in fact due to crevice corrosion which occurs even when the graphite is replaced by a nonconductive gasket material.<sup>44</sup>

## 2.18.4 Carbon Steels

Carbon steels are widely used in seawater applications because of their ready availability, extensive range of mechanical properties, ease of fabrication, and usually lowest initial cost. However, carbon steels are very susceptible to corrosion in marine environments, and hence require some form of corrosion control. As stated earlier, corrosion rate is affected by a complex interaction of factors that include DO, temperature, depth, flow rate, and microbiological activity.

**Figure 13** illustrates the typical corrosion profile of steel piling subjected to various marine zones. The highest corrosion rate in the splash and spray zone is attributed to constant wetting that produces a thin film of seawater through which oxygen diffuses readily. The high corrosion rate, constant wetting conditions, and the mechanical effects of splashing preclude development of protective corrosion products. Even if coatings are applied prior to installation, they are virtually impossible to maintain in this zone. However, successful long-term protection has been achieved with metallic sheathing<sup>46,47</sup> (e.g., using alloys such as NiCu alloy 400 and 90/10 CuNi). Nonmetallic wraps have also been used for protection in the splash zone.<sup>48,49</sup>

In the tidal zone, the structure is exposed to alternate immersion. The lower general corrosion rates in this zone are ascribed to oxygen shielding by macrofouling. However, localized attack can be aggressive if SRB activity under anaerobic macrofouling



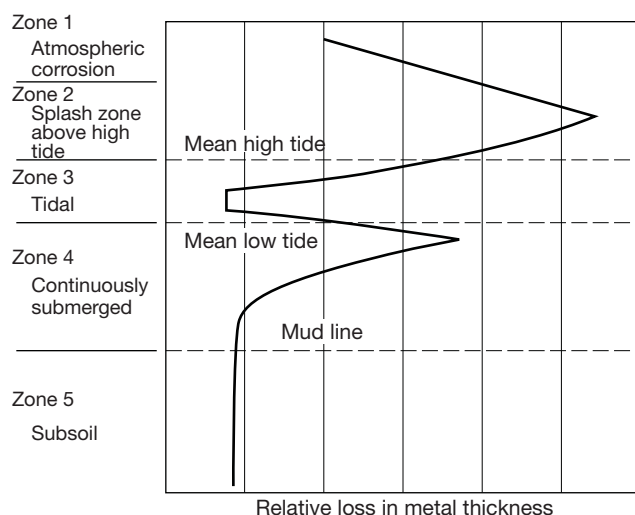


**Figure 13** Corrosion profile of steel piling exposed to various zones in a natural marine environment for 5 years. Reproduced from Humble, H. A. *Corrosion* **1948**, 5(9), 23–28.

conditions is high. A particularly severe form of attack known as ‘accelerated low water corrosion (ALWC)’ afflicts steel sheet piling in some ports and harbors at areas just above the lowest astronomical tide.<sup>50–52</sup> The phenomenon is not fully understood presently. However, empirical evidence suggests a strong influence of microbiological organisms, especially SRB possibly synergized by acid producing bacteria; corrosion penetration can exceed  $1 \text{ mm year}^{-1}$  on a given steel surface. Apparently, structures affected by ALWC are usually exposed to tidal and brackish waters.

As discussed earlier, reduction of DO is the primary cathodic reaction controlling corrosion of steel in aerated marine environments. Although oxygen solubility decreases with increasing temperature, corrosion of steel immersed in seawater generally increases with temperature and with flow rate. The data in **Table 5** illustrate the increase in corrosion rate of steel in warmer seawater during the summer months despite the lower oxygen content. **Figure 14** depicts increase in corrosion rate with flow velocity in ambient temperature seawater in the absence of significant corrosion products.<sup>53</sup> Adherent corrosion products can diminish the effect of flow. However, above a critical wall shear stress, corrosion products are prevented from forming and existing ones removed by erosion.

The corrosion rate of steel, based on mass loss, in quiescent seawater is typically on the order of  $\sim 0.13 \text{ mm year}^{-1}$  after several years of exposure. A 5-year worldwide seawater corrosivity test program

**Table 5** Seasonal variations in corrosion rate of steel in natural seawater at  $\sim 0.2 \text{ m s}^{-1}$

Period	Ave temp (°C)	Ave dissolved oxygen (ppm)	pH	Ave corrosion rate ( $\mu\text{m year}^{-1}$ )
Jan–Mar	10.5	9.2	8.0	100
Apr–Jun	22.4	6.9	8.0	130
Jul–Sep	27.2	6.0	8.0	140
Oct–Dec	14.1	8.2	8.1	110

indicated that local conditions can exert a strong influence on corrosion rate and types of attack.<sup>54</sup> In some cases, pitting rates were much higher than general corrosion rates, as illustrated by the data in **Figure 15**. Complete localized penetration of the 6-mm plate thickness occurred on some, but not all test panels at specific exposure locations. This type of accelerated localized attack resulting in large, round pits has been attributed previously to sea urchins<sup>55</sup> – which apparently ‘scrub’ corrosion products, and thus expose fresh metal surface to enhanced corrosion rate. Extensive data analysis and modeling on corrosion of steel in seawater have been performed by Melchers<sup>56</sup>; the primary conclusions were that velocity affects corrosion in the early stages until marine fouling and corrosion products develop – thereafter, influence of fouling thickness is significantly reduced. DO and temperature rather than depth *per se* affect corrosion; for a given exposure period, test specimens first exposed during autumn and winter exhibited less corrosion than those first exposed in spring and summer.

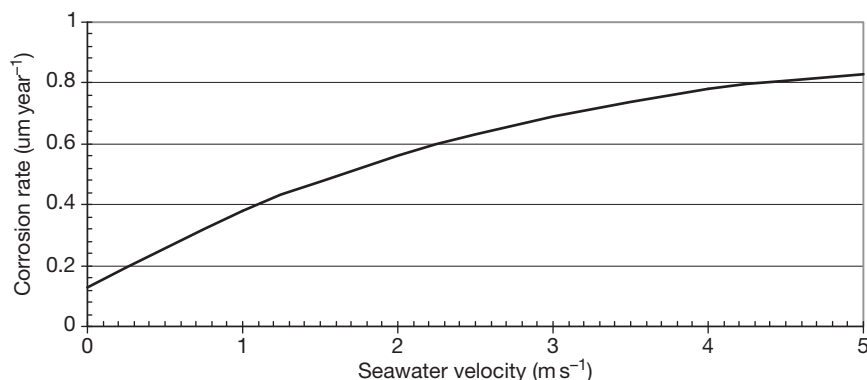


**Figure 14** Corrosion rate of clean carbon steel in ambient temperature flowing natural seawater on 38 days. Reproduced from Oubner, R.; Beech, I. In *Corrosion/1999*; NACE International: Houston, TX, 1999; Paper No. 99318.

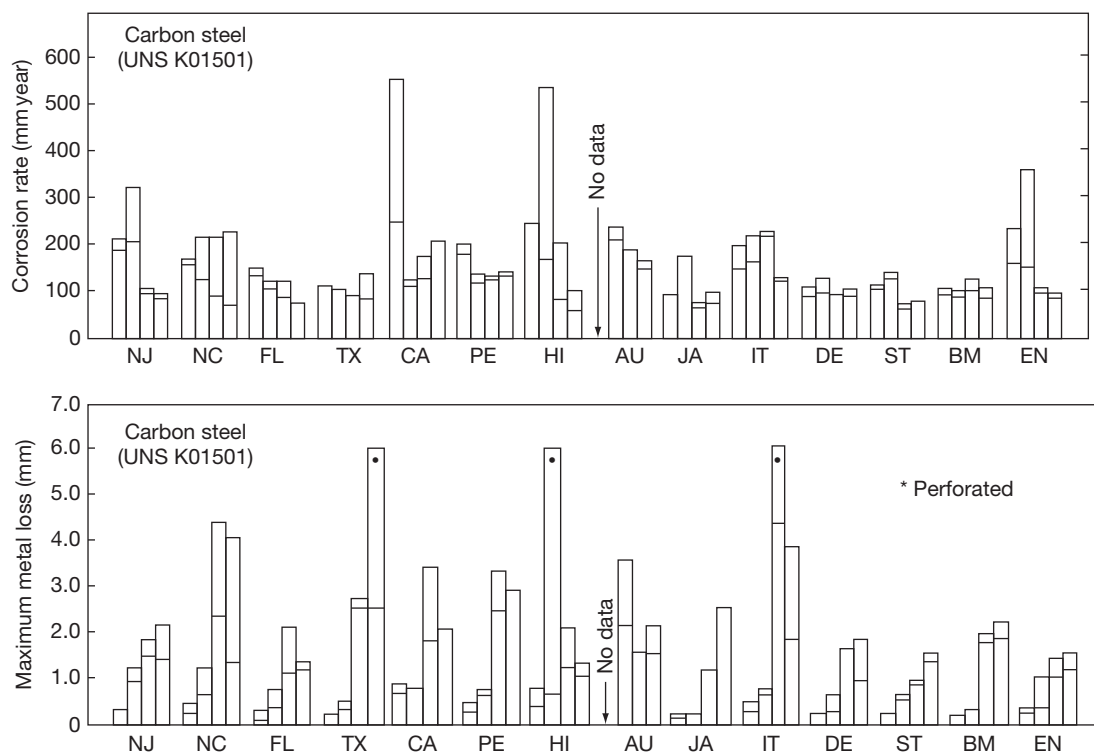


**Figure 15** Mass loss corrosion rate and maximum depth of pitting attack on carbon steel in seawater at 14 worldwide test locations. For each location, the bars represent (from the left) 0.5, 1, 3 and 5-year exposures. NJ – New Jersey, NC – North Carolina, FL – Florida, TX – Texas, CA – California, HI – Hawaii, AU – Australia, JA – Japan, IT – Italy, DE – Denmark, ST and BM – Sweden, EN – England. Reproduced from Phull, B. S.; Pikul, S. J.; Kain, R. M. *ASTM STP 1300*; American Society for Testing and Materials: West Conshohocken, PA, 1997; pp 34–73.

It is commonly believed that macrofouling reduces oxygen transport and, consequently, overall corrosion rate of steel in seawater. However, data from tests indicate similar corrosion behavior for carbon steel in filtered and unfiltered seawater – suggesting that microfouling may be more important than macrofouling in controlling corrosion behavior. This appears

contradictory to the view that biofilms enhance the oxygen reduction reaction, for example, in microbiologically influenced corrosion of stainless steels.

In shallow immersion, pitting depths on carbon steel can be an order of magnitude higher than general corrosion rates calculated from mass loss as illustrated in [Figure 16](#).<sup>57</sup> Determination of pitting rates

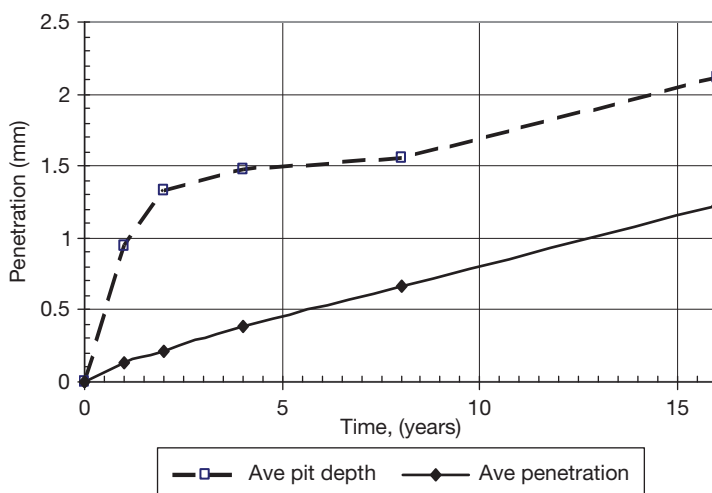


**Figure 16** Corrosion of carbon steel in natural seawater. Average penetration calculated from mass loss of six replicate test panels – slope corresponds to  $\sim 0.07 \text{ mm year}^{-1}$  corrosion rate; average pit depth is the mean of 60 measured pits, five deepest pits on each surface of six test panels. Reproduced from Southwell, C. R.; Alexander, A. L. *Mater. Prot.* **1970**, 9(1), 14–23.

can be an onerous task. A common but mistaken practice involves measuring the maximum or average pit depth and calculating a pitting rate. There are a number of flaws with this approach. First, pitting is not linear with time, especially for long-term exposures in seawater. Second, the data are usually based on measuring different pits on different test samples, that is, specific pits are not monitored as a function of time owing to the obvious experimental shortcomings of this approach. Pitting is a statistical process; the number, size, and locations of pits on a given metal surface can vary over a wide range. Thus, computing pitting rates from limited data, and assuming linear growth rate with time is fraught with problems.

**Figure 17** shows the general corrosion rate of carbon steels exposed for 1 year and DO content as a function of seawater depth.<sup>58</sup> It is apparent that the corrosion profile closely follows that of the oxygen concentration. The following relationship derived from linear regression analysis<sup>59</sup> indicates a greater dependence on oxygen content compared to temperature:

$$\text{Corrosion rate } (\mu\text{m year}^{-1}) = 21.3 + 25.4[\text{O}_2(\text{ml l}^{-1})] + 0.356[T(^{\circ}\text{C})]$$

Other data have indicated more complex corrosion behavior. For example, in unpolluted seawater, corrosion rate was dependent on oxygen content, whereas in polluted seawater, temperature had a greater influence.<sup>60</sup> Polluted seawater typically has the following characteristics (compared to unpolluted seawater):

lower oxygen content, lower pH, higher sulfide and sulfate-reducing bacteria concentrations, and higher ammonia content. Corrosion data suggest that at similar temperatures, the effect of lower oxygen content in polluted seawater is offset by the presence of pollutants,<sup>60</sup> especially sulfides.

Under immersion conditions, low alloy steels behave fairly similar to carbon steels. Small amounts of alloying additions do not evidently alter the corrosion rate of steel significantly in seawater. However, as the alloy content is increased further (e.g.,  $>5 \text{ wt\%}$ , especially Cr addition), a reduction in general corrosion rate is often replaced by deep, localized pits. It has been reported that low-alloy steels can cause galvanic corrosion of plain carbon steels despite a small difference in their corrosion potentials.<sup>61</sup>

Higher strength carbon steels are susceptible to hydrogen embrittlement (HE) in seawater, especially when polarized to excessively negative potentials. Factors that affect the susceptibility of steels in seawater to HE include yield strength (which is influenced by composition and heat treatment), electrochemical potential, and pollutants (especially sulfide). In general, susceptibility increases with increasing yield strength. High-strength steels are generally considered to be those with  $\text{YS} > 700 \text{ MPa}$ . Steels with  $\text{YS} < 700 \text{ MPa}$  are generally considered resistant to hydrogen embrittlement. Since alloying additions affect yield strength, it is difficult to delineate their influence on HE behavior. However, limited data<sup>62</sup> on steels of varying compositions but similar yield strengths indicate negligible

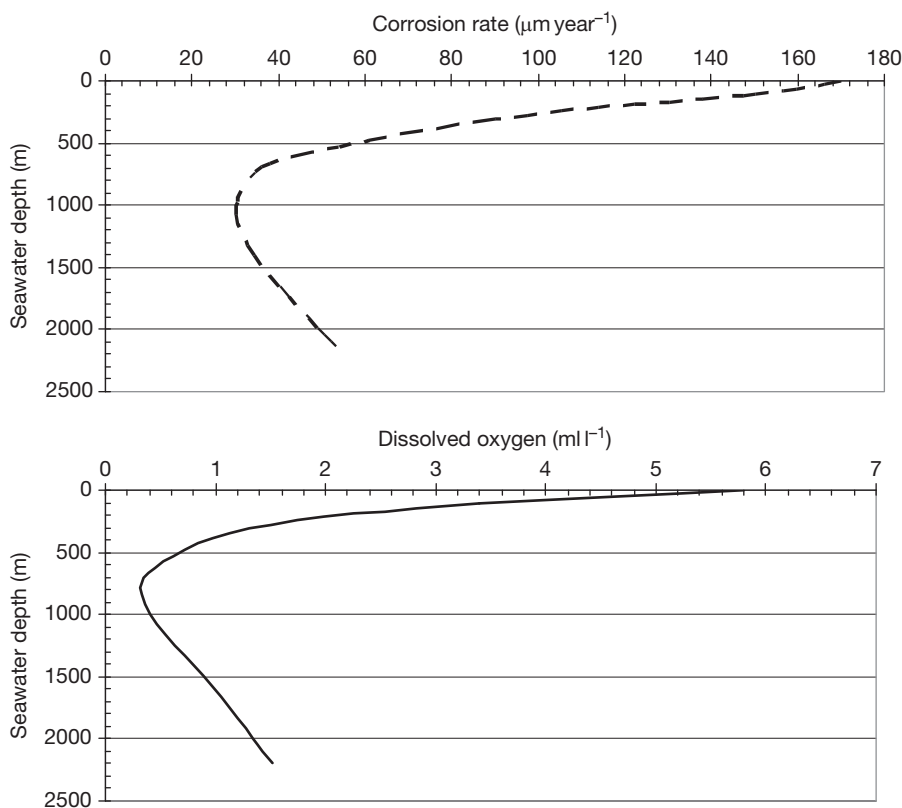


**Figure 17** Corrosion rate of carbon steel exposed for 1 year and DO concentration versus seawater depth ( $\text{DO ml l}^{-1} \times 1.429 = \text{mg l}^{-1}$ ); note similarity in profiles versus depth. Reproduced from Reinhart, F. M. *Corrosion of Metals and Alloys in the Deep Ocean*, Technical Report No. R-834, Civil Engineering Laboratory, Port Hueneme, CA, 1976; p 14.

effects of S or P (each  $<0.03\%$ ), Si or Cr (each  $<2.1\%$ ), Mo ( $<1.2\%$ ), and Co ( $<3\%$ ). Detrimental effects were indicated for C ( $0.3\text{--}0.4\%$ ), Mn ( $0\text{--}3\%$ ), and slightly deleterious for Ni ( $>6\%$ ). Tempering or aging heat-treatments at higher temperatures lower yield strengths and hence typically increase HE resistance. Ultra high-strength steels (e.g., with  $\text{YS} \geq \sim 1400$  MPa) can suffer HE even in distilled water. Elevated temperatures increase crack growth rates, probably as anodic dissolution rate increases, following Arrhenius behavior.<sup>63</sup>

Polarization of high-strength steel to more noble potentials than the free corrosion potential can markedly increase HE propensity as indicated by significantly shorter time to failure. Cathodic polarization to a narrow potential range (e.g.,  $-0.8$  to  $-0.9$  V SCE) is generally beneficial since anodic dissolution processes are stifled. However, cathodic polarization to more active potentials (especially more negative than  $-1$  V, SCE) again lowers cracking resistance. Pollutants, in particular sulfur-containing species, have been found to increase susceptibility to HE.

Carbon steel has been used extensively in the past for construction of flash chambers in thermal desalination plants. In principle, the corrosion rate should be negligible if DO is completely stripped from the seawater used in the process. However, in practice, it is very difficult to deoxygenate the seawater fully. Typically, oxygen concentration is reduced from ppm to ppb levels. However, increasing temperature has a far greater effect on corrosion than low oxygen levels. For example, data from a thermal desalination pilot-plant test revealed that even at a 100 ppb DO level and seawater flow-rate of  $\sim 1.7 \text{ m s}^{-1}$ , the corrosion rate of carbon steel doubled from  $0.3 \text{ mm year}^{-1}$  at  $81^\circ\text{C}$  to  $0.6 \text{ mm year}^{-1}$  at  $120^\circ\text{C}$ .<sup>64</sup> Oldfield and Todd<sup>65</sup> developed the following expression for calculating corrosion rate:

$$\text{Corrosion rate (mm year}^{-1}\text{)} =$$

$$(0.0117 \times C_o \times U_o^{0.9}) / Pr^{0.75}$$

where  $C_o$  is bulk concentration of oxygen in moles  $\text{cm}^{-3}$ ,  $U_o$  is bulk flow rate in  $\text{cm s}^{-1}$ , and  $Pr$  is the

Prandtl number (defined as ratio of kinematic viscosity,  $\nu$ , to diffusion coefficient,  $D$ ). The predicted corrosion trends were in good agreement with previously published field and test data; lower actual corrosion rates in the field were attributed to presence of corrosion products and scaling.

Millscale on steel surfaces is cathodic to the substrate. While the general corrosion rate of steel, based on mass loss data, may not appear significantly different, the presence of millscale can produce deep pitting by galvanic action due to the adverse cathode (millscale) to anode (exposed steel) area ratio.

## 2.18.5 Cast Irons

The initial corrosion behavior and corrosion rates of unalloyed gray and ductile cast irons in seawater are similar to those of carbon steels. However, in gray cast irons, as corrosion progresses, dissolution of the ferrite phase exposes increasing the amounts of the flake graphite network. This dealloying phenomenon is known as graphitic corrosion. It is commonly but incorrectly referred to as graphitization – which is really a metallurgical term used to describe decomposition of iron carbide ( $\text{Fe}_3\text{C}$ ) to iron (Fe) and graphite (C) at elevated temperatures. At low velocities, the iron corrosion products are often ‘trapped’ by the flake graphite network. In such cases, visual inspection can greatly underestimate material degradation because reduction in section thickness is not apparent. Ultrasonic inspection and/or destructive examination are usually necessary to monitor graphitic corrosion before catastrophic failure occurs.

Graphitic corrosion may advance to a stage where it can induce galvanic corrosion of other materials coupled to the cast iron. For example, initially steels are galvanically compatible with gray cast iron, while copper alloys are cathodic. However, graphitic corrosion of the cast iron can eventually generate or reverse the galvanic couple where the exposed graphite behaves cathodically to steels and copper alloys and accelerate their dissolution by galvanic action.<sup>66</sup> Graphitic corrosion and its consequences are not a major problem with ductile irons because the graphite is present as discrete nodules instead of a flake graphite network.

Addition of  $\sim 20\%$  Ni to cast iron increases toughness and shock resistance. However, the austenitic microstructure is still susceptible to graphitic corrosion, if the graphite is present in the flake

form. Depending on alloy composition, small Mg additions (e.g.,  $\sim 0.1\%$ ) during production convert the flake graphite to nodular form. This significantly increases the tensile strength, impact resistance, and graphitic corrosion resistance. Corrosion rates of austenitic cast irons (commonly referred to by a trade name, NiResist<sup>®</sup>) in seawater are often an order or magnitude lower than gray or ductile irons. The benefit of increasing Ni content in the cast iron is particularly notable for erosion–corrosion resistance in seawater at high velocities as illustrated by the data in Table 6. Sporadic stress corrosion cracking (SCC) problems observed in austenitic cast iron seawater pumps have been attributed to improper stress-relief heat treatment.<sup>67</sup>

## 2.18.6 Stainless Steels

The addition of  $>11\%$  Cr to Fe generates a Cr- and Fe-containing passive oxide film on the metal surface. There is a very marked reduction in general corrosion rate in seawater compared to carbon steel or low alloy steels. However, the stainless steels are highly susceptible to localized corrosion unless much more Cr and/or other alloying additions such as Mo, N, and Ni are also present. Thus, determination of general corrosion rates of stainless steels in seawater from weight loss results can be misleading because most of the metal dissolution is typically associated with pitting and crevice corrosion.

There are several hundred commercial grades of stainless steels, with widely ranging compositions and properties. Obviously, a large number of grades are unsuitable for seawater applications. Typically, stainless steels are divided into several broad classifications, *viz.* martensitic, ferritic, austenitic, superaustenitic, duplex, superduplex, and precipitation hardening

**Table 6** Effect of increasing Ni content in cast irons on erosion–corrosion behavior in seawater at  $8 \text{ m s}^{-1}$  at  $28^\circ\text{C}$  for 60 days

Alloy	% Ni content	Ave corrosion rate ( $\text{mm year}^{-1}$ )
Cast iron	–	6.9
2% Ni cast iron	2	6.1
Type 1 Ni-Resist	13.5–17.5	0.74
Type 2 Ni-Resist	18–22	0.79
Type 3 Ni-Resist	28–32	0.53

Source: Shreir, L. L., Ed. *Corrosion*; Newnes Butterworths, 1979; Vol. 1, pp 3–106.



(PH). Even within each classification, there can be a wide range of compositions.

Martensitic stainless steels are susceptible to pitting, crevice corrosion, SCC, and hydrogen embrittlement (especially under cathodic protection) in seawater.

High-Cr ferritic grades, such as Type 29-4C (29Cr-4Mo), are considered to have much greater resistance to localized corrosion compared to more leaner grades such as Type 430 (17Cr). Ferritic grades are resistant to chloride stress corrosion cracking ( $\text{Cl}^-$  SCC), but susceptible to hydrogen embrittlement, especially when subjected to cathodic protection, unintentional or otherwise.

Despite their popularity, particularly for marine atmospheres, many austenitic grades (such as many of the 300-series) are unsuitable for seawater service; unfortunately, they are often selected because of their attractive mechanical and welding properties, that is, without a complete understanding of their limitations, especially corrosion resistance. They are susceptible to  $\text{Cl}^-$  SCC; susceptibility trend decreases with increasing Cr or Cr + Ni content. They are resistant to hydrogen embrittlement except in the severely cold-worked condition. Type 304 is highly susceptible to pitting corrosion in seawater; Type 316 is more resistant due to the Mo addition but certainly not immune. The biggest limitation of these grades is their high propensity to crevice corrosion, for example, under gaskets, O-rings, washers, sleeves, macrofouling deposits, silt, and so on which are discussed later. Superaustenitic grades have higher alloy content ( $\sim 20\%$  Cr,  $25\%$  Ni, and  $\sim 6\%$  Mo, or more) for increased resistance to crevice corrosion; their higher Ni content also enhances resistance to SCC.

In seawater, the localized corrosion resistance of duplex stainless steels is similar or slightly better than many austenitic grades. They are slightly magnetic and susceptible to hydrogen embrittlement, for example, under cathodic over-protection conditions, or in the presence of hydrogen sulfide. Superduplex stainless steels have higher Cr and nitrogen contents (e.g., alloy 2705; 27Cr-5Ni-3Mo-0.2N), which improve corrosion resistance notably, but does not make them immune under all conditions. They are much more resistant to chloride SCC than austenitic stainless steels.

PH stainless steels are susceptible to pitting, crevice corrosion, SCC, and hydrogen embrittlement (especially under cathodic protection) in seawater.

The highly-oxygenated thin liquid film environment, and absence of biofouling in the splash zone

represent conditions under which stainless steels generally perform well at ambient temperatures and if critical crevices are not present. Leaner compositions may develop superficial rust staining. Stainless steel sheathing fabricated from 300-series austenitic stainless steel (e.g., Types 304 and 316) has been successfully used for long-term splash-zone protection at ambient temperatures.

The leaner grades of stainless steel are susceptible to localized attack under biofouling attachments that usually proliferate in the intertidal zone. **Figure 18** shows classical crevice corrosion of Type 304 stainless steel under barnacles.

The data in **Table 7** show localized corrosion penetration for several stainless steels after 16 years exposure in the intertidal and full immersion zones in Panama.<sup>69</sup> There was complete perforation of the 6-mm thick plate material by localized corrosion for all the grades tested under full immersion conditions. In the intertidal zone, the martensitic Type 410 material was also completely perforated, while the deepest pits on the other three grades ranged from  $\sim 1$  to  $\sim 3$  mm. Type 304 stainless steel pits in seawater like Type 302 and Type 321 (Type 321 is an analog of Type 304L, but stabilized with Ti for averting sensitization in lieu of lowering the carbon content). Attack typically initiates under biofouling attachments and at cut edges where inclusions in the material are exposed prominently. The acidic environment generated in the pits by metal-ion hydrolysis often leads to subsurface attack in the form of tunneling. On stationary structures, such attack often progresses vertically downward due to gravity. The addition of 2–3% molybdenum in Type 316 stainless steel imparts some resistance, but

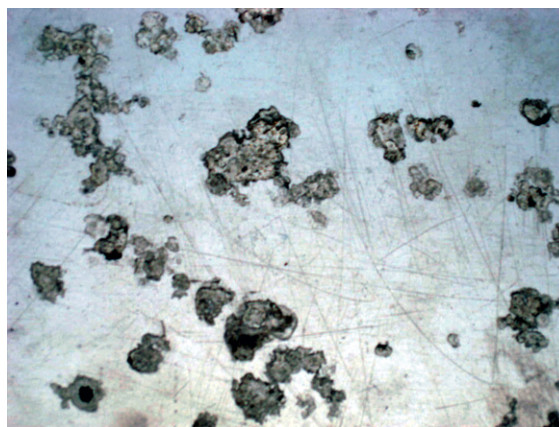


**Figure 18** Crevice corrosion of Type 304 stainless steel under barnacles in natural seawater.

**Table 7** Depth of localized corrosion attack on various stainless steels in natural seawater intertidal and immersion zones after 16 years' exposure

Alloy	Exposure zone	Ave of 20 deepest pits 1 year	Ave of 20 deepest pits 8 years	Ave of 20 deepest pits 16 years	Deepest pit over 16 years
410 SS	Tidal	1.17	1.70	2.72	P*
	Immersion	1.55	4.08	5.38	P
302 SS	Tidal	0.15	1.47	1.27	2.79
	Immersion	1.78	3.56	3.84	P
321 SS	Tidal	0.18	1.42	1.40	2.36
	Immersion	1.63	4.90	6.02	P
316 SS	Tidal	0.13	0.41	0.33	0.91
	Immersion	1.14	3.96	2.41	P

Source: Southwell, C. R.; Bultman, J. D.; Alexander, A. L. *Mater. Prot.* **1976**, 15(7), 9–26.  
P – Perforation (of 6-mm plate).

not immunity to pitting in seawater compared to Type 304. Sufficiently high flow rates that prevent macrofouling attachments would be expected to mitigate pit initiation. However, even in the absence of macrofouling, attack can initiate if the inclusion (e.g., MnS) concentration is high. For example, rampant pitting is encountered in Type 303 'free machining' stainless steels because they contain sulfur or selenium alloying additions, which produce copious electrochemically active inclusions in the microstructure.

Localized corrosion experienced with Type 304 stainless steel often leads to selection and specification of Type 316 stainless steel in many seawater applications. This is unfortunate despite a wealth of available information in the published literature. Virtually all 300-series stainless steels are susceptible to crevice corrosion in seawater. It is not widely appreciated that Type 316 stainless steel is just as susceptible to this form of localized corrosion as Type 304 in typical seawater applications containing crevices, for example, at flange faces, under gaskets, under O-rings, under washers, at threaded connections, under lap joints, and so on. Crevice corrosion can also occur under disbonded paint films, under biofouling, under silt, and so forth. There is another mistaken, but again, unfortunately, widely held view that low carbon 'L' grades of 300-series stainless steels are somehow more resistant to pitting and crevice corrosion in seawater. This is simply not the case. The 'L' grades are beneficial for mitigating intergranular attack, which would otherwise occur at sensitized areas of the microstructure, for example, heat-affected zones associated with welds. **Figure 19** shows typical crevice corrosion of a Type 316L stainless steel pump shaft bearing sleeve in seawater service. Thus, if crevices are present, and some form of corrosion-control,



**Figure 19** Crevice corrosion of Type 316L stainless steel pump shaft sleeve in natural seawater.

for example, cathodic protection, is not applied, Type 316 stainless steel will crevice corrode in most aerated seawater applications. This fact is used in crevice corrosion testing in seawater where Type 316 specimens are routinely used as susceptible controls. In other words, the test is invalid if the Type 316 stainless steel controls do not crevice corrode.

Crevice corrosion of stainless steels in seawater has been investigated extensively over the past 30 years. The importance of DO transport to the stainless steel surface to maintain passivity is widely accepted. For example, the following minimum velocity relationship was derived from one laboratory study<sup>70</sup> on smooth-wall, Type 316 stainless steel tubes to prevent fouling in seawater:

$$v = 2.74 + 0.56 \log d$$

where  $v$  is the velocity ( $\text{m s}^{-1}$ ) and  $d$  is the tube inside diameter (m).

Another rule-of-thumb  $\sim 2 \text{ m s}^{-1}$  minimum seawater velocity is commonly recommended to prevent settlement of silt and macrofouling under which localized attack can initiate and propagate. This type of approach is fraught with problems in practice because it is virtually impossible to maintain flow without interruptions. Experience indicates that macrofouling which attaches during extended stoppages is not usually removed when flow is resumed. Furthermore, it is very difficult to eliminate 'man-made' crevices completely in most components and seawater applications. The seawater electrolyte in the crevice is stationary even if high flow conditions exist outside the crevice. Thus, if a material is susceptible to crevice corrosion, maintaining sufficient flow to prevent fouling (outside the crevice) will not prevent attack within the crevice, as also discussed earlier.

The data in **Table 8** show that the maximum depth of crevice attack in seawater for three stainless steel alloys at 28 °C seawater temperature is greater than at 12 °C, but decreases markedly at 50 °C.<sup>71</sup> As discussed earlier, this behavior is often attributed to enhanced biofilm activity in warm seawater compared to cold or hot seawater.

As stated earlier, Cr and Mo are the primary alloying elements that influence localized corrosion resistance of stainless steels in seawater. Service experience<sup>72</sup> and tests<sup>73</sup> have shown that significant crevice corrosion resistance in ambient temperature seawater is attained with austenitic stainless steels of the nominal composition 20Cr–25–Ni–6Mo. However, even these 6Mo alloys have been shown to be prone to crevice attack if the seawater temperature exceeds their critical crevice corrosion temperatures (CCT), typically in the 30–45 °C range depending on the exact composition. Crevice attack on these alloys has also been demonstrated in tests conducted on painted panels even with relatively small areas left uncoated.<sup>74</sup>

**Table 8** Maximum depth of crevice attack in natural seawater in 30-day test at three temperatures

Alloy	Maximum depth of crevice attack (mm)		
	12 °C	28 °C	50 °C
304 SS	0.56	0.81	0.12
316 SS	0.34	0.57	0.05
Alloy 20	0.18	0.20	0

Source: Asphahani, A. I.; Manning, P. E.; Silence, W. L.; Hodge, G. F. In *Corrosion/80*; NACE International: Houston, TX, 1980; Paper No. 29.

Duplex stainless steels are also potentially susceptible to crevice corrosion depending on alloy composition, crevice geometry, and service or test conditions. The higher Cr-containing alloy 2507 is generally more resistant to crevice corrosion than the lower Cr alloy 2205. Successful use of higher Cr duplex stainless steel has been reported in offshore and desalination seawater pumps, valves, and piping systems<sup>75</sup> normally at temperatures below their CCT ( $\sim 40^\circ\text{C}$ ) and chlorine levels of 0.5 ppm or less.

Critical crevice corrosion temperatures of stainless steels are usually determined using the ASTM G 48 standard test.<sup>76</sup> Test conditions are accelerated by using an aggressive test solution consisting of 6%  $\text{FeCl}_3 + 1\%$  HCl. Test specimens are fitted with PTFE multiple crevice assembly (MCA) washers torqued to 0.28 N m and exposed to the test solution at various thermostatically controlled temperatures. The CCT of the test alloy is the temperature at which crevice attack  $\geq 0.025 \text{ mm}$  is detected after 72 h immersion. Critical pitting temperatures (CPT) also commonly reported in the literature refer to pitting corrosion observed in the absence of artificial crevices; any edge attack on the test specimens is discounted. For any given alloy, the CPT is always greater than the CCT. However, the latter is generally considered more meaningful for practical applications because it takes into account the unavoidable crevices that are either man-made (e.g., gaskets, O-rings, sleeves) or naturally occurring (e.g., barnacles, thermal scale, silt).

In addition to CCT, stainless steels are also frequently ranked for likely crevice corrosion behavior in seawater based on their pitting resistance number (PREN). The following is a typical empirical expression for PREN based on alloy (wt%) composition:

$$\text{PREN} = \% \text{Cr} + 3.3\% \text{Mo} + A\% \text{N}$$

where the value of  $A$  is typically chosen to be 30 for austenitic stainless steels, and 16 for duplex stainless steels. **Table 9** shows the PREN and CCT values for a number of stainless steels.<sup>77</sup> It is apparent that as the PREN increases, the CCT increases. The following expression was proposed<sup>78</sup> for austenitic stainless steels:

$$\text{CCT} = (2.7 \times \text{PREN}) - 0.81$$

At first sight, this appears to be a very convenient method for ranking alloy performance in terms of expected localized corrosion resistance. However, for reliable materials selection, neither the PREN nor the CCT (as determined by the ASTM G 48

**Table 9** Typical PRE numbers versus CCT and CPT values for various stainless steels

Alloy	UNS No.	PRE	CCT (°C)
316L	S31603	26	<5
317L	S31783	28	0
2205	S31803	34	17.5–25
904L	N08904	36	15–25
2507	S32750	43	35–43
254SMO	S31254	46	30–60
AL-6XN	N08367	47	43
654SMO	S32654	63	60+

Source: Davies, M.; Scott, P. J. B. *Guide to Use of Materials in Waters*; NACE International: Houston, TX, 2003; p 90.

test method) provides a consistently accurate prediction of actual crevice corrosion resistance in seawater service. In other words, even alloys with high PREN and CCT values have been shown to crevice corrode, for example, in tests with severe crevice geometries.<sup>74</sup>

In crevice corrosion testing in seawater, crevice geometries can be created in a number of ways. For example, for flat sheet or plate stock, nonmetal or metal crevice-forming washers are commonly used as bolted assemblies; rubber O-rings and vinyl sleeves are used for tubular and round bar, and so on. Some of these devices and methods are described in ASTM standard G 78.<sup>79</sup> For irregular-shaped components or surfaces, for example, protruding weld beads, that do not readily permit the use of conventional crevice-formers, the use of paint coatings as crevice-formers has been proposed.<sup>80</sup> This methodology is based on the observation of crevice attack under coatings (e.g., marking inks, paint overspray, disbonded coatings, etc. on stainless steel surfaces) in actual practical applications.

Surface finish can also affect crevice corrosion resistance of stainless steels. The generally greater resistance of rough-ground surfaces to crevice attack, compared to smooth polished ones, is explained in terms of crevice tightness with respect to the crevice former. A certain degree of surface grinding and/or pickling is considered essential to remove the surface layer that is considered to have suffered some Cr depletion during manufacturing and/or fabrication (e.g., hot rolling, annealing, welding, etc.). The surface treatment is also intended to remove any extraneous particles (e.g., embedded iron) from tools, which can impair corrosion resistance; removal of embedded iron by immersion in acid solution (e.g., HNO<sub>3</sub>) is often erroneously referred to as 'passivation.' Chromium

carbide (Cr<sub>23</sub>C<sub>7</sub>) precipitation occurs at grain boundaries, typically in the 500–800 °C temperature range during welding and heat treatment of austenitic stainless steels. Corrosion resistance of areas adjacent to the carbide particles is lowered because of Cr depletion. However, despite this, no significant incidences of intergranular corrosion in ambient temperature seawater have been reported. On the other hand, precipitation of sigma phase (FeCr intermetallic), which can form in the temperature range 565–925 °C in Mo-containing austenitic steels, is considered more deleterious for seawater corrosion resistance.<sup>81</sup> Although their compositions are not exactly the same, cast stainless steels often exhibit lower resistance to localized corrosion than the corresponding wrought material. In the case of austenitic stainless steels, this is generally due to the residual ferrite phase in castings (necessary to counteract shrinkage during solidification). Welds represent 'miniature' castings, and hence their corrosion resistance can be lower than the parent material of similar nominal composition. Laboratory tests have shown that pickling of welds increased the critical pitting temperature of a 25-Cr duplex stainless steel by ~20 °C<sup>82</sup>; presumably, the reason for this is elimination of heat tint and surface Cr depletion. A 'soft' start up has been recommended in situations where pickling is not possible in piping systems; apparently the procedure consists of initial exposure to cold seawater for at least 2 days, followed by exposure to cold chlorinated seawater for at least 5 days, before turning on the heat exchangers.<sup>75</sup> This method may not be very practical in geographical areas where cold seawater is not readily available.

As stated earlier, the type of crevice geometry and its dimensions can play a critical role in the determining crevice corrosion resistance of stainless steels. Generally, crevice corrosion severity increases with decreasing crevice gap (tightness) and increasing crevice depth. This has been demonstrated by mathematical modeling<sup>83</sup> and by experimental evaluations.<sup>84,85</sup> The critical values of pH and chloride concentration of crevice solutions to initiate crevice attack have also been determined<sup>83</sup>; results for four different stainless steels are depicted in Table 10. In crevice corrosion testing, ideally, the actual crevice geometry (gap and depth) and crevice-formers (gaskets, washers, O-rings, etc.) intended for the service environment should be used. Lack of proper simulation could result in incorrect indication of corrosion behavior in service, for example, insufficiently tight and deep crevices could lead to a false prediction of corrosion resistance and vice versa.



**Table 10** Critical crevice corrosion solution values

Alloy	$[Cl^-] (M)$	pH
430 SS	1.0	2.90
304 SS	2.5	2.10
316 SS	4.0	1.65
904L	4.0	1.25

Source: Oldfield, J. W.; Sutton, W. H. *Br. Corros. J.* **1980**, 15(1), 31–34.

Polluted seawater containing sulfides have not adversely affected the performance of stainless steels in seawater,<sup>86,87</sup> both at moderate ( $2.4 \text{ m s}^{-1}$ ) as well as high velocities<sup>88</sup> (up to  $50 \text{ m s}^{-1}$ ). This observed corrosion resistance is based on the results of testing and experience in seawater, which either already contained sulfide or to which sulfide was deliberately added. Lean stainless steel grades can however, be subjected to microbially influenced corrosion (e.g., especially at welds) where the sulfide is generated biogenically as a byproduct, especially under quiescent conditions.

In the absence of solid particulate matter (e.g., entrained sand), stainless steels can generally tolerate seawater velocities in the order of  $40 \text{ m s}^{-1}$  without any erosion–corrosion problems.<sup>88</sup> However, in service application such as pumps and valves, proper hydraulic design and operation are essential to preclude cavitation problems. Stainless steels are not immune to cavitation, but typically exhibit greater resistance than ‘softer’ materials such as carbon steels, copper-base alloys, and aluminum-based alloys.

In the passive condition, stainless steels are galvanically compatible with each other in seawater despite their somewhat different positions in the galvanic series. In the passive condition, stainless steels are not usually adversely affected by galvanic corrosion when coupled to more noble materials, for example, titanium, gold, graphite, etc. As stated earlier, when localized corrosion of stainless steel is observed at areas in intimate contact with such noble materials, there is a common tendency to attribute attack on the stainless steel to galvanic corrosion. Tests conducted with inert gasket materials, such as PTFE and graphite-impregnated gaskets have shown that attack on 300-series stainless steel flanges is just as severe as, or more so, with the PTFE gaskets compared to graphite-containing ones.<sup>44</sup> The attack on the stainless steel can be explained as crevice corrosion with both types of gasket. Conversely, it can be argued that if it was galvanic corrosion,

graphite should produce attack on even those stainless steels that exhibit resistance to crevice attack with PTFE gaskets. It has been shown that high alloy stainless steels are adversely affected when coupled to graphite in chlorinated but not natural seawater.<sup>89</sup> But this is also the case when stainless steels with nonabsorbent inert gasket materials are subjected to chlorine levels  $>2 \text{ ppm}$ .<sup>90</sup> It has been reported that crevice corrosion associated with synthetic fiber gasket materials which absorb water is less severe because of dilution of the crevice electrolyte.<sup>91</sup> This phenomenon has been used to advantage in the design of an electrochemical corrosion cell where crevice corrosion of a flat-stock test specimen is eliminated by flooding the specimen sealing gasket with distilled water.<sup>92</sup>

Crevice corrosion has been investigated electrochemically in a number of ways.<sup>80</sup> For example, in a remote crevice assembly, crevice formers are used to sandwich a small specimen (anode) which is then coupled to a separate, larger cathode specimen made of the same alloy as the anode. In an alternative compartmentalized cell design, the anode and cathode are exposed to two different solutions (anode – acidic, deaerated, high  $Cl^-$  solution; cathode – neutral, aerated solution), respectively. In both these designs, the crevice corrosion current associated with the couple is usually measured using a zero-resistance ammeter (ZRA). Although, the anode and cathode members are made from single pieces of the test alloy to eliminate unwanted crevices and immersed connections, unfortunately localized attack is sometimes observed on one or both electrodes at the waterline. Such attack is usually associated with salting out due to evaporation of the test solutions.

Comparisons have been made between pitting corrosion of stainless steels and crevice attack. This stems from the similarity observed between chemistry (low pH, high  $Cl^-$ ) of the electrolyte trapped in a pit and in a crevice. Pits can be regarded as microcrevices (e.g., initiating at sulfide, inclusions) associated with the microstructure, extraneous embedded particles (e.g., iron), under heat tints, ‘peaks’ folded over by mechanical processes such as coarse machining, grinding, and so on. **Table 11** shows that pitting corrosion of Type 316 stainless steel is reduced by more than an order of magnitude in ‘deaerated’ seawater at  $105^\circ\text{C}$ , but not eliminated because  $25 \text{ ppb } O_2$  is probably sufficient to initiate and sustain some attack. The degree of localized corrosion attack on susceptible stainless steels shows a decreasing trend with exposure depth in the ocean



**Table 11** Maximum pit depths on stainless steel in natural and deaerated seawater<sup>93</sup>

<i>Alloy</i>	<i>Seawater conditions</i>	<i>Exposure (days)</i>	<i>Max. pit depth (mm)</i>
316 SS	Aerated, natural, ambient temperature	486	2.4
316 SS	Deaerated, 105 °C, 25 ppb DO	547	0.12
304 SS	Deaerated, 105 °C, 25 ppb DO	547	0.60

as the dissolved O<sub>2</sub> content decreases in the deeper water; however, this trend is general but not necessarily always one-to-one, indicating that other factors are probably implicated in the corrosion process.

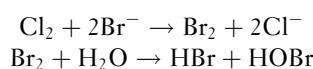
In ambient temperature seawater, nonsensitized austenitic and ferritic stainless steels are considered resistant to stress corrosion cracking (SCC). SCC of Type 316 stainless steel was reported in the vapor zone above boiling seawater, but not on fully immersed specimens.<sup>81</sup> Since oxygen is usually essential for SCC, the likely explanation is that boiling eliminated dissolved O<sub>2</sub> from the seawater. Other data indicated that SCC of Type 316 stainless steel in hot seawater (126 °C) containing 600 ppb O<sub>2</sub> was mitigated when the O<sub>2</sub> level was reduced to 30 ppb.<sup>93</sup>

Martensitic and precipitation-hardening (PH) stainless steels are more prone to SCC. In deep-ocean water tests,<sup>94</sup> SCC of 15–7PH in the RH950 and RH1150 condition, and 17–7PH in the RH1050 condition, was reported. No correlation between SCC susceptibility and tensile strength was observed. These failures occurred at low O<sub>2</sub> levels, leading to the inference that hydrogen embrittlement may be the operative mechanism, for example, due to acidity generation associated with localized corrosion. Extrapolation of results of accelerated SCC tests in boiling NaCl and MgCl<sub>2</sub> solutions (e.g., per ASTM standard G 38) to seawater applications should be done very cautiously. Although temperatures >50 °C are often cited as necessary for SCC of stainless steels, experience indicates that failures can occur even at ambient temperatures where localized corrosion (e.g., crevice attack) generates low-pH conditions; of course, the material has to be in a susceptible condition, for example, sensitized, containing martensite, or containing high tensile stresses, and so on. Dynamic tests such as slow strain rate and crack growth rate are now strongly favored over static tests which may otherwise falsely indicate resistance, because the former expose the base metal

by almost constantly deforming and cracking the passive film above certain strain rates. Another major attribute of the dynamic SCC tests is the much shorter testing time compared to the static tests.

The greater SCC resistance of cast stainless steels over wrought material is usually ascribed to residual ferrite phase in the former. Polluted or putrid seawater containing sulfides may increase the susceptibility to hydrogen embrittlement of martensitic and PH and stainless steels; this propensity is increased when the material is deliberately or inadvertently under cathodic protection. Duplex stainless steels may also be susceptible under the latter condition. If SCC propensity decreases above a certain threshold temperature, especially in sulfide environments, it is reasonable to infer that the cracking mechanism is hydrogen embrittlement since outward diffusion of atomic hydrogen is temperature dependent. On the other hand, cathodic polarization increases the susceptibility to hydrogen embrittlement.

SCC failure of Type 316 stainless steel in venting systems of MSF desalination plants has been attributed to bromine.<sup>95</sup> Chlorination of seawater for biofouling control converts the bromide ions present in the seawater to bromine, which dissolves to produce hypobromous and bromic acids. If ammonia is present, bromoamines are also produced. Acidification of the seawater downstream for scale control releases hydrogen bromide into the vapor, which can then attack the susceptible stainless steels such as Type 316 in the venting system:



Cavitation susceptibility and ranking are often performed in laboratory tests in which the test specimen is vibrated ultrasonically in seawater by a magnetostrictive transducer. Cavitation resistance is based on mass loss per unit time and visual examination. Results for a number of alloys are discussed in the literature.<sup>96–98</sup> Such laboratory tests have shown decreased cavitation damage due to cathodic protection.<sup>97</sup>

## 2.18.7 Copper Alloys

Copper alloys rely on the formation of protective corrosion product films for corrosion control in marine environments. These films are sometimes described as ‘passive.’ In the author’s opinion, the term ‘passive film’ should be reserved for situations

(materials and conditions) where the film is very thin (typically <100 nm), optically transparent, extremely adherent, ennobles the potential of the metal appreciably, and not formed as a 'voluminous' deposit by the incorporation of species from the environment. For example, films on stainless steel, titanium, and aluminum would be considered as passive. The protective corrosion product films on copper alloys are much thicker and also quite complex; in clean seawater, copper hydroxychloride is often a major component.

In the splash and intertidal zones, 90/10 copper–nickel sheathing has been successfully used for corrosion control on offshore platforms. Unlike paint coatings, such sheathing requires little maintenance – which is extremely difficult in the splash zone as discussed earlier. Because of high resistance to macrofouling, copper–nickel has also been used for the construction of small boat hulls and as adhesive-backed foils on ferries and fireboats.<sup>99</sup> Macrofouling resistance is apparently reduced when the copper–nickel is galvanically coupled to a more anodic material such as steel, or if it is subjected to cathodic protection, *albeit* inadvertently. However, the macrofouling attachments are relatively easily removed compared to bare or coated steel.

Copper alloys are very desirable for seawater applications because of high resistance to biofouling. They have been widely used for heat exchanger tubing because of high heat transfer properties. However, they are relatively soft and hence subject to erosion–corrosion in seawater above certain velocities. The high turbulence in seawater pumps restricts the choice of copper alloys largely to nickel–aluminum–bronze. As a general rule of thumb critical velocities for small diameter heat exchanger tubing determined from laboratory testing and field experience are shown in [Table 12](#).<sup>100</sup> These values are still widely used in design and operation of copper-alloy heat exchangers. It has been postulated that each copper-based alloy has a critical shear stress associated with it.<sup>101</sup> When this shear stress exceeds the adhesion strength of the protective corrosion product film, attack of the base metal ensues. Critical shear stresses, depicted in [Table 13](#),<sup>101</sup> determined using fluid mechanics and evaluated by laboratory testing now support the view that as the piping diameter increases, higher critical velocities than those shown in [Table 12](#) can be used without increasing the risk of erosion–corrosion for the alloy in question.

One of the most important corrodents toward copper alloys in seawater service is sulfide. Sulfide can be entrained in the seawater (e.g., from bottom

**Table 12** Rule of thumb maximum velocities for copper alloy heat exchanger tubing in seawater

Alloy	Suggested max. design velocity ( $\text{m s}^{-1}$ ) <sup>a</sup>
Copper	0.9
S-bronze	0.9
Admiralty brass	1.5
Aluminum brass	2.4
90/10 CuNi	3.0
70/30 CuNi	3.7

<sup>a</sup>Velocities may be increased by  $0.3\text{--}0.6 \text{ m s}^{-1}$  in deaerated brines encountered in heat recovery exchangers in desalination plants. Source: LaQue, F. L. *Marine Corrosion: Causes and Prevention*; Wiley, 1975; p 267.

**Table 13** Critical velocities and shear stresses for copper alloys in seawater

Alloy	UNS No.	Test temp ( $^{\circ}\text{C}$ )	Critical velocity ( $\text{m s}^{-1}$ )	Critical shear stress ( $\text{N m}^{-2}$ )
DHP Copper	C12200	17	1.3	9.6
As-inhibited Al brass	C68700	12	2.2	19.2
90/10 CuNi	C70600	27	4.5	43.1
70/30 CuNi	C71500	12	4.1	47.9
Cr-modified 90/10 CuNi	C72200	27	12.0	296.9

Source: Efrid, K. D. *Corrosion* **1977**, 33(1), 3–8.

sediment or polluted harbors) or generated *in situ* by sulfate-reducing bacteria, as discussed previously. The latter mechanism is very common when initially clean seawater putrefies after a few days of stagnation, for example, in heat exchangers, pumps, and piping systems during outages or shutdowns. The role of sulfides has been extensively investigated.<sup>102–108</sup> The evidence suggests that protective corrosion product films allowed to form on copper alloys in clean seawater for several months can resist short subsequent exposure to sulfides. Conversely, exposure to sulfide conditions from the outset interferes with the formation of desirable protective films. In such cases, sulfides have a deleterious effect on pitting corrosion and erosion–corrosion resistance. Thus, commissioning of copper alloy equipment such as heat exchangers using clean seawater for several months initially appears to be critical. However, this task should not be underestimated as access to large quantities of clean seawater at coastal areas is difficult

at best. Experience indicates that once incorporated in the corrosion product film, sulfides are very difficult to remove completely and problems continue.

A classical laboratory study<sup>102</sup> of the effects of sulfide on 90/10 and 70/30 CuNi in seawater disclosed the following: corrosion rate increased as the sulfide content was increased from 7 to 250 ppb; attack was localized at lower sulfide concentrations, and more general at higher ones; once attack initiated, there was minimal seawater velocity effect over the 0.5–5.3 m s<sup>-1</sup> range; attack continued even in clean seawater after initial exposure to 1000 ppb sulfide for 1–5 days, or 10 ppb sulfide for 30 days. Addition of 0.2 ppm ferrous ions which is sometimes used to mitigate erosion–corrosion was found to reduce but not eliminate sulfide-related corrosion of the CuNi alloys.<sup>103</sup>

Protective corrosion product films reduce the corrosion rate markedly in clean seawater with time.<sup>109</sup> In the ambient temperature range, the corrosion rate increases with increasing temperature. However, at high temperatures, such as in MSF desalination plants, the corrosion rate decreases with increasing temperature<sup>110</sup> in the 54–121 °C temperature range as illustrated in **Figure 20**. This may be due to the lower oxygen levels and precipitation of scales due to inverse solubility. However, at elevated temperature, corrosion rate increases with increasing dissolved O<sub>2</sub> even in the ppb range as depicted in **Figure 21**.<sup>111</sup> Decrease in corrosion rate has also been reported for deep waters where oxygen levels were lower.<sup>112</sup>

It should be emphasized that copper alloys with >70% copper are resistant to biofouling compared, for example, to carbon steel, stainless steels, aluminum, titanium, but not completely immune. Macrofouling resistance of copper alloys is usually explained in terms of either continuous, but slow release of copper ions, or presence of copper-rich corrosion products on the metal surface – both of which are purportedly ‘toxic’ toward macroorganisms.<sup>113,114</sup> The situation is confounded by the fact that while increasing alloy content lowers the copper ion release (and hence likelihood of fouling), it also affects the nature of corrosion products. It is not known why, for instance, barnacles attach at some but not most areas of such copper alloys. It has been suggested that attack on the metal under macrofouling occurs after the organisms die.<sup>113</sup> Fouling is more likely in quiescent than flowing seawater. A minimum velocity of 1–2 m s<sup>-1</sup> was proposed to mitigate macrofouling.<sup>115</sup> Higher velocities to prevent macrofouling may increase the risk of erosion–corrosion.

Pitting corrosion of copper alloys can occur under deposits due to differential aeration, and is often exacerbated by sulfides. Another factor that can increase pitting susceptibility is the presence of residual carbon films on the copper surface.<sup>116</sup> The carbon is believed to derive from oxidation of lubricating oil residues left behind from manufacturing (e.g., tube drawing) and subsequent annealing heat treatment. It has been hypothesized that the carbon film acts as a cathode and promotes localized corrosion of the base metal at exposed areas in the film. Ideally, the carbon film should be removed after

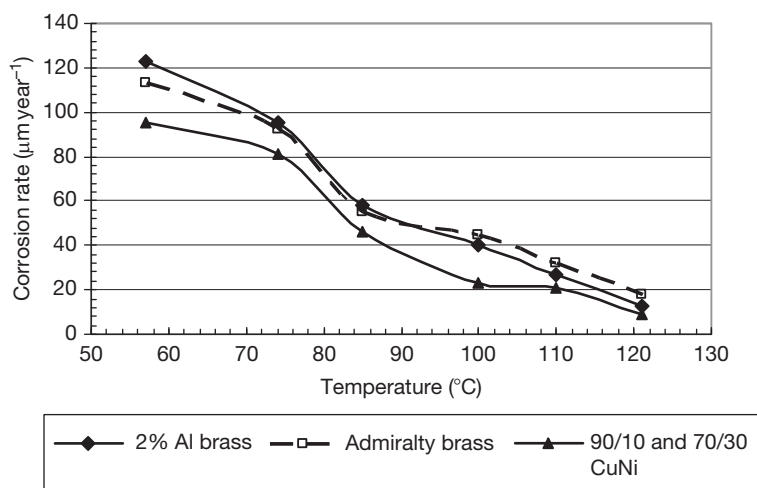


**Figure 20** Corrosion rate versus temperature for three copper-base alloys in seawater; DO 40–600 ppb, pH 6.2–7.8, 156 days. Reproduced from Mattson, M. E.; Fuller, R. M. A study of materials of construction in distillation plants, Joint report by Office of Saline Water and the International Nickel Company, Research report No. 163, 1965.

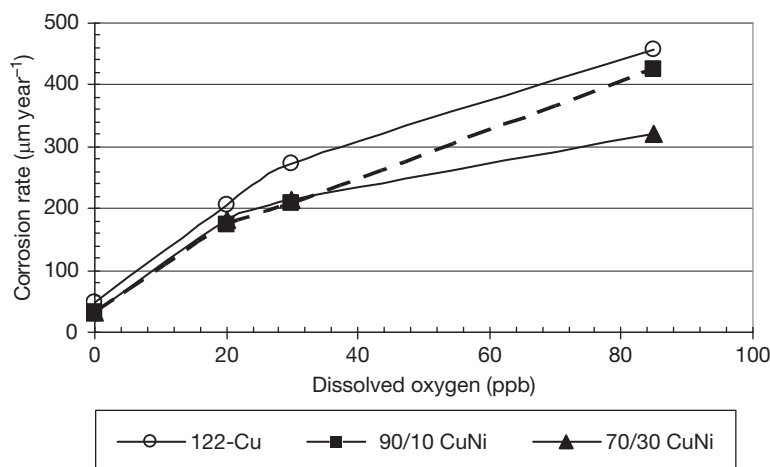


**Figure 21** Corrosion rate versus DO in seawater for three copper-base alloys at 107 °C in a once-through desalination system; seawater flow rate  $\sim 2 \text{ m s}^{-1}$ , pH 7.2–7.5,  $\text{CO}_2 < 10 \text{ ppm}$ , 15–30 days. Reproduced from Schreiber, C.; Osborn, O.; Coley, F. H. *Mater. Perform.* **1968**, 7(10), 20–25; NACE International: Houston, TX.

manufacturing. Detection of the carbon film is not always easy. Since the carbon film is insoluble, one method involves placing a drop of nitric acid on the test surface and visually observing any flakes of thin gray/black matter float up to the top. The films are often even more difficult to detect after corrosion failures have occurred. Potential measurement has been proposed as a detection method in such cases.<sup>117</sup>

A number of copper-based alloys tested concurrently in an ancillary seawater condenser operated for over 8 months revealed that Admiralty brass (70/30 Cu/Zn) suffered from impingement corrosion at the inlet and outlet ends as well as adjacent to deposits.<sup>118</sup> Iron and manganese additions to copper–nickel alloys have been shown to enhance erosion–corrosion resistance.<sup>119</sup> However, some other tests indicated iron additions to be deleterious,<sup>120</sup> especially  $>1\%$ .<sup>121</sup> This was probably related to the distribution of iron in the microstructure. Uniform distribution improves corrosion resistance, while segregation increases susceptibility to localized attack. A simple magnetic permeability test is used to detect iron segregation.<sup>122</sup> Small Cr additions to copper–nickel alloys improves erosion–corrosion resistance; however, localized corrosion resistance in quiescent conditions may be impaired by Cr segregation. Any restrictions on flow caused by macrofouling (e.g., shells) or pebbles lodged in the tube can cause severe local turbulence, and hence erosion–corrosion or impingement attack at associated (usually immediately downstream) areas. Experience shows that less protective scales are formed as the seawater pH is

lowered, for example, by pollutants or dissolved  $\text{CO}_2$ . This is not unexpected since corrosion products and mineral scales are more difficult to form at lower pH values. Absence of protective scales at lower pH will increase erosion–corrosion tendency.

The role of gas bubbles in promoting erosion–corrosion has been discussed.<sup>121,123</sup> In rotating spindle and disc tests, air bubbles in the seawater were stated to be beneficial toward CuNi alloys.<sup>121,124</sup> However, results of impingement attack in flowing loop tests indicated that both air and nitrogen bubbles were harmful.<sup>121</sup> Since collapsing bubbles are thought to be the cause of cavitation damage, copper alloys, being considerably softer are more likely to be affected by this form of damage compared to, say, stainless steels, nickel-based alloys, and titanium.

Investigations on the effect of entrained sand particles on erosion–corrosion resistance of aluminum brass indicated the following: erosion–corrosion increased with increasing sand content ( $>300 \text{ ppm}$ ) and particle size<sup>125</sup>; cathodic protection with or without ferrous iron injection was beneficial when the sand particles were  $50 \mu\text{m}$  in size, but not when they were  $250 \mu\text{m}$ <sup>126</sup>; less attack in polluted seawater containing sand was attributed to protective sulfide films.

Galvanic corrosion of copper alloys is problematic in seawater when they are coupled to cathodic materials such as stainless steels, nickel-based alloys, titanium, and graphite, especially for small anode/cathode area ratios. In chlorinated seawater, a reduction in galvanic corrosion of copper alloys coupled to stainless steels has been observed<sup>43,128</sup> and ascribed to reduced biofilm

activity, which affects cathodic polarization kinetics, and hence galvanic corrosion rate.

Copper alloys are cathodic to many materials, and can thus cause unacceptable galvanic corrosion of anodic materials such as carbon steel, cast iron, aluminum, and zinc – particularly for large cathode/anode area ratios. Gray cast irons are initially anodic to copper; however, graphitic corrosion of gray cast iron can eventually expose enough graphite at the exposed surface so as to reverse the galvanic couple and accelerate corrosion of the copper alloy. In principle, the free corrosion potentials of copper-based alloys in seawater are fairly close to one another, and thus one might expect them to be galvanically quite compatible. In principle, this is the case. However, regardless of potentials, an adverse cathode/anode area ratio between two copper alloys can produce unacceptable galvanic attack on the more anodic material. Increasing flow rate and temperature typically accelerates galvanic corrosion of copper alloys. Presence of sulfides (especially 50 ppb) in seawater was found to promote galvanic attack on Naval M-bronze and nickel aluminum bronze fittings coupled to 90/10 or 70/30 CuNi piping.<sup>128</sup> The effect of sulfides appears to be greater at lower seawater temperatures.<sup>129</sup>

Electrically isolated copper components in a system can undergo self-corrosion in seawater environments. The release of even imperceptible amounts of copper ions can pose an indirect problem for anodic materials that come in contact with them. For instance, copper ions can plate out on aluminum, steel, and zinc, leading to deposition or cementation corrosion. In other words, copper ions plate out on the anodic material (as a cathodic reaction) and cause corrosion of the base metal. However, once the ions have plated out, galvanic corrosion (usually as pitting) of the base metal ensues even if the original source of the copper ions is removed. Copper-colored areas surrounding pits in the anodic material are usually a telltale sign of this phenomenon. For example, it has been observed in aluminum fuel tanks on pleasure boats, particularly those operating in seawater environments. Copper corrosion products enter the tank from water condensate in copper piping and/or copper alloy valves in the fuel system.

Copper-based alloys are quite resistant to SCC in clean seawater. SCC of brasses is generally associated with ammonia, amines, or nitrates that are either entrained as pollutants or can form *in situ* under decaying biofouling attachments. Copper–nickel alloys are considered resistant to such environments. Stress relief

of cast nickel aluminum bronze alloys is recommended to minimize the risk of SCC failure in critical seawater service applications.

Dealloying is quite common in many copper-base alloys. It is often observed in marine artifacts submerged for long periods in seawater. Reddish coloration due to copper deposition is a telltale sign of dealloying. Alpha brasses (e.g., 85/15 Cu/Zn) can be inhibited against dealloying with Sn or As additions. Unfortunately, such additions are usually not considered to be as effective in beta brasses (e.g., 60/40 Cu/Zn). Unlike in brasses, dealloying in copper–nickels is usually superficial. In nickel aluminum bronzes, dealloying involves the selective dissolution of aluminum from the alloy. Proper heat treatment to minimize the beta phase alleviates this problem.

Copper-base alloys can suffer from another form of localized attack known as metal-ion concentration cell corrosion. Attack usually occurs at the mouth of a crevice, in contrast to localized corrosion that occurs inside the crevice, for example, in susceptible stainless steels and nickel-base alloys.

## 2.18.8 Nickel-Based Alloys

The primary nickel-based materials used in seawater include nickel–copper alloys (e.g., the 70/30 NiCu alloy 400, or its high strength version, alloy K-500) and Ni–Cr–Mo–Fe alloys (e.g., alloy 625, C-276, alloy 59, alloy 686, etc.). As with stainless steels, these nickel-based alloys are also believed to depend on the formation of passive films for corrosion resistance.

Because of its established record of good performance in the splash zone, alloy 400 has been successfully used as sheathing for protection of carbon steel in the splash zone.<sup>46</sup> Unlike the copper–nickel alloys described in the previous section, the NiCu and other nickel-based alloys are not resistant to macrofouling in the tidal and immersion zones. In fact, nickel-base alloys tend to behave more like stainless steels. General corrosion rates in clean seawater are low to negligible, and when attack occurs, it is usually as pitting and/or crevice corrosion; corrosion initiation is more likely in quiescent or low flow seawater.

For unalloyed nickel and nickel–copper alloys (e.g., alloys 400 and K-500), pitting in low flow seawater is common. Unlike with susceptible stainless steels, the pits tend to be open, hemispherical, and do not grow significantly in depth, for instance, after ~1 year in seawater.<sup>130</sup> Alloying nickel with copper appreciably improves the pitting resistance. Seawater



temperature has been shown to dramatically affect pitting corrosion behavior of alloy 400; maximum pit depth increased in the 18 to 30 °C range, but then decreased markedly at 50 °C.<sup>131</sup> A similar trend was discussed earlier for crevice corrosion of stainless steels and attributed to 'degraded' biofilms at 50 °C. The pitting potential of alloy 400 determined electrochemically decreased with temperature.

Corrosion rate of alloy 400 has been shown to increase as the sulfide concentration in seawater increased from 0 to 5 ppm.<sup>128</sup> Ni–Cr alloys were not affected by sulfides in ambient temperature seawater.

Alloying additions of ~20% Cr and ~8% Mo to nickel-based alloys (e.g., in alloy 625) impart significant resistance to pitting and crevice corrosion in seawater. As with stainless steels, addition of ~20% Cr alone does not ameliorate localized attack. **Table 14** provides a comparison of relative corrosion resistance of several nickel-based alloys immersed in quiescent seawater for ~18 months.<sup>132</sup> Apparently, from a corrosion resistance viewpoint, cobalt in Ni-based alloys behaves like nickel. Alloy C-276 was found to be highly-resistant to localized and general corrosion in seawater up to 288 °C<sup>71</sup>; it also exhibited crevice corrosion resistance at 107 °C in deaerated seawater (DO 28 ppb).

Crevice corrosion of alloy 400 is not generally as severe as, say, for 300-series stainless steels. This can be explained by the fact that hydrolysis of Ni and Cu ions from alloy 400 does not produce a highly acidic and aggressive crevice solution compared to Cr and Mo ions from susceptible stainless steels.

The erosion–corrosion behavior of nickel-based alloys is quite similar to that of stainless steels, that is, notably superior to that of copper–nickel alloys. Thus, nickel alloys can tolerate high velocities, turbulence, and impingement which makes them candidates for seawater pumps, valves, piping systems, and so on. Test data summarized in **Table 15**<sup>133,134</sup> show that, like stainless steels, most nickel-based alloys exhibit acceptably low erosion–corrosion rates up to ~40 m s<sup>-1</sup>. With the exception of the NiCu alloys, their cavitation resistance is also expected to be similar to that of stainless steels.

Nickel–copper alloys are often selected for seawater service because their higher Ni content provides enhanced resistance to chloride stress corrosion cracking (Cl<sup>-</sup> SCC) compared to stainless steels. Deep ocean tests of 2 years duration confirmed the SCC resistance of Alloy 825 and Alloy C.<sup>135</sup> Alloys G-3, 625, and C-276 were resistant to SCC in U-bend tests of several hundred hours duration in synthetic seawater.<sup>81</sup>

**Table 14** Localized corrosion resistance of some Ni-based alloys after ~18 months' exposure in quiescent ambient-temperature seawater

<i>Alloy</i>	<i>Max depth of crevice attack (μm)</i>
Unalloyed Ni	2.06
400	432
K-500	51
600	457
825	229
625	0
C 276	0

Source: Lennox, T. J., Jr. In *Corrosion/82*; NACE International: Houston, TX, 1982; Paper No. 64.

**Table 15** Corrosion resistance of Ni-base alloys at ambient-temperature high velocity seawater

<i>Alloy</i>	<i>Seawater velocity (m s<sup>-1</sup>)</i>	<i>Corrosion rate (μm year<sup>-1</sup>)</i>
C	39	50
825	43	75
718	41	50
X-750	41	50
600	41	75
400	43	100
K-500	41	100

Source: Boyd, W. K.; Fink, F. W. *Corrosion of Metals in Marine Environments*, Battelle Columbus Labs, OH, Report No. MCIC-78-37, 1978; p 103.  
Moller, G. E. *Soc. Pet. Eng. J.* **1977**, 17(2), 101–110.

Because of their austenitic microstructure, nickel-based alloys are generally resistant to hydrogen embrittlement in the annealed condition. However, risk of hydrogen embrittlement (HE) increases as the strength level increases due to cold work or heat treatment. At similar strength levels, increasing aging temperature is apparently favorable in lowering HE risk. HE of 70/30 NiCu alloy K-500 bolts has been reported for an offshore platform application under cathodic protection conditions.<sup>136</sup> Susceptibility to HE was traced to high hardness and subsequent cathodic protection. Annealing after rolling the threads to alleviate high hardness before precipitation hardening was recommended to mitigate the problem.

Accelerated attack would be predicted for active materials coupled to Ni-based alloys because of the noble positions of the latter in the galvanic series. However, the successful use of alloy 400 sheathing on carbon steel in the splash and tidal zones, even in the

absence of cathodic protection, suggests galvanic compatibility which has been attributed to easy cathodic polarization of the nickel alloy.<sup>137</sup> It should be emphasized that this would not be the case if the steel/nickel-alloy area ratio was small. Pitting and crevice corrosion of NiCu alloy trim in pumps and valves is mitigated by cast iron bodies. Although nickel-based alloys are anodic to titanium, they are galvanically compatible because the increased corrosion rates are still very small from a practical viewpoint.<sup>138</sup>

### 2.18.9 Titanium Alloys

Titanium alloys are among the most corrosion resistant materials in seawater service. The general corrosion rate in seawater is extremely low, for example,  $0.8 \text{ nm year}^{-1}$ ,<sup>140</sup> not surprisingly, it is often reported as 'nil.' Titanium alloys are immune to pitting and crevice corrosion in all marine environments at ambient temperatures. Thus, no localized corrosion is encountered in the atmospheric, splash, tidal, immersion, or mud zones. Titanium is not resistant to biofouling. Therefore, macrofouling attachments similar to those on carbon steel, stainless steel, and aluminum alloys are also commonly observed on titanium alloys. However, unlike the other alloys, there is no localized corrosion of titanium under the biofouling or any silt deposits. No corrosion allowance is necessary for titanium because of its very high corrosion resistance in ambient-temperature seawater. Thus, titanium is widely used for heat exchanger applications, especially retubing in shell-and-tube heat exchangers. Grade-1 titanium is the premier material of choice for plate-and-frame heat exchangers because of high corrosion resistance and easy fabrication properties. However, because of extensive demand, there is currently a worldwide shortage of grade-1 titanium. Other materials such as Ni–Cr–Mo alloys and superaustenitic stainless steels are being evaluated as alternatives.

Crevice corrosion of titanium in seawater has been reported in tight crevices at temperatures  $>70^\circ\text{C}$ .<sup>141,142</sup> The crevice electrolyte was also found to be acidic, suggesting that a similar oxygen-depletion and metal-ion hydrolysis mechanism (as discussed earlier for stainless steels) may be operative. However, the actual mechanism is probably more complex since crevice corrosion resistance is increased by small additions of Pd, Mo, or Ni to the titanium. Iron, carbon steel or low-alloy steel particles embedded accidentally into a titanium surface can lead to

localized attack at temperatures  $>80^\circ\text{C}$ . This has been proposed as a special case of crevice corrosion,<sup>142</sup> that is, occlusion by titanium metal smears or laps may create micro crevices that allow the generation of acidic conditions, preventing repassivation and localized attack, and possibly hydrogen adsorption. Thus, the mechanism is probably more complex than the presence of just micro crevices, since the attack has not apparently been observed if austenitic stainless steel, nickel, or copper particles are embedded in the titanium surface. Evidently, the Pd-containing grades exhibit significant resistance to attack associated with smeared iron particles.

Titanium is quite noble in the galvanic series for seawater. It can sometimes exhibit potentials anodic to graphite, platinum, zirconium, Ni–Cr–Mo–Fe alloy C, and NiCu alloy 400, and even some 300-series stainless steels in the passive condition. However, titanium is galvanically compatible with these materials. Any attack on the titanium is more likely to be crevice corrosion in tight crevices at temperatures  $>70^\circ\text{C}$ , as discussed earlier. In fact, despite being slightly more noble than titanium, attack is much more likely on the 300-series stainless steels, alloy 400, and even alloy C, at crevices regardless of galvanic coupling to titanium. Corrosion of the more active materials such as copper-base alloys, carbon steels, cast irons, aluminum alloys, zinc, and magnesium will be accelerated if galvanically coupled to titanium. The degree of attack acceleration will depend on the relative anode/cathode area ratio, system geometry, and cathodic reduction reaction kinetics on the titanium, which are influenced by seawater temperature, velocity, fouling, and so on. **Figure 12** shows that in seawater, titanium is more easily polarized than copper due to its higher overvoltage for oxygen reduction. Consequently, galvanic attack on carbon steel coupled to titanium is less severe compared to corrosion of steel coupled to copper, in each case for the same anode/cathode area ratio. The potential difference between titanium and steel is nearly double that between steel and copper – affirming that potential difference is not reliable for predicting galvanic attack on the anodic material. The free corrosion potential of titanium in aerated and deaerated seawater is fairly steady in the  $\sim 20\text{--}135^\circ\text{C}$  temperature range. However, as temperature increases further, the potential shifts in the electronegative direction by  $\sim 500 \text{ mV}$  at  $\sim 200^\circ\text{C}$ . Potentials of other alloys also exhibit electronegative shifts.<sup>143</sup>

Unfortunately, titanium is susceptible to hydriding when its potential shifts more electronegative

than  $-0.7$  V (SCE) at elevated temperature.<sup>144</sup> This can happen when titanium is cathodically polarized by coupling to anodic materials such as steel, aluminum, or zinc, or by impressed current cathodic protection. In ambient temperature seawater applications, a potential shift to no more than  $-1$  V (SCE) has been suggested.<sup>144</sup> Hydrogen is generated by a two-step process: (1) discharge of  $H^+$  to atomic H by electron consumption, and (2) H recombination to generate molecular  $H_2$  gas bubbles. If excessive hydrogen is generated, there is an increasing uptake of atomic hydrogen, which diffuses into the titanium, reacts with the  $\alpha$  phase, and precipitates as brittle, acicular, titanium hydride ( $TiH_2$ ) needles at grain boundaries. Hydriding is exacerbated at temperatures  $>80^\circ\text{C}$ . About 500–600 ppm, hydrogen can cause excessive hydriding which embrittles the titanium, causing potentially significant reduction in ductility and fracture toughness. Anodizing reduces hydrogen uptake. The beta titanium alloys do not hydride easily because of considerably higher solubility of hydrogen (several 1000 ppm) in the beta phase.

It was prematurely concluded from early tests that unwelded titanium was highly resistant to stress corrosion cracking (SCC) in seawater<sup>145</sup> even when stressed to 75% of the yield strength. However, those tests used smooth test specimens. Subsequent tests disclosed that while alloy composition and heat treatment influenced SCC resistance, presence of notches simulating stress risers was essential. Environmental variables did not greatly affect the SCC behavior, this is not surprising because of the very high resistance of titanium to corrosion in seawater. Generally, all the  $\alpha$  alloys (e.g., Ti–8Al–1Mo–1V and Ti–7Al–3Nb–2Sn), and near  $\alpha$  alloys that contain small amounts of  $\beta$  phase stabilizers such as Al, Zr, Sn, and O (e.g., Ti–6Al–5Zr–0.5Mo–0.2Si and Ti–8Al–1V–1Mo) are susceptible to SCC in seawater. SCC resistance is markedly reduced when Al  $>5\%$  and oxygen  $>0.4\%$  in  $\alpha$  alloys. For the  $\alpha + \beta$  alloys, such as grade 5, oxygen concentration  $<0.1\%$  is necessary to preclude SCC; commercial alloys contain typically 0.15% oxygen. In  $\alpha + \beta$  alloys, cracking occurs primarily in the  $\alpha$  phase. Contradictory behavior has been indicated for the effect of  $\beta$  stabilizers on SCC resistance in seawater. In some cases, V and Nb additions were detrimental, in others,  $>2\%$  V was advantageous when Al in the 7–8% range was present in the alloy. In  $\alpha + \beta$  alloys, Si and Mn were apparently deleterious.<sup>146</sup>

The SCC resistance of titanium alloys in seawater is greatly affected by heat treatment. Generally, small

grain size is attained by aging just below the  $\beta$  transus (above the  $\beta$  transus,  $\alpha$  or  $\alpha + \beta$  phases transform to  $\beta$ ) which enhances SCC resistance. For the susceptible alloys, the SCC behavior is also highly influenced by stress concentration; for example, there is a significant decrease in fracture stress in seawater at a notch radius of 125  $\mu\text{m}$  compared to 250  $\mu\text{m}$ . In slow strain rate tests in simulated seawater, SCC behavior of a number of titanium alloys was found to be highly influenced by the strain rate<sup>147</sup>; typically, they were most susceptible at strain rates of  $\sim 7 \times 10^{-5} \text{ s}^{-1}$ . Other laboratory tests revealed that crack velocity decreased linearly with cathodic polarization of titanium alloys over the  $-400$  to  $-900$  mV (SCE) potential range<sup>148</sup>; the opposite behavior would be expected if there is sufficient uptake of hydrogen, for example, due to extended precharging time and/or polarization to more negative potentials in test. Crack velocity was found to increase with temperature, exhibiting Arrhenius behavior.<sup>149</sup> In tests performed in surface seawater and at depths of  $\sim 800$  and  $\sim 2000$  m, only butt-welded, nonstress relieved, Ti–13V–11Cr–3Al alloy stressed to 75% of yield strength exhibited SCC.<sup>150</sup>

The passive oxide film, its ability to reheal, and high inherent hardness of titanium confer high resistance to erosion–corrosion and cavitation in seawater. Velocities as high as  $\sim 37 \text{ m s}^{-1}$  can be tolerated in clean seawater. Minimum velocities of the order of  $>2 \text{ m s}^{-1}$  are necessary to prevent attachment of macrofouling in seawater heat exchanger tubing and piping. Provided they are galvanically compatible, titanium inserts can be used in the inlet ends of heat exchanger tubing experiencing erosion–corrosion at those locations. Ordinary silt in seawater does not lower erosion–corrosion appreciably. Higher-strength titanium alloys, such as grade 5 (Ti–6Al–4V), can be substituted for enhanced resistance if large, angular, abrasive particles produce erosion of the commercial purity (CP) grades.

The anodic breakdown potential of titanium in ambient temperature seawater is  $\sim 10$  V. This allows titanium to be used as a substrate for platinum in impressed current anodes. If higher breakdown voltages are necessary in specific applications, niobium is substituted for titanium.

## 2.18.10 Aluminum Alloys

The low density of aluminum alloys ( $\sim 2700 \text{ kg m}^{-3}$ ) makes them attractive for marine engineering

applications such as seacraft. However, the corrosion resistance is quite variable depending on alloy composition and heat treatment. **Table 16** summarizes a commonly used designation system for aluminum alloys. For some applications, 'Alclad' products are specified. Alclad refers to a composite wrought (e.g., sheet) material which has an aluminum-alloy core with a metallurgically bonded thin 'skin' of either pure aluminum or another aluminum alloy on its surface for corrosion protection, for example, high-purity (more corrosion resistant) aluminum over alloy 2024, or alloy 7072 applied over alloy 6061 as sacrificial coating.

Aluminum relies on the formation of a passive aluminum oxide ( $\text{Al}_2\text{O}_3$ ) film for corrosion resistance. However, the film properties are affected by alloy composition, metallurgical condition, and environmental factors, and widely ranging corrosion behavior is exhibited in seawater. In seawater immersion, the major corrosion concerns with aluminum alloys are galvanic corrosion when electrically coupled to cathodic materials, crevice corrosion and pitting under macrofouling and silt deposits, exfoliation, stress corrosion cracking, and metal-ion (especially Cu) deposition corrosion. The high strength 2xxx series and the 7xxx series aluminum alloys are widely used in aerospace applications. However, the alloying additions of Cu (in 2xxx) and Zn (in 7xxx) also make them more susceptible to corrosion in seawater.

Unalloyed aluminum has very low general corrosion rate in the splash zone because DO diffuses easily through the thin seawater layer to sustain passivity associated with the  $\text{Al}_2\text{O}_3$  film. However, pure aluminum is considered too 'soft' for many splash-zone applications. The stronger 5xxx and 6xxx alloys are more suitable. In the tidal zone, aluminum alloys

are subject to biofouling and localized attack (pitting and/or crevice corrosion) underneath macrofouling attachments. Long-term exposure tests<sup>133</sup> showed that the average penetration for alloys 1100 and 6061 in the tidal zone after 16 years exposure was very low,  $<15\text{ }\mu\text{m}$ ; however, the maximum pit depths were  $\sim 1\text{--}1.5\text{ mm}$ . Under immersion conditions, the average penetration increased but was still very low from a practical viewpoint,  $<30\text{ }\mu\text{m}$ ; however, maximum pit depths were in the range  $\sim 1\text{--}2\text{ mm}$ .

The effect of alloying additions is complex. For example, depending on specific alloy,  $<0.2\%$  Cu and  $\sim 0.5\text{--}1.2\%$  Mn were beneficial, but  $0.4\text{--}0.8\%$  Fe was detrimental toward corrosion resistance of aluminum in synthetic seawater.<sup>151</sup> Heat treatment affects the distribution and size of the intermetallic particles that influence mechanical properties by precipitation hardening. The desired mechanical properties of 5xxx alloys cannot be attained by conventional heat treatment alone; instead, they are strain hardened by mechanical working and, depending on alloy, may be subjected to some annealing treatment. The selected data in **Table 17** show that the general corrosion rate of alloy 5052 in the H22 temper was an order of magnitude lower than in the annealed 'O' condition; the H32 temper reduced the corrosion rates of alloys 5086 and 5456 by half, but the H113 temper did not significantly affect the corrosion rate of alloy 5085.<sup>152</sup>

**Table 16** Aluminum wrought alloy designations

Series	UNS No.	Major alloying element(s)	Heat treatable
1xxx	A91xxx	None	No
2xxx	A92xxx	Cu	Yes
3xxx	A93xxx	Mn	No
4xxx	A94xxx	Si	No
5xxx	A95xxx	Mg	No
6xxx	A96xxx	Mg, Si	Yes
7xxx	A97xxx	Zn, Mg	Yes
8xxx	A98xxx	Ti, Li	No
<i>Temper (heat treatment) designations</i>			
O	Annealed		
H (e.g., H1, H2, etc.)	Strain-hardened only		
T (e.g., T4, T6, etc.)	Solution heat treated; aged		

**Table 17** Corrosion rates of 5xxx aluminum alloys in seawater

Alloy	Exposure duration (months)	Exposure depth (m)	Corrosion rate ( $\mu\text{m year}^{-1}$ )
5052-O	35	1700	78
5052-H22	35	1700	10
5052-H34	13	770	5
5454-H32	6.5	760	18
5454	13	770	15
5456-H321	13	770	28
5456-H32	13	770	15
5456-H343	6.5	770	10
5085	13	770	13
5085-H113	13	770	15
5086	13	770	20
5086-H32	13	770	10
5086-H34	13	770	15
5086-H112	6	2	28

Source: Reinhart, F. M. Corrosion of Metals and Alloys in the Deep Ocean, Technical Report No. R-834, Civil Engineering Laboratory, Port Hueneme, CA, 1976; pp 204–209.

The increase in corrosion rate of aluminum alloys with seawater depth is often attributed to lower oxygen content of seawater, which presumably prevents rehealing of the aluminum oxide film. Lower seawater pH (and hence less likelihood of calcareous deposit formation) in deep water has been proposed as an alternative explanation.<sup>153</sup> However, this rationalization appears to be contradicted by data<sup>154</sup> from artificial seawater tests indicating that corrosion rate of Al–3Mg alloy decreased with decreasing pH in the 6–9 range. The mechanism is probably much more complex since alloy composition appears to affect corrosion behavior even at the same seawater depth. For example, maximum depth of pitting was <50  $\mu\text{m}$  for alloys 5086-H34 and 5083-H113 exposed for 1 year at a depth of  $\sim 250$  m, whereas the maximum pit depths for alloys 2219-T81 and 6061-T6 at the same depth were almost 2 mm.

Tests on alloys 3004, Alclad 3004, Alclad 3003, and 5052 exhibited less mass loss, but more pitting in cold seawater ( $\sim 10^\circ\text{C}$ ); in warm seawater ( $\sim 27^\circ\text{C}$ ), overall mass loss was greater but corrosion was uniform with no discernible pitting.<sup>155</sup> It was shown electrochemically that the pitting potential was not significantly altered by temperature,<sup>153</sup> however, ennoblement of the free corrosion potential indicated greater propensity to pitting in colder seawater. Data for Al–3Mg alloy indicate that corrosion rate increased steadily with temperature in the  $\sim 20$  to  $\sim 70^\circ\text{C}$  range, it then decreased somewhat with a minimum at  $\sim 90^\circ\text{C}$ , and finally increased rapidly above boiling to  $\sim 125^\circ\text{C}$ .<sup>154</sup> Increased corrosion at the lower temperatures was attributed to DO. A significant decrease in pitting corrosion of alloy 5052 was reported for hot, flowing seawater environment associated with desalination when the temperature increased from 82 to  $108^\circ\text{C}$ .<sup>156</sup>

Alloy composition and heat treatment appear to affect pitting corrosion behavior as illustrated by the data in Table 18 which show maximum depths of

**Table 18** Maximum depths of attack on some aluminum alloy plate specimens after 10 years immersion in natural seawater at ambient temperature

Alloy	Maximum pit depth (mm)
1100-H14	1.02
3003-H14	0.53
6061-T4	0.36
6061-T6	2.41
7072	1.42 (perforated)
7075-T6	1.68

attack on selected aluminum alloy plate specimens after 10 years exposure in seawater. Electrochemical studies have indicated that alloying additions of Zn lower the pitting potential of aluminum; Cu additions raise it, while Mg additions exhibit a minor effect. However, heat treatment to attain maximum hardness lowered the pitting potential of Al–Cu alloys; this is probably related to grain boundary depletion of Cu associated with precipitation of  $\text{CuAl}_2$  intermetallics particles at grain boundaries. Figure 22 shows an interesting relationship between pitting propensity and free corrosion potential for a number of aluminum alloys.<sup>175</sup> There is no general agreement on the growth rate of pits with time. Some data suggest that pit depth decreases with time; other data imply opposite behavior. Despite wide variations in pitting corrosion behavior, aluminum alloys are highly susceptible to crevice corrosion, and therefore require protection, especially when tight crevices are present. It is not known with certainty whether the crevice corrosion mechanism in aluminum alloys is similar to that in stainless steels because it has not been studied as extensively.

Aluminum alloys have been reported to be generally resistant to seawater up to velocities of  $\sim 6 \text{ m s}^{-1}$ .<sup>157,158</sup> However, critical velocities vary with alloy composition, heat treatment, and exposure time<sup>159,160</sup>; and attack morphology can change from pitting to increased general metal loss as velocity increases. Aluminum alloys being relatively soft are more susceptible to cavitation damage under turbulent flow conditions than, for example, stainless steels, nickel-based alloys, and titanium alloys. This means

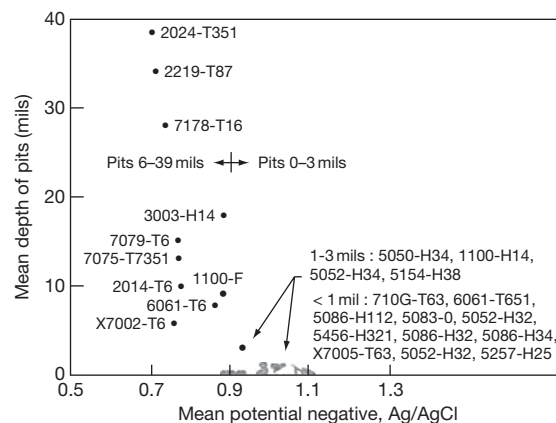


**Figure 22** Depth of pitting on Al alloys versus free corrosion potential in seawater. Reproduced from Schumacher, M., Ed. *Seawater Corrosion Handbook*; Noyes Data Corporation: NJ, USA, 1979; p 61.



that aluminum alloys can be used, for example, in the construction of seacraft hulls operating at moderately high velocities, but not for seawater pump applications.

Aluminum alloys have high thermal conductivities, which should make them very attractive for heat transfer surfaces, for example, in seawater heat exchanger applications. However, several factors limit their widespread utility. For example, aluminum alloys are highly susceptible to galvanic corrosion when coupled to components made of cathodic materials such as copper-based alloys, stainless steels, nickel-based alloys, and titanium alloys. Even if they are electrically isolated, only tens of ppb levels of copper ions (e.g., generated by self-corrosion of copper-based alloys upstream) are sufficient to cause severe corrosion by the cementation mechanism<sup>161</sup> (also known as deposition corrosion). Aluminum alloys are prone to biofouling such that sufficient velocities would be required to prevent crevice corrosion under macrofouling attachments.

An extensive study was performed in simulated seawater on galvanic corrosion rates determined from current density measurements for a number of aluminum alloys coupled to dissimilar materials as well as between the aluminum alloys themselves.<sup>162</sup> The data showed that all of the aluminum alloys tested were incompatible with Cu, Ag, and Ni. In addition, alloys 1100, 6061, and 7075 were not compatible with all the stainless steels, nickel alloy 718, low alloy steel 4130, and Ti-6Al-4V. However, surprisingly, alloy 2024 and 2219 were compatible with these materials (low alloy 4130 excepted). The aluminum alloys were compatible with each other except alloy 1100 with alloy 7075. In another test, alloy 5086-H32 incurred accelerated attack when coupled to carbon steel, 90/10 CuNi, Type 304 stainless steel, and 60/40 brass.<sup>163</sup> The degree of galvanic attack is influenced by the anode/cathode area ratio. Laboratory tests<sup>164</sup> have confirmed that increasing seawater velocity will increase galvanic attack on aluminum alloys in seawater because the most common cathodic reaction is oxygen reduction, which is under diffusion control.

Pure Al is generally considered resistant to stress corrosion cracking (SCC) in seawater. Aluminum 5xxx alloys are prone to intergranular SCC failure when the Mg addition is >5% which results in supersaturation and allows precipitation of a continuous  $Mg_2Al_3$  intermetallic phase at the grain boundaries; this phase is anodic to the matrix. Restricting the Mg addition to <4% results in discontinuous  $Mg_2Al_3$  phase and SCC resistance. This was

confirmed by immersion tests in seawater.<sup>165</sup> In Mg additions >5%, addition of small amounts of Bi, Cr, Zr, B, and Be have been found to enhance SCC resistance. Alloy 6061 in the fully aged T6 temper is resistant to SCC in seawater.<sup>165</sup>

Several of the highest strength 7xxx aluminum alloys were found to be susceptible to SCC in natural seawater,<sup>166</sup> especially in the T6 temper to attain maximum strength.

Lithium additions lower the density of the aluminum alloy but increase strength and elastic modulus. However, fracture toughness and SCC resistance are lowered.

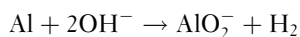
Alloy 6061 is susceptible to SCC in the T4 temper if slow quench follows high heat treat temperature. However, the T6 temper (fully aged) imparts high SCC resistance.

Exfoliation is a form of corrosion that occurs along grain boundaries in rolled aluminum alloy sheet and plate products. Corrosion often initiates at exposed grain boundaries (end-grain attack) or at pit sites that have exposed the elongated grain microstructure to the environment. The voluminous corrosion products of aluminum,  $Al(OH)_3$ , introduce internal stresses that are sufficiently to cause exfoliation, that is, lifting off of material in layers that comprise corrosion products and unaffected metal. Exfoliation resistance is derived from the absence of second phase precipitates, especially at grain boundaries, and where the free corrosion potentials of the precipitates and matrix are closely matched. The 5xxx aluminum alloys are resistant to exfoliation in seawater at Mg additions <3%. 6xxx series are resistant to intergranular corrosion (IGC) except when excess Si is present. Al alloys 5456-H116 and H117 have been used for boat hull plates to resist IGC in H321 temper.

As-quenched T3 or T-4 tempers, or naturally aged 2xxx alloys are prone to SCC and exfoliation, but only slightly to IGC, whereas 7xxx alloys are more susceptible to IGC. Overaging to T6 and T8 tempers improves SCC and exfoliation resistance but not IGC. As for 2xxx alloys, rapid quenching and overaging increases resistance significantly, for example, 7075-T63 and T-73, 7178-T76.

Cathodic protection can mitigate SCC of aluminum alloys when they are polarized to a potential in the -1.2 to -1.4 V (SCE) range. However, overprotection, for example, with Mg anodes, and especially quiescent conditions raise the surface pH significantly as  $OH^-$  ions accumulate at the aluminum alloy surface. The high-pH conditions can result in 'cathodic corrosion' of the aluminum alloy by the

formation of an aluminate complex:



Seawater flowing at moderate velocities can prevent build-up of  $\text{OH}^-$ , and hence reduce risk of cathodic corrosion. Even in quiescent conditions, the cathodic corrosion issue for aluminum alloys can be almost entirely eliminated by the use of zinc anodes for cathodic protection.

Aluminum is an active metal in the galvanic series. Therefore, in principle, it could be considered for cathodic protection of carbon steel and other engineering alloys. However, the application is not straightforward. As stated earlier, a passive  $\text{Al}_2\text{O}_3$  film usually forms on aluminum and its structural alloys. This is contrary to the requirements of a sacrificial anode material which must corrode efficiently to provide protective current for cathodic protection. Thus aluminum is alloyed with small amounts of Zn or Sn and trace levels of In or Sn (although Hg was used previously) to activate the aluminum surface. Aluminum alloys find widespread usage as sacrificial anodes in seawater, for example, on offshore platforms and pipelines because of their significant weight advantage and high current capacity ( $\text{A h kg}^{-1}$ ) compared to zinc. The development and performance of aluminum anodes have been reviewed extensively in the literature.

### 2.18.11 Magnesium

Magnesium and its alloys are not normally utilized in seawater because they are highly reactive. Reduction of DO is not normally the primary cathodic reaction, but rather the reduction of water to evolve hydrogen.

This reaction occurs particularly easily on cathodic impurities in Mg such as Fe, Cu, Cd, Zn, Ni, and so on. Being anodic and very reactive, corrosion of Mg is greatly accelerated by galvanic coupling to most other engineering materials, for example, carbon steel, stainless steels, nickel-based alloys, copper-based alloys, titanium alloys, and so on. In fact, Mg sacrificial anodes are widely used for cathodic protection of steel used in soil environments. Use of Mg for cathodic protection in seawater environments is rare because of the risk of overprotection of steel, which can cause hydrogen embrittlement in high strength steels, cathodic blistering and disbondment of coatings, and cathodic corrosion of amphoteric materials such as aluminum alloys, and high rate of self corrosion of the magnesium.

Mg alloys have been used in a very limited capacity for deep-sea diving suits – the main attraction being

very light weight due to the low density of Mg. However, the Mg has to be properly coated to prevent direct contact with seawater which would otherwise result in severe corrosion. This could be especially catastrophic at any holidays in the coating if the Mg was inadvertently coupled to a cathodic material.

The very high corrosion rate of Mg can be used to advantage in special applications, for example, ‘time release’ links on oceanographic instruments deployed in deep ocean environments.

### 2.18.12 Zinc

Although zinc is also an active metal in the galvanic series, it is much less reactive than magnesium. While the self corrosion of zinc is surprisingly low, its other major limitations are similar, that is, susceptibility to galvanic attack when coupled to steel, stainless steels, copper alloys, and so on. Historically, zinc is the most common sacrificial material used for cathodic protection in seawater.

### 2.18.13 Nonmetallic Materials

Nonmetallic materials do not generally corrode in the same manner as metals and alloys in seawater, that is, by thinning. Instead, they may suffer marine borer attack which is usually not very deep, except in wood. In addition, nonmetallics may undergo swelling and some reduction in mechanical strength – which is usually less for synthetic materials than those derived from nature (e.g., to make ropes). Deterioration is generally greater in warm seawater and close to the seabed. Other hazards are fish bites, for example, on cables. Results of long-term exposures of polymeric materials have been reviewed.<sup>167,168</sup> Nonmetallic materials are often reinforced to increase strength, for example, glass fibers in epoxy resins, carbon fibers in epoxies and aluminum, steel in concrete, and so on. Reinforcements can affect the performance of the composite material in seawater, for instance, carbon fibers can accelerate galvanic corrosion of aluminum and corrosion of steel reinforcement can lead to spalling of concrete. Rubber linings and reinforced polymer (e.g., flake glass polyester) coatings applied to metal substrates can provide corrosion protection. However, elastomers exhibit reduction in elongation with prolonged exposures; silicone–rubber and ester-based polyurethanes deteriorate more extensively. Thus, meticulous attention to selection, application, inspection, and maintenance is essential for successful

usage. While they may provide adequate corrosion protection, the major limitations of polymeric materials include elevated service temperatures, high pressure containment, and fatigue life.

For seawater service, concrete with sulfate resistance (Type V cement) must be specified. The steel reinforcement requires corrosion protection for long-term performance, for example, by cathodic protection. Ceramics are generally considered resistant to seawater.

### 2.18.14 Corrosion Protection Methods

In principle, most of the methods used for corrosion control in other aqueous environments are applicable to seawater. However, the major factors contributing to the corrosivity of seawater that must be taken into consideration include high chloride and sulfate content, presence of microorganisms, biofouling, and putrefaction.

Carbon steel corrodes in aerated seawater at rates that require either a corrosion allowance or other means of corrosion control if a long service life is required. Corrosion allowance requires careful monitoring to avoid unexpected failures. It is probably most useful for applications where some areas of localized perforation caused by seawater can be tolerated without loss or mixing of fluids, or reduction in structural (load-bearing) properties, for example, nontubular structural support members.

Coatings are the most common method of corrosion control. Apart from suitability for seawater service, the single most important requirement for a successful coating is proper surface preparation and application conditions – which are often best achieved under shop conditions. Once a coating system is applied, even under initially optimal conditions, repairing or replacing it in service can be extremely challenging. For applications such as the underwater areas of ship hulls, it is fairly easy to perform coating inspections, repairs, and replacements during periodic dry docking. In the case of fixed structures, such as offshore platforms and pipelines, similar access to the underwater areas is almost impossible. Building cofferdams around the structure and evacuating them to carry out repairs and replacements can only be done more economically in very shallow waters. Although some coatings that can be applied underwater (e.g., by divers) are available, they are fraught with problems, for example, surfaces cannot usually be adequately cleaned and prepared, and coating application and inspection are very difficult.

Hence, such coatings are typically only considered for emergency situations. Antifouling coatings are utilized on ships for controlling macrofouling. Presently, most antifouling coatings contain either copper or cuprous oxide as the antifouling agent. Other coatings based on low surface energy are also available to minimize adhesion of macrofouling, but they are more expensive. Both types of coatings are consumed with time and lose their effectiveness, and thus need replacement periodically.

As mentioned previously, it is possible to protect simple structural steel shapes by sheathing. For example, splash-zone areas on offshore platforms have been successfully protected by alloy 400 (nickel–copper) or 90/10 CuNi sheathing. Hot risers are not usually protected by sheathing because of periodic visual inspection requirements that would require removal of the sheathing. Metallurgically cladding steel with a more corrosion resistant alloy can also be used but is again applicable to only relatively simple geometries such as piping.

The most widely used method for corrosion control of steel structures immersed in seawater is cathodic protection using sacrificial zinc or aluminum anodes. Cathodic protection is only effective below the waterline, regardless of tide level. Cathodic protection and coatings complement each other if they can be used together for corrosion control. The coating reduces the area of metal requiring protection; conversely, cathodic protection can extend the coating life. However, it is essential to select a coating that is compatible with cathodic protection to obviate cathodic disbondment (blistering) of the coating. The anode material must meet tight alloy composition and performance requirements before it is specified. Sacrificial anodes generally require no maintenance, except replacement when consumed. However, it must be recognized that replacement of anodes on stationary structures is difficult and very costly; thus, in such cases, the original anodes are typically designed to last the life of the structure (e.g., 30 years). Impressed current cathodic protection systems serve the same function but, contrary to popular belief, require more attention, for example, in monitoring proper operation of rectifiers and reference electrodes, especially for systems with automatic control, stray current effects, diver safety concerns, and so on. Impressed current anodes based on platinized niobium are now preferred in seawater over platinized titanium because of the much higher breakdown voltage of niobium ( $\sim 70$  V) compared to titanium ( $\sim 9$  V). Cathodic protection of structures

and components in seawater is extensively covered in the published literature.

Calcareous deposits (discussed previously), formed in seawater on cathodically protected metal surfaces are essential for polarization of the structure, and to achieve significant reduction in current demand by the structure. Although used extensively for carbon steels, cathodic protection can also be used to mitigate corrosion of nonferrous materials in seawater, for example, for pitting and crevice corrosion of stainless steels. In fact, carbon steel can be used as sacrificial anode material. Cathodic protection can also be effective for controlling galvanic corrosion between dissimilar materials, for example, between waterbox, tube sheet, and tubes; and erosion-corrosion of copper alloys, for example, inlet-end impingement in heat exchangers.

Cathodic protection for corrosion control in the interior of pipes has been investigated but is not commonly used for a variety of reasons. The biggest problem is limited 'throwing power' of the protective current. Thus, depending on pipe size, an anode may be required, say, every few meters for protecting bare steel. Continuous anodes along the length of the pipe for internal cathodic protection have also been investigated but present many limitations including economics.

Modification of the seawater by deoxygenation is an effective method of corrosion control. As discussed previously, it is used in a number of applications, for example, MSF desalination and seawater injection during secondary recovery. For steels, while corrosion rate decreases with oxygen content, it increases markedly at elevated temperatures even when only a few hundred parts per billion oxygen is present. Thus, effective control and monitoring of oxygen is essential for this method of corrosion control, especially at high temperatures. Deaeration has not been found to be harmful for passive materials such as stainless steels that often rely on oxygen for film healing.

Conflicting requirements often preclude use of a single material in most engineering applications. Since dissimilar materials are often unavoidable, the issue of galvanic corrosion must be addressed. In principle, electrical isolation between anode and cathode members can be effected by using nonconductive (insulating) hardware to mitigate galvanic corrosion. However, in many applications, this is difficult to achieve because alternative electrical grounding paths exist, for example, hangers or pedestal supports in piping systems. In many systems, however, even if electrical

isolation is possible, it is not permitted for personnel safety reasons, for example, electrical safety codes may preclude galvanic isolation in systems where ground fault currents would otherwise pose potential electrical shock hazards. In design, a small cathode/anode area ratio is usually selected to minimize galvanic corrosion. Coating either the cathode or both the cathode and anode can be a practical means of controlling galvanic corrosion. The anode alone should not be coated since inevitable holidays and flaws in the coating can severely accelerate corrosion attack at those locations because of the resulting very adverse anode/cathode area ratio. However, it should be recognized that coatings for galvanic corrosion control have limitations where they are difficult to apply and maintain, and where they can incur damage rather easily, for example, in pumps.

Mitigation of galvanic corrosion in piping systems at dissimilar-metal flanged-joints, without electrical isolation, has been addressed in a number of ways. Since the galvanic corrosion damage of the anodic material is restricted over a relatively short distance that is either known from experience or can be determined by mathematical modeling, one approach is to insert a heavier-wall waster spool between the original anode and cathode. The length of the spool piece is a function of the pipe diameter and polarization characteristics of the cathode.<sup>169</sup> Consumption of the waster spool piece can be monitored, for example, by ultrasonic thickness gauging from the outside, so that it can be replaced in a timely manner. A novel technique known as the 'bi-electrode' method<sup>170,171</sup> has been proposed to control galvanic corrosion. Two ring or sleeve electrodes with inert metal surfaces are inserted in the piping system on either side of the joint. The sleeves which are electrically isolated from the piping system are polarized with respect to each other by an external DC power supply, such that the electrical field created by current flow annuls the galvanic current. Since the galvanic current can vary with operating conditions such as flow, temperature, oxygen content, and so on, the externally applied counter current between the bielectrodes has to adjust automatically – a problem that has been found to be challenging to date.

For many components, coatings and/or cathodic protection are not practical methods of corrosion control, for example, pumps, valves, entire heat exchanger tubing in shell-and-tube heat exchangers, plates in plate-and-frame heat exchangers, internal piping, and so on. In such cases, corrosion resistant materials must be selected. The selection is based on

practical experience and test data. For example, as discussed earlier, Type 304 and 316 stainless steels are unsuitable materials for seawater service because of extreme susceptibility to crevice corrosion in aerated seawater; in other words, they should not be used for immersion service in seawater without protection (e.g., cathodic protection) if crevices are present. The use of a resistor-controlled cathodic protection system has been proposed for controlling internal corrosion in chlorinated stainless steel piping systems.<sup>172,173</sup>

Unfortunately, selection of more highly alloyed grades such as Type 317 stainless steel or alloy 825 that contain greater amounts of Cr and Mo does not bestow sufficient resistance to crevice corrosion. Crevice corrosion initiation time is usually longer in cold seawater. Conversely, it is known that localized corrosion susceptibility increases with increasing temperature. Critical pitting and critical crevice corrosion temperature data are used to provide guidelines for the upper limits of alloys. For example, it is generally recommended that superaustenitic 20Cr–25Ni–6Mo stainless steels should not be subjected to seawater temperatures  $> \sim 35^{\circ}\text{C}$  for prolonged periods. Pitting resistance equivalent numbers (PREN) based on alloy composition (primarily Cr, Mo, and N) have been advocated as indicators of localized corrosion resistance of stainless steels and nickel-based alloys in seawater and other chloride environments. However, crevice corrosion resistance does not depend just on alloy content; it is also affected by crevice geometry, tightness, depth, crevice-forming materials, their deformability, and surface finish of both the crevice formers and the alloy in question.<sup>174</sup> Thus, although many materials, such as Ni–Cr–Mo–Fe alloy C-276, have very high resistance to crevice corrosion in seawater, they are by no means completely immune under all crevice conditions. This is also the case with titanium, which is very resistant to localized attack in seawater at ambient temperatures, but is susceptible to crevice corrosion at  $> 70^{\circ}\text{C}$ . Titanium alloys containing noble metals additions, such as palladium in grade 7, are more resistant to crevice corrosion.

Copper–nickel alloys have been successfully used for heat exchanger piping, waterbox and sheathing applications in clean seawater. In the freely corroding condition, they are resistant to macrofouling but not entirely immune. Their major limitations are high susceptibility to accelerated corrosion by sulfides, for example, in polluted seawater and bottom silt; or generated *in situ* as a result of putrefaction of stagnant

seawater by sulfate reducing bacteria. Avoiding contact with polluted seawater is difficult in certain situations, for example, when shipboard piping and heat exchangers are commissioned in harbors. Guidelines based on practical experience suggest that the risk of sulfide production and consequent initiation of corrosion of copper–nickel alloys increases when they are exposed to stagnant seawater in closed systems for more than  $\sim 2$  days. Thus, it is imperative that such conditions be avoided by draining the system, flushing with fresh water and drying, if possible. Alternatively, the water can be treated with suitable biocides that are compatible with the alloy. Nickel aluminum bronze pumps have been used successfully in unpolluted seawater. This is not a good choice of material for auxiliary pumps because of the risk of seawater putrefaction during protracted standby periods and hence sulfide attack. However, heat treatment is necessary to preclude dealloying, especially in the heat-affected zones associated with welds, and the consequent increased risk of fatigue cracking. Such areas are often beyond the reach of cathodic protection from bare steel piping that might be beneficial in other situations where the current ‘throwing power’ is more effective.

Other factors that need to be considered in the selection of copper-base alloys include sensitivity to erosion–corrosion at high flow rates and galvanic corrosion when coupled to stainless steels, titanium, and Ni–Cr–Mo alloys. For instance, copper–nickel heat exchanger tubes that have suffered from sulfide and/or erosion–corrosion attack are often retubed with titanium. This results in unacceptable galvanic corrosion of the copper–nickel tube sheet. This situation is usually alleviated by the application of cathodic protection which must be controlled and monitored carefully to preclude hydriding of the titanium tubes that can be caused by overprotection. Tube support plate spacing also has to be addressed to preclude vibration of the low-modulus, thin-walled titanium tubes, and subsequent mechanical fatigue failure.

Chlorination is widely used for controlling biofilms and macrofouling; the latter interferes with seawater flow. Both biofouling and macrofouling can initiate corrosion of engineering materials such as many stainless steels, nickel–copper alloys, and even some copper-based alloys. At low levels,  $\sim 0.5$  ppm residual, chlorine does not accelerate corrosion of these materials or carbon steel significantly. However, as the chlorine concentration increases to  $\sim 1$ – $2$  ppm, risk of general corrosion on the active metals and localized corrosion on certain passive metals



increases. Reduction of galvanic corrosion of certain materials, for example, copper-alloys coupled to stainless steels and nickel alloys, has been observed especially in laboratory tests and explained on the basis of biofilm suppression and attendant reduction reaction kinetics on the cathode. As the chlorine content increases to ~5 ppm or more, corrosion propensity of many stainless steels and nickel-copper alloys increases noticeably. Titanium is unaffected by even very high levels of chlorine in seawater – in fact, titanium electrodes are commonly used in the electrolytic cells to generate chlorine from seawater.

## 2.18.15 Test Methods

Test methods for assessing materials performance in seawater are extensively described in the literature and standards. In principle, most of these test methods are not applicable exclusively to seawater. However, it is important to recognize the important differences between natural seawater that contains micro and macroorganisms that can influence corrosion behavior of materials, and synthetic seawater that does not contain representative species which mimic biological effects. The equipment used for testing in seawater must also be corrosion resistant to prevent test interruptions or confounding of results by extraneous corrosion products introduced into the system.

## References

- Lyman, J.; Abel, R. B. *J. Chem. Educ.* **1958**, 35(3), 113–115.
- Reinhart, F. M. Corrosion of Metals and Alloys in the Deep Ocean, Technical Report No. R-834; Civil Engineering Laboratory: Port Hueneme, CA, 1976; p 2.
- Dexter, S. C.; Culberson, C. *Mater. Perform.* **1980**, 19(9), 23.
- Compton, K. G., *Corrosion* **1970**, 26, 448.
- Korbin, G., Ed. *Microbiologically Influenced Corrosion*; NACE International: Houston, TX, 1993; p 5.
- Korbin, G., Ed. *Microbiologically Influenced Corrosion*; NACE International: Houston, TX, 1993; p 48.
- Whitfield, M.; Jagner, D., Eds. *Marine Electrochemistry, A Practical Introduction*; Wiley, 1981; p 513.
- Tomashov, N. D. *Theory of Corrosion and Protection of Metals*; Macmillan: New York, 1966; p 470.
- ASM Handbook, Vol. 13A: Corrosion, Fundamentals, Testing, and Protection*; ASM International: Materials Park, OH, 2003; pp 398–416.
- Uhlig, H. E.; Revie, R. W. *Corrosion and Corrosion Control*, 3rd ed.; Wiley: New York, 1985; p 94.
- ASM Handbook, Vol. 13A: Corrosion, Fundamentals, Testing, and Protection*; ASM International: Materials Park, OH, 2003; p 648.
- Cox, G. C. US Patent 2,200,469, May 14, 1941.
- Cox, G. C. US Patent 2,417,009, March 11, 1947.
- Humble, H. A. *Corrosion* **1948**, 4(7), 358–370.
- Guillen, M. A.; Feliu, S. *Rev. Metall.* **1966**, 2(6), 519–532.
- Shigeno, H.; Umino, T.; Fukazawa, H. In *Proceedings of the 5th International Congress on Metallic Corrosion*; NACE International: Houston, TX, 1975; pp 619–623.
- Wolfson, S. L.; Hartt, W. H. *Corrosion* **1981**, 37, 70–76.
- Phull, B. S. PhD Thesis, University of Manchester, UK, 1981.
- Hartt, W. H.; Culberson, C. H.; Smith, S. W. In *Corrosion/83*; NACE International: Houston, TX, 1983; Paper No. 59.
- Ambrose, J. R.; Yaniv, A. E.; Lee, U. R. In *Corrosion/83*; NACE International: Houston, TX, 1983; Paper No. 60.
- Culberson, C. H. In *Corrosion/83*; NACE International: Houston, TX, 1983; Paper No. 61.
- Fisher, K. P.; Finnegan, J. E. In *Corrosion/89*; NACE International: Houston, TX, 1989; Paper No. 581.
- Fisher, K. P.; Finnegan, J. E. *Corrosion/89*; NACE International: Houston, TX, 1989; Paper No. 582.
- de Oliveira, R.; de Souza Pimenta, G. In *12th International Corrosion Congress*; NACE International: Houston, TX, 1993; pp 2278–2284.
- Pytkowich, R. M. *J. Geology* **1965**, 73(1), 196.
- Philipponeau, G. In *8th International Congress on Metallic Corrosion*; DEHEMA: Frankfurt, Germany, 1981; pp 196–199.
- Doremus, E. P.; Doremus, G. L. *Corrosion* **1950**, 6(7), 216–224.
- Uhlig, H. E.; Revie, R. W. *Corrosion and Corrosion Control*, 3rd ed.; Wiley: New York, 1985; pp 69–71.
- Oldfield, J. W.; Sutton, W. H. *Br. Corros. J.* **1978**, 13(1), 13.
- Oldfield, J. W.; Sutton, W. H. *Br. Corros. J.* **1978**, 13(3), 104.
- Kain, R. M. *Mater. Perform.* **1984**, 23(2), 24–30.
- Kain, R. M.; Lee, T. S. In *ASTM STP 866*; Haynes, G. S., Baboian, R., Eds.; American Society for Testing and Materials: West Conshohocken, PA, 1985; pp 299–323.
- Kain, R. M. Seawater crevice corrosion testing of stainless steel, Ni-base and Cu-Ni alloys: Perspectives on methodologies and interpretation of results, EUROCORR/2006.
- Kain, R. M. Private communication.
- Dexter, S. C.; Gao, G. Y. *Corrosion* **1988**, 44(10), 717–723.
- Johnsen, R.; Bardal, E. *Corrosion* **1985**, 41(5), 296.
- Suzuki, T.; Yamake, M.; Kitamura, Y. *Corrosion* **1973**, 29, 18.
- Lei, M. K.; Zhu, X. M. *J. Electrochem. Soc.* **2005**, 152(8), B291–B295.
- Ellis, O. B.; LaQue, F. L. *Corrosion* **1951**, 7(11), 362.
- LaQue, F. L. *Marine Corrosion: Causes and Prevention*; Wiley, 1975; p 195.
- Dexter, S. C.; LaFontaine, J. P. *Corrosion* **1998**, 54(11), 851–861.
- Ferrara, R. J.; Taschenberg, L. E.; Moran, P. J. *Corrosion/85* Paper No. 211; NACE International: Houston, TX, 1985.
- Wallen, B.; Henrikson, S. *Werkst. Korros.* **2004**, 40(10), 602–615.
- Kain, R. M. In *Corrosion/98*; NACE International: Houston, TX, 1998; Paper No. 702.
- Humble, H. A. *Corrosion* **1948**, 5(9), 292–302.
- Kirk, W. W. *Mater. Perform.* **1987**, 26(9), 23–28.
- Phull, B. S.; Kain, R. M. In *Applications and Materials Performance*; Proceedings of the Nickel-Cobalt/97 International Symposium; Smith, F. N., McGurn, J. F., Lai, G. Y., Sastri, V. S., Eds.; Canadian Institute of Mining, Metallurgy and Petroleum, 1997; Vol. IV, pp 141–150.
- Chaker, V.; Lindemuth, D. In *Corrosion/90*; NACE International: Houston, TX, 1990; Paper No. 376.

49. Smith, M.; Bowley, C.; Williams, L. In *Corrosion/2002*; NACE International: Houston, TX, 2002; Paper No. 02214.
50. Linder, B. Cathodic protection of sheet steel piling in seawater, containing sulfate-reducing bacteria, particularly with respect to accelerated low water corrosion (ALWC), Swedish Corrosion Institute Report No. 55467, 1999.
51. Oubner, R.; Beech, I. In *Corrosion/1999*; NACE International: Houston, TX, 1999; Paper No. 99318.
52. Breakell, J. E.; Foster, K.; Siegwart, M. *Management of Accelerated Low Water Corrosion in Steel Maritime Structures*; CIRIA: London, 2005; publ. no. C634.
53. LaQue, F. L. *Marine Corrosion: Causes and Prevention*; Wiley, 1975; p 143.
54. Phull, B. S.; Pikul, S. J.; Kain, R. M. *ASTM STP 1300*; American Society for Testing and Materials: West Conshohocken, PA, 1997; pp 34–73.
55. LaQue, F. L. *Marine Corrosion: Causes and Prevention*; Wiley, 1975; p 14.
56. Melchers, R. E. *ASTM STP 1300*; American Society for Testing and Materials: West Conshohocken, PA, 1997; pp 20–33.
57. Southwell, C. R.; Alexander, A. L. *Mater. Prot.* **1970**, 9(1), 14–23.
58. Reinhart, F. M. *Corrosion of Metals and Alloys in the Deep Ocean, Technical Report No. R-834*; Civil Engineering Laboratory: Port Hueneme, CA, 1976; p 14.
59. Beavers, J. A. Koch, G. H.; Berry, W. E., Eds. *Corrosion of Metals in Marine Environments*; MCIC Report MCIC-86-50, 1986, pp 6–33.
60. Beavers, J. A.; Koch, G. H.; Berry, W. E., Eds. *Corrosion of Metals in Marine Environments*; MCIC Report MCIC-86-50; pp 6–42–6–45.
61. Preiser, H. S. In *Handbook of Corrosion Protection for Steel Pile Structures in Marine Environments*; American Iron and Steel Institute, 1981; pp 67–100.
62. Beavers, J. A. Koch, G. H.; Berry, W. E. Eds. *Corrosion of Metals in Marine Environments*; MCIC Report MCIC-86-50, 1986, pp 6–49.
63. Van Der Sluys, W. A. *Eng. Fract. Mech.* **1969**, 1, 447.
64. Schrieber, C. F.; Coley, F. H. *Mater. Perform.* **1976**, 15(7), 47–54.
65. Oldfield, J. W.; Todd, B. Corrosion considerations in selecting metals for flash chambers, *Eurocorr/77*, 1977.
66. LaQue, F. L. *Marine Corrosion: Causes and Prevention*; Wiley, 1975; p 8.
67. Shreir, L. L., Ed. *Corrosion*; Newnes Butterworths, 1979; Vol. 1, p 3.106.
68. Miyasaka, M.; Ogure, N. In *Corrosion/86*; NACE International: Houston, TX, 1986; Paper No. 324.
69. Southwell, C. R.; Bultman, J. D.; Alexander, A. L. *Mater. Prot.* **1976**, 15(7), 9–26.
70. Mollica, A.; Trevis, A. In Proceedings of the 4th International Congress on Marine Corrosion and Fouling; Juan-les-Pins: France, 1976.
71. Asphahani, A. I.; Manning, P. E.; Silence, W. L.; Hodge, G. F. In *Corrosion/80*; NACE International: Houston, TX, 1980; Paper No. 29.
72. Deverell, H. E.; Maurer, J. R. *Mater. Perform.* **1978**, 17(3), 15–20.
73. Bond, A. P.; Dundas, H. J. *Mater. Perform.* **1984**, 23(7), 39–43.
74. Kain, R. M. In *ASTM STP1399*; Dean, S. W., Delgadillo, G. H., Bushman, J. B., Eds.; American Society for Testing and Materials: West Conshohocken, PA, 2000; pp 284–299.
75. Francis, R.; Byrne, G. In *Corrosion/2003*; NACE International: Houston, TX, 2003; Paper No. 03255.
76. ASTM Standard G 48.
77. Davies, M.; Scott, P. J. B. *Guide to Use of Materials in Waters*; NACE International: Houston, TX, 2003; p 90.
78. Kovach, C. W.; Redmond, J. D. In *Corrosion/93*; NACE International: Houston, TX, 1993; Paper No. 267.
79. ASTM Standard G 78.
80. *ASM Handbook Vol. 13A Corrosion: Fundamentals, Testing, and Protection*; ASM International, 2003; pp 549–561.
81. Sedriks, A. J. *Int. Met. Rev.* **1982**, 27(6), 321–353.
82. Francis, R.; Burton, G. R. In *Corrosion/2000*; NACE International: Houston, TX, 2000; Paper No. 630.
83. Oldfield, J. W.; Sutton, W. H. *Br. Corros. J.* **1980**, 15(1), 31–34.
84. Kain, R. M. In *Corrosion/81*; NACE International: Houston, TX, 1981; Paper No. 200.
85. Kain, R. M. In *Corrosion/82*; NACE International: Houston, TX, 1982; Paper No. 66.
86. Deverell, H. E.; Davis, J. A. In *Corrosion/78*; NACE International: Houston, TX, 1978; Paper No. 27.
87. Kain, R. M.; Zeuthen, A. W.; Maurer, J. R. In *Corrosion/97*; NACE International: Houston, TX, 1997; Paper No. 97423.
88. Weber, J. In *Materials to Supply Demand*; Proceedings of ASM International Conference; Harrison, B. C., Ed.; 1981; pp 49–80.
89. Turnbull, A. *Corrosion* **1999**, 55(2), 206.
90. Wallen, B. *Some Factors Affecting Stainless Steel Corrosion in Seawater*; ACOM: Avesta Sheffield, 1990; Vol. 4, pp 1–8.
91. Rogne, T.; Drugli, J. M. In *Stainless Steel World'99 Conference*; KCI, 1999; p 527.
92. ASTM Standard G 160.
93. Oldfield, J. W.; Todd, B. *Desalination* **1979**, 31(3), 365–383.
94. Reinhart, F. M. *Corrosion of Metals and Alloys in the Deep Ocean, Technical Report No. R-834*, Civil Engineering Laboratory, Port Hueneme, CA, 1976; p 174.
95. Lee, W. S. W.; Oldfield, J. W.; Todd, B. *Desalination* **1983**, 44(5), 209–221.
96. Plessset, M. S. *Corrosion* **1962**, 18(5), 181t–188t.
97. Simoneau, R.; Fihey, R.; Roberge, R. In *Cavitation Erosion in Fluid Systems Conference Proceedings*, June 1981; pp 71–81.
98. Al Hashem, A. H.; Tarish, H.; Akbar, A. A. In *Corrosion/2007*; NACE International: Houston, TX, 2007; Paper No. 07253.
99. Powell, C. A.; Michels, H. T. In *Corrosion/2000*; NACE International: Houston, TX, 2000; Paper No. 00627.
100. LaQue, F. L. *Marine Corrosion: Causes and Prevention*; Wiley, 1975; p 267.
101. Efird, K. D. *Corrosion* **1977**, 33(1), 3–8.
102. Gudas, J. P.; Hack, H. P. *Corrosion* **1979**, 35(6), 259–264.
103. Gudas, J. P.; Hack, H. P. *Mater. Performance* **1980**, 19(4), 49–54.
104. Syrett, B. C. *Corros. Sci.* **1981**, 21(3), 187–209.
105. Sanchez, S. R.; Schiffrin, D. J. *Corros. Sci.* **1981**, 22(6), 245–248.
106. Eiselstein, L. E.; Syrett, B. C.; Wing, S. S.; Caliguirri, R. D. *Corros. Sci.* **1981**, 23(3), 223–239.
107. Francis, R. *The effect of sulfide and chlorine on the corrosion of copper alloy heat exchanger tubes*, INCRA Project, 289A/3, final report 1984.
108. Al Hajji, J. N.; Reda, M. R. *Corros. Sci.* **1992**, 34(1), 163–177.
109. Efird, K. D.; Anderson, D. B. *Mater. Perform.* **1975**, 14(11), 37–40.
110. Mattson, M. E.; Fuller, R. M. A study of materials of construction in distillation plants, Joint report by Office of

- Saline Water and the International Nickel Company, Research report No. 163, 1965.
111. Schreiber, C.; Osborn, O.; Coley, F. H. *Mater. Perform* **1968**, 7(10), 20–25.
  112. Reinhart, F. M. Corrosion of Metals and Alloys in the Deep Ocean, Technical Report No. R-834, Civil Engineering Laboratory, Port Hueneme, CA, 1976; p 56.
  113. LaQue, F. L.; Clapp, W. F. *Trans. Electrochem. Soc.* **1945**, 87, 103–125.
  114. Efird, K. D. In *Corrosion/75*; NACE International: Houston, TX, 1975; Paper No. 124.
  115. Clapp, W. F. In *Corrosion Handbook*; Uhlig, H. H., Ed.; Wiley, 1948; p 443.
  116. Retief, R. *Br. Corros. J.* **1973**, 8(4), 264–269.
  117. Shone, E. B.; Grim, B. C. *Trans. Inst. Mar. Eng. UK* **1985**, 98, Paper No. 11.
  118. Otsu, T.; Sato, S. *Comparative corrosion test of condenser tube materials by model condenser at Meiko power station*, Sumitomo Light Metal Technical reports, Oct 1961, 2(4), pp 299–322.
  119. Tracy, A. W.; Hungerford, R. L. *Proc. ASTM* **1945**, 45, 591.
  120. Stewart, W. C.; LaQue, F. L. *Corrosion* **1977**, 8(8), 259–277.
  121. Syrett, B. C. *Corrosion* **1976**, 32(6), 242–252.
  122. ASTM Standard A 342.
  123. Anderson, D. B. *Mater. Perform.* **1971**, 10(11), 26.
  124. Danek, G. J., Jr. *Naval Eng. J.* **1966**, 78(5), 763–769.
  125. Sato, S.; Nagata, K. Factors affecting corrosion and fouling of condenser tubes of copper alloys and titanium, Sumitomo Light Metal Technical reports, July 1978, 19(3–4), pp 83–94.
  126. Sato, S.; Nosetani, T.; Yamaguchi, Y.; Onda, K. *Factors affecting the sand erosion of aluminum brass condenser tubes*; Sumitomo Light Metal Technical reports, Jan 1975, 16(1–2), pp 23–37.
  127. Maligas, M.; Vivic, J. In *Corrosion/97*; NACE International: Houston, TX, 1997; Paper No. 426.
  128. Hack, H. J. *Test. Eval.* **1980**, 8(2), 74–79.
  129. Gehring, G. A., Jr. Effects of sulfide, sand and cathodic protection on condensers, EPRI Report No. CS-4562, Electric Power Research Institute, Palo Alto, May, 1986.
  130. Southwell, C. R.; Alexander, A. L. *Mater. Prot.* **1969**, 8(3), 39–44.
  131. Tipton, D. G.; Kain, R. M. In *Corrosion/80*; NACE International: Houston, TX, 1980; Paper No. 36.
  132. Lennox, T. J., Jr. In *Corrosion/82*; NACE International: Houston, TX, 1982; Paper No. 64.
  133. Boyd, W. K.; Fink, F. W. Corrosion of Metals in Marine Environments, Battelle Columbus Labs, OH, Report No. MCIC-78-37, 1978; p 103.
  134. Moller, G. E. *Soc. Pet. Eng. J.* **1977**, 17(2), 101–110.
  135. Reinhart, F. M. Corrosion of Metals and Alloys in the Deep Ocean, Technical Report No. R-834, Civil Engineering Laboratory, Port Hueneme, CA, 1976; p 126.
  136. Efird, K. D. *Mater. Performance* **1985**, 24(4), 37–40.
  137. LaQue, F. L. *Marine Corrosion: Causes and Prevention*; Wiley, 1975; p 115.
  138. Bomberger, H. B. *J. Electrochem. Soc.* **1954**, 101(9), 442–447.
  139. Ross, R. W., Jr.; Tuthill, A. H. *Mater. Performance* **1990**, 29(4), 65–69.
  140. Feige, N. G.; Murphy, T. J. *Corrosion* **1966**, 22(11), 320–324.
  141. Griess, J. C., Jr. *Corrosion* **1968**, 24(4), 96–109.
  142. Covington, L. C. *Corrosion* **1979**, 35(8), 378–382.
  143. Smith, C. A.; Compton, K. G. *Corrosion* **1975**, 31(9), 320–326.
  144. *ASM Metals Handbook Vol. 13: Corrosion*; ASM International, 1987; p 673.
  145. Brown, B. F. *Mater. Res. Stand.* **1966**, 6(3), 29–133.
  146. Beavers, J. A.; Koch, G. H.; Berry, W. E. Eds. *Corrosion of Metals in Marine Environments*; MCIC Report MCIC-86-50, 1986, pp 3–27.
  147. Powell, D. T.; Scully, J. C. *Corrosion* **1968**, 24(6), 151.
  148. Beck, T. R. *J. Electrochem. Soc.* **1967**, 114, 551–556.
  149. Beck, T. R. In *Theory of Stress Corrosion Cracking in Alloys*; Scully, J. C., Ed.; NATO Scientific Affairs Division: Brussels, 1971; pp 64–85.
  150. Reinhart, F. M. Corrosion of Metals and Alloys in the Deep Ocean, Technical Report No. R-834, Civil Engineering Laboratory, Port Hueneme, CA, 1976; pp 228–238.
  151. Beavers, J. A.; Koch, G. H.; Berry, W. E. Eds. *Corrosion of Metals in Marine Environments*; MCIC Report MCIC-86-50, 1986; pp 2–31.
  152. Reinhart, F. M. Corrosion of Metals and Alloys in the Deep Ocean, Technical Report No. R-834, Civil Engineering Laboratory: Port Hueneme, CA, 1976; pp 204–209.
  153. Dexter, S. C. *Corrosion* **1980**, 36(8), 423–432.
  154. Konstantinova, E. V.; Nazarova, N. P. *Prot. Met.* **1976**, 12(3), 279–281.
  155. Larsen-Basse, J. *Mater. Perform.* **1984**, 23(7), 16–21.
  156. Ahmed, Z. *Anti-Corros. Methods Mater.* **1981**, 28(7), 4–10.
  157. Davis, J. A.; Gehring, G. A., Jr. *Mater. Performance* **1975**, 14(4), 32–39.
  158. Herrigel, H. R. *Mater. Perform.* **1976**, 15(3), 43–45.
  159. Davis, J. A.; Gehring, G. A., Jr. In *Corrosion/75*; NACE International: Houston, TX, 1975; Paper No. 123.
  160. Gehring, G. A., Jr.; Peterson, M. H. *Corrosion* **1981**, 37(4), 232–242.
  161. Dexter, S. C. *J. Ocean Sci. Eng.* **1981**, 6(1), 109–148.
  162. Mansfeld, F.; Hengstenberg, D. H.; Kenkel, J. V. *Corrosion* **1974**, 30(10), 343–353.
  163. Lennox, T. J., Jr.; Peterson, M. H.; Smith, J. A.; Groover, R. E. *Mater. Perform.* **1974**, 13(2), 31–36.
  164. Mansfeld, F.; Kenkel, J. V. *Corrosion* **1977**, 33(7), 236–240.
  165. Beavers, J. A.; Koch, G. H.; Berry, W. E., Eds. *Corrosion of Metals in Marine Environments*; MCIC Report MCIC-86-50, 1986, pp 2–64.
  166. Reinhart, F. M. Corrosion of Metals and Alloys in the Deep Ocean, Technical Report No. R-834, Civil Engineering Laboratory, Port Hueneme, CA, 1976; pp 221–223.
  167. Connolly, R. A.; DeCoste, J. B.; Gaupp, H. L. *J. Mater.* **1970**, 5, 339.
  168. Munitz, A. J. *Undersea Technol.* **1966**, 7, 45.
  169. Francis, R. A. *Galvanic Corrosion: A Practical Guide for Engineers*; NACE International, 2001; pp 120–124.
  170. Shifler, D. A.; Hack, H. P.; Melton, D. G. In *Corrosion/98*; NACE International: Houston, TX, 1998; Paper No. 706.
  171. Tossey, B. M.; Beavers, J. A. In *Corrosion/2007*; NACE International: Houston, TX, 2007; Paper No. 07244.
  172. Bardal, E.; Johnsen, R.; Gartland, P. O. In *Corrosion/92*; NACE International: Houston, TX, 1992; Paper No. 408.
  173. Johnsen, R.; Gartland, P. O.; Valen, S.; Drugli, J. *Mater. Performance* **1996**, 35(7), 17.
  174. Kain, R. M. In *Corrosion/91*; NACE International: Houston, TX, 1991; Paper No. 508.
  175. Schumacher, M., Ed. *Seawater Corrosion Handbook*; Noyes Data Corporation: NJ, USA, 1979; p 61.

## 2.19 Corrosion in Soils

**J. F. D. Stott and G. John**

Intertek-CAPCIS Ltd, Bainbridge House, 86-90 London Road, Manchester M1 2PW, UK

© 2010 Elsevier B.V. All rights reserved.

<b>2.19.1</b>	<b>Introduction</b>	1152
<b>2.19.2</b>	<b>The Nature of Soils</b>	1153
2.19.2.1	General Soil Texture and Structure	1154
2.19.2.2	The Clay Fraction	1154
2.19.2.3	Aeration and Oxygen Diffusion	1154
2.19.2.4	Water Relations	1155
2.19.2.4.1	Free ground water	1156
2.19.2.4.2	Gravitational water	1156
2.19.2.4.3	Capillary water	1156
2.19.2.5	Variable Conditions	1156
2.19.2.6	Effect of Bacterial Activity on Corrosion in Soils	1156
<b>2.19.3</b>	<b>Corrosion Rates in Soils</b>	1157
2.19.3.1	Carbon and Low Alloy Steels	1157
2.19.3.2	Other Metals and Alloys	1158
2.19.3.3	Influence of Soil Parameters on Corrosion Rate	1158
2.19.3.4	Long-Term Corrosion Rates in the Soil Environment	1159
2.19.3.5	Disturbed and Undisturbed Soils	1159
<b>2.19.4</b>	<b>Corrosivity (Aggressivity) Assessment</b>	1161
2.19.4.1	General	1161
2.19.4.2	Resistivity	1161
2.19.4.3	Influence of SRB	1161
2.19.4.4	DIN 50 929 Part 3 Criteria	1162
2.19.4.5	Eyre and Lewis System	1162
2.19.4.6	AWWA/DIPRA	1162
2.19.4.7	Mean Time Before Failure (MTBF)	1163
2.19.4.8	Direct Measurement Approach	1164
2.19.4.9	Summary	1164
<b>2.19.5</b>	<b>Metallic Coatings in Soils</b>	1165
<b>2.19.6</b>	<b>Corrosion Control Options</b>	1166
<b>References</b>		1167

### Glossary

**Aerobic** The presence of oxygen in an environment (including oxygen from the air).

**Anaerobic** The absence of oxygen in an environment (including oxygen from the air).

**Backfill** Material that is applied around the component that is buried.

**Bacteria** Unicellular microorganisms, typically a few micrometers in length and having many shapes including spheres, rods, and spirals.

**Biogenic** Arising from living processes.

**Brownfield site** Former commercial or industrial site, earmarked for commercial development

or industrial projects. Potentially contaminated land.

**Cathodic protection** A decrease of corrosion rate of a metal by cathodic polarization such that the net anodic current is decreased.

**Clay** Natural constituent of soil. Comprises particles of less than 0.005 mm mean diameter ( $<5\ \mu\text{m}$ ).

**Conductivity** The specific ability of a material to conduct ionic or electronic charge. In SI units, the conductivity is defined as the conductance (in Siemens or  $\text{Ohms}^{-1}$ ) between the opposing faces of a cube of side  $1\ \text{m}^2$  (SI units:  $\text{Sm}^{-1}$ ).

**Corrosion product** A species formed as a result of corrosion; most commonly a solid (e.g., rust) but may be liquid, gaseous, or ionic.

**Corrosion protection** A process of modification to a material or its corrosive environment such as to decrease its corrosion rate.

**Corrosion rate** The rate at which corrosion proceeds. It may be expressed as loss of thickness or cross-section (e.g.,  $\mu\text{m year}^{-1}$ ), as a rate of mass loss per unit area (e.g.,  $\text{g m}^{-2} \text{d}^{-1}$ ), or via Faraday's Law, as a current density (e.g.,  $\text{A m}^{-2}$ ). Although the term implies that corrosion rate is constant, this is not always the case.

**Corrosivity assessment or aggressivity**

**assessment** Estimation of likely corrosion rates that will occur on metal/alloys in a particular soil environment on the basis of consideration of soil type, resistivity, soil and groundwater chemistry, etc. Also referred to as aggressivity assessment.

**Disturbed soils** Soils that are mechanically disturbed, for example, by excavation.

**Electrical resistance (ER)** Method for measuring corrosion rate where metal loss of a probe element is determined by measurement of electrical resistance of the element.

**General corrosion or uniform corrosion** A form of corrosion that results in a more-or-less uniform thickness loss from the surface of a material.

**Graphitic corrosion** A form of corrosion of grey cast iron in which the metallic constituents are selectively removed leaving the graphite (often called 'graphitization,' although the latter term is deprecated because of its alternate use to describe the formation of graphite, for example, by the decomposition of carbides in steel).

**Greenfield site** Agricultural or forest land or undeveloped (virgin) site earmarked for commercial development or industrial projects.

**Groundwater** Natural water contained within soil.

**Hot-dip coating or galvanizing** A method of application of a coating by immersion of a material in a bath of molten metal: for example, hotdip galvanizing, for the formation of a zinc coating on steel.

**Linear polarization** (1) The approximate linear dependence between current density and

potential at low values of electrode polarization (typically less than  $\sim \pm 10 \text{ mV}$ ).

(2) An electrochemical test method that uses the principle of linear polarization to derive an estimate of the electrode reaction (e.g., the corrosion rate). Not the same as Ohm's law.

**Long-line corrosion** Form of differential concentration corrosion, occurring on pipelines crossing different soil conditions or for piles crossing different soil layers. The large surface area in benign/aerated conditions causes increased corrosion in more active/deaerated conditions. See also macro-cell corrosion.

**Macro-cell corrosion** Form of differential concentration corrosion.

**Metabolism** The complete set of chemical reactions that occur in living cells. These processes are the basis of life, allowing cells to grow and reproduce, maintain their structures, and respond to their environments.

**Microbially influenced corrosion (MIC)** A form of corrosion that is associated with the presence of microorganisms, including bacteria, fungi, and algae. Corrosion is commonly influenced by the metabolites of the organism and/or by the production of a biofilm.

**Microorganism or microbe** An organism that is microscopic (too small to be seen by the human eye). The study of microorganisms is called microbiology. Microorganisms can be bacteria, fungi, archaea, or protists, but not viruses and prions, which are generally classified as nonliving.

**Moisture-holding capacity of a soil** A term applied to the ability of a soil to hold water present in the form of capillary water.

**Nondisturbed soils** Soils in the natural state that have not been affected by excavation.

**pH** The negative logarithm of the hydrogen ion activity defined as  $\text{pH} = -\log_{10} a_{\text{H}^+}$ , where  $a_{\text{H}^+}$  is the activity of the hydrogen ion in an electrolyte.

**Pit** A cavity in the surface of a material that extends into its interior.

**Pitting (corrosion)** A form of localized corrosion that results in the formation of pits, often associated with a cover of corrosion product or perforated metal over the pit.



**Polarization resistance** The slope ( $dE/di$ ) at the corrosion potential of the current density versus electrode potential under Linear Polarization. The polarization resistance is inversely proportional to the corrosion rate provided that charge transfer is the controlling electrode reaction. See also Charge Transfer Resistance.

**Redox** An abbreviation for reduction–oxidation.

**Redox potential** The equilibrium potential of an inert electrode (such as platinum) in a solution; a measure of the oxidizing or reducing tendency of the solution.

**Reference electrode** An equilibrium half-cell electrode of reproducible potential against which an unknown electrode potential can be measured. Commonly used examples include the standard hydrogen electrode (Pt,  $H_2/H^+$ ), the calomel electrode ( $Hg/Hg_2Cl_2/Cl^-$ ), and the silver/silver chloride electrode ( $AgCl/Cl^-$ ).

**Resistivity** The inverse of the conductivity of a material or solution.

**Sabkha** A flat area between a desert and an ocean, characterized by a crusty surface consisting of evaporite deposits (including salt, gypsum, and calcium carbonate), windblown sediments, and tidal deposits.

**Sand** Natural constituent of soil. Comprises particles of mean diameter 0.07–~2 mm in size (70–2000  $\mu m$ ).

**Selective backfill** Backfill material that has been selected to exhibit specific properties, particularly material of low corrosivity.

**Silt** Natural constituent of soil. Comprises particles of mean diameter 0.005–0.07 mm (5–70  $\mu m$ ).

**Sulfate-reducing bacteria (SRB)** Term describing several groups of anaerobic bacteria that use sulfate as an oxidizing agent for their energy-generating metabolism, reducing it to sulfide, which appears as  $H_2S$ , sulfide ions, metal sulfides, or a combination of these forms according to the conditions.

**Standard hydrogen electrode (SHE)** A redox electrode which forms the basis of the thermodynamic scale of oxidation–reduction potentials. The potential of platinum electrode in an acid solution with  $aH^+ = 1 \text{ mol kg}^{-1}$ , purged with hydrogen at a pressure of 101 325 Pa, which is declared to be zero at all temperatures.

**Stray-current corrosion** A corrosion process caused by unwanted currents flowing through paths other than the intended circuit and usually arising from an adjacent direct current source (e.g., traction supply, welding station, cathodic protection supply) or from an induced alternating current source (e.g., power transmission conductors).

**Substrate** (1) The base material on which a coating is present. (2) Any substance (other than materials required in trace quantities only) required for the growth or metabolism of a microorganism.

**Thermal spraying** A process for the application of a coating to a substrate by forming an atomized spray of small particles of molten material and directing onto a substrate with a suitable profile.

**Underground corrosion** A process involving corrosion of a buried material where the earth's soil forms a component of the corrosive environment.

## Abbreviations

**ASTM** American Society for Testing and Materials

**AWWA** American Water Works Association

**BC** Before Christ

**BS** British Standards

**DC** Direct current

**DIN** Deutsches Institut für Normung e.V. (German Institute for Standardization)

**DIPRA** Ductile Iron Pipe Research Association

**DMM** Design decision model

**EN** EuroNorm (European Standard)

**ER** Electrical resistance

**HDPE** High density polyethylene

**LPR** Linear polarization resistance

**MIC** Microbiologically influenced corrosion

**MTBF** Mean time before failure

**NACE** National Association of Corrosion Engineers

**NBS** National Bureau of Standards

**PREN** Pitting resistance equivalent numbers

**PVC** Polyvinyl chloride

**SHE** Standard hydrogen electrode

**SRB** Sulfate reducing bacteria

**TS** Tank size

**UNS** Unified Numbering System

**Symbols** **$k_W$ ,  $k_P$**  Scale constants (mm, mil,  $\text{g m}^{-2}$ , or  $\text{oz ft}^{-2}$ ) **$m$ ,  $n$**  Shape constants, with  $n, m \leq 1$  (typically  $n, m \approx 0.33\text{--}0.67$ )**pH** Soil pH **$t$**  Period of exposure (years) **$y$**  Typical variable**Cl** Chloride ion content **$E(\text{age})$**  Unconditional predicated age to corrosion failure **$M$**  Moisture content **$P$**  Pit depth (mm or mil) **$P$**  Tank structure-to-soil potential **$R$**  Resistivity **$S$**  Sulfide content**SC** Stray current magnitude **$W$**  Uniform metal loss (measured as mm, mil,  $\text{g m}^{-2}$ , or  $\text{oz ft}^{-2}$ ) **$\epsilon$**  Standard error**2.19.1 Introduction**

Corrosion in soils (also referred to as ‘underground corrosion’) is applicable to a wide range of different components (e.g., pipelines, underground storage tanks, tubular and sheet steel piles, ground anchors, power and telecommunication cables, etc.), which are either directly buried, driven, or otherwise positioned underground (sometimes referred to as ‘below grade’) and which can, therefore, be exposed to a wide range of different conditions (ranging from dry aerated sand to water-logged anaerobic clay). Any consideration of the subject of corrosion in soils must address both natural and contaminated (‘green field’ and ‘brown field’) sites and must consider ferrous alloys (such as cast iron, ductile iron, carbon/low-alloy steels, various stainless steels), as well as alloys of copper, aluminum, zinc, and lead. It must also include the performance of metallic coatings (e.g., galvanizing and thermally sprayed coatings). However, in all cases, the basic corrosion mechanisms are the same as for corrosion in natural waters. Examples of corrosion in soils for different components are shown in Figures 1–4.

Degradation of buried nonmetallic components (such as polyvinyl chloride (PVC) or high density polyethylene (HDPE) pipe) and concrete (including corrosion of reinforcing steel in buried concrete foundations) are not considered here.



**Figure 1** Corrosion of cast iron pipe (due to external stray current).



**Figure 2** Burst failure of carbon steel oil pipeline (due to lack of cathodic protection).



**Figure 3** Corrosion of buried copper pipe exposed to  $\text{H}_2\text{S}$  containing ground water. Reproduced from *Corrosion Atlas*, 3rd ed.; compiled by Durning, E. D. D.; Elsevier Science Publishers: London, 1997; (Item 06.05.05.01).



**Figure 4** Bronze spearheads (Knossos, Crete, ca. 1500 BC).

The main aspect that differentiates corrosion in soils from corrosion in other natural environments is the contribution that the soil (and associated ground water) plays in modifying the corrosion mechanism and in particular the corrosion rate. In practice, cast iron, ductile iron, and carbon/low-alloy steels behave essentially in the same manner for a given soil type and condition; their corrosion rates can range from negligible ( $<0.005 \text{ mm year}^{-1}$ ) to extremely rapid (with localized corrosion of  $>1 \text{ mm year}^{-1}$ ). The differences are related to soil type, soil resistivity, ground water composition, soil condition, and the activity of bacteria, especially sulfate-reducing bacteria (SRB).

It is not the intention here to provide full details of soil genesis, for which the reader is directed to specialist publications<sup>1</sup> for a detailed description. However, an outline description of different soil types and methods of classification is included, in order to assist in the understanding of the variations in soil that directly relate to the corrosion processes.

Corrosion in soils has been studied worldwide over many years; to date, the most extensive and comprehensive study was conducted by Romanoff, for the National Bureau of Standards (NBS) in the US in the 1950s and 1960s. This work was published as a series of NBS circulars and presentations,<sup>2,3</sup> covering the results of over 37 000 different samples, comprising numerous different metals/alloys and 95 different soils, exposed for up to 17 years. The work is still relevant today as the benchmark for describing performance of various metals and alloys exposed to a wide range of soils and is the ultimate source for much of the published data relating to the subject.

Other studies have been carried out since the work by Romanoff up to the present day in North

America,<sup>4,5</sup> the United Kingdom,<sup>6,7</sup> Sweden,<sup>8</sup> Germany,<sup>9</sup> and Russia<sup>10</sup> and elsewhere. Whilst these different studies provide further information on specific local soils and on alternative/new alloys, the overall results are complementary to the original findings of Romanoff.

The original studies of corrosion in soil mainly concerned pipelines; this was later expanded to include driven piles. However, since the 1980s significant interest has also been focused on underground storage tanks, because of increased concern about environmental damage caused by leaking tanks, especially for small scale (retail) storage facilities at petrol (gasoline) stations, domestic fuel storage facilities, etc. The long-term performance of ground anchorage systems (high stressed anchorages, soil nails, tie-bars, etc.) is another area where there is an increasing requirement to demonstrate long-term performance, especially for systems that provide stabilization for major critical civil structures such as flood defense, dams, bridges, tunnels, etc.

In archaeology, the extent of deterioration of metals over millennia of exposure is of interest. The condition of bronze and iron artifacts can vary greatly depending on local ground conditions.

## 2.19.2 The Nature of Soils

Encarta Dictionary defines soil as “The top layer of most of the Earth’s land surface, consisting of the unconsolidated products of rock erosion and organic decay, along with bacteria and fungi.” While demonstrating the natural variability in soils, such a definition does not fully convey an impression of the countless variations in soil that occur. The type and condition of the soil are directly affected by moisture, principally entering through rainfall, but also from flooding, tidal action, and human interaction (e.g., from irrigation schemes, dewatering, or land reclamation schemes), as well as by contamination from industrial processes. It is the combination of the genesis of the soil and the source of moisture within the soil that leads to variations in soil chemistry.

Often locations are classed as ‘green field’ or ‘brown field’ sites; green field sites are those where there has been no previous industrial use, while brown field sites are locations of former industrial use (factories, storage yards, waste tips, etc.). For brown field sites there is, therefore, also the possibility that contaminated soil may be present, the soil being contaminated by the presence of man-made chemicals or

other human alteration in the natural soil environment. In addition to the direct discharge of industrial wastes to the soil, contamination often occurs from the rupture of underground storage tanks, application of pesticides, percolation of contaminated surface water, oil dumping or leaching of wastes from landfill sites. The most common chemicals involved are petroleum hydrocarbons, pesticides, and heavy metals.

An important consideration is that statutory or other routine surveys of contaminated land for data acquisition are carried out primarily for public health and environmental reasons and are rarely, if ever, intended for corrosivity assessment. Most of the data, thereby, generated are of little or no consequence for soil corrosivity evaluation, whereas other data of vital importance for appraisal of soil corrosivity are often not generated by such surveys. A soil corrosivity survey is, therefore, a distinct exercise from a general contaminated land survey.

### 2.19.2.1 General Soil Texture and Structure

In any assessment of potential corrosivity, it is important that the nature of the soil itself is considered; however, this is a vast topic.<sup>1</sup> The more important aspects on soil texture and structure that follow are based on the corresponding chapter, by Harris and Eyre, in the previous edition.<sup>11</sup>

Soils are commonly named and classified according to the general size range of their particulate matter. Thus, sandy, silt, and clay types derive their names from the predominant size range of inorganic constituents. Particles between 0.07 mm and ~2 mm are classed as sands. Silt particles range from 0.005 to 0.07 mm, and clay particle size ranges from 0.005 mm mean diameter down to that of colloidal matter.

The proportion of the three size groups will determine many of the properties of the soil. Although a number of systems have been used to classify soils according to texture, the one shown in **Figure 5** represents the most commonly used terminology for various proportions of sand, silt, and clay.

As soils contain organic matter, moisture, gases, and living organisms as well as mineral particles, it is apparent that the relative size range does not determine the whole nature of the soil structure. In fact, most soils consist of aggregates of particles within a matrix of organic and inorganic colloidal matter rather than of separate individual particles. This aggregation gives a crumb-like structure to the soil and leads to friability, more ready penetration of moisture, greater

aeration, less erosion by water and wind, and generally greater biological activity. The loss of the aggregated structure can occur as the result of mechanical action, or by chemical alteration such as excess alkali accumulation. Destruction of the structure or 'puddling' greatly alters the physical nature of the soil.

Mention should be made of the soil profile (section through soil showing various layers) because it is important to recognize that the soil's surface gives a very poor indication of the underlying strata. Pipelines are buried a meter or so and foundations/anchorages typically more than 10 m below surface soils and corrosion surveys based on surface observations give little information as to the actual environs of the pipe when buried.

### 2.19.2.2 The Clay Fraction

Clays make up the most important inorganic constituents of soil. They consist of various minerals depending on the mineral composition of the parent material, and on the type and degree of weathering. Often clays may be grouped in a family series, depending upon the weathered condition, as, for example, montmorillonite → illite → kaolinite. Weathering of montmorillonite causes loss of potassium and magnesium, which alters the crystalline structure, and eventually kaolinite results. In this example (and also for other clay mineral groups) marked changes occur in the physical properties of a soil as clay minerals undergo the weathering process.

Montmorillonite clays absorb water readily, swell greatly, and confer highly plastic properties to a soil. Thus soil stress occurs most frequently in these soils and less commonly in predominantly kaolinitic types. Similarly, a soil high in bentonite will show more aggressive corrosion than a soil with a comparable percentage of kaolinite. A chalky soil usually shows low corrosion rates. Clay mineralogy and the relation of clays to corrosion deserve attention from corrosion engineers.

### 2.19.2.3 Aeration and Oxygen Diffusion

The pore space of a soil may contain either water or a gaseous atmosphere. Therefore, the aeration of a soil is directly related to the amount of pore space present and to the water content. Soils of fine texture due to high clay content contain more closely packed particles and have less pore capacity for gaseous diffusion than an open-type soil such as sand.

Oxygen content of soil atmosphere is of special interest in corrosion. It is generally assumed that the



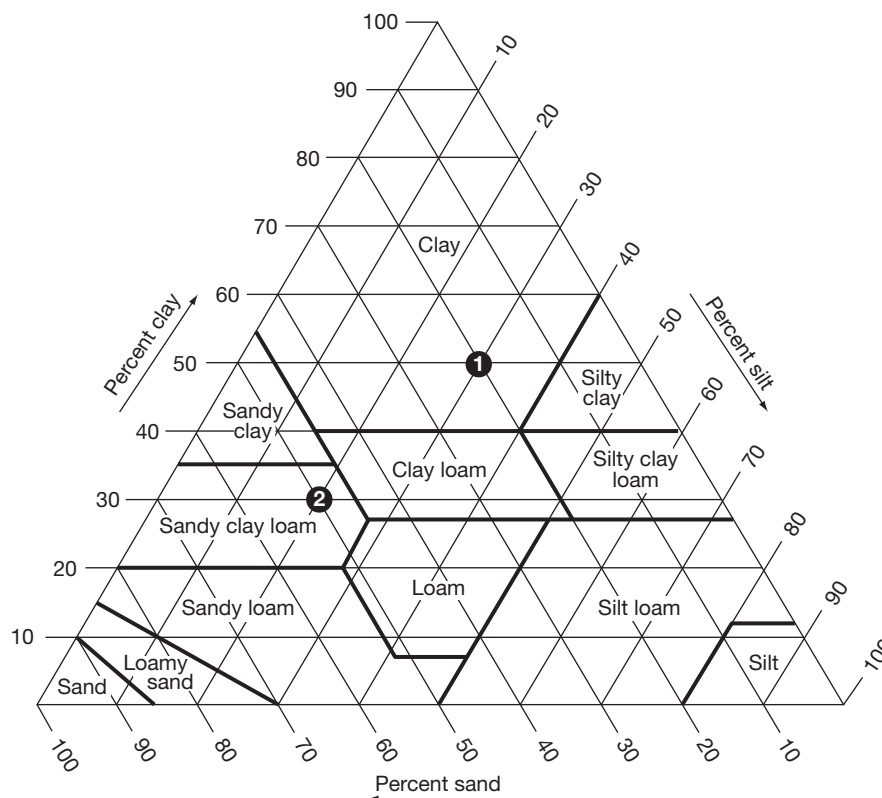


**Figure 5** Proportions of sand, silt and clay making up the various groups of soils classified on the basis of particle size <sup>(\*)</sup>. Reproduced from *Soil Survey Manual* 1993. Soil Conservation Service. U.S. Department of Agriculture Handbook 18. United States Government Printing Office, Washington, DC. (ISBN-10: 1410204170) (<http://soils.usda.gov/technical/manual/>).

<sup>(\*)</sup> The corresponding percentages of clay, silt, and sand present in the soil are located on relevant axis of the triangle.

The values are then projected inwards (along the lines as indicated on the axis). The name of the area in which the lines intersect is the class name for the particular soil. For example, a soil with 50% clay, 30% silt, and 20% sand (location ❶) is a 'clay,' while a soil with 30% clay, 20% silt, and 50% sand (location ❷) is a 'sandy clay loam,' etc.

gases of the upper layers of soil are similar in composition to the atmosphere above the soil, except for a higher carbon dioxide content. However, biological activity within the soil tends to decrease the oxygen content and replace the oxygen with gases from metabolic activity, such as carbon dioxide. Most of the biological activity occurs in the upper 150 mm of soil, and it is in this region that diffusion would be most rapid. Factors which tend to increase microbial respiration, such as the addition of large amounts of readily decomposed organic matter, or factors which decrease diffusion rates (water saturation) will lead to development of anaerobic conditions within the soil. Anaerobic conditions favor the proliferation of SRB, which produce hydrogen sulfide, sulfide ions, or inorganic sulfides according to the conditions and may give rise to very high rates of localized corrosion under conditions of near neutral pH and low oxygen concentration,

which would normally be considered benign. Such situations are discussed in [Section 2.19.2.6](#) below.

The main difference between 'buried' and 'driven' components relates to the availability or otherwise of oxygen. Where the components are exposed to 'back-fill,' the soil will normally be aerated (at least initially), whereas for driven components (i.e., where the item is placed in 'undisturbed soil') the oxygen content can be negligible and in these cases corrosion of the bulk of the item will also be negligible (see [Section 2.19.3.5](#) below).

#### 2.19.2.4 Water Relations

No soil corrosion occurs in a completely dry environment. Water is needed for ionization of the oxidized state at the metal surface. Water is also needed for ionization of soil electrolytes, thus completing the



circuit for flow of a current maintaining corrosive activity. Apart from its participation in the fundamental corrosion process, water markedly influences most of the other factors relating to corrosion in soils. Its role in weathering and soil genesis has already been mentioned.

#### **2.19.2.4.1 Free ground water**

At some depth below the surface, water is constantly present. This distance to the water table may vary from a <1 m to >100 m, depending upon the geological formations present. Only a small amount of the metal used in underground service is present in the ground water zone. Such structures, as well as casings and under-river pipelines, are surrounded by ground water. The corrosive conditions in such a situation are essentially those of an aqueous environment.

#### **2.19.2.4.2 Gravitational water**

Water entering soil at the surface from rainfall or some other source will tend to move downwards. This gravitational water will flow at a rate governed largely by the physical structure regulating the pore space at various zones in the soil profile. An impervious layer of clay, a 'puddled' soil, or other layers of material resistant to water passage may act as an effective barrier to the gravitational water and cause zones of water accumulation and saturation. This is often the situation in highland swamp and bog formation. Usually, gravitational water percolates rapidly to the level of the permanent ground water.

#### **2.19.2.4.3 Capillary water**

Most soils contain considerable amounts of water held in the capillary spaces of the silt and clay particles. The actual amount present depends on the soil type and weather conditions. Capillary moisture represents the important reservoir of water in soil, which supplies the needs of organisms living in or on the soil. Only a portion of capillary water is available to plants. The moisture-holding capacity of clay is much greater than that of a sandy type soil. Likewise, the degree of corrosion that occurs in soil will be related to its moisture-holding capacity, although the complexities of the relationships do not allow any direct and simple quantitative predictive application.

#### **2.19.2.5 Variable Conditions**

An important aspect of corrosion in soil is the effect that varying soil type and composition have on corrosion, giving rise to different conditions on different sections of a buried structure; this could be due to

changes in moisture content, soil structure (clay to sand), or soil chemistry (pH, chloride concentration, oxygen content, etc.), resulting in galvanic corrosion.

For horizontal systems (i.e., pipelines, metallic cable sheaths, etc.), such processes are often referred to as 'long-line corrosion' where the pipeline crosses from one soil condition to another. Vertical changes in conditions are equally important, principally for driven components (such as piles or soil nails). The effect can be extensive, with the section of a structure in the higher pH, low chloride, or more aerated ground acting as a large cathode over tens or even hundreds of meters in length, leading to accelerated corrosion in the lower pH, deaerated, or higher chloride areas. A classic example is that of a pipeline running in normally high resistance, well aerated sand crossing an area of *sabkha* (i.e., salt rich desert area). *Sabkha*, being very high in salt content and generally low resistivity ground, is naturally more corrosive than the surrounding sand and hence would result in naturally higher corrosion rates. However, for a continuous pipeline, the line sections in the adjacent, normal sand also act as a good cathode, increasing the rate of attack in the *shabka* area.

#### **2.19.2.6 Effect of Bacterial Activity on Corrosion in Soils**

Microorganisms or 'microbes' are commonly defined as living entities that are too small to be visible to the human eye. Soils that contain more than a few percent moisture abound with an incalculable variety of microbial activity. However, fundamentally, the vast majority of those microbes perform a single overall metabolic function to mineralize organic matter of plant and animal origin and ultimately to convert it to carbon dioxide, inorganic nitrates, inorganic phosphates, etc. Such microbes, termed 'heterotrophs,' have little direct relevance to corrosion of buried metal.

A more detailed account of microbially-influenced corrosion (MIC) is presented in **Chapter 2.20, Corrosion in Microbial Environments** of this work, to which the reader is referred. In the context of soils, the most important group of microorganisms associated with corrosion belongs to the specialized group of bacteria known as sulfate reducing bacteria (SRB); the vast majority of MIC failures are related to their activities.

SRB thrive in oxygen-free soils and other anaerobic environments, where they obtain their required carbon from organic nutrients and their energy from the reduction of sulfate ions to sulfide. Waterlogged

soils often provide ideal environments for SRB proliferation, especially in brackish or estuarine water areas, which contain abundant sulfate ions. Sulfide appears as hydrogen sulfide ( $\text{H}_2\text{S}$ ), sulfide ions, metal sulfides, or a combination of these according to conditions. Sulfides are highly corrosive to many metals, mainly because they form complex semiprotective layers that are also conductive and cathodic to the parent metal, leading to intense localized (shallow pitting) attack in areas of film breakdown. In the case of ferrous metal corrosion, the characteristic black iron sulfide ( $\text{FeS}$ ) corrosion products liberate  $\text{H}_2\text{S}$  on acid treatment, distinguishing it from black iron oxide (magnetite). The corrosion products are often loose and when dislodged exhibit pits lined with bright metal corresponding to areas of anodic dissolution, but are sometimes also hard and adherent. Typical pictures of the morphology of this type of attack are shown in **Chapter 2.20, Corrosion in Microbial Environments**.

The effect of high SRB activity to corrosion rates in soils and corrosivity assessments are described in the relevant sections of this chapter (below). Suffice to say at this point that the most severe conditions with respect to MIC typically occur under conditions of low oxygen content and near-neutral pH, which would be otherwise regarded as benign. In this respect, low oxidation/reduction (redox) potential is an important indicator of intense SRB activity.

## 2.19.3 Corrosion Rates in Soils

### 2.19.3.1 Carbon and Low Alloy Steels

The monumental work of Romanoff,<sup>2</sup> which still forms the basis of much of our understanding of corrosion in soils, demonstrated that, in practice, all ferrous alloys (cast iron, wrought iron, mild steel, low carbon steel, etc.) are attacked at essentially the same rate in a particular soil. However, the rate of attack is not normally linear with time and can generally be modeled by an exponential relationship, as shown in eqn [1]:

$$W = k_w \cdot t^m \text{ or } P = k_p \cdot t^n \quad [1]$$

where  $t$  is period of exposure (years);  $W$ , uniform metal loss (measured as mm, mil,  $\text{g m}^{-2}$  or  $\text{oz ft}^{-2}$ );  $P$ , pit depth (mm or mil);  $k_w$ ,  $k_p$ , scale constants (mm, mil,  $\text{g m}^{-2}$  or  $\text{oz ft}^{-2}$ );  $m$ ,  $n$ , shape constants, with  $n$ ,  $m \leq 1$  (typically  $n$ ,  $m \approx 0.33$ – $0.67$ ).

The scale and shape constants are dependent on the soil. For example, data for different ferrous materials exposed to two different soil types (sand and

clay respectively) over a 17 year period are shown in **Figure 6**, which presents both the raw data and the calculated regression lines for the two conditions. The shape constants are 0.702 in clay and 0.809 in sand (independent of units), with scale constants of 0.636 and 0.215 mm for clay and sand, respectively. The error bands shown in **Figure 6** are the 95% prediction range from linear regression analysis of the data which gives factors of  $\times 10^{\pm 0.094}$  for clay and of  $\times 10^{\pm 0.236}$  for sand. Because the data follow an exponential relationship, a plot of  $\log(y)$  versus time takes the form of a straight line, which allows the standard error ( $\varepsilon$ ) of the predicted value of  $\log(y)$  to be obtained. The 95% prediction limit (for  $\log(y)$ ) is given as  $\pm 1.96 \cdot \varepsilon$ ; the corresponding limit is for  $y$  is then given by  $10^{\pm 1.96 \cdot \varepsilon}$ .

However, while Romanoff found that, in general, all ferrous material alloys behaved similarly in the same soil, some low alloy steels did show variable performances in specific soil types. Generally steels with chrome content of  $\sim 5\%$  (with or without molybdenum, at  $\sim 0.5\%$ ) exhibited corrosion rates (weight loss or pitting) of about half of that plain low alloy/low carbon steels, except in very poorly aerated conditions, where they exhibited greater pitting, as shown in **Figure 7** (steels *D*, *E*, and *H*).

In the presence of high SRB activity, see **Section 2.19.2.6**, special considerations apply and localized, shallow pitting corrosion may be much higher than would otherwise be expected. In some instances, cast

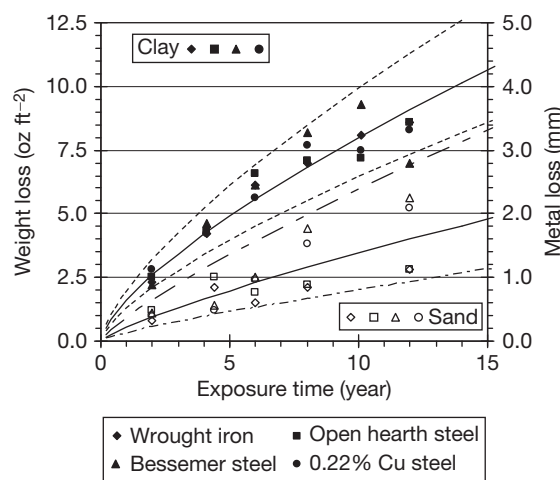


**Figure 6** Comparison of measured metal loss for a range of steels in different soil types (clay and sand). Reproduced from Romanoff, M. *Underground Corrosion*; National Bureau of Standards, Circular 579 (April 1957). [Republished by NACE International, Houston, Texas, USA, 1989 ISBN 0-915567-47-4].

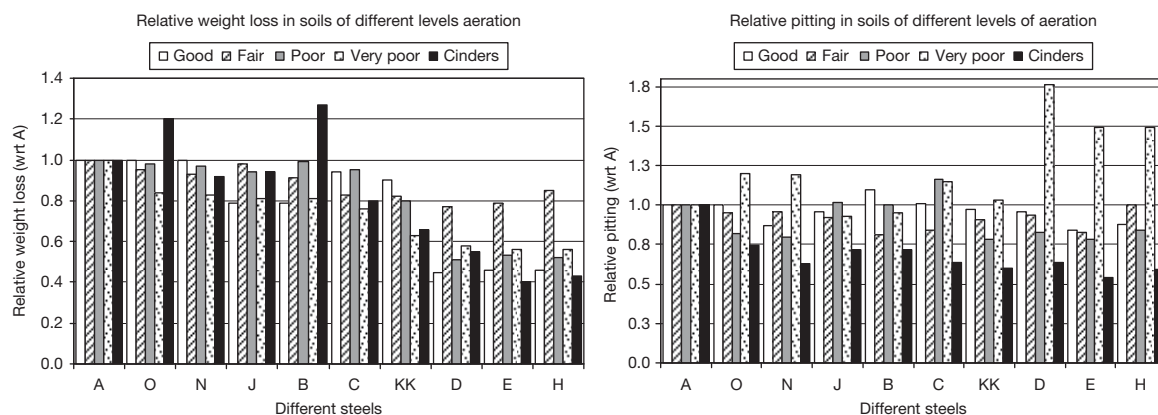


**Figure 7** Relative performance of different low alloy steels in different soil types. Reproduced from Romanoff, M. *Underground Corrosion*; National Bureau of Standards, Circular 579 (April 1957). [Republished by NACE International, Houston, Texas, USA, 1989 ISBN 0-915567-47-4].

iron pipes of 8mm thickness have become perforated within a year under such conditions, while perforation rates of 1–2 mm year<sup>-1</sup> at ambient temperature are not uncommon. Under anaerobic/aerobic cycling conditions, where SRB mediated sulfide corrosion may be exacerbated by the production of elemental sulfur, and/or at elevated temperatures corrosion rates of 3–5 mm year<sup>-1</sup> may be encountered.

### 2.19.3.2 Other Metals and Alloys

Romanoff obtained only limited experimental data for stainless steels in soils, as summarized in Table 1, which shows improved performance with regards to both general metal loss and pitting except for ferritic steels (grade UNS S41000/EN 1.4006 and UNS S43000/EN 1.4016), which were still relatively high at 0.75 and 0.31 mm year<sup>-1</sup>, respectively.

**Table 1** Corrosion performance of some stainless steels

Stainless steel grade		General metal loss ( $\mu\text{m year}$ )	Pitting rate ( $\mu\text{m year}$ )
UNS system	EN system		
S41000	1.4006	750 $\pm$ 650	68 $\pm$ 44
S43000	1.4016	310 $\pm$ 280	65 $\pm$ 31
S30400	1.4301	7.8 $\pm$ 7.2	15 $\pm$ 8.0
S31600	1.4401	1.3 $\pm$ 0.88	0.42 $\pm$ 0.82
S30200	1.4319	0.37 $\pm$ 0.30	0.91 $\pm$ 1.8
S30900	1.4822	0.15 $\pm$ 0.11	0.91 $\pm$ 1.8

Source: Modified from Romanoff, M. *Underground Corrosion*; National Bureau of Standards, Circular 579 (April 1957); [Republished by NACE International, Houston, Texas, USA, 1989 ISBN 0-915567-47-4].

Since the work carried out by Romanoff, a wider range of stainless steels are now available for pipework, tanks, and anchorage systems. Typically, the higher the pitting resistance equivalent number (PREN) the better the corrosion resistance for stainless steels in soils and with the main factor being consideration of chloride content and resistivity, SRB can also attack stainless steels.<sup>12</sup>

The corrosion behaviors of other metals, including copper, lead, and zinc obtained by Romanoff<sup>2</sup> are summarized in Figure 8 for exposure in a combination of several different soil types and for tidal marsh, clay, and sandy loam.

### 2.19.3.3 Influence of Soil Parameters on Corrosion Rate

Romanoff concluded that the main parameter that influenced the corrosion rate of ferrous materials was the extent of aeration, with the highest corrosion rates occurring in soils with poor or very poor aeration (poor or very poor drainage) compared to lower corrosion in soils possessing good aeration (good drainage). Pooled data for steel samples from 47 test sites<sup>2</sup> grouped by degree of aeration as defined by Romanoff are shown in Figure 9. However, it is clear that aeration alone is insufficient to account for the variability among different soils.

The same pooled data from Romanoff, if grouped by resistivity, soil type, pH, or salt content, show similar levels of correlation. Consequently, these factors have been incorporated into the development of various methods for assessing corrosivity, as described later.

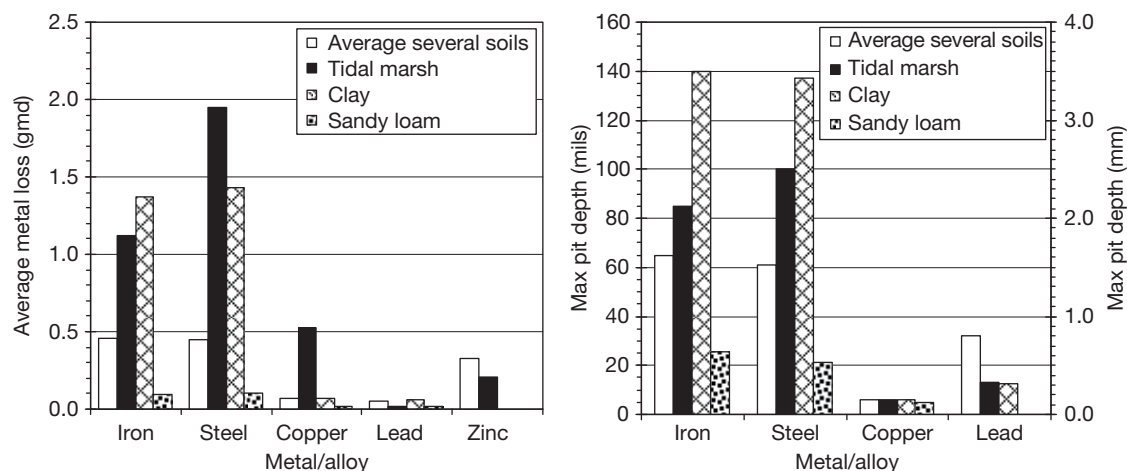


**Figure 8** Average metal loss rate ( $\text{g m}^{-2} \text{ day}^{-1}$ ) and maximum pit depth (normalized to 12 years exposure) for iron, steel, copper, lead and zinc. Reproduced from Romanoff, M. *Underground Corrosion*; National Bureau of Standards, Circular 579 (April 1957). [Republished by NACE International, Houston, Texas, USA, 1989 ISBN 0-915567-47-4].

#### 2.19.3.4 Long-Term Corrosion Rates in the Soil Environment

For most engineering applications, the rate of deterioration is considered over periods ranging from 20 to 100 years; however, corrosion in soils is a rare instance where exposure periods of more than 1000 years may also be relevant, both for strategic storage facilities (nuclear fuel storage, national archives, etc.) and with regard to archaeological artifacts.

In fact, ancient historical periods are defined by the metallurgy that was available at the time, from the Copper Age (4000–3500 BC), various Bronze Ages (Early 3500–2000 BC, Middle 2000–1600 BC, and Late 1600–1100 BC), and Iron Age (from 1100 BC to 500 AD). Lead was also widely used from 3000 BC onward. The different natural corrosion rates for the various metals and alloys, together with the soil conditions in which the metallic items were left, lead to a wide variation in the quantity and condition of artifacts found in archaeological sites, with some older artifacts fabricated from bronze being preserved in better condition than newer iron artifacts.

Studies over recent years have examined the impact of different soil parameters on bronze artifacts<sup>13</sup> and have shown that aeration and pH are the main factors, with highly aerated and/or acidic soils leading to the most severe deterioration, while low aeration (i.e., clay soils) leads to best preservation. These findings have wider implications as environmental changes, and in particular impact of acid rain on soils, could lead to deterioration of artifacts that

have been reasonably preserved for thousands of years but are located in soils of poor buffering capacity.

For iron artifacts, while acidic conditions will also lead to severe attack, poorly aerated/clay soils tend to lead to the converse condition,<sup>14</sup> which is consistent with the experience on modern ferrous materials as described above. Another factor that is important is the presence of soot in the soil, formed for example, from a funeral pyre or from destruction of a dwelling by fire, which can also lead to more extensive corrosion of the artifact.

#### 2.19.3.5 Disturbed and Undisturbed Soils

One of the main factors relating to corrosion rate in soils is whether the component is placed in disturbed or undisturbed condition. Disturbed soil is defined as one that has been mechanically moved and replaced (e.g., backfill used in laying a pipeline, burying a tank, etc.), whereas in the case of undisturbed soils the component has been driven directly into soil, for example, driven sheet steel piles, H-piles, tubular steel piles, or soil nails.

The process of mechanically moving the soil affects it by breaking up the soil (which can affect the cohesiveness of the soil) and also aerates the soil. Conversely, for driven components, the mechanical property and cohesive form of the soil are unaffected. Separate work by Romanoff in the 1960s<sup>3</sup> found that a soil which, if disturbed, would be considered corrosive, resulted in negligible corrosion if undisturbed.

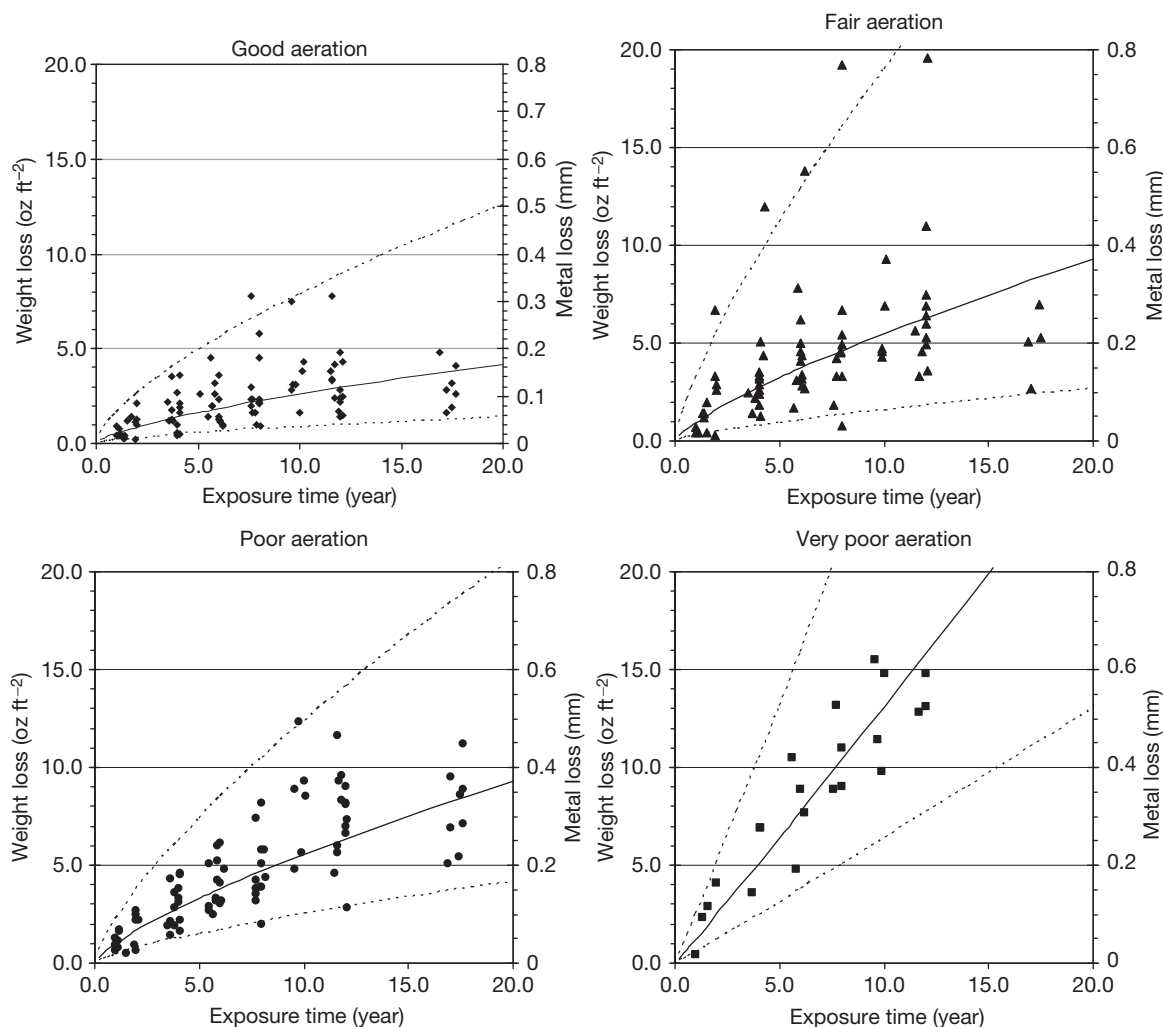


**Figure 9** Pooled weight loss data for Bessemer steel (3" Pipe) from 47 different test sites, group by degree of aeration. Reproduced from Romanoff, M. *Underground Corrosion*; National Bureau of Standards, Circular 579 (April 1957). [Republished by NACE International, Houston, Texas, USA, 1989 ISBN 0-915567-47-4] – with regression lines and 95% prediction limits.

This work combined specific field trials plus observations of steel piling that were removed after 50 years exposure.

In many cases, the extent of metal loss was minimal and only limited isolated pitting observed, which for most types of piling is not structurally significant. In some cases, it was reported that the original mill scale was still intact when the pile was removed.

Examination of piling removed from permafrost<sup>15</sup> also showed that no corrosion occurred on the section of pile that was permanently in frozen conditions, with little corrosion occurring in the area above the frozen ground.

A survey carried out in 2000<sup>4</sup> confirmed Romanoff's overall findings relating to steel piling for most soils. However, cases of significant corrosion of steel piling (single side metal loss rates of  $0.06\text{--}0.11\text{ mm year}^{-1}$ ) were found where the ground was either contaminated by cinders/coal, or had low resistivity ( $<20\ \Omega\text{ m}$ ) or where acidic ( $\text{pH} < 4$ ) conditions occurred. In particular, this study identified problems at the interface between disturbed and nondisturbed areas, where differential concentration cells (macro-cells) are formed, as described above and as shown in [Figure 10](#). Here the corrosion is concentrated on the section of pile in the nondisturbed soil at the interface.



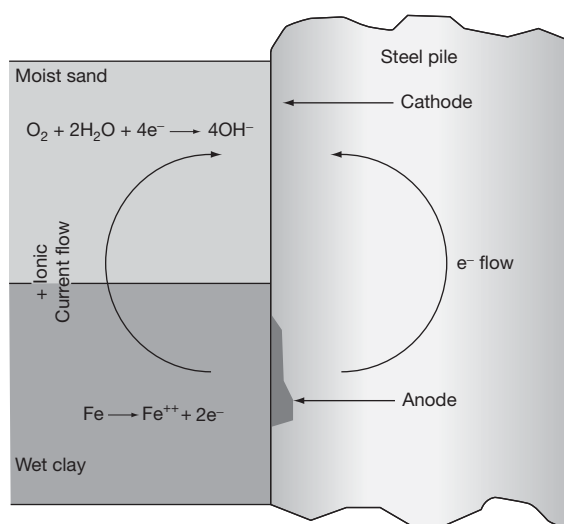


**Figure 10** Creation of differential concentration (differential aeration) cells between disturbed and nondisturbed soils. NACE Technical report 05101 *State-of-the-Art Survey on corrosion of steel piling in soils* (Dec-2001); published by NACE International (item no 24216); Houston, TX, USA.

## 2.19.4 Corrosivity (Aggressivity) Assessment

### 2.19.4.1 General

Various different methods for assessing the likely corrosivity of soils have been developed. In most cases, the different procedures assign ratings (values) to the various influencing factors and the sum of the ratings is used to assess aggressiveness. Schemes have also been proposed that incorporate a statistical approach, whilst others provide general guidance based on generic conditions or rely on direct measurement of corrosion rate in the soil.

The methodology used most extensively in the UK and Europe is on the basis of original work carried out in Germany<sup>9</sup> and first published in English in Beakman and Swenk.<sup>16</sup> In Germany, the system has evolved into DIN 50 929 Part 3.<sup>17</sup> The Eyre & Lewis system,<sup>18</sup> which is a derivative of the original German system, has been adopted by the UK Highways Authority for assessment of new bridge and road projects.

### 2.19.4.2 Resistivity

The simplest method of assessing soil corrosivity is solely on the basis of resistivity measurements. There

**Table 2** Assessment of soil corrosivity based on soil resistivity

Soil resistivity ( $\Omega m$ )	Corrosivity rating
>200	Essentially noncorrosive
100–200	Mildly corrosive
50–100	Moderately corrosive
30–50	Corrosive
10–30	Highly corrosive
<10	Extremely corrosive

Source: Reproduced from NACE Resource Centre (<http://events.nace.org/library/corrosion/SoilCorrosion/Severity.asp>).

are several different resistivity criteria; the most widely used method is summarized in **Table 2**.

Sandy soils are high up on the resistivity scale and therefore considered the least corrosive on the basis of this simplistic criterion. Clay soils, especially those contaminated with saline water, are at the opposite end of the spectrum. The soil resistivity parameter is widely used in practice and generally considered to be the dominant variable in the absence of microbial activity. However, it is widely acknowledged that resistivity alone does not determine overall soil corrosivity and hence most systems include assessment of other parameters.

### 2.19.4.3 Influence of SRB

A large scale study of many factors at 59 sites in the United Kingdom<sup>6</sup> lead to the finding that aggressive sites were characterized by soil resistivity of less than  $20 \Omega m$  or a mean redox potential more negative than +400 mV (the redox potential is defined as the potential difference measured between a platinum electrode and a suitable reference electrode in contact with the soil, normalized to standard hydrogen potential (SHE) and a pH of 7<sup>19</sup>). Low redox potential is attributed to reduced sulfur compounds, particularly sulfides, produced by the activities of SRB. 'Borderline' cases were classified according to water content – those containing more than 20% water being deemed aggressive soils. Similarly, all soils with a mean soluble iron content of over  $120 \text{ mg kg}^{-1}$  were found to be aggressive.

It is the authors' experience that, in addition to redox measurements (which should, be performed on undisturbed soil *in situ*), it is also useful to test small samples of soil for the direct presence of SRB. A pragmatic procedure, developed by the authors, involves two different sized samples inoculated (in triplicate) into vials of SRB culture medium

(see Chapter 2.20, Corrosion in Microbial Environments), which are then immediately resealed. One set of samples (milli-sample) would comprise 100–200 mg of soil material, the other set (micro-sample) less than 10 mg of material (i.e., literally only a few grains). If, after 14 days incubation at  $\sim 30^\circ\text{C}$ , all the milli- and micro-sample test vials turn black, the soil is designated as moderate to severely infected with SRB, and likely to present a high threat of MIC. If the micro-samples only turn black, the soil may be designated as low to moderately infected with SRB and hence, as a lower threat of MIC.

#### 2.19.4.4 DIN 50 929 Part 3 Criteria

DIN 50 929 Part 3<sup>17</sup> provides by far the most comprehensive methodology and has been validated on many different projects, following comparison of predicted metal loss to actual metal loss.

In DIN 50 929 Part 3, the aggressiveness of soil is determined by consideration of soil type, extent of contamination, resistivity, pH, moisture content, soil condition (i.e., disturbed/undisturbed), total alkalinity/acidity (buffer capacity), combined chloride/sulfate content (aqueous extract), sulfate content (acid extract), sulfide content, presence of ground water, vertical/horizontal homogeneity, and external stray current.

DIN 52 929 Part 3 also assesses ground water in a similar manner to soil by considering water mobility, position (fully submerged, at water/air interface or in splash zone), chloride and sulfate content, buffer capacity, calcium content, pH, and external stray current.

The individual parameters are assigned values ranging from +4 (nonaggressive) to –12 (strongly aggressive), on the basis of defined criteria. The sum of the various items can range from a best case of +4 to a worst case of –47, and from this the overall corrosivity (aggressivity) is assessed. This also allows an estimate of the expected corrosion rate and the practical range (essentially a factor of  $\times 2$  on the median corrosion rate), as shown in Table 3.

#### 2.19.4.5 Eyre and Lewis System

The Eyre and Lewis system<sup>18</sup> is a development of the original German assessment method<sup>9</sup> and has been adopted by the UK Highway Agency<sup>20</sup> for determining corrosion protection requirements for all highway structures.

The main differences between the two systems is that the Eyre and Lewis system of assessment includes the redox potential of the soil and assesses the buffering capacity (i.e., the extent to which the pH could change if acid or alkali is added) by measuring the bicarbonate content of soil as opposed to the analysis required in DIN 50 929 part 3.

#### 2.19.4.6 AWWA/DIPRA

DIPRA (Ductile Iron Pipe Research Association, formally CIPRA – Cast Iron Pipe Research Association) developed a classification for assessing soils for determining whether protective measures are required for ductile iron pipes for use in water and waste water applications, which was first published in 1968.<sup>21</sup> This method was adopted by AWWA (American Water Works Association) and is now more commonly referred to as the ‘AWWA 10-point system.’<sup>22</sup> It is used widely in North America, where it defines whether or not the minimal level of protection as required by AWWA, that is either no protection or application of plastic liner, for cast iron water and sewer pipes. It has also been adopted as part of other assessment schemes.<sup>7</sup>

The system assigns scores dependent on resistivity, pH, redox, sulfides, and moisture content, with a total score greater than 10 considered corrosive and requiring application of plastic liner. While it would appear to be similar to other systems as described above,<sup>9,17,18</sup> and there is evidence of good correlation between the predicted score and actual performance,<sup>5</sup> there is also evidence that it can underestimate the soil corrosivity.<sup>23,24</sup> This is on the basis of the observed corrosion performance being at

**Table 3** Assignment of aggressiveness and expected corrosion rates for soils

Sum of ratings	Aggressiveness	General corrosion rate ( $\text{mm year}^{-1}$ )	Localized attack ( $\text{mm year}^{-1}$ )
$\geq 0$	Ia Virtually nonaggressive	0.005 (range 0.0025–0.01)	0.03 (range 0.015–0.06)
–1 to –4	Ib Weakly aggressive	0.01 (range 0.005–0.02)	0.05 (range 0.025–0.1)
–5 to –10	II Aggressive	0.02 (range 0.01–0.04)	0.2 (range 0.1–0.4)
$< -10$	III Strongly aggressive	0.06 (range 0.03–0.12)	0.4 (range 0.2–0.8)

Source: Reproduced from DIN 50 929 Part 3. Probability of Corrosion of Metallic Materials when Subject to Corrosion from the Outside. Buried and Underwater Pipelines and Structural Components, Sep-1985.

variance to the predicted corrosion condition. Similar variances between predicted corrosivity by the DIPRA method and actual experience, where other systems (e.g., DIN 50 929 part 3) showed good correlation, have also been observed by the authors. This is, in part, because most assessments only take into account the point scores, while the full procedure (as detailed in AWWA C105) actually requires the soil type to be taken into consideration as well. It is this omission that, in the authors' opinion, is one of the reasons for the variable results of the system.

DIPRA has recognized the limitations in its original system and published an extended methodology in 2004, referred to as Design Decision Model™ (or DDM™).<sup>23,24</sup> This extends the general hazard assessment to include the effect of chlorides, bimetallic effects, and known corrosive environments (i.e., soil type) and also now includes a risk assessment as shown in **Figure 11** (i.e., considering the combination of both likelihood of failure and consequence of failure, used in corrosion risk assessments as described in other chapters of this publication).

As the risk of corrosion increases the required level of protection (as outlined in **Section 2.19.6** below) is then increased, as follows:

1. Negligible – install the pipe as-manufactured with its protective standard shop coating/annealing oxide system.

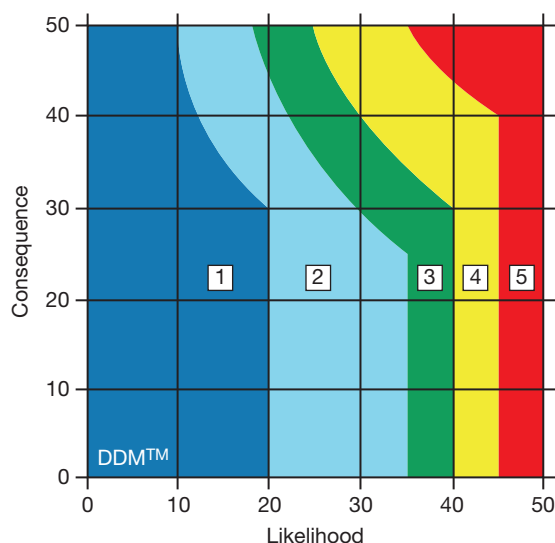


**Figure 11** Design decision method (DDM™) corrosion risk assessment. Reproduced from Kroon, D. H.; Lindermuth, D. L. *Corrosion Protection of Ductile Iron Pipe*, Paper no 04046, NACE Corrosion 2003, New Orleans, March 2004; NACE International; Houston, Texas.

2. Low – encase the pipe in polyethylene.
3. Medium – encase the pipe in polyethylene or encase the pipe and provide bonded joints.
4. High – encase the pipe in polyethylene and provide bonded joints or provide life-extension cathodic protection currents, with or without encasement.
5. Severe – apply cathodic protection.

#### 2.19.4.7 Mean Time Before Failure (MTBF)

As noted previously, there has been increasing concern relating to environmental contamination due to leaking underground storage tanks caused by corrosion, especially in North America. This led to the development of ASTM standard G 158<sup>25</sup> for assessing the condition of buried tanks and applying remedial measures to ensure integrity, which is now mandated in the United States.

One of the methods described in the standard is the so called MTBF method, which determines the likely time to failure (through wall pitting in this case) of buried storage tanks, on the basis of a statistical assessment of various soil parameters and was developed from previous published work.<sup>26</sup> The parameters used in the assessment are obtained either directly on site or from samples analyzed in a laboratory and compared to a data set of corrosion rates obtained from a number of other sites, so as to be able to demonstrate a statistical confidence level of 99%.

The standard indicates that a multivariate nonlinear regression analysis that contains the following minimum essential variables may be used, for example, as shown in **eqn [2]**:

$$E(\text{age}) = f(R, M, Cl, pH, S, SC, TS, P) \quad [2]$$

where  $E(\text{age})$  = unconditional predicated age to corrosion failure;  $R$  = resistivity;  $M$  = moisture content;  $Cl$  = chloride ion content;  $pH$  = soil pH;  $S$  = sulfide content;  $SC$  = stray current magnitude;  $TS$  = tank size; and  $P$  = tank structure-to-soil potential.

However, the standard also allows other parameters such as redox potential, sulfate content and others tests as may be considered appropriate to be included.

It is clear that while the overall procedure as described in ASTM G 158 is generally sound, it first requires the user to develop a sufficiently large data set of soil types, environmental conditions, and associated measured corrosion rates of actual structures before any assessment for further tanks can be carried out. Several commercial organizations have

developed data sets and are therefore able to carry out such assessments. The requirement for a 99% confidence level would normally be sufficient to compensate for any limitation of data for a particular parameter. In the absence of a specific database to allow an assessment, the extensive data from the original work by Romanoff<sup>2</sup> could be utilized.

Other statistical approaches to the development of predicting corrosion rates and time to failure have also been proposed by other workers.<sup>27,28</sup>

#### 2.19.4.8 Direct Measurement Approach

As an alternative (or in support of) assessment of soil corrosivity by consideration of relevant parameters, several workers have carried out direct measurement of corrosion in soils, either in the field or on soil samples brought back to the laboratory. Such measurements have used a wide range of different procedures including, for example, corrosion coupons, linear polarization resistance (LPR), electrical resistance (ER), and other electrochemical techniques.

As would by now be realized the most extensive use of exposure coupons to date was carried out by Romanoff,<sup>2,3</sup> who also described some of the earliest electrochemical measurements using what was essentially a LPR measurement, which was reported as giving very good correlation to weight loss measurements.

More recently, the use of ER and LPR probes has been applied to corrosion testing in soils, either directly<sup>29,30</sup> or as part of assessing performance of cathodic protection systems.<sup>31,32</sup>

In any system using buried probes, it should be self-evident that for meaningful information to be obtained the probes must be buried in the same soil and under the same conditions as the structure (pipeline/foundation) they are intended to represent; this is particularly important if they are being used to assess corrosivity for driven components (such as soil nails, driven piles, etc.). It should also be self-evident that an isolated probe/exposure coupon will provide only information on the inherent corrosivity of the soil. If there is a concern relating to either long-line (macro-cell) corrosion or external stray current corrosion, the probe must be electrically connected to the structure of concern. However, there must also be a method of temporarily disconnecting the probe from the structure<sup>31</sup> to allow measurements to take place (when using ER probes) or some other means of isolation (when using LPR probes).

#### 2.19.4.9 Summary

The key features associated with any of the different methods of assessment as applied to soils are the following:

- All soils contaminated with coal, coke, industrial waste, and so on are strongly aggressive.
- The lower the resistivity the more aggressive the conditions, with very low resistivity soil ( $<10 \Omega \text{ m}$ ) normally associated with strongly aggressive conditions.
- While soil/groundwater pH can range from  $<4.5$  to  $>9.5$ , its effect can be less important than the buffering capacity of the soil. Soils which are strongly alkaline buffered (measured as alkalinity to  $K_{S\ 4.3}$  of  $>1000 \text{ mmol kg}^{-1}$  or carbonate content  $>1500 \text{ mmol kg}^{-1}$ ) have sufficient residual alkalinity to be beneficial. Soils which are strongly acidic buffered (as measured by acidity to  $K_{B\ 7.0} > 20 \text{ mmol kg}^{-1}$ ) are very corrosive, while a low buffering capacity (e.g.,  $K_{B\ 7.0} < 5 \text{ mmol kg}^{-1}$ ) has little impact on overall aggressiveness.
- Where a metal component passes through different soils (e.g., a pipeline running from one soil to another or a pile/anchorage driven vertically through different soil layers) the main concern relates to the formation of differential aeration and/or concentration cells, where corrosion will be located at or just below the interfacial layer.
- Buried structures are also at risk from stray current sources (e.g., from neighboring cathodic protection systems, dc welding, dc railway systems, etc.). This risk is assessed by the change in potential on site and hence measurements of structure-to-soil potential (as required in DIN 50 929 part 3 and others systems) are only directly applicable to existing facilities. Other methods are available to assess stray current risks on site or during the design stage, using computer modeling.<sup>33</sup>
- Where the soil contains active SRB, which can be determined by the presence of sulfides, measurement on site of redox potential or bacterial assay, it can lead to microbiologically influenced corrosion (MIC) which can be severe.

It should also be noted that while some assessment methods (in particular DIN 50 929 Part 3) state that they cover both disturbed and undisturbed soil conditions, in practice the rate of corrosion of components in undisturbed soil is significantly lower. As noted previously, Romanoff<sup>3</sup> concluded that for driven piles the

portion in the undisturbed soil did not suffer significant attack. This concept has been adopted in the recent Eurocode 3 Part 5<sup>34</sup> where projected corrosion rates for a particular soil show essentially a doubling of corrosion rate depending on whether the soil conditions are compacted, driven or noncompacted.

In the case of ground anchorages,<sup>35</sup> the appropriate method of determining aggressiveness will be dependent on the type of anchor. For high strength prestressed ground anchors, the aggressiveness of soils (disturbed or undisturbed) is directly relevant, for example, in ground anchorage systems where the steel component is in direct contact with the soil (e.g., where the tendon has lost its cement grout cover) or the protective system fails (e.g., tie bars with damaged protective tape wrapping). For other anchor types, for example, soil nails or drilled piles, the steel component is inserted into undisturbed soil. For permanent anchorages, where the components are protected by a corrosion protection system, in accordance with most national standards, the steel tendon is not in direct contact with the ground; hence, it is the aggressiveness of the ground water that is most relevant, as it is the ingress of ground water through any breaks in the protective system that is of concern.

There are also many more published soil corrosivity assessment methods than just those described here, with varying degrees of acceptance and success.

Where stainless steels are being considered, their use should be on the basis of chloride content and soil resistivity. In the absence of external stray currents and for soils with groundwater pH > 4.5, suitable stainless steel grades that can be used without coatings or cathodic protection are shown in **Table 4**.

**Table 4** Use of stainless steels in soils

	<500	500–1500	1500–6000
Chloride level (mg kg <sup>-1</sup> )			
Resistivity (Ω m)	>10	>10	5–10
Suitable grades (UNS/EN)	S30400/ 1.4301	S31600/ 1.4401	S32750/ 1.4410
	S31600/ 1.4401	S44400/ 1.4521	S31254/ 1.4547
	S44400/ 1.4521		

Source: from Pierrie-Jean Cnat, *Corrosion Resistance of Stainless Steels in Soils and in Concrete*; paper presented at CECOR, Biarritz, Oct-2001.

## 2.19.5 Metallic Coatings in Soils

Several different metallic coatings have been used to provide protection to ferrous components in soils, principally galvanizing but also thermal spray coatings of zinc, aluminum, and zinc–aluminum alloys.

The performance of zinc coatings is interesting in that the mechanism of protection in soils differs from that provided in other environments (in particular natural waters and the atmosphere). In soils, initially the zinc acts as a barrier with a generally lower natural corrosion rate (compared to iron or steel) and also provides galvanic protection at any damage site where substrate is exposed. However, the longer term protection from the zinc coating is also provided by the *de facto* formation of insoluble corrosion product comprising zinc salts (mainly sulfates and carbonates), which forms as a semi protective film *in situ*. This extends the level of protection, even when the bulk of the zinc has been consumed.<sup>36</sup>

The overall corrosion rate of zinc is dependent on soil pH and resistivity, the performance of the metal being less efficient in acidic soils. The method for determining the rate of deterioration of zinc in galvanized steel sheets used, for example for culverts, was developed by California Division of Highways<sup>37</sup> (based on the work by Romanoff), as shown in **Figure 12**. Note 16 Gage galvanized steel sheet is nominally 0.06 inch (1.5 mm) thick with 3.5 mil (88 μm) thick zinc coating. Gage 14, 12, 10, and 8 galvanized sheets are respectively 0.075, 0.105, 0.135, and 0.165 inch (1.9, 2.7, 3.4, and 4.2 mm) all with nominal 3.5 mil (88 μm) zinc coating.

Aluminum coatings act only as a barrier, with no significant long term protection once the aluminum has been consumed (which can occur rapidly in alkaline soils).

The use of thermal spray zinc–aluminum alloy, in particular Zn85–Al15, has been shown to provide improved performance, compared to pure zinc coatings, in many soil environments, particularly when used with a finishing layer (typically an thin, semiporous, epoxy coating). The research indicates that the presence of the aluminum reduces the self corrosion of the coating, while still allowing the formation of *in situ* insoluble zinc salts. In fact, by slowing the rate of formation of the zinc salts the protective nature of the film is improved.<sup>38,39</sup> This allows a zinc/aluminum coating to be used in an extended range of soil types compared to a zinc



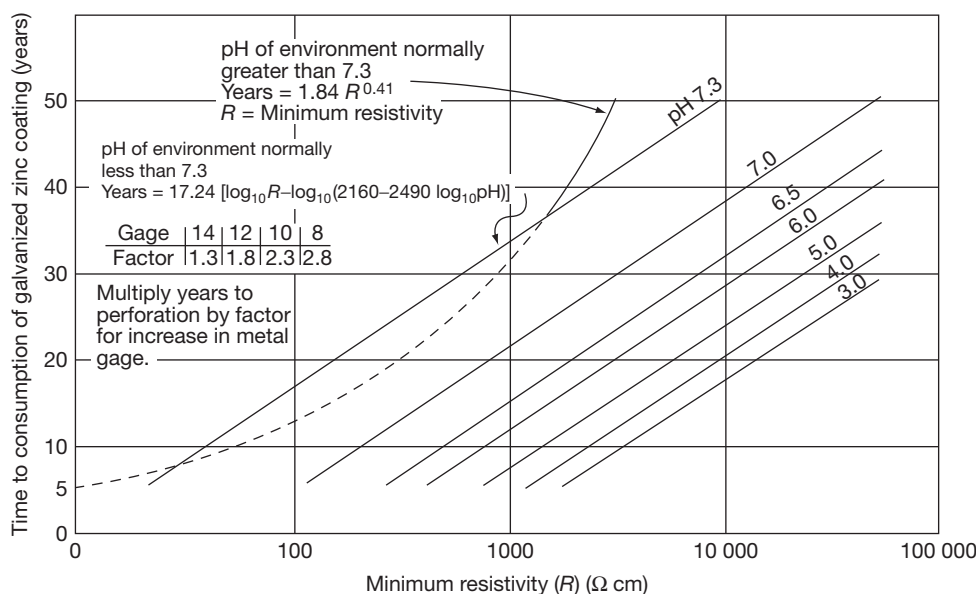


**Figure 12** Estimating service life of galvanized steel in soils. Reproduced from *NACE Corrosion Engineers Reference Book*, 3rd ed.; Baboian, R. Ed., ISBN 1-57590-127-7.

coating. However, it is not suitable for very aggressive soils, for example, acidic peaty soils ( $\text{pH} < 5$ ), polluted/contaminated soils (with cinders, slag, etc.), or marine soils below the water table (with resistivity  $< 5 \Omega \text{ m}$ ).

### 2.19.6 Corrosion Control Options

Practical corrosion control options for buried components are dependent on the structure/component type, soil environment, and impact of any resultant corrosion, and will normally comprise one or more of the following:

- do nothing
- application of a corrosion allowance
- use of selected backfill
- use of protective sheeting (for ductile iron pipe)
- application of organic protective coating (bitumen, epoxy, polyurethane, etc.)
- application of metallic coating (galvanizing, flame sprayed zinc/aluminum alloy)
- cathodic protection (galvanic or impressed current).

As can be seen, the option of do-nothing and/or inclusion of a corrosion allowance can be a practical consideration for some structures/components, where the soil aggressivity may be classed as negligible or low

(i.e., general metal loss rates of  $< 0.01 \text{ mm year}^{-1}$  or localized pitting rates of  $< 0.05 \text{ mm year}^{-1}$ ) and where the consequence of any corrosion is acceptable.

The use of a corrosion allowance is normally applied to piles where protective coatings are not suitable (see below). The corrosion allowance is an additional thickness over that necessary for structural strength to allow for metal loss over the design life (as detailed in the new Eurocode 3<sup>34</sup>).

The use of selective backfill, for pipelines or buried tanks, is another method of reducing the corrosion threat for buried components. Any backfill should be sifted to remove stones, which could damage the protective coating. Where the local soil is aggressive, for example, clay based, contaminated with cinders, low pH, or high salt content, imported material should always be used, although it has to be recognized that this is not always practical in remote sites. When selected backfill is used it is also important to ensure that the same material is applied across all components. This is because if backfills of significantly different compositions are used in different locations long-line (macro-cell) corrosion could develop. For example, in 1980 in Ortuella, near Bilbao, Spain, a butane gas tank, which was buried in predominantly limestone fill and connected to a poorly protected small bore pipe, was buried in nonselective backfill. This led to severe corrosion of the pipe causing a leak. This in turn resulted in an explosion in a school

basement and the deaths of forty-seven children and three adults.

Protective plastic sheeting has been used extensively for ductile iron pipes and, where the soil is moderately aggressive, it can provide benefit. It should be noted however, that there is a major variance between European and North American practice; in Europe plastic sheeting is applied over galvanized or thermally sprayed zinc coating plus bitumen, while in North America it has been applied over otherwise uncoated pipe.<sup>40</sup>

Protective coatings are widely applied as the principle method of corrosion control for buried components especially pipelines and buried tanks. They can also be applied to driven components (sheet steel piles, H-piles, soil nails, etc.); however, because the driving process is likely to cause significant mechanical damage to any applied coating, it cannot, in such circumstances, be considered as a primary protection measure. Nonetheless, the use of protective coating can still be beneficial, especially where cathodic protection will also be applied, as it will significantly reduce the current demand. There are a wide range of protective coatings that can be used for buried components (especially pipelines). These include tape wrap systems, bitumen, liquid applied epoxies and polyurethanes, fusion bonded epoxy, and multilayer epoxy/polyurethane coatings. Selection of an appropriate coating depends on the specific soil condition (in particular, whether the component will be below or above the water table). Mechanical damage of coatings from the soil (so called soil stress) can also be a major concern, especially for tape wrap and some epoxy systems).

For small components and cast iron, increasing use is made of metallic coatings (as summarized in Section 2.19.5) comprising galvanizing and flame sprayed zinc or zinc–aluminum alloys. However, it should be recognized that metallic coatings are more sensitive to soil pH than organic coatings; in particular, zinc coatings are not suitable for soils with  $\text{pH} < 5$  and aluminum coatings are unsuitable for  $\text{pH} > 9$ .

Successful cathodic protection can be defined as where the effective corrosion rate is  $< 0.01 \text{ mm year}^{-1}$ ; consequently use of cathodic protection may not be considered necessary for soils which are classed as ‘noncorrosive.’ However, for high risk assets (e.g., high pressure oil and gas pipelines, buried hydrocarbon storage tanks, etc.) with unacceptable consequences of failure, cathodic protection is almost universally applied, even in areas where soil aggressivity is negligible; its application to other assets is variable across the world. In some areas, in particular

in the tropics, the Middle East, North Africa and elsewhere, cathodic protection is applied to the majority (if not all) of buried facilities, for the simple reason that soils in these areas are often very aggressive.

Cathodic protection can be applied by either galvanic or impressed current systems, the decision being dependent on ground resistivity (zinc galvanic anodes are normally only used in soils with resistivity  $< 30 \Omega \text{ m}$ ; magnesium anodes  $< 150 \Omega \text{ m}$  and impressed current otherwise); but selection of the most appropriate system will be influenced by the availability of power supplies, access (for maintenance), required design life, and whether there are any concerns relating to over protection (which can lead to stress corrosion cracking).

## References

1. *Soil Survey Manual* 1993. Soil Conservation Service. U.S. Department of Agriculture Handbook 18. United States Government Printing Office, Washington, DC. (ISBN-10: 1410204170) (<http://soils.usda.gov/technical/manual>)
2. Romanoff, M. *Underground Corrosion*; National Bureau of Standards, Circular 579 (April 1957); Republished by NACE International, Houston, Texas, USA, 1989 ISBN 0-915567-47-4
3. Romanoff, M. *Performance of steel piling in soils*; Paper no 82; presented at NACE Corrosion/69: Houston, TX, 1969.
4. NACE Technical report 05101 *State-of-the-Art Survey on corrosion of steel piling in soils* (Dec-2001); published by NACE International (item no 24216): Houston, TX, USA.
5. Bonds, R. W.; Barnard, L. M.; Horton, A. M.; Oliver, G. L. *J. Amer. Water Works Assoc.* **2005**, 97(6), 88–98.
6. Booth, G. H.; Cooper, A. W.; Cooper, P. M.; Tiller, A. K.; Wakerley, D. S. *Brit. Corr. J.* **1967**, 2, 104–118.
7. Jarvis, M. G.; Hedges, M. R. *Water Environ. J.* **1994**, 8(1), 68–75.
8. Camitz, G.; Vinka, T. G. *Corrosion of Steel and Metal Coated Steel in Swedish Soils – Effects of Soil Parameters* In *ASTM STP 1013, Effects of Soil Characteristics on Corrosion*; Chaker, V., Palmer, J. D., Eds.; ASTM: Philadelphia, 1989; pp 37–53. [ISBN 0-80321-1189-4].
9. DVGW Arbeitsblatt GW9 *Merklblatt für die Beurteilung der Korrosionsgefährdung von Eisen und Stahl im Erdboden (Instruction sheet for the assessment of corrosion risk of steel and iron in contact with soil)* Aug-1971.
10. Krasnoyarskii, V. V.; Larionov, A. K. *Podzemnaya korroziya metallov i metody bor'by s nei (underground corrosion of metals and corrosion protection)*, Moscow, Ministry of Municipal Economy of the Russian Federation, 1962.
11. Harris, J. O.; Erye, D. Chapter 2.6 *Shrier Corrosion*, 3rd ed.; Butterworth-Heinemann: Oxford, 1994.
12. Pierrie-Jean Cunat *Corrosion Resistance of Stainless Steels in Soils and in Concrete*; paper presented at CEOCOR, Biarritz, Oct-2001.
13. Tylecote, R. F. *J. Archaeol. Sci.* **1979**, 6, 345–368.
14. Neffa, D.; Dillmann, P.; Bellot-Gurlet, L.; Berangere, G. *Corros. Sci.* **2005**, 47(2), 515–535.
15. Romanoff, M. *Corrosion Evaluation of Steel Test Piles Exposed to Permafrost Soils*, Paper no 81; presented at NACE Corrosion/69: Houston, March 1969.

16. Von Baeckmann, W.; Schwenk, W. *Handbook of Cathodic Protection*, 1st ed.; Portcullis Press: England, 1975.
17. DIN 50 929 Part 3. *Probability of Corrosion of Metallic Materials when Subject to Corrosion from the Outside. Buried and Underwater Pipelines and Structural Components*, Sep-1985.
18. Eyre, D.; Lewis, D. A. *Soil Corrosivity Assessment* (Contractor Report 54); Transport and Road Research Laboratory: Crowthorne, UK, 1987.
19. BS 1377-3: 1990 *Method of test for soils for civil engineering purposes – Part 3: Chemical and Electrochemical tests*.
20. DMRB BD 42/00 *Design Manual for Roads and Bridges*, Vol. 2 *Highway Structures: Design (Substructures, Special Structures and Materials)*, Section 1 *Substructures*, Part 2 *Design of embedded retaining walls and bridge abutments*, UK Highways Agency (2000) <http://www.standardsforhighways.co.uk>.
21. Smith, W. H. J. *Am. Wat. Wks. Ass.* **1968**, 60, 221–227.
22. ANSI/AWWA C105/A21.5–05 *American National Standard for Polyethylene Encasement for Ductile-Iron Pipe Systems* Dec-2005 (Appendix 1).
23. *The Design Decision Model™ for corrosion control of ductile iron pipelines* "DIPRA DDM/7–06/5 M, July 2006. <http://www.dipra.net>.
24. Kroon, D. H.; Linderemuth, D. L. *Corrosion Protection of Ductile Iron Pipe*, Paper no 04046, NACE Corrosion 2004, New Orleans, March 2004; NACE International; Houston, Texas.
25. ASTM G 158 – 98 (2004) *Standard Guide for Three Methods of Assessing Buried Steel Tanks*.
26. Bushman, J. B.; Mehalick, T. E. Statistical Analysis of Soil Characteristics to Predict Mean Time to Corrosion Failure of Underground Metallic Structures. In *Effects on Soil Characteristics on Corrosion*; ASTM STP 1013; Chakar, V., Palmer, J. D., Eds.; ASTM: Philadelphia, 1989; pp 107–118 [ISBN 0–80321–1189–4].
27. Song, G. L.; Cao, C. N.; Lin, H. C. *Corrosion* **1995**, 51(7), 491–497.
28. Kajiyama, F.; Koyama, Y. *Corrosion* **1997**, 53(2), 156–162.
29. Ansuini, F.; Yaffe, M.; Chaker, V. *Corrosion Rate Sensors for Soil, Water and Concrete*; Paper 14; presented at NACE Corrosion/95 conference: Houston, TX, 1995.
30. Li, M. C.; Han, Z.; Lin, H. C.; Cao, C. N. *Corrosion* **2001**, 57(10), pp 913–917.
31. NACE Technical Report 05017 *Report on Corrosion Probes in Soil or Concrete* Aug-2007; NACE International: Houston, TX, USA.
32. Sun, X. *Real-Time Monitoring of Corrosion in Soil Utilizing Coupled Multi-Electrode Array Sensors*, Paper no 05381; presented at NACE Corrosion/2005: Houston, TX, Apr- 2005.
33. Aylott, P.; Cotton, I.; Hassanein, A. *The Application of Modelling Systems at the Design Stage to the Mitigation of Stray Current Interference*, paper no 03706; NACE Corrosion/2003: San Diego, CA, USA, 2003.
34. EN 1993–5: 2007, *Eurocode 3: Design of steel structures – Part 5: Piling*.
35. John, G.; Littlejohn, G. S. Durability of Buried and Encased Ground Anchorages and Structural Components; Requirements for Corrosivity Assessment and Protection to Ensure Service Life, In *Ground Anchorages and Anchored Structures in Service*; Littlejohn, G. S., Ed.; Thomas Telford: London, 2008, pp 263–272.
36. A Comprehensive Ductile Iron Pipeline System; Pont-a-Mousson SA: France, 1992.
37. *NACE Corrosion Engineers Reference Book*, 3rd ed.; Baboian, R. Ed., ISBN 1–57590–127–7.
38. Nouail, G. *A New Coating for Ductile Iron Pipes based on Zinc-Aluminium 85–15 alloy*; 3R International: Rohre Rohrleitungsbau Rohrleitungstransport, 2001; Vol. 40, Chapter 2, pp 120–124.
39. Nouail, G.; Tournier, A. *Utilisation des alliages de zinc-aluminium comme protection anticorrosion - application au revêtement des tuyaux en fonte*, paper presented at CEOCOR Colloque Biarritz, 2001.
40. Rajani, B.; Kleiner, Y. J. *Am. Wat. Wks Assoc.* **2003**, 95(11), 110–125.
41. *Corrosion Atlas*, 3rd ed.; Compiled by Doring, E. D. D.; Elsevier Science: London, 1997; (Item 06.05.05.01).

## Further Reading

Chaker, V.; Palmer, J. D., Eds.; *Effects of Soil Characteristics on Corrosion*; ASTM STP 1013 1989, ISBN 0–8031–1189–4.

Escalante, E., Ed.; *Underground Corrosion*, ASTM STP 741, 1981, ISBN: 0–8031–0703-X.

*Handbook of Corrosion Engineering*, Roberge, P. R.; McGraw-Hill Professional, 1999. ISBN 0070765162.

Littlejohn, G. S., Ed. *Ground Anchorages and Anchored Structures in Service*, Institute of Civil Engineers; Thomas Telford Publishing: London, 2008, ISBN 978–07277–3561–4.

*Practical Handbook of Corrosion Control in Soils*, 1st ed.; Bradford, S. A., Ed.; CASTI Publishing Inc.: Edmonton, Alberta, 2006. ISBN 1-894038-48-7.

Romanoff, M. *Underground Corrosion*, National Bureau of Standards, Circular 579 (April 1957); Republished by NACE International: Houston, TX, USA, 1989. ISBN 0–915567–47–4.

Wilmott, M. J.; Jack, T. R. Corrosion by Soils. In *Uhlig's Corrosion Handbook*, 2nd ed.; Winston, R. R. Ed.; John Wiley & Sons, 2000, ISBN 978–0–471–15777–9.

## 2.20 Corrosion in Microbial Environments

**J. F. D. Stott**

CAPCIS Ltd., CAPCIS House, 1 Echo Street, Manchester M1 7DP, UK

© 2010 Elsevier B.V. All rights reserved.

---

<b>2.20.1</b>	<b>Introduction</b>	1171
<b>2.20.2</b>	<b>Microorganisms</b>	1171
2.20.2.1	General	1171
2.20.2.2	Bacteria	1171
2.20.2.3	Fungi	1172
2.20.2.4	Algae	1172
2.20.2.5	Biofilms	1172
<b>2.20.3</b>	<b>Types of MIC</b>	1173
<b>2.20.4</b>	<b>Corrosion by the Sulfate-Reducing Bacteria</b>	1174
2.20.4.1	Situations Effected	1174
2.20.4.2	Mechanism of SRB Corrosion of Iron and Low-Alloy Steel	1176
2.20.4.3	SRB-Mediated Corrosion of Stainless Steel Alloys	1176
2.20.4.4	MIC of Copper and Copper Alloys	1178
<b>2.20.5</b>	<b>Microbially Influenced Acid Corrosion</b>	1179
2.20.5.1	Sulfuric Acid Corrosion by Sulfur-Oxidizing Bacteria	1179
2.20.5.2	Acid Attack on Concrete	1180
2.20.5.3	Acid Corrosion by Fungi	1181
<b>2.20.6</b>	<b>MIC of Higher Alloys by General Aerobic Biofilms in Natural Seawaters</b>	1182
<b>2.20.7</b>	<b>Other Microorganisms Associated with MIC</b>	1182
<b>2.20.8</b>	<b>Testing for MIC Activity</b>	1183
<b>2.20.9</b>	<b>MIC Risk Assessment Based on Operating Conditions</b>	1185
2.20.9.1	Presence of Water	1185
2.20.9.2	Salinity	1185
2.20.9.3	Temperature	1185
2.20.9.4	pH	1185
2.20.9.5	Anaerobic Conditions	1186
2.20.9.6	Nutrient Status of Water Phase	1186
2.20.9.7	Flow Rate	1186
2.20.9.8	Cleaning Frequency	1186
2.20.9.9	Use of Antimicrobial Chemical Treatments	1186
<b>2.20.10</b>	<b>Control of MIC</b>	1186
2.20.10.1	General Principles	1186
2.20.10.1.1	Provision of a nonaggressive surround	1186
2.20.10.1.2	Cathodic protection	1186
2.20.10.1.3	Protective coatings	1186
2.20.10.1.4	Biocides	1187
2.20.10.2	Biocide Treatments	1187
2.20.10.3	Alternatives to Biocide Treatments	1188
<b>References</b>		1189

---

## Glossary

**Anaerobic** In the absence of oxygen, cf. aerobic.

**Autotroph** An organism that produces complex organic compounds from inorganic carbon dioxide and an external source of energy, such as sunlight or chemical reactions of inorganic compounds. All green plants and certain specialized bacteria are autotrophs.

**Bacteria** Unicellular microorganisms, typically a few micrometers in length and having many shapes, including spheres, rods, and spirals.

**Biocide** Usually refers to a chemical agent that is intended to kill microbiological life, as distinct from sterilization by heat or radiation.

**Biofilm** A complex aggregation of microorganisms marked by the excretion of a protective and adhesive matrix and also often characterized by surface attachment, structural heterogeneity, genetic diversity, and complex community interactions.

**Biogenic** Arising from living processes.

**Biostud** One of a set of small, replaceable metal coupons mounted inside a side stream, used to monitor biofilm.

**Chlorination** The process of adding elemental chlorine, hypochlorous acid, or hypochlorite ions in solution to water as a biocide to reduce the prevalence of microorganisms.

**Fungi** Microorganisms with cells much larger than bacteria that digest their food externally, absorbing nutrient molecules into their cells. They were originally classified as simple plants; however, they have been separated as heterotrophs.

**Heterotroph** An organism that requires organic substrates to get its carbon for growth and development in contrast with autotrophs, which use inorganic carbon dioxide as their sole carbon source. All animals are heterotrophic, as well as fungi and many but not all bacteria.

**Mesophilic** Microorganisms that grow optimally within the temperature range 20–40 °C.

**Metabolism** The complete set of chemical reactions that occurs in living cells. These processes are the basis of life, allowing cells to grow and reproduce, maintain their structures, and respond to their environments.

**Microbially-influenced corrosion (MIC)** The deterioration of the essential properties of a

material due to reactions caused or promoted by the activity of microorganisms.

**Microorganism** Or *microbe* is an organism that is microscopic (too small to be seen by the human eye). The study of microorganisms is called microbiology. Microorganisms can be bacteria, fungi, archaea, or protists, but not viruses and prions, which are generally classified as nonliving.

**mg l<sup>-1</sup>** A concentration term to define the amount of a substance which is the practical numerical equivalent to the derived SI unit of milligrams per cubic decimeter (mg dm<sup>-3</sup>).

**Nitrate-reducing bacteria (NRB)** Nitrate-reducing bacteria, comprising many groups of bacteria that use nitrate as an oxidizing agent for their energy-generating metabolism, reducing it to nitrogen gas, sometimes with the generation of nitrite or other nitrogen oxides as by-products.

**Planktonic** Bacteria that are suspended or free floating in a liquid environment.

**Redox** Reduction/oxidation potential. High redox potentials ( $E_h$  positive) reflect oxidizing conditions, whereas low redox potentials ( $E_h$  negative) reflect reducing conditions.

**Sessile** Stationary bacteria that are permanently attached to a surface as a biofilm.

**Side stream** A small test pipe, generally equipped with a series of isolation valves, through which water flows and designed to hold multiple flush mounted, replaceable metal studs for the measurement, analysis, or testing of biofilms in industrial water systems.

**Souring** The appearance of hydrogen sulfide (H<sub>2</sub>S) in production fluids as a consequence of the introduction and activity of sulfate-reducing bacteria, which generate H<sub>2</sub>S within a waterflooded zone of (particularly) a subsurface petroleum reservoir.

**Sulfate-reducing bacteria (SRB)** Sulfate-reducing bacteria, comprising several groups of anaerobic bacteria that use sulfate as an oxidizing agent for their energy-generating metabolism, reducing it to sulfide, which appears as H<sub>2</sub>S, sulfide ions, metal sulfides, or a combination of these forms according to the conditions.

**Substrate** Any substance required for the growth or metabolism of a microorganism, other than materials required in trace quantities only.



**Thermophilic** Microorganisms that grow optimally at temperatures above the mesophilic range and most typically at greater than 55 °C.

**Water injection** A method used in crude oil production where water is injected back into the subsurface petroleum reservoir to increase pressure and thereby stimulate production.

### 2.20.1 Introduction

‘Microbiologically-induced corrosion,’ nowadays more commonly termed ‘microbially-influenced corrosion’ (MIC), is a rather special case of the widespread occurrence of biodeterioration of materials. It is important to recognize that MIC of metals is not fundamentally different from other types of aqueous electrochemical corrosion. Microorganisms do not directly consume metals in the way that they do various types of organic substances; it is rather that aggressive environments are created by certain types of microorganisms as by-products of their energy-obtaining metabolism.

Microorganisms can be viewed as ‘catalytic’ entities, bringing about chemical reactions that would otherwise not occur because of their high activation energy. Such processes may involve the production of aggressive chemical agents, such as acids, or the consumption of substances that are important in corrosion reactions, such as oxygen or nitrite corrosion inhibitors. Alternatively, the physical presence of microorganisms may form a slime or poultice, leading to differential aeration corrosion or crevice corrosion. Some microorganisms also chemically break down the desirable physical properties of lubricating oils and protective coatings.<sup>1–3</sup>

Microorganisms, including the corrosion-inducing microorganisms, are present almost everywhere in soils, freshwater, seawater, and air. Therefore, the mere presence of microorganisms in an environment does not necessarily indicate a corrosion problem. What is important is the number of microorganisms of the relevant types. The salient characteristics of these microorganisms from the engineer’s viewpoint are that they are small, ubiquitous, potentially very rapid-growing, and subject to certain common restraints such as temperature, pH, and nutrient availability. A corrosion problem exists only when conditions become favorable for a specific microbial population to ‘explode,’ giving rise to millions of cells per gram of environmental material. Even then, most microorganisms are harmless from the standpoint of corrosion;

therefore, it is important that microbiological assessment be type specific.

The role of microorganisms in the corrosion of metals was the subject of a number of classic review articles in the 1970s and 1980s<sup>4–7</sup>; though now somewhat dated, they are still worth reading for their clarity and objectivity. For more detailed recent reviews of the subject, the reader is referred to European Federation of Corrosion Report, number 29, published in 2000,<sup>8</sup> the ‘*Practical Manual on Microbiologically Influenced Corrosion*,’ published by NACE in 2001,<sup>9</sup> the very practical and engineering-orientated report titled ‘*Microbiologically Influenced Corrosion and Biofouling in Oilfield Equipment*,’<sup>10</sup> also published by NACE, and the ‘*Microbiologically Influenced Corrosion Handbook*’ published by the Industrial Press, USA.<sup>11</sup> For a detailed review of emerging tools and modern trends in MIC technology, the reader is referred to the research review article by Videla and Herrera.<sup>12</sup>

### 2.20.2 Microorganisms

#### 2.20.2.1 General

Microorganisms or ‘microbes’ are commonly defined as living entities that are too small to be visible to the human eye. The main differentiating feature, other than size alone, between microorganisms and larger, more complex organisms is that there is little or no degree of cell differentiation, one cell being able to emulate the functions of the whole organism. The microorganisms traditionally comprise bacteria, fungi, algae, and small unicellular animal-like protists, but not the minute and very simple (in biological terms) viruses and prions, which are now generally classified as ‘nonliving.’ Microorganisms are often described as single-celled (unicellular) organisms; however, some unicellular protists are visible to the human eye, and some multicellular species are microscopic. It seems to be a general biological principal that every criterion we devise for defining and classifying things breaks down at some point. We need to remember that classification – the process of putting objects into ‘pigeon holes’ – is something fundamental to human beings rather than nature. However, such classification is useful and necessary in reducing chaos to some semblance of order.

#### 2.20.2.2 Bacteria

The true bacteria are unicellular microorganisms, neither animals nor plants, but belonging to a separate and more primitive domain of organisms called

prokaryotes. They are a few micrometers in size and have many different shapes, including spheres, rods, and spirals. Though often occurring in pairs, clusters, or chains owing to incomplete separation after cell division, such aggregates are not essential to their existence. Bacteria are ubiquitous, living in almost every possible habitat on the planet, including soil, underwater, and even deep inside the earth's crust. Some types are aerobic, requiring oxygen, whereas other types are anaerobic, growing in the absence of oxygen.

The defining characteristic of bacterial cells, apart from their very small size, is that they do not contain a nucleus or other membrane-bound discrete structures having specialized functions (organelles). Bacteria are also far more metabolically varied than higher organisms, and the various diverse species are able to obtain energy by carrying out a wide range of chemical reactions. Most types of bacteria are heterotrophs, meaning that they do not fix their own carbon through photosynthesis, but use the oxidation of organic carbon fixed by other organisms. However, a few specialized bacteria carry out inorganic reactions involving oxidation or reduction of nitrogen, sulfur, or iron. It is the activities of these latter groups, the so-called chemolithotrophic bacteria, that most concern the corrosion engineer, even though they represent a tiny minority of the bacteria in the biosphere.

### 2.20.2.3 Fungi

Fungi were originally classified as plants; however, they have more recently been separated, as they are heterotrophs and are now thought to be more closely related to animals than to plants. The fungi are now placed in their own kingdom. Fungal cells are much larger than those of bacteria and always contain nuclei. The simplest fungi are yeasts, which are completely unicellular, as are bacteria, and reproduce by 'budding.' Most fungi are filamentous organisms, often referred to as moulds, comprising a tangled mass of filaments (hyphae), known collectively as a mycelium. The higher fungi include most common mushrooms, which are clearly large and multicellular, at least in one phase of their life cycle, but are biochemically and genetically closely related to the microscopic fungi. The fungi of most interest to the corrosion engineer are those that attack some types of polymers and paints and the 'kerosene fungus,' which secretes organic acids and is implicated in the corrosion of aircraft integral fuel tanks.

### 2.20.2.4 Algae

Algae are pigmented organisms (most commonly green, brown, or red) possessing the same photosynthetic mechanism as higher plants but having no true tissues, despite the enormous size of some marine algae (seaweeds). Their main interest to the engineer is the development of fouling masses in environments where light can penetrate, giving rise to microenvironments beneath which harmful bacteria may proliferate.

### 2.20.2.5 Biofilms

Though bacteria and other microorganisms can and do exist in the free floating state, they all have a propensity to attach to surfaces, where they proliferate, giving rise to slime and deposit formation. Microorganisms that float or swim in water are called *planktonic* bacteria. Microorganisms that attach to a substrate (e.g., metal) surface are called *sessile* bacteria. Biofilms comprise accumulations of living and dead microorganisms and their secretions together with entrained organic and inorganic debris. Microbial corrosion generally occurs beneath such biofilms. In addition to corrosion, biological fouling in industrial water systems can, for example, result in decreased efficiency of heat exchangers and plugging of tubes; slimes in cooling towers can cause rot of timber slats. Biofilm that detaches from surfaces can plug pumps and pipe work in cooling systems.

Most of the microorganisms present in industrial systems are present in biofilms and the most common types of biofilms are largely bacterial in nature. As noted earlier, various types of bacteria can grow with or without oxygen. Bacteria that need oxygen to grow are called *aerobes* or aerobic bacteria. Bacteria that need little or no oxygen to grow are called *anaerobes* or anaerobic bacteria. All these broad types of bacteria have a role in a typical biofilm. [Figure 1](#) shows the steps in biofilm.

Biofilm formation begins when (1) small amounts of organic material attach to the metal surface; (2) microbes then attach onto the organic layer; (3) a thick biofilm develops; (4) the biofilm becomes thick enough to exclude oxygen from the metal surface and forms an anaerobic zone near the surface; (5) aerobic and anaerobic bacterial species develop where conditions are most favorable for them; the biofilm thickens until parts of it are torn away by flowing water. The process begins again when the detached biofilm adsorbs onto another part of the

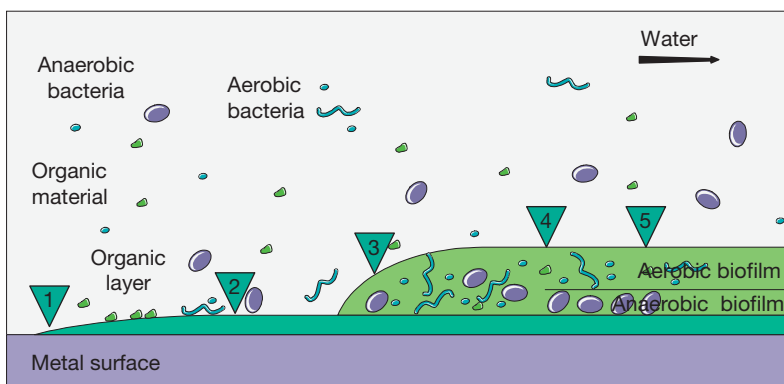


**Figure 1** Steps in biofilm formation.

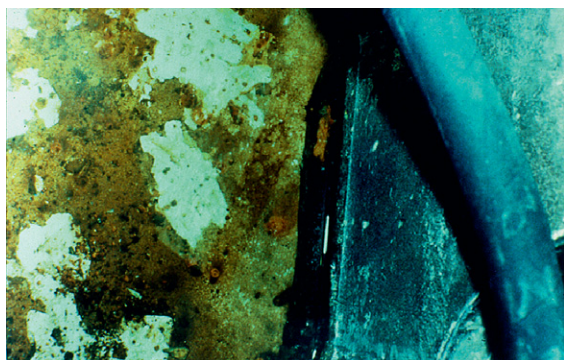


**Figure 2** Dense biofilm on a metallic surface.

metal surface. The time required for this process is very much dependent on temperature and nutrient availability, but may be as short as 10–14 days under favorable conditions. The biofilm can thus provide very favorable conditions for both anaerobic and aerobic bacteria, growing in consort. Localized corrosion can develop on the metal surface and can cause corrosion pitting. An example of dense biofilm formation in an industrial water system is shown in [Figure 2](#).

Although it is true that corrosion-inducing microorganisms do not exist in isolation, but rather they form part of the complex microbiological consortia of biofilms, there has nevertheless been a tendency by recent reviewers to approach the subject of MIC from the point of view of the microbiologist rather than the engineer and to emphasise the complexity and diversity of such communities. It is not really necessary to either identify or to understand in detail these multifarious microbial populations in order to

comprehend the presence and activity of specific problem microbes.

### 2.20.3 Types of MIC

As emphasized in [Section 2.20.1](#), the immediate cause of corrosion is electrochemical in all cases we are about to consider. The ways in which metabolic activities of certain microorganisms are believed to bring about or contribute to electrochemical corrosion may be broadly categorized as follows:

- (a) Direct chemical action of metabolic products such as organic acids, sulfuric acid, or reduced sulfur compounds, especially sulfides or chelating agents.
- (b) Generation of an electrochemical cell by deposition of cathodic and conducting metal sulfides, often in conjunction with mechanism (a).
- (c) Cathodic depolarization by removal of hydrogen associated with anaerobic growth, frequently suggested to occur in conjunction with mechanisms (a) or (b) or both. This proposed mechanism is contentious and is now less widely believed than it formerly was.
- (d) Localized electrochemical effects because of changes in oxygen concentration, pH, etc., which establish local differential cells often in conjunction with mechanisms (a) and (b). The physical presence of the biomass in itself contributes to this mechanism.
- (e) Removal of inhibitory substances, most notably nitrite corrosion inhibitors but also possibly amines.

- (f) Direct degradation of protective coatings by utilization of one or more of their constituents as a source of carbon, thereby reducing the efficiency of the protective system.

The most important of these mechanisms will now be considered in turn, with brief reference to illustrative case histories and with a particular emphasis on the monitoring of trends and the identification of remedial measures.

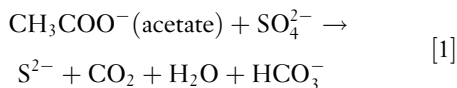
## 2.20.4 Corrosion by the Sulfate-Reducing Bacteria

### 2.20.4.1 Situations Effected

The most important group of microorganisms associated with corrosion belongs to the rather diverse group of bacteria known as the sulfate-reducing bacteria (SRB); the vast majority of MIC failures are related to their activities.

SRB live in oxygen-free environments (i.e., SRB are anaerobic bacteria), where they obtain their required carbon from organic nutrients and their energy from the reduction of sulfate ions to sulfide. SRB will only flourish and cause damage if they can obtain sufficient sulfate, which is abundant in many freshwaters, seawater, and soils. Sulfide appears as dissolved or gaseous hydrogen sulfide ( $\text{H}_2\text{S}$ ),  $\text{HS}^-$  ions,  $\text{S}^{2-}$  ions or metal sulfides, or a combination of these according to conditions. Sulfides are highly corrosive to many metals. In the case of iron and mild steel, the characteristic black iron sulfide ( $\text{FeS}$ ) corrosion products liberate  $\text{H}_2\text{S}$  on acid treatment, distinguishing it from black iron oxide (magnetite). The corrosion products are often loose and when dislodged exhibit pits lined with bright metal corresponding to areas of anodic dissolution, but are sometimes also hard and adherent.

The most commonly encountered SRB type belongs to the genus *Desulfovibrio* (Figure 3). In natural conditions, SRB grow in association with other microorganisms and use a range of carboxylic acids and fatty acids, which are the common by-products of other microorganisms. They couple the oxidation of these carbon sources to sulfate reduction. For example:



Bacteria of this type can also use molecular hydrogen instead of organic carbon, to sulfate reduction:

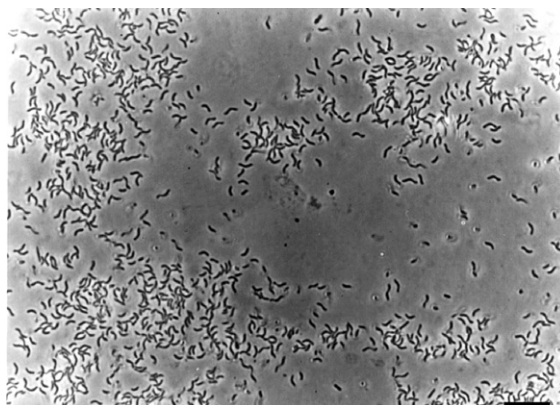
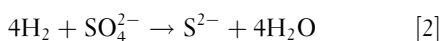


**Figure 3** *Desulfovibrio*, a common genus of SRB as viewed under a phase contrast microscope. Bar = 10  $\mu\text{m}$  in length.

Conditions at the base of even thin biofilms can be ideal for growth of SRB, with high organic nutrient status, no oxygen, low oxidation–reduction (redox) potential, and protection from biocidal agents. SRB activity can thereby produce active sulfide-mediated corrosion even in systems where the bulk liquid phase has a low nutrient status, a high oxygen concentration, and will not support growth of anaerobic bacteria.

Most types of SRB will only grow in the pH range 5–10 and the temperature range 5–45  $^{\circ}\text{C}$ , up to a pressure limit of  $\sim 500$  atm,<sup>13</sup> although some less common groups of SRB have the ability to grow at elevated temperatures (thermophiles) up to at least 70  $^{\circ}\text{C}$ . The thermophiles are most commonly encountered in produced water from hot petroleum reservoirs; however, Postgate,<sup>14</sup> in his definitive monograph on the microbiology of the SRB, cites two cases of corrosion by thermophilic SRB activity, one case being in a tank of hot molasses at a sugar refinery, the second being a transformer tank buried in London clay, where the temperature was 60–80  $^{\circ}\text{C}$  for long periods.

The muddy bottoms of any relatively stagnant bodies of water with a high biological oxygen demand often support massive growth of SRB, as may waterlogged soils. Any metallic installations buried or immersed in such environments can be expected to suffer badly from SRB-mediated external MIC. The most serious economic problem is to pipelines, though sheet piles, hulls of ships, piers, etc., are also frequently attacked. In some instances, cast iron pipes of 0.25 in. thick have become perforated within a year under such conditions, while perforation rates 1–2 mm year<sup>-1</sup> at ambient temperature are not uncommon. Under anaerobic/aerobic cycling



conditions, where SRB-mediated sulfide corrosion may be exacerbated by the production of elemental sulfur, and/or at elevated temperatures, corrosion rates (CRs) of several millimeters per year may be encountered. This type of corrosion typically takes the form of shallow pitting attack, which may be either widespread or highly localized. A classic example of such morphology is shown in [Figure 4](#); this is a case of unprotected sheet steel piling attack in highly SRB-infested estuarine mud. The metal surface was grit blasted to remove the copious black iron sulfide corrosion product.

Oil field water handling systems, especially wet crude oil production pipelines and water injection pipe work, are beset by internal corrosion problems due to SRB-mediated internal MIC, most commonly at the bottom of line locations of water and particulate drop out. Low-velocity lines and storage tanks, aircraft jet fuel tanks and lines, hydrotest waters, cooling waters, and facilities handling wastewaters suffer similarly.

The petroleum production industry has been particularly plagued by the activities of SRB, because it handles large volumes of deaerated water. These waters can become very 'sour' with  $\text{H}_2\text{S}$  if infection with SRB occurs. The phenomenon of unexpected increase in  $\text{H}_2\text{S}$  concentrations in produced fluids from petroleum reservoirs (reservoir souring) has been observed over a period of many years in different areas of the world.<sup>15–18</sup> It is a very serious problem for that industry and considerable money has been invested in biocide-treatment programs for water injection, with the principal aim of killing or controlling this group of microorganisms. For a more

detailed modern appraisal of the problems of microbiological control in oilfield water systems, the reader is referred to the book by Davies and Scott.<sup>19</sup>

A large-scale study of external MIC of buried steel structures at 59 sites in the United Kingdom<sup>20,21</sup> lead to the suggestion that aggressive sites were characterized by soil resistivity of less than  $2000\ \Omega\text{ cm}$  or a mean redox potential more negative than  $+400\text{ mV}$  (on the hydrogen scale) at pH 7. Borderline cases were classified according to the water content – those containing more than 20% water being deemed aggressive soils. Similarly, all soils with a mean soluble iron content of over  $120\ \mu\text{g g}^{-1}$  were found to be aggressive. A particularly corrosive situation occurs when  $\text{H}_2\text{S}$  diffuses upwards into the aerated zone, where it becomes oxidized by air to elemental sulfur.<sup>22</sup> An example of external MIC of a cast iron water main is shown in [Figure 5](#). This was one of the most rapid incidences of its kind that has been observed and was accompanied by deposition of elemental sulfur. The site was made-up ground on a new housing estate in the south of England, where the soil type should have been 'nonaggressive' by the foregoing criteria. In fact, the lower horizons were waterlogged with sulfate-rich spring water and the SRB were highly active.  $\text{H}_2\text{S}$  diffused upwards into the aerated zone, where it became partly oxidized by the air to elemental sulfur.

Numerous examples of corrosion of stainless steel and higher active/passive alloys involving sulfide production by SRB have been published.<sup>23,24</sup> The mechanism is discussed in [Section 2.20.4.3](#).

Copper alloys are highly susceptible to rapid and severe biogenic sulfide corrosion if conditions allow the growth of SRB (see [Section 2.20.4.4](#)).



**Figure 4** Typical morphology of SRB-mediated MIC of carbon steel, an example from sheet steel piling.

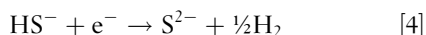
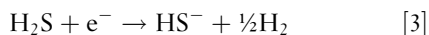


**Figure 5** Massive 'black water' corrosion of pipe work under wet lay up because of SRB activity.



### 2.20.4.2 Mechanism of SRB Corrosion of Iron and Low-Alloy Steel

The mechanism of SRB-mediated sulfide corrosion of ferrous metals<sup>25</sup> involves both  $\text{H}_2\text{S}$  and  $\text{FeS}$ . CRs tend to be slow at first and then accelerate with time.<sup>26</sup> Initially, semiprotective iron sulfide layers form, which typically reduce the generalized CR compared with sulfide-free environments. Later, sometimes after an exposure period of months, the iron sulfide layer spalls locally and never reforms; in the case of petroleum production pipelines, this localized spalling may be initiated by sand erosion. The remaining iron sulfide film is both electrically conducting and cathodic to carbon steel, thus galvanic attack initiates at the site of the iron sulfide film breakdown, driven by the huge surface area of the  $\text{FeS}$  cathode. Costello<sup>20</sup> has argued convincingly that the principal cathodic reactions are as follows rather than the mechanism of hydrogen ion reduction:



This postulate is supported by the relative pH independence of SRB-mediated sulfide corrosion, except where the pH of the environment is too high or too low to permit SRB growth.

This mechanism is thus a combination of ‘Type (a)’ MIC, direct chemical action of a metabolic product, in this case  $\text{H}_2\text{S}$ , and ‘Type (b)’ MIC (see [Section 2.20.3](#)), the generation of an electrochemical cell, in this case an iron or steel anode with an iron sulfide cathode.

Furthermore, the hydrogen evolved from the cathodic part of the reaction can be used as a source of reducing power by many strains of SRB and coupled to sulfate reduction to generate even more sulfide, a process that is catalyzed by the hydrogenase enzyme. The overall process thus becomes a type of feedback loop: the more the hydrogen available, the more the sulfide generation; the more the sulfide, the more the corrosion; the more the corrosion, the more the hydrogen generated; and so forth. A classic example of this is the so-called ‘black water corrosion’ of carbon steel pipe work under long-term wet lay up (most especially, following hydrostatic testing), in which more iron sulfide may be generated compared with the stoichiometric amount of organic carbon that is available to ‘fuel’ sulfate reduction ([Figure 6](#)). A schematic representation of the mechanism of SRB-mediated MIC of iron or low-alloy steels is presented in [Figure 7](#).



**Figure 6** SRB-mediated external MIC of a cast iron water pipe accentuated by elemental sulfur.

Some workers have suggested that hydrogenase can even directly depolarize steel surfaces by removal of bound atomic hydrogen. This suggested mechanism, the ‘direct cathodic depolarization theory’ (‘Type (c)’ MIC – see [Section 2.20.3](#)), was very prominent in the early literature on SRB-related corrosion and is still cited by some workers, though it has lost widespread acceptance in the light of work showing that hydrogenase extracts are only active on combined, molecular hydrogen ( $\text{H}_2$ ).

[Figure 8](#) shows a longitudinal section of oilfield water gathering line, which suffered a through wall internal perforation because of SRB-mediated MIC. Note the thick layer of black, iron sulfide corrosion product, which has broken down locally to allow massively concentrated localized corrosion at the resulting anodic site surrounded by an overwhelmingly large volume of cathodic and conductive  $\text{FeS}$ . The surface oxidation of the thick  $\text{FeS}$  layer to give a layer of brown rust (with included elemental sulfur) is due to air exposure of the specimen and is typical.

### 2.20.4.3 SRB-Mediated Corrosion of Stainless Steel Alloys

The phenomenon of severe SRB-mediated MIC of stainless steels and higher active/passive alloys is best termed as microbially assisted, chloride-induced pitting attack. It should not be confused with the related but separate mechanism of pitting and crevice corrosion of these materials promoted by aerobic biofilms in seawater, which is discussed in [Section 2.20.6](#). SRB-mediated effects are generally more rapid and severe.

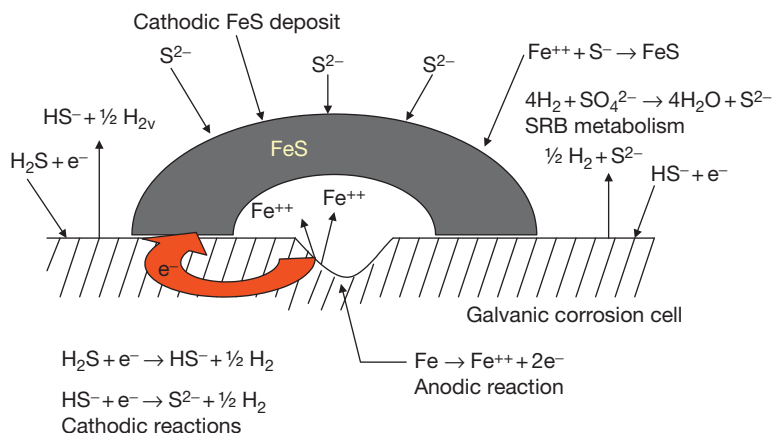


**Figure 7** SRB-mediated galvanic corrosion cell.



**Figure 8** SRB-mediated internal MIC of an oilfield water gathering line.

Active/passive alloys are susceptible to localized pitting by chloride ions. Reduced sulfur compounds produced by SRB, primarily sulfide but also traces of other substances such as thiosulfate, are believed to bind to the metal surface and catalyze the initiation of the stable pitting process at much lower chloride concentrations and at lower temperatures than would otherwise be the case. Once a pit is established, the anodic reaction generates acidic conditions, accelerating the CR and causing flask-shaped cavities to form. This is totally different from the shallow pitting attack of low-alloy materials exemplified in [Figures 4, 5 and 8](#). The pits may be concealed beneath ferric hydroxide and the process is often associated with copious amounts of brown colored biological slime, containing iron-oxidizing bacteria known as *Gallionella*. Bacterial metabolism is only

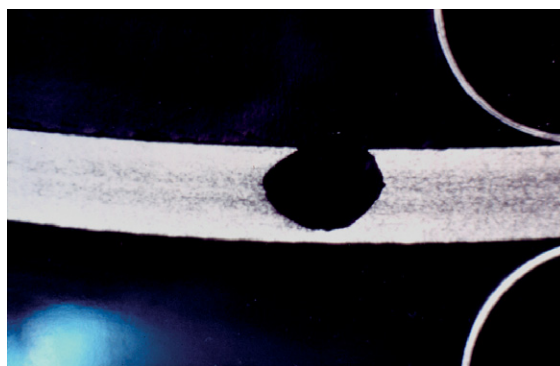


**Figure 9** Microbially assisted chloride-induced internal pitting attack on AISI 304 stainless steel pipe work showing classic flask-shaped pit.

involved in the pit initiation stage. Once the pit has formed and acidic chloride conditions develop within, the pit propagation process is the same as with any other case of chloride-induced pitting. Claims that MIC of stainless steels is characterized by a particular pit morphology that is different from conventional chloride-induced pitting attack should therefore be viewed with scepticism.

An example of this type of corrosion occurred when AISI 304 grade stainless steel pipe work was installed at a newly built chemical plant in the tropics ([Figure 9](#)). A hydrostatic pressure test was made using local water, which was subsequently left *in situ* in a static condition for several weeks. The 5 mm thick wall pipe work began to leak in hundreds of places at the 6 o'clock position. Initially, futile attempts were made to clamp the pits but much of

the pipe work eventually had to be replaced. The pipes were found to contain slime masses of iron-oxidizing bacteria of the genus *Gallionella* (Figure 10). The aerobic iron bacteria had depleted all the dissolved oxygen, allowing SRB to become active, giving rise to sulfide formation. The water was warm, stagnant, but relatively low with respect to chloride ion concentration ( $20\text{--}30\text{ mg l}^{-1}$ ); the presence of the extensive slime had allowed an inorganic chemical mechanism to initiate and run rife at chloride levels that would conventionally be regarded as relatively safe. This case history stands as a good example of the interaction of 'microbiological' and 'conventional' corrosion processes.

#### 2.20.4.4 MIC of Copper and Copper Alloys

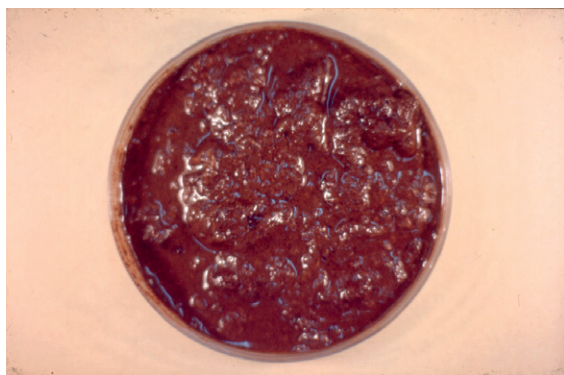
There is a widespread belief that copper and its alloys are toxic to microorganisms and are therefore not susceptible to MIC. This notion is false; copper alloys are much less toxic to bacteria than they are to macrofouling organisms such as seaweed or shellfish; they suffer severe attack by sulfide if conditions allow the growth of SRB. 'Under-deposit' or 'under-fouling' pitting corrosion of copper–nickel heat exchanger tubes due to biogenic sulfide, produced by SRB, has frequently been observed.

Figure 11 shows a gunmetal impeller located in a polluted harbor, which failed in a matter of weeks after the pump was switched off because of growth of SRB in the stagnant pump. The component had previously given 2 years of trouble-free operation in aerated seawater.

Numerous cases of mysterious 'under-deposit' or 'under-fouling' pitting corrosion of copper–nickel heat exchanger tubes have been observed, especially

in marine environments. Many of these failures are demonstrably due to biogenic sulfide produced by SRB. Copper–nickel alloys are much more susceptible to the initiation of MIC by SRB-generated sulfides during the first few weeks of exposure to the operating environment, at which time the protective oxide film is incompletely formed. MIC of aged copper–nickel alloys, with a well-formed oxide film, is also known, but is much less common than for newly exposed material and seems to require considerably more severe conditions, that is exposure of higher concentration of sulfide for a longer duration. The promotion of protective oxide films and avoidance of exposure to stagnant contaminated water during early exposure is critical in order to avoid such problems. If wet lay up with contaminated water is unavoidable, the use of an organic biocide treatment is highly recommended.

Although the most severe corrosive effects on copper alloys, including cupronickel, have typically been associated with microbially generated sulfides, attention has also been drawn to other activities of surface-associated microbial populations, which in some cases can lead to localized corrosion. These are the production of acidic metabolites, the binding of copper by microbial cells and their extracellular slimes, and the alteration of the nature and porosity of the oxide layer because of biofilm penetration. In particular, it should be recognized that the level of acidity at the biofilm metal interface may be much higher than that of the bulk fluid. It has been reported that a biofilm-forming marine bacterial species increased the corrosion potential of copper by 145 mV and the CR fivefold in a seawater medium and that electrochemical impedance spectroscopy data has shown CRs under biofilms in water of pH



**Figure 10** *Gallionella* slime mass from corroded AISI 304 stainless steel pipe work.

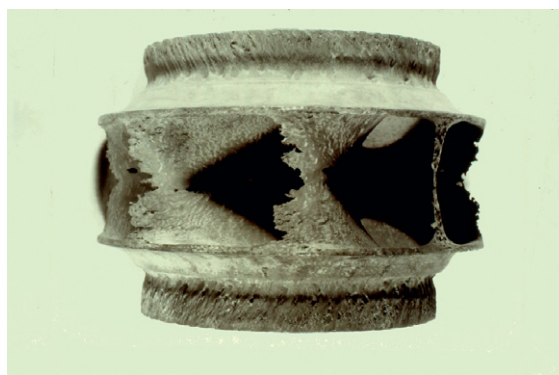


**Figure 11** SRB-mediated sulfide corrosion of a gunmetal pump impeller.

8 to be equivalent to those observed under abiotic conditions at pH 6.8.

It is worth noting that when copper alloys are electrically linked into a cathodic protection system they tend to lose their antifouling properties and become highly susceptible to attack by biogenic sulfide produced by SRB colonies underneath the consequent fouling 'mat.'

From the mid 1980s onward, a distinctive type of localized corrosion has been seen in copper pipes carrying potable water, which Campbell and coworkers<sup>27</sup> termed 'Type 1½' pitting. Type 1 and Type 2 are relatively well-known forms of pitting corrosion in copper water pipes; Type 1 occurs in cold water and is associated with the presence of residual carbon films, whereas Type 2 occurs only at temperatures above 60°C, in copper pipes carrying soft water with a sulfate content exceeding the bicarbonate content. The newly identified type of pitting was found to be associated with relatively large mounds of corrosion product and occurred at relatively low temperatures, as in the case of Type 1, but the products consisted principally of basic copper sulfates and black cupric oxide, as in Type 2. The phenomenon was initially reported from Britain, Germany, Sweden, and the Middle East, and in all cases, a gelatinous film of microbial origin and consisting largely of polysaccharides was present.

This occurrence has since been reported from numerous other locations<sup>28</sup> and is commonly associated with blue water, in which the copper concentration in solution can reach tens of milligrams per liter. This should not be confused with 'Type 3' pitting, associated with soft waters and elevated pH (above 8.0), which is also known as blue water corrosion.

The occurrence of this type of copper corrosion has been convincingly demonstrated to be associated with the presence of biofilms comprising extracellular polymeric products of various types of aerobic heterotrophic bacteria, particularly members of the genera *Pseudomonas*, *Sphingomonas*, or *Acidovorax*.<sup>28,29</sup> When the corroded copper surfaces are treated with 25% nitric acid in a similar manner to a carbon film test, a clear gelatinous membrane of biofilm floats on the surface of the acid. This corrosion mechanism is also critically dependent on water composition and operating conditions. Soft waters with less than 40 mg l<sup>-1</sup> hardness expressed as CaCO<sub>3</sub>, low bicarbonate alkalinity (< 20 mg l<sup>-1</sup>), high organic content, mean temperatures of between 20 and 45°C, frequent stagnation, and lack of chlorination or chlorine depletion are factors that favor this

mechanism. One distinctive characteristic is that this type of copper tube corrosion does not have the likelihood of failure at maximum between 1 and 3 years of installation, unlike other common mechanisms.

The mechanism of copper tube failure associated with non-SRB biofilms is still uncertain. Certainly, the uronic acid carboxyl residues of the extracellular biopolymers are rather acidic (typical pK<sub>a</sub> values are in the range 4.2–5.6)<sup>28</sup> and their uronic acid or pyruvyl substitutions are known to possess high affinity binding sites for copper.<sup>30</sup> Furthermore, the heterogeneous nature of aerobic biofilm distribution is certain to create oxygen concentration cells. Siedlarek et al.<sup>31</sup> called attention to the property that oxygen and carbon dioxide, but not chloride ions, can readily pass through the biofilm layer. This allows the formation of copper oxides or hydroxides beneath the biofilm coating but not the deposition of copper (I) chloride. Therefore, it is argued, amorphous copper (I) oxide, which inhibits anodic metal dissolution, cannot readily be formed from hydrolysis of copper (I) chloride in the presence of chloride impermeable biofilm. It is likely that all the foregoing mechanisms play a role to a greater or lesser extent and that they are interactive with one another.

Optimization of the anion ratio in the water with regard to chloride, sulfate, and bicarbonate, minimizing stagnation, ensuring adequate chlorination, and avoiding warming of cold water pipes from proximity to hot water pipe runs are considered to be appropriate measures to minimize the risk of biofilm-related corrosion of copper pipework in potable water systems.<sup>28</sup>

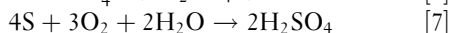
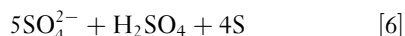
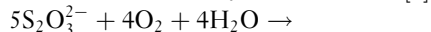
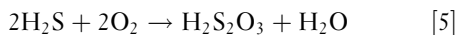
## 2.20.5 Microbially Influenced Acid Corrosion

### 2.20.5.1 Sulfuric Acid Corrosion by Sulfur-Oxidizing Bacteria

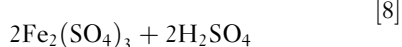
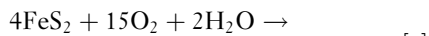
Massive and rapid general corrosion of metal, concrete, or limestone under aerobic conditions may be caused by the action of sulfuric acid formed by the oxidation of sulfur or sulfide by members of the bacterial genus *Thiobacillus*. The sulfur-oxidizing bacteria belong to an unusual group of microorganisms called chemolithotrophs. These microorganisms obtain energy not by oxidation of organic compounds but by oxidation of inorganic sulfur compounds (including sulfides) to sulfuric acid; they build up their cell material by fixation of carbon dioxide, and hence they are classed as autotrophs. Purkiss<sup>32</sup> stated that the following interlinked reactions are



performed by mixed cultures of *Thiobacillus* acting on elemental sulfur or sulfides:



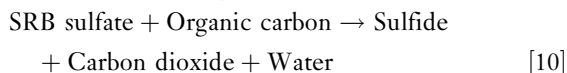
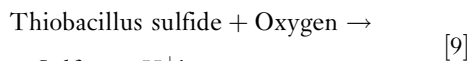
Certain of the *Thiobacillus* species will also leach sulfide mineral ores according to the following reaction<sup>33</sup>:



The important points to note are that these bacteria require oxygen (the opposite of the situation with SRB) and a source of reduced sulfur. The end product is sulfuric acid; one species (*Thiobacillus thiooxidans*) has been claimed to remain active at a pH value as low as 0.7, corresponding to more than 5% sulfuric acid.<sup>34</sup> In the author's experience, such an observation would be very unusual, a pH limit in the order of 1.5–2.0 being more common.

Thiobacilli are fairly commonly encountered in nature; it is believed that they obtain their energy from simple sulfur-containing breakdown products of sulfide minerals or from sulfide produced in an adjacent locality (or in the same locality under anaerobic conditions) by SRB. Normally, they are not found in large numbers, but if a high concentration of a suitable nutrient substrate occurs locally, their activity may be great and result in a zone of intense acidity. Such conditions can most commonly arise in sewage, in which sulfide concentration may be high owing to the action of putrefactive bacteria, unless aeration is efficient. Suitable conditions can also arise locally in paper mill effluents, damp or wet sulfur cargos, and 'made-up' ground into which industrial waste material sometimes finds its way. For this reason, sulfuric acid corrosion of underground pipelines is sporadic and unpredictable. Though *Thiobacillus*-mediated corrosion is occasionally encountered in other industrial situations, such as cooling water systems, such instances are surprisingly uncommon.

At first sight, it might seem inconsistent that various microorganisms can obtain energy both from the oxidation of sulfide to sulfate and from the oxidation of sulfate to sulfide. However, the answer is that one chemical reaction is not simply the reverse of the other: sulfur oxidizers consume oxygen, whereas SRB consume organic carbon. The two reactions can be summarized as follows:



Combining reactions [9] and [10] one derives the following overall reaction [11], a variant of the familiar air oxidation of organic carbon to  $\text{CO}_2$ .

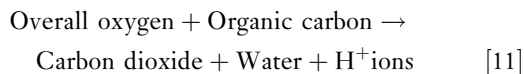


Figure 12 shows a severe example of internal corrosion of a mortar-lined ductile iron sewage water pipe, which failed by sulfuric acid corrosion due to the activity of *Thiobacillus* sulfur-oxidizing bacteria. As it is typical, the attack has occurred in the air gap at the top of the pipe where there is no actual sewage contact. Figure 13 explains how this occurs. The rate of microbial activity in the sewage effluent is sufficiently high that the rate of consumption of oxygen exceeds its rate of replenishment by diffusion from the air space. SRB then become active and produce  $\text{H}_2\text{S}$  – some of which diffuses into the air space at the top of the line where it redissolves in a surface film of condensed moisture. The sulfur oxidizers convert the  $\text{H}_2\text{S}$  containing solution to sulfuric acid, which then attacks the metal. Corrosion takes the form of generalized thinning around the '12 o'clock' position.

#### 2.20.5.2 Acid Attack on Concrete

Attack on concrete by sulfuric acid produced by sulfur-oxidizing bacteria of the genus *Thiobacillus* can be a severe problem. The most widely studied problem is the collapse of concrete sewers. As in the case of attack



**Figure 12** Corrosion of a mortar-lined ductile iron wastewater pipe because of activity of *Thiobacillus*.



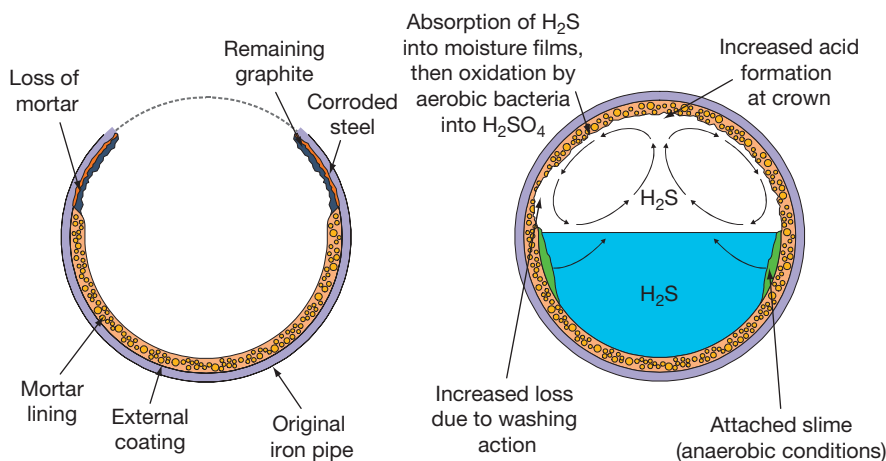


**Figure 13** MIC processes leading to collapse of iron or steel sewer pipes.

on metallic sewer pipes, this occurs due to growth of SRB in the anaerobic sewage, giving rise to  $H_2S$ . The gaseous  $H_2S$  migrates to the air space at the top of the pipes where it is converted to sulfuric acid by the sulfur oxidizers, leading to low pH, rapid dissolution of the concrete, and collapse of the sewer from the top. Under favorable conditions for the bacteria, average concrete dissolution can be greater than 12.5 mm in 50 years, with higher local rates at the air/sewage interface.<sup>36</sup>

When steel reinforcing bars are exposed, metal corrosion occurs, leading to spalling and cracking of the concrete.<sup>35</sup> Corrosion of reinforced concrete on offshore installations is a more recent problem. In seawater displaced crude oil storage tanks, crude oil stimulates SRB, with sulfur oxidizers again producing sulfuric acid in aerobic zones.<sup>37</sup>

### 2.20.5.3 Acid Corrosion by Fungi

A completely different type of microorganism to the various groups of bacteria is the fungi. The cells are much larger and grow in dense mats of material. Filamentous fungi are aerobic in nature and are involved in a wide range of biodeterioration problems; timber, paper, fuel oils, cloth, etc., can all be attacked by fungi. Fungal activity generates organic acids, leading to a low pH in the surrounding water and under the microbial mat. In addition to direct acid corrosion, oxygen concentration cells are set up between zones of metal covered with oxygen-depleted fungal mats and those areas where no fungi are present. This electrochemical cell drives the metal dissolution reaction beneath the fungal mat. A further complication is that SRB can sometimes proliferate in the oxygen-depleted niches beneath the fungal mats, giving rise to a

combination of acid corrosion enhanced by sulfide corrosion and differential aeration effects.

By far the most troublesome fungus in engineering systems is a type regularly called *Cladosporium resinae*, though now formally reclassified as *Hormoconis resinae*. *H. resinae* has the ability to thrive in the presence of kerosene and other hydrocarbons, which it uses as a carbon source for oxidation. It also produces spores that can survive extremes of temperature, only to germinate when more moderate conditions prevail. *H. resinae* is a continuing problem in fuel storage tanks and in aluminum integral fuel tanks of aircraft.

Brown slimy mats of *H. resinae* may cover large areas of aluminum alloy, causing pitting, exfoliation, and intergranular attack because of the organic acids produced by the microbes and differential aeration cells. This type of problem is largely confined to tropical, humid locations and is particularly severe in short-haul aircraft and those that experience a lot of idle time where condensation builds up.

The above problem was unknown until the 1950s, when it became prevalent after the introduction of gas-turbine-engined aircraft that use kerosene rather than gasoline as a fuel and the adoption of integral or 'wet wing' fuel tanks to replace the earlier rubberized fabric 'bay tanks.'<sup>38</sup> The problem of fungal growth in the fuel tanks of jet aircraft has generally diminished as the design of fuel tanks has improved to facilitate better drainage of condensed water and as biocides such as organoboranes have gained acceptance as fuel additives. However, this type of corrosion has reappeared in recent years, due to increasingly stringent environmental restrictions of biocides in fuel, combined with certain aircraft designs in which the lessons that were learned during the 1950s and 1960s

about the importance of efficient water drainage in integral fuel tanks have seemingly been forgotten.

### 2.20.6 MIC of Higher Alloys by General Aerobic Biofilms in Natural Seawaters

While the most rapid and severe MIC attack of stainless steels and higher active/passive alloys is commonly associated with SRB (see [Section 2.20.4.3](#)), several investigators<sup>39–42</sup> have reported positive shifts in the open circuit potentials for metals exposed to natural seawater. This positive shift has been attributed to the development of general mixed bacterial slimes on the exposed metal surface. A wide range of bacteria (e.g., *Pseudomonads* and *Flavobacteria*) can secrete large amounts of slime-like organic material under both aerobic and anaerobic conditions. Although the exact mechanism by which the bacterial film enhances the oxygen reduction kinetics is not fully understood, it has been postulated that the oxygen reduction is catalyzed by enzyme action, leading to either an increase in the exchange current density or a decrease in the cathodic Tafel constant.

In the absence of corrosion, the free corrosion potential of high molybdenum austenitic and duplex stainless steels in artificial seawater was found to rise from  $\sim -100$  to  $0$  mV and reach a stable value of  $\sim 130$  mV (vs saturated calomel electrode) after  $\sim 10$  days.<sup>42</sup> In microbially active seawater, however, there appears to be fairly common agreement that the potential continues to rise and reaches stable values of  $300 \pm 50$  mV after 20 days. There are indications, however, that the final potential is relatively independent of composition but is dependent on factors such as temperature and flow rate.

The length of time to reach the steady potentials has been shown to be closely related to the time necessary for microorganisms to settle and grow on the metal surface. Close examination of some of the potential versus time curves reported in the literature reveals that there is an initial rise in potential in the first 2–3 days, followed by a more rapid rise until the potential stabilizes after  $\sim 20$  days. This is consistent with the time found by Gunderson *et al.* for the bacterial count to reach a level of  $\sim 10^6$  cells  $\text{cm}^{-2}$ .

The effect of the potential rise because of bacterial slime is to increase the susceptibility of these alloys to crevice corrosion, but this is accompanied by an increase in the cathodic reaction rate, and therefore,

once crevice initiation occurs, there can be a marked increase in the crevice propagation rate.

Temperature has a number of important effects. First, the rate at which a critical crevice solution (CCS) is achieved is believed to be a function of the passive current density within the crevice, which may be increased by 2–3 orders of magnitude because of the positive potential shift caused by bacterial slimes compared with sterile seawater. It may also increase by 1–2 orders of magnitude because of an increase in temperature from  $10$  to  $35^\circ\text{C}$ . Second, it is reported that there is a maximum temperature for biofilm growth of  $\sim 30$ – $32^\circ\text{C}$ , although this may be higher in warm climates such as the Mediterranean because of greater natural tolerance.

This phenomenon explains why the crevice CRs for 254 SMO and SAF 2507 have been found to be 2–3 decades higher at  $25^\circ\text{C}$  than at  $40^\circ\text{C}$ . At lower temperature, the biofilm activity increases the potential, and therefore increases the risk of crevice initiation, but also increases the cathodic reaction efficiency and consequently increases the rate of propagation. At  $40^\circ\text{C}$ , the higher temperature also increases the risk of crevice initiation but the loss of the biofilm activity results in lower cathodic efficiencies and lower propagation rates. The anodic current densities were found to be 2–3 decades higher at the lower temperature. Mathematical modeling was used to show that, in the absence of biofilms, a much larger cathode-to-anode area ratio was required to sustain high CRs, and that improved mass transport of oxygen because of higher flow rates had a greater effect on the propagation rate than in the presence of the biofilm.

### 2.20.7 Other Microorganisms Associated with MIC

As already discussed, biological slimes are commonly found in the water phases of industrial process plant. Conditions at the base of even thin slimes can be anaerobic and therefore ideal for the growth of SRB, with high organic nutrient status, oxygen depletion, low redox potential, and protection from biocidal agents. In such situations, SRB-mediated sulfide corrosion can be exacerbated by fermentative acid production. An illustration of how easy it is for anaerobic conditions to develop even beneath thin microbiological slime layers is provided by the well-known process of tooth decay; the secretion of organic acids, which leads to such dental decay, is a completely anaerobic process – in the presence of oxygen, sugars

are oxidized to carbon dioxide instead of being fermented to produce acids. Given that even a thin layer of tooth plaque can give rise to anaerobic conditions, it can be appreciated how colonies of the strictly anaerobic SRB can similarly thrive beneath slimes in the nominally fully aerated environments of industrial water systems.

A particularly common type of biological slime is that produced by iron bacteria, which are found in freshwaters with a high concentration of reduced iron compounds. The bacteria require aerobic conditions and form colonies that are impregnated with ferric oxides. *Sphaerotilus* forms dense, cotton wool like growths in organically polluted rivers, the bacteria forming filaments, which are surrounded by a sheath of slime and iron oxide. The base of the colony may be highly anaerobic and SRB can develop under certain conditions. Another genus of iron bacteria, *Gallionella*, is able to use iron sulfides as a source of reduced iron, and is therefore commonly found in association with SRB. The consortium, in the form of tubercle, is one of the classic examples of growth of organisms inside ferrous water pipes.

Some components of slimes also use nitrogen-containing compounds as an energy source. They are involved in the cycling of nitrogen in the environment. Ammonia and amines are produced by microbial decomposition of organic matter under both aerobic and anaerobic conditions (ammonification). These compounds are oxidized to nitrite and nitrate by aerobic bacteria such as *Nitrosomonas* or *Nitrobacter* species. *Nitrobacter* is very efficient at destroying the corrosion-inhibition properties of nitrite-based inhibitors by oxidation of nitrite to nitrate, unless a biocidal agent is included in the inhibitor formulation.<sup>43</sup> Whereas under anaerobic conditions, a wide range of bacteria can reduce nitrite to nitrogen gas, sometimes with the production of ammonia as a by-product. The detrimental effects on brass by the release of ammonia at the surfaces of heat exchanger tubes have also been highlighted.<sup>44</sup>

### 2.20.8 Testing for MIC Activity

Assessment of a microbial population in industrial fluids is normally carried out by the use of well-established culture techniques involving specific growth media; this test format was developed for oil-field water systems, but is suitable for other industrial situations as well. Enumeration of SRB and total viable bacteria is most commonly by a 'serial extinction

dilution technique' in liquid media, using vials containing specially formulated SRB growth medium.<sup>45</sup> The test comprises initially a *serial dilution step*, followed by an *incubation step*. Ideally, the serial dilution part of the test should be carried out within a few hours of obtaining the subject samples (typically done on site); however, this is frequently not possible. The results become less reliable with increasing sample age. At the end of the incubation period, the SRB population density in the original sample is determined to the nearest order of magnitude by the number of vials in each dilution series that turn black because of bacterial sulfide production. According to current standards, the prescribed incubation period for SRB is a minimum 28 days, but a very good indication of the SRB count can usually be obtained after 10–14 days of incubation.

An example of an SRB serial extinction dilution set is shown in **Figure 14**. Similar serial dilution tests, using a different type of growth medium, are used to enumerate total bacteria; the vials that show growth turn cloudy rather than black, often accompanied by a color change of an indicator dye to indicate organic acid production.

For the most accurate assessment, threefold or fivefold replicate serial dilution enumeration is carried out; this allows the mean probable number (MPN) of bacteria to be derived from standard MPN tables. Test kits of this type are commercially available, sometimes in a simplified form. There are also some rapid assay kits based on antibody reactions to SRB enzymes, which do not require an incubation period to obtain a result. All simplified and rapid kits compromise accuracy and reliability to a greater or lesser degree. They should be regarded as no more than crude indicators, unless calibrated against standard serial dilution techniques for a specific environment.

Most of the SRB and other bacteria present in industrial systems are sessile. Planktonic bacterial



**Figure 14** Serial dilution test for SRB, blacking (positive SRB count) to 5 orders of magnitude demonstrates heavy infestation.

counts are often misleadingly low, whereas much larger populations may be concealed in sediments, deposits, and biofilms on metal surfaces. Increasingly, there is a trend to monitor SRB, and microorganisms generally, using metal coupons similar to corrosion test coupons. Such coupons are sometimes termed 'bioprobes' or 'biostuds,' and for ease of recovery, are often placed in side-stream devices in flowing pipelines (Figure 15).

If surface deposits or coupons are available, they should be sonicated or scraped into vials of culture media, serially diluted on site, then incubated in the manner of water samples. In order of priority, samples from industrial systems should be taken from bottom, metal surfaces, dead ends, and sumps. Sampling should be on a regular basis, weekly, monthly, or quarterly, depending on the extent of concern.

Low sessile population counts of below  $\sim 1000$  SRB colony forming units (cfu) per gram of deposit or per square centimeter of surface are not levels about which much concern need be expressed. However, periodic testing should be undertaken to check trends. Populations will oscillate, but if they show a general upward drift, then action will be necessary sooner or later.

Planktonic SRB counts provide a less reliable indicator than do sessiles. However, recurrent counts of greater than  $\sim 10$  cfu ml<sup>-1</sup>, any general upward trend, or any positive planktonic SRB counts in a nominally biocide-treated system are a cause at least for further investigation of sessiles. Any planktonic SRB counts above  $\sim 1000$  cfu ml<sup>-1</sup> is indicative of a heavy

proliferation somewhere in the system, probably in deposits on surfaces, especially in stagnant or low flow areas.

Total viable bacteria counts (TVCs) are usually much higher than SRB counts. Planktonic TVCs of up to 100 000 per milliliter are common in many natural waters and industrial systems. Higher population densities, greater than 100 000 per milliliter probably, indicate a significant build-up of slime somewhere. In biocide-treated systems, TVCs should be several orders of magnitude lower than in the untreated water. The incubation period for TVCs is only  $\sim 3$  days, considerably shorter than for SRB. Therefore, these counts can give a useful early warning of any problem with biocide-treatment efficiency.

SRB counts and TVCs are relatively straightforward, routine analytical techniques. Tests for nitrite-utilizing bacteria or sulfur oxidizers are more complex, specialist techniques. However, problems associated with these organisms are usually clearly evident from the undesirable chemical changes they bring about.

As a supplement to microbiological testing, it is useful to carry out some chemical analyses. An important test is for sulfide in corrosion deposits. In the case of iron sulfide, a simple test is to warm a small sample of the solid with a few milliliters of 50% hydrochloric acid in a glass test tube. If sulfide is present in the deposit, a slightly moistened strip of lead acetate paper in the mouth of the tube will turn brown, indicating H<sub>2</sub>S evolution. If a lot of sulfide is present, the characteristic 'rotten egg' odor will also be apparent.

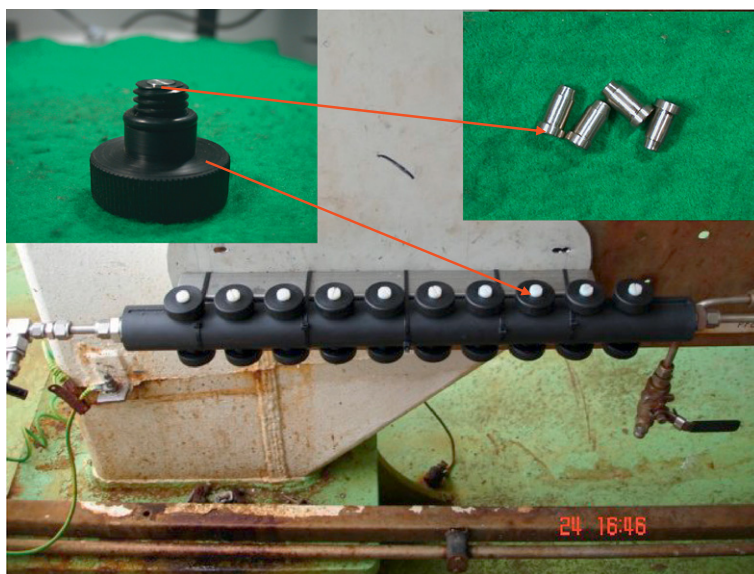


**Figure 15** A typical side stream device incorporating 'biostuds' for monitoring of biofilms.



This test needs to be undertaken within a short time of removing samples of deposit from the corrosion site, because wet or damp iron sulfide will eventually oxidize in air to brown rust. The color change of corrosion deposits from black to brown is, in itself, a good indication of sulfide corrosion product. Any such deposits that are taken back to the laboratory for more sophisticated chemical analysis should be preserved in anaerobic bags to prevent the oxidation of FeS, which would otherwise occur.

Tests for sulfate, total organic carbon (TOC), pH, and oxygen concentration are also useful indicators of the potential for SRB growth. If sulfate concentration is low, then there is little hazard of SRB activity. The pH range most suited to SRB growth is 5–10. Outside these limits, bulk phase growth of SRB is very limited. Oxygen concentration will also affect SRB growth in bulk phases but a high value does not mean that SRB are not present in pockets or under debris. A high oxygen concentration may allow other organisms to develop. The interpretation of those tests, together with other operating parameters, is discussed in [Section 2.20.9](#).

## 2.20.9 MIC Risk Assessment Based on Operating Conditions

It is frequently the case that the engineer is required to make an appraisal of MIC risk with limited information on the corrosion history and little or no historic microbiological test data. The conclusions that may be drawn about the risk of MIC in such cases are largely based on consideration of operating parameters. This is often the situation for the assessment of internal corrosion risk of pipelines, water handling systems, or process plant. The discussion that follows refers specifically to SRB-related problems, which are by far the most common MIC issue.

A group of researchers at Shell Petroleum Co. have developed an approach to risk assessment of carbon steel pipelines, based on the details of water chemistry and operation parameters.<sup>46</sup> Their MIC CR calculation is based on the following equation:

$$\text{CR}(\text{mm year}^{-1}) = C \times F^p \quad [12]$$

with

$$F = f_1 \times f_2 \times \cdots \times f_n \quad [13]$$

where  $C$  is a constant ( $C = 2 \text{ mm year}^{-1}$ ), the  $f$ s are factors for the various influencing parameters and  $p$  is a power law index (0.57).

Although such an approach does provide a valuable empirical recognition of the relative contribution of the factors that encourage or inhibit MIC, the calculation of actual CRs on such a basis should be viewed with extreme caution, given our present limited understanding of the effects of the various factors, the most important of which are discussed below.

### 2.20.9.1 Presence of Water

All bacteria require free water in order to proliferate. In the case of oil pipelines, MIC is to be considered only under separated flow conditions; if all water is entrained in the hydrocarbon, there is no risk of MIC.<sup>46</sup> In the author's experience, it is unwise to rely on dispersions to provide fully oil-wetted surfaces when the bottom solids and water content (BS and W) is in the order of 2% or greater, except under very turbulent hydrodynamic conditions. It is best to take an empirical and conservative view as to whether lines may be wet enough to sustain SRB growth at the present time and during their future operating life.

### 2.20.9.2 Salinity

According to results presented by Postgate,<sup>14</sup> if the salinity of water, expressed as w/w percentage NaCl, is more than ~7%, there is unlikely to be any SRB growth. That observation broadly agrees with the author's own experience and similar statement is reiterated in the more recent Shell Petroleum Co. work.<sup>39</sup> However, it should be noted that other workers have suggested that some SRB strains may tolerate considerably higher salt concentrations.

### 2.20.9.3 Temperature

Most types of bacteria grow optimally at temperatures between 10 and 45 °C, which is the highest risk temperature range. However, there are thermophilic strains of SRB and some other microorganisms that grow at higher temperatures up to at least 70 °C and their activity cannot be discounted.

### 2.20.9.4 pH

Generally, there is unlikely to be SRB proliferation below pH 5 or above pH ~10, though the pH range for SRB that are protected in heavy deposits may be somewhat wider.



### 2.20.9.5 Anaerobic Conditions

SRB will only proliferate and produce sulfide in the absence of oxygen. Clearly, deaerated environments are at greatest risk; however, there are many cases of problems in slimes and deposits where the bulk water phase is essentially aerobic, for example, in cooling waters. This is especially the case for static or slow flow conditions.

### 2.20.9.6 Nutrient Status of Water Phase

SRB growth is much less likely if the aqueous sulfate concentration or the organic carbon content is below  $\sim 10 \text{ mg l}^{-1}$  or the ammoniacal nitrogen (not nitrate or nitrite) is below  $\sim 1 \text{ mg l}^{-1}$ . An exception, in the author's experience, is the case of plant under long-term lay up with static, high-sulfate water (e.g., seawater), where a corrosive 'black water' condition may develop over a period of months even with very low organic carbon content. This is believed to be due to reduction of sulfate by SRB using cathodic hydrogen formed by corrosion on steel surfaces.

### 2.20.9.7 Flow Rate

Flow rate influences the nature of biofilm formation and the rate of nutrient delivery. As flow rate increases, biofilms become less bulky and only the more adherent films remain on the metal surface. However, above a certain threshold, the initiation of biofilm formation is severely limited. The transition zone is considered to be between 2 and  $3 \text{ m s}^{-1}$ . At the other extreme, stagnation is often associated with the severest MIC incidents.

### 2.20.9.8 Cleaning Frequency

As discussed earlier, in order to initiate the MIC process, the free-floating ('planktonic') SRB cells need to attach to a metal surface (i.e., become 'sessile') and proliferate to form a biofilm with its own entrained microenvironment. It is that process that is disturbed by regular mechanical cleaning, such as brush 'pigging' of pipelines. The incipient biofilm is disrupted and largely removed and this *is the most* effective means of minimizing SRB growth and obviating MIC. MIC is uncommon in pipelines that are frequently pigged, even without biocide treatment. The more frequent the pig runs, the less time the biofilm has to recover.

### 2.20.9.9 Use of Antimicrobial Chemical Treatments

Any operation that disrupts the biofilm and thereby limits its proliferation will act to alleviate MIC. The application of periodic or continuous biocide or other antimicrobial chemical treatment is one such factor, which is discussed in more detail in [Section 2.20.10](#).

## 2.20.10 Control of MIC

### 2.20.10.1 General Principles

For situations where chemical treatment of the environment by biocides is not possible (e.g., soils, harbors, marine fouling, etc.), the remedies available reflect measures taken to obviate other forms of corrosion and may be summarized as follows.

#### 2.20.10.1.1 Provision of a nonaggressive surround

For buried steel, provision of a backfill of sand or chalk around the material to ensure good drainage and aeration is helpful. Incorporation of a very sparingly soluble biocide into the backfill material has been tried with some success. Another method is to incorporate biocide into protective coatings, the best-known example probably being the use of strontium chromate primers, which are very effective in controlling the kerosene fungus in aircraft wing integral fuel tanks, until such time as the chromate becomes deleted by leaching into the condensed water phase. However, the use of such treatments is both expensive and becoming increasingly less acceptable for environmental reasons.

#### 2.20.10.1.2 Cathodic protection

This may be in the form of sacrificial anodes or impressed voltage, sometimes in conjunction with a coating. There is a long-standing precept, current in the industry, that structures need to be held at potentials more negative than  $\sim -0.9 \text{ V}$  (vs Ag/AgCl) in order to protect against anaerobic corrosion by SRB. Horvath and Novak<sup>47</sup> presented the most reasoned argument for this view, which has appeared numerous times in print, though the evidence is not very convincing.

#### 2.20.10.1.3 Protective coatings

The coating must be resistant to biodegradation and to chemical attack by the metabolic products of microbial activity, principally  $\text{H}_2\text{S}$  and sulfuric

acid. Biodegradation resistance of the more long-established wrappings and coatings forms a separate study and was the subject of a site study by British Gas in the 1970s.<sup>48</sup>

#### 2.20.10.1.4 Biocides

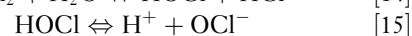
For internal protection of pipelines, cooling systems, vessels under hydrotest, etc., biocide treatment is the obvious remedial measure, in combination with cleaning techniques. Their selection use is explained in more detail below.

### 2.20.10.2 Biocide Treatments

A microbiocide must first be effective in greatly inhibiting microbial activity; second, it must be economical in a treatment program; and third, it must meet the constraints imposed by increasingly stringent environmental legislation. In Europe, the availability of biocides is now restricted to a limited range of substances that are registered under the European Union's 'Biocidal Substances Directive,' which was primarily intended for control of agricultural pesticides but has caught industrial biocides within its net.

Biocides can be broadly divided into two types: oxidizing and nonoxidizing. Commonly accepted oxidizing biocides are 'chlorine' (actually mainly hypochlorous acid plus hypochlorite ion), chlorine dioxide, chlorine donors, bromine, ozone, and hydrogen peroxide. Chlorine is by far the single most prevalent industrial biocide in use today; it is popular because of its efficiency, low cost, and relative environmental acceptability. The disadvantages of chlorine are its high reactivity with many other chemicals, short half-life, necessitating continuous dosing of flowing systems, and difficulties with dosage control – there is a narrow window between the effective dose and an overdose, which can give rise to serious corrosion problems for a wide range of materials. Achieving a continuous chlorine dose with that 'window,' typically 0.2–1.0 mg l<sup>-1</sup>, is complicated by the 'chlorine demand' of natural waters. During continuous chlorination practice, sufficient chlorine must be generated to overcome the chemical demand and leave a free chlorine residual. This is variously expressed as free residual chlorine (FRC), free available chlorine (FAC), total residual chlorine (TRC), or total available chlorine (TAC). In each case, it is a measure of the residual oxidizing power rather than the true concentration of dissolved chlorine, since a number of different 'free chlorine species' are produced during water chlorination.

Chlorination can be achieved by dosing with chlorine gas or sodium hypochlorite solution and in the case of treating large volumes of saline water by electrolytic chlorine generation. When water is chlorinated, whether by chlorine gas, addition of sodium hypochlorite ('bleach') solution, or by electrolytic generation, it very quickly reacts to establish the equilibrium:



One of the by-products is H<sup>+</sup> and therefore the concentration of OCl<sup>-</sup>, HOCl, and Cl<sub>2</sub> are pH dependent. At a pH of greater than 8, chlorine is present predominantly as OCl<sup>-</sup> (hypochlorite ion), whereas at pH 7.5 there is a mixture of hypochlorite and hypochlorous acid (HOCl) and at lower pH values hypochlorous acid predominates. HOCl is ~80 times more effective as a biocide than OCl<sup>-</sup>, which means that chlorination is more effective as a biocidal treatment for neutral or slightly acidic 'soft' waters than it is for alkaline 'hard' waters. The exception is seawater, which has an alkaline pH of ~8.2 but can, nevertheless, be effectively chlorinated due to the presence of bromide ions, which react with hypochlorous acid to form hypobromous acid (HOBr); 'chlorination' of seawater is really therefore bromination. HOBr has a different pH-dependent dissociation profile to HOCl, making it much less dissociated into OBr<sup>-</sup> ions under mildly alkaline conditions and therefore effective as a biocide in seawater.

Continuous chlorination of industrial water systems might seem prudent for control of MIC as well as slime control on heat exchangers and for public health reasons, particularly the control of the waterborne pathogen *Legionella*, the causative organisms of legionnaire's disease. However, in some high demand systems with process leaks maintaining a continuous 'FRC' level is not economically feasible. The alternative is to maintain a 'FRC' concentration from 0.3 to 0.8 mg l<sup>-1</sup> for up to 2 h per treatment period in order to kill as much as possible of the sessile biofilm. The rate of recontamination will suggest the frequency of treatment.

The shortcomings of chlorination for certain systems with high pH and/or high chlorine demand have led to an increase in the popularity of chlorine dioxide (ClO<sub>2</sub>) as an alternative oxidizing biocide. Chlorine dioxide has more oxidizing power than 'chlorine,' yet is less affected by the chemical composition of the water than is chlorine and it forms a true nonionized solution of a gas, which is not pH dependent. ClO<sub>2</sub> is usually generated at plant site by

the reaction of chlorite and hypochlorite, with the addition of acid to ensure the optimal pH for the reaction. For this reason, it is somewhat more complex and expensive than chlorination. Other oxidizing biocides are less extensively used in industrial water systems, but their mode of action is similar to chlorine and chlorine dioxide.

The alternative approach to the use of oxidizing biocides is to use much higher concentrations of organic, nonoxidizing biocides,<sup>49</sup> often blended with surfactants to increase their penetrating power into biofilms and other deposits. Some of the most common organic biocides are THPS (tetrakis hydroxy phosphonium sulfate),<sup>50</sup> aldehydes (glutaraldehyde and formaldehyde),<sup>51</sup> quaternary ammonium compounds,<sup>52</sup> biguanides,<sup>53</sup> isothiazolones,<sup>54</sup> chlorinated phenols, methylene-bis-(thiocyanate), dithiocarbamates, sulfones, and thiones. All the various types of organic biocides have advantages and disadvantages relative to one another and to oxidizing biocides, which are beyond the scope of this chapter. However, it is worthwhile to elucidate some general principles about biocide selection.

First, where some form of biocide treatment is in use, it should not necessarily be assumed that it must be effective. Biocides have very limited ability to penetrate existing deposits and are therefore much more effective when used in conjunction with frequent mechanical cleaning processes such as brush cleaning or 'pigging' of pipelines.

The first stage of biocide selection is a laboratory evaluation of candidate biocides. For plant under wet lay-up, recirculating water systems, or other batch processes, there are only two parameters that need to be optimized: type of biocide and concentration. However, for oilfield water systems, such as secondary recovery water injection systems, continuous treatment with biocides at an effective dose is not feasible. Continuous low-level injection of organic biocide is of no value; indeed continuous low-level exposure may possibly be detrimental in the long term, because there is some possibility that it may encourage the development of more biocide tolerant strains of bacteria. Periodic batch treatment is therefore required to treat biofilms and this means that there is a substantial matrix of parameters: type of biocide, concentration, duration of batch, and frequency of treatment. The first three factors may be optimized by means of a laboratory 'time kill test'<sup>45</sup> using real or simulated system water at system temperature, bacteria such as mixed cultures of SRB, isolated from the system for which the treatment is

being selected, and most importantly, sessile rather than planktonic populations. More realistic, though more complex and expensive, tests can be performed on side stream units at site. As with batch chlorination, the rate of recontamination will suggest the frequency of treatment and this parameter can only be optimized on the basis of site experience.

Given the relative complexity of optimizing biocide dosages properly, it is not surprising that organic biocides are commonly either underdosed or overdosed. Underdosing ultimately results in lack of control of MIC, possibly involving biocide-resistant strains of microorganisms and negates the whole purpose of the treatment strategy. Conversely, overdosing involves not only unnecessary expenditure over a prolonged period but also the introduction of unnecessarily large amounts of toxic substances into the environment.

### **2.20.10.3 Alternatives to Biocide Treatments**

Given the shortcomings of biocide treatments, specific antimicrobial treatments based on manipulation of microbial ecology have long been mooted; one such alternative, continuous nitrate treatment, has recently become commonplace for selective control of SRB in oilfield water systems. Though mainly employed as an agent against H<sub>2</sub>S generation in deep petroleum reservoirs ('souring'), nitrate (or, less commonly, nitrite) based treatments have also been used in some locations as anti-MIC agents in topside facilities, either alone or in combination with biocide.

The objective of these treatments is the suppression of sulfide generation by the selective manipulation of indigenous bacteria through nutrient addition. There are several possible mechanisms by which nitrate can suppress the accumulation of sulfide.

Nitrate-reducing bacteria (NRB) generally 'out-compete' SRB for common carbon and energy sources such as acetate and longer chained fatty acids. This shifts the flow of electrons in energy-generating metabolism of bacteria away from sulfate reduction toward nitrate reduction. Ideally, this process gives rise to nitrogen as the end product, but sometimes it also results in the production of nitrite.

SRB themselves may preferentially use nitrate instead of sulfate as the electron acceptor in their energy-generating metabolism.

NRB may produce traces of compounds (nitrogen oxides and/or nitrites) that raise the oxidation-reduction (redox) potential of the environment to a

level that is inhibitory to the growth of SRB or these substances may act as toxins to SRB.

Finally, specialized nitrate-reducing sulfide oxidizing bacteria may use the sulfide produced by SRB as the electron donor for nitrate or nitrite reduction. In this case, the production of sulfide is not completely inhibited, but the consumption of sulfide by NRB prevents its accumulation.

Depending on the microbial populations present, any of the above mechanisms or combinations of mechanisms may be operative. The addition of nitrate does not directly kill SRB and, in some cases, will not inhibit their activity, but will still achieve the desired effect – the reduction or removal of sulfide. Several field tests have also demonstrated the potential usefulness of nitrate for controlling SRB. The Institute of Petroleum (now the Energy Institute) in the United Kingdom published a useful introductory review about use of nitrate treatments to control SRB, MIC, and reservoir souring.<sup>55</sup> Certainly, in laboratory tests, these treatments have proven very effective for suppression of SRB activity compared with conventional biocide treatments.

Unfortunately, in practice the use of these agents is by no means always problem free; in particular, the production of nitrites as a by-product of the treatment may itself induce pitting corrosion in a minority of applications; furthermore, nitrate is only active against SRB rather than the wider range of other MIC microorganisms. In summary, it continues to be the case that no single treatment can provide a definitive solution to MIC; the choice of most appropriate agent is very situation specific and will remain, like most decisions relating to living organisms, a challenging compromise.

## References

- Ross, R. T.; Sladen, J. R.; Wienart, L. A. In *Biodeterioration of Materials*; Walters, A. H., Elphick, J. J. Eds.; Elsevier: London and New York, 1975; pp 127–136.
- Hill, E. C. In *Biodeterioration of Materials*; Walters, A. H., Elphick, J. J. Eds.; Elsevier: London and New York, 1975; pp 157–172.
- Hill, E. C. In *Microbial Aspects of the Deterioration of Materials*; Lovelock, D. W., Gilbert, R. J. Eds.; Academic Press: London and New York, 1975; pp 127–136.
- Miller, J. D. A.; Tiller, K. A. In *Microbial Aspects of Metallurgy*; Miller, J. D. A. Ed.; Medical & Technical Publishing: Aylesbury, 1971; pp 61–105.
- Iverson, W. P. In *Microbial Iron Metabolism*; Niedlands, J. B. Ed.; Academic Press: New York, 1974.
- Kucera, V. *Microbial Corrosion – A Literature Survey*; Swedish Corrosion Institute: Stockholm, 1980.
- Pope, D. H.; Duquette, D.; Wayner, P. C.; Arland, H. J. *Microbially Influenced Corrosion, a State-of-the-Art Review*, Materials Technology Institute, Columbus, OH, Publication Number 13, 1984.
- Sequeira, C. A. C. Ed.; *Microbial Corrosion*; European Federation of Corrosion, Report Number 29; Institute of Materials: London, 2000.
- Stoeckler, J. G. II, Ed.; *A Practical Manual on Microbiologically Influenced Corrosion*; NACE International: Houston, TX, 2001; Vol. 2.
- Anon. *Microbiologically Influenced Corrosion and Biofouling in Oilfield Equipment*; NACE International: Houston, TX, 1990; TCP 3.
- Borenstein, S. W. *Microbiologically Influenced Corrosion Handbook*; Industrial Press: USA, 1994.
- Videla, H. A.; Herrera, L. K. *Int. Microbiol.* **2005**, *8*, 169–180.
- Stott, J. F. D.; Herbert, B. N. J. *Appl. Bacteriol.* **1986**, *60*, 57–66.
- Postgate, J. R. *The Sulphate-Reducing Bacteria*; Cambridge University Press, 1979.
- Ginter, R. L. *Bull. Am. Assoc. Petrol. Geol.* **1930**, *14*, 139.
- Gates, G. L.; Parent, C. F. *Oil Gas J.* **1976**, 115.
- Al Sawaf, F. D. S. *Econ. Geol.* **1977**, *72*, 608.
- Ege, S. L.; Houghton, C. J.; Tucker, P. T. Second Annual Workshop on Secondary Recovery Technology, June 1985, London.
- Davies, M.; Scott, P. J. B. *Oilfield Water Technology*; NACE International: Houston, TX, 2006.
- Booth, G. H.; Cooper, A. W.; Cooper, P. M. *Br. Corros. J.* **1967**, *2*, 104.
- Booth, G. H.; Cooper, A. W.; Wakerley, D. S. *Br. Corros. J.* **1967**, *2*, 109.
- Schaschl, E. *Mater. Perform.* **1980**, *19*, 9.
- Kobrin, G. *Mater. Perform.* **1976**, *15*, 38–43.
- Tatnall, R. E. *Mater. Perform.* **1980**, *19*, 88.
- Costello, J. A. Ph.D. thesis, University of Cape Town, South Africa, 1975.
- King, R. A.; Miller, J. D. A. *Nature* **1972**, *233*, 491.
- Campbell, H. S.; Chamberlain, A. H. L.; Angel, P. J. In *Corrosion and Related Aspects of Material for Potable water Supplies*; McIntyre, P., Mercer, A. D. Eds.; Institute of Materials: London, 1993; pp 222–231.
- Wagner, D.; Chamberlain, A. H. L. *Biodegradation* **1997**, *8*, 177–187.
- Critchley, M. M.; Pasetto, R.; O'Halloran, R. J. *J. Appl. Bacteriol.* **2004**, *97*, 590–597.
- Geesey, G. G.; Beamer, P. J. *Mar. Technol. Soc.* **1990**, *24*, 36–43.
- Siedlarek, H.; Wagner, D.; Fischer, W. R.; Paradies, H. H. *Corros. Sci.* **1994**, *34*(1), 50–54.
- Purkiss, B. E. In *Microbial Aspects of Metallurgy*; Miller, J. D. A. Ed.; Medical & Technical Publishing: Aylesbury, 1971; pp 107–128.
- Kempner, E. S. J. *Bacteriol.* **1966**, *92*, 1842.
- Le Roux, N. W.; North, A. A.; Wilson, J. C. Tenth International Mineral Processing Congress, London, Institute of Mining and Metallurgy **1974**, 1051.
- White, G. C. *Handbook of Chlorination and Alternative Disinfectants*, 4th ed.; Wiley: New York, 1999.
- Thistlethwayte, D. K. B. Ed.; *The Control of Sulphides in Sewerage Systems*; Butterworth: Sydney, Australia, 1972.
- Morgan, T. O. B.; Steele, A. D.; Gilbert, P. D. Concrete Durability in Acidic Stagnant Water, Proceedings of Congress on Microbial Corrosion, Teddington, March 1983; The Metals Society: London, 1983.
- Elphink, J. J. In *Microbial Aspects of Metallurgy*; Miller, J. D. A. Ed.; Medical & Technical Publishing: Aylesbury, 1971; pp 157–172.

39. Jurinski, M. P.; Scully, J. R.; Lillard, R. S. Corrosion 1993 Conference, National Association of Corrosion Engineers (NACE), Paper Number 501.
40. Kain, R. D. Corrosion 1987 Conference, National Association of Corrosion Engineers (NACE), Paper Number 348.
41. Kain, R. D. Corrosion 1993 Conference, National Association of Corrosion Engineers (NACE), Paper Number 67.
42. Gallagher, P.; Malpas, R. E. Corrosion 1989 Conference, National Association of Corrosion Engineers (NACE), Paper Number 113.
43. Tarbuck, L. A.; Wyborn, C. H. E. Proceedings of Condenser Biofouling Control Symposium., Electric Power Research Institute, Atlanta, U.S.A., March, 1979.
44. Hoar, T. P. *Corrosion* **1957**, *14*, 1036–1046.
45. Standard Test Method, TM0-194-94. Field Monitoring of Bacterial Growth in Oilfield Systems; NACE International: Houston, TX, 1994.
46. Pots, B. F. M.; John, R. C.; Rippon, I. J.; Maarten, J. J.; Thomas, S.; Kapusta, S. D.; Girgis, M. M.; Whitham, T. Corrosion 2002 Conference, National Association of Corrosion Engineers (NACE), Paper Number 2235.
47. Horvath, J.; Novak, M. *Corros. Sci.* **1976**, *4*, 159.
48. Pankhurst, E. C.; Nicolle, H. G. M.; Allan, K. In *Microbial Aspects of the Biodeterioration of Materials; Society for Applied Bacteriology, Technical Series 9*; Academic Press: London, 1975; pp 137–152.
49. Romero, J. M.; Amaya, M.; Hernandez, J. A. *Mater. Perform.* **2004**, 38–40.
50. Larsen, J.; Sanders, P. F.; Talbot, R. E. Corrosion 2000 Conference, National Association of Corrosion Engineers (NACE), Paper Number 123.
51. Gorman, S. P.; Scott, E. M.; Russell, A. D. *J. Appl. Bacteriol.* **1980**, *48*, 161–190.
52. Bessems, E.; Clemmit, A. F. Chemicals in the Oil Industry, Proceedings of a Symposium Organised by Royal Society of Chemistry, Manchester, United Kingdom; Ogden, P. H. Ed.; March 1983; pp 159–170.
53. Gilbert, P.; Pemberton, D.; Wilkinson, D. E. *J. Appl. Bacteriol.* **1990**, *69*, 593–598.
54. Collier, P. J.; Ramsay, A. J.; Austin, P.; Gilbert, P. *J. Appl. Bacteriol.* **1990**, *69*, 569–577.
55. The Energy Institute. The Stimulation of Nitrate-Reducing Bacteria (NRB) in Oilfield Systems to Control Sulfate-Reducing Bacteria (SRB), Microbiologically Influenced Corrosion and Reservoir Souring – An Introductory Review. The Energy Institute (formerly The Institute of Petroleum): London, 2003.



## 2.21 Corrosion in Alkalis

**J. A. Richardson**

Anticorrosion Consulting, 5 Redhills Lane, Durham DH1 4AL, UK

© 2010 Elsevier B.V. All rights reserved.

2.21.1	Introduction	1191
2.21.2	Steels and Cast Irons	1192
2.21.3	Stainless Steels	1196
2.21.4	Nickel and Nickel Alloys	1200
2.21.5	Other Metals and Alloys	1204
2.21.6	Nonmetallic Materials	1204
2.21.6.1	Thermoplastic and Reinforced Thermosetting Materials	1204
2.21.6.2	Elastomers	1205
2.21.6.3	Inorganic Materials	1205
References		1205

### Abbreviations

**ASTM** American Society for Testing Materials

**CPVC** Chlorinated polyvinyl chloride

**ECTFE** Ethylene chlorotrifluoroethylene

**ETFE** Ethylene tetrafluoroethylene

**FEP** Fluorinated ethylene propylene

**FRP** Fiber reinforced plastic

**HDPE** High density polyethylene

**IGSCC** Intergranular stress corrosion cracking

**LME** Liquid metal embrittlement

**PE** Polyethylene

**PFA** Perfluoroalkoxy

**PP** Polypropylene

**ppm** Parts per million

**PTFE** Polytetrafluoroethylene

**PVC** Polyvinyl chloride

**PVDF** Polyvinylidene fluoride

**PWHT** Postweld heat treatment

**PWR** Pressurized water reactor

**SCC** Stress corrosion cracking

**SCE** Saturated calomel electrode

**SHE** Standard hydrogen electrode

**XPS** X-ray photoelectron spectroscopy

### Symbols

$\Delta T$  Temperature difference (°C)

### 2.21.1 Introduction

Sodium hydroxide (caustic soda) is one of the world's most commercially important chemicals. It is produced in huge quantities worldwide, mostly as a by-product of the electrolysis of brine to produce chlorine, historically in mercury cells but increasingly in diaphragm or membrane cells. Diaphragm cells are used to produce the majority of the world's caustic soda which leaves the cells at ~10–12% (w/w) concentration, and is subsequently evaporated to produce commercial grades, typically at 50% and 73% (w/w) concentration, or anhydrous. Potassium hydroxide (caustic potash) also has some commercial significance but it is more expensive than and, in volume terms, well-behind caustic soda.

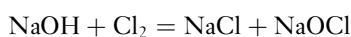
Both sodium and potassium hydroxides are strong bases that are highly dissociated in water at all concentrations to release the metal cation and the hydroxide anion as follows:



Their aqueous solutions have pHs above 7, and pHs 10, 11, and 12 are equivalent to concentrations of 4, 40, and 400 ppm (w/w) sodium hydroxide respectively at 25 °C.

Depending mostly on the method of manufacture, sodium hydroxide may contain contaminants that are potentially significant from the corrosion standpoint, in particular:

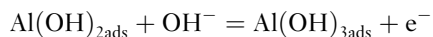
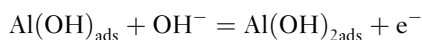
1. Chlorides, particularly in the case of the sodium hydroxide produced in diaphragm cells that may contain up to 1% (w/w) sodium chloride, in contrast to mercury or membrane cells that deliver sodium hydroxide with much lower levels of sodium chloride, typically 10 s of ppm.
2. Chlorates,  $\text{ClO}_3^-$ , are produced at the anode during electrolysis and are normally removed before or during the evaporation stage in the manufacturing process, so are of significance mostly to the performance of manufacturing equipment.
3. Chlorine and hypochlorite that is formed when chlorine, a coproduct of electrolysis, dissolves in sodium hydroxide:



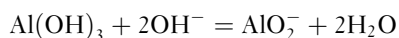
4. Mercury, entrained in the sodium hydroxide produced in mercury cells.

Alkalis differ fundamentally from acids in the mechanism of the metal dissolution process. In acids, soluble metal cations are produced anodically, supported by hydrogen evolution as the primary cathodic process. In alkalis, soluble oxyanions containing the metal are produced by reaction between the metal and hydroxide anions. In the case of the so-called amphoteric metals such as aluminum, zinc, tin and lead, and their alloys, these processes are so strongly favored as to render the metals unsuitable for service under alkaline conditions because of the formation of soluble aluminates, zincates, stannates, and plumbates respectively. For example, a simplified Pourbaix diagram for the aluminum–water system at 25 °C is shown in **Figure 1**, and confirms that the metal will be potentially vulnerable to corrosion above a pH of  $\sim 9$  as well as below a pH of  $\sim 4$ .

The reactions that give rise to this alkaline vulnerability in aluminum are thought to consist of the initial formation of aluminum hydroxide in a series of three single electron transfers<sup>1</sup>:



The final step is believed to be the chemical dissolution of aluminum hydroxide to form soluble aluminate<sup>1</sup>:



The supporting cathodic process is the direct reduction of water molecules on the aluminum surface with the liberation of hydrogen:

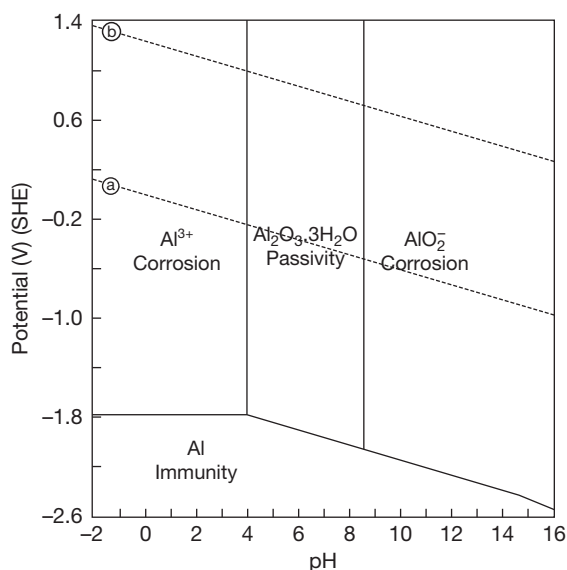
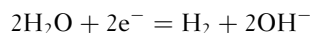


**Figure 1** Simplified potential/pH diagram for the Al–H<sub>2</sub>O system at 25 °C, based on an equilibrium activity of  $10^{-6}$  g ion per litre.



Thus, and somewhat counter-intuitively, hydrogen is produced in the corrosion processes occurring adjacent to the metal surface despite the tiny concentration of protons in the bulk fluid.

The corrosion performances of the various classes of material in alkalis have been reviewed extensively elsewhere.<sup>2–5</sup> Much of the data relates to sodium hydroxide, reflecting its commercial significance. There is relatively little data for potassium hydroxide in the public domain. Readers whose main interest is to identify ‘what works where’ are referred to these sources and the relevant chapters on specific materials in this book. In this chapter, the corrosion performances of materials are reviewed with an emphasis on the principles and mechanisms that underpin their corrosion performances in alkalis.

## 2.21.2 Steels and Cast Irons

The Pourbaix diagram for the iron–water system at 25 °C shown in **Figure 2**<sup>6</sup> suggests that steels should form protective oxide films, probably composed of magnetite ( $\text{Fe}_3\text{O}_4$ ), at pH up to  $\sim 14$ , approximately equivalent to  $\sim 4\%$  (w/w), or 1 M, sodium hydroxide.

When the pH is above 14 the diagram indicates that there is a potential corrosion zone arising from

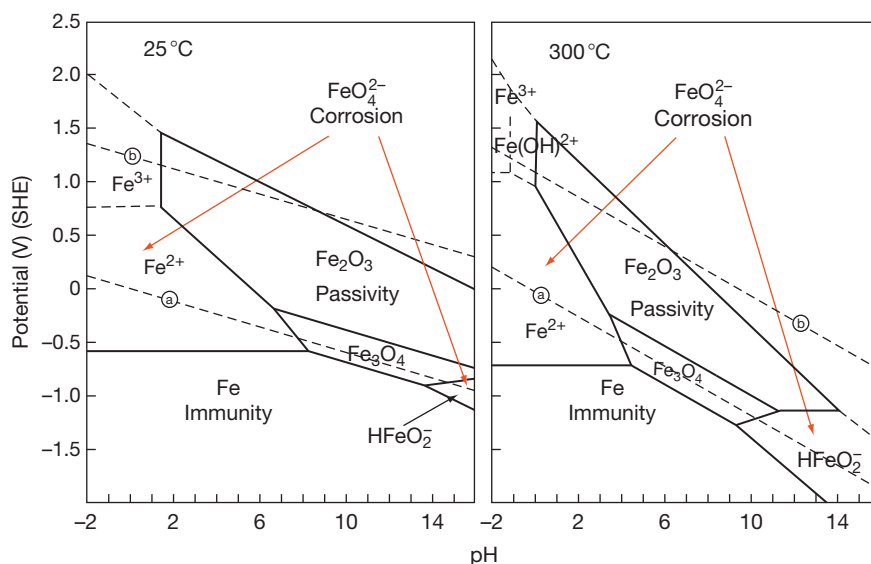
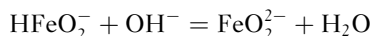


**Figure 2** Simplified potential/pH diagrams for the Fe–H<sub>2</sub>O system at 25 °C and 300 °C, based on an equilibrium activity of 10<sup>−6</sup> g ion per litre. Adapted from Chen, C. M.; Aral, K.; Theus, G. J. Computer Calculated Potential–pH Diagrams to 300 °C, Report NP-3137, Electric Power Research Institute, 1983.

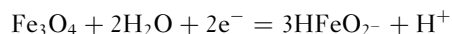
the stability of the dihypoferrite anion,  $\text{HFeO}_2^-$ , that forms by the anodic dissolution of the metal in a sequence of steps similar to those for aluminum above, culminating in the dissolution of ferrous hydroxide as the dihypoferrite anion, rather than its further oxidation to solid magnetite on the surface. The overall process can be written as follows:



As in the case of aluminum, the supporting cathodic process is the reduction of water to hydrogen. The dihypoferrite anion is in equilibrium with the hypoferrite (ferroate) anion as follows:



This equilibrium moves to the right as the alkalinity increases. Dissolution of the magnetite film also contributes to metal dissolution under alkaline conditions:



In practice, carbon steel is widely used for the storage, handling, and transport of sodium hydroxide solutions at concentrations and temperatures well beyond the limits suggested in the Pourbaix diagram, indicative of a kinetic rather than thermodynamic control over the stability of passivity. Although measured corrosion rates vary with purity, velocity, and other factors, the general experience is that corrosion rates are acceptably low in concentrations up

to ~75% (w/w) at temperatures up to ~80 °C and perhaps even beyond,<sup>5</sup> assuming that some degree of iron contamination is acceptable. Of the potential contaminants, only chlorates present a significant threat, having the potential to accelerate the corrosion of steel by up to an order of magnitude, depending on the concentration.<sup>5</sup>

The major concern across these concentrations and temperatures is not general corrosion but the risk of intergranular stress corrosion cracking (SCC) to which carbon steels are vulnerable in the presence of tensile residual stresses arising from welding and cold working operations during fabrication. These risks can be mitigated by thermal stress relief following fabrication and some well-established guidelines for determining the need, or otherwise, for postweld heat treatment (PWHT) are available and are summarized in [Figure 3](#).<sup>7</sup>

The presence of carbon/carbides in the steel and the segregation of phosphorus at grain boundaries increase the risks of cracking.<sup>8</sup> Low alloy steels vary in their vulnerability to caustic-induced SCC. Tests have suggested that nickel-containing steels are more resistant than carbon steels, molybdenum additions are detrimental and the effects of chromium additions vary with temperature.<sup>9</sup>

At higher temperatures and concentrations, the zone of dihypoferrite stability increases considerably, extending to lower pH values, as shown in the Pourbaix diagram for the iron–water system at 300 °C in

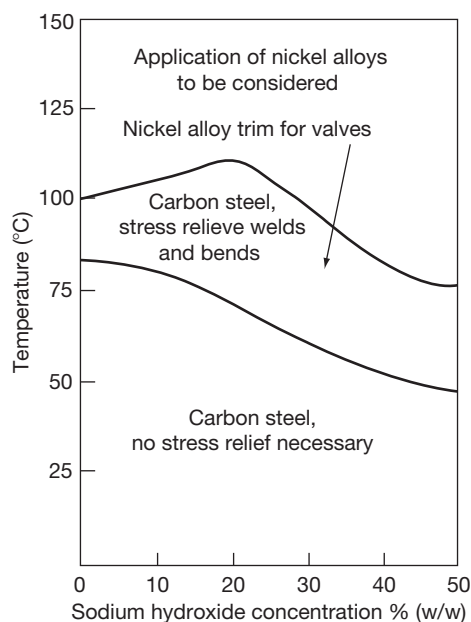


**Figure 3** Temperature and concentration limits for stress corrosion cracking susceptibility of carbon steels in sodium hydroxide solutions. Adapted from NACE Standard Practice SP0403–2008. Avoiding Caustic Stress Corrosion Cracking of Carbon Steel Refinery Equipment and Piping; NACE International: Houston, TX, 2008.

**Figure 2**, which suggests that the alkaline corrosion of steels is possible at a pH down to  $\sim 9$ , equivalent to lightly alkalized water. Kinetic studies suggest that the magnetite film on carbon steels begins to lose its protective properties as temperatures increase above the atmospheric boiling point, depending on concentration. Anodic polarization curves for AISI 1020 steel in stagnant 2.75 M ( $\sim 11\%$  w/w) sodium hydroxide at temperatures in the range 95–175 °C are shown in **Figure 4**.

The active regions of the curves are thought to be attributable to active iron dissolution as ferroate rather than dihypoferrite, because of the greater solubility of the former in alkaline solutions. Although passivation behavior is evident at all four test temperatures, the passive current increases by around an order of magnitude between the lowest and highest temperatures. Additional studies on rotating electrodes suggest that this is due to magnetite film thinning due to increased solubility as the temperature rises. Film formation competes with film dissolution, and turbulence accelerates film dissolution and corresponding corrosion rates.<sup>10</sup>

Although the corrosion risks that are presented at high temperatures by increased concentrations of sodium hydroxide solutions are well understood,

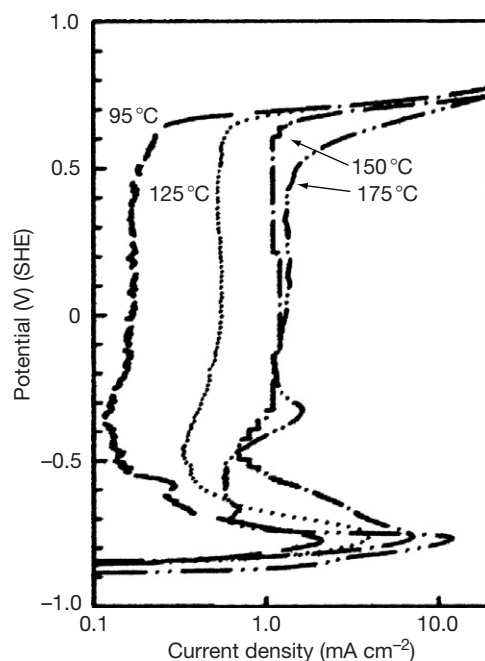


**Figure 4** Potentiodynamic polarization curves for AISI 1020 steel in stagnant 2.75 M ( $\sim 11\%$  w/w) sodium hydroxide at temperatures in the range 95–175 °C. Adapted from Giddey, S.; Cherry, B.; Lawson, F.; Forsyth, M. *Corros. Sci.* **2001**, 43, 1497–1517.

problems can arise in practice in situations where nominally benign concentrations can increase locally under the influence of high heat fluxes and/or adverse geometries, particularly in steam raising equipment. Corrosion control in boilers is based on maintaining the pH of boiler waters, typically in the pH range 9–10, by the addition, at the ppm level, of either free sodium hydroxide or combinations of sodium phosphates that buffer the pH in the required range but have the potential to release free sodium hydroxide, depending on the Na:P ratio. The concentration of these alkaline species can be increased by several orders of magnitude from the ppm to the percent level in films of boiler water on heat transfer surfaces when the metal skin temperature exceeds the boiling temperature of the water at the prevailing pressure. The driving force for concentration is related to the temperature difference between the two,  $\Delta T$ , as illustrated in **Figure 5**.<sup>11</sup>

Heat transfer into a crevice, as might exist at a tube/tubesheet joint in a boiler, can exacerbate the driving force for concentration.<sup>12</sup> These concentration processes at local sites in steam raising equipment can result in the on-load, caustic corrosion, sometimes described as ‘caustic gouging,’ of utility<sup>13</sup> and process plant<sup>14</sup> steel boiler tubes, and also give

rise to caustic-induced SCC of carbon, low alloy and stainless steels, and nickel alloy components, exemplified by the caustic cracking of a carbon steel stub attached to an alloy 825 (N08825) bellows that is illustrated in **Figure 6**. The root cause of the problem was a malfunctioning desuperheater upstream of the bellows that injected periodic slugs, rather than the

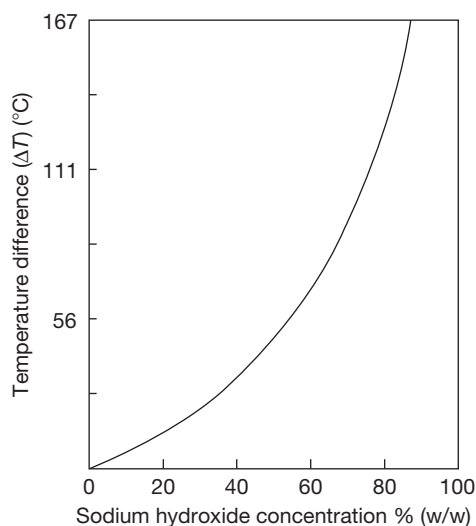


**Figure 5** Concentration of sodium hydroxide attainable in a film of boiler water on a heat transfer surface as a function of the temperature difference,  $\Delta T$ , between the surface temperature and the boiling point of the water. Adapted from *Betz Handbook of Industrial Water Conditioning*, 9th ed.; Betz Laboratories, 1991.

intended spray, of water containing a few ppm of sodium hydroxide into the pipe. The water collected in the crevice between the stub and the bellows and successive wetting/drying events resulted in concentration of the caustic in the crevice, leading ultimately to SCC of the stub, driven by the residual stresses around the attachment weld to the bellows.

Grey and ductile cast irons have corrosion resistances broadly similar to steels in sodium hydroxide. Ductile irons, in contrast to grey irons, are vulnerable to SCC. A comparative study of pure iron and white cast iron in 14 M ( $\sim 56\%$  w/w) acid in the temperature range 20–60°C suggested that iron carbide is detrimental to corrosion performance in relatively concentrated sodium hydroxide.<sup>15</sup> Nickel has the most significant influence on the corrosion resistance of cast irons, as shown by the corrosion rate data in **Figure 7** for cast irons with varying nickel contents in boiling 50–65% (w/w) sodium hydroxide.<sup>16</sup>

In particular, the austenitic irons containing >15% nickel (such as F41000, F41002, and F43000) have very good resistance to sodium hydroxide solutions of up to  $\sim 70\%$  (w/w) concentration, but can be vulnerable to SCC, particularly if chlorides are present, for which stress relief provides appropriate mitigation.<sup>5</sup> High silicon cast irons, containing typically 14–16% Si (such as F 47003), are not resistant to relatively concentrated sodium hydroxide at elevated temperatures because the siliceous films that provide their resistance to erosion–corrosion are soluble in the alkali.

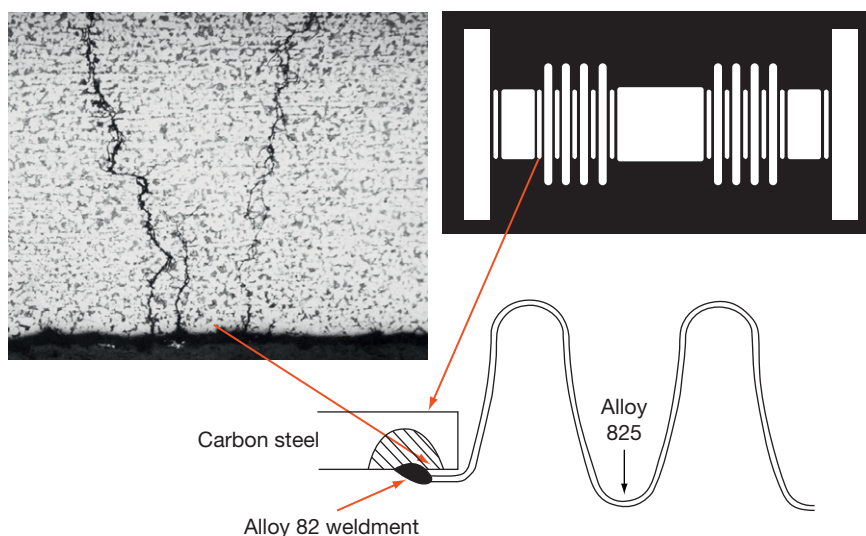


**Figure 6** Section through carbon steel bellows stub downstream of a desuperheater in a steam main operating at  $\sim 16$  bar and 250°C that has suffered caustic SCC due to sequential wetting/drying in the crevice between the stub and the alloy 825 convolutions.



Although there is very little specific data in the public arena, the performances of steels and cast irons in potassium hydroxide are very similar to their equivalent performances in sodium hydroxide.

### 2.21.3 Stainless Steels

Potentiodynamic polarization curves in stagnant 15% (w/w) sodium hydroxide solution at 90 °C for the key constituent elements of stainless steels, pure

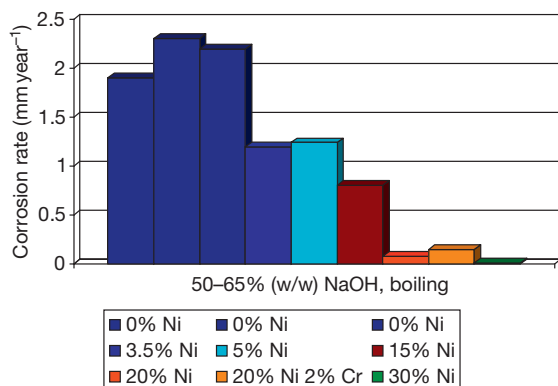


**Figure 7** Corrosion rates for cast irons containing varying quantities of nickel tested in boiling 50–65% (w/w) sodium hydroxide solution. Adapted from Corrosion Resistance of Nickel and Nickel-Containing Alloys in Caustic Soda and Other Alkalis; CEB-2, International Nickel Company, 1973.

iron, nickel, chromium, and molybdenum, are shown in **Figure 8**.<sup>17</sup> Iron has the most active corrosion potential, and in the early stages of anodic polarization, it dissolves at progressively increasing rates. At a relatively high, critical current density, it exhibits classic passivation behavior due to the formation of magnetite,  $\text{Fe}_3\text{O}_4$  which shows gradually increasing rates of dissolution as the potential is further increased to a secondary passivation peak, probably associated with the oxidation of  $\text{Fe}_3\text{O}_4$  to  $\text{Fe}_2\text{O}_3$ . The current density shows little tendency to increase in response to further polarization up to a potential >300 mV at which transpassive breakdown as soluble ferrate,  $\text{FeO}_4^{2-}$ , occurs.

Molybdenum has a corrosion potential more noble than iron but more active than chromium or nickel. However, under anodic polarization, molybdenum dissolves at progressively faster rates as soluble molybdate,  $\text{MoO}_4^{2-}$ , and shows no tendency to passivate. Chromium, on the other hand, has the most noble corrosion potential, and its initial anodic polarization behavior is consistent with the presence of a protective passive film of chromium oxide,  $\text{Cr}_2\text{O}_3$ , from the outset with no evidence of an active dissolution peak prior to the onset of passivity. When present, the film is more protective than the corresponding films on iron and nickel, having the lowest current density requirement for maintenance in its passive potential range. However, transpassive breakdown to soluble chromate,  $\text{CrO}_4^{2-}$ , occurs at a potential

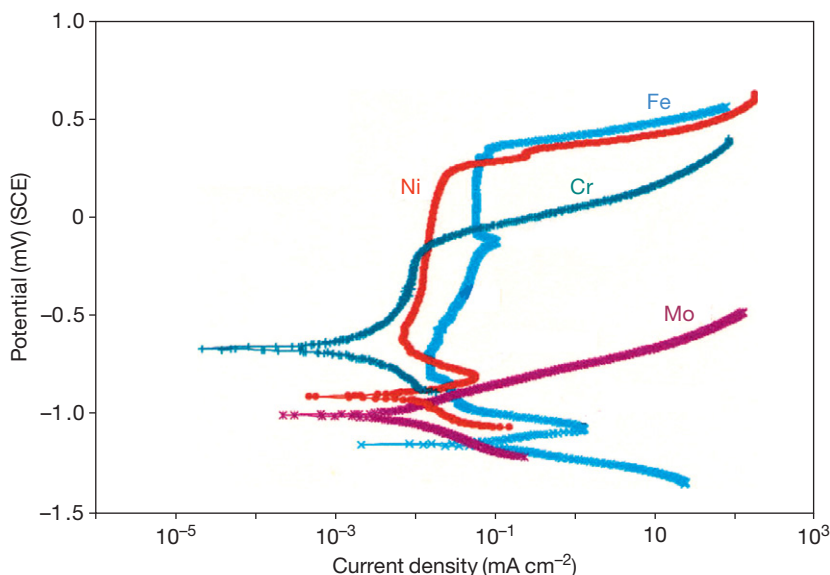


**Figure 8** Potentiodynamic polarization curves for pure iron, nickel, chromium, and molybdenum in stagnant 15% (w/w) sodium hydroxide at 90 °C. Adapted from Bhattacharya, A.; Preet, M. S. In *Corrosion 2008, Corrosion of Duplex Stainless Steels in High pH Caustic Solution*, New Orleans, LA; NACE International: Houston, TX, 2008; Paper 08194.

well below the corresponding breakdown potentials for iron and nickel.

The corrosion potential of nickel is more noble than either iron or molybdenum but less noble than chromium. Nickel's anodic polarization behavior attests to the importance of the element in providing resistance to strongly alkaline environments. The critical current density for passivation is an order of magnitude lower than that for iron. The passive zone extends over a wide potential range within which nickel is protected by nickel oxide, NiO. As the potential increases in the passive range, the current density also increases gradually but the current densities for the maintenance of passivity are only marginally higher than for chromium. Ultimately, transpassive breakdown does occur at a similar potential in iron due to the formation of a soluble species, probably  $\text{HNO}_2 \cdot \text{H}_2\text{O}$ , well beyond the transpassive breakdown potential of chromium.

The polarization curves for the individual alloying elements explain their effects on the performances of stainless steels. The compositions of the commercial grades of stainless steels that are relevant to alkali applications are summarized in Table 1.

Nickel delivers the most significant benefits, providing additional resistance to anodic dissolution at lower potentials and robust passivity across a

potential range wide enough to limit the possible promotion of transpassivity by oxidizing agents. Chromium also delivers significant benefits by inhibiting dissolution and promoting passivity at lower potentials but introduces a vulnerability to transpassive dissolution in the presence of oxidizing agents. Molybdenum's benefits are confined to additional resistance to anodic dissolution in the active potential range.

These roles for the individual alloying elements are apparent in the formation of the passive films that form spontaneously on stainless steels in alkalis. Film formation was studied recently<sup>18</sup> in an X-ray photoelectron spectroscopic (XPS) study of the progressive formation of the naturally formed passive films on types 304 (S30400) and 2205 (S32205) stainless steel in 0.4% (w/w) sodium hydroxide solution at ambient temperatures, in which the natural corrosion potential of both increases with time. On first immersion, iron dissolves preferentially and is present in the film ultimately as  $\text{Fe}^{3+}$  oxy-hydroxide, the content of which decreases with time. Chromium accumulates with time in the film as  $\text{Cr}^{3+}$  oxy-hydroxide, and the combined effect of iron and chromium depletion is that the metal layer beneath the film becomes enriched in nickel, which accumulates in the film as nickel hydroxide, to a greater extent on

**Table 1** Compositions of some wrought stainless steels that are relevant to alkali applications

UNS no	Common name	Fe	Ni	Cr	Mo	Cu	Si	Other
S43000	430	Balance		16–18				
S43035	439	Balance		17–19				
S44627	E-brite	Balance		26	1			
S44735	29–4C	Balance		29	4			
S32304	2304	Balance	4–5	23				
S31803 S32205	2205	Balance	4.5–6.5	21–23	2.5–3.5			N
S32750 S32760	2507	Balance	6–8	24–26	3–4.5 3–4	<0.5 0.5–1.0		N W, N
S32900		Balance	4.5	28	1.5			
S30400	304	Balance	8–10.5	18–20				<0.08C
S30403	304L	Balance	8–12	18–20				
S30500	305	Balance	10.5–13	17–19				<0.12C
S31600	316	Balance	10–14	16–18	2–3			<0.08C
S31603	316L	Balance	10–14	16–18	2–3			
S31254	254SMO	Balance	17.5–18.5	19.5–20.5	6–6.5	0.5–1.0		N
S30900	309	Balance	12–15	22–24				Mn
S31000	310	Balance	19–22	24–26				Mn
S32654	654SMO	Balance	22	24	7.3			Mn
N08904	904L	Balance	23–28	19–23	4–5	1–2		
N08926	25–6MO	Balance	24–26	19–21	6–7	0.5–1.5		N
S31277	27–7MO	Balance	26–28	20.5–23.0	6.5–8.0	0.5–1.5		Mn, N
N08020	20	Balance	32–35	19–21	2–3	3–4		
N08800	800	Balance	30–35	19–23				
N08028	28	Balance	31	27	3.5	1		
R20033	33	Balance	30–33	31–35	0.5–2.0	0.3–1.2		N

type 304 (S30400) than the 2205 (S32205) stainless steel. The molybdenum in the 2205 (S32205) stainless steel is present as an oxy-hydroxide in the film and in the metallic form at the metal/film interface at the same level as in the parent material. The dealloying effects are exacerbated in more aggressive conditions at higher temperatures and in more concentrated solutions to the extent that 'nickel' layers have been reported on austenitic stainless steel surfaces. It has been shown that, in reality, the dealloying of iron from the surface of type 316 stainless steel proceeds as far as a solid solution with a nickel/iron atomic ratio of  $\sim 1.3$ , equivalent to  $\sim 56\%$  nickel, in 50% (w/w) sodium hydroxide solution at  $140^\circ\text{C}$ .<sup>19</sup>

In practice, the relative contribution of chromium and nickel to the corrosion resistances of stainless steels in alkalis depends on and varies with the grade. The standard ferritic grades of stainless steel such as types 430 (S43000) and 439 (S43035), containing up to  $\sim 19\%$  chromium, do not find significant application in alkalis. However, the so-called super-ferritic grades containing typically 26–29% chromium with controlled carbon + nitrogen levels or stabilized with titanium or niobium to control vulnerability to intergranular corrosion due to sensitization, typified by the proprietary grades E-brite 26–1 (S44627) and AL 29–4C (S44735), have significant, potentially useful resistance. The corrosion rate data in Figure 9 demonstrate the superior performance of the super-ferritic grades relative to conventional austenitic grades of stainless steel in tests in 50% (w/w) sodium hydroxide at  $140^\circ\text{C}$  in which a conventional ferritic grade performed relatively badly.<sup>20</sup> Superferritic stainless steels have found commercial application as tubing materials

in caustic evaporators, and are not adversely affected to any significant extent by the presence of contaminants. Indeed, they require a sustained supply of oxidizing contaminants such as chlorates to maintain passivity at the prevailing high temperatures and concentrations.<sup>5</sup>

Isocorrosion diagrams for the basic types 304 (S30400) and 316 (S31600) austenitic stainless steels in sodium hydroxide are shown in Figure 10.<sup>21</sup> There is little to choose between the grades and their low carbon equivalents, all of which are resistant up to  $\sim 20\%$  (w/w) boiling sodium hydroxide solutions. Corrosion rates for some duplex stainless steels in boiling sodium hydroxide solutions are shown in Figure 11<sup>22</sup> and suggest that duplex alloys are resistant up to  $\sim 30\%$  (w/w) boiling sodium hydroxide solutions, depending on the chromium and nickel contents of the specific grade.

The corrosion rates of various grades of duplex stainless steels in 30–70% (w/w) sodium hydroxide solutions are in the order S32906 < 2507 (S32750) < 2205 (S32205) < 2304 (S32304), confirming that their resistances are determined largely, but not exclusively, by their chromium contents.<sup>23</sup> However, the vulnerability of chromium to transpassive dissolution was confirmed in studies of austenitic and duplex alloys in 30% (w/w) sodium hydroxide at  $150^\circ\text{C}$ . Under deaerated conditions, the strong, passivating effects of both chromium and nickel were confirmed. However, in more strongly oxidizing conditions, chromium was dissolved resulting in thicker, less protective oxide films containing only nickel and iron.<sup>24</sup>

The overall effects of additions of the major alloying elements nickel, chromium, and molybdenum on the corrosion of austenitic and duplex stainless steels

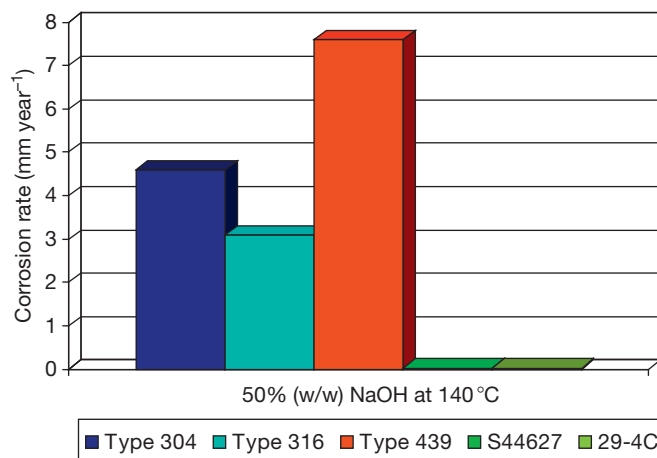


**Figure 9** Corrosion rates for various stainless steels in 50% (w/w) sodium hydroxide at  $140^\circ\text{C}$ . Adapted from Deverell, H. E.; Franson, I. A. *Mater. Perform* **1989**, 28, 52–57.

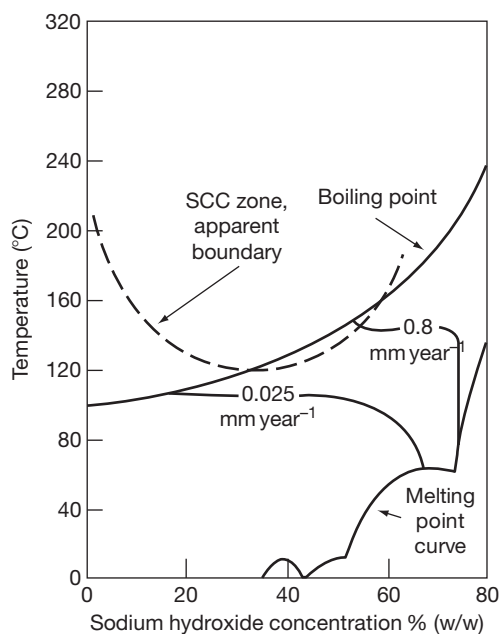


**Figure 10** Isocorrosion diagram for types 304 and 316 stainless steels in sodium hydroxide. Adapted from Corrosion Resistance of Nickel and Nickel-Containing Alloys in Caustic Soda and Other Alkalies; CEB-2, International Nickel Company, 1973.

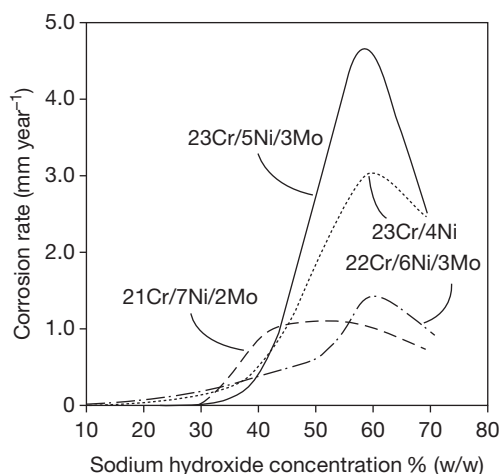


**Figure 11** Corrosion rates of duplex stainless steels as a function of concentration of boiling NaOH solutions. Adapted from Horn, E. M. *Corrosion and Environmental Degradation*; Schutze, M., Ed.; Wiley-VCH: London, 2000; Vol. 2, pp 69–111.

in sodium hydroxide are summarized in Figure 12, based on an analysis of the threshold temperature in the range 85–146 °C at which the corrosion rate in 50% (w/w) sodium hydroxide exceeds 0.13 mm

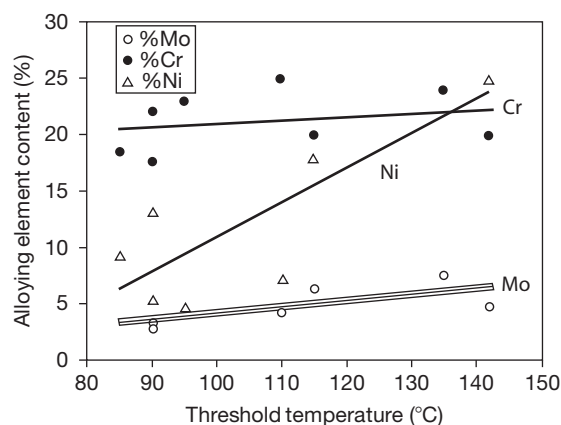


**Figure 12** Effects of nickel, molybdenum, and chromium contents of stainless steels on the threshold temperature at which the corrosion rate in 50% (w/w) sodium hydroxide exceeds 0.13 mm year<sup>-1</sup>. Adapted from Davies, M. *Corrosion by Alkalies*. In *ASM Handbook: Corrosion: Environments and Industries*; ASM International: Materials Park, OH, 2006; Vol. 13C, pp 710–726.

year<sup>-1</sup> for the grades 304 (S30400), 316L (S31603), 2205 (S32205), 2304 (S32304), 2507 (S32750), 254SMO (S31254), 654SMO (S32654), and 904L (N08904).<sup>5</sup>

The most significant alloying element is clearly nickel, with both chromium and molybdenum demonstrating only minor benefits within the relevant composition ranges. The beneficial effects of nickel additions were demonstrated in a study of stainless steels and nickel alloys in 50% (w/w) sodium hydroxide at 300 °C in the presence and absence of oxygen, the results of which are shown in Figure 13.<sup>25</sup> Clearly, corrosion rates are very sensitive to the presence or otherwise of oxygen but in all conditions, the resistance increases with nickel addition up to a content of ~20%, but not beyond under these relatively aggressive conditions.

At lower temperatures, alloys with >20% nickel such as 904L (N08904) and alloys 20 (N08020), 800 (N08800), and 33 (R20033) provide much improved resistance to sodium hydroxide relative to the basic austenitic grades and cheaper alternatives to nickel based alloys. For example, Figure 14 shows corrosion rates for alloy 33 relative to nickel alloys 600 (N06600) and 625 (N06625) in 50% (w/w) sodium hydroxide solution at 180 °C. Although not as resistant as alloy 600 (N06600), alloy 33 (R20033) corrodes at a rate of <0.1 mm year<sup>-1</sup> that is acceptable for most applications and is much more resistant than the molybdenum-containing alloy 625 (N06625). Additionally, alloy 33 (R20033) shows no evidence of dealloying after 153 days exposure, in contrast to

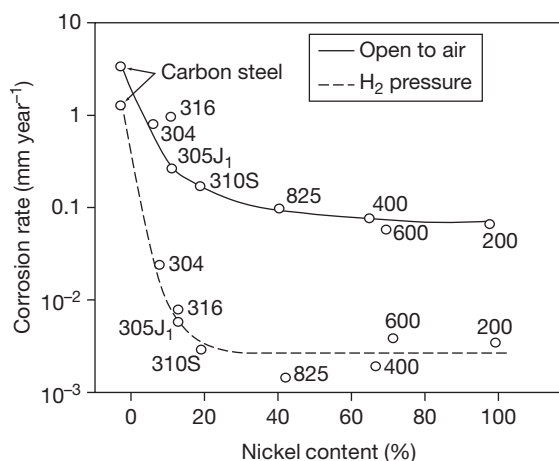


**Figure 13** Effect of nickel content on the corrosion rates of stainless steels and nickel alloys in 50% (w/w) sodium hydroxide at 300 °C in the presence and absence of oxygen. Adapted from Yasuda, M.; Fukumoto, K.; Koizumi, H.; Ogata, Y.; Hine, F. *Corrosion* **1987**, 43, 492–498.

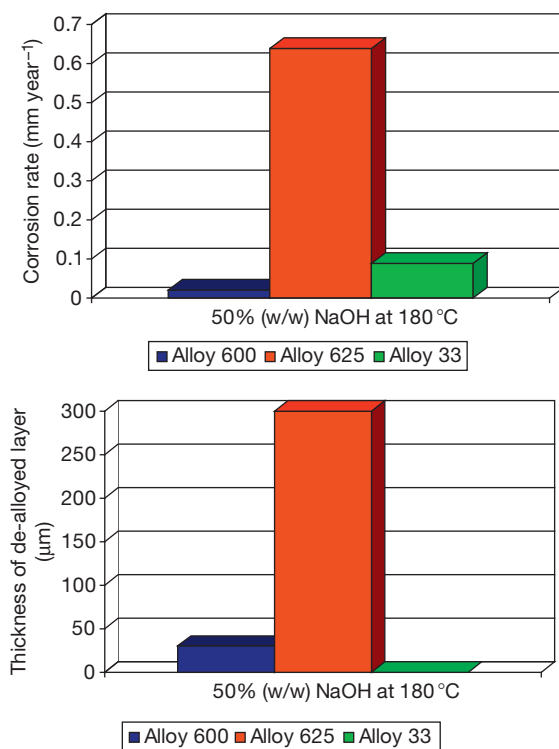


**Figure 14** Corrosion rates and dealloyed layer thicknesses for alloys 600, 625 and 33 tested in 50% (w/w) sodium hydroxide solution at 180 °C. Adapted from Paul, L.; Alves, H. *Corrosion 2004, Alloy 33: A Versatile Alloy for Mineral Acid and Other Applications*, New Orleans, LA; NACE International: Houston, TX, 2004; Paper 04226.

both of the nickel alloys that are significantly dealloyed after 35 days exposure.<sup>26</sup>

Stainless steels are vulnerable to SCC in alkaline solutions. It has been proposed that the vulnerability is due to the iron and chromium dealloying processes that occur on stainless steel surfaces in alkaline exposures<sup>19</sup> and this is described in more detail in **Chapter 2.05, Dealloying** in this volume. The conditions of concentration and temperature that present risks to the basic types 304 (S30400) and 316 (S31600) austenitic stainless steels are shown in **Figure 9** which confirms that SCC is possible at temperatures above ~100 °C, depending on concentration. Tests on duplex stainless steels have revealed no evidence of SCC in boiling 20–70% (w/w) solutions, suggesting that they are at least as resistant as the basic austenitic grades.<sup>21,23</sup> Various studies have indicated that chromium is more important than nickel in determining the resistance to SCC in alkaline solutions. For example, in 30% (w/w) sodium hydroxide at 200 °C, the resistances to cracking in separate studies were in the order 2205 (S32205) > 316L (S31603) > 904L (N08904) and 33 (R20033) > 28 (N08028) > 825 (N08825) > 904L (N08904).<sup>27,28</sup>

Overall, contaminants do not appear to have any significant adverse effects on either the corrosion rates or the vulnerability to SCC of stainless steels in sodium hydroxide solutions. The oxidizing chlorates at the normal levels of contamination appear to be beneficial toward stainless steels in helping to promote and sustain passivity. There is no evidence that SCC risks are exacerbated in sodium hydroxide solutions by the presence of chlorides up to their maximum contaminant levels. However, if the sodium hydroxide is neutralized, the risks of chloride-induced SCC are reintroduced.

Although there is very little specific data in the public arena, the performances of stainless steels in potassium hydroxide are broadly similar to their equivalent performances in sodium hydroxide. A specific study of type 304L (S30403) austenitic stainless steel showed potassium hydroxide to be less aggressive than sodium hydroxide in promoting caustic-induced SCC.<sup>29</sup>

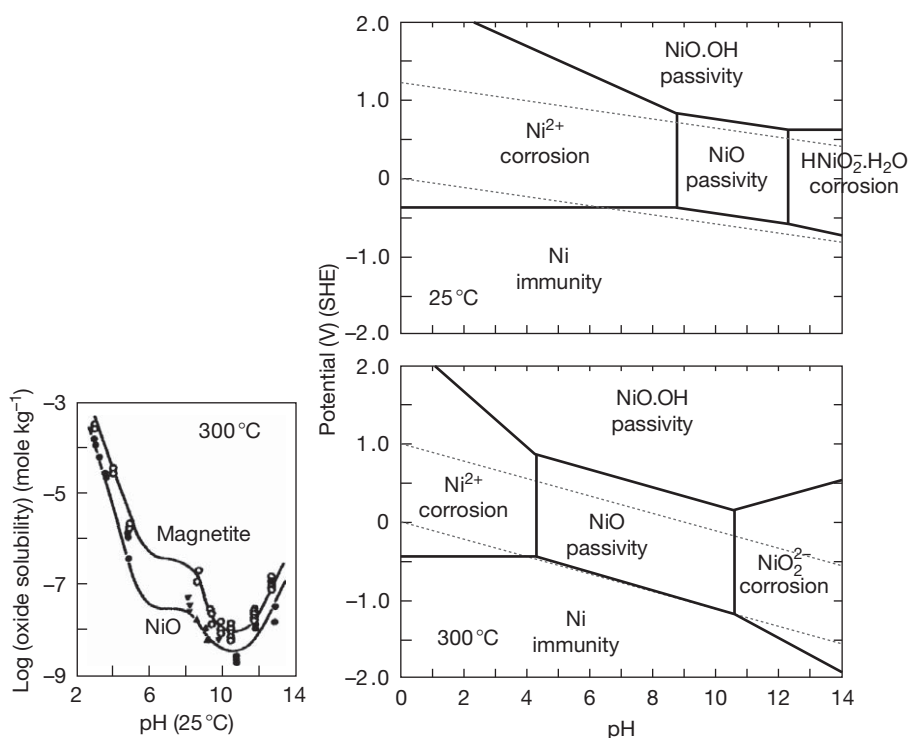
## 2.21.4 Nickel and Nickel Alloys

The compositions of the commercial nickel alloys that are relevant to alkali applications are summarized in **Table 2**. Nickel is second only to silver in its resistance to concentrated alkalis at elevated



**Table 2** Compositions of some wrought nickel alloys that are relevant to alkali applications

UNS no	Common name	Fe	Ni	Cr	Mo	Cu	Si	Other
N02200	200		>99					<0.15C
N02201	201		>99					<0.02C
N04400	400	<2.5	Balance			28–34		Mn
N05500	500	<2.0	Balance			27–33		Al, Mn
N08825	825	>22	Balance	19.5–23.5	2.5–3.5	1.5–3.0		Ti
N06600	600	6–10	Balance	14–17				
N06690	690	7–11	Balance	27–31				
N10276	C-276	4–7	Balance	14.5–16.5	15–17			W, Co
N06022	C-22	2–3	Balance	20.5–22	13–14			W, Co
N06059	59		Balance	23	16			
N06686	686	<5	Balance	19–23	15–17			W
N06625	625	<5	Balance	20–23	8–10			Nb
N10665	B-2	<2	Balance		28			
N10675	B-3	1.5	Balance	1.5	28.5			W, Co

**Figure 15** Simplified potential/pH diagrams for the Ni-H<sub>2</sub>O system at 25 °C and 300 °C, based on an equilibrium activity of 10<sup>-5</sup> molal, calculations performed using HSC Chemistry V6.12, Outotec Research, Finland. Oxide solubility data adapted from Turnbull, A.; Psaila-Dombrowski, M. *Corros. Sci* **1992**, 33, 1925–1966.

temperatures where nickel and its alloys find significant commercial application. The temperature range up to ~300 °C is of particular significance because evaporator tubes that are used for the commercial manufacture of 73% (w/w) sodium hydroxide and steam generator tubes in pressurized water reactors (PWR) in the nuclear industry both operate at

~300 °C. The basis of the good performance of nickel and its alloys under these conditions is the formation and maintenance of highly insoluble, nickel oxide, NiO, films. The Pourbaix diagrams for the nickel-water system shown in Figure 15 confirm the existence of the NiO passivation zone and define its thermodynamic boundaries at 25 °C and 300 °C.

Despite the apparent threat to passivity due to the encroachment of corrosion zones based on the formations of soluble  $\text{H}\text{NiO}_2 \cdot \text{H}_2\text{O}$  and  $\text{NiO}_2^-$  at 25 °C and 300 °C respectively, in practice a kinetic passivation zone extends much further into the alkaline pH region. The passive film forms much more rapidly than it dissolves because of the low solubility of NiO, exemplified by the comparative data for magnetite and NiO at 300 °C<sup>30</sup> that is also shown in Figure 15. In practice, both of the commercial purity grades of nickel, 200 (N02200) and 201 (N02201), have excellent resistance to sodium hydroxide across wide ranges of concentration and temperature, as shown in Figure 16, and find significant application in caustic evaporation equipment. The low carbon grade 201 is generally preferred for service above 300 °C to avoid problems associated with loss of ductility and intergranular attack due to the precipitation of graphite in the alloy.

However, the corrosion rates of commercially pure nickel are very sensitive to the presence and concentration of oxidizing chlorates and hypochlorites that have a significant influence on the life of caustic evaporation equipment. The test results in Figure 17 are corrosion rates for a duplex stainless steel (S32906) and nickel 200 (N02200) in boiling 50% (w/w) sodium hydroxide solution with different

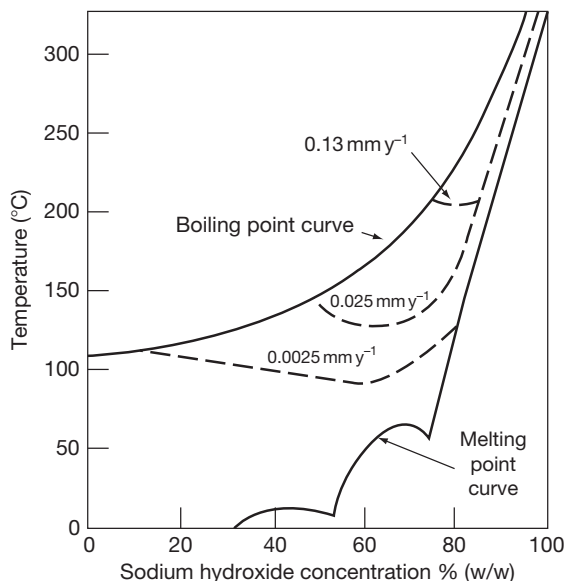


**Figure 16** Isocorrosion diagram for nickel 200 and low carbon nickel 201 in sodium hydroxide. Adapted from Corrosion Resistance of Nickel and Nickel-Containing Alloys in Caustic Soda and Other Alkalies; CEB-2, International Nickel Company, 1973.

levels of chloride and chlorate contaminants. The differing effects of oxidizing contaminants on stainless steels and nickel are apparent.

The chromium-free nickel alloys that find significant applications in sodium hydroxide, particularly in evaporation equipment, are the nickel copper alloys 400 (N04400) and 500 (N05500) that have equivalent corrosion resistance to sodium hydroxide up to ~73% (w/w) concentration. However, in keeping with nickel 200 (N02200) and 201 (N02201), their corrosion resistance is very sensitive to the presence of oxidizing agents such as chlorates and hypochlorites that have to be controlled below threshold levels to avoid excessive corrosion and contamination of the product sodium hydroxide with nickel and copper corrosion products.<sup>5,31</sup> The alloys 400 (N04400) and 500 (N05500) are also vulnerable to caustic-induced SCC and liquid metal embrittlement (LME) by mercury in the case of components that handle mercury cell caustic prior to final separation of mercury and its salts from the product caustic.<sup>21</sup> The chromium-free B family of alloys also has good resistance to sodium hydroxide in the absence of oxidizing agents but the advantages they offer over cheaper alternatives are marginal and they have found little application.

The preferred chromium-bearing alloy for sodium hydroxide applications at higher temperatures is alloy 600 (N06600) that has comparable, arguably better, resistance to corrosion than the commercially pure nickel alloys exemplified by the corrosion rates in boiling solutions for the two materials that are shown in Figure 18.<sup>5</sup>

Alloy 600 (N06600) has two additional advantages over commercially pure nickel. It is more resistant to

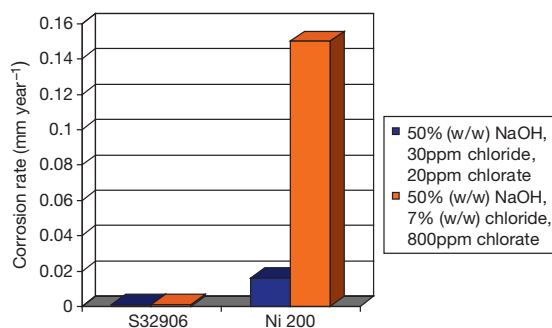


**Figure 17** Corrosion rates for a duplex stainless steel and nickel 200 in boiling 50% (w/w) sodium hydroxide solution with different levels of chloride and chlorate contaminants. Adapted from Leander, D. Corrosion Characteristics of Different Stainless Steels, Austenitic and Duplex, in NaOH Environments Stainless Steel World Conference Maastricht, Stainless Steel World, 2003.

the presence of sulfur-containing contaminants in the sodium hydroxide that can promote intergranular penetration of nickel due to the formation of a low melting point nickel/nickel sulfide eutectic. It is also more tolerant to the presence of oxidizing agents such as chlorate and hypochlorite due to the passivation reinforcing effects of the chromium in the base metal. However, on the downside, the alloy 600 (N06600) is vulnerable to caustic-induced SCC at temperatures above  $\sim 190^\circ\text{C}$  in concentrated sodium hydroxide. In principle, the risk of SCC can be mitigated by appropriate thermal stress relief but this requires exposure to relatively high temperatures for significant time periods (for example,  $\sim 900^\circ\text{C}$  for 1 h) and is not always practicable for complex equipment items.

Few corrosion problems have been studied as intensively as the SCC vulnerability of alloy 600 (N06600) that has been used extensively as a steam generator tube material in PWRs in the nuclear industry. This is a complex topic that is described in more detail elsewhere<sup>32</sup> and in **Chapter 2.09, Stress Corrosion Cracking** in this volume. The research has included detailed investigations of the intergranular cracking (IGSCC) of alloy 600 (N06600) in concentrations of  $\sim 10\%$  (w/w) sodium hydroxide at  $\sim 300^\circ\text{C}$ . The IGSCC occurs in a relatively narrow band of corrosion potentials close to the Ni/NiO equilibrium that are adopted by the alloy in the deaerated boiler water. Carbon content and carbide morphology play an important role. Intergranular carbides improve

IGSCC resistance, and heat treatments for alloy 600 that develop preferred microstructures have been proposed and adopted. Operating experience has established that alloys 800 (N08800) and 690 (N06690) are much more resistant to IGSCC than alloy 600 (N06600). Recently, it has been proposed that internal, intergranular oxidation of chromium is the initiating process for IGSCC in alloy 600 (N06600). In contrast, alloy 690 (N06690) resists IGSCC because its much higher chromium content allows it to form a protective external oxide, and alloy 800 (N08800) has sufficient nickel to resist the dealloying processes that might render it vulnerable to the mechanism for caustic-induced SCC in stainless steels and sufficient chromium to form an external oxide and resist the internal oxidation route to crack initiation.<sup>33,34</sup>

The nickel–chromium–molybdenum alloys such as alloys 625 (N06625), 59 (N06059), and the C family do not find significant application in alkalis because, at the margin, they are less resistant than other nickel based alloys and in conditions where they have useful resistance, there are cheaper alternatives.

The corrosion rates shown in **Figure 19** for various nickel alloys in 70% (w/w) sodium hydroxide solution at  $170^\circ\text{C}$ <sup>35</sup> confirm that the two nickel–chromium–molybdenum alloys are outperformed by the nickel–copper and nickel–chromium–iron alloys. The nickel–chromium–molybdenum alloys are also vulnerable to caustic-induced SCC.<sup>36</sup> Arguably, the nickel–chromium–molybdenum alloys might be more tolerant to the presence of oxidizing agents such as chlorates and hypochlorites, but this has to be offset against the vulnerability of molybdenum to transpassive dissolution in alkaline media. In practice,

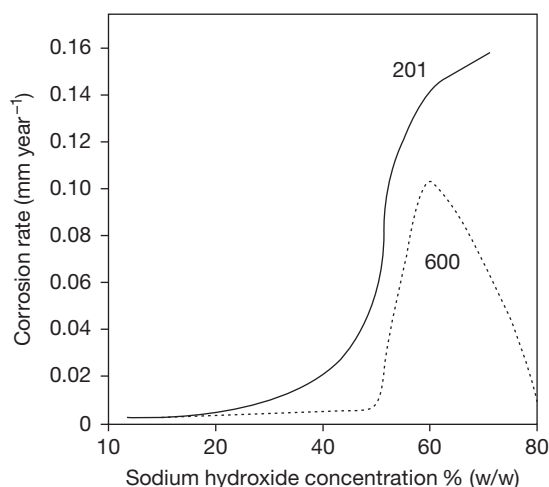


**Figure 18** Corrosion rates of alloys 201 and 600 in boiling 50% (w/w) sodium hydroxide solution. Adapted from Davies, M. *Corrosion by Alkalies*. In *ASM Handbook: Corrosion: Environments and Industries*; ASM International: Materials Park, OH, 2006; Vol. 13C, pp 710–726.

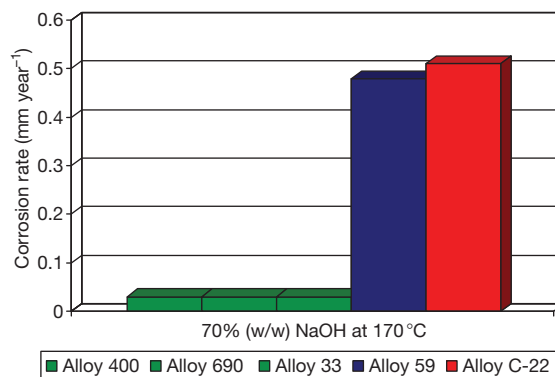


**Figure 19** Corrosion rates for various nickel alloys in 70% (w/w) sodium hydroxide solution at  $170^\circ\text{C}$ . Adapted from Heubner, U.; Kohler, M. *High Alloy Materials for Aggressive Environments*; ThyssenKrupp VDM GmbH 1998; VDM Report No 26.

the nickel–chromium–molybdenum alloys are specified only when their corrosion resistance to other fluids are required simultaneously, such as in heat exchange duties for alkaline fluids where the heating or cooling fluid is sufficiently corrosive as to require a nickel–chromium–molybdenum alloy.

Although there is very little specific data in the public arena, the performances of nickel alloys stainless steels in potassium hydroxide are broadly similar to their equivalent performances in sodium hydroxide.

## 2.21.5 Other Metals and Alloys

Commercial purity zirconium (Zr702, R60702) is protected by a surface oxide film, composed mainly of  $\text{ZrO}_2$ , that is extremely resistant to alkaline attack, as a result of which zirconium has excellent resistance to alkalis, both aqueous and fused. Thus, it resists 73% (w/w) sodium hydroxide up to 138 °C and molten sodium hydroxide at temperatures above 1000 °C. It is resistant to the presence of oxidizing contaminants unless significant amounts of chlorides are present. It is resistant to SCC in boiling solutions but is very vulnerable to LME if contaminant mercury is present.<sup>5</sup> More detailed information is given in **Chapter 3.14, Corrosion of Zirconium and its Alloys**.

Titanium and its alloys are also dependent on the formation of protective oxide films consisting mostly of titanium dioxide,  $\text{TiO}_2$ , for their resistances to corrosion. However, the  $\text{TiO}_2$  film on titanium is more soluble in alkaline conditions than the equivalent  $\text{ZrO}_2$  film on zirconium. In practice, commercially pure titanium (ASTM grade 2, R50400) is resistant over a wide range of concentrations at ambient temperatures but increases in temperature increase the film dissolution rate. Titanium's performance limits are determined as much by vulnerability to the hydriding caused by the hydrogen released in the corrosion process as by the corrosion rate *per se* that might otherwise be acceptable. Hydrogen absorption is particularly prevalent in the 20–40% (w/w) concentration range and at 50% (w/w) sodium hydroxide, the temperature has to be limited to ~80 °C to avoid excessive hydriding and embrittlement.<sup>37</sup>

Copper piping has been used for handling sodium hydroxide solutions in the absence of oxidizing agents and tolerates temperatures up to ~100 °C at 73% (w/w) concentration. The cupronickels (grades 90–10, C70600 and 70–30, C71500) have improved resistance and have found application in caustic evaporation up to 50% (w/w) concentration if some

copper contamination is acceptable.<sup>5</sup> However, copper contamination is not acceptable in several major uses of the sodium hydroxide product and this inevitably limits the usage of copper and its alloys in alkaline applications.

Silver has exceptional resistance to sodium hydroxide at temperatures well beyond boiling but its cost precludes other than niche use. The amphoteric metals are clearly precluded from significant application, and tantalum has very poor resistance to caustic solutions and finds no application.

## 2.21.6 Nonmetallic Materials

### 2.21.6.1 Thermoplastic and Reinforced Thermosetting Materials

In practice, chemical compatibility is, but, one factor that determines the suitability or otherwise of a thermoplastic material for a specific application. Other factors such as mechanical and fabrication properties, thermal expansion characteristics, permeation properties, etc. are significant design considerations. In practice, other than for small scale equipment, thermoplastics are used more commonly as linings on stronger substrates rather than in solid form, because of reliability and integrity concerns. The application of these materials is covered in more detail in the relevant chapters in this book but the more significant materials are as follows:

1. Polyethylene (PE) and polypropylene (PP) have good resistance. High density polyethylene (HDPE) and PP resist concentrations up to ~70% (w/w) at temperatures up to ~60 °C and ~100 °C respectively.
2. Polyvinyl chloride (PVC) resists concentrations up to ~70% (w/w) at temperatures up to ~40 °C, although PVC-lined fiber reinforced plastic (FRP) construction is generally preferred to solid PVC on safety grounds. Chlorinated polyvinyl chloride (CPVC) tolerates higher temperatures.
3. Fluoroplastics are very resistant to alkaline solutions, depending upon their degree of fluorination. The highly fluorinated materials polytetrafluoroethylene (PTFE), fluorinated ethylene propylene (FEP), and perfluoroalkoxy (PFA) resist concentrations up to ~70% (w/w) at temperatures up to 150 °C and beyond. The less highly fluorinated materials ethylene chlorotrifluoroethylene (ECTFE), ethylene tetrafluoroethylene (ETFE), and polyvinylidene fluoride (PVDF) are also very resistant but have lower temperature limits for service than the fully fluorinated grades.

FRP constructions can be used, but the common isophthalate and phenolic resins are not resistant to, and glass is attacked by, caustic solutions. FRP construction is therefore based on the use of specific resins such as epoxy, bisphenol-A fumarate, and vinyl ester resins and special surfacing veils of materials such as polyesters and acrylics. Dual laminate construction is also common, involving the use of resistant, thermoplastic liners supported by FRP. Materials selection needs care and experience, and suppliers should always be consulted in the selection of thermoplastic or thermosetting construction for caustic applications.

### 2.21.6.2 Elastomers

Natural rubber is resistant to concentrations up to 70% (w/w) at temperatures up to  $\sim 60^{\circ}\text{C}$ , and in the case of hard natural rubber up to temperatures as high as  $\sim 90^{\circ}\text{C}$ . Several synthetic rubbers, including chlorosulfonated PE (such as Hypalon), butyl, nitrile butadiene, and butadiene rubbers also have good resistance up to  $\sim 60^{\circ}\text{C}$  and beyond. Silicone and polysulfide rubbers are restricted to temperatures close to ambient.

### 2.21.6.3 Inorganic Materials

Impervious graphite finds application depending on the impregnant. Of the common impregnants, carbon tolerates up to 80% (w/w) concentration at temperatures up to  $\sim 80^{\circ}\text{C}$ . The PTFE impregnant is also tolerant to relatively demanding conditions, but phenolic resins are limited to much lower concentrations and are substituted with furane resins for more demanding applications.

Ceramics find only limited application. Borosilicate glass is very restricted in the concentrations and temperatures that it can handle, and glass linings are restricted essentially to dilute solutions at low temperatures.

## References

- Doche, M. L.; Rameau, J. J.; Duran, R.; Novel-Cattin, F. *Corros. Sci.* **1999**, *41*, 805–826.
- Materials Selector for Hazardous Chemicals. Ammonia and Caustic Soda; MTI Publication MS-6, Materials Technology Institute of the Process Industries Inc.: St Louis, MO, 2004; Vol. 6.
- DECHEMA *Corrosion Handbook: Sodium Hydroxide, Mixed Acids*; Wiley-VCH: London, 2004; Vol. 1.
- DECHEMA *Corrosion Handbook: Potassium Hydroxide, Ammonia, Ammonium Hydroxide*; Wiley-VCH: London, 2007; Vol. 9.
- Davies, M. Corrosion by Alkalies. In *ASM Handbook: Corrosion: Environments and Industries*; ASM International: Materials Park, OH, 2006; Vol. 13C, pp 710–726.
- Chen, C. M.; Aral, K.; Theus, G. J. Computer Calculated Potential-pH Diagrams to  $300^{\circ}\text{C}$ , Report NP-3137, Electric Power Research Institute, 1983.
- NACE Standard Practice SP0403–2008. Avoiding Caustic Stress Corrosion Cracking of Carbon Steel Refinery Equipment and Piping; NACE International: Houston, TX, 2008.
- Bandyopadhyay, N.; Briant, C. L. *Corrosion* **1985**, *41*, 274–280.
- Poulson, B. S. Effect of Alloying Elements on the SCC of Ferritic Steels; Ph.D. Thesis, University of Newcastle-on Tyne, 1972.
- Giddey, S.; Cherry, B.; Lawson, F.; Forsyth, M. *Corros. Sci.* **2001**, *43*, 1497–1517.
- Betz Handbook of Industrial Water Conditioning*, 9th ed.; Betz Laboratories, 1991.
- Lumsden, J. B.; Stocker, J. B.; Pollock, G. A.; Millet, P. J. *Corrosion'96, Heated Crevice Investigation of the Effects of Feedwater Chemistry on Crevice Chemistry and Potential*, Denver, CO; NACE International: Houston, TX, 1996; Paper 111.
- Staehle, R. W.; Gorman, J. A. *Corrosion'96, Status and Issues in Corrosion on the Secondary Side of Steam Generators*, Denver, CO; NACE International: Houston, TX, 1996; Paper 122.
- Wood, S. P.; Algeo, W. J.; Call, R. A.; Laronge, T. M. In *Corrosion 2007, Caustic Gouging in a Refinery Boiler – Root Cause and Remediation*, Nashville, TN; NACE International: Houston, TX, 2007; Paper 07451.
- Bouzek, K.; Bergmann, H. *Corros. Sci.* **1999**, *41*, 2113–2128.
- Corrosion Resistance of Nickel and Nickel-Containing Alloys in Caustic Soda and Other Alkalies; CEB-2, International Nickel Company, 1973.
- Bhattacharya, A.; Preet, M. S. In *Corrosion 2008, Corrosion of Duplex Stainless Steels in High pH Caustic Solution*, New Orleans, LA; NACE International: Houston, TX, 2008; Paper 08194.
- Addari, D.; Elsener, B.; Rossi, A. *Electrochim. Acta* **2008**, *53*, 8078–8086.
- Deacon, J.; Dong, Z.; Lynch, B.; Newman, R. C. *Corros. Sci.* **2004**, *46*, 2117–2133.
- Deverell, H. E.; Franson, I. A. *Mater. Perform.* **1989**, *28*, 52–57.
- Schillmoller, C. M. NiDI Technical Report 10019: Alloy Selection for Caustic Soda Service Nickel Development Institute, 1988.
- Horn, E.M. *Corrosion and Environmental Degradation*; Schutze, M., Ed.; Wiley-VCH: London, 2000; Vol. 2, pp 69–111.
- Leander, D. Corrosion Characteristics of Different Stainless Steels, Austenitic and Duplex, in NaOH Environments Stainless Steel World Conference Maastricht, Stainless Steel World, 2003.
- Cassagne, T.; Combrade, P. *Innovation Stainless Steels* **1993**, *3*, 215–220.
- Yasuda, M.; Fukumoto, K.; Koizumi, H.; Ogata, Y.; Hine, F. *Corrosion* **1987**, *43*, 492–498.
- Paul, L.; Alves, H. *Corrosion 2004, Alloy 33: A Versatile Alloy for Mineral Acid and Other Applications*, New Orleans, LA; NACE International: Houston, TX, 2004; Paper 04226.
- Rondelli, G.; Vincenti, B.; Sivieri, E. *Corros. Sci.* **1997**, *39*, 1037–1049.



28. Rondelli, G.; Vincenti, B. *Mater. Corros.* **2002**, 53, 813–819.
29. Dean, S.; Abayarathna, D.; Kane, R. D. *Corrosion'98, Stress Corrosion Cracking of 304L Stainless Steel and 1.25Cr 0.5Mo in Caustic Environments in Syn Gas Service*, San Diego, CA; NACE International: Houston, TX, 1998; Paper 590.
30. Turnbull, A.; Psaila-Dombrowski, M. *Corros. Sci.* **1992**, 33, 1925–1966.
31. Yasuda, M.; Takeya, F.; Hine, F. *Corrosion* **1983**, 39, 10.
32. Staehle, R. W.; Gorman, J. A. *Corrosion* **2004**, 60, 5–63.
33. Newman, R. C.; Gendron, T. S.; Scott, P. M. *Proceedings of the Ninth International Symposium on Environmental Degradation of Materials in Nuclear Power Systems – Water Reactors*, Warrendale; TMS-AIME: Warrendale, PA, 2000; pp 79–93.
34. Coull, Z. L.; Newman, R. C. *Corrosion 2007, Selective Dissolution and Oxidation Zones in Ni-Cr-Fe Space and Their Relationship to Stress Corrosion Cracking*, Nashville, TN; NACE International: Houston, TX, 2007; Paper 07487.
35. Heubner, U.; Kohler, M. *High Alloy Materials for Aggressive Environments*; ThyssenKrupp VDM GmbH 1998; VDM Report No 26.
36. Rebak, R. B. In *Corrosion 2005, Environmentally Assisted Cracking of Commercial Ni-Cr-Mo Alloys: A Review*, Houston, TX; NACE International: Houston, TX, 2005; Paper 05457.
37. Popa, M. V.; Vasilescu, E.; Mirza-Rosca, I.; Gonzalez, S.; Llorente, M. L.; Drob, P.; Anghel, M. *Eurocorr'97*, Trondheim: Norway, 1997; Vol. 2, pp 687–692.

## 2.22 Corrosion in Hydrogen Halides and Hydrohalic Acids

**J. A. Richardson**

Anticorrosion Consulting, 5 Redhills Lane, Durham DH1 4AL, UK

© 2010 Elsevier B.V. All rights reserved.

2.22.1	Introduction	1207
2.22.2	Steels and Cast Irons	1209
2.22.3	Stainless Steels	1211
2.22.4	Nickel and Nickel Alloys	1212
2.22.5	Other Metals and Alloys	1220
2.22.5.1	Copper and Copper Alloys	1220
2.22.5.2	Titanium and Titanium Alloys	1220
2.22.5.3	Zirconium and Zirconium Alloys	1221
2.22.5.4	Tantalum and Tantalum Alloys	1222
2.22.5.5	Noble Metals	1223
2.22.6	Nonmetallic Materials	1223
2.22.6.1	Thermoplastic and Reinforced Thermosetting Materials	1223
2.22.6.2	Elastomers	1224
2.22.6.3	Inorganic Materials	1224
References		1224

### Abbreviations

**AHF** Anhydrous hydrogen fluoride  
**AES** Auger electron spectroscopy  
**ASTM** American Society for Testing Materials  
**CPVC** Chlorinated polyvinyl chloride  
**ECTFE** Ethylene chlorotrifluoroethylene  
**EIS** Electrochemical impedance spectroscopy  
**EPDM** Ethylene propylene diene terpolymer  
**ETFE** Ethylene tetrafluoroethylene  
**FEP** Fluorinated ethylene propylene  
**GRP** Glass reinforced plastic  
**HAZ** Heat affected zone  
**HIC** Hydrogen-induced cracking  
**HSC** Hydrogen stress cracking  
**PE** Polyethylene  
**PFA** Perfluoroalkoxy  
**PP** Polypropylene  
**ppm** Parts per million  
**PTFE** Polytetrafluoroethylene  
**PVC** Polyvinyl chloride  
**PVDF** Polyvinylidene fluoride  
**PWHT** Postweld heat treatment  
**SCC** Stress corrosion cracking  
**SCE** Saturated calomel electrode  
**SHE** Standard hydrogen electrode  
**SIMS** Secondary ion mass spectrometry

**SOHIC** Stress-oriented hydrogen-induced cracking

**TOF** Time of flight

**XPS** X-ray photoelectron spectroscopy

### Symbols

$E_{\text{corr}}$  Corrosion potential (V)

$i_{\text{corr}}$  Corrosion current density ( $\text{mA cm}^{-2}$ )

### 2.22.1 Introduction

The hydrohalic acids comprise the group of monobasic acids that are formed when the hydrogen halide gases are dissolved in water, with strengths in descending order:

hydroiodic (HI) > hydrobromic (HBr) > hydrochloric (HCl) > hydrofluoric (HF)

The differences in strength arise from the differing sizes of the relevant halide ion. Thus, the largest iodide anion interacts relatively weakly with its complementary proton, leaving it relatively free to dissociate. In practice, the differences amongst HI, HBr, and HCl acids are not great, and all are strong acids that are highly dissociated in water at all concentrations to

release protons and the corresponding halide anion as follows:



The result, in relation to the pHs of hydrohalic acids, is that at the higher end of the pH range the solutions are effectively acidified waters. Thus, the pHs 2, 3, and 4 are equivalent to concentrations of 360, 36, and 3.6 ppm (w/w) hydrochloric acid, respectively at 25 °C. However, HF acid is an exception to this behavior. There is very strong hydrogen bonding between the nonionized HF and water molecules, and the small fluoride anion imposes a high degree of order on the surrounding protons and water molecules as a result of which HF acid is a very weak acid, the pH of which varies in a complicated manner with concentration as shown in Figure 1.<sup>1</sup>

Hydrogen chloride, bromide, and iodide are all gases at ambient temperatures and available commercially in nominally anhydrous specifications, containing trace quantities of water. Anhydrous hydrogen fluoride (AHF) is a liquid that boils at ~20 °C, and is normally specified as containing < 400 ppm water. The significant commercial grades of the acids are as follows:

1. HI acid, the least significant acid commercially, is supplied at various concentrations, typically 47% or 55% (w/w), but concentrated grades in the range 90–98% (w/w) are also available.
2. Hydrobromic acid is manufactured in significant quantities and supplied at various concentrations, most commonly at ~47–49% (w/w).
3. Hydrochloric acid is manufactured in the greatest quantities at concentrations up to ~38% (w/w), above which the fuming nature of the acid

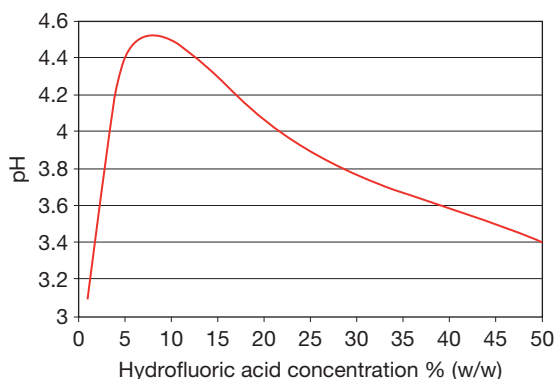
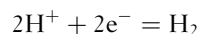


**Figure 1** pH of hydrofluoric acid solutions. Adapted from *Hydrofluoric Acid Properties*; Honeywell Specialty Materials Products, 2002.

introduces problems in relation to storage and transport. Most bulk commercial grades have concentrations in the range 30–35% (w/w).

4. HF acid is also significant commercially, and is available in bulk at concentrations of 49% and 70% (w/w).

From the corrosion standpoint, the hydrohalic acids are commonly classified as inherently ‘reducing’ acids because the only cathodic process that the pure acids can deliver is the reduction of protons to evolve hydrogen:



This is in contrast to ‘oxidizing’ acids such as sulfuric and nitric acid in which reductions of the acid itself, or its constituent species, occur at potentials more noble than hydrogen evolution, and to an extent that can determine the behaviors of materials exposed to the acid, as described in the separate chapters devoted to the two acids in this book. In the case of the hydrohalic acids, their ‘reducing’ characteristics are compounded by the aggressive properties of the halide anions that inhibit the formation of, and attack preexisting, protective passive layers on metals and alloys. Indeed, both HCl and HF acids find significant commercial applications in the cleaning and pickling of metals and alloys because of their ability to dissolve metal oxides.

In practice, alternative cathodic processes to hydrogen evolution may be available due to the presence of specific contaminants in the acid, in particular oxidants such as dissolved oxygen and metal cations in a higher oxidation state such as ferric,  $\text{Fe}^{3+}$  or cupric,  $\text{Cu}^{2+}$  ions. The presence of the corresponding halogen gas, for example chlorine in the case of hydrochloric acid, can also have a significant effect. The effects of oxidizing agents that raise the potentials of metals and alloys are almost invariably detrimental to corrosion performance in the hydrohalic acids, in which metals and alloys are mostly unable or struggle to form protective, passive films, as will emerge below.

The corrosion performances of the various classes of material in hydrohalic acids have been reviewed extensively elsewhere.<sup>2–8</sup> Much of the data relate to hydrochloric and HF acids, reflecting their commercial significance. There is relatively little data for hydrobromic, and virtually none for HI acid in the public domain. Readers whose main interest is to identify ‘what works where’ are referred to these sources and the relevant chapters on specific materials in this book. In this chapter, the corrosion

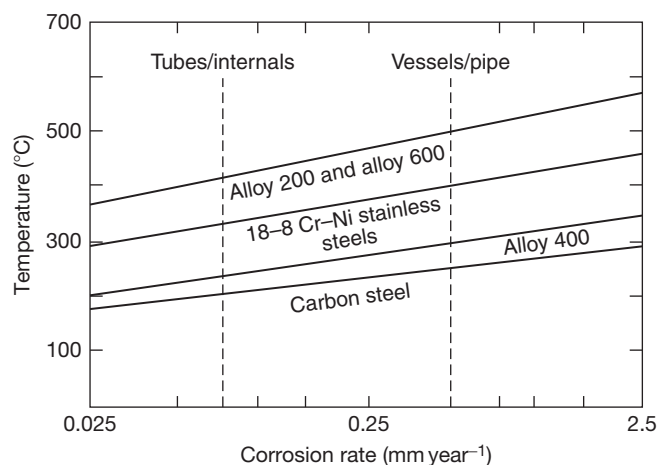


**Figure 2** Proposed design limits for various alloys in anhydrous hydrogen chloride. Adapted from Schillmoller, C. M. *Chem. Eng.* **1980**, 87, 161–163.

performances of materials are reviewed with an emphasis on the principles and mechanisms that underpin their corrosion performances in the acids.

### 2.22.2 Steels and Cast Irons

Steels react with anhydrous hydrogen halide gases to form the corresponding iron halide and hydrogen. In AHF, the fluoride films are protective and steels have acceptable corrosion rates at temperatures up to  $\sim 200^\circ\text{C}$  and velocities up to  $10\text{ m s}^{-1}$ , and arguably to higher temperatures at lower velocities.<sup>3,6</sup> The velocity limitations arise because the fluoride films are vulnerable to detachment which not only increases the corrosion rates, but also adversely affects the operability of equipment due to accumulations of solid iron fluoride in seals and joints in valves, pumps, and elsewhere. In anhydrous hydrogen chloride gas, the growth of a film of  $\text{FeCl}_2$  obeys parabolic kinetics up to temperatures of  $500\text{--}600^\circ\text{C}$ , above which the vaporization of  $\text{FeCl}_2$  results in a switch to linear, nonprotective kinetics. As in the case of the analogous fluoride films, the chloride films on steels are protective within specific temperature and velocity constraints,<sup>5,9,10</sup> and some widely used design temperature limits for carbon steel, austenitic stainless steels, and specific nickel alloys in anhydrous hydrogen chloride are shown in **Figure 2**.<sup>10</sup>

Aqueous hydrohalic acids are very aggressive toward steels and grey or ductile cast irons. A typical polarization curve for carbon steel in stagnant, aqueous 3M ( $\sim 10\%$ , w/w) hydrochloric acid is shown in **Figure 3**.

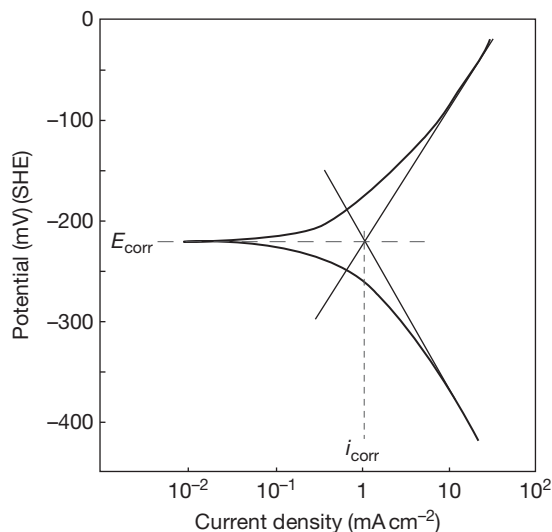
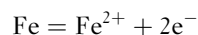


**Figure 3** Potentiodynamic polarization curve for carbon steel in stagnant, 3M ( $\sim 10\%$ , w/w) hydrochloric acid open to air at ambient temperature. Adapted from Poorqasemi, E.; Abootalemi, O.; Peikari, M.; Haqdar, F. *Corros. Sci.* **2009**, 51, 1043–1054.

The anodic curve shows classic Tafel behavior, characteristic of active dissolution of iron:



The cathodic curve also shows classic Tafel behavior, characteristic of hydrogen evolution. In more dilute acids, curves are obtained that are time dependent to a small extent, and electrochemical impedance spectroscopic (EIS) measurements suggest the presence of highly nonprotective films that present limited

barriers to anodic dissolution.<sup>11</sup> Such films that do exist are likely to consist of iron chloride, which is very soluble in hydrochloric acid and the degree of protection that they can provide is therefore very marginal. The general experience of steels in aqueous HCl, HBr, and HI acids is of active corrosion across the full concentration range at rates that preclude practical application.

In aqueous HF acid, corrosion rates are generally lower, but acceptable only at concentrations above ~70% (w/w), as shown in Figure 4. The corrosion resistance of steels in concentrated aqueous and liquid AHF arises from the spontaneous formation of protective iron fluoride films on steel surfaces that are much less soluble than the corresponding chloride films. Studies of the growth of fluoride films in vapors over dilute HF acids at ambient temperature have shown that the kinetics is linear, and controlled by reaction at the metal–film interface, resulting in the formation of porous, nonprotective films. However, when the HF acid concentration rises to 40% (w/w), the initial film that forms in the vapor phase has been identified as  $\text{FeF}_2 \cdot 4\text{H}_2\text{O}$ , and it grows with a parabolic dependence on time. With increasing film thickness, a product identified as nonstoichiometric  $\text{Fe}_2\text{F}_5 \cdot 7\text{H}_2\text{O}$  occurs. The change to parabolic kinetics indicates a switch to diffusion control of reaction rate through a thickening, potentially protective film.<sup>12</sup>

The significance of such films is evident in the polarization curves for two steels in 90% (w/w) acid at 90 °C, shown in Figure 5.

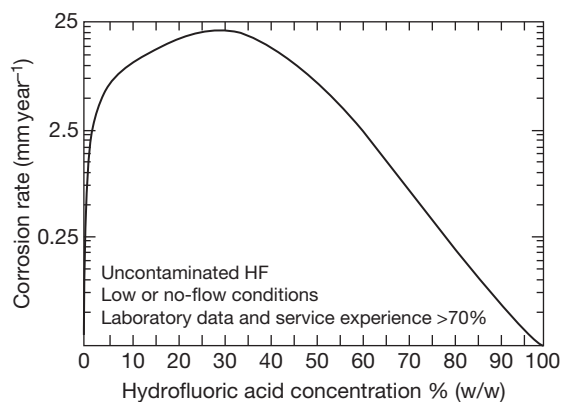


**Figure 4** Corrosion rate of carbon steel in hydrofluoric acid at 21–38 °C as a function of concentration. Adapted from NACE International Publication 5A–171 *Materials for Storing and Handling Commercial Grades of Aqueous Hydrofluoric Acid and Anhydrous Hydrogen Fluoride*; NACE International: Houston, TX, 2007.

In both cases, the anodic kinetics is clearly influenced strongly by diffusion due to the presence of the fluoride film, while the cathodic reactions obey Tafel-type kinetics, characteristic of hydrogen evolution beneath the film.<sup>13</sup> The adherence and protection afforded by the fluoride film has been shown to depend upon several factors. Although the laboratory test in Figure 5 demonstrates the existence of a film at 90 °C, temperatures and limiting velocities are typically restricted to ~65 °C and  $\sim 1.6 \text{ m s}^{-1}$  in liquid AHF, reducing to ~30 °C and  $0.6 \text{ m s}^{-1}$  in 70% (w/w) acid.<sup>6</sup> The carbon and residual element content of the steel, in particular the copper and nickel contents, also appear to influence the persistence of the fluoride films that form and the corresponding corrosion rates that are experienced,<sup>13</sup> and recommendations have been formulated relating to the control of such elements.<sup>14</sup> Corrosion rates have also been shown to be higher in the presence of oxygen in both the laboratory<sup>10</sup> and in the field.<sup>6</sup>

Steels are vulnerable to damage due to hydrogen uptake in HF acid service that is similar to the types of damage that can be experienced in wet  $\text{H}_2\text{S}$  such as hydrogen stress cracking (HSC) of stronger materials and hard welds and heat affected zones (HAZ), and hydrogen-induced cracking (HIC), stress-oriented hydrogen-induced cracking (SOHIC), and blistering of plate materials. General approaches to mitigating these risks are available<sup>7,15</sup> based on the

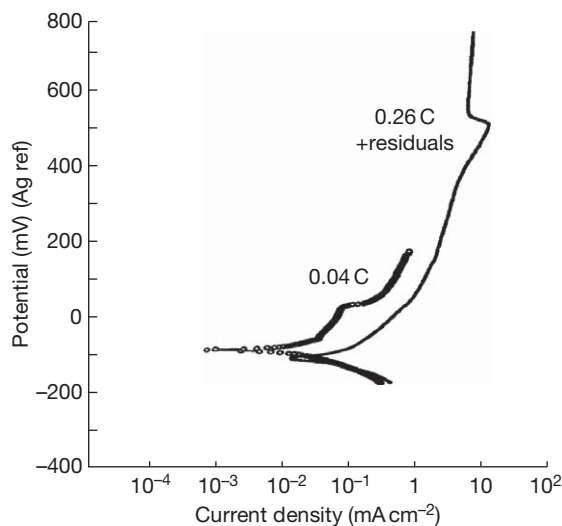


**Figure 5** Potentiodynamic polarization curves for steels in 90% (w/w) hydrofluoric acid at 90 °C. Adapted from Chirinos, G.; Turgoose, S.; Newman, R. C. *Effects of Residual Elements on the Corrosion of Steels in HF*, Paper 97513, Corrosion '97; NACE International: Houston, TX, 1997.



practices that have been developed for the control of the similar problems that are experienced in wet  $\text{H}_2\text{S}$ , including the control of base metal chemistry and the hardness of welds and HAZs within threshold levels and, if appropriate, postweld heat treatment (PWHT).<sup>16</sup> The risks of HIC and SOHIC in the base materials are mitigated by controlling steel chemistry and microstructure (including limits on sulfur content and inclusion shape control) and manufacture (in particular rolling conditions), and confirming resistance by appropriate testing.<sup>17–19</sup>

Gray and ductile cast irons have corrosion resistances broadly similar to steels in hydrohalic acids, but find no application in HF acid service, not least in the case of gray irons because of safety concerns relating to their poor ductility. High-silicon cast irons, containing typically 14–16% Si, are resistant to all concentrations of hydrochloric acid up to 40% (w/w) at ambient temperatures and at higher temperatures in more dilute acids, as shown in the isocorrosion curves for some metals and alloys with exceptional corrosion resistance to aqueous hydrochloric acid, described later in Figure 14. Their exceptional corrosion resistance is due to the formation of robust, siliceous films that have considerable resistance to erosion and abrasion. However, they find relatively limited application due to their poor ductility that renders them difficult to fabricate and requires them to be protected from thermal and/or mechanical shock.

### 2.22.3 Stainless Steels

The compositions of the relevant commercial grades of stainless steels are summarized in Table 1.

In anhydrous hydrogen chloride gas, stainless steels perform in a similar manner to steels in that they form chloride films that obey parabolic kinetics up to temperatures of 500–600 °C, above which the vaporization of the chlorides results in a switch to linear kinetics. However, the films contain  $\text{CrCl}_3$  and  $\text{NiCl}_2$  in addition to, or instead of  $\text{FeCl}_2$ , depending on the alloy and the temperature.<sup>10</sup> They form more slowly and are much more protective than the corresponding films on steels at temperatures below ~500 °C. As a result, the corrosion rates for stainless steels are lower than for steels, and the design temperature limits are correspondingly higher, exemplified by those reported in Figure 2.<sup>10</sup> At temperatures above ~500 °C, stainless steels offer no significant advantage over carbon or low alloy steels in anhydrous hydrogen chloride gas.

The performances of austenitic stainless steels in AHF liquid and vapor are good up to a temperature of ~100 °C. All of the basic grades 304 (S30400), 304L (S30403), 316 (S31600) and 316L (S31603), and their cast equivalents show good resistance and find significant application, although due caution to prevailing velocities is necessary as in the case of steels. However, austenitic stainless steels that can develop  $\alpha$ -martensite as a result of cold working are vulnerable

**Table 1** Compositions of some wrought stainless steels that are relevant to hydrohalic acid applications

UNS no.	Common name	Fe	Ni	Cr	Mo	Cu	Si	Other
S31803	2205	Balance	4.5–6.5	21–23	2.5–3.5			N
S32205								
S32750	2507	Balance	6–8	24–26	3–4.5	<0.5		N
S32760					3–4	0.5–1.0		W, N
S30400	304	Balance	8–10.5	18–20				<0.08C
S30403	304L	Balance	8–12	18–20				
S34700	347	Balance	9–13	17–19				Nb/Ta < 0.08C
S31600	316	Balance	10–14	16–18	2–3			<0.08C
S31603	316L	Balance	10–14	16–18	2–3			
S31700	317	Balance	11–15	18–20	3–4			<0.08C
S31703	317L	Balance	11–15	18–20	3–4			
S31254	254SMO	Balance	17.5–18.5	19.5–20.5	6–6.5	0.5–1.0		N
S30900	309	Balance	12–15	22–24				Mn
S31000	310	Balance	19–22	24–26				Mn
N08904	904L	Balance	23–28	19–23	4–5	1–2		
N08926	25–6MO	Balance	24–26	19–21	6–7	0.5–1.5		N
S31277	27–7MO	Balance	26–28	20.5–23.0	6.5–8.0	0.5–1.5		Mn, N
N08020	20	Balance	32–35	19–21	2–3	3–4		
N08031	31	Balance	30–32	26–28	6–7	1.4		N
R20033	33	Balance	30–33	31–35	0.5–2.0	0.3–1.2		N

to HSC, and some users favor the higher nickel 316/316L grades for this reason.<sup>8</sup> Above  $\sim 100^\circ\text{C}$ , the rates of corrosion of austenitic stainless steels in AHF increase to unacceptable levels and they are outperformed by carbon steel, as shown in **Figure 6**.

The performances of stainless steels in aqueous hydrohalic acids are generally poor because they are unable to form and sustain the passive, chromium oxide films upon which they depend for corrosion resistance and, as a result, corrode actively. Ferritic and martensitic stainless steels have poor resistance under all conditions. Austenitic and duplex stainless steels offer some limited resistance, as shown in the isocorrosion diagrams for various grades in HCl and HF acids in **Figures 7 and 8** respectively.

The basic 316L (S31600) grade is clearly limited to very dilute acids at relatively low temperatures. The grades with higher levels of nickel, molybdenum, and copper offer progressive extension of the boundaries for stable passivity, but more than 30% nickel and significant contents of molybdenum and copper are required to provide resistance to hydrochloric acid at all concentrations up to 40% (w/w) at close to ambient temperatures, exemplified by the isocorrosion diagram for alloy 31 (N08031) which is shown in **Figure 9**.<sup>20</sup>

Overall, taking into account the additional risks of localized corrosion and stress corrosion cracking (SCC) presented by the halide anions, stainless steels are weak options for aqueous, hydrohalic acid service.

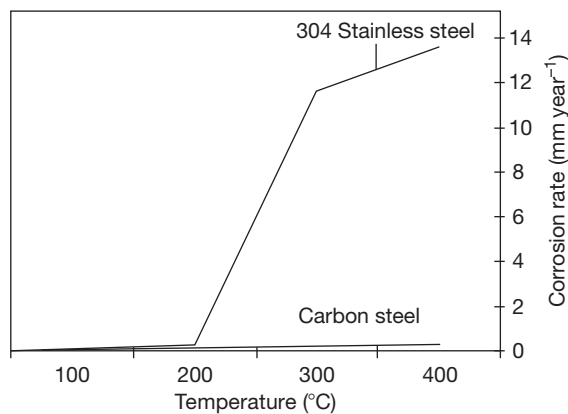


**Figure 6** Corrosion rates of carbon steel and type 304 stainless steel as a function of temperature in static, anhydrous hydrofluoric acid. Adapted from Jennings, H. S. *Corrosion by Hydrogen Fluoride and Hydrofluoric Acid*. In *ASM Handbook Corrosion: Environments and Industries*; ASM International, 2006; pp 690–703, Vol. 13C.

## 2.22.4 Nickel and Nickel Alloys

The compositions of the relevant commercial grades of nickel and its alloys are summarized in **Table 2**.

The reaction of nickel with anhydrous hydrogen chloride gas as a function of temperature is shown in **Figure 10**.<sup>21</sup>

Evidently, reaction kinetics is parabolic up to a temperature of  $\sim 450^\circ\text{C}$ , associated with the formation of protective  $\text{NiCl}_2$ . In the temperature range of  $450\text{--}550^\circ\text{C}$ , there is a transition to linear kinetics associated with the relatively high vapor pressure and progressive evaporation of  $\text{NiCl}_2$ . Alloying, in general, reduces the temperature at which there is a transition to unacceptable evaporation rates. The effects are relatively small for the commercial nickel–chromium

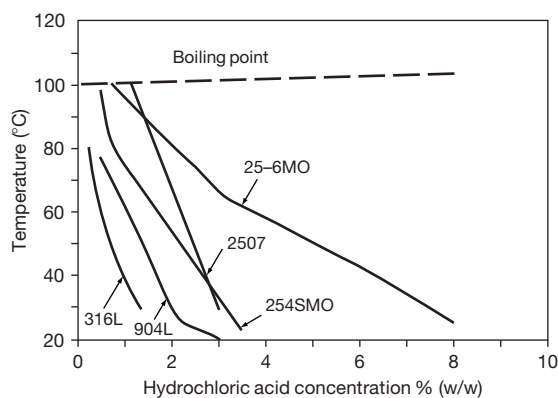


**Figure 7** Isocorrosion charts ( $0.1\text{ mm year}^{-1}$ ) for austenitic and duplex stainless steels in hydrochloric acid. Adapted from *Corrosion Handbook, Stainless Steels*; AB Sandvik Steel, 1994.

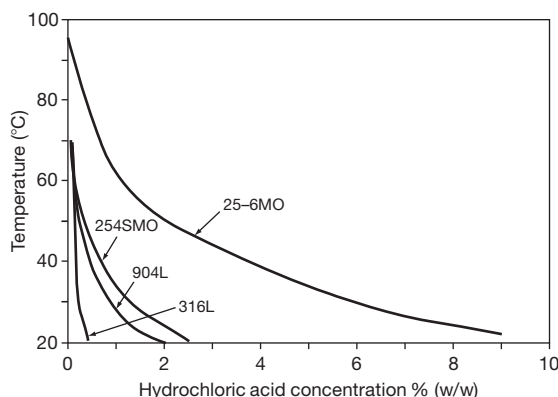


**Figure 8** Isocorrosion charts ( $0.1\text{ mm year}^{-1}$ ) for austenitic stainless steels in hydrofluoric acid. Adapted from *Corrosion Handbook, Stainless Steels*; AB Sandvik Steel, 1994.

and nickel–chromium–molybdenum alloys, but more significant for nickel–molybdenum and particularly nickel–copper alloys because of the relatively low melting point and high volatility of copper chloride. This is reflected in the relatively high, proposed, design temperature limits proposed in **Figure 2** for nickel 200 (N02200) and alloy 600 (N06600) compared with alloy 400 (N04400) for which the proposed limits are little better than those for carbon steel.<sup>10</sup>

The resistance of nickel and its alloys to AHF gas at elevated temperatures is dependent on the formation

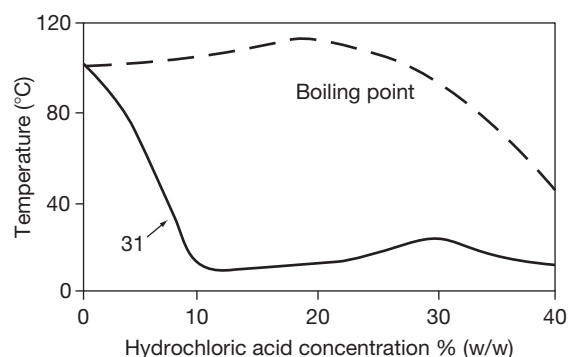


**Figure 9** Isocorrosion chart ( $0.13 \text{ mm year}^{-1}$ ) for austenitic alloy 31 in hydrochloric acid. Adapted from Agarwal, D. C., Alves, H. *Applications of Alloys 59 (UNS N06059) and 31 (UNS N08031) in Mitigating Corrosion Risks in the CPI and Petrochemical Industries*, Paper 07186, Corrosion 2007; NACE International: Houston, TX, 2007.

of protective metal fluoride films. Nickel and molybdenum fluorides are stable and protective relative to chromium and iron fluorides that have lower melting points and higher volatilities, and this is reflected in the corrosion rates for various metals and alloys in AHF at  $600^\circ\text{C}$  that are charted in **Figure 11**<sup>22</sup> which links to the data reported in **Figure 6**.

Alloys can suffer internal as well as external attack in high temperature hydrogen fluoride related to fluoride diffusivity and solubility in the metal and, in addition to chromium and iron, the elements niobium, tantalum, and titanium also exacerbate the vulnerability of an alloy to internal attack due to the lower melting points and higher volatilities of their fluorides. **Figure 11** confirms that the chromium-rich types 309 (S30900) and 310 (S31000) and the niobium/tantalum-containing type 347 (S34700) stainless steel suffer extremely high rates of corrosion. Type 304 (S30400) stainless steel is confirmed as having unacceptable rates relative to steel, and the most resistant materials are nickel 200 (N02200) and nickel alloys 400 (N04400) and 600 (N06600).

In AHF liquid, the leaner nickel alloys such as alloys 20 (N08020), 825 (N08825), and the G family are highly resistant to corrosion at temperatures up to  $\sim 125^\circ\text{C}$ , even under flowing conditions, and find significant application, subject to appropriate mitigation of risks relating to preferential weld corrosion and HSC of heavily cold-worked material.<sup>6</sup> The more

**Table 2** Compositions of some wrought nickel alloys that are relevant to hydrohalic acid applications

UNS no.	Common name	Fe	Ni	Cr	Mo	Cu	Si	Other
N02200	200		>99					<0.15C
N02201	201		>99					<0.02C
N04400	400	<2.5	Balance			28–34		Mn
N05500	500	<2.0	Balance			27–33		Al, Mn
N08825	825	>22	Balance	19.5–23.5	2.5–3.5	1.5–3.0		Ti
N06007	G	18–21	Balance	21–23.5	5.5–7.5	1.5–2.5		Co, Nb
N06985	G-3	18–21	Balance	21–23.5	6–8	1.5–2.5		Co W
N06030	G30	13–17	Balance	28.0–31.5	4–6	1.0–2.4		W
N06600	600	6–10	Balance	14–17				
N06690	690	7–11	Balance	27–31				
N10276	C-276	4–7	Balance	14.5–16.5	15–17			W, Co
N06455	C-4	3	Balance	14–18	14–17			Co
N06022	C-22	2–3	Balance	20.5–22	13–14			W, Co
N06200	C-2000		Balance	23	16	2		
N06059	59		Balance	23	16			
N06686	686	<5	Balance	19–23	15–17			W
N06625	625	<5	Balance	20–23	8–10			Nb
N10001	B	5.5	Balance		28			Co
N10665	B-2	<2	Balance		28			
N10675	B-3	1.5	Balance	1.5	28.5			W, Co
	Hybrid BC-1	2	Balance	15	22			

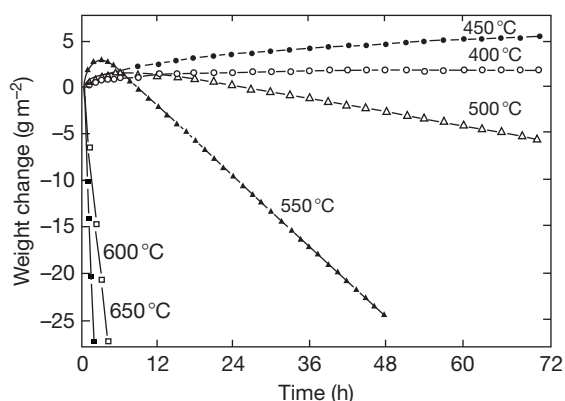


**Figure 10** Weight change of nickel exposed to anhydrous hydrogen chloride gas as a function of temperature. Adapted from Ihara, Y.; Ohgame, S.; Sakiyama, K.; Hashimoto, K. *Corros. Sci.* **1982**, 22, 901.

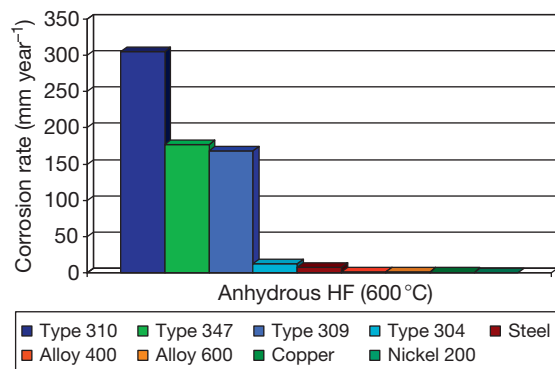


**Figure 11** Corrosion rates for various metals and alloys tested for 4–15 h in anhydrous hydrogen fluoride (AHF) at 600°C. Adapted from Myers, W. R.; Delong, W. B. *Chem. Eng. Prog.* **1948**, 44, 359.

nickel-rich alloys 600 (N06600), C-22 (N06022), and C-276 (N10276) are even more resistant, as illustrated in **Figure 12** that shows corrosion rates for various metals and alloys tested for 6–40 days in AHF at 15–40°C.<sup>6</sup>

The nickel–chromium and nickel–chromium–molybdenum alloys are used at temperatures up to at least ~150°C, but appropriate precautions are also necessary with the nickel-rich alloys to avoid environmental cracking. Thus, the nickel–copper alloys 400 (N04400) and 500 (N05500) have excellent general corrosion resistance but are vulnerable to environmental cracking in the presence of air. Alloy 600 (N06600) has shown a vulnerability to cracking in the presence of chlorine and copper fluoride after cold forming.

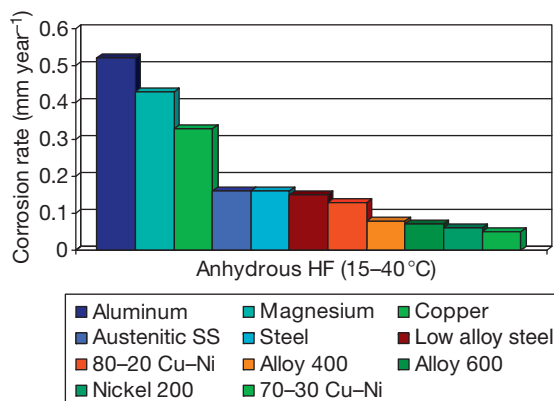
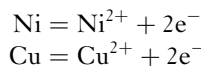


**Figure 12** Corrosion rates for various metals and alloys tested for 6–40 days in AHF at 15–40°C. Adapted from Jennings, H. S. *Corrosion by Hydrogen Fluoride and Hydrofluoric Acid*. In *ASM Handbook. Corrosion: Environments and Industries*; ASM International, 2006; pp 690–703, Vol. 13C.

Such risks can be mitigated by appropriate heat treatment procedures.<sup>6</sup>

The basic electrochemistry of the classes of alloys of commercial significance for aqueous hydrohalic acid duties is illustrated by the polarization curves in **Figure 13** for nickel and three nickel alloys in aqueous hydrochloric acid.

Evidently, the corrosion potentials and polarization characteristics of nickel 200 (N02200) and the nickel–copper alloy 400 (N04400) in deaerated 5N (~18%, w/w) hydrochloric acid at room temperature are very similar.<sup>23</sup> Both display very active corrosion potentials and anodic polarization behavior characteristic of active dissolution of the base elements with no tendency to passive film formation:



The polarization curves in **Figure 13** and **Figure 3** confirm the much greater resistance to active, anodic dissolution that nickel displays relative to iron under similar conditions. That is the basis of the generally better performances of nickel-based compared with iron-based alloys in hydrochloric acid. Regarding the specific effects of alloying with copper, the curves in **Figure 13** suggest slightly more polarization of both anodic and cathodic processes in the case of alloy 400 (N04400) than for nickel 200 (N02200), but this depends very much on acid concentration and temperature. Alloy 400 (N04400) is more sensitive to increases in concentration and less sensitive to increases in temperature than nickel 200. In practice, both alloys

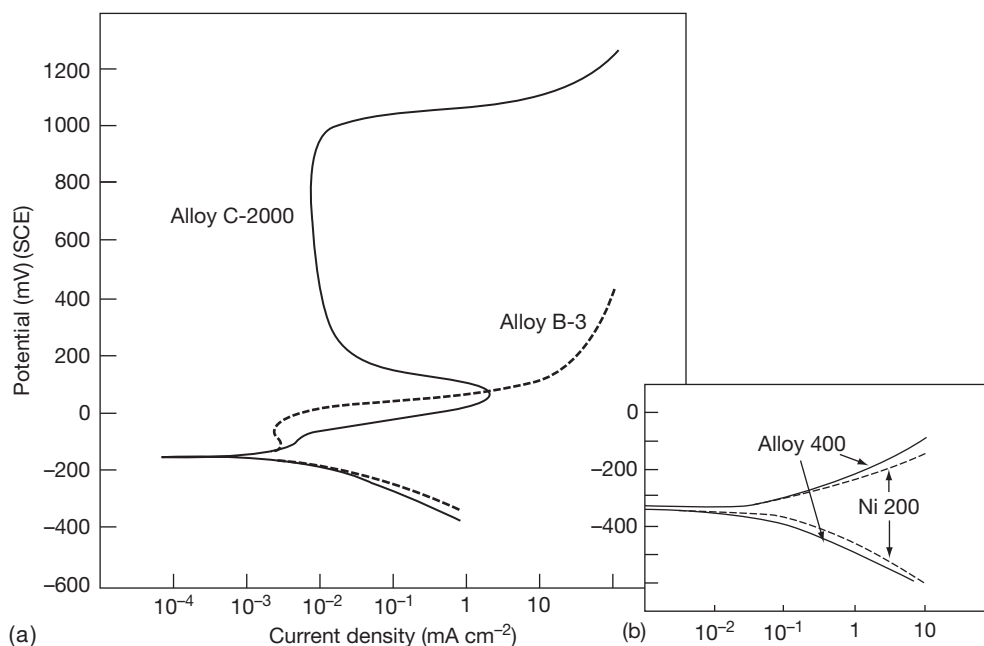
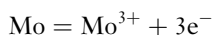


**Figure 13** Polarization behavior of (a) alloys B-3 and C-2000 in deaerated 20% (w/w) hydrochloric acid at 25 °C. Adapted from Nacera, S. M.; Crook, P.; Klarstrom, D. L.; Rebak, R. B. *Effect of Ferric Ions on the Corrosion Performance of Nickel Alloys in Hydrochloric Acid Solutions*, Paper 04430, Corrosion 2004: NACE.

have acceptable resistance to corrosion in relatively dilute ( $<10\%$ , w/w) acids at ambient temperatures but at higher concentrations and temperatures, and particularly if oxygen or other oxidizing agents are present, their application is limited.

The more important alloying elements for resistance to aqueous hydrochloric acid are molybdenum and chromium, exemplified by the polarization curves in [Figure 13](#) for the nickel–molybdenum alloy B-3 (N10675) and the nickel–chromium–molybdenum alloy C-2000 (N06200) in deaerated 20% (w/w) hydrochloric acid at 25 °C.<sup>24</sup> Both alloys exhibit relatively active corrosion potentials, albeit more noble than for nickel 200 (N02200) or the nickel–copper alloy 400 (N04400) under similar conditions. Active dissolution is clearly inhibited in the nickel–molybdenum alloy B-3 (N10675) relative to nickel 200 (N02200), arising from the significant contribution of molybdenum to overall dissolution:



The mechanism via which molybdenum inhibits dissolution has been variously attributed to the relatively high Mo–Mo bond energy that blocks active sites<sup>25,26</sup> and the promotion of salt film formation due to the relative insolubility of molybdenum chlorides.<sup>27</sup> It has been suggested that the pseudo-passive behavior,

exemplified by the anodic polarization curve for alloy B-3 (N10675) in [Figure 13](#), may be due to the formation of a molybdenum dioxide ( $\text{MoO}_2$ ) and/or trioxide ( $\text{MoO}_3$ ) film<sup>24</sup> that breaks down under further anodic polarization. Whatever the mechanism, the inhibiting effect of molybdenum on the anodic dissolution of nickel in hydrochloric acid is of significant practical benefit, exemplified by the isocorrosion diagrams in [Figure 14](#) that show the performance of alloy B-2 (N10665) relative to other metals and alloys with exceptional resistance to aqueous hydrochloric acid.<sup>28</sup> However, the absence of the capacity of nickel–molybdenum alloys to passivate, which is apparent in the anodic polarization curve for alloy B-3 (N10675) in [Figure 13](#) signals a sensitivity to the presence of oxidizing agents which limits their practical application, as described later.

In contrast to alloy B-3 (N10675), the anodic polarization curve for the chromium-containing alloy C-2000 (N06200) in [Figure 13](#) shows a pronounced capacity to passivate, which offers the prospect of useful corrosion performance in environments that have sufficient oxidizing capacity to exceed the critical current density for passivation and raise the potential into the passivation range. The active portion of the curve describes active dissolution of the alloy to produce, in addition to  $\text{Ni}^{2+}$  and  $\text{Mo}^{3+}$ , soluble



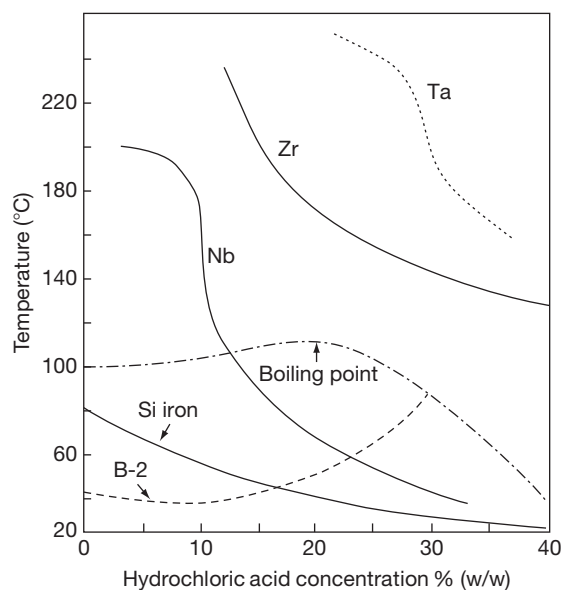
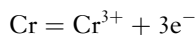


**Figure 14** Isocorrosion charts ( $0.13 \text{ mm year}^{-1}$ ) for various metals and alloys in hydrochloric acid. Adapted from Hunkeler, F. J. Tantalum and Niobium. In *Process Industries Corrosion*; Moniz, B. J., Pollock, W. J., Eds.; NACE International: Houston, TX, 1986.

chromous ions as follows:



The active dissolution curve is less polarized than alloy B-3 (N10675) due to its lower molybdenum content. At a potential in the 50–100 mV range, the current density drops by more than two orders of magnitude, signaling the formation of a protective passive film. The passive films that form on nickel–chromium and nickel–chromium–molybdenum alloys have been shown to be thin ( $<10 \text{ nm}$ ), and to consist mostly of chromium oxide,  $\text{Cr}_2\text{O}_3$ . An Auger electron spectroscopic (AES) study showed the presence of outer nickel and iron oxides over an inner chromium oxide layer on alloy 600 (N06600), but nickel oxide only in the case of alloy C-4 (N06455).<sup>29</sup> An X-ray photoelectron spectroscopic (XPS) study differentiated inner chromium oxide and outer hydroxide layers.<sup>30</sup> A study using both XPS and time of flight secondary ion mass spectrometry (TOF SIMS) suggested a threshold concentration of chromium in an alloy of  $\sim 20\%$  to promote strong passivity, above which thicker oxides developed with layered structures consisting of inner Cr–Ni and outer Cr–Mo oxides. Molybdenum and tungsten exert little discernible effect on passivation at potentials below  $\sim 200 \text{ mV}$ , when  $\text{Cr}^{3+}$  is the only possible chromium dissolution

product. However, they appear to suppress passive film dissolution at potentials  $> \sim 500 \text{ mV}$ , when transpassive oxidation to  $\text{Cr}^{6+}$  is possible.<sup>31</sup>

The relative performances of nickel–chromium and nickel–chromium–molybdenum alloys in aqueous hydrochloric acid will depend on their compositions, as illustrated in the isocorrosion diagrams in **Figure 15** for a range of alloys relative to the stainless steel 25–6MO (N08926) (note that these are isocorrosion diagrams for a corrosion rate of  $0.5 \text{ mm year}^{-1}$  which is not an acceptable corrosion rate for most practical applications).<sup>32</sup>

Clearly, all of the alloys have significant limitations and none perform as well as the nickel–molybdenum, B family of alloys at concentrations above  $\sim 25\%$  (w/w) pure acid. Alloy 825 (N08825) is the leanest in relation to both nickel and molybdenum contents, and is, therefore, the poorest performer. Alloy 625s (N06625) poor performance relates mainly to its relatively low molybdenum content. The remainder has similar resistances, the marginal differences amongst them reflecting mainly their relatively high, but differing molybdenum and tungsten contents.

There is relatively little published data on the behavior of nickel alloys in aqueous hydrobromic acid, but such data suggest that their relative performances are broadly similar to those in hydrochloric acid. However, hydrobromic acid appears to be less aggressive than hydrochloric acid, despite being a stronger acid, exemplified by the isocorrosion diagrams ( $0.1 \text{ mm year}^{-1}$  for alloy C-22 (N06022) in hydrochloric and hydrobromic acids at concentrations up to  $\sim 5\text{M}$  that are shown in **Figure 16**.<sup>33</sup>

In practice, the performances of nickel alloys in aqueous hydrohalic acids are very often determined by the presence of oxygen or other oxidizing agents that can accelerate markedly the corrosion rates of nickel–molybdenum alloys, or reduce the corrosion rates of chromium-containing alloys by promoting passivity. For example, corrosion rates for alloy B (N10001) tested in aerated and deaerated aqueous hydrochloric acid at  $65\text{--}70^\circ\text{C}$  are shown in **Figure 17**, and the pronounced accelerating effects of aeration, particularly at concentrations below  $\sim 25\%$  (w/w), are evident.<sup>34</sup>

The most pronounced effects are produced by stronger oxidizing agents such as ferric ions, the effects of which on the corrosion of alloys B-3 (N10675) and C-2000 (N06200) in deaerated  $20\%$  (w/w) hydrochloric acid at  $25^\circ\text{C}$  are summarized in **Figure 18**.

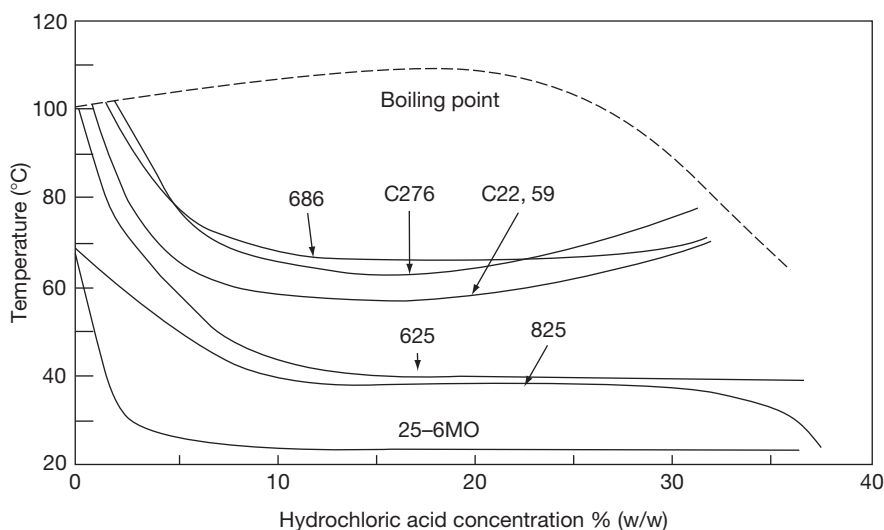


**Figure 15** Isocorrosion charts ( $0.5 \text{ mm year}^{-1}$ ) for nickel alloys in hydrochloric acid. Adapted from *High Performance Alloys for Resistance to Aqueous Corrosion*; Publication SMC-026, Special Metals Corporation, 2000.

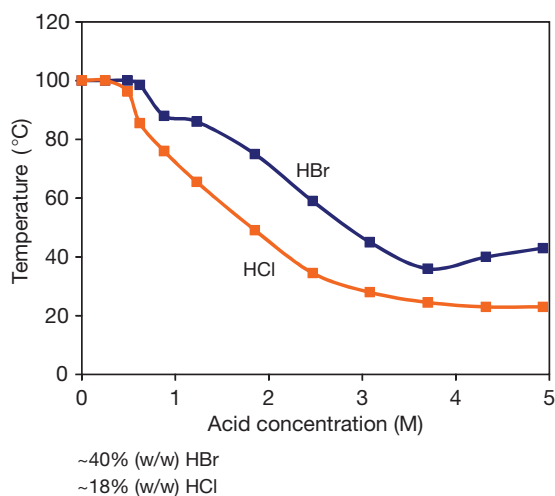


**Figure 16** Isocorrosion charts ( $0.1 \text{ mm year}^{-1}$ ) for alloy C-22 in hydrochloric and hydrobromic acids at concentrations up to  $\sim 5 \text{ M}$ . Adapted from Meck, N. S.; Pike, L.; Crook, P. Corrosion Performance of a New Age-Hardenable Ni-Cr-Mo Alloy, Paper 08181, Corrosion 2008; NACE International: Houston, TX, 2008.

Evidently, the addition of up to  $\sim 200 \text{ ppm Fe}^{3+}$  increases the corrosion rates of both alloys by increasing their corrosion potentials in the active potential range. Further additions produce progressive increases in the corrosion potential and corrosion rate of alloy B-3 (N10675) which remains active throughout the full potential range, as revealed in the polarization curves for the alloy with and without

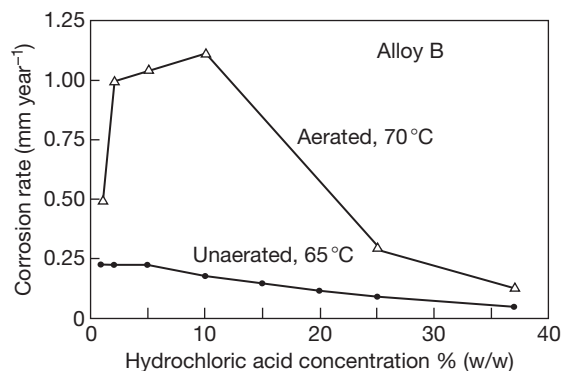


**Figure 17** Corrosion rates for alloy B tested in aqueous hydrochloric acid at  $65\text{--}70^\circ\text{C}$ . Adapted from Friend, W. Z. *Corrosion of Nickel and Nickel-Base Alloys*; John Wiley & Sons: London, 1980.

$1000 \text{ ppm Fe}^{3+}$  in **Figure 18**. In the case of alloy C-2000 (N06200), further additions also produce progressive and significant increases in the corrosion potential, but reductions in the corrosion rate by promoting passivation. This is apparent in the polarization curve in **Figure 18** for alloy C-2000 (N06200) in the presence of  $1000 \text{ ppm Fe}^{3+}$  which shows no evidence of an active/passive transition because the material is spontaneously passivated at the outset of the test, as confirmed by its relatively high corrosion potential and the correspondingly low applied current densities required to raise the potential above the corrosion potential.<sup>24</sup>

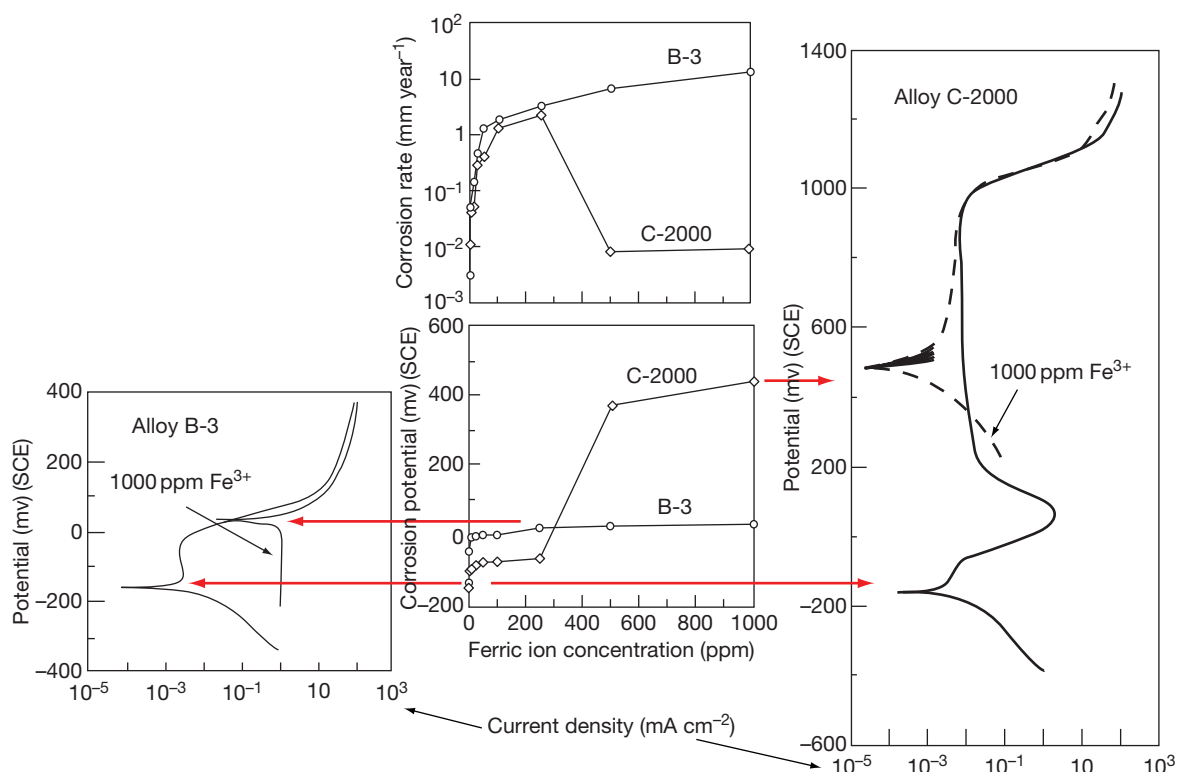


**Figure 18** Corrosion rates, corrosion potentials, and polarization behaviors of alloys B-3 and C-2000 in deaerated 20% (w/w) hydrochloric acid with various additions of ferric ions at 25 °C. Adapted from Nacera, S. M.; Crook, P.; Klarstrom, D. L.; Rebak, R. B. *Effect of Ferric Ions on the Corrosion Performance of Nickel Alloys in Hydrochloric Acid Solutions*, Paper 04430, Corrosion 2004; NACE International: Houston, TX, 2004.

Nickel and its alloys are among the more corrosion resistant materials in aqueous HF acid, and their relative performances up to the relevant atmospheric boiling point are summarized relative to the stainless steel type 316L (S31603) in the isocorrosion diagrams in [Figure 19](#) (note that these are isocorrosion diagrams for a corrosion rate of  $0.5 \text{ mm year}^{-1}$  which is not an acceptable corrosion rate for most practical applications).<sup>35</sup>

Corrosion rates increase generally with concentration and temperature, and the nickel–copper and nickel–molybdenum alloys outperform significantly the nickel–chromium–molybdenum alloys in the pure acid. Behavior is influenced strongly by the formation and persistence or otherwise of pseudo-passive, fluoride films. However, as with the other acids, the presence of oxygen and other oxidizing agents play a key role and can dominate materials performance, particularly in the cases of nickel–copper and nickel–molybdenum alloys. As a result, the performances of alloys can vary significantly between

liquid and vapor phases as shown in the corrosion rates for various nickel alloys tested in and above 10% (w/w) HF acid at 24 and 76 °C that are charted in [Figure 20](#).<sup>36</sup>

Thus, all the alloys perform relatively well in the liquid phase but nickel 200 (N02200) and alloys 400 (N04400) and 600 (N06600) perform very poorly in the vapor phase at both temperatures. The corrosion rates of alloy C-22 (N06022) also increase in the vapor phase, but not to the same extent as the other alloys that were tested.

These effects are all due to the increased availability of oxygen in the thin, liquid films that condense in the vapor phase. In the case of the chromium-free alloys 200 (N02200) and 400 (N04400) or chromium-deficient alloy 600 (N06600), corrosion product accumulation in the liquid films promotes progressively increased rates of corrosion. Thus, in the case of alloy 400 (N04400), cuprous ions ( $\text{Cu}^+$ ) that are the initial products of dissolution are oxidized by oxygen to the cupric state ( $\text{Cu}^{2+}$ ) in which they induce further

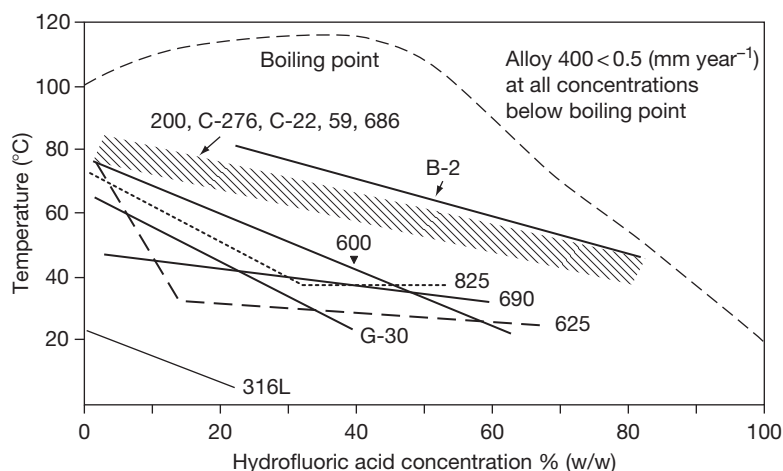


**Figure 19** Isocorrosion charts ( $0.5 \text{ mm year}^{-1}$ ) for nickel alloys in aqueous hydrofluoric acid. Adapted from Crum, J. R.; Smith, G. D.; McNallan, M. J.; Hirnyj, S. *Characterisation of Corrosion Resistant Materials in Low and High Temperature HF Environments*, Paper 382, Corrosion '99; NACE International: Houston, TX, 1999.

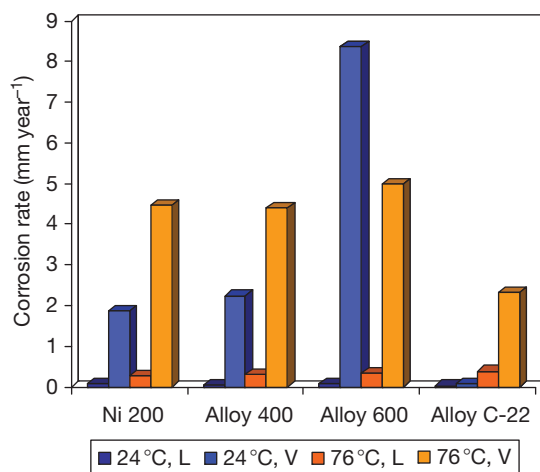


**Figure 20** Corrosion rates for various nickel alloys tested in (liquid, L) and above (vapor, V) 10% (w/w) hydrofluoric acid at 24°C and 76°C. Adapted from Pawel, S. J. *Corrosion* **1994**, 50, 963–971.

increases in corrosion potential and corrosion rate. In contrast, the chromium-containing alloy C-22 (N06022) performs better in the vapor phase because passive film formation, albeit relatively non-protective, is possible. Clearly, this is a significant consideration in selecting nickel alloys for aqueous HF acid duties. Other significant factors include:

1. Niobium has an adverse effect on the corrosion resistance of nickel alloys, exemplified by the relatively poor performance of alloy 625 (N06625) that

contains a nominal 3.7% niobium, as shown in [Figure 19](#).

2. Segregation of specific elements, not least niobium, can result in preferential corrosion of welds in nickel alloys.<sup>6</sup>
3. SCC is a significant threat to nickel alloys in aqueous HF acid. Nickel 200 (N02200) and alloys 400 (N04400), 500 (N05500), 600 (N06600), B-2 (N10665), and C-276 (N10276) have all been reported as vulnerable under specific environmental conditions, in particular in vapors over 48% (w/w) acid. The risks of SCC are exacerbated by cold work, and the presence of oxygen and  $\text{Cu}^{2+}$  and can be mitigated by appropriate heat treatment.<sup>6</sup>

The very different behaviors of the nickel–molybdenum B and nickel–chromium–molybdenum C families of alloys have stimulated interest in alloy compositions that might provide both the resistance to anodic dissolution of the B family and the capacity to passivate of the C family. For example, a proprietary alloy Hybrid BC-1 has recently been developed<sup>37</sup> containing 22% molybdenum and 15% chromium that outperforms significantly the other members of the C family of alloys in aqueous hydrochloric and hydrobromic acid solutions, and maintains its performance in the presence of oxygen. For example, corrosion rates for the new alloy and various members of the C family of alloys in tests in hydrochloric acid at concentrations in the range 5–20% (w/w) at  $\sim 80^\circ\text{C}$  are shown in [Figure 21](#). Clearly, the

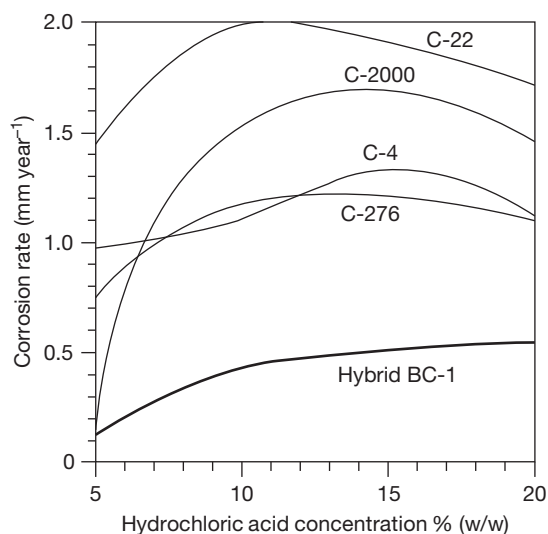


**Figure 21** Corrosion rates for various nickel–chromium–molybdenum alloys tested in aqueous hydrochloric acid at 79 °C. Adapted from Crook, P.; Meck, N. S.; Koon, N. E. *The Corrosion Characteristics of a Uniquely Versatile Nickel Alloy*, Paper 08190, Corrosion 2008; NACE International: Houston, TX, 2008.

new alloy performs significantly better than any of the other alloys tested, but the prevailing rates of  $\sim 0.5 \text{ mm year}^{-1}$  that apply across much of the concentration range are of limited practical benefit.

## 2.22.5 Other Metals and Alloys

### 2.22.5.1 Copper and Copper Alloys

Copper has limited resistance to anhydrous hydrogen chloride gas, with a suggested upper temperature limit for continuous service below 100 °C. Copper and some of its alloys are, however, much more resistant to AHF gas and liquid, as shown in [Figures 11 and 12](#). Copper has been used at ambient temperatures to handle AHF liquid and vapor and the cupro–nickels (C71000, C71500), in particular, have useful resistance, and have been used for heat exchanger tubing because of their relative resistance to flowing AHF.<sup>6</sup>

Copper might be expected to resist aqueous hydrochloric acid because it is relatively noble and does not normally displace hydrogen from acid solutions. However, its resistance is reduced significantly in the presence of air or other oxidizing agents, not least its own corrosion product,  $\text{Cu}^{2+}$ , which can stimulate corrosion autocatalytically. Silicon bronzes (for example, C65500) have found some use at

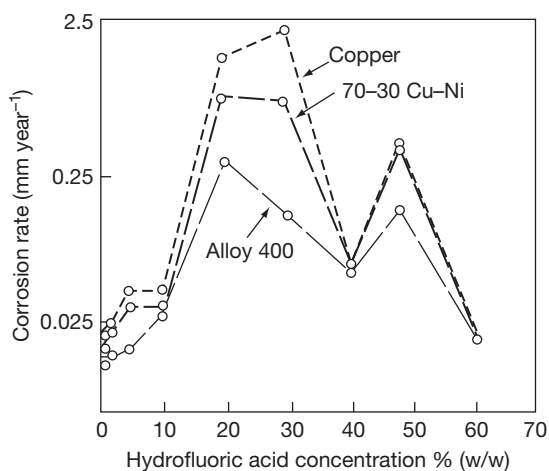


**Figure 22** Corrosion rates for copper alloys in static, aqueous hydrofluoric acid under air at 60 °C. Adapted from Materials Selector for Hazardous Chemicals. In *Hydrogen Fluoride and Hydrofluoric Acid*; MTI Publication MS-4, Materials Technology Institute of the Process Industries Inc., 2000; Vol. 4.

concentrations  $< 20\%$  (w/w) at moderate temperatures<sup>5</sup> but, in general, applications for copper and its alloys in aqueous hydrochloric acid are limited.

Some copper alloys have useful resistance to aqueous HF acid but only at relatively low velocities in the absence of oxygen or other oxidizing agents. Corrosion rates for some copper alloys in static, aqueous HF acid under air at 60 °C are shown in [Figure 22](#).<sup>3</sup>

Other tests have shown increased rates of corrosion in vapors over aqueous acids due to the presence of oxygen. Copper, cupronickels (C71000, C71500), and aluminum/aluminum–silicon bronzes have all found some application in aqueous acids, but there have been problems with dealloying and SCC.<sup>6</sup>

### 2.22.5.2 Titanium and Titanium Alloys

Titanium and its alloys are dependent on the formation of protective oxide films consisting mostly of titanium dioxide,  $\text{TiO}_2$ , for their resistances to corrosion. Such films require the presence of oxygen or water to form, and as a general rule anhydrous conditions are best avoided. Titanium and its alloys thus have useful resistance to hydrogen chloride gas containing water but anhydrous gas or condensates from water-containing gas can present significant corrosion risks, depending on the temperature.<sup>2</sup>

One of the conditions for protective film formation in aqueous hydrohalic acids, namely the availability of a



cathodic process to elevate the corrosion potential above the potential for passive oxide formation, is satisfied under most conditions because this potential is below the hydrogen evolution potential. However, the solubility of the passive film increases with concentration and temperature. It has also been shown that the protection afforded by the film depends on the conditions under which it forms, in particular the formation rate.<sup>38</sup> Titanium dioxide is attacked strongly by HF acid to a degree that precludes the application of titanium and its alloys in acidic environments containing HF acid or fluorides. The performance of titanium and its alloys in other hydrohalic acids is dominated by the stability of the titanium dioxide film, and applications are limited to relatively weak acids.

**Figure 23** shows isocorrosion curves ( $0.13 \text{ mm year}^{-1}$ ) for commercially pure titanium (ASTM grade 2, R50400), a titanium–nickel–molybdenum alloy (ASTM grade 12, R53400), and a titanium–palladium alloy (ASTM grade 7, R52400) in naturally aerated hydrochloric acid at concentrations up to 35% (w/w).<sup>39</sup> Evidently, pure titanium is restricted

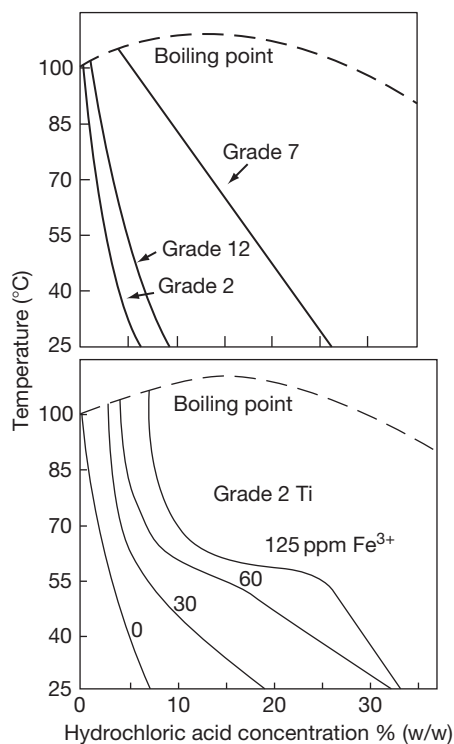


**Figure 23** Isocorrosion charts ( $0.13 \text{ mm year}^{-1}$ ) for titanium and various titanium alloys in hydrochloric acid and in hydrochloric acid containing various levels of ferric ions. Adapted from *Corrosion Resistance of Titanium*; Timet Metals Corporation, 1997.<sup>39</sup>

to concentrations below  $\sim 5\%$  (w/w) even at ambient temperatures. Alloying with palladium significantly improves the corrosion resistance arising from the well established cathodic modification effects of palladium on promoting and sustaining the passivity of titanium, which are described elsewhere in this book.

There is little published data relating to the performance of titanium and its alloys in hydrobromic acid. Apart from the order of hydrohalic acid strengths, it is known that the breakdown potentials of titanium in aqueous halide-containing solutions are in the order: chlorides  $>$  bromides  $>$  iodides,<sup>40</sup> so hydrobromic acid might be expected to be more aggressive than hydrochloric acid. Notwithstanding that, titanium and its alloys do find commercial application in processes that involve exposure to hydrobromic acid, such as in the manufacture of terephthalic acid from *p*-xylene using metal bromide catalysts.

Oxidizing agents in the acid such as dissolved oxygen, chlorine, nitric and chromic acids, and metal cations in higher oxidation states such as ferric,  $\text{Fe}^{3+}$  or cupric,  $\text{Cu}^{2+}$  ions also promote significant increases in corrosion resistance by promoting and sustaining passivity. For example, the effects of progressive additions of up to 125 ppm ferric ions on the performance of commercially pure titanium, (ASTM grade 2, R50400), in aqueous hydrochloric acid is also shown in **Figure 23**. Evidently, the addition of 125 ppm ferric ions extends the acceptable performance boundary to match the performance of the titanium–palladium alloy, (ASTM grade 7, R52400), at lower temperatures.<sup>39</sup> However, even the temporary absence of oxidizing agents can result in a loss of passivity and the addition of palladium to titanium provides a much more robust mechanism for the mitigation of corrosion risk than additions of oxidizing agents to the acid.

### 2.22.5.3 Zirconium and Zirconium Alloys

Zirconium and its alloys are similar to titanium in their dependence on oxide films, composed mainly of  $\text{ZrO}_2$ , to resist corrosion. They are less resistant to anhydrous hydrogen halide gases than titanium and they find no practical application. Zirconium dioxide is also attacked strongly by HF acid to a degree that also precludes the application of zirconium and its alloys in acidic environments containing HF acid or fluorides.

The performance of zirconium and its alloys in other aqueous hydrohalic acids is superior to titanium because the zirconia film is much less soluble than the corresponding titania film on titanium.

Indeed, zirconium is second only to tantalum in its resistance to aqueous hydrochloric acid, exemplified by the isocorrosion diagram for commercial purity zirconium (Zr702, R60702) in [Figure 14](#). The performances of the commercial alloys containing tin (Zr704, R60704) and niobium (Zr705, R60705) are broadly similar, but they may display inferior resistance toward the performance boundary for commercial purity zirconium (Zr702, R60702) in [Figure 14](#). The main threats to the successful performance of zirconium and its alloys in hydrochloric acid are:

1. Strongly oxidizing conditions can result in the potential exceeding the breakdown potential, resulting in the initiation of localized corrosion. Aeration does not present a significant threat in this respect but stronger oxidizing agents such as cupric and ferric ions in sufficient quantities can stimulate significant pitting attack. Galvanic coupling with nobler materials such as graphite can present a similar threat.
2. Galvanic coupling to more active materials can result in the uptake of cathodically produced hydrogen, resulting in the embrittlement and hydriding of zirconium and its alloys, with a consequential loss of ductility.

These risks and their mitigation are described in more detail in the chapter on zirconium and its alloys in this book.

As with titanium, there is little published data relating to the performance of zirconium and its alloys in hydrobromic acid. However, in contrast to titanium, the breakdown potentials of zirconium in aqueous halide-containing solutions are in the order: iodides > bromides > chlorides<sup>41</sup> and it might thus be expected to be less vulnerable to oxidizing agents than in hydrochloric acid.

#### 2.22.5.4 Tantalum and Tantalum Alloys

Tantalum and its alloys are similar to zirconium and titanium in their dependence on the formation of a protective oxide, specifically tantalum pentoxide ( $\text{Ta}_2\text{O}_5$ ), to resist corrosion. Tantalum is resistant to hydrogen chloride and bromide gases up to at least 150 °C, and even at higher temperatures if the gases contain some water. However, in keeping with the other reactive metals, tantalum's protective oxide is attacked strongly by anhydrous and aqueous HF acid to a degree that precludes its application in acidic environments containing HF acid or fluorides.

Tantalum pentoxide is very stable in aqueous hydrochloric acid, and tantalum (R05200) has exceptional corrosion resistance to the acid, as illustrated in [Figure 14](#). Niobium is similar to tantalum, being protected from corrosion by a film of niobium pentoxide,  $\text{Nb}_2\text{O}_5$ . The film is less protective than tantalum pentoxide, as a result of which niobium is considerably less resistant to corrosion in hydrochloric acid than tantalum or zirconium, as shown in [Figure 14](#). Binary alloys of tantalum and niobium deliver performances intermediate between those of the parent metals. The performance of the commercial 2.5% tungsten alloy (R05252) is broadly similar to tantalum metal.

The main threat to the successful performance of tantalum and its alloys in hydrochloric acid is hydrogen embrittlement due to uptake of cathodic hydrogen from the corrosion of tantalum itself or a more active metal to which tantalum is coupled electrically. Tantalum has a high solubility for hydrogen and forms hydrides. It can absorb hydrogen at ambient temperatures but embrittlement arising from the self corrosion of tantalum and its alloys is usually associated with higher temperatures at which significant corrosion rates are experienced. The rate of embrittlement depends on the corrosion rate but the effects are cumulative, and it has been reported<sup>5</sup> in 25% (w/w) hydrochloric acid at 190 °C in which the corrosion rate is no more than 0.025 mm year<sup>-1</sup>.

Hydrogen embrittlement of tantalum can be prevented by electrical isolation from more active equipment items using insulated flanges or by coupling with a more noble metal with a low hydrogen overvoltage such as platinum, either mechanically, or by resistance or spot welding, or brush plating.<sup>2</sup> An area ratio of ~1000:1 Ta:Pt has been shown to be effective, not only in eliminating embrittlement, but also in reducing the corrosion rates of both tantalum and the noble metal, as shown in [Figure 24](#).<sup>42</sup> The presence of oxidizing agents also prevents hydrogen embrittlement by raising the potential of the tantalum. Thus, embrittlement does not occur in chlorine-saturated hydrochloric acid.<sup>2</sup>

Tantalum is also highly resistant to hydrobromic acid but there is much less data in the public arena than for hydrochloric acid. Like titanium, the breakdown potentials of tantalum in aqueous halide-containing solutions are in the order: chlorides > bromides > iodides,<sup>40</sup> so tantalum might be expected to be more vulnerable to the presence of oxidizing agents in hydrobromic than in hydrochloric acid.

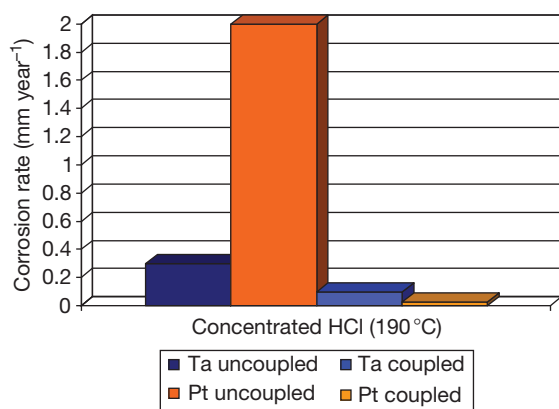


**Figure 24** Corrosion rates for uncoupled and coupled tantalum and platinum in concentrated hydrochloric acid at 15–40 °C. Adapted from Bishop, C. R.; Stern, M. *Hydrogen Embrittlement of Tantalum in Aqueous Media*; 17th Annual NACE Conference; National Association of Corrosion Engineers, 1966.

### 2.22.5.5 Noble Metals

Silver, gold, and platinum are highly resistant to the anhydrous hydrogen halides. In anhydrous hydrogen chloride, upper temperature limits of 230, 870, and 1200 °C have been suggested for silver, gold, and platinum, respectively.<sup>5</sup> Silver has found significant application in equipment for AHF in the absence of oxidizing agents and sulfides.<sup>6</sup>

Silver has good but not unlimited resistance to the aqueous hydrohalic acids below the atmospheric boiling point, depending on the temperature, velocity, and the presence or otherwise of oxidizing agents. Gold and platinum are highly resistant below the atmospheric boiling point, although gold is vulnerable to the presence of very strong oxidants such as ferric ions or nitric acid, and platinum is slightly attacked in 36% (w/w) acid at the boiling point<sup>5,6</sup> and more significantly so at higher temperatures, exemplified by the data in Figure 24.

### 2.22.6 Nonmetallic Materials

Given the limitations of most classes of alloys that might be considered for handling hydrohalic acid, and the high cost of the more resistant materials such as nickel, zirconium, and tantalum alloys, it is inevitable that nonmetallic materials play major roles in hydrohalic acid applications. The application of these materials is covered in more detail in the relevant chapters in this book but the more significant materials are as follows.

#### 2.22.6.1 Thermoplastic and Reinforced Thermosetting Materials

In practice, chemical compatibility is but one factor that determines the suitability or otherwise of a thermoplastic material for a specific application. Other factors such as mechanical and fabrication properties, thermal expansion characteristics, permeation properties, etc. are significant design considerations. In practice, other than for small scale equipment, thermoplastics are used more commonly as linings on stronger substrates rather than in solid form, because of reliability and integrity concerns. Permeation is a particular issue in the case of HF acid at higher concentrations and temperatures, and needs to be managed by, for example, the use of manifolded vent holes through the metal<sup>7</sup> in the case of lined metal systems.

Most thermoplastics of commercial significance find applications in the handling of hydrohalic acids. Readers interested in specific applications should consult materials suppliers and the more detailed sources are referenced,<sup>2–8</sup> but the more significant materials are as follows:

1. Polyethylene (PE), depending upon its molecular weight, and polypropylene (PP) have useful resistance. PE tends to be restricted to temperatures close to ambient, but PP has been used at much higher temperatures as a lining material in the handling, for example, of hydrochloric acid.
2. Polyvinyl chloride (PVC) and chlorinated polyvinyl chloride (CPVC) also find uses at lower temperatures, for example, as linings in glass reinforced plastic tanks for the storage of hydrochloric acid. Unplasticized grades are normally specified because plasticized grades have lower chemical resistance.
3. Fluoroplastics are highly resistant to hydrohalic acids, depending upon their degree of fluorination. The highly fluorinated materials polytetrafluoroethylene (PTFE), fluorinated ethylene propylene (FEP), and perfluoroalkoxy (PFA) are resistant to all concentrations of the acids up to and well-beyond their atmospheric boiling points. The less highly fluorinated materials ethylene chlorotrifluoroethylene (ECTFE), ethylene tetrafluoroethylene (ETFE), and polyvinylidene fluoride (PVDF) are also highly resistant but tend to have lower temperature limits for service than the fully fluorinated grades.

Reinforced polyester, epoxy, phenolic, and furane resins all find application in the handling of hydrohalic

acids. Glass reinforced materials (GRP) based on polyester or vinyl ester resins, possibly lined with PVC (so called dual laminate construction), are widely used for the storage and handling of hydrochloric acid at temperatures up to  $\sim 90^{\circ}\text{C}$ , depending on the acid concentration and the specific resin. Glass is attacked by HF acid but constructions using epoxy vinyl esters and corrosion resistant barriers such as carbon veils can be used for handling weaker acids at lower temperatures.

### 2.22.6.2 Elastomers

Natural rubber is used widely as a lining for carbon steel in the storage, transport, and handling of hydrochloric acid. Softer rubbers tend to be restricted to lower temperatures, but hard rubber can tolerate temperatures as high as  $\sim 90^{\circ}\text{C}$ . Natural rubbers are limited to ambient temperatures in HF acid. Chloro- or bromobutyl rubbers are preferred as linings on carbon steel for the storage and transport of up to 70% (w/w) HF acid, up to maximum service temperatures that depend on concentration.

Other elastomers such as butyl, ethylene propylene diene terpolymer (EPDM), and chlorosulphonated PE (such as Hypalon) find niche applications in hydrohalic acids where, for example, the resistance of natural rubber is limited by factors such as the presence of organic contaminants, higher temperatures, or flexibility requirements. Additives such as silica or magnesia compounds are unsuitable for HF acid service, and have to be substituted by materials such as carbon in special grades.

Fluoro- and perfluoroelastomers provide the best resistance to hot and/or concentrated hydrohalic acids, but their high cost tends to limit their use to smaller components such as gaskets and other sealing components.

### 2.22.6.3 Inorganic Materials

Borosilicate glass is highly resistant to hydrochloric and hydrobromic acids up to temperatures well beyond their atmospheric boiling points, and solid or glass lined equipment finds significant use for handling the acids. However, glass is heavily attacked by HF acid for which it is unsuitable.

Impervious graphite, filled with impregnants such as phenolic resins, PTFE, or carbon, is highly resistant to hydrohalic acids and finds significant use in heat exchange duties for temperatures well-beyond atmospheric boiling. Carbon-carbon composites have excellent resistance to hydrohalic acids and found application for internal components, particularly in

HF acid duties. Carbon bricks with appropriate mortars and fluoroplastic membranes have found applications as linings for steel in high temperature duties. Silicon carbide also has excellent hydrohalic acid resistance and has been used in heat exchange duties.

## References

1. *Hydrofluoric Acid Properties*; Honeywell Specialty Materials Products, 2002: [http://www51.honeywell.com/sm/hfacid/common/documents/HF\\_Properties\\_Graph\\_technical\\_doc.pdf](http://www51.honeywell.com/sm/hfacid/common/documents/HF_Properties_Graph_technical_doc.pdf)
2. Materials Selector for Hazardous Chemicals. *Hydrochloric Acid, Hydrogen Chloride and Chlorine*; MTI Publication MS-3: Materials Technology Institute of the Process Industries Inc.: St Louis, MO, 1999; Vol. 3.
3. Materials Selector for Hazardous Chemicals. *Hydrogen Fluoride and Hydrofluoric Acid*; MTI Publication MS-4: Materials Technology Institute of the Process Industries Inc.: St Louis, MO, 2000; Vol. 4.
4. DECHEMA Corrosion Handbook. *Hydrochloric Acid, Nitric Acid*; Wiley-VCH: London, 2004; Vol. 2.
5. Crum, J. R. Corrosion by Hydrogen Chloride and Hydrochloric Acid. In *ASM Handbook. Corrosion: Environments and Industries*; ASM International: Materials Park, OH, 2006; pp 682–689, Vol. 13C.
6. Jennings, H. S. Corrosion by Hydrogen Fluoride and Hydrofluoric Acid. In *ASM Handbook. Corrosion: Environments and Industries*; ASM International: Materials Park, OH, 2006; pp 690–703, Vol. 13C.
7. NACE International Publication 5A-171. *Materials for Storing and Handling Commercial Grades of Aqueous Hydrofluoric Acid and Anhydrous Hydrogen Fluoride*; NACE International: Houston, TX, 2007.
8. Jennings, H. S. *Materials for HF Service in the New Millennium*, Paper 01345, Corrosion 2001; NACE International: Houston, TX, 2001.
9. Foroulis, Z. A. *Anticorros. Methods Mater.* **1988**, 35(11), 4–12.
10. Schillmoller, C. M. *Chem. Eng.* **1980**, 87, 161–163.
11. Poorqasemi, E.; Abootalemi, O.; Peikari, M.; Haqdar, F. *Corros.Sci.* **2009**, 51, 1043–1054.
12. Crouse, P. L. *Corros. Sci.* **1993**, 34, 295–305.
13. Chirinos, G.; Turgoose, S.; Newman, R. C. *Effects of Residual Elements on the Corrosion of Steels in HF*, Paper 97513, Corrosion '97; NACE International: Houston, TX, 1997.
14. Gysbers, A.; Hasim, H.; Clarida, D.; Chirinos, G.; Marsh, J.; Palmer, J. *Specification for Carbon Steel Materials for Hydrofluoric Acid Alkylolation Units*, Paper 03651, Corrosion 2003; NACE International: Houston, TX, 2003.
15. API Recommended Practice RP751. *Safe Operation of Hydrofluoric Acid Alkylolation Units*; American Petroleum Institute: Washington, DC, 1999.
16. NACE Publication 8X194. *Materials and Fabrication Practices for New Pressure Vessels Used in Wet H<sub>2</sub>S Refining Service*; NACE International: Houston, TX, 2006.
17. NACE Standard Test Method TM0177–2005. *Laboratory Testing of Metals for Resistance to Sulphide Stress Cracking and Stress Corrosion Cracking in H<sub>2</sub>S Environments*; NACE International: Houston, TX, 2005.
18. NACE Standard Test Method TM0284–2003. *Evaluation of Pipeline and Pressure Vessel Steels to Hydrogen Induced Cracking*; NACE International: Houston, TX, 2003.

19. NACE Standard Test Method TM0103–2003. *Laboratory Test Procedures for Evaluation of SOHIC Resistance of Plate Steels Used in Wet H<sub>2</sub>S Service*; NACE International: Houston, TX, 2003.
20. Agarwal, D. C.; Alves, H. *Applications of Alloys 59 (UNS N06059) and 31 (UNS N08031) in Mitigating Corrosion Risks in the CPI and Petrochemical Industries*, Paper 07186, Corrosion 2007; NACE International: Houston, TX, 2007.
21. Ihara, Y.; Ohgame, S.; Sakiyama, K.; Hashimoto, K. *Corros. Sci.* **1982**, 22, 901.
22. Myers, W. R.; Delong, W. B. *Chem. Eng. Prog.* **1948**, 44, 359.
23. Trabanelli, G.; Zucchi, F.; Felloni, L. *Corros. Sci.* **1965**, 5, 211.
24. Nacera, S. M.; Crook, P.; Klarstrom, D. L.; Rebak, R. B. *Effect of Ferric Ions on the Corrosion Performance of Nickel Alloys in Hydrochloric Acid Solutions*, Paper 04430, Corrosion 2004; NACE International: Houston, TX, 2004.
25. Marcus, P. *Corros. Sci.* **1994**, 36, 2155.
26. Newman, R. C. *Corros. Sci.* **1985**, 25, 331–341.
27. Schneider, A.; Kuron, D.; Hofmann, S.; Kirchhein, R. *Corros. Sci.* **1990**, 31, 191.
28. Hunkeler, F. J. Tantalum and Niobium. In *Process Industry Corrosion*; Moniz, B. J., Pollock, W. J., Eds.; NACE International: Houston, TX, 1986; pp 545–549.
29. Lorang, G.; Jallerat, N.; Vu Kwang, K.; Langeron, J.-P. *Surf. Interface Anal.* **1990**, 16, 325.
30. Jabs, T.; Borthen, P.; Strehblow, H.-H. *J. Electrochem. Soc.* **1997**, 144, 1231–1243.
31. Lloyd, A. C.; Noel, J. J.; McIntyre, N. S.; Shoesmith, D. W. *Electrochim. Acta.* **2004**, 49, 3015–3027.
32. *High Performance Alloys for Resistance to Aqueous Corrosion*; Publication SMC-026, Special Metals Corporation, 2000.
33. Meck, N. S.; Pike, L.; Crook, P. *Corrosion Performance of a New Age-Hardenable Ni-Cr-Mo Alloy*, Paper 08181, Corrosion 2008; NACE International: Houston, TX, 2008.
34. Friend, W. Z. *Corrosion of Nickel and Nickel-Base Alloys*; John Wiley & Sons, 1980.
35. Crum, J. R.; Smith, G. D.; McNallan, M. J.; Hirnyj, S. *Characterisation of Corrosion Resistant Materials in Low and High Temperature HF Environments*, Paper 382, Corrosion '99; NACE International: Houston, TX, 1999.
36. Pawel, S. J. *Corrosion* **1994**, 50, 963–971.
37. Crook, P.; Meck, N. S.; Koon, N. E. *The Corrosion Characteristics of a Uniquely Versatile Nickel Alloy*, Paper 08190, Corrosion 2008; NACE International: Houston, TX, 2008.
38. Blackwood, D. J.; Peter, L. M. *Electrochim. Acta.* **1989**, 34, 1505–1511.
39. *Corrosion Resistance of Titanium*; Timet Metals Corporation, 1997.
40. Dugdale, I.; Cotton, J. B. *Corros. Sci.* **1964**, 4, 397–411.
41. Yau, Te-Lin *Understanding Corrosion Behavior From Electrochemical Measurements*, Paper 04227, Corrosion 2004; NACE International: Houston, TX, 2004.
42. Bishop, C. R.; Stern, M. *Hydrogen Embrittlement of Tantalum in Aqueous Media*, 17th Annual NACE Conference; National Association of Corrosion Engineers: Houston, TX, 1966.



## 2.23 Corrosion in Sulfuric Acid

**J. A. Richardson**

Anticorrosion Consulting, 5 Redhills Lane, Durham DH1 4AL, UK

© 2010 Elsevier B.V. All rights reserved.

2.23.1	Introduction	1226
2.23.2	Steels and Cast Irons	1228
2.23.3	Stainless Steels	1230
2.23.3.1	Mechanisms of Protection	1230
2.23.3.2	Performances of Stainless Steels	1235
2.23.4	Nickel Alloys	1238
2.23.4.1	Mechanisms of Protection	1238
2.23.4.2	Performances of Nickel Alloys	1241
2.23.5	Other Metals and Alloys	1242
2.23.5.1	Aluminum and Aluminum Alloys	1242
2.23.5.2	Copper and Copper Alloys	1243
2.23.5.3	Titanium and Titanium Alloys	1243
2.23.5.4	Lead and Lead Alloys	1244
2.23.5.5	Zirconium and Zirconium Alloys	1244
2.23.5.6	Tantalum and Tantalum Alloys	1246
2.23.6	Nonmetallic Materials	1246
2.23.6.1	Organic Materials	1246
2.23.6.2	Inorganic Materials	1248
References		1248

### Abbreviations

**ASTM** American Society for Testing Materials  
**CPVC** Chlorinated polyvinyl chloride  
**CR** Corrosion rate ( $\text{mm year}^{-1}$ )  
**ECTFE** Ethylene chlorotrifluoroethylene  
**ETFE** Ethylene tetrafluoroethylene  
**FEP** Fluorinated ethylene propylene  
**FRP** Fiber reinforced plastic  
**MSE** Mercurous sulfate electrode  
**ppm** Parts per million  
**PE** Polyethylene  
**PFA** Perfluoroalkoxy  
**PP** Polypropylene  
**PTFE** Polytetrafluoroethylene  
**PVC** Polyvinyl chloride  
**PVDF** Polyvinylidene fluoride  
**SCE** Saturated calomel electrode  
**SHE** Standard hydrogen electrode  
**XPS** X-ray photoelectron spectroscopy

### Symbols

**$C_{\text{surface}}$**  Solubility of ferrous sulfate in the acid (mass %)  
 **$C_{\text{bulk}}$**  Initial concentration of ferrous sulfate in the acid (mass %)  
 **$d$**  Diameter (m)  
 **$E$**  Electrode potential (V)  
 **$i$**  Current density ( $\text{mA cm}^{-2}$ )  
 **$M_{\text{H}_2\text{O}}$**  Molarity of free water  
 **$M_{\text{species}}$**  Molarity of species  
 **$\rho$**  Density ( $\text{kg m}^{-3}$ )  
 **$T$**  Temperature (K)  
 **$u$**  Velocity ( $\text{m s}^{-1}$ )  
 **$\mu$**  Viscosity (cp)

### 2.23.1 Introduction

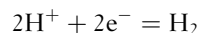
Sulfuric acid ( $\text{H}_2\text{SO}_4$ ) is a major feedstock for many chemical processes and is manufactured in greater quantities than any other chemical, most commonly

by the contact process, in which sulfur or sulfur-containing waste is burned to form sulfur dioxide ( $\text{SO}_2$ ), which is converted to sulfur trioxide ( $\text{SO}_3$ ) by contact with a vanadium catalyst and absorbed in acid to increase its strength. The structure of sulfuric acid solutions as a function of concentration is summarized in Figure 1.<sup>1</sup> From the corrosion standpoint, acids are conventionally classified into three concentration ranges:

1. Weak acids with concentrations  $< \sim 25\%$  by weight (w/w). The dominant species are water molecules in which the acid is dissociated into protons ( $\text{H}^+$ ) and bisulfate ( $\text{HSO}_4^-$ ) and sulfate ( $\text{SO}_4^{2-}$ ) anions. Below a concentration of  $\sim 5\%$  (w/w), acid strengths are commonly defined by pH. At the higher end of the pH range, the solutions are effectively acidified waters. Thus, pHs of 2, 3, and 4 are equivalent to concentrations of 490, 49, and 4.9 ppm (w/w) sulfuric acid respectively at  $25^\circ\text{C}$ .
2. Medium-strength acids with concentrations in the range 25–80% (w/w), toward the upper end of which the thermodynamic activity of water decreases to low values while acid molecules are dissociated into protons and bisulfate ( $\text{HSO}_4^-$ ) anions.
3. Concentrated acids, with strengths  $> \sim 80\%$  (w/w), which contain little free water. At the lower end of the concentration range, acid molecules are dissociated into protons and bisulfate ( $\text{HSO}_4^-$ ) anions but undissociated  $\text{H}_2\text{SO}_4$  molecules dominate as

the concentration increases. This includes all of the significant commercial grades of acid, the commonest of which have strengths within the range 93–99% (w/w). Oleums are fuming acids that contain an excess of uncombined  $\text{SO}_3$ , defined in terms of either the free  $\text{SO}_3$  content or the concentration of sulfuric acid equivalent to the contained  $\text{H}_2\text{SO}_4$  plus the acid content that would form if the  $\text{SO}_3$  were reacted with water to form additional acid. Thus, 20% oleum is equivalent to 104.5% (w/w) sulfuric acid.

Sulfuric acid can be either ‘reducing’ or ‘oxidizing’ depending on its concentration. These are rather loose terms, not least because their common usage invariably fails to define the material to which the adjective applies. Conventionally, a reducing acid is one in which cathodic activity is confined to the reduction of protons to evolve hydrogen:



An oxidizing acid is one in which reductions of the acid itself, or its constituent species, occur at potentials more noble than hydrogen evolution and to an extent that can determine the behaviors of materials exposed to the acid. The terms have some validity as descriptors of the hydro-halic acids as inherently reducing and nitric acid as inherently oxidizing, but otherwise they are rather imprecise terms that are potentially misleading. Notwithstanding that, sulfuric acid exhibits inherently reducing or oxidizing properties, depending

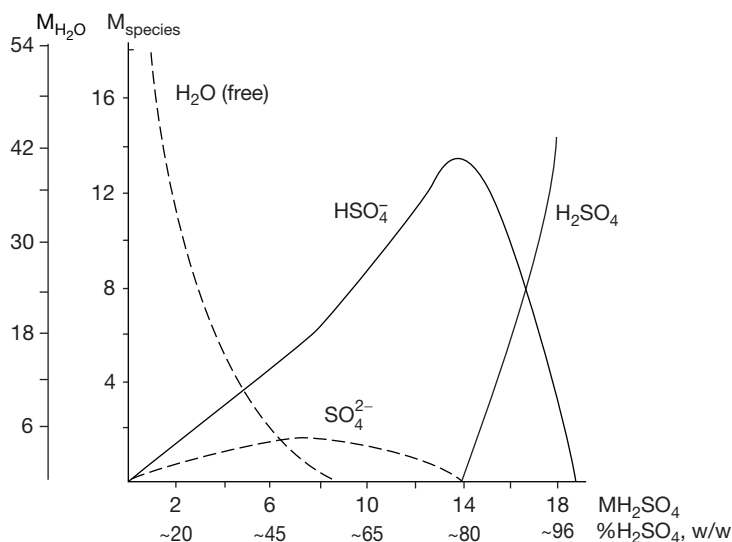
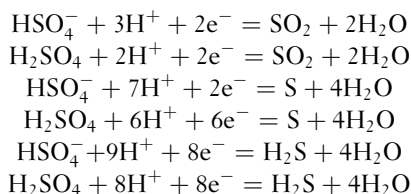


**Figure 1** Structure of sulfuric acid solutions. Adapted from Hammer, W. J. *The Structure of Electrolyte Solutions*; J. Wiley, 1959.

on the concentration and temperature. Thus, weak sulfuric acid is inherently reducing but concentrated sulfuric acid is inherently oxidizing, because both bisulfate anions and undissociated acid molecules contain sulfur in the  $S^{6+}$  oxidation state that can be reduced to sulfur dioxide, sulfur, or hydrogen sulfide, in which sulfur is in the  $S^{4+}$ ,  $S^0$ , and  $S^{2-}$  oxidation states, respectively. These reductions can be described stoichiometrically as follows:



Medium-strength acids can be inherently reducing or oxidizing. Dillon<sup>1</sup> has pointed out that 25% (w/w) acid is reduced to sulfur by finely divided nickel at ambient temperatures and by alloy 400 (Ni–30%Cu) at the boiling point, and on that basis, would be classified as oxidizing. However, 25% (w/w) acid corrodes steels and stainless steels rapidly at and above ambient temperatures supported by hydrogen evolution, which classifies it as reducing. As a general rule, hotter, more concentrated acids in the medium concentration range are more likely to exhibit oxidizing properties.

In practice, the extent to which a particular strength of acid is reducing or oxidizing at a particular temperature is also influenced and possibly dominated by the presence or otherwise of specific contaminants, in particular, oxidants, such as dissolved oxygen, nitric acid, and metal cations in a higher oxidation state, such as  $\text{Fe}^{3+}$  or  $\text{Cu}^{2+}$ , that can be beneficial or detrimental to corrosion performance, depending upon the circumstances. However, the presence of reducing agents, such as sulfites and sulfides, is usually detrimental, and halides, notably the ubiquitous chlorides, can have significant adverse effects on the corrosion performances of specific materials, particularly in weak- and medium-strength acids.

The corrosion performances of the various classes of material in sulfuric acid have been reviewed extensively elsewhere<sup>2–7</sup>, and readers whose main interest is to identify ‘what works where’ are referred to these sources and the relevant chapters on specific materials in this book. An exhaustive literature survey of corrosion in sulfuric acid has also been published.<sup>8</sup> In this chapter, the corrosion performances of materials are reviewed with an emphasis on the principles and

mechanisms that underpin their corrosion performances in sulfuric acid.

## 2.23.2 Steels and Cast Irons

Steels and gray or ductile cast irons are active and corroded rapidly by weak- and medium-strength acids. However, they have useful corrosion resistance in concentrated acids under static or low flow conditions as illustrated by the corrosion rate (CR) data in **Figure 2** relating to the performances of steel and gray or ductile cast irons in acid concentrations above 80% (w/w) at a temperature of 27 °C under stagnant conditions.<sup>2</sup>

The corrosion resistance arises from the spontaneous formation of protective films on steel and cast iron surfaces in concentrated acids. The potential to form such films is illustrated in **Figure 3** that shows anodic polarization curves for gray cast iron in stagnant 20% (w/w) sulfuric acid at 30 and 60 °C.<sup>9</sup> Gray cast iron corrodes rapidly at its natural corrosion potential in 20% (w/w) sulfuric acid at both temperatures, but the CR is reduced significantly in stages by anodic polarization, initially as the potential increases through a less protective sulfation region into a much more protective passivation region. The sulfation process involves the formation of a supersaturated

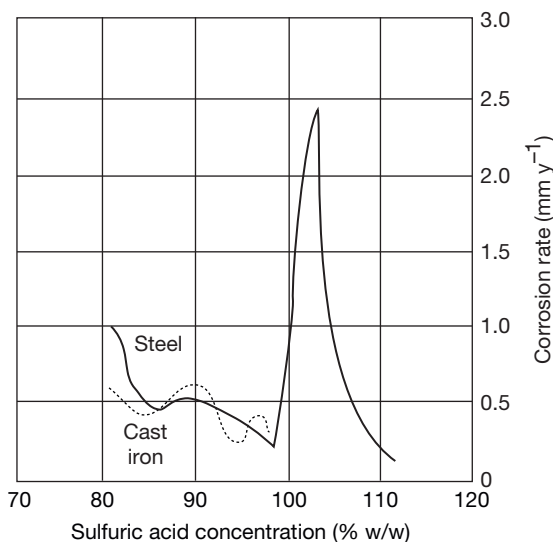


**Figure 2** Corrosion rates of steel and cast iron in concentrated sulfuric acid under stagnant conditions. Adapted from Materials Selector for Hazardous Chemicals. *Concentrated Sulphuric Acid and Oleum*, 2nd Ed.; MTI Publication MS-1, Materials Technology Institute of the Process Industries Inc., 2005; Vol. 1.

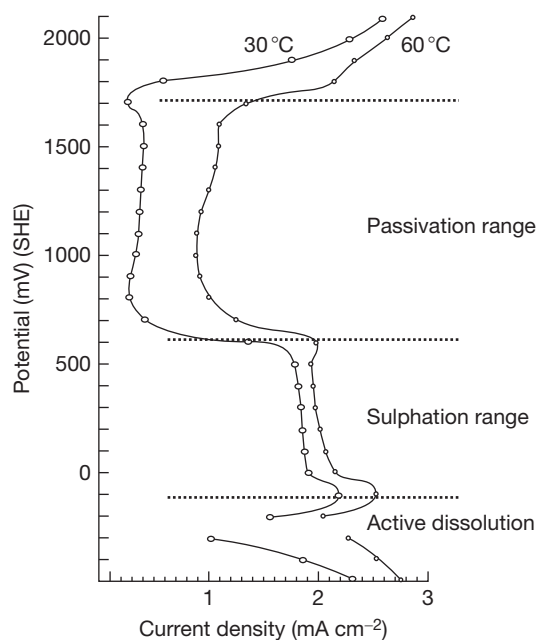


**Figure 3** Anodic polarization curves for grey cast iron in 20% (w/w) sulfuric acid. Adapted from Breakell, J. E. *The Corrosive Wear of Cast Irons in Marine Diesel Engine Cylinder Environments*; Ph. D. Thesis, University of Manchester, October, 1980.<sup>9</sup>

solution of ferrous sulfate, from which a crystalline film nucleates and grows. The degree of hydration of this film is thought to vary with acid strength as the concentration of water reduces from the heptahydrate ( $\text{FeSO}_4 \cdot 7\text{H}_2\text{O}$ ) in dilute acids through the monohydrate ( $\text{FeSO}_4 \cdot \text{H}_2\text{O}$ ) in the 60–70% (w/w) concentration range to  $2\text{FeSO}_4 \cdot \text{H}_2\text{SO}_4 \cdot \text{H}_2\text{O}$  in the 75–85% (w/w) concentration range and  $\text{FeSO}_4 \cdot 3\text{H}_2\text{SO}_4$  in 96% (w/w) acid.<sup>10</sup> This is the archetypal process underpinning the more general salt-film formation on metals, which may (as in this case) limit the CR by providing a diffusion barrier to reactive species.

As electrochemical potentials increase further into the passivation range, the ferrous salts are thought to oxidize progressively to ferric salts such as  $\text{Fe}_2(\text{SO}_4)_3 \cdot \text{H}_2\text{O}$  and  $\text{Fe}_2(\text{SO}_4)_3 \cdot 5\text{H}_2\text{SO}_4$  in concentrated solutions and ferric oxide centers nucleate and grow in the mixed ferrous–ferric salt film.<sup>10</sup> The passive film has been shown by X-ray photoelectron spectroscopy (XPS) to consist of a hydrated oxy-hydroxide layer across all acid concentrations. In weak acids, the film is thin as a result of the reaction of iron with water. As the acid concentration increases, progressively thicker, less hydrated films with higher contents of oxide phase are formed containing sulfates ( $\text{S}^{6+}$ ) at their surfaces but sulfur species in oxidation state  $\text{S}^{2-}$

in their bulks, confirming that acid reduction plays an integral role in the passivation process.<sup>11</sup>

In practice, the natural, open circuit potentials of steels and gray or ductile cast irons in concentrated acids are confined to the sulfation potential range, and their corrosion behaviors are determined essentially by the dissolution rates of the iron sulfate films on their surfaces. These are determined in practice by mass transport control of the diffusion of dissolved iron sulfate away from the surface in the prevailing conditions of acid concentration, temperature, velocity, and the presence or otherwise of dissolved iron in the acid. Convective mass transfer rates have been modeled for turbulent flow in a variety of geometries and for the case of a steel pipe protected by a layer of iron sulfate that remains constant with time (ie any loss of the layer is compensated for by further corrosion of the steel), the following expression for calculating the corrosion rate (CR) can be derived.<sup>12</sup>

$$\text{CR} = 1.42 \times 10^{-4} T^{-0.654} u^{0.913} \rho^{1.567} \mu^{-1.221} d^{-0.087} (C_{\text{surface}} - C_{\text{bulk}})$$

Since  $T$ ,  $u$ ,  $\rho$ ,  $\mu$  and  $d$ , and  $C_{\text{surface}}$  are all known for the concentration of acid at the temperature in question, the CR can be calculated if  $C_{\text{bulk}}$  is known.  $C_{\text{bulk}}$  could be assumed to be zero, in which case a maximum CR would be calculated. However, in practice commercial acid always contains some ferrous sulfate, having been produced and handled in carbon steel equipment, and therefore,  $C_{\text{bulk}}$  can either be measured, or assumed to be typically  $\sim 100$  ppm ( $\sim 0.01\%$  w/w), in which case a rate correspondingly lower than the zero case is calculated. In practice, an excellent correlation between calculated and observed CRs in pipes is obtained, confirming that the corrosion of steel is dominated by mass transport control of the diffusion of dissolved iron sulfate away from the corroding surface.<sup>12</sup>

The CRs in Figure 2 underpin the widespread use of carbon steels and gray/ductile irons for the storage and piping of commercial grades of sulfuric acids with concentrations in the range 93–99% (w/w) at near-ambient temperatures. However, the protective sulfate films are very vulnerable to disturbance. Velocities in steel piping systems have to be restricted<sup>2</sup> to  $\sim 0.6 \text{ m s}^{-1}$  or less. In steel storage tanks, if roof inlet nozzles are too close to the shell wall, during filling, turbulence adjacent to the wall can promote rapid dissolution of the protective iron sulfate film, resulting in accelerated local corrosion. Bubbles of cathodically produced hydrogen ascend vertically, disrupting the

protective film, causing vertical corrosion grooves at CRs up to several millimeters per year, as shown in **Figure 4**. Gray and ductile cast irons perform in a manner similar to that of steels in concentrated acids, as confirmed in **Figure 2**. However, gray irons have slightly better temperature and velocity tolerances that have been attributed to an ennoblement of corrosion potential by the graphite flake network, resulting in a sulfate film that is more resistant to dissolution and disturbance.

High-silicon cast irons, containing typically 14–16% Si (e.g., F47003), are very resistant to all concentrations of sulfuric acid up to 100% (w/w) at temperatures up to their boiling points at atmospheric pressure. Their corrosion resistance is due to the formation of robust, siliceous films that have considerable resistance to erosion and abrasion. Unfortunately, their exceptional resistance finds relatively limited application because of their poor ductility that renders them difficult to fabricate and requires them to be protected from thermal and/or mechanical shock.

Electrochemical anodic protection can be used to reinforce passivity steel in concentrated acids, as described in the separate chapter on anodic protection in this book. CRs can be reduced by up to 80%, which can be beneficial, for example, in controlling the iron content of acids in steel storages. However, anodic protection of gray cast irons can result in cracking by a

mechanism similar to that described in oleum in the following paragraph.

In oleum, steel experiences relatively high rates of corrosion in the 100–101% (w/w) acid concentration range at near-ambient temperatures that drop to acceptable levels as the concentration increases, arguably beyond  $\sim 102.5\%$  and certainly beyond 105% acid (w/w). Ductile irons behave similarly, but gray flake irons cannot be used in oleum, because they are vulnerable to cracking, triggered, it is thought, by the oxidation of graphite flake surfaces by free  $\text{SO}_3$  resulting in penetrating volumetric expansion and associated strains. High-silicon cast irons are also rapidly attacked by  $\text{SO}_3$  in oleum.

## 2.23.3 Stainless Steels

### 2.23.3.1 Mechanisms of Protection

The compositions of some of the more important stainless steels for sulfuric acid applications are summarized in **Table 1**. The behavior of stainless steels in sulfuric acid is determined by the presence or otherwise of passive surface films that are composed mostly of chromium oxide formed from the chromium in the alloy. The compositions and structures of the films can be modified by other alloying elements, in particular, molybdenum and silicon, resulting in changes in the

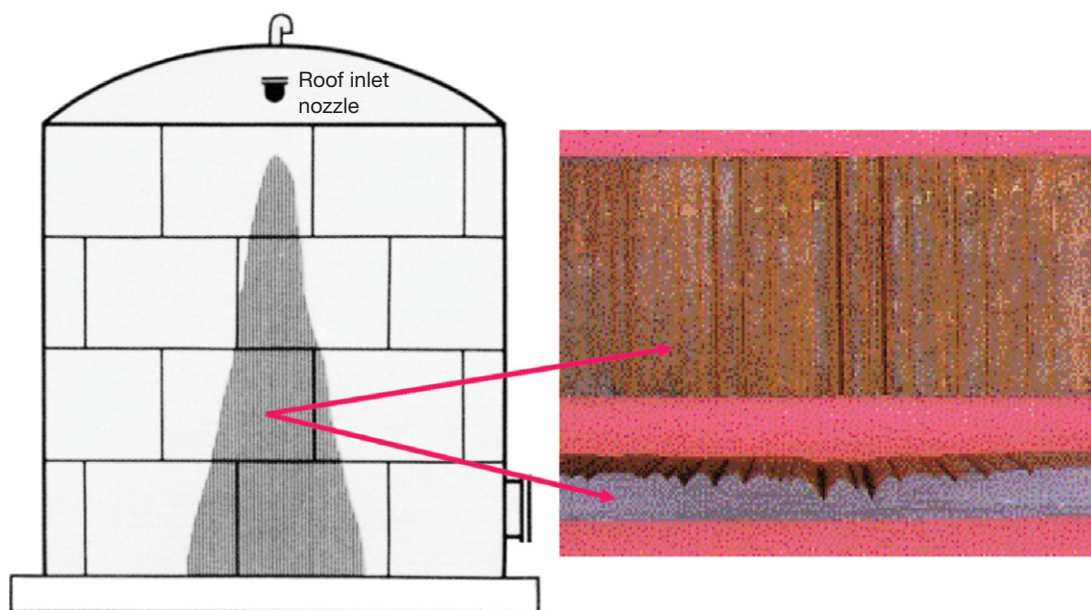


**Figure 4** Hydrogen grooving of the wall of a concentrated sulfuric acid storage tank. Adapted from *Materials Selector for Hazardous Chemicals Vol. 1: Concentrated Sulphuric Acid and Oleum (2nd ed.)*; MTI Publication MS-1, Materials Technology Institute of the Process Industries Inc., 2005.



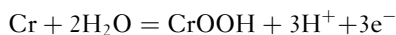
**Table 1** Compositions of some wrought stainless steels that are significant for sulfuric acid applications

UNS no	Common name	Fe	Ni	Cr	Mo	Cu	Si	Other
S43000	430	Balance		16–18				
S31803	2205	Balance	4.5–6.5	21–23	2.5–3.5			N
S32205								
S32750	2507	Balance	6–8	24–26	3–4.5	<0.5		N
S32760					3–4	0.5–1.0		W,N
S30400	304	Balance	8–10.5	18–20				<0.08
S30403	304L	Balance	8–12	18–20				
S31600	316	Balance	10–14	16–18	2–3			<0.08
S31603	316L	Balance	10–14	16–18	2–3			
S31700	317	Balance	11–15	18–20	3–4			<0.08C
S31703	317L	Balance	11–15	18–20	3–4			
S30601		Balance	17–18	17–18			5–5.6	
S31254	254SMO	Balance	17.5–18.5	19.5–20.5	6–6.5	0.5–1.0		N
S31000	310	Balance	19–22	24–26				
N08904	904L	Balance	23–28	19–23	4–5	1–2		
N08926	25–6MO	Balance	24–26	19–21	6–7	0.5–1.5		N
S31277	27–7MO	Balance	26–28	20.5–23.0	6.5–8.0	0.5–1.5		Mn, N
N08020	20	Balance	32–35	19–21	2–3	3–4		
N08031	31	Balance	30–32	26–28	6–7	1.4		N
R20033	33	Balance	30–33	31–35	0.5–2.0	0.3–1.2		N

behaviors of the films under specific conditions of concentration and temperature.

The potential benefits that alloying with chromium provides are illustrated by the polarization curves in [Figure 5](#) for iron, chromium, and type 430 (S43000) ferritic stainless steel that were obtained in agitated, 93.5% (w/w) sulfuric acid at 60 °C.<sup>13</sup> All the three anodic curves show an initial limiting current plateau preceding an active–passive transition as the potential is increased. The limiting current in all the cases results from the convective diffusion of  $\text{Fe}^{2+}$  and  $\text{Cr}^{2+}$  into the bulk liquid from a saturated sulfate salt layer. However, the plateau persists over a much wider potential range for iron than for chromium and the type 430 stainless steel, both of which show well developed passivity at much lower potentials and at current densities several orders of magnitude lower than for iron.

XPS studies of the passive layer on chromium in sulfuric acid<sup>14,15</sup> have shown it to consist of chromium oxy-hydroxides across the full range of acid concentrations. As in the case of iron, in weak- and medium-strength acids, passivation results from the reaction of chromium with water molecules from the acid:



However, in concentrated acids, bisulfate ( $\text{HSO}_4^-$ ) anions and undissociated acid molecules provide the oxygen:

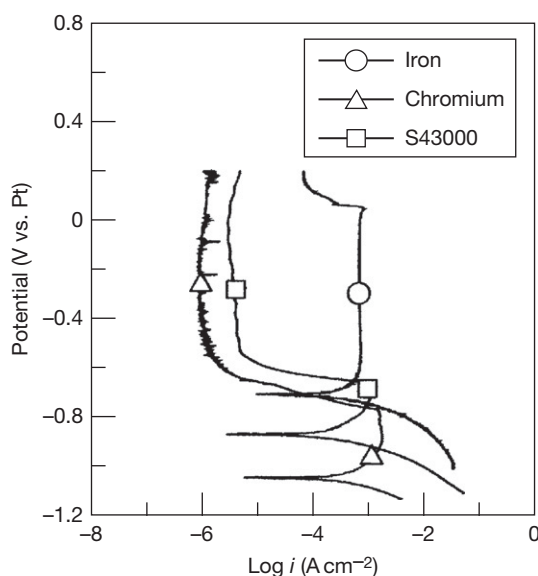
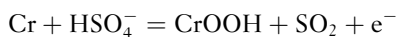


**Figure 5** Potentiodynamic anodic polarization behavior of iron, chromium and S43000 (Fe~18%Cr) ferritic stainless steel in stirred 93.5% (w/w) sulfuric acid at 60 °C. Adapted from Kish, J. R.; Ives, M. B.; Rodda, J. R. *Corros. Sci.* **2003**, *45*, 1571–1594.



The films formed in concentrated acids contain sulfur species in lower oxidation states ( $\text{S}^{2-}$ ) than in the acid ( $\text{S}^{6+}$ ), confirming that acid reduction plays an integral role in the passivation process.

The passive films that form on stainless steels in sulfuric acid are very similar in structure and thickness to the chromium oxy-hydroxide films that form on chromium metal.<sup>16,17</sup> However, the formation or otherwise of the films depends on the presence and concentration of elements other than chromium in the base material. Thus, it is clear from the polarization curve shown in **Figure 5** for type 430 stainless steel that the steel does not passivate spontaneously under the conditions tested, because the reductions of bisulfate anions and undissociated acid molecules cannot occur at sufficient rates to exceed the limiting current density for passivation. However, under the same conditions, type 304 (S30400) austenitic stainless steel exhibits spontaneous, periodic oscillations of corrosion potential between the active and passive states, as shown in **Figures 6(a) and 6(b)** on different time bases.<sup>18</sup> These oscillations have been studied by several workers<sup>19–22</sup>, and it is generally agreed that they result from the formation of an intermediate corrosion product in the active state that promotes passivation, which is subsequently redissolved resulting in reactivation. Since only nickel-containing steels exhibit oscillations, the intermediate corrosion product is believed to be a nickel salt, probably nickel sulfide, and a sequence of reactions that give rise to the oscillations has been proposed in four stages, as in **Figure 6(b)**:

1. The potential decrease from zero time to point one results from the dissolution of the nickel sulfide film and subsequently, the passive film.
2. The rapid potential drop between points one and two is associated with the active dissolution of the alloying elements as  $\text{Fe}^{2+}$ ,  $\text{Ni}^{2+}$ , and  $\text{Cr}^{3+}$  supported by acid reduction to sulfide,  $\text{S}^{2-}$ .
3. The gradual rise in potential between points two and three is associated with the nucleation and growth of nickel sulfide on the active surface.
4. Nickel sulfide increases the exchange current density for acid reduction to levels at which passivation occurs spontaneously, signaled by a rapid rise in potential between points three and four.

This sequence is the basis for the significant improvements in corrosion resistance of stainless steels in sulfuric acid that result from alloying with nickel at modest levels, although as the level in the alloy increases, nickel's effect in retarding active dissolution of the alloy also becomes significant. Three other alloying elements bring additional improvements:

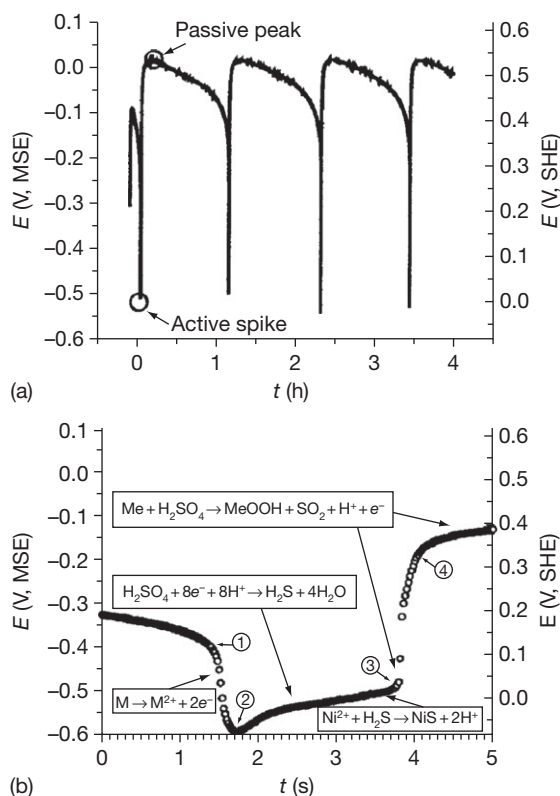


**Figure 6** Potential of type 304L austenitic stainless steel in 93.5% (w/w) sulfuric acid at 60 °C as a function of time (a) typical active passive oscillations (b) dominant reactions in a single oscillation. Adapted from Li, Y.; Ives, M. B.; Coley, K. S. *Corros. Sci.* **2006**, 48, 1560–1570.

1. Copper promotes the formation of passive films, partly by retarding active dissolution and reducing the critical current density required to form a film, but mostly by depolarizing cathodic processes, including hydrogen evolution, in the form of copper films that redeposit rapidly on active surfaces.<sup>23</sup> The beneficial effect is similar to that delivered by nickel sulfide films, and increases up to a level of 2–3% copper, as illustrated in **Figure 7**.
2. Molybdenum also promotes the formation of passive films by depolarizing cathodic processes, in particular hydrogen evolution. It also retards active dissolution in sulfuric acid by the formation of a molybdenum-rich, stable oxide film in the active region that acts as a diffusion barrier to metal dissolution, thereby reducing the critical current density and lowering the potential required to form a passive film.<sup>24</sup> Molybdenum also modifies the composition and structure of the passive film, being incorporated in the  $\text{Mo}^{6+}$  oxidation state as

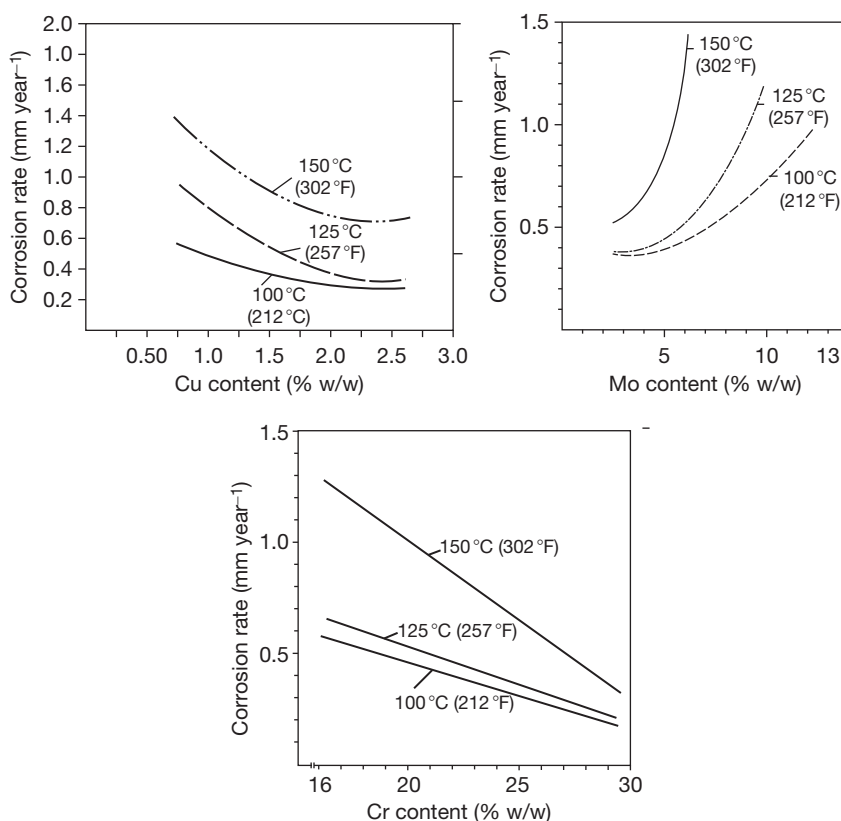


**Figure 7** Influence of copper, molybdenum, and chromium contents on corrosion rates of stainless steels and nickel alloys in stagnant 95% sulfuric acid solutions at 100–150 °C. Adapted from Coppolechia, V. D.; Renner, M. H. W.; Rockel, M. B. *Corrosion Resistance of Stainless Steels and Nickel Alloys in Concentrated Sulphuric Acid*; Paper 189, Corrosion '86, NACE International, 1986.

either  $\text{MoO}_3$  or  $\text{MoO}_4^{2-}$ , particularly in the outer regions.<sup>24,25</sup> However, molybdenum increases the vulnerability of the alloy and film to transpassive dissolution,<sup>25</sup> and as a result, molybdenum-containing alloys become vulnerable to corrosion in very concentrated acids and oleum, particularly as temperatures increase, and at levels above ~5% molybdenum, as illustrated in Figure 7.

3. Silicon additions, typically in the range 5–6% (w/w), modify the composition and structure of the passive film, producing silicon-rich films that confer high resistance to corrosion and erosion corrosion in hot acids with concentrations in the 93–99% (w/w) range. However, corrosion resistance drops steeply on either side of this range, and as in the case of high-silicon cast irons, the silicon-rich films are attacked by  $\text{SO}_3$  in oleums, rendering the materials unsuitable for service.

The ease and sustainability of passivation of stainless steels is also a function of the chromium content

itself, as illustrated in Figure 7. This has an influence on the range of sulfuric acid conditions that specific grades of stainless steel can withstand. Most of the widely used materials, such as alloys 304L (S30403), 316L (S31603), 904L (N08904), and 20 (N08020) contain ~20% chromium but are limited by concentration and/or temperature to varying degrees, depending on their contents of other alloying elements. Increased tolerance of temperature and/or concentration is provided by alloys, such as 31 (N08031) and 33 (R20033), that contain ~27% and ~31% chromium, respectively.

Oxidizing agents and aggressive anions exert strong influences on the corrosion of stainless steels in sulfuric acid. Dissolved oxygen has a pronounced effect on the presence or otherwise of passivity, particularly in relatively weak acids, as confirmed in Figure 8, which demonstrates that rates of corrosion for types 304 (S30400), 316 (S31600), 317 (S31700), and 310 (S31000) stainless steels are all higher at

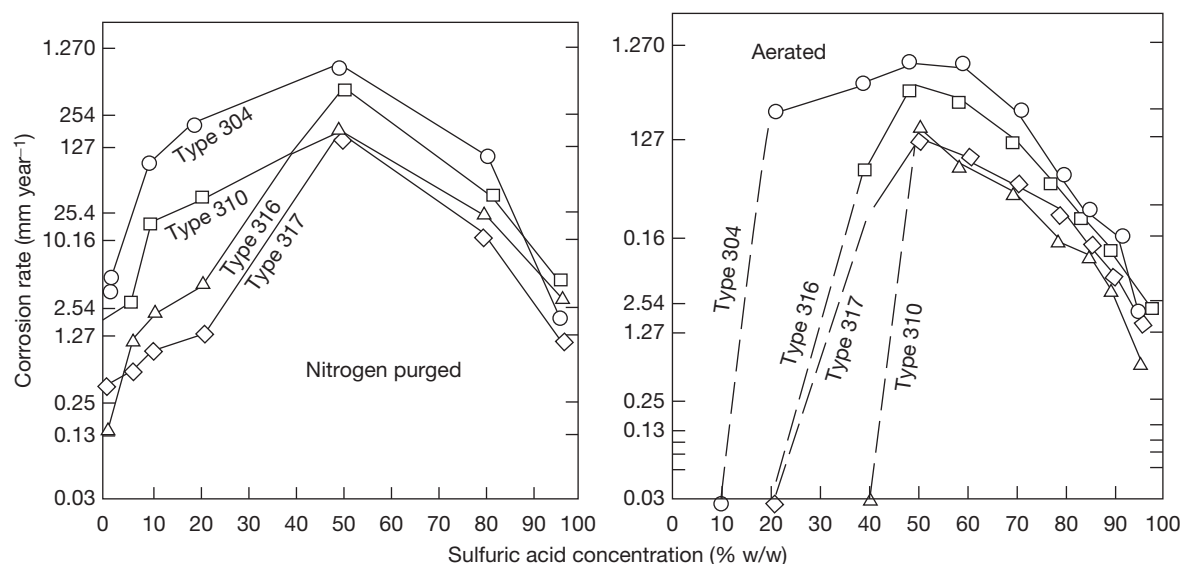


**Figure 8** Effects of aeration on corrosion rates of stainless steels in sulfuric acid solutions at 70°C. Adapted from Phelps, E. H., Vreeland, D. C. *Corrosion* **1957**, 13, 619–624.

concentrations below 30–40% acid at 70 °C when oxygen is absent.<sup>26</sup> Figure 9(a) shows the beneficial effects of additions of Fe<sup>3+</sup> and Cu<sup>2+</sup> as sulfates on the corrosion of type 316L (S31603) stainless steel in 75% and 85% acids at 100 °C.<sup>27</sup> Figure 9(b) confirms the dramatic effect of sufficient (2%) nitric acid that effectively stifles the corrosion of type 316L (S31603) stainless steel in 30% sulfuric acid at 90 °C, but also illustrates that insufficient oxidizing agent, in this case nitric acid (1%), can accelerate, rather than inhibit, corrosion.<sup>28</sup> Other oxidizing agents have been shown to have similar effects, including Cr<sup>6+</sup> added as chromic oxide or chromates and Sn<sup>2+</sup> added as sulfate, which is effective by being reduced to the metallic state.<sup>7</sup> Figure 9(c) shows the significant accelerating effects of 5% sodium chloride additions on the CRs of alloys 316L (S31603), 20 (N08020) and 825 (N08825) in 10% acid at 66 °C, and in practice, much lower levels of chloride can exert significant accelerating effects on corrosion.<sup>7</sup>

The passive films that form on stainless steels are in general much less vulnerable to acid velocity than the sulfate films that form on steels. Thus, maximum velocities up to  $\sim 3.3 \text{ m s}^{-1}$  are recommended for stainless piping systems for commercial grades of sulfuric acids with concentrations in the range 93–99% (w/w) at near-ambient temperatures compared with  $\sim 0.6 \text{ m s}^{-1}$  for steels.<sup>2</sup> Brubaker<sup>4</sup> has pointed out that the sensitivity of CRs of passive stainless steels to velocity depends on how close they are operating to the transitions to

activity or transpassivity, with ‘solidly’ passive stainless steels tolerating relatively high velocities. A good example of this is shown in Figure 10 that shows CRs for different stainless steels in 98.7% (w/w) sulfuric acid at 100 °C as a function of velocity. Clearly, the CRs of alloys 316 (S31600) and 825 (N08825) are very dependent on velocity, whereas the CR of the proprietary alloy 1815LCSi, an austenitic stainless steel containing 4% silicon, is independent of velocity, reflecting the tenacious nature of the passive film formed on high Si-containing stainless steels under these conditions.

Some of the main factors that influence the formation and stability of passive films on stainless steels are summarized schematically in Figure 11. The anodic polarization curves show the familiar active dissolution, passive, and transpassive regions. As the temperature and/or the concentration of aggressive anions, such as chloride increase, the capacity of materials to passivate is squeezed by extended active dissolution and less protective passive regions. Under nonoxidizing conditions, the prevailing cathodic process, hydrogen evolution, anchors the corrosion potential in the active dissolution region of the anodic polarization curve of the material. Under oxidizing conditions, cathodic processes arising from reduction of the acid itself or from the presence of oxidizing agents, such as dissolved oxygen, nitric acid, or metal cations in higher oxidation states, such as Fe<sup>3+</sup> or Cu<sup>2+</sup>, are able to promote passivity.

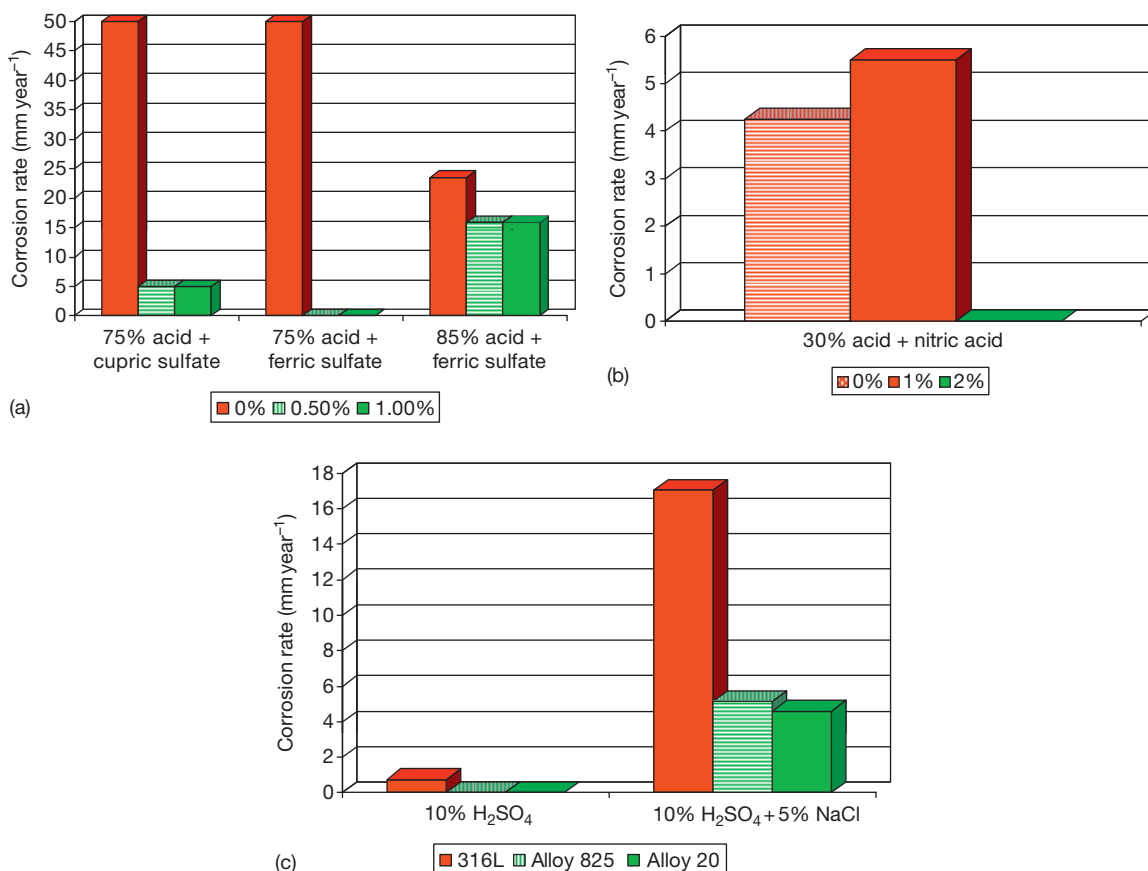


**Figure 9** Effects of contaminants on the corrosion of 316L stainless steel and other alloys in sulfuric acid (a)  $\text{Cu}^{2+}$  and  $\text{Fe}^{3+}$  additions at 100 °C, adapted from Berglund, G.; Martenson, C. *Application of a High Alloyed Stainless Steel in Sulphuric Acid Environments*; Paper 21, Corrosion '87, NACE International, 1986 (b)  $\text{HNO}_3$  additions at 93 °C, adapted from Kiefer, G. C.; Renshaw, W. G. *Corrosion* **1950**, 6, 235–244 (c)  $\text{Cl}^-$  additions at 66 °C. Adapted from *The Corrosion Resistance of Nickel-Containing Alloys in Sulphuric Acid and Related Compounds*; Corrosion Engineering Bulletin 1, The International Nickel Company, 1983.

Under strongly oxidizing conditions, the cathodic polarization curve intersects the anodic polarization curves at relatively high potentials well into the passive region, and stable passivity is promoted that may well survive the moderate increases in temperature and/or the concentrations of aggressive anions, such as chloride. However, further increases may move the corrosion potential into the transpassive region in the case of temperature, or above a film breakdown potential in the case of aggressive ions, such as chloride, resulting in accelerated corrosion.

Moderately oxidizing conditions may be sufficient to promote passivity at low temperatures and/or concentrations of aggressive anions, such as chloride. However, moderate increases in either can result in multiple intersections of the cathodic and anodic polarization curves, which are indicative of unstable passivity.

Under such borderline conditions, the corrosion potential may oscillate between the passive and active regions, and the CR will lie between the rates that are characteristic of passive and active behavior, depending on the period and frequency of the oscillations.

### 2.23.3.2 Performances of Stainless Steels

The performances of some of the more important stainless steels for sulfuric acid applications are summarized in **Figures 12–14**. The basic austenitic grades, such as 304L (S30403) and 316L (S31603), provide useful resistance to relatively weak, and in particular, strong acids where they find frequent use for storage and transport equipment at concentrations  $>\sim 93\%$  (w/w). The molybdenum-containing 316L (S31603) grade expands the region of stable



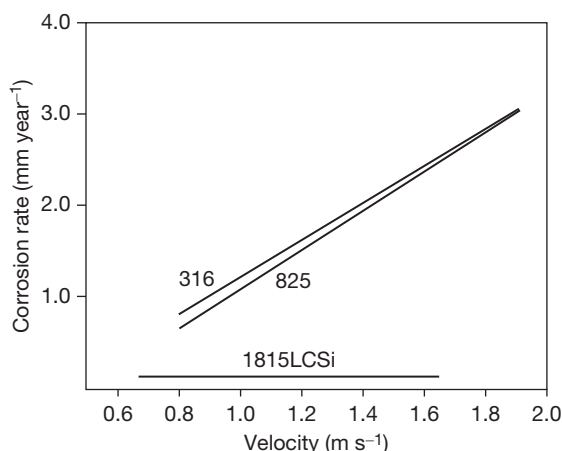


**Figure 10** Corrosion rates of different stainless steels in 98.7% (w/w) sulfuric acid at 100 °C as a function of velocity. Adapted from Coppolechia, V. D., Renner, M. H. W., Rockel, M. B. *Corrosion Resistance of Stainless Steels and Nickel Alloys in Concentrated Sulphuric Acid*; Paper 189, Corrosion '86, NACE International, 1986.

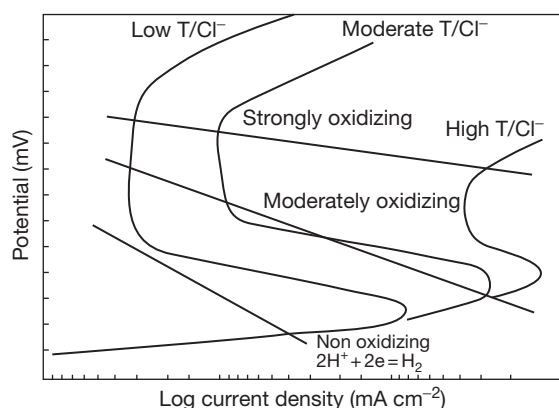


**Figure 11** Schematic polarization characteristics of stainless steels in sulfuric acid as a function of temperature ( $T$ ), chloride content ( $\text{Cl}^-$ ) and the inherent oxidizing potential of the acid, and/or the presence of oxidizing contaminants, such as dissolved oxygen, nitric acid or metal cations in higher oxidation states, such as  $\text{Fe}^{3+}$  or  $\text{Cu}^{2+}$ .

passivity relative to type 304L (S30403) and is a candidate, for example, for service in the 90–93% (w/w) concentration range at ambient temperatures, where 304L (S30403) is at greater risk of unstable passivity. In concentrated acids, the upper temperature limit for stable passivity increases with concentration from  $\sim 40^\circ\text{C}$  at 93% to above  $100^\circ\text{C}$  above 99% (w/w), in line with the much greater oxidizing potential of the more concentrated acid. Anodic protection, which is the subject of a separate chapter in this book, can

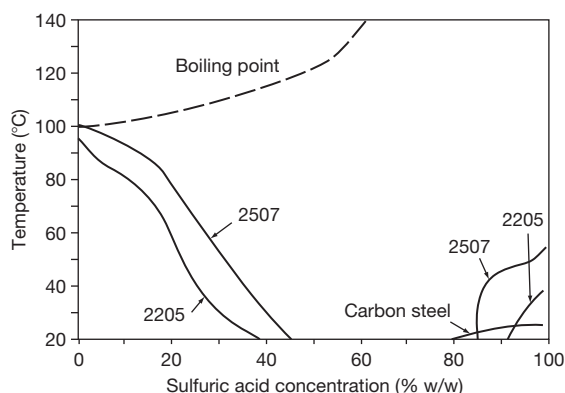


**Figure 12** Isocorrosion charts ( $0.1 \text{ mm year}^{-1}$ ) for carbon steel and duplex stainless steels in naturally aerated sulfuric acid. Adapted from *Corrosion Handbook, Stainless Steels*; AB Sandvik Steel, 1994.

be of significant benefit in reducing CRs in concentrated acids, as illustrated for type 316 (S31600) stainless steel in Figure 15, and is used routinely for the protection of concentrated acid coolers in sulfuric acid plants.

In weak acids, the molybdenum-containing 316L (S31603) grade shows significantly expanded resistance relative to type 304L (S30403) that has a limited resistance to solutions other than very dilute solutions at temperatures close to ambient, and both grades are vulnerable to loss of passivity in the absence of oxygen. The duplex grades, 2205 (S32205) and 2507 (S32750) grades offer significantly enhanced resistance to weaker acids than the basic austenitic grades, in line with their higher contents of chromium, molybdenum, and copper. However, none of the basic austenitic or duplex grades contains sufficient nickel to provide serviceable corrosion performances in medium-strength acids.

Stainless steel grades that offer useful corrosion resistance to medium strength as well as weak and concentrated acids, contain a minimum of  $\sim 18\%$  nickel, supplemented by significant molybdenum and/or copper contents. The grades that are leaner in nickel, relying more on molybdenum and copper to promote passivation, such as alloys 254SMO (S31254), 25–6MO (N08926), and 27–7MO (S31277), perform particularly well in weaker acids but have lower temperature limits for stable passivity as the concentration rises and relatively poor performances in concentrated acids. The stainless steel grades that offer the most stable passivity across the whole concentration range are alloys 20 (N08020) and 31 (N08031), which contain a minimum of  $\sim 30\%$  nickel

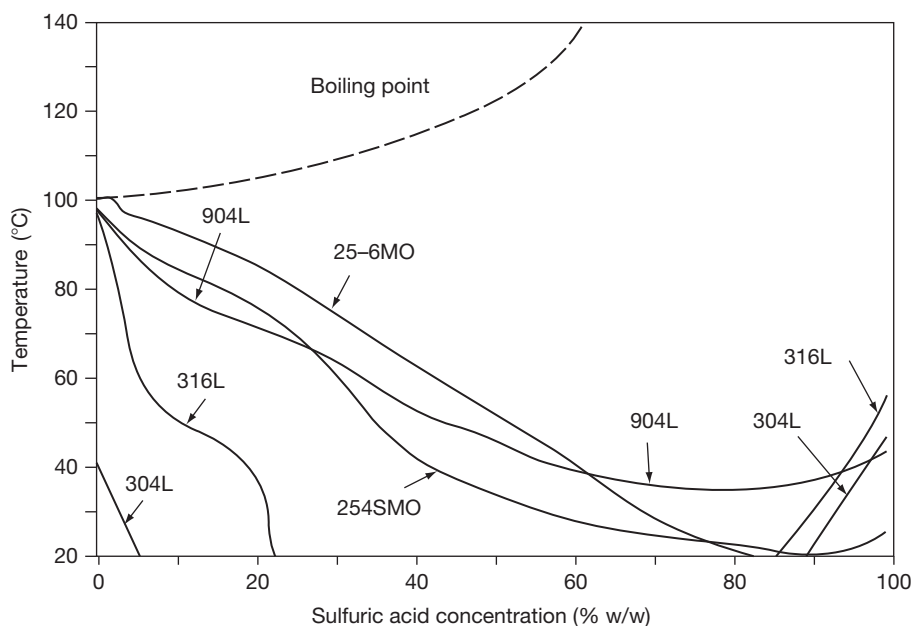


**Figure 13** Isocorrosion charts ( $0.1 \text{ mm year}^{-1}$ ) for austenitic stainless steels in naturally aerated sulfuric acid. Adapted from *Corrosion Handbook, Stainless Steels*; AB Sandvik Steel, 1994.

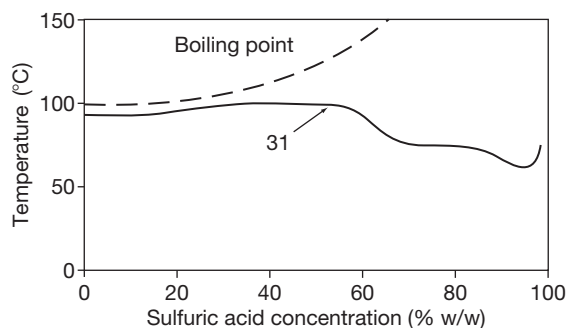


**Figure 14** Isocorrosion chart ( $0.1 \text{ mm year}^{-1}$ ) for austenitic alloy 31 in lightly aerated sulfuric acid. Adapted from *Material Data Sheet No 4031*, Thyssenkrupp VDM, 2002.

supplemented by molybdenum and copper additions, exemplified by the temperature limits for stable passivity of alloy 31 (N08031) shown in [Figure 14](#).

Acid strengths above 98% (w/w) and oleum are very oxidizing, and the CRs of most stainless steels are correspondingly lower. However, alloys with particularly high molybdenum contents are vulnerable to transpassive corrosion and can underperform the more basic grades of stainless steel, as illustrated in the ranking of various materials in tests under static conditions in 99% (w/w) acid at 100–120 °C shown in [Figure 16](#). Evidently, the most resistant material was type 304L (S30403) stainless steel that outperformed

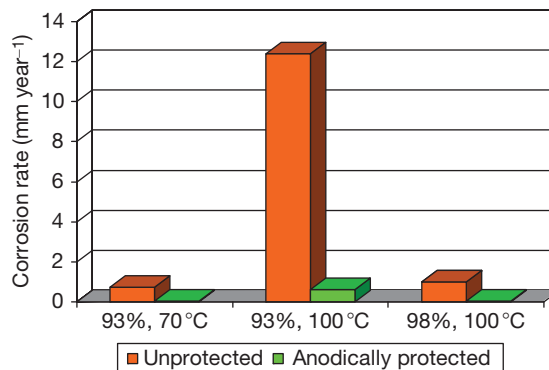


**Figure 15** Effects of anodic protection on corrosion rates of type 316 stainless steel in 93–98% sulfuric acid at 70 and 100 °C. Adapted from Walker, R. *Anodic protection*. In *Corrosion*, 3rd ed.; Shreir, L. L., Jarman, R. A., Burstein, G. T., Eds.; Butterworth-Heinemann, Oxford, 10.155-10.170, 1994.

not only the molybdenum-containing alloys 904L (N08904), 20 (N08020), C-276 (N10276), and B-2 (N10665), but also the silicon-containing material S30601. Notwithstanding that, high-silicon stainless steels, such as S30601, have found significant applications in equipment handling concentrated acids at elevated temperatures, as long as there is no risk of oleum formation, to which their resistance is poor. Brubaker<sup>4</sup> has drawn attention to the care that is required in selecting stainless steels for acid concentrations above 98% (w/w) where variations in velocity, oxidant

content and transient acid dilution can adversely affect performance. For oleum duties in particular, stainless steels with high chromium and low molybdenum contents are least vulnerable to such risks. Thus, alloy 33 (R20033) provides very high resistance to hot, concentrated, oxidizing acids, as illustrated in Figure 17, and this extends into the oleum concentration range.

## 2.23.4 Nickel Alloys

### 2.23.4.1 Mechanisms of Protection

The CR of nickel in aerated sulfuric acid as a function of concentration at room temperature is shown in Figure 18.<sup>29</sup> Evidently, CRs peak at  $\sim 1.5 \text{ mm year}^{-1}$  in  $\sim 80\%$  (w/w) acid in the concentration range 0–96% (w/w) acid, which, although unacceptable from the engineering standpoint, is indicative of the

much slower rates of active dissolution of nickel in weak and medium-strength acids compared with iron. Nickel can be used in deaerated sulfuric acid solutions at low temperatures, but in practice, its significant applications in sulfuric acid are alloy form, and the compositions of some of the more important alloys for sulfuric acid service are summarized in Table 1.

The mechanisms of protection of nickel alloys in sulfuric acid are illustrated by the anodic polarization curves for nickel and binary alloys of nickel with copper, molybdenum and chromium in deaerated sulfuric acid in Figure 19.<sup>30–33</sup> The active region for pure nickel is generally much smaller and the passivation potential lower than for iron, but the current density in the passive range remains relatively high, indicative of relatively unprotective passivity. XPS studies of the passive film indicate a duplex structure with an inner NiO and outer  $\text{Ni}(\text{OH})_2$  layers, the solubility of the latter increasing as the pH drops in weak acids.<sup>34</sup> At higher potentials, transpassive dissolution of nickel occurs, particularly at grain boundaries. The effects of alloying elements are as follows:

1. Copper additions move the corrosion and the active/passive transition potentials to more noble values and increase the current densities required to form and sustain passivity, so that in the case of the curve for alloy 400 (N04400), the commercial  $\sim 30\%$  copper alloy, shown in Figure 19(a), the remaining passivity is even less protective than the relatively unprotective films that are characteristic of pure nickel.<sup>31</sup> These curves not only suggest the significant benefits of alloying with copper at potentials in the active region, but also that in the passive region, alloying with copper alone is deleterious to corrosion resistance.

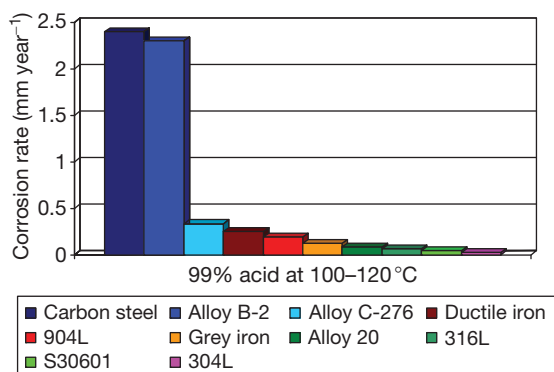


**Figure 16** Corrosion rates for various materials under static conditions in 99% (w/w) acid at 100–120°C. Adapted from Brubaker, S. K., H. Corrosion by Sulfuric Acid. In *ASM Handbook Vol. 13C Corrosion: Environments and Industries*; ASM International, 2006; pp 659–667.

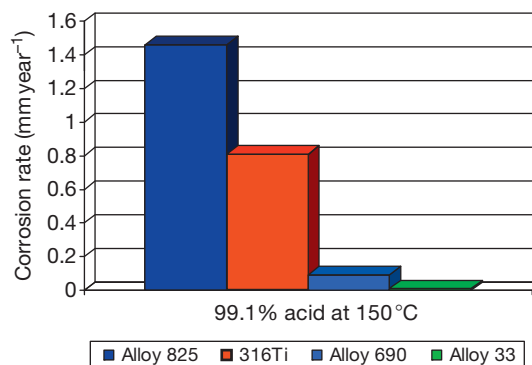
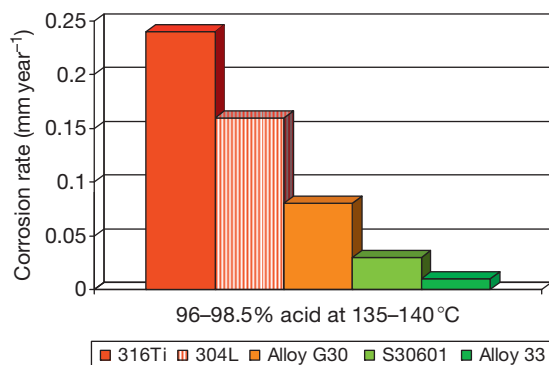


**Figure 17** Corrosion rates for various materials in hot, concentrated sulfuric acids. Adapted from Renner, M. H.; Michalski-Vollmer, D. *Stainless Steel World* **2000**, 12, 53–61.

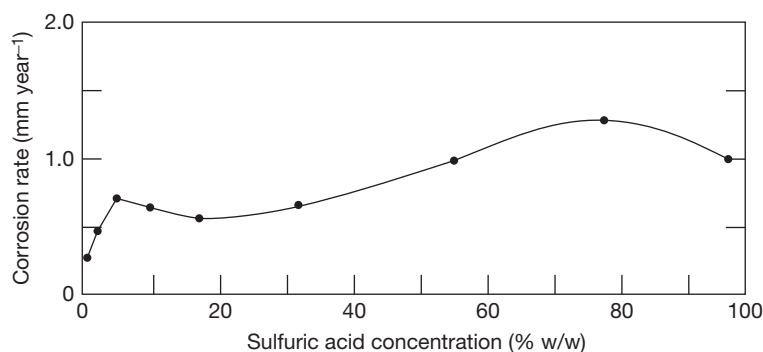


**Figure 18** Corrosion rate of nickel in aerated sulfuric acid at room temperature. Adapted from Fink, C. G.; DeCroly, C. M. *Trans. Am. Electrochem. Soc.* **1929**, 56, 239.

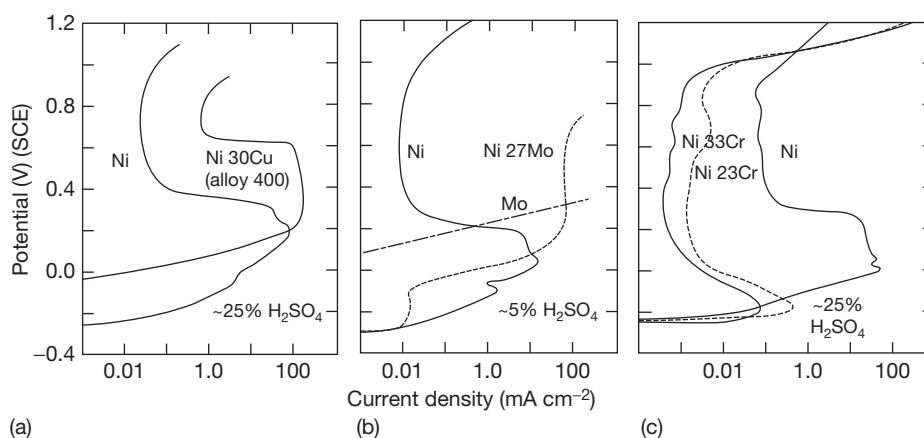


**Figure 19** Anodic polarization curves in deaerated sulfuric acid at 25 °C for nickel and (a) nickel–copper. Adapted from TrabANELLI, G.; Zucchi, F.; Felloni, L. *Corros. Sci.* **1965**, 5, 211. (b) nickel–molybdenum. Adapted from Greene, N. D. *The Passivity of Nickel and Nickel-Base Alloys*; Proceedings of the 1st International Congress on Metallic Corrosion; Butterworth: London, 1962. (c) Nickel–chromium alloys, adapted from Myers, J. R.; Beck, F. H.; Fontana, M. G. *Corrosion* **1965**, 21, 277.

2. Molybdenum additions have effects similar to those of copper additions. The polarization curve for pure molybdenum shown in [Figure 19\(b\)](#), shows no evidence of passive behavior in ~5% (w/w) acid. Alloys with molybdenum additions of up to ~20% (w/w) continue to display passive characteristics but with progressively increasing passive current densities with respect to pure nickel.<sup>32</sup> However, at the 27% (w/w) level that is representative of the commercial B family of alloys, there is no evidence of passivation in the polarization curve shown in [Figure 19\(b\)](#) and the current density increases progressively with potential in a manner similar to that of pure molybdenum. As with copper, the main benefit of molybdenum alloying is in the active region, and in the passive

region, molybdenum is also deleterious to corrosion resistance.

3. Chromium additions confer very pronounced benefits in both active and passive regions of the polarization curve, as shown in [Figure 19\(c\)](#). In practice, levels of chromium of ~9% or more produce significant reductions in the current density in the active region, the potential at which passivation occurs, and the passive current density.<sup>33</sup> At the 23% and 33% (w/w) levels depicted in [Figure 19\(c\)](#), chromium reduces the potential required to form passivity by ~400 mV and the current densities required to form and sustain passivity by up to two orders of magnitude relative to pure nickel.
4. Silicon additions in the range 5–6% (w/w) modify the composition and structure of the passive

film on nickel–chromium alloys by a similar mechanism as in the case of stainless steels, producing silicon-rich films that confer high resistance to corrosion and erosion corrosion in hot acids with concentrations in the 93–99% (w/w) range.

Oxidizing agents and aggressive anions exert influences on the corrosion of nickel alloys that are similar to those observed with stainless steels in sulfuric acid. Thus, the effects of dissolved oxygen and oxidizing agents on nickel–chromium alloys are broadly beneficial in that they help to promote and sustain the formation of protective passive films. However, dissolved oxygen has a significant accelerating effect on the corrosion of nickel metal and nickel–copper and nickel–molybdenum alloys that do not passivate in

the acid. For example, CRs for alloy 400 (N04400) across the concentration range in gently moving acid at 30 °C and alloy B at various acid concentrations and temperatures<sup>7</sup> are shown in **Figure 20(a) and (b)**. The accelerating effects of air in weak and medium-strength acids and the dramatic accelerations in CR in strongly oxidizing, concentrated/hot acids are evident in both cases. Other oxidizing agents, such as metal cations in higher oxidation states, in particular  $\text{Fe}^{3+}$  or  $\text{Cu}^{2+}$ , chromates, nitrates/nitrites, and peroxides exert similar effects, depending on the alloy. Thus, the CR of alloy B-2 (N10665) in boiling 30% (w/w) acid is increased dramatically by  $\text{Fe}^{3+}$  additions at levels in the range of 10s–100s ppm, whereas the CR of alloy C-276 (N10276) is, if anything, lowered under similar conditions as shown in **Figure 21(a) and 21(b)**.<sup>7</sup>

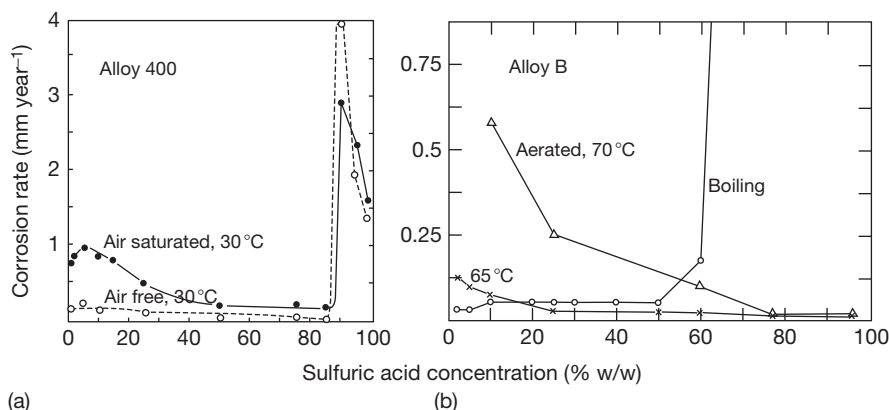


**Figure 20** Effects of aeration on corrosion rates in sulfuric acid of (a) alloy 400 and (b) alloy B. Adapted from *The Corrosion Resistance of Nickel-Containing Alloys in Sulphuric Acid and Related Compounds*; Corrosion Engineering Bulletin 1, The International Nickel Company, 1983.

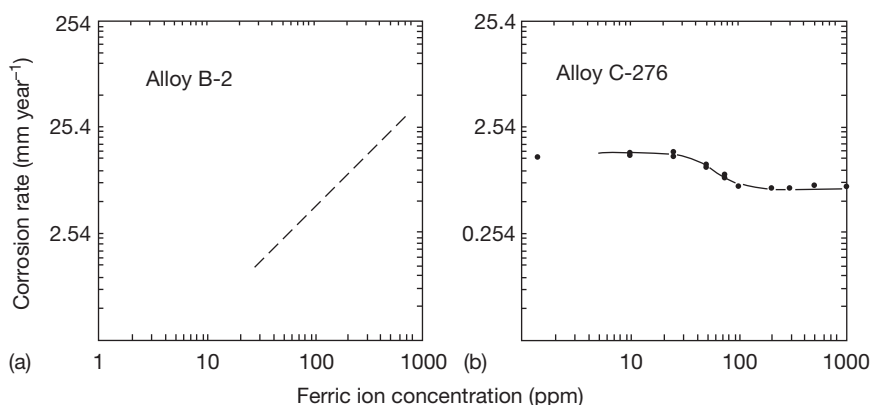


**Figure 21** Effects of additions of  $\text{Fe}^{3+}$  on the corrosion rate of alloys B-2 and C-276 in boiling 30% (w/w) sulfuric acid. Adapted from *The Corrosion Resistance of Nickel-Containing Alloys in Sulphuric Acid and Related Compounds*; Corrosion Engineering Bulletin 1, The International Nickel Company, 1983.



Chloride contaminants have a general accelerating effect on the CRs but the magnitude of the effect varies, depending on the alloy, as illustrated in **Figure 22** that shows CRs for alloys B-3 (N10675) and C-2000 (N06200) in boiling weak and medium-strength acids in the presence and absence of 200 ppm chloride.<sup>35</sup> Although the presence of chloride increases the CRs of both alloys at all concentrations, the effects are significantly greater for alloy C-2000 (N06200), which depends on passivity for its corrosion resistance. In contrast, for alloy B-3 (N10675) depends on its intrinsic resistance to anodic dissolution in the nonoxidizing environment that is only marginally affected by the presence of a relatively small amount of chloride.

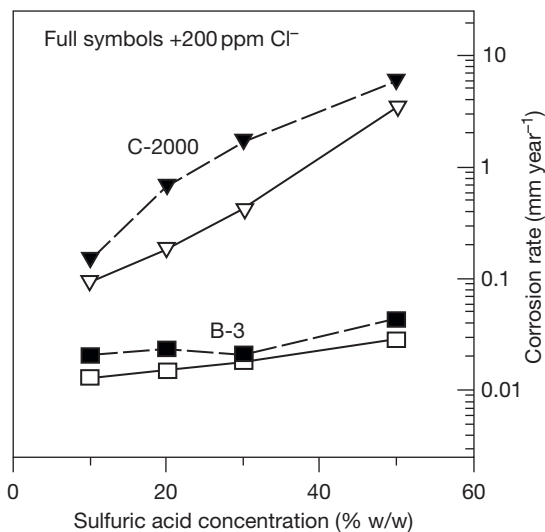
The sensitivity of CRs to acid velocity also varies with the alloy. The CRs of nickel–copper and nickel–molybdenum alloys that do not form passive films are sensitive to the relatively low velocities that determine the rates of mass transfer of oxidants and soluble corrosion products to/from the alloy surface, as illustrated for alloy 400 (N04400) in 5% (w/w) acid in **Figure 23**. Also evident in **Figure 23** is a limiting CR beyond which velocity has little effect, because the relevant anodic and cathodic processes are activation controlled. In contrast, the passive films that form on chromium-containing alloys are less vulnerable to

relatively low acid velocities away from conditions close to transitions to activity or transpassivity and the films that form on silicon-containing alloys, as in the case of stainless steels, are relatively resistant to acid velocity.

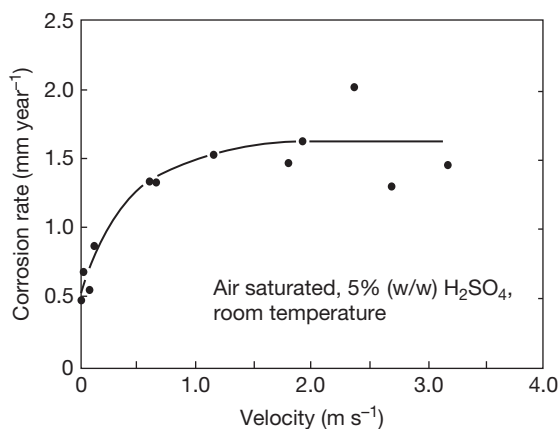
#### 2.23.4.2 Performances of Nickel Alloys

The compositions of some wrought nickel alloys that are significant for sulfuric acid applications are summarized in **Table 2**. The substantial nickel contents of all the alloys provide significant improvements in corrosion resistance relative to the iron-based alloys across most of the concentration range. The nickel–copper alloy 400 (N04400) can be used to handle weak- and medium-strength acids up to ~60% concentration (w/w) and ~95 °C in the absence of air and other oxidizing agents, but other materials are generally preferred and the alloy has no application in the strong acid concentration range. The B family of alloys show the greatest resistances across a wide range of temperatures and concentrations in the pure acid, exemplified by alloy B-2 (N10665) in **Figure 24**, but in practice are very vulnerable to the presence of even small quantities of oxidizing agents that can promote corrosion at unacceptable rates, and therefore, great care is needed in their application.

The most versatile alloys for handling sulfuric acid are the passivable nickel–chromium and nickel–chromium–molybdenum alloys that range from alloy 825 (N08825), which bridges the gap to stainless steels, to the more nickel-rich 690 (N06690) and the



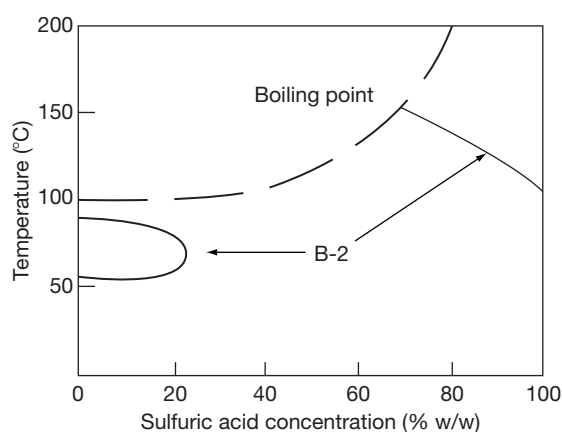
**Figure 22** Effects of chloride contamination on the corrosion rates of alloy B-3 and C2000 in boiling sulfuric acid. Adapted from Rebak, R. B.; Crook, P. *Influence of Alloying Elements, Temperature and Electrolyte Composition on the Corrosion Behaviour of Nickel-based Alloys*, Paper 00499, Corrosion 2000; NACE International, 2000.



**Figure 23** Effect of velocity on the corrosion rate of alloy 400 in sulfuric acid. Adapted from *The Corrosion Resistance of Nickel-Containing Alloys in Sulphuric Acid and Related Compounds*; Corrosion Engineering Bulletin 1, The International Nickel Company, 1983.

**Table 2** Compositions of some wrought nickel alloys that are significant for sulfuric acid applications

UNS no	Common name	Fe	Ni	Cr	Mo	Cu	Si	Other
N08825	825	>22	Balance	19.5–23.5	2.5–3.5	1.5–3.0		Ti
N06007	G	18–21	Balance	21–23.5	5.5–7.5	1.5–2.5		Co, Nb
N06985	G-3	18–21	Balance	21–23.5	6–8	1.5–2.5		Co W
N06030	G30	13–17	Balance	28.0–31.5	4–6	1.0–2.4		W
N06690	690	7–11	Balance	27–31				
N10276	C-276	4–7	Balance	14.5–16.5	15–17			W, Co
N06455	C-4	3	Balance	14–18	14–17			Co
N06022	C-22	2–3	Balance	20.5–22	13–14			W, Co
N06200	C-2000		Balance	23	16	2		
N06059	59		Balance	23	16			
N06686	686	<5	Balance	19–23	15–17			W
N06625	625	<5	Balance	20–23	8–10			Nb
N10001	B	5.5	Balance		28			Co
N10665	B-2	<2	Balance		28			
N10675	B-3	1.5	Balance	1.5	28.5			W, Co
N04400	400	<2.5	Balance			28–34		
	Lewmet 55	16	Balance	31		3		Co
	Lewmet 66	16	Balance	32	4	3	0.5	Co, Mn
	Ilium B		Balance	28	8	5	3.5	
	D205	6	Balance	20	2.5	2	5	

**Figure 24** Isocorrosion chart ( $0.13 \text{ mm year}^{-1}$ ) for Ni-Mo alloy B-2 in sulfuric acid. Adapted from *The Corrosion Resistance of Nickel-Containing Alloys in Sulfuric Acid and Related Compounds*; Corrosion Engineering Bulletin 1, The International Nickel Company, 1983.

C family of alloys. The performances of alloys 825 (N08825), 625 (N06625), G (N06007), and C-276 (N10276), shown in [Figure 25](#), bear comparison with the equivalent performances of the more highly alloyed stainless steels that are exemplified in [Figures 13 and 14](#). The leanest alloy 825 (N08825) offers little advantage over the 904L/26–5MO/27–7MO grades of stainless steel. The C family of alloys, exemplified by alloy C-276 (N10276) in [Figure 25](#), provides the most consistent resistance to temperature in

weak and medium-strength acids into the strong acid concentration range, and their performances are generally enhanced by the presence of oxidizing agents. However, they are vulnerable to the presence of chlorides, particularly in more concentrated acids at higher temperatures.<sup>2,4</sup>

A number of proprietary alloys have found significant usage for niche applications, particularly in relatively hot, concentrated acids. Lewmet alloys 55 and 66, and Ilium B are cast alloys containing relatively high levels of chromium and copper, and in the case of Ilium B, a significant level of silicon, and they are used for pumps and valves. Alloy D-205 is a silicon-containing nickel alloy that was developed to withstand acids in the concentration range of 93–99% (w/w) at temperatures of 90 °C and above, depending on acid strength, and which is more easily formed in thin sections than the equivalent stainless steels for components such as heat exchanger plates.

## 2.23.5 Other Metals and Alloys

### 2.23.5.1 Aluminum and Aluminum Alloys

Aluminum and its alloys have limited resistance to sulfuric acid other than in weak acids at relatively low temperatures and find no significant applications as constructional materials. However, thick, porous coatings can be formed on aluminum and some of its

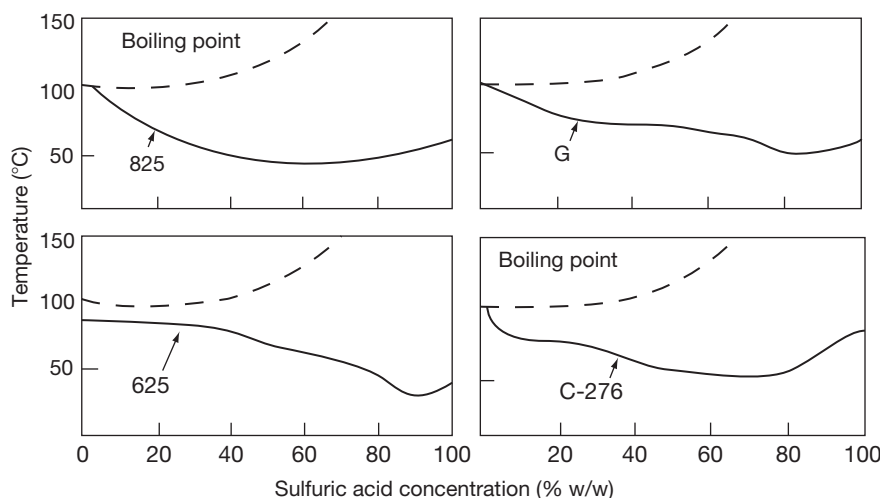


**Figure 25** Isocorrosion charts ( $0.13 \text{ mm year}^{-1}$ ) for Ni-Cr-Mo alloys in sulfuric acid. Adapted from *The Corrosion Resistance of Nickel-Containing Alloys in Sulphuric Acid and Related Compounds*; Corrosion Engineering Bulletin 1, The International Nickel Company, 1983.

alloys by anodic polarization to voltages up to  $\sim 25 \text{ V}$  in 5–10% sulfuric acid. These are of commercial significance for corrosion protection and decoration in architectural and other applications and are the subject of a separate chapter in this book.

### 2.23.5.2 Copper and Copper Alloys

Copper is relatively noble and does not normally displace hydrogen from acid solutions and thus has a relatively good resistance to sulfuric acid in nonoxidizing conditions. However, its resistance is reduced significantly in the presence of air or other oxidizing agents, not least its own corrosion product,  $\text{Cu}^{2+}$ , which can stimulate corrosion autocatalytically. The brasses are vulnerable to dezincification in sulfuric acid solutions. The tin, silicon, and aluminum bronzes have useful resistances in weak and medium-strength acids at moderate temperatures,<sup>2,4</sup> but, in general, applications for copper and its alloys in sulfuric acid are limited.

### 2.23.5.3 Titanium and Titanium Alloys

Titanium and its alloys are dependent on passive film formation to resist corrosion in sulfuric acid. One of the conditions for film formation, viz. the availability of a cathodic process to elevate the corrosion potential above the potential for passive oxide formation, is satisfied across the concentration range, even in weak acids, because this potential is below the hydrogen evolution potential. However, film formation also

depends on the availability of free water, the concentration of which is progressively limited in concentrated acids and in weak and medium-strength acids, the solubility of the passive film increases with the concentration and temperature and dominates performance. It has been shown that the protection afforded by the film depends on the conditions under which it forms, in particular the formation rate.<sup>36</sup> As a result, the resistances of titanium and its alloys are limited to relatively weak acids.

**Figure 26(a)** shows isocorrosion curves ( $0.13 \text{ mm year}^{-1}$ ) for commercially pure titanium (ASTM grade 2, R50400), a titanium–nickel–molybdenum alloy (ASTM grade 12, R53400), and a titanium–palladium alloy (ASTM grade 7, R52400) in naturally aerated sulfuric acid. Evidently, pure titanium is restricted to concentrations below  $\sim 5\%$  (w/w) even at ambient temperatures. Alloying with palladium significantly improves the corrosion resistance at lower temperatures but, as shown in **Figure 26(b)**, not much beyond  $\sim 5\%$  (w/w) at the boiling temperature. The improvements in corrosion resistance of ASTM grade 7 (R52400) arise from the well-established cathodic modification effects of palladium on promoting and sustaining the passivity of titanium, described elsewhere in this book.

Oxidizing agents in the acid, such as dissolved oxygen, chlorine, nitric and chromic acids, and metal cations in higher oxidation states, such as  $\text{Fe}^{3+}$  or  $\text{Cu}^{2+}$ , also promote significant increases in corrosion resistance by promoting and sustaining passivity. Some of the largest, titanium-clad process vessels ever

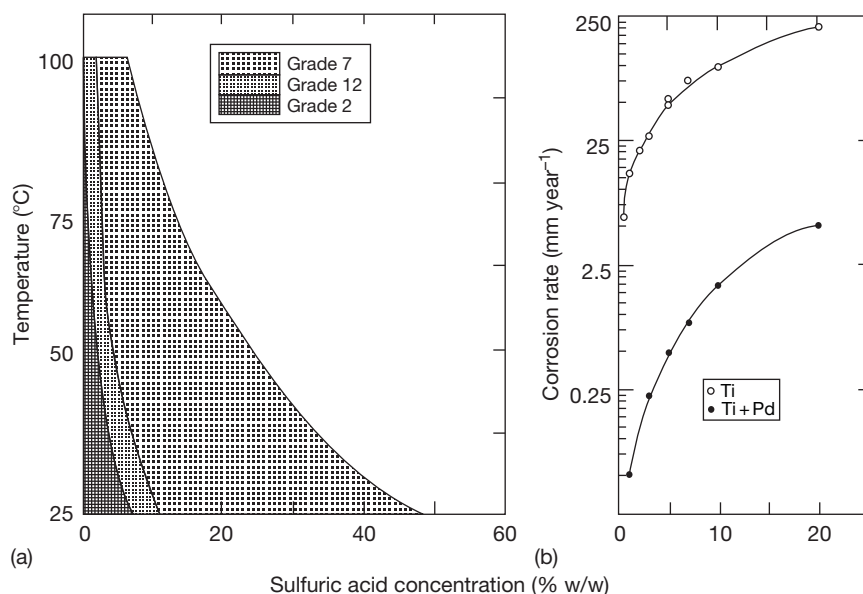


**Figure 26** (a) Isocorrosion chart (0.13 mm year<sup>-1</sup>) for ASTM grades 2 (commercially pure Ti), 7 (Ti 0.12–0.25%Pd) and 12 (Ti 0.6–0.9%Ni 0.2–0.4%Mo) alloys in naturally aerated sulfuric acid (b) corrosion rates of Ti and Ti 0.2%Pd alloy in boiling acid. Adapted from *Handbook of Corrosion Data*; ASM International, 1995.

constructed are used for the acid leaching of ores to recover gold, nickel, and other metals, involving exposure to several % (w/w) sulfuric acid in the presence of significant partial pressures of oxygen at temperatures as high as 200–250 °C.<sup>37</sup> However, even the temporary absence of oxidizing agents can result in a loss of passivity and a risk of very high CRs, and this inevitably limits the wider application of titanium and its alloys in sulfuric acid applications.

#### 2.23.5.4 Lead and Lead Alloys

The lead–sulfuric acid system is the basis of the ubiquitous lead-acid accumulator battery in which lead electrodes are exposed to acid in the concentration range of 27–39% (w/w) when fully charged. As a result, the prevailing anodic and cathodic processes have been studied intensively. The anodic reaction during discharge is the dissolution of lead in the divalent state followed by the precipitation of lead sulfate on the anode, and this is also the mechanism via which lead and its alloys resist corrosion in sulfuric acid. The effects of temperature and concentration on the CR of lead in stagnant sulfuric acid are shown in Figure 27.<sup>38</sup> Evidently, lead is very resistant to corrosion at temperatures up to boiling in 50% (w/w) acid and ~80 °C in 85% (w/w) acid, beyond which the film dissolves at rates that increase progressively. However, as in the case of the equivalent

films on steels, sulfate films on lead are vulnerable to erosion and abrasion resulting in excessive rates of attack, particularly at conditions close to the boundary for acceptable corrosion. For this reason, lead has often been used as a corrosion resistant membrane behind acid-resistant brick linings that separate the lead from any potentially damaging velocity and abrasion effects.

Historically, lead and its alloys found significant application in equipment for the manufacture and storage of sulfuric acid, but its use has declined because of its relatively poor mechanical properties, and health and toxicity concerns, resulting in a shortage of skilled craftsmen.

#### 2.23.5.5 Zirconium and Zirconium Alloys

Zirconium and its alloys are similar to titanium and its alloys in their dependence on passive film formation to resist corrosion in sulfuric acid. The key difference is that the passive films on zirconium and its alloys are much less soluble in sulfuric acid across the weak and medium-strength concentration range. The effects of concentration on the anodic polarization behavior of zirconium near the boiling point are shown in Figure 28(a).<sup>39</sup> Evidently, at concentrations below 20% (w/w), zirconium shows no active region and no tendency to transpassive breakdown at potentials significantly above 1 V relative to the saturated

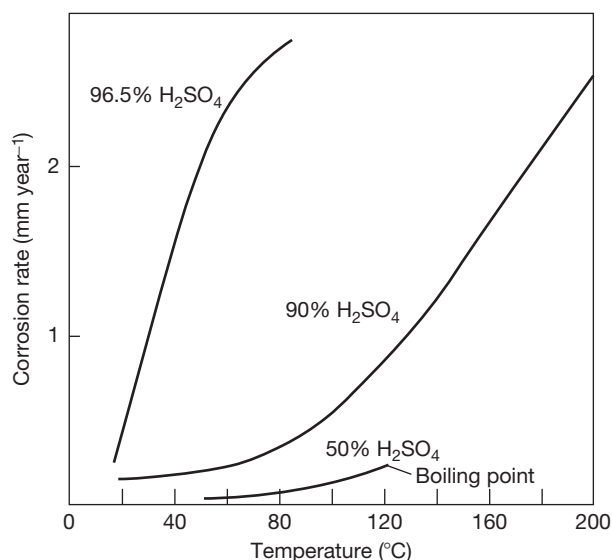


**Figure 27** Effects of temperature and concentration on corrosion rates of lead in sulfuric acid. Adapted from Hofmann, W. *Lead and Lead Alloys: Properties and Technology*; Vibranos, G., Ed.; Springer-Verlag, 1970.

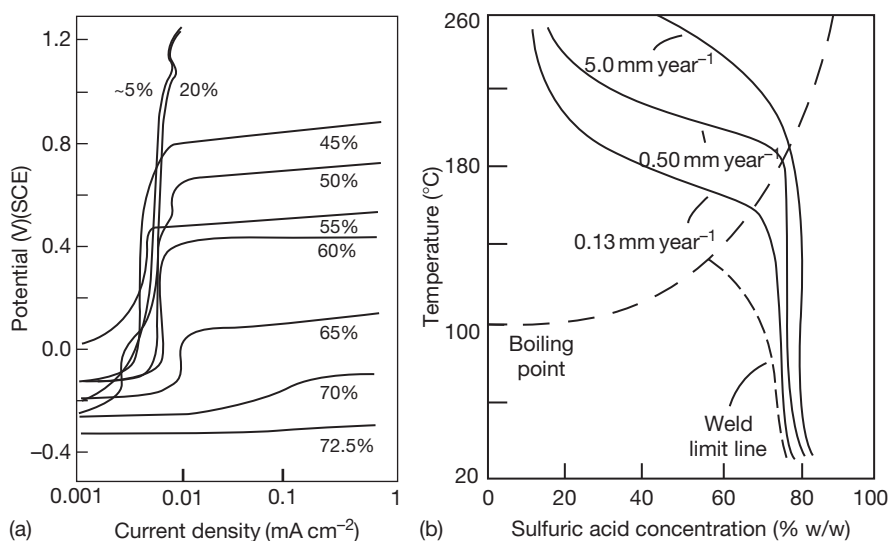


**Figure 28** Effects for zirconium in sulfuric acid of (a) concentration (% w/w) on anodic polarization behavior near the boiling point. Adapted from Yau, Te-Lin *Understanding Corrosion Behaviour From Electrochemical Measurements*; Paper 04227, Corrosion 2004; NACE International, 2004 (b) temperature and concentration on corrosion rate. Adapted from *Handbook of Corrosion Data*; ASM International, 1995.

calomel electrode (SCE). At higher concentrations, transpassive breakdown behavior is exhibited at potentials that reduce with increasing concentration and at 70% (w/w) concentration and beyond, zirconium reverts to active behavior with no evidence of stable passivity.

This behavior is reflected in the performance of commercial purity zirconium (Zr702, R60702) in

sulfuric acid as a function of concentration and temperature, which is summarized in [Figure 28\(b\)](#).<sup>40</sup> Evidently, at concentrations up to 20% (w/w), zirconium resists attack at temperatures well above the boiling point, beyond 200 °C. The limiting temperature for passivity decreases as the concentration increases beyond 20% (w/w) but remains above the boiling point in pure acid up to >60% (w/w).



In 70–80% (w/w) acid, the limiting temperature for passivity falls off rapidly with increasing concentration due to the formation of nonprotective zirconium sulfate films. **Figure 28(b)** indicates that the resistance of zirconium welds to >55% (w/w) acid is marginally lower than for parent material due to the presence and morphology of second-phase particles, related to tin content, but appropriate heat treatment can restore the corrosion resistance of weld metal. The performances of the commercial grades containing tin (Zr704, R60704) and niobium (Zr705, R60705) are broadly similar, except in the near boiling region above ~60% (w/w) acid concentration, where Zr702 outperforms Zr704 and Zr705.

The polarization curves in **Figure 28(a)** suggest that zirconium and its alloys may be vulnerable to the presence of oxidizing agents in higher concentration acids that might elevate the potential above the corresponding transpassive breakdown potential. In practice, zirconium is relatively tolerant to oxidizing agents over most of its useful concentration range but in >60% (w/w) acid, becomes sensitive to the presence of oxidizing agents.<sup>41</sup> Chlorides can also accelerate CRs if oxidizing agents are present, and zirconium and its alloys are acutely sensitive to the presence of even small quantities of fluorides in acids of all strengths.

Zirconium is vulnerable to stress corrosion cracking in 64–69% (w/w) sulfuric acid, the mechanism and remedies for which have been described elsewhere.<sup>42</sup>

### 2.23.5.6 Tantalum and Tantalum Alloys

Tantalum forms very stable, oxide films in sulfuric acid across the concentration range. For example, films formed galvanostatically in 95% (w/w) acid at 25 °C continue to thicken to support an applied potential of ~50 V before breaking down.<sup>43</sup> It is thus not surprising that tantalum (R05200) has an exceptional corrosion resistance to sulfuric acid, as illustrated by the CR data in **Figure 29**, which shows that tantalum has exceptionally low CRs at concentrations up to 98% (w/w) acid at temperatures up to ~150 °C and corrodes very slowly in 98% (w/w) acid at temperatures up to ~200 °C. However, tantalum is much less resistant to fuming acids, as illustrated by the data for oleum in **Figure 29**.<sup>42</sup> Long-term tests have suggested temperature limits for unalloyed tantalum of 200 °C and 150 °C for acid concentrations of 96 and 97% (w/w), respectively, and temperature limits for the 2.5% tungsten alloy (R05252) of

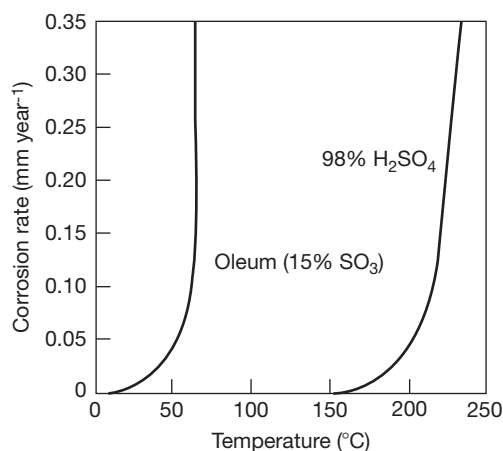


**Figure 29** Effects of temperature on corrosion rates of tantalum in 98% (w/w) sulfuric acid and oleum. Adapted from *Handbook of Corrosion Data*; ASM International, 1995.

210 °C and 175 °C for acid concentrations of 96 and 97.5% (w/w), respectively. The same tests have suggested that the tungsten alloy has superior resistance to hot, concentrated acids that contain oxidizing agents such as nitrates.<sup>44</sup>

A guide to the uniquely wide ranging corrosion resistance of tantalum and its alloys to sulfuric acid is illustrated by the test data in **Figure 30** for a range of metals and alloys in boiling acids across the concentration range up to 80% (w/w). It is clear that only tantalum and its alloys provide acceptable resistance across the full concentration range tested.

### 2.23.6 Nonmetallic Materials

Given the limitations of most classes of alloy that might be considered for handling sulfuric acid, and the high cost of the more resistant materials, such as nickel, zirconium, and tantalum alloys, it is inevitable that nonmetallic materials play significant roles in sulfuric acid applications. The application of these materials is covered in more detail in the relevant chapters in this book, but the more significant materials are as follows:

#### 2.23.6.1 Organic Materials

Concentrated sulfuric acid is a strong oxidizing and dehydrating agent, and hence, organic materials have inevitable performance limitations in concentrated and hot acids.

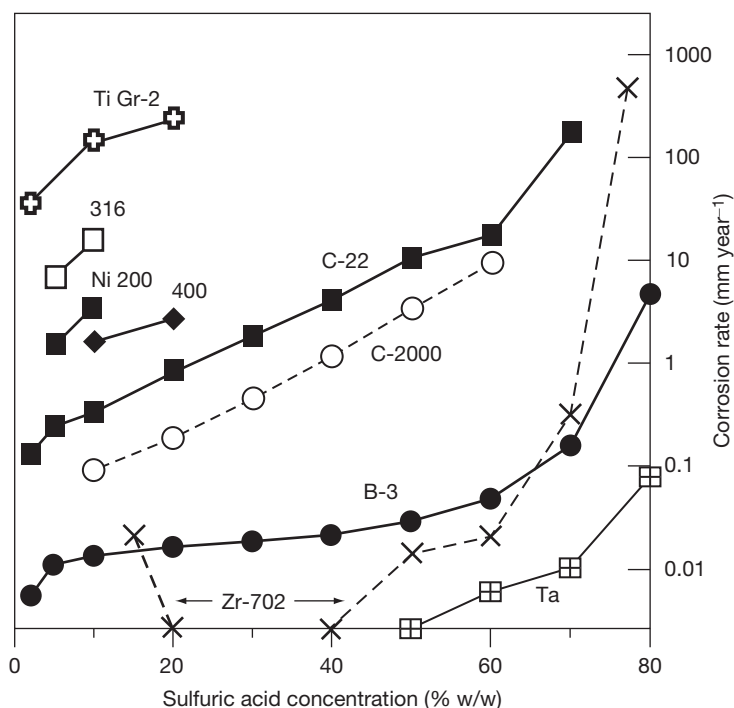


**Figure 30** Effects of concentration on corrosion rates in boiling sulfuric acid. Adapted from Rebak, R. B.; Crook, P. *Influence of Alloying Elements, Temperature and Electrolyte Composition on the Corrosion Behaviour of Nickel-based Alloys*, Paper 00499, Corrosion 2000; NACE International, 2000.

In relation to chemical compatibility, the major thermoplastics perform broadly as follows:

1. Polyethylene (PE), depending upon its molecular weight, can resist weak and medium-strength sulfuric acid at temperatures up to  $\sim 60^\circ\text{C}$ , depending on concentration and concentrated acids at ambient temperature.
2. Polypropylene (PP) is more resistant than PE and can tolerate weak acids up to  $\sim 90^\circ\text{C}$ , and medium-strength and concentrated acids at temperatures that reduce with increasing concentration.
3. Polyvinyl chloride (PVC) and chlorinated polyvinyl chloride (CPVC) resist concentrated acids at ambient temperatures and medium and weak acids at temperatures that increase as the concentration decreases.
4. Fluoroplastics are very resistant to sulfuric acid, depending upon their degree of fluorination. The highly fluorinated materials polytetrafluoroethylene (PTFE), fluorinated ethylene propylene (FEP), and perfluoroalkoxy (PFA) are resistant to all concentrations of sulfuric acid and oleum at temperatures up to at least  $200^\circ\text{C}$ . The less highly fluorinated materials ethylene chlorotrifluoroethylene

(ECTFE) and ethylene tetrafluoroethylene (ETFE) resist up to 98% (w/w) acid at temperatures up to  $\sim 150^\circ\text{C}$ . Polyvinylidene fluoride (PVDF) also resists up to 98% (w/w) acid but at temperatures that vary from  $\sim 120^\circ\text{C}$  at the lower end of the concentration range to  $\sim 50^\circ\text{C}$  at 98% (w/w) acid.<sup>2,4</sup>

In practice, chemical compatibility is but one factor that determines the suitability or otherwise of a thermoplastic material for a specific application. Other factors, such as mechanical and fabrication properties, thermal expansion characteristics, permeation properties, etc., are significant design considerations. In practice, except for small scale equipment, thermoplastics are used more commonly as linings on stronger substrates rather than in solid form, because of reliability and integrity concerns.

The more common natural and synthetic elastomers are unsuitable for concentrated acids. Thus, butyl rubber and neoprene are generally limited to weak and medium-strength acids, but chlorosulfonated PE elastomers (e.g., Hypalon) can be used in concentrated acids. Some grades of fully fluorinated elastomers (e.g., some Kalrez grades) can be used in

concentrated acids and even oleum, depending on the filler materials.

The common glass reinforced polyester and vinyl ester resins find significant use in the storage and handling of weak acids up to temperatures of  $\sim 90^{\circ}\text{C}$  and medium-strength acids up to lower temperatures, depending on the acid strength. However, these materials are not suitable for concentrated acids.

Thin paint coatings are unsuitable for the protection of substrates that would corrode at significant rates if exposed. However, some high-performance coatings, for example, heat-cured phenolic coatings, are used to prevent contamination of concentrated acids that are stored in steel containers.

### 2.23.6.2 Inorganic Materials

Borosilicate glass is highly resistant to acids across the concentration range up to temperatures well beyond their boiling points and solid- or glass-lined equipment finds significant use for handling sulfuric acid.

Impervious graphite, filled with impregnants such as phenolic resins or PTFE, finds significant use in heat exchange duties and is resistant to all but the most oxidizing conditions at temperatures well beyond boiling. Silicon carbide also has an excellent sulfuric acid resistance and has been used in heat exchange duties.

Acid-resistant brick linings on steel are widely used to handle sulfuric acid. Below  $\sim 70\%$  (w/w) concentration, corrosion-resistant membranes are required behind the brick, which can be metallic, such as lead, or nonmetallic, such as fluoroplastic linings or asphaltic or other coatings. In concentrated acids, the bricks can be used directly onto steel, although in practice, fluoroplastic or other membranes are often installed. Carbon bricks find occasional use in very hot, concentrated acid duties.

## References

1. Hammer, W. J. *The Structure of Electrolyte Solutions*; J. Wiley: London, 1959.
2. Materials Selector for Hazardous Chemicals In *Concentrated Sulphuric Acid and Oleum*, 2nd ed.; MTI Publication MS-1, Materials Technology Institute of the Process Industries Inc: St. Louis, MO, 2005; Vol. 1.
3. DECHEMA Corrosion Handbook. *Sulphuric Acid*; Wiley-VCH: London, 2008; Vol. 11.
4. Brubaker, S. K. H. Corrosion by Sulphuric Acid. In *ASM Handbook Corrosion: Environments and Industries*; ASM International: Materials Park, OH, 2006; Vol. 13C, pp 659–667.
5. NACE Recommended Practice RP0391–2001. *Materials for Handling and Storage of Commercial Concentrated (90–100%) Sulphuric Acid at Ambient Temperatures*; NACE International: Houston, TX, 2001.
6. NACE Standard Practice SP0254–2006. *Design, Fabrication and Inspection of Storage Tank Systems for Concentrated Fresh and Process Sulphuric Acid and Oleum at Ambient Temperatures*; NACE International: Houston, TX, 2006.
7. *The Corrosion Resistance of Nickel-Containing Alloys in Sulphuric Acid and Related Compounds*; Corrosion Engineering Bulletin 1, The International Nickel Company, 1983.
8. Renner, M. H. W. *Metallic Materials for Concentrated Sulphuric Acid Service*, Paper 01342, Corrosion 2001; NACE International: Houston, TX, 2001.
9. Breakell, J. E. *The Corrosive Wear of Cast Irons in Marine Diesel Engine Cylinder Environments*; Ph. D. Thesis, University of Manchester, October, 1980.
10. Williamson, R. C.; Hines, J. G. *Corros. Sci.* **1964**, *4*, 221–235.
11. Mazurkiewicz, B. *Electrochim. Acta* **1993**, *38*, 495–502.
12. Dean, S. W.; Grab, G. D. *Mater. Perform.* **1985**, 21–25.
13. Kish, J. R.; Ives, M. B.; Rodda, J. R. *Corros. Sci.* **2003**, *45*, 1571–1594.
14. Stypula, B.; Banas, J. *Electrochim. Acta* **1993**, *38*, 2309–2314.
15. Stypula, B.; Stoch, J. *Corros. Sci.* **1994**, *36*, 2159–2167.
16. Bera, S.; Rangarajan, S.; Narasimhan, S. V. *Corros. Sci.* **2000**, *42*, 1709–1724.
17. Olsson, C. O. A.; Landolt, D. *Electrochim. Acta* **2003**, *48*, 1093–1104.
18. Li, Y.; Ives, M. B.; Coley, K. S. *Corros. Sci.* **2006**, *48*, 1560–1570.
19. Chang, Y. S. *Periodic Active-Passive Corrosion Behaviour*; Ph. D. Thesis, Fitzwilliam College, Cambridge University, 1984.
20. Mitsuhashi, R. *Corros. Eng.* **1990**, *39*, 89.
21. Renner, M. H. W. *Corrosion Behaviour of Stainless Steels and Nickel Alloys in Hot, Concentrated Static and Flowing Sulphuric Acid*; Ph. D. Thesis, University of Teesside, 1991.
22. Li, Y.; Ives, M. B.; Coley, K. S.; Rodda, J. R. *Corros. Sci.* **2004**, *46*, 1969–1979.
23. Hermas, A. A.; Ogura, K.; Adachi, T. *Electrochim. Acta* **1995**, *40*, 837–844.
24. Pardo, A.; Merino, M. C.; Coy, A. E.; Viejo, F.; Arrabal, R.; Matykina, E. *Corros. Sci.* **2008**, *50*, 780–794.
25. Bojinov, M.; Fabricius, G.; Laitinen, T.; Makela, K.; Saario, T.; Sundholm, G. *Electrochim. Acta* **2001**, *46*, 1339–1358.
26. Phelps, E. H.; Vreeland, D. C. *Corrosion* **1957**, *13*, 619–624.
27. Berglund, G.; Martenson, C. Application of a High Alloyed Stainless Steel in Sulphuric Acid Environments; Paper 21, Corrosion '87; NACE International: Houston, TX, 1986.
28. Kiefer, G. C.; Renshaw, W. G. *Corrosion* **1950**, *6*, 235–244.
29. Fink, C. G.; DeCroly, C. M. *Trans. Am. Electrochem. Soc.* **1929**, *56*, 239.
30. Friend, W. Z. *Corrosion of Nickel and Nickel-Base Alloys*; John Wiley & Sons: New York, 1980.
31. Trabanelli, G.; Zucchi, F.; Felloni, L. *Corros. Sci.* **1965**, *5*, 211.
32. Greene, N. D. *The Passivity of Nickel and Nickel-Base Alloys*; Proceedings of the 1st International Congress on Metallic Corrosion; Butterworth: London, 1962.
33. Myers, J. R.; Beck, F. H.; Fontana, M. G. *Corrosion* **1965**, *21*, 277.
34. Hoppe, H. W.; Strehblow, H. H. *Surf. Interface Anal.* **2004**, *14*, 121–131.

36. Blackwood, D. J.; Peter, L. M. *Electrochim. Acta* **1989**, *34*, 1505–1511.
37. Banker, J. G. *Hydrometallurgical Applications of Titanium Clad Steel*; Conference Reactive Metals in Corrosive Applications, Sun River, OR, Sept. 12–16 1999.
38. Hofmann, W. *Lead and Lead Alloys: Properties and Technology*; Vibranos, G., Ed.; Springer: Verlag, 1970; pp 274.
39. Yau, Te-Lin *Understanding Corrosion Behavior From Electrochemical Measurements*, Paper 04227, Corrosion 2004; NACE International: Houston, TX, 2004.
40. *Handbook of Corrosion Data*; ASM International: Materials Park, OH, 1995.
41. Yau, Te-Lin *Effects of Impurities in  $H_2SO_4$  on the Corrosion Resistance of Zirconium*; ASTM STP 830, ASTM, 1984, pp 203.
42. Fitzgerald, B. J.; Yau, Te-Lin *The Mechanism and Control of Stress Corrosion Cracking of Zirconium in Sulfuric Acid*, Paper 092, 12th International Corrosion Congress, Houston, TX, September 19–24 1993.
43. Shimizu, K.; Brown, G. M.; Habazaki, H.; Kobayashi, K.; Skeldon, P.; Thompson, G. E.; Wood, G. C. *Corros. Sci.* **1998**, *40*, 963–973.
44. Coscia, M.; Renner, M. H. W. *Mater. Perform.* **1998**, *37*, 52–57.

## 2.24 Corrosion in Nitric Acid

**G. O. H. Whillock and S. E. Worthington**

National Nuclear Laboratory Ltd., B170, Sellafield, Seascale, Cumbria CA20 1PG, UK

© 2010 Elsevier B.V. All rights reserved.

<b>2.24.1</b>	<b>Uses of Nitric Acid</b>	1251
<b>2.24.2</b>	<b>Chemical Attack by Nitric Acid</b>	1251
2.24.2.1	Pure Nitric Acid	1251
2.24.2.2	Aqueous Nitric Acid	1251
2.24.2.2.1	Base metals in aqueous nitric acid	1251
2.24.2.2.2	Noble metals in aqueous nitric acid	1251
2.24.2.2.3	Passive metals	1252
<b>2.24.3</b>	<b>Materials for Nitric Acid Containment</b>	1252
2.24.3.1	Stainless Steels	1253
2.24.3.2	Titanium	1254
2.24.3.3	Zirconium, Niobium, Hafnium, and Tantalum	1255
2.24.3.4	Aluminum	1255
<b>2.24.4</b>	<b>Corrosion Mechanisms of Passive Metals in Nitric Acid</b>	1255
2.24.4.1	General Corrosion and Intergranular Corrosion	1255
2.24.4.2	End Grain Corrosion	1257
2.24.4.3	Crevice Corrosion	1257
2.24.4.4	Stress Corrosion Cracking	1258
2.24.4.5	Corrosion Fatigue	1258
2.24.4.6	Erosion Corrosion and Fretting Corrosion	1258
2.24.4.7	Galvanic Corrosion	1259
<b>2.24.5</b>	<b>Factors Affecting Corrosion Processes in Nitric Acid</b>	1259
2.24.5.1	Welding	1259
2.24.5.2	Cold Work	1260
2.24.5.3	NO <sub>x</sub> Gases	1260
2.24.5.4	Dissolved Oxidizing Species and Corrosion Products	1261
2.24.5.4.1	Stainless steel	1261
2.24.5.4.2	Other passive metals	1263
2.24.5.5	Dissolved Reducing Species	1263
2.24.5.6	Radiation	1264
2.24.5.7	Solution Boiling	1265
2.24.5.8	Heat Transfer	1266
2.24.5.9	Liquor-Line and Vapor Regions	1267
<b>2.24.6</b>	<b>Corrosion Testing Methods</b>	1267
2.24.6.1	Ranking Tests	1267
2.24.6.2	Prediction of In-Service Corrosion Rates	1267
<b>References</b>		1268

### Glossary

**18/13/1** A niobium-stabilized stainless steel used in UK nuclear reprocessing plant, conforming approximately to the top end of the AISI 347 specification range.

**End grain** The cross-section perpendicular to the hot-working direction of a fabricated component.

**Grain dropping** Dislodgement of metal grains as they are undermined by intergranular



corrosion. Dropped stainless steel grains have the appearance of fine soot.

**Magnox** A magnesium alloy containing 0.8% aluminum, used to clad uranium metal fuel for CO<sub>2</sub>-cooled Magnox reactors.

**NAG 18/10L** A proprietary stainless steel used in UK nuclear reprocessing plant, similar to AISI 304L but with tighter control of residuals.

**Radiolysis** Chemical change resulting from the absorption of ionizing radiation.

**R-SUS 304ULC** A proprietary stainless steel used in Japanese nuclear reprocessing plant. Similar to NAG 18/10L.

**20Cr25Ni1Nb** A proprietary stainless steel used in UK Advanced Gas-Cooled Reactor fuel.

**Uranus 65** A proprietary stainless steel, conforming approximately to AISI 310L, but with added niobium. Used in UK and French nuclear reprocessing plant.

## Abbreviations

**AISI** American Iron and Steel Institute

**AR** As-received

**Gy** Grays (unit of absorbed radiation dose;  
1 Gy = 1 J kg<sup>-1</sup>)

**mpy** Thousandths of an inch per year

**M** Molar or metal

**NAG** Nitric acid grade

**SCC** Stress corrosion cracking

**ss** Stainless steel

## Symbols

**E** Electrode potential

**i** Current density

**V<sub>SCE</sub>** Electrode potential, volts with respect to the Standard calomel electrode

**X(Y)** Element X present in valency state Y; for example, Cr(VI) is Cr<sub>2</sub>O<sub>7</sub><sup>2-</sup> or CrO<sub>4</sub><sup>2-</sup>

## 2.24.1 Uses of Nitric Acid

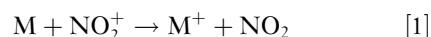
Nitric acid is used in salt formation, preparation of organic nitrates and nitro compounds, and oxidation of organic compounds.<sup>1</sup> Major applications include the production of agricultural fertilizers and reprocessing of nuclear fuels.

## 2.24.2 Chemical Attack by Nitric Acid

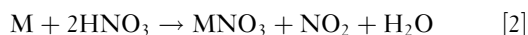
### 2.24.2.1 Pure Nitric Acid

At greater than about 96–97% concentration, HNO<sub>3</sub> chemistry is dominated by the NO<sub>2</sub><sup>+</sup> ion. The acid undergoes no proton transfer to water molecules and it cannot be considered as an acid in the protionic sense at this concentration.<sup>2</sup>

The initial electron transfer reaction with a metal, M:



leads to the overall reaction



with nitrates produced at the metal surface.<sup>2</sup>

The reaction of some metals with pure HNO<sub>3</sub> is given in Table 1.

There is no correlation between apparent reactivity and position of the metal in the periodic table. In some instances, there is evidence of cohesive film formation (e.g., Ca) while some metals are either inert (e.g., Pt) or form protective oxide films (e.g., Al).

### 2.24.2.2 Aqueous Nitric Acid

In practice, most nitric acid corrosion occurs in aqueous mixtures of <96% concentration.

#### 2.24.2.2.1 Base metals in aqueous nitric acid

These generally dissolve extremely rapidly to form nitrates, cathodically discharging hydrogen, which reacts with the nitric acid to give compounds such as ammonia, ammonium nitrate, hydroxylamine nitrate, nitrogen, and nitrous oxide.<sup>3</sup>

#### 2.24.2.2.2 Noble metals in aqueous nitric acid

The dominant cathodic reaction in this case is the reduction of the nitrate ion. This is a complex process, proceeding via an autocatalytic mechanism involving a charge transfer reaction and various chemical reactions leading to the regeneration of the active species (nitrous acid). The autocatalytic nature of the reaction can readily be demonstrated by simple observation of the corrosion rate of copper, for example, in nitric acid solutions: the rate, as evinced by NO<sub>x</sub> evolution, is initially low, but accelerates rapidly if the copper is placed in contact with a surface, thus forming a crevice, which traps the nitrous acid generated, or if a little nitrite is added

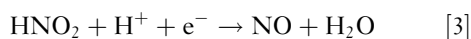
**Table 1**     Reaction of pure HNO<sub>3</sub> with metals

<i>Solution complete within</i>			<i>Evidence of inhibition by film</i>	<i>No evidence of reaction</i>
<i>1 day</i>	<i>1 week</i>	<i>1 month</i>		
Mg	Cr powder	Fe	Ca	Be
Sc		Mn	Cu	Al
V	Ni		Ag	Ti
Co	Cd		Bi	Pt
Zn	U			Sn
Hg				

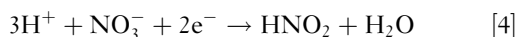
Reprinted with permission from Addison, C. C. *Chem. Rev.* **1980**, 80, 21–39. Copyright 1980 American Chemical Society.

to the solution; conversely, the rate is retarded by agitation or stirring of the acid, which displaces the nitrous acid generated, or by the addition of a chemical such as urea, which impedes the autocatalytic reaction by destroying nitrous acid.<sup>3</sup>

Two basic mechanisms have been proposed: one heterogeneous<sup>4</sup> leading to NO<sub>2</sub> formation and one homogeneous<sup>5</sup> leading to NO. Both mechanisms have been shown to be consistent with experimental data collected over different potential ranges.<sup>6</sup> More recently, a modified mechanism has been suggested, which results in two limiting cases, one applicable for low nitric acid concentrations (<8 M) leading to NO formation, the other for high nitric acid concentrations (>8 M) leading to NO<sub>2</sub>.<sup>7</sup> According to this scheme, the major species involved in the reduction of nitric acid at low overvoltages are nitrous acid (HNO<sub>2</sub>), NO, and NO<sub>2</sub>, and the charge transfer reaction is the reduction of HNO<sub>2</sub>:



The product of the overall cathodic reaction is HNO<sub>2</sub>, thus giving rise to autocatalysis:



Whatever the precise mechanism, the important point is that nitrate reduction is autocatalytic, being strongly affected by HNO<sub>2</sub>, NO, and NO<sub>2</sub>. Reactions [3] and [4] indicate that H<sup>+</sup> is required, but in all but the most dilute solutions it is the nitrate concentration that is important; thus, the addition of neutral nitrate salts to nitric acid generally increases the liquor corrosivity.

Iron can show both base and noble metal characteristics in its corrosion reactions. It is attacked at an increased rate in crevices, but its corrosion products include nitrous oxide, ammonia, and nitrogen as well as nitrogen dioxide and nitric oxide. In concentrated acids of >~40%, after an initial reaction, iron

becomes passive (although this can be disrupted relatively easily, by agitation, for example), whereas in dilute acids, reactions are rapid.<sup>8</sup>

#### 2.24.2.2.3 Passive metals

Highly reactive metals such as chromium, titanium, hafnium, niobium, and zirconium rapidly form thin insoluble surface oxides in air. These films may grow slightly on immersion in oxidizing acids, but then prevent further corrosion or reduce it to negligible rates in a wide range of nitric acid conditions. These metals or their alloys, as in the case of stainless steels, where alloying of iron with chromium confers much greater passivity, are the most important class of metals for the industrial handling of nitric acid.

This behavior is illustrated for stainless steels in Figure 1.<sup>9</sup> The polarization curve shows three distinct regions of active, passive, and transpassive corrosion. The effect of temperature on the anodic reaction is important, as demonstrated in Figure 2. Although increasing the temperature of stainless steel in nitric acid produces only a small increase in corrosion potential (due to augmentation of the cathodic reaction), the anodic polarization curve changes significantly; the passive region is effectively lost, and therefore, a small increase in potential leads to significantly increased corrosion. This is pertinent when considering the effect of oxidizing species or galvanic effects, which will therefore be more pronounced at high temperatures (see Sections 2.24.4.7 and 2.24.5.4.1).

### 2.24.3 Materials for Nitric Acid Containment

The primary materials used for nitric acid environments are stainless steels, titanium, and zirconium. Aluminum can also be used in some circumstances. The austenitic stainless steel, AISI 304L, and its

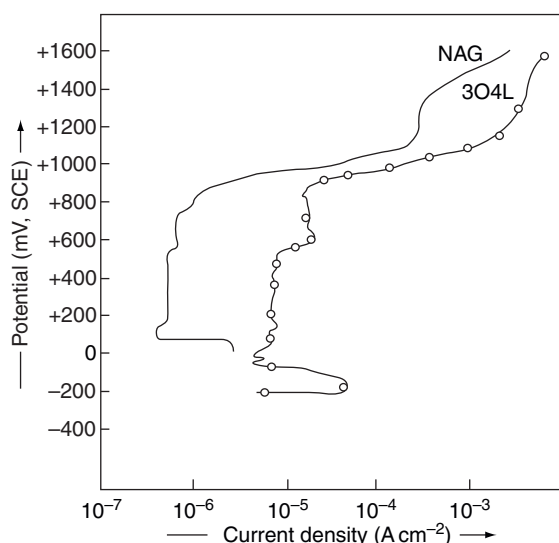


**Figure 1** Anodic polarization of stainless steel in 1 M nitric acid at room temperature. Reproduced from Kain, V.; Shinde, S.; Gadiyar, H. J. *Mater. Eng. Perform.* **1994**, *3*, 699–705, with permission from ASM International.

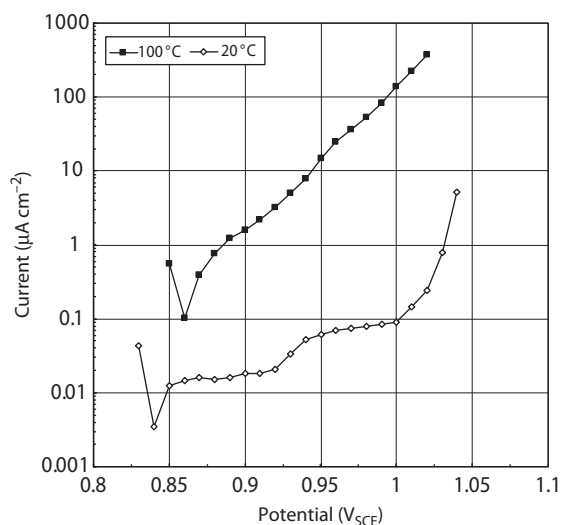


**Figure 2** Effect of temperature on polarization behavior of NAG 18/10L stainless steel in 8M nitric acid (measured by step-wise potentiostatic polarization, 10 mV steps each of 1 h duration). Takeuchi, M.; Whillock, G. O. H. BNFL unpublished work.

variants are now the most commonly used, although much early plant has been made from stabilized austenitic steels such as AISI 321, AISI 347, and 18/13/1. In more oxidizing conditions, higher alloy steels such as AISI 310L or possibly high Si stainless may be preferred. In the most aggressively oxidizing conditions, titanium, zirconium, niobium, hafnium, or tantalum may be used. In the past, titanium has

**Table 2** Indicative corrosion rates of various metals subject to testing in boiling 65% nitric acid

Metal	Corrosion rate ( $\text{mm y}^{-1}$ )
18/13/1 stainless steel <sup>a</sup>	0.2–0.5
NAG 18/10L stainless steel <sup>b</sup>	0.1–0.2
NAG 18/10L stainless steel <sup>c</sup>	0.1–0.3
310L stainless steel	0.05–0.1
Ti <sup>d</sup>	0.7
Zr	<0.001
Ta	<0.001

<sup>a</sup>Similar to AISI 347.

<sup>b</sup>As-received.

<sup>c</sup>Sensitized.

<sup>d</sup>The high corrosion rate is due to the test conditions employed (see [Section 2.24.3.2](#)).

Source: Quayle, B. E. BNFL unpublished work.

been the most widely used, but the use of zirconium in preference has increased in recent years. The others find only occasional use, despite their excellent corrosion resistance, because of high cost and fabrication difficulties. [Table 2](#) provides indicative corrosion rates for some of these metals.

### 2.24.3.1 Stainless Steels

The industrial use of stainless steel for nitric acid containment seeks to ensure that it operates in the passive regime where corrosion rates are typically  $<0.01 \text{ mm year}^{-1}$ . However, it is also possible to operate stainless steel plant successfully for extended periods in the potential regime between passivity and full transpassivity where intergranular corrosion occurs and the corrosion rate is significant (see [Section 2.24.4.1](#)). In practice, all stainless steel plant handling hot nitric acid operates in the intergranular corrosion regime.

Corrosion rates show Arrhenius behavior over a large range of acid concentrations and temperatures, as illustrated in [Figure 3](#), indicating that electron transfer is the rate-determining step in the corrosion mechanism.

Austenitic stainless steels are the most widely used for nitric acid containment. Reasonable or good nitric acid resistance can be achieved with ferritic, super ferritic, and ferritic–austenitic (duplex) steels, but they are generally less resistant than the austenitics, and factors such as compositional variation, heat treatment, and welding can lead to reduction in corrosion resistance.<sup>11</sup> Ferritic stainless steels with  $>14\%$  Cr resist corrosion in nitric acid at room temperature, and high Cr/Mo ferritics such as 26Cr1Mo, and 29Cr4Mo resist nitric acid up to 65% boiling. Duplex

stainless steels have similar resistance to ferritics, but the ferritic phase can be preferentially attacked.<sup>11</sup>

AISI 300 series stainless steels (i.e., austenitic) are adequate for a wide range of applications up to about 70% acid concentration. AISI 304L is now commonly used and improvements in its performance can be achieved by improved manufacturing processes to reduce elements such as Si, P, S, and C, as illustrated

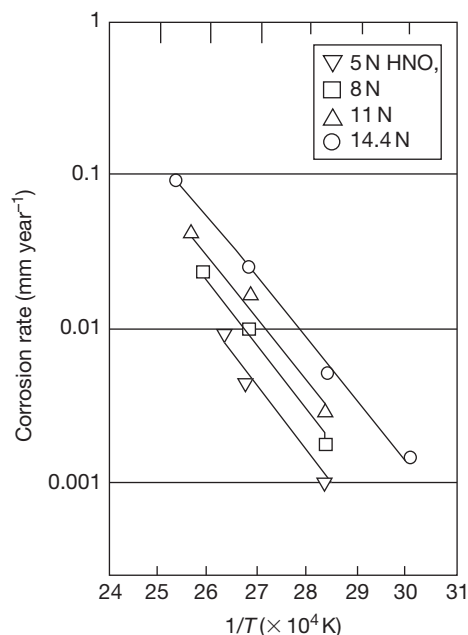


**Figure 3** Corrosion rate of stainless steel (R-SUS 304ULC) as functions of temperature and nitric acid molarity. Reproduced from Onoyama, M.; Nakata, M.; Hirose, Y.; Nakagawa, Y. In *Proceedings of the RECOD'91, Japan Atomic Industrial Forum: Japan, 1991*; Vol II, pp 1066–1071.

in **Figure 1**. Here, a nitric acid grade version of 304L shows improved corrosion resistance in the passive and lower transpassive region. However, it is doubtful whether significant corrosion differences persist under more aggressive oxidizing conditions where higher chromium steels such as 310L may be required.<sup>12</sup> Alternatively, in extremely oxidizing conditions stainless steels containing Si at  $>\sim 4\%$  (e.g., Uranus S1N) may find application, although such steels are more problematic to join because some ferrite needs to be maintained in the welds to avoid cracking.<sup>13</sup>

### 2.24.3.2 Titanium

Titanium has a high corrosion resistance to a range of nitric acid concentrations, provided there is sufficient concentration of dissolved titanium or other oxidizing ions present.<sup>14,15</sup> In the absence of such dissolved ions, corrosion rates can reach or exceed  $1 \text{ mm year}^{-1}$ . Hence, corrosion rates in the vapor regions of operating plant handling condensing nitric acid, where continuous washing prevents the accumulation of dissolved titanium, can be significant even though the metal below liquor is unaffected. Titanium is accordingly no longer recommended for use in condensing nitric acid. Owing to the sensitivity of titanium corrosion rates to the presence of dissolved titanium, account must be taken of the suppressing effect of corrosion product accumulation when assessing corrosion rate data. The susceptibility of titanium to corrosion in pure acid can be mitigated by alloying with tantalum; at  $>5\%$  Ta, corrosion is significantly reduced.<sup>14</sup> These effects are illustrated by the corrosion data in **Table 3**.

**Table 3** Effect of test conditions on the corrosion rate of titanium and titanium–tantalum alloys

Metal	Nitric acid concentration plus additions	Liquor renewal (h)	Corrosion rate ( $\text{mm year}^{-1}$ )	Source
Ti	6 M	14	0.6	(a)
	6 M	65	0.43	(b)
	6 M	280	0.15	(a)
	6 M + $0.1\% \text{ Fe}^{3+}$	65	0.14	(b)
	6 M + $0.1\% \text{ Ce}^{4+}$	65	$<0.01$	(b)
	40%	24	0.75	(c)
	40% + $40 \text{ mg l}^{-1} \text{ Ti}$	24	0.05	(c)
	Condensing acid	24	0.33	(c)
	40%	4	0.74	(c)
Ti–6.1%Ta	40%	4	0.02	(c)

<sup>a</sup>Quayle, B. E. BNFL unpublished work.

<sup>b</sup>Shimogori, K.; Satoh, H.; Kamikubo, F. In *Titanium Science and Technology*; Proceedings of the 5th International Conference on Titanium, Munich, Germany, 10–14 Sept; 1984; Lutherling, G., Ed., Vol. 4, pp 1111–1114.

<sup>c</sup>Takamura, A.; Arakawa, K.; Moriguchi, Y. In *The Science Technology and Application of Titanium*; Jafee, R. I., Promisel, N. E., Eds.; Pergamon Press: Oxford, 1970; pp 209–216.

Titanium can also be susceptible to enhanced corrosion in both weld metal and heat-affected zones. This has generally been attributed to the redistribution of iron impurities during the welding operation so that the iron originally present in discrete stringers or well-distributed particles is deposited on grain boundaries either as iron–titanium intermetallic compounds or as  $\beta$ -phase. The formation of a continuous grain boundary network can lead to intergranular corrosion and grain dropping in certain conditions. This is likely to become more significant in marginally passive environments where these iron-rich phases may become soluble. To avoid this problem, it is now recommended that iron levels in titanium are specified to be  $<0.05\%$ .<sup>16</sup>

### 2.24.3.3 Zirconium, Niobium, Hafnium, and Tantalum

These materials are generally highly resistant to nitric acid corrosion (see Table 2), although operating experience of these materials is less extensive than that of titanium. There are no reported materials issues affecting corrosion performance, although stress corrosion cracking (SCC) of zirconium cannot be entirely discounted in extremely oxidizing conditions (see Section 2.24.4.4). In addition, zirconium is very susceptible to trace levels of fluoride ions (see Section 2.24.5.5). There have been no reported instances of enhanced vapor phase corrosion and they do not require the presence of dissolved ions to achieve passivity.

### 2.24.3.4 Aluminum

The corrosion rate of aluminum and its alloys is appreciable in all but very concentrated nitric acid, reaching  $3\text{--}5\text{ mm year}^{-1}$  at room temperature in 30% acid, whereas rates of  $<0.1\text{ mm year}^{-1}$  can be achieved in  $>85\%$  acid. This is illustrated in Figure 4<sup>17</sup>. The corrosion rate is strongly temperature dependent and increases with the level of copper impurity. However, a number of aluminum alloys containing magnesium silicon or manganese have corrosion rates comparable with those of pure aluminum in 98.5% acid.<sup>18</sup> As would be expected from its decreased corrosion resistance in dilute acids, aluminum corrodes more quickly where dilute acid condensates are formed above concentrated acids.<sup>19</sup> Hence, although aluminum can be suitable for room temperature storage of concentrated nitric acid, the vapor regions of storage vessels may undergo increased corrosion.

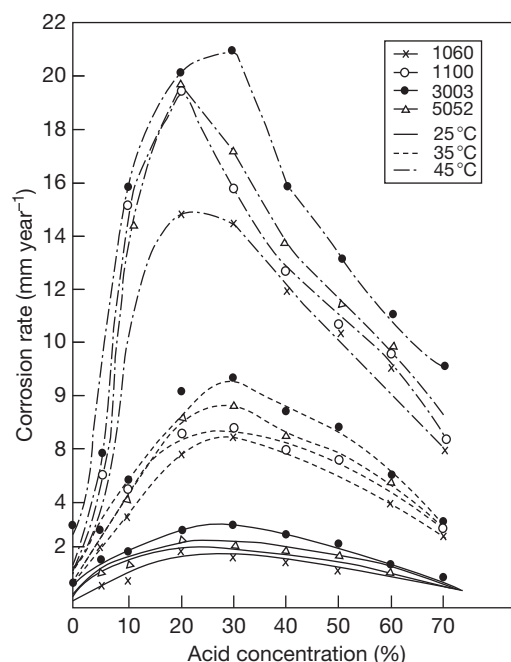


**Figure 4** Corrosion rate of various aluminum alloys as a function of nitric acid concentration and temperature. Reproduced from Singh, D. D. N.; Chaudhary, R. S.; Agarwal, C. V. J. *Electrochem. Soc.* **1982**, 129, 1869–1874, with permission from The Electrochemical Society.

## 2.24.4 Corrosion Mechanisms of Passive Metals in Nitric Acid

### 2.24.4.1 General Corrosion and Intergranular Corrosion

For stainless steels, full transpassivity occurs when the  $\text{Cr}_2\text{O}_3$ -based passive film becomes unstable in extremely oxidizing conditions, allowing corrosion to proceed by the formation of soluble  $\text{CrO}_3$ ; this occurs at  $\sim 1.0\text{ V}_{\text{SCE}}$ .<sup>20</sup> However, grain boundaries are more vulnerable to corrosion. This is largely due to impurities in the metal, with the segregation of silicon and phosphorus being particularly implicated.<sup>21,22</sup> The transpassive corrosion process therefore proceeds primarily by grain boundary dissolution, but is manifest as general corrosion owing to grain dropping. Owing to the high corrosion rates encountered, stainless steels are unsuitable for use in extremely oxidizing conditions where transpassive corrosion occurs.

In the potential band between full passivity and transpassivity (i.e., between  $\sim 0.9$  and  $\sim 1.0\text{ V}_{\text{SCE}}$ ), intergranular corrosion occurs. This is the principal mechanism affecting stainless steels handling nitric



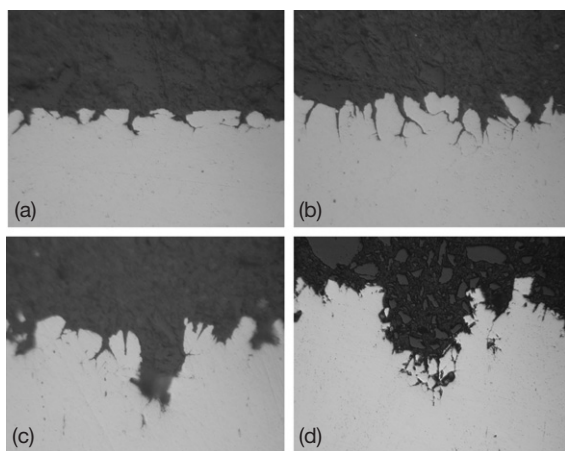


**Figure 5** Morphology of intergranular corrosion of 18/13/1 stainless steel exposed to 8 M nitric acid containing  $25 \text{ g l}^{-1}$  Fe(III) at  $100^\circ\text{C}$ . The sections show penetration into (a) plate, (b) side and (c) end surfaces after 340 h exposure. (d) Shows end grain pitting after 1000 h exposure. Magnification: (a)–(c)  $\times 360$ ; (d)  $\times 150$ . Dunnett, B. F. BNFL unpublished work.

acid solutions which are too oxidizing for the maintenance of passivity. Intergranular attack increases significantly if the steel has become sensitized by heat treatment,<sup>23</sup> but sensitization is not a prerequisite, intergranular corrosion occurring in the fully solution-annealed condition even in very clean stainless steels providing potentials in excess of  $\sim 0.9 V_{\text{SCE}}$  are achieved in hot solutions. The intergranular corrosion rate can be strongly anisotropic, depending on the orientation of the exposed face to the underlying microstructure (see also Section 2.24.4.2). Figure 5 illustrates this. The effects tend to be less pronounced in modern ultraclean stainless steels, but are still evident.

General corrosion curves derived for stainless steels from weight loss are broadly characterized by two regions, as illustrated in Figure 6.<sup>24</sup> In the early stages, grain boundaries are etched, but no grains are lost, and weight loss is by chemical dissolution only. The apparent corrosion rate rises as the grain boundaries are penetrated more deeply because a greater area of metal is opened to corrosion. As time progresses, grains begin to drop out of the metal surface as their boundaries are completely corroded. Eventually, a relatively stable corrosion rate is reached, which is a combination of chemical dissolution and grain dropping. For AISI 304L stainless steel and related steels, grain dropping accounts for only  $\sim 25\%$  of the total metal loss, chemical dissolution of the grain boundary regions accounting for the rest.<sup>25</sup> It is therefore important in deriving corrosion

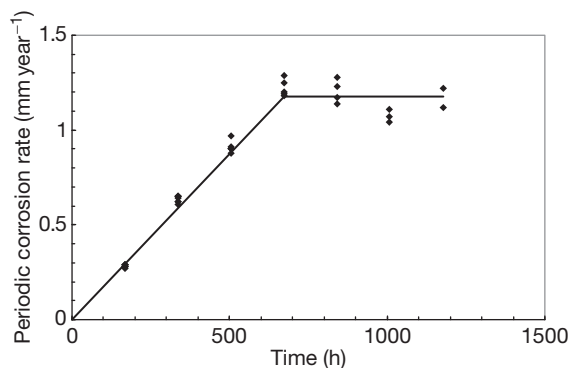


**Figure 6** Effect of immersion time on the corrosion rate of 18/13/1 stainless steel in 8 M nitric acid containing  $25 \text{ g l}^{-1}$  Fe(III) at a solution temperature of  $100^\circ\text{C}$ . Reproduced from Dunnett, B. F.; Whillock, G. O. H. *Corrosion* **2003**, 59, 274–283, with permission from NACE International.

rates from analysis of dissolved species to allow for grain dropping.

Corrosion rates derived from weight loss averaged over the specimen area will tend to be underestimated in the early stages of corrosion. In practice, the corrosion curve is an artifact of the measurement process; if measurements of penetration are made, then it is found that the rate of penetration is constant and corresponds to the corrosion rate derived from weight loss once steady grain dropping is established.<sup>24</sup> The time to reach this state depends on the corrosion resistance of the steel, its grain size, and the corrosivity of the medium.

This problem can be addressed either by numerical models to predict the long-term rate from short-term data<sup>26,27</sup> or by pre-corroding test samples in aggressive media to establish grain dropping before reverting to the required test media.<sup>24,28</sup> The validity of numerical models is still to be fully established. Pre-corrosion appears to be a valid method, although it appears that care needs to be taken in selecting the pre-corrosion conditions, otherwise reasonably prolonged testing in the liquor of interest may be required in order to establish the true corrosion rate. In practice, it is found that the overall metal loss by intergranular corrosion is fairly uniform even in plants operating with relatively aggressive environments. Hence, extrapolation of the steady-state corrosion rate to predict plant life is valid, provided there are no localized mechanisms acting, such as crevice/underdeposit corrosion (see Section 2.24.4.3).

Intergranular corrosion in stainless steels can be suppressed by alloying with silicon.<sup>13</sup> At  $>4\%$  Si, intergranular corrosion is suppressed, but general

corrosion rates at most nitric acid concentrations are higher at least in the early stages of corrosion compared with the equivalent AISI 300 series stainless steel. In particular, high Si stainless steels show a significant improvement in corrosion resistance in super-azeotropic solutions. However, welding of these alloys can be problematical; ferrite needs to be maintained in the welds to avoid cracking, and welds can be susceptible to enhanced corrosion.<sup>13</sup>

Intergranular corrosion of other passive metals such as zirconium and tantalum has not been reported. Of these metals, only titanium shows a transpassive breakdown in normal operating conditions, although a form of transpassivity (breakaway oxidation) can be induced in zirconium and its alloys under extreme conditions (in excess of  $\sim 2 V_{SCE}$ ).<sup>29</sup> Titanium can also exhibit intergranular corrosion at welds; this propensity tending to be associated with the presence of  $\beta$ -phase (see Section 2.24.3.2).

#### 2.24.4.2 End Grain Corrosion

The rate of intergranular penetration depends on the orientation of the exposed face to the underlying microstructure. In general, the corrosion rate increases in the order: plate < side < end (see Figure 5). The effects of end grain corrosion are clearly seen in boiling nitric acid testing (the Huey test, see Section 2.24.6) if specimens are cut so as to vary the percentage of exposed end grain in a susceptible material. Figure 7 shows an example, clearly demonstrating a significant effect for end grain fractions exceeding  $\sim 10\%$ .

In addition to this pronounced effect of end grain on the general corrosion rate, localized pitting-like

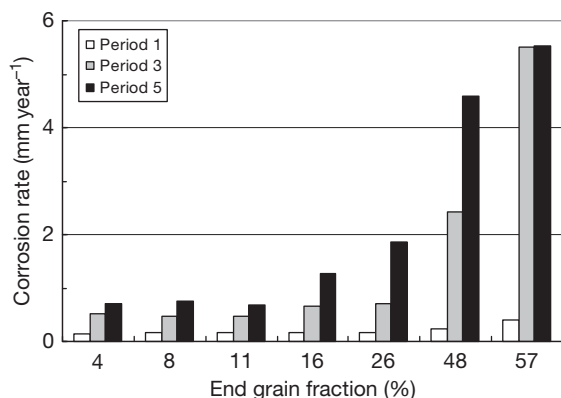


**Figure 7** Effect of end grain fraction on the corrosion rate obtained from successive 48 h test periods of 18/13/1 stainless steel in boiling 65% nitric acid. Quayle, B. E. BNFL unpublished work.

attack can develop parallel to the hot-working direction. This is known as ‘end grain’ or ‘tunneling’ corrosion. Figure 8 shows an example. Older stabilized steels appear to be most vulnerable, and the phenomenon is extremely variable even within the same grade of steel. However, extremely clean stainless steels such as R-SUS 304ULC and Uranus 65 also exhibit end grain pitting.<sup>30,31</sup> In such steels, the mechanism is considered to be a consequence of the exposure of segregated material in the original ingot, which has been distributed, producing bands with more susceptible grain boundaries.<sup>31</sup> In stabilized steels, stringers of magnesium sulfide and precipitates of niobium or titanium carbide mark out the regions of maximum segregation as they solidify late from the melt. The outer regions of the ingots solidify first, and hence contain little impurity segregation conferring superior corrosion resistance to the as-formed plate surface.

In practice, end grain corrosion of stainless steels is usually more of a problem for corrosion testing (see Section 2.24.6) than for operating plant where most end grain is welded over in pipe or plate joints, although issues can arise, for instance, with forgings where outcropping end grain can be present.

End grain corrosion of other passive metals has not generally been reported, although at least one instance on titanium is known.

#### 2.24.4.3 Crevice Corrosion

Although crevice corrosion is not widely reported in nitric acid, austenitic stainless steels are known to be susceptible to this mechanism in certain circumstances. One such example is corrosion testing of heat transfer surfaces, where corrosion focuses at



**Figure 8** End grain corrosion pits: 18/13/1 stainless steel stirrer paddle in nitric acid media. Green, D. S. BNFL unpublished work.

the mouth of the crevice on the external surface; for instance, under nucleate boiling at a heat flux of  $50 \text{ kW m}^{-2}$ , the depth of attack was twice that on the free surface.<sup>32</sup> Crevice corrosion appears to be possible only in more aggressive conditions, although indications of it have been found in isothermal tests at temperatures as low as  $90^\circ\text{C}$ ,<sup>33</sup> and in a nitric acid reboiler where corrosion rates increased from  $\sim 0.02$  to  $0.1 \text{ mm year}^{-1}$  on a heat transfer surface at  $\sim 90^\circ\text{C}$  in 12 M nitric acid. The mechanism may have several origins depending on the circumstances. For heat-transfer surfaces, the inhomogeneity provided by the crevice may simply lead to increased local surface temperatures, and hence increased local corrosion rate. The entrapment of stainless steel corrosion products is also possible (see [Section 2.24.5.4.1](#)), as is entrapment of  $\text{NO}_x$  species (see [Section 2.24.5.3](#)). The mechanism is oxidative rather than reductive in contrast to crevice corrosion brought about by chloride ions in water systems. The operation of a crevice in nitric acid systems is capable of adversely affecting the potential outside the crevice and increases the external corrosion rate. Care is therefore required in interpreting corrosion test data where the operation of a crevice is suspected.

Crevice corrosion has not been found on zirconium, titanium, or niobium under similar heat-transfer conditions in nitric acid. However, it has been recorded on zirconium in laboratory trials in acid contaminated by fluoride ions (see also [Section 2.24.5.5](#)) and also under cathodic polarization. It is probable that here the phenomenon is one of active corrosion in localized reducing conditions in the crevice. Crevice corrosion has not been reported for these metals in operating plant.

#### **2.24.4.4 Stress Corrosion Cracking**

Despite the intergranular nature of nitric acid attack of stainless steels, SCC of stainless steels in nitric acid is almost unknown. This is not due to a simple absence of stress, as postfabrication stresses at welds in austenitic stainless steels invariably approach yield. SCC is known to occur in weak nitric acid solutions and is facilitated by severe sensitization, the only known example in practice being intergranular SCC of irradiated stainless steel nuclear fuel cladding exposed to moist air, the corrosive agent being generated by nitrogen radiolysis (see [Section 2.24.5.6](#)). Slow strain rate testing reveals a link between the oxidizing power of the acid (i.e., the repassivation rate) and the metal rupturing rate (i.e., the strain rate).

SCC can occur in a critical regime where repassivation kinetics are such that the crack tip remains active; otherwise, crack blunting occurs at one extreme, with the absence of sufficient crack advancement at the other. The absence of SCC of stainless steel in stronger nitric acid solutions is accordingly attributed to too rapid repassivation rates relative to practically achievable strain rates.

SCC has also been induced in zirconium by slow strain rate testing.<sup>34</sup> However, this only occurs above the azeotrope and is therefore unlikely to be relevant other than in extremely oxidizing conditions. SSC of zirconium has not been reported in plant operating in nitric acid media.

#### **2.24.4.5 Corrosion Fatigue**

Normal air fatigue processes can be exacerbated in the presence of corrosive media, leading to corrosion fatigue. As in SCC, the process is complex, requiring conditions where a crack tip is continuously formed by fatigue and its propagation is accelerated by corrosion of the exposed metal. However, in passivating media, crack blunting is also possible.<sup>35</sup> Test rig data indicate that corrosion fatigue of stainless steel in nitric acid solutions is feasible in some circumstances, indicating that careful assessment may be required. However, corrosion fatigue in nitric acid plant appears not to have been encountered in practice.

There is no indication that zirconium or similar passive metals are susceptible to corrosion fatigue in nitric acid.

#### **2.24.4.6 Erosion Corrosion and Fretting Corrosion**

These mechanisms proceed in passive metals by removing the protective oxide film, leading to oxidation of the underlying reactive metal. Erosion corrosion requires the surface oxide to be scoured by a slurry of abrasive particles. The erosion corrosion rate depends on a variety of factors, including particle weight and sharpness, but is especially sensitive to particle velocity, with attrition rates typically increasing as  $(\text{velocity})^n$  where  $n$  is  $\sim 4$ .<sup>36</sup> A dynamic process ensues in which oxide is continuously removed and regrown. In metal–environment combinations where transient metal dissolution rather than simple repassivation of the scoured surface is possible, considerable enhancement of metal loss can occur.<sup>37</sup> For stainless steel abraded in water and in dilute nitric acid, the attrition rates have been found to be similar.

Although repassivation kinetics will differ for the two media, they will be rapid in both cases, and therefore, unless the erosion rate approached the repassivation rate, it is probable that full repassivation occurs at any given point before it is re-eroded, and therefore, no difference between the attrition rates in the two media is apparent.

It is, however, anticipated that a corrosive element will be more significant in erosion corrosion at transpassive potentials or where nitric acid is contaminated with halides (see [Section 2.24.5.5](#)) or other species, which lead to active dissolution of bared metal.

Fretting corrosion is possible when loaded surfaces move against each other in a corrodant. The process depends on loading, displacement, and cycling frequency and tends to be exacerbated if debris remains between the moving faces. Some studies in nitric acid show high attrition rates, but the relative contribution of wear and corrosion was not established and it is likely that similar processes and considerations to erosion corrosion apply.

#### 2.24.4.7 Galvanic Corrosion

Galvanic corrosion effects can occur in nitric acid in much the same way as other media. The consequence depends on the strength and direction of the resulting potential shift and may thus be beneficial, neutral, or deleterious to the half-couple of interest. Coupling with an actively corroding base metal, such as Magnox or uranium, tends to reduce the corrosion rate of stainless steels in hot nitric acid solutions. The behavior of aluminum is more complex, ranging from slight reduction in the corrosion rate of stainless steel in concentrated nitric acid solutions,<sup>38</sup> to marked enhancement in the stainless steel corrosion rate if the potential shift is sufficient to move stainless steel into its active region.<sup>39</sup> Caution is therefore needed in predicting the effect of coupling with base metals. Deleterious effects on stainless steel arise from coupling with lead<sup>40</sup> and noble metals, such as, for example, platinum catalyst fragments (fertilizer plant) or fission product solids rich in platinum metals (nuclear reprocessing plant). Less obvious is the effect of coupling stainless steels with markedly different chromium contents; coupling 18% and 25% Cr stainless steels (i.e., 304L and 310L) results in significant increase in corrosion rate of the former and decrease in corrosion rate of the latter in hot nitric acid solution. This arises because the corrosion potential of 25% Cr stainless steel is  $\sim 20$  mV higher than that of 18% Cr stainless steel in hot nitric acid, illustrating the

extreme sensitivity of corrosion rate to potential close to the onset of full transpassivity. In less oxidizing liquors, the effects of coupling noble metals to stainless steel are much less pronounced.<sup>41</sup>

Connections between other passive metals tend not to be problematic. For example, connections between stainless steel and zirconium plant have minimal effects on the corrosion of the junction below transpassivity; similarly, measurements on titanium/stainless steel couples show no enhanced corrosion.<sup>42</sup>

### 2.24.5 Factors Affecting Corrosion Processes in Nitric Acid

#### 2.24.5.1 Welding

Sensitization can occur during welding of stainless steels even if they are stabilized or low carbon grades, although the effects are much less pronounced than is the case for nonstabilized or high carbon steels. The formation of chromium-rich carbides at grain boundaries leaves chromium-depleted steel in their vicinity, creating a band of corrosion susceptible material running parallel to the weld but displaced a few millimetres from it. Such zones are more susceptible to intergranular corrosion in hot nitric acid, leading to heat-affected zone corrosion (weld decay). In niobium-stabilized stainless steels, the enhancement appears to be modest, amounting to at most  $\sim 10\%$  of the parent metal corrosion rate. [Figure 9](#) shows an example.

Knife-line corrosion is also possible in some circumstances. This is manifest as a sharp band of corrosion penetrating along the weld-parent metal interface where temperatures exceed  $1150^\circ\text{C}$  during

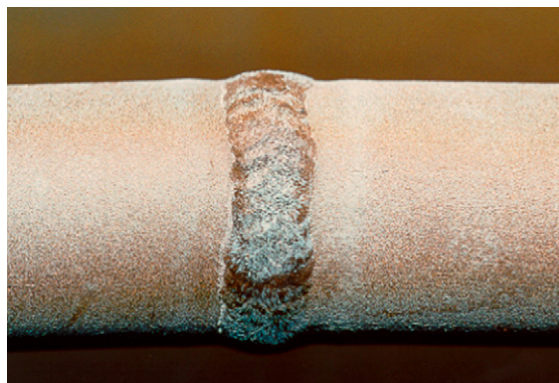


**Figure 9** Weld metal and heat affected zone corrosion: 18/13/1 stainless steel tube (steam-heated) in nitric acid media. Green, D. S. BNFL unpublished work.



the welding process. In most nitric acid solutions, this is an issue primarily for stabilized stainless steels such as AISI 321, since titanium carbides are susceptible to dissolution releasing carbon into solid solution, which then reacts with chromium, resulting in a chromium-deficient narrow band at the weld interface. Niobium-stabilized stainless steels such as AISI 347 and 18/13/1 do not exhibit knife-line corrosion in most nitric acid solutions, but are susceptible in mixed acid systems such as nitric acid/fluoride.

In general, welds in austenitic stainless steels are at least as corrosion resistant in nitric acid as the parent metal (see [Figure 9](#)). Their coarse-grained structure may delay the onset of grain dropping relative to the parent material, but overall penetration rates are similar. Occasionally preferential attack of weld roots may be seen.

Titanium welds can be susceptible to enhanced corrosion, both the weld metal and the heat-affected zone, in hot nitric acid solutions (see [Section 2.24.3.2](#)).

### 2.24.5.2 Cold Work

Most information on the effects of cold work on corrosion in nitric acid relates to austenitic stainless steels. The effect of cold work is intimately linked to the thermal and mechanical history of the steel and can lead to an increase or reduction in corrosion rate depending on the circumstances. Data can appear to be contradictory, and the mechanisms by which cold work affects corrosion are not fully explained, although processes such as carbon diffusion, precipitation, and martensite formation appear to be involved.<sup>43,44</sup> The relevance of the process by which cold work is achieved appears not to have been assessed and both compression by cold rolling, and tension by tensometer have been used in studying the phenomenon.

Cold work on the as-received material has generally been found to produce little effect or a marginal decrease in corrosion resistance; steels with an intrinsically lower corrosion resistance (including high Si stainless steels) and greater susceptibility to sensitization tending to fall into the latter category.<sup>43,45–47</sup> [Figure 10](#) illustrates this.

The order of cold working and thermal treatments seems to be important. Austenitic stainless steels, either sensitized<sup>46</sup> or partly sensitized as a result of cooling after prolonged solution treatment,<sup>44,48</sup> have been found to exhibit improved corrosion resistance when subsequently cold worked, although at very high levels of cold work the corrosion resistance can begin to decrease again due to martensite formation.<sup>44</sup>

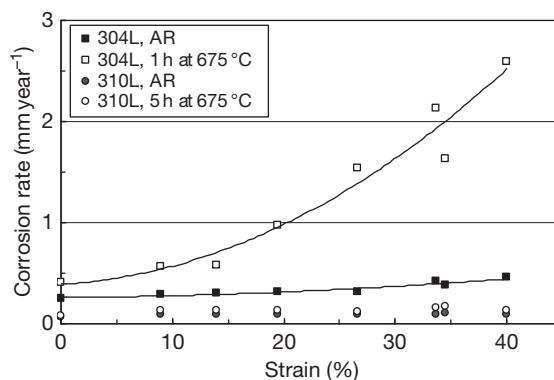


**Figure 10** Effect of cold work and subsequent thermal treatment on the corrosion resistance of austenitic stainless steels in boiling 65% nitric acid. Quayle, B. E. BNFL unpublished work.

Conversely, if austenitic stainless steels are first cold worked and then sensitized, those steels having a susceptibility to sensitization show decreased corrosion resistance with increasing levels of cold work (see [Figure 10](#)), although the effect can reach a peak at relatively low deformation for some stainless steels.<sup>43</sup>

In practice, cold work is only likely to be problematical, at least for austenitic stainless steels, if they are in fact subsequently sensitized, for instance, by welding or by operation for prolonged periods at temperatures exceeding  $\sim 300^\circ\text{C}$ .<sup>43</sup>

### 2.24.5.3 NO<sub>x</sub> Gases

NO<sub>x</sub> gases dissolve in aqueous nitric acid producing nitrous acid. The resulting concentration of nitrous acid depends on temperature and it has been shown that steady state is established relatively quickly owing to solution saturation.<sup>49</sup> In the absence of other dissolved species, the redox potential of a given aqueous nitric acid solution is determined by its nitrous acid content and is amenable to calculation over a wide temperature range for a wide range of nitric acid concentrations.<sup>50</sup> Increasing nitrous acid concentration leads to an essentially perfect Nernstian decrease in solution redox potential. Nitrous acid is thus more reducing in nature than nitric acid. Metals such as zirconium exhibit the same behavior as platinum, the corrosion potential decreasing upon NO<sub>x</sub> addition. However, because nitrous acid catalyses nitrate reduction (see [Section 2.24.2.2.2](#)), the effect on stainless steels is a significant rise in the metal's corrosion potential (see [Figure 11](#)). These opposing effects on solution redox potential and stainless steel corrosion potential are explained in [Figure 12](#).



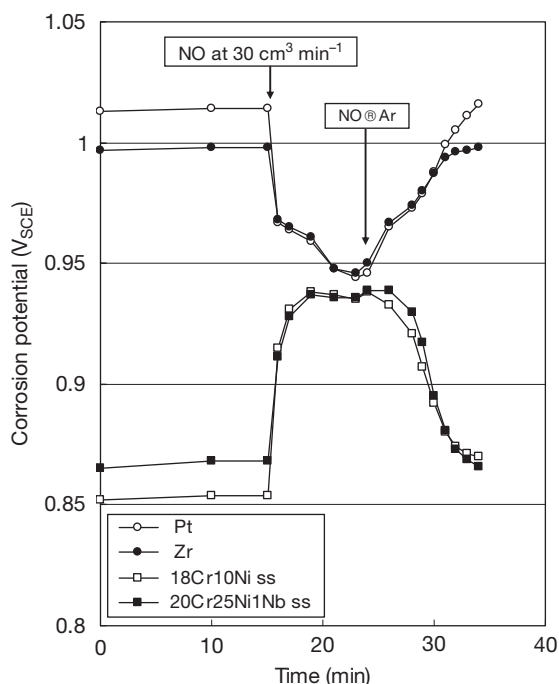


**Figure 11** Effect of  $\text{NO}_x$  purging on the corrosion potential of the indicated metals in 8 M nitric acid at 100 °C Takeuchi, M.; Whillock, G. O. H. BNFL unpublished work.

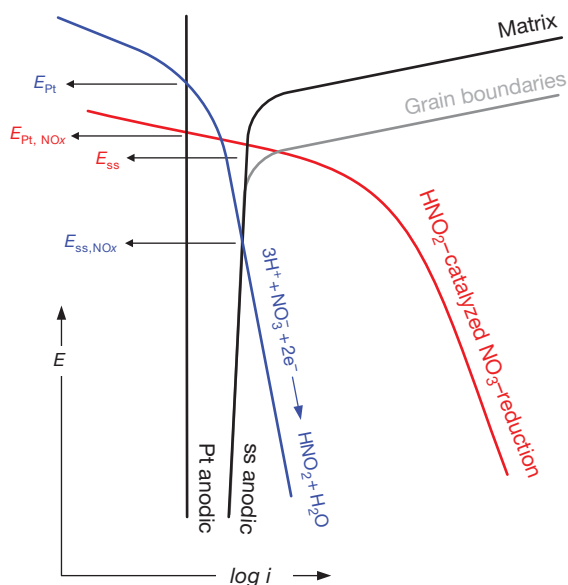


**Figure 12** Evans diagram accounting schematically for the observed effect of  $\text{NO}_x$  purging on corrosion processes occurring in nitric acid. Adapted from Takeuchi, M.; Whillock, G. O. H. *Br. Corros. J.* **2002**, 37, 199–205, with permission from Maney Publishing.

Because  $\text{NO}_x$  addition increases the corrosion potential of stainless steels in pure aqueous nitric acid solutions, the corrosion rate rises.<sup>49</sup> However, in the presence of more powerful oxidants, such as  $\text{Cr(VI)}$  or  $\text{Ce(IV)}$ ,  $\text{NO}_x$  purging significantly lowers the corrosion rate of stainless steel by reducing these strong accelerators to innocuous valency states. A similar effect was observed by Truman,<sup>51</sup> indicating the importance of considering the effect of  $\text{NO}_x$  gases in experimental design (see [Section 2.24.6](#)). In addition, the operating pressure and state of solution boiling could be of significance in some circumstances (see [Section 2.24.5.7](#)); lowering the partial pressure of  $\text{NO}_x$  gases would favor solution oxidation reactions, which would have the potential to exert a significant effect in solutions containing dissolved species such as chromium and cerium, particularly when the conditions were otherwise just insufficiently oxidizing to give significant equilibrium concentrations of  $\text{Cr(VI)}$  and  $\text{Ce(IV)}$  (see [Sections 2.24.5.4.1](#) and [2.24.5.6](#)).

## 2.24.5.4 Dissolved Oxidizing Species and Corrosion Products

### 2.24.5.4.1 Stainless steel

Many dissolved species capable of existing in more than one valency state can increase the corrosion rate of stainless steel in nitric acid; for instance in boiling 12 M nitric acid,  $\text{Cr(VI)}$ ,  $\text{Ce(IV)}$ ,  $\text{Au(III)}$ ,  $\text{V(V)}$ ,  $\text{Ru(VIII)}$ , and  $\text{I(VII)}$  are strong corrosion accelerators.<sup>52</sup> The effect of oxidizing species like these is to provide a facile cathodic reaction, essentially replacing nitrate reduction, which is capable of polarizing stainless steel to a potential where breakdown of the passivating film occurs (specifically,  $\text{Cr}_2\text{O}_3$  to  $\text{CrO}_3$  conversion). It was proposed that any species that forms a redox couple lying in the range 1.05–1.30  $V_{\text{SCE}}$  will produce the same effect, and hence would act as a strong accelerator.<sup>52</sup> This appears to provide a means of assessing the likely effect of species that cannot be tested easily (e.g., Pu, Np, Tc, etc).

However, this theory is incomplete in that it fails to predict the accelerating effect of a number of dissolved species, notably  $\text{Fe(III)}$  (see [Figure 13](#)<sup>53</sup>),  $\text{Np(VI)}$ ,  $\text{Ru(III)}$ , and  $\text{Pu(VI)}$ , the redox potentials of which are all too low to induce transpassivity, ranging between 0.53  $V_{\text{SCE}}$  ( $\text{Fe(II)/(III)}$ ) and 0.89  $V_{\text{SCE}}$  ( $\text{Np(V)/Np(VI)}$ ). The failure of Evans's approach<sup>52</sup> is due in part to oversimplification of the anodic metal dissolution reaction: commercial stainless steels do not remain passive until  $\text{Cr}_2\text{O}_3$  to  $\text{CrO}_3$  conversion

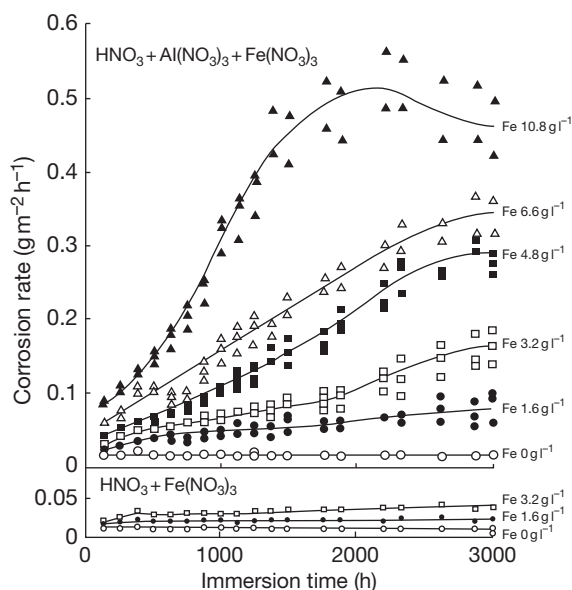


**Figure 13** Effect of dissolved iron on the corrosion rate of R-SUS 304ULC stainless steel in (i) 8 M nitric acid containing 1.53 M (Al+Fe) and (ii) 9 M nitric acid, both at 100 °C. Reproduced from Hirose, Y.; Suzuoki, A.; Sukekawa, M. In *1994 Fall Meeting of Atomic Energy Society of Japan*; Japan Atomic Energy Society: Japan, 1994; 70, with permission from Atomic Energy Society of Japan.

occurs; instead, grain boundary attack sets in at significantly lower potential (see [Figure 12](#)). Thus, corrosion accelerators can be considered to fall into two classes:

- species capable of polarizing stainless steel to very high potential, sufficient to promote  $\text{Cr}_2\text{O}_3$  to  $\text{CrO}_3$  conversion (i.e., Cr(VI), Ce(IV), Au(III), Ru(VIII) and I(VII));
- species capable of polarizing stainless steel to slightly lower potential where intergranular attack occurs (i.e., Fe(III), V(V), Ru(III), Np(VI), and Pu(VI)), but  $\text{Cr}_2\text{O}_3$  to  $\text{CrO}_3$  conversion does not (except perhaps at very high concentrations).

The mechanism whereby species belonging to the latter type act to elevate the corrosion potential of stainless steel has not been rigorously established. However, it is probably due to catalysis of nitrate reduction. This has previously been suggested to account for the action of dissolved iron<sup>54</sup> and neptunium,<sup>55</sup> but kinetic studies demonstrating this unequivocally have not been reported. The catalysis mechanism, if this is correct, is obscure, as Fe(II) should be unobtainable even transiently in hot nitric

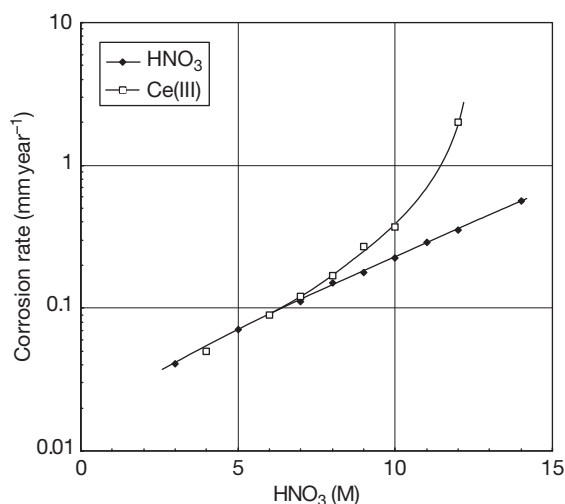


**Figure 14** Effect of 0.01 M Ce (added as Ce(III)) on the corrosion rate of 18/13/1 stainless steel in boiling nitric acid solutions. Jones, F. BNFL unpublished work.

acid; it may be the case that the thermodynamic properties of the transitional complex have not been properly considered.

An important feature of species such as dissolved iron is that they will produce a persistent effect, because, in nitric acid solutions of sufficient strength and temperatures to pose a corrosion threat, they will be ever-present in their highest oxidation state. Conversely, deliberate additions of species such as Cr(VI) and Ce(IV) would not be capable of creating a persistent effect (provided the solution volume to metal surface area ratio was sufficient to preclude a complicating effect from released iron corrosion product) except in extremely oxidizing conditions where the oxidation of the reduced species proceeds reasonably quickly, because the reduced forms (i.e., Cr(III) and Ce(III)) are not corrosion accelerators *per se*, but can be converted to their oxidized forms by reaction with nitric acid if the conditions are sufficiently oxidizing. [Figure 14](#) illustrates this effect for dissolved cerium (added as Ce(III)), indicating that cerium accelerates corrosion in boiling nitric acid stronger than ~7 M. However, at lower temperature (100 °C), 8 M nitric acid can be tolerated without significant effect of dissolved cerium, since these conditions are just insufficiently oxidizing for the production of Ce(IV) in solution. But at still lower temperature (70 °C), significant production of Ce(IV) occurs in 10 M nitric acid, but Cr(III) does not act as an accelerator under these conditions because the oxidation of Cr(III) is more difficult than the oxidation of Ce(III) owing to

the more complicated chemical rearrangements required. These examples demonstrate the complex effect of temperature, nitric acid (i.e., nitrate) concentration, and dissolved species on solution oxidizing power, and hence the corrosive effect on stainless steels.

Although in hot, concentrated solutions, nitric acid is usually the most powerful oxidant present, it is not capable of polarizing stainless steel to as high a potential as can be achieved in the presence of species such as Fe(III), Cr(VI), etc.; this must be due to the kinetics of the various reduction reactions, as illustrated in [Figure 15](#). Redox potentials alone therefore provide no certain guide to the corrosive effect of dissolved species in nitric acid solutions. The valency state of potential corrosion accelerators is of critical importance (i.e., the equilibrium concentration of the most oxidized form) and this is governed by the balance between the solution oxidation rate and the reduction rate by reaction with stainless steel. It is therefore a prerequisite of successful corrosion testing that the valency states that would be present in an operating plant liquor are maintained during the course of testing.

#### 2.24.5.4.2 Other passive metals

Similar considerations can be applied to other metals as to stainless steels in terms of the effect of dissolved species on polarization behavior. The need for oxidants to be present for titanium to achieve passivity has already been noted ([Section 2.24.3.2](#)). Although the very passive metals such as zirconium and tantalum will be polarized by the presence of dissolved species, the absence of a low breakdown potential in nitric acid ensures that this is of little consequence for corrosion in most circumstances. Hence, these materials are generally suitable for use in oxidizing plant conditions where stainless steel would suffer an unacceptably high corrosion rate.

#### 2.24.5.5 Dissolved Reducing Species

Dissolved ions such as chloride and fluoride in sufficient quantity can lead to weakening of passivity in nitric acid. The process is dynamic, depending on the relative concentration of halide to nitrate and appears to occur more readily at lower temperatures as the passivating tendency of the nitric acid decreases.

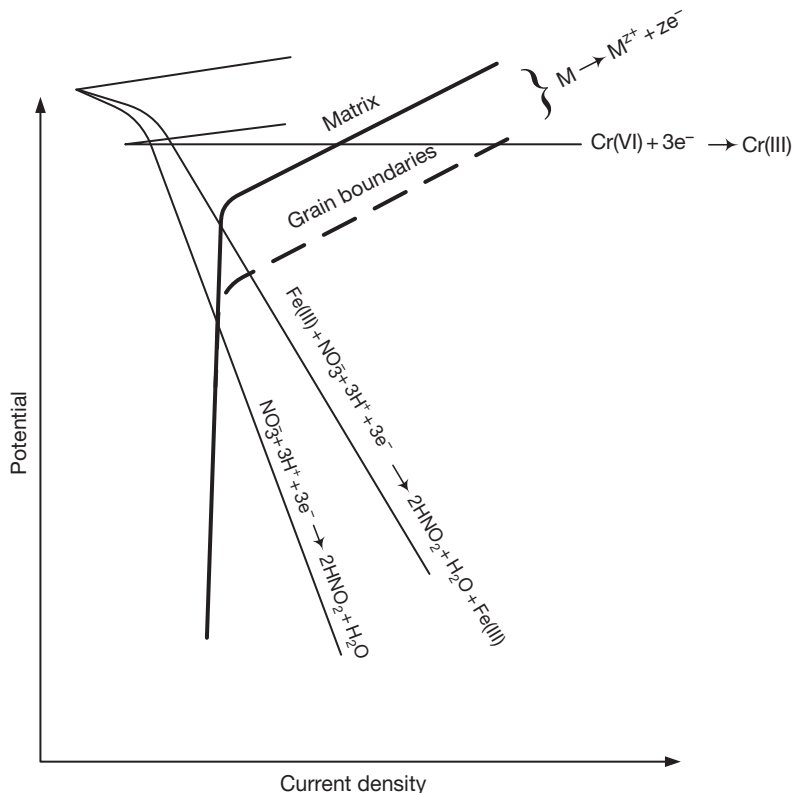


**Figure 15** Schematic Evans diagram, showing increased corrosion rate due to Fe(III) and Cr(VI).

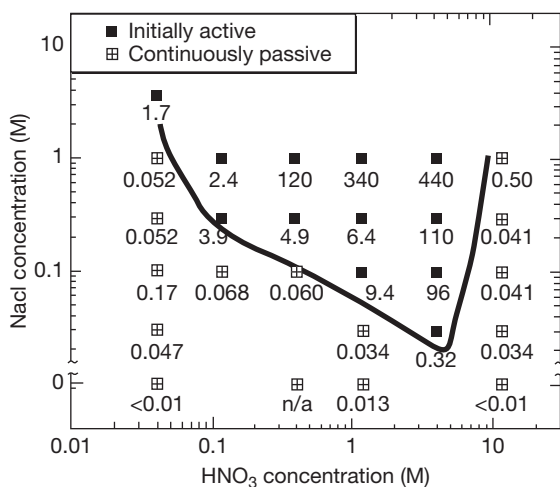


**Figure 16** Plot of corrosion state and average corrosion rate (mpy) determined from immersion tests for 1 week of 304 stainless steel in aerated HNO<sub>3</sub>/NaCl liquors at 22 °C. Reproduced from Kolman, D. G.; Ford, D. K.; Butt, D. P.; Nelson, T. O. *Corros. Sci.* **1997**, 39, 2067–2093, with permission from Elsevier.

The breakdown in passivity is readily indicated by a fall in the corrosion potential, which is intermittent at low concentrations (i.e., downward spikes are observed, increasing in frequency and duration as the halide concentration increases), but sustained at high concentrations leading to rapid active corrosion. Figure 16 maps out regions of active corrosion and passivity for AISI 304 stainless steel in nitric acid/chloride mixtures.<sup>56</sup> On the borderline between activity and passivity, sustained active corrosion can be induced by the application of ultrasound.<sup>57</sup> Although SCC, corrosion fatigue, and erosion/fretting corrosion appear not to have been reported for nitric acid/halide systems, susceptibility to all such chemicomechanical processes is expected.

An effect of chloride ions on corrosion in nitric acid is not reported for other passive metals such as zirconium and tantalum. However, zirconium, and, to much lesser extent, tantalum are sensitive to attack by fluoride ions in nitric acid. For zirconium, a significant effect is observed as low as 1 µg ml<sup>-1</sup> F<sup>-</sup>, as illustrated in Figure 17. For tantalum and Ta–40Nb alloy, an increase in corrosion rate is not seen for fluoride concentrations <10 µg ml<sup>-1</sup>.<sup>58</sup> The effect of fluoride ions can be reduced by the addition of ions such as Zr<sup>4+</sup> or Al<sup>3+</sup>, which form strong fluoride complexes, although in high fluoride concentrations, the effect appears to be difficult to suppress completely. The corrosion of zirconium is thus amenable to self-inhibition to some

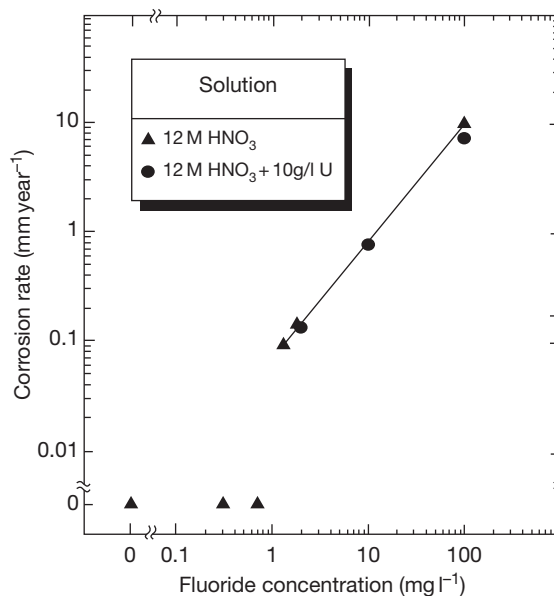
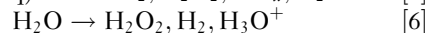
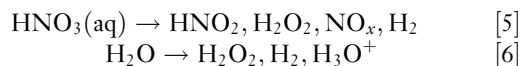


**Figure 17** Effect of fluoride ion additions on the corrosion rate of zirconium 702 in boiling nitric acid solutions. Herbert, D. BNFL unpublished work.

extent, although this would not be expected in a frequently-washed situation such as condensing vapor regions. Table 4 illustrates the major effects observed.

#### 2.24.5.6 Radiation

An overview of the basic effects of ionizing radiation of all types on corrosion processes is given by Byalobzhetskii.<sup>59</sup> For nuclear reprocessing plant, the most important result of radiation is the formation of a large number of short-lived radical species, which react to produce stable molecular products. This is known as radiolysis. Radiolysis of the nitrate ion and water produces the following molecular products, although the reaction chains are long and complex involving a great number of intermediate species<sup>60,61</sup>:



Radiolytic reactions will be affected by the nitrate concentration, dissolved species, temperature and the radiation type. At high dose rates, appreciable levels of nitrous acid (up to ~0.5 g l<sup>-1</sup>) are formed, though the nitrous acid would be expected to become increasingly unstable at higher temperatures. Although the action of hydrogen peroxide has not been exhaustively assessed, it probably has little direct impact on

corrosion in hot nitric acid as it decomposes by reaction with nitric acid, producing nitrous acid.

Although data are sparse, the overall effect of the irradiation of nitric acid on corrosion appears to be similar to that produced by nitrous acid. Analogous to the effect of  $\text{NO}_x$  purging (Figure 11), in pure nitric acid solutions the corrosion potential of stainless steel is increased and hence the corrosion rate is increased slightly, as illustrated by Figure 18.<sup>62</sup> The effects of irradiation are more pronounced when nitric acid contains dissolved oxidizing species where reduction

**Table 4** Effect of fluoride ion concentration and various additions on the corrosion rate of zirconium 702 in boiling nitric acid solutions

Solution			Corrosion rate ( $\text{mm y}^{-1}$ )	
$\text{HNO}_3$ (M)	$\text{F}^-$ ( $\text{mg l}^{-1}$ )	Additions	Period 1	Period 2
12	0	—	0.001	0.001
	0.1	—	18.9	10.5
	0.1	$10 \text{ g l}^{-1} \text{ U}$	13.9	8.0
	0.1	$3.5 \text{ g l}^{-1} \text{ Bi}$	12.9	7.3
	0.1	$1.1 \text{ g l}^{-1} \text{ Al}$	1.6	1.4
3	1.8	—	29.6	29.6
	1.8	$1.8 \text{ g l}^{-1} \text{ Zr}$	19.1	20.1
	0.5	$2.4 \text{ g l}^{-1} \text{ Zr}$	1.7	1.4
	0.5	$4.8 \text{ g l}^{-1} \text{ Zr}$	0.002	0.001

Two 24 h test periods without solution renewal.  
Source: Herbert, D. BNFL unpublished work.

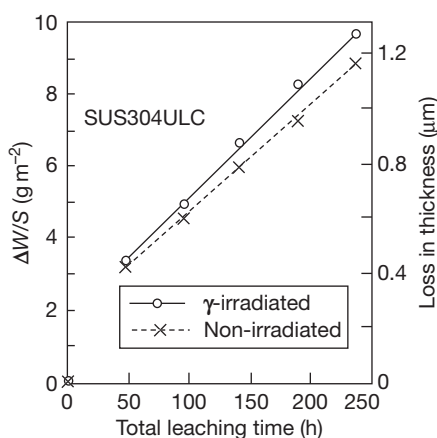


**Figure 18** Effect of Co-60 radiation ( $40 \text{ kGy h}^{-1}$ ) on the corrosion rate of SUS 304ULC stainless steel in boiling (at atmospheric pressure) 9M nitric acid. Reproduced from Yamamoto, T.; Tsukui, S.; Okamoto, S.; Nagai, T.; Takeuchi, M.; Takeda, S.; Tanaka, Y. *J. Nucl. Mater.* **1996**, 228, 162–167, with permission from Elsevier.

of oxidizing species such as  $\text{Cr(VI)}$  and  $\text{Ce(IV)}$  can profoundly reduce corrosion rates by maintaining the corrosion potential below transpassivity.<sup>52</sup> Whether the oxidation by the acid or reduction by irradiation predominates depends on the nitric acid concentration and temperature, increase of either favoring oxidation, and radiation dose rate, increase of which favors reduction. The effect of radiation on the corrosion of stainless steels in nitric acid containing the oxidizing species  $\text{Cr(VI)}$ ,  $\text{Ce(IV)}$  and  $\text{Ru(III)}$  is demonstrated in Figure 19.<sup>63</sup> It is notable that in the case of  $\text{Ru(III)}$  the effect is less than for  $\text{Cr(VI)}$  and  $\text{Ce(IV)}$ .

By analogy with the behavior of  $\text{Ce(IV)}$  and  $\text{Cr(VI)}$ , it is expected that other species of the same type (i.e.,  $\text{Ru(VIII)}$ ,  $\text{I(VII)}$  and  $\text{Au(III)}$ )<sup>52</sup> would also be reduced by high radiation fields and thus exert negligible corrosive effect towards stainless steels. Redox potential considerations indicate that nitrous acid is incapable of reducing either  $\text{Fe(III)}$  or  $\text{V(V)}$ ; hence, no effect of radiation on their corrosive effect results.

Because the corrosion resistance of metals such as zirconium and tantalum is unaffected by oxidizing species in solution (Section 2.24.5.4.2), no effect of radiation is apparent. No effect of radiation on the corrosion resistance of titanium has been reported, although a deleterious effect might be expected if reliance were placed on oxidizing ions, rather than dissolved titanium, for the maintenance of passivity.

### 2.24.5.7 Solution Boiling

The effects, if any, of boiling on corrosion processes on passive metals appear to be minimal in simple nitric acid systems. This is demonstrated by the failure of Arrhenius data to show a marked discontinuity at the boiling point (see, e.g., Figure 3). Other studies found no difference between corrosion rates measured in boiling (under reduced pressure) and nonboiling nitric acid solutions containing dissolved iron.

However, in a more complex nitric acid solution containing many dissolved species a reduction in corrosion rate is apparently found in the boiling solution. Such systems are very corrosive and there are several possible mechanisms which could occur once boiling commences including enhanced mass transport, reduction in dissolved  $\text{NO}_x$  by mechanical stripping from solution, removal of reactants and corrosion products from the reacting metal surface by agitation, local concentration effects in nucleating bubbles, limitation of corrodant access to the metal surface by gas blanketing and facilitation of interaction between dissolved species. It may be the case



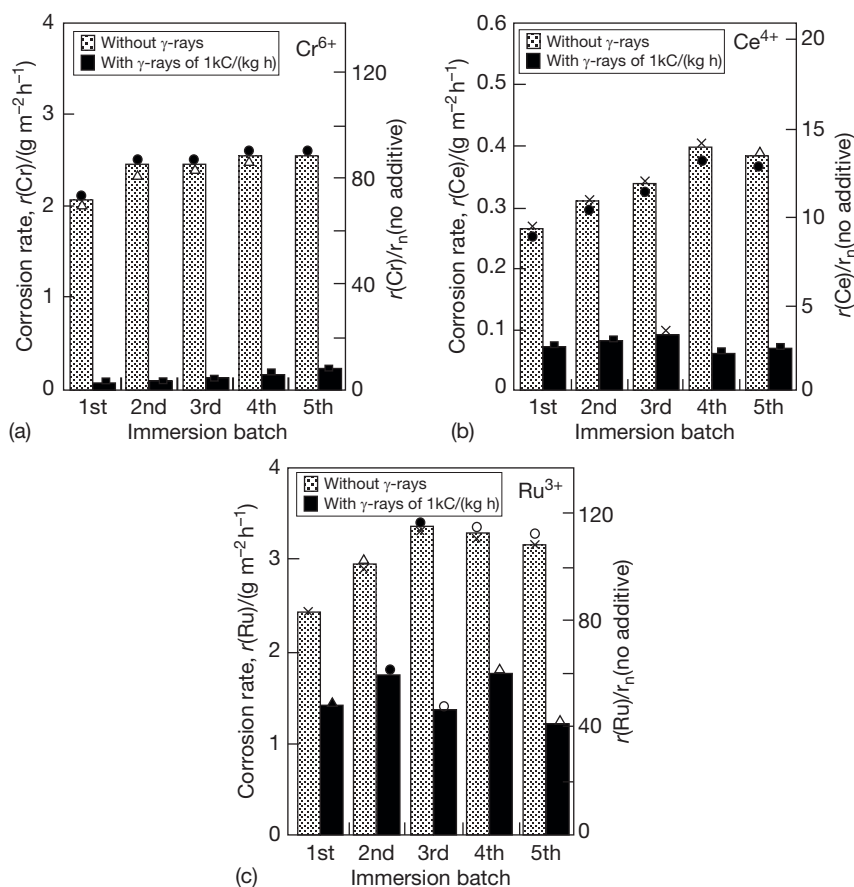


**Figure 19** Effect of Co-60 radiation ( $40 \text{ kGy h}^{-1}$ ) on the corrosion rate of SUS 304ULC stainless steel in boiling 9 M nitric acid containing: (a) 0.02M Cr(VI); (b) 0.01 M Ce(IV); (c) 0.004 M Ru(III). Reproduced from Yamamoto, T.; Tsukui, S.; Okamoto, S.; Nagai, T.; Takeuchi, M.; Takeda, S.; Tanaka, Y. *J. Nucl. Sci. Technol.* **1998**, 35, 353–356, with permission from Atomic Energy Society of Japan.

that removal of iron and chromium corrosion products from the corrosion surface by agitation reduces corrosion.

In practice, individual systems may need to be tested if the possibility of a boiling effect is of interest.

#### 2.24.5.8 Heat Transfer

It would not be expected that the transfer of heat *per se* would affect corrosion processes and to date heat flux has not been demonstrated to have an effect on the corrosion process which cannot be assigned to the metal/liquor interface temperature. However, consequent processes such as changes of interface temperatures, modification of the Helmholtz layer, effects on diffusion/mass transport, solute concentration and gas blanketing under boiling could affect corrosion processes.

Data, which are limited, are principally derived from either heated disc<sup>32,64,65</sup> or heated tube rigs<sup>25,66</sup> and can be difficult to interpret. The former suffer from crevice corrosion effects on stainless steel, and the latter from difficulties in maintaining controlled and even heating.

In most simple nitric acid systems, the predominant factor determining the corrosion rate is the effective interface temperature; this will lie between that of the metal heat transfer surface and that of the liquid, but can be difficult to determine with precision. So at a constant metal surface temperature the presence of cooler acid at the metal surface under heat flux reduces the corrosion rate compared to a fully isothermal system.<sup>32,64</sup>

However, it is plausible that oxidation processes such as Cr(III) to Cr(VI) could proceed on heat transfer surfaces with a consequent increase in corrosion providing the surface is of sufficient temperature

even if the liquors are significantly cooler. When boiling occurs on the heat transfer surface, the effects may be further complicated. Although no effect of nucleate boiling on austenitic stainless steel corrosion was found at a heat flux of  $9 \text{ kW m}^{-2}$ ,<sup>32</sup> other workers indicate that boiling improves heat transfer and leads to a reduction in metal surface temperature with a consequent reduction in corrosion rate.<sup>64</sup> Conversely, other workers suggest an increased oxidizing effect on heated surfaces, generally consistent with solute rejection from nucleating voids.<sup>65</sup> It is evident that further, carefully controlled, studies are required to resolve the debate.

Industrial experience tends to support the view that corrosion processes on heated surfaces can be affected relative to isothermal surfaces, but that the effects can vary from increasing the corrosion rate where temperatures are increased at the heat transfer face to decreasing them where heating and boiling are so rapid as to create gas-blanketing effects.

### 2.24.5.9 Liquor-Line and Vapor Regions

No significant liquor-line corrosion effects have been found for stainless steel exposed to nitric acid liquors, either in operating plant or in test conditions.<sup>25</sup> Significant effects would not be expected on other passive metals.

Enhanced corrosion effects can occur in vapor-condensate phases, however. This can occur for instance where condensing films run onto heated tubes in boiler systems and are reevaporated allowing high solute concentrations to build up. In some circumstances transpassivity can be reached with consequent rapid corrosion. Instances have occurred in situations as diverse as stainless steel nitric acid transport tankers and industrial acid boilers. For stainless steels, such thin liquor film effects are considered largely to be due to corrosion product build-up, since both Fe(III) and Cr(VI) are corrosion accelerators (Section 2.24.5.4.1). Conversely, titanium is prone to corrosion in condensing systems owing to continuous removal of its corrosion products (-Section 2.24.3.2), as is aluminum (Section 2.24.3.4).

In mixed acid systems, enhanced corrosion can occur in vapor regions if preferential partitioning of the active species occurs. For stainless steels in nitric acid/chloride solutions, the formation of volatile nitrosyl chlorides may be implicated.<sup>67</sup> Preferential partitioning of fluoride to vapor occurs, hence enhanced corrosion of zirconium in vapor regions above nitric acid/fluoride liquors might be

expected; however, the absence of reports of any such effect in operating plant points to the presence of fluoride complexants that prevent or limit fluoride partitioning.

## 2.24.6 Corrosion Testing Methods

### 2.24.6.1 Ranking Tests

These are intended to indicate general trends of corrosion resistance for different materials or to show the effect of, for example, different heat treatments. They are also used to screen different batches of material procured for plant construction to ensure consistency of supply.

For stainless steels in nitric acid, the Huey test,<sup>68</sup> which is covered in both ASTM<sup>69</sup> and European standards,<sup>70</sup> is the most frequently used procedure for the assessment of intergranular or general corrosion of stainless steel. It can also form the basis of assessing general corrosion rates of other metals intended for nitric acid service. In this test, a prepared coupon is subjected to five successive 48 h test periods in boiling 65% nitric acid with the solution renewed at each period, the periodic corrosion rate being determined by weight loss. It is noted that the acid specification is more stringently controlled in the ASTM specifications with  $\text{F}^-$  limited to  $<0.1 \text{ ppm}$  as opposed to  $<3 \text{ ppm}$  in the European standard. This could be significant for some passive materials such as zirconium.

Even with such a simple test, care must be taken to ensure consistency of apparatus (e.g., the type of condenser used affects the results obtained<sup>51</sup>) and the selection of a consistent ratio of liquor volume to metal surface area, since this affects the rate of corrosion product build-up. Maintenance of a constant end, to side, to face grain ratio is essential in materials that have any susceptibility to end grain corrosion; in particular, care is needed in the selection of a consistent coupon design which avoids the exposure of excessive or varying end grain fraction (see Figure 7). Although not recommended in the test procedures, some assessment and recording of the attack on the end grain is usually worthwhile. Additional periods of testing may be required to discriminate between similar materials.

### 2.24.6.2 Prediction of In-Service Corrosion Rates

Owing to the dependence of the corrosion rate of stainless steels in nitric acid on microstructural

orientation (see [Section 2.24.4.1](#)), corrosion rates derived from periodic weighing of immersed coupons can significantly overestimate in-service corrosion rates and can also be subject to considerable variability if different coupon designs are used; the latter in particular prevents meaningful comparison of test data in a great many instances. Conversely, owing to the progressive nature of intergranular attack, short-term tests can lead to significant underestimation of in-service corrosion rates. These problems can be overcome in a number of ways:

- direct measurement of the corrosion rate by metallurgical sectioning transverse to the surface of interest (this works only for relatively short test times otherwise grain dropping removes the initial surface)<sup>30</sup>;
- short-term weight loss measurements made on specially-prepared coupons where the surface of interest has been corroded to the grain dropping stage, but all other surfaces are freshly-ground<sup>24</sup>;
- weight loss measurements made on a series of coupons specially prepared to have very different ratios of plate, side and end surfaces, all these previously having been corroded to the grain-dropping stage.<sup>30</sup>

In addition, it is possible to seal exposed end grain by overlaying it with weld metal,<sup>71</sup> but this can produce undesirable metallurgical changes and usually requires excessively large coupons unless laser techniques are employed.

All these methods are time consuming, but are necessary where a high confidence of plant life prediction is required. However, none are effective at predicting pit depths where tunneling occurs on the end grain,<sup>30</sup> so prediction of forging life, for instance, is difficult.

Great care must of course be paid to reproducing anticipated plant conditions as closely as possible owing to the many factors which affect the corrosion rate (see [Section 2.24.5](#)).

## References

1. Miles, F. D. *Nitric Acid Manufacture and Uses*; Oxford University Press: London, 1961; Chapter VI, pp 61–73.
2. Addison, C. C. *Chem. Rev.* **1980**, *80*, 21–39.
3. Evans, U. R. *An Introduction to Metallic Corrosion*, 3rd ed.; Edward Arnold: London, 1981; Chapter III, pp 70–72.
4. Vetter, K. J. *Electrochemical Kinetics – Theoretical and Experimental Aspects*; Academic Press: New York, 1967; pp 490–493.
5. Schmid, G.; Lobeck, M. A. Z. *Elektrochem. Ber. Busenges physik. Chem.* **1969**, *73*, 89–199.
6. Razygraev, V. P.; Lebedeva, M. V.; Kabakchi, S. A.; Ponomareva, E. Yu.; Balovneva, R. S.; Lobanova, L. P. *J. Appl. Chem. USSR* **1988**, *61*, 67–73.
7. Balbaud, F.; Sanchez, G.; Santarini, G.; Picard, G. *Eur. J. Inorg. Chem.* **2000**, 665–674.
8. Pakhomov, V. S. *Trans. Mosk. Inst. Khim. Mashinostr.* **1975**, *67*, 102–109.
9. Kain, V.; Shinde, S.; Gadiyar, H. J. *Mater. Eng. Perform.* **1994**, *3*, 699–705.
10. Onoyama, M.; Nakata, M.; Hirose, Y.; Nakagawa, Y. In *Proceedings of the RECOD'91*, Japan Atomic Industrial Forum: Japan, 1991; Vol II, pp 1066–1071.
11. Kreysa, G.; Eckermann, R. Eds. *Dechema Corrosion Handbook: Corrosive Agents and their Interaction with Materials*; VCH Publishers: New York, 1991; pp 142–147.
12. Blom, U.; Kvarnback, B. *Mater. Perform.* **1975**, *14*, 43–46.
13. Donat, H.; Schäfer, K. *Schweissen Schneiden* **1975**, *27*, 343–351.
14. Takamura, A.; Arakawa, K.; Moriguchi, Y. In *The Science Technology and Application of Titanium*; Jafee, R. I., Prom, N. E., Eds.; Pergamon Press: Oxford, 1970; pp 209–216.
15. Shimogori, K.; Satoh, H.; Kamikubo, F. In *Titanium Science and Technology*; Proceedings of the 5th International Conference on Titanium, Munich, Germany, Sept 10–14; 1984; Luthering, G., Ed., Vol. 4, pp 1111–1114.
16. Bomberger, H. B. In *Titanium and Zirconium*, Proceedings of the 3rd International Conference, STP 830, 1984; 143.
17. Singh, D. D. N.; Chaudhary, R. S.; Agarwal, C. V. *J. Electrochem. Soc.* **1982**, *129*, 1869–1874.
18. Horn, E. M.; Schoeller, K.; Dölling, H. *Werkst. Korros.* **1990**, *41*, 308–329.
19. Zhuravleva, L.; Rebrunov, V. P. *Zasch. Met.* **1970**, *6*, 224–227.
20. Pourbaix, M. *Atlas of Electrochemical Equilibria in Aqueous Solutions*, 2nd ed.; NACE: Houston, 1974; Chapter 10, pp 256–271.
21. Hosoi, K.; Yokosuka, T.; Honda, T.; Yoshida, T.; Masaoka, I. In *Proceedings of the RECOD 91*, Japan Atomic Industrial Forum: Japan, 1991; Vol. 2, 1060.
22. Kolotyrlin, Y. M.; Kasparova, O. V.; Bogolyubski, S. D. In *Proceedings International Congress on Metallic Corrosion*; National Research Council of Canada: Canada, 1984; Vol. 3, 130.
23. Cihal, V. *Intergranular Corrosion of Steels and Alloys*; Elsevier: Amsterdam, 1984; Chapter 3, pp 67–129.
24. Dunnett, B. F.; Whillock, G. O. H. *Corrosion* **2003**, *59*, 274–283.
25. Rowland, S. M.Sc. thesis, University of Manchester: UK, 1998.
26. Kiuchi, K.; Yanagihara, T.; Kato, T.; Takizawa, M. *JAERI Rev.* **2001**, *10*, 211–213.
27. Ohno, A.; Isoo, H.; Akashi, M. In *Plant Aging and Life Predictions of Corrodible Structures*; Proceedings of the International Symposium, Sapporo, Japan, May 15–18, 1995; Shoji, T., Shibata, T., Eds.; NACE: Houston, TX, 1997; pp 869–874.
28. Balbaud, F.; Sanchez, G.; Fauvet, P.; Santarini, G.; Picard, G. *Corros. Sci.* **2000**, *42*, 1685–1707.
29. Clark, A. T.; Meyer, L. H.; Owen, J. H.; Rust, F. G. Idaho Chemical Processing Plant Report DP-647, 1961.
30. Whillock, G. O. H.; Dunnett, B. F.; Takeuchi, M. *Corrosion* **2005**, *61*, 58–67.
31. Nagano, H.; Kajimura, H. In *Proceedings of the 12th International Corrosion Congress*, September 19–24, 1993 NACE International: Houston, TX, 1993; pp 1341–1352.

32. Andon, R. J. L.; Pemberton, R. C.; Thomas, J. G. N.; Harrison, J. M.; Worthington, S. E.; Shaw, R. D. *Br. Corros. J.* **1986**, 21, 119–128.
33. Maslov, V. A.; Semenova, A. A. *Svar. Proiz.* **1980**, 11, 29–30.
34. Nagano, H.; Kajimura, H. *Corros. Sci.* **1996**, 38(5), 781–792.
35. Turnbull, A. In *Comprehensive Structural Integrity (Fracture of Materials from Nano to Macro)*, Environment-Assisted Fracture; Petit, J., Scott, P., Eds.; Elsevier, 2003; Vol. 6, pp 163–210.
36. Hutchings, I. M. The Erosion of Materials by Liquid Flow; Materials Technology Institute of the Chemical Industries Inc.: Columbus, USA, 1986; MTI publication No. 25.
37. Burstein, G. T.; Ashley, G. W.; Marshall, P. I.; Misra, R. D. K. In *Proceedings of the 6th International Conference on Erosion by Liquid and Solid Impact* Field, R., Corney, J., Eds.; Cambridge, UK, 1983.
38. Miki, M. *Corros. Eng. (Boshoku Gijutsu)* **1983**, 32, 701–706.
39. Brunet, S.; Coriou, H.; Grall, L.; Mahieu, C.; Pelras, M.; Sanatine, O. *Mém. Sci. Rev. Metallurg.* **1970**, LXVII, 12, 781–786.
40. Gorelik, G. N.; Anikonova, E. A. *Zasch. Met.* **1970**, 6, 416–419.
41. Casarini, G.; Colonna, C.; Songa, T. *Metall. Ital.* **1970**, 62, 183–186.
42. Shvarts, G. L.; Glazkova, S. A.; Moroz, V. A. *Chem. Petroleum Eng.* **1986**, 22, 25–29.
43. Cihal, V. *Intergranular Corrosion of Steels and Alloys*; Elsevier: Amsterdam, 1984; Chapter 4, pp 144–156.
44. Hahin, C.; Stoss, R. M.; Nelson, B. H.; Reucroft, P. J. *Corrosion* **1976**, 32, 229–238.
45. Uhlig, H. H. Ed. *Corrosion Handbook*; John Wiley & Sons: New York, 1948; pp 159–160.
46. Mahla, E.; Nielsen, N. *Trans. ASM* **1951**, 43, 290–297.
47. Herbsleb, G.; Jäkel, U.; Schwaab, P. *Werkst. Korros.* **1990**, 41, 170–176.
48. Hahin, C. *Corrosion* **1982**, 38, 116–119.
49. Takeuchi, M.; Whillock, G. O. H. *Br. Corros. J.* **2002**, 37, 199–205.
50. Takeuchi, M.; Whillock, G. O. H. *Zairyo-to-Kankyo* **2002**, 51, 549–554.
51. Truman, J. E. *J. Appl. Chem.* **1954**, 4, 273–283.
52. McIntosh, A. B.; Evans, T. E., *Peaceful Uses of Atomic Energy*; In Proceedings of the 2nd International Conference, Geneva, Switzerland, Sept 1958; UN: Geneva, Switzerland, 1958; pp 206–225.
53. Hirose, Y.; Suzuoki, A.; Sukekawa, M. In *1994 Fall Meeting of Atomic Energy Society of Japan*; Japan Atomic Energy Society: Japan, 1994; 70.
54. Cleland, G. E. Ph.D. Thesis, University of Newcastle upon Tyne, 1998.
55. Motooka, T.; Kiuchi, K. *J. Nucl. Sci. Technol.* **2002**, 3, 367–370.
56. Kolman, D. G.; Ford, D. K.; Butt, D. P.; Nelson, T. O. *Corros. Sci.* **1997**, 39, 2067–2093.
57. Whillock, G. O. H.; Harvey, B. F. *Ultrason. Sonochem.* **1996**, 3, 111–118.
58. Klas, W.; Herpers, U.; Reich, M.; Michel, R.; Droste, R.; Holm, R.; Horn, E.-M.; Müller, G. *Werkst. Korros.* **1991**, 42, 570–575.
59. Byalobzheskii, A. V. *Radiation Corrosion*; Israel Programme for Scientific Translations Ltd.: Jerusalem, Israel, 1970.
60. Kazanjian, A. R.; Miner, F. J.; Brown, A. K.; Hagan, P. G.; Berry, J. W. *Trans. Faraday Soc.* **1970**, 66, 2192–2198.
61. Spinks, J. W. T.; Woods, R. J. *An Introduction to Radiation Chemistry*, John Wiley: New York, 1990.
62. Yamamoto, T.; Tsukui, S.; Okamoto, S.; Nagai, T.; Takeuchi, M.; Takeda, S.; Tanaka, Y. *J. Nucl. Mater.* **1996**, 228, 162–167.
63. Yamamoto, T.; Tsukui, S.; Okamoto, S.; Nagai, T.; Takeuchi, M.; Takeda, S.; Tanaka, Y. *J. Nucl. Sci. Technol.* **1998**, 35, 353–356.
64. Honda, T.; Hirose, Y.; Sasada, Y.; Furutani, Y.; Suzuki, K.; Fujita, H. In *Proceedings of the RECOD 91*, Japan Atomic Industrial Forum: Japan, 1991; Vol. 2, pp 558–563.
65. Kiuchi, K.; Kikuchi, M. In *Plant Aging and Life Predictions of Corrodible Structures*; Proceedings of the International Symposium, Sapporo, Japan, May 15–18, 1995; Shoji, T., Shibata, T., Eds.; NACE: Houston, TX, 1997; pp 861–867.
66. Yanagihara, T.; Kiuchi, K. *JAERI Rev.* **2001**, 010, 208–210.
67. Shashi Gupta, M. V. D.; Pandey, G. N. *Corros. Prev. Control* **1986**, 33, 47–50.
68. Huey, W. R. *Trans. Am. Soc. Steel Treating* **1930**, 18, 1126–1143.
69. *Annual Book of ASTM Standards*; ASTM International: West Conshohocken, PA, 1985; pp 7–10.
70. ISO 3651–1; Determination of Resistance to Intergranular Corrosion of Stainless Steels – Part 1: Austenitic and Ferritic-Austenitic (Duplex) Stainless Steels – Corrosion Test in Nitric Acid Medium by Measurement of Loss in Mass (Huey Test), ISO 1998.
71. Jeng, J. Y.; Quayle, B. E.; Modern, P. J.; Steen, W. M.; Bastow, B. D. *Corros. Sci.* **1993**, 35, 1289–1296.

## 2.25 Corrosion in Acid Gas Solutions

**S. Nesic**

Institute for Corrosion and Multiphase Technology, Ohio University, Athens, OH, USA

**W. Sun**

ExxonMobil Upstream Research Company, Houston, TX, USA

© 2010 Elsevier B.V. All rights reserved.

<b>2.25.1</b>	<b>Introduction</b>	1273
<b>2.25.2</b>	<b>Aqueous CO<sub>2</sub> Corrosion of Mild Steel</b>	1273
2.25.2.1	Chemistry of CO <sub>2</sub> Saturated Aqueous Solutions – Equilibrium Considerations	1273
2.25.2.2	Electrochemistry of Mild Steel Corrosion in CO <sub>2</sub> Saturated Aqueous Solutions	1277
2.25.2.2.1	Oxidation of iron	1278
2.25.2.2.2	Reduction of hydronium ion	1278
2.25.2.2.3	Reduction of carbonic acid	1278
2.25.2.2.4	Reduction of water	1279
2.25.2.3	Transport Processes in CO <sub>2</sub> Corrosion of Mild Steel	1279
2.25.2.4	Calculation of Mild Steel CO <sub>2</sub> Corrosion Rate	1280
2.25.2.5	Successes and Limitations of Modeling of Aqueous CO <sub>2</sub> Corrosion of Mild Steel	1280
2.25.2.6	Key Factors Affecting Aqueous CO <sub>2</sub> Corrosion of Mild Steel	1281
2.25.2.6.1	Effect of pH	1281
2.25.2.6.2	Effect of CO <sub>2</sub> partial pressure	1281
2.25.2.6.3	Effect of temperature	1282
2.25.2.6.4	Effect of flow	1283
2.25.2.6.5	Effect of corrosion inhibition	1284
2.25.2.6.6	Effect of organic acids	1285
2.25.2.6.7	Effect of glycol/methanol	1285
2.25.2.6.8	Effect of condensation in wet gas flow	1285
2.25.2.6.9	Nonideal solutions and gases	1286
2.25.2.7	Localized CO <sub>2</sub> Corrosion of Mild Steel in Aqueous Solutions	1286
<b>2.25.3</b>	<b>Aqueous H<sub>2</sub>S Corrosion of Mild Steel</b>	1286
2.25.3.1	Chemistry of H <sub>2</sub> S Saturated Aqueous Solutions – Equilibrium Considerations	1287
2.25.3.2	Mild Steel Corrosion in H <sub>2</sub> S and Mixed H <sub>2</sub> S/CO <sub>2</sub> Saturated Aqueous Solutions	1289
2.25.3.3	Calculation of Mild Steel H <sub>2</sub> S Corrosion Rate	1291
2.25.3.3.1	Pure H <sub>2</sub> S aqueous environment	1291
2.25.3.3.2	Mixed CO <sub>2</sub> /H <sub>2</sub> S environments	1292
2.25.3.4	Limitations of Modeling of Aqueous H <sub>2</sub> S Corrosion of Mild Steel	1292
2.25.3.5	Key Factors Affecting Aqueous H <sub>2</sub> S Corrosion of Mild Steel	1293
2.25.3.5.1	Effect of H <sub>2</sub> S partial pressure	1293
2.25.3.5.2	Effect of flow	1295
2.25.3.5.3	Effect of time	1295
2.25.3.6	Localized H <sub>2</sub> S Corrosion of Mild Steel in Aqueous Solutions	1297
<b>References</b>		1297

### Abbreviations

**CR** Corrosion rate (mm year<sup>-1</sup>)

### Symbols

**A** Surface area of the steel (m<sup>2</sup>)

**A/V** Surface to volume ratio (m<sup>-1</sup>)

**A<sub>(FeCO<sub>3</sub>)</sub>** Constant in the Arrhenius-type equation for  
 $k_{r(FeCO_3)}$

**A<sub>H<sub>2</sub>S</sub>** Solid state diffusion kinetic constant for H<sub>2</sub>S  
 through mackinawite film,

$$A_{H_2S} = 2.0 \times 10^{-5} \text{ mol m}^{-2} \text{ s}^{-1}$$



**$A_{H^+}$**  Solid state diffusion kinetic constant for  $H^+$  through mackinawite film,  
 $A_{H^+} = 4.0 \times 10^{-4} \text{ mol m}^{-2} \text{ s}^{-1}$

**$A_{CO_2}$**  Solid state diffusion kinetic constant for  $CO_2$  through mackinawite film,  
 $A_{CO_2} = 2.0 \times 10^{-6} \text{ mol m}^{-2} \text{ s}^{-1}$

**$b_{a(Fe)}$**  Anodic Tafel slope for Fe oxidation (V)

**$b_{c(H^+)}$**  Cathodic Tafel slope for  $H^+$  ion reduction (V)

**$b_{c(H_2CO_3)}$**  Cathodic Tafel slope for  $H_2CO_3$  reduction (V)

**$b_{c(H_2O)}$**  Cathodic Tafel slope for  $H_2O$  reduction (V)

**$B_{(FeCO_3)}$**  Constant in the Arrhenius-type equation for  $k_{r(FeCO_3)}$  ( $\text{kJ mol}^{-1}$ )

**$c_{CO_2}$**  Bulk aqueous concentration of  $CO_2$  ( $\text{kmol m}^{-3}$ )

**$c_{CO_3^{2-}}$**  Bulk aqueous concentration of  $CO_3^{2-}$  ions ( $\text{kmol m}^{-3}$ )

**$c_{Fe^{2+}}$**  Bulk aqueous concentration of  $Fe^{2+}$  ions ( $\text{kmol m}^{-3}$ )

**$c_{H^+}$**  Bulk aqueous concentration of  $H^+$  ions ( $\text{kmol m}^{-3}$ )

**$c_{s(H^+)}$**  'Near-zero' concentration of  $H^+$  underneath the mackinawite film at the steel surface, set to  $1.0 \times 10^{-7}$  ( $\text{kmol m}^{-3}$ )

**$c_{HCO_3^-}$**  Bulk aqueous concentration of  $HCO_3^-$  ions ( $\text{kmol m}^{-3}$ )

**$c_{H_2CO_3}$**  Bulk aqueous concentration of  $H_2CO_3$  ( $\text{kmol m}^{-3}$ )

**$c_{H_2S}$**  Bulk aqueous concentration of  $H_2S$  ( $\text{kmol m}^{-3}$ )

**$c_{HS^-}$**  Bulk aqueous concentration of  $HS^-$  ions ( $\text{kmol m}^{-3}$ )

**$c_i$**  Bulk aqueous concentration of a given aqueous species ( $\text{kmol m}^{-3}$ )

**$c_{i(H_2S)}$**  Aqueous concentration of  $H_2S$  at the inner sulfide film/outer sulfide layer interface ( $\text{kmol m}^{-3}$ )

**$c_{S^{2-}}$**  Bulk aqueous concentration of  $S^{2-}$  ions ( $\text{kmol m}^{-3}$ )

**$c_{s(H_2S)}$**  'Near-zero' aqueous concentration of  $H_2S$  underneath the mackinawite film at the steel surface, set to  $1.0 \times 10^{-7}$  ( $\text{kmol m}^{-3}$ )

**$c_{o(H_2S)}$**  Aqueous concentration of  $H_2S$  at the outer sulfide layer/solution interface ( $\text{kmol m}^{-3}$ )

**$c_{s(CO_2)}$**  Aqueous concentration of  $CO_2$  underneath the mackinawite film at the steel surface

**$d$**  Characteristic dimension for a given flow geometry (m)

**$d_p$**  Diameter of a pipe (m)

**$d_c$**  Diameter of a rotating cylinder (m)

**$D$**  Diffusion coefficient of a given species ( $\text{m}^2 \text{ s}^{-1}$ )

**$D_{H_2CO_3}$**  Aqueous diffusion coefficient of  $H_2CO_3$  ( $\text{m}^2 \text{ s}^{-1}$ )

**$D_{\text{ref}(H_2CO_3)}$**  Reference aqueous diffusion coefficient of  $H_2CO_3$ ,  $D_{\text{ref},H_2CO_3} = 1.3 \times 10^{-9} \text{ m}^2 \text{ s}^{-1}$  at  $25^\circ \text{C}$

**$D_{H^+}$**  Aqueous diffusion coefficient for  $H^+$

**$D_{\text{ref}(H^+)}$**  Reference aqueous diffusion coefficient for  $H^+$ ,  $D_{\text{ref}(H^+)} = 2.80 \times 10^{-8} \text{ m}^2 \text{ s}^{-1}$  at  $25^\circ \text{C}$

**$D_{H_2S}$**  Aqueous diffusion coefficient for dissolved  $H_2S$

**$D_{CO_2}$**  Aqueous diffusion coefficient for dissolved  $CO_2$ ,  $D_{CO_2} = 1.96 \times 10^{-9} \text{ m}^2 \text{ s}^{-1}$

**$E$**  Potential (V)

**$E_{\text{corr}}$**  Corrosion (open circuit) potential (V)

**$E_{\text{rev}(Fe)}$**  Reversible potential of Fe oxidation,  
 $E_{\text{rev}(Fe)} = -0.488 \text{ V}$

**$E_{\text{rev}(H^+)}$**  Reversible potential for  $H^+$  ion reduction (V)

**$E_{\text{rev}(H_2CO_3)}$**  Reversible potential for  $H_2CO_3$  reduction (V)

**$E_{\text{rev}(H_2O)}$**  Reversible potential for  $H_2O$  reduction ( $\text{A m}^{-2}$ )

**$f_{H_2CO_3}$**  Flow factor for the chemical reaction boundary layer

**$F$**  Faraday's constant,  $F = 96485 \text{ C mol}^{-1}$

**$\text{Flux}_{H_2S}$**  Flux of  $H_2S$  ( $\text{kmol m}^{-2} \text{ s}^{-1}$ )

**$\text{Flux}_{H^+}$**  Flux of  $H^+$  ions ( $\text{kmol m}^{-2} \text{ s}^{-1}$ )

**$\text{Flux}_{CO_2}$**  Flux of  $CO_2$  ( $\text{mol m}^{-2} \text{ s}^{-1}$ )

**$H_{\text{sol}(CO_2)}$**  Henry's constant for dissolution of  $CO_2$  ( $\text{bar kmol m}^{-3}$ )

**$\Delta H_{Fe}$**  Activation enthalpy for Fe oxidation,  
 $\Delta H_{Fe} = 50 \text{ kJ mol}^{-1}$

**$\Delta H_{(H^+)}$**  Activation enthalpy for  $H^+$  ion reduction,  
 $\Delta H_{(H^+)} = 30 \text{ kJ mol}^{-1}$

**$\Delta H_{(H_2CO_3)}$**  Activation enthalpy for  $H_2CO_3$  reduction,  
 $\Delta H_{(H_2CO_3)} = 57.5 \text{ kJ mol}^{-1}$

**$\Delta H_{(H_2O)}$**  Activation enthalpy for  $H_2O$  reduction,  
 $\Delta H_{(H_2O)} = 30 \text{ kJ mol}^{-1}$

**$i$**  Current density ( $\text{A m}^{-2}$ )

**$i_{\text{corr}}$**  Corrosion current density ( $\text{A m}^{-2}$ )

**$i_{a(Fe)}$**  Anodic current density of iron oxidation ( $\text{A m}^{-2}$ )

**$i_{c(H^+)}$**  Cathodic current density for  $H^+$  ion reduction ( $\text{A m}^{-2}$ )

**$i_{c(H_2CO_3)}$**  Cathodic current density for  $H_2CO_3$  reduction ( $\text{A m}^{-2}$ )

**$i_{c(H_2O)}$**  Cathodic current density for  $H_2O$  reduction ( $\text{A m}^{-2}$ )

**$i_{\text{lim}(H^+)}^d$**  Mass transfer (diffusion) limiting current density for  $H^+$  ion reduction ( $\text{A m}^{-2}$ )

**$i_{\text{lim}(H_2CO_3)}^r$**  Chemical reaction limiting current density for  $H_2CO_3$  reduction ( $\text{A m}^{-2}$ )

$i_{o(\text{Fe})}$  Exchange current density of iron oxidation ( $\text{A m}^{-2}$ )

$i_{o(\text{H}^+)}$  Exchange current density for  $\text{H}^+$  ion reduction ( $\text{A m}^{-2}$ )

$i_{o(\text{H}_2\text{CO}_3)}$  Exchange current density for  $\text{H}_2\text{CO}_3$  reduction ( $\text{A m}^{-2}$ )

$i_{o(\text{H}_2\text{O})}$  Exchange current density for water reduction ( $\text{A m}^{-2}$ )

$i_{o(\text{Fe})}^{\text{ref}}$  Reference exchange current density of Fe oxidation,  $i_{o(\text{Fe})}^{\text{ref}} = 1 \text{ A m}^{-2}$

$i_{o(\text{H}^+)}^{\text{ref}}$  Reference exchange current density of  $\text{H}^+$  oxidation,  $i_{o(\text{H}^+)}^{\text{ref}} = 0.03 \text{ A m}^{-2}$  at  $T_{\text{c,ref}} = 25^\circ\text{C}$  and pH 4

$i_{o(\text{H}_2\text{CO}_3)}^{\text{ref}}$  Reference exchange current density for  $\text{H}_2\text{CO}_3$  reduction,  $i_{o(\text{H}_2\text{CO}_3)}^{\text{ref}} = 0.06 \text{ A m}^{-2}$  at  $T_{\text{c,ref}} = 25^\circ\text{C}$ , pH 5, and  $c_{\text{H}_2\text{CO}_3,\text{ref}} = 10^{-4} \text{ kmol m}^{-3}$

$i_{o(\text{H}_2\text{O})}^{\text{ref}}$  Reference exchange current density for  $\text{H}_2\text{O}$  reduction,  $i_{o(\text{H}_2\text{O})}^{\text{ref}} = 3 \times 10^{-5} \text{ A m}^{-2}$  at  $T_{\text{c,ref}} = 20^\circ\text{C}$

$i_{\alpha(\text{H}^+)}$  Charge transfer current density for  $\text{H}^+$  ion reduction ( $\text{A m}^{-2}$ )

$i_{\alpha(\text{H}_2\text{CO}_3)}$  Charge transfer current density for  $\text{H}_2\text{CO}_3$  reduction ( $\text{A m}^{-2}$ )

$I$  Ionic strength  $\text{kmol m}^{-3}$

$k_{\text{hyd}}^{\text{b}}$  Backward reaction rate of  $\text{H}_2\text{CO}_3$  dehydration reaction ( $1 \text{ s}^{-1}$ ),  $k_{\text{hyd}}^{\text{b}} = k_{\text{hyd}}^{\text{f}} / K_{\text{hyd}}$

$k_{\text{hyd}}^{\text{f}}$  Forward reaction rate for the  $\text{CO}_2$  hydration reaction ( $1 \text{ s}^{-1}$ )

$k_{\text{m}(\text{H}^+)}$  Aqueous mass transfer coefficient for  $\text{H}^+$  ( $\text{A m}^{-2}$ )

$k_{\text{m}(\text{H}_2\text{CO}_3)}$  Aqueous mass transfer coefficient for  $\text{H}_2\text{CO}_3$  ( $\text{A m}^{-2}$ )

$k_{\text{m}(\text{H}_2\text{S})}$  Aqueous mass transfer coefficient for  $\text{H}_2\text{S}$  ( $\text{A m}^{-2}$ )

$k_{\text{m}(\text{CO}_2)}$  Aqueous mass transfer coefficient for  $\text{CO}_2$  ( $\text{A m}^{-2}$ )

$k_{\text{r}(\text{FeCO}_3)}$  Kinetic constant in the ferrous carbonate precipitation rate equation ( $1 \text{ mol}^{-1} \text{ s}^{-1}$ )

$K_{\text{hyd}}$  Equilibrium hydration constant for  $\text{CO}_2$ ,  $K_{\text{hyd}} = k_{\text{hyd}}^{\text{f}} / k_{\text{hyd}}^{\text{b}} = 2.58 \times 10^{-3}$

$K_{\text{bi}}$  Equilibrium constant for dissociation of  $\text{HCO}_3^-$  ( $\text{kmol m}^{-3}$ )

$K_{\text{bs}}$  Equilibrium constant for dissociation  $\text{HS}^-$  ( $\text{kmol m}^{-3}$ )

$K_{\text{ca}}$  Equilibrium constant for dissociation of  $\text{H}_2\text{CO}_3$  ( $\text{kmol m}^{-3}$ )

$K_{\text{hs}}$  Equilibrium constant for dissociation  $\text{H}_2\text{S}$  ( $\text{kmol m}^{-3}$ )

$K_{\text{sol}(\text{H}_2\text{S})}$  Solubility constant for dissolution of  $\text{H}_2\text{S}$  ( $\text{kmol m}^{-3} \text{ bar}^{-1}$ )

$K_{\text{sol}(\text{CO}_2)}$  Solubility constant for dissolution of  $\text{CO}_2$  ( $\text{kmol m}^{-3} \text{ bar}^{-1}$ )

$K_{\text{sp}(\text{FeCO}_3)}$  Solubility product constant for ferrous carbonate ( $\text{kmol m}^{-3} \text{ bar}^{-1}$ )

$K_{\text{sp}(\text{FeS})}^{\text{mackin}}$  Solubility product constant for mackinawite ( $\text{kmol m}^{-3} \text{ bar}^{-1}$ )

$m_{\text{os}}$  Mass of the outer sulfide layer (kg)

$M_{\text{Fe}}$  Molecular mass of iron ( $\text{kg kmol}_{\text{Fe}}^{-1}$ )

$M_{\text{FeS}}$  Molecular mass of ferrous sulfide ( $\text{kg kmol}_{\text{FeS}}^{-1}$ )

$n$  Number of electrons used in reducing or oxidizing a given species ( $\text{kmol}_e \text{ kmol}^{-1}$ )

$p_{\text{CO}_2}$  Partial pressure of  $\text{CO}_2$  (bar)

$p_{\text{H}_2\text{S}}$  Partial pressure of  $\text{H}_2\text{S}$  (bar)

$R$  Electrochemical reaction rate ( $\text{kmol m}^{-2} \text{ s}^{-1}$ )

$R_{\text{FeCO}_3}$  Precipitation rate for iron carbonate ( $\text{kmol m}^{-3} \text{ s}^{-1}$ )

$R$  Universal gas constant,  $R = 8.314 \text{ J mol}^{-1} \text{ K}^{-1}$

$Re$  Reynolds number,  $Re = v \rho_{\text{H}_2\text{O}} d / \mu_{\text{H}_2\text{O}}$

$Sc$  Schmidt number of a given species,  $Sc = \mu_{\text{H}_2\text{O}} / (\rho_{\text{H}_2\text{O}} D)$

$Sh_p$  Sherwood number of a given species for a straight pipe flow geometry,  $Sh_p = k_m d_p / D$

$Sh_r$  Sherwood number of a given species for a rotating cylinder flow geometry,  $Sh_r = k_m d_c / D$

$SS_{(\text{FeCO}_3)}$  Supersaturation of iron carbonate

$ST$  Scaling tendency

$T_{\text{c}}$  Temperature ( $^\circ\text{C}$ )

$T_{\text{c,ref}}$  Reference temperature,  $T_{\text{c,ref}} = 25^\circ\text{C}$

$T_{\text{f}}$  Temperature ( $^\circ\text{F}$ )

$T_{\text{k}}$  Temperature (K)

$v$  Water characteristic velocity ( $\text{m s}^{-1}$ )

$z_i$  Species charge of various aqueous species

$\delta_{\text{m}(\text{H}_2\text{CO}_3)}$  Thickness of the mass transfer layer for  $\text{H}_2\text{CO}_3$  (m)

$\delta_{\text{r}(\text{H}_2\text{CO}_3)}$  Thickness of the chemical reaction layer for  $\text{H}_2\text{CO}_3$  (m)

$\delta_{\text{os}}$  Thickness of the outer sulfide layer (m),  $\delta_{\text{os}} = m_{\text{os}} / (\rho_{\text{FeS}} A)$

$\Delta t$  Time interval (s)

$\mu_{\text{H}_2\text{O}}$  Water dynamic viscosity (Pa s)

$\mu_{\text{H}_2\text{O,ref}}$  Reference water dynamic viscosity (Pa s) at a reference temperature,  $\mu_{\text{H}_2\text{O,ref}} = 1.002 \times 10^{-4} \text{ Pa s}$  at  $20^\circ\text{C}$

$\zeta_{\text{H}_2\text{CO}_3}$  Ratio of the mass transfer layer and chemical reaction thicknesses for  $\text{H}_2\text{CO}_3$

$\epsilon$  Outer sulfide layer porosity

$\psi$  Outer sulfide layer tortuosity factor  
 $\rho_{\text{H}_2\text{O}}$  Density of water ( $\text{kg m}^{-3}$ )  
 $\rho_{\text{Fe}}$  Density of iron ( $\text{kg m}^{-3}$ )  
 $\rho_{\text{FeS}}$  Density of ferrous sulfide ( $\text{kg m}^{-3}$ )

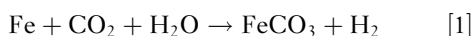
## 2.25.1 Introduction

As oil and gas emerge from the geological formation, they are always accompanied by some water and varying amounts of 'acid gases': carbon dioxide,  $\text{CO}_2$ , and hydrogen sulfide,  $\text{H}_2\text{S}$ . This is a corrosive combination, which affects the integrity of mild steel. This has been known for over 100 years; aqueous  $\text{CO}_2$  and  $\text{H}_2\text{S}$  corrosion of mild steel still represents a significant problem for the oil and gas industry.<sup>1</sup> Although corrosion resistant alloys that are able to withstand this type of corrosion exist, mild steel is often the most cost effective construction material used in this industry for these applications. All the pipelines, many wells, and much of the processing equipment in the oil and gas industry are built out of mild steel. The cost of equipment failure due to internal  $\text{CO}_2/\text{H}_2\text{S}$  corrosion is enormous, both in terms of direct costs such as repair costs and lost production, as well as in indirect costs such as environmental cost, impact on the downstream industries, etc.

The following section summarizes the degree of understanding of the so-called 'sweet'  $\text{CO}_2$  corrosion and the so-called 'sour' or  $\text{H}_2\text{S}$  corrosion of mild steel exposed to aqueous environments. It also casts the knowledge in the form of mathematical equations whenever possible. This should enable corrosion engineers and scientists to build entry level corrosion simulation and prediction models.

## 2.25.2 Aqueous $\text{CO}_2$ Corrosion of Mild Steel

Aqueous  $\text{CO}_2$  corrosion of carbon steel is an electrochemical process involving the anodic dissolution of iron and the cathodic evolution of hydrogen. The overall reaction is



$\text{CO}_2$  corrosion of mild steel is reasonably well understood. A number of chemical, electrochemical, and transport processes occur simultaneously. They are briefly described below.

### 2.25.2.1 Chemistry of $\text{CO}_2$ Saturated Aqueous Solutions – Equilibrium Considerations

$\text{CO}_2$  gas is soluble in water:



For ideal gases and ideal solutions in equilibrium, Henry's law can be used to calculate the aqueous concentration of dissolved  $\text{CO}_2$ ,  $c_{\text{CO}_2}$ , given that the respective concentration in the gas phase (often expressed in terms of partial pressure,  $p_{\text{CO}_2}$ ) is known:

$$H_{\text{sol}(\text{CO}_2)} = \frac{1}{K_{\text{sol}(\text{CO}_2)}} = \frac{p_{\text{CO}_2}}{c_{\text{CO}_2}} \quad [3]$$

The  $\text{CO}_2$  solubility constant,  $K_{\text{sol}(\text{CO}_2)}$ , is a function of temperature,  $T_f$ , and ionic strength,  $I$ :<sup>2</sup>

$$K_{\text{sol}(\text{CO}_2)} = \frac{14.5}{1.00258} \times 10^{-(2.27 + 5.65 \times 10^{-3} T_f - 8.06 \times 10^{-6} T_f^2 + 0.075 I)} \quad [4]$$

Ionic strength,  $I$ , can be calculated as

$$I = \frac{1}{2} \sum_i c_i z_i^2 = \frac{1}{2} (c_1 z_1^2 + c_2 z_2^2 + \dots) \quad [5]$$

The concentration of  $\text{CO}_2$  in the aqueous phase is of the same order of magnitude as the one in the gas phase. For example, at  $p_{\text{CO}_2} = 1$  bar, at  $25^\circ\text{C}$ , the gaseous  $\text{CO}_2$  concentration is  $\sim 4 \text{ mol l}^{-1}$  ( $\text{kmol}^{-1} \text{ m}^{-3}$ ) while in the water it is about  $3 \text{ mol l}^{-1}$ . Since the solubility of  $\text{CO}_2$  decreases with temperature, at  $100^\circ\text{C}$ , the respective concentrations are  $3.3 \text{ mol l}^{-1}$  in the gas and  $1.1 \text{ mol l}^{-1}$  in water.

A rather small fraction (about 1 in 500) of the dissolved  $\text{CO}_2$  molecules hydrates to make a 'weak' carbonic acid,  $\text{H}_2\text{CO}_3$ :



due to a relatively slow forward (hydration) rate. Assuming that the concentration of water remains unchanged, the equilibrium concentration  $c_{\text{H}_2\text{CO}_3}$  is determined by:

$$K_{\text{hyd}} = \frac{c_{\text{H}_2\text{CO}_3}}{c_{\text{CO}_2}} \quad [7]$$

The equilibrium hydration/dehydration constant,  $K_{\text{hyd}} = 2.58 \times 10^{-3}$ , does not change much across the typical temperature range of interest ( $20$ – $100^\circ\text{C}$ ).<sup>3</sup>

Carbonic acid is considered to be 'weak' because it only partially dissociates in water to produce

hydronium,  $H^+$  ions and bicarbonate ions,  $HCO_3^-$ :



The  $HCO_3^-$  dissociates further to give some more  $H^+$  and carbonate ion,  $CO_3^{2-}$ :



The respective equilibrium relations can be written as

$$K_{ca} = \frac{c_{H^+} c_{HCO_3^-}}{c_{H_2CO_3}} \quad [10]$$

$$K_{bi} = \frac{c_{H^+} c_{CO_3^{2-}}}{c_{HCO_3^-}} \quad [11]$$

The equilibrium constants can be calculated as functions of temperature  $T_f$ , and ionic strength,  $I$  as<sup>2</sup>

$$K_{ca} = 387.6 \times 10^{-6} \frac{-(6.41 - 1.594 \times 10^{-3} T_f + 8.52 \times 10^{-6} T_f^2 - 3.07 \times 10^{-5} p \times 14.7 - 0.4772 I^{0.5} + 0.118 I)}{T_f} \quad [12]$$

$$K_{bi} = 10^{-\frac{(10.61 - 4.97 \times 10^{-3} T_f + 1.331 \times 10^{-5} T_f^2 - 2.624 \times 10^{-5} p \times 14.7 - 1.166 I^{0.5} + 0.3466 I)}{T_f}} \quad [13]$$

One can use the equations above to calculate the pH for a pure aqueous  $CO_2$  saturated system. Assuming that the concentration of  $CO_2$  (or partial pressure,  $p_{CO_2}$ ) in the gas phase is known, one can calculate the concentration of aqueous/dissolved  $CO_2$   $c_{CO_2}$ , via eqn [3]. Then the concentration  $c_{H_2CO_3}$  can be determined via eqn [7]. However, in the remaining

two eqns [12] and [13], there are three unknowns:  $c_{H^+}$ ,  $c_{HCO_3^-}$ , and  $c_{CO_3^{2-}}$ , and therefore one more equation is needed to close the system: a constraint that describes charge conservation, that is, electroneutrality of the solution. Clearly, chemical reactions [8] and [9], which involve ions, always remain balanced with respect to charge and therefore one can write

$$c_{H^+} = c_{HCO_3^-} + 2c_{CO_3^{2-}} \quad [14]$$

Now, the system of equations is closed and concentrations of all the aqueous species can be determined, including the  $c_{H^+}$  and the corresponding pH. The pH of pure water as a function of  $p_{CO_2}$  at room temperature is shown in Figure 1.

If there are other ions in the aqueous solution, such as for example  $Fe^{2+}$  produced by corrosion of steel, then eqn [14] is extended to read

$$2c_{Fe^{2+}} + c_{H^+} = c_{HCO_3^-} + 2c_{CO_3^{2-}} \quad [15]$$

By inspecting the equations above, one can see that, as iron dissolution causes an increase in  $c_{Fe^{2+}}$ , it is accompanied by a decrease of  $c_{H^+}$  due to the cathodic reaction and a corresponding increase in pH. Other cations and anions as well as other chemical reactions can be introduced into the mix in a similar way. An example of a  $CO_2$  aqueous species distribution as a function of pH for an open system is given in Figure 2.

It is worth noting that this simple water chemistry calculation procedure is valid only for the case when the concentration of gaseous  $CO_2$ , i.e., the partial

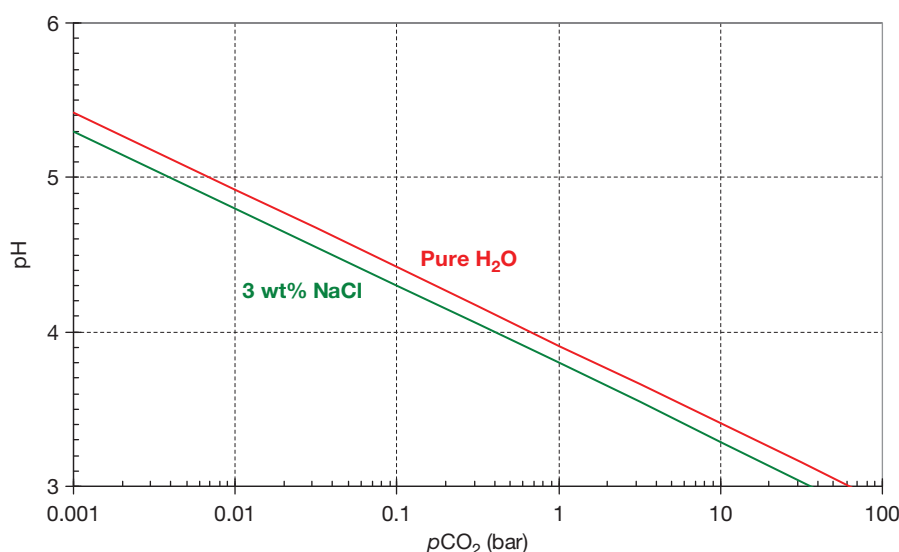


**Figure 1** Calculated pH of a pure aqueous solution saturated with  $CO_2$  as a function of partial pressure of  $CO_2$ ;  $T = 25^\circ C$ , 1 wt% NaCl.

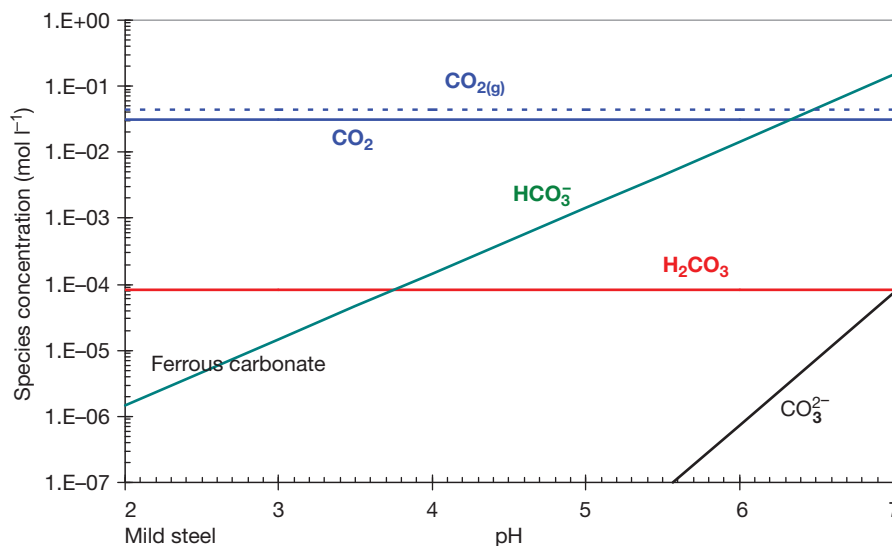


**Figure 2** Calculated carbonic species concentrations as a function of pH for a  $\text{CO}_2$  saturated aqueous solution;  $p_{\text{CO}_2}=1$  bar,  $25^\circ\text{C}$ , 1 wt% NaCl.

pressure,  $p_{\text{CO}_2}$  is known, constant, and independent from what is happening in the aqueous phase. This is often referred to as an *open* system. It is relevant to field situations where there is an overwhelming amount of  $\text{CO}_2$  in the gas phase (such as seen in wet gas lines, multiphase pipelines, gas/liquid separators, etc.). In the lab setting, this condition is easily achieved by continuous purge of a vessel with gaseous  $\text{CO}_2$ .

In contrast, there are many systems where there is a limited amount of  $\text{CO}_2$  in the gas phase compared to the amount in the liquid phase, such as in oil well tubing, oil transportation lines, liquid/liquid separators, etc. In the lab, aqueous systems with a limited gas phase are frequently found in high-pressure autoclaves and flow loops. Consequently they are often referred to as *closed* systems, and in principle can have varying gas/liquid volume ratios. An *open* system can be seen as a *closed* system with an infinitely large gas/liquid volume ratio. In *closed* systems, the concentration of gaseous  $\text{CO}_2$ , that is, the partial pressure,  $p_{\text{CO}_2}$ , is not known explicitly and typically depends on the aqueous chemistry. In mathematical terms, this means that there is one more unknown:  $p_{\text{CO}_2}$ , and therefore one needs one more equation to be able to solve for species concentrations. The extra equation comes from the additional constraint: in a *closed* system, the total amount of carbonic species remains constant; they are just redistributed between the gas and aqueous

phases as conditions change. When one accounts for this, an extra equation is obtained:

$$n_{\text{CO}_2(\text{g})} + n_{\text{CO}_2(\text{aq})} + n_{\text{H}_2\text{CO}_3(\text{aq})} + n_{\text{HCO}_3^-(\text{aq})} + n_{\text{CO}_3^{2-}(\text{aq})} = \text{Const.} \quad [16]$$

where  $n$  denotes the number of moles of a particular species in a gaseous or aqueous phase of a *closed* system.

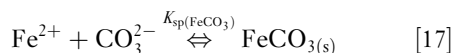
The dissociation steps [8] and [9] are very fast compared to all other processes occurring simultaneously in corrosion of mild steel, thus preserving chemical equilibrium. However, the  $\text{CO}_2$  dissolution reaction [2] and the hydration reaction [6] are much slower. When such chemical reactions proceed slowly, other faster processes (such as electrochemical reactions or diffusion) can lead to local nonequilibrium in the solution.

Either way, the occurrence of chemical reactions can significantly alter the rate of electrochemical processes at the surface and the rate of corrosion. This is particularly true when, due to high local concentrations of species, the solubility limit of salts is exceeded and precipitation of a surface layer occurs. In a precipitation process, heterogeneous nucleation occurs first on the surface of the metal or within the pores of an existing layer since homogenous nucleation in the bulk requires a much higher concentration of species. Nucleation is followed by crystalline layer growth.



Under certain conditions, surface layers can become very protective and reduce the rate of corrosion.

In  $\text{CO}_2$  corrosion, when the concentrations of  $\text{Fe}^{2+}$  and  $\text{CO}_3^{2-}$  ions exceed the solubility limit, they form solid ferrous carbonate according to



where the solubility product constant for ferrous carbonate  $K_{\text{sp}}(\text{FeCO}_3)$  is<sup>4</sup>

$$K_{\text{sp}}(\text{FeCO}_3) = 10^{-\frac{(59.3498 - 0.041377 T_k - (2.1963/T_k))}{+24.5724 \log T_k + 2.5187^{0.5} - 0.6571}} \quad [18]$$

Actually ferrous and carbonate ions are frequently found in the aqueous solution at concentrations much higher than predicted by the equilibrium  $K_{\text{sp}}(\text{FeCO}_3)$ . This is termed *supersaturation* and is a necessary condition before any substantial precipitation can occur. The ferrous carbonate supersaturation,  $\text{SS}_{(\text{FeCO}_3)}$ , is defined as:

$$\text{SS}_{(\text{FeCO}_3)} = \frac{c_{\text{Fe}^{2+}} c_{\text{CO}_3^{2-}}}{K_{\text{sp}}(\text{FeCO}_3)} \quad [19]$$

The precipitation process can be seen as the process of the solution returning to equilibrium and is driven by the magnitude of supersaturation. The rate of the precipitation ( $\mathfrak{R}_{\text{FeCO}_3}$ ) is therefore often expressed as

$$\mathfrak{R}_{\text{FeCO}_3} = k_{\text{r}}(\text{FeCO}_3) \frac{A}{V} K_{\text{sp}}(\text{FeCO}_3) (\text{SS}_{(\text{FeCO}_3)} - 1) \quad [20]$$

where  $k_{\text{r}}(\text{FeCO}_3)$  is a kinetic constant, which can be derived from the experimental results as a function of temperature, using an Arrhenius' type equation<sup>5</sup>

$$k_{\text{r}}(\text{FeCO}_3) = \exp\left(A_{(\text{FeCO}_3)} - \frac{B_{(\text{FeCO}_3)}}{RT_k}\right) \quad [21]$$

where  $A_{(\text{FeCO}_3)} = 28.2$  and  $B_{(\text{FeCO}_3)} = 64851 \text{ J mol}^{-1}$ .

SEM images of a crystalline ferrous carbonate layer formed on a mild steel substrate are shown in **Figure 3**. The ferrous carbonate layer can slow down the corrosion process by presenting a diffusion barrier for the species involved in the corrosion process, thereby changing the conditions at the steel surface. The effective protectiveness of a solid ferrous carbonate layer depends on its porosity, which hangs in the balance of the precipitation rate and the underlying corrosion rate. For high precipitation rates, and low corrosion rates, a dense and protective ferrous carbonate layer is obtained, and conversely, low precipitation rates and high corrosion rates lead to the formation of porous unprotective ferrous carbonate layers. A non-dimensional parameter termed 'scaling

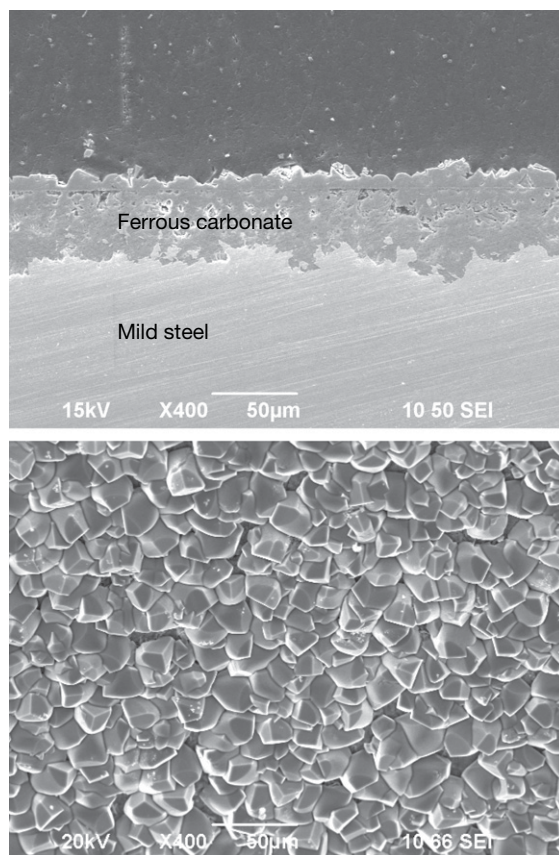


**Figure 3** SEM images showing a cross-section and a top view of a ferrous carbonate layer formed on mild steel;  $80^\circ\text{C}$ ,  $\text{pH } 6.6$ ,  $p_{\text{CO}_2} = 0.5 \text{ bar}$ , stagnant conditions.

tendency' (ST) can be used to quantify the relative rates of precipitation ( $\mathfrak{R}_{\text{FeCO}_3}$ ) and corrosion (CR) expressed in the same volumetric units:

$$\text{ST} = \frac{\mathfrak{R}_{\text{FeCO}_3}}{\text{CR}} \quad [22]$$

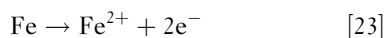
For  $\text{ST} \ll 1$ , porous and unprotective films are likely to form. Conversely, for  $\text{ST} \geq 1$ , conditions become favorable for the formation of dense, protective ferrous carbonate films. However, the use of scaling tendency is not as straightforward as it appears, as it requires simultaneous calculation of  $\mathfrak{R}_{\text{FeCO}_3}$  and corrosion CR.

In some cases, other salts can be detected in the surface layers that form on mild steel. In high temperature  $\text{CO}_2$  corrosion magnetite ( $\text{Fe}_3\text{O}_4$ ) has been detected. In the presence of oxygen, a ferric oxide hematite ( $\text{Fe}_2\text{O}_3$ ), which is very insoluble but offers little protection from corrosion forms. Oilfield scales also include calcium carbonate, calcium sulfate,

barium sulfate, strontium sulfate, etc. The presence of calcium carbonate, in particular, can have a beneficial effect upon corrosion and upon the stability of the  $\text{FeCO}_3$  scale. Finally, in the presence of  $\text{H}_2\text{S}$ , various types of sulfides form as discussed in a separate section below.

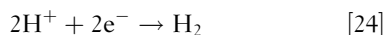
### 2.25.2.2 Electrochemistry of Mild Steel Corrosion in $\text{CO}_2$ Saturated Aqueous Solutions

The electrochemical dissolution of iron in a water solution:



is the dominant anodic reaction in  $\text{CO}_2$  corrosion. The reaction is pH dependent in acidic solutions with a reaction order with respect to  $\text{OH}^-$  between 1 and 2, decreasing toward 1 and 0 at  $\text{pH} > 4$ , which is the typical range for  $\text{CO}_2$  corrosion. Measured Tafel slopes are typically 30–80 mV. This subject, which is still somewhat controversial with respect to the mechanism, has been reviewed for acidic corrosion<sup>6,7</sup> and  $\text{CO}_2$  solutions.<sup>8</sup>

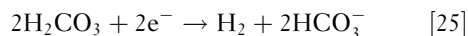
The presence of  $\text{CO}_2$  increases the rate of corrosion of mild steel in aqueous solutions primarily by increasing the rate of the hydrogen evolution reaction. It is well known that in *strong* acids, which are fully dissociated, the rate of hydrogen evolution occurs according to



and is, for the case of mild steel corrosion, limited by the rate at which  $\text{H}^+$  ions are transported from the bulk solution to the steel surface (mass transfer limitation). In  $\text{CO}_2$  solutions, where typically  $\text{pH} > 4$ , this limiting flux would be small, and therefore it is the presence of  $\text{H}_2\text{CO}_3$  which enables hydrogen evolution at a much higher rate. Thus, for  $\text{pH} > 4$ , the presence of  $\text{CO}_2$  leads to a much higher corrosion rate than would be found in a solution of a *strong* acid at the same pH.

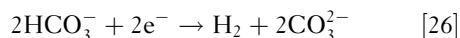
This can be readily explained by considering that the homogenous dissociation of  $\text{H}_2\text{CO}_3$ , as given by reaction [8], serves as an additional source of  $\text{H}^+$  ions, which are subsequently adsorbed at the steel surface and reduced according to reaction [24].<sup>1</sup> A different pathway is also possible, where the  $\text{H}_2\text{CO}_3$  first adsorbs at the steel surface followed by heterogeneous dissociation and reduction of the  $\text{H}^+$  ion. This is

often referred to as ‘direct’ reduction of carbonic acid<sup>9–11</sup> and is written as



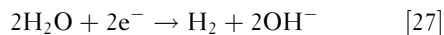
Clearly, the addition of the reactions [8] and [24] gives the reaction [25] proving that the overall reaction is the same and the distinction is only in the pathway, that is, in the sequence of reactions. The rate of reaction [25] is limited primarily by the slow hydration step [6]<sup>11,12</sup> and in some cases by the slow  $\text{CO}_2$  dissolution reaction [2].

It can be conceived that in  $\text{CO}_2$  solutions at  $\text{pH} > 5$  the direct reduction of the bicarbonate ion becomes important<sup>13</sup>:



which seems plausible, as the concentration of  $\text{HCO}_3^-$  increases with pH and can exceed that of  $\text{H}_2\text{CO}_3$  as seen in Figure 2. However, it is difficult to distinguish experimentally the effect of this particular reaction pathway for hydrogen evolution from the two previously discussed (eqns [8] and [25]). In addition, evidence exists that suggests that the rate of this reaction is comparatively low and can be neglected. For example, as the pH increases, the amount of  $\text{HCO}_3^-$  increases as well (see Figure 2), suggesting that the corrosion rate should follow the same trend, if one is to believe that the direct reduction of the bicarbonate ion [26] is a significant cathodic reaction. Experimental evidence does not support this scenario and shows the opposite trend: the corrosion rate actually decreases with an increasing pH, even if no protective ferrous carbonate layer forms.

Hydrogen evolution by direct reduction of water:



is always possible, but is comparatively very slow and is important only at  $p_{\text{CO}_2} \ll 0.1$  bar and  $\text{pH} > 6$ .<sup>14,15</sup> Therefore, this reaction is rarely a factor in practical  $\text{CO}_2$  corrosion situations.

The various electrochemical processes described above can be quantified using the well established electrochemical theory. The rate of the electrochemical reactions,  $\mathcal{R}$  in  $\text{kmol m}^{-2} \text{s}^{-1}$ , can be readily expressed in terms of current density,  $i$  in  $\text{A m}^{-2}$ , since the two are directly related: for example, during hydrogen evolution [24] for every kmol of  $\text{H}^+$  1 kmol of electrons is used ( $n = 1 \text{ kmol}_e \text{ kmol}^{-1}$ ), while for every kmol of iron dissolved [23] two

kmols of electrons are used ( $n = 2 \text{ kmol}_e \text{ kmol}^{-1}$ ). Therefore, one can write

$$i = nF\mathfrak{R} \quad [28]$$

### 2.25.2.2.1 Oxidation of iron

In the corrosion of mild steel, the oxidation (dissolution) of iron [23] is the dominant anodic reaction. The anodic dissolution of iron at the corrosion potential (and up to 200 mV above) is under charge transfer control. Thus, pure Tafel behavior can be assumed close to the corrosion potential:

$$i_{\text{a(Fe)}} = i_{\text{o(Fe)}} 10^{(E_{\text{corr}} - E_{\text{rev(Fe)}})/b_{\text{a(Fe)}}} \quad [29]$$

The exchange current density of iron oxidation is a function of temperature:

$$i_{\text{o(Fe)}} = i_{\text{o(Fe)}}^{\text{ref}} \exp\left(\frac{-\Delta H_{\text{Fe}}}{R} \left(\frac{1}{T_{\text{c}} + 273.15} - \frac{1}{T_{\text{c,ref}} + 273.15}\right)\right) \quad [30]$$

The Tafel slope of this reaction is given by

$$b_{\text{a(Fe)}} = \frac{2.303R(T_{\text{c}} + 273.15)}{1.5F} \quad [31]$$

### 2.25.2.2.2 Reduction of hydronium ion

In general, the  $\text{H}^+$  ion reduction reaction [24] can be either under charge transfer or mass transfer (diffusion) control, therefore, one can write:

$$\frac{1}{i_{\text{c(H}^+)}} = \frac{1}{i_{\alpha(\text{H}^+)}} + \frac{1}{i_{\text{lim(H}^+)}}^{\text{d}} \quad [32]$$

The charge transfer current density can be calculated by

$$i_{\alpha(\text{H}^+)} = i_{\text{o(H}^+)}} \times 10^{(-E_{\text{corr}} - E_{\text{rev(H}^+)})/b_{\text{c(H}^+)}} \quad [33]$$

The exchange current density  $i_{\text{o(H}^+)}}$  is a function of pH and temperature. The pH dependence is

$$\frac{\partial \log i_{\text{o(H}^+)}}{\partial \text{pH}} = -0.5 \quad [34]$$

The temperature dependence of the exchange current density can be calculated via an Arrhenius-type relation:

$$\frac{i_{\text{o(H}^+)}}{i_{\text{o(H}^+)}}^{\text{ref}} = \exp\left(-\frac{\Delta H_{\text{(H}^+)}}{R} \left(\frac{1}{T_{\text{c}} + 273.15} - \frac{1}{T_{\text{c,ref}} + 273.15}\right)\right) \quad [35]$$

The reversible potential for  $\text{H}^+$  reduction  $E_{\text{rev(H}^+)}$  is a function of temperature and pH:

$$E_{\text{rev(H}^+)}} = -\frac{2.303R(T_{\text{c}} + 273.15)}{F} \text{pH} \quad [36]$$

The cathodic Tafel slope  $b_{\text{c(H}^+)}$  is calculated as

$$b_{\text{c(H}^+)}} = \frac{2.303R(T_{\text{c}} + 273.15)}{0.5F} \quad [37]$$

The limiting mass transfer current density  $i_{\text{lim(H}^+)}}^{\text{d}}$  is related to the rate of transport of  $\text{H}^+$  ions from the bulk of the solution through the boundary layer to the steel surface:

$$i_{\text{lim(H}^+)}}^{\text{d}} = k_{\text{m(H}^+)}} F c_{\text{H}^+} \quad [38]$$

where the mass transfer coefficient,  $k_{\text{m(H}^+)}}$  can be calculated from a correlation of the Sherwood, Reynolds, and Schmidt numbers as explained in the following section.

### 2.25.2.2.3 Reduction of carbonic acid

The carbonic acid reduction reaction [25] can be under charge transfer control or limited by the slow chemical reaction–hydration step [6], preceding it.<sup>11,12</sup> The rate of this reaction in terms of current density is

$$\frac{1}{i_{\text{c(H}_2\text{CO}_3)}} = \frac{1}{i_{\alpha(\text{H}_2\text{CO}_3)}} + \frac{1}{i_{\text{lim(H}_2\text{CO}_3)}}^{\text{r}} \quad [39]$$

The charge transfer current density  $i_{\alpha(\text{H}_2\text{CO}_3)}$  is calculated as

$$i_{\alpha(\text{H}_2\text{CO}_3)} = i_{\text{o(H}_2\text{CO}_3)}} \times 10^{(-E_{\text{corr}} - E_{\text{rev(H}_2\text{CO}_3)}})/b_{\text{c(H}_2\text{CO}_3)}} \quad [40]$$

The exchange current density  $i_{\text{o(H}_2\text{CO}_3)}}$  depends on pH,  $\text{H}_2\text{CO}_3$  concentration, and temperature:

$$\frac{\partial \log i_{\text{o(H}_2\text{CO}_3)}}{\partial \text{pH}} = 0.5 \quad [41]$$

$$\frac{\partial \log i_{\text{o(H}_2\text{CO}_3)}}{\partial c_{\text{H}_2\text{CO}_3}} = 1 \quad [42]$$

$$\frac{i_{\text{o(H}_2\text{CO}_3)}}{i_{\text{o(H}_2\text{CO}_3)}}^{\text{ref}} = \exp\left(-\frac{\Delta H_{\text{(H}_2\text{CO}_3)}}{R} \left(\frac{1}{T_{\text{c}} + 273.15} - \frac{1}{T_{\text{c,ref}} + 273.15}\right)\right) \quad [43]$$

The cathodic Tafel slope  $b_{\text{c(H}_2\text{CO}_3)}}$  is

$$b_{\text{c(H}_2\text{CO}_3)}} = \frac{2.303R(T_{\text{c}} + 273.15)}{0.5F} \quad [44]$$

Since the reductions of  $\text{H}_2\text{CO}_3$  and  $\text{H}^+$  are equivalent

thermodynamically, the reversible potential for  $\text{H}_2\text{CO}_3$  reduction  $E_{\text{rev}(\text{H}_2\text{CO}_3)}$  is calculated as

$$E_{\text{rev}(\text{H}_2\text{CO}_3)} = -\frac{2.303R(T_c + 273.15)}{F} \text{pH} \quad [45]$$

The chemical reaction limiting current density  $i_{\text{lim}(\text{H}_2\text{CO}_3)}^r$  can be calculated from<sup>16</sup>:

$$i_{\text{lim}(\text{H}_2\text{CO}_3)}^r = F \dot{c}_{\text{CO}_2} f_{\text{H}_2\text{CO}_3} \sqrt{D_{\text{H}_2\text{CO}_3} K_{\text{hyd}} k_{\text{hyd}}^f} \quad [46]$$

The diffusion coefficient for carbonic acid  $D_{\text{H}_2\text{CO}_3}$  as a function of temperature can be calculated using Einstein's relation:

$$D = D_{\text{ref}} \left( \frac{T_c + 273.15}{T_{c,\text{ref}} + 273.15} \right) \left( \frac{\mu_{\text{H}_2\text{O},\text{ref}}}{\mu_{\text{H}_2\text{O}}} \right) \quad [47]$$

where  $T$  is temperature and  $\mu$  is dynamic viscosity. The forward reaction rate for the  $\text{CO}_2$  hydration reaction  $k_{\text{hyd}}^f$  is calculated as

$$k_{\text{hyd}}^f = 10^{169.2 - 53.0 \log(T_c + 273.15) - (11715/(T_c + 273.15))} \quad [48]$$

The flow factor  $f_{\text{H}_2\text{CO}_3}$  is

$$f_{\text{H}_2\text{CO}_3} = \coth \zeta_{\text{H}_2\text{CO}_3} \quad [49]$$

where

$$\zeta_{\text{H}_2\text{CO}_3} = \frac{\delta_{\text{m}(\text{H}_2\text{CO}_3)}}{\delta_{\text{r}(\text{H}_2\text{CO}_3)}} \quad [50]$$

and

$$\delta_{\text{m}(\text{H}_2\text{CO}_3)} = \frac{D_{\text{H}_2\text{CO}_3}}{k_{\text{m}(\text{H}_2\text{CO}_3)}} \quad [51]$$

$$\delta_{\text{r}(\text{H}_2\text{CO}_3)} = \sqrt{\frac{D_{\text{H}_2\text{CO}_3}}{k_{\text{hyd}}^b}} \quad [52]$$

The carbonic acid mass transfer coefficient  $k_{\text{m}(\text{H}_2\text{CO}_3)}$  is discussed in [Section 2.25.2.3](#).

#### 2.25.2.2.4 Reduction of water

Unless water is mixed with methanol or glycol to prevent hydrate formation or somehow diluted otherwise, it can be assumed that water molecules are present in virtually unlimited quantities at the steel surface, and the reduction rate of  $\text{H}_2\text{O}$  is controlled by the charge-transfer process and, hence, pure Tafel behavior:

$$i_{\text{c}(\text{H}_2\text{O})} = i_{\text{o}(\text{H}_2\text{O})} 10^{-(E_{\text{corr}} - E_{\text{rev}(\text{H}_2\text{O})})/b_{\text{c}(\text{H}_2\text{O})}} \quad [53]$$

Since the reduction of  $\text{H}_2\text{O}$  and  $\text{H}^+$  are equivalent thermodynamically, they have the same reversible potential at a given pH:

$$E_{\text{rev}(\text{H}_2\text{O})} = -\frac{2.303R(T_c + 273.15)}{F} \text{pH} \quad [54]$$

The exchange current density for water reduction  $i_{\text{o}(\text{H}_2\text{O})}$  depends on temperature:

$$\frac{i_{\text{o}(\text{H}_2\text{O})}}{i_{\text{o}(\text{H}_2\text{O})}^{\text{ref}}} = \exp \left( -\frac{\Delta H_{(\text{H}_2\text{O})}}{R} \left( \frac{1}{T_c + 273.15} - \frac{1}{T_{c,\text{ref}} + 273.15} \right) \right) \quad [55]$$

The Tafel slope for  $\text{H}_2\text{O}$  reduction was found to be the same as that for  $\text{H}^+$  reduction:

$$b_{\text{c}(\text{H}_2\text{O})} = \frac{2.303R(T_c + 273.15)}{0.5F} \quad [56]$$

#### 2.25.2.3 Transport Processes in $\text{CO}_2$ Corrosion of Mild Steel

From the description of the electrochemical processes above, it is clear that certain species in the solution are 'produced' at the metal surface (e.g.,  $\text{Fe}^{2+}$ ) while others are depleted (e.g.,  $\text{H}^+$ ). The established concentration gradients lead to molecular diffusion of the species toward and away from the surface. In cases when the diffusion processes are much faster than the electrochemical processes, the concentration change at the metal surface is small. In contrast, when the diffusion is unable to 'keep up' with the rate of the electrochemical reactions, the concentration of species at the metal surface can become very different from that in the bulk solution. The rate of the electrochemical processes depends on the concentration of the reactants at the surface. Therefore, there exists a two-way coupling between the electrochemical processes at the metal surface (corrosion) and processes in the adjacent solution layer (i.e., diffusion in the boundary layer). The same is true for chemical reactions, which interact with both the transport and electrochemical processes in a complex way.

In most practical systems, the water solution moves with respect to the metal surface. Therefore, the effect of convection on transport processes cannot

be ignored. Turbulent eddies can penetrate deep into the hydrodynamic boundary layer and significantly alter the rate of species transport to and from the surface. Very close to the surface no turbulence can exist and the species are transported solely by diffusion. The effect of turbulent flow is captured most easily by using the concept of mass transfer coefficient, described below.

In turbulent flow of dilute ideal solutions, a mass transfer coefficient  $k_m$  for a given species ( $H^+$  ions,  $H_2CO_3$  etc.) can be calculated from a correlation, such as the straight pipe correlation of Berger and Hau<sup>25</sup>:

$$Sb_p = 0.0165 Re^{0.86} Sc^{0.33} \quad [57]$$

or the rotating cylinder correlation of Eisenberg *et al.*<sup>26</sup>:

$$Sb_r = 0.0791 Re^{0.7} Sc^{0.356} \quad [58]$$

or any other similar correlation for the flow geometry at hand. It should be noted that most of the mass transfer correlations found in the literature (including the two listed above) are suited only for single-phase flow. Therefore, extension of this approach to multiphase flow situations needs to be done with careful consideration.

Overall,  $CO_2$  corrosion of mild steel is not very sensitive to flow, at least not so when compared to mild steel corrosion in strong acids. This is due to the fact that the main corrosive species in  $CO_2$  corrosion is  $H_2CO_3$  which can easily be depleted due to a slow chemical step which precedes it: the hydration reaction [6]. Therefore, the limiting rate of  $CO_2$  corrosion is primarily affected by the rate of this chemical reaction [46], which is a function of temperature and  $CO_2$  partial pressure and not very sensitive to flow.

#### 2.25.2.4 Calculation of Mild Steel $CO_2$ Corrosion Rate

Leading to this point, the main processes underpinning  $CO_2$  corrosion were defined: the speciation of the aqueous  $CO_2$  solution using the thermodynamic approach outlined in Section 2.25.2.1, the electrochemical theory described in Section 2.25.2.2, and the transport processes as covered in Section 2.25.2.3. Using this information, the corrosion rate of mild steel can now be calculated. The unknown corrosion potential  $E_{corr}$  in [33], [40], [53], and [29] can be found from the current (charge) balance equation at the steel surface:

$$i_{c(H^+)} + i_{c(H_2CO_3)} + i_{c(H_2O)} = i_{a(Fe)} \quad [59]$$

which expresses the simple fact that at steady state all the electrons generated by the oxidation processes are consumed by the sum of the reduction processes. By substituting the expressions for the various currents given by eqns [33], [40], [53], and [29] into eqn [59] a single nonlinear equation is now obtained with  $E_{corr}$  as the only unknown, which can be easily solved. When the calculated value of  $E_{corr}$  is now returned to eqns [33], [40], [53], and [29], the rate of each individual reaction can be explicitly computed. This also includes the corrosion current density obtained from eqn [29]:

$$i_{corr} = i_{a(Fe)} \quad [60]$$

Finally, the  $CO_2$  corrosion rate is recovered by using Faraday's law:

$$CR = \frac{i_{corr} M_{Fe}}{\rho_{Fe} n F} \quad [61]$$

where  $M$  is the molecular mass and  $\rho$  is the density. If the unit amperes per square meters is used for the corrosion current density  $i_{corr}$ , then conveniently the corrosion rate for iron and steel expressed in millimeter per year takes almost the same numerical value, precisely,  $CR = 1.155 i_{corr}$ .

#### 2.25.2.5 Successes and Limitations of Modeling of Aqueous $CO_2$ Corrosion of Mild Steel

Evidence that our basic understanding of the processes underlying  $CO_2$  corrosion of mild steel is reasonably sound can be found by comparing the predictions made by the mechanistic model outlined above with experimental values. In Figure 4, below, one can see the comparison of a potentiodynamic sweep obtained in the experiments and the one predicted by the model. Many other comparisons of the predicted and measured corrosion rates are given in the following section, where the effect of key factors in  $CO_2$  corrosion of mild steel is discussed.

Despite the relative progress we have made in understanding and modeling of aqueous  $CO_2$  corrosion of mild steel, many questions persist. One is the issue of localized  $CO_2$  corrosion, which is still a topic of intense ongoing research. Effect of other factors such as steel metallurgy, organic acids, oxygen, multiphase flow, and inhibitors are challenges that need further effort. Some of those are discussed in the following sections.



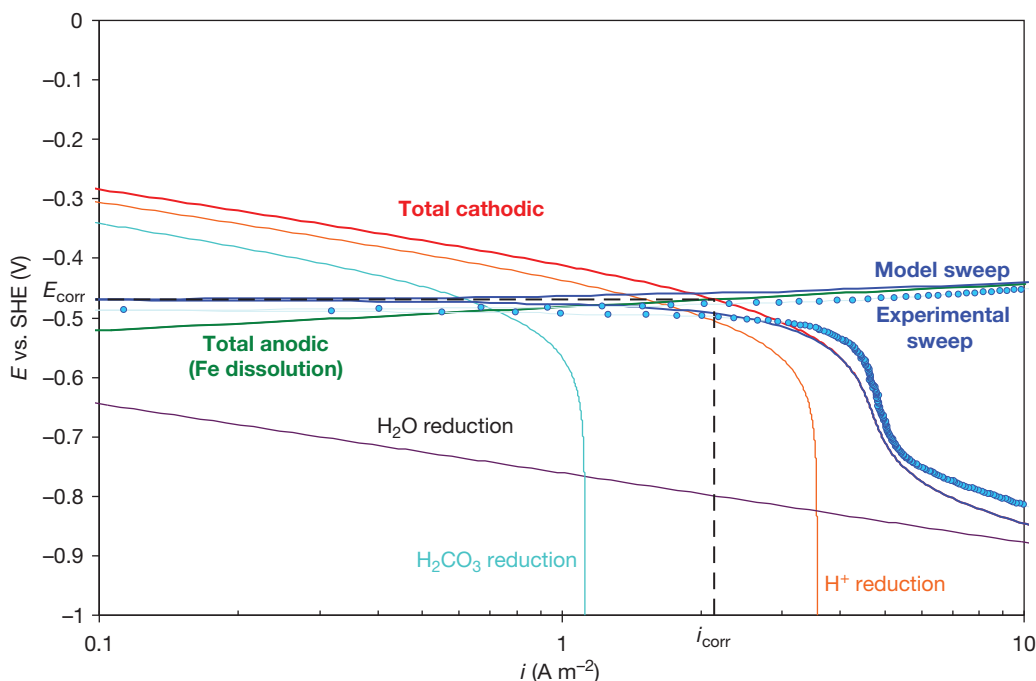


**Figure 4** Potentiodynamic sweep, experimental (points) vs. model (lines); 20 °C,  $p_{\text{CO}_2} = 1$  bar, pH 4,  $2 \text{ ms}^{-1}$ .

### 2.25.2.6 Key Factors Affecting Aqueous $\text{CO}_2$ Corrosion of Mild Steel

Armed with the understanding and the ability to calculate  $\text{CO}_2$  corrosion rates, as described in the sections above, in this section, the effect of key factors which affect the rate of  $\text{CO}_2$  corrosion are discussed, and the predictions made by the model are compared to empirical results.

#### 2.25.2.6.1 Effect of pH

The pH has a significant influence on the  $\text{CO}_2$  corrosion rate. Lower pH leads to higher corrosion rates and vice versa, just like in many other acidic solutions. Typical pH in  $\text{CO}_2$  saturated condensed water is about pH 4 while in buffered brines, one frequently encounters  $5 < \text{pH} < 7$ . At pH 4 or below, direct reduction of  $\text{H}^+$  ions, reaction [24], is important, particularly at lower partial pressures of  $\text{CO}_2$ , when direct reduction of carbonic acid, reaction [25], can be ignored. In that case, the pH has a direct effect on the corrosion rate. Another important effect of pH is indirect and relates to how pH changes conditions for the formation of ferrous carbonate layers. Higher pH ( $5 < \text{pH} < 7$ ) results in a decreased solubility of ferrous carbonate and leads to an increased precipitation rate and a higher scaling tendency. The effect of various pH and

supersaturations are shown in Figure 5. At lower supersaturations obtained at the lower pH of 6, shown in Figure 5, the corrosion rate does not change much with time, even if some ferrous carbonate precipitation occurs, reflecting the fact that a relatively porous, detached and unprotective layer is formed (low scaling tendency ST). The higher pH of 6.6 results in higher supersaturation, faster precipitation, and formation of more protective ferrous carbonate, reflected by a rapid decrease of the corrosion rate with time. There are other indirect effects of pH, and by almost all accounts, higher pH leads to a reduction of the corrosion rate, making the ‘pH stabilization’ (meaning: pH increase) technique an attractive way of managing  $\text{CO}_2$  corrosion. The drawback of this technique is that it can lead to excessive scaling and can rarely be used with formation water systems.

#### 2.25.2.6.2 Effect of $\text{CO}_2$ partial pressure

In the case of scale-free  $\text{CO}_2$  corrosion, an increase of  $p_{\text{CO}_2}$  typically leads to an increase in the corrosion rate. The commonly accepted explanation is that with increasing  $p_{\text{CO}_2}$  the concentration of  $\text{H}_2\text{CO}_3$  increases and accelerates the cathodic reaction, eqn [25], and ultimately the corrosion rate. The detrimental effect of  $p_{\text{CO}_2}$  at a constant pH is illustrated in Figure 6. The model described above reasonably

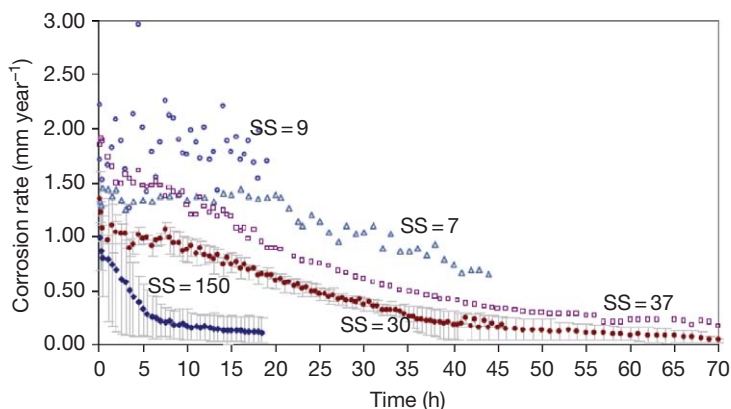


**Figure 5** Effect of ferrous carbonate supersaturation  $SS_{(FeCO_3)}$  on corrosion rate obtained at a range of pH 6.0–6.6, for  $5 \text{ ppm} < c_{Fe^{2+}} < 50 \text{ ppm}$  at  $T = 80^\circ\text{C}$ , under stagnant conditions. Error bars represent minimum and maximum values obtained in repeated experiments. Data taken from Chokshi *et al.*<sup>17</sup>

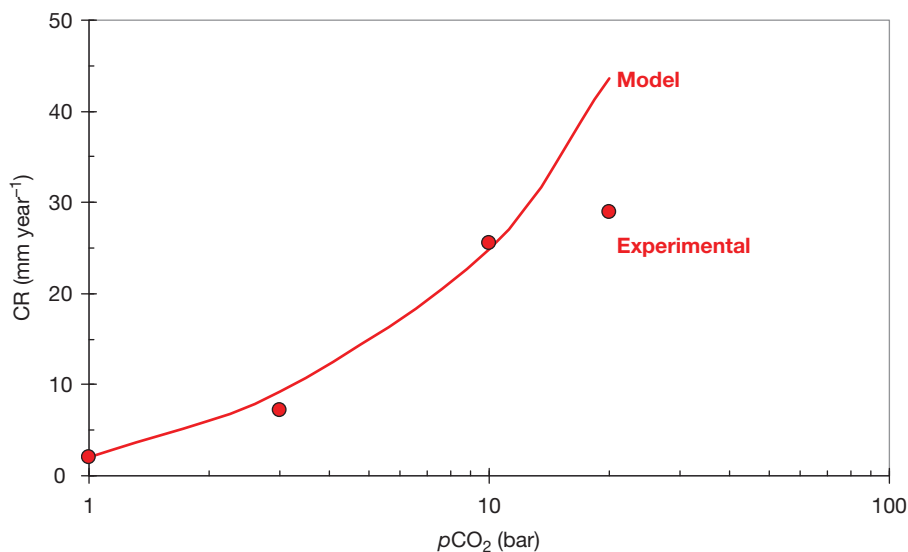


**Figure 6** The effect of  $\text{CO}_2$  partial pressure,  $p_{\text{CO}_2}$  on bare steel corrosion rate, comparison of experimental results (points) and model (line);  $60^\circ\text{C}$ , pH 5,  $1 \text{ m s}^{-1}$ , 100 mm ID single-phase pipe flow.

captures well this trend up to approximately  $p_{\text{CO}_2} = 10 \text{ bar}$ . However, when other conditions are favorable for the formation of ferrous carbonate layers, increased  $p_{\text{CO}_2}$  can have a beneficial effect. At a high pH, higher  $p_{\text{CO}_2}$  leads to an increase in bicarbonate and carbonate ion concentration and a higher supersaturation which accelerates precipitation and protective layer formation. The effect of  $p_{\text{CO}_2}$  on the corrosion rate in the presence of ferrous carbonate precipitation is illustrated in Figure 7 where in stratified wet gas flow, corrosion rate is reduced both at top and bottom of the pipe with the increase partial pressure of  $\text{CO}_2$ .

#### 2.25.2.6.3 Effect of temperature

Temperature accelerates all the processes involved in corrosion: electrochemical, chemical, transport, etc. One would expect then that the corrosion rate steadily increases with temperature, and this is the case at low pH when precipitation of ferrous carbonate or other protective layers does not occur. An example is shown Figure 8. The situation changes markedly when solubility of ferrous carbonate is exceeded, typically at a higher pH. In that case, increased temperature rapidly accelerates the kinetics of precipitation and protective layer formation, decreasing the corrosion rate. The peak in the

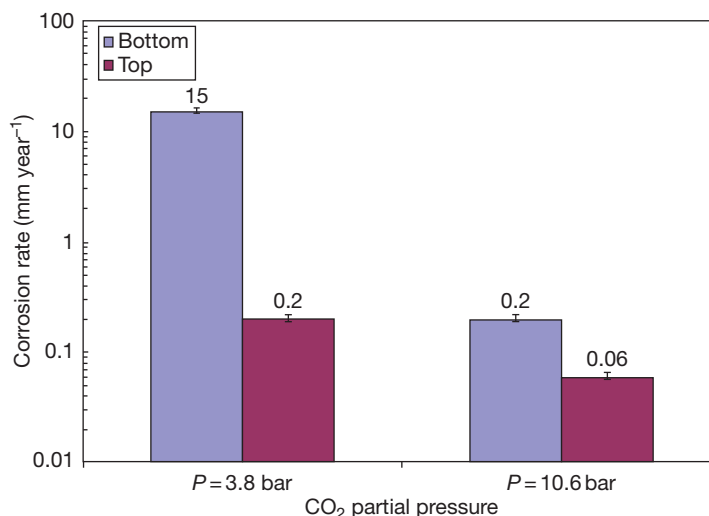


**Figure 7** Experimental measurements of the corrosion rate at the top and bottom of the pipe in stratified gas–liquid flow showing the effect of CO<sub>2</sub> partial pressure,  $p_{\text{CO}_2}$ , on formation of ferrous carbonate layer. Test conditions: 90 °C, pH 6, 100 mm ID,  $V_{\text{sg}} = 10 \text{ m s}^{-1}$ ,  $V_{\text{sl}} = 0.1 \text{ m s}^{-1}$ . Data taken from Sun and Nešić.<sup>18</sup>

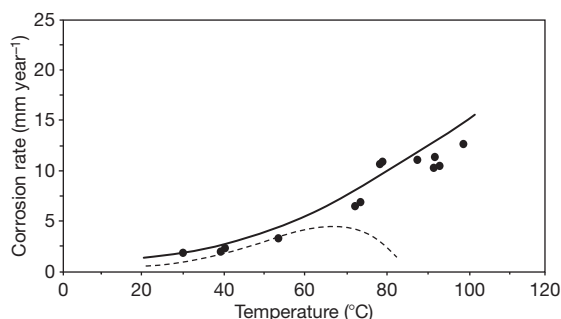


**Figure 8** The effect of temperature on CO<sub>2</sub> corrosion rate of mild steel; pH 4,  $p_{\text{CO}_2} = 1 \text{ bar}$ , 100 mm ID single phase pipe flow. Points are experimental values and the solid line is the model. The dotted line is a model simulation of the same conditions at pH 6.6 accounting for protective ferrous carbonate film formation.

corrosion rate is usually seen between 60 and 80 °C depending on water chemistry and flow conditions as shown in Figure 8 (dotted line).

#### 2.25.2.6.4 Effect of flow

There are two main ways in which flow may affect CO<sub>2</sub> corrosion, which can be distinguished based on whether or not other conditions are conducive to protective layer formation or not.

In the case of corrosion where protective layers do not form (typically at low pH as found in condensed water and in the absence of inhibitors), the main role of turbulent flow is to enhance transport of species toward and away from the metal surface. This may

lead to an increase in the corrosion rate as illustrated in Figure 9. At lower pH 4, the effect is much more pronounced as the dominant cathodic reaction is direct H<sup>+</sup> ion reduction [24], which is under mass transfer control (see eqn [38]).

When protective ferrous carbonate layers form (typically at higher pH in produced water) or when inhibitor films are present on the steel surface, the above-mentioned effect of flow becomes insignificant as the main resistance to corrosion is now in the surface layer or inhibitor film. In this case, the effect of flow is to interfere with the formation of protective surface layers or to remove them once they are in place, often leading to an increased risk of localized attack.

The two flow accelerated corrosion effects discussed above are frequently aggravated by flow disturbances such as valves, constrictions, expansions, bends, etc. where local increases of near-wall turbulence and wall-shear stress are seen. However, flow can lead to onset of localized attack only when given the ‘right’ set of circumstances as discussed in a separate heading below.

The effect of multiphase flow on CO<sub>2</sub> corrosion is complicated by the different flow patterns that exist, the most common being *stratified*, *slug*, and *annular-mist* flow. In the liquid phase, water and oil can flow separated or mixed with either phase being continuous with the other flowing as a dispersed phase. Different flow patterns lead to a variety of steel surface wetting mechanisms: stable water wetting, stable oil wetting, intermittent wetting, etc., which

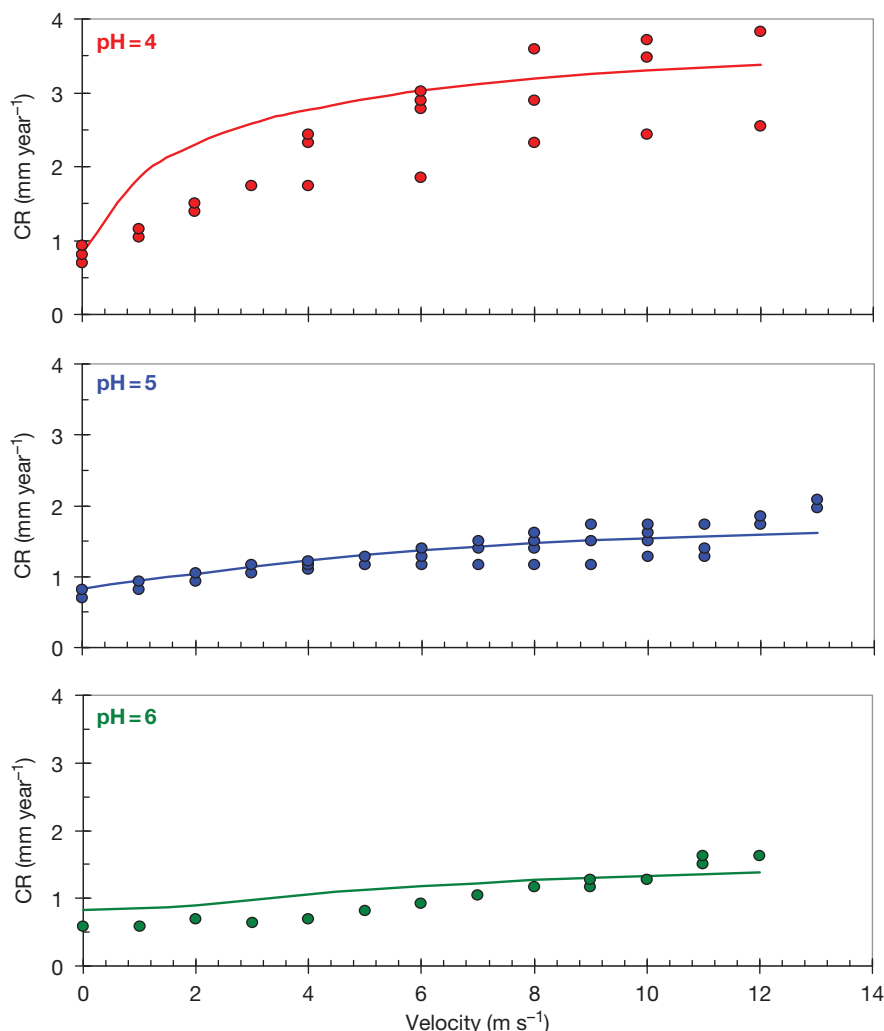


**Figure 9** Predicted (line) and experimentally measured corrosion rates (points) showing the effect of velocity in the absence of ferrous carbonate layers. Test conditions: 20 °C,  $p_{\text{CO}_2} = 1$  bar, 15 mm ID single-phase pipe flow. Experimental data taken from Nešić *et al.*<sup>19</sup>

greatly affect corrosion. In annular mist flow, the liquid droplets move at high velocity and can lead to protective layer damage at points of impact such as bends, valves, tees, constrictions/expansions, and other pipe fittings. Slug flow can lead to significant short-lived fluctuations in the wall-shear stress, which can help remove a protective surface layer of ferrous carbonate or possibly affect an inhibitor film.

#### 2.25.2.6.5 Effect of corrosion inhibition

The two most common sources of corrosion inhibition need to be considered:

- inhibition by addition of corrosion inhibitors and
- inhibition by components present in the crude oil.

#### Corrosion inhibitors

Describing the effect of corrosion inhibitors is not a straightforward task due to the enormous complexity of the subject. Quantifying them and predicting their behavior are even harder. There is a plethora of approaches in the open literature, varying from the use of simple *inhibitor factors* and *inhibition efficiencies* to the application of complicated *molecular modeling* techniques to describe inhibitor interactions with the steel surface and ferrous carbonate layer. A middle-of-the-road approach is based on the assumption that corrosion protection is achieved by *surface coverage*, that is, that the inhibitor adsorbs onto the steel surface and slows down one or more electrochemical reactions by ‘blocking.’ The degree of protection is

assumed to be directly proportional to the fraction of the steel surface blocked by the inhibitor. In this type of model, one needs to establish a relationship between the surface coverage  $\theta$  and the inhibitor concentration in the solution  $c_{\text{inh}}$ . This is most commonly done by the use of adsorption isotherms.

#### Corrosion inhibition by crude oil

It has been known for a while that  $\text{CO}_2$  corrosion rates seen in the field in the presence of crude oil are much lower than those obtained in laboratory conditions where crude oil was not used or synthetic crude oil was used. One can identify two main effects of crude oil on the  $\text{CO}_2$  corrosion rate.

The first is a *wettability* effect and relates to a hydrodynamic condition where crude oil entrains the water and prevents it from wetting the steel surface (continuously or intermittently).

The second effect is *corrosion inhibition* by components of the crude oil that reach the steel surface either by direct contact or by first partitioning into the water phase. Various surface active organic compounds found in crude oil (typically oxygen, sulfur and nitrogen containing molecules) have been identified to directly inhibit corrosion of mild steel in  $\text{CO}_2$  solutions.

#### 2.25.2.6.6 Effect of organic acids

The low molecular weight organic acids are primarily soluble in water and can lead to corrosion of mild steel. Higher molecular weight organic acids are not water soluble, but are typically soluble in the oil phase and pose a corrosion threat at higher temperatures in the refineries. Acetic acid  $\text{CH}_3\text{COOH}$  (denoted as HAc in the text below) is the most prevalent low molecular weight organic acid found in brines. Other acids typically found in the brine are propionic, formic, etc.; however, their behavior and corrosiveness is very similar to that of HAc and therefore HAc can be used as a 'surrogate' for all the organic acids found in the brine. HAc is a weak acid; however, it is stronger than  $\text{H}_2\text{CO}_3$  ( $pK_a$  4.76 vs. 6.35 at 25 °C), and it is the main source of  $\text{H}^+$  ions when the two acid concentrations are similar. The effect of HAc is particularly pronounced at higher temperatures and low pH when the abundance of undissociated HAc can increase the  $\text{CO}_2$  corrosion rate dramatically as seen in Figure 10. Solid iron acetate does not precipitate in the pH range of interest since its solubility is much higher than that of ferrous carbonate. There are some indications that the presence of organic acids impairs

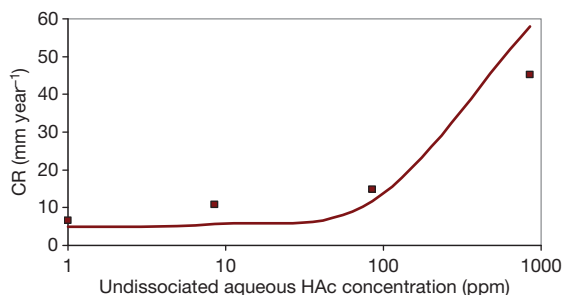


**Figure 10** Predicted (line) and experimentally measured data (points) showing the effect of the concentration of undissociated acetic acid (HAc) on the  $\text{CO}_2$  corrosion rate, 60 °C,  $p_{\text{CO}_2}$  = 0.8 bar, pH 4, 12 mm OD rotating cylinder flow at 1000 rpm. Experimental data taken from Sun *et al.*<sup>20</sup>

the protectiveness of ferrous carbonate layers; however, the mechanism is still not clear.

#### 2.25.2.6.7 Effect of glycol/methanol

Glycol and methanol are often added to flowing systems in order to prevent hydrates from forming. The quantities are often significant (50% of total liquid phase is not unusual). In the very few studies available, it has been assumed that the main 'inhibitive' effect of glycol/methanol on corrosion comes from dilution of the water phase, which leads to a decreased activity of water. However, there are many unanswered questions such as the changes in mechanisms of  $\text{CO}_2$  corrosion in water/glycol mixtures which are yet to be discovered.

#### 2.25.2.6.8 Effect of condensation in wet gas flow

When transporting humid natural gas, due to the cooling of the stream, condensation of water vapor occurs on the internal pipe wall. The condensed water is pure and, due to dissolved  $\text{CO}_2$ , typically has a  $\text{pH} < 4$ . This leads to the so-called *top-of-the-line corrosion* (TLC) scenario. If the rate of condensation is high, plenty of acidic water flows down the internal pipe walls leading to a very corrosive situation. If the condensation rate is low, the water film is not renewed and flows down very slowly and the corrosion process can release enough  $\text{Fe}^{2+}$  to raise the local pH and saturate the solution, leading to the formation of protective ferrous carbonate layer. The layer is often protective; however, incidents of localized attack in TLC were reported.<sup>21</sup> Either way, the stratified or stratified-wavy flow regime, typical for TLC, does not lead to a good opportunity for inhibitors to reach the upper portion of the internal pipe wall and protect it. A very limited



range of corrosion management options for TLC exists. To qualitatively and quantitatively describe the phenomenon of corrosion occurring at the top of the line, a deep insight into the combined effect of the chemistry, hydrodynamics, thermodynamics, and heat and mass transfer in the condensed water is needed. A full description exceeds the scope of this review, and the interested reader is directed to some recent articles published on this topic.<sup>21,22</sup>

#### 2.25.2.6.9 Nonideal solutions and gases

In many cases produced, water has very high dissolved solids content (>10 wt%). At such high concentrations, the infinite dilution theory used above does not hold, and corrections need to be made to account for solution nonideality. A simple way to account for the effect on nonideal homogenous water chemistry is to correct the equilibrium constants by using the concept of ionic strength as indicated above. This approach seems to work well only for moderately concentrated solution (up to a few weight percentage of dissolved solids). For more concentrated solutions, a more accurate way is to use activity coefficients as described by Anderko *et al.*<sup>23</sup> The effect of concentrated solutions on heterogeneous reactions such as precipitation of ferrous carbonate and other layers is still largely unknown. Furthermore, it is unclear how the highly concentrated solutions affect surface electrochemistry. Some experience suggests that corrosion rates can be dramatically reduced in very concentrated brines; nevertheless a more systematic study is needed.

At very high total pressure, the gas–liquid equilibria cannot be accounted for by Henry's law. A simple correction can be made by using a fugacity coefficient, which accounts for nonideality of the CO<sub>2</sub>/natural gas mixture<sup>24</sup> and can be obtained by solving the equation of state for the gas mixture. Those cases, in which critical point for CO<sub>2</sub> is approached or exceeded, warrant a separate analysis and are not covered by the considerations discussed above.

#### 2.25.2.7 Localized CO<sub>2</sub> Corrosion of Mild Steel in Aqueous Solutions

As illustrated above, significant progress has been achieved in understanding uniform CO<sub>2</sub> corrosion, without or with protective layers, and hence successful uniform corrosion models can be built. However, much less is known about localized CO<sub>2</sub> corrosion. It is thought that one of the main factors that 'triggers' localized attack is flow, tempered by other environmental variables such as pH, temperature, partial

pressure of CO<sub>2</sub>, etc. It seems that localized attack occurs when the conditions are such that partially protective ferrous carbonate layers form. It is well known that when fully protective ferrous carbonate forms, low general corrosion rates are obtained and vice versa: when no protective layers form, a high rate of general corrosion is seen. It is when the corrosive environment is 'in between,' in the so-called 'gray zone,' that localized attack can be initiated most often by some extreme flow conditions. There are many combinations of environmental and metallurgical parameters that define the grey zone, making this sound like a difficult proposal. However, there is a single parameter which is easy to calculate: ferrous carbonate supersaturation,  $SS_{(FeCO_3)}$  (see eqn [19] above), which can be successfully used as a good delineator for the gray zone and as such a predictor for the probability for localized attack. When bulk ferrous carbonate supersaturation is in the range  $0.5 < SS_{(FeCO_3)} < 2$  there is a risk of localized attack. The further away the solution is from these boundaries, the lower the risk. The scaling tendency  $ST$  (see equation [22] above) is conceptually even better suited as a predictor of localized corrosion risk, however, its calculation is much more difficult and uncertain as it involves calculation of both the uniform corrosion rate and the precipitation rate.

Based on mostly anecdotal evidence (field experience), the presence of H<sub>2</sub>S and HAc is related to the onset of localized attack, however, little is understood about how and when this may happen.

#### 2.25.3 Aqueous H<sub>2</sub>S Corrosion of Mild Steel

Corrosion of mild steel in the presence of hydrogen sulfide (H<sub>2</sub>S) also represents a significant problem for the oil and gas industry.<sup>27–33</sup> Many fields have been developed that in addition to CO<sub>2</sub> have high concentrations of H<sub>2</sub>S. In CO<sub>2</sub>/H<sub>2</sub>S corrosion of mild steel, thermodynamic considerations suggest that both ferrous carbonate and ferrous sulfide layers could theoretically form on the steel surface. However, studies have demonstrated that the formation of the ferrous sulfide layers is dominant and presents one of the most important factors governing the H<sub>2</sub>S corrosion rate. The sulfide layer growth depends primarily on the kinetics of the corrosion process as it is described below.

Despite the relative abundance of experimental data on H<sub>2</sub>S corrosion of steel, most of the literature is still confusing and somewhat contradictory.

Therefore, the mechanism of  $\text{H}_2\text{S}$  corrosion remains much less understood when compared to that of  $\text{CO}_2$  corrosion. This uncertainty makes it more difficult to develop a model to predict the corrosion rate of mild steel in  $\text{H}_2\text{S}$  saturated aqueous solution.

### 2.25.3.1 Chemistry of $\text{H}_2\text{S}$ Saturated Aqueous Solutions – Equilibrium Considerations

Similar to  $\text{CO}_2$  discussed above,  $\text{H}_2\text{S}$  gas is also soluble in water:

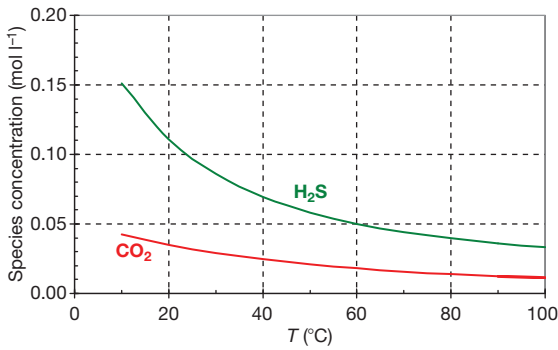


**Figure 11** Calculated solubility of  $\text{H}_2\text{S}$  and  $\text{CO}_2$  as a function of temperature;  $25^\circ\text{C}$ ,  $p_{\text{H}_2\text{S}} = 1 \text{ bar}$ ,  $p_{\text{CO}_2} = 1 \text{ bar}$ .

where  $K_{\text{H}_2\text{S}}$  is the solubility constant of  $\text{H}_2\text{S}$  in  $\text{mol l}^{-1} \text{ bar}^{-1}$ :

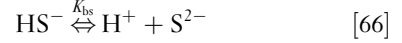
$$K_{\text{sol}(\text{H}_2\text{S})} = \frac{c_{\text{H}_2\text{S}}}{p_{\text{H}_2\text{S}}} \quad [63]$$

and can be found from<sup>34</sup>

$$K_{\text{sol}(\text{H}_2\text{S})} = 10^{\frac{(634.27 + 0.2709 T_K - 0.11132 \times 10^{-3} T_K^2 - (16719/T_K))}{-261.9 \log T_K}} \quad [64]$$

As shown in **Figure 11**, the solubility of  $\text{H}_2\text{S}$  decreases with temperature, as it is observed for  $\text{CO}_2$ . However, for the same partial pressure and temperature, the concentration of dissolved  $\text{H}_2\text{S}$  actually exceeds that in the gas phase as shown in **Figure 12**.

Aqueous  $\text{H}_2\text{S}$  is another weak acid which partly dissociates in two steps:



where  $K_{\text{hs}}$  is the dissociation constant of  $\text{H}_2\text{S}$ :

$$K_{\text{hs}} = \frac{c_{\text{H}^+} c_{\text{HS}^-}}{c_{\text{H}_2\text{S}}} \quad [67]$$

and can be calculated as<sup>35</sup>

$$K_{\text{hs}} = 10^{\frac{782.43945 + 0.361261 T_K - 1.6722 \times 10^{-4} T_K^2 - (20565.7315/T_K)}{-142.741722 \ln T_K}} \quad [68]$$

and  $K_{\text{bs}}$  is the dissociation constant of  $\text{HS}^-$ :

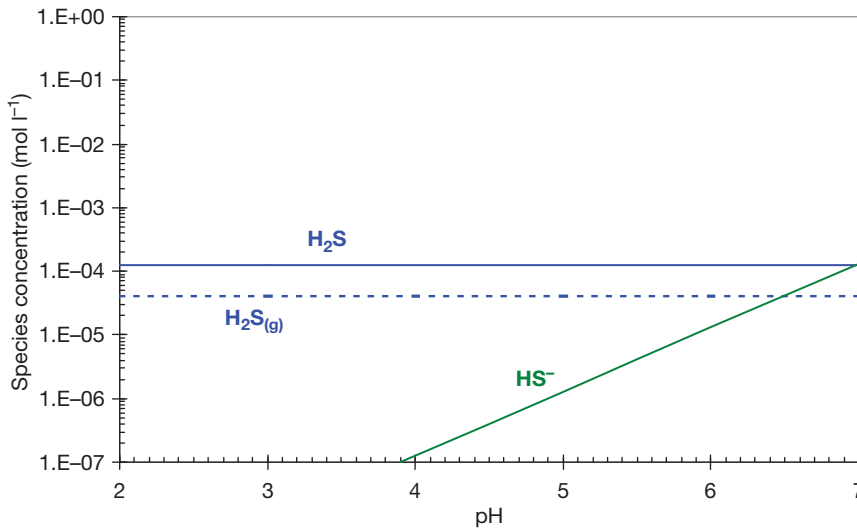


**Figure 12** Calculated sulfide species concentrations as a function of pH for an  $\text{H}_2\text{S}$  saturated aqueous solution at  $p_{\text{H}_2\text{S}} = 1 \text{ mbar}$ ,  $25^\circ\text{C}$ , 1 wt% NaCl.

$$K_{bs} = \frac{c_{H^+} c_{S^{2-}}}{c_{HS^-}} \quad [69]$$

There is a very large discrepancy in the reported values for  $K_{bs}$ , varying from  $1.0 \times 10^{-19}$  to  $1.1 \times 10^{-12} \text{ kmol m}^{-3}$  at room temperature (seven orders of magnitude). In addition, these values are very small compared with other equilibrium constants, all suggesting that using  $K_{bs}$  to calculate the concentration of sulfide species,  $c_{S^{2-}}$  and further to predict the solubility product constants for ferrous sulfides should be avoided.

Given the same gaseous concentrations of  $H_2S$  and  $CO_2$ , one obtains a similar aqueous concentration of dissolved  $H_2S$  and  $CO_2$  (see Figure 11) and the resulting pH is within 0.1 pH unit, therefore, values shown in Figure 1 for  $CO_2$  can be used for  $H_2S$  as the first approximation. The equilibrium distribution of sulfide species as a function of pH for an open system is shown in Figure 12. The concentration of bisulfide ion,  $c_{HS^-}$ , becomes significant only above pH 4, while the concentration of the sulfide ion,  $c_{S^{2-}}$ , is not even shown as it is very low and unreliable to calculate.

Many types of iron sulfides, such as amorphous ferrous sulfide (FeS), mackinawite ( $Fe_{1+x}S$ ), cubic ferrous sulfide (FeS), troilite (FeS), pyrrhotite ( $Fe_{1-x}S$  or  $FeS_{1+x}$ ), smythite ( $Fe_{3+x}S_4$ ), greigite ( $Fe_3S_4$ ), and pyrite ( $FeS_2$ ) occur. Studies have suggested that some of these are stoichiometric such as cubic ferrous sulfide, troilite, greigite, and pyrite, while others such as mackinawite, pyrrhotite, and smythite are not. Some are electrically nonconductive, others apparently behave as semiconductors. However, there is no consensus on these issues and the interested reader is directed to the vast literature on iron sulfides for a more in-depth treatment. The thermodynamics of these systems is very complicated; depending on environmental conditions and time, transformation from one type of ferrous sulfide into the other occurs. Limited information exists on aqueous solubility of the various sulfides. Avoiding the usage of the sulfide ion concentration,  $c_{S^{2-}}$ , one can write a general equation for precipitation of ferrous sulfide as



where the solubility constant for one type of

ferrous sulfide – mackinawite is known as a function of temperature<sup>36,37</sup>

$$K_{sp(FeS)}^{mackin} = 10^{(2848.779)/T_k - 6.347} \quad [71]$$

For other ferrous sulfides, only the values at room temperature are known, as listed in Table 1 below. It is convenient to show various ferrous sulfide solubilities in terms of an equilibrium concentration of the  $Fe^{2+}$  as a function of pH at a given  $H_2S$  partial pressure (concentration). An example is presented in Figure 13 where it can be seen that the much less soluble pyrrhotite and troilite are thermodynamically more stable forms compared to mackinawite and amorphous ferrous sulfide. For a typical ferrous ion concentration of  $c_{Fe^{2+}} = 1 \text{ ppm}$ , the saturation with respect to troilite and pyrrhotite is reached already at pH 5.4, while for mackinawite it is pH 6 and for amorphous ferrous sulfide pH 6.7. Keeping in mind that the concentration of  $Fe^{2+}$  at a corroding steel surface can easily be much higher than in the bulk (e.g., 10 ppm or even higher) and that the pH is also higher at the surface than in the bulk (typically above pH 6), using Figure 13 one can expect a whole range of different ferrous sulfides to form on a corroding steel surface at this  $H_2S$  concentration at different points in time.

SEM images of a ferrous sulfide surface layer formed on mild steel after a week long exposure are shown in Figure 14. The layered structure of the sulfide is prominent, and it can be identified as mackinawite. In longer exposures, the ferrous sulfide layer thickens and eventually becomes more protective. An image of a ferrous sulfide layer after a month long exposure is shown in Figure 15. The composition of the layer is a mixture of mackinawite and pyrrhotite. Another layered structure composed of a mixture of ferrous carbonate and ferrous sulfide is shown in Figure 16.

**Table 1** Solubility product constants for various ferrous sulfides at 25 °C<sup>38</sup>

Type of ferrous sulfide	$-\log K_{sp(FeS)}$
Amorphous (FeS)	2.95
Mackinawite ( $Fe_{1+x}S$ )	3.6
Pyrrhotite ( $Fe_{1-x}S$ or $FeS_{1+x}$ )	5.19
Troilite (FeS)	5.31

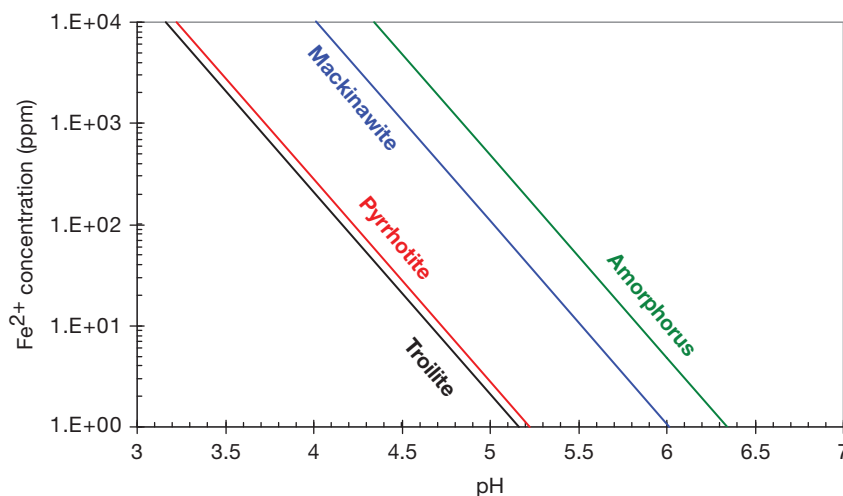


**Figure 13** Calculated solubility of various iron sulfides as a function of pH shown in terms of the equilibrium concentration of  $\text{Fe}^{2+}$ ,  $p_{\text{H}_2\text{S}} = 1 \text{ mbar}$ ,  $25^\circ\text{C}$ ,  $1 \text{ wt\% NaCl}$ .

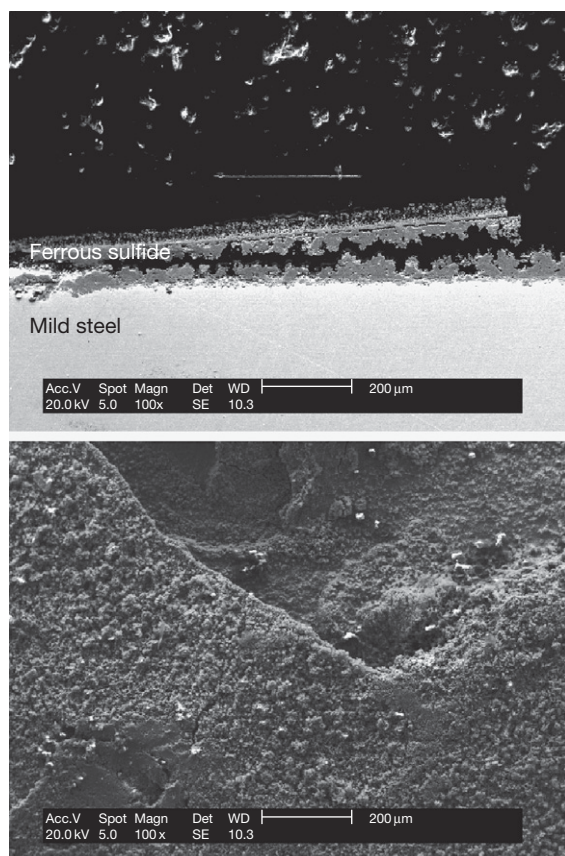


**Figure 14** SEM images showing a cross-section and a top view of a ferrous sulfide layer formed on mild steel;  $60^\circ\text{C}$ ,  $\text{pH } 6$ ,  $p_{\text{CO}_2} = 7.7 \text{ bar}$ ,  $p_{\text{H}_2\text{S}} = 0.25 \text{ mbar}$ ,  $1 \text{ m s}^{-1}$  single phase flow in a  $100 \text{ mm ID}$  pipe, 7 days exposure.

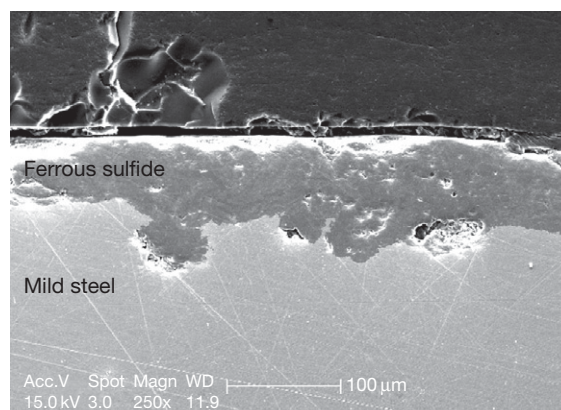


**Figure 15** SEM images showing a cross-section view of a ferrous sulfide layer formed on mild steel;  $60^\circ\text{C}$ ,  $\text{pH } 6$ ,  $p_{\text{CO}_2} = 7.7 \text{ bar}$ ,  $p_{\text{H}_2\text{S}} = 0.25 \text{ mbar}$ ,  $1 \text{ m s}^{-1}$  single phase flow in a  $100 \text{ mm ID}$  pipe, 30 day exposure.

### 2.25.3.2 Mild Steel Corrosion in $\text{H}_2\text{S}$ and Mixed $\text{H}_2\text{S}/\text{CO}_2$ Saturated Aqueous Solutions

As aqueous  $\text{H}_2\text{S}$  is another weak acid, it can be seen as an additional reservoir of  $\text{H}^+$  ions according to reaction [65], similar to  $\text{H}_2\text{CO}_3$ . Therefore, stimulation of the hydrogen evolution reaction could also be expected in the presence of  $\text{H}_2\text{S}$ . Using the analogy with  $\text{CO}_2$  corrosion, one must also allow the possibility of direct reduction of  $\text{H}_2\text{S}$ , that is, that the  $\text{H}_2\text{S}$  molecule can be adsorbed at the steel surface,



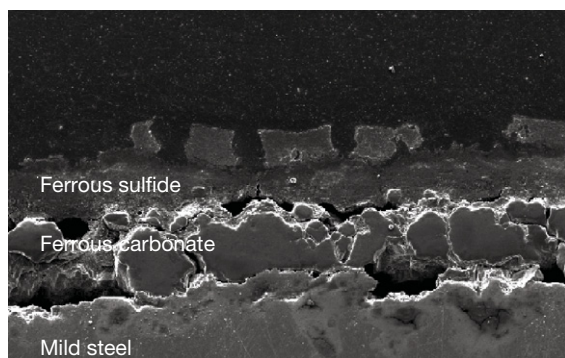
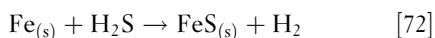


**Figure 16** SEM images showing a cross-section view of a mixed ferrous carbonate and ferrous sulfide layer formed on mild steel; 60 °C, pH 6,  $p_{\text{CO}_2} = 7.7$  bar,  $p_{\text{H}_2\text{S}} = 1.2$  mbar,  $1 \text{ m s}^{-1}$  single phase flow in a 100 mm ID pipe, 25 day exposure.

followed by a reduction of the  $\text{H}^+$  and oxidation of iron in the steel. One can write the overall corrosion reaction as



As solid ferrous sulfide (mackinawite) is always found on the corroding steel surface in the presence of  $\text{H}_2\text{S}$ , even below the solubility limit, this can be referred to as a direct ‘solid state’ reaction pathway as both the initial and final state of Fe are solid(s).<sup>39</sup>

Experimental evidence suggests that corrosion of mild steel by  $\text{H}_2\text{S}$  initially proceeds by adsorption of  $\text{H}_2\text{S}$  to the steel surface followed by a very fast redox reaction at the steel surface to form an adherent mackinawite film (much like a tarnish). This initial mackinawite film is very thin ( $\ll 1 \mu\text{m}$ ) but apparently rather dense and acts as a solid state diffusion barrier for the species involved in the corrosion reaction. Therefore, this thin mackinawite film is one of the most important factors governing the corrosion rate in  $\text{H}_2\text{S}$  corrosion. It also impedes the mobility of other species in reaching the steel surface and therefore corrosion rates due to  $\text{CO}_2$  are affected even if very small amounts of  $\text{H}_2\text{S}$  are present in the gas phase (as little as  $10^{-5}$  bar).

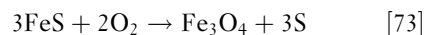
The thin mackinawite film continuously goes through a cyclic process of growth, internal stress growth, cracking, and delamination that generates an outer sulfide layer, which thickens over time (typically  $\gg 1 \mu\text{m}$ ) and forms an additional diffusion barrier. However, this outer sulfide layer is very porous and rather loosely attached to the steel surface. Over time it cracks, peels, and spalls, a process accelerated by turbulent flow. If the pH

of the solution is below saturation level, the outer sulfide layer will undergo a process of chemical dissolution. Conversely, when the saturation is exceeded, ferrous sulfide precipitation from the bulk is possible. Eventually, the amount and protectiveness of the outer sulfide layer is determined by the balance of the various formation and removal processes.<sup>39</sup>

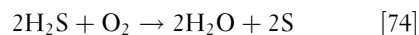
The transformation of mackinawite into other forms of less soluble and more stable ferrous sulfide (pyrrhotite and troilite, see Figure 13) may happen over time. Among the various ferrous sulfides, mackinawite is the prevalent ferrous sulfide that forms in the corrosion of mild steel at low  $\text{H}_2\text{S}$  concentration and low temperature. At increased levels of  $\text{H}_2\text{S}$ , mackinawite is less prevalent and pyrrhotite is the main corrosion product. At very high  $\text{H}_2\text{S}$  concentrations, pyrite and elemental sulfur appear. While thermodynamics of ferrous sulfides may favor other types of sulfide over mackinawite as the corrosion product, the rapid kinetics of mackinawite formation favors it as the initial corrosion product seen in most situations. Overall, however, there is currently no clearly defined relationship between the nature of the sulfide layer and the underlying corrosion process. It is generally thought that all types of ferrous sulfide layers offer some degree of corrosion protection for mild steel.

At very high  $\text{H}_2\text{S}$  concentrations, elemental sulfur can appear and lead to severe localized corrosion. Large amounts of elemental sulfur can precipitate out of the gas stream and can even block the line, due to the changes in pressure and temperature. Alternatively, when there is  $\text{O}_2$  present, the most likely pathways for formation of elemental sulfur are as follows:

- ferrous sulfide reacts with  $\text{O}_2$  and converts to iron oxide forming elemental sulfur probably via:



- at very high  $\text{H}_2\text{S}$  concentration, the following reaction can occur to yield elemental sulfur:



At very high temperatures, an alternative pathway is



Localized corrosion by elemental sulfur occurs via a reaction with the iron in the steel, represented by the



overall reaction



It is not very clear at this stage what the detailed mechanism of this reaction is. It appears that rapid attack is seen only when direct contact of sulfur with the steel is achieved in the presence of water. A more in-depth discussion about the corrosion mechanisms of mild steel involving elemental sulfur exceeds the scope of this review.

### 2.25.3.3 Calculation of Mild Steel H<sub>2</sub>S Corrosion Rate

Due to the complexity of the underlying processes and a lack of mechanistic understanding, predictive models of H<sub>2</sub>S corrosion were not readily available until recently. One approach<sup>40</sup> which has the capability to address a few simple H<sub>2</sub>S corrosion scenarios is presented below. A pure H<sub>2</sub>S corrosion environment is described first followed by a mixed H<sub>2</sub>S/CO<sub>2</sub> corrosion scenario.

#### 2.25.3.3.1 Pure H<sub>2</sub>S aqueous environment

Due to the presence of the inner mackinawite film and the outer porous sulfide layer, it is assumed that the corrosion rate of steel in H<sub>2</sub>S solutions is always under mass transfer control. One can then write the flux of H<sub>2</sub>S due to:

- convective diffusion through the mass transfer boundary layer as

$$\text{Flux}_{\text{H}_2\text{S}} = k_{\text{m}(\text{H}_2\text{S})} (c_{\text{H}_2\text{S}} - c_{\text{o}(\text{H}_2\text{S})}) \quad [77]$$

- molecular diffusion through the liquid in the porous outer sulfide layer as

$$\text{Flux}_{\text{H}_2\text{S}} = \frac{D_{\text{H}_2\text{S}} \varepsilon \psi}{\delta_{\text{os}}} (c_{\text{o}(\text{H}_2\text{S})} - c_{\text{i}(\text{H}_2\text{S})}) \quad [78]$$

- solid state diffusion through the inner mackinawite film as

$$\text{Flux}_{\text{H}_2\text{S}} = A_{\text{H}_2\text{S}} \exp\left(-\frac{B_{\text{H}_2\text{S}}}{RT_k}\right) \ln\left(\frac{c_{\text{i}(\text{H}_2\text{S})}}{c_{\text{s}(\text{H}_2\text{S})}}\right) \quad [79]$$

In a steady state, the three fluxes are equal to each other and are equivalent to the corrosion rate as

$$\text{CR}_{\text{H}_2\text{S}} = \text{Flux}_{\text{H}_2\text{S}} M_{\text{Fe}} / \rho_{\text{Fe}} \quad [80]$$

further corrected for appropriate corrosion rate unit.

By eliminating the unknown interfacial concentrations  $c_{\text{o}(\text{H}_2\text{S})}$  and  $c_{\text{i}(\text{H}_2\text{S})}$  from eqns [77] to [79], the following equation is obtained for the flux (corrosion rate) due to H<sub>2</sub>S:

$$\text{Flux}_{\text{H}_2\text{S}} = A_{\text{H}_2\text{S}} \ln \frac{c_{\text{H}_2\text{S}} - \text{Flux}_{\text{H}_2\text{S}} \left( \frac{\delta_{\text{os}}}{D_{\text{H}_2\text{S}} \varepsilon \psi} + \frac{1}{k_{\text{m}(\text{H}_2\text{S})}} \right)}{c_{\text{s}(\text{H}_2\text{S})}} \quad [81]$$

This is an algebraic nonlinear equation with respect to  $\text{Flux}_{\text{H}_2\text{S}}$ , which does not have an explicit solution but can be solved by using a simple numerical algorithm such as the interval halving method or similar methods. These are available as ready-made routines in spreadsheet applications or in any common computer programming language. The prediction for  $\text{Flux}_{\text{H}_2\text{S}}$  depends on a number of constants used in the model which can be either found in handbooks (such as  $D_{\text{H}_2\text{S}}$ ), calculated from the established theory (e.g.,  $k_{\text{m}(\text{H}_2\text{S})}$ ) or are determined from experiments (e.g.,  $A_{\text{H}_2\text{S}}$ ,  $c_{\text{s}(\text{H}_2\text{S})}$ ). The unknown thickness of the outer sulfide layer change with time and need to be calculated as described below.

It is assumed that the amount of layer retained on the metal surface at any point in time depends on the balance of:

- layer formation kinetics (as the layer is generated by spalling of the thin mackinawite film underneath it and by the precipitation from the solution), and
- layer damage kinetics (as the layer is damaged by intrinsic or hydrodynamic stresses and/or by chemical dissolution):

$$\underbrace{\text{SRR}}_{\text{Sulfide layer retention rate}} = \underbrace{\text{SFR}}_{\text{Sulfide layer formation rate}} - \underbrace{\text{SDR}}_{\text{Sulfide layer damage rate}} \quad [82]$$

where all the terms are expressed in  $\text{kmol m}^{-2} \text{s}^{-1}$ . In order to simplify the calculations, it can be assumed that in the typical range of application ( $4 < \text{pH} < 7$ ), precipitation and dissolution of ferrous sulfide layer do not play a significant role and so it can be written

$$\text{SRR} = \text{CR} - \text{SDR}_{\text{m}} \quad [83]$$

Some experiments involving mackinawite have shown that even in stagnant conditions about half of the outer sulfide layer that forms is lost from the steel surface due to intrinsic growth stresses by internal cracking and spalling, that is,  $\text{SDR}_{\text{m}} \approx 0.5\text{CR}$ , so one obtains:

$$\text{SRR} = 0.5\text{CR} \quad [84]$$

that is, about half of the iron corroded is found on the steel surface in the form of mackinawite. It is not known if and how this ratio is different when other types of ferrous sulfide layers form, for example, the more adherent and protective pyrrhotite. Moreover, additional experimentation is required to determine how the mechanical layer damage is affected by hydrodynamic forces.

Once the layer retention rate SRR is known, the change in mass of the outer sulfide layer can be easily calculated as

$$\Delta m_{os} = SRR M_{FeS} A \Delta t \quad [85]$$

The porosity of the outer sulfide layer was determined to be very high ( $\varepsilon \approx 0.9$ ) by comparing the weight of the layer with the cross-sectional SEM images showing its thickness. On the other hand, this layer has proven to be rather protective (i.e., impermeable to diffusion) which can only be explained by its low tortuosity arising from its layered structure. By comparing the measured and calculated corrosion rates in the presence of the outer sulfide layer, the tortuosity factor was calculated to be  $\psi = 0.003$ .

A time-marching explicit solution procedure could now be established where

1. the corrosion rate  $\text{Flux}_{H_2S}$  in the absence of outer sulfide layer can be calculated by using eqn [81], and assuming  $\delta_{os} = 0$ ;
2. the amount of sulfide layer  $\delta m_{os}$  formed over a time interval  $\Delta t$  is calculated by using eqn [85];
3. the new corrosion rate  $\text{Flux}_{H_2S}$  in the presence of sulfide layer can be recalculated by using eqn [81];
4. a new time interval  $\Delta t$  is set and steps 2 and 3 repeated.

At very low  $H_2S$  gas concentrations (ppm<sub>w</sub> range), there is very little dissolved  $H_2S$  and the corrosion rate is directly affected by pH. A mackinawite layer still forms and controls the corrosion rate; however, the corrosion process is largely driven by the reduction of  $H^+$  ions, rather than of  $H_2S$ . By analogy with the approach laid out above, the following expression is obtained for the flux of  $H^+$  ions controlled by the presence of the ferrous sulfide layers:

$$\text{Flux}_{H^+} = A_{H^+} \ln \frac{c_{H^+} - \text{Flux}_{H^+} \left( \frac{\delta_{os}}{D_{H^+} \varepsilon \psi} + \frac{1}{k_m(H^+)} \right)}{c_s(H^+)} \quad [86]$$

The flux  $\text{Flux}_{H^+}$  is directly related to the corrosion rate by  $H^+$  ions:

$$CR_{H^+} = \frac{\text{Flux}_{H^+} M_{Fe}}{2 \rho_{Fe}} \quad [87]$$

further adjusted for the appropriate corrosion rate unit.

By solving eqns [81] and [86] sequentially in time, the total corrosion rate in mixed pure  $H_2S$  aqueous environments can be calculated as

$$CR = CR_{H_2S} + CR_{H^+} \quad [88]$$

### 2.25.3.3.2 Mixed $CO_2/H_2S$ environments

For mild steel corrosion in mixed  $CO_2/H_2S$  containing environments, one can account for the effect of  $CO_2$  by assuming that the rate controlling step in this additional process is the diffusion of  $CO_2$  through the ferrous sulfide layers. Then a similar expression can be obtained for the corrosion rate due to  $CO_2$ :

$$\text{Flux}_{CO_2} = A_{CO_2} \ln \frac{c_{CO_2} - \text{Flux}_{CO_2} \left( \frac{\delta_{os}}{D_{CO_2} \varepsilon \psi} + \frac{1}{k_m(CO_2)} \right)}{c_s(CO_2)} \quad [89]$$

The flux  $\text{Flux}_{CO_2}$  is equivalent to the corrosion rate by  $CO_2$ :

$$CR_{CO_2} = \frac{\text{Flux}_{CO_2} M_{Fe}}{2 \rho_{Fe}} \quad [90]$$

further adjusted for appropriate corrosion rate unit.

By solving eqns [81], [86], and [89], the total corrosion rate in mixed  $CO_2/H_2S$  environments can be calculated as

$$CR = CR_{H_2S} + CR_{H^+} + CR_{CO_2} \quad [91]$$

### 2.25.3.4 Limitations of Modeling of Aqueous $H_2S$ Corrosion of Mild Steel

The calculation model presented above covers uniform  $H_2S$  and  $CO_2/H_2S$  corrosion. There are numerous limitations:

- It does not predict localized corrosion in either environment.
- While it covers a very broad range of  $H_2S$  partial pressures, it is not recommended to use this model below  $p_{H_2S} = 0.01$  mbar or above  $p_{H_2S} = 10$  bar. Similar limits apply to the  $CO_2$  partial pressure.

This leaves a very broad area of applicability for the present model.

- This H<sub>2</sub>S model does not account for any precipitation of ferrous sulfide, ferrous carbonate, or any other scale; therefore, in cases where this is deemed important for corrosion, the model should be used with caution. The model also does not account for various transformations of sulfide layer from one type to another which are known to happen over time.
- The present model does not account for dissolution of the sulfide layer that may occur at very low pH. Therefore, the use of this model at pH < 3 is not recommended. Similarly, the model should be used with caution for pH > 7 where it has not been tested.
- The model in its present state does not cover the effect of organic acids on mixed H<sub>2</sub>S and CO<sub>2</sub>/H<sub>2</sub>S corrosion, and therefore it should not be used when organic acids are present in the system. A practical threshold for the validity of the present model is <1 ppm of organic acids in the brine.
- The model does not account for the effect of high chloride concentrations, oxygen, elemental sulfur or any other unspecified condition, which is known to affect the corrosion rate and is not explicitly covered in the theoretical underpinnings discussed above.

While this calculation model is clearly not inclusive of all the important processes in aqueous H<sub>2</sub>S corrosion of mild steel, it is believed that the

main underlying assumptions about the formation and protective nature of a mackinawite layer are correct. The comparison of the performance of this model with experimental data is given in the following section, which covers the main factors affecting CO<sub>2</sub>/H<sub>2</sub>S corrosion of mild steel.

### 2.25.3.5 Key Factors Affecting Aqueous H<sub>2</sub>S Corrosion of Mild Steel

Some of the key factors affecting aqueous H<sub>2</sub>S corrosion are discussed in these sections, and the experimental results are compared with the model described above.

#### 2.25.3.5.1 Effect of H<sub>2</sub>S partial pressure

Corrosion rate of mild steel at extremely low H<sub>2</sub>S partial pressures is seen in Figure 17 wherein atmospheric glass cell experiments  $p_{\text{H}_2\text{S}}$  ranged from 0.0013–0.32 mbar, corresponding to 1–250 ppm<sub>m</sub> in the gas phase at 1 bar CO<sub>2</sub>. Clearly, this is a CO<sub>2</sub> dominated corrosion scenario ( $p_{\text{CO}_2}/p_{\text{H}_2\text{S}}$  ratio is in the range  $10^3$ – $10^6$ ); however, the presence of H<sub>2</sub>S controls the corrosion rate. Even when present in such minute amounts, H<sub>2</sub>S reduces the pure CO<sub>2</sub> (H<sub>2</sub>S-free) corrosion rate by 3–10 times due to the formation of a thin mackinawite film. The model presented above successfully captures this effect as shown in Figure 17.

At higher H<sub>2</sub>S partial pressures, the same effect is observed as shown in Figure 18, which shows results from autoclave experiments conducted at a very high

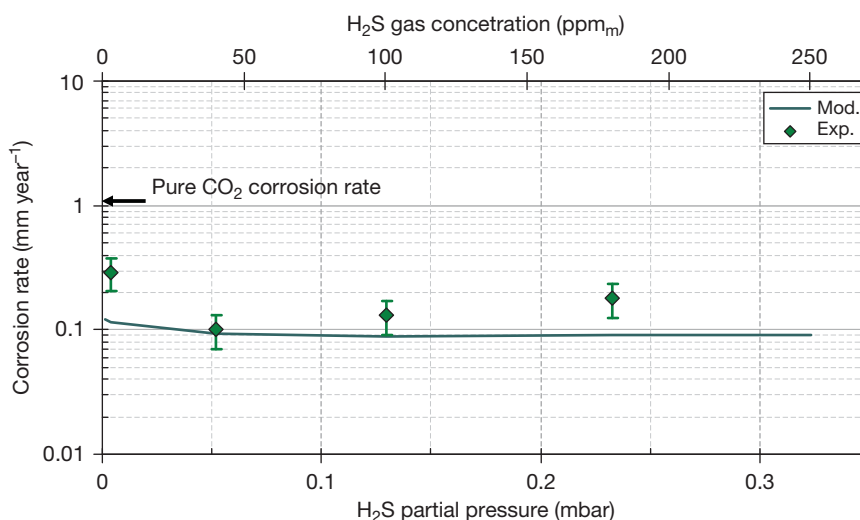


**Figure 17** The corrosion rate vs. partial pressure of H<sub>2</sub>S; experimental data (exp.) shown as points, model predictions (mod.) shown as lines; conditions: total pressure  $p = 1$  bar,  $p_{\text{CO}_2} = 1$  bar,  $p_{\text{H}_2\text{S}} = 0.0013$ – $0.32$  mbar,  $T = 20^\circ\text{C}$ , reaction time 24 h, pH 5, 1000 rpm. For reference: pure CO<sub>2</sub> corrosion rate is measured to be  $1\text{ mm year}^{-1}$ . Data taken from Lee.<sup>41</sup>

total pressure ( $p = 138$  bar) and a high  $\text{CO}_2$  partial pressure ( $p_{\text{CO}_2} = 13.8$  bar). When comparing the predictions with the experimental results, it can be seen that the model underpredicts the observed rate of steel corrosion by approximately a factor of 2. However, when this is compared with a pure  $\text{CO}_2$  ( $\text{H}_2\text{S}$ -free) corrosion rate under the same conditions (which is not reported but can be predicted to be almost  $20 \text{ mm year}^{-1}$ ), the accuracy of the model can be considered as reasonable. At the highest  $p_{\text{CO}_2}/p_{\text{H}_2\text{S}}$

ratio of 3500 ( $p_{\text{CO}_2} = 13.8$  bar,  $p_{\text{H}_2\text{S}} = 40$  mbar),  $\text{CO}_2$  accounts for  $\sim 70\%$  of the corrosion rate and 30% can be ascribed to  $\text{H}_2\text{S}$ . At the lowest  $p_{\text{CO}_2}/p_{\text{H}_2\text{S}}$  ratio of 1180 ( $p_{\text{CO}_2} = 13.8$  bar,  $p_{\text{H}_2\text{S}} = 116$  mbar),  $\text{CO}_2$  accounts for  $\sim 57\%$  of the corrosion rate and 43% can be ascribed to  $\text{H}_2\text{S}$ .

Corrosion rates of mild steel at very high partial pressures of  $\text{H}_2\text{S}$  ( $p_{\text{H}_2\text{S}} = 3\text{--}20$  bar) and  $\text{CO}_2$  ( $p_{\text{CO}_2} = 3\text{--}12.8$  bar) for exposures lasting up to 4 days are shown in Figure 19. This is a situation where the

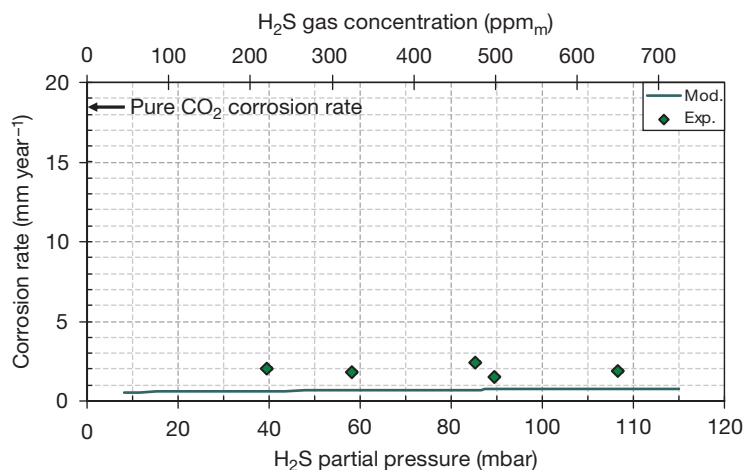


**Figure 18** The corrosion rate vs.  $\text{H}_2\text{S}$  partial pressure; experimental data (exp.) shown as points, model predictions (mod.) shown as lines; conditions: total pressure  $p = 137.9$  bar,  $p_{\text{CO}_2} = 13.8$  bar,  $p_{\text{H}_2\text{S}} = 40\text{--}120$  mbar,  $T = 50^\circ\text{C}$ , experiment duration 3 days, pH 4.0–6.2, stagnant. Experimental data taken from Smith and Pacheco *et al.*<sup>31</sup>

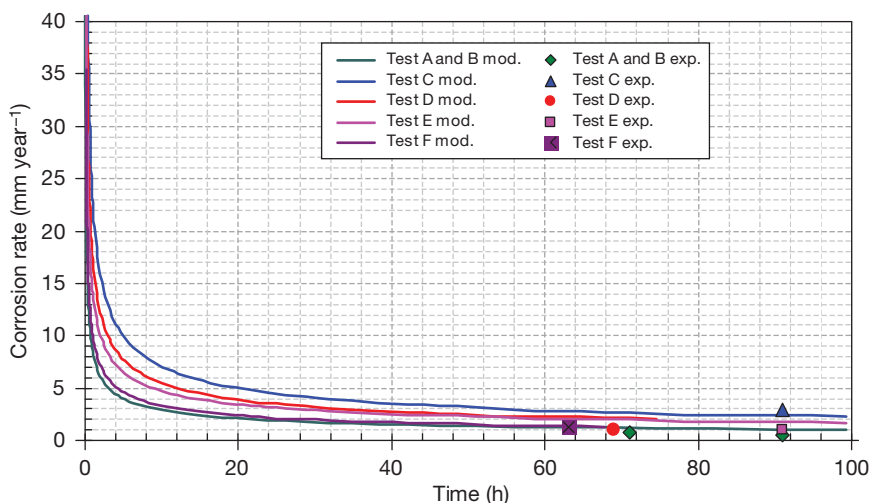


**Figure 19** The corrosion rate vs. time; experimental data (exp.) shown as points, model predictions (mod.) shown as lines; Test A and B:  $p = 8.3$  bar,  $p_{\text{CO}_2} = 5.3$  bar,  $p_{\text{H}_2\text{S}} = 3$  bar,  $T = 60^\circ\text{C}$ , 71 h (a) and 91 h (b); Test C:  $p = 24$  bar,  $p_{\text{CO}_2} = 4$  bar,  $p_{\text{H}_2\text{S}} = 20$  bar,  $T = 70^\circ\text{C}$ , 91 h; Test D:  $p = 15.7$  bar,  $p_{\text{CO}_2} = 3.5$  bar,  $p_{\text{H}_2\text{S}} = 12.2$  bar,  $T = 65^\circ\text{C}$ , 69 h; Test E:  $p = 20.8$  bar,  $p_{\text{CO}_2} = 12.8$  bar,  $p_{\text{H}_2\text{S}} = 8$  bar,  $T = 65^\circ\text{C}$ , 91 h; Test F:  $p = 7.2$  bar,  $p_{\text{CO}_2} = 3$  bar,  $p_{\text{H}_2\text{S}} = 4.2$  bar,  $T = 65^\circ\text{C}$ , 63 h; experimental data taken from Bich and Goerz.<sup>43</sup>

H<sub>2</sub>S was the dominant corrosive species. At the highest  $p_{\text{CO}_2}/p_{\text{H}_2\text{S}}$  ratio of 1.8 ( $p_{\text{CO}_2} = 5.3$  bar,  $p_{\text{H}_2\text{S}} = 3$  bar), H<sub>2</sub>S generated ~86% of the corrosion rate. At the lowest  $p_{\text{CO}_2}/p_{\text{H}_2\text{S}}$  ratio of 0.2 ( $p_{\text{CO}_2} = 4$  bar,  $p_{\text{H}_2\text{S}} = 20$  bar), H<sub>2</sub>S generated 97% of the overall corrosion rate. It is also noted that the model predictions show that the corrosion rate in the first reaction hour is on average 20 mm year<sup>-1</sup> with an initial corrosion rate of 60 mm year<sup>-1</sup> and a final corrosion rate of 10 mm year<sup>-1</sup>. The pitting corrosion rate was reported to be 30 mm year<sup>-1</sup> in a field case with similar conditions, which is related to the very high, H<sub>2</sub>S-driven corrosion seen at the beginning of experiments before a thick protective ferrous sulfide film forms.

### 2.25.3.5.2 Effect of flow

The effect of flow velocity in H<sub>2</sub>S corrosion is shown in Figure 20 for the three long-term experiments reported by Omar *et al.*<sup>44</sup> Flow loop experiments lasting 15–21 days were conducted at severe conditions: high partial pressure of H<sub>2</sub>S ( $p_{\text{H}_2\text{S}} = 10$ –30 bar), high partial pressure of CO<sub>2</sub> ( $p_{\text{CO}_2} = 3.3$ –10 bar) and low pH 2.9–3.2. No effect of velocity on the uniform corrosion rate could be observed in these long-term exposures, which is due to the build-up of a thick protective sulfide layer. The model predictions also shown in Figure 20 confirm this trend and show a remarkable agreement with the experimental results

in the less extreme experiments 1 and 2 ( $p_{\text{CO}_2} = 3.3$  bar;  $p_{\text{H}_2\text{S}} = 10$  bar) both at low (25 °C) and high temperature (80 °C). In experiment 3 which was conducted at the most extreme set of conditions ( $p_{\text{CO}_2} = 10$  bar;  $p_{\text{H}_2\text{S}} = 30$  bar) and high temperature (80 °C) the model overpredicts the corrosion rate by a factor of 2.5. In all three experiments reported by Omar *et al.*,<sup>44</sup> the  $p_{\text{CO}_2}/p_{\text{H}_2\text{S}}$  ratio was about 0.3, that is, the corrosion process and corrosion rate were completely dominated by H<sub>2</sub>S, which contributed ~95% of the corrosion rate.

### 2.25.3.5.3 Effect of time

A marked decrease of corrosion rate with time was seen in autoclave tests as reported in Figure 19 above; the same was observed in stratified pipe flow experiments where pure CO<sub>2</sub> corrosion rate decreased with time due to the presence of H<sub>2</sub>S, as shown in Figure 21 below. The latter is also a mixed CO<sub>2</sub>/H<sub>2</sub>S corrosion scenario. At a  $p_{\text{CO}_2}/p_{\text{H}_2\text{S}}$  ratio of 200 ( $p_{\text{CO}_2} = 2$  bar,  $p_{\text{H}_2\text{S}} = 4$  mbar), the CO<sub>2</sub> contribution to the corrosion rate is 75% with most of the balance provided by H<sub>2</sub>S. At the  $p_{\text{CO}_2}/p_{\text{H}_2\text{S}}$  ratio of 28 ( $p_{\text{CO}_2} = 2$  bar,  $p_{\text{H}_2\text{S}} = 70$  mbar), both CO<sub>2</sub> and H<sub>2</sub>S account for ~50% of the overall corrosion rate.

Corrosion experiments at high temperature (120 °C), high partial pressures of CO<sub>2</sub> ( $p_{\text{CO}_2} = 6.9$  bar), and H<sub>2</sub>S ( $p_{\text{H}_2\text{S}} = 1.38$ –4.14 bar) in exposures

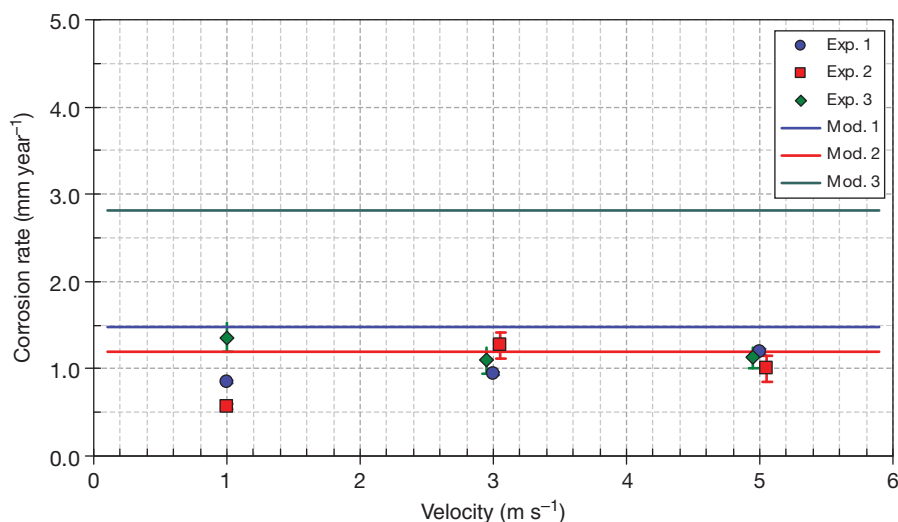


**Figure 20** The corrosion rate vs. velocity; experimental data (exp.) shown as points, model predictions (mod.) shown as lines; exp 1.: 19 days,  $p = 40$  bar,  $p_{\text{CO}_2} = 3.3$  bar,  $p_{\text{H}_2\text{S}} = 10$  bar,  $T = 80$  °C, pH 3.1,  $v = 1$ –5 m s<sup>-1</sup>; exp 2.: 21 days,  $p = 40$  bar,  $p_{\text{CO}_2} = 3.3$  bar,  $p_{\text{H}_2\text{S}} = 10$  bar,  $T = 25$  °C, pH 3.2,  $v = 1$ –5 m s<sup>-1</sup>; exp 3.: 10 days,  $p = 40$  bar,  $p_{\text{CO}_2} = 10$  bar,  $p_{\text{H}_2\text{S}} = 30$  bar,  $T = 80$  °C, pH 2.9,  $v = 1$ –5 m s<sup>-1</sup>; experimental data taken from Omar *et al.*<sup>44</sup>



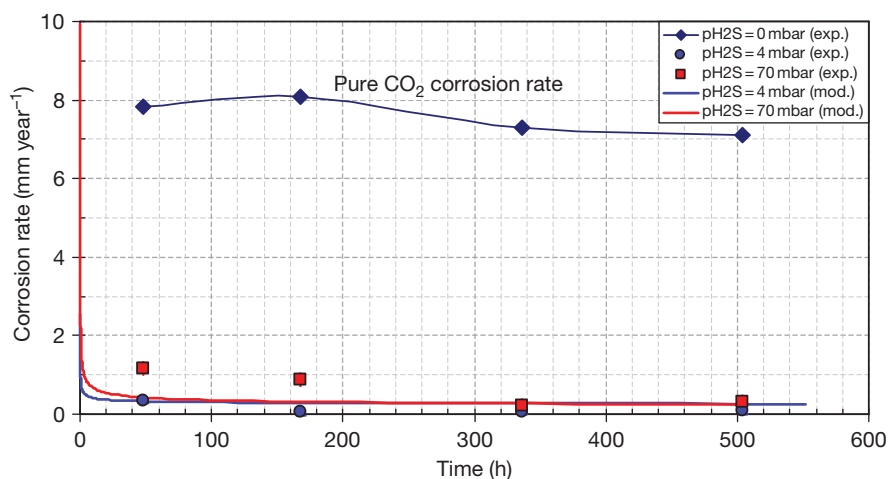


**Figure 21** The corrosion rate vs. time; experimental data (exp.) shown as points, model predictions (mod.) shown as lines; conditions: total pressure  $p = 3$  bar,  $p_{\text{CO}_2} = 2$  bar,  $p_{\text{H}_2\text{S}} = 3\text{--}70$  mbar,  $T = 70^\circ\text{C}$ , experiment duration 2–21 days, pH 4.2–4.9, liquid velocity  $0.3\text{ m s}^{-1}$ . Experimental data taken from Singer *et al.*<sup>42</sup>

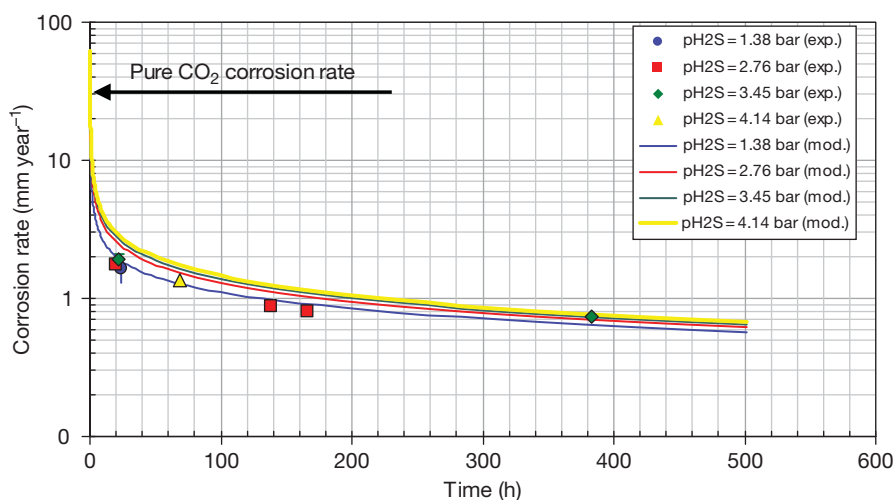


**Figure 22** The corrosion rate vs. time; experimental data (exp.) shown as points, model predictions (mod.) shown as lines; conditions: total pressure  $p = 7$  bar,  $p_{\text{CO}_2} = 6.9$  bar,  $p_{\text{H}_2\text{S}} = 1.38\text{--}4.14$  bar,  $T = 120^\circ\text{C}$ , experiment duration 1–16 days, pH 3.95–4.96, liquid velocity  $10\text{ m s}^{-1}$ . Experimental data taken from Kvarekval *et al.*<sup>45</sup>

lasting up to 16 days are shown in Figure 22. A steadily decreasing corrosion rate was observed due to build-up of a protective ferrous sulfide layer. The effect of  $p_{\text{H}_2\text{S}}$  increase on corrosion rate was very small and practically vanished over time. Both these effects were readily captured by the model with very good accuracy as seen in Figure 22. In this case, the  $\text{H}_2\text{S}$  is the dominant corrosive species. At the highest  $p_{\text{CO}_2}/p_{\text{H}_2\text{S}}$  ratio of 5 ( $p_{\text{CO}_2} = 6.9$  bar,  $p_{\text{H}_2\text{S}} = 1.38$  bar),  $\text{H}_2\text{S}$  generated  $\sim 70\%$  of the corrosion rate. At the

lowest  $p_{\text{CO}_2}/p_{\text{H}_2\text{S}}$  ratio of 1.67 ( $p_{\text{CO}_2} = 6.9$  bar,  $p_{\text{H}_2\text{S}} = 4.14$  bar),  $\text{H}_2\text{S}$  generated 82% of the overall corrosion rate.

The longest  $\text{H}_2\text{S}$  containing corrosion experiments which are practically achievable in the lab are of the order of a few weeks or at best a few months, while predictions are meant to cover a period of at least a decade, in order to be meaningful. With this in mind, it is interesting to take the experimental conditions above ( $p_{\text{CO}_2} = 6.9$  bar,  $p_{\text{H}_2\text{S}} = 3.45$  bar,

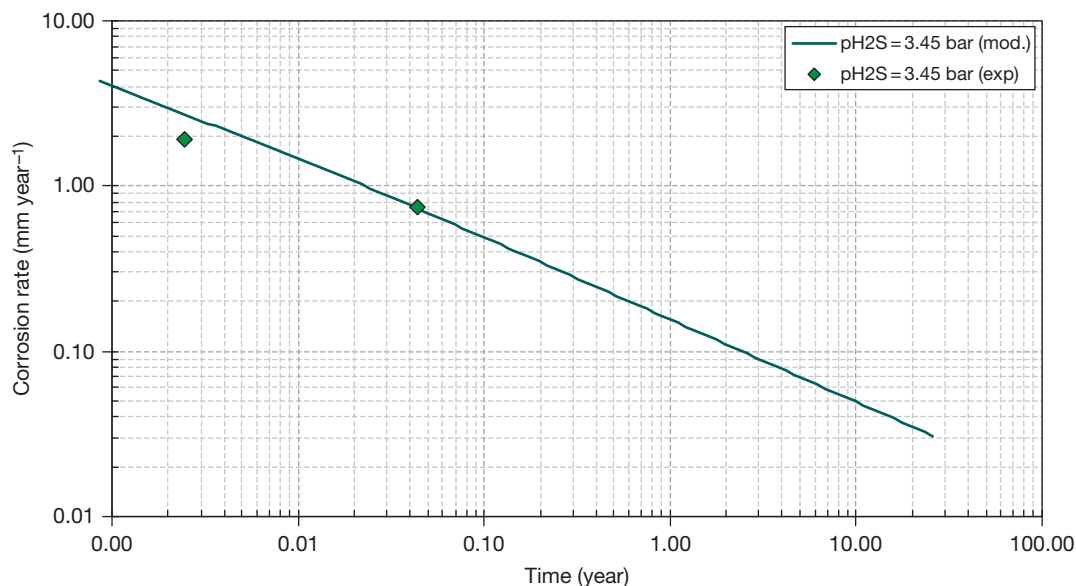


**Figure 23** Extension of corrosion prediction to a 25-year lifetime; experimental (points), predicted (lines); conditions:  $p_{\text{CO}_2} = 6.9$  bar,  $p_{\text{H}_2\text{S}} = 3.45$  bar,  $T = 120^\circ\text{C}$ , pH 4, liquid velocity  $10\text{ m s}^{-1}$ . Data from Kvarekval *et al.*<sup>45</sup>

$T = 120^\circ\text{C}$ , pH 4,  $v = 10\text{ m s}^{-1}$ ) and extend the simulation to 25 years. The result is shown in Figure 23. The corrosion rate was predicted to start out rather high as observed in the experiments; however, it was reduced to below  $0.1\text{ mm year}^{-1}$  after 2 years and was as low as  $0.03\text{ mm year}^{-1}$  after 25 years. The average corrosion rate over this period was only  $0.06\text{ mm year}^{-1}$ , which amounts to a wall thickness loss of only 1.5 mm over the 25 years, an acceptable amount by any practical account. Actually, most of the other conditions simulated have shown that rather low  $\text{H}_2\text{S}$  uniform corrosion rates are obtained for very long exposures, which agrees with general field experience as recently discussed by Bonis *et al.*<sup>33</sup> Nevertheless, no quantitative long-term lab data are currently available to back-up these long-term predictions, and therefore they should be used with caution.

#### 2.25.3.6 Localized $\text{H}_2\text{S}$ Corrosion of Mild Steel in Aqueous Solutions

Localized  $\text{H}_2\text{S}$  corrosion of mild steel is even less understood than its uniform counterpart. While it is not very common, anecdotal evidence exists that has linked localized  $\text{H}_2\text{S}$  corrosion in aqueous environments to other factors such as high chloride content, the presence of elemental sulfur and the transformation of one type of sulfide into another. Intense research of these topics is ongoing with a breakthrough in understanding expected in the decade to come.

## References

1. Bonis, M. R.; Crolet, J. L. In *Corrosion/89*; NACE International: Houston, TX, 1989; Paper no. 466.
2. Oddo, J.; Tomson, M. In *SPE of AIME*; Society of Petroleum Engineers: Richardson, TX, 1982; pp 1583–1590.
3. Palmer, D. A.; van Eldik, R. *Chem. Rev.* **1983**, 83, 651.
4. Sun, W.; Nešić, S.; Woollam, R. C. *Corros. Sci.* **2009**, 51(6), 1273–1276.
5. Sun, W.; Nešić, S. *Corrosion* **2008**, 64, 334.
6. Drazic, D. M. In *Aspects of Electrochemistry*; Plenum Press, 1989; Vol. 19, p 79.
7. Lorenz, W.; Heusler, K. In *Corrosion Mechanisms*; Mansfeld, F., Ed.; Marcel Dekker: New York, 1987.
8. Nešić, S.; Thevenot, N.; Crolet, J. L. In *Corrosion/96*; NACE International: Houston, TX, 1996; Paper no. 3.
9. de Waard, C.; Williams, D. E. *Corrosion* **1975**, 31, 131.
10. Gray, L. G. S.; Anderson, B. G.; Danysh, M. J.; Tremaine, P. R. In *Corrosion/89*; NACE International: Houston, TX, 1989; Paper no. 464.
11. Eriksrud, E.; Sontvedt, T. In *Advances in  $\text{CO}_2$  Corrosion*, Proceedings of the Corrosion/83 Symposium on  $\text{CO}_2$  Corrosion in the Oil and Gas Industry; Hausler, R. H., Goddard, H. P., Eds.; NACE: Houston, TX, 1984; Vol. 1, p 20.
12. Schmitt, G.; Rothman, B. *Werkst. Korros.* **1977**, 28, 816.
13. Gray, L. G. S.; Anderson, B. G.; Danysh, M. J.; Tremaine, P. R. In *Corrosion/90*; NACE International: Houston, TX, 1990; Paper no. 40.
14. Delahay, P. *J. Am. Chem. Soc.* **1952**, 74, 3497.
15. Nešić, S.; Postlethwaite, J.; Olsen, S. In *Corrosion/95*; NACE International: Houston, TX, 1995; Paper no. 131.
16. Nešić, S.; Pots, B. F. M.; Postlethwaite, J.; Thevenot, N. *J. Corros. Sci. Eng.* **1995**, 1 Paper no. 3. Available at [http://www.cp.umist.ac.uk/JCSE/Vol1/PAPER3/V1\\_p3int.htm](http://www.cp.umist.ac.uk/JCSE/Vol1/PAPER3/V1_p3int.htm)
17. Chokshi, K.; Sun, W.; Nešić, S. In *Corrosion/05*; NACE International: Houston, TX, 2005; Paper no. 285.
18. Sun, Y.; Nešić, S. *Corrosion/2004*; NACE International: Houston, TX, 2004; Paper no. 380.

19. Nešić, S.; G.Solvi, T.; Enerhaug, J. *Corrosion* **1995**, *51*, p 773.
20. Sun, Y.; George, K.; Nešić, S. In *Corrosion/2003*; NACE International: Houston, TX, 2003; Paper no. 3327.
21. Gunaltun, Y. M.; Larrey, D. In *Corrosion/2000*; NACE International: Houston, TX, 2000; Paper no. 71.
22. Vitse, F.; Nešić, S.; Gunaltun, Y.; Larrey de Torreben, D.; Duchet-Suchaux, P. *Corrosion* **2003**, *59*, 1075.
23. Anderko, A.; Young, R. In *Corrosion/99*; NACE International: Houston, TX, 1999; Paper no. 31.
24. de Waard, C.; Lotz, U. *Corrosion/93*; NACE International: Houston, TX, 1993; Paper no. 69.
25. Berger, F. P.; Hau, K.-F. F.-L. *Int. J. Heat Mass Transfer* **1977**, *20*, 1185.
26. Eisenberg, M.; Tobias, C. W.; Wilke, C. R. *J. Electrochem. Soc.* **1954**, *101*, 306.
27. Shoesmith, D. W.; Taylor, P.; Bailey, M. G.; Owen, D. G. J. *Electrochem. Soc.* **1980**, *125*, 1007–1015.
28. Shoesmith, D. W. Formation, transformation and dissolution of phases formed on surfaces, In Lash Miller Award Address, Electrochemical Society Meeting, Ottawa, 27 November 1981.
29. Smith, S. N. In Twelfth International Corrosion Congress, Houston, TX, 19–24 September 1993; Paper no. 385.
30. Smith, S. N.; Wright, E. J. In *Corrosion/94*; NACE International: Houston, TX, 1994; Paper no. 11.
31. Smith, S. N.; Pacheco, J. L. In *Corrosion/2002*; NACE International: Houston, TX, 2002; Paper no. 02241.
32. Smith, S. N.; Joosten, M. In *Corrosion/2006*; NACE International: Houston, TX, 2006; Paper no. 06115.
33. Bonis, M.; Girgis, M.; Goerz, K.; MacDonald, R. In *Corrosion/2006*; NACE International: Houston, TX, 2006; Paper no. 06122.
34. Suleimenov, O. M.; Krupp, R. E. *Geochim. Cosmochim. Acta* **1994**, *58*, 2433–2444.
35. Suleimenov, O. M.; Seward, T. M. *Geochim. Cosmochim. Acta* **1997**, *61*, 5187–5198.
36. Benning, L. G.; Wilkin, R. T.; Barnes, H. L. *Chem. Geol.* **2000**, *167*, 25–51.
37. Sun, W.; Nescic, S.; Young, D.; Woollam, R. *Ind. Eng. Chem. Res.* **2008**, *47*(5), 1738–1742.
38. Criaud, A.; Fouillac, C.; Marty, B. *Geothermics* **1989**, *18*(5–6), 711–727.
39. Sun, W.; Nescic, S.; Papavinasam, S. *Corrosion* **2008**, *64*(7), 586–599.
40. Sun, W.; Nescic, S. *Corrosion* **2009**, *65*(5), 291–307.
41. Lee, K. J. Ph.D. dissertation. Ohio University, 2004.
42. Singer, M.; Brown, B.; Camacho, A.; Nešić, S. In *Corrosion/07*; NACE International: Houston, TX, 2007; Paper no. 07661.
43. Bich, N. N.; Goerz, K. In *Corrosion/1996*; NACE International: Houston, TX, 1996; Paper no. 26.
44. Omar, I. H.; Gunaltun, Y. M.; Kvarekval, J.; Dugstad, A. In *Corrosion/05*; NACE International: Houston, TX, 2005; Paper no. 05300.
45. Kvarekval, J.; Nyborg, R.; Choi, H. In *Corrosion/03*; NACE International: Houston, TX, 2003; Paper no. 03339.

## 2.26 Corrosion in Lubricants/Fuels

**R. W. Wilson**

Capcis House, 1 Echo Street, Manchester, M1 7DP, UK

**S. B. Lyon**

Corrosion and Protection Centre, School of Materials, The University of Manchester, Oxford Road, Manchester, M13 9PL, UK

This article is a revision of the Third Edition article 2.11 by R.W. Wilson, volume 1, pp 2:143–2:154, © 2010 Elsevier B.V.

<b>2.26.1</b>	<b>The Nature of Lubricating Oils and Greases</b>	1300
2.26.1.1	Introduction	1300
2.26.1.2	Lubricating Oils	1300
2.26.1.3	Greases	1301
<b>2.26.2</b>	<b>Deterioration of Lubricants</b>	1301
2.26.2.1	Deterioration by Combustion Products	1301
2.26.2.2	Oxidative Degradation	1301
2.26.2.3	Biodeterioration	1302
<b>2.26.3</b>	<b>Lubricant Additives</b>	1302
2.26.3.1	Types of Additive	1302
2.26.3.2	Extreme Pressure Additives	1302
2.26.3.3	Interactions Between Additives	1303
2.26.3.4	Additives in Greases	1303
2.26.3.5	Sulfur-Containing Additives	1303
<b>2.26.4</b>	<b>Corrosion in Specific Lubricant Systems</b>	1304
2.26.4.1	Internal Combustion Engine Lubricants	1304
2.26.4.2	Corrosive Wear	1304
2.26.4.3	Steam Turbine Lubricants	1305
2.26.4.4	Gear Lubricants	1305
2.26.4.5	Cavitation and Erosion	1305
2.26.4.6	Metal-Working Lubricants	1305
2.26.4.7	Water Base Lubricants	1306
2.26.4.8	Lubricants for Other Applications	1306
<b>2.26.5</b>	<b>Monitoring and Testing</b>	1306
2.26.5.1	Oil Condition Monitoring	1306
2.26.5.2	Testing	1306
2.26.5.3	Health and Safety	1307
<b>References</b>		1307

### Glossary

**Aromatic** A hydrocarbon containing one or more conjugated (i.e., repeated single and double) bonds in the form of a ring (e.g., benzene – C<sub>6</sub>H<sub>6</sub>).

**Asphaltenes** Molecular substances found in crude oil that have some of the properties of asphalt, with high viscosity and melting point. Practically they are defined as crude oil fractions that are generally insoluble in *n*-heptane (C<sub>7</sub>H<sub>14</sub>) but soluble in toluene (CH<sub>3</sub>·C<sub>6</sub>H<sub>5</sub>).

**Grease** A solid or semi-solid lubricant material that consists of calcium, sodium or lithium soap that is emulsified with mineral or vegetable oil.

**Oligomer** A compound containing a limited (generally small) number of monomer units (as opposed to a polymer, which in principle contains a large number of monomer units).

**Olefin** A hydrocarbon that contains unsaturated bonds (e.g., ethene – C<sub>2</sub>H<sub>4</sub>).

**Paraffin** A hydrocarbon that contains no unsaturated bonds (e.g., ethane – C<sub>2</sub>H<sub>6</sub>).

**Soap** A metallic salt of a fatty acid.

**Abbreviations****ASTM** American Society for Testing and Materials**BS** British Standard**EP** Extreme pressure**VI** Viscosity index (L, M, or H – low, medium, or high)**TAN** Total acid number**TBN** Total base number**SOA** Spectrographic oil analysis**2.26.1 The Nature of Lubricating Oils and Greases****2.26.1.1 Introduction**

Lubricants and fuels are not generally regarded as being corrosive, and therefore, in order to appreciate how corrosion can occur in lubricant systems, it is necessary to understand something of their nature. Once lubricants were almost exclusively derived from animal (e.g., whale) or vegetable (e.g., castor) oils or fats but modern requirements by way of volume and special properties have made petroleum the main source of supply. The production of lubricants represents between 1 and 2% of all petroleum products by volume but considerably more by value and type.

The main function of most lubricants is to reduce friction and wear between moving surfaces and to abstract heat. They also have to remove debris from the contact area (e.g., combustion products in an engine cylinder) or swarf in metal-cutting operations (e.g., in metal-working fluids). They may also be required to protect the lubricated or adjacent parts against corrosion, but this is not a prime function of most lubricants. On the other hand, many lubricants do contain corrosion inhibitors and some lubricating oils, greases, mineral fluids, and compounds are specially formulated to prevent the corrosion of machinery or machine parts, particularly when these components are in storage or in transit (e.g., temporary protectives).

**2.26.1.2 Lubricating Oils**

There are many hundreds of different varieties of lubricants, many of them tailored to meet specific requirements. For some applications, vegetable oils (especially those derived from the castor oil plant) are still preferred. However, due to the volume requirements petroleum-derived (mineral) lubricant base oil stocks predominate.<sup>1</sup>

Mineral base oils may be distillates or from residues and are derived from the vacuum distillation of a primary distillate with a boiling point range generally above that of gas oils (i.e., above about 200°C). They are mixtures of hydrocarbons, generally containing more than about 20 carbon atoms per molecule, and range from thin, easily flowing long-chain ‘spindle’ molecules to thick, branched, ‘cylinder’ oils. For hydrocarbons having the same number of carbon atoms per molecule, generally, the higher the proportion of carbon to hydrogen, the more viscous the oil and the lower the viscosity index.

Distillate lubricating oils can be conveniently divided into three groups: low viscosity index oils (LVI oils), medium viscosity index oils (MVI oils), and high viscosity index oils (HVI oils). LVI oils are made from naphthenic distillates with low wax contents so that costly dewaxing is not required. MVI oils are produced from both naphthenic and paraffinic distillates; generally, the paraffinic distillates have to be dewaxed (i.e., those fractions that are solid at room temperature need to be removed from the base oil). The residues from the vacuum distillation can also be refined to provide very viscous lubricants; thus, residues from paraffinic base oils are generally solvent extracted and dewaxed. The main use of these products (bright stocks) is as blending components for heavy lubricants.

The mineral base oil fractions may be further categorized as predominantly long-chain aliphatic (paraffinic) hydrocarbons or aromatic hydrocarbons, depending on the crude feedstock. For higher performance, base oils may be synthesized to produce a more tightly specified range of compounds such as olefin oligomers and polyolefinic aromatics that are not present in the original crude oil feedstock. Although such materials can cost 5–10 times more than the conventional materials, their properties are more predictable and their performance (e.g., thermal and chemical stability) is significantly improved.

The primary component of a lubricant, which commonly comprises over 70% and generally up to 98% of the volume of the material, is the base oil stock. To this are added further components that modify and improve the overall performance of the lubricant for specific purposes. Additives that are present in most formulations include: viscosity modifiers, detergents and dispersants, antifoaming agents, oxidation inhibitors, and corrosion inhibitors (often called ‘rust inhibitors’). Additives for specific purposes include biocides and antiwear and extreme pressure (EP) components, which are formulated to react with metal bearing surfaces under extreme conditions to produce a low friction surface.



### 2.26.1.3 Greases

Greases, in contrast to oils, are solid or semisolid lubricants that are made by thickening lubricating base oils with gelling agents such as metal ion salts of long-chain fatty acids (i.e., soaps), lubricious solids such as talc, mica, graphite, and molybdenum disulfide, as well as the conventional additives mentioned above. Typical greases are formulated from approximately a 1:1 ratio of lubricating base oil with emulsifying agent (usually calcium, sodium, or lithium soaps of long-chain fatty acids) plus additives. Greases are used where lubrication may be infrequent and/or where the lubricant is required to remain in place over a significant length of time. Greases are essentially emulsions of the base oil with the soap as the emulsifying agent and second phase and are thixotropic; that is under high shear the viscosity falls to values more representative of the base oil used in the formulation. Thus, they are ideal for lubrication of bearings and similar components. Since many vegetable oils are long-chain hydrocarbons and contain reactive functionality (i.e., double bonds or hydroxyl groups) they may be easily processed into fatty acids. Hence, many greases use fatty acid soaps derived from vegetable oils (e.g., castor oil).

## 2.26.2 Deterioration of Lubricants

### 2.26.2.1 Deterioration by Combustion Products

Lubricating oils deteriorate in service in two primary ways: they become contaminated and they undergo physical and chemical changes due to oxidation.<sup>2</sup> In engines the common contaminants are airborne dust and wear products, unburnt fuel, fuel combustion products, and water. The oxidation products are mainly acidic materials and asphaltenes. Asphaltenes in association with fuel contaminants and water tend to form solids such as sludges and lacquers that can coat component parts and become entrained in the lubricant. The acidic materials resulting from oxidation of the lubricant oil are generally weak organic acids. However, contamination by fuel combustion products (i.e., oxides of sulfur and nitrogen) is the source of almost all strong-acid contamination in lubricants. Recent trends in fuel compositions have resulted in the amount of sulfur, particularly in diesel fuels for automotive use, being reduced considerably. However, heavy fuel oils and residual diesel fuels can contain several percent of sulfur by weight. This sulfur is oxidized to sulfur acids, and sulfuric acid condensate

may be encountered on the cooler surfaces. In petrol (gasoline) the sulfur content is now generally very small to negligible. Historically, halogen compounds added to gasoline as scavengers for lead-based anti-knock compounds could be oxidized to halogen acids; however, with the general elimination of lead in this role, this is no longer of significant concern.

Water, absorbed from the environment or as a product of combustion, exacerbates the problem of acids in oils as the presence of water both promotes corrosion and solvates any ions present, including hydrogen ions from combustion acids. For this reason, lubricant oils for internal combustion engines frequently contain additives to combat acidity. Generally however, provided the water content in lubricating oil remains below about 0.1%, few problems occur.

### 2.26.2.2 Oxidative Degradation

Apart from unusual and highly specialized materials (i.e., lubricants based on silicone chemistry or fully fluorinated hydrocarbons) lubricants, being hydrocarbon based, are relatively susceptible to deterioration by oxidation.<sup>3</sup> Oxidation, being a thermally activated process, will increase in rate with temperature although this will depend on the nature of the compound being oxidized. Thus, oils with a high aromatic content (LVI and some MVI oils) tend to oxidize to give sludge-forming compounds, although some naphthenic oils give organic acids. Paraffinic (long-chain) oils (HVI and some MVI oils) oxidize more slowly to give weak acids.<sup>4</sup> In a plentiful supply of oxygen, oxidation proceeds at a significant rate at temperatures above about 60–130°C depending on the composition of the lubricant. This oxidation is a complex process that typically involves the formation of organic peroxides as intermediates, which facilitate further hydrocarbon chain scission (breaking) or polymerization to form tars, sludges, and varnishes. Oxidation of hydrocarbons is catalyzed by the presence of transition metals with multiple oxidation states, such as copper, iron, and lead.

Oxidative degradation of hydrocarbons will, of course, lead eventually to the formation of carbon dioxide and water. Generally, however, lubricants form intermediate oxidation products, including aldehydes, ketones, and alcohols, with carboxylic acids as the common final oxidation products. Thus, the acidity of lubricating oils during use tends to increase as a function of time. Also, the intermediates, especially ketones and aldehydes, can polymerize, especially in the presence of strong acids from the

products of combustion (nitric and sulfuric). The presence of acidity is clearly corrosive to components and will form metal ion carboxylates (soaps) that are catalytic to oxidation. Thus, the oxidation of octane is accelerated from 5–10 times in the presence of 500 ppm iron octanoate<sup>3</sup> and excessive copper or iron will generally significantly enhance oxidation of lubricants at higher temperatures.<sup>5</sup> Lubricant (and fuel) additives may be formulated to control oxidation, corrosion, acidity, and radical formation in order to limit the degradation of the lubricant. However, such additives will themselves degrade (or be consumed) with time, hence the importance of regular changes of engine lubricants.<sup>6</sup>

### 2.26.2.3 Biodeterioration

Hydrocarbons provide a potential nutrient source of carbon for microorganisms and, consequently, lubricants and fuels are susceptible to biodeterioration by a range of fungal and microbial species.<sup>7</sup> Indeed, selection of specific microbial strains is of increasing interest as a mechanism of bioremediation of waste hydrocarbons. Lubricants are not normally susceptible to biodegradation unless they contain a significant separated water phase. However, the presence of 10–100 ppm water is sufficient to permit microbial growth on interfaces; thus, apparently water-free – (<0.1%) lubricants can contain significant microbial contamination. Lubricants can be particularly susceptible to biodeterioration since they contain essential elements for microbial activity (e.g., phosphorus, sulfur, nitrogen, etc.) in significant quantities. Engine and machinery lubricants that operate at a sufficiently high temperature in a closed environment will be essentially sterile. However, significant problems occur where lubricants are used at lower temperatures. Thus, metal-working lubricants (cutting fluids, etc.) that are left, for periods of time, open to the air at room temperature have increased susceptibility to microbial attack<sup>8</sup> unless a suitable biocide is present in the formulation.

## 2.26.3 Lubricant Additives

### 2.26.3.1 Types of Additive

The progressive development of engines and general machinery resulting in more arduous operating conditions, and particularly the use of longer oil-change periods, means that neither straight mineral oils nor compounded oils (mineral oils to which a proportion of an animal or vegetable oil has been added) are adequate for modern service requirements.

Despite the introduction of new, improved methods of refining, it has been necessary to enhance the performance of lubricants by the use of additives, either to reinforce existing qualities or to confer additional properties. Thus, almost all quality lubricants on sale today contain one or more additives. An enormous range of additives are available for use in lubricants, some produced by the oil companies and others provided by specialist manufacturers.<sup>9</sup> Additives are usually named after their particular function, but many additives are multifunctional. Thus, an antiwear additive may also protect a surface against corrosion. The main types of additive that can enhance the behavior of lubricants are listed in [Table 1](#).

As can be seen from [Table 1](#), many compounds are multipurpose and can act in a number of ways, some beneficial, some detrimental. The selection of additives thus involves a careful balance of properties for the required application.

### 2.26.3.2 Extreme Pressure Additives

Many additives, essential to the performance of the lubricant, provide no corrosion protection and some additives may become corrosive in certain circumstances. Thus, extreme pressure (EP) antiwear additives contain chemical groups which are designed to react chemically with metal surfaces when normal lubrication fails, forming easily sheared layers of metal oxides, sulfides, chlorides, or phosphates, thereby preventing catastrophic wear and seizure. Reaction between EP compounds and metal surfaces should only occur at local hot spots and the layers formed are extremely thin.<sup>10</sup> However, if the operating conditions are very severe these layers are continually generated and removed as they fulfill their antiwear function. A process of this nature is sometimes called ‘chemical’ wear, and if sliding surfaces operate continually under these conditions loss of metal from the rubbing surfaces can ultimately result in failure. Alternatively, all the EP additive may be used up (depleted) and then failure by seizure will occur. EP agents are intended to cater for the occasional overload condition and it must be emphasized that machinery should be designed so that it does not require the continual action of EP agents to function satisfactorily. Obviously, the selection of an EP additive requires great care; if it is too active, it may give rise to excessive metal removal (effectively corrosion) under normal operating conditions. Also, if a component is prone to ‘fatigue pitting’ (a form of contact fatigue in which fatigue cracks grow in such a way as

**Table 1** Lubricant oil additives that can enhance anticorrosive function

<i>Additive</i>	<i>Function</i>	<i>Chemical types</i>
Antioxidant	To increase oxidation resistance of lubricants by interfering with the reactions that give rise to acid and asphaltene (polymer) formation	Oil-soluble amine and phenol derivatives (<120°C), dialkyldithiophosphates and compounds listed below as metal deactivators (>120°C)
Metal deactivator	To form inactive protective films on metal surfaces which would otherwise catalyze oxidation and corrosion reactions	Trialkyl and triaryl phosphites, organic dihydroxyphosphines, some active sulfur compounds, diamines; for greases mercaptobenzothiazole and phosphites
Corrosion/rust inhibitors	To protect metal surfaces, particularly bearing surfaces, against corrosion/to eliminate rusting in the presence of moisture	Zinc dialkyldithiophosphates; esters and derivatives of dibasic acids (e.g., barium and calcium sulphonates)
Water repellents	To impart water-resistant properties, particularly in greases	Aliphatic amines, hydroxyl fatty acids and organosilicone polymers
Basic compounds	To neutralize acids	Barium and calcium salts of sulphonic acids and alkyl salicylic acid
Dispersants/detergents	To keep insoluble combustion and oxidation products in suspension and dispersed	Salts of phenolic derivatives, polymers containing barium, sulfur and phosphorus; calcium or barium salts of sulphonic acids
Antiwear/extreme pressure	To protect metal surfaces from binding together (seizure) by formation of a surface reaction product that is easily sheared under local high pressures and temperatures	Sulfur or phosphate esters/amines, halogenated compounds (the latter are decreasing in use)

to cause ‘chips’ of metal to detach from the surface) in service the presence of an overactive EP agent may result in corrosion fatigue.

### 2.26.3.3 Interactions Between Additives

Modern high-performance lubricants contain a number of additives, each with a particular, special function. Thus, a turbine lubricant may contain an oxidation inhibitor, a rust inhibitor, an EP agent, and an anti-foam compound. A high-grade diesel-engine lubricant may contain a viscosity improver, a dispersant, an antioxidant, a corrosion inhibitor, a basic compound, a pour-point depressant, and an antifoam compound. Sometimes, these additives may have undesirable side effects or interact adversely; in turbine oil, the rust inhibitor may act as an emulsifier, interfering with demulsification; in a diesel lubricant, the dispersant may promote oil oxidation. Frequently anticorrosion additives may not be able to exert their maximum effect because they are competing for sites on metal surfaces. The development of successful new lubricating oils requires skill and experience and always necessitates considerable laboratory and field testing in order to strike the right balance between the various additives.

### 2.26.3.4 Additives in Greases

All classes of additive mentioned earlier may be incorporated in the oil phase of greases and have similar function. However, with greases there is also the opportunity to employ oil-insoluble species that will partition to the emulsifying (soap) phase. The complete range of conventional water-soluble corrosion inhibitors, for example, nitrites and molybdates, can thus be easily incorporated into greases. However, care is required to avoid unwanted antagonistic interactions with other additives.

### 2.26.3.5 Sulfur-Containing Additives

Sulfur compounds occur naturally in most lubricants and many oil additives contain sulfur. In a properly formulated lubricant, these sulfur compounds should be inactive at ambient temperature. At elevated temperatures, they may decompose to give more active materials which can stain and corrode metals, particularly silver and copper. However, these same sulfur compounds have many beneficial qualities; this is why they are not removed completely in refining and why they are used as additives.

Thus, sulfur compounds in lubricants generally act as antioxidants, preventing acid and sludge formation. They can also adsorb or react to form thin films on metal surfaces protecting them from acid or peroxide attack. In addition, sulfur compounds are often used as EP agents. The oil chemist must try to strike a balance; the activity of the sulfur must be high enough for it to exert a beneficial effect and yet not so high as to stimulate corrosion.

All too frequently lubricants containing sulfur are exposed to more severe operating conditions than intended, and staining and corrosion may result. With traditional bearing materials, such as those containing silver and copper, significant corrosion can result, particularly where the sulfur-containing species have partially degraded. A more widespread problem is the corrosion of phosphor-bronze alloys (containing about 10% tin) particularly where temperatures can exceed 200°C. Two important metallurgical factors affecting the corrosion resistance of phosphor-bronze alloys are the amount of alloying element in solution in the copper-rich phase and the porosity of the alloy. For example, if the amount of tin in the solution can be increased by special casting techniques or heat treatments, the corrosion resistance is greatly increased. Similarly, zinc or silicon in solution also increases the resistance of copper to sulfur corrosion. If the alloy is porous the lubricant is drawn into the pores where it stagnates, and, at high temperatures, becomes very corrosive. Thus, as noted above, copper catalyzes oil oxidation with the consequent formation of corrosive sulfur compounds.

The most satisfactory solution to such problems is to employ corrosion-resistant bearing alloys. Traditional alloys with relatively high levels of tin and alloys of the gunmetal type, containing 2–4% zinc, have proved completely satisfactory. The substitution of zinc for phosphorus gives sounder castings and improves the corrosion resistance of the copper-rich matrix. More modern bearing materials such as thermally sprayed aluminum-copper-tin-(indium) have much improved resistance to such corrosion.<sup>11</sup>

## **2.26.4 Corrosion in Specific Lubricant Systems**

### **2.26.4.1 Internal Combustion Engine Lubricants**

Engine lubricants are exposed to severe operating conditions, being subjected to high temperatures, the products of combustion and a plentiful supply

of oxygen. Consequently, unless the oil is changed at appropriate intervals, strong mineral acids and weak organic acids may accumulate. In addition, droplets of water may be formed and these can contain strong mineral acids derived from the fuel combustion gases. These droplets sometimes give rise to emulsions which deposit in the colder portions of an engine, for example, on the rocker-box covers; ferrous surfaces are most affected by this condensed moisture. A special dynamic corrosion test has been developed to study corrosion in these two-phase (water-in-oil) systems.<sup>12</sup> Problems associated with the retention of water in engine lubricants are likely to become more acute as antipollution devices are fitted to engines. The harmful effects are best countered by antirust and basic additives, and in diesel engines burning high-sulfur fuels, for example, marine diesel engines, very high levels of lubricant basicity are required.

Cast or sintered copper-lead or lead-bronze alloys are still widely used for engine bearings. The lead phase in such bearings is readily attacked by weak organic acids and almost all the lead can be leached out unless preventive measures are employed. However, the lead may be protected by an overlay of a lead-tin or lead-indium alloy.<sup>13</sup> About 3% tin or 5% indium in lead will render the lead resistant to attack by oil-oxidation acids. One reason why leaded bearings are protected by an overlay, and not by incorporating the protective alloying elements in the underlying lead, is that both tin and indium dissolve preferentially in copper.<sup>14</sup> In a cast or sintered bearing, therefore, any tin or indium will be found in solution in the copper-rich phase, leaving the lead-rich phase susceptible to attack. Aluminum-copper-tin alloys, which are increasingly used in modern automotive applications, are significantly more resistant to corrosion than conventional copper and lead-based alloys.

### **2.26.4.2 Corrosive Wear**

Modern efficient engines that require extended service intervals and minimum maintenance, and that are able to accept a wide range of fuels whilst meeting strict exhaust emission standards, present special lubrication problems. In particular it is essential that the lubricant can prevent corrosion from fuel combustion products retained in the engine. Corrosive wear can be reduced or prevented by alkaline additives that can neutralize the acids responsible, by additives that prevent the acids reaching metal surfaces and by antirust additives that are adsorbed on metal surfaces and prevent the access

of water and oxygen.<sup>15</sup> Often all three additive types will be used in association although their relative concentrations will depend on the nature of the corrosive agents. In spark-ignition engines the use of nonconventional fuels such as compressed natural gas (methane), liquefied petroleum gas (propane and butane), methanol, ethanol and lead-free gasoline can give specific corrosion problems.<sup>16</sup> Broadly, organic acids of shorter chain length and greater acidity (lower  $pK_a$ ) are generated from such fuels compared with normal gasoline, so higher additive levels are required.

Diesel-fuel sulfur levels can range from about 0.2% to 5.0%. The higher levels only occur in low- and medium-speed engines operating on residual fuels, but because of the high combustion pressures, sulfuric acid condensate forms at temperatures up to 200°C. On cross-head engines, which have independent cylinder lubrication systems the neutralizing power of the fresh oil depends on both oil feed rate and alkalinity.<sup>17</sup> The alkalinity of the lubricant is measured as the total base number (TBN) and lubricants with a TBN exceeding 100 are now available. This means that the lubricant has an acid neutralizing capacity equivalent to a 10% aqueous solution of KOH in oil-soluble form. Experience shows that when fuels with sulfur contents of 2.0% or more are used, the TBN of oils draining from the cylinders should not fall below 10 if excessive wear rates are to be avoided. However, the use of highly alkaline cylinder oils with low sulfur fuels is not recommended; not only is it needlessly expensive, it can also give rise to high wear rates.<sup>15,17</sup> In splash-lubricated piston engines running on high sulfur fuels, the copious quantities of oil splashed up from the crank case provide a greater reservoir of alkalinity and an initial TBN of 25–30 is generally adequate. Nevertheless, the TBN of the oil should not fall below about 3 times the sulfur content of the fuel.

#### 2.26.4.3 Steam Turbine Lubricants

Lubricants in steam turbines are not exposed to such arduous conditions as those in engines. Thus, their main requirement is for high oxidation stability. However, they may be exposed to aqueous condensate or, in the case of marine installations, to sea water contamination, so they have to be able to separate from water easily and to form a rust-preventing film on ferrous surfaces, and it is usual to employ rust inhibitors. The problem of tin oxide formation on white-metal bearings is associated with the presence of water condensate in lubricants and can be

overcome by keeping the lubricant dry or by the incorporation of appropriate inhibitors.<sup>18</sup>

#### 2.26.4.4 Gear Lubricants

In addition to the usual oxidation and corrosion inhibitors, lubricants for heavily loaded gears almost always contain EP additives containing sulfur, chlorine, or phosphorus. In order to function, these additives must react locally with the metal surfaces, and yet the extent of the reaction should not be such that it could be described as corrosive, or promote fatigue pitting. These EP additives may be quite safe with ferrous surfaces, but may cause severe corrosion on copper alloys, for example, on bronze worm wheels, if for any reason excessive temperatures arise. Some turbine lubricants have to lubricate the turbine gears as well as the turbine; in these circumstances, any EP additives employed should not be corrosive in the presence of moisture.

#### 2.26.4.5 Cavitation and Erosion

Cavitation and consequent erosion are an insidious cause of failure in plain bearings and hydraulic systems.<sup>19</sup> Vapor cavities form locally in reduced pressure areas of the lubricating fluid and then collapse rapidly in higher pressure regions. The shock waves generated by the vapor collapse can result in mechanical (impact) damage on surfaces. Common causes of cavitation are pressure fluctuations associated with the flow of the liquid and the vibration of a surface in contact with it. Unlike other kinds of damage, vapor cavitation is generally encountered on the unloaded areas of bearings. When the damage is due solely to cavitation, the damaged surfaces are rough: when foreign particles are present they are smooth (cavitation–erosion). Vapor cavitation can remove protective films, such as oxides, from metals and so initiate corrosion. In addition, the very high local pressures and temperatures associated with the final stage of cavity collapse can induce chemical reactions that would not normally occur. Thus certain additives are damaged by cavitation and their decomposition products can be corrosive.

#### 2.26.4.6 Metal-Working Lubricants

Metal-working lubricants can be divided into two categories: metal cutting lubricants and metal forming lubricants.<sup>20</sup> Three types of cutting fluids are widely



used: soluble oils, water base fluids and straight cutting oils. Soluble oils are low-viscosity mineral oils (containing emulsifying agents) that, when added to water, form stable oil-in-water emulsions. Their main function is to cool the workpiece rather than to lubricate, but they should contain rust inhibitors to prevent corrosion of both the workpiece and the machine. Water base fluids contain no oil and employ the normal corrosion inhibitors used in coolants, for example, sodium nitrite, sodium benzoate, and triethanolamine phosphate. Straight cutting oils are used in severe operations where good lubrication is essential, and generally contain EP additives that should be carefully selected so that they do not corrode (stain) the workpiece or the machine tool. For example, very active sulfur compounds should not be employed with copper alloys. Chlorinated additives should be stable in moist air to avoid the risk of hydrochloric acid formation.

Metal-forming lubricants include formulations for rolling, drawing, extruding and forging. A vast range of compounds including fatty oils and compounded oils are used in these operations, and a major requirement is that they should not stain the workpiece during the forming operation or during subsequent annealing or in storage. Consequently, all oils and additives employed should be completely volatile, in addition to affording protection against rusting.

#### **2.26.4.7 Water Base Lubricants**

In some applications, for example, mining machinery, nonflammable lubricants are specified and water base or water-containing fluids are used. Standard corrosion inhibitors are used to combat corrosion but even a small amount of water in a mineral oil lubricant can adversely affect the fatigue life of components such as rolling bearings and gears.<sup>21</sup> Worthwhile improvements in fatigue life can be achieved by using additives of a completely different nature and by special heat-treatment techniques.<sup>22</sup>

#### **2.26.4.8 Lubricants for Other Applications**

Specially formulated lubricants are required for steam engines, compressors and exhausters, refrigerators, hydraulic equipment, textile machinery, transformers and switchgear, nuclear power plants, and many other diverse applications. Most of these lubricants will contain a carefully balanced set of additives, including some to prevent corrosion either directly by protecting the metal surface, or indirectly by

preventing deterioration of the lubricant and combating the action of contaminants. When corrosion is encountered with a specialized lubricant, the cause is not likely to be any weakness on the part of the lubricant; it is probable that the lubricant is being exposed to extreme operating conditions, far more than those for which it was designed.

### **2.26.5 Monitoring and Testing**

#### **2.26.5.1 Oil Condition Monitoring**

Historically, regular changes in lubricant ensured that they remained in optimum condition. However, lubricants are expensive and users have no wish to change them until necessary. Thus, much greater attention is now given to intermittent or continuous (online) monitoring of the condition of the oil and associated machinery.<sup>23</sup> Oil condition monitoring is often extended to include techniques that give advance warning of the deterioration or impending breakdown of the machinery, whether or not this is associated with loss of performance of the lubricant. Conventional condition monitoring collects particulate debris, for example, by magnetic filtration, and subjects these to *ex situ* analysis, typically for elemental components. Such methods include ferrography and spectrographic oil analysis SOA.<sup>24</sup> More recent techniques have been developed for online (*in situ*) use and these include particle counting, infrared analysis,<sup>25</sup> electrical methods<sup>26</sup> as well as online viscosity<sup>27</sup> measurement.

#### **2.26.5.2 Testing**

Methods for the testing and analysis of lubricants are the subject of many Company, National, and International Standards.<sup>28</sup> Typical tests for used diesel engine oils include viscosity, fuel dilution, flash point, water content, ash level, insoluble species, and neutralization value. Neutralization value is a measure of the acidity (total acid number, TAN), or alkalinity (total base number, TBN) of the oil. Laboratory examination of used oil samples and reporting results takes time and the simpler tests can be used in the field. Extensive tests for the performance (oxidation resistance) as well as for the corrosivity of oils and greases also exist and lie within the BS2000 series (now generally superseded) and the ASTM 'D' series. Thus, the most commonly known test for corrosivity of lubricants is the copper strip corrosion test specified in

BS 2000-112:2005; "Methods of test for petroleum and its products: Determination of corrosiveness to copper of lubricating grease (copper strip method)," which is broadly equivalent to ASTM D 130.

### 2.26.5.3 Health and Safety

The solvent action of mineral oil base stocks can cause skin problems and prolonged exposure has been found to be carcinogenic.<sup>29</sup> Thus, the use of additives that might be in any way harmful to health, for example orthotricresyl phosphate (antiwear) and sodium mercaptobenzothiazole (anticorrosion), is discouraged and discontinued where skin contact is likely. The presence of fungi and bacteria in water base or water-contaminated lubricants such as machining fluids and marine diesel crankcase lubricants may promote corrosion and are potentially of concern to health.<sup>30</sup> More broadly, increasing environmental concerns in recent years is driving research on environmentally friendly disposal of used lubricants and substitution of nonbiodegradable mineral oils with fully biodegradable oils that are often plant derived.<sup>31</sup>

## References

1. Pisso, D. M.; Wessel, A. A. *Lubrication Fundamentals*, 2nd ed.; Dekker Mechanical Engineering Series, Vol. 137, Marcel Dekker, 2001.
2. Fox, M. F. In *Handbook of Lubrication and Tribology*, 2nd ed.; Totten, G. E. Ed.; CRC Press, 2006; Chapter 29.
3. Cochrane, G. J.; Rizvi, S. Q. A. In *Fuels and Lubricants Handbook: Technical Properties, Performance and Testing*; Totten, G. E., Westbrook, S. R., Shah, R. J., Eds.; ASTM, 2003; Chapter 30.
4. Murray, D. W.; McDonald, J. M.; Wright, P. G. *Petroleum Rev.* **1982**, 36, 36.
5. Clark, D. B.; Klaus, E. E.; Hsu, S. M. *Lubric. Eng.* **1985**, 41, 280.
6. Barcroft, F. T.; Park, D. *Wear* **1986**, 108, 213.
7. Allsopp, D.; Seal, K.; Gaylarde, C. *Introduction to Biodeterioration*, 2nd ed.; Cambridge University Press, 2003; Chapter 3.
8. Taylor, G. T.; Knee, N. D.; Keep, M. J. H.; Freestone, V. C. M. In Proceedings of the "Waste Management '99" Conference, Tucson, Arizona, USA, 1999.
9. Rudnick, L. R. Ed. *Lubricant Additives: Chemistry and Applications*; CRC Press, 2003.
10. Farnig, L. O. In *Lubricant Additives: Chemistry and Applications*; Rudnick, L. R. Ed.; CRC Press, 2003; Chapter 8.
11. Kato, K.; Adachi, K. In *Modern Tribology Handbook*; Bhushan, B. Ed.; CRC Press, 2001; Vol. 2, Chapter 21.
12. Hughes, R. I. *Corros. Sci.* **1969**, 9, 535.
13. Forrester, P. G. *Trans. Inst. Metal Finishing* **1961**, 38, 52.
14. Wilson, R. W.; Shone, E. B. *Anti-Corros. Meth. Mater.* **1970**, 17(8), 9.
15. Wilson, R. W. In Proceedings 6th International Congress on Metallic Corrosion; Australasian Corrosion Association, 1981; Vol. 2 p 1479.
16. Thring, R. H. *SAE J. Automot. Eng.* **1984**, 92(1), 60.
17. Golothan, D. W. K. *Trans. Inst. Mar. Engrs: Tech. Rep.* **1978**, 90A(Pt 3), 137.
18. Hiley, R. W. *Trans. Inst. Mar. Engrs.* **1979**, 91, 52.
19. Dowson, D.; Godet, M.; Taylor, C. M. In 1st Leeds-Lyon Symposium on Tribology, Section 7 Institution of Mechanical Engineers, 1975; p 177.
20. Savoit, R. E. *Lubrication - Texaco* **1969**, 55(7), 65.
21. Grunberg, L.; Jamieson, D. T.; Scott, D.; Lloyd, R. A. *Nature* **1960**, 188, 1182.
22. Hollox, G. E.; Hobbs, R. A.; Hampshire, J. M. *Wear* **1981**, 68, 229.
23. Collacott, R. A. In *Industrial Tribology*; Jones, M. H., Scott, D. Eds.; Elsevier, 1983; Chapter 18.
24. Hoffmann, W. *Wear* **1981**, 65, 307.
25. Agoston, A.; Ötsch, C.; Zhuravleva, J.; Jakoby, B. In Proceedings of IEEE Sensors; **2004**; Vol.1, P. 463 art. no. M4L-5.
26. Turner, J. D.; Austin, L. *Meas. Sci. Technol.* **2003**, 14, 1794.
27. Agoston, A.; Ötsch, C.; Jakoby, B. *Sensors Actuators A: Phys.* **2005**, 121, 327.
28. Hunter, M. E.; Baker, R. F. In *Fuels and Lubricants Handbook: Technical Properties, Performance and Testing*; Totten, G. E., Westbrook, S. R., Shah, R. J., Eds.; ASTM, 2003; Chapter 31.
29. Warne, T. M.; Halder, C. A. *Lubric. Eng.* **1986**, 42, 97.
30. Bennett, E. O. *Tribology Int.* **1983**, 16, 133.
31. Chen, B.; Fang, J.; Dong, L.; Xia, S.; Wang, J. *Lubric. Sci.* **2008**, 20, 311.

## Further Reading

*Lubrication*; Texaco/Chevron, since 1925. Back issues available for download from Chevron: [www.lubricantsuniversity.com](http://www.lubricantsuniversity.com).  
Totten, G. E. Ed. *Handbook of Lubrication and Tribology*, 2nd ed.; CRC Press, 2006.  
Totten, G. E.; Westbrook, S. R.; Shah, R. J. Eds.; *Fuels and Lubricants Handbook: Technical Properties, Performance and Testing*; ASTM, 2003.  
Bhushan, B. Ed.; *Modern Tribology Handbook*; CRC Press, 2001; Vol. 2.

## 2.27 Corrosion in Body Fluids

**D. J. Blackwood**

Department of Materials Science and Engineering, National University of Singapore, 9 Engineering Drive 1, Singapore 117576, Singapore

© 2010 Elsevier B.V. All rights reserved.

2.27.1	Introduction	1309
2.27.2	Historical Development	1309
2.27.3	Health Effects Related to Corrosion in Body Fluids	1310
2.27.4	Environments Encountered in Biomedical Applications	1311
2.27.5	Metals and Alloys Used in Biomedical Applications	1313
2.27.5.1	Titanium and Titanium Alloys	1313
2.27.5.2	Cobalt–Chromium–Molybdenum Alloys	1314
2.27.5.3	Stainless Steels	1314
2.27.5.4	Nickel–Titanium Alloy	1314
2.27.5.5	Porous Materials and Metallic Foams	1315
2.27.5.6	Magnesium Alloys	1315
2.27.5.7	Rare Earth Magnets	1316
2.27.5.8	Dental Amalgams	1316
2.27.5.9	Titanium Nitride Coatings	1316
2.27.6	Corrosion Types Encountered in Biomedical Applications	1316
2.27.6.1	General Corrosion	1316
2.27.6.2	Pitting Corrosion	1317
2.27.6.3	Crevice Corrosion	1317
2.27.6.4	SCC and Hydrogen Embrittlement	1317
2.27.6.5	Corrosion Fatigue	1318
2.27.6.6	Fretting Corrosion and Wear	1318
2.27.6.7	Galvanic Corrosion	1319
2.27.7	Conclusions	1319
References		1320

### Glossary

**Biocompatibility** The extent to which an implanted material elicits an immune response in a host.

**Carcinogen** Cancer causing.

**Cardiac** Related to the function of the heart.

**Cytotoxicity** Toxic towards cells.

**Extracellular** The space outside the plasma membranes of cells and occupied by fluid; literally means outside the cell as opposed to intracellular which is inside the cell.

**Hematoma** A collection of blood, usually partially clotted, that results from the breakage of veins or blood vessels.

**Inflammatory response** Part of the human body's initial response to injury or infection.

**In vitro** Experiments conducted outside the body; literally means in-glass.

**In vivo** Data collected from materials implanted within a live subject, human or animal.

**Orthodontic** An area of dentistry concerned with treatment of the inability to bite correctly, due to the misalignment of teeth, irregular tooth growth or disproportionate relationship between the upper and lower jaws.

**Oral lesions** Abnormal tissue in or around the mouth, usually caused by disease or trauma.

**Oral mucosa** Mucous membranes of the mouth.

**Osteoporosis** Thin or porous bones caused by lack of calcium or stress shielding by load-bearing implants.

**Prosthesis** An artificial device that replaces a missing body part.

**Pathological changes** The human body's initial response to injury or infection.

**Pulmonary** Related to the function of the lungs.

**Serum** Blood plasma from which clotting factors have been removed.

**Shape-memory alloy** A material that, after it has been deformed, regains its original geometry by heating, due to temperature-dependent martensitic phase transformation.

**Sherman plates** Metal plates used to hold fractured bones in place to allow them to heal; typically the plate is screwed to the bone.

## Abbreviations

**ASTM** American Society for Testing and Materials

**FCC** Face Centered Cubic

**ISO** International Standards Organization

**L** Low carbon

**PREN** Pitting resistance equivalent number  

$$= \%Cr + (3.3\% \times Mo) + (16 \times \%N)$$

**SCC** Stress corrosion cracking

**SHE** Standard hydrogen electrode

**VM** Vacuum melted

## 2.27.1 Introduction

Corrosion is of concern to the biomedical industry for two reasons. The first is common to all industries, being ‘how will a device’s lifetime/performance be impacted by corrosion?’ However, the second concern is specific to the biomedical industry, being ‘will the metallic ions that leach out of the device build up to levels sufficient to harm the patient, for example, by causing tumors to develop?’ There is little known about what represents longterm safe limits for metallic ion concentrations in the body, and therefore, these could well be exceeded at corrosion rates that are insignificant with respect to the physical performance of the implant. Corrosion problems in dental applications are more common, mainly due to the high acidity and chloride contents of many foodstuffs. Fortunately, fixtures in the oral cavity are readily accessible for repair or replacement, but the toxicity of the metals leaching out is a major concern.

In most industries, corrosion is typically controlled by either coatings or altering the local environment. Unfortunately, until recently, coatings were of limited use for protecting surgical implants, since many of these (especially orthopedic devices) are

subjected to wearing and abrasion processes. Likewise, the environment within the human body is essentially fixed, and therefore, it is not possible to lower the temperature or raise the pH. As a result, the only available method of reducing corrosion rates within the human body has been to fabricate the biomedical devices from a corrosion-resistant material. Nevertheless, since the late 1970s, this approach has been extremely successful, at least with respect to extending the lifetime of biomedical devices, thanks to the development of a range of corrosion-resistant alloys that have reduced the number of failures to extremely low levels. Besides, many of the few corrosion failures that still occur can be traced either to poor quality control or to an unexpected and unusually aggressive local environment around the implant, due to pathological changes in the surrounding tissue as this reacts to the surgical procedure. The remaining early failures of surgical implants are due to either fatigue or fretting, which may or may not be accelerated by corrosion.

Nevertheless, the lack of consensus over what represents safe levels for metallic ion concentrations within the body, or even which metals are toxic, means that the concerns about extended exposure to even very low levels of corrosion products resulting in medical complications remain. Furthermore, average life expectancies are increasing and the average age of patients receiving implants is decreasing. Ironically, this is both in part due to the modern popularity of physical sports, which place a large strain on joints, and therefore, the required performance lifetime of devices, and with it, the likelihood of both the corrosion-related failures and health problems instigated by elevated metallic levels is increasing. Additionally, a number of advanced materials, such as shape-memory alloys, are being introduced into the biomedical industry often with very little prior thought given to corrosion protection.

## 2.27.2 Historical Development

The earliest use of metallic materials in dental applications was over 4000 years ago in ancient Egypt; although initially for aesthetic purposes, by about 700 BC, this had developed to the level of using gold bridgeworks to secure false teeth formed out of ivory and bone. However, the modern era of using metallic surgical implants to fix damaged bones only began at the beginning of the twentieth century. Of the metals and alloys available at that time, vanadium

steel, developed in 1912, offered the best combination of corrosion resistance and mechanical strength. Although this alloy had poor tissue compatibility, it was not until the 1930s that austenitic stainless steels became sufficiently available as a viable alternative, first with compositions similar to that of grade 304 and later with molybdenum additions, that is, evolving towards grade 316L, which was endorsed by the American College of Surgeons in 1946.<sup>1</sup> In 1981, a 22Cr13Ni5Mo stainless steel was introduced for hip implants, but this was rapidly superseded by the introduction of high-nitrogen austenitic stainless steel, which offered the same corrosion resistance but without the need for a high-nickel content to maintain the FCC structure, dramatically reducing costs. In response to fears of nickel toxicity, the beginning of this millennium saw the introduction of nickel-free or low-nickel austenitic stainless steels implants, such as the nitrogen-strengthened 23Mn21Cr1Mo (ASTM F2229-02).

Cobalt–chromium–molybdenum alloys were first used in dentistry in the late 1920s and then for surgical implants in the late 1930s. The high corrosion resistance and apparent good biocompatibility made these alloys a favored material for orthopedic devices, but during the 1950s, the better strength-to-weight ratio of titanium meant that it started to increase in popularity; CoCrMo alloys remained the preferred choice in the United States up to the late 1960s. In 1974, the Ti6Al4V alloy,

which has a much higher ultimate tensile strength than the commercial purity titanium, was introduced for trauma implants, and by the end of that decade, it had become the material of choice in orthopedic surgery, although CoCrMo alloys were still regularly used.

The late 1980s and 1990s saw the beginning of the introduction of advanced materials for biomedical applications, including rare earth magnets and NiTi shape-memory alloys. In the present decade, zirconium alloy joint prostheses were introduced and important advances have been made in the application of wear-resistant titanium nitride coatings.<sup>1</sup> Undoubtedly, the nature of surgical and dental implant materials will continue to evolve in the coming decades.

### 2.27.3 Health Effects Related to Corrosion in Body Fluids

There is no doubt that surgical implants do raise the level of metallic elements in the body, as illustrated by the data displayed in Table 1.<sup>2–4</sup> However, the form of the metal released into the body is often uncharacterized, for example, particulate matter or soluble ions, with the role of serum protein binding being virtually unknown. Furthermore, there is still no agreement over what constitutes safe levels for metals within human body fluids and tissues. Although cobalt,

**Table 1** Approximate concentrations of metals in the human body with and without a total-joint replacement implant<sup>2–4</sup>

		<i>Metal ion concentrations: body fluids (μM); tissues (ppm)</i>						
		<i>Co</i>	<i>Cr</i>	<i>Mo</i>	<i>Ni</i>	<i>Ti</i>	<i>Al</i>	<i>V</i>
Serum	Normal	0.003	0.001	–	0.007	0.06	0.08	<0.02
	Implant	0.007	0.006	–	<0.16	0.09	0.09	0.03
Blood	Normal	0.002	0.058	0.009	0.078	0.35	0.48	0.12
	Implant	0.33	2.1	0.104	0.50	1.4	8.1	0.45
Liver	Normal	120	<14	–	–	100	890	14
	Implant	15 200	1130	–	–	560	680	22
Lung	Normal	–	–	–	–	710	9830	26
	Implant	–	–	–	–	980	8740	23
Spleen	Normal	30	10	–	–	70	800	<9
	Implant	16 000	180	–	–	1280	1070	12
Lymphatic	Normal	10	690	–	–	–	–	–
	Implant	390	690	–	–	–	–	–
Heart	Normal	30	30	–	–	–	–	–
	Implant	280	90	–	–	–	–	–

Source: Hallab, N. J.; Jacobs, J. J.; Gilbert, J. L. In Joint Replacement and Bone Resorption; Shanbhag, A., Rubash, H. E., Jacobs, J. J., Eds.; Taylor & Francis: New York, 2006; pp 211–254.



chromium, and nickel are essential trace elements, in excess, all these lead to carcinogenesis as well as other ailments;<sup>2</sup> likewise, vanadium leads to cardiac dysfunction and hypotension,<sup>2</sup> while iron has been linked with Parkinson's disease.<sup>5</sup> Excess aluminum can cause anaemia,<sup>2</sup> but claims that it causes Alzheimer's disease have been proved to be completely unfounded.<sup>6</sup> Titanium is a nonessential element, which is usually considered inert, but pulmonary disease has been reported in titanium production workers as well as in rats exposed to TiO<sub>2</sub> dust.<sup>2</sup>

The potential to cause cancer is obviously a major concern with metallic implants. Memoli *et al.*<sup>7</sup> reported a slight increase in sarcoma cancers in rats when implanted with devices with high Cr, Co, or Ni contents, and a significant number of implant site tumors have been reported in cats and dogs with stainless steel implants, but fortunately to date, malignant tumors associated with implants in humans are rare.<sup>8</sup> Nevertheless, the number of reported cases is increasing and is likely to continue to do so as the patient age decreases and the life-expectancy increases.<sup>9</sup>

Health concerns with orthodontic devices are also mainly associated with metal release, particularly nickel from stainless steels and the NiTi shape-memory alloy.<sup>10</sup> With respect to amalgams, apart from the release of toxic mercury, the main concern is the development of lesions of the oral mucosa that can lead to leukoplakia, lichen planus, and oral cancers. Early reports linked these lesions to the potential associated with galvanic cells that can exist between amalgams and precious metal restoration, and hence these have been termed galvanic lesions.<sup>11,12</sup> However, galvanic cells appear to be commonplace among healthy populations; Phillips *et al.*<sup>13</sup> did not find any evidence of leukoplakia in rats that were subjected to galvanic currents.<sup>14</sup> More recent studies have found that the lesions are usually caused by contact hypersensitivity to mercury<sup>15</sup>; the oral mucosa may be either in direct contact with an amalgam or contain some mercury deposits resulting from amalgam corrosion.<sup>16</sup> Clinical signs of amalgam corrosion have been reported to be significantly more frequent in patients suffering from oral lichen planus than in controlled groups, and of course, any galvanic cells between amalgams and precious metals would accelerate the corrosion and thus exacerbate the problem.<sup>17</sup> Nevertheless, lesions of the oral mucosa caused by amalgam restorations are rare and can usually be solved by replacement of the amalgam.<sup>15</sup>

## 2.27.4 Environments Encountered in Biomedical Applications

Upon detecting the presence of a foreign entity, the body will produce enzymes and attempt to ingest the foreign object. If the foreign object is too large to be ingested, such as a surgical implant, the body will isolate and encapsulate the object in a fibrous tissue membrane. As such, the implant remains continuously exposed to extracellular tissue fluid. Although the actual compositions of body fluids are complicated, in terms of corrosiveness, the most important characteristics are the chloride, dissolved oxygen, and pH levels. The biological components in body fluids, for example, phosphates, cholesterol, and phospholipids, are usually considered either to play no role in the corrosion process or to exist at insignificant levels. Figure 1(a) shows the typical environmental conditions expected within a range of different body fluids, superimposed on the Pourbaix diagram for chromium in the presence of chloride ions.<sup>18,19</sup> From this diagram, it can be predicted that stainless steels and cobalt–chromium–molybdenum alloys are likely to suffer corrosion in many of the environments found within the body, but titanium would be in the passive state for virtually all physiological solutions (Figure 1(b)). Fortunately, the body fluid most likely to be encountered by an implant is blood, which contains ~0.9% NaCl and under normal conditions is at pH 7.4, with a redox potential in the vicinity of 0.0 V versus standard hydrogen electrode (SHE) and body temperature of ~37 °C. Under these conditions, many stainless steels and cobalt–chromium–molybdenum alloys can be expected to be in the passive state.

A review by Solar<sup>20</sup> in 1979 concluded that inorganic solutions based on 0.9% NaCl were satisfactory substitutes for human body fluids when studying the behavior of passive metals. As a result, the majority of *in vitro* corrosion experiments have been conducted in either 0.9% NaCl or standard isotonic solutions, such as SBF-K9, Ringer's, or Hank's solution, in which additions of bicarbonate and calcium chloride tend to be the main difference to a simple NaCl solution. Dissolved oxygen levels in blood are lower than in saline solutions exposed to air atmospheres, by factors of about 2 and 6 for arterial blood and for venal blood, respectively. Conversely, bicarbonate levels are about 20 times higher in blood than in saline solutions (Table 2).<sup>21–23</sup> Usually, no attempt is made to lower the dissolved oxygen content of the isotonic NaCl solutions to that of the venal blood, which may

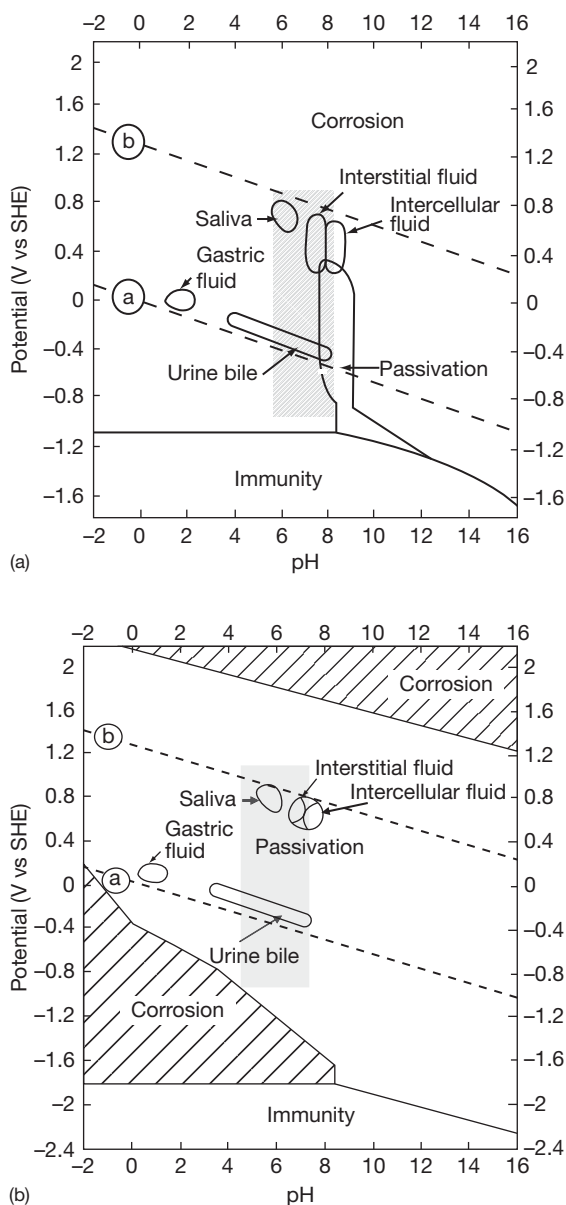


**Figure 1** Representative environmental conditions for various body fluids superimposed on Pourbaix diagrams for (a) chromium in solutions containing chloride and (b) titanium. The shaded zones represent the conditions for physiological solutions as suggested by Schenk.<sup>19</sup> Adapted from Blackwood, D.J.; Seah, K.H.W.; Teoh, S.H. In *Engineering Materials for Biomedical Applications*; Teoh, S.H., Ed.; World Scientific: Singapore, 2004; pp 3.1–3.56, with permission from World Scientific.

explain some of the minor differences between the *in vitro* and *in vivo* corrosion behaviors of surgical implant materials.<sup>22,24</sup> In addition, the minor components in blood, which are usually ignored in *in vitro* studies, have occasionally been blamed for accelerated

**Table 2** Comparison of oxygen and carbon dioxide levels in real and simulated human body fluids.<sup>21–23</sup>

	$P_{O_2}$ (mmHg)	$P_{CO_2}$ (mmHg)	$HCO_3^-$ (mM)
Human artery blood	85–100	35–45	25
Human veinal blood	40	42–48	25
Rabbit artery blood	78	31	20
Rabbit veinal blood	28	39	23
NaCl solution	160	2	–

*in vivo* corrosion rates, for example, it has been reported that proteins can lower the pitting potential of 304L stainless steel.<sup>25</sup> Overall, it appears that typical body fluids are slightly less aggressive than is seawater, indeed Zitter<sup>26</sup> recommends that if a stainless steel is to be used to fabricate a biomedical device, it should have a pitting resistance equivalent number (PREN) not less than 26, somewhat below the value of 40 usually required for stagnant seawater.

Finally, it needs to be understood that the surgical operation plus the presence of the implant itself may cause the surrounding tissue to undergo severe pathological changes that can result in the development of a more corrosive environment. For example, Laing<sup>27</sup> reported that the buildup of hematomas, a condition that could last several weeks, can force the pH in the vicinity of a freshly inserted surgical implant down to as low as pH 4.0. Likewise, the initial stages of the inflammatory response can lead to the generation of hydrogen peroxide and elevated protein levels, both of which may favor the initiation of pitting and crevice corrosion.<sup>21,28,29</sup> Furthermore, the degree to which pathological changes occur depends not only on the biological activity of any released corrosion products, but also on the size and shape of the implant, which means that the extent of the pathological changes will vary across the surface of an implant. This could lead to the development of electrochemical cells and the potential gradients necessary to drive localized corrosion.

The environment within the oral cavity is not well defined. There are a number of recipes for artificial saliva, of which the most common is that of Fusayama<sup>30</sup> (NaCl, 0.400 g dm<sup>-3</sup>; KCl, 0.400 g dm<sup>-3</sup>; CaCl<sub>2</sub>·H<sub>2</sub>O, 0.795 g dm<sup>-3</sup>; NaH<sub>2</sub>PO<sub>4</sub>·H<sub>2</sub>O, 0.69 g dm<sup>-3</sup>; Na<sub>2</sub>S·9H<sub>2</sub>O, 0.005 g dm<sup>-3</sup>; pH 5.5), which may be acidified with citric acid to pH 4.0. However, in reality, the makeup of human saliva varies considerably between individuals, especially in the sulfide

content, which can cause tarnishing of both silver- and gold-based amalgams. In any case, many food-stuffs are acidic with high-chloride levels, and are thus far more corrosive than saliva. Moreover, oral hygiene has a strong affect on the corrosiveness of the oral environment. Many dental products also contain fluoride, some of the specialist varnishes used by dentists being over 2 wt% fluoride, which can cause corrosion even in commercial purity titanium.<sup>31</sup> An example of the problem of defining the environment for the oral cavity is illustrated in the work of Schiff *et al.*,<sup>32</sup> who investigated the corrosion performance of different orthodontic wires. All showed excellent resistance in artificial saliva, but in monofluorophosphate-containing mouthwashes, NiTi-based alloys were found to suffer strong corrosion, while TiNb alloys and TiMo-based alloys gave satisfactory performance. However, when a mouthwash containing stannous fluoride was used, the NiTi alloys outperformed the other two alloys, the TiMo alloys corroding badly.

### 2.27.5 Metals and Alloys Used in Biomedical Applications

In addition to an alloy's mechanical and corrosion resistance properties, its surface finish is also an important aspect for biomedical devices. The type of surface finish required on an implant is very much dependent on its final use. For example, on the one hand, for prostheses implants usually a rough surface is desirable, as this promotes attachment to the surrounding bone or cement. On the other hand, implants that come into contact with the blood stream, such as vials or reservoirs used to hold the chemicals required in chemotherapy, need to have smooth surfaces to prevent provoking thrombus or crystal formation of the applied chemotherapeutics. As a result, the compositions, mechanical properties, and surface finish of the major types of metals and alloys available are governed by a range of international and national standards, most notably, the various parts of ISO 5832.

#### 2.27.5.1 Titanium and Titanium Alloys

Titanium has excellent corrosion resistance to most environments likely to be found *in vivo*, with the possible exception of acid anoxic regions (e.g., gastric fluids) where the protective passive oxide may not form. The ability of the passive oxide film to provide corrosion

protection can be improved by anodizing; note that earlier concerns that anodizing may reduce titanium's resistance to stress corrosion cracking (SCC) and corrosion fatigue appear to be unfounded.<sup>33</sup>

Titanium alloys have even better strength-to-weight ratios than does pure titanium, but not quite as high a resistance to pitting corrosion as the parent metal has, and problems can be encountered if the local redox potential is high and the pH low. Theoretically, these conditions could exist during the initial stages of the inflammatory response following surgery, when both a reduction in pH and hydrogen peroxide production can occur, but the author is not aware of any such clinical cases.<sup>21,27–29</sup> Overall, titanium alloys have better corrosion resistance than do cobalt–chromium–molybdenum alloys and stainless steels.

In the previous decade, concerns about the cytotoxicity of vanadium have led to the development of a number of new alloys as potential replacements for the dual phase ( $\alpha + \beta$  phases) Ti6Al4V alloy; there have been reports of elevated metal levels in soft tissues and bones surrounding implants fabricated from this alloy.<sup>34</sup> Many of the potential replacements are  $\beta$  stabilized, which allows a lower elastic modulus and thus should aid bone growth, but at the cost of lower wear and fatigue resistances. However, two replacement alloys, Ti15Mo5Zr3Al and Ti6Al2Nb1Ta0.8Mo, have already been used in hip prostheses in cemented and noncemented applications, respectively, with apparently excellent clinical results.<sup>35</sup>

Despite their excellent corrosion resistance and biocompatibility, titanium and its alloys are still not the perfect biomedical materials, as their poor shear strength makes them unsuitable for screws and other forms of fastener devices. This can lead to fixation problems if galvanic corrosion is to be avoided between the titanium alloys and attaching screws. In addition, titanium alloys also have a high coefficient of friction, which means that wear particles may form if rubbing against bone or another implant surface occurs; the latter case has led to failures due to fretting corrosion, in which the passive oxide film is worn away.<sup>36</sup> The poor fretting resistance of the Ti6Al4V alloy represents its most serious drawback for use in load-bearing prosthesis, and therefore, considerable effort has been made to find possible solutions.<sup>37–40</sup> Encouraging results have been reported for both anodizing and titanium nitride coatings.<sup>37,41</sup> Anodization has the advantages of low cost and ease of operation, while the nitride-coated Ti6Al4V has the better fretting resistance<sup>38</sup>; both techniques have demonstrated

biocompatibility.<sup>37,42</sup> Recently, a zirconium alloy containing 2.5% niobium has been introduced for joint prosthesis. A thick oxide layer formed on the Zr2.5Nb by heating to 535°C gives it a far superior wear resistance to that of titanium alloys.<sup>43</sup> Zr alloys have similar corrosion resistance properties to titanium, but are difficult to machine as they show pyrotechnic tendencies.

### 2.27.5.2 Cobalt–Chromium–Molybdenum Alloys

The main alloys used are based on either CoCrMo alloy, which has been used extensively in dentistry and more recently for artificial joints, or CoCrNiMo, which has a very high ultimate tensile strength and thus is used for making the stems of prostheses for heavily loaded joints. Molybdenum is added to improve the mechanical properties by decreasing the grain size, rather than to improve the corrosion resistance. These alloys have excellent resistance to most forms of corrosion, including crevice corrosion and corrosion fatigue, but fretting corrosion can cause failures. The nickel-containing alloys have the better corrosion resistance, and ASTM F1058 (40Co20Cr15Ni7Mo) has a long track record as a permanent implant alloy.<sup>44</sup> However, concerns about the release of toxic Ni<sup>2+</sup> ions have resulted in the CoCrMo alloy, ASTM F75 being the dominant cobalt–chromium–molybdenum alloy in use today. A final concern with using CoCrMo alloys is the potential release of chromate, a known carcinogen, into the body. This worry also applies to stainless steels, since these too contain chromium, although at lower levels.

### 2.27.5.3 Stainless Steels

Early attempts to use 12% Cr Sherman plates with type 304 stainless steel screws led to predictable galvanic corrosion problems; nonetheless, some of these plates remained in patients for over 30 years, only being removed when tumors (nonmalignant) develop over the corroding implants.<sup>45</sup> The galvanic corrosion problem was solved by using an all type 304 stainless steel construction, but this did not prevent problems associated with pitting and crevice corrosion. Nevertheless, small type 304 stainless steel Sherman plates have been removed from patients after ~30 years of service without any sign of corrosion; possibly the low oxygen content of body fluids prevented the pitting potential from being exceeded.<sup>21</sup> In contrast, a

number of cases of larger type 304 stainless steel implants developing localized corrosion problems shortly after implantation have been reported.<sup>46</sup> These apparently contradictory results bear testament to the importance of the pathological changes that accompany the healing process in the first few weeks after surgery, and the extent of the healing process can be expected to be dependent on the size of the implant.<sup>21</sup>

The development of the molybdenum-containing type 316L stainless steel led to a significant decrease in the number of failures related to localized corrosion. However, from a review of failures during the years 1980–1989, Zitter<sup>26</sup> suggested that a PREN greater than 26 was required to prevent *in vivo* pitting corrosion, which is slightly above the PREN of most type 316L stainless steels produced, making this grade more suitable for temporary implant devices. The PREN value can be pushed above the recommended threshold of 26 by the addition of nitrogen, which also has the advantage of increasing the ultimate tensile strength of the material, but at the expense of a lower elongation at fracture. During the last two decades, the importance of sulfide and phosphide inclusions in pit initiation processes has been recognized and this has led to the development of type 316LVM stainless steel, in which the nonmetallic inclusion content is reduced by vacuum melting. The composition of the 316LVM grade is usually slightly above the normal 316 specification, typically being 18Cr14Ni3Mo, such that its PREN value of ~28 is above Zitter's threshold limit. The recently developed low-nickel stainless steels such as 23Mn21Cr1Mo (ASTM F2229-02) are nitrogen strengthened, which can also push their PREN beyond 26.

The superior mechanical and formability properties of stainless steels over titanium alloys are a great advantage in orthodontic applications. However, the consumption of acidic food and beverages means that there is a much greater risk of localized corrosion in the oral cavity than inside the body. To counter this threat, ultraclean high-nitrogen austenitic stainless steels have been developed, for example, 21Cr10Ni3Mo0.3Nb0.4N.<sup>47</sup>

### 2.27.5.4 Nickel–Titanium Alloy

NiTi is a shape-memory alloy with super-elasticity, a property that is of interest in both surgical and dental applications. Mantovani<sup>48</sup> reviewed the possible uses of NiTi in medical appliances, typical applications

including dental braces, medical staples, and nails. The most likely form of corrosion on NiTi is pitting; its resistance to pitting in body fluids appears to be similar to that of 316L stainless steel type.<sup>49</sup> However, NiTi fares worse than stainless steel orthodontic wires in acidified artificial saliva.<sup>50</sup> Given that there is some evidence that nickel initiates cancer, the high nickel content of NiTi is a matter of concern.<sup>2</sup> To date, studies indicate that the amount of nickel released into the body from the corrosion of NiTi depends on the local environment and the tests in artificial saliva showed similar Ni release rates to 316L stainless steel,<sup>51</sup> while in simulated body fluids, the NiTi released three times as much nickel as in artificial saliva.<sup>52</sup> Rather alarmingly, Heintz *et al.*<sup>53</sup> found that when fibroblast cells adhere to the NiTi alloy, they damage the oxide film, leading to rapid localized corrosion and that this has caused failures in stent wires of explanted endovascular grafts. Hashimoto and Morita<sup>54</sup> have also reported significantly higher nickel ion release rates in the presence of living fibroblast cells. The mechanism by which this accelerated corrosion occurs is not yet known, possibly the attached fibroblasts lead to the development of occluded electrochemical cells. Nevertheless, the biocompatibility of NiTi, as determined in short-term *in vivo* tests on guinea pigs, was reported to be comparable with type 316LVM stainless steel.<sup>55</sup> This view appears to be supported by the largely favorable surgical clinical evidence available to date, including excellent biocompatibility in tendon tissue, minimal corrosion on retrieved implants, and nickel concentrations in the major organs at levels similar to those for stainless steel devices.<sup>56</sup> However, the concerns about potential Ni release and its poor performance in dental applications have led to a number of efforts aimed at improving the NiTi alloys' resistance to pitting corrosion, the most promising techniques being diamond-like carbon coatings and nitriding.<sup>57–59</sup> Recently, a new nickel-free shape-memory alloy has been developed, Ti18Nb4Sn, with a corrosion resistance in simulated body fluids apparently comparable with that of commercial titanium.<sup>60</sup> Once acceptable biocompatibility of this alloy has been demonstrated, there is a good chance of it eventually replacing NiTi, at least in orthodontics.

### 2.27.5.5 Porous Materials and Metallic Foams

As demonstrated earlier, titanium alloys and CoCrMo alloys have excellent corrosion characteristics for the

construction of surgical implants. However, the elastic moduli of these solid metallic alloys are much higher than those of human bone, which means that stresses are not transferred to the surrounding bone effectively, leading to irregular bone growth and osteoporosis. One possible solution to this problem is to use porous implant materials that have lower elastic moduli closer to those of human bone. Such porous materials not only have the advantage of a more suitable elastic modulus, but also open up the possibility of allowing bone growth into the implant itself, thereby improving the adhesion and thus reducing the likelihood of fatigue or fretting failures. Unfortunately, the corrosion rates of porous titanium, porous CoCrMo, and porous NiTi in simulated body fluids have all been reported as being significantly higher than those of their solid counterparts, possibly due to crevice corrosion within the pore matrix.<sup>61–64</sup>

Very recently, interest has been shown in metallic foams, in which a foaming agent helps to control the porosity that can be up to 80%.<sup>65</sup> It has been reported that, for such titanium foams, corrosion rate as low as  $0.07 \mu\text{m year}^{-1}$  can be obtained after aging for 6 days in a simulated body fluid (0.01 M phosphate buffer pH 7.4, 0.027 M KCl + 0.137 M NaCl), which is comparable with or even better than that of solid titanium.<sup>66</sup> However, since the wetted surface area of a foam is more than 1000 times its geometric area, the concentration of metallic ions released is still much higher from foams than from solid materials, increasing the risk of health problems related to elevated metal levels in body tissues.

### 2.27.5.6 Magnesium Alloys

At first sight, most readers will be surprised at the suggestion of fabricating biomedical devices out of a material that corrodes as readily as magnesium; however, corrosion can in fact be a desirable feature! Preliminary investigations are being conducted into the use of magnesium alloys as degradable implants for musculoskeletal surgery,<sup>67</sup> the idea being that magnesium ions encourage bone cell activation so that the bone slowly regenerates as the metal corrodes. This represents an interesting new challenge to corrosion scientist: how to tailor the corrosion rate of the Mg alloy to match the bone regrowth rate? However, it should be noted that Witte *et al.*<sup>67</sup> reported that *in vivo* corrosion rates were four orders of magnitude lower than *in vitro* rates, and that the order of relative performance between the various Mg alloys tested changed with environment, leading these



authors to conclude that the present ASTM standard *in vitro* corrosion tests are unable to predict the *in vivo* corrosion rates of magnesium alloys.

### 2.27.5.7 Rare Earth Magnets

There are a number of ternary alloys containing rare earth elements that have remarkably strong magnetic properties, such as the samarium–cobalt family. Although originally developed for the magnetic storage industry, these alloys are used in a number of specialized medical applications, for example, as dental keepers; the strong magnetization is used to keep dental fixtures in place. Unfortunately, these rare earth magnets have very poor corrosion resistances and cannot be directly inserted into any body fluid. One solution is to completely seal the magnet inside a stainless steel cladding, but this must not reduce the effectiveness of the magnetization, which rules out the austenitic steels. In the case of dental keepers, ferritic stainless steels with chromium levels as high as 55% have been used, sufficient to withstand the most corrosive foodstuffs. The magnets hold the dental fixture to a ferromagnetic material usually cemented into a residual tooth root; typically this is a Pd–Co alloy offering good corrosion resistance, but there are concerns about the leaching of cobalt ions, which are cytotoxic at high concentrations.<sup>68</sup>

### 2.27.5.8 Dental Amalgams

Dental amalgams are high-strength multiphase alloys, which makes them vulnerable to localized galvanic or intergranular corrosion between the different phases. The majority of modern dental amalgams are prepared from two types of alloys: conventional silver tin amalgam and high-copper amalgams. The high-copper amalgams have superior clinical properties with a higher resistance to corrosion.<sup>69</sup> The corrosion of any amalgam is of concern, as it leads to the release of mercury into the body, and in rare cases, can cause oral lesions if this redeposits in the oral mucosa.<sup>15</sup> In conventional silver tin amalgams, the most base phase is  $\gamma_2$  ( $\text{Sn}_7\text{Hg}$ ), which releases mercury when it corrodes.<sup>70</sup> Conversely, the most corrosion-prone phase in high-copper amalgams is  $\eta'$  ( $\text{Cu}_6\text{Sn}_5$ ), preferential corrosion of which does not release mercury into the body and thus these alloys have recently been favored.<sup>71</sup> However, Joska *et al.*<sup>72</sup> found that mercury release rates from conventional silver amalgams and high-copper amalgams were very similar, the method of preparation being

critical. Furthermore, it has been shown that for most people, the major route for mercury to be taken into the body is via food, less than 10% coming from dental amalgams.<sup>73</sup>

### 2.27.5.9 Titanium Nitride Coatings

Very hard yet smooth, low friction coatings of titanium nitride, typically a few microns thick, can now be produced by a variety of methods, including ion implantation,<sup>38</sup> nitriding,<sup>39,40</sup> physical vapor deposition,<sup>41</sup> and magnetron sputtering.<sup>74</sup> These coatings have been shown to have excellent biocompatibility and have been successfully used on Ti6Al4V to protect against fretting corrosion and other forms of wear, allowing the world's first collar bone replacement to be preformed in 2003,<sup>41</sup> as well as on NiTi alloy and stainless steels to provide protection against pitting and crevice corrosion.<sup>59,75</sup> The excellent combination of biocompatibility with corrosion and wear resistance means that TiN coatings will undoubtedly find increased usage in biomedical applications.

One potential concern about nitride coatings that has yet to be fully investigated is the possibility of galvanic corrosion of the underlying metal at holidays or damaged areas of the coating. This has already been shown to be a problem at microstructural defects in TiN coatings on type 304 stainless steel in saline solutions.<sup>76</sup> Variations on titanium nitride coatings are also being developed, such as titanium aluminum nitride, that reportedly provide better protection to stainless steels without any loss of biocompatibility.<sup>76,77</sup>

## 2.27.6 Corrosion Types Encountered in Biomedical Applications

### 2.27.6.1 General Corrosion

For a successful implant material, the longterm general corrosion rate should certainly fall to much less than  $1\mu\text{m year}^{-1}$ ; for almost any other application, such low corrosion rates would be considered insignificant. Nevertheless, even at these rates, it has been reported that after implantation the nickel, chromium, and cobalt levels in surrounding tissues can be significantly higher than normal values (Table 1).<sup>2</sup> It has also been shown that the presence of metallic ions released from nonmolybdenum-containing high-nitrogen stainless steels suppresses cell growth of human gingival fibroblasts.<sup>78</sup>

### 2.27.6.2 Pitting Corrosion

Although cases of pitting corrosion were common with the early stainless steel implants fabricated from grade 304, the addition of Mo (2–3%) to form 316L grade stainless steel has greatly reduced the number of failures. Zitter<sup>26</sup> has suggested that a PREN greater than 26 is required to prevent *in vivo* pitting corrosion. Stainless steel biomedical devices should thus be manufactured from at least high-quality 316L, preferably from ultraclean grades such as 316LVM or grades containing nitrogen additions. The risk of pitting corrosion of stainless steels in the oral cavity is higher than that in implants because of the number of chloride-containing acidic foodstuffs regularly introduced into the mouth. Although this is partly compensated by the ease by which orthodontic devices can be retrieved, it is still recommended that ultraclean high-nitrogen austenitic stainless steels be used rather than the standard 316L grade.

One of the major concerns about the use of surgical implants based on cobalt–chromium–molybdenum alloys is that pitting corrosion could lead to carcinogens being released into the body. This has resulted in numerous *in vitro* investigations into the pitting behavior of these alloys in pseudo-body fluids, all of which have reported excellent resistance to pitting as long as static conditions are maintained.<sup>64,79</sup> However, pitting corrosion has been observed when the CoCrMo alloys were subjected to either cyclic loads or severe cold working.<sup>80</sup>

Titanium metal is immune to pitting corrosion in any *in vivo* environment likely to be encountered. Although Ti alloys are less resistant, no *in vivo* pitting-related failures have been reported. The pitting behavior of nickel–titanium shape-memory alloys has already been discussed earlier.

### 2.27.6.3 Crevice Corrosion

The most common location of crevice corrosion found in biomedical applications is beneath the heads of fixing screws and it is a very serious problem with stainless steel devices, even when fabricated from high-grade molybdenum and nitrogen-containing alloys. In a survey conducted in 1959, Scales *et al.*<sup>81</sup> found that 24% of grade 316 stainless steel bone plates and screws removed from patients revealed signs of crevice corrosion. Although the introduction of the low nonmetallic inclusion type 316LVM stainless steel and the use of an austenitic microstructure free of any  $\delta$ -ferrite phase have reduced the level of

crevice corrosion problems, these have not been eliminated.

Crevice corrosion on CoCrMo alloys appears to be less of a problem than on stainless steels. Syrett and Davis<sup>82</sup> found no crevice corrosion on specimens removed from dogs and rhesus monkeys after 2 years of implantation. Similarly, Galante and Rostoker<sup>83</sup> found no crevice corrosion on CoCrMo alloy implants removed from rabbits after 1 year, although the latter authors did find single pits in the crevice regions that might have eventually developed into crevice corrosion if given sufficient time.

Crevice corrosion of titanium in neutral chloride environments has only been reported at temperatures in excess of 70°C, that is, it is not expected *in vivo*. As with pitting corrosion, titanium alloys are less resistant to crevice corrosion than is pure titanium, and Galante and Rostoker<sup>83</sup> have reported single pits in the crevice regions of Ti6Al4V specimens implanted in rabbits for 1 year, but no actual crevice corrosion. Despite titanium's excellent resistance to crevice corrosion, it is not the answer to the problem, since its poor shear strength makes it unsuitable for screws and other fasteners, which are the main crevice formers.

Finally, some total-joint implant designs contain metal-on-metal press-fit conical tapers, which are subjected to stress and motion. Retrieval studies have found crevice corrosion at taper connections consisting of CoCrMo alloy heads with both CoCrMo alloy and Ti6Al4V stems.<sup>2,84</sup> Occasionally, titanium alloy stems have been attacked, which suggests that the wearing away of the passive film plays a role, that is, the mechanism is a combination of fretting and crevice corrosion.<sup>36</sup>

### 2.27.6.4 SCC and Hydrogen Embrittlement

To the best of the author's knowledge, neither SCC nor hydrogen embrittlement has been observed on recovered surgical implants. Although retrieved implants may show evidence of cracks, they do not show the physical characteristics associated with SCC, and thus almost certainly, result from mechanical damage either during manufacturing or during the recovery process. The laboratory experiments conducted to date support the presumption that the three classes of common implant alloys (Ti, CoCrMo alloys, and stainless steels) are not susceptible to SCC in *in vivo* environments. The only counter evidence comes from *in vitro* tests conducted under experimental conditions that are highly unlikely to ever exist in any true *in vivo* situation, such as extreme

negative potentials or acidic  $\text{MgCl}_2$  solutions. However, Rodrigues *et al.* have very recently reported the first evidence of hydrogen absorption being implicated in the corrosion of retrieved titanium alloy hip implants.<sup>106</sup>

### 2.27.6.5 Corrosion Fatigue

One of the features that distinguish corrosion fatigue from mechanical fatigue is that the former is strongly dependent on the frequency of the applied loaded, with low-frequency cycles causing the most damage. Unfortunately, many medical devices are subjected to low-frequency loads, for example, simply walking represents a cyclic loading at about 1 Hz on a hip implant, so the threat of corrosion fatigue might be expected to be high. However, in 1975, Bechtol<sup>85</sup> reviewed all types of clinical fatigue-related failures and claimed that the most common root cause of failure was not related to corrosion, but rather to a breakdown of the bone–cement support interface. This leads to a widening of the separation between the metal prosthesis and bone–cement and finally to the deformity of the metal stem. This mechanism was recently supported by von Knock *et al.*,<sup>86</sup> who found no evidence of corrosion on 11 CoCrMo alloy femoral components retrieved after 2–15 years of service and suggested that the majority of the micromotion between the prosthesis and bone occurs at the bone–cement/bone interface.

Likewise, reviews of the literature related directly to corrosion fatigue of prostheses implants by Leclerc<sup>87</sup> in 1982 and Zitter<sup>26</sup> in 1991 both concluded that as long as the manufacture and metallurgical condition of the device conformed to international standards (e.g., ISO 5832 or ASTM F 138), corrosion played only a minor role in most fatigue failures. However, in contrast, Morita *et al.*<sup>22</sup> reported that the fatigue strengths of 316 stainless steel and a CoCrNiFe alloy were considerably less *in vivo* (rabbits) than in air and proposed that this was due to the low dissolved oxygen concentration in body fluids, causing a corrosive action on the alloys. Furthermore, in his 1982 review, Leclerc did note that the longer the prosthesis was implanted in the patient, the greater the role of corrosion, which is significant giving that, as explained in the introduction, it is anticipated that the required service life of surgical prosthesis will increase in the coming decades.

If corrosion fatigue does become an important issue in the future, the importance of material selection and design were emphasized by Piehler *et al.*,<sup>88</sup>

who tested hip nail plates and found that large plates had better corrosion fatigue resistance than did small ones and that Ti6Al4V outperformed 316L stainless steel. The good performance of titanium alloys was also highlighted by Hughes *et al.*,<sup>24</sup> who reported that the corrosion fatigue resistance of titanium was virtually independent of pH over the range 2–7, whereas that of stainless steel declines rapidly below pH 4. These observations are consistent with the findings of Yu *et al.*<sup>89</sup> that corrosion fatigue in stainless steels can be initiated by pitting corrosion. The latter authors also reported that the corrosion fatigue resistance of the common implant alloy Ti6Al4V can be enhanced by nitrogen implantation and heat treatments to produce fine prior- $\beta$  grain sizes.

### 2.27.6.6 Fretting Corrosion and Wear

Because all the successful surgical implant alloys are based on passive metals, any process that wears away the protective oxide film is of major concern. As a result, fretting corrosion represents the most important form of attack on load-bearing prosthesis and all three major classes of alloys used, namely, Ti alloys, CoCrMo alloys, and stainless steels, suffer fretting corrosion, sometimes in combination with crevice corrosion.<sup>90</sup> Fretting corrosion not only results in metal loss but also alters the dimensions of the prosthesis, causing fixation problems and allowing additional micromotions. This in turn can increase mechanical wear and lead to the loss of the surrounding bone–cement or bone, which, besides being a serious problem in itself, increases further the amount of movement of the implant, thereby increasing the likelihood of fatigue-related failures.<sup>85</sup> The situation is made worse by the fact that the corrosion products collect locally as particles that can cause further abrasion of the implant; for example, black titanium oxide debris is often found in the vicinity of implants.<sup>91</sup> The main cause of the shearing micromovements that eventually lead to the fretting corrosion is believed to be the large difference between the elastic moduli of solid metallic implants and the surrounding bone or bone–cement.

Morita *et al.*<sup>92</sup> investigated the wear resistances of a high-nickel version of 316L stainless steel (Fe17Cr14Ni2Mo), a cobalt–chromium–molybdenum alloy (Co28Cr6Mo), and the titanium alloy Ti6Al4V and found that rubbing between metal and ultra-high-molecular weight polyethylene, commonly used as a liner for the sockets into which the ball of hip implants are inserted, only caused the oxide on the Ti6Al4V alloy to suffer damage, that is, the titanium alloy was

the least resistant. Worse, when metal rubbed metal, the oxides on all the three implant alloys were destroyed, even at low loads. Furthermore, the addition of calcium chloride and/or hydrogen peroxide to saline solutions has also been shown to lead to increased fretting corrosion of Ti6Al4V.<sup>93</sup> Since  $H_2O_2$  can be produced as part of the inflammatory response of damaged body tissues, it can be postulated that new load bearing prosthesis are at the most risk of developing fretting corrosion, although the corrosion may subside as the  $H_2O_2$  production ceases, sufficient loosening of the device might occur to induce mechanical fatigue. Efforts to reduce the effects of fretting are based mainly on coatings, usually titanium nitride or aluminum oxide.<sup>38–41,74,94</sup>

Besides wear-resistant coatings, endeavors have been made to reduce the threat of fretting corrosion by improving the binding between the implant and its surroundings, be it bone or bone–cement. Proposals of how to achieve this include engineering the shape, topography, porosity, or composition of the implant to provide either in-growth of tissue or enhanced on-growth of mineralized bone<sup>61,95</sup>; plasma spraying a titanium coating with a specific surface roughness on the surface of the Ti6Al4V<sup>96</sup>; or depositing strongly adhered hydroxyapatite coatings that can fuse with the growing bone. Encouraging results have recently been obtained for silicon-doped hydroxyapatite coatings.<sup>97</sup> Although some reports have suggested that hydroxyapatite coatings do not provide any longterm improvement in fixation,<sup>98</sup> overall clinical results indicate that coated implants perform well, especially in young patients.<sup>2,99</sup> Occasionally, erosion–corrosion problems are encountered on implanted valves and pumps, as with nonbiomedical application, the solution to this problem is to use a more resistant material, such as titanium.<sup>100</sup>

#### 2.27.6.7 Galvanic Corrosion

Galvanic corrosion has certainly caused the failure of a number of biomedical devices. However, the vast majority of these cases were caused by poor quality control or a lack of appreciation of the existence of galvanic couple between apparently similar materials. There have even been examples of galvanic corrosion-related failures arising, because just a single grade 304L screw was used in what was otherwise an all grade 316L construction<sup>101</sup>; since it is not possible to visually distinguish one grade of stainless steel from another, the solution to the problem is careful quality control. When the correct materials

have been used, galvanic corrosion is not normally a problem; however, the poor shear strength of titanium alloys means that it is not suitable for use as fasteners, so there may be times when the production of a galvanic couple is unavoidable. In the event that titanium and any cobalt–chromium–molybdenum alloys or stainless steels are coupled together, it is likely that the former will become the cathode and thus accelerated corrosion of the latter alloys may be anticipated. However, titanium and its alloys are easily polarized and their passive films make them poor cathodes, which in practice means that the extent of accelerated corrosion caused to any metal from coupling to a titanium alloy can be expected to be small. This argument has been confirmed in a literature review by Mears<sup>102</sup> and also for titanium/cobalt–chromium–molybdenum alloy combinations by the *in vitro* experiments of Lucas *et al.*<sup>80</sup> and in clinical use as reported by Jackson-Burrows *et al.*<sup>103</sup> Nevertheless, Rostoker *et al.*<sup>104</sup> found that type 316L stainless steel suffered pitting corrosion in 1% NaCl solution at 37°C when it was coupled to either Ti6Al4V, CoCrMo alloy, or graphite, but no pitting corrosion was found when any two of the other three materials were coupled together.

There is also one further aspect of galvanic corrosion to be considered, that is, any bimetallic couple is of course a small battery in which a current flows between the anode and cathode. Even if this current is too small to cause any significant corrosion problems, these could be sufficient to cause the patient pain, indeed persistent pain resulting from such situations has led to the need to retrieve some biomedical devices.<sup>105</sup> In dental applications, galvanic corrosion of amalgams has been linked to causing oral lesions, which can develop into cancer, particularly in patients with a hyposensitivity to mercury.<sup>15</sup>

#### 2.27.7 Conclusions

The knowledge of corrosion and mechanical properties of materials has allowed the development of a number of extremely successful biomedical alloys. As a result, as long as the chosen materials match the requirements of national and international standards, the likelihood of a surgical implant suffering a corrosion-related failure is very low. The most important remaining areas of concern are fretting and corrosion fatigue. Even here, recent advances in titanium nitride coatings and fixation techniques are extremely encouraging, suggesting that a solution to

at least some of the problems is close at hand. The TiN coatings probably represent the most important advance in the protection of biomedical devices since Leclerc<sup>87</sup> wrote his chapter on surgical implants for the third edition of *Shrier's Corrosion* in 1994. However, TiN coatings have yet to be demonstrated in the tapered joints of some total-joint replacements where a combination of fretting and crevice corrosion can cause failures even in titanium alloys. Moreover, device failure is not the only concern; now that younger patients are receiving implants, the concern that extended exposure to even very low levels of corrosion products could result in medical complications, including cancer, is becoming more and more important. So there is still a continuing need to further reduce corrosion rates.

Furthermore, in recent years advanced materials have been developed that possess properties considered highly desirable for biomedical devices, for instance, porosity, shape-memory, and high magnetism. This trend is likely to continue, as the recent upsurge in funding on life science-related research will produce a number of new materials and devices specifically designed for biomedical applications, such as implanted sensors, automatic drug dispensers, and even micromachines. Techniques to protect these materials without interfering with the very functional properties that make them so desirable have been, and will have to be continually, developed, and occasionally, the biomedical industry will continue to throw out more unusual challenges to the corrosion scientist, as in the case of the sacrificial magnesium alloys being proposed to stimulate bone growth where a controlled corrosion rate is deemed desirable.

## References

- Blanchard, C. R.; Medlin, D. J.; Shetty, R. In *Joint Replacement and Bone Resorption*; Shanbhag, A., Rubash, H. E., Jacobs, J. J., Eds.; Taylor & Francis: New York, 2006; pp 559–592.
- Hallab, N. J.; Jacobs, J. J.; Gilbert, J. L. In *Joint Replacement and Bone Resorption*; Shanbhag, A., Rubash, H. E., Jacobs, J. J., Eds.; Taylor & Francis: New York, 2006; pp 211–254.
- Urban, R. M.; Jacobs, J. J.; Gilbert, J. L.; Galante, J. O. *J. Bone Joint Surg. Am.* **1994**, *76*, 1345–1349.
- Jacobs, J. J.; Skipor, A. K.; Patterson, L. M.; Paprosky, W. G.; Black, J.; Galante, J. O. *J. Bone Joint Surg. Am.* **1998**, *80*, 1447–1458.
- Thong, P. S. P.; Watt, F.; Ponraj, D.; Leong, S. K.; He, Y.; Lee, T. K. Y. *Nucl. Instrum. Methods Phys. Res. B* **1999**, *158*, 349–355.
- Landsberg, J. P.; McDonald, B.; Watt, F. *Nature* **1992**, *360*, 65–68.
- Memoli, V. A.; Urban, R. M.; Alloy, J.; Galante, J. O. *J. Orthop. Res.* **1986**, *4*, 346–355.
- Jacobs, J. J.; Rosenbaum, D. H.; Hay, R. M.; Gitelis, S.; Black, J. *J. Bone Joint Surg. Br.* **1992**, *74*, 740–744.
- Goodfellow, J. *J. Bone Joint Surg. Br.* **1992**, *74*, 645.
- Wataha, J. C. *J. Prosthet. Dent.* **2000**, *83*, 223–234.
- Solomon, H. A.; Reinhard, M. C. *J. Cancer* **1934**, *22*, 606–610.
- Schiodt, M. *Oral Surg. Oral Med. O.* **1984**, *57*, 281–293.
- Phillips, R. W.; Schnell, R. J.; Shafer, W. G. *J. Dent. Res.* **1968**, *47*, 666.
- Muller, A. W.; Van Loon, L. A.; Davidson, C. L. *J. Oral Rehabil.* **1990**, *17*, 419–424.
- Holmstrup, P. *J. Oral Pathol. Med.* **1991**, *20*, 1–7.
- Ostman, P. O.; Anneroth, G.; Skoglund, A. *Scand. J. Dent. Res.* **1994**, *102*, 172–179.
- Lundstrom, I. M. *Int. J. Oral Surg.* **1982**, *12*, 1–9.
- Blackwood, D. J.; Seah, K. H. W.; Teoh, S. H. In *Engineering Materials for Biomedical Applications*; Teoh, S. H., Ed.; World Scientific: Singapore, 2004; pp 3.1–3.56.
- Schenk, R. In *Titanium in Medicine*; Brunette, D. M., Tengvall, P., Textor, M., Thomsen, P., Eds.; Springer-Verlag: Berlin, 2001; pp 145–170.
- Solar, R. J. In *Corrosion and Degradation of Implant Materials*; Syrett, B. C., Acharya, A., Eds.; ASTM Special Technical Publication, ASTM International: Philadelphia, 1979; Vol. 684, pp 259–273.
- Blackwood, D. J.; Pereira, B. P. *J. Mater. Sci. Mater. Med.* **2004**, *15*, 755–758.
- Morita, M.; Sasada, T.; Hayashi, H.; Tsukamoto, Y. *J. Biomed. Mater. Res.* **1988**, *22*, 529–540.
- Moxham, J.; Costello, J. In *Textbook of Medicine*, 2nd ed.; Souhami, R. L., Moxham, J., Eds.; Churchill Livingstone: Edinburgh, UK, 1994; pp 444–534.
- Hughes, A. N.; Jordan, B. A.; Orman, S. *Eng. Med.* **1978**, *7*, 135–141.
- Kocjan, A.; Milosev, I.; Pihlar, B. *J. Mater. Sci. Mater. Med.* **2003**, *14*, 69–77.
- Zitter, H. *Werkst. Korros.* **1991**, *42*, 455–466.
- Liang, P. G. *Orthop. Clin. North Am.* **1973**, *4*, 249–273.
- Hadjigaryrou, M.; Ahrens, W.; Rubin, C. T. *J. Bone Miner. Res.* **2000**, *15*, 1014–1023.
- Tengvall, P.; Lundstrom, I. *Clin. Mater.* **1992**, *9*, 115–134.
- Fusayama, T.; Katayori, T.; Nomoto, S. *J. Dent. Res.* **1963**, *42*, 1183–1197.
- Joyston-Bechal, S.; Kidd, E. A. M. *Dent. Update* **1994**, *21*, 366–371.
- Schiff, N.; Groszogeat, B.; Lissac, M.; Dalard, F. *Biomaterials* **2004**, *25*, 4535–4542.
- Zardiackas, L. D.; Roach, L. D.; Williamson, R. S. In *Titanium, Niobium, Zirconium, and Tantalum for Medical and Surgical Applications*; Zardiackas, L. D., Kraay, M., Freese, H., Eds.; ASTM Special Technical Publication, ASTM International: Philadelphia, 2006; Vol. 1471, pp 166–182.
- Zaffe, D.; Bertoldi, C.; Consolo, U. *Biomaterials* **2004**, *25*, 3837–3844.
- Maehara, K.; Doi, K.; Matsushita, T.; Sasaki, Y. *Mater. Trans.* **2002**, *43*, 2936–2942.
- Heimgartner, P.; Schenk, R. In *Critical Factors in Localized Corrosion IV*, Proceedings of the 202nd Meeting of the Electrochemical Society, Salt Lake City, USA, Oct. 20–25, 2002; Virtanen, S., Schmuki, P., Frankel, G. S., Eds.; Electrochemical Society: New Jersey, 2003; Vol. 2002–24, pp 631–639.
- Disegi, J. A. In Proceedings of the 16th Southern Biomedical Engineering Conference, Biloxi, Mississippi, USA, Apr. 4–6, 1997; Bumgardner, J. D., Puckett, A. D.,



- Eds.; Institute of Electrical and Electronics Engineers: New York, 1997; pp 129–132.
38. Buchanan, R. A.; Rigney, E. D.; Williams, J. M. *J. Biomed. Mater. Res.* **1987**, *21*, 355–366.
  39. Shenhar, A.; Gotman, I.; Radin, S.; Ducheyne, P.; Gutmanas, E. Y. *Surf. Coat. Technol.* **2000**, *126*, 210–218.
  40. Starosvetsky, D.; Shenhar, A.; Gotman, I. *J. Mater. Sci. Mater. Med.* **2001**, *12*, 145–150.
  41. Burslem, R. *Mater. World* **2004**, *12*, 31–32.
  42. Manso-Silvan, M.; Martinez-Duart, J. M.; Ogueta, S.; Garcia-Ruiz, P.; Perez-Rigueiro, J. *J. Mater. Sci. Mater. Med.* **2002**, *13*, 289–293.
  43. Mishra, A. K.; Davidson, J. A. *Mater. Tech.* **1993**, *8*, 16–21.
  44. Clerc, C. O.; Jedwab, M. R.; Mayer, D. W.; Thompson, P. J.; Stinson, J. S. *J. Biomed. Mater. Res.* **1997**, *38*, 229–234.
  45. Blackwood, D. J. *Corros. Rev.* **2003**, *21*, 97–124.
  46. Zitter, H.; Schaschl-Outschar, D. *Werst. Korros.* **1981**, *32*, 324–331.
  47. Pan, J.; Karlen, C.; Ulfvin, C. *J. Electrochem. Soc.* **2000**, *147*, 1021.
  48. Mantovani, D. J. *Mater.* **2000**, *52*, 36–44.
  49. Rondelli, G.; Torricelli, P.; Fini, M.; Rimondini, L.; Giardino, R. *J. Biomed. Mater. Res. B* **2006**, *79*, 320–324.
  50. Huang, H.-H. *J. Biomed. Mater. Res. A* **2003**, *66*, 829–839.
  51. Barrett, R. D.; Bishara, S. E.; Quinn, J. K. *Am. J. Orthod. Dentofacial Orthop.* **1993**, *103*, 8–14.
  52. Rondelli, G. *Biomaterials* **1996**, *17*, 2003–2008.
  53. Heintz, C.; Riepe, G.; Birken, L.; Kaiser, E.; Chakfe, N.; Morlock, N.; Delling, G.; Imig, H. J. *Endovasc. Ther.* **2001**, *8*, 248–253.
  54. Hashimoto, T.; Morita, M. *Mater. Sci. Forum* **2005**, *475–479*, 2075–2078.
  55. Wever, D. J.; Veldhuizen, A. G.; Sanders, M. M.; Schakenraad, J. M.; van Horn, J. R. *Biomaterials* **1997**, *18*, 1115–1120.
  56. Ryhanen, J.; Shabalovskaya, S.; Yahia, L. *Mater. Sci. Forum* **2002**, *394–395*, 139–144.
  57. Kobayashi, S.; Ohgoe, Y.; Ozeki, K.; Gei, L.; Hirakuri, K. K.; Aoki, H. *Key Eng. Mater.* **2005**, *284–286*, 783–786.
  58. Starosvetsky, D.; Gotman, I. *Biomaterials* **2001**, *22*, 1853–1859.
  59. Yeung, K. W. K.; Poon, R. W. Y.; Liu, X. M.; Chu, P. K.; Chung, C. Y.; Liu, X. Y.; Chan, S.; Lu, W. W.; Chan, D.; Luk, K. D. K.; Cheung, K. M. C. *Surf. Coat. Technol.* **2007**, *201*, 5607–5612.
  60. Kawashima, A.; Watanabe, S.; Asami, K.; Hanada, S. *Mater. Trans.* **2003**, *44*, 1405–1411.
  61. Seah, K. H. W.; Thampuran, R.; Chen, X.; Teoh, S. H. *Corros. Sci.* **1995**, *37*, 1333–1340.
  62. Blackwood, D. J.; Chua, A. W. C.; Seah, K. W. H.; Thampuran, R.; Teoh, S. H. *Corros. Sci.* **2000**, *42*, 481–503.
  63. Becker, B. S.; Bolton, J. D. *Powder Metall.* **1995**, *38*, 305–313.
  64. Li, Y.-H.; Rao, G.-B.; Rong, L.-J.; Li, Y.-Y.; Ke, W. *Mater. Sci. Eng. A* **2003**, *363*, 356–359.
  65. Wen, C. E.; Yamada, Y.; Shimojima, K.; Chino, Y.; Asahina, T.; Mabuchi, M. *J. Mater. Sci. Mater. Med.* **2002**, *13*, 397–401.
  66. Menini, R.; Dion, M. J.; So, S. K. V.; Gauthier, M.; Lefebvre, L. P. *J. Electrochem. Soc.* **2006**, *153*, B13–B21.
  67. Witte, F.; Fischer, J.; Nellesen, J.; Crostack, H. A.; Kaese, V.; Pisch, A.; Beckmann, F.; Windhagen, H. *Biomaterials* **2006**, *27*, 1013–1018.
  68. Angelini, E.; Pezzoli, M.; Zucchi, F. *J. Prosthet. Dent.* **1991**, *65*, 848–853.
  69. Sarker, N. K.; Eyer, C. S. *J. Oral. Rehabil.* **1987**, *14*, 27–33.
  70. von Fraunhofer, J. A.; Staheli, P. *J. Nature* **1972**, *240*, 304–306.
  71. Eley, B. M. *Br. Dent. J.* **1997**, *182*, 247–249.
  72. Joska, L.; Bystrainsky, L.; Novak, P. *Mater. Corros.* **2003**, *54*, 152–156.
  73. Newton, T. *Chem. Br.* **2002**, *38*(10), 24–27.
  74. Hubler, R. *Surf. Coat. Technol.* **1999**, *116–119*, 1111–1115.
  75. Neumann, H. G.; Beck, U.; Drawe, M.; Steinback, J.; Rostock, H. *Surf. Coat. Technol.* **1998**, *98*, 1157–1161.
  76. Ibrahim, M. A. M.; Korablov, S. F.; Yoshimura, M. *Corros. Sci.* **2002**, *44*, 815–828.
  77. Freeman, C. O.; Brook, I. M. *J. Mater. Sci. Mater. Med.* **2006**, *17*, 465–470.
  78. Endo, K.; Abiko, Y.; Suzuki, M.; Ohno, H.; Kaku, T. *Zairyo Kankyo* **1998**, *47*, 570–576.
  79. Syrett, B. C.; Wing, S. S. *Corrosion* **1978**, *34*, 138–145.
  80. Lucas, L. C.; Buchanan, R. A.; Lemons, J. E.; Griffin, C. D. *J. Biomed. Mater. Res.* **1982**, *16*, 799–810.
  81. Scales, J. T.; Winter, G. D.; Shirley, H. T. *J. Bone Joint Surg.* **1959**, *41B*, 810–820.
  82. Syrett, B. C.; Davis, E. E. In *Corrosion and Degradation of Implant Materials*; Syrett, B. C., Acharya, A., Eds.; ASTM Special Technical Publication, ASTM International: Philadelphia, 1979; Vol. 684, pp 229–244.
  83. Galante, J.; Rostoker, W. *Clin. Orthop. Relat. Res.* **1972**, *86*, 237–244.
  84. Gilbert, J. L.; Buckley, C. A.; Jacobs, J. J. *J. Biomed. Mater. Res.* **1993**, *27*, 1533–1544.
  85. Bechtol, C. O. *Orthop. Rev.* **1975**, *4*, 23–29.
  86. von Knoch, M.; Bluhm, A.; Morlock, M.; von Förster, G. *J. Arthroplasty* **2003**, *18*, 471–477.
  87. LeClerc, M. F. In *Corrosion*, 3rd ed.; Shrier, L. L., Jarman, R. A., Burstein, G. T., Eds.; Butterworth Heinemann: Oxford, 1994; Vol. 1, pp 2:164–2:180.
  88. Piehler, H. R.; Portnoff, M. A.; Slotter, L. E.; Vegdahl, E. J.; Gilbert, J. L.; Weber, M. J. In *Corrosion and Degradation of Implant Materials: 2nd Symposium*; Fraker, A. C., Griffin, C. D., Eds.; ASTM Special Technical Publication, ASTM International: Philadelphia, 1985; Vol. 859, pp 93–104.
  89. Yu, J.; Zhao, Z. J.; Li, L. X. *Corros. Sci.* **1993**, *35*, 587–597.
  90. Syrett, B. C.; Wing, S. S. *Corrosion* **1978**, *34*, 379–386.
  91. Engh, C. A., Jr.; Moore, K. D.; Vinh, T. N.; Engh, G. N. *J. Bone Joint Surg. Am.* **1997**, *79*, 1721–1725.
  92. Morita, M.; Inoue, Y.; Sasada, T. *Toraiborajisuto* **1998**, *43*, 429–435.
  93. Montague, A.; Merritt, K.; Brown, S.; Payer, J. *J. Biomed. Mater. Res.* **1996**, *32*, 519–526.
  94. Sella, C.; Martin, J. C.; Lecoeur, J.; Bellier, J. P.; Davidas, J. P. *Adv. Biomater.* **1987**, *7*, 119–124.
  95. Lemons, J. E. *Surf. Coat. Technol.* **1998**, *103–104*, 135–137.
  96. Normand, B.; Renaud, F.; Coddet, C.; Tourenne, F. In *Thermal Spray: Practical Solutions for Engineering Problems*, Proceedings of the 9th National Thermal Spraying Conference, Cincinnati, USA, Oct. 7–11, 1996; Berndt, C. C., Ed.; ASM International: Materials Park, OH, 1996; pp 73–78.
  97. Thian, E. S.; Huang, J.; Best, S. M.; Barber, Z. H.; Bonfield, W. *Mater. Sci. Eng. C* **2007**, *27*, 251–256.
  98. Parvizi, J.; Sharkey, P. F.; Hozack, W. J.; Orzoco, F.; Bissett, G. A.; Rothman, R. H. *J. Bone Joint Surg. Am.* **2004**, *86A*, 783–786.

99. Dumbleton, J.; Manley, M. T. *J. Bone Joint Surg. Am.* **2004**, 86A, 2526–2540.
100. Andersen, T. S.; Johansen, P.; Paulsen, P. K.; Nygaard, H.; Hasenkam, J. M. *J. Heart Valve Dis.* **2003**, 12, 790–796.
101. Jedwab, J.; Burny, F.; Wollast, R.; Naessens, G.; Opdecam, P. *Acta Orthop. Belg.* **1974**, 40, 877–886.
102. Mears, D. C. *J. Biomed. Mater. Res. (Symp.)* **1975**, 6, 133–148.
103. Jackson-Burrows, H.; Wilson, J. N.; Scales, J. T. *J. Bone Joint Surg.* **1975**, 57B, 148–159.
104. Rostoker, W.; Pretzel, C. W.; Galante, J. O. *J. Biomed. Mater. Res.* **1974**, 8, 407–419.
105. Park, J. B.; Lakes, R. S. *Biomaterials: An Introduction*; Plenum: New York, 1992; pp 108–110.
106. Rodrigues, D. C.; Urban, R. M.; Jacobs, J. J.; Gilbert, J. L. *J. Biomed. Mater. Res. B* **2009**, 88, 206–219.

## 2.28 Corrosion by Wood

**M. J. Schofield**

CAPCIS Ltd, 1 Echo Street, Manchester M1 7DP, UK

© 2010 Elsevier B.V. All rights reserved.

2.28.1	Corrosion of Metals by Wood	1323
2.28.2	Structure and Composition of Wood	1323
2.28.2.1	Mechanisms of Corrosion by Wood	1324
2.28.2.1.1	Contact corrosion	1324
2.28.2.1.2	Corrosion by acidic vapor	1326
2.28.2.1.3	Corrosion of other metals	1326
2.28.2.2	Corrosion Testing	1326
2.28.2.3	Corrosion Modeling	1327
2.28.2.4	Industrial Significance of Corrosion of Metals by Wood	1327
2.28.2.4.1	Building	1327
2.28.2.4.2	Water tanks	1328
2.28.2.4.3	Water cooling towers	1328
2.28.2.4.4	Wood cutting tools	1328
2.28.2.4.5	Conservation	1328
References		1328

### Glossary

**Cellulose** A complex polymeric carbohydrate, the chief constituent of the cell walls of all plants.

**Creosote** Oily liquid containing phenols and creosols, obtained from coal tar or by the destructive distillation of wood tar.

**Heartwood** The inner region of wood in a tree, it is dead.

**Hemicellulose** Plant cell-wall polysaccharides.

**Lignin** A polymeric organic compound consisting of various aromatic alcohols.

**Lumber** Wood that has been cut and surfaced for construction use.

**Lumen** The cavity bounded by a plant cell wall.

**Moisture content** The weight of water in wood expressed as a percentage of the weight of wood fibrous material (which is considered to be the oven dry weight of the sample).

**Polyphenols** Alcohols containing two or more benzene rings, each of which have at least one hydroxyl group (OH) attached.

**Sapwood** The outer layer of wood in a tree, next to the bark.

**Tannins** Soluble astringent complex phenolic substances of plant origin.

**Timber** Lumber whose smallest dimension is not less than 5 in.

**Wood** The hard, fibrous substance that forms the major part of the trunk and branches of a tree.

### Abbreviations

**ACQ** Alkaline copper quat

**AWPA** American Wood Preservers' Association

**CCA** Copper–chromium–arsenic

**DOT** Disodium octaborate

### 2.28.1 Corrosion of Metals by Wood

Wood can cause corrosion of metals with which it is in contact, and nearby metals by emission of acidic vapors. The most important practical consequence of contact corrosion is the failure of fasteners in wood. Vapor corrosion affects mainly items that are packaged, stored, or displayed in wooden containers.

### 2.28.2 Structure and Composition of Wood

Wood is an organic material with a cellular structure and open spaces (lumens) between the cells. There

are many constituents in wood; the structural constituents are cellulose and hemicellulose fibers and lignin. Woods show great variability in terms of mechanical properties and chemical composition between species and within individual samples. Wood is very anisotropic in respect of most of its properties.

In dry wood, water is present only in the cell walls and within the cells; this water is bound and hence not available to support a corrosion process. However, dry wood is hygroscopic and it readily absorbs further water, becoming damp or wet. This water is present in the cell walls and in the lumens; it is free water and is usually present in sufficient quantities to support corrosion of metals in contact with the wood.

Woods are more or less resistant to biological attack; preservative chemicals are used to treat it to control fungal decay and insect attack. It is also flammable and therefore often treated with fire-retardant chemicals.

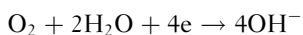
Woods contain organic acids, principally acetic acid with smaller quantities of formic, propionic, and butyric acids. Indeed, in the early twentieth century, most acetic acid was obtained by distillation from wood.<sup>1</sup> Wood also contains some natural corrosion inhibitors such as tannins. The water, acid, inhibitor, and treatment chemical contents of wood influence its corrosivity toward metallic materials.

### 2.28.2.1 Mechanisms of Corrosion by Wood

Two distinct mechanisms have been identified for the corrosion of metals by wood. These are conventionally called contact corrosion and corrosion by acidic vapor. This discussion applies primarily to the corrosion of iron and steel; corrosion of other metals is addressed in [Section 2.28.2.1.3](#). Indirectly, some of the constituents of wood contribute to corrosion in pulping plants, but this subject is not addressed in this chapter.

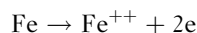
#### 2.28.2.1.1 Contact corrosion

Damp wood can be considered as an electrolyte or a slightly acidic solution,<sup>2</sup> hence metals in contact with wood are subject to conventional electrochemical corrosion in which electrons are released at anodic sites and consumed at cathodic sites. Pinion<sup>3</sup> demonstrated the production of alkali ( $\text{OH}^-$ ) at the exposed end of a steel nail in wet wood. This is formed as a result of oxygen reduction in the cathodic reaction of the corrosion process



This process occurs most readily at areas of greatest oxygen access, for example, on the heads of fasteners embedded in wood.

The anodic reaction is metal dissolution, which in the case of iron and steel is



This process occurs on the shanks of fasteners embedded in wood, resulting in damage that is not visible from the outside.

The corrosion of fasteners in wood is often described as a form of crevice corrosion, since metal loss occurs primarily in the area that is shielded from the higher oxygen content environment on the external surface of the wood (and the head of the fastener). However, differential aeration cell corrosion is a better description, because the term crevice corrosion is most commonly applied to corrosion-resistant alloys, for example, stainless steels. Differential aeration cells are reported to occur also on fasteners that connect two different woods,<sup>3,4</sup> resulting in corrosion within the wood of lower oxygen diffusivity.

#### Moisture content

The moisture content of wood is the dominant factor in controlling contact corrosion. As explained by Zelinka *et al.*,<sup>5</sup> in wood with moisture content below ~15–18%, the water in wood is bound to the hydroxyl sites within the cell walls; there is no free water, and therefore, the ionic conductivity of wood is very low and corrosion is minimal. Increasing the moisture content of wood results in free water within the cell walls; this supports the ionic conductivity, permitting corrosion to occur. This critical moisture content of the wood is equivalent to a relative humidity of the atmosphere around the wood of approximately 80–85%, depending on temperature.<sup>6</sup> Note that the critical moisture content varies between woods and a wider range of 10–20% is given in some references.<sup>2,7</sup> This critical moisture content is often described as the threshold for corrosion to occur, but the transition between dry and wet wood, or no corrosion and corrosion, is not so marked as the term implies.

The threshold moisture content for corrosion is also the minimum moisture content required for fungal decay (for which there is an upper limit of ~60% and oxygen must also be present), hence wood that is to be exposed to wet conditions is typically treated with preservatives to prevent such decay.

#### Acid content

The organic acid content of wood is an important factor in contributing to contact corrosion and vapor

corrosion of metals by wood. Acetic acid is the main acid involved, since it is present at significantly higher levels than are the other acids in wood. Acetic acid is formed by the hydrolysis of acetylated polysaccharides in the wood. As little as 0.5 ppmw is sufficient to influence corrosion,<sup>8</sup> with corrosivity increasing roughly in line with acid content, but it is to be noted that pH and other measured properties of wood can vary significantly between samples, between heartwood and sapwood, and across small distances in a single sample.

**Table 1** shows the variable nature of the acidity of woods;<sup>9–11</sup> the pH of aqueous extracts from eucalyptus woods have been found to be 2.5 or even lower.<sup>12</sup> As a rough guide, woods of pH below 4 are very corrosive and woods of pH greater than 5 are low in corrosivity, but other factors are also relevant.

### Salts

Woods naturally have a small salt content, notably sulfate and chloride, but this can increase by a number of means, including marine aerosol deposition, the floating of logs in seawater,<sup>13</sup> the introduction of chemical treatments such as preservatives and fire retardants, and even by the process of salt seasoning.<sup>13</sup> Salts contribute to corrosion by increasing the conductivity of the wood. The role of copper ions, which are an important component of many preservative treatments, is discussed in [Section 2.28.2.4.1](#).

### Polyphenols

Polyphenolic compounds that possess two or three adjacent hydroxyl groups are reported to be capable of forming iron chelates. This chelation, along with the acidity of the wood, is considered to be a contributing factor in the corrosion of steel saw blades.<sup>14</sup>

### Bimetallic corrosion

Contact between dissimilar metals in damp wood results in bimetallic corrosion.<sup>2,15</sup> An example is that of steel-framed boats with wooden planking attached by copper alloy fasteners.<sup>11</sup> This is easily avoided by preventing such contact or selecting compatible fasteners.

### Effect of corrosion on wood

The alkali ( $\text{OH}^-$ ) that is formed at the cathodic site during the corrosion process degrades the wood. Hemicelluloses and lignins are readily attacked by alkali, making the wood spongy. This effect is commonly known as nail sickness<sup>3,16</sup> and results in a loss of holding power of nails and other fasteners in the wood.

At anodic sites, iron corrosion products react with tannin to form blue-black staining. This is a common problem in wooden railway sleepers and it affects other materials of cellulosic structure, including textiles.<sup>17</sup> It also occurs where iron corrosion products from steel wool (used to finish wood) and handling chains come into contact with the wood. Tannate

**Table 1** Relative corrosivity of woods by vapor corrosion

Wood	Classification in Defence Guide-3A <sup>10</sup>	Typical pH values
Oak	Most corrosive	3.35, 3.45, 3.85, 3.9
Sweet chestnut	Most corrosive	3.4, 3.45, 3.65
Steamed European beech	Moderately corrosive	3.85, 4.2
Birch	Moderately corrosive	4.85, 5.05, 5.35
Douglas fir	Moderately corrosive	3.45, 3.55, 4.15, 4.2
Gaboon	Moderately corrosive	4.2, 4.45, 5.05, 5.2
Teak	Moderately corrosive	4.65, 5.45
Western red cedar	Moderately corrosive	3.45
Parana pine	Least corrosive	5.2–8.8
Spruce	Least corrosive	4.0, 4.45
Elm	Least corrosive	6.45, 7.15
African mahogany	Least corrosive	5.1, 5.4, 5.55, 6.65
Walnut	Least corrosive	4.4, 4.55, 4.85, 5.2
Iroko	Least corrosive	5.4, 6.2, 7.25
Ramin	Least corrosive	5.25, 5.35
Obeche	Least corrosive	4.75, 6.75

Source: Rance, V. E.; Cole, H. G. *Corrosion of Metals by Vapours from Organic Materials*, 3rd edn.; HMSO: London, 1958.

DG-3A *Defence Guide for the Prevention of Corrosion of Cadmium and Zinc Coatings by Vapours from Organic Materials*; HMSO: London, 1966.

Gray, V. R. J. *Inst. Wood Sci.* **1958**, 1, 58.



staining is generally restricted to a depth of 0.4 mm<sup>18</sup> and hence is not a significant form of degradation.

Some sources suggest that acidic conditions develop at the site of the anodic reaction, by reaction between chloride ions and ferrous ions (though more accurately the acidity will be produced by metal ion hydrolysis),<sup>19</sup> but the significance of this is not well documented.

### 2.28.2.1.2 Corrosion by acidic vapor

The organic acids in wood are volatile and can cause corrosion of some metals in confined spaces. It is principally acetic acid that is responsible for this form of corrosion. The mechanical properties of woods can be enhanced by thermal treatment, but this increases the volatility of organic acids, which increases the risk of vapor corrosion at least in the short term. This form of corrosion was traditionally associated with the use of wooden packaging and pallets, but more recently, it has become a serious issue in conservation.

Aoyama *et al.*<sup>20</sup> attributed the corrosion of nickel-plated brass to acetic acid released from wooden storage boxes. In extreme conditions of heat and humidity, sufficient acetic acid vapor is produced from wood to cause stress corrosion cracking of quenched and tempered AISI 1035 carbon steel nails.<sup>21</sup> The imposition of hardness and tensile strength limits was found to be necessary to prevent such cracking. Volatile corrosion inhibitors such as *m*-dinitrobenzene and anthraquinone have been shown to be effective in suppressing acetic acid vapor corrosion of mild steel in wooden boxes in hot, humid conditions.<sup>22</sup>

A common problem in conservation is the corrosion of artifacts stored in wooden boxes or displayed in wooden showcases. As summarized by Berndt,<sup>23</sup> corrosion is due mostly to the presence of acetic acid vapor, although other chemicals, including formic acid, formaldehyde (which is oxidized by atmospheric oxygen to formic acid), and esters (which hydrolyze to form alcohols and acids) can also contribute. Work conducted at the British Museum has shown that Egyptian bronze artifacts corroded when stored in wooden cupboards due to the presence of acetic acid vapor at levels in the range 1000–2500 mg m<sup>-3</sup>. Subsequent work found that corrosion did not occur on a range of lead and copper alloys when the acid vapor was reduced to below ~350 mg m<sup>-3</sup> in showcases, but this limit is a function of humidity and temperature.<sup>24</sup> Humidity control and acid-scavenging chemicals are used to control this form of corrosion, but the preferred solution is to select materials of construction that release less acidic vapor.

### 2.28.2.1.3 Corrosion of other metals

#### Aluminum

Aluminum alloys have reasonable resistance to corrosion in wood of low moisture content, but it is recommended that they should be protected by coatings or other technique if the wood becomes wet in service.<sup>25</sup> Specific corrosion risks are posed by wood that contains chloride ions (e.g., by absorption from salt water) and by copper-containing and mercury-containing preservative treatment chemicals. This corrosion risk extends to flashing that is exposed to water runoff from treated wood. Some preservatives such as pentachlorophenol and chromates are considered to be innocuous to aluminum, but note that chromate treatments have been largely phased out for environmental reasons. Coal tar creosote is considered to have corrosion-inhibiting properties toward aluminum, but some corrosion testing that forms the basis of some reports has failed to separate out other effects, such as water repellency, associated with creosote.

#### Brass and other copper alloys

Copper and its alloys are susceptible to corrosion by acetic acid, as noted in [Section 2.28.2.1.2](#), and are therefore subject to corrosion in most woods. Brass screws were reported to suffer dezincification in damp wood that had been treated with zinc chloride and sodium dichromate.<sup>26</sup> Copper and its alloys are susceptible to corrosion by ammonia, which is released from ammonium salt fire-retardant treatments in some circumstances.

#### Lead

Lead roofs have been corroded by acetic and formic acid released from wood that has been wet by condensation in poorly ventilated conditions.<sup>27</sup>

### 2.28.2.2 Corrosion Testing

A number of corrosion test methods are applicable to contact corrosion; these are reviewed by Zelinka *et al.*<sup>28</sup>

Simple exposure tests have been standardized by the American Wood Preservers' Association (AWPA). AWPA standard method E12-94 'Standard Method of Determining Corrosion of Metal in Contact with Treated Wood,' is an accelerated test method, in which a metal coupon is placed between two pieces of preservative-treated wood and exposed for 240 h at 49 ± 1 °C, 90 ± 1% relative humidity. The assessment of the test coupons is based on mass loss

and visual appearance. Because the test is accelerated, it cannot be used to predict a service life for a metal component in contact, rather, it is used to rank the corrosivity of preservative treatments. The industry is currently working to develop new tests that will be more directly applicable to the corrosion of fasteners in treated wood. ASTM subcommittee G01.14.01 'Corrosion of Metals in Treated Lumber' is also addressing this issue.

A further AWPAs test is E17-99 'Standard Method for Determining Corrosion Rates of Metals in Contact With Treating Solutions,' in which metal coupons are exposed in the preservative treatment chemicals. This method is applicable to corrosion in treatment plant equipment, and not to corrosion on contact with treated wood.

Electrochemical corrosion test methods have also been employed. Linear polarization resistance measurement has been used successfully to study the corrosion behavior of carbon steel, stainless steel, and zinc in solutions of preservative treatment chemicals<sup>29</sup> and in aqueous extracts prepared from wood.<sup>5</sup> However, it is not a suitable technique for corrosion in contact with wood because of the relatively poor ionic conductivity of wood and it is not capable of measuring localized corrosion effects such as pitting. Alternating current impedance testing is more appropriate for the study of contact corrosion; it has been used with some success on preservative-treated wood.<sup>30</sup> However, Zelinka *et al.*<sup>31</sup> reported that results obtained in their tests could not be related to corrosion rate 'because of gaps in understanding the impedance properties of wood.'

### 2.28.2.3 Corrosion Modeling

The modeling of the corrosivity of wood toward embedded fasteners has been undertaken in Australia,<sup>32</sup> taking into account several factors, including the moisture content and acidity of the wood, temperature, local sheltering, and weathering, in addition to climatic and atmospheric factors. The objective of this modeling is the prediction of the service life of fasteners in wooden structures.

### 2.28.2.4 Industrial Significance of Corrosion of Metals by Wood

Wood is the oldest construction material known to man. It has long been used to construct dwellings, boats, and structures such as bridges, and to manufacture weapons. In the first stages of the Industrial

Revolution, most machines were made of wood.<sup>33</sup> Although its industrial use has declined in recent years, it is expected to increase again now that it has been recognized<sup>34</sup> that wood is an environmentally friendly material with significantly lower energy cost and carbon footprint than steel and concrete in many building applications.

#### 2.28.2.4.1 Building

The most important use of wood within the purview of this book is its use as a construction material for buildings. Wood in ground contact, or exposed to rain or to humid air, has a moisture content sufficient to sustain contact corrosion of metallic fasteners. Corrosion in this condition is often dominated by the effects of preservative or fire-retardant chemicals. The following discussion also applies to other wood in ground contact such as railway sleepers and utility poles, which are routinely treated with these chemicals.

#### Preservative treatments

A range of preservative chemicals are used for the treatment of wood against fungal decay and insect attack. Traditional preservatives include creosotes. Creosotes are low in corrosivity toward most metallic materials except lead,<sup>8</sup> and are often reported as having corrosion inhibiting properties. Coal tar creosote is reported to be less corrosive than is wood tar creosote toward carbon steel.<sup>35</sup> Other organic chemicals such as pentachlorophenol are considered to be noncorrosive.

Many modern preservatives are based on copper compounds, since copper is a potent fungicide. Copper ions introduced into wood are a major contributing factor to corrosion in treated wood, but their role has not been established with certainty. Baker<sup>2</sup> proposed a form of galvanic corrosion between the copper and less noble fastener materials. However, work by Simm *et al.*<sup>36</sup> failed to find metallic copper on the surface of steel fasteners that had corroded in copper–chromium–arsenic (CCA) treated wood, implying that the possible cathodic reaction of  $\text{Cu}^{2+}$  ion reduction was not operative. Copper salts in common use include copper naphthenate, copper azoles, CCA, and alkaline copper quat (ACQ).

CCA preservatives are now less commonly used, since the U.S. Environmental Protection Agency has concluded that their arsenic content may threaten human health. They have been largely replaced by ACQ formulations, which are more corrosive toward steel and galvanized steel. This is considered to be due to the higher level of copper ions in the newer formulations, and because the chromium and arsenic

in CCA acted as corrosion inhibitors. Tests conducted on galvanized steel in accordance with AWWA E12 standard (see [Section 2.28.2.2](#)) showed corrosion rates  $< 0.03 \text{ mm year}^{-1}$  for DOT,  $\sim 0.03\text{--}0.08 \text{ mm year}^{-1}$  for CCA, and  $0.08\text{--}0.16 \text{ mm year}^{-1}$  for ACQ types. Types 304 (UNS S30400) and 316 (UNS S31600) stainless steels performed well in all treatments.<sup>37</sup>

Recommended fasteners<sup>36</sup> for use in wood treated with modern copper-containing preservatives are galvanized steel, with at least  $0.9 \text{ oz ft}^{-2}$  ( $45 \mu\text{m}$ ) of zinc, or stainless steels. Aluminum alloy fasteners are not recommended for this application. Previous work<sup>2</sup> showed that the corrosion resistance of copper and Monel (UNS N04400) in CCA-treated wood was intermediate between that of stainless steels and galvanized (and bare) steel.

Copper-free formulations such as zinc naphthenate<sup>11</sup> and disodium octaborate (DOT,  $\text{Na}_2\text{B}_8\text{O}_{13}\cdot 4\text{H}_2\text{O}$ ) are reported to be noncorrosive.

#### Fire-retardant chemicals

Common fire-retardant treatment chemicals are based on boron compounds (boric acid or sodium tetraborate), zinc chloride, or ammonium salts (sulfate or phosphate). Corrosion inhibitors such as sodium dichromate and ammonium thiocyanate are present in some formulations.

Boron-based treatments are considered not to pose a risk of corrosion to metallic materials in contact with treated wood.<sup>8</sup> Zinc chloride is corrosive, but reports for the ammonium-based treatments are variable.<sup>11</sup>

#### 2.28.2.4.2 Water tanks

Wood is still used for tank construction and may have “the best life cycle cost of any material in handling water, acidic wastewaters, and weak acid solutions up to temperatures of  $60^\circ\text{C}$ .”<sup>38</sup> Corrosion-resistant materials should be used for fasteners and fittings in such tanks.

#### 2.28.2.4.3 Water cooling towers

Wood is the most economic material of construction for some components of water-cooling towers of certain design and capacity. Wood degrades in this service, but fastener failure by corrosion does not appear to be an issue.

#### 2.28.2.4.4 Wood cutting tools

In use, saw blades<sup>11</sup> and other wood cutting tools<sup>39</sup> suffer corrosion and corrosive wear that has an

electrochemical component that ‘is not negligible and can be very important.’

#### 2.28.2.4.5 Conservation

In addition to the issues discussed in [Section 2.28.2.1.2](#), corrosion of metals by wood endangers some of our cultural heritage. Sánchez-Gómez *et al.* report that steel bars embedded in a wooden door to a belfry tower dating back to 1724 corroded, damaging the door.<sup>40</sup>

## References

1. [http://en.wikipedia.org/wiki/Acetic\\_acid](http://en.wikipedia.org/wiki/Acetic_acid) (viewed on 13/07/2009).
2. Baker, A. J. *Durability of Building Materials and Components*; ASTM STP 691; American Society for Testing and Materials: West Conshohocken, 1980; pp 981–993.
3. Pinion, L. C. The degradation of wood by metal fastenings and fittings; Timberlab 174–183, 1968–1972, Paper No. 27, Forest Products. Research Laboratory: Princes Risborough, Aylesbury, Bucks, England, 1970; pp 61–66.
4. Causes of Metal Corrosion in Timber Fixings; British Stainless Steel Association. <http://www.bssa.org.uk> (viewed on 13/07/2009).
5. Zelinka, S. L.; Rammer, D. R.; Stone, D. S. *Corrosion of Metals in Contact with Treated Wood: Developing Test Methods*; Proceedings of Corrosion 2008, New Orleans, March 16–20, 2008; NACE International: Houston, 2006.
6. *Technical Notes. Treated Wood News*; Western Wood Preservers Institute, 2001.
7. Hof, T.; Van der Elburg, J. *TNO Nieuws* **1967**, 22(4), 217–218.
8. Davis, R. I. *Timber and Metal – The Connection*; Proceedings of the Pacific Timber Engineering Conference; Timber Research and Development and Advisory Council: Gold Coast, Australia, 1994; pp 439–448.
9. Rance, V. E.; Cole, H. G. *Corrosion of Metals by Vapours from Organic Materials*; HMSO: London, 1958.
10. DG-3A Defence Guide for the prevention of corrosion of cadmium and zinc coatings by vapours from organic materials; HMSO: London, 1966.
11. Gray, V. R. J. *Inst. Wood Sci.* **1958**, 1, 58.
12. Hillis, J. A. F. *Wood Extractives and Their Significance to the Pulp and Paper Industries*; Academic Press: New York, 1962; pp 389–392.
13. Corrosion of Metals by Wood. Guides to Practice in Corrosion Control; National Physical Laboratory: Teddington, UK, 1979 (available online at <http://www.npl.co.uk>).
14. Krilov, A.; Gref, R. *Wood Sci. Technol.* **1986**, 20(4), 363–370.
15. Packman, D. F. *Wood* **1954**, 19(9), 358–359.
16. Baker, A. J. Degradation of wood by products of metal corrosion, U.S.D.A. Forest Service Research Paper FPL 229; U.S. Department of Agriculture Forest Service Forest Products Laboratory: Madison, WI, 1974.
17. Bell, W. A.; Gibson, J. M. *Nature* **1957**, 180, 1056.
18. Wengert, E. M. Causes and Cures for Stains in Dried Lumber. [http://www.woodweb.com/knowledge\\_base/](http://www.woodweb.com/knowledge_base/)

- [Causes\\_and\\_Cures\\_for\\_Stains\\_In\\_Dried\\_Lumber.html](#) (viewed on 13/07/2009).
19. Crossman, M.; Simm, J. *Manual on the Use of Timber in Coastal and River Engineering*; Thomas Telford Publishing: London, 2004.
  20. Aoyama, Y.; Kamioka, M. *Corros. Eng.* **1965**, 14(9), 381–401. (Article in Japanese with English abstract.)
  21. Fox, S. P.; Barton, G. M.; Hawbolt, E. B. *Mater. Perform.* **1977**, 16(10), 36–40.
  22. Srivastava, K.; Dwivedi, S. K. *J. Corrosion Sci. Eng.* **2007**, 10, Paper 21. <http://www.jcse.org> (viewed on 13/07/2009).
  23. Berndt, H. Assessing the detrimental effects of wood and wood products on the environment inside display cases. American Institute for Conservation 15th Annual Meeting, Vancouver, Washington, DC.
  24. Bradley, S.; Thickett, D. *The Pollutant Problem in Perspective*; IAP, 1998.
  25. Hatch, J.E. *Aluminum – Properties and Physical Metallurgy*; ASM, 1984.
  26. Baechler, R. H. *Proc. Am. Wood-Preservers' Assoc.* **1939**, 35, 56–63.
  27. Edwards, R.; Bordass, W.; Farrell, D. *Analyst* **1997**, 122, 1517–1520.
  28. Zelinka, S. L.; Rammer, D. R. Review of test methods used to determine the corrosion rate of metals in contact with treated wood. United States Department of Agriculture Forest Service, Forest Products Laboratory, General Technical Report, FPL–GTR–156, 2005.
  29. Zelinka, S. L.; Rammer, D. R.; Stone, D. S.; Gilbertson, J. T. *Corros. Sci.* **2007**, 49(3), 1673–1685.
  30. Bailey, G.; Schofield, M. J. *J. Inst. Wood Sci.* **1984**, 10(1), 14–18.
  31. Zelinka, S. L.; Rammer, D. R. Proceedings 9th World Conference on Timber Engineering, Portland, USA, August 6–10, 2006.
  32. Nguyen, M. N.; Leicester, R. H.; Wang, C. Embedded corrosion of fasteners in timber structures. Manual No. 6. Forest and Wood Products Australia, 2008.
  33. [http://www.puhsd.k12.ca.us/chana/staffpages/eichman/Adult\\_School/us/fall/industrialization/1/industrial\\_revolution.htm](http://www.puhsd.k12.ca.us/chana/staffpages/eichman/Adult_School/us/fall/industrialization/1/industrial_revolution.htm) (viewed on 13/07/2009).
  34. Bowyer, J. L.; Shmulsky, R.; Haygreen, J. G. *Forest Products and Wood Science*, 4th ed.; Blackwell: Oxford, UK, 2003; p 506.
  35. Paes, J. B.; Vital, B. R.; Della Lucia, R. M.; Della Lucia, T. M. C. *R. Arvore, Viçosa-MG* **2002**, 26(5), 621–627.
  36. Simm, D. W.; Button, H. E. *Corros. Prevent. Control* **1985**, 32(2), 25–35.
  37. Technical Bulletin. Preservative treated wood. <http://www.strongtie.com> (viewed on 13/07/2009).
  38. Smallwood, R. E. *Life Cycle Maintenance Considerations of Non-Metallic Process Equipment Compared to Metallic Equipment*; Proceedings of Corrosion 2006, San Diego, USA, March 12–16, 2006; NACE International: Houston, 2006.
  39. Gauvent, M.; Rocca, E.; Meausoone, P. J.; Brenot, P. *Wear* **2006**, 261(9), 1051–1055.
  40. Sánchez-Gómez, M. A.; Estesó, M. A. *Corrosion Effects on the Cultural Heritage*; Proceedings of Corrosion 2002, Denver, USA, April 7–11, 2002; NACE International: Houston, 2002.

## Further Reading

Nguyen, M. N.; Leicester, R. H.; Wang, C. *Atmospheric Corrosion of Fasteners in Timber Structures*. Manual No. 5. Forest and Wood Products Australia, 2008.

## 2.29 Corrosion in Radiolysis Induced Environments

**G. O. H. Whillock**

National Nuclear Laboratory, B170 Sellafield, Cumbria CA20 1PG, UK

© 2010 Elsevier B.V. All rights reserved.

2.29.1	The Nature of Ionizing Radiation	1330
2.29.2	Corrosion Effects Arising from Radiation Absorbance	1331
2.29.2.1	The Effect on Metals and Surface Films	1331
2.29.2.2	The Effect on the Environment – Radiolysis	1331
2.29.2.2.1	Water radiolysis	1331
2.29.3	The Effect of Radiolysis on the Corrosion of Metals in Aqueous Environments	1332
2.29.3.1	High Temperature Water – LWRs	1333
2.29.3.2	Chemical Plant Heating/Cooling Waters and Related Environments	1334
2.29.3.3	Nitric Acid Solutions	1337
2.29.3.4	Polymer Degradation Products	1337
2.29.4	The Effect of Radiolysis on the Corrosion of Metals in Atmospheric Environments	1337
2.29.5	Corrosion Test Considerations	1338
References		1338

### Glossary

**Gray** SI unit of absorbed radiation;  $1 \text{ Gy} = 1 \text{ J kg}^{-1}$ .

**G-value** Radiolytic yield in terms of the number of particles formed per 100 eV of absorbed energy.

**LET** Linear energy transfer; measures the energy deposited by ionizing radiation per unit path length in the absorbing medium.

**Rad** Non-SI unit of absorbed radiation dose;  $100 \text{ rad} = 1 \text{ Gy}$ .

**Radiolysis** Chemical decomposition brought about by the absorbance of ionizing radiation.

**$V_{\text{NHE}}$**  Electrode potential, volts with respect to the normal hydrogen electrode

**$X(Y)$**  Element X present in valency state Y; for example, Cr(VI) is  $\text{Cr}_2\text{O}_7^{2-}$  or  $\text{CrO}_4^{2-}$

### Abbreviations

**IASCC** Irradiation-assisted stress corrosion cracking

**LET** Linear energy transfer

**LWR** Light water reactor

**PWR** Pressurized water reactor

### Symbols

**$V_{\text{SCE}}$**  Electrode potential, volts with respect to the saturated calomel electrode

### 2.29.1 The Nature of Ionizing Radiation

Ionizing radiation is produced by a number of processes, such as radioactive decay, nuclear fission, and nuclear fusion. There are many types of ionizing radiation, including neutrons, protons,  $\alpha$ -particles (helium nuclei),  $\beta$ -particles (electrons),  $\gamma$ -radiation, X-rays, and cosmic rays. Ionizing radiation imparts energy to matter with which it interacts, sufficient, by definition, to displace electrons from the matter. The amount of energy absorbed,  $\phi_{\text{ads}}$ , obeys the exponential decay law, depending on the energy of the incident radiation flux, the nature of the radiation, the physical properties of the matter (such as its density), and the depth of the matter through which the radiation passes:

$$\phi_{\text{ads}} = \phi_0 - \phi_0 e^{-\mu x} \quad [1]$$

where  $\phi_0$  is the incident flux,  $\mu$  is the attenuation coefficient (which is specific to the type of radiation and depends on the density of the absorbing matter), and  $x$  is the depth of the absorbing matter.<sup>1</sup> It is



immediately clear why thick sections of dense materials such as lead are used to shield ionizing radiation in order to limit occupational exposures to acceptable levels. The range of charged particles, that is, electrons, protons,  $\alpha$ -particles, and heavier ions, is much shorter and decreases with particle mass. For example,  $\alpha$ -particles will not penetrate through a sheet of paper, and  $\beta$ -radiation is typically completely absorbed by a few millimeters of a light metal such as aluminum. However, heavy charged particles deposit significantly more energy per unit path length than do lighter uncharged particles. This is termed the linear energy transfer (LET) value<sup>2</sup>; LET values for 3 MeV  $\beta$ -radiation, protons, and  $\alpha$ -radiation in water are 0.2, 20, and 150 keV  $\mu\text{m}^{-1}$  respectively.<sup>1</sup>

The SI unit of absorbed radiation is the gray (Gy), which is defined to be the absorbance of 1 J  $\text{kg}^{-1}$  of matter. However, a unit termed 'rad' is still frequently used (1 Gy = 100 rad). Absorbed dose rates are measured in grays per second or, more conveniently, grays per hour. A related unit is the sievert (Sv), which is used to measure absorbed dose equivalents in biological samples, using weighting factors to take into account the different damage effects of the various types of ionizing radiation.

## 2.29.2 Corrosion Effects Arising from Radiation Absorbance

### 2.29.2.1 The Effect on Metals and Surface Films

The majority of the effects of ionizing radiation on corrosion processes are associated with radiolytic alteration of the environment (see Section 2.29.2.2), but a brief mention is made here of effects on the metal substrate and surface films, which may be important, sometimes critically so, in some circumstances.

All types of ionizing radiation may affect the semi-conducting properties of passive films (termed the photoradiation effect) by altering the number and type of charge carriers.<sup>3,4</sup> Cathodic processes may consequently be affected, leading to change in the corrosion rate. However, the photoradiation effect is small and can be confused with the much more significant effect on cathodic processes arising from solution radiolysis.

Heavy, energetic particles (i.e., neutrons and protons) promote atomic displacement and the formation of increased numbers of defects, both in metal lattices and oxide films. A number of important physical properties are affected as a result (e.g., electrical resistivity

and hardness), but as far as corrosion processes are concerned, there are two principal effects, both deriving, in very simplistic terms, from increased defect density arising from atomic displacements:

- the thickness and porosity of oxide films forming on metals such as aluminum and zirconium increases<sup>5,6</sup>;
- some alloying elements may preferentially segregate to grain boundaries at elevated temperatures (i.e., in nuclear reactors), leading, in the case of stainless steels, to radiation-induced sensitization.<sup>7</sup> This may either have significant *in situ* corrosion consequences in the form of susceptibility to irradiation-assisted stress corrosion cracking (IASCC),<sup>8–10</sup> or introduce a legacy effect when, for example, reactor-irradiated stainless steel is subsequently exposed to water containing very low chloride concentrations.

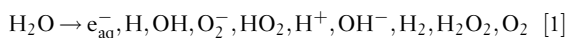
The other principal types of ionizing radiation,  $\alpha$ ,  $\beta$ ,  $\gamma$ , X-rays, and cosmic rays, do not detectably affect the metal microstructure.

### 2.29.2.2 The Effect on the Environment – Radiolysis

Radiolysis is defined as chemical decomposition brought about by the absorbance of ionizing radiation. Significant corrosion consequences can arise from the products resulting from the decomposition of water, solutes, gases, and polymers and, in some circumstances, from the alteration of the valence state of certain solutes.

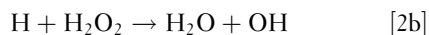
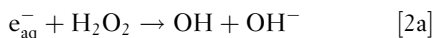
#### 2.29.2.2.1 Water radiolysis

Water is fragmented by ionizing radiation, resulting in the formation of a range of short-lived intermediates, which react with themselves, water, and some solutes to generate hydrogen, hydrogen peroxide, and to a much lesser extent, oxygen, as stable molecular products<sup>11–13</sup>:

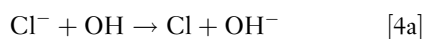
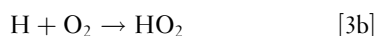
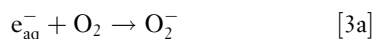


In a completely closed single-phase situation, almost never encountered in practice, the irradiation of pure water produces no overall oxidizing or reducing effect. When, however, the gaseous products are able to escape, a net oxidizing or reducing effect is produced depending on the composition of the cover gas; the former results in the presence of air, oxygen, or argon, whereas the latter results in the presence of excess hydrogen.

Radiolytic reaction schemes are complex, involving a host of interactions that limit the ultimate yield of the molecular products. For example,



It therefore follows that any solute that preferentially reacts with the reducing radicals acts to increase the overall yield of hydrogen peroxide by suppressing reactions [2a] and [2b]; in such circumstances, the radiolytic yield of hydrogen is suppressed. Oxygen does this directly, reactions [3a] and [3b], and  $Cl^-$  does this indirectly, reactions [4a]–[4b].<sup>11,12</sup> The term radical scavenger is used to denote species that act like this.



$Cl^-$  is not consumed in the process, so low concentrations exert a pronounced effect.

The yield of radiolytic species is quantified by *G*-values, which measure the number of molecules decomposed or the number of molecules, ions, or radicals formed per 100 eV of absorbed radiation energy. *G*-values depend on the type of radiation (i.e., its LET value); fast neutrons and  $\alpha$ -radiation produce higher yields of the molecular products than do  $\beta$ - and  $\gamma$ -radiation, the last two being essentially equivalent. Table 1 illustrates these effects for high-purity, high temperature water.<sup>14</sup> The effect of radical scavengers also depends on the type of radiation, it being more pronounced for neutrons than for  $\beta/\gamma$ -radiation. Hence, considerable care must be taken in applying the findings of studies carried out with one type of radiation ( $\gamma$ -rays being frequently used) to situations where other types of radiation may dominate (e.g., reactor cores).

*G*-values are of fundamental importance in elucidating radiolytic mechanisms, usually done using pulse radiolysis techniques, but from a corrosion viewpoint, have little direct relevance, since it is the steady-state concentration of certain species, primarily hydrogen peroxide, that is important. The steady-state concentration depends not only on the net rate of radiolytic formation, which from the *G*-value concept can be seen to be dose rate dependent, but also on any nonradiolytic consumption mechanisms (including corrosion reactions). However, radiolytic production rates, along with kinetic data for relevant chemical and electrochemical (i.e., corrosion) reactions, do have an important application in forming the basis for mechanistic models predicting the corrosion potential in light water reactors (LWRs) (see Section 2.29.3.1).

### 2.29.3 The Effect of Radiolysis on the Corrosion of Metals in Aqueous Environments

A number of important effects of radiolysis on corrosion processes have been discovered as a consequence of the exploitation of nuclear energy, ranging from energy production in water-cooled power reactors, through reprocessing operations, to the disposal of nuclear wastes.

Upon initial irradiation, the potential of platinum and stainless steel electrodes initially falls toward the reversible hydrogen potential, but then rises with increasing dose uptake toward potentials dominated by hydrogen peroxide redox reactions.<sup>15</sup> This behavior reflects the faster diffusion rate of hydrogen to the electrode compared with hydrogen peroxide and the greater radiolytic yield of hydrogen peroxide compared with hydrogen. For most corrosion processes, the oxidizing effect due to the production of hydrogen peroxide dominates.

**Table 1** Radiolytic yields in high-purity, high temperature water

Energy source	LET (eV Å <sup>-1</sup> )	Yields of species (number per 100 eV)							
		–H <sub>2</sub> O	H <sub>2</sub>	H+e <sub>aq</sub> <sup>–</sup>	H	e <sub>aq</sub> <sup>–</sup>	H <sub>2</sub> O <sub>2</sub>	OH	HO <sub>2</sub>
β, γ	0.02	3.74	0.44	2.86	0.55	2.31	0.70	2.34	0.00
Neutrons	4.0	2.79	1.12	0.72	0.36	0.36	1.00	0.47	0.17
<sup>10</sup> B(n,α) <sup>7</sup> Li	24	3.30	1.70	0.20	0.16 <sup>a</sup>	0.04 <sup>a</sup>	1.30	0.10	0.30

<sup>a</sup>Estimated.

Source: Hart, E. J.; Boag, J. W. *Nuclear Chemistry – Theory and Applications*; Pergamon Press: Oxford, 1980; Chapter 15, pp 323–324.

### 2.29.3.1 High Temperature Water – LWRs

The major application here is the primary coolant circuit of LWRs (i.e., normal, as opposed to heavy, water), of which there are two principal types: boiling water reactor (BWR) and pressurized water reactor (PWR), differentiated by whether steam is raised directly in the core or indirectly via separate steam generators. The water temperature varies a little from reactor to reactor, but is  $\sim 300^\circ\text{C}$ . High-purity water is used in BWRs, whereas in PWRs, additions of boric acid are made to control the reactivity of the fuel as it burns (i.e., undergoes fission) with the acidity counteracted by lithium hydroxide.

Various corrosion processes affect reactor operations, the principal ones being

- fuel cladding corrosion, leading to the formation of adherent oxides, which impact on heat transfer;
- general corrosion of stainless steels and inconels, the latter are used in PWR steam generators, leading to the formation of deposits (termed cruds), which can impact on heat transfer rates and also pose a dose uptake issue in areas that require maintenance, since the corrosion products become radioactive as a result of the ingrowth of various isotopes; and
- stress corrosion cracking (SCC), intergranular or transgranular, of structural stainless steels and inconels.

All of the above are affected by water radiolysis. Corrosion in LWRs arguably constitutes the most important application of water radiolysis, and consequently, LWR chemistry has been extensively studied, and continues to be so as new problems emerge and new reactor designs are being considered. The interested reader is directed to the proceedings of recent international conferences on the subject.<sup>16,17</sup>

Within the core of a BWR operating under normal water chemistry (i.e., deoxygenated pure water), water radiolysis results in oxidizing conditions arising from the greater radiolytic yield of hydrogen peroxide compared with hydrogen. Complex models considering the various radiolytic and electrochemical processes and the flow conditions, coupled with direct measurement in a number of instances, indicate that the free corrosion potential of stainless steels is elevated significantly by as much as 250 mV compared with out-of-core exposure.<sup>18,19</sup> This renders 304 stainless steel susceptible to SCC, particularly if sensitized; if not already present as a result of welding operations, sensitization tends to grow in as a result of neutron damage. Irradiation-assisted SCC is

therefore influenced both by microstructural changes and water radiolysis.<sup>8–10</sup> To counteract the radiolytic oxidizing effect, hydrogen–water chemistry has been introduced to BWRs. **Figure 1** shows that small concentrations of hydrogen, of the order of  $5\text{ cm}^3$  of  $\text{H}_2$  per kg, act to suppress almost completely the radiolytic production of oxidizers in the bulk water.<sup>20</sup> In PWRs, a hydrogen overpressure is similarly used, thus ensuring that conditions within the core are generally sufficiently reducing to prevent the attainment of potentials where SCC of stainless steel can occur,  $-230\text{ mV}_{\text{NHE}}$  being accepted commonly as the safe limit.

The effect of crevices (i.e., occluded regions) requires careful consideration, since local electrochemical conditions within the crevice can differ significantly from the bulk. Complex models considering the rates of radiolytic reactions, transport processes, fluid flow, and electrochemical reactions are

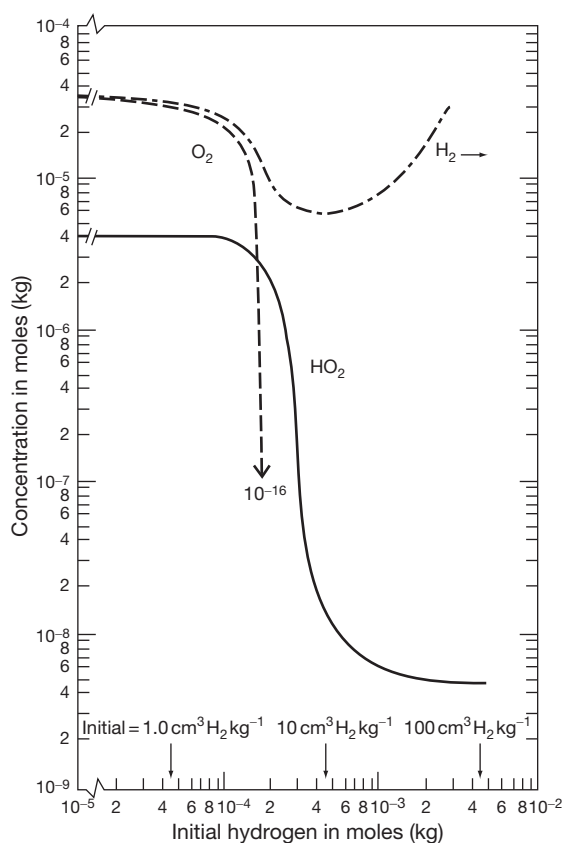


**Figure 1** Computed steady-state concentrations of the indicated radiolytic products in PWR conditions as a function of initial hydrogen concentration. Reproduced from Solomon, Y. In *Water Chemistry of Nuclear Reactor Systems*, Bournemouth, UK, 24–27 October 1978; BNES, London, UK, 1979; pp 101–109, with permission from BNES.

used to estimate the potential distribution, since *in situ* direct measurement is not possible. Such models indicate that higher bulk hydrogen concentrations, that is, 20–25 cm<sup>3</sup> of H<sub>2</sub> per kg, are needed to ensure that the corrosion potential at the tip of long crevices does not exceed –230 mV<sub>NHE</sub>; still higher hydrogen concentrations, that is, 50 cm<sup>3</sup> of H<sub>2</sub> per kg, are required to prevent significant acidification at the crevice tip.<sup>21</sup>

High hydrogen concentrations and slightly alkaline conditions also act to reduce the general corrosion rate of stainless steels and inconels, thus reducing activity build-up in the coolant circuit. However, increasing hydrogen concentration appears to increase the SCC susceptibility of inconel alloy 600. There is, thus, a drive to reduce hydrogen concentrations in PWRs slightly in order to limit SCC of alloy 600, while not compromising on either SCC control of stainless steels or crud deposition due to general corrosion within the reactor circuit.<sup>22</sup>

### 2.29.3.2 Chemical Plant Heating/Cooling Waters and Related Environments

Stainless steels, almost exclusively austenitic grades, are widely used in the construction of nuclear reprocessing plant and ancillary items associated with the storage and disposal of radioactive wastes. In these applications, stainless steels are exposed to a variety of environments, including irradiated waters containing low to moderately high concentrations of chloride at ambient to moderately high temperatures. A strong susceptibility to localized corrosion propagating in the form of pitting corrosion has been noted in some circumstances where such tendency would otherwise not be expected, that is, at <10 mg l<sup>-1</sup> Cl<sup>-</sup> and temperatures as low as 30 °C.

All localized corrosion processes consist of discrete initiation and propagation phases, both of which are influenced by the adopted corrosion potential, and hence the redox potential exerted by the environment. **Table 2** shows that the corrosion potential of passive stainless steel in water is strongly elevated by exposure to  $\gamma$ -radiation, but that the corrosion potential is insensitive to the dose rate.<sup>23</sup> This effect is known to be attributable to water radiolysis rather than subtle modification of the metal's passive film, since the corrosion potential shift is reproduced in nonirradiated stainless steels exposed to previously irradiated water. In addition, in contradiction to early interpretation of the radiolytic corrosive effect,<sup>24</sup> it is clear that the observed oxidizing

**Table 2** Effect of  $\gamma$ -radiation on the corrosion potential of 304L stainless steel in 10 mg l<sup>-1</sup> Cl<sup>-</sup> at 30 °C

Dose rate (Gy h <sup>-1</sup> )	Potential (mV <sub>SCE</sub> )
0	–150 to 80
10	250–300
200	250–300
1000–2000	260–380

Source: Ferreira, M. G. S.; Simoes, A. M. P. Eds.; *Mater. Sci. Forum* **1995**, 192–194, 469–476; Work carried out by Marsh, G. P.; and Taylor, K. J. AERE Harwell, under contract to BNFL, reported by Herbert, D.; Whillock, G. O. H.; Worthington, S. E. In *Electrochemical Methods in Corrosion Research V*; Proceedings of the 5th International Symposium, Sesimbra, Portugal, September 5–8, 1994.

effect is due to stable molecular products, rather than the short-lived intermediates, since the latter do not persist outside of the directly irradiated region. Chemical additions of hydrogen peroxide to nonirradiated waters, in fact, produce essentially the same effect on the corrosion potential, including independence on concentration, as illustrated in **Figure 2**.<sup>23</sup> The behavior of hydrogen peroxide in fixing the potential of (passive) stainless steel is consistent with mechanistic studies, which indicate that the potential of inert (i.e., noble or passive) surfaces is determined by the discharge of hydroxyl radicals, OH, resulting from the decomposition of hydrogen peroxide; the hydrogen peroxide concentration in solution is unimportant, provided it is sufficient to give full surface coverage of adsorbed OH.<sup>25</sup> **Figure 2** indicates that for stainless steel, the critical hydrogen peroxide concentration is less than 0.5 mg l<sup>-1</sup>. This mechanism also explains the reported independence of stainless steel corrosion potential on ozone concentration,<sup>26</sup> since OH radicals also arise from the decomposition of ozone in water.<sup>27</sup>

At Cl<sup>-</sup> concentrations of the order of 10 mg l<sup>-1</sup> and temperatures up to 80 °C at least, the elevation of corrosion potential promoted by water radiolysis (or hydrogen peroxide additions) is not, however, sufficient to initiate true pitting corrosion, since the pitting breakdown potential is far too high. The breakdown potential of commercial grades of stainless steel is, in fact, elevated a little, on average, by ionizing radiations due to the elimination of low breakdown potentials from the distribution.<sup>24</sup> The origin of this effect is not known for certain; it may possibly reflect slight passive film thickening or the removal of surface-breaking inclusions, which might otherwise act as pitting sites, or it might somehow be related to the photoinhibition effect.<sup>28</sup> However, if a suitable crevice

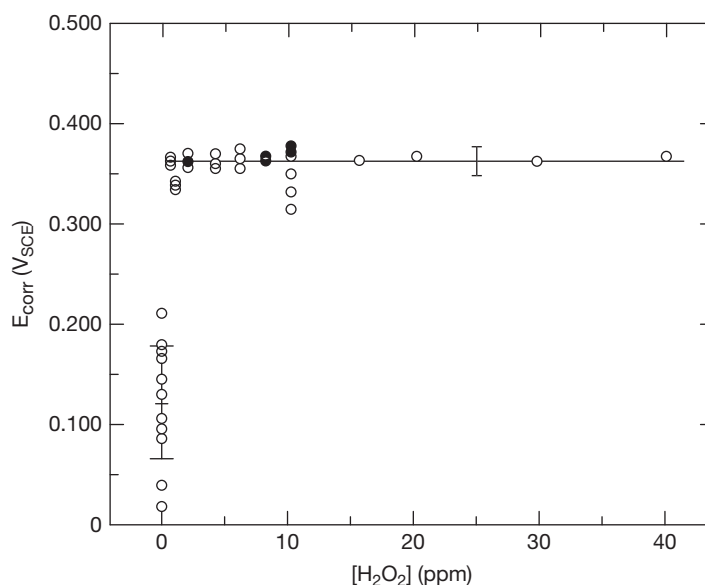


**Figure 2** Effect of hydrogen peroxide on the free corrosion potential of 304L stainless steel in 300 mg L<sup>-1</sup> Cl<sup>-</sup> solution at ambient temperature. Adapted from Ferreira, M. G. S.; Simoes, A. M. P. Eds.; *Mater. Sci. Forum* **1995**, 192–194, 469–476; Herbert, D.; Whillock, G. O. H.; Worthington, S. E. In *Electrochemical Methods in Corrosion Research V*; Proceedings of the 5th International Symposium, Sesimbra, Portugal, September 5–8, 1994.

is present, the elevation in corrosion potential promoted by water radiolysis is sufficient to initiate breakdown within the crevice. **Table 3** demonstrates the effect of  $\gamma$ -radiation on the ease of crevice initiation. These data refer to engineered crevices manufactured from 304L stainless steel, tested in water containing 10 mg L<sup>-1</sup> Cl<sup>-</sup> at 30 °C.<sup>23</sup> Although the dataset is incomplete, hampering unequivocal interpretation, a wealth of other data collected on different stainless steels at different temperatures and dose rates confirms a dose rate effect. The dependence on dose rate, despite the independence of the initial potential elevation, is due to the metastable nature of crevice initiation; without sufficient maintenance of the potential provided by the cathode, an incipient crevice can be switched off by the potential fall accompanying the burst of anodic dissolution.

In the propagation phase of crevice/pitting corrosion, the additional cathodic reaction provided by the reduction of hydrogen peroxide, generated either radiolytically or due to deliberate addition, increases the propagation rate. This is illustrated in **Figure 3** by recording the current flow from a large passive stainless steel surface to an engineered crevice in the presence and absence of  $\gamma$ -radiation.

Once initiated, crevice corrosion propagates in essentially the same manner as pitting corrosion. However, the existence of the crevice is crucial;

**Table 3** Effect of  $\gamma$ -radiation on the ease of crevice initiation: 304L stainless steel engineered crevices, 10 mg L<sup>-1</sup> Cl<sup>-</sup> at 30 °C

Dose rate (Gy h <sup>-1</sup> )	Initiation frequency <sup>a</sup>
0	2/16
2.8	1/2
25	1/2
200	2/2
1000	3/3
1600	1/1

<sup>a</sup>n/m indicates *n* corroded out of *m* tested.

Source: Ferreira, M. G. S.; Simoes, A. M. P. Eds.; *Mater. Sci. Forum* **1995**, 192–194, 469–476; Work carried out by Marsh, G. P.; and Taylor, K. J. AERE Harwell, under contract to BNFL, reported by Herbert, D.; Whillock, G. O. H.; Worthington, S. E. In *Electrochemical Methods in Corrosion Research V*; Proceedings of the 5th International Symposium, Sesimbra, Portugal, September 5–8, 1994.

without it, the deleterious effect of the ionizing radiation on stainless steel exposed to low Cl<sup>-</sup> concentrations does not happen. Experience indicates that even very minor defects such as a slight rolling lap or microporosity at a weld, which would not be expected to be detectable at the manufacturing stage, can act as the required crevice, provided the radiation dose rate is high enough. **Figure 4** presents an example. At lower radiation dose rates, a more



severe crevice would be expected to be required to initiate sustained propagation (all other factors such as  $\text{Cl}^-$  concentration and temperature being equal). There are insufficient data and the interactions are too complex to be definitive as to whether there is a dose rate threshold, below which crevice effects cease to be of practical significance. However, as noted earlier, the transition from initiation to stable propagation requires a vigorous cathode, otherwise, the potential drops too far and the corrosion switches off.

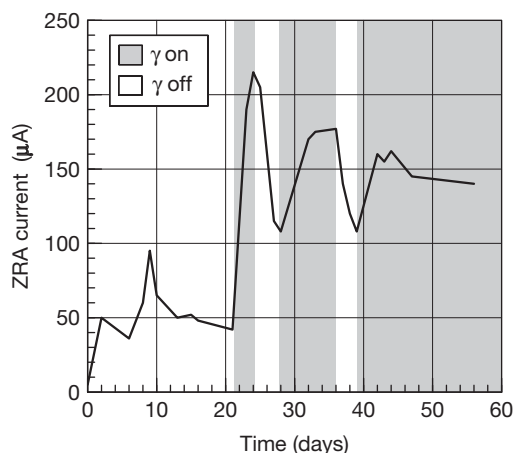


**Figure 3** Effect of  $\gamma$ -radiation ( $1 \text{ kGy h}^{-1}$ ) on the current flowing to an AISI 347 crevice in  $100 \text{ mg L}^{-1} \text{ Cl}^-$  solution at ambient temperature. Reproduced from Ferreira, M. G. S., Simoes, A. M. P., Eds.; *Mater. Sci. Forum* **1995**, 192–194, 469–476; Work carried out by Marsh, G. P.; and Taylor, K. J. AERE Harwell, under contract to BNFL, reported by Herbert, D.; Whillock, G. O. H.; Worthington, S. E. In *Electrochemical Methods in Corrosion Research V*; Proceedings of the 5th International Symposium, Sesimbra, Portugal, September 5–8, 1994.

It is in fact the case that all examples, known to the author, of a clear effect on crevice initiation/propagation come from high dose rate environments ( $>100 \text{ Gy h}^{-1}$ ).

Mitigation options are essentially the same as those that pertain to nonirradiated situations. Reducing the  $\text{Cl}^-$  concentration and temperature have strong beneficial effects in reducing the likelihood of crevice initiation; the former has a secondary effect on radiolyzed waters if reduced low enough, since the radical scavenging action of  $\text{Cl}^-$  is eliminated. Inhibitors such as hydroxide and nitrate can also be effective if applied at the outset, but for the latter, at least, consideration needs to be given to its radiation stability (which also precludes organic inhibitors from serious consideration). The selection of a more resistant alloy, such as 316L stainless steel, would also eliminate irradiation-assisted crevice corrosion except at high  $\text{Cl}^-$  concentration.

Although the earlier discussion focuses on stainless steels, there is no reason to suppose that similar radiation effects would not be manifest in other alloy systems where the elevation of the corrosion potential by a few hundred millivolts is required to initiate crevice. However, there appear to be no reported occurrences owing, presumably, to an absence of industrial applications. Likewise, a deleterious effect of radiolysis on other localized corrosion mechanisms, notably SCC and corrosion fatigue, would be expected, but appears not to be reported except in high temperature, high-purity waters (see [Section 2.29.3.1](#)) and for the pond-storage of some types of spent nuclear fuel where the stainless steel cladding is highly sensitized as a consequence of in-reactor damage.<sup>29</sup>

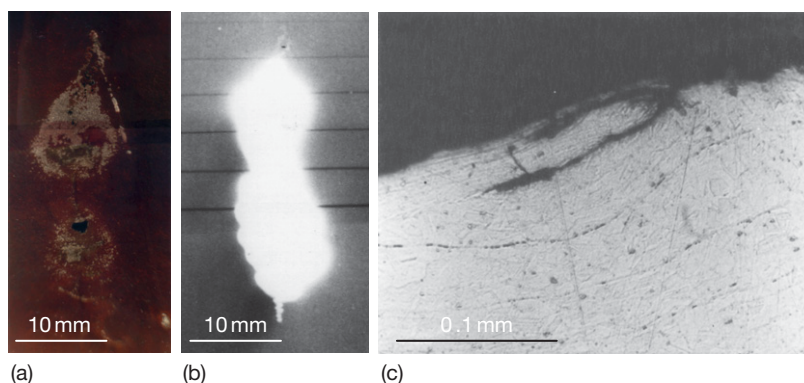


**Figure 4** Corrosion pit resulting from crevice corrosion at a rolling lap on an AISI 321 stainless steel plate exposed for 13 Gy to irradiated water ( $\sim 500 \text{ Gy h}^{-1}$ ) containing  $\sim 10 \text{ mg L}^{-1} \text{ Cl}^-$  at  $\sim 40^\circ \text{C}$ : (a) external appearance (the bright scratch-like feature is the initiating defect); (b) radiograph showing the extent of pit growth; (c) cross-section through the initiating defect. The plate in question was only 4.7 mm thick and the pit did not penetrate to the outside; instead, a relatively large exit hole formed on the same side as the corrosion started from about half way down the pit.

### 2.29.3.3 Nitric Acid Solutions

Nitric acid solutions are used in nuclear fuel reprocessing, exploiting the propensity of uranium and plutonium to form nitrate complexes that dissolve in nucleophilic solvents such as tri-*n*-butyl phosphate. Stainless steels, mainly austenitic grades, are commonly used in the construction of reprocessing plant and are either passive or suffer intergranular corrosion (leading to grain dropping, and hence general wastage rather than cracking), depending on the oxidizing power of the solution, which is strongly increased at high temperatures ( $>70^{\circ}\text{C}$ ) and in the presence of certain dissolved species, which act as oxidants. A more detailed exposition is given elsewhere (see **Chapter 2.24, Corrosion in Nitric Acid**).

Radiolysis of aqueous nitric acid, and indeed, neutral nitrate solutions, produces the nitrite ion as the principal dissolved product,<sup>30</sup> along with varying amounts of hydrogen peroxide, depending on the acidity, since nitrous acid is oxidized by hydrogen peroxide (at least, at room temperature; in hot nitric acid solutions, hydrogen peroxide decomposes with the production of  $\text{NO}_x$  gases, indicating the reduction of the nitrate ion, that is, reversal of the redox couple). The reaction schemes are complex, involving various linked chemical reactions as well as radiolytic ones, and the yields depend strongly on the LET of the radiation.<sup>30</sup>

The presence of significant concentrations of nitrous acid modifies the corrosive behavior of nitric acid considerably, the overall effect depending on the circumstances. In pure aqueous nitric acid solutions, nitrous acid catalyzes nitrate reduction and, therefore, acts to elevate the corrosion potential of stainless steel, increasing its corrosion rate a little if the temperature is high enough to support intergranular corrosion, even though the redox potential of the solution falls, since nitrous acid is less oxidizing than nitric acid (see **Figure 12** in **Chapter 2.24, Corrosion in Nitric Acid**). In more complex liquors containing certain dissolved species such as  $\text{Cr(VI)}$  and  $\text{Ce(IV)}$ , the effect of nitrous acid production can be profound, sharply reducing the corrosion rate if a complete reduction to  $\text{Cr(III)}$  and  $\text{Ce(III)}$  occurs, since the corrosion potential moves back toward passivity.<sup>31</sup> In such liquors, the corrosion potential and hence the corrosion rate attained depends on the overall redox balance; whether oxidation by the acid or reduction by irradiation predominates depends on the nitric acid concentration and temperature, the increase of either of which favors oxidation, and radiation dose rate, the increase of which favors reduction.

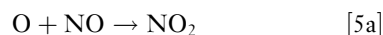
Owing to the fact that the corrosion resistance of metals such as zirconium and tantalum is unaffected by oxidizing species in solution, no effect of radiolysis is apparent. No effect of radiolysis on the corrosion resistance of titanium has been reported, although a deleterious effect might be expected if reliance were placed on oxidizing ions, rather than dissolved titanium ions, for the maintenance of passivity (see **Chapter 2.24, Corrosion in Nitric Acid**).

### 2.29.3.4 Polymer Degradation Products

Polymeric materials are susceptible to radiolytic degradation and some, notably halogenated ones, release species capable of exerting strong corrosive effects in some circumstances. For example, the radiolysis of polyvinyl chloride (PVC) produces hydrogen and chlorine free radicals as primary products, which combine producing  $\text{HCl}$ ,  $\text{Cl}_2$ , and  $\text{H}_2$ .<sup>32</sup> Likewise, fluoropolymers produce  $\text{F}_2$  and  $\text{HF}$  (if either hydrogen is present within the polymer or water is present) as potential corrodants. In general, owing to the fact that the release rates are relatively low, significant corrosive effects arise only in situations where the corrodants are able to accumulate. For example, the use of PVC tape to attach temporary signage during the construction of stainless steel plant, which will subsequently be irradiated, is usually banned owing to concerns over the possibility of chloride-induced SCC.

### 2.29.4 The Effect of Radiolysis on the Corrosion of Metals in Atmospheric Environments

In addition to hydrogen peroxide production due to radiolysis of condensed water films, atmospheric corrosion processes may be affected by the production of ozone, nitrogen oxides, and nitric acid from radiolysis of air. In air, most of the observed effects are attributable to nitric acid production, hence, the corrosion rate of metals, which are attacked by dilute nitric acid (e.g., iron, copper, lead, aluminum, zinc, nickel), is increased, whereas metals passivated by nitric acid, such as stainless steels (but see later text), are unaffected.<sup>33</sup> The radiolytic reaction scheme is complex, but nitric acid results from interactions such as



Nitric acid is produced only if water, nitrogen, and oxygen are simultaneously present. Hence, no corrosion acceleration results in irradiated dry air,<sup>33,34</sup> or in irradiated moist oxygen-free nitrogen.<sup>33</sup> Radiation shifts the critical relative humidity required to support atmospheric corrosion to much lower value, 10–20%, compared with 60–70% in the absence of radiation.<sup>35</sup> In general, increasing dose rate increases the corrosive effect, although at very high dose rates, surface temperatures can increase sufficiently to prevent the formation of condensed water films, in which case, no corrosion results.<sup>33</sup> It is also reported that there is a lower dose rate threshold ( $\sim 50 \text{ Gy h}^{-1}$ ), below which negligible corrosive effect results on iron,<sup>33</sup> although the evidence presented to support that assertion appears weak.

Subtle effects arising from the radiolysis of air have been noted, such as an inhibiting effect (due to the nitrate ion) on the initiation of crevice corrosion in stainless steels tested in low  $\text{Cl}^-$  water. However, the principal application relates to potential, deleterious effects during the storage and disposal of spent nuclear fuels and wastes.<sup>36</sup> Stainless steel fuel cladding, if severely sensitized as a consequence of neutron damage, is known to be susceptible to intergranular attack in moist air; the corrosion mechanism appears to be SCC, constituting the only practical example, known to the author, of the occurrence of this failure mechanism in the stainless steel–nitric acid system. In the absence of severe sensitization (i.e., in excess of that produced by normal welding operations), no corrosion occurs.

## 2.29.5 Corrosion Test Considerations

Careful consideration needs to be given to the design of tests employing radiation if representative radiolytic effects are to be adequately produced. This includes the selection of the dose rate and the type of radiation, since the steady-state radiolytic yield of hydrogen peroxide (which is the principal active agent modifying aqueous corrosion) depends on both. However, it appears to be generally the case that sufficiently representative effects are produced by radiation dose rates of the same order of magnitude as those that pertain in the environment being simulated. Likewise, it is the case that different types of radiation generally produce similar radiolytic effects, although the exact effect may be more or less pronounced depending on LET values.

Consideration also needs to be given to the selection of suitably radiation-resistant materials for

the construction of the test apparatus to avoid inadvertent contamination of test liquors by released polymeric degradation products or, in the case of electrochemical tests, to avoid problems arising from the breakdown of electrical insulation. Where necessary, local shielding can be employed to protect items that cannot be made intrinsically more robust. With regard to electrochemical testing, it appears to be the case that  $\gamma$ -radiolysis exerts negligible effect on the stability of saturated calomel or silver/silver chloride reference electrodes.

## References

1. Choppin, G. R.; Rydberg, J. *Nuclear Chemistry – Theory and Applications*; Pergamon Press: Oxford, 1980; Chapter 14, pp 265–307.
2. Choppin, G. R.; Rydberg, J. *Nuclear Chemistry – Theory and Applications*; Pergamon Press: Oxford, 1980; Chapter 15, pp 308–331.
3. Gorse, D.; Rondot, B.; da Cunha Belo, M. *Corr. Sci.* **1990**, *30*, 23–36.
4. Byalobzheskii, A. V. *Radiation Corrosion*; Israel Program for Scientific Translations: Jerusalem, 1970; pp 79–93.
5. Byalobzheskii, A. V. *Radiation Corrosion*; Israel Program for Scientific Translations: Jerusalem, 1970; pp 70–79.
6. Simnad, M. T. In *The Effects of Radiation on Materials*; Harwood, J. J. Ed.; Reinhold: New York, 1958; pp 129–133.
7. Norris, D. I. R. Ed. Radiation-Induced Sensitisation of Stainless Steels, Proceedings of the Symposium held at Berkeley Nuclear Laboratories on 23 September 1986, CEBG.
8. Andresen, P. L. In *Stress Corrosion Cracking – Material Performance and Evaluation*; Jones, R. H. Ed.; ASM International: Materials Park, OH, 1992; pp 181–210.
9. Scott, P. J. *Nucl. Mat.* **1994**, *211*, 101–122.
10. Was, G. S. In *Radiation Effects in Solids*; Sickafus, K. E., Kotomin, E. A., Uberuaga, B. P., Eds.; Proceedings of the NATO Advanced Study Institute on Radiation Effects in Solids, held in Erice, Sicily, Italy, 17–29 July 2004; Springer: Netherlands, 2007; pp 421–447.
11. Byalobzheskii, A. V. *Radiation Corrosion*; Israel Program for Scientific Translations: Jerusalem, 1970; pp 11–15.
12. Spinks, J. W. T.; Woods, R. J. *An Introduction to Radiation Chemistry*, 3rd ed.; John Wiley & Sons: New York, 1990.
13. Burns, W. G.; Moore, P. B. *Rad. Effects* **1976**, *30*, 233–242.
14. Hart, E. J.; Boag, J. W. Reported by Choppin, G. R.; Rydberg, J. *Nuclear Chemistry – Theory and Applications*; Pergamon Press: Oxford, 1980; Chapter 15, pp 323–324.
15. Airey, P. L. *Radiat. Res. Rev.* **1973**, *5*, 341–371.
16. Swann, T. Ed. *Water Chemistry of Nuclear Reactor Systems 7: Proceedings of the Conference Organized by the British Nuclear Energy Society and Held in Bournemouth on 13–17 October 1996*; Thomas Telford: London, 1998.
17. 5th International Workshop on LWR Coolant Water Radiolysis and Electrochemistry, San Francisco, 15 October 2004.
18. Indig, M. E.; Nelson, J. L.; Wozadlo, G. P. Proceedings of the 5th International Symposium on Environmental Degradation of Materials in Nuclear Power Systems – Water Reactors, Monterey, California, 25–29 August 1991;

- Cubicciotti, D., Simonen, E. P., Gold, R., Eds.; ANS: La Grange Park, IL, 1992; pp 941–952.
19. Indig, M. E.; Nelson, J. L. *Corrosion* **1991**, *47*, 202–209.
20. Solomon, Y. *Water Chemistry of Nuclear Reactor Systems*, Bournemouth, UK, 24–27 October 1978, BNES, London, UK, 1979; pp 101–109.
21. Vankeerberghen, M.; Weyns, G.; Gavrilov, S.; Henshaw, J.; Deconinck, J. J. *Nucl. Mater.* **2009**, *385*(3), 517–526.
22. Feron, D.; Corbel, C.; Hickel, B. 5th International Workshop on LWR Coolant Water Radiolysis and Electrochemistry, San Francisco; 15 October 2004.
23. Herbert, D.; Whillock, G. O. H.; Worthington, S. E. In *Electrochemical Methods in Corrosion Research V*, Proceedings of the 5th International Symposium, Sesimbra, Portugal, September 5–8, 1994; Ferreira, M. G. S., Simoes, A. M. P. Eds. *Mater. Sci. Forum* **1995**, *192–194*, 469–476.
24. Marsh, G. P.; Taylor, K. J.; Bryan, G.; Worthington, S. E. *Corr. Sci.* **1986**, *26*, 971–982.
25. Bockris, J. O'M.; Oldfield, L. F. *Trans. Faraday Soc.* **1955**, *51*, 249–259.
26. Lu, H. H.; Duquette, D. J. *Corrosion* **1990**, *46*, 843–852.
27. Rice, R. G.; Wilkes, J. F. Fundamental Aspects of Ozone Chemistry in Recirculating Cooling Water Systems, paper 205 in *Corrosion '91*, 11–15 March 1991, Cincinnati, NACE, Houston, TX, 1991.
28. Macdonald, D. D.; Heaney, D. F. *Corr. Sci.* **2000**, *42*, 1779–1799.
29. Hands, B. J. *Conference on Materials and Nuclear Power*, Proceedings of EuroMat 96, Bournemouth, UK, 21–23 October, 1996; Institute of Materials: London, 1997; pp 459–468.
30. Kazanjian, A. R.; Miner, F. J.; Brown, A. K.; Hagan, P. G.; Berry, J. W. *Trans. Faraday Soc.* **1970**, *66*, 2192–2198.
31. McIntosh, A. B.; Evans, T. E. *Peaceful Uses of Atomic Energy*, Proceedings of the 2nd International Conference, Geneva, Switzerland, September, 1958; UN: Geneva, Switzerland, 1958; pp 206–225.
32. Clough, R. L.; Gillen, K. T. *Radiat. Phys. Chem.* **1981**, *18*, 661–669.
33. Byalobzhetskii, A. V. *Radiation Corrosion*; Israel Program for Scientific Translations: Jerusalem, 1970; Chapter 5, pp 141–162.
34. Shatalov, I. V.; Nikitina, V. A. *Peaceful Uses of Atomic Energy*, Proceedings of the 2nd International Conference, Geneva, Switzerland, September, 1958; UN: Geneva, Switzerland, 1958; pp 284–296.
35. Vernon, W. H. J. *Trans. Faraday Soc.* **1935**, *31*, 1668–1700.
36. Reed, D. T.; Van Konynenburg, R. A. *Effect of ionizing radiation on moist air systems*, Lawrence Livermore Laboratory report UCRL 97936, 1987.

## 2.30 Electrochemical Methods

**R. A. Cottis**

University of Manchester, Manchester, UK

© 2010 Elsevier B.V. All rights reserved.

<b>2.30.1</b>	<b>Introduction</b>	1343
<b>2.30.2</b>	<b>Basics of Electricity</b>	1343
2.30.2.1	Charge	1343
2.30.2.2	Current	1343
2.30.2.3	Current Density	1343
2.30.2.4	Potential	1343
2.30.2.5	Potential Difference and Voltage	1343
2.30.2.6	Resistance and Resistivity	1343
2.30.2.7	Conductivity and Conductance	1344
2.30.2.8	Capacitance	1344
2.30.2.9	Inductance	1344
2.30.2.10	Impedance	1344
2.30.2.11	Admittance	1345
2.30.2.12	Measurement Fundamentals	1345
2.30.2.12.1	Time and frequency domains	1346
2.30.2.12.2	Instrumentation fundamentals	1346
2.30.2.12.3	Amplifiers	1346
2.30.2.12.4	Filters	1346
<b>2.30.3</b>	<b>Measurement and Control Methods</b>	1347
2.30.3.1	Measurement of Voltage	1347
2.30.3.1.1	Fundamentals	1347
2.30.3.1.2	Single-ended and differential measurements	1347
2.30.3.1.3	Instruments	1347
2.30.3.1.4	Earthing and shielding	1348
2.30.3.2	Measurement of Current	1348
2.30.3.2.1	Fundamentals	1348
<b>2.30.4</b>	<b>Instruments</b>	1348
2.30.4.1	Measurement of Resistance	1349
2.30.4.1.1	Fundamentals	1349
2.30.4.1.2	Instruments	1349
2.30.4.2	Measurement of Impedance	1349
2.30.4.2.1	Fundamentals	1349
2.30.4.3	Control of Potential – The Potentiostat	1349
2.30.4.3.1	Operational amplifier model	1350
2.30.4.3.2	Principle of negative feedback	1350
2.30.4.3.3	Simple potentiostat circuit	1350
2.30.4.3.4	Some potentiostat configurations	1351
2.30.4.3.5	Control of current	1351
2.30.4.3.6	Measurement of current	1351
2.30.4.3.7	Problems in potentiostatic measurements	1352
2.30.4.4	Control of Current	1352
<b>2.30.5</b>	<b>Electrochemical Methods</b>	1353
2.30.5.1	Potential Monitoring	1353
2.30.5.2	Galvanic Current	1353
2.30.5.3	Polarization Curves	1353
2.30.5.3.1	Introduction	1353



2.30.5.3.2	Measurement methods	1354
2.30.5.3.3	Interpretation	1354
2.30.5.4	Linear Polarization Resistance	1355
2.30.5.4.1	Interpretation	1358
2.30.5.4.2	Errors	1358
2.30.5.5	Electrochemical Impedance Spectroscopy	1358
2.30.5.5.1	Presentation of EIS data	1359
2.30.5.5.2	Interpretation of EIS measurements	1360
2.30.5.5.3	Advanced impedance measurements	1360
2.30.5.6	Harmonic Analysis	1361
2.30.5.7	Intermodulation Distortion	1361
2.30.5.8	Transient Techniques	1363
2.30.5.9	Electrochemical Noise	1363
2.30.5.9.1	Interpretation of electrochemical noise	1363
2.30.5.9.2	Measurement	1364
2.30.6	Electrode Design	1366
2.30.7	Cell Design	1370
2.30.8	Reference Electrode	1370
2.30.9	Counter Electrode	1372
References		1372

## Abbreviations

**ADC** Analog to digital converter  
**CE** Counter electrode  
**CSE** Copper sulfate reference electrode  
**EIS** Electrochemical impedance spectroscopy  
**EN** Electrochemical noise  
**IR** Voltage produced by current  $I$  passing through resistance  $R$   
**K-K** Kramers-Kronig  
**OCPD** Open circuit potential decay  
**PSD** Power spectral density  
**RE** Reference electrode  
**SCE** Saturated calomel reference electrode  
**WE** Working electrode

## Symbols

**A** Area ( $\text{m}^2$ ), gain of operational amplifier  
 **$b$**  Bandwidth of measurement ( $\text{s}^{-1}$ )  
 **$B$**  Stern-Geary coefficient (V)  
**C** Capacitance (F)  
 **$C_{dl}$**  Double layer capacitance ( $\text{F m}^{-2}$  or F)  
 **$d$**  Separation between conductors (m)  
 **$e_-$**  Inverting input to operational amplifier  
 **$e_+$**  Non-inverting input to operational amplifier  
 **$e_o$**  Output from operational amplifier  
 **$E_n$**  Electrochemical potential noise (V)

**$f$**  Frequency ( $\text{s}^{-1}$ )  
 **$f_n$**  Characteristic frequency ( $\text{s}^{-1}$ )  
**G** Amplifier gain  
 **$i$**  Current density ( $\text{A m}^{-2}$ )  
 **$i_{corr}$**  Corrosion current density ( $\text{A m}^{-2}$ )  
 **$I_n$**  Electrochemical current noise (A)  
 **$I$**  Current (A)  
**L** Inductance (H)  
 **$q$**  Characteristic charge (C)  
**Q** Charge (C)  
**R** Resistance ( $\Omega$ )  
 **$R_n$**  Electrochemical noise resistance ( $\Omega \text{ m}^2$  or  $\Omega$ )  
 **$R_p$**  Polarization resistance ( $\Omega \text{ m}^2$  or  $\Omega$ )  
 **$R_s$**  Solution resistance ( $\Omega$ )  
**V** Voltage (V)  
 **$V_C$**  Control voltage (V)  
 **$V_{CE}$**  Voltage of counter electrode (V)  
 **$V_i$**  Input voltage (V)  
 **$V_o$**  Output voltage (V)  
 **$V_{RE}$**  Voltage of reference electrode (V)  
**Z** Impedance (complex)  
 **$\Delta E$**  Small change in potential (V)  
 **$\Delta i$**  Small change in current density ( $\text{A m}^{-2}$ )  
 **$\epsilon$**  Relative permittivity  
 **$\epsilon_0$**  Permittivity of free space ( $8.854187817 \times 10^{-12} \text{ F m}^{-1}$ )  
 **$\rho$**  Resistivity ( $\Omega \text{ m}$ )  
 **$\sigma_E$**  Standard deviation of potential (V)

$\sigma_I$  Standard deviation of current (A)  
 $\Psi_E$  Power spectral density of potential ( $V^2 \text{ Hz}^{-1}$ )  
 $\Psi_I$  Power spectral density of current ( $A^2 \text{ Hz}^{-1}$ )  
 $\omega$  Angular frequency ( $\text{s}^{-1}$ )

### 2.30.1 Introduction

This chapter commences by providing a brief summary of the basics of electricity and electrical measurements. It then considers the various measurements involved in the study of electrochemistry and how these can be applied to the study of corrosion. Finally the design of test electrodes and electrochemical cells is discussed. For a more comprehensive introduction to electrochemical methods for corrosion studies, the readers are referred to Kelly *et al.*<sup>1</sup>

### 2.30.2 Basics of Electricity

#### 2.30.2.1 Charge

Charge is the most fundamental electrical property. It derives from the charge inherent in the electrons and protons that make up the atoms and molecules of metals, solutions, and gases that we are concerned with. The unit of charge is the Coulomb, named after Charles Augustin de Coulomb, with the symbol C. The charge on the electron is  $1.602176487 \times 10^{-19}$  C, and therefore, one coulomb corresponds to  $6.24151 \times 10^{18}$  electrons (strictly, the charge on the electron is negative, and therefore, that should really be  $-1$  C).

#### 2.30.2.2 Current

Current is the flow of charge and a current of one Ampere (named after André Marie Ampère, and usually abbreviated to Amp) corresponds to 1 C passing a given point in an electrical circuit in 1 s. Currents in metals invariably consist of movement of the mobile valence electrons. The movement is surprisingly slow (typically of the order of  $10^{-4} \text{ m s}^{-1}$ ), since there are a lot of valence electrons available. Note that the electrons move in the opposite direction to the ‘conventional current,’ which is treated as being due to the movement of positive charges. Currents in solutions consist of the flow of ions, both positively and negatively charged, with positive ions moving in the direction of the conventional current and negative ions moving in the opposite direction.

#### 2.30.2.3 Current Density

In electrochemical systems in which reactions are occurring at the same rate over the entire electrode surface, it is useful to normalize measured currents by dividing by the area to give the current density (units  $\text{A m}^{-2}$ ). In this chapter, we use the convention that  $I$  stands for current, while  $i$  stands for current density. Note that it is not always reasonable to quote current densities; for example, in electrochemical noise measurements (see the following section), current is not expected to be proportional to area, and hence current density is area-dependent. Similarly, it is misleading to refer to current density in relation to pitting or crevice corrosion (except when referring to true current densities, such as the local current density at the corroding surface within the pit or crevice, or the cathodic current density at the external surface).

#### 2.30.2.4 Potential

The potential at a point is defined as the work done in moving unit positive charge to that point from infinity. It is clearly a theoretical concept rather than anything that can really be used! The unit of potential is volt (named after Alessandro Volta), abbreviated as V, and the potential at a point is 1 V if 1 W is required to move a positive charge of 1 C to that point.

#### 2.30.2.5 Potential Difference and Voltage

The potential difference or voltage between two points is the difference between the potentials at the two points. The basic principles of thermodynamics imply that this is identical to the work done in moving unit charge from one point to the other (which we can measure, at least in principle).

#### 2.30.2.6 Resistance and Resistivity

It is commonly found that the voltage across a component is proportional to the current passing through the component. This behavior is known as Ohm’s Law (named after Georg Simon Ohm), given by the well-known formula  $V = IR$ , where  $V$  is the voltage (V),  $I$  the current (A), and  $R$  is the conventional symbol for the *resistance* of the component, with the unit Ohm and the symbol  $\Omega$ . It should be appreciated that, like many laws, Ohm’s Law is an

approximation to reality, and many components (including semiconductors and metal–solution interfaces) do not exhibit a linear relationship between current and potential. When Ohm's Law is not obeyed, we can still talk about the resistance of a component, defined as the slope of the voltage-versus-current curve, but the value of the resistance will vary according to the applied voltage or current.

The resistance of a uniform conductive solid decreases as the cross-sectional area increases and as the length decreases. We can define the *resistivity* of the solid as the resistance across opposite faces of a unit cube of the solid. Then the resistance of a section of wire will be  $l\rho/A$ , where  $l$  is the length of the wire (unit m),  $A$  the cross-sectional area ( $\text{m}^2$ ), and  $\rho$  the *resistivity* ( $\Omega \text{ m}$ ).

### 2.30.2.7 Conductivity and Conductance

In some situations, it is convenient to work in terms of the conductance of a component or the conductivity of a metal or solution. These are simply the inverse of the resistance and resistivity respectively. The unit of conductance is  $\Omega^{-1}$ , also known as Siemens (after Ernst Werner von Siemens), with the symbol S, while conductivity has the unit  $\Omega^{-1}\text{m}^{-1}$  or  $\text{Sm}^{-1}$ .

A particular application of conductance is found in the relationship of the conductivity of a solution to the composition. For dilute solutions, each ion contributes a specific amount to the conductivity, and therefore, the conductivity can be derived by summing the conductivities due to the individual ions making up the solution (see **Chapter 2.38, Modeling of Aqueous Corrosion** for further details).

### 2.30.2.8 Capacitance

If two conductors are placed close together, a change in the voltage between the conductors will lead to a separation of charge, and the amount of charge will be proportional to the voltage. This leads to the concept of a capacitor, a device that stores charge, the governing equation being  $Q = CV$ , where  $Q$  is the stored charge (C),  $V$  the voltage across the capacitor (V), and  $C$  the capacitance (it is unfortunate but inescapable that  $C$  is commonly used as both the symbol for capacitance and for the unit of charge). The unit of capacitance is Farads with the symbol F (after Michael Faraday), and a 1 F capacitor will store 1 C when 1 V is applied across it.

Note that if we differentiate the governing equation for a capacitor with respect to time, we obtain

$$\frac{dQ}{dt} = I = C \frac{dV}{dt}$$

that is, the current is proportional to the rate of change of voltage across the capacitor.

One of the simplest forms of capacitor consists of two parallel plates of conductor separated by an insulator, known as a 'parallel plate capacitor.' In this case, the capacitance is defined by  $C = A\epsilon\epsilon_0/d$ , where  $A$  is the area ( $\text{m}^2$ ),  $\epsilon$  is the relative permittivity of the insulator (dimensionless),  $\epsilon_0$  is the permittivity of free space ( $8.854187817 \times 10^{-12} \text{ F/m}$ ), and  $d$  is the separation between the conductors (m) (strictly this formula is approximate, because it ignores edge effects).

An example of a parallel plate capacitor that is found in electrochemical systems is metals covered with insulating films immersed in solution. In this case, the metal and the solution form the two plates, while the coating provides the layer of insulator.

In the absence of an insulator, there is also a capacitance between a metal and a solution, known as the double-layer capacitance (see **Chapter 1.02, Electrochemistry** for further information).

### 2.30.2.9 Inductance

As current flows along a conductor, it induces a magnetic field. When the current changes, this magnetic field must also change and a voltage is required to cause this change. The inductance,  $L$  (unit Henry, symbol H, named after Joseph Henry), of a component is defined by

$$V = L \frac{dI}{dt}$$

While a capacitor can be thought of as storing charge, an inductor effectively stores current (i.e., once a current is flowing, the inductor tries to keep it flowing). This leads to problems when switching inductive loads, such as motors, as the inductor will develop a large voltage as it tries to keep the current flowing through the switch. This can lead to arcing and damage to the switch contact, together with the production of high-frequency electromagnetic radiation that can be picked up as interference.

### 2.30.2.10 Impedance

Resistance, capacitance, and inductance all represent the response of a component to applied voltage or current, and they can be combined into a single property, the impedance of the component. We can consider a simple example of impedance by thinking

about the properties of a paint-coated metal immersed in solution. An ideal paint will be a perfect insulator, but real paints will display some conductivity. Thus, a paint of thickness  $d$  and area  $A$ , together with the metal and solution either side of it, will exhibit a resistance given by  $\rho d/A$ , while the capacitance, which will be in parallel with the resistance, will be given by  $A\epsilon\epsilon_0/d$ . Note that the resistance decreases with increasing area, whereas the capacitance increases.

The impedance of a resistor is independent of frequency and has a magnitude that is equal to the resistance, and a phase shift of zero.

The magnitude of the impedance of a capacitor decreases with increasing frequency, being given by  $1/\omega C$ , where  $\omega$  is the angular frequency, and the phase shift is  $-\pi/2$  radians ( $-90^\circ$ ).

The magnitude of the impedance of an inductor increases with increasing frequency, being given by  $\omega L$ , and the phase shift is  $\pi/2$  radians ( $90^\circ$ ).

### 2.30.2.11 Admittance

Just as we can consider conductance to be the inverse of resistance, admittance is the inverse of impedance.

### 2.30.2.12 Measurement Fundamentals

All electrochemical studies involve the measurement and/or control of current and voltage. In this section, the fundamental requirements for accurate measurements are presented. Measurements come in a variety of forms:

- Analog or digital

Analog signals have a continuous range of possible values; almost all real variables (current, voltage, velocity, etc.) are analog. It is essentially impossible to measure the value of an analog variable completely, as this would require an infinite resolution. The term analog, when applied to measurements, therefore implies not that the measurement reproduces the measured property completely, but rather that it does not have clearly defined measurement limits. Thus, a conventional electromechanical chart recorder can be described as analog, in that the pen can adopt any position across the chart and the chart paper nominally moves continuously. In practice, the resolution is limited by many factors, including the size of the pen tip, the grain in the chart paper, noise in the measurement electronics, and steps in the chart motion (it is common for the chart drive to use a stepper motor which moves in small discrete steps).

Digital signals have a well-defined set of possible values. The number of values is frequently defined by the number of bits (binary digits) used to represent all of the possible values (since digital instruments often use binary arithmetic internally). One bit can have two possible values (0 and 1), eight bits can have 256 ( $2^8$ ) possible values (00000000 to 11111111), and in general  $n$ -bit numbers provide  $2^n$  possible values. Common resolutions that are available in measuring systems are indicated in [Table 1](#). Not all instruments use binary arithmetic, and many devices such as multimeters that are primarily intended for human interpretation use decimal arithmetic. In this case, the resolution is defined in terms of the number of decimal digits.

- Continuous or sampled

Besides having a finite set of possible values, real measurements also have limited resolution in time. In the case of analog measurements, this usually corresponds to a drop in sensitivity to rapid changes, while for digital measurements, it corresponds to a finite sampling rate. Note that the process of sampling data has important consequences on their quality. In particular, all signal frequencies at or above half the sampling frequency will be converted to false signals below the sampling frequency by a process known as aliasing, and these must be removed by analog filtering ([Section 2.30.2.12.4](#)) before sampling.

**Table 1** Common digital measurement resolutions (as is common, for binary measurements 1 bit is assumed to be used to signify the sign of the measured voltage, while for decimal instruments the sign is additional to the number of digits)

<b>Binary</b>		
Number of bits	Number of values	Resolution for $\pm 1$ V full scale
8	256	7.8 mV
10	1024	2 mV
12	4096	400 $\mu$ V
16	65 536	30 $\mu$ V
20	1 048 576	2 $\mu$ V
24	16 777 216	120 nV
<b>Decimal</b>		
Number of Digits	Number of values	Resolution for $\pm 1$ V full scale
3	1000	1 mV
3.5	1999	500 $\mu$ V
4	10 000	100 $\mu$ V
4.5	19 999	50 $\mu$ V
5	100 000	10 $\mu$ V
6	1 000 000	1 $\mu$ V
7	10 000 000	100 nV
8	100 000 000	10 nV

### 2.30.2.12.1 Time and frequency domains

We experience the world as a sequence of events that follow on in time, and it is natural to think in the ‘time domain,’ that is, the variation of the measured parameters with time. However, the properties of many systems can be understood and interpreted more easily when expressed as the behavior at different frequencies, that is, in the ‘frequency domain’ (the brain works in the frequency domain when processing sound – we hear the different frequencies in the sound, rather than the moment to moment fluctuations in air pressure).

### 2.30.2.12.2 Instrumentation fundamentals

In this section, we shall briefly review the various components that make up modern electronic instruments. This is not intended to be a full coverage of the subject, for which the readers are referred to specialist works, but rather to give a general understanding of the basis.

### 2.30.2.12.3 Amplifiers

A common requirement in instruments is to change the amplitude of a signal or to convert from a current to a voltage or vice versa. This function is performed by amplifiers. In general, the relationship between the input and the output of an amplifier can be defined by its ‘transfer function.’ To simplify the discussion, we shall just consider voltage amplifiers (i.e., devices that take an input voltage  $V_i$  and produce an output voltage  $V_o$ ). Then the transfer function of an amplifier can simply be defined by  $V_o = G(V_i)$ , where  $G$  is the gain of the amplifier. We have written  $G$  as a function in order to emphasize that  $G$  may not be a constant multiplier. Thus the amplifier may be nonlinear over voltage and/or frequency. However, amplifiers are often designed to be linear for voltages and frequencies within their design range, and we can therefore write  $V_o = GV_i$ , where  $G$  is a constant. Thus, an amplifier with a gain of 1000 will convert a 1 mV signal to a 1 V signal.

There is no reason why  $G$  must be positive or greater than 1; thus, it is perfectly feasible to design an amplifier with a gain of  $-0.1$ , which would convert a 1 mV signal to  $-0.1$  mV.

Other important properties of an amplifier are the input and output impedance. The input impedance is the impedance that the input presents to the circuit to which it is connected – for voltage amplifiers we often want this to be very high so that the connection of the amplifier does not affect the system to which it is connected. The output impedance is an indication of the way in which the output voltage is affected by the impedance of the circuit to which it is connected.

We usually want amplifiers to have a low output impedance so that the output voltage is unaffected by the circuit to which it is connected. An important type of amplifier is the ‘unity-gain buffer’; this has a gain of 1 (so the output is the same as the input), but the input impedance is very high, and the output impedance very low. This allows us to connect high-impedance voltage sources (such as the potential measured on a painted sample) to low-impedance measuring devices. A practical realization of a unity-gain buffer is described in the following section.

In contrast to voltage amplifiers, a current amplifier takes an input current, and we want it to have a very low input impedance, so that connecting the amplifier does not affect the current, while a current output should have a very high output impedance, so that the current is not affected by the impedance of the system to which it is connected. Note that there is no reason why an amplifier should not have a current input and a voltage output; indeed this is exactly the characteristics of a ‘zero-resistance amplifier’ (in a later section). Similarly, an amplifier can be designed with a voltage input and a current output, producing a device that provides a current that is controlled by an input voltage (i.e., a voltage-controlled galvanostat).

### 2.30.2.12.4 Filters

Another important building block of modern instruments is the filter. This is a device that responds differently to different frequencies. The simplest filter consists of a resistor and a capacitor (Figure 1). At high frequencies (above  $1/2\pi RC$  Hz), the capacitor has a low impedance compared with the resistor, while at low frequencies it has a high impedance. Then a low pass filter (one that allows low frequencies to pass but removes high frequencies) can be obtained by placing the resistor in the signal path and the capacitor across it (Figure 1(a)). Swapping the two components produces a high pass filter (Figure 1(b)). (The black triangle at the bottom of each figure is a conventional symbol for the earth or ground connection, voltages being assumed to be measured with respect to ground.)

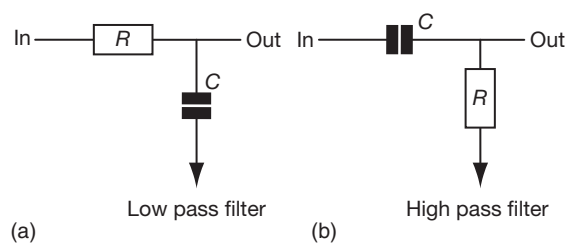


Figure 1 RC filter circuits.



Simple filters using only passive components (resistors, capacitors, or inductors) are rather limited, and many practical filters will use either analog amplifier circuits or digital techniques, which permit a wide range of transfer functions to be produced (see Horowitz and Hill<sup>2</sup> for further information).

## 2.30.3 Measurement and Control Methods

### 2.30.3.1 Measurement of Voltage

#### 2.30.3.1.1 Fundamentals

An ideal voltage-measuring instrument will determine the voltage between two points without drawing any current (since this could modify the measurement). In practice, all voltage-measuring instruments will draw a small amount of current, and this is usually defined in terms of the input impedance of the instrument. Many lower-cost multimeters will have an input impedance of 10 M $\Omega$ , and if such a meter is used to measure a voltage of 1 V, it will draw a current of 0.1  $\mu$ A. Whether or not this is acceptable will depend on the system being measured, but for many corrosion applications, the impedance would be too low, and a value of 1 G $\Omega$  or above is recommended (an even higher input impedance may be necessary for some systems, such as intact paint-coated metals or passive alloys).

A second consideration in the selection of voltage measurement instruments is the measurement quality required. There are several aspects to this, and we can define three terms with slightly different meaning:

- Resolution or precision is the ability to detect small changes in a large value (e.g., if the meter can measure a maximum of 1 V and can resolve 1 mV the resolution is one part in one thousand).
- Sensitivity is the ability to measure small values, irrespective of the range being used (it is relatively easy to measure changes of 1 mV in a signal with a maximum of 1 V, but it is much more difficult if the maximum is 1 kV).
- Accuracy is the ability to measure the 'true' value (this is often much less well-defined than resolution, as it depends on how well the instrument is maintained and calibrated as well as its initial specification).

An important aspect of voltage measuring devices is the speed with which they can adjust to and measure changes. For 'manual' instruments (i.e., instruments where the only output is viewing by a human, who

may or may not choose to write down the result), changes occurring over periods of less than a second cannot be resolved by the observer, and speed is a minor limitation. However, when the output is being recorded, whether by a computer or on a chart recorder, then the measurement speed is also important. For corrosion studies most information tends to be at rather low frequencies (rarely more than 1 kHz), although impedance measurements may go to higher frequencies.

#### 2.30.3.1.2 Single-ended and differential measurements

Voltage-measuring devices may have one input terminal connected to earth, known as a 'single-ended input,' or both input terminals may be independent of ground, known as a 'differential input.' In general, differential inputs are to be preferred, as they help to avoid problems associated with earth loops (see the following section).

#### 2.30.3.1.3 Instruments

A range of instruments is available to measure voltage:

- Moving coil meters are actuated by current but can be adapted to measure voltage by adjusting the resistance of the coil (plus a series resistor if necessary) to give an appropriate calibration. However, they generally have too low an impedance to be useful for corrosion measurements, and they have limited resolution (usually about 1% of full scale).
- Electronic voltmeters use a semiconductor circuit to amplify and convert the voltage to a suitable form for display, either on a moving coil meter or on a digital display (in which case the term digital voltmeter is normally used). Whichever form of display is used, the input impedance is a function of the amplifier used and can be very high (values of  $10^{14}$   $\Omega$  are commercially available, usually termed electrometers).
- Chart recorders provide a means of recording the variation of voltage with time. They are gradually becoming less widely used, both because they are relatively expensive, and, unlike computer-based data acquisition systems, the recorded data cannot easily be further processed. As with electronic voltmeters, the input impedance is a function of the electronics used, a value of 10 M $\Omega$  being common.
- Oscilloscopes can be thought of as specialized chart recorders that are optimized for viewing high-speed signals. Electrochemical measurements are only rarely concerned with high-speed measurements, and hence oscilloscopes are not widely used,

especially as their input impedance is usually rather low (1–10 M $\Omega$  being common). However, they can be useful for checking for high-frequency oscillation or viewing transient behavior (but note that modern computer-based data acquisition systems may provide similar or enhanced functionality for lower cost).

- Computer data-acquisition systems can be thought of as being similar to digital voltmeters, but with the display components being replaced by a connection to the computer, which can take over the display functions (as well as doing many other things). Unfortunately, the majority of computer data acquisition systems are optimized for rapid data acquisition ( $10^5$  or  $10^6$  samples per second being common), rather than high input impedance or high precision, and consequently they are not ideal for corrosion measurements.

#### **2.30.3.1.4 Earthing and shielding**

Induced interference is a common problem in electrical measurements. This arises because the signal circuits act as aerials for the pick-up of electromagnetic radiation. Much of this interference can be eliminated by appropriate earthing (also known as grounding) and screening of the signal circuits. An electrical earth (or ground) is a connection to a stable voltage at approximately the potential of the local soil. It is common to use the safety earth associated with mains power sockets to earth an appropriate part of the measuring circuit. In electrochemical measurements, it is common to earth the working electrode, although there may be circumstances in which this is not desirable. When configuring earth connections, it is very important to avoid an 'earth loop,' which involves two separate connections to earth. This results in a loop of wire, with earth forming part of the loop, and this loop can act as a very effective aerial for the pickup of mains frequency interference.

Interference pickup can be significantly reduced by screening the signal circuits. This involves surrounding the circuits with a metallic conductor that is connected to earth. Electromagnetic radiation cannot penetrate this conductor, and consequently cannot interact with circuits inside the screen. It is common to screen cables by using a coaxial cable, in which the inner conductor is screened by an outer braided screen, which is earthed (note that the comments above about earth loops also apply to the screen connection of coaxial cables). Larger circuits, such as electrochemical cells, can be enclosed in an earthed, conductive box, known as a Faraday cage.

### **2.30.3.2 Measurement of Current**

#### **2.30.3.2.1 Fundamentals**

An ideal ammeter will measure the current between the two input terminals while maintaining the voltage between the terminals at zero. In many modern instruments, current is measured by measuring the voltage across a resistor (known as a current shunt) that is inserted in the current path. This results in a small but significant voltage being developed (this is known as the 'voltage burden' and is typically of the order of 100 mV for a full-scale reading to allow the voltage to be measured with an acceptable accuracy), and such meters are unsuitable for many electrochemical measurements. The capabilities of an ammeter can be defined in terms of the input impedance (essentially the resistance across which the voltage is measured) and ideally we want the input impedance to be zero. An alternative current measurement method uses a form of amplifier known as a current amplifier (essentially an amplifier with a current input and a voltage output) that can measure current with a very low input impedance, and this is preferred for corrosion studies. In the corrosion field the term 'zero-resistance ammeter' is used to describe a current amplifier coupled with a suitable voltage measuring device.

### **2.30.4 Instruments**

Many current-measuring methods use similar instruments to those described earlier for voltage measurement. Such instruments normally use the method of measuring the voltage drop across a resistor to measure currents, but even if the instrument offers such a capability internally (as in the case of cheaper digital multimeters), it may be better to use it in voltage measurement mode with an external resistor, as this allows a greater control of the compromise between sensitivity and input impedance (i.e., a smaller resistor, and hence a smaller voltage, may be used, giving a less sensitive measurement, but one that is less affected by the input impedance of the measuring system).

There are three main classes of instrument that can measure current with negligible voltage drop. All of these use essentially the same current amplifier circuit, the only real difference being the packaging and primary function of the device:

- Electrometers normally include a very high input impedance voltage amplifier and a very low input impedance current amplifier capable of measuring

very small currents with a very low voltage burden (typically less than 1 mV).

- Zero-resistance ammeters are normally designed specifically to measure currents in the range of concern for electrochemistry.
- Potentiostats (see [Section 2.30.4.3](#)) can be configured to measure current with negligible voltage burden.

A limitation of all devices based on the current amplifier circuit is the limited maximum current that can be measured, as the full measured current must be supplied by an internal amplifier, and once the current exceeds the capability of the amplifier, the current amplifier will behave as a very high resistance.

### 2.30.4.1 Measurement of Resistance

#### 2.30.4.1.1 Fundamentals

In general, resistance is measured by applying a current to the circuit in question and measuring the voltage developed across it. Then the resistance is computed from Ohm's Law,  $V = IR$ , making the tacit assumption that the behavior of the component is correctly described by this law. Note that Ohm's Law does not apply to electrochemical interfaces, and somewhat more complex methods must be used.

#### 2.30.4.1.2 Instruments

Most digital multimeters can measure resistance, normally by applying a constant current, which will vary according to the resistance range selected, and measuring the voltage developed. This is generally satisfactory for larger resistances, but for accurate measurements, especially for small resistances, it is necessary to compensate for the resistance of the connecting cables. This is done using a 4-terminal measurement ([Figure 2](#)), in which the current is applied to the component using one set of cables, and the voltage is measured using a second set of cables. More sophisticated multimeters provide the separate current and voltage connections that are required for this method. When measuring

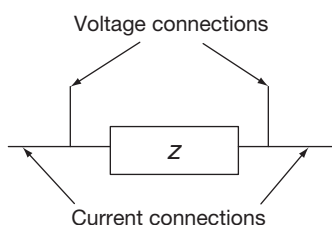


**Figure 2** Four-terminal method for resistance or impedance measurement.

the resistance of electrochemical interfaces, a variant of the 4-terminal measurement method must be used (see the discussion on the measurement of polarization resistance).

### 2.30.4.2 Measurement of Impedance

#### 2.30.4.2.1 Fundamentals

Impedance measurement can be seen as an extended form of resistance measurement in that a current is applied to the component in question and the resulting voltage is measured. In the case of impedance measurement, however, the current must be a sine wave and the voltage measurement must determine both the amplitude and the phase (with respect to the current) of the resulting voltage. In the general case, it is also necessary to vary the frequency of the sine wave and to account for nonlinearity and noise in the measurement. These aspects are discussed further in the following section.

### 2.30.4.3 Control of Potential – The Potentiostat

In the general case, the control of the potential of an electrode in an electrochemical cell can be achieved using a four terminal method that is similar to the 4-terminal method of measuring resistance, the current being supplied through one pair of connections and the voltage measured through a second pair. Then a control circuit can adjust the current to maintain a constant potential difference (or a potential difference that follows an independent control signal) between the two voltage measuring connections. However, one of the two connections (to the working electrode) is generally very low resistance and can use a single connecting wire in most cases, whereas the other (to the solution) has a high resistance (and other problems), and must use two connections, one for current (supplied to a separate conductor known as the counter electrode or secondary electrode or auxiliary electrode) and the other to measure the potential using a reference electrode. This leads to the three-terminal device (though it may have more connections to provide additional facilities) known as a potentiostat. In essence, a potentiostat is a very simple voltage amplifier that amplifies the difference between a control potential and the potential of the reference electrode by a very large amount and then applies it to the counter electrode (with the working electrode being connected to ground). Then if the control potential

differs from the reference electrode potential, the counter electrode potential will be changed in the opposite direction, tending to bring the reference electrode potential back to being the same as the control potential. This process is known as ‘negative feedback.’ A very basic potentiostat can be constructed for a few pounds (Steinberg and Lowe<sup>3</sup> provides an example circuit, although the method of current measurement is more complex than is necessary for most applications, and the circuit could be even simpler). Commercial potentiostats typically provide higher currents, better facilities for the measurement of current and potential, more controlled frequency response, etc.

#### 2.30.4.3.1 Operational amplifier model

The very simplest potentiostat can be constructed from a single operational amplifier (op-amp). (Nowadays the operational amplifier is a standard integrated circuit component that is available with a wide variety of specifications, costing less than £1 for lower specification devices.) The ideal op-amp is a device with three terminals (plus power supply connections – typical op-amp designs use power supplies with three outputs,  $-15$ ,  $0$ , and  $+15$  V, the  $0$  V output providing the reference for voltage measurements) as shown in Figure 3.

The relationship between the output of the amplifier ( $e_o$ ) and the noninverting ( $e_+$ ) and inverting ( $e_-$ ) inputs is given by

$$e_o = A(e_+ - e_-)$$

where  $A$ , the gain of the amplifier, is very large (typically of the order of  $10^6$  or more, although it falls with increasing frequency). For the ideal amplifier, the input impedance is infinite and therefore no

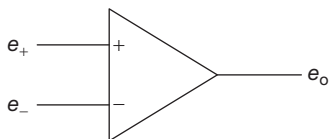


**Figure 3** Operational amplifier (power supply connections omitted for simplicity).

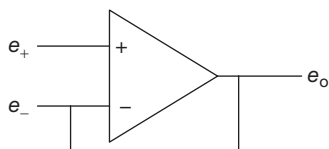


**Figure 4** Unity gain buffer.

current will flow into the inputs of the amplifier; for real amplifiers, it is normal to specify the input leakage current rather than the input impedance, and typical values range from  $100$  nA down to less than  $1$  pA, depending on the technology used to construct the amplifier.

#### 2.30.4.3.2 Principle of negative feedback

Most operational amplifier circuits rely on ‘negative feedback’ to provide the required function. In essence, this means that a signal derived from the amplifier output is fed back to the input such that the desired relationship between the input and the output is obtained.

The simplest negative feedback circuit is the unity gain buffer:

In this circuit, the input signal is connected to  $e_+$  and  $e_o$  is connected back to  $e_-$  (Figure 4). We can analyze the behavior by substituting for  $e_-$  in the op-amp gain equation:

$$e_o = A(e_+ - e_o)$$

Hence

$$e_o = e_+[A/(1 + A)]$$

As  $A$  is very large,  $[A/(1 + A)]$  is very close to  $1$ , so  $e_o \approx e_+$ .

By design, the input impedance of the operational amplifier is very large, and the output impedance is very low (and made lower still by the action of the negative feedback), thus providing an amplifier with a gain of one, very high input impedance and very low output impedance.

#### 2.30.4.3.3 Simple potentiostat circuit

The basic circuit to provide control of potential is also very simple (Figure 5).

Again, we can see how the circuit works by putting the various voltages into the gain equation for the op-amp (using  $V_{CE}$  for the potential at the counter electrode terminal and  $V_{RE}$  for the reference electrode,

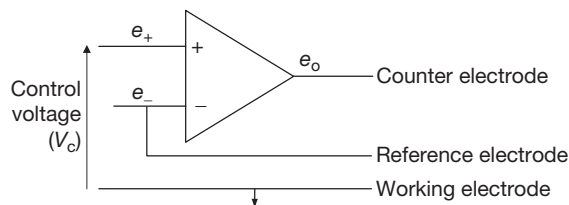


**Figure 5** Operational amplifier circuit for potential control.

both relative to the working electrode, which is connected to the power supply ground):

$$V_{\text{CE}} = A(V_c - V_{\text{RE}})$$

Hence

$$V_{\text{RE}} = V_c - V_{\text{CE}}/A$$

As  $A$  is very large (usually  $> 10^6$ ), this implies that  $V_{\text{RE}} \approx V_c$ . As the electrode potential of the working electrode is measured relative to  $V_{\text{RE}}$ , this means that the potential of the sample will be  $-V_c$ .

Somewhat more detailed descriptions of potentiostat circuits are presented in **Chapter 1.02, Electrochemistry**. Note that the circuits for the unity gain buffer and the potentiostat illustrate a general fact for operational amplifier designs, namely that when operating with correct negative feedback, the voltage at the two input terminals is the same, that is,  $e_+ = e_-$ , and this provides a simple way of working out how the circuit will behave.

#### 2.30.4.3.4 Some potentiostat configurations

For simplicity, we shall draw the potentiostat as a box with three connections, labeled CE, RE, and WE (for Counter Electrode, Reference Electrode, and Working Electrode respectively), and a control input that permits control of the potential with an external input. Then the simplest potentiostat circuit controls potential, optionally following an external device, such as a sweep generator that provides a potential that varies with time (**Figure 6**).

The potentiostat may provide a means of monitoring the current, but if this is not available, then the current can be measured by inserting an ammeter in the lead from the potentiostat to the counter electrode or by inserting a resistor and measuring the voltage across it (note that the potentiostat automatically compensates for the voltage drop across the ammeter/resistor, and hence this is not a problem, providing it is not excessive; up to 1 V is reasonable).

#### 2.30.4.3.5 Control of current

If a potentiostat is configured to control the potential across a fixed resistor, this will produce a controlled

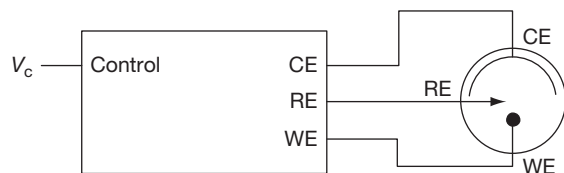


**Figure 6** Potentiostat used for control of potential.

current from the CE terminal to the RE terminal (**Figure 7**). It should be noted that in this circuit, the RE is at a voltage of  $V_c$  relative to instrument ground (the WE terminal), while the CE terminal is at whatever potential is necessary (within the capability of the potentiostat of course) to supply the current. (The term 'instrument ground' is used to refer to the 0 V connection of the power supply. This may or may not be connected to a true local ground (e.g., the earth pin of the mains connector).) It is often required to measure the potential that results from the application of a controlled current; note that the reference electrode must not be connected to the RE terminal to achieve this; some potentiostats may provide a mechanism for measuring the potential in galvanostatic mode (check the manual); alternatively an independent voltmeter must be used.

#### 2.30.4.3.6 Measurement of current

If a potentiostat is configured to control the potential between the RE and WE terminals at 0 V, then the current required to do this can be measured between the CE and RE terminals (**Figure 8**). The voltage burden is not particularly important, as the potentiostat will adjust the voltage at the CE terminal to supply the required current. An ammeter is shown in **Figure 8**, but this can, of course, be replaced by a resistor and voltmeter (providing the voltage across the resistor is within the capability of the potentiostat). Note that one current measuring connection is connected to instrument earth in this configuration, while the other (connected to the RE terminal) is a 'virtual earth' (i.e., it is at earth potential, but not actually connected to earth).

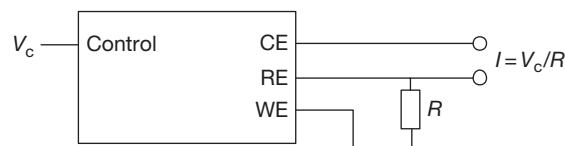


**Figure 7** Potentiostat configuration for current control.

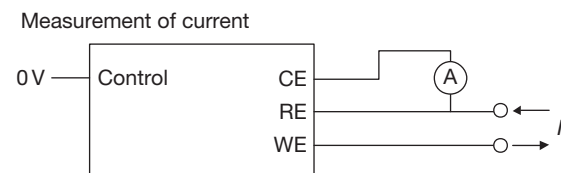


**Figure 8** Configuration of potentiostat to measure current.



#### **2.30.4.3.7 Problems in potentiostatic measurements**

The potentiostat is a very useful device, but users should be aware of a number of possible problems:

- **Overloading**

The potential of the working electrode is controlled by current supplied from the amplifier in the potentiostat. The current and voltage available will be determined by the design of the amplifier and the power supply in the potentiostat. The voltage limit is very often  $\pm 15$  V, as this is the normal maximum supply voltage range for integrated circuit operational amplifiers (though higher voltage potentiostats are available). The current limit will vary from  $\pm 10$  mA for standard operational amplifiers, up to many amps for power devices. If the required potential demands more current or voltage than the potentiostat can supply, then the potential control will break down; this can usually be recognized by an unchanging current, corresponding to either the current limit of the potentiostat or the voltage limit in conjunction with the total circuit resistance.

- **Instability**

As already explained, the operation of the potentiostat depends on negative feedback. However, at higher frequencies, elements in the circuit (including the cable from the reference electrode to the potentiostat and circuits internal to the potentiostat) can introduce delays between a change in the potential being applied to counter electrode and the resultant potential appearing at the inverting amplifier input. At a frequency where the delay corresponds to half of the period of one cycle, the delay will convert negative feedback into positive feedback, which can result in strong oscillation of the potentiostat (this is essentially the same as the 'howl' when the microphone picks up the sound from the public address system). Very often the only measurements taken from a potentiostatic experiment are the potential and current – if these are made using dc instruments, the 'howl' will not be detected, and the potentiostat will just appear not to be working, as the dc value of the potential will typically not be what is intended. In this situation, it is important to check the current using an ac meter; alternatively check the cell voltage with an ac meter – do not try to measure the ac voltage between the reference electrode and the working electrode, as this will typically be very small (remember that it will be amplified by the

gain of the amplifier in the potentiostat before it is applied to the counter electrode). Such oscillations can usually be stopped (at the expense of slowing down the response of the potentiostat) by connecting a capacitor from the counter electrode terminal to the reference electrode terminal, which provides strong negative feedback at higher frequencies (1  $\mu$ F is usually sufficient). It may also be useful to reduce the effective impedance of the reference electrode at higher frequencies (especially when using high-resistivity solutions) by coupling it with a capacitor to a length of platinum wire wrapped around the tip of the Luggin probe (see [Section 2.30.8](#)).

- **Frequency response**

Many applications of potentiostats are concerned with 'near-dc' conditions, and the frequency response is not particularly important. For this reason and to avoid problems with instability, some potentiostats have a relatively low frequency response. Some applications, however, such as the measurement of electrochemical impedance or transient measurements with scratching electrodes, demand a response at high frequencies. Users should therefore take care to select an appropriate instrument for their application.

#### **2.30.4.4 Control of Current**

In principle, the control of current is simpler than the control of voltage, as we are not concerned with the source of any voltages developed in the external circuit. Thus, the simplest galvanostat is a two-terminal device, and many laboratory power supplies offer a controlled current mode of operation that may be suitable for some corrosion experiments (though they are typically not very easy to set accurately, especially for smaller currents). Alternatively, a potentiostat can be used very easily as a galvanostat by using it to control the voltage across a resistor ([Figure 7](#) and also in the Chapter **Electrochemistry** for an example circuit). Note that there can be earthing issues with galvanostats, as the simplest circuits (including potentiostats used as galvanostats) do not connect either of the output terminals to earth.

As with potentiostats, galvanostats have limits on the output current and voltage, but they are less susceptible to oscillation and similar problems (as the feedback is contained within the instrument, it is much easier to avoid the positive feedback that could give problems).

## 2.30.5 Electrochemical Methods

### 2.30.5.1 Potential Monitoring

The measurement of potential is very simple – a reference electrode is placed in the same solution as the working electrode and a voltmeter with suitable (high) input impedance is connected to measure the voltage difference between the two. Note that the negative terminal of the voltmeter should be connected to the reference electrode in order for the measured voltage to have the correct polarity. However, if the working electrode is connected to earth (as is quite likely in the case of plant measurements), this configuration may compromise the input impedance of the meter (since the negative input terminal of a voltmeter often has a much lower impedance to earth than the positive terminal), and in this case it is better to connect the meter ‘the wrong way round’ (i.e., connect the higher impedance positive terminal to the reference electrode) and reverse the sign of the measured potential.

Provided no current is being applied to the working electrode, it is not particularly important where the reference electrode is situated, and it is not necessary to use a Luggin probe (see [Section 2.30.8](#)). The only exception to this is for measurements of the distribution of potential over the surface of the sample, when the design and location of the reference electrode is critical.

While the measurement of potential is relatively easy, the interpretation may present problems. The corrosion potential is affected by many factors, and in the absence of additional information (such as a detailed understanding of the system in question), it is not possible to deduce anything about what is happening. As an example of a situation where the potential does provide useful information, the potential of carbon steel in concrete drops markedly when it starts to corrode, but even here, there is a wide range of potential over which the behavior is considered as uncertain, as indicated in [Table 2](#).

**Table 2** Determination of condition of steel in concrete from measured potential (from Tullmin *et al.*<sup>4</sup>)

Potential/V(CSE)	Condition
> -0.20	Passive
-0.20 to -0.35	Active or passive
< -0.35	Active (i.e., corroding)

### 2.30.5.2 Galvanic Current

As with the potential, the coupling current between two electrodes is relatively easy to measure, but more difficult to interpret. With a well-defined galvanic couple, the current may provide a useful indication of some feature of the environment, but it is difficult to be sure in the general case whether it will provide useful information and how to extract that information from the measured data.

Note that galvanic currents must be measured with a low potential drop, and therefore an electrometer, zero-resistance ammeter, or potentiostat should be used as described earlier.

### 2.30.5.3 Polarization Curves

#### 2.30.5.3.1 Introduction

One of the most common electrochemical methods in corrosion research and testing is the determination of the polarization curve – the relationship between the current and the potential, usually over a relatively wide range (of the order of a volt). It is normally the objective to determine polarization curves under near steady-state conditions (i.e., the measured current at each potential is essentially that that would be obtained after a long period at a constant potential). For at least two reasons, this is not really possible:

- When corrosion reactions are occurring, the electrode will change with time, especially in the anodic region of the curve, and hence there is really no such thing as steady-state.
- It is not usually feasible to use more than a few samples, and therefore measurements must be made at different potentials on the same sample; the prior history of the sample is thus likely to influence the behavior.

Thus, the measurement of a polarization curve involves an element of compromise, and the optimum method and parameters to use will depend on the system being studied. As a general rule, systems exhibiting a low corrosion rate benefit from slow measurement methods (since the electrodes will change only slowly by corrosion and the low currents involved will be more easily perturbed in the short term by factors such as double-layer charging currents and currents associated with thickening of passive oxide films), while systems exhibiting rapid corrosion can (and should) be measured more quickly, since the actively corroding surface will reach near-steady state quickly and will change more quickly as a result of corrosion.

### 2.30.5.3.2 Measurement methods

Polarization curves can be measured either by controlling the current and measuring the potential or by controlling the potential and measuring the current. Since control of current is somewhat easier than control of potential, early measurements tended to use controlled current, but it has a number of disadvantages; in particular, it is not possible to control the potential in the passive region of active-passive polarization curves using controlled current (Figure 9). Thus, modern approaches almost invariably use controlled potential.

The polarization curve is notionally a continuous function, in that the potential can be held at any value and the current measured. In practice, however, there are two approaches to the measurement – the potential can be swept smoothly through the range of values of interest (leading to a *potentiodynamic* polarization curve) or it can be stepped over a range of reasonably small steps (typically in the range of 10–50 mV and leading to a *potentiostep* curve). The advantage of the potentiodynamic method is that it provides an essentially continuous curve. The advantage of the potentiostep method is that the measured current can be taken at the end of the step hold period, and therefore it approaches steady-state a little more

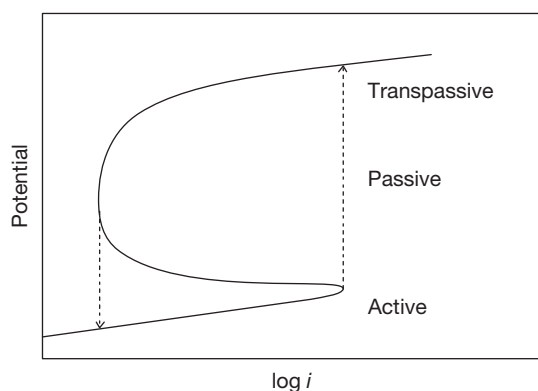


**Figure 9** Potentiostatic and galvanostatic measurement of polarization curve (schematic). Note that there is only one current density for each potential, so potentiostatic measurement gives the complete curve. In contrast there are three possible potentials (only two of which are stable) corresponding to much of the range of current densities, so galvanostatic measurement cannot reach some parts of the curve, and flips from the active peak to transpassive corrosion on the positive-going scan direction, and from the passive current density to the active curve in the negative-going direction (denoted by the dashed arrows). Note also that it is impossible to hold the system in the passive region using galvanostatic polarization, as slight changes in condition will cause a transition to active corrosion.

closely for the same overall measurement time. It also permits the use of new specimens for each potential, which minimizes effect due to the prior history of the specimen (though it also much more time-consuming and expensive, and introduces questions about sample-to-sample reproducibility).

The potentiodynamic method requires a potentiostat, a linear sweep generator (to produce the potential sweep) and a recording device of some kind to record the current and potential. In principle, the latter can be an  $X$ - $Y$  recorder (possibly with a log converter on one axis to record  $\log(\text{current})$ ), or a conventional recorder with a hard-working research student to extract and process the information. However, most modern systems will use a computer data acquisition system to manage the measurement and facilitate the processing of the data. The wide dynamic range of the measured current presents something of a problem here, and it is common for dedicated systems to use automatic range switching in order to permit the measurement of both large and small currents.

The sweep rate is an important parameter, as it controls the closeness with which steady-state is approached. Typical values of sweep rate are of the order of  $1 \text{ mVs}^{-1}$ ; as indicated earlier, a slow sweep rate is required for low corrosion rates, while a faster sweep can be used (and may be necessary to avoid excessive modification of the working electrode by corrosion) for systems that are corroding rapidly.

### 2.30.5.3.3 Interpretation

The simplest approach to the interpretation of polarization curves is to model the curve as the summation of a series of curves corresponding to the individual electrochemical reactions that can occur. As activation-controlled reactions exhibit a linear relationship between potential and  $\log(\text{current density})$ , it is normal to plot potential using linear axes and current density using log axes (strictly the absolute value of current density, since  $\log(x)$  does not exist for  $x < 0$ ). Since the potential is usually the controlled variable and current density the measured variable, polarization curves should strictly be plotted with potential on the  $x$ -axis. However, early workers controlled current and therefore plotted current density on the  $x$ -axis, and many workers still use this convention.

**Figure 10** (taken from ASTM Standard G5:1998, which provides a standard method for determining polarization curves) shows an example polarization curve, in this case for a ferritic stainless steel in sulfuric acid (the curve displays as a band because

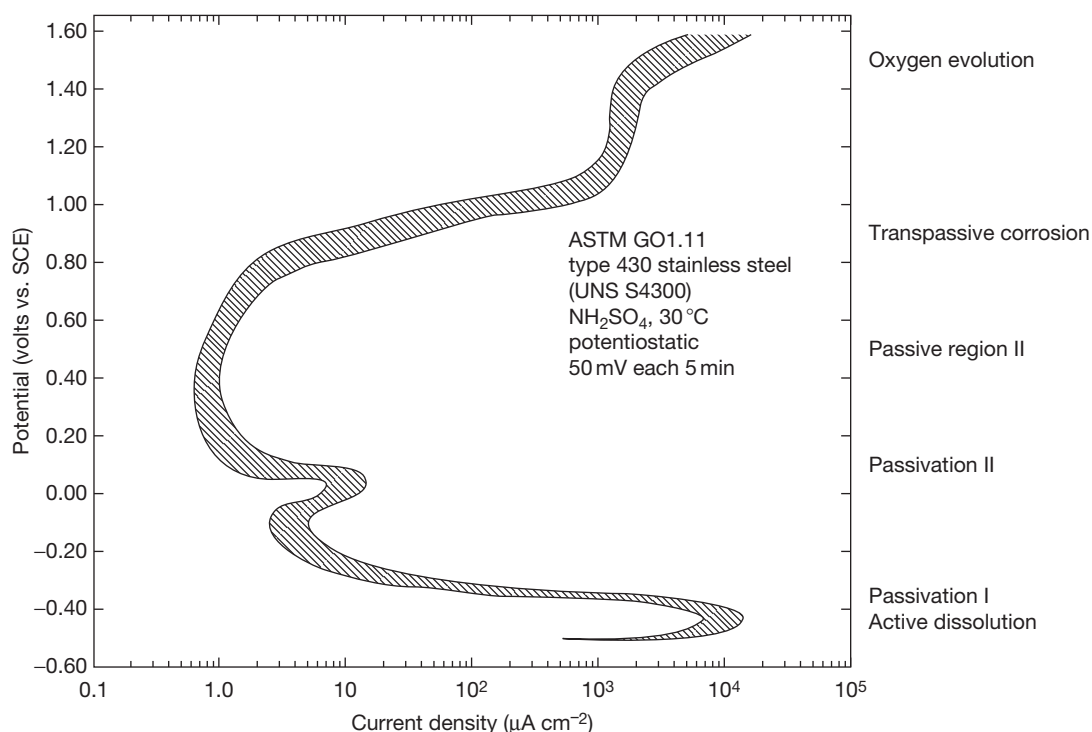


**Figure 10** Polarization curve for ferritic stainless steel in sulfuric acid (from ASTM standard<sup>5</sup>).

this figure shows the range of curves obtained by different labs on a particular batch of steel). The labels on the right of **Figure 10** indicate what is happening in each region of the curve. Note that there are two passivation reactions; the first corresponds to passivation by  $\text{Cr}_2\text{O}_3$ , while the second corresponds to passivation by  $\text{Fe}_2\text{O}_3$  as well as  $\text{Cr}_2\text{O}_3$ .

An important process in the analysis of polarization curves is the estimation of the Tafel slope (the slope of the linear region of the  $E-\log|i|$  curve). For an ideal activation controlled reaction, this is straightforward (though easy for beginners to miscalculate the slope, for example by taking  $\log(i_1-i_2)$  rather than  $\log(i_1)-\log(i_2)$ ). However, real polarization curves tend not to show a clear Tafel region, and it can be impossible to determine the Tafel slope. As a guide, a Tafel slope should be considered to be reliable only if it meets the following conditions:

- The polarization curve is straight for at least one decade of current (i.e., the current changes by a factor of ten).
- The straight region of the polarization curve should start at about one Tafel slope away from the open circuit potential (i.e., if the Tafel slope is

60 mV, then the curve should become linear at about 60 mV from the corrosion potential). This is not an exact rule, as it depends on the relationship between the anodic and cathodic slopes; if in doubt, a good check is to overlay the calculated curve onto the measured curve.

- The Tafel slope should not ‘undercut’ the polarization curve between the open circuit potential and the start of the Tafel region. If this occurs, it suggests that the Tafel slope corresponds to a different reaction from the one that is dominant at the open circuit potential; a common student error is to fit a Tafel slope to the hydrogen evolution reaction when the dominant reaction at the open circuit potential is oxygen reduction (**Figure 11**). The Tafel slope may be correct in this situation, but it is not relevant to the corrosion process (therefore, it cannot be used, for example, to compute the Stern–Geary coefficient).

#### 2.30.5.4 Linear Polarization Resistance

The linear polarization resistance is the slope of the  $E-i$  relationship at the open circuit potential (OCP) (i.e., at zero current), and it provides a method of

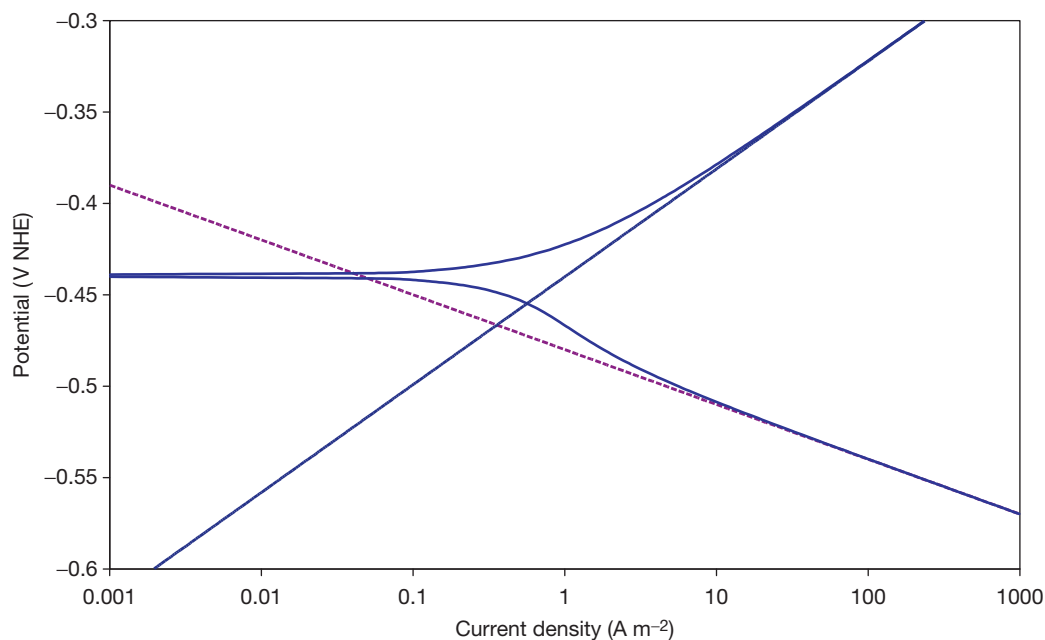


**Figure 11** Calculated polarization curve exhibiting ‘undercutting’ of cathodic Tafel region due to multiple cathodic reactions. This graph is based on the idealized behavior of iron in a neutral solution, where the primary cathodic reaction is oxygen reduction at the OCP, which gives rise to the ‘bump’ in the cathodic curve. Note that the anodic and cathodic Tafel slopes do not intersect at the corrosion potential, and the current density at the intersection is less than the corrosion current density (which is defined by the limiting current density for oxygen reduction, set to  $1 \text{ A m}^{-2}$  for this model).

estimating the instantaneous corrosion rate. It can be measured in a number of ways:

- The potential can be swept through a narrow range either side of the OCP, the current recorded, and the slope determined. This method is commonly used in laboratory measurements, as it has a number of advantages – the  $E-i$  plot produced provides an indication of measurement problems such as high noise levels (Figure 12), and it makes a true measurement of  $dE/di$  at  $i=0$ . However, it is relatively difficult to automate, as it is necessary both to compensate for changes in the OCP and to determine the slope of the curve at  $i=0$ .
- The current can be swept through a small range about zero and the potential measured. This has the advantage of automatically making a measurement that is centered on zero current, but the current range needs to be adjusted to compensate for changes in the measured resistance. This method also reveals measurement noise.
- The potential can be stepped between  $\text{OCP} - \Delta E/2$  and  $\text{OCP} + \Delta E/2$ , where  $\Delta E$  is a small potential difference (typically 10 to 20 mV). Then  $R_p$  can be determined as  $\Delta E/\Delta i$ , where  $\Delta i$  is the change in current density. This suffers from the difficulty of compensating for changes in the OCP, and errors can be introduced if the anodic and cathodic Tafel slopes are markedly different.
- An applied current can be stepped between  $-\Delta i/2$  and  $+\Delta i/2$  and the corresponding potential step,  $\Delta E$ , measured. This is the simplest approach for corrosion monitoring, as it automatically makes the measurement centered on the OCP, and the polarization resistance is directly proportional to  $\Delta E$  (since  $R_p = \Delta E/\Delta i$  and  $\Delta i$  is constant). The current amplitude should ideally be adjusted to keep  $\Delta E$  in a reasonable range, but this is not too problematic unless the corrosion rate varies over quite a wide range. This method is also subject to error if the anodic and cathodic Tafel slopes are markedly different.
- A more sophisticated approach to the measurement of polarization resistance is to apply a sine wave of current or potential and measure the amplitude of the potential or current respectively. Essentially, this consists in making a single frequency impedance measurement – see the following section for further information. This method has two main advantages: it is easier to account for extraneous noise, and the frequency at which the measurement is made is well-defined, which



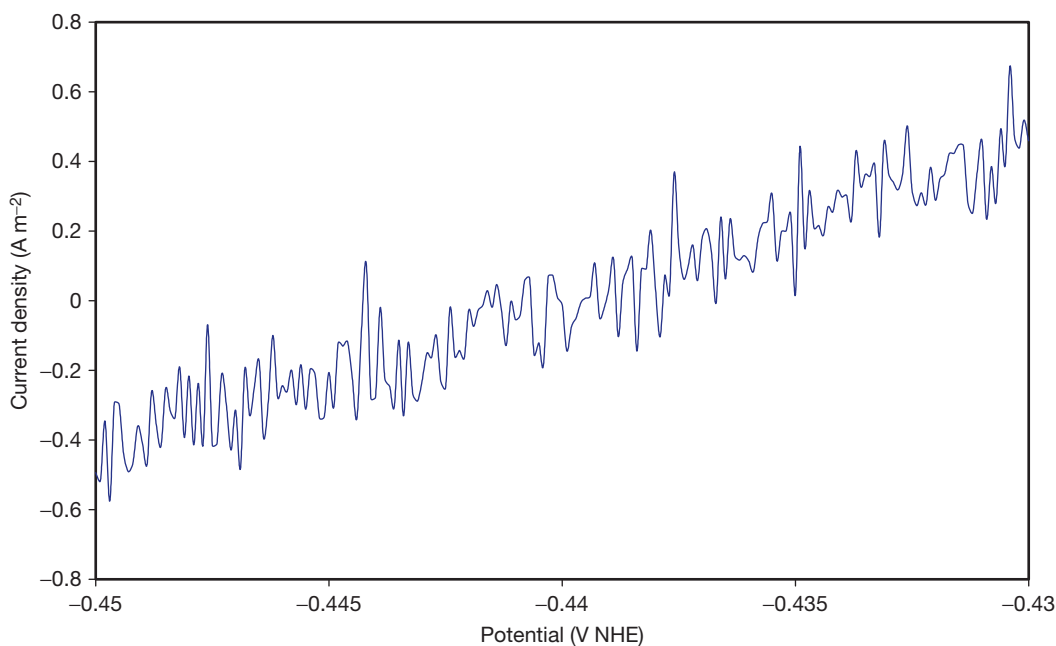


**Figure 12** Linear polarization resistance measurement using a potential sweep and exhibiting measurement noise. In this case the amplitude of the noise is low enough that we can make a reasonable estimate of the polarization resistance.

facilitates interpretation. With the low cost of sophisticated electronics, this has become a good method for corrosion monitoring, especially as it can easily be combined with Harmonic Analysis for the estimation of the Stern–Geary coefficient (see [Section 2.30.5.6](#)).

In addition to the variety of methods of polarization that are available, polarization resistance can be measured either as the resistance between two equivalent electrodes (this has some practical advantages, notably the fact that the expected dc potential difference is zero) or as the resistance of a single electrode, using a reference electrode to connect to the solution in a reproducible fashion ([Figure 13](#)).

Note that the normal unit of  $R_p$  is  $\Omega\text{m}^2$ , that is, it is not, strictly speaking, a resistance, but a resistance times area.

A question for all of the measurement methods is the optimum cycle time for the measurement. The basic theory on which the polarization resistance method is based assumes that  $R_p$  is measured at a low frequency, such that capacitive and other time varying currents can be neglected. However, in some situations diffusion processes can change very slowly (notably in environments such as soil and concrete), and it is not feasible to measure  $R_p$  at sufficiently low frequencies. In this case it has been found that relatively fast

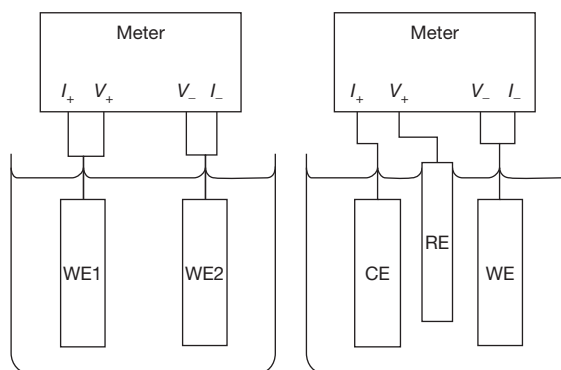


**Figure 13** Two- and three-electrode methods for polarization resistance and impedance measurement. Generic connections have been indicated on the measuring device – if a potentiostat is used for the measurement,  $I_+$  will correspond to the counter electrode terminal,  $V_+$  the reference electrode and  $V_-$  and  $I_-$  the working electrode (this will be one terminal unless the potentiostat has separate current and voltage measuring connections for the working electrode).

measurements (with a typical measurement cycle time of 30 s) still give good correlation with corrosion rate. This is attributable to the measurement of the charge transfer resistance with only a small contribution from the diffusional impedance (see Cottis and Turgoose<sup>6</sup> for further explanation), but note that this does lead to a  $B$ -value different than for very low frequency measurements.

#### 2.30.5.4.1 Interpretation

The interpretation of the polarization resistance is normally based on the Stern–Geary relationship:<sup>7</sup>

$$R_p = \frac{B}{i_{\text{corr}}}$$

where  $B$  is the Stern–Geary coefficient (it is often called the Stern–Geary constant, but it is not a true constant, being dependent on the metal and environment being studied), or simply the  $B$ -value; its unit is V.

Note that the  $B$ -value cannot be derived from the measured data (but see the sections on harmonic analysis and intermodulation distortion) and must be obtained from separate experiments, either by measuring the anodic and cathodic Tafel slope from a polarization curve or by using a practical calibration against corrosion rates measured by an alternative method, such as weight loss. In the absence of a suitable  $B$ -value, it is common to use 26 mV for activation controlled systems and 52 mV for systems with the cathodic reaction being limited by diffusion. These values correspond to typical Tafel slopes for these two cases, and the calculated corrosion rates will usually be within a factor of two or three of the true value, which is usually tolerable for corrosion monitoring, where the objective of the electrochemical corrosion monitoring is primarily to detect major changes in behavior.

#### 2.30.5.4.2 Errors

The polarization resistance method makes a number of assumptions about the system under investigation, and errors arise if these assumptions are invalid.

- It is assumed that there is only one anodic reaction (metal dissolution) and one cathodic reaction (oxygen reduction or hydrogen evolution). Note that this implies that the rates of the reverse reactions are negligible. This is not always valid: relatively noble metals such as copper and nickel may be close to equilibrium at their corrosion potential, and it is possible for  $R_p$  to be dominated by the metal–metal ion exchange reaction; similarly, the kinetics of hydrogen–hydrogen ion reaction typically control the potential of nickel–base alloys in hydrogen-containing high temperature water, and electrochemical measurements give little information about the corrosion reaction.
- It is assumed that both anodic and cathodic reactions obey Tafel’s Law, which implies that they must be under activation control. Truly diffusion limited reactions (i.e., reactions that are at the limiting current density) can also be regarded as

obeying Tafel’s Law, with a Tafel slope of infinity, but intermediate cases (where the current is at a significant fraction of the limiting current density) do not obey the Stern–Geary equation and will give errors. Similarly, passive alloys will have an anodic behavior that does not obey Tafel’s Law. Fortunately in the case of passive systems, the cathodic reaction will often obey Tafel’s Law, while the anodic reaction can be regarded as having a very high Tafel slope; consequently, they may obey the Stern–Geary relationship. This is not a major problem for corrosion monitoring, as the passive alloy will always have a high polarization resistance, and the exact corrosion rate is not usually of concern.

- The electrochemical reactions are uniformly distributed over the electrode (i.e., uniform corrosion is occurring). Polarization resistance measurements on electrode that are subject to localized corrosion are normally considered to estimate the average corrosion rate. This is justified if the corrosion process consists solely of a cathodic reaction (either obeying Tafel’s Law or fully diffusion controlled) on the passive surface and an anodic reaction at the localized corrosion site (e.g., within the pit or crevice) that obeys Tafel’s Law. However, this is not necessarily the case, and polarization resistance should be regarded as more of a qualitative measure if localized corrosion is occurring. Note that it is not possible to identify purely from the measured value whether or not the corrosion is localized or uniform.
- It is generally assumed that the relatively small current or potential perturbation that is applied as a result of the measurement of polarization resistance does not change the corrosion behavior. This is not necessarily correct, and the perturbation may change the behavior somewhat. This is more likely when using controlled potential methods, as these are more likely to apply a nonzero mean current to the electrodes.
- Polarization resistance measurements are necessarily performed on probe electrodes when used for corrosion monitoring. It is assumed that the probes have the same behavior as the plant, but there are several reasons why this may not be valid.<sup>8</sup>

#### 2.30.5.5 Electrochemical Impedance Spectroscopy

Electrochemical impedance spectroscopy, EIS, extends the polarization resistance method by measuring how the impedance varies with frequency. There are a

number of ways in which this measurement can be made (see Turgoose and Cottis<sup>9</sup> and Orazem and Tribollet<sup>10</sup> for further information on the technique), but in essence the measurement consists in applying a series of ac currents and measuring the ac potential response or applying a series of ac potentials and measuring the current response. The impedance is then calculated by dividing the potential by the current at each frequency (using complex arithmetic in order to maintain the phase information). There are a number of criteria that must be satisfied in order to make a valid measurement,<sup>11</sup> including:

- **Linearity:** the response of the system must be proportional to the perturbation (this is rarely true for electrochemical systems, but we approach it by using small amplitude perturbations).
- **Causality:** the response of the system must be a direct result of the perturbation (power line noise and similar interference would result in a breach of this requirement, as would randomly occurring currents associated with localized corrosion).
- **Stability:** this requirement requires that the system does not exhibit characteristics such as multiple values for a given perturbation, or (equivalently) regions of negative resistance (electrochemical systems are often not stable, including any systems that include an active–passive transition).

It is possible to test EIS data for failure to meet these requirements, the most common method being to use the Kramers–Kronig (K–K) transform; this allows for the calculation of the phase response from the amplitude response and vice versa. If the calculated and measured data do not match up, this implies that the data are not valid (note that this is a necessary, but not sufficient, condition – valid data will not fail the K–K transform test, but it is possible for invalid data to pass it).

#### 2.30.5.5.1 Presentation of EIS data

The EIS measurement produces a set of amplitude and phase values for a range of frequencies, and there are two main ways of presenting these:

- The Bode plot presents  $\log(\text{amplitude})$  and phase against  $\log(\text{frequency})$ . Figure 15 presents a Bode plot for the equivalent circuit of Figure 14 (this is known as the Randles equivalent circuit and has three components:  $R_s$  is the resistance of the solution,  $R_p$  is the polarization resistance of the metal–solution interface, and  $C_{dl}$  is the double-layer capacitance of the metal–solution interface).

On the Bode plot, a resistor produces a horizontal line on the amplitude plot with amplitude equal to the resistance and a constant phase of zero on the phase plot. A capacitor produces an amplitude that falls with a slope of  $-1$  as the frequency increases (the amplitude of the impedance is  $1/(2\pi fC)$ , where  $f$  is the frequency and  $C$  the capacitance), and a constant phase of  $-90^\circ$ ; as we are normally dealing with resistors and capacitors, it is common to invert the phase axis (i.e., plot  $-\text{phase}$ ) so that capacitive circuit elements give data above zero.

- The Nyquist plot normally plots the imaginary part of the impedance against the real part (Figure 16). The Nyquist plot invariably inverts the imaginary axis (i.e., it plots the imaginary component of impedance with increasingly negative values on the  $y$ -axis), so that capacitive circuit elements plot above the  $x$ -axis. One weakness of the Nyquist plot compared with the Bode plot is that it does not implicitly include the frequency of each measurement point, so at least some points should have their frequency indicated.

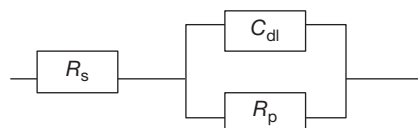


**Figure 14** The Randles equivalent circuit for a corroding interface.

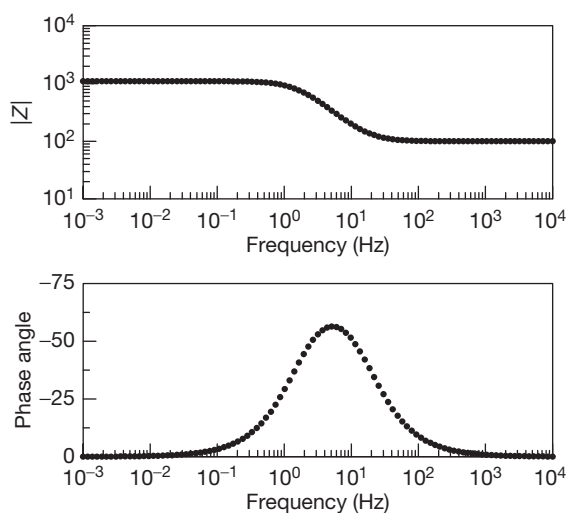


**Figure 15** Example Bode plot for the equivalent circuit of Figure 14, with component values of  $R_s = 100\ \Omega$ ,  $R_p = 1000\ \Omega$ ,  $C_{dl} = 0.0001\ \text{F}$  (from Cottis<sup>8</sup>). Note that  $|Z|$  tends to  $R_s$  at high frequency and to  $R_s + R_p$  at low frequency.

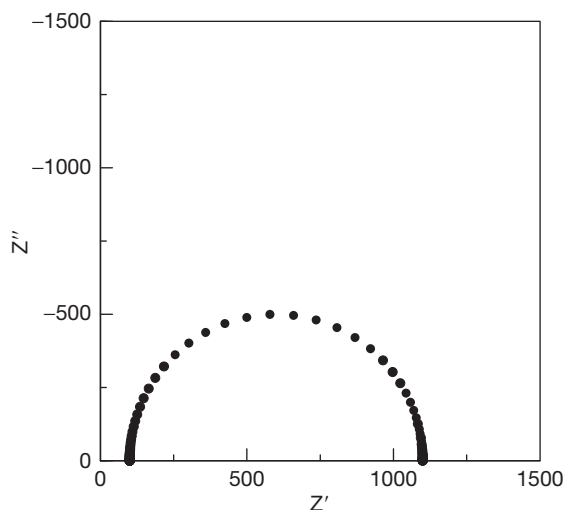


**Figure 16** Example Nyquist plot (from Cottis<sup>8</sup>).

#### 2.30.5.5.2 Interpretation of EIS measurements

The interpretation of EIS data is essentially concerned with determining the components inside a sealed 'black box' with just two leads connected to the outside. It is relatively easy to determine the values of internal components if we know what their configuration is, but if we do not know the configuration or the number of components there is no unique solution to the problem, as there are an infinite number of circuits that could produce the observed behavior. The simplest example of this is circuits that contain only resistors. Any resistor network will appear from the outside as a pure resistor (i.e., the measured impedance will have constant amplitude and zero phase). Consequently, in order to obtain a valid interpretation, it is important to use prior knowledge of the expected behavior in order to model the real physical system.

There are two basic approaches to model EIS performance, and hence to determine the properties of the elements of the electrochemical interface by adjusting the parameters of the model to match the measured data:

- The response of the chemical and electrochemical processes to a fluctuating potential is analyzed with a mathematical or numerical model in order to produce a simulated spectrum, and the parameters of the model are adjusted to fit the measured spectrum. This is technically an ideal approach, as it provides a direct relationship between the physical processes occurring and the observed spectrum, and can include the effects of

nonlinearity in response, but it is very demanding of time and skill, and it is therefore used only infrequently.

- A much more common approach is for the components of the system under investigation to be modeled by electrical equivalent circuit elements that have similar characteristics to the actual processes concerned. Thus, a paint film can be modeled as a resistor (corresponding to ionic current passing through the film) in parallel with a capacitor (corresponding to the capacitance of the paint film acting as a parallel plate capacitor); underneath the paint film the metal–solution interface gives rise to a resistor (corresponding to the charge transfer resistance) in parallel with a capacitance (the double-layer capacitance). The response of the resultant electrical circuit is then modeled using conventional methods from electrical engineering, and the parameter values adjusted to optimize the fit between the model and real data. Note that the equivalent circuit is derived first, based on the physical processes occurring; it may then be necessary to modify the equivalent circuit to fit features of the measured data. It is important that the added elements are linked to a physical process; some less-experienced workers try different equivalent circuits to find the one that best fits the measured data and then try to work out what the elements correspond to; while this may provide a good fit to the data, the circuit may have the wrong configuration so that the values of circuit elements give no information about the real processes occurring.

#### 2.30.5.5.3 Advanced impedance measurements

Significant advances have been made in the EIS technique in recent years. These are largely related to the detection and handling of errors in the measurement and enhancing the speed of measurement.

In a conventional EIS measurement, the impedance is acquired sequentially at each of a set of frequencies. The frequencies are normally arranged as a geometric series (i.e., each frequency in the series is the product of the immediately preceding sample and a multiplier (the latter is typically chosen to give around seven frequencies per decade). With this analysis scheme, the time taken to determine a full spectrum is dominated by the lowest frequency included in the measurement. It is not uncommon for the lowest frequency to be 1 mHz, implying that the measurement of an impedance spectrum takes

several hours. Besides leading to long measurement times, this leads to questions about the stationarity of the system. Van Gheem *et al.*<sup>12,13</sup> have developed a measurement method that uses multiple simultaneous sine waves, permitting the simultaneous measurement of a full spectrum (the use of multiple sinewaves is not new; Van Gheem *et al.*'s method is novel in the way that it allocates measurement frequencies in such a way that the measurement of the power at frequencies that are not present in the applied signal permits the estimation of the impact of noise and nonlinearity on the measurement).

In a similar vein, Orazem<sup>14</sup> has developed a method to use the error structure of EIS data to optimize the fitting of equivalent circuit models to the data.

Unfortunately, the methods developed by Van Gheem and Orazem were not available in commercial EIS measurement systems at the time of writing, but they provide an important advance in the development of reliable EIS analysis methods.

### 2.30.5.6 Harmonic Analysis

Harmonic analysis may be thought of as a single-frequency impedance measurement that is extended to measure the first and second harmonics of the input signal.

When a sine wave voltage is applied to a linear system (see the definition of linearity given earlier), the resultant current consists only of a sine wave at the same frequency. However, if the system is nonlinear, as is the case with electrochemical interfaces, this produces some distortion of the sine wave, which creates harmonics of the input signal. Using similar assumptions to those used by Stern and Geary,<sup>7</sup> Dévay and Mészáros<sup>15,16</sup> showed that the amplitudes of the first and second harmonics can be used to determine the Tafel slopes of the anodic and cathodic reactions, and hence determine the  $B$ -value to be used in the estimation of  $i_{\text{corr}}$ . Thanks to the low cost and power of modern electronics, this approach has been adopted as a corrosion monitoring technique with the claimed advantage (based on the theoretical analysis, but not yet really validated in practice) that it does not depend on prior knowledge of the  $B$ -value.

In his analysis Mészáros showed that the double layer capacitance could be allowed for by taking measurements at two frequencies. However, this requires the assumption that the equivalent circuit is a simple Randles circuit, which is often not the case, and as far as the author is aware, all practical implementations of

this method depend on the measurement being made at a low frequency, such that the capacitive components of the equivalent circuit can be neglected.

### 2.30.5.7 Intermodulation Distortion

A further development of the harmonic analysis technique applies two sine waves to the corroding sample. These interact with the nonlinear interface to produce a rather more complex set of output frequencies (Figures 17 and 18). Besides the harmonics of the two input signals, intermodulation components are formed at the sum and difference frequencies. The method was first proposed by Mészáros and Dévay,<sup>17</sup> and the method was subsequently developed by Bosch *et al.*,<sup>18</sup> who termed it 'Electrochemical Frequency Modulation,' although the process by which the output signals are produced is termed 'intermodulation distortion' in the signal processing literature (and in Mészáros and Dévay's paper). (Intermodulation has been widely used in electronic systems for many years as a method for changing the frequency of a signal. Thus in a modern satellite TV system, the LNB (Low Noise Block downconverter) takes the microwave signal picked up by the satellite dish (with a frequency in the range 5–20 GHz) and mixes it through a nonlinear device with a locally generated signal to convert it to a lower frequency (which will be the difference between the incoming frequency and the local signal frequency) that can be handled more easily in the receiver itself, the original signals and all the other intermodulation components being removed by filtering.)

Analysis of the signals produced permits, in theory, the extraction of the Tafel slopes in much the same way as harmonic analysis, but in addition, certain pairs of frequencies can be shown to have constant ratios, and these have been proposed as a test of the reliability of the data (Bosch *et al.*, who first drew attention to these relationships, termed them 'causality factors' 2 and 3 on the basis that they should have values of 2 and 3 if the outputs are caused by the inputs, rather than being random noise). This is potentially a very attractive ability, but at the time of writing this method had been relatively little used, and it is unclear whether or not real systems follow the theoretical behavior well enough for the results to be relied upon.

The theoretical derivation of the analysis procedures for this method implicitly assumes that the measurement is made at a low enough frequency that capacitive effects can be ignored. The relevant



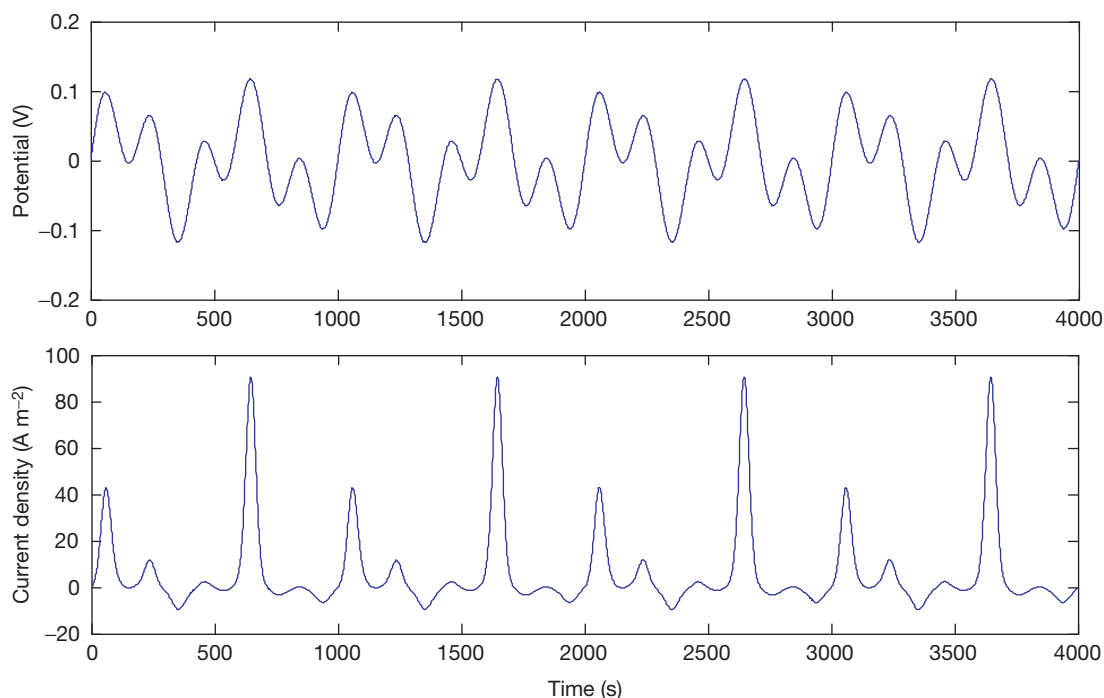


**Figure 17** Potential and current versus time for a simulated intermodulation measurement (controlled potential, cathodic Tafel slope 120 mV anodic slope 60 mV). Note the much lower amplitude of the cathodic currents as a result of the larger Tafel slope, and the resultant distortion of the signal compared to the input signal.

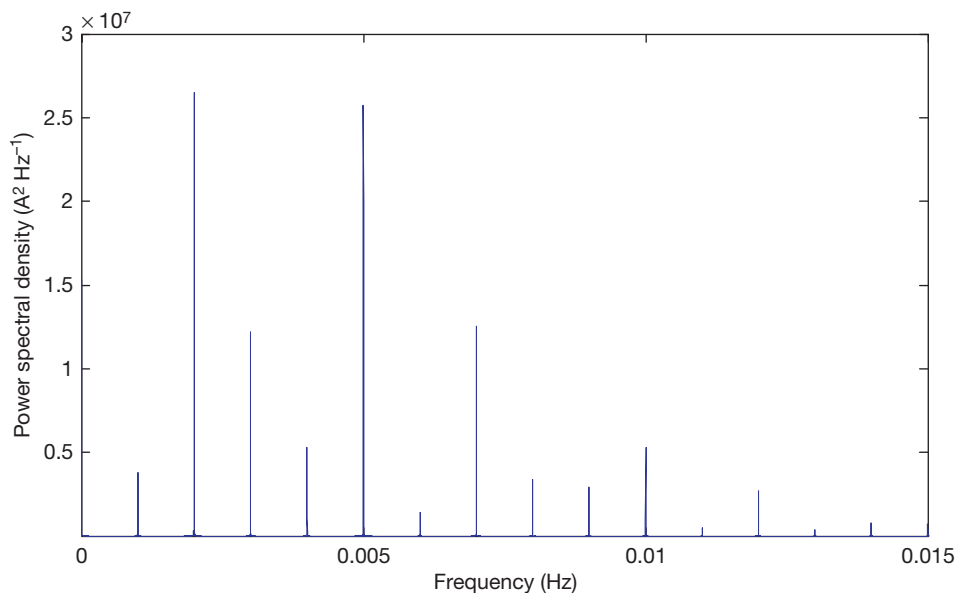


**Figure 18** Illustration of intermodulation distortion (the two input frequencies used were 0.002 and 0.005 Hz ( $f_1$  and  $f_2$ ); the signal at 0.003 and 0.007 Hz are the difference ( $f_2 - f_1$ ) and sum ( $f_2 + f_1$ ) signals; the signals at 0.004 and 0.01 Hz are the first harmonics of  $f_1$  and  $f_2$ ; the remaining signals result from intermodulation between  $f_1$ ,  $f_2$ , and harmonics and intermodulation components. The current was based on a 1 m<sup>2</sup> electrode, which is why the observed power spectral density is so high).

frequency is that of the highest component used in the analysis, and this typically requires the use of very low frequencies for the two input signals. It may be possible to analyze the phase and amplitude of the various output components in order to test for, and possibly to correct for, capacitive components, but this had not been done at the time of writing.

### 2.30.5.8 Transient Techniques

A number of transient techniques have been developed to probe the properties of electrochemical interfaces. Several of these are essentially attempting to determine the properties of elements of an assumed equivalent circuit. These have largely been superseded by EIS, since this obtains the same information in a more accurate and more general way. An example of such a technique is open circuit potential decay (OCPD). In this method, the metal–solution interface is charged by the application of a constant current until a steady potential is achieved. Then the current source is disconnected, and the potential allowed to decay back to its open circuit value, giving a potential–time curve similar to that shown in Figure 18.

Various methods can be used to interpret the resultant curve (see Bosch *et al.*<sup>18</sup> for details); most of these depend on the assumption that the interface can be described by a simple equivalent circuit and that the interface has been charged for long enough that the charging current into the double layer capacitance,  $C_{dl}$ , can be neglected.

### 2.30.5.9 Electrochemical Noise

Electrochemical noise (EN) can be defined as naturally occurring fluctuations in the current and/or potential of corroding electrodes.<sup>20</sup> Early workers regarded these fluctuations as merely a nuisance, to be removed by filtering or averaging if possible, but Iverson<sup>21</sup> realized that they may contain information about the rate and nature of the corrosion process. A number of techniques have been devised for the measurement of electrochemical noise,<sup>8</sup> but most measurements now determine the potential noise as either the fluctuation of the electrochemical potential relative to a low-noise reference electrode or the fluctuation of the potential between two nominally identical working electrodes, while the current noise is measured as the current between two nominally identical working electrodes. An extension of the method measures the potential and current noise

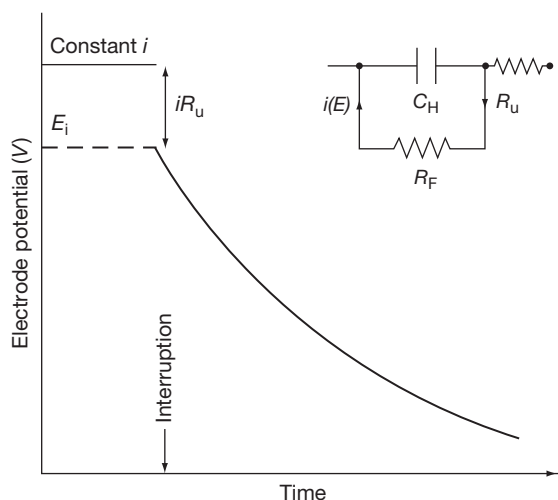


Figure 19 Typical OCPD plot (from Kelsall<sup>19</sup>).

simultaneously using three electrodes (Figure 19). This has a number of advantages, including the ability to determine the electrochemical noise resistance (see the following paragraph).

#### 2.30.5.9.1 Interpretation of electrochemical noise

Early work on electrochemical noise used largely heuristic methods to analyze the data, that is, a number of analysis procedures were tried, and the ones that seemed to work determined by experiment. More recently, more detailed theoretically-based analyses have been developed.<sup>19,22</sup>

One of the most useful parameters to come out of the early heuristic work was the electrochemical noise resistance,  $R_n$ . This can be defined as  $A\sigma_E/\sigma_I$ , where  $A$  is the area of each electrode and  $\sigma_E$  and  $\sigma_I$  are the standard deviations of current and potential respectively, assuming the conventional three-electrode configuration. (Throughout this chapter we take  $R_p$ ,  $R_n$ , and  $R_{ct}$  as being normalized to unit area (i.e., their unit is  $\text{Ohm m}^2$ .) This convention has not always been used (including by the author) and care should be taken to ensure that area effects are properly handled.) This result was first suggested by Dawson *et al.*<sup>23</sup> The result can be proved theoretically with relatively few assumptions:

- The current noise sources on the two working electrodes have the same mean and standard deviation and are uncorrelated.
- The measurements are made at a low enough frequency that capacitive and other effects can be ignored.

- The response of the two working electrodes to an applied current is defined by  $AR_p$ , where  $R_p$  is the polarization resistance.

With these assumptions, it can be shown that  $R_n = R_p$  (strictly we should say the expected value of  $R_n$  is  $R_p$ , since this is a statistical result that is only true on average). Thus,  $i_{\text{corr}}$  can be estimated as  $B/R_n$ , where  $B$  is the Stern–Geary coefficient.

The simplest theoretical analysis of the expected amplitude of the potential and current noise is based on the premise that the electrochemical process consists of a series of events that are characterized by a pulse of charge. At the lowest level, this pulse might be two electrons produced by the oxidation of one iron atom to  $\text{Fe}^{2+}$  or four electrons consumed by the reduction of one molecule of oxygen. (Note that corrosion texts often state that the anodic and cathodic processes associated with corrosion are tightly coupled, such that every oxygen molecule reduced requires two iron atoms to be dissolved. However, this is not strictly correct, and the coupling only occurs indirectly through the change in electrochemical potential that occurs as the double-layer capacitance is discharged. Thus the anodic and cathodic events are uncorrelated in the short term, and we can therefore treat them as independent noise sources.) Larger events would correspond to such processes as the anodic charge produced by the initiation, growth, and death of a metastable pit.

If we assume that individual events are uncorrelated (i.e., the occurrence of one event does not change the probability of a subsequent event occurring), we can use the shot noise analysis produced by Shottky<sup>24</sup> to describe noise production in thermionic valves. Individual events are treated as pulses of zero duration, but nonzero charge,  $q$ . Then if the mean current is  $I$ , the average number of events occurring each second is  $I/q$ . (Note that we use  $I$ ,  $I_n$ ,  $I_{\text{corr}}$ , etc. to indicate total current, rather than current density, because current noise is not expected to be proportional to specimen area, and therefore it is more meaningful to talk about the current for a given specimen area, rather than considering the current density.  $R_n$  on the other hand is expected to be inversely proportional to specimen area and it is therefore appropriate to normalize it to unit area (giving the unit of  $\Omega \text{ m}^2$ .) Analysis of the statistics of this process leads to the shot noise formula  $\overline{I_n^2} = 2qIb$ , where  $\overline{I_n^2}$  is the variance of the current noise signal and  $b$  the bandwidth of the measurement (the range of frequencies included in the measurement).

For a corroding electrode two processes must be occurring simultaneously (e.g., metal dissolution and oxygen reduction). In principle, we can estimate the noise due to each source and sum them to derive the total noise amplitude. However, it will commonly be the case that one of the processes produces significantly more noise than the other, in which case we only need to consider that process. Thus, for pitting corrosion driven by oxygen reduction, the pitting process is expected to produce much more noise than oxygen reduction under normal circumstances, and therefore, we can simply treat oxygen reduction as providing a constant current that brings the net current to zero. With this assumption, and assuming that we can apply the Stern–Geary equation to estimate  $I_{\text{corr}}$  from  $R_n$ , it can be shown<sup>19</sup> that we can estimate  $I_{\text{corr}}$ , the charge,  $q$ , in the transient events, and the frequency,  $f_n$  of those events:

$$\begin{aligned} I_{\text{corr}} &= \frac{B}{R_n} = \frac{B\sigma_I}{\sigma_E} \\ q &= \frac{\sigma_I\sigma_E}{Bb} \\ f_n &= \frac{I_{\text{corr}}}{q} = \frac{B^2b}{\sigma_E^2} \end{aligned}$$

where  $B$  is the Stern–Geary coefficient;  $\sigma_I$ , the standard deviation of current;  $\sigma_E$ , standard deviation of potential, and  $b$  is the bandwidth of measurement.

Note that these equations assume that only low frequencies are included in the calculation of standard deviation, and it is arguably better to use an estimate of the power spectral density (PSD) at a low frequency:

$$\begin{aligned} I_{\text{corr}} &= \frac{B}{R_n} = B\sqrt{\frac{\Psi_I}{\Psi_E}} \\ q &= \frac{\sqrt{\Psi_I\Psi_E}}{B} \\ f_n &= \frac{I_{\text{corr}}}{q} = \frac{B^2}{\Psi_E} \end{aligned}$$

where  $\Psi_I$  is the PSD of current and  $\Psi_E$  is the PSD of potential.

### 2.30.5.9.2 Measurement

Electrochemical noise is almost invariably measured as digitized time records. Thus, the measurement process consists of a number of steps, illustrated in [Figure 20](#). Potential noise typically has a low amplitude, and it is therefore common to amplify it – this is done as the first step in order to minimize the effects of other processes on the instrument noise. If the potential is measured with respect to a reference

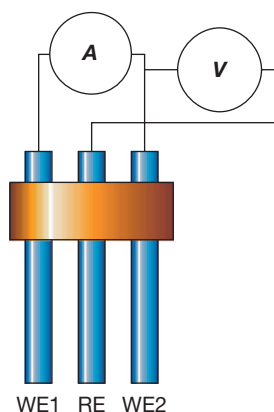


**Figure 20** Three electrode EN measurement configuration.

electrode, it will typically have a relatively large dc value, and the voltage amplifier may also incorporate a dc offset to allow a larger gain to be used without exceeding the output voltage range of the amplifier.

Current noise is normally converted to a voltage signal using a current amplifier. It is not usually necessary to provide for a current offset as the current noise normally has an expected mean of zero.

Following amplification, the voltage and current noise signal should be filtered to remove unwanted frequency components (although the amplifier and filter circuits may be combined in a practical instrument). In particular, a low-pass antialiasing filter should be included to remove frequency components that could give rise to aliasing in the sampling process. A high-pass filter may also be incorporated to remove the dc level (as an alternative to the use of a fixed dc offset), although it is difficult to produce good analog filters with a very low frequency, and even good quality filters present ‘issues’ associated with the filter settling time when first switching on.

The continuous analog signal must then be sampled to convert it to a regular sequence of samples, and these sampled values must be converted from analog to digital values. These two processes may be combined if certain types of analog to digital convertor are used. Most electrochemical noise information is present at low frequencies (typically below about 10 Hz), and hence EN measurement systems do not have particularly stringent sampling rate requirements, and it is more important to have a high resolution. Most computer data acquisition systems are optimized for high-speed, relatively low-resolution sampling, and they are therefore unsuitable for EN measurements. Conventional digital

multimeters or electrometers usually provide more suitable measurement capabilities, and they may also provide some of the required signal conditioning (although for the best results separate signal conditioning systems are normally required).

Finally the sampled digital time series is either recorded for subsequent processing (this is typically done for research purposes) or processed online to produce summary parameters (typically used for corrosion monitoring).

The measurement of electrochemical noise requires care in order to avoid sources of noise other than true electrochemical noise. Some of the more likely sources of error are:

- **Instrument noise** – electrochemical noise often has a very low amplitude, and high-quality current and potential measuring systems are necessary in order to minimize the addition of electronic noise from the instrument. Instrument noise levels should be checked to ensure that the level of such noise is significantly below that of the measured signals. Instrument noise levels are influenced by the impedance of the system being measured, and a dummy cell with a similar impedance to that of the corroding system should be used in the calibration process (**Figure 21**, based on Ritter *et al.*<sup>25</sup>).
- **Quantization noise** – virtually all electrochemical noise analysis methods involve converting the analog noise signal to a sampled digital time record. If the resolution of the analog to digital convertor is inadequate, steps will be observed in the time record (**Figure 22**). These add a form of noise, known as quantization noise, to the data; providing the measured signal is changing sufficiently rapidly, the contribution of the quantization noise is to add white noise (noise with a constant PSD) to the signal. (If the signal is changing slowly compared with the quantization step size, the measured value may be constant for long periods, and in this case the effect of the quantization may be to reduce the apparent noise.)
- **Aliasing** – during the sampling process, signals with a frequency above half the sampling frequency are transformed into samples that appear to have a lower frequency (**Figure 23**). (Some digital-to-analog conversion methods reduce the sensitivity to aliasing by averaging the measured signal over the sample period. However, this does not completely prevent aliasing, and it is good practise to use antialiasing filters for all EN measurements.) It is important to use antialiasing filters to remove these frequencies

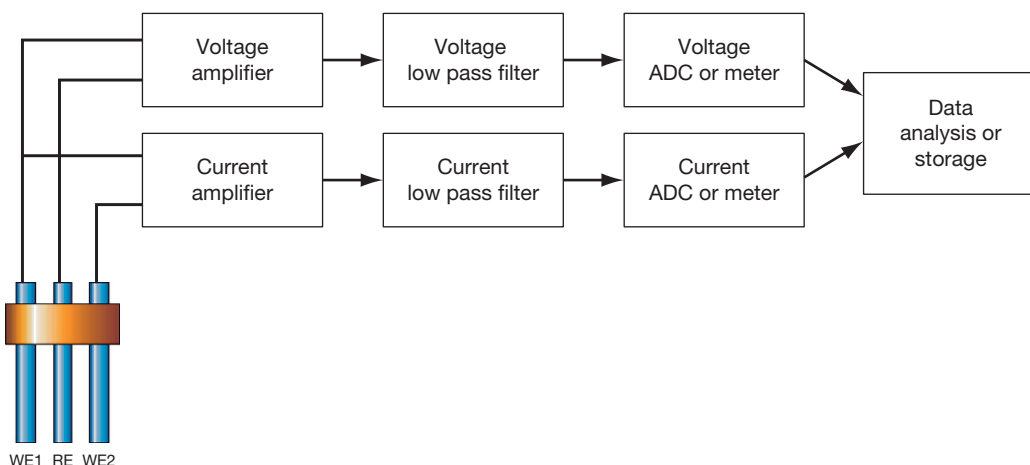


**Figure 21** EN Measurement System (ADC = Analog to Digital Converter) (from Cottis<sup>8</sup>).

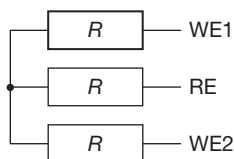


**Figure 22** Dummy cell for determination of instrument noise levels (from Schottky<sup>24</sup>).

before sampling occurs, as it is impossible to distinguish the resultant sampled data from real low-frequency signals. It should also be appreciated that aliasing does not just occur within electronic devices; it can also be created in software. Thus, if the sampling frequency of a signal is reduced by decimation (selecting every  $n$ th sample), this will also produce aliasing, and a low-pass software filter should be applied to the original data before decimation. (As software filters can be constructed to have essentially ideal properties, this can be a useful approach. Indeed there are arguments that the most effective approach to the development of instrumentation for EN is to sample at a fixed, relatively high frequency and then deliver data at the required rate by filtering and decimation. Besides avoiding expensive, low-frequency analog filters, this tends to reduce the amplitude of quantization noise (this process is known as oversampling in the electronics literature).)

- Interference – electromagnetic interference from a number of sources may be picked up and amplified by the EN measurement system. This leads to two main types of error: mains frequency (power-line) noise (50 or 60 Hz depending on location) and relatively rapid transients

(duration of the order of ms) due to inductive effects associated with the switching of high currents (the laboratory refrigerator is a common source of the latter). While both of these types of interference can be identified relatively easily, it may be more difficult to do this once the data have been sampled. Thus, mains frequency noise will typically be aliased to a much lower frequency, and transients will appear to be at least one sample period long. Thus, it is always best to prevent such interference from getting into the measurement system. This is normally achieved by careful shielding and earthing.

### 2.30.6 Electrode Design

Specimens for corrosion electrochemistry can take many forms, and much will depend on factors such as the form in which the material is available, the objective of the measurement, and the type of corrosion behavior that is expected. Typical electrode constructions are shown in [Figure 24](#).

Factors that should be taken into account in the design of the electrode include:

- Surface to be studied  
Different planes in an alloy tend to behave differently as a result of segregation occurring during casting and subsequent thermo-mechanical treatment. Consequently, it may be important to study a particular surface, in which case only planar electrodes, [Figures 25\(b\), 25\(d\), 25\(e\), and 25\(f\)](#), are suitable ([Figure 25\(a\)](#) is not suitable, as the edges of the specimen are necessarily exposed as well as



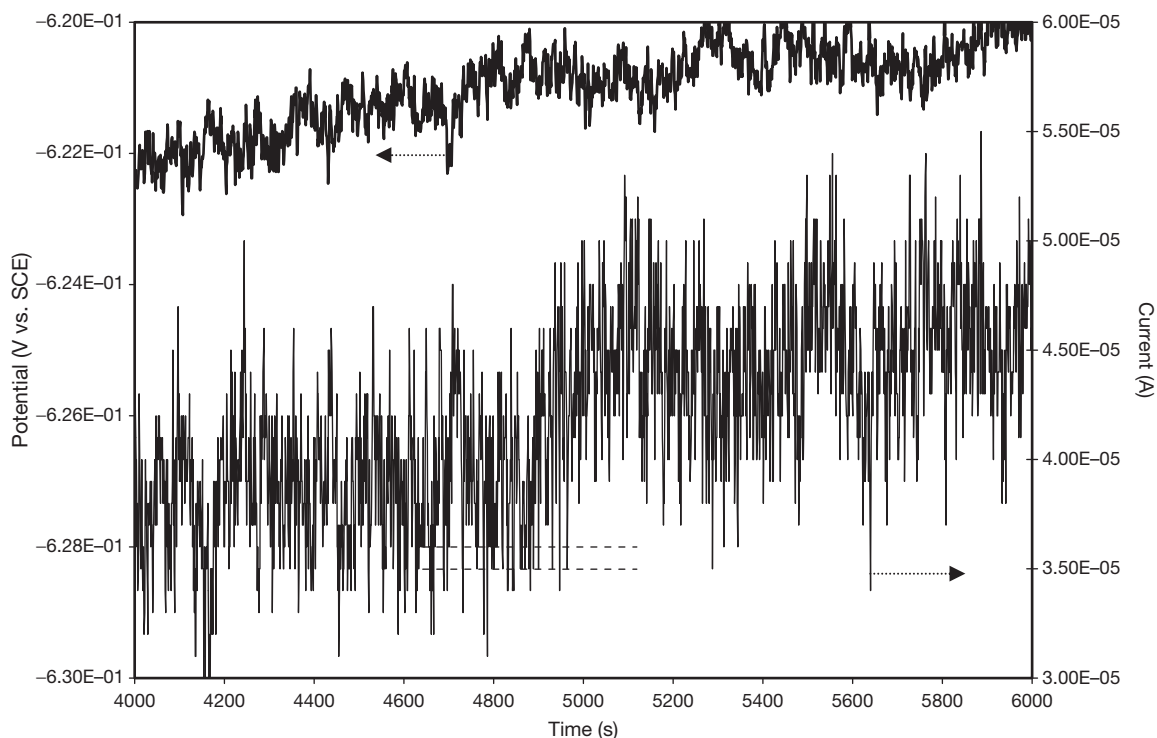


**Figure 23** EN time record showing quantization noise in the current signal (from Cottis<sup>8</sup>). The quantization can be seen as the 'banding' in the plot, illustrated by the two dotted lines superimposed on the plot at two adjacent quantization levels. This level of quantization is tolerable, and is not going to have a very large impact on the analysis.

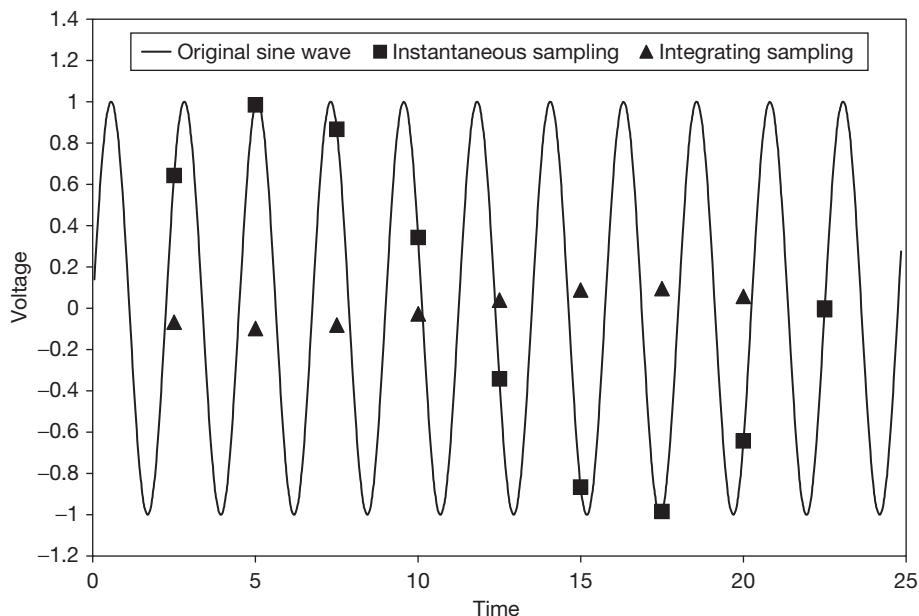


**Figure 24** Illustration of aliasing (from Cottis<sup>8</sup>). Integrating sampling is used by many voltmeters, and averages the voltage over the sample period; instantaneous sampling just takes value of the voltage at the sample time, and is much more seriously affected by aliasing.

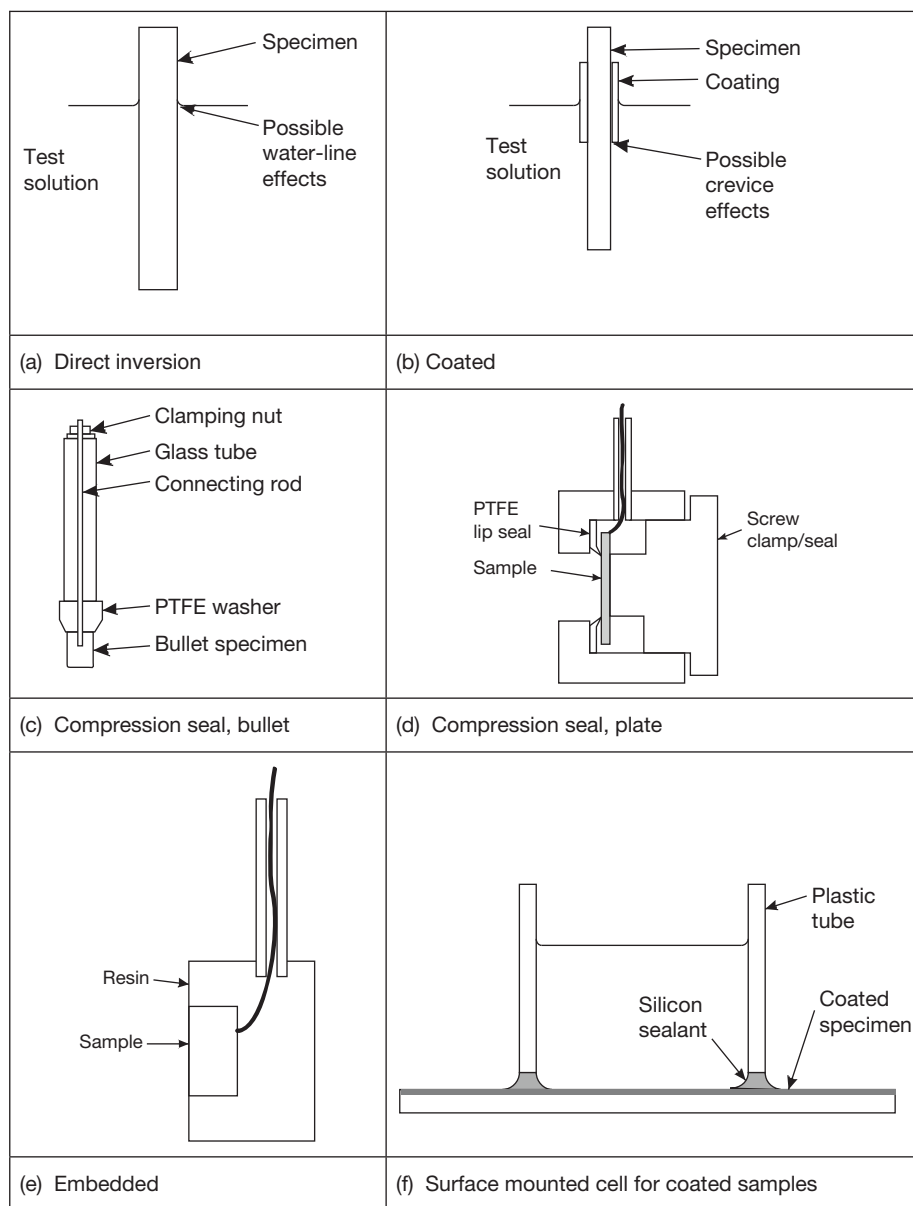


**Figure 25** Typical electrode designs for corrosion studies.

the surface of interest). Thought should also be given to the state of the surface (ground, polished, as received, etc.) as this can have a marked effect on the electrochemical behavior (the embedded electrode of [Figure 25\(e\)](#) is suitable for studying a specific plane, but not a preexisting surface, as the electrode preparation must include grinding and/or polishing of the embedded electrode to remove resin from the surface).

- **Susceptibility to crevice corrosion**

Passive alloys, including stainless steels, are susceptible to crevice corrosion. It is almost inevitable that electrode designs expose metal–insulator junctions to the test solution ([Figure 25\(a\)](#) is an exception, but it has its own problems associated with the waterline) and these are potential sites for crevice corrosion. Besides blatant damage to the specimen, this can lead to apparent passive current densities

that are much higher than the true values (Figure 26). A number of approaches have been used to minimize the risk of crevice corrosion:

1. The use of a PTFE-metal compression seal<sup>26</sup> can prevent crevice corrosion, but careful design and manufacture are necessary (PTFE-metal contacts have also been used as crevice-formers<sup>27</sup>).
2. Embedding a metal sample in epoxy or similar resin can lead to the formation of a crevice as the resin cracks away from the metal. The risk of this happening can be minimized by maximizing the adhesion of the resin to the metal by using an appropriate pretreatment (contact the resin manufacturer for advice), and by using a thin layer of resin (this minimizes the shrinkage stress between the resin and the metal; if a thick resin layer is required to facilitate surface preparation, this can be added as a second layer, when cracking will usually occur harmlessly between the two resin layers). Another
3. Some coatings are particularly liable to act as a crevice at the edge of the coating, while others, particularly those with a very good adhesion, may be less susceptible. Wax-based coatings may be useful, as the wax can usually be removed easily after the test.<sup>28</sup>
4. Crevice corrosion arises because of chemical changes (normally acidification) that occur in the crevice, and a method of avoiding crevice corrosion is to flush the crevice so that an aggressive solution cannot build up. (There are systems where the dominant factor involved in crevice corrosion is the potential drop down the crevice, but this is relatively unusual.) This is the basis of the Avesta Cell,<sup>29</sup> which uses a seal fabricated from filter paper that is flushed with distilled water.

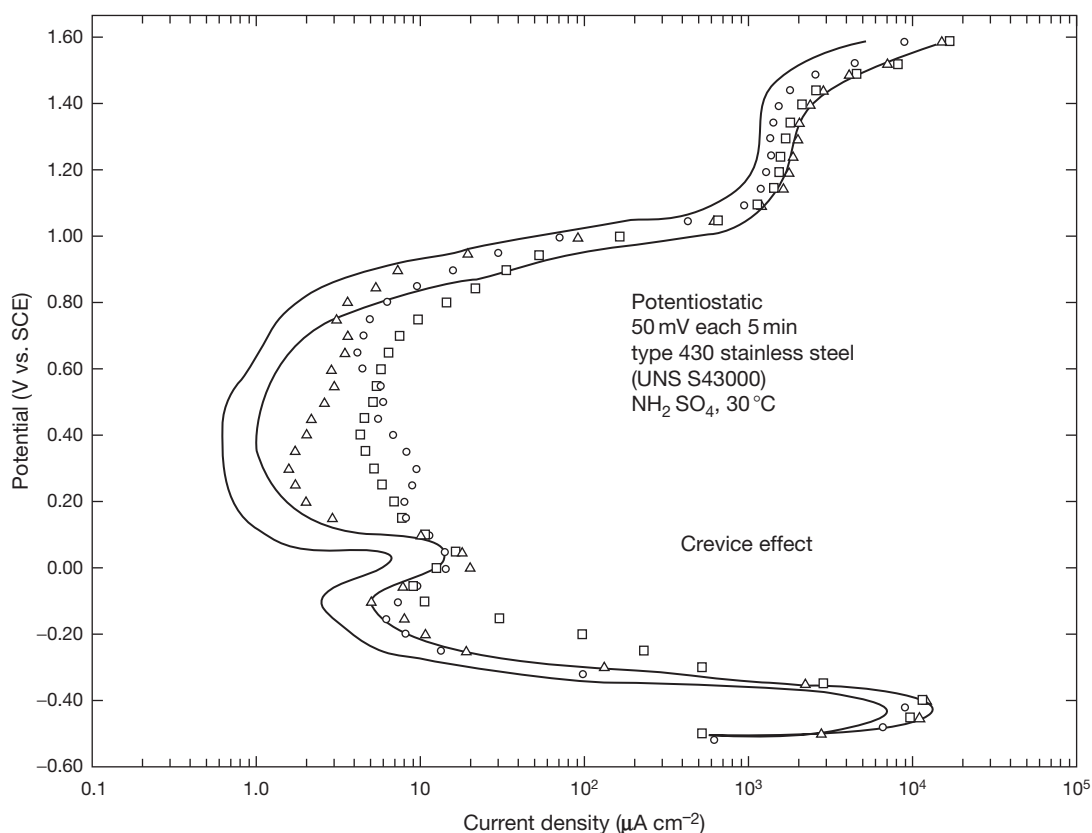


**Figure 26** Effect of crevice corrosion on passive current density, revealed by the increase in passive current density (markers) compared to the standard curve (solid lines) (from Tullmin *et al.*<sup>4</sup>).

### 2.30.7 Cell Design

The design of cells for electrochemical corrosion measurements should take a number of factors into account:

- **Current distribution**  
In most cases, one objective for an electrochemical measurement will be to make the measurement at a uniform current density and potential over the surface of the specimen. In general, this is facilitated by ensuring a uniform current path between the WE and the CE (e.g., using by a cylindrical WE at the center of a cylindrical CE or by using two parallel plates). It is often suggested that the CE should be large compared with the WE, but this is not necessarily beneficial from the point of view of the current distribution. In general, it becomes more difficult to achieve a uniform current distribution as the solution conductivity decreases, since the IR drop will have a larger relative influence on the current distribution.
- **Mass transport**  
Besides the distribution of current, it is also important to consider mass transport effects, particularly when applying relatively large overpotentials, as in the case of the measurement of a polarization curve. If well-characterized flow conditions are required, a variety of configurations is available (see the Chapter on **Flow Assisted Corrosion** for further information). Where mass transport is less critical, stirring of the solution may be sufficient. Gas bubbling serves both to stir the solution and to control the gas concentration in the solution. Note that of the range of controlled flow configurations that are available, only a few offer mass transport conditions that are the same across the electrode, the rotating cylinder electrode probably being the best from this perspective.
- **Influence of reaction products**  
Any electrochemical reaction will induce a change in the local chemistry, and it is generally desirable to minimize the influence of such changes on the measurement. The nature and significance of such changes will vary according to the system under study, concentrated solutions typically being less seriously affected than dilute solutions. The local concentration at the metal surface will be influenced by mass transport, while the bulk concentration will be influenced by the solution volume and the applied current. The reaction products at the counter electrode should also be considered, and

in critical cases, it may be necessary to separate the working electrode and the counter electrode compartments.

- **Control of gas composition of solution**  
Dissolved gases, notably oxygen, can be very important in corrosion reactions, and it is important to control the gas concentration of the solution. For aerated solutions this can be simply achieved by bubbling air through the solution. Deaeration is much more difficult, both because commercial gases typically contain traces of oxygen and because oxygen diffuses very rapidly (it even diffuses relatively rapidly through many polymers). Consequently, for rigorous deaeration, it is necessary to take great care to prevent oxygen access (e.g., by sealing the cell, bubbling the exhaust gas from the cell through water to restrict back diffusion, and possibly by purging the gas used to deaerate the solution by passing it through a suitable solution such as vanadous chloride). Any gases produced at the counter electrode must also be considered, as noted earlier.
- **Temperature**  
Chemical and electrochemical processes are generally rather sensitive to temperature (for typical activation energies corrosion rates double every 10 °C). Consequently for accurate measurements, the temperature should be controlled (or at least recorded). Temperature control is easier when the temperature is above ambient, and it is usual to perform tests somewhat above room temperature (e.g., at 30 °C). Tests at temperatures approaching boiling point become difficult, with respect to the maintenance of the solution composition (especially for dissolved gases) and because condensed moisture from the test can cause electrical leakage problems. For tests at above ambient pressure, it is necessary to use an autoclave, and electrochemical measurements become far more difficult and are beyond the scope of this article.

### 2.30.8 Reference Electrode

A range of reference electrodes is available (see [Table 3](#) and the Chapter **Electrochemistry**).

Note that the solution in the reference electrode plays an important part in controlling the potential of the electrode. Thus, a saturated calomel electrode must have saturated KCl as the solution in contact with the Hg/Hg<sub>2</sub>Cl<sub>2</sub> paste. This means that the SCE

**Table 3** Common reference electrodes

Common Name	Electrode	V vs NHE	Notes
Saturated* Calomel Electrode (SCE)	Hg/Hg <sub>2</sub> Cl <sub>2</sub> /sat. KCl	+0.241	Probably the most common electrode in the laboratory, but use of mercury presents safety hazards
Calomel	Hg/Hg <sub>2</sub> Cl <sub>2</sub> /1 M KCl	+0.280	Better temperature stability than SCE
Mercurous sulfate	Hg/Hg <sub>2</sub> SO <sub>4</sub> /sat. K <sub>2</sub> SO <sub>4</sub>	+0.640	Useful for avoiding Cl <sup>-</sup> contamination of test solution
	Hg/Hg <sub>2</sub> SO <sub>4</sub> /0.5M H <sub>2</sub> SO <sub>4</sub>	+0.680	
Mercurous oxide	Hg/HgO/1M NaOH	+0.098	Good for alkaline solutions
Silver chloride	Ag/AgCl/sat. KCl	+0.197	Very easy to make, but light sensitive, tending to replace SCE as most commonly used
Copper sulfate	Cu/sat. CuSO <sub>4</sub>	+0.316	Robust, commonly used for cathodic protection in soils (best avoided in chlorides because of precipitation of CuCl <sub>2</sub> )
Zinc/seawater	Zn/seawater	-0.8	Not a true reference electrode, but robust and quite stable

\*Note that the S in SCE stands for Saturated (not Standard) owing to the use of a saturated solution of KCl.

tends to leach chloride (and potassium of course, although this is usually less significant for corrosion) into the solution in contact with it. This leaching will contaminate the solution in contact with the reference electrode. Whether or not this leads to a serious problem depends on the test solution and the configuration of the reference electrode. In general, it is beneficial to use reference electrodes based on anions that are already present in the test solution. Thus, SCE is fine for seawater and other solutions containing high concentrations of chloride, but would be undesirable in chloride-free solutions.

It is a general objective of electrochemical measurements to measure the potential of the working electrode relative to the solution immediately adjacent to it. If there is no current applied to the working electrode, then this is not a problem, as there will not normally be significant currents in the test solution, and hence the potential will be essentially constant throughout the solution. However, when the working electrode is polarized, there will be potential drops in the solution (commonly called 'IR-drops') due to the interaction of the applied current and the resistance of the solution. There are several approaches to minimizing or correcting for the IR-drop:

- The reference electrode can be placed close to the surface of the working electrode. In practice this is usually undesirable due to the relatively large size of most reference electrodes (although micro electrodes are available) and the contamination of the working electrode by species leaching from the reference electrode. A way around both of these problems is the use of a Haber–Luggin probe (also

known as a Luggin probe), which is an electrically insulating tube with a fine tip that is placed close to the surface of the working electrode. The other end of the tube is connected to an electrode holder into which the reference electrode is inserted, and the tube and electrode holder are filled with the test solution. (A tube filled with solution is known as a 'salt bridge' and is essentially the ionic conduction equivalent of an insulated metal wire (although the resistance is, of course, much higher).) This provides a small probe that can be placed close to the surface of the working electrode (but not too close, about 3 tip diameters is generally recommended to avoid shielding part of the surface), and it also reduces the significance of leaching of the reference electrode solution into the test solution.

- The potential drop can be compensated for in one of a number of ways. The simplest method is to correct the measured potential based on an estimate of the solution resistance, but this may have undesirable consequences for some measurements, such as the measurement of polarization curves, where the effective sweep rate may be very different from that intended as a result of changes in the IR-drop during the measurement. Alternatively the estimated resistance can be used by the potentiostat to compensate for the IR drop. In essence, the applied current is passed through a resistor with the same value as the estimated solution resistance, and the resultant voltage is added to the control voltage. This is a form of positive feedback, and will result in instability in the potentiostat if the estimated resistance is too large; consequently, it is difficult to compensate completely



for the IR-drop. Another approach is to use the fact that the metal–solution potential tends to decay relatively slowly when the current is disconnected (due to the effect of the double-layer capacitance), whereas the IR-drop disappears essentially instantaneously. This leads to the current-interruption method, whereby the true potential is estimated when the current is briefly switched off.

### 2.30.9 Counter Electrode

In some cases, typically when working with micro-electrodes, or when the current is very small for some other reason, it is possible to use the reference electrode as the counter electrode. The use of a specific counter electrode can also be avoided by using two working electrodes, and this may be useful in the measurement of polarization resistance or electrochemical impedance (seen already). In all other cases where current is applied to the working electrode, a counter electrode is required as the second connection to the test solution.

In most cases, the counter electrode should not affect the measurement, and it should therefore have the following properties:

- It should have a relatively low polarization resistance so that the potential drop between the counter electrode and the solution does not limit the polarization that can be applied.
- It should not contaminate the solution. In practice, there will always be some electrochemical reaction at the counter electrode, and what we really need is for the products of that reaction to be harmless or easily removed. Inert electrodes, such as platinum or graphite are often used, in which case the reaction products are usually gases (oxygen or chlorine when anodic or hydrogen when cathodic) that can be removed by bubbling air or nitrogen past the counter electrode (although there may also be a pH change at the counter electrode). In closed systems (e.g., in autoclave studies), it is more difficult to dispose of gaseous reaction products, and it may be better to use a reactive electrode and trap the reaction products close to the counter electrode (e.g., by using an ion-exchange membrane between the counter electrode and the working electrode). It is also wise to check that supposedly inert electrodes are actually inert – some platinum dissolution can occur at high enough anodic current densities and graphite electrodes tend to release

traces of impurities into the solution as the graphite is oxidized to CO<sub>2</sub>. Note that many metals, including carbon steels and stainless steels, are essentially inert when cathodically polarized, and they can therefore be used as counter electrodes when only anodic polarization of the working electrode is required (e.g., when studying pitting breakdown potentials of stainless steel).

- It is often stated that the area of the counter electrode should be large compared with the working electrode, but this may be less important than ensuring that the overall cell configuration provides the required current density distribution. Thus, a counter electrode of the same size as the working electrode, mounted parallel to it, may optimize the current distribution without significant adverse effects from the size of the counter electrode.

## References

1. Kelly, R. G.; Scully, J. R.; Shoesmith, D. W.; Buchheit, R. G. *Electrochemical Techniques in Corrosion Science and Engineering*. Boca Raton FL: CRC Press, 2002.
2. Horowitz, P.; Hill, W. *The Art of Electronics*, 2nd edn. Cambridge: Cambridge University Press, 1989.
3. Steinberg, M. D.; Lowe, C. R. *Sens. Actuators B* **2004**, *97*, 284–289.
4. Tullmin, M. A. A.; Hansson, C. M.; Roberge, P. R. The Corrosion of Steel, and its Monitoring, in Concrete contribution to Intercorr/96, from [www.corrosionsource.com](http://www.corrosionsource.com) viewed on 22nd April 2009.
5. ASTM Standard G5: 1998.
6. Cottis, R. A.; Turgoose, S. In *Electrochemical and Optical Techniques for the Monitoring of Metallic Corrosion*; Ferreira, M. G. S., Melendres, C. A., Eds.; Dordrecht: Kluwer, 1991; pp 123–133.
7. Stern, M.; Geary, A. L. *J. Electrochem. Soc.* **1957**, *104*(1), 56–63.
8. Cottis, R. A. “Corrosion Monitoring – What’s the Point”, in “Corrosion Monitoring in Nuclear Systems”, ed. S. Ritter, European Federation of Corrosion, in press.
9. Turgoose, S.; Cottis, R. A. *Corrosion Testing Made Easy: Electrochemical Impedance and Noise*. NACE: Houston, 1999.
10. Orazem, M. E.; Tribollet, B. *Electrochemical Impedance Spectroscopy*, Wiley: New York, 2008.
11. Urquidí-Macdonald, M.; Real, S.; Macdonald, D. D. *Electrochim. Acta* **1990**, *35*(10), 1559–1566.
12. Van Gheem, E.; Pintelon, R.; Vereecken, J.; Schoukens, J.; Hubin, A.; Verboven, P.; Blajiev, O. *Electrochim. Acta* **2004**, *49*(26), 4753–4762.
13. Van Gheem, E.; Pintelon, R.; Hubin, A.; Schoukens, J.; Verboven, P.; Blajiev, O.; Vereecken, J. *Electrochim. Acta* **2006**, *51*(8–9), 1443–1452.
14. Orazem, M. E.; Tribollet, B. *Electrochim. Acta* **2008**, *53*(25), 7360–7366.
15. Dévay, J.; Mészáros, L. *Acta Chimica Academiae Scientiarum Hungaricae* **1979**, *100*(1–4), 183–202.
16. Mészáros, L.; Dévay, J. *Acta Chimica Academiae Scientiarum Hungaricae* **1980**, *104*(3), 311–316.

17. Mészáros, L.; Dévay, J. *Acta Chimica Academiae Scientiarum Hungaricae* **1980**, 105(1), 1–17.
18. Bosch, R. W.; Hubrecht, J.; Bogaerts, W. F.; Syrett, B. C. *Corrosion* **2001**, 57(1), 60–70.
19. Kelsall, G. H. In *Techniques in Electrochemistry, Corrosion and Metal Finishing*; Kuhn, A. T., Ed.; New York: Wiley, 1987; pp 75–94.
20. Cottis, R. A. *Corrosion* **2001**, 27(3), 265–285.
21. Iverson, W. P. *J. Electrochem. Soc.* **1968**, 115(6), 617–618.
22. Gabrielli, C.; Huet, F.; Keddam, M. *J. Appl. Electrochem.* **1985**, 15(4), 503–508.
23. Eden, D. A.; John, D. G.; Dawson, J. L. Corrosion Monitoring UK Patent 8611518 1986, US Patent 5139627 (filed 1987, granted 1992).
24. Schottky, W. *Ann. Phys.* **1918**, 57, 541–567.
25. Ritter, S.; Huet, F.; Cottis, R. A. Reliability of electrochemical noise measurements – part 2: First ECG-COMON guideline for an assessment of electrochemical noise measurement devices to be presented to Eurocorr 2009.
26. Stern, M.; Makrides, A. C. *J. Electrochem. Soc.* **1960**, 107, 782.
27. Carranza, R. M. In *Proc. MRS Fall Meeting*; Rebak, R. B., Hyatt, N. C., Pickett, D. A., Eds.; 2008, 1124; Paper 1124-Q09-01 2008.
28. Fonseca, C.; Barbosa, M. A. *Corrosion Sci.* **2001**, 43(3), 547–559.
29. Qvarfort, R. The Avesta Cell – a New Tool for Studying Pitting **1988**, acom, no. 2–3, pp 2–5.

## 2.31 Spectroscopies, Scattering and Diffraction Techniques

### H.-H. Strehblow

Institut für Physikalische Chemie und Elektrochemie, Heinrich-Heine-Universität Düsseldorf, Universitätsstr. 1, 40225 Düsseldorf, Germany

### D. Lützenkirchen-Hecht

Fachbereich C – Physik, Bergische Universität Wuppertal, Gauß-Str. 20, 42097 Wuppertal, Germany

© 2010 Elsevier B.V. All rights reserved.

2.31.1	Introduction	1375
2.31.2	Methods Working in the Vacuum and Sample Transfer	1376
2.31.3	X-ray Photoelectron Spectroscopy	1378
2.31.4	Ultraviolet Photoelectron Spectroscopy	1382
2.31.5	Auger Electron Spectroscopy	1384
2.31.6	Ion Spectrometry	1385
2.31.6.1	Ion Scattering Spectrometry or Low Energy Ion Scattering	1385
2.31.6.2	Rutherford Back Scattering	1386
2.31.6.3	SIMS and Related Methods	1387
2.31.7	Methods Using Hard X-rays: X-ray Diffraction (XRD), X-ray Reflectivity (XRR), and X-ray Absorption Spectroscopy (XAS)	1388
2.31.7.1	X-ray Diffraction	1390
2.31.7.2	X-ray Reflectivity	1393
2.31.7.3	X-ray Absorption Spectroscopy	1395
2.31.8	Glow Discharge Optical Emission Spectroscopy (GDOES)	1398
2.31.9	Infrared Spectroscopy	1402
2.31.9.1	Attenuated Total Reflection	1402
2.31.9.2	IR Reflection Absorption Spectroscopy	1403
2.31.10	Summary	1403
References		1404

### Abbreviations

**AES** Auger electron spectroscopy  
**ATR** Attenuated total reflection  
**EXAFS** Extended X-ray absorption fine structure  
**GDOES** Glow discharge optical emission spectroscopy  
**IR** Infrared  
**IRAS, IRRAS** IR reflection absorption spectroscopy  
**ISS** Ion scattering spectrometry  
**MALDI** Matrix assisted laser desorption  
**MEIS** Medium energy ion scattering  
**NEXAFS** Near edge X-ray absorption fine structure  
**RBS** Rutherford back scattering  
**SEM** Scanning electron microscopy  
**SIMS** Secondary ion mass spectrometry  
**TOF** Time of flight  
**UHV** Ultrahigh vacuum  
**UPS** UV-photoelectron spectroscopy  
**XANES** X-ray absorption near edge structure

**XAS** X-ray absorption spectroscopy  
**XPS** X-ray photoelectron spectroscopy  
**XRD** X-ray diffraction  
**XRR** X-ray reflectivity

### Symbols

**$a_i$**  Base vector of the elementary unit cell  
 **$b_i$**  Base vector of the reciprocal lattice  
 **$d$**  Lattice spacing, layer thickness  
 **$D$**  Particle size, atomic density  
 **$E_B$**  Binding energy  
 **$E_{kin}$**  Kinetic energy  
 **$E_P$**  Passivation potential  
 **$E_{Pass}$**  Pass energy  
 **$e\Phi_W$**  Work function  
 **$e\Phi_{Th}$**  Threshold energy  
 **$F_{hkl}$**  Structure factor  
 **$f_n$**  Atomic form factor  
 **$h$**  Planck's constant

$h\nu$	Photon energy
$I$	Intensity of radiation
$m$	Mass of projectile ions in ISS, MEIS, RBS
$M$	Mass of a target atom
$n$	Complex index of refraction
$Q$	Reciprocal lattice vector
$Q_z$	Transferred momentum
$R_n$	Lattice vector of atom $n$ in real space
$T$	Spectrometer transmission function
$\beta$	Imaginary part of the refractive index
$\delta$	Real part of the refractive index
$\Delta\theta$	Width of a diffraction peak
$\phi$	Incidence angle
$\phi_c$	Critical angle of total reflection
$\lambda$	Wavelength (X-ray, photon, photoelectron)
$\Lambda$	Photoelectron mean free path
$\mu$	Absorption coefficient
$\Theta$	Scattering angle in RBS, ISS, Bragg angle in a diffraction experiment
$\sigma$	Photoionization cross section
$\omega$	Angle of acceptance of an analyzer

### 2.31.1 Introduction

Corrosion is the attack of solid material by the environment, which could be liquid or gas phase. The pertinent reactions involve oxidation or reduction of the material's surface which yield products that are transferred, at least temporarily, into the surrounding phase, that is, species into the gas phase, species dissolved into the electrolyte, or deposits on the surface. Corrosion studies usually involve weight loss or weight gain measurements, electrochemical studies, and the analysis of the electrolyte and the solid surface with spectroscopic methods. Most of these investigations start with assumptions about a corrosion process and its chemistry. The analysis of the data may be very accurate and sensitive like in the case of electrochemical methods. However, the nature of the process itself often remains uncertain. Thermodynamic data provide a reasonable basis for assumptions of the processes occurring at the surface, which may be deduced from potential–pH diagrams, the so-called Pourbaix diagrams.<sup>1</sup> They give the first insight into the most likely chemical and electrochemical processes, but they are uncertain because they are based on pure equilibrium data and thus do not account for the kinetic characteristics of the system which may dominate the process. As a result, any study on the basis of electrochemical and other

physicochemical data requires the application of surface analytical methods to learn about the nature of the chemical processes which then may be used for their interpretation. Besides the knowledge of the chemical processes, one needs information on the structure of the surface and of surface compounds and their changes which may significantly influence surface reactions. Similar to the information on the surface and the surface compounds, one needs knowledge of the chemistry and the structure of soluble or gaseous corrosion products, which may be obtained by appropriate methods such as rotating ring disc studies or spectroscopic investigation of the electrolyte or the gas phase.

Spectroscopic methods, which are sensitive to the surface chemistry and structure, may be applied *ex situ* and/or *in situ*. Although *in situ* methods are often preferred because they allow one to follow the surface reaction in its natural environment, several *ex situ* methods give such rich and detailed chemical and structural information that they are widely used and well accepted for the interpretation of a corroding system. Of course, one has to be sure that the transfer of the specimen from its environment to the spectrometer does not introduce changes, which then are studied and lead to misinterpretation. The loss of contact with an aggressive atmosphere or an electrolyte solution, the loss of potential control after electrochemical treatment and sample transfer to a vacuum, which is necessary for several methods, should not introduce artifacts to the composition and structure of the specimen's surface. Experience to date indicates that there are methods and equipments that largely meet these requirements.

All spectroscopic methods involve excitation of the solid surface or the homogeneous medium in front (gas or liquid phase) which then induces a response from the system under study. Exciting radiation may consist of electrons, atoms, ions or electromagnetic radiation from the infrared (IR) to the hard X-ray range. Emission of electrons, ions, molecules, or electromagnetic radiation is the response. This chapter intends to give a brief summary of important spectroscopic methods which have been applied successfully to corrosion research and to the solution of practical corrosion problems. The principle, the strength, and the limits of these methods will be discussed and an example in each case will illustrate their application. **Table 1** presents a summary and a comparison of the various techniques. A more detailed description of surface analytical methods and their application to corrosion are discussed elsewhere.<sup>2,3</sup>

**Table 1** Characteristics of some surface analytical methods for corrosion in research and practice

<i>Method</i>	<i>Depth resolution</i>	<i>Lateral resolution</i>	<i>Information</i>
XPS (X-ray photoelectron spectroscopy)	2 nm	100 nm	Composition of surface and surface films, binding, and oxidation state, <i>ex situ</i>
UPS (UV photoelectron spectroscopy)	1 nm	>1 nm	Work function, threshold energies, band structure, and binding orbitals, <i>ex situ</i>
AES, SAES ([scanning] auger electron spectroscopy)	2 nm	20 nm	Composition of surface and surface films, and high lateral resolution, <i>ex situ</i>
ISS (ion scattering spectroscopy)	0.3 nm	20 nm	Composition of surface and surface films, modest lateral information, and high depth resolution (monolayer), <i>ex situ</i>
RBS (Rutherford back scattering)	5 nm	0.1 mm	Quantitative quasi-nondestructive depth profile, thick films, modest depth resolution, <i>ex situ</i>
SEM (scanning electron microscopy)	2 nm	1 nm	Surface topography with high lateral resolution, <i>ex situ</i>
EMA (electron microprobe analysis)	2 $\mu$ m	2 $\mu$ m	Composition of surfaces and surface layers, <i>ex situ</i>
SIMS (secondary ion mass spectroscopy), TOF SIMS	0.5 nm	20 nm	Composition of surfaces and surface layers, high sensitivity and mass resolution, isotopes, large molecules detection, <i>ex situ</i>
X-ray reflectivity	0.1 nm	>1 mm	Surface roughness, <i>in situ</i>
XRD (X-ray diffraction)	2–3 nm	100 nm	Atomic structure, (micro) crystalline materials (>3 nm), surface sensitive for grazing incidence, <i>in situ</i>
XAS (X-ray absorption spectroscopy)	2–3 nm	100 nm	Near range order also of amorphous structures by EXAFS, analysis of electrode surfaces and electrolyte films, chemical information by XANES, <i>in situ</i>
GDOES (glow discharge optical emission spectroscopy)	~1 nm	1 mm	Fast elemental analysis of surfaces and thin layer depth profiling, <i>ex situ</i>
IR (infrared spectroscopy), ATR (attenuated total reflection) IR spectroscopy, and IRAS or IRRAS (IR reflection absorption spectroscopy)	~0.5 nm	10 $\mu$ m	Chemical information via oscillation modes of adsorbates and thin layers, <i>in situ</i> by grazing incidence or total reflection from the rear side of thin vapor deposited films despite water absorption

### 2.31.2 Methods Working in the Vacuum and Sample Transfer

Many valuable spectroscopic methods function only in vacuum, for example, X-ray photoelectron spectroscopy (XPS), Auger electron spectroscopy (AES), secondary ion mass spectroscopy (SIMS), ion scattering spectroscopy (ISS) for low energy ions (1–5 keV) or high energy ions, and Rutherford backscattering (RBS). Indeed, typically, the evaluation of energy and mass of emitted electrons and ions requires ultra-high vacuum (UHV) conditions. There has been a strong debate on the usefulness of these methods, with their application in corrosion research being compared to experiments in surface physics. In physics, mostly single crystals were investigated, and the UHV equipment was not flexible enough for a rapid

specimen exchange. However, since the mid-1970s, when spectrometers were equipped with effective sample transfer systems, these methods have been applied very successfully to studies in surface chemistry, corrosion science, catalysis, and practical surface problems in industry. Any kind of surface, such as metals, semiconductors, insulators, and polymers may be studied as long as it is stable under vacuum conditions and does not contaminate the spectrometer. The wide application of these methods in various fields has shown that the achieved data are extremely useful, and one almost cannot avoid his or her use for the solution of many problems in research and industry. However, one has to keep in mind that they require sample transfer to UHV, and as a result, the specimen loses contact with a gaseous environment or the electrolyte and potential control during



sample transfer. Furthermore, exposure to the laboratory atmosphere may cause contamination of the surface and oxidation of surface compounds and corrosion products. In addition to this, the structure of the surface and surface layers may change due to dehydration and oxidation. These problems may be minimized or avoided in corrosion research by an electrochemical specimen preparation within a closed system and its transfer via a protecting inert gas atmosphere.

Several systems have been described in the literature with a shuttle taking specimens from the preparation stage to the UHV environment of the spectrometer, or a specimen preparation facility within a special vessel attached to the spectrometer and an appropriate transfer system to the analyzer chamber.<sup>4,5</sup> Figure 1 presents an example of the equipment that has been used successfully for corrosion research and the investigation of passive layers in the laboratory of the authors during the last 25 years. In addition to the three chambers of a commercial spectrometer, the analyzer chamber, preparation chamber, and the fast entry lock, an electrochemical preparation chamber is attached which contains a small electrochemical vessel of  $\sim 3\text{ cm}^3$  volume for electrochemical specimen preparation under well controlled conditions and under the protection of a purified argon atmosphere.<sup>4,5</sup> Water and the electrolyte are degassed by purified argon and are introduced from the containers to the electrochemical vessel, which is equipped with a counter electrode and the reference electrode. The specimen is contacted to the electrolyte surface using a hanging meniscus geometry. Pulse programs given to the

potentiostat allow a specimen preparation at the potential of choice in the range of milliseconds or less up to hours. A typical specimen preparation starts with cleaning by argon ion sputtering within the preparation chamber. Then the sample is transferred to the electrochemical chamber and contacted to the electrolyte at sufficiently negative potentials so that one starts with an oxide free clean surface. The potential is then pulsed to a value of interest and then returned to a value where the sample is not expected to change further. Finally, it is washed with degassed water and transferred to the analyzer chamber for its surface analytical investigation. This system has been applied to many studies of corrosion and passivity. It is even suited for the study of the electrochemical double layer by XPS when the electrode can be removed from the electrolyte under water repelling (i.e., hydrophobic) conditions.<sup>4,7</sup> In this case, the surface is not washed by water after its preparation. For these studies, one may follow with XPS, both qualitatively and quantitatively, changes in the chemical composition of the double layer with the electrode potential and may also investigate the changes in the energy of XPS features with the potential, which is related to the position of the species within the double layer.<sup>8</sup> The system also contains an additional port on the fast entry lock to allow for introduction from a transfer vessel of samples which have been prepared within a glove box or in an *ex situ* experimental stage, enabling exposure to aggressive gases, such as HCl. Together with a shuttle, the spectrometer has been applied successfully for high temperature corrosion research in aggressive gas phases.<sup>9</sup>

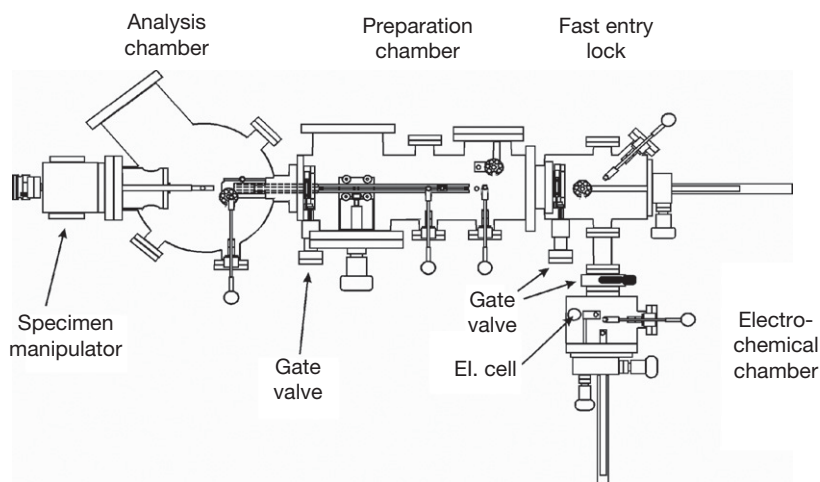


**Figure 1** Schematic representation of a commercial XPS Spectrometer with three vacuum chambers, and an attached electrochemical chamber with an electrochemical vessel. A rack and pinion drive system permits a fast and flexible specimen transfer.<sup>4-6</sup>

### 2.31.3 X-ray Photoelectron Spectroscopy

XPS is a widely used soft surface analytical method, which usually does not introduce changes due to the analysis itself. An XP-spectrometer consists of an X-ray source, an energy analyzer, and a detector. A monochromatic X-ray beam leaves the X-ray source, strikes the specimen surface, and ejects electrons. Typically, a twin anode X-ray source is used, providing either Mg  $K_{\alpha}$  ( $E = 1253.6 \text{ eV}$ ) or Al  $K_{\alpha}$  ( $E = 1486.6 \text{ eV}$ ) radiation. The kinetic energy of the photoelectrons is measured by an electrostatic energy analyzer. Modern spectrometers use a spherical or a spherical sector analyzer and an electrostatic lens focusing the electrons to its entrance slit (see [Figure 2](#)). The standard detector is a channeltron, an electron multiplier of special design with a potential drop of 3–4 keV across its surface. In most cases, an array of several channeltrons is used, or a channel plate with a two-dimensional arrangement of many small channeltrons on a plate to increase the sensitivity. The spectral data emerging from the channeltrons are sorted out with respect to their energy and added to each other appropriately with the help of the computer. The analyzer consists of a spherical

condenser supplied with a voltage which allows electrons with the appropriate pass energy to travel through it via its entrance and exit slits. It may be seen as a band pass filter which permits the transfer of only those electrons with the correct energy, the so-called pass energy  $E_{\text{pass}}$ . A linearly changing retardation voltage between the specimen, usually at ground, and the entrance slit is applied, so that all electrons have the chance to get successively through the analyzer when a spectrum is taken. Due to the specific energetic situation between the specimen and the analyzer, the energy balance of the photoelectrons follows [eqn \[1\]](#).

$$h\nu = E_B + E_{\text{kin}} + e\Phi_A \quad [1]$$

The energy  $h\nu$  of an absorbed X-ray photon is used to ionize an electron with binding energy  $E_B$  from an atom at the surface. For solid specimens,  $E_B$  is measured relative to the Fermi level  $E_F$ . Any excess  $h\nu$  energy, beyond that required for ejection, provides the electron with its kinetic energy  $E_{\text{kin}}$ , which is measured relative to the energy analyzer. [Figure 3\(a\)](#) illustrates the energy balance of the photoelectron of [eqn \[1\]](#). It contains the work function  $e\Phi_A$  of the analyzer, which is a constant of the spectrometer that is compensated internally after its calibration. With all

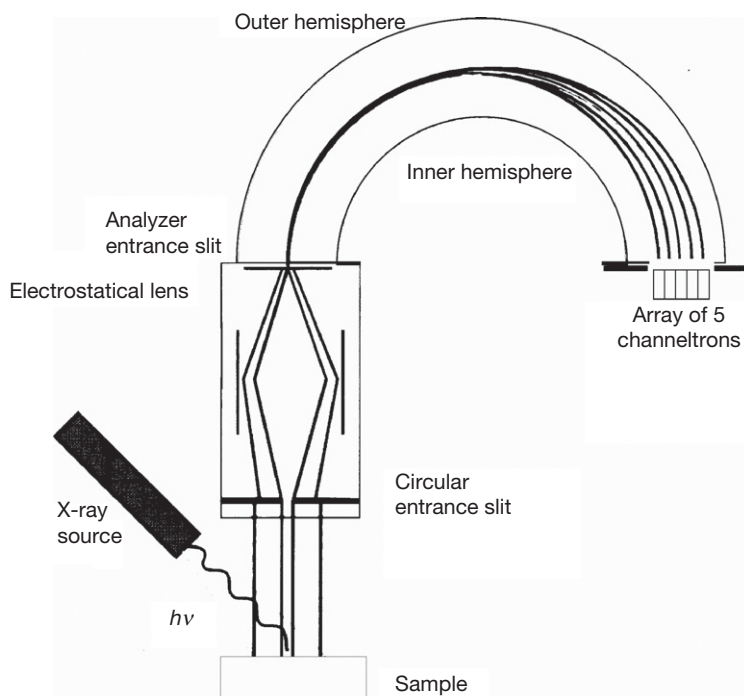


**Figure 2** Schematic diagram of an XPS spectrometer with an X-ray source, focusing electrostatic lens, spherical sector analyzer, and a channeltron array as detector.<sup>6</sup>

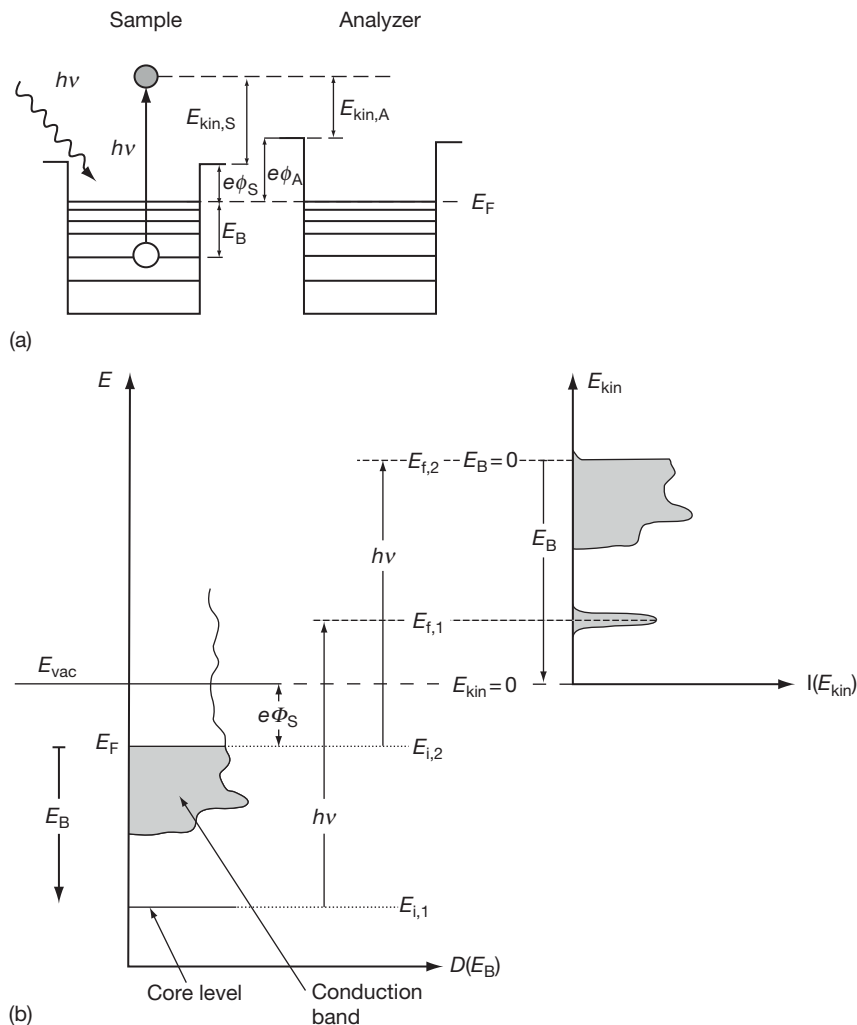


**Figure 3** (a) Energy diagram for XPS showing the potential wells of the specimen and the analyzer along with electronic levels, Fermi energy  $E_F$ , the related work functions  $e\phi_S$  and  $e\phi_A$ , contact potentials difference  $\phi_A - \phi_S$ , and the related kinetic energies  $E_{kin,S}$  and  $E_{kin,A}$ . A contact situation between analyzer and the specimen is shown with equal Fermi energies  $E_F$ .<sup>10</sup> (b) Mechanism of XPS with exciting X-rays of energy  $h\nu$  and electrons emitted from a core level (a) and from the conduction band (b) with initial energies  $E_i$  and final state energies of  $E_f$ . The resulting XP-spectrum is displayed, indicating the binding energy  $E_B$  and kinetic energy  $E_{kin}$  of the photoelectrons. For simplicity, the contact potential difference of the specimen and the analyzer as well as the retardation voltage are omitted.<sup>10</sup>

other quantities known,  $E_B$  is given by eqn [1]. Usually, a spectrometer is calibrated relative to the XPS-signals of well characterized standards mostly of pure metals such as  $E_B$  ( $\text{Au}4f_{7/2}$ ) = 84.00 eV,  $E_B$  ( $\text{Ag}3d_{5/3}$ ) = 368.26 eV,  $E_B$  ( $\text{Cu}2p_{3/2}$ ) = 932.67 eV.

In most cases, a spectrum contains several XP signals from each of the elements at the surface of a specimen due to their characteristic electronic levels, as indicated in Figure 3(b). It also contains X-ray induced Auger features, which arise through filling of the ejected photoelectron's core hole with an electron

from a higher energy level. As shown in Figure 4, the excess energy resulting from this transition may lead to the ejection of a third electron, the Auger electron. Another competing process is the emission of a photon, that is, X-ray fluorescence. Heavier elements ( $Z > 35$ ) have a high Auger yield so that their XPS spectra contain strong Auger lines.

The energy resolution of the XP-spectra is limited by the width of the excitation lines, which is  $\sim 0.8$  eV for Mg  $K_\alpha$  and 1.0 eV for Al  $K_\alpha$  radiation. The exact position of an XPS-signal contains a chemical shift

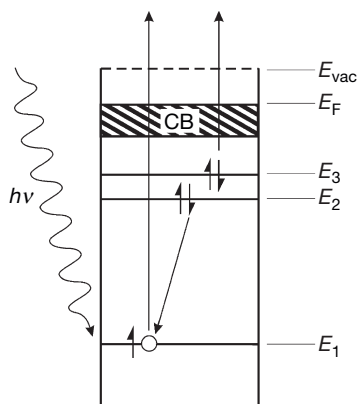


**Figure 4** Auger process with photoionization at level  $E_1$ , transfer of an electron from  $E_2$  to  $E_1$  and ejection of an Auger electron from level  $E_3$ .<sup>10</sup>

which has been found and interpreted first by Kai Siegbahn. An increasing charge on the atom causes a slightly higher ionization energy for any core level and thus a smaller kinetic energy or a higher binding energy  $E_B$ . As a result, one may measure energy shifts of the XP-signal, the so-called chemical shifts, which informs one about the charge of an ion or the oxidation number of an element. Electronegative binding partners similarly induce a more positive charge and thus a higher  $E_B$ . The chemical shift is often in the range of the width of the signals. The natural width of the exciting X-rays may be improved with an X-ray monochromator to  $\sim 0.5$  eV, *albeit* at the expense of intensity loss. Modern energy analyzers and sensitive detector arrays and channel plates will compensate for these losses. In many cases, one has to deconvolute a measured signal in order to separate it into the contributions of the different species. The integration of these contributing peaks yields a quantitative measure for the amount of the related species.

XPS analysis usually starts with a background subtraction, which is often achieved by a linearly increasing line or a correction according to Shirley,<sup>11</sup> that is, a curve with background contributions proportional to the preceding part of the signal. The background corrected signal is then synthesized with peaks of well characterized standards, which are usually described by Gauss–Lorentzians with appropriate parameters. The energy and shape of these peaks are usually kept constant with an adjustment of their height to get the best fit of the synthesized to the measured signal.<sup>10</sup> Usually, relative signal intensities are used (i.e., intensity ratios) in order to compensate for spectrometer characteristics such as sensitivity of the detector, the intensity of the X-ray

source, or the intensity/energy performance of the energy analyzer. The intensity ratio of two elements A and B is given by eqn [2]:

$$\frac{I_A}{I_B} = \frac{\sigma_A T_A \lambda_A D_A}{\sigma_B T_B \lambda_B D_B} \quad [2]$$

$D$  is the atomic density of components A and B. The photoionization cross-section  $\sigma$  takes care of the relative sensitivity of elements A and B to the photoionization process and is given by the data of Scofield.<sup>12</sup> The mean free path of the electrons  $\lambda$  within the specimen generally increases with kinetic energy and is given by the empirical relation of Seah and Dench<sup>13</sup> (eqn [3]).

$$\lambda = B\sqrt{E_{\text{kin}}} \quad [3]$$

Parameter  $B = 0.054 \text{ nm eV}^{-0.5}$  for elements,  $B = 0.097 \text{ nm eV}^{-0.5}$  for inorganic compounds, and  $B = 0.087 \text{ nm eV}^{-0.5}$  for organic compounds. The transmission function  $T$  depends on the specific design of the spectrometer and changes with the pass energy  $E_{\text{pass}}$  and the kinetic energy  $E_{\text{kin}}$  of the photoelectrons. Equation [4] gives the transmission function  $T$  for the VG ESCALB Mk2 analyzer as an example.

$$T = \omega^2 0.01 E_{\text{pass}}^{1.5} E_{\text{kin}}^{-0.5} \quad [4]$$

$\omega$  is the angle of acceptance of the analyzer for the electrons. In this case, the square root dependence of  $T$  and  $\lambda$  on  $E_{\text{kin}}$  cancel each other for eqn [2].

A frequent problem in corrosion is the examination of thin passive layers, that is, some few nanometers thick anodic oxide films on a metal substrate. The XPS intensity ratio of the cations and the metal atoms provides a possibility to calculate the oxide thickness. The parameters  $\sigma$ ,  $\lambda$ , and  $T$  in eqn [2] cancel, in this case due to the ratio of the same element. However the signal  $I_{\text{ox}}^{\text{Me}}$  from the cations of Me within the oxide are submitted to a self attenuation factor  $[1 - \exp(-d/\lambda_{\text{ox}}^{\text{Me}} \cos\theta)]$ , and the substrate signal  $I_{\text{Me}}^{\text{Me}}$  is attenuated by a factor  $\exp(-d/\lambda_{\text{ox}}^{\text{Me}} \cos\theta)$  due to the oxidic layer above. This attenuation is a consequence of inelastic energy losses of the photoelectrons on their way through the surface layers to the vacuum.  $d$  is the layer thickness, and  $\theta$  the angle between the direction of the detector and the surface normal of the specimen. The intensity ratio of eqn [5] indicates an increase with increasing angle  $\theta$ . This is simply due to increased masking of the electrons from the substrate, because their path through the thin oxide layer increases with  $\theta$ . Equation [6] permits the calculation of the thickness  $d$  of the passive layer.

$$\frac{I_{\text{ox}}^{\text{Me}}}{I_{\text{Me}}^{\text{Me}}} = \frac{D_{\text{ox}}^{\text{Me}}}{D_{\text{Me}}^{\text{Me}}} \cdot \frac{[1 - \exp(-d/\lambda_{\text{ox}}^{\text{Me}} \cos\theta)]}{[\exp(-d/\lambda_{\text{ox}}^{\text{Me}} \cos\theta)]} \quad [5]$$

$$d = \lambda_{\text{Me}}^{\text{ox}} \cos\theta \ln \left[ \frac{I_{\text{ox}}^{\text{Me}} D_{\text{Me}}^{\text{Me}}}{I_{\text{Me}}^{\text{Me}} D_{\text{ox}}^{\text{Me}}} + 1 \right] \quad [6]$$

In the case of an oxide layer on a metal substrate, such a calculation is quite trivial, but in a multilayered system, one must decide where the various cations and anions are located relative to each other. Angular resolved XPS measurements (ARXPS) can be used to decide the distribution of species perpendicular to the surface plane. As an example, Figure 5 presents ARXPS results from a passive layer on Fe formed at  $E = -0.16$  V in 1 M NaOH for various times in the range of 100 ms to 100 s. It is clear that a majority of Fe(III) ions are located above the Fe(II) ions, as suggested on the basis of thermodynamics.<sup>15</sup> One may further see that the passive film develops over this period of time. At 100 ms, almost no Fe(III) is present, and the bilayer structure is still not developed. With increasing time, the intensity ratio and the upward bending increase due to the growth of Fe(III) on top of Fe(II), and the Fe(II) to Fe(III) oxidation.

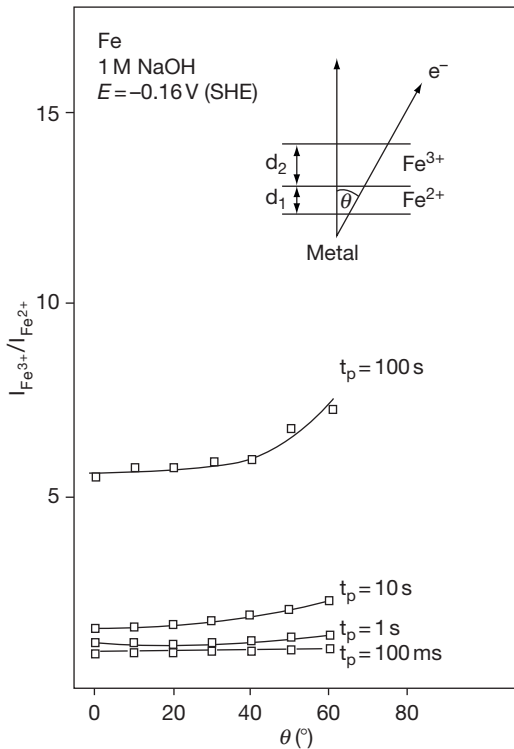


**Figure 5** ARXPS intensity ratio of Fe(III)/Fe(II) intensities for Fe passivated at  $E = -0.160$  V (SHE) in 1 M NaOH for different times  $t_p$  as indicated.<sup>6,14</sup>

At 100 s, the passive film has its final form and thickness. These data have been evaluated to obtain the thickness of the Fe(II) and Fe(III) layers for anodic oxidation at all potentials from the prepasive to the transpassive range as presented in Figure 6.<sup>14</sup> The film composition follows the characteristic peaks of the polarization curve of sputter cleaned iron in 1 M NaOH, which is also displayed in Figure 6. Film growth starts in this alkaline electrolyte at  $E_{P1} = -0.80$  V. Below  $E = -0.20$  V, the film contains a large fraction of Fe(II) which is oxidized at  $E_{P2} = -0.20$  V to Fe(III). At  $E > 0.20$  V, only a small residue of Fe(II) ions remain located below a growing Fe(III) film, which is at the detection limits of the method. These XPS results confirm the thermodynamic predictions of the composition of the passive layer.  $E_{P2}$  is the passivation potential of Fe in acidic

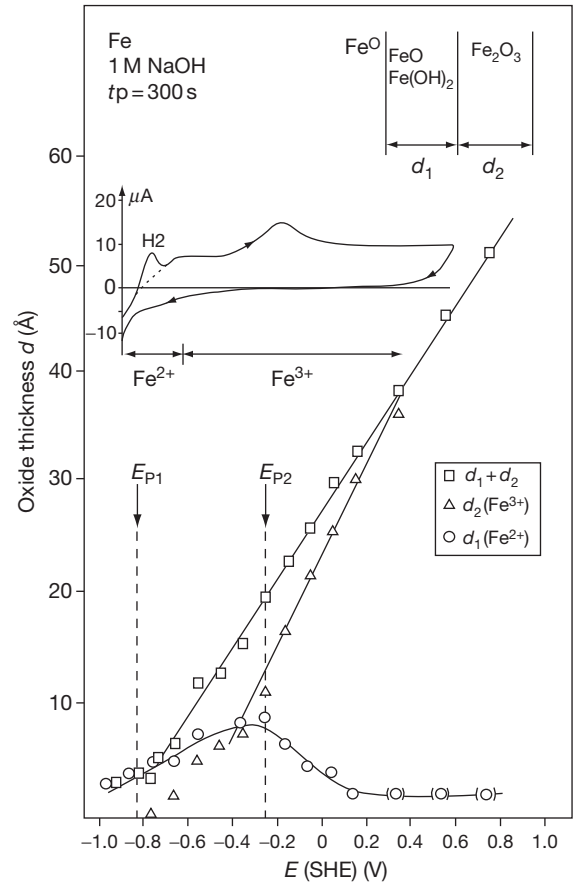


**Figure 6** Evaluation of XPS studies of Fe passivated in 1 M NaOH for 300 s on the basis of a bilayer model with Fe(II) and Fe(III) layer thicknesses of  $d_1$  and  $d_2$ , respectively. Polarization curve of sputter cleaned Fe within the spectrometer with indication of the passivation potentials  $E_{P1}$  and  $E_{P2}$ .<sup>6,14</sup>



solution, the so-called Flade potential extrapolated to pH = 13 with a  $-0.059 \text{ V/pH}$  dependence. It was interpreted as the  $\text{Fe}_3\text{O}_4$  to  $\text{Fe}_2\text{O}_3$  oxidation with thermodynamic data, which is confirmed by the XPS results.<sup>14,15</sup> In acidic electrolytes, the Fe(II) rich layer between  $E_{P1}$  and  $E_{P2}$  is not protective and dissolves immediately. However, it is protective in alkaline solution. These results may be obtained by the exclusion of air only, that is, by an investigation in the closed XPS system as described above. Fe(II) would be oxidized immediately to Fe(III) by traces of oxygen so that this species otherwise could not be found. Many passive layers have been examined in detail on pure metals and binary alloys as a function of the potential, time of passivation and electrolyte composition, in particular pH. A compilation of data and literature can be found elsewhere.<sup>6</sup> Figure 7 presents schematically the multilayered structure of passive layers on several different pure metals and binary alloys obtained by a detailed XPS analysis along with ion scattering measurements for completion. Higher valent species are found for sufficiently positive potentials only. Usually, hydroxides are outside and oxides inside. Higher valent cations are located in the outer part of the films.

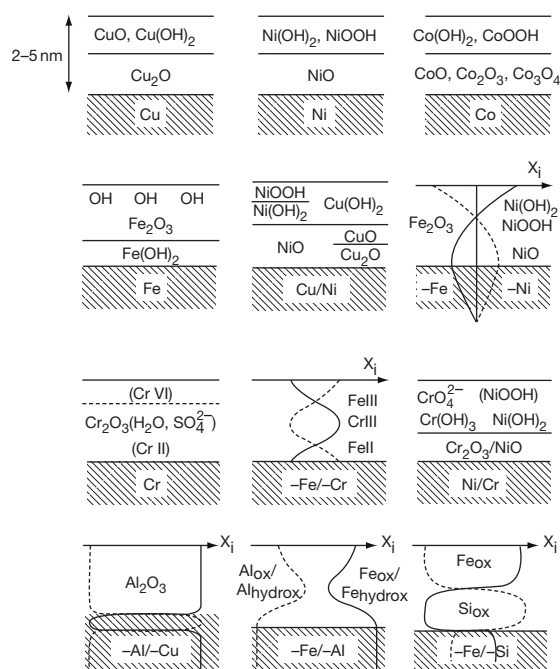


**Figure 7** Schematic diagram of passive layers on various metals and binary alloys deduced from XPS and ion scattering measurements demonstrating their multilayer character.<sup>6</sup>

The lateral resolution of XPS is usually poor and corresponds to the diameter of the exciting X-ray beam (several mm). The inlet slit to the analyzer may reduce the accepted surface area of the sample to some extent. Furthermore, the beam may be focused, especially together with a monochromator, with an ellipsoidal diffracting crystal down to several micrometers only. New instruments also contain an imaging option. This can be achieved by rastering a focused X-ray beam across the sample surface. Another design uses lenses at the entrance and exit of the analyzer to focus an image of the whole specimen or a major part of it onto a channel plate, which registers an image of the elemental distribution at the surface. Modern spectrometers allow a switching from a spectroscopic mode registering XPS to an imaging mode registering the elemental distribution of any element, which is chosen by its binding energy at the spectrometer control unit.

In addition to the basic research, XPS may also be used for a wide variety of industry problems. Besides the investigation of corrosion problems and corrosion layers, it may be used to study polymers, semiconductors, and insulators. One may investigate contaminations and surface problems in the production of any kind. Many laboratories of surface analysis help the industry and other institutes to provide a fast solution for their problems. A serious component of such activity is, ensuring that the specimen is obtained and prepared without the contamination of its surface in order to get results which are relevant to the technical situation.

## 2.31.4 Ultraviolet Photoelectron Spectroscopy

In ultraviolet photoelectron spectroscopy (UPS), a surface is irradiated with UV light, usually the He I (21.2 eV) or the He II line (40.8 eV), from a lamp attached to the analysis chamber of a spectrometer. The UV-light of the helium discharge is transmitted via a capillary to the specimen's surface, which permits a sufficiently high transmission without ruining the vacuum. As the excitation energy is low compared to the XPS, one only gets contributions to the photoelectron spectrum from low binding energy levels, including the valence band. Thus, UPS mirrors the broad distribution of states of the conduction band of a metal and the valence band of a semiconductor or insulator. Consequently, interpretation of the data can rather be more involved than

for XPS. One straightforward, but important, application of UPS is the determination of the work function  $e\Phi_W$  of a metal, or the threshold energy  $e\Phi_{Th}$  of a semiconductor or insulator ( $e\Phi_{Th}$  = difference between the upper valence band edge and the vacuum level). **Figures 8(a) and 9** show UP-spectra of Cu-metal without and with a thin passive layer of  $\text{Cu}_2\text{O}$ , respectively. One may see clearly the contribution of the surface oxide to the spectrum. **Figures 8(b) and 8(c)** show the potential wells of Cu metal and the analyzer with the related work functions similar to **Figure 3(a)**. Application of a negative bias to the specimen of  $\sim U = -5\text{ V}$  ensures that all photoelectrons reach the analyzer (**Figure 8(c)**). This bias negates a potential barrier which the electrons would otherwise have to overcome, as presented in **Figure 8(b)**, causing a drop off of the UV-spectrum at the low energy side close to  $E_{kin} = 0\text{ eV}$ . There exists

the obvious relationship, indicated in **eqn [7]**, between the work function  $e\Phi_W$ , the kinetic energy  $E_{kin}$ , and the width  $\Delta E$  of the spectrum. The cutoff edge in the biased spectra corresponds to photoelectrons with  $E_{kin} = 0\text{ eV}$ , which have been excited from deeper levels within the valence band, or which have lost their kinetic energy due to inelastic interactions. Similarly, **eqn [8]** allows one to deduce the threshold energy  $e\Phi_{Th}$  of a semiconductor or insulator. These equations and data have been used to determine  $e\Phi_W$  of Cu and  $e\Phi_{Th}$  of its anodic oxides and thus the absolute value of the Fermi energy of a bare Cu electrode immersed from the electrolyte at appropriate potentials and of the upper valence band edge of its anodic oxides.<sup>6</sup>

$$e\Phi_W = h\nu - \Delta E \quad [7]$$

$$e\Phi_{Th} = h\nu - \Delta E \quad [8]$$

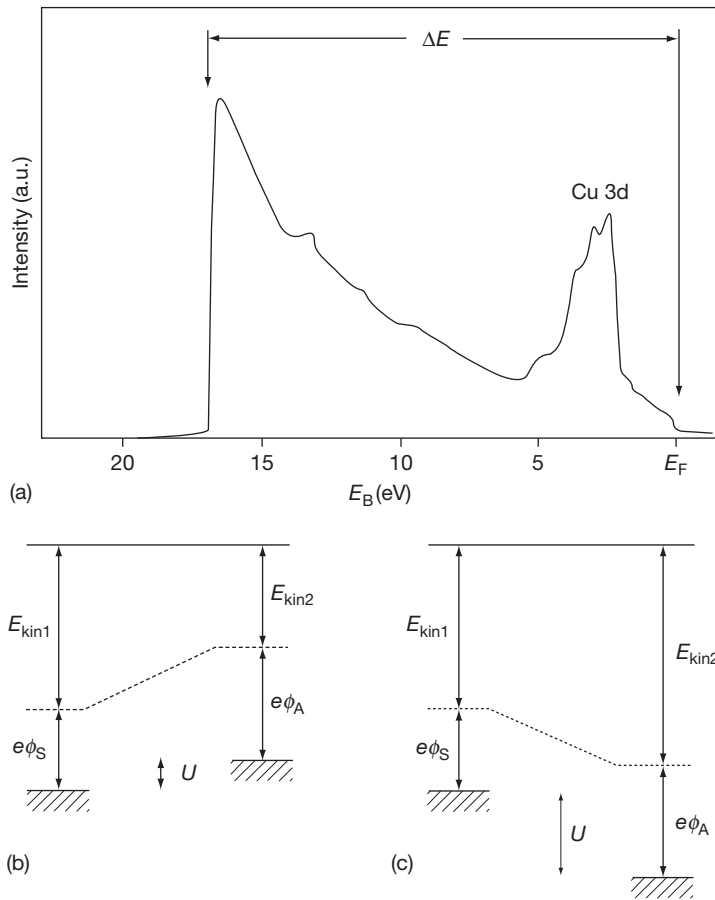


**Figure 8** (a) UP-spectrum of sputter cleaned copper with a width  $\Delta E$ . (b) and (c) Energy diagrams showing the work functions of the specimen  $e\phi_S$  and the analyzer  $e\phi_A$  and the related kinetic energies in direct contact, and with the application of a negative bias  $U$  to overcome the contact potential difference.<sup>10</sup>

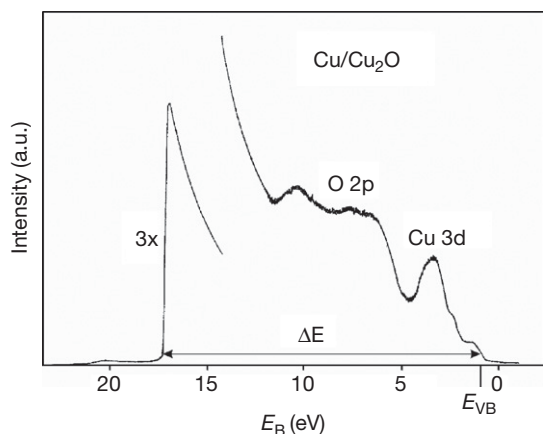


**Figure 9** UP-spectrum of an anodic  $\text{Cu}_2\text{O}$  layer on Cu showing the O bands and a step related to the valence band edge.

### 2.31.5 Auger Electron Spectroscopy

If an electron is emitted from its orbital, the remaining hole may be filled by a more energetic electron. The energy difference between the two electrons leads to characteristic X-ray fluorescence or to the ejection of a third electron, the Auger electron, as competing processes (Figure 3). Such emission may be initiated by X-rays or incoming electrons, corresponding to the X-ray and electron induced AES. In the XPS subsection, it has been mentioned briefly that Auger lines are present in XP-spectra. These Auger lines are sometimes relied upon for the determination of the chemical state, when the chemical shift of XP lines is so small that it cannot be resolved with XPS, as is the case for Cu metal and Cu(I) oxide. In Figure 10, the Cu LMM line acquired from a thin  $\text{Cu}_2\text{O}$  film on Cu has been deconvoluted with the aid of the Auger lines from appropriate Cu reference compounds. From these quantitative data for the two Cu species, the thickness of the  $\text{Cu}_2\text{O}$  layer has been determined in good agreement with electrochemical results.<sup>16</sup> However, the AES lines are usually more complicated due to the three electron process of AES which requires more effort for a reliable quantitative evaluation. Therefore, AES is used for a chemical analysis mainly if the chemical shift for XPS is too small to distinguish between the two species.

Electron induced AES is of greater importance for surface analysis. The beam from an electron source may be focused by a lens to a sufficiently small spot, so that one may get AE-spectra with very high lateral resolution of  $\sim 10$  nm. Modern high intensity electron

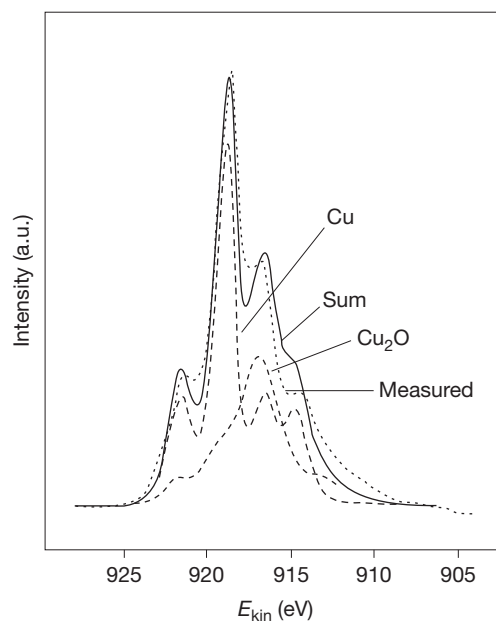


**Figure 10** X-ray induced LMM Auger signal of a Cu specimen passivated in 1 M NaOH with a  $\sim 2$  nm  $\text{Cu}_2\text{O}$  overlayer, and its separation into contributions from Cu and  $\text{Cu}_2\text{O}$ , respectively,<sup>10,16</sup> using reference compound data.

sources use thermoionic emission or field assisted emission of electrons as, for example, from  $\text{LaB}_6$  filaments or pin shaped Schottky emitters. Given these source characteristics, AES has been used for local spot analysis, line profiles, or even an elemental mapping, that is, imaging with respect to the elements of interest by scanning the beam. In corrosion, many localized effects are of decisive importance like inclusions and local attack at these sites, pitting and crevice corrosion, and grain boundary segregation and grain boundary attack. In all these cases, information on the distribution of metal components, impurities, and corrosion products is important to understand the leading mechanisms which require surface analysis with high lateral resolution.

Conventional electron induced AES yields the first derivative of the Auger lines. This is a consequence of modulation of the pass energy of the energy analyzer, usually by 5–10 mV together with the application of lock-in techniques. The obtained signal is therefore the first derivative of the Auger line with respect to the energy scale. The advantage is removal of a large and especially seriously changing background, which is the case for Auger signals of elements like Si at low kinetic energy. The disadvantage of differentiated signals is the loss of some

information. In modern spectrometers, the sensitivity is high enough to measure the nondifferentiated signal, which provides the advantages mentioned above.

Auger lines are named using the electronic levels involved in the process, for example, KLL. The first letter describes the orbital which is ionized by the impinging electrons or X-rays, the second is associated with the level from which an electron falls into the hole, and the third is the level from where the Auger electron is emitted. A KLL process starts with the ionization of a K shell, followed by a transfer of a L-electron to the core hole, and finally transfer of the energy difference to a third electron from the L-shell. The energy of the Auger electron is thus determined by the three involved energy levels. Due to spin-orbit coupling, the p- and d-electrons of the L and M shells are split into different levels, for example, L<sub>1</sub>–L<sub>3</sub> (s, 2p<sub>1/2</sub> and 2p<sub>3/2</sub>), leading to the nomenclature KL<sub>1</sub>L<sub>2,3</sub> for an Auger line. Thus, Auger lines are more complicated compared to XPS and therefore a quantitative evaluation including different oxidation states requires more effort. If electrons of the valence band are involved, their description contains V, for example, LVV for an electron ejected from the L shell with two additional electrons involved from the valence band.

## 2.31.6 Ion Spectrometry

The backscattering of noble gas ions has been developed into techniques for elemental analysis of surfaces and surface films. Two main approaches are described here: the backscattering of He- or Ne-ions with a primary energy of 1–5 keV (ISS, or low energy ion scattering (LEIS)) and the backscattering of He with a primary energy of 2 MeV (RBS). In addition, SIMS will also be discussed in this subsection.

### 2.31.6.1 Ion Scattering Spectrometry or Low Energy Ion Scattering

In ISS, only impinging ions, which are backscattered by the outermost atomic layer of a surface, have a small, but significant, probability of emerging charged. At the second or any deeper layer, essentially all noble gas ions pick up an electron and are scattered as neutral atoms. Given that only charged particles are detected, using an electrostatic energy analyzer as employed for XPS but with reversed polarity, ISS detects the composition of the outermost surface layer. A soft sputter process yields a depth profile of the surface region

with a monolayer resolution. The energy loss suffered by scattered ions of mass  $m$  is described by eqn [9a], where  $E$  is the ion energy after scattering, and  $E_0$  the primary energy. If the backscattering angle between the primary beam and the scattered ions is  $\Theta = 90^\circ$ , eqn [9a] simplifies to eqn [9b]. In this geometry, each target mass  $M$  will lead to an energy loss with a characteristic  $E/E_0$  ratio depending on the involved masses  $m$  and  $M$  only.

$$\frac{E}{E_0} = \frac{m^2}{(m+M)^2} \left\{ \left[ \cos\theta + \left( \frac{M^2}{m^2} - \sin^2\theta \right) \right]^{1/2} \right\}^2 \quad [9a]$$

$$\frac{E}{E_0} = \frac{M-m}{M+m} \quad [9b]$$

Thus, the energy spectrum of the backscattered ions leads to a peak for each target mass  $M$ . The integrated peak areas provide a measure of the amount of atoms within the surface. After calibration for the backscattering cross section, that is, the relative sensitivity of the elements, one may calculate quantitative results for surface concentrations. In combination with sputtering, one gets a quantitative depth profile. Figure 11 shows the depth profiles of Cr for a Fe15Cr

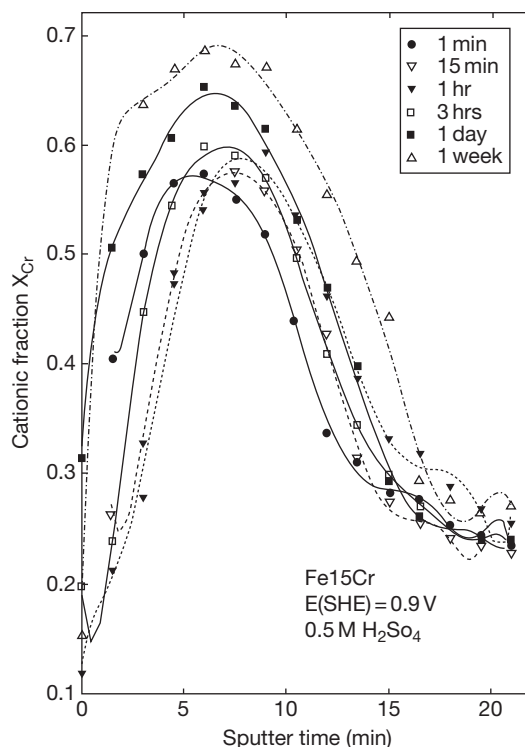


**Figure 11** Quantitative ISS depth profiles of Fe15Cr passivated at  $E = 0.90$  V in  $0.5$  M  $\text{H}_2\text{SO}_4$  for different times in the range of 1 min to 1 week.<sup>6</sup>

electrode passivated in 0.5 M  $\text{H}_2\text{SO}_4$  at  $E = 0.90$  V for different times in the range of 1 min to 1 week.<sup>6</sup> The profile demonstrates that the passive layer is significantly enriched in Cr. At the right side, it levels off to 15% Cr for the bulk metal alloy. The outermost surface is only slightly enriched in Cr. Apparently, the Cr content accumulates on the surface region during passivation. Also, the maximum gets slightly higher with time from 58% for 1 min to 70% Cr for 1 week. These results agree well with those obtained by XPS. In contrast to XPS, which provides chemical information, the advantage of ISS is the high depth resolution for this 2 nm film. Therefore, both methods are complementary to each other. The high enrichment of Cr(III) ions within the layer is a consequence of their extremely slow dissolution rate, 1–2 orders of magnitude smaller than Fe(III). This property in turn is the reason for the excellent stability of FeCr alloys and FeCrNi stainless steel in comparison to iron.

### 2.31.6.2 Rutherford Back Scattering

For RBS He ions are accelerated by a high voltage to 2 MeV, provided by a Van der Graaf generator. These high energy ions may penetrate materials to a

maximum depth of  $\sim 1 \mu\text{m}$ . They are backscattered at the nuclei of atoms at different depths and then get back to the surface where they are measured at a backscattering angle of  $\Theta = 175^\circ$  by a solid state detector. The ring shaped Si-detector contains a hole for the primary impinging beam. Two kinds of energy losses are obtained, the loss by the backscattering process which follows eqn [9], and the losses due to 'inelastic' processes of the ions on their way in and out. The latter depend on the kinetic energy and may be taken from tables for the stopping cross sections. As a result, one obtains broad signals whose leading edge is characteristic of the mass of the target atoms and whose width corresponds to the depth. The height is proportional to the concentration of the atoms when corrected for the element's sensitivity. The intensity increases with the square of the atomic number. Figure 12 shows an example of RBS from an Al 1%Cu vapor deposited film, before and after anodization to 100 V in citrate buffer pH 6.0.<sup>6,17</sup> The leading edge of Cu is at high energy due to its larger mass well separated from the light metal Al. A step in the Al signal after anodization corresponds to the grown  $\text{Al}_2\text{O}_3$  anodic film with a smaller Al-concentration compared to the metal substrate. Its width is a measure of the oxide thickness.

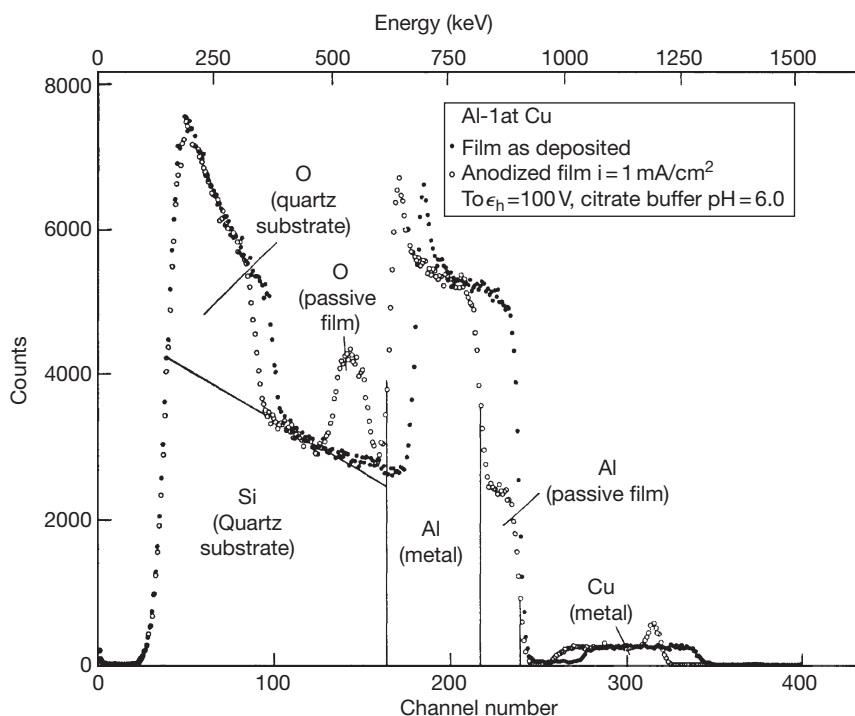


**Figure 12** RBS spectrum of vapor deposited Al 1 at. % Cu film on quartz substrate before and after passivation with  $i = 1 \text{ mA cm}^{-2}$  at 100 V in citrate buffer pH = 6.0.<sup>17</sup>



The oxygen signal of the anodic oxide is superimposed on the signal of Si from the quartz substrate for the vapor deposited metal film. The leading edge of the Cu signal shows a shift to smaller energies, due to the formation of the anodic oxide which is Cu free. A superimposed small peak close to its leading edge corresponds to Cu accumulation at the metal surface underneath the oxide. In the case of anodization of these Al/Cu films Cu accumulation at the metal surface finally causes a film breakthrough and a destruction of the vapor deposited metal film. This example demonstrates that one obtains nondestructive depth profiles of corroding surfaces by RBS which explain the details of elemental distribution and their changes during the reactions.

### 2.31.6.3 SIMS and Related Methods

If an ion beam strikes a surface, the energy of the impact is transmitted to atoms and molecules of the specimen, which causes their transfer to the vacuum. These ions may be submitted to mass analysis for their identification. For the mass separation, quadrupole mass analyzers may be used instead of magnetic sector analyzers. Another possibility is time-of-flight mass spectrometers (TOF-SIMS). In this case, a pulsed ion beam creates bunches of secondary species, which are accelerated to a fixed kinetic energy. Given  $E_{\text{kin}} = 1/2mv^2$ , lighter ions travel faster, and so arrive at the detector quicker than the heavier ones. These ions are detected by a channeltron or a channel plate. Mass spectrometry is very sensitive, so traces of species may be detected. Furthermore, the method may distinguish between the various isotopes of one element and may also separate species with only slight mass changes, less than one unit due to the mass defect. It is also one of the few methods which may detect hydrogen which is not seen by methods such as XPS or AES. A frequent application is the determination of dopants in semiconductors and their depth profiles which may be measured by ion sputtering and SIMS. The method is also important for electrode kinetics and corrosion research. As isotopes may be separated by the method, one may study the incorporation of oxygen during anodic film growth on an already preexisting layer by SIMS depth profiling. The distribution of the  $\text{O}^{18}$ -isotope within anodic oxide grown in  $\text{O}^{18}$ -enriched water may help distinguish, where new oxide is formed at the metal surface or at the oxide-electrolyte interface. This enables the measurement of transfer rates of oxygen anions versus metal cations

within the preexisting anodic oxide film. It has been found that oxygen ions can migrate inward<sup>18</sup> while metal cations are moving outward. These results have been confirmed by the study of the movement of Xe-implants in oxide films by RBS during further oxide growth. High intensity ion sources like liquid metal ion sources with Cs and Ga permit a very small focus of the beam from 5  $\mu\text{m}$  to <20 nm. These ion guns facilitate the study of corrosion processes with high lateral resolution and allow imaging by SIMS showing the lateral distribution of elements with appropriate resolution.

SIMS may be used as a quantitative method. However, the SIMS signal depends strongly on the matrix, that is, the electronic conditions at the specimen's surface. A metal with a high concentration of electrons at the Fermi level causes a high probability of neutralization via tunnel processes for the ions immediately in front of the surface. Therefore, the SIMS signal of cations is very small for pure metal surfaces, whereas it gets much higher if the specimen is covered with a thin semiconducting or insulating oxide film, due to its band gap where no electrons are available. The SIMS signal may vary for the same concentration of species by orders of magnitude. However, it will be fixed if the interesting species is a dopant in a matrix which does not change during ion impact. This is the case for the analysis of dopant implants in semiconductors. One possibility to stabilize the SIMS efficiency is the inlet of small amounts of oxygen to the surface of the metal forming a thin layer of semiconducting oxide. Another is the ionization of the neutrals after their sputtering with an electron beam, or by the stabilized formation of secondary ion species by a glow discharge (GD).

An ion beam may also be used to remove large ionized molecules from a metal surface. These processes have been studied in detail by SIMS of large organic molecules deposited on Ag. In this case, one obtains the  $\text{M}^+$ , the  $[\text{M} + \text{H}]^+$  and the  $\text{AgM}^+$  signals, besides fractions of the molecule M. Apparently, the energy of the ion beam is distributed via a cascade to the site of the molecule, which then finally is responsible for its transfer to the vacuum. The chemical interaction of the molecules with the silver surface causes the  $\text{AgM}^+$  peak. A very similar mass spectrometry of organic molecules is matrix assisted laser desorption (MALDI). For this analytical method, the organic molecules are codeposited with a matrix molecule at a metal surface, mostly a derivative of benzoic acid. The matrix is vaporized by a pulsed laser beam which ionizes and transfers the embedded molecules together with the matrix to the vacuum.

After acceleration by a voltage in the range of 10–30 keV, the molecules are analyzed and detected by a TOF-mass spectrometer. Very large masses have been detected by MALDI-TOF up to  $10^6$  mass units. TOF mass spectrometry is an excellent tool to study organic films, inhibitors and polymers due to the high mass range of up to  $10^6$  atomic mass units which is accessible to this method.

### 2.31.7 Methods Using Hard X-rays: X-ray Diffraction (XRD), X-ray Reflectivity (XRR), and X-ray Absorption Spectroscopy (XAS)

In the laboratory, sealed X-ray tubes are the most widely used X-ray sources, which emit continuous Bremsstrahlung-radiation as well as characteristic X-ray emission lines. The X-rays are excited by an accelerated electron beam impinging on a metal target within a vacuum tube. Although the maximum electrical input power of such an X-ray tube is typically about several kilowatts, the resulting X-ray intensities which are measured on a sample surface are relatively weak, because typically, only fractions of a percent of this electric input power is transformed into X-ray radiation leaving the tube through X-ray windows (typically beryllium). This is a serious drawback for *in situ* investigations of electrodes and related corrosion processes, since the parasitic absorption by the electrolyte further reduces the intensity which is available for the experiments. Assuming, for example, a rotating anode X-ray tube which provides  $\sim 10^6$  monochromatic X-ray photons per second per square millimeter, a Bragg reflectivity of a real sample (such as a passive film on a metal substrate) of  $\sim 10^{-3}\%$  and a transmission of the electrochemical cell of  $\sim 10\%$ , we end up with a single photon per second only. In a practical diffraction experiment, thus, an extremely large accumulation time is required for each data point in order to achieve a useful signal to noise ratio even in the photon counting mode using sophisticated detector equipment. Nevertheless, some few *in situ* experiments with laboratory equipment have been reported in literature.

Much more intense X-ray beams are provided by synchrotron radiation (SR).<sup>19</sup> SR is generated when charged high energy particles (usually electrons or positrons with kinetic energies of  $\sim 2$ – $8$  GeV) are moving on a curved path which is induced by a magnetic structure. Compared to X-ray anodes, SR has a continuous emission spectrum ranging from the

IR to hard X-rays. It is well defined and can be calculated from the knowledge of the local curvature of the electron path and the energy of the stored electrons or positrons.<sup>19</sup> The quality of the emitted radiation is characterized by its brightness and brilliance. The latter parameter is defined by the number of photons which is emitted in one second from a source area of  $1 \text{ mm}^2$  into a cone defined by  $1 \text{ mrad}^2$  normalized to a spectral band width of  $0.1\%$ .<sup>19</sup> In Figure 13, the brilliance of some synchrotron sources is illustrated as a function of the photon energy. For comparison, the radiation emitted by a rotating anode with a point focus is  $\sim 10^{10}$  photons/( $\text{s mm}^2 \text{ mrad}^2 0.1\%$ ), which is at the lower end of the scale of Figure 13. In contrast to the discrete line spectrum which is provided by the emission lines of an X-ray anode, the SR storage ring emits over a large range of energy from the IR to hard X-rays. Thus, the energy (wavelength) for the experiments can be selected freely from this continuum and allows an optimization depending on the actual sample or problem

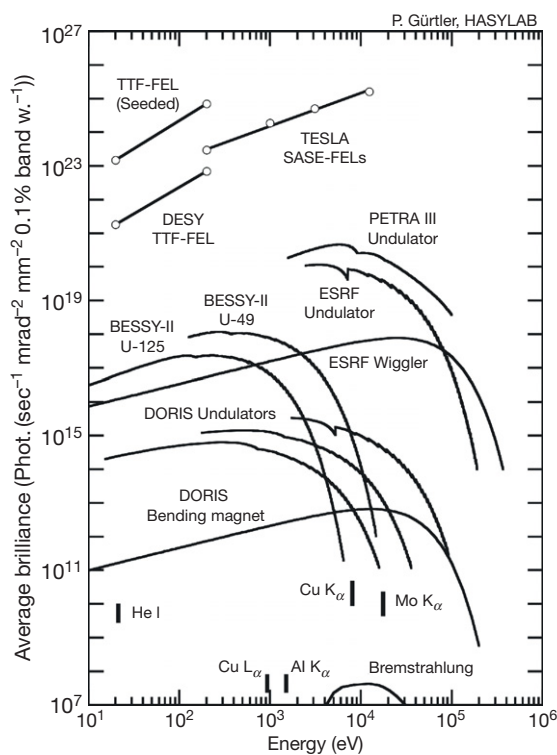


**Figure 13** Average brilliance for different radiation sources at HASYLAB (DESY, Germany), BESSY (Berlin, Germany) and the ESRF (Grenoble, France). For comparison, the brilliance expected for future sources (free electron lasers) is also depicted. Courtesy of P. Gürtler, HASYLAB.

under investigation. For the application of extended X-ray absorption spectroscopy (EXAFS, see below), the use of SR is mandatory, since the photon energy is scanned over  $\sim 1$  keV in these experiments. Here, even for a simple transmission mode experiment, the Bremsstrahlung-continuum of X-ray tubes is much too weak in intensity.

While second generation SR sources make use of the radiation emitted by bending magnets, sophisticated periodic magnet-structures (insertion devices, wigglers, and undulators) are installed at third generation synchrotron sources. The periodic field inside these devices forces the passing electrons and positrons on a sinusoidal path. Depending on the magnetic field strength, the magnetic gap and the number of antiparallel arranged magnets, the individual emission processes are without any phase relation (wiggler: strong field, small number of periods) or in phase (undulator: weak field, large number of undulator periods), improving the spectral brightness by at least two orders of magnitude compared to a bending magnet (see [Figure 13](#)). This means that SR is able to provide highly intense monochromatic radiation with extremely small lateral and horizontal divergence. These properties are an indispensable prerequisite for example, for surface X-ray scattering or diffraction experiments, especially in an electrochemical environment.

The charge carriers in a storage ring are generally accumulated in small bunches, the size of which is measured in terms of the time which is necessary to pass the focal point of the experiment. While the length of an individual bunch is of the order of several picoseconds, the distance between two bunches amounts to several nanoseconds. Therefore, SR enables time resolved experiments using this periodic bunch structure. Furthermore, due to the fact that the accelerated particles are kept in the orbit plane, the emitted synchrotron light is generally linearly polarized in this plane. This is important with regard to investigations of highly anisotropic systems such as adsorbates on single crystal surfaces. In addition, slightly below and above the orbit plane, SR-light is circularly polarized, which gives unique experimental opportunities for the investigation of magnetic materials and newly constructed insertion devices provide circularly polarized light with extremely high brilliance even in the orbit plane.

The increased availability of intense SR light sources, especially those of the new third generation, has its benefit for *in situ* investigations of corrosion processes, such as localized corrosion or passivation. *In situ* studies of electrode surfaces with X-rays

generally suffer from the parasitic absorption by the electrolyte. While this effect can be tolerated at high X-ray energies of  $\sim 15$  keV or more, the absorption of the electrolyte increases dramatically with decreasing photon energy. For example, for energies  $\sim 25$  keV, a 10 mm electrolyte (water) layer has an X-ray transmission of  $\sim 65\%$ , while at the energy of the Cu  $K_{\alpha}$ -emission line ( $\sim 8.0$  keV), the transmission of an electrolyte layer of only 3 mm decreases to  $\sim 12\%$ . While for X-ray scattering or diffraction experiments, this parasitic absorption by the electrolyte can be circumvented simply by using higher photon energies, it is a crucial drawback for XAS, since the electrode material with its characteristic absorption edges predefines the energy range which is necessary for the experiments. Depending on the scientific problem and the chosen experimental technique, different types of *in situ* cells have been applied, meeting both the experimental requirements for electrochemistry and the chosen analytical methods and techniques. A schematic representation of several different cell geometries is given in [Figure 14](#). Simple transmission type cells ([Figure 14\(a\)](#)) may be used for XRD and XRR experiments, and they are also suited to the study of corrosion products within the electrolyte.<sup>20</sup> A number of studies of pitting corrosion applied this geometry for the investigation of artificial pits also.

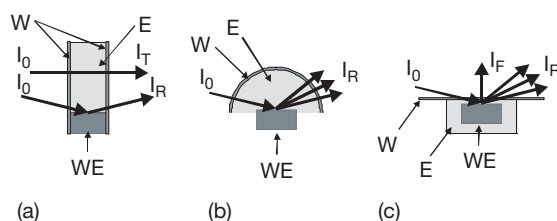


**Figure 14** Schematic representations of different electrochemical cells for *in situ* studies of corrosion processes. (a) Transmission type cells which may be used for investigations of the electrode using X-ray diffraction (XRD), reflection mode X-ray spectroscopy as well as for the characterization of the electrolyte in front of the electrode, for example, for the spectroscopic identification of corrosion products. (b) Cell geometry which is optimized for diffraction experiments. (c) Thin layer cell favorable for fluorescence spectroscopy or diffraction experiments of electrode surfaces. While the electrochemical preparation is performed with an inflated window allowing an unhindered mass transport from and to the electrode surface, the thin elastic window is pressed onto the surface of the electrode for the X-ray measurements with a thin electrolyte layer remaining in order to retain potential control. WE – working electrode, W – X-ray window, E – electrolyte.

A second type of cell is optimized for XRD experiments (**Figure 14(b)**).<sup>21</sup> It mainly consists of a cylindrical body with a sample holder and a hemispherical X-ray window of fused silica. Due to its symmetry, all solid angles in the hemisphere above the sample surface are accessible for the incident and reflected beam. Since the X-ray path length in the electrolyte and the window material are angle independent, this cell design is ideal for diffraction, surface diffraction as well as for XRR studies.<sup>21</sup>

A third type of electrochemical cells reduces the electrolyte to a thin film with a typical thickness well below 10–20  $\mu\text{m}$ , which is trapped between the sample (working electrode, WE) and an organic polymer film (polypropylene, Mylar, Kapton, etc.) of a few  $\mu\text{m}$  thickness.<sup>22</sup> Such a cell, presented schematically in **Figure 14(c)**, is well suited for fluorescence mode detection experiments and X-ray standing wave techniques<sup>22,23</sup> since the path length of the detected fluorescence photons is minimized and independent from the incidence angle  $\Theta$ . However, for surface sensitive studies, the grazing incidence geometry with glancing angles of typically below  $0.5^\circ$  is mandatory, so that the path length of the X-rays in the electrolyte and the window material increase dramatically causing an enhanced parasitic absorption of the impinging and also the emerging radiation accordingly. As a result, *in situ* studies of electrode surfaces are currently limited to X-ray energies of above  $\sim 6000$  eV, even if state of the art detector equipment such as multielement solid state detectors<sup>22,24</sup> and high flux insertion device beamlines at third generation storage rings are used. For investigations of dynamical processes consuming species from the solution or generating significant amounts of soluble reaction products, cells with a thin layer geometry cannot be used due to the strongly restrained mass transfer from and to the WE. In this case, cells without mass transfer limitations such as the transmission type cells (**Figure 14(a) and 14(b)**) have to be applied or the electrode has to reach a stationary state with low reaction rates prior to the measurement in order to avoid erroneous results or misinterpretation.

### 2.31.7.1 X-ray Diffraction

The XRD technique is based on the elastic scattering of X-rays from structures that have long range order as schematically shown in **Figure 15**. X-rays reflected at net planes parallel to the surface may lead to constructive interference (Bragg-peak) if the incidence angle  $\Theta$  (Bragg-angle) between the

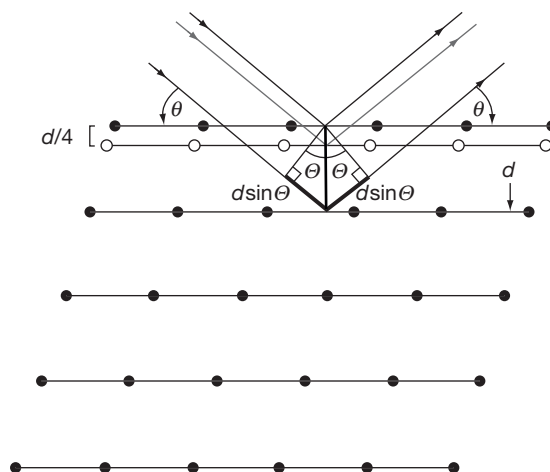


**Figure 15** Basic principle of XRD. For constructive interference, that is, the observation of a Bragg-peak, the path length difference between the interfering X-rays has to be an integer multiple of the X-ray wavelength  $\lambda$  as shown for the lattice planes with the black atoms. If a second net plane (white atoms) is inserted, the diffracted intensities are influenced accordingly. See text for more details.

impinging radiation and the lattice planes satisfies the relation

$$n\lambda = 2d\sin\Theta, \quad [10]$$

where  $\lambda$  is the X-ray wavelength, and  $d$  the lattice spacing of the sample under investigation. In general, not only the fundamental wave ( $n = 1$ ) but also higher harmonics ( $n > 1$ ) are observed in a diffraction experiment. The interpretation of eqn [10] is illustrated in **Figure 15**, that is, constructive interference only occurs, if the optical path difference between the X-rays which are diffracted from neighboring lattice planes is equal to an integer multiple of the X-ray wavelength  $\lambda$ . The resulting diffraction pattern is representative of the crystal structure because each crystal structure is characterized by the distribution of its lattice atoms in the unit cell. If, for example, a second lattice plane is present in between those considered as first (open dots in **Figure 15**), this inserted plane may alter the diffraction pattern significantly as follows. If the distance between the two planes is equal to a quarter of the original  $d$ -spacing, then the path difference for the inserted net-plane equals half of the wavelength for  $n = 2$ , that is, destructive interference occurs. This is the case, for example, for the (222)-reflections of Si and Ge. In general, this behavior is mathematically described by the so-called structure factors  $F_{hkl}$ , which include the positions of all the atoms in the crystal structure under investigation as well as their occupation by different types of atoms according to eqn [11].

$$F_{hkl} = \sum_n f_n \exp(2\pi i Q R_n) \quad [11]$$

$$R_n = n_1 a_1 + n_2 a_2 + n_3 a_3 \quad [12]$$

$$Q = b_1 b_1^* + b_2 b_2^* + b_3 b_3^* \quad [13]$$

Here  $R_n$  is the lattice vector of the  $n$ th atom (eqn. [12]), with  $a_1$ ,  $a_2$ , and  $a_3$  as the basis of the unit cell unit and  $n_1$ – $n_3$  are integer numbers.  $Q$  is the reciprocal lattice vector which corresponds to the scattering processes at the  $(hkl)$ -lattice planes (eqn [13]).<sup>25</sup> Again,  $b_1$ – $b_3$  are integer numbers, and the reciprocal lattice is connected to the real space representation by  $a_i b_j^* = 2\pi \delta_{ij}$  (for  $i = 1, 2, 3$ ,  $\delta_{ij} = 1$  for  $i = j$ ,  $\delta_{ij} = 0$  for  $i \neq j$ ).

If  $Q$  is given by the difference between the  $K$ -vector of the scattered X-rays and the impinging radiation, that is,  $Q = K_f - K_i$  as can be seen in Figure 16, where a schematic representation of different diffraction geometries is given, then we may expect a Bragg-peak for the corresponding angles. The summation in eqn [11] includes all the atoms in

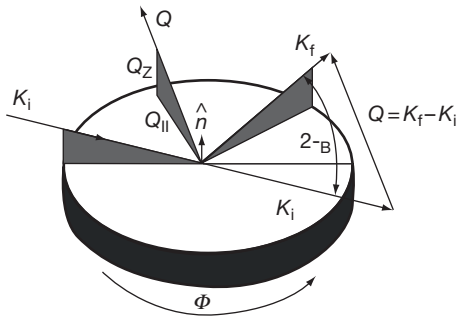


**Figure 16** Schematic presentation of the scattering geometry in an XRD experiment (Laue-case). A Bragg peak is observed if the difference between the wave vector of the Bragg-reflected beam  $K_f$  and the impinging radiation  $K_i$  is identical to a reciprocal lattice vector  $Q$ . The Bragg angle  $\theta_B$  is identical to the angle between the diffracted wave and the  $(hkl)$ -lattice plane, which is not necessarily parallel to the surface of the crystal under investigation. Three different types of scans are indicated. (a) Out-of-plane scan ( $Q_z$  or  $Q_{\perp}$ -scan): the rotation ( $\Phi$ ) of the crystal is fixed, and data are measured by varying the component of  $Q$  normal to the surface (which is named  $Q_z$  or  $Q_{\perp}$ ) while the component parallel to the surface ( $Q_{\parallel}$ ) is fixed. (b) In-plane radial scan ( $Q_{\parallel}$ -scan): the component of  $Q$  along the surface is varied. The direction of  $Q$  is kept, but its magnitude is varied by changing the incident and diffracted angles ( $\theta$  and  $2\theta$ ) symmetrically. (c) Phi-scan: the crystal rotates about its surface normal with the positions of the incident and diffracted beams fixed. The magnitude of  $Q$  is fixed for this scan while the direction of  $Q$  rotates.

the unit cell, and  $f_n$  is the atom form factor, which represents the scattering power of an individual atom. Basically,  $f_n$  is determined by the number and the distribution of the electrons belonging to a single atom.<sup>25</sup> Values for  $f_n$  are tabulated elsewhere.<sup>26</sup> The diffracted intensity then is given by eqn [14]

$$I \propto |F_{hkl}|^2 \quad [14]$$

and thus not only the positions of the diffraction peaks are representative of the crystal structure, but also their intensities, and characteristic diffraction patterns result for each individual crystal structure.

As an example from corrosion research, we present results determined from a diffraction experiment of passive layers on iron in borate buffer solution.<sup>27,28</sup> It should be mentioned here that a long and controversial discussion has been carried out and that contradicting results have been obtained.<sup>6,24</sup> Both amorphous as well as different crystalline structures have been proposed. Thus, an *in situ* diffraction experiment is very helpful for a structure determination. Due to the weak scattering intensities, focused SR as well as sophisticated detector equipment was used to obtain reliable data quality.<sup>27,28</sup> In Figure 17(a), the structure factors obtained for different diffraction peaks for the passive film on Fe(110) are compared to those of several different model compounds. Based on the measured symmetry, lattice constants and the detected Bragg-peak intensities, the passive layer data are most consistent with oxides of the spinel type (e.g.,  $\text{Fe}_3\text{O}_4$  and  $\gamma\text{-Fe}_2\text{O}_3$ ), while all other crystalline iron oxides, hydroxides or oxy-hydroxides are not compatible to the measured diffractograms. As can easily be seen, however, there are statistically significant deviations between the  $F_{hkl}$  of the measured data and those of the model compounds  $\text{Fe}_3\text{O}_4$  and  $\gamma\text{-Fe}_2\text{O}_3$ . Furthermore, linear combinations of the  $\text{Fe}_3\text{O}_4$  and  $\gamma\text{-Fe}_2\text{O}_3$  model compounds are not able to fit the experimental data sufficiently, and thus, a refinement of the structure was performed, yielding the structure presented in Figure 17(b), that is, the LAMM phase. Without going too much into the details, it should be mentioned here that the spinel unit cell which contains 32 oxygen anions, 16 octahedral, and eight tetrahedral cation sites is fully occupied in  $\text{Fe}_3\text{O}_4$ . For  $\gamma\text{-Fe}_2\text{O}_3$ , a quarter of the octahedral sites have only 33% occupancy, the remaining octahedral and tetrahedral sites being fully occupied. Both spinel reference compounds do not contain any interstitial ions. The authors found an octahedral site occupancy of  $(80 \pm 10)\%$  and a tetrahedral site occupancy of  $(66 \pm 10)\%$  for the passive film. While no evidence



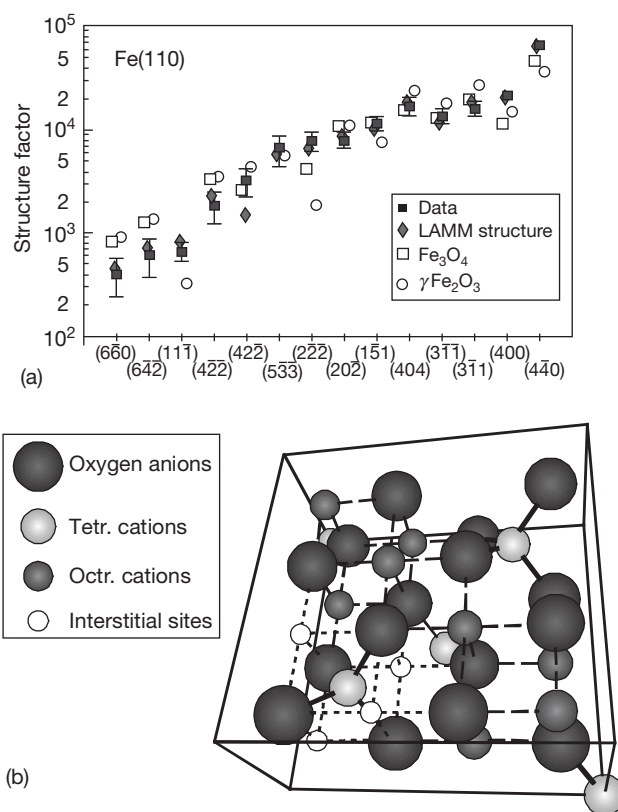


**Figure 17** (a) Comparison of the experimental structure factors (filled squares) with those of selected Fe-oxide model compounds for the passive layer on Fe(110): open squares for  $\text{Fe}_3\text{O}_4$ , open circles for  $\gamma\text{-Fe}_2\text{O}_3$ , and filled diamonds for the 'LAMM'-phase. Reproduced from Toney, M. F.; Davenport, A. J.; Oblonsky, L. J.; Ryan, M. P.; Vitus, C. M. *Phys. Rev. Lett.* **1997**, 79, 4282–4285. (b) Schematic illustration of the passive film structure (LAMM-structure). The solid black lines are the borders of the bottom half of the unit cell (big spheres: oxygen anions, fully occupied; smaller light grey spheres: tetrahedral cation sites, 66% occupancy; dark grey spheres: octahedral cation sites, 80% occupancy). Four of the eight octahedral interstitial sites are indicated by small white spheres, four additional sites are located in the upper right hand section which is not shown. Note that the interstitials are shown in well defined positions for clarity, while in the LAMM-structure used for the fitting of the diffractograms, they are distributed randomly in the structure. Bonds are also indicated for clarity: bold, dashed, and dotted lines for the tetrahedral, octahedral, and octahedral interstitial bonds, respectively. Adapted from Toney, M. F.; Davenport, A. J.; Oblonsky, L. J.; Ryan, M. P.; Vitus, C. M. *Phys. Rev. Lett.* **1997**, 79, 4282–4285.

for tetrahedral interstitials was found, there are cations occupying  $(12 \pm 4)\%$  of the available octahedral interstitial sites.<sup>27,28</sup> The large Debye–Waller factors (0.01 nm up to 0.028 nm) which are needed to fit the experimental data are the indication of the static disorder in the film, which results from the bond length variations induced by the interstitials and vacancies, and may explain why previous X-ray absorption spectroscopic investigations also found evidence for amorphous structures.

For real corroding systems, the interpretation of diffraction patterns in comparison to the data for passive layers on single crystal Fe-electrodes is even more complicated. A sample in practice consists of crystallites of different but eventually some preferential orientation, that is, a certain texture at the

surface. As a consequence, the Bragg reflexes of all other orientations are suppressed in their intensity compared to those expected from the calculated structure factors. Such a behavior is well known for example, for vapor deposited thin films. Furthermore, a diffraction pattern is also modified by the presence of defects in the crystal lattice. For example, stacking faults in the sample cause systematic shifts and a characteristic broadening of the diffraction peaks.<sup>29</sup> Some of the peaks remain stable in position and half width, while others systematically move toward larger or smaller Bragg angles in conjunction with broadening. Even peak splitting is observed for special defect structures. Stress and strain also cause systematic Bragg peak shifts.<sup>30</sup> Therefore, the detailed analysis of peak positions shifts, their widths, and

intensities can be used for the identification of existing defects, as shown elsewhere.<sup>27,31</sup> For example, in the case of the passive film on Ni single crystal electrodes in sulfuric acid, a tilt of the oxide structure with respect to the underlying Ni-metal was found.<sup>31</sup>

When finite size effects are included, the width of measured Bragg peaks are found to be inversely related to the dimension of the diffracting region of the crystal. Thus, line broadening provides information about the particle size  $D$  of small crystallites which may be calculated by the application of the Scherrer formula of eqn [15]:

$$D = \frac{K\lambda}{\Delta\theta \cos\theta} \quad [15]$$

where  $K$  is the Scherrer constant, which depends on the shape of the crystallites under investigation and in most cases is close to 0.9, and  $\Delta\theta$  is the line width at half maximum in radians after correction for instrumental broadening.<sup>30</sup> Although it is not trivial to separate the different contributions, information about the particle size distribution can be obtained from a more complete line shape Fourier-analysis.<sup>30</sup> In this regard, the use of SR may simplify the data interpretation. Compared to a laboratory experiment, the experimental line width is drastically reduced due to the extremely small divergence of SR-beams. In the case of the Fe passive layers presented above, the lateral crystallite size can be calculated to  $\sim 4.5$  nm for films on Fe(110), whereas for Fe(001), a slightly larger size of

$\sim 6$  nm was found.<sup>27,28</sup> Therefore the passive film is best described as a nanocrystalline material. In the case of passive films on Ni(111) in sulfuric acid, slightly larger crystallite sizes of  $\sim 8$ – $10$  nm were found.<sup>31</sup>

Even with the use of SR, XRD is limited to particles or domain sizes of at least 2–3 nm to yield a measurable diffraction pattern in the sense of the Bragg equation. Thus, particles or domains with smaller size will appear as X-ray amorphous in an XRD experiment and will not reveal any sharp Bragg reflexes. In conclusion, XRD is an excellent method for very detailed information on crystalline structures, although in practice, the interpretation of the measured diffraction patterns may be very complicated.

### 2.31.7.2 X-ray Reflectivity

Due to the large penetration depth of hard X-rays in matter, X-ray techniques are in general not surface sensitive; that is, they are not suited for the investigation of surface phenomena such as passive oxide film formation, adsorption, corrosion, etc. without any special precautions. However, the whole spectrum of X-ray analytical methods (e.g., XAS, XRD, X-ray fluorescence, X-ray topography) can be made surface sensitive using the grazing incidence geometry, which is schematically shown in the insert of Figure 18. The energy dependent index of refraction  $n(E)$  in the

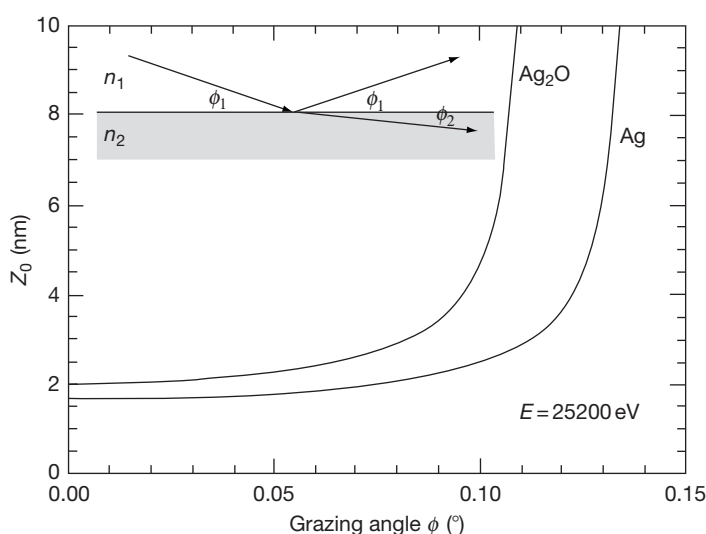


**Figure 18** X-ray penetration depth  $z_0$  for metallic silver and silver oxide  $\text{Ag}_2\text{O}$  at  $h\nu = 25\,200$  eV, as a function of incidence angle. The critical angle is  $\approx 0.13^\circ$  for Ag, and  $\approx 0.11^\circ$  for  $\text{Ag}_2\text{O}$ . In the insert, a schematic presentation of the grazing incidence geometry is given: the refracted beam is diffracted toward the surface.

hard X-ray regime is given by eqn [16],

$$n(E) = 1 - \delta(E) - i\beta(E) \quad [16]$$

where  $\beta$  and  $\delta$  are small positive quantities. Depending on the material and the photon energy, typical values for  $\beta$  and  $\delta$  range from  $\sim 10^{-4}$  to  $10^{-8}$ . The absorptive correction  $\beta$  is proportional to the linear absorption coefficient  $\mu$ , through  $\beta = \lambda\mu/4\pi$ . Therefore, condensed matter is optically thinner than vacuum, and X-rays entering into the samples surface are refracted away from the surface's normal, as indicated in the insert of Figure 18. The application of Snell's law of refraction, which has the same form as in the visible spectral range (eqn [17]),

$$n_1 \cos \phi_1 = n_2 \cos \phi_2 \quad [17]$$

suggests the existence of a glancing angle  $\phi_c$ , the critical angle, for which  $\phi_2 = 0$ . Assuming  $n_1 = 1$  for vacuum,  $\phi_c$  can be calculated from  $\cos \phi_c = n_2$ . If the absorption term  $\beta$  can be neglected, a simple calculus leads to  $\phi_c \approx (2\delta_2)^{1/2}$ . Typical values for  $\phi_c$  are  $0.39^\circ$  for Cu and  $0.22^\circ$  for Al for 8600 eV photon energy, so that total reflection can only be observed for grazing incidence angles below  $0.5^\circ$ .<sup>32</sup> In this case, there is no X-ray wave propagation inside the material, and the electric field amplitude within the sample is damped exponentially with depth. The decay constant, that is, the penetration depth  $z_0$ , amounts to only few nm below the critical angle. This relation is illustrated in Figure 18 for Ag and Ag<sub>2</sub>O, where a value of  $\sim 2$ – $3$  nm is obtained below the critical angle, while a steep increase is observed above  $\phi_c$ . This behavior generally leads to a steep decrease of the XRR for angles larger than the critical angle, and a detailed evaluation of such angle dependent specular reflectivities may yield the density and the surface roughness of the material.<sup>32</sup> In the case of a thin film on a substrate, the X-rays that have penetrated the surface layer will be reflected at the inner interface and interfere with those beams that have been reflected at the outer side, that is, the air–vacuum surface, leading to a systematic variation of the measured reflectivity profiles. Their detailed analysis yields to the thickness of the film and the roughness of the inner interface, in addition to the densities of the film and the substrate and the surface roughness.<sup>32</sup> Without going into great detail, it should be mentioned here that multilayered film structures can be treated and analyzed in a straightforward manner, so that specular reflectivity measurements are ideal tools for the *in situ* observation of electrochemical growth of oxide and passive layers and their reduction.<sup>33</sup> In Figure 19,

specular reflectivity profiles recorded in the course of several oxidation–reduction cycles of a thin film Cu electrode in borate buffer (pH 8.4) are shown for a photon energy of 7700 eV ( $\lambda = 0.148$  nm). The incidence angle scale was transferred to the transferred momentum ( $Q_z$ ) scale by  $Q_z = 4\pi/\lambda \sin \phi$  (see also Figure 16). As can be seen in Figure 19, the reflectivity profiles change considerably upon the oxidation and reduction of the Cu electrode. For example, the thickness oscillations are much more pronounced for the

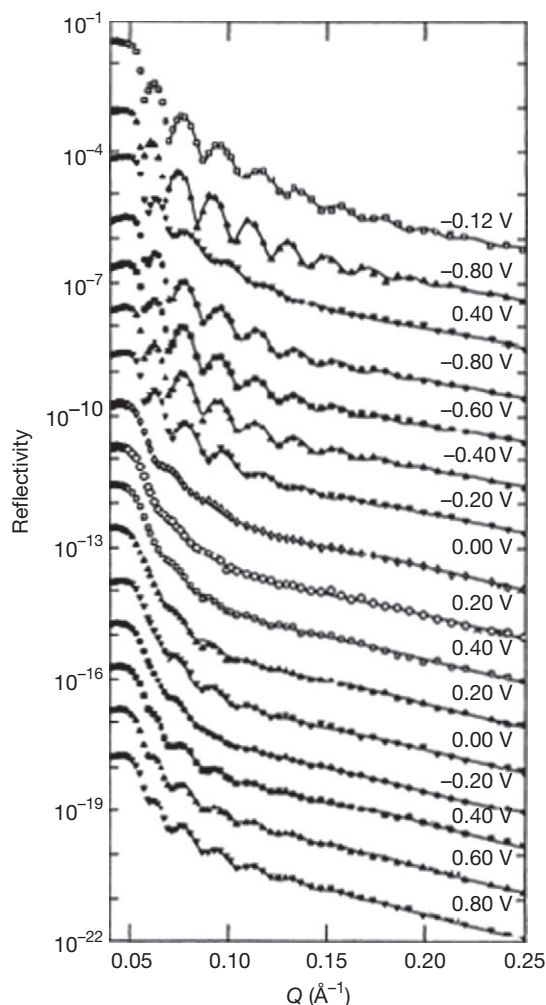


**Figure 19** A series of specular X-ray reflectivity profiles measured *in situ* in the course of the anodic oxidation and reduction of a Cu thin film electrode in borate buffer solution (pH 8.4). The measurements were performed at the potentials indicated, and the curves are vertically offset for easier visualization. Reproduced from You, H.; Melendres, C. A.; Nagy, Z.; Maroni, V. A.; Yun, W.; Yonco, R. M. *Phys. Rev. B* **1992**, 45, 11288–11298, with permission from American Physical Society.

reduced electrode, while only weak thickness fringes can be identified in the case of the oxidized sample, which are the first indication of an increased roughness at the interface to the electrolyte. Moreover, it can already be seen in these raw specular reflectivity data that the original state of the electrode is not recovered after completion of several oxidation/reduction cycles. The quantitative analysis of the presented data allows a microscopic access to the processes at the electrode/electrolyte interface. For example, the surface roughness of the electrode/electrolyte surface is  $\sim 1.1$ – $1.2$  nm in the reduced state prior to the oxidation, while it increases to  $\sim 2.5$  nm in the fully oxidized state. After a completed oxidation–reduction cycle, the electrode remains with an irreversibly increased roughness of  $\sim 1.6$  nm, which can be further increased by prolonged cycling between anodic oxidation and cathodic reduction conditions.<sup>33</sup> Such a behavior has been previously found for Cu and Ag electrodes in alkaline media using SEM and quartz microbalance techniques and is important with regard to surface enhanced Raman scattering (SERS). Furthermore, the increase of the oxide layer thickness with increasing potential at the expense of the thickness of the thin film metal electrode is evident. The thickness of the fully developed oxide layer on Cu amounts to  $\sim 3.0$  nm, in agreement with previous *ex situ* XPS, UPS, and ISS experiments<sup>5,10,16</sup> and *in situ* Raman spectroscopy.<sup>34</sup> However, the reduction is fully reversible, as the initial thickness of the metal layer is recovered after a complete oxidation–reduction cycle. Such a behavior can be anticipated from the cyclic voltammogram, where balanced anodic and cathodic charges were found. In conclusion, we would like to mention that specular XRR measurements can be used for the *in situ* investigation of gaseous oxidation and corrosion processes in a similar way.

### 2.31.7.3 X-ray Absorption Spectroscopy

The basic process underpinning XAS is identical to that of the XPS-technique, that is, an incident photon with sufficient energy is absorbed by an atom and excites a core electron to unoccupied levels (bands) or to the continuum. This excited atom can relax by filling the empty core level with an electron from a higher occupied core level. The energy difference of the involved electronic levels can be released as a photon or may lead to emission of an Auger-electron. XAS is governed by the details of this photon absorption process. In a XAS experiment, the absorption of X-rays within the sample is measured as a function

of the X-ray energy ( $E = h\nu$ ). More specifically, the X-ray absorption coefficient,  $\mu(E) = -d \ln I/dx$ , is determined from the decay in the X-ray beam intensity  $I$  with distance (sample thickness)  $x$ . Monochromatic radiation is used, the energy of which is increased to the point at which core electrons can be excited to unoccupied states close to the continuum. In **Figure 20**, an absorption spectrum of a gold metal foil is shown for an extended photon energy range. The experimental data show three general features: (1) an overall decrease in X-ray absorption with increasing energy; (2) the presence of sharp rises at certain energies called edges, which roughly resemble step-function increases in the absorption (i.e., K-, L-, and M-edges in **Figure 20**); and (3) above the edges, a series of wiggles or an oscillatory structure occurs which modulates the absorption typically by a few percent of the overall absorption cross section as can be seen in the insert of **Figure 20**. It should be already stressed at this stage that the availability of intense new synchrotron X-ray sources permits the investigation of highly dilute systems such as impurities or trace elements within an alloy, or adsorbates and thin films on a surface of a foreign substrate. This capability of the XAS-technique is important and somehow unique with regard to the investigation of corrosion processes, where the

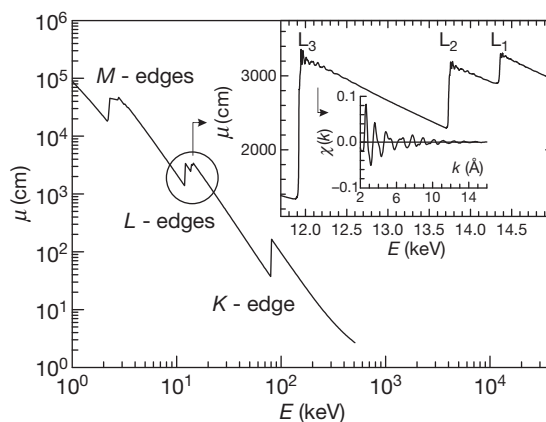


**Figure 20** Schematic view of the absorption spectrum of a gold metal foil over a wide energy range. Steep increases of the absorption coefficient are related to the K-, L-, and M-edges, respectively. The inset shows the absorption at the Au-L edges on a magnified scale. The oscillatory behavior of the absorption coefficient  $\mu(E)$  above the edge, known as EXAFS, is clearly resolved at each of the L-edges. The extracted fine structure oscillations  $\chi(k)$  measured at the  $L_3$ -edge after the removal of the smooth background function  $\mu_0(E)$  are also displayed as a function of the photoelectron wave vector.

alloyed elements often have a dramatic influence on the resulting corrosion protection properties. Various alloyed elements of a specimen can be investigated separately by XAS due to their different X-ray absorbing edges. However, for the investigation of flat electrode surfaces, a simple transmission mode experiment is not adequate. Fluorescence mode detection and/or grazing incidence techniques are required, which are well suited even for samples in an electrochemical environment.<sup>22,24</sup>

The general decrease of  $\mu$  with  $E$  can be related to the well-understood quantum mechanical phenomenon of X-ray absorption by atoms, which can be described by Fermi's golden rule. As with the energy of fluorescence photons, the energy of the absorption edge is characteristic of the absorbing material and hence the measured edges are signatures of the atomic species present in a material. For example, for the transition metals Fe, Co, Ni and Cu, the K edges are located at 7112, 7709, 8333, and 8979 eV, that is, there is a separation of 600 eV between consecutive edges, while, for example, the Mo K edge is located at 20 000 eV. Each edge corresponds to a quantum-mechanical transition that excites a particular atomic core-orbital electron to free or unoccupied levels. The nomenclature for the X-ray absorption edges reflects the origin of the core electron; that is, K edges refer to transitions that excite the innermost 1s electron, while L edges are related to those of 2p<sub>3/2</sub> (L<sub>3</sub>), 2p<sub>1/2</sub> (L<sub>2</sub>), and 2s (L<sub>1</sub>) initial states. These transitions always occur in unoccupied states, that is, in states with an excited photoelectron above the Fermi energy leaving behind a core hole. In a solid, such a photoelectron generally has enough kinetic energy to propagate freely through the material and independent from the structure and the state of matter of the sample under investigation. From the change of the absorption coefficient at the edge, the concentration of the respective element can easily be calculated (see, e.g., Ref. 20). For example, if a metal is corroded and dissolved in an electrolyte, the specific absorption of the element of interest within the electrolyte can be used for the analysis of soluble corrosion products in the active, passive or transpassive state of a metal or the selective dissolution of a single element in a multielement specimen such as an alloy.

Similar to an XPS experiment, the exact energy of the absorption edge is a sensitive function of the valency of the excited atom. In general, a shift of the absorption edge toward higher photon energies is observed as the chemical valency of the absorber atom is increased, i.e., with increasing oxidation

state.<sup>35,36</sup> In many cases, a more or less linear shift of the edge with typically 1–3 eV per unit of the valency can be found in the literature for different elements. This effect provides an easy access to determine the valency of a selected element (see, e.g., Refs. 35–37) even for trace elements in complex systems. In addition, in some special cases, there are also features in the absorption spectrum below the edge. These so-called pre-edge peaks can be attributed to transitions from the excited photoelectron into unoccupied electronic levels of the sample, that is, an X-ray absorption spectrum probes the density of unoccupied states of the absorbing element.

The detailed structure of the absorption coefficient within ~50 eV above the edge is referred to as near edge X-ray absorption fine structure (NEXAFS) or X-ray absorption near edge structure (XANES). Besides the above mentioned transitions into unoccupied states, the near edge structure also involves transitions of the photoelectron into the continuum, that is, into states above the vacuum level. In the latter case, the photoelectron has a low kinetic energy and accordingly a large (inelastic) mean free path (see, e.g., Ref. 13), so that it can undergo multiple scattering events.<sup>38</sup> The shape of the edge is thus highly sensitive to both the valency and the coordination of the absorbing atoms, including also the angular arrangement of the neighboring atoms. Although the complexity of the involved processes makes a full theoretical treatment very difficult, it is currently possible to calculate near edge X-ray absorption spectra on an *ab initio* basis, that is, based on the assumption of a model structure.<sup>38</sup> This approach works quite well for molecules and complexes – which is an interesting feature for the investigation of corrosion products within the electrolyte as shown in Ref. 37. However, for crystalline materials it is still a quite challenging task to fit an experimental spectrum using *ab initio* calculations since the theory of XANES is not fully quantitative and requires several physical considerations.<sup>38</sup> Thus, for the practical analysis the near edge spectra are most commonly used as fingerprint techniques. Edges are collected for a number of standard compounds with known valence and crystal structure and these are compared to the spectra of the actual samples. Certain compounds such as Cr<sup>6+</sup> or Mo<sup>6+</sup> give rise for distinct pre-edge peaks, so that these species can be identified qualitatively and quantitatively. For the application of fingerprint techniques to electrochemical probes, see for example, 24, 37. As an example for the application of XANES spectroscopy in



corrosion research, we present a study dealing with the initial stages of high temperature corrosion of Y-implanted Fe–Cr steels.<sup>39</sup> This study intends to examine the so-called ‘rare-earth effect.’ It is well-known that the presence of a small percentage of active elements, especially rare-earth elements, may have a beneficial effect on the properties and the adherence of protective scales to the substrate. In the present experiment, the rare earth element was inserted into the Ni–Cr alloy by means of 200 keV Y<sup>+</sup>-ion implanting, and the resulting samples were oxidized at 700 °C in a dilute oxygen atmosphere (1% O<sub>2</sub>, 99% Ar) for varying times. In **Figure 21**, grazing incidence XANES spectra acquired from the as-implanted sample and samples oxidized for different times are compared with the reference spectra from metallic Y and Y<sub>2</sub>O<sub>3</sub>.<sup>39</sup> A progressive oxidation of the samples is observed as the oxidation time increases, as directly evidenced by the shift of the absorption edge toward increasing energy values. Furthermore, after ~2 min of oxidation, the obtained spectra closely resemble those of yttria Y<sub>2</sub>O<sub>3</sub>. A more detailed investigation of the extended X-ray absorption structure suggests that the formed crystallites are of nanosize, and parallel XRD experiments revealed

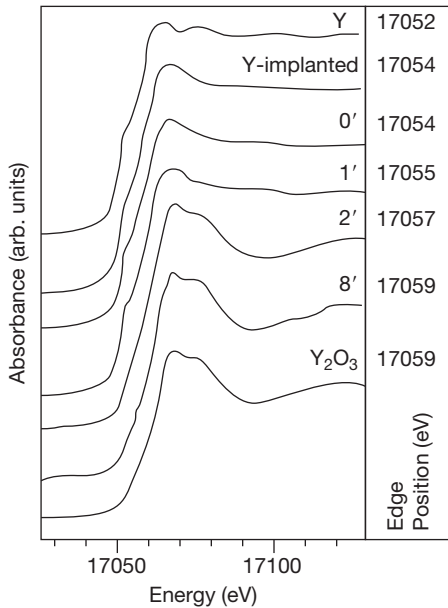


**Figure 21** Near edge X-ray absorption spectra at the Y K-edge of a Y-implanted Ni–20Cr alloy in the as-prepared state as well as after oxidation in a gas atmosphere of 1% O<sub>2</sub> in Ar at 700 °C for 1, 2, and 8 min, respectively. (Metallic Y and Y<sub>2</sub>O<sub>3</sub> reference spectra are also shown). Reproduced from Gibson, P. N.; Crabb, T. A. *Nucl. Instrum. Methods B*, **1995**, 97, 495–498.

that the crystallization is *initiated* at the interface between the oxide scale and the bare alloy, proving in this case the positive effect of the dispersed rare earth element on the formation of a well ordered oxide.<sup>39</sup>

The third general feature in XAS spectra are the oscillations of the absorption coefficient which are visible up to ~1000 eV above the edge. This so-called extended X-ray absorption fine structure (EXAFS) originates from scattering of the emitted photoelectrons by neighboring atoms. The photoelectron, which is ejected from the absorbing atom, can be described as a propagating electron wave with a wave vector  $k$  and a de Broglie wavelength  $\lambda$  (eqn [18]):

$$k = \frac{\sqrt{2m(E - E_0)}}{\hbar}, \lambda = 2\pi/k \quad [18]$$

$E$  is the actual photon energy,  $E_0$  the edge energy,  $m$  the electron mass,  $\hbar = h/2\pi$  and  $h$  is Planck's constant. This wave can be scattered by neighboring atoms, so that the outgoing wave interferes with the backscattered wave. Depending on the distance,  $r_j$ , to the scattering atoms and the wavelength of the photoelectron, this interference can be constructive or destructive, resulting in an increase or a decrease of the absorption coefficient by some few percentage points. This phenomenon was first theoretically described by the short range order theory developed by Sayers, Stern, and Lytle.<sup>40</sup> In contrast to the near edge structures in the absorption coefficient, the theory of the EXAFS is today well understood with acceptable tolerances from the experimental results.<sup>38</sup> The EXAFS spectrum  $\chi(E)$  above a given absorption edge is defined as the oscillatory part of the X-ray absorption:

$$\chi(E) = \frac{\mu(E) - \mu_0(E)}{\mu_0(E)} \quad [19]$$

$\mu(E)$  is the energy dependent absorption coefficient, and  $\mu_0(E)$  is the smoothly varying, atomic-like background absorption.  $\mu_0(E)$  contains all the contributions from other edges and other elements and their absorption edges within the sample. According to the plane-wave concept and the single-scattering approximation, the EXAFS oscillations  $\chi(\kappa)$  can be expressed by eqn [20]:

$$\chi(\kappa) = \sum_j S_0^2 N_j \frac{|f_j(k)|}{\kappa r_j^2} \sin(2\kappa r_j + \delta_j(k)) e^{-2r_j/\lambda(k)} e^{-\sigma_j^2 \kappa^2} \quad [20]$$

$N_j$  is the coordination number of the central atom in the  $j$ th shell,  $f_j(k)$  the backscattering amplitude,  $\sigma_j$  the mean relative displacement of the atoms in the  $j$ th

shell, and  $\delta_j$  a phase shift associated with the interactions of the photoelectron wave with the potential of the absorbing and the backscattering atoms. Since different backscattering atoms have their own characteristic backscattering phases and amplitudes, EXAFS enables identification of the nature of the atoms in each coordination sphere around the absorbing atom. In contrast to XRD, EXAFS is very sensitive toward light backscattering atoms, which justifies its use for the investigation of, for example, oxides and passive layers. The disorder  $\sigma^2$  is partly due to thermal effects, which cause all the atoms to oscillate around their equilibrium positions. Effects of structural disorder are similar, giving an additional contribution to  $\sigma^2$ . Both effects can be separated by means of temperature dependent measurements. As a consequence of the  $1/r_j^2$  dependence of  $\chi(k)$  and the limited mean free path of the photoelectrons characterized by  $\lambda(k)$ , EXAFS is useful in providing information about the local short-range order around the absorbing atom, that is, the fine structure contains precise information about the local atomic structure around the atom that absorbed the X-rays. The structural information is typically obtained by Fourier-filtering of the experimental  $\chi(k)$  data into distance-space, giving a radial distribution function from which coordination numbers, interatomic distances, and the local disorders are determined.<sup>40</sup> Similar to the XANES, this turns out to be a unique signature of a given material, since it depends on both the detailed atomic structure and its vibrational properties. For this reason, EXAFS has become an important probe especially for disordered materials, where XRD can hardly be applied due to the absence of any long range order correlations. A complete data analysis comprises the separation of the individual shells contributing to the radial distribution function, and the fitting of these peaks with phases and amplitude functions.<sup>41</sup>

In this contribution, we will not show a detailed data evaluation, but only focus on the main features of EXAFS. As an example, in Figure 22, we show the *in situ* evolution of the EXAFS at the Ni K-edge (8333 eV) of a metallic Ni-layer on an  $\text{Al}_2\text{O}_3$ -substrate during the formation of a spinel-type oxide in an  $\text{O}_2$ -containing atmosphere at elevated temperatures.<sup>42</sup> First, the thin Ni film was oxidized to NiO at 700 °C, and the resulting X-ray absorption fine structure of this Ni-oxide thin film is similar to that of the crystalline NiO-reference material, as can be seen in Figure 22. In a second oxidation step at an elevated temperature of  $\sim 1000$  °C, this NiO-layer interacts with the Al-oxide substrate, and a spinel-type

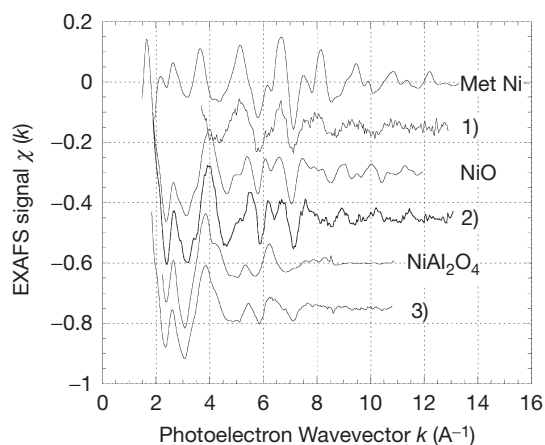


**Figure 22** EXAFS of a Ni thin-film sample on a single crystal  $\text{Al}_2\text{O}_3$  substrate after (a) initial deposition, (b) 20 min in 60 mbar  $\text{O}_2$  at 973 K, and (c) additional 9 h oxidation at 1273 K. For comparison, spectra of metallic Ni and crystalline NiO and  $\text{NiAl}_2\text{O}_4$  spinel are also presented. Reproduced from d'Acapito, F.; Davoli, I.; Ghigna, P.; Mobilio, S. *J. Synchrotron Rad.* **2003**, *10*, 260–264.

$\text{NiAl}_2\text{O}_4$ -layer is formed as can be deduced by comparing this high temperature spectrum with that of the related spinel reference material.<sup>42</sup> In a similar way, the oxidizing effect of elevated temperatures on high- $T_c$  superconductors has also been proven, showing clearly the further oxygenation of the superconductor as well as the appearance of new phases.<sup>43</sup> It is important to mention here that several *in situ* EXAFS studies have also dealt with electrochemically formed passive layers on various metals and alloys (see Refs. 24, 27, 28, 37, 44). Finally, due to the fact that XAS experiments are element specific and not restricted to investigations of crystalline materials (such as XRD studies), it is possible to investigate in detail the structure and the chemical state of corrosion products dissolved in the electrolyte in front of a corroding electrode.<sup>20,37</sup> The use of the state of the art detectors and stable monochromators also enables the investigation of highly dilute solutions, and time resolved investigations are easily possible, so that the change in concentration in solution can be followed in tandem with changes in the structure of the solid.

### 2.31.8 Glow Discharge Optical Emission Spectroscopy (GDOES)

If a sufficiently high voltage is applied, a GD can be generated between two physically separated

electrodes in a gas filled vacuum vessel with a pressure of typically 10–1000 Pa. Depending on the gas type and pressure, the distance of the electrodes and the applied voltage, electrical currents, and characteristic light emissions are observed. We will only focus on the most relevant points here; for more detailed information on the fundamentals of GDs, the reader can refer to the literature, for example, Ref. 45. As a result of the physical processes, GD plasma shows several luminous and dark regions. For analytical use of the GD, the optical emission in the luminous regions are studied and analyzed quantitatively. It is also essential that the cathode (sample under study) is exposed to a bombardment of ions and fast neutral species from the plasma, and therefore, the cathode is eroded and cathode material is released into the gas phase continuously – this effect is known as cathode sputtering. This sputtering of the cathode is the basis for analytical exploitation of GD. The sputtered species from the sample arrive in the plasma where they are subject to ionization and excitation. If the corresponding ions are measured in a mass spectrometer, they can be identified quantitatively. This method is called glow discharge mass spectrometry (GDMS) in literature. On the other hand, the excited atoms emit characteristic photons during their deexcitation which in principle allow their identification, if they are detected with an optical spectrometer. This technique is called GDOES. It should also be mentioned here that the sputtered

atoms and ions can also be excited with an external light source for atomic absorption (GDAAS) or fluorescence (GDAFS) spectroscopy. Given that the sample is continuously eroded, a depth profiling of the sample is possible, if the erosion rate is calibrated properly. In contrast to other depth profiling techniques, matrix effects only play a minor role here because of the spatial separation of the sputtering and excitation of the sputtered atoms, as well as their dilution in the plasma. Using the Monte-Carlo simulation techniques, it is possible to calculate the profile of the sputtered crater on the sample, where reasonable agreement to the experiment was found for direct current GDs. These simulations also show that a homogeneous electrical field distribution in the active (sputtering) region is required to ensure that the sample surface is evenly eroded, resulting in a sputter crater with a nearly flat bottom. Only in this case, a well resolved depth profile of the sample can be obtained. It is noteworthy to mention here that for analytical GDs argon is most commonly used as the discharge gas, in order to avoid chemical reactions of the sputter gas with the sample and the system. In addition, a small but continuous flow is applied to ensure a clean atmosphere during the process of analysis.

A schematic representation of a GDOES analytical system is shown in Figure 23. The hollow anode configuration is composed of a grounded metal tube. An appropriate window confines the vacuum vessel on one side, while the flat sample closes the

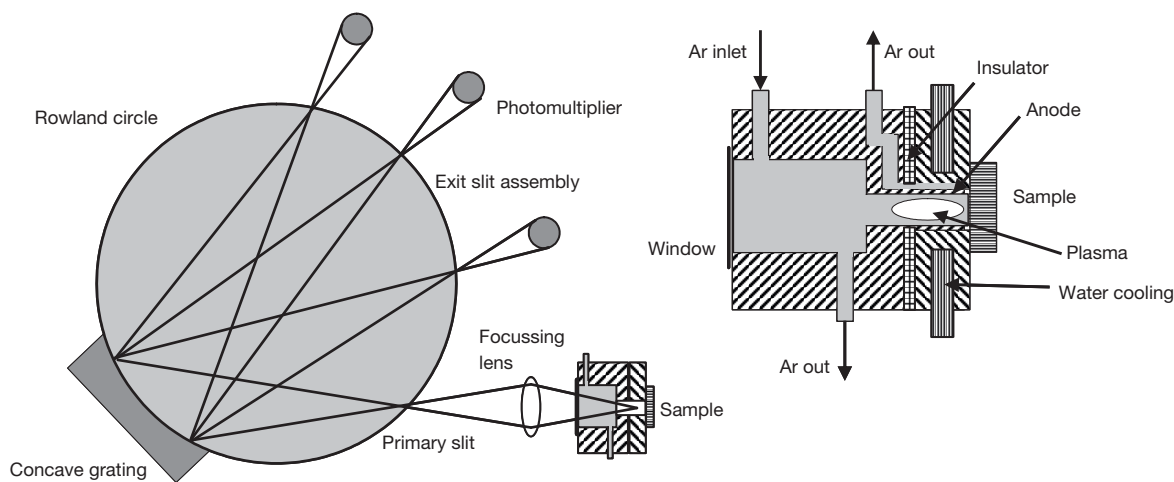


**Figure 23** Schematic representation of a spectrometer for glow discharge optical emission spectroscopy (GDOES). The sample, cathode, is placed in a hollow, as shown, in an expanded view in the insert. Ions from the plasma are accelerated against the sample, and material is eroded and subsequently diffuses into the plasma. Here excitation of these atoms may occur, leading to the emission of characteristic photons during relaxation to the ground state. These optical emissions of the plasma are focused onto the primary slit of a grating spectrometer, where the spectrum is analyzed by means of a grating spectrometer, and the spectral contributions of different species are detected by an array of photomultipliers.

discharge cavity on the other side. This way, sample introduction or change is easy, and the electrical power that is needed for ignition and maintenance of the plasma is simply supplied to the sample. The sample holder is water cooled in order to limit the heating of the samples. Usually, a quartz window is used because of its transparency for photons of lower wavelength.

In the case of a conducting (metal) sample, a regulated DC-voltage of typically some hundred volts is applied. As for sputtering, etching, and coating processes, however, the GD can also be energized by alternating radiofrequency (RF) fields in order to investigate in particular poor/bad or nonconducting samples.<sup>45</sup> Assuming the presence of a nonconducting sample, a DC-discharge would cause a positive charging of the cathode because of the recombination of positive ions and electrons coming from the near surface region of the sample. As a consequence, the potential drop between the two electrodes would decrease and the discharge would extinguish, within some few milliseconds, with a positive charge remaining on the sample. If the direction of the voltage is reversed, the same processes will occur, resulting in a decrease of the positive charge on the sample, which in this case acts as an anode until a negative charge is accumulated so that the discharge is stopped again. If the switching of the voltage polarity is repeated continuously with a high frequency, that is, RF with a power of typically up to  $\sim 30$  W, the discharge can be maintained continuously even for nonconducting samples. Using frequencies in the mega-Hertz range, the plasma with typical frequencies of the order of 1 kHz is not able to decay but will glow permanently. One may argue that the use of an RF-discharge could be disadvantageous for GDOES-investigations because the material of the hollow electrode will be sputtered as well and thus contribute to the measured optical emissions. However, due to the characteristic design of the two electrodes, the sputtered area on the sample is limited to some few square millimeter while on the other hand the area of the hollow tube exposed to electrons and ions is not restricted at all and can be extended as much as required by the size of the GD plasma, thus reducing the related contributions accordingly.

The spectrometer displayed in [Figure 23](#) employs a concave grating that is fixed in the Rowland geometry, and the light emissions from the GD are focused onto the entrance slit of the spectrometer using a lens of suitable focal length. Several photomultiplier tubes are mounted at well defined positions on the Rowland

circle for light detection related to some few specific excitation lines, as it is not possible to measure a full spectrum in this configuration. However, due to the fast erosion of the samples, it is important to make use of an extremely fast and reliable detection method for the excited photons. State of the art systems employ up to 60 individual detectors in parallel. The use of solid state detectors, charged coupled devices or photo diode arrays have become a common alternative to photomultiplier tubes. These detectors allow the acquisition of the entire spectrum, or at least a large portion of it, but are usually slower than photomultiplier tubes and therefore not suitable in those cases where extremely short acquisition times are required, for example, for the analysis of adsorbates or very thin surface films. Light elements such as hydrogen, carbon, nitrogen, oxygen, or sulfur have important spectral lines in the vacuum ultraviolet (UV) region with wavelengths below  $\sim 200$  nm. For example, oxygen species are in many cases identified using an oxygen emission line at 130.2 nm. Spectrometers in this spectral range are usually operated under vacuum, or at least a purged nitrogen atmosphere to obtain a sufficient transparency in this spectral range.

GDOES, as an analytical technique, was introduced by Grimm in 1968 with first applications being the determination of the bulk atomic compositions of metal alloys.<sup>46</sup> The capabilities of GDOES for surface analytical studies was proven a few years later with oxidation studies of steels being one of the first areas of research interest. In a depth profiling experiment, the intensities of the spectral lines of interest are measured as a function of the sputter time. For a quantitative analysis, these have to be converted to an analyte concentration and a sputter depth. Although the detection limits for GDOES are generally small with typical values in the range of 1–10 ppm, an exact determination of atomic concentration and film thicknesses is in many cases not straightforward and the use of more sophisticated calibration procedures for example, using certified materials in a wide range of elemental compositions, is recommended. Furthermore, spurious hydrogen in the plasma, either from a contamination of the plasma gas or the sample, may affect the measured concentrations of the analytes and have to be corrected accordingly. Nevertheless, in combination with the numerous efforts that have been made for quantitative modeling and understanding of GD-plasmas and sputtering for analytical purposes, and because of its easy use, GDOES has become an

interesting and important method for routine depth-profiling analysis in a wide range of applications, including corrosion phenomena.

Corrosion protection coatings – in particular on steel – are an important topic. The depth profiling capabilities of GDOES give a fast and direct access to a simple determination of the composition of the coating as well as its thickness. This is of special importance in those cases where the coating contains the same chemical elements as the underlying steel, such as for Fe/Zn-coating on iron based steels. For industrial applications, it is in many cases important to know the structure and the composition of a material in order to accomplish reproducible physico-chemical properties such as, mechanical elasticity and plasticity, or corrosion resistance of metal sheets. These properties are often influenced by the pre-treatment of the metal, such as milling or hot-rolling which alter the microstructure and the composition of the metal significantly. Depending on the details of the processing conditions, trace elements, impurities, or rolled-in oxide particles are located especially in the near surface region of the metal. In [Figure 24\(a\)](#), GDOES depth profile of a hot-rolled steel surface is presented.<sup>47</sup> As can be seen, the oxide layer on the steel has a rather complex substructure, and even the alloyed elements Mn and Si are detectable, although their atomic concentrations are only in the 1% range. Besides the near surface region of some 10 nm, where Si is significantly enriched, the outer oxide scale has a lower Fe-content compared to the inner part of the duplex layer, which contains significantly more iron. The manganese concentration is smaller in the outer layer, and increases in the inner layer, but it is still depleted compared to the bulk concentration. While

the entire oxide is almost free of Si and C, both elements are significantly enriched at the interface between the oxide and the bulk material.

In a similar manner, GDOES has fostered our understanding of high temperature corrosion processes and materials. Very recently, first studies on materials and coatings that are used in biological environments and biocorrosion have been published. The thickness and the composition of passive oxide layers were determined using GDOES for a variety of different materials and for various electrochemical environments – here the most important aspect of GDOES is its easy operation and data interpretation. This is also true for samples of archeological interest, where GDOES can easily be applied to conducting as well as to nonconducting samples such as, ancient bronzes, ceramics, pottery, etc., and GDOES may give information which is important for the conservation of such objects.

In conclusion, when considering GDOES for a practical application, one should always have in mind that the recorded depth profiles are destructive, which is sometimes critical for example, in the case of archeological objects. Furthermore, GDOES is always an *ex situ* method, that is, it relies on the assumption that the sample is not affected or altered by the transfer to the spectrometer and the bombardment with electrons and ions, which seems to be true for metals and alloys. Compared to UHV-techniques such as XPS or SIMS, GDOES is not very time-consuming, and the repetition of each experiment allows one to apply statistical techniques to the results, for example, to elemental concentrations or thickness *values*, which is again important for industrial applications. On the other hand, however,

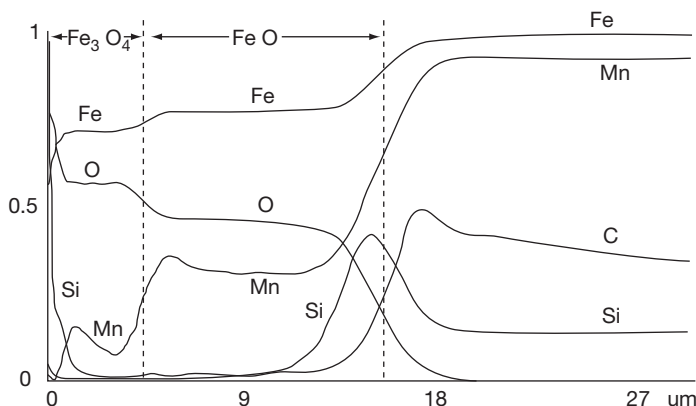


**Figure 24** GDOES depth profile of an oxide layer on hot-rolled carbon steel. The concentration scale for each of the elements is given in relation to the following values: 100% for Fe, 50% for O, 0.5% for Mn, 0.2% for C, and 2% for Si. Reproduced from Weiss, Z.; Musil, J.; Vlcek, J., *Fresenius J. Anal. Chem.* **1996**, 354, 188–192.



GDOES is not able to specify the binding state of an element, that is, GDOES is not able to distinguish between a metal cation and the reduced metal. Thus, it is useful to combine GDOES with other techniques in order to strengthen the conclusions drawn.

### 2.31.9 Infrared Spectroscopy

Infrared spectroscopy applies electromagnetic radiation of wavelength  $\lambda$  or wave number  $\tilde{\nu}$  of the middle-IR range ( $\lambda = 2.5\text{--}50\ \mu\text{m}$ ,  $\tilde{\nu} = 4000\text{--}200\ \text{cm}^{-1}$ ) to a sample. Typically, the near-IR range ( $\lambda = 0.8\text{--}2.5\ \mu\text{m}$ ,  $\tilde{\nu} = 13\,000\text{--}4000\ \text{cm}^{-1}$ ) or the far-IR range ( $\lambda = 5\text{--}1000\ \mu\text{m}$ ,  $\tilde{\nu} = 200\text{--}10\ \text{cm}^{-1}$ ) are of minor importance for this spectroscopic method. The absorption of IR-radiation in the middle range by a sample leads to excitation of vibrational modes of its molecules as a whole (fingerprint region,  $\tilde{\nu} = 600\text{--}1200\ \text{cm}^{-1}$ ) or of characteristic groups such as C=O and O–H (group frequency region,  $\tilde{\nu} = 1200\text{--}3600\ \text{cm}^{-1}$ ). The excitation of vibrations is controlled by selection rules. For IR absorption, the dipole moment should change with the oscillation mode. Therefore, polar groups like C=O are IR-active. If, however, the changes in the dipole moment compensate internally within a molecule, the IR mode is inactive, for example, the symmetric stretch of O=C=O. The asymmetric stretching and the bending vibrations of O=C=O are IR-active. We note that the selection rules for Raman Spectroscopy depend on the polarizability of groups and molecules. Under the selection rules for Raman, the symmetric stretching of the O=C=O molecule, which has an inversion center, is active, whereas the asymmetric stretching and the bending mode are Raman-inactive. Thus, IR and Raman can give complimentary results.

An IR spectrometer usually has a strong light source like a Nernst Glower, which is an electrically heated rod of rare earth oxides, or a Globar, a heated rod of silicon carbide. A very intense IR source is SR. In this case, polarized light of high intensity is also available.

A more conventional IR spectrometer uses a monochromator, separating the incoming polychromatic radiation into its components and thus taking sequentially a wavelength dispersive spectrum. A Fourier transform IR (FTIR) spectrometer uses a Michelson Interferometer which creates an interferogram due to the different optical path length of the two interfering beams. Its Fourier transform leads to an IR spectrum. The advantages of this approach are

a much better signal to noise ratio and the short time required to record a spectrum. Here the whole spectrum is obtained in parallel, rather than sequentially, with no loss of radiation at the entrance and exit slits of a monochromator. A spectrum may be obtained within a second, and thus it is possible to follow the kinetics of corrosion processes. An additional advantage of FTIR spectroscopy is the high spectral resolution of  $0.1\ \text{cm}^{-1}$ .

A variety of detectors are utilized in IR spectroscopy, based either on thermal or photonic response. Thermal detectors are IR absorbers that measure the produced heat via thermocouples, or bolometers, which measure the change of heat via the resistance change of a platinum wire. Pyroelectric detectors are also employed. They use chopped IR light, which changes the polarization of a condenser whose capacity is a measure of the absorbed radiation and the thereby produced heat. They have the advantage of suppressing background radiation efficiently. As regards photonic detectors, low band gap semiconductors such as  $\text{Cd}_x\text{Hg}_{1-x}\text{Te}$  (CMT) are typically used, where the incoming IR radiation excites electrons from the valence to the conduction band leading to photocurrents which are a measure of its intensity. CMT detectors are very sensitive and have a fast response so that they are widely used for FTIR spectrometers.

IR spectroscopy is routinely employed by synthetic chemists in the transmission mode, with specimens pressed as pellets often in KBr as an IR transparent medium or in solution with appropriate organic solvents. In aqueous corrosion and electrochemistry, the chemistry of a metal surface and its changes with the corrosion process are of decisive importance. Therefore, one needs to investigate the surface preferably in its natural environment. Two main problems arise. First, water strongly absorbs IR-radiation. Therefore, the transmission path in water should be avoided or made as short as possible. Furthermore, thin films or absorption layers are often of interest and not the substrate metal or the bulk electrolyte and the information should come from the electrode/electrolyte interface. Therefore two main approaches are used in electrochemistry and corrosion science, namely attenuated total reflection spectroscopy (ATR) and IR-Reflection-Absorption Spectroscopy (IRAS and IRRAS).

#### 2.31.9.1 Attenuated Total Reflection

In ATR spectroscopy, the IR beam travels through a crystal such as Ge or ZnSe with total reflection at its

interfaces, that is, the angle of incidence, measured against the normal surface, is above its critical value of total reflection. One surface of the ATR crystal may be covered with a very thin metal layer which then is exposed to the electrolyte. Although the radiation is totally reflected, the electrical field vector penetrates the metal and samples the electrode–electrolyte interface with a depth of  $\sim 0.1\text{--}5\text{ }\mu\text{m}$  (evanescent wave). It thus picks up the IR spectrum of adsorbed molecules and thin layers and may follow changes at the interface even for well controlled electrochemical conditions with a potentiostat and counter and reference electrode.

### 2.31.9.2 IR Reflection Absorption Spectroscopy

In IRAS, the IR-beam strikes the specimen surface from the front side at grazing incidence, i.e., at a large angle relative to the surface normal. This geometry permits an intense interaction of the beam with the electrode–electrolyte interface. For IR radiation polarized parallel to the plane of incidence (containing the incoming beam and the surface normal), that is, p-type radiation, the electrical field vector changes in the direction of the axis of at least partially perpendicularly oriented molecules and thus gives its characteristic interaction and absorption lines. For perpendicularly oriented, s-type radiation one does not get a signal, for due to a  $90^\circ$  phase shift during reflection it cancels with the incoming radiation. These surface selection rules lead to an IRAS-signal for those molecules oriented on the surface with a component of a changing dipole moment in the direction of the normal surface. These characteristics permit one to distinguish between the randomly oriented molecules within the electrolyte and those adsorbed with a characteristic orientation at the metal surface. IR spectroscopy may also contribute to the monitoring and understanding of atmospheric corrosion.<sup>48</sup> In this case, the electrolyte is a thin water containing film and thus does not cause too many problems for the application of the method.

### 2.31.10 Summary

This chapter describes the most important surface analytical methods which provide information on the chemistry and structure of corroding surfaces and surface layers. Many methods work in vacuum, and one should be aware that the specimen has lost the contact with its environment and the electrode

potential for the case of electrochemical corrosion systems. However, such broad and valuable information is urgently needed for an understanding of surface reactions and corrosion phenomena. It has been shown by numerous detailed studies that the results follow the systemically changed experimental parameters, for more extensive studies, when one examines the reaction, free of artifacts. *In situ* methods are free of this problem, but they cannot replace the rich information provided by the methods functioning only in vacuum. Generally, it is the combination of many methods which ensures understanding and a correct interpretation of the reactions and their mechanisms. XPS is a soft method and gives excellent data on the chemistry at the surface. AES allows a high lateral resolution, which is extremely important if localized corrosion phenomena occur. ISS may improve the depth profiles of thin films, and RBS will give a detailed insight into reactions on thick films, however, with a poor depth resolution of  $\sim 5\text{ nm}$  only. IR methods may give *in situ* information on the chemistry of the surface whereas XRD and XAS provide information on the structure, that is, the long range and the near range order of surfaces and surface films. In addition, *in situ* scanning tunneling microscopy and atomic force microscopy give exact information on their structure. Thus, all these methods supply details of the characteristics and the reactions occurring at a solid surface. Furthermore, some methods add spectroscopic information of the dissolved species in solution or in the gas phase like XAS in transmission mode. Table 1 summarizes the methods which have been discussed in this chapter and presents their advantages and disadvantages. A group might not have experts in all these methods, but laboratories may collaborate and thus the expertise and the equipment of the laboratories may be complementary. A collaboration will be useful when the different backgrounds of the scientists involved still allows them to communicate, which is a difficult task, as the methods range from corrosion and electrochemistry to surface physics and the application of SR facilities. It is often observed in science that different communities work parallel to each other, largely ignoring each other. However, the situation is improving. One requirement is crucial in all cases. The application of a sophisticated surface method to a system requires the full knowledge of its electrochemistry. Any study without a careful and reliable specimen preparation is useless. On the other hand, all these surface methods are needed to understand the surface reactions. Therefore, the surface physicist

should understand to some extent electrochemistry, corrosion, and materials science, and the corrosion engineer and electrochemist to some extent surface science and its related methods, which would be an excellent basis for a fruitful collaboration of experts.

## References

1. Pourbaix, M. *Atlas of Electrochemical Equilibria in Aqueous Solutions*; Pergamon: Oxford, 1966.
2. Briggs, D.; Seah, M. P. *Practical Surface Analysis*; Wiley, 1983.
3. Marcus, P.; Mansfeld, F. Eds. *Analytical Methods in Corrosion Science and Engineering*; Taylor & Francis: Boca Raton FL, 2006.
4. Haupt, S.; Collisi, U.; Speckmann, H. D.; Strehblow, H.-H. *J. Electroanal. Chem.* **1985**, *194*, 179–190.
5. Haupt, S.; Calinski, C.; Collisi, U.; Speckmann, H. D.; Strehblow, H.-H. *Surf. Interface Anal.* **1986**, *9*, 357–365.
6. Strehblow, H.-H. In *Advances in Electrochemical Science and Engineering*; Alkire, R. C., Kolb, D. M., Eds.; Wiley-VCH: Weinheim, 2003; pp 271–378.
7. Hecht, D.; Strehblow, H.-H. *J. Electroanal. Chem.* **1997**, *436*, 109–118.
8. Strehblow, H.-H. In *Bergmann Schäfer, Lehrbuch der Experimentalphysik, Gase, Nanosysteme Flüssigkeiten* de Gryter: Berlin, New York, 2006; Vol. 5, pp 551–555.
9. Abels, J. M.; Strehblow, H.-H. *Corros. Sci.* **1997**, *39*, 115–132.
10. Strehblow, H.-H.; Marcus, P. In *Analytical Methods in Corrosion Science and Engineering*; Taylor & Francis: Boca Raton FL, 2006; pp 1–37.
11. Shirley, D. A. *Phys. Rev. B* **1972**, *5*, 4709–4714.
12. Scofield, H. J. *Electron Spectrosc.* **1976**, *8*, 129–137.
13. Seah, M. P.; Dench, W. A. *Surf. Interface Anal.* **1979**, *1*, 2–11.
14. Haupt, S.; Strehblow, H.-H. *Langmuir* **1987**, *3*, 873–885.
15. Vetter, K. J. *Electrochemical Kinetics*; Academic Press: New York, 1967; pp 780–783.
16. Speckmann, H. D.; Haupt, S.; Strehblow, H.-H. *Surf. Interface Anal.* **1988**, *11*, 148–155.
17. Strehblow, H.-H.; Melliar Smith, C. M.; Augustyniak, W. M. *J. Electrochem. Soc.* **1978**, *125*, 915–919.
18. McIntyre, N. S.; Graham, M. J. In *Analytical Methods in Corrosion Science and Engineering*; Taylor & Francis: Boca Raton, FL, 2006; pp 65–102.
19. Margeritondo, G. *Introduction to Synchrotron Radiation Research*; Oxford University Press: Oxford, 1988.
20. Lützenkirchen-Hecht, D.; Frahm, R. *J. Phys. Chem. B* **2001**, *105*, 9988–9993.
21. Scherb, G.; Kazimirov, A.; Zegenhagen, J. *Rev. Sci. Instrum.* **1998**, *69*, 512–516.
22. Shi, Z.; Wu, S.; Lipkowski, J. *Electrochim. Acta* **1995**, *40*, 9–15.
23. Zegenhagen, J. *Surf. Sci. Rep.* **1993**, *18*, 200–271.
24. Davenport, A. J.; Sansone, M.; Bardwell, J. A.; Aldykiewicz, A. J., Jr.; Taube, M.; Vitus, C. M. *J. Electrochem. Soc.* **1994**, *141*, L6–8.
25. Kittel, C. *Introduction to Solid State Physics*, 7th ed.; Wiley: New York, 1996.
26. *International Tables for X-ray Crystallography: Mathematical Tables*; Kynoch Press: Birmingham, 1962; Vol. 3. (Published for the International Union of Crystallography.).
27. Davenport, A. J.; Oblonsky, L. J.; Ryan, M. P.; Toney, M. F. *J. Electrochem. Soc.* **2000**, *147*, 2162–2173.
28. Toney, M. F.; Davenport, A. J.; Oblonsky, L. J.; Ryan, M. P.; Vitus, C. M. *Phys. Rev. Lett.* **1997**, *79*, 4282–4285.
29. Paterson, M. S. *J. Appl. Phys.* **1952**, *23*, 805–811.
30. Klug, H. P.; Alexander, L. E. *X-ray Diffraction Procedures*; Wiley: New York, 1974.
31. Magnussen, O. M.; Scherer, J.; Ocko, B. M.; Behm, R. J. *J. Phys. Chem. B* **2000**, *104*, 1222–1226.
32. Parratt, L. G. *Phys. Rev.* **1954**, *95*, 359–369.
33. You, H.; Melendres, C. A.; Nagy, Z.; Maroni, V. A.; Yun, W.; Yonco, R. M. *Phys. Rev. B* **1992**, *45*, 11288–11298.
34. Schwartz, D. T.; Müller, R. H. *Surf. Sci.* **1991**, *248*, 349–358.
35. Chiu, N. S.; Bauer, S. H.; Johnson, M. F. L. *J. Catal.* **1984**, *89*, 226–243.
36. Ressler, T.; Wong, J.; Roos, J. J. *Synchrotron Rad.* **1999**, *6*, 656–658.
37. Lützenkirchen-Hecht, D.; Strehblow, H.-H. In *Analytical Methods in Corrosion Science and Engineering*; Marcus, P., Mansfeld, F., Eds.; Taylor & Francis: Boca Raton FL, 2006.
38. Rehr, J. J.; Albers, R. C. *Rev. Mod. Phys.* **2000**, *72*, 621–654.
39. Gibson, P. N.; Crabb, T. A. *Nucl. Instrum. Methods B* **1995**, *97*, 495–498.
40. Sayers, D. E.; Stern, E. A.; Lytle, F. W. *Phys. Rev. Lett.* **1971**, *27*, 1204–1207.
41. Koningsberger, D.; Prins, R. *X-ray Absorption: Principles, Applications, Techniques of EXAFS, SEXAFS and XANES*; Wiley: New York, 1988.
42. d'Acapito, F.; Davoli, I.; Ghigna, P.; Mobilio, S. *J. Synchrotron Rad.* **2003**, *10*, 260–264.
43. Salluzzo, M.; Natali, F.; Aruta, C.; Maglione, M. G.; Ricci, F.; Koller, E.; Fischer, O.; Saini, N. L. *Eur. Phys. J. B* **2002**, *27*, 467–472.
44. Kruger, J.; Long, G. G.; Zhang, Z.; Tanaka, D. K. *Corros. Sci.* **1990**, *31*, 111–120.
45. Bogaerts, A.; Neyts, R.; Gijbels, R.; van der Mullen, J. J. A. M. *Spectrochim. Acta B* **2002**, *57*, 609–658.
46. Grimm, W. *Spectrochim. Acta B* **1968**, *23*, 443–454.
47. Weiss, Z.; Musil, J.; Vlcek, J.; Fresenius, J. *Anal. Chem.* **1996**, *354*, 188–192.
48. Leygraf, C.; Johnson, M. In *Analytical Methods in Corrosion Science and Engineering*; Taylor & Francis: Boca Raton, FL, 2006; pp 237–268.

## 2.33 Scanning Probe Microscopies

**P. Marcus and V. Maurice**

Laboratoire de Physico-Chimie des Surfaces, CNRS (UMR 7045) – Université Pierre et Marie Curie, Ecole Nationale Supérieure de Chimie de Paris, 11 rue Pierre et Marie Curie, 75231 Paris Cedex 05, France

© 2010 Elsevier B.V. All rights reserved.

2.33.1	Introduction	1431
2.33.2	Scanning Tunneling Microscopy	1431
2.33.2.1	Principle and Operation	1431
2.33.2.2	Scanning Tunneling Spectroscopy	1432
2.33.2.3	Application to the Solid–Gas Interface and Limitations	1432
2.33.3	Electrochemical STM	1433
2.33.3.1	Electrochemical Implementation and Limitations	1433
2.33.3.2	Application to Corrosion Analysis at the Solid–Liquid Interface	1434
2.33.3.2.1	Active dissolution of metals	1434
2.33.3.2.2	Growth and structure of passive films	1436
2.33.3.3	Electrochemical Tunneling Spectroscopy	1438
2.33.4	Atomic Force Microscopy	1439
2.33.4.1	Principle and Operation	1439
2.33.4.2	Electrochemical Implementation and Limitations	1440
2.33.4.3	Application to Corrosion Analysis at the Solid–Liquid Interface	1440
2.33.5	Conclusion	1441
References		1441

### Glossary

**Adsorption** The first stage of interaction between a surface and its environment (gaseous or liquid), in which atoms or molecules are bound to the surface of a material.

**Corrosion** The degradation of a metallic material under the effect of the environment.

**Dissolution** The electrochemical reaction in which the metal is ionized and the cation thus formed goes into solution where it is hydrolyzed.

**Localized corrosion** Limitation of the corrosion of a metal surface to local areas.

**Passivation** The property of a metal to form a thin, continuous, compact, and adherent layer of oxide or oxyhydroxide (the passive film) at its surface that blocks the reaction of dissolution of metal atoms.

**Passivity breakdown** The local breakdown of the passive film.

**Pitting** The result of localized corrosion of passivated metal surfaces in local areas.

**Reconstruction** The change of atomic position when the surface of a material has a structure different from a bulk termination.

**Superstructure** The specific structure formed at the surface of a material.

### Abbreviations

**AFM** Atomic force microscopy

**CB** Conduction band

**DOS** Density of states

**ECAFM** Electrochemical atomic force microscopy

**ECSTM** Electrochemical scanning tunneling microscopy

**ECTS** Electrochemical tunneling spectroscopy

**SECM** Scanning electrochemical microscope

**SPM** Scanning probe microscopy

**STM** Scanning tunneling microscopy

**STS** Scanning tunneling spectroscopy

**UHV** Ultrahigh vacuum

**VB** Valence band

### Symbols

***d*** Distance between tip and sample surface (m)

***d<sub>z</sub>*** Deflection along the axis *Z* (m)

$e$	Charge of proton ( $1.6 \times 10^{-19}$ C)
$E_F$	Fermi level energy (eV)
$h$	Planck's constant ( $6.63 \times 10^{-34}$ J s)
$I$	Tunneling current (A)
$I_T$	Tip current (A)
$k$	Spring constant ( $\text{N m}^{-1}$ )
$m_e$	Mass of the electron ( $9.11 \times 10^{-31}$ kg)
$P_X, P_Y, P_Z$	Components of the piezoelectric scanner controlling $x, y, z$ position
$T$	Tunneling transmission probability
$U$	Intermolecular potential
$U_S$	Sample electrochemical potential (V vs. reference electrode)
$U_T$	Tip electrochemical potential (V vs. reference electrode)
$V_{\text{bias}}$	Bias potential between sample and tip (V)
$V_X, V_Y, V_Z$	Voltages applied to $P_X, P_Y, P_Z$ (V)
$X, Y, Z$	Orthogonal scan axes
$\phi$	Electron tunneling barrier height (eV)
$\kappa$	Tunneling decay constant ( $\text{m}^{-1}$ )
$\rho_s(E)$	Density of states of the sample at the energy $E$ ( $\text{m}^{-2}$ )
$\rho_t(E)$	Density of states of the tip at the energy $E$ ( $\text{m}^{-2}$ )

## 2.33.1 Introduction

Scanning probes microscopies (scanning tunneling microscopy (STM) and atomic force microscopy (AFM)) allow direct three-dimensional (3D) imaging of the surface structure and topography of materials at high resolution (atomic or molecular resolution). Their advent in the 1980s has opened up new prospects for the structural analysis of corroded surfaces, as these microscopes can be applied to both solid–gas interfaces under controlled environments (ultrahigh vacuum (UHV)) and to solid–liquid interfaces under electrochemical control. Moreover, time-resolved imaging allows the investigation of the dynamics of structure modifications produced by corrosion processes. The coupling of STM with spectroscopic measurements (scanning tunneling spectroscopy (STS)) provides information on a local scale on the electronic properties of surfaces.

This chapter describes the principles and operation of STM/STS and AFM and their electrochemistry implementation (ECSTM and ECAFM) for the analysis of corrosion processes at surfaces. Applications of ECSTM, ECTS, and ECAFM are illustrated by selected examples, emphasizing data obtained *in situ* at the solid–liquid interface on the anodic dissolution

of metals, the growth mechanism and structure of passive oxide layers and their electronic properties at the (sub)nanometer scale, and on the initiation of localized corrosion at the (sub)micrometer scale.

## 2.33.2 Scanning Tunneling Microscopy

This technique is unique in that it provides 3D real space images and allows localized measurements of geometric and electronic structures at high resolution. The first atomically resolved images were published in 1983.<sup>[1]</sup>

### 2.33.2.1 Principle and Operation

STM is based on tunneling of electrons between two electrodes separated by a potential barrier and biased by a voltage  $V_{\text{bias}}$  (Figure 1). Electrons within  $eV_{\text{bias}}$  of the Fermi level tunnel from the occupied states of the negatively biased electrode to the unoccupied states of the positively biased electrode. Assuming constant density of these electronic states, the tunneling current through the planar barrier increases linearly with  $V_{\text{bias}}$  and decreases exponentially with the barrier width  $d$  according to eqn. [1]

$$I \propto V_{\text{bias}} \exp(-2\kappa d) \quad [1]$$

where  $\kappa$  is the tunneling decay constant in the barrier, given by eqn. [2]

$$\kappa = \frac{2\pi}{h} \sqrt{2m_e\phi} \quad [2]$$

with  $h$  being the Planck's constant,  $m_e$  the electron mass, and  $\phi$  the tunnel barrier height. For electrons at the Fermi level,  $\phi$  is the work function of the negatively biased electrode. Since most work functions are 4–5 eV,  $\kappa \sim 1 \text{ \AA}^{-1}$  we find that for a bias of 0.1 V, a tunneling current of  $\sim 1.5$  nA can be observed for a separation between the two electrodes of  $\sim 0.9$  nm. The tunneling current drops by nearly one order of magnitude for every increase of 0.1 nm of the barrier width. A direct consequence of this exponential decay is that if one electrode is a tip terminated by an atomic asperity protruding by  $\sim 0.1$  nm at the apex (Figure 1),  $\sim 90\%$  of the current is spatially limited to this atomic asperity.

STM operation is based on precise control of the position of the tip with respect to the surface to be analyzed. The tip is placed on a tripod formed by three independent piezoelectric elements,  $P_X, P_Y, P_Z$ , controlled by the voltages  $V_X, V_Y, V_Z$  respectively (Figure 1). At a given bias voltage, the tip is scanned



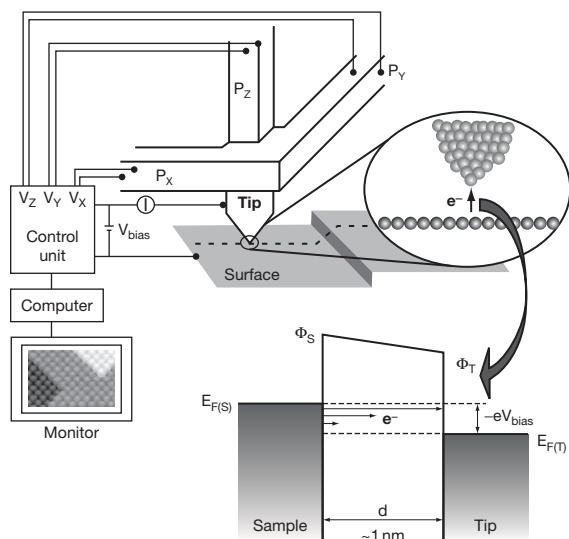


**Figure 1** Schematic diagram of the scanning tunneling microscope and principle of electron tunneling through a biased potential barrier between sample and tip.

along the two lateral directions  $X$  and  $Y$  parallel to the surface, while a feedback loop constantly adjusts the tip vertical position along the  $Z$ -axis, so as to keep the current to a constant setpoint value chosen by the operator. This is the ‘constant current’ mode where  $\kappa d$  is kept constant. If the local work function  $\phi$  remains constant, a constant current corresponds to a constant distance  $d$  between tip and surface. The shape of the surface is then reproduced by the path of the tip. The values of  $V_Z = f(V_X, V_Y)$  are used to produce a 3D image of the surface most often displayed on the monitor, using a color or gray scale. The microscope can also be operated in ‘constant height’ mode with the feedback slowed down or switched off, but at the risk of tip damage, as the tip height is not adjusted.

The setpoint current used can vary from a few tens of picoamperes for poorly conductive surfaces to a few nanoamperes for metal or doped semiconductor surfaces. Bias voltages can vary from a few volts to a few millivolts. High quality tips can be prepared from tungsten or Pt–Ir wires by electrochemical etching.<sup>2</sup> The lateral (spatial) resolution of the instrument depends on the quality of tip preparation; it is, at best, typically  $\sim 0.1$  nm. The vertical (depth) resolution depends on the quality of the damping system used to isolate the instrument from external vibrations and on the precision of the control of the tip–sample distance; it is  $\sim 0.001$  nm at best. Most commercial instruments adhere to specifications that allow imaging at atomic resolution on reference samples.

### 2.33.2.2 Scanning Tunneling Spectroscopy

STM images also contain information on the local electronic structures of the surface and tip. According to the theory of STM,<sup>3</sup> the tunneling current is expressed as (eqn. [3])

$$I = \int_0^{eV_{\text{bias}}} \rho_s(r, E) \rho_t(r, E - eV_{\text{bias}}) T(E, eV_{\text{bias}}) dE \quad [3]$$

where  $\rho_s(r, E)$  and  $\rho_t(r, E)$  are respectively the density of states (DOS) of the sample and tip at location  $r$  and energy  $E$ , measured with respect to their individual Fermi levels.  $T(E, eV_{\text{bias}})$  is the tunneling transmission probability for electrons with energy  $E$  at applied bias voltage  $V_{\text{bias}}$ . For a fixed surface-to-tip distance and assuming to a first approximation, a constant  $\rho_t(r, E)$ , eqn. [4] can be deduced:

$$\frac{d \ln I}{d \ln V_{\text{bias}}} = \frac{dI}{dV_{\text{bias}}} \times \frac{V_{\text{bias}}}{I} \propto \rho_s(E) \quad [4]$$

It follows that  $\rho_s(E)$  can be extracted from measurements of the tunneling current as a function of the bias voltage applied to the tunneling barrier, that is, from tunneling spectroscopy  $I$ – $V_{\text{bias}}$  measurements.<sup>4</sup>

In tunneling spectroscopy (TS), quantitative information on surface electronic states is obtained using either modulation techniques or numerical techniques to measure  $dI/dV_{\text{bias}}$  at constant average tunneling distance as a function of  $V_{\text{bias}}$  at a single point of the surface. Such measurements can reveal structures in the surface density of states that can arise from critical points in the surface-projected bulk band structure or from true surface states associated with surface reconstructions, adsorbates, or ultrathin films formed on the surface. In scanning tunneling spectroscopy (STS), spectroscopic  $I$ – $V_{\text{bias}}$  measurements are combined with topographic measurements to extract laterally resolved information and map  $\rho_s(E)$  spatially. In the so-called current imaging tunneling spectroscopy (CITS) mode,  $I$ – $V_{\text{bias}}$  curves are recorded for every pixel of the topographic image with the feedback loop switched off in order to operate at a fixed surface-to-tip distance. The interest of corrosion science in these techniques is the possibility of acquiring laterally resolved chemical information on surfaces.

### 2.33.2.3 Application to the Solid–Gas Interface and Limitations

STM was originally designed for application at the solid–gas interface under UHV. The environmental control of the interface inherent to UHV allows one to

locally characterize, at the atomic scale, the surface structure of semiconductors, superconductors, and metallic materials, along with the modifications induced by the adsorption of atoms and molecules or by the deposition of nanoparticles. The technique is also widely used to study nanostructuring processes resulting from surface modifications. Operation at low temperature (down to 4 K) permits manipulation of atoms, molecules, and nanoparticles. Operation at high temperature (up to  $\sim 900$  K) limits space resolution due to acceleration of surface diffusion and thermal drift (uncontrolled variation of tip position with respect to the surface), and the time resolution due to activation of surface reactions.

For corrosion related studies, UHV-STM is mostly applied to study the initial stages of oxidation of metallic materials. The adsorption of oxygen on metallic materials has been the most studied topic. A review of data obtained on Cu, Ni, and Ag single-crystal surfaces has been published.<sup>5</sup> The technique allows one to determine the adsorption site of the adsorbate, the adsorbate superstructure including the reconstruction of the substrate possibly induced by adsorption, and the nature and role of defects.

The growth mechanism of the superstructure and surface diffusion can be studied by acquiring consecutive images from a selected area as a function of time (time-resolved imaging). However, the time resolution is of the order of several tens of seconds per image with most commercial microscopes and the application is restricted to relatively slow processes. Relatively fast physical processes can be slowed down by operating at low temperature, or alternatively, fast-scanning microscopes with a time resolution better than one second per image can be used. One such example of fast-scan STM applied to the solid–liquid interface is presented further on.

Time-resolved UHV-STM can also be applied to the solid–gas interface to study the mechanism of phase transformation from metals to oxides. The local nature of measurement is then most effective to characterize the sites of nucleation of the oxide phase and the role of surface defects, the growth mechanism of the nuclei until full coverage of the surface, and the structure of the oxide nuclei. STS can be combined with STM to locally characterize the oxide nuclei and the unmodified metallic areas.<sup>6</sup>

Because of its sensitivity to the topmost surface atomic layer only, STM is less effective in characterizing the structure of 3D films formed by oxidation at the surface of metals and alloys. Indeed, neither the inner structure of the film nor the buried metal–oxide

interface can be accessed, thereby preventing a detailed investigation of the mechanism of 3D growth of the oxide film. Rare exceptions of imaging of the buried metal–oxide interface have been reported when an ultrathin oxide film transparent to the tunneling electrons is formed on the metallic substrate.<sup>7</sup> In most cases, only the surface of the 3D oxide films can be characterized, including its atomic structure and nanostructural defects. However, the technique is well suited to locally characterize the reactivity of 3D oxide films and their resulting surface structural modifications. It has been applied, for example, to the interaction of water vapor with thermal oxide films of chromia grown on Cr surfaces<sup>8</sup> and alumina on NiAl surfaces.<sup>9</sup>

### 2.33.3 Electrochemical STM

STM was first applied in solution in 1986<sup>10</sup> and to corrosion studies in 1988.<sup>11</sup> A major difference with UHV operation is the decrease of the tunneling barrier height in solution. Experimental values ranging from 0.1 to 0.3 eV have been reported,<sup>12,13</sup> which is much smaller than the values of  $\sim 4$  eV for UHV operation.

#### 2.33.3.1 Electrochemical Implementation and Limitations

In ECSTM, the tip is immersed in the electrolyte and acts as a fourth electrode added to a conventional three electrode cell with working reference and counter electrodes (Figure 2). Charging of the double layer and electrochemical reactions take place at the tip–electrolyte interface. They generate capacitive and faradic currents at the tip that superimpose onto the tunneling current and must be minimized as they affect STM operation based on the measurement of the total tip current. The most effective minimization is obtained by reduction of the tip surface in contact with the electrolyte. This is done by covering most of the immersed portion of the tip by an insulating coating. Glass, epoxy varnish, silicone polymer, Apiezon wax, nail polish, or electrophoretic paint can be used. Well-prepared coatings will leave only  $\sim 10$   $\mu\text{m}$  or less, uncoated at the very end of the tip. Further minimization of the electrochemical currents at the tip is achieved by polarizing the tip in the double layer charging region (PtIr) or at the corrosion potential (W). This combined minimization allows one to decrease the electrochemical current to values of 50 pA or less, extremely small relative to the usual set-point current of 0.5–10 nA used in ECSTM,

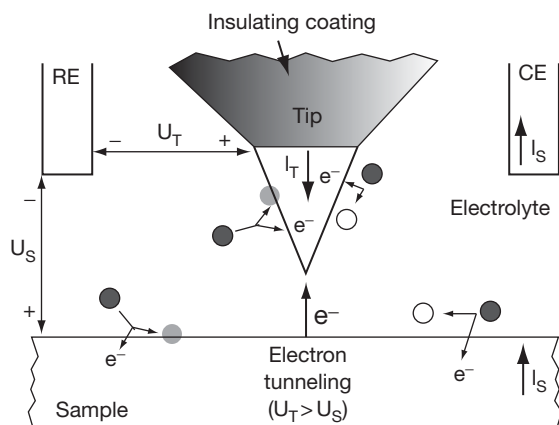


**Figure 2** Schematic diagram of the four electrode cell used in ECSTM. RE is the reference electrode. CE is the counter electrode.  $U_S$  and  $U_T$  are electrochemical potentials applied to the sample and tip, respectively.  $I_S$  and  $I_T$  are the sample current and tip currents, respectively. For  $U_T > U_S$ , electrons tunnel from the occupied states of the sample to the empty states of the tip.

thus ensuring no interference with the functioning of the STM.

ECSTM, performed in a four-electrode cell, requires the use of a bipotentiostat that enables one to control independently the electrochemical potentials of the tip ( $U_T$ ) and sample ( $U_S$ ) relative to a common reference electrode. The bias voltage for STM operation is then given by the difference between  $U_T$  and  $U_S$ . The current resulting from the electrochemical reaction taking place at the sample–electrolyte interface is measured by the counter electrode, as in a conventional electrochemical cell.

There are limitations related to the local nature of the measurements. The high spatial resolution capability of the instrument, which provides the basis for the ability to image individual atoms or molecules, brings down the analyzed area to a tiny fraction of the total surface area (typically  $1 \times 1 \mu\text{m}^2$ ) or less. A correlation between STM-derived and electrochemical information (integrated over areas of  $1 \text{ cm}^2$  or less) is really meaningful only if the area probed by STM is representative of the whole electrode surface. Limitations can also arise from the possible interference of the tip with the electrochemical process at the working electrode surface. The close proximity of the tip can cause shielding effects for reaction at the sample–solution interface. An interference of sample and tip electric double layer is also possible.<sup>12,14</sup> Tip-induced corrosion processes can also occur.<sup>14,15</sup> Corrosion studies by ECSTM may also be limited by the small volume of the electrochemical STM cells. It is

indeed not possible to investigate the substrate modifications resulting from extensive corrosion processes as the observation of the substrate surface would be masked by redeposition of corrosion products.

Despite these limitations, ECSTM investigations can provide invaluable information, in particular molecular scale information, on the structural modifications related to corrosion processes such as the active dissolution and passivation of metallic surfaces as illustrated below, as well as the adsorption of corrosion inhibitors<sup>16</sup> or the reactivity of anodic oxide films determining the initial stages of localized corrosion of passivated metallic materials.<sup>17</sup>

### 2.33.3.2 Application to Corrosion Analysis at the Solid–Liquid Interface

The high resolution provided by ECSTM allows structural characterization of corrosion processes at the molecular level. This requires appropriate control of electrochemical conditions in order to minimize the rate of corrosion processes to a point compatible with the STM time resolution. In contrast with UHV-STM, corrosion reactions cannot be slowed down by operating at low temperatures because of the liquid environment, but electrochemical potential can be used to control the reaction kinetics. High resolution ECSTM also requires high quality of surface preparation and control, that is, atomically flat surfaces of well-defined structure. This can be achieved with single-crystals of known orientation whose surface has been appropriately prepared to have a terrace and step topography.

#### 2.33.3.2.1 Active dissolution of metals

ECSTM is very effective to study *in situ* the active dissolution of metals because the surface is free of passivating oxides and for pure metals, the electrode surface remains terminated by an atomically flat terrace and step topography during the corrosion process. This is a very favorable situation for atomic-scale imaging of dynamic processes at surfaces. Investigations can focus on the structural modifications of atomically flat surfaces resulting from adsorption of anions in the double layer potential region preceding the onset of dissolution and on the dissolution of metal atoms at specific sites. The formation of well-ordered superstructures, more corrugated than the metallic lattice, facilitates high resolution ECSTM imaging of the surface structure. For alloys,

dealloying can be studied. The dynamics of these processes can be studied by time-resolved imaging of a selected region. High-resolution ECSTM has been applied to the anodic dissolution of pure metals, Cu,<sup>18–20</sup> Ni,<sup>21,22</sup> Ag,<sup>23</sup> Co,<sup>24</sup> and Pd,<sup>25</sup> and alloys, CuAu.<sup>26</sup>

**Figure 3** illustrates the process of dissolution, proceeding layer-by-layer *via* a step-flow mechanism at moderate potentials (i.e., slow etching rate). It was observed in this case at atomic resolution for Cu(001) in HCl<sub>aq</sub> with a fast-scan ECSTM.<sup>20</sup> Preferential etching of the surface takes place at the defects

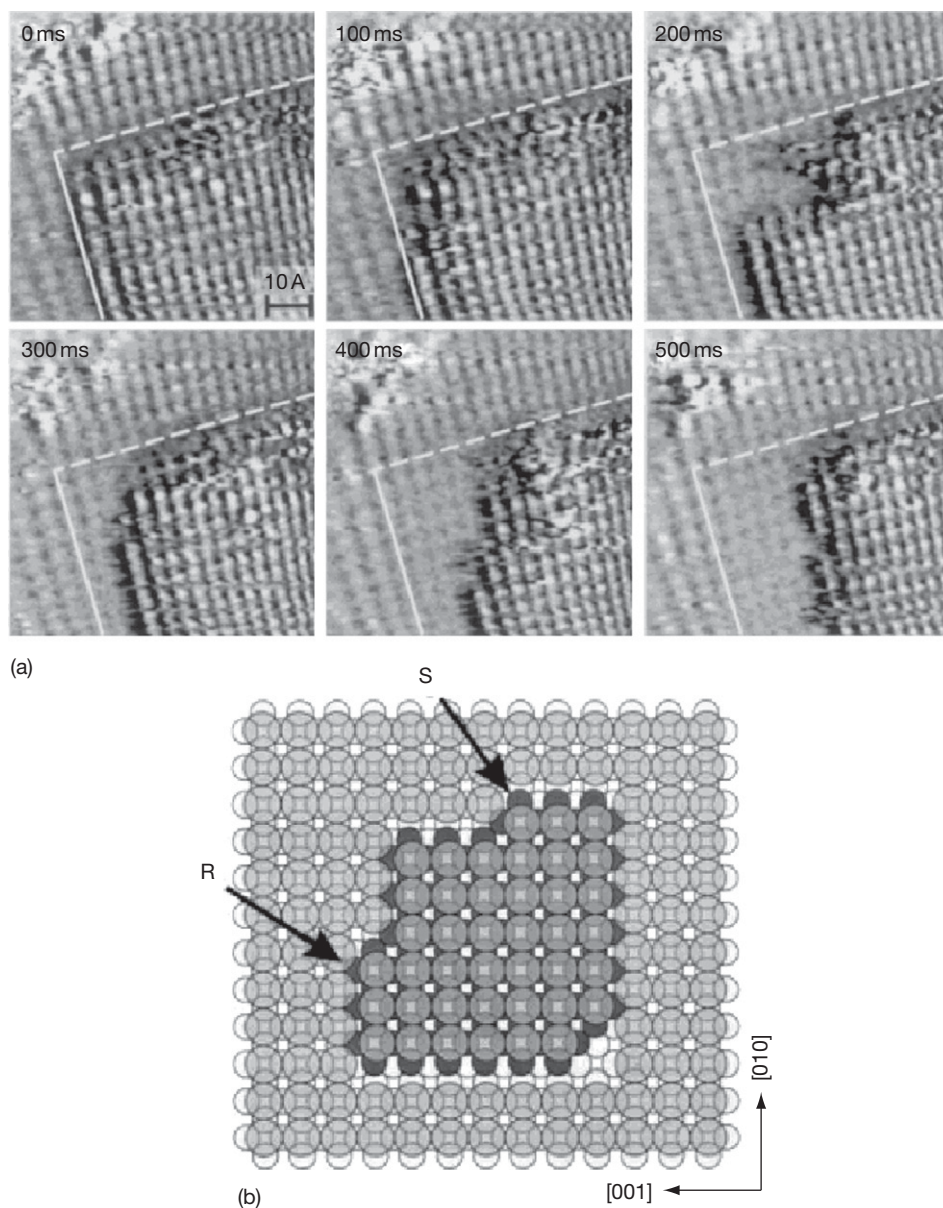


**Figure 3** (a) Sequence of fast-scan ECSTM images (0.1 s per image) recorded on Cu(001) in 0.01 M HCl<sub>aq</sub> at  $-0.17$  V/SCE showing dissolution of a Cu terrace starting at the outer terrace corner. The observed lattice is formed by adsorbed chlorine. The markedly different dissolution behavior at the active and stable steps whose initial position is marked by solid and dashed lines, respectively, is clearly visible. (b) Model of the (001) surface of a face-centered cubic metal (e.g., Cu) covered by an ordered  $c(2 \times 2)$  adlayer (e.g., Cl) showing different structure of steps and kinks along the [010] and [001] directions. R and S mark the reactive and stable Cu atoms at the outer kinks, respectively. Reproduced from Magnussen, O. M.; Zitzler, L.; Gleich, B.; Vogt, M. R.; Behm, R. J. *Electrochimica Acta* **2001**, 46, 3725–3733.



corresponding to preexisting step edges. Selective etching of atoms at these sites results from their lower coordination to nearest neighbor atoms.

The superstructure formed by strongly adsorbed ions in the double layer region influences the anisotropy of the etching. In the absence of strongly adsorbed anions, the etching process, at moderate overpotentials, stabilizes the step edges oriented along the close-packed directions of the crystal where the nearest neighbor coordination of the atoms is maximum, e.g., along the atomically smooth  $\langle 1-10 \rangle$  and  $\langle 10-10 \rangle$  directions for (111)-oriented fcc metals and (0001)-oriented hcp metals respectively. On Cu(001), a highly ordered  $\alpha(2 \times 2)$  adlayer (observed in Figure 3) is formed in  $\text{HCl}_{\text{aq}}$  solutions. It stabilizes the step edges along the close-packed directions of the superstructure corresponding to the  $\langle 100 \rangle$  substrate directions. Atomic-scale imaging shows that the dissolution proceeds at structurally well-defined kinks of the [100]- and [010]-oriented steps *via* removal of the primitive unit cells of the Cl adlayer. Another effect of the  $\alpha(2 \times 2)$  adlayer is an induced anisotropy of the dissolution process along the symmetrical  $\langle 100 \rangle$  directions of the step edges. This is also visible in Figure 3 where one orientation of the step edges dissolves more rapidly than the other. This results from the structural anisotropy of the  $\langle 100 \rangle$  step edges induced by the presence of the  $\alpha(2 \times 2)$  adlayer, as illustrated by the model shown in Figure 3. This has been tentatively explained by the coordination of the outmost Cu atom forming the dissolving kink to the adjacent Cl adsorbates.<sup>20</sup>

In the double layer potential range, equilibrium fluctuations of these step edges are observed, which result from local removal/redeposition processes. These fluctuations are also illustrated by the sequence of fast-scan images shown in Figure 3. At more anodic potentials, the dissolution process prevails and a net removal is observed; but re-deposition still occurs.

### 2.33.3.2.2 Growth and structure of passive films

In the area of passivation, high-resolution ECSTM measurements have also been obtained with well-prepared single-crystal surfaces, bringing new insight into the mechanisms of self-protection of metal and alloys against corrosion in aqueous solutions. Data on this topic are available for Cu,<sup>27–29</sup> Ni,<sup>21,22,30,31</sup> Ag,<sup>32</sup> Co,<sup>33</sup> Fe,<sup>34</sup> Cr,<sup>35</sup> Al,<sup>36</sup> and ferritic<sup>37</sup> and austenitic<sup>38</sup> stainless steels.

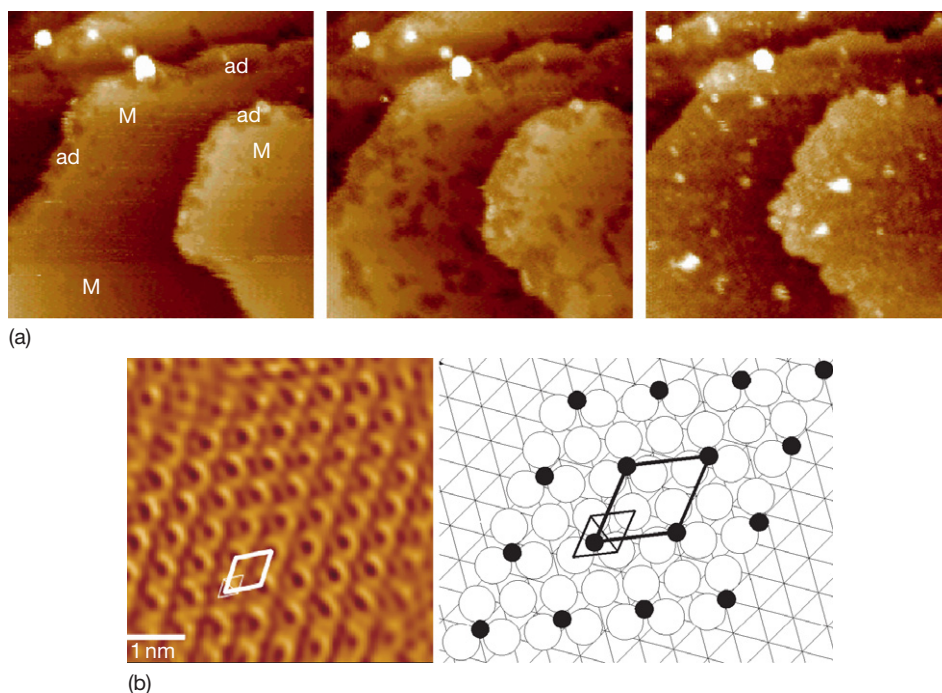
The structural modifications of the electrode occurring at the active/passive transition as well as in the

potential range preceding oxide formation are illustrated here for Cu(111) in aqueous sodium hydroxide solution.<sup>27–29</sup> Figure 4 illustrates the growth of the adsorbed hydroxide layer on Cu(111) at potentials below that at which copper oxide is formed. The sequence of images shown in Figure 4(a) was obtained after stepping anodically the potential to  $-0.6 \text{ V}_{\text{SHE}}$ , below the active/passive transition at  $\sim -0.2 \text{ V}_{\text{SHE}}$ . The atomically smooth terraces of the surface (marked M) become progressively covered by darker-appearing islands (marked ad) that grow laterally and coalesce to cover the terraces completely. The darker appearance of these ad-islands is a typical effect of adsorbed O species also observed at the solid-gas interface.<sup>5</sup> The adsorbed layer preferentially grows at the step edges, confirming the preferential reactivity of these defect sites of the surface. The terraces grow laterally due to displacement of the step edges, and monoatomic ad-islands are formed at the end of the growth process. These two features are indicative of the reconstruction of the topmost Cu plane induced by the adsorption of the OH groups. The reconstruction causes ejection of Cu atoms from the original metallic surface layer. These ejected atoms diffuse on the surface and aggregate at step edges, which cause the observed lateral displacement of the step edges. In the final stages of the adsorption process, when most of the surface is already covered by the adlayer, the ejected atoms have reduced mobility on the OH-covered terraces and aggregate to form the observed monoatomic ad-islands.

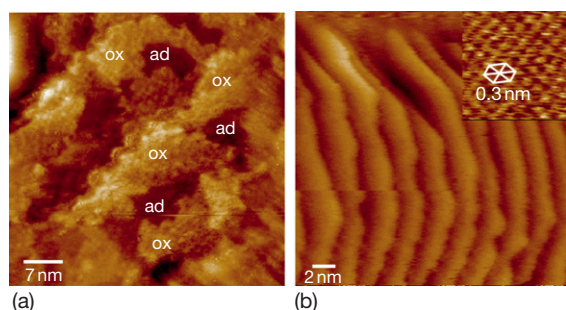
Figure 4(b) shows an atomically-resolved image and model of the ordered  $\text{OH}_{\text{ads}}/\text{Cu}(111)$  surface that confirm the reconstruction of the Cu(111) topmost atomic plane. A hexagonal lattice with a parameter of  $0.6 \pm 0.02 \text{ nm}$  is measured. The interatomic distance between the Cu atoms is  $\sim 0.3 \text{ nm}$ , which is larger than the interatomic spacing of  $0.256 \text{ nm}$  in Cu(111), and confirms the reconstruction of the topmost Cu plane into a plane of lower atomic density. A coverage of  $\sim 0.2 \text{ OH}$  per Cu(111) atom is deduced from the density of the  $\text{OH}_{\text{ads}}$ , in excellent agreement with the coverage of 0.19 obtained from the electrochemical charge transfer measurements. In addition, the STM data show that the  $\text{OH}_{\text{ads}}$  sit in the three-fold hollow sites of the reconstructed Cu plane on which they form a  $(2 \times 2)$  structure.

Figure 5 illustrates the influence of the potential on nucleation, growth, crystallization, and structure of the  $\text{Cu}_2\text{O}$  oxide film formed in the potential range of Cu(I) oxidation. At low oversaturation (Figure 5(a)), mono-layer thick islands poorly crystallized and partially





**Figure 4** (a) Sequence of ECSTM images (38 s per image) showing growth of an adlayer of OH groups on Cu(111) at  $-0.6 V_{\text{SHE}}$  in 0.1 M  $\text{NaOH}_{\text{aq}}$ . Adapted from Maurice, V.; Strehblow, H.-H.; Marcus, P. *Surface Science* **2000**, 458, 185–194. (b) ECSTM image and model of the ordered structure of adsorbed OH groups formed on Cu(111). The large and small cells mark the lattice of adsorbed OH and reconstructed copper, respectively. Adapted from Kunze, J.; Maurice, V.; Klein, L. H.; Strehblow, H.-H.; Marcus, P. *Electrochimica Acta* **2003**, 48, 1157–1167.



**Figure 5** ECSTM images showing the effect of the potential on the growth and structure of the Cu(I) oxide formed on Cu(111) in 0.1 M  $\text{NaOH}_{\text{aq}}$  at  $-0.25 V_{\text{SHE}}$  (a) and  $-0.20 V_{\text{SHE}}$  (b). In (a), noncrystalline oxide islands (ox.) separated by the adsorbed OH layer (ad) partially cover the substrate. In (b), a crystalline oxide layer fully covers the substrate. Its atomic lattice (shown in the inset) corresponds to  $\text{Cu}_2\text{O}(111)$ . Adapted from Kunze, J.; Maurice, V.; Klein, L. H.; Strehblow, H.-H.; Marcus, P. *Journal of Physical Chemistry B* **2001**, 105, 4263–4269, with permission from American Chemical Society.

covering the substrate, are formed after preferential nucleation at step edges. They are separated by islands of the ordered hydroxide adlayer. At higher

oversaturation (Figure 5(b)), a well crystallized multi-layer thick film is formed, and the step edges are not preferential sites of nucleation. The equivalent thickness of the oxide layer can be deduced from subsequent measurements of the charge transfer during cathodic reduction scans. It was  $\sim 0.5$  and 7 equivalent monolayers (ML) of  $\text{Cu}_2\text{O}(111)$  after growth at  $-0.25$  and  $-0.2 V_{\text{SHE}}$ , respectively. The observed lattice of the ordered oxide layer is hexagonal with a parameter of  $\sim 0.3$  nm, consistent with the Cu sublattice in the (111)-oriented cuprite. The oxide grows in parallel (or antiparallel) epitaxy ( $\text{Cu}_2\text{O}(111) [\bar{1}\bar{1}0]||\text{Cu}(111) [\bar{1}\bar{1}0]$  or  $[\bar{1}\bar{1}0]$ ).

The crystalline Cu(I) oxide layer has a nanostructured surface consisting of facets. The surface faceting results from a tilt of a few degrees of the orientation of the oxide lattice with respect to the Cu lattice. A possible origin of the tilt is the relaxation of the epitaxial stress at the metal–oxide interface resulting from the large mismatch between the two lattices. The height of the surface steps of the oxide layer corresponds to 1 ML of cuprite, indicating an identical chemical termination of the  $\text{Cu}_2\text{O}(111)$  oxide terraces. It is thought that the surface of

the oxide layer is hydroxylated in the aqueous solution and that the measured lattice corresponds to OH and/or OH<sup>-</sup> groups forming a (1 × 1) layer on the Cu<sup>+</sup> planes of the (111)-oriented cuprite layers.

### 2.33.3.3 Electrochemical Tunneling Spectroscopy

With the potential of the substrate fixed by the electrochemical process under study and that of the tip adjusted to minimize the electrochemical tip current and optimize the STM measurement, the tunnel voltage can no longer be adjusted in a wide range as in UHV conditions. Thus, spectroscopic  $I$ - $V_{\text{bias}}$  measurements (TS) are most often restricted to a few hundreds millivolts range in an ECSTM cell.<sup>12</sup> However, recent developments allowing *in situ* single-point spectroscopic measurements (ECTS) over a larger range of tunnel voltage of nearly 3 V have been applied to Fe in a borate buffer solution.<sup>13</sup> The developments are based on the use of noble metals for tips (PtIr) combined with improved performance in tip isolation using electrophoretic coating. Ultrafast voltage ramps (up to 20 V s<sup>-1</sup>) are applied to vary the tip potential ( $U_T$ ) at a fixed sample potential ( $U_S$ ) and at a tunneling distance defined by the initial set-point conditions. The tip current ( $I_T$ ) is measured during the  $U_T$  ramp with the feedback loop switched off.  $I_T$ - $U_T$  curves measured at distances beyond the tunneling gap (with the tip retracted) are subtracted from  $I_T$ - $U_T$  curves measured at predefined tunneling distances. This procedure is used to eliminate capacitive and faradaic contributions to the tip current.

Tunneling spectra obtained by scanning  $U_T$  between -800 and +1500 mV/SCC at five different  $U_S$  values corresponding to various oxidation states of the Fe electrode versus  $U_T$  are plotted in Figure 6. The lower panel shows the tunneling conductance  $dI_T/dU_T$ , proportional to the Fe electrode DOS. It is obtained by numerical differentiation of the curves in the upper panel. The upper panel shows linear spectra for iron polarized at -800 and -650 mV. This results from a high and nearly constant density of surface states (or high surface conductance) of the metallic Fe(0) electrode. At -400 mV, an hydrated Fe(II) layer, a few nanometers thick and with unknown electronic properties, formed on the electrode surface in the specific conditions used in this study. A double exponential behavior is measured revealing a region of low current due to a decrease of the DOS. At 500 mV, the oxide layer is oxidized to

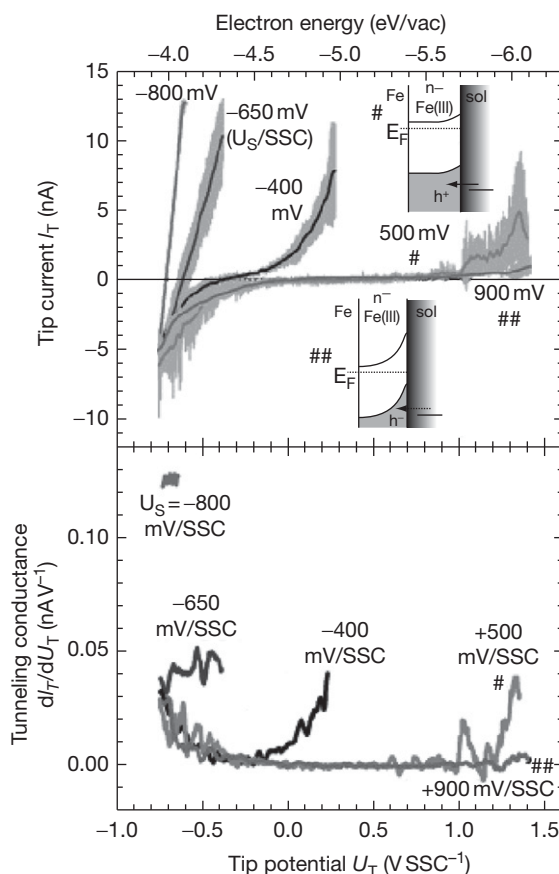


**Figure 6** ECTS spectra of Fe polarized at  $U_S = -800$ ,  $-650$ ,  $-400$ ,  $+500$ , and  $+900$  mV in a borate buffer aqueous solution. The upper panel shows tip current vs. tip potential curves. Solid lines and gray bands show average curves and standard deviations, respectively. The lower panel shows the conductance curves. See text for details. Adapted from Díez-Pérez, I.; Güell, A. G.; Sanz, F.; Gorostiza, P. *Analytical Chemistry* **2006**, 78, 7325–7329, with permission from American Chemical Society.

Fe(III) with well-characterized n-type semiconductive properties. A band gap in the DOS increases the separation between the exponential current branches. Its width is consistent with values reported for passivated iron ( $E_g = 1.6$ – $1.9$  eV). The positive current branch results from hole injection from the tip to the valence band (VB). At 500 mV, it is maintained by the slight depletion of the Fe(III) oxide film (upper inset marked #). At 900 mV, the positive current branch becomes extinguished due to stronger depletion conditions and demonstrates low density of charge carriers (upper inset marked ##). Both at 500 and 900 mV, the negative current branches result from electron injection from the tip to the conduction band (CB) of the oxide.

This spectroscopic data demonstrates the capability of ECTS to obtain *in situ* the electronic structure of the solid/electrolyte interface and measure the availability of charge carriers at the electrode surface. Series of tunneling spectra can be acquired stepwise over a large range of polarization potential and used to plot so-called conductograms (map of the conductance (i.e., the charge exchange properties) of the electrode as a function of potential), to study modifications resulting from a variation of the pH of the electrolyte or from the presence of chlorides. Up to now, such tunneling spectra have only been obtained in single-point mode, without combined imaging of the surface.

### 2.33.4 Atomic Force Microscopy

In contrast with STM, AFM, invented in 1986,<sup>39</sup> does not require conductive samples and tips. It can measure and image local forces between a surface and a tip, including van der Waals, Born repulsion, electrostatic and magnetic forces, friction, and adhesion.<sup>40</sup> The following presentation is restricted to topographic data derived from measurement of local forces on a length scale of  $10^{-10}$  to  $10^{-8}$  m.

#### 2.33.4.1 Principle and Operation

AFM is based on the variation of the interactions between two atoms or molecules. At very short distances, the interaction is repulsive and dominated by the electrostatic repulsion felt by the electrons as the orbitals start to overlap. At larger distances, the interaction is attractive and dominated by the dipole-dipole interaction between molecules. These interactions vary as inverse power laws of the distance,  $1/d^{12}$  and  $1/d^6$  for repulsive and attractive interactions, respectively. Their sum defines the total intermolecular potential  $U$ .

In AFM, this is the force ( $(-\partial U/\partial d)$ ) that is measured. The tip is positioned at the end of a cantilever spring (Figure 7). The deflection,  $d_z$ , of the cantilever is measured by an optical setup consisting of a laser beam reflected from the back side of the cantilever and impinging on a partitioned photodiode. The force on the cantilever is simply  $-k \cdot d_z$ ,  $k$  being the cantilever's spring constant. As in STM, a piezoelectric setup allows precise control of the tip position relative to the surface. A feedback loop is used to adjust the tip-surface distance in order to maintain the deflection (force) of the cantilever at a set-point

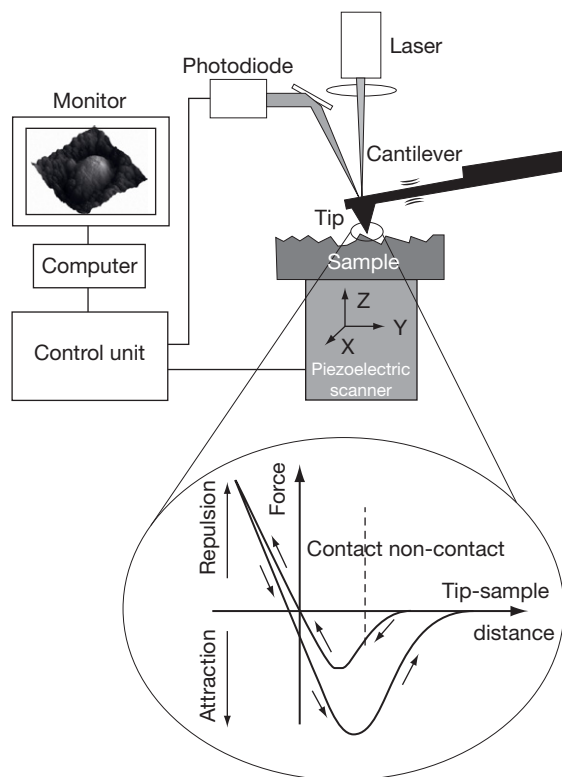


**Figure 7** Schematic diagram of the atomic force microscope and typical force curve showing the force on the cantilever as the tip-sample distance is varied.

value chosen by the operator when scanning the  $X$  and  $Y$  axes. This is the 'constant force' mode of imaging in which the tip reproduces the topographic profile of the surface. The lateral spatial resolution of the instrument is  $\sim 0.1$  nm when the interaction can be spatially limited to the atomic asperities of the tip. The vertical resolution is  $\sim 0.02$  nm.

The AFM user can choose to operate the microscope at any point along the typical force curve obtained when varying tip-sample distance (Figure 7). Contact occurs at the inflection point of the approaching curve where the curvature (i.e., derivative) changes from attractive to repulsive. Contact increases after this point as the tip-sample distance decreases. Contact-mode imaging is at risk of a potentially destructive interaction that can damage tip and/or sample. In air, stray adhesive forces ( $10^{-7}$  to  $10^{-8}$  N), resulting mostly from the presence of a condensed layer of water or other contaminants forming a capillary bridge between tip and surface, and at the origin of the hysteresis in the force curve, interfere to decrease the spatial resolution of the imaging. In addition, the dragging motion of the tip on the surface involves lateral shear force that can

distort measurement severely and induce lateral motion and/or tearing of surface features. The adhesive force is drastically reduced ( $\leq 10^{-9}$  N) in liquid applications where the whole cantilever–tip/surface assembly is immersed in solution. However the energy dissipated ( $\leq 1$  eV) by local interaction remains of the order of the energy of chemical bonds, and imaging in these conditions remains potentially destructive.

In the resonant (or Tapping®) mode, the cantilever–tip assembly oscillates at or near its resonance frequency with an amplitude of several nanometers. The oscillating tip is then moved toward the surface until contact. During scanning, the vertically oscillating tip alternately contacts the surface for force measurement and lifts off for implementation of the  $X, Y$  scan. This avoids dragging of the tip across the surface. The tip–sample separation is adjusted *via* the feedback loop of the microscope to maintain a constant oscillation amplitude and force on the sample. This resonant mode inherently prevents the tip from sticking to the surface and causing damage during scanning.

The noncontact mode is obtained for tip–surface distances larger than the one where the curvature of the force curve in **Figure 7** changes from negative to positive. Unfortunately, the attractive van der Waals forces are substantially weaker than forces used in contact mode and force resolution is poor. The consequences are a poor spatial resolution and a problematic thermal drift. The noncontact mode is more appropriate for UHV operation where the sample and tip can be cleaned from contaminants and the thermal drift is much less problematic. True atomic resolution can then be achieved when the tip–sample attractive force is such that the interaction is limited to a single atom at the tip apex.

#### 2.33.4.2 Electrochemical Implementation and Limitations

In ECAFM (electrochemical atomic force microscopy) the cantilever–tip assembly does not constitute a fourth electrode through which the electrochemical currents could flow, interfering with the signal used to probe the surface. Immersing the cantilever tip assembly and surface in solution allows better control of the adhesive force in contact mode (see above). In resonant contact mode, the fluid medium tends to damp the normal resonance frequency of the cantilever, which complicates this mode of operation. The noncontact mode becomes impractical because the van der Waals forces are even smaller, which can be a substantial limitation (e.g., for biological applications).

The limitations of ECAFM regarding the correlation between local information and integrated macroscopic information, possible tip-shielding effects on the corrosion behavior, kinetics of mass transport and small volume of the electrochemical cell are the same as those described for ECSTM.

#### 2.33.4.3 Application to Corrosion Analysis at the Solid–Liquid Interface

The application of ECAFM to corrosion analysis is much more widespread than that of ECSTM. ECAFM is often preferred because of its easier setup and because the obtained topographic information is independent of the conductivity of corrosion products. Moreover, ECAFM is most often used at the (sub) micrometer scale, i.e., at a lower level of spatial resolution that does not require preparation of atomically smooth surfaces as for ECSTM studies. ECAFM or AFM is often combined with a variety of other techniques to analyze corrosion and optimize corrosion protection properties. Corrosion protection by inhibitors<sup>41</sup> and coatings,<sup>42</sup> atmospheric corrosion,<sup>43</sup> passivation,<sup>44</sup> passivity breakdown,<sup>45</sup> localized corrosion,<sup>46,47,48,49</sup> and stress corrosion cracking<sup>50</sup> have been studied. We present examples of application to localized corrosion at inclusions.

The lower spatial resolution of AFM is appropriate to study pitting corrosion at microstructural defects (inclusions, grain boundaries, interphase boundaries) of metallic materials. **Figure 8** shows two images of localized corrosion observed *in situ* at the inclusion–matrix interface on an Al–Si(7.7 wt%) alloy under anodic polarization close to breakdown potential in 10 mM NaCl<sub>aq</sub> + 50 mM KI<sub>aq</sub>. **Figure 8(a)** shows localized dissolution occurring at the boundary surrounding a round-shaped particle of  $\sim 1$   $\mu$ m, whereas **Figure 8(b)** shows localized dissolution occurring between two irregular shaped particles (1–2  $\mu$ m size), while the boundary region to the matrix remains intact. The different nature of the particles present in the alloy (predominantly AlFeSi and eutectic Si phases) was advanced to explain the different corrosion behaviors of these particle/matrix boundaries.<sup>49</sup> A commonly advanced explanation for the formation of trenches around inclusions in Al alloys is that the inclusions act as cathodic sites for reduction of oxygen, causing the formation of an alkaline environment in the immediate vicinity of each inclusion, confirmed by local pH measurements.<sup>46</sup> This local increase of pH promotes local dissolution of the Al matrix.



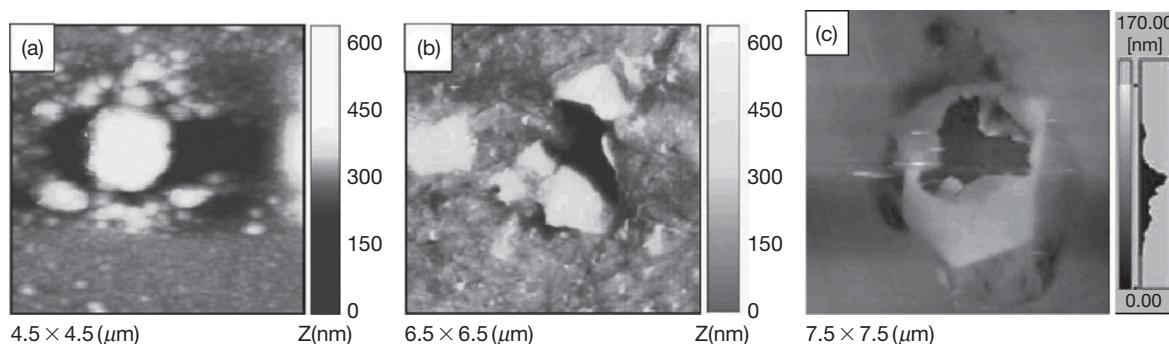


**Figure 8** (a,b) ECAFM images of an Al-7.7 wt% Si alloy under anodic polarization close to breakdown potential in 10 mM NaCl<sub>aq</sub> + 50 mM KI<sub>aq</sub>. Localized corrosion around (a) and in between (b) inclusions is observed. Reproduced from Davoodi, A.; Pan, J.; Leygraf, C.; Norgren, S. *Applied Surface Science* **2006**, 252, 5499–5503. (c) ECAFM image of SUS304 stainless steel treated at a current density of 5 mA cm<sup>-2</sup> for 1500 s in 0.6 M NaCl<sub>aq</sub>. A crust of corrosion product is observed above a pit. Reproduced from Zhang, Q.; Wang, R.; Kato, M.; Nakasa, K. *Scripta Materialia* **2005**, 52, 227–230.

On stainless steels, studies have focused on the initiation of pitting near or at sulfide and carbide inclusions. On 304 SS, *ex situ* AFM combined with scanning electrochemical microscopy (SECM) and EDX analysis has shown that certain inclusions (sulfides) concentrate chloride, by electromigration, under a sulfur crust as a result of their dissolution evidenced by AFM. It has been proposed that the high local current density (evidenced by SECM), the electromigration of chloride, and the sulfur crust (evidenced by EDX) generate an occluded extreme environment in which stainless steel depassivates.<sup>47</sup> **Figure 8(c)** shows a crust of corrosion product on a small pit observed *in situ* on SUS304 treated anodically in NaCl (3.5 wt%) to trigger localized corrosion.<sup>48</sup> A part of the crust was destroyed, possibly by the scanning probe, and the pit hole remained shallow indicating repassivation. This was explained by the decrease of the concentration of chloride and hydrogen ions in the pit due to the destruction of the crust and stirring of the solution in the initially occluded environment in the pit.

### 2.33.5 Conclusion

The principles, instrumentation, and electrochemical implementation of STM and AFM have been presented. Both methods can provide 3D imaging of surfaces in direct space during corrosion processes. ECSTM is better suited for high resolution studies at the (sub)nanometer scale but is restricted to conductive surfaces. Atomic scale studies require a high level of control to produce atomically smooth

surfaces. ECSTM can be combined with ECTS to characterize the electronic properties of surface layers *in situ*. ECAFM is well-suited for (sub)micrometer scale studies of surfaces irrespective of their conductivity. Selected examples of applications to corrosion analysis show that both methods can greatly contribute to corrosion analysis and an improved understanding and control of corrosion of metals and alloys.

### References

1. Binnig, G.; Rohrer, H.; Gerber, Ch.; Weibel, E. *Phys. Rev. Lett.* **1983**, 50, 120–123.
2. Rohrer, G. In *Scanning Tunneling Microscopy and Spectroscopy. Theory, Techniques and Applications*; Bonnell, D. A., Ed.; Wiley-VCH: New York, 1993; pp 155–187.
3. Tersoff, J. In *Scanning Tunneling Microscopy and Spectroscopy. Theory, Techniques and Applications*; Bonnell, D. A., Ed.; Wiley-VCH: New York, 1993; pp 31–50.
4. Hamers, R. J. In *Scanning Tunneling Microscopy and Spectroscopy. Theory, Techniques and Applications*; Bonnell, D. A., Ed.; Wiley-VCH: New York, 1993; pp 51–103.
5. Besenbacher, F.; Nørskov, J. K. *Prog. Surf. Sci.* **1993**, 44, 5–66.
6. Wiame, F.; Maurice, V.; Marcus, P. *Surf. Sci.* **2007**, 601, 1193–1204.
7. Maurice, V.; Despert, G.; Zanna, S.; Bacos, M.-P.; Marcus, P. *Nature Materials* **2004**, 3, 687–691.
8. Maurice, V.; Cadot, S.; Marcus, P. *Surf. Sci.* **2001**, 471, 43–58.
9. Maurice, V.; Cadot, S.; Marcus, P. *Surf. Sci.* **2005**, 581, 88–104.
10. Sonnenfeld, R.; Hansma, P. K. *Science* **1986**, 232, 211–213.
11. Lev, O.; Fan, F.-R.; Bard, A. J. *J. Electrochem. Soc.* **1988**, 135, 783–784.
12. Halbritter, J.; Repphun, G.; Vinzelberg, S.; Staikov, G.; Lorenz, W. J. *Electrochim. Acta* **1995**, 40, 1385–1394.
13. Diéz-Pérez, I.; Guell, A. G.; Sanz, F.; Gorostiza, P. *Anal. Chem.* **2006**, 78, 7325–7329.



14. Xie, Z.-X.; Kolb, D. M. *J. Electroanal. Chem.* **2000**, *481*, 177–182.
15. Garcia, S. G.; Salinas, D. R.; Mayer, C. E.; Lorenz, W. J.; Staikov, G. *Electrochim. Acta* **2003**, *48*, 1279–1285.
16. Vogt, M. R.; Nichols, R. J.; Magnussen, O. M.; Behm, R. J. *J. Phys. Chem. B* **1998**, *102*, 5859–5865.
17. Maurice, V.; Klein, L. H.; Marcus, P. *Surf. Interf. Anal.* **2002**, *34*, 139–143.
18. Suggs, D. W.; Bard, A. J. *J. Am. Chem. Soc.* **1994**, *116*, 10725–10733.
19. Broekmann, P.; Anastasescu, M.; Spaenig, A.; Lisowski, W.; Wandelt, K. *J. Electroanal. Chem.* **2001**, *500*, 241–254.
20. Magnussen, O. M.; Zitzler, L.; Gleich, B.; Vogt, M. R.; Behm, R. *J. Electrochim. Acta* **2001**, *46*, 3725–3733.
21. Suzuki, T.; Yamada, T.; Itaya, K. *J. Phys. Chem.* **1996**, *100*, 8954–8961.
22. Seyeux, A.; Maurice, V.; Klein, L. H.; Marcus, P. *J. Electrochem. Soc.* **2006**, *153*, B453–B463.
23. Dietterle, M.; Will, T.; Kolb, D. M. *Surf. Sci.* **1995**, *327*, L495–L500.
24. Ando, S.; Suzuki, T.; Itaya, K. *J. Electroanal. Chem.* **1997**, *431*, 277–284.
25. Itaya, K. In *Interfacial Electrochemistry – Theory, Experiments and Applications*; Wieckowski, A., Ed.; Marcel Dekker, New York, 1999; pp 187–210.
26. Stratmann, M.; Rohwerder, M. *Nature* **2001**, *410*, 420–423.
27. Maurice, V.; Strehblow, H.-H.; Marcus, P. *Surf. Sci.* **2000**, *458*, 185–194.
28. Kunze, J.; Maurice, V.; Klein, L. H.; Strehblow, H.-H.; Marcus, P. *J. Phys. Chem. B* **2001**, *105*, 4263–4269.
29. Kunze, J.; Maurice, V.; Klein, L. H.; Strehblow, H.-H.; Marcus, P. *Electrochim. Acta* **2003**, *48*, 1157–1167.
30. Zuili, D.; Maurice, V.; Marcus, P. *J. Electrochem. Soc.* **2000**, *147*, 1393–1400.
31. Scherer, J.; Ocko, B. M.; Magnussen, O. M. *Electrochim. Acta* **2003**, *48*, 1169–1191.
32. Kunze, J.; Strehblow, H.-H.; Staikov, G. *Electrochem. Comm.* **2004**, *6*, 132–137.
33. Foelske, A.; Kunze, J.; Strehblow, H.-H. *Surf. Sci.* **2004**, *554*, 10–24.
34. Ryan, M. P.; Newman, R. C.; Thompson, G. E. *J. Electrochem. Soc.* **1995**, *142*, L177–L179.
35. Zuili, D.; Maurice, V.; Marcus, P. *J. Phys. Chem. B* **1999**, *103*, 7896–7905.
36. Bhardwaj, R. C.; Gonzalez-Martin, A.; Bockris, J. O. M. *J. Electrochem. Soc.* **1992**, *139*, 1050–1058.
37. Ryan, M. P.; Newman, R. C.; Thompson, G. E. *Philos. Mag. B* **1994**, *70*, 241–251.
38. Maurice, V.; Yang, W. P.; Marcus, P. *J. Electrochem. Soc.* **1998**, *145*, 909–920.
39. Binnig, G.; Quate, C. F.; Gerber, Ch. *Phys. Rev. Lett.* **1986**, *56*, 930–933.
40. Burnham, N. A.; Colton, R. J. In *Scanning Tunneling Microscopy and Spectroscopy. Theory, Techniques and Applications*; Bonnell, D. A., Ed.; Wiley-VCH: New York, 1993; pp 191–249.
41. Rocca, E.; Bertrand, G.; Rapin, C.; Labrune, J. C. *J. Electroanal. Chem.* **2001**, *503*, 103–140.
42. Donley, M. S.; Mantz, R. A.; Khramov, A. N.; Balbyshev, V. N.; Kasten, L. S.; Gaspar, D. J. *Prog. Org. Coat.* **2003**, *47*, 401–415.
43. Kleber, C. H.; Hilfrich, U.; Schreiner, M. *Appl. Surf. Sci.* **2007**, *253*, 3712–3731.
44. Ikemiya, N.; Kubo, T.; Hara, S. *Surf. Sci.* **1995**, *323*, 81–90.
45. Maurice, V.; Nakamura, T.; Klein, L. H.; Strehblow, H.-H.; Marcus, P. In *Local Probe Techniques for Corrosion Research*; Woohhead Publishing and Maney Publishing, CRC Press, 2007; pp 71–83. EFC Publications Number 45.
46. Park, J. O.; Paik, C.-H.; Huang, Y. H.; Alkire, R. C. *J. Electrochem. Soc.* **1999**, *146*, 517–523.
47. Williams, D. E.; Mohiuddin, T. F.; Zhu, Y. Y. *J. Electrochem. Soc.* **1998**, *145*, 2664–2672.
48. Zhang, Q.; Wang, R.; Kato, M.; Nakasa, K. *Scr. Mater.* **2005**, *52*, 227–230.
49. Davoodi, A.; Pan, J.; Leygraf, C.; Norgren, S. *Appl. Surf. Sci.* **2006**, *252*, 5499–5503.
50. Prades, S.; Bonamy, D.; Dalmas, D.; Bouchaud, E.; Guillot, C. *Int. J. Solids Struct* **2005**, *42*, 637–645.

## 2.32 Electron and Photon Based Spatially Resolved Techniques

**X. Zhou and G. E. Thompson**

School of Materials, University of Manchester, PO Box 88, Manchester M60 1QD, UK

© 2010 Elsevier B.V. All rights reserved.

<b>2.32.1</b>	<b>Introduction</b>	1405
<b>2.32.2</b>	<b>Optical Microscopy</b>	1407
<b>2.32.3</b>	<b>Electron Microscopy</b>	1408
2.32.3.1	Introduction	1408
2.32.3.2	Scanning Electron Microscopy	1409
2.32.3.2.1	Electron backscatter diffraction	1411
2.32.3.2.2	Environmental scanning electron microscopy	1412
2.32.3.3	Transmission Electron Microscopy	1412
2.32.3.3.1	High-resolution TEM	1415
2.32.3.3.2	Scanning transmission electron microscopy	1416
2.32.3.3.3	TEM tomography	1416
2.32.3.3.4	Electron diffraction	1417
<b>2.32.4</b>	<b>Chemical Analysis in the Electron Microscope</b>	1417
2.32.4.1	X-ray Analysis	1418
2.32.4.2	Electron Probe Microanalysis	1420
2.32.4.3	Electron Energy Loss Spectroscopy	1421
<b>2.32.5</b>	<b>Specimen Preparation Techniques</b>	1424
2.32.5.1	TEM Specimen Preparation	1424
2.32.5.2	SEM Specimen Preparation	1425
<b>2.32.6</b>	<b>Other Techniques</b>	1425
2.32.6.1	X-ray Microscopy	1425
2.32.6.1.1	Introduction	1425
2.32.6.1.2	X-ray tomography	1426
2.32.6.2	Infrared Microscopy	1426
2.32.6.3	Raman Microscopy	1427
<b>2.32.7</b>	<b>Concluding Remarks</b>	1428

### Abbreviations

**BF** Bright field  
**BSE** Backscattered electron  
**CBED** Convergent beam electron diffraction  
**CCD** Charge-coupled device  
**DF** Dark field  
**EBSD** Electron backscatter diffraction  
**EDS** Energy dispersive spectrometer  
**EDX** Energy dispersive X-ray  
**EELS** Electron energy loss spectroscopy  
**EPMA** Electron probe microanalysis  
**ESEM** Environmental scanning electron microscopy  
**FIB** Focused ion beam

**HRTEM** High resolution transmission electron microscopy  
**SAD** Selected area diffraction  
**SE** Secondary electron  
**SEM** Scanning electron microscopy  
**STEM** Scanning transmission electron microscopy  
**TEM** Transmission electron microscopy  
**WDS** Wavelength dispersive spectrometer

### 2.32.1 Introduction

Understanding the corrosion and protection of materials often requires examination of the morphology,

composition and structure of the surface and near-surface regions of a material, as well as their relationship to the bulk material. The knowledge gained allows definition of features that may increase susceptibility to degradation, and hence, routes for their removal.

Electron- and photon-based, spatially resolved techniques are widely used in corrosion studies. The selection of a technique for corrosion studies requires consideration of various factors, including:

- sensitivity/detection limit,
- elemental range,
- spatial resolution,
- depth penetration,
- quantitative/qualitative information,
- sample preparation,
- destructive/nondestructive procedure, and
- cost.

Usually, a single technique will provide only a part of the required information. For example, common approaches for morphological characterization include

- visual observation,
- optical microscopy (resolution  $\sim 1\ \mu\text{m}$ ),
- scanning electron microscopy (SEM) (resolution  $\sim 1\text{--}2\ \text{nm}$ ), and
- transmission electron microscopy (TEM) (resolution  $\sim 0.1\ \text{nm}$ ).

Typically, a combination of the techniques provides the comprehensive information required for the corrosion studies. **Figure 1** displays a set of optical, SEM and TEM images and an energy dispersive X-ray (EDX) spectrum obtained from a friction-stir-welded AA7108 aluminum alloy following corrosion testing for 72 h. The images reveal the propagation path of intergranular corrosion and the associated sensitized microstructure.

**Figures 1(a) and 1(b)** show the optical micrographs of the weld surface after corrosion testing. Semicircular marks created by the tool shoulder on the weld surface, evident at the center of the weld, are revealed as a series of ridges in the cross-section of the weld. Severe localized attack is evident in the heat-affected zone (HAZ),

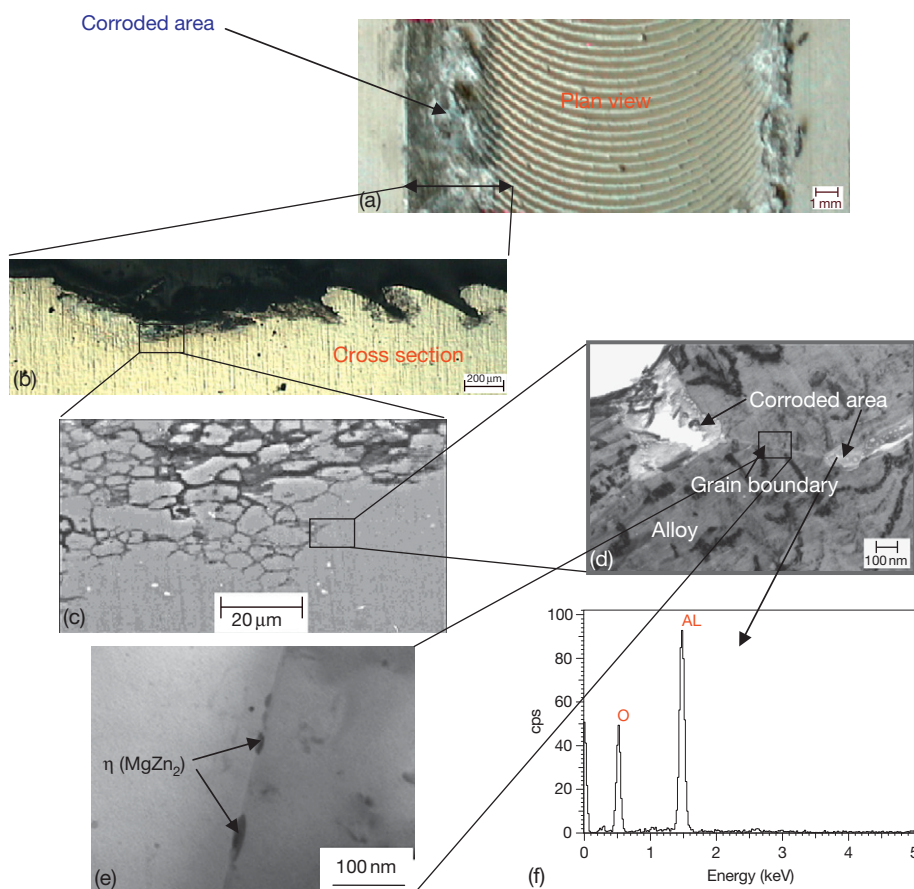


**Figure 1** Corroded AA7108 aluminum alloy weld: (a) and (b) optical images; (c) scanning electron micrograph; (d) and (e) transmission electron micrograph; and (f) EDX spectrum taken from corrosion front.

where some ridges at the surface have been completely removed, with the attack extending through the HAZ to a depth of about 300  $\mu\text{m}$  from the original surface. However, the corrosion path is not resolved in the optical images. A scanning electron micrograph of the framed region in **Figure 1(b)** displays intergranular corrosion within the HAZ (**Figure 1(c)**). The dark lines in this backscattered electron image represent areas associated with relatively light elements compared with those of the adjacent regions. In this case, the dark lines represent corroded areas as corrosion products (i.e., aluminum oxide/hydroxide) contain oxygen and hydrogen, which are lighter than aluminum.

**Figure 1(d)** shows a transmission electron micrograph of an ultramicrotomed section taken from the corrosion front located in the framed region in **Figure 1(c)**. Significant attack of the region between the grains is evident, with the alloy bulk now being penetrated by the resin used to embed the specimen. Further, corrosion of the individual grains has resulted in the development of hydrated alumina of thickness about 90 nm; EDX analysis of the corrosion products gives the yields of aluminum and oxygen as expected (**Figure 1(f)**).

**Figure 1(e)** displays a transmission electron micrograph of an electropolished foil taken from the HAZ. At the grain boundary, distinct  $\text{MgZn}_2$  particles, about 100 nm length and 20 nm width, are evident, indicating sensitization of the HAZ that has led to the intergranular attack due to microgalvanic action.

### 2.32.2 Optical Microscopy

Optical microscopy is still a major tool in corrosion studies, being relatively cheap, readily available, and easy to use. Specimens can be observed in air. The images are of natural appearance, that is, color, with available resolution up to 1  $\mu\text{m}$  (**Figures 1(a) and 1(b)**). Optical microscopy is generally a reflection technique. A visible light beam is focused onto the area of interest. Reflected light beams pass through a single lens, or multiple lenses, to produce a magnified view of the examined area. The resultant image is detected directly by the eye, recorded on photographic film or captured by digital devices.

However, optical microscopes are limited in their ability to resolve fine detail by a phenomenon called diffraction. The resolution ( $\delta$ ) of an optical microscope is given by

$$\delta = \frac{0.5\lambda}{\text{NA}} \text{ NA} = \mu \sin \alpha \quad [1]$$

where NA or  $A_N$  is the numerical aperture of the optical microscope. Thus, the resolution is controlled by three factors:

- $\mu$  – the refractive index of the medium between the lens and the specimen;
- $\lambda$  – the wavelength of illuminating radiation;
- $\alpha$  – the half angle subtended by the maximum cone of rays entering the objective lens.

The resolution can be improved by increasing  $\mu$ ; for example,  $\mu$  can be increased from 1 to 2 by oil immersion. However, decreasing  $\lambda$  has the greatest potential to improve resolution. Visible light has wavelengths of 400–700 nm; with air as the medium, the highest practical NA is 0.95. Thus, the highest achievable resolution is  $\sim 0.2\text{--}0.4 \mu\text{m}$ .

In addition to the limitation on resolution, the depth of field is also relatively poor in optical microscopy. The depth of field is the portion of the object that can be seen acceptably sharply. The depth of field decreases as the magnification increases. Typically, the depth of field is 250  $\mu\text{m}$  at a magnification of  $15\times$  compared with 0.08  $\mu\text{m}$  at the magnification of  $1200\times$ .

In an optical micrograph taken at a relatively high magnification, only a section of the radiolarian is in sharp focus. Thus, flat specimens are required for optical microscopy. Therefore, metallography is employed to prepare a flat surface. Generally, metallic specimens that are to be examined in an optical microscope are mechanically polished to a 1- $\mu\text{m}$  finish. Examination in the as-polished condition reveals structural features such as porosity, cracks, and inclusion of foreign matter. Etching with appropriate chemical agents may be used to reveal the microstructural features such as grain size and phase distribution as grain boundaries are preferentially attacked by the etchants. **Figure 2** displays an optical micrograph of an AZ91D magnesium alloy after etching in a mixed etching solution (5 ml acetic acid, 10 ml water, 6 g picric acid, and 100 ml ethanol). The typical  $\alpha$  and  $\beta$  phases are clearly revealed.

A further limitation of conventional optical microscopy is that only dark or strongly reflecting objects can be imaged effectively. This limitation has, to some extent, been overcome by specific microscopy techniques using differences in the refractive indices of objects. To improve image contrast in optical microscopy, dark field or oblique illumination may be employed, but with no improvement in resolution. Other approaches include phase contrast microscopy, interference microscopy, and polarized light microscopy.

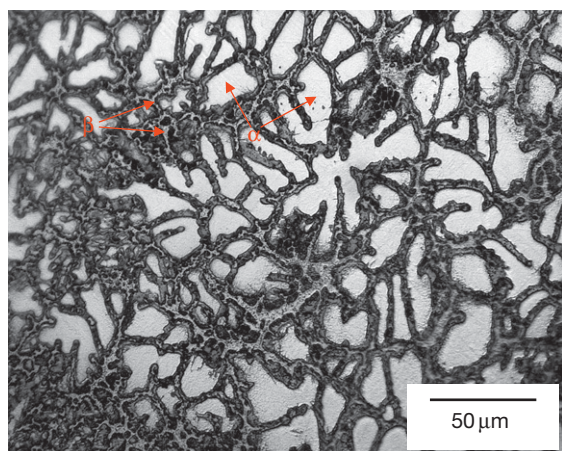


**Figure 2** Optical micrograph of AZ91D magnesium alloy after etching in a mixed solution (5 ml acetic acid, 10 ml water, 6 g picric acid, and 100 ml ethanol).

## 2.32.3 Electron Microscopy

### 2.32.3.1 Introduction

The limitations of optical microscopy are, to an extent, overcome in electron microscopy. From eqn [1], it is evident that the resolution is determined by the wavelength ( $\lambda$ ) of the radiation and the NA of the objective. To overcome the limitations set by the diffraction limit of visible light, electron microscopes that use electrons in place of light have been developed. This gives much increased resolution because the wavelength of the electrons is shorter, and hence, the diffraction limit is lower. At an accelerating voltage of 100 kV,  $\lambda$  is 0.0037 nm, giving the potential for significantly increased resolution in an electron microscope. Theoretically, a resolution of 0.02 nm is achievable in an electron microscope operated at 100 kV. Practically, however, such resolution cannot be obtained because of lens aberrations. The resolution limit presently is around 0.05 nm.

Further, the depth of field is also improved by using electrons for imaging. It is not unusual that the macroscopic specimen surface is in focus in a scanning electron microscope (SEM) because of the relevant large depth of field. However, as electrons can be readily scattered or absorbed in air, vacuum is required for electron microscopy, which makes the system more expensive with the need for effective maintenance.

Typically, an electron microscope consists of two components: the illumination system and the imaging system. The illumination system comprises the electron gun and the lenses that transfer the electrons from the gun to the specimen. Electrons are thermally

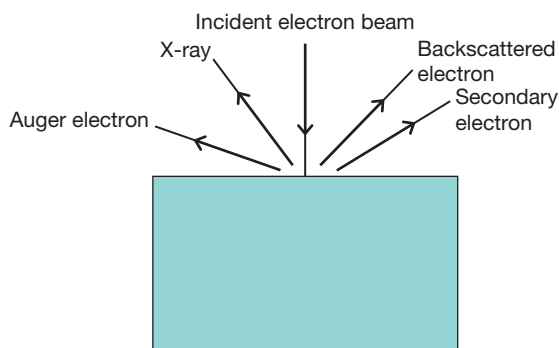


**Figure 3** Schematic diagram illustrating the generation of electrons and X-rays by a bulk specimen.

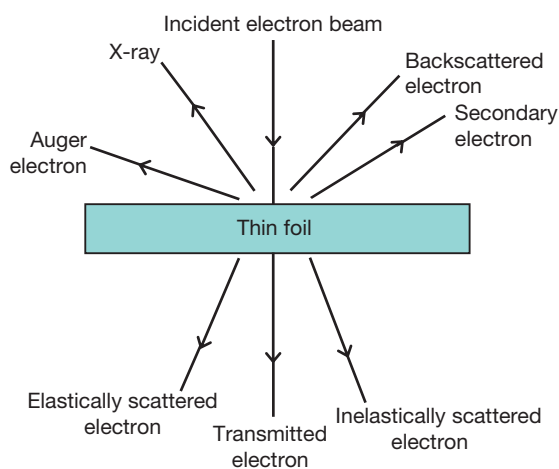


**Figure 4** Schematic diagram illustrating the interaction between the incident beam and the thin foil.

generated from a tungsten or lanthanum hexaboride ( $\text{LaB}_6$ ) cathode and are accelerated towards an anode. Alternatively, electrons can be emitted by field emission (FE). The latter produces an electron beam of fine size, increased brightness, and well-defined energies. The smaller energy spread of the FE gun, typically less than 0.5 eV compared with 1–2 eV for a thermionic source (e.g., tungsten or lanthanum hexaboride filament), is particularly important for electron energy loss spectroscopy (EELS).

In an electron microscope, incident electrons enter the specimen, interact with the material, and result in various secondary emissions, as illustrated in Figures 3–5. Each of the emissions may provide useful and different information about the material. Most of these emissions are used for imaging and analysis in the electron microscopy. Thus, electron microscopes generally require a source of incident electrons and a detector to collect the emitted



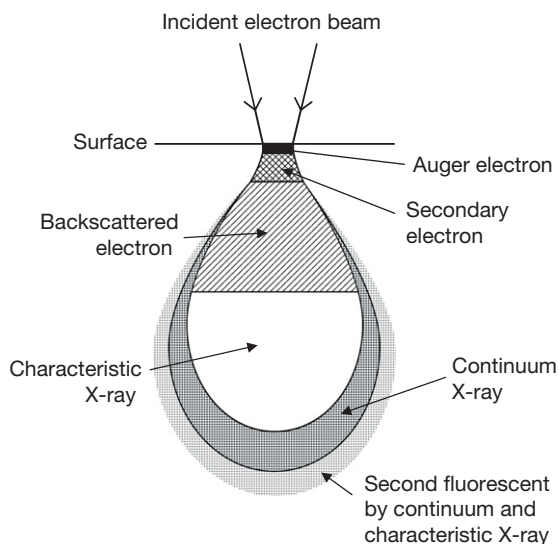


**Figure 5** Schematic diagram illustrating the regions where electrons and X-rays are generated.

radiation; often several detectors are combined in one system using a common incident electron beam.

When an electron beam is projected onto a specimen, various interactions between the incident electrons and the atoms of the specimen occur, including (i) elastic scattering, (ii) inelastic scattering, and (iii) combinations of (i) and (ii). Elastic scattering, which is the main contributor to the electron diffraction patterns, is due to the Coulombic interaction between the incident electrons and the atoms of the specimen, resulting in a change of direction, but not the energy, of the incident electrons. Inelastic scattering leads to energy transfer from the incident electrons to the electrons or atoms of the specimen. A small proportion of the lost energy may escape from the specimen as secondary electrons or X-rays, which are very useful for imaging and compositional analysis. Further, the detection of energy losses of the incident electrons is the basis of EELS.

As illustrated in **Figures 3 and 4**, in scanning electron microscopes, the images are generally generated by secondary and backscattered electrons, and in transmission electron microscope, the images are produced by the transmitted electrons. Determined by the image generation mechanism, SEM is used for studying the surface and near-surface regions of bulk specimens, and TEM is employed to investigate the internal structure of thin foil specimens.

The electrons lose energy by inelastic scattering within a region that is termed the interaction volume, which has a typical onion shape and extends approximately up to a few micrometres into the examined

material, as shown in **Figure 5**. The size of the interaction volume depends on the electron beam accelerating voltage, the atomic number of the elements in the specimen, and the material density.

### 2.32.3.2 Scanning Electron Microscopy

The application of SEM in corrosion studies is widespread, including (i) determination of structure–property relationships; (ii) location of corrosion; (iii) study of surface topography; (iv) examination of fracture sections and cracks; (v) and determination of the morphology of oxides, scales, corrosion products, etc.

In a typical SEM, a finely focused electron beam, of diameter down to 1 nm, is scanned across the surface of the specimen of interest. The scanning of the focused electron beam is achieved by controlling the current to the associated scan coils. The accelerating voltage in an SEM is typically in the range of a few hundred electron volts to 30 keV.

**Figure 3** illustrates schematically the electrons and X-rays generated through the interaction of an electron beam with the examined material. Although all resultant radiations can be used to produce an image, for SEM the images of surfaces are formed by collecting the low-energy secondary electrons (SEs) and backscattered electrons (BSEs). SEs are electrons that are ejected from atoms which interacted with the incident electrons and to which a small amount of energy has been transferred by the incident electrons during inelastic scattering; consequently, SEs have relatively low energies, below 50 eV, and escape only from regions up to 50 nm depth below the surface. The yield of secondary electrons is heavily influenced by the nature of the surface. BSEs are incident electrons that are backscattered from the specimen interaction volume. BSEs carry relatively high energies and, therefore, emerge from deeper regions within specimens. BSEs are used for imaging and generation of diffraction patterns for structure and texture analyses. These electrons may be used to provide compositional information by detecting the contrast between areas with different chemical compositions, especially when the average atomic number of elements in various areas is different, since the yield of BSEs varies with the atomic number of the elements in the examined specimen. Further, as illustrated in **Figure 3**, the relatively high-energy BSEs, emerging from deeper regions in the specimen, have an increased sampling volume; thus, generally, the surface sensitivity and resolution

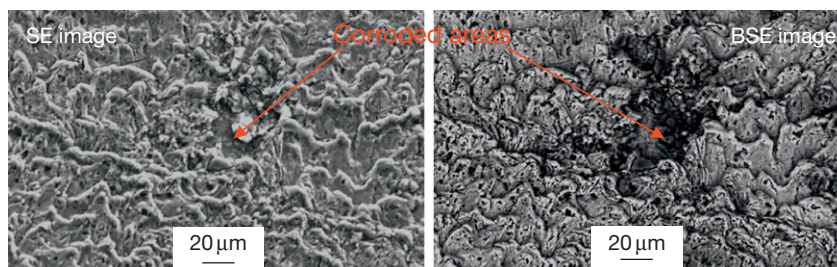


**Figure 6** Corresponding secondary electron and backscattered electron images of a laser-surface-treated AA2024 aluminum alloy following accelerated corrosion testing.

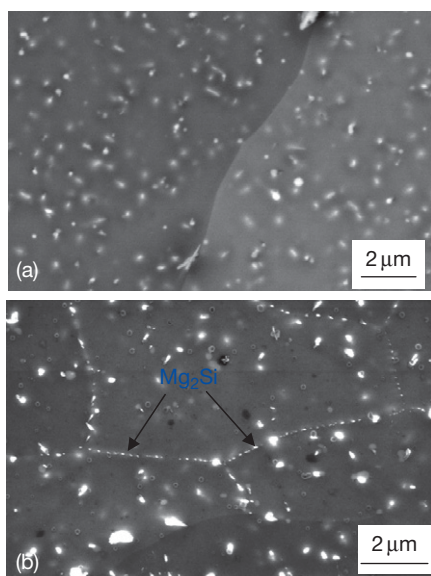


**Figure 7** Backscattered electron images taken from (a) the parent alloy and (b) the HAZ of friction-stir-welded AA6082 aluminum alloy.

of the BSE approach are lower compared to that of the SE approach.

**Figure 6** shows the corresponding SE and BSE electron images of the surface of a laser-treated AA2024 aluminum alloy following accelerated corrosion testing. The SE image reveals clearly the typical wavy appearance generated by laser treatment, but with little evidence of development of corrosion. The contrast in the BSE image readily shows localized corrosion. The relatively dark areas represent the areas where corrosion has occurred, since corrosion products (i.e., mainly aluminum oxides/hydroxides in this case) consist of relatively light elements of oxygen and hydrogen compared to metallic aluminum, thereby generating a relatively low intensity of BSEs.

**Figures 7–9** display further BSE images taken from various specimens. **Figure 7** shows the BSE images from the parent alloy and the HAZ of a friction-stir-welded AA6082 aluminum alloy, revealing

the difference in the distribution, size and population density of intermetallics caused by thermal exposure during the welding process. Within the HAZ, a continuous network of  $\beta$  phase ( $\text{Mg}_2\text{Si}$ ) is clearly evident along grain boundaries, indicating sensitization of the HAZ. Such information assists in the understanding of the reasons for the HAZ of the friction-stir-welded AA6082 aluminum alloy displaying a relatively high susceptibility to intergranular corrosion.

The backscattered electron image of **Figure 8** displays the cross section of an AZ91D magnesium alloy after immersion in 3.5% NaCl for 4 h. As stated previously, the dark regions in this backscattered electron image represent areas of relatively light elements. In this case, the dark regions indicate corrosion products (i.e., magnesium oxides/hydroxides). It is clearly evident that corrosion occurred nonuniformly, with the areas of the  $\alpha$  phase being preferentially attacked and the  $\beta$  phase remaining generally intact.

**Figure 9** illustrates the backscattered electron images of a friction-stir-welded AA2024-T3 aluminum alloy following the immersion in an EXCO solution (ASTM G 34-01, a standard testing method for exfoliation susceptibility in 2xxx and 7xxx series aluminum alloys) for 8 h. Again, the dark regions in these BSE images represent corroded areas. At the surface, a severely corroded band is evident. On the right side of the corrosion band (**Figure 9(a)**), that is, in the parent alloy, little development of corrosion is observed. Conversely, on the left side of the corrosion band, that is, within the thermomechanically affected zone (TMAZ), a large number of randomly distributed pits, of dimension about 50–300  $\mu\text{m}$ , is evident. Further, the weld cross-section revealed clearly that localized corrosion has penetrated into the alloy from both top and bottom surfaces.

A topographic image may be obtained using SEM. **Figure 10(a)** displays an SE image of an oxide film formed on a binary Al–Cu alloy, revealing the different topographies of the oxide film formed on three individual alloy grains of different crystallographic

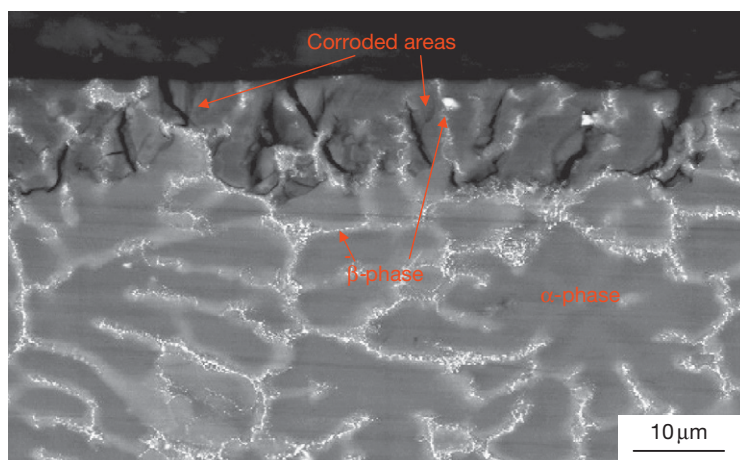


**Figure 8** Backscattered electron image of the cross section of AZ91D magnesium alloy after immersion testing in 3.5% NaCl solution for 4 h.

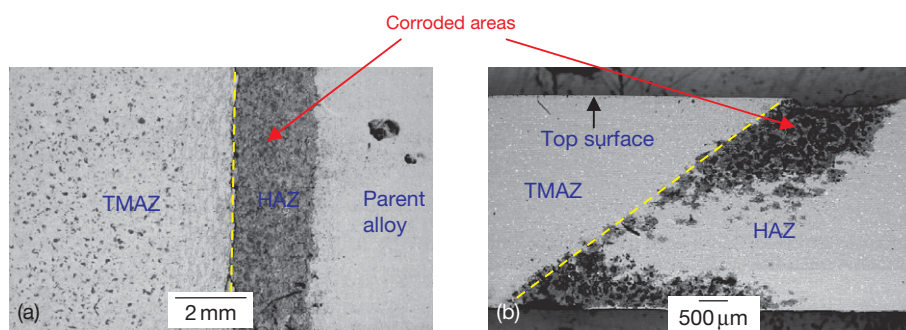


**Figure 9** Backscattered electron images of friction-stir-welded AA2024-T3 aluminum alloy following corrosion testing in the EXCO solution for 8 h, revealing corrosion susceptible zones where the alloy was sensitized during welding: (a) plan view and (b) cross sectional view of (a).

orientations. Since the shape and size of the SE sampling volume is related to the angle between the surface and the incident electron beam, as the angle increases, the escape distance of one side of the beam will decrease and, consequently, more SEs will be emitted. Thus, steep surfaces and edges tend to be brighter than flat surfaces, resulting in images with a well-defined topographic contrast. It is essential to tilt the specimen to obtain the desirable topographic contrast, avoiding signals emitted from deeper regions within the specimen, and thereby enhancing the surface sensitivity in topographic studies. For example, **Figure 10(b)** was obtained from the framed area in **Figure 10(a)** without tilting the specimen, revealing little topographic contrast although features of subsurface regions of the specimen (i.e., voids in the oxide film in this case) are clearly displayed. This is because the surface topographic contrast is overwhelmed by internal features since a relatively large portion of signal is emitted from deeper regions

within the specimen. **Figure 10(c)** illustrates schematically the cross section of the oxide film, revealing the distribution of the voids. It is clearly evident that the internal features of the oxide film overwhelmed the surface topographic features.

#### 2.32.3.2.1 Electron backscatter diffraction

Electron backscatter diffraction (EBSD), also known as backscattered Kikuchi diffraction (BKD), allows crystallographic information to be obtained from any crystalline material using BSEs in the scanning electron microscope. EBSD can be used to determine grain sizes and shapes, as well as orientations and misorientations. Such information is very useful for corrosion studies. For example, the sensitization of an alloy may be correlated to misorientations between alloy grains. Because of the relatively weak channeling contrast used for EBSD, a carefully prepared surface is essential to obtain satisfactory information. Normally, a flat and strain-free surface is desirable.



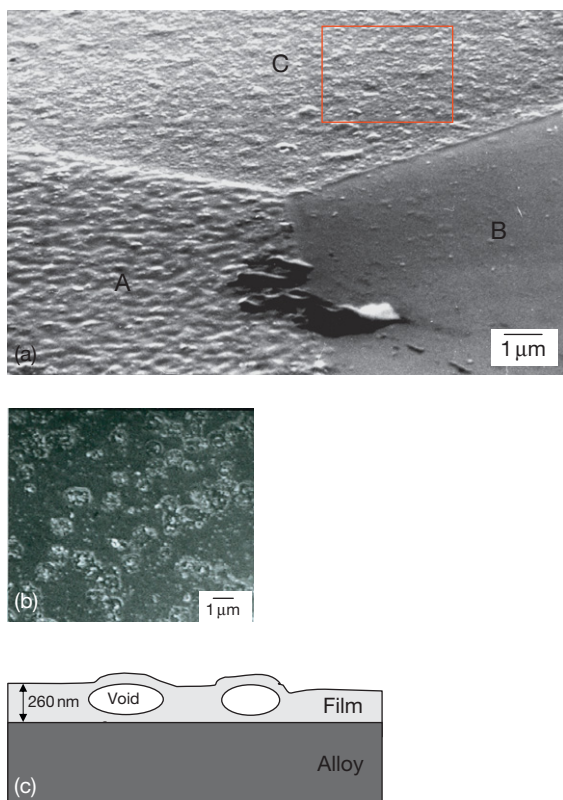


**Figure 10** (a) and (b) Scanning electron micrographs of an oxide film formed on an Al-Cu binary alloy; and (c) schematic illustration of the cross section of the oxide film.

Such a surface may be produced by electropolishing. Mechanical polishing should be avoided in EBSD specimen preparation since a near-surface layer of deformed microstructure is normally introduced into the materials during the process. **Figure 11** displays the EBSD maps recorded in various weld zones of a friction-stir-welded AA2024 aluminum alloy, revealing grain size and orientations. The parent alloy and the HAZ were shown to consist of a relatively coarse, elongated grain structure, ranging from approximately  $20 \times 30 \mu\text{m}$  to  $50 \times 150 \mu\text{m}$  in dimensions that were generated during fabrication. The nugget region, that is, the center of thermomechanically affected zone (TMAZ), displays relatively small, equiaxed grains of size about  $1\text{--}10 \mu\text{m}$ . Outside the nugget, within the TMAZ, a heavily deformed parent microstructure is revealed.

### 2.32.3.2.2 Environmental scanning electron microscopy

Environmental scanning electron microscopy (ESEM), developed in the 1980s, allows operation in increased pressure gaseous environments, in the range of 1–10 torr,

compared to a vacuum below  $10^{-5}$  torr in a conventional SEM. This is achieved by the development of an SE detector that is capable of operating in the presence of gases and by the use of electron apertures and differential pumping systems to separate the high-vacuum regions around the gun and the column from the low-vacuum sample chamber. Therefore, in corrosion studies, ESEM allows imaging of specimens with a vapor or volatile component, or while *in situ* examinations involve gas or liquid phases. Additionally, ESEM allows examination of nonconductive specimens without coating since the excess electrons are dissipated by the collision between the electrons and gas molecules.

### 2.32.3.3 Transmission Electron Microscopy

The application of TEM in corrosion studies includes (i) structure–property relationships determination; (ii) sites of corrosion and surface roughness determination, (iii) morphological determination of oxides, scales, corrosion products, etc.

TEM forms images following the transmission of an electron beam through an electron-transparent specimen. An image is formed, magnified, and directed to appear either on a fluorescent screen or photographic film, or detected by a sensor such as a CCD (charge-coupled device) camera. In a typical TEM, electrons are generated from a tungsten or lanthanum hexaboride ( $\text{LaB}_6$ ) filament or a FE gun which accelerates electrons through voltages in the range 40–300 kV. Over the years, high-voltage (up to 3 MV) TEMs have been developed to achieve improved resolution and increased penetration, but they have become rarer since the resolution of relatively low-voltage TEMs being improved through improved lens design, and thin specimen preparation techniques being developed. Further, FE guns are now becoming increasingly widespread because of the capability of producing electron beams of very fine diameter (0.2 nm), increased brightness, and well-defined energies. In a TEM, a parallel or convergent beam can be generated. The former is used for imaging and diffraction, and the latter is used for scanning transmission electron microscopy (STEM), microanalysis, and convergent beam electron diffraction (CBED).

As illustrated in **Figure 4**, when an electron beam is projected onto a thin foil specimen, various processes occur, including (i) the straight passage of electrons through the specimen, (ii) elastic scattering, (iii) inelastic scattering, and (iv) combinations of (ii) and (iii). The intensity of the transmitted beam is affected

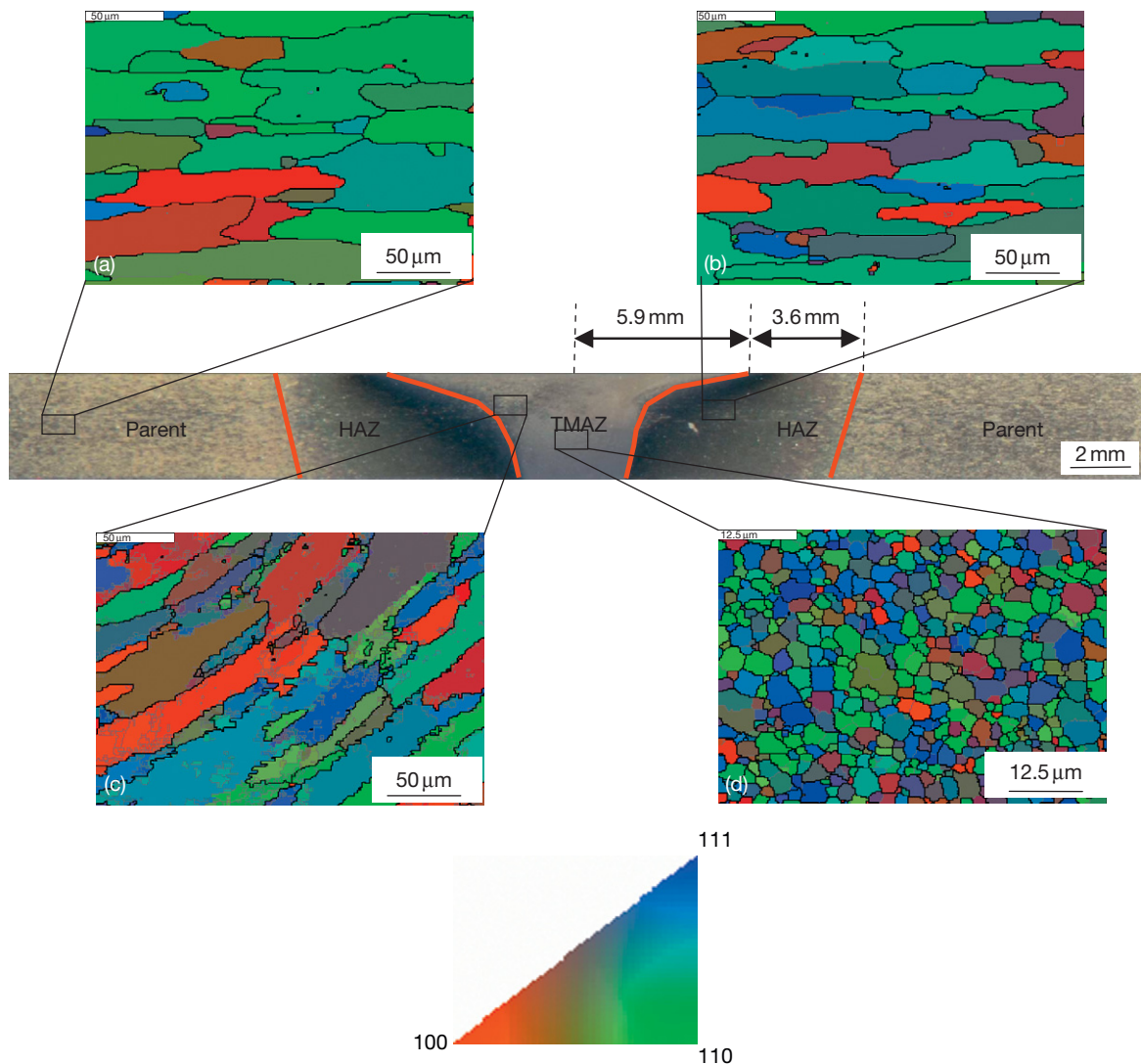


**Figure 11** Electron backscatter diffraction (EBSD) maps recorded in various weld regions of friction-stir-welded AA2024 alloy: (a) the parent alloy; (b) the HAZ; (c) the TMAZ; and (d) the nugget region.

by the volume and density of the material through which the beam passes. The thick regions, or regions of increased density, scatter electrons strongly and appear dark in the image. This gives a mass-thickness contrast. However, a crystalline material can also interact with the electron beam by diffraction. The intensity of the diffraction depends on the orientation of the planes of atoms in a crystal relative to the incident electron beam. This is known as diffraction contrast.

In TEM, an objective aperture is placed at the focal plane of the objective lens to select electrons to form the image. The objective aperture can then be used to allow either the unscattered beam or the diffracted beam to form images. If the objective aperture is

centered at the optical axis, the electrons that are deflected away from the optical axis are blocked, and only unscattered electrons pass through to form an image. This is known as a bright field (BF) image since in the absence of a specimen a bright background is seen on the screen. It is also possible to produce an image from electrons that are deflected by particular crystal planes. By either moving the objective aperture to the position to block the unscattered electrons and allow a particular diffracted beam to pass through, or tilting the incident electron beam so that a particular diffracted beam passes through the centered aperture, an image can be formed by the deflected electrons. This is known as a dark field (DF) image



since in the absence of a specimen the background appears dark. BF and DF images provide valuable complementary microstructural information.

**Figure 12** shows a pair of BF and DF images of an ultramicrotomed section of an AA6111 aluminum alloy that was solution-heat-treated (SHT) at 813 K for 30 min followed by rapid quenching in ice water before mechanical grinding with 220 grit SiC paper and heat treatment at 180 °C for 30 min. The mechanical grinding introduced a deformed layer microstructure, which is characterized by very fine grains, approximately 50–150 nm diameter. Further, the DF image (**Figure 12(b)**), achieved by choosing the electrons deflected by a particular set of planes in the precipitate to form the image, reveals precipitate particles of approximately 20 nm diameter distributed along grain boundaries.

Using an annular detector to collect electrons that have been inelastically scattered through relatively

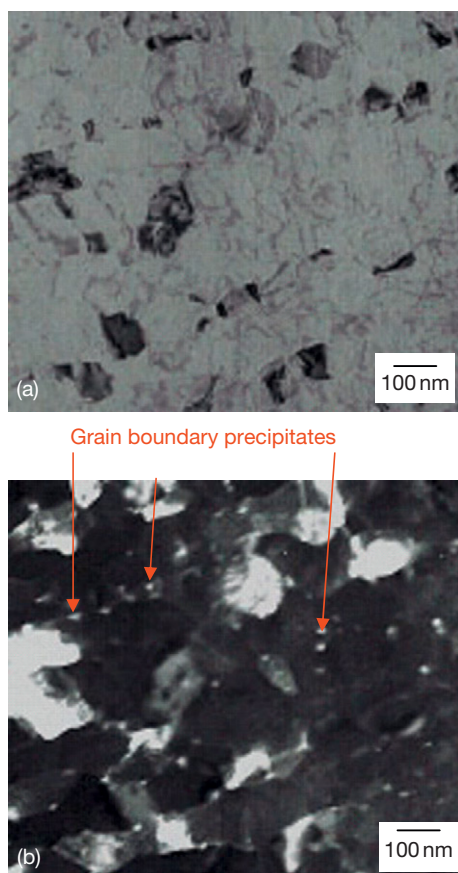


**Figure 12** Transmission electron micrographs of ultramicrotomed section of the AA6111 alloy: (a) bright field image and (b) dark field image.

large angles, compositional information of the specimen may be obtained by acquiring a Z-contrast image since the inelastic scattering is proportional to the square of the atomic number  $Z$ . Thus, areas with higher average atomic number elements appear brighter and areas with lower average atomic number elements appear darker. For example, etching or anodizing of copper-containing aluminum alloys normally results in the formation of a thin layer of alloy, about 2 nm thick, immediately beneath the residual or anodic alumina film, which is highly enriched in copper. Such enrichment arises from the less negative Gibbs free energy per equivalent for formation of copper oxide compared to alloys. **Figure 13(a)** shows a high angle annular dark field (HAADF) image of a cross-section of an AA6111 aluminum alloy after anodizing, revealing the Z contrast from the copper-rich band located at the alumina–aluminum interface. However, such a copper-rich band appears as a dark band in the BF image (**Figure 13(b)**) because of the mass contrast, that is, enhanced electron scattering by copper compared to aluminum.

A further example of the use of TEM in corrosion studies is given in **Figure 14**. A scanning electron micrograph of a cross-section taken from an AA6111 aluminum alloy is shown in **Figure 14(a)**, revealing localized corrosion which has proceeded into the alloy to a depth of  $\sim 4 \mu\text{m}$ . However, the SEM image provides little information about the corrosion initiation sites and propagation paths. **Figure 14(b)** displays the transmission electron micrograph of an ultramicrotomed section taken from the region indicated with the frame in **Figure 14(a)**. It is now clearly revealed that the corrosion is intergranular and develops preferentially along grain boundaries.

However, TEM requires consideration of the means of preparation of electron-transparent specimen. Thus, many materials require extensive specimen

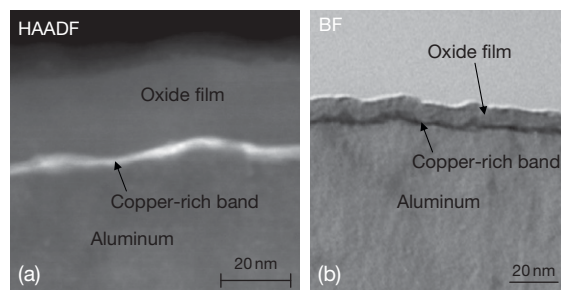


**Figure 13** Transmission electron micrographs of cross-sections of AA6111 aluminum alloy after (a) anodizing and (b) caustic etching.

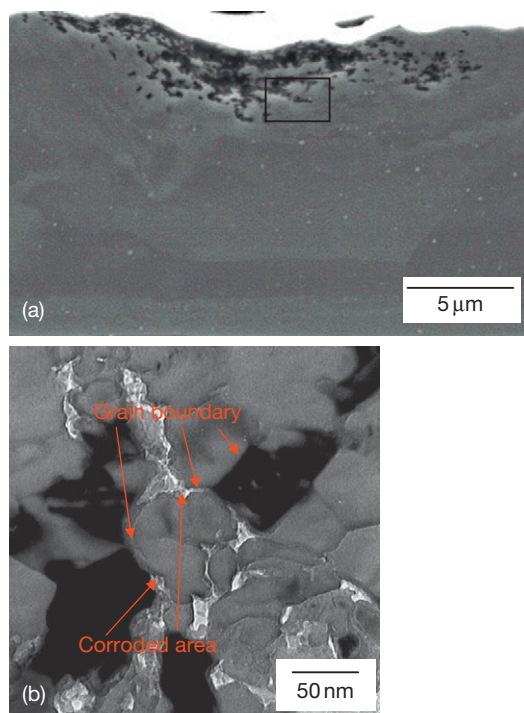


**Figure 14** (a) Scanning electron micrograph of cross-section of corroded AA6111 aluminum alloy and (b) transmission electron micrograph of an ultramicrotomed section taken from corrosion front as indicated by the frame in (a).

preparation to produce a specimen sufficiently thin to be transparent to electrons. Often, the specimen preparation is a time-consuming process with low throughput. Further, the composition and structure of the material may be changed during specimen preparation processes. Additionally, the sampling volume in TEM is relatively small, raising the possibility that the region examined may not be characteristic of the bulk material.

As stated previously, inelastic scattering generates useful signals. However, there is also the potential that the specimen may be damaged by the high-energy electron beam during inelastic scattering. Electron beam damage changes the structure and chemistry of the examined materials. Certain materials are more susceptible to damage than others. Inelastic scattering may break the chemical bonds of materials such as polymers. Further, the kinetic energy that is carried by the incident electrons may be transferred to heat in the specimen during the inelastic scattering processes. Electron-beam heating of thermally conductive materials such as metals is negligible under standard condition but can be quite

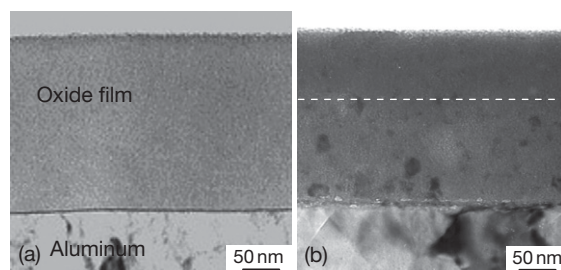


**Figure 15** Transmission electron micrographs of an ultramicrotomed section of the anodic film formed to 200 V on the Al-2 wt% Cu alloy: (a) upon immediate examination in electron microscope, revealing a featureless amorphous film attached to the substrate and (b) after continued exposure to the electron beam in the microscope, the inner film region showing crystallization of alumina.

substantial if thermal conduction is poor. For example, in [Figure 15](#), a transmission electron micrograph of an ultramicrotomed section of the anodic film formed on the Al-2 wt% Cu alloy reveals a featureless amorphous film attached to the substrate. With continued exposure to the electron beam, the inner region of the anodic oxide film is crystallized to  $\gamma'/\gamma$  alumina, as shown in [Figure 15\(b\)](#). However, such changes are not always problematic and advantage may be taken from such changes. From [Figure 15\(b\)](#), it is evident that the thickness of the crystalline region adjacent to the alloy substrate is about 60% of the total film thickness; the outer region, representing about 40% of the total film thickness, showed delayed crystallization. This suggests that about 40% of the total film thickness is formed at the film–electrolyte interface by cation migration, and the remainder formed at the aluminum–film interface by anion migration since the outer region of the film contains incorporated, immobile electrolyte species that retard crystallization of the contaminated amorphous alumina under electron irradiation.

### 2.32.3.3.1 High-resolution TEM

High-resolution TEM (HRTEM) allows the imaging of the crystallographic structure of materials at an atomic scale. The image formation in HRTEM relies on phase contrast. As mentioned in [Section 2.32.1](#), theoretically, a resolution of 0.02 nm is achievable in an electron microscope. However, such resolution cannot be obtained because of lens aberrations. At present, the highest resolution achieved is 0.05 nm on HRTEM with aberration correctors.

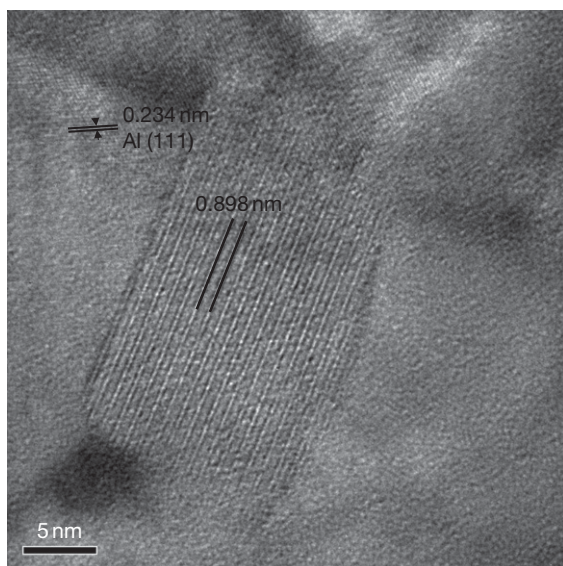


**Figure 16** HRTEM image of a Q-phase particle in AA6111 aluminum alloy.

**Figure 16** shows an HRTEM lattice image of a grain boundary precipitate in AA6111 aluminum alloy. The particle extends through the thickness of the section, with no consequent interference from the surrounding aluminum matrix. The lattice fringe spacing was determined accurately by using the (111) lattice plane spacing of the aluminum matrix as a reference. The measured fringe spacing of the precipitate is 0.898 nm, in good agreement with the  $d$  value of 0.899 nm for the  $\{100\}_Q$  set of planes, thereby confirming that the precipitate is the quaternary Q phase ( $\text{Cu}_2\text{Mg}_8\text{Si}_7\text{Al}_4$ ). The revelation of the Q phase at the grain boundary helps in explaining the occurrence of intergranular corrosion of the same alloy, as revealed in **Figure 14**. Where the Q-phase particles are formed at grain boundaries, the microgalvanic coupling between the particles and the adjacent matrix to the particles provides the driving force for localized corrosion.

Further, although the high-angle annular dark field and BF image of **Figure 13** revealed that a copper-enriched layer of 2 nm thickness formed at the aluminum–oxide interface by anodizing and caustic etching of the AA6111 aluminum alloy, it is impossible to tell how the copper species exist in the band from **Figure 13**. Such information can be readily obtained by using HRTEM. **Figure 17** displays a lattice image of the copper-enriched layer, revealing clearly the lattice fringe spacing and confirming the presence of a  $\text{CuAl}_2$  particle within the copper-enriched layer.

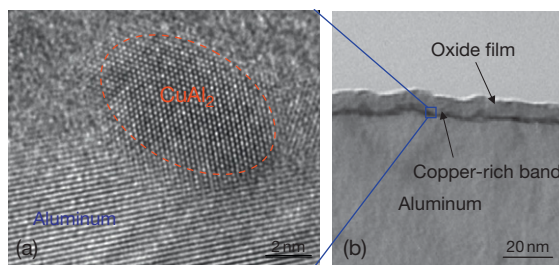


**Figure 17** (a) Transmission electron micrograph of cross-section of AA6111 aluminum alloy after caustic etching, revealing a copper-rich band at the aluminum–oxide film interface; and (b) HRTEM lattice image of a  $\text{CuAl}_2$  particle in the copper-rich band.

### 2.32.3.3.2 Scanning transmission electron microscopy

Scanning transmission electron microscopy (STEM) is a combination of SEM and TEM: that is, a transmission image is obtained using a scanning method. A TEM can be modified into an STEM by the addition of a system that scans a focused beam across the specimen to form the image. Further, by fitting a transmission stage and a detector, an SEM can also be operated in the STEM mode. Thus, a STEM combines some of the advantages of the SEM and the TEM. The image obtained in an STEM is similar to that obtained in a TEM, but the data are acquired serially.

In recent years, dedicated STEMs have also been built. In a dedicated STEM, since no objective or projector lenses are needed after the specimen, a relatively large space is available for various signal detectors to be positioned in. Thus, the dedicated STEM is normally used as a multisignal analytical microscope with high spatial resolution. Since the resolution of an STEM is determined by the diameter of the focused electron beam, the beam is focused to as small a size as possible. Nowadays, in a dedicated STEM, using a FE electron gun, an electron beam of diameter 0.2 nm can be generated. This is sufficient to image heavy single atoms. The employment of dedicated STEMs is limited since they are comparatively expensive and the improvement in the electron beam size in TEMs equipped with a FE gun has significantly reduced the difference in the resolution of the two types of microscope.

### 2.32.3.3.3 TEM tomography

Typically, TEM microscopy generates two-dimensional (2-D) images which locate the position of an internal feature in the examined specimen both vertically



and horizontally but with no information on the depth of that feature within the specimen being obtained. However, information concerning the depth of the feature can be obtained by tilting the specimen in small steps (small angle) and acquiring a series of 2-D images at each angle and subsequently reconstructing 3-D images by merging the individual 2-D images into a single 3-D block that can then locate any feature in the specimen in any direction. This technique is termed TEM tomography.

#### 2.32.3.3.4 Electron diffraction

Electron diffraction is a technique that allows determination of the crystal structure of materials. When the electron beam is projected onto a specimen, its crystal lattice acts as a diffraction grating, scattering the electrons in a predictable manner, and resulting in a diffraction pattern. Electron diffraction patterns are mainly contributed by elastic scattering. In an electron microscope, the diffraction pattern appears either on a fluorescent screen or is recorded on a photographic film or detected by a sensor such as a CCD (charge-coupled device) camera. From the diffraction pattern, the arrangement of the atoms in a material can be determined. Electron diffraction can be acquired with either TEM or SEM (electron back-scattered diffraction).

Selected area diffraction (SAD) is often employed to obtain a diffraction pattern from the area of interest, such as one grain in a polycrystalline specimen or a second phase embedded in the matrix. SAD is achieved by either inserting an aperture in the plane of the specimen itself or the first image produced by the objective lens, or illuminating only the area of interest. By using a convergent electron beam, diffraction patterns can also be obtained from fine regions. This technique is called convergent beam electron diffraction (CBED).

There are many reasons for obtaining diffraction patterns in corrosion studies. For example, by obtaining diffraction patterns, an unknown material may be identified, or the relationship between the grain orientations and the surface properties of a material may be established. **Figure 18** displays diffraction patterns obtained from (a) a single crystal of tin along the  $[001]_{Sn}$  zone axis, revealing a regular array of sharp spots since several sets of planes that are approximately parallel to the incident electron beam diffract electrons, thereby giving rise to a diffraction pattern; (b) a fine-grained polycrystalline AA 6111 aluminum alloy, exhibiting a ring-like diffraction pattern since the

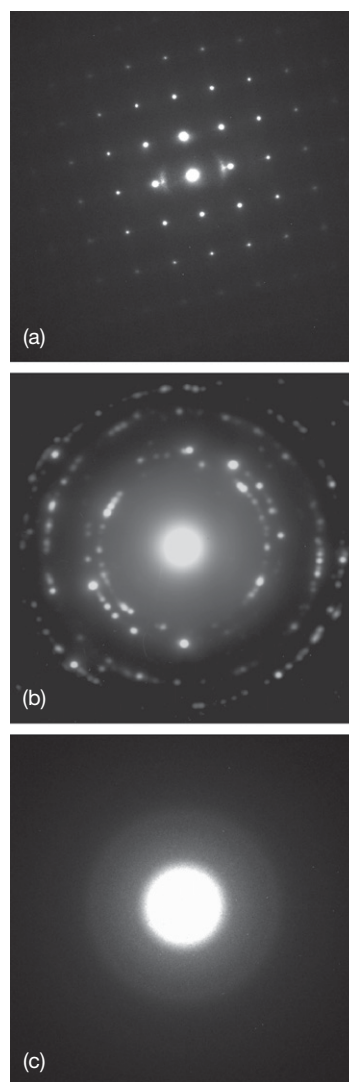


**Figure 18** Electron diffraction patterns: (a) a single crystal of tin along the  $[001]_{Sn}$  zone axis, (b) a fine-grained polycrystalline AA6111 aluminum alloy, and (c) amorphous carbon.

diffraction pattern is the sum of individual crystals of random orientations and (c) amorphous carbon, showing amorphous diffusion rings.

### 2.32.4 Chemical Analysis in the Electron Microscope

Chemical analysis in the electron microscope provides spatially resolved compositional information which is not available in conventional chemical or spectrographic methods.

### 2.32.4.1 X-ray Analysis

As stated previously, in an electron microscope, the energy lost by the incident electrons during inelastic scattering may escape from the specimen as X-rays. If an inner-shell electron has been knocked out of an atom during the inelastic scattering of an incident electron by that atom, the atom is in an excited high-energy state. The vacancy will be filled by an electron from an outer higher energy shell and the atom will relax. The excess energy of that electron is released in the form of an X-ray or an Auger electron. The X-rays are highly specific to individual elements, known as characteristic X-rays. For example, if a K shell electron has been removed from an iron atom and the vacancy is filled by an L shell electron, the energy difference,  $\Delta E$ , is 6400 eV. The corresponding wavelength of the emitted X-ray can be calculated from  $\lambda = hc/\Delta E$  to be 0.193 nm. The energy (wavelength) can be measured to determine the composition of the examined material since the energy (wavelength) is characteristic to a particular element. Thus, the emitted X-rays can be processed by two different approaches: using an energy dispersive spectrometer (EDS) or a wavelength dispersive spectrometer (WDS). Further, X-ray analysis is non-destructive and may be quantitative.

In an EDS, semiconducting silicon or germanium is used as the X-ray detector. The detector converts each absorbed X-ray photon into an electrical current pulse that is proportional to the energy of the X-ray photon. Each current pulse is amplified by a computerized analyzer. A histogram of energies of all X-rays arriving at the detector is collected and displayed as a smooth curve, which is the EDS spectrum. Normally, a window is necessary to separate the detector from the specimen chamber to prevent condensation on the detector since the detector works at very low temperatures. Unfortunately, such windows can absorb a significant portion of low-energy X-rays, thereby making light elements particularly difficult to be detected. However, windowless detectors or detectors with ultrathin windows are available to detect elements down to boron in the periodic table.

The main drawbacks of EDS systems are the relatively poor energy resolution, typically within the range of 100–200 eV, and a low signal-to-noise ratio, which make it difficult to resolve characteristic X-rays with sufficiently close energies and affect the detection, and therefore its use for quantitative analysis. The minimum detection limit for any element is about 0.1% using an EDS system and an order of

magnitude lower using a WDS system. As an EDS detector can be placed very close to the specimen, thereby collecting X-rays very efficiently, a spectrum for qualitative analysis can be acquired within a couple of minutes.

In WDS, the arriving X-rays are filtered by a crystal spectrometer using diffraction to separate the X-rays on the basis of their wavelength. Then, X-rays of the energy resolution and signal-to-noise ratio are achieved, making it possible to resolve characteristic X-rays of close energies and to undertake more accurate quantitative analysis. Thus, the main drawbacks of EDS are overcome in a WDS system. However, since only one wavelength is detected at a time, it is very time consuming to acquire a spectrum.

Further, a characteristic X-ray is most efficiently generated when the primary electrons carry approximately 3 times the energy of the X-ray. Therefore, by using a SEM operating at 30 keV all elements are readily detectable since they have at least one strong characteristic X-ray line with energy less than 10 keV. In SEM, the surface sensitivity of X-ray analysis is related to the accelerating voltage since the penetration of the primary electrons is dependent on the beam energy: that is, accelerating voltage. With reducing accelerating voltage, electrons have less energy and hence penetrate to shallower depths; thus, X-rays are generated from regions close to the specimen surface.

Although secondary emission is generated throughout the entire interaction volume, which extends approximately a few micrometers into the examined materials, only that escaping from the specimen is detected. Most X-rays generated can escape from the specimen since X-rays are not readily absorbed. Thus, in the SEM, the X-rays are generated from a relatively large volume of material, of typical dimensions 2–3  $\mu\text{m}$ . As illustrated in [Figure 3](#), the sampling volume of X-rays is similar to the interaction volume, but the sampling volume of SEs and BSEs are significantly smaller. A large portion of X-ray signals are contributed by materials that are not seen in SE or BSE images. Thus, in SEM, an unseen phase below the surface may be detected during X-ray analysis, as illustrated in [Figure 19](#).

Therefore, the spatial resolution of X-ray analysis in SEM or electron probe microanalysis is limited to the sampling volume of the X-rays, which is typically at the level of micrometers although the imaging resolution of SEMs can achieve 1 nm. It is difficult to reduce the sampling volume below  $\sim 1 \mu\text{m}^3$  without reducing the energy of the incident electron



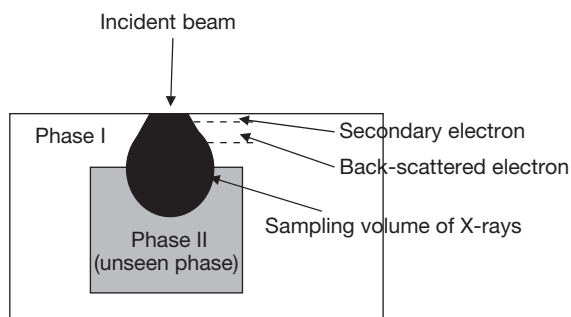


**Figure 19** Schematic diagram illustrating the sampling volumes of imaging and X-ray analysis in SEM.

beam to the degree that no useful X-rays are generated. However, as illustrated in [Figure 5](#), the lateral spread of the interaction volume and X-ray sampling volume increases with the depth of penetration. Thus, the problem can be overcome by using a sufficiently thin specimen in the TEM. With the use of such a specimen in the TEM, the X-ray sampling volume is approximately equivalent to the imaging region. Thus, the spatial resolution of X-ray analysis in the TEM is approximately the probe size, typically of diameter down to  $\sim 1$  nm. However, the small amount of X-rays generated by the low current of such a small probe from a small sampling volume of the thin specimen makes meaningful analysis difficult. Practically, it is difficult to achieve meaningful analysis with a probe size of diameter much less than 10 nm for a typical specimen.

Further, in a TEM, the specimen is closely surrounded by the specimen holder and supporting grid, which can interfere with the analysis since X-rays can also be generated by BSEs from the specimen holder and the supporting grid. Such interference can be minimized by using a beryllium specimen holder which generates X-rays that are not detectable and by using grids made of a material that is irrelevant to the specimen. It is also critical to ensure that the grid is placed in a direction such that the specimen faces the incident beam, thereby minimizing interference.

If only one spot or area is analyzed, quantification of the relative proportions of elements under that spot or area is possible, which is known as point analysis ([Figures 1](#) and [20](#)). If a line of pixels is analyzed, changes in the proportions of elements with distance along the line can be determined, which is termed X-ray line scanning. Each pixel in an image can also be analyzed, illustrating the locations and amounts of a selected element across the image, which is known as X-ray mapping.

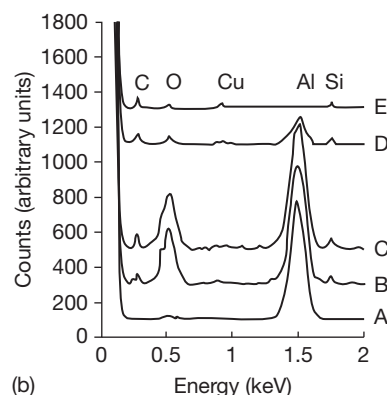
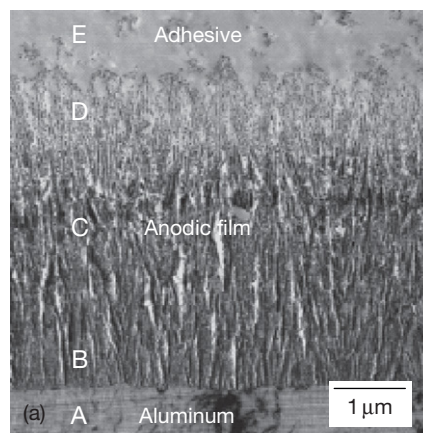


**Figure 20** (a) Transmission electron micrograph of the cross section of the interface between the adhesive and the anodic porous alumina film formed on aluminum substrate and (b) EDX spectra taken from the areas indicated in (a).

[Figure 20\(a\)](#) illustrates the TEM image of the cross section taken from the interface region of adhesively bonded aluminum that was pretreated by chromic acid anodizing (CAA). The morphology of the porous anodic film formed by CAA is readily revealed from observation of the cross-section displayed in [Figure 20\(a\)](#). The anodic film is well wetted by the adhesive, and the relatively open morphology of the outer region of the anodic film allows significant penetration of the adhesive. However, the extent of penetration of the adhesive into the pores of the anodic film cannot be determined precisely from the micrograph. Hence, energy dispersive analysis of X-rays was performed by placing an electron probe at various locations across the section of the anodic film/adhesive interface. [Figure 20\(b\)](#) shows the EDX spectra. Spectrum A, taken from the aluminum substrate, indicates that only aluminum is detected. Spectra B, C and D were taken within the

anodic film close to the interface with the aluminum substrate and in the middle and the outer region of section of the anodic film, respectively, indicated the presence of Al, O and, additionally, C and Si; C and Si arise from the adhesive (spectrum (E) taken from the bulk adhesive) that had penetrated into the film. This suggests that the adhesive penetrated significantly into the porous anodic film.

**Figure 21(a)** shows a transmission electron micrograph of an ultramicrotomed section of an AA5182 aluminum alloy after accelerated corrosion testing, revealing the corrosion front and the intact grain boundaries ahead of the corrosion front. Significant attack along a grain boundary is evident. **Figure 21(b)** shows the EDX spectra generated from a probe located at the grain boundary and within the bulk grains. For an electron probe of a nominal diameter 20 nm located on the boundary, an increased yield of magnesium was detected compared with that from the bulk grain, suggesting the presence of a magnesium-rich phase at the grain boundary since the relative peak height (area) is generally proportional to the concentration of individual elements in the specimen. The revelation of the magnesium-rich phase, probably  $\beta$  phase ( $\text{Mg}_2\text{Al}_3$ ), at the grain boundary helps in explaining the occurrence of intergranular attack of the alloy. Since the magnesium-rich phase is anodic with respect to bulk grain, when such phases are formed at grain boundaries, the microgalvanic coupling between the magnesium-rich phase and the adjacent grain matrix provides the driving force for localized corrosion.

**Figure 22** illustrates the line scan profiles across a precipitate revealed in the DF image of the AA6111 aluminum alloy shown in **Figure 12**. By scanning with an electron probe of nominal diameter  $\sim 2$  nm across the precipitate and the adjacent grain matrix, changes in the proportions of elements with distance along the line are determined. Increased yields of copper, magnesium and silicon at the grain boundary particles are detected with respect to the grain matrix, suggesting the presence of the Q phase ( $\text{Cu}_2\text{Mg}_8\text{Si}_7\text{Al}_4$ ). Notably, no solute-depleted zones are readily detected in the vicinity of the grain boundary precipitates or at the grain boundary itself.

#### 2.32.4.2 Electron Probe Microanalysis

Electron probe microanalysis (EPMA) is a nondestructive technique that allows determination of the composition of small volumes of a solid material. In an electron probe microanalyzer, an electron beam is

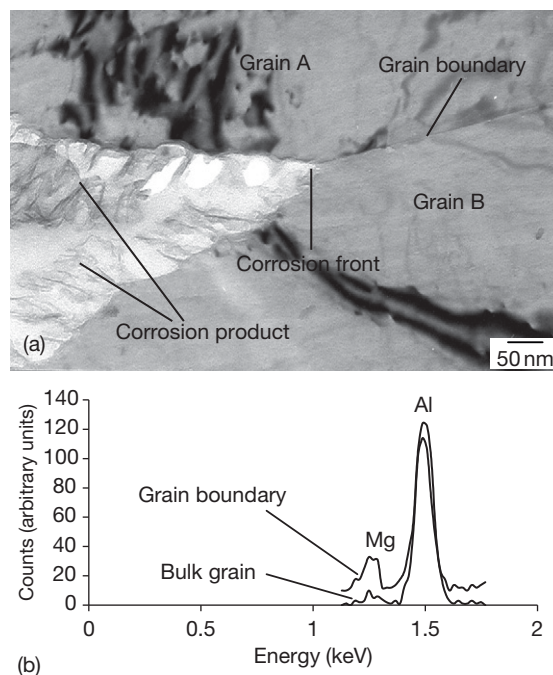


**Figure 21** (a) Transmission electron micrograph of ultramicrotomed section of AA5182 aluminum alloy after accelerated corrosion testing, revealing the corrosion front and (b) EDX spectra taken from the intact grain boundary and bulk grain.

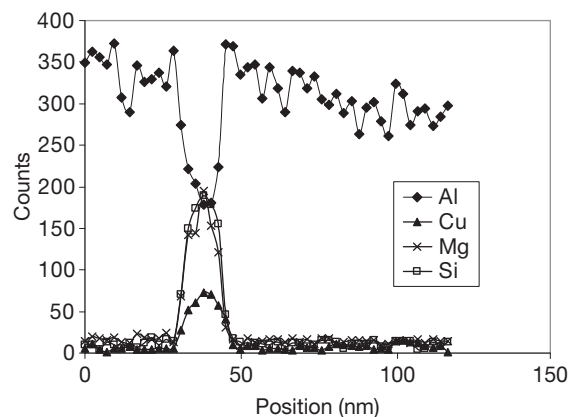


**Figure 22** EDX line scanning profiles across a precipitate revealed in **Figure 12** of the dark field image of AA6111 aluminum alloy.

generated and directed to a specimen to be examined and a wavelength dispersive spectrometer is employed to detect the X-rays emitted from the specimen. By scanning the electron beam and fitting an electron detector, complementary images may also be obtained. In this mode, an EPMA is similar to the SEM. As stated

previously, WDS provides much improved energy resolution and signal-to-noise ratio compared to EDS. However, to achieve more accurate quantitative analysis and to cover the full X-ray spectrum, a range of crystals of different lattice spaces is required. Further, the mechanics of WDS place strict geometric restrictions on the positions of the specimen, crystal spectrometer, and the detector. These make it difficult, but not impossible, to fit such a system into an electron microscope. Thus, a purpose-built electron probe microanalyzer is necessary. Typically, four computer-controlled crystal spectrometers containing a range of crystals of different lattice spacing are installed in a dedicated EPMA system. Such equipment can achieve more accurate quantitative analysis than X-ray analyses in a standard electron microscope. EPMA can quantitatively analyze elements down to boron in the periodic table at levels as low as 100 ppm.

Mapping of elemental distributions by EPMA in the cross-section of a coating formed on an aluminum substrate anodized for 1800 s at  $5 \text{ A dm}^{-2}$  in 0.05 M potassium hydroxide/0.15 M sodium metasilicate electrolyte is shown in **Figure 23**. Oxygen is revealed in all regions of the coating thickness, apart from cavities. Other elements are less uniformly distributed. Notably, aluminum is largely absent in some regions of size up to  $50 \mu\text{m}$ , which are enriched in silicon. These regions were found at various depths within the coating, including regions close to the metal.

#### 2.32.4.3 Electron Energy Loss Spectroscopy

As discussed previously, a primary electron that undergoes any inelastic interaction with the examined material loses energy. EELS determines the losses of electron energy. The most commonly used EELS is transmission EELS, in which the energy loss of incident electrons with a known, narrow range of kinetic energy passing through a thin specimen is determined by an electron spectrometer that is mounted after the specimen in the TEM.

Typically, an EELS spectrum consists of three regions: (i) zero loss peak, resulting from electrons that have suffered negligible inelastic scattering; (ii) low loss region, containing electrons that have suffered inelastic scatterings including phonon excitations, inter- and intraband transitions, plasmon excitations, and have lost up to  $\sim 50 \text{ eV}$  energy and (iii) high loss region, containing electrons that have suffered interaction with tightly bound inner shell electrons and caused inner shell ionization, which is characteristic of the element. Although each region of

the EELS spectrum provides complementary information, it is the characteristic edges in the high energy loss region that are most commonly used. In TEM, EELS is capable of obtaining spatially resolved information on composition, chemical bonding as well as valence and conduction band electronic structure since the spectra for an element in different compounds are different. This ability is a strong advantage of EELS compared with EDX.

A further advantage of EELS compared to EDX is its capability of detecting light elements that generate X-rays that are too soft to be detected, such as helium, lithium, and beryllium. The probability that a particular electron will be scattered by an atom is defined as the cross-section, which decreases for elements of high atomic number. Thus, light element edges are far more intensive than those of elements with higher atomic number. Thus, EELS is very powerful for the analysis of light elements.

In corrosion studies, spatially resolved EELS has been successfully applied, for example, to the study of local chemistry of anodic oxide films. A correlation between flaws in the oxide film and changes in the oxygen gas generation has been established via spatially resolved EELS. **Figure 24** shows a transmission electron micrograph of ultramicrotomed section of the anodic film formed at a constant current density of  $50 \text{ A m}^{-2}$  on a binary Al-4 at.% Cr alloy in 0.01 M ammonium pentaborate solution to 32 V, revealing an anodic film of  $\sim 40 \text{ nm}$  thickness. Variation of film morphology is clearly evident. Light regions of different sizes are revealed within the film section. **Figure 25** displays the EELS spectra at the oxygen K-shell electron ionization energy region acquired from locations across the film from the film surface to the alloy/film interface; the separation of the spectrum line is  $0.8 \text{ nm}$ . The spatially resolved oxygen K-edge fine structure encompassing a region of light film materials reveals a sharp pre-edge peak at  $529 \text{ eV}$  before the OK edge; such pre-edge peaks are characteristic of oxygen gas. Thus, it is concluded that the light regions in the film are bubbles filled with oxygen gas.

Further, the valence state of chromium species that have been incorporated into the film from the substrate alloy has also been determined by EELS. Using the data generated from anodic alumina,  $\text{Cr}_2\text{O}_3$  and  $\text{K}_2\text{Cr}_2\text{O}_7$ , spectra have been simulated for anodic alumina with associated  $\text{Cr}^{3+}$  or  $\text{Cr}^{6+}$  species. From the simulation and measurement of the experimental spectrum acquired at a location in the anodic film, as shown in **Figure 26**, it is evident



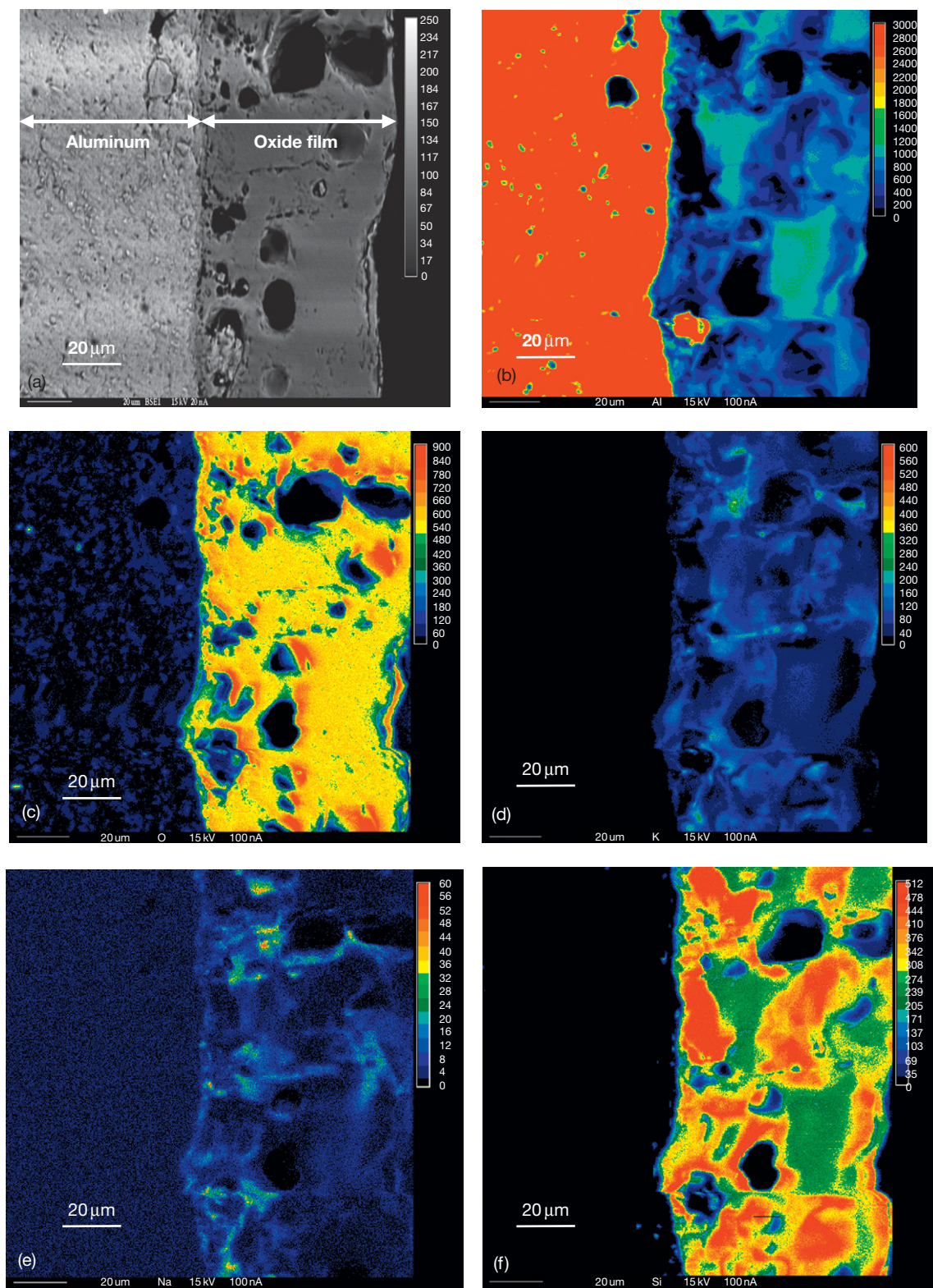


**Figure 23** EPMA of the cross section of aluminum anodized for 1800 s at  $5 \text{ A dm}^{-2}$  in  $0.05 \text{ M}$  potassium hydroxide/ $0.15 \text{ M}$  sodium metasilicate electrolyte at  $293 \text{ K}$ : (a) scanning electron micrograph, (b) aluminum map, (c) oxygen map, (d) potassium map, (e) sodium map, and (f) silicon map.

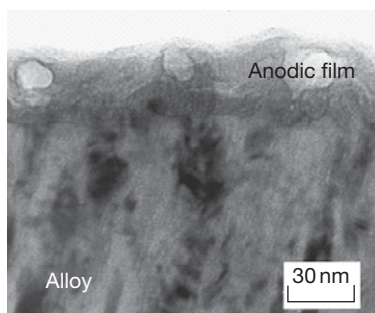


**Figure 24** Transmission electron micrograph of an ultramicrotomed section of the anodic film formed at a constant current density of  $50 \text{ A m}^{-2}$  on a binary Al-4 at.% Cr alloy in 0.01 M ammonium pentaborate solution to 32 V.

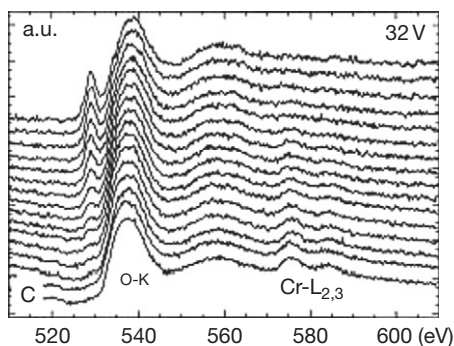


**Figure 25** EELS spectra acquired at a series of locations from close to the film surface to the alloy-film interface for the film displayed in [Figure 24](#).

that  $\text{Cr}^{3+}$  species was incorporated into the anodic film during the anodization of Al-4 at.% Cr alloy.

If EELS spectra are acquired from each pixel in an image, the distribution of a chosen element at certain oxidation state across the image can be analyzed, which is known as EELS mapping. For example, the DF image of [Figure 12\(b\)](#) reveals precipitate particles of  $\sim 20 \text{ nm}$  diameter distributed along grain boundaries in the examined AA6111 aluminum alloy. However, no compositional information is revealed in [Figure 12\(b\)](#). Such information can be readily obtained by EELS mapping. [Figure 27](#) shows EELS maps of precipitates in the AA6111 aluminum alloy revealed in [Figure 12\(b\)](#). The bright areas represent relatively high intensities of signals. Mapping images of  $508 \times 508$  pixels were acquired, giving a pixel size of  $0.92 \times 0.92 \text{ nm}$  for the selected magnification. The images were selected at the Al K, Cu  $L_{2,3}$ , Mg K and Si K edges, with onsets at 1560, 931, 1305 and 1839 eV, respectively, and energy resolution of about 0.6 eV. The EELS maps of [Figure 27](#) confirm

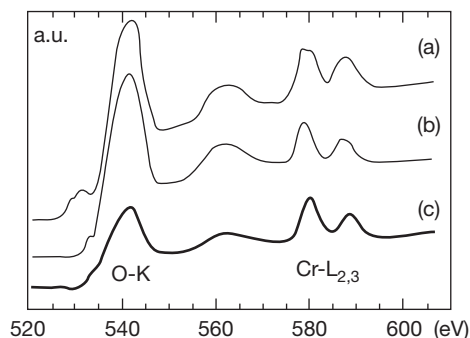


**Figure 26** Simulated and experimental EELS spectra: (a) simulated spectrum for anodic alumina containing  $\text{Cr}^{3+}$  species, (b) simulated spectrum for anodic alumina containing  $\text{Cr}^{6+}$  species, (c) experimental spectrum acquired at a location in the anodic film close to the alloy-film interface.

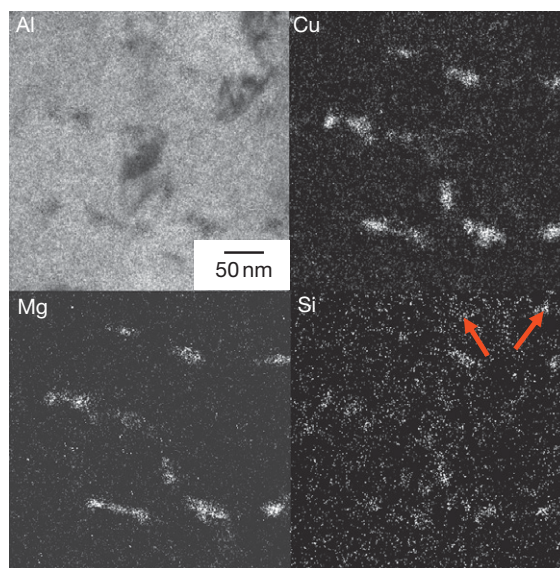


**Figure 27** EELS maps showing the distribution of precipitates in AA6111 aluminum alloy. The bright areas represent relatively high intensity of signals.

that the fine particles contain increased levels of copper, magnesium and silicon compared to the matrix. Examination of the images also reveals regions in which only silicon was detected, as shown by arrows, indicating the presence of two different types of precipitates in the alloy.

Comparing [Figure 27](#) with the X-ray maps (EPMA or EDX, [Figure 23](#)), it is clearly evident that EELS mapping has significantly improved the spatial resolution. This is because the spatial resolution of X-ray analysis in SEM or electron probe



microanalysis is limited to the sampling volume of the X-rays, which is typically at the level of micrometers although the imaging resolution of the SEMs is as high as 1 nm.

### 2.32.5 Specimen Preparation Techniques

Successful electron microscopy is essentially dependent on the employment of appropriate specimen preparation techniques that can produce revealing specimens and avoid, or minimize, change to the materials.

#### 2.32.5.1 TEM Specimen Preparation

Since TEM forms images following transmission of an electron beam through the specimen, thin foil specimen of thickness from a few nanometers to a few hundred nanometers must be prepared. For example, at an accelerating voltage of 100 kV, the maximum thickness of a transparent specimen is about 100 nm depending on the density of the material. The task is made even harder by the need to precisely prepare thin foil specimens from interesting regions within a large sample. Thus, preparation of TEM specimen can be a very challenging and time-consuming operation. The commonly employed TEM specimen preparation techniques include

- electropolishing,
- chemical polishing,
- ion beam thinning,
- deposition,
- film stripping,
- ultramicrotomy, and
- replication.

Depending on the type of materials being studied, appropriate preparation techniques should be chosen to generate an electron-transparent specimen.

TEM specimens from materials that have dimensions sufficiently small to be transparent to an electron, such as powders or nanotubes, can be quickly produced by the deposition of a suspension containing the material onto support grids. The suspension is normally made by diluting the sample in a volatile solvent such as ethanol. The solvent rapidly evaporates after depositing the suspension onto support grids, thereby producing a specimen that is suitable for TEM. Dry powder may also be directly dusted onto support grids.

The surface of a solid sample cannot be observed in TEM directly. The examination of a surface of a solid sample is achieved by replication. The replication process typically involves molding the surface of interest in a thin replica material which is transparent to electrons and subsequently removing the replica from the surface. Then the replica, which has copied the features on the surface, is ready for examination in the TEM.

Thin oxide films can be stripped from metal substrates by a chemical stripping process and transferred to supporting grids for TEM examination. Electropolishing is the most commonly employed technique for preparing thin foil specimen from electrically conductive materials such as metals. Chemical polishing is frequently used for generating TEM specimens from nonconductive materials such as semiconductors and ceramics. The main drawback of both electropolishing and chemical polishing is that a certain component of the material may be preferentially leached to change the specimen, thereby leading to inaccuracies in the subsequent TEM characterization.

Ion beam thinning is widely used to prepare an electron-transparent foil from hard materials including metals and ceramics. Focused ion beam (FIB) thinning is a relatively new technique that can be employed to prepare thin foils from precisely selected regions in a relatively large sample of any material. However, the highly energetic ion beam may introduce artifacts such as amorphization of the materials or contamination to the resultant thin foil specimen. Such artifacts introduce noticeable effects when lattice images are examined in HRTEM or EELS analysis is carried out.

In corrosion studies, ultramicrotomy is a very powerful tool. With experience, very revealing specimens can be produced. The principal advantages of ultramicrotomy are that it can create uniform thin foils and maintain the integrity of a multiphase sample ([Figure 20\(a\)](#)), for example, enabling thin foil specimens to be generated displaying the interface between the metal and its protective coatings ([Figure 13](#)) or exhibiting corrosion sites with corrosion products being kept in its original location ([Figures 1, 14, and 21](#)). However, ultramicrotomy may introduce mechanical damage, mainly compression, to the thin foil specimen; also reaction may occur between the materials and water in the bath behind the diamond knife employed in ultramicrotomy. The latter can be used to advantage in corrosion studies in the case of employing thin foil specimen to investigate the relationship between the microstructure and corrosion initiation.

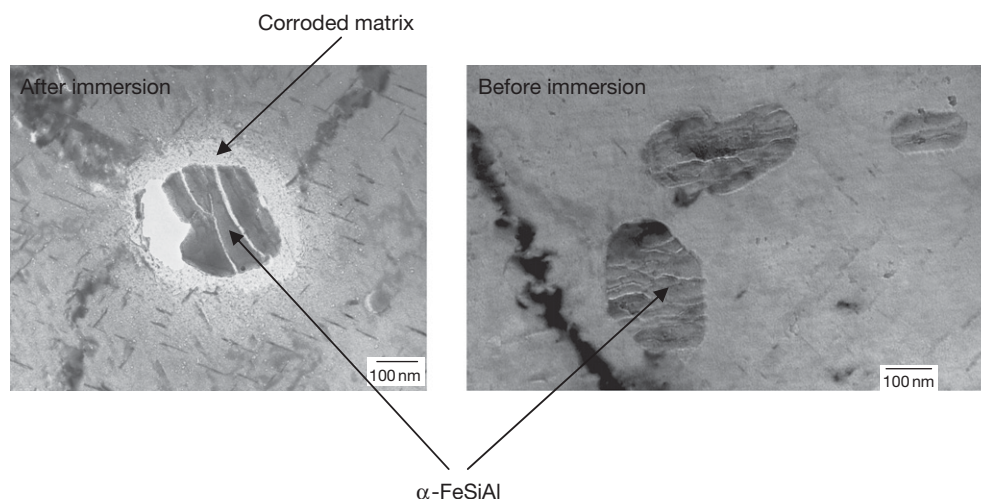


**Figure 28** Transmission electron micrographs of an ultramicrotomed section of an aluminum alloy before/after immersion in water.

**Figure 28** shows transmission electron micrographs of the ultramicrotomed section of an aluminum alloy before and after the immersion in water;  $\alpha$ -FeSiAl-particle-induced localized corrosion of the alloy matrix, due to the cathodic nature of the particle with respect to surrounding matrix, is revealed.

### 2.32.5.2 SEM Specimen Preparation

Compared to TEM, SEM allows much larger specimens to be examined, and specimen preparation is much simpler. Examination of bulk specimens makes it possible to image a comparatively large area. In corrosion studies, it is often needed to examine the cross-section of a specimen to determine corrosion propagation paths, the extent of corrosion beneath the surface, the thickness of a protective coating and its morphology in inner regions, its composition profile and adhesion to substrate, etc. In addition to conventional methods, such as mechanical polishing, for the preparation of the cross-section, new methods such as ultramicrotomy are increasingly employed to produce cross-section specimens with significantly reduced roughness, mechanical damage and contamination, thereby producing revealing specimens for the new generation of SEMs that provides very high surface sensitivity by avoiding interference between signals from different depths of specimens.

Further, with the typical operation voltages (20–30 kV), the number of electrons that escape from the specimen is smaller than that of electrons that hit the specimen. Consequently, there is a

buildup of electrons at the specimen surface if the excess electrons are not conducted away from the specimen, leading to the specimen surface becoming negatively charged. As a result, the incident electrons are repelled, and the image is distorted. Thus, for a nonconductive specimen surface, such as a metal with corrosion products or oxides films on the surface, the surface must be coated with a thin conducting layer, such as carbon or gold–palladium, which does not readily form an insulating oxide layer in air during its transport from the coating unit to the microscope. Thus, the build-up of electrons at the specimen surface is avoided by conducting the excess electrons away from the specimen by the conducting coating. However, there are drawbacks for the employment of such coatings. The coatings may mask fine surface features. The coating may also absorb some of the X-rays emitted from the specimen during X-ray analysis. The absorption is more pronounced by coating with elements of higher atomic number such as gold/palladium. An alternative approach to the surface charging problem is to operate the SEM at a relatively low voltage (1–5 kV) so that excessive electron build-up at the specimen surface is minimized.

### 2.32.6 Other Techniques

#### 2.32.6.1 X-ray Microscopy

##### 2.32.6.1.1 Introduction

X-ray microscopy is a nondestructive technique that generates an image of the internal features of the

examined materials, with the image contrast being determined by the difference in absorption of X-rays by the different components in the materials. The first X-ray microscope was developed in the late 1940s. In the X-ray microscope, images are recorded on photographic film or detected by a sensor such as a CCD camera. Similar to visible light, X-rays are a form of electromagnetic energy, but with much shorter wavelength and much higher energy. The resolution of X-ray microscopy lies between that of light microscopy and electron microscopy since an X-ray microscope uses soft X-rays with a wavelength in the range of 10 to 0.01 nm. Resolutions of nanometer level are achievable using the Fresnel zone plate lens which forms the image using the soft X-rays emitted from a synchrotron or from a laser-produced plasma. Further, because of their high energy, X-ray microscopes have the ability to penetrate relatively deep into materials, allowing images to be generated from the internal features. Compared to TEM, X-ray microscopy can generate images from relatively thick samples. A further advantage over electron microscopy is that X-ray microscopy does not require particular specimen preparation or a high-vacuum sample chamber.

#### 2.32.6.1.2 X-ray tomography

Standard X-ray microscopy can generate 2-D images which locate the position of an internal feature in the examined specimen both vertically and horizontally but with no information on the depth of that feature within the specimen being obtained. However, the information concerning the depth of the feature can be obtained by X-ray tomography. X-ray tomography is a 3-D scanning technique that allows nondestructive, high-definition scans of a specimen to be made. 3-D tomography requires the collection of a series of 2-D X-ray images on all sides of the specimen. Subsequently, highly detailed 3-D images are reconstructed by merging the individual 2-D X-ray images into a single 3-D block which can then locate any feature in the specimen in any direction. Systems with zone plate lenses can provide spatial resolution better than 50 nm.

The ability of nondestructive imaging of the internal features of materials in three dimensions gives X-ray tomography critical advantages in applications such as failure analysis as well as fundamental research. For example, internal cracks can be observed in three dimensions and correlated to the microstructure of a material; intergranular corrosion may be examined and correlated to grain boundary compositions; the

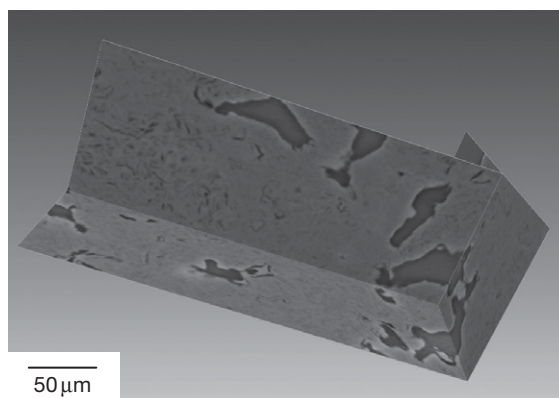


**Figure 29** X-ray tomography image of isotropic nuclear graphite, revealing porosity introduced by the fabrication process. Courtesy D. James, A. Jone, T.J. Marrow, and N. Stevens, Materials Performance Centre, School of Materials, The University of Manchester.

3-D approach can also lead to an improved understanding of interfacial reactions that occur at the intermetallics–matrix interface during pitting. This may lead to significant insight and understanding of the relationship between the microstructure and performance, that is, susceptibility to corrosion. X-ray tomography may also be extended to the observation of real-time processes of crack growth and corrosion propagation. **Figure 29** shows an image of isotropic nuclear graphite obtained on the Swiss Light Source TOMCAT synchrotron, revealing the porosity introduced by the fabrication process.

#### 2.32.6.2 Infrared Microscopy

Infrared spectroscopy is a technique based on the specific resonant frequencies of molecules, that is, the frequencies at which they rotate or vibrate. The resonant frequencies can be related to the strength of specific bonds and the mass of the atoms forming the bonds. Thus, the frequency of the vibrations can be associated with a particular bond type. When an infrared beam is directed to the material to be examined, the rotation or vibrations can lead to infrared absorptions at characteristic frequencies that are related to specific chemical groups in the material. The infrared spectrum is obtained by measuring the absorption at each wavelength. Thus, infrared spectroscopy can provide direct molecular identification of the examined materials.

In an infrared microscope, spatially resolved infrared spectra are obtained to form images, with the contrast being determined by the response of

individual specimen regions to particular wavelengths, generating a molecular fingerprint from the specimen. For infrared microscopy, as well as Raman microscopy, which is discussed in the next section, there are two approaches to acquire the spectrum. These approaches are known as parallel acquisition and serial acquisition. For parallel acquisition, the area of interest is fully illuminated by the incident beam; then, a micrograph is generated at a chosen wavelength which is characteristic of a molecular compound. For the serial mode, a finely focused incident beam is rastered across the surface of the materials to be examined, generating spatially resolved spectra. Subsequently, the micrograph is reconstructed to display the locations and amount of molecular compounds within the area of interest. Infrared microscopy employs focal plane array detection for infrared chemical imaging. The spatial resolution of infrared microscope is limited to about 10  $\mu\text{m}$  depending on the wavelength of light and the aperture. A typical infrared microscope operates over the range 650–4000  $\text{cm}^{-1}$ .

In corrosion studies, infrared microscopy can provide valuable information on interfacial reactions such as inhibition of metals and chemical bonding between a protective coating and the substrate. Further, by measuring at a specific frequency over time, changes in the character or quantity of a particular bond can be measured. This is especially useful in measuring the degree of polymerization in an organic protective coating. The infrared microscope operates in three different modes, transmission, reflection, and absorbance, depending on the transparency of the material to be examined. Materials that are transparent to infrared may be investigated in the transmission mode, which usually requires that the specimen is polished on both sides. For the reflectance mode, little specimen preparation is required.

### 2.32.6.3 Raman Microscopy

Like infrared spectroscopy, Raman spectroscopy is also based on the vibration or rotation of molecules within the material of interest. Thus, similar information is generated by Raman spectroscopy. However, infrared spectroscopy and Raman spectroscopy yield complementary information since they are based on different physical principles. Raman spectroscopy is based on inelastic scattering, or Raman scattering, of the incident monochromatic radiation by the material. Normally, a monochromatic source of light is used as the incident radiation. Highly

monochromatic and intense lasers in the visible, near-infrared or near-ultraviolet regions are usually employed as incident radiation in a modern Raman spectroscope. The interaction between the material and the laser beam results in phonons or other excitations, leading to the energy of the laser photons being shifted. Thereafter, the laser beam is collected with a lens and transferred through a monochromator. Wavelengths close to that of the incident radiation, due to elastic Rayleigh scattering, are filtered out, while the rest of the collected light is dispersed onto a detector to generate the spectrum. Thus, Raman spectroscopy allows the molecular identification of species present in the examined materials since the energy shift of the laser beam is associated with specific molecules in the materials.

A typical Raman microscope consists of a standard optical microscope, a laser, a monochromator, and a detector. A CCD or photomultiplier tube (PMT) is normally used as the detector. Relatively long acquisition times are required when a photomultiplier tube is used. The acquisition time is significantly reduced with CCD detectors. In Raman microscopy, the micrograph is obtained by generating spatially resolved spectra in the parallel or serial acquisition mode. The spectra are then analyzed and used to form a corresponding chemical image that shows the location and amount of different components within the examined area. Raman microscopy has relatively high spatial resolution. The lateral and depth resolutions are approximately 0.3 and 2  $\mu\text{m}$ , respectively. Raman microscopy cannot be performed on materials that exhibit fluorescence, since fluorescence yields a much more intense signal than Raman scattering and, therefore, masks any Raman bands that might be present. For incident radiation of wavelengths less than 785 nm, fluorescence interference can be very common. Moving to long-wavelength lasers can mitigate much of the fluorescence interference. However, the efficiency of Raman scattering decreases as the fourth power of wavelength, making long-wavelength Raman microscopes much less sensitive than systems based on visible wavelengths. Since Raman spectroscopy is a scattering technique, specimens do not need to be specially prepared.

Recently, Raman spectroscopy has been successfully combined with SEM and scanning probe microscopy (SPM), allowing morphological, compositional, structural and chemical analyses without moving the specimen between instruments. The features of interest are precisely located using the SEM and SPM and are chemically identified using Raman spectroscopy.

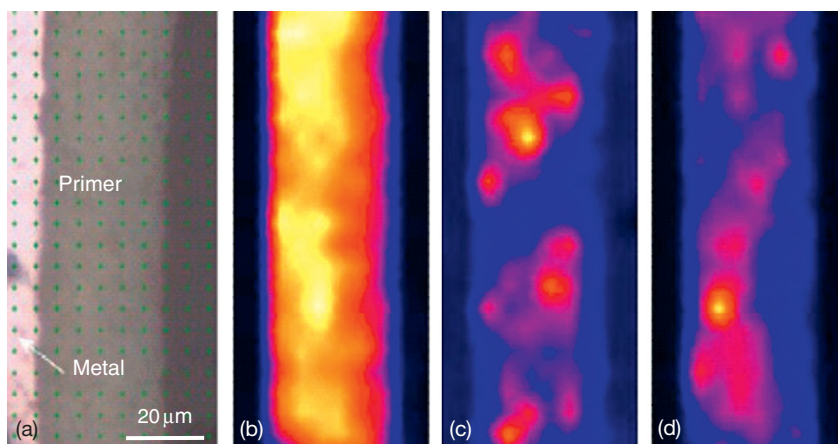


**Figure 30** Raman micrograph of chromate-inhibited primer: (a) optical image, (b)  $\text{TiO}_2$ , (c)  $\text{BaSO}_4$ , and (d)  $\text{SrCrO}_4$ . Courtesy Dr A.E. Hughes, CSIRO Manufactory and Infrastructure Technology, Australia.

**Figure 30** displays the Raman micrographs of a cross-section of the interface between an AA2024 aluminum alloy and chromate-inhibited epoxy polyamide primer, revealing the distribution of various components, including  $\text{TiO}_2$ ,  $\text{BaSO}_4$  and  $\text{SrCrO}_4$  in the primer. Raman micrographs were generated using peaks at  $866$ ,  $987$ , and  $638\text{ cm}^{-1}$  for  $\text{SrCrO}_4$ ,  $\text{BaSO}_4$  and  $\text{TiO}_2$ , respectively. It is clearly evident that  $\text{TiO}_2$  is distributed relatively uniformly throughout the primer, whereas  $\text{BaSO}_4$  and  $\text{SrCrO}_4$  exhibit locally high concentration corresponding to relatively large particles of these two phases in the primer.

### 2.32.7 Concluding Remarks

This chapter is written mainly on the basis of experiences in the Corrosion and Protection Centre at The University of Manchester. The authors acknowledge the many colleagues who have also contributed significantly to the application of electron- and photon-based spatially resolved techniques in corrosion studies.

Leading scientists around the world continue to raise expectation for electron microscopy, and the manufacturers of electron microscopes continue to meet the expectation with improved design of the electron microscope. The introduction of the FEI Titan TEM in 2005 is a good example. In the Titan microscope, aberration correction breaks through the fundamental optical limitations of magnetic lenses. The Titan's extra wide column was specifically designed to give the mechanical stability required by the added height of probe and image correctors.

Its proprietary constant power lenses and advanced power supplies provide the necessary thermal and electronic stability. Titan enables sub-Angstrom microscopy in both TEM and STEM modes. The Titan can also achieve energy resolution down to  $0.1\text{ eV}$  for EELS, obtaining information of the electronic properties of materials, such as bonding states or band gaps, with unprecedented spatial resolution. Titan ETEM extends the capabilities of conventional TEM by permitting gas in the specimen chamber (up to  $4\text{ kPa}$ ) along with specimen heating (up to  $1000^\circ\text{C}$ ), thereby allowing investigation of interactions between the material and the local gaseous environment.

Although this chapter is entitled 'electron- and photon-based spatially resolved techniques,' it would not be complete without mentioning the increasing sophistication in microscopy, for example, the recently developed Carl Zeiss ORION helium ion microscope. The scanning ion microscope uses a beam of helium ions as the incident radiation. Like a conventional SEM, in a scanning helium ion microscope the ion beam is rastered across the surface of the material to be examined. Since ion beam can be focused to a finer size, with less surface interaction than electrons, the scanning ion microscope can generate images with increased resolution and better contrast, more surface sensitivity, and better depth of field. Further, as in the case of Rutherford backscattering spectroscopy, backscattered helium ions can be collected in the helium ion microscope, with the total backscattered ion yield being directly proportional to the mass of the sample atoms. Thus, it is possible to easily differentiate between elements.



For those who wish to pursue the subject further, there are many textbooks that provide much more detailed information on electron- and photon-based spatially resolved techniques.

## Further Reading

Clarke, A. R.; Eberhardt, C. N. *Microscopy Techniques for Materials Science*; CRC Press: Boca Raton and Cambridge, 2002.

Egerton, R. F. *Physical Principles of Electron Microscopy: An Introduction to TEM, SEM, and AEM*; Springer: Boston, 2005.

Goodhew, P. J.; Humphreys, J.; Beanland, R. *Electron Microscopy and Analysis*, 3rd ed.; Taylor & Francis: London, 2001.

Lawes, G. In *Scanning Electron Microscopy and X-ray Microanalysis*; James, A. M., Ed.; Wiley: Chichester, 1987.

Reimer, L. *Transmission Electron Microscopy: Physics of Image Formation and Microanalysis*, 4th ed.; Springer: Berlin and London, 1997.

Reimer, L. *Scanning Electron Microscopy: Physics of Image Formation and Microanalysis*, 2nd ed.; Springer: Berlin and London, 1998.

Stuart, B. H. *Infrared Spectroscopy: Fundamentals and Applications*; Wiley: Chichester, 2004.

Turrell, G.; Corset, J. *Raman Microscopy: Developments and Applications*; Academic Press: London, 1996.

Williams, D. B.; Carter, C. B. *Transmission Electron Microscopy*; Plenum Press: New York and London, 1996.

## 2.34 Corrosion Testing and Determination of Corrosion Rates

**P. J. McIntyre**

NPL, Hampton Road, Teddington, Middlesex TW11 0LW, UK

**A. D. Mercer**

Formerly NPL, Hampton Road, Teddington, Middlesex TW11 0LW, UK

This article is a revision of the Third Edition article 19.1 by P. McIntyre and A. D. Mercer, volume 2, pp 19:3–19:118,  
© 2010 Elsevier B.V.

---

<b>2.34.1</b>	<b>Introduction</b>	1445
<b>2.34.2</b>	<b>Test Procedures</b>	1446
2.34.2.1	Preparation of Surface	1446
2.34.2.2	Marking Specimens for Identification	1448
2.34.2.3	Number of Replicate Specimens	1448
2.34.2.4	Test of Fusion Welds	1448
2.34.2.5	Duration of Exposure	1449
2.34.2.6	Heat Treatment	1450
2.34.2.7	Stress Effects	1451
2.34.2.8	Appraisal of Damage	1451
2.34.2.9	Removal of Corrosion Products	1454
<b>2.34.3</b>	<b>Laboratory Corrosion Tests</b>	1455
2.34.3.1	Total-Immersion Tests	1455
2.34.3.1.1	Solution composition	1455
2.34.3.1.2	Temperature control	1456
2.34.3.1.3	Aeration	1456
2.34.3.1.4	Velocity	1457
2.34.3.1.5	Volume of testing solution	1460
2.34.3.1.6	Support of specimens	1460
2.34.3.2	Alternating-Immersion Tests	1460
2.34.3.3	Water-Line Tests	1460
2.34.3.4	Heat-Flux Effects	1461
2.34.3.5	Composition of Testing Solution	1462
<b>2.34.4</b>	<b>Electrochemical Measurements (General)</b>	1462
2.34.4.1	Techniques	1462
2.34.4.2	Instruments	1463
2.34.4.3	Electrochemical Cells	1463
2.34.4.4	Measurements of the Corrosion Potential	1465
<b>2.34.5</b>	<b>Polarization Resistance</b>	1466
2.34.5.1	Tafel Constants	1467
2.34.5.2	Applications	1467
2.34.5.3	Derivation of Linear Polarization Method for Determining Corrosion Rates	1468
2.34.5.4	Simultaneous Determination of Tafel Slopes and Corrosion Rates from $R_p$	
	Determinations	1469
<b>2.34.6</b>	<b>Tests for Bimetallic Corrosion</b>	1470
<b>2.34.7</b>	<b>Soil Tests</b>	1471
<b>2.34.8</b>	<b>Accelerated Tests – Electrolytic Tests</b>	1471
2.34.8.1	Electrolytic Oxalic Acid Etching Test	1472
2.34.8.2	The Electrolytic Corrosion (EC) Test	1472

---

2.34.8.3	Impedance (Aztac) Test	1472
<b>2.34.9</b>	<b>Accelerated Tests – Simulated Environments</b>	1472
2.34.9.1	Spray Tests	1472
2.34.9.2	Corrodkote Test <sup>162,166</sup>	1473
2.34.9.3	Sulfur Dioxide Tests	1474
2.34.9.4	General Considerations of Spray and SO <sub>2</sub> Tests	1475
2.34.9.5	Accelerated Tests for Weathering Steels	1475
<b>2.34.10</b>	<b>Intergranular Attack of Cr–Ni–Fe Alloys</b>	1478
2.34.10.1	Boiling HNO <sub>3</sub> Test	1478
2.34.10.2	Boiling H <sub>2</sub> SO <sub>4</sub> + CuSO <sub>4</sub> Tests	1481
2.34.10.3	HNO <sub>3</sub> –HF Test	1482
2.34.10.4	H <sub>2</sub> SO <sub>4</sub> + Fe <sub>2</sub> (SO <sub>4</sub> ) <sub>3</sub> Test (Streicher Test)	1482
2.34.10.5	Electrolytic Oxalic Acid Etching Test	1483
2.34.10.6	Electrochemical Tests	1483
2.34.10.7	EPR Test	1485
2.34.10.7.1	Single loop EPR test	1485
2.34.10.7.2	Double loop EPR test	1485
2.34.10.7.3	Reactivation ratio EPR test <a href="#">Figure 20c</a>	1485
2.34.10.8	EPR Tests for Ferritic Stainless Steels	1486
<b>2.34.11</b>	<b>Crevice Corrosion and Pitting</b>	1486
<b>2.34.12</b>	<b>Impingement Tests/Erosion Corrosion</b>	1489
<b>2.34.13</b>	<b>Corrosion Fatigue</b>	1491
<b>2.34.14</b>	<b>Cavitation-Erosion</b>	1493
<b>2.34.15</b>	<b>Fretting Corrosion</b>	1495
<b>2.34.16</b>	<b>Corrosion Testing in Liquid Metals and Fused Salts</b>	1495
2.34.16.1	Chemical Reaction	1496
2.34.16.2	Simple Solution	1496
2.34.16.3	Mass Transfer	1496
2.34.16.4	Impurity Reactions	1496
2.34.16.5	Testing	1497
2.34.16.5.1	Static tests	1497
2.34.16.5.2	Refluxing capsules	1497
2.34.16.5.3	Dynamic tests	1498
2.34.16.5.4	Loop tests	1498
2.34.16.6	Liquid–Metal Embrittlement	1500
<b>2.34.17</b>	<b>Tests in Plant</b>	1500
2.34.17.1	Corrosion Racks	1501
2.34.17.2	Specimens	1502
<b>2.34.18</b>	<b>Atmospheric Tests</b>	1502
<b>2.34.19</b>	<b>Atmospheric Galvanic Tests</b>	1503
<b>2.34.20</b>	<b>Tests in Natural Waters</b>	1506
<b>2.34.21</b>	<b>Field Tests in Soil</b>	1507
2.34.21.1	Other Tests	1508
<b>2.34.22</b>	<b>Corrosion Testing of Organic Coatings</b>	1508
2.34.22.1	Behavior of Organic Coatings	1508
2.34.22.2	Preparation	1509
2.34.22.3	Exposure Conditions	1509
2.34.22.3.1	Laboratory tests	1509
2.34.22.3.2	Field and plant tests	1510
2.34.22.4	Coating Evaluation	1510
2.34.22.4.1	Distensibility	1511
2.34.22.4.2	Abrasion tests	1511
2.34.22.4.3	Hardness	1511

2.34.22.4.4	Impact tests	1511
<b>2.34.23</b>	<b>Test Methods for Corrosion Inhibitors</b>	1511
2.34.23.1	Immersed Conditions	1511
2.34.23.2	Vapor Phase Conditions	1513
<b>Appendix A:</b>	<b>Methods of Removal of Corrosion Product</b>	1513
<b>Appendix B:</b>	<b>Standards</b>	1515
<b>References</b>		1522

## Glossary

**$\sigma$ -phase** A brittle intermetallic phase that forms in stainless steels in some heat treatment conditions.

**$R$**  Electrical resistance

**$R_p$**  Polarization resistance

**$\beta_a, \beta_c$**  Slopes of anodic and cathodic polarization curves

**$\Delta\psi$**  Potential drop across the double layer

**$\Delta K$**  Stress intensity factor range

**$\rho$**  Density

## Abbreviations

**ASTM** American Society for Testing and Materials

**BS** British Standard

**CCT** Critical crevice temperature

**CPT** Critical pitting temperature

**EC** Electrolytic corrosion

**EPR** Electrochemical potentiokinetic reactivation

**gma** g per m<sup>2</sup> per annum

**IEC** International Electrotechnical Commission

**ISO** International Organization for Standardization

**LME** Liquid–metal embrittlement

**mdd** mg per dm<sup>2</sup> per day

**mpy** mils (0.001 inch) per year

**NACE** National Association of Corrosion Engineers

**PTFE** Polytetrafluoroethylene

**SCE** Saturated calomel electrode

**SHE** Standard hydrogen electrode

## 2.34.1 Introduction

Corrosion tests provide the basis for the practical control of corrosion and therefore deserve a more exhaustive discussion than limitations of space will permit. A detailed description of all the procedures and devices that have been employed in corrosion studies in many countries will not be attempted. Instead, attention will be directed principally to underlying principles and to comments on the significance and limitations of the results of the test methods that are considered. Further details may be obtained from the references and from the comprehensive works by Champion<sup>1</sup> and Ailor.<sup>2</sup> (See also: Baboian, R.; Dean, S. W. *Corrosion Testing and Evaluation: Silver Anniversary Volume*, ASTM STP1000-EB; ASTM: Philadelphia, 1990; 436 p. and Cramer, S. D.; Covino, B. S., Jr., Eds. *ASM Handbook Volume 13A: Corrosion: Fundamentals, Testing, and Protection*, ASM International, Ohio, 2003; 1135 p.)

Tests may be classified conveniently under three headings.

1. Laboratory tests, in which conditions can be precisely defined and controlled.
2. Field tests (tests in real environments), in which replicate test samples of metals or alloys – referred to as test coupons or specimens – are exposed to the actual environmental conditions expected in service, for example, the atmosphere, the ground, the sea, etc.
3. Service tests, in which the test specimens – which may often take the form of manufactured components – are exposed to the particular conditions in which they are to be used, for example, in process streams of chemical plant.

## Symbols

**$b_a, b_c$**  Tafel constants for anodic and cathodic processes

**$E$**  Potential

**$E_b$**  Pitting breakdown potential

**$E_{corr}$**  Corrosion potential

**$E_p$**  Pit repassivation potential

**$i$**  Current density

**$i_a, i_c$**  Net anodic and cathodic current densities

**$i_{corr}$**  Corrosion current density

**$i_L$**  Limiting current density

**$i_o$**  Exchange current density

**$I$**  Total current

**$Q$**  Electrical charge

Laboratory tests, although often necessarily conducted under conditions that are not met in service, have a number of advantages over the other types of tests. Since conditions can be controlled at will, it is possible to identify the separate effects of a number of factors on the corrosion behavior. These factors include the type and condition of the metal surface, the environmental composition, temperature and pressure, movement of the specimen relative to the environment, time of exposure, and so on. Laboratory tests, at least in principle, also enable comparisons to be made under identical conditions of the relative corrosion behavior of different metals and alloys and different protective schemes, for example, coatings, environmental treatments, etc.

In many cases, attempts will be made to accelerate the test to produce results in a shorter time than might otherwise be possible in field or service tests. Such acceleration is usually achieved by intensifying one or more of the controlling factors. Tests might be conducted at a higher temperature, with more corrosive media, with activation of the corrosion process by electrochemical methods, etc., with the object of enhancing the aggressivity of the test conditions. While accelerated test procedures are often used, the results should always be treated with careful consideration. It is not unknown for a protective system to fail to meet the requirements of an accelerated test, although showing satisfactory performance in normal conditions of use. Nevertheless, a number of such tests, particularly for atmospheric corrosion, in which rates of corrosion in real conditions are often low, are accepted and correlations have been established with real conditions. (Such tests are typically designed and standardized for very specific conditions, such as the performance of nickel–chromium-plated components for automotive applications, and care should be taken when applying them for other situations. A key requirement for any accelerated test is that it should produce the same type of corrosion (uniform, pitting, etc.) as in the service exposure.)

Field tests do not have the uncertainties attached to accelerated laboratory tests, since there is no attempt to adjust the controlling environmental conditions. The chief problem is obtaining reproducible conditions from one test to another. This is particularly the case with tests in the atmosphere. While broad classes of terrestrial atmospheres have long been recognized, for example, tropical, rural, urban, marine, etc., difficulties remain that are associated with variations within these classes. In the 1980s, steps were taken within ISO to rationalize the situation by producing a standard on the classification of atmospheres (ISO 9223). Other

standards that provide guidance on the mounting and disposition of specimens for field tests (ISO 8565) and for the statistical treatment of results where large numbers of specimens are used (see Ailor<sup>2</sup> and ASTM G 16) are available.

Service tests will be used: (1) where the operating conditions cannot be successfully reproduced in laboratory tests, (2) where the environment does not occur naturally, (3) where real components, as opposed to test specimens, need appraisal, and (4) to confirm laboratory and/or field tests.

Often, all the three types of test will be used sequentially. An example might be the development of a coating to protect suspension cables for use on a bridge in a coastal region. The test program could involve salt spray testing of candidate treatments in the laboratory, followed by field trials of the most successful materials at a site similar in aggressivity to the location of the final product and eventual testing at the site with loadings and positioning matching those of the end use. It would be expected that the number of candidate materials would decrease through this sequence of tests.

Irrespective of the method of test or the purpose for which it is made, there are certain practical features that require attention and will be necessary to achieve good reproducibility (by one operator) and repeatability (by different operators).

## **2.34.2 Test Procedures**

### **2.34.2.1 Preparation of Surface**

When the test is to predict the performance of a material in a particular service, the ideal procedure would be to have the surface of the test-pieces duplicate the surface of the material as it would be used. Here, however, a complication is presented by the fact that materials in service are commonly used in several forms with different conditions of surface. Where the number of materials to be compared is large, it will usually be impractical to test all the conditions of surface treatment of possible interest. The best practical procedure, then, is to choose some condition of surface more or less arbitrarily to allow the materials to perform near the upper limits of their ability. If all the materials to be tested are treated in this way, and preferably with uniform surface treatment, the results of the test will indicate the relative abilities of the different materials to resist the test environment when in a satisfactory condition of surface treatment. Then, if it should be considered prudent or desirable to do so, the most promising materials can be subjected to



further tests in a variety of surface conditions so that any surface sensitivity can be detected.

These remarks apply as well to the treatment of the surfaces of specimens to be used in tests in corrosion research projects, except that here, selection of a particular method of surface preparation is required to achieve reproducibility of results from test to test and among different investigators. Methods of preparing specimens are described in ASTM G 1 and ISO 7539-1.

The final step in surface preparation should ordinarily be a cleaning and degreasing treatment to remove any dirt, oil, or grease that might interfere with the inception or distribution of corrosion. The simplest test of a satisfactory surface condition in this respect is for the specimens to be free from 'water break' when rinsed with water after cleaning. As a final treatment for specimens to be weighed prior to exposure, a dip in a mixture of water and acetone or of alcohol and ether will facilitate quick drying and avoid water-deposited films. Specimens to be stored prior to weighing should be placed in a desiccator, which, in best practice, should be sealed without grease.<sup>3</sup>

In addition to the preparation of the principal surfaces of the specimen, it is essential to machine or grind any cut or sheared edges, since these could become sites of preferential attack. As a general rule, edge effects should be kept to a minimum by using specimens in which the ratio of surface area to edge area is large. With flat specimens, a disc is best from this point of view, but other shapes may be more convenient and acceptable in many practical instances. When mass loss is to be used as a measure of corrosion, precision will be improved by providing a large ratio of exposed area to mass, and thin flat specimens or fine wires have obvious advantages. (Wires also have the disadvantage of a metallurgical structure that is usually not typical of bulk material.)

For accuracy of weighing, it is usually necessary to restrict the dimensions of specimens to what can be accommodated on the common analytical balances. It must be borne in mind that where attack occurs in the form of a very few pits or in crevices under supports, the extent of this localized attack may be determined by the total area of the test-piece as it establishes the area of passive metal acting as a cathode to the few anodic areas. Thus, larger specimens, or the much larger surfaces that will often be involved in field or service tests, may give rise to much more severe localized attack under nominally the same conditions of exposure.

In certain tests, it is sometimes desirable to eliminate any effects of a mechanically achieved surface

condition by chemical treatment or pickling of the surface prior to test. This may be done in a pickling solution; alternatively, the test itself may be interrupted after sufficient corrosion has occurred to remove the original surface, the specimen then being cleaned and reweighed and the test started over again. Wesley<sup>4</sup> found it to be desirable to pickle off about 0.008 mm from the surface of specimens in acid to improve the reproducibility of the tests.

With materials the stainless steels that may be either active or passive in a test environment, it is common practice to produce a particular initial level of passivity or activity by some special chemical treatment prior to exposure. With stainless steels this objective may be subsidiary to eliminating surface contamination, such as iron from processing tools, by treatment in a nitric acid solution, which might also be expected to achieve substantial passivity incidental to the cleaning action (ASTM A 380).

In studies of the behavior of materials that may be either active or passive in the test environment, there would seem to be a real advantage in starting with specimens in an activated state to see whether they will become passive, and to ascertain how fast they are corroded if they remain active. If passivity should be achieved after such an activated start, the material can be considered to be more reliable in the test environment than would be the case if by chance it managed to retain an originally induced passivity for all, or most of, the test period. It may also be valuable to know how fast the metal will be corroded by the test medium if activity should persist.

A procedure for testing previously activated specimens applied in studies of titanium was described by Bayer and Kachik.<sup>5</sup> Renshaw and Ferree<sup>6</sup> also employed prior activation in their studies of the passivation characteristics of stainless steels.

In many cases, there is a need to test metal-coated specimens, for example, galvanized steel, tin-plated copper, nickel-plated zinc, etc. It will then be necessary to test specimens in the completely coated condition and also with the coating damaged so that the basis metal is exposed. The latter condition will provide the conditions for galvanic action between the coating and the basis metal. With sheet specimens, this condition is most readily achieved by leaving cut edges exposed to the test environment.

There may also be a need to consider the performance of pre-corroded test specimens. Apart from the fact that these conditions frequently arise in service, it is also important for other reasons:

- The presence of corrosion products or other surface layers may affect the access of constituents of the environment to the underlying metal surface where the corrosion process occurs.
- In the case of alloys, some precorrosion may lead to compositional changes in the surface.

(Additionally, in the case of inhibitor tests, preexisting corrosion product often absorbs a significant proportion of the inhibitor, leading to a lower inhibition efficiency than for a clean surface.) These factors should be taken into account in the application of any test method.

#### **2.34.2.2 Marking Specimens for Identification**

The simplest way to identify a specimen is to mark it with letters or numbers applied by stamping with a stencil or number punch. (Both of these methods have potential problems – in the case of stenciled identification the paint used may act as a crevice-former, while stamping leads to an area of higher plastic strain, which may modify its corrosion behavior.) There is, of course, always the danger that the identification marks will be obliterated by corrosion. To guard against this, the several specimens in a test should be identified further by a record of their positions relative to each other or to their supporting device. Before specimens are taken from test, their identity should be established in this manner unless inspection has already shown that the identification marks have been preserved.

Other means of identification can be used on specimens exposed to atmospheric corrosion. For example, where stamped letters cannot be expected to persist, identification may be provided by holes drilled in particular positions or by notching the edges of specimens in particular places, both in accordance with a template. Where severe corrosion is encountered, the identification by drilled holes is more permanent than that achieved by notching edges.

Other means of identification sometimes used satisfactorily involve chemical etching of the surface (not to be generally recommended), or the formation of letters or numbers by means of a vibrating stylus. The former is advantageous in studies of stress-corrosion cracking, in which stamped symbols could lead to regions of stress concentration.

#### **2.34.2.3 Number of Replicate Specimens**

Practical considerations usually limit the number of replicate specimens of each kind that can be exposed

for each period of test. At least two are recommended for obvious reasons, and if a larger number can be accommodated in the program more valuable results can be secured – especially when it is desired to establish the reality of small differences in performance. For statistical analysis, five replicates are desirable. Accounts of statistical planning and analysis are given by F. H. Haynie in Ailor<sup>2</sup> and in ASTM G 16.

In providing replicates for tests to be subjected to statistical analysis, it is necessary, in the original sampling of the materials to be tested, to ensure that normal variations in those qualities of the metals that might affect the results are represented in each set of samples.

In order to secure information as to changes in corrosion rates with time, as in atmospheric exposure tests, it is necessary to expose sufficient specimens to allow sets to be taken from test after at least three time intervals.

For preliminary tests where the number of test specimens that can be accommodated is limited, yet numerous materials are of possible interest, it is in order to expose single specimens. This may be more advantageous than limiting the compositions that can be investigated by exposing half the number of materials in duplicate. Probably the greatest advantage in exposing two specimens of a material instead of only one is in detecting gross errors, as in weighing, etc. rather than in any considerable improvement in the precision of the observations that may be made as to the relative behaviors of the metals tested.

#### **2.34.2.4 Test of Fusion Welds**

In view of the widespread use of welded joints in equipment and structures exposed to corrosion, it is necessary to know whether such welded joints will demonstrate satisfactory resistance to attack. It is not necessary to include welded specimens of all materials in a preliminary study to discover which of them have satisfactory resistance to a particular environment. Weld tests can be postponed until the preliminary selection has been made, or alternatively, those materials expected in advance to be most likely to be resistant can be exposed in the welded condition to expedite the final answer.

There are several reasons for testing welded specimens. The first is to discover whether the weld itself will resist corrosion satisfactorily. A second purpose is to discover whether the heat effects associated with welding operations have been in any way detrimental to the corrosion resistance of the parent metal near the

weld as in the case of the so-called 'weld decay' of stainless steels. Since weld deposits may themselves be subject to a weld thermal cycle, it is necessary to include cross welds in the design of welded specimens for such corrosion tests. Further, a weld will generally constitute a stress concentration, and unless postweld heat treated, will contain residual contraction stress. Thus, testing may be necessary to generate appropriate corrosion fatigue or stress-corrosion cracking data. The latter may follow ASTM standard G 58, 'Standard Practice for the Preparation of Stress-Corrosion Test Specimens for Weldments,' for example.

A weld bead included in a test-piece is, to some extent, peculiar to itself and may not necessarily be representative of nominally similar welds to be made by other welders under other circumstances. To this extent, results of tests on welds must be subject to some qualification in interpretation, having in mind that what will be disclosed principally will be the overall ability of the composition of the weld metal to resist the corrosive environment. In some cases, entrapped flux, craters, fissures, folds, surface oxides, etc. may introduce localized corrosion that may or may not occur with all welds of the type studied.

The heat effects of welding are to an even greater extent peculiar to the particular test specimens used. They will be influenced by the welding process, by the skill of the welder, by the thickness of the metal welded, by the type of joint made, and by the geometry and mass of the surrounding structure insofar as they affect heating and cooling rates and areas over which these effects apply. Consequently, what happens to a particular welded test-piece has a questionable general significance, especially when the result shows no apparent damage to a material known to be susceptible to welding heat effects in corrosive environments. It should not be assumed that high heat input during welding will represent the worst case. For example, with ferritic steels that are sensitive to hydrogen embrittlement stemming from environmental action, low welding heat input can be most detrimental because of the formation of hardened structures in the weld area. Moreover, the possible effects of multipass welding with attendant repeated thermal cycles must be recognized in the design of a suitable test-piece.

With some materials, there are specific heat treatments that are known to reproduce the worst effects of the heat of welding. It is recommended, therefore, that in tests made to qualify a material for a particular service environment, in addition to the exposure of welded test specimens in order to observe effects of

welding heat, specimens that have been given a controlled abusive or sensitizing heat treatment should be included. As an illustration, austenitic stainless steels may be held at 650–700 °C for 0.5–1 h, followed by testing for susceptibility to intercrystalline attack as in ISO 3651-1 or-2.

If such sensitized specimens remain as free from accelerated corrosion as the welded specimens do, then it can be concluded that no detrimental effects of the heat of welding need to be anticipated in the environment covered by the test. However, if the sensitized specimens are corroded while the welded specimens are not, there will remain the possibility that, under some conditions of welding, difficulties due to the effects of the welding heat may be encountered, and appropriate action or the substitution of more reliable compositions will be required. Having in mind the effect of time in damage of this sort, it will be necessary to make a careful examination of the corroded specimens to detect the first signs of attack before it can be concluded that none has occurred. In assessing the significance of attack observed on drastically sensitized specimens, it is necessary to keep in mind that no similar sensitization may result from good welding practice. Likewise, it should not be concluded that attack in a specific test environment will occur to a similar extent or will not occur at all, in some quite different environment.

The evaluation of heat treatments or the effectiveness of stabilization by limiting carbon content of these stainless steels can be determined by subjecting specimens to the ASTM standardized acid copper sulfate test or boiling nitric acid test (ASTM A 262).

#### 2.34.2.5 Duration of Exposure

The duration of a particular test is likely to be determined by practical factors such as the need for some information within a particular limit of time, or the nature of the operation or process with which the test is concerned. Tests are rarely run too long; however, this can happen, particularly in laboratory tests where the nature of the corrosive environment may be changed drastically by the exhaustion of some important constituent initially present in small concentration, or by the accumulation of reaction products that may either stifle or accelerate further attack. In either case, the corrosivity of the environment may be altered considerably. Gross errors may result from the assumption that the results apply to the original conditions of the test rather than to

some uncertain and continually changing conditions that may exist during the course of too extended a test period.

Rates of corrosion rarely remain constant with time. More often than not, rates of attack tend to diminish as a result of the formation of adherent insoluble corrosion products or other protective films originating in the environment (Figure 1). Therefore, extrapolation of results of tests that are too short is more likely to indicate a lower resistance to attack than will actually be observed over a prolonged period of exposure. To this extent, such extrapolation may be considered as conservative. At the worst, it may lead to the use of a more resistant material or a heavier section than is actually needed, or to the exclusion from consideration of some materials that might be much better than the short-time test results would indicate.

Tests should be of sufficiently long duration to permit demonstration of the possible protective nature of films. Lengthy tests would not normally be required for materials that experience severe corrosion, although there are cases where this is not so. For example, lead exposed to sulfuric acid corrodes at an extremely high rate initially, while building up a protective film, then the rate decreases considerably and further corrosion is negligible. Short tests on such materials would indicate a high corrosion rate and would be completely misleading. Short-term tests can also give misleading results on alloys such as stainless steels that form passive films. With borderline conditions, a prolonged test may be needed to permit breakdown of the passive film and the subsequent more rapid attack. Consequently, tests run for long periods are considerably more realistic than those conducted for short periods.

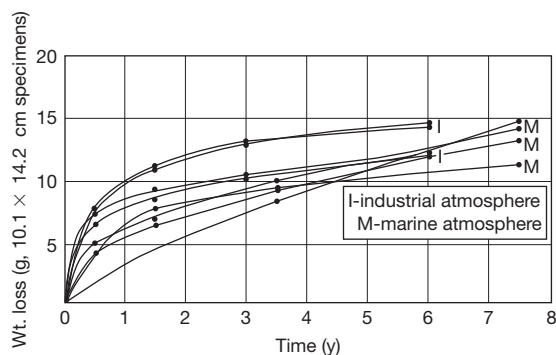


**Figure 1** Corrosion rate vs. time curve showing diminishing rate of attack. Reproduced from *Proc. ASTM* 1951, 51, 500.

Where anticipated corrosion rates are moderate or low, ASTM G 31 suggests that the following equation be used to estimate a suitable test duration:

$$\text{Test duration (h)} = 50 / (\text{Corrosion rate, mm year}^{-1})$$

For example, where the corrosion rate is 0.25 mm year<sup>-1</sup>, the test should run for at least 200 h.

Due to the relatively slow rate of the atmospheric corrosion process, it is recommended in ISO 8565 that test exposures be on a schedule such as 1, 2, 5, 10, and 20 years, depending on the corrosion resistance of the metal or coating being tested. In some cases, a total exposure of less than 2 years may be suitable. It should be noted that, especially for short-term testing, the results may depend on the season of initiation of exposure. Therefore, it is recommended that exposures are commenced in the period of highest corrosivity (usually autumn).

Tests in waters and soils should ordinarily be allowed to run for extended periods in excess of 3 years, with removals of specimens in groups after different time intervals. A desirable schedule for any extended test in a natural environment is one in which the interval between successive removals is doubled each time. For example, the first removal would be after 1 year, the second after 3 years, and the third after 7 years, and so on. On the other hand, test periods should not be significantly longer than the process or exposure time of the end-use requirement. The testing of inhibitors for use in pickling or cleaning treatments should be of a period commensurate with the practical requirement, which may be for only a few minutes.

In any event, the actual duration of a test must be reported along with the results, so that those who may wish to make predictions based on them will have an accurate idea of the extent to which they may undertake any extrapolation or interpolation.

#### 2.34.2.6 Heat Treatment

Many alloys are subject to drastic changes in their response to the effects of corrosive media when they have undergone certain heat treatments. The principal effect of interest is a loss of corrosion resistance to some degree. This commonly takes the form of concentration of corrosion in particular regions or along certain paths – as in the vicinity of grain boundaries – where phases formed by heat treatment are most likely to be concentrated. In other instances, and particularly in castings, homogenizing heat treatments may improve corrosion resistance by

eliminating 'coring' or major differences in composition from point to point in the original dendritic cast structure. Heat treatments that eliminate internal stresses are obviously helpful in connection with stress corrosion, but may induce structural changes that can affect corrosion in other forms.

Heat treatments involving heating to a temperature high enough to take harmful phases into solution, followed by cooling (e.g., by quenching) at a rate high enough to hold such phases in solution, may also be helpful in improving resistance to corrosion by avoiding attack that would otherwise be associated with a precipitated phase or compound.

Obviously, some knowledge of the possible effects of such heat treatments is essential for a complete understanding of the corrosion behavior of an alloy. Studies along this line should follow the initial selection of a material considered to be possibly useful for a particular service. Thus, it should be tested in the condition most likely to resist corrosion. Sometimes the obtaining of this condition may require annealing at a temperature sufficiently high to take any possibly harmful phases or compounds into solution followed by quenching to prevent them from precipitating. Following this preliminary selection, it would be prudent to carry out additional corrosion tests on specimens that have been deliberately subjected to any possibly detrimental heat treatments to which the material may be subjected during processing, fabrication, or use.

Heat treatment may also affect the extent and distribution of internal stresses. These may be eliminated by appropriate annealing treatments that can remove susceptibility to stress-corrosion cracking. This must be explored in any study of the performance of materials in environments where stress-corrosion cracking is a hazard. In particular cases, stress-relief annealing treatments may result in the appearance of new phases that, while eliminating the stress-corrosion effects, will induce another type of path of attack. This possibility must be kept in mind in assessing the overall benefits of heat treatments applied primarily for stress relief.

In other instances, heat treatments involving quenching, tempering, or holding at some temperature to precipitate an age-hardening compound are employed to secure some desired level of hardness or other mechanical properties. It is obviously necessary to explore what effects such heat treatments may have on the corrosion resistance of the material in the condition, or conditions, of heat treatment in which it is to be used.

### 2.34.2.7 Stress Effects

Techniques for studying the effects of stress on corrosion are covered in some detail elsewhere in this work. So far as attention to stress effects in a general materials-selection program is concerned, it is suggested that this should be a supplement to the initial selection of processing materials by exposing specimens to what approaches their best condition to resist corrosion, that is, free from stresses. Materials found to be worthy of further consideration in this way can be subjected to tests for stress effects. Where it is desired to discover whether severe internal stresses can be satisfactorily accepted, it will suffice to expose specimens in such a condition of stress. For example, a crucial test can be made by using a specimen in the form of a heavily cold-drawn tube in the as-drawn condition flattened on one end to introduce some additional multiaxial stresses. If such a severely cold-worked specimen suffers no stress-corrosion cracking in a test, then the danger of this occurring on any structure of that metal in the environment represented by the test is extremely remote.

### 2.34.2.8 Appraisal of Damage

There are many ways of determining the extent or progress of corrosion. The choice may be determined either by convenience or on the basis of some special interest in a particular result of corrosion or in a particular stage of a corrosion process.

Probably the most frequently made observation is the change in mass of a test-piece. This may take the form of a mass gain or a mass loss.

Mass-gain determinations are most common in studies of the extent and rate of oxidation or scaling at elevated temperatures. Very precise studies of this sort can be made by continuous observation of mass changes, as in the use of microbalances, such as used and described by Gulbransen.<sup>7</sup> Such data have quantitative significance only when the exact composition (metal content) of the scale is known or can be determined and when there has been no loss of loose scale during or after the test. Fundamental studies of the initial stages of corrosion when films of a few monolayers are formed have made use of an ellipsometer to follow the increase of thickness of corrosion products without disturbing the specimen.<sup>8</sup>

In most other cases, data on gains in mass due to the accumulation of corrosion products have little quantitative significance, since there is usually a question as to how much of the corroded metal is



represented in the corrosion products that remain attached to the specimen at a particular time. There are also uncertainties as to the chemical composition of corrosion products, which may consist of mixtures of several compounds with varying amounts of combined or uncombined water, depending on the humidity of the atmosphere at the time.

For these reasons, it is much better to determine the amount of metal removed by corrosion by weighing what is left after the removal of all adherent corrosion products by some method that will not cause further attack in the process, or by making proper correction for losses in the cleaning process. (Removal of corrosion products is dealt with in detail in [Appendix A](#).) Subtracting this final mass from the original mass will give the loss in mass during the test. Since the extent of this loss in mass will be influenced by the area exposed, as well as by the duration of exposure, it is desirable, to facilitate comparisons between different tests and different specimens, to report the loss in mass in a unit that includes both area and time. A most commonly used unit of this sort is milligrams weight loss per square decimeter of exposed surface per day (24 h) (mdd).

The unit gram per square meter per annum (gma) is sometimes used in atmospheric corrosion tests (see ISO 9226) where 'a' represents 'year.' It must be recognized that these units embody two assumptions that may not, in fact, be true. The first is that corrosion has occurred at a constant rate throughout the test period. This is rarely the case, since most rates of attack tend to diminish with time, but if the duration of the test and the actual loss in mass are also reported, the user of the data can take this into account. The second probable error in a mass loss/unit area unit is that it implies that corrosion has proceeded uniformly over the whole surface. These units, therefore, will give the wrong impression as far as the probable depth of attack is concerned, if corrosion has occurred at only a few spots on the surface of the specimen. Obviously, the mdd and gma units have limited significance when corrosion has taken the form of scattered pits or has been confined to the crevices where the specimen was supported. This should be covered by appended notes describing the nature and location of the corrosion represented and should be supplemented by data on the actual depths of the pitting or crevice attack. Here, again, the report should include data on the actual mass losses and duration of exposure.

Expression of mass loss in terms of a percentage of the original mass of a test-piece is usually

meaningless except for comparing specimens of the same size and shape, since it does not take into account the important relationship between surface and mass.

As indicated, it is necessary to measure and report the depths of any pitting or other localized corrosion, such as in crevices, that may have occurred. It is also useful to provide information on the frequency of occurrence, distribution, and shape of pits, since these features are likely to have practical significance. Champion<sup>1</sup> has produced charts in which the number of pits/unit area, the size of pits, the depth of pitting, cracking, and general attack can each be rated by the numbers 1–7. Where the number of pits is very large, it is obviously impracticable to measure the depths of all of them. Consequently, the practice of choosing 10 of the deepest pits and reporting their average depth and that of the deepest of them has developed. All surfaces of the specimen should be examined in selecting the 10 deepest pits.

There are several ways of measuring pit depths, but in all cases these measurements are facilitated if corrosion products are first removed (see [Appendix A](#)). If the pits are large enough, their depths may be measured directly with a pointed micrometer or with an indicating needle-point depth gauge. Otherwise, they may be measured optically with a microscope by focusing in turn on the surface of the specimen and, on the bottom of the pit using a calibrated wheel on the fine-focus adjustment rack for this focusing operation. In some instances, the small dimensions or shapes of pits may require metallographic examination of a cross-section for a precise measurement of depth. Such metallographic examination may also be useful in detecting an association of pitting with a structural feature of the metal.

Since it is often difficult to visualize the extent of attack in terms of depth from such mass-loss units as mdd, it is common practice to convert these mdd figures into others to indicate depth of penetration, for example, millimeter per year or mils per year (mpy), where 1 mil = 0.001 in. Such calculations suffer from the same defects as the mdd figures in that they take into account neither changes in corrosion rates with time nor nonuniform distribution of corrosion. However, since such conversions are often made, it is desirable for the initial reporter of the test results to make the calculations accurately and to report corrosion rates in both mdd and  $\text{mm year}^{-1}$  or similar units.

The basic formula for making such calculation is:

$$\text{mdd} \times 0.0365/\rho = \text{mm year}^{-1}$$

where  $\rho$  is the density of the metal ( $\text{g cm}^{-3}$ ). Some values showing the relationship between mdd, and mpy and  $\text{mm year}^{-1}$  are given in Table 1.

Losses in mass will also not disclose the extent of deterioration that may result from the distribution of a very small amount of attack concentrated along grain boundaries or in transgranular paths (as in some cases of stress-corrosion cracking). In such instances, an apparently trivial or even undetectable loss in mass may be associated with a practically complete loss of the strength or ductility of the corroded metal. Where this may be suspected, or in any doubtful cases, the mass-loss determinations must be supplemented by other means of detecting

this sort of damage, including simple bend tests followed by visual or metallographic examination to disclose surface cracking, quantitative tension tests, and direct metallographic examination of cross-sections. Changes in electrical resistance have been used as a measure of intergranular attack.<sup>9</sup> Because of the nature of such resistance determinations,<sup>10,11</sup> they have been more useful for comparing specimens of a particular kind and size than as a basis for quantitative expression of rates of attack.

The characteristic mode of corrosion of some alloys may be the formation, as a corrosion product, of a redeposited layer of one of the alloy constituents, as in the case of the brasses that dezincify, or of a residue of one of the components, as in the case of the graphitic corrosion of cast iron. Particularly in the case of the dezincified brass, the adherent copper is not likely to be removed with the other corrosion products, and therefore, the mass-loss determination will not disclose the total amount of brass that has been corroded. This is especially important because the copper layer has very little strength and ductility and the extent of weakening of the alloy will not be indicated by the mass loss. In these cases, also, the mass-loss determinations must be supplemented by, or replaced by, mechanical tests or metallographic examination, or both, to reveal the true extent of damage by corrosion. Difficulties in obtaining accurate mass losses of heavily graphitized specimens have been reported.<sup>12</sup>

Whenever changes in mechanical properties, such as performance in tension tests, fatigue tests, and impact tests, are to be used as a measure of corrosion damage, it is obviously necessary to provide test data on the relevant properties of the uncorroded metal. When tests extend over long periods during which the alloys being tested may be subject to changes in mechanical properties due to ageing effects, entirely aside from corrosion, it will be necessary to provide sets of specimens that may be subjected to similar ageing in a noncorrosive environment so that by direct comparison with corroded specimens of the same age the changes due to corrosion can be separated from those due to ageing. Preferably the control specimens should be stored so that they will be subjected to the same thermal experience as the specimens undergoing corrosion. This is usually very difficult to accomplish while maintaining the control specimens completely protected from corrosion.

In calculating the strength properties of the corroded specimens and comparing them with those of the uncorroded control specimens after appropriate

**Table 1** Relationship between corrosion rate in  $\text{mg dm}^{-2} \text{d}^{-1}$  (mdd) and penetration in mpy and  $\text{mm y}^{-1}$

Material	Density ( $\text{g cm}^{-3}$ )	Penetration equivalent to a corrosion rate of 1 mdd	
		mpy	$\text{mm year}^{-1} \times 10^2$
Aluminum 2S	2.72	0.528	1.342
Ambrac (Cu-6.5Si)	8.86	0.162	0.412
Brass (admiralty)	8.54	0.168	0.427
Brass (red)	8.75	0.164	0.416
Brass (yellow)	8.47	0.170	0.432
Bronze, phosphor (5% Sn)	8.86	0.162	0.412
Bronze (silicon)	8.54	0.168	0.427
Bronze, cast (85-5-5-5)	8.70	0.165	0.419
Cast iron	7.20	0.200	0.508
Copper	8.92	0.161	0.409
Cu-30Ni	8.95	0.161	0.409
Hastelloy A	8.80	0.163	0.414
Hastelloy B	9.24	0.155	0.394
Hastelloy C	8.94	0.161	0.409
Inconel 600	8.42	0.171	0.434
Iron-silicon alloy	7.0	0.205	0.521
Lead (chemical)	11.35	0.127	0.323
Monel	8.84	0.163	0.414
Nickel	8.89	0.162	0.412
Nickel silver (18% Ni)	8.75	0.164	0.417
Ni-resist	7.48	0.192	0.488
Silver	10.50	0.137	0.348
Stainless steel Type 304	7.92	0.181	0.462
Stainless steel Type 430	7.61	0.189	0.480
Steel (mild)	7.86	0.183	0.465
Tin	7.29	0.197	0.500
Zinc	7.15	0.201	0.510

mechanical tests, it will be necessary to take into account the actual area of the cross-section of the corroded metal and report results on this basis instead of, or as well as, on the basis of the original cross-section before exposure, such as would be represented by the uncorroded control specimens.

In view of possible or probable variations in mechanical properties among different specimens of the same metal cut from different sheets or other pieces, or even from different sections of the same sheet or piece, it is necessary to pay careful attention to the initial sampling of stock to be used for control, as well as exposure, specimens. An interesting case in which several of these considerations were involved was provided by the long-time atmospheric exposure tests of nonferrous metals carried out by Subcommittee VI of ASTM Committee B-3 on Corrosion of Non-Ferrous Metals and Alloys<sup>13</sup> in which changes in tensile properties were used as one of the means of measuring the extent of corrosion.

Tests carried out for particular purposes may make use of other special means to measure the progress of corrosion. For example, changes in the reflectivity of polished surfaces<sup>14,15</sup> have been used as a sensitive means of following changes in the very early stages of corrosion in laboratory studies. A similar technique has been applied on a practical scale in connection with the direct evaluation of the relative merits of different alloys as used for mirrors in searchlights exposed to corrosive natural atmospheres.

Kruger,<sup>16</sup> at the then US National Bureau of Standards, used an ellipsometer to follow the growth of very thin corrosion-product films (oxides) during the initial stages of corrosion. This requires a knowledge of the composition of the oxide and its refractive index.

In some cases, the principal interest is in the possibility of undesired contamination or other alteration of an environment rather than in the rate of destruction of the metals being tested. Here, in addition to paying attention to the usual factors that influence rates of corrosion, it is also necessary to consider the ratio of the area of the test specimen to the volume or mass of test solution, and the time of contact. All of these factors may be quite different in a test from what would be obtained in a practical case, and any distortions of the test in these ways must be taken into account in planning the test and in interpreting the results.

In cases such as this, the possible contamination of the solution by corrosion products may be estimated from the loss in mass of the test specimen. This,

however, does not make any distinction between soluble and insoluble corrosion products, which may have different effects and which can be studied best by chemical analysis of the test solution and the materials filtered from it. Similarly, chemical analysis may be required to detect any other changes in the composition of the test solution that may be of interest.

Particularly in theoretical studies of corrosion processes, it has been useful to measure the progress of corrosion in terms of the rate or extent of consumption of oxygen in the corrosion reactions. This technique has been very useful in following the progress of wet corrosion or of oxidation in its initial stages.<sup>17</sup>

Somewhat along the same lines is the measurement of the volume of hydrogen generated as corrosion proceeds.<sup>18,19</sup> This technique has been used not only in theoretical studies, but also as a means of comparing some corrosion-resisting characteristics of different lots of steel that seem to affect their behavior when used as a base metal for tin cans.<sup>20-22</sup>

The polarograph has been found to be a very useful tool for following the progress of corrosion, especially in its early stages, by measuring minute changes in the composition of the solution, as in the consumption of some constituent, such as oxygen, or by the accumulation of metal salts or other reaction products, such as hydrogen peroxide.<sup>23</sup>

An electrical resistance method that directly measures loss of metal from a probe installed in the corrosive system under study is described as follows. It is reported that corrosion equivalent to a thickness loss of as little as  $2.5 \times 10^{-7}$  cm can be detected.<sup>24,25</sup> This technique is most useful as a means of monitoring steps taken to reduce corrosion, for example, by inhibitors, or to detect changes in the corrosivity of process streams. Electrical methods of determining corrosion rates are considered subsequently.

Temperature effects may also be used in test methods, notably for assessing the effects of inhibitors in acid solutions. The technique is based on the one first proposed by Mylius,<sup>26</sup> which records the temperature-time behavior associated with the exothermic reaction resulting from the initial contact of a metal with a corrosive acid solution. The effectiveness of inhibitors may then be determined from their effects on the temperature-time behavior.<sup>27</sup>

#### **2.34.2.9 Removal of Corrosion Products**

An ideal method for removing corrosion products would be one that would remove them completely

without causing any further corrosion or other deterioration of a test specimen in the process. Procedures that achieve this ideal or approach it very closely have been developed for many of the common alloys.

There are numerous satisfactory methods of cleaning corroded specimens, but whatever the method, its effect in removing base metal should be determined for each material<sup>28–30</sup> taking into account possible differences between the behavior of ‘as-new’ and corroded base metal (see [Appendix A](#)). The various methods may be classified as follows:

1. Mechanical treatment:
  - a. scrubbing with bristle brush,
  - b. scraping,
  - c. wire brushing,
  - d. grit, shot, sand blasting;
2. Chemical treatments:
  - a. organic solvents,
  - b. chemical reagents;
3. Electrolytic treatments as cathode in solutions of the following:
  - a. sulfuric acid, usually inhibited,
  - b. citric acid,
  - c. potassium cyanide,
  - d. sodium hydroxide.

Further details of removing corrosion products are given in [Appendix A](#).

## 2.34.3 Laboratory Corrosion Tests

### 2.34.3.1 Total-Immersion Tests

The total-immersion corrosion test is most adaptable to rigorous control of the important factors that influence results. This control may be achieved in different ways and it is unnecessary and undesirable to seek a standardized method or apparatus for universal use. All that is required is a recognition of what is essential, as covered, for example, by the ASTM procedure G 31. This represents a code of minimum requirements without insisting on the use of any particular kind of apparatus or specifying the exact conditions of aeration, temperature or velocity to be used. Since different metals respond differently to effects of aeration, temperature and velocity, the setting up of standard test conditions in terms of these factors would be inappropriate. Depending on the environment, such standardized testing conditions would favor maximum corrosion of some materials and minimum corrosion of others and thus lead to gross errors in indicating any general order of

merit applicable under conditions differing from those of a standardized test.

In some instances, it may be possible, although it is usually very difficult, to undertake laboratory corrosion tests under conditions that will be the same as those encountered in some practical application and thus to secure some directly applicable data. More often, the conditions of service are so variable or so difficult to appraise accurately and duplicate in the laboratory that it is impractical and probably unwise to attempt to do so. A better procedure is to examine the individual effects of the several controlling factors by varying them one at a time so as to provide a picture of their influence on the behavior of the materials of interest in the corrosive medium being investigated. This information will be helpful in deciding whether the conditions of a particular use are favorable or unfavorable to the materials being considered. It will also serve as a guide to account for behavior in service and to suggest changes in the operating conditions that may be expected to reduce corrosion of a material being used.

In many cases, and particularly in aqueous solution, the most important controlling factors will be solution composition, temperature, aeration, and velocity.

#### 2.34.3.1.1 Solution composition

When designing tests to determine the effects of solution composition on corrosion, it is important to understand the nature of the controlling process. In the case of many metals and alloys, the rate-determining step will be the supply of cathodic reactant to the metal surface. This is particularly true in neutral solutions where corrosion will often be under oxygen diffusion control. Thus, tests in stagnant (unstirred, quiescent) conditions may be inappropriate, since the effects of solution composition will be insignificant compared with the oxygen diffusion effect. In stagnant conditions, corrosion rates of mild steel in, for example, sodium chloride, sodium sulfate and other salt solutions will be effectively the same over a range of concentrations. The effects of anion type and concentration begin to be shown only with movement of the solution, that is, when oxygen access to the metal surface is facilitated to the point where it may be no longer rate controlling. Specific effects of anions in stagnant solutions will, however, be found when the anion has oxidizing properties, as in the case of nitrate and in systems where the dominant cathodic reaction is hydrogen evolution.

Care must therefore be taken in designing tests to study the effects of solution composition since

different results will be obtained depending on the degree of aeration and/or movement of the solution.

Variations in solution composition throughout a test should be monitored and, if appropriate, corrected. Variations may occur as a result of reactions of one or more of the constituents of the solution with the test specimen, the atmosphere or the test vessel. Thus, it is important that the composition of the testing solution is what it is supposed to be. Carefully made-up solutions of pure chemicals may not act in the same way as nominally similar solutions encountered in practice, which may, and usually do, contain other compounds or impurities that may have major effects on corrosion. This applies particularly to 'artificial' seawater, which is usually less corrosive than natural seawater. This subject is discussed in detail in a Special Technical Publication of ASTM,<sup>31</sup> and tests with natural, transported, and artificial seawater have been described.<sup>32</sup> Suspected impurities may be added to the pure solutions in appropriate concentrations or, better still, the testing solutions may be taken directly from plant processes whenever this is practical.

It should also be pointed out that in exploring the effects of the concentration of a particular acid or other chemical on its corrosivity, it is necessary to cover the full possible variation of concentrations thoroughly, since it frequently happens that particular ranges of concentration are especially corrosive to some metals. This extends to the highest degrees of concentration where sometimes the complete elimination of water may increase corrosion a great deal – as in the case of aluminum in acetic acid. On the other hand, the presence of a trace of water may make other chemicals much more corrosive – as in the case of bromine and other halogens.

It should be noted, also, that exposing a specimen to a solution of some chemical while it is being concentrated by evaporation practically to dryness will not suffice to explore the effects of the complete range of concentration, simply because the period in which any particular concentration range exists is not likely to be long enough to permit any especially corrosive effects to be detected in the overall result.

#### 2.34.3.1.2 Temperature control

Of the factors mentioned, temperature is probably the easiest to control; this can be accomplished by means of a thermostat or by operating at the boiling point of the testing solution with an appropriate reflux condenser to maintain the solution at a constant concentration. Control to  $\pm 1^\circ\text{C}$  is not hard to accomplish.

The need for temperature cycling should be taken into account when designing or conducting tests. The nature of the test vessel should be considered for tests in aqueous solutions at temperatures above about  $60^\circ\text{C}$  since soluble constituents of the test vessel material can inhibit or accelerate the corrosion process. An inhibiting effect of soluble species from glass, notably silica, on the behavior of steel in hot water has been shown.<sup>33</sup> Pure quartz or polymeric materials are often more appropriate for test vessel construction. (It should also be recognized that the control of gas concentrations becomes more difficult as temperature approaches the boiling point of the solution.)

#### 2.34.3.1.3 Aeration

Control of aeration is more difficult. Aeration here means the amount of oxygen supplied either as such or, more commonly, in air. In some situations, it may not require a large amount of air bubbled through a solution to accommodate even a modest rate of corrosion of a small test-piece. Figure 2 shows the relationship between the rate of supply of air used for aeration and the rate of corrosion of Monel alloy in 5% sulfuric acid.

To facilitate rapid solution of oxygen from air bubbles it is desirable to make these as small as possible, for example, by having the air enter through a porous thimble or sintered glass disc. Much less satisfactory results are secured by simply letting air escape into the solution from a tube drawn to a fine tip.

It is also undesirable to permit air bubbles to impinge directly on the test-pieces. This can be avoided by placing the aerator inside a chimney.

When it is desired to study effects of various degrees of aeration, it is better to do this by varying the oxygen content of the saturating gas (e.g., by using controlled mixtures of oxygen and nitrogen)

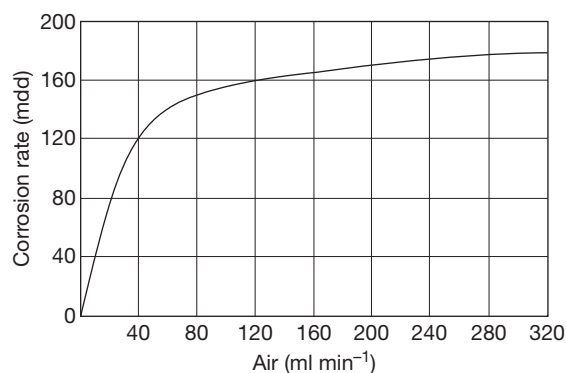


**Figure 2** Effect of rate of supply of air used for aeration on corrosion of Monel alloy in 5% sulfuric acid.



introduced at a constant and adequate rate than by attempting to vary the rate of admission of a gas (such as air) of constant composition. This extends as well to zero aeration, which can best be accomplished by saturating the test solution with deoxygenated nitrogen or other inert gas. It is unwise to assume that, because no air is purposely added, oxygen has been excluded from a test solution in a vessel open to air. Such a practice provides a low oxygen availability that is not sufficiently under control to ensure reproducible results.<sup>3</sup>

#### 2.34.3.1.4 Velocity

Controlled flow conditions can be achieved either by having the test-piece move through a notionally stationary liquid or by having a moving liquid come into contact with a stationary test-piece. Occasionally tests may involve both types of exposure. Details of test procedures are presented elsewhere.

The achievement of zero velocity in a test set-up is about as difficult as the accurate control of some high velocity. It is a common mistake to assume that by not making any attempt to move either the specimen or the testing liquid, the relative velocity between them will be zero. This neglects such effects as convection currents and the agitation due to the effects of corrosion products streaming under the influence of gravity. The most common difficulty arising from this situation is that these uncontrolled effects in tests made under presumably quiet or stagnant conditions make it very difficult to secure reproducible results from test to test. Therefore, even when there is no practical interest in the effects of any appreciable velocity, it is desirable to provide for some controlled movement of either the specimens or the solution at some velocity such as  $7.5 \text{ cm s}^{-1}$ , readily achieved with a vertical circular-path machine.

Equipment of this type in which the specimens are moved in a vertical circular path with all portions of the surface of a specimen moving at the same speed has been used in instances where such moderate test velocities are required. Statistical analysis of data from tests with an apparatus by Wesley<sup>4</sup> has demonstrated satisfactory reproducibility of results not only among specimens in a particular test, but also from test to test undertaken at different times.

Where effects of much higher velocities are to be studied, various devices have been used to move test-pieces through the testing solution at high velocity.

One procedure is to use test specimens in the form of discs, which can be rotated at the desired speed while either wholly or partly immersed in the testing

solution, and Freeman and Tracy described a device of this sort in a contribution to the ASTM Symposium on Corrosion Testing Procedures.<sup>28</sup> With their apparatus the specimen discs were mounted on horizontal shafts and were partially immersed in the testing solution.

A similar method of test was used at the International Nickel Company's Corrosion Laboratory at North Carolina. The specimen discs are mounted on insulated vertical spindles and submerged in seawater, which is supplied continuously to the tank in which the specimens are immersed. The maximum peripheral speed of the spinning disc is about  $760 \text{ cm s}^{-1}$ , and the characteristic pattern of attack is shown in **Figure 3(a)**. Studies of variation of depth of attack with velocity indicate that at low velocities (up to about  $450 \text{ cm s}^{-1}$ ) alloys such as Admiralty brass, Cu-10Ni and cupronickel alloys containing iron maintain their protective film with a consequent small and similar depth of attack for the different alloys. At higher velocities the rate increases due to breakdown of the film.

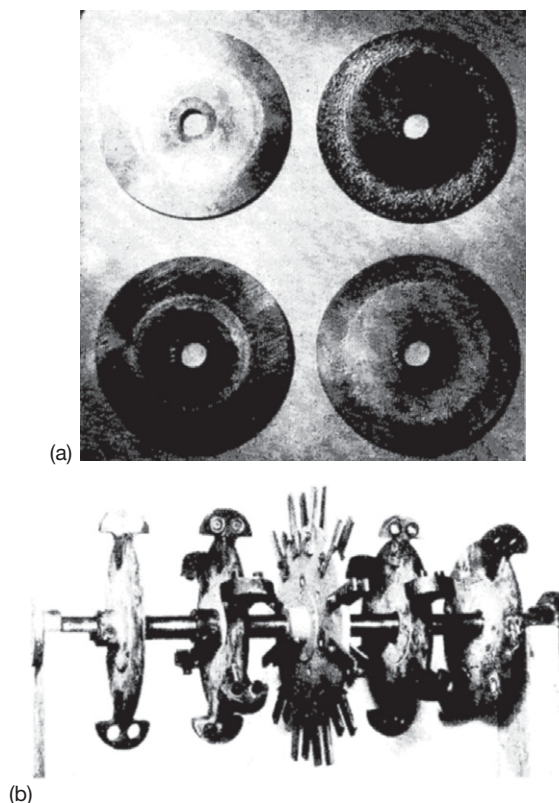


**Figure 3** (a) Distribution of corrosion on surfaces of rotating disc specimens and (b) assembly of specimens attached to rotating discs.

Tests of this sort indicate a sort of critical velocity for each material that marks the boundary between the maintenance and loss of protective films. These apparently 'critical' velocities must be considered as relative and only applicable to the conditions of test in which they are measured. Because of the complex effects associated with the differences in velocity from point to point on such rotating specimens, the apparent 'critical velocity' obtained in a given test may be quite different from what might be indicated by another test in which the same velocity is achieved in some other way – as by moving the liquid past a stationary specimen at a uniform velocity from point to point. The apparent 'critical velocity' indicated by this latter method of test will likely be higher for many materials than that shown by the spinning disc test. Thus, the establishment of critical velocities by a particular method of test will afford only qualitative data regarding the relative abilities of a number of materials to resist the destructive effects of high velocity. Furthermore, the critical velocity at which severe attack commences has been found to depend on the diameter of the disc so that no quantitative significance can be attached to it. This restriction extends as well to tests with iron discs, where attack is concentrated at the centre of the disc rather than at the periphery, irrespective of its diameter. (Small variations in solution composition may also affect the value of any critical velocity. In laboratory tests using recirculating artificial seawater the presence of dissolved copper from copper alloy test-pieces has been shown to affect the critical velocity for such materials.)<sup>34</sup>

Somewhat similar tests may be made by attaching specimens to discs that can be rotated at some desired velocity in the testing medium. A machine of this sort that is used extensively in studying corrosion of metals by seawater at high velocity was developed by the staff of the US Naval Engineering Experiment Station at Annapolis, Maryland.<sup>35</sup> A typical assembly of discs and specimens is shown in **Figure 3(b)**.

The action of the rotating discs with their attached specimens causes violent agitation of the liquid in the tank. Depending on the height of liquid above the specimens, as determined by the location of the overflow pipe, there may be considerable whipping of air bubbles into the liquid or none at all, as desired. The heat of agitation causes the temperature to rise. This may be controlled readily by adjusting the amount of fresh cold liquid, for example seawater, allowed to pass into the tank and out through the overflow pipe. It is not difficult to hold the temperature within 1–2 °C of the desired value.

The use of rotating discs to carry test specimens has been extended to studies of protective coatings in what are considered to be 'accelerated' tests of such coatings for service underwater.<sup>36</sup>

Velocity effects involving a high differential in velocity between adjacent areas are achieved simply by exposing a test specimen to the action of a submerged jet. This sort of test has been very popular and very useful in studying impingement attack or erosion of condenser tube alloys. It was introduced originally by Bengough and May<sup>37</sup> and later modifications were described subsequently by May and Stacpoole.<sup>38</sup> The appearances of typical specimens from this test are shown in **Figure 4**. In this test the dimensions of test specimens should be standardized, since the depth of attack has been found to be influenced by the extent of the immersed area of the specimen that is outside the impingement zone.

Along the same general lines is an apparatus employed by Brownsdon and Bannister<sup>39</sup> in which a stream of air at high velocity is directed against the surface of a submerged test specimen.

A straightforward way to study velocity effects is to force the testing liquid through tubular specimens, which may be arranged to form model piping systems for studying the peculiar corrosion that may result from severe turbulence effects downstream of valves, reducers, branch connections, elbows, and other fittings. In such systems the rates of flow can be measured by suitable orifice meters and regulated by control valves. A somewhat similar technique applied to condenser-tube alloys is to test them as installed in model tube-bundle assemblies.<sup>40</sup> Butler and Ison have described a laboratory test rig for studying the effects of flowing water on steel pipework.<sup>41</sup>

Other methods involve holding specimens in suitable fixtures so that they form the walls of channels through which the test solution can be passed at controlled rates of flow. Such devices have been used at the Harbor Island Test Station in North Carolina primarily for studying the electrode potential and polarization characteristics of metals and alloys, but they are also suitable for observing effects of velocity on corrosion. This is illustrated in **Figure 5** in which the specimen and Pt electrode are of the same size and are placed parallel to one another in the holder. When required potentials are measured by inserting a capillary through the hole in the Pt, it is removed to avoid shielding effect.

Effects of velocity are sometimes aggravated by the presence of abrasive solids in suspension, which increases deterioration by straight mechanical abrasion as well as accelerating corrosion by continually

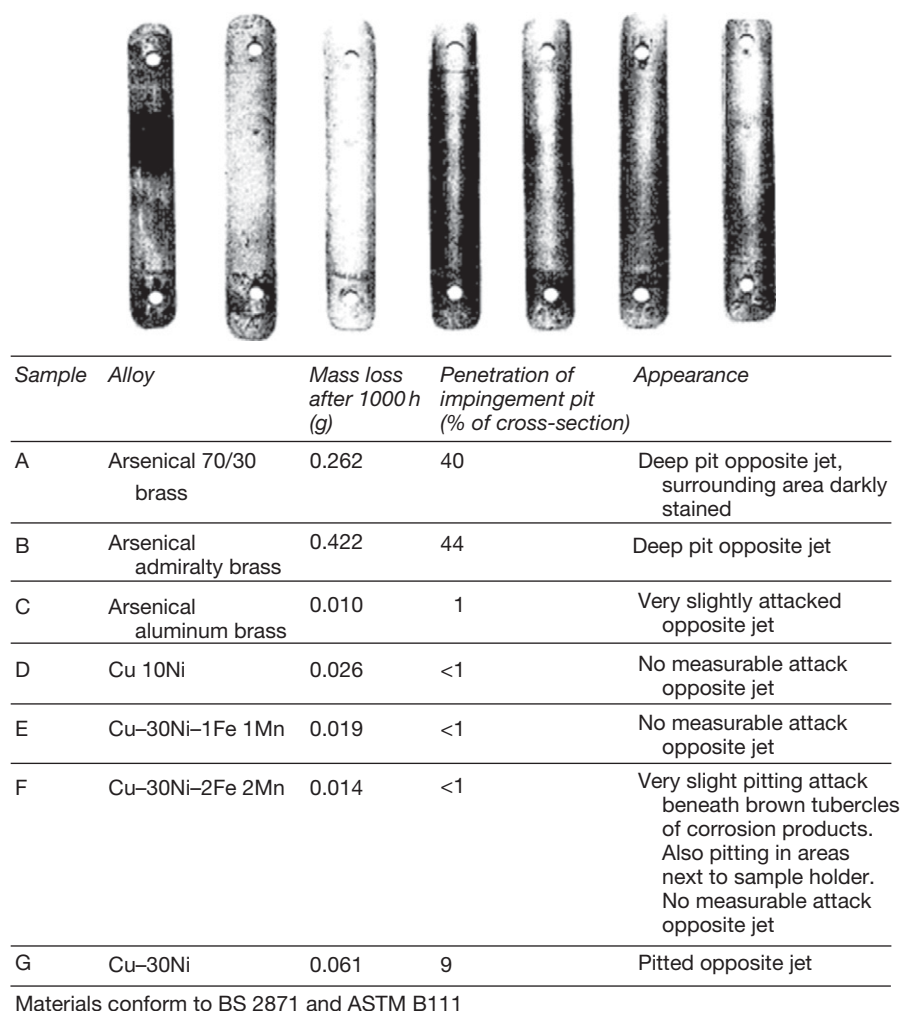


**Figure 4** (Top) Pattern of corrosion of jet-impingement test specimens and (bottom) sample test data and results.

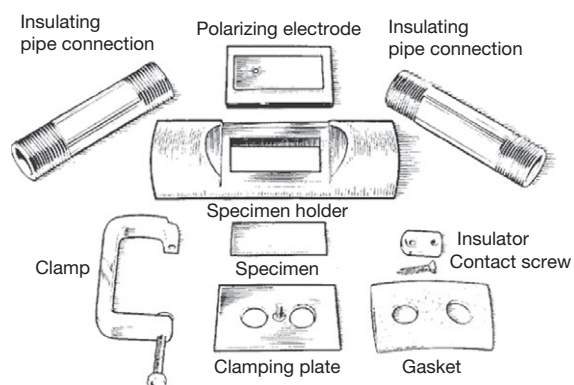


**Figure 5** Components of apparatus in which specimens form walls of channel for test solution.

exposing fresh surfaces to attack. Such attack is especially serious with pumps, agitators, and piping systems. Special apparatus has been designed to measure the performance of materials under such conditions, as described, for example, by Fontana.<sup>42</sup>

Special devices have been used to study erosion-corrosion by boiler water moving at high velocity, and an example is the method used by Wagner *et al.*<sup>43</sup>

Where high rates of flow are desired with a small volume of testing liquid, a specimen may be mounted in the form of a tube inside a large glass tube and a small mass of liquid may be forced to flow through the restricted annular space between the two tubes. Such a method was used successfully in

studying corrosion by milk where the volume of milk was small, the required movement being achieved simply by the use of an air lift to return the milk to an overhead reservoir from which it flowed by gravity through the test set up.<sup>44</sup> Velocities as high as  $0.6 \text{ m s}^{-1}$  were studied in this way.

#### 2.34.3.1.5 Volume of testing solution

If exhaustion of corrosive constituents that may be present in minute concentrations and the accumulation of reaction products which may either accelerate or stifle further attack are to be avoided, the volume or mass of testing solution must be sufficiently large to avoid effects caused by these factors. In laboratory tests, however, practical considerations limit the volume of testing solution that can be provided for. A minimum of 250 ml of testing solution for each  $6.3 \text{ cm}^2$  of specimen area is suggested in NACE TM0169.

#### 2.34.3.1.6 Support of specimens

Since crevices set up where specimens are in contact with their supports and may become the seats of accelerated corrosion by concentration cell effects, special attention should be given to this detail in setting up tests. The area screened by the supporting members should be kept to a minimum, for example, by making contact at a point or along a line rather than over any appreciable area. In some instances it may be desirable to apply some protective coating to the areas that are in contact with the supporting members. In any event, any corrosion that has occurred in the area of the supports should be taken into account in appraising and reporting the results of a test.

Somewhat along the same lines are techniques that have been employed to avoid edge effects by having the specimen come into contact only with a pool of testing solution, which does not cover its complete surface – as described, for example, by Brenner.<sup>45</sup> A more elaborate technique in which the pool of testing solution was circulated by thermal currents was described by Smith.<sup>46</sup>

#### 2.34.3.2 Alternating-Immersion Tests

One means of ensuring aeration of a testing solution in contact with a specimen is provided by an alternating-immersion corrosion test in which the specimen is alternately immersed in a solution and withdrawn from it in some predetermined cycle. This procedure also has the effect of allowing the test solution that clings to the specimen to become concentrated by evaporation while the specimen is out of the liquid,

and in addition it permits corrosion products to remain and reach greater concentrations and undergo more chemical changes in immediate contact with the metal than can occur in continuous-immersion tests. In these ways, an alternating-immersion test may simulate certain circumstances of practical corrosion better than a continuous-immersion test and may, therefore, be preferred.

Since the conditions of this test can be standardized fairly readily, it has also been used as a routine test in comparing different alloys of the same general kind in the course of studies of effects of composition on properties, as, for example, in the researches by Hanawalt *et al.* on the corrosion of magnesium.<sup>47</sup>

The ASTM have established a recommended procedure for alternating-immersion stress corrosion tests in 3.5% NaCl solution (ASTM G 44).

The alternating immersion may be accomplished either by moving specimens held in a suitable suspension rack into and out of containers holding the test solution, by leaving the specimens fixed and raising and lowering the solution containers around them so as to immerse them or leave them suspended above the solution, or by using a combination of pump and siphon to move the solution between two reservoirs.

To favor reproducibility of results, the cycles of immersion and withdrawal must be kept the same from test to test. It is necessary to control the temperature and humidity of the atmosphere surrounding the test setup as these affect the rate of evaporation of the solution and of drying of the specimens when they are out of the solution. It is also necessary to provide for replenishing losses of water from the test solution resulting from evaporation.

#### 2.34.3.3 Water-Line Tests

Materials may be subject to intense localized attack at the liquid level when they are partially immersed in a solution under conditions where the water line remains at a fixed position for long periods. This attack may be the result of concentration cell effects complicated by differences in the nature and adherence of corrosion-product films as they form in the water-line region as compared with those that form above or below this region.

The testing technique is very simple since it involves no more than providing means of supporting a specimen or specimens in a fixed position of partial immersion, and of maintaining the liquid level constant by the continuous addition of distilled water to



make up for evaporation losses. For maximum reproducibility of results, the dimensions of the specimens, and especially the ratio of areas above and below the liquid level, should be held constant, as should be the depth of immersion.

#### 2.34.3.4 Heat-Flux Effects

When heat flows into or out of a fluid through a containing wall, the wall surface reaches a temperature that differs from that of the bulk of the fluid. The wall's corrosion resistance at this temperature may be significantly different from its resistance at the bulk-fluid temperature. Tubes or tank walls heated by steam or direct flame have failed in service in which similar materials, not so heated, performed acceptably.

The name 'hot wall effect' was given to this phenomenon by Benedicks<sup>48</sup> who observed separation of dissolved gas from aerated water in boiler tubes. The metal wall was insulated from the cooler boiler water by the gas, its temperature rose substantially, and the more severe corrosion took the form of pitting. It was recognized subsequently that even without such gas formation, a hot-wall effect resulted when heat flowed through a wall into a fluid. The temperature difference that had to exist in order for heat to flow was increased by the insulating effect of the thin film of almost stagnant fluid at the wall surface. This film is thinned by rapid flow of a fluid through a tube, but is not eliminated at any finite velocity. Boiling of a liquid, by either bubble nucleation or coverage of the heating surface by a vapor film, increases the skin temperature further; the second mechanism provides much more severe insulation and greater temperature rise.<sup>49</sup>

High rates of heat flow through heat-transfer surfaces in atomic energy installations studied by Groves made him develop an appropriate corrosion test method.<sup>50</sup> In this, a small sheet specimen in contact with a hot liquid, usually boiling, is heated externally so that its surface reaches the desired test temperature. The surface or skin temperature is close to the temperature at mid-thickness, which is measured by a thermocouple inserted in a drilled hole. The heating source is an electric soldering iron in which the tip is replaced by a flat-surfaced metal block. The voltage to the heat source is controlled by a variable transformer. Supplementary heating may be provided to the liquid in the test vessel by winding the liquid container with resistance wire, or by an immersion heater (Figure 6).

A similar unit, modified in details such as location of condenser, use of an agitator, and shape of the

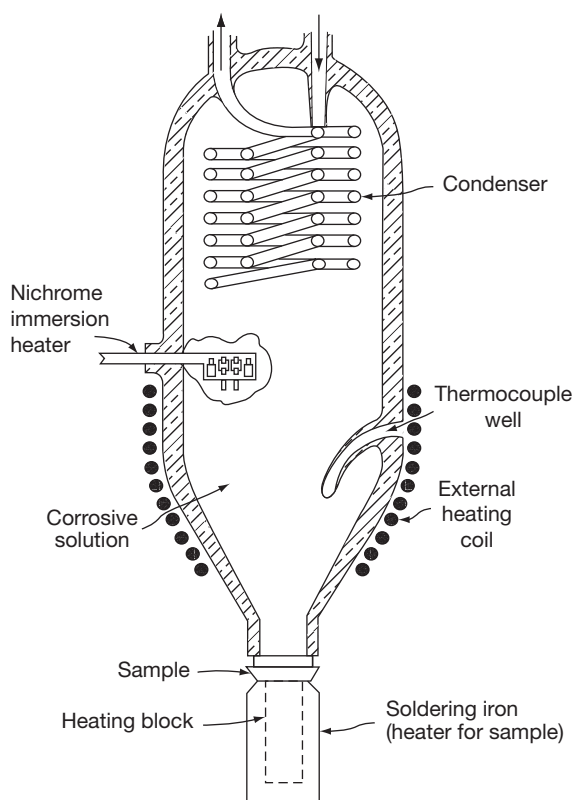


**Figure 6** Device for studying hot wall effects.

vessel, was used by Fisher and Whitney.<sup>51</sup> Further substantial modifications to permit interface location of specimens, cooling of specimens and operation under applied pressure, have been described by Fisher.<sup>52</sup> Earlier laboratory test methods tried by Fisher and Whitney<sup>51</sup> included exposure of specimens heated by their own electrical resistance and of tubular specimens containing a pencil-type resistance-wire heater in a quartz tube.

To investigate corrosion in heated crevices filled with wetted paste a sandwich test assembly was designed by Gleekman and Swandby<sup>347</sup> simulating a slotted cylindrical steam-heated drier. Two plates are bolted together, the lower being heated by an electric hot plate.

It has been concluded from data reported in these studies that the skin temperature is the major controlling factor in corrosion, not the rate of heat flow through the metal.<sup>51</sup> It has also been concluded, however, that corrosion rates at a given mid-specimen temperature do depend on the presence or absence of thermal flux.<sup>53</sup> The difference between temperatures at skin and mid-specimen positions may account for this discrepancy.



Heat-flux corrosion rates can also be determined in plant tests using steam-heated tubular specimens which are weighed or callipered.

In addition to the direct effect of film temperature on corrosion rate, an indirect effect has been observed in the heating of some foods and chemicals, in which insulating solid corrosion films on different metals. By raising the metal surface temperature, these films may, when pervious, lead to further corrosion.

Apparatus and procedures for testing the corrosion resistance of alloys in brines at temperatures up to 120–150 °C are described by Hart.<sup>54</sup>

Testing procedures for corrosion inhibitors in heat flux conditions are discussed later.

### 2.34.3.5 Composition of Testing Solution

Changes in corrosivity with time may be observed by exposing fresh specimens to a solution that has already been used for testing. Where such changes are known to occur, or are suspected, it will be necessary to arrange for replacement of the testing solution after appropriate intervals or replenishment of constituents that may be consumed in the corrosion processes.

## 2.34.4 Electrochemical Measurements (General)

In view of the electrochemical nature of corrosion it is not surprising that measurements of the electrical properties of the interface metal–solution (electric double layer) are used extensively in fundamental studies of the mechanism of corrosion, in corrosion testing and in monitoring the control in service. In the context of this section, electrical measurements in the laboratory are used to assess the corrosion behavior of metals and alloys in service and to avoid the more tedious and prolonged field testing. Determinations of the corrosion rate, susceptibility of a metal to bimetallic corrosion, pitting, intergranular attack, stress-corrosion cracking, etc. are examples of corrosion phenomena that are studied in the laboratory by means of electrochemical methods in order to anticipate behavior in service.

Progress in this field has been made possible with increase in knowledge of the detailed mechanism of corrosion and by the developments that have taken place in instrumentation. The widespread use of potentiostatic control and the availability of a range of commercial potentiostats have given a tremendous

impetus to electrochemical testing, and have perhaps led to the unfortunate belief that corrosion testing in the laboratory and in the field can be replaced completely by electrochemical measurements in the laboratory under conditions of controlled potential. Indeed, La Que<sup>55</sup> in 1969 was prompted to express concern about the proliferation of publications describing electrochemical techniques for corrosion testing and to advise caution regarding the extrapolation of results obtained in the laboratory with a potentiostat for the performance of metals in service.

Although important contributions in the use of electrical measurements in testing have been made by numerous workers, it is appropriate here to refer to the work of Stern and his coworkers<sup>56,57</sup> who have developed the important concept of linear polarization, which led to a rapid electrochemical method for determining corrosion rates, both in the laboratory and in plant. Pourbaix<sup>58</sup> and his coworkers on the basis of a purely thermodynamic approach to corrosion constructed potential–pH diagrams for the majority of metal–H<sub>2</sub>O systems, and by means of a combined thermodynamic and kinetic approach developed a method of predicting the conditions under which a metal will (a) corrode uniformly, (b) pit, (c) passivate, or (d) remain immune. Laboratory tests for crevice corrosion and pitting, in which electrochemical measurements are used, are discussed later.

### 2.34.4.1 Techniques

Electrochemical methods of testing involve the determination of specific properties of the electrical double layer formed when a metal is placed in contact with a solution, and these can be summarized as follows.

1. The potential difference across the electric double layer  $\Delta\psi$ . This cannot be determined in absolute terms but must be defined with reference to another charged interface, that is, a reference electrode. In the case of a corroding metal, the potential is the corrosion potential which arises from the mutual polarization of the anodic and cathodic reactions constituting the overall corrosion reaction.
2. The reaction rate per unit area, expressed as the current density  $i$ . For a corroding metal the partial anodic and cathodic current densities cannot be determined directly by means of an ammeter unless the anodic and cathodic areas can be separated physically, for example, as in a bimetallic couple. If the metal is polarized a net current  $i_c$

for cathodic polarization, and  $i_a$  for anodic polarization, will be obtained and can be measured by means of an ammeter.

3. The capacitance. The electrical double layer may be regarded as a resistance and capacitance in parallel, and measurements of the electrical impedance by the imposition of an alternating potential of known frequency can provide information on the nature of a surface. Electrochemical impedance spectroscopy is now well established as a powerful technique for investigating electrochemical and corrosion systems.

The most commonly used measurements are as follows:

1. determination of the steady-state corrosion potential  $E_{\text{corr}}$ ;
2. determination of the variation of  $E_{\text{corr}}$  with time;
3. determination of the  $E-i$  relationships during polarization at constant current density (galvanostatic), the potential being the variable;
4. determination of the  $E-i$  relationships during polarization at constant potential (potentiostatic), the current being the variable;
5. determination of the electrochemical impedance under alternating potential conditions as a function of frequency;
6. determination of electrochemical noise: fluctuations of the free potential or fluctuations of the current when a constant potential is maintained.

#### 2.34.4.2 Instruments

The techniques and instruments used may be classified as follows:

1. *Potential measurements*: a reference electrode and a potentiometer or electrometer that require only a small current to give a measurement of e.m.f. and thus minimize polarization of the electrodes.
2. *Current measurements*: milliammeters or the measurements of the  $IR$  drop across a conductor of known resistance.
3. *Galvanostatic polarization*: constant direct current power units, or banks of accumulators or dry cells used in conjunction with a variable resistance.
4. *Potentiostatic polarization*: potentiostats with varying output currents.
5. *Determination of impedance*: dedicated instruments for the measurement of impedance as a function of frequency.

Impedance measurements, originally used in fundamental studies of anodic oxidation, have great power for deriving corrosion rates and information about reaction mechanisms for processes that occur at a corroding surface using readily available instrumentation. Armstrong *et al.*<sup>59</sup> have used impedance measurements for studying the active-passive transition of chromium and Epelboin *et al.*<sup>60</sup> describe its use for determining the instantaneous corrosion rate of a metal. Sathyaharayana<sup>61</sup> has described a method using Faradaic rectification to determine the instantaneous corrosion rate, in which no reference electrode is required; the electrodes consist of the metal under study and a counter electrode of a large area of the same metal. Macdonald<sup>62</sup> in a review of electrochemical impedance spectroscopy has highlighted the enormous advantage it offers over other electrochemical methods of being able to evaluate the validity of the data using the Kramers–Kronig transforms. While the use of impedance techniques is usually restricted to homogenous corrosion situations, applications to localized corrosion have been reported. These included pitting,<sup>63–65</sup> abrasion,<sup>66</sup> other types of corrosion<sup>67–69</sup> and stress-corrosion cracking.<sup>70</sup> The potentiostatic technique has a number of variations and the potential may be increased or decreased incrementally, changed continuously at a predetermined rate (potential sweep) or applied as pulses of very short duration.

The application of a stochastic approach to the study of pitting was pioneered by Sato.<sup>71</sup> Shibata and Takeyama<sup>72</sup> then developed stochastic theory to study the statistical variation of the pitting potential determined by the potential sweep method. Subsequently, Williams and his coworkers<sup>73–75</sup> described how electrochemical noise (current fluctuations in systems under potentiostatic control or potential fluctuations at the corrosion potential) can be analyzed to provide information on the initiation and propagation of pitting corrosion on stainless steels. In a review Gabrielli *et al.*<sup>76</sup> discuss published results for both stable pitting, where statistical counting is the major technique of investigation, and unstable pitting during the pre-pitting stage, where the techniques that can be applied include statistical counting, ensemble averages, and spectral analysis.

#### 2.34.4.3 Electrochemical Cells

Since the single potential of a metal cannot be measured, it is necessary to use a suitable reference

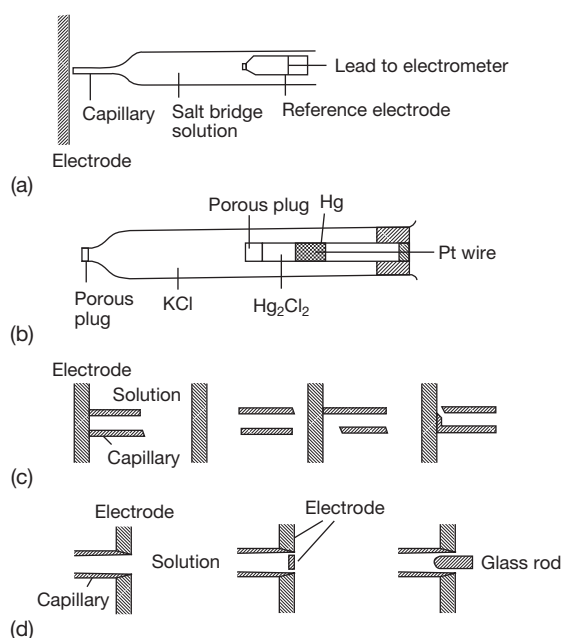
electrode such as the  $\text{Hg}/\text{Hg}_2\text{Cl}_2/\text{KCl}$  electrode or the  $\text{Ag}/\text{AgCl}/\text{KCl}$  electrode, and although potentials are commonly expressed with reference to the standard hydrogen electrode (SHE), the use of this electrode in practice is confined to fundamental studies rather than testing. Details of the preparation of reference electrodes, salt bridges, capillaries, etc. are given in the book by Ives and Janz<sup>77</sup> and elsewhere.<sup>78–81</sup>

Measurements of the corrosion potential of a single metal corroding uniformly do not involve an  $IR$  drop, but similar considerations do not apply when the metal is polarized by an external e.m.f., and under these circumstances the  $IR$  drop must be minimized by using a Luggin capillary placed close to the surface of the electrode. Even so, the  $IR$  drop is not completely eliminated by this method, and a further error is introduced by the capillary shielding the surface from the current flow with a consequent decrease in current density. At high current density this error due to the  $IR$  drop can conceal the Tafel region by distorting the measured overpotentials, a difficulty that can be overcome by determining the resistance of the solution at the capillary tip and by making an appropriate correction for each value of the current density. Alternatively, electronic feedback circuits may be employed for automatic compensation of the  $IR$  drop, and this method is attractive if rapid variations in overpotential are being studied.<sup>82–85</sup> Other methods include using a Piontelli capillary<sup>86,87</sup> or a rearside capillary<sup>88</sup> (Figure 7). However, in testing in electrolyte solutions of low resistivity these errors are normally small, and the conventional Luggin capillary is used in conjunction with a salt bridge and reference electrode.

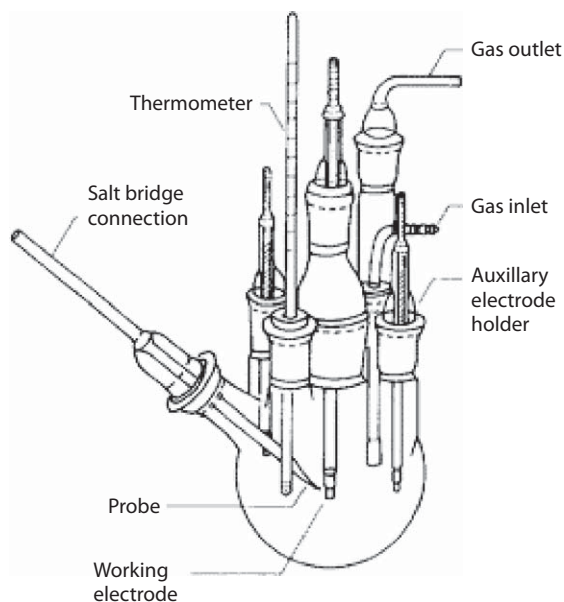
For polarization studies, the cell must make provision for the metal electrode under study, an auxiliary or counter electrode, and a Luggin capillary. Provision must also be made for introducing a gas such as oxygen-free nitrogen or argon, which serves to remove dissolved oxygen and to prevent its introduction during the test (or to introduce it if required at predetermined partial pressures) and to agitate the solution; additional agitation if required can be obtained by means of a stirrer (electric or magnetic).

Figure 8 shows the design of an all-glass cell, which has been listed as the standard polarization cell in the ASTM Recommended Practice G 5, which makes provision for the essential requirements listed earlier; this cell is typical of those used for fundamental studies and for testing, although details of design may vary.

The metal electrode to be studied must be carefully prepared, attached to an electrical lead and mounted so that a known surface area of one face is



**Figure 7** Reference electrodes and capillaries. (a) Reference electrode, salt bridge and Luggin capillary, (b) calomel electrode, (c) frontal types of capillaries and positions, and (d) rearside capillaries. Reproduced from von Fraunhofer J. A.; Banks, C. A. *Potentiostat and Its Applications*; Butterworths: London, 1972.



**Figure 8** All-glass cell for studies of polarization of metal electrodes. Reproduced from ASTM G 5–94 (2004).

presented to the solution. Several procedures such as mounting in a cold curing epoxy or polyester resin or inserting into a close-fitting holder of PTFE are used. In the case of metal–solution systems that have a

propensity for pitting, care must be taken to avoid a crevice at the interface between metal specimen and the mounting material (discussion of approaches to the solution of this problem is provided elsewhere). In view of the widespread use of the cell shown in **Figure 8** suitable electrode holders, based on the use of a compression gasket of PTFE or a similar inert polymer, have been designed for bulk metal

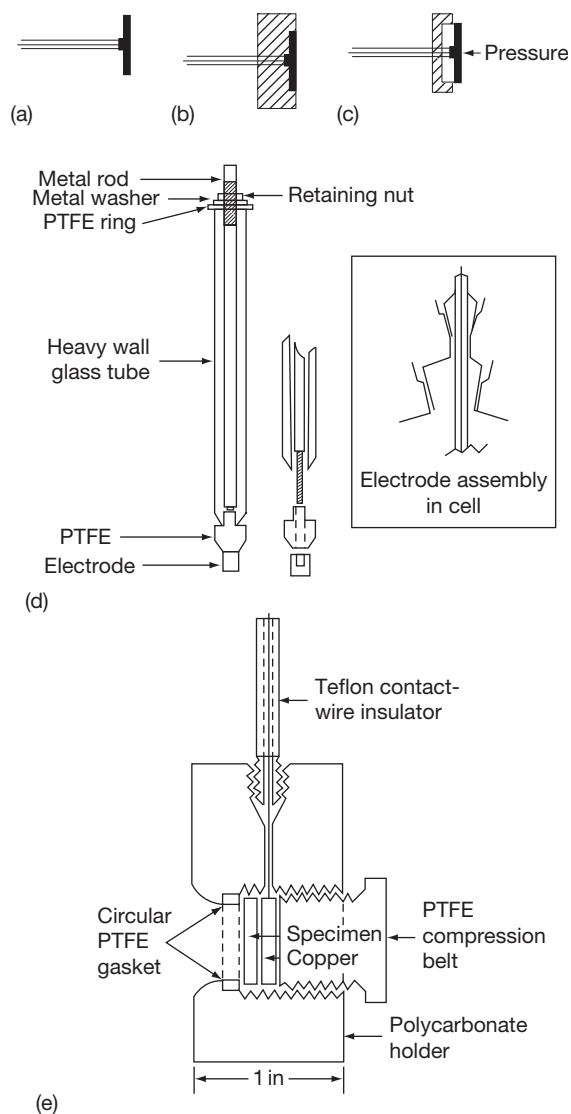


**Figure 9** Methods of mounting specimens. (a) Wire soldered to metal specimen, wire being enclosed in glass tube; (b) specimen completely encapsulated in cold-setting resin that is ground down to expose one face; (c) specimen clipped into machined PTFE holder; (d) Stern Makrides pressure gasket for cylindrical specimen; and (e) pressure gasket for sheet or foil. (d) Reproduced from Stern, M.; Makrides, A. C. *J. Electrochem. Soc.* **1960**, *107*, 782. (e) Reproduced from France, W. D., Jr.; *J. Electrochem. Soc.* **1967**, *114*, 818.

specimens,<sup>89,90</sup> wires,<sup>91</sup> tubes,<sup>92</sup> sheets and foil,<sup>93</sup> and for high temperature high-pressure assemblies.<sup>94</sup> Examples of methods of mounting specimens to give a defined area of surface are shown in **Figure 9**.<sup>88</sup>

Various types of reference electrodes are available of which the saturated calomel electrode (SCE), the silver–silver chloride electrode and the copper–copper sulphate electrode are the most widely used in corrosion testing and monitoring. It is appropriate, however, to point out here that the saturated calomel electrode (SCE), the silver–silver chloride electrode and the copper–copper sulfate electrode are the most widely used in corrosion testing and monitoring.

To avoid contamination of the solution under study, and to minimize the liquid-junction potential, it is usual to use a salt bridge, but in many cases this can be dispensed with; thus, if corrosion in a chloride-containing solution is being studied a Ag/AgCl electrode immersed directly in the solution could be used; similarly a Pb/PbO<sub>2</sub> electrode could be used for studies of corrosion in H<sub>2</sub>SO<sub>4</sub>.

#### 2.34.4.4 Measurements of the Corrosion Potential

Pourbaix<sup>58</sup> has provided a survey of potential measurements in relation to the thermodynamics and kinetics of corrosion, and an example of how they can be used to assess the pitting propensity of copper in water.

The determination of the corrosion potential of the two metals constituting a bimetallic couple will provide information on which one of the two will be predominantly anodic and will suffer enhanced corrosion when they are coupled. Similarly the effect of microscopic heterogeneities in alloys on corrosion has been investigated by measuring the corrosion potentials of selected small areas of the surface of the metal. Smith and Pingel<sup>95</sup> coated the surface of the metal with a lacquer of ethyl cellulose (deposited from a volatile solvent), allowed it to dry and then perforated selected areas with a microhardness tester using a steel stylus ground to a truncated cone, and Budd and Booth<sup>96</sup> using a similar technique were able to produce punctures in the film down to 35  $\mu\text{m}$  diameter. Microelectrodes for potential measurements were described by Cleary<sup>97</sup> who used a Ag/AgCl/Cl-electrode with capillary tips down to 15  $\mu\text{m}$ ; Cleary also described microglass electrodes of approximately 30  $\mu\text{m}$  diameter for the determination of pH. Doig and Edington<sup>98</sup> used microelectrodes with an internal diameter at the tip of about 0.2  $\mu\text{m}$  to measure localized corrosion potentials in the grain boundary regions of aged Al–Mg and Al–Cu alloys,

and Davis<sup>99</sup> used microelectrodes with a tip diameter of 1  $\mu\text{m}$  to measure pH during stress corrosion of aluminum alloys.

Potential–time relationships have been widely used for studying film formation and film breakdown, as indicated by an increase or decrease in the corrosion potential, respectively. May<sup>100</sup> studied the corrosion of 70/30 brass and aluminum brass in seawater and showed how scratching the surface resulted in a sudden fall in potential to a more negative value followed by a rapid rise due to reformation of the film; conversely, the pitting of stainless steel in chemical plant may be detected by a sudden decrease in potential.<sup>101</sup>

Hoar and his coworkers<sup>102,103</sup> used potential changes to study film breakdown and repair during the stress-corrosion cracking of austenitic stainless steels in boiling saturated  $\text{MgCl}_2$  solution. Horst, *et al.*<sup>104</sup> have used potential measurements as a test to predict, the stress-corrosion susceptibility of 2219 aluminum alloy products (alloys containing approximately 6% Cu and tempered to give maximum strength and resistance to stress-corrosion cracking). The test solution used was methanol plus carbon tetrachloride and, it was shown that susceptible alloys were 200–500 mV more positive than nonsusceptible alloys, and that this difference in potential was revealed in less than 1 h. They claim that the test is more sensitive than that in which sodium chloride plus hydrogen peroxide is used as the test solution, since the latter gives potential differences of only 20 mV.

ASTM G 5 outlines standard methods for making potentiostatic and potentiodynamic anodic polarization measurements and ASTM G 3 gives conventions applicable to electrochemical measurements in corrosion testing. Further information and references are provided elsewhere.

### 2.34.5 Polarization Resistance

It is evident from previous considerations that the corrosion potential  $E_{\text{corr}}$  provides no information on the corrosion rate, and it is also evident that in the case of a corroding metal in which the anodic and cathodic sites are inseparable (cf. bimetallic corrosion) it is not possible to determine  $i_{\text{corr}}$  by means of an ammeter. The conventional method of determining corrosion rates by mass-loss determinations is tedious and over the years attention has been directed to the possibility of using instantaneous electrochemical methods. Thus, based on the Pearson derivation,<sup>105</sup>

Schwerdtfeger, *et al.*<sup>106,107</sup> have examined the logarithmic polarization curves for ‘potential breaks’ that can be used to evaluate the corrosion rate; however, the method has not found general acceptance.

Skold and Larson<sup>108</sup> in studies of the corrosion of steel and cast iron in natural water found that a linear relationship existed between potential and the applied anodic and cathodic current densities, provided the values of the latter were low. However, the recognition of the importance of these observations is due to Stern and his coworkers<sup>56,57</sup> who used the term ‘linear polarization’ to describe the linearity of the  $E$  versus  $i$  curve in the region of  $E_{\text{corr}}$ , the corrosion potential. The slope of this linear curve,  $\Delta E$  versus  $\Delta i$  or  $\Delta E$  versus  $\Delta i$ , is termed the polarization resistance,  $R_p$ , since it has dimensions of ohms, and this term is synonymous with ‘linear polarization’ in describing the ‘Stern–Geary’ technique for evaluating corrosion rates.

Stern and Geary<sup>56,57</sup> on the basis of a detailed analysis of the polarization curves of the anodic and cathodic reactions involved in the corrosion of a metal, and on the assumption that both reactions were charge-transfer controlled (transport overpotential negligible) and that the  $IR$  drop involved in determining the potential was negligible, derived the expression:

$$\frac{1}{R_p} = \left[ \frac{\Delta i}{\Delta E} \right]_{E_{\text{corr}}} = 2.3 \left[ \frac{b_a + |b_c|}{b_a |b_c|} \right] i_{\text{corr}} \quad [1]$$

where  $R_p$  is the polarization resistance determined at potentials close to  $E_{\text{corr}}$ , and  $b_a$ ,  $b_c$  are the Tafel constants; note that in the case of  $b_c$  the negative sign is disregarded. This equation shows that the corrosion rate is inversely proportional to  $R_p$  (or directly proportional to the reciprocal slope of the  $\Delta E$  versus  $\Delta i$  curve) at potentials close to  $E_{\text{corr}}$  (typically within 10 mV), and that  $i_{\text{corr}}$  can be evaluated provided the Tafel constants are known. For a process that is controlled by diffusion of the cathode reactant (transport control) and in which the anodic process is under activation control a similar linear relationship applies:

$$\frac{1}{R_p} = \left[ \frac{\Delta i}{\Delta E} \right]_{E_{\text{corr}}} = \frac{2.3 i_L}{b_a} = \frac{2.3 i_{\text{corr}}}{b_a} \quad [2]$$

where  $i_L$  is the limiting current density of the cathodic reaction and it is assumed that  $i_L = i_{\text{corr}}$

Stern and Weisert<sup>109</sup> by taking arbitrary values of the Tafel constants showed that corrosion rates



determined by the polarization resistance techniques are in good agreement with corrosion rates obtained by mass loss methods.

The importance of the method in corrosion testing and research has stimulated other work, and since the appearance of Stern's papers there have been a number of publications many of which question the validity of the concept of linear polarization. The derivation of linearity polarization is based on an approximation involving the difference of two exponential terms, and a number of papers that have attempted to define the range of validity of polarization resistance measurements have appeared. Barnatt<sup>110,111</sup> derived an analytical expression for the deviations from linearity and concluded that it varied widely between different systems. Leroy,<sup>112</sup> using mathematical and graphical methods, concluded that linearity was sufficient for the technique to be valid in many practical corrosion systems. Most authors emphasize the importance of making polarization resistance measurements at both positive and negative overpotentials.

Oldham and Mansfeld<sup>113</sup> approached the problem of linearity in a different way and their derivation avoids the approximation used by Stern and Geary. They conclude that although linearity is frequently achieved, this is due to three possible causes: (a) ohmic control due to the  $IR$  drop rather than control according to linear polarization, (b) the similarity of the values of  $b_a$  and  $b_c$ , and (c) a predisposition by the experimenter to assume that the  $\Delta E$  versus  $\Delta i$  curves near  $E_{\text{corr}}$  must be linear. In a later paper Oldham and Mansfeld<sup>114</sup> showed that linearity of the  $\Delta E$  versus  $\Delta i$  curve is not essential and that  $i_{\text{corr}}$  can be evaluated from the slopes of the tangents of the nonlinear curve determined at potentials of about 20–30 mV more positive and negative than  $E_{\text{corr}}$ .

Hickling,<sup>115</sup> in attempting to study the corrosion of steels under thin film conditions that simulate atmospheric exposure, took into account the time-dependence of polarization measurements, and developed a technique using galvanostatic transients.

### 2.34.5.1 Tafel Constants

It is evident from eqns [1] and [2] that the evaluation of  $i_{\text{corr}}$  from  $R_p$  determinations requires a knowledge of the Tafel constants  $b_a$  and  $b_c$ , which may not be available for the system under study and which may change in value during the progress of the determination. The determination of the Tafel constants from complete  $E$  versus  $i$  curves for each system

studied is time consuming, and may not be particularly accurate owing to resistance and mass transfer effects. Hoar<sup>116</sup> has criticized the method on these grounds and has pointed out that the complete Tafel equations for the anodic and cathodic reactions, which have to be determined to evaluate the Tafel slopes, can be used to calculate  $i_{\text{corr}}$  without resorting to the polarization resistance technique. Mansfeld<sup>117–120</sup> suggests that polarization curves obtained in the  $R_p$  region can be fitted to various theoretical curves, preferably by computer analysis, to give the separate value of both  $b_a$  and  $b_c$ , which since they are determined simultaneously with the  $R_p$  values avoids the criticism that they may change substantially during the corrosion test. (An alternative approach uses the distortion of a small amplitude sine wave as a means of estimating the Tafel constants.)

The controversy that arises owing to the uncertainty of the exact values of  $b_a$  and  $b_c$  and their variation with environmental conditions, partial control of the anodic reaction by transport, etc. may be avoided by substituting an empirical constant for  $(b_a + |b_c| / b_a |b_c|)$  in eqn [1], which is evaluated by the conventional mass-loss method. This approach has been used by Makrides<sup>121</sup> who monitors the polarization resistance continuously, and then uses a single mass-loss determination at the end of the test to obtain the constant. Once the constant has been determined it can be used throughout the tests, providing that there is no significant change in the nature of the solution that would lead to markedly different values of the Tafel constants.

### 2.34.5.2 Applications

The method, in spite of its limitations, has a number of significant advantages and provides a method of rapidly monitoring the instantaneous corrosion rates; furthermore, it has the advantage of the small changes in potential required in the determination not disturbing the system significantly. It is capable of measuring both high and low corrosion rates with accuracy, and may be used as a laboratory tool for testing or research, or for monitoring corrosion rates of plant.

Stern<sup>57</sup> pointed out that the polarization resistance method could be of value for determining the effect of the changes of environment (composition, temperature, velocity) and alloy composition on the corrosion rate and for evaluating inhibitors, and since his original publications the method has been widely used for a variety of studies. Thus, Legault and Walker<sup>122</sup> used the method for studying the

inhibition of the corrosion of steel in chloride solutions by  $\text{NaNO}_2$ , and Walker and France<sup>123</sup> extended this approach to a study of the in situ corrosion of the various metals in automotive-engine cooling systems. Jones and Greene<sup>124</sup> developed the theory of transient linear polarization to study very low corrosion rates, such as those that occur with surgical implant materials, and have shown how polarization resistance data can be used to monitor the onset of pitting or other forms of localized corrosion.

Wilde<sup>125</sup> has applied the Jones d.c.-bridge technique<sup>126</sup> to compensate for errors due to the  $IR$  drop, and has obtained meaningful corrosion rates from polarization resistance data in high temperature high-purity water in nuclear reactors.

Bureau<sup>127</sup> and others<sup>128</sup> have tried to apply the technique for evaluating the corrosion rate of painted metals, and although the results are controversial, the method has also been used successfully in the study of canning materials and lacquered surfaces.<sup>129–131</sup>

Rowlands and Bentley<sup>132</sup> have provided an account of the possibilities for continuously monitoring corrosion rates by polarization resistance measurements, and they also describe the development of a commercial instrument, which uses low-frequency square-wave current to polarize the test specimens.

### 2.34.5.3 Derivation of Linear Polarization Method for Determining Corrosion Rates

It is assumed that

1. The corrosion current  $i_{\text{corr}}$  (it is also assumed that the area of the metal is  $1 \text{ cm}^2$  so that  $I_{\text{corr}} = i_{\text{corr}}$ ) occurs at a value within the Tafel region for the anodic and cathodic reaction, that is, transport overpotential is negligible.
2.  $E_{\text{corr}}$  is remote from the reversible potentials of the anodic and cathodic reactions.
3. The  $IR$  drop in measuring the polarized potential is negligible.

Following Oldham and Mansfeld,<sup>113</sup> but using the symbols that have been adopted in the present work, it is required to show that

$$\left(\frac{di}{dE}\right)_{E_{\text{corr}}} = Z = i_{\text{corr}} \left[ \frac{1}{\beta_a} + \frac{1}{\beta_c} \right] \quad [3]$$

where  $\beta_a$ ,  $\beta_c$  are the Tafel slopes of anodic and cathodic reactions constituting the overall corrosion reaction, that is,  $i_{\text{corr}}$  is linearly related to the polarization resistance ( $dE/di$ ) at potentials close to  $E_{\text{corr}}$ .

(Note that  $\beta$  is used to represent the Tafel slope expressed in terms of natural logarithms, so  $b = 2.3\beta$ .)

At any potential  $E$  the net current is given by

$$i = \bar{i}_1 - |\vec{i}_1| + \bar{i}_2 - |\vec{i}_2| \quad [4]$$

where  $\bar{i}_1$  is the anodic current for metal dissolution and  $\vec{i}_1$  is the reverse cathodic current, and  $\bar{i}_2$  is the cathodic current for the reduction of the cathode reactant (dissolved  $\text{O}_2$ ,  $\text{H}^+$ ,  $\text{H}_2\text{O}$ , etc.) and  $\vec{i}_2$  the reverse current.

The rate of the anodic reaction at a potential  $E$  is given by

$$\bar{i}_1 = i_{0,1} \exp\left(\frac{E - E_{r,1}}{\beta_a}\right) \quad [5]$$

where  $E_{r,1}$  is the reversible potential for the anodic dissolution reaction,  $\beta_a$  is the Tafel slope and  $i_{0,1}$  is the exchange current density. Similarly for the cathodic reaction

$$\vec{i}_2 = i_{0,2} \exp\left(\frac{E_{r,2} - E}{\beta_c}\right) \quad [6]$$

Similar expressions may be written for the partial reverse rates  $\vec{i}_1$  and  $\bar{i}_2$ , but under the conditions assumed here they may be neglected. Hence, substituting eqns [5] and [6] in eqn [4]:

$$i = i_{0,1} \exp\left(\frac{E - E_{r,1}}{\beta_a}\right) - i_{0,2} \exp\left(\frac{E_{r,2} - E}{\beta_c}\right) \quad [7]$$

At the corrosion potential  $E_{\text{corr}}$  the net current  $i$  becomes zero, since  $\bar{i}_1 = |\vec{i}_2|$ . Thus, the two terms on the right-hand side of eqn [7] become equal to one another and equal to  $i_{\text{corr}}$ , the corrosion current density. Thus, replacing  $E$  in eqn [7] by  $E_{\text{corr}}$  gives

$$i = i_{0,1} \exp\left(\frac{E_{\text{corr}} - E_{r,1}}{\beta_a}\right) - i_{0,2} \exp\left(\frac{E_{r,2} - E_{\text{corr}}}{\beta_c}\right) \quad [8]$$

Differentiating eqn [7] with respect to  $E$  gives

$$\frac{di}{dE} = \frac{i_{0,1}}{\beta_a} \exp\left(\frac{E - E_{r,1}}{\beta_a}\right) + \frac{i_{0,2}}{\beta_c} \exp\left(\frac{E_{r,2} - E}{\beta_c}\right) \quad [9]$$

which for  $E = E_{\text{corr}}$  becomes

$$\begin{aligned} \left(\frac{di}{dE}\right)_{E_{\text{corr}}} &= \frac{i_{0,1}}{\beta_a} \exp\left(\frac{E_{\text{corr}} - E_{r,1}}{\beta_a}\right) \\ &+ \frac{i_{0,2}}{\beta_c} \exp\left(\frac{E_{r,2} - E_{\text{corr}}}{\beta_c}\right) \end{aligned} \quad [10]$$

Combining eqns [8] and [10] gives eqn [3] the Stern–Geary equation by simple algebra. However, Oldham and Mansfield point out that further differentiation of eqn [9] gives

$$\frac{d^2 i}{dE^2} = \frac{i_{0,1}}{\beta_a^2} \exp\left(\frac{E - E_{r,1}}{\beta_a}\right) - \frac{i_{0,2}}{\beta_c^2} \exp\left(\frac{E_{r,2} - E}{\beta_c}\right) \quad [11]$$

an equation that demonstrates that there is only one point (a point of inflection, corresponding to a minimum slope) at which the  $i$ – $E$  curve has no curvature and is linear. It follows that

$$\left(\frac{d^2 i}{dE^2}\right)_{E_{\text{corr}}} = \frac{i_{0,1}}{\beta_a^2} \exp\left(\frac{E_{\text{corr}} - E_{r,1}}{\beta_a}\right) - \frac{i_{0,2}}{\beta_c^2} \exp\left(\frac{E_{r,2} - E_{\text{corr}}}{\beta_c}\right) \quad [12]$$

and combining this equation with eqn [8] gives

$$\left(\frac{d^2 i}{dE^2}\right)_{E_{\text{corr}}} = i_{\text{corr}} \left( \frac{1}{\beta_a^2} - \frac{1}{\beta_c^2} \right) \quad [13]$$

For the  $E$  versus  $i$  plot to be linear at  $E \approx E_{\text{corr}}$  ( $d^2 i/dE^2$ ) <sub>$E_{\text{corr}}$</sub>  must be zero, but eqn [13] shows that this will be true only if  $\beta_a = \beta_c$ . (Note that this does not invalidate the basic Stern–Geary equation, it merely shows that the  $d^2 E/di^2$  is only zero at  $E_{\text{corr}}$  if  $\beta_a = \beta_c$ , so that it could be argued that the use of the word ‘linear’ is not strictly accurate.)

#### 2.34.5.4 Simultaneous Determination of Tafel Slopes and Corrosion Rates from $R_p$ Determinations

Mansfield<sup>120</sup> points out that a major limitation of the polarization resistance is that the factor  $b_a b_c / 2.3(b_a + b_c)$  must be determined in order to evaluate  $I_{\text{corr}}$  and has devised a procedure in which this can be achieved by a graphical method.

The Stern–Geary equation can be written in the form

$$I_{\text{corr}} = \frac{b_a b_c}{2.3(b_a + b_c)} \times \frac{1}{R_p} = \frac{B}{R_p} \quad [14]$$

where  $B = b_a b_c / 2.3(b_a + b_c)$  and  $R_p = (dE/dI)$  at  $E_{\text{corr}}$ . Equation [14] is valid only if the relationship between  $I$  and  $E$  can be expressed as

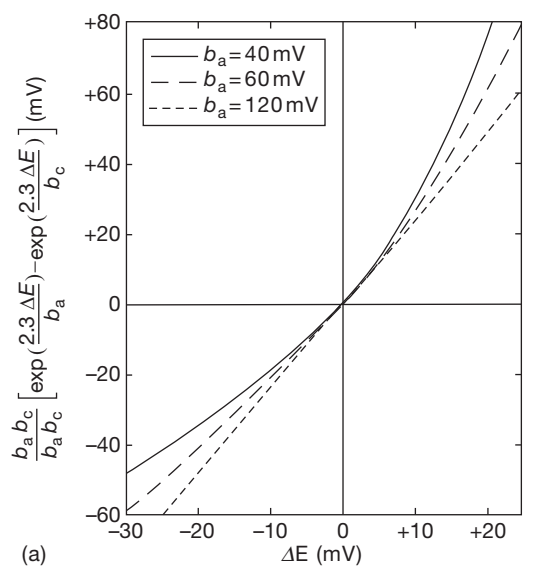
$$I = I_{\text{corr}} \left\{ \exp\left(\frac{2.3(E - E_{\text{corr}})}{b_a}\right) - \exp\left(\frac{-2.3(E - E_{\text{corr}})}{b_c}\right) \right\} \quad [15]$$

Combining eqns [14] and [15] and rearranging gives

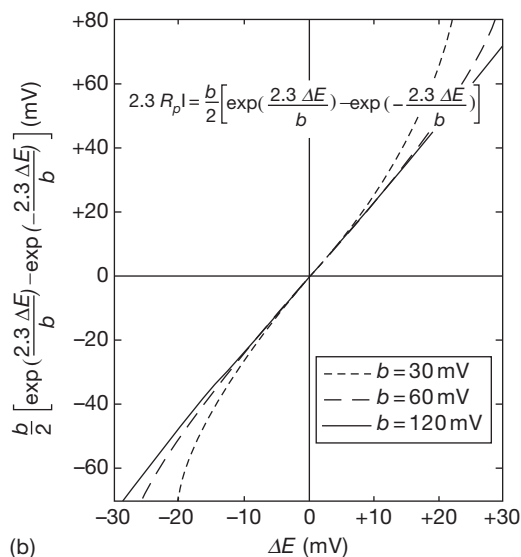
$$2.3 R_p I = \frac{b_a b_c}{b_a + b_c} \left\{ \exp\left(\frac{2.3 \Delta E}{b_a}\right) - \exp\left(-\frac{2.3 \Delta E}{b_c}\right) \right\} \quad [16]$$

where  $\Delta E = E - E_{\text{corr}}$ . Since the right-hand side of eqn [16] depends only upon the Tafel slopes it should be possible to evaluate  $b_a$  and  $b_c$  from plots of  $R_p I$  versus  $\Delta E$ .

Figure 10(a) shows a theoretical plot of the right-hand side of eqn [16] versus  $\Delta E$  in which the cathodic



(a)



(b)

**Figure 10** Plots of right-hand side of equation 16 versus  $\Delta E = E - E_{\text{corr}}$  for various combinations of Tafel slopes. (a)  $b_c$  constant at 120 mV,  $b_a$  varied and (b)  $b_a = b_c = b$ . Reproduced from Mansfield, F. J. *Electrochem. Soc.* **1973**, 120, 515.

Tafel slope has been assumed to be constant at 120 mV and the anodic Tafel slope to have the arbitrary slopes of 40, 60, and 120 mV. It can be seen that linearity over a range of positive and negative potentials  $\Delta E$  is achieved only when  $b_a = b_c$  and that linearity is confined to  $\Delta E \approx 0$  when  $b_a$  and  $b_c$  differ.

In **Figure 10(b)** it has been assumed that the Tafel slopes are equal, that is,  $b_a = b_c = b$  and the modified expression for the right-hand side of eqn [16] has been plotted against  $\Delta E$  for different values of  $b$  (e.g., 30, 60, and 120 mV). Comparison of **Figure 10(a)** and **10(b)** shows how the curvature of the plots differs at cathodic potentials, that is,  $\Delta E < 0$ . Thus, the kinetic behavior of a corroding metal, as expressed by different combinations of Tafel slopes, can be organized by this method of plotting curves. This theoretical approach has been confirmed experimentally by Mansfeld for the system Fe/H<sub>2</sub>SO<sub>4</sub>.

Mansfeld points out that  $I_{\text{corr}}$  can be calculated from the measured polarization curve by the following four steps, which are based on eqns [14] and [15]. (With the advent of low cost computing power, and computerized systems for the acquisition of polarization data, this process can be automated by fitting eqn [8] (or rather a simplified form of this equation, taking account of the fact that  $i_{0,1}$  and  $E_{r,1}$  (and  $i_{0,2}$  and  $E_{r,2}$ ) can be replaced by any current–potential pair that lies on the Tafel line, one such pair being  $i_{\text{corr}}$  and  $E_{\text{corr}}$  for both anodic and cathodic reactions), or a more sophisticated model of the  $E$ – $i$  relationship, to the measured data by adjusting the variable parameters (for a recent example see Guinea, D. M.; Moreno, B.; Chinarro, E.; Guinea, D.; Jurado, J. R. *Int. J. Hydrogen Energy* **2008**, 33(11), 2774–2782). Alternatively the harmonic analysis and electrochemical frequency modulation methods provide other approaches to obtain this information.)

1. Determine  $R_p$  from:

$$\left[ \frac{\partial I}{\partial E} \right]_{E_{\text{corr}}} = \frac{1}{R_p}$$

by drawing a tangent at  $\Delta E = 0$  that is, at  $E_{\text{corr}}$ .

2. Multiply the current  $I$  measured at a certain value of  $\Delta E$  by  $2.3 R_p$  and plot  $2.3 R_p I$  versus  $\Delta E$  for various values.
3. Determine from this plot the Tafel slopes  $b_a$  and  $b_c$  by curve fitting using the theoretical curves calculated for various values of  $b_a$  and  $b_c$ .
4. Calculate  $I_{\text{corr}}$  from eqn [14] using the  $R_p$  value evaluated in Step 1 and the Tafel slopes determined in Step 3.

## 2.34.6 Tests for Bimetallic Corrosion

The extent of galvanic effects will be influenced by, in addition to the usual factors that affect corrosion of a single metal, the potential relationships of the metals involved, their polarization characteristics, the relative areas of anode and cathode, and the internal and external resistances in the galvanic circuit.

The results of a galvanic corrosion test on a small scale are as a general rule no more than semiquantitative. A principal reason for this is that the magnitude of the galvanic effect is a function of galvanic current density which is usually determined by the relative areas of the metals forming the couple. There may also be major differences in circuit resistances in tests as compared with practice – especially if current-measuring shunts of substantial resistance are made part of the circuit in the test. The geometric relationship between the metals in the test will also influence the result through effects on electrolyte resistance and the distribution of the galvanic currents.

The simplest procedure in studying galvanic corrosion is a measurement of the open-circuit potential difference between the metals in a couple in the environment under consideration. This will at least indicate the probable direction of any galvanic effect, although no information is provided on the rate. A better procedure is to make similar open-circuit potential measurements between the individual metals and some appropriate reference electrode, which will yield the same information and will also permit observations of any changes in the potential of the individual metals with time that will affect the overall potential difference in the couple. For most practical laboratory testing, the saturated calomel half cell is most convenient. The precision of the determinations is adequate and it is easy to maintain a constant concentration of potassium chloride.

The preferred potential-measuring instruments are high-input impedance voltmeters that permit measurements to be made without flow of sufficient current to polarize the electrodes during the determinations.

Open-circuit potential measurements do not indicate the all important effects of continued current flow, and much more information is derived from frequent or continuous determinations of the magnitude of the galvanic current. In making these measurements it is necessary to avoid the use of instruments that will introduce sufficient resistance to exert a controlling effect on the magnitude of the galvanic current being measured. Instruments (zero-resistance ammeters) that permit current measurements to be made with

zero resistance in the measuring circuit (see Ailor)<sup>2</sup> are available.

In less critical cases it will suffice to include in the circuit a low value resistance over which  $IR$ -drop potential measurements can be made for calculation of the current. This technique permits measurements to be made as required without opening the circuit even momentarily for the introduction of current-measuring devices.

An obvious method for studying galvanic corrosion either with or without supplementary electrical measurements is to compare the extent of corrosion of coupled and uncoupled specimens exposed under identical conditions. Such measurements may use the same techniques for estimating corrosion damage, such as mass-loss determinations, as have been described in connection with ordinary corrosion tests.

A convenient method of carrying out such a galvanic test in the laboratory has been described by Wesley<sup>133</sup> in which the vertical circular-path machine is used. Each assembly includes two pairs of dissimilar metals – one pair coupled galvanically while the other pair is left uncoupled to determine the normal corrosion rates under the same environmental conditions. The type of motion provided (specimens moving in a vertical circular path) enables electrical connections to be made without mercury cup or commutator and the leads can be connected to a calibrated resistance for current measurements attached to the specimen carrier.

It is often of interest also to measure both the external and internal resistances of the galvanic circuit by the use of appropriate resistance-measurement bridges or by even more elaborate techniques such as those described by Pearson.<sup>105</sup>

It is often desirable to know something about the probable distribution of galvanic effects in a galvanic couple. This will be determined, of course, by the size and shape of the different metals and how they are placed relative to each other – whether more or less parallel in the electrolyte, close together or far apart, or joined along some line of contact. The distribution from such a line of contact may be observed directly if the test couples are exposed in this way and for long enough for sufficient corrosion to occur for it to be observed and measured. Alternatively, the distribution of the galvanic currents in terms of the current density on different portions of both the anode and cathode surfaces may be estimated from data derived from surveys of the potential field in the electrolyte around the couple. Such a potential survey may be made using a fixed and a movable reference electrode so that equipotential lines in several planes may be measured

and plotted as was done by Copson<sup>134</sup> using a technique originally proposed by Hoar. By analysing the data from the potential surveys, it is possible to calculate the current distribution over different areas near and remote from the contact of the dissimilar metals. This technique has been used by Rowe<sup>135</sup> to study the corrosion behavior of coated and uncoated couples.

Guidance on conducting and evaluating galvanic corrosion tests in electrolytes is given in ASTM G 71.

## 2.34.7 Soil Tests

Soil corrosion does not lend itself readily to direct study in the laboratory. However, indirect methods involving the action of differential aeration cells have yielded valuable information in comparing the probable corrosivities of different soils towards steel. The details of this technique were described by Denison,<sup>136</sup> Ewing,<sup>137</sup> Schwerdtfeger,<sup>138–141</sup> and by Logan *et al.*<sup>142</sup>

The Schwerdtfeger<sup>138–141</sup> ‘polarization break’ and the polarization resistance methods have been studied by Jones and Lowe<sup>143</sup> in relation to their effectiveness in evaluating corrosion rates of buried metals. A Holler bridge circuit was used to remove  $IR$  contributions during the measurement of the polarized potential. Jones and Lowe, on the basis of their studies of buried steel and aluminum specimens, concluded that the polarization resistance was the most useful, and that the polarization break had the serious limitation difficult to making it identify the breaks in the curve.

## 2.34.8 Accelerated Tests – Electrolytic Tests

In view of the electrochemical nature of corrosion, it has seemed reasonable to many investigators to assume that suitable accelerated corrosion tests could be made by observing the response to electrolytic stimulation of the corrosion processes, or by attaching particular significance to the results of quickly made electrode potential and current measurements.

Acceleration of corrosion by electrolytic stimulation has sometimes been found to distort normal corrosion reactions to such an extent that the results bear no consistent relationship to ordinary corrosion and are, therefore, quite inconsistent and unreliable. This was shown, for example, by a series of tests sponsored by ASTM Committee B-3.<sup>144,145</sup> Nevertheless, considerable success has been achieved with the development



of the electrochemical potentiokinetic reactivation (EPR) test as an accelerated method for the detection of sensitization in austenitic stainless steels. This is discussed subsequently in the section concerned with intergranular attack of Cr–Ni–Fe alloys.

Measurements of open-circuit potentials relative to a reference electrode have been assumed on occasion to provide a means of rating metals as to their relative resistance to corrosion on the basis that the more negative the measured potential, the higher will be the rate of corrosion, but this assumption is obviously invalid, since it disregards polarization of the anodic and cathodic areas. (More importantly, it ignores the possibility of passivation, which leads to a more positive potential, but a reduced corrosion rate compared to active corrosion.)

Some examples of the use of potential measurements in corrosion tests have been given and it is of interest to outline here certain test procedures that are used industrially to supplement or replace the more tedious and prolonged laboratory and field tests. These tests frequently rely on changing the potential as a means of accelerating the test, and although, as emphasized earlier, this is capable of distorting the mechanism, it is less likely to do so than a change in the nature of the environment, an increase of temperature, etc. The majority of these tests are used for evaluating electrodeposits, anodized coatings, and paint films.

#### 2.34.8.1 Electrolytic Oxalic Acid Etching Test

This test has been developed and used by Streicher<sup>146–149</sup> as a screening test to be used in conjunction with the tedious boiling nitric acid test for assessing the susceptibility of stainless steels to intergranular attack as specified in ASTM A 262, and will be considered subsequently in the section concerned with intergranular attack of Cr–Ni–Fe alloys.

#### 2.34.8.2 The Electrolytic Corrosion (EC) Test

The EC test was developed by Saur and Basco<sup>150–153</sup> for decorative Cu (optional) + Ni + Cr electrodeposits. After an appropriate area is masked off and cleaned with a slurry of MgO, the specimen is immersed in test solution A or B (Table 2). It is held by means of a potentiostat at +0.3 V (versus SCE) and taken through cycles of 1 min anodically polarized, 2 min unpolarized.

The extent of pitting is estimated by a special microscopic technique, or by the attack on the

**Table 2** Electrolytic corrosion test: composition of test solutions (A, B) and indicators (C, D)

	Concentration			
	A	B	C	D
NaNO <sub>3</sub> (g l <sup>-1</sup> )	10	10		
NaCl (g l <sup>-1</sup> )	1.3	1.0		
HNO <sub>3</sub> (conc.; g l <sup>-1</sup> )	5	5		
1,10-Phenanthroline hydrochloride (g l <sup>-1</sup> )		1.0		
KCNS			3	3
Acetic acid (glacial, ml l <sup>-1</sup> )			2	2
Quinoline (ml l <sup>-1</sup> )			8	
H <sub>2</sub> O <sub>2</sub> (30%) (ml l <sup>-1</sup> )				3

Source: Saur, R. L.; Basco, R. P. *Plating* **1966**, 53, 33.  
 Saur, R. L.; Basco, R. P. *Plating* **1966**, 53, 320.  
 Saur, R. L.; Basco, R. P. *Plating* **1966**, 53, 981.  
 Saur, R. L. *Plating* **1966**, 54, 393.

substrate using an appropriate indicator. Thus, in the case of steel 1,10-phenanthroline hydrochloride is added to the electrolyte (solution B) to detect the formation of Fe<sup>2+</sup> ions. Alternatively, the specimens can be removed from the corrosion test solution and placed in an indicator solution, that is, solution C for zinc-base die castings and solution D for steels.

The test is much faster than the CASS test and is probably more reproducible; more important is the fact that it has been correlated with service exposure.

#### 2.34.8.3 Impedance (Aztac) Test

The impedance test<sup>154</sup> for anodized aluminum (ASTM B 457) employs a 1 V r.m.s. 1 kHz source applied to a test cell in an impedance bridge; the electrolyte solution is 3.5% NaCl. The results are expressed as kilohms, and while a bare Al specimen will give a value of about 1 kΩ, a well scaled anodized coating will give a value of 100 kΩ. The admittance test (BS BS EN 12373-5 and BS 3987) is essentially the same as the impedance test but uses 3.5% K<sub>2</sub>SO<sub>4</sub> rather than 3.5% NaCl. An admittance of < 500/*t* μS (where *t* is the thickness of the film in micrometers) denotes good sealing. It should be noted that thickness of the sealed coating should be specified in both tests.

### 2.34.9 Accelerated Tests – Simulated Environments

#### 2.34.9.1 Spray Tests

The most common of the spray tests is the salt-spray or salt-fog test, which was developed originally by

Capp<sup>155</sup> in 1914 for studying the protective values of metallic coatings on steel under conditions that he hoped would simulate exposure to a sea-coast atmosphere. Since then, the test has been used for a number of purposes, for many of which it is not well suited.<sup>156–158</sup>

Although there is no standard size or shape of salt-spray box, certain other features of the test have been standardized in ASTM B 117. Various factors affect the rate of attack and **Figure 11** shows the effect of the angle of exposure of the specimen to the salt droplets, which fall vertically from the spray nozzle, based on early work by May and Alexander.<sup>159</sup> It can be seen that maximum corrosion occurs at angles between about 30° and 80° to the horizontal; vertical exposures were found to give erratic results.

There may be variations from box to box, depending on differences in fog characteristics as influenced by the design of the spray nozzles, the pressure at which the brine enters the nozzle, and the constancy of this pressure.<sup>160</sup>

The results will also be influenced by the concentration of NaCl solution sprayed, some metals are affected more by one concentration than another, for example, zinc is corroded most by a concentrated brine (20%), while iron is corroded most by a dilute brine (3%); synthetic seawater is less corrosive to these metals than either brine. In view of the many other ways by which the conditions within a salt-spray box differ from those of exposure to a natural sea-coast environment, there seems to be no great advantage in making-up complicated synthetic seawaters for use in salt-spray testing. However, tablets for this purpose are commercially available.

Some modified brines have been used in salt-spray boxes for particular purposes, such as the acetic acid-modified brine developed by Nixon<sup>161</sup> to

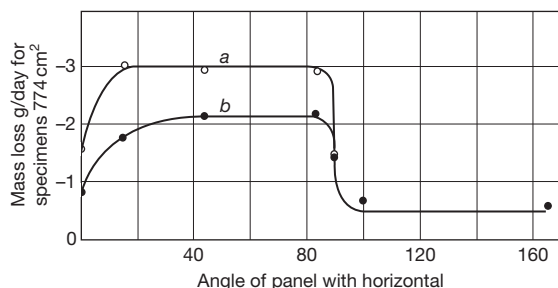


**Figure 11** Effect of cold-rolled steel specimen position on corrosion in salt-spray test; a is 20% NaCl and b is synthetic seawater.

reproduce the type of blistering frequently encountered on chromium-plated zinc-base die castings. An acetic acid-salt-spray test has been adopted by ASTM (ASTM G 85) and other modifications of the spray test covered by the same standard practice include the cyclic acidified salt spray test, the acidified synthetic seawater spray test and the SO<sub>2</sub> salt spray test. Corresponding tests in the BS series are covered by BS EN 12540. In addition, the original acetic acid-salt-spray test has been modified by including cupric chloride in the brine. This is called the CASS (Copper Accelerated Acetic Acid Salt-Spray) Test; ASTM B 368 test. It is used extensively for testing nickel–chromium coatings on steel and zinc. The original acetic acid-salt-spray test, is modified in an important aspect by the addition of 0.25 g l<sup>-1</sup> of CuCl<sub>2</sub>·2H<sub>2</sub>O, to the 5% NaCl test solution, which substantially increases the corrosivity of the solution, especially to nickel. The addition of FeCl<sub>3</sub> to the acetic acid-salt-spray solution, such as is used in the Corrodokote test, was earlier noted to be troublesome in that it tended to precipitate. For this reason, ferric iron is not included in the CASS test solution. Essential details<sup>162,163</sup> include control of cabinet temperature at 49 °C, control of saturation temperature at 57 °C, control of collection rate at 1.5 ± 0.5 ml h<sup>-1</sup> per 80 cm<sup>2</sup> of specimen surface, control of pH by addition of acetic acid to 3.2 ± 0.1, and an operating air pressure of 103.4 ± 6.9 kN m<sup>-2</sup>. Higher pressure may be required to achieve the specified collection rate in ‘walk-in’ cabinets.

It has been shown that chromium is virtually unattacked by the CASS test solution.<sup>164</sup> Nickel, on the other hand, is corroded at a substantial rate (about 0.072 mm year<sup>-1</sup>), the presence of the copper ions tending to maintain the nickel in an active state.<sup>164,165</sup> Thus, in the CASS test (and in the Corrodokote test as well) accelerated galvanic corrosion of the nickel occurs at any discontinuity in the chromium layer. Good correlation between the results of the CASS test and the performance of plated parts in service has been reported.<sup>164</sup>

#### 2.34.9.2 Corrodokote Test<sup>162,166</sup>

This is a refinement of an earlier test in which melted street slush together with its contained dirt, salts, etc. was splashed upon plated parts by means of a rotating paddle wheel. Parts soiled in this manner were then exposed to a warm, humid atmosphere. The results were striking and significant in that they closely paralleled service experience. The ‘paddle-wheel test’ was

intended to simulate the conditions to which plated parts on automobiles are subjected when cars are garaged, unwashed, after being driven over salted slush-covered city streets on typical winter days. Platings of inadequate thickness and quality have frequently been observed to show signs of failure after only a few weeks' or even a few days' use under such circumstances. Despite certain limitations, good correlation has been reported between the results of the Corrodokote test and service performance of plated components,<sup>133</sup> and it is now included in ASTM B 380 and BS EN 12540 and ISO 4541. Reagents for use in this test are prepared as follows.

1. The cupric nitrate reagent contains 2.5 g  $\text{CuNO}_3 \cdot 3\text{H}_2\text{O}$ , dissolved in 500 ml distilled water.
2. The ferric chloride reagent contains 2.5 g  $\text{FeCl}_3 \cdot 6\text{H}_2\text{O}$ , dissolved in 500 ml distilled water. This reagent should not be kept longer than 2 weeks.
3. The ammonium chloride reagent contains 50 g  $\text{NH}_4\text{Cl}$ , dissolved in 500 ml distilled water.
4. The Corrodokote slurry is prepared by mixing 7 ml of the cupric nitrate reagent, 33 ml of the ferric chloride reagent, and 10 ml of the ammonium chloride reagent with 30 g of kaolin to form a homogeneous slurry, which is sufficient to cover about  $2.79 \text{ m}^2$  of plated surface. A fresh batch of slurry should be made up each day.
5. The surfaces to be tested should be coated with the slurry by brushing in circular motion, finishing with brush strokes in one direction. The coating should then be allowed to dry for 1 h, after which the coated specimen should be put into a noncondensing humidity cabinet at  $38^\circ\text{C}$  and from 90 to 95% RH. After 20 h in the cabinet the specimen should be removed for inspection. Zinc die castings should be cleaned with running water and dried before inspection. Steel specimens should be examined before cleaning and the number of rust spots counted. Since most of the rust will come off with the Corrodokote coating, it may be difficult to distinguish between surface pits and pin holes reaching the basis metal after cleaning. Steel parts may be returned to a condensing humidity cabinet for 24 h or to a salt-spray cabinet for 4 h. Either supplementary exposure will bring out rust spots again.

One cycle of the Corrodokote test will reliably reveal coatings that will not endure one winter's normal use in a typical city that uses salt to deice its streets. In contrast, several cycles of the Corrodokote test are generally required to 'fail' coatings which will withstand one or more such winter's use.

In this connection, there is some indication that while the Corrodokote test can be depended upon to reveal coatings of unsatisfactory durability, there has been some question of its ability to distinguish between, or to predict the relative protective value or length of useful life of different coating systems in the very good or excellent durability range.

Also of questionable significance is the practice of shortening the Corrodokote cycle, to say 4 h, for the purpose of evaluating the durability of relatively thin coatings intended for use under comparatively mild conditions such as indoors or the interiors of automobiles, since by far the greatest amount of corrosion (of the nickel) appears to occur during the early part of the Corrodokote humidity cycle. Good correlation between the Corrodokote test and service performance has been obtained by Bigge.<sup>166</sup>

### 2.34.9.3 Sulfur Dioxide Tests

Historically, two tests in which sulfur dioxide is the principal corroding agent have been used, that is, the BNFMRSA sulfur dioxide test<sup>167,168</sup> and the Kesternich test.<sup>169</sup> These tests were investigated by the American Electroplaters' Society Research Project 15 Committee early in its search for an acceptable accelerated corrosion test. They were soon abandoned, however, largely because the types of corrosion failures developed did not resemble those that occurred in actual service. Furthermore, the extreme corrosivity of the test environment to nickel (some  $8.38 \text{ mm year}^{-1}$ ) appeared to place an undue premium on the integrity of the overlying chromium deposit, which is virtually unattacked in the test. Thus, coatings that were substandard in respect of nickel or copper-nickel thicknesses might easily pass the test provided the chromium topcoat was completely continuous and remained so for the duration of the test. Conversely, coatings of proven merit on the basis of service experience, such as 0.039 mm of semibright plus bright nickel (duplex) with 0.00025 mm of conventional chromium, could be expected to fail in these  $\text{SO}_2$  tests relatively quickly at any discontinuities in the chromium. In this connection, it is well to keep in mind that, even though the chromium may be non-porous initially, it can hardly be expected to remain so in service on an automobile for example, where it is subject to impact from sand, gravel, etc.

The BNFMRSA test was used in Europe for testing Ni + Cr coatings, but since 1970 it has been omitted from revisions of BS 1224. The test was also used to ensure the quality of anodic coatings on aluminum, but in the current British Standard (BS EN 12373) the

acetic acid salt spray test or the copper-accelerated salt spray test are specified for corrosion testing (BS EN ISO 9227). In the United Kingdom, the Kesternich test, which has obtained the status of an ISO Standard (ISO 6988), is only specified for checking the extent of porosity in tin (BS 1872), tin/lead (BS 6137) and tin/nickel (BS 3597) coatings. In the United States, another version with a much more aggressive atmosphere is used to detect porosity in gold coatings on copper, nickel or silver (ASTM B 735) but the equivalent British Standard (BS EN ISO 27874) specifies electrographic tests for this purpose.

Sulfur dioxide is not included as a corrosion test medium in the current ISO Standard for electrodeposited coatings of nickel + chromium and of copper + chromium (ISO 1456). However, one important use of sulfur dioxide atmospheres as a controlled accelerated test has been for electrical (and, particularly, electronic) contacting surfaces. In this case, the concentration of SO<sub>2</sub> is much less than for the Kesternich test and the time of testing is much longer (IEC 60068-2-49).

Because moist air containing sulfur dioxide quickly produces easily visible corrosion on many metals in a form resembling those that occur in industrial environments, ASTM have issued a Standard Practice for conducting tests in moist SO<sub>2</sub> (G 87). This suggests that such tests are well suited to detect pores or other sources of weakness in protective coatings and deficiencies in corrosion resistance associated with unsuitable alloy composition or treatments. However, it is stressed that the results obtained should only be taken as a general guide to the relative corrosion resistance of these materials in moist SO<sub>2</sub> service.

#### 2.34.9.4 General Considerations of Spray and SO<sub>2</sub> Tests

The salt-spray test has seemed to yield the most consistent results when used to establish the relative merits of different aluminum alloys in resisting attack by marine atmospheres. The best results have been secured when the spray has been interrupted for many hours each day.<sup>170</sup>

Salt-spray boxes are also used for studying the deterioration and protective value of organic coatings, although this test is of doubtful value for such purposes, since it fails to include many factors, for example, sunlight, which affects the life of such coatings. Methods of testing organic coatings are discussed elsewhere. The variable responses of different metals and coatings to the conditions that can be set up in salt-spray boxes, as well as to the conditions that

exist in natural atmospheres, make it impossible to determine the equivalent in some natural atmosphere of say an hour in a salt-spray box.

For additional information on some of the features of the salt-spray test and its limitations in respect of certain purposes for which it may be used, reference should be made to the book *Corrosion Testing for Metal Finishing*<sup>171</sup> prepared by the Institute of Metal Finishing.

There have been several attempts to develop rather elaborate testing machines in which specimens may be subjected to various sprays of fogs with cycles of condensation, heating, and drying. The object has been to reproduce the conditions encountered by metals exposed in polluted industrial atmospheres. Such devices have been experimented with in the United Kingdom<sup>172</sup> and the United States.<sup>173</sup> While it is sometimes possible for such tests to rate steels in a rough order of resistance to atmospheric corrosion, it should be appreciated that the nature of rust formed may differ from that obtained during actual exposure. It is only in rare cases that the resistance to attack by the sprays is analogous to their resistance in the natural atmosphere, which the tests seek to simulate. Such parallelism is not common enough to make these tests very reliable.<sup>174</sup>

Dennis and Such<sup>175</sup> point out that the BNFMRASO<sub>2</sub> test was really a means of detecting discontinuities in the chromium layer of a Cr + Ni coating system and it therefore gave unfavorable results when used for testing microcracked or microporous Cr, since the Cr was rapidly undermined, with consequent flaking. Conversely, the test exaggerates the beneficial effect of crack-free Cr. The test also fails to indicate the improved corrosion resistance of duplex Ni when compared with bright Ni. A critical account of laboratory corrosion testing methods for Ni-Cr coatings is given by Dennis and Such.<sup>176</sup>

#### 2.34.9.5 Accelerated Tests for Weathering Steels

Interest in weathering steels has stimulated work on accelerated laboratory tests that can be used to investigate the effect of alloy composition on performance. It is well established that a wetting and drying cycle should be an integral part of any laboratory test in which the characteristic properties of weathering steels are revealed,<sup>177</sup> and Bromley, Kilcullen, and Stanners<sup>178</sup> have designed a test rig (Figure 12) that provides results that can be correlated with actual atmospheric exposure data. The rig has been designed to investigate

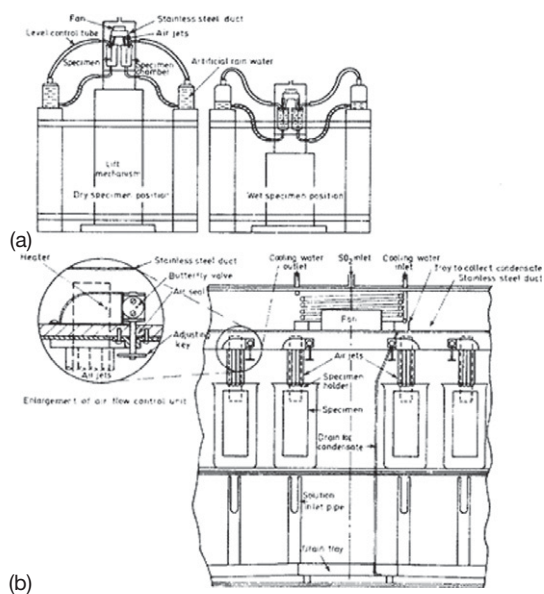


**Figure 12** Rig used for laboratory evaluation of weathering steels. (a) General layout showing unimmersed and immersed positions and (b) detailed view of central position of cabinet. Reproduced from Bromley, A. F.; Kilcullen, M. B.; Stanners, J. F. In 5th European Congress of Corrosion, Paris, September 1973.

a wide range of alloying elements in a development program on slow-weathering steels for which it was essential to have a rapid, reliable and reproducible test that incorporated the specific atmospheric factors responsible for rust formation.

The results obtained with this equipment show that the corrosion rate in the rig is about four times that encountered in an industrial UK atmosphere. This acceleration, however, is not achieved by accentuating any of the environmental factors, but rather by holding them near the worst natural conditions for as long as possible. The procedure used ensures that the rust film is completely dried for short periods, thus simulating the conditions that bring out the beneficial effects of protective rust films on the steels under study.

The use of electrochemical tests for rapid assessment of the performance of these steels has attracted interest, and Pourbaix<sup>179</sup> has devised an apparatus in which potential measurements are used to evaluate the protective nature of corrosion products formed on low-alloy steels, such as the weathering steels, during periodic wetting and drying. The apparatus (Figure 13) consists of a glass tank containing an appropriate electrolyte, such as a natural or artificial water. Two specimens of the metal or alloy under study are attached to a spindle that rotates slowly

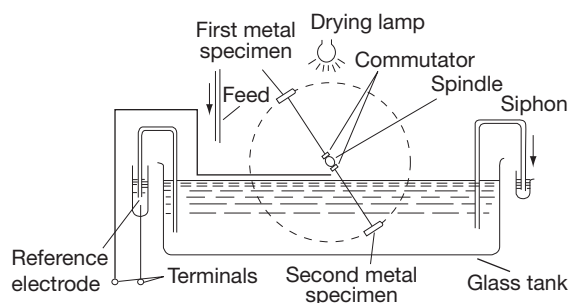


**Figure 13** Equipment for studying patina formation on low alloy steels. Reproduced from Pourbaix, M. CEBELCOR RT; 1969, 160.

(about  $1 \text{ rev h}^{-1}$ ) so that the specimen is immersed in the solution for approximately half the time and exposed to the atmosphere for the remaining time. An electric lamp is placed above the tank so that the specimens remain wet for a time after withdrawal from the solution, but are completely dried during the cycle. Measurement of the potentials of the specimens at the beginning and end of the immersion period is effected by means of the commutators, which are attached to the spindle but electrically insulated from it, and a reference electrode. The e.m.f. taken from the terminals can be fed to a multipoint recorder so that a recording of the  $E$ -time relationship may be obtained for each specimen. The solution can be made to circulate slowly by allowing it to drip from a feed and overflow via a siphon. In a variation of the apparatus, a Luggin capillary is attached to the sample so that the potentials can be measured during the period when the specimen has emerged from the solution but is still wet.

Figure 14 shows results obtained from the apparatus for different steels some of which (nos. 1, 2, 3, and 7) form a protective patina for corrosion products, while others (nos. 4, 5, and 6) form patinas that are nonprotective; the criterion adopted is that the more positive the potential the more protective is the rust patina.<sup>179</sup>

Legault *et al.*<sup>180,181</sup> have used open-circuit potential versus time measurements and cathodic reduction of rust patinas for the rapid laboratory evaluation of the performance of low-alloy weathering steels. The steel specimens are first exposed for 48 h to the vapor of an  $0.001 \text{ mol dm}^{-3}$  sodium bisulfite solution maintained at  $54^\circ\text{C}$  (humid  $\text{SO}_2$ -containing atmosphere) to stimulate corrosion under atmospheric conditions. They are then subjected to two types of test: (a) open-circuit potential-time tests for periods up to 3000 s in either distilled



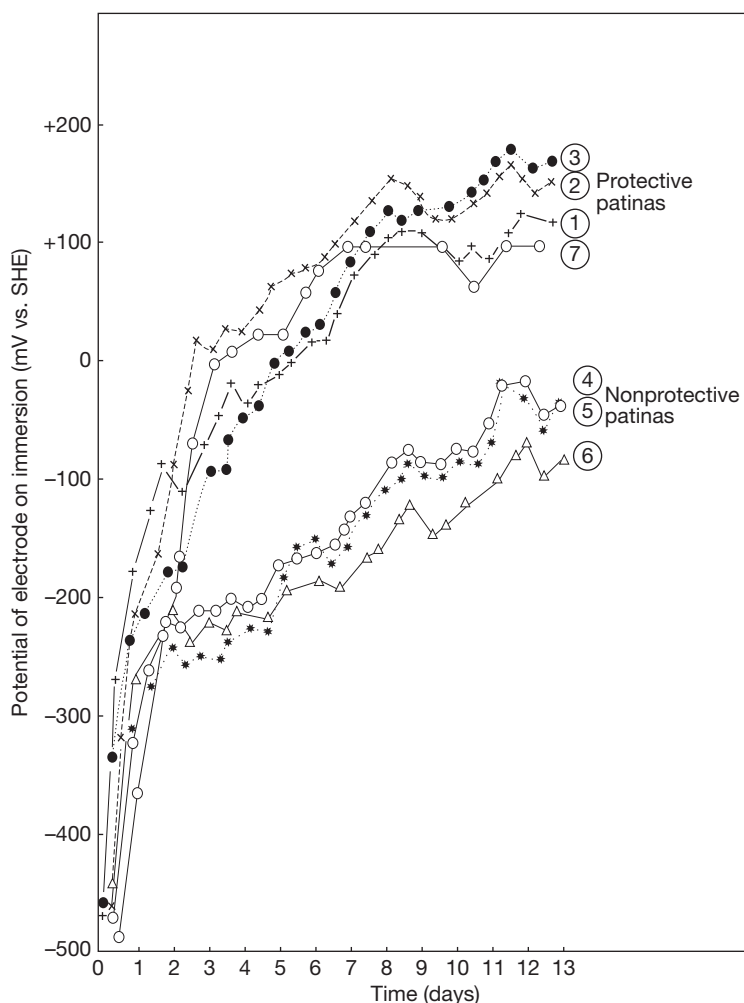


**Figure 14** Relationship between potential (determined during initial immersion using the equipment in **Figure 13**) and time for steels that form protective (1, 2, 3, 7) or nonprotective (4, 5, 6) patinas. Reproduced from Pourbaix, M. CEBELCOR RT; 1969, 160.

water or  $0.1 \text{ mol dm}^{-3} \text{ Na}_2\text{SO}_4$  and (b) cathodic reduction in  $0.1 \text{ mol dm}^{-3} \text{ Na}_2\text{SO}_4$  at  $1 \text{ mA cm}^{-2} \text{ c.d.}$  In the cathodic reduction experiments, which provide a means of evaluating the degree of rusting,<sup>182</sup> both the potential and time are recorded, the onset of hydrogen evolution at constant potential being taken as the end point and giving the oxide-reduction time.

In order to evaluate the tests, determinations were carried out on the steels that had been exposed to the atmosphere for 1, 2, 3, 4, and 6-month periods. It was established that the initial open-circuit potential and the decrease in potential (more negative) with time varied with the nature of the steel and the time of exposure to the atmosphere, and the maximum negative potential was taken as a measure of corrosion

resistance; the more negative the potential the lower the resistance of the alloy. In the case of three alloy steels that differed only in copper content it was found that the open-circuit potential was related to the corrosion rate as assessed by conventional weight loss.

A relationship was also established between the oxide-reduction time and time of exposure, and the results for a mild steel and a 1Cu–3Ni weathering steel were similar to those obtained by mass loss. The authors give various expressions that relate oxide-reduction time (min) with corrosion rate ( $\text{mm year}^{-1}$ ), and claim that a short exposure to a laboratory  $\text{SO}_2$  atmosphere followed by determining the  $E$  versus time and oxide-reduction time provides a rapid method of evaluating weathering steels.

### 2.34.10 Intergranular Attack of Cr-Ni-Fe Alloys

Early in the history of stainless steels it was recognized that they were highly susceptible to intergranular attack resulting from the precipitation of Cr-Fe carbides with the consequent depletion in the chromium content at grain boundaries when the alloy was heated in a specific range of temperature. It was necessary, therefore, to develop methods of testing that would detect susceptibility to intergranular attack as influenced by variations in processing and/or composition. As will be seen, most reagents used for these tests are highly aggressive, and it is important to note that an alloy found to be susceptible during testing will not necessarily be attacked intergranularly under the milder environmental conditions that may prevail in service.

Brown<sup>183</sup> has pointed out that Du Pont used evaluation tests for (a) as-received unstabilized alloys containing more than 0.03% C to check the effectiveness of the final heat treatment and (b) stabilized or special low-carbon grades after a sensitizing treatment (1 h at 677°C) to determine whether susceptibility might develop during a subsequent welding operation.

Intergranular corrosion of Fe-Ni-Cr alloys has been the subject of a comprehensive review by Cowan and Tedmon<sup>184</sup> who summarized the various tests used for determining susceptibility (Table 3).

Of these tests, nos. 1-5, which are regarded as reliable test procedures by the ASTM, have been incorporated into ASTM A 262 'Standard Practices for Detecting Susceptibility to Intergranular Attack in Austenitic Stainless Steels' as follows:

Practice A – 10% oxalic acid, electrolytic etching at ambient temperatures;

Practice B – Boiling 50%  $\text{H}_2\text{SO}_4$  + 25 g  $\text{l}^{-1}$   $\text{Fe}_2(\text{SO}_4)_3$ ;

Practice C – Boiling  $\text{HNO}_3$ ;

Practice D – 10%  $\text{HNO}_3$  + 3% HF at 70°C;

Practice E – Boiling 16 wt%  $\text{H}_2\text{SO}_4$  + 5.7%  $\text{CuSO}_4$  + metallic copper.

It should be noted that although ASTM A 262 provides details of test procedures, no information is given on typical corrosion rates or acceptable limits for various heat-treated alloys, which are regarded as outside the province of a specification that describes test procedures. Table 4, taken from a paper by Brown,<sup>183</sup> shows the maximum acceptable evaluation test rates specified by the Du Pont Company for various alloys

tested by the acid ferric sulfate test and by the Huey test. It should be noted that evaluation tests are specified by Du Pont when it is known or suspected that the environmental conditions in service are conducive to intergranular attack of susceptible material.

All the reagents used in Practice B to E have a high redox potential and Cowan and Tedmon<sup>184</sup> have presented schematic  $E$ -log  $i$  curves (Figure 15) showing the range of potentials of the various tests and the relative rates of attack on the matrix (Fe-18Cr-10Ni) and the chromium-depleted alloy at the grains boundaries, which has been assumed for this purpose to have a composition Fe-10Cr-10Ni, in a hot reducing acid. Although this diagram cannot show the effect of alloy composition, nature of test solution, conditions of test, etc. on intergranular attack, it serves to illustrate the electrochemical principles involved in the test procedures, all of which are based on reagents that attack the intergranular sensitized areas at a higher rate than the matrix; this may lead to the dislodgement of whole grains with a consequent high mass loss.

#### 2.34.10.1 Boiling $\text{HNO}_3$ Test

This test, which is commonly referred to as the Huey test, was first described and used by Huey<sup>185</sup> in 1930, and since that time it has had wide application, particularly in the United States. The test consists of exposing the specimens (20–30  $\text{cm}^2$ ) to fresh boiling 65%  $\text{HNO}_3$  (constant boiling mixture) for five successive periods of 48 h each under a reflux condenser. The specimens are cleaned and weighed after each period, and the corrosion rate (as a rate of penetration) is calculated for each period of test and for the average over the five periods; corrosion rates are expressed as millimeter per year. The reason for this procedure is the fact that Cr(VI) ions, produced from the oxidation of  $\text{Cr}^{2+}$  and  $\text{Cr}^{3+}$  by the  $\text{HNO}_3$ , if allowed to accumulate in the  $\text{HNO}_3$  markedly increase its aggressiveness so that severe intergranular attack with grain dislodgement can occur even with solution-annealed steel free from precipitated carbides; hence, the necessity for the periodic changing of the solution and for a minimum ratio of solution volume to area of specimen (at least 20 ml  $\text{HNO}_3/\text{cm}^2$  of stainless steel). Brown<sup>183</sup> points out that during a normal test the Cr(VI) content will not reach a level where an acceleration in rate occurs unless the specimen is in the sensitized condition, and under these circumstances the presence of Cr(VI) is an advantage in discriminating between sensitized and unsensitized material.

**Table 3** Summary of chemical tests used for the determination of susceptibility to intergranular corrosion of iron–nickel–chromium alloys (Data from Cowan and Tedmon)

Test name	Usual solution composition	Test procedure	Quantitative measure	Potential range (V vs. SHE)	Species selectivity attacked
1. Nitric acid test <sup>a</sup>	65 wt% HNO <sub>3</sub>	Five 48-h exposures to boiling solution; refreshed after period	Average mass loss per unit area of five testing periods	+0.99 to +1.20	1. Chromium-depleted areas 2. $\sigma$ -phase 3. Chromium carbide
2. Acid ferric sulfate (Streichet) test <sup>b,c</sup>	50 wt% H <sub>2</sub> SO <sub>4</sub> + 25 g l <sup>-1</sup> ferric sulfate	120 h exposure to boiling solution	Mass loss per unit area	+0.7 to +0.9	1. Chromium-depleted areas 2. $\sigma$ -phase in some alloys
3. Acid copper sulfate test <sup>b,d</sup>	16 wt% H <sub>2</sub> SO <sub>4</sub> + 100 g l <sup>-1</sup> CuSO <sub>4</sub> (+ metallic copper)	72 h exposure to boiling solution	1. Appearance of sample upon bending 2. Electrical resistivity change 3. Change in tensile properties	+0.30 to +0.58	Chromium-depleted area
4. Oxalic acid etch <sup>b</sup>	100 g H <sub>2</sub> C <sub>2</sub> O <sub>4</sub> ·2H <sub>2</sub> O + 900 ml H <sub>2</sub> O	Anodically etched at 1 A/cm <sup>2</sup> for 1.5 min	1. Geometry of attack on polished surface at $\times 250$ or $\times 500$	+1.70 to +2.00 or greater	Various carbides
5. Nitric-hydrofluoric acid test <sup>e</sup>	10% HNO <sub>3</sub> + 3% HF	4 h exposure to 70 °C solution	Comparison of ratio of mass loss of laboratory annealed and as-received samples of same material	Corrosion potential of 304 steel = +0.14 to +0.54	1. Chromium-depleted areas 2. Not for $\sigma$ -phase 3. Used only for Mo-bearing steels
6. Hydrochloric acid test <sup>e</sup>	10% HCl	24 h in boiling solution	1. Appearance of sample after bending around mandril 2. Mass loss per unit area	(a) Redox potential = +0.32 (b) Corrosion potential = $-0.2 \pm 0.1$	1. Alloy-depleted area 2. Not for $\sigma$ -phase
7. Nitric acid Cr <sup>6+</sup> test <sup>f</sup>	5N H <sub>2</sub> SO <sub>4</sub> + 0.5 N KCr <sub>2</sub> O <sub>2</sub>	Boiling with solution renewed every 2–4 h for up to 100 h	1. Mass loss per unit area 2. Electrical resistivity 3. Metaflographic examination	(a) Redox potential = +1.37 (b) Corrosion potential of 304 steel = +1.21	Solute segregation to grain boundaries

<sup>a</sup>Data after Cowan and Tedman.<sup>184</sup><sup>b</sup>A262-02a (2008) and Practice G 28-02 (2008).<sup>c</sup>M. A. Streicher, ASTM Bulletin No. 229, 77–86 (1958) G28-1985.<sup>d</sup>A262-02a (2008).<sup>e</sup>D. Warren, ASTM Bulletin No. 230, 45–56 (1958).<sup>f</sup>J. S. Armijo, *Corrosion*, **24** (1968).

Maximum corrosion rates used by Du Pont for various alloys are given in Table 4, and most users of the test consider average corrosion rates of 0.46–0.61 and 0.76 mm year<sup>-1</sup> to represent the upper limits for satisfactory resistance for wrought austenitic alloys and cast austenitic alloys, respectively. Streicher<sup>148</sup> considers that if the corrosion rate for each period increases over that for the previous period the alloy is susceptible.

The mechanism of the corrosion reaction is not clear, particularly in view of the changes in composition of the HNO<sub>3</sub> that take place during the 48 h period of the test. Streicher<sup>148</sup> reports that the corrosion potential of the steel ranges from 1.00 to 1.20 V (versus SHE) during the test owing to the accumulation of Cr(VI), and it can be seen from Figure 15 that the sensitized areas will have a higher corrosion rate than the matrix throughout this potential range, although they will become similar at the higher potentials. The high corrosion rates obtained in the test are due partly to intergranular attack and partly to the undermining and dislodgement of grains.

Stainless steels and Ni-base alloys containing Mo, such as Type 316L (0.03% C max.) and Hastelloy C, are found to give very high corrosion rates in the HNO<sub>3</sub> test even when they are immune to intergranular attack when subjected to other tests that reveal sensitization due to chromium-depleted zones; furthermore, such alloys even after being subjected to a

sensitizing heat-treatment do not give rise to intergranular attack in most conditions of service. This high corrosion rate is considered to be due to the formation of a submicroscopic  $\sigma$ -phase, and although positive proof is not available, its presence is substantiated by the fact that the phase becomes identifiable after longer periods of sensitizing temperatures, although in this form it has little effect on the corrosion rate. It would appear that the  $\sigma$ -phase dissolves rapidly during the HNO<sub>3</sub> test, and since it has a high chromium content, the solution becomes enriched in Cr(VI) with a consequent increase in the corrosion rate of the alloy. It follows that the test is unsuitable for evaluating the behavior of stainless steels that may precipitate  $\sigma$ -phase, unless the alloy is to be used in service for nitric acid plant.

Henthorne,<sup>186</sup> in considering the corrosion testing of weldments, points out that the test will also give high rates due to (a) end-grain attack, which is particularly prevalent in resulfurized or heavily cold-worked material and (b) dissolution of Ti(C, N) such as occurs in Type 321 weldments and leads to knife-line attack. Since most service conditions do not cause attack on the alloy in these conditions the test can be misleading.

Thus, under the circumstances already outlined, the test can be misleadingly severe, but it is

**Table 4** Maximum acceptable evaluation test rates specified by Du Pont for services where susceptible material would be intergranularly attacked

Type	Condition	Max. corrosion rate (mm year <sup>-1</sup> )
120 h acid Fe <sub>2</sub> (SO <sub>4</sub> ) <sub>3</sub> test (ASTM A.262, Practice B)		
304	As received	1.22
304L	20 min at 677 °C	1.22
316	As received	1.22
316L	20 min at 677 °C	1.22
317L	20 min at 677 °C	1.22
CF-8	As received	1.22
CF-8M	As received	1.22
240 h HNO <sub>3</sub> test (ASTM A-262, Practice C)		
304	As received	0.457
304L	20 min at 677 °C	0.305
304L	1 h at 677 °C	0.610
309S	As received	0.305
316	As received	0.457
347	1 h at 677 °C	0.610
CF-8	As received	0.610
CF-8M	As received	0.762

Source: Brown, M. H. *Corrosion* 1974, 30, 1.

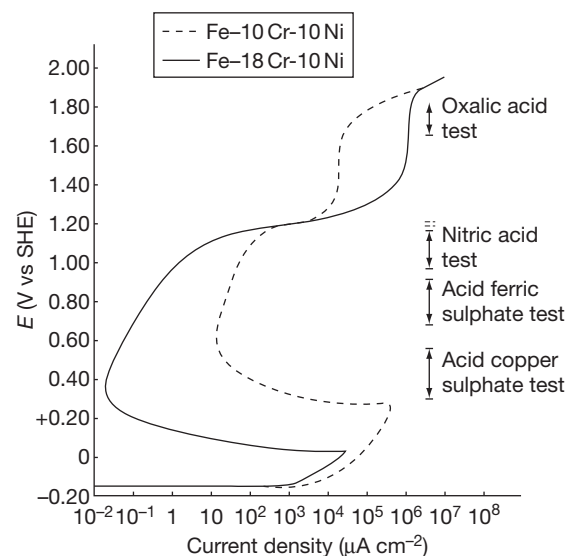


**Figure 15** Schematic representation of ranges of corrosion potential expected from various chemical tests for sensitization in relation to the anodic dissolution kinetics of parent (Fe-18Cr-10Ni) and grain boundary (assumed Fe-10Cr-10Ni) material in a hot, reducing acid. Reproduced from Cowan, R. L.; Tedmon, C. S., Jr. In Fontana, M. G., Staehle, R. W., Eds.; *Advances in Corrosion Science and Technology*; Plenum Press: New York, 1973; Vol. 3.

particularly valuable for evaluating alloys for use in  $\text{HNO}_3$  or in other strongly oxidizing acid solutions to ensure that they have received the correct heat treatment and have an appropriate composition, that is, a low carbon content or the correct ratio of (Ti or Nb)/C.

### 2.34.10.2 Boiling $\text{H}_2\text{SO}_4 + \text{CuSO}_4$ Tests

The use of boiling  $\text{H}_2\text{SO}_4 + \text{CuSO}_4$  for detecting intergranular sensitivity was first described by Strauss, *et al.*<sup>187</sup> in 1930, and is frequently referred to as the Strauss test, although the conditions of the test have been modified; whereas the Huey test is most widely used in the United States the Strauss test has been the preferred test in Europe. The test is mild compared to the Huey test and intergranular attack takes place with little grain dislodgement.

The use of metallic copper chips placed in contact with the steel to speed up the test and thus decrease the time of testing was first described by Rocha,<sup>188</sup> and subsequent work by Streicher<sup>148</sup> showed that its presence significantly increased the rate of intergranular attack even when it was not in contact with the steel. Approximate mass losses for a sensitized Type 316 stainless steel during a 240 h testing in boiling  $\text{H}_2\text{SO}_4 + \text{CuSO}_4$  are as follows:

- No metallic copper present  $0.1 \text{ g dm}^{-2}$ ;
- Metallic copper present but not in contact with the steel  $1.0 \text{ g dm}^{-2}$ ;
- Metallic copper in contact with steel  $4.0 \text{ g dm}^{-2}$ .

As used in Germany the composition of the solution is  $110 \text{ g CuSO}_4 \cdot 5\text{H}_2\text{O}$ ,  $100 \text{ ml H}_2\text{SO}_4$  (spec. grav. 1.84) and  $1 \text{ l}$  of water, the test being conducted for  $168 \text{ h}$  in the boiling solution. The ASTM Tentative Procedure A393–63T specified a similar composition containing  $100 \text{ g CuSO}_4 \cdot 5\text{H}_2\text{O}$ ,  $100 \text{ ml H}_2\text{SO}_4$  (spec. grav. 1.84) with water added to make a total volume of  $1 \text{ l}$ . The test time was  $72 \text{ h}$ , and with the high carbon contents of the earlier steels this was adequate for detecting susceptibility. However, with the decrease in the carbon contents of stainless steels a more prolonged boiling time was found to be necessary, and Scharfstein and Eisenbrown<sup>189</sup> showed that a Type 304 stainless steel containing  $0.068\% \text{ C}$  would pass the  $72\text{-h}$  Strauss test even after a sensitizing treatment of up to  $4 \text{ h}$  at  $677^\circ\text{C}$ . For this reason, A393–63T has been discontinued and in ASTM A 262 Practice E, the specimens are placed in contact with metallic copper chips to increase the rate of intergranular attack.<sup>148,183</sup> This test is of comparable

sensitivity to the other tests, and is far more discriminating than the older tentative standard; furthermore, it is more severe so that the testing time is decreased from  $72$  to  $24 \text{ h}$ . This test has been incorporated in the international standard ISO 3651–2.

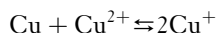
Figure 15 shows that the corrosion potential of stainless steel in the  $\text{H}_2\text{SO}_4 + \text{CuSO}_4$  test lies in the range  $0.30\text{--}0.58 \text{ V}$ , and that while the corrosion rate of the unsensitized alloy is approximately  $10^{-1} \mu\text{A cm}^{-2}$ , that of the sensitized material is  $10 \mu\text{A cm}^{-2}$ ; for heavily sensitized material the ratio of rates<sup>184</sup> of sensitized:unsensitized alloy may be as high as  $10^5:1$ . This large difference in rates leads to rapid attack, which is confined to the depleted zone having a thickness of the order of  $1 \mu\text{m}$ , and under these circumstances there will be little grain dislodgement. Thus, the mass change will be so small that it cannot be used as a criterion of susceptibility. For this reason assessment of intergranular attack is normally carried out (ASTM 262 Practice E) by bending the specimen around a mandrel through  $180^\circ$  and inspecting the bend surface for cracks. Measurements of changes in electrical resistivity<sup>146</sup> and in ultimate tensile strength<sup>190</sup> are used as quantitative methods of assessment, but according to Ebling and Scheil<sup>191</sup> they are not as discriminating as the qualitative bend test.

The  $\text{H}_2\text{SO}_4\text{--CuSO}_4$  test, unlike the Huey test, is specific for susceptibility due to chromium depletion and is unaffected by the presence of submicroscopic  $\sigma$ -phase in stainless steels containing molybdenum or carbide stabilizers. It can be used, therefore, with confidence to test susceptibility in austenitic (300 series) and ferritic (400 series) stainless steels and in duplex austenoferritic stainless steels such as Types 329 and 326.

The mechanism of the action of metallic copper was investigated by Streicher<sup>148</sup> who determined the potential of a Type 314 stainless steel, the redox potential of the solution (as indicated by a platinized-Pt electrode) and the potential of the copper. The actual measurements were made with a saturated calomel electrode, but the results reported below are with reference to SHE. In the absence of copper the corrosion potential of the stainless steel was  $0.58 \text{ V}$ , whereas the potential of the Pt electrode was approximately  $0.77 \text{ V}$ . When metallic copper was introduced into the solution (not in contact with the steel) both the corrosion potential of the steel and that of the Pt electrode attained the same high negative potential of  $0.37 \text{ V}$ , the copper attaining a steady value of  $0.30 \text{ V}$ . Finally, when the stainless steel was placed in contact with the copper it took up



a more negative potential of 0.30 V, the potential of the copper being unaffected. These potentials have been interpreted by Streicher and have been expressed in  $E$ - $I$  diagrams (Figure 16) showing how the corrosion potential and the corrosion rate varies with conditions of the test. Introduction of metallic copper into the solution results in the disproportionation reaction:



and the accumulation of the  $\text{Cu}^+$  ions in the solution produces a decrease in the polarization of the local anodes on the stainless steel, which are polarized to the redox potential of the solution (Figure 16). Contact of copper with the stainless steel results in a further decrease in the corrosion potential of the stainless steel to that of copper, indicating that cathodic polarization of the steel has occurred since the steel is the cathode of the stainless steel/copper bimetallic couple. Simultaneously, there is a reduction in the anodic polarization of the susceptible grain boundaries, and a consequent increase in the corrosion rate (Figure 16). Thus, contact of the steel with the copper results in intergranular attack of the steel at constant potential, the copper acting in the same way as a potentiostat.

The Huey test is widely used in the United States while the  $\text{H}_2\text{SO}_4$ - $\text{CuSO}_4$  test is preferred in the United Kingdom, with an increasing tendency to

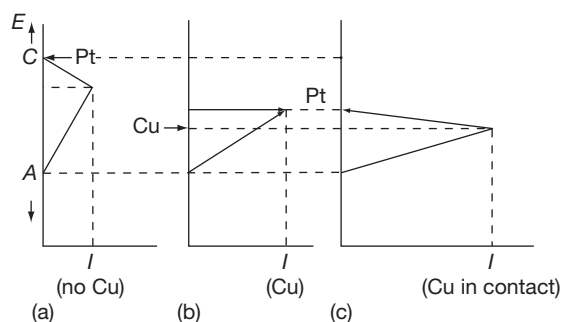


**Figure 16** Schematic  $E$ - $I$  diagrams of local cell action on stainless steel in  $\text{CuSO}_4 + \text{H}_2\text{SO}_4$  solutions showing the effects of metallic copper on corrosion rate. C and A are the open-circuit potentials of the local cathodic and anodic areas and  $I$  is the corrosion current. The potentials of platinized platinum and copper in the same solution are indicated by arrows. (a) Corrosion of stainless steel in isolation. (b) The rate when copper is introduced into the acid without contact with the steel. (c) The rate when copper contacts the steel. Reproduced from Streicher, M. A. *J. Electrochem. Soc.* 1959, 106, 161.

use the metallic copper variant. The  $\text{H}_2\text{SO}_4$ - $\text{CuSO}_4$ -Cu test procedure is given in BS EN ISO 3651-2.

### 2.34.10.3 $\text{HNO}_3$ -HF Test

This test was first described by Warren<sup>192</sup> in 1958, and consists of two 2-h periods in 10%  $\text{HNO}_3 + 3\%$  HF solution at 70 °C using fresh solution for each period. The test is therefore more rapid than the others, and it is specific for chromium depletion by carbide precipitation since it is unaffected by the submicroscopic  $\sigma$ -phase formed in molybdenum-bearing steels; as described in A262, its use is confined to Types 316, 316L, 317, and 317L stainless steels.<sup>183</sup> Since the corrosion rates of stainless steels in the acid are high and vary greatly from test to test, it is necessary to run two tests and to compare the corrosion rates of the specimen to be evaluated ('as received' for Types 316 and 317 and in the sensitized condition for Types 316L and 317L) and another laboratory-annealed specimen of the same alloy shown to be free from precipitated carbides by the step structure produced after electrolytic etching in oxalic acid. Intergranular attack is assessed by the rate of penetration evaluated from the mass loss, and if the mass loss of the specimen to be evaluated is greater than 1.5 times that of the standard, the former is considered to be susceptible.

The solution has a low redox potential and the corrosion potentials for austenitic stainless steels will be in the range 0.14–0.54 V, according to composition. Thus, it can be seen from Figure 15 that all but the highest chromium steels will be in the active region, so that the test relies on vigorous corrosion of the grain boundary zones while the matrix remains somewhat passive and corrodes at a slower rate.<sup>184</sup> Although the test gives constant and reliable results, it has not been used widely for routine evaluations for the following reasons: (a) the need to use a ratio of two test rates, (b) inconvenience of handling solution containing HF, and (c) the availability of the  $\text{H}_2\text{SO}_4 + \text{Fe}_2(\text{SO}_4)_3$  test.

### 2.34.10.4 $\text{H}_2\text{SO}_4 + \text{Fe}_2(\text{SO}_4)_3$ Test (Streicher Test)

This was described in 1959 by Streicher,<sup>148</sup> and consists of one period of exposure to a boiling solution of 50 mass%  $\text{H}_2\text{SO}_4 + 25 \text{ g l}^{-1} \text{ Fe}_2(\text{SO}_4)_3$  for 120 h, assessment being based on mass loss (see Table 4). Streicher, however, usually reports a ratio of mass

loss of sample to be assessed/weight loss of annealed sample, and as for the  $\text{HNO}_3$ –HF test considers that a ratio  $>1.5$ – $2.0$  indicates susceptibility; for Type 304 Streicher considers a rate  $>0.76 \text{ mm year}^{-1}$  to indicate susceptibility, but Brown considers a higher figure to be acceptable (see [Table 4](#)).

Accumulation of corrosion products does not stimulate attack and so several specimens may be tested in the same solution, but additional  $\text{Fe}_2(\text{SO}_4)_3$  may have to be added (or the solution changed) if there is considerable attack on severely sensitized specimens, as indicated by a color change of the solution from brown to dark green.

The redox potential of the solution is that of the  $\text{Fe}^{3+}/\text{Fe}^{2+}$  equilibrium and lies within the range  $0.80$ – $0.85 \text{ V}$  (versus SHE). The severe weight loss of susceptible alloys is due to undermining and grain dislodgement at the sensitized zones, which occurs at about twice the rate of that in the Huey test. Another difference is that while in the Huey test corrosion products  $[\text{Cr(VI)}]$  increase the rate by raising the potential of the alloy into the transpassive region, the converse applies in the acid ( $\text{Fe}_2(\text{SO}_4)_3$ ) test, since reduction of  $\text{Fe}^{3+}$  to  $\text{Fe}^{2+}$  during the test will result in a decrease in the redox potential and the whole sample will corrode with hydrogen evolution.

According to Cowan and Tedmon<sup>184</sup> the test can selectively attack some types of  $\sigma$ -phase. Those of Types 321 and 347 are readily attacked, whereas the molybdenum-bearing  $\sigma$ -phase of Type 316 is unattacked. The test will also show Hastelloys and Inconels to be susceptible to intergranular attack when there are either chromium- (or molybdenum-) depleted grain boundaries or grain-boundary  $\sigma$ -phase present. Ferritic (200 series) and austenoferritic stainless steels can also be tested for chromium-depletion sensitization in this reagent, but whether  $\sigma$ -phases formed in these alloys affect the test has not been established.

In conclusion it must be emphasized again that all the tests used are accelerated tests and only provide information on susceptibility to intergranular attack under the prevailing precise test conditions. They are quality control tests that may be used to demonstrate either that heat treatment has been carried out adequately or that a steel will withstand the test for a certain sensitizing heat treatment.

#### 2.34.10.5 Electrolytic Oxalic Acid Etching Test

This test, which was developed by Streicher,<sup>148</sup> is used as a preliminary screening test to be used

in conjunction with the more tedious testing procedures such as the boiling  $\text{HNO}_3$  test. The specimens are polished (3/0 grit paper) and then anodically polarized for  $1.5 \text{ min}$  at  $1 \text{ A cm}^{-2}$  at room temperature in a solution prepared by dissolving  $100 \text{ g}$  of  $\text{H}_2\text{C}_2\text{O}_4 \cdot 2\text{H}_2\text{O}$  in  $900 \text{ ml}$  of distilled water. The surface is then examined at about  $\times 500$  magnification and the structure is classified as ‘step,’ ‘ditch,’ or ‘dual’ (both ‘step’ and ‘ditch’). If the surface shows a ‘step’ structure it is immune to intergranular attack and no further testing is necessary; if the structure is ‘ditch,’ further testing by the Huey test or some other chemical test is necessary; if ‘dual’ further testing may be necessary. Thus, the test, by identifying structures that are immune to intergranular attack, eliminates unnecessary testing, although where a ‘ditch’ (or possibly a ‘dual’ structure) is obtained, final confirmation by the Huey test is essential. [Figure 17](#) shows the ‘ditch’ and ‘step’ structures diagrammatically, and [Figure 18](#) shows photomicrographs of these structures and a ‘dual’ structure.<sup>193</sup>

The test operates at a potential above  $2.00 \text{ V}$  (versus SHE), and the ‘ditch’ structure obtained with sensitized alloys must be due, therefore, to the high rate of dissolution of the sensitized areas as compared with the matrix. The ‘step’ structure is due to the different rates of dissolution of different crystal planes, and the ‘dual’ structure is obtained when chromium carbides are present at grain boundaries, but not as a continuous network.

#### 2.34.10.6 Electrochemical Tests

The difficulties associated with the ASTM ‘Standard Practices for Detecting Susceptibility to Intergranular Attack in Austenitic Stainless Steels’ (A 262) are that the methods are destructive and qualitative in nature. Early attempts to develop quantitative, non-destructive electro-chemical techniques to detect

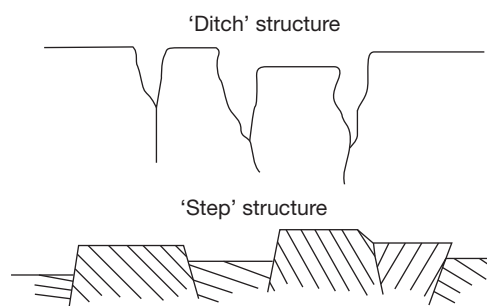


**Figure 17** ‘Ditch’ and ‘step’ structures. Reproduced from Streicher, M. A. J. *Electrochem. Soc.* **1959**, *106*, 161.

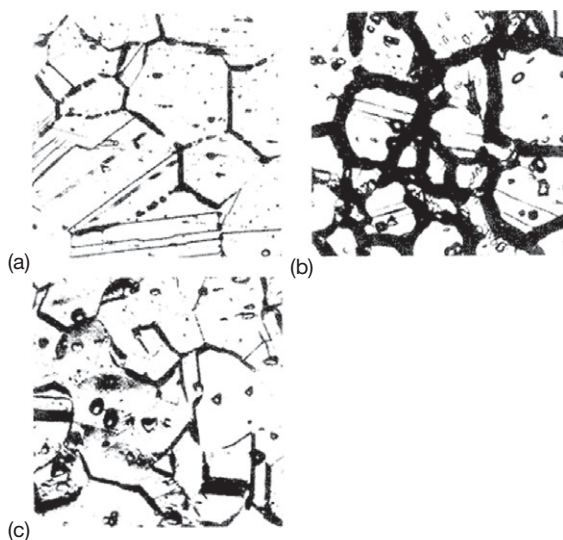


**Figure 18** Micrographs of (a) step, (b) ditch, and (c) dual structures. Reproduced from Streicher, M. A. *J. Electrochem. Soc.* **1959**, *106*, 161; Cowan, R. L.; Tedmon, C. S., Jr. In Fontana, M. G., Staehle, R. W., Eds.; *Advances in Corrosion Science and Technology*; Plenum Press: New York, 1973; Vol. 3.

sensitization by Clerbois *et al.*<sup>194</sup> employed potentiostatic techniques and it was observed that sensitized 18–8 stainless steel when anodically polarized potentiostatically in 1.0 mol dm<sup>-3</sup> H<sub>2</sub>SO<sub>4</sub> gave rise to a secondary active peak in the range 0.14–0.24 V (versus SHE) that was not present in the curve for the annealed alloys. This observation was criticized by France and Greene,<sup>195</sup> who consider that the active peak is due to the dissolution of Ni that had accumulated at the surface during active dissolution at lower potentials. Clerbois, *et al.*<sup>194</sup> also noted that if a sensitized sample is held at 0.14 V in 1.0 mol dm<sup>-3</sup> H<sub>2</sub>SO<sub>4</sub> for 24 h and then bent around a mandrel, it fissures and cracks, and it can be seen from Figure 15 that at this potential the chromium-depleted grain boundary will corrode actively, whereas the matrix will be passive. The potentiostatic test using cracking to detect susceptibility is thus analogous to the acid-copper sulfate test.

France and Greene<sup>195</sup> proposed that it should be possible to predict service performance by potentiostatic studies of steels in the environments encountered in practice coupled with metallographic examination of the surfaces. They argued that many environments do not selectively attack the grain boundaries of sensitized stainless steels so that the use of costly preventative measures is unnecessary. Since the intergranular attack of austenitic stainless

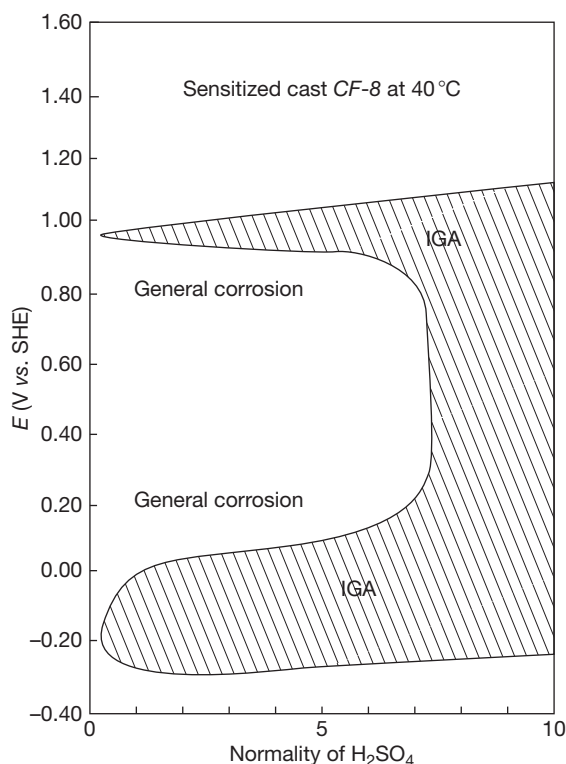


**Figure 19** Intergranular corrosion plot for a sensitized cast CF-8 stainless steel (0.08% max C 8–11% Ni 18–21% Cr) in H<sub>2</sub>SO<sub>4</sub> at 40°C as a function of potential and acid concentration. Reproduced from France, W. D.; Greene, N. D. *Corros. Sci.* **1968**, *8*, 9.

steels occurs only in limited potential regions it should be possible to predict service performance provided these regions are precisely characterized.

In their studies, specimens of different sensitized steels were held at various constant potentials in different concentrations of the acid under study at various temperatures and the surfaces were then examined metallographically for intergranular attack. Data obtained in this way enabled E-concentration of acid diagrams to be produced showing the zones of general corrosion, fine intergranular corrosion and coarse intergranular corrosion for a given sensitized stainless steel in a given acid at various constant temperatures (Figure 19).

Streicher,<sup>196</sup> however, considered this approach to be unsound and pointed out that the short duration of the potentiostatic studies carried out by France and Greene cannot be used to predict long-term behavior in service. The prolonged dialogue between these workers<sup>197,198</sup> was well summarized in the review article by Cowan and Tedmon<sup>184</sup> who concluded that these particular potentiostatic tests cannot be

regarded as accelerated tests for service environments and that predicting future industrial service for periods longer than the test is not advisable.

### 2.34.10.7 EPR Test

The electrochemical potentiokinetic reactivation (EPR) test was proposed by Cihal *et al.*<sup>199</sup> and developed by Novak and others<sup>200–202</sup> as a fast, quantitative and nondestructive technique for establishing the degree of sensitization of austenitic stainless steels.

The test is accomplished by a potentiodynamic sweep from the passive to the active regions of electrochemical potential (a process referred to as reactivation) for a given alloy in a specific electrolyte, during which the amount of current resulting from the corrosion of the chromium-depleted regions surrounding the precipitated chromium carbide particles is measured. In a sensitized microstructure, the bulk of these particles are located at the grain boundaries and are particularly susceptible to corrosion in oxidizing acids. Proposed national and international standards on EPR testing specify 0.5 M H<sub>2</sub>SO<sub>4</sub> + 0.01 M KSCN at 30°C as the EPR test environment for sensitized austenitic stainless steels.

Three different forms of EPR test can be employed, designated as the single loop, double loop and reactivation ratio methods in Figure 20.

#### 2.34.10.7.1 Single loop EPR test

The single loop method requires the sample to be polished to a 1 μm finish and then passivated at +200 mV (SCE) for 2 min following which the potential is decreased at 1.67 mV s<sup>-1</sup> until the corrosion potential of approximately -400 mV (SCE) is reached. The reactivation process results in the preferential breakdown of the passive film in the chromium-depleted grain boundaries of sensitized material and an increase in the current through the cell. The area under the *E* versus log *I* curve (Figure 20a) is proportional to the electric charge, *Q*, measured during the reactivation process. On nonsensitized materials, the current density during the reactivation step is very low because the passive film remains essentially intact. A measure of the degree of sensitization is obtained by calculating the normalized charge, *P<sub>a</sub>*, where:

$$P_a(C\ m^{-2}) = Q/A$$

where *Q* = integrated charge during the reactivation scan, and *A* = grain boundary area ( $5.1 \times 10^{-3}$  exp

0.35 *G*, where *G* is the ASTM grain size at 100 × magnification).

Pitting caused by the dissolution of nonmetallic inclusions can increase the *P<sub>a</sub>* value. Consequently, the microstructures of specimens with a high *P<sub>a</sub>* value must be examined to identify the source of the elevated value. In general, *P<sub>a</sub>* values below 0.10 are characteristic of unsensitized microstructures, while sensitization is indicated if *P<sub>a</sub>* exceeds 0.4. Single loop tests are sensitive to mild degrees of sensitization but do not readily distinguish between medium and severely sensitized materials.

#### 2.34.10.7.2 Double loop EPR test

Details of this procedure are given in Japanese Industrial Standard JIS G 0580. The sample is ground to a 100 grit finish then placed in the test solution for about 2 min to establish the rest potential (about -400 mV (SCE) for AISI Types 304 and 304L stainless steel).

The sequence of polarization steps is shown in Figure 20b. The surface is first polarized anodically from the corrosion potential to +300 mV (SCE) at a rate of 1.67 mV s<sup>-1</sup>. As soon as this potential is reached, the scanning direction is reversed and the potential is decreased at the same rate to the corrosion potential. The ratio of the maximum current in the reactivation loop, *I<sub>r</sub>*, to that in the larger anodic loop, *I<sub>a</sub>*, is used as a measure of the degree of sensitization.

#### 2.34.10.7.3 Reactivation ratio EPR test

##### Figure 20c)

This is a simpler and more rapid method than the single or double loop tests, and depends on the fact that the value of *I<sub>a</sub>* determined during the anodic scan of a double loop test (which produces general dissolution without intergranular attack on sensitized material) is essentially the same for all AISI Type 304 and 304L steels.

The specimen is ground to a 100 grit finish then, after 2 min at the corrosion potential (about -400 mV (SCE)), it is conditioned by a 2-min treatment at -230 mV (SCE) in order to eliminate the need for polishing prior to the reactivation procedure. Passivation is then accomplished at +200 mV (SCE) for 2 min after which the specimen is reactivated by scanning back to the corrosion potential at 1.67 mV s<sup>-1</sup>. During this reactivation scan, the maximum current, *I<sub>r</sub>*, is measured and is divided by the surface area as an indication of the degree of sensitization.

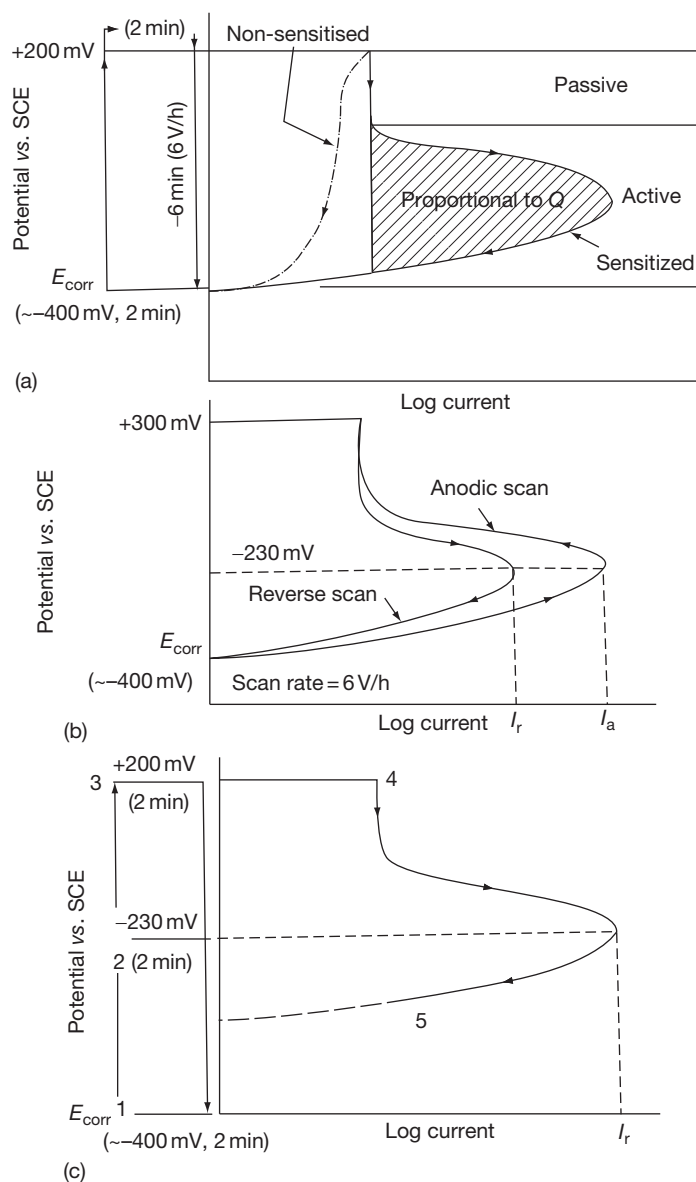


**Figure 20** Schematics of reactivation polarisation curves. (a) Single loop EPR test method, and (b) double loop EPR test method, and (c) reactivation ratio EPR test method.

### 2.34.10.8 EPR Tests for Ferritic Stainless Steels

Lee<sup>203</sup> has demonstrated that in slightly modified forms the single loop EPR test can be used to quantify the degree of sensitization in ferritic stainless steels. For AISI Types 430, 430Ti, 430Nb, and 446 stainless steels, the test consists of passivating the specimen in deaerated 3 N  $\text{H}_2\text{SO}_4$  solution at 30 °C at +400 mV (SCE) for 10 min, followed by a reactivation at a scan rate of 250  $\text{mV min}^{-1}$ . The EPR test for AISI Type 434 stainless steel requires a

reactivating scan rate of 150  $\text{mV min}^{-1}$  (the other test conditions remaining unchanged). For AISI Type 444 stainless steel, the test is conducted in deaerated 5 N  $\text{H}_2\text{SO}_4$  solution at 30 °C and involves passivation at +400 mV (SCE) for 2 min followed by a reactivation at a scan rate of 100  $\text{mV min}^{-1}$ .

### 2.34.11 Crevice Corrosion and Pitting

Crevice corrosion and pitting are dealt with in some detail elsewhere, and it is not appropriate here to



discuss the nature of the phenomena nor the methods that have been used to determine the mechanisms of these forms of localized attack. However, it should be noted that many of the methods of testing follow directly from the concepts such as  $E_b$  (the critical pitting potential),  $E_p$  (the protection potential) have been investigated by a number of workers as possible criteria for the resistance of metals and alloys to pitting and crevice corrosion in service. It should also be noted that since crevice corrosion and pitting have similar mechanisms and since the presence of a crevice is conducive to pitting of alloys that have a propensity, to this form of attack, it is appropriate to consider them under the same heading. (Editor's note: A group of tests that have gained favor in recent years are based on the observation that, providing the solution is sufficiently oxidizing (or, equivalently, the potential is held at a suitably positive value), there is a critical temperature below which pitting will not occur, and a (more negative) critical temperature below which crevice corrosion will not occur. These are known as the critical pitting temperature (CPT) and critical crevice temperature (CCT), respectively, and the higher the temperature, the greater the resistance to pitting or crevice corrosion. There are various methods of measuring these temperatures (see ISO 17864, ASTM G 48, and G 150).)

In general, the tests may be classified as follows:

1. Laboratory tests, in which the specimen is immersed in a solution conducive to pitting, such as an acidified  $\text{FeCl}_3$  solution (redox potential above the critical pitting potential  $E_b$ ).
2. Laboratory tests, in which the specimen is anodically polarized in a chloride-containing solution to evaluate  $E_b$  and  $E_p$ .
3. Field tests, in which the specimen (with or without a crevice) is exposed to the environment that it will encounter in service.

As far as tests for crevice corrosion are concerned, all that is required is a geometrical configuration that simulates a crevice, which may be achieved in a variety of ways using either the metal itself or the metal and a nonmetallic material. Streicher<sup>204</sup> studied the crevice corrosion of Cr–Ni–Fe alloys, in which two plastic cylinders are held on the two opposite faces of a sheet metal specimen by two rubber bands, thus providing three different types of crevice in duplicate. A simple method of testing for crevice corrosion produced by contact with different materials is to use a horizontal strip of the metal under study and place on its upper surface at

intervals small piles of sand, small piles of sludge, pieces of gasket material, rubber, etc. More precise crevices can be produced by bolting together two discs of the metal, which are machined on the facing surfaces so that there is a flat central portion followed by a taper to the periphery of the disc, the flat central portion providing a very fine crevice and the tapered portion a coarser one.<sup>205</sup>

Figure 21 shows the types of crevices used by Wilde<sup>206</sup> for studying crevice corrosion and pitting of Cr–Ni–Fe alloys in the laboratory and in the field. Types 1 and 5 were used for anodic polarization studies in nitrogen-saturated  $1 \text{ mol dm}^{-3}$  NaCl and in aerated 3.5 wt% NaCl, respectively, and it can be seen that attachment to the conducting lead is by means of a Stern-Makrides pressure gasket; Types 3 and 4 were used for field tests in seawater for periods up to 4½ years; Type 2 was used for laboratory studies in which the specimens were immersed in acidified  $\text{FeCl}_3$  ( $108 \text{ g l}^{-1}$   $\text{FeCl}_3 \cdot 6\text{H}_2\text{O}$  with the pH adjusted to 0.9 with HCl).

The value of electrochemical evaluation of the critical pitting potential as a rapid method of determining pitting propensity is controversial. France and Greene<sup>207</sup> studied the pitting of a ferritic steel (Type 430) using a controlled potential test in 1 M NaCl and a conventional immersion test in oxygen-saturated 1 M NaCl but found that at the same potential ( $-0.17$  to  $0.09 \text{ V}$  versus SCE) the corrosion rates were  $390$  and  $5.2 \text{ mm year}^{-1}$ , respectively. Similar studies were carried out on Zr using  $0.5 \text{ M H}_2\text{SO}_4 + 1 \text{ M NaCl}$  for the controlled potential test and  $0.5 \text{ M H}_2\text{SO}_4 + \text{FeCl}_3 \cdot 6\text{H}_2\text{O}$  for the immersion test, and again the former gave a much higher corrosion rate than the latter. France and Greene conclude that these two types of test give rise to significantly different results under identical test conditions. To explain the results obtained with the ferritic stainless steel, they pointed out that, during the controlled potential test, the anodic reaction occurs at the metal's surface whereas the interdependent cathodic reaction takes place at the counter-electrode. Under these circumstances, the metal ions produced anodically result in increased migration of  $\text{Cl}^-$  to maintain electro-neutrality, and this in turn results in a higher concentration of  $\text{Cl}^-$  at the metal–solution interface with consequent increase in the rate of pitting. A similar situation does not arise during the immersion test where the anodic and cathodic sites are in close proximity, and charge balance is maintained without the migration of  $\text{Cl}^-$  from the bulk solution.

Potentiostatic tests<sup>208–210</sup> have been used, and Wilde and Williams<sup>208</sup> in potentiokinetic studies of

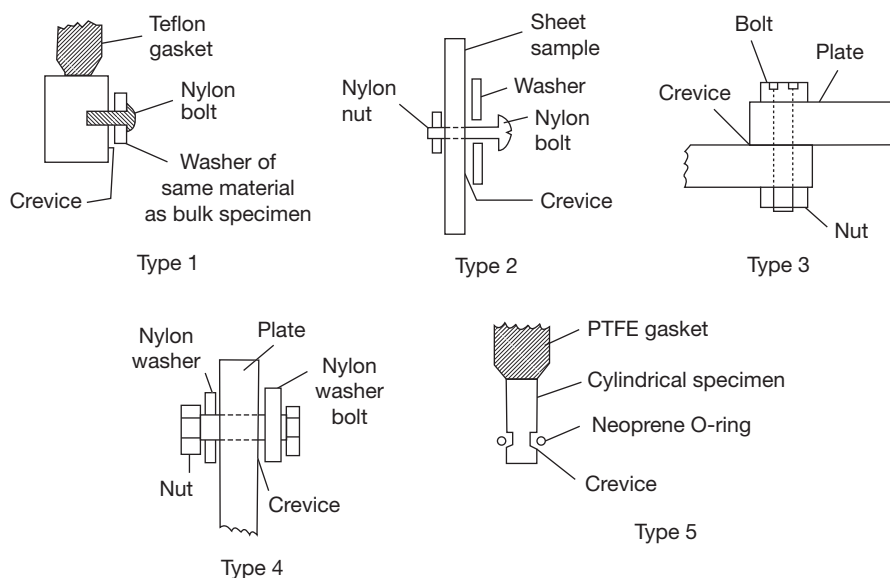


**Figure 21** Various types of crevices used for investigating crevice corrosion of stainless steels. Reproduced from Wilde, B. E. *Corrosion* **1972**, 28, 283.

the critical breakdown potential of stainless steels (Types 430 and 304) in 1.0 M NaCl showed that the nature of the gas used to purge the solution has a pronounced effect on the value of  $E_b$  (Table 5). In particular, they have established that the presence of dissolved  $O_2$  enhances passivity thus causing  $E_b$  to become more positive, and consider that this explains the failure of France and Greene to obtain accord between controlled potential tests in hydrogen-saturated chloride solutions and immersion tests in oxygenated chloride solutions at the same potentials.

Wilde and Williams<sup>208</sup> have used the redox system  $0.1 \text{ M } \text{Fe}(\text{CN})_3^{6-}/\text{Fe}(\text{CN})_4^{6-}$  for their immersion tests, which for Type 403 stainless steel gives a corrosion potential of  $-0.100 \text{ V}$  (versus SCE); selection of this system was based on the premise that being large anions they would be less likely than dissolved  $O_2$  to be involved in the adsorption processes that stabilize the passive state. Pitting occurred within 60 s, and equivalent tests on the same alloy conducted potentiostatically at  $-0.1 \text{ V}$  (versus SCE) in hydrogen-saturated 1.0 M NaCl gave similar results. They conclude that these two tests give comparable results, but that extreme caution must be used in utilizing  $E_b$  as an index of pitting, since its value is dependent upon environmental variables and in particular the nature of the dissolved gas in the corrodent. Wilde and Williams<sup>211</sup> have also shown that the critical pitting potential can be used to predict the behavior of alloys

**Table 5** Variation in  $E_b$  (V) for stainless steels in 1.0 mol  $\text{dm}^{-3}$  NaCl at 25 °C with nature of dissolved gas ( $E_b$  vs. SCE)

Gas	Type 430 stainless steel	Type 304 stainless steel
Hydrogen	-0.185	-0.050
Nitrogen	-0.130	-0.020
Argon	-0.100	+0.050
Oxygen	-0.035	+0.065

Data after Wilde and Williams<sup>208</sup>

exposed for long periods to seawater or to industrial chemical environments.

In a subsequent paper, Wilde<sup>206</sup> pointed out that although  $E_b$  is qualitatively related to resistance of a material to breakdown of passivity and pit initiation, it is of questionable value in predicting performance when crevices are present. Wilde found that although the Fe-30Cr-3Mo alloy appeared to indicate total immunity to breakdown when tested anodically in 1 M NaCl and in the freely corroding condition in 10%  $\text{FeCl}_3$ , it pitted within the crevice when an artificial crevice was present. Exposure in seawater for a 16-month period showed that AISI Types 304 and 316 stainless steels and the Fe-30Cr-3Mo alloy all pitted to the same extent when a crevice was present, although the former two alloys are considered to be less resistant to pitting than the Fe-30Cr-3Mo alloy. Pourbaix *et al.* have defined the protection

potential  $E_p$  as the potential below which no pits can initiate and preexisting pits cannot propagate, since they are passive at that potential. However, Wilde, using cyclic potentiodynamic sweeps at varying sweep rates, has established that  $E_p$  is not a unique parameter and that it varies in a semilogarithmic manner with the extent of localized attack produced during the anodic polarization, that is,  $E_p$ -log(extent of pit propagation) is linear. Thus, at a sweep rate of  $10 \text{ V h}^{-1}$ ,  $E_p$  was found to be  $-0.290 \text{ V}$  (versus SCE) while it fell to a more negative value of  $-0.410 \text{ V}$  at the slower sweep rate of  $1 \text{ V h}^{-1}$ . This was explained by Wilde as being due to the chemical changes that occur in the growing pit by hydrolysis of corrosion products and by the increased migration of  $\text{Cl}^-$  ions. Since  $E_p$  is a variable that depends upon experimental procedures, it cannot be used on its own as a criterion for protection against the propagation of preexisting pits or crevices in an engineering structure. Wilde considers that a more useful parameter appears to be the 'difference potential' ( $E_b - E_p$ ), which is used as a rough measure of the hysteresis loop area produced during the cyclic determination of  $E_b$  and  $E_p$ . (Editor's note: The parameter  $E_b - E_p$  has recently formed the basis of a predictive model of localized corrosion of Alloy 22 for the storage of nuclear waste over periods of up to a million years.) The area of the hysteresis loop obtained in a potentiodynamic sweep using a specimen with an artificial crevice provides a measure of the resistance to crevice corrosion in service, that is, the greater the area the lower the resistance. **Figure 22** shows the linear relationship between the 'difference potential' and the mass losses of various stainless alloys containing an artificial crevice that have been exposed to seawater for  $4\frac{1}{2}$  years.

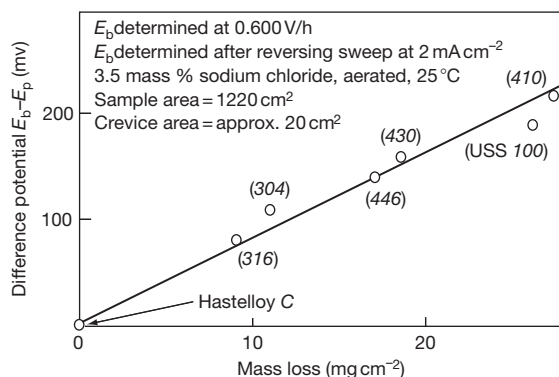


**Figure 22** Linear correlation between difference potential and mass loss of various stainless steels containing crevices exposed to seawater for 4.25 years. Reproduced from Wilde, B. E. *Corrosion* **1972**, 28, 283.

These considerations show that although considerable advances have been made in developing laboratory controlled potential tests for evaluating crevice corrosion and pitting, the results must be interpreted with caution.

Guidance on crevice corrosion testing of iron-base and nickel-base stainless alloys in seawater and other chloride-containing aqueous environments is given in ASTM G 78, while ASTM G 61 provides a standard test method for conducting cyclic potentiodynamic polarization measurements for localized corrosion susceptibility (i.e., pitting and crevice corrosion) of iron-, nickel-, and cobalt-based alloys. Guidance on the selection of procedures for the identification and examination of pitting corrosion to determine the extent of its effect is available in ASTM G 46.

### 2.34.12 Impingement Tests/Erosion Corrosion

The method most commonly used for testing condenser materials is the BNFMR May jet impingement test<sup>212</sup> in which small sections of tube, abraded to a standard finish, are immersed in seawater and subjected to an underwater jet of seawater containing air bubbles. However, at high velocities, cavitation can occur in the water box in this test. An alternative design has been described to overcome this.<sup>213</sup> Resistance to impingement attack is also assessed by the Brownsdon and Bannister test<sup>214</sup> in which a stream of air bubbles is directed onto the surface of the test specimens immersed in seawater or sodium chloride solution. Special tests for resistance to corrosion under localized heat transfer conditions (hot-spot corrosion) have been described by Breckon and Gilbert<sup>215</sup> and by Bem and Campbell,<sup>216</sup> but temperature effects are usually ignored when comparing condenser tube materials.

Campbell<sup>217</sup> points out that in evaluating condenser tube materials a test apparatus is required that will include all the principal hazards likely to be encountered in service and should thus cater for the following conditions: impingement, slow moving water, heat transfer, and shielded areas. Furthermore, the internal surfaces should not be abraded, as in the jet impingement test, but should be tested in the 'as-manufactured' condition, particularly in view of the deleterious effect of carbon films produced during manufacture. LaQue has pointed out the importance of specimen area in impingement tests.<sup>218</sup>

The general arrangement of the apparatus is shown in **Figure 23**. It accommodates 10 vertical

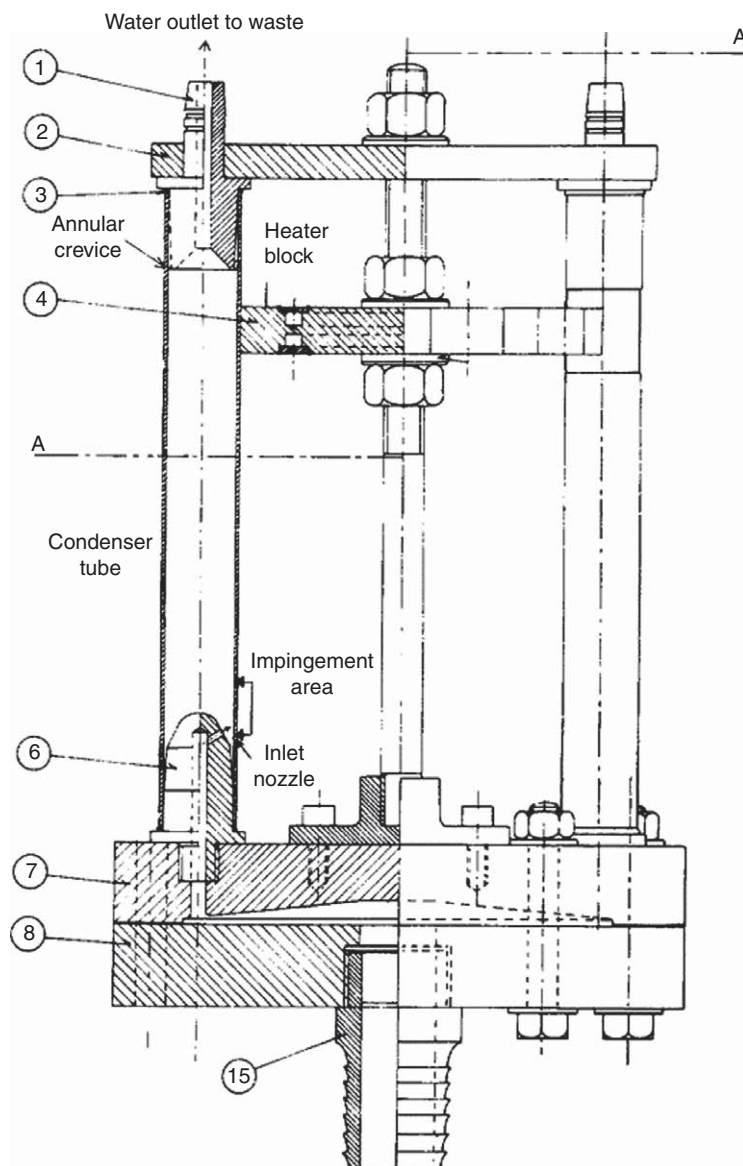


**Figure 23** Campbell test apparatus for determining the various forms of attack suffered by condenser tubes in service. Reproduced from Campbell, H. S. MP577, BNFMR, 1973.

200 mm lengths of condenser tube spaced equally around a 125-mm diameter circle. Water enters the bottom of each tube through an inlet nozzle (Part No. 6 in Figure 23) which fits inside the tube and also locates it. The nozzle has a 5-mm diameter blind hole up the center connecting with a 2.4-mm diameter hole, set at 45° to the vertical, through which the water emerges at a velocity of  $10 \text{ m s}^{-1}$  to impinge on the wall of the tube. The water then rises up through the tube at a mean velocity of  $0.1 \text{ m s}^{-1}$  (in a 22–24-mm diameter condenser tube) and leaves

through an outlet nozzle (Part No. 1) fitted into the top end of the tube. Half the length of each outlet nozzle has a 2° taper on the outside to provide a reproducible annular crevice between it and the inside of the condenser tube. Neoprene 'O'-rings (Part No. 3) provide seals between the tube and the top and bottom nozzles, and the tubes are held in place by a common clamping plate (Part No. 2) at the top. The 10 inlet nozzles are fed with water through a distributor (Part Nos. 7, 8, and 15) of the design used in the May jet impingement apparatus, which ensures equal

distribution of water between them. The distributor and nozzles are all of nonmetallic materials. The part of each test piece between 40 and 65 mm from the top is fine-machined externally to fit a semicircular notch in a 15-mm thick brass heater block (Part No. 4), the tubes being held in contact with the block by a circumferential clip to ensure efficient and equal heat transfer between the block and each tube. The diameter of the inlet and outlet nozzles and that of the semicircular notches in the heater block are made to suit the size of condenser tube to be tested.

The common heater block shown in [Figure 23](#) can itself be subject to corrosion leading to different heat transfer conditions for different tubes, and in some later versions of the apparatus, individual short heating jackets are used for each tube, which are heated with oil from either a steam-heated or electrically heated heat exchanger. This modification not only avoids corrosion problems but also obviates the necessity to machine a length of the outside of each tube to fit the semicircular notches in the single heater block. The oil flow is adjusted to give an oil temperature of 95 °C at each outlet.

The test usually lasts 8 weeks, after which the tubes are sectioned longitudinally and their interiors inspected for accumulated deposits. Loose deposits are then removed by washing in water and the internal surfaces are examined for impingement attack, pitting and blistering or flaking of the corrosion-product film, using a low-power binocular microscope. After cleaning the section in 10% H<sub>2</sub>SO<sub>4</sub>, the depth of impingement attack, pitting, or other localized corrosion, is determined. Observations and measurements are recorded for each of the following five areas of the section: (a) impingement area opposite the inlet nozzle where water velocity and turbulence are greatest, (b) the slow-moving cold water area from the impingement area upward to the heated area, (c) the heated area including the heat-transfer area itself and the warm-water area above, and (d) the two annular crevices formed between the tapered portions of the cold-water inlet and warm-water outlet nozzles and the tube wall.

The Campbell apparatus is cheap to construct and easy to use and can be installed on site to assist the selection of condenser or heat-exchanger tube materials, or to monitor changes in the corrosivity of the cooling water. The information that it provides on the various forms of attack is more comprehensive than that of any other existing apparatus for corrosion testing condenser tubes, and it is therefore particularly suitable also for assessing new materials or the effect of surface conditions arising from changes in manufacture.

Impingement and erosion–corrosion forms of attack will usually be intensified by the presence of solid particles in the fluid. Variations of the jet test have been proposed to take this effect into account.<sup>219</sup>

Test equipment for the study of erosion–corrosion by liquids with sand content, as met in formation waters in oil and gas production, has been described by Kohley and Heitz.<sup>220</sup>

### 2.34.13 Corrosion Fatigue

The simultaneous action of alternating stresses and corrosion usually has a greater effect than when either is operating separately, and in this respect corrosion fatigue is analogous to stress–corrosion cracking. The important factors in corrosion fatigue include the following:

1. environmental conditions;
2. magnitude of the alternating stress;
3. magnitude of mean stress;
4. frequency of reversal of the stress;
5. load-versus-time waveform;
6. characteristics of the metal.

Depending on the intended purpose, corrosion fatigue tests can be conducted on smooth, notched or precracked specimens as well as on components and parts joined by welding. Because of the time-dependent nature of corrosion processes, it is essential that the mechanical variables employed during corrosion fatigue testing, including cyclic frequency and load-versus-time waveform, as well as the chemical and electrochemical conditions, are relevant to the intended application. For example, it is unlikely that data generated in a laboratory test at a frequency of 10 Hz would be applicable for predicting corrosion fatigue behavior in a structure that is cycled at 0.1 Hz.

Laboratory corrosion fatigue tests can be classified as either cycles to failure (crack initiation) or crack propagation tests.<sup>221</sup> Cycles to failure tests employ plain or notched specimens to provide data on the intrinsic corrosion fatigue crack initiation behavior of a metal or alloy. Crack propagation tests use precracked specimens to provide information on the threshold conditions for the propagation of preexisting defects by corrosion fatigue and on the rates of corrosion fatigue crack growth.

It is often difficult to conduct laboratory tests in which both the environmental and stressing conditions approximate to those encountered in service.



This applies particularly to the corrosive conditions, since it is necessary to find a means of applying cyclic stresses that will also permit maintenance around the stressed areas of a corrosive environment in which the factors that influence the initiation and growth of corrosion fatigue cracks may be controlled. Among these factors are electrolyte species and concentration, temperature, pressure, pH, flow rate, dissolved oxygen content, and potential (free corrosion potential or applied).

For tests on plain or notched specimens, a simple approach can be to use a conventional Wöhler rotating cantilever beam modified so as to permit the specimen to be brought into contact with the corrodent. This may be achieved by surrounding the specimen with a cell through which the corrosive solution is circulated or by applying it by a pad,<sup>222</sup> wick,<sup>223</sup> or drip feed.<sup>224</sup> Four-point loading or push-pull machines can be used in a similar way and have the advantage over the Wöhler machine when testing plain specimens that the length of the test-piece between the two points of loading is subjected to an approximately uniform stress.

Rawdon<sup>225</sup> used flat specimens that were subjected to repeated flexure while they were being immersed periodically in the corrosive solution. Kenyon<sup>226</sup> used a rotating wire specimen in the form of a loop, the upper part of which was attached to the motor while the lower part of the loop passed through the corrodent, and a somewhat similar device was developed by Haigh-Robertson and used in several studies.<sup>227,228</sup> Gough and Sopwith<sup>229,230</sup> used this machine in their studies, the corrodent being applied as a spray.

Figure 24 shows a slow fatigue machine<sup>231</sup> that has been developed to study the performance of welded butt and fillet joints for steels used in the construction of North Sea oil drilling rigs; the bending stress and frequency have been selected to simulate the forces produced by the wave motion. The specimens,  $1500 \times 100 \times 12.5$  mm with the weld 25 cm from the base, are clamped at the lower end, and the stress is applied as a variable bending moment at the upper end by rams. The rams, which are attached to a sliding frame, are activated by a pneumatic cylinder that can be automatically programmed for stroke and frequency and the stress level is monitored by strain gauges. The stress range is up to 300 MPa, and the frequency can be varied from 0.5 to 0.05 Hz. The corrodent is artificial seawater, and provision is made for studying the effect of cathodic protection by means of Zn anodes.

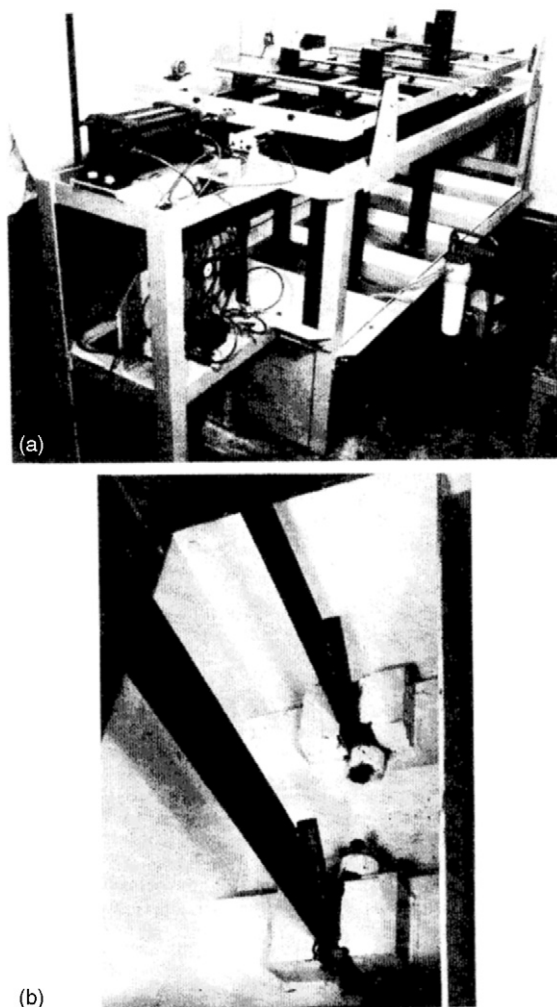


**Figure 24** (a) Rig for the laboratory study of corrosion fatigue of welded joints in seawater and (b) view of the test pieces showing welded joint. Reproduced from Jarman, R. A.; Smith, S.; Williams, R. A. *Br. Corros. J.* **1978**, *13*, 195.

Hoeppner<sup>232</sup> pointed out that until the early 1970s, most investigators conducted fatigue tests utilizing rotating bending, flat-plate bending or torsion-type loading configurations, which have the disadvantage that tests at positive or negative mean-stress values are difficult to achieve. In addition, the rotating bending and flat-plate bending tests create complex stress states upon crack initiation, for example, a shifting neutral axis. For these reasons, axial load fatigue machines, as recommended by the ASTM Committee E9, are preferred.

The results obtained from the tests described earlier are presented in the form of the conventional S-N curve, where S is the stress and N the number of cycles to cause fracture. Curves of this type are

obtained for the metal in air and for the metal in the corrodent, and comparison provides information on the effect of the corrosive environment on the fatigue life. Hoepfner points out that even though the S-N curve for either notched or unnotched specimens may be useful for certain applications it cannot always be employed to evaluate the effect of the environment on the fatigue life. This is because in some materials the inherent metallurgical and fabrication discontinuities, which may be undetectable by nondestructive testing will be so large that the only factor of engineering significance will be the rate of propagation of a crack from the initial defect, that is, the fatigue-crack propagation rate may play the dominant rôle in the useful life of the component. For this reason, it is important to conduct fatigue crack growth tests on precracked specimens, and the data are then presented in the form of curves showing crack growth rate,  $da/dN$ , versus stress intensity factor range,  $\Delta K$ .

The NACE publication *Corrosion Fatigue*<sup>232</sup> gives a comprehensive account of all aspects of the subject, and in this work, a review of the application of fracture mechanics for studying the phenomenon has been presented by McEvily and Wei,<sup>233</sup> while Kitagawa<sup>234</sup> has given a detailed account of crack propagation in unnotched steel specimens. This work should be consulted for details of testing and interpretation of results.

Special requirements for fatigue testing in aqueous environments are addressed in the Annexe to ASTM E 647 'Standard Test Method for Measurement of Fatigue Crack Growth Rates.'

### 2.34.14 Cavitation-Erosion

In considering these tests, it should be remembered that the phenomenon of cavitation-erosion is often accompanied by corrosion effects and that a synergistic effect may operate between the mechanically and chemically induced forms of attack. In fact the term cavitation-erosion-corrosion may often be more applicable in describing the requirements of a test procedure. The subject has been discussed by Wood and Fry.<sup>235</sup>

The methods used have been classified by Lichtman, *et al.*<sup>236</sup> as follows:

1. High-velocity flow.
  - a. Venturi tubes.
  - b. Rotating discs.
  - c. Ducts containing specimens in throat sections.

2. High-frequency vibratory devices.
  - a. Magnetostriction devices.
  - b. Piezoelectric devices.
3. Impinging jet.
  - a. Rotating specimens pass through continuous, stationary jets or droplets.
  - b. Stationary specimens exposed to high-speed jet or droplet impact.

All tests are designed to provide high erosion rates on small specimens so that the test can be conducted in a reasonable time, and although vibratory and high-velocity jet methods may not simulate flow conditions, they give rise to high-intensity erosion and can be used, therefore, for screening materials.

The essential component of many high-velocity flow rigs is a venturi-type section in which cavitation occurs in the low-pressure high-velocity region created by the venturi throat. Typical of this type is the double-weir arrangement used by Schroter,<sup>237</sup> but since this technique requires very large volumes of water, it is not readily adaptable to laboratory use. Hobbs<sup>238</sup> and others have used a uniform-area, rectangular-cross-section duct in which a cylinder of small diameter is inserted; cavitation occurs in the wake of the cylinder, which may be used as the test specimen or the specimen may be set in the side wall of the duct near the cylinder. The cavitation intensity will be dependent on the configuration of the test section and the velocity, pressure, temperature, viscosity, surface tension, corrosivity, gas content, and density of the liquid.

Devices in which cavitation is achieved by vibrating a test specimen at high frequencies are often used. The original apparatus was developed by Gaines<sup>239</sup> and was adapted for cavitation-erosion studies by Hunsaker and Peters, as described in the paper by Kerr,<sup>240</sup> and it has been used also by Beeching,<sup>241</sup> Rheingans,<sup>242</sup> and Leith and Thompson.<sup>243</sup> In this method, cavitation is produced by attaching the specimen to the vibrating source or by means of a partially immersed probe vibrating axially at a high velocity and low amplitude and placed close to the test specimen. Although originally magnetostriction oscillators were used,<sup>239</sup> these have now been largely superseded by piezoelectric oscillators, which are more efficient. The apparatus consists basically of a conventional ultrasonic generator, a piezoelectric transducer and a resonating horn or probe, and tests are typically carried out at a frequency of 20 kHz.

Originally, the test specimen was fastened to the end of the ultrasonic probe, and this is still specified

in ASTM D 2809 which describes a method of testing aluminum in antifreeze solution. However, this arrangement also subjects the test-piece to high alternating stresses as a result of the high accelerations associated with vibration at ultrasonic frequencies, which may be overcome by using a stationary test-piece and locating it immediately below a dummy tip placed on the end of the ultrasonic probe.

Vibratory test apparatuses are relatively cheap to build and run and have low power consumption, while flow rigs are bulky, expensive to build and run, and have high power consumptions but have the advantage that they simulate more closely practical conditions of hydrodynamic cavitation. On the other hand, the damage rate is higher in the vibratory tests than in the flow test, although whether this is advantageous depends on the objectives of the test. A further criticism of the vibratory test is that the mechanical component is overemphasized in relation to the effect produced by corrosion. For this reason Plesset<sup>244</sup> uses a technique in which cavitation is intermittent with short bursts of vibration followed by longer static periods, which significantly increases the erosion rate of materials with poor corrosion resistance but has little effect on materials with good corrosion resistance. Tests of this type have distinguished readily between materials having the same hardness but different resistances to corrosion, and between corrosive and noncorrosive solutions.

Figure 25 shows an apparatus for studying cavitation-corrosion using the magnetostriction

principle for vibration. A nickel tube is made the core of a magnetic field tuned to the natural frequency of the tube assembly, and since nickel changes its length as it is magnetized and demagnetized, it will vibrate with the frequency of the magnetizing current. The specimen under test vibrates with the nickel tube, and a commonly used frequency is 6500 Hz with an amplitude of 0.008–0.009 cm. Damage is increased by the amplitude of vibration, and the more resistant the material the greater the amplitude to achieve substantial attack. Increase in temperature decreases damage by increasing the vapor pressure within the cavitation bubbles, thus reducing the force of their collapse, but in opposition to this effect is the increased damage resulting from the lower solubility of gases which cushion the collapse of the cavitation bubbles. Consequently, under many circumstances damage reaches a maximum at a test temperature of about 46–52 °C.

Assessment of cavitation-erosion is based on mass loss, and the results are expressed as curves showing cumulative mass (or volume) loss versus the time of the test. Eisenberg and Preiser<sup>245</sup> have expressed the cumulative mass-loss plot on the basis of the rate versus time curve as follows:

1. Incubation zone (little or no mass loss).
2. Accumulation zone (increasing rate to a maximum).
3. Attenuation zone (decreasing loss rate to a steady-state value).
4. Steady-state zone (loss rate at a constant value).

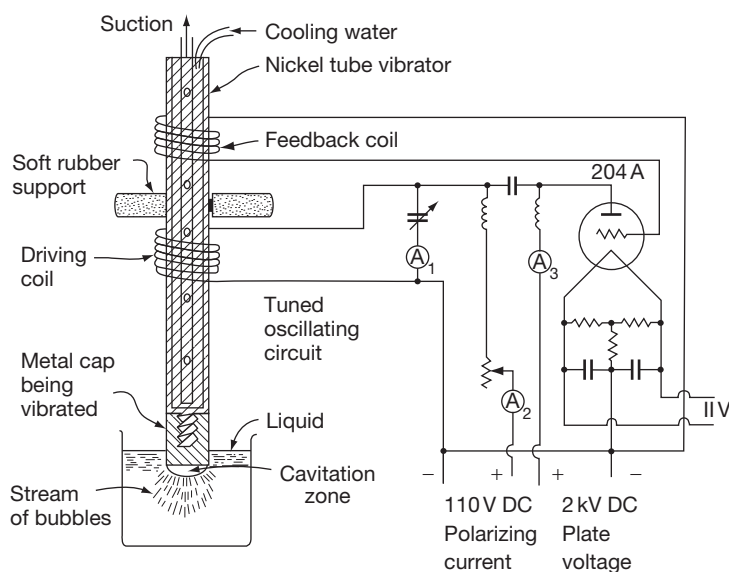


Figure 25 Vibratory cavitation-erosion test using magnetostriction.

It has been proposed that evaluation of the resistance of materials, or the study of experimental variables, should be based on the results obtained for the attenuation zone. Other methods of assessment have been proposed by Hobbs,<sup>246</sup> and by Plesset and Devine.<sup>247</sup>

Examples of various vibratory test procedures for studying cavitation-erosion of metals in inhibited engine coolants have been given in an ASTM Special Technical Publication.<sup>248–250</sup>

### 2.34.15 Fretting Corrosion

The deterioration of surfaces that occurs when parts supposedly tightly fitted together nevertheless move slightly relative to each other in some sort of cycle under load is called fretting corrosion. With ferrous materials, the characteristic corrosion product is a finely divided cocoa-colored oxide. The general state of knowledge of the subject was reviewed in a symposium on fretting corrosion held by the ASTM in 1952<sup>251</sup> and more recently by Waterhouse.<sup>252,253</sup>

Several techniques for reproducing fretting corrosion have been used. All involve some means for controlling contact pressure, and for achieving and measuring small-amplitude cyclic motion or slip between the contacting surfaces; some control of the environment, particularly moisture, which has a considerable effect on the extent of damage, is also desirable. Fink<sup>254</sup> used an Amsler wear machine. Another early series of tests on fretting corrosion arose from a study of the bottom bearings of electricity meters by Shotter.<sup>255</sup> Tomlinson *et al.*<sup>256</sup> adapted a Haigh alternating-stress machine by which annular specimens were pressed together under load while being subjected to vibration to achieve the required slip. These investigators also used apparatus in which a specimen having a spherical surface was moved cyclically through a small amplitude while in contact under load with a plane surface. A further modification involved an upper specimen machined to provide an annulus which was oscillated under load in contact with a lower plane specimen. A similar technique was used by Wright.<sup>257</sup> The area of damage was measured optically, and the maximum depth of damage was calculated by carefully lapping the lower surface and determining the change in mass. In addition, the amount of oxidized debris was determined chemically.

Uhlig *et al.*<sup>258</sup> measured fretting damage by mass loss of recessed 25.4-mm diameter steel cylinders subjected to radial oscillating motion. The specimens were loaded pneumatically, frequency was varied,

and slip was adjusted up to 0.020 mm. Mass loss was determined after debris had been removed by pickling the specimens in inhibited acid.

McDowell<sup>259</sup> used a setup that took advantage of the elastic modulus of one of the test materials to provide a definite deflection subject to control. A rotating-beam fatigue-testing machine was used to produce an alternating compressive and tensile deflection on the surface of the rotating specimen. A sliding specimen slipped back and forth on the rotating specimen as the outer fibers were strained alternately in tension and compression in proportion to the extent of deflection of the rotating specimen.

Horger<sup>251</sup> undertook rotating-beam fatigue tests of press-fitted assemblies using specimens as large as 305-mm diameter shafts.

Warlow-Davies<sup>260</sup> used a technique in which specimens were subjected to fretting corrosion and then tested in fatigue to show the effect of fretting damage in lowering resistance to fatigue.

Herbeck and Strohecker<sup>251</sup> used machines designed particularly for comparing the merits of lubricants in preventing fretting corrosion of anti-friction bearings. One provided for both oscillating conditions and combination radial and thrust loads to simulate service. Another was concerned primarily with thrust bearings and correlated satisfactorily with the radial load tester.

An interesting approach involved microscopic observation of fretting corrosion; a glass slide mounted on the stage of a microscope was used for the bearing surface which pressed against a spherical specimen being vibrated by a solenoid.<sup>261</sup>

Other testing machines and techniques have been described by Gray and Jenny,<sup>262</sup> de Villemeur,<sup>263</sup> Wright,<sup>264,265</sup> Barwell and Wright,<sup>266</sup> Field and Waters,<sup>267</sup> and Waterhouse.<sup>268</sup>

### 2.34.16 Corrosion Testing in Liquid Metals and Fused Salts

Liquid metals have high heat capacities and heat transfer coefficients, and these and other properties make them attractive as coolants for high temperature nuclear reactors and as heat-transfer and working fluids in power-generation systems that operate in conjunction with nuclear reactors. However, austenitic cladding and ferritic structural steels can suffer rapid corrosion when exposed to liquid metals at high temperatures (e.g., in liquid sodium at temperatures above 600 °C or in liquid Pb-17 at %-Li eutectic alloy at

temperatures above 500°C). Similar corrosion processes affect numerous solid–liquid metal systems, including molybdenum in liquid sodium or lithium, stainless steel in liquid aluminum, platinum in liquid sodium, and carbon steel in liquid zinc.

Corrosion by liquid metals is usually controlled by diffusion processes in the solid and liquid phases and, unlike aqueous corrosion, does not generally involve galvanic effects, and, even where electrochemical phenomena are known to occur, it has not, in general, been demonstrated that they have been responsible for a significant portion of the corrosion observed.<sup>269</sup> In fused salts, there is evidence that electrochemical factors are involved.<sup>270,271</sup> Nevertheless, the corrosion process in relation to liquid metals and fused salts may conveniently be considered under one of the following processes, which do not directly include electrochemical factors: (1) chemical reaction, (2) simple solution, (3) mass transfer, and (4) impurity reactions. Several of these processes may be involved in a single corrosion reaction, but for simplicity, they will be treated separately.

#### 2.34.16.1 Chemical Reaction

This involves the formation of distinct compounds by reaction between the solid metal and the fused metal or salt. If such compounds form an adherent, continuous layer at the interface, they tend to inhibit continuation of the reaction. If, however, they are nonadherent or soluble in the molten phase, no protection will be offered. In some instances, the compounds form in the matrix of the alloy, for example, as grain-boundary intermetallic compound, and result in harmful liquid metal embrittlement (LME), although no corrosion loss can be observed.

#### 2.34.16.2 Simple Solution

The liquid phase may simply dissolve the solid metal, or the liquid may go into solid solution with the metal to form a new phase. In some instances, only a single constituent of an alloy will dissolve in the liquid phase; in this case, a network of voids extending into the metal will result, with obvious deleterious effects.

#### 2.34.16.3 Mass Transfer

This phenomenon manifests itself as the physical transport of a metal from one portion of the system to another, and may occur when there is an alloy compositional difference or a temperature gradient

between parts of the unit joined by the flowing liquid phase. An exceedingly small solubility of the metal component or corrosion product in the molten metal or salt appears sufficient to permit mass transfer to proceed at a fairly rapid pace.

#### 2.34.16.4 Impurity Reactions

Small amounts of impurities in the liquid phase or on the surface of the solid metal may result in the initiation of attack or in increased severity of attack by one of the mechanisms just outlined.

In general, it is fair to state that one of the major difficulties in interpreting, and consequently in establishing definitive tests of, corrosion phenomena in fused metal or salt environments is the large influence of very small, and therefore not easily controlled, variations in solubility, impurity concentration, temperature gradient, etc.<sup>272</sup> For example, the solubility of iron in liquid mercury is of the order of  $5 \times 10^{-5}$  at 649°C, and static tests show iron and steel to be practically unaltered by exposure to mercury. Nevertheless, in mercury boiler service, severe operating difficulties were encountered, owing to the mass transfer of iron from the hot to the cold portions of the unit. Another minute variation was found substantially to alleviate the problem: the presence of 10 ppm of titanium in the mercury reduced the rate of attack to an inappreciable value at 650°C; as little as 1 ppm of titanium was similarly effective at 454°C.<sup>273</sup>

In the case of the alkali metals, impurities, such as oxygen and carbon, can have a significant effect on the corrosion of steel and refractory metals. Borgstedt and Frees<sup>274</sup> have shown that for the corrosion of both stabilized and unstabilized austenitic stainless steels in flowing liquid sodium at 700°C, there is an almost linear dependence of the corrosion constant,  $k$ , on the oxygen content of the sodium, as follows:

$$\log k = -5.6637 + 0.919 \log [\text{O}] \quad [17]$$

where,  $k$  is in  $\text{mg cm}^{-2} \text{h}^{-1}$  and  $[\text{O}]$  is in ppm. Barker *et al.*<sup>275</sup> have demonstrated that oxygen exerts a similarly deleterious effect on the corrosion of AISI Type 316 austenitic stainless steel in liquid Pb–17Li eutectic by increasing the depth of the ferritic corrosion layer and the extent of chromium depletion within the layer.

The effect of carbon on the corrosion of stainless steels in liquid sodium depends upon the test conditions and the composition of the steels.<sup>274</sup> Stabilized stainless steels tend to pick up carbon from sodium,



leading to a degree of carburization that corresponds to the carbon activity in the liquid metal. Conversely, unstabilized stainless steels suffer slight decarburization when exposed to very pure sodium. The decarburization may promote corrosion in the surface region of the material<sup>276</sup> and, under creep rupture conditions, can lead to cavity formation at the grain boundaries and decreased strength.

### 2.34.16.5 Testing

As in all corrosion testing, the procedure that most nearly duplicates the conditions anticipated in service will provide the most satisfactory and useful information for those aspects of corrosion under consideration here. In fact, in view of the extraordinary sensitivity of fused metal and salt corrosion phenomena to minute variations in operating conditions and purity of components, as already discussed, failure to reproduce these conditions with considerable accuracy may well make any test results completely unrealistic and worthless. In all of the following, then, it should be understood, if not explicitly stated, that all extraneous matter must be carefully excluded from the system and that only materials closely simulating those to be employed in service (including prior history and surface preparation of the metals) should be used. Other factors affecting the corrosion in liquid metals and fused salts include the heat flux of the corroding surface, the volume of liquid to the surface area of the solid, and the liquid flow rate. If, however, screening tests to establish the compatibility of a relatively large number of metals with a given molten metal or salt are to be run, it is often useful to commence with static tests even though the ultimate application involves a dynamic system. This is desirable because static tests are comparatively simple to conduct and interpret, and considerably more economical to operate, and because experience has shown that a metal that fails a static test is not likely to survive the more severe dynamic test.<sup>277</sup> Static tests have been used by Grabner *et al.*<sup>278</sup> to investigate the compatibility of metals and alloys in liquid Pb–Li eutectic at temperatures up to 650°C.

#### 2.34.16.5.1 Static tests

Ideally, a static test would consist of immersing a test sample in the liquid medium held in an inert container under isothermal conditions. Tests in mercury, for example, may be contained in glass at temperatures of several hundred degrees.<sup>279</sup> Unfortunately, at the higher temperatures and with the aggressive

metals and salts of interest, there are few readily available inert container materials, and results will often vary according to the nature of the container. The most satisfactory solution is to make the container of the same material as the test sample or, even in some cases, to let it be the sample. Klueh used small capsules for determining the effect of oxygen on the compatibility of Nb and Ta with sodium<sup>280</sup> and potassium.<sup>281</sup> For the Nb–K tests, the Nb specimen was approximately  $2.5 \times 1.4 \times 0.1$  cm and was contained in a Nb capsule surrounded by another capsule of welded Type 304 stainless steel. It was demonstrated that the oxygen concentration, added as K<sub>2</sub>O, markedly increased the solubility of the Nb in the molten K. DiStefano<sup>282</sup> studied the interaction of Type 316 stainless steel with Nb (or Nb–1Zr) in Na and Na–K by exposing tensile specimens of Nb (Nb–1Zr) to the liquid metal in a stainless steel container. Carbon and nitrogen from the stainless steel were transferred to the Nb, resulting in carbide-nitride at the surface and diffusion of nitrogen into the metal, thus producing an increase in tensile strength and a decrease in ductility. Close control of temperature is also essential if reproducible results are to be obtained, because of differential solubility as a function of temperature. For example, the corrosion rate for Cu–Bi at  $500 \pm 5.0^\circ\text{C}$  is several times its rate at  $500 \pm 0.5^\circ\text{C}$ .<sup>283</sup>

#### 2.34.16.5.2 Refluxing capsules

In systems in which a liquid metal is used as the working fluid, the liquid is converted to vapor in one part of the system, while the converse takes place in another, and the effect of a boiling-condensing metal on the container materials is most readily studied in a refluxing capsule. DiStefano and De Van<sup>284</sup> used a system in which the lower part of the capsule was surrounded by a heating coil, while the upper part was water cooled. Specimens were inserted in the upper part of the capsule and thus exposed to the condensing vapor, the rate of condensation being controlled by the water flow rate.

When close control of purity is essential, it may be necessary to assemble the test specimens in a dry box under an inert atmosphere and to weld the containers shut under inert gas or vacuum before placing on test. With some environments, even the small amount of oxygen and moisture adsorbed on the component surfaces will significantly affect the test results. In one laboratory, this problem was eliminated by maintaining within the dry box a container of molten sodium at  $250^\circ\text{C}$ <sup>277</sup>; it is a rather cumbersome procedure, but one that emphasises again the importance of purity.

Static test results may be evaluated by measurement of change of mass or section thickness, but metallographic and X-ray examinations to determine the nature and extent of attack are of greater value because difficulty can be encountered in removing adherent layers of solidified corrodent from the surface of the specimen on completion of the exposure, particularly where irregular attack has occurred. Changes in the corrodent, ascertained by chemical analysis, are often of considerable value also. In view of the low solubility of many construction materials in liquid metals and salts, changes in mass or section thickness should be evaluated cautiously. A limited volume of liquid metal could become saturated early in the test, and the reaction would thus be stifled when only a small corrosion loss has occurred, whereas with a larger volume, the reaction would continue to destruction.<sup>283,285</sup>

### 2.34.16.5.3 Dynamic tests

Various tests have been devised to study the effects of dynamic conditions, and one of the simplest tests is to use a closed capsule that contains a sample at each end and is partially filled with the liquid metal or salt.<sup>286</sup> A temperature gradient is maintained over the length of the tube, and the capsule is rocked slowly so that the liquid metal passes from one end to the other. After the test, the extent of mass transfer is determined from the two specimens placed at each end of the capsule. Tests of this type are useful to establish whether thermal-gradient mass transfer (or concentration-gradient mass transfer if dissimilar metals are incorporated in the system) will occur, but although the method is useful for screening purposes, the dynamic nature of the heating and cooling cycles prevents a rigorous analysis of mass transfer in terms of time and temperature.

High velocity effects can also be studied in spin tests using cylindrical specimens of the solid metal and rotating them at high velocities in an isothermal-metal bath. Although, strictly speaking, only a single alloy should be tested at a time, it is generally satisfactory to include a variety of alloys since the velocity effects become manifest at considerably shorter times than does mass transfer.

Kassner<sup>287</sup> used a rotating disc, for which the hydrodynamic conditions are well defined, to study the dissolution kinetics of Type 304 stainless steel in liquid Bi-Sn eutectic. He established a temperature and velocity dependence of the dissolution rate that was consistent with liquid diffusion control with a transition to reaction control at 860 °C when the speed of the

disc was increased. The rotating disc technique has also been used to investigate the corrosion stability of both alloy and stainless steels in molten iron sulfide and a copper/65% calcium melt at 1220 °C.<sup>288</sup> The dissolution rate of the steels tested was two orders of magnitude higher in the molten sulfide than in the metal melt.

### 2.34.16.5.4 Loop tests

Loop test installations vary widely in size and complexity, but they may be divided into two major categories: (1) thermal-convection loops and (2) forced-convection loops. In both types, the liquid medium flows through a continuous loop or harp mounted vertically, one leg being heated, while the other is cooled to maintain a constant temperature across the system. In the former type, flow is induced by thermal convection, and the flow rate is dependent on the relative heights of the heated and cooled sections, on the temperature gradient and on the physical properties of the liquid. The principle of the thermal convective loop is illustrated in **Figure 26**. This method was used by De Van and Sessions<sup>289</sup> to study mass transfer of niobium-based alloys in flowing lithium, and by De Van and Jansen<sup>290</sup> to determine the

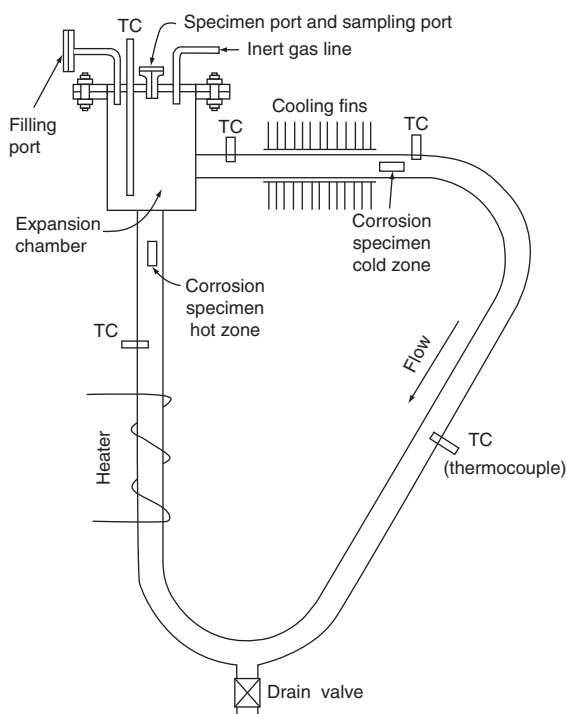


**Figure 26** Loop test for studying corrosion in molten metals or salts.

transport rates of nitrogen and carbon between vanadium alloys and stainless steels in liquid sodium.

The thermal-convection loops are limited to flow velocities up to about  $6 \text{ cm s}^{-1}$ . Where higher velocities are required, the liquid must be pumped, either mechanically or electromagnetically; the latter is usually preferred as it avoids the problem of leakage at the pump seal. Basically, these forced-convection systems<sup>290–293</sup> consist of (1) a hot leg, where the liquid metal is heated to the maximum temperature, (2) an economiser or regenerative heat exchanger, and (3) a cold leg, where the liquid is cooled to its minimum temperature. The economiser consists of concentric tubes with the hotter liquid flowing through the inner tube, while the cooler liquid flows in the opposite direction through the annulus between the two tubes, thus minimizing power requirements. The material under test may be used for constructing all parts of the loop, and the loop is then destructively examined after a given period of test. However, this is costly, and it is now a usual practice to use the loop as a permanent testing facility and to test specimens that are generally placed in the hot leg. Assessment of corrosion is based on changes in weight, dimensions, composition, mechanical properties, and microstructure.

The final stage in a testing program is the design, construction, and testing of loops that simulate the type of system for which data are required.

Since sodium, which is liquid between about  $100^\circ\text{C}$  and  $881^\circ\text{C}$ , has excellent properties as a heat-transfer medium, with a viscosity comparable with that of water and superior heat conductivity,<sup>294</sup> much attention has been paid to liquid sodium corrosion testing of metal and alloys. Indeed, there was an ASTM Standard Practice, which was used for the determination of the corrosion of ferrous alloys, austenitic stainless steels, high nickel alloys, and refractory metals in pumped flowing sodium (ASTM G 68, now withdrawn). This included guidance on the monitoring and control of impurity levels in liquid sodium. The oxygen content of the liquid sodium can be measured continuously by an electrochemical oxygen meter.<sup>295</sup> Similar electrochemical sensors have been used to monitor the carbon content of liquid sodium<sup>296</sup> and the oxygen content of liquid Li–17Bi eutectic.<sup>297</sup> The purity of the liquid metal can be maintained by means of a cold trap through which a small part of the flow is continuously bypassed, the purity level being determined by the temperature of the trap. The ASTM Standard Practice gave the following relationship between the cold trap temperature and

oxygen content of the liquid sodium:

$$\log_{10} C(\text{ppm oxygen content}) = 7.0058 - 2820/T(^{\circ}\text{K}) \quad [18]$$

and recommended that the oxygen level of liquid sodium be lowered to 2.85 ppm or less, corresponding to a cold trap temperature of about  $150^\circ\text{C}$ . Borgstedt and Frees<sup>274</sup> found that a cold trap operating at  $125^\circ\text{C}$  further reduced the oxygen content of liquid sodium to 1–2 ppm and acted as a sink for carbon, reducing the level of this element to about 0.01 ppm. The maintenance of low impurity levels in the liquid metal is facilitated if the inert cover gas in the expansion chamber is of high purity (e.g.,  $\geq 99.996\%$  argon).

Although the thermal loop test approximates to the conditions that obtain in a dynamic heat-transfer system, in evaluating the results, it is necessary to be aware of those aspects in which the test differs from the full-scale unit, as otherwise unwarranted confidence may be placed in the data. Assuming that adequate attention has been paid to the purity and condition of components, etc., the following factors will, according to ASTM G 68, influence the observed corrosion behavior:

1. liquid metal temperature;
2. degree of nonisothermality of the liquid metal system;
3. liquid metal flow rate;
4. heat flux at the corroding surface;
5. surface-area/volume ratio of solid metal/liquid metal;
6. relative sizes of dissimilar metal surface areas exposed to the liquid metal at the various system temperatures.

The relation between corrosion, and maximum temperature and temperature gradient is obvious, since solubility varies as a function of temperature. If the results are to be useful, these factors should match those anticipated in service. Erratic temperature cycling should be avoided as this can also modify the corrosion behavior. The effect of surface-to-volume ratio will be more pronounced in thermal convection than in pump loops. It can readily be seen that if a relatively small volume of liquid passes through a given isothermal segment of loop per unit time, it will become saturated quickly, and the corrosion rate will appear lower than would be the case if a substantially larger volume of liquid were passing at the same velocity. In a pumped loop, the velocity can be maintained sufficiently high to prevent the attaining of equilibrium between the solid and liquid

phases, and the rate of dissolution of the solid will be the controlling step. The flow velocity, or Reynolds number, will affect this step too, in that increased velocity will decrease the stagnant or lamellar layer adjacent to the tube wall and decrease the diffusion path that particles must negotiate to enter the rapidly moving stream.<sup>283</sup> The turbulence of the flow may also be modified by the manner in which test specimens are inserted in the loop, and this should also be considered carefully in designing a test unit.

The corrosion rates of the materials of construction are always of importance, but it has been found that, the uniform removal of metal from the hot leg may not impair the load-carrying ability of the container, whereas the deposition of metal in the cold leg can cause the cessation of flow, and the measure of the suitability of an alloy is often the time, under given conditions, that it takes for plugging to occur. Again, the flow velocity and the cross-sectional area are of primary importance in relating test results to operating conditions.

The ultimate test, short of constructing a full-scale unit, is to build a small-scale system in which each item to be incorporated in the final device is represented. Such programs are too specialized to warrant discussion here, and are fully described in the literature.<sup>298–301</sup>

#### 2.34.16.6 Liquid–Metal Embrittlement

Metals have sometimes been observed to crack almost instantaneously when wetted by certain molten metals and subjected to plastic strain at temperatures far below those at which the diffusion-ruled processes involved in liquid–metal corrosion attain significance.<sup>302</sup> The fracture appears to be more brittle than in the absence of the liquid metal, leading to decreased elongation and reduction of area values and, in severe cases, brittle intergranular fracture. Like other forms of environmental cracking, liquid–metal embrittlement is highly specific according to alloy and environment. For example, molten zinc can cause liquid–metal embrittlement of stainless steel if the oxide film is damaged, and because of this molten zinc from associated galvanized parts poses the greatest hazard in welding stainless steel equipment.<sup>303</sup> Other well known examples of liquid–metal embrittlement include the effects of solder on copper alloys and carbon steels and those of mercury on aluminum and nickel alloys. It is generally accepted that most cases of liquid–metal embrittlement arise from the effects of chemisorption of liquid–metal atoms and

the consequent reduction of the tensile strength of interatomic bonds at the crack tip since rates of crack growth (up to  $10 \text{ cm s}^{-1}$ ) are usually rapid compared with rates of diffusion of embrittling atoms ahead of cracks or dissolution of the solid in the liquid metal.<sup>304</sup> However, there are a few cases in which diffusion of embrittling atoms ahead of cracks or selective dissolution of a particular phase of an alloy can produce degradation of materials in liquid–metal environments.<sup>305</sup>

Prerequisites for liquid–metal embrittlement are that a solid metal should be subjected to tensile plastic strain while wetted by a liquid metal in which it has low solubility. It has been suggested that such embrittlement may be a general phenomenon occurring under appropriate conditions and to varying degrees between all solid–metal/liquid–metal couples and that a single mechanism may be responsible for all liquid metal embrittlement failures.<sup>306</sup> The occurrence and severity of the embrittlement are governed by:

1. the particular solid–metal/liquid–metal combination;
2. the temperature;
3. the strain rate;
4. the initial mechanical and metallurgical state of the solid metal.

The most commonly used method for assessing liquid–metal embrittlement is by tensile deformation at a slow strain rate. During testing, the specimen should be immersed in the liquid metal in a sealed autoclave to avoid contamination by atmospheric gases.<sup>302</sup> Electrochemical probes similar to those employed in liquid metal corrosion testing can be used to monitor the purity of the liquid metal. Susceptibility to liquid–metal embrittlement can be assessed in terms of the uniform elongation, reduction in area, and fracture appearance of the specimen relative to that determined under similar testing conditions in an inert environment at the same temperature. Where information on crack-propagation behavior is required, use can be made of precracked specimens. These can be tested under static or cyclic loading conditions to determine threshold stress intensity factors and crack growth rates.<sup>307</sup>

#### 2.34.17 Tests in Plant

Although laboratory tests (NACE TMO 169, and Thompson)<sup>308</sup> are obviously of value in selecting materials, they cannot simulate conditions that

occur in practice, and although an initial sorting may be made on the basis of these tests, ultimate selection must be based on tests in the plant. This is particularly important where the process streams may contain small concentrations of unknown corrosive species whose influence cannot be assessed by laboratory trials. Testing is also important for monitoring various phenomena such as embrittlement, hydrogen uptake, corrosion rates, etc.

### 2.34.17.1 Corrosion Racks

Exposure of coupons or specimens to the process stream cannot be achieved satisfactorily unless they are rigidly supported in a rack, although in some cases, it may be possible to simply hang them in by means of a wire. Methods of exposure of coupons are described in ASTM Method G4.

In the birdcage rack, disc specimens are mounted on a central rod and are insulated from each other and from the rod by insulating spacers and an insulating tube, respectively. PTFE has been found to be suitable for this purpose in aggressive media, particularly at high temperatures. Plates at the end of the rack act as bumpers to prevent the specimens touching the side walls, and the assembly is constructed from a corrosion resistant material such as Monel. Advantages of this method are the following: (1) electrical insulation avoids galvanic effects, and (2) the method of holding the specimen at the centre avoids losses because of corrosion around the point of support. The disadvantages are as follows: (1) specimens are not subjected to either heating or cooling effects and thus will not disclose 'hot-wall' effects and may also escape corrosive condensates when the

specimens are in a vapor stream above the dew point, and (2) the corrosivity of the environment may be affected by the presence of corrosion products of the construction material of the racks or by corrosion products of adjacent specimens. A further disadvantage is that because of its size and shape, it must be inserted into the process stream when the plant is out of service. Special devices are required for mounting specimens within pipelines so that they will be subjected to velocity effects.

The insert rack is designed for easy installation and removal through an unused nozzle. The supporting rods (one for each specimen) are welded to a single support plate that is of a width that enables it to be introduced through the nozzle. However, this too cannot be inserted unless the equipment is out of service, although its introduction does not require removal of gas.

A slip-in rack (**Figure 27**) that is designed to be inserted and removed during the operation of the plant through a full-port gate valve attached to a nozzle of suitable diameter (3.8–5.1 cm) is described by Dillon *et al.*<sup>309</sup>. It consists of a short length of pipe flanged at one end to match the gate valve and has a backing-gland arrangement at the other. The coupons are mounted on a rod of small diameter welded to a long heavier rod. The valve is opened, and the support rod is pushed through the packing gland so that the specimen is introduced into the process stream. The specimens are removed by withdrawing the rod until they are again within the pipe section, the gate valve is closed, and the rack removed from the valve.

Access fittings that enable specimens to be introduced into plant that is operating at high pressures, but can also be used for ambient pressures are available. In some instances, it is possible to secure valuable information by substituting experimental materials for parts

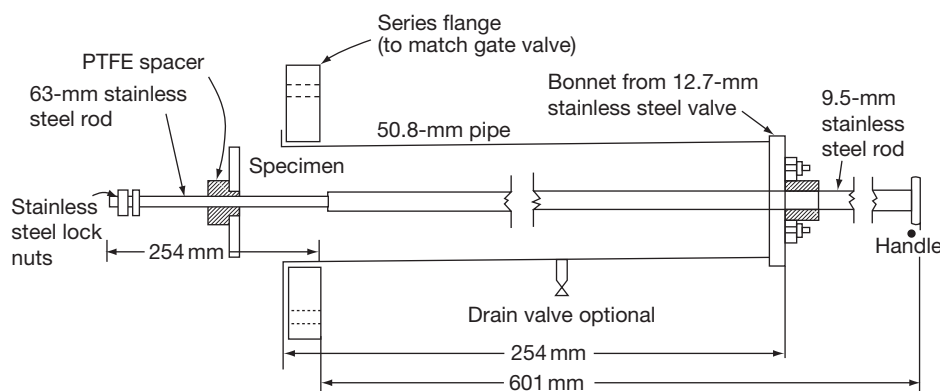


**Figure 27** Slip-in corrosion test rack. Reproduced from Dillon, C. P.; Krisher, A. S.; Wissenburg, H. In: Ailor, W. H., Ed.; *Handbook on Corrosion Testing and Evaluation*; John Wiley, 1971.



of the operating equipment, a practice that is used most frequently with condenser tubes, evaporators or other heat exchangers or sections of piping systems.

The prediction of materials performance in plant conditions using modeling and corrosion test methods has been discussed by Strutt and Nichols.<sup>310</sup>

### 2.34.17.2 Specimens

A convenient size for a circular coupon is 3.8-cm diameter, a thickness of 0.32 cm, and a central hole of 1.1 cm. Although inherent in the philosophy of corrosion testing, the use of coupons with surfaces that simulate those in service has been found to be unsatisfactory owing to irreproducibility, and the standard procedure normally adopted is to abrade down to 120 grit. ASTM Method G4 gives details of preparation of specimens, evaluation of replicate exposures, and the application of statistical methods.

### 2.34.18 Atmospheric Tests

More or less standardized techniques have been developed for the exposure of specimens to atmospheric weathering. ASTM G 50 and ISO 8565 provide guidance on conducting atmospheric corrosion tests on metals, alloys, and metallic coatings. Procedures for recording data from atmospheric corrosion tests on metallic-coated steel specimens are given in ASTM G 33. The usual practice in the USA<sup>311</sup> is to mount bare specimens on racks that slope 30° from the horizontal and painted specimens on racks that slope 45° from the horizontal. The usual orientation is to have the specimens face south. In coastal exposures, it is not uncommon to have the specimens face the ocean. Steel specimens exposed vertically have been found to corrode about 25% more than similar specimens exposed at the 30° angle.<sup>312</sup> Vertical exposure was used in the large-scale tests of nonferrous metals undertaken by Subcommittee VI of ASTM Committee B-3.<sup>313</sup> Vertical exposure is also favored by Hudson.<sup>314</sup>

A typical test installation uses a frame to support racks on which the specimens are mounted by means of porcelain or plastics insulators. The insulators may be spaced to take specimens varying in size from 10.1 × 13.4 cm to 10.1 × 32 cm and even larger specimens may be used for certain tests. Special types of exposure have been devised to take into account important effects of partial shelter and accumulation of pools of water, as in the case of the specimen and method of support used by Pilling and Wesley<sup>315</sup> to compare steels for roofing.

Copson<sup>316</sup> has described in considerable detail the several factors that require attention in studying atmospheric corrosion, particularly of steels.

Several sizes and shapes of specimen have been used in addition to the common ones already mentioned. In the long-time test of bare and zinc-coated steels undertaken by ASTM Committee A-5 on Corrosion of Iron and Steel, full-size sheets were used.<sup>317</sup> This Committee has also exposed specimens in the form of hardware<sup>318</sup> and wire and fencing.<sup>319</sup>

The extent of deterioration may be measured by one or more of the following methods: visual examination, change in weight, or change in tensile properties. Visual inspection was depended primarily upon the A-5 tests of steel sheets.<sup>319</sup> Here, visible perforation more than 6 mm from an edge was the criterion of failure. This leaves much to be desired for close comparisons because of the frequency with which perforations may be obscured by heavy coats of rust.<sup>312</sup> Other shortcomings of the use of time to visible perforation as the criterion of corrosion resistance are as follows.

1. The removal of rust films or other corrosion products to facilitate inspection for perforation prior to termination of the exposure will change the natural performance of the material and is therefore not tolerable.
2. The recording of a perforation establishes only the time to failure and provides no idea of the progress of corrosion up to the point of failure.
3. The time to perforation may be influenced considerably by the random occurrence of pits that happen to meet after starting from opposite sides of a sheet. This chance meeting of pits may be determined only to a slight extent by the composition of the material and, therefore, will interfere with observations of the effects of composition.

Where changes in appearance are of paramount interest, as in the case of metallic and organic coatings on steel or other metals, visual examination is most desirable. To facilitate ratings on such a basis, photographic standards have been employed, for example, in tests on chromium-plated steel undertaken by ASTM Committee B-8 on Electrodeposited Metallic Coatings.<sup>320</sup> These ratings are supplemented by a shorthand description of the nature of the deterioration observed.

Similarly, photographic standards are recommended for rating organic coatings with respect to different modes of deterioration in ASTM D 610.

The most precise measurements of corrosion resistance require the use of specimens that can be

weighed accurately after careful removal of corrosion products by the techniques described earlier.

A sufficient number of specimens should be exposed initially to permit their withdrawal from test in appropriate groups, for example, 3 to 5 duplicates after at least three time intervals. For long-time tests, a suitable schedule would call for removals after 1, 2, 5, 10, and 20 years. (Editor's note: As with all weight loss tests, it is desirable to retain some specimens in an inert environment to provide a control for the evaluation of systematic errors (such as those due to changes in balance calibration).)

It is good practice to determine depths of pitting as well as mass loss.

As is the case with other types of corrosion testing, mass-loss determinations may fail to indicate the actual damage suffered by specimens that are attacked intergranularly or in such a manner as dezincification. In such cases, mechanical tests or microscopic examination will be required as discussed already in the section on evaluation techniques.

It is desirable for reporting of atmospheric corrosion tests to include a precise description of the climatic conditions that prevailed at the test site during the test so that the weather factors can be tied in with the results of exposure. Progress toward this aim has been made with the development of international standards that provide guidance on evaluating the corrosivity of atmospheric environments. Atmospheric corrosivity can be expressed in terms of environmental factors, the most important of which have to do with contaminants of the atmosphere and the time that the specimens are actually wetted by condensed moisture. In the case of organic coatings, the interacting effects of sunlight and moisture, and their sequence, complicate this problem even more.<sup>321</sup> Methods of measuring pollution (deposition rates of sulfur compounds and chlorides) are provided in ISO 9225. ISO 9223 defines five different categories of atmospheric corrosivity based on time of wetness and pollution. An alternative approach is to express atmospheric corrosivity in terms of the corrosion rate of standard materials, including carbon steel, weathering steel, zinc, copper, and brass. Methods of determining the corrosion rates for this purpose are given in ISO 9226, while ISO 9224 provides a classification of atmospheric corrosivity based on both the average and the steady-state corrosion rates of the standard metals.

Sereda<sup>322</sup> has described a method of determining time of wetness in which a strip of platinum foil ( $0.8 \times 7$  cm) is mounted on a zinc panel ( $10.1 \times 13.4$  cm) on both the skyward and groundward face.

Condensed moisture from dew, or rain or snow, results in a galvanic cell, the potential of which is monitored on a recorder, thus giving the time of wetness. Guttman and Sereda<sup>323</sup> found that if the  $\text{SO}_2$  content remained essentially constant, the corrosion rate of zinc was related to time of wetness; furthermore, the dew detector registered the presence of moisture on the panel when the relative humidity ranged between 82% and 89%, thus providing a means of estimating from long-term weather data, such as temperature and relative humidity, the time a specimen is likely to be wet.

## 2.34.19 Atmospheric Galvanic Tests

Studies of galvanic corrosion in the atmosphere are experimentally simpler than those conducted in solution in the laboratory. The environment is taken as it comes, and the relatively high electrical resistance of the rain and moisture films that serve as electrolytes restricts the distance through which the galvanic action can extend and thus limits the relative area effects that complicate galvanic corrosion in solutions of high conductivity. Standard test methods for assessing galvanic corrosion caused by the atmosphere are given in ASTM G 104 and in ISO 7441.

Because of the limited proportion of the areas of a couple that actually participates in the galvanic action, it is difficult to make quantitative measurements that separate the galvanic action from the total effects of exposure. Thus, many of the observations are likely to be qualitative ones, and often no more than what can be determined by visual inspection or measurements of changes in strength, etc. as a result of any localized galvanic action.

An idea of the distribution of galvanic corrosion in the atmosphere is provided by the location of the corrosion of magnesium exposed in intimate contact with steel in the assembly shown in [Figure 28](#) after exposure in the salt atmosphere 25 m from the ocean at Kure Beach, North Carolina, for 9 years. Except where ledges or crevices may serve to trap unusual amounts of electrolyte, it may be assumed that, even with the most incompatible metals, simple galvanic effects will not extend more than about 4–5 mm from the line of contact of the metals in the couple.

The extent of galvanic action in atmospheric exposure may also be restricted by the development of corrosion products of high electrical resistance between the contacting surfaces: this is especially likely to occur if one of the metals in the couple is an iron or steel that will rust. In long-time tests, such

possible interruptions in the galvanic circuit should be checked by resistance measurements from time to time so as to determine the actual periods in which galvanic effects could operate.

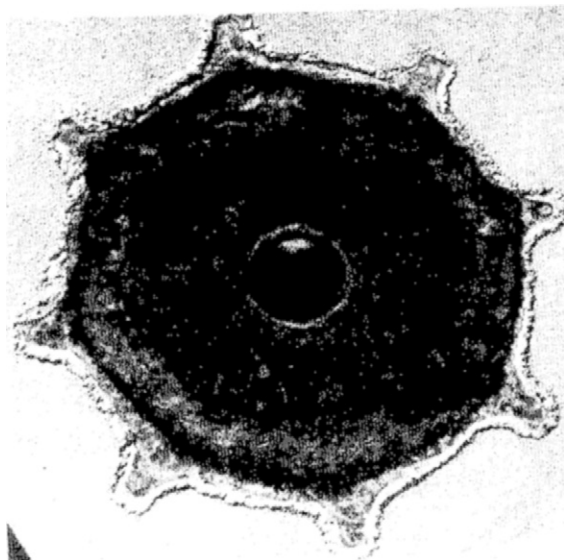


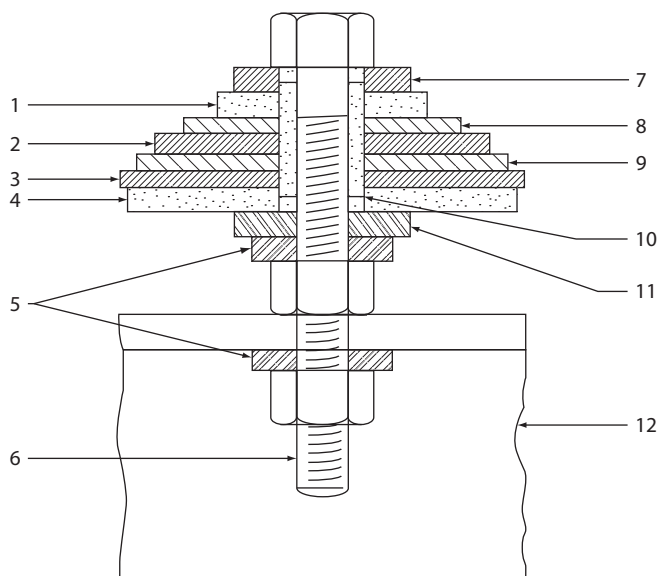
**Figure 28** Distribution of galvanic effects around contact of a magnesium casting and a steel core.

The test assembly used originally by Subcommittee VIII of ASTM Committee B-3 in its comprehensive studies of atmospheric galvanic corrosion<sup>324</sup> had the disadvantage that it depended on paint coatings to confine corrosion to the surfaces in actual contact with each other. In interpreting the results, it was frequently difficult to decide how much corrosion was due to galvanic action and how much to a variable amount of normal corrosion through failure of the paint system.

These difficulties were overcome in a design developed by Subcommittee VIII of ASTM Committee B-3<sup>325</sup> (**Figure 29**). In this assembly, each of the two middle specimens has a specimen of the other metal each side of it, and only these middle specimens are considered in appraising the results.

A fairly direct way of observing galvanic effects, which also permits changes in mechanical properties to be measured, involves the preparation of a composite specimen formed by attaching a strip, or strips, of one metal to a panel of another one. Tensile test specimens that include the areas of galvanic action can be cut from these panels after exposure, as shown in **Figure 30**.

A modification of the specimen shown in **Figure 30** may be made simply by lapping a panel of one material over a panel of another one. The greatest effects may



**Key**

- (1) Bakelite washer 19.0 × 3.2 mm. (2) Metal B disc 30 × 1.6 mm. (3) Metal B disc 36.6 × 1.6 mm.
- (4) Bakelite washer 35.5 × 3.2 mm. (5) Stainless steel lock washer. (6) Stainless steel bolt 4.8 × 38.1 mm.
- (7) Stainless steel washer 15.9 mm o.d. (8) Metal A disc 25.4 × 1.6 mm. (9) Metal A disc 35.5 × 1.6 mm. (10) 11.1 mm bakelite bushing, 5.2 mm i.d. × 7.9 mm o.d. (11) Stainless steel washer 15.9 mm o.d. (12) Galvanised angle support.

**Figure 29** Atmospheric galvanic couple test assembly.

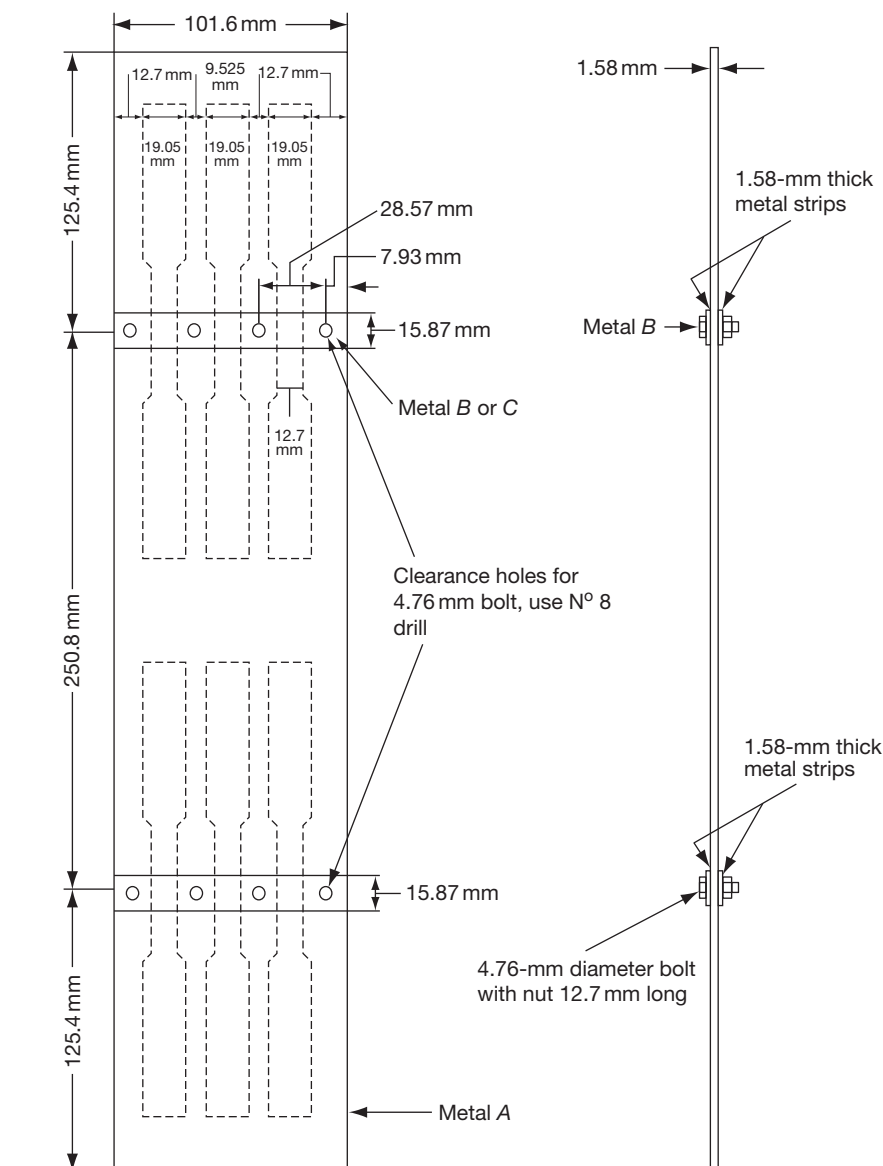


**Figure 30** Plate and fastening type galvanic couple test specimen.

be observed when such panels are exposed with the laps facing up so as to favor retention of corrosive liquids along the line of contact. To permit observations of secondary effects of corrosion products, or exhaustion of corrosive constituents, the relative positions of the dissimilar metals should be changed from top to bottom in duplicate test assemblies.

Where the practical interest is in possible galvanic effects of fastenings, it is simple to make up specimens to include such couple assemblies as illustrated in [Figure 31](#).

A type of assembly calculated to favor maximum galvanic action was developed by the Bell Telephone Laboratories and is illustrated in [Figure 32](#). Here, the less noble metal is in the form of a wire wound in the grooves of a threaded specimen of the metal believed to be more noble. Good electrical contact is achieved by means of set screws covered with a protective coating. This assembly favors accumulation of corrosive liquids around the wire in the thread grooves. Corrosive damage is also favored by the high ratio of surface to mass in the wire specimens.

To determine whether a protective metallic coating will retard or accelerate corrosion of a basis metal, and to what distance either effect will extend, specimens in which strips of various widths are left bare or made bare have been used by Subcommittee 11 of ASTM Committee B-8.<sup>325</sup> The extent of corrosion in and near the bare strips as compared with that on a completely bare or completely coated specimen will provide a measure of the extent of galvanic action and the distance through which the effect is able to extend from the edges of the bare strips.

### 2.34.20 Tests in Natural Waters

The corrosion testing of metals in natural waters is usually conducted in field or service tests since the

conditions of flow are important and often rate-determining. Testing will be concerned with mains water (potable water), river-water and seawater, or combinations of these as in estuarine conditions. Test specimens of various geometries will be used, for example, in the form of wires, plates, tubes, etc., and certain general precautions should be followed.

1. The specimens should be mounted so that they are insulated from their supporting racks and from each other. Such insulation can be achieved by the use of fastening assemblies, such as those illustrated in [Figure 33](#). Occasional difficulties have been encountered with this sort of assembly for tests of copper and high-copper alloys because of deposition of copper from corrosion products along the surfaces of the insulating tubes, which provided a metallic bridge between the specimens and the rack and introduced undesired galvanic effects. The required insulation and support can be provided by use of porcelain or plastic knob insulators in much the same manner as used on atmospheric test racks. A modified design has the advantage of offering less resistance to the flow of water and is less likely to serve as a form of screen to catch debris floating on, or suspended in, the water. Additional details of rack design may be found in the section on seawater tests in *The Corrosion Handbook* (Uhlig, Selective Bibliography).
2. In the case of corrosion tests in the sea or in other large volumes of water, that is, as opposed to tests in waters flowing within pipes, all the specimens to be compared should be suspended at the same depth or should pass through the same range of depths. Isolated specimens exposed at different depths will not be corroded in the same way as continuous specimens that extend through the total range of depth to be studied. This is especially the case with specimens exposed to seawater

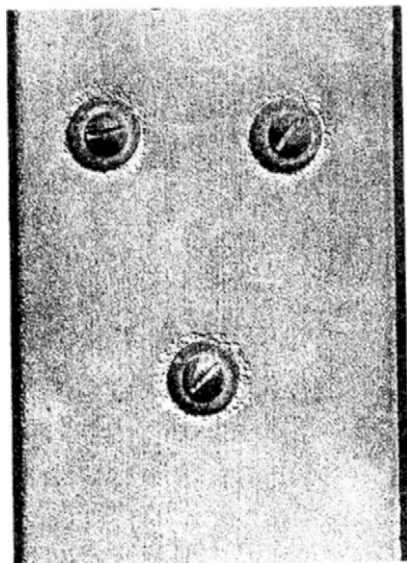


**Figure 31** Specimen for studying galvanic corrosion resulting from fasteners.

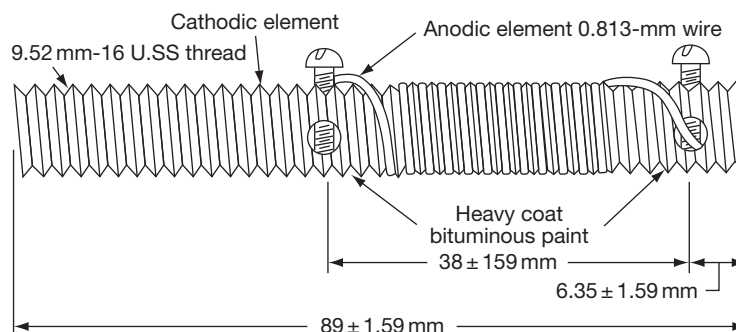


**Figure 32** Bolt and wire type atmospheric galvanic couple test specimen.



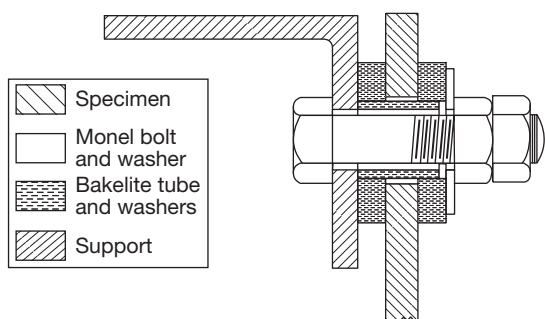


**Figure 33** Scheme for insulating specimens from metal test racks.

from above high tide to below low tide. Where the behavior of structures, such as piling, that pass through these zones is to be investigated, the test specimens must be continuous and large enough to extend through the total range in order to take into account differential aeration and other possible concentration cells that may have such a tremendous effect on the results secured.<sup>326</sup> For example, in seawater exposure, isolated specimens of steel exposed in the tidal zone have corroded 10 times as fast as portions of continuous specimens of the same steel in the same zone that extended also below low-tide level.<sup>312</sup>

3. The specimens should be oriented so that their flat surfaces are parallel to the direction of water flow and so that one specimen will neither shield an adjacent specimen from effects of water velocity nor create any considerable extra turbulence upstream of it.
4. In tests in seawater where accumulations of marine organisms are likely, specimens exposed parallel to each other should be spaced far enough apart to ensure that the space between specimens will not become completely clogged by fouling organisms. A minimum spacing of 100 mm is suggested.
5. Wooden racks used in seawater tests are likely to be subject to severe damage by marine borers. The wood used, therefore, must be treated with an effective preservative, for example, creosote applied under pressure, if the test is to extend for several years. Organic copper compound preservatives may suffice for shorter tests, for example, 2 or 3 years. Since the leaching of such preservatives may have some effects on corrosion, metal racks fitted with porcelain or plastic insulators have an advantage over wooden racks.
6. Where constant depth of immersion is desired in spite of tidal action, it is necessary to support the test racks from a float or raft.

Recommended methods for assessing the corrosivity of waters, including flowing potable waters, are described in ASTM D 2688. Three procedures are described in which test specimens in the form of wires, sheets, or tubes are placed in pipes, tanks, or other equipment. The test assembly for the first of these consists of three helical wire coils mounted in series on, and electrically insulated from, a supporting frame. The assembly must be installed so that flow is not disturbed and turbulence and high velocities, for example, of more than  $1.53 \text{ m s}^{-1}$ , are avoided. A minimum test period of 30 days is recommended. Procedures for the other specimen forms are given in the standard.

An extensive study of the corrosion of metals in tropical environments has been carried out by Southwell.<sup>327</sup> Tests have included atmospheric exposure, and exposure in seawater under mean tide and fully immersed conditions for a range of ferrous and non-ferrous metals and alloys.

The Marine Corrosion Working Party of the European Federation of Corrosion has published valuable advice on corrosion testing in service.<sup>328</sup>

### 2.34.21 Field Tests in Soil

The precautions generally applicable to the preparation, exposure, cleaning, and assessment of metal test specimens in tests in other environments will also apply in the case of field tests in the soil, but there will be additional precautions because of the nature of this environment. In the case of aqueous, particularly seawater, and atmospheric environment, the physical and chemical characteristics will be reasonably constant over distances covering individual test sites, whereas this will not necessarily be the case in soils, which will almost inevitably be of a less homogeneous nature. The principal factors responsible for the corrosive nature of soils are the presence of bacteria, the chemistry (pH and salt content), the redox potential, electrical resistance, stray currents, and the formation of concentration cells. Several of these factors are interrelated.

These considerations will significantly affect the location of test specimens in field testing. It is clearly important to ensure that the conditions of exposure are accurately known so that the corrosion test results may be interpreted with respect to the end-use requirements.

Two civil engineering operations require particular attention when soil corrosion tests in the field are

required. These are (1) the use of reinforced earth structures in which the corrosion conditions will differ from those at the site from which the soil has been taken and which may take some time to come to equilibrium in the new site, and (2) the use of reclaimed or contaminated land where unusual corrosive agents may be present in irregular distribution. In both these situations, considerable thought should be given to the corrosion test procedures.

Soil burial tests are popular despite the precautions that are needed. It is also important that a sufficient number of specimens are exposed so that statistical treatment of the results may be applied to compensate for some of the inevitable variations in the exposure conditions. Certain precautions originally set out in 1937<sup>329</sup> are still valid, and are as follows:

1. A sufficient number of specimens to yield a reliable coverage should be included.
2. The test site should be typical of the type of soil to be investigated.
3. The depth of burial should be that which will be occupied by the structure of interest. Specimens to be compared should be buried at the same depth. Ideally, tests for structures, such as piling, that will extend through several horizons would require the use of test specimens long enough to extend to the same depth.
4. Specimens should be separate so that they will not affect the corrosion of each other. A minimum spacing of two diameters was proposed.
5. Cylindrical specimens should be laid horizontally.
6. Sheet or plate specimens should be placed on edge.
7. The ends of pipe specimens should be closed to prevent internal corrosion.
8. Sufficient specimens should be provided to allow withdrawals after several time intervals so as to permit observations of changes in corrosion rates with time.
9. A portion of the original surface should be protected so as to provide a datum line for the measurement of pit depths.
10. In applying results of tests on small specimens to estimating corrosion, particularly by pitting on large structures, the effect of the increased area in increasing the depth of pitting must be taken into account.<sup>330</sup>

#### **2.34.21.1 Other Tests**

Other tests to determine bacterial—notably sulfate reducing—activity, soil resistivity, pH, redox potential,

etc. will provide valuable data to supplement the results obtained with test specimens. A useful account of some of these was given in.<sup>331</sup> A scheme for assessment of corrosivity of soils based on some of these parameters has been given by Tiller.<sup>332</sup>

A number of standards exist for the determination of some of these parameters. BS 1377: Part 3 refers to methods of tests for soils for civil engineering purposes, and Part 9 refers to these and corrosivity tests in situ. It is significant that the standard draws attention to the fact that the results of the tests that are described should be interpreted by a specialist. ASTM tests for pH and resistivity of soil used for corrosion testing are covered by G51 and G57, respectively.

#### **2.34.22 Corrosion Testing of Organic Coatings**

Programs to evaluate the corrosion protection by organic coatings on metals are intended to establish relationships between coating properties and performance. Such knowledge is essential to the most effective use of organic coating systems in corrosion control. Depending on the detail with which such studies are performed, light may be shed on the mechanism of coating deterioration as well.

If valid and useful relationships are to be established, it is essential that the factors affecting performance be recognized and form part of the test record. Since the performance is determined by interactions between the coating, the substrate and the surrounding environment against which protection is sought, significant factors and their interrelationships will vary with the nature of the service.

Care in designing and conducting the test in no way reduces the need for discrimination on the part of the person using the test data in the selection of a coating for a particular purpose. Test environments must reflect the deteriorating influences of the service for which they are applicable. A coating system cannot reliably be selected for service in a chemical plant on the basis of performance determined in a rural atmosphere.

Thus, both the proper conduct of the testing program and the valid use of the data depend on an understanding of the nature of organic coatings and of the forces through which they are degraded.

#### **2.34.22.1 Behavior of Organic Coatings**

An organic coating provides corrosion protection through the interposition of a continuous, adherent,

high-resistance film between the metal surface and its environment. In principle, its function is the mechanical exclusion of the environment from the metal surface. It seldom, if ever, succeeds practically in achieving this since all continuous organic films are permeable to some degree to moisture, and many coatings either have occasional physical defects or acquire them in service. Surface conversion treatments, such as phosphate and chromate dips, are used to supplement the physical protective properties of coatings, as are chemically inhibiting primers and wash primers. When such treatments are used, they must be included in the record as constituting a part of the coating system.

Critical parts of the test program are the preparation of test specimens, the selection of the exposure conditions (both in laboratory and field tests), and the selection of significant coating properties to be evaluated as a measure of deterioration with time.

### 2.34.22.2 Preparation

Specimens will normally be flat panels, large enough to avoid any effects caused by nearby edges of the specimen. Edges and backs are usually coated unless the effect of uncoated edges is an intended test variable. Panels may include the structural features of plates, channels, welds, sharp edges, pits, or depressions, depending on the service for which the data are to be applicable.

The composition of the basis metal has been found to influence the performance of organic finishes in many cases. Thus, composition is a significant test variable and must be considered in comparing test data.

It is particularly important that surface roughness and cleanness, which greatly affect adhesion, should be carefully controlled and that the procedures used to achieve them be a part of the test record. A high degree of cleanliness is normally sought. If, however, the data are to be applicable to the painting of outdoor structures, a certain amount of outdoor weathering becomes a part of the specimen preparation prior to coating. Specimens again will be of the basis metal appropriate for the related service application.

The thickness of a coating plays an important part in determining its physical characteristics. Uniformity of thickness among specimens is therefore necessary, particularly when coating deterioration is to be assessed by changes in such properties. For the preparation of reproducible specimens, methods of

applying coatings in uniform thicknesses are available, as are methods for accurately measuring film thickness.

### 2.34.22.3 Exposure Conditions

In considering exposure tests, whether in the form of laboratory, field, or service tests, it is important to consider the purpose of the test and the relevance of the data to the anticorrosion function of the coating. Thus, in the case of paint coatings, factors such as gloss deterioration, chalking, and color retention are of considerable importance in some industries, for example, the automotive industry, but perhaps of minor importance in the painting of structural steelwork. These assessment factors can nevertheless be of significance, since they may be the precursors of corrosion of the basis metal.

#### 2.34.22.3.1 Laboratory tests

Laboratory tests are often conducted with the purpose of providing an accelerated test procedure and if intelligently used, that is, with proper respect for their limitations, they are of value in determining the probable order of durability, and hence, by implication, corrosion protection of a group of paints. They can also be of value in assessing the quality of a range of similar compositions where there is already some knowledge of the performance of the general composition. Although continuing attention is given to the correlation of accelerated tests with field trials and service performance, caution must always be exercised in attempting to predict the type of failure likely to occur under conditions of natural exposure. Certainly, an approach based on 'the rougher the treatment, the better the test' cannot be justified. Three main classes of laboratory test can be identified and may be conveniently classified under the headings of (1) electrochemical, (2) coating adherence, and (3) exposure cabinets – including weatherometers.

#### *Electrochemical tests*

This group includes the various electrochemical tests that have been proposed and used over the last fifty years or so. These tests include a number of techniques ranging from the measurement of potential–time curves, electrical resistance, and capacitance to the more complex electrochemical impedance methods. The various methods have been reviewed by Walter.<sup>333</sup> As the complexity of the technique increases, that is, in the mentioned order, the data

that are produced will provide more types of information for the metal-paint system. Thus, the impedance techniques can provide information on the water uptake, barrier action, damaged area, and delamination of the coating as well as the corrosion rate and corroded area of the metal. However, it must be emphasized that the more comprehensive the technique, the greater the difficulties that will arise in interpretation and in reproducibility.

#### **Adherence tests**

This group of techniques involves the testing of the metal-to-paint adherence. These techniques are covered by descriptions such as cohesion,<sup>334</sup> blister,<sup>335</sup> pull off (BS EN 24624), and cross-cut (BS EN ISO 2409). Detailed descriptions of these techniques will be found in the appropriate references.

#### **Exposure cabinets**

This group of laboratory tests include the so-called exposure cabinets, salt-spray, and weatherometer tests in which the paint-coated panels are subjected to various cycles of wetting and exposure to ultraviolet light to simulate atmospheric conditions of exposure. BS 3900: Part F3 describes a weatherometer consisting of a 1.2 m diameter drum that rotates at 1 rev/20 min, and has facilities for spraying the panels (100 × 150 mm) periodically during a 24 h cycle and exposing them to ultraviolet light by means of an enclosed carbon arc. Spraying with distilled water is effected by means of an atomizer and fan using the following 24-h cycle: 4 h off, 2 h on, 10 h off, 2 h on and 1 h off; the final 1 h is used for checking the arc. The test is continued for 7 days, at the end of which the panels are examined visually for change of color, loss of gloss and blistering, and for checking, cracking, and chalking by means of a lens (×25).

An appraisal of artificial weathering methods was given in a report by Hoey and Hipwood<sup>336</sup> who described the effectiveness of various weatherometer tests such as those described in BS 3900: Part F3 and ASTM G 152/52. Although these tests simulate atmospheric exposure, it is not possible to obtain a direct correlation owing to variation in outdoor exposure conditions from place to place, but they serve a very useful purpose in providing a preliminary sorting of paints that can then be tested in the field.

#### **2.34.22.3.2 Field and plant tests**

Field exposure of test panels offers the benefit of a high degree of control over surface preparation and application. Moreover, through standardized

exposure conditions, broader comparisons between both paint systems and locations are possible. More importantly, since replicates may be removed and laboratory tested periodically, changes in properties can be followed in considerable detail. At least four replicates should be examined for each exposure period to minimize the effects of atypical specimens.

The exposure site is selected according to the service for which the data are to be applicable. For atmospheric service, such factors as marine and industrial contaminants, sunlight, dew, and sand abrasion must be considered. Atmospheric specimens are normally mounted at 45°, facing south. This has been shown to provide about a 2:1 acceleration of failure compared with a vertical exposure. Whether this or other standardized positions are used, the details of the exposure are an important part of the test record.

The degree of deterioration experienced over a given test period varies with climatic conditions. Since these differ significantly from one season to another, a standard specimen, the performance of which is well known, should be included with each exposure to increase the validity of coating comparisons.

For other environments, such as in seawater or in chemical plants, exposure conditions that most nearly duplicate those of the related service, and are at the same time reproducible, are used. Impingement by water or water carrying entrained solids, thermal effects, and physical abuse are among the factors to be considered.

#### **2.34.22.4 Coating Evaluation**

The performance of organic finishes on test is evaluated by visual observation and by physical tests made upon coated specimens that have been exposed for various periods of time to natural or accelerated weathering conditions. Electrical tests are sometimes used on immersed specimens.

Inspection of test panels at the test sites consists of visual observations of blistering (see ASTM D 714) and the appearance of rust (see ASTM D 610). For these, photographs showing various degrees of degradation that serve as observational standards greatly reduce variations between observers. Results of consecutive observations entered on charts provide visual records of the trend of these features with time.

These more serious evidences of degradation, however, are preceded by invisible physical alterations within the coatings, which can be detected readily and quantitatively by suitable physical tests of replicate specimens removed from tests at periodic

intervals. The use of such tests to reveal incipient coating changes is, in a sense, a means of accelerating the test program without distortion of the test environment. This approach is especially dependent on uniformity of properties among replicates, hence on reproducible application techniques. Moreover, since many coating properties are highly sensitive to changes in temperature and relative humidity, equilibrium of the specimens during testing is necessary. Testing conditions are commonly 25 °C and 50% RH.

Physical tests appropriate for this type of evaluation are not necessarily limited to those properties that the coating may be called upon to display in service. A coating that shows a decrease in distensibility from 20% to 10% is still quite capable of withstanding the expansion and contraction of the substrate in atmospheric temperature cycling, yet such a coating can be expected to fail in service earlier than one that shows no decrease. Thus, the properties of value are those that have been established as reliable indices of deterioration.

Besides providing early comparative data on coating performance, physical tests in dealing with intrinsic coating properties provide much-needed quantitative information on the relationships between the several factors affecting the ageing of organic films. The tests cited as follows are those that have been shown to indicate reliably significant changes in the condition of coatings on tests.

#### **2.34.22.4.1 Distensibility**

This property is very sensitive to chemical changes within the coating. Its measurement thus shows the beginning of normal ageing or of deterioration through reaction with the environment. Distensibility is generally determined by bending the test panels over a conical mandrel of known radius and calculating the % elongation at first rupture.

#### **2.34.22.4.2 Abrasion tests**

In these tests, the end point is normally taken as the amount of abrasion required to penetrate the coating. The results thus reflect the strength of the coating, its cohesion, and in some cases, its adhesion to the basis metal as well as resistance to abrasion.

#### **2.34.22.4.3 Hardness**

Coating hardness is related to the method of measurement. Results reflect the resistance to scratching as well as to indentation.

#### **2.34.22.4.4 Impact tests**

Such tests reveal the resistance of coatings to deformation and destruction by concentrated sudden stresses. They thus throw considerable light on the integrity of the metal-coating bond. Changes in adhesion through chemical reaction at the paint/metal interface will be reflected in the impact-test values.

These tests for characterizing coating properties necessarily continue to involve a certain amount of empiricism. The intelligent use of these tests, however, has shown that wide variations of physical and electrochemical characteristics of coatings as a function of composition may be obtained, and further, that significant changes in these characteristics, that can be measured before the usual evidence of failure appears, occur upon natural and accelerated ageing.

### **2.34.23 Test Methods for Corrosion Inhibitors**

#### **2.34.23.1 Immersed Conditions**

Since corrosion inhibitors are used in a wide range of applications, no universal test method exists. Recognized methods tend to relate to a product or process in which the inhibitor forms a part rather than to the inhibitor *per se*. Thus, tests exist for inhibited coolants, cooling waters, cutting oils, pickling liquids, etc.

The considerations applicable to corrosion test methods also apply to tests for inhibited products. The metals and alloys used, their surface preparation, the temperature, flow rate, composition of the test medium, the presence of heat transfer, and so on must all be relevant to the proposed use of the inhibited product. As with other test methods, there are those tests that have been developed in particular laboratories for the development of inhibitors for particular purposes and those that have acquired national or international recognition by appropriate standards-writing bodies.

The three types of test procedure discussed in this chapter may often be identified in testing of inhibitors or inhibited products. The testing of inhibited engine coolants provides a suitable example.

Laboratory tests used in the development of inhibitors can be of various types and are often associated with a particular laboratory. Thus, in one case, simple test specimens, either alone or as bimetallic couples, are immersed in inhibited solutions in a relatively simple apparatus, as illustrated in [Figure 34](#). Sometimes, the test may involve heat transfer, and a simple test arrangement is shown in [Figure 35](#). Tests of



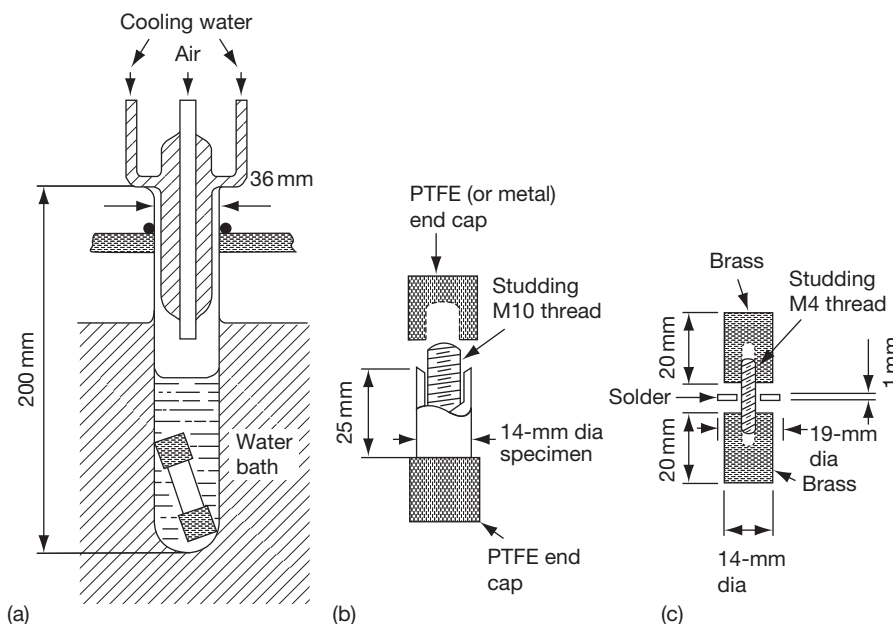


**Figure 34** Experimental arrangements for corrosion tests without heat transfer. (a) Test vessel and specimen, (b) assembly for single or bimetallic specimens, and (c) assembly for brass/solder/brass specimens.

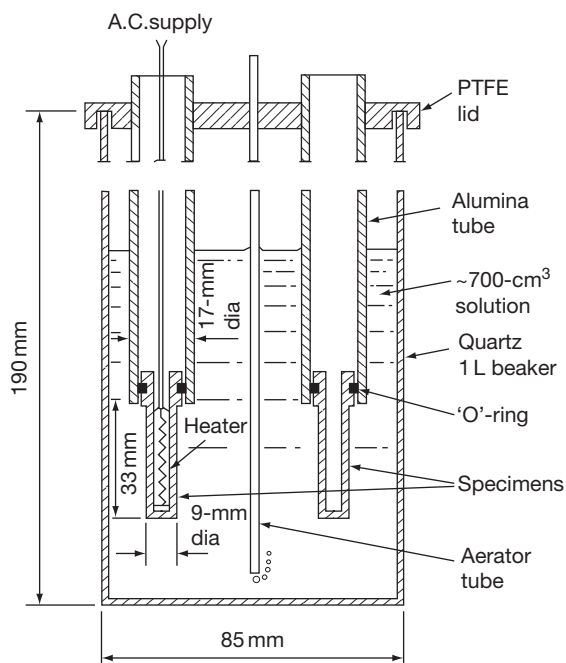


**Figure 35** Apparatus for testing inhibitors with metal-to-coolant heat transfer.

these types have been described in the literature.<sup>337,338</sup> However, national standards also exist for this type of test approach. BSI and ASTM documents describe laboratory test procedures and, in some cases, provide recommended pass or fail criteria (BS

5117: Part 2: Section 2.2; BS 6580; ASTM D 1384). Laboratory testing may involve a recirculating rig test in which the intention is to assess the performance of an inhibited coolant in the simulated flow conditions of an engine cooling system. Although test procedures have been developed (BS 5117: Part 2: Section 2.3, ASTM D 2570), problems of reproducibility and repeatability exist, and it is difficult to quote numerical pass or fail criteria.

These laboratory tests may be followed by engine dynamometer tests (BS5117: Section 2.4) and finally by road tests in working vehicles (BS 5117: Part 2: Section 2.5), thus completing the sequence of laboratory, field, service testing.

The problems that have been experienced in the recirculating rig test are indicative of those often met in performance testing. Attempts to reproduce the service conditions in a laboratory test inevitably involve attempting to reproduce each of the controlling conditions that exist in the real situation. Variations, which may be relatively small, in these simulations can lead to significant differences in test results. There is therefore much to be said for keeping test conditions as simple as possible rather than attempting to reproduce accurately the conditions in practice. A balance between reproducibility and realism has to be struck.

The testing of inhibitors for use in oil and gas production, transport, and processing normally involves two-phase oil–water fluids with, sometimes, a solid

phase, for example, entrained sand particles. Tests are usually of the dynamic variety with continuous movement so that test specimens contact all phases present. A well known laboratory test procedure is the so-called wheel test in which bottles of about 200-cm<sup>3</sup> volume containing weighed test specimens and a two-phase fluid saturated with an appropriate gas (CO<sub>2</sub> or H<sub>2</sub>S) rotate inside a temperature-controlled chamber.<sup>339</sup> For many applications in these technologies, data are required for high temperature high-pressure conditions, and the use of autoclaves then becomes essential.<sup>340</sup> Two reviews on test procedures for corrosion inhibitors have been published.<sup>341,342</sup>

### 2.34.23.2 Vapor Phase Conditions

The testing of vapor phase inhibitors, usually referred to as volatile corrosion inhibitors, is essentially a matter of placing a test specimen in the vapor space of a closed vessel containing an aggressive atmosphere – frequently water vapor, perhaps with SO<sub>2</sub> present – and a quantity of the inhibitor. Variations on the basic technique include provision for circulation of the vapor, the use of paper impregnated with inhibitor, provision for temperature cycling, etc.

In the early 1950s, Wachter *et al.*,<sup>343</sup> in the USA, described a humidity cabinet test in which metal specimens were supported inside inverted glass tubes containing a slip of inhibitor-impregnated paper in the lower end. The test was conducted at 37.7 °C and 100% RH. In the UK, Stroud and Vernon<sup>344</sup> described two types of test: (1) with a single test specimen suspended from a cork in the neck of a 250-cm<sup>3</sup> conical flask containing 25 cm<sup>3</sup> of water with 5 mass% of the inhibitor, which was held at 35 °C during the day and at room temperature overnight; and (2) with specimens suspended in the upper part of glass tubes containing water and inhibitor with the lower part of the tubes immersed in a thermostatted bath so that condensation occurred in the upper part of the tubes. Other forms of test using a climatic cabinet with tropical or industrial atmospheres have also been described.<sup>345</sup>

## Acknowledgements

Acknowledgements are made to Dr. R. Francis, Dr. T. G. Gooch, Prof. J. S. Llewelyn Leach, Dr. T. C. Lindley, Mr. G. O. Lloyd, Dr. D. Mills, Mr. T. E. Such, Mr. A. K. Tiller, and Mr. P. J. Trant for their helpful comments in connection with the updating of this section, which is based on the original by Dr. L. L. Shreir and Dr. F. L. LaQue.

## Appendix A: Methods of Removal of Corrosion Product

This appendix provides information on chemical and electrochemical treatments, which have been recommended for the removal of corrosion products. In using these methods the following points need to be borne in mind:

1. The duration of chemical or electrochemical treatment should be kept to the minimum necessary to remove the corrosion product. Loosely adherent material should be removed beforehand by suitable mechanical means, for example, scrubbing.
2. The combined action of chemical (or electrochemical) treatment and scrubbing is often more effective than either method alone. It is frequently advantageous to alternate short periods of immersion with scrubbing to remove any corrosion product that has become loosened by the action of the chemical reagent.
3. The rate of attack of the chemical reagent on sound metal should be determined on a separate uncorroded sample of the material being cleaned, and if necessary a correction should be applied to the loss in weight of the corroded specimen. However, where a metal, and particularly an alloy, is heavily corroded, thus exposing a surface structure different from that of an uncorroded surface, it will be necessary to check the reliability of the cleaning method (Mercer, A. D.; Butler, G.; Warren, G. M. *Br. Corrosion J.* **1977**, *12*(2), 122–126). A procedure for obtaining more accurate weight loss data in these circumstances has been described [ISO 8407].
4. The possibility of redeposition of metal from the dissolved corrosion product or, if electrochemical treatment is employed, from the anode material should always be kept in mind. If there is reason to believe this has occurred during removal of the corrosion product, further treatment to remove the redeposited metal will be necessary before the weight loss due to corrosion is measured.

### A.1 Procedures for Removing Corrosion Products

The removal of corrosion products from metal specimens is described in Reference 1 and in ASTM G 1 and ISO 8407 and certain of these procedures are described as follows.

**A.1.1 Electrolytic cathodic cleaning**

After scrubbing to remove loosely attached corrosion products, cathodically polarize in hot dilute sulfuric acid under the following conditions:

Electrolyte-sulfuric acid (5 wt. %) plus an inhibitor ( $0.5 \text{ kg m}^{-3}$ ) such as diorthotolyl thiourea, quinoline ethiodide, or  $\beta$ -naphthol quinoline. The temperature should be  $75^\circ\text{C}$ , the cathode current density  $2000 \text{ Am}^{-2}$ , and the time of cathodic polarization 3 min. The anode should be carbon or lead. If lead anodes are used, lead may deposit on the specimens and cause an error in the weight loss. If the specimen is resistant to nitric acid the lead may be removed by a flash dip in 1:1 nitric acid. Except for this possible source of error, lead is preferred as an anode, as it gives more efficient corrosion product removal.

After the electrolytic treatment, scrub the specimen with a brush, rinse thoroughly and dry.

Electric treatment may result in the redeposition of a metal, such as copper, from reducible corrosion products and thus decrease the apparent weight loss.

**A.1.2 Chemical Cleaning****A.1.2.1 Copper and nickel alloys**

Dip for 1–3 min in 1:1 HCl or 1:10  $\text{H}_2\text{SO}_4$  at room temperature. Scrub lightly with bristle brush under running water, using fine scouring powder if needed.

**A.1.2.2 Aluminum alloys**

Dip for 5–10 min in an aqueous solution containing 2 wt. % chromic acid ( $\text{CrO}_3$ ) plus 5 vol. % orthophosphoric acid ( $\text{H}_3\text{PO}_4$ , 85%) maintained at  $80^\circ\text{C}$ . Ultrasonic agitation will facilitate this procedure.

Rinse in water to remove the acid, brush very lightly with a soft bristle brush to remove any loose film, and rinse again. If film remains, immerse for 1 min in concentrated nitric acid and repeat previous steps. Nitric acid may be used alone if there are no deposits. (See comments on this method when used for corroded specimens in the paper by Mercer, A. D.; Butler, G.; Warren, G. M. *Br. Corrosion J.* 1977, 12, 122.)

**A.1.2.3 Tin alloys**

Dip for 10 min in boiling trisodium phosphate solution (15%). Scrub lightly with a bristle brush under running water, and dry.

**A.1.2.4 Lead alloys**

Preferably use the electrolytic cleaning procedure just described. Alternatively, immerse for 5 min in boiling 1% acetic acid. Rinse in water to remove the acid and brush very gently with a soft bristle brush to remove any loosened matter.

Alternatively, immerse for 5 min in hot 5% ammonium acetate solution, rinse and scrub lightly. This removes  $\text{PbO}$  and  $\text{PbSO}_4$ .

**A.1.2.5 Zinc**

Immerse the specimens in warm ( $60$ – $80^\circ\text{C}$ ) 10%  $\text{NH}_4\text{Cl}$  for several minutes. Then rinse in water and scrub with a soft brush. Then immerse the specimens for 15–20 s in a boiling solution containing 5% chromic acid and 1% silver nitrate. Rinse in hot water and dry.

Note: in making up the chromic acid solution it is advisable to dissolve the silver nitrate separately and add it to the boiling chromic acid to prevent excessive crystallization of the silver chromate. The chromic acid must be free from sulfate to avoid attack on the zinc. Immerse each specimen for 15 s in a 6% solution of hydriodic acid at room temperature to remove the remaining corrosion products. Immediately after immersion in the acid bath, wash the samples first in tap water and then in absolute methanol, and dry in air. This procedure removes a little of the zinc and a correction may be necessary.

**A.1.2.6 Magnesium alloys**

Dip for approximately 1 min in boiling 15% chromic acid to which 1% silver chromate solution has been added with agitation.

**A.1.2.7 Iron and steel**

Preferably use the electrolytic cleaning procedure, or else immerse in Clark's solution (hydrochloric acid 100 parts, antimonious oxide 2 parts, stannous chloride 5 parts) for up to 25 min. The solution may be cold but it should be vigorously stirred. Remove scales formed under oxidizing conditions on steel in 15 vol. % concentrated phosphoric acid containing 0.15 vol. % of an organic inhibitor at room temperature.

**A.1.2.8 Stainless steels**

Clean stainless steels in 20% nitric acid at  $60^\circ\text{C}$  for 20 min. In place of chemical cleaning, use a brass scraper

or brass bristle brush or both, followed by scrubbing with a wet bristle brush and fine scouring powder.

Other methods of cleaning iron and steel include immersion in molten sodium hydride and cathodic treatment in molten caustic soda. These methods may be hazardous to personnel, and should not be carried out by the uninitiated, or without professional supervision.

### A.1.3 General Note

Whatever cleaning method is used, the possibility of removal of solid metal is present. This will result in error in the determination of the corrosion rate. One or more cleaned and weighed specimens should be recleaned by the same method and reweighed. Loss due to this second treatment may be used as a correction to that indicated by the first weighing.

## Appendix B: Standards

### B.1 ISO Standards

ISO standards are managed by the International Organization for Standardization, known as ISO for short (the short name is taken from the Greek 'iso' meaning equal, rather than being an abbreviation of the name of the organization, which would, of course be different in different languages). ISO standards have a simple naming convention, ISO nnnn-pp:yyyy, where nnnn is the standard number, pp the optional part number and yyyy the year of publication. For standards published in collaboration with national bodies, ISO may be supplemented with the abbreviation of the body (as in ISO/ASTM ...). In the main text we have just given the standard number and part number; here we list the current version at the time of writing.

ISO 1456:2003 Metallic coatings – Electrodeposited coatings of nickel plus chromium and of copper plus nickel plus chromium

ISO 2160:1998 Petroleum products – Corrosiveness to copper – Copper strip test

ISO 2810:2004 Paints and varnishes – Natural weathering of coatings – Exposure and assessment

ISO 3651-1:1998 Determination of resistance to intergranular corrosion of stainless steels – Part 1: Austenitic and ferritic-austenitic (duplex) stainless steels – Corrosion test in nitric acid medium by measurement of loss in mass (Huey test)

ISO 3651-2:1998 Determination of resistance to intergranular corrosion of stainless steels – Part 2: Ferritic, austenitic and ferritic-austenitic (duplex) stainless steels – Corrosion test in media containing sulfuric acid

ISO 4536:1985 Metallic and nonorganic coatings on metallic substrates – Saline droplets corrosion test (SD test)

ISO 4538:1978 Metallic coatings – Thioacetamide corrosion test (TAA test)

ISO 4539:1980 Electrodeposited chromium coatings – Electrolytic corrosion testing (EC test)

ISO 4541:1978 Metallic and other nonorganic coatings – Corrodokote corrosion test (CORR test)

ISO 4543:1981 Metallic and other nonorganic coatings – General rules for corrosion tests applicable for storage conditions

ISO 4623-1:2000 Paints and varnishes – Determination of resistance to filiform corrosion – Part 1: Steel substrates

ISO 4623-2:2003 Paints and varnishes – Determination of resistance to filiform corrosion – Part 2: Aluminum substrates

ISO 6251:1996 Liquefied petroleum gases – Corrosiveness to copper – Copper strip test

ISO 6314:1980 Road vehicles – Brake linings – Resistance to water, saline solution, oil and brake fluid – Test procedure

ISO 6315:1980 Road vehicles – Brake linings – Seizure to ferrous mating surface due to corrosion – Test procedure

ISO 6505:2005 Rubber, vulcanized or thermoplastic – Determination of tendency to adhere to and corrode metals

ISO 6509:1981 Corrosion of metals and alloys – Determination of dezincification resistance of brass

ISO 6988:1985 Metallic and other nonorganic coatings – Sulfur dioxide test with general condensation of moisture

ISO 7120:1987 Petroleum products and lubricants – Petroleum oils and other fluids – Determination of rust-preventing characteristics in the presence of water

ISO 7384:1986 Corrosion tests in artificial atmosphere – General requirements

ISO 7441:1984 Corrosion of metals and alloys – Determination of bimetallic corrosion in outdoor exposure corrosion tests

ISO 7539-1:1987 Corrosion of metals and alloys – Stress corrosion testing,

Part 1: General guidance on testing procedures  
ISO 7539-2:1989 Corrosion of metals and alloys – Stress corrosion testing,  
Part 2: Preparation and use of bent-beam specimens  
ISO 7539-3:1989 Corrosion of metals and alloys – Stress corrosion testing,  
Part 3: Preparation and use of U-bend specimens  
ISO 7539-4:1989 Corrosion of metals and alloys – Stress corrosion testing,  
Part 4: Preparation and use of uniaxially loaded tension specimens  
ISO 7539-5:1989 Corrosion of metals and alloys – Stress corrosion testing,  
Part 5: Preparation and use of C-ring specimens  
ISO 7539-6:2003 Corrosion of metals and alloys – Stress corrosion testing,  
Part 6: Preparation and use of precracked specimens for tests under constant load or constant displacement  
ISO 7539-7:2005 Corrosion of metals and alloys – Stress corrosion testing,  
Part 7: Slow strain rate testing  
ISO 7539-8:2000 Corrosion of metals and alloys – Stress corrosion testing, Part 8: Preparation and use of specimens to evaluate weldments  
ISO 7539-9:2003 Corrosion of metals and alloys – Stress corrosion testing,  
Part 9: Preparation and use of pre-cracked specimens for tests under rising load or rising displacement  
ISO 8044 1999 Corrosion of metals and alloys – Basic terms and definitions  
ISO 8407:1991 Corrosion of metals and alloys – Removal of corrosion products from corrosion test specimens  
ISO 8565:1992 Metals and alloys – Atmospheric corrosion testing – General requirements for field tests  
ISO 9223:1992 Corrosion of metals and alloys – Classification of corrosivity of atmospheres  
ISO 9224:1992 Corrosion of metals and alloys – Guiding values for the corrosivity categories of atmospheres  
ISO 9225:1992 Corrosion of metals and alloys – Corrosivity of atmospheres – Methods of measurement of pollution  
ISO 9226:1992 Corrosion of metals and alloys – Corrosivity of atmospheres – Methods of determination of corrosion rate of standard specimens for the evaluation of corrosivity  
ISO 9227:2006 Corrosion tests in artificial atmospheres – Salt spray tests

ISO 9400:1990 Corrosion of metals and alloys – Nickel-based alloys – Determination of resistance to intergranular corrosion  
ISO 9591:2004 Corrosion of aluminum alloys – Determination of resistance to stress corrosion cracking  
ISO 10062:2006 Corrosion tests in artificial atmosphere at very low concentrations of polluting gas(es)  
ISO 10270:1995 Corrosion of metals and alloys – Aqueous corrosion testing of zirconium alloys for use in nuclear power reactors  
ISO 10270:1995 Corrigendum 1:1997  
ISO 11130:1999 Corrosion of metals and alloys – Alternate immersion test in salt solution  
ISO 11303:2002 Corrosion of metals and alloys – Guidelines for selection of protection methods against atmospheric corrosion  
ISO 11306:1998 Corrosion of metals and alloys – Guidelines for exposing and evaluating metals and alloys in surface sea water  
ISO 11463:1995 Corrosion of metals and alloys – Evaluation of pitting corrosion  
ISO 11474:1998 Corrosion of metals and alloys – Determination of corrosion resistance through accelerated outdoor atmosphere testing  
ISO 11782-1:1998 Corrosion of metals and alloys – Corrosion fatigue tests, Part 1: Cycles to failure testing  
ISO 11782-2:1998 Corrosion of metals and alloys – Corrosion fatigue tests, Part 2: Crack propagation testing  
ISO 11844-1:2006 Corrosion of metals and alloys – Classification of low corrosivity in indoor atmospheres – Part 1: Determination and estimation of indoor corrosivity  
ISO 11844-2:2006 Corrosion of metals and alloys – Classification of low corrosivity of indoor atmospheres – Part 2: Determination of corrosion attack in indoor atmospheres  
ISO 11844-3:2006 Corrosion of metals and alloys – Classification of low corrosivity of indoor atmospheres – Part 3: Measurement of environmental parameters affecting indoor corrosivity  
ISO 11845:1995 Corrosion of metals and alloys – General principles for corrosion testing  
ISO 11846:1995 Corrosion of metals and alloys – Determination of resistance to intergranular corrosion of solution heat treatable aluminum alloys  
ISO 11881:1999 Corrosion of metals and alloys – Determination of resistance to exfoliation corrosion of high strength aluminum alloys



ISO 11881:1999 Corrigendum 1:1999

ISO 12732:2006 Corrosion of metals and alloys – Electrochemical potentiokinetic reactivation measurement using the double loop method (based on Cihal's method)

ISO 14993:2001 Corrosion of metals and alloys – Accelerated testing involving cyclic exposure to salt-mist, 'dry' and 'wet' conditions

ISO 15324:2000 Corrosion of metals and alloys – Evaluation of stress corrosion cracking by the drop evaporation test

ISO 15329:2006 Corrosion of metals and alloys – Anodic test for evaluation of intergranular corrosion susceptibility of heat-treatable aluminum alloys

ISO 16151:2005 Corrosion of metals and alloys – Accelerated cyclic tests with exposure to acidified salt-spray, 'dry' and 'wet' conditions

ISO 16701:2003 Corrosion of metals and alloys – Corrosion in artificial atmosphere – Accelerated corrosion test involving exposure under controlled conditions of humidity cycling and intermittent spraying of a salt solution

ISO 16784-1:2006 Corrosion of metals and alloys – Corrosion and fouling in industrial cooling water systems – Part 1: Guidelines for conducting pilot-scale evaluation of corrosion and fouling control additives for open recirculating cooling water systems

ISO 16784-2:2006 Corrosion of metals and alloys – Corrosion and fouling in industrial cooling water systems – Part 2: Evaluation of the performance of cooling water treatment programs using a pilot-scale test rig

ISO 17081:2004 Method of measurement of hydrogen permeation and determination of hydrogen uptake and transport in metals by an electrochemical technique

ISO 17475:2005 Corrosion of metals and alloys – Electrochemical test methods – Guidelines for conducting potentiostatic and potentiodynamic polarization measurements

ISO 17864:2005 Corrosion of metals and alloys – Determination of the critical pitting temperature under potentiostatic control

ISO 21207:2004 Corrosion tests in artificial atmospheres – Accelerated corrosion tests involving alternate exposure to corrosion-promoting gases, neutral salt-spray and drying

ISO 21610:2009 Corrosion of metals and alloys – Accelerated corrosion test for intergranular corrosion susceptibility of austenitic stainless steels.

## B. 2 IEC Standards

IEC standards are produced by the International Electrotechnical Commission. They use a naming convention similar to ISO.

IEC 60068-2-11: Edition 3, 1981: Environmental testing – Part 2: Tests. Test – Ka: Salt mist

IEC 60068-2-42: Edition 3, 2003: Environmental testing – Part 2-42: Tests – Test Kc: Sulfur dioxide test for contacts and connections

IEC 60068-2-43: Edition 2, 2003: Environmental testing – Part 2-43: Tests – Test Kd: Hydrogen sulfide test for contacts and connections

IEC 60068-2-46: Edition 1, 1982 Environmental testing – Part 2: Tests. Guidance to Test – Kd: Hydrogen sulfide test for contacts and connections

IEC 60068-2-60: Edition 2, 1995: Environmental testing – Part 2: Tests – Test Ke: Flowing mixed gas corrosion test

IEC 60068-2-49: Edition 1, 1983: Environmental testing – Part 2: Tests. Guidance to Test – Kc: Sulfur dioxide test for contacts and connections

IEC 60068-2-52: Edition 2, 1996: Environmental testing – Part 2: Tests – Test Kb: Salt mist, cyclic (sodium chloride solution).

## B. 3 ASTM Standards

ASTM standards use names of the form Xnnn-yy (yyyy), where X is a letter that indicates the general area of the standard (most corrosion standards start with G), nnn is the standard number, yy is the last two digits of the year in which the standard was last revised and yyyy (if present) is the year in which the standard was last reapproved. In the main text we have given only the standard letter and number; here we list the version of the standard that is current at the time of writing (May 2009).

A262-02a (2008) Standard Practices for detecting susceptibility to intergranular attack in austenitic stainless steels

A380-06 Standard Practice for Cleaning, Descaling, and Passivation of Stainless Steel Parts, Equipment, and Systems

A763-93(2009) Standard practices for detecting susceptibility to intergranular attack in ferritic stainless steels

B117-07a Standard practice for operating salt-spray (fog) apparatus

B154-05 Standard test method for mercurous nitrate test for copper alloys

B368–97(2003)e1 Standard method for copper-accelerated acetic acid-salt-spray (fog) testing (CASS test)

B380–97(2008)e1 Standard test method for corrosion testing of decorative electrodeposited coatings by the Corrodikote procedure

B457–67(2008)e1 Standard test method for measurement of impedance of anodic coatings on aluminum.

B537–70(2007) Standard practice for rating of electroplated panels subjected to atmospheric exposure

B735–06 Standard test method for porosity in gold coatings on metal substrates by nitric acid vapor

D130–04e1 Standard test method for corrosiveness to copper from petroleum products by copper strip test

D610–08 Standard practice for evaluating degree of rusting on painted steel surfaces

D714–02e1 Standard test method for evaluating degree of blistering of paints

D807–05 Standard practice for assessing the tendency of industrial boiler waters to cause embrittlement (USBM Embrittlement Detector Method)

D849–05 Standard test method for copper strip corrosion by industrial aromatic hydrocarbons

D1014–09 Standard practice for conducting exterior exposure tests of paints and coatings on metal substrates

D1280–00(2007) Standard guide for total immersion corrosion test for soak tank metal cleaners

D1384–00(2005) Standard test method for corrosion produced by leather in contact with metal

D1654–08 Standard test method for evaluation of painted or coated specimens subjected to corrosive environments

D1743–05ae1 Standard test method for determining corrosion preventive properties of lubricating greases

D1748–02(2008) Standard test method for rust protection by metal preservatives in the humidity cabinet

D1838–07 Standard test method for copper strip corrosion by liquefied petroleum (LP) gases

D2059–03 Standard test method for resistance of zippers to salt spray (fog)

D2247–02 Standard practice for testing water resistance of coatings in 100% relative humidity

D2251–96(2004) Standard test method for metal corrosion by halogenated organic solvents and their admixtures

D2570–08 Standard test method for simulated service corrosion testing of engine coolants

D2688–05 Standard test methods for corrosivity of water in the absence of heat transfer (weight loss methods)

D2758–94(2003) Standard test method for engine coolants by engine dynamometer

D2803–03 Standard guide for testing filiform corrosion resistance of organic coatings on metal

D2809–04e2 Standard test method for cavitation corrosion and erosion-corrosion characteristics of aluminum pumps with engine coolants

D2847–07 Standard practice for testing engine coolants in car and light truck service

D2943–02(2007) Standard test method for aluminum scratch of 1,1,1-trichloroethane to determine stability

D3310–00(2006) Standard test method for determining corrosivity of adhesive materials

D3843–00(2008) Standard practice for quality assurance for protective coatings applied to nuclear facilities

D3911–08 Standard test method for evaluating coatings used in light-water nuclear power plants at simulated design basis accident (DBA) conditions

D3912–95(2001) Standard test method for chemical resistance of coatings used in light-water nuclear power plants

D3929–03 Standard test method for evaluating stress cracking of plastics by adhesives using the bent-beam method

D4340–96(2007) Standard test method for corrosion of cast aluminum alloys in engine coolants under heat-rejecting conditions

D4350–00(2005) Standard test method for corrosivity index of plastics and fillers

D4627–92(2007) Standard test method for iron chip corrosion for water-dilutable metalworking fluids

D4798–08 Standard practice for accelerated weathering test conditions and procedures for bituminous materials (Xenon-Arc method)

D5144–08 Standard guide for use of protective coating standards in nuclear power plants

E647–08 Standard test method for measurement of fatigue crack growth rates

F363–99(2004) Standard test method for corrosion testing of gaskets

F482–03 Standard test method for corrosion of aircraft metals by total immersion in maintenance chemicals

F483–08 Standard test method for total immersion corrosion test for aircraft maintenance chemicals

F981–04 Standard practice for assessment of compatibility of biomaterials for surgical implants with respect to effect of materials on muscle and bone  
F1110–08 Standard test method for sandwich corrosion test

G1–03 Standard practice for preparing, cleaning, and evaluating corrosion test specimens

G2/G2M–06 Standard test method for corrosion testing of products of zirconium, hafnium, and their alloys in water at 680°F [360°C] or in steam at 750°F [400°C]

G3–89 (2004) Standard practice for conventions applicable to electrochemical measurements in corrosion testing

G4–01 (2008) Standard guide for conducting corrosion tests in field applications

G5–94 (2004) Standard reference test method for making potentiostatic and potentiodynamic anodic polarization measurements

G7–05 Standard practice for atmospheric environmental exposure testing of nonmetallic materials

G11–04 Standard test method for effects of outdoor weathering on pipeline coatings

G15–08 Standard terminology relating to corrosion and corrosion testing

G16–95 (2004) Standard guide for applying statistics to analysis of corrosion data

G28–02 (2008) Standard test methods for detecting susceptibility to intergranular corrosion in wrought nickel-rich, chromium-bearing alloys

G30–97 (2003) Standard practice for making and using U-bend stress corrosion test specimens

G31–72 (2004) Standard practice for laboratory immersion corrosion testing of metals

G32–06 Standard test method for cavitation erosion using vibratory apparatus

G33–99 (2004) Standard practice for recording data from atmospheric corrosion tests of metallic-coated steel specimens

G34–01 (2007) Standard test method for exfoliation corrosion susceptibility in 2XXX and 7XXX series aluminum alloys (EXCO test)

G35–98 (2004) Standard practice for determining the susceptibility of stainless steels and related nickel–chromium–iron alloys to stress corrosion cracking in polythionic acids

G36–94 (2006) Standard practice for evaluating stress corrosion cracking resistance of metals and alloys in a boiling magnesium chloride solution

G37–98 (2004) Standard practice for use of Mattson's solution of pH 7.2 to evaluate the stress corrosion cracking susceptibility of copper–zinc alloys

G38–01 (2007) Standard practice for making and using C-ring stress corrosion test specimens

G39–99 (2005) Standard practice for preparation and use of bent-beam stress corrosion test specimens

G41–90 (2006) Standard practice for determining cracking susceptibility of metals exposed under stress to a hot salt environment

G44–99 (2005) Standard practice for exposure of metals and alloys by alternate immersion in neutral 3.5% sodium chloride solution

G46–94 (2005) Standard guide for examination and evaluation of pitting corrosion

G47–98 (2004) Standard test method for determining susceptibility to stress corrosion cracking of 2XXX and 7XXX aluminum alloy products

G48–03 Standard test method for pitting and crevice corrosion resistance of stainless steels and related alloys by the use of ferric chloride solution

G49–85 (2005) Standard practice for preparation and use of direct tension stress corrosion test specimens

G50–76 (2003) Standard practice for conducting atmospheric stress corrosion tests on metals

G51–95 (2005) Standard test method for measuring pH of soil for use in corrosion testing

G52–00 (2006) Standard practice for exposing and evaluating metals and alloys in surface seawater

G57–06 Standard test method for field measurement of soil resistivity using the Wenner four-electrode method

G58–85 (2005) Standard practice for the preparation of stress corrosion test specimen for weldments

G59–97 (2003) Standard test method for conducting potentiodynamic polarization resistance measurements

G60–01 (2007) Standard practice for conducting cyclic humidity exposures

G61–86 (2003)e1 Standard test method for conducting cyclic potentiodynamic polarization measurements for localized corrosion susceptibility of iron-, nickel-, or cobalt-based alloys

G64–99 (2005) Standard classification of resistance to stress corrosion cracking of heat treatable aluminum alloys

G66–99 (2005)e1 Standard test method for visual assessment of exfoliation corrosion susceptibility of 5XXX series aluminum alloys (ASSET test)

G67–04 Standard test method for determining the susceptibility to intergranular corrosion of 5XXX series aluminum alloys by mass loss after exposure to nitric acid (NAMLT test)

- G69–97 (2003) Standard test method for measurement of corrosion potentials of aluminum alloys
- G71–81 (2003) Standard guide for conducting and evaluating galvanic corrosion tests in electrolytes
- G 73–04 Standard practice for liquid impingement erosion testing
- G78–01 (2007) Standard guide for crevice corrosion testing of iron base and nickel base stainless steels in seawater and other chloride-containing aqueous environments
- G82–98 (2003) Standard guide for development and use of a galvanic series for predicting galvanic corrosion performance
- G84–89 (2005) Standard practice for measurement of time-of-wetness on surfaces exposed to wetting conditions as in atmospheric corrosion testing
- G85–02e1 Standard practice for modified salt spray (fog) testing
- G87–02 (2007) Standard practice for conducting moist SO<sub>2</sub> test
- G90–05 Standard practice for performing accelerated outdoor weathering of nonmetallic materials using concentrated natural sunlight
- G91–97 (2004) Standard practice for monitoring atmospheric SO<sub>2</sub> using sulfation plate technique
- G92–86 (2003) Standard practice for characterization of atmospheric test sites
- G96–90(2008) Standard guide for online monitoring of corrosion in plant equipment (electrical and electrochemical methods)
- G97–97(2007) Standard test method for laboratory evaluation of magnesium sacrificial anode test specimens for underground applications
- G100–89(2004) Standard test method for conducting cyclic galvanostaircase polarization
- G101–04 Standard guide for estimating the atmospheric corrosion resistance of low-alloy steels
- G102–89 (2004)e1 Standard practice for calculation of corrosion rates and related information from electrochemical measurements
- G103–97 (2005) Standard practice for evaluating stress-corrosion cracking resistance of low copper 7XXX series Al-Zn-Mg-Cu alloys in boiling 6% sodium chloride solution
- G104:1989 Test method for assessing galvanic corrosion caused by the atmosphere
- G106–89(2004) Standard practice for verification of algorithm and equipment for electrochemical impedance measurements
- G107–95(2008) Standard guide for formats for collection and compilation of corrosion data for metals for computerized database input
- G108–94(2004)e1 Standard test method for electrochemical reactivation (epr) for detecting sensitization of AISI type 304 and 304L stainless steels
- G109–07 Standard test method for determining effects of chemical admixtures on corrosion of embedded steel reinforcement in concrete exposed to chloride environments
- G110–92(2003)e1 Standard practice for evaluating intergranular corrosion resistance of heat treatable aluminum alloys by immersion in sodium chloride + hydrogen peroxide solution
- G111–97(2006) Standard guide for corrosion tests in high temperature or high pressure environment, or both
- G112–92(2003) Standard guide for conducting exfoliation corrosion tests in aluminum alloys
- G116–99(2004) Standard practice for conducting wire-on-bolt test for atmospheric galvanic corrosion
- G123–00(2005) Standard test method for evaluating stress-corrosion cracking of stainless alloys with different nickel content in boiling acidified sodium chloride solution
- G129–00(2006) Standard practice for slow strain rate testing to evaluate the susceptibility of metallic materials to environmentally assisted cracking
- G135–95(2007) Standard guide for computerized exchange of corrosion data for metals
- G139–05 Standard Test method for determining stress-corrosion cracking resistance of heat-treatable aluminum alloy products using breaking load method
- G140–02(2008) Standard test method for determining atmospheric chloride deposition rate by wet candle method
- G142–98(2004) Standard test method for determination of susceptibility of metals to embrittlement in hydrogen containing environments at high pressure, high temperature, or both
- G146–01(2007) Standard practice for evaluation of disbonding of bimetallic stainless alloy/steel plate for use in high-pressure, high temperature refinery hydrogen service
- G148–97(2003) Standard practice for evaluation of hydrogen uptake, permeation, and transport in metals by an electrochemical technique
- G150–99(2004) Standard test method for electrochemical critical pitting temperature testing of stainless steels
- G152–06 Standard practice for operating open flame carbon arc light apparatus for exposure of nonmetallic materials

G153–04 Standard practice for operating enclosed carbon arc light apparatus for exposure of nonmetallic materials

G157–98(2005) Standard guide for evaluating the corrosion properties of wrought iron- and nickel-based corrosion resistant alloys for the chemical process industries

G158–98(2004) Standard guide for three methods of assessing buried steel tanks

G162–99(2004) Standard practice for conducting and evaluating laboratory corrosion tests in soils

G165–99(2005) Standard practice for determining rail-to-earth resistance

G168–00(2006) Standard practice for making and using precracked double beam stress corrosion specimens

G170–06 Standard guide for evaluating and qualifying oilfield and refinery corrosion inhibitors in the laboratory

G180–07 Standard test method for initial screening of corrosion inhibiting admixtures for steel in concrete

G184–06 Standard practice for evaluating and qualifying oil field and refinery corrosion inhibitors using rotating cage

G185–06 Standard practice for evaluating and qualifying oil field and refinery corrosion inhibitors using the rotating cylinder electrode

G186–05 Standard test method for determining whether gas-leak-detector fluid solutions can cause stress corrosion cracking of brass alloys

G187–05 Standard test method for measurement of soil resistivity using the two-electrode soil box method

G188–05 Standard specification for leak detector solutions intended for use on brasses and other copper alloys

G189–07 Standard guide for laboratory simulation of corrosion under insulation

G192–08 Standard test method for determining the crevice repassivation potential of corrosion-resistant alloys using a potentiodynamic-galvanostatic-potentiostatic technique.

## B. 4 NACE Standards

NACE standards are produced by NACE International (formerly the National Association of Corrosion Engineers). They use the naming convention NACE XXnnnn-yyyy, where XX is the type of

standard, nnnn the standard number and yyyy the year of publication. Here we list only the TM (Test Method) standards; the full list can be found on the NACE website ([www.nace.org](http://www.nace.org)).

TM0101–2001 Measurement techniques related to criteria for cathodic protection on underground or submerged metallic tank systems

TM0102–2002 Measurement of protective coating electrical conductance on underground pipelines

TM0103–2003 Laboratory test procedures for evaluation of SOHIC resistance of plate steels used in wet H<sub>2</sub>S service

TM0104–2004 Offshore platform ballast water tank coating system evaluation

TM0105–2005 Test procedures for organic-based conductive coating anodes for use on concrete structures

TM0106–2006 Detection, testing, and evaluation of microbiologically influenced corrosion (MIC) on external surfaces of buried pipelines

TM0108–2008 Testing of catalyzed titanium anodes for use in soils or natural waters

TM0109–2009 Above ground survey techniques for the evaluation of underground pipeline coating condition

TM0169–2000 Laboratory corrosion testing of metals

TM0172–2001 Determining corrosive properties of cargoes in petroleum product pipelines

TM0173–2005 Methods for determining quality of subsurface injection water using membrane filters

TM0174–2002 Laboratory methods for the evaluation of protective coatings and lining materials on metallic substrates in immersion service

TM0177–2005 Laboratory testing of metals for resistance to sulfide stress cracking and stress corrosion cracking in H<sub>2</sub>S environments

TM0183–2006 Evaluation of internal plastic coatings for corrosion control of tubular goods in an aqueous flowing environment

TM0185–2006 Evaluation of internal plastic coatings for corrosion control of tubular goods by autoclave testing

TM0186–2002 Holiday detection of internal tubular coatings of 250- to 760- $\mu$ m (10 to 30 mils) dry-film thickness

TM0187–2003 Evaluating elastomeric materials in sour gas environments

TM0190–2006 Impressed current laboratory testing of aluminum alloy anodes



TM0192–2003 Evaluating elastomeric materials in carbon dioxide decompression environments

TM0193–2000 Laboratory corrosion testing of metals in static chemical cleaning solutions at temperatures below 93°C (200°F)

TM0194–2004 Field monitoring of bacterial growth in oil and gas systems

TM0197–2002 Laboratory screening test to determine the ability of scale inhibitors to prevent the precipitation of barium sulfate and/or strontium sulfate from solution (for oil and gas production systems)

TM0198–2004 Slow strain-rate test method for screening corrosion-resistant alloys (CRAs) for stress corrosion cracking in sour oilfield service

TM0199–2006 Standard test method for measuring deposit mass loading (deposit weight density) values for boiler tubes by the glass-bead-blasting technique

TM0204–2004 Exterior protective coatings for seawater immersion service

TM0208–2008 Laboratory test to evaluate the vapor-inhibiting ability of volatile corrosion inhibitor materials for temporary protection of ferrous metal surfaces

TM0284–2003 Evaluation of pipeline and pressure vessel steels for resistance to hydrogen-induced cracking

TM0286–2001 Cooling water test unit incorporating heat transfer surfaces

TM0294–2007 Testing of embeddable impressed current anodes for use in cathodic protection of atmospherically exposed steel-reinforced concrete

TM0296–2002 Evaluating elastomeric materials in sour liquid environments

TM0297–2008 Effects of high temperature, high-pressure carbon dioxide decompression on elastomeric materials

TM0298–2003 Evaluating the compatibility of FRP pipe and tubulars with oilfield environments

TM0304–2004 Offshore platform atmospheric and splash zone maintenance coating system evaluation

TM0374–2007 Laboratory screening tests to determine the ability of scale inhibitors to prevent the precipitation of calcium sulfate and calcium carbonate from solution (for oil and gas production systems)

TM0384–2002 Holiday detection of internal tubular coatings of less than 250- $\mu\text{m}$  (10 mils) dry-film thickness

TM0397–2002 Screening tests for evaluating the effectiveness of gypsum scale removers

TM0399–2005 Standard test method for phosphonate in brine

TM0404–2004 Offshore platform atmospheric and splash-zone new construction coating system evaluation

TM0497–2002 Measurement techniques related to criteria for cathodic protection on underground or submerged metallic piping systems

TM0498–2006 Evaluation of the carburization of alloy tubes used for ethylene manufacture

TM0499–99 Immersion corrosion testing of ceramic materials.

## B. 5 Other National Standards

Most other national standards have been subsumed into ISO standards. Thus, the British Standards Institute (BSI) now markets standards as BS EN ISO xxxx (for British Standard, European Norm, ISO xxxx).

## References

1. Champion, F. A. *Corrosion Testing Procedures*, Chapman and Hall: London, 1964.
2. Ailor, W. H. Ed.; *Handbook on Corrosion Testing and Evaluation*; Wiley: New York, 1971.
3. Gilroy, D.; Mayne, J. E. O. *Corros. Sci.* **1965**, 5, 55.
4. Wesley, W. A. *Proc. Am. Soc. Test. Mater.* **1943**, 43, 649.
5. Bayer, R. O.; Kachik, E. A. *Corrosion* **1949**, 5, 308.
6. Renshaw, W. G.; Ferree, J. A. *Corrosion* **1951**, 7, 353.
7. Gulbransen, E. A. *Miner. Metall. N.Y.* **1944**, 25, 172.
8. Kruger, J. J. *Electrochem. Soc.* **1959**, 106, 847; Kruger, J.; Hayfield, P. C. S. In *Handbook on Corrosion Testing and Evaluation*; Ailor, W. H., Ed.; Wiley: New York, 1971.
9. Rutherford, J. J. B.; Aborn, R. H. *Trans. Am. Inst. Miner. (Metall.) Eng.* **1932**, 100, 293.
10. Burns, R. M.; Campbell, W. E. *Trans. Electrochem. Soc.* **1929**, 55, 271.
11. Hudson, J. C. *Proc. Phys. Soc. Lond.* **1928**, 40, 107.
12. Mercer, A. D.; Butler, G.; Warren, G. M. *Br. Corrosion J.* **1977**, 12, 122.
13. Finkeldey, W. H. *Proc. Am. Soc. Test. Mater.* **1932**, 32, 226.
14. Kenworthy, L.; Waldram, J. M. *J. Inst. Met.* **1934**, 55, 247.
15. Tronstad, L. *Trans. Faraday Soc.* **1933**, 29, 502.
16. Kruger, J. J. *Electrochem. Soc.* **1959**, 106, 847, and **1961**, 108, 504.; Kruger, J. In *Symp. Proc.* Bashara, N. M., Buckman, A. B., Hall, A. C., Eds.; University of Nebraska: Lincoln, 1969; p 16.
17. Bengough, G. D.; Stuart, J. M.; Lee, A. R. *Proc. Roy. Soc. A.* **1928**, 116, 425; 121, 89.
18. Shipley, J. W.; McHaffie, I. R.; Clare, N. D. *Ind. Eng. Chem.* **1925**, 17, 381.
19. Bloom, M. C.; Krulfeld, M. J. *Electrochem. Soc.* **1957**, 104, 264.
20. Vaurio, V. W.; Clark, B. S.; Lueck, R. H. *Ind. Eng. Chem. (Anal.)* **1938**, 10, 368.
21. Hudson, R. M.; Stragland, G. L. *Corrosion* **1959**, 15, 135t.

22. Willey, A. R.; Krickl, J. L.; Hartwell, R. R. *Corrosion* **1956**, 12, 433t.
23. Burns, R. M. *J. Appl. Phys.* **1937**, 8, 398.
24. Dravnieks, A.; Cataldi, H. A. *Corrosion* **1954**, 10, 224.
25. Marsh, G. A.; Schaschl, E. *Corrosion* **1958**, 14, 155t.
26. Mylius, F. Z. *Metallkd.* **1922**, 14, 233.
27. El-Kot, A. M.; Al-Suhbani, Br. *Corros. J.* **1987**, 22, 29.
28. Am. Soc. Test. Mater. Spec. Tech. Publ. No. 32, 1937.
29. Knapp, B. B. In *The Corrosion Handbook*; Uhlig, H. H., Ed.; Wiley/Chapman and Hall: New York/London, 1948; p 1077.
30. Teeple, H. O. *Am. Soc. Test. Mater. Spec. Tech. Publ.* No. 175, 1956, 89.
31. Am. Soc. Test. Mater. Spec. Tech. Publ. No. 970, 1988.
32. Gallagher, P.; Malpas, R. E.; Shone, E. B. *Br. Corros. J.* **1988**, 23, 229.
33. Mercer, A. D.; Brook, G. M. *La Tribune de Cebedeau*. **1978**, 299, 417–418.
34. Cheung, W. K.; Thomas, J. G. N. In *The Use of Synthetic Environments for Corrosion Testing*; ASTM STP; ASTM: Philadelphia, 1988; Vol. 970, p 190.
35. LaQue, F. L.; Stewart, W. C. *Métaux Corros.* **1948**, 23, 147.
36. Vernon, W. H. *J. Soc. Chem. Ind. Lond.* **1947**, 66, 137; *Corrosion* **1948**, 4, 141.
37. Bengough, G. D.; May, R. *J. Inst. Met.* **1924**, 32, 81.
38. May, R.; Stacpoole, R. W. de Vere, *J. Inst. Met.* **1950**, 77, 331.
39. Brownsdon, H. W.; Bannister, L. C. *J. Inst. Met.* **1932**, 49, 123.
40. Freeman, J. R., Jr.; Tracy, A. W. *Corrosion* **1949**, 5, 245.
41. Butler, G.; Ison, H. C. K. *J. Appl. Chem.* **1960**, 10, 80.
42. Fontana, M. G. *Ind. Eng. Chem.* **1947**, 39, 87A.
43. Wagner, H. A.; Decker, J. M.; Marsh, J. C. *Trans. Am. Soc. Mech. Eng.* **1947**, 69, 389.
44. Trembler, H. A.; Wesley, W. A.; LaQue, F. L. *Ind. Eng. Chem.* **1932**, 24, 339.
45. Brenner, S. *J. Iron Steel Inst.* **1937**, 135, 101P.
46. Smith, H. A. *Metal Prog.* **1938**, 33, 596.
47. Hanawalt, J. D.; Nelson, C. E.; Peloubet, J. A. *Trans. Am. Inst. Miner. (Metall.) Eng.* **1942**, 147, 273.
48. Benedicks, C. *Trans. Am. Inst. Miner. (Metall.) Eng.* **1925**, 71, 597.
49. McAdams, D. J. *Heat Transmission*, 3rd ed.; McGraw-Hill: New York, 1954; p 370.
50. Groves, N. D.; Eisenbrown, C. M. *Metal Prog.* **1959**, 75, 78.
51. Fisher, A. O.; Whitney, F. L., Jr. *Corrosion* **1959**, 15, 257t.
52. Fisher, A. O. *Corrosion* **1961**, 17, 215t.
53. Groves, N. D.; Eisenbrown, C. M.; Scharfstein, L. R. *Corrosion* **1961**, 17, 173t.
54. Hart, R. J. In *Handbook on Corrosion Testing and Evaluation*; Ailor, W. H., Ed.; Wiley: New York, 1971; p 367.
55. LaQue, F. L. *J. Electrochem. Soc.* **1969**, 116, 73C.
56. Stern, M.; Geary, A. L. *J. Electrochem. Soc.* **1957**, 104, 56.
57. Stern, M. *Corrosion* **1958**, 14, 440t.
58. Pourbaix, M. *Lectures on Electrochemical Corrosion* Plenum Press; 1973; see also references to potential-pH diagrams given in Section.
59. Armstrong, R. D.; Henthorne, M.; Thirsk, H. R. *J. Electroanal. Chem.* **1972**, 35, 119.
60. Epelboin, I.; Keddam, M.; Takenouti, H. *J. App. Electrochem.* **1972**, 2, 71.
61. Sathyaharayana, S. *Electroanal. Chem. Interfacial Electrochem.* **1974**, 50, 411.
62. Macdonald, D. D. *Corrosion* **1990**, 46, 229.
63. Kendig, M. W.; Mansfield, F. Proc. Fall Meeting, Detroit, Electrochem. Soc., 82–2, **1982**, p 105.
64. Ferreira, M. G. S.; Dawson, J. L. In *Passivity of Metals and Semiconductors*; Froment, M., Ed.; **1980**, p 359.
65. Ferreira, M. G. S.; Dawson, J. L. *J. Electrochem. Soc.* **1983**, 132, 760.
66. Keddam, M.; Oltra, R.; Colson, J. C.; Desestret, A. *Corros. Sci.* **1983**, 23, 441.
67. Isaacs, H. S.; Kendig, M. W. *Corrosion* **1980**, 36, 269.
68. Park, J. K.; Macdonald, D. D. *Corros. Sci.* **1983**, 23, 293.
69. Epelboin, I.; Gabrielli, C.; Keddam, M.; Takenouti, H. Z. *Physik. Chem.* **1975**, 98, 215.
70. Oltra, R.; Keddam, M. *Corros. Sci.* **1988**, 28, 1.
71. Sato, N. *J. Electrochem. Soc.* **1976**, 123, 1197.
72. Shibata, T.; Takeyama, T. *Corrosion* **1977**, 33, 243.
73. Williams, D. E. Proc. In *Electrochemical Corrosion Testing*, Ferrara. 10–14 September 1985 DEHEMA 1986.
74. Williams, D. E.; Wescott, C.; Fleischmann, M. *J. Electrochem. Soc.* **1985**, 132, 1796.
75. Williams, D. E.; Wescott, C.; Fleischmann, M. *J. Electrochem. Soc.* **1985**, 132, 1804.
76. Gabrielli, C.; Huet, F.; Keddam, M.; Oltra, R. *Corrosion* **1990**, 46, 266.
77. Ives, D. J. G.; Janz, G. J. *Reference Electrodes*; Academic Press: London, 1961.
78. Compton, K. G. *Mater. Res. Standards* **1970**, 10, 13.
79. Covington, A. K. In *Electrochemistry*; The Chemical Society: London, 1970; Vol. 1, p 56.
80. Meites, L.; Moros, S. A. *Analyt. Chem.* **1959**, 31, 25.
81. European Federation of Corrosion Publication No. 4, A WP report Guidelines on Electrochemical Corrosion Measurements; The Institute of Metals: London, 1990.
82. Berzins, T.; Delahay, P. *J. Am. Chem. Soc.* **1955**, 77, 6448.
83. Pouli, D.; Huff, J. R.; Pearson, J. C. *Anal. Chem.* **1966**, 38, 382.
84. Kooijman, D. J.; Sluyters, J. H. *Electrochim. Acta.* **1966**, 11, 1147.
85. Bewick, J. *Electrochim. Acta.* **1968**, 13, 825.
86. Piontelli, R.; Bianchi, G. Proc. 2nd. Meeting C.I.T.C.E., Milan 1951.
87. Piontelli, R. Proc. 4th Meeting C.I.T.C.E., London and Cambridge, 1952.
88. von Fraunhofer, J. A.; Banks, C. A. *Potentiostat and its Applications*; Butterworths: London, 1972.
89. Stern, M.; Makrides, A. C. *J. Electrochem. Soc.* **1960**, 107, 782.
90. Greene, N. D.; France, W. D.; Wilde, B. E. *Corrosion* **1965**, 21, 275.
91. Greene, N. D.; Acello, S. J.; Greif, A. J. *J. Electrochem. Soc.* **1962**, 109, 1001.
92. Cleary, H. J.; Greene, N. D. *Electrochim. Acta.* **1965**, 10, 1107.
93. France, W. D., Jr. *J. Electrochem. Soc.* **1967**, 114, 818.
94. Wilde, B. E. *Corrosion* **1967**, 23, 331.
95. Smith, L. W.; Pingel, V. J. *J. Electrochem. Soc.* **1951**, 98, 48.
96. Budd, M. K.; Booth, F. F. *Metallurgia* **1962**, 66, 245.
97. Cleary, H. J. *Corrosion* **1968**, 24, 159.
98. Doig, P.; Edington, J. W. *Br. Corros. J.* **1974**, 9, 88.
99. Davis, J. A. Proc. Conf. on Localised Corrosion; NACE: Williamsburg, 1971; p 168.
100. May, R. *J. Inst. Metals* **1928**, 40, 141.
101. Hines, J. private communication.
102. Hoar, T. P.; Hines, J. G. *J. Iron Steel Inst.* **1965**, 182(124), 156.
103. Hoar, T. P.; West, J. M. *Proc. Roy. Soc.* **1962**, A268, 304.
104. Horst, R. L., Jr.; Hollingsworth, E. H.; King, W. *Corrosion* **1969**, 25, 199.

105. Pearson, J. M. *Trans. Electrochem. Soc.* **1942**, 81, 485.
106. Schwerdtfeger, W. J. *Corrosion* **1963**, 19, 17t.
107. Schwerdtfeger, W. J.; Manuele, R. J. *Corrosion* **1963**, 19, 59t.
108. Skold, R. V.; Larson, T. E. *Corrosion* **1957**, 13, 139t.
109. Stern, M.; Weisert, E. D. *Proc. Am. Soc. Test. Mater.* **1959**, 59, 1280.
110. Barnartt, S. *Corrosion* **1971**, 27, 467.
111. Barnartt, S. *Corrosion Sci.* **1969**, 9, 145.
112. Leroy, R. L. *Corrosion* **1973**, 29, 272.
113. Oldham, K. B.; Mansfeld, F. *Corrosion* **1971**, 27, 434.
114. Oldham, K. B.; Mansfeld, F. *Corrosion Sci.* **1973**, 13, 811.
115. Hickling, J. Ph.D. Thesis, University of Cambridge, 1974.
116. Hoar, T. P. *Corrosion Sci.* **1967**, 7, 455.
117. Mansfeld, F. *Corrosion* **1973**, 29, 397.
118. Mansfeld, F. *Corrosion* **1974**, 30, 92.
119. Mansfeld, F. J. *Electrochem. Soc.* **1971**, 118, 545.
120. Mansfeld, F. J. *Electrochem. Soc.* **1973**, 120, 515.
121. Makrides, A. C. *Corrosion* **1969**, 25, 455.
122. Legault, R. A.; Walker, M. S. *Corrosion* **1963**, 19, 222.
123. Walker, M. S.; France, W. D. *Mat. Protect.* **1969**, 8, 47.
124. Jones, D. A.; Greene, N. B. *Corrosion* **1969**, 25, 367.
125. Wilde, B. E. *Corrosion* **1967**, 23, 379.
126. Jones, D. A. *Corros. Sci.* **1968**, 8, 19.
127. Bureau, M. 9th Fatigue Congress 1968, 79.
128. Mikhailovskii, Y. N.; Leonev, V. V.; Tomashov, N. D. *Korrozya Metallov i Splavov Sbornik 2*; Metallurgizdat: Moscow, 1965.
129. Butler, T. J.; Carter, P. R. *Electrochem. Tech.* **1963**, 1, 22.
130. Walpole, J. F. *Bull. Inacol.* **1972**, 23, 22.
131. Bird, D. W. *Bull. Inacol.* **1971**, 22, 149.
132. Rowlands, J. C.; Bentley, M. N. *Br. Corros. J.* **1972**, 7, 42.
133. Wesley, W. A. *Trans. Electrochem. Soc.* **1938**, 73, 539.
134. Copson, H. R. *Ind. Eng. Chem.* **1945**, 37, 721.
135. Rowe, L. C. *J. Mater.* **1970**, 5, 323.
136. Denison, I. A. *J. Res. Nat. Bur. Stand.* **1936**, 17, 363.
137. Ewing, S. P. *Am. Gas. Assoc. Mon.* **1932**, 14, 356.
138. Schwerdtfeger, W. J. *J. Res. Nat. Bur. Stand.* **1953**, 50, 329.
139. Schwerdtfeger, W. J. *J. Res. Nat. Bur. Stand.* **1954**, 52, 265.
140. Schwerdtfeger, W. J. *J. Res. Nat. Bur. Stand.* **1957**, 58, 145.
141. Schwerdtfeger, W. J. *J. Res. Nat. Bur. Stand.* **1961**, 65C, 271.
142. Logan, R. H.; Ewing, S. P.; Denison, I. A. *Am. Soc. Test. Mater. Spec. Tech. Publ.*; No. 32, 1937, 95.
143. Jones, D. A.; Lowe, T. A. *J. Mater.* **1969**, 4, 600.
144. Fuller, T. S. *Proc. Am. Soc. Test. Mater.* **1924**, 27, 281.
145. Lathrop, E. C. *Proc. Am. Soc. Test. Mater.* **1924**, 24, 281.
146. Streicher, M. A. *ASTM Bull* No. 188, **1953**, p 35.
147. Streicher, M. A. *ASTM Bull* No. 195, **1954**, p 63.
148. Streicher, M. A. *J. Electrochem. Soc.* **1959**, 106, 161.
149. Streicher, M. A. *Corrosion* **1963**, 19, 272t.
150. Saur, R. L.; Basco, R. P. *Plating* **1966**, 53, 33.
151. Saur, R. L.; Basco, R. P. *Plating* **1966**, 53, 320.
152. Saur, R. L.; Basco, R. P. *Plating* **1966**, 53, 981.
153. Saur, R. L. *Plating* **1966**, 54, 393.
154. Englehart, E. T.; George, D. J. *Mater. Prot.* **1964**, 3, No. 11, 25.
155. Capp, J. A. *Proc. Am. Soc. Test. Mater.* **1914**, 14, 474.
156. LaQue, F. L. *Proc. Am. Soc. Test. Mater.* **1951**, 51, 495.
157. LaQue, F. L. *Mater. Meth.* **1952**, 35, No. 2, 77.
158. Sample, C. H. *Bull. Am. Soc. Test. Mater.*, **1943**, 123, 19.
159. May, T. P.; Alexander, A. L. *Proc. Am. Soc. Test. Mater.* **1950**, 50, 1131.
160. Darsey, V. M.; Cavanaugh, W. R. *Proc. Am. Soc. Test. Mater.* **1948**, 48, 153.
161. Nixon, C. F. *Mon. Ren. Am. Electropl. Soc.* **1945**, 32, 1105.
162. Pinner, W. L. *Plating* **1957**, 44, 763.
163. Nixon, C. F.; Thomas, J. D.; Hardesty, D. W. *46th Ann. Tech. Proc. Am. Electropl. Soc.* **1959**, 159.
164. Thomas, J. D.; Hardesty, D. W.; Nixon, C. F. *47th Ann. Tech. Proc. Am. Electropl. Soc.* **1960**, 90.
165. LaQue, F. L. *46th Ann. Tech. Proc. Am. Electropl. Soc.* **1959**, 141.
166. Bigge, D. M. *46th Ann. Tech. Proc. Am. Electropl. Soc.* **1959**, 149.
167. Edwards, J. *46th Ann. Tech. Proc. Am. Electropl. Soc.* **1959**, 154.
168. Edwards, J. *Trans. Inst. Metal Finish.* **1958**, 35, 55.
169. Kesternich, W. *Stahl u. Eisen* **1951**, 71, 587.
170. Dix, E. H., Jr.; Bowman, J. J. *Am. Soc. Test. Mater. Spec. Tech. Publ.* No. 32, **1937**, 57.
171. Carter, V. E., Ed. *Corrosion Testing for Metal Finishing*; Butterworths: London, 1982.
172. Swinden, T.; Stevenson, W. W. *J. Iron St. Inst.* **1940**, 142, 165P.
173. Lloyd, T. E. *J. Metals NY* **1950**, 188, 1092.
174. Evans, U. R.; Britton, S. C. *J. Iron St. Inst. Spec. Rept. No.* **1931**, 1, 139.
175. Dennis, J. K.; Such, T. E. *Trans. Inst. Metal Finish.* **1963**, 40, 60.
176. Dennis, J. K.; Such, T. E. *Nickel and Chromium Plating*, 2nd ed.; Butterworths: London, 1986.
177. Chandler, K. A.; Kilcullen, M. B. *Br. Corros. J.* **1970**, 5, 1.
178. Bromley, A. F.; Kilcullen, M. B.; Stanners, J. F. In 5th European Congress of Corrosion, Paris, September 1973.
179. Pourbaix, M. *CEBELCOR RT*; **1969**, 160.
180. Legault, R. A.; Mori, S.; Leckie, H. P. *Corrosion* **1970**, 26, 121.
181. Legault, R. A.; Mori, S.; Leckie, H. P. *Corrosion* **1973**, 29, 169.
182. Okada, H.; Hosio, U.; Naito, H. *Corrosion* **1970**, 26, 429.
183. Brown, M. H. *Corrosion* **1974**, 30, 1.
184. Cowan, R. L.; Tedmon, C. S., Jr. In Fontana, M. G., Staehle, R. W., Eds.; *Advances in Corrosion Science and Technology*; Plenum Press: New York, 1973; Vol. 3.
185. Huey, W. R. *Trans. Am. Soc. Steel Treat.* **1930**, 18, 1126.
186. Henthorne, M. *Corrosion* **1974**, 30, 39.
187. Strauss, B.; Schottky, H.; Hinnüber, J. Z. *Anorg. Allgem. Chem.* **1930**, 188, 309.
188. Rocha, H. J. in discussion of paper by Brauns, E., Pier, G., Stahl, U. *Eisen* **1955**, 75, 579.
189. Scharfstein, L. R.; Eisenbrown, C. M. *ASTM STP* No. 369, **1963**, 253.
190. Tedmon, C. S., Jr.; Vermilyea, D. A.; Rosolowski, J. H. *J. Electrochem. Soc.* **1971**, 118, 192.
191. Ebling, H.; Scheil, M. A. *ASTM Special Tech. Publ.* No. 93, **1949**, 121.
192. Warren, D. *ASTM Bulletin*. No. 230, **1958**, 45.
193. Streicher, M. A. *ASTM Bulletin*. No. 188, **1953**, 35.
194. Clerbois, L.; Clerbois, F.; Massart, J. *Electrochem. Acta.* **1959**, 1, 70.
195. France, W. D.; Greene, N. D. *Corros. Sci.* **1968**, 8, 9.
196. Streicher, M. A. *Corros. Sci.* **1969**, 9, 55.
197. France, W. D.; Greene, N. D. *Corros. Sci.* **1970**, 10, 379.
198. Streicher, M. A. *Corros. Sci.* **1971**, 11, 275.
199. Cihal, V.; Desestret, A.; Froment, M.; Wagner, G. H. *Proc. Conf. European Federation on Corrosion, Paris, France 1973*; p 249.
200. Novak, P.; Stefec, R.; Franz, F. *Corrosion* **1975**, 31, 344.

201. Kolotyrkin, Ya. M. *Zashch. Met.* **1975**, 11, 699.
202. Clark, W. L.; Cowan, R. L.; Walker, W. L. *Comparative Methods for Measuring Degree of Sensitisation in Stainless Steel* ASTM STP; ASTM: Philadelphia, 1978; Vol. 656, p 99.
203. Lee, J. B. *Corrosion* **1986**, 42, 106.
204. Streicher, M. A. *Corrosion* **1974**, 30, 77.
205. Fontana, M. G.; Greene, N. D. *Corrosion Engineering*; McGraw-Hill: New York, 1967.
206. Wilde, B. E. *Corrosion* **1972**, 28, 283.
207. France, W. D.; Greene, N. D. *Corrosion* **1970**, 26, 1.
208. Wilde, B. E.; Williams, E. J. *Electrochem. Soc.* **1970**, 117, 775.
209. Wilde, B. E.; Greene, N. D. *Corrosion* **1969**, 25, 300.
210. Henry, W. D.; Wilde, B. E. *Corrosion* **1969**, 25, 515.
211. Wilde, B. E.; Williams, E. J. *Electrochem. Soc.* **1971**, 118, 1058.
212. May, R.; Stacpoole, R. W. de V. J. *Inst. Met.* **1950**, 77, 331.
213. Efrid, K. D. *Corrosion* **1977**, 33, 347.
214. Brownsdon, H. W.; Bannister, L. C. J. *Inst. Met.* **1932**, 49, 123.
215. Breckon, C.; Gilbert, P. T. 1st Int. Congress on Met. Corrosion, Butterworths, London, **1962**, p 624.
216. Bem, R. S.; Campbell, H. S. 1st Int. Congress on Met. Corrosion, Butterworths, London, **1962**, p 630.
217. Campbell, H. S. MP577, BNFMR, 1973.
218. LaQue, F. L. *Marine Corrosion*; Wiley: New York, 1975; p 62.
219. Grant, A. A.; Phillips, L. *The Application of Advanced Materials Technology in Fluid Engineering*; Institute of Mechanical Engineering: London, 1990.
220. Kohley, T.; Heitz, E. In *The Use of Synthetic Environments for Corrosion Testing* ASTM STP; Francis. P. E., Lee, T. S., Eds., ASTM: Philadelphia, 1988; Vol. 970, pp 235–245.
221. Sprowls, D. O. In *ASM Metals Handbook*, 9th ed. 1987; Vol. 13, pp 291–302.
222. Haigh, B. P. J. *Inst. Metals* **1971**, 18, 55.
223. Huddle, A. U.; Evans, U. R. J. *Iron Steel Inst.* **1944**, 149, 109P.
224. Inglis, N.; Lake, G. F. *Trans. Faraday Soc.* **1931**, 17, 803.
225. Rawdon, H. S. *Proc. Am. Soc. Test. Mater.* **1929**, 19, 314.
226. Kenyon, J. N. *Proc. Am. Soc. Test. Mater.* **1940**, 40, 705.
227. Gould, A. J.; Evans, U. R. *Iron Steel Inst. Spec. Report* No. 24, **1939**, 235.
228. Evans, U. R.; Simnad, M. T. *Proc. Roy. Soc.* **1947**, A188, 372.
229. Gough, H. J.; Sopwith, D. G. J. *Iron Steel Inst.* **1933**, 127, 301.
230. Gough, H. J.; Sopwith, D. G. *Engineering* **1933**, 136, 75.
231. Jarman, R. A.; Smith, S.; Williams, R. A. *Br. Corros. J.* **1978**, 13, 195.
232. Hoepfner, D. W. Corrosion Fatigue, NACE-2 University of Connecticut, 1972; p 3.
233. McEvily, A. J.; Wei, R. P. Corrosion Fatigue, NACE-2 University of Connecticut, 1972; p 381.
234. Kitigawa, H. Corrosion Fatigue, NACE-2 University of Connecticut, 1972; p 521.
235. Wood, R. J. K.; Fry, S. A. J. *Fluids Eng.* **1989**, 111, 271.
236. Lichtman, J. Z.; Kallas, D. H.; Rufola, A. In *Handbook on Corrosion Testing and Evaluation*; Ailor, W. H., Ed.; Wiley: New York, 1971; p 453.
237. Schroter, H. Z. *Ver. Dtsch. Ing.* **1934**, 78, 349.
238. Hobbs, J. M. *Proc. Cavitation Forum*, ASME **1966**, 1.
239. Gaines, N. *Physics* **1932**, 3, 209.
240. Kerr, S. L. *Trans. Am. Soc. Mech. Eng.* **1937**, 59, 373.
241. Beeching, R. *Trans. Inst. Eng. Shipb. Scot.* **1946**, 90, 203.
242. Rheingans, W. J. In *Engineering Approach to Surface Damage*; Lipson, C., Colwell, L. V., Eds.; University of Michigan: Ann Arbor, MI, 1958; p 249.
243. Leith, W. C.; Thompson, A. L. *Trans. Am. Soc. Mech. Eng. J. Basic Eng.* **1960**, 82, 795.
244. Plesset, M. S. *Trans. ASME Series D, J. Basic. Eng.* **1963**, 85, 360.
245. Eisenberg, P.; Preiser, H. S.; Thiruyengadam, A. *Trans. SNAME* **1965**, 73, 241.
246. Hobbs, J. M. In *ASTM STP*; 1967, Vol. 408; p 159.
247. Plesset, M. S.; Devine, R. D. J. *Basic Eng. Trans. ASME*; **1966**, 692, Dec.
248. Schulmeister, R.; Speckhardt, H. In *ASTM STP* **1980**; Vol. 705, p 81.
249. Hudgens, R. D.; Carver, D. P.; Hercamp, R. D.; Lauterback, J. In *ASTM STP*; 1980, Vol. 233.
250. Chance, R. L. In *ASTM STP*; 1980, Vol. 270.
251. In *ASTM STP*; 1953, Vol. 144.
252. Waterhouse, R. B. *Fretting Corrosion*; Pergamon Press: New York, 1972.
253. Waterhouse, R. B. Proc. 10th International Conference on Metallic Corrosion, Madras, India, 7–11 November 1987, 5, Oxford and IBH Publishing Co. New Delhi, 1987; p 63.
254. Fink, M. *Trans. Am. Soc. Steel Treat.* **1930**, 18, 1026.
255. Shotton, G. F. J. *Inst. Elec. Eng.* **1934**, 75, 755.
256. Tomlinson, G. A.; Thorpe, P. L.; Gough, H. J. J. *Inst. Mech. Eng.* **1939**, 141, 233.
257. Wright, K. H. R. *Proc. Instn. Mech. Eng.* **1952–1953**, 1B, 556.
258. Uhlig, H. H.; Tierney, W. D.; McClellan, A. In *ASTM STP* **1953**; Vol. 144, p 71.
259. McDowell, J. R. In *ASTM STP*; 1953, Vol. 24.
260. Warlow-Davies, E. J. J. *Inst. Mech. Eng.* **1941**, 146, 32.
261. Godfrey, D. *Tech. Note 2039, Natl. Advisory Comm. Aeronaut* 1950.
262. Gray, A. C.; Jenny, R. W. S.A.E.J. **1944**, 52, 511.
263. de Villemeur, Y. *Metaux. Paris* **1959**, 34, 413.
264. Wright, K. H. R. *Proc. Instn. Mech. Eng.* **1952–1953**, 1B, 556.
265. Wright, K. H. R. *Proc. Instn. Mech. Eng.* **1966–1967**, 181 (30), 256.
266. Barwell, F. T.; Wright, K. H. R. J. *Res. Br. Cast Iron. Ass.* **1958**, 7, 190.
267. Field, J. E.; Waters, D. M. *N.E.L. Rep. No.* **1967**, 275.
268. Waterhouse, R. B. *J.I.S.I.* **1961**, 197, 301.
269. Epstein, L. F. *Proc. Int. Conf. Peaceful Uses of Atomic Energy*, New York **1956**, 9, 311.
270. Bakish, R.; Kern, F. *Corrosion* **1960**, 9, 533t.
271. Edeleanu, C.; Gibson, J. G. J. *Inst. Met.* **1960**, 88, 321.
272. Brasunas, A.; de, S. *Corrosion* **1953**, 9, 78.
273. Miller, E. C. In *Liquid Metals Handbook*; Lyon, R. N., Ed.; Atomic Energy Comm. and Dept. of the Navy: Washington DC, 1952; p 144.
274. Borgstedt, H. U.; Frees, G. Proc. 10th Int. Cong. on Metallic Corrosion, Madras, India, 7–11 Nov. 1987, 3, **1988**; p 1843.
275. Barker, M. G.; Coen, V.; Kolbe, H.; Lees, J. A.; Orecchia, L.; Sample, T. J. *Nucl. Mater.* **1988**, 155–157B, 732.
276. Borgstedt, H. U.; Frees, G. *Werkst. Korros.* **1990**, 41, 1.
277. Vreeland, D. C.; Hoffman, E. E.; Manly, W. D. *Nucleonics* **1953**, 11, 36.
278. Grabner, H.; Feurstein, H.; Oschinski, J. J. *Nucl. Mater.* **1988**, 155–157B, 702.
279. Strachan, J. F.; Harris, N. L. J. *Inst. Met.* **1956–1957**, 85, 17.
280. Klueh, R. L. Proc. Int. Conf. Sodium Technol. Large Fast Reactor Design, Nov. 7–9 ANL-7520, Pt. 1, 171, Argonne National Laboratory, 1968.
281. Klueh, R. L. *Corrosion* **1969**, 25, 416.
282. DiStefano, J. R. ORNL-4028 Oak Ridge Laboratory, 1966.
283. Manly, W. D. *Corrosion* **1956**, 12, 336t.

284. DiStefano, J. R.; De Van, J. H. *Nuclear Appl. Tech.* **1970**, 8, 29.
285. Koenig, R. F.; Vandenberg, S. R. *Metal. Prog.* **1952**, 61, 71.
286. Hoffman, E. E. *Corrosion of Materials by Lithium at Elevated Temperatures*, ORNL-2924; Oak Ridge National Laboratory, 1960.
287. Kassner, T. F. *AIIME Met. Soc. Trans.* **1967**, 239, 1643.
288. Shibanova, L. N.; Vostryakov, A. A.; Lepinskikh, B. M. *Zashch. Met.* **1986**, 22, 124.
289. De Van, J. H.; Sessions, C. E. *Nucl. Appl.* **1967**, 3, 102.
290. De Van, J. H.; Jansen, D. H. Progr. Report 30 September 1968, ORNL-4350, Oak Ridge National Laboratory, p 91.
291. Bonilla, C. F. In *Reactor Handbook*; McInain, S. ED.; Interscience: New York, 1964; Vol. IV, p 107.
292. Romana, A. J.; Fleitman, A. H.; Klamut, C. J. Proc. AEC-NASA Liquid Metals Inform. Meeting, CONF-650411 1965.
293. Fuller, L. C.; MacPherson, R. E. ORNL-TM-2595 Oak Ridge National Laboratory, 1967.
294. Borgstedt, H. U.; Frees, G. *Werkst. Korros.* **1987**, 38, 732.
295. RDT Standard C8-5T, Electrochemical Oxygen Meter for Service In *Liquid Sodium*, RDT Standards Office, Oak Ridge National Laboratory, Tennessee.
296. Pillai, S. R.; Mathews, C. K. J. *Nucl. Mater.* **1986**, 137, 107.
297. Schutter, F.; De Dekeyser, J. A.; Tas, H.; Burbure, S. de. *J. Nucl. Mater.* **1988**, 155, 744.
298. Roy, P.; Wozaldo, G. P.; Comprelli, F. A. In *Proc. Int. Conf. Sodium Technol. Large Fast Reactor Design*, 7-9 November 1968; ANL-7520, Pt. 1, Argonne National Laboratory, p 131.
299. Roy, P.; Gebhardt, M. F. GEAP-13548 General Electric Company, 1969.
300. Hoffmann, E. E.; Harrison, R. W. *Metallurgy and Technology of Refractory Metal Alloys*; Plenum Press: New York, 1969; p 251.
301. Harrison, R. W. GESP-258. General Electric Company, 1969.
302. Borgstedt, H. U.; Grundman, M. Preprints of Eurocorr 87th conference, Karlsruhe, Germany, 6-10 April 1987, DECHEMA, Frankfurt **1987**; p 141.
303. Dillon, C. P. *Mater. Perform.* **1990**, 29(11), 54.
304. Lynch, S. P. Proceedings of 2nd International Conference on Environmental Degradation of Engineering Materials, Blacksburg, Virginia, September 31-23 1981 Virginia Polytechnic Institute, 1981; p 229.
305. Old, C. F. *Metal Science* **1980**, 14, 433.
306. Preece, C. M. In Proceedings of International Conference on Stress Corrosion Cracking and Hydrogen Embrittlement of Iron Base Alloys, Unieux-Firminy, France, June 12-16 1973 NACE: Houston, 1977; p 625.
307. Kapp, J. A.; Duquette, D.; Kamdar, M. H. *J. Eng. Mater. Technol.* **1986**, 108, 37.
308. Thompson, D.H. in Ref. 2
309. Dillon, C. P.; Krisher, A. S.; Wissenburg, H. *Ref.* **1971**, 2, 599.
310. Strutt, J. E.; Nichols, J. R. Eds. *Plant Corrosion: Prediction of Materials Performance*; Ellis Horwood: Chichester, 1987.
311. Rawdon, H. S. *ASTM STP* **1937**, 32, 36.
312. LaQue, F. L. *Proc. Am. Soc. Test. Mater.* **1951**, 51, 495.
313. Finkeldey, W. H. *Proc. Am. Soc. Test. Mater.* **1932**, 32, 226.
314. Hudson, J. C. J. *Iron Steel. Inst.* **1943**, 161P, 148.
315. Pilling, N. B.; Wesley, W. A. *Proc. Am. Soc. Test. Mater.* **1940**, 40, 643.
316. Copson, H. R. *Proc. Am. Soc. Test. Mater.* **1948**, 48, 591.
317. Gibboney, J. H. *Proc. Am. Soc. Test. Mater.* **1919**, 19, 181.
318. Mendizza, A. *Proc. Am. Soc. Test. Mater.* **1950**, 50, 114.
319. Passano, R. F. *Proc. Am. Soc. Test. Mater.* **1934**, 34, 159.
320. Pinner, W. L. *Proc. Am. Soc. Test. Mater.* **1953**, 53, 256.
321. Wirshing, R. J.; McMaster, W. D. *Paint Varn. Prod.* **1951**, 41, 13.
322. Sereda, P. J. *Bull. Am. Soc. Test. Mater. No.* **1958**, 228, 53.
323. Guttman, H.; Sereda, P. J. *ASTM STP* **1968**, 435.
324. Gorman, L. J. *Proc. Am. Soc. Test. Mater.* **1939**, 39, 247.
325. Pray, H. A. *Proc. Am. Soc. Test. Mater.* **1944**, 44, 280.
326. Humble, H. A. *Corrosion* **1949**, 5, 292.
327. Southwell, C. R. NRL Reports, Naval Research Laboratory, Washington, D.C.
328. Ijsseling, F. P. *Br. Corros. J.* **1989**, 24, 55.
329. Logan, R. H.; Ewing, S. P.; Denison, I. A. *ASTM STP* **1937**, 32, 95.
330. Scott, G. N. *Proc. Am. Petrol. Inst.* **1937**, 95.
331. Escalante, E. Ed. *Underground Corrosion* ASTM STP; ASTM: Philadelphia, 1981; Vol 741.
332. Tiller, A. K. *Biocorrosion in Civil Engineering*; Cranfield Institute of Technology, 1990.
333. Walter, G. W. *Corros. Sci.* **1986**, 26, 681.
334. Timmins, F. D. J. *Oil Col. Chem. Assoc.* **1979**, 62, 131.
335. Ali Elbasir; Scantlebury, J. D.; Callow, L. M. J. *Oil Col. Chem. Assoc.* **1985**, 67, 282.
336. Hoey, C. E.; Hipwood, H. A. J. *Oil Col. Chem. Assoc.* **1974**, 57, 151.
337. Butler, G.; Mercer, A. D.; Warren, G. M. In Eurocorr 77, 6th Eur. Congr. Metall. Corros., Soc. Chem. Ind., London **1977**; pp 349-355.
338. Mercer, A. D. In *Engine Coolant Testing: State of the Art 1979*, ASTM STP; Ailor, W. H., Ed., ASTM: Philadelphia, 1980; Vol. 705, pp 53-80.
339. NACE Publication. *Mater. Perform.* **1982**, 21(12), 45.
340. Schmitt, G.; Bruckhoff, W. In Proc. 5th European Conference on Corrosion Inhibitors (5 SEIC) University of Ferrara, 1980; p 323.
341. Mercer, A. D. *Br. Corros. J.* **1985**, 20, 61.
342. Mercer, A. D. In Proc. 6th European Symposium on Corrosion Inhibitors, (6 SEIC), University of Ferrara, N.S. Sez. V, Suppl. N8 1985.
343. Wachter, A.; Skei, T.; Stillman, N. *Corrosion* **1951**, 7, 284.
344. Stroud, E. G.; Vernon, W. H. J. *J. Appl. Chem.* **1982**, 2, 178.
345. Levin, S. Z.; Gintzberg, S. A.; Dinner, S. M.; Kuchinsky, V. N. 2nd Ferrara Conference on Corrosion Inhibitors (2SEIC) 1965 University of Ferrara, 1966; p 765.
346. Romeo, A. J.; Skrinde, R. T.; Eliassen, R. *Proc. Am. Soc. Civ. Eng.* **1958**, 84(SA4).
347. Gleekman, L. W.; Swandby, R. K. *Corrosion* **1961**, 17, 144t.
348. Makar, D. R.; Francis, H. T. J. *Electrochem. Soc.* **1955**, 102, 669.
349. Todt, F. Z. *Elektrochem.* **1928**, 34, 586.
350. Todt, F. Z. *Ver. Dtsch. Zuckerind.* **1929**, 79, 680.



## 2.35 Environmentally Assisted Cracking Test Methods

**R. N. Parkins**

Department of Metallurgy and Engineering Materials, Newcastle University, Newcastle-upon-Tyne NE1 7RU, UK

This article is a revision of the Third Edition article 8.10 by R. N. Parkins, volume 1, pp 8:215–8:242, © 2010 Elsevier B.V.

<b>2.35.1</b>	<b>Introduction</b>	1527
2.35.1.1	Stressing Systems	1527
2.35.1.2	Constant Total-Deflection Tests	1528
2.35.1.3	Constant-Load Tests	1530
2.35.1.4	Slow Strain-Rate Tests	1531
<b>2.35.2</b>	<b>Testpiece</b>	1534
2.35.2.1	Precracked Samples	1534
2.35.2.2	Comparison of the Results from Plain and Precracked Specimens	1536
2.35.2.3	Crack Velocity Measurements	1537
2.35.2.4	Effects of Surface Finish	1538
<b>2.35.3</b>	<b>Choice of Environment</b>	1538
<b>2.35.4</b>	<b>Stress Corrosion Test Methods</b>	1540
2.35.4.1	Types of Test Cells	1540
2.35.4.2	Initiation of Stress Corrosion Tests	1541
2.35.4.3	Hydrogen Embrittlement Tests	1541
2.35.4.4	Dynamic Tests	1542
2.35.4.5	Static Tests	1543
<b>Appendix A</b>	<b>Stresses in Bent Specimens</b>	1545
<b>References</b>		1545

### Abbreviations

**ASTM** American Society for Testing and Materials

**EAC** Environmentally assisted cracking

**UTS** Ultimate tensile strength

### Symbols

**$E$**  Modulus of elasticity

**$E_{\text{corr}}$**  Corrosion potential

**$h$**  Height

**$I$**  Current density

**$K_{\text{ISCC}}$**  Threshold stress intensity factor for the onset  
of stress corrosion cracking

**$t$**  Specimen thickness

**$t_f$**  Time to failure

**$V$**  Potential

**$\sigma$**  Maximum tensile stress

**$\sigma_{\text{th}}$**  Threshold stress for the onset of stress  
corrosion cracking

**$\sigma_y$**  Lower yield strength

### 2.35.1 Introduction

#### 2.35.1.1 Stressing Systems

Many different methods<sup>1–4</sup> have been used for the stressing of specimens (or testpieces), from which it may be reasonably assumed that there is no single method that is markedly superior to all the others. Each method may have its peculiar advantages in a given situation, but ideally, a test method should not be so severe that it leads to the condemnation of a material that would prove adequate for service or so trifling as to permit the use of materials in circumstances where rapid failure ensues. Methods of stressing testpieces, whether initially plain, notched, or precracked, can be conveniently grouped according to whether they involve:

1. a constant total strain or deflection;
2. a constant load;
3. an imposed strain or deflection rate.

Constant deflection tests usually have the attraction of employing simple and, therefore, often cheap

specimens and straining frames and of simulating the fabrication stresses that are most frequently associated with stress corrosion failure. Constant load tests may simulate failure from applied or working stresses more closely. Although tests involving the application of a constant deflection rate (strain rate) are commonly used, their relevance to service failures continues to be debated.

### 2.35.1.2 Constant Total-Deflection Tests

Prismatic beams stressed by bending offer a simple means of testing sheet or plate material, typical arrangements being shown in Figure 1(a)–1(e). Below the elastic limit, the stresses may be calculated<sup>1,5</sup> or

determined from the response of strain gauges attached to the surface at an appropriate position.

Plastic bending of strip specimens to produce a ‘U’-bend, Figure 1(d) and 1(e), will usually allow the use of a lighter restraining system, although some of the effects of the plastic deformation, if not removed by subsequent heat treatment, may be to influence cracking response, and the stress obtained in the outer fibers of the specimen is usually less reproducible than with more sophisticated specimens. Tubular material may be tested in the form of ‘C’- or ‘O’-rings, the former being stressed by partial closing of the gap, Figure 1(c), and the latter by the forced insertion of a plug that is appropriately oversized for the bore. The circumferential stress at the outer

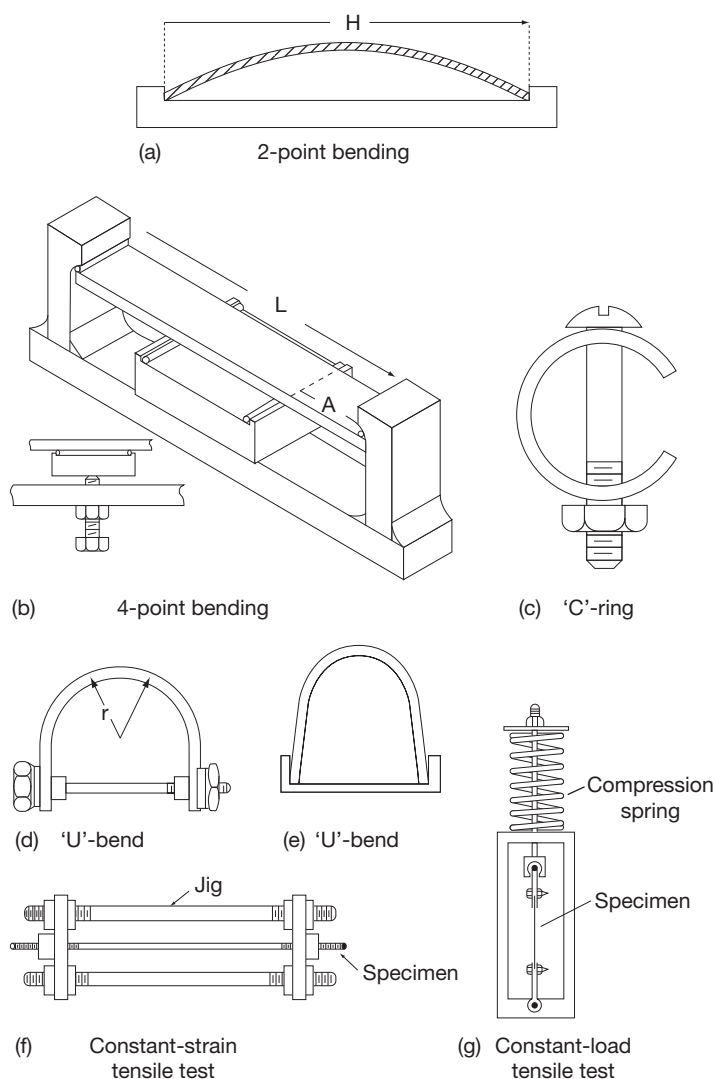


**Figure 1** Stressing systems for stress corrosion test specimens; (a) to (f) constant strain, (g) constant load.

surface of a 'C'-ring is maximal midway between the bolt holes, but for the 'O'-ring, it is constant over the periphery, the stresses being readily calculated in terms of measured deflections.<sup>1,2</sup>

Constant-deflection tensile tests, **Figures 1(f) and 1(g)**, are sometimes preferred to bend tests, but for similar cross sections, require a more massive restraining frame. In principle, this problem may be surmounted by the use of internally stressed specimens containing residual stresses as the result of inhomogeneous deformation. The latter may be introduced by plastic bending, for example, by producing a bulge in sheet or plate material, or by welding, but such tests cause problems in the systematic variation of the initial stress, which will usually be in the region of the yield stress. Moreover, elastic spring-back, in introducing residual stresses by bulging plate or partially flattening tube, may introduce problems, and where welding is involved, the structural modifications may raise difficulties unless the test is simulative of a practical situation.

At least as important as the choice of methods of stressing is the realization of the limitations of the various methods, these having been considered in a review of stress corrosion test methods.<sup>6</sup> The stiffness of the stressing frame in constant-deflection tests may influence results because of relaxation in the specimen during the initial loading stage and during subsequent crack propagation. Especially in testing ductile materials, the initial elastic strain is converted in part to plastic strain, even if the total deflection remains constant during cracking. This is because, as the crack propagates, the stress increases on the remaining uncracked portion of the specimen section beyond the crack, eventually reaching the effective yield stress. Yielding will then occur, accompanied by yawning of the crack and frequently, with the propagation of a Lüders band that results in a sharp load drop, which is sometimes mistaken as an indication of the crack having advanced by a burst of mechanical fracture. Once load relaxation has been initiated, the extent to which it proceeds can vary from specimen to specimen. Thus, **Figure 2** shows load relaxation curves for two specimens of the same maraging steel in the same stressing frame, which had a facility for load recording throughout the test. The specimens differed in the extent to which they showed load relaxation prior to sudden fracture, this difference being related to the number of cracks that developed in the specimens. Marked load relaxation was associated with the development of many cracks in the specimen and little relaxation, with only a few cracks.

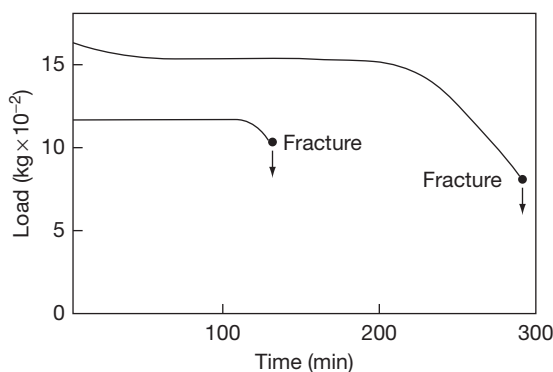


**Figure 2** Load relaxation curves for a maraging steel stress corroded in 0.6 M NaCl at pH 2. Reproduced from Parkins, R. N.; Haney, E. G. *Trans. Metall. Soc., AIME* **1968**, 242, 1943.

This can influence the time to failure, as is apparent from **Figure 2**, where the specimen stressed at the initially higher load took longer to fail than that at the initially lower one. This is because, when only a single stress corrosion crack develops, it will not need to grow to large dimensions before sudden, final failure occurs, since the applied load remains high, whereas with the marked load relaxation associated with the multicroaked specimen, one of the cracks will need to propagate much further before it reaches the size for sudden fracture at the reduced load. Such an explanation conforms to the observations<sup>7</sup> that the load at fracture is related to the area of stress corrosion cracking upon the final fracture surface and to the number of cracks initiated.

This type of result will depend upon the nature of the stress corrosion system being studied, that is, upon such properties as the fracture toughness of the material and even upon the aggressiveness of the environment employed. It will also vary according to the stiffness of the restraining jig employed, since the stiffer the frame, the less the elastic strain that is likely to remain in the specimen after the propagation of a Lüders band, so that a stress-corrosion crack may cease to propagate in some circumstances, especially if the initial stress is in the vicinity of the threshold stress. This indicates some of the dangers inherent in comparing stress corrosion resistances in terms of times to failure at a given initial stress, an approach that is often practiced but can be misleading. **Figure 3** shows the results from some tests in which the time to failure of specimens previously cold worked in varying amounts is plotted against initial stress. Comparison of the effects of different amounts of cold work by tests at an initial

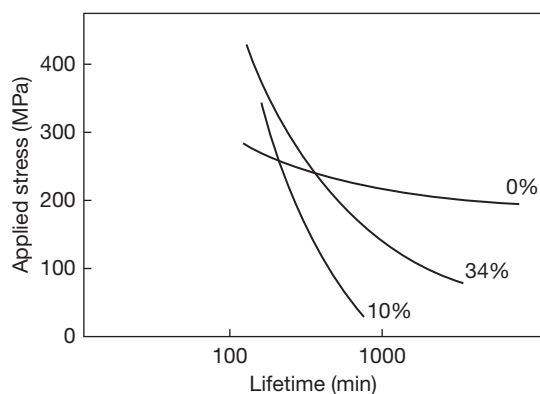


**Figure 3** Effects of different amounts of prior cold work (0, 10 and 34%) on the stress corrosion of a 0.07% C steel in boiling 4 M  $\text{NH}_4\text{NO}_3$ .

**Table 1** Relative susceptibilities to cracking of a mild steel in boiling 4 M  $\text{NH}_4\text{NO}_3$  after various amounts of cold work

Initial stress	Susceptibility of different cold-worked conditions		
	Most (%)	Intermediate (%)	Least (%)
280 MPa	0	10	34
155 MPa	10	34	0
100% of yield stress	34	10	0
30% of yield stress	10	34	0

stress of 280 or 155 MPa gives different orders of susceptibility, as shown in **Table 1**. It could be argued that neither of these results is correct because the prior cold work would result in different yield strengths being developed in the three different conditions and that the results should be rationalized by making the comparison a function of the respective yield strengths. Here again, however, the order of susceptibility varies according to the rationalized stress at which the comparison is made, as the results in **Table 1** show. It is difficult to escape the conclusion that a more satisfactory basis of comparison is the threshold, but even the latter may not be a basis for comparison of results obtained using different restraining frames.

The simplicity of the rigs used in the constant-strain tests is an advantage in the application of the corrosive solution. Thus, in the case of two-point bending, **Figure 1(a)**, several specimens may be strained in the same rig, which can be constructed of plastic and immersed in a tank containing the test solution.

### 2.35.1.3 Constant-Load Tests

Dead-weight loading (with or without the assistance of levers to reduce the load requirements) of tensile specimens has the advantage of avoiding some of the difficulties already discussed, not the least in allowing accurate determination of the stress if the specimen is uniaxially loaded. The relatively massive machinery usually required for such tests upon specimens of appreciable cross section is sometimes circumvented by the use of a compression spring, **Figure 1(g)**, chosen with characteristics that ensure that it does not change significantly in length during testing, thereby approximating to a constant-load application. For immersion tests, the frame may be coated in polymer and the specimen insulated from the shackles by plastic sleeves and washers to avoid bimetallic effects; alternatively, the specimen may be enclosed in a glass cell containing the test solution. The alternative approach of minimizing the size of the loading system by reducing the cross section of the specimen to the dimensions of a wire is dangerous unless failure by stress corrosion cracking is confirmed by, say, metallography. This is because failure may result from pitting and an attendant increase in the effective stress to the ultimate tensile strength (UTS) in some stress corrosion environments. Indeed, there is evidence for some systems that before stress corrosion cracking proper can begin, a pit must form wherein certain chemical or electrochemical conditions are established that permit cracks to be initiated, and in such systems, the use of fine wires has obvious pitfalls.

The load relaxation that accompanies some, if not all, constant-deflection tests is replaced in constant-load tests by an increasing stress condition, since the effective cross section of the test piece is reduced by crack propagation. This suggests that it will be less likely that cracks will cease to propagate once initiated, as may happen with constant deflection tests at initial stresses in the region of the threshold stress, and therefore, the threshold stresses are likely to be lower when determined under constant-load conditions than under conditions of constant deflection. Some results attributed to Brenner and Gruhl<sup>8</sup> for an aluminum alloy, **Figure 4**, confirm this expectation. These results also show shorter times to failure for the same initial stress with constant load testing and, as already indicated for constant-deflection tests, raise queries as to the significance of time to failure, the parameter so frequently used in assessing cracking susceptibility.

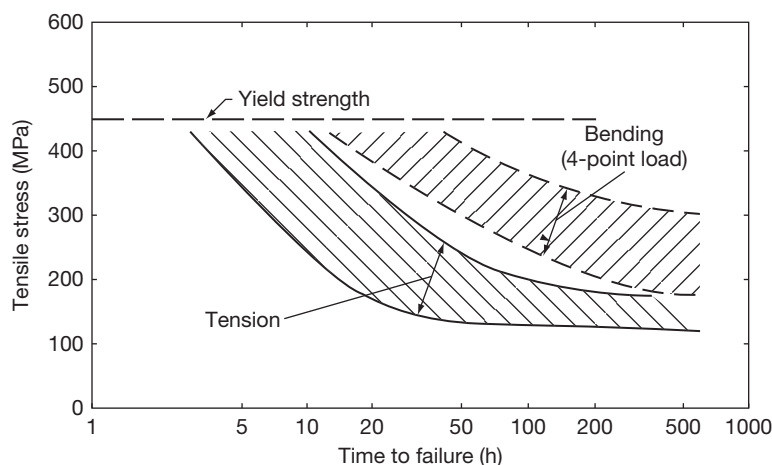


**Figure 4** Comparison of test results from bend and tension tests upon Al-Zn-Mg alloy in 3% NaCl plus 0.1% H<sub>2</sub>O<sub>2</sub>. Reproduced from Brenner, P.; Gruhl, W. Z. *Metall.* **1961**, 52, 599.

#### 2.35.1.4 Slow Strain-Rate Tests

While this method of testing has been in use in some laboratories for two decades or more and has increased in use considerably in very recent years, there remain some skepticism and unfamiliarity with the method. In essence, it involves the application of a relatively slow strain or deflection rate ( $\sim 10^{-6} \text{ s}^{-1}$ ) to a specimen<sup>9</sup> subjected to appropriate electrochemical conditions. It should be emphasized that the strain rates employed are very much lower than those involved in straining electrode experiments where the object, the measurement of current transients, is totally different. In slow strain-rate corrosion tests, the object is to produce stress corrosion cracks that are metallographically indistinguishable from those produced in constant-load or constant-deflection experiments. The object in all these laboratory tests is normally to obtain data in a relatively shorter period of time, and this is frequently achieved by adopting an approach that increases the severity of the test. In stress corrosion testing, this usually takes the form of increasing the aggressiveness of the environment by changing its composition, temperature, or pressure, stimulating the corrosion reactions (galvanostatic or potentiostatic), increasing the susceptibility of the alloy through changes in structure, or increasing the severity of the stress by the introduction of a notch or precrack. The application of dynamic straining to a stress corrosion test specimen also comes into this last category, and, like all of the other accelerating approaches, its justification will vary according to the circumstances in which it is used.

Most stress corrosion crack velocities fall in the range from  $10^{-3}$  to  $10^{-6} \text{ mm s}^{-1}$ , which implies that failures in laboratory test specimens of usual dimensions occur in not more than a few days. This is found to be so if the system is one in which stress corrosion cracks are readily initiated, but it is common experience to find that some testpieces do not fail even after extended periods of testing, which are then terminated at some arbitrarily selected time. The consequences are that considerable scatter may be associated with replicate tests, and the arbitrary termination of the test leaves an element of doubt concerning what the outcome would have been if it had been allowed to continue for a longer time. Just as the use of precracked specimens assists in stress corrosion crack initiation, so does the application of slow dynamic strain, which has the further advantage that the test is not terminated after some arbitrary time, since the conclusion is always achieved by the specimen fracturing, and the criterion of cracking susceptibility is then related to the mode of fracture. Thus, in the form in which it is normally employed, the slow strain-rate method will result in failure in not more than  $\sim 2$  days, either by ductile fracture or by stress corrosion cracking, according to the susceptibility towards the latter, and metallographic or other parameters may then be assigned in assessing the cracking response. The fact that the test concludes in this positive manner in a relatively shorter period of time constitutes one of its main attractions.

Early use of the test was in providing data whereby the effects of such variables as alloy



composition and structure or inhibitive additions to cracking environments could be compared, and also for promoting stress corrosion cracking in combinations of alloy and environment that could not be caused to fail in the laboratory under conditions of constant load or constant strain. Thus, they constitute a relatively severe type of test in the sense that they frequently promote stress corrosion failure in the laboratory where other modes of stressing plain specimens do not promote cracking, and in this sense, they are in a category similar to tests on precracked specimens. In recent years, an understanding of the implications of dynamic strain testing has developed, and it now appears that this type of test may have much more relevance and significance than just that of an effective and rapid sorting test. It may, at first sight, be argued that laboratory tests involving the pulling of specimens to failure at a slow strain-rate show little relation to the reality of service failures. In point of fact, in constant-strain and constant-load tests, crack propagation also occurs under conditions of slow dynamic strain, to a greater or lesser extent depending upon the initial value of stress, the point in time during the test at which a stress corrosion crack is initiated, and various metallurgical parameters that govern creep in the specimen. Moreover, there is an increasing amount of evidence for some systems which suggests that the function of stress in stress corrosion cracking is to promote a strain rate which, rather than stress *per se*, is the parameter that really governs crack initiation or propagation. In these cases, the minimum creep rate for cracking is as much an engineering design parameter as is the threshold stress or stress-intensity factor obtained from constant-load tests on plain or precracked specimens.

The point may be illustrated by data for a ferritic steel exposed to a carbonate-bicarbonate solution as fatigue precracked cantilever beams subjected to constant loads. Deformation in the plastic zone associated with the precrack is time dependent following load applications and can be measured, and the threshold conditions for stress corrosion cracking defined, in terms of a limiting average creep rate over a specific time interval. That limiting creep rate may then be used in subsequent experiments to calculate the threshold stress from creep data determined independently, these calculated threshold stresses then being compared with values determined experimentally. The creep properties of ferritic steels may be varied by prior strain aging, following different amounts of cold work, and Figure 5 shows the observed and calculated threshold stresses from tests on specimens subjected to various strain aging treatments. Clearly,

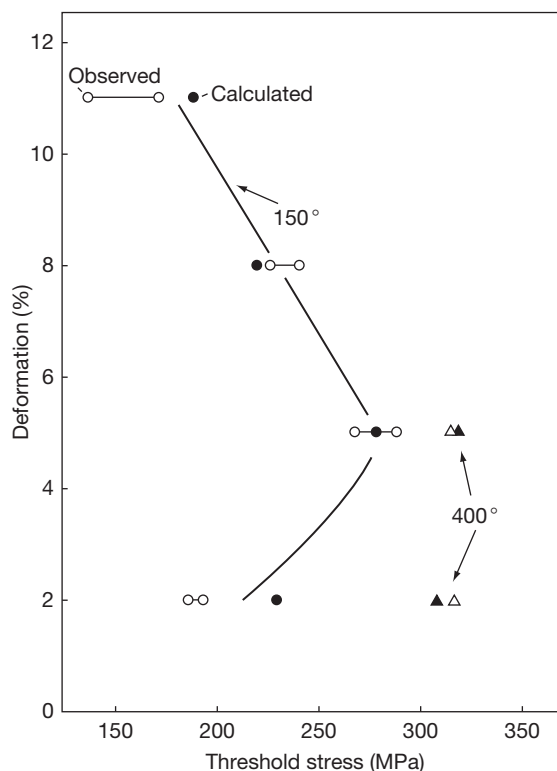


**Figure 5** Observed and calculated values of the threshold net section stresses for stress corrosion cracking of a C-Mn steel after various prior deformations and aging treatments.

the general trend of the experimentally determined curve showing the effects of the amount of prior deformation is reflected in the calculated results.

The equipment required for slow strain-rate testing is simply a device that permits a selection of deflection rates while being powerful enough to cope with the loads generated. Plain or precracked specimens in tension may be used, but if the cross section of these needs to be large or the loads high for any reason, cantilever bend specimens with the beam deflected at appropriate rates may be used. It is important to appreciate that the same deflection rate does not produce the same response in all systems and that the rate has to be chosen in relation to the particular system studied.

The representation of the results from slow strain-rate tests may be through the usual ductility parameters, such as reduction in area, the maximum load achieved, the crack velocity, or even the time to failure, although as with all tests, metallographic or fractographic examination, while not readily quantifiable, should also be involved. Since stress corrosion failures are usually associated with relatively little

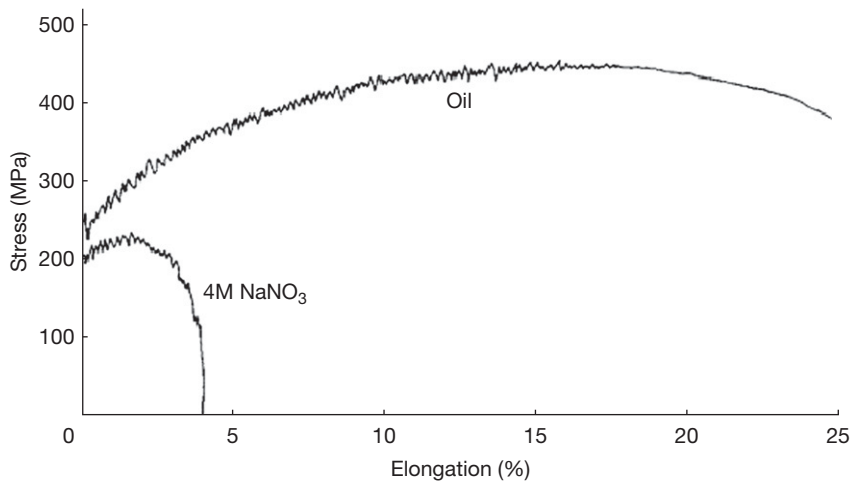


**Figure 6** Nominal stress–extension curves for mild steel in oil giving ductile failure, and in 4 M NaNO<sub>3</sub> producing stress corrosion failure, at the same test temperature (104 °C).

plastic deformation, the ductility of specimens will be variable according to the extent to which stress corrosion contributes to the fracture process. This will also influence the shape of the load–extension curve that may be obtained by continuous monitoring of the response of a load cell incorporated in the system; **Figure 6** shows the forms of curves obtained with and without attendant stress corrosion. It is apparent from these curves that not only is the extension to fracture dependent upon the presence or otherwise of stress corrosion cracks, but so also is the maximum load achieved. The latter may be used for expressing cracking susceptibility in some systems, as also may the area bounded by the load–extension curve. However, the variations in maximum load achieved in slow strain-rate tests in circumstances of varying cracking severity are not always large enough for significant distinctions to be made. Even measurements of ductility, such as reduction in area, are readily invariably not made, if only because the final fracture of the specimen does not always follow a simple path, and the fitting of the two broken pieces together is not easy. Probably, the easiest quantity to measure with reasonable accuracy is the time to failure, which has as much significance in a slow strain-rate test as it does in constant-load or constant-deflection tests. Indeed, the time to failure in slow strain-rate tests is simply related to ductility parameters, a not very surprising result when it is remembered that the less the intensity of stress corrosion cracking, the greater will be the ductility to fracture and therefore, the greater the time to failure for a given strain rate.

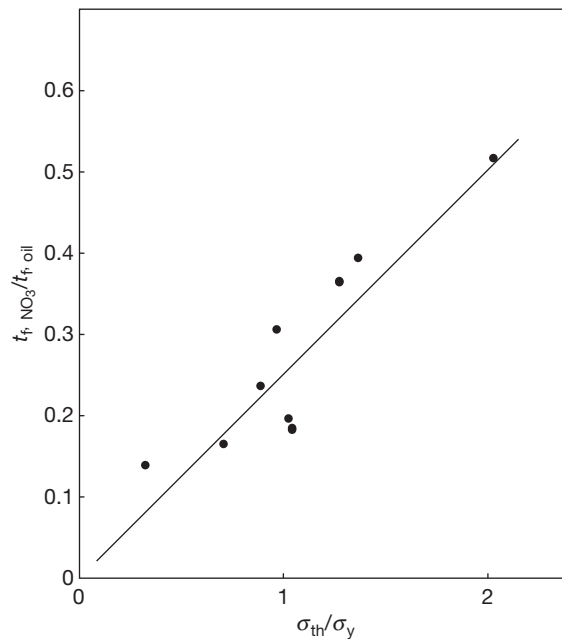


**Figure 7** Time to failure ratios from constant-deflection rate tests and normalized threshold stresses  $\sigma_{th}/\sigma_y$  obtained from constant-strain tests for a series of low-alloy ferritic steels in boiling 4 M NH<sub>4</sub>NO<sub>3</sub>.

Clearly, for slow strain-rate testing to have credence, it should give results that are comparable with those obtained by other methods. **Figure 7** shows some results for tests upon low-alloy ferritic steels in boiling 4 M NH<sub>4</sub>NO<sub>3</sub>, the various alloying elements producing a range of cracking susceptibilities as measured by the threshold stresses obtained from constant-strain tests. These results have been

normalized by dividing the threshold stress  $\sigma_{th}$  by the lower yield strength  $\sigma_y$  for each steel, while the slow strain test results have been normalized by dividing the time to failure in the 4 M  $NH_4NO_3$  by the time to failure in oil at the same temperature, so that increasing departure from unity indicates increasing cracking susceptibility. The general trend of the results in Figure 7 is clear in indicating reasonable agreement between the two types of tests in placing the steels in essentially the same order of merit.

Although slow strain-rate tests are most frequently taken to total failure in order to produce a 'go/no-go' type of result in which threshold stresses are not defined, they can be conducted in a manner that allows such definition. Specimens are preloaded to various initial stresses in the absence of the cracking environment or at a potential that prevents cracking, after which they are allowed to creep until the latter falls below the strain rate to be applied. The applied straining is continued for a sufficient time only to allow cracks to grow to a measurable size. During straining, the stress upon the specimen varies in a manner dependent upon the magnitude of the applied strain-rate, hence the importance of restricting the test time to no longer than that necessary to produce measurable cracks. The cracks are probably most conveniently measured by microscopy on longitudinal sections of the gauge lengths, the length of the deepest detectable crack divided by the test time giving an average crack velocity. Figure 8 shows some results from tests upon a cast nickel–aluminum bronze exposed to seawater<sup>10</sup> and clearly it is possible to define a threshold stress below which cracking is not observed. However, that threshold stress depends upon the strain-rate applied, as is to be expected. Another approach to defining threshold stresses in slow strain-rate tests that may sometimes be useful is to use tapered specimens, with the taper angle minimized to avoid complications by resolved components of the tensile load.<sup>11</sup> Applied to the cracking of  $\alpha$ -brass exposed to sodium nitrite solutions, a single tapered specimen gave threshold stresses close to those obtained by the use of a number of plain specimens loaded at a given strain rate to various stress levels.

## 2.35.2 Testpiece

### 2.35.2.1 Precracked Samples

The literature contains many references to the use of notched, as opposed to precracked or plain specimens

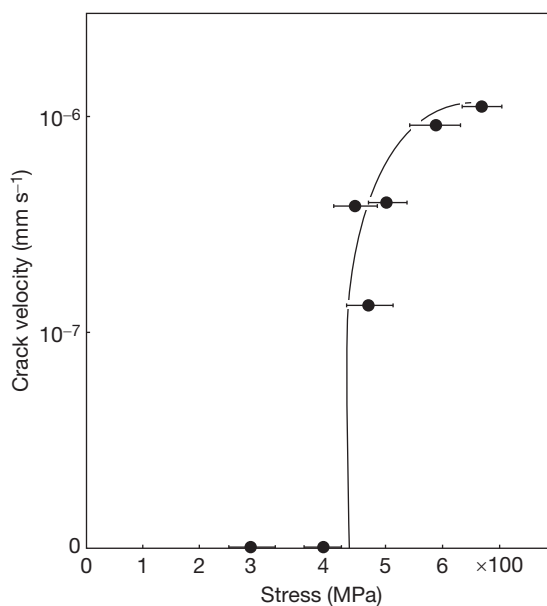


**Figure 8** Average stress corrosion crack velocity from monotonic slow strain rate tests at  $1.5 \times 10^{-7} \text{ s}^{-1}$  conducted over various restricted ranges of stress on a cast Ni–Al bronze in seawater at 0.15 V(SCE). The stress range traversed in each test is shown by the length of the bar. Reproduced from Parkins, R. N.; Suzuki, Y. *Corros. Sci.* **1983**, *23*, 577.

in laboratory studies of stress corrosion, for reasons of improved reproducibility, inability to crack plain specimens under otherwise identical conditions or ease of measuring some parameters, such as crack growth rate, when the crack location is predetermined. However, the developments in fracture mechanics have resulted in a whole new field of stress corrosion testing involving the use of specimens containing a sharp pre-crack, usually produced from a notch by subjecting the specimen to fatigue. The application of fracture mechanics to stress corrosion cracking is the subject of an admirable review by Brown,<sup>12</sup> and various aspects of the method are considered in papers presented at an Advisory Group for Aerospace Research and Development (AGARD) conference.<sup>13</sup>

The problems associated with the choice of plain specimens for assessing stress corrosion resistance may, at first sight, appear equally large in relation to pre-cracked specimens in the sense that in the relatively shorter time during which such tests have been in use, a large number of specimen types have been used (Figure 9). However, the differing specimen geometries are rationalized through the stress–intensity factor, with the result that data from different testpieces are comparable, provided appropriate precautions are taken in

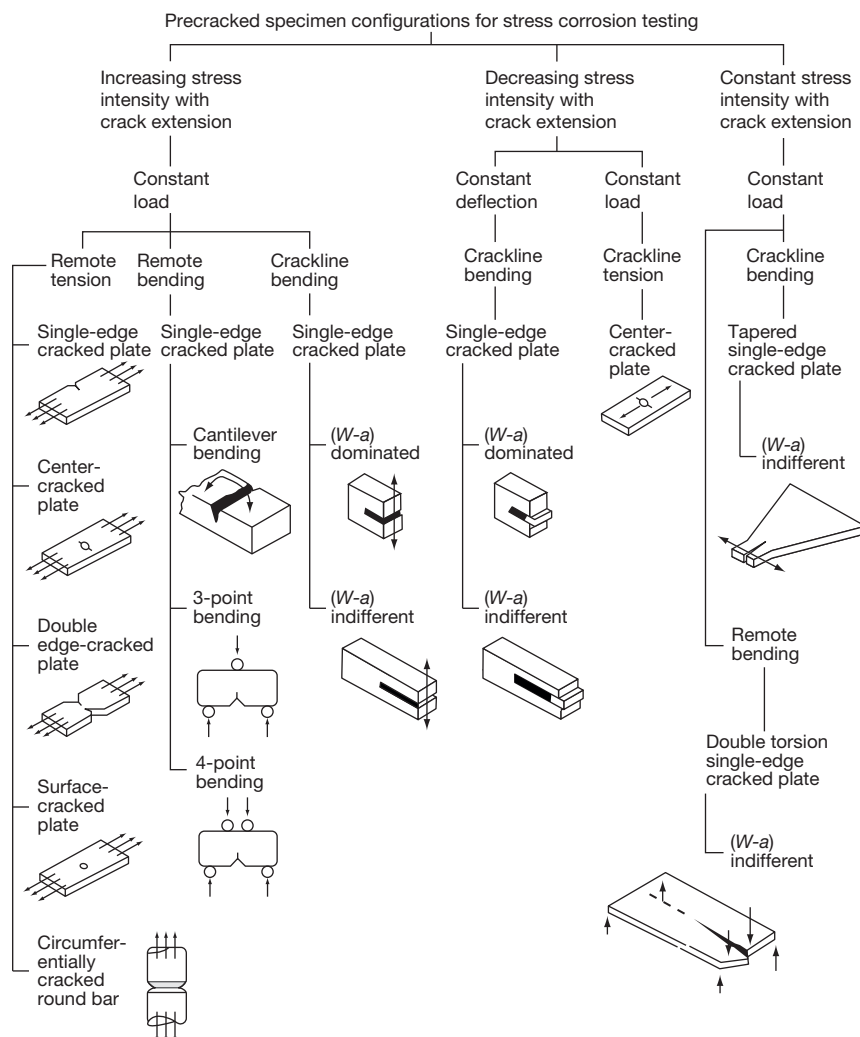


**Figure 9** Classification of precracked specimens for stress corrosion testing. Reproduced from Smith, H. R.; Piper, D. E. Stress Corrosion Testing with Precracked Specimens, The Boeing Co, D6-24872, ARPA 878, June, 1970.

specimen preparation. The biggest single difficulty is in relation to the large size of specimen that is necessary for highly ductile materials if the concepts of linear elastic analysis are to be applicable. Since it is probable that most service stress corrosion failures occur in highly ductile materials in relatively thin sections, it is clear that there are problems here, but the use of precracked specimens that do not conform dimensionally to the requirements for linear elastic analysis to be strictly valid is still worthwhile in some instances, and in any case, developments in fracture mechanics over the last decade or so allow alternative approaches than that of linear elastic analysis.

Precracked specimens are sometimes useful for other reasons than the analysis that they afford in relation to stress-intensity factors. Such applications

may be associated with the simulation of service situations, the relative ease with which stress-corrosion cracks can be initiated at precracks, or the advantages that sometimes accrue from the propagation of a single crack. The claim that has sometimes been made of precracked specimen tests – that they circumvent the initiation stage of cracking in plain specimens, erroneously assumed invariably to be related to the creation of a corrosion pit that provides a measure of stress concentration approaching that achieved at the outset with a precrack – is rarely entirely valid. Thus, the geometries of a pit, notch, or precrack are often as important for electrochemical reasons as they are for any reason associated with their influences upon stress distribution. This is because a geometrical discontinuity may be necessary

to provide the localized electrochemical conditions, in terms of environment composition or electrode potential, that are necessary for stress corrosion crack propagation. The objections that have sometimes been made against the use of precracked specimens, for example, to the validity of introducing a transgranular precrack into a specimen that suffers intergranular stress corrosion cracking, or of the necessity of incurring a considerable expense to produce a very sharp crack when the introduction of a corrosive environment may blunt the crack by the dissolution, miss the point that such sharp discontinuities do indeed exist in some real materials. Indeed, one of the major attractions of precracked specimen testing is that it can provide data that allow the designation of the maximum allowable defect sizes in structures for the latter to remain in a safe condition.

In view of the significance of strain rate in stress corrosion cracking, mentioned earlier, it is good to remember that its significance is as applicable to precracked specimens as it is to initially plain specimens, in relevant systems. This has a number of implications, not the least of which is the possible influence of time delay between loading precracked specimens and exposing them to the test environment. Moreover, the limiting stress–intensity factor  $K_{ISCC}$ , above which cracks grow relatively rapidly (Figure 10) may well depend upon the conditions under which it is determined, and it should not be regarded as some property of the material equivalent to, say, a yield stress. There is now a considerable volume of data that shows how relatively small fluctuating stresses may reduce the threshold stresses or stress-intensity factors for stress corrosion cracking, and some of these effects are probably related to cyclic loading sustaining creep-related effects. Crack-tip strain rates have consequently become a topic of interest, and expressions are available for cyclically loaded precracked specimens<sup>14,15</sup> and also for multicracked specimens<sup>16</sup> of the form that initially plain specimens take during slow strain-rate tests.

### 2.35.2.2 Comparison of the Results from Plain and Precracked Specimens

It is clear that an initially plain specimen that develops a stress corrosion crack may, if the geometry is appropriate, conform to the conditions obtaining in an initially precracked specimen. This raises a question, despite the opposing views of the protagonists of the two types of testpieces, as to the comparability of the result from each. Figure 11 shows the results<sup>17</sup>

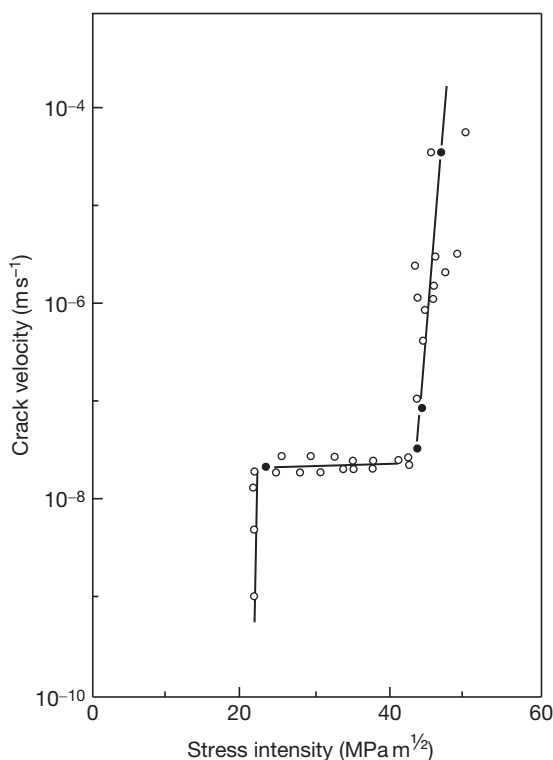


**Figure 10** Effect of applied stress intensity upon crack velocity for high-strength (1800 MPa UTS) quenched and tempered steel (AFC 77) in distilled water. Reproduced from Spiedel, M. O.; In Conference on *Hydrogen in Metals*; National Association of Corrosion Engineers, Houston, TX, 1975.

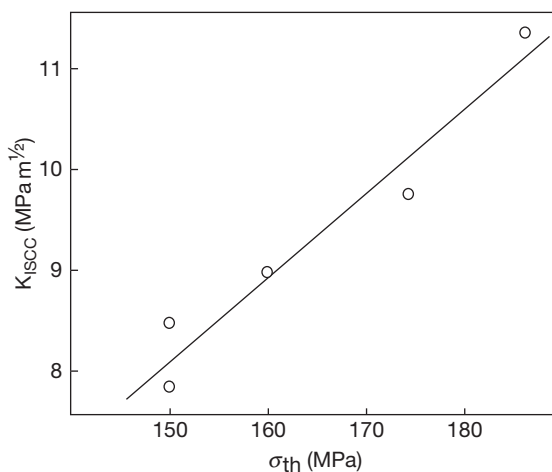


**Figure 11** Threshold stress intensities  $K_{ISCC}$  from precracked specimen tests, and threshold stresses  $\sigma_{th}$  from plain specimen tests, for a Mg–7Al alloy in various structural conditions tested in chromate–chloride solution. Reproduced from Wearmouth, W. R.; Dean, G. P.; Parkins, R. N. *Corrosion* **1973**, 29, 251.



obtained from stress corrosion tests upon a Mg–7Al alloy exposed to a chromate–chloride solution, the cracking susceptibility of the alloy being varied by different heat treatments. The implication of Figure 11 is that the threshold stress  $\sigma_{th}$ , determined upon initially plain specimens of small cross section, is related to the threshold stress intensity  $K_{ISCC}$  obtained from precracked specimens of relatively large section. Since  $K_{ISCC}$  represents the stress intensity below which an existing crack does not propagate, it would appear that the threshold stress given by tests on plain specimens corresponds to values below which cracks do not propagate to give total failure, that is, the threshold stress for plain specimens is not necessarily the stress below which cracks do not form. Examination of plain specimens stressed below the threshold stress revealed the presence of small stress corrosion cracks that had ceased to propagate and moreover, the maximum sizes of the cracks that did not propagate to total failure were quadratically related to the threshold stress, as would be expected if the concepts of fracture mechanics were applicable to these initially plain specimens. Nonpropagating cracks have also been observed at stresses below the threshold stress in other systems, such as low-alloy ferritic steels exposed to various environments, and would therefore, support the suggestion that what are being measured in tests upon plain and precracked specimens are not as different as has sometimes been suggested.

### 2.35.2.3 Crack Velocity Measurements

In mechanistic studies of stress corrosion and also in the collection of data for remaining-life predictions for plants there is need for stress corrosion crack velocity measurements to be made. In the simplest way, these can be made by microscopic measurements at the conclusion of tests, the assumption being that the velocity is constant throughout the period of exposure, or, if the crack is visible during the test, *in situ* measurements may be made by visual observation, the difficulty then being that it is assumed that the crack visible at a surface is representative of the behavior below the surface. Indirect measurements must frequently be resorted to, and these have involved observation of the elongation of the specimen, crack-opening displacement, changes in the electrical resistivity of the specimen, and acoustic emissions that sometimes accompany crack extension.

Measurement of the elongation of the specimen is probably the least satisfactory of all these, even though it is often the simplest, requiring a transducer

that responds to dimensional change. Multiple cracking of initially plain specimens raises problems in interpreting the data in terms of crack velocities, and so the technique has been frequently used for attempting to determine the point in time when cracking was initiated, the preceding time during which the transducer shows no response being equated to an incubation period for cracking. However, such results can be completely misleading because the sensitivity of most transducers is such that they will only detect change when the specimen undergoes some plastic deformation, resulting from the propagation of a crack to the size where the remaining uncracked portion of the section beyond the crack is raised to its yield strength. Consequently, crack propagation can occur during the (so-called) incubation period when the stress is insufficient to cause the propagation of a deformation band. The latter frequently occurs suddenly, producing a sharp response by the transducer, which has sometimes been interpreted as evidence of a burst of fast mechanical fracture but which may, in fact, be nothing of the sort. It is much more satisfactory to use a crack-opening displacement gauge<sup>18</sup> located across a precrack. These gauges usually take the form of two thin cantilever beams to which strain gauges are attached, the beams being located at opposite sides of the extremity of the precrack. As crack extension occurs and the sides of the crack undergo relative displacement, the strain gauges respond to the unbending of the beams.

Changes in the electrical resistivity of a specimen containing a propagating crack<sup>19</sup> depend upon applying a high constant direct current at each end of the specimen and measuring the potential difference across electrical leads situated at the opposite sides of the crack. The potential field in the region of the crack is disturbed by the presence of the latter and as the crack extends, the potential difference between the leads on opposite sides increases, the total current remains constant. This requires a reliable constant current source, and the technique is dependent in some degree upon the exact positioning of the leads and gives less reproducible results if crack branching occurs. The initial thought that the application of DC to the specimen may influence the electrochemistry of the stress corrosion reactions is not sustained in practice, and the technique can provide reliable data.

High-frequency stress waves are generated when stress corrosion cracks propagate in some materials, especially the high-strength steels when these undergo

hydrogen-induced cracking. The detection of these acoustic signals, which are filtered from lower amplitude background noise, affords a means of studying crack propagation.<sup>20</sup> While the technique involves the use of sophisticated and relatively costly equipment if it is to be correctly practiced, it has been suggested that it may also offer a means of distinguishing between active paths and hydrogen-embrittlement mechanisms of cracking.<sup>21</sup> However, that is not universally accepted, and the data from acoustic signals need treating with caution.<sup>22</sup>

#### **2.35.2.4 Effects of Surface Finish**

It is hardly surprising that the preparation of surfaces of plain specimens for stress corrosion tests can sometimes exert a marked influence upon the results. Heat treatments carried out on specimens after their preparation is otherwise completed can produce barely perceptible changes in surface composition, for example, decarburization of steels or dezincification of brasses, that promote quite dramatic changes in stress corrosion resistance. Similarly, oxide films, especially if formed at high temperatures during heat treatment or working, may influence results, especially through their effects upon the corrosion potential.

However, quite apart from these chemical changes at surfaces occasioned by the method of specimen preparation, physical effects may be important. Paxton and Procter<sup>23</sup> have prepared a review of what little is known about the effects of machining and grinding upon stress corrosion susceptibility, the most obvious effects being related to surface topography and the introduction of residual stresses into the surface layers. The former is more likely to be important in the higher strength notch-sensitive materials, while surface compressive stresses are likely to have the general effect of delaying or preventing failure.

#### **2.35.3 Choice of Environment**

Although the list of environments reported as promoting stress corrosion cracking in any alloy continues to grow with time, the concept of solution specificity remains in that not all corrosive environments will initiate or sustain stress corrosion cracking in all alloys. While it is inevitable that the environment will always remain as one of the variables that may need to be assessed by stress corrosion tests, nevertheless certain solutions, by their widespread use over many years, have tended to become standard test solutions for certain types of alloys. Thus, boiling

MgCl<sub>2</sub> solution for stainless steels, boiling nitrate solutions for carbon steels, and 3.5% NaCl for aluminum alloys, to mention but a few, have been extensively used, for example, in comparing the effects of metallurgical variables upon cracking propensities. Such approaches raise two questions: the first concerned with the extent to which 'standard' solutions prepared in different laboratories may be regarded as identical, and the second with the extent to which degrees of susceptibility of a range of alloys to cracking in one environment are related to cracking in a different environment.

While the relatively small differences that may be expected to occur between laboratories preparing a solution to the same specification often will not influence stress corrosion test results, there are situations where relatively small changes in environment can promote marked changes in cracking response. Thus, Streicher and Casale<sup>24</sup> have pointed to the potential problems associated with the use of nominally 42% boiling MgCl<sub>2</sub> in testing stainless steels. Since the hydrate of MgCl<sub>2</sub> is hygroscopic, solution preparation by weighing may lead to appreciable differences in boiling point and hence, times to failure in a stress corrosion test, so that it is preferable to prepare the solution by adding water to the hydrate to achieve a particular boiling point.

Similarly, pH variations resulting from either the initial preparation or from changes during a stress corrosion test may exert a marked influence upon results in some systems. Thus, the cracking of carbon steels in nitrates is markedly pH sensitive and, depending upon the volume of solution and the surface area of the specimen exposed, as well as upon the time involved in making the test, significant pH rises can occur, and cracking can cease as a result. Moreover, if tests are carried out with anodic stimulation, these effects may be aggravated, especially if the counter electrode is immersed in the test cell. In other cases, for example, the medium and higher strength steels, the initiation and maintenance of cracking frequently requires localized pH changes within the confines of the crack, and these can only occur if the initial conditions of exposure are appropriate.

The oxygen concentration of the solution, as in many instances of corrosion, can also be critical in stress corrosion cracking tests. Instances are available in the literature that show very markedly different test results according to the oxygen concentration in systems as widely different as austenitic steels immersed in chloride-containing phosphate-treated boiler water<sup>25</sup> and aluminum alloys<sup>26</sup> immersed in 3% NaCl.

The assumption that the relative cracking responses of a series of alloys will be the same irrespective of the environment to which they are exposed can be extremely dangerous. Many examples could be quoted of the dangers of drawing conclusions from tests in a given environment and applying these to a different situation, but some results by Lifka and Sprowls<sup>27</sup> will suffice. The results for the relative cracking susceptibilities of three aluminum alloys subjected to different exposure conditions are shown in **Figure 12**, which indicate that an intermittent spray test using acidified 5% NaCl solution gives the same order of susceptibility for the three alloys as was observed in outdoor exposure tests at three different locations. On the other hand, an alternate immersion test in 3.5% NaCl, widely used for testing aluminum alloys, places the alloys in a completely different order of susceptibility. This single example will suffice to indicate the necessity for simulating service conditions as closely as possible where laboratory data are to be used for selection or design in relation to industrial equipment.

While the dangers inherent in using standardized environments in relation to environment-sensitive fracture are readily indicated by many examples that can be quoted, there remains a problem in relation to alloy development where possible service environments may not always be identifiable at the time of the development program. In such circumstances, it appears desirable that an alloy should be assessed in a range of environments, but even then, it is necessary for realism to be injected into the program if an excessively large number of test environments are

not to be involved. The potential dependence of cracking, with its implications for dissolution and film-forming reactions or the discharge of hydrogen, suggests that the solution pH is also likely to exert significant influence upon cracking. Plots of cracking domains on potential–pH diagrams sometimes indicate correlations with certain reactions, and this may be useful in guiding a testing program,<sup>28</sup> that is, involving solutions of different pH values and exploring the cracking propensity as a function of potential.

The importance of potential cannot be over emphasized, and some aspects of this part of stress corrosion testing may be conveniently discussed in the context of **Figure 13**. This shows the different potential ranges for the cracking of ferritic steel according to the environment in tests involving potentiostatic control. Also shown are the free corrosion potentials for that steel in the different solutions. These indicate that while failure would occur in the nitrate at the free corrosion potentials, this would not be so in the hydroxide or carbonate–bicarbonate solution. This does not mean that carbon steels will never fail by stress corrosion in these two environments at the free corrosion potential, since the latter is, of course, dependent upon the composition of the steel, its surface condition, the composition of the environment, and other factors. It is possible, therefore, that as the result of, say, small additions to the environments, added intentionally or present as impurities, the corrosion potential can be caused to be within the cracking range, or that as a result of small additions to a steel, the corrosion potential may fall outside the cracking range. Quite small changes in

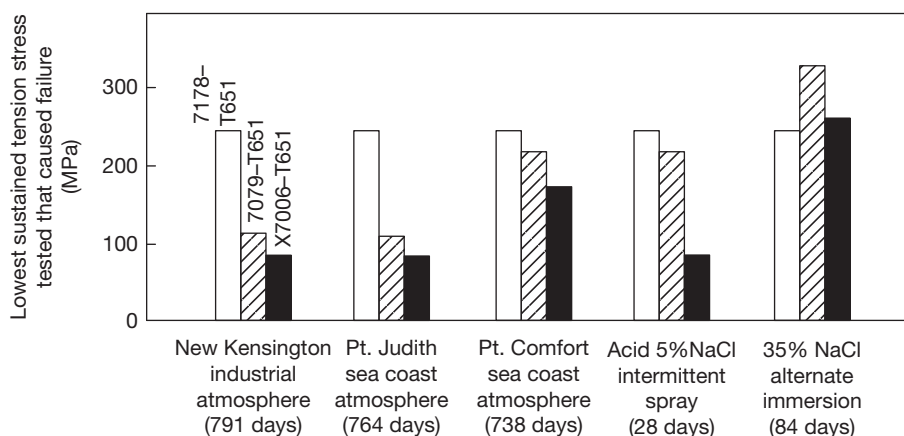


**Figure 12** Relative resistance to stress corrosion cracking of three aluminum alloys subjected to different environments. The stress levels employed corresponded to 75, 50, and 25% of the respective transverse yield strengths. Reproduced from Lifka, B. W.; Sprowls, D. O. Stress Corrosion Testing, ASTM STP No. 425, 1966; p. 342.

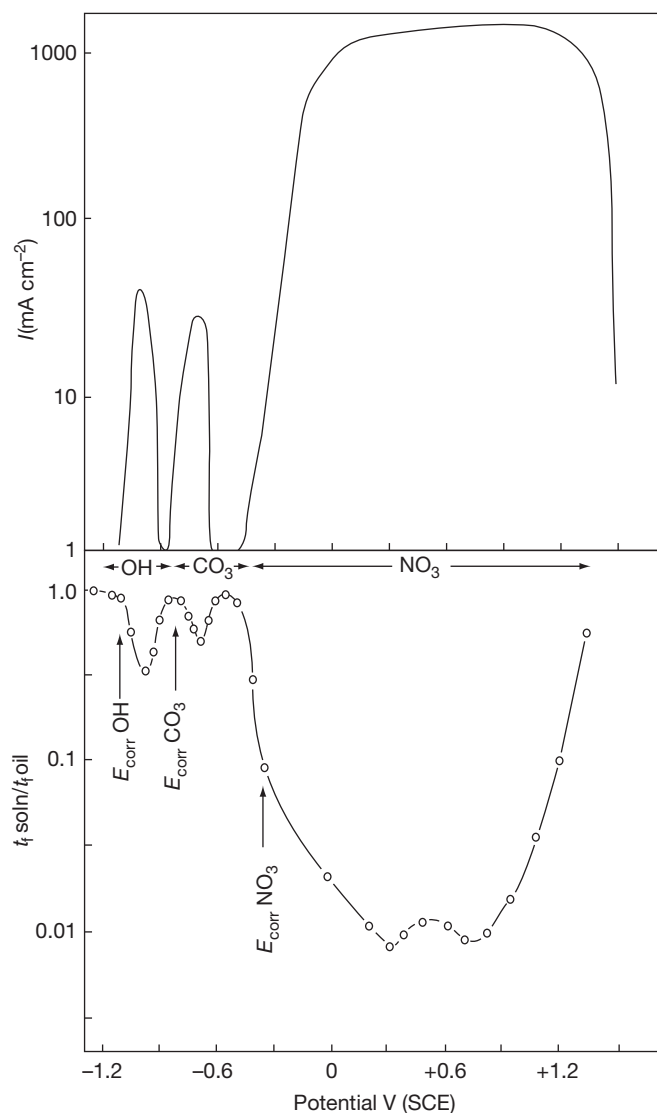


**Figure 13** Current density differences between fast and slow sweep rate polarisation curves and stress corrosion cracking susceptibility as a function of potential for C-Mn steel in nitrate, hydroxide, and carbonate-bicarbonate solutions.

potential, often only a few tens of millivolts, can therefore produce dramatic changes in cracking response and point to the necessity, especially in laboratory tests attempting to simulate a service failure, of reproducing the potential with precision.

## 2.35.4 Stress Corrosion Test Methods

### 2.35.4.1 Types of Test Cells

The cells that contain the specimen and environment for stress corrosion tests often need to be more than a

vessel made in some substance, usually glass, that is inert to the environment and which produces no electrical response upon the test specimen. Where cracking is initiated at surfaces through which heat transfer occurs, it may be necessary to design a cell in which such an effect is incorporated, since the concentration of substances in solution that may occur at an interface through which heat passes, may play a significant role in promoting cracking, especially if surface deposits allow concentration by evaporation while preventing mixing with the bulk or the environment. The cracking of riveted mild-steel boilers and the concentration of carbonate-bicarbonate

solutions under pipeline coatings to produce cracking in high-pressure gas transmissions lines are significant examples. Dana<sup>29</sup> has developed a method for simulating the conditions for cracking of stainless steels in contact with thermal insulating materials, while concentration in leaking boiler seams is simulated in the 'embrittlement detector' developed by Schroeder and Berk.<sup>30</sup>

Such test cells involve, among other things, a crevice, the essence of which is that the volume of solution that it contains is relatively small compared with the area of exposed metal, a ratio that may influence stress corrosion test results determined in more conventional cells where crevices do not exist. The experiments of Pugh *et al.*,<sup>31</sup> on the stress corrosion of 70–30 brass in ammoniacal solutions of various volumes are particularly instructive in indicating how this ratio may influence results, the time to failure varying by about an order of magnitude for a similar change in solution volume. Changes in the surface area of exposed specimens, apart from the effects already implied, may influence the cracking response for other reasons, as shown by the results of Farmery and Evans<sup>32</sup> for an Al–7Mg alloy immersed in a chloride solution. They found that coupling unstressed to stressed specimens of varying area ratio influences failure times, relatively shorter times being obtained when the area of unstressed to stressed specimen was large.

#### 2.35.4.2 Initiation of Stress Corrosion Tests

It may be felt that the initiation of a stress corrosion test involves no more than bringing the environment into contact with the specimen in which a stress is generated, but the order in which these steps are carried out may influence the results obtained, as may certain other actions at the start of the test. Thus, in outdoor exposure tests, the time of the year at which the test is initiated can have a marked effect upon the time to failure,<sup>26</sup> as can the orientation of the specimen, that is, according to whether the tension surface in bend specimens is horizontal upwards or downwards or at some other angle. However, even in laboratory tests, the time at which the stress is applied in relation to the time at which the specimen is exposed to the environment may influence results. Figure 14 shows the effects of exposure for 3 h at the applied stress before the solution was introduced to the cell, upon the failure of a magnesium alloy immersed in a chromate–chloride solution. Clearly, such prior creep extends the lifetime of specimens and raises the

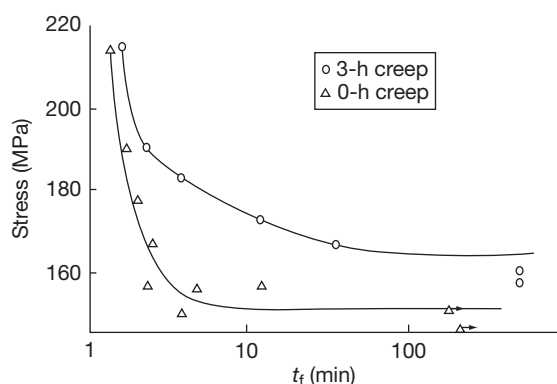


**Figure 14** Effect of delay period between application of load and introduction of solution to test cell in the failure of a Mg–7Al alloy exposed to a chromate–chloride solution. Reproduced from Wearmouth, W. R.; Dean, G. P.; Parkins, R. N. *Corrosion* **1973**, 29, 251.

threshold stress very considerably, and since other metals are known to be strain-rate sensitive in their cracking response, it is likely that the type of result apparent in Figure 14 is more widely applicable.

#### 2.35.4.3 Hydrogen Embrittlement Tests

The absorption of hydrogen by various materials, including high-strength steels, results in loss of ductility, which in turn can result in cracking and fracture when the metal is subjected to a sustained tensile stress. Hydrogen may be introduced into these various alloys from the gas phase (during manufacture or welding), or from aqueous solution during surface treatment (pickling, plating, and phosphating) or from the environment during a spontaneous corrosion process in which the development of acidity within the crack results in hydrogen evolution and absorption. Various test methods<sup>33</sup> may be used to evaluate the effect of hydrogen on the properties of alloys, including some *ad hoc* tests that were specifically developed for high strength steels.

Although similar constant-load test rigs are used for both active-path corrosion and hydrogen stress cracking, there is one fundamental difference in the test procedure. In the case of active-path corrosion testing, it is always carried out in the presence of the corrosive environment, but in the case of hydrogen-related cracking, testing may be carried out after hydrogen has been introduced into the alloy either deliberately by gaseous or cathodic charging, or following processes such as welding, pickling, or electroplating. However, with precharged specimens, loss



of hydrogen may occur<sup>34</sup> when they are removed from the environment, resulting in the entry of that substance and so, sustained-load tests are also carried out in the presence of an environment (gaseous or aqueous) so that hydrogen is introduced into the test piece during the application of the tensile stress.

#### 2.35.4.4 Dynamic Tests

All of the properties evaluated by the conventional tensile test (yield strength, tensile strength, elongation, and reduction in area) are affected by the presence of hydrogen, but in the case of the tensile strength and yield strength, the effect is significant only when the steel has a very high tensile strength and has been severely embrittled. On the other hand, the reduction in area, and, to a lesser extent, the elongation may be used for detecting embrittlement. Hobson and Sykes<sup>35</sup> found that with low-carbon steels there was an almost linear relationship between reduction in area and hydrogen content of the steel. Slow strain-rate tests are sometimes employed in testing materials (and not only steels) after preexposure to a source of hydrogen. The strain rate may be critical in that not only can it be too high but also, if it is too low the hydrogen may diffuse out of the specimen before cracking occurs.

Various types of bend tests have been used to evaluate embrittlement. Beck *et al.*<sup>36</sup> used thin strip specimens and determined the decrease in height,  $\Delta h$ , at fracture when the specimen was bent by compressing it at a constant rate in a tensile testing machine (Figure 15). The decrease in height,  $\Delta h$ , gives a measure of the embrittlement, the maximum elongation of the outside fiber of the specimen being calculated from the radius of curvature at maximum bending. In general, the ductility is found to increase with the rate of straining, and for this reason, high-strain-rate tests, such as impact tests, are insensitive to hydrogen embrittlement. Where the material is available only in the form of tubing, semicircular specimens may be used in place of flat strips in the compression bend test. The total cross-head travel from the unstressed height along the diameter to the point of fracture gives a measure of embrittlement, which may be compared with that obtained from an unembrittled specimen of the same steel.

A constant-rate bend-test machine, which provides an effective method for testing highly embrittled steel wires of high-tensile strength, was designed by Zapffe and Haslem<sup>37</sup> (Figure 16). The motor *A* pulls a chord attached to the traveling arm *D* that rotates about a

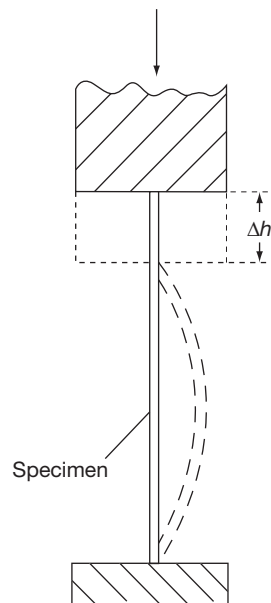


**Figure 15** Bend test using a tensile testing machine. Reproduced from Beck, W.; Klier, E. P.; Sachs, G. *Trans. AIME* 1956, 206, 1263.

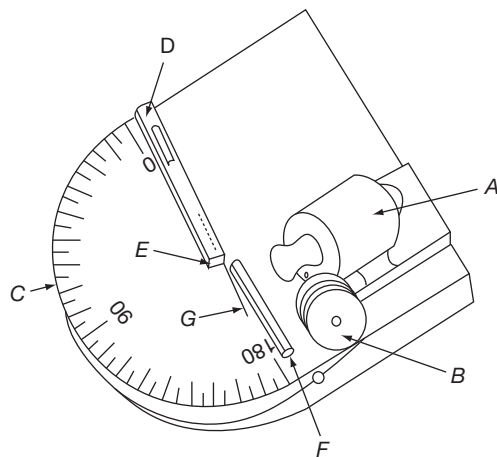


**Figure 16** Constant-rate bend-test for determining hydrogen embrittlement of wires. *A*, drive unit; *B*, pulley; *C*, semicircular base; *D*, traveling arm; *E*, axial pin; *F*, fixed arm; *G*, wire specimen. Reproduced from Zapffe, C. A.; Haslem, M. E. *Trans. AIME* 1946, 167, 281.

pivot pin. The wire specimen *G* (1.6 × 100 mm) is inserted in *D* and is supported by the fixed arm *F*, the arrangement being so designed that tensile or torsional stresses are avoided. The specimen is thus bent around the pivot pin *E* (radius 1.6 mm) at a constant rate, the angle of bend to cause fracture giving a measure of its ductility. Since ductility increases with rate of straining, the bending rate must be slow and (4%) is

considered to be suitable for detecting embrittlement. A similar machine has been used for studying the embrittlement of spring steel strip after hydrogen has been introduced by cadmium plating.

An alternative procedure is the reverse-bend test in which the specimen in the form of wire or strip is bent repeatedly backward and forward over a mandrel until it fractures, the number of bends

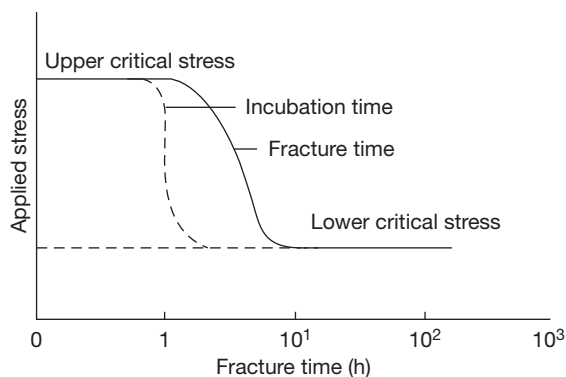


**Figure 17** Schematic representation of delayed failure characteristics of a hydrogenated high-strength steel.

indicating the degree of embrittlement. However, this method is considered to be less sensitive than the single-bend test.

#### 2.35.4.5 Static Tests

Whereas ductile materials, such as iron and mild steel, are often considered not to crack when charged with hydrogen and subjected to a tensile stress below the yield stress, the position is different with high-strength ferrous alloys where, depending on the strength of the steel and the hydrogen content, failure may occur well below the yield stress. However, the fracture process is not instantaneous, and there is a time delay before cracks are initiated; for this reason, the phenomenon is sometimes referred to as 'delayed failure.'

In the majority of cases, the tests are conducted using a dead-weight lever-arm stress-rupture rig with an electric timer to determine the moment of fracture, but a variety of test rigs similar to those shown in [Figure 1\(g\)](#) are also used. The evaluation of embrittlement may be based on a delayed-failure diagram in which the applied nominal stress versus time to

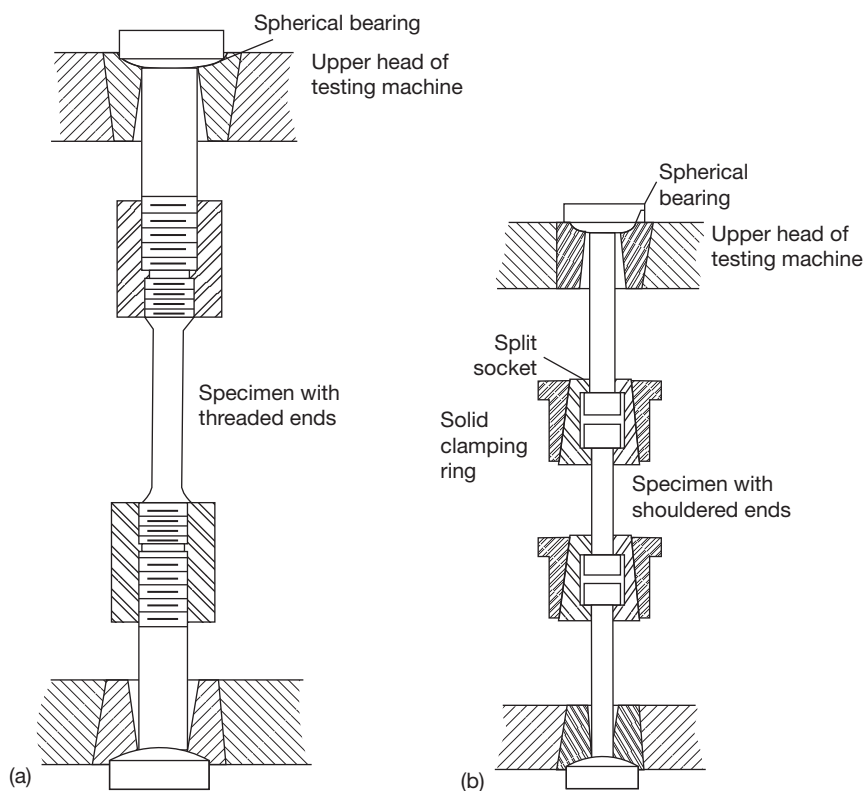


**Figure 18** Methods of gripping specimens in order to avoid bending stresses: (a) Device for threaded end specimens, and (b) device for shouldered-end specimens. Reproduced from Stress Corrosion Testing, ASTM STP No. 425, 1967.

failure is plotted, [Figure 17](#), or the specimen may be stressed to a predetermined value (say 75% of the ultimate notched tensile strength) and is considered not to be embrittled if it shows no evidence of cracking within a predetermined time (say 500 h). Troiano<sup>38</sup> considers that the nature of delayed fracture failure can be described by four parameters (see [Figure 17](#)):

1. the upper critical stress corresponding to the fracture stress of the unembrittled notched specimen;
2. the lower critical stress, which is the applied stress below which failure does not occur;
3. the incubation period or the time required for the formation of the first crack;
4. the failure time or the time for specimen failure at a given applied stress; in the intermediate stress range, this includes a period of relatively slow crack growth.

During the constant-load test, it is essential that only axial tensile stresses are applied, as any bending stresses that are introduced will result in a higher true stress than that calculated. For this reason, the ends of the specimens and the grips must be designed to avoid bending stresses. The ASTM Standard E8 (Standard Test Methods for Tension Testing of Metallic Materials) specifies that in the case of specimens with threaded ends the grips should be attached to the heads of the testing machine through properly lubricated spherical-seated bearings and that the distance between the bearings should be as great as is feasible ([Figure 18](#)).

In order to simplify the test procedure, a number of investigators have designed test rigs in which the bulky lever arm is replaced by a loading nut, the stress in the specimen being determined by means of strain gauges; these rigs are similar in principle to those shown in [Figure 1\(g\)](#). [Figure 19](#) shows a spring-loaded rig that was used by Cavett and van Ness<sup>39</sup> to study the embrittlement produced by hydrogen gas at high pressures, in which the tensile load is applied by compressing a heavy-duty spring.

Raring and Rinebold<sup>40</sup> have devised a method in which the specimen is supported along the diameter of a steel loading ring, [Figure 20](#), and the stress is applied by tightening the bottom nut until the diameter corresponds with the required load. The sudden release of elastic energy stored within the ring when the specimen fractures results in displacement of the tightening nut, and this is used to actuate a micro-switch and timer. Williams *et al.*<sup>41</sup> have used notched 'C'-rings, the stress being applied by tightening the

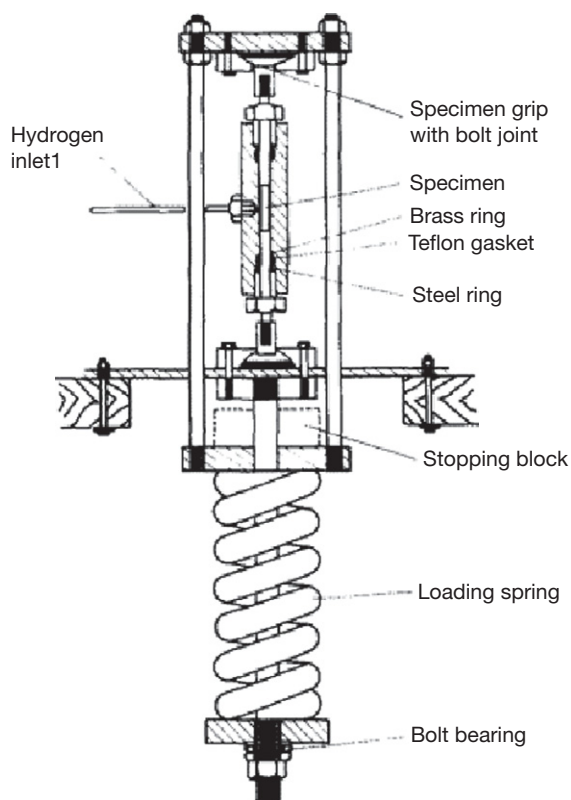


**Figure 19** Spring-loaded rig for sustained load testing of a steel specimen in gaseous hydrogen at high pressure. Reproduced from Cavett, R. H.; van Ness, H. C. *Welding J.* (research supplement) **1967**, 42, 317.

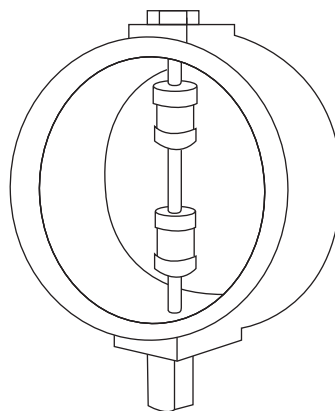


**Figure 20** Loading-ring method of stressing a specimen. Reproduced from Raring, R. H.; Rinebold, J. A. *ASTM Bulletin No. 213*, 1956.

nut of a calibrated loading bolt that passes through the diameter of the 'C' ring, [Figure 21](#). The strain gauges attached to the bolt form two arms of a Wheatstone bridge circuit and to compensate for temperature

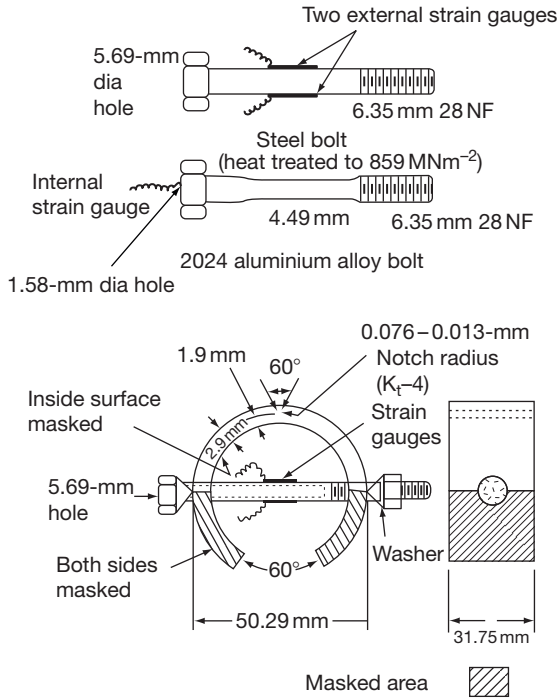


**Figure 21** Notched 'C'-ring specimen with attached strain gauges.

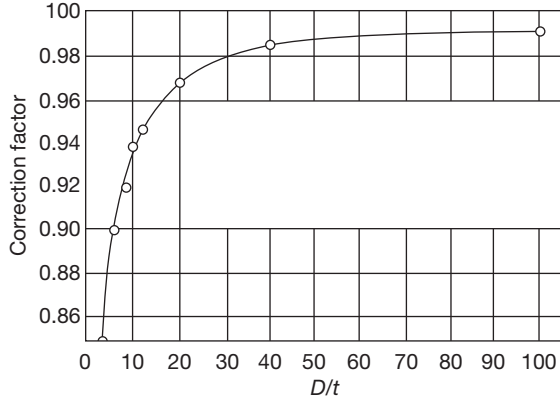


**Figure 22** Correction factor Z for calculating stress in 'C'-ring tests.

changes, the other two arms consist of two identical strain gauges attached to a similar unstrained bolt.

## Appendix A: Stresses in Bent Specimens

In each of the following equations:  $\sigma$  = maximum tensile stress,  $E$  = modulus of elasticity, and  $t$  = specimen thickness.

### A.1 Two-point bending, Figure 1(a):

$$L = \frac{k.t.E}{\sigma} \sin^{-1} \left( \frac{H.\sigma}{k.t.E} \right)$$

where  $L$  = specimen length,  $k$  = constant (1.280), and  $H$  = holder span.

### A.2 Four-point bending, Figure 1(b):

$$\sigma = \frac{12E.t.y}{3L^2 - 4A^2}$$

where  $y$  = maximum deflection,  $L$  = distance between outer supports, and  $A$  = distance between inner and outer supports.

### A.3 'U'-bends, Figures 1(d) and 1(e):

Applied strain  $\epsilon = t/2r$ , when  $t < r$ , where  $r$  = radius of curvature at section of interest.

### A.4 'C'-rings, Figure 1(c):

$$\sigma = \frac{4E.t.Z.\Delta}{\pi D^2}$$

where  $\Delta = OD_f - OD_i$ ,  $OD_f$  = final outside diameter of stressed 'C'-ring,  $OD_i$  = initial outside diameter of unstressed 'C'-ring,  $D$  = mean diameter, that is,  $(OD - t)$ , and  $Z$  = a correction factor, related to  $D/t$  as indicated in Figure 22.

## References

1. Ailor, W. H. Ed.; *Handbook on Corrosion Testing and Evaluation*; Wiley: New York, 1971.
2. *Stress Corrosion Testing*, ASTM STP No. 425, 1967.
3. BS 6980, Stress corrosion testing, Parts 1–7, (ISO 7539–1/7) BSI, Milton Keynes.
4. Logan, H. L. *The Stress Corrosion of Metals*; Wiley: New York, 1966; p 273.
5. Haaijer, G.; Loginow, A. W. *Corrosion* **1965**, 21, 105.
6. Parkins, R. N.; Mazza, F.; Royuela, J. J.; Scully, J. C. *Br. Corr. J.* **1972**, 7, 154.
7. Parkins, R. N.; Haney, E. G. *Trans. Metall. Soc., AIME* **1968**, 242, 1943.
8. Brenner, P.; Gruhl, W. Z. *Metall.* **1961**, 52, 599.
9. Ugianski, G. M.; Payer, J. H. Eds., *Stress Corrosion Cracking – The Slow Strain Rate Technique*, ASTM STP 665; ASTM: Philadelphia, 1975.
10. Parkins, R. N.; Suzuki, Y. *Corros. Sci.* **1983**, 23, 577.
11. Yu, J.; Holroyd, N. J. H.; Parkins, R. N. In *Environment-Sensitive Fracture: Evaluation and Comparison of Test Methods*, ASTM STP 821; Dean, S. W., Pugh, E. N., Ugianski, G. M., Eds.; ASTM: Philadelphia, 1984; p 288.
12. Brown, B. F. *Met. Rev.* **1968**, 13, 17.
13. Specialists Meeting on Stress Corrosion Testing Methods, AGARD Conference Proceedings, No. 98 NATO, 1972.

14. Lidbury, D. P. G. *Embrittlement by the Localized Crack Environment*; Gangloff, R. P., Ed.; AIME: New York, 1983; p 149.
15. Parkins, R. N. *Corrosion* **1987**, 43, 130.
16. Congleton, J.; Shoji, T.; Parkins, R. N. *Corros. Sci.* **1985**, 25, 633.
17. Wearmouth, W. R.; Dean, G. P.; Parkins, R. N. *Corrosion* **1973**, 29, 251.
18. Fisher, D. M.; Bubsey, R. T.; Srawley, J. E. Design and Use of a Displacement Gauge for Crack Extension Measurements, NASA IN-D 3724, 1966.
19. Barnett, W. J.; Troiano, A. R. *Trans. AIME* **1957**, 209, 486.
20. Gerberich, W. W.; Hartblower, C. E. Proceedings of the Conference on Fundamental Aspects of Stress Corrosion Cracking NACE, 1986; p 420.
21. Okada, H.; Yukawa, K.; Tamura, H. *Corrosion* **1974**, 30, 253.
22. Pollock, W. J.; Hardie, D.; Holroyd, N. J. H. *Br. Corros. J.* **1982**, 17, 103.
23. Paxton, H. W.; Proctor, R. P. M. Paper No. EM68-520 presented at American Society of Tool and Manufacturing Engineers Symposium on Surface Integrity in Machining and Grinding, Pittsburgh 1968.
24. Streicher, M. A.; Casale, I. B. Proceedings of Conference on Fundamental Aspects of Stress Corrosion Cracking NACE: Houston, 1969; p 305.
25. Williams, W. I. *Corrosion* **1957**, 13, 539.
26. Romans, H. B. *Stress Corrosion Testing*, ASTM STP No. 425, 1966, p 182.
27. Lifka, B. W.; Sprowls, D. O. *Stress Corrosion Testing*, ASTM STP No. 425 1966, p 342.
28. Parkins, R. N. In *The Use of Synthetic Environments for Corrosion Testing*, ASTM STP 970; Francis, P. E., Lee, T. S., Eds.; ASTM: Philadelphia, 1988; p 132.
29. Dana, A. W. *ASTM Bulletin No. 225, TP 196* 1957, p 46.
30. Schroeder, W. C.; Berk, A. A. *Bull. US Bur. Mines* 1941, p 443.
31. Pugh, E. N.; Montague, W. G.; Westwood, A. R. *Trans. Am. Soc. Met.* **1965**, 58, 665.
32. Farmery, H. K.; Evans, U. R. *J. Inst. Met.* **1956**, 84, 413.
33. Smialowski, M. *Hydrogen in Steel*; Pergamon Press: London, 1962.
34. Hardie, D.; Holroyd, N. J. H.; Parkins, R. N. *Met. Sci.* **1979**, 13, 603.
35. Hobson, J. D.; Sykes, C. *J. Iron Steel Inst.* **1951**, 169, 209.
36. Beck, W.; Klier, E. P.; Sachs, G. *Trans. AIME* **1956**, 206, 1263.
37. Zapffe, C. A.; Haslem, M. E. *Trans. AIME* **1946**, 167, 281.
38. Troiano, A. R. *Trans. Am. Soc. Met.* **1960**, 52, 54.
39. Cavett, R. H.; van Ness, H. C. *Welding J.* (research supplement) **1967**, 42, 317.
40. Raring, R. H.; Rinebold, J. A. *ASTM Bulletin No. 213* 1956.
41. Williams, F. S.; Beck, W.; Jankowsky, E. J. *Proc. ASTM* **1960**, 60, 1192.



## 2.36 Applications of Statistical Analysis Techniques in Corrosion Experimentation, Testing, Inspection and Monitoring

### **N. Laycock**

Shell Todd Oil Services, Private Bag 2035, New Plymouth, New Zealand

### **P. Laycock**

School of Mathematics, Alan Turning Building, University of Manchester, Oxford Road, Manchester, M13 9PL, UK

### **P. Scarf**

Centre for OR and Applied Statistics, Salford Business School, University of Salford, The Crescent, Manchester, M5 4WT, UK

### **D. Krouse**

Industrial Research Limited, Gracefield Research Centre, PO Box 31-310, Lower Hutt, New Zealand

© 2010 Elsevier B.V. All rights reserved.

<b>2.36.1</b>	<b>Introduction</b>	1549
<b>2.36.2</b>	<b>Basic Terminology and Methods</b>	1550
2.36.2.1	The Normal Distribution and Associated Distributions	1550
2.36.2.2	Linear Regression	1553
2.36.2.3	Poisson Process Modeling	1553
2.36.2.4	Extreme Value Distributions	1554
2.36.2.5	Threshold Techniques	1555
2.36.2.6	Wiener Process Modeling	1555
2.36.2.7	Sampling Theory and Sample Surveys	1556
2.36.2.8	Experimental Design	1556
2.36.2.9	Bayes' Theory	1557
2.36.2.9.1	Bayes' theorem	1557
2.36.2.9.2	Probability	1557
2.36.2.9.3	Prior and posterior probabilities	1558
2.36.2.9.4	Specifying the prior	1558
2.36.2.9.5	Robust Bayes	1559
<b>2.36.3</b>	<b>Corrosion Science</b>	1559
2.36.3.1	Pitting Potentials and Induction Times	1559
2.36.3.2	Coupon Testing	1559
2.36.3.2.1	Straight-line regression analysis of weight loss data	1560
2.36.3.2.2	Extreme value analysis of pit depth measurements	1560
2.36.3.2.3	Response surface regression analysis of LPRM data	1562
2.36.3.3	Crack Depth Modeling	1563
2.36.3.3.1	Two-stage modeling of crack growth	1563
<b>2.36.4</b>	<b>Corrosion Engineering</b>	1565
2.36.4.1	Sample Inspection of Heat Exchanger Tubes	1565
2.36.4.2	Thickness Measurement Locations	1566
2.36.4.2.1	Straight-line regression	1567
2.36.4.2.2	Extreme value analysis	1567
2.36.4.2.3	Bayesian methods	1569
2.36.4.3	Pit Depth Data	1570
2.36.4.3.1	Extreme value analysis for life prediction	1570
2.36.4.3.2	Life prediction models transformable to linearity	1571
2.36.4.4	Intelligent Pigging Data	1573
2.36.4.4.1	Untracked features: Pareto distribution example	1573
2.36.4.4.2	Tracked feature comparison	1573
2.36.4.5	Optimizing Inspection and Repair Intervals	1574
2.36.4.5.1	Planning inspections for cracks	1574

2.36.4.5.2	Optimizing inspections with unknown cost of failure	1575
2.36.4.5.3	Crack inspection case study	1575
<b>2.36.5</b>	<b>Corrosion Monitoring</b>	1577
2.36.5.1	Threshold Techniques	1577
<b>2.36.6</b>	<b>Summary and Conclusions</b>	1579
<b>References</b>		1579

## Glossary

- Exceedance** The amount by which a data value exceeds a selected threshold.
- Extrapolation** The process of predicting the value of some quantity of interest over a region (interval of space and/or time) that is outside the region of observation or inspection.
- Extreme value** The largest (else smallest) number in a data set.
- Likelihood** The joint probability distribution for the sampled data, considered as a function of the parameters of this distribution.
- Operational failure rate** The reciprocal of the mean time between operational failures of the function of a system that is subject to preventive maintenance such as inspection and repair.
- Outlier** A discordant or suspect data value.
- Poisson process** A sequence of events occurring purely at random in time or over an area at a constant mean rate.
- Probability** The relative 'long-run' frequency of occurrence of an outcome from many repetitions of a test or experiment, or the degree of one's current belief that a statement is true. Measured on a scale from 0 to 1, where 0 indicates that the outcome of interest cannot occur and 1 indicates that it must occur.

## Abbreviations

- CDF** Cumulative distribution function
- EV** Extreme value distribution
- F dn** Fisher's variance-ratio distribution
- GEV** Generalized extreme value distribution
- GPD** Generalized pareto distribution
- IRIS** Internal rotary inspection system
- LOTIS** Laser optical tube inspection system
- MAT** Minimum allowable thickness
- ML** Maximum likelihood
- MTBOF** Mean time between operational failures

**NDT** Nondestructive testing (also known as nondestructive examination, NDE)

**NWT** Nominal wall thickness

**PDF** Probability density function

**RWT** Remaining wall thickness

**S-IDAP** Shell inspection design analysis and plotting package

**t dn** Student's  $t$  distribution

**TML** Thickness measurement location

**WT** Wall thickness

## Symbols

- A** Extrapolation area
- a, b** Intercept and slope for data regression line
- C<sub>f</sub>** Cost of failure due to a crack
- C<sub>p</sub>** Cost of inspection for cracks including the repair of crack defects
- C(T)** Long-run cost per unit time of policy that inspects every  $T$  time units
- F<sub>max,τ</sub>(z)** Distribution function of the maximum crack depth at inspection at time  $T$
- F<sub>T</sub>(z)** Unconditional distribution of the crack depth at inspection at time  $T$
- F(y)** Probability model cumulative frequency distribution (cdf,  $\Pr(Y < y)$ )
- f(x, θ), F(x, θ)** Density and distribution function with parameter  $\theta$
- F(x), f(x), f(x|·)** Distribution function, density, and conditional density
- F<sub>n</sub>(y)** Sample cdf for  $n$  data values
- G<sub>T</sub>(z; T - x)** The distribution of crack depth at inspection at time  $T$  conditional on initiation of a crack at time  $x$
- G(Z; τ)** Distribution of crack depth for a crack that has been growing for time  $\tau$
- N<sub>t</sub>** Number of cracks at time  $t$
- P<sub>WT</sub>( )** Density function of initial wall thickness
- p( )** Posterior or prior density function
- Pr(A)** Probability that event A occurs
- Pr(A|B)** Probability that A occurs given that B occurs

<b>Pr(A &amp; B), Pr(A, B)</b>	Probability that both A and B occur
<b>R</b>	Half-width of uniform error range
<b>S(t)</b>	Survivor function ( $\Pr(T > t) = 1 - F(t)$ )
<b>S<sup>2</sup></b>	Sample variance of data
<b>T</b>	Optimum inspection interval
<b>u</b>	Threshold wall loss
$\bar{x}, \bar{y}$	Means or averages for sample data
<b>X<sub>(p)</sub></b>	The $p$ th quantile of the maximum wall loss distribution
<b>y(i)</b>	$i$ 'th order statistic, the $i$ 'th sample value in ordered data $y(1) < y(2) < \dots$
<b>z<sub>f</sub></b>	Critical crack depth: if $Z > z_f$ , then failure occurs
<b><math>\alpha\alpha</math></b>	Intercept for model regression line or similar <i>else</i> scale parameter for Extreme Value distribution
<b><math>\beta\beta</math></b>	Slope for model regression line or similar
<b><math>\delta, \alpha</math></b>	Location and scale parameters of a GEV or GPD
<b><math>\Delta, \hat{\Delta}</math></b>	Change and estimated change in extreme value mode between inspections
<b><math>\varepsilon</math></b>	Measurement error effect on the mode of a Gumbel distribution
<b><math>\gamma\gamma</math></b>	Euler constant, 0.57721...
<b><math>\gamma, \alpha_0, \beta</math></b>	Parameters of Weibull distribution for $G_T(z; T - x)$
<b><math>\kappa</math></b>	Shape parameter of a GEV or GPD
<b><math>\lambda\lambda</math></b>	Mean event rate for a Poisson process (e.g. pit initiation or crack initiation)
<b><math>\mu</math></b>	Mean of a probability distribution
<b><math>\hat{\mu}, \hat{\sigma}</math></b>	Maximum likelihood estimates of distribution parameters
<b><math>\varphi()</math></b>	Density of wall loss measurement error
<b><math>\Theta, \theta, \theta_1, \theta_2</math></b>	Possible values of the Bernoulli parameter
<b><math>\rho\rho</math></b>	Coefficient of Variation, $\sigma/\mu$
<b><math>\sigma</math></b>	Standard deviation (square-root of variance) <i>else</i> scale parameter for a distribution
<b><math>\sigma^2, \sigma_c^2, \sigma_e^2</math></b>	Variance and variance components of a Normal distribution, $N(\mu, \sigma^2)$
<b><math>\xi</math></b>	Bound for extreme value distribution

## 2.36.1 Introduction

Statistical techniques are used extensively across the full range of scientific and engineering disciplines. More often than not, the results of experimental studies are reported in terms of averages, best-fit lines, confidence limits, and distribution functions. The special relevance of statistics to corrosion was

identified as early as 1933,<sup>1</sup> and the application of extreme value analysis techniques to some corrosion engineering problems was introduced in the 1950s.<sup>2,3</sup> Statistical approaches were then more widely adopted and developed in Japan, both in the study of localized corrosion processes<sup>4,5</sup> and for remnant life prediction in an engineering context.<sup>6</sup> The 1980s and 1990s saw increasing academic activity,<sup>7-9</sup> and recently there have appeared a small number of guidelines and standards for the practical applications of these techniques.<sup>10-12</sup>

Other chapters in this book describe the state of the art in corrosion modeling, but here we briefly mention a few examples where in statistical techniques have proved particularly useful. In modeling pitting corrosion of stainless steels, it is common to assume that pit initiation is a *Poisson process* occurring randomly in time and at sites distributed randomly across the sample surface,<sup>13-15</sup> although interactions between pits are now being considered more significant.<sup>16,17</sup> Similarly, *percolation theory*<sup>18</sup> has been used to explain the critical Cr concentration for the passivation of stainless steels in dilute acids,<sup>19,20</sup> the degree of grain boundary sensitization required for intergranular SCC of 304 stainless steel in thiosulfate solutions,<sup>21</sup> the mechanism of pit initiation for stainless steels in chloride solutions,<sup>22</sup> and the critical compositional thresholds associated with dealloying processes.<sup>23,24</sup> Of course, *Monte-Carlo (MC) techniques*<sup>25</sup> are frequently applied to enable the computer simulation of these and other corrosion processes; for example, **Figure 1** shows the results of an MC simulation of the passivation of Fe–Cr alloys.

Statistical approaches are frequently applied to the analysis of the results from the experimental studies of pitting corrosion, and the so-called ‘electrochemical noise’ monitoring is fundamentally dependent on statistical theory. Both these application areas are covered in some detail later. However, the most economically important use of statistics in corrosion is undoubtedly in the analysis of inspection results to estimate the in-service corrosion rate of industrial plants. These results are used to determine the planned replacement and future inspection strategies for plants all over the world, with enormous safety, financial, and environmental consequences potentially arising from poor decisions. In this context, it is natural to consider extreme corrosion events so that extreme value analysis has found wide application. In this chapter, we provide a basic introduction to the underlying mathematics behind the most commonly used techniques in the statistical

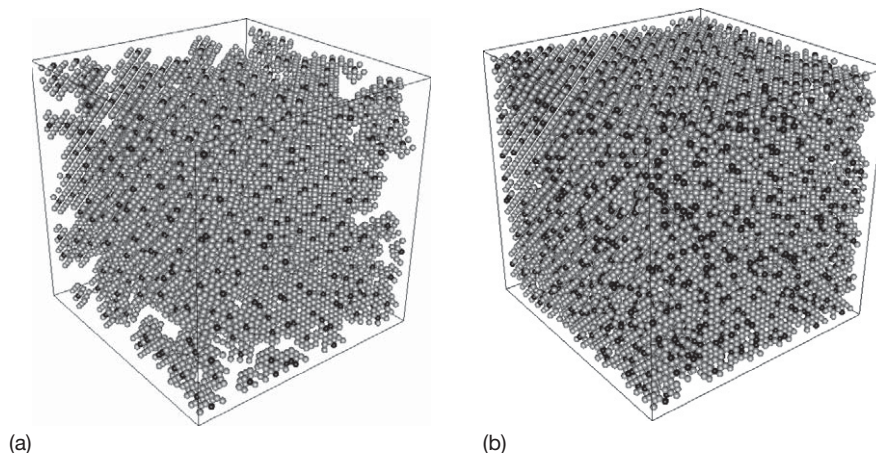


**Figure 1** Surface exposed Fe (grey) and Cr (black) atoms after 100 000 time steps in a dissolution simulation involving 17 261 atoms in a bcc lattice: (a) 3 at.% Cr; (b) 18 at.% Cr. This simulation is based on the method described in Qian *et al.*,<sup>20</sup> and it shows passivation when the Cr concentration is above the relevant percolation threshold,  $P_c(1,2) = 17.2$  at.%.

evaluation of corrosion data, but we focus, in particular, on those methods that have either been customized to a significant extent for specific applications in corrosion, or seem most likely to be further developed by the corrosion community in the future.

### 2.36.2 Basic Terminology and Methods

This is an introduction to the relevant statistical terminology and methods discussed in this chapter, as can be found in a fuller form in an introductory text book or at online resources.<sup>26,27</sup> Dedicated statistical software packages, such as SPSS, MINITAB, SAS, or GENSTAT, are also widely available and are usually preferable for implementing statistical techniques. Extensions of these ideas and nomenclature to allow for other probability distributions and contexts are introduced as and when they appear in this chapter.

#### 2.36.2.1 The Normal Distribution and Associated Distributions

Statistical methods are designed to explore the interface between data and models. The simplest standard model is the Normal (or Gaussian) distribution, as illustrated in **Figure 2** with an example dataset comprising 75 measurements of crack depth on circumferential welds on piping at various locations inside a nuclear power plant facility.

Note that although the data are clearly not ‘a perfect fit’ to the model, they can nevertheless be shown to be compatible with these model assumptions.

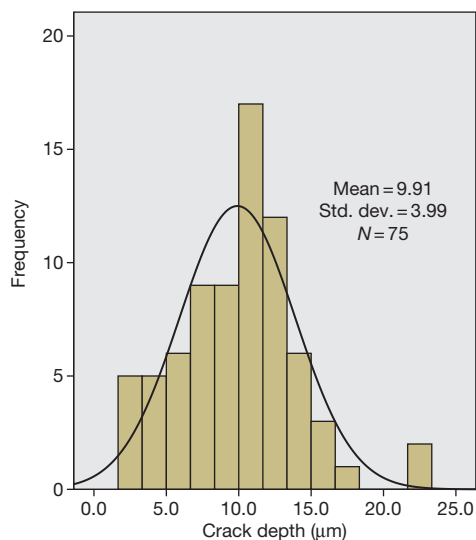


**Figure 2** An example of a Normal (or Gaussian) distribution. The dataset comprises 75 measurements of crack depth on circumferential welds on piping inside a nuclear power plant.

We write  $Y \sim N(\mu, \sigma^2)$  to be read as ‘the random variable  $Y$  has a Normal distribution with mean  $\mu$  and variance  $\sigma^2$ .’ However, there are two possible ‘outliers’ in the right-hand ‘tail’ of the distribution at a depth of 22  $\mu\text{m}$ , which might warrant a validity check and an assessment of any special circumstances at that measurement location. The model allows us to make statements such as ‘There is a 95% probability that the next observation on  $Y$  will lie in the interval  $\mu \pm 1.96\sigma$ .’ Note that  $\sigma$  is called the standard deviation of  $Y$  and is measured in the same units. Replacing

1.96 ( $\sim 2$ ) with 1.64 produces a 90% interval size, while 3.29 ( $\sim 3$ ) produces 99%, and 4.89 ( $\sim 5$ ) leaves just a one in a million chance of landing outside of the interval. The smooth curve drawn in **Figure 2** is called the probability density function (PDF), and for the Normal distribution, this has formula

$$f(y) = \frac{1}{\sqrt{2\pi}\sigma} \exp \left[ -\left( \frac{y - \mu}{\sigma} \right)^2 \right] \quad [1]$$

Probabilities for this or any other random variable are obtained by integrating the relevant PDF over the chosen interval. In particular, the cumulative distribution function (CDF) is defined by

$$\Pr(Y \leq y) = F(y) = \int_{-\infty}^y f(y) dy \quad [2]$$

This probability may or may not have a simple formula. For the Normal distribution, access is required to a table of values for the standard distribution with mean zero and standard deviation one. When the measured variate is time, especially a failure time, then  $S(t) = \Pr(T > t) = 1 - F(t)$  is commonly called the Survivor function.

A random sample of observations  $y_1, y_2, \dots, y_n$  on any such random variable  $Y$  has sample mean (or average)  $\bar{y} = (y_1 + y_2 + \dots + y_n)/n$ , which can be used to estimate the population mean,  $\mu$ , and we write  $\hat{\mu} = \bar{y}$ . The distinction between capital letters ( $Y$ , standing for the name of the random variable) and lower-case letters ( $y$  for the collected data) is frequently dropped, whereas the distinction between Latin letters (such as  $y$  and  $s$  for data) and Greek letters (such as  $\mu$  and  $\sigma$  for model parameters) is always vital and should only be discarded when the context and intent is clear – although for simplicity of presentation, this will usually be assumed to be the case in most of this chapter. By the Central Limit Theorem, almost all sample means,  $\bar{y}$ , have approximately (although exactly so if  $Y$  is itself Normal) a Normal distribution, with mean  $\mu$  and variance  $\sigma^2/n$  – and hence standard deviation (or ‘standard error’) equal to  $\sigma/\sqrt{n}$ , which tends to zero as  $n$  increases.

The data will also have their own sample variance, given by

$$s^2 = \frac{1}{(n-1)} \sum_{i=1}^n (y_i - \bar{y})^2 \quad [3]$$

which provides an ‘unbiased’ estimate of the population variance  $\sigma^2$ , where we write  $\tilde{\sigma}^2 = s^2$ , which then provides an estimate  $s/\sqrt{n}$  of the ‘standard error of the mean’. The divisor ‘ $n - 1$ ’ is called the ‘degrees of freedom’ for the numerator and will change as more

parameters (currently only one, namely  $\mu$ ) are introduced into the model of the population mean. When  $Y$  is Normal, a 95% (say) ‘confidence interval’ for the true mean,  $\mu$ , is  $\hat{\mu} \pm t\sigma/\sqrt{n}$ , where  $t$  comes from tables for the  $t$ -distribution, with  $t = 1.96$  for a large  $n$  when this can also be used for other sampled distributions.

Proposed values of  $\mu$  (such as zero, for example), which lie outside of this interval, are said to be rejected at a 5% significance level. Conversely, the confidence interval could alternatively be derived from the formalities of the significance test.

The mean  $\mu$  represents the deterministic part of the model and can be expanded – as can the noise (or random) component  $\sigma^2$  – to incorporate covariate data  $x_1, x_2, \dots, x_n$  collected along with  $y$  on a  $p$ -vector  $x = (x_1, x_2, \dots, x_p)^T$ . Such information was available for the data on  $Y$ , as summarized in **Figure 2**, namely ‘location,’  $x_1 = 1$  or  $2$ , and  $x_2 =$  ‘working hours’; and this was initially absorbed into a more complex model of  $Y$ , incorporating parallel linear relationships between  $Y$  and  $x_2$ . The effect of location (reactor number) was found to be statistically nonsignificant, leaving just the simple regression line through the data displayed in **Figure 3**. The fitted model is

$$y_i = 4.7609 + 0.1875x_{2i} + e_i, \text{ where}$$

$$e_i \sim N(0, 0.993^2), i = 1, \dots, n \quad [4]$$

The histogram of the fitted residuals  $\{e_i\}$  is shown in **Figure 4**, where it can be seen that the visual fit for a Normal distribution is superior to that for the original  $y$  data seen in **Figure 2** – as is often the case with the residuals from more complex models, thereby making the assumption of Normality of the random component of the model more plausible. However, the two outliers are still noticeable and may warrant special attention. A typical definition of an outlier is any data point for which the modulus of the associated residual term in the fitted model exceeds  $3\sigma$ ; refer to the book on outliers by Barnett and Lewis.<sup>28</sup>

Note that when modeling the variance in a corrosion context, it can be important to distinguish between system or corrosion noise,  $\sigma_c^2$ , and measurement error,  $\sigma_e^2$ . These may add to give  $\sigma^2 = \sigma_c^2 + \sigma_e^2$ ,  $\sigma^2 = t\sigma_c^2 + \sigma_e^2$ , or  $\sigma^2 = t^2\sigma_c^2 + \sigma_e^2$ , depending on the context or assumptions – where  $t$  is the exposure time.

It is often useful to reorder the data by size, with notation  $y_{(1)} \leq y_{(2)} \leq \dots \leq y_{(n)}$ , implying that  $y_{(1)}$  is the data minimum,  $y_{(n)}$  is the data maximum, and more generally,  $y_{(i)}$  is called ‘the  $i$ th’-order statistic. Plotting  $y_{(i)}$  against  $i/n$  gives the sample cumulative distribution function,  $F_n$  where



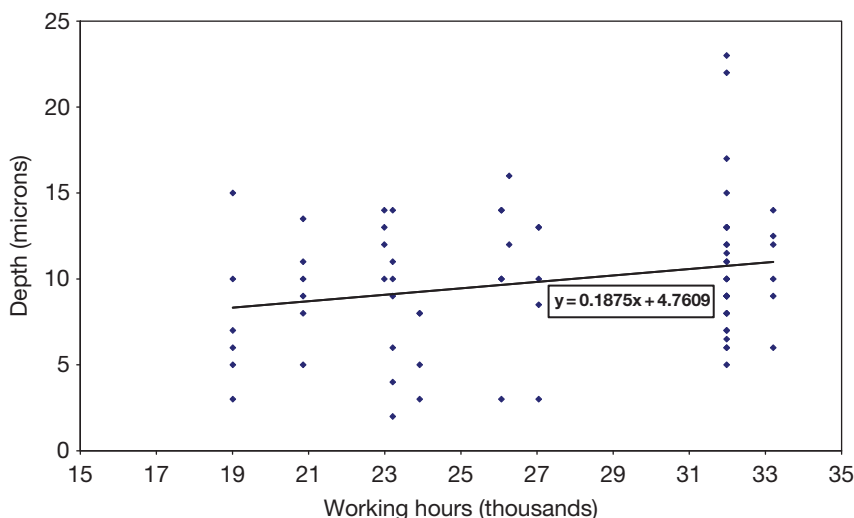


**Figure 3** For the data shown in Figure 2, the effect of location on crack depth was found to be statistically nonsignificant, leaving just the simple regression line shown here for the effect of ‘working hours.’

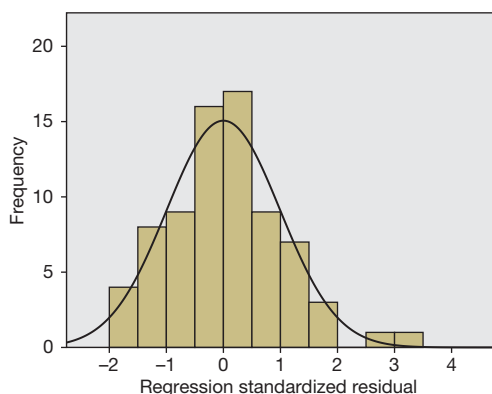


**Figure 4** The histogram for the fitted residuals  $e_i$  from the linear regression of Figure 3. The visual fit for a Normal distribution is superior to that for the original crack depth data seen in Figure 2. However, the two outliers are still noticeable and may warrant special attention.

$$F_n(y) = i/n, \mathcal{Y}_{(i)} < y \leq \mathcal{Y}_{(i+1)} \quad i = 0, 1, 2, \dots, n,$$

with  $\mathcal{Y}_{(0)} = -\infty, \mathcal{Y}_{(n+1)} = \infty$

Alternatively, since  $E[F(\mathcal{Y}_{(i)})] = i/(n+1)$ ,  $i = 1, 2, \dots, n$ , plotting  $\mathcal{Y}_{(i)}$  against  $i/(n+1)$  and connecting points directly by straight lines or a smooth curve will provide an approximately unbiased estimate  $\hat{F}$  of the population cumulative distribution function,  $F$ , with  $\hat{S} = 1 - \hat{F}$  for the Survivor function. Also, plotting  $\mathcal{Y}_{(i)}$  against  $F^{-1}(i/(n+1))$ , when  $F$  is known (perhaps only up to location and scale), should give an approximately straight line if the assumed distributional form is correct. The intercept and slope of

this line can provide estimates of the unknown location and scale parameters. This technique can be implemented algorithmically or *via* the appropriate probability paper.

Discrete probability distributions can be used for counting pits, failures, or other corrosion-induced events. A standard model is the Binomial distribution

$$p_r = \Pr(X = r) = {}^nC_r p^r q^{n-r},$$

$$q = 1 - p, r = 0, 1, \dots, n \quad [5]$$

for the number of ‘successes’  $X$  in  $n$  independent trials with a constant probability of success,  $p$ . This distribution has mean  $\mu = np$  and variance  $\sigma^2 = npq$ , and for a large  $n$ , this can be approximated by a Normal distribution with the same mean and variance by replacing ‘ $r$ ’ with the interval  $r \pm \frac{1}{2}$  – except for ‘rare events’ with  $\mu < 5$  when a Poisson distribution can be used. For event counts in random samples of  $n$  objects from a finite population of  $N$  objects, such as a boiler with  $m$  ‘failed tubes’ out of  $N$ , we can use the hypergeometric distribution

$$p_r = {}^mC_r {}^{N-m}C_{n-r} / {}^NC_n, \max\{0, m+n-N\}$$

$$\leq r \leq \min\{m, n\} \quad [6]$$

This distribution has mean  $\mu = mn/N$  and variance  $\sigma^2 = npq[(N-n)/(N-1)]$ , where  $p = (m/N)$ ,  $q = 1 - p$ , and this can be approximated by a binomial – and hence by Normal or Poisson distributions as appropriate – for a large enough  $N$ .

### 2.36.2.2 Linear Regression

The statistical methods in 'linear regression' cover a very wide range of models though the default assumption is a simple 'straight line regression,' which has the form  $y = \alpha + \beta x$ . The textbook by Freund and Wilson<sup>29</sup> provides an introduction to this topic, with a more extensive treatment in Neter *et al.*<sup>30</sup> The standard *straight line regression* model can be written as

$$y_i = \alpha + \beta x_i + e_i, \text{ where } e_i \sim N(0, \sigma^2),$$

$$i = 1, \dots, n \quad [7]$$

The least-squares estimates  $a$  and  $b$  of the intercept  $\alpha$  and slope  $\beta$  and the unbiased estimate of the residual variance  $\sigma^2$  are given by

$$b = \sum (x_i - \bar{x})(y_i - \bar{y}) / \sum (x_i - \bar{x})^2;$$

$$a = \bar{y} - b\bar{x}; \hat{\sigma}^2 = \sum (y_i - \hat{y}_i)^2 / (n - 2) \quad [8]$$

where  $\hat{y}_i = a + bx_i$  is the predicted value of  $y_i$  from the fitted model. Confidence limits about the line and prediction limits for future observations can be constructed. Formulae with further explanatory discussion are supplied in an example of straight line regression analysis of weight loss data, as is given later in [Section 2.36.3.2.1](#). Variants on this model are parallel regressions  $y_j = \alpha_j + \beta x_i, j = 1, 2$  or broken-line regressions

$$y = \alpha_1 + \beta_1 x \text{ for } x < x^* \text{ then } y = \alpha_2 + \beta_2 x \text{ for}$$

$$x \geq x^* = (\alpha_2 - \alpha_1) / (\beta_1 - \beta_2) \quad [9]$$

When duplicate observations are available for at least one fixed value of  $x$  and there are more than two distinct  $x$  values, then this will provide an independent estimate of the residual variance, enabling 'analysis of variance' techniques to be used to test the 'goodness-of-fit' of a straight line to the data. This method can be extended to more complex models.<sup>30</sup>

The *polynomial regression* model is given by

$$y_i = \alpha + \beta_1 x_i + \dots + \beta_k x_i^k + e_i \quad (i = 1, \dots, n) \quad [10]$$

In this model,  $x$  is called a *genuine* variable, while its powers,  $x^2, \dots, x^k$  are called *carrier* variables. This model can be used when searching for a local optimum in a dataset, and the most important special case is *quadratic regression*, for which  $k = 2$ .

Finally, we have *general linear regression*, for which

$$y_i = \alpha + \beta_1 x_{1i} + \beta_2 x_{2i} \dots +$$

$$\beta_k x_{ki} + e_i \quad (i = 1, \dots, n) \quad [11]$$

where some of the  $x_j^i$  s may be *genuine* physically distinct variables (such as temperature or pressure) and some may be *carriers* (such as powers or interaction terms such as temperature.pressure) or *indicators* of qualitative variates (such as location or manufacturer). When all the  $x_j^i$  s ( $j = 1, \dots, k$ ) are genuine, this model is called *multiple linear regression*.

These models are best fitted using a standard statistical package, which will supply the fitted parameters along with their standard errors, confidence intervals, and tests for goodness of fit. Note that in a model-fitting context, a nonlinear model is one where the unknown parameters (conventionally denoted by Greek letters) occur in a nonlinear fashion, as, for example, in the models  $y = \alpha e^{\beta x}$  or  $y = \alpha x / (\beta + x)$ .

### 2.36.2.3 Poisson Process Modeling

If 'events,' such as pits or cracks, occur 'purely at random' along a line, or in time, or over a surface – but at a constant mean rate, say  $\lambda$  – then they are said to follow a (homogeneous) 'Poisson process.' The count, say  $X$ , of events in any fixed interval/area of size  $t$  then follows a Poisson distribution:

$$\Pr(X = r) = \mu^r \exp(-\mu) / r!,$$

$$r = 0, 1, \dots; \mu = \lambda t \quad [12]$$

This distribution has mean and variance equal to  $\mu$  and can be approximated by a Normal distribution for a large  $\mu$ . The gaps,  $t$ , between such events along a single axis will follow an exponential distribution with PDF

$$f(t) = \lambda e^{-\lambda t}, t > 0 \quad [13]$$

This distribution has mean and standard deviation equal to  $1/\lambda$ . If the mean event rate  $\lambda$  varies, then this is called a nonhomogeneous Poisson process, in which case, if the variation is known, the (time) axis can be transformed to produce a homogeneous process (i.e., by squeezing and stretching the axis appropriately). This type of approach was used in Laycock *et al.*<sup>31</sup> to model the initiation of crevice corrosion of stainless steels *via* metastable pitting events in open-circuit conditions.

A standard all-purpose technique for estimating the unknown parameters in these and more extensive models is the method of maximum likelihood (ML), which directly enables the production of standard errors, confidence intervals, and prediction intervals for estimated parameters and predictions about future values for  $Y$ . An application of all these techniques in a corrosion context can be found elsewhere.<sup>32</sup>

### 2.36.2.4 Extreme Value Distributions

Extreme value (EV) distributions are typically applied in a corrosion context to maximum pit depths measured on a set of test coupons or from sampled areas on a large metal structure. They may have been recorded at one moment in time or at several distinct times, and interest may center on extrapolation in time and/or over larger areas. Relevant environmental parameters may have been measured along with the measured maxima. The models can be applied to single maxima or extended to include the largest two or largest three *et cetera* on each coupon or sampled area. An introductory text for the application of these methods can be seen elsewhere.<sup>33</sup>

Gnedenko<sup>34</sup> fully characterized the limit (implying a large amount of unrecorded data, such as smaller pits) distribution of the maximum (or minimum) as being one of three types: I, II, or III. One textbook<sup>6</sup> suggests that the maximum pit-depth is often described by the Type I distribution, although Type III with a finite upper bound has been found elsewhere.<sup>35</sup> Gnedenko's limit theorems on the maximum are analogous to the celebrated 'Central Limit theorem' on the mean. These distributions reproduce their form under maximization of further data in the same way that the Normal distribution reproduces itself under summation. The Type I distribution is more commonly known as the Gumbel or, simply, the EV distribution. The Type II is known as a Fréchet distribution, and the Type III for maxima can be described as a reversed three parameter Weibull distribution. The distribution function of the EV with location parameter  $\delta$  and scale parameter  $\alpha$  – EV( $\delta, \alpha$ ) – is

$$F(y) = \exp[-\exp[-(y - \delta)/\alpha]],$$

$$-\infty < y < \infty, \alpha > 0 \quad [14]$$

The mode is  $\delta$ , and the mean is  $\mu = \delta + \gamma\alpha$ , where  $\gamma$  is the Euler constant, 0.57721... , while the standard deviation is  $\sigma = \alpha\pi/\sqrt{6}$ .

The generalized extreme value distribution (GEV) subsumes the Type I, II, and III distributions into a single three parameter distribution – GEV( $\delta, \alpha, \kappa$ ) – with distribution function (for maxima)

$$F(y) = \exp\{-[1 - \kappa(y - \delta)/\alpha]^{1/\kappa}\},$$

$$\alpha > 0, \kappa y \leq \kappa\xi = \alpha + \kappa\delta \quad [15]$$

and shape parameter  $\kappa < 0$  for Type II with lower bound  $\xi$ ,  $\kappa > 0$  for Type III with upper bound  $\xi$ , and when the  $\kappa$  parameter reaches zero, the GEV

becomes the unbounded EV. The mapping  $y \rightarrow -y$  recovers the form for minima. The mean is

$$\mu = \delta + \frac{\alpha}{\kappa}[1 - \Gamma(1 + \kappa)]$$

$$= \xi - \frac{\alpha}{\kappa}\Gamma(1 + \kappa), \text{ provided } \kappa > -1, \quad [16]$$

and the standard deviation is

$$\sigma = \frac{\alpha}{\kappa}[\Gamma(1 + 2\kappa) - \Gamma(1 + \kappa)^2]^{1/2},$$

$$\text{provided } \kappa > -\frac{1}{2} \quad [17]$$

Note that some references use  $\xi$  or  $\gamma = -\kappa$  for the shape parameter. Most, but not all, continuous distributions have a limiting form that is a member of the GEV family. In particular, both tails of the Normal distribution (i.e., maximum or minimum values) have a limiting Type I distribution, as have maxima from a Weibull distribution, while minima from a Weibull distribution have exactly a Type III distribution.

The joint generalized extreme value (JGEV) multivariate density function for the  $r$  largest order statistics  $\mathcal{Y}_{(1)}^* > \mathcal{Y}_{(2)}^* > \dots > \mathcal{Y}_{(r)}^*$  (e.g., from a single coupon at one moment in time) is

$$f(\mathcal{Y}_{(1)}^*, \mathcal{Y}_{(2)}^*, \dots, \mathcal{Y}_{(r)}^*) = \alpha^{-r}$$

$$\exp\left\{-(1 - \kappa(\mathcal{Y}_{(r)}^* - \delta)/\alpha)^{1/\kappa} - \left(\frac{1}{\kappa} - 1\right)\right.$$

$$\left.\sum_{j=1}^r \log\left(1 - \kappa(\mathcal{Y}_{(j)}^* - \delta)/\alpha\right)\right\} \quad [18]$$

with bounds as for the GEV and a limiting form when  $\kappa = 0$ , but the joint cumulative distribution function does not have a simple closed form expression.

These distributions can be fitted to data using ML techniques. For the EV distribution, suitable starting values for iterative ML can be obtained by plotting the order statistics  $\mathcal{Y}_{(1)} \leq \mathcal{Y}_{(2)} \leq \dots \leq \mathcal{Y}_{(n)}$  against  $F^{-1}(i/(n+1) = -\ln(-\ln(i/(n+1))))$ ,  $i = 1, 2, \dots, n$ , which can be done using EV plotting paper. The intercept and slope of the line then provide estimates of  $\delta$  and  $\alpha$ , respectively, while deviations downwards from the line at the upper end may indicate a Type III distribution with  $\kappa > 0$  and hence an absolute upper bound. By extending the EV fitted line, extrapolated values for percentiles such as

$$\hat{y}_N = \hat{F}^{-1}(N/(N+1)) = \hat{\delta} - \hat{\alpha}\ln$$

$$(-\ln(N/(N+1))) \approx \hat{\delta} + \hat{\alpha}\ln(N) \quad [19]$$

can be read directly off the graph. In hydrology and meteorology, where data are typically annual maxima, ‘ $N = T$  years’ is described as ‘the return period,’ and setting  $T = 100$  years leads to the so-called ‘hundred year storm’ prediction. In corrosion, where data are more typically from sampled areas of size  $a$ , say,  $\hat{y}_N$  becomes an extrapolation over the extrapolation area  $A = Na$ . The  $N$ th return level  $\hat{y}_N$  is that value which would be exceeded, on average, once every  $N$  time or area units. Alternatively, since  $y_N$  is the maximum of a set of maxima, it will also have a distribution from the GEV family. This will be  $\text{GEV}(\delta_N, \alpha_N, \kappa)$  where

$$\delta_N = \delta + \alpha(1 - N^{-\kappa})/\kappa, \alpha_N = \alpha N^{-\kappa}$$

and bound  $\xi = \delta + \alpha/\kappa, \kappa \neq 0$ , unchanged [20]

The mean of this distribution is a best estimator for  $y_N$  in the usual mean-squared error sense

$$\begin{aligned} \mu_N &= \delta_N + \frac{\alpha_N}{\kappa} [1 - \Gamma(1 + \kappa)], \text{ provided } \kappa > -1 \\ &= \delta + \alpha(\gamma + \ln(N)) \text{ when } \kappa = 0 \\ &\rightarrow \delta + \alpha \ln(N), \text{ as seen before} \\ &\text{for the EV ‘return period’ method} \end{aligned} \quad [21]$$

When covariates, such as time, are measured along with each maximum, a regression model for the mean – and possibly the variance or scale parameter – is required. Given a covariate vector  $\mathbf{x} = (x_1, x_2, \dots, x_p)^T$  at each maximum, a multiple regression model might set  $\delta_i = \beta^T \mathbf{x}_i = \beta_1 x_{1i} + \beta_2 x_{2i} + \dots + \beta_k x_{ki}, i = 1, 2, \dots, n$  implying modeled mean

$$\begin{aligned} E[y_i | \mathbf{x}_i] &= \beta_0 + \beta^T \mathbf{x}_i \text{ with intercept} \\ \beta_0 &= \frac{\alpha}{\kappa} [1 - \Gamma(1 + \kappa)] \end{aligned} \quad [22]$$

and constant residual variance

$$\begin{aligned} \text{Var}[y_i | \mathbf{x}] &= \sigma_e^2 \\ &= (\alpha/\kappa)^2 [\Gamma(1 + 2\kappa) - \Gamma(1 + \kappa)^2] \end{aligned} \quad [23]$$

After fitting such a model using ordinary least-squares, the fitted intercept and residual variance could be equated to the above formulae and solved for  $\alpha$  and  $\kappa$ , enabling an estimate of the bound  $\xi$  to be obtained as a function of the covariates. The alternative of a constant coefficient of variance model can be achieved by additionally setting  $\alpha_i = \rho \beta^T \mathbf{x}_i$ , where  $\rho = \sigma/\mu$ , so 100 $\rho\%$  is the percentage variability in the data, independent of mean size. When the only covariate is time,  $t$ , and a fixed ‘corrosion rate’ parameter,  $\beta$ , is desired,

then we must set  $\delta_i = \beta t_i$ . Alternatively, setting  $\delta_i = \beta t_i^b$  allows for square-root, cube-root, or other nonlinear dependency on time, as referenced elsewhere in this chapter.

### 2.36.2.5 Threshold Techniques

These techniques can be applied in situations wherein we are interested in the statistical properties of extremes from a single large sample, such as feature depths from an Intelligent Pigging run or current noise measurements obtained by online corrosion monitoring.

Given a large random sample of measurements on such a  $y$  for a given threshold value  $u$ , the exceedances,  $x$ , are defined by  $x = y - u$  for  $y > u$ . It can be shown, see for example Smith and Davison,<sup>36</sup> that for sufficiently high thresholds and for a wide variety of initial distributions, the number,  $n$ , of these exceedances has asymptotically a Poisson distribution, while their sizes have a generalized pareto distribution (GPD) with CDF

$$F(x) = 1 - (1 - \kappa x/\sigma)^{1/\kappa}, x > 0 \quad [24]$$

The mean is  $\sigma/(1 + \kappa), \kappa > 1$ , and the variance is  $\sigma^2/[(1 + \kappa)^2(1 + 2\kappa)], \kappa > 1/2$ . Maxima from this distribution have a GEV distribution with shape parameter  $\kappa$ . A suitable value of the minimum threshold, above which the GPD will hold, can be found by plotting the mean exceedances in the data against the increasing threshold. This plot should eventually follow a straight line with slope  $-\kappa/(1 + \kappa)$  and intercept  $\sigma/(1 + \kappa)$ . A horizontal plot corresponds to  $\kappa = 0$  and a simple exponential distribution for this tail area distribution.

### 2.36.2.6 Wiener Process Modeling

Successive pigging runs along a corroding pipeline or successive surveys over any corroding structure will, in general, exhibit an increasing spread, as measured by range or variance,  $\sigma^2$ . Models with variance proportional to time are a consequence of incrementally additive assumptions for corrosion – which assumption is used, for example, in the theoretical ‘shot noise’ models for electrochemical noise measurements in pitting and crevice corrosion, as proposed by Cottis and other workers.<sup>37,38</sup> A statistical model incorporating linear growth in the mean and additive corrosion noise plus

instrument noise for tracked feature depths on two successive runs or surveys is

$$y_{ji} = \beta t_j + \omega_{ji} + \varepsilon_{ji}, \text{ where } \omega_{ji} \sim W(0, t_j \sigma_w^2)$$

is a Wiener additive (corrosion) noise process

and  $\varepsilon_{ji} : N(0, \sigma_M^2)$  is measurement noise;

$j = 1, 2$  runs or surveys;  $i$  = feature identifier.

[25]

A Wiener process has the simple property that its additive increments are normally distributed. It follows that the model for the corrosion increment  $y_{(2-1)i}$  is

$$y_{(2-1)i} = \beta(t_2 - t_1) + \omega_{(2-1)i} + \varepsilon_{(2-1)i}$$

$$\sim N(\beta(t_2 - t_1), (t_2 - t_1)\sigma_w^2 + 2\sigma_M^2),$$

where  $\omega_{(2-1)i} \sim N(0, (t_2 - t_1)\sigma_w^2)$  and  $\varepsilon_{(2-1)i}$

$$\sim N(0, 2\sigma_M^2); i = \text{feature identifier.} \quad [26]$$

Since we know  $(t_2 - t_1)$ , the sample mean for  $y_{(2-1)}$  will provide an estimate  $\hat{\beta} = \bar{y}_{(2-1)} / (t_2 - t_1)$ , which can then be scaled to a yearly rate if the time units are not years.

Given the sample variance  $s_{(2-1)}^2$  for  $y_{(2-1)}$ , the estimated variance for this estimated  $\beta$  will be  $\hat{\sigma}_\beta^2 = s_{(2-1)}^2 / [N(t_2 - t_1)^2]$ , which can then be used to provide a confidence bound on this mean rate. Because the sample count,  $N$ , for pigging runs and oil platform or chemical plant surveys is typically large or very large, this particular adjustment may prove minor. However, feature tracking with successive pigging runs is technically and practically difficult, and this may lead to concentration on just a few of the measured features. In particular, discarded data, here, will include features that appear in one run but not in the other. Assuming a constant probability in time for such omissions (note that dependence on size will not matter for the differenced data), discarding these data will clearly not bias the subsequent estimates, although including such discarded data in a full likelihood analysis could improve the precision of such estimates. Given an independent estimate of  $\sigma_M$  – as supplied by the manufacturer of the measuring instrument, say, and the sample variance  $s_{(2-1)}^2$  for  $y_{(2-1)}$ , we can then estimate  $\sigma_w^2$  to be equal to  $(s_{(2-1)}^2 - 2\sigma_M^2) / (t_2 - t_1)$ . Assuming the time units are years, a (two-sided) prediction interval for  $y_\delta$  – the (true, as opposed to measured) corrosion increment after 1 year – will therefore be  $y_\delta = \hat{\beta} \pm t \sqrt{(\sigma_\beta^2 + \sigma_w^2)}$ , where ‘ $t$ ’ comes from Student’s  $t$ -distribution on  $(N - 1)$  degrees of

freedom. Dropping the minus sign converts this into a one-sided (upper bound) prediction interval with an appropriately adjusted probability level. A set of  $n$  successive runs or surveys will provide a set of  $(n - 1)$  independent increments with means and variances to be pooled appropriately, which can then be used in the formulae mentioned earlier.

### 2.36.2.7 Sampling Theory and Sample Surveys

The statistical methods in sampling theory are principally designed for sampling large inhomogeneous populations of discrete items, such as motor vehicles, books in libraries, or populations of people. Two key ideas that can be useful when measuring corrosion on large structures such as an oil platform or pipeline are ‘stratification’ and ‘clustering.’ The strata of a population arise from dividing the whole population into identifiable groups such that the between-groups variability is likely to be larger than that within the groups. So elbows, joints, verticals, horizontals, and valves might form such a stratification on a large industrial structure. Clusters arise from grouping the whole of each such stratum into convenient and identifiable clumps of items for subsequent ease of sampling within each cluster. This process can be extended in a nested fashion. In a two-stage procedure, one or more clusters are chosen at random from every stratum, and then one or more items are chosen at random from each of the selected clusters. Practical introductions to these ideas, along with their theoretical justification, can be found elsewhere.<sup>39,40</sup>

### 2.36.2.8 Experimental Design

When used, the statistical principles and methods of experimental design can both help to justify the assumptions made in the standard analyses of experimental results and also improve the efficiency of the information gathering for a given amount of experimental effort. Two reference books on this subject are Cobb<sup>41</sup> and Cox and Reid.<sup>42</sup> Randomization, blocking, factorials, and fractions, Latin Squares, central composite, and optimal design are names of some of the main ideas in this area of statistics. For an illustrative example in corrosion, consider an experiment wherein metal coupons made of a particular alloy are to be corroded in a controlled environment with two flow rates F1 and F2, two temperatures T1 and T2, and two levels of acidity pH1 and pH2. In a full factorial experiment, a ‘single replicate’ would consist



of one experiment at each of the  $2 \times 2 \times 2 = 8$  combinations of the three 'factors' flow, temperature, and acidity. Repeats would consist of exposing a further set of eight coupons to the same conditions. The addition of a base position or 'central point' at F0.T0.pH0 is often useful. This method can be contrasted with the so-called one-at-a-time experimentation, wherein each factor is altered one at a time from the base position, with repeats at each such selection. This implies a basic set of  $2 + 2 + 2 = 6$  experimental combinations. For a given number of coupons used, most analyses would show that the factorial system provides a significantly more useful set of results. Alternatively, consider a situation wherein, say for financial reasons, only four of the above eight possible factorial combinations can be attempted (though, as usual, repeats might be more easily available). There are  ${}^8C_4 = 70$  possible selections of four experiments from the eight possible, of which just two form a  $2^{3-1}$  fractional factorial (which is also a simple Latin Square in this instance). The two experiments are (F1.T1.pH1, F1.T2.pH2, F2.T2.pH1, F2.T1.pH2) and its complement. These two have the unique property that all possible pairings appear. Selecting levels at random would have a chance of just 2/70 of achieving this property. With more factors or more levels, the potential gains increase markedly.

### 2.36.2.9 Bayes' Theory

The specific relevance of Bayesian methods to engineering applications is the ability to update subjective information with data for decision-making. Although the mathematical theory dates back to 1774, the numerical integration routines required to solve practical problems were not available until the 1980s. Since then, Bayesian techniques have increasingly been used in reliability and risk applications and are likely to become indispensable tools for corrosion risk management. Bolstad<sup>43</sup> is a suitable introductory text for 'Bayesian Statistics,' while Gelman *et al.*<sup>44</sup> provide the computational details necessary to implement the methods to practical problems.

#### 2.36.2.9.1 Bayes' theorem

The essential mathematical content of the theory is 'Bayes' theorem' also known as 'Bayes' rule,' which was discovered in a restricted form by the amateur mathematician the Reverend Thomas Bayes and was subsequently published posthumously in 1763.<sup>45</sup> A more

general formula first appeared in a 1774 paper by Pierre-Simon de Laplace.<sup>46</sup> In present-day notation,

$$\Pr(B|A) = \frac{\Pr(A|B)\Pr(B)}{\Pr(A)} \quad [27]$$

or, in words, the probability that  $B$  occurs given that  $A$  occurs (i.e.,  $\Pr(B|A)$ ) is equal to the probability that  $A$  occurs given that  $B$  occurs (i.e.,  $\Pr(A|B)$ ) times the probability that  $B$  occurs (i.e.,  $\Pr(B)$ ) divided by the probability that  $A$  occurs (i.e.,  $\Pr(A)$ ).

This rather simple-looking formula hides a deep mathematical subtlety that must be thoroughly understood if we are to make proper use of Bayesian methods. As a formula in probability calculus, it is mathematically rigorous, yet ever since its first enunciation, there have been divergent interpretations of its meanings, leading to intense philosophical debate and controversy in applications. The problem lies in the interpretation of 'probability,' and we must devote some time and effort to comprehending its various meanings.

#### 2.36.2.9.2 Probability

Bayes' formula can be rearranged to give the symmetrical form

$$\Pr(B|A)\Pr(A) = \Pr(A|B)\Pr(B), \quad [28]$$

where, in fact, the quantity,  $\Pr(B|A)\Pr(A)$ , is the probability that both  $A$  and  $B$  occur, denoted by  $\Pr(A \& B)$  or  $\Pr(A, B)$ .

The generic probabilities appearing in the above formulae have the following special names:

- $\Pr(A)$  – the *total probability* that  $A$  occurs
- $\Pr(B|A)$  – the *conditional probability* that  $B$  occurs given that  $A$  occurs
- $\Pr(A \& B)$  – the *joint probability* that  $A$  and  $B$  occur

In 'frequentist' statistics, such as that presented in previous sections, these probabilities are all interpreted as long-run frequencies that occur in repeated sampling. Thus, the probability that a coin lands heads is expressed as  $\Pr(C=b) = 1/2$ , with the informal interpretation that in a 100 tosses of the coin, the frequency of heads will be 'approximately' 50.

The alternative, 'Bayesian,' interpretation is that probabilities can express degrees of belief. Thus,  $\Pr(C=b) = 1/2$ , quantifies one's current belief that the coin is fair – *a statement that can be made even without any data!* Note, however, that an *Empirical Bayesian* would be allowed to use previously collected data to calculate a direct estimate of such a probability. The chief use of Bayes' Theorem in the context of *Bayesian*

*methods* is to revise such beliefs given data. We will illustrate this procedure, assuming that the coin has landed tails-up in a single toss; that is, the event  $C = t$  has occurred.

### 2.36.2.9.3 Prior and posterior probabilities

The probability of tails is given by the Bernoulli data model,  $\Pr(C = t|\Theta = \theta) = 1 - \theta$ , where  $\Theta$  is the probability of heads. Notice that we use a capital Greek letter for the Bernoulli parameter, which is, according to the Bayesian paradigm, a *random variable* and not a *fixed unknown value*. This is an essential point of difference between Bayesian and frequentist data modeling. Most statisticians currently use both methods according to convenience, but *true Bayesians* will never use frequentist methods.

To avoid unnecessary technical details, we assume that it is known that  $\Theta$  has only two possible values  $\theta_1$  and  $\theta_2$ , which are known *a priori*. Then, applying Bayes' rule,

$$\begin{aligned}\Pr(\Theta = \theta|C = t) &= \frac{\Pr(C = t|\Theta = \theta)\Pr(\Theta = \theta)}{\Pr(C = t)} \\ &= \frac{(1 - \theta)}{\Pr(C = t)}\Pr(\Theta = \theta)\end{aligned}\quad [29]$$

To calculate the probability in the denominator, we use *the total probability formula*

$$\begin{aligned}\Pr(C = t) &= \Pr(C = t|\Theta = \theta_1)\Pr(\Theta = \theta_1) \\ &\quad + \Pr(C = t|\Theta = \theta_2)\Pr(\Theta = \theta_2)\end{aligned}\quad [30]$$

which gives

$$\begin{aligned}\Pr(\Theta = \theta|C = t) &= \frac{(1 - \theta)}{(1 - \theta_1)\Pr(\Theta = \theta_1) + (1 - \theta_2)\Pr(\Theta = \theta_2)}\Pr(\Theta = \theta)\end{aligned}\quad [31]$$

In Bayesian statistics, the probability  $\Pr(\Theta = \theta)$  is known as the *prior probability* and  $\Pr(\Theta = \theta|C = t)$  is the *posterior probability* (having observed tails). Many of the problems that arise applying Bayes' rule can be traced to inappropriate specification of the prior. The key point to note here is that it cannot be specified independently of the data model, that is, the Bernoulli model, because in using the total probability formula, it must be true that

$$\Pr(\Theta = \theta_1) + \Pr(\Theta = \theta_2) = 1 \quad [32]$$

Hence, the prior itself cannot be entirely subjective nor can it be an arbitrary quantification of degrees of belief as some Bayesian analysts insist.

### 2.36.2.9.4 Specifying the prior

We are now faced with the problem of specifying the prior, since, evidently, it cannot be arbitrary. Laplace's own prescription for the prior – now known as an *uninformative prior* – has  $\Pr(\Theta = \theta_1) = \Pr(\Theta = \theta_2) = 1/2$ , giving the posterior

$$\Pr(\Theta = \theta|C = t) = \frac{1 - \theta}{2 - \theta_1 - \theta_2} \quad [33]$$

and the *prior predictive probability*

$$\begin{aligned}\Pr(C = b) &= \Pr(C = b|\Theta = \theta_1)\Pr(\Theta = \theta_1) \\ &\quad + \Pr(C = b|\Theta = \theta_2)\Pr(\Theta = \theta_2) \\ &= (\theta_1 + \theta_2)/2\end{aligned}\quad [34]$$

In the special case that  $\theta_1 + \theta_2 = 1$ , the uninformative prior also gives  $\Pr(C = b) = 1/2$ , and is therefore in accord with our prior belief in a fair coin. However, in all other cases, the uninformative prior gives  $\Pr(C = b) \neq 1/2$ .

An alternative to the uninformative prior is to use a customized prior that matches both the total probability constraint and our prior predictive constraint. Effectively, with  $\Pr(\Theta = \theta_1) = p$ , we must take

$$\theta_1 p + \theta_2 (1 - p) = 1/2 \quad [35]$$

and hence

$$\begin{aligned}\Pr(\Theta = \theta_1) &= \\ p &= \begin{cases} 1/2 & \theta_1 = \theta_2 \\ (1/2 - \theta_2)/(\theta_1 - \theta_2) & \theta_1 \neq \theta_2 \end{cases}\end{aligned}\quad [36]$$

Such a prior is consistent with the data model and belief in a fair coin even when, *a priori*, it is known that neither  $\theta_1$  nor  $\theta_2$  is equal to  $1/2$ . This is because the parameter  $\Theta$  in the Bernoulli data model is a *random variable* and *not some fixed unknown value*.

Now, however, there is a degenerate case in which one, but not both, of  $\theta_1$  or  $\theta_2$  is equal to  $1/2$ . In this case, the prior becomes  $\Pr(\Theta = \theta) = \delta(\theta - 1/2)$  ( $\delta$  is the delta function:  $\delta(0) = 1$  and  $\delta(x) = 0$  for  $x \neq 0$ ). The prior no longer has a nonzero value on all possible values, and, therefore, there is no possibility of updating the prior, since Bayes' rule gives  $\Pr(\Theta = \theta|C = t) = \Pr(\Theta = \theta|C = b) = \Pr(\Theta = \theta)$ .

This phenomenon has been called the 'zero preservation problem.' It actually points to an inconsistency between our prior belief and the data model and requires revision of one or more of our models. Clearly, the quantification of even the most uncontroversial beliefs – here, simply that a coin is fair – is

fraught with technicalities, and it is no wonder that Bayesian methods are often controversial.

### 2.36.2.9.5 Robust Bayes

The coin example reveals how, in the Bayesian paradigm, consistency between prior beliefs and a data model is obtained by randomization over the parameters using the prior. At the limits of this randomization process are degenerate cases in which the prior has zero probability, and there is no possibility of updating prior beliefs by data. Although Bayes' rule is still formally applicable, there is really too great an inconsistency to proceed with the analysis, without a major revision of either our beliefs or the data model.

These issues, especially the 'zero preservation problem,' are especially relevant in applying Bayesian methods to engineering risk, where risks can be seriously underestimated. There is now increasing recognition by practitioners that some form of sensitivity analysis is required to augment the standard Bayesian analysis.

Currently under development are 'robust Bayes' methods that address many of the problems identified. The most promising methods employ *classes of priors*, which are appealing from a mathematical viewpoint, because Bayes' rule maps classes of priors to *multivalued predictive probabilities*. Thus, in the coin example, a prior class such as

$$\{\delta(\theta - \theta_1), \delta(\theta - \theta_2), [\delta(\theta - \theta_1) + \delta(\theta - \theta_2)]/2\} \quad [37]$$

yields the multivalued prior predictive probability

$$\Pr(C = b) \in \{\theta_1, \theta_2, (\theta_1 + \theta_2)/2\} \quad [38]$$

Such multivalued probabilities have a clear interpretation in terms of prior belief – here simply, that the probability of heads takes on one of the three values.

## 2.36.3 Corrosion Science

This section demonstrates the application of some of the above techniques to the analysis of experimental data, primarily from laboratory studies.

### 2.36.3.1 Pitting Potentials and Induction Times

One common method for the experimental study of pitting corrosion is the measurement of 'pitting potentials.' Typically, multiple repeat experiments are carried out for each given set of experimental conditions, using a freshly prepared sample for each

test. This produces several measurements of the pitting potential for the given set of conditions, and these measurements will be spread over a range of potentials that is much wider than that of the inherent measurement error and can be attributed to the mechanistic details of the pit initiation process. Following Shibata and Takeyama,<sup>5</sup> such data are often presented as sample cumulative probability distribution functions, as shown in Figure 5.

Similarly, another common experiment is to measure the 'induction time' before stable pitting is observed on a given sample. Results of these experiments on multiple samples can be presented as the (estimated) survival probability function,  $S(t)$ , by plotting the  $i$ th-order statistic against  $1 - i/(n + 1)$ , as described in the basic terminology and methods section. Further examples and discussion on these methods can be found elsewhere.<sup>5,7,14</sup>

### 2.36.3.2 Coupon Testing

Corrosion coupons are often exposed in a test environment for significant periods of time and then examined to enable the determination of their corrosion rate. Usually, the examination consists of removing solid corrosion products and then measuring both the depth of any pits and the total weight lost from the coupon during the exposure. Sometimes, electrochemical methods may also be used to obtain corrosion rate information at certain times during the exposures. This section describes some examples of statistical approaches to the analysis of the resulting data.

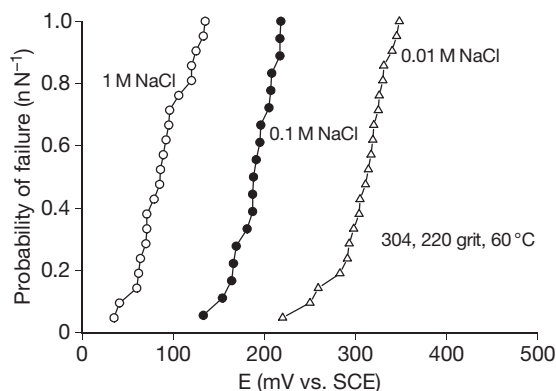


**Figure 5** Typical results from potentiodynamic pitting potential measurements for 304 stainless steel with a 220 grit surface finish, in sodium chloride solutions at 60 °C. Each datapoint is the pitting potential of an individual test on a freshly prepared sample.

### 2.36.3.2.1 Straight-line regression analysis of weight loss data

Figure 6 shows the metal loss from carbon steel coupons exposed at two statistically similar sites along the River Thames over a period of 5 years.<sup>47</sup> The metal loss (mm) was calculated from the weight loss by assuming one-side uniform corrosion and applying Faraday's Second Law, and the slope of the 'best fit' line gives an estimate of the 'corrosion rate' (mm year<sup>-1</sup>) over the measurement period.

Although a formal approach to corrosion might suggest omitting the intercept,  $a$ , to give a simple regression through the origin, that is  $y = bx$ , it is rarely sensible to do this in practice for the whole of a data set unless an appropriate significance test on  $a$  suggests that the intercept can be safely omitted, even though  $a$  may have no metallurgical validity at time zero. By forcing  $y$  to be zero at time zero, it may extend the formal range of validity of the model, but it will then almost certainly predict a higher (possibly much higher) corrosion rate, and it is the validity of the model for extrapolation into the future, not the past, which is important in practice.

In this case, the calculation of a prediction interval is also appropriate. This has the form

$$y_x = \hat{y}_x \pm t\hat{\sigma} \sqrt{\left(1 + \frac{1}{n} + \frac{(x - \bar{x})^2}{\sum(x_i - \bar{x})^2}\right)} \quad [39]$$

for a future observation on  $y$  at  $x$ , with  $t$  selected appropriately from  $t$ -tables with  $(n - 2)$  degrees of

freedom. A confidence interval about the line (which omits the '1' inside the bracket above – as this term relates not to the line itself, but to future noise in the observations as they appear about the line) and the prediction interval for future observations are demonstrated in Figure 6.

### 2.36.3.2.2 Extreme value analysis of pit depth measurements

Figure 7 shows the maximum pit depth as a function of immersion time for 316L stainless steel coupons in a 10% ferric chloride solution at 50 °C, as reported by Pierpoline *et al.*<sup>48</sup> Laycock *et al.*<sup>32</sup> have fitted to this data a constant coefficient of variance model with nonlinear time dependence, using ML. This had location parameter  $\delta_i = \beta t_i^b$  and scale parameter  $\alpha_i = \rho \beta t_i^b$  (where  $\rho = \sigma/\mu$ ), and produced the following parameter estimates (with associated standard errors in brackets)

$$\begin{aligned} \tilde{\alpha} &= 1.004(\pm 0.317), \tilde{\delta} = 6.322(\pm 1.721), \\ \tilde{\kappa} &= 0.401(\pm 0.162), b = 0.376(\pm 0.047) \end{aligned} \quad [40]$$

This implies the following formula for the extrapolated mean for maxima as a function of extrapolation area  $A$  in square inches and time  $t$  in days

$$\begin{aligned} \tilde{\mu} &= (29.16 - 14.404/A^{0.401})t^{0.376} \rightarrow \\ 29.16t^{0.376} &= \xi t^{0.376} \text{ for large } A \end{aligned} \quad [41]$$

When the two or three largest (etc.) maxima are collected at each location, this can afford greater

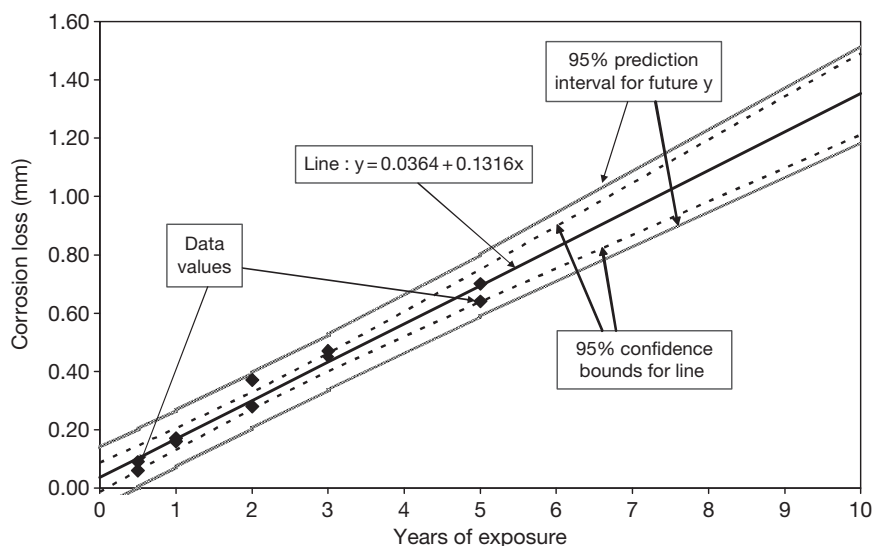


**Figure 6** Corrosion loss from carbon steel coupons exposed in the River Thames for 5 years,<sup>47</sup> with the best-fit line obtained by straight-line regression and extrapolated for a further 5 years. Also, shown are the 95% confidence bounds for the fitted line, and the 95% prediction interval for future 'corrosion loss.'

precision for the same estimated parameters, as demonstrated for the earlier data.<sup>49</sup>

Another example is provided by a set of 1800 maximum pit depths extracted from  $8 \times 8$  grids over experimental coupons of a corrosion-resistant alloy subjected to a complex cyclic testing regime, involving hold periods at 350 °C (for between 1 and 23 h), with and without exposure to salt, for total test durations of 1 year. The statistical package Genstat was used to prepare an analysis of variance table for the data, with the results shown in [Table 1](#).

Inspection of a half-normal plot for the residuals showed good linearity, suggesting that the standard model assumptions, for this particular analysis, were sound. It can be seen that the variation of maximum pit depths between days of exposure (3, 4, or 11, treated as a factor with three levels) and temperature cycles

(either 1 or 23 h at 350 °C) and salt treatments (Yes or No) was highly significant ( $P < 0.001$ ), but the other two factors (salt replenishment and measurement position) were definitely nonsignificant ( $P > 0.5$ ) although not so small as to cast doubt on the validity of the model or data. Therefore, four experimental conditions, defined by the two temperature cycle schemes and exposure to or not to salt, were found to give statistically different results in terms of maximum pit depths, though no detectable growth of pits could be found for the cycle with 23 h at 350 °C and no salt exposure. Hence, the Fortran program described in Laycock *et al.*<sup>32</sup> was used to fit four-parameter GEV distributions to the three sets of data, which had significant upward time trends. [Figure 8](#) shows a plot against time of one of these fitted GEV mean functions, which were all Type III, for a selection of extrapolated

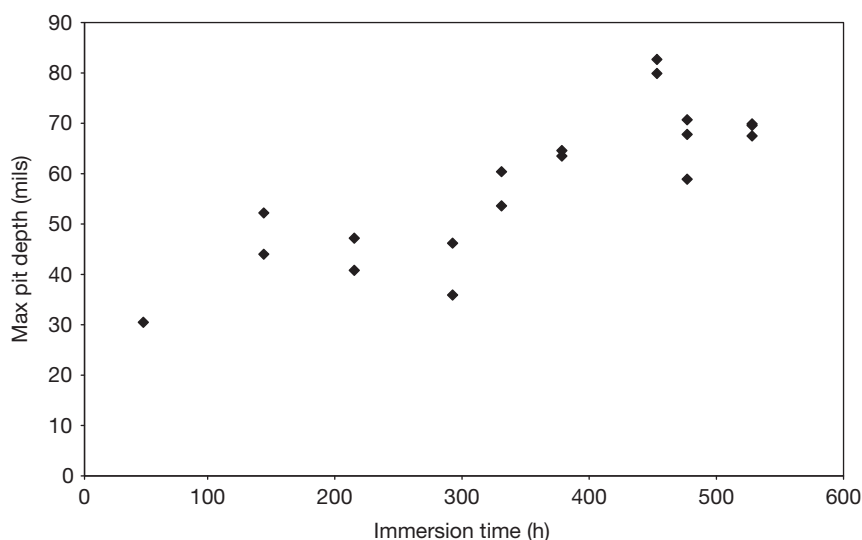


**Figure 7** Maximum pit depth as a function of immersion time for 316L stainless steel coupons in a 10% ferric chloride solution at 50 °C. Reproduced from Pierpoline, R.; White, R. J.; Wrong, C.; Cornwell, L.; Griffin, R. In *NACE-9: Advances in Localised Corrosion*; Isaacs, H., Bertocci, U., Kruger, J., Smialowska, S., Eds.; NACE: Houston, TX, 1990; pp 123–126.

**Table 1** Analysis of variance for pit depth data from coupons of a corrosion-resistant alloy subjected to a complex cyclic testing regime

Source of variation	Degrees of freedom	Sum-of-squares	Mean-square	Variance-ratio	F dn probability
Cycles(2)	1	79 644.4	79 644.4	548.74	<.001
Days(3)	2	19 183.6	9 591.8	66.09	<.001
Salt(Y/N)	1	10 339.5	10 339.5	71.24	<.001
Replication	1	0.1	0.1	0.00	0.975
Position	24	2 666.2	111.1	0.77	0.784
Residual	1770	256 898.0	145.1	–	–
Total	1799	368 757.5	–	–	–

1800 maximum pit depths were extracted as internal  $5 \times 5$  grids (to remove edge effects) from  $8 \times 8$  grids over experimental coupons. The statistical package Genstat was used to prepare this table.



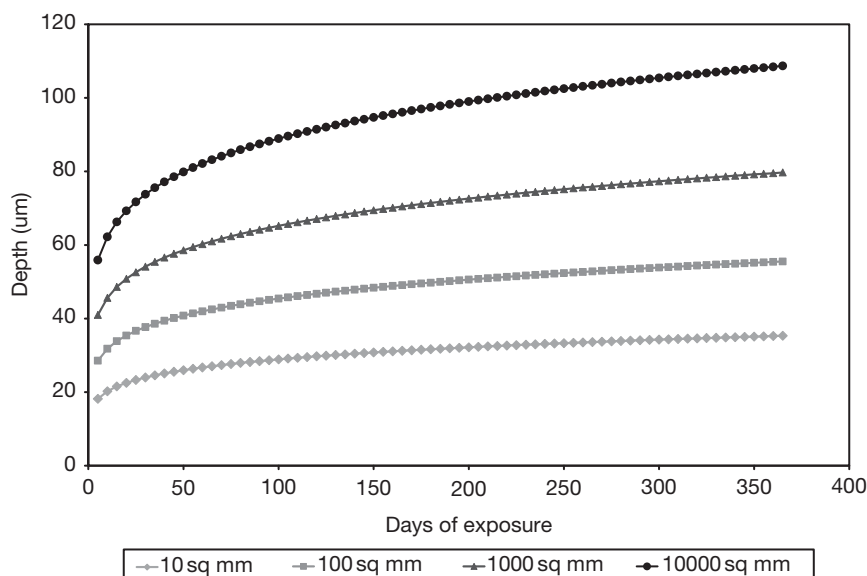


**Figure 8** A Fortran program<sup>32</sup> was used to fit four-parameter GEV distributions to pit depth data from cyclic testing of corrosion-resistant alloy coupons. This figure shows a plot against time of one of these fitted GEV mean functions for a selection of exposure areas.

exposure areas related to operational requirements for this alloy, which was to be used inside jet engines operating in a marine environment.

### 2.36.3.2.3 Response surface regression analysis of LPRM data

Sometimes, experiments are carried out to determine the influence of various parameters (such as alloy composition) on the corrosion rate in a given environment. In one such set of experiments, linear polarization resistance measurements (LPRM) were used to measure corrosion rates for a selection of different carbon steels in a concentrated HF environment. The steels were selected because they had small differences in residual element (nickel, chromium, copper) and carbon content, and it was suspected that such variations were responsible for unexpected failures due to corrosion in HF alkylation plants. To determine the optimum steel composition for corrosion resistance in this environment, the data were analyzed using response surface regression. The most popular version of this is the bivariate second order model:

$$y_i = \beta_{00} + \beta_{10}x_{1i} + \beta_{01}x_{2i} + \beta_{20}x_{1i}^2 + \beta_{02}x_{2i}^2 + \beta_{11}x_{1i}x_{2i} + e_i \quad (i = 1, \dots, n), \quad [42]$$

which can be described as the *quadratic* version of *bivariate linear regression*, and it represents a smooth hill, or valley, or saddle-point in the response surface.

The general  $n$ th-order,  $k$ -variate, model has the form

$$y_i = \sum_{0 \leq i_1 + i_2 + \dots + i_k \leq t} \beta_{i_1 + i_2 + \dots + i_k} x_{1i}^{i_1} x_{2i}^{i_2} \dots x_{ki}^{i_k} + e_i \quad (i = 1, \dots, n) \quad [43]$$

This model has  $k$  *genuine* variables, the rest being *carrier* variates.

The fitted model was a second-order response surface for LPRM regressed on carbon, chromium, copper, and nickel content, based on 45 determinations of LPRM. This model gave a good fit to the data, with a squared multiple correlation coefficient of  $\sim 80\%$  and 30 degrees of freedom for the residual. A contour plot for the raw data is shown in [Figure 9\(a\)](#), while the corresponding contour plot for the fitted model but controlled for the hidden variates (nickel and copper at their median values) is shown in [Figure 9\(b\)](#). From this saddle-point figure, the qualitative conclusions for this application were that when copper and nickel are at their median levels (0.06% and 0.04%, respectively), a decreasing carbon content is good for corrosion resistance, provided chromium is low, while an increasing carbon content will be good when chromium is high. This analysis supported a recommendation for new guidelines on the residual element and carbon content of steels for concentrated HF service.

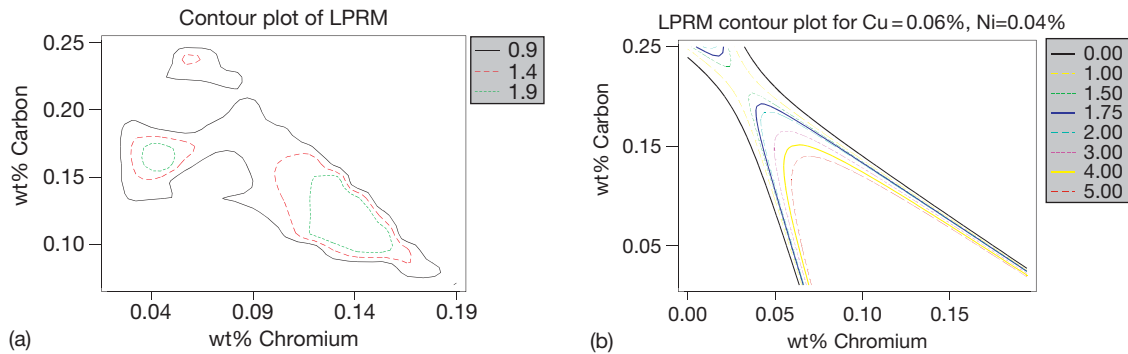


**Figure 9** LPRM data for carbon steels of different alloy content in deaerated 60% HF (by volume) at 71 °C, with 5 ppm of predissolved iron. The fitted model is a second-order response surface regressed on carbon, chromium, copper, and nickel content, based on 45 determinations of LPRM. A contour plot for the raw data is shown in (a), while the corresponding contour plot for the fitted model but controlled for the hidden variates (nickel and copper at their median values) is shown in (b). Data produced in a multiclient project at CAPCIS Ltd, Manchester, UK.

### 2.36.3.3 Crack Depth Modeling

Cracks in engineered structures, whether they are caused by (corrosion) fatigue or stress-corrosion cracking, can be considered, in general, as defects, which initiate and 'grow' according to some random mechanism. Hence, there is much scope for modeling. There is, of course, an extensive literature on crack growth, and, in particular, fracture mechanics has been extensively used to study the principle and nature of fatigue crack growth. Many authors present purely theoretical considerations in an attempt to provide a model to predict crack growth, and such methods have been reviewed.<sup>50,51</sup> Dolinski<sup>52</sup> is skeptical as to whether theoretical considerations alone can provide an adequate model for prediction. On the other hand, when data are presented, they are often experimental in nature,<sup>53</sup> from which it is extremely difficult to infer useful practical models for the prediction of crack growth in real complex systems. For this reason, an empirical model, which makes reasonable assumptions, and which can be evaluated or fitted using data on the nature and extent of cracks observed at inspection may be more useful in practice. This empirical approach will suppose that the physical properties of the system, such as loading history and material characteristics, are inherent in the field data and also suppose that data are available in sufficient quantity and in a form that allows the fitting of a statistical model. This model can then be used to predict fatigue crack growth and to investigate the consequences of various inspection policies. This philosophical contrast between a physical model and an empirical one based on the observation of

large scale effects is not uncommon and not easily resolved. Although the model in this section is not based strictly on fracture mechanics, the approach and the assumptions made are simple, and the approach taken is a practical one.

#### 2.36.3.3.1 Two-stage modeling of crack growth

Detailed models of crack growth will consider crack development in stages. Suppose a crack initiates according to one random process, and subsequent to initiation, it grows according to another random process independently of the initiation process. Given a simple model for each stage, the distribution of crack depths at some time  $T$  can be formulated. The simplest model that can capture the randomness of the initiation process is the homogeneous Poisson process.<sup>54</sup> This supposes that cracks initiate purely at random but at an average rate of  $\lambda$  crack initiations per unit of time. Then, the number of crack initiation events in the time period  $[0, T]$ ,  $N_T$ , will be Poisson distributed with mean  $\lambda T$ , that is,  $E(N_T) = \lambda T$  and  $\Pr(N_T = n) = e^{-\lambda T} (\lambda T)^n / n!$ .

Next, let the distribution of crack depth for a crack that has been growing for some time  $\tau$  be  $G(z; \tau) - G$ , which will be specified later. For now, put simply, not all cracks that have been growing for the same time would be expected to be of the same size – some will propagate more quickly than others. Thus, the depth of a crack  $Z$  that has been growing for a particular time will be a random variable, and this random variable will have distribution  $G$ .

Suppose a structure or an area on a structure is inspected for cracks at some time  $T$ , and a number of

cracks are observed. If any of these cracks is selected at random (with no size-related selection bias), then it is a property of the Poisson process of initiation events that the time of initiation of the crack is uniformly distributed over the interval  $[0, T]$  – that is, the crack could have initiated in any equal interval of time within  $[0, T]$  with equal probability. This can be thought of as the defining property of the Poisson process and one that characterizes events that occur ‘purely at random.’ With inspection carried out at time  $T$ , conditional on initiation of a crack at time  $x$ , the distribution of crack depth at time  $T$  will be  $G_T(z; T - x)$ . However, we do not observe  $x$ , and, therefore, predictions have to be made unconditionally. To do this, we appeal to the law of total probability so that the unconditional distribution of the crack depth at time  $T$  (with no regard to the initiation time),  $F_T(z)$ , is

$$\begin{aligned} F_T(z) &= \int_0^T \Pr(Z_T \leq z | x = x) f(x) dx \\ &= \frac{1}{T} \int_0^T G_T(z; T - x) dx, \end{aligned} \quad [44]$$

where  $f$  is the probability density function of the initiation time. This expression is interpreted as follows: the distribution of the depth  $Z$  is a weighted average of the distribution of depth, given the initiation time with weights given by the probabilities of particular initiation times. We have already stated that for the Poisson process, these initiation times are uniformly distributed on  $[0, T]$  so that  $f(x) = 1/T$ .

For  $n$  crack depths  $z_1, \dots, z_n$  observed at time  $T$ , the log-likelihood function is given by

$$\sum_{i=1}^n \log \left[ \frac{d}{dz} \left\{ \int_0^T G_T(z_i; T - x) dx \right\} \right] \quad [45]$$

From this, we can estimate the parameters of  $G$  and  $F$  by implication, and make predictions about  $Z_t$  for  $t > T$ .

It may be natural to focus on the maximum crack depth. Only the maximum crack depth may be recorded. In this case, given  $n$  crack initiations in the interval  $[0, T]$ , the distribution function of the maximum crack depth is  $F_{\max, T}(z | N_T = n) = \{F_T(z)\}^n$ , given the assumption that the  $n$  crack depths are independent and identically distributed. If, in general, the number of cracks at a location at an inspection is unknown, it follows, arguing unconditionally on  $N_t$ , that the distribution function of the maximum crack depth is given by  $F_{\max, T}(z) = \sum_{n=0}^{\infty} \{F_T(z)\}^n \Pr(N_t = n)$ , and the likelihood for

an observed maximum crack depth  $z_{(1)}$  is  $\log \left[ \frac{d}{dz} F_{\max, T}(z_{(1)}) \right]$  if  $z_{(1)} > 0$  and  $\log[\Pr(N_t = 0)] = -\lambda T$  if  $z_{(1)} = 0$  (i.e., if no cracks have initiated).

With  $F_T(z)$  given by eqn [44], it then follows that

$$\begin{aligned} F_{\max, T}(z) &= \sum_{n=0}^{\infty} \left\{ \frac{1}{T} \int_0^T G_T(z; T - x) dx \right\}^n e^{-\lambda T} (\lambda T)^n / n! \\ &= \exp \left\{ -\lambda \int_0^T 1 - G_T(z; T - x) dx \right\} \end{aligned} \quad [46]$$

As to the form of the distribution function for  $G_T(z; T - x)$ , for simplicity, the two-parameter Weibull distribution is recommended. This distribution is widely used in reliability for modeling failure times.<sup>55</sup> Taking the scale parameter  $\alpha$  of the Weibull to be a power function of the ‘growing time,’  $\tau = T - x$ ,  $G$  becomes

$$G_T(z; \tau) = 1 - \exp[-\{z/(\alpha_0 \tau^\gamma)\}^\beta], \quad [47]$$

where  $\beta$  is the shape parameter. This implies that the mean depth grows according to  $\mu = \alpha_0 \Gamma(1 + 1/\beta) \tau^\gamma$ , and where  $\Gamma(\cdot)$  is the gamma function. This power law function for the scale parameter, while having no immediate physical justification, provides, along with the Weibull distribution, a flexible family of growth laws and also implies power law growth in the mean. The implied distribution of the maximum crack depth is then

$$\begin{aligned} F_{\max, T}(z; \lambda, \alpha_0, \beta, \gamma) \\ = \exp \left[ -\lambda \int_0^T \exp \left[ -\left\{ \frac{z}{\alpha_0 (T - x)^\gamma} \right\}^\beta \right] dx \right] \end{aligned} \quad [48]$$

Extrapolation in space and time now proceeds as follows. Suppose the estimation of the maximum is carried out using maxima from sampled regions of area  $A$  at time  $T$ , if we wish to determine the distribution of the maximum over an area  $a > A$  at time  $t > T$ , then it is required to scale up the initiation rate  $\lambda$  to  $\lambda(a/A)$ , and, therefore, the distribution of the maximum over an area  $a$  at time  $t$  is then

$$\begin{aligned} F_{\max, t, a}(z; \lambda, \alpha_0, \beta, \gamma) \\ = \exp \left[ -\lambda \left( \frac{a}{A} \right) \int_0^t \exp \left[ -\left\{ \frac{z}{\alpha_0 (t - x)^\gamma} \right\}^\beta \right] dx \right]. \end{aligned} \quad [49]$$

If  $X$  is the time for the maximum crack depth to reach some critical level,  $z_f$ , then the expected value of  $X$  can be determined from this distribution, since  $\Pr(X > t) = \Pr(Z_{\max, t, a} < z_f)$  and  $E(X) = \int_0^\infty \Pr(X > t) dt$ .

### 2.36.4 Corrosion Engineering

Statistical data analysis techniques have long been used in the assessment of corrosion damage to industrial plant. Such techniques can be applied to *condition assessment*, wherein there typically are concerns about the influence of measurement error and the extrapolation of sample inspection results to uninspected areas; and *life prediction*, wherein the goal is to determine the remaining life of the equipment.

#### 2.36.4.1 Sample Inspection of Heat Exchanger Tubes

Heat exchanger tubes are often inspected using non-destructive testing (NDT) methods – such as IRIS (internal rotary inspection system) or LOTIS (laser optical tube inspection system) – and the results are typically reported in terms of the maximum pit depth in each inspected tube. However, in many such cases, no more than 10 or 20% of the tubes are tested, at least initially, and the sample data must be used to estimate the overall condition of the tube bundle. The hypergeometric distribution – as described in the introductory section – can be applied here to determine the required level of inspection for a given detection requirement.

ASTM G46<sup>10</sup> describes a procedure based on the Type-I EV (Gumbel) distribution for extrapolating maximum pit depths over areas larger than the inspected area, and this technique is described in the following example. A carbon steel ammonia condenser with cooling water on the tube-side was inspected after ~2 years service. The exchanger contained 773 nominally identical tubes, of which 54 were inspected, and the maximum measured pit depth from each inspected tube was recorded. The method described in G46 was

then applied to this dataset, as shown in [Figure 10](#). In this case, the extent of inspection was ~7%, and the maximum measured pit depth was 0.99 mm, while the maximum predicted pit depth was 1.32 mm.

The previous example provides no validation that the analysis has produced an accurate estimate of the condition for the uninspected tubes. However, the next example concerns another exchanger with cooling water on the tube side, in which 357 out of 410 tubes were inspected (with the remaining 53 tubes being uninspectable due to obstructions). To assess the accuracy of the GEV analysis technique, the full dataset was randomly sampled to create simulated inspection datasets of different sizes from 5 to 100 tubes. For each of these simulated datasets, the GEV technique was used to estimate the maximum pit depth in the entire 410 tube bundle, with 95% confidence limits also determined for each prediction. As shown in [Figure 11](#), for sample sizes over ~50 tubes (or ~25% inspection), the estimated maximum pit depth is both quite stable and in excellent agreement with the maximum measured pit depth from all the inspected tubes.

In the latter example, it is also instructive to consider the measurement error. For the NDT technique used in this case, the stated accuracy on clean tubes was  $\pm 0.05$  mm, but this varies for other inspection methods. For a sample size of 10% (40 tubes), [Figure 12](#) shows the impact of taking this effect into account. The ML estimates for the Gumbel parameters were obtained using the Xtremes software of Reiss and Thomas.<sup>56</sup> To allow for small sample calculations, we use the parametric bootstrap method to obtain standard errors and confidence limits.<sup>57</sup> The bootstrap method is implemented in the Xtremes software. Therefore, all we need to do is adjust the ML estimates to allow for the measurement error.

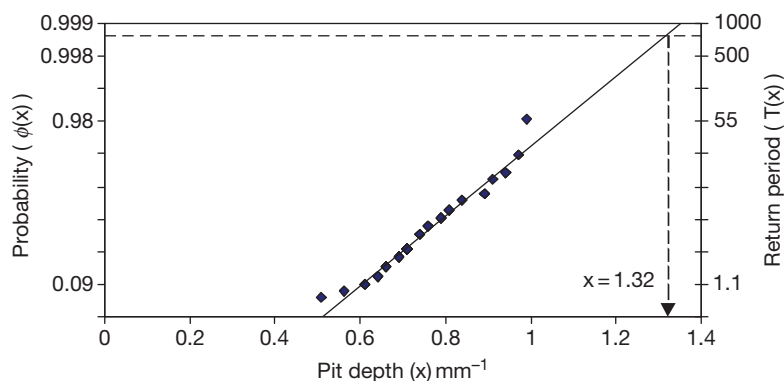


**Figure 10** ASTM G46 extrapolation method for maximum pit depth in an ammonia condenser with 54 tubes inspected out of 773 in total. The return period is 773, and the maximum expected pit depth is 1.32 mm.

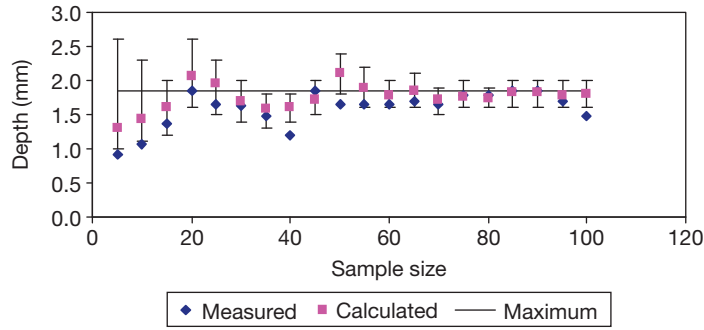


**Figure 11** For a cooler with pitting corrosion on the internal surface of the tubes, this figure compares the maximum measured pit depth in samples of varying size (up to 100 sampled tubes); the calculated maximum pit depth based on GEV analysis of the given sample size; and the maximum measured pit depth in the 357 inspected tubes from the 410 tube bundle (1.85 mm).

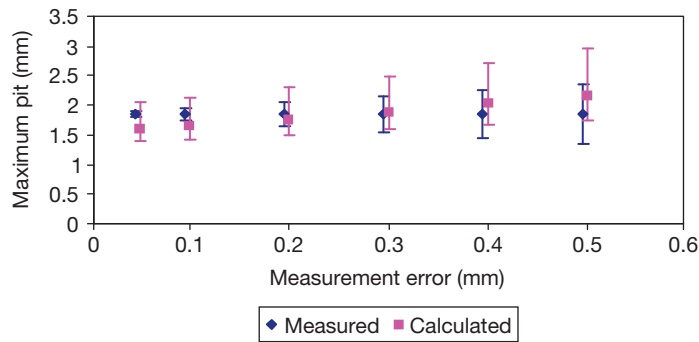


**Figure 12** For a cooler with pitting corrosion on the internal surface of the tubes. As a function of the assumed inherent measurement error, this figure compares; the maximum calculated pit depth based on inspection of a random 10% sample of the tubes; and the maximum measured pit depth in the 357 inspected tubes from the 410 tube bundle (1.85 mm).

In the special case that the measurement error is uniform, we use the following method.

The (ideal) genesis of the Gumbel is as follows:

1. The distribution of deep pits follows an exponential distribution,  $1 - \exp(-(x - \theta)/\sigma)$ .
2. The number of deep pits follows a Poisson distribution with mean  $\lambda$ .

Then, the distribution of the maximum pit depth follows the Gumbel distribution,  $\exp[-\exp\{-(x - \theta)/\sigma + \ln(\lambda)\}]$ , which has mode  $\theta + \sigma \ln(\lambda)$  and scale  $\sigma$ .

If, in fact, the pits are measured with uniform error between  $-R$  and  $R$ , then the distribution of measured depths  $x$  is exponential with distribution function  $1 - \exp[-(x - \theta - \varepsilon)/\sigma]$ , where

$$\varepsilon = \sigma \ln \left[ \frac{\sinh(R/\sigma)}{R/\sigma} \right] \quad [50]$$

The resulting distribution of the maximum measured pit follows the Gumbel distribution,  $\exp[-\exp\{-(x - \theta - \varepsilon)/\sigma + \ln(\lambda)\}]$ , which has mode  $\theta + \varepsilon$

+  $\sigma \ln(\lambda)$  and scale  $\sigma$ . Therefore, the effect of the measurement error is to increase the mode by an amount  $\varepsilon$ . Hence, given the ML estimates,  $\hat{\mu}$  and  $\hat{\sigma}$ , the appropriate adjustment for uniform error is to *reduce* the mode by an amount

$$\hat{\varepsilon} = \hat{\sigma} \ln \left[ \frac{\sinh(R/\hat{\sigma})}{R/\hat{\sigma}} \right] \quad [51]$$

while leaving the scale estimate as  $\hat{\sigma}$ . The usual parametric bootstrap can now be applied with the adjusted parameters to obtain the required standard errors and confidence limits. Further discussion on these techniques can be found elsewhere.<sup>58</sup>

#### 2.36.4.2 Thickness Measurement Locations

Corrosion engineers are frequently faced with the situation wherein they have inspection data showing the change in wall thickness (or increase in pit depth) at certain locations on a given piece of equipment



over several months or years, and are now being asked to predict the remaining useful life of this equipment. Here, we ignore the various possible different definitions for 'end-of-useful-life' and assume that there is a defined minimum allowable wall thickness, and that reaching this thickness at any one location constitutes the end-of-life for the given piece of equipment. In-service inspection codes<sup>59,60</sup> describe simple ways of calculating corrosion rates for a single thickness measurement location (TML); for example, the long-term corrosion rate is determined from the wall loss between the first measurement and the most recent measurement, while the short-term corrosion rate is obtained using only the two most recent measurements. However, there are also several different statistical approaches to this problem.

#### 2.36.4.2.1 Straight-line regression

Figure 13 shows the wall thickness data obtained by ultrasonic testing at one particular location on a wet gas flowline over a period of several years.

In this case, the observed erosion-corrosion damage was restricted to the outside of a bend, and the inspections always covered 100% of the damaged area such that there is no concern here about extrapolation of the results to other locations. As in the

earlier examples concerning coupon testing data, the slope of this 'best fit' line gives an estimate of the 'corrosion rate' over the measurement period, and a confidence interval about the line and the prediction interval for future observations are also shown. The corresponding graphic produced for these data by the Shell inspection design analysis and plotting (S-IDAP) package<sup>61</sup> is presented in Figure 14, where it is seen to present much the same predictions out to the same time point in 2008.

#### 2.36.4.2.2 Extreme value analysis

In this example, ultrasonic testing has been used to map the extent of internal corrosion damage to a carbon steel Benfield process vessel.<sup>62</sup> Inspections were carried out ~1 year apart, the measurements made using continuous scans of 50 mm × 50 mm grids and the minimum measured wall thickness being reported for each grid. For the worst case (thinnest) locations at the first inspection, the maximum measured wall loss between the two inspections was 0.6 mm, but, on average, there was negligible change (Table 2). It might be assumed, therefore, that the apparent differences between results at specific TMLs are all due to the measurement error (which has a mean of zero). However, for 8 of the 11

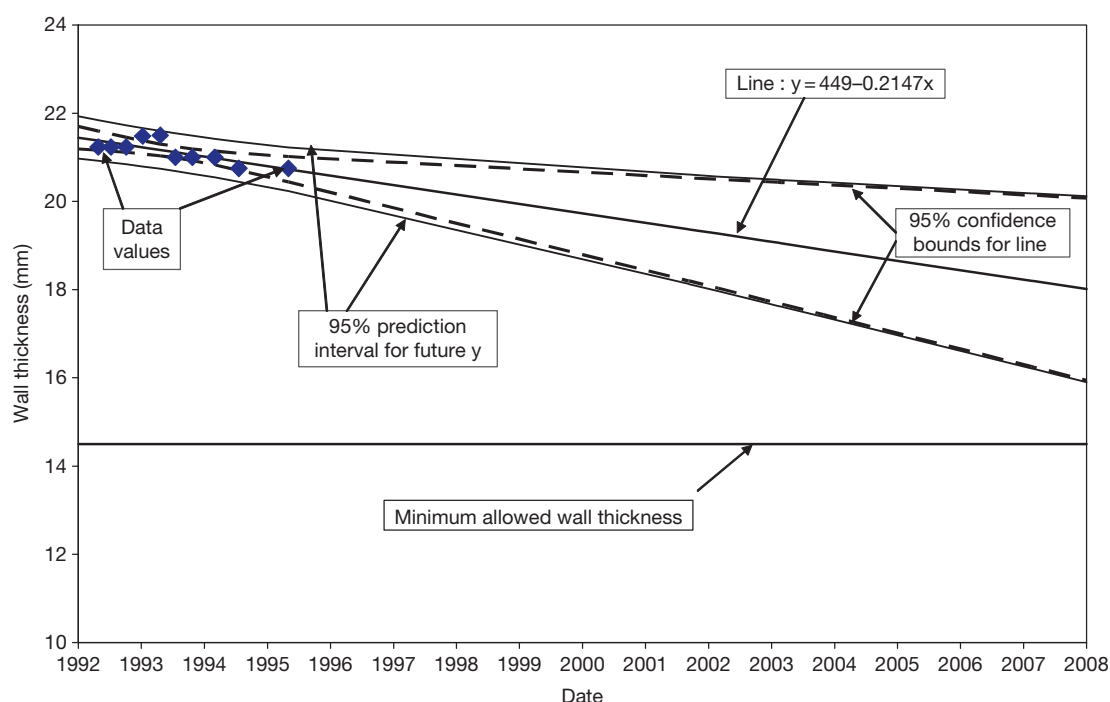


**Figure 13** Minimum wall thickness data from ultrasonic testing measurements on the outside of a bend in an offshore gas flowline, with confidence and prediction intervals around the best fitting line.

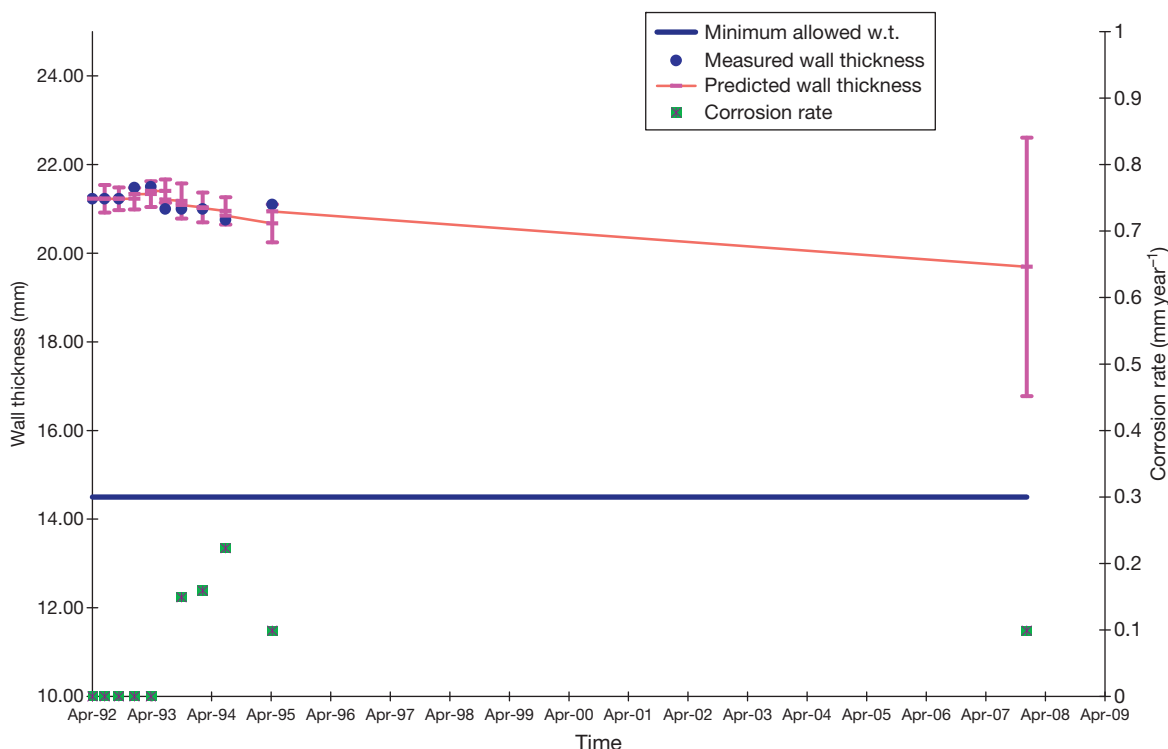


**Figure 14** The same measurement data as in Figure 13, with the extrapolation in time carried out using the S-IDAP package described by Hoeve *et al.*<sup>61</sup>

**Table 2** Ultrasonic testing results from inspection of a Benfield Process vessel at several thickness measurement locations in 2001 and 2002<sup>62</sup>

TML	Wall loss Aug 01–Nov 02 (mm)
1	–0.4
2	0
3	–0.9
4	0.1
5	–0.5
6	0.3
7	0.6
8	0.6
9	–0.1
10	0.2
11	0.3
Mean	0.01

The selected locations are those where the minimum wall thicknesses were found in 2001. Note that negative values indicate an apparent increase in wall thickness.

circumferential rows making up the inspected area, the minimum measured thickness was found in a different grid in the two inspections. This happens partly because of inherent measurement errors and partly because the highest corrosion rates are not necessarily experienced at the same locations at all times.

An alternative approach to this problem again takes advantage of extreme value analysis methods. In Figure 15, the maximum wall loss in each circumferential row is plotted for each inspection time. This is done in such a way that data conforming to a Type-I EV distribution would fall along a straight line. Hence, it is clear that the data from each inspection follow a Type-I EV distribution, but the entire distribution has shifted to higher wall loss values over time, as might reasonably be expected in a vessel suffering from corrosion. The corresponding corrosion rate can be calculated from the change in the Gumbel mode (assuming the same scale). Thus, we consider  $x \sim \text{EV}(\mu, \sigma)$  for the wall loss data from August 2001 and  $x \sim \text{EV}(\mu + \Delta, \sigma)$  for the data from November 2002. As the data are based on minima from different locations, we can assume that the wall loss results are statistically independent, yielding two independent samples, each of size 11. Using the ML estimation procedure, we obtain the parameter estimates  $\hat{\mu} = 5.05$ ,  $\hat{\sigma} = 0.36$ , and  $\hat{\Delta} = 0.43$ . In general, ML estimates are biased in small samples. To estimate the bias-corrected estimate and its standard error, we use the two-sample *jackknife* procedure, which gives  $\hat{\Delta} = 0.46$  with

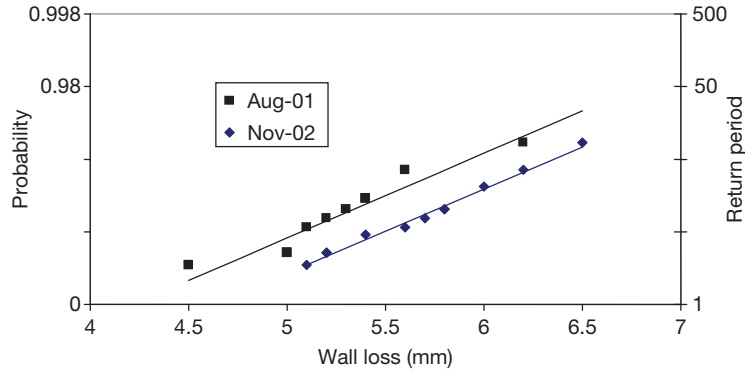


**Figure 15** EV analysis of minimum wall thickness data from surveys of a Benfield process vessel in August 2001 and November 2002. The progression of the distribution from left to right shows the rate at which the minimum wall thickness is decreasing, which is a practical definition of the corrosion rate. Reproduced from Wilson, P. T.; Krouse, D. P.; Moss, C. J. Proceedings of Corrosion Control and NDT; ACA, Melbourne, Australia, 23–26 November 2003; ACA: Melbourne, 2003; Paper no. 45.

standard error 0.22. Note that the *large sample* standard error for the ML estimate of the mode is  $\sigma\sqrt{\frac{1.11}{n}}$ .

In the present case, this is estimated by  $0.36\sqrt{1.11/11} = 0.114$ . Hence, the standard error for the difference of two independent ML estimates is  $0.114\sqrt{2} = 0.16$ , which is, as expected, somewhat less than that obtained using the jackknife procedure.<sup>57</sup> Thus, we conclude that a wall loss of  $0.46 \pm 0.22$  mm occurred over a period of 457 days, yielding a corrosion rate estimate of  $0.37 \pm 0.18$  mm year<sup>-1</sup>.

#### 2.36.4.2.3 Bayesian methods

In many corrosion applications, fitness for purpose is assessed using the remaining wall thickness (RWT). However, the RWT varies with the initial wall thickness, WT, independently of the corrosion process. The primary corrosion damage measure is actually the wall loss, which is independent of the initial wall thickness. For a given wall loss,  $X = x$ , the determination of the RWT depends on the measurement method. Generically, measurement methods determine either the material remaining or the material lost. In the first case, the RWT is measured directly as

$$y^{(1)} = (WT - x) + e^{(1)} \quad [52]$$

(for some error  $e^{(1)}$ ), and in the second case, the wall loss is measured directly as  $x + e^{(2)}$  (for some error  $e^{(2)}$ ), giving the apparent RWT

$$y^{(2)} = \text{NWT} - (x + e^{(2)}) \quad [53]$$

where NWT is the nominal wall thickness. However, noting that  $y^{(2)} = (WT - x) + [(NWT - WT) - e^{(2)}]$ , in general, the RWT is given by  $y = (WT - x) + e$ .

Bayesian methods are ideally suited to the problem of varying wall thickness. Wall loss  $X$  is assumed to be independent of the initial wall thickness, WT, and to have a continuous distribution function  $F(x)$ . Hence, conditional on the initial wall thickness,  $WT = w$ , the wall loss has the truncated distribution function  $F(x)/F(w)$  and differentiation gives the conditional density,

$$f(x|WT = w) = \frac{f(x)}{F(w)} \quad [54]$$

Hence, the first application of Bayes' rule is to obtain the posterior as

$$p(\theta, WT = w|x) = \frac{1}{c(x)} \frac{f(x, \theta)}{F(w, \theta)} p(\theta) p_{WT}(w) \quad [55]$$

where the normalizing constant is given by

$$c(x) = \int \left[ \int \frac{p_{WT}(w)}{F(w, \theta)} dw \right] f(x, \theta) p(\theta) d\theta \quad [56]$$

Now the posterior density  $p(\theta|x)$  can be obtained by integrating over the initial wall thickness to give

$$p(\theta|x) = \frac{f(x, \theta)}{c(x)} p(\theta) \int \frac{p_{WT}(w)}{F(w, \theta)} dw \quad [57]$$

This formula explicitly quantifies the effect of uncertainty in initial wall thickness. In cases wherein the wall loss is small compared with the initial wall thickness,  $F(w, \theta) \cong 1$ , and the posterior reduces to

$$p(\theta|x) = \frac{f(x, \theta) p(\theta)}{\int f(x, \theta) p(\theta) d\theta} \quad [58]$$

Having obtained the posterior, the posterior predictive probability of wall loss exceeding a

threshold,  $u$ , is given by integrating over the posterior, that is,

$$\Pr(X > u|x) = 1 - \int F(u, \theta)p(\theta|x)d\theta \quad [59]$$

These results can be extended to the case when the wall loss is measured directly with measurement-error density,  $\varphi(z)$ , since the likelihood conditional on the wall thickness is now given by

$$f(y|WT = w) = \frac{1}{F(w)} \int_{y-w}^y f(y-z)\varphi(z)dz \quad [60]$$

The case in which the RWT is measured directly gives a similar result,

$$f(y|WT = w) = \frac{1}{F(w)} \int_{y-w}^y f(w-y+z)\varphi(z)dz \quad [61]$$

In cases wherein the wall loss can be localized to a 'defect' and there are a large number per component, the problem reduces to considering the maximum wall loss. In case the number of defects is Poisson with mean  $\lambda$ , the maximum wall loss has distribution function  $\exp\{\lambda[1 - F(x)]\}$ .

In many practical situations, the GEV distribution can be used to approximate the distribution of the maximum wall loss. A question of special interest is whether the distribution has an upper bound, which is given by

$$\delta + \frac{\alpha}{\kappa} = X_{(1/e)} + \frac{X_{(0.5)} - X_{(1/e)}}{1 - (\ln 2)^\kappa} \quad [62]$$

where  $X_{(p)}$  denotes the  $p$  the quantile of the distribution. Evidently, since the quantiles are readily estimated by the sample values, uncertainty in the putative upper bound is dominated by uncertainty in the shape parameter,  $\kappa$ . Indeed, any Bayesian analysis using the GEV is very sensitive to the shape-parameter prior, and more experience is required to assess whether the results are suitably robust for practical application.

**Figure 14** shows an analysis of wall thickness data produced by the S-IDAP package described by Hoeve *et al.*<sup>61</sup> S-IDAP makes Bayesian predictions based on a number of alternative models in addition to the linear or constant corrosion rate model. These include a genuine change in corrosion rate as well as other data anomalies such as an outlier or incorrect measurement. Given prior probabilities for the candidate models, Bayes' rule can be used to calculate the posterior probability of each model, thereby indicating the most probable model. Such information is useful for reviewing the data to ensure a robust prediction. The final prediction is a weighted

combination of the predictions from each model. According to Bayes' rule, the optimal prediction is obtained by weighting the predictions from each model with the model's posterior probability.

### 2.36.4.3 Pit Depth Data

For pitting corrosion, analysis of inspection data is generally focused on predicting the time at which the deepest pit is expected to penetrate through the complete thickness of the inspected item. Of course, extreme value techniques are naturally suited to this problem. Furthermore, pits in engineering metals and alloys generally initiate at defects, such as nonmetallic inclusions or intermetallic particles, such that the number of potential pit initiation sites is typically very large. It is also well known that many pits will initiate and propagate for short periods, producing only small pits, while a relatively small number of pits may become 'stable' and grow to significant depths from an integrity perspective. For example, experimental data presented by Bhakta and Solomon<sup>63</sup> show pit densities for low carbon steel in the range 100–350 cm<sup>-2</sup>. Coupled with the resolution of the measuring instrument, this implies that data sets consisting of all practicably measurable pits at a given site may inherently consist of data incorporating a known and (relative to the majority of the initiated pits) large threshold.

#### 2.36.4.3.1 Extreme value analysis for life prediction

**Figure 16** shows all pit depths over 6  $\mu\text{m}$ , as found by inspection of two copper-plated 316L stainless steel college roofs in the south of England. The first roof had been exposed for 1523 days and the second for 883 days. The mean exceedance plots for these data gave a slope that was not significantly different from zero after applying the usual least-squares criteria, implying a simple exponential distribution for these exceedances, and hence a Type-I EV for maxima.

Time dependence can be incorporated into the fitted GPD models by assuming the square root law for growth (see other comments in this chapter), which then had exponential type probability density functions

$$f(y) = 2.893t^{-0.5} \exp[-2.893(y-6)t^{-0.5}], \quad y > 6 \text{ Roof 1} \quad [63]$$

with mean  $0.346t^{0.5}$ , and

$$f(y) = 1.062t^{-0.5} \exp[-1.062(y-6)t^{-0.5}], \quad y > 6 \text{ Roof 2} \quad [64]$$

with mean  $0.0941t^{0.5}$ .

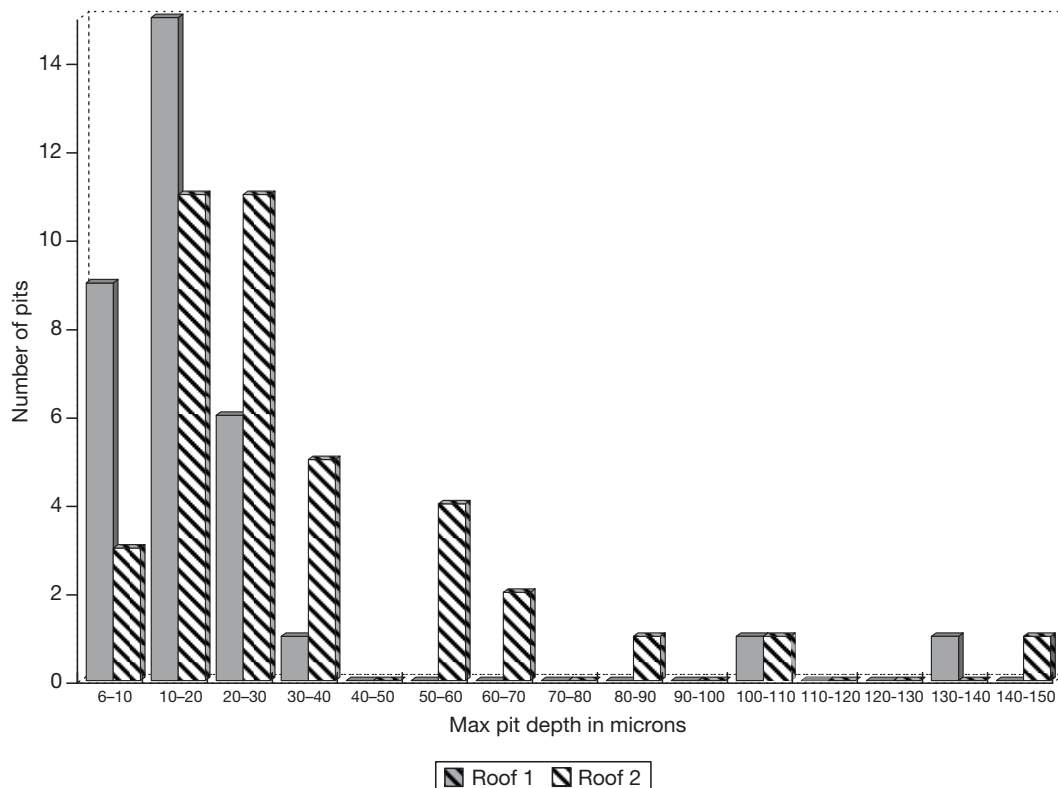


**Figure 16** All pit depths over 6  $\mu\text{m}$ , as found by inspection of two copper plated 316L stainless steel college roofs in the south of England. The first roof had been exposed to the weather for 1523 days and the second for 883 days.

The count of exceedances over the specified value will follow a Poisson distribution with mean rates over the whole roof

$$\begin{aligned}
 &= 4.3A \exp[-2.893(\gamma - 6)t^{-0.5}] \text{ for Roof 1} \\
 &= 3.9A \exp[-1.062(\gamma - 6)t^{-0.5}] \text{ for Roof 2} \quad [65]
 \end{aligned}$$

where  $A = 5\,000\,000\text{ cm}^2$ . Given that the roof (cover) thickness is 400  $\mu\text{m}$ , this reaches a mean count of 1 after 12 years for Roof 1, and after 3 years for Roof 2. This analysis gives the expected time to the first penetration for each roof covering.

In the majority of cases, life prediction based on the analysis of historical data involves the key assumption that the environmental conditions in the future can reasonably be considered similar to those in the past. However, even if this assumption is reasonable on average, over long time periods, the environmental conditions usually vary quite significantly over time. For example, Figure 17 shows the variation of the chloride concentration in an open recirculating cooling water system over several years. Despite this variation, which will be not limited to the chloride level but will extend to many other factors such as pH and inhibitor concentration,

a Japanese survey of carbon steel heat exchangers in cooling water circuits found that the depth of the deepest pit tends to increase with the square root of time over many years of service.<sup>64</sup> From their survey data, they calculated the variation of EV model parameters over time and used this to produce remaining life estimates for exchanger tube bundles in this type of service. Some further discussion and alternative approaches to this problem are provided elsewhere.<sup>65</sup>

#### 2.36.4.3.2 Life prediction models transformable to linearity

A model with profound implications for the extrapolation of long-term corrosion rates in time is the power-law model  $y = at^b$ , as reported in Laycock *et al.*,<sup>32</sup> Aziz and Godard,<sup>66</sup> and de la Fuente,<sup>67</sup> and elsewhere, all with  $b < 1$  and  $b = 0.5$  or  $0.67$  typical. It is important to note that the corrosion rate, that is,  $dy/dt$ , is now time dependent and cannot be reported in isolation as a single number. By assuming a multiplicative error, taking logs of this model produces a straight line regression model, which can be fitted by ordinary least-squares with dependent variable  $y' = \log(y)$ , intercept  $a' = \log(a)$ , slope  $b$ , and



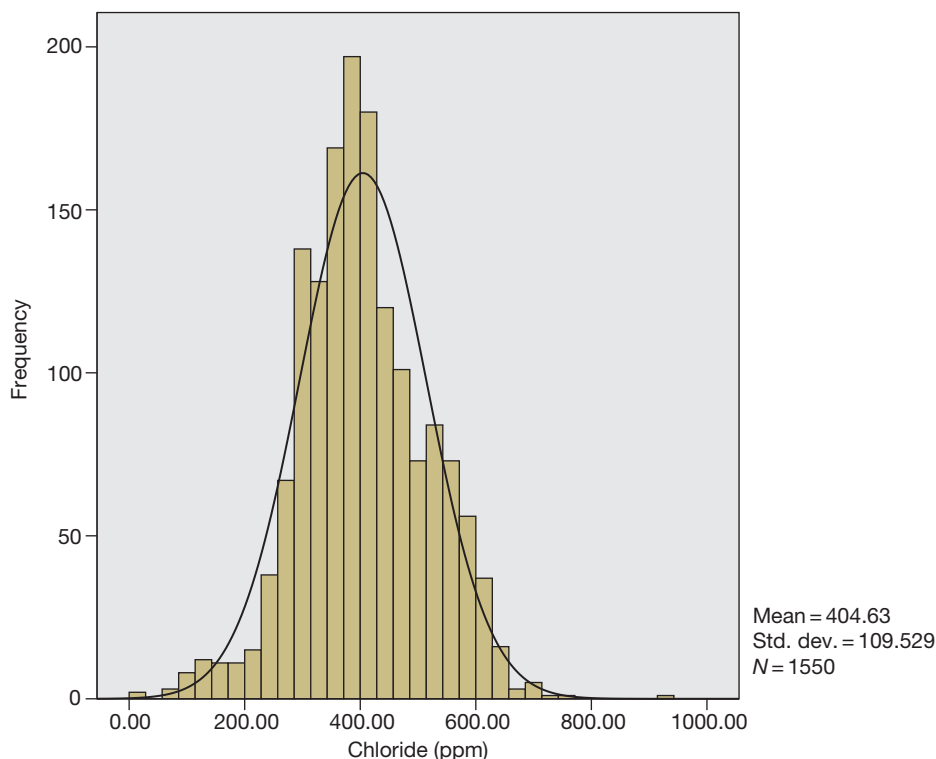


**Figure 17** Distribution of measured chloride concentrations (ppm) in an open recirculating cooling water system, obtained from 1550 measurements over 12 years of operation.

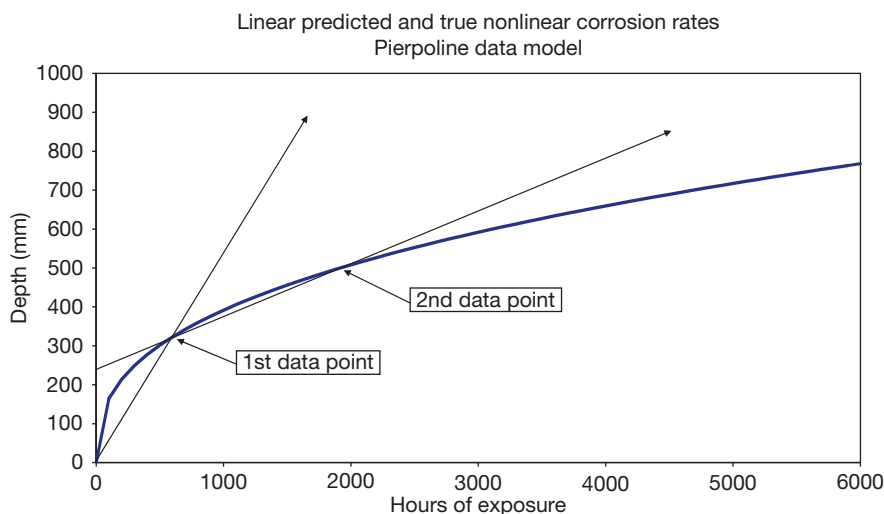


**Figure 18** A true power-law growth curve, with decreasing corrosion rate, fitted through the pit depth data of Pierpoline *et al.*,<sup>48</sup> using the method described in Scarf *et al.*<sup>49</sup> This is compared with fitted straight lines based on (a) first data point plus origin; then (b) first and second data points, both extrapolated to show how prediction errors decrease.

covariate  $x = \log(t)$ , except that  $b$  is of course no longer the corrosion rate. Now, suppose that corrosion is progressing according to such a law, as illustrated in Figure 18, but we only have some current data, collected at time  $t = t_1$ , say. Then, fitting a simple straight line through the origin with these

data will produce the straight line superimposed on the curve as shown in Figure 18, and an extrapolated corrosion rate much in excess of future corrosion rates. Now, suppose that we collect some more data, at a later time  $t_2$  and fit a straight line regression through the two time points we now have, as again

illustrated in [Figure 18](#). This time the predicted corrosion rates are much closer to reality for reasonable extrapolations into the future. This suggests that, where it is convenient to have just a single reportable ‘corrosion rate,’ straight-line regression should be used, with an intercept, utilizing just the latest two or three time points. If more points are available, then the tests for deviations from linearity (as described earlier) can be used to assist in model determination.

#### 2.36.4.4 Intelligent Piggings Data

Pipeline inspections by Intelligent Pigs can produce vast amounts of data, which are typically summarized in lists of ‘features’ with depths greater than some predefined reporting threshold. When comparing the data from two different inspections of the same pipeline, it is often attempted to match the ‘corrosion features’ from the two runs and thereby determine a corrosion rate for each feature. However, for various reasons, such as changes in technology over time, it is often difficult to match all the reported features in this way. Here, we describe methods for analysis of both ‘tracked’ and ‘untracked’ features.

##### 2.36.4.4.1 Untracked features: Pareto distribution example

Suppose that the results of two piggings runs down a large and actively corroding pipeline are presented as two sets of untracked feature depths  $y_{11}, y_{12}, \dots, y_{1n_1}$  at time  $t_1$  and  $y_{21}, y_{22}, \dots, y_{2n_2}$  at time  $t_2$  with  $n_2 \geq n_1$ . Because the later survey may have new features, the two data mean  $\bar{y}_1$  and  $\bar{y}_2$  may not provide a sound

estimate of the corrosion rate. Indeed, if there are enough fresh features, the second mean could be smaller than the first. Instead, consider the  $n < \min(n_2, n_1)$  largest order statistics  $y_{(11)}^* > y_{(12)}^* > \dots > y_{(1n)}^*$  and  $y_{(21)}^* > y_{(22)}^* > \dots > y_{(2n)}^*$  for the two series. Since interest will center on the growth rate of the largest values, it seems sensible to use a mean exceedance plot to decide on a common cutoff point for the two ordered series based on the same count of measurements to maintain rough comparability and equivalence to a fully tracked sequence. A plot of the two fitted GPD distributions for a simulated set of piggings data that has been filtered and processed in this manner can be seen in [Figure 19](#). The modal shift between these two roughly parallel curves is 2.85 mm and the runs were 6 months apart, implying a corrosion rate of  $5.7 \text{ mm year}^{-1}$ .

##### 2.36.4.4.2 Tracked feature comparison

[Figure 20](#) shows a set of 22 tracked feature depths from two piggings runs of a subsea gas pipeline. The tracked features are all from one pipe spool known to have suffered some internal damage early in service life, many years before these two piggings runs. However, there was also a risk of ongoing internal corrosion due to upsets in dewpoint control. The piggings data are expressed as percentage wall thickness lost, with the difference between the two sets of data converted to an implied wall loss in millimeters – based on a nominal original wall thickness of 15.9 mm. Since 7 of the 22 values are negative, with a maximum absolute value of 1.27 mm, there is substantial measurement error involved. The average

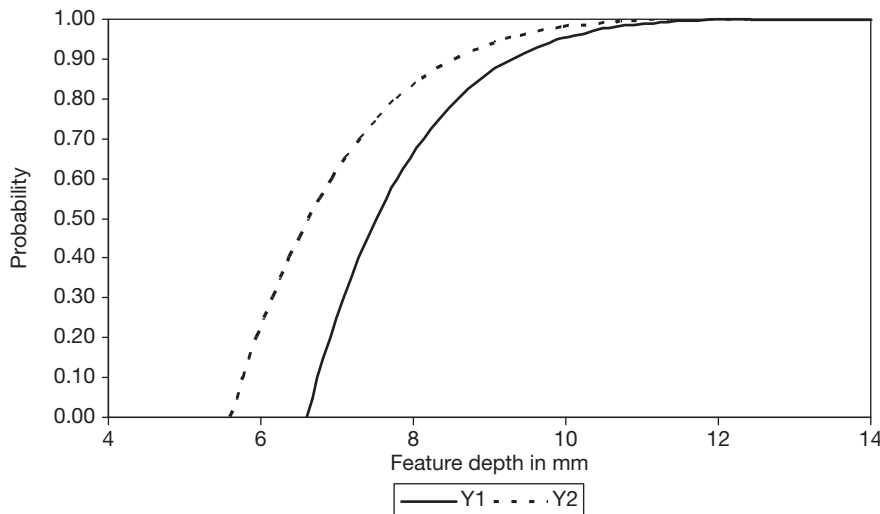


**Figure 19** Fitted Pareto distributions for the largest 1500 order statistics from two successive piggings runs (simulated data only). The modal shift between these two roughly parallel curves is 2.85 mm, and the runs were 6 months apart, implying a corrosion rate of  $5.7 \text{ mm year}^{-1}$ .

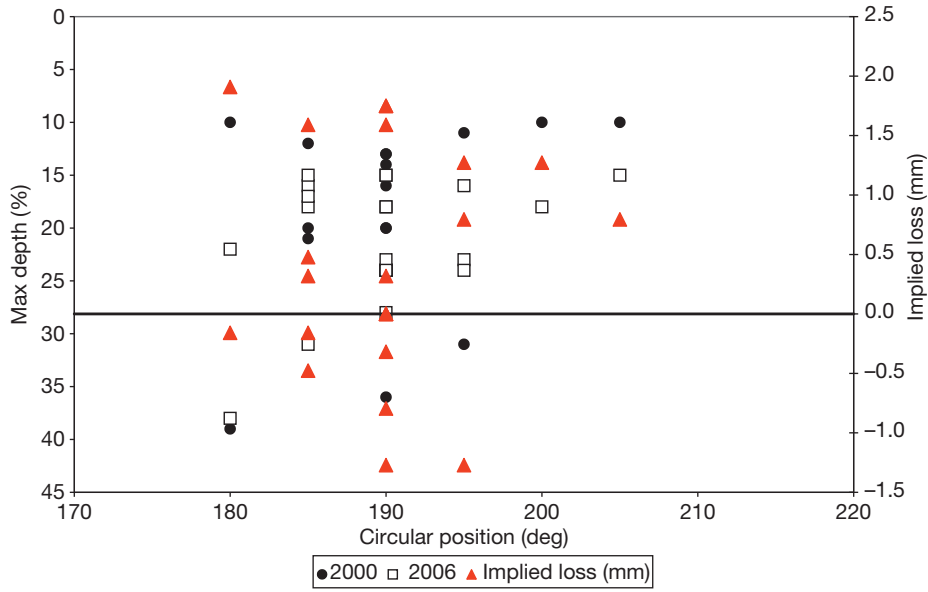


**Figure 20** A set of 22 tracked feature depths from two pigging runs of a subsea gas pipeline. These features are all from one pipe spool known to have suffered some internal damage early in service life, many years before these two pigging runs.

implied wall loss is  $-0.426$  mm with a standard error of  $0.208$  mm (so an implied corrosion rate of  $-0.065$  mm year $^{-1}$  with standard error of  $0.032$  mm year $^{-1}$ ). Note that this average loss is based on all the 22 values. Discarding the seven negative values as ‘erroneous’ would produce a severely biased estimate of the true corrosion rate – since, without further information, it must be assumed that the unknown measurement errors are as likely to be positive as negative. An inferred tolerance for these measurements of  $\pm 1.3$  mm implies a measurement error standard deviation of  $0.65$  mm with variance of  $0.4225$ . The variance of the recorded wall loss data is  $0.9520$ ; hence if we assume an additive corrosion process, the implied Wiener noise variance (see Section 2.36.1) is  $(0.9520 - 2 \times 0.4225) = 0.1070$  over the 2393 days between the pigging runs, or  $0.0163$  scaled to 1 year – so a standard deviation of  $0.13$  mm year $^{-1}$ . Since the 95% (one-sided) point from Student’s  $t$ -distribution on  $(22 - 1) = 21$  degrees of freedom is  $1.72$ , and a 95% upper prediction bound on future values for the corrosion rate will be  $-0.065 - 1.72 \times \sqrt{(0.032^2 + 0.0163)} = -0.29$  mm year $^{-1}$ , which coincides with the single (so  $\sim 5\%$ ) maximum observed corrosion rate found in the 22 measured annual corrosion rates.

#### 2.36.4.5 Optimizing Inspection and Repair Intervals

Corrosion damage and cracks detected by nondestructive inspection may be subject to repair. Such

maintenance will, in general, need to be carried out within an effective maintenance program.<sup>68–70</sup> Based on assumptions about the rate of corrosion or crack growth, the consequences of failure, the cost of inspection and repair, and data to estimate parameters relating to these quantities, maintenance decision-making can follow. In particular, the optimum time between inspections may be determined.

##### 2.36.4.5.1 Planning inspections for cracks

In the simplest case, assume that an inspection is carried out at  $T$  time units since the last inspection or failure; inspections are perfect (all crack defects are detected at inspection and repaired) so that they renew the system; on failure, all crack defects are repaired, and the system is renewed; the cost inspection including the repair of crack defects is fixed at  $C_p$ ; and the cost of failure is  $C_f$ . Denote the time to failure by  $X$ , then

$$\begin{aligned} F_X(t) &= \Pr(X \leq t) = \Pr(Z_{\max,t} > z_f) \\ &= 1 - F_{\max,t}(z_f) \end{aligned} \quad [66]$$

where  $F_{\max,t}(z_f)$  is the distribution of the maximum crack depth at time  $T$ . The long-run cost per unit time is given by the renewal-reward theorem<sup>71</sup>:

$$C(T) = E(U)/E(V) \quad [67]$$

where  $E(U)$  is the expected cost of an renewal interval, and  $E(V) = E\{\min(X, T)\}$  is the expected

length of a renewal interval. The renewal interval is defined as the time between successive renewals. Now

$$E(U) = C_f - (C_f - C_p)F_{\max,T}(z_f) \quad [68]$$

since the cost of a renewal interval is  $C_p$  if the renewal interval ends with an inspection that occurs with probability  $F_{\max,T}(z_f)$ , and  $C_f$  if the renewal interval ends with a failure that occurs with probability  $1 - F_{\max,T}(z_f)$ . Also,

$$\begin{aligned} E(V) &= E\{\min(X, T)\} = \int_0^T \{1 - F_X(t)\} dt \\ &= \int_0^T F_{\max,t}(z_f) dt \end{aligned} \quad [69]$$

Thus,

$$C(T) = \{C_f - (C_f - C_p)F_{\max,T}(z_f)\} / \int_0^T F_{\max,t}(z_f) dt \quad [70]$$

This is the classic age-based replacement policy of Barlow and Proschan [72].  $C(T)$  is minimized with respect to  $T$  to obtain  $T^*$ , the cost-optimal age limit for inspection (or more generally, preventive maintenance). For this purpose,  $F_{\max,t}(z_f)$ ,  $C_p$ , and  $C_f$  must be specified and  $C(T)$  minimized. Differentiating eqn [70] with respect to  $T$  and setting the derivative equal to zero, we obtain

$$\begin{aligned} \{f_{\max,T^*}(z_f)/F_{\max,T^*}(z_f)\} \int_0^{T^*} F_{\max,t}(z_f) dt \\ + F_{\max,T^*}(z_f) = C_f/(C_f - C_p) \end{aligned} \quad [71]$$

where  $f_{\max,t}(z_f)$  is the density function of the maximum crack depth.  $T^*$  can be found by solving eqn [71] numerically, or by plotting  $C(T)$  against  $T$  for various values of  $T$ .

If the cost of crack repairs is additional to the cost of inspection, the cracks costing  $C_r$  each to repair, then the optimum inspection interval does not depend on  $C_r$ , because the expected cost of a renewal interval  $E(U)$  increases by  $\lambda C_r \times E(V)$ , where  $\lambda$  is the rate of crack initiation – a longer inspection interval will result in more cracks developing. Thus, the long-run cost per unit time,  $C(T)$ , increases by a factor  $\lambda C_r$  that does not depend on  $T$ .

#### 2.36.4.5.2 Optimizing inspections with unknown cost of failure

Often in practice, it is difficult to specify the cost of failure. Engineers may be happier to prescribe a required reliability. Such a required reliability is best expressed in terms of the operational reliability, which is defined as the distribution of the time

between operational failures of the system. Assuming that system renewal intervals are independent of one another, the time of any failure can be taken as time origin, and events up to the first subsequent failure can be considered without loss of generality. Thus, if the time to the first operational failure of the system is denoted by  $Y_1$  and subsequent time to second operational failure by  $Y_2, \dots$ , then  $Y_1, Y_2, \dots$  are independent and identically distributed with distribution function  $F_Y(y)$ , say. It follows that

$$\begin{aligned} R_Y(y) &= R_X(y - nT)\{R_X(T)\}^n, \\ (nT \leq y < (n+1)T, n = 0, 1, \dots) \end{aligned} \quad [75]$$

where  $R_Y(y) = 1 - F_Y(y)$  is the operational reliability function. This result is given in this form by Lewis.<sup>73</sup> The mean and variance of this distribution can be determined explicitly:

$$\begin{aligned} E(Y) &= \mu_T + T\{1 - F_X(T)\}/F_X(T) \\ &= \int_0^T (1 - F_X(x))dx/F_X(T) \\ \text{var}(Y) &= \sigma_T^2 + T^2\{1 - F_X(T)\}/\{F_X(T)\}^2 \end{aligned} \quad [76]$$

where  $\mu_T = E(X|X < T)$  and  $\sigma_T^2 = \text{var}(X|X < T)$ . We call  $E(Y)$  the mean time between operational failures (MTBOF). For small  $T$ ,  $\mu_T \sim 0$  and  $\sigma_T^2 \sim 0$ . Therefore,  $E(Y) \sim T/F_X(T)$ ,  $\text{var}(Y) \sim \{T/F_X(T)\}^2$ , and  $Y$  has approximately an exponential distribution with mean  $T/F_X(T)$ . This approximation is supported by the results of Xie *et al.* [74]. Furthermore,

$$F_X(T)/T = \Pr(Z_{\max,T} > z_f)/T \quad [77]$$

can be interpreted as the operational failure rate.

Thus, given a reliability constraint that is expressed in terms of the MTBOF, the required inspection interval  $T^*$  can be obtained from eqn [77] and using the fact that  $F_X(t) = 1 - F_{\max,t}(z_f)$ . Note that an implied cost of failure,  $C_f$ , can be determined by substitution of  $T^*$  in eqn [71].  $T^*$  can also be determined by specifying the operational failure rate in eqn [77].

#### 2.36.4.5.3 Crack inspection case study

Maximum crack depths were measured on identical circular welds at locations in two identical plants after varying amounts of operating time (Figure 21). A number of welds were subjected to repeated inspection by NDT, but here, only the first inspections are considered. The complete dataset is presented in Scarf *et al.*<sup>75</sup> Where a weld was inspected and no crack found, this was recorded as a zero. At inspection, welds were repaired. It was of interest

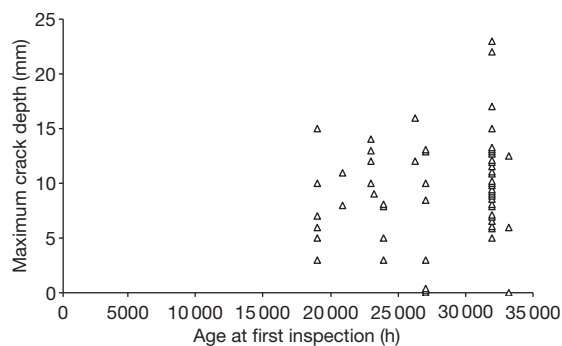


**Figure 21** Maximum crack depth against age-at-first-inspection for 59 circular welds from two identical plants – jitter added to depths to distinguish all datapoints.

**Table 3** Parameter estimates for the model: Poisson process of crack initiation (rate  $\lambda$ ) with distribution of crack depth given by eqn [47]

Parameter	Estimate
$\alpha_0$	7.092
$\beta$	1.645
$\gamma$	0.00079
$\lambda$	0.00013

to the engineers operating the plant to determine if there was some positive trend in crack depth with age (or time since last inspection), and if so, at what rate cracks were ‘growing’; and also to determine how often they should carry out costly inspections.

The crack depth data are used here to demonstrate the estimation of the maximum crack depth distribution (eqn [49]). The estimated parameters are shown in Table 3. These imply that visible cracks initiate at a rate per weld of one every 7937 operating hours and then subsequently grow at a mean rate given by  $\mu = \alpha_0 \Gamma(1 + 1/\beta) \tau^\gamma = 6.32 \tau^{0.000785}$ . This growth rate implies that, for example, the mean depth of a crack that has been growing for 10 000 h is 6.37 mm. The estimated growth rate is extremely slow, suggesting that the cracks were in fact not growing at all and were present in the welds from new.

To demonstrate the methods of this section further, the growth rate parameter is taken to be  $\gamma = 0.3$ , and  $\alpha_0$  is rescaled. Taking  $\alpha_0 = 0.4$  implies that the mean depth of a crack that has been growing for 10 000 h is 6.34 mm, and 9.23 mm for one growing for 35 000 h. The distribution of the maximum crack depth over the entire system (assuming 60 welds on the system) at time  $T$  is then as shown in Figure 22.

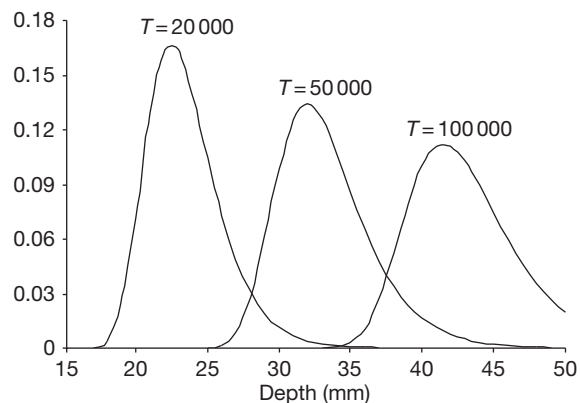


**Figure 22** The distribution (probability density) of the maximum crack depth over the system at various times,  $T$ , in operating hours.

The probability density is drawn here for various values of  $T$ . The mean maximum depth and the standard deviation of the maximum crack depth are increasing as expected.

The probability of observing a maximum crack depth that is at least as big as some specified threshold can be determined. For example, from Figure 22, there is a significant risk that a maximum crack depth in a weld is larger than 40 mm after 50 000 h ( $P=0.033$ ). This probability rises to 0.727 after 100 000 h of operation.

To consider an optimum time between inspections, assuming perfect inspection and repair (weld renewal), the cost of inspection and repair of welds,  $C_p$ , can be considered as the unit of cost. Then, the cost of failure,  $C_f$ , need only be specified in terms of the cost of inspection and repair. The failure-critical threshold for the maximum crack depth must also be specified. This is taken to be 40 mm. Then, the long-run cost per unit time can be determined for various  $T$ . This is shown in Figure 23(a) with  $C_f = 4C_p$ . The optimum inspection interval is  $\sim 55$  000 h. The sensitivity to  $C_f$  and  $z_f$  may be investigated simply by determining  $T^*$  for various values of  $C_f$  and  $z_f$ . For example, for a scenario in which the cost of failure is considerably higher than the cost of inspection, say  $C_f = 10C_p$ ,  $T^*$  reduces to  $\sim 45$  000 h. Where an operational reliability is required, this is done most simply by specifying an operational failure rate, eqn [77], and solving for  $T^*$  by trial and error. In Figure 23(b), the operational failure rate is plotted against  $T$ . Given a required operational reliability,  $T^*$  may be read off this graph. Note that this  $T^*$  then implies a cost of



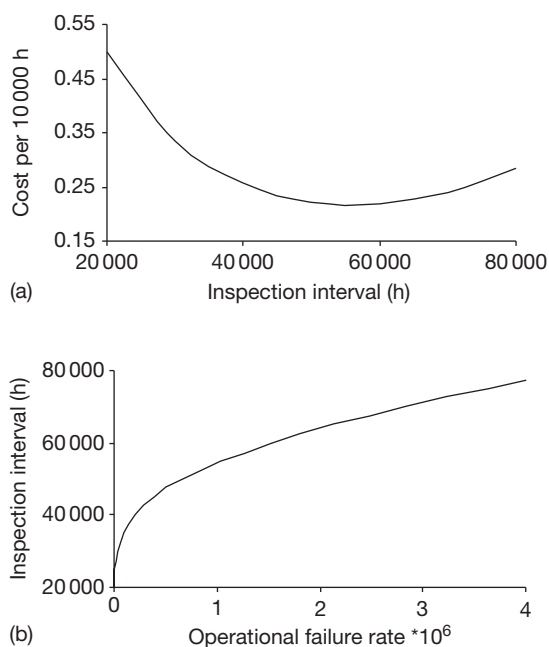


**Figure 23** (a) The long-run cost per unit time,  $C(T)$ , against  $T$ , with  $C_f = 4C_p$  and  $z_f = 40\text{mm}$ . (b) Time between inspections against operational failure rate,  $\Pr(Z_{\max,T} > z_f)/T$  with  $z_f = 40\text{mm}$ .

failure that may be calculated and used to confirm engineering judgment about these quantities. An operational reliability of (at most) one failure for every  $5 \times 10^6$  operating hours requires that the inspections take place every 40 000 h, which in turn implies that  $C_f = 20C_p$  (approximately).

The calculations mentioned earlier may be performed on a spreadsheet. The integral in eqn [49] may be evaluated most simply using Simpson's rule. For the calculation of the long-run cost (eqn [70]), the integral in the denominator can be calculated likewise and noting that  $F_{\max,t}(z_f) \approx 1$  for small  $t$  (here for  $t \leq 20\,000$ ). These approximations provide sufficient accuracy for optimization purposes, given that the cost function is relatively flat in the region of the optimum.

### 2.36.5 Corrosion Monitoring

The science of electrochemical noise monitoring began in the 1980s<sup>76,77</sup> and has since extended into commercially available corrosion monitoring techniques. The standard noise analysis techniques are typically built on incrementally additive assumptions for corrosion, as in the theoretical 'shot noise' models for pitting and crevice corrosion proposed by Eden, Cottis, and other workers.<sup>37,38</sup> These result in Poisson

models and consequently have variance equal to the mean, which can be approximated by Normal distributions. More generally, statistical analysis methods may ignore the ordering of the measured potential or current values by using sequence-independent parameters such as the mean, standard deviation, skew, and kurtosis, or they may take the sequencing into account by computing the autocorrelation function, power spectral density PSD –  $\psi_E$  for potential, or  $\psi_I$  for current – or higher-order spectra. When potential and current noise are measured simultaneously, electrochemical noise resistance  $R_n$ , electrochemical noise impedance, characteristic charge  $q$ , and characteristic frequency  $f_n$  can be calculated. The  $R_n$  is obtained as the ratio of the standard deviation of potential to the standard deviation of current, justified by appealing to the definition of electrical power for an alternating current. The PSD referred to is that at low frequencies, where the noise is white (hence, the PSD is frequency-independent). Electrochemical noise impedance can be estimated in essentially the same way as the  $R_n$ , by dividing the PSD of the potential noise by the PSD of the current noise. Several researchers have analyzed the relationship between  $R_n$  and the polarization resistance  $R_p$ , and some claim to have proved that the two are equivalent.<sup>78</sup>

#### 2.36.5.1 Threshold Techniques

When this technique is used on a correlated time-series, such as the current noise plot in Figure 24(a), preliminary filtering of the data is required so as to produce a set of statistically independent measured maxima. The most widely adopted method is declustering (see Coles<sup>33</sup>, p. 99). In this, an empirical rule is used to define isolated clusters of exceedances, followed by extraction of the maximum within each such cluster. In meteorology, this is sometimes described as 'rainstorm identification'. The empirical spreadsheet formula with a bandwidth of 10 units used to extract the maxima in Figure 24(b) from the noise data in Figure 24(a) was

```
IF(AND(((MAX(F11:F20)–AVERAGE(F11:F20))<1),
((MAX(F10:F20)–AVERAGE(F10:F20))>1)),1,0)
*F20IF(AND((MAX(F11:F20)–AVERAGE
(F11:F20))<1),
((MAX(F10:F20)–AVERAGE(F10:F20))>1)),1,0)
*F20
```

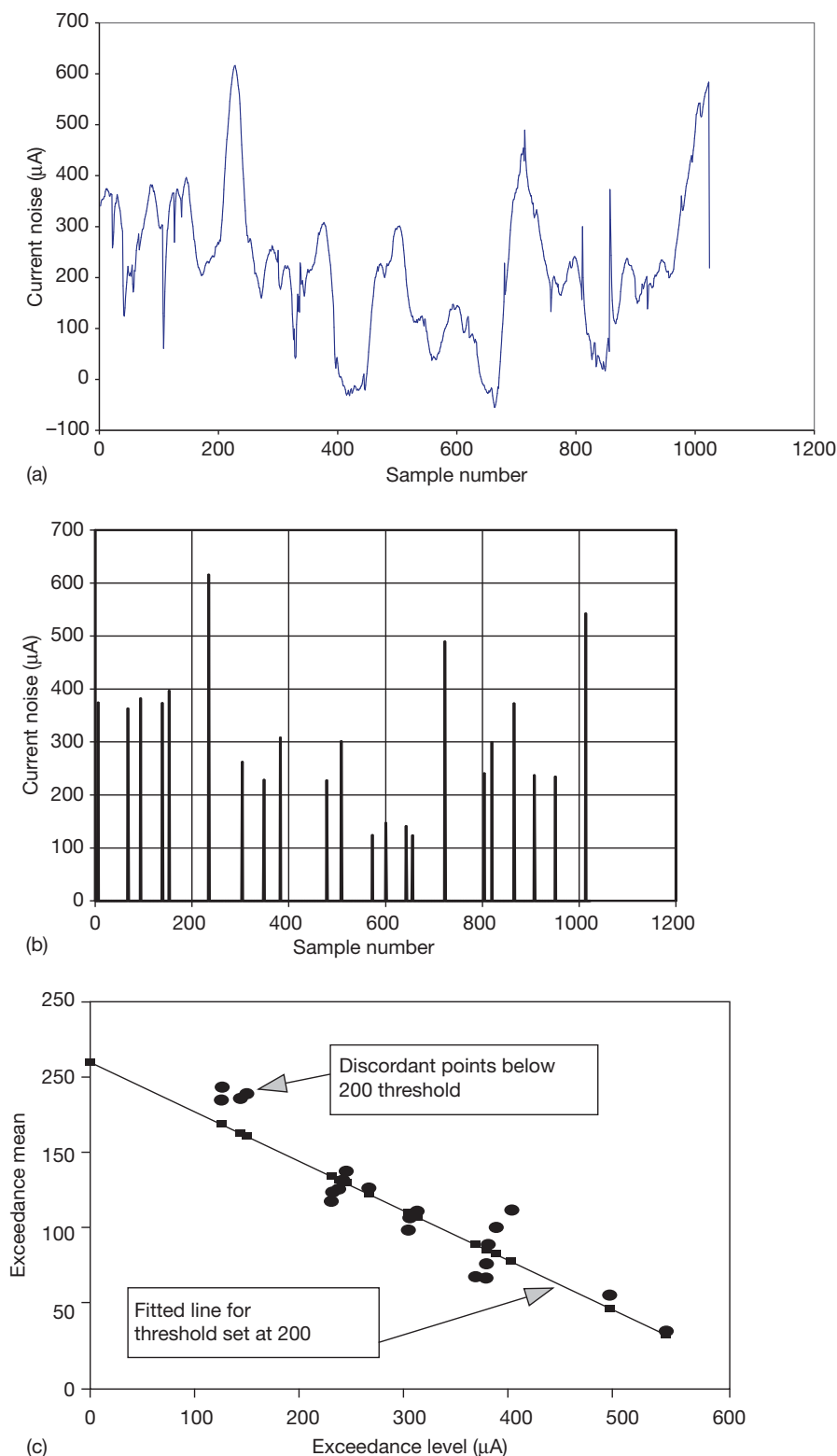


**Figure 24** Threshold analysis techniques applied to electrochemical noise measurements. (a) Raw current noise data, (b) extracted peaks, and (c) mean exceedance plot for the current noise measurements, with fitted straight line at selected threshold.

This is for data row 20 updated as usual for other rows. The mean exceedance plot for these data can be seen in **Figure 24(c)**, in which a threshold of 200  $\mu\text{A}$  was used as a cutoff point for fitting the straight line. The statistical package Xtremes, which is supplied with the book by Reiss and Thomas,<sup>56</sup> offers an automated procedure for selecting this threshold.

### 2.36.6 Summary and Conclusions

Statistical techniques have long been used in both corrosion science and engineering. Rigorous data analysis can help to ensure that the maximum possible benefit is achieved from analysis of corrosion data, be it from laboratory experiments, or plant inspection programs. However, the full range of available methods is not widely used in either field. For corrosion engineering in particular, modern computer technology and readily available statistical software packages present a considerable opportunity for wider use of advanced analysis methods that will make better use of limited inspection data and provide quantitative measures of uncertainty, thereby enabling improved decision making. Key applications include estimating the maximum extent of damage from sample inspections and estimating corrosion rates from wall thickness measurements at different times. While values extrapolated far beyond the sampling region have to be interpreted with care, extreme value analysis provides an established method for carrying out such predictions. Also, when combined with risk-based inspection and reliability engineering methodologies, statistical techniques can be used to guide decisions on the required extent of inspection, especially in relation to piping systems wherein only relatively small sample inspections are practically feasible.

## References

1. Evans, U. R.; Mears, R. B.; Queneau, P. E. *Engineering* **1933**, 136, 689–701.
2. Aziz, P. M. *Corrosion* **1956**, 12, 495t–506t.
3. Eldredge, G. G. *Corrosion* **1957**, 13, 51t–60t.
4. Sato, N. J. *Electrochem. Soc.* **1976**, 123, 1197–1199.
5. Shibata, T.; Takeyama, T. *Corrosion* **1997**, 33, 243–251.
6. Kowaka, M. Ed. *Introduction to Life Prediction of Industrial Materials: Application of the Extreme Value Statistical Method for Corrosion Analysis*; Allerton Press: New York, 1994. [First published in Japanese in 1984].
7. Gabrielli, C.; Huet, F.; Keddam, M.; Oltra, R. In *NACE-9: Advances in Localised Corrosion*; Isaacs, H., Bertocci, U., Kruger, J., Smialowska, S., Eds.; NACE: Houston, TX, 1990; pp 93–108.
8. Bertocci, U. In *NACE-9: Advances in Localised Corrosion*; Isaacs, H., Bertocci, U., Kruger, J., Smialowska, S., Eds.; NACE: Houston, TX, 1990; pp 127–130.
9. Laycock, P. J.; Scarf, P. A. *Corros. Sci.* **1993**, 35, 135–145.
10. ASTM G 46-94: Standard Guide for Examination and Evaluation of Pitting Corrosion; American Society for Testing and Materials: West Conshohocken PA, 1994.
11. ASTM G 16-95: Standard Guide for Applying Statistics to Analysis of Corrosion Data; American Society for Testing and Materials: West Conshohocken PA, 1995.
12. Guidelines for Use of Statistics for Analysis of Sample Inspection of Corrosion, Health and Safety Executive, UK, 2001.
13. Williams, D. E.; Westcott, C.; Fleischmann, M. *J. Electrochem. Soc.* **1985**, 132, 1796–1811.
14. Baroux, B. *Corros. Sci.* **1988**, 28, 969–986.
15. Laycock, N. J.; Noh, J. S.; White, S. P.; Krouse, D. P. *Corros. Sci.* **2005**, 47, 3140–3177.
16. Wu, B.; Scully, J. R.; Hudson, J. L.; Mikhailov, A. S. *J. Electrochem. Soc.* **1997**, 144, 1614–1629.
17. White, S. P.; Krouse, D. P.; Laycock, N. J. *ECS Trans.* **2005**, 1(16), 37–45.
18. Grimmer, G. *Percolation*, 2nd ed.; Springer-Verlag: Berlin, 1999.
19. Sieradzki, K.; Newman, R. C. *J. Electrochem. Soc.* **1986**, 133, 1979–1980.
20. Qian, S.; Newman, R. C.; Cottis, R. A.; Sieradzki, K. *J. Electrochem. Soc.* **1990**, 137, 435–439.
21. Wells, D. B.; Stewart, J.; Herbert, A. W.; Scott, P. M.; Williams, D. E. *Corrosion* **1989**, 45, 649–660.
22. Williams, D. E.; Newman, R. C.; Song, Q.; Kelly, R. G. *Nature* **1991**, 350, 216–219.
23. Sieradzki, K.; Kim, J. S.; Cole, A. T.; Newman, R. C. *J. Electrochem. Soc.* **1987**, 134, 1635–1639.
24. Sieradzki, K.; Corderman, R. R.; Shukla, K.; Newman, R. C. *Philos. Mag. A* **1989**, 59, 713–746.
25. Fishman, G. S. *Monte Carlo: Concepts, Algorithms, and Applications*; Springer Verlag: New York, 1995.
26. <http://onlinestatbook.com>
27. [www.statsoft.com](http://www.statsoft.com)
28. Barnett, V.; Lewis, T. *Outliers in Statistical Data*, 3rd ed.; Wiley Series in Probability & Statistics: New York, 1994.
29. Freund, R. J.; Wilson, W. J. *Regression Analysis*; Academic Press: New York, 1998.
30. Neter, J.; Kutner, M. H.; Wasserman, W.; Nachtsheim, C. J. In *Applied Linear Statistical Models*; 4th ed.; Richard, D., Ed.; Irwin: Illinois, 1996.
31. Laycock, N. J.; Stewart, J.; Newman, R. C. *Corros. Sci.* **1997**, 39, 1791–1809.
32. Laycock, P. J.; Cottis, R. A.; Scarf, P. A. *J. Electrochem. Soc.* **1990**, 137, 64–69.
33. Coles, S. *An Introduction to Statistical Modelling of Extreme Values*; Springer-Verlag: London, 2001.
34. Gnedenko, B. V. *Ann. Math.* **1943**, 44, 423–453.
35. Cottis, R. A.; Laycock, P. J.; Holt, D.; Moir, S. A.; Scarf, P. A. In *NACE-9: Advances in Localised Corrosion*; Isaacs, H., Bertocci, U., Kruger, J., Smialowska, S., Eds.; NACE: Houston, TX, 1990; pp 117–122.
36. Smith, R. L.; Davison, A. C. *J. Roy. Stat. Soc. B.* **1990**, 52, 393–442.
37. Eden, D. A. *Electrochemical Noise – the First Two Octaves*; CORROSION/98, NACE International: Houston, TX, 1998; Paper no. 386.
38. Cottis, R. A.; Turgoose, S. *Mater. Sci. Forum* **1995**, 192–194, 663–672.
39. Barnett, V. *Sample Survey: Methods and Principles (Mathematics)*, 3rd ed; Hodder Arnold: London, 2002.

40. Thompson, M. *Theory of Sample Surveys (Monographs on Statistics and Applied Probability)*; Chapman & Hall: London, 1997.
41. Cobb, G. W. *Introduction to Design and Analysis of Experiments*; Springer-Verlag: New York, 1998.
42. Cox, D. R.; Reid, N. *The Theory of the Design of Experiments*; CRC Press: London, 2000.
43. Bolstad, W. M. *Introduction to Bayesian Statistics*, 2nd ed.; Wiley: New York, 2007.
44. Gelman, A.; Carlin, J. B.; Stern, H. S.; Rubin, D. B. *Bayesian Data Analysis*; 2nd ed.; Chapman & Hall/CRC: London, 2003.
45. Bayes, T. *Philos. Trans. R. Soc.* **1763**, 330–418. Reprinted in *Biometrika* **1958**, 45, 293–315.
46. Laplace, P. S. *Memoires de Mathematique et de Physique* **1774**. Tome Sixieme. English translation by Stigler, S.M. *Statist. Sci.* **1986**, 1(19), 364–378.
47. Melchers, R. E. *Corros. Sci.* **2007**, 49, 3149–3167.
48. Pierpoline, R.; White, R. J.; Wong, C.; Cornwell, L.; Griffin, R. In *NACE-9: Advances in Localised Corrosion*; Isaacs, H., Bertocci, U., Kruger, J., Smialowska, S., Eds.; NACE: Houston, TX, 1990; pp 123–126.
49. Scarf, P. A.; Laycock, P. J.; Cottis, R. A. *J. Electrochem. Soc.* **1992**, 9, 2621–2627.
50. Maddox, S. J. *Int. J. Fract.* **1975**, 11, 389–408.
51. Hoepfner, D. W.; Krupp, W. E. *Eng. Fract. Mech.* **1974**, 6, 47–70.
52. Dolinski, K. *Eng. Fract. Mech.* **1992**, 43, 195–216.
53. To, S.; Lambert, S. B.; Burns, D. J. *Int. J. Fatigue* **1993**, 15, 333–340.
54. Karlin, H. M.; Taylor, S. *An Introduction to Stochastic Modeling*, revised ed.; Academic Press: San Diego, 1994.
55. Crowder, M. J.; Kimber, A. C.; Smith, R. L.; Sweeting, T. J. *Statistical Analysis of Reliability Data*; Chapman & Hall: London, 1991.
56. Reiss, R. D.; Thomas, M. *Statistical Analysis of Extreme Values with applications to Insurance, Finance, Hydrology and Other Fields*; 2nd ed.; Birkhauser: Berlin, 2001.
57. Efron, B.; Tibshirani, R. J. *An Introduction to the Bootstrap*; Chapman & Hall: London, 1993.
58. Krouse, D.; Laycock, N. J. Proceedings of Corrosion & Protection, Auckland, New Zealand, November 2000; ACA: Melbourne, 2000; Paper # 70.
59. API Publication 510, Pressure Vessel Inspection Code: In-Service Inspection, Rating, Repair, and Alteration, 9th ed.; API: Washington DC, 2006.
60. API Publication 570, Piping Inspection Code: Inspection, Repair, Alteration, and Rating of In-Service Piping Systems, 2nd ed.; API: Washington DC, 1998.
61. Hoeve, F.; Terpstra, S.; van de Camp, P.; Paleja, R. Proceedings of World Congress on Asset Management, Gold Coast, Australia, 11–14 July, 2006.
62. Wilson, P. T.; Krouse, D. P.; Moss, C. J. Proceedings of Corrosion Control and NDT; ACA, Melbourne, Australia, 23–26 November, 2003; ACA: Melbourne, 2003; Paper # 45.
63. Bhakta, P.; Solomon, A. In *NACE-9: Advances in Localised Corrosion*; Isaacs, H., Bertocci, U., Kruger, J., Smialowska, S., Eds.; NACE: Houston, TX, 1990; pp 445–452.
64. Nakahara, M. Proceedings of the International Symposium on Plant Aging and Life Prediction of Corrodible Structures; NACE: Houston TX, 1997; pp 169–174.
65. Laycock, N. J.; Hodges, S.; Krouse, D.; Keen, D.; Laycock, P. J. Proceedings of Corrosion Science in the 21st Century; UMIST, Manchester, UK, 6–11 July, 2003; *J. Corros. Sci. Eng.* 2003; CO54; [www.jcse.org](http://www.jcse.org).
66. Aziz, P. M.; Godard, H. P. *Ind. Eng. Chem.* **1952**, 1791–1795.
67. de la Fuente, D.; Otero-Huerta, E.; Morcillo, M. *Corros. Sci.* **2007**, 49, 3134–3148.
68. Christer, A. H.; Waller, W. M. *J. Opl. Res. Soc.* **1984**, 35, 401–406.
69. Thoft-Christensen, P.; Sorensen, J. D. *Civil Eng. Sys.* **1987**, 4, 94–100.
70. Fujimoto, Y.; Swilem, S. A. M. *OMAE Vol II, Safety and Reliability*; Guedes Soares, C., Ed.; ASME: New York, 1992; pp 219–226.
71. Tijms, H. C. *Stochastic Models: An Algorithmic Approach*; Wiley: New York, 1994.
72. Barlow, R.; Proschan, F. *Mathematical Theory of Reliability*; SIAM: Philadelphia, 1996.
73. Lewis, E. E. *Introduction to Reliability Engineering*; Wiley: New York, 1987.
74. Xie, M.; Kong, H.; Goh, T. N. *J. Qual. Maintenance Eng.* **2000**, 6, 260–268.
75. Scarf, P. A.; Wang, W.; Laycock, P. J. *Reliab. Eng. Syst. Saf.* **1996**, 51, 331–339.
76. Hladky, K.; Dawson, J. *Corros. Sci.* **1981**, 21, 317–322.
77. Hladky, K.; Dawson, J. *Corros. Sci.* **1982**, 22, 231–237.
78. Cottis, R. A. *Corrosion* **2001**, 27(3), 265–285.

## 2.37 Introduction to the Modeling of Corrosion

**R. A. Cottis**

School of Materials, University of Manchester, Manchester M60 1QD, UK

© 2010 Elsevier B.V. All rights reserved.

2.37.1	Introduction	1581
2.37.2	Applications of Modeling	1581
2.37.3	Modeling Methods	1582
2.37.4	Approaches to Modeling Spatial and Time Distribution	1582
2.37.4.1	Finite Difference Methods	1583
2.37.4.2	Finite Element Method	1583
2.37.4.3	Boundary Element Method	1584
References		1584

### Symbols

$V[x,y]$  Voltage at position  $x,y$  on a regular 2-D grid

### 2.37.1 Introduction

For the purposes of this chapter, modeling is defined as the construction of a mathematical-based description of the corrosion process that permits the calculation of expected corrosion behavior for arbitrary conditions within a specified range. While physical models (i.e., practical systems that are expected to have the same behavior as a real corrosion system) have been used (e.g., to study current distribution in cathodic protection), these have received relatively little attention recently. In contrast, the rapidly increasing power of computer hardware and software has led to a huge growth in the use of mathematical models, usually using numerical methods to solve the complex systems of equations that govern most corrosion processes.

### 2.37.2 Applications of Modeling

There are two distinct reasons for the development of models of corrosion processes:

1. *Prediction of behavior:* Many would expect that the construction of predictive models (i.e., models that can predict corrosion behavior over a range of conditions) would be the most important aspect of corrosion modeling, and this is certainly a common view. For some well-defined problems,

such as the distribution of cathodic protection current in a uniform conductive environment such as seawater, predictive models based on ‘first-principles’ methods can be very accurate and form an important tool in the corrosion engineer’s armoury. However, many corrosion processes are very complex and the construction of first-principles predictive models is currently difficult (but see **Chapter 2.38, Modeling of Aqueous Corrosion** and **Chapter 2.39, Predictive Modeling of Corrosion**), and practical predictive models often use relatively simple functions (possibly, but not necessarily, based on theoretically expected dependencies) that are calibrated using measured data. Thus, such models are often concerned more with fitting functions to data than with real understanding of the corrosion process. One such method, the use of neural networks, is discussed in **Chapter 2.40, Neural Network Methods for Corrosion Data Reduction**, while other data-based models may be discussed in the context of the specific corrosion process.

2. *Testing and developing understanding:* While it may not be appreciated by those who have not attempted to develop models, one of the most powerful applications of modeling is to test understanding of mechanisms. One of the fundamental reasons for this is that the construction of a theoretically-based model requires every aspect of a mechanism to be exactly defined and quantified, which is often not done (and may be essentially impossible without constructing a model, due to the complexity of corrosion processes) in the absence of the rigorous analysis required by the modeling process. Then the comparison of the output of the model with



observations provides a challenging test of the precision of understating of the mechanism. Furthermore, the process of creating a model almost inevitably enhances the understanding of the process by those involved in the creation – a challenge for modelers is often to convey their enhanced understanding to others.

### 2.37.3 Modeling Methods

This section covers a number of modeling methods:

1. Modeling of electrochemical reactions  
Electrochemical kinetic theory is well-developed, and accurate models of the behavior of pure metals in reasonably simple environments can be developed. This is covered in **Chapter 2.38, Modeling of Aqueous Corrosion** and **Chapter 2.39, Predictive Modeling of Corrosion**, which demonstrates the detail required for the construction of accurate first-principles models.
2. Modeling of spatial distribution  
For a number of corrosion processes, such as galvanic corrosion, pitting corrosion, crevice corrosion, and cathodic protection, the challenge is to evaluate the distribution of reaction over the surface of a component. In the simplest cases, such as cathodic protection, it is sufficiently accurate to treat the problem as that of potential and current distribution in a uniform resistive medium. In more challenging cases, such as pitting and crevice corrosion, it is necessary to account for changes in the chemistry of the solution and the consequent changes in reaction kinetics. In this case, the techniques in the previous section become important, although most work in this area tends to use rather simplified models of interfacial chemistry. Such models have been developed for many years, but the advent of general-purpose finite element programs has made these methods much more accessible. **Chapter 2.39, Predictive Modeling of Corrosion** provides examples of the state-of-the art in such modeling, but does not go into the details of the principles underlying the spatial aspects of the models, which are described in outline in the following section.
3. Data-based modeling  
Owing to the complexity of the interactions between metallurgical structure, environment and mechanical stress, many corrosion processes are not yet amenable to theoretically-based modeling, and predictive models must therefore be based on measured data. Such models are then highly

dependent on both the quality and the quantity of the measured data on which they are based. We can define the ‘problem domain’ for a particular set of measured data as being a region in a multidimensional space where each dimension represents one of the variables that have a significant effect on the behavior. For accurate models, it is important that the measured data provide an adequate coverage of the problem domain and that the measured data have well-defined values for all of the dimensions of the multidimensional space. Unfortunately, this is rarely achieved, especially where real service data are concerned. The modeling of the data then becomes a problem of fitting the ‘best’ function to the measured values. For small data sets, it is usually necessary to make some simplifying assumptions about the behavior, such as assuming linear dependencies and neglecting interactions between variables. If sufficient information is available, more complex functions can be fitted, such as higher-order polynomials. Neural network methods (introduced in **Chapter 2.40, Neural Network Methods for Corrosion Data Reduction**) provide a particularly interesting approach, whereby the functional relationship is effectively determined by the fitting process, rather than being defined in advance.

### 2.37.4 Approaches to Modeling Spatial and Time Distribution

When we are concerned with the spatial distribution of corrosion (e.g., when attempting to model crevice corrosion or pitting corrosion), either for the final steady state or for incorporating the evolution over time, the problem can almost invariably be expressed as requiring the solution of a set of partial differential equations over the space and time concerned (the ‘problem domain’) with specified boundary conditions. Occasionally, it is possible to obtain an analytical solution, but usually only in highly simplified cases. Consequently, it is normally necessary to use a numerical method to obtain a solution. As a generalization, many of the numerical methods aim at converting the differential equations into a finite (but usually large) set of simultaneous difference equations. These can then be solved by conventional methods for the solution of simultaneous equations (essentially these write the simultaneous equations as a matrix equation that can be solved by matrix inversion). There are three approaches to this.

### 2.37.4.1 Finite Difference Methods

In the finite difference method, the problem domain is covered by a regular grid of points, the objective then being to determine the values corresponding to the solution to the system of differential equations at the grid points. These will be points with a constant spacing along a line for a 1-dimensional problem, crossing points of a square grid for a 2-dimensional problem and points on a cubic grid for a 3-dimensional problem. (Some finite difference methods use grid spacings that vary according to a regular pattern, and these may offer advantages for electrochemical problems.<sup>1</sup>) Then the solution can be approximated by replacing the differential equations by the corresponding difference equations. For the detailed mathematics of the process (and an indication of the large variety of methods that have been developed to obtain a solution), the readers are referred to Britz,<sup>1</sup> but we can illustrate the method by a simplified explanation.

We shall consider one of the simplest classes of problems, that of determining the steady-state potential distribution in a uniform 2-dimensional conductor (e.g., a conductive sheet). If we consider a grid point somewhere in a 2-dimensional array (Figure 1), it is easy to see that the best estimate of the true value of the potential at a point is the average of the corresponding potentials in the four nearest neighbors. Thus, if  $V[x,y]$  is the potential at point  $x, y$ , we can write

$$V[x,y] = (V[x-1,y] + V[x+1,y] + V[x,y-1] + V[x,y+1])/4$$

Edge and corner points and internal boundaries will obviously have to be handled specially (and this is where the boundary conditions will be introduced). Writing the appropriate equations for all grid points leads to a set of simultaneous equations, which can be solved by matrix inversion or by a range of alternative

techniques (iterative solution methods are usually used, because the arrangement of grid points in the problem domain is normally very regular; these effectively implement the matrix inversion in a very efficient manner by taking advantage of the regularity). The method has the advantage of conceptual simplicity and relatively easy implementation without specialist software. However, it does not handle complex geometries very well and it is inefficient for problems where small regions need to be analyzed in detail in a large problem domain (since this requires a very large number of very closely spaced points).

### 2.37.4.2 Finite Element Method

The limitations of the finite difference method are, to an extent, a result of the requirement to use an array of elements of constant size and shape. The finite element method provides the ability to use elements of arbitrary (and variable) size and shape, although at the expense of more complex mathematics; we shall not attempt to explain the mathematical basis here (see the Comsol web site<sup>2</sup> for extensive documentation on the method and its application to electrochemical problems). Fortunately several programs, both commercial and open-source, are available to handle finite element problems. Most of these are targeted to well-defined problems such as stress analysis and the analysis of heat flow in uniform media. Heat flow is slightly more complex than current flow, due to the heat capacity of the material, but the steady-state temperature distribution will be identical to the steady-state voltage distribution. Because of the greater generality and greater practical significance, program literature will usually refer to the analysis of thermal rather than electrical problems.

Some programs<sup>3</sup> are able to handle problems involving multiple physical processes (such as diffusion, migration, and reaction) and provide a simple

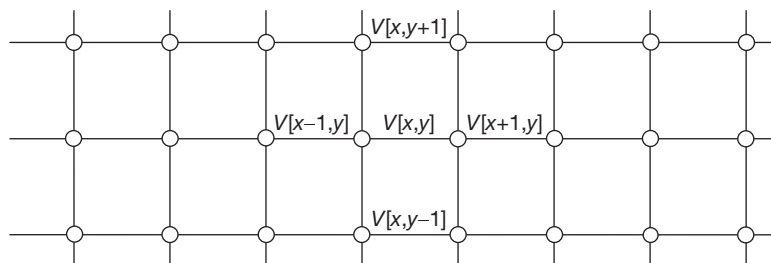


**Figure 1** 2-Dimensional grid for finite difference analysis of potential distribution.

way to analyze problems associated with the distribution of corrosion processes.

#### **2.37.4.3 Boundary Element Method**

Both the finite difference and finite element methods need to fill the problem domain with elements, and consequently, it is often necessary to use very large numbers of elements, with the result that very large matrices need to be inverted (the matrix size required is approximately proportional to the square of the number of elements). The boundary element method is based on analyzing only elements on the boundaries of the problem domain. This leads to a major reduction in the number of elements required, and hence the size of matrix that needs to be inverted. However, the computational benefits are not quite as significant as this would suggest, as the matrix that needs to be inverted is usually much more completely filled than for the other methods, and the inversion is consequently much slower for given matrix dimensions. Furthermore, the boundary element method can only be used for a subset of possible characteristics within the

problem domain; fortunately the electrical behavior of a uniform conductive material can be handled. Hence this method is popular for the solution to current distribution problems in cathodic protection. A subsidiary benefit of the method is that it can handle problem domains with no exterior boundary (i.e., the conductive medium can extend to infinity), which is particularly useful for cathodic protection problems. It is beyond the scope of this article to describe the mathematical basis of the boundary element method and the readers are referred to appropriate texts.<sup>4</sup> As with the finite element method, commercial software is available to implement the boundary element method.

### **References**

1. Britz, D. *Digital Simulation in Electrochemistry*, 3rd ed.; Springer: Berlin, 2005.
2. Pepper, D. W.; Heinrich, J. C. *The Finite Element Method: Basic Concepts and Applications*; Hemisphere Publishing: New York, 1992.
3. <http://www.comsol.com/> (viewed 5 March 2009).
4. Beer, G. *Programming the Boundary Element Method: An Introduction for Engineers*; Wiley Blackwell, 2002.

## 2.38 Modeling of Aqueous Corrosion

**A. Anderko**

OLI Systems Inc., 108 American Road, Morris Plains, NJ 07950, USA

© 2010 Elsevier B.V. All rights reserved.

<b>2.38.1</b>	<b>Introduction</b>	1586
<b>2.38.2</b>	<b>Thermodynamic Modeling of Aqueous Corrosion</b>	1587
2.38.2.1	Computation of Standard-State Chemical Potentials	1588
2.38.2.2	Computation of Activity Coefficients	1588
2.38.2.3	Electrochemical Stability Diagrams	1591
2.38.2.3.1	Diagrams at elevated temperatures	1594
2.38.2.3.2	Effect of multiple active species	1594
2.38.2.3.3	Diagrams for nonideal solutions	1595
2.38.2.3.4	Diagrams for alloys	1596
2.38.2.3.5	Potential–concentration diagrams	1597
2.38.2.4	Chemical Equilibrium Computations	1597
2.38.2.5	Problems of Metastability	1599
<b>2.38.3</b>	<b>Modeling the Kinetics of Aqueous Corrosion</b>	1600
2.38.3.1	Kinetics of Charge-Transfer Reactions	1601
2.38.3.2	Modeling Adsorption Phenomena	1604
2.38.3.3	Partial Electrochemical Reactions	1605
2.38.3.3.1	Anodic reactions	1605
2.38.3.3.2	Cathodic reactions	1607
2.38.3.3.3	Temperature dependence	1609
2.38.3.4	Modeling Mass Transport Using Mass Transfer Coefficients	1609
2.38.3.4.1	Example of electrochemical modeling of general corrosion	1611
2.38.3.5	Detailed Modeling of Mass Transport	1611
2.38.3.5.1	Effect of the presence of porous media	1614
2.38.3.6	Active–Passive Transition and Dissolution in the Passive State	1614
2.38.3.7	Scaling Effects	1618
2.38.3.8	Modeling Threshold Conditions for Localized Corrosion	1620
2.38.3.8.1	Breakdown of passivity	1621
2.38.3.8.2	Repassivation potential and its use to predict localized corrosion	1622
2.38.3.9	Selected Practical Applications of Aqueous Corrosion Modeling	1624
<b>2.38.4</b>	<b>Concluding Remarks</b>	1626
<b>References</b>		1626

### Abbreviations

**CCT** Critical crevice temperature

**CR** Corrosion rate

**HKF** Helgeson–Kirkham–Flowers equation of state

**Me** Metal

**MSA** Mean spherical approximation

**NRTL** Nonrandom two-liquid (equation)

**Ox** Oxidized form

**Re** Reduced form

**SHE** Standard hydrogen electrode

**UNIFAC** Universal functional activity coefficient  
(equation)

**UNIQUAC** Universal quasi-chemical (equation)

### Symbols

$a_i$  Activity of species  $i$

$A$  Surface area

$A_{ij}$  Surface interaction coefficient for species  $i$  and  $j$

$b$  Tafel coefficient using decimal logarithms

$c_{i,b}$  Bulk molar concentration of species  $i$   
 $c_{i,s}$  Surface molar concentration of species  $i$   
 $C_p$  Heat capacity at constant pressure  
 $d$  Characteristic dimension  
 $D_i$  Diffusion coefficient of species  $i$   
 $D_t$  Turbulent diffusion coefficient  
 $e^-$  Electron  
 $E$  Potential  
 $E_b$  Passivity breakdown potential  
 $E_{\text{corr}}$  Corrosion potential  
 $E_{\text{crit}}$  Critical potential for localized corrosion  
 $E_{\text{rp}}$  Repassivation potential  
 $E_0$  Equilibrium potential  
 $f$  Friction factor  
 $f_i$  Fugacity of species  $i$   
 $F$  Faraday constant  
 $G^{\text{ex}}$  Excess Gibbs energy  
 $i$  Current density  
 $i_a$  Anodic current density  
 $i_{a,\text{ct}}$  Charge-transfer contribution to the anodic current density  
 $i_{a,L}$  Limiting anodic current density  
 $i_c$  Cathodic current density  
 $i_{c,\text{ct}}$  Charge-transfer contribution to the cathodic current density  
 $i_{c,L}$  Limiting cathodic current density  
 $i_{\text{corr}}$  Corrosion current density  
 $i_p$  Passive current density  
 $i_{\text{rp}}$  Current density limit for measuring repassivation potential  
 $i_0$  Exchange current density  
 $i^*$  Concentration-independent coefficient in expressions for exchange current density  
 $J_i$  Flux of species  $i$   
 $k_{\text{ads}}$  Adsorption rate constant  
 $k_{\text{des}}$  Desorption rate constant  
 $k_i$  Reaction rate constant for reaction  $i$   
 $k_{m,i}$  Mass transfer coefficient for species  $i$   
 $K$  Equilibrium constant  
 $K_{\text{ads}}$  Adsorption equilibrium constant  
 $K_{\text{sp}}$  Solubility product  
 $l_i$  Reaction rate for  $i$ th reaction  
 $m_i$  Molality of species  $i$   
 $m_0$  Standard molality of species  $i$   
 $n_i$  Number of moles of species or electrons  
 $Nu$  Nusselt number  
 $Pr$  Prandtl number  
 $R$  Gas constant  
 $R_k$  Rate of production or depletion of species  $k$   
 $Re$  Reynolds number  
 $S$  Supersaturation  
 $Sc$  Schmidt number

$Sh$  Sherwood number  
 $t$  Time  
 $T$  Temperature  
 $u_i$  Mobility of species  $i$   
 $v_i$  Rate of reaction  $i$   
 $V$  Linear velocity  
 $z$  Direction perpendicular to the surface  
 $z_i$  Charge of species  $i$   
 $\alpha$  Thermal diffusivity  
 $\alpha_i$  Electrochemical transfer coefficient for species  $i$   
 $\beta$  Tafel coefficient using natural logarithms  
 $\gamma_i$  Activity coefficient of species  $i$   
 $\delta_i$  Nernst layer thickness for species  $i$   
 $\Delta G_{\text{ads},i}$  Gibbs energy of adsorption for species  $i$   
 $\Delta H^\ddagger$  Enthalpy of activation  
 $\Delta\Phi$  Potential drop  
 $\epsilon$  Dielectric permittivity  
 $\eta$  Dynamic viscosity  
 $\theta_i$  Coverage fraction of species  $i$   
 $\theta_p$  Coverage fraction of passive layer  
 $\lambda$  Thermal conductivity  
 $\mu_i$  Chemical potential of species  $i$   
 $\mu_i^0$  Standard chemical potential  
 $\bar{\mu}_i$  Electrochemical potential of species  $i$   
 $\nu$  Kinematic viscosity  
 $\nu_i$  Stoichiometric coefficient of species  $i$   
 $\rho$  Density  
 $\Phi$  Electrical potential  
 $\xi_i$  Electrochemical transfer coefficient for reaction  $i$   
 $\omega$  Rotation rate  
 $\nabla$  Vector differential operator  
 $\equiv X$  Surface species  $X$

### 2.38.1 Introduction

Aqueous corrosion is an extremely complex physical phenomenon that depends on a multitude of factors including the metallurgy of the corroding metal, the chemistry of the corrosion-inducing aqueous phase, the presence of other – solid, gaseous, or nonaqueous liquid – phases, environmental constraints such as temperature and pressure, fluid flow characteristics, methods of fabrication, geometrical factors, and construction features. This inherent complexity makes the development of realistic physical models very challenging and, at the same time, provides a strong incentive for the development of practical models to understand the corrosion phenomena, and to assist in their mitigation. The need for tools for simulating aqueous corrosion has been recognized in various industries including oil and gas production and



transmission, oil refining, nuclear and fossil power generation, chemical processing, infrastructure maintenance, hazardous waste management, and so on. The past three decades have witnessed the development of increasingly sophisticated modeling tools, which has been made possible by the synergistic combination of improved understanding of corrosion mechanisms and rapid evolution of computational tools.

Corrosion modeling is an interdisciplinary undertaking that requires input from electrolyte thermodynamics, surface electrochemistry, fluid flow and mass transport modeling, and metallurgy. In this chapter, we put particular emphasis on corrosion chemistry by focusing on modeling both the bulk environment and the reactions at the corroding interface. The models that are reviewed in this chapter are intended to answer the following questions:

1. What are the aqueous and solid species that give rise to corrosion in a particular system? What are their thermophysical properties, and what phase behavior can be expected in the system? These questions can be answered by thermodynamic models.
2. What are the reactions that are responsible for corrosion at the interface? How are they influenced by the bulk solution chemistry and by flow conditions? How can passivity and formation of solid corrosion products be related to environmental conditions? How can the interfacial phenomena be related to observable corrosion rates? These questions belong to the realm of electrochemical kinetics and mass transport models.
3. What conditions need to be satisfied for the initiation and long-term occurrence of localized corrosion? This question can be answered by electrochemical models of localized corrosion.

These models can be further used as a foundation for larger-scale models for the spatial and temporal evolution of systems and engineering structures subject to localized and general corrosion. Also, they can be combined with probabilistic and expert system-type models of corrosion. Models of such kinds are, however, outside the scope of this review, and will be discussed in companion chapters.

### 2.38.2 Thermodynamic Modeling of Aqueous Corrosion

Historically, the first comprehensive approach to modeling aqueous corrosion was introduced by Pourbaix in the 1950s and 1960s on the basis of purely thermodynamic considerations.<sup>1</sup> Pourbaix<sup>1</sup> developed the  $E$ -pH stability diagrams, which indicate

which phases are stable on a two-dimensional plane as a function of the potential and pH. The potential and pH were originally selected because they play a key role as independent variables in electrochemical corrosion. Just as importantly, they made it possible to construct the stability diagrams in a semianalytical way, which was crucial before the advent of computer calculations. Over the past four decades, great progress has been achieved in the thermodynamics of electrolyte systems, in particular for concentrated, mixed-solvent, and high temperature systems. These advances made it possible to improve the accuracy of the stability diagrams and, at the same time, increased the flexibility of thermodynamic analysis so that it can go well beyond the  $E$ -pH plane.

The basic objective of the thermodynamics of corrosion is to predict the conditions at which a given metal may react with a given environment, leading to the formation of dissolved ions or solid reaction products. Thermodynamics can predict the properties of the system in equilibrium or, if equilibrium is not achieved, it can predict the direction in which the system will move towards an equilibrium state. Thermodynamics does not provide any information on how rapidly the system will approach equilibrium, and, therefore, it cannot give the rate of corrosion.

The general condition of thermodynamic equilibrium is the equality of the electrochemical potential,  $\bar{\mu}_i$  in coexisting phases,<sup>2</sup> that is,

$$\bar{\mu}_i = \mu_i + z_i F \phi = \mu_i^0 + RT \ln a_i + z_i F \phi \quad [1]$$

where  $\mu_i$  is the chemical potential of species  $i$ ;  $\mu_i^0$ , its standard chemical potential;  $a_i$ , the activity of the species;  $z_i$ , its charge;  $F$ , the Faraday constant; and  $\phi$  is the electrical potential. The standard chemical potential is a function of the temperature and, secondarily, pressure. The activity depends on the temperature and solution composition and, to a lesser extent, on pressure. The activity is typically defined in terms of solution molality  $m_i$ ,

$$a_i = (m_i/m^0) \gamma_i \quad [2]$$

where  $m^0$  is the standard molality unit ( $1 \text{ mol kg}^{-1} \text{ H}_2\text{O}$ ), and  $\gamma_i$  is the activity coefficient. It should be noted that the molality basis for species activity becomes inconvenient for concentrated solutions because molality diverges to infinity as the concentration increases to the pure solute limit. Therefore, the mole fraction basis is more generally applicable for calculating activities.<sup>3</sup> Nevertheless, molality remains the most common concentration unit for aqueous systems and is used here for illustrative purposes.

Computation of  $\mu_i^0$  and  $\gamma_i$  is the central subject in electrolyte thermodynamics. Numerous methods, with various ranges of applicability, have been developed over the past several decades for their computation. Several comprehensive reviews of the available models are available (Zemaitis *et al.*,<sup>4</sup> Renon,<sup>5</sup> Pitzer,<sup>6</sup> Rafal *et al.*,<sup>7</sup> Loehe and Donohue,<sup>8</sup> Anderko *et al.*<sup>3</sup>). In the next section, the current status of modeling  $\mu_i^0$  and  $\gamma_i$  is outlined as it applies to the thermodynamics of corrosion.

### 2.38.2.1 Computation of Standard-State Chemical Potentials

The computation of the standard chemical potential  $\mu_i^0$  requires the knowledge of thermochemical data including

1. Gibbs energy of formation of species  $i$  at reference conditions (298.15 K and 1 bar).
2. Entropy or, alternatively, enthalpy of formation at reference conditions.
3. Heat capacity and volume as a function of temperature and pressure.

For numerous species, these values are available in various compilations (Chase *et al.*,<sup>9</sup> Barin and Platzki,<sup>10</sup> Cox *et al.*,<sup>11</sup> Glushko *et al.*,<sup>12</sup> Gurvich *et al.*,<sup>13</sup> Kelly,<sup>14</sup> Robie *et al.*,<sup>15</sup> Shock and Helgeson,<sup>16</sup> Shock *et al.*,<sup>17,18</sup> Stull *et al.*,<sup>19</sup> Wagman *et al.*,<sup>20</sup> and others). In general, thermochemical data are most abundant at near-ambient conditions, and their availability becomes more limited at elevated temperatures.

In the case of individual solid species, the chemical potential can be computed directly from tabulated thermochemical properties according to the standard thermodynamics.<sup>2</sup> In the case of ions and aqueous neutral species, the thermochemical properties listed above are standard partial molar properties rather than the properties of pure components. The standard partial molar properties are defined at infinite dilution in water. The temperature and pressure dependence of the partial molar heat capacity and the volume of ions and neutral aqueous species are quite complex because they are manifestations of the solvation of species, which is influenced by electrostatic and structural factors. Therefore, the computation of these quantities requires a realistic physical model.

An early approach to calculating the chemical potential of aqueous species as a function of temperature is the entropy correspondence principle of Criss and Cobble.<sup>21</sup> In this approach, heat capacities of various types of ions were correlated with the reference-state entropies of ions, thus making it

possible to predict the temperature dependence of the standard chemical potential.

A comprehensive methodology for calculating the standard chemical potential was developed by Helgeson *et al.* (Helgeson *et al.*,<sup>22</sup> Tanger and Helgeson<sup>23</sup>). This methodology is based on a semi-empirical treatment of ion solvation, and results in an equation of state for the temperature and pressure dependence of the standard molal heat capacities and volumes. Subsequently, the heat capacities and volumes are used to arrive at a comprehensive equation of state for standard molal Gibbs energy and, hence, the standard chemical potential. The method is referred to as the HKF (Helgeson–Kirkham–Flowers) equation of state. An important advantage of the HKF equation is the availability of its parameters for a large number of ionic and neutral species (Shock and Helgeson,<sup>16</sup> Shock *et al.*,<sup>18</sup> Sverjensky *et al.*<sup>24</sup>). Also, correlations exist for the estimation of the parameters for species for which little experimental information is available. The HKF equation of state has been implemented both in publicly available codes (Johnson *et al.*<sup>25</sup>) and in commercial programs. A different equation of state for standard-state properties has been developed on the basis of fluctuation solution theory (Sedlbauer *et al.*,<sup>26</sup> Sedlbauer and Majer<sup>27</sup>). This equation offers improvement over HKF for nonionic solutes and in the near-critical region. However, the HKF remains as the most widely accepted model for ionic solutes.

### 2.38.2.2 Computation of Activity Coefficients

In real solutions, the activity coefficients of species deviate from unity because of a variety of ionic interaction phenomena, including long-range Coulombic interactions, specific ion–ion interactions, solvation phenomena, and short-range interactions between uncharged and charged species. Therefore, a practically-oriented activity coefficient model must represent a certain compromise between physical reality and computational expediency.

The treatment of solution chemistry is a particularly important feature of an electrolyte model. Here, the term ‘solution chemistry’ encompasses ionic dissociation, ion pair formation, hydrolysis of metal ions, formation of metal–ligand complexes, acid–base reactions, and so on. The available electrolyte models can be grouped in three classes:

1. models that treat electrolytes on an undissociated basis,
2. models that assume complete dissociation of all electrolytes into constituent ions, and

3. speciation-based models, which explicitly treat the solution chemistry.

The models that treat electrolytes as undissociated components are analogous to nonelectrolyte mixture models. They are particularly suitable for supercritical and high temperature systems, in which ion pairs predominate. Although this approach may also be used for phase equilibrium computations at moderate conditions (e.g., Kolker *et al.*<sup>28</sup>), it is not suitable for corrosion modeling because it ignores the existence of ions. The models that assume complete dissociation are the largest class of models for electrolytes at typical conditions. Compared with the models that treat electrolytes as undissociated or completely dissociated, the speciation-based models are more computationally demanding because of the need to solve multiple reactions and phase equilibria. Another fundamental difficulty associated with the use of speciation models lies in the need to define and characterize the species that are likely to exist in the system. In many cases, individual species can be clearly defined and experimentally verified in relatively dilute solutions. At high concentrations, the chemical identity of individual species (e.g., ion pairs or complexes) becomes ambiguous because a given ion has multiple neighbors of opposite sign, and, thus, many species lose their distinct chemical character. Therefore, the application of speciation models to concentrated solutions requires a careful analysis to separate the chemical effects from physical nonideality effects.

It should be noted that, as long as only phase equilibrium computations are of interest, comparable results could be obtained with models that belong to various classes. For example, the overall activity coefficients and vapor–liquid equilibria of many transition metal halide solutions, which show appreciable complexation, can be reasonably reproduced using Pitzer's<sup>29</sup> ion-interaction approach without taking speciation into account. However, it is important to include speciation effects for modeling the thermodynamics of aqueous corrosion. This is due to the fact that the presence of individual hydrolyzed forms, aqueous complexes, and so on is often crucial for the dissolution of metals and metal oxides. It should be noted that activity coefficients of individual species are different in fully speciated models than in models that treat speciation in a simplified way. Therefore, it is important to use activity coefficients that have been determined in a fully consistent way, that is, by assuming the appropriate chemical species in the solution.

The theory of liquid-phase nonideality is well-established for dilute solutions. A limiting law for activity

coefficients was developed by Debye and Hückel<sup>30</sup> by considering the long-range electrostatic interactions of ions in a dielectric continuum. The Debye–Hückel theory predicts the activity coefficients as a function of the ionic charge and dielectric constant and density of the solvent. It reflects only electrostatic effects and, therefore, excludes all specific ionic interactions. Therefore, its range of applicability is limited to  $\sim 0.01$  M for typical systems. Several modifications of the Debye–Hückel theory have been proposed over the past several decades. The most successful modification was developed by Pitzer<sup>29</sup> who considered hard-core effects on electrostatic interactions. A more comprehensive treatment of the long-range electrostatic interactions can be obtained from the mean-spherical approximation (MSA) theory,<sup>31,32</sup> which provides a semianalytical solution for ions of different sizes in a dielectric continuum. The MSA theory results in a better prediction of the long-range contribution to activity coefficients at somewhat higher electrolyte concentrations.

The long-range electrostatic term provides a baseline for constructing models that are valid for electrolytes at concentrations that are important in practice. In most practically-oriented electrolyte models, the solution nonideality is defined by the excess Gibbs energy  $G^{\text{ex}}$ . The excess Gibbs energy is calculated as a sum of the long-range term and one or more terms that represent ion–ion, ion–molecule, and molecule–molecule interactions:

$$G^{\text{ex}} = G_{\text{long-range}}^{\text{ex}} + G_{\text{specific}}^{\text{ex}} + \cdots \quad [3]$$

where the long-range contribution is usually calculated either from the Debye–Hückel or the MSA theory, and the specific interaction term(s) represent(s) all other interactions in an electrolyte solution. Subsequently, the activity coefficients are calculated according to standard thermodynamics<sup>2</sup> as

$$\ln \gamma_i = \frac{1}{RT} \left( \frac{\partial G^{\text{ex}}}{\partial n_i} \right)_{T,P,n_{j \neq i}} \quad [4]$$

**Table 1** lists a number of activity coefficient models that have been proposed in the literature, and shows the nature of the specific interaction terms that have been adopted. In general, these models can be subdivided into two classes:

1. models for aqueous systems; in special cases, such models can also be used for other solvents as long as the system contains a single solvent;
2. mixed-solvent electrolyte models, which allow multiple solvents as well as multiple solutes.

The aqueous electrolyte models incorporate various ion interaction terms, which are usually defined

**Table 1** Summary of representative models for calculating activity coefficients in electrolyte systems

Reference	Terms	Features
<i>Aqueous (or single-solvent) electrolyte models</i>		
Debye and Hückel <sup>30</sup>	Long-range	Limiting law valid for very dilute solutions
Guggenheim <sup>33,34</sup>	Long-range + ion interaction	Simple ion interaction term to extend the Debye–Hückel limiting law; applicable to fairly dilute solutions
Helgeson <sup>35</sup>	Long-range + ion interaction	Ion interaction term to extend the limiting law; applicable to fairly dilute solutions
Pitzer <sup>29</sup>	Long-range + ion interaction	Ionic strength-dependent virial coefficient-type ion interaction term; revised Debye–Hückel limiting law; applicable to moderately concentrated solutions (~6 m)
Bromley <sup>36</sup>	Long range + ion interaction	Ionic strength dependent ion interaction term; applicable to moderately concentrated solutions (~6 m)
Zemaitis <sup>37</sup>	Long-range + ion interaction	Modification of the model of Bromley <sup>36</sup> to increase applicability range with respect to ionic strength
Meissner <sup>38</sup>	One-parameter correlation as a function of ionic strength	Generalized correlation to calculate activities based on a limited amount of experimental information
Pitzer and Simonson, <sup>39</sup> Clegg and Pitzer <sup>40</sup>	Long-range + ion interaction	Mole fraction-based expansion used for the ion interaction term; applicable to concentrated systems up to the fused salt limit
<i>Mixed-solvent electrolyte models</i>		
Chen <i>et al.</i> <sup>41</sup>	Long-range + short-range	Local-composition (NRTL) short-range term
Liu and Watanasiri <sup>42</sup>	Long-range + short-range + electrostatic solvation (Born) + ion interaction	Modification of the model of Chen <i>et al.</i> <sup>41</sup> using a Guggenheim-type ion interaction term for systems with two liquid phases
Abovsky <i>et al.</i> <sup>43</sup>	Long-range + short-range	Modification of the model of Chen <i>et al.</i> <sup>41</sup> using concentration-dependent NRTL parameters to extend applicability range with respect to electrolyte concentration
Chen <i>et al.</i> <sup>44</sup>	Long-range + short-range + ion hydration	Modification of the model of Chen <i>et al.</i> <sup>41</sup> using an analytical ion hydration term to extend applicability with respect to electrolyte concentration
Chen and Song <sup>45</sup>	Long-range + short-range + electrostatic solvation (Born)	Modification of the model of Chen <i>et al.</i> <sup>41</sup> by introducing segment interactions for organic molecules
Sander <i>et al.</i> <sup>46</sup>	Long-range + short-range	Local composition model (UNIQUAC) with concentration-dependent parameters used for short-range term
Macedo <i>et al.</i> <sup>47</sup>	Long-range + short-range	Local composition model (UNIQUAC) with concentration-dependent parameters used for short-range term
Kikic <i>et al.</i> <sup>48</sup>	Long-range + short range	Local composition group contribution model (UNIFAC) used for short-range term
Dahl and Macedo <sup>49</sup>	Short-range	Undissociated basis; no long-range contribution; group contribution model (UNIFAC) used for short-range term
Iliuta <i>et al.</i> <sup>50</sup>	Long-range + short-range	Local composition (UNIQUAC) model used for short-range term
Wu and Lee <sup>31</sup>	Extended long-range (MSA)	Mean-spherical approximation (MSA) theory used for the long-range term
Li <i>et al.</i> <sup>51</sup>	Long range + ion interaction + short range	Virial-type form used for the ion interaction term; local composition used for short-range term
Yan <i>et al.</i> <sup>52</sup>	Long-range + ion interaction + short range	Group contribution models used for both the ion interaction term and short-range term (UNIFAC)
Zerres and Prausnitz <sup>53</sup>	Long-range + short range + ion solvation	Van Laar model used for short-range term; stepwise ion solvation model
Kolker <i>et al.</i> <sup>28</sup>	Short-range	Undissociated basis; no long-range contribution
Wang <i>et al.</i> <sup>54,55</sup>	Long range + ion interaction + short range	Ionic strength-dependent virial expansion-type ion interaction term; local composition (UNIQUAC) short-range term; detailed treatment of solution chemistry
Papaiconomou <i>et al.</i> <sup>32</sup>	Extended long-range (MSA) + short-range	MSA theory used for the long-range term; local composition model (NRTL) used for the short-range term

in the form of virial-type expansions in terms of molality or mole fractions (see [Table 1](#)). Among these models, the Pitzer<sup>29</sup> molality-based model has found wide acceptance. Parameters of the Pitzer<sup>29</sup> model are available in the open literature for a large number of systems.<sup>6</sup>

The mixed-solvent electrolyte models are designed to handle a wider variety of chemistries. They invariably use the mole fraction and concentration scales. A common approach in the construction of mixed-solvent models is to use local-composition models for representing short-range interactions. The well-known local-composition models include NRTL, UNIQUAC, and its group-contribution version, UNIFAC (see Prausnitz *et al.*<sup>56</sup> and Malanowski and Anderko<sup>57</sup> for a review of these models). The local composition models are commonly used for nonelectrolyte mixtures and, therefore, it is natural to use them for short-range interactions in electrolyte systems. The combination of the long-range and local-composition terms is typically sufficient for representing the properties of moderately concentrated electrolytes in any combination of solvents. For systems that may reach very high concentrations with respect to electrolyte components (e.g., up to the fused salt limit), more complex approaches have been developed. One viable approach is to explicitly account for hydration and solvation equilibria in addition to using the long-range and short-range local composition terms (Zerres and Prausnitz,<sup>53</sup> Chen *et al.*<sup>44</sup>). A particularly effective approach is based on combining virial-type ion interaction terms with local composition models (Li *et al.*,<sup>51</sup> Yan *et al.*,<sup>52</sup> Wang *et al.*<sup>54,55</sup>). In such combined models, the local-composition term reflects the nonelectrolyte-like short-range interactions, whereas the virial-type ion interaction term represents primarily the specific ion–ion interactions that are not accounted for by the long-range contribution. These and other approaches are summarized in [Table 1](#). Among the models summarized in [Table 1](#), the models of Pitzer,<sup>29</sup> Zemaitis,<sup>37</sup> Chen *et al.*<sup>41</sup> (including their later modifications),<sup>44,45</sup> and Wang *et al.*<sup>54,55</sup> have been implemented in publicly available or commercial simulation programs.

### 2.38.2.3 Electrochemical Stability Diagrams

The  $E$ -pH diagrams, commonly referred to as the Pourbaix<sup>1</sup> diagrams, are historically the first, and remain the most important class of electrochemical stability diagrams. They were originally constructed for ideal solutions (i.e., on the assumption that  $\gamma_i = 1$ ),

which was the only viable approach at the time when they were introduced.<sup>1</sup> The essence of the procedure for generating the Pourbaix diagrams is analyzing all possible reactions between all – aqueous or solid – species that may exist in the system. The simultaneous analysis of the reactions makes it possible to determine the ranges of potential and pH at which a given species is stable. The reactions can be conveniently subdivided into two classes, that is, chemical and electrochemical reactions. The chemical reactions can be written without electrons, that is

$$\sum v_i M_i = 0 \quad [5]$$

Then, the equilibrium condition for the reaction is given in terms of the chemical potentials of individual species by

$$\sum v_i \mu_i = 0 \quad [6]$$

According to [eqn \[1\]](#), [eqn \[6\]](#) can be further rewritten in terms of species activities as

$$\sum v_i \ln a_i = -\frac{\sum v_i \mu_i^0}{RT} = \ln K \quad [7]$$

where the right-hand side of [eqn \[7\]](#) is defined as the equilibrium constant because it does not depend on species concentrations.

In contrast to the chemical reactions, the electrochemical reactions involve electrons,  $e^-$ , as well as chemical substances  $M_i$  that is

$$\sum v_i M_i + n e^- = 0 \quad [8]$$

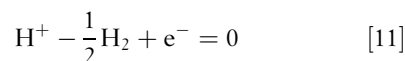
The equilibrium state of an electrochemical reaction is associated with a certain equilibrium potential. Since electrode potential cannot be measured on an absolute basis, it is necessary to choose an arbitrary scale against which the potentials can be calculated. If a reference electrode is selected, the equilibrium state of the reaction that takes place on the reference electrode is given by an equation analogous to [eqn \[8\]](#), that is

$$\sum v_{i,\text{ref}} M_{i,\text{ref}} + n e^- = 0 \quad [9]$$

Then, the equilibrium potential  $E_0$  of [eqn \[8\]](#) is given with respect to the reference electrode as

$$E_0 - E_{0,\text{ref}} = \frac{\sum v_i \mu_i - \sum v_{i,\text{ref}} \mu_{i,\text{ref}}}{nF} \quad [10]$$

According to a generally used convention, the standard hydrogen electrode (SHE) (i.e.,  $H^+(a_{H^+} = 1)/H_2(f_{H_2} = 1)$ ) is used as a reference. The corresponding reaction that takes place on the SHE is given by





Then, eqn [10] becomes

$$E_0 - E_{0,\text{ref}} = \frac{\sum v_i \mu_i - n \left( \mu_{\text{H}^+}^0 - \frac{1}{2} \mu_{\text{H}_2}^0 \right)}{nF} \quad [12]$$

In eqn [12], the standard chemical potentials  $\mu_{\text{H}}^0$  and  $\mu_{\text{H}_2}^0$  as well as the reference potential  $E_{0,\text{ref}}$  are equal to zero at  $T = 298.15$  K. For practical calculations at temperatures other than 298.15 K, two conventions can be used for the reference electrode. According to a universal convention established by the International Union of Pure and Applied Chemistry (the ‘Stockholm convention’), the potential of SHE is arbitrarily defined as zero at all temperatures (i.e.,  $E_{0,\text{ref}} = 0$ ). When this convention is employed, eqn [12] is used as a working equation with  $E_{0,\text{ref}} = 0$ . In an alternate convention, the SHE reference potential is equal to zero only at room temperature, and its value at other temperatures depends on the actual, temperature-dependent values of  $\mu_{\text{H}^+}^0$  and  $\mu_{\text{H}_2}^0$ . In this case, it is straightforward to show (see Chen and Aral,<sup>58</sup> Chen *et al.*,<sup>59</sup>) that eqn [12] becomes

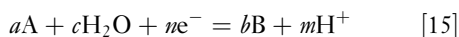
$$E_0 = \frac{\sum v_i \mu_i}{nF} \quad [13]$$

at all temperatures. Equation [13] can be further rewritten in terms of activities as

$$E_0 = \frac{\sum v_i \mu_i^0}{nF} + \frac{RT}{nF} \sum v_i \ln a_i = E_0^0 + \frac{RT}{nF} \sum v_i \ln a_i \quad [14]$$

where  $E_0^0$  is the standard equilibrium potential, which is calculated from the values of the standard chemical potentials  $\mu_i^0$ .

For a brief outline of the essence of the Pourbaix diagrams, let us consider a generic reaction in which two species, A and B, undergo a transformation. The only other species that participate in the reaction are hydrogen ions and water, that is:



If eqn [15] is a chemical reaction (i.e., if  $n = 0$ ), then its equilibrium condition (eqn [7]) can be rewritten as

$$m\text{pH} = \log \left( \frac{a_B^a}{a_A^a} \right) - \log K - \log a_{\text{H}_2\text{O}}^c \quad [16]$$

where  $\text{pH} = -\log a_{\text{H}^+}$ , and decimal rather than natural logarithms is used. For dilute solutions, it is appropriate to assume that  $a_{\text{H}_2\text{O}} = 1$ , and the last term on the right-hand side of eqn [16] vanishes. If we assume that the components A and B are aqueous dissolved species and their activities are equal, eqn [16] defines the boundary between the predominance areas of species A and B. If one of the species (A or B) is a pure

solid and the other is an aqueous species, the activity of the solid is equal to one and the activity of the aqueous species can be set equal to a certain predetermined, typically small, value (e.g.,  $10^{-6}$ ). Then, eqn [16] represents the boundary between a solid and an aqueous species at a fixed value of the dissolved species activity. Similarly, for a boundary between two pure solid phases, the activities of the species A and B are equal to one. Such a boundary is represented by a vertical line in a potential–pH space, and its location depends on the equilibrium constant according to eqn [16].

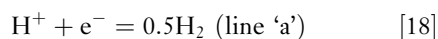
If eqn [15] represents an electrochemical reaction (i.e.,  $n \neq 0$ ), the equilibrium condition (eqn [14]) becomes

$$E_0 = E_0^0 + \frac{RT}{nF} \ln \frac{a_A^a}{a_B^b} + \frac{RT}{nF} \ln a_{\text{H}_2\text{O}} + \frac{RT \ln 10}{F} \frac{m}{n} \text{pH} \quad [17]$$

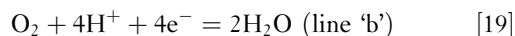
As with the chemical reactions, the term that involves the activity of water vanishes for dilute solutions, and the ratio of the activities of species A and B can be fixed to represent the boundary between the predominance areas of two species. Under such assumptions, the plot of  $E$  versus pH is a straight line with a slope determined by the stoichiometric coefficients  $m$  and  $n$ .

Thus, for each species, boundaries can be established using eqns [16] and [17]. As long as the simplifying assumptions described above are met, the boundaries can be calculated analytically. By considering all possible boundaries, stability regions can be determined using an algorithm described by Pourbaix.<sup>1</sup> Sample  $E$ –pH diagrams are shown for iron in Figure 1.

One of the main reasons for the usefulness of stability diagrams is the fact that they can illustrate the interplay of various partial processes of oxidation and reduction. The classical  $E$ –pH diagrams contain two dashed lines, labeled as ‘a’ and ‘b,’ which are superimposed on the diagram of a given metal (see Figure 1). The dashed line ‘a’ represents the conditions of equilibrium between water (or hydrogen ions) and elemental hydrogen at unit hydrogen fugacity, that is



The ‘b’ line describes the equilibrium between water and oxygen, also at unit fugacity,



Accordingly, water will be reduced to form hydrogen at potentials below line ‘a,’ and will be oxidized to form oxygen at potentials above line ‘b.’ The location

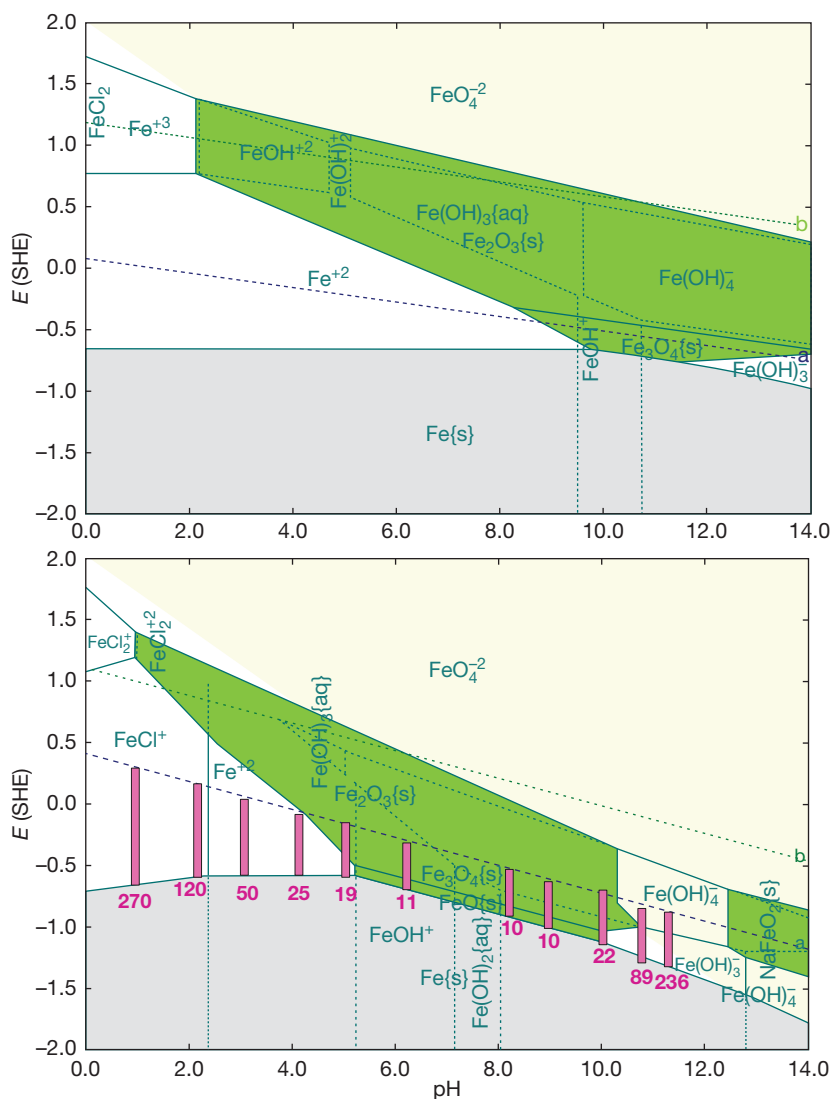


**Figure 1**  $E$ -pH (Pourbaix) diagrams for iron at 25 °C (upper diagram) and 300 °C (lower diagram). At 300 °C, the conditions of the experiments of Partridge and Hall<sup>60</sup> are superimposed on the diagram. The vertical bars show the range between the equilibrium potentials for the reduction of  $H^+$  and oxidation of Fe, thus bracketing the mixed potential in the experiments. The numbers under the bars denote the experimentally determined relative attack. The diagrams have been generated using the Corrosion Analyzer software<sup>61</sup> using the algorithm of Anderko *et al.*<sup>62</sup>

of the 'a' and 'b' lines on the diagram indicates whether a given redox couple is thermodynamically possible. For example, in the region between the line 'a' and the upper edge of the stability region of  $Fe(s)$  in Figure 1, the anodic reaction of iron oxidation can be coupled with the cathodic reaction of water or hydrogen ion reduction. In such a case, the measurable open-circuit potential of the corrosion process will establish itself between the line 'a' and the equilibrium potential for the oxidation of iron (i.e., the upper edge of the  $Fe(s)$  region). If the potential lies above

line 'a,' then water reduction is no longer a viable cathodic process, and the oxidation of iron must be coupled with another reduction process. In the presence of oxygen, reaction eqn [19] can provide such a reaction process. In such a case, the open-circuit (corrosion) potential will establish itself at a higher value for which the upper limit will be defined by line 'b.'

Pourbaix<sup>1</sup> subdivided various regions of the  $E$ -pH diagrams into three categories, that is, immunity, corrosion, and passivation. The immunity region

encompasses the stability field of elemental metals. The corrosion region corresponds to the stability of dissolved, either ionic or neutral species. Finally, passivation denotes the region in which solid oxides or hydroxides are stable. In **Figure 1**, the immunity and passivation regions are shaded, whereas the corrosion region is not. It should be noted that this classification does not necessarily reflect the actual corrosion behavior of a metal. Only immunity has a strict significance in terms of thermodynamics because in this region the metal cannot corrode regardless of the time of exposure. The stability of dissolved species in the 'corrosion' region does not necessarily mean that the metal rapidly corrodes in this area. In reality, the rate of corrosion in this region may vary markedly because of kinetic reasons. Passivation is also an intrinsically kinetic phenomenon because the protectiveness of a solid layer on the surface of a metal is determined not by its low solubility alone. The presence of a sparingly soluble solid is typically a necessary, but not sufficient condition for passivity.

Although the  $E$ -pH diagrams indicate only the thermodynamic tendency for the stability of various metals, ions, and solid compounds, they may still provide useful qualitative clues as to the expected trends in corrosion rates. This is illustrated in the lower diagram of **Figure 1**. In this diagram, the vertical bars denote the difference between the equilibrium potentials for the reduction of water and oxidation of iron. Thus, the bars indicate the tendency of the metal to corrode in deaerated aqueous solutions with varying pH. They bracket the location of the corrosion potential and, thus, indicate whether the corrosion potential will establish itself in the 'corrosion' or 'passivation' regions. The numbers associated with the bars represent the experimentally determined relative attack. It is clear that the observed relative attack is substantially greater in the regions where a solid phase is predicted to be stable than in the regions where no solid phase is predicted. Thus, subject to the limitations discussed above, the stability diagrams can be used for the qualitative assessment of the tendency of metals to corrode, and for estimating the range of the corrosion potential.

Following the pioneering work of Pourbaix and his coworkers, further refinements of stability diagrams were made to extend their range of applicability. These refinements were made possible by the progress of the thermodynamics of electrolyte solutions and alloys. Specifically, further developments focused on

1. generation of diagrams at elevated temperatures,
2. taking into account the active solution species other than protons and water molecules,
3. introduction of solution nonideality, which influences the stability of species through realistically modeled activity coefficients,
4. introduction of alloying effects by accounting for the formation of mixed oxides and the nonideality of alloy components in the solid phase, and
5. flexible selection of independent variables, other than  $E$  and pH, for the generation of diagrams.

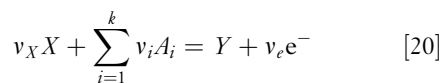
### 2.38.2.3.1 Diagrams at elevated temperatures

The key to the construction of stability diagrams at elevated temperatures is the calculation of the standard chemical potentials  $\mu_i^0$  of all individual species as a function of temperature. In earlier studies, the entropy correspondence principle of Criss and Cobble<sup>21</sup> was used for this purpose. Macdonald and Cragnolino<sup>63</sup> reviewed the development of  $E$ -pH diagrams at elevated temperatures until the late 1980s.

The HKF equation of state<sup>22,23</sup> formed a comprehensive basis for the development of  $E$ -pH diagrams at temperatures up to 300 °C for iron, zinc, chromium, nickel, copper, and other metals (Beverkog and Puigdomenech,<sup>64-69</sup> Anderko *et al.*<sup>62</sup>) An example of a high temperature  $E$ -pH diagram is shown for Fe at 300 °C in the lower diagram of **Figure 1**. Comparison of the Fe diagrams at room temperature and 300 °C shows a shift in the predominance domains of cations to lower pH values and an expansion of the domains of metal oxyanions at higher pH values. Such effects are relatively common for metal-water systems.

### 2.38.2.3.2 Effect of multiple active species

The concept of stability diagrams can be easily extended to solutions that contain multiple chemically active species other than  $H^+$  and  $H_2O$ . In such a general case, the simple reaction **eqn [15]** needs to be extended as



where the species  $X$  and  $Y$  contain at least one common element and  $A_i$  ( $i = 1, \dots, k$ ) are the basis species that are necessary to define equilibrium equations between all species containing a given element. Reaction **eqn [20]** is normalized so that the stoichiometric coefficient for the right-hand side species ( $Y$ ) is equal to 1. Such an extension results in generalized

expressions for the boundaries between predominance regions (eqns [16] and [17]). The equilibrium expression for the chemical reactions (eqn [20] with  $v_e = 0$ ) then becomes

$$\begin{aligned}\ln K &= \left( \ln a_Y - v_X \ln a_X - \sum_{i=1}^k v_i \ln a_{A_i} \right) \\ &= \frac{1}{RT} \left( \mu_Y^0 - \mu_X^0 - \sum_{i=1}^k v_i \mu_{A_i}^0 \right) \quad [21]\end{aligned}$$

and the expression for an electrochemical reaction (eqn [20] with  $v_e \neq 0$ ) takes the form:

$$E_0 = E_0^0 + \frac{RT}{Fv_e} \left( \ln a_Y - v_X \ln a_X - \sum_{i=1}^k v_i \ln a_{A_i} \right) \quad [22]$$

Thus, the expression for the boundary lines become more complicated but the algorithm for generating the diagrams remains the same, that is, the predominance areas can still be determined semianalytically.

The strongest effect of solution species on the stability diagrams of metals is observed in the case of complex-forming ligands and species that form stable, sparingly soluble solid phases other than oxides or hydroxides (e.g., sulfides or carbonates). Several authors focused on stability diagrams for metals such as iron, nickel, or copper in systems containing sulfur species (Biernat and Robbins,<sup>70</sup> Froning *et al.*,<sup>71</sup> Macdonald and Syrett,<sup>72</sup> Macdonald *et al.*,<sup>73,74</sup> Chen and Aral,<sup>58</sup> Chen *et al.*,<sup>59</sup> Anderko and Shuler<sup>75</sup>). This is due to the importance of iron sulfide phases, which have a strong tendency to form in aqueous environments even at very low concentrations of dissolved hydrogen sulfide. The stability domains of various iron sulfides can be clearly rationalized using *E*-pH diagrams. Diagrams have also been developed for metals in brines (Pourbaix,<sup>76</sup> Macdonald and Syrett,<sup>72</sup> Macdonald *et al.*,<sup>73,74</sup> Kesavan *et al.*,<sup>77</sup> Muñoz-Portero *et al.*<sup>78</sup>). The presence of halide ions manifests itself in the stability of various metal-halide complexes. Typically, the effect of halides on the thermodynamic stability is less pronounced than the effect of sulfides. However, concentrated brines can substantially shrink the stability regions of metal oxides and promote the active behavior of metals. An example of such effects is provided by the diagrams for copper in concentrated bromide brines (Muñoz-Portero *et al.*<sup>78</sup>). Effects of formation of various carbonate and sulfate phases have also been reported (Bianchi and Longhi,<sup>79</sup> Pourbaix<sup>76</sup>).

The formation of complexes of metal ions with organic ligands (e.g., chelants) frequently leads to a

significant decrease in the stability of metal oxides, which may, under some conditions, indicate an increased dissolution tendency in the passive state (Silverman,<sup>80,81</sup> Kubal and Panacek,<sup>82</sup> Silverman and Silverman<sup>83</sup>). An important example of the importance of complexation is provided by the behavior of copper and other metals in ammoniated environments. **Figure 2** (upper diagram) illustrates an *E*-pH diagram for copper in a 0.2 m NH<sub>3</sub> solution. As shown in the figure, the copper oxide stability field is bisected by the stability area of an aqueous complex. The formation of a stable dissolved complex indicates that the passivity of copper and copper-base alloys may be adversely affected in weakly alkaline NH<sub>3</sub>-containing environments. In reality, ammonia attack on copper-base alloys is observed in steam cycle environments.<sup>63</sup> Stability diagrams are a useful tool for the qualitative evaluation of the tendency of metals to corrode in such environments.

### 2.38.2.3.3 Diagrams for nonideal solutions

As long as the solution is assumed to be ideal (i.e.,  $\gamma_i = 1$  in eqn [2]), the chemical and electrochemical equilibrium expressions can be written in an analytical form, and the *E*-pH diagrams can be generated semianalytically. For nonideal solutions, the analytical character of the equilibrium lines can be preserved if fixed activity coefficients are assumed for each species (see Bianchi and Longhi<sup>79</sup>). However, such an approach does not have a general character because the activities of species change as a function of pH. This is due to the fact that, in real systems, pH changes result from varying concentrations of acids and bases, which influence the activity coefficients of all solution species. In a nonideal solution, the activities of all species are inextricably linked to each other because they all are obtained by differentiating the solution's excess Gibbs energy with respect to the number of moles of the individual species.<sup>2</sup> Therefore, in a general case, the equilibrium expressions (eqns [21] and [22]) can no longer be expressed by analytical expressions. This necessitates a modification of the algorithm for generating stability diagrams. A general methodology for constructing stability diagrams of nonideal solutions has been developed by Anderko *et al.*<sup>62</sup>

In general, the nonideality of aqueous solutions may shift the location of the equilibrium lines because the activity coefficients may vary by one or even two orders of magnitude. Such effects become pronounced in concentrated electrolyte solutions and in mixed-solvent solutions, in which water is not necessarily the predominant solvent.

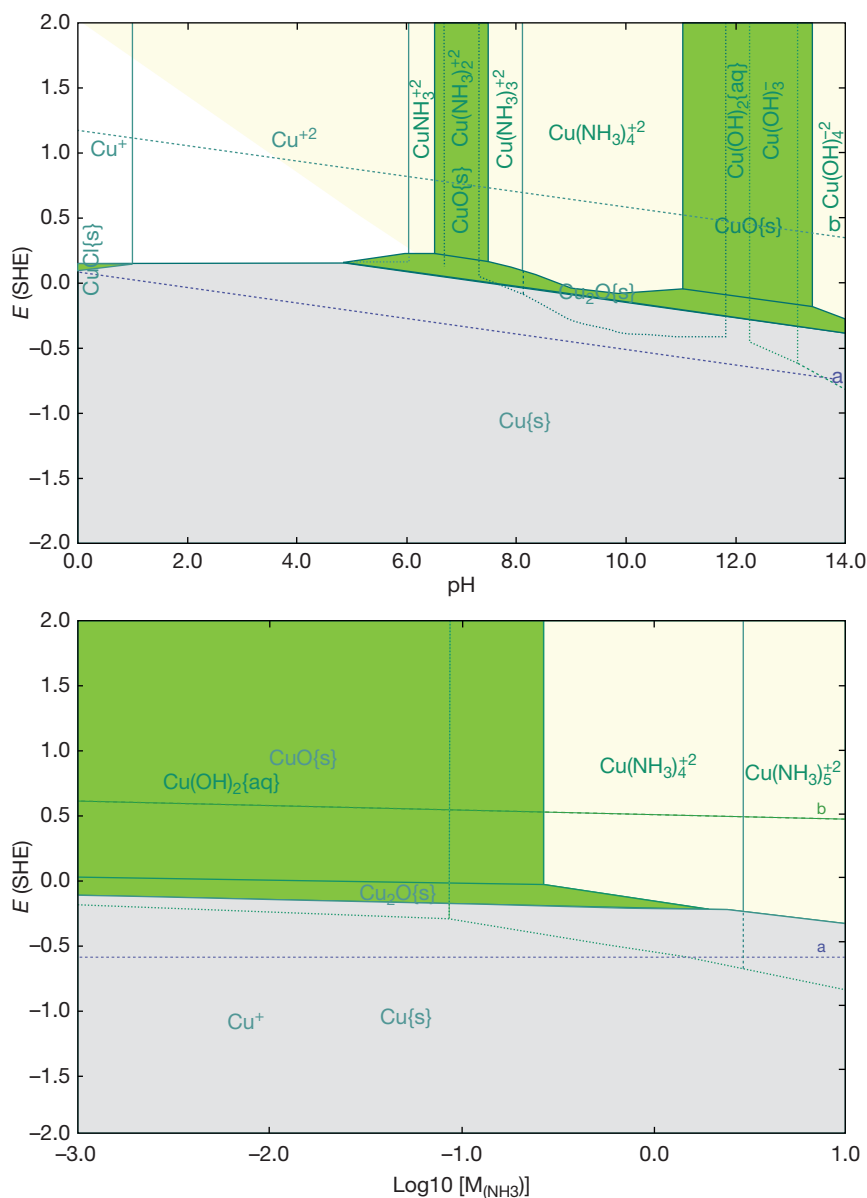


**Figure 2** Use of thermodynamic stability diagrams to analyze the effect of ammonia on the corrosion of copper. The upper plot is an  $E$ -pH diagram for Cu in a 0.2 m  $\text{NH}_3$  solution. The lower plot is a potential-ammonia molality diagram.

#### 2.38.2.3.4 Diagrams for alloys

The vast majority of the published stability diagrams have been developed for pure metals. However, several studies have been devoted to generating stability diagrams for alloys, particularly those from the Fe-Ni-Cr-Mo family (Cubicciotti,<sup>84,85</sup> Beverskog and Puigdomenech,<sup>69</sup> Yang *et al.*,<sup>86</sup> Anderko *et al.*<sup>87</sup>). In general, a stability diagram for an alloy is a superposition of partial diagrams for the individual components of the alloy.<sup>69</sup> However, the partial diagrams

are not independent because the alloy components form a solid solution and, therefore, their properties are linked. The superposition of partial diagrams makes it possible to analyze the tendency of alloy components for preferential dissolution. This may be the case when a diagram indicates that one alloy component has a tendency to form a passivating oxide, whereas another component has a tendency to form ions. Also, stability diagrams indicate in a simple way which alloy component is more anodic.



There are two key effects of alloying on thermodynamic equilibrium, that is, the formation of mixed solid corrosion products and the nonideality of alloy components in the solid phase. The formation of mixed solid corrosion products may be particularly significant for passive systems. Fe–Ni–Cr alloys may form mixed oxides, including  $\text{NiFe}_2\text{O}_4$ ,  $\text{FeCr}_2\text{O}_4$ , and  $\text{NiCr}_2\text{O}_4$ . Such oxides may be more stable than the single oxides of chromium, nickel, and iron, which appear in stability diagrams for pure metals.  $E$ –pH diagrams that include mixed oxide phases have been reported by Cubicciotti,<sup>84,85</sup> Beverskog and Puigdomenech,<sup>69</sup> and Yang *et al.*<sup>86</sup> for Fe–Ni–Cr alloys in ideal aqueous solutions.

Another fundamental effect of alloying on the thermodynamic behavior results from the nonideality of the solid solution phase. In contrast to pure metals, the activity of a metal in an alloy is no longer equal to 1. This affects the value of the equilibrium potential for metal dissolution, which determines the upper boundary of the stability field of an alloy component on an  $E$ –pH diagram. As with the liquid phase, the activity of solid solution components can be obtained from a comprehensive excess Gibbs energy model of the solid phase. Thermodynamic modeling of alloys is a very wide area of research, which is beyond the scope of this chapter (see Lupis<sup>88</sup> and Saunders and Miodownik<sup>89</sup> for reviews). Detailed models have been developed for the thermodynamic behavior of alloys on the basis of high temperature data that are relevant to metallurgical processes. These models can be, in principle, extrapolated to lower temperatures that are of interest in aqueous corrosion. Despite the inherent uncertainties associated with extrapolation, estimates of activities of alloy components can be obtained in this way and incorporated into the calculation of stability diagrams. Such an approach was used by Anderko *et al.*<sup>87</sup> in a study in which solid solution models were coupled with an algorithm for generating stability diagrams for Fe–Ni–Cr–Mo–C and Cu–Ni alloys. In that work, the solid solution models of Hertzman,<sup>90</sup> Hertzman and Jarl,<sup>91</sup> and Anderson and Lange<sup>92</sup> were implemented to estimate the activities of alloy components.

It should be noted that the effect of varying activities of alloy components on  $E$ –pH diagrams is relatively limited. This is due to the fact that alloy phase nonideality, while crucial for modeling alloy metallurgy, is only a secondary contribution to the energetics of reactions between metals and aqueous species. The effect of alloy solution nonideality manifests itself in a limited shift of the upper boundary of

the metal stability area in  $E$ –pH diagrams. The effect of mixed oxide phases is usually much more pronounced on stability diagrams.

### 2.38.2.3.5 Potential–concentration diagrams

Once the thermodynamic treatment of solution chemistry is extended to allow for the effect of species other than  $\text{H}^+$  and  $\text{H}_2\text{O}$  (see eqns [21] and [22]), other independent variables become possible in addition to  $E$  and pH. The chemical and electrochemical boundaries can then be calculated as a function of concentration variables other than pH. In particular, the stability diagrams can be generated as a function of the concentration of active solution species that may react with metals through precipitation, complexation, or other reactions. Thus, an extension of  $E$ –pH diagrams to  $E$ –species concentration diagrams is relatively straightforward. The algorithm developed by Anderko *et al.*<sup>62</sup> for nonideal solutions is equally applicable to  $E$ –pH and  $E$ –concentration diagrams. An example of such a diagram is provided in the lower plot of Figure 2. This plot is an  $E$ – $\text{NH}_3$  molality diagram and illustrates the thermodynamic behavior of copper when increasing amounts of ammonia are added to an aqueous environment. In this simulation, pH varies with ammonia concentration. However, pH is less important in this case than the concentration of  $\text{NH}_3$  because the stability of copper oxide is controlled by the formation of copper–ammonia complexes. The diagram indicates at which concentration of ammonia the copper oxide film becomes thermodynamically unstable, thus increasing the tendency for metal dissolution.

### 2.38.2.4 Chemical Equilibrium Computations

While the  $E$ –concentration diagrams are merely an extension of Pourbaix's original concept of stability diagrams, a completely different kind of thermodynamic analysis can also be performed using electrolyte thermodynamics. This kind of analysis relies on solving the chemical equilibrium expressions without using the potential as an independent variable. Assuming that temperature, pressure, and starting amounts of components (both metals and solution species) are known, the equilibrium state of the system of interest can be found by simultaneously solving the following set of equations:

1. chemical equilibrium equations (eqn [6]) for a linearly independent set of reactions that link all the species that exist in the system; this set of

- equations also includes solid–liquid equilibrium reactions (or precipitation equilibria);
2. if applicable, vapor–liquid and, possibly, liquid–liquid equilibrium equations (i.e., the equality of chemical potentials of species in coexisting phases),
  3. material balance equations for each element in the system, and
  4. electroneutrality balance condition.

Once the solution is found, the potential can be calculated using the Nernst equation for any redox pair in the equilibrated system. It should be noted that procedures for solving these equations are very involved and require sophisticated numerical techniques. Methods for solving such electrolyte equilibrium problems were reviewed by Zemaitis *et al.*<sup>4</sup> and Rafal *et al.*,<sup>7</sup> and will not be discussed here.

The solution of the chemical equilibrium conditions provides detailed information about the thermodynamically stable form(s) of the metal in a particular system. This is in contrast with the information presented on the  $E$ –pH diagrams, which essentially indicate whether a given oxidation reaction (e.g., dissolution of a metal) can occur simultaneously with a given reduction reaction (e.g., reduction of water). In the chemical equilibrium algorithm outlined above, all possible reduction and oxidation equilibria are solved simultaneously. This provides very detailed information about the chemical identity of all species and their concentrations. On the other hand, this kind of information is less

conductive to gaining qualitative insight into the key anodic and cathodic reactions that occur in the system.

To visualize the information obtained from detailed chemical equilibrium computations, stability diagrams can be constructed by selecting key independent variables. Such diagrams can be referred to as ‘chemical’ as opposed to ‘electrochemical’ because they do not involve the potential as an independent variable. An example of such a diagram is shown in **Figure 3**, which shows the stability areas of solid corrosion products of iron as a function of the amount of dissolved iron and hydrogen sulfide in 1 kg of water. Diagrams of this type can be generated by repeatedly solving the chemical equilibrium expressions outlined above and tracing the stability boundaries of various species (Lencka *et al.*,<sup>94</sup> Sridhar *et al.*<sup>93</sup>). Such diagrams are useful for illustrating the transition between various corrosion products (e.g., iron sulfide and magnetite in **Figure 3**) as a function of environmental conditions. Diagrams of this kind have been generated by Sridhar *et al.*<sup>95</sup> to identify the conditions under which  $\text{FeCO}_3$ ,  $\text{Fe}_3\text{O}_4$ , and  $\text{Fe}_2\text{O}_3$  coexist as corrosion products of carbon steel. This approach was used to elucidate conditions that are conducive to intergranular stress corrosion cracking in weakly alkaline carbonate systems, which has been associated with the transition between iron carbonate, iron (II), and iron (III) corrosion products.

It should be noted that simplified ‘chemical’ diagrams can be generated using activities rather than

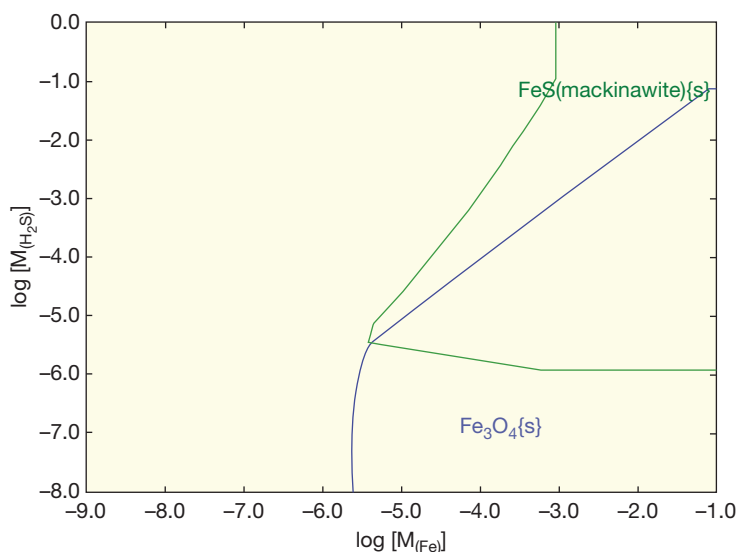


**Figure 3** Stability diagram for solid iron corrosion products as a function of the molality of dissolved Fe and the total number of moles of  $\text{H}_2\text{S}$  per 1 kg of  $\text{H}_2\text{O}$ . The diagram has been constructed by computing the equilibrium states of solid–liquid–vapor reactions.<sup>93</sup>

concentrations of species as independent variables. Such an approach makes it possible to obtain the 'chemical' diagrams in a semianalytical way, as with the classical Pourbaix diagrams. An example of such diagrams is provided by Mohr and McNeil<sup>96</sup> for the Cu–H–O–Cl system. However, such simplified 'chemical' diagrams suffer from the fundamental disadvantage that species activities are not directly measurable and are, therefore, much less suitable as independent variables than concentrations. Comprehensive 'chemical' diagrams can be obtained only by simultaneously solving the chemical and phase equilibrium expressions for each set of conditions, preferably with the help of a realistic model for liquid-phase activity coefficients.

### 2.38.2.5 Problems of Metastability

The main strength of the stability diagrams lies in their purely thermodynamic nature. Accordingly, they can be generated using equilibrium thermochemical properties that are obtained from a variety of classical experimental sources (e.g., solubility, vapor pressure, calorimetric or electromotive force measurements for bulk systems) without recourse

to any electrochemical kinetic studies of surfaces. At the same time, the purely thermodynamic nature of the diagrams is also their main weakness. An important limitation of the stability diagrams is the fact that they predict the equilibrium phases, whereas the actual corrosion behavior may be controlled by metastable phases. The same limitation applies to the detailed thermodynamic computations outlined earlier.

To illustrate the problems of metastability, it is instructive to examine how  $E$ –pH diagrams can be used to rationalize the Faraday paradox of iron corrosion in nitric acid, which historically played a great role in establishing the concept of passivity (Macdonald<sup>97</sup>). Faraday's key observation was that iron easily corroded in dilute nitric acid with the evolution of hydrogen. However, it did not corrode with an appreciable rate in concentrated  $\text{HNO}_3$  solutions despite their greater acidity. When scratched in the solution, an iron sample would corrode for a short time and, then, rapidly passivate. A stability diagram for this system is shown in Figure 4. This figure presents a superposition of an  $E$ –pH diagram for iron species and another one for nitrogen species. Dilute nitric acid is a weak oxidizing agent and, therefore, the main cathodic reaction in this case is

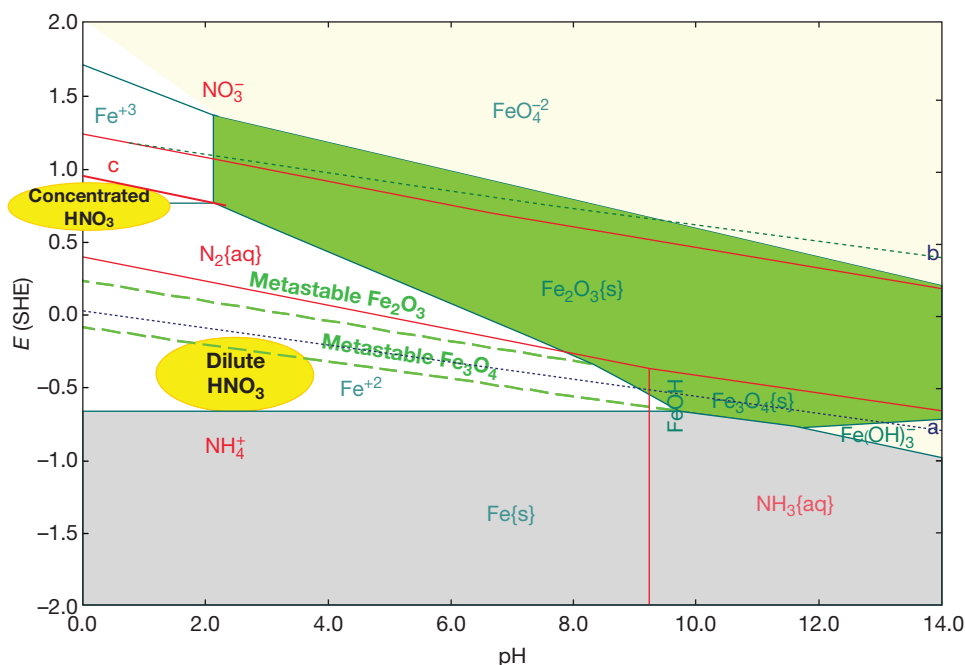
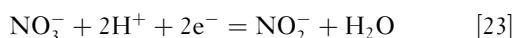


**Figure 4** Metastability on the  $E$ –pH diagram and the interpretation of the Faraday paradox of iron corrosion in dilute and concentrated nitric acid. The stability fields of the oxides ( $\text{Fe}_3\text{O}_4$  and  $\text{Fe}_2\text{O}_3$ ) are extended into the metastable region (long dashed lines). An  $E$ –pH diagram for nitrogen is superimposed on the diagram for Fe. The line 'c' is a metastable equilibrium line for the reduction of  $\text{HNO}_3$  to  $\text{HNO}_2$ . The ovals marked as 'concentrated  $\text{HNO}_3$ ' and 'dilute  $\text{HNO}_3$ ' indicate the mixed potential ranges that are expected for iron in concentrated and dilute  $\text{HNO}_3$ , respectively.

the common reaction of reduction of  $H^+$  ions. The equilibrium potential for this reaction is given by the dotted line marked as 'a' in the diagram. The anodic process is the oxidation of Fe, for which the equilibrium potential is given by the equilibrium line between Fe(s) and  $Fe^{2+}$  in the diagram. Thus, the corrosion potential will establish itself between the 'a' line and the upper limit of the stability field of elemental iron. This corrosion potential range is approximately shown by the lower ellipsoid in **Figure 4**. In this region, the stable iron species is  $Fe^{2+}$  and, therefore, the stability diagram predicts the dissolution of iron with the formation of  $Fe^{2+}$  ions. Unlike dilute nitric acid, concentrated  $HNO_3$  is a strong oxidizing agent. The main reduction reaction in this case is



The equilibrium potential for this reaction is shown by a line marked as 'c' in **Figure 4**. It should be noted that the nitrite ions ( $NO_2^-$ ) are metastable and, therefore, a stability field of nitrites does not appear on an  $E$ -pH diagram of nitrogen. Nevertheless, the equilibrium potential for reaction eqn [21] can be easily calculated as described above. It lies within the stability field of elemental nitrogen  $N_2(aq)$ . The corrosion potential will then establish itself at a much higher potential, relatively close to the dominant cathodic line 'c.' The likely location of the corrosion potential is outlined in **Figure 4** by an ellipsoid marked 'concentrated  $HNO_3$ .' However, the stable species in this region are the  $Fe^{2+}$  and  $Fe^{3+}$  ions. Thus, the stability diagram does not explain the Faraday paradox as long as only stable species are considered. As indicated by Macdonald,<sup>97</sup> the  $E$ -pH diagram becomes consistent with experimental observation when the existence of metastable phases is allowed for. The dashed lines in **Figure 4** show the metastable extensions of the  $Fe^{2+}/Fe_3O_4$  and  $Fe_3O_4/Fe_2O_3$  equilibrium lines into the acidic range. Thus, it is clear that the corrosion potential of iron in concentrated  $HNO_3$  is likely to establish itself in a potential range in which metastable iron oxides are stable. In contrast, the metastable solids are not expected to form at the low potentials that correspond to dilute  $HNO_3$  environments (i.e., below the  $Fe^{2+}$ /metastable  $Fe_3O_4$  boundary). If the surface is scratched, the large supply of  $H^+$  ions near the scratch will create conditions under which the potential will be below the 'a' line and short-term hydrogen evolution will follow. However, this will lead to a rapid depletion of the  $H^+$  ions, and the potential will shift to higher values, at which metastable phases can lead to passivation.

The formation of metastable solid phases is fairly common. The metastability of chromium oxide phases is important for the passivity of Fe-Ni-Cr alloys in acidic solutions. Although the  $E$ -pH diagrams indicate that chromium oxides/hydroxides cease to be stable in relatively weakly acidic solutions, the practical passivity range extends to a more acidic range for numerous alloys. Also, the metastability of iron sulfide phases plays an important role in the behavior of corrosion products in  $H_2S$  containing environments. Anderko and Shuler<sup>75</sup> used stability diagrams to evaluate the natural sequence of formation of various iron sulfide phases (e.g., amorphous FeS, mackinawite, pyrrhotite, greigite, marcasite, or pyrite). The sequence of formation of such phases could be predicted on the basis of the simple but reasonably accurate rule that the order of formation of solids is the inverse of the order of their thermodynamic stability. Stability diagrams are then used to predict the conditions under which various metastable phases are likely to form.

Thermodynamics provides a convenient starting point in the simulation of aqueous corrosion. Although it is inherently incapable of predicting the rates of interfacial phenomena, it is useful for predicting the final state toward which the system should evolve if it is to reach equilibrium. Furthermore, the computation of the final, thermodynamic equilibrium state can be refined by taking into account the metastable phases. In addition to determining the equilibrium state in metal-environment systems, electrolyte thermodynamics provides information on the properties of the environment. Such information, including speciation in the liquid phase, concentrations and activities of individual species, and phase equilibria, is necessary for constructing kinetic models of corrosion.

### 2.38.3 Modeling the Kinetics of Aqueous Corrosion

Aqueous corrosion is intrinsically an electrochemical process that involves charge transfer at a metal-solution interface. Because aqueous corrosion is a heterogeneous process, it involves the following fundamental steps:

1. reactions in the bulk aqueous environment,
2. mass transport of reactants to the surface,
3. charge transfer reactions at the metal surface,
4. mass transport of reaction products from the surface, and
5. reactions of the products in the bulk environment.

Reactions in the bulk environment (1 and 5) can be considered, with some important exceptions, to be equilibrium. As long as they are treated as equilibrium phenomena, they remain within the domain of electrolyte thermodynamics. On the other hand, the charge transfer reactions at the surface (3), and their coupling with mass transport (2 and 4) require the tools of electrochemical kinetics. In this section, we review the fundamentals of modeling approaches to electrochemical kinetics.

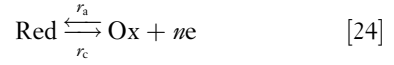
The objective of modeling the kinetics of aqueous corrosion is to relate the rate of electrochemical corrosion to external conditions (e.g., environment composition, temperature, and pressure), flow conditions, and the chemistry and metallurgical characteristics of the corroding interface. The two main quantities that can be obtained from electrochemical modeling are the corrosion rate ( $v_{\text{corr}}$  often expressed as the corrosion current density  $i_{\text{corr}}$ ) and corrosion potential ( $E_{\text{corr}}$ ). For practical applications, the calculation of the corrosion rate is of primary interest for simulating general corrosion and the rate of dissolution in occluded environments such as pits or crevices. The value of the corrosion potential ( $E_{\text{corr}}$ ) is also of interest because there is often a relationship between the value of the corrosion potential and the type of corrosion damage that occurs. In general, if the corrosion potential is above a certain critical potential ( $E_{\text{crit}}$ ), a specific form of corrosion that is associated with  $E_{\text{crit}}$  can occur, typically at a rate that is determined by the difference  $E_{\text{corr}} - E_{\text{crit}}$ . This general observation applies to localized corrosion including pitting, crevice corrosion, intergranular stress corrosion cracking, and so on. An internally consistent model for general corrosion should simultaneously provide reasonable values of the corrosion rate and corrosion potential. Thus, the computation of the corrosion potential is of interest not so much for modeling general corrosion but for predicting other forms of corrosion.

### 2.38.3.1 Kinetics of Charge-Transfer Reactions

The theory of charge-transfer reactions is well developed and has been reviewed in detail by a number of authors including Vetter,<sup>98</sup> Bockris and Reddy,<sup>99</sup> Kaesche,<sup>100</sup> Bockris and Khan,<sup>101</sup> and Gileadi.<sup>102</sup> Here, we summarize the key relationships that form the basis of modeling.

Considering a simple reaction of transfer of  $n$  electrons between two species, a reduced form ‘Red’

and an oxidized form ‘Ox’:



the current density associated with this reaction is, according to Faraday’s law, equal to the difference between the anodic rate  $v_a$  and the cathodic rate  $v_c$ , multiplied by  $nF$ :

$$i = nF(v_a - v_c) \quad [25]$$

According to the theory of electrochemical kinetics,<sup>98</sup> the rates of the anodic and cathodic reactions are related to the potential and the concentrations of the reacting species at the phase boundary, that is

$$i_a = nFv_a = nFk_a c_{r,s}^{x,r} \exp\left(\frac{\alpha_a nFE}{RT}\right) \quad [26]$$

$$i_c = -nFv_c = -nFk_c c_{o,s}^{x,o} \exp\left(-\frac{\alpha_c nFE}{RT}\right) \quad [27]$$

where  $k_a$  and  $k_c$  are the anodic and cathodic rate constants,  $\alpha_a$  and  $\alpha_c$  are the anodic and cathodic electrochemical transfer coefficients,  $c_{r,s}$  and  $c_{o,s}$  are the concentrations of the reduced (r) and oxidized (o) forms at the surface, respectively, and  $x,r$  and  $x,o$  are the reaction orders with respect to the reduced and oxidized species. For a given individual redox process, the anodic and cathodic electrochemical transfer coefficients are interrelated as  $\alpha_c = 1 - \alpha_a$ . The total current density for reaction eqn [24] is then

$$i = nFk_a c_{r,s}^{x,r} \exp\left(\frac{\alpha_a nFE}{RT}\right) - nFk_c c_{o,s}^{x,o} \exp\left(-\frac{\alpha_c nFE}{RT}\right) \quad [28]$$

At the equilibrium (reversible) potential  $E_0$ , the current density  $i$  is equal to zero. In the absence of a net current, the concentrations of the species at the surface are equal to their bulk concentrations (i.e.,  $c_{r,s} = c_{r,b}$  and  $c_{o,s} = c_{o,b}$ ). Then, the current density of the anodic process is equal to that of the anodic process and is defined as the exchange current density  $i_0$ , that is,

$$i_0 = nFk_a c_{r,b}^{x,r} \exp\left(\frac{\alpha_a nFE_0}{RT}\right) = nFk_c c_{o,b}^{x,o} \exp\left(-\frac{\alpha_c nFE_0}{RT}\right) \quad [29]$$

Using eqn [29], the equation for the current density [28] can be expressed in terms of the exchange current density and the overvoltage  $\eta = E - E_0$ :

$$i = i_0 \left(\frac{c_{r,s}}{c_{r,b}}\right)^{x,r} \exp\left(\frac{\alpha_a nF(E - E_0)}{RT}\right) - i_0 \left(\frac{c_{o,s}}{c_{o,b}}\right)^{x,o} \exp\left(-\frac{\alpha_c nF(E - E_0)}{RT}\right) \quad [30]$$



The ratios  $c_{r,s}/c_{r,b}$  and  $c_{o,s}/c_{o,b}$  depend on the transport of reactants and products to and from the corroding interface. If the mass transport is slow compared to charge transfer, the surface concentrations become different from those in the bulk. Conversely, if charge transfer is slow relative to mass transfer, the reaction is under charge transfer control and the ratios are equal to one not only at the equilibrium potential. In such a case, eqn [30] takes a particularly simple form and is usually referred to as the Butler–Volmer equation for charge-transfer reactions:

$$i = i_0 \exp\left(\frac{\alpha_a nF(E - E_0)}{RT}\right) - i_0 \exp\left(-\frac{\alpha_c nF(E - E_0)}{RT}\right) \quad [31]$$

The electrochemical transfer coefficient  $\alpha$  depends on the mechanism of the charge transfer reaction. For some reactions, its value can be deduced from mechanistic considerations. However, in many cases, it needs to be determined empirically. It can be determined in the form of empirical Tafel coefficients defined as the slope of a plot of potential against the logarithm of current density, that is

$$\beta_a = \frac{dE}{d \ln i_a}; \quad \beta_c = \frac{dE}{d \ln i_c} \quad [32]$$

which yields

$$\beta_a = \frac{RT}{\alpha_a nF}; \quad \beta_c = \frac{RT}{\alpha_c nF} \quad [33]$$

or, in a more traditional decimal logarithm form:

$$b_a = \frac{2.303RT}{\alpha_a nF}; \quad b_c = \frac{2.303RT}{\alpha_c nF} \quad [34]$$

Then, the Tafel coefficients  $b_a$  or  $b_c$  can be used in eqns [28] or [30] instead of the electrochemical transfer coefficient.

The above formalism includes both the cathodic and anodic process for a particular redox couple. However, in practical corrosion modeling, it is usually entirely sufficient to include only either a cathodic or an anodic partial current for a given redox process. Specifically, the cathodic partial process can be neglected for metal-ion reactions because the deposition of metal ions (i.e., the reverse of metal dissolution) is typically not of practical significance in corrosion. Similarly, the anodic partial process can be usually neglected for oxidizing agents because it is only their reduction that is of interest for corrosion. There are some exceptions to this rule, for example, in the case of relatively noble metals whose ions can be reduced under realistic conditions. Nevertheless, in the remainder of this review, we will separately consider partial anodic and cathodic processes for corrosion-related reactions.

As mentioned above, the concentrations of reactants and products at the surface depend on the mass transport to and from the corroding interface. In general, three mechanisms contribute to mass transport, that is, diffusion, migration, and convection. In many practical applications, migration can be neglected. This is the case for the transport of neutral molecules in any environment and, also, for the transport of charged species in environments that contain appreciable amounts of background electrolytic components (e.g., as supporting electrolyte). Migration becomes important in ionic systems in which there is no supporting electrolyte. We will return to the treatment of migration later in this review. If migration is neglected, the treatment of mass transfer by diffusion and convection can be simplified by using the concept of the Nernst diffusion layer. According to this concept, the environment near the corroding surface can be divided into two regions. In the inner region, called the Nernst diffusion layer, convection is negligible and diffusion is the only mechanism of transport. In the outer region, concentrations are considered to be uniform and equal to those in the bulk solution. Thus, the concentration changes linearly from the surface concentration to the bulk concentration over a distance  $\delta$ , which is the thickness of the diffusion layer. In such a model, the flux of a species  $i$  in the vicinity of a corroding interface is given by Fick's law

$$\mathcal{J}_i = -D_i \left( \frac{\partial c_i}{\partial z} \right)_{z=0} \quad [35]$$

where  $D_i$  is the diffusion coefficient of species  $i$  and  $z$  in the direction perpendicular to the surface. Integration of eqn [35] over the thickness of the diffusion layer gives:

$$\mathcal{J}_i = -D_i \frac{c_{i,b} - c_{i,s}}{\delta_i} \quad [36]$$

It should be noted that the diffusion layer thickness  $\delta$  is not a general physical property of the system. Rather, it is a convenient mathematical construct that makes it possible to separate the effects of diffusion and convection. It depends on the flow conditions, properties of the environment, and the diffusion coefficient of individual species. Thus, it may be different for various species. Methods for calculating  $\delta$  will be outlined later in this review. Equation [36] can be applied to both the reactants that enter into electrochemical reactions at the interface and to corrosion products that leave the interface. Then, it can be combined with Faraday's law to obtain the current

density. For an oxidant  $o$ , eqn [36] yields an expression for a cathodic partial current density:

$$i_c = nF\mathcal{J}_o = -nFD_o \frac{c_{o,b} - c_{o,s}}{\delta_o} \quad [37]$$

According to eqn [37], the current density reaches a maximum, limiting value when the surface concentration  $c_{o,s}$  decreases to zero. This condition defines the limiting current density, that is

$$i_{c,L} = -\frac{nFD_o c_{o,b}}{\delta_o} \quad [38]$$

For a corrosion product (e.g., Me ions), an analogous equation can be written for an anodic current density

$$i_a = nF\mathcal{J}_{Me} = -nFD_{Me} \frac{c_{Me,b} - c_{Me,s}}{\delta_{Me}} \quad [39]$$

In eqn [39], the surface concentration is typically limited by the solubility of corrosion products. Thus, a limiting anodic current density can be reached when the surface concentration of metal ions corresponds to the metal solubility, that is

$$i_{a,L} = -nFD_{Me} \frac{c_{Me,b} - c_{Me,sat}}{\delta_{Me}} \quad [40]$$

Combination of eqns [26]–[28] for charge-transfer processes and the simplified mass-transport equations (eqns [37] and [39]) yields a general formalism for electrochemical processes that are influenced by both charge transfer and mass transport. For example, for a cathodic process, the current density obtained from eqn [37] is equal to that obtained from eqn [27]. Thus, the surface concentration of the diffusing species can be obtained from eqn [37] and substituted into eqn [27]. The resulting equation can be solved analytically for  $i_c$  for some values of the reaction order  $x_o$ . If the reaction order is equal to one (i.e.,  $x_o = 1$  in eqn [27]), a particularly simple relationship is obtained for  $i_c$ , that is

$$\frac{1}{i_c} = \frac{1}{i_{c,ct}} + \frac{1}{i_{c,L}} \quad [41]$$

where  $i_{c,L}$  is the limiting current density (eqn [38]) and  $i_{c,ct}$  is the charge-transfer contribution to the current density. The latter quantity is given by eqn [27] with the bulk concentration  $c_{o,b}$  replacing the surface concentration, that is

$$i_c = -nFk_c c_{o,b}^{x_o} \exp\left(-\frac{\alpha_c nFE}{RT}\right) \quad \text{with } x_o = 1 \quad [42]$$

An analytical formula can also be obtained when  $x_o = 0.5$ .<sup>103</sup> For an arbitrary value of the reaction

order, the current density can be computed numerically by solving a single equation.

It should be noted that eqns [26] and [27] are particularly simple forms for reactions of the type [24], in which no species other than *Red* and *Ox* participate. In general, the preexponential part of eqns [26] and [27] depends on the mechanism of a particular electrochemical reaction. In general, the preexponential terms of eqns [26] and [27] can be generalized using the surface coverage factors,  $\theta_i$ , for reactive species that participate in electrochemical processes, that is,

$$i_a = nFk_a \theta_1^{x_1} \theta_2^{x_2} \dots \theta_m^{x_m} \exp\left(\frac{\alpha_a nFE}{RT}\right) \quad [43]$$

$$i_c = -nFk_c \theta_1^{x_1} \theta_2^{x_2} \dots \theta_m^{x_m} \exp\left(-\frac{\alpha_c nFE}{RT}\right) \quad [44]$$

The surface coverage factors,  $\theta_i$ , are further related to the concentrations (or, more precisely, activities) of individual species at the metal surface through appropriate adsorption isotherms. In general, analysis of reaction mechanisms on the basis of experimental data leads to a substantial simplification of eqns [43] and [44]. In many cases, activities of species can be directly used in the kinetic expressions rather than the surface coverage fractions.

The above formalism makes it possible to set up a model of electrochemical kinetics on a corroding metal surface by considering the following steps:

1. determining all possible partial cathodic and anodic processes that may occur in a given metal-environment combination;
2. writing equations for the partial cathodic or anodic current densities associated with charge transfer reactions (eqns [43] and [44] or simplifications thereof); and
3. writing equations for the mass transport of the species that participate in the charge-transfer reactions (eqns [37] and [39]). In some simple, but realistic cases a combination of the charge-transfer and mass-transport equations results in analytical formulas such as eqn [41] for partial electrochemical processes.

Once the equations for the partial anodic and cathodic processes are established, the behavior of a corroding surface can be modeled on the basis of the Wagner–Traud<sup>104</sup> theory of metallic corrosion, often referred to as the mixed potential theory. According to the mixed potential theory, the sum of all partial anodic currents is equal to the sum of all cathodic

currents. Further, it is assumed that the electrical potential of the metal at an anodic site is equal to that at a cathodic site. These assumptions follow from the requirement that charge accumulation within a metal cannot occur and, therefore, the electrons produced as a result of oxidation processes must be consumed in the reduction processes. Therefore, in a freely corroding system, we have

$$\sum_j A_a i_{a,j} + \sum_j A_c i_{c,j} = 0 \text{ at } E = E_{\text{corr}} \quad [45]$$

where  $A_a$  and  $A_c$  are the areas over which the anodic and cathodic reactions occur, respectively. The first sum in eqn [45] enumerates all anodic partial reactions and the second sum pertains to all cathodic reactions. Equation [45] is written using the sign conventions introduced earlier, in which the cathodic processes are written with a negative sign.

Equation [45] can be solved to obtain the corrosion potential,  $E_{\text{corr}}$ . Then, the corrosion current density and, equivalently, the corrosion rate, can be computed from the anodic current density for metal dissolution at the corrosion potential, that is

$$i_{\text{corr}} = i_{a,\text{Me}}(E_{\text{corr}}) \quad [46]$$

At potentials that deviate from the corrosion potential, the left-hand side of eqn [45] represents the predicted current. Such a computed current versus potential relationship can be compared with experimentally determined polarization behavior.

In the case of general corrosion,  $A_a = A_c$  and the solution of eqns [45] and [46] yields the corrosion potential and general corrosion rate. For localized corrosion, there is usually a great disparity between the areas on which the anodic and cathodic processes operate.

### 2.38.3.2 Modeling Adsorption Phenomena

Before discussing partial electrochemical reactions, it is necessary to outline the treatment of adsorption because the presence of adsorbed species is frequently assumed to derive expressions for electrochemical processes.

Adsorption of neutral molecules and ions on metals has been reviewed in detail by Gileadi,<sup>105</sup> Damaskin *et al.*,<sup>106</sup> and Habib and Bockris.<sup>107</sup> In general, adsorption leads to the reduction of the surface area that is accessible to electrochemical reactions. In such cases, adsorption results in a reduction in the rate of both anodic and cathodic processes. Thus, the rates of electrochemical reactions become modified

by the factor  $(1 - \sum \theta_j)$ , in which  $\theta_j$  is a coverage fraction by species  $j$ . At the same time, adsorption may result in the formation of surface complexes that have different dissolution characteristics. An example of such a dual effect is provided by halide ions on Fe-group metal surfaces corroding in the active state. At relatively low or moderate halide concentrations, adsorption of halides leads to a reduction in electrochemical reaction rates. However, at higher halide concentrations, the adsorbed halide ions interfere with the mechanism of anodic dissolution of iron, which may lead to an increase in the corrosion rate.

A general formalism for modeling the effect of adsorption on electrochemical reactions is provided by the Frumkin isotherm. The Frumkin formalism takes into account the interactions between the species adsorbed on the surface. It results from the requirement that the rate of adsorption is equal to the rate of desorption in the stationary state,<sup>105</sup> that is

$$v_{\text{ads},i} = v_{\text{des},i} \quad [47]$$

where the subscript  $i$  denotes any adsorbable species. The rate of adsorption is given by

$$v_{\text{ads},i} = k_{\text{ads},i} \left( 1 - \sum_j \theta_j \right) a_i \exp \left( -\beta \sum_j A_{ij} \theta_j \right) \quad [48]$$

where  $k_{\text{ads},i}$  is an adsorption rate constant,  $\theta_i$  is a fraction of the surface covered by species  $i$ ,  $a_i$  is the activity of species  $i$  in the solution,  $\beta$  is a transfer coefficient, and  $A_{ij}$  is a surface interaction coefficient between species  $i$  and  $j$ . The first term in parentheses on the right-hand side of eqn [48] represents the available surface, and the second term represents the effect of pairwise interactions between adsorbed species. The rate of desorption is given by

$$v_{\text{des},i} = k_{\text{des},i} \theta_i \exp \left( (1 - \beta) \sum_j A_{ij} \theta_j \right) \quad [49]$$

where  $k_{\text{des},i}$  is the desorption rate constant. Combination of eqns [48] and [49] yields the Frumkin isotherm, that is

$$K_{\text{ads},i} a_i = \frac{k_{\text{ads},i}}{k_{\text{des},i}} a_i = \frac{\theta_i}{1 - \sum_j \theta_j} \exp \left( \sum_j A_{ij} \theta_j \right) \quad [50]$$

where  $K_{\text{ads},i}$  is an adsorption equilibrium constant. Equation [50] can be simplified if it is assumed that the species are independently adsorbed. Then, the interactions between the species become zero, and eqn [50] takes the form of the well-known Langmuir isotherm:

$$K_{\text{ads},i}a_i = \frac{\theta_i}{1 - \sum_j \theta_j} \quad [51]$$

The Langmuir isotherm is extensively used in electrochemical kinetics. The Frumkin isotherm has been used in some studies when more accurate modeling of adsorption is warranted by experimental data, for example, in the case of corrosion in very concentrated brines (Anderko and Young<sup>108</sup>).

It should be noted that detailed modeling of adsorption requires taking into account the effect of potential on adsorption. Equations [50] and [51] are strictly valid only when adsorption is not significantly influenced by metal dissolution. An approach to include the effect of dissolution and, hence, potential on adsorption has been developed by Heusler and Cartledge<sup>109</sup> who proposed an additional process in which a metal atom from an uncovered area  $(1 - \sum \theta_j)$  reacts with an adsorbed ion from the covered area  $\theta_i$  to dissolve as ferrous ion. The adsorbed ion is then postulated to leave the surface during the reaction, thus contributing to the desorption process. Accordingly, eqn [49] is rewritten by adding an additional term, that is

$$v_{\text{des},i} = k_{\text{d},i}\theta_i \exp\left((1 - \beta) \sum_j A_{ij}\theta_j\right) + i_{\text{des},i} \quad [52]$$

where the desorption current  $i_{\text{des},i}$  is given by

$$i_{\text{des},i} = k_{\text{r},i}\theta_i \left(1 - \sum_j \theta_j\right) a_X \exp\left(\frac{\beta FE}{RT}\right) \quad [53]$$

where  $a_X$  is the activity of possible additional species (e.g.,  $\text{OH}^-$ ) that participate in the dissolution. In eqn [53], the desorption current is potential-dependent because it involves the dissolution of the metal. Equation [53] can be combined with eqns [48] and [52] to form a system of  $n$  equations for a solution with  $n$  adsorbable species. This system can be solved numerically for the coverage fractions  $\theta_i$  of each adsorbed species. Because of the potential dependence, the model predicts that the adsorption coverage rapidly decreases above a certain potential range.

It should be noted that a detailed treatment of adsorption is not always necessary for modeling aqueous corrosion. In particular, the potential dependence of adsorption can be often neglected. In most cases, simplified approaches are warranted. Specifically, for low surface coverage, the fraction  $\theta_i$  can be assumed to be proportional to the activity of the species  $i$  as shown by eqn [51]. Thus, eqns [43] and

[44] can often be simplified by using activities of species rather than their surface coverages.

### 2.38.3.3 Partial Electrochemical Reactions

The behavior of a corroding system results from the interplay of at least two and, frequently, many partial electrochemical reactions. Such reactions include:

1. anodic dissolution of pure metals and alloys in both the active and passive state;
2. reduction of protons, which is usually the primary cathodic reaction in acid corrosion;
3. reduction of water molecules, which is frequently the main cathodic reaction in deaerated neutral and alkaline solutions;
4. reduction of dissolved species that can act as proton donors such as undissociated carboxylic acids, carbonic acid, hydrogen sulfide, and numerous ions that contain protons (e.g., bicarbonates, bisulfides, etc.);
5. reduction of oxygen, which is a common cathodic process in aerated solutions;
6. reduction of metal ions at high oxidation states such as Fe(III) or Cu(II), which can be reduced to a lower oxidation state;
7. reduction of oxyanions such as nitrites, nitrates, or hypochlorites in which a nonmetallic element is reduced to a lower oxidation state;
8. oxidation of water to oxygen, which occurs at high potentials and, therefore, is rarely important in freely corroding systems; and
9. oxidation of metals to higher oxidation states, for example, Cr(III) to Cr(VI), which may occur in the transpassive dissolution region of stainless steels and nickel base alloys.

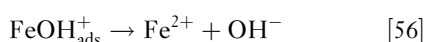
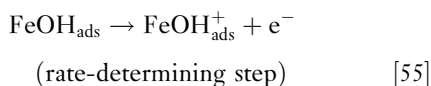
In this section, we present illustrative examples of how these reactions can be modeled in practice.

#### 2.38.3.3.1 Anodic reactions

The dissolution of several pure metals such as iron, copper, or nickel has been extensively investigated. Thus, it is possible to construct practical equations for the partial anodic dissolution processes on the basis of mechanistic information. For most alloys, detailed mechanistic information is not available and, therefore, it is necessary to establish kinetic expressions on a more empirical basis.

For iron dissolution, various multistep reaction mechanisms have been proposed. They have been reviewed in detail by Lorenz and Heusler,<sup>110</sup> Drazic,<sup>111</sup> and Keddam.<sup>112</sup> From the point of view of

modeling, particularly important parameters are the electrochemical transfer coefficient and reaction orders with respect to the ions that participate in anodic dissolution. Although there are substantial differences between the various proposed mechanisms, the dependence of the iron dissolution rate in acidic solutions on the activity of hydroxide ions is generally accepted. The mechanism proposed by Bockris *et al.*,<sup>113</sup> that is



predicts that the reaction order with respect to the  $\text{OH}^-$  ion is one because of the intermediate step of  $\text{OH}^-$  adsorption. The validity of this prediction has been verified for acidic solutions. Other mechanisms yield reaction orders between one and two. Additionally, the current density for iron dissolution has been found to depend on the activity of water (Smart and Bockris<sup>114</sup>). The mechanism of Bockris *et al.*<sup>113</sup> also predicts that the anodic transfer coefficient is  $\alpha_{\text{Fe}} = 1.5$ , which is consistent with experimentally observed Tafel slopes of 30–40 mV. Thus, the current density for Fe dissolution in acidic solutions can be expressed as

$$i_{\text{Fe,OH}} = i_{\text{Fe,OH}}^* a_{\text{OH}} a_{\text{H}_2\text{O}}^c \exp\left(\frac{\alpha_{\text{Fe}} F(E - E_{0,\text{Fe}})}{RT}\right) \quad [57]$$

where  $i_{\text{Fe,OH}}^*$  is a temperature-dependent coefficient, the subscript Fe,OH indicates that the dissolution reaction is mediated by  $\text{OH}^-$  ions, and  $c$  is an empirically determined reaction order with respect to the activity of water. According to Smart and Bockris<sup>114</sup>  $c = 1.6$ . The effect of the activity of water on the current density becomes significant for concentrated solutions, for which the activity of water is usually significantly lower than 1.

Although the reaction order with respect to the  $\text{OH}^-$  ions is valid for acidic solutions, it has been found that iron dissolution proceeds with little influence of pH for solutions with pH above  $\sim 4$ . Bockris *et al.*<sup>113</sup> explained this phenomenon by assuming a certain nonzero reaction order with respect to  $\text{Fe}^{2+}$  and by considering the hydrolysis of the  $\text{Fe}^{2+}$  ions that result from the dissolution. Alternatively, the change in the reaction order with respect to  $\text{OH}^-$  ions can be reproduced by assuming that the exchange current density is proportional to the surface coverage

by  $\text{OH}^-$  ions. This assumption is consistent with the reaction mechanism (see eqns [54]–[56]). Thus, eqn [57] can be generalized as<sup>108</sup>:

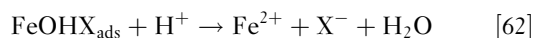
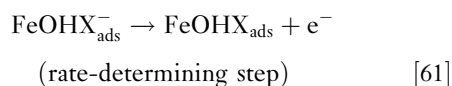
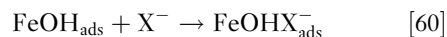
$$i_{\text{Fe,OH}} = i_{\text{Fe,OH}}^* \theta_{\text{OH}} a_{\text{H}_2\text{O}}^c \exp\left(\frac{\alpha_{\text{Fe}} F(E - E_{0,\text{Fe}})}{RT}\right) \quad [58]$$

Assuming that  $\theta_{\text{OH}}$  follows the Langmuir adsorption model, eqn [58] can be rewritten as

$$i_{\text{Fe,OH}} = i_{\text{Fe,OH}}^* \frac{a_{\text{OH}}}{1 + K_{\text{OH}} a_{\text{OH}}} a_{\text{H}_2\text{O}}^c \exp\left(\frac{\alpha_{\text{Fe}} F(E - E_{0,\text{Fe}})}{RT}\right) \quad [59]$$

Equation [59] reduces to eqn [57] for low activities of  $\text{OH}^-$ , that is, for acidic solutions. For higher concentrations of hydroxide ions, the reaction order with respect to  $\text{OH}^-$  becomes zero. This is consistent with the lack of a dependence of the Fe oxidation reaction on pH in  $\text{CO}_2$  corrosion of mild steel, which occurs at pH values above  $\sim 4$  (Nešić *et al.*,<sup>115</sup> Nordsveen *et al.*<sup>116</sup>).

The effect of halide ions on the dissolution of iron and carbon steel is of particular interest. Adsorbed halide ions may accelerate the anodic dissolution, especially in concentrated halide solutions. A number of reaction mechanisms have been proposed to explain this phenomenon. In particular, Chin and Nobe<sup>117</sup> and Kuo and Nobe<sup>118</sup> developed a mechanism that postulates a reaction route that is parallel to eqns [52]–[54]. An essentially identical mechanism has also been proposed by Drazic and Drazic.<sup>119</sup> According to this mechanism, a halide-containing surface complex is responsible for the dissolution. Thus, eqn [54] is followed by the following parallel route:



The mechanism eqns [60]–[62] results in a dissolution current density that depends on the activities of both halide and hydroxide ions. In acidic solutions, an equation analogous to eqn [57] can be written as

$$i_{\text{Fe,X}} = i_{\text{Fe,X}}^* a_{\text{X}^-}^s a_{\text{OH}^-}^t \exp\left(\frac{\alpha_{\text{Fe}} F(E - E_{0,\text{Fe}})}{RT}\right) \quad [63]$$

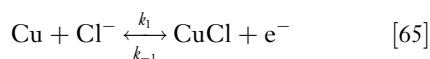
where the subscript X indicates the halide ions that mediate the reaction. For chloride systems,  $s = 0.4$  and  $t = 0.6$  when concentrations are used instead of



activities.<sup>118</sup> Since the mechanism described by eqns [60]–[62] is assumed to be parallel to the mechanism under halide-free conditions, the total current density of anodic dissolution can be assumed to be a sum of the contributions of two mechanisms. Also, eqn [63] can be generalized to neutral solutions in analogy with eqn [59]. Additionally, the desorption current density (eqn [53]) contributes to the total current, although it becomes important only at relatively high potentials, and its numerical significance is usually limited. Thus, the expression for the total active Fe dissolution current in halide solutions becomes<sup>108</sup>

$$i_{\text{Fe}} = i_{\text{Fe,OH}} + i_{\text{Fe,X}} + i_{\text{des,i}} \quad [64]$$

As with iron, anodic dissolution of copper has also been extensively investigated. Kear *et al.*<sup>120</sup> reviewed the mechanisms and associated expressions for the current density of anodic dissolution of copper in the active state in chloride environments. Copper dissolution is generally thought to proceed through the formation of cuprous chloride complexes and to be under mixed, charge-transfer and transport, control close to the corrosion potential. Several authors (Lee and Nobe,<sup>121</sup> Deslouis *et al.*,<sup>122</sup> King *et al.*<sup>123</sup>) assumed the following mechanism:



The expression for the anodic current density derived from eqns [65] and [66] is

$$\frac{i_{\text{Cu}}}{nF} = \frac{k_1 k_2}{k_{-1}} a_{\text{Cl}}^2 \exp\left(\frac{F(E - E_{0,\text{Cu}})}{RT}\right) - k_{-2} a_{\text{CuCl}_2^-} \quad [67]$$

Since the reaction rate depends on the activity of the reaction products ( $\text{CuCl}_2^-$ ) at the surface (see the second term on the right-hand side of eqn [67]), the reaction is partially controlled by the mass transport of the  $\text{CuCl}_2^-$  ions, and the anodic current density is simultaneously equal to

$$\frac{i_{\text{Cu}}}{nF} = D_{\text{CuCl}_2^-} \frac{a_{\text{CuCl}_2^-}}{\delta_{\text{CuCl}_2^-}} \quad [68]$$

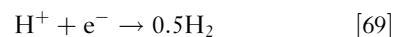
Equation [68] is a special case of eqn [39] when the bulk concentration of  $\text{CuCl}_2^-$  is negligible.

Much less mechanistic information is available for the anodic dissolution of alloys in the active state. In the case of stainless steels and nickel-base alloys, this is due to the fact that dissolution of these metals in

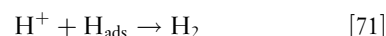
the passive state is more important than in the active state. For these alloys, active dissolution is of importance only in acidic solutions. In this case, expressions for anodic dissolution need to be established on an empirical basis. For stainless steels and nickel-base alloys, a positive reaction order between one and two with respect to hydroxide ions is observed. While such values are similar to those observed for Fe, the exchange current densities are very different and need to be determined separately for individual alloys.

### 2.38.3.3.2 Cathodic reactions

Among the numerous possible partial cathodic processes, the reduction of protons, water molecules, and dissolved oxygen is ubiquitous in aqueous corrosion. Reduction of protons is an important cathodic process in acidic solutions. The overall reaction is given by

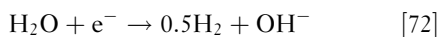


The mechanisms of this reaction have been reviewed by Vetter<sup>98</sup> and Kaesche.<sup>100</sup> Proton reduction proceeds in two steps according to two alternative mechanisms. The Volmer–Heyrovsky mechanism applies to most metals, whereas the Volmer–Tafel mechanism may be observed on certain noble metals. The Volmer–Heyrovsky mechanism can be represented as a sequence of two elementary reactions, that is



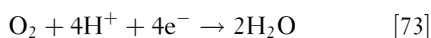
It is generally accepted that the  $\text{H}^+$  reduction reaction may proceed under activation or mass transfer control. The cathodic process of  $\text{H}^+$  reduction can be modeled assuming that the reaction order with respect to the protons is equal to one. Then, eqns [41] and [42] can be directly used for modeling. In addition to its dependence on the activity of protons, there is empirical evidence that the  $\text{H}^+$  reduction depends on the activity of water. According to Smart *et al.*,<sup>124</sup> the reaction order with respect to water activity is 2.2 on iron. The electrochemical transfer coefficient can be assumed to be equal to  $\sim 0.5$  for carbon steels and many corrosion-resistant alloys, which corresponds to a Tafel slope of 118 mV at 25 °C.

As the pH of a solution increases, the importance of the proton reduction reaction rapidly decreases. In neutral and alkaline solutions, the reduction of water molecules becomes predominant unless stronger oxidizing agents (e.g., oxygen) are present in the system. The water reduction is given by

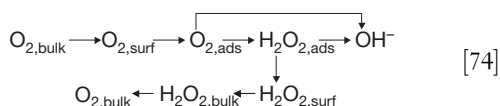


and is thermodynamically equivalent to the reduction of protons. However, its kinetic characteristics are different. Unlike the reduction of protons, the water reduction reaction typically does not exhibit a limiting current density because there are no diffusion limitations for the transport of  $\text{H}_2\text{O}$  molecules to the surface. This remains true as long as the system is predominantly aqueous. The water reduction process can be modeled by assuming the same reaction order with respect to  $\text{H}_2\text{O}$  as that for proton reduction. Also, practically the same value of the electrochemical transfer coefficient can be assumed.

Reduction of oxygen, that is



is the predominant cathodic reaction in aerated aqueous solutions unless the solution contains stronger oxidizing agents such as ferric, cupric, or hypochlorite ions. The mechanism of oxygen reduction is substantially more complex than the mechanisms of  $\text{H}^+$  or  $\text{H}_2\text{O}$  reduction. Oxygen reduction on iron and carbon steel has been reviewed by Jovancicevic and Bockris,<sup>125</sup> Zecevic *et al.*,<sup>126</sup> and Jovancicevic.<sup>127</sup> On stainless steels, it has been analyzed by Le Bozec *et al.*,<sup>128</sup> Kapusta,<sup>129</sup> and in papers cited therein. On copper, it has been studied by King *et al.*<sup>130</sup> In general, it has been established that the reaction may proceed either through a four-electron pathway, which leads to the reduction of  $\text{O}_2$  to  $\text{H}_2\text{O}$ , or through a two-electron pathway, which leads to the formation of  $\text{H}_2\text{O}_2$  as an intermediate. An overall reaction scheme may be represented as



where the subscripts 'surf' and 'ads' denote the oxygen in the diffusion layer close to the surface and oxygen adsorbed on the surface, respectively. The absorbed intermediate  $\text{H}_2\text{O}_2$  can be either further reduced to  $\text{OH}^-$  or desorbed and dissolved in the solution or converted back to oxygen through decomposition or reoxidation. The actual reaction pathway is influenced by many factors such as the surface treatment of the electrode.<sup>128</sup> However, the four-electron reduction path from  $\text{O}_2$  to  $\text{OH}^-$  seems to predominate.<sup>129</sup> Oxygen reduction may be under charge transfer or mass transfer control, due to the diffusion of dissolved oxygen molecules. For passive metals, the process is usually under charge transfer control because the limiting

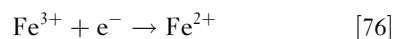
current density for oxygen reduction is usually greater than the passive current density at typical dissolved oxygen concentrations.

For modeling purposes, the key parameters are the electrochemical transfer coefficient and the reaction orders with respect to dissolved oxygen and protons. These parameters determine the dependence of the reduction reaction on dissolved oxygen concentration (or, equivalently, the partial pressure of oxygen) and on pH. Once these parameters are known, the oxygen reduction process can be modeled on a semi-empirical basis. The current density for oxygen reduction can be written as:

$$i_{\text{O}_2} = i_{\text{O}_2}^* a_{\text{O}_2,s}^q a_{\text{H}^+,s}^r \exp \left[ \frac{-\alpha_{\text{O}_2} F (E - E_{0,\text{O}_2})}{RT} \right] \quad [75]$$

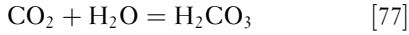
Equation [75] needs to be coupled with eqn [37] with  $n=4$  for mass-transfer limitations. The reaction orders  $q$  and  $r$  in eqn [75] are, in general, specific to the metal surface although they are expected to be similar within families of alloys. For stainless steels, there seems to be a consensus that the reaction order with respect to dissolved oxygen is 0.5 (Kapusta,<sup>129</sup> Sridhar *et al.*<sup>131</sup>), whereas the order with respect to protons ranges from 0.5 to 1 (or, equivalently, the order with respect to hydroxide ions varies from  $-0.5$  to  $-1$ ). For passive iron or carbon steel, the reaction order with respect to  $\text{O}_2$  has been reported as 0.5 (Calvo and Schiffrin<sup>132</sup>) or 1 (Jovancicevic and Bockris,<sup>125</sup> Jovancicevic<sup>127</sup>). For copper, a value of 1 has been reported (King *et al.*<sup>130</sup>).

Another important cathodic reaction is the reduction of transition metal ions such as  $\text{Fe}^{3+}$  and  $\text{Cu}^{2+}$  to lower oxidation states, for example

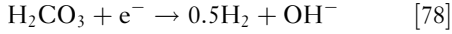


This process can be modeled as a first-order reaction with respect to the activity of ferric ions by taking into account the mass transport limitations (eqn [37]).

All the cathodic reactions discussed above may proceed under mass transfer limitations due to the diffusion of reactants to the corroding surface. However, cathodic limiting current densities may also arise because of limitations due to homogeneous reactions in the solution. A prominent example of such a reaction is the reduction of carbonic acid, which is the key cathodic process in  $\text{CO}_2$  corrosion of carbon steel. This reaction accounts for the substantially higher corrosivity of  $\text{CO}_2$  solutions than mineral acid solutions at the same pH. Carbonic acid results from the hydration of dissolved  $\text{CO}_2$ , that is



Reaction eqn [77] is followed by the reduction of  $\text{H}_2\text{CO}_3$  on the surface, that is



which is thermodynamically equivalent to the reduction of protons, but is characterized by different kinetics. The  $\text{H}_2\text{CO}_3$  reduction is under activation or chemical reaction control, and can be modeled using eqn [41]. The charge transfer current is expressed as (Nešić *et al.*<sup>115</sup>):

$$i_{\text{H}_2\text{CO}_3} = i_{\text{H}_2\text{CO}_3}^* a_{\text{H}_2\text{CO}_3} a_{\text{H}^+}^{-0.5} \exp \left[ \frac{-\alpha_{\text{H}_2\text{CO}_3} F (E - E_{0,\text{H}})}{RT} \right] \quad [79]$$

where the transfer coefficient can be assumed to be equal to that for  $\text{H}_2\text{O}$  reduction. The limiting current density can be calculated from an equation developed by Nešić *et al.*<sup>115</sup> on the basis of a formula derived by Vetter<sup>98</sup> for processes with a rate-determining homogeneous reaction in the solution. Here, the rate-determining reaction is the hydration of  $\text{CO}_2$  and the limiting current density is:

$$i_{\text{H}_2\text{CO}_3,\text{L}} = F a_{\text{H}_2\text{CO}_3} \left( D_{\text{H}_2\text{CO}_3} K_{\text{H}_2\text{CO}_3} k_{\text{H}_2\text{CO}_3}^f \right)^{1/2} \quad [80]$$

where  $D_{\text{H}_2\text{CO}_3}$ ,  $K_{\text{H}_2\text{CO}_3}$ , and  $k_{\text{H}_2\text{CO}_3}^f$  are the diffusion coefficient of  $\text{H}_2\text{CO}_3$ , equilibrium constant for the hydration of  $\text{CO}_2$ , and forward reaction constant for the hydration reaction, respectively.

### 2.38.3.3.3 Temperature dependence

The rates of the majority of partial anodic and cathodic processes are strongly dependent on temperature. This temperature dependence can be modeled by assuming that the concentration-independent part of the exchange current density (here denoted by  $i^*$ ) is expressed as

$$i^*(T) = i^*(T_{\text{ref}}) \exp \left[ -\frac{\Delta H^\ddagger}{R} \left( \frac{1}{T} - \frac{1}{T_{\text{ref}}} \right) \right] \quad [81]$$

Equation [81] is equivalent to assuming a constant enthalpy of activation  $\Delta H^\ddagger$  for each partial process.

### 2.38.3.4 Modeling Mass Transport Using Mass Transfer Coefficients

To calculate the mass-transport effects on electrochemical kinetics according to eqns [37]–[40], it is necessary to predict the diffusion layer thickness  $\delta_i$

or, equivalently, the limiting current density. Theoretical formulas for these quantities cannot be obtained for arbitrary flow conditions and, therefore, empirical approaches are necessary for most practical applications.

In the case of a rotating disk electrode, a theoretical solution has been derived by Levich.<sup>133</sup> It is noteworthy that Levich's solution preceded experimental results. The thickness of the diffusion layer on a rotating disk electrode is

$$\delta_i = 1.61 D_i^{1/3} \nu^{1/6} \omega^{-1/2} \quad [82]$$

where  $D_i$  is the diffusion coefficient of the reacting species,  $\omega$  is the rotation rate, and  $\nu$  is the kinematic viscosity, which is the ratio of the dynamic viscosity and density, that is

$$\nu = \eta / \rho \quad [83]$$

In view of the relationships between the thickness of the diffusion layer and the limiting current density (eqns [38] and [40]), a physically equivalent predictive expression can be written for the limiting current density. For example, the limiting current density of a cathodic reaction (eqn [38]) then becomes:

$$i_{\text{c,L}} = -0.6205 n F c_{0,\text{b}} D_o^{2/3} \nu^{-1/6} \omega^{1/2} \quad [84]$$

For many other flow geometries, mass transport can be calculated using empirical correlations expressed in terms of the mass transfer coefficient  $k_m$ . In general, the mass transfer coefficient is defined as

$$k_m = \frac{\text{Reaction rate}}{\text{Concentration driving force}} \quad [85]$$

For an electrochemical reaction, the reaction rate is expressed using the current density, and eqn [36] for a mass transport-limited reaction can be rewritten in terms of the mass transfer coefficient  $k_m$  as

$$\mathcal{J}_i = \frac{i_i}{n_i F} = -D_i \frac{c_{i,\text{b}} - c_{i,\text{s}}}{\delta_i} = -k_{m,i} (c_{i,\text{b}} - c_{i,\text{s}}) \quad [86]$$

This indicates a relationship between  $\delta_i$  and  $k_{m,i}$  that is

$$k_{m,i} = \frac{D_i}{\delta_i} \quad [87]$$

Mass transport rates can be expressed using dimensionless groups, for which empirical correlations can be developed for a number of flow patterns. The mass transfer coefficient  $k_m$  enters into the Sherwood number  $Sh$ , which is defined as

$$Sh = \frac{k_m d}{D} \quad [88]$$

where  $d$  is a characteristic dimension (e.g., a pipe or rotating disk diameter);  $D$ , a diffusion coefficient; and the subscript  $i$  has been dropped for convenience as it is understood that eqn [88] is written for individual reacting species. The Sherwood number can be correlated with the Reynolds ( $Re$ ) and Schmidt ( $Sc$ ) numbers, which are defined as

$$Re = \frac{Vd}{\nu} \quad [89]$$

$$Sc = \frac{\nu}{D} \quad [90]$$

where  $V$  is the linear velocity. It can be shown by dimensional analysis that  $Sb$  is a function of  $Re$  and  $Sc$ . This function typically has the form<sup>134,135</sup>

$$Sb = \text{Const} \times Re^x \times Sc^y \quad [91]$$

where  $x$  is usually between 0.3 and 1 and  $y$  is about 1/3. For example, the theoretically derived results for the rotating disk can be recast in terms of the mass transfer coefficient as

$$Sb = 0.6205 Re^{0.5} Sc^{0.33} \quad [92]$$

Empirical expressions for other flow geometries have been reviewed by Poulson<sup>134,135</sup> for single-phase flow conditions. Equations of the type eqn [91] exist for the rotating cylinder, impinging jet, nozzle or orifice, and pipe flow. For the rotating cylinder, the correlation of Eisenberg *et al.*<sup>136</sup> is widely used

$$Sb = 0.0791 Re^{0.70} Sc^{0.356} \quad [93]$$

For single-phase flow in a straight pipe, several correlations have been developed. Among these equations, Berger and Hau<sup>137</sup> correlation has found use in a number of corrosion modeling studies:

$$Sb = 0.0165 Re^{0.86} Sc^{0.33} \quad [94]$$

The earlier pipe flow formulas have been reviewed by Poulson,<sup>134</sup> and the use of more recent equations has been discussed by Lin *et al.*<sup>138</sup> Equations of this kind are not as well developed for multiphase flow. Correlations are available for stratified flow (Wang and Nešić<sup>139</sup>), but a comprehensive treatment is not available for various regimes of multiphase flow. Therefore, a convenient alternative is to base the computation of mass transfer coefficients on the well-known analogy between heat and mass transfer.

The analogies between the transport of mass, momentum, and heat can be understood by considering the similarity between their respective mathematical formulations, namely, Fick's law of diffusion, Newton's law of viscosity, and Fourier's law of heat conduction.

Thus, once a relationship has been established for a given phenomenon in terms of dimensionless numbers, it can further serve for the calculation of another phenomenon that takes place under the same geometric and physical conditions but with different velocities, dimensions, and physical properties of the system. In particular, the correlations established for heat transfer can be used for mass transfer calculations. The analogy between the heat, mass, and momentum transfer has been stated in a dimensionless form by Chilton and Colburn<sup>140</sup> as

$$\frac{Sb}{Re Sc^{1/3}} = \frac{Nu}{Re Pr^{1/3}} = \frac{f}{2} \quad [95]$$

where the Nusselt number,  $Nu$ , and the Prandtl number,  $Pr$ , are the heat transfer equivalents of the Sherwood and Schmidt numbers in mass transfer, respectively, and  $f$  is a friction factor. Correlations for the friction factor are available as a function of pipe roughness, its diameter, and the Reynolds number (Frank<sup>141</sup>). The exponent 1/3 in eqn [95] can be replaced with a generalized exponent  $n$ . The Nusselt and Prandtl numbers are defined as

$$Nu = \frac{bd}{\lambda} \quad [96]$$

$$Pr = \frac{\nu}{\alpha} \quad [97]$$

where  $b$  is the convection heat transfer coefficient;  $\lambda$ , the thermal conductivity; and  $\alpha$ , the thermal diffusivity ( $\alpha = \lambda/\rho C_p$ ).

This relationship makes it possible to determine the mass transfer coefficient in two-phase flow systems for which experimental heat transfer correlations are available. Heat transfer correlations take the form

$$Nu = \text{Const} \times Re^x Pr^y \quad [98]$$

They have been reviewed by Kim *et al.*<sup>142</sup> and Adsani *et al.*<sup>143,144</sup> for annular, slug, and bubbly flow in horizontal and vertical tubes. Also, Adsani *et al.*<sup>143,144</sup> developed a correlation for calculating the two-phase Nusselt number, which is a generalization of the Chilton-Colburn<sup>140</sup> heat transfer expression (i.e., the second equality of eqn [95]):

$$Nu_{\text{two-phase}} = C_1 f_L^{C_2} \left( \frac{V_L d}{\nu} \right)^{C_3} Pr_L^{1/3} \quad [99]$$

where the liquid-phase friction factor  $f_L$  and velocity  $V_L$  are calculated using flow models for annular, slug, and bubbly flow, and  $C_1$ ,  $C_2$ , and  $C_3$  are fitting constants. Subsequently, the Sherwood number and the

mass transfer coefficient can be obtained from the first equality in eqn [95].

As shown in the above equations, the computation of the mass transfer coefficient requires the diffusion coefficients, viscosity, and density. Density is a thermodynamic property and, as such, can be calculated from any comprehensive thermodynamic model for electrolyte systems. For example, Wang *et al.*<sup>54</sup> describe how to calculate densities in a way that is consistent with other thermodynamic properties. The computation of viscosities and diffusion coefficients requires separate models, which are beyond the scope of this chapter. Viscosity and diffusivity models have been reviewed and critically evaluated by Corti *et al.*<sup>145</sup> with particular emphasis on systems at elevated temperatures.

### 2.38.3.4.1 Example of electrochemical modeling of general corrosion

To illustrate the application of the principles described earlier, Figure 5 shows the computation of the corrosion rate and potential of type 316 stainless steel in aqueous solutions of HF. These calculations have been made using the model of Anderko *et al.*<sup>108,146</sup> as implemented in the Corrosion Analyzer software.<sup>61</sup> The upper diagram shows the partial cathodic and anodic processes in a 2 m HF solution. Three cathodic processes are taken into account in this system: reduction of protons ( $H^+$ ), reduction of undissociated HF molecules, and reduction of water molecules. These partial processes are marked in Figure 5(a) as (1), (2), and (3), respectively. The  $H^+$  reduction reaction is modeled using eqns [41] and [42] as described earlier. The HF reduction process is calculated using the same equations, but with a different exchange current density. Both the  $H^+$  and HF reduction processes show partial current densities because of mass transport limitations for the transport of  $H^+$  and HF to the surface. Because of the low degree of dissociation of HF, the reduction of HF (line two in Figure 5(a)) plays a much more important role than the reduction of  $H^+$  ions (line 1). The partial anodic curve for the oxidation of 316 SS is labeled as (4). It is assumed that the alloy components dissolve congruently, and the dependence of the partial anodic current density on the acidity of the solution is analogous to that observed for Fe (see eqn [59]), but with a different exchange current density. The superposition of the partial cathodic and anodic processes yields a predicted polarization curve, which is shown by a thick line in Figure 5(a). The location of the mixed potential is calculated

according to eqn [45] with  $A_a = A_c$  and marked with a triangle. The complete model reproduces the experimental corrosion rates (Figure 5(b)) and corrosion potentials (Figure 5(c)) as a function of HF concentration and temperature.

### 2.38.3.5 Detailed Modeling of Mass Transport

The treatment of mass transport by the use of mass transfer coefficients is computationally efficient and is capable of reproducing steady-state corrosion behavior with good accuracy. However, it is subject to some limitations including:

1. it is suitable for calculating only steady-state behavior and, therefore, it is not appropriate for modeling time-dependent corrosion,
2. it neglects migration which introduces errors especially for dilute systems without a background electrolyte, and
3. it is not convenient for modeling transport in systems with geometrical constraints, especially when the cathodic and anodic areas are spatially separated; thus, it is not well suited for modeling the propagation of localized corrosion.

These limitations can be eliminated by a more comprehensive (but much more computationally demanding) treatment of transport phenomena. This treatment is based on the conservation laws for each species in the solution (Newman<sup>150</sup>):

$$\frac{\partial c_k}{\partial t} = -\nabla \mathcal{J}_k + R_k \quad k = 1, \dots, K \quad [100]$$

where  $C_k$  is the concentration of species  $k$ ,  $t$  is the time,  $\mathcal{J}_k$  is the flux of species  $k$ ,  $\nabla$  is the vector differential operator (which reduces to  $\partial/\partial x$  in a one-dimensional case), and  $R_k$  is the rate of production (source) or depletion (sink) of this species as a result of chemical reactions. In the vast majority of practical applications, the dilute solution theory is used to calculate the flux of the species, that is

$$\mathcal{J}_k = -D_k \nabla c_k - z_k F u_k c_k \nabla \varphi + c_k v \quad [101]$$

where  $u_k$  is the mobility of species  $k$ ,  $\varphi$  is the electrostatic potential in the solution,  $v$  is the fluid velocity, and the other symbols were defined previously. In eqn [101], the first term on the right-hand side represents the contributions of diffusion, the second term describes migration, and the third term is a contribution of convection. In the migration term, the mobility can be calculated from the diffusivity using the Nernst–Einstein equation:



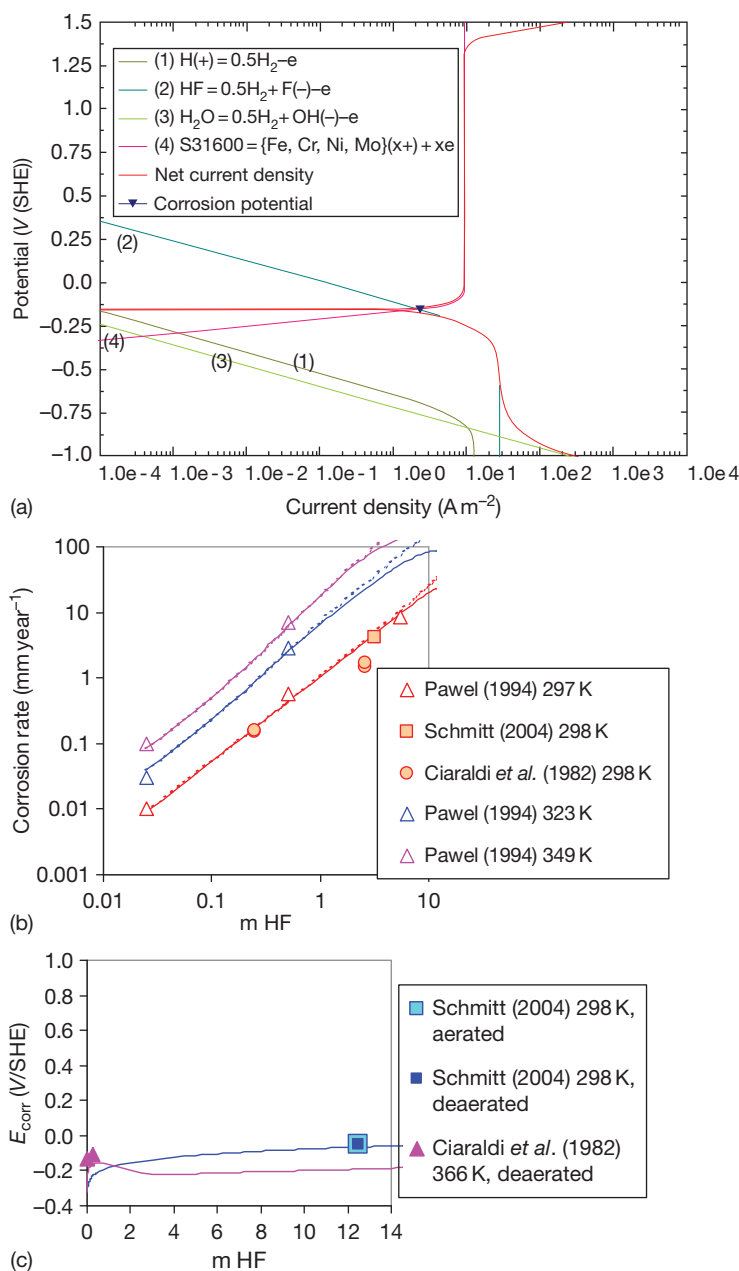


**Figure 5** Application of an electrochemical model of general corrosion<sup>108,146</sup> to type 316L stainless steel in aqueous HF solutions. The upper diagram (a) shows the partial cathodic and anodic processes in a 2 m HF solution. The middle (b) and lower (c) diagrams compare the calculated and experimental<sup>147–149</sup> corrosion rates and potentials, respectively.

$$u_k = \frac{D_k}{RT} \quad [102]$$

which is exact for species at infinite dilution and provides a good approximation at finite concentrations. An additional condition for determining the potential in eqn [101] is given by the Poisson equation:

$$\nabla^2 \varphi = -\frac{F}{\varepsilon} \sum_k z_k c_k \quad [103]$$

where  $\varepsilon$  is the dielectric permittivity of the solution. It can be shown<sup>150</sup> that, due to the large value of the ratio  $F/\varepsilon$ , even a very small separation of charges (i.e.,  $\sum z_k c_k \neq 0$ ) results in a large potential gradient,

which in turn prevents any appreciable separation of charge. Therefore, eqn [103] is very often replaced in practice by the simple electroneutrality condition, that is

$$\sum z_k c_k = 0 \quad [104]$$

which is one of the basic equations for computing equilibrium properties of electrolytes.

It should be noted that eqn [101] is rigorous only for dilute solutions. For concentrated solutions, its more general counterpart is<sup>150</sup>

$$\mathcal{F}_k = c_k v_k \quad [105]$$

where the velocities  $v_k$  of species  $k$  are determined by the multicomponent diffusion equations:

$$c_k \nabla \mu_k = RT \sum_j \frac{c_k c_j}{c_{\text{tot}} D_{kj}} (v_j - v_k) \quad [106]$$

where  $D_{kj}$  are the mutual diffusion coefficients, and  $c_{\text{tot}}$  is the total concentration of all components. The application of eqns [105] and [106] is very difficult due to the lack of a general methodology for computing  $D_{kj}$  and computational complexity. Therefore, eqns [105] and [106] have found few applications in practical models. However, a practical simplified form can be obtained for moderately dilute solutions for which the concentrations of solute species are smaller than the concentration of the solvent. Then, eqns [105] and [106] simplify to

$$\mathcal{F}_k = -\frac{D_k}{RT} c_k \nabla \mu_k + c_k v \quad [107]$$

Considering that  $\mu_k = \mu_k^0 + RT \ln c_k \gamma_k + z_k F \varphi$ , the flux equation becomes<sup>150</sup>

$$\mathcal{F}_k = -D_k \nabla c_k - z_k F u_k c_k \nabla \varphi + c_k v - D_k c_k \nabla \ln \gamma_k \quad [108]$$

which is only moderately more complex than the dilute-solution eqn [101], but benefits from the information on solution nonideality that is embedded in the activity coefficient and can be calculated from an electrolyte thermodynamic model.

In the convective term of eqn [101] or [108], the instantaneous fluid velocity ( $v$ ) can be calculated, in principle, by the methods of computational fluid dynamics. However, such calculations involve a large computational effort and are, in practice, limited with respect to flow geometries and conditions. For turbulent flow, a practical approach relies on introducing turbulent diffusion. Accordingly, instantaneous velocity is divided into steady and turbulent components. The steady component is parallel to the surface and does not contribute to transport to and from the surface. Then, the convection term in eqn [101] or [108],

$c_k v$ , is approximated by a turbulent diffusivity term,  $-D_t \nabla c_k$ , which can be lumped with the molecular diffusion term thus defining an effective diffusion coefficient (Davis,<sup>151</sup> Nordsveen *et al.*<sup>116</sup>)

$$D_k^{\text{eff}} = D_k + D_t \quad [109]$$

where  $D_t$  can be obtained from empirical correlations with fluid properties.<sup>151,152</sup> For example, Davis's<sup>151</sup> correlation has been used in the CO<sub>2</sub> corrosion model of Nordsveen *et al.*<sup>116</sup>:

$$D_t = 0.18 \left( \frac{z}{\delta} \right)^3 \frac{\eta}{\rho} \quad [110]$$

where  $z$  represents the distance from the surface (either a metal surface or a surface covered with corrosion products),  $\eta$  is the viscosity,  $\rho$  is the density, and  $\delta$  is the thickness of the laminar boundary layer, which can be calculated for a pipe with a diameter  $d$  as

$$\delta = 25 Re^{-7/8} d \quad [111]$$

It is noteworthy that this formalism can be shown to be physically equivalent to the treatment of turbulent flow through mass transfer coefficients as described in the previous section. Specifically, Wang and Nešić<sup>139</sup> showed a relationship between the mass transfer coefficient and  $D_t$ :

$$\frac{1}{k_{m,i}} = \int_0^\delta \frac{dz}{D_i + D_t} \quad [112]$$

The computation of the rates of production or depletion  $R_k$  is necessary in order to apply eqn [100]. A general matrix formalism for calculating the  $R_k$  terms in a system with multiple reactions has been developed by Nordsveen *et al.*<sup>116</sup> The main limitation here is the fact that rate data are available only for a very limited number of reactions such as precipitation of common scales (CaCO<sub>3</sub>, FeCO<sub>3</sub>) and selected homogeneous reactions (e.g., hydration of H<sub>2</sub>CO<sub>3</sub>). For the vast majority of reactions, only equilibrium equations are available and, in fact, there is no physical need for kinetic expressions for most homogeneous reactions because they are fast relative to mass transport. Therefore, arbitrary rate expressions may be assumed as long as they are constrained by the equilibrium constant (i.e., the ratio of the forward and reverse rate constants is equal to the equilibrium constant), give appropriately fast reaction rates and change direction as the equilibrium point is crossed. A convenient expression for the production or depletion rate for species  $k$  can be defined in terms of the departure of the ionic product from equilibrium (Walton<sup>153</sup>):

$$R_k = \sum_{m=1}^M \left[ -r_m v_{km} \ln \left( \frac{\prod c_k^{v_{km}}}{K_m} \right) \right] \quad [113]$$

where  $r_m$  is an adjustable numerical rate parameter for reaction  $m$ ,  $K_m$  is the equilibrium constant for reaction  $m$ , and  $v_{km}$  is the stoichiometric coefficient for species  $k$  in the  $m$ th reaction. Alternatively, the transport equations can be first solved separately from the chemical effects and, then, at the end of each sufficiently small time step, thermodynamic equilibrium calculations can be performed in each elementary volume.

To solve the system of transport eqns [100] and [101] or [108], boundary conditions are required. In the bulk solution, the equilibrium concentrations are the natural boundary conditions. For each species involved in electrochemical reactions, the flux at the metal surface is determined from

$$\mathcal{J}_k = -\frac{i_k}{n_k F} \quad [114]$$

where the current density  $i_k$  is calculated from appropriate expressions for cathodic and anodic partial processes as a function of concentrations at the metal surface. This provides a link to the mechanistic or empirical electrochemical expressions described above. For the species that are not involved in the reactions, the flux at the interface is zero. It should be noted that the application of this formalism of mass transport can become quite computationally involved, especially for systems with numerous species, because it requires solving a system of differential equations (eqns [100] and [101] or [108]) with constraints (eqns [103] or [104] and chemical terms).

### 2.38.3.5.1 Effect of the presence of porous media

The above transport equations need to be modified when mass transport occurs through porous media such as corrosion products, calcareous deposits, soil or sand, and various man-made environments, including concrete and ceramics. Such a generalization can be formulated in terms of two characteristic quantities, porosity and tortuosity. Porosity ( $\varepsilon$ ) is the volumetric void fraction of the medium, whereas tortuosity ( $\tau$ ) is defined as the ratio of the distance that an ion or molecule travels around solid particles to the direct path. For practical applications, tortuosity can be correlated with porosity thus leaving porosity as the only parameter to affect transport equations. The generalization of transport equations to porous media has been

discussed by Newman<sup>150</sup> and Bear.<sup>154</sup> A detailed corrosion model that includes the transport in porous corrosion products has been developed for CO<sub>2</sub> corrosion by Nordsveen *et al.*<sup>116</sup> and Nešić and Lee.<sup>155</sup>

### 2.38.3.6 Active–Passive Transition and Dissolution in the Passive State

The expressions for anodic partial current densities discussed above (eqns [54]–[68]) are limited to the dissolution in the active state. However, dissolution in the passive state and the transition between the active and passive state are equally important for modeling aqueous corrosion. In fact, passivity is the key to our metal-based civilization (Macdonald<sup>97</sup>) and has been extensively investigated since the pioneering work of Faraday and Schönbein in the 1830s. Theories of passivity have been reviewed by many investigators (Frankenthal and Kruger,<sup>156</sup> Froment,<sup>157</sup> Marcus and Oudar,<sup>158</sup> Natishan *et al.*,<sup>159</sup> Macdonald<sup>97,160</sup>) and are beyond the scope of this chapter. In this section, we focus solely on practical models for calculating the anodic current density in the passive and active–passive transition regions as a function of solution chemistry.

Passivity manifests itself by a sharp drop in the anodic current density at a certain critical potential as the metal is polarized in a negative-to-positive potential direction. For calculation purposes, empirically determined anodic polarization curves can be reproduced using a suitable fitting function. For example, such a function has been developed by Macdonald.<sup>161</sup> Then, empirical fitting functions can be used within the framework of the mixed potential theory as described above.

A convenient way to introduce the active–passive transition into a computational model is to consider a current that leads to the formation of a passive layer in addition to the current that leads to active dissolution (Ebersbach *et al.*,<sup>162</sup> Anderko and Young<sup>108</sup>). For this purpose, a certain fraction of the surface  $\theta_p$  can be assumed to be covered by a passive layer. The change of the passive layer coverage fraction with time can be expressed as

$$\left( \frac{\partial \theta_p}{\partial t} \right)_{E, a_i} = c i_{\text{MeO}} (1 - \theta_p) - K \theta_p \quad [115]$$

where  $i_{\text{MeO}}$  is the current density that contributes to the formation of a passive layer. The second term on the right-hand side of eqn [115] represents the rate of dissolution of the passive layer, which is

proportional to the coverage fraction. Solution of this equation in the steady-state limit yields an expression for the anodic dissolution current:

$$i_{\text{Me,TOT}} = \frac{i_{\text{Me}} + i_{\text{MeO}}}{1 + (i_{\text{MeO}}/K)} = \frac{i_{\text{Me}} + i_{\text{MeO}}}{1 + (i_{\text{MeO}}/i_{\text{p}})} \quad [116]$$

where  $i_{\text{Me}}$  is the dissolution current density in the active state and the ratio  $i_{\text{p}} = c/K$  constitutes the passive current density. The current  $i_{\text{Me}}$  is calculated using the active dissolution models described above. The current  $i_{\text{MeO}}$  is expressed using the usual expression for process under activation control, that is

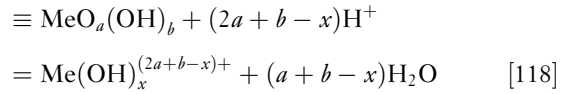
$$i_2 = i_2^0 \exp\left(\frac{\alpha_2 F(E - E_{\text{F}})}{RT}\right) \quad [117]$$

in which the parameters can be adjusted to reproduce the observable characteristics of the active-passive transition including the critical current density ( $i_{\text{crit}}$ ) and Flade potential ( $E_{\text{F}}$ ).<sup>146</sup> Equation [116] can be then used for the anodic process of metal dissolution within the framework of the mixed-potential theory (eqns [45] and [46]).

An example of mixed-potential calculations for a passive metal is shown in **Figure 6**. This figure illustrates the computation of the corrosion potential of alloy 600 in a dilute LiOH solution as a function of dissolved oxygen concentration. As in **Figure 5**, the upper and middle diagrams of **Figure 6** show the predicted partial  $E$  versus  $i$  curves for the anodic and cathodic processes. The upper diagram (**Figure 6(a)**) shows the predictions for a very low  $\text{O}_2$  concentration (0.013 ppm), whereas the concentration in the middle diagram is somewhat higher (0.096 ppm). In a weakly alkaline solution, the alloy is passive as indicated by the vertical portion of the anodic curve (line labeled as (3)). Two main cathodic processes are taken into account in this system, that is, the reduction of  $\text{H}_2\text{O}$  (line (1)) and the reduction of  $\text{O}_2$  (line (2)). At the lower  $\text{O}_2$  concentration, the limiting current density is lower than the passive current density, and the main cathodic process is the reduction of  $\text{H}_2\text{O}$  (i.e., the mixed potential lies at the intersection of the lines (1) and (3) in **Figure 6(a)**). As the  $\text{O}_2$  concentration increases, the  $\text{O}_2$  reduction reaction becomes predominant and determines the mixed potential, which then lies at the intersection of lines (2) and (3). This behavior explains the experimentally determined s-shaped dependence of  $E_{\text{corr}}$  on  $\text{O}_2$  concentration as shown in **Figure 6(c)**. The s-shape is due to the transition from  $\text{H}_2\text{O}$  reduction to  $\text{O}_2$  reduction as the dominant cathodic process. The transition

depends on flow conditions because the  $\text{O}_2$  reduction is partially under mass transport control.

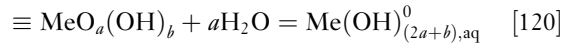
Passive dissolution and active-passive transition strongly depend on solution chemistry. In the absence of specific active ions, the dissolution of oxide films depends primarily on the pH of the solution. Appropriate kinetic expressions can be constructed by considering dissolution reactions between the passive oxide/hydroxide surface layers and solution species (Anderko *et al.*,<sup>146</sup> Sridhar *et al.*<sup>131,164</sup>) In acidic solutions, the key reaction involves the protons from the solution:



where the symbol ‘ $\equiv$ ’ denotes surface species. The corresponding kinetic equation is

$$i_{\text{p,H}^+} = k_{\text{H}^+} a_{\text{H}^+,s}^q \quad [119]$$

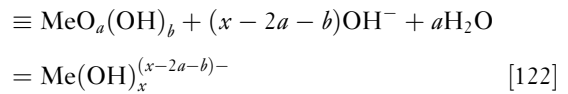
where  $a_{\text{H}^+,s}$  denotes the surface concentration of hydrogen ions and  $q$  is a reaction order, which is not necessarily related to the stoichiometric coefficient in the dissolution reaction. In neutral solutions, the predominant dissolution reaction can be written as



where the predominant species on the right-hand side of eqn [120] is a neutral complex as indicated by the superscript 0. The corresponding kinetic equation is

$$i_{\text{p,H}_2\text{O}} = k_{\text{H}_2\text{O}} a_{\text{H}_2\text{O},s}^r \quad [121]$$

where the reaction order with respect to water indicates that dissolution may be affected by water activity. Similarly, the predominant reaction in alkaline solutions is



with a corresponding kinetic equation given by

$$i_{\text{p,OH}^-} = k_{\text{OH}^-} a_{\text{OH}^-,s}^c \quad [123]$$

The total passive current density as a function of pH is given by

$$i_{\text{p}} = i_{\text{p,H}^+} + i_{\text{p,H}_2\text{O}} + i_{\text{p,OH}^-} \quad [124]$$

It should be noted that the passive dissolution may be influenced by mass transport. For example, aluminum dissolution in alkaline solutions is known to be partly under mass transport control due to the transport of

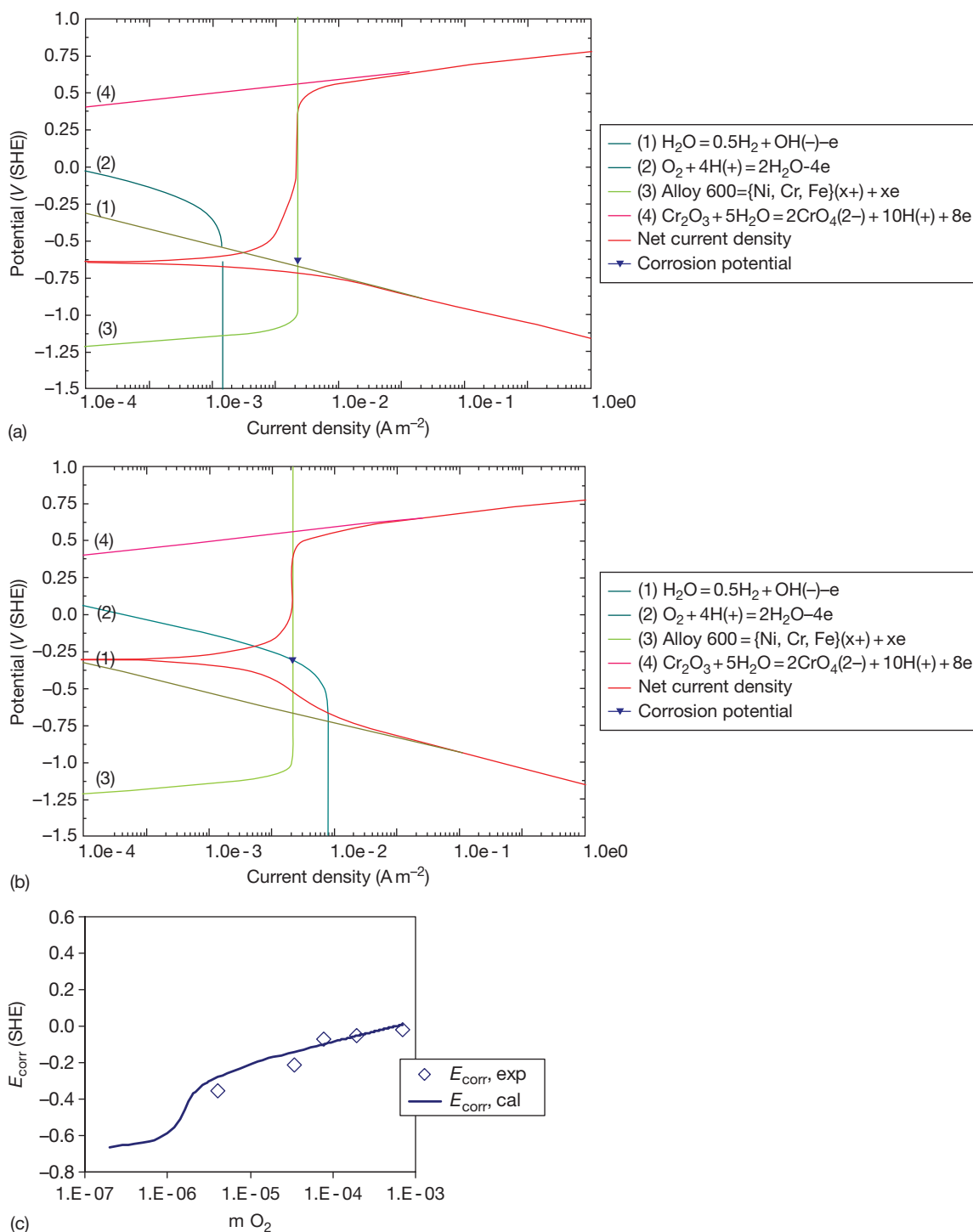


**Figure 6** Modeling of the corrosion potential of alloy 600 in a 0.1 M LiOH solution at 200 °C as a function of dissolved oxygen concentration. The upper and middle diagrams (a and b) show the calculated partial electrochemical reactions and predicted polarization curve for solutions containing  $4 \times 10^{-7}$  m ( $0.013$  ppm) and  $3 \times 10^{-6}$  m ( $0.096$  ppm)  $O_2$ , respectively. The lower diagram (c) compares the calculated corrosion potential with experimental data<sup>163</sup> at 200 °C as a function of dissolved oxygen molality.



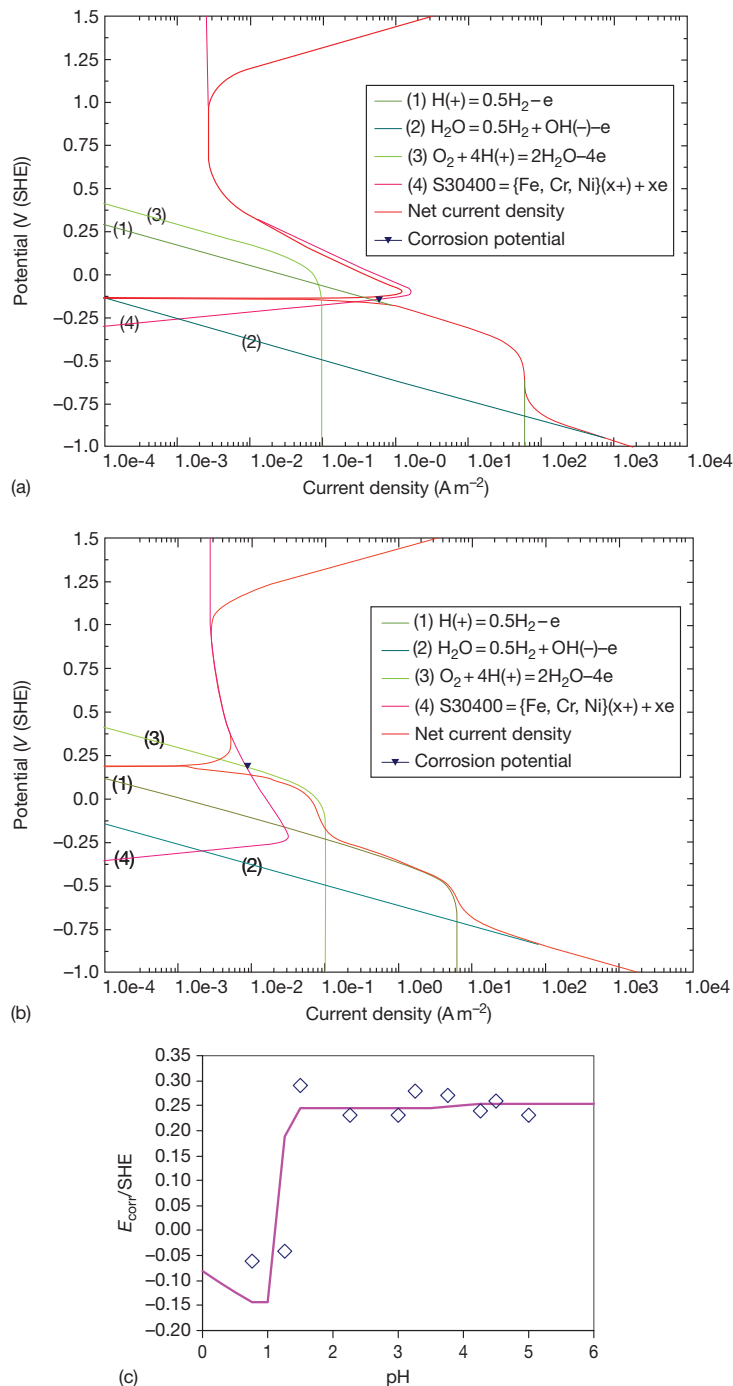


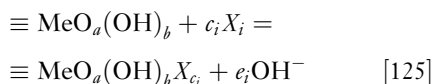
**Figure 7** Electrochemical modeling of the depassivation pH and corrosion potential of type 304 stainless steel in aerated 0.1 M Na<sub>2</sub>SO<sub>4</sub> + H<sub>2</sub>SO<sub>4</sub> solutions. The upper (a) and middle (b) diagrams show the calculated partial electrochemical processes and predicted polarization curve for pH = 0.8 and 1.8, respectively. The lower diagram (c) compares the calculated corrosion potentials with experimental data.<sup>165</sup>

OH<sup>-</sup> ions from the bulk to the interface. Then, the contributions to the passive current density (eqn [124]) should be coupled with mass-transfer equations such as eqn [36].<sup>131</sup>

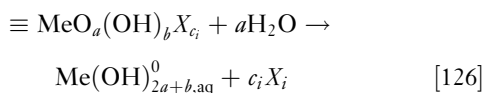
Figure 7 illustrates the electrochemical modeling of the pH dependence of the active-passive transition of type 304 stainless steel. The upper and middle diagrams in Figure 7 show the partial electrochemical

processes in  $\text{Na}_2\text{SO}_4$  solutions with  $\text{pH}=0.8$  and  $1.8$ , respectively. The anodic curve (line 4) was modeled using a model based on eqns [116] and [117]. The main cathodic process is the reduction of  $\text{O}_2$ . Because of the pH effect on the active–passive transition, the mixed potential moves from the active dissolution region for  $\text{pH}=0.8$  to the passive region for  $\text{pH}=1.8$ . This explains the dependence of the experimentally determined corrosion potential on pH (Figure 7(c)). The pH value at which an abrupt change of  $E_{\text{corr}}$  occurs can be identified with the depassivation pH.

In addition to pH effects, some active ions may influence the magnitude of the passive current density. The effect of active species on the dissolution in the passive state can be modeled by considering surface reactions between the metal oxide film and solution species (Blesa *et al.*,<sup>166</sup> Anderko *et al.*<sup>146</sup>):



where  $X_i$  is the  $i$ th reactive species in the solution, and the subscripts  $a$ ,  $b$ ,  $c_i$  and  $e_i$  represent the reaction stoichiometry. In general, eqn [125] may be written for any active, aggressive, or inhibitive species  $i$  in the solution ( $i=1, \dots, n$ ). It is reasonable to assume that eqn [125] is in quasi-equilibrium. The surface species that forms as a result of reaction eqn [125] may undergo irreversible dissolution reactions such as:



in which dissolved metal species are formed in analogy to those described by eqns [118], [120], and [122]. Mathematical analysis of reactions eqns [125] and [126]<sup>108,146</sup> yields a relationship between the passive current density and activities of reactive species:

$$i_p = i_p^0(\text{pH}) \frac{1 + \sum_i l_i (a_{X_i}^{e_i} / a_{\text{OH}^-}^{e_i})}{1 + \sum_i K_i (a_{X_i}^{e_i} / a_{\text{OH}^-}^{e_i})} \quad [127]$$

where  $i_p^0(\text{pH})$  is given by eqn [124],  $l_i$  is the forward rate of reaction eqn [126], and  $K_i$  is the equilibrium constant of reaction eqn [125].

Figure 8 illustrates the effect of active ions on the rate of general corrosion using alloy 22 in mixed  $\text{HNO}_3 + \text{HF}$  solutions as an example. The upper diagram (Figure 8(a)) shows the predicted partial electrochemical processes in a 20%  $\text{HNO}_3$  solution and the middle diagram (Figure 8(b)) shows how

these processes change when a moderate amount of HF (1.57%) is added. A 20 wt.%  $\text{HNO}_3$  solution is an oxidizing medium, and, therefore, reduction of  $\text{NO}_3^-$  ions in an acidic environment is the main cathodic process. This results in a high corrosion potential as shown in Figure 8(a). The corrosion rate is controlled by the dissolution rate of the oxide film. When HF is added, the dissolution rate of the oxide substantially increases even though a moderate amount of HF has practically no effect on the acidity of the system. This effect is reproduced by eqn [127] and manifests itself by the increased passive current density in Figure 8(b). The predicted effects can be compared with the observed corrosion rates in 20%  $\text{HNO}_3$  solution as a function of HF concentration (Figure 8(c)).

### 2.38.3.7 Scaling Effects

In addition to passive dissolution and active–passive transition, modeling of surface scale formation is of great practical importance. Scales form as a result of deposition of corrosion products (e.g., iron carbonate or sulfide) or other solids that reach supersaturation near metal interfaces (e.g., calcareous deposits). Scales can be distinguished from passive films in that they do not give rise to the classical active–passive transition such as that shown in Figure 7. Rather, they reduce the rate of dissolution by providing a barrier to the diffusion of species to and from the surface and by partially blocking the interface, thus reducing the overall rate of electrochemical reactions. In general, there may be multiple mechanisms of scale formation depending on the chemistry of the precipitating solids.

One mechanism of scale formation can be quantified in terms of the competition between the rate of scale formation, which results in the precipitation of a corrosion product, and the rate of corrosion under the scale, which leads to the ‘undermining’ of the scale. When the rate of precipitation exceeds the rate of corrosion, dense protective films are formed. Conversely, when the corrosion rate is greater than the precipitation rate, the scale still forms, but the precipitation rate is not fast enough to fill the growing voids. Then, the scale becomes unprotective even though it may be thick. Nešić and Lee<sup>155</sup> developed a model to represent this phenomenon for  $\text{FeCO}_3$  scale formation. In Nešić and Lee’s<sup>155</sup> model, the local change in the volumetric concentration of the scale-forming solid is given by a redefined eqn [100]:

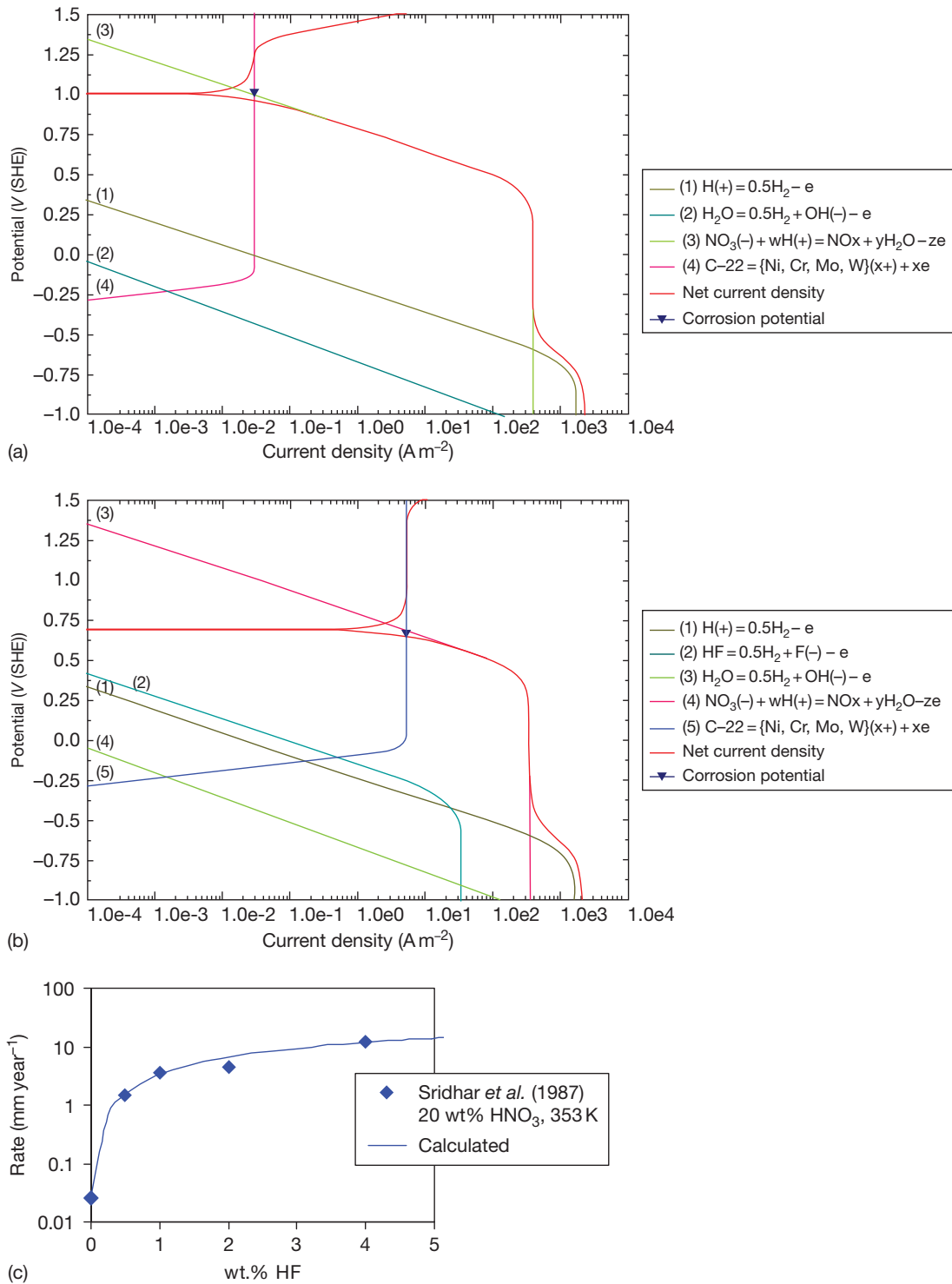


**Figure 8** Electrochemical modeling of the effect of HF concentration on the corrosion rate of alloy 22 in  $\text{HNO}_3 + \text{HF}$  solutions. The upper (a) and middle (b) diagrams show the partial electrochemical processes in 20 wt%  $\text{HNO}_3$  solutions without HF and with 1.57% HF, respectively. The lower diagram compares the calculated results with experimental data<sup>167</sup> as a function of HF concentration.

$$\frac{\partial c_{\text{solid}}}{\partial t} = R_{\text{solid}} - \text{CR} \frac{\partial c_{\text{solid}}}{\partial z} \quad [128]$$

where the first term on the right-hand side represents the rate of the scale formation and the second term is the scale undermining rate. In eqn [128], CR is the corrosion rate and  $z$  is a direction perpendicular to the surface. The rate of formation of the scale is, in general, a product of the scale particles' surface area-to-volume ratio  $A/V$ , a function of temperature, the thermodynamic solubility product  $K_{\text{sp}}$  and an empirical function of supersaturation  $S$ :

$$R_{\text{solid}} = \frac{A}{V} f(T) K_{\text{sp}} f(S) \quad [129]$$

where supersaturation is defined as

$$S = \frac{\prod a_i^{v_i}}{K_{\text{sp}}} = \frac{\prod c_i^{v_i}}{K_{\text{sp}}} \quad [130]$$

While the  $f(T)$  and  $f(S)$  functions can be, in principle, derived from precipitation kinetics data that are independent of corrosion, Sun and Nešić<sup>168</sup> have determined that much more reliable precipitation rates can be obtained from corrosion weight loss and gain measurements than from kinetic measurements that start from dissolved metal ions. The  $A/V$  ratio depends on the porosity of the scale on the metal surface. Nešić and Lee<sup>155</sup> developed an empirical function of porosity that is consistent with the experimental data for  $\text{FeCO}_3$  scale formation.

A different model is necessary for scales whose formation does not follow the kinetics of precipitation processes. For example,  $\text{FeS}$  scales form very fast in highly undersaturated solutions, in which they would be thermodynamically unstable in the bulk, and their formation appears not to be influenced by solution supersaturation. Thus, the effect of  $\text{FeS}$  scales can be modeled by assuming a solid-state reaction at the metal surface that is mediated by the adsorption of  $\text{H}_2\text{S}$  (Anderko and Young,<sup>169</sup> Nešić *et al.*<sup>170</sup>) The formation of  $\text{FeS}$  scales is further complicated by the existence of an outer layer that results from the growth, cracking, and delamination of the  $\text{FeS}$  film. A model that accounts for these phenomena was developed by Sun and Nešić.<sup>171</sup>

### 2.38.3.8 Modeling Threshold Conditions for Localized Corrosion

Modeling of the evolution of localized corrosion has been the subject of extensive research during the past three decades, and a number of important models have been developed for the initiation, stabilization,

propagation, and stifling of individual pits, crevices, and cracks and for the statistical behavior of their ensembles in corroding structures. However, this topic is outside the scope of this chapter and will be reviewed in the chapter 'Predictive Modeling of Corrosion' in this volume.

In this chapter, we focus solely on models that predict the conditions for the occurrence of localized corrosion without going into the treatment of the evolution of localized corrosion events in time and space. Such models are designed to find the threshold criteria for localized corrosion. In general, localized corrosion occurs when the corrosion potential of an alloy in a given environment exceeds a critical potential. The meaning, experimental determination, and interpretation of the key potentials that characterize localized corrosion have been reviewed by Szklarska-Smialowska.<sup>172</sup> While this general concept is well accepted, what constitutes a critical potential continues to be debated. The selection of the critical potential depends on the particular phenomenon that is to be modeled.

The applicability of the critical potential concept to modeling localized corrosion is qualitatively illustrated in Figure 9. In this figure, the arrows indicate the conditions at which localized corrosion is expected. For a given alloy, the critical potential decreases with an increase in the concentration of aggressive species (e.g., halide ions) as shown in Figure 9(a). The shape of the  $E_{\text{crit}}$  curve corresponds to that of the repassivation potential curve, but the qualitative pattern is more general. Unlike the critical potential, the corrosion potential is usually not a strong function of aggressive ion concentration unless significant localized corrosion occurs. The critical aggressive species concentration for localized corrosion is observed when  $E_{\text{corr}}$  exceeds  $E_{\text{crit}}$ . Similarly, for a given aggressive chemical environment, a critical temperature exists (see Figure 9(b)). The critical potential is also strongly affected by the presence of inhibitors. As shown in Figure 9(c), this gives rise to a critical inhibitor concentration. In many environments, the presence of oxidants may increase  $E_{\text{corr}}$  so that localized corrosion may occur beyond a critical concentration of redox species (Figure 9(d)). The actual conditions in a system may be a combination of the four idealized cases shown in Figure 9. Thus, the key is to predict both the corrosion potential and the repassivation potential. The corrosion potential can be obtained from a general-corrosion, mixed-potential model for passive metals as described above. For the critical potential, separate models are necessary.

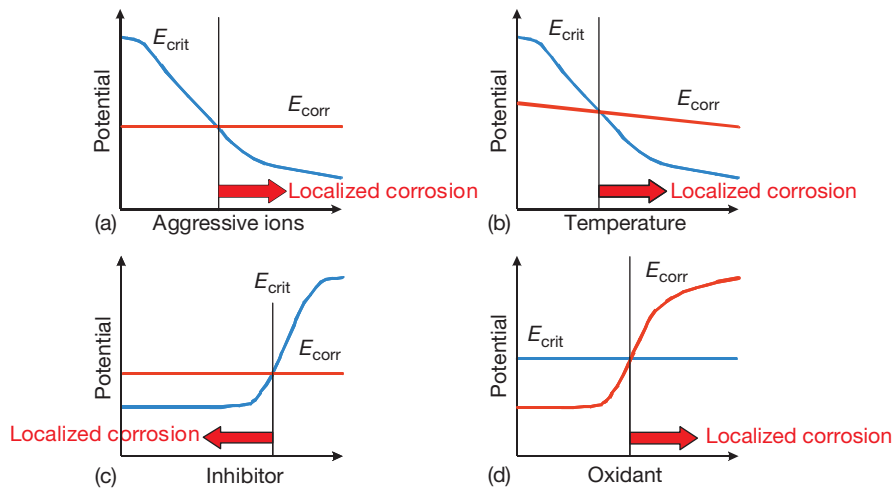


**Figure 9** A general conceptual scheme of the use of the corrosion potential ( $E_{\text{corr}}$ ) and critical potential ( $E_{\text{crit}}$ ) to predict the effect of aggressive ions, temperature, inhibitors, and oxidizing redox species on localized corrosion. The arrows marked 'localized corrosion' denote the potential ranges in which localized corrosion can be expected.

In this chapter, we briefly review the computation and applicability of the passivity breakdown potential and the repassivation potential.

### 2.38.3.8.1 Breakdown of passivity

To predict the initiation of localized corrosion, it is necessary to calculate the critical passivity breakdown potential. Several theories have been developed to relate the breakdown potential to the concentration of aggressive species in the solution (Heusler and Fischer,<sup>173</sup> Strehblow and Titze,<sup>174</sup> Lin *et al.*,<sup>175</sup> Okada,<sup>176</sup> McCafferty,<sup>177</sup> Haruna and Macdonald,<sup>178</sup> Macdonald,<sup>97</sup> Yang and Macdonald,<sup>179</sup> and papers cited therein). A common theoretical result, confirmed by experimental data, is the linear dependence of the passivity breakdown potential on the logarithm of the concentration of aggressive ions. While this observation is generally accepted, its generalization to systems with multiple aggressive and inhibitive ions is not immediately obvious.

A particularly comprehensive treatment of passivity breakdown is provided by the point defect model of Macdonald and coworkers (Lin *et al.*,<sup>175</sup> Haruna and Macdonald,<sup>178</sup> Macdonald,<sup>97</sup> Yang and Macdonald<sup>179</sup>). According to the point defect model, passivity breakdown results from the condensation of cation or metal vacancies at the interface between the metal and the passive barrier layer. The vacancies are envisaged to be generated at the barrier layer–solution interface in an autocatalytic, anion-induced process. For systems containing only aggressive (halide) ions  $X$ , the critical breakdown potential is expressed as

$$E_b = \frac{4.606RT}{\chi\alpha F} \log \left[ \frac{\mathcal{J}_m}{\hat{a}Du^{-\chi/2}} \right] - \frac{2.303RT}{\alpha F} \log a_X \quad [131]$$

where  $\mathcal{J}_m$  is the rate of annihilation of cation vacancies at the metal/barrier layer interface,  $\hat{a}$  and  $u$  are thermodynamic parameters related to the absorption of an aggressive ion into an oxygen vacancy,  $D$  is the cation vacancy diffusivity, and  $\alpha$  is the polarizability of the film–solution interface. Yang and Macdonald<sup>179</sup> extended eqn [131] to systems containing both aggressive ions  $X^-$  and inhibitive ions  $Y^{z-}$ :

$$E_b = E_b^0 - \frac{\beta}{\alpha} \text{pH} - \frac{2.303}{\alpha\alpha_0 F} \log \frac{a_{X^-}}{a_{Y^{z-}}} \quad [132]$$

where the constant  $E_b^0$  is a function of adsorption and elementary reaction rate parameters that is derived from a competitive adsorption model for the  $X^-$  and  $Y^{z-}$  species,  $\beta$  is the dependence of the potential drop across the barrier layer–solution interface on pH, and  $\alpha_0$  is a transfer coefficient. The predictions of the point defect model have been found to be in agreement with experimental phenomena including the linear dependence of the breakdown potential on the concentrations of aggressive and inhibitive ions, the dependence of the induction time on potential and chloride concentration, dependence of the breakdown potential on the scan rate and the inhibition of pitting by Mo and W in the alloy. It should be noted that the breakdown potential is a distributed quantity that can be described with a normal distribution function. The distribution in  $E_b$  has been reproduced by assuming that the cation diffusivity is normally distributed.<sup>97</sup>



While the logarithmic dependence of the breakdown potential on the aggressive species concentration is predicted by most passivity breakdown models, the induction time provides a more stringent criterion for testing alternative models. Accordingly, Milošev *et al.*<sup>180</sup> tested the validity of the point defect model, the two-dimensional nucleation model of Heusler and Fischer,<sup>173</sup> and the halide nuclei model of Okada<sup>176</sup> for the pitting of copper. The point defect model was found to yield the best agreement with experimental data.

### 2.38.3.8.2 Repassivation potential and its use to predict localized corrosion

While the breakdown potential is the critical parameter for the initiation of pitting, the repassivation potential ( $E_{rp}$ ) has been used for predicting the long-term occurrence of pitting and crevice corrosion. The repassivation potential (also called protection potential) is the potential at which a stably growing pit or crevice corrosion will cease to grow. Thus, localized corrosion cannot occur at potentials below  $E_{rp}$ . The use of  $E_{rp}$  for engineering predictions can be justified by the fact that only the fate of stable pits or crevice corrosion is important for predicting the possibility of failure, and metastable pits do not adversely affect the performance of engineering structures. It has been shown by Dunn *et al.*<sup>181,182</sup> that  $E_{rp}$  is practically independent of the amount of charge passed in a localized corrosion process as long as it is above a certain minimum amount of charge. As a result, the repassivation potential is relatively insensitive to prior pit depth and surface finish. As a corollary, it has been shown that the repassivation potential for pitting (i.e., measured on an open sample) and the repassivation potential for crevice corrosion (i.e., measured on a creviced sample) coincide at high pit depths. This has demonstrated the utility of the repassivation potential for engineering design as it provides a reproducible and inherently conservative threshold for the occurrence of localized corrosion. Thus, the prediction of long-term occurrence of localized corrosion can be separated into two independent parts, that is, the calculation of the repassivation and the corrosion potentials. The separation of localized corrosion modeling into these two steps is valid as long as the initial stages of stable localized corrosion are considered because the corrosion potential is not affected at this stage by the progress of the localized corrosion process and the interaction between pits can be ignored. The separation remains valid as long as significant pit or crevice corrosion growth does not occur and the area of an actively

corroding pit does not become significant compared to the overall area.

A model for calculating the repassivation potential has been developed by Anderko *et al.*<sup>183</sup> by considering the electrochemistry of a metal M that undergoes dissolution underneath a layer of concentrated metal halide solution MX. The concentrated solution may or may not be saturated with respect to a hydrous solid metal halide. In the process of repassivation, a thin layer of oxide forms at the interface between the metal and the hydrous metal halide. The model assumes that, at a given instant, the oxide layer covers a certain fraction of the metal surface. This fraction increases as repassivation is approached. Further, the model includes the effects of multiple aggressive and nonaggressive or inhibitive species, which are taken into account through a competitive adsorption scheme. The aggressive species form metal complexes, which dissolve in the active state. On the other hand, the inhibitive species and water contribute to the formation of oxides, which induce passivity. The model assumes that the measurable potential drop across the interface can be expressed as a sum of four contributions, that is

$$E = \Delta\Phi_{M/MX} + \Delta\Phi_{MX} + \Delta\Phi_{MX/S} + \Delta\Phi_S \quad [133]$$

where  $\Delta\Phi_{M/MX}$  is the potential difference at the interface between the metal and metal halide, which may be influenced by the partial coverage by the metal oxide,  $\Delta\Phi_{MX}$  is the potential drop across the hydrous halide layer,  $\Delta\Phi_{MX/S}$  is the potential difference across the metal halide–solution interface, and  $\Delta\Phi_S$  is the potential drop across the boundary layer within the solution. Expressions for the potential drops can be derived using the methods of nonequilibrium thermodynamics.<sup>184</sup> In general, these expressions are complex and can be solved only numerically. However, a closed-form equation has been found in the limit of repassivation, that is, when the current density reaches a predetermined low value  $i_{rp}$  (typically  $i_{rp} = 10^{-2} \text{ A m}^{-2}$ ) and the fluxes of metal ions become small and comparable to those for passive dissolution. Then, eqn [133] can be used to arrive at a closed-form expression for the repassivation potential. This closed-form expression, which can be solved numerically to calculate  $E_{rp}$  is given by:

$$1 + \sum_k \left[ \left( \frac{i_{rp}}{i_p} - 1 \right) \frac{l_k''}{i_{rp}} \theta_k^{n_k} \exp\left(\frac{\zeta_k F E_{rp}}{RT}\right) \right] = \sum_j \frac{k_j''}{i_{rp}} \theta_j^{n_j} \exp\left(\frac{\alpha_j F E_{rp}}{RT}\right) \quad [134]$$

where  $i_p$  is the passive current density,  $T$  is the temperature,  $R$  is the gas constant, and  $F$  is the Faraday constant. The partial coverage fraction of a species  $j$  is related to the activity of this species in the bulk solution by

$$\theta_j = \frac{K_{\text{ads},j} a_j}{1 + \sum_k K_{\text{ads},k} a_k} \quad [135]$$

where

$$K_{\text{ads},j} = \exp\left(-\frac{\Delta G_{\text{ads},j}}{RT}\right) \quad [136]$$

and  $\Delta G_{\text{ads},j}$  is the Gibbs energy of adsorption. The parameters  $k'_j$  and  $l''_k$  in eqn [134] are rate constants for surface reactions mediated by the adsorption of aggressive and inhibitive species, respectively. The inhibitive species include water, as it is necessary for oxide formation. The parameter  $n_j$  is the reaction order with respect to species  $j$ , and  $\alpha_j$  and  $\xi_k$  are the electrochemical transfer coefficients for reactions mediated by aggressive and inhibitive species, respectively. Some parameters ( $\Delta G_{\text{ads},i}$ ,  $\alpha_j$ , and  $n_k$ ) can be assigned default values. The remaining parameters need to be regressed from a limited amount of experimental  $E_{\text{rp}}$  measurements. Since  $E_{\text{rp}}$  data are most abundant for chloride solutions, the rate constant for the chloride ions ( $k'_{\text{Cl}}$ ), reaction order with respect to chlorides ( $n_{\text{Cl}}$ ), rate constant for water ( $l''_{\text{H}_2\text{O}}$ ), and electrochemical transfer coefficient for water ( $\xi_{\text{H}_2\text{O}}$ ) are determined based on the data for chloride solutions. The determination of parameters is greatly simplified by the fact that the parameters for Fe–Ni–Cr–Mo–W–N alloys can be correlated with alloy composition,<sup>185,186</sup> thus enhancing the predictive value of the model. The  $k'_j$  and, if necessary,  $n_j$  parameters are determined for other aggressive species  $j$  (e.g., bromide ions) using  $E_{\text{rp}}$  data for either pure or mixed

solutions containing such ions. Finally, the  $l''_k$  parameters for inhibitive ions  $k$  are determined on the basis of data for mixed solutions containing chlorides and inhibitors. Data for mixed systems are necessary because  $E_{\text{rp}}$  is undefined in solutions containing only inhibitors.

The repassivation potential model has a limiting character, that is, it accurately represents the state of the system in the repassivation potential limit. In addition to the value of the repassivation potential, the model predicts the correct slope of the current density versus potential relationship as the potential deviates from  $E_{\text{rp}}$ .<sup>183</sup> The current density predicted by the model as a function of potential is given by

$$i = \frac{\sum_j k'_j \theta_j^{n_j} \exp\left(\frac{\alpha_j FE}{RT}\right) + \sum_j l''_j \theta_j^{n_j} \exp\left(\frac{\xi_j FE}{RT}\right)}{1 + \frac{1}{i_p} \sum_j l''_j \theta_j^{n_j} \exp\left(\frac{\xi_j FE}{RT}\right)} \quad [137]$$

Equation [137] reduces to eqn [134] for  $E = E_{\text{rp}}$  and  $i = i_{\text{rp}}$ . Since eqn [137] is a limiting law, its accuracy gradually deteriorates as the potential increasingly deviates from  $E_{\text{rp}}$ . Equation [137] cannot be regarded as a model for the propagation rate of an actively growing pit or crevice because it does not take into account the factors such as the ohmic potential drop, transport limitations, and so on. However, the current density predicted using eqn [137] for  $E > E_{\text{rp}}$  is useful because it provides an estimate of the maximum propagation rate of an isolated pit as a function of potential. Such an upper estimate is convenient because it relies only on parameters that are calibrated using repassivation potential data.

Figure 10 shows the application of the repassivation potential model to alloy CuNi 7030 in chloride

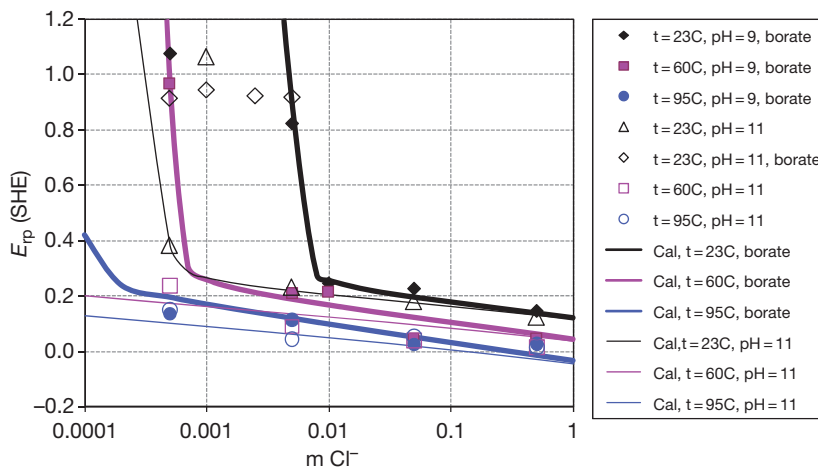


**Figure 10** Modeling the repassivation potential of alloy CuNi 7030 (UNS C71500).<sup>217</sup> as a function of chloride activity at various temperatures.

solutions at three temperatures. As shown in the figure, the slope of the repassivation potential changes as a function of chloride activity. A steeper slope is observed at low chloride concentrations. This is a general phenomenon for alloys and becomes more pronounced for more corrosion-resistant alloys.<sup>183</sup> The transition between the low-slope and high-slope segments of the curves strongly depends on the alloy and temperature.

A particularly useful application of the repassivation potential model is for investigating the competing effects of aggressive and inhibitive species. For example, Figure 11 shows the inhibitive effect of nitrate ions on localized corrosion of alloy 22 in concentrated chloride solutions. The  $E_{rp}$  versus  $\text{NO}_3^-$  concentration curves have a characteristic shape with two distinct slopes. As the concentration of the  $\text{NO}_3^-$  ions is increased, the slope of the  $E_{rp}$  versus  $\text{NO}_3^-$  concentration curve initially slowly increases with a low slope. At a certain concentration of  $\text{NO}_3^-$ , the slope of the  $E_{rp}$  curve rapidly increases and the repassivation potential attains a high value. At  $\text{NO}_3^-$  concentrations that lie beyond the high-slope portion of the  $E_{rp}$  versus  $\text{NO}_3^-$  curve, localized corrosion becomes impossible even in systems with a high corrosion potential. Thus, there is a fairly narrow range of inhibitor concentrations over which the  $E_{rp}$  curve transitions from a low-slope region (in which localized corrosion is possible depending on the value of the corrosion potential) to a high-slope region that constitutes the upper limit of inhibitor concentrations for localized corrosion. The exact location of the transition region depends on the temperature and chloride concentration and can be accurately reproduced using the repassivation potential model.

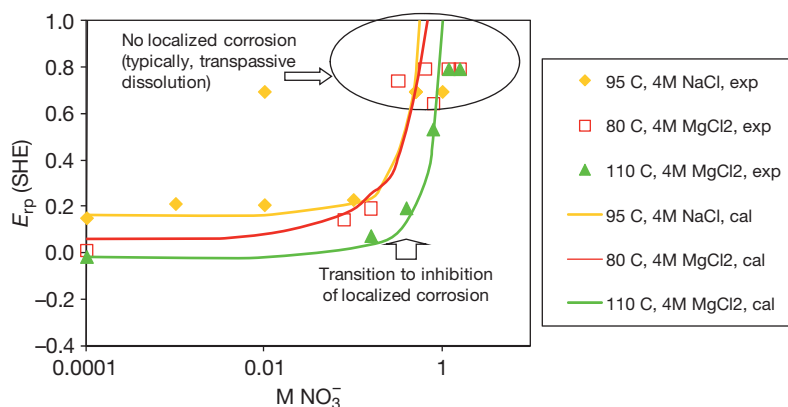


**Figure 11** Modeling the effect of nitrate ions on the repassivation potential of alloy 22 in concentrated chloride solutions. The experimental data are from Dunn *et al.*<sup>187</sup>

Figure 12 illustrates an application of the corrosion potential and repassivation potential models to predict the critical crevice temperature. At temperatures below critical crevice temperature (CCT), the calculated corrosion potential ( $E_{corr}$ ) should lie below the repassivation potential, whereas it should exceed  $E_{rp}$  above CCT. Thus, the intersection of the  $E_{corr}$  and  $E_{rp}$  curves versus temperature provides an estimate of CCT. Figure 12 shows the results of such calculations for alloy C-276 in 6%  $\text{FeCl}_3$  solutions.<sup>188</sup> The repassivation potential shows an initially steep decrease followed by a moderate decrease at higher temperatures. On the other hand, the corrosion potential shows a much weaker temperature dependence. The intersection points of the  $E_{corr}$  and  $E_{rp}$  curves can be compared with experimental critical crevice temperatures (Hibner<sup>189</sup>).

It should be noted that while the approach based on computing  $E_{corr}$  and  $E_{rp}$  can predict the long-term occurrence and maximum propagation rate of localized corrosion, it gives no spatial or temporal information. For predicting the spatial and temporal evolution of localized corrosion, models are required that include a detailed treatment of mass transport and take into account the geometric constraints of crevices, pits, and so on. Such models are outside the scope of this chapter.

### 2.38.3.9 Selected Practical Applications of Aqueous Corrosion Modeling

In this section, we briefly outline selected models that have been developed for practical applications on the basis of the principles discussed above.

Extensive efforts have been devoted to the modeling of aqueous corrosion in oil and gas environments.

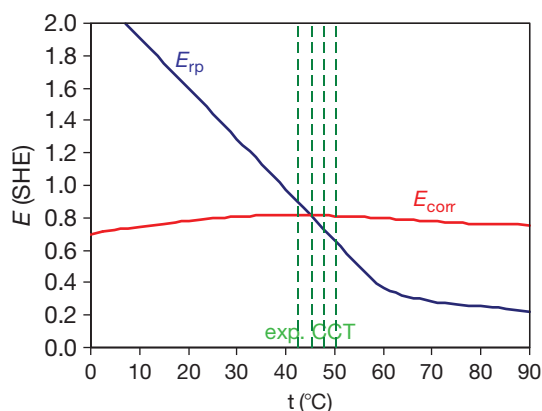


**Figure 12** Prediction of the critical crevice temperature (CCT) for various alloys in a 6%  $\text{FeCl}_3$  solution using corrosion potential and repassivation potential models.<sup>188</sup> The vertical lines show the location of the experimental CCT values.<sup>189</sup> The intersection of the calculated corrosion potential and repassivation potential lines shows the predicted critical crevice temperature.

This is due to the great practical importance of corrosion in oil and gas production and transmission, and to the fact that the number of key corrosive components in such environments is relatively limited (primarily to  $\text{CO}_2$ ,  $\text{H}_2\text{S}$ , acetic acid, and  $\text{O}_2$ ), thus making the modeling task manageable despite the inherent complexity of corrosion mechanisms and their dependence of flow conditions. Corrosion modeling in this area has been reviewed by Nešić *et al.*,<sup>190</sup> Nyborg,<sup>191</sup> and Papavisanam *et al.*<sup>192–194</sup> The  $\text{CO}_2/\text{H}_2\text{S}$  models range from expert systems based on laboratory and field data to mechanistic models that recognize the partial electrochemical processes in an explicit way. Among the electrochemical models, the treatment of flow effects using mass transfer coefficients has found wide applicability for both single-phase and two-phase flow (Nešić *et al.*,<sup>115</sup> Dayalan *et al.*,<sup>195</sup> Anderko and Young,<sup>169</sup> Pots and Kapusta,<sup>196</sup> Deng *et al.*<sup>197</sup>). While the methodology for modeling  $\text{CO}_2$  corrosion is well established, the modeling of  $\text{H}_2\text{S}$  effects is still in a state of flux and is a subject of significant research efforts (Anderko and Young,<sup>169</sup> Nešić *et al.*,<sup>170</sup> Sun and Nešić<sup>171</sup>). A  $\text{CO}_2$  corrosion model based on a detailed treatment of transport (eqns [100]–[103]) has been developed by Nordsveen *et al.*,<sup>116</sup> Nešić *et al.*,<sup>198</sup> and Nešić and Lee.<sup>166</sup> This model has been further extended to  $\text{CO}_2/\text{H}_2\text{S}$  corrosion by considering mechanistic aspects of  $\text{FeS}$  scale formation (Nešić *et al.*,<sup>170</sup> Sun and Nešić<sup>171</sup>). The model has been integrated with a multiphase flow model, which made it possible to predict the effect of water entrainment and water wetting in oil–water

systems (Nešić *et al.*<sup>170</sup>). Also, a stochastic algorithm for predicting localized corrosion due to partially protective  $\text{FeCO}_3$  scales has been integrated with this model (Nešić *et al.*<sup>199</sup>).

Another area in which electrochemical models have found wide applicability is the prediction of the corrosion potential in dilute aqueous solutions that exist in power generation industries. In particular, mixed-potential models have been developed for stainless steels in water as a function of oxygen and hydrogen content (Macdonald,<sup>161</sup> Lin *et al.*,<sup>138</sup> Kim<sup>103</sup>). Such models are useful for calculating  $E_{\text{corr}}$  in boiling water reactors and related environments.  $E_{\text{corr}}$  is then further used for localized corrosion modeling. In such systems, modeling of the initiation and evolution of crevice corrosion, stress corrosion cracking, and corrosion fatigue is of primary importance. For this purpose, several electrochemical models that are suitable for alloys in high temperature and low-conductivity water have been developed (see Betts and Boulton,<sup>200</sup> Turnbull,<sup>201–203</sup> Engelhardt *et al.*<sup>204,205</sup> and references therein).

Corrosion in halide-containing natural and industrial environments such as seawater, deliquescent liquids, or production brines is another important application for modeling. For example, King *et al.*<sup>123</sup> developed a model for calculating the corrosion potential of copper in aerated chloride solutions. Anderko and Young<sup>108</sup> modeled general corrosion of steel in concentrated bromide brines used in absorption cooling. Sridhar *et al.*<sup>131</sup> developed a model that predicts both the general corrosion and the occurrence of localized corrosion for stainless steels and aluminum in seawater. A mixed-potential model has been developed to predict the behavior of nuclear fuel in steel containers (Shoesmith *et al.*<sup>206</sup>). Models for the initiation, stabilization, and propagation of pitting, crevice corrosion, and cracking in halide systems have been developed by a number of authors (Turnbull and Ferris,<sup>207</sup> Turnbull,<sup>203,208</sup> Betts and Boulton,<sup>200</sup> Engelhardt *et al.*,<sup>209,210</sup> Cui *et al.*,<sup>211</sup> and references therein).

Modeling corrosion in the process industries is a potentially fruitful area but is subject to great difficulties because of the complex and variable nature of the chemical environments. In principle, acid systems are amenable to modeling because of their well-defined chemistry. In particular, corrosion in acids has been modeled by Sridhar and Anderko<sup>212</sup> in the moderate concentration range. Rahmani and Strutt<sup>213</sup> developed a model for very concentrated sulfuric acid solutions, in which corrosion can be assumed to

be exclusively under mass transport control. Veawab and Arronwilas<sup>214</sup> developed a model for the general corrosion in amine-CO<sub>2</sub> systems. Models are also available for the corrosivity in wet porous media (Huet *et al.*<sup>215</sup>). Anderko *et al.*<sup>216</sup> applied the localized corrosion model based on calculating the repassivation and corrosion potentials to predict the occurrence of pitting and estimate the worst-case propagation rates of localized corrosion in a process environment.

### 2.38.4 Concluding Remarks

Over the past three decades, tremendous progress has been achieved in the development of computational models of aqueous corrosion. A number of practically important models have been developed for applications as diverse as oil and gas production and transmission, nuclear and fossil power generation, seawater service, and various chemical processes.

Thermodynamic models of electrolyte systems have reached a level of sophistication that extended their applicability range from dilute aqueous solutions to multiphase, multicomponent systems ranging from infinite dilution to solid saturation or pure solute limits. Although they were originally developed mostly for applications other than corrosion (especially chemical processing and geology), they are increasingly used to predict the solution chemistry of corrosive environments and to understand the effect of phase behavior on corrosion. Electrochemical models of corroding interfaces have been developed to predict the kinetics of anodic and cathodic reactions that are responsible for corrosion and to relate them to bulk solution chemistry and flow conditions. Semiempirical and mechanistic models of passivity have been developed to predict the behavior of passive metals and the breakdown of passivity. Also, models are available to predict the threshold conditions for localized corrosion.

The main focus of the models reviewed in this chapter is on relating the chemistry of the environment to electrochemical corrosion phenomena on metal surfaces. However, this is often only the first stage of corrosion modeling. Beyond this stage, the models discussed here serve as a basis for simulating the spatial and temporal evolution of localized and general corrosion damage in various engineering structures subject to localized and general corrosion. This level of modeling will be discussed in other chapters of this volume.

### Acknowledgments

The work reported in this paper has been supported by the Department of Energy (award number DE-FC36-04GO14043) and cosponsored by Chevron-Texaco, DuPont, Haynes International, Mitsubishi Chemical, Shell, and Toyo Engineering.

### References

1. Pourbaix, M. *Atlas of Electrochemical Equilibria in Aqueous Solutions*; Pergamon Press: New York, NY, 1966.
2. Pitzer, K. S. *Thermodynamics*, 3rd ed.; McGraw-Hill: New York, NY, 1995.
3. Anderko, A.; Wang, P.; Rafal, M. *Fluid Phase Equil.* **2002**, *194–197*, 123–142.
4. Zemaitis, J. F., Jr.; Clark, D. M.; Rafal, M.; Scrivner, N. C. *Handbook of Aqueous Electrolyte Thermodynamics*; DIPPR, AIChE: New York, NY, 1986.
5. Renon, H. *Fluid Phase Equil.* **1986**, *30*, 181–195.
6. Pitzer, K. S. Ed. *Activity Coefficients in Electrolyte Solutions*, 2nd ed.; CRC Press: Boca Raton, FL, 1991.
7. Rafal, M.; Berthold, J. W.; Scrivner, N. C.; Grise, S. L. In *Models for Thermodynamic and Phase Equilibria Calculations*; Sandler, S. I., Ed.; Marcel Dekker: New York, NY, 1994; pp 601–670.
8. Loehe, J. R.; Donohue, M. D. *AIChE J.* **1997**, *43*, 180–195.
9. Chase, M. W.; Davies, C. A.; Downey, J. R.; Frurip, D. J.; McDonald, D. A.; Syverud, A. N. *JANAF Thermochemical Tables*, 3rd ed., supplement no. 1, *J. Phys. Chem. Ref. Data* **1985**, *14*, 1–1856.
10. Barin, I.; Platzki, G. *Thermochemical Data of Pure Substances*, 3rd ed.; Wiley-VCH: Verlag, 1997.
11. Cox, J. D.; Wagman, D. D.; Medvedev, V. A. *CODATA Key Values for Thermodynamics*; Hemisphere Publishing: New York, 1989.
12. Glushko, V. P.; Medvedev, V. A.; Bergman, G. A.; Vasil'ev, B. P.; Kolesov, V. P.; Gurvich, L. V.; Yungman, V. S.; Khodakovskii, I. L.; Resnitskii, L. A.; Smirnova, N. L.; *et al.* *Thermal Constants of Compounds*; Academy of Sciences: Moscow, USSR, 1965–1981.
13. Gurvich, L. V.; Veyts, I. V.; Alcock, C. B.; Iorish, V. S. *Thermodynamic Properties of Individual Substances*; Hemisphere Publishing: New York, 1988–1998; Vols 1–5.
14. Kelly, K. K. Contribution to the Data on Theoretical Metallurgy XIII. High Temperature Heat Content, Heat Capacity and Entropy Data for the Elements and Inorganic Components, Bull. 584, Bureau of Mines, US Dept. of Interior, 1960.
15. Robie, R. A.; Hemingway, B. S.; Fisher, J. R. *US Geol. Survey Bull* **1978**, 1452.
16. Shock, E. L.; Helgeson, H. C. *Geochim. Cosmochim. Acta* **1988**, *52*, 2009–2036; *Geochim. Cosmochim. Acta* **1990**, *54*, 915–943.
17. Shock, E. L.; Helgeson, H. C.; Sverjensky, D. A. *Geochim. Cosmochim. Acta* **1989**, *53*, 2157–2183.
18. Shock, E. L.; Sassani, D. C.; Willis, M.; Sverjensky, D. A. *Geochim. Cosmochim. Acta* **1997**, *61*, 907–950.
19. Stull, D. R.; Westrum, E. F., Jr.; Sinke, G. L. *The Chemical Thermodynamics of Organic Compounds*; R. F. Krieger: Malabara, FL, 1987.



20. Wagman, D. D.; Evans, W. H.; Parker, V. B.; Shum, R. H.; Halow, I.; Bailey, S. M.; Churney, K. L.; Nuttal, R. L. *J. Phys. Chem. Ref. Data* **1982**, *11*(2), 1–392.
21. Criss, C.; Cobble, J. *J. Am. Chem. Soc.* **1964**, *86*, 5385–5390; *J. Am. Chem. Soc.* **1964**, *86*, 5390–5393.
22. Helgeson, H. C.; Kirkham, D. H.; Flowers, G. C. *Am. J. Sci.* **1974**, *274*, 1089–1198; *Am. J. Sci.* **1974**, *274*, 1199–1261; *Am. J. Sci.* **1976**, *276*, 97–240; *Am. J. Sci.* **1981**, *281*, 1241–1516.
23. Tanger, J. C., IV; Helgeson, H. C. *Am. J. Sci.* **1988**, *288*, 19–98.
24. Sverjensky, D. A.; Shock, E. L.; Helgeson, H. C. *Geochim. Cosmochim. Acta* **1997**, *61*, 1359–1412.
25. Johnson, J. W.; Oelkers, E. H.; Helgeson, H. C. *Comput. Geosci.* **1992**, *18*, 899–947.
26. Sedlbauer, J.; O'Connell, J. P.; Wood, R. H. *Chem. Geol.* **2000**, *163*, 43–63.
27. Sedlbauer, J.; Majer, V. *Eur. J. Mineral.* **2000**, *12*, 1109–1122.
28. Kolker, A.; de Pablo, J. J. *Ind. Eng. Chem. Res.* **1996**, *35*, 228–233; *Ind. Eng. Chem. Res.* **1996**, *35*, 234–240.
29. Pitzer, K. S. *J. Phys. Chem.* **1973**, *77*, 268–277.
30. Debye, P.; Hückel, E. *Physik. Z.* **1923**, *24*, 185–206; *Physik. Z.* **1923**, *24*, 305–325; *Physik. Z.* **1924**, *25*, 97–107.
31. Wu, R.-S.; Lee, L. L. *Fluid Phase Equil.* **1992**, *78*, 1–24.
32. Papaiconomou, N.; Simonin, J.-P.; Bernard, O.; Kunz, W. P. *Phys. Chem. Chem. Phys.* **2002**, *4*, 4435–4443.
33. Guggenheim, E. A. *Philos. Mag* **1935**, *19*, 588–643.
34. Guggenheim, E. A.; Turgeon, J. C. *Trans. Faraday Soc.* **1955**, *51*, 747–761.
35. Helgeson, H. C. *Am. J. Sci.* **1969**, *267*, 729.
36. Bromley, L. A. *AIChE J.* **1973**, *19*, 313–320.
37. Zemaitis, J. F., Jr. *ACS Symp. Series* **1980**, *133*, 227–246.
38. Meissner, H. P. *ACS Symp. Series* **1980**, *133*, 495–511.
39. Pitzer, K. S.; Simonson, J. M. *J. Phys. Chem.* **1986**, *90*, 3005–3009.
40. Clegg, S. L.; Pitzer, K. S. *J. Phys. Chem.* **1992**, *96*, 3513–3520.
41. Chen, C.-C.; Britt, H. I.; Boston, J. F.; Evans, L. B. *AIChE J.* **1982**, *28*, 588–596.
42. Liu, Y.; Watanasiri, S. *Fluid Phase Equil.* **1996**, *116*, 193–200.
43. Abovsky, V.; Liu, Y.; Watanasiri, S. *Fluid Phase Equil.* **1998**, *150*, 277–286.
44. Chen, C.-C.; Mathias, P. M.; Orbey, H. *AIChE J.* **1999**, *45*, 1576–1586.
45. Chen, C.-C.; Song, Y. *AIChE J.* **2004**, *50*, 1928–1941.
46. Sander, B.; Fredenslund, A.; Rasmussen, P. *Chem. Eng. Sci.* **1986**, *41*, 1171–1183.
47. Macedo, E. A.; Skovborg, P.; Rasmussen, P. *Chem. Eng. Sci.* **1990**, *45*, 875–882.
48. Kikic, I.; Fermeglia, M.; Rasmussen, P. *Chem. Eng. Sci.* **1991**, *46*, 2775–2780.
49. Dahl, S.; Macedo, E. A. *Ind. Eng. Chem. Res.* **1992**, *31*, 1195–1201.
50. Iliuta, M. C.; Thomsen, K.; Rasmussen, P. *Chem. Eng. Sci.* **2000**, *55*, 2673–2686.
51. Li, J.; Polka, H.-M.; Gmehling, J. *Fluid Phase Equil.* **1994**, *94*, 89–114.
52. Yan, W.; Topphoff, M.; Rose, C.; Gmehling, J. *Fluid Phase Equil.* **1999**, *162*, 97–113.
53. Zerres, H.; Prausnitz, J. M. *AIChE J.* **1994**, *40*, 676–691.
54. Wang, P.; Anderko, A.; Young, R. D. *Fluid Phase Equil.* **2002**, *203*, 141–176.
55. Wang, P.; Anderko, A.; Springer, R. D.; Young, R. D. *J. Molec. Liq.* **2006**, *125*, 37–44.
56. Prausnitz, J. M.; Lichtenthaler, R. N.; Gomes de Azevedo, E. *Molecular Thermodynamics of Fluid Phase Equilibria*; Prentice-Hall: Englewood Cliffs, NJ, 1998.
57. Malanowski, S.; Anderko, A. *Modeling Phase Equilibria: Thermodynamic Background and Practical Tools*; Wiley: New York, 1992.
58. Chen, C. M.; Aral, K. *Corrosion* **1982**, *38*, 183–190.
59. Chen, C. M.; Aral, K.; Theus, G. J. *Computer Calculated Potential-pH Diagrams to 300 °C*, EPRI NP 3137; Electric Power Research Institute: Palo Alto, CA, 1983; Vols. 1–2.
60. Partridge, E.; Hall, R. *Trans. Am. Soc. Mech. Eng* **1939**, *61*, 597.
61. OLI Systems Inc. Corrosion Analyzer software version 2.0, [www.olisystems.com](http://www.olisystems.com), 2007.
62. Anderko, A.; Sanders, S. J.; Young, R. D. *Corrosion* **1997**, *53*, 43–53.
63. Macdonald, D. D.; Cragolino, G. A. In *The ASME Handbook on Water Technology for Thermal Power Systems*; Cohen, P., Ed.; American Society of Mechanical Engineers: New York, 1989; Chapter 9.
64. Beverskog, B.; Puigdomenech, I. *Corros. Sci.* **1996**, *38*, 2121–2135.
65. Beverskog, B.; Puigdomenech, I. *J. Electrochem. Soc.* **1997**, *144*, 3476–3483.
66. Beverskog, B.; Puigdomenech, I. *Corros. Sci.* **1997**, *39*, 43–57.
67. Beverskog, B.; Puigdomenech, I. *Corros. Sci.* **1997**, *39*, 969–980.
68. Beverskog, B.; Puigdomenech, I. *Corros. Sci.* **1997**, *39*, 107–114.
69. Beverskog, B.; Puigdomenech, I. *Corrosion* **1999**, *55*, 1077–1087.
70. Biernat, R. J.; Robbins, R. G. *Electrochim. Acta* **1972**, *17*, 1261–1283.
71. Froning, M. H.; Shanley, M. E.; Verink, E. D., Jr. *Corros. Sci.* **1976**, *16*, 371–376.
72. Macdonald, D. D.; Syrett, B. C. *Corrosion* **1979**, *35*, 471–474.
73. Macdonald, D. D.; Syrett, B. C.; Wing, S. S. *Corrosion* **1979**, *35*, 1–11.
74. Macdonald, D. D.; Syrett, B. C.; Wing, S. S. *Corrosion* **1979**, *35*, 367–378.
75. Anderko, A.; Shuler, P. J. *Comput. Geosci.* **1997**, *23*, 647–658.
76. Pourbaix, M. In *Localized Corrosion*; Staehle, R. W., Brown, B. F., Kruger, J., Agarwal, A., Eds.; NACE: Houston, TX, 1974; pp 12–33.
77. Kesavan, S.; Mozhi, T. A.; Wilde, B. E. *Corrosion* **1989**, *45*, 213–214.
78. Muñoz-Portero, M. J.; Garcia-Anton, J.; Guiñón, J. L.; Perez-Herranz, V. *Corrosion* **2004**, *60*, 749–756.
79. Bianchi, G.; Longhi, P. *Corros. Sci.* **1973**, *13*, 853–864.
80. Silverman, D. C. *Corrosion* **1982**, *38*, 541–549.
81. Silverman, D. C. *Corrosion* **1988**, *44*, 606–610.
82. Kubal, M.; Panacek, F. *Br. Corros. J.* **1995**, *30*, 309–311.
83. Silverman, D. C.; Silverman, A. L. *Corrosion/2007*; NACE International: Houston, TX, 2007; Paper no. 07616.
84. Cubicciotti, D. J. *Nucl. Mat.* **1989**, *167*, 241–248.
85. Cubicciotti, D. J. *Nuclear Mat.* **1993**, *201*, 176–183.
86. Yang, L. X.; Yang, X. Z.; Pourbaix, A. *Corrosion/2007*; NACE International: Houston, TX, 2007; Paper no. 01084.
87. Anderko, A.; Wang, P.; Young, R. D.; Riemer, D. P.; McKenzie, P.; Lencka, M. M.; Babu, S. S.; Angelini, P. Prediction of Corrosion of Alloys in Mixed-Solvent Environments, Final report, DE-FC07-00CH11019, DOE OIT, 2003, [www.osti.gov/servlets/purl/811533-wUQQwz/native/](http://www.osti.gov/servlets/purl/811533-wUQQwz/native/).
88. Lupis, C. H. *Chemical Thermodynamics of Materials*; North Holland: New York, 1983.

89. Saunders, N.; Miodownik, A. P. *CALPHAD – Calculation of Phase Diagrams – A Comprehensive Guide*; Pergamon/Elsevier Science: New York, 1998.
90. Hertzman, S. *Metall. Trans. A* **1987**, *18A*, 1753–1766; *Metall. Trans. A*, **1987**, *18A*, 1767–1778.
91. Hertzman, S.; Jarl, M. *Metall. Trans. A* **1987**, *18A*, 1745–1752.
92. Andersson, J.-O.; Lange, N. *Metall. Trans. A* **1988**, *19A*, 1385–1394.
93. Sridhar, N.; Dunn, D. S.; Anderko, A.; Lencka, M. M.; Schutt, H. U. *Corrosion* **2001**, *57*, 221–235.
94. Lencka, M. M.; Nielsen, E.; Anderko, A.; Riman, R. E. *Chem. Mater.* **1997**, *9*, 1116–1125.
95. Sridhar, N.; Dunn, D. S.; Anderko, A. In *Environmentally Assisted Cracking: Predictive Methods for Risk Assessment and Evaluation of Materials, Equipment and Structures*; ASTM STP 1401; Kane, R. D., Ed.; American Society for Testing and Materials: West Conshohocken, PA, 2000; p 241.
96. Mohr, D. W.; McNeil, M. B. *J. Nucl. Mater.* **1992**, *190*, 329–342.
97. Macdonald, D. D. *Pure Appl. Chem.* **1999**, *71*, 951–978.
98. Vetter, K. J. *Electrochemical Kinetics*; Academic Press: New York, London, 1967.
99. Bockris, J. O'M.; Reddy, A. K. N. *Modern Electrochemistry*; Plenum Press: New York, 1970.
100. Kaesche, H. *Metallic Corrosion*; NACE International: Houston, TX, 1985.
101. Bockris, J. O'M.; Khan, S. U. M. *Surface Electrochemistry: A Molecular Level Approach*; Plenum Press: New York, London, 1993.
102. Gileadi, E. *Electrode Kinetics*; VCH Publishers: New York, 1993.
103. Kim, Y. J. *Corrosion* **2002**, *58*, 208–215.
104. Wagner, C.; Traud, W. Z. *Elektrochem* **1938**, *44*, 391–402.
105. Gileadi, E. Ed. *Electrosorption*; Plenum Press: New York, 1967.
106. Damaskin, B. B.; Petrii, O. A.; Batrakov, V. V. *Adsorption of Organic Compounds on Electrodes*; Plenum Press: New York, 1971.
107. Habib, M. A.; Bockris, J. O'M. In *Comprehensive Treatise of Electrochemistry*; Bockris, J. O'M., Conway, B. E., Yeager, E., Eds.; Plenum Press: New York, 1980; Vol. 1.
108. Anderko, A.; Young, R. D. *Corrosion* **2000**, *56*, 543–555.
109. Heusler, K. E.; Cartledge, G. E. *J. Electrochem. Soc.* **1961**, *108*, 732–740.
110. Lorenz, W.; Heusler, K. In *Corrosion Mechanisms*; Mansfeld, F., Ed.; Marcel Dekker: New York, 1987.
111. Drazic, D. M. In *Modern Aspects of Electrochemistry*; Conway, B. E., Bockris, J. O'M., White, R. E., Eds.; Plenum Press: New York, 1989; Vol. 19, pp 69–192.
112. Keddah, M. In *Corrosion Mechanisms in Theory and Practice*; Marcus, P., Oudar, J., Eds.; Marcel Dekker: New York, 1995.
113. Bockris, J. O'M.; Drazic, D.; Despic, A. R. *Electrochim. Acta* **1961**, *4*, 325–361.
114. Smart, N. G.; Bockris, J. O'M. *Corrosion* **1992**, *48*, 277–280.
115. Nešić, S.; Postlethwaite, J.; Olsen, S. *Corrosion* **1996**, *52*, 280–294.
116. Nordsveen, M.; Nešić, S.; Nyborg, R.; Stangeland, A. *Corrosion* **2003**, *59*, 443–456.
117. Chin, R. J.; Nobe, K. J. *Electrochem. Soc.* **1972**, *119*, 1457–1461.
118. Kuo, H. C.; Nobe, K. J. *Electrochem. Soc.* **1978**, *125*, 853–860.
119. Drazic, V. J.; Drazic, D. M. *J. Serb. Chem. Soc.* **1992**, *57*, 917–926.
120. Kear, G.; Barker, B. D.; Walsh, F. C. *Corros. Sci.* **2004**, *46*, 109–135.
121. Lee, H. P.; Nobe, K. J. *Electrochem. Soc.* **1986**, *133*, 2035–2043.
122. Deslouis, C.; Tribollet, B.; Mengoli, G.; Musiani, M. M. *J. Appl. Electrochem* **1988**, *18*, 374–383.
123. King, F.; Litke, C. D.; Quinn, M. J.; LeNeveu, D. M. *Corros. Sci.* **1995**, *37*, 833–851.
124. Smart, N. G.; Gamboa-Aldeco, M.; Bockris, J. O'M. *Corros. Sci.* **1993**, *34*, 759–777.
125. Jovancicevic, V.; Bockris, J. O'M. *J. Electrochem. Soc.* **1986**, *133*, 1797–1807.
126. Zecevic, S.; Drazic, D.; Gojkovic, S. *Electrochim. Acta* **1991**, *36*, 5–14.
127. Jovancicevic, V. In *Electrochemistry in Transition*; Murphy, O., Ed.; Plenum Press: New York, 1992; p 127.
128. Le Bozec, N.; Compere, C.; L'Her, M.; Laouenan, A.; Costa, D.; Marcus, P. *Corros. Sci.* **2001**, *43*, 765–786.
129. Kapusta, S. D. *Corrosion/2004*; NACE International: Houston, TX, 2004; Paper no. 04655.
130. King, F.; Quinn, M. J.; Litke, C. D. *J. Electroanal. Chem* **1995**, *385*, 45–55.
131. Sridhar, N.; Brossia, C. S.; Dunn, D. S.; Anderko, A. *Corrosion* **2004**, *60*, 915–936.
132. Calvo, E. J.; Schiffrin, D. J. *J. Electroanal. Chem* **1988**, *243*, 171–185.
133. Levich, V. G. *Physicochemical Hydrodynamics*; Prentice-Hall: Englewood Cliffs, NJ, 1962; p 700.
134. Poulson, B. *Corros. Sci.* **1983**, *23*, 391–430.
135. Poulson, B. *Corros. Sci.* **1993**, *35*, 655–665.
136. Eisenberg, M.; Tobias, C. W.; Wilke, C. R. *J. Electrochem. Soc.* **1954**, *101*, 306–319.
137. Berger, F. P.; Hau, K.-F. F. *Int. J. Heat Mass Trans.* **1977**, *20*, 1185–1194.
138. Lin, C. C.; Kim, Y.-J.; Niedrach, L. W.; Ramp, K. S. *Corrosion* **1996**, *52*, 618–625.
139. Wang, S.; Nešić, S. *Corrosion/2003*; NACE International: Houston, TX, 2003; Paper no. 03631.
140. Chilton, T. H.; Colburn, E. I. *Ind. Eng. Chem* **1934**, *26*, 1183–1187.
141. Frank, M. W. *Viscous Fluid Flow*, 2nd ed.; McGraw-Hill: New York, 1991.
142. Kim, D.; Sofya, Y.; Ghajar, A. J.; Dougherty, R. L. ASME Proceedings, National Heat Transfer Conference **1997**; Vol. 34, pp 119–130.
143. Adsani, E.; Shirazi, S. A.; Shadley, J. R.; Rybicki, E. R. *Corrosion/2002*; NACE International: Houston, TX, 2002; Paper no. 02492.
144. Adsani, E.; Shirazi, S. A.; Shadley, J. R.; Rybicki, E. R. *Corrosion/2006*; NACE International: Houston, TX, 2006; Paper no. 06573.
145. Corti, H.; Trevani, L.; Anderko, A. In *Aqueous Systems at Elevated Temperatures and Pressures; Physical Chemistry in Water, Steam and Hydrothermal Solutions*; Palmer, D. A., Fernandez-Prini, R., Harvey, A. H., Eds.; Academic Press, 2004; Chapter 10, p 752.
146. Anderko, A.; McKenzie, P.; Young, R. D. *Corrosion* **2001**, *57*, 202–213.
147. Ciaraldi, S. W.; Berry, M. R.; Johnson, J. M. *Corrosion/82*; NACE International: Houston, TX, 1982; Paper no. 98.
148. Pawel, S. J. *Corrosion* **1994**, *50*, 963–971.
149. Schmitt, G.; Losacker, S.; Renner, M. H. W.; Horn, E. M. *Corrosion/2004*; NACE International: Houston, TX, 2004; Paper no. 04229.
150. Newman, J.; Thomas-Alyea, K. E. *Electrochemical Systems*, 3rd ed.; Prentice Hall: Englewood Cliffs, NJ, 2004.
151. Davis, J. T. *Turbulence Phenomena*; Academic Press: London, 1972.

152. Lin, C. S.; Moulton, R. W.; Putnam, G. L. *Ind. Eng. Chem* **1953**, *45*, 636–640.
153. Walton, J. C. *Corros. Sci.* **1990**, *30*, 915–928.
154. Bear, J. *Dynamics of Fluids in Porous Media*; Dover Publications: New York, NY, 1972.
155. Nešić, S.; Lee, K.-L. *J. Corrosion* **2003**, *59*, 616–628.
156. Frankenthal, R. P.; Kruger, J. Eds. *Passivity of Metals*; The Electrochemical Society: Princeton, NJ, 1978.
157. Froment, M. Ed. *Passivity of Metals and Semiconductors*; Elsevier: Amsterdam, 1983.
158. Marcus, P.; Oudar, J. Eds. *Corrosion Mechanisms in Theory and Practice*; Marcel Dekker: New York, 1995.
159. Natishan, P. M. Ed. *Passivity and its Breakdown*; The Electrochemical Society: Princeton, NJ, 1998; Vol. PV97-26.
160. Macdonald, D. D. *J. Electrochem. Soc* **2006**, *15*, B213–B224.
161. Macdonald, D. D. *Corrosion* **1992**, *48*, 194–205.
162. Ebersbach, U.; Schwabe, K.; Ritter, K. *Electrochim. Acta* **1967**, *12*, 927–938.
163. Park, H. Y.; Tsuruta, T.; Macdonald, D. D. EPRI Project RP 1166-1 report Electric Power Research Institute: Palo Alto, CA, 1980.
164. Sridhar, N.; Brossia, C. S.; Dunn, D. S.; Buckingham, J. P.; Anderko, A. *Corrosion/2002*; NACE International: Houston, TX, 2002; Paper no. 2204.
165. Leckie, H. P. *Corrosion* **1968**, *24*, 70–74.
166. Blesa, M. A.; Morando, P. J.; Regazzoni, A. E. *Chemical Dissolution of Metal Oxides*; CRC Press: Boca Raton, FL, 1994.
167. Sridhar, N.; Wu, J. B. C.; Corey, S. M. *Mater. Perform.* **1987**, *26*(10), 17–23.
168. Sun, W.; Nešić, S. *Corrosion/2006*; NACE International: Houston, TX, 2006; Paper no. 06365.
169. Anderko, A.; Young, R. D. *Corrosion/99*; NACE International: Houston, TX, 1999; Paper no. 31.
170. Nešić, S.; Cai, J.; Lee, K.-L. *J. Corrosion/2005*; NACE International: Houston, TX, 2005; Paper no. 05556.
171. Sun, W.; Nešić, S. *Corrosion/2007*; NACE International: Houston, TX, 2007; Paper no. 07655.
172. Szklarska-Smialowska, Z. *Pitting and Crevice Corrosion*; NACE International: Houston, TX, 2005.
173. Heusler, K. E.; Fischer, L. *Werkst. Korros* **1976**, *27*, 551–556; *Werkst. Korros.* **27**, 788–791.
174. Strehblow, H. H.; Titze, B. *Corros. Sci.* **1977**, *17*, 461–472.
175. Lin, L. F.; Chao, C. Y.; Macdonald, D. D. *J. Electrochem. Soc* **1981**, *128*, 1194–1198.
176. Okada, T. *J. Electrochem. Soc* **1984**, *131*, 241–247.
177. McCafferty, E. J. *Electrochem. Soc* **1990**, *137*, 3731–3737.
178. Haruna, T.; Macdonald, D. D. *J. Electrochem. Soc* **1997**, *144*, 1574–1581.
179. Yang, S.; Macdonald, D. D. *Electrochim. Acta* **2007**, *52*, 1871–1879.
180. Milošev, I.; Metikoš-Huković, Drogowska, M.; Ménard, H.; Brossard, L. *J. Electrochem. Soc.* **1992**, *139*, 2409–2418.
181. Dunn, D. S.; Sridhar, N.; Cragnolino, G. A. *Corrosion* **1996**, *52*, 1583–1612.
182. Dunn, D. S.; Cragnolino, G. A.; Sridhar, N. *Corrosion* **1996**, *56*, 90–104.
183. Anderko, A.; Sridhar, N.; Dunn, D. S. *Corros. Sci.* **2004**, *46*, 1583–1612.
184. Okada, T. *J. Electrochem. Soc.* **1984**, *131*, 1026–1032.
185. Anderko, A.; Sridhar, N.; Brossia, C. S.; Dunn, D. S. *Corrosion/2004*; NACE International: Houston, TX, 2004; Paper no. 04061.
186. Anderko, A.; Sridhar, N.; Tormoen, G.; Brossia, C. S. *Corrosion/2006*; NACE International: Houston, TX, 2006; Paper no. 06215.
187. Dunn, D. S.; Pensado, O.; Pan, Y.-M.; Pabalan, R. T.; Yang, L.; He, X.; Chiang, K. T. Report CNWRA 2005-02 Southwest Research Institute: San Antonio, TX, 2005.
188. Anderko, A.; Sridhar, N.; Brossia, C. S. *Corrosion/2005*; NACE International: Houston, TX, 2005; Paper no. 05053.
189. Hibner, E. L. *Corrosion/86*; NACE International: Houston, TX, 1986; Paper no. 181.
190. Nešić, S.; Postlethwaite, J.; Vrhovac, M. *Corros. Rev* **1997**, *15*, 211–240.
191. Nyborg, R. *Corrosion/2002*; NACE International: Houston, TX, 2002; Paper no. 02233.
192. Papavinasam, S.; Revie, R. W.; Doiron, A. *Corrosion/2005*; NACE International: Houston, TX, 2005; Paper no. 05643.
193. Papavinasam, S.; Revie, R. W.; Doiron, A. *Corrosion/2005*; NACE International: Houston, TX, 2005; Paper no. 05644.
194. Papavinasam, S.; Revie, R. W.; Friesen, W. I.; Doiron, A.; Paneerselvam, T. *Corros. Rev.* **2006**, *24*, 173–230.
195. Dayalan, E.; de Moraes, F. D.; Shadley, J. R.; Shirazi, S. A.; Rybicki, E. F. *Corrosion/98*; NACE International: Houston, TX, 1998; Paper no. 51.
196. Pots, B. F. M.; Kapusta, S. D. *Corrosion/2005*; NACE International: Houston, TX, 2005; Paper no. 05550.
197. Deng, C.; Sand, K.; Teevens, P. J. *Corrosion/2006*; NACE International: Houston, TX, 2006; Paper no. 06565.
198. Nešić, S.; Nordsveen, M.; Nyborg, R.; Stangeland, A. *Corrosion* **2003**, *59*, 489–497.
199. Nešić, S.; Xiao, Y.; Pots, B. F. M. *Corrosion/2004*; NACE International: Houston, TX, 2004; Paper no. 04628.
200. Betts, A. J.; Boulton, L. H. *Br. Corros. J.* **1993**, *28*, 2121–2135.
201. Turnbull, A. *Corros. Sci.* **1993**, *34*, 921–960.
202. Turnbull, A. *Corros. Sci.* **1997**, *39*, 789–805.
203. Turnbull, A. *Corrosion* **2001**, *57*, 175–189.
204. Engelhardt, G.; Macdonald, D. D.; Millett, P. J. *Corros. Sci.* **1999**, *41*, 2165–2190.
205. Engelhardt, G.; Macdonald, D. D.; Urquidi-Macdonald, M. *Corros. Sci.* **1999**, *41*, 2267–2302.
206. Shoesmith, D. W.; Kolar, M.; King, F. *Corrosion* **2003**, *59*, 802–816.
207. Turnbull, A.; Ferris, D. H. *Corros. Sci.* **1987**, *27*, 1323–1350.
208. Turnbull, A. *Br. Corros. J.* **1993**, *28*, 297–308.
209. Engelhardt, G.; Urquidi-Macdonald, M.; Macdonald, D. D. *Corros. Sci.* **1997**, *39*, 419–441.
210. Engelhardt, G.; Urquidi-Macdonald, M.; Macdonald, D. D. *Corros. Sci.* **2004**, *46*, 1159–1187.
211. Cui, F.; Presuel-Moreno, F.; Kelly, R. G. *Corros. Sci.* **2005**, *47*, 2987–3005.
212. Sridhar, N.; Anderko, A. *Corrosion/2001*; NACE International: Houston, TX, 2001; Paper no. 1348.
213. Rahmani, M.; Strutt, J. E. *Hydrodynamic Modeling of Corrosion of Carbon Steels and Cast Irons in Sulfuric Acid*, Materials Technology Institute; NACE International: Houston, TX, 1992.
214. Veawab, A.; Aroonwilas, A. *Corros. Sci.* **2002**, *44*, 967–987.
215. Huet, B.; L'hostis, V.; Santarini, G.; Feron, D.; Idrissi, H. *Corros. Sci.* **2007**, *49*, 1918–1932.
216. Anderko, A.; Sridhar, N.; Yang, L. T.; Grise, S. L.; Saldanha, B. J.; Dorsey, M. H. *Corros. Eng. Sci. Technol* **2005**, *40*, 33–42.
217. Jakab, M. A.; Sridhar, N.; Anderko, A. *Corrosion/2007*; NACE International: Houston, TX, 2007; Paper no. 07243.

## 2.40 Neural Network Methods for Corrosion Data Reduction\*

R. A. Cottis

Corrosion and Protection Centre, School of Materials, University of Manchester, Manchester M60 1QD, UK

This article is a revision of an article that appeared in *Material and Design* by R. A. Cottis, Li Qing, G. Owen, S. J. Garland and I. A. Helliwell, volume 20(4), pp 169–178, © 2010 Elsevier B.V.

2.40.1	Introduction	1680
2.40.2	Interpolation Techniques	1680
2.40.3	Application of Neural Networks to Corrosion	1682
2.40.4	Variability of Corrosion Data	1684
2.40.5	Confidence in Fitted Function	1684
2.40.6	Inconsistent Data Sets	1686
2.40.7	Training Data Requirements	1686
2.40.8	A Particular Example	1687
2.40.9	Conclusions	1690
	References	1691

### 2.40.1 Introduction

The reliable prediction of corrosion behavior is a fundamental requirement for the effective control of corrosion. At first sight, this is relatively easy. There is an extensive corrosion literature, and we can simply look up the relevant information. Unfortunately, real world corrosion never seems to involve quite the same conditions as have been tested before, and there is also the difficult question of the inherent variability of the corrosion process. If we are concerned with only one variable such as the effect of temperature on the corrosion of a particular grade of stainless steel in a specific concentration of sulfuric acid, we can plot all the data that we can find and estimate the behavior for the temperature that we are interested in. However, this approach is limited. If we are interested in 22% H<sub>2</sub>SO<sub>4</sub>, we shall find very few data points, such that we shall probably not be able to plot a reasonable curve. We can extend the number of points available by considering a spread of values, but even then we shall be using only a very small fraction of the relevant data available.

However, in the particular case where we do have a large collection of information, we need techniques to make efficient use of that information. In this chapter, we are concerned with techniques that rely only on the available data. It is important to appreciate that such techniques are necessarily limited to conditions

that lie within the region for which we have data. In order to extrapolate outside the range of the available data, we need to use techniques that take advantage of the knowledge of the controlling processes.

### 2.40.2 Interpolation Techniques

In its simplest form, the problem is one of interpolation. Given the data for points around the point that we are interested in, how do we estimate data for our point? For one or two variables, it is relatively easy to plot graphs, fit lines or surfaces to the graph, estimate standard error and so forth. However, in corrosion, we generally need to consider more than two controlling variables. Even for the very simple case of austenitic stainless steels corroding in sulfuric acid, our data set has a minimum of six controlling variables (Cr, Ni, and Mo content of the steel, temperature and concentration of the acid, and flow conditions). We could easily and justifiably increase the number of variables, for example, by considering minor alloying elements, such as sulfur, phosphorus, and carbon. In the absence of a good model of the behavior, it is difficult to know which variables are significant. If we ignore the effects of significant variables, we introduce uncertainty into the prediction; if we reject data that do not have the ‘correct’

\*This article is based on a paper originally published in *Materials and Design*.<sup>1</sup>

values of parameters, we ignore much of the information contained within our data set.

We therefore need interpolation methods that can accommodate large numbers of input variables. The most obvious approach is to assume that the corrosion rate ( $y$ ) depends linearly on the  $n$  controlling variables ( $x_1, x_2, \dots, x_n$ ) and that the effects of the variables are independent.

Then, we can write

$$y = a_0 + a_1x_1 + a_2x_2 + \dots + a_nx_n$$

where  $a_0$  to  $a_n$  are coefficients that we must estimate from the available data.

This approach is quite widely used, and provided we have more data points than controlling variables, it is relatively easy to find the values of  $a_0$  to  $a_n$  that minimize the error, using techniques of regression analysis. Unfortunately, the underlying assumptions are rather questionable. Corrosion rate often has a rather non-linear dependence on the controlling variables, and the effects of the variables are rarely independent. In theory, we can reduce this limitation by fitting higher-order functions, for example, the second-order function

$$y = a_0 + a_1x_1 + a_2x_2 + \dots + a_nx_n + a_{11}x_1^2 + a_{12}x_1x_2 + \dots + a_{1n}x_1x_n + \dots + a_{nn}x_n^2$$

Note, however, that the second-order function has a large number of coefficients (for  $n = 6$ , there are 28 coefficients) and the second-order function is not

particularly flexible (in one dimension, it is a quadratic). We can get more flexibility by using higher-order functions, but the number of coefficients involved increases markedly.

A better approach is to use rather more flexible functions that can adapt to the data, and thereby fit it better with fewer coefficients. In effect, this is the approach used by artificial neural networks (so-called because they are based on simplified models of animal nervous systems). However, we tend not to describe the artificial neural network by the function that is used to model the data, because the overall function used is very complicated. Rather, we describe the neural network as an assembly of connected components, where each component implements a somewhat simpler function. The components are known as nodes or neurons, and each node has one or more inputs and one output. Several transfer functions can be used for the nodes, but a common one is the sigmoidal function (see [Figure 1](#)):

$$y = \frac{1}{1 + (1/\exp x')}$$

where  $x' = a_0 + a_1x_1 + \dots + a_nx_n$ . Then a neural network is constructed by assembling nodes in a network. In principle, the network can be arbitrarily complex, but in practice we generally use fairly simple layered structures, such as that shown in [Figure 2](#). Each node of the network takes a number of inputs; each input value ( $x_1$  to  $x_n$ ) is multiplied by a weight

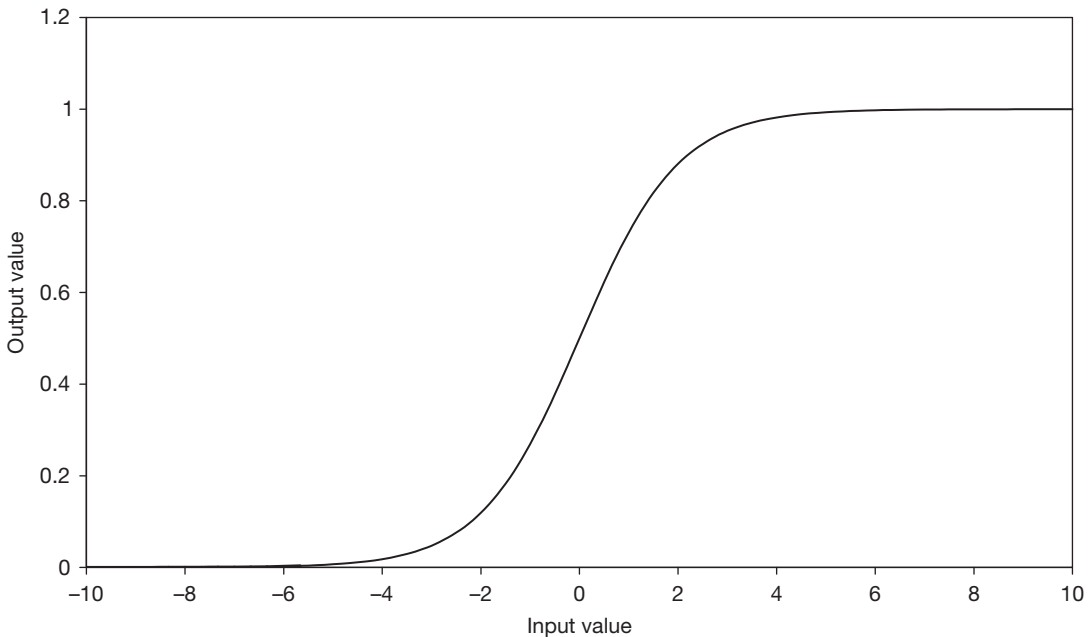


**Figure 1** Sigmoidal transfer function typically used by neural network nodes or neurons.



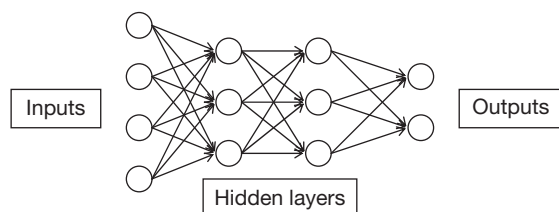


**Figure 2** Layered structure of typical artificial neural network.

( $a_1$  to  $a_n$ ) and the sum of all the weighted inputs plus a bias ( $a_0$ ) is used as the input ( $x'$ ) to the sigmoidal function.

As with simpler linear and polynomial functions, the problem is then to find the values of the coefficients that give the 'best' fit between the output of the neural network and the known data. Owing to the complexity of the function implemented by the neural network, we cannot define an analytical method to find the coefficients, and a range of heuristic methods are used to search for the values of the coefficients that give the best fit, usually starting from randomized values. The process of seeking the coefficients is known as 'training' the network (by analogy with the training of biological neural networks).

It is important to appreciate the limitations of neural network methods:

- Neural networks cannot produce reliable predictions for input conditions that are a long way from the data used to train them. The precise meaning of 'a long way' in this context is rather difficult to define, but it is clear that extrapolation beyond the bounds of the training data is unlikely to be reliable (except by good luck).
- If there are insufficient training data for the complexity of the network, the network may 'learn' the individual data points very precisely, but the behavior between the training points will be unpredictable. It has been suggested that there should always be more training points than weights in the network in order to avoid this problem. While this seems plausible, the rule has often been broken, apparently without problems. However, it is difficult to inspect the multidimensional function implemented by the network, and it may therefore be the case that problems with the fit produced by the network have simply not been detected.
- Neural networks are purely phenomenological and do not inherently produce a mechanistic understanding of the process being modeled. However, the generalization of the behavior that is

achieved with a well-fitted neural network may well contribute to the development of mechanistic understanding.

- Large training data sets are required, especially when the data are noisy (it might be considered that this should advise against their use to model corrosion processes).

The training of a neural network involves the iterative refinement of the weights for all of the nodes. Typically, this involves applying inputs to the network for which the output values are known. Then, the error (the difference between the value predicted by the network and the known value) is passed back through the network and used to modify the weights so as to reduce the error. In order to help in deciding when to stop training the network, a number of data points (called the validation or selection set) are normally held back, and the network is deemed to be trained as well as possible when the error for the validation set starts to increase. A further set may also be reserved (the test set) to test the error performance of the network on data that have not been used in any way in the training.

### 2.40.3 Application of Neural Networks to Corrosion

An early published attempt to apply a neural network to a corrosion problem was that of Smets and Bogaerts.<sup>2</sup> They developed a series of neural networks to predict the SCC of type 304 stainless steel in near-neutral solutions as a function of chloride content, oxygen content and temperature. They found that the neural network approach outperformed traditional regression techniques (this should always be the case with a well-fitted network, as it is always possible for the network to model a linear fit). The network used had almost as many weights (35) as the number of examples in the data set used to train it (39). Thus, there may have been a tendency for the network to fit the 'noise' in the data as well as the mean behavior.

Urquidi-Macdonald *et al.*<sup>3</sup> developed a neural network model for predicting the number and depth of pits in heat exchangers. No information was given about the network size (other than that it had two hidden layers) or the number of training points, although there appear to be rather few. Hence, there must be some uncertainty about the reliability of the predictions obtained. On the other hand, the predicted evolution of pit depth and number do appear plausible.

Ben-Hain and Macdonald<sup>4</sup> describe the use of neural network models to predict the influence of various parameters on the acidity of simulated geological brines. The solutions were based on NaCl plus MgCl<sub>2</sub>; the network inputs were the Na<sup>+</sup> and Mg<sup>2+</sup> concentration and the temperature, and the output was the predicted pH value. A relatively large training set was available (101 points, of which 90 were used for training, with the remaining 11 retained as a test set), and a very simple network was used (just two hidden nodes in a single layer), and it is perhaps not surprising that the network achieved a good result. The prediction error was of the same order as the experimental uncertainty.

Silverman and Rosen<sup>5</sup> combined artificial neural networks with an expert system in order to predict the type of corrosion from a polarization curve. Inputs to the networks included the passive current density, the pitting potential and the repassivation potential, while outputs were the risks of crevice, pitting and general corrosion. Two approaches were used: independent networks for each type of corrosion, and a single combined network producing all three outputs. The expert system was used to interpret the outputs produced by the two approaches. This combination of neural network with an expert system 'supervisor' offers interesting possibilities, although in this particular case it seems probable that the available training set (87 examples) was not really adequate to describe the dependence of the type of corrosion on the seven input variables. Hence, a larger training set could have led to neural networks that were sufficient by themselves.

Silverman<sup>6</sup> also applied neural network methods to the prediction of service behavior of polymeric linings from laboratory test data. Inputs to the network were parameters obtained from a short-term solvent-uptake test, while the output was a pass-fail description of service behavior. Taking into account the inherent difficulty of this problem, the results obtained seem promising. For example, the neural network was able to produce a correct prediction for three out of four examples of a lining material that was not included in the training data. Silverman's neural network models have since been adapted for web access.<sup>7</sup>

Ramamurthy *et al.*<sup>8</sup> used a neural network to analyze impedance data for automobile paint finishes subjected to stone impacts. The paper contains very little detail on the data set or the network, and it is difficult to assess the performance of the network. However, the data presented suggest that

the network is too large, and fits the noise in the training data rather than the mean behavior.

Trasatti and Mazza<sup>9</sup> developed a neural network for the prediction of crevice corrosion behavior of stainless steels. The network was trained from long-term laboratory and field tests. Seventeen input variables were used with one hidden layer of five nodes. Six hundred training examples were available; 450 of these were used for training and the remaining 150 as a test set. The performance of the network was reasonably good, but the very large number of input variables might be expected to present difficulties in training with a relatively small data set. A 17-dimensional hypercube has 2<sup>17</sup> (about 130 000) 'corners,' so the data space is inevitably very sparsely populated.

Nesic and Vrhovac<sup>10</sup> have studied the prediction of corrosion of steel in CO<sub>2</sub>-containing solutions. The prediction ability was found to be significantly better than conventional models, although there are some questions about the number of coefficients used in the network.

Neural network methods have been used to fit the corrosion rate of austenitic stainless steels in sulfuric acid using the data set described earlier.<sup>11</sup>

Since the paper on which this chapter is based was published in 1999, there have been about 100 articles published on the application of neural network methods to corrosion. The subject areas that have been covered include:

- atmospheric corrosion<sup>12-23</sup>
- corrosion and degradation of steel-reinforced concrete<sup>24-35</sup>
- marine corrosion<sup>36-45</sup>
- erosion-corrosion<sup>46</sup>
- organic coatings<sup>47-51</sup>
- corrosion fatigue<sup>52-56</sup>
- pipeline and oilfield corrosion<sup>37,39,57-63</sup>
- alloy optimization<sup>64</sup>
- damage assessment<sup>65</sup>
- pitting corrosion<sup>66-68</sup>
- general corrosion<sup>69-73</sup>
- interpretation or simulation of polarization curves<sup>74-77</sup>
- corrosion in aircraft<sup>78-85</sup>
- refinery corrosion<sup>86-88</sup>
- corrosion monitoring and inspection<sup>89-91</sup>
- stray current corrosion<sup>92</sup>
- metallic coatings<sup>93</sup>
- CO<sub>2</sub> corrosion<sup>94-96</sup>
- cathodic protection anode performance<sup>97</sup>
- oxidation in high temperature water and steam<sup>98-100</sup>

- stress corrosion cracking<sup>63,101</sup>
- identification of corrosion type<sup>102–104</sup>
- high temperature oxidation and corrosion<sup>105,106</sup>
- hydrogen effects.<sup>107</sup>

One of the difficulties of working with prediction in multiple dimensions is that of representing the results. All that can be done on two-dimensional paper is to plot representative sections through the data, either as simple two-dimensional plots, or as pseudo-three-dimensional plots. The only complete way of reporting the results of a neural network fit is to present the coefficients of the individual nodes, together with a description of the network. Clearly, this is not a very helpful representation for the casual reader. The alternative representation would be a computer program that implements the neural network, and thereby provides means of interrogating the network. However, even this is not very effective in representing the essence of the neural network model in a way that provides a general view of the relationships involved. We do not, as yet, have a good method of achieving this.

#### 2.40.4 Variability of Corrosion Data

While it is useful to represent the expected corrosion rate as a function of the controlling parameters, this is not a complete representation of the corrosion behavior. Corrosion is inherently variable; as well as knowing the average corrosion rate, it is also important to know the variability of the behavior, as it is the

extreme behavior that will typically cause a corrosion failure, rather than the average. Methods are currently being developed to derive the variability of the training data. A simple approach illustrated in **Figure 3** is to assume that the deviation of the training data points from the fitted neural network is an indication of the inherent variance of the training data. Then, a second network can be fitted to this variance information to derive a model of the variance of the corrosion rate as a function of the controlling variables. While this is a relatively transparent way of obtaining an estimate of the variance, there may be better ways of achieving this and this is the subject of current research. One thing that is clear is that a larger data set is required to obtain a good prediction of the variance as a function of the input variables, since the training data for variance are inherently noisy. In the absence of sufficient data points to model the variance as a function of the input variables, the best that can be done to overcome this problem is to estimate the average behavior as the mean-square residual, although it may be better to use the residual as a proportion of the mean at each point (i.e., to assume that the coefficient of variation is constant over the problem domain).

#### 2.40.5 Confidence in Fitted Function

In general, one limitation of fitting techniques is the way in which they isolate the user from the original

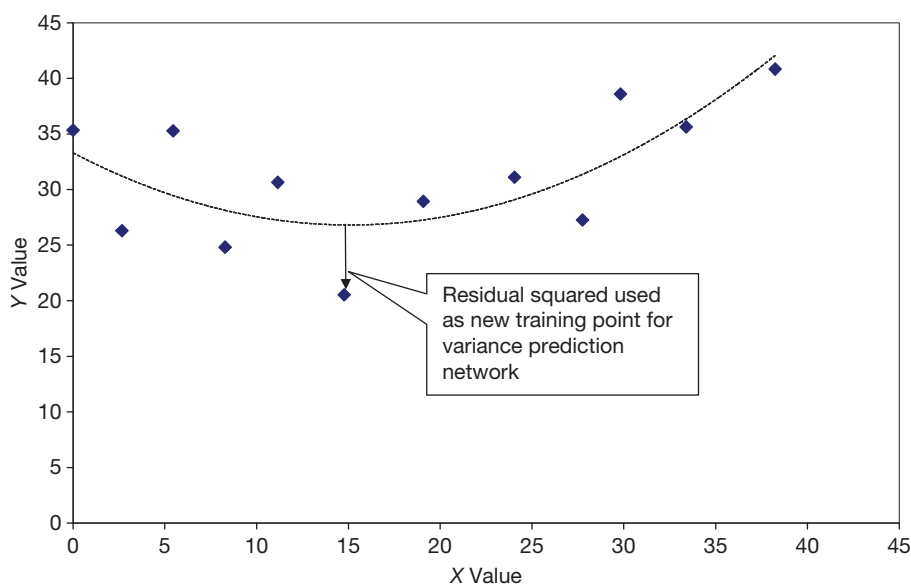


**Figure 3** Estimation of variance.

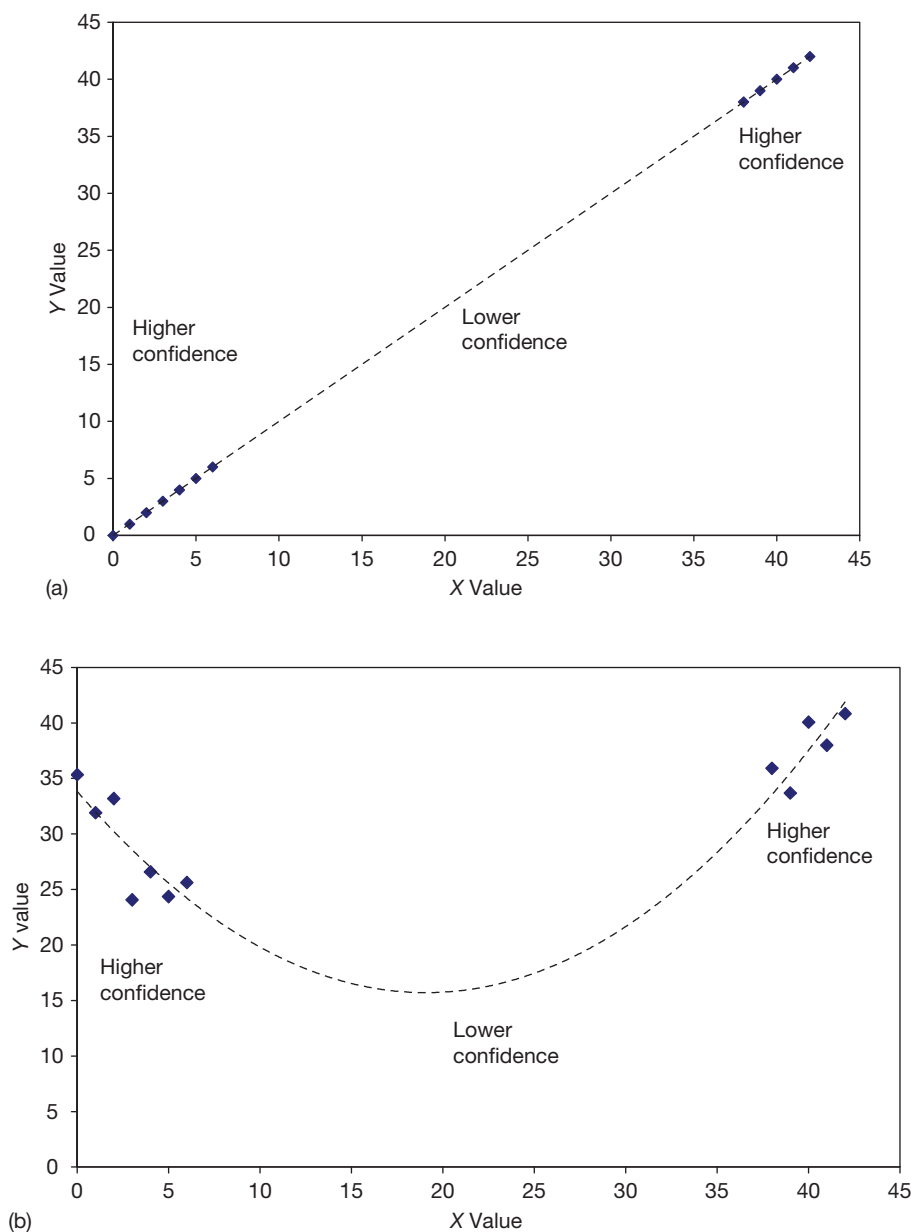


**Figure 4** Regions of low confidence in a neural network prediction: (a) More reliable interpolation? and (b) Less reliable interpolation?

data. It is apparent from [Figure 4](#) that any attempt to predict the corrosion rate in the central region is unlikely to be reliable. However, when the corrosion rate is produced as an output from a neural network or any other fitting function, this limitation is lost, and a naive user may assume that the prediction is as reliable as a prediction from regions with a high density of training data. Indeed, the imagined infallibility of computer programs may lead users to place greater faith in the prediction of the neural network.

Consequently, it is important to provide some indication of the confidence that can be placed in the prediction of the network. If the original training data are available, the 'distance' from the nearest training points can be determined, and this can be used as an indicator of confidence. Alternatively, an additional network can be trained on the local density of points. This may not be an entirely accurate estimate. [Figure 4](#) shows cases with equivalent distance between the training points, but with a somewhat

different perceived confidence in the interpolation or extrapolation. The continuous, consistent slope in **Figure 4(a)** gives a strong expectation that the line will continue between the two data regions. On the other hand, the inconsistent slopes in **Figure 4(b)** lead to uncertainty about the intervening region and hence a much lower confidence than in **Figure 4(a)**. These perceptions may, of course, be misleading, but this just underscores the difficulty of estimating the confidence that can be placed in the prediction of a neural network (or any other interpolation method). With a simple two-dimensional system such as that shown in **Figure 4**, it is relatively easy to see the implications of the interpolation process. However, in six-dimensional space it is much more difficult to visualize the relationship between the training data points and the interpolated result, and consequently it is important to develop a quantitative estimate of the confidence that can be placed in the prediction. Again, this is the basis of ongoing research.

### 2.40.6 Inconsistent Data Sets

As several groups have shown, neural network techniques can be very effective for modeling corrosion behavior. However, these methods require consistent data sets. To look at another example, work on pitting corrosion of austenitic stainless steels has used a number of measurement techniques, including the measurement of pitting potential, the ferric chloride exposure test (ASTM G 48) for critical pitting temperature (CPT) or various electrochemical methods for the measurement of CPT. If we are interested in the effect of steel composition, we can use neural network methods to fit the individual types of measurement (this has been done for the particular groups mentioned above<sup>108</sup>). This provides useful information, but fails to take full advantage of the ‘relatedness’ of the three data sets. In this case, it is apparent that we should be able to get better estimates if we could take account of all the data in the related data sets. We do not, as yet, have ways of doing this.

A similar problem is concerned with the relatively poor quality of many corrosion results. In this context, poor quality may indicate one or more of many limitations in the recorded data:

- Errors in the data arising from poor experiment design, faulty equipment or miscalculation. It is hoped such errors are rare.

- Failure to measure, control or report significant variables. For any work concerned with the effect of alloy composition on corrosion behavior, the reporting of nominal, rather than actual, compositions introduces a significant uncertainty, and degrades the value of the result. Similarly, failure to report or control environmental variables such as flow rate, oxygen concentration or temperature restrict the value of the data recorded.
- The summarization of data, for example, by plotting lines without the data points on which the line is based, seriously limits the use of such data for further analysis, and, in particular, tends to lose information about the variability and reliability of the data. It is less of a problem to report mean and standard deviation (e.g., as ‘error bars’) for measured data, as examples of the original data can be recreated by Monte Carlo methods. However, it is still better to know the exact data.

### 2.40.7 Training Data Requirements

In the introduction to prior work, we have placed significant emphasis on the number of training points, the number of input variables and the number of weights in the network. The significance of these values has often been misunderstood in the application of neural methods to corrosion problems. Even the neural network literature is somewhat unclear about what is acceptable for a good performance from a network. It may therefore be useful to examine this in a little more detail, although it should be appreciated that there is only a limited theoretical basis for this discussion.

We can consider the basic objective of the training of the neural network to be the accurate modeling of the expected value of the outer parameters (in the statistical sense of most likely value) over the relevant regions of the problem domain. By the problem domain we mean the multidimensional space defined by all the input parameters, with the ‘relevant region’ being the range of input parameters for which we want the output to be valid. Note that in many problems there may be strong correlation between input parameters, such that only a limited region of the problem domain is significant. In effect, this means that the effective dimensionality of the problem is less than the number of input variables would imply. This has important consequences for the number of training points that will be required, but the general analysis of this problem requires further work. We shall therefore consider only the case



where there is little correlation between the input variables, other than through possible clustering.

In general, an  $M$ -dimensional hypercube has  $2^M$  'corners.' A reasonable objective of a training data set would be to have a point on each corner of the hypercube. In experimental terms, this corresponds to taking two values of each variable and performing experiments for every combination of the two values. Thus, for one input variable this corresponds to taking one measurement at each of the maximum and minimum values of the input parameter and drawing a straight line between them. On this basis, two points might be rather low, and 3, 4, or more points might be better. However, the application of this approach over multiple dimensions leads to rapidly escalating requirements for the number of training points. If we cover all the possible combinations of  $N$  values for each  $M$  variable, we require  $N^M$  measurements. For example, for the relatively modest case of six input parameters we need 64 729 and 4096 measurements to provide 2, 3, and 4 points along each axis.

Unfortunately, corrosion data are generally expensive to produce, and large corrosion data sets with sufficient consistency to be suitable for training neural networks are rare. It is therefore generally the case that neural networks for corrosion data reduction must be trained on fewer points than is ideal. This leads to questions about acceptable network architectures, dimensions and training methods. This is a complex subject, and one that has not been fully defined.

From a simple information theory viewpoint, each weight used in the network provides one degree of freedom for the function produced by the network, and there should be at least one training point for each degree of freedom. If the training data are noisy, more training data (or fewer weights) will be required, otherwise the network will model the noise rather than the average behavior. On this basis, a good rule of thumb would appear to be that there should be at least twice as many training points as weights in the network. However, this rule is frequently broken, apparently without ill-effects, and it appears that over-large networks may produce acceptable behavior if the training method used is not too aggressive. Furthermore, methods have been proposed that allow the less important connections to be 'pruned' (their weights set at or near zero), thereby permitting a more complex network to be used while still retaining a good generalization ability. This is another area that merits further study. Until these questions have been clarified, we suggest that the

guideline of two training points for every weight<sup>109</sup> should be taken as the ideal.

Recently, Liu *et al.*<sup>52</sup> have used Newton interpolation to create artificial data points between existing points in order to increase the number of training points and the density of points in the problem domain. However, at first sight, this is effectively training the network to perform Newton interpolation, and it is questionable whether it offers real advantages.

## 2.40.8 A Particular Example

To conclude this introduction to the use of neural networks for the handling of corrosion data, we shall show the results obtained for a 'purpose-built' experimental data set that examined the pitting potential for type 304 austenitic stainless steel as a function of solution composition and temperature. The input variables were the concentrations of  $\text{Cl}^-$ ,  $\text{I}^-$ ,  $\text{Br}^-$ ,  $\text{F}^-$ ,  $\text{SO}_4^{2-}$ ,  $\text{CO}_3^{2-}$ ,  $\text{OH}^-$ ,  $\text{NO}_3^-$ , and  $\text{S}_2\text{O}_3^{2-}$  and the temperature of the solution, and the output was the pitting potential (the latter term being interpreted rather imprecisely as that potential at which the anodic current started to increase rapidly – this may therefore correspond to transpassive corrosion or oxygen evolution).

The data set consisted of 200 measurements distributed at random through the 10-dimensional problem domain. Various network architectures and training methods were examined, but for the results reported here, 2/3 of the data were used for training, with the remaining 1/3 being used as a validation set to determine when to terminate training. A very simple network was used with only four nodes in a single hidden layer. This produced a network with a total of 75 weights, just over half the number of training points.

As noted previously, it is very difficult to represent or test the properties of a 10-dimensional function. The best that we have been able to do so far is to compare the predictions for simple situations, in which only one variable is changed with the corresponding experimental data. The results of this exercise are shown in **Figures 5–10**, in which the network predictions are compared with the experimental results of Man and Gabe<sup>110</sup> and with data measured using the same material and test method as were used to produce the training data (these results were not included in the training or validation data). In general, it can be seen that the network predictions are reasonable, but not

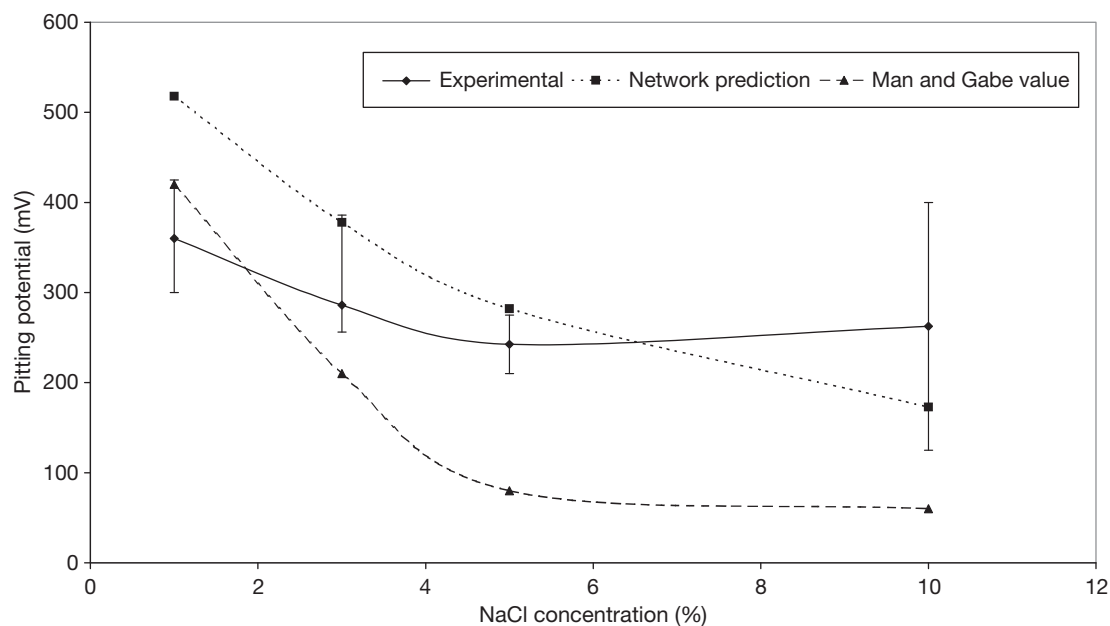


**Figure 5** Effect of chloride concentration on pitting potential.

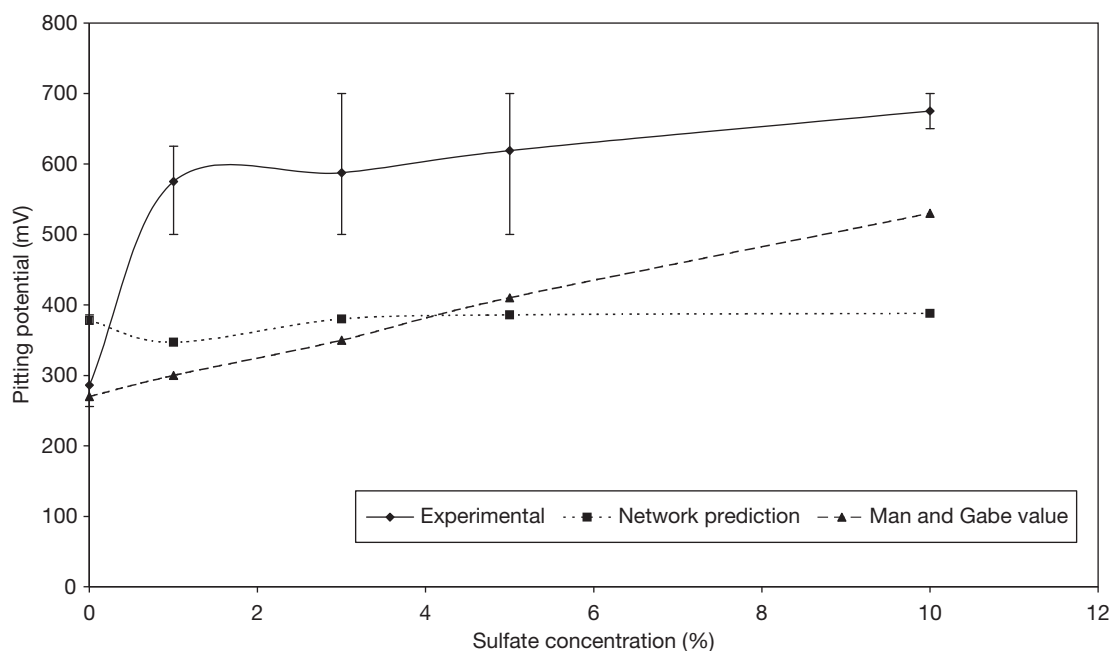


**Figure 6** Effect of sulfate on pitting potential in 3% NaCl solution.

outstanding. The failure to provide completely accurate predictions is understandable, and demonstrates the fundamental problems of this approach to corrosion prediction. The training data set is small by comparison to the size of the problem (the 10-dimensional

hypercube has 1024 corners, compared to our training data set of only 133 points). This, then, requires the use of a small network in order to avoid the possibility of memorizing the data, rather than generalizing. The conditions used for plotting, with 7 or 8 of the 9

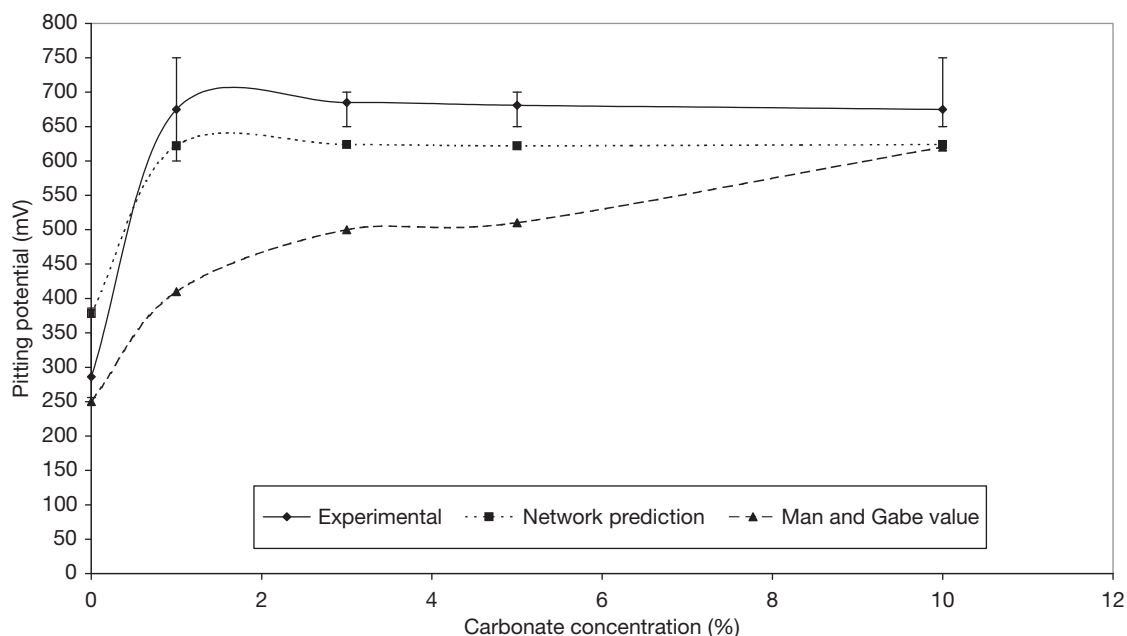


**Figure 7** Effect of carbonate concentration on pitting potential in 3% NaCl solution.

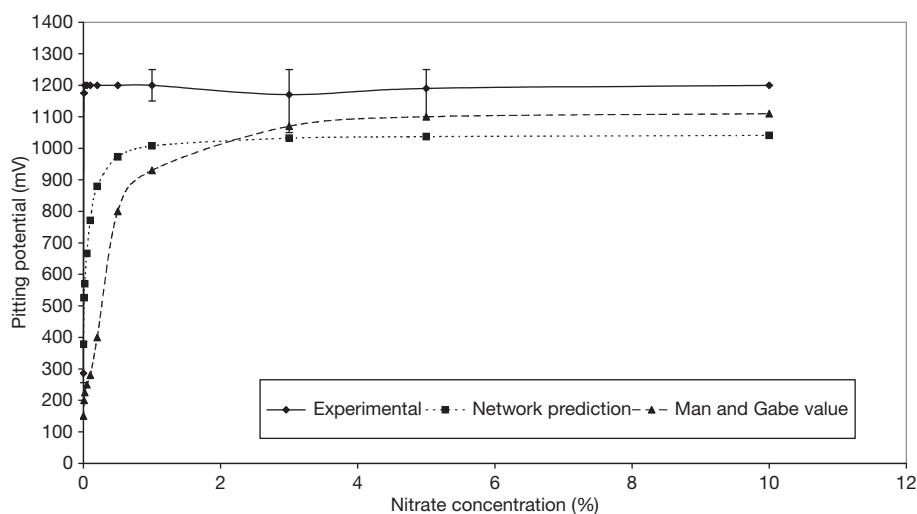


**Figure 8** Effect of nitrate concentration on pitting potential in 3% NaCl solution.

concentrations set to 0 (modeled as  $10^{-6}$  M to accommodate the log scaling used for concentration) lie right at the 'edges' of the problem domain, implying that an element of extrapolation is inevitably occurring. When these difficulties are taken into account, it seems reasonable to suggest that the neural network model performs remarkably well.

Owing to the rather small training set relative to the size of the problem, it is not realistic, at least with

our current methods, to try to extract the variance information from the network. However, the residual error (that part of the training data that is not accounted for by the network) is of the same order (around 100 mV) as the standard deviation found when repeating experiments for the same conditions, which suggests that the network is modeling the mean behavior reasonably well, and that the residual errors are largely a result of real variability in the

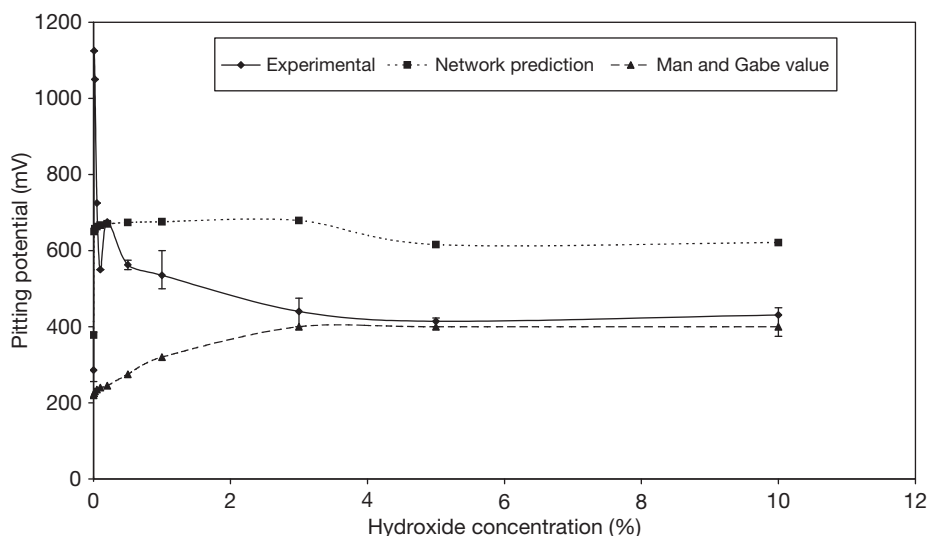


**Figure 9** Effect of hydroxide concentration on pitting potential in 3% NaCl solution.

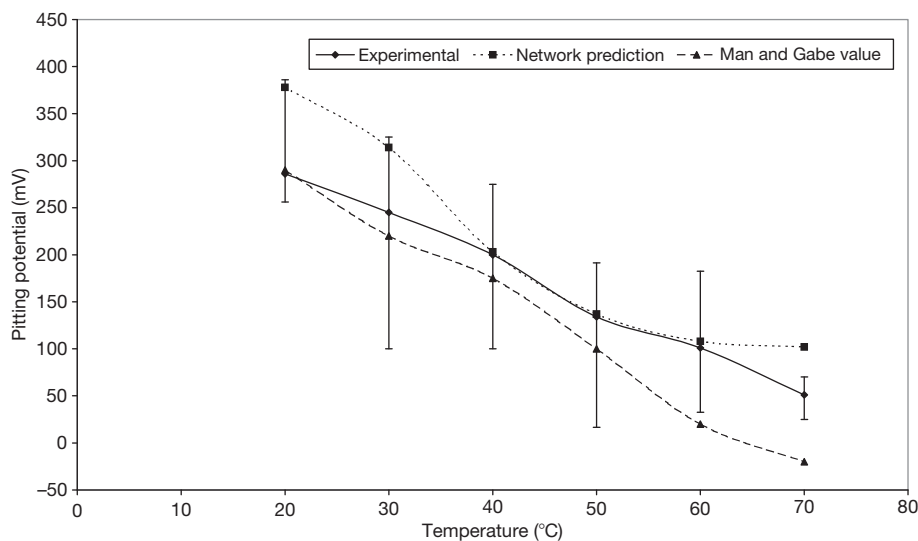


**Figure 10** Effect of temperature on pitting potential in 3% NaCl solution.

measured value. As the training data have been deliberately distributed throughout the problem domain in a relatively uniform way, there is no point in assessing the confidence that can be attributed to the prediction of the network.

### 2.40.9 Conclusions

- Artificial neural networks have generally been claimed to be successful in modeling various types of corrosion behavior. However, it is difficult to evaluate the quality of the model that is provided by a neural network with many input variables, and many studies have only validated the performance of the neural network to a limited extent.
- There is a need to model the variability in the corrosion behavior as well as the mean behavior. This can be done, but requires rather larger training data sets than the modeling of the mean.
- There is a need to provide an indication of the confidence that can be placed in the prediction of a neural network. This requires further work towards developing the necessary techniques.

## References

- Cottis, R. A.; Li Qing; Owen, G.; Gartland, S. J.; Helliwell, I. A.; Turega, M. *Mater. Des.* **1999**, 20(4), 169–178.
- Smets, H. M. G.; Bogaerts, W. F. L. *Mater. Perform.* **1992**, 31(a), 64–67.
- Urquidi-Macdonald, M.; Eiden, M. N.; Macdonald, D. D. In *Modifications of Passive Films, Paris*, 1993, pp 336–343.
- Ben-Hain, M.; Macdonald, D. D. *Corros. Sci.* **1994**, 36(2), 385–393.
- Silverman, D. C.; Rosen, E. M. *Corrosion* **1992**, 48, 734–745.
- Silverman, D. C. *Corrosion* **1994**, 50(6), 411–418.
- Silverman, A. L.; Silverman, D. C. In *Corrosion/2005*; Houston, TX, 3–7 April 2005; p 12.
- Ramamurthy, A. C.; Lorenzen, W. I.; Urquidi-Macdonald, M. *Electrochim. Acta.* **1993**, 14(14), 2083–2091.
- Trasatti, S. P.; Mazza, F. *Br. Corros. J.* **1996**, 31(2), 105–112.
- Nesic, S.; Vrhovac, M. *J. Corros. Sci. Eng.* **1998**, 1 Paper 6.
- Cottis, R. A.; Helliwell, I.; Turega, M. In *Corrosion/96*; NACE, 1996; Paper 379.
- Fang, S. F.; Wang, M. P.; Qi, W. H.; Zheng, F. *Comput. Mater. Sci.* **2008**, 44(2), 647–655.
- Diaz, V.; Veronica; Lopez, C. *Corros. Sci.* **2007**, 49(3), 949–962.
- Wang, H.-T.; Han, E.-H.; Ke, W. *J. Chin. Soc. Corros. Protect.* **2006**, 26(5), 272–274281.
- Wang, H.-T.; Han, E.-H.; Ke, W. *Corros. Sci. Protect. Technol.* **2006**, 18(2), 144–147.
- Wang, S.; Song, S. *J. Chin. Soc. Corros. Protect.* **2005**, 25(5), 257–261.
- Abdul-Wahab, S. A.; Bakheit, C. S.; Siddiqui, R. A.; Al-Alawi, S. M. *J. Corros. Sci. Eng.* **2004**, Vol. 5, 1–17.
- Song, S.; Wang, G.; Wang, S. *J. Chin. Soc. Corros. Protect.* **2003**, 23(1), 56–64.
- Diaz, V.; Lopez, C.; Rivero, S. *Revista de Metalurgia*. no. Extraordinario. **2003**, Vol. 39, 188–193.
- Ma, X.; Qu, Z.; Li, C. *Corros. Sci. Protect. Technol. (China)* **2002**, 14(1), 52–54.
- Ma, X.; Qu, Z.; Li, C. *J. Univ. Sci. Technol. Beijing (China)* **2001**, 23(2), 123–126.
- Pintos, S.; Queipo, N. V.; Troconis de Rincon, O.; Rincon, A.; Morcillo, M. *Corros. Sci.* **2000**, 42(1), 35–52.
- Cai, J.; Cottis, R. A.; Lyon, S. B. *Corros. Sci.* **1999**, 41(10), 2001–2030.
- Ukrainczyk, N.; Ukrainczyk, V. *Mag. Concr. Res.* **2008**, 60(7), 475–486.
- Shu, Y.; Du, Y.-P.; Wang, X.-M.; Yan, S.-W.; Yan, C.-H. *Gongcheng Lixue (Eng. Mech.)* **2008**, 25(suppl. 1), 102–106.
- Fan, L.; Niu, D.-T.; Dong, Z.-P.; Qin, H.-F. *Hunningtu (Concrete)* **2008**, 3, 27–29.
- Ukrainczyk, N.; Pecur, I. B.; Bolf, N. *Civil Eng. Environ. Syst.* **2007**, 24(1), 15–32.
- Sun, L.; Wang, T. *Jianzhu Jiegou Xuebao/J. Build. Struct.* **2006**, 27(suppl. 1), 713–716.
- Sun, L.-Z.; Wang, T.-C.; Zhang, H.-B. *Tianjin Daxue Xuebao (J. Tianjin Univ. Sci. Technol.)* **2006**, 39(3), 284–288.
- Parthiban, T.; Ravi, R.; Parthiban, G. T.; Srinivasan, S.; Ramakrishnan, K. R.; Raghavan, M. *Corros. Sci.* **2005**, 47(7), 1625–1642.
- Morcous, G.; Lounis, Z. *Comput. Aided Civil Infrastruct. Eng.* **2005**, 20(2), 108–117.
- Hou, H.-B.; Zhang, G.-Z. *J. Wuhan Univ. Technol. (Mater. Sci. Ed.)* **2004**, 19(4), 6–8.
- Otsuki, N.; Yodsudjai, W.; Nishida, T.; Yamane, H. *ACI Mater. J.* **2004**, 101(2), 146–453.
- Fan, Y.-F.; Zhou, J.; Feng, X. *Key Eng. Mater.* **2004**, 274–276(Part 2), 667–672.
- Iitsuka, Y.; Iyoda, T.; Kato, Y.; Uomoto, T. *Seisan-Kenkyu (J. Inst. Ind. Sci., Univ. Tokyo) (Japan)* **2000**, 52(2), 34–37.
- Liu, W.; Zhao, X.; Deng, C.; Li, W. *J. Chin. Soc. Corros. Protect.* **2008**, 28(4), 201–204.
- Kong, T.; Wang, J.; Zhong, L. *Corros. Sci. Protect. Technol.* **2008**, 20(1), 58–61.
- Du, C.-W.; Zhao, Y.-Y.; Lu, L.; Gao, J.; Li, X.-G. *Zhuangbei Huanjing Gongcheng (Equip. Environ. Eng.)* **2007**, 4(3), 85–87.
- Deng, C.-L.; Sun, M.-X.; Li, W.-J.; Lin, Z.-J.; Chen, G.-Z.; Guo, W.-M.; Liu, W.; Mu, Z.-J. *Zhuangbei Huanjing Gongcheng (Equip. Environ. Eng.)* **2006**, 3(3), 58–62, 88.
- Deng, C.-L.; Li, W.-J.; Shun, M.-X. *Corros. Sci. Protect. Technol.* **2006**, 18(1), 54–57.
- Liu, X.; Tang, X.; Wang, J. *J. Chin. Soc. Corros. Protect.* **2005**, 25(1), 11–14.
- Wang, S.; Song, S. *J. Chin. Soc. Corros. Protect.* **2004**, 24(2), 108–111.
- Kong, D.; Wang, S.; Song, S. *J. Chin. Soc. Corros. Protect. (China)* **2001**, 21(6), 352–356.
- Owen, G.; Cottis, R. A.; Turega, M. In *Corrosion 2000*; NACE, 2000; Paper 489.
- Kong, D.; Hou, G.; Song, S. *Corros. Sci. Protect. Technol. (China)* **2000**, 12(1), 16–19.
- Pai, P. S.; Mathew, M. T.; Stack, M. M.; Rocha, L. A. *Tribol. Int.* **2008**, 41(7), 672–681.
- Zhao, X.; Wang, J.; Kong, T.; Zhang, W.; Wang, Y.-H.; Pan, G.-Y. *Corros. Sci. Protect. Technol.* **2008**, 20(4), 275–278.
- Yao, D.; Gong, L.-H.; Wang, H.-L.; Wang, H.-X. *Jiefangjun Ligong Daxue Xuebao (J. PLA Univ. Sci. Technol. (Nat. Sci. Ed.) (China)* **2004**, 5(5), 67–69.
- Kumar, G.; Buchheit, R. G. In *Corrosion/2004*, New Orleans, LA, 28 March–1 April 2004; p 24.
- Gao, Z.; Wang, S.; Song, S. *Corros. Sci. Protect. Technol. (China)* **2001**, 13(suppl), 464–466.
- Castaneda, H.; Urquidi-Macdonald, M. In *Corrosion 2000*, Orlando, FL, 26–31 March 2000; pp 00768.1–00768.13.
- Liu, Z.-G.; Mu, Z.-T.; Jin, P. *Zhuangbei Huanjing Gongcheng (Equip. Environ. Eng.)* **2008**, 5(3), 24–27, 57.
- Fan, C.; He, Y.; Zhang, H.; Li, H.; Li, F. *Key Eng. Mater.* **2007**, 353–358(Part 2), 1029–1032.
- Ji, D.-M.; Zhou, C.-Y.; Hu, Y.-R. *Chuanbo Lixue (J. Ship Mech.)* **2005**, 9(6), 103–112.
- Haque, M. E.; Sudhakar, K. V. *Int. J. Fatigue* **2001**, 23(1), 1–4.
- Pleune, T. T.; Chopra, O. K. *Nucl. Eng. Des. (Switzerland)* **2000**, 197(1–2), 1–12.
- Xu, S.-H.; Ma, K.; Liu, X.-D. *Jisuanji Yingyong Yanjiu/ Appl. Res. Computers* **2008**, 25(6), 1673–1675.
- Zhang, Z.; Liu, X.; Li, Z. *J. Chin. Soc. Corros. Protect.* **2008**, 28(3), 173–176.
- Huang, Y.; Ji, D.-W. ISOPE-2007: Seventeenth (2007) International Offshore and Offshore and Polar Engineering Conference Proceedings, 2007.
- Castaneda, H.; Urquidi-Macdonald, M. *Corrosion* **2004**, 60(6), 538–547.
- Gao, Z.; Song, S.; Wang, S.; Chen, S.; Lai, G. *J. Chin. Soc. Corros. Protect.* **2004**, 24(2), 100–104.



62. Sinha, S. K.; Pandey, M. D. *Comput. Aided Civil Infrastruct. Eng.* **2002**, 17(5), 320–329.
63. Cassidy, J. M.; McCoy, T. H. In *Corrosion/2002*, Denver, CO, 7–11 April 2002; p 12.
64. Yan, G.-F.; Zhang, Y.; Wu, J.-J. *Hebei Gongye Daxue Xuebao/J. Hebei Univ. Technol.* **2007**, 36(6), 18–22.
65. Pidaparti, R. M. *Structural Health Monitor.* **2007**, 6(3), 245–259.
66. Liang, C.; Zhang, W. J. *Wuhan Univ. Technol. (Mater. Sci. Ed.)* **2007**, 22(3), 389–393.
67. Zhang, W.; Liang, C.-H. *J. Iron Steel Res. Int.* **2005**, 12(6), 59–62.
68. Leifer, J.; Mickalonis, J. I. *Corrosion (USA)* **2000**, 56(6), 563–571.
69. Shang, J.; Hu, Z.-L. *Corros. Sci. Protect. Technol.* **2007**, 19(3), 225–228.
70. Mahjani, M. G.; Jalili, S.; Jafarian, M.; Jaber, A. In *EUROCORR 2004: Long Term Prediction and Modelling of Corrosion*; Nice: France, 12–16 September 2004.
71. Tan, X.; Chen, Y.; Mu, Z.; Wei, Z. *J. Chin. Soc. Corros. Protect.* **2004**, 24(4), 218–221.
72. Wang, H.-T.; Han, E.-H.; Ke, W. *Corros. Sci. Protect. Technol.* **2004**, 16(3), 147–150.
73. Mao, X.-H.; Gan, F.-X.; Wang, D.-H. *Mater. Protect. (China)* **2001**, 34(9), 55–56.
74. Aleksanyan, A. Y.; Reformatskaya, I. I.; Podobaev, A. N. *Protect. Met. (Russia)* **2007**, 43(2), 125–128.
75. Kiselev, V. D.; Ukhlovstev, S. M.; Podobaev, A. N.; Reformatskaya, I. I. *Protect. Met. (Russia)* **2006**, 42(5), 452–458.
76. Nor, A. M.; Cottis, R. A. In *Corrosion/2004*, New Orleans, LA, 28 March–1 April 2004; p 8.
77. Sundara Raj, A.; Ravi, R.; Parthiban, T.; Radhakrishnan, G. *Bull. Electrochem. (India)* **1999**, 15(12), 552–555.
78. Pidaparti, R. M.; Neblett, E. J. *Comput. Mater. Continua.* **2007**, 5(1), 1–10.
79. Yu, D.; Chen, Y.; Duan, C. *J. Chin. Soc. Corros. Protect.* **2006**, 26(1), 19–21.
80. Kumar, M.; Ramuhalli, P.; Liu, Z. *Rev. Progr. Quant. Nondestruct. Eval.* **2005**, 24A, 720–727.
81. Chen, Y.; Lu, G.; Duan, C. *Xibe Gongye Daxue Xuebao* **2002**, 20(3), 368–372.
82. Pidaparti, R. M.; Jayanti, S.; Sowers, C. A.; Palakal, M. J. *J. Aircraft* **2002**, 39(3), 486–492.
83. Pidaparti, R. M.; Jayanti, S.; Palakal, M. J. *J. Aircraft* **2002**, 39(1), 175–180.
84. Palakal, M. J.; Pidaparti, R. M. V.; Rebbapragada, S.; Jones, C. R. *AIAA J.* **2001**, 39(10), 1936–1943.
85. Bailey, R. A.; Pidaparti, R. M.; Jayanti, S.; Palakal, M. J. In *AIAA/ASME/ASCE/AHS/ASC Structures, Structural Dynamics, and Materials Conference and Exhibit*, 41st, Atlanta, GA, 3–6 April 2000.
86. Trasatti, S. P.; Gabetta, G. *Corros. Eng. Sci. Technol.* **2006**, 41(3), 200–211.
87. Fu, D.; Li, X.; Dong, C.; Li, M. *J. Univ. Sci. Technol. Beijing (China)* **2001**, 23(2), 189–192.
88. Li, X.; Fu, D.; Dong, C.; Jin, Y. *Corros. Sci. Protect. Technol. (China)* **2001**, 13(1), 56–59.
89. Prateepasen, A.; Kaewtrakulpong, P.; Jirarungsatean, C. *Key Eng. Mater.* **2006**, Vol. 321–323(Part 1), 549–552.
90. Coates, C. W.; Olanubi, O. O.; Sokoloski, R. D.; Singleton, J. In *45th AIAA/ASME/ASCE/AHS/ASC Structures, Structural Dynamics and Materials Conference*, Palm Springs, CA, 19–22 April 2004.
91. Spanner, J.; Udpal, L.; Polikar, R.; Ramuhalli, P. *J. Nondestruct. Testing Ultrasonics (Germany)*; **2000**, 5(7).
92. Li, W.; Wang, Y.-Q. *Corros. Sci. Protect. Technol.* **2005**, 17(6), 438–441.
93. Xu, J.; Liu, W.; Xu, Z. *Surf. Rev. Lett.* **2005**, 12(4), 569–572.
94. Hernandez, S.; Nesic, S.; Weckman, G.; Ghai, V. In *Corrosion/2005*, Houston, TX, 3–7, April 2005; p 33.
95. Wu, J.; Li, M.; Li, X. *J. Chin. Soc. Corros. Protect.* **2003**, 23(1), 26–29.
96. Nesic, S.; Nordsveen, M.; Maxwell, N.; Vrhovac, M. *Corros. Sci. (USA)* **2001**, 43(7), 1373–1392.
97. Lai, Y.-Q.; Chen, X.-T.; Qin, Q.-W.; Li, J.; Liu, Y.-X. *Zhongnan Daxue Xuebao (Ziran Kexue Ban)/J. Central South Univ. (Sci. Technol.)* **2004**, 35(6), 896–901.
98. Osgerby, S.; Fry, A. In *Fourth International Conference on Advances in Materials Technology for Fossil Power Plants*; Hilton Head Island, SC, 25–28 October 2004; pp 388–401.
99. Guo, H.; Lu, Z.; Feng, G.; Cai, X.; Yang, W. *J. Chin. Soc. Corros. Protect.* **2004**, 24(1), 25–28.
100. Zhou, J.-M.; Liu, D.-Z.; Bai, Z.-Q. *Corros. Sci. Protect. Technol.* **2003**, 15(6), 342–344351.
101. Ye, H.; Xiong, J.-P.; Zhao, J.-M.; Zuo, Y. *Corros. Sci. Protect. Technol.* **2003**, 15(6), 365–368.
102. Song, G.-X.; He, S.-F.; Cao, H.; Zhang, Z.; Zhong, Q.-P. *Trans. Mater. Heat Treatment (China)* **2003**, 24(1), 82–8489.
103. Verma, A.; Ibragimov, A.; Ramachandran, S. *Neural Parallel Sci. Computat.* **2003**, 11(1–2), 19–40.
104. Howell, P. A.; Winfree, W. P. *AIP Conf. Proc.* **2003**, 657A (22), 568–574.
105. Simms, N. J.; Oakey, J. E.; Saunders, S. R. J.; Osgerby, S. *Mater. High Temp.* **2003**, 20(2), 137–151.
106. Makkonen, P. In *BALTICA V, Porvoo*, Finland, 6–8 June 2001; pp 185–195.
107. Jin, Y.; Dong, C.; Fu, D.; Li, X. *J. Chin. Soc. Corros. Protect. (China)* **2001**, 21(6), 368–373.
108. Gartland, S. J. Ph.D. Thesis, UMIST 1998.
109. Tarrasenko, L. *Guide to Neural Computing Applications*; Wiley, 1998.
110. Man, H.; Gabe, D. *Corros. Sci.* **1981**, 21(9), 713.

## 2.39 Predictive Modeling of Corrosion

**D. D. Macdonald**

Center for Electrochemical Science and Technology, Department of Materials Science and Engineering, Pennsylvania State University, University Park, PA 16802, USA

**G. R. Engelhardt**

OLI Systems, Inc., 108 The American Road, Morris Plains, NJ 07950, USA

© 2010 Elsevier B.V. All rights reserved.

2.39.1	Introduction	1632
2.39.2	Definition of Corrosion Damage	1633
2.39.3	Damage Function Analysis	1636
2.39.4	Mixed Potential Model	1638
2.39.5	Rate of Pit Nucleation	1641
2.39.5.1	Empirical Models	1641
2.39.5.2	Point Defect Model	1641
2.39.6	Rate of Pit (Cavity) Propagation	1648
2.39.6.1	General Approach for Calculating Propagation Rates	1648
2.39.6.2	Coupled Environment Corrosion Cavity Growth Models	1653
2.39.6.3	Simplified Approach for Calculating Propagation Rates	1657
2.39.7	Rate of Pit Repassivation and Transition of Pits into Cracks	1661
2.39.8	Statistical Properties of the Damage Function	1662
2.39.9	Monte Carlo Simulation	1665
2.39.10	Examples of Deterministic Prediction of Corrosion Damage in Complicated Industrial Systems	1669
2.39.10.1	Cracking in Nuclear Reactors	1670
2.39.10.2	Low Pressure Steam Turbines	1674
2.39.11	Conclusions	1676
References		1677

### Abbreviations

**BWR** Boiling water reactor  
**CDF** Cumulative distribution function  
**CEFM** Coupled environment fracture model  
**CEM** Coupled environment model  
**CEP** Corrosion evolutionary path  
**CF** Corrosion fatigue  
**CGR** Crack growth rate  
**CT** Compact tension  
**DAH** Differential aeration hypothesis  
**DFA** Damage function analysis  
**ECL** Electrochemical crack length  
**ECP** Electrochemical corrosion potential  
**EVD** Extreme value distribution  
**HWX** Hydrogen water chemistry  
**IGSCC** Stress corrosion cracking  
**LPST** Low-pressure steam turbines  
**MCL** Mechanical crack length  
**MPM** Mixed potential model

**NWC** Normal water chemistry

**PDM** Point defect model

**SCC** Stress corrosion cracking

### Symbols

***a*** Depth of a corrosion event  
***a<sub>max</sub>*** Deepest corrosion event  
***a<sub>cr</sub>*** Critical depth  
***b*** Bulk  
***b*** Inverse Tafel constant  
***C<sub>k</sub>*** Concentration of species *k*  
***d*** Thickness of the wall  
 ***$\bar{D}$***  Average diffusivity of breakdown sites  
***D<sub>k</sub>*** Diffusion coefficient of species *k*  
***D<sub>t</sub>*** Turbulent diffusion coefficient  
***E*** Potential  
***E<sub>corr</sub>*** Corrosion potential

$E_{\text{crit}}$  Critical potential for localized corrosion  
 $E_{\text{rp}}$  Repassivation potential  
 $E_0$  Equilibrium potential  
 $F$  Faraday's constant  
 $F_k$  Integral damage function for corrosion event,  $k$   
 $f_k$  Differential damage function for corrosion event,  $k$   
 $G^{\text{ex}}$  Excess Gibbs energy  
 $I$  Current density  
 $I_{\text{ss}}$  Steady-state passive current density  
 $i_a$  Anodic current density  
 $i_c$  Cathodic current density  
 $i_{\text{corr}}$  Corrosion current density  
 $i_p$  Passive current density  
 $i_0$  Exchange current density  
 $i_{\text{corr}}^0$  Current density on the bare surface  
 $i^*$  Current density calculated in the absence of a potential drop in the cell  
 $J_{\text{ca}}$  Flux of cation vacancies  
 $J_{\text{m}}$  Annihilation flux of metal vacancies  
 $j_k$  Flux of species  $k$   
 $K$  Constant in [eqn \[70\]](#)  
 $k_i$  Reaction rate for  $i$ th reaction  
 $K$  Equilibrium constant  
 $K_I$  Stress intensity factor  
 $K_{\text{ISCC}}$  Critical stress intensity factor  
 $k_m$  Rate of chemical reaction  $m$   
 $K_v$  Electrochemical equivalent volume  
 $L$  Thickness of barrier layer  
 $L_{\text{ss}}$  State thickness of barrier layer  
 $m$  Constant in [eqn \[70\]](#)  
 $N$  Total number of nucleated stable pits  
 $n_k$  Rate of nucleation of defect  $k$   
 $Q$  Quasipotential  
 $P_f$  Probability of failure  
 $R$  Gas constant  
 $R_k$  Rate of production or depletion of species  $k$   
 $Re$  Reynolds number  
 $s$  Surface  
 $S$  Surface area  
 $Sc$  Schmidt number  
 $T$  Temperature  
 $t$  Time  
 $t_s$  Service time  
 $t_{\text{in}}$  Incubation time  
 $t_{\text{pr}}$  Propagation time  
 $u$  Central parameter  
 $u_i$  Mobility of species  $i$   
 $U_0$  Open circuit potential  
 $v$  Hydrodynamic velocity

$V_k$  Rate of propagation of corrosion defect  $k$   
 $V_0$  Initial pit propagation rate  
 $\bar{V}_0$  Mean initial pit propagation rate  
 $V_{\text{app}}$  Applied voltage  
 $V_c$  Critical voltage  
 $V_m$  Electrode potential  
 $X_i$  Internal independent variable  
 $X_m$  Average depth of the largest pit  
 $x$  Depth of penetration  
 $x_0$  Characteristic depth  
 $Y_i$  External independent variable  
 $z$  Direction perpendicular to the surface  
 $z_k$  Charge of species  $k$   
 $\alpha$  (1) Anodic transfer coefficient, (2) scale parameter, (3) polarizability of the barrier layer/solution (outer layer) interface  
 $\beta$  (1) Tafel coefficient using natural logarithms, (2) dispersion in Laplace's distribution  
 $\Delta G_s^0$  Standard Gibbs energy change for the chloride absorption reaction  
 $\Delta G_s^0$  Change of Gibbs energy for the Schottky-pair reaction  
 $\Delta K$  Stress intensity factor range  
 $\epsilon$  (1) Dielectric permittivity, (2) electric field strength within the barrier layer  
 $\dot{\epsilon}_{\text{ct}}$  Crack tip strain rate  
 $\epsilon_f$  Fracture strain  
 $\gamma$  Delay repassivation constant  
 $\gamma_k$  Activity coefficient of species  $k$   
 $\Gamma$  Ratio of the bare surface of the crack tip to the total geometric surface  
 $\eta$  Dynamic viscosity  
 $\Delta K_{\text{th}}$  Threshold stress intensity factor range  
 $\kappa$  Conductivity  
 $\lambda$  (1) Constant in [eqn \[83\]](#), (2) function defined by [eqn \[97\]](#)  
 $\mu_k$  Chemical potential of species  $k$   
 $\nu$  Kinematic viscosity  
 $\nu_k$  Stoichiometric coefficient of species  $k$   
 $\rho$  Density  
 $\xi$  Critical areal concentration of vacancies  
 $\zeta$  Survival probability  
 $\sigma$  Standard deviation  
 $\tau$  Dissolution time  
 $\Phi$  Cumulative distribution function  
 $\varphi$  Electrical potential  
 $\Psi$  Extreme value distribution  
 $\psi$  Laplace's distribution function  
 $\Omega$  Mole volume of the barrier layer per cation

### 2.39.1 Introduction

As our industrial and infrastructure systems (refineries, power plants, pipelines, etc.) age, there is a considerable economic incentive to avoid unscheduled outages and to extend operation beyond the design lifetime. The avoidance of unscheduled outages is of particular interest, because the failure of even a minor component can result in the complete shutdown of a facility. For example, the unscheduled shutdown of a 1000 MWe nuclear power plant due to the failure of a valve may cost the operator between \$1 million and \$3 million per day, depending upon the cost of replacement power and other factors. However, if component failures could be accurately predicted, maintenance could be performed during scheduled outages, the cost of which has already been built into the price of the product, thereby minimizing the economic impact of the failure. With regard to life extension, the successful extension of operation beyond the design life translates into enhanced profits and the avoidance of costly licensing and environmental impact assessments associated with the development and construction of a new facility. However, in this case as well, the key to successful operation is the ability to avoid unscheduled downtime and hence maintain continuity of production. However, eventually, the frequency and severity of unscheduled outages render continued operation uneconomic and, at that point, replacement of the facility becomes necessary.

Corrosion is a major cause of component failure, and hence the occurrence of unscheduled downtime, in complex industrial systems. In particular, the various forms of localized corrosion, including pitting corrosion, crevice corrosion, stress corrosion cracking (SCC), and corrosion fatigue (to name the common forms), are particularly deleterious, because they frequently occur without any outward sign of accumulating damage and because they often result in sudden and catastrophic failures. Thus, the development of effective general and especially localized corrosion damage prediction technologies is essential for the successful avoidance of unscheduled downtime and for the successful implementation of life extension strategies.

There are two main approaches for predicting corrosion damage – empiricism and determinism. ('Determinism' is used here in the physics sense to describe a model whose predictions are constrained to the 'physically viable' realm by the natural laws. The term 'determinism' is often used in engineering disciplines to indicate a model that provides a definite output in response to a definite input.) Empiricism is the philosophy that everything we

can ever know must have been experienced. On the other hand, determinism is the philosophy that we may predict the future from the past via the natural laws. Within these two classes, there exist numerous subclasses. For example, within the empirical class, there are functional models, in which (discrete) data are represented by continuous mathematical functions; statistical models; and artificial neural networks, to name a few. Within the broad class of 'deterministic' models, there can exist 'definite' models that yield a single output for a given set of input values; and probabilistic models, in which the inputs are distributed resulting in a distributed output from which the probability of an event occurring can be estimated.

It must be noted that, up to now, the prediction of corrosion damage has been largely based on the application of empirical models and only in the past decade, or so, have deterministic models been developed.

It is important to note that there are particular difficulties in using purely empirical models for predicting corrosion damage in real industrial systems, caused by the following factors: (i) Empirical models are generally expensive, because of the need for large databases covering many independent variables for calibration. Complex industrial systems are unique, even when they are of the same design, because they endure different operating conditions and histories. Thus, for example, an airplane that has been operating in a hot, humid environment might require more inspection and maintenance than an identical aircraft based in a desert environment. (ii) Failures are rare events. Accordingly, it is generally impossible to develop an effective database for model calibration based on the failure statistic of any given system. (iii) Empirical models also fail to capture the mechanism of failure.

Of course, deterministic models also pose many challenges. The most important of these are as follows: (i) Corrosion is an extremely complex phenomenon that depends on a multitude of factors, including the chemistry of the environment, metallurgy, and thermomechanical history of the corroding metal, hydrodynamics of multiphase flow, geometry, stress, temperature, pressure, and so on; (ii) the lack of information on kinetic parameters of the corroding system; and (iii) the need to define the corrosion evolutionary path (CEP). Because any model that is developed to describe the damaging process, and on which the deterministic prediction of damage is based, is only a figment of our imagination, and is based upon inputs from imperfect senses that are interpreted through an imperfect intellect, it is clear

that a working deterministic model can yield only an approximate description of a real system. Accordingly, pure ‘determinism’ is an ideal concept that is probably never achieved in reality, and the complementary, use of deterministic and empirical model provides the most effective method for predicting corrosion damage. Nevertheless, through the application of the ‘scientific method,’ in which a model is continually revised as it is cyclically tested against new observations, many deterministic models evolve toward providing accurate descriptions of real systems.

At this point, it is necessary to contrast the philosophical bases of ‘mechanistic models’ and ‘deterministic models,’ because great confusion exists in the literature on this issue. A mechanistic model is based upon a realistic mechanism for the process that is underpinned by a valid theory that, ideally, accounts for all of the observed properties. There is no requirement that the output must be constrained by the natural laws, as is the case for a deterministic model. Frequently, it is found that the values of unknown parameters are simply determined by calibration, whereas, in a deterministic model those same parameter values would be determined by the constraints. Given sufficient complexity and enough unknown parameters, a mechanistic model can be made to fit any data set imaginable and then yield predictions that are frequently at odds with reality. This cannot happen in the case of a deterministic model because the constraints, which are expressions of scientific generality (i.e., the ‘natural laws’), limit the predictions to a realm that is consistent with the constraints themselves (i.e., to physical ‘reality’).

The need to define the CEP has been explained above. The CEP is defined as the path taken by the system in terms of those independent variables that have a significant impact on the rate of damage accumulation in transitioning from the present state to the future state. This path must be continuous and is required for both deterministic and empirical damage prediction models. Examples of defining the CEP are given later in this chapter, when we discuss the prediction of damage in practical systems.

In this article, we review recent advances in the development of some deterministic models for predicting corrosion damage (the review of some empirical models, including statistical models and artificial neural networks can be found in other articles in this volume). This subject is much too broad for justice to be done in a single chapter of the current length, but, by limiting the scope, the authors wish to illustrate the essential elements of theory and deterministic

model-building and to demonstrate how the models can make useful predictions. The cases discussed have been chosen to address practical problems in current science and engineering, and, where possible, applications of the models to real engineering problems have been selected.

## 2.39.2 Definition of Corrosion Damage

As is well known, corrosion damage can be classified into two categories: uniform (general) corrosion and localized corrosion, and the quantitative description of these two cases are quite different. In this review, principal attention will be devoted to the case of localized corrosion. However, it must be noted that, in the general case, it is impossible to describe the propagation of localized corrosion damage without having reliable deterministic models for general corrosion, because the latter models yield the most important value for predicting the rate of localized corrosion; namely, the corrosion potential,  $E_{\text{corr}}$ .

In the case of general corrosion, it is natural to define corrosion damage at a given point on a metal surface as being the thickness of the metal layer that has corroded,  $a$ . This definition means that we can predict general corrosion damage if we can calculate  $a$  as a function of time and of the independent variables controlling the damaging process, that is,  $a$  is predicted in the form:

$$a = a(t, X_i, Y_i) \quad [1]$$

Here,  $X_i$  and  $Y_i$  are internal and external independent variables, respectively, that determine the damage propagation rate. Examples of internal variables are grain size and orientation, texture, electrochemical kinetic parameters, and other microstructural properties. The external variables include loading and environmental conditions.

Even the term ‘uniform corrosion’ shows that, usually, the corroding layer thickness,  $a$ , depends slightly on the coordinates on the metal surface, if internal and external variables can be considered to be approximately constant for different parts of the system. In other words, it is assumed that, for a given set of conditions, uniform corrosion damage can be characterized for a given time and for given environmental conditions by a single value – average thickness of the corroded layer. Accordingly, for the case of general corrosion, the service life of the system,  $t_s$ , can be defined as the duration before the corroding



layer thickness achieves some average critical thickness,  $a_{cr}$ , (or reaches some minimum allowed value). Usually, the uniform corrosion data are analyzed by using the normal distribution. It is also assumed that the standard deviation of the thickness of the corroded layer,  $\sigma$ , can be estimated by using eqn [1], if the standard deviations of values  $X_i$  and  $Y_i$  are known by using, for example, the standard method for calculating the propagation of error.

In the case of localized corrosion, the situation becomes more complicated. Generally speaking, the accumulation of localized corrosion damage in a system is completely defined if we know how many pits or other corrosion events (per square centimeter) have depths between  $x$  and  $x + dx$  for a given observation time,  $t$ , at a given location on the metal surface. We will denote this quantity as  $f_k(x, t)dx$  where  $f_k(x, t)$  is the so-called differential damage function.<sup>1</sup> Here, the index  $k$  denotes different types of localized defects, such as active and passive pits, cracks, crevices, and so on.

However, in the overwhelming majority of practical cases, such complete information is not required to effectively predict the failure time due to the penetration of the deepest event. Thus, very often, it is sufficient to obtain information about only the deepest corrosion event (pit, crack), because failure in the system commonly occurs when the depth of the deepest corrosion event  $a_{max}$  exceeds some critical value,  $a_{cr}$ . Usually,  $a_{cr}$  is the thickness of the wall of a pipe, for example, or the depth of a pit transitioning into an unstable crack. With regard to the first case, in order to describe the damage, we can use an equation of the previous form, that is,

$$a_{max} = a_{max}(t, X_i, Y_i) \quad [2]$$

Accordingly, the service life of the system,  $t_s$  (that is sometimes denoted as being the time to failure,  $t_f$ ) can be expressed as the sum of incubation period,  $t_{in}$ , and propagation period,  $t_{pr}$ , in order for the defect to attain a critical depth:

$$t_s = t_{in} + t_{pr} \quad [3]$$

The period of propagation,  $t_{pr}$ , can be divided into periods corresponding to different forms of propagating of the corrosion defect; for example, in the form of pit,  $t_{pit}$ , or in the form of crack,  $t_{cr}$ , if the crack nucleates from the pit. In turn, for example,  $t_{cr}$  can be subdivided into the period  $t_{cr,c}$  (the time required for the surface crack to grow into a through crack) and  $t_{cr,g}$  (the time for a through crack to grow to a prescribed critical length), and so on.

It is important to understand that even if relation [2] can be obtained, its applicability would be questionable. The problem is that eqn [2] yields a single number for  $a_{max}$  for a given value for  $t$  and for other parameters of the system. However, in the general case, it is impossible to describe available experimental data by a single number. Thus, Table 1 shows typical data for the depths of the deepest pits experimentally measured<sup>2</sup> on 20 sampled areas of  $300 \times 300$  mm on the bottom outer surface near the periphery of a circular tank made of SS41 carbon steel, storing heavy petroleum, after 7 years of service; all of the pit depths not smaller than 0.5 mm were recorded, and the maximum pit depth in each sampled area was noted. The experimental data were taken from Harlow and Wei.<sup>3-7</sup>

We see that the difference between the observed values is greater than 280%. It is clear that, in the general case, prediction of corrosion damage can be done only in probabilistic terms. Apparently, the best form of predicting localized corrosion damage would be prediction of the probability of failure,  $P_f$ :

$$P_f = P_f(a_{cr}, t, X_i, Y_i, S) \quad [3]$$

that is, the probability that at least one corrosion event of any form (pit, stress corrosion crack, fatigue crack) reaches some critical depth,  $a_{cr}$ , at a given observation time,  $t$ , for any given set of environmental conditions. It is essential that  $P_f$  must be a function of the total area of the system, because the larger the area of the system, the larger will be the number of corrosion events and hence the greater the probability that a deeper event will exist. Accordingly,  $P_f$  must increase with area.

**Table 1** Maximum pit depth distribution,  $a_{max,i}$  (in ascending order) for oil storage tank

	<i>i</i>								
	12	13	14	15	16	17	18	19	20
$a_{max,i}$ (mm)	0.65	0.71	0.75	0.84	0.90	1.07	1.18	1.25	1.82

Index  $i$  numerates samples. Samples with  $i < 12$  have maximum pit depth of  $< 0.5$  mm.

Let us consider possible ways for theoretically estimating this probability. The most intensive work that has been reported on predicting corrosion (in aluminum alloys) is that of Harlow and Wei,<sup>3-7</sup> whose important achievement has been to insert into prediction technology the realization that an analytical description (not necessarily a deterministic description) of the accumulation of damage is possible. Their approach is as follows: It is assumed that a pit is nucleated at an initial moment,  $t = 0$ , with an initial depth of  $a_0$ , and that the depth increases with increasing observation time,  $t$ . At some critical depth,  $a_{cr}$ , the pit transitions into a crack. By using mechanically-based models for calculating pit or crack propagation rates, an analytical expression for the depth of the corrosion event,  $a$  (in the form of a pit or crack), as a function of time is found in analytical form, as described by eqn [1]. All variables  $X_i$  and  $Y_i$  (where only temperature has been included in the environmental variables) are subdivided into two parts: deterministic parameters (in the engineering sense, i.e., parameters with fixed values) and random parameters, with the latter obeying, for example, the Weibull distribution. Subsequently, eqn [1], together with the change-of-variable theorem, or standard Monte Carlo technique, may be used to estimate the probability of failure,  $Pr(a > a_{cr}, t)$ , that is, the probability that the crack length,  $a$ , exceeds the prescribed critical length of the crack,  $a_{cr}$ , at given observation time,  $t$ . The obvious problem with this approach is that it is completely devoid of environmental effects, such as those of potential, pH,  $[Cl^-]$ , and solution conductivity on pit and crack nucleation and growth, even though these effects have been established experimentally and are consistent with field observations. Accordingly, the underlying model for damage propagation fails to explain all of the experimental observations and hence is not viable. The second problem is that, by selecting a single pit, the significant literature demonstrating that pitting, which leads to cracking, is a progressive phenomenon in which new pits nucleate as existing pits grow and die (repassivate), is ignored. Thus, by selecting a particular pit initially, there is no way of knowing, *a priori*, whether that pit will survive to grow to a critical depth and hence, nucleate a crack. Indeed, the approach taken by Harlow and Wei is, in form, very similar to that employed by Liu and Macdonald<sup>8,9</sup> in the early 1990s to describe the failure of low pressure steam turbines, except that the latter study incorporated environmental effects, and the predictions of the component models were

constrained by the appropriate natural laws (including the conservation of charge, recognizing the electrochemical nature of the damaging processes).

The question then arises whether the models of Harlow and Wei, for example, can be generalized by including the influence of environmental parameters, other than temperature, in explicit form. Even if they were able to do so, which, in itself, would require a massive reformulation of the models to incorporate environmental effects, in our opinion, the applicability of their approach would remain highly questionable, because environmental effects cannot be included in an *ad hoc* fashion. In addition, as noted above, the current Harlow and Wei<sup>3-7</sup> models consider only a single event, whereas it is well known that corrosion damage due to pitting, stress corrosion cracking, and corrosion fatigue accumulates progressively (that is, new pits/cracks nucleate while existing pits/cracks grow and die). In other words, it is impossible, in the general case, to attribute corrosion damage to a single corrosion event on the surface in isolation from all other events. Instead, the development of damage must be described in terms of an ensemble of localized corrosion events.

This thesis is confirmed by the following: The probability that any particular pit will repassivate (die) during the service life of a system is generally very high. Thus, let us consider the classical measurements of pit depth distribution versus time performed by Aziz<sup>10</sup> on Alcan aluminum alloy 2S-O in Kingston tap water (Figure 1). This study showed that by the end of 2 months, the bulk of the pits represented by the bell-shaped curve had ceased to grow (i.e., they had 'died') and only the deeper pits continued to propagate. In other words, by the end of two months from the beginning of the corrosive attack (in this particular case), the overwhelming majority of the pits repassivate (die). Accordingly, there is no way of knowing whether the pit selected had the necessary characteristics to grow to the critical length. In the general case, the probability that the depth of the deepest pit will exceed some critical value depends on the number of nucleated, stable pits and on the probability of repassivation. In some extreme cases, the probability that the depth of the deepest pit increases beyond some critical value is vanishingly small,<sup>11</sup> with the result that cracks will not nucleate. Obviously, this is a scenario that can only be described in terms of a large ensemble of events, rather than in terms of a single event.

In addition, the interaction between growing pits must be taken into account. The presence of existing

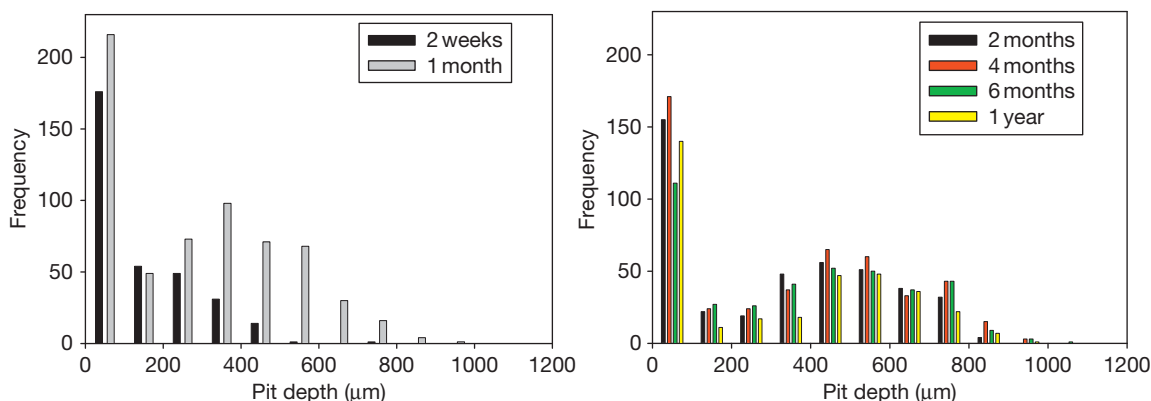


**Figure 1** Pit depth distributions for Alcan 2S-O aluminum alloy immersed in Kingston water for different periods of time. The increment in pit depth is 100  $\mu\text{m}$ . Reproduced from Aziz, P. M. *Corrosion* **1956**, 12, 35–46.

pits impacts the probability of nucleation of other stable pits within the neighboring region. This phenomenon has been experimentally reported by Macdonald<sup>12</sup> and is explained by the competition of the pits for the available resources on the external surfaces (oxygen reduction) or because the existing pit cathodically protects the neighboring surface and hence inhibits the nucleation of the second pit. The interaction between the ‘hemispheres of influence’ (subtending the external area over which the cathodic reaction occurs) of growing, stable pits can also reduce the propagation rate of each of the pits, simply by reducing the metal potential at the pit bottom. Finally, we also have to take into account the overlapping between growing pits that also influences the shape and propagation rate. All of this shows that any method for estimating the probability of failure on the basis of the propagation of a single corrosion event (pit or crack) cannot be general.

### 2.39.3 Damage Function Analysis

One of the approaches that considers the accumulation of corrosion damage in terms of the evolution of an ensemble of pits and cracks is damage function analysis (DFA).<sup>1,13,14</sup> (The other possible method, that based on the Monte Carlo simulation of movement of ensemble of corrosion events will also be described below). As mentioned above, the differential damage function,  $f_k(x, t)$  yields the complete description of corrosion damage. It is easy to obtain the differential equation for this function. The function  $f_k$  has a dimension of  $\#/(\text{cm}^2 \text{ cm}) = \#/\text{cm}^3$ , analogous to the concentration of particles. Accordingly, it is very convenient to regard each defect as a ‘particle’ that

moves in the  $x$  direction (perpendicular to the surface, with  $x = 0$  being at the metal surface). The coordinate of this particle,  $x$ , coincides with the depth of penetration into the surface. Accordingly,  $f_k$  must obey the law of mass conservation

$$\frac{\partial f_k}{\partial t} + \frac{\partial j_k}{\partial x} = R_k, \quad k = 1, 2, \dots, K \quad [4]$$

where  $j_k$  and  $R_k$  are the flux density and the bulk source (sink) of the ‘particle’  $k$  respectively. Thus, the subscript  $k$  enumerates the corrosion defect (e.g., pit or crack) and  $K$  is the total number of different corrosion defects in the system. By definition,  $R_k(x, t)dxdt$  yields the number of defects  $k$  (per square centimeter) with depths between  $x$  and  $x+dx$  that arise (or disappear) during the period of time between  $t$  and  $t+dt$ , due to transformation (repassivation, in the case of pits).

The system of eqns [4] can be solved with the appropriate boundary and initial conditions.

$$j_k = n_k(t) \quad \text{at } x = 0, t > 0 \quad [5]$$

and

$$f_k = f_{k0}(x) \quad \text{at } x \geq 0, t = 0 \quad [6]$$

where  $f_{k0}(x)$  is the initial distribution of defect  $k$  (usually we can assume that  $f_{k0}(x) = 0$ , i.e., no damage exists at zero time) and  $n_k(t)$  is the nucleation rate of the same defect (i.e.,  $n_k(t)dt$  is the number of stable defects (per square centimeter) that nucleate in the induction time interval between  $t$  and  $t+dt$ ).

Thus, because the defect propagation flux,  $j_k$ , must be nonnegative (the depth of a corrosion event can only increase with time), the following, simplest numerical upwind finite difference scheme can be used for numerically solving eqns [4]–[6].

$$f_{k,m}^{n+1} = f_{k,m}^n - \frac{\Delta t}{\Delta x} (j_{k,m}^n - j_{k,m-1}^n) + R_k^n \Delta t \quad [7]$$

Here, we use the straightforward approach of choosing equally spaced points along both the  $t$ - and  $x$ -axes:  $x_j = x_0 + m\Delta x$ ,  $m = 0, 1, \dots, J$  and  $t_j = t_0 + n\Delta x$ ,  $n = 0, 1, \dots, N$ , and we denote  $f_{k,m}^n = f_k(t_n, x_m)$ . The values  $f_{k,0}^n$  and  $f_{k,m}^0$  are calculated from the boundary and initial conditions [4] and [5]. Of course, it is assumed that we know (i.e., can calculate) fluxes,  $j_k$ , and sources/sinks,  $R_k$ , as functions of the spatial coordinates and time, and, in nonlinear cases, as functions of the unknown values of  $f_k$ .

It is important to note that, sometimes, the equation of continuity is presented in the simplified form<sup>15,16</sup>

$$\frac{\partial f_k}{\partial t} + \frac{\partial [V_k(x)f_k]}{\partial x} = R_k, k = 1, 2, \dots, K \quad [8]$$

This expression implies that the rate of  $k$ th defect,  $V_k$ , depends only on the depth of penetration,  $x$ , and accordingly, for the flux density,  $j_k$ , we have

$$j_k(x, t) = f_k(x, t) V_k(x) \quad [9]$$

In the simplest cases, it is even possible to obtain analytical solutions for the damage functions. As an example, let us consider the case of pitting corrosion under constant external conditions. In this instance, we have two kinds of defects ( $K = 2$ ): active pits with the damage function,  $f_a$ , and passivated pits (i.e., those that have ‘died’ through delayed repassivation) with the damage function,  $f_p$ . Let us assume that the flux density of active pits is described by eqn [8] with  $V_a(x) = V(x)$ . By definition, the flux of passivated pits is zero (i.e., these pits are ‘dead’). It is evident that functions  $R_a$  and  $R_p$  must obey the relation  $R_p = -R_a$  (a pit must be either alive or dead). If, in addition, we assume that the pit repassivation process obeys a first order decay law, the function  $R_a$  has the form

$$R_a(x, t) = -\gamma f_a(x, t) \quad [10]$$

where  $\gamma$  is the delayed repassivation (‘death’) constant (i.e., the rate constant for repassivation of stable pits). In the general case,  $\gamma$  depends on the depth of the pit,  $x$ , and on time,  $t$ , when the external conditions depend on time. However, in this example, we assume that  $\gamma$  is a constant, that is, we suppose that pits repassivate accidentally and that the probability of repassivation does not depend on pit depth. (This is clearly a gross oversimplification, since the probability of delayed repassivation is expected to increase with pit age, but

this does not change the logic of the argument). Accordingly, the system of equations for calculating the DFs has the form

$$\frac{\partial f_a}{\partial t} + \frac{\partial [V(x)f_a]}{\partial x} = -\gamma f_a \quad [11]$$

and

$$\frac{\partial f_p}{\partial t} = \gamma f_a \quad [12]$$

The boundary and initial conditions are given as

$$Vf_a = n(t) \text{ at } x = 0, t > 0 \text{ and } f_a = f_p = 0 \text{ at } t = 0 \quad [13]$$

where  $n(t)$  is the nucleation rate of pits on the surface. Analytical solutions to this system of linear partial first-order differential equations can be obtained by using the characteristic method<sup>17</sup> and have the following form:

$$f_a = \frac{\exp[-\gamma\theta(x)]n[t - \theta(x)]}{V(x)} \text{ and} \quad [14]$$

$$f_p = \frac{\gamma \exp[-\gamma\theta(x)]N[t - \theta(x)]}{V(x)}$$

where

$$\theta_{\text{pit}}(x) = \int_0^x \frac{dx'}{V(x')} \quad [15]$$

is the age of a pit with depth  $x$  and

$$N(t) = \int_0^t n(t')dt' \quad [16]$$

is the number of stable pits (per square centimeter) that nucleate in the time interval between 0 and  $t$ .

In some cases, it is convenient to use the so-called integral damage function

$$F_k(x, t) = \int_x^\infty f_k(x', t)dx' \quad [17]$$

which yields the number (per square centimeter) of corrosion events with depths larger than  $x$  for a given observation time,  $t$ . It is important to note that, experimentally, only the sum of the damage functions for active and passive pits  $f = f_a + f_p$  is determined and in many instances the integral damage function only is measured. Accordingly, it is important for practical reasons to obtain the equation for the integral damage function,  $F = F_a + F_p$ , for the sum of the active and passive pits. Note that, for the considered case, the integral damage function corresponds to the

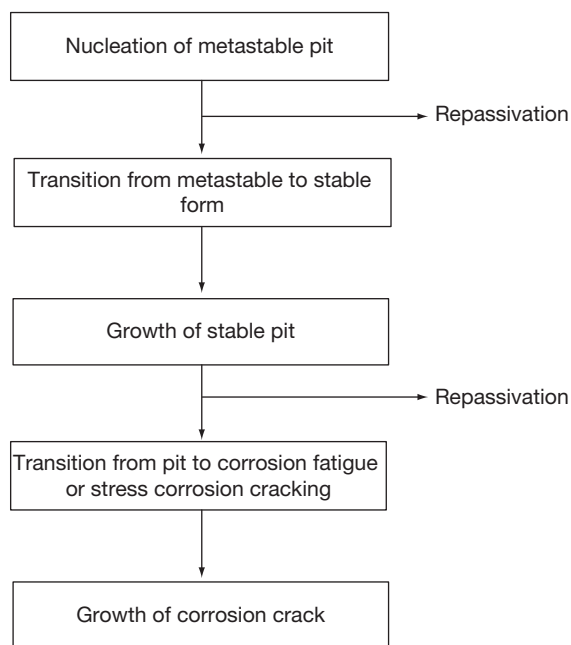


**Figure 2** Schematic history of the nucleation and propagation of corrosion damage.

number of remaining pits on a surface, as the surface is removed layer by layer in preestablished increments. From eqns [14] and [17], we therefore have

$$F(x, t) = \exp[-\gamma\theta(x)]N[t - \theta(x)] \quad [18]$$

According to the theory outlined above, calculation of the damage functions requires the determination of three independent functions for each kind of corrosion defect,  $k$ : (1) the rate of defect nucleation,  $n_k$ ; (2) the flux density (growth rate) of the defect,  $j_k$ ; and (3) the rate of transition of one kind of defect into another,  $R_k$  (e.g., the transition of an active pit into a passivated pit or the transition of a pit into a crack). In other words, we need to have quantitative models for describing each stage of corrosion damage as indicated in Figure 2. Below, we will discuss the feasibility of calculating each of these three functions. However, as noted above, the detailed deterministic description of any phase of corrosion propagation is impossible without reliable information about the corrosion potential of the system,  $E_{\text{corr}}$ . Accordingly, in the first step, the methods for calculating  $E_{\text{corr}}$  will be considered.

### 2.39.4 Mixed Potential Model

In 1937, Wagner and Traud<sup>18</sup> formulated their mixed potential theory in electrochemistry, in which the

potential adopted by an electrode in contact with an aqueous solution containing both oxidizing and reducing species is determined by a balance of the cathodic (reduction) and anodic (oxidation) partial processes occurring at the surface. If the electrode is inert, the resulting potential is known as the redox potential,  $E_{\text{redox}}$ . On the other hand, if the electrode is electroactive and undergoes electrooxidation (corrosion), thereby contributing to the total partial anodic current, the potential is known as the electrochemical corrosion potential, ECP (or  $E_{\text{corr}}$ ), of the substrate. Thus, if the partial current densities do not depend on the coordinate on the metal surface, the charge conservation condition for the interface may be written as

$$\sum_k i_{a,k} + \sum_m i_{c,m} = 0 \text{ at } E = E_{\text{corr}} \quad [19]$$

where  $i_{a,k}$  and  $i_{c,m}$  are partial anodic and cathodic current densities, corresponding to the  $k$ th anodic and  $m$ th cathodic reaction correspondingly. This simple theory has proved to have a profound impact on how we interpret the corrosion of metals and alloys in a wide variety of systems.

As an example, let us consider one of the first comprehensive applications of the mixed potential theory in corrosion science to an industrial system, namely the calculation of ECP in the coolant circuits of water-cooled nuclear reactors, particularly boiling water reactors (BWRs), using a mixed potential model (MPM).<sup>19,20</sup> In this complex chemical system (the reactor coolant circuit), radiolysis of the coolant water by ionizing radiation ( $\gamma$ -photons and neutrons) produces a myriad of electroactive species, some of which are oxidizing species (e.g.,  $\text{O}_2$ ,  $\text{H}_2\text{O}_2$ ,  $\text{OH}$ ) and others that are reducing species ( $\text{H}_2$ ,  $\text{H}$ ). These species all contribute to the current flow across the interface, but the mixed potential theory predicts that the contribution that any given species can make to the potential is roughly proportional to its concentration. Thus, in BWR primary coolant circuits, the only species of practical importance are  $\text{O}_2$ ,  $\text{H}_2\text{O}_2$ , and  $\text{H}_2$ , since the concentrations of these species are orders of magnitude greater than those of the other radiolytic species. The reactions describing each of the electroactive species are described as redox reactions, which can be written in the general form as



where R and O are reduced and oxidized species, respectively, with the kinetics of the reaction being



described in terms of the generalized Butler–Volmer equation

$$i_{R/O,j} = \frac{e^{b_{a,j}\eta_j} - e^{-b_{c,j}\eta_j}}{\frac{1}{i_{0,j}} + \frac{e^{b_{a,j}\eta_j}}{i_{l,f,j}} - \frac{e^{-b_{c,j}\eta_j}}{i_{l,r,j}}} \quad [21]$$

where  $b_a$  and  $b_c$  are the anodic (oxidation) and cathodic (reduction) inverse Tafel constants,  $i_0$  is the exchange current density,  $i_{l,f}$  and  $i_{l,r}$  are the mass transport limiting current densities, and  $\eta$  is the overpotential that is defined as the difference between the potential and the equilibrium potential for reaction  $j$ . The parameters  $b_a$  and  $b_c$  are normally measured in separate experiments, but in principle can be calculated *ab initio*. The exchange current density,  $i_0$ , is almost always measured directly, as theory is not sufficiently well developed to calculate this quantity from first principles. In addition to the redox partial reactions (oxidation and reduction processes), the anodic oxidation of the substrate also contributes to the total current density. In this case, the point defect model (PDM)<sup>21</sup> (the PDM will be considered in detail in the next section) provides the functional form of the anodic oxidation current density as

$$i_a = A + Be^{CE} \quad [22]$$

where  $A$ ,  $B$ , and  $C$  are constants that depend upon the values of fundamental parameters in the model and upon the properties of the system (e.g., pH). For metals and alloys that form n-type passive films, in which cation interstitials and/or oxygen vacancies are the dominant defects,  $B=0$ , and the anodic oxidation current density is independent of potential, unless there is a change in the oxidation state of the metal ion (cation or interstitial) being ejected from the barrier oxide layer at the barrier layer–solution interface. Systems of this type include iron and carbon steel, the stainless steels, and the chromium-containing, nickel-based alloys, such as Alloys 600 and 22. On the other hand, for metals that form p-type passive films (e.g., nickel),  $A=0$ , and  $B$  and  $C$  are greater than zero. In this case, the passive current density is described by the Tafel equation.

The conservation of charge requires that the sum of the partial current densities at the interface be zero, with this condition being expressed as

$$i_a(E) + \sum_{j=1}^{\mathcal{J}} \frac{e^{b_{a,j}\eta_j} - e^{-b_{c,j}\eta_j}}{\frac{1}{i_{0,j}} + \frac{e^{b_{a,j}\eta_j}}{i_{l,f,j}} - \frac{e^{-b_{c,j}\eta_j}}{i_{l,r,j}}} = 0 \quad [23]$$

where  $\mathcal{J}$  is the total number of redox reactions in the system. Note that in eqn [19], the summation takes place over the anodic and cathodic reactions

separately, whereas in eqn [23], index  $j$  enumerates the redox reactions, each comprising conjugate partial anodic and cathodic partial reactions. Solution of eqn [23] yields the ECP or the corrosion potential,  $E_{\text{corr}}$ . Note that  $\eta_j = E - E_j^e$ , where  $E_j^e$  is the equilibrium potential for the  $j$ th redox reaction. The limiting currents can be written in terms of the mass transfer correlations for the flow geometry and flow regime of interest.<sup>22</sup>

$$i_{l,j} = \pm n_j F A' Re^\lambda Sc^\gamma C_{O/R}^b \quad [24]$$

where  $n_j$  is the number of electrons involved in the reaction,  $A'$  is a constant,  $Re = dV/v$  is Reynolds number,  $d$  is the hydrodynamic diameter of the channel,  $V$  is the flow velocity,  $v = \hat{\eta}/\rho$  is the kinematic viscosity,  $\hat{\eta}$  and  $\rho$  are the dynamic viscosity and the density, respectively, of the medium, and  $C_{O/R}^b$  is the concentration of the reactive species in the bulk environment. The Schmidt number is defined as  $Sc = v/D$ , where  $D$  is the diffusivity of the reacting species. The sign convention is ‘+’ for the forward direction (left to right) of the reaction [20], as written, and ‘−’ for the reverse direction. Mass transfer correlations of the type expressed by eqn [24] are available in the literature for a wide variety of flow geometries and regimes (Selman and Tobias,<sup>22</sup> and citations therein), with the latter corresponding to specific ranges in  $Re$  and  $Sc$ . Once the corrosion potential is known (by solving eqn [23]), the corrosion current density is readily calculated using eqn [22].

As noted above, the MPM has been used extensively to calculate the corrosion potentials of stainless steel components in the coolant circuits of BWRs, and we will use this case to illustrate the power of this model in defining the response of metals and alloys to the properties of the environment in a complex industrial system. The typical measured and calculated ECP data for a cell attached to the recirculation piping of the Liebstadt BWR in Switzerland as a function of the amount of hydrogen added to the feedwater are plotted in Figure 3. This represents a ‘double blind’ comparison in that those who performed the calculations<sup>19,23</sup> did not have access to the data measured on the reactor, and those who measured the ECP on the reactor (Sierra Nuclear) did not have access to the calculated values. As shown, the measured and predicted corrosion potential data are in good agreement, except for the initial point (zero added hydrogen). However, in this case, it was found that the level of agreement could be greatly improved by changing the mass transport parameters (flow velocity, hydrodynamic diameter, etc.).

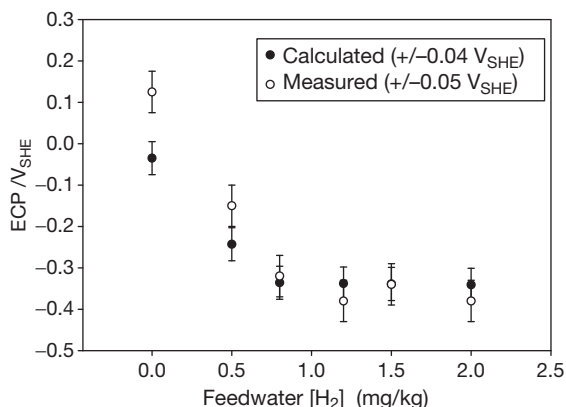


**Figure 3** Comparison of calculated and measured ECP for the Leibstadt BWR in Switzerland. The ‘measured’ data were acquired in a test cell attached to the recirculation piping. The data employed in the calculation are summarized in Macdonald and Urquidi-Macdonald<sup>19</sup> and Macdonald *et al.*<sup>23</sup> The estimated accuracies of the calculated and measured data are indicated in the box in the figure.

Since these parameters are poorly characterized for an autoclave at very low flow rates, the disagreement in the absence of added hydrogen is of little consequence.

The accuracy of any MPM model for predicting  $E_{\text{corr}}$  and the rate of uniform corrosion depends on the accuracy of modeling of the rates of particular electrochemical reactions along with the completeness of the set of reactions included in the summation in eqn [19]. A detailed review of different models for the kinetics of corrosion can be found in the corresponding chapter of this book **Chapter 2.38, Modeling of Aqueous Corrosion**. Here we would only like to mention that already existing commercial software yields reliable prediction of the corrosion potential and, correspondingly, the rate of uniform corrosion under relatively complicated conditions, including the influence of adsorption, active–passive transition effects, scaling, transport in porous media, and so on.

Thus, the models of Anderko *et al.*<sup>24–26</sup> and those of others<sup>8,9,19–21,23</sup> have been developed for simulating the rates of general corrosion of selected metals (including carbon steels, stainless steels, aluminum, and nickel-based alloys) in aqueous solutions. The model consists of thermophysical and electrochemical modules. The thermophysical module is used to calculate the speciation of aqueous solutions and to obtain concentrations, activities, and the transport properties of individual species. The electrochemical module simulates partial oxidation and reduction processes on the surface of the metal. It is capable of reproducing the active–passive transition and the

effect of solution species on passivity. The model has been implemented in a program that can be used to simulate the effects of various conditions, such as temperature, pressure, pH, component concentrations, and flow velocity on the corrosion potential and corrosion rate. The model clearly demonstrates the influence of inhibitors on corrosion rate. Good agreement with experimental data has been obtained.

Other comprehensive models have been developed for describing general corrosion under specific conditions. Thus, Nordsveen *et al.*<sup>27</sup> developed a mechanistic model of uniform carbon dioxide (CO<sub>2</sub>) corrosion that takes into account such phenomena as diffusion of species between the metal surface and the bulk including diffusion through porous surface films, migration due to the establishment of potential gradients, and the existence of homogenous chemical reactions, including the precipitation of surface films. Nešić *et al.*<sup>28</sup> developed a comprehensive model for calculating internal uniform corrosion rates under multiphase flow conditions in mild steel pipelines.

However, it is important to note that, in the general case, for calculating ECP and uniform corrosion rate, where extensive localized corrosion may exist on a surface, thereby imparting significant nonuniformity in the current densities, we have to use, instead of eqn [19], the following equation.

$$\int_S \sum_m i_{a,m} dS + \int_S \sum_k i_{c,k} dS = 0 \quad \text{at } E = E_{\text{corr}} \quad [25]$$

It is evident that eqn [25] reduces to eqn [19] when we can assume that the partial current densities do not depend on the coordinates (location) on the metal surface, or if we can neglect any such dependencies. Thus, let us consider the case of pitting corrosion. Of course, the anodic current density inside pits can exceed the passive corrosion current density by several orders of magnitude. However, if the area of the active dissolution (area of pit surfaces) is much smaller than the total area of the metal surface (active corrosion current is much smaller than the passive corrosion current), it may be possible to use eqn [19] instead of eqn [25]; otherwise, such a simplification would be incorrect.

Experiments show that, often, both possibilities can be realized in an industrial system.<sup>29,30</sup> Thus, in the case of the corrosion of Alloy 20Kh13 (the Russian analog of Type 403 SS) in NaCl solutions, the corrosion potential is observed to decrease with time.<sup>30</sup> This reduction occurs due to the intensive growth of corrosion pits, because the total cathodic partial current has

to increase in order to compensate the increasing total partial anodic current, to conserve charge in the system. At some point, this growth stops due to the transport limitation for the cathodic reactant (oxygen), that is, the system is now limited by the lack of cathodic resources to support the ever-increasing corrosion current. On the other hand, such reduction is not observed in cases where the total area of observed pits is very small and hence, the nonuniformity in the partial current densities is minor and can be ignored.

These examples clearly show that, in the general case, eqn [25] must be used for predicting corrosion potential, at least in the case of steels that are not highly resistant to localized corrosion in the prevailing environment. It is evident that because of the statistical character of pit distribution in size and position, the imposition of charge conservation can be done correctly only by considering propagation of pitting damage as the evolution of an ensemble of pits that initiate, propagate, and repassivate on the metal surface.

## 2.39.5 Rate of Pit Nucleation

### 2.39.5.1 Empirical Models

It would be natural to assume, and experiment confirms this at least for the case of stainless steels, that the rate of nucleation of stable pits,  $n$ , is proportional to the rate of nucleation of metastable pits,  $n_{mp}$ <sup>31–33</sup> that is,

$$n = \zeta n_{mp} \quad [26]$$

where coefficient,  $\zeta$ , can be considered as the probability of nucleation of a stable pit from a metastable pit and is termed the ‘survival probability.’ This parameter can be measured experimentally. Thus, for example, for Type 304L stainless steel in chloride-containing solution, the experimentally measured survival probability has a value of the order of  $10^{-2}$  to  $10^{-4}$ ,<sup>31,32</sup> depending upon the potential and solution conditions. Accordingly, the most probable number of stable pits (per square centimeter),  $N_0$ , will be  $N_0 = \zeta N_{mp,0}$ , where  $N_{mp,0}$  is the most probable number of available sites (per square centimeter) for metastable pits.

In many practical cases, it is possible to assume that all stable pits on a given surface nucleate during an initial period of time that is much smaller than the observation time,  $t$ , or the service life of the system,  $t_s$ . In this case, the process is termed ‘instantaneous nucleation.’ For example, for the case of the pitting

corrosion of aluminum in tap water, as described by Aziz,<sup>10</sup> practically all the pits were found to nucleate within the first 2 weeks (see Figure 1). Under these conditions, the total number of nucleated stable pits (per square centimeter) that nucleate in the time interval between 0 and  $t$  can be simply represented as

$$N(t) = N_0 U_+(t) \quad [27]$$

where  $U_+(t)$  is the asymmetrical unit function ( $U_+ = 0$  at  $t \leq 0$  and  $U_+ = 1$  at  $t > 0$ ).

If pit nucleation cannot be regarded as being ‘instantaneous,’ the simplest assumption concerning the pit nucleation rate of metastable sites,  $n_{mp}(t) = dN_{mp}/dt$ , is that  $n_{mp}(t)$  is proportional to the number of available metastable sites, that is,  $dN_{ms}/dt = [N_{ms,0} - N_{mp}(t)]/t_0$ ,<sup>32</sup> which yields

$$N(t) = N_0 [1 - \exp(-t/t_0)] \quad [28]$$

where  $t_0$  is some characteristic time. It is evident that  $t_0$  must depend on the corrosion potential, temperature, and electrolyte composition, and some experimental data indicating such dependencies can be found in the literature.<sup>31–34</sup> However, no theoretical (deterministic) model has been reported for estimating  $t_0$  as a function of the environmental conditions and the kinetic parameters of the system.

### 2.39.5.2 Point Defect Model

A comprehensive model, in the form of the PDM<sup>35–39</sup> has been developed for estimating the nucleation rate of metastable pits which, when combined with eqn [26], yields the sought-after nucleation rate of stable pits. (Note that only the growth of stable pits gives rise to pitting damage on a surface.) The PDM was originally developed in the early 1980s to provide an atomic scale description of the growth of passive films on a metal surface, but was subsequently expanded to describe metastable passivity breakdown. Thus, it is clearly evident that any deterministic model for describing pit nucleation rate must simultaneously describe the properties of passive films existing on the metal surface and clearly specify the criteria for passivity breakdown itself. The conditions under which passive films exist on metal surfaces are a matter of great theoretical and practical interest, because the phenomenon of passivity is the enabler for our current, metals-based civilization.<sup>21</sup> Thus, our industrial systems and machines are fabricated primarily from the reactive metals and their alloys, including iron, nickel, chromium, aluminum, titanium, copper, zinc, zirconium, stainless steels, nickel-base alloys, and

aluminum alloys, to name a few. Although the phenomenon of ‘passivity’ has been known for about 170 years,<sup>40</sup> and the conditions under which metals and alloys become passive have been systematically explored over the past 70 years, until recently no reasonably unifying theoretical treatment of the limits of passivity has emerged. While many theories and models for the passive state have been developed,<sup>21</sup> most of the presently available models describe an already existing passive film and do not address the conditions under which the film may form or disappear. One of the few attempts to address this issue is the one by Engell,<sup>41</sup> who postulated that passive films can be thermodynamically stable or metastable, with film formation being governed by equilibrium thermodynamics in the first case and by the relative rates of formation and dissolution in the second. While Engell’s work<sup>41</sup> made a valuable contribution to the theory of passivity, it did not resolve the theoretical issues with sufficient precision to allow specification of the exact conditions under which passivation/depassivation might occur (see below).

A comprehensive review of the conditions under which passivity may occur and be lost has been explored within the framework of the PDM by using phase-space analysis (PSA) and can be found in Macdonald.<sup>42</sup> It has been shown that the PDM provides a comprehensive basis for describing the formation and destruction of passive films and hence allows specification of the conditions for the use of reactive metals in our metals-based civilization. A brief description of some results is given below.

The PDM postulates that passive films that form on metal and alloy surfaces in contact with oxidizing environments are bilayer structures comprising a highly (point) defective barrier layer, which grows into the metal and an outer layer that forms via the hydrolysis of cations transmitted through the barrier layer and the subsequent precipitation of a hydroxide, oxyhydroxide, or oxide, depending upon the formation conditions, or by transformation of the outer surface of the barrier layer itself (an ‘Ostwald ripening’ process). In many systems (e.g., Ni and Cr), the barrier layer appears to be substantially responsible for the phenomenon of passivity. In other systems, such as the valve metals and their alloys (Al, Ta, Ti, Nb, Zr), and iron (particularly at elevated temperatures), for example, the outer layer may form a highly resistive coating that effectively separates the reactive metal and the barrier layer from the corrosive environment. The ‘sealing’ of anodized aluminum is an example of how the outer layer may be manipulated to achieve high corrosion resistance. In the present analysis, only the barrier layer is considered, because the passivity of chromium-containing alloys appears to be due to a thin barrier layer of defective  $\text{Cr}_2\text{O}_3$  that forms on the surface in contact with the alloy. Thus, in these cases, the barrier layer is clearly ‘the last line of defense.’

The PDM further postulates that the point defects present in a barrier layer are, in general, cation vacancies ( $V_M^{\chi'}$ ), oxygen vacancies ( $V_O^{\bullet\bullet}$ ), and cation interstitials ( $M_i^{\chi+}$ ), as designated by the Kroger–Vink notation (Figure 4). Cation vacancies are electron acceptors, which result in doping the barrier layer

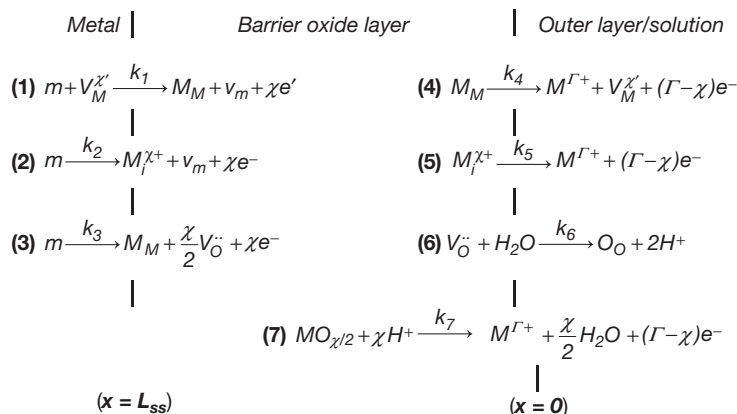


**Figure 4** Interfacial defect generation/annihilation reactions that are postulated to occur in the growth of anodic barrier oxide films according to the point defect model.<sup>35</sup> M, metal atom;  $V_M^{\chi'}$ , cation vacancy on the metal sublattice of the barrier layer;  $M_i^{\chi+}$ , interstitial cation;  $M_M$ , metal cation on the metal sublattice of the barrier layer;  $V_O^{\bullet\bullet}$ , oxygen vacancy on the oxygen sublattice of the barrier layer;  $O_O$ , oxygen anion on the oxygen sublattice of the barrier layer;  $M^{\Gamma+}$ , metal cation in solution.

p-type, whereas oxygen vacancies and metal interstitials are electron donors, resulting in n-type doping. Thus, on both pure metals and alloys, the barrier layer is essentially a highly doped, point defect semiconductor, as demonstrated by Mott–Schottky analysis<sup>21</sup> for example. Not unexpectedly, the situation with regard to alloys is somewhat more complicated than that for the pure metals. Thus, while the barrier layers on pure chromium and on Fe–Cr–Ni alloys (including the stainless steels) are commonly described as being ‘defective Cr<sub>2</sub>O<sub>3</sub>,’ those on pure chromium are normally p-type in electronic character<sup>43</sup> and those on the stainless steels<sup>44</sup> are n-type. The latter can be described as Cr<sub>2+x</sub>O<sub>3-y</sub>, recognizing that the barrier layer may be metal rich (via metal interstitials) or oxygen-deficient (via oxygen vacancies), or both, whereas that on pure chromium apparently is metal- and oxygen-deficient, or Cr<sub>2-x</sub>O<sub>3-y</sub>, with the cation vacancy being the dominant defect in the system. It is not known whether the apparent differences in the barrier layers on pure chromium and on chromium-containing alloys are due to doping of the barrier layer by other alloying elements, or the inhibition of cation vacancy generation relative to the generation of oxygen vacancies and metal interstitials, in the barrier layer on the alloys compared with that on pure chromium.

The defect structure of the barrier layer can be understood in terms of the set of defect generation and annihilation reactions occurring at the metal–barrier layer interface and at the barrier layer–outer layer (solution) interface, as depicted in Figure 4.<sup>42</sup> Regardless of the electronic type, that is, irrespective of the identity of the dominant defect in the system, reactions [3] and [7] (Figure 4) are responsible for the growth and destruction of the barrier layer and any analysis of the stability of the layer must focus on these two reactions. That the barrier layer always contains oxygen vacancies is self-evident, since the rate of dissolution at the barrier layer–solution interface is always finite.

As noted elsewhere,<sup>21,42</sup> the rate of change of the barrier layer thickness for a barrier layer that forms irreversibly on a metal or alloy surface can be expressed as

$$\frac{dL}{dt} = \Omega k_3^0 e^{a_3 V} e^{b_3 L} e^{c_3 \text{pH}} - \Omega k_7^0 (C_{\text{H}^+} / C_{\text{H}^+}^0)^n e^{a_7 V} e^{c_7 \text{pH}} \quad [29]$$

where  $a_3 = \alpha_3(1 - \alpha)\chi\gamma$ ,  $a_7 = \alpha_7\alpha(\Gamma - \chi)\gamma$ ,  $b_3 = -\alpha_3\chi\epsilon\gamma$ ,  $c_3 = -\alpha_3\chi\beta\gamma$ , and  $c_7 = \alpha_7\beta(\Gamma - \chi)\gamma$ . In these expressions,  $\Omega$  is the mole volume of the barrier layer per cation,  $\epsilon$  is the electric field strength within the

barrier layer (postulated to be a constant and independent of the applied voltage in the steady state, because of the buffering action of Esaki tunneling),<sup>21</sup>  $k_i^0$  and  $\alpha_i$  are the standard rate constant and transfer coefficient, respectively, for the appropriate reactions depicted in Figure 4 (i.e., reactions [3] and [7]),  $\alpha$  is the polarizability of the barrier layer–solution (outer layer) interface (i.e., the dependence of the voltage drop across the interface,  $\phi_{\text{f/s}}$ , on the applied voltage,  $V$ ),  $\beta$  is the dependence of  $\phi_{\text{f/s}}$  on pH (assumed to be linear),  $\gamma = F/RT$ ,  $\chi$  is the oxidation state of the cation in the barrier layer,  $\Gamma$  is the corresponding quantity for the cation in solution,  $C_{\text{H}^+}$  is the concentration of hydrogen ion,  $C_{\text{H}^+}^0$  is the standard state hydrogen ion concentration, and  $n$  is the kinetic order of the barrier layer dissolution reaction with respect to H<sup>+</sup>.

By setting the left side of eqn [29] equal to zero, the steady state thickness of the barrier layer,  $L_{\text{ss}}$ , is readily derived as

$$L_{\text{ss}} = \left[ \frac{1 - \alpha}{\epsilon} - \frac{\alpha\alpha_7}{\alpha_3\epsilon} \left( \frac{\Gamma}{\chi} - 1 \right) \right] V + \left[ \frac{2.303n}{\alpha_3\epsilon\chi\gamma} - \frac{\alpha_7\beta}{\alpha_3\epsilon} \left( \frac{\Gamma}{\chi} - 1 \right) - \frac{\beta}{\epsilon} \right] \text{pH} + \frac{1}{\alpha_3\epsilon\chi\gamma} \ln \left( \frac{k_3^0}{k_7^0} \right) \quad [30]$$

Note that in deriving these expressions, the convention has been adopted that, for the rate of barrier layer dissolution,  $C_{\text{H}^+}$  and  $C_{\text{H}^+}^0$  have units of mol cm<sup>-3</sup>, but when used for defining pH, the units are the conventional mol l<sup>-1</sup>. Thus, the standard states for the dissolution reaction (second term on the right side of eqn [39]) and for the pH are 1.0 mol cm<sup>-3</sup> and 1.0 mol l<sup>-1</sup>, respectively. The introduction of a standard state into the dissolution rate renders the units of  $k_7^0$  independent of the kinetic order,  $n$ , without altering the numerical value of the rate.

The steady state passive current density is readily derived<sup>21</sup> as

$$I_{\text{ss}} = \Gamma F \left[ k_2^0 e^{a_2 V} e^{b_2 L_{\text{ss}}} e^{c_2 \text{pH}} + k_4^0 e^{a_4 V} e^{c_4 \text{pH}} + k_7^0 e^{a_7 V} e^{c_7 \text{pH}} \cdot (C_{\text{H}^+} / C_{\text{H}^+}^0)^n \right] \quad [31]$$

where the first, second, and third terms arise from the generation and transport of cation interstitials, cation vacancies, and oxygen vacancies, respectively, with the term due to the latter being expressed in terms of the rate of dissolution of the barrier layer.<sup>21</sup> This expression is derived, in part, by noting that the fluxes of a given defect at the two interfaces under steady-state conditions are equal; in this way, the



expression for the current can be formulated so as to avoid the defect concentrations at the interfaces.

The passive state is not perfectly protective and, for a variety of reasons, passivity breakdown occurs, resulting in enhanced corrosion rates. Of particular concern is localized passivity breakdown, which results in the nucleation and growth of pits and subsequently, the nucleation and growth of cracks if, the requisite tensile stress is present in the system. A review of the literature reveals the following generalizations of the experimental data for passivity breakdown of metals and alloys in a wide variety of environments<sup>21</sup>:

1. Localized corrosion is initiated by passivity breakdown and occurs on a wide variety of passive metals and alloys in a wide variety of environments.
2. Certain species (e.g.,  $\text{Cl}^-$  and  $\text{Br}^-$ ) induce passivity breakdown by interacting with the barrier layer. These aggressive species apparently do not penetrate through the barrier layer but may be incorporated into the precipitated outer layer.
3. Passivity breakdown occurs at a wide variety of sites on metal and alloy surfaces.
4. Passivity breakdown is a dynamic deterministic process, being predetermined and (in principle) predictable on the basis of known physical laws.
5. The transition of a metastable event to a stable event is a rare event.
6. Two fundamentally different repassivation phenomena may be identified: (i) 'Prompt' repassivation and (ii) 'delayed' repassivation (sometimes referred to as 'stifling').
7. A single passivity breakdown site is characterized by a critical voltage ( $V_c$ ) and induction time ( $t_{\text{ind}}$ ).  $V_c$  is found to be near-normally distributed while  $t_{\text{ind}}$  displays a left acute distribution. The parameters  $V_c$  (and  $\bar{V}_c$ ) and  $t_{\text{ind}}$  exhibit highly characteristic dependencies on the activities of the breakdown-inducing aggressive species ( $a_x$ ) and on the applied voltage ( $t_{\text{ind}}$  only) for a wide variety of systems, suggesting commonality in mechanism.
8.  $V_c$  (and  $\bar{V}_c$ ) is found to depend on the identity of the aggressive ion within a homologous series. Thus, in the case of iron and nickel, the propensities of the halide ions for inducing passivity breakdown lie as  $\text{F}^- < \text{Cl}^- > \text{Br}^- < \text{I}^-$ , whereas, in the case of titanium, bromide ion is the most aggressive. These trends are readily explained by the absorption of the halide into oxygen vacancies in the surface of the barrier layer, with the extent of absorption being determined by the competitive needs to dehydrate the ion and expand the vacancy.<sup>21</sup>
9. The mean breakdown voltage,  $\bar{V}_c$  is found to decrease linearly with  $\log(a_x)$  with a slope that exceeds  $2.303RT/E$  which is attributed to the value of the polarizability of the barrier layer–solution interface lying between 0 and 1, for essentially all systems (metal–solution) that have been investigated. Likewise, the induction time for essentially all systems investigated display a common form of the dependencies of  $\log(t_{\text{ind}})$  on potential and  $[X^-]$ . These relationships strongly suggest commonality in breakdown mechanism.
10. Certain oxyanions (e.g., nitrate, borate, and nitrite) strongly inhibit passivity breakdown, with the effect being accounted for by competitive absorption with the aggressive anion into surface oxygen vacancies in the barrier layer.<sup>21</sup>
11. In many systems (e.g., Al, Ga, Zr, stainless steel), blister formation is observed to be the precursor to passivity breakdown.
12. Certain alloying elements (e.g., Mo in Ni) cause a positive shift in  $V_c$  (and  $\bar{V}_c$ ) and in a lengthening of the induction time. The effect is greater for a larger difference in the oxidation states between the solute and host.
13. Incident electromagnetic radiation, with a photon energy that is greater than the bandgap of the barrier layer oxide also results in a positive shift in  $V_c$  (and  $\bar{V}_c$ ) and in a lengthening of the induction time. The defect (electronic and crystallographic) structures of the barrier layer are modified by irradiation.

It has been shown that PDM is able to explain all the experimental data for passivity breakdown of metals and alloys mentioned above and accordingly, can be considered as providing a suitable theoretical basis for a deterministic model treatment of passivity breakdown and the nucleation of metastable pits in a metal surface.<sup>21</sup>

The PDM, as it relates to passivity breakdown, postulates that certain aggressive anions, for example,  $\text{F}^-$ ,  $\text{Cl}^-$ ,  $\text{Br}^-$ , and  $\text{I}^-$  absorb into oxygen vacancies in the surface of the barrier layer, resulting in the generation of cation vacancies and hence, to an enhanced flux of the same species across the barrier layer toward the metal–barrier layer interface, as depicted in **Figure 5**. The PDM postulates that if the cation vacancies arriving at the metal–barrier layer interface

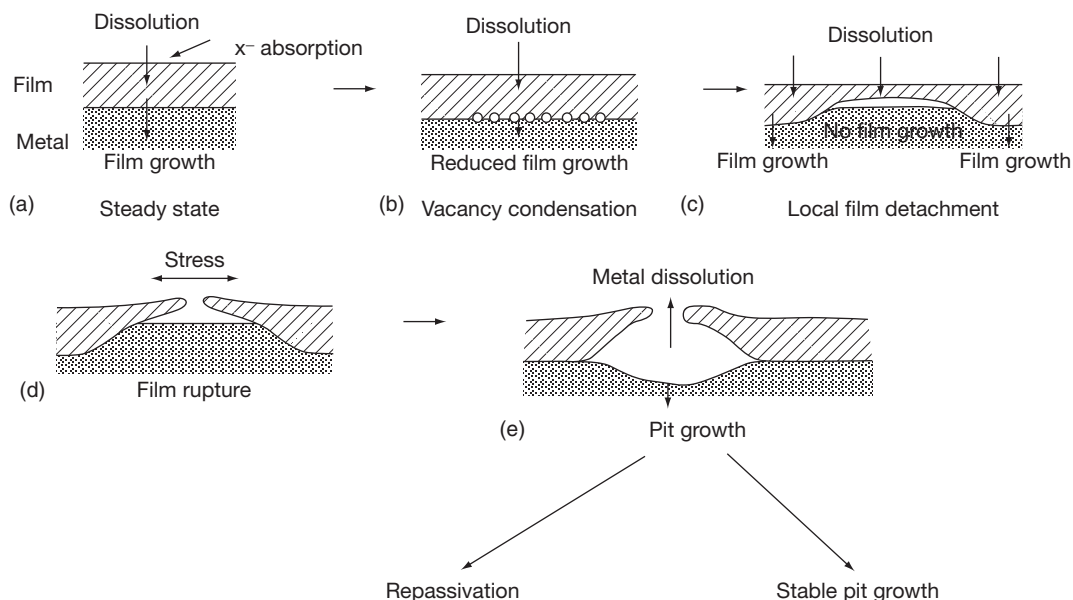


**Figure 5** Sequence of events in passivity breakdown, according to the point defect model.<sup>21</sup> Note that the initial event is the absorption of an aggressive anion into an oxygen vacancy at the film–solution interface (a), resulting in an enhanced flux of cation vacancies across the film and eventually in condensation of cation vacancies at the metal–film interface (b). The film stops growing into the metal beneath the cation vacancy condensate while it continues to dissolve at the film–solution interface (c), eventually resulting in rupture (d) and repassivation or the formation of a stable pit (e).

cannot be annihilated at a sufficiently high rate via reaction [1] (Figure 5), the excess vacancies will condense locally and hence cause local separation of the barrier layer from the substrate metal. Once separation has occurred, reaction [3] (Figure 5) can no longer occur so that the barrier layer at that locale is prevented from growing into the metal. However, the barrier layer continues to grow into the metal at the periphery of the cation vacancy condensate and also continues to dissolve at the barrier layer–solution interface. This results in local thinning of the ‘cap’ over the cation vacancy condensate with the cap eventually rupturing because of the growth stresses in the film and in the near-surface substrate. The ‘weak points’ on the surface where passivity breakdown is predicted to occur correspond to regions of high cation vacancy flux. These regions are assumed to be regions of high local discontinuity in the barrier layer, such as the points of intersection of the barrier layer with precipitates, inclusions (e.g., MnS), and other ‘second phase’ particles. Support for this mechanism stems from the almost general observation of the formation of blisters (‘cation vacancy condensate’) as precursors to passivity breakdown on a wide variety of metals and alloys, the passivity breakdown on liquid versus solid gallium, and the potential sweep rate dependence of the apparent breakdown voltage.<sup>21</sup>

The latter evidence is particularly convincing because the test involves no adjustable parameters and yields a quantity (the concentration of condensed vacancies) that can be compared with the same quantity calculated from fundamental principles (crystal structure of the barrier layer).

The description of possible mechanisms for the generation of cation vacancies at the barrier layer–solution interface upon the absorption of the aggressive anion into a positively charged oxygen vacancy in the surface of the barrier layer can be found in Macdonald.<sup>21</sup>

Mathematically, the condition for the initial formation of the cation vacancy condensate can be expressed as<sup>35</sup>

$$(\mathcal{J}_{ca} - \mathcal{J}_m)(t - \tau) \geq \xi \quad [32]$$

where  $\mathcal{J}_{ca}$  is the flux of cation vacancies across the barrier layer at the breakdown site,  $\mathcal{J}_m$  is the annihilation flux (i.e., the rate of reaction [1], Figure 5),  $t$  is the time,  $\tau$  is the dissolution time (see below), and  $\xi$  is the critical areal concentration of vacancies ( $\#/\text{cm}^2$ ). Noting that  $\mathcal{J}_{ca}$  is voltage dependent, the critical breakdown voltage corresponds to that at which breakdown takes an infinite time to occur that is, when  $\mathcal{J}_{ca} = \mathcal{J}_m$ . This condition, in turn, leads to the following expressions for the breakdown voltage and

the induction time for passivity breakdown at a single site on the metal surface as<sup>35</sup>

$$V_C = \frac{4.606RT}{\chi\alpha F} \log \left[ \frac{\mathcal{F}_m}{\mathcal{F}^0 u^{-\chi/2}} \right] - \frac{2.303RT}{\alpha F} \log a_X \quad [33]$$

$$t_{\text{ind}} = \zeta' \left[ \exp \left( \frac{\chi\alpha F \Delta V}{2RT} \right) - 1 \right]^{-1} + \tau \quad [34]$$

where

$$\mathcal{F}^0 = \chi K D [N_v/\Omega]^{1+\chi/2} \exp[-\Delta G_S^0/RT] \quad [35]$$

and

$$u = (N_A/\Omega) \exp[\Delta G_A^0/RT] \exp[-F(\beta pH + \varphi_{f/s}^0)/RT] \quad [36]$$

where  $N_A$  is the Avogadro number,  $\Delta G_S^0$  is the Gibbs energy change for the Schottky-pair reaction,  $\beta$  is the dependence of the potential drop across film–solution interface on pH,  $\varphi_{f/s}^0$  is a constant (potential drop at the film–solution interface for  $V_{\text{app}} = 0$ , and pH = 0) and  $\Delta G_A^0$  is the standard Gibbs energy change for the chloride–oxygen vacancy absorption reaction.

Additionally, the ‘relaxation’ time,  $\tau$ , which is now identified with the time taken for the cap over the vacancy condensate to thin sufficiently for rupture to occur<sup>21</sup> from the point of initial cation vacancy condensation, can be expressed as

$$\tau \leq L_{\text{ss}}/(dL/dt)_{\text{dissolution}} = L_{\text{ss}}/\Omega k_s (C_{\text{H}^+}/C_{\text{H}^+}^0)^n \quad [37]$$

In these expressions,  $L_{\text{ss}}$  is the steady-state thickness

of the barrier layer at the voltage at which cation vacancy condensation just begins. This value is given by eqn [30]. The other parameters are as defined above.

Typical plots of breakdown voltage versus chloride activity, plotted in accordance with eqn [33] are presented in Figure 6. The data labeled ‘PDM’ were calculated from eqn [33] using parameter values estimated by different experiments (primarily from electrochemical impedance spectroscopy, EIS). It should be noted that the PDM has been subjected to numerous experimental tests and, to the authors’ knowledge, no substantial discrepancies have been noted.<sup>21</sup> The model has also been extended to account for transients in barrier layer thickness and passive current in response to potential step and linear potential sweep perturbations. The model has also been extended to account for electrochemical impedance data and, indeed, optimization of the model on impedance data as a function of frequency and voltage has proven to be a very effective way of determining values for various model parameters. Finally, the PDM has also been used to describe the cathodic formation of metal hydride films on metals, such as Li and Zr, and, again, optimization has proven to be an effective means of determining values for model parameters. Discussion of these topics is beyond the

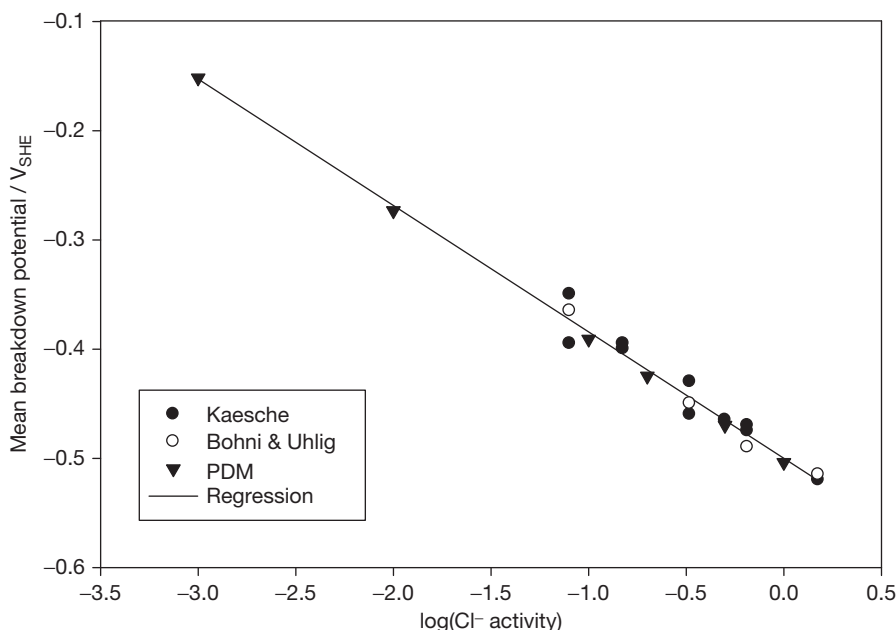


**Figure 6** Plot of the mean critical breakdown potential vs.  $\log(\text{Cl}^- \text{ activity})$  for aluminum in sodium chloride solutions at 25 °C. Experimental data are taken from Kaesche<sup>45</sup> and Böhni and Uhlig.<sup>46</sup>

scope of the present chapter, and the reader is referred to the literature for additional information.<sup>21</sup>

On any real surface, a large number of potential breakdown sites exist, corresponding to a distribution in the properties of the ‘weak spots.’ Thus, examination of data reported by Shibata<sup>47</sup> and Fratesi,<sup>48</sup> among others, suggests that the breakdown voltage is nearly normally distributed. The PDM assumes that the breakdown sites, with respect to the diffusivity of cation vacancies, are described approximately by a normal distribution function,<sup>39</sup> that is,

$$\frac{dN(D)}{dD} = -A \exp \left[ -\frac{(D - \bar{D})^2}{2\sigma_D^2} \right] \quad [38]$$

Here,  $N(D)$  is the number of breakdown sites (per square centimeter) that have diffusivities larger than  $D$ , and  $\bar{D}$  and  $\sigma_D$  are the average value and the standard deviation, respectively, of the diffusivity for the population of the breakdown sites. The negative sign in eqn [38] means that  $N(D)$  decreases with increasing  $D$ . Parameter  $A$  does not depend on  $D$ , so that normalization of the diffusivity distribution using the condition  $N(0) = N_{mp,0}$ , where  $N_{mp,0}$  is the total number of breakdown sites (per square centimeter), yields

$$N(D) = N_{mp,0} \operatorname{erfc} \left( \frac{D - \bar{D}}{\sqrt{2}\sigma_D} \right) / \operatorname{erfc} \left( -\frac{\bar{D}}{\sqrt{2}\sigma_D} \right) \quad [39]$$

Because the transport of cation vacancies across the barrier layer from the barrier layer–solution interface to the metal–barrier layer interface occurs primarily by electro-migration, the cation vacancy flux density,  $\mathcal{J}_{ca}$ , is proportional to the diffusion coefficient of the vacancies,  $D$ , that is,

$$\mathcal{J}_{ca} = DB \quad [40]$$

where the function  $B$  depends on the external conditions (applied voltage,  $V_{app}$ , temperature,  $T$ , chloride activity,  $a_{cl}$ , etc.) and on the electric field strength within the film. Thus, for the case of passivity breakdown in a solution containing an aggressive anion,  $X^-$  (e.g., chloride ion), the PDM yields

$$B = \hat{a} u^{-\chi/2} \exp \left( \frac{\chi F \alpha V_{app}}{2RT} \right) a_x^{\chi/2} \quad [41]$$

where  $\alpha$  is the polarizability of the film–solution interface (i.e., dependence of the potential drop across the barrier layer–solution interface on the applied potential),  $\chi$  is the cation oxidation state in the barrier layer,  $R$  is the gas constant, and  $F$  is

Faraday’s constant. In turn, parameters  $\hat{a}$  and  $u$  are defined as<sup>35</sup>

$$\hat{a} = \chi(F\varepsilon/RT)[N_A/\Omega]^{1+\chi/2} \exp(-\Delta G_s^0/RT) \quad [42]$$

where parameter  $u$  is defined by eqn [36].

Substituting eqns [40] into eqn [32] yields the following criterion for metastable pit nucleation as

$$D \geq D_{cr} = \frac{\xi + \mathcal{J}_m(t - \tau)}{B(t - \tau)} \quad [43]$$

Criterion [43] states that the nucleation of metastable pits occurs within the observation time,  $t$ , on those and only those sites that have  $D \geq D_{cr}$ . From Equations [26], [39], and [43], we have

$$N(t) = N_0 \operatorname{erfc} \left( \frac{a}{t - \tau} + b \right) / \operatorname{erfc}(b) \quad [44]$$

where  $a = \xi/(B\sqrt{2}\sigma_D)$ , and  $b = (\mathcal{J}_m/B - \bar{D})/(\sqrt{2}\sigma_D)$ . Accordingly, for the rate of pit nucleation, we obtain the following expression,

$$n(t) = \frac{dN}{dt} = \frac{N_0 2a}{\operatorname{erfc}(b)\sqrt{\pi}} \frac{\exp \left[ -\left( \frac{a}{t - \tau} + b \right)^2 \right]}{(t - \tau)^2} \quad [45]$$

It is important to note that, in accordance with eqn [28], the maximum pit nucleation rate must be observed at the beginning of corrosion attack, that is, at  $t = 0$ . On the other hand, in accordance with PDM, as follows from eqn [45], the maximum pit nucleation rate must be observed at

$$t_{max} = a \left( b + \sqrt{b^2 + 4} \right) / 2 \quad [46]$$

Accordingly, if observation time,  $t$  (service life  $t_s$ ), satisfies the condition

$$t \gg t_{max} \quad [47]$$

practically all pits nucleate during a very short period of time at the beginning of the observation time, that is, the PDM predicts the case of instantaneous nucleation. Calculation shows<sup>13</sup> that, in some cases (especially at high concentrations of  $Cl^-$ ) criterion [47] holds very well and the nucleation of pits on a metal surface may be regarded as an ‘instantaneous nucleation’ phenomenon. However,  $t_{max}$ , increases very sharply with decreasing chloride concentration, leading to the case of progressive nucleation, in which new pits nucleate on the surface as existing pits grow and die (repassivate). The fact that the surface concentration of pits grows at a maximum rate after the appearance of the first pit has been experimentally observed, for example,

the case of the pitting corrosion of passive iron in borate buffer solution containing chloride ion.<sup>49</sup>

### 2.39.6 Rate of Pit (Cavity) Propagation

The quantitative description of pit (or cavity) growth remains one of the key problems in predicting corrosion damage in many practical systems. This follows from the fact that the calculated corrosion damage that is based only on this (growth) stage can be compared with experiments in many limiting cases. For example, in the case of pitting corrosion, when all pits nucleate ‘instantaneously,’ or when the induction time for pit nucleation is much smaller than the observation time, it is possible to ignore the initial stage of pit nucleation when estimating the damage. In addition, if the probability of survival of a corrosion defect is sufficiently high, we must take into account the possibility that a stable corrosion defect (pit or crack) nucleates immediately after the start of operation and propagates without repassivation and hence, the same defect that nucleated in the beginning is still active at the end of the observation time. In any case, calculations based only on the growth stage yield the most conservative estimate of the service life,  $t_{s,\min}$ , of the system. We can be sure that if calculation of the service life is based on growth alone, the real service life,  $t_s$ , will at least be not less than  $t_{s,\min}$ .

Moreover, it is also natural to assume that the rate of propagation of an individual pit (crack) without neighbors will be greater than that for the same pit (crack) with neighbors (i.e., within an ensemble of pits (cracks)), because the neighboring pits reduce the potential at the surface and multiple, neighboring cracks are expected to reduce the stress intensity factor experienced by a single crack for a given loading stress. Accordingly, the proper modeling of propagation of individual corrosion defects can yield the possible minimum survival time for the system as a whole (e.g., a machine). If this time extends beyond the projected service life of the system, we can be sure that the system will survive under real conditions.

#### 2.39.6.1 General Approach for Calculating Propagation Rates

Apparently, one of the main theoretical problems in describing localized corrosion damage is the prediction of the shape and dimensions of corrosion

cavities at any time as a function of the parameters controlling the process (potential of the metal, species concentrations, such as velocity of the electrolyte, thickness of the passive film, diameter of the pit mouth, etc.). It seems obvious that mathematical models describing the pit (cavity) growth should start with the assumption that the pit form and size are not known *a priori*, but should be found during the solution of the appropriate equations.

From the mathematical point of view, the problem of determining the shape and size of a developing pit belongs to the class of Stefan problems.<sup>50</sup> These problems are reduced to the solution of the system differential equations of parabolic or elliptic type with unknown boundary conditions because the velocity of this boundary is connected to the sought after solution by some differential relationship.

The implicit equation  $\Phi(t, x_1, x_2, x_3) = 0$  shall describe the pit surface with time, relative to the Cartesian coordinate system  $x_1, x_2, x_3$ . This expression fulfills the relation  $d\Phi = (\partial\Phi/\partial t + \nabla\Phi \cdot V_s)dt = 0$ , where  $V_s(t, dx_1/dt, dx_2/dt, dx_3/dt)$  is the velocity of the dissolving metal surface. In this formulation, subscript refers to the electrode surface and subscript  $\infty$  to the bulk of the solution. Let  $\vec{n} = \nabla\Phi/|\nabla\Phi|$  be a unit vector pointing normally from the solution to the metal surface. According to Faraday’s law,  $V_s = K_v i_{\text{corr}} \vec{n}$ , where  $i_{\text{corr}}$  is the current density for metal dissolution, and  $K_v$  is the electrochemical equivalent volume, that is, the volume of dissolving metal when one Faraday of charge (96 487 int. coulombs) passes through the interface.

Introducing the correlation for  $V_s$  into the expression for the differential  $d\Phi$  yields an equation describing the change of the electrode surface

$$\frac{\partial\Phi}{\partial t} + K_v i_{\text{corr}} |\nabla\Phi| = 0 \quad [48]$$

Equation [48] is frequently used to describe some important processes in electrochemical technology, for example, electrochemical machining of metals, electrochemical shape formation, and so on.<sup>51</sup> Of course, we can also expect that, in the general case, some additional component, not connected with metal dissolution (e.g., due to mechanical spallation at very high fluid velocities or hydrogen embrittlement) should be incorporated into the expression for the  $V_s$ , but this issue is not germane to the present discussion and will not be considered further here.

Besides the information about the boundary position in the initial period,  $\Phi(0, x_1, x_2, x_3)$ , the integration of eqn [48] requires information about the



dissolution current density,  $i_{\text{corr}}$  that is, eqn [48] must be solved with a set of nonstationary equations for mass balance for each component in the solution, namely

$$\frac{\partial c_k}{\partial t} = -\nabla \cdot \vec{J}_k + R_k; \quad k = 1, \dots, K \quad [49]$$

where  $C_k$  is the concentration of species  $k$ ,  $\vec{J}_k$  is the flux density of species  $k$ , and  $R_k$  is the rate of production (source) or depletion (sink) of this species as a result of homogeneous chemical reactions. The current density,  $\vec{i}$ , in the electrolyte solution is defined as

$$\vec{i} = F \sum_k z_k \vec{J}_k \quad [50]$$

In the vast majority of practical applications, dilute solution theory is used to calculate the flux of the species, that is,

$$\vec{J}_k = -D_k \nabla C_k - z_k F u_k C_k \nabla \phi + C_k \vec{v} \quad [51]$$

where  $\phi$  is the electrostatic potential in the solution,  $v$  is the fluid (hydrodynamic) velocity, and  $u_k$  is the mobility of species  $k$ , which can be estimated by using the Nernst–Einstein equation:

$$u_k = \frac{D_k}{RT} \quad [52]$$

In eqn [51], the first term on the right-hand side represents the contributions of diffusion, the second term describes migration, and the third term is a contribution of convection. An additional condition for determining the electrostatic potential is the equation

$$\sum_k z_k C_k = 0 \quad [53]$$

It must be noted that, generally speaking, the condition of electroneutrality is not a law of nature and can be considered as an approximation of Poisson's equation:

$$\nabla^2 \phi = -\frac{F}{\varepsilon} \sum_k z_k C_k \quad [54]$$

where  $\varepsilon$  is the dielectric permittivity (dielectric constant multiplied by the permittivity of free space) of the solution. However, due to the large value of the ratio  $F/\varepsilon$ , an appreciable separation of charge would require unrealistically large electric forces. Visible deviation from electroneutrality can be observed only in a very thin double layer near an electrode surface (which is of the order of 1–10 nm in thickness) or within a doped semiconductor junction that can be taken into account in the boundary

conditions for the problem. Accordingly, the electro-neutrality approximation is fulfilled very well, and is widely accepted by the electrochemical community.<sup>52</sup> In spite of this fact, some papers where Poisson's equation is used directly can be found in the literature.<sup>53</sup> In accordance with our opinion, this approach introduces only unnecessary complications, due to excessive calculational time.

The hydrodynamic velocity,  $\vec{v}$ , within the framework of dilute solution theory, can be found apart from the solution of the mass transfer problem by using the corresponding mechanical equations (e.g., the Navier–Stokes equations, in the case of laminar flow<sup>52,54</sup>). In the case of turbulent flow, which often exists outside the corrosion cavity, it is convenient to use some effective diffusion coefficient instead of the usual diffusion coefficient,  $D_k$ ,

$$D_k^{\text{eff}} = D_k + D_t \quad [55]$$

where diffusion coefficient  $D_t$  depends on the distance from the wall, hydrodynamic conditions, and the physical properties of the liquid. Some empirical correlations for  $D_t$  can be found in the literature.<sup>52,54,55</sup>

Strictly speaking, eqn [51] for species flux densities is valid in the case of dilute solutions. In the case of concentrated solutions, eqn [51] should be replaced by

$$\vec{J}_k = C_k \vec{v}_k \quad [56]$$

where the velocity,  $\vec{v}_k$ , of species  $k$  can be found from the equation of multicomponent diffusion.<sup>52</sup>

$$C_k \nabla \mu_k = RT \sum_i \frac{C_k C_i}{C_T D_{ki}} (\vec{v}_i - \vec{v}_k) \quad [57]$$

where  $\mu_k$  is the electrochemical potential of species  $k$ ,  $D_{ij}$  are diffusion coefficients, and  $C_T$  is the sum of all concentrations of all components, including the solvent. However, in the literature, there are no significant applications of the theoretical principles describing transport in concentrated solutions for the case of corrosion, with the exception of the preliminary work of Popov *et al.*<sup>56</sup> The reasons for this state of affairs are the increased complexity of the theory and the lack of appropriate input data for practical application.

However, it is important to note that, in the overwhelming majority of corroding systems, the concentrations of all solute species,  $C_k$ , are much smaller than the concentration of the solvent,  $C_0$ . Under these

conditions, only one term on the right side of eqn [50] is important. Accordingly, eqn [57] can be rewritten in the following form for the theory of moderately dilute solutions<sup>52</sup>

$$\vec{J}_k = -D_k \nabla \mu_k + C_k \vec{v} \quad [58]$$

If we present  $\mu_k$  in the form

$$\mu_k = RT \ln(\gamma_k C_k) + z_k F \varphi \quad [59]$$

where the activity coefficient,  $\gamma_k$ , depends on the concentration of all species in the solution, the equation of the flux becomes

$$\vec{J}_k = -D_k \nabla C_k - \frac{D_k z_k F}{RT} C_k \nabla \phi + C_k \vec{v} - D_k C_k \nabla \ln(\gamma_k) \quad [60]$$

This equation for ion flux densities has been used, for example, in Walton *et al.*<sup>57</sup> for describing crevice corrosion. However, the activity coefficients in Walton *et al.*<sup>57</sup> are calculated within the framework of Debye–Hückel theory that, is strictly speaking, applicable only for the case of dilute solutions.

We would like to emphasize that, in many real corrosion systems, the concentration drops within a corroding cavity may be not very high, because corrosion is not a fast process. Accordingly, eqn [1] can be used with sufficient accuracy in relatively concentrated solutions, assuming that  $D_k$  is referred to the bulk electrolyte, but not to infinitely dilute solutions.

In accordance with the rules, the homogeneous terms,  $R_k$ , in the balance equations can be written in general form as

$$R_k = \sum_{m=1}^M \left[ -k_m v_{km} \left\{ \prod_{v_{km}>0} C_k^{v_{km}} - K_m \prod_{v_{km}<0} C_k^{-v_{km}} \right\} \right] \quad [61]$$

where  $k_m$  is the rate constant of reaction  $m$ ,  $\sum_k v_{km} M_k = 0$  ( $m=1,2,\dots,M$ ),  $K_m$  is the equilibrium constant for reaction  $m$ ,  $v_{km}$  is the stoichiometric coefficient for species  $k$  in  $m$ th chemical reaction, and  $M_k$  is the symbol for the chemical formula of species  $k$ .

The presence of the chemical terms in balance eqns [49] greatly complicates their solution. First of all, we have practically no information about the rates of homogeneous reactions (usually, we only have information about their equilibrium constants). However, we can reasonably assume that these reactions are fast and they are practically in equilibrium at any given point and time. The most widely applied

method for dealing with these problems is to eliminate chemical terms by adding or subtracting balance eqns [49]. The new set of governing equations is then supplemented by equations of equilibrium.<sup>58</sup> The great disadvantage of this approach is as follows. Every time, we want to add or delete from consideration any chemical reaction, we have to completely change the computer code for numerical solution of balance equations because of their change in form. Moreover, the forms of these equations do not coincide with the standard form of the equation of mass balance, and this adds to the complexity of the process of numerical solution.

The alternative approach for modeling the equilibrium state is to keep the governing equation in rate format (i.e., in the form of eqn [49]), and hence to assume that reactions are very fast. As long as reaction rates are large, relative to the rates of mass transport, the reactions will remain at equilibrium, and the solution composition will be independent of the kinetics assumed. All kinetic expressions that are physically consistent (i.e., are stoichiometrically true) yield zero net reaction at equilibrium, change sign as the equilibrium point is crossed, and give sufficiently fast reaction rates that can be used.<sup>59</sup> The choice becomes a matter of numerical stability and convenience. Therefore, Walton<sup>60</sup> used the following expression for the rate of production or depletion of species  $k$  by the chemical reaction

$$R_k = \sum_{m=1}^M \left[ -r_m v_{km} \ln \left\{ \prod_{k=1}^K C_k^{v_{km}} / K_m \right\} \right] \quad [62]$$

which satisfies all of the conditions noted above.

Another alternative approach is the following.<sup>57,61</sup> It is assumed that characteristic times of chemical reactions in aqueous solution are much shorter than those of the mass transport or corrosion processes, which is equivalent to assuming high reaction rates. Accordingly, the set of transport equations are first solved separately from the chemical terms. After that, at the end of each sufficiently small time step, the resulting aqueous solution composition, within each elementary volume, is solved to equilibrium by calling an equilibrium solver. For example Walton *et al.*<sup>57</sup> determined the equilibrium composition of the solution by Gibbs free energy minimization.

The homogeneous terms,  $R_k$ , in the balance equations can be written in a general form as: It is assumed that at a point far away from the mouth of a pit or crevice, the concentrations and potentials have their bulk values, that is,

$$C_k = C_{k,\infty}; \phi = \phi_\infty = 0 \quad [63]$$

It is also assumed that the normal fluxes on the solid surface,  $\mathcal{J}_{ks}$ , can be expressed as a known function of surface temperature,  $T_s$ , surface concentrations,  $C_{ks}$ , and surface potential,  $E_{\text{corr}} - \phi_s$ , (on the metal surface), that is,

$$-D_k \frac{\partial C_k}{\partial n} = \mathcal{J}_{ks}(E_{\text{corr}} - \phi, C_{1,s}, C_{2,s}, \dots, C_{K,s}, T_s) \quad [64]$$

If some component does not participate in any heterogeneous reaction (chemical or electrochemical), its flux density will be equal to zero. Of course, on an insulator, all fluxes are equal to zero.

In formulating the initial conditions, it would be natural to assume that concentrations of all species and potentials coincide with the corresponding bulk values at  $t = 0$ . However, simple calculation shows that, under normal conditions, the velocity of the interface is so slow that the steady-state approximation can be used for describing the transport processes for the anodic dissolution of the metal.<sup>50,51</sup>

The sense of this approximation is as follows: The movement of the metal surface is so slow that the concentration distribution in the solution is approximately that corresponding to steady flow at a given position of the boundary and for given boundary conditions. In this case, it is possible to omit the derivative over time in balance, eqn [49]. Accordingly, it is possible to separate the solution of the mass transfer problem from the movement of the boundary. After solving the steady-state problem in the region with the fixed boundaries, and after calculating the corrosion current density, the new position of the metal surface is found by using Faraday's law (see eqn [48]). After that, the solution of the steady problem for the new boundary is found, and the process is repeated until the desired time is achieved. Of course, it is not possible to omit the derivative over time in the balance equation in the case of corrosion fatigue, caused by the sharply changing hydrodynamic velocity, which is a result of periodic loading.

However, it must be noted that there are a very limited number of studies where the problem of pit propagation is regarded as a problem having a free boundary in multidimension space. Practically, (in multidimension space) consideration of a moving boundary is limited to the simplest cases, when the system of transport equations can be reduced to the solution of a single Laplace equation for the

relative concentration of a single species<sup>62</sup> or electric potential.<sup>63</sup>

On the other hand, such problems are successfully solved in heat transfer studies, for example, in connection with the problem of metal ingot solidification.<sup>64</sup> The presence of migration is the fundamental difference between the problems of ionic transport and those in nonelectrolyte solutions or problems in heat transfer. This difference does not permit the direct use of a wide range of methods and computer programs that have been developed in connection with the problems of heat transfer for solving ion transport problems. As a result, to solve each ion transport problem, for example, using the so-called Newman method,<sup>52</sup> it is necessary to create new programs that require substantial expenditure of time and effort.

It is also possible to use iterative methods to reduce ion transport problems to a sequence of transport problems for nonelectrolyte solutions, which enables one to directly use the methods and even the existing computer programs available in heat engineering.<sup>65-67</sup>

The very useful method of quasipotential transformation for modeling transport processes in dilute electrochemical systems has been developed by Pillay and Newman.<sup>68</sup> It can be shown that, under steady-state quiescent conditions, with equilibrium homogeneous chemical reactions, and for a single electrochemical reaction, the electrostatic potential and all concentration distributions can be represented as a single-valued harmonic function of the quasipotential,  $q$ . This harmonic function vanishes at infinity and satisfies the following boundary conditions

$$\frac{\partial q}{\partial n} = 0 \quad [65]$$

at an insulating surface, and

$$-\frac{\partial q}{\partial n} = i \quad [66]$$

at an electrode (conducting) surface, where  $\mathbf{n}$  is the unit normal vector at the electrode surface pointed towards the solution. Accordingly, the set of coupled second-order, nonlinear partial differential equations governing mass transfer by diffusion and migration in electrochemical systems is transformed into Laplace's equation for the quasipotential and hence, into a set of coupled, first-order nonlinear ordinary differential equations. This method has been applied to the case of the development of an active hemispherical pit.<sup>69</sup> Unfortunately, this method cannot be generalized, for example, for the nonstationary case, for the case of

multiple electrochemical reactions, or for mass transfer in flowing electrolytes.

It is also important to note that, at the present time, commercial software is available for solving transport equations with migration terms with fixed boundaries (see, e.g., COMSOL software),<sup>70</sup> although some algorithms also handle moving boundaries now. Accordingly, the most difficult problem that arises very often during the solution of mass transfer problems is not the solution of the differential equations themselves, but in defining the transport coefficients (e.g., diffusion coefficients) in multicomponent systems, rates of chemical reactions, and especially in establishing real kinetic relations for the species fluxes on the metal surfaces (particularly for the rate of metal dissolution), such as those contained in eqn [64]. The concrete dependencies of the rates of corrosion propagation as a function of potential, concentrations of species near the metal surface, and mechanical conditions for the cases of pitting corrosion, stress corrosion cracking, corrosion fatigue, crevice corrosion, etc. are discussed in the corresponding chapters of this book. Commercial software for calculating transport properties (diffusion coefficients, activities, viscosities, density rates of particular electrochemical reactions on particular metals and alloys) is also available (see, e.g., OLI Systems software).<sup>71</sup>

A detailed review of a great number of papers dealing with mathematical modeling of transport phenomenon in pitting and crevice corrosion is presented, for example, in Turnbull,<sup>58</sup> Sharland,<sup>61</sup> Papavinosan *et al.*<sup>72</sup> In the majority of these models, instead of boundary conditions [64], the boundary conditions of the Type II kind (i.e., prescription of current density on the metal surface) are employed. In the latter case, the principal aim of these models is not to predict corrosion damage (corrosion rates are assumed to be known in advance), but to estimate species concentrations, and the potential distribution in corrosion cavities, as a function of many parameters like cavity dimension, bulk solution composition, temperature, and so on. Very often such models serve to aid in the understanding of results of particular experimental systems. However, at present, the overwhelming majority of the models devoted to estimating the size of a corrosion cavity have adopted the one-dimensional approximation, that is, they are reduced to calculating the depth of the cavity,  $a$ , as a function of time, when eqn [48] is reduced to the simplest relation

$$\frac{da}{dt} = K_V i_{\text{corr}} \quad [67]$$

Because of the mathematical complexity of the problem, analyses of the transfer processes occurring within corrosion cavities have generally employed the one-dimensional approximation. For example, it is often assumed, in the case of corrosion pits, that the cavity has a cylindrical shape with a depth  $a$ , which is much larger than the radius,  $r$ . Likewise, crevices and cracks are often viewed as being one-dimensional slots of length  $a$ , such that  $a$  is much greater than the opening displacement,  $w$ .<sup>57,60,61,73–82</sup> Very often, only metal dissolution at the bottom is assumed. However, two-dimensional analyses of corroding hemispherical pits have been described for the case of a well mixed electrolyte by Newman *et al.*,<sup>83</sup> and for the case of a quiescent system, in which concentration gradients exist.<sup>63,69,84</sup> In many cases, the results obtained by mathematical simulation or by experimental studies of ‘ideal’ cells (one-dimensional or hemispherical) have been used to describe corrosion processes under real conditions.

In the one-dimensional case, the balance equations are reduced to the form

$$\frac{\partial(wC_k)}{\partial t} = -\frac{\partial w\mathcal{F}_k}{\partial x} + wR_k + \mathcal{F}_{S1} + \mathcal{F}_{S2}, \quad [68]$$

$$k = 1, 2, \dots, K$$

where  $\mathcal{F}_k$  is the flux density along the direction down the crevice,  $x$ , averaged over the width of the crevice,  $w$ ,  $\mathcal{F}_{S1}$  and  $\mathcal{F}_{S2}$  are the flux densities at a metal–solution interface or on the side walls (usually it is assumed that  $\mathcal{F}_{S1} = \mathcal{F}_{S2}$ ). In the case of the cylindrical pit of radius,  $r$ , we simply have

$$\frac{\partial C_k}{\partial t} = -\frac{\partial \mathcal{F}_k}{\partial x} + R_k + 2\mathcal{F}_S/a, \quad k = 1, 2, \dots, K \quad [69]$$

It must be emphasized that, in the overwhelming majority of the work devoted to describing localized corrosion in the one-dimensional approximation, it has been tacitly assumed that it is possible to neglect the potential drop in the external environment (outside the corrosion cavity), that is, to assume that boundary conditions [56] are fulfilled at the mouth of the crevice. The following section will show that such an approximation is incorrect from the physical point of view and in many cases can lead to significant errors in the estimation of corrosion damage.

### 2.39.6.2 Coupled Environment Corrosion Cavity Growth Models

Many localized corrosion processes, including pitting, stress corrosion cracking, corrosion fatigue, and crevice corrosion may be described within the framework of the differential aeration hypothesis (DAH), which was first postulated by U. R. Evans in the 1920s.<sup>85</sup> This postulate attributes localized corrosion to a spatial separation of the local anode and local cathode, with the local anode occurring in that region of the system that has the least access to the cathodic depolarizer (e.g., oxygen), while the local cathode occurs in that region that has the greatest access to the cathodic depolarizer. In the case of a pit or a crack, as depicted schematically in Figure 7, the local anode exists within the cavity, whereas the local cathode exists on the bold external surfaces.

The voltage difference generated between the cavity and the external surface causes a positive current to flow through the solution from the local anode to the local cathode. Negative electron current flows through the metal in the reverse direction and the two currents mutually annihilate at the

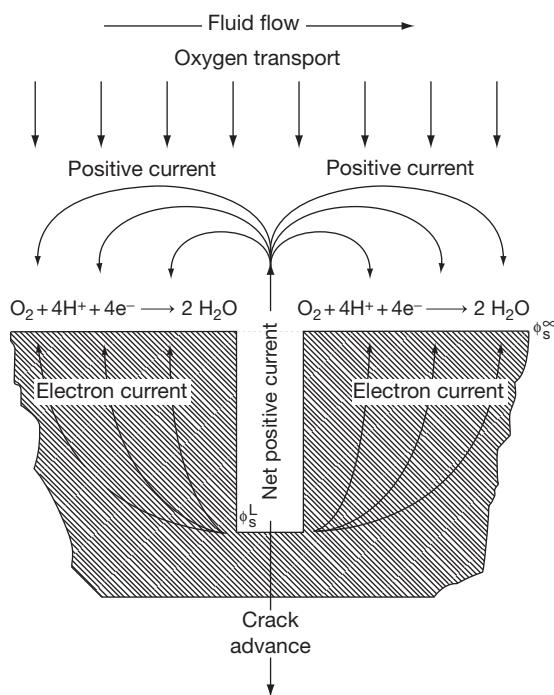


**Figure 7** Coupling of crack internal and external environments. Note that in the steady state, the crack can grow only as fast as the positive current flowing from the crack can be consumed on the external surfaces by oxygen reduction. Reproduced from Macdonald, D. D.; Lu, P.-C.; Urquidí-Macdonald, M.; Yeh, T.-K. *Corrosion* **1996**, 52, 768.

external surface via a charge transfer reaction, in this case, the reduction of oxygen. The current is known as the ‘coupling current’ and is easily measured.<sup>86</sup> The coupling current has been shown to contain a wealth of information concerning the processes that occur within the cavity. The coupling current is generated within the cavity by anodic oxidation of the metal that may be unassisted by mechanical processes (pitting corrosion and crevice corrosion) or assisted by the presence of a constant stress (stress corrosion cracking, SCC) or a cyclic stress (corrosion fatigue, CF). In any event, the flow of positive current out of the cavity occurs because of the existence of a potential gradient in the solution from the cavity tip to the cavity mouth, such that  $\phi_t > \phi_m > \phi_\infty$ , where  $\phi_t$ ,  $\phi_m$  and  $\phi_\infty$  are the corresponding electrostatic potentials in the solution at the cavity tip, cavity mouth, and at a point on the external surface that is at an effectively infinite distance from the mouth (i.e., the ‘throwing power,’ which turns out to be about 10–20 crack mouth opening displacements, but which also depends upon the conductivity of the environment). The sign of this potential gradient is such that anions are transported into the crack, where they neutralize the positive charge that is injected into the cavity solution in the form of metal cations. The metal cations hydrolyze to produce protons that acidify the environment. The concentration factors for both  $\text{Cl}^-$  and  $\text{H}^+$  from electromigration and hydrolysis, respectively, can exceed  $10^4$ . Thus, for an environment containing 10 ppb of chloride ion and having a pH of 7, the chloride concentration and pH in the cavity may exceed 100 ppm and below 3, respectively. Accordingly, noting the propensity of chloride ions to induce passivity breakdown, the DAH accounts for the development of aggressive conditions within the cavity, even though the external conditions might be quite benign.

It is evident that, under free corrosion conditions, the conservation of charge requires that the charge passed by the cathodic reaction be matched by the charge passed by the partial anodic reaction (see eqn [25]). Recognizing that, at sufficiently large distances from the crack mouth on the external surface, the net current,  $i_N = i_a + i_c$  ( $i_a$  and  $i_c$  are the local anodic and cathodic partial current densities) must be zero, corresponding to ‘free,’ general corrosion, the partial current density distributions are such that eqn [25] must be satisfied. Note that eqn [25] does not stipulate that cathodic partial reactions cannot occur within the cavity or that anodic partial reactions cannot occur on the external surfaces; only that, in the ‘cathodic’ and



‘anodic’ regions, the net current densities are negative and positive, respectively, and the total currents integrated over the respective areas are equal.

It is also important to glean an understanding of the critical nature of the properties that exist at the crack mouth. Thus, note that solving the entire problem involves solving two closely coupled sub problems, one for the external environment and the other for the crack enclave. These two problems are coupled because they share common boundary conditions in potential,  $\phi_m$ , and in current,  $i_m$ . The objective in all coupled environment models (CEMs) developed to date has been to find the appropriate values for  $\phi_m$  and  $i_m$ , such that eqn [25] is satisfied. It is the constraint imposed by eqn [25] that imparts determinism to the model.

Traditionally, models for localized corrosion cavity growth have assumed that the electrical potential in the solution at the crack mouth is the negative of the free corrosion potential or that the external environment presents no impedance to current flow (i.e., the current may flow to infinity). Neither postulate is correct. In the first case, no potential gradient would exist in the external environment and hence, the coupling current must be zero, contrary to experimental observation. Indeed, these models actually predict that SCC cannot occur. In the second case, if there exists no impedance for current flow to infinity, then there should be no dependence of the coupling current and crack growth rate on the catalytic properties of neighboring external surfaces, again contrary to experiment. The requirement that the underlying theory must account for all of the experimental observations is therefore not met by both classes of models. However, the authors note that the assumptions may be valuable approximations in solving the mass transport equations for the cavity, but, in doing so, it must be recognized that in ignoring the external environment, the physical description of the system is incomplete. Accordingly, and emphasizing again that a viable model must account for all experimental observations, such an approach would fail to recognize the important impact that catalysis or inhibition of oxygen reduction on the external surfaces has on crack growth rate in sensitized Type 304 SS in high temperature water, as noted above.<sup>87,88</sup>

To date, we<sup>86,89–95</sup> and others<sup>96,97</sup> have developed ‘coupled environment’ models for stress corrosion cracking (coupled environment fracture model, CEFM<sup>89,90,92,93</sup>), corrosion fatigue (coupled environment corrosion fatigue model, CECFM<sup>94</sup>), pitting

(coupled environment pitting model, CEPF<sup>91</sup>), and crevice corrosion (coupled environment crevice model, CECM<sup>95</sup>). Details of the algorithms are not given here as they have been adequately described in the literature. In the interests of space, only a brief outline of some of the results from the CEFM is given. We note that alternate models for crack growth in sensitized stainless steels have been developed by others, most notably by Ford and coworkers,<sup>98,99</sup> Shoji,<sup>100,101</sup> and Vankeerberghen and Gavrilov.<sup>102</sup> Of these models, only the model of Vankeerberghen and Gavrilov<sup>102</sup> constrains the solution by the conservation of charge and hence, can be regarded as being deterministic. The models of Shoji<sup>100,101,103</sup> are essentially mechanical in form, with any electrochemistry being introduced ‘inadvertently,’ and, like Ford *et al.*’s models,<sup>98,99</sup> while they are ‘mechanistic,’ they fail to be constrained by the relevant natural law (conservation of charge), recognizing that IGSCC is primarily an electrochemical phenomenon.

The first of the CEMs to be developed was the coupled environment models (CEMs) in 1991.<sup>89</sup> Since then, the model has been extensively developed by the authors and their colleagues as a deterministic model for predicting stress corrosion crack growth rate in a variety of systems, including the coolant circuits of water-cooled nuclear reactors.<sup>104</sup> The models are based upon the following general experimental observations that apply strictly to the growth of intergranular cracks in sensitized Type 304 SS in high temperature water, but that are believed to be general correlations for SCC and other forms of localized corrosion in other systems:

- Localized corrosion generally follows the differential aeration hypothesis, first proposed by Evans in the 1920s.<sup>85</sup>
- A positive coupling current is observed to flow through the solution from the crack mouth to the external surfaces, while an equal but opposite electron current flows through the metal in the reverse direction.<sup>86</sup>
- The crack growth rate increases roughly exponentially with the potential of the metal if it is sufficiently high. At lower potentials, the CGR is potential-independent, corresponding to the mechanical creep (Figure 8).<sup>90–101,103</sup>
- The CGR depends upon the electrochemical crack length, which is defined as the shortest distance between the crack front and the exposed external surface. This length is generally different from the mechanical loading crack length.<sup>90,102</sup>

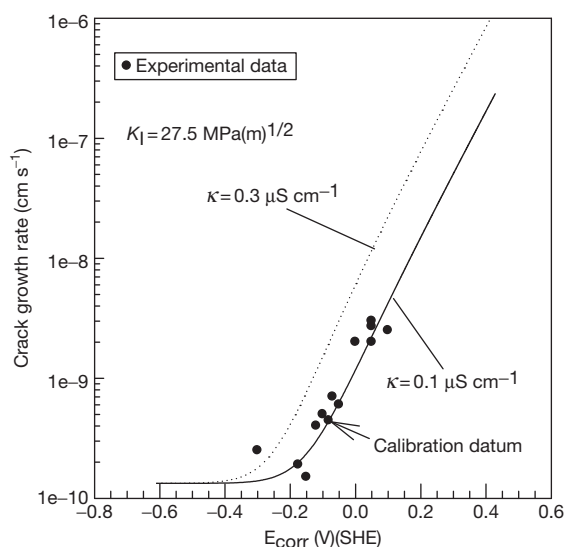


**Figure 8** Measured and analytically calculated crack growth rate of sensitized Type 304 stainless steel as a function of corrosion potential. Calculations were done using the Congleton's correlation for the crack-tip strain rate. Experimental data were taken from Ford *et al.*<sup>99</sup>

- The environmentally-mediated CGR is proportional to the magnitude of the coupling current.<sup>87,105</sup>
- Coating the external surfaces with an insulator, and hence inhibiting the reduction of oxygen, causes the coupling current to decrease sharply and stops the crack from growing.<sup>87</sup>
- Catalyzing the reduction of oxygen on the external surface results in an increase in the coupling current and hence, an increase in the CGR.<sup>86,88</sup>
- The crack growth rate passes through a maximum with increasing temperature at about 175 °C.<sup>106</sup>

It is well known that, in the fracture of sensitized stainless steels and nickel alloys in high temperature (250–300 °C), oxidizing aqueous media, the CGR becomes independent of potential at sufficiently negative ECP values (see [Figure 8](#)) and that the fracture morphology changes from intergranular brittle fracture to ductile failure. The ductile fracture surfaces frequently yield evidence of microvoid coalescence, with ductile tearing of the matrix between the voids. These voids appear to nucleate at intergranular precipitates, such as carbides (e.g., Cr<sub>23</sub>C<sub>7</sub>) on the grain boundaries, but nucleation at intragranular precipitates is also observed. Thus, in the CEFM, which was developed originally to describe fracture in sensitized stainless steels in BWR primary heat

transport circuits,<sup>83,84,90</sup> it seemed appropriate to describe crack growth at the 'creep' limit in terms of a cavitation model.

A modified version of the cavitation model developed by Wilkinson and Vitek<sup>107</sup> was used to estimate CGR at sufficiently negative potentials, where environmental effects are not evident. A detailed account of the creep model will not be given here and the reader is referred to the original paper by Wilkinson and Vitek<sup>107</sup> and papers by Macdonald *et al.*<sup>90,93,108</sup> describing the application of the model in the CEFM. It suffices to note that the Wilkinson–Vitek model accurately describes creep crack growth in stainless steels over the temperature range of interest (25–300 °C).

The numerical and analytical solutions employed in the CEFM yield very reasonable results for the environmentally assisted and creep fracture of sensitized Type 304 SS,<sup>89</sup> and have yet to yield a prediction of crack growth rate that is at odds (i.e., lies outside the experimental error range) with experiment. The calibration factor appears to take care of a number of simplifying assumptions in the numerical CEFM (e.g., inert crack walls and linear potential drop down the crack) and compensates for some less quantified effects (e.g., parameters associated with the crack tip process). Nevertheless, it is only necessary to calibrate the model with a single crack growth rate under specified conditions (see [Figure 8](#)) and to choose an appropriate activation energy for the crack tip strain rate (this is actually equivalent to calibrating the model with CGR data at two temperatures), in order to accurately describe crack growth rate in sensitized Type 304 SS over temperatures ranging from 25 to 288 °C.

One of the persistent issues that is raised in debates on the basis of the CEFM concerns the role of the external environment in determining the crack growth rate. If the differential aeration hypothesis (DAH) is accepted as the basis for localized corrosion, including SCC, then the importance of the external environment is unequivocal. That the external environment is intimately involved has been demonstrated experimentally by detecting and measuring the coupling current that flows from the crack to the external surfaces where it is consumed by oxygen reduction.<sup>88,89</sup> Furthermore, unless the cathodic processes are confined to the crack, in which case the measured coupling current would be zero, and hence at odds with experiment,<sup>86</sup> the conservation of charge *requires* consideration of the external environment in any deterministic

description of crack growth. Finally, catalysis<sup>88</sup> and inhibition<sup>87</sup> of the oxygen reduction reaction on the external surface is found to increase and decrease the crack growth rate, respectively. In the case of inhibition, which was affected by depositing Zirconia on the external surfaces, the extent of inhibition was in agreement with that calculated by the CEFM by reducing the exchange current density for the oxygen electrode reaction by the amount indicated by electrochemical impedance spectroscopy measurements of the specific interfacial impedance using a fast redox couple  $[\text{Fe}(\text{CN})_6^{3-/4-}]$ .<sup>87</sup> These studies unequivocally demonstrate the importance, and possibly the dominance, of the processes occurring, on the external surfaces in determining the crack growth rate in sensitized Type 304 SS in high temperature aqueous systems.

The role of the external environment is further demonstrated by the calculated polarization data plotted in Figure 9.<sup>93,108</sup> Thus, it is seen that, at low temperatures (e.g., 50 °C), significant polarization is predicted to occur in the external environment (170 mV). As the temperature increases, the polarization in the external environment is predicted to decrease, but nevertheless remains significant at temperatures up to 250 °C. Even at higher temperatures, where the external polarization has been decreased to

small values, because of increased conductivity of the external environment and increased rate of oxygen reduction on the external surfaces, the external environment must still be considered because of the need for charge conservation. The temptation has been to assume that, in this case, the potential at the crack mouth can be equated to  $\phi_m = -E_{\text{corr}}$ , and hence to eliminate the need to consider the external environment altogether. However, this would be to assume that no potential gradient exists in the external environment, in which case no coupling current should be detected, again at odds with experiment,<sup>89</sup> leading to the prediction that SCC cannot occur. Finally, it is interesting to note that the decrease in the polarization in the external environment is predicted to be at the expense of an increase in the potential drop down the crack.

As noted elsewhere,<sup>90,104</sup> the CEFM predicts that the crack growth rate for given values of stress intensity, ECP, conductivity, etc. depends upon the crack length. This prediction is consistent with the available experimental data.<sup>19,88,105</sup> In discussing this topic, it is necessary to differentiate between the mechanical crack length (MCL), which is traditionally referred to as the 'crack length' in fracture studies, and the 'electrochemical crack length' (ECL), as noted previously.<sup>19,88,105</sup> The electrochemical

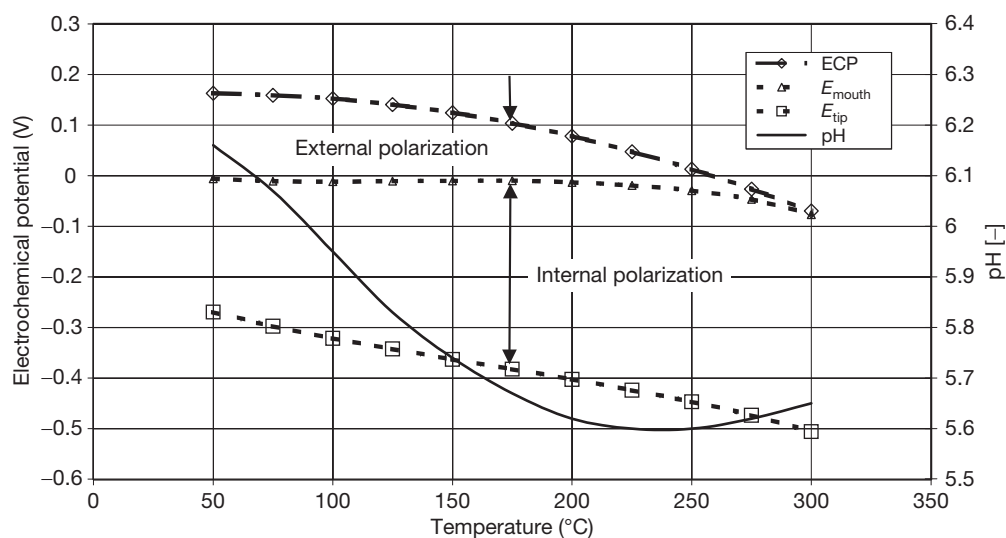


**Figure 9** The calculated effect of temperature on the pH of the external environment, the electrochemical potential at the crack tip,  $E_{\text{tip}}$ , the potential at the crack mouth,  $E_{\text{mouth}}$ , and on the potential in the external environment (ECP), during crack growth in Type 304 stainless steel in dilute sulfuric acid solution having an ambient temperature (25 °C) conductivity of  $0.27 \mu\text{S cm}^{-1}$  and a dissolved oxygen concentration of 200 ppb. The data were calculated using the CEFM after calibration at 288 °C and assuming a crack tip strain rate thermal activation energy of  $100 \text{ kJ mol}^{-1}$  (Congleton crack tip strain rate model).<sup>93</sup>

crack length is defined as the shortest path through the solution from the crack front, where the coupling current is generated, to the external surface, where the current is consumed. For a CT specimen, the MCL corresponds physically to the distance between the load line (for example) and the crack tip, and this distance increases as the crack grows through the specimen. On the other hand, because of the through thickness nature of a crack in a CT specimen, the ECL is constant and is essentially independent of the MCL. Furthermore, a CT geometry yields a distribution in ECL, depending upon where the current originates at the crack front. This dependence is such that the crack growth rate is highest at the crack edges (smallest ECL), but is lowest for the coupling current that originates from the crack front in the center of the specimen (largest ECL) by virtue of the dependence of crack growth rate on the electrochemical crack length.<sup>90,102,104</sup> This phenomenon is responsible for the generation of convex crack fronts, when the crack grows by SCC, in contrast to the concave crack front obtained for creep crack growth.<sup>105</sup>

Finally, we note that the CEFM is used extensively in various corrosion damage codes developed by Macdonald and coworkers (DAMAGE PREDICTOR, ALERT, REMAIN, FOCUS)<sup>19,23</sup> to predict stress corrosion cracking damage in BWR primary coolant circuits, as described below. To date, fourteen BWRs have been modeled and, where comparison is possible, the predicted damage is found to be in excellent agreement with that observed in the field.

### 2.39.6.3 Simplified Approach for Calculating Propagation Rates

It is well known from experiment that the rates of individual pit (crack) propagation as a function of time at constant environmental conditions can be approximated by a relatively simple function of time. Thus, for the case of pitting corrosion, the power function,

$$a = kt^m \quad [70]$$

has been suggested, where  $k$  and  $m$  are empirical constants.<sup>11,58,109</sup> Here,  $a$  is the characteristic pit size (e.g., pit depth or radius of the pit mouth). Published values of  $m$  are very often approximately equal to 1/3, 1/2, 2/3 or 1, but they can also vary over wider ranges.<sup>11,109–111</sup>

However, this dependence of  $a$  on  $t$  cannot be used directly in mathematical calculations for small times,

because of the nonphysical limit

$$V_s = \frac{da}{dt} = km t^{m-1} \rightarrow \infty, \text{ at } t \rightarrow 0 \text{ for } m < 1 \quad [71]$$

This is why, instead of eqn [70], the following interpolation equation for pit propagation rate,  $V_s$ , has been suggested<sup>91</sup>

$$V_s = \frac{da}{dt} = V_0(1 + t/t_0)^n \quad [72]$$

where  $n = m - 1$  and  $t_0$  are constants, and  $V_0$  is the initial, finite rate of pit propagation. Equation [72] yields  $V = V_0$  at  $t/t_0 \ll 0$  and  $V = V_0(t/t_0)^n$  at  $t \gg t_0$ .

Integration of eqn [72] with the boundary condition  $a = 0$  at  $t = 0$  yields

$$a = x_0[(1 + t/t_0)^m - 1] \quad [73]$$

where  $x_0 = t_0 V_0/m$ . For small times, as follows from eqn [73],  $a$  can be presented as the linear function of  $t$ ,  $a = V_0 t$  and for large times,  $a$  takes the form of eqn [70]. In many cases, the period of time over which the approximation

$$V(t)V_0 = \text{Constant} \quad [74]$$

is valid can be comparable with the observation time (or even with the service life of the system). The reason is that corrosion is, generally speaking, a slow process and under real, practical conditions, values of the critical pit depth of the system,  $x_{cr}$ , and typical service life,  $t_s$ , impose significant restrictions on the values of the initial and average corrosion current densities and, thus, on the potential and concentration drops that might be observed in a corrosion cavity.<sup>112</sup>

For constant external conditions, the dependence of cavity propagation rate as a function of the cavity depth,  $x$ , can be written in the form

$$V_s = \frac{da}{dt} = V_0 \varsigma(x) \quad [74]$$

where function  $\varsigma(x)$  satisfies the evident boundary condition  $\varsigma(x) \rightarrow 1$  at  $x \rightarrow 0$ . For the particular case when eqn [72] holds,  $\varsigma(x)$  can be expressed in the form:

$$\varsigma(x) = \frac{1}{(1 + x/x_0)^{(1-m)/m}} \quad [75]$$

where  $x_0 = v_0 t_0/m$ .

The general approach based on the numerical solution of the system of mass transfer equations does not present the depth of pit in the form of eqn [70] or [73]. As noted in Turnbull,<sup>58</sup> the mechanistically based models are complex to set up and, at the

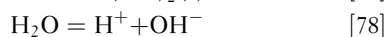
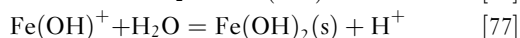
present stage of development, are not user-friendly. For us, it is most important that the solution of the full system of mass transfer equations for the ensemble of pits is practically unrealistic for usual systems, from the point of view of the required computation time. One way to deal with this problem is to perform numerous calculations of pit propagation in advance and approximate the obtained results by eqns [70] or [73]. The other way is to try, after some simplification that does not significantly reduce the accuracy of calculations, to develop a model that can yield a cavity propagation law of the form of eqns [70] or [73], and that may even yield analytical expressions for parameters  $k$  and  $m$ . The principal concept in this simplification is that, if the rate of corrosion reaction depends explicitly only on the local potential and some surface concentrations of particular species (e.g.,  $\text{Cl}^-$  and  $\text{H}^+$ ), the pit growth rate depends only on the concentrations of those species that determine the value of electrostatic potential near the corroding surface.

Below, we will consider the example of such an approach for the simplest (but perhaps the most important, from the practical point of view) case of the corrosion of steels in neutral solutions. Thus, it has been suggested that, in the mathematical simulation of the corrosion of Fe in NaCl solutions, at least six species in the solution must be taken into the account.<sup>91</sup>

$$S_1 \equiv \text{Fe}^{2+}; S_2 \equiv \text{Fe}(\text{OH})^+; S_3 \equiv \text{Na}^+; S_4 \equiv \text{Cl}^-;$$

$$S_5 \equiv \text{H}^+; \text{ and } S_6 \equiv \text{OH}^-$$

These species include iron ions from the dissolution process, sodium and chloride ions (for example) that are commonly included to control the bulk conductivity, hydrogen and hydroxyl ions from the dissociation of water, and a metal hydrolysis product (for example). In the simplest case, the following homogeneous hydrolysis reactions are assumed to occur



with  $\text{Fe}(\text{OH})_2(\text{s})$  representing the precipitated hydrolysis product. Homogeneous reactions include hydrolysis processes and also precipitation processes. If the degree of supersaturation is sufficiently high, direct precipitation will occur in the solution itself; otherwise, precipitation will tend to occur on the walls preferentially. However, if an appropriate balance is obtained between the rate of production of the

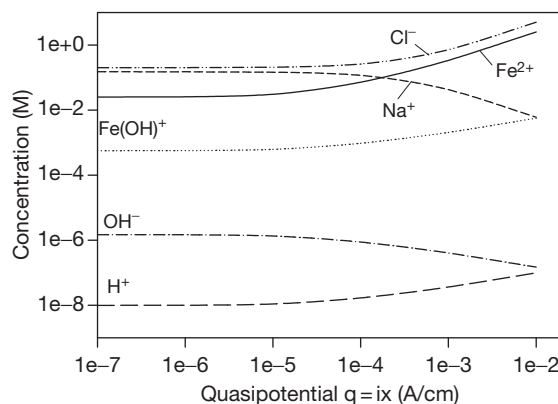
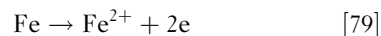


**Figure 10** The concentration of species down a corroding cavity (crevice) in 0.1 M NaCl at 25 °C as functions of the quasipotential.

hydrolyzing species and the rate of precipitation, general saturation is expected to occur.<sup>60</sup>

We will assume that a single electrochemical reaction



occurs on the walls of the cavity.

Numerical solution of the corresponding boundary problem has been performed<sup>91</sup> by using the values of kinetic parameters from Sharland *et al.*<sup>78</sup> Figure 10 shows the concentrations profiles as a function of the quasipotential,  $q$ .<sup>68</sup> Please note that, for the case of a deep, one-dimensional cylindrical pit with passive walls or for a crevice with parallel passive sides,  $q = ix$ , where  $x$  is the distance down the cavity, and  $i$  is the current density in the crevice that is determined by the dissolution rate.<sup>91,112</sup> We can see that there are three species that dominate in the pit,  $\text{Fe}^{2+}$ ,  $\text{Cl}^-$ , and  $\text{Na}^+$ , and only these species determine the electrostatic field in the cavity.

Let us now assume in addition, that, the electro-dissolution reaction occurring in the cavity due to oxidation of the metal, can be described in terms of the Tafel equation as

$$\begin{aligned} i &= i_0 \exp \left\{ \frac{\alpha F (V_m - U_0 - \phi_s)}{RT} \right\} \\ &= i^* \exp \left\{ -\frac{\alpha F \phi_s}{RT} \right\} \end{aligned} \quad [80]$$

Here,  $i_0$  is the exchange current density,  $\alpha$  is the anodic transfer coefficient,  $V_m$  is the local electrode potential,  $U_0$  is the open-circuit potential (measured on the external surface remote from the pit),  $\phi_s$  is the electrostatic potential in the solution near the



electrode surface, all referred to a reference electrode at infinity, and  $i^* = i_0 \exp \{ \alpha F (V_m - U_0) / RT \}$  is the current density calculated in the absence of a potential drop in the cell ( $\phi_s = 0$  corresponding to the maximum possible current density on the electrode surface at the given potential of the metal).

Hence, if we only want to calculate the potential distribution and rate of corrosion in this system, we can approximate the complete system involving six species ( $\text{Fe}^{2+}$ ,  $\text{Fe}(\text{OH})^+$ ,  $\text{Na}^+$ ,  $\text{Cl}^-$ ,  $\text{H}^+$  and  $\text{OH}^-$ ) by a reduced system involving only three species ( $\text{Fe}^{2+}$ ,  $\text{Na}^+$  and  $\text{Cl}^-$ ).

In this case, the solution of the mass transfer equations for this simplified system can be easily performed even in analytical form. In particular, if the polarization curve for reaction [79] can be described by Tafel's law [80] with the symmetry factor,  $\alpha$ , it was shown that the depth of one dimensional pit with passive walls can be described by eqn [73] with

$$m = \frac{\alpha + 1}{2\alpha + 1} \quad [81]$$

and

$$x_0 = 3FD_1 C_{\text{Cl}^-}^b / i^*, \quad V_0 = K_V i^*, \quad t_0 = mx_0 / V_0 \quad [82]$$

where  $D_1$  is the diffusion coefficient of  $\text{Fe}^{2+}$ , and  $C_{\text{Cl}^-}^b$  is the bulk concentration of chloride ions. Moreover, if  $\alpha = 1$  (typical value for corrosion of steels), eqn [81] yields  $m = 2/3$ .

If, for example,  $C_{\text{Cl}^-}^b = 0.6 \text{ M}$  (which corresponds approximately in the case of seawater),  $i^* = 10^{-4} \text{ A cm}^{-2}$  (which corresponds to an initial propagation rate,  $V_0$ , of  $\sim 1 \text{ mm year}^{-1}$ ) and  $D_1 = 0.72 \text{ cm}^2/\text{s}$ , eqn [82] yields  $x_0 \approx 12 \text{ cm}$ . Accordingly, if the critical depth of the pit penetration  $x_{\text{cr}}$  is of the order of 1 cm, as follows from eqns [74] and [75], it is possible to conclude that the pit will propagate at a constant rate because, when  $x_0$  is a large number  $\zeta(x)$  becomes equal to one. The physical reason for this uniform propagation is that the potential (and concentration) drops are very small in this system for the adopted values of dimensions, kinetic parameters, and environmental conditions. We can also state that the mere fact that hemispherical (or approximately hemispherical) pits exist can be explained by the insignificance of the potential drop in the corrosion cavity. Otherwise, the corrosion current density on the edge of the pit becomes higher than that on the bottom, and the pit will quickly assume a shallow ('saucer') form. This initial rate can be determined by using the experimentally measured polarization curves in the region of active dissolution, and can be calculated

for certain metals and alloys for different environmental conditions by using available software.<sup>71</sup>

However, it is also possible that pits can propagate with a constant rate, in spite of the fact that significant potential drops may exist down the cavity. In many cases, the rate of corrosion depends on the concentration of aggressive anions (e.g., chloride ions) near the metal surface. This dependence is usually approximated by the following relation<sup>11</sup>:

$$i = k_a C_{\text{As}}^\lambda \exp \left\{ \frac{\alpha F (V_m - U_0 - \phi_s)}{RT} \right\} \quad [83]$$

where  $C_{\text{As}}$  is the surface concentration of the aggressive anion,  $k_a$  is the rate constant for the reaction proceeding in the anodic direction, and  $\lambda$  is the effective kinetic order of the metal dissolution reaction with respect to the anion concentration. The value of  $\lambda$  is usually restricted to  $0 \leq \lambda \leq 1$ .<sup>11</sup> It was shown that, in this case, instead of eqn [81], we can use the alternate equation<sup>91,112</sup>

$$m = \frac{\alpha_{\text{eff}} + 1}{2\alpha_{\text{eff}} + 1} \quad [84]$$

where

$$\alpha_{\text{eff}} = \alpha - \lambda \quad [85]$$

It is clear that if  $\alpha \approx \lambda$ , we have  $m \approx 1$ , and the pit propagates with an approximately constant rate.

Generally speaking, under real, practical conditions, values of the critical pit depth of the system,  $x_{\text{cr}}$ , and typical service life,  $t_s$ , impose significant restrictions on the corrosion current densities (averaged and initial) and thus on the potential and concentration drops that might be observed in the corrosion cavity. Thus, if  $x_{\text{cr}}$  does not exceed the order of 1–10 mm, and if the order of  $t_s$  is not less than 1 year, initial corrosion current densities in real, open pits cannot exceed values of  $10^{-4}$  to  $10^{-3} \text{ A cm}^{-2}$ , with the understanding that the polarization curve (corrosion current density versus potential) and the surface concentrations of the species do not change as the pit propagates.<sup>112</sup> Simple analytical expressions for predicting the potential and concentration drops in open corrosion cavities and for predicting cavity propagation rate in systems containing uni- and bivalent anions in stagnant electrolytes under well mixed, external conditions have been obtained.<sup>112</sup>

After the transition of a pit into a crack or into a corrosion fatigue crevice, the total rate of corrosion cavity propagation,  $V_s$ , cannot be described simply by Faraday's law, but also has to contain mechanical

and, in the general case, some additional environmental component (e.g., hydrogen embrittlement component). It would be natural to assume that  $V_s$  is a known function of the environmental (concentration of species near metal surface, temperature) and mechanical parameters (stress), and so on. The explicit forms of these dependences are discussed in the corresponding chapters of this book. Here, only the most general relations will be discussed.

**Figure 8** clearly shows that at low corrosion potential, the crack propagation rate does not depend on  $E_{\text{corr}}$ , that is,  $V_s$  reduces to the mechanical (creep) component. It is also clear that at high values of  $E_{\text{corr}}$ , crack propagation rate does not depend on creep rate and is described by an exponential dependence of the Tafel type. Accordingly, in the first approximation, we can present  $V_s$  as the sum of two contributions

$$V = V_{\text{env}} + V_{\text{mech}} \quad [86]$$

where  $V_{\text{env}}$  is the environmental/electrochemical component, which is often determined by Faraday's law, and  $V_{\text{mech}}$  is the mechanical component (crack advance associated with mechanical fatigue/creep). Of course, in some cases, the synergistic interaction of mechanical and environmental attack can play a role and a simple summation, as expressed by [eqn \[86\]](#), may not be appropriate.<sup>113</sup>

A review of many models for describing environment-induced cracking based directly or indirectly on anodic reaction processes or on hydrogen embrittlement can be found.<sup>114,115</sup> Thus, in accordance with the slip-dissolution model, the average crack growth velocity will be given by

$$V_{\text{env}} = K_v i_{\text{corr}}^0 \Gamma \quad [87]$$

where  $i_{\text{corr}}^0$  is the current density on the bare surface, and  $\Gamma$  is the ratio of the bare surface of the crack tip to the total geometrical surface. It can be shown that

$$\Gamma = \frac{t_0''}{(1-n)\varepsilon_f''} (\dot{\varepsilon}_{\text{ct}})^n \quad [88]$$

where  $\varepsilon_v$  is the fracture strain of the passive film at the crack apex,  $\dot{\varepsilon}_{\text{ct}}$  is the crack tip strain rate, and  $t_0$  and  $n$  are material constants. It is evident that  $\Gamma \leq 1$ . In turn, the expressions for  $\dot{\varepsilon}_{\text{ct}}$  can be found as described in Engelhardt *et al.*,<sup>92</sup> Turnbull,<sup>114</sup> and Peng *et al.*<sup>116</sup>

In the case of corrosion fatigue, the crack growth rate is usually expressed in terms of the increment of crack growth during each fatigue cycle,  $da/dN = V_s/f$  (where  $f$  is the frequency of the applied stress). Very often, this rate follows the well known power-law

relationship (Paris' law)

$$\frac{da}{dN} = C(\Delta K)^n \quad [89]$$

for both fatigue (no corrosion) and corrosion fatigue. Here,  $\Delta K$  is the stress intensity factor range and  $C$  and  $n$  are empirical parameters that depend, in the general case, on environmental conditions. While the dependencies of the Paris equation parameters on environmental conditions is well recognized through numerous experimental studies, few of the models for corrosion fatigue developed to date incorporate environmental effects in an explicit, mechanistic manner. This is another example of where the underlying (mechanical) theory fails to account for the experimental data, and the resultant models fail to meet the requirements of determinism.

Until now, it has been tacitly assumed that the rate of pit (crack) propagation is unequivocally determined by its depth and by the external conditions, that is, there is no distribution in cavity propagation rate for pit cavities of equal depth. However, as noted above, a distribution in pit (crack) propagation rate might be observed in practical systems because of underlying distributions in system parameters that affect the growth rate. Usually, such problems are considered in the following way. In the case of pitting corrosion, it is assumed that the pit depth is described by [eqn \[70\]](#) with distributed parameters  $k$  and  $m$ .<sup>117</sup> However, in Turnbull *et al.*,<sup>118</sup> it is assumed for simplicity, that only parameter  $k$  is normally distributed; parameter  $m$  is assumed to be fixed, and its value is obtained by fitting the model to the experimental data. In contrast, in Harlow and Wei,<sup>3</sup> it is assumed that the pit maintained a hemispherical geometry and grew at a constant volumetric rate. From this fact, it immediately follows that  $m = \text{const} = 1/3$ . On the other hand, it was assumed that parameter  $k$  is described by a Weibull distribution.

Analogously, in Turnbull *et al.*,<sup>118</sup> for the case of SCC, the crack propagation rate was assumed to be given by

$$\frac{da}{dt} = C\sigma^p a^q \quad [90]$$

where  $\sigma$  is the applied stress. It was assumed that parameters  $p$  and  $q$  are fixed and were determined by fitting [eqn \[90\]](#) to the experimental data, but parameter  $C$  was assumed to be normally distributed. Additionally, for example, in Harlow and Wei,<sup>3</sup> for the case of corrosion fatigue, it was assumed that crack propagation is described by [eqn \[89\]](#) with

fixed crack growth exponent,  $n$ , and distributed parameter  $C$ .

Of course, few of the models that are discussed in this section are ‘deterministic’ in nature, although they are certainly ‘mechanistic’ in form. Determinism is readily introduced by first identifying the relevant natural laws and then ensuring that the predictions are constrained by these laws. In many cases, this would be most effectively done by introducing the models, which for the most part, describe the ‘anodic’ part of the corrosion cell, into a ‘coupled environment’ framework to impose the conservation of charge. This again illustrates the important difference between ‘mechanistic’ and ‘deterministic’ models, with only the latter constraining the output (‘predictions’) to those that are ‘physically real’ (i.e., that are consistent with scientific knowledge).

### 2.39.7 Rate of Pit Repassivation and Transition of Pits into Cracks

As noted above, we assume that the repassivation process obeys a first-order decay law

$$R_a(x, t) = -\gamma f_a(x, t) \quad [91]$$

where  $\gamma$  is the delayed repassivation (‘death’) constant (i.e., the rate constant for repassivation of stable pits), and  $f_a$  is the differential damage function for active pits. The repassivation constant,  $\gamma$ , is, in general, expected to be a function of the external conditions, including the corrosion potential, temperature, and electrolyte composition. Generally speaking,  $\gamma$  is also expected to be a function of the depth of the pit,  $x$ , because the local potential in the solution at the cavity surface depends on the IR potential drop in the cavity, that is,  $\gamma$  might be a function of both the spatial coordinates and time. Of course, if the potential and concentration drops inside the corrosion cavity are insignificant during pit propagation, it is possible to neglect changes in  $\gamma$  (see above). However, the value of this constant still depends on the external conditions, such as potential, pH, and concentration of aggressive species in the bulk electrolyte. Finally, active pits may no longer be viable if the potential,  $E$ , at the pit internal surface is less than the repassivation value,  $E_{rp}$ . Accordingly, if the value of  $E_{rp}$  is reached at some pit depth,  $x_{rp}$ , active pits passivate and cannot penetrate further into the metal. The value of repassivation potential  $E_{rp}$  is a function of the metal potential and surface concentrations at the pit tip. It can be

calculated, for example, by using methodology described in Anderko *et al.*<sup>119</sup>

Regarding the transition of a pit into a crack, we assume that a pit immediately transforms into a crack if its depth exceeds some critical value  $x_{tc}$ . As of now, the most widely accepted set of criteria for the transition of a pit into crack are the Kondo criteria.<sup>120</sup> According to these criteria, two conditions must be satisfied for crack nucleation to take place from a pit, namely,

$$K_I > K_{ISCC}(\text{for SCC}) \text{ or } \Delta K > \Delta K_{th}(\text{for CF}) \quad [92]$$

and

$$V_{crack} > V_{pit} \quad [93]$$

Here,  $K_I$  and  $K_{ISCC}$  are the stress intensity factor and critical stress intensity factor for propagation of a stress corrosion crack, respectively;  $\Delta K$  is the stress intensity factor range, and  $\Delta K_{th}$  is the threshold stress intensity factor range for fatigue crack propagation, respectively.

The first requirement defines the mechanical (fracture mechanics) condition that must be met for the prevailing stress and geometry, while the second simply says that the nucleating crack must be able to ‘outrun’ the pit.

It is important to note the following circumstance. At high values of corrosion potential,  $E_{corr}$ , the environmental component of crack propagation rate,  $V_{env}$ , could be much higher than the mechanical component,  $V_{mech}$  (see [Figure 8](#)). Accordingly, the crack propagation rate,  $V_{crack}$  will practically coincide with its environmental part,  $V_{env}$ .

In accordance with the slip dissolution model, the crevice tip is partially blocked by the passive film. Accordingly, for a given set of tip conditions (metal potential, pH, etc.),  $V_{env}$  must be smaller than that corresponding to the pit propagation rate,  $V_{pit}$ , with the tip surface being bare (see [eqn \[87\]](#)). This means that, under these conditions, the transition from a pit into a crack occurs if (1) the depth of the pit exceeds some critical length,  $x_{mech}$  (where  $K_I \geq K_{ISCC}$  or  $\Delta K_I \geq \Delta K_{I,th}$ ); and (2) the pit is passivated (when  $V_{pit}$  is very small). Thus, this latter criterion suggests that cracks will nucleate only from ‘dead’ pits. This example shows how important repassivation phenomena may be for predicting corrosion damage.

### 2.39.8 Statistical Properties of the Damage Function

There exists a close correspondence between damage function analysis (DFA), which has been described at some length above, and extreme value statistics (EVS). The latter technique has been used extensively to extrapolate damage (maximum pit or crack depth) from small samples in the laboratory to larger area samples in the field. Furthermore, DFA provides a means of calculating the central and scale parameters and their time-dependencies in EVS from first principles, and hence represents a unification of the two prediction philosophies.

From a statistical point of view, all distributed properties of the system are completely determined by the cumulative distribution function (CDF),  $\Phi(x)$ . By definition,  $\Phi(x)$  is the probability that the depth of a randomly selected pit (crack) is  $\leq x$ . We postulate that the pit distribution on the metal surface is uniform. Accordingly, the total number of nucleated pits in the entire system is  $SN(t)$ , where  $S$  is the area of the system and, from the definition of the integral damage function,  $F$ , the number of pits that have the depth  $\geq x$ , is  $S[N(t) - F(x, t)]$ . Accordingly, from the definition of probability, we have

$$\Phi(x, t) = \frac{S[N(t) - F(x, t)]}{SN(t)} = 1 - \frac{F(x, t)}{N(t)} \quad [94]$$

We see that the CDF for a given observation time,  $\Phi(x, t)$ , can be predicted if we know (can calculate) the integral damage function of the system (note that the number of nucleated, stable pits,  $N(t)$  simply equals  $F(0, t)$ ). This relationship can be regarded as being the bridge between the statistical and deterministic approaches for estimating the accumulation of localized corrosion damage on a surface.

As noted above, from the practical point of view, the most important value for characterizing corrosion damage is the failure probability,  $P_f$ , of the system. By definition,  $P_f$  is the probability that at least one corrosion event in any form (pit, crevice, stress corrosion crack, or fatigue crack) reaches a depth,  $x$ , at a given observation time,  $t$ , where  $x$ , in this case, is the critical dimension. It can be shown<sup>14</sup> that

$$P_f(x, t) = 1 - \exp\{-SF(x, t)\} \quad [95]$$

Equation [95] allows us to calculate the probability of failure if the integral damage function,  $F$ , is known. The latter function can be found as a solution of eqn [4]. However, here we will reject the equal velocities for all

pits with a given depth assumption that was adopted previously (see eqn [9]). Thus, it is well known that the morphology of pits on any given surface can vary significantly, with some shapes favoring more rapid mass and charge transfer, and hence, a greater propagation rate.<sup>121</sup> In addition, some pits will initiate at metallurgical features that may favor more rapid propagation, for example, at MnS inclusion.<sup>121</sup> The distribution in pit propagation rate might also be explained, for example, by the spatial distribution in electrochemical activity of the anodic and cathodic sites on the corroding surface.<sup>122</sup>

Here, we will assume that the pits that propagate with initial rate  $V_0$  are nucleated in accordance with the equation.

$$n(t) = \int_0^\infty \lambda(t, V_0) dV_0 \quad [96]$$

The function  $\lambda(t, V_0)$  yields the number of pits (per square centimeters) that have initial propagation rates between  $V_0$  and  $V_0 + dV_0$  and that nucleate in the period of time between  $t$  and  $t + dt$ . Further propagation of the pits takes place in accordance with eqn [74]. It can be shown that, in this case, the expression for the flux of active pits can be expressed in general form as<sup>123</sup>

$$j_a(x, t) = \int_0^\infty \exp[-\gamma g(x)/V_0] \lambda[t - g(x)/V_0, V_0] dV_0 \quad [97]$$

where

$$g(x) = \int_0^x \frac{dx'}{\zeta(x')} \quad [98]$$

(compare with eqn [9]). Accordingly, the expressions for the differential damage functions for active and passive pits and the integral damage function have the following forms<sup>123</sup> as solutions of eqn [4]

$$f_a = \int_0^\infty \frac{\exp[-\gamma g(x)/V_0] \lambda[t - g(x)/V_0, V_0]}{V_0 \zeta(x)} dV_0 \quad [99]$$

and

$$f_p = \int_0^\infty \frac{\gamma \exp[-\gamma g(x)/V_0] A[t - g(x)/V_0, V_0]}{V_0 \zeta(x)} dV_0 \quad [100]$$

Furthermore, for the case of pitting corrosion, the total integral damage function,  $F$ , is<sup>123</sup>

$$F = \int_0^{\infty} \exp[-\gamma g(x)/V_0] A[t - g(x)/V_0, V_0] dV_0 \quad [101]$$

where  $A(t, V_0) = \int_0^t \lambda(t', V_0) dt'$  yields the number of pits (per square centimeters) that have initial propagation rates between  $V_0$  and  $V_0 + dV_0$  and nucleate in the period of time between 0 and  $t$ .  $F$  is the sum of the integral damage functions for active and passive pits for the given case.

Let us assume that the distribution in initial pit propagation rate does not depend on time, that is,

$$\lambda(t, V_0) = n(t)\psi(V_0) \quad [102]$$

To move further, we must assume a distribution function,  $\psi(V_0)$ , for the pit growth rate, in order to account for those factors that result in a distribution in growth rate that is not captured by the (present) deterministic models. For our purposes, it is most convenient to approximate  $\psi(V_0)$  by Laplace's distribution function

$$\psi(V_0) = \frac{\exp(-|V_0 - \bar{V}_0|/\beta)}{2\beta} \quad [103]$$

where  $\bar{V}_0$  is the mean initial pit propagation rate and  $\sigma^2 = 2\beta^2$  is the dispersion.

If eqn [102] holds, we have, for the integral damage function and the cumulative damage function, the following expressions

$$F(x, t) = \int_0^{\infty} N[t - g(x)/V_0] \exp[-\gamma g(x)/V_0] \psi(V_0) dV_0 \quad [104]$$

and

$$\Phi(x, t) = 1 - \int_0^{\infty} N[t - g(x)/V_0] \exp[-\gamma g(x)/V_0] \psi(V_0) dV_0 / N(t) \quad [105]$$

respectively. In particular, for the case of instantaneous nucleation, we have

$$\Phi(x, t) = 1 - \int_{x/t}^{\infty} \exp[-\gamma g(x)/V_0] \psi(V_0) dV_0 \quad [106]$$

As has been shown experimentally, in many practical cases, the asymptotic behavior (for large values of  $x$ ) of the CDF can be described by the exponential relationship<sup>58,121</sup>

$$\Phi(x, t) = 1 - \exp[-(x - u)/\alpha] \quad [107]$$

where  $u$  is the central parameter (the most frequent value), and  $\alpha$  is the scale parameter, which defines the width of the distribution. Accordingly, as follows from eqn [107], the extreme value distribution (EVD),  $\psi(x, t)$  (the probability that the largest value of pit depth  $\leq x$ ), is described by a double exponent (Gumbel Type I extreme value distribution) in the form<sup>58</sup>:

$$\Psi(x, t) = 1 - P_f = \exp[-\exp(-y)] \quad [108]$$

where

$$y = (x - b)/\alpha \quad [109]$$

and  $b = u + \alpha \ln(SN)$ .

Numerical calculation<sup>14</sup> shows that the dependencies of  $\ln(1 - \text{CDF})$  on pit depth,  $x$ , can be approximated by straight lines, at least for sufficiently large values of  $x$ , and therefore provide a theoretical basis for applying the Type I extreme value distributions to real corrosion systems. In some cases, parameters  $\alpha$  and  $b$  can be expressed in analytical form. Thus, for the case of instantaneous nucleation and constant pit propagation rate, these parameters can be presented in the form<sup>14</sup>:

$$\alpha = \frac{\beta t}{1 + \gamma \beta t / \bar{V}_0} \quad \text{and} \quad b = \frac{[\bar{V}_0 + \beta L n(0.5 S N_0)] t}{1 + \gamma \beta t / \bar{V}_0} \quad [110]$$

We see that, for small values of  $t$ , the parameters  $\alpha$  and  $b$  can be described by  $\alpha = \beta t$  and  $b = [\bar{V}_0 + \beta L n(0.5 S N_0)] t$ , that is, they are proportional to time. Such dependencies were actually observed, for example, for the case of the pitting corrosion of manganese steel in CO<sub>2</sub>-acidified seawater.<sup>122</sup> On the other hand, for large observation times, the parameters  $\alpha$  and  $b$  approach the following limits

$$\alpha = \bar{V}_0 / \gamma \quad \text{and} \quad b = [\bar{V}_0 + \beta L n(0.5 S N_0)] t \bar{V}_0 / \gamma \quad [111]$$

that are independent of time. This fact can be regarded as being physically evident, because at sufficiently large times, all pits become passive (the damage function becomes 'frozen'), and further propagation of damage cannot occur, provided that  $\gamma > 0$ . This conclusion concerning the achievement of limiting pitting depth also follows from a formal statistical treatment of experimental data for underground carbon steel pipelines.<sup>11</sup> The 'freezing' of damage functions can also be seen in the propagation of corrosion damage on aluminum in tap water.<sup>10</sup>

Equation [110] with eqn [108] can be used for calculating the probability of the failure of a system. Unfortunately, very often it can be the case that not



all, or even none, of the kinetic parameters that determine the pit (crack) nucleation rate, pit propagation rate, and pit repassivation rate, are known. However, unknown parameters are determined by comparing the results of analytical or numerical calculations of the depths of the deepest pits (cracks) with the corresponding experimentally observed values for short-term experiments. After determining values for the unknown parameters, the depths of the deepest pit (crevice) for the total system (i.e., for the system with arbitrary surface area) for long-term exposure are predicted.

Usually therefore, in the case when none of the kinetic parameters are known, the following expression, based on the Gumbel type-I distribution is used for predicting perforation probability in the large systems with the total area,  $S$ , by using the results of measurements of the depth of the deepest pits on the series coupons with area,  $s$ <sup>124</sup>

$$P_f = 1 - \exp\{-\exp[-(d - u + \alpha \ln(S/s))/\alpha]\} \quad [112]$$

where  $d$  is the thickness of the wall.

For predicting probability of failure in long-term experiments by using the results of measurements in short-term experiments, it is necessary to assume some functional dependence of the location parameter,  $u$ , and scale parameters,  $\alpha$ , on time. For the case when eqn [110] is valid, these parameters are described by hyperbolic relations of the form

$$u = \frac{a_1 t}{1 + a_2 t}, \quad \alpha = a_3 u \quad [113]$$

where,  $a_1$ ,  $a_2$ , and  $a_3$  are unknown parameters that must be fitted by using the short term experiments. The procedure of such fitting by using the maximum likelihood method is described in Laycock *et al.*<sup>125</sup>

Figure 11 illustrates the applicability of the hyperbolic dependencies for predicting the results of experiments measuring the depth of the deepest pits in the corrosion of aluminum Alloy 2S-O in Kingston tap water.<sup>10</sup> The mean depth of the deepest corrosion event,  $X_m$ , and standard deviation of this value,  $\sigma$ , can be calculated by using the following relations<sup>125</sup>:

$$X_m = b + \alpha[E + \ln(S/s)] \quad \text{and} \quad \sigma = \pi\alpha/\sqrt{6} \quad [114]$$

We see that applicability of the hyperbolic functions can be considered as being very satisfactory. Note that only the data for  $t = 1$  week and 1 month were used for calibration and hence, for prediction over a period of up to 1 year, providing accurate extrapolation over a range of 12 times that of the calibration range.

However, the typical time-relations that are usually used for estimating the location and scale parameters in extreme value distributions are of the power law type:

$$b = a_1 t^{a_2}, \quad \alpha = a_3 b \quad [115]$$

or logarithmic:

$$b = a_1 \log(t) + a_2, \quad \alpha = a_3 b \quad [116]$$

Figure 12 shows that application of the power law functions for fitting experimental data to the short

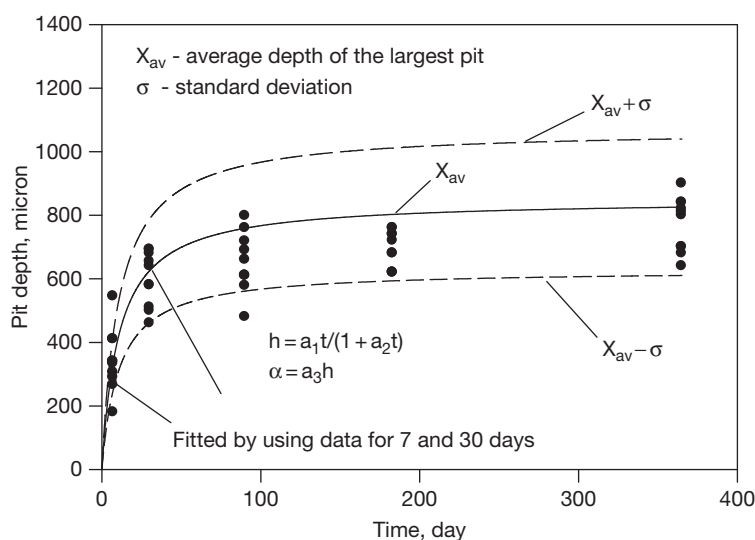


**Figure 11** The mean depth of the deepest pit as a function of time. Fitting to experimental data (black circles) has been performed by using the hyperbolic dependencies [113].

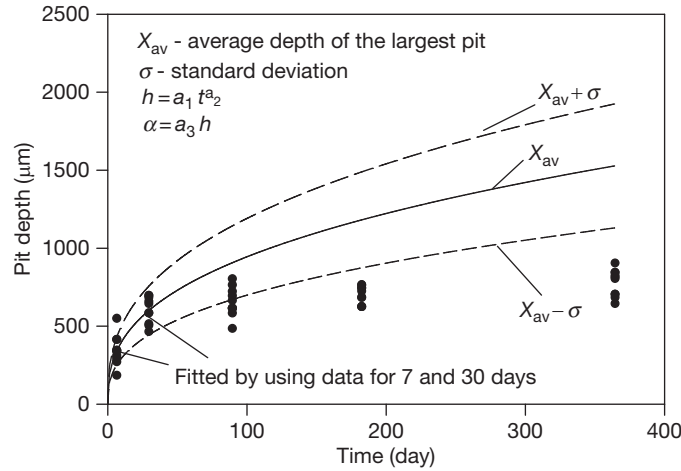


**Figure 12** Fitting to experimental data (black circles) has been performed by using power law dependencies [114].

term experiments yields results that are not as good as application of hyperbolic law, at least for the considered experimental data. This happens, because the power law [115] does not take into account the repassivation of pits that plays a substantial role in determining the results of Aziz's experiments.

From the above, it is evident that the application of the logarithmic law yields much more acceptable results than does the application of the power law (Figure 13). However, at present, there is no physical model that could explain a logarithmic law of pit growth. In reality, if we assume that the growth law of individual pits can be described by a logarithmic function, it can be easily shown that the rate of the pit growth must decrease in accordance with the exponential law ( $da/dt \sim \exp(-\zeta a)$ ). This dependence is substantially stronger than the maximum possible decrease of the rate of open pit growth under diffusion control when  $da/dt \sim 1/a$ . Accordingly, it might be suggested that the logarithmic dependence of pit growth is formally introduced for effectively describing pit propagation in the presence of repassivation phenomena.

A generalization of the hyperbolic function [113] in the form

$$b = \frac{a_1 t^{a_4}}{1 + a_2 t^{a_4}}, \quad \alpha = a_3 b \quad [117]$$

appears to offer some advantages. The principal advantage of the general hyperbolic dependence [117] is that it coincides with the power law at short times and yields the accurate transition:  $u, \alpha \rightarrow \text{constant}$  as  $t \rightarrow \infty$  as it must, due to the repassivation. It is interesting to note that calculation

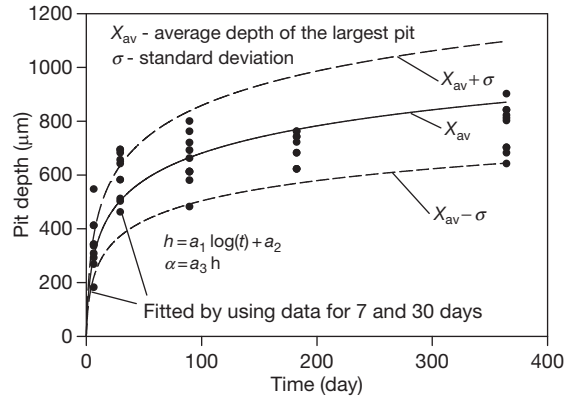


**Figure 13** Fitting to experimental data (black circles) has been performed by using logarithmic dependencies [116].

shows that the parameter  $a_4 = 1.0093 \approx 1$ , that is, fitting by using the general hyperbolic dependencies yields, for the given case, practically the same results as the simple hyperbolic dependencies.

### 2.39.9 Monte Carlo Simulation

The existence of deterministic models to describe nucleation, propagation, and repassivation of localized corrosion processes allows us to replace the current DFA, which reduces to the direct solution of the balance eqns [2], with an alternative approach – Monte Carlo simulation of corrosion damage. However, it is worthwhile to develop this alternative

approach for describing corrosion damage for the following reasons. It is important to note that, frequently, under real conditions, only a few pits (or cracks), or sometimes only a single pit (or crack), may be alive (propagating) on the corroding metal surface (see the upper extremes in [Figure 1](#)). In this case, the differential equations for the damage function, which are equivalent to a balance equation for particles in discontinuous media, lose their strict physical meaning.

The main idea of the Monte Carlo method is to keep track of each stable pit (or crack) that nucleates, propagates and repassivates on the metal surface. A great advantage of this method lies in the fact that it allows us to take into account the interactions between particular individual pits (cracks) in an explicit manner. By doing so, it becomes possible to reduce the number of unknown parameters that describe the interaction between individual pits (cracks). Preliminary calculation shows that both approaches (DFA and Monte Carlo) yield the same results, if the same physical assumptions are made for describing the propagation of corrosion damage. At this point, it is important to note that, in the Monte Carlo method described here, the stages in the life of an individual pit or crack are described deterministically (i.e., in terms of models whose predictions are constrained by the natural laws), while the ensemble of pits is described statistically in terms of a Monte Carlo algorithm. Below, the current version of the deterministic Monte Carlo simulation (DMCS) algorithm that has been developed for predicting the accumulation of localized corrosion damage will be briefly described.

Let us denote by  $N_0$  the total number (not per square centimeters) of stable pits that can nucleate on a metal surface having a total area of  $S$ . We number these pits by the index  $k = 1, 2, \dots, N_0$ , and we will track each of these pits individually. Initially, we suggest that there are no stable pits on the metal surface. We proceed by calculating the probability that a pit will nucleate in stable form during the time step  $dt$  as

$$P_{\text{nuc}} = \frac{N(t+dt) - N(t)}{N_0 - N(t)} \quad [118]$$

where,  $N(t)$  is the number of stable pits that nucleate within the time interval between 0 and  $t$ . (Note that  $P_{\text{nuc}}$  is defined as a ratio of the number of pits that nucleate in the time interval between  $t$  and  $t+dt$  to the number of available remaining sites at moment  $t$ ).

For each pit,  $k$ , that has not yet been born, we generate a random number  $0 \leq G_k \leq 1$ . If  $G_k \leq P_{\text{nuc}}$ , a pit is proclaimed to have been born with a depth of penetration  $x = 0$ ; otherwise, it is considered not to have been born and will be interrogated in the following step. In the case of instantaneous nucleation, all pits in the amount of  $N_0$  are born during the first time step. In the more general 'progressive nucleation' case, the function  $N(t)$  can be calculated by using, for example, the PDM, as noted above. The Cartesian coordinates of the centers of the nucleated pits,  $X_k$  and  $Y_k$ , are also established by using the random number generator, but this will be modified in the future to correspond to particular metallurgical, microstructural, and microchemical features on the surface (e.g., emergent precipitates or second phase particles) that may not be randomly distributed (e.g.,  $\text{Cr}_{23}\text{C}_7$  precipitates on emergent grain boundaries in stainless steels). This innovation will introduce, surface structural factors for the first time, in the deterministic prediction of localized corrosion damage. Practically, if the surface is rectangular with area  $a \times b$ , the Cartesian coordinates  $X_k$  and  $Y_k$  are declared to be  $X_k = G_m$  and  $Y_k = G_b$ , where  $0 \leq G \leq 1$  is a random number. If the surface is not rectangular, we insert the surface into a sufficiently large rectangle so that all points on the actual surface are included, and then repeat the described procedure. However, in this case, we declare  $X_k$  and  $Y_k$  as a center of a newly-born pit only if the point  $(X_k, Y_k)$  lies inside the actual surface. Otherwise, the procedure is repeated until success is achieved, that is, until  $(X_k, Y_k)$  lie inside the actual surface.

At each time step, the depth of the  $j$ -th stable, living pit,  $a_j$ , is calculated sequentially by using Faraday's law

$$a_j(t+dt) = a_j(t) + K_V i_j(t) dt \quad [119]$$

We assume that  $i_j$  is described by Tafel's law for the active metal dissolution current density as a function of potential, that is,

$$i_j = i_0 \exp\left(-\frac{\alpha F \Delta\phi_j}{RT}\right) \text{ at } \Delta\phi_j < \Delta\phi_{\text{cr}} \text{ and} \quad [120]$$

$$i_j = 0 \text{ at } \Delta\phi_j \geq \Delta\phi_{\text{cr}}$$

where  $\Delta\phi_j$  is the averaged potential drop on the active surface (relative to a point that is remote from the hemispherical pit of index  $j$ ),  $\alpha$  is the transfer coefficient of the metal dissolution reaction,  $i_0$  is the corrosion current density at the corrosion potential,  $T$  is the Kelvin temperature,  $F$  is Faraday's constant, and  $R$  is

the gas constant. The physical meaning of the value  $\Delta\phi_{cr}$  is as follows. We can assume that the pit should continue to grow (be alive) if the metal potential at the bottom of the pit,  $E$ , is larger than the repassivation potential,  $E_{rp}$ , that is, at  $E = E_{corr} - \Delta\phi_j > E_{rp}$  or at  $\Delta\phi_j < E_{corr} - E_{rp}$ . In other words  $\Delta\phi_{cr} = E_{corr} - E_{rp}$  is the difference between corrosion and repassivation potentials. Of course, it is assumed that  $E_{corr} > V_{crit}$ , which in turn is greater than  $E_{rp}$ , otherwise pitting corrosion cannot be initiated.

It can be shown<sup>126</sup> that the average potential drop on the active surface of a hemispherical pit (relative to a point far away from it),  $\Delta\phi_j$ , can be estimated by the following relation

$$\Delta\phi_j = \frac{ba_j i_j}{\kappa} + \sum_{k \neq j} \frac{i_k a_k^2}{\kappa d_k} \quad [121]$$

Here, the index  $k$  denotes the pits on the surface (the pit of interest is denoted by the index  $j$ ),  $a_k$  is the radius of the hemispherical pit,  $i_k$  is the average current density inside the pit,  $\kappa$  is the conductivity, and  $b \approx 2.1$  is a constant. Equation [121] can be obtained as an approximate solution of Laplace's equation for the electrical potential for the ensemble of hemispherical pits embedded in a plane under the condition that pits are far apart, that is, when the contribution of each pit can be considered independently. Noting that  $\Delta\phi_j$  corresponds to the potential drop from some point within the pit and a remote point on the external surface, the first term in eqn [121] describes the contribution of the central pit to the total potential drop; this contribution can be found, for example, by using the method described in Pistorius and Burstein.<sup>32</sup> The second term describes the contribution of all other pits on the corroding surface.<sup>50</sup>

Accordingly,  $i_j$  is calculated by using eqn [121], where  $\Delta\phi_j$  is determined by a numerical solution of the equation

$$\Delta\phi_j = \frac{ba_j i_0}{\kappa} \exp\left(-\frac{\alpha F \Delta\phi_j}{RT}\right) + \sum_{k \neq j} \frac{i_0 a_k^2}{\kappa} \exp\left(-\frac{\alpha F \Delta\phi_k}{RT}\right) \quad [122]$$

By solving this equation, we assume that all  $\Delta\phi_k$  in the second term on the right-hand side of eqn [122] are known and are equal to their previous (in the iteration sense) values.

After each time step, the repassivated (dead) pits are excluded from the population of actively growing

pits. A pit is considered dead if  $\Delta\phi_j > \Delta\phi_{cr}$ . In addition, if two pits touch each other, that is, if

$$d_{ij} \leq a_i + a_j \quad [123]$$

where  $d_{ij}$  is the distance between the centers of the  $i$ th and  $j$ th pits, the smallest pit is declared repassivated (dead). A more correct assumption might be that, instead of two touching hemispherical pits, we have a single ellipsoidal pit with the depth of the deepest pit and a dimension obtained, for example, from the condition  $\pi a^2 = \pi a_i^2 + \pi a_j^2$ . Also, the entities that encroach on one another are the 'hemispheres of influence' (HOI), such that the pits begin to compete for the same resources (oxygen reduction). However, such an approach would substantially complicate the problem, but these factors will eventually be included in the analysis. To justify the adopted simplification, we note that the total area occupied by the active pits,  $S_a$ , must be much smaller than the area of the sample,  $S$ , in order to sustain differential aeration. Accordingly, overlap of the pits must be a relatively rare event. Moreover, our simplification can only decrease the value of  $\Delta\phi_j$  for any given pit  $j$ . Thus, if interactions between pits were substantial in the corrosion process, the conclusion would be all the more true than without the simplification.

In addition, we consider the probability that pits can repassivate accidentally (by chance). It is assumed that the probability of a pit repassivating during each time step is proportional to the magnitude of this step, that is,  $P_\gamma = \gamma dt$ , where  $\gamma$  is the delayed repassivation constant. Practically, for the  $j$ th living pit in each time step, we generate the random number  $0 \leq G \leq 1$ . If  $G \leq P_\gamma$ , the pit is declared to be dead (passivated) and is excluded from the further consideration; otherwise, the pit is considered to be alive on entering the next time step. We see that our Monte Carlo simulation method describes all three stages of the pit propagation damage – nucleation, propagation, and repassivation of stable pits.

**Table 2** Parameter values for model calculations

$i_0$	$1.5 \times 10^{-2} \text{ A cm}^{-2}$
$K_v$	$3.44 \times 10^{-5} \text{ cm}^3 \text{ C}^{-1}$
$\alpha$	1
$\kappa$	$0.3 \times 10^{-3} \Omega^{-1} \text{ cm}^{-1}$
$\Delta\phi_{cr}$	200 mV
$T$	25 °C
$\tau$	3 days
$a$	3.65 days
$b$	1
$\gamma$	0.066 day <sup>-1</sup>

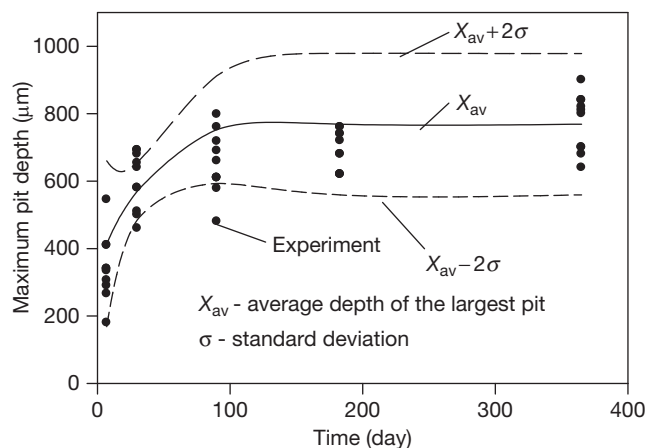


**Figure 14** The mean depth of the deepest pit as a function of time. Experimental data are taken from Aziz<sup>10</sup> and are for aluminum alloy Alcan 2S-O in Kingston, Ontario tap water. Note that no calibration was performed on short term data, as was the case for Figure 11.

As an example of the application of this Monte Carlo simulation method within DFA, we consider again, the corrosion of aluminum alloy Alcan 2S-O in Kingston, Ontario tap water.<sup>10</sup> In this paper, for the purpose of numerically simulating the accumulation of pitting damage on the alloy surface, we will assume the values of various model parameters that are shown in Table 2. The parameters for the PDM ( $\tau$ ,  $a$ , and  $b$ ) were chosen somewhat arbitrarily. The aim was only to ensure that, by the end of two weeks, practically all stable pits had nucleated, as indicated by the experimental data.<sup>10</sup> The value of  $K_V$  corresponds to that for aluminum and the value of  $\kappa$  corresponds to that typically assumed for tap water. The value for the delayed repassivation constant,  $\gamma$ , was chosen to ensure that, by the end of 2 months, the bulk of the pits represented by the bell-shaped curve have ceased to grow (see Figure 1). The value of  $\alpha$  has been chosen as being typical for metal dissolution, and only the value of  $i_0$  has been fitted to the experimentally measured values of maximum pit depth at  $t = 1$  week after metal exposure.<sup>10</sup> Finally, the sample is considered to be rectangular with the dimensions  $7 \times 18$  cm and  $N_0 = 450$ .<sup>10</sup>

Figure 14 shows a comparison of results of the Monte Carlo simulation with experimental data.<sup>10</sup> For a given observation time,  $t$ , we perform  $M$  simulations as described above and, accordingly, receive  $M$  values  $x_1^*(t)$ ,  $x_2^*(t)$ ,  $\dots$ ,  $x_M^*(t)$  for the depth of the deepest pits. After that, we calculate the average (mean) value of the depth of the deepest pit as

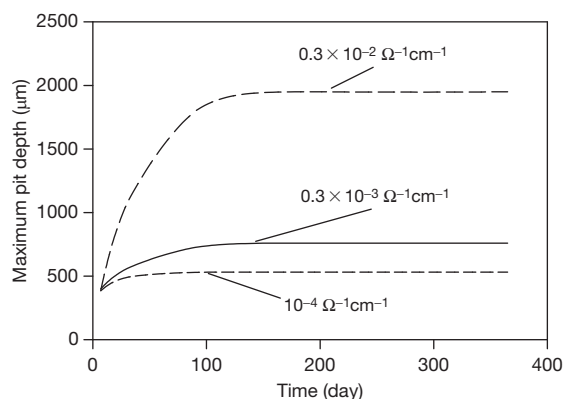


**Figure 15** The mean depth of the deepest pit as a function of time for different conductivities of the electrolyte for aluminum alloy Alcan 2S-O in Kingston, Ontario tap water. Reproduced from Aziz, P. M. *Corrosion* 1956, 12, 35–46.

$$X_{av}(t) = \frac{1}{M} \sum_{m=1}^M x_m^*(t) \quad [124]$$

and the standard deviation as

$$\sigma(t) = \sqrt{\frac{1}{M-1} \sum_{m=1}^M (X_{av}(t) - x_m^*(t))^2} \quad [125]$$

For the sufficiently large value of  $M$  ( $M \geq 40$ , in our case), the results do not depend practically on the value of  $M$ . Because 95% of all experimental measurements usually lie in the interval  $(X_{av} - 2\sigma, X_{av} +$



$2\sigma$ ), we posit that excellent agreement is observed between the experimental and simulation results.

It is important to emphasize that **Figures 11 and 14** were obtained by using absolutely different approaches. While **Figure 11** was obtained as a result of extrapolating data from short term experiments, without any assumption of kinetic parameters, **Figure 14** was obtained assuming that we have the complete set of required parameters without directly using data of short term experiments.

As noted previously, the main advantage of deterministic models over the statistics-based models lies in the fact that deterministic models allow us to make predictions for environmental conditions that lie beyond the available experimental (calibration) data, because the predictions are analytic and based upon a sound physical model and because the prediction is constrained by the natural laws to that which is physically real. As an example, **Figure 15** shows the influence of electrolyte conductivity on the mean depth of the deepest pits from multiple, identical sample areas on the surface as a function of time. It is seen that the mean of the deepest pits on multiple, but equal, areas on the alloy surface is a very sensitive function of the external environment conductivity; this probably reflects primarily an enhanced throwing power of the coupling current from the pit mouth to the external surface where it is consumed by oxygen reduction. Thus, increasing the conductivity of the external environment allows the coupling current to be thrown a greater distance from the mouth because of the lower IR potential drop in the solution, with the result that the pit can access a larger area for oxygen reduction. Because the pit growth rate is related to the magnitude of the coupling current through Faraday's law, the pit depth is also predicted to increase. It is also important to note that, in all cases, the mean of the deepest pits on the surface is predicted to become constant after  $\sim 100$  days of exposure, simply reflecting that, at longer times, all the pits on the surface are 'dead' (repassivated). The critical question then is whether the deepest dead pits are sufficiently deep to nucleate cracks under the prevailing loading conditions.

The version of the Monte Carlo model that is described above deals only with the propagation of pitting corrosion damage. The example of Monte Carlo simulation that considers the transition of a pit into a crack can be found, for example, in Turnbull *et al.*<sup>118</sup> This model is based on mechanistic equations for pit and crack propagation rates (see eqns [70] and

[90]), with statistically distributed input parameters, and no models were assumed for the pit or crack growth processes. These unknown parameters are fitted to the available experimental data, and accordingly, it will be impossible to use this model for predicting corrosion damage under different environmental conditions.

It is important to note that, in the models that consider deterministically the propagation of ensemble of cracks, it would be necessary, in the general case, to take into account the possible mechanical interactions between multiple cracks.<sup>127</sup>

### 2.39.10 Examples of Deterministic Prediction of Corrosion Damage in Complicated Industrial Systems

In this section, we present two examples of the deterministic prediction of corrosion damage in complex industrial systems. The two systems chosen are both from the electric power industry, where corrosion has proven to be an important factor in determining the availability of the power generating facilities. Indeed, it has long been recognized that the management of

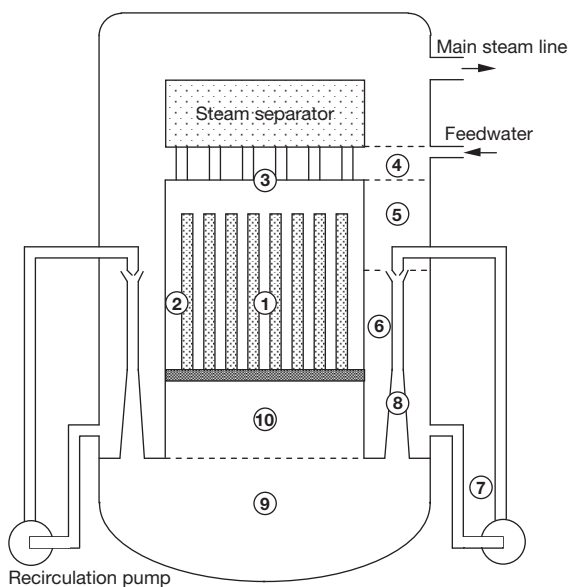


**Figure 16** Schematic of the primary coolant circuit of a BWR having external coolant pumps. The regions are identified as (1) core channels; (2) core bypass; (3) upper plenum; (4) mixing plenum; (5) upper downcomer; (6) lower downcomer; (7) recirculation system; (8) jet pump; (9) bottom of lower plenum; (10) top of lower plenum. Reproduced from Macdonald, D. D.; Balachov, I.; Engelhardt, G. R. *Power Plant Chem.* **1999**, 1, 9–16.

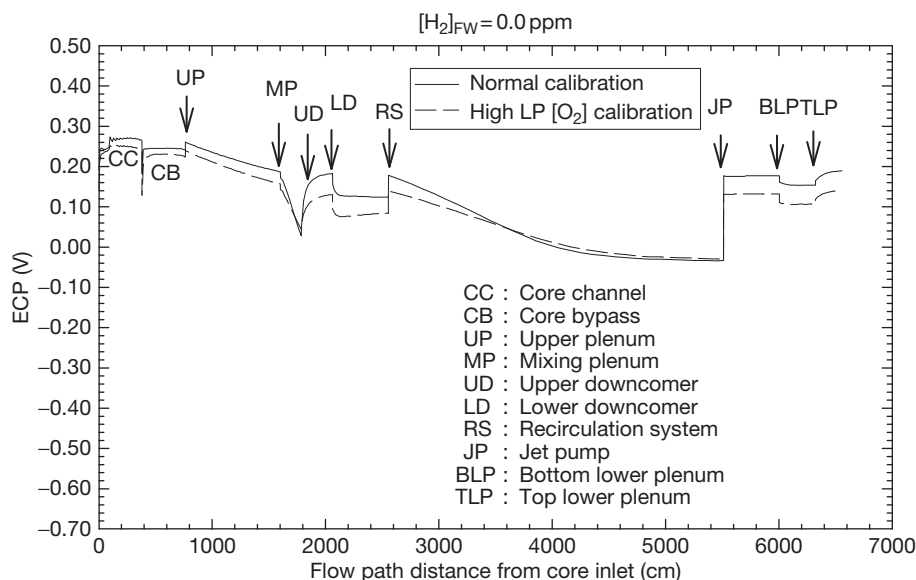


**Figure 17** Calculated ECP (versus SHE) for the primary coolant circuit in the Leibstadt BWR operating under 'normal water chemistry' conditions (no hydrogen added to the feedwater). Reproduced from Macdonald, D. D.; Urquidí-Macdonald, M. *Corrosion* **1992**, *48*, 354–366.

the accumulation of corrosion damage, such that maintenance can be performed during scheduled outages, is an effective strategy for enhancing availability and for life extension. The primary purpose, here, however, is to convince the reader that the deterministic prediction of damage is practical and that such models may form the basis for the effective management of damage.

### 2.39.10.1 Cracking in Nuclear Reactors

The first example of the application of deterministic modeling of damage localized corrosion that we have chosen to describe in our work on modeling the accumulation of damage due to intergranular stress corrosion cracking (IGSCC) in sensitized Type 304 SS in the primary (liquid water) coolant circuit of a BWR.<sup>23</sup> This case is important because it illustrates the integration of the damage over the CEP taken by the reactor during normal operation. The reader will recall that the CEP is the path taken by the system in terms of those independent variables that have a significant impact on the rate of accumulation of damage as the system changes from the present state to the future state.

A schematic of the primary coolant circuit of a BWR with external coolant pumps is shown in [Figure 16](#), and the various components and regions in the flow circuit are identified in the caption.<sup>128</sup>

Plotted in [Figure 17](#) is the ECP calculated using the MPM (see [Section 2.39.4](#)) by first calibrating the radiolysis model (not the MPM) on Dresden II (a completely different reactor in Illinois) field data for the oxygen content of the coolant during operation and on another reactor (Duane–Arnold); these two reactors define the extremes of the US fleet of BWRs in their response to hydrogen added to the reactor feedwater.<sup>20,31,99</sup> These calculations predict that the ECP varies by about 250 mV around the entire coolant circuit when no hydrogen is added to the feedwater.

On the other hand, if significant hydrogen is added to the feedwater (e.g., 0.5 ppm), the corrosion potential is predicted to vary by about 0.9 V around the circuit. The Nuclear Regulatory Commission (NRC) has proposed a critical potential for intergranular stress corrosion cracking (IGSCC) in sensitized Type 304 SS of  $-0.23 \text{ V}_{\text{SHE}}$ ; if the corrosion potential lies below this value, no cracking will occur but for more positive values, cracks will nucleate and grow, and the utility cannot take credit for a 'no cracking environment.' In the case of 'normal water chemistry (NWC)' ([Figure 17](#), zero feedwater hydrogen), all components in the primary (liquid water) coolant circuit are predicted to be susceptible to IGSCC. Under 'hydrogen water chemistry (HWC)' ([Figure 18](#),  $[\text{H}_2]_{\text{FW}} = 0.50 \text{ ppm}$ ), significant regions of the coolant circuit are protected by the added hydrogen, including much of the recirculation piping system

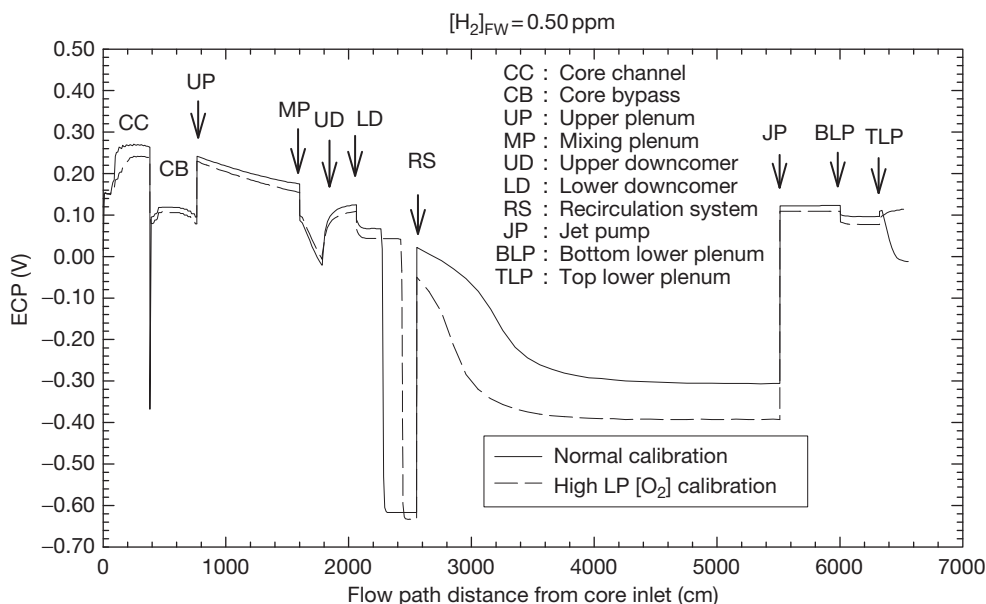
and the Lower Downcomer, while other regions are not. This example demonstrates how modern modeling techniques (i.e., reaction kinetic analysis, RKA) can be used to specify the conditions that must be achieved in a complex chemical system in order to protect components against corrosion.

As indicated above, the CEP describes the path taken by the system in terms of the independent variables that have a significant impact on the process, resulting in corrosion damage as the system changes from the present state to the future state. Once this path is defined, the corrosion rate is integrated along the path to yield the integral damage. This concept is illustrated below with reference to intergranular stress corrosion cracking in the core shroud of a boiling water nuclear reactor. (The shroud is a stainless steel drum that surrounds the core containing the fuel rods. The shroud contains a circumferential weld (the 'H-3 weld') at the top, and the steel adjacent to the weld, in the so-called heat-affected zone, HAZ, is sensitized and hence is susceptible to IGSCC. The phenomenon of IGSCC has been responsible for billions of dollars of losses in the nuclear power industry during a period extending over 30 years.) For IGSCC in sensitized Type 304 SS, the important independent variables in determining the crack growth rate are stress, degree of sensitization (DOS), crack length, temperature, conductivity of the water, oxygen, hydrogen, and hydrogen

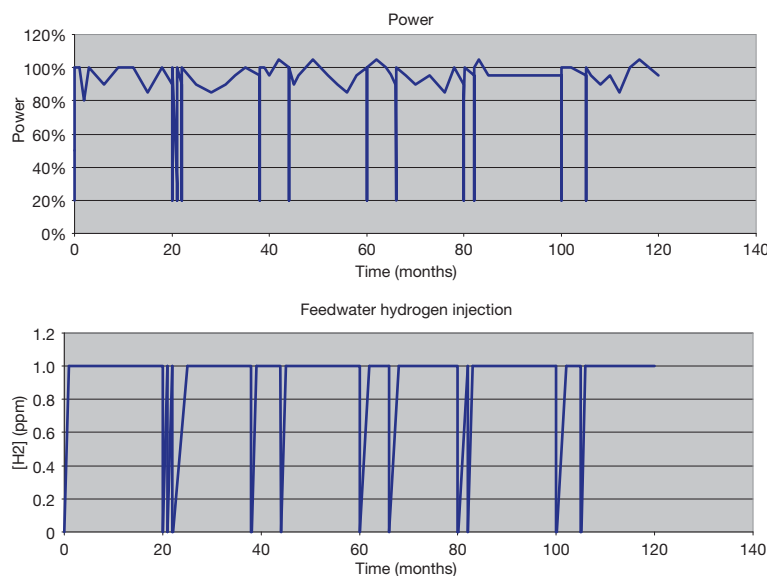
peroxide concentrations (all produced by the radiolysis of water or added, as in the case of  $H_2$ , for a reactor operating on hydrogen water chemistry), and water flow velocity. In turn, the concentrations of the redox species ( $H_2$ ,  $O_2$ , and  $H_2O_2$ ) determine the electrochemical corrosion potential (ECP), upon which the crack growth rate is exponentially dependent. Accordingly, the independent variables defining the CEP for the crack in the shroud ID surface within the HAZ of the weld are temperature, degree of sensitization (DOS) of the steel, crack length, tensile stress (residual and operational), water conductivity, ECP, and flow velocity. Thus, the CEP is defined in terms of the variations in each of these quantities as the reactor changes during the ten years of operation.

Figure 19 shows the operating history of the reactor in terms of reactor power (which defines the temperature and the bulk coolant flow rate) and hydrogen added to the feedwater ( $H_2$  has a large impact on the ECP – see Figures 17 and 18). This generic reactor was operating on HWC, with hydrogen being added only when the reactor is operating, not during shutdown, and the damage, in terms of the crack length, was calculated by integrating the crack growth rate over the CEP for a period of 10 years.

The predicted damage is summarized in Figure 20, in which are plotted crack length (in centimeters) versus time curves for three operating protocols:



**Figure 18** Calculated ECP (vs. SHE) for the primary coolant circuit in the Leibstadt BWR operating under 'hydrogen water chemistry' conditions (0.50 ppm hydrogen added to the feedwater). Reproduced from Macdonald, D. D.; Balachov, I.; Engelhardt, G. R. *Power Plant Chem.* **1999**, 1, 9–16.



**Figure 19** Corrosion evolutionary path (CEP) defined in terms of the prime variables of reactor power and hydrogen added to the reactor feedwater. Reproduced from Macdonald, D. D.; Balachov, I.; Engelhardt, G. R. *Power Plant Chem.* **1999**, 1, 9–16.

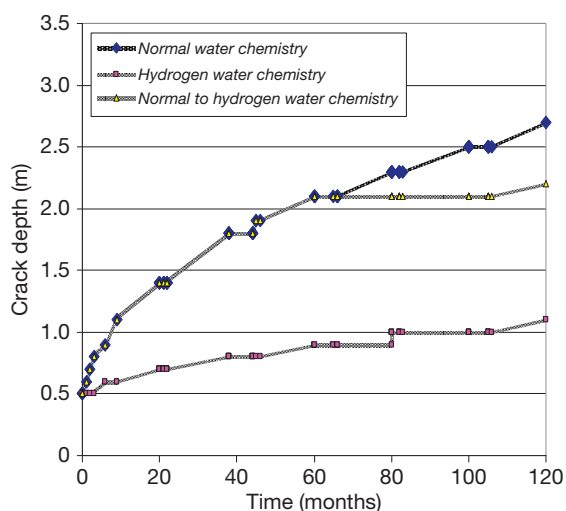


**Figure 20** Integrated damage functions (crack length) versus reactor operating time for three operating scenarios: (1) normal water chemistry, (2) hydrogen water chemistry (1 ppm H<sub>2</sub> in the reactor feedwater), (3) NWC for 5 years followed by HWC for the remaining 5 years. Reproduced from Macdonald, D. D.; Balachov, I.; Engelhardt, G. R. *Power Plant Chem.* **1999**, 1, 9–16.

(1) normal water chemistry (NWC), where no hydrogen is added to the reactor coolant (diamonds), (2) hydrogen water chemistry (1 ppm H<sub>2</sub> in the reactor feedwater over the entire 10-year operating period, squares), and (3) NWC for 5 years followed by HWC for the remaining 5 years (triangles). The various ‘jigs

and jogs’ in the data are not artifacts caused by imprecise calculation, but represent changes in crack growth rate with the changing conditions along the CEP, particularly when the reactor is shut down and started up. During entering and exiting a shutdown period, some of which occur for refueling of the reactor, the hydrogen concentration, coolant conductivity, temperature, coolant flow velocity, and stress (although the stress on the crack was assumed to be primarily residual and hence, is assumed to be constant in the simulations described above) change markedly, but the impact on the overall damage is only small, because the shutdown and start up periods are short. It is seen from **Figure 20** that the crack growth rate (gradient of the curve) decreases with time. This is the consequence of coupling between the internal and external environments of the crack, as postulated in the coupled environment fracture model (CEFM) (see Macdonald *et al.*<sup>23</sup> and citations therein and the corresponding section of this article). Thus, as the crack grows in length under constant potential conditions, a larger IR potential drop occurs down the crack, resulting in a lower potential drop being available on the external surface for the reduction of oxygen or the evolution of hydrogen, thereby resulting in a reduction of the coupling current and hence, a lower crack growth rate. (Note that the crack cannot grow faster than the coupling current can be consumed on the external surface by oxygen reduction and/or hydrogen evolution, and it has been established experimentally

that the crack growth rate is linearly related to the coupling current.)

Under NWC, the crack is predicted to grow by about 2.2 cm over the 10 years of operation (note that we assume an initial crack length of 0.5 cm). If HWC (where 1 ppm of  $H_2$  is added to the reactor coolant water only during operation, see Figure 19), the crack is estimated to grow by only 0.6 cm over the 10-year operating period, a substantial reduction in the damage. If, on the other hand, the reactor operated for the first 5 years on NWC (no added hydrogen) and then switched to HWC, the damage (increase in crack length) is predicted to be 1.7 cm. The progression of damage is clearly governed by the 'law of decreasing returns,' in that the damage avoided in the last 5 years by implementing HWC (0.5 cm) is substantially less than that incurred under NWC in the first 5 years (1.6 cm). This is entirely due to the dependence of the crack growth rate on crack length, a dependence that was never previously recognized in crack growth-rate studies. Clearly, predictions of this type are of considerable value, because they allow the benefits to be defined in a cost/benefit analysis. The cost of installing HWC in a BWR is significant because of the need to store considerable amounts of hydrogen on site and because of the need to shield personnel against the production of radioactive  $^{16}NH_3$  that forms by neutron bombardment of oxygen in water ( $^1n_0 + ^{16}O_8 \rightarrow ^{16}N_7 + ^1p_1$ ) under the reducing conditions that exist in the coolant circuit under HWC operating

conditions. Note that  $^{16}N_7$  is a strong  $\gamma$ -photon emitter.

At this point, it is worthwhile to enquire how accurate the prediction might be for a system that is as complex as an operating BWR. Data published by Tang *et al.*<sup>129</sup> (see also Macdonald *et al.*<sup>23</sup>) for a crack adjacent to the H-3 weld in a reactor operating in Taiwan affords an opportunity to assess the accuracy, as depicted in Figure 21. The depth of the crack was assessed by inspection at times of 10 and 20 months after Outage 11 and the ALERT code was fit to the datum for the shorter time, essentially by adjusting the time of nucleation of the crack, such that the calculated and measured crack depth coincided. ALERT was then used to calculate the crack depth at the longer, 20-month time after Outage 11, and the comparison with the measured value is displayed in the figure. Excellent agreement is obtained, with the small residual difference being attributed to uncertainty in the operating history of the reactor.

This example has been presented because it illustrates the application of damage function analysis (DFA) to the deterministic prediction of damage in a complex industrial system. It also illustrates the role of, and the need for, careful characterization of the CEP. It is the opinion of the authors that a water-cooled nuclear reactor is comparable in complexity to, say, an oil production system, and that meaningful damage prediction calculations are possible on the basis of DFA (or any other deterministic protocol), provided that the CEP is carefully defined.

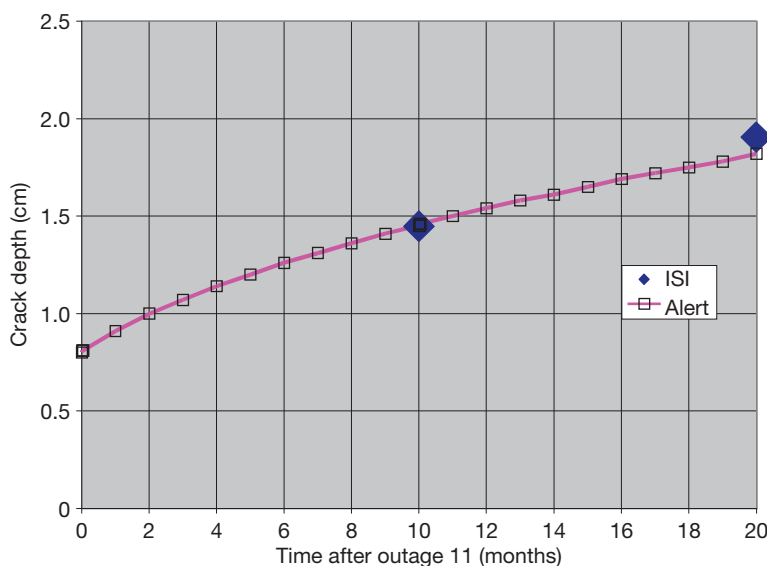


**Figure 21** Depth of a crack at the H3 weld in the shroud as a function of time after Outage 11. (♦) Values calculated by ALERT.<sup>19,23</sup> Experimental data reported by Tang *et al.*<sup>129</sup>



Of course, the reward for being able to make such calculations is that it then becomes possible to answer the all-important ‘what if’ questions, such as: ‘What damage will I incur if I operate in this manner?’ or ‘If I take this corrective measure, can I operate with reasonable certainty to the next outage?’ Answers to questions of this type can have significant economic implications.

### 2.39.10.2 Low Pressure Steam Turbines

Another complex industrial system that has been modeled deterministically with regard to the accumulation of localized corrosion damage is low pressure steam turbines (LPSTs). Failure of LPSTs generally occurs via the cracking of the rotor, disk, or blades, from cracks that nucleate at pits.

Below we will show some results of calculating the probability of failure,  $P_f$ , of LPSTs by using the deterministic Monte Carlo simulation method that has been described above.<sup>130</sup> By definition,  $P_f$  is the probability that at least one corrosion event in any form (pit, stress corrosion crack, or fatigue crack) reaches a depth,  $a_{cr}$ , at a given observation time,  $t$ , where  $a_{cr}$  in this case, is the critical dimension (e.g., the stress corrosion crack length at which unstable, rapid mechanical fracture and sudden failure occurs). Using the Monte Carlo simulation method, we can calculate  $P_f$  in a straightforward way. Let us assume that we make  $M$  calculations of the depth of the deepest corrosion event,  $x^*$ , and, in  $M_f$  cases ( $M_f \leq M$ ),  $x^* > a_{cr}$  for a given observation time,  $t$ . In this case,  $P_f(a_{cr}, t)$  is defined as

$$P_f = \frac{M_f}{M} \quad [126]$$

for sufficiently large  $M$ .

In particular, it was found that the failure probability is a very sensitive function of the conditions that exist in a low pressure steam turbine (LPST)

**Table 3** Assumed operational cycle parameters for the development of corrosion fatigue in low pressure steam turbine blades

Shutdown	Operation cycle
$t = 100$ h	$t = 500$ h
$\sigma = 0$	$\sigma = \sigma_m + 0.5 \Delta \sigma \sin(2\pi ft)$
	$\sigma_m = 84$ ksi, $\Delta \sigma = 4$ ksi, $f = 60$ Hz
$T = 25^\circ\text{C}$	$T = 95^\circ\text{C}$
$[\text{O}_2] = 8$ ppm	$[\text{O}_2] < 1$ ppb
$[\text{Cl}^-] = 3500$ ppm	$[\text{Cl}^-] < 100$ ppm
pH = 6	pH = 6

**Table 4** Assumed operational cycle parameters for the development of corrosion fatigue in low-pressure steam turbine discs

Shutdown	Operation cycle
$t = 100$ h	$t = 500$ h
$\sigma = 0$	$\sigma = 95$ ksi
$T = 25^\circ\text{C}$	$T = 160^\circ\text{C}$
$[\text{O}_2] = 8$ ppm	$[\text{O}_2] < 1$ ppb
$[\text{Cl}^-] = 3500$ ppm	$[\text{Cl}^-] < 100$ ppm
pH = 6	pH = 6

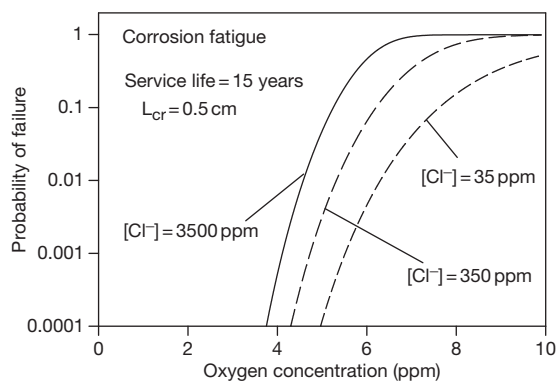


**Figure 22** Calculated failure probability for LP steam turbine blades as a function of oxygen concentration for different chloride concentrations in the electrolyte film during the shutdown period. Other parameters are the same as in Table 3.

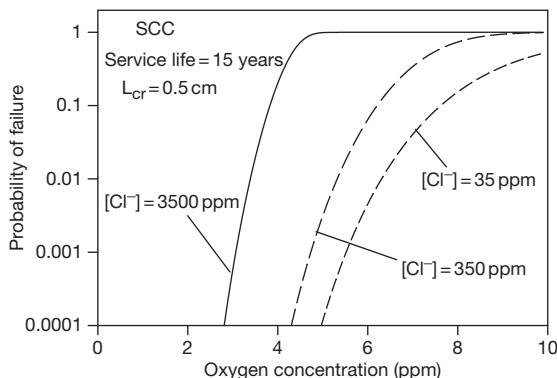


**Figure 23** Calculated failure probability for LP steam turbine discs as a function of oxygen concentration for different chloride concentrations in the electrolyte film during the shutdown period. Other parameters are the same as in Table 4.

during shutdown, including the oxygen concentration, chloride concentration, and the fraction of the time spent under shutdown versus operation, if the shutdown environment is not deaerated, and the steel

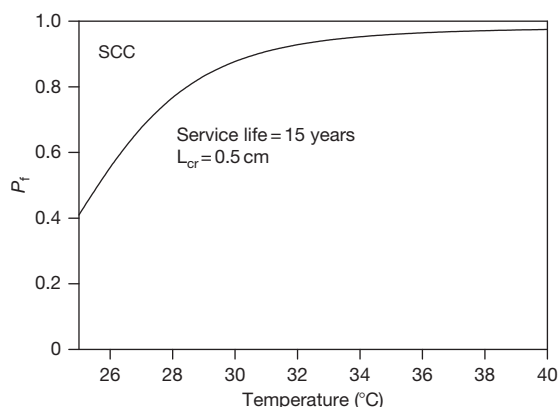


**Figure 24** Probability of failure of a turbine disk as a function of temperature during the shutdown period. The oxygen concentration during shutdown period is 4.5 ppm. Other parameters are the same as in Table 4.

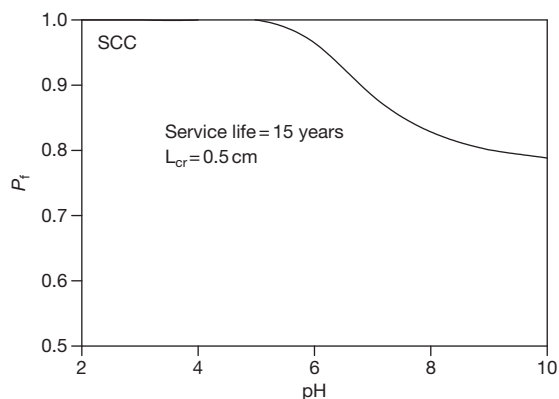


**Figure 25** Probability of failure of a turbine disk as a function of pH during the shutdown period. The oxygen concentration during shutdown period is 5.2 ppm. Other parameters are the same as in Table 4.

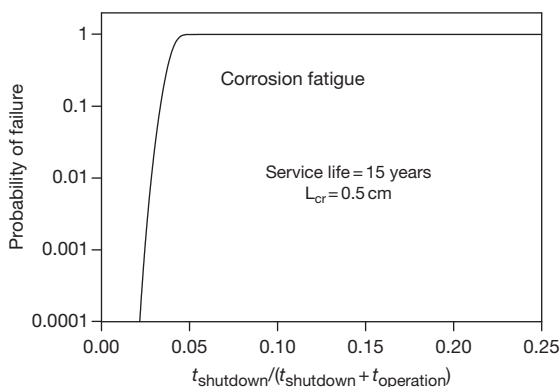


**Figure 26** Calculated failure probability for LP steam turbine blades versus the fraction of the time spent in shutdown.

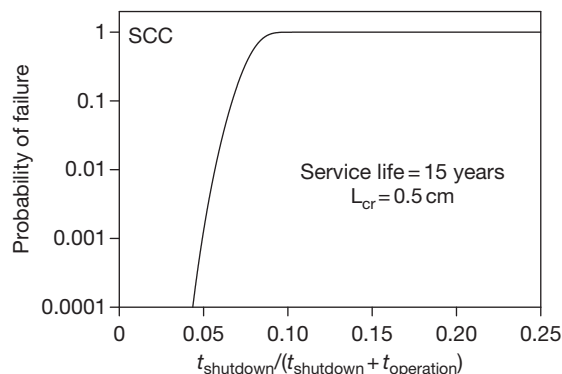


**Figure 27** Calculated failure probability for LP steam turbine discs versus the fraction of the time spent in shutdown.

surfaces are not washed free of chloride ion. It is important to note that the calculations were made by using experimentally determined electrochemical parameters for Type 403 SS in the case of determining failure in blades (where CF takes place) and A470/471 steels in the case of determining failure in discs and rotors (where SCC takes place).<sup>131</sup>

For illustrative purposes, we present below only some examples of the influence of environmental parameters on the probability of failure of blades and discs in low pressure steam turbines. The assumed operating cycle parameters for the case of stress corrosion cracking can be found in Tables 3 and 4. This information defines the CEP.

The failure probabilities plotted in Figures 22–27 as a function of  $[O_2]$ ,  $[Cl^-]$ , temperature, pH, and fraction of the time spent in shutdown under aerated conditions all during the shutdown period, were calculated for 219 shutdown–operation cycles over 15 years, assuming instantaneous nucleation (all pits nucleating during the first shut down) and that all cycles are identical. This particular CEP was chosen for modeling convenience; more complicated CEPs, in which the cycle time and other parameters are varied over realistic ranges, are easily enacted. The critical crack length was assumed to be 0.5 cm, and crack growth was determined to occur primarily by mechanical fatigue during operation.

The calculated failure probabilities plotted in Figures 22 and 23 are clearly sensitive functions of both the oxygen concentration and the chloride concentration in the condensate on the blade or disk surface left over from operation. Increasing the oxygen concentration under open shutdown (i.e., opening the turbine to the atmosphere) displaces the corrosion potential in the positive direction and hence

increases the pit nucleation and propagation rates, thereby resulting in enhanced pitting damage. Upon subsequent startup, the pits act as stress-raisers for the nucleation of cracks (SCC and corrosion fatigue) and hence lead to an increase in the failure probability. The important lesson to be learned from this plot, and from many simulations of this type, is that deaeration of the turbine upon shutdown should be an effective method of protecting low pressure steam turbines against blade and disc failure after subsequent start-up.

**Figures 22 and 23** also show that the failure probability,  $P_f$ , decreases sharply to a very low value (essentially zero) as  $[\text{Cl}^-]$  is lowered below 35 ppm. This provides a second strategy for reducing, or even eliminating the failure of discs and blades, reducing the chloride concentration of  $\text{Cl}^-$  on the surfaces immediately upon shutdown. This would be most easily instituted by washing the blade and disc surfaces with pure (chloride-free) water immediately upon shutdown of the turbine. In fact, an even more effective strategy would be to combine turbine surface washing with nitrogen blanketing. Given that turbine failure costs anywhere between \$10 million and \$100 million per event, depending upon the nature of the failure, an incentive certainly exists for the utilities to explore the strategies identified above.

The temperature of shutdown is also predicted, in certain situations, to have a visible effect on the failure probability (see **Figure 24**), primarily through the pit growth rate. While this is a substantial reduction, the investment in the necessary facilities to cool a turbine after shutdown is possibly too great to be cost effective, but the desired effect might be achieved through conventional air conditioning.

The remaining environmental variable that is amenable to change is the pH. This variable may be changed by doping the boiler water of the steam with pH buffers, including ammonia, various amines, and systems such as boric acid–hydroxide systems. However, our predictions are that pH has relatively little impact on the failure probability (see **Figure 25**). Thus, the gain that might be achieved in turbine service life possibly would not warrant instituting a major chemistry change upon the basis of enhancing turbine blade and disc life alone.

**Figures 26 and 27** clearly show that the probability of failure increases rapidly with the time spent under aerated conditions during shutdown. That is why the reduction of this time could be an effective method of protecting low pressure steam turbines against blade and disc failure.

It must be emphasized that prediction of the probability of failure in LPTS can also be done on the basis of damage function analysis. Examples of the corresponding calculations can be found in Engelhardt *et al.*<sup>132</sup> and Engelhardt and Macdonald.<sup>131</sup>

## 2.39.11 Conclusions

The purpose of this chapter is to introduce the reader to deterministic methods that have been developed to predict the accumulation of corrosion damage in complex industrial systems. That such predictions can be made is now well beyond question, and it is expected that determinism will rapidly develop as the philosophy of choice in making damage predictions. Because practicing scientists and engineers have seldom taken a course on the philosophies of prediction, few have been exposed to the modeling choices that are available, ranging from empiricism, to ‘mechanistic models,’ to models that are characterized by varying degrees of determinism. This latter caveat recognizes that, in practice, ‘determinism’ is an ideal concept that is seldom, if ever, achieved in modeling in pure form. From a practical viewpoint, however, determinism offers a methodology that means minimal calibration, because the dependent/independent variable relationships are captured within the constitutive equations of the model, rather than by calibration, as is the case for an empirical model. As noted above, failure in industrial systems is, by and large, a very rare event, so that almost no chance exists for establishing reliable dependent–independent variable relationships by direct calibration.

Another great advantage of deterministic models is that they draw upon the wealth of scientific experience by constraining the solutions of the constitutive equations to that which is ‘physically real’ via the natural laws. This feature cannot be overemphasized, as it greatly reduces the need for calibration, provides a condition that must be satisfied and does not arise from the model itself (the model is described by the constitutive equations). If the constraints are absent, or are not imposed, the model may still be ‘mechanistic,’ but it clearly lacks the predictive power offered by determinism.

In making predictions with any model, be it empirical or deterministic, it is essential to define the CEP, which is the path taken by the system in terms of those independent variables that have a significant impact on the damage accumulation rate as the system changes from the present state

to the future state. Because, the future cannot generally be predicted with certainty, the CEP is most often synthesized to present 'what if' scenarios of operation. These scenarios coupled with economic analyses, may be used to identify the most cost-effective modes of operation and hence, are a valuable financial planning tool. Similarly, the CEP may be designed to ascertain the probability that failure will not have occurred by the time of the next scheduled inspection, which, given the deleterious cost of unscheduled outages, again becomes a valuable financial planning tool. Finally, it is evident that the tools discussed in this chapter are capable of providing valuable input to the design of complex industrial systems, particularly in the light of the fact that corrosion issues are seldom, if ever, given more than cursory examination.

One of the significant advantages of integrating the damage along the CEP to yield the damage function (DF) is that the process may be applied to historical data from which the CEP may be defined with considerable accuracy. In this mode, the predicted damage function becomes a means of accessing the veracity of the model and the damage prediction process. In fact, this type of calculation should always be performed, if for no other reason than that it affords a means of customizing the algorithm to the system of interest. Customization may require the adjustment of values for poorly known parameters in the model or may even require modification of the code itself. In any event, the code becomes the 'alter ego' of the system and provides a means of accurately predicting the accumulation of damage under conditions where the CEP can be defined with historical accuracy.

## References

- Macdonald, D. D.; Urquidi-Macdonald, M. *Corrosion* **1992**, *48*, 354–366.
- Kowaka, M.; Tsuge, H.; Akashi, M.; Masamura, K.; Ishimoto, H. *Introduction to Life Prediction of Industrial Plant Materials: Application of the Extreme Value Statistical Method for Corrosion Analysis*; Allerton Press, 1994.
- Harlow, D. G.; Wei, R. P. *AIAA J.* **1994**, *32*, 2073–2079.
- Harlow, D. G.; Wei, R. P. *Eng. Fract. Mech.* **1998**, *59*, 305–325.
- Harlow, D. G.; Wei, R. P. *Fatigue Fract. Eng. Mater. Struct.* **2001**, *22*, 427–436.
- Harlow, D. G.; Wei, R. P. *Fatigue Fract. Eng. Mater. Struct.* **2001**, *24*, 523–535.
- Harlow, D. G.; Wei, R. P. *Model. Simul. Mater. Sci. Eng.* **2005**, *13*, R33–R51.
- Macdonald, D. D.; Liu, C. In *Proceedings of the 12th International Corrosion Congress*; NACE International, Houston, TX, 1993; Vol. 5A, pp 3446–3459.
- Liu, C.; Macdonald, D. D. *J. Press. Vessel Technol.* **1997**, *119*, 393–400.
- Aziz, P. M. *Corrosion* **1956**, *12*, 35–46.
- Freiman, L. I. In *Progress in Science and Technology. Corrosion and Corrosion Protection* VINITI, 1985; Vol. 11, pp 3–71 [in Russian].
- Macdonald, D. D. *Proceedings of Corrosion and Prevention-2000*; Australasian Corrosion Association: Auckland, NZ, Nov 2000; pp 19–22; Paper **42**.
- Engelhardt, G. R.; Macdonald, D. D. *Corrosion* **1998**, *54*, 469–479.
- Engelhardt, G. R.; Macdonald, D. D. *Corros. Sci.* **2004**, *46*, 2755–2780.
- McCartney, L. N. *Int. J. Fract.* **1979**, *15*, 477–487.
- Turnbull, A.; McCartney, L. N.; Zhou, S. *Corros. Sci.* **2006**, *48*, 2084–2105.
- Polyanin, A. D.; Zaitsev, V. F.; Moussiaux, A. *Handbook of First Order Partial Differential Equations*; Taylor & Francis: London, 2002.
- Wagner, C.; Traud, W. Z. *Elektrochem.* **1938**, *44*, 391–402.
- Macdonald, D. D.; Urquidi-Macdonald, M. In *Encyclopedia of Electrochemistry*; Bard, A. J., Stratmann, M., Eds.; Wiley-VCH: Weinheim, 2006; *Electrochemical Engineering*, Vol. 5, Macdonald, D. D., Schmuki, P., Eds., pp 665–720.
- Macdonald, D. D. *Corrosion* **1992**, *48*, 194–205.
- Macdonald, D. D. *Pure Appl. Chem.* **1999**, *71*, 951–978.
- Selman, J. R.; Tobias, C. W. *Advan. Chem. Eng.* **1978**, *10*, 211.
- Macdonald, D. D.; Balachov, I.; Engelhardt, G. R. *Power Plant Chem.* **1999**, *1*, 9–16.
- Anderko, A.; Young, R. D. *Corrosion* **2000**, *56*, 543–555.
- Anderko, A.; McKenzie, P.; Young, R. D. *Corrosion* **2001**, *57*, 202–213.
- Sridhar, N.; Brossia, C. S.; Dunn, D. S.; Anderko, A. *Corrosion* **2004**, *60*, 915–936.
- Nordsveen, M.; Nešić, S.; Nyborg, R.; Stangeland, A. *Corrosion* **2003**, *59*, 443–456.
- Nešić, S.; Cai, J.; Lee, K.-L. *Corrosion/2005*; NACE International: Houston, TX, 2005; Paper no. 05556.
- Davydov, A. D.; Shaldaev, V. S.; Engelhardt, G. R. *Russian J. Electrochem.* **2006**, *42*, 121–128.
- Davydov, A. D. *Russian J. Electrochem.* **2008**, *44*(7), 835–839.
- Stewart, J.; Williams, D. E. In *Advances in Localized Corrosion*; Isaacs, H. S., et al. Eds.; NACE International: Houston, TX, 1990; pp 131–136.
- Pistorius, P. S.; Burstein, G. T. *Philos. Trans. R. Soc. Lond. A* **1992**, *341*, 531–559.
- Williams, D. E.; Stewart, J.; Balkwill, P. H. *Corros. Sci.* **1994**, *36*, 1213–1235.
- Williams, D. E.; Westcott, C.; Fleischmann, M. *J. Electrochem. Soc.* **1985**, *132*, 1796, 1804.
- Lin, L. F.; Chao, C. Y.; Macdonald, D. D. *J. Electrochem. Soc.* **1981**, *128*, 1194.
- Macdonald, D. D.; Urquidi-Macdonald, M. *Electrochim. Acta* **1986**, *31*, 1079.
- Macdonald, D. D.; Urquidi-Macdonald, M. *J. Electrochem. Soc.* **1987**, *134*, 41.
- Macdonald, D. D.; Urquidi-Macdonald, M. *J. Electrochem. Soc.* **1989**, *136*, 961.
- Macdonald, D. D.; Urquidi-Macdonald, M. *J. Electrochem. Soc.* **1992**, *139*, 3434–3449.

40. Uhlig, H. In *Passivity of Metals*; Frankenthal, R. P., Kruger, J., Eds.; The Electrochemical Society: Princeton, NJ, 1978; p 1.
41. Engell, H. *Electrochim. Acta* **1977**, *22*, 987.
42. Macdonald, D. D. *J. Electrochem. Soc.* **2006**, *153*, B213–B224.
43. Kong, D.-S.; Chen, S.-N.; Wang, C.; Yang, W. *Corros. Sci.* **2003**, *45*, 747.
44. Tsuchiya, H.; Fujimoto, O.; Chinara, O.; Shibata, T. *Electrochim. Acta* **2002**, *47*, 4357.
45. Kaesche, H. Z. *Phys. Chem. (Neue Folge)* **1962**, *34*, 87.
46. Böhm, H.; Uhlig, H. H. *J. Electrochem. Soc.* **1969**, *116*, 906–910.
47. Shibata, T. *Trans ISIJ* **1983**, *23*, 785.
48. Fratesi, R. *Corrosion* **1985**, *41*, 114.
49. Reuter, M.; Heusler, K. E. *Electrochim. Acta* **1990**, *35*, 1809–1814.
50. Carslaw, H. S.; Jaeger, J. C. *Conduction of Heat in Solids*, 2nd ed.; Oxford Press: London, 1959.
51. McGeough, J. A. *Principles of Electrochemical Machining*; Chapman and Hall: London, 1974.
52. Newman, J.; Thomas-Alyea, K. E. *Electrochemical Systems*, 3rd ed.; Prentice Hall: Englewood Cliffs, NJ, 2004.
53. Chang, H.-Y.; Park, Y.-S.; Hwang, W.-S. *J. Mater. Process. Technol.* **2000**, *103*, 206–217.
54. Bird, B. R.; Stewart, W. E.; Lightfoot, E. N. *Transport Phenomena*, Wiley: New York, 2002.
55. Davis, J. T. *Turbulence Phenomena*; Academic Press: London, 1972.
56. Popov, Yu. A.; Alekseev, Yu. V.; Kolotykin, Ya. M. *Sov. Electrochem.* **1979**, *14*, 1260.
57. Walton, J. C.; Grangolino, G.; Kalandros, S. K. *Corros. Sci.* **1996**, *38*, 1–18.
58. Turnbull, A. *Br. Corros. J.* **1993**, *28*, 297–308.
59. Lasaga, A. C.; Kirkpatrick, R. J. *Kinetics of Geochemical Processes*; Mineralogical Society of America: Washington, 1981.
60. Walton, J. C. *Corros. Sci.* **1990**, *30*, 915–928.
61. Sharland, S. M. *Corros. Sci.* **1992**, *33*, 183.
62. Engelhardt, G. R.; Strehblow, H.-H. *Corros. Sci.* **1994**, *34*, 1171–1175.
63. Laycock, N. J.; White, S. P. *J. Electrochem. Soc.* **2001**, *148*, B264–B275.
64. Yao, L. S.; Prusa, J. *Adv. Heat Transfer* **1989**, *19*, 1.
65. Engelhardt, G. R.; Davydov, A. D. *Russian J. Electrochem.* **1994**, *30*, 865.
66. Engelhardt, G. R.; Strehblow, H.-H. *J. Electroanal. Chem.* **1994**, *365*, 7.
67. Engelhardt, G. R.; Strehblow, H.-H. *J. Electroanal. Chem.* **1995**, *394*, 7.
68. Pillay, B.; Newman, J. *J. Electrochem. Soc.* **1993**, *140*, 414.
69. Verbrugge, M. V.; Bakker, D. R.; Newman, J. *J. Electrochem. Soc.* **1993**, *140*, 2530.
70. COMSOL software, [www.comsol.com](http://www.comsol.com).
71. OLI Systems software, [www.olisystems.com](http://www.olisystems.com).
72. Papavinosan, S.; Revie, W.; Friesen, W. *Corrosion Reviews* **2006**, *24*, 173–230.
73. Isaacs, H. S. *J. Electrochem. Soc.* **1973**, *120*, 1456.
74. Doig, P.; Flewitt, E. J. *Metall. Trans. A* **1981**, *12*, 927.
75. Ateya, D. G.; Pickering, H. W. *J. Appl. Electrochem.* **1981**, *11*, 453.
76. Gravano, S.; Galvele, J. R. *Corros. Sci.* **1984**, *24*, 517.
77. Sharland, S. M.; Tasker, P. W. *Corros. Sci.* **1988**, *28*, 603.
78. Sharland, S. M.; Jackson, C. P.; Diver, A. J. *Corros. Sci.* **1989**, *29*, 1149.
79. Sharland, S. M. *Corros. Sci.* **1992**, *33*, 183.
80. Alkire, R.; Sittary, D. *J. Electrochem. Soc.* **1979**, *126*, 15.
81. Galvele, J. R. *J. Electrochem. Soc.* **1976**, *123*, 464.
82. Galvele, J. R. *Corros. Sci.* **1981**, *21*, 551.
83. Newman, J.; Hanson, D. B.; Vetter, K. *Electrochim. Acta* **1977**, *22*, 829.
84. Harb, J. N.; Alkire, R. C. *J. Electrochem. Soc.* **1991**, *138*, 2594.
85. Evans, U. R. *J. Inst. Met.* **1923**, *30*, 239.
86. Manahan, M. P.; Macdonald, D. D.; Peterson, A. J. *Corros. Sci.* **1995**, *37*, 189.
87. Zhou, X.; Balachov, I.; Macdonald, D. D. *Corros. Sci.* **1998**, *40*, 1349.
88. Yeh, T.-K.; Tsai, C.-H.; Chang, C.-Y. In Proceedings of the 11th International Symposium on Environmental Degradation of Materials in Nuclear Power Systems – Water Reactors : ANS, WA, USA, 10–14, August 2003; pp 500–511.
89. Macdonald, D. D.; Urquidi-Macdonald, M. *Corros. Sci.* **1991**, *32*, 51.
90. Macdonald, D. D.; Lu, P.-C.; Urquidi-Macdonald, M.; Yeh, T.-K. *Corrosion* **1996**, *52*, 768.
91. Engelhardt, G. R.; Urquidi-Macdonald, M.; Macdonald, D. D. *Corros. Sci.* **1997**, *39*, 419–441.
92. Engelhardt, G. R.; Macdonald, D. D.; Urquidi-Macdonald, M. *Corros. Sci.* **1999**, *41*, 2267–2302.
93. Vankeerberghen, M.; Macdonald, D. D. *Corros. Sci.* **2002**, *44*, 1425.
94. Engelhardt, G. R.; Macdonald, D. D. In *Corrosion/2000*, Orlando, FL, March 2000, Paper no. 00227, pp 1–12.
95. Engelhardt, G. R.; Macdonald, D. D.; Millet, P. *Corros. Sci.* **1999**, *41*, 2165–2190.
96. Turnbull, A. *Corros. Sci.* **1999**, *41*, 2267.
97. Gavrilov, S.; Vankeerberghen, M.; Deconinck, J.; Vereecken, J. In 4th Workshop LWR Coolant Water: Radiolysis and Electrochemistry Avignon: 2002, 26 April France.
98. Ford, F. P. In *Corrosion sous contrainte-phénoménologie et mécanismes*; Desjardins, D., Oltra, R., Eds.; Bombannes, 1990.
99. Ford, F. P.; Taylor, D. F.; Andresen, P. L.; Ballinger, R. G. Corrosion-assisted cracking of stainless and low-alloy steels in LWR environments, EPRI Final Report NP-5064M, Project 2006-6; Palo Alto: Electric Power Research Institute, CA, 1987.
100. Shoji, T. Quantitative prediction of environmentally assisted cracking based on crack tip strain rate *American Society of Mechanical Engineers, Pressure Vessels and Piping Division (Publication) PVP* **1985**, Vol. 99, 127–142.
101. Shoji, T.; Moriya, S.; Arai, H.; Higashi, M. In *Fracture Mechanics Applications*; American Society of Mechanical Engineers, Pressure Vessels and Piping Division (Publication) PVP, 1994; Vol. 287, pp 107–113.
102. Vankeerberghen, M.; Gavrilov, S. In EUROCORR 2001, Riva del Garda: Italy, 30 September–4 October 2001.
103. Peng, Q. J.; Kwon, J.; Shoji, T. *J. Nucl. Mater.* **2004**, *324*, 52.
104. Macdonald, D. D.; Lvov, S. N.; Kelkar, G.; Magalhaes, J. F.; Kwon, H.-K.; Wuensche, A.; Biswas, R.; Ahmad, Z.; Engelhardt, G. R.; Urquidi-Macdonald, M. The development of deterministic methods for predicting corrosion damage in water-cooled nuclear reactors, Final Report EP93–33 Empire State Electric Energy Research Corporation (ESEERCO): New York, NY, November 1996.



105. Wuensche, A.; Macdonald, D. D. In CORROSION 2001, Houston, TX, 2001, Paper no. 01236.
106. Andresen, P. L. *Corrosion* **1993**, 49, 714.
107. Wilkinson, D. S.; Vitek, V. *Acta Metall.* **1982**, 30, 1723.
108. Macdonald, D. D. In Proceedings of the Chimie 2002 (French Nuclear Society) Avignon: France, April 2002.
109. Szklarska-Smialowska, Z. *Pitting Corrosion of Metals*; National Association of Corrosion Engineers: Houston, TX, 1986.
110. Engell, H. J.; Stolica, N. D. *Z. Phys. Chem., NF* **1959**, 20, 113.
111. Macdonald, D. D.; Lui, C.; Urquidi-Macdonald, M.; Stickford, G. H.; Hindin, B.; Agrawal, A. K.; Krist, K. *Corrosion* **1994**, 50, 761.
112. Engelhardt, G. R.; Macdonald, D. D. *Corros. Sci.* **2004**, 46, 1159–1187.
113. Wei, R. P. In *Fracture Mechanics: Microstructure and Micromechanics*; Nair, S. V., et al. Ed.; ASM International: Metals Park: OH, 1989.
114. Turnbull, A. *Corros. Sci.* **1993**, 34, 921–960.
115. Unger, D. J. *Analytical Fracture Mechanics*; Academic Press: San Diego, 1995.
116. Peng, O. J.; Kvon, J.; Shoji, T. *J. Nucl. Mater.* **2004**, 324, 52–61.
117. Turnbull, A.; Zhou, S. *Corros. Sci.* **2004**, 46, 1239–1264.
118. Turnbull, A.; McCartney, L. N.; Zhou, S. *Corros. Sci.* **2006**, 48, 2084–2105.
119. Anderko, A.; Sridhar, N.; Dunn, D. S. *Corros. Sci.* **2004**, 46, 1583–1612.
120. Kondo, Y. *Corrosion* **1989**, 45, 7–11.
121. Marsh, G. P.; Bland, I. D.; Tabor, K. J. *Br. Corros. J.* **1988**, 23, 157.
122. Strutt, J. E.; Nicholls, J. R.; Barbier, B. *Corros. Sci.* **1985**, 25, 305.
123. Engelhardt, G. R.; Macdonald, D. D.; Zhang, Y.; Dooley, B. *PowerPlant Chem.* **2004**, 6, 647.
124. Shibata, T.; Akoshi, M.; Ikematsu, K.; Nakajima, H.; Tsuge, H. *Corros. Eng.* **1988**, 37, 699–705.
125. Laycock, P. J.; Cottis, R. A.; Scarf, P. A. *J. Electrochem. Soc.* **1990**, 137, 64–69.
126. Engelhardt, G. R.; Macdonald, D. D. In CORROSION/2008, New Orleans, April 2008; Paper no. 08270.
127. Kamaya, M.; Totsuka, N. *Corros. Sci.* **2002**, 44, 2333.
128. Yeh, T. K.; Macdonald, D. D.; Motta, A. T. *Nucl. Sci. Eng.* **1995**, 121, 468–482.
129. Tang, J. R.; Kao, L.; Shiau, D.-Y.; Chao, L.-Y.; Yao, C.-C.; Chiang, S. C. *Nucl. Technol.* **1998**, 121, 324–336.
130. Engelhardt, G. R.; Macdonald, D.; Dooley, B. *PowerPlant Chem.* **2007**, 9, 454–462.
131. Engelhardt, G. R.; Macdonald, D. D. Development of code to predict stress corrosion cracking and corrosion fatigue of low pressure turbine components, EPRI Report 1004190, 2004.
132. Engelhardt, G. R.; Macdonald, D. D.; Zhang, Y.; Dooley, B. *PowerPlant Chem.* **2004**, 6, 647–662.

# COMPREHENSIVE CORROSION



ELSEVIER  
CORROSION  
ELSEVIER

## 3.01 Corrosion of Carbon and Low Alloy Steels

**S. B. Lyon**

Corrosion and Protection Centre, School of Materials, University of Manchester, Oxford Road, Manchester M13 9PL, UK

© 2010 Elsevier B.V. All rights reserved.

<b>3.01.1</b>	<b>Introduction</b>	1695
3.01.1.1	Historical Perspective	1695
3.01.1.2	Iron–carbon Alloys	1695
3.01.1.2.1	Phase diagram	1695
3.01.1.2.2	Equilibrium microstructures	1697
3.01.1.2.3	Nonequilibrium microstructures	1697
3.01.1.3	Mechanical and Physical Properties	1699
3.01.1.4	Processing	1699
3.01.1.4.1	Heat treatment	1699
3.01.1.4.2	Mechanical deformation	1700
3.01.1.4.3	Metallurgical influences on corrosion	1700
<b>3.01.2</b>	<b>Electrochemistry</b>	1702
3.01.2.1	Thermodynamics	1702
3.01.2.2	Anodic Dissolution	1704
3.01.2.2.1	Oxygen-free (deaerated) conditions	1704
3.01.2.2.2	Oxygen containing (aerated) conditions	1704
3.01.2.2.3	Anion adsorption effects on the mechanism of dissolution	1704
3.01.2.3	Passivity	1705
3.01.2.3.1	Passive oxide films	1705
3.01.2.3.2	Nonoxide passive films	1706
3.01.2.4	Cathodic Reactions	1707
3.01.2.4.1	Hydrogen evolution reaction	1707
3.01.2.4.2	Oxygen reduction reaction	1707
3.01.2.5	Corrosion in Aqueous Environments	1708
3.01.2.5.1	Anode and cathode separation	1708
3.01.2.5.2	Mass transport	1708
3.01.2.5.3	Effect of flow rate on corrosion	1708
<b>3.01.3</b>	<b>Corrosion Processes</b>	1709
3.01.3.1	Corrosion Products	1709
3.01.3.2	Aqueous Corrosion	1710
3.01.3.2.1	General corrosion	1710
3.01.3.2.2	Concentration cell corrosion: Differential aeration	1710
3.01.3.2.3	Pitting and crevice corrosion	1711
3.01.3.2.4	Galvanic corrosion	1711
3.01.3.2.5	Flow-assisted corrosion (FAC)	1712
3.01.3.2.6	Erosion–corrosion	1712
3.01.3.3	Environmentally Assisted Cracking	1712
3.01.3.3.1	Environments	1712
3.01.3.3.2	Hydrogen embrittlement	1713
3.01.3.4	Microbiologically Influenced Corrosion	1713
3.01.3.5	Aqueous Corrosion Protection	1713
3.01.3.6	High Temperature Oxidation	1713
<b>3.01.4</b>	<b>Atmospheric Corrosion</b>	1714
3.01.4.1	Environmental Influences	1714
3.01.4.1.1	Humidity	1714
3.01.4.1.2	Air-borne pollutants	1715

3.01.4.1.3	Particulates	1717
3.01.4.2	Mechanism of Atmospheric Corrosion of Iron	1718
3.01.4.2.1	Acid regeneration cycle	1718
3.01.4.2.2	The electrochemical mechanism	1719
3.01.4.2.3	The wet–dry cycle	1719
3.01.4.3	Corrosion Product Composition	1719
3.01.4.4	Atmospheric Corrosion Kinetics	1720
3.01.4.4.1	Climatic variation	1720
3.01.4.4.2	Conditions of exposure	1721
3.01.4.4.3	Damage functions	1722
3.01.4.5	Weathering Steel	1723
3.01.4.5.1	Alloying effects	1723
3.01.4.5.2	Wetting and drying	1723
3.01.4.5.3	Applications	1724
3.01.4.5.4	Next generation weathering steels	1725
3.01.4.6	Classification of Atmospheres	1725
3.01.5	Corrosion in Water	1726
3.01.5.1	Water Composition	1726
3.01.5.1.1	Dissolved gases	1726
3.01.5.1.2	Dissolved solids	1727
3.01.5.1.3	Microbial effects	1728
3.01.5.2	Deposits and Scales	1728
3.01.5.2.1	Fouling of surfaces	1728
3.01.5.2.2	Under-deposit corrosion	1728
3.01.5.3	Natural Waters	1728
3.01.5.3.1	Corrosion rates	1728
3.01.5.3.2	Piped fresh water systems	1729
3.01.5.3.3	Structural steel in waters	1729
3.01.5.3.4	Variation of corrosion with height	1730
3.01.5.4	Process Waters	1730
3.01.5.4.1	Heating and cooling systems	1730
3.01.5.4.2	Boiler waters	1731
3.01.6	Underground Corrosion	1731
3.01.6.1	Controlling Factors	1731
3.01.6.2	Corrosion of Buried Steel	1732
3.01.6.2.1	Piling	1732
3.01.6.2.2	Pipelines	1733
3.01.6.2.3	Long-term burial	1733
References		1733

---

## Glossary

**Akaganeite** Hydrated iron oxide,  $\beta$ -FeO(OH,Cl), that is stable in the presence of chloride ions and thus generally forms in seawater.

**Goethite** Stable form of hydrated iron oxide, FeOOH and thus commonly found in nature.

**LAMM phase** The structure of the passive film on iron.

**Lepidocrocite** Metastable form of hydrated iron oxide, FeOOH and commonly found during atmospheric corrosion of iron-based alloys.

## Abbreviations

**ALWC** Accelerated low water corrosion

**BISRA** British Iron and Steel Research Association

**BS EN** British Standard European Norm

**FAC** Flow-assisted corrosion  
**ISO** International Standards Organisation  
**MIC** Microbiologically assisted corrosion  
**NACE** National Association of Corrosion Engineers  
**NBS** National Bureau of Standards  
**RH** Relative humidity  
**SIMS** Secondary ion mass spectrometry

## Symbols

**ads** Adsorbed  
**C** Concentration of species  
**F** The Faraday or Faraday's constant  
 **$i_{lim}$**  Diffusion limited current density  
 **$k$**  Mass transfer coefficient  
 **$n$**  Number of electrons transferred in an electrochemical reaction  
 **$t$**  Time  
 **$\alpha$**  Ferrite  
 **$\gamma$**  Austenite  
 **$\omega$**  Angular velocity

## 3.01.1 Introduction

### 3.01.1.1 Historical Perspective

Prior to the sustained and deliberate production of iron, there is some evidence that ferrous materials (i.e., iron–nickel) derived from meteors were used intermittently in antiquity although they must have been relatively rare. The development of iron production dates back more than 3000 years (1500–1200 BC) when ferrous ores began to be smelted in the ancient Near East civilizations (i.e., Iran, India, Mesopotamia, and Anatolia), which apparently coincided with a shortage of tin for the production of bronze. In Europe, iron began to be produced somewhat later, in the period from the eighth to the sixth century BC.<sup>1</sup>

A feature of early iron production was the relatively limited temperature that the furnaces of the time could achieve. In practice, this was not necessarily a disadvantage as the process involved the use of wood charcoal to reduce iron ore in the solid state leaving a porous mass of relatively pure solid iron (of variable composition) mixed with the ore residues (slag) resulting in a 'bloom.' Subsequently, the skill of the smith was required to repeatedly forge the hot bloom in order to remove the majority of the slag inclusions, resulting in a product known as 'wrought' (i.e., forged) iron. Subsequent adjustments in carbon

content were made by cementation type processes, effectively by successively placing the semifinished object in hot charcoal or air.

This method of iron production remained, essentially unchanged in Europe, for 1500 years. However, in China development of iron smelting techniques that were able to reach temperatures of  $\sim 1150^{\circ}\text{C}$  and, consequently, were able to melt cast iron (when combined with  $\sim 4\%$  carbon) was achieved in  $\sim 500$  BC. Methods for reducing the carbon content of such cast irons were necessary in order to achieve a malleable material, and this was achieved by heating the molten material in air with stirring. During this process iron oxide, formed by oxidation of the molten metal, was stirred into the melt and reacted with dissolved carbon producing carbon monoxide, thus lowering the overall carbon content. In Europe, the development of water power was applied to the bloomery forging process in order to increase production of steels from 1000 AD onwards. However, cast irons were not generally produced as knowledge of how to reliably reduce their carbon content was not introduced until the Middle Ages (i.e., from 1100 to 1300 AD onwards) where a process similar to the Chinese one was used in so-called 'puddling' furnaces. Later developments included the manufacture of limited quantities of high quality steels via crucible and similar methods.

Large scale cast iron manufacture in blast furnaces developed only after the switch from wood charcoal (a limited resource) to coke derived from coal in the late seventeenth and early eighteenth centuries, while mass production of steel had to wait until Bessemer's invention of the converter in 1855, which utilized a hot air draught from below to remove carbon by reaction with oxygen. Until these developments, steel was an expensive commodity used only for niche applications where its combination of properties was essential. The widespread production of steel lowered its cost such that it could be used for an increasing number of applications, and eventually mild steel completely replaced wrought iron. Advances in the production of steel to further lower costs have continued as have alloy developments to further expand the use of ferrous materials. Nowadays, steel is a ubiquitous and essential component of modern life.

### 3.01.1.2 Iron–carbon Alloys

#### 3.01.1.2.1 Phase diagram

Carbon is generally present in steel at room temperature as iron carbide ( $\text{Fe}_3\text{C}$  or cementite). This phase



is strictly metastable to decomposition to graphite and iron, however, the reaction is very sluggish at lower carbon contents although graphite evidently forms preferentially in, for example, grey cast irons. The iron–carbon phase diagram (drawn with cementite as the stable phase) is reproduced in **Figure 1**. The room temperature allotrope of unalloyed iron is known as ferrite ( $\alpha$ -iron) and has a body-centered cubic structure; above 910 °C, this transforms to  $\gamma$ -iron or austenite (face-centered cubic) that, in turn, transforms to  $\delta$ -iron (also body-centered cubic) above 1394 °C prior to melting at 1538 °C. Alloying with carbon lowers the melting point, eventually to the Fe–C eutectic temperature of 1140 °C forming effectively cast iron. Note that the solubility of carbon in ferrite is extremely low (around 0.03% at 723 °C and <0.01% at room temperature).

For practical purposes, iron may be defined as a material that contains carbon only up to its solubility limit in ferrite (i.e., <0.03% C by mass), while steel contains carbon within its solubility limits in austenite (i.e., from ~0.03% to 2.05% C by mass). In practice, most steels contain typically from 0.05% to 1.0% of carbon, with the majority of alloys lying at the lower end of this scale (i.e., 0.05–0.5% carbon),

although some specialized alloys may have compositions that lie outside these values. Steel also contains elements such as silicon, phosphorus, and sulfur that arise inevitably from the steel-making process and which may affect properties detrimentally unless limited or controlled. For example, sulfur forms a low melting point eutectic with iron, and hence, limits the ability of the steel to be processed at higher temperatures. Thus, plain carbon steels traditionally contain sufficient added manganese (15–20 times that of sulfur) to ‘mop-up’ the sulfur via the formation of MnS precipitates. However, increased amounts of manganese are also beneficial in, for example, solid solution hardening of ferrite, and improving the ductility and toughness of the alloy.

‘Plain carbon steel’ may be defined as an alloy of iron with carbon where the total quantity of alloying elements is less than 2% by mass with compositional limits of 0.6% for copper, 1.65% for manganese, 0.04% for phosphorus, 0.6% for silicon, and 0.05% for sulfur and where no other elements are deliberately added in order to provide a specific property or attribute. This somewhat convoluted definition is necessary to exclude some low-alloyed steels (e.g., with small amounts of chromium, cobalt, niobium, molybdenum, nickel,

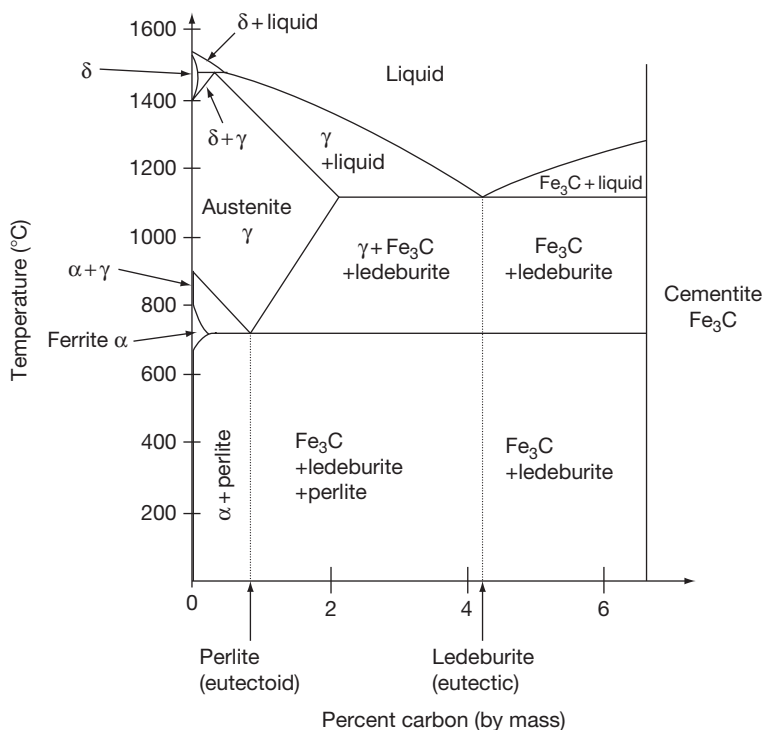


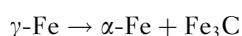
**Figure 1** Iron–carbon phase diagram (note ‘perlite’ is an alternative spelling of ‘pearlite’). Reproduced here under the Gnu Free Documentation License from its original source at [www.wikipedia.org](http://www.wikipedia.org).

titanium, vanadium, etc.) that otherwise might be classed as 'plain carbon.' In contrast, 'low alloy steels' contain deliberate additions of alloying elements up to 10% by weight so as to develop enhanced mechanical properties. Finally, 'high alloy steels' contain more than 10% by weight of alloying additions and include materials such as stainless, tool, and maraging steels. Alloying additions may also be classed with respect to their effects on the stability of the ferrite and austenite phase regions. Thus, carbon, nitrogen, manganese, nickel, and cobalt all tend to expand the austenite phase region (i.e., are austenite stabilizers), while silicon, chromium, molybdenum, niobium, vanadium are ferrite stabilizers.

Carbon steels typically comprise more than 85% of steels produced and shipped worldwide and are, therefore, by far the most frequently used iron-carbon alloy. It is usual to categorize steels by their carbon content, but the specific boundaries are not well-defined. Generally, low-carbon steel ('dead mild' steel) contains up to ~0.15% carbon and 0.3–0.6% manganese by mass. It has relatively low strength but high formability, and is used typically in sheet and strip products. Mild steel contains from 0.15% to 0.3% carbon and is used in flat rolled products where higher strengths are required. For structural steelwork, plates and rolled sections, forgings and stampings of the manganese content can be increased to ~1.5% to improve toughness. Medium-carbon steels with 0.3–0.6% carbon and 0.60–1.65% manganese allow the use of quenched and tempered heat treatments with applications in axles, gears, forgings, rails, etc. Finally high-carbon steels containing 0.6–1.0% carbon and 0.3–0.6% manganese are used for high strength applications such as springs and wires. Materials with carbon content greater than 1% are typically insufficiently tough to be used for structural purposes, but find application where high hardness and abrasion resistance is required, for example, as machine tools, saw blades, etc.

### 3.01.1.2.2 Equilibrium microstructures

The iron-carbon phase diagram can be seen to be dominated by the pearlite eutectoid reaction (important for steel) and the ledeburite eutectic reaction (important for cast iron, and not considered further here). The pearlite reaction comprises the diffusion-controlled decomposition of austenite to ferrite and iron carbide at the eutectoid composition (~0.8% C by mass) and temperature (723 °C):



At carbon content below the eutectoid composition (hypoeutectoid <0.8% C), ferrite will form first, while at higher carbon content cementite will form first (hypereutectoid >0.8% C); both phases nucleating preferentially at the austenite grain boundaries. Pearlite (or perlite) is not a phase itself but it is rather a two-phase mixture of ferrite (~88%) and cementite (~12%) that forms in alternating laths (strips); it is so-called because of its characteristic pearl-like appearance. **Figure 2** shows representative steel microstructures of varying compositions. The individual laths of ferrite and cementite are often not easily resolved in commercial alloys using optical microscopy, however, they are visible in the higher carbon content material, **Figure 2(c)**.

Since the transformation is diffusion controlled, the spacing between the ferrite and cementite laths in pearlite varies as a function of cooling rate with slow (i.e., furnace) cooling giving the widest spacing and faster cooling giving closer spacing. Ferrite itself has a rather low yield stress, so the overall strength of the steel is dependent on the nature and spacing of second phase particles, including the individual pearlite colonies as well as the pearlite lamellae and any other phase that happens to be present.

### 3.01.1.2.3 Nonequilibrium microstructures

If steel is cooled faster than the rate at which carbon can be rejected by diffusion from the austenite lattice, the consequent formation of equilibrium iron carbide is partially or wholly suppressed. Under these circumstances, the austenite cannot retain the excess of carbon within its structure due to its thermodynamic instability and must transform via an alternative mechanism. At sufficiently low temperatures where essentially no significant diffusion of carbon can occur, the thermodynamic driving force is able to overcome the lattice strains inherent in a diffusionless (shear) transformation and martensite, which is a distorted body-centered tetragonal structure, will form directly. At intermediate temperatures where limited diffusion of carbon can still occur, the bainite structure forms by transformation of austenite to carbon-supersaturated ferrite with the subsequent diffusion of carbon and the precipitation of carbides either in untransformed austenite (upper bainite) or within the ferrite (lower bainite). The detailed mechanisms of these transformations and their microstructures are complex and beyond the scope of this work, however, the concept is important in understanding the properties of steel and particularly how they may be altered beneficially by heat treatment.

The advantage in rapid cooling (or quenching) of steel is that carbon is then held uniformly in the martensite phase in supersaturated solid solution. Martensite itself is very brittle and hard and, consequently, has limited uses. However, when martensite is reheated sufficiently, the retained carbon is able to diffuse and precipitate as fine carbides that are relatively evenly distributed in the material. In contrast, in pearlitic steel, the strengthening phase is both unevenly distributed (i.e., in pearlite

colonies) and present in thin strips that are more likely to act as crack initiators. **Figure 3(a)** shows a quenched martensitic structure, while **Figure 3(b)** shows the same material but after aging (tempering) at an elevated temperature in order to precipitate the carbide particles. The even distribution of carbides is evident and compared with a pearlitic microstructure of similar carbon content, results in greatly increased fracture toughness at similar yield stress.

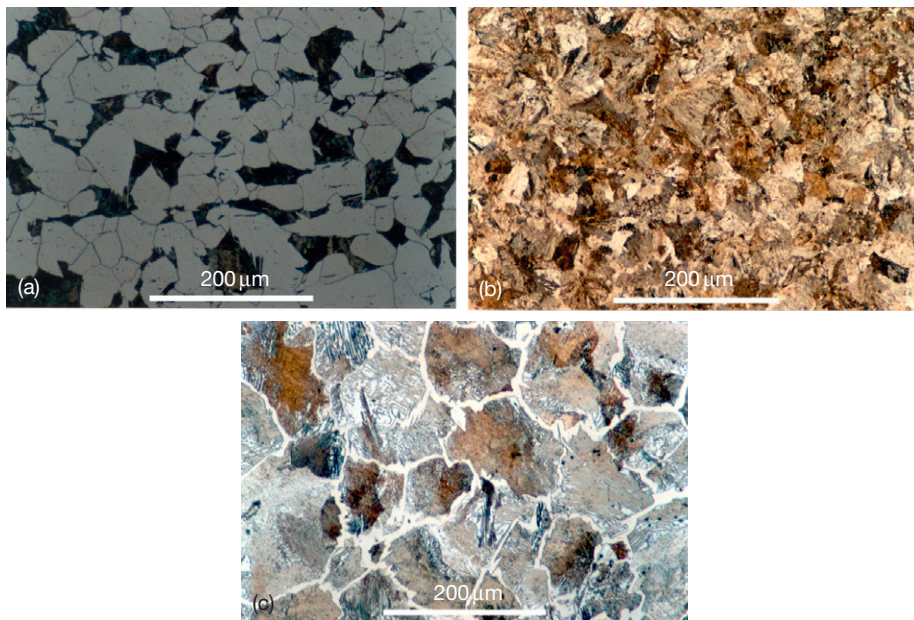


**Figure 2** Pearlitic microstructures in steel (air cooled) (a) Hypoeutectoid (0.2% C; ferrite, light, with pearlite colonies, dark, elsewhere in the structure). (b) Eutectoid composition (0.8% C; fully pearlitic). (c) Hypereutectoid (1.3% C; cementite has nucleated on former austenite grain boundaries with pearlite elsewhere in the structure). Reproduced by kind permission of Cochrane, R. F. University of Leeds and the DoITPoMS Micrograph Library ([www.doitpoms.ac.uk](http://www.doitpoms.ac.uk)).

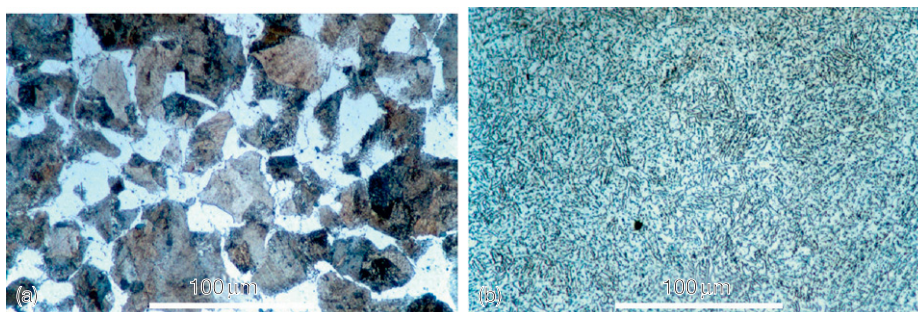


**Figure 3** Annealed, compared with quenched and tempered, steel microstructures. (a) 0.31% C annealed showing pearlite colonies of ferrite and cementite between grains of ferrite. (b) as (a) but quenched to form martensite then tempered to precipitate a fine carbide distribution of cementite. Reproduced by kind permission of Cochrane, R. F. University of Leeds and the DoITPoMS Micrograph Library ([www.doitpoms.ac.uk](http://www.doitpoms.ac.uk)).

### 3.01.1.3 Mechanical and Physical Properties

Alloying greatly decreases the thermal and electrical conductivities of pure iron but has little effect on other physical properties such as the elastic modulus. Regarding mechanical properties, pure iron (ferrite) is soft and malleable but work-hardens rapidly, **Table 1**. Ferrite can be solid-solution strengthened by either interstitial (e.g., C, N, and P) or substitutional (e.g., Si and Mn) alloying additions. Silicon and manganese, which are always present in iron at levels of  $\sim 0.3$ – $0.5\%$ , provide some solid-solution strengthening of the ferrite; phosphorus gives much stronger solid-solution strengthening but is not commonly added deliberately as it can greatly reduce toughness. Carbon and nitrogen have the greatest potential effect but have very low solubilities in ferrite.

As noted above, carbon-containing alloys (i.e., steels) are mainly strengthened by the formation of second phase carbide precipitates. In plain carbon steels, these comprise iron carbides that may form as pearlite colonies or, after quenching and tempering, as a fine carbide distribution in the microstructure. In low alloy steels, the addition of elements such as molybdenum, titanium, vanadium, chromium, niobium, and nickel either promote the formation of alloy carbides or control the formation of martensite and/or the favorable precipitation of iron carbides.

Like other body-centered cubic metals, steels are subject to a ductile-to-brittle transition and this may occur close to ambient temperatures depending upon the type of steel, its alloying contents (including carbon, manganese, etc.), and how it has been processed. Clearly, it is usually advisable for the ductile-to-brittle transition temperature to fall well below operating temperatures in order to ensure adequate fracture toughness during service. Key factors that influence the transition temperature include microstructure, carbide distribution, internal stress, and the composition of the ferrite phase.

It is beyond the scope of this chapter to discuss the detailed effect of microstructure, composition, etc. on the overall mechanical properties of steels and, hence, interested readers are directed to Llewellyn *et al.*<sup>3</sup> and Bhadeshia *et al.*<sup>4</sup> for further information.

### 3.01.1.4 Processing

#### 3.01.1.4.1 Heat treatment

The main purpose of heat treatment is to optimize the mechanical properties of a particular steel grade. This typically involves a single or a series of heating and cooling operations designed to produce an optimum microstructure for the particular end use. These processes can be divided conveniently into: softening (or annealing), normalizing, hardening, and tempering treatments.

General process annealing is carried out on cold-worked materials in order to relieve internal stresses and/or to soften them prior to further cold work. Full annealing is carried out by heating the steel into the austenite phase region (if a hypoeutectoid steel), or just above the eutectoid temperature (if hypereutectoid) followed by slow (e.g., furnace) cooling that results in a relatively coarse lamellar pearlite. Normalizing involves the same heat treatment, however, the cooling is more rapid and carried out in air, which results in a decrease in the size of microstructural features (grain size and pearlite lamellae spacing) and consequent increased final hardness.

Hardening of hypoeutectoid steels involves heating into the austenite phase region followed by rapid cooling (or quenching). As the cooling rate is increased, the formation of pearlite occurs at lower temperatures resulting in an increasingly finer lamellar structure, until at a critical cooling rate that depends on the alloy content of the steel, martensite is formed directly. Tempering of hardened steel is achieved by reheating to various temperatures below the austenite boundary with the intention to relieve internal stresses

**Table 1** Generic properties for annealed ferrous alloys

Property	Iron (>99.9% Fe)	Carbon steel (0.15%C)	Stainless steel (18%Cr, 10%Ni)
Density ( $\text{Mg m}^{-3}$ )	7.86	7.86	8.00
Elastic modulus (GPa)	200	200	195
Thermal conductivity ( $\text{W m}^{-1} \text{K}^{-1}$ )	76.2	20–65	16.2
Electrical conductivity ( $10^6 \Omega^{-1} \text{m}^{-1}$ )	11.2	6.23	1.45
Ultimate tensile strength (MPa)	>200	385	565
Proof Stress at 0.2% strain (MPa)	$\sim 70$	285	210
Elongation (%)	>40	35	55

Source: Data taken from Smithells Metals Handbook.



induced by quenching and to permit the diffusion of carbon retained in the martensite matrix in order to precipitate a relatively even distribution of carbides. Tempering at 100–200 °C is sufficient to relieve quenching stresses only. However, at temperatures between 200 °C and 450 °C the martensite will decompose into ferrite by precipitation of fine particles of carbide throughout the structure decreasing yield strength but increasing toughness. At higher temperatures still (i.e., 450–650 °C) fewer but larger carbide particles are produced further increasing the toughness and reducing the strength. Microstructures formed in this way are known as tempered martensites and vary in microstructure from relatively large ferrite grains containing second phase carbides to small, fine-grained structures similar to bainite. Generically, these steels are known as quenched and tempered.

The details for steel heat treatments are complex and those given above merely summarize the main elements; further details can be found in *Steel Heat Treatment Handbook*.<sup>5</sup> In some cases, heat treatment alone cannot provide the desired structure, and some form of thermo-mechanical treatment is necessary. For example, some low alloy and microalloyed steels (high-strength low-alloy steels) develop exceptional combinations of strength, toughness, and low ductile-to-brittle transition temperature by virtue of a controlled process combining a gradually decreasing temperature with simultaneous rolling of the steel.

After processing (rolling, forging, forming, etc.) at elevated temperatures, a layer of oxide, called millscale, inevitably would have formed on the metal surface. The structure of millscale consists of three superimposed layers of iron oxides in progressively higher states of oxidation from the metal side outwards: ferrous oxide (FeO) on the inside, magnetite (Fe<sub>3</sub>O<sub>4</sub>) in the middle, and ferric oxide (Fe<sub>2</sub>O<sub>3</sub>) on the outside. The relative portions of the three oxides vary with the processing temperatures. A typical millscale on 9.5 mm mild steel plate would be ~50 µm thick, and contain ~70% FeO, 20% Fe<sub>3</sub>O<sub>4</sub>, and 10% Fe<sub>2</sub>O<sub>3</sub>. If millscale was perfectly adherent, continuous, and impermeable, it would form a good protective coating, but in practice millscale is liable to crack and flake off exposing the underlying metal. During atmospheric exposure, the presence of millscale on the steel may reduce the corrosion rate over comparatively short periods, but over longer periods, the rate tends to rise as the oxide flakes off the surface. In water, severe pitting of the steel may occur if large amounts of millscale are present on the surface.

For example, pits up to 1.25 mm deep were found on as-rolled steel specimens after 6 months immersion in sea-water at Gosport.<sup>6</sup> It follows that for most practical purposes where steel is exposed without a protective coating, or indeed to achieve effective coatings adhesion to the substrate, it is essential to remove all millscale either before putting components into service or prior to application of a protective coating.

#### **3.01.1.4.2 Mechanical deformation**

The vast majority of steel products are produced by mechanical deformation either while ‘hot’ (i.e., above the recrystallization temperature of the alloy) or ‘cold’ (i.e., below the recrystallization temperature); in the latter case, if continued processing is required, periodic annealing is necessary in order to remove the effects of work-hardening. Such processes include: rolling (plate, strip, and bar products, etc.), forging, stamping, wire drawing, etc. Both hot and cold deformation will produce a varying degree of banding and texture in the resultant microstructure, which may result in properties that vary according to the deformation direction, [Figure 4](#). Nonmetallic second-phase inclusions that originally derive typically from slag materials incorporated during the steel-making process will tend to form stringers in the metal during rolling operations. These can form planes of weakness in the steel, although modern clean steel making technology has greatly reduced the volume fraction and distribution of such unwanted second phases.

#### **3.01.1.4.3 Metallurgical influences on corrosion**

Generally, the process of manufacture has no appreciable effect on the corrosion characteristics of carbon steel. Slight variations in composition that inevitably occur from batch to batch in steels of the same quality have little effect with the exception of a limited number of elements in a small (but important) number of applications. For example, the addition of ~0.2% of copper results in a two- to threefold reduction in the atmospheric corrosion rate compared with a copper-free steel.<sup>7,8</sup> Variation in other alloying additions in carbon steel affects the corrosion rate to a marginal degree, the tendency being for the rate to decrease with increasing content of carbon, manganese, and silicon. Thus, steel containing 0.2% of silicon rusts in air ~10% slower than an otherwise similar steel containing 0.02% of silicon. Otherwise, all ordinary ferrous structural materials, that is, carbon and low-alloy steels, corrode at virtually the same rate when immersed in natural waters.



As shown in the historic data of **Table 2**, the process of manufacture and the composition of mild steel do not affect its corrosion rate appreciably.<sup>9</sup>

In carbon steels, the effect of microstructural anisotropy caused by processing is also generally not significant. Thus, in seawater immersion tests, carried out to determine the effects of rolling direction and tensile stress on the corrosion of a steel containing 0.14% C, 0.47% Mn and 0.04% Si,<sup>10</sup> specimens were cut from plates parallel to and perpendicular to the rolling direction. There was little difference in general corrosion performance, although pitting was somewhat worse on the plate cut parallel to rolling.

For low alloy steels generally under immersed conditions, alloying additions of at least 3% (e.g., of chromium, nickel, etc.) are necessary to obtain any marked improvement in the corrosion-resistance.

The main elements that alter the rate of corrosion of low alloy steels when immersed in natural waters are aluminum, copper, chromium, molybdenum, and nickel, but other additions, for example, manganese, silicon, phosphorus, and sulfur, may have minor roles. The action of some alloying elements can be beneficial, neutral, or detrimental, depending upon whether localized or uniform corrosion is being considered and whether the steel is fully, partially, or intermittently immersed. A large program of work between a number of research laboratories in Europe was carried out over an extended period to study the influence of alloying elements on corrosion of low alloy steel<sup>11</sup> and the main findings, which are summarized in **Table 3**, are still relevant.

From a consideration of **Table 3**, steel containing copper and phosphorus might be chosen for its resistance to corrosion in the critical tidal and splash zone.

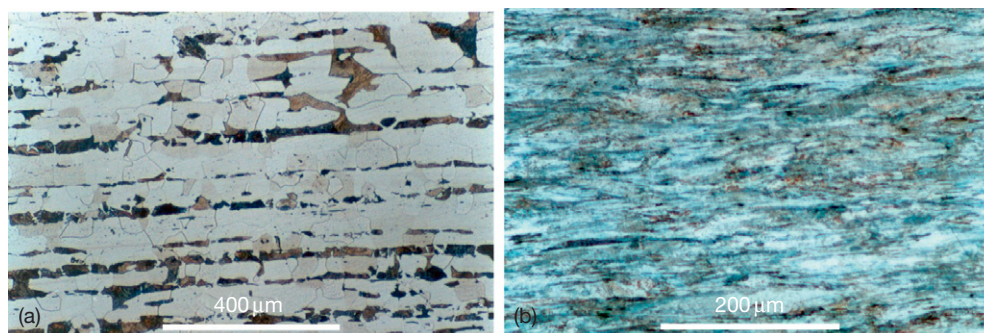


**Figure 4** Directionality in microstructure after mechanical deformation. (a) 0.2% C steel after hot rolling showing banded carbide microstructure. (b) 0.6% C steel after cold wire drawing showing highly deformed grain structure. Reproduced by kind permission of Cochrane, R. F. University of Leeds and the DoITPoMS Micrograph Library ([www.doitpoms.ac.uk](http://www.doitpoms.ac.uk)).

**Table 2** Corrosion rates of mild steels in seawater, total immersion for 203 days at Plymouth

Type of steel <sup>a</sup>	Analysis (%)				Average general penetration (mm year <sup>-1</sup> )
	C	Mn	P	S	
Basic Bessemer, rimming ordinary	0.05	0.64	0.06	0.02	0.143
High phosphorus	0.03	0.31	0.14	0.04	0.143
High phosphorus and sulfur	0.03	0.30	0.10	0.07	0.148
Open-hearth, rimming ordinary	0.13	0.33	0.03	0.03	0.143
From haematite pig	0.06	0.32	0.01	0.03	0.140
Open-hearth, killed ordinary	0.10	0.35	0.03	0.02	0.140
From haematite pig	0.11	0.34	0.01	0.03	0.136
Open-hearth, killed ordinary	0.22	0.71	0.03	0.03	0.143
From haematite pig	0.21	0.58	0.02	0.03	0.158

<sup>a</sup>The copper contents of the steels, which were supplied through the courtesy of l'Office Technique pour l'Utilisation de l'Acier (France), varied from 0.03 to 0.11%. The killed steels contained 0.04% Al and 0.1% Si.

Source: After Hudson, J.C. *J. Iron Steel Inst.* **1950**, 166, 123.

**Table 3** Effect of alloying elements on marine corrosion resistance

Corrosion type	Environment	Favorable	Neutral	Unfavorable
Uniform corrosion	Marine immersion	Mn, Si, Al, Mo (> 4 years), Cr (< 4 years)	Ni	P, S, Cu, Mo (> 4 years), Cr (< 4 years)
Uniform corrosion	Tidal and splash zone	P	Cu, Cr, Ni	–
Uniform corrosion	Marine atmosphere	P, Si, Mn, Cu, Cr, Ni	–	–
Pitting corrosion	Marine immersion	–	Cu, Cr	Ni
Pitting corrosion	Tidal and splash zone	Cu	Ni	Cr

Source: After Songa, T. International Conference on Steel in Marine Structures, Paris, ECSC: Luxembourg, 1981.

However, in practice the sample-to-sample variation in corrosion rate is much greater than the difference between various alloy steels, so it is improbable that low-alloy steels will corrode more slowly than mild steel in most practical environments. This conclusion was supported by Forgeson *et al.* in the 1960s who concluded from extensive tests in fresh and salt waters of the Panama Canal Zone that: “proprietary low-alloy steels were not in general more resistant to underwater corrosion than the mild unalloyed carbon steel.”<sup>12</sup> In any case, it is rare to expose unprotected steel in this way without a reliable corrosion control method such as cathodic protection also being applied.

The generally negligible effects of alloying additions on the corrosion of low alloy steels under immersed conditions were also reported in historic work from the 1930s to 1950s by the former British Iron and Steel Research Association (BISRA) in the UK<sup>13</sup> and the National Bureau of Standards (NBS) in the USA.<sup>14</sup> The latter work was rather extensive and involved ten varieties of steel (as well as cast irons), which were buried in 15 typical American soils from 1937 to 1950. The results showed that, with few exceptions, the corrosion of low-alloy steels containing copper, nickel, and molybdenum in various combinations did not differ by more than 20% from that of ordinary carbon steel. The main exception was chromium, where additions of 2% or 5% of chromium did increase the corrosion resistance somewhat, as is indicated in Figure 5.

### 3.01.2 Electrochemistry

#### 3.01.2.1 Thermodynamics

Iron is a relatively active element whose domain of stability resides completely below that of the domain of stability for water. Thus, in principle, iron can evolve hydrogen from aqueous solutions at all pH, Figure 6. In practice, hydrogen evolution occurs readily only at low pH (i.e., below ~pH 3); at higher pH, although it

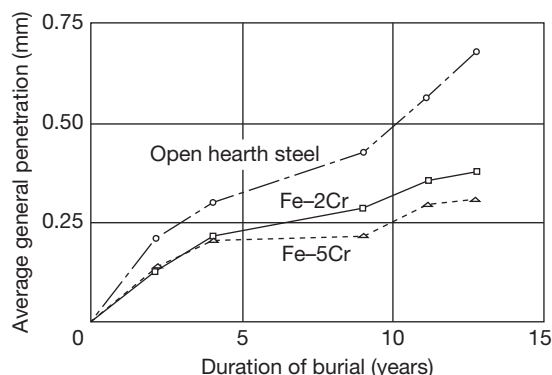


**Figure 5** Effect of chromium content on the corrosion of buried steel. Reproduced from Romanoff, M. Underground Corrosion, National Bureau of Standards Circular 579, US Government Printing Office, Washington, 1957.

is thermodynamically possible, hydrogen evolution is very slow at ordinary temperatures due to the low driving force and sluggish kinetics. At intermediate pH, iron passivates and at higher pH iron may dissolve as the ferroate oxyanion, although this reaction is sluggish and passive iron is practically stable to pH 13 and above (e.g., in concrete). Iron corrodes readily, therefore, in near-neutral oxidizing environments, including: the atmosphere, natural waters in equilibrium with atmospheric carbon dioxide and seawater, however, the rate of corrosion in oxygen-free neutral waters is much less and controlled by the stability of the passive film. Iron is more active than elements such as nickel, copper, cobalt, etc. but is more noble than zinc, aluminum, magnesium, etc. Thus, the latter elements are, in practice, important for use as sacrificial anodes for the cathodic protection of steel. Apart from a few exceptions in specific circumstances, minor variations in the composition of steel generally have minimal effect on the overall electrochemistry and, hence, the corrosion rates.

Iron has two stable oxidation states: ferrous (+2) and ferric (+3). Typically, divalent ferrous species are

considerably more soluble in aqueous solution than the trivalent ferric species, which have significant solubility only at low and high pH. The oxides and hydroxides of iron are complex and interrelated crystallographically; furthermore, many of the ferric

oxides undergo reductive dissolution to soluble ferrous species, such as the  $\text{Fe}(\text{OH})^+$  ion. **Figures 6 and 7** show a Pourbaix diagram for the limits of stability of soluble iron species at a concentration of  $10^{-5}$  M.

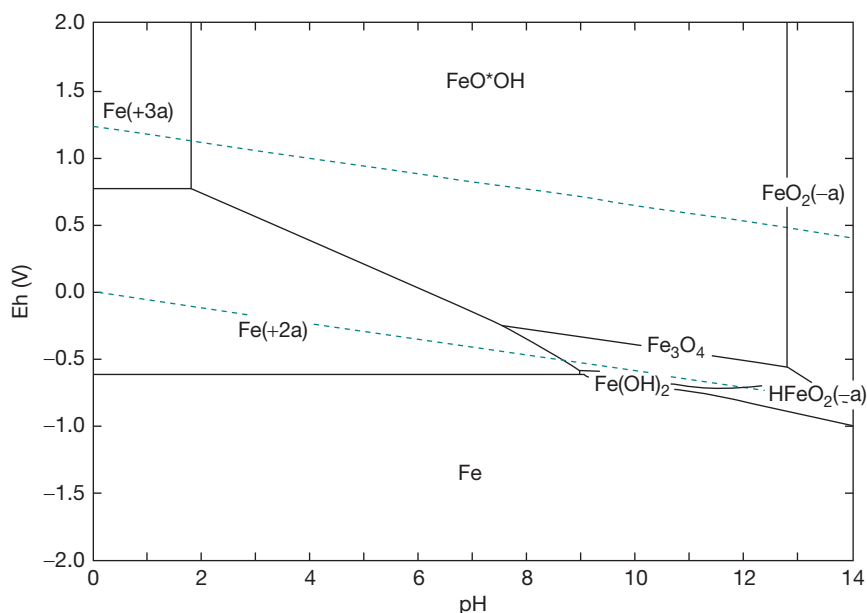


**Figure 6** Pourbaix diagram for iron with soluble species at concentration of  $10^{-5}$  M, and with the most frequent stable oxide species present. Calculated using HSC version 6.12 thermochemical modelling software, Outotec, Finland.

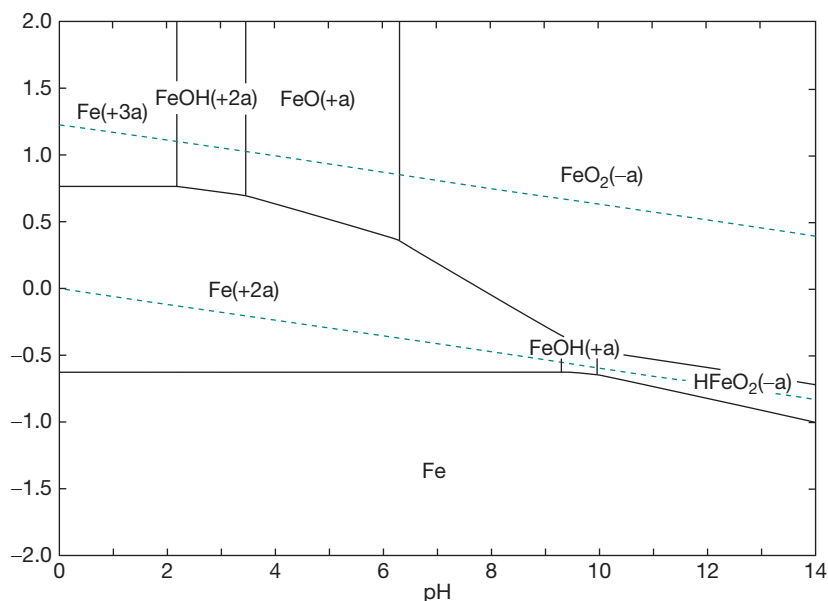
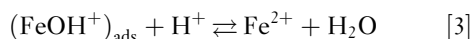
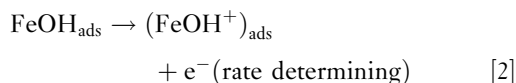


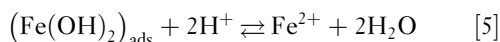
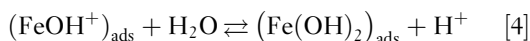
**Figure 7** Pourbaix diagram for soluble species only (i.e., excluding solid species) at a concentration of  $10^{-5}$  M. Calculated using HSC version 6.12 thermochemical modelling software, Outotec, Finland.

**3.01.2.2 Anodic Dissolution****3.01.2.2.1 Oxygen-free (deaerated) conditions**

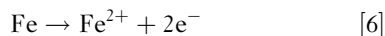
The mechanism for the dissolution of iron, whether in aerated or deaerated conditions, varies as a function of pH and, despite extensive investigation by Bockris,<sup>15–18</sup> Drazic,<sup>19,20</sup> Lorenz,<sup>21,22</sup> Hackerman,<sup>23</sup> and others, is still not entirely resolved. One of the complications is that the mechanism is greatly influenced by a number of factors including the nature of the anions present in solution. The most commonly accepted generic reaction sequence in deaerated acid conditions is due to Bockris, Drazic, and Despic<sup>17</sup> where a reaction order of  $\sim 1$  with respect to hydroxide ion concentration (i.e., the kinetics are a function of pH) was determined for the anodic dissolution of iron at pH < 4. This broadly fits the following reaction sequence:



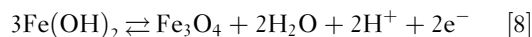
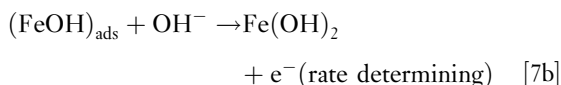
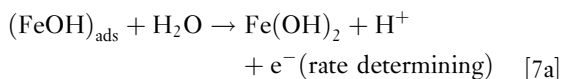
Thus, adsorption of water initially occurs onto the iron surface together with the first single electron transfer step giving rise to a transient intermediate ( $\text{FeOH}_{\text{ads}}$ ). The second electron transfer step, giving rise to the stable  $\text{Fe}(+2)$  oxidation state, occurs subsequently and is rate determining. In near neutral solution ( $4 < \text{pH} < 9$ ) this sequence is modified slightly<sup>24</sup> and after reaction [2] above, the following sequence holds:



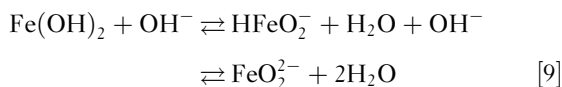
In both cases, the overall reaction is the familiar:



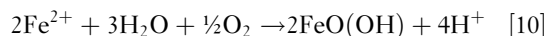
In alkaline solution ( $\text{pH} > 9$ ), and in the absence of oxygen, passivation of the iron surface occurs after reaction [4] with the initial formation of ferrous hydroxide, reactions [7] below and subsequent oxidation to magnetite:



Finally, strong alkali ferrous hydroxide can chemically dissolve as the dihypoferrite anion that is in equilibrium with the hypoferrite (ferroate) anion:

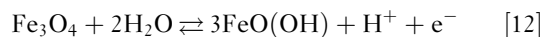
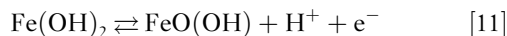
**3.01.2.2.2 Oxygen containing (aerated) conditions**

When dissolved oxygen is present, ferrous species are unstable to further oxidation in solution to ferric species, which have considerably lower solubility products and are liable to precipitation giving rise to the familiar rust corrosion product. Thus, in aerated near-neutral to acid conditions, ferrous ions are oxidized by dissolved oxygen in solution, with  $\text{FeO}(\text{OH})$  as the end product (other oxides/hydroxides are possible):



Any formed ferric oxide will immediately precipitate giving rise to the familiar brown staining that denotes rusting. If precipitation occurs close to the metal surface (as is likely in aerated solution), oxide will tend to build up on the iron, although this will not be in a coherent and impermeable manner. Hence, rust layers formed in this way can only provide a diffusion restriction for the corrosion of iron and steel and do not result in passivation.

In alkaline environments at  $\text{pH} > 9$ , passive ferrous hydroxide and magnetite (in which 1/3 of the iron atoms are in the ferrous state and 2/3 ferric) are also susceptible to further oxidation to ferric hydroxide:



However, in these cases, the reaction occurs in the solid state and the iron remains passive with the advantage that ferric hydroxide has a greater thermodynamic stability range. Note that the oxidation of ferrous hydroxide and magnetite to ferric hydroxide is reversible and, hence, the passive film is unstable to electrochemical reduction.

**3.01.2.2.3 Anion adsorption effects on the mechanism of dissolution**

As key steps in the anodic dissolution mechanism for iron involve the adsorption of water or hydroxyl ions,

it is evident that the presence of other anions that compete for adsorption will influence the concentration of the adsorbed hydroxyl intermediate and, in consequence, the corrosion rate. For example, the effect of halide ions on the corrosion rate of iron in acid media has been known for over 80 years.<sup>25</sup> Although, it is widely assumed that halides are uniformly aggressive (i.e., increase corrosion rates), this is not universally the case, and at low-to-intermediate concentrations in acid, they can act as effective inhibitors. For example, iodide ions inhibit corrosion of mild steel in 0.5 M H<sub>2</sub>SO<sub>4</sub> at concentrations less than  $\sim 10^{-2}$  M with an inhibition efficiency (i.e., percentage reduction in corrosion rate) of up to 90%.<sup>26</sup> The effectiveness of inhibition decreases in the order: I<sup>-</sup>, Br<sup>-</sup>, and Cl<sup>-</sup>, which is consistent with the adsorption efficiency of the anions and confirmed by electrochemical impedance spectroscopy measurements of surface capacitance. Species that are only weakly absorbing (such as perchlorate) have no significant effect on the corrosion rate. Of course, a distinction here has to be made between species that interfere directly with the anodic dissolution process and species that interfere with a cathodic reaction such as hydrogen evolution. A large class of organic inhibitors for corrosion in acids (e.g., pickling inhibitors) act by adsorbing onto the surface of the steel and, hence, block either or both of the electrochemical reactions.<sup>27</sup>

### 3.01.2.3 Passivity

#### 3.01.2.3.1 Passive oxide films

The phenomenon of passivity was probably first recorded by James Keir in 1790 on the exposure of iron to concentrated nitric acid.<sup>28</sup> He noticed that if the concentration of nitric acid was sufficiently high, gas evolution appeared to cease and the iron appeared to be in a quiescent state. This 'passive' state of iron was later explained by Michael Faraday in 1836 and, given the undeveloped state of knowledge at the time, his comments are immensely prescient<sup>29</sup>:

... my impression is that the surface of the metal is oxidised or else that the superficial particles of the metal are in such relation to the oxygen of the electrolyte as to be equivalent to oxidation ...

Passivity is now known to be caused by the formation of an oxidized species on a metal surface under the correct conditions of potential and pH. Thus, on formation of a more-or-less thermodynamically stable, compact, and continuous film on a metal surface,

the kinetic processes involved in corrosion (e.g., electron and ion charge transfer, diffusion of reacting species, etc.) are slowed by many orders of magnitude. For ferrous alloys, and as indicated above, passivity occurs at intermediate pH and at sufficiently high oxidizing potentials and results in the formation of an oxide film. The literature on passivity in general, and on passivity of iron in particular, is extensive. Of interest are the mechanisms of passive oxide film formation, its structure and composition, the long-term stability of the film, and its local breakdown in the presence of species such as chloride ions and others (i.e., pitting).

Passive iron oxide is thermodynamically stable at sufficiently high potentials. Thus, the passive film on iron can itself participate in the corrosion process as a cathodic reactant, and is consequently destroyed in the process. In this way the passivity of iron is fundamentally more unstable than, for example, that of chromium or of aluminum. Also, unlike other passive films which are generally insulating, the passive oxide on iron (e.g., magnetite) is an electronically conducting n-type semiconductor<sup>30</sup> and forms an effective electrode for, for example, oxygen reduction.

Regarding the nature of the film, it was historically proposed to consist of a Fe<sub>3</sub>O<sub>4</sub> inner layer with an outer layer of  $\gamma$ -Fe<sub>2</sub>O<sub>3</sub>,<sup>31,32</sup> results that appeared to be consistent with electrochemical data. However, later Mössbauer studies demonstrated that the passive film contained only ferric species with no evidence of significant Fe<sup>2+</sup> present. Also, the films were likely to be microcrystalline or amorphous and did not appear to change structurally on drying in air.<sup>33,34</sup> For passive films formed on iron by anodic polarization in borate buffer solution at pH 8.4, the hydroxyl content of the film was shown by secondary ion mass spectrometry (SIMS) to be effectively zero,<sup>35</sup> thus confirming that the film was an oxide only and not a hydroxide.

A criticism of most research of this type is that it is necessarily carried out *ex situ* (i.e., the passive film was formed in solution the sample was removed and then analyzed elsewhere). Truly *in situ* measurements of the passive film structure were only achieved in the 1990s by use of X-ray absorption near edge fine structure<sup>36</sup> and scanning tunneling microscopy,<sup>37</sup> which showed that the film is either amorphous or a crystalline spinel (i.e., similar to Fe<sub>3</sub>O<sub>4</sub> and  $\gamma$ -Fe<sub>2</sub>O<sub>3</sub>), thus confirming the previous results but leaving open the question of precisely which structure is correct.

The controversy on the structure of passive iron oxide appears now to have been solved by Toney *et al.* using careful *in situ* and *ex situ* synchrotron X-ray



diffraction measurements on high purity iron.<sup>38</sup> This confirmed that the diffraction peaks were similar to spinel, but that the structure factors did not conform to either  $\text{Fe}_3\text{O}_4$  or  $\gamma\text{-Fe}_2\text{O}_3$ , or indeed any other known oxide or hydroxide of iron. Full X-ray structure refinement determined that the passive film consists of a nano-crystalline spinel unit cell (containing 32 oxide anions) with cation occupancy of  $\sim 80\%$  for octahedral sites,  $66\%$  for tetrahedral sites, and with  $\sim 12\%$  of cations occupying octahedral interstitial sites. Note that despite the superficial similarities to both the magnetite ( $\text{Fe}_3\text{O}_4$ ) and maghemite ( $\gamma\text{-Fe}_2\text{O}_3$ ) structures, it is a distinctly different material, termed the LAMM phase. Later work by the same authors, using a molecular modeling approach, has indicated that the LAMM phase is metastable.<sup>39</sup> However, this may not be so surprising considering that the film is formed under nonequilibrium conditions and, since it is thin, surface and interfacial free energies will dominate over the free energy of the macroscopic phase.

Similar experimental problems exist for determining the mechanism for passive oxide film growth. This is commonly assumed to occur via ion conduction caused by the electric field between the metal and the electrolyte. A clever experiment using isotopically labeled reagents studied the film formed after sequential anodizing of iron in ordinary and  $^{18}\text{O}$  enriched water, using SIMS to monitor the  $^{18}\text{O}/^{16}\text{O}$  ratio.<sup>35</sup> The results were consistent with the majority

transport mechanism during film growth consisting of inward oxygen ion transport in the lattice; however, some  $^{18}\text{O}$  was detected at the interface indicating that some short-circuit diffusion paths exist in the structure, presumably at crystalline boundaries.

### 3.01.2.3.2 Nonoxide passive films

In the strict sense, passivity relates to the process of oxidation leading to a solid corrosion product that forms in such a way (i.e., thermodynamically, or at least kinetically, stable, continuous, without substantive defects, relatively insoluble, and generally resistant to further oxidation or reduction) as to provide a significantly protective film. This definition does not have anything to say about the chemical nature of the passive film. Indeed, although passive oxide films are by far the most important type, passive films may also consist of sulfides, chlorides, etc.

In sulfide environments, for example, steel may passivate by the formation of an iron sulfide film, **Figure 8**. However, this film has distinctly different properties to passive oxides.<sup>40</sup> Firstly, the initially formed film is nonstoichiometric ( $\text{FeS}_{1-x}$ ) and, like  $\text{Fe}_3\text{O}_4$  (but unlike  $\text{FeO}(\text{OH})$ ) is electronically conducting and is an excellent cathode, especially for the hydrogen evolution reaction. Secondly, the film is unstable to further oxidation to  $\text{FeO}(\text{OH})$  and  $\text{FeS}_2$ , which, due to volume expansion, disrupts the film and results in damage, including cracking. Cracks and

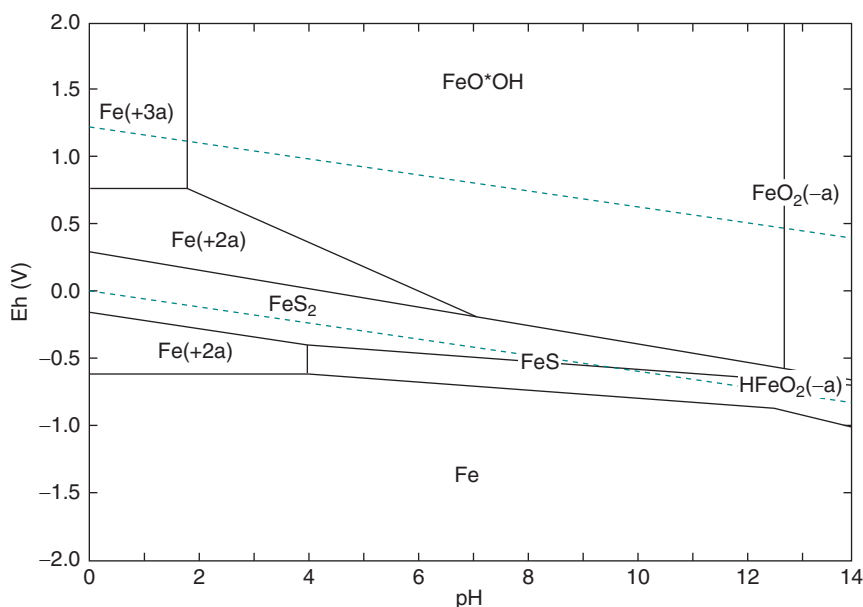


**Figure 8** Pourbaix diagram for iron and sulfur at  $10^{-5}$  M metal ion and  $10^{-3}$  M sulfur species. Calculated using HSC version 6.12 thermochemical modelling software, Outotec, Finland.

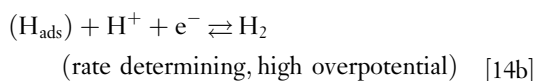
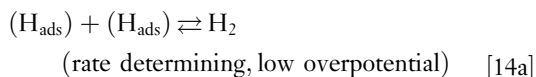
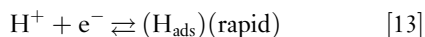
other defects in the sulfide film effectively result in small local anodes that, when coupled to the large efficient external cathode (the remnant sulfide film), causes severe localized (pitting) corrosion.

Other forms of corrosion that result in the formation of surface films with significant protective properties are often the result not of direct oxidation to a solid species, but rather by precipitation of an insoluble salt that covers the metal surface, for example, iron phosphate. In the strict sense, this is not 'passivity,' although it is often described as such, particularly, if the end result (a greatly reduced corrosion rate and a tendency for corrosion to occur in a localized manner) is similar. In some cases, however, it is unclear whether the film forms by direct oxidation or by precipitation. For example, a protective ferrous sulfate film forms during corrosion of steel in concentrated sulfuric acid,<sup>41</sup> since iron sulfate is relatively insoluble in this environment. Also, corrosion of steel in environments containing dissolved carbon dioxide (so-called 'sweet' corrosion in the oil and gas industry) can result in a protective film of ferrous carbonate under some conditions.<sup>42</sup> Such films may either form by precipitation (salt films) or may form by direct oxidation to a solid product where the solubility of the species is extremely low. However, whether this is really passivity or not is ultimately a matter of semantics.

### 3.01.2.4 Cathodic Reactions

#### 3.01.2.4.1 Hydrogen evolution reaction

The hydrogen evolution reaction is one of the most studied electrochemical processes partly due to its technological interest but also due to the relative ease of investigation (one only needs to place some zinc in sulfuric acid to observe hydrogen bubbles being produced). The mechanism for hydrogen evolution on iron involves initial discharge of hydrogen ions on the metal surface with corresponding adsorption of a hydrogen atom followed by the rate determining reaction<sup>43</sup>: most commonly, chemical desorption of adsorbed hydrogen [14a] or, at high overpotential, electrochemical desorption of adsorbed hydrogen [14b]:

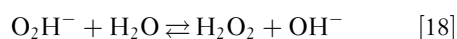
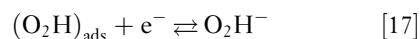
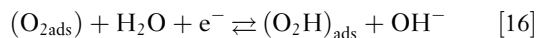
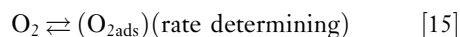


Chemical desorption of adsorbed hydrogen [14a] is a potential independent reaction and consequently, the surface coverage of hydrogen may build up to a high equivalent thermodynamic fugacity (i.e., equivalent pressure or chemical activity). This has the important consequence that the atomic hydrogen has sufficient residence time on the metal surface to enter the metal lattice (and cause embrittlement, hydrogen induced cracking, and other related phenomena) before combining to give molecular hydrogen that leaves the surface.

#### 3.01.2.4.2 Oxygen reduction reaction

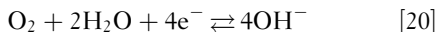
The oxygen reduction reaction on iron is important in all aerated conditions and particularly so in near-neutral to alkaline solutions where, in the majority of technologically important corrosion problems, oxygen is the dominant cathodic reactant. Unlike reduction of hydrogen ions, which is a 2-electron process that occurs via two successive single electron transfer reactions, the mechanism for the reduction of dissolved oxygen is intrinsically more complex due to the overall required transfer of four electrons. The initial step for the reduction of oxygen is generally believed to involve one or both of a superoxide or a peroxide intermediate species. However, hydrogen peroxide once formed is easily reduced in a 2-electron process that cleaves the central O–O bond.

The overall reaction for oxygen reduction differs according to whether the iron is passive (i.e., the reduction process occurs on an oxide or hydroxide surface) or whether the surface of iron is oxide-free (i.e., bare iron). An extensive investigation of the oxygen reduction reaction on iron in neutral solution was carried out by Jovancicevic.<sup>44</sup> For passive iron, the reaction scheme that best fits the observations involves rate determining adsorption of oxygen followed by stepwise reduction of the adsorbed intermediate initially to an adsorbed superoxide species ( $\text{O}_2\text{H}$ ) then to peroxide ion ( $\text{O}_2\text{H}^-$ ). This reacts immediately in water to form hydrogen peroxide, which may be detected in solution using a rotating ring disc electrode, and which is relatively easily reduced to hydroxide:

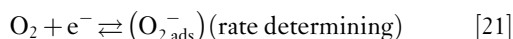




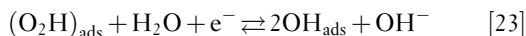
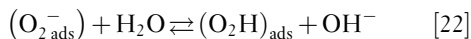
The overall reaction being the familiar:



On bare iron, the situation differs in that no hydrogen peroxide species are detectable in solution; also, the kinetics of reduction are slower. In this case, therefore, the partly reduced intermediaries are expected to exist as adsorbed species on the metal surface. The rate-determining step is, in this case, consistent with adsorption and reduction of oxygen to an adsorbed superoxide species ( $\text{O}_2^-$ ):



After this, the sequence is unclear but one that is consistent involves stepwise reduction, via an adsorbed peroxide intermediate, to hydroxide:



### 3.01.2.5 Corrosion in Aqueous Environments

#### 3.01.2.5.1 Anode and cathode separation

During corrosion, the local electrochemical potential at an anode is different from that at a cathode. Also, the local electrochemical reactions at anodes and cathodes result in significant chemical changes in their vicinity that encourage and maintain their spatial separation. Furthermore, the potential difference in solution gives rise to a voltage gradient, which attracts oppositely charged ions (or repels similarly charged ions), a process known as electro-migration. Additionally, there is the requirement for electro-neutrality in the electrolyte (by which is meant that an anion cannot exist in solution without a corresponding cation). The overall process for corrosion of iron with oxygen as the cathodic reaction is shown schematically in Figure 9, with migration and diffusion of ions carrying the flow of current.

#### 3.01.2.5.2 Mass transport

For many, if not the majority, of the technical applications of carbon steel, the aqueous corrosion rate is controlled by the diffusion of reacting oxygen to the metal surface and/or the diffusion of dissolved species away from the surface. Under these conditions, mass transport in the solution becomes critical. In general, mass transport occurs by three fundamental processes:

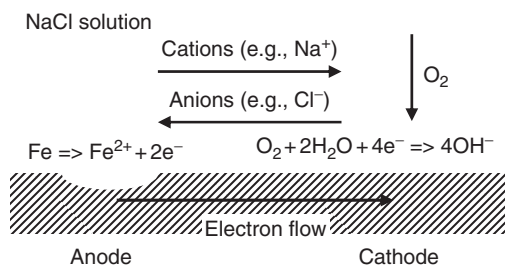


**Figure 9** Schematic diagram showing spatial separation of anode from cathode with corresponding migration of ions in solution.

- Diffusion (i.e., movement under a concentration gradient)
- Migration (i.e., movement under an electric field gradient)
- Convection (i.e., natural or forced solution flow)

The total flux of reactant to a surface or interface (i.e., the total mass transport) is obtained simply by addition of the components of diffusion and migration to that of convection:

$$\text{Flux} = \text{Diffusional} + \text{Migrational} + \text{Convective}$$

In all flow conditions, a region of fluid exists adjacent to the surface of the electrode in which no convection occurs and only diffusion and migration occur; this is called the boundary layer, and may be equated with the diffusion distance in Fick's Law. Generally, as the convection rate increases, the boundary layer is compressed and reduced in extent and, hence, the overall rate of mass transport increases.

#### 3.01.2.5.3 Effect of flow rate on corrosion

For corroding systems, under mass transport control, the flux of species to a surface where the rate-controlling reaction is occurring is described in the steady-state by Fick's first Law. This flux may be also measured electrochemically by the limiting current for that reaction (e.g., oxygen reduction). In this way, a mass transfer coefficient,  $k$ , may be defined by:

$$k = \frac{i_{\text{lim}}}{nFC_b} \quad [25]$$

where:  $i_{\text{lim}}$  is the limiting current density for a cathodic reaction,  $C_b$  is the bulk concentration of cathodic reactant,  $F$  is Faraday's constant and  $n$  is the number of electrons transferred in the reaction. For a corrosion process whose rate is controlled by mass transfer of cathodic reactant, for example carbon steel in neutral, oxygen-containing solutions,

knowledge of the mass transfer coefficient,  $k$ , enables prediction of corrosion rate.

Measurement of the diffusion flux may be carried out using standard electrochemical techniques as a function of fluid flow rate, either via rotating electrode systems, or via electrodes placed in flow channels. For laminar flow, the analytical solution predicts that the limiting current ( $i_{\text{lim}}$ ) at a rotating electrode is proportional to the concentration of reacting species in solution and the square root of the rotation speed, the Levich equation<sup>45</sup>:

$$i_{\text{lim}} = A C \omega^{0.5}$$

where:  $\omega$  is the angular rotation rate of the electrode (radians  $\text{s}^{-1}$ ),  $C$  is the concentration of reacting species, and  $A$  is a constant that depends on the fluid properties and diffusion rate of the reacting species. Thus, if a plot of  $i_{\text{lim}}$  v.  $\omega^{0.5}$  is a straight line, then the reaction is mass-transport controlled and the diffusion coefficient for the reacting species can be obtained from the slope of the straight line. This general kind of relationship holds for fluid flow in more complex geometries, including turbulent flow, where analytical solutions are not possible. Hence,

experimental analogies for particular situations must be developed, commonly in terms of dimensionless parameters such as the Sherwood number (related to mass transport), the Reynold number (related to the fluid flow rate), and the Schmidt number (related to the fluid properties). For more detailed information on corrosion in flowing systems, the reader is referred to the relevant chapter of this book.

### 3.01.3 Corrosion Processes

Some of the technically more important corrosion processes for steel are summarized in this section. Note, however, that this is not intended as a comprehensive treatment and more detailed descriptions of these processes (both in general and in specific situations) will be found in the relevant chapters elsewhere in this book.

#### 3.01.3.1 Corrosion Products

For general information, common compounds associated with the corrosion of steel are listed in [Table 4](#).<sup>46</sup>

**Table 4** Corrosion products formed on carbon steel in various environments

Compound	Comments
<i>Oxides:</i>	
FeO (wüstite)	Formed during high temperature oxidation, present in millscale with $\text{Fe}_2\text{O}_3$ and $\text{Fe}_3\text{O}_4$
$\alpha\text{-Fe}_2\text{O}_3$ (hematite)	Iron ore mineral, also formed at elevated temperatures
$\text{Fe}_3\text{O}_4$ (magnetite)	Corrosion product formed in reducing aqueous conditions
$\gamma\text{-Fe}_2\text{O}_3$ (maghemite)	Oxidized form of magnetite and with the same crystal structure
<i>Oxy-hydroxides:</i>	
$\alpha\text{-FeO(OH)}$ (goethite)	Stable mineral, commonly found in nature
$\gamma\text{-FeO(OH)}$ (lepidocrocite)	Metastable phase, formed during atmospheric corrosion
$\beta\text{-FeO(OH,Cl)}$ (akaganéite)	Formed during corrosion in seawater – characteristic orange color
$\text{Fe}_5\text{O}_3(\text{OH})_9$ (ferrihydrite)	Common iron mineral: metastable to hematite and goethite
<i>Hydroxides:</i>	
$\text{Fe(OH)}_2$ (ferrous hydroxide)	Intermediate corrosion product formed under reducing conditions
$\text{Fe(OH)}_3$ (ferric hydroxide)	Hydrated iron oxy-hydroxide, more properly written as: $\text{FeO(OH)} \cdot \text{H}_2\text{O}$
<i>Sulfides:</i>	
$\text{FeS}_{1-x}$ (mackinawite)	Anion deficient FeS (troilite) formed during microbially influenced corrosion
$\text{Fe}_{1-x}\text{S}$ (pyrrhotite)	Iron sulfide mineral, cation deficient form of FeS (troilite)
$\text{FeS}_2$ (pyrite)	Iron sulfide mineral, known as ‘fool’s gold’
<i>Carbonates:</i>	
$\text{FeCO}_3$ (siderite)	Corrosion product that forms as a protective film in some forms of ‘sweet’ corrosion at high $\text{CO}_2$ partial pressures; occasionally also found as part of the corrosion product layer on archaeological iron objects after long-term burial
<i>Phosphates:</i>	
$3\text{FeO} \cdot \text{P}_2\text{O}_5 \cdot 8\text{H}_2\text{O}$ (vivianite)	Occasionally found within the corrosion product layer on archaeological iron objects after long-term burial in strongly anaerobic, typically water-logged, environments
<i>Green rusts:</i>	
$[\text{Fe}_3^{2+} \text{Fe}^{3+} (\text{OH})_8]^+ [\text{Cl} \cdot \text{H}_2\text{O}]^-$	Series of corrosion products that comprise mixed ferrous/ferric species together with incorporated anions, in particular: carbonates, sulfates and chlorides

### 3.01.3.2 Aqueous Corrosion

#### 3.01.3.2.1 General corrosion

In the absence of inhibiting species, carbon and low alloy steel are not passive in most aqueous environments at pH less than  $\sim 9$ . Thus, for the majority of natural environments likely to be encountered in service, steel will undergo general corrosion. It is important to note that the term 'general corrosion' does not imply uniform thickness loss across a corroding surface rather it defines an active corrosion process that occurs in the absence of a passive film.

In practice, the general corrosion of uncoated steel in high conductivity media such as seawater will generally lead to an overall macroscopic roughening of the surface. This is exacerbated by the presence of surface-breaking second phase particles, the most important of which are sulfide inclusions that are always present in steels. For example, partial dissolution of sulfide inclusions results in aqueous sulfide species and the possible formation of adjacent iron sulfide films resulting in a surface electrochemical heterogeneity.<sup>47–49</sup> Hence, heterogeneity in the

corrosion rate is developed across the material surface eventually resulting in variations in the thickness loss over the surface.

In low conductivity environments such as natural waters, the resistivity of the electrolyte is sufficiently large that the spatial separation of anodes and cathodes is greatly reduced. This tends to result in the localization of corrosion to specific regions of the surface with associated local precipitation of corrosion product giving the appearance of small protuberances. Such corrosion is often called tuberculation corrosion and can result in local attack underneath the precipitated corrosion product,<sup>50</sup> **Figure 10**. Although giving the appearance of pitting, the mechanism is in essence an extremely localized form of general corrosion combined with differential aeration corrosion. In the fullness of time, such regions will tend to merge together giving a macroscopically roughened surface.



**Figure 10** Tuberculation corrosion of steel; corrosion is localized beneath rust protuberances (known as tubercles).

#### 3.01.3.2.2 Concentration cell corrosion: Differential aeration

Where differences in concentration of an electrochemically active species are present in an environment then corrosion is likely to result. For example, for a buried structure, the local oxygen concentration will vary according to whether the soil is well-aerated or not, with the degree of aeration also varying as a function of soil depth. Thus, cathodes are likely to be localized at regions of relatively higher oxygen availability with anodes localized in regions of lower oxygen content. This is effectively a corrosion cell that is driven by a spatial variation in oxygen concentration in the environment (and is thus known as a concentration cell). Localization of the corrosion reactions can be readily demonstrated in a droplet of salt water on steel by the use of indicators that show the high pH generated at a cathode (e.g., by use of phenolphthalein, which turns pink) and the ferrous ions generated at an anode (e.g., by use of ferricyanide, which turns blue), **Figure 11**.

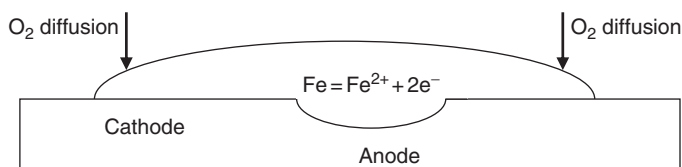


**Figure 11** Corrosion in a salt water droplet showing the cathodic reaction localized at the droplet periphery (due to oxygen availability) and the anodic reaction localized in the droplet centre (due to oxygen depletion).



Differential aeration is an important factor in many corrosion processes where local oxygen depletion is present. For example, corrosion that is localized underneath deposits, and between mating surfaces, etc., is almost always caused by a differential aeration mechanism. In general, those localities that have a plentiful supply of oxygen will become cathodes with anodes occurring in regions of oxygen depletion.

### 3.01.3.2.3 *Pitting and crevice corrosion*

At alkaline pH and in the region where passivity of carbon steel is possible, then classical pitting and crevice corrosion mechanisms, that is, those involving local breakdown of a passive film, are possible. Localized corrosion may also result where the surface has been passivated by other means, such as oxidizing inhibitors (e.g., nitrite, etc.) or in sulfide environments.

For the pitting of pure iron in neutral electrolytes with a passive oxide film, pit initiation was found to be associated with a stage in the development of the film corresponding to a particular film thickness. This was found to be potential independent but dependent on the halide ion type (i.e.,  $\text{Cl}^-$  or  $\text{Br}^-$ ) and concentration as well as the anodic charge passed prior to pitting.<sup>51,52</sup> No incorporation of halide into the passive film was observed, which is in stark contrast to stainless steel, where halide ions do incorporate into the chromium passive film.<sup>53</sup> This is an evidence of the structural stability of the passive film on iron (which once formed is relatively stable) compared with the passive film on Fe–Cr alloys (which changes with time in accommodation to the environment). Note, of course, that passive iron oxide is unstable to reductive dissolution, which is not the case with stainless steel and is one of the reasons for the improved passivity of stainless alloys. Overall, iron (at a given pH in a given supporting electrolyte) appears to be susceptible to halide-induced pitting, if and only if, the passive oxide has reached a certain critical stage of growth.

Pitting can be generally prevented if there are sufficient alternative anion species present (e.g., nitrate, sulfate, and hydroxide). Thus, pitting generally is only feasible if the ratio of chloride to other anions exceeds certain critical values, which are environment, pH, and temperature dependent; for example, the chloride-to-hydroxide ratio for pitting corrosion of steel reinforcement in concrete.<sup>54,55</sup> Also, for a propagating pit, the chemistry must be consistent with the active regime of corrosion as indicated in the Pourbaix diagram. Given that the cathode area is large while that of the anode is small, the anodic current density

(and hence the local rate of dissolution) in a pit must necessarily be high.

Pitting of steel also occurs in the presence of passive sulfide films such as mackinawite ( $\text{FeS}_{1-x}$ ). Sulfide films are inherently unstable to oxidation with consequent disruption that results in the generation of defects and flaws in the film.<sup>56</sup> Since the film is an excellent cathode, anodes localize at the defects where the substrate is exposed thus resulting in severe local pitting.

Pitting and crevice corrosion are therefore associated with local development of chemical heterogeneity on the surface at the pit site. Furthermore, their occluded geometry, once formed, tends to maintain the solution at a significantly different local chemistry than the environment. This form of localized corrosion is much more likely to occur in stagnant conditions where the development of diffusion-driven solution heterogeneity over the metal surface is encouraged. Conversely, under flowing conditions, local diffusion-driven chemical changes cannot be maintained so effectively and pitting is less likely. Pumps and valves that operate intermittently with long periods of nonoperation are particularly prone to internal pitting and crevice corrosion.

### 3.01.3.2.4 *Galvanic corrosion*

Although the electrochemical series forms an outline guide for the tendency or not for galvanic corrosion, it is important to note that the position of alloys in the series is altered in specific environments and a galvanic series developed for the environment should therefore be consulted. Galvanic series for metals and alloys in seawater and potable waters are well-known and easily available.<sup>57</sup>

There are two necessary requirements for galvanic corrosion to occur: firstly, electrical connection to another electronically conducting material of a different electrochemical potential (commonly a metal, although conducting films such as magnetite and mackinawite as well as graphite can also act as electrodes) and secondly connection through the electrolyte solution (in order to permit ionic current to flow). Galvanic corrosion can also occur in a macroscopic sense between components differing materials, but may also occur microscopically at preexisting metallurgical features in the steel or, more commonly, where metal ions of a more noble element are present in solution and plate out locally on the steel surface. Thus, where copper ions plate out onto steel, for example from corrosion of a brass component elsewhere in the system, then local galvanic corrosion will initiate at such locations.

### 3.01.3.2.5 Flow-assisted corrosion (FAC)

The phenomenon of flow-assisted (or flow-accelerated) corrosion (FAC) is of fundamental importance and occurs particularly in high performance boilers and heat exchangers such as are used in power generating facilities (both conventional and nuclear), but also elsewhere.<sup>58</sup> The general mechanism of FAC is not limited to steel and involves the removal of a protective corrosion product, generally by dissolution, in a flowing environment. The process has long been known to occur in high flow rate systems, for example in copper alloy condenser tubing where the relatively soft and poorly adherent protective surface films are stripped from the surface by the shear stress across the boundary layer between the pipe wall and the moving turbulent fluid.

For carbon steel, the latter mechanism does not operate as the protective magnetite layer adheres strongly to the substrate. However, in common with all minerals, iron oxides are sparingly soluble in water and FAC involves the local or general thinning of the protective oxide film that forms on carbon steel in high temperature water. However, oxides where iron is entirely in the ferric (+3) oxidation state are considerably less soluble than magnetite as can be seen from Table 5.

In traditional boiler water treatment, the dissolved oxygen concentration is kept as low as possible (a few parts per billion, ppb) where magnetite is the stable oxide phase. It is thus susceptible to enhanced dissolution under high flow rate conditions. This leads both to unwanted deposition of oxide elsewhere in the system but, more importantly, enhanced corrosion of steel and often unexpected failures with typical scalloped surfaces.<sup>59</sup> However, if the oxygen concentration is controlled at a slightly higher level hematite becomes the stable phase. This is

advantageous as it is considerably less soluble than magnetite and, hence, much more resistant to flow-accelerated corrosion (FAC).

### 3.01.3.2.6 Erosion-corrosion

In the presence of two-phase flow in solution (i.e., solid particles, slurries, entrained gas, etc.) enhanced corrosion will generally occur due to a number of mechanisms including: increased mass transport of reacting species and impact of the 2nd phase onto the surface, see for example.<sup>60</sup> The latter process is the most important in causing erosion-corrosion as its effect on the protective surface film is critical. Thus, protective films may be thinned by abrasion or removed altogether causing rapid corrosion of the underlying material. This process is particularly prevalent where sharp changes in flow direction (e.g., pipe bends, etc.) or flow velocity (e.g., valves and chokes, etc.) occur. Careful design of plant components can minimize this form of attack.

### 3.01.3.3 Environmentally Assisted Cracking

#### 3.01.3.3.1 Environments

Carbon steel is susceptible to stress corrosion cracking in a range of environments, often where it shows passivity or marginal passivity. These include anhydrous liquid ammonia, nitrate/nitrite, strong alkali and in carbonate/bicarbonate systems. Stresses in the steel can either arise from externally applied forces or be the result of processing, deformation, welding, etc. giving rise to a residual stress that is present at all times.

Historically the most important of these processes was caustic cracking prevalent in low-to-medium pressure riveted steel boilers. In such systems boiler waters that were traditionally dosed with carbonate or bicarbonate for pH control lost CO<sub>2</sub> to the steam resulting in a gradual increase in pH. Although in well-controlled systems, the bulk pH would be maintained within correct limits, local concentration in crevices or under deposits could give rise to a strongly alkaline region that initiated intergranular stress corrosion.<sup>61</sup> The phenomenon is not restricted to boilers but can occur in any system that handles strong alkali, for example during purification of bauxite via the Bayer process<sup>62</sup> or in Kraft process paper digesters.<sup>63</sup> The morphology of caustic cracking is intergranular with a lower limit for cracking of carbon steel in the range 1–5% NaOH (additions of nickel improve resistance). Cracking is observed to be potential dependent<sup>64</sup> occurring only in the passive region

**Table 5** Solubility products for various iron oxides

Reaction	Solubility product at 25°C	Solubility product at 300°C
$\text{Fe}(\text{OH})_2 \rightleftharpoons \text{Fe}^{2+} + 2\text{OH}^-$	$10^{-15.04}$	$10^{-17.54}$
$\text{Fe}_3\text{O}_4 + \text{H}_2\text{O} \rightleftharpoons \text{Fe}^{2+} + 2\text{FeO}(\text{OH})$	$10^{-20.25}$	$10^{-21.40}$
$\text{Fe}_3\text{O}_4 + 4\text{H}_2\text{O} \rightleftharpoons \text{Fe}^{2+} + 2\text{Fe}^{3+} + 8\text{OH}^-$	$10^{-33.68}$	$10^{-33.59}$
$\text{Fe}(\text{OH})_3 \rightleftharpoons \text{Fe}^{3+} + 3\text{OH}^-$	$10^{-37.94}$	$10^{-36.87}$
$\text{FeO}(\text{OH}) + \text{H}_2\text{O} \rightleftharpoons \text{Fe}^{3+} + 3\text{OH}^-$	$10^{-41.58}$	$10^{-39.62}$
$\text{Fe}_2\text{O}_3 + 3\text{H}_2\text{O} \rightleftharpoons 2\text{Fe}^{3+} + 6\text{OH}^-$	$10^{-40.40}$	$10^{-39.68}$

Source: Buecker, B. *Power Eng.* **2007**, 111(7), 20–24.

and predominating in the region of the active-to-passive transition (i.e., from  $-800$  to  $-600$  mV vs. the Standard Hydrogen Electrode in 10% NaOH). Steels with lower carbon content appear to be more susceptible.<sup>65</sup> The failure mechanism is not thought to be associated with hydrogen embrittlement but is consistent with a slip dissolution model.<sup>66</sup>

Stress corrosion cracking of carbon and low alloy steels also occurs on buried structures under cathodic protection due to generation of alkalinity at coating defects by cathodic reduction. In aerated soil, carbon dioxide migrates to the cathodes in order to buffer the alkalinity thus producing the critical carbonate/bicarbonate environment. Failure surfaces are characterized by multiply branched intergranular cracks that tended to align along the principle stress axis of the pipe; fracture surfaces are often observed to be covered with magnetite.<sup>67</sup>

Transgranular stress corrosion cracking in anhydrous liquid ammonia is a separate phenomenon that unfortunately, because it was not understood, led to some catastrophic failures and loss of life.<sup>68</sup> The predominant risk factor for cracking in anhydrous ammonia is the presence of dissolved oxygen at  $>5$  ppm (or  $>1$  ppm in the presence of  $\text{CO}_2$ ). Cracking can be inhibited effectively provided that the ammonia contains more than 0.1% of water to encourage passivity of the steel.<sup>69</sup>

#### 3.01.3.3.2 Hydrogen embrittlement

Ferrite, like most body centered structures, has a high diffusivity and solubility for interstitial hydrogen in its lattice. Thus, carbon and low alloy steel are highly susceptible to hydrogen embrittlement and hydrogen-induced cracking. The former is caused by reduction in macroscopic ductility due to the presence of lattice hydrogen resulting in transgranular cleavage fracture, while the latter is due to the formation of hydrogen gas bubbles at extremely high pressure within the steel microstructure. There are numerous mechanistic models in the literature for the causes of hydrogen embrittlement and it is not clear whether a single mechanism prevails or whether several mechanisms coexist. A more detailed discussion of hydrogen embrittlement mechanisms and effects can be found elsewhere in the relevant chapter of this book.

#### 3.01.3.4 Microbiologically Influenced Corrosion

In nonsterile systems (i.e., generally at temperatures below  $\sim 60$ – $70^\circ\text{C}$ ) the growth and multiplication of a

wide range of microbial species is possible. For a microorganism to initially establish itself and then to grow and flourish, the environmental conditions must be favorable including a supply of a carbon food source and other trace essential nutrients (e.g., nitrogen, phosphorous, etc.) Many of the microbial species that have influence on the corrosion of carbon steel are anaerobic. Of these, sulfate reducing bacteria are the most frequently encountered. These metabolize oxidized sulfur species in their environment producing sulfide species in solution: that is,  $\text{H}_2\text{S}$ ,  $\text{HS}^-$ , or  $\text{S}^{2-}$ , depending on pH. These will form sulfide corrosion product films on steel that are nonprotective and unstable, resulting in severe and often local corrosion.<sup>70</sup>

Other problematic families of anaerobic bacteria include: the nitrate-reducers (that metabolize nitrite corrosion inhibitors, reducing their concentration), the organic acid producers (acetic and other acids can be aggressive to carbon steel depending on the environment), and iron oxidizers that metabolize ferrous ions resulting in unwanted deposition of ferric oxides. Anaerobic bacteria can survive (but not metabolize) in aerobic environments and can often tolerate low levels of oxygen. Thus, they may colonize benign environments in locations of low oxygen concentration (i.e., under deposits of corrosion product, dirt, etc., and under bio-films of oxygen-tolerant species), even though the overall environment may be relatively well-oxygenated.

#### 3.01.3.5 Aqueous Corrosion Protection

Although unprotected (bare) carbon and low alloys steel may be exposed without corrosion protection provided suitable allowances are made for corrosion losses during service, most steel is protected in some way. Methods available include: metallic coatings (e.g., galvanizing, electroplating, etc.), inorganic coatings (e.g., phosphate conversion coatings, etc.), organic coatings (i.e., paint coatings and linings) and cathodic protection. These topics are dealt with in detail elsewhere in this book and will not be considered further here.

#### 3.01.3.6 High Temperature Oxidation

Plain carbon steels cannot be used at temperatures close to the lower critical temperature for austenite formation, as the microstructure becomes unstable, with spheroidization of pearlite and graphitization of iron carbide. Also, significant grain growth and creep occurs. In practice, plain carbon steel has an effective

temperature limit of  $\sim 400\text{--}420^\circ\text{C}$ . For higher temperature service, low-alloy steels hardened by stable alloy carbides should be used.

Iron readily oxidizes at elevated temperatures in air (and other oxidizing environments) resulting in a relatively adherent layered scale. Above  $570^\circ\text{C}$  the ferrous oxide phase wüstite is stable and the oxide scale has three layers: a relatively thick inner layer of wüstite, a relatively thin intermediate layer of magnetite and a thin outer layer of hematite. The oxidation kinetics are controlled by diffusion of species through the scale thickness and are thus parabolic in nature. Wüstite has a large number of cation defects and is more properly written as  $\text{Fe}_{1-x}\text{O}$ . The oxide growth mechanism in wüstite is controlled by cation transport outwards,<sup>71</sup> resulting in relatively rapid oxidation rates. In view of this, the service temperature for carbon and low alloy steel should be below the formation temperature of wüstite.

Below  $\sim 570^\circ\text{C}$ , where wüstite is thermodynamically unstable, the oxide scale on iron contains an outer region of  $\text{Fe}_2\text{O}_3$  (hematite) with an inner region of  $\text{Fe}_3\text{O}_4$  (magnetite) adjacent to the metal. Since the transport processes (diffusion) through these phases is much less rapid, the oxidation rates are also less.<sup>72</sup> At these lower temperatures, the oxidation kinetics are not purely parabolic and are dependent on the surface preparation and degree of cold work present in the material; larger amounts of cold work resulting in more rapid oxidation. Plain carbon steel oxidizes somewhat (10–20%) more slowly than pure iron, which is almost certainly due to the presence of other alloying elements (e.g., silicon, manganese, and aluminum).<sup>72</sup> Below  $570^\circ\text{C}$ , increased carbon content generally results in an increased oxidation rate because the scale formed over carbide particles and especially pearlite colonies is finer with a higher iron diffusion rate.

The high temperature oxidation and corrosion of iron and steel is discussed in greater depth elsewhere in this book, to which the interested reader is referred.

### 3.01.4 Atmospheric Corrosion

#### 3.01.4.1 Environmental Influences

##### 3.01.4.1.1 Humidity

Relative humidity (RH) is defined as the ratio of partial pressure of water vapor to the saturated water vapor pressure at the same temperature. Thus, the RH is a thermodynamic quantity that is equivalent to the fugacity of water vapor in the gas phase.

Consequently, an RH of 100% defines a gas phase fugacity of 1, which is by definition in equilibrium with liquid phase water also at an activity of 1. In theory, therefore, atmospheric corrosion cannot occur at RH below 100% because no liquid water is present. However, in practice, water absorption readily occurs on bare metal surfaces at RH below 100% because, apart from gold, all metals are generally covered at standard conditions by hydrophilic thin oxide or hydroxide (passive) films.

Water adsorption on electropolished, uncontaminated surfaces as a function of RH from 0% to 80% was studied in the context of metrology in the precision weighing of stainless steel, silicon and platinum–iridium mass standards.<sup>73,74</sup> On these materials, water adsorption can be described well by a Brunauer–Emmett–Teller (BET) isotherm appropriate to multilayer adsorption on hydrophilic surfaces. On 20% Cr, 25%Ni stabilized stainless steel the water layer thickness was found to vary approximately linearly from 0% RH to 80% RH where it reached  $\sim 0.6$  nm, corresponding to about three monolayers of water.

Generally, the corrosion of metals in the atmospheric environment is possible if and only if there is sufficient water present on the metal surface to solvate the ions produced during corrosion reactions. This was first demonstrated by Vernon<sup>75</sup> in a series of classical experiments, some of which are summarized graphically in [Figure 12](#). He showed that rusting occurs at a low rate in pure air of less than 100% RH but that in the presence of minute concentrations of impurities, such as sulfur dioxide, serious rusting can occur without visible precipitation of moisture once the RH of the air rises above a critical and comparatively low value. This value depends to some extent upon the nature of the atmospheric pollution, but, when sulfur dioxide is present, it is in the region of 70–80%. Below the critical humidity, rusting is inappreciable, even in polluted air.

The results of Vernon have been confirmed many times. For example, more recent work has studied the integrity of carbon steel materials as a function of humidity in air at  $65^\circ\text{C}$ .<sup>76</sup> On clean, uncontaminated steel, the corrosion at and below 75% RH was negligible and consistent with a dry oxidation mechanism. However, at 85% and above, the corrosion rate rapidly increased, consistent with a critical RH for the onset of aqueous atmospheric corrosion of  $\sim 80\%$ .

The critical humidity for the onset of atmospheric corrosion varies considerably as a function of surface condition. Two factors are paramount in controlling this. Firstly, physical adsorption on porous surfaces

will occur below the expected bulk equilibrium value (i.e., the saturated vapor pressure) due to capillary condensation. This is of obvious relevance in the development of corrosion product (rust) layers, which will retain water in their pores well below the RH of condensation. Secondly, and importantly, liquid condensation will tend to occur at reduced RH where surface chemical contamination exists. This is because the activity of water at the saturated concentration of the solute, is lowered significantly, **Table 6**.

Thus, in the absence of other factors, a surface that is contaminated with sodium chloride will condense an aqueous phase at  $RH > 75\%$  while for seawater (containing magnesium and calcium cations) condensation of an aqueous phase might be expected at all  $RH > 33\%$ . In the presence of porous corrosion products, capillary condensation will lower these values further.

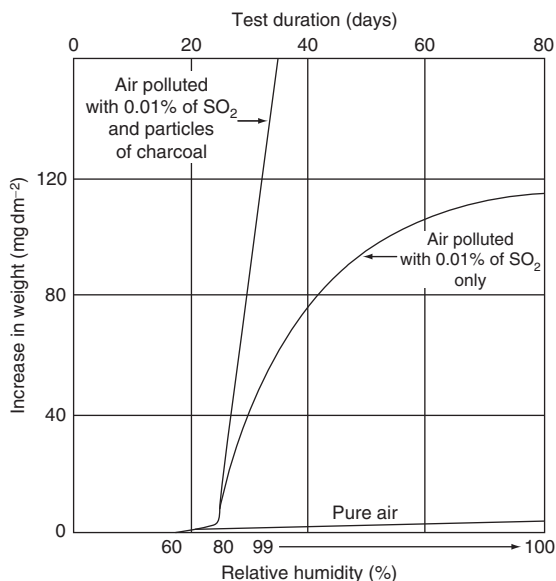


**Figure 12** Effect of relative humidity and atmospheric pollution on the rusting of iron, after Vernon. Reproduced from Vernon, W. H. J. *Trans. Faraday Soc.* **1935**, 31(1), 668.

**Table 6** Equilibrium RH for saturated solutions of various solute species

Solute species	Equilibrium RH in saturated solution
$(\text{NH}_4)_2\text{SO}_4$	81.3% (20 °C); 79.0% (50 °C)
NaCl	75.5% (20 °C); 74.4% (50 °C)
$\text{MgCl}_2$	33.1% (20 °C); 30.5% (50 °C)
LiCl	11.3% (20 °C); 11.1% (50 °C)

Source: Greenspan, L. J. *Res. Natl. Bur. Stand.* **1977**, 81A(1), 89–96.

### 3.01.4.1.2 Air-borne pollutants

Historically, the combustion-derived air-borne sulfur dioxide and nitrogen oxides have been the most important pollutant species in the atmosphere. Other air-borne pollutants including hydrochloric acid vapor, ammonia, dust, soot and salt aerosol particles are also of importance. However, given extensive pollution controls that are now placed on industry and transportation, combustion-derived species have been greatly reduced. For example, current European Union legislation<sup>77</sup> sets down limits for  $\text{SO}_2$ ,  $\text{NO}_x$  and particulates of less than  $10 \mu\text{m}$  for implementation no later than 2010, **Table 7**. Annual global sulfur dioxide emissions are estimated to have peaked at the end of the 1970s (75 Mtonnes) and have since dropped  $\sim 20\%$ .<sup>78</sup> In Europe, emissions have dropped much further and by 2010 are expected to be less than half their peak value. The impact on ground level pollutant concentrations is clearly considerable with a consequent reduction in atmospheric corrosion rates.

The significance of the amount of sulfur dioxide available for reaction at the metal surface (its presentation rate), rather than the concentration in the atmosphere, has been demonstrated by studying the effects of atmospheric flow rate. Thus, an increase in steel corrosion with increase in atmospheric flow rate at a constant volume concentration of sulfur dioxide has been observed by Vannerberg<sup>79</sup> and Walton *et al.*<sup>80</sup> Notwithstanding these findings, the effect of sulfur dioxide on the corrosion of steel is clearly seen in **Figure 13**, which plots historic data from the Sheffield area of the UK. This illustrates a clear relationship between sulfur dioxide in the atmosphere and the corrosion of steel exposed to it; the atmospheric  $\text{SO}_2$  concentration accounting for  $\sim 50\%$  of the observed variation in corrosion rate.<sup>81</sup>

The corrosion of steel in the presence of  $\text{SO}_2$  has been studied as a function of RH by a number of

**Table 7** EU air-borne pollution limits for 2010

Species	Averaging period	Limit value
$\text{SO}_2$	1 h	$350 \mu\text{g m}^{-3}$
	24 h	$125 \mu\text{g m}^{-3}$
	365 days	$20 \mu\text{g m}^{-3}$
$\text{NO}_x$	1 h	$200 \mu\text{g m}^{-3}$
	24 h	$40 \mu\text{g m}^{-3}$
	365 days	$30 \mu\text{g m}^{-3}$
Particulates < $10 \mu\text{m}$	24 h	$50 \mu\text{g m}^{-3}$
	365 days	$20 \mu\text{g m}^{-3}$

European Council Directive 1999/30/EC of 22 April 1999: Limit values for sulphur dioxide, nitrogen dioxide and oxides of nitrogen, particulate matter and lead in ambient air.



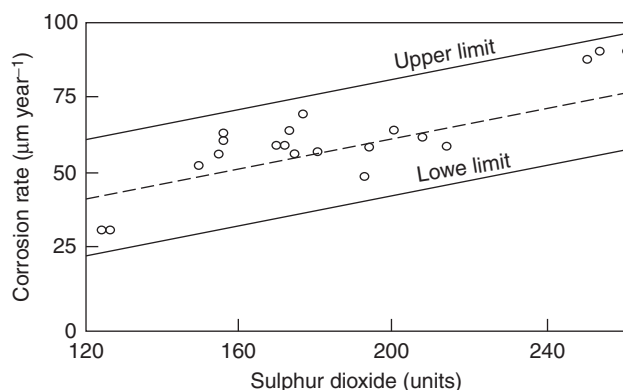


**Figure 13** Relationship between sulfur dioxide ( $\text{mg of SO}_2 \text{ per m}^3$ ) and corrosion, after. Reproduced from Chandler, K. A.; Kilcullen, M. B. *Br. Corr. J.* **1968**, 3.

workers, the first being Vernon whose data are reproduced in [Figure 12](#). Sydberger and Vannerberg later repeated this work extending it to include corroded surfaces.<sup>82</sup> Using isotopic labeling, they confirmed that on uncontaminated, polished iron, in 0.1 ppm  $\text{SO}_2$  little or no  $\text{SO}_2$  was absorbed at RH below 80% and no corrosion was observed. On pre-corroded iron at RH greater than 80% and in 0.10 ppm  $\text{SO}_2$ , sulfur was absorbed quantitatively.

This explains the historic observation that rust films formed in industrial atmospheres contain considerable amounts (5% or more) of ferrous sulphate.<sup>83,84</sup> However, the formation of iron sulfate only accounts for a small percentage of the overall metal loss and this does not explain fully the effect of  $\text{SO}_2$  on iron corrosion.<sup>85,86</sup> For example, there is evidence that steel that has been allowed to corrode in an atmosphere containing sulfur dioxide, continues to corrode at a similar rate, at least for a time, after transferring it to a clean atmosphere.<sup>87</sup>

Historically, a cyclic variation in the amount of sulfate found in rust formed on steel exposed at different times of the year [Figure 14](#), has been observed. The quantity present depends on the month of the year rather than on the period of exposure, at least for periods of up to 2 years.<sup>88</sup> Consequently, the month of initial exposure will have an important influence on the corrosion rate. For example, in one test, specimens exposed for 2 months from September corroded at  $35 \mu\text{m year}^{-1}$  compared with  $136 \mu\text{m year}^{-1}$  for specimens exposed from May. This effect was of importance in planning for atmospheric exposure tests for steel since different annual corrosion rates would be obtained depending on whether the initial exposure was carried out in the summer or the winter months. The observed variation was historically

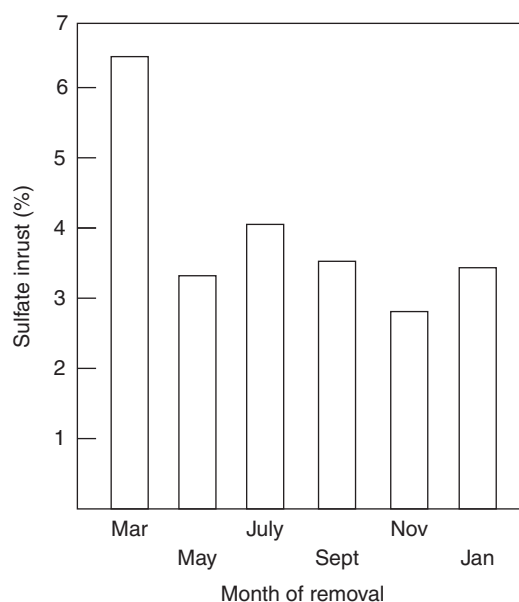


**Figure 14** Sulfate in adherent rust on steel exposed at Battersea in January after. Reproduced from Chandler, K. A.; Stanners, J. F. *Proceedings of 2nd International Congress of Metallic Corrosion*; NACE: Houston, 1963; 325.

related to the quantity of ground-level atmospheric  $\text{SO}_2$  present at different times of the year, which varied according to the burning of domestic coal for space and water heating. However, this source of  $\text{SO}_2$  is no longer present and it might be assumed that the observed difference is now considerably less.

Historically, sulfur dioxide was the most important gaseous pollutant present in the atmosphere. However, given the considerable reduction in ground level  $\text{SO}_2$  concentration over the last 30 years other species, particularly oxides of nitrogen ( $\text{NO}_x$ ), have increased in importance.<sup>89</sup> Nitrogen oxides are

produced during combustion as a consequence of direct reaction between nitrogen and oxygen in the air at high temperature. Increased thermal efficiency of plant, where the combustion temperature is raised, inevitably increases the production of  $\text{NO}_x$ . Thus, at elevated temperatures the following reactions occur:



The ratio of NO to  $\text{NO}_2$  is controlled by the reaction temperature and by the cooling time; faster cooling rates favoring  $\text{NO}_2$  over NO.

Several attempts have been made to study the influence of nitrogen oxides alone and in combination with sulfur dioxide, on the corrosion of steel, however no clear answer exists. In multiregression studies under atmospheric exposure in Japan no significant correlation with measured  $\text{NO}_x$  levels was found.<sup>90</sup> Likewise Haynie, in laboratory tests, found no correlation with  $\text{NO}_x$  levels and the corrosion or weathering steel.<sup>91</sup> Later work by Johansson clarified this situation. He found that, on its own, the increase in the atmospheric corrosion rate of steel, which was not large, was independent of RH.<sup>92</sup> However, a strong synergism was found with small levels of  $\text{NO}_x$  in combination with  $\text{SO}_2$ , which were much more corrosive than either pollutant on its own. This behavior is believed to be caused by the considerably more rapid solution-phase oxidation of sulfite to sulfate species in the presence of  $\text{NO}_x$  as oxidizer.<sup>93</sup>

One of the confusing aspects to the effect of  $\text{NO}_x$  pollutant is that it is a mixture of NO and  $\text{NO}_2$ . In order to separate the effects of these species on steel, Oesch carried out a series of laboratory experiments<sup>94</sup> in controlled pollutant gas mixtures. He found that NO had almost no effect on corrosion irrespective of RH, which is no doubt due to its low solubility in water. Conversely,  $\text{NO}_2$  caused a significant increase in corrosion rate although its effect was much lower than for  $\text{SO}_2$  (the corrosion rate in 10 ppm  $\text{NO}_2$  was about one-half that in 0.5 ppm  $\text{SO}_2$ ).

Hydrochloric acid gas is produced during the combustion of coals containing chloride species. Given its high solubility in water it might be expected also to influence corrosion although in rainwater its presence will only be evident from a higher chloride concentration than expected from sea salt and a lower pH. Askey *et al.* studied the effect of hydrochloric acid gas on corrosion of steel at varying atmospheric

presentation rates.<sup>95</sup> They found that the influence on corrosion of steel was high but reached a plateau where further increases in concentration did not increase the rate of corrosion. This was explained by the formation of iron chloride on the surface that oxidized to iron oxy-hydroxide liberating chloride. Thus, once sufficient chloride is present, further increases should have no additional effect.

Many other pollutant species are present in the atmosphere, including:  $\text{H}_2\text{S}$ ,  $\text{NH}_3$ , etc. Most of these arise from biological processes and are present at low concentration or have limited effects. Ammonia, the only significant basic atmospheric constituent, is produced via biological activity (e.g., primarily farming) and industrially. It has an extremely high solubility in water and consequently has a low residence time in the air. It is, however, a significant component of atmospheric aerosols typically forming ammonium sulfate or chloride.

#### 3.01.4.1.3 Particulates

Solid particles suspended in the atmosphere may also have influence on corrosion. They generally comprise three classes of material: dusts (e.g., from erosion of soil or sand), soots (i.e., derived from incomplete combustion) and aerosols (primarily sea salt and ammonium sulfate). Particles of all types play an important role in atmospheric corrosion as was found by Vernon and shown in Figure 12. They act as nuclei for the initial corrosion attack and as some particles are hygroscopic their presence tends to increase the periods of wetness of the steel surface. The most important particulate species in industrial atmospheres was historically ammonium sulfate, although chlorides<sup>96</sup> also have an effect. In marine environments (and as the ground-level  $\text{SO}_2$  concentrations decrease, increasingly in most environments) sea-derived chlorides have the most pronounced effect. In the presence of chlorides, rusting can continue at humidities as low as 35%.<sup>97,98</sup> As a rule, the chloride concentration in the air falls off rapidly with distance inland, but steel rusts at almost incredible rates on surf beaches where it is exposed to a continuous spray of sea salts. This is shown by the results of some tests made in Nigeria that are given in Table 8 and are confirmed in numerous other tests by other workers over many years. Cole and co-workers have developed a holistic model of atmospheric corrosion that considers the generation of salt in the ocean, its long-range transport and final deposition on materials as a function of distance from the sea.<sup>99,100</sup>

The number and composition of particulate matter in the atmosphere has changed markedly in view

of the change in overall pollution levels. Thirty years ago in the UK, the most aggressive species were: salt and salt/sand from marine or deiced locations, emitted ash from iron smelters, plume ash from incinerators and coal-fired boilers, and coal mine soot and dust.<sup>101</sup> However, the first of these sources now dominates the impact on corrosion. Detailed analysis of the nature and form of particulates is possible provided care is taken to separate and secure the water-soluble aerosol component. A recent analysis of air-borne solids in Hong Kong<sup>102</sup> has identified, for that location, three principle sources of ions derived from atmospheric particulates: fine aerosols derived from atmospheric transformations (e.g., the reaction of sulfate with ammonia to produce ammonium sulfate); coarse particles derived from soils and sea salt derived aerosol, **Table 9**.

Particles were found to have a bimodal size distribution with the larger particles in the size range 2–10 µm and the smaller particles in the range 0.1–1 µm. The effect on corrosion was found to depend on the size of the aerosols, which was also related to their composition. Thus, rusts formed from the finer aerosol particles have composition related to sulfates, while those from coarse particles are mainly related to

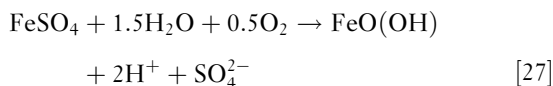
chloride. Sea salt was found to contribute most to the corrosion of mild steel while calcium ions inhibited corrosion. Ammonium, potassium, and magnesium ions had much less of an effect on the corrosion of steel.

The effect on corrosion of combustion derived ashes (fly-ash) from coal and oil, as well as inert glass powder of similar size range as studied by Askey *et al.*<sup>103</sup> They found that the ashes from oil combustion were considerably more corrosive than those derived from coal combustion due to the much higher acidity of the former. In general, the effect of the fly-ash particulates was in approximate proportion to the quantity of ions that were released into solution indicating that a primary mechanism controlling corrosion was the resistance of the surface electrolyte. The presence of inert borosilicate glass particles on the steel surface was found to have a small, but statistically significant affect on the corrosion rate, increasing it by between 50% and 100% compared with the clean, uncontaminated surface. This effect was ascribed to a mechanism involving local differential aeration at the microcrevice formed between the particle and the surface.

### 3.01.4.2 Mechanism of Atmospheric Corrosion of Iron

#### 3.01.4.2.1 Acid regeneration cycle

Atmospheric corrosion of steel tends to initiate at local sites on the metal surface. The initial distribution of corroding sites is correlated with the presence of active surface-breaking manganese sulfide inclusions. These dissolve to form sulfide species that react locally with iron forming sulfide films that promote local corrosion.<sup>104,105</sup> As noted previously, sulfur dioxide from the air also absorbs onto the surface of clean steel, and into rust layers, and reacts to form a sulfate-containing electrolyte in the rust. During corrosion, ferrous sulfate is formed, which then reacts with atmospheric oxygen to form iron oxy-hydroxide:



In this way, the sulfate is regenerated and the local acidity is increased. Nests of sulfate species are frequently found in corrosion products after atmospheric exposure and the mechanism is consistent with these observations. Recent work using high-resolution analytical studies have found that the initial absorption of sulfur dioxide, and subsequent corrosion of steel, was local in nature. Importantly, it was found that SO<sub>2</sub> on its own is insufficient to

**Table 8** Effect of sea salts on the rate of corrosion of ingot iron<sup>a</sup>

Distance from surface	Salt content of air <sup>b</sup>	Rate of rusting (mm year <sup>-1</sup> )
50 yd	11.1	0.950
200 yd	3.1	0.380
400 yd	0.8	0.055
1300 yd	0.2	0.040
25 miles	–	0.048

Supply Tests in Nigeria carried out on behalf of BISRA.

Source: Sixth Report of the Corrosion Committee, Spec. Rep. No. 66, Iron and Steel Institute, London, 1959.

<sup>a</sup>The specimens were of ingot iron and were exposed for 1 year.

<sup>b</sup>The salt content of the air was determined by exposing wet cloths, and is expressed as mg NaCl per day (100 cm<sup>2</sup>)<sup>-1</sup>.

**Table 9** Principle atmospheric particulate species collected in Hong Kong

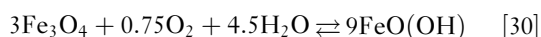
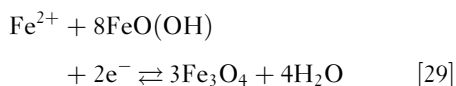
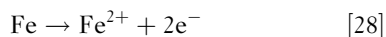
Particle group	Major ionic species	Variance of composition accounted
Fine particles	SO <sub>4</sub> <sup>2-</sup> , NH <sub>4</sub> <sup>+</sup> , K <sup>+</sup>	31%
Nonsea salt coarse particles	NO <sub>3</sub> <sup>-</sup> , Mg <sup>2+</sup> , Ca <sup>2+</sup>	30%
Sea salt	Cl <sup>-</sup> , Na <sup>+</sup>	22%

Source: Ngai T. Lau; Chak K. Chan; Lap I. Chan; Ming Fang *Corros. Sci.* **2008**, 50(10), 2927–2933.

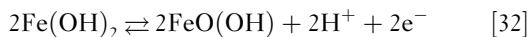
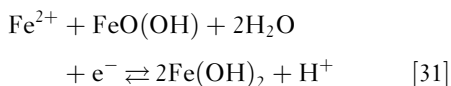
form sulfate nests and the presence of an additional oxidant ( $\text{NO}_2$  or  $\text{O}_3$ ) was essential for the detection of sulfate nests.<sup>106</sup>

### 3.01.4.2.2 The electrochemical mechanism

An electrochemical mechanism for atmospheric rusting was first proposed by Evans in 1963, but was not accepted at the time.<sup>107</sup> Its basic conception is that an electrochemical cell is formed between iron and iron oxy-hydroxide. At the anode, ferrous ions are produced in the normal way while at the cathode  $\text{FeO}(\text{OH})$  is reduced. At some later point, the reduced iron oxide is reoxidized by atmospheric oxygen<sup>108</sup>; hence, a net increase in the amount of  $\text{FeO}(\text{OH})$  ensues. Evans' original cycle is reproduced below:



The above mechanism is now generally accepted although the indicated role of magnetite as the reduced species is probably only true under relatively reducing conditions. Thus, electrochemical reduction of lepidocrocite,  $\gamma\text{-FeO}(\text{OH})$ , results in a thin surface layer containing  $\text{Fe}^{2+}$  species which may either dissolve into the electrolyte or, at more negative potentials, may form magnetite.<sup>109</sup> The reduced surface layer, containing ferrous hydroxide, is easily reoxidized back to  $\gamma\text{-FeO}(\text{OH})$ . Hence, reactions [29] and [30] become:



On the other hand, magnetite oxidizes preferentially to maghemite,  $\gamma\text{-Fe}_2\text{O}_3$ , which is relatively resistant to reduction, as is magnetite. Likewise, goethite,  $\alpha\text{-FeO}(\text{OH})$ , is considerably more resistant to electrochemical reduction compared with lepidocrocite.<sup>110</sup> Hence, the electrochemical mechanism will only operate where there is sufficient lepidocrocite present while rusts largely containing goethite would be expected to be resistant to reduction and, hence, dimensionally more stable and more protective.

### 3.01.4.2.3 The wet-dry cycle

During atmospheric exposure of any material, a repeated, endless, and chaotic cycle of wetting and drying occurs, caused by precipitation, heat and wind drying of wetted surfaces, absorption and deposition of pollutants and wetting and drying of surfaces as a function of the RH. The cycles of wetting and drying strongly influence the corrosion of materials. For steel that this cycle is an essential part of the electrochemical mechanism described above was confirmed by an elegant series of experiments by Stratmann and co-workers.<sup>111–114</sup> In these studies, the mass loss of iron and the oxygen consumption rate were measured simultaneously as a function of the wetting and drying of the iron surface. The outstanding feature of the variation in corrosion rate with wetting and drying cycle, **Figure 15**, is the surprisingly large contribution that occurs during the drying part of the cycle. This was the first experimental evidence to demonstrate this unexpectedly large effect, which has since been confirmed for other materials during atmospheric corrosion.<sup>115</sup>

Notable from **Figure 15** is the profound effect on the corrosion rate during drying that is a result of the alloying copper with iron. This work thus provides insight into the well-known beneficial effect of copper on the atmospheric corrosion of low alloys steels. This is discussed in more detail below.

### 3.01.4.3 Corrosion Product Composition

Until quite recently, it was not thought useful to analyze rusts in detail partly because X-ray diffraction indicated that they were poorly crystalline. Notwithstanding this, it was known that corrosion products on steel during atmospheric exposure were similar to those formed in immersed conditions as might be expected by consideration of the electrochemical mechanism of corrosion. Thus, corrosion products on plain carbon steel after atmospheric rusting contain magnetite,  $\text{Fe}_3\text{O}_4$ , lepidocrocite,  $\gamma\text{-FeO}(\text{OH})$  and goethite,  $\alpha\text{-FeO}(\text{OH})$  in varying amounts, the last being thermodynamically the most stable.

Recently, rather detailed studies have begun to be performed using a variety of techniques. A Mössbauer analysis of the corrosion products on mild steel after 35 years exposure in a semirural Japanese location found that the rusts were composed mostly of goethite with minor amounts of lepidocrocite and trace amounts of magnetite.<sup>116</sup> In addition, the crystallite size of the goethite component was found to be

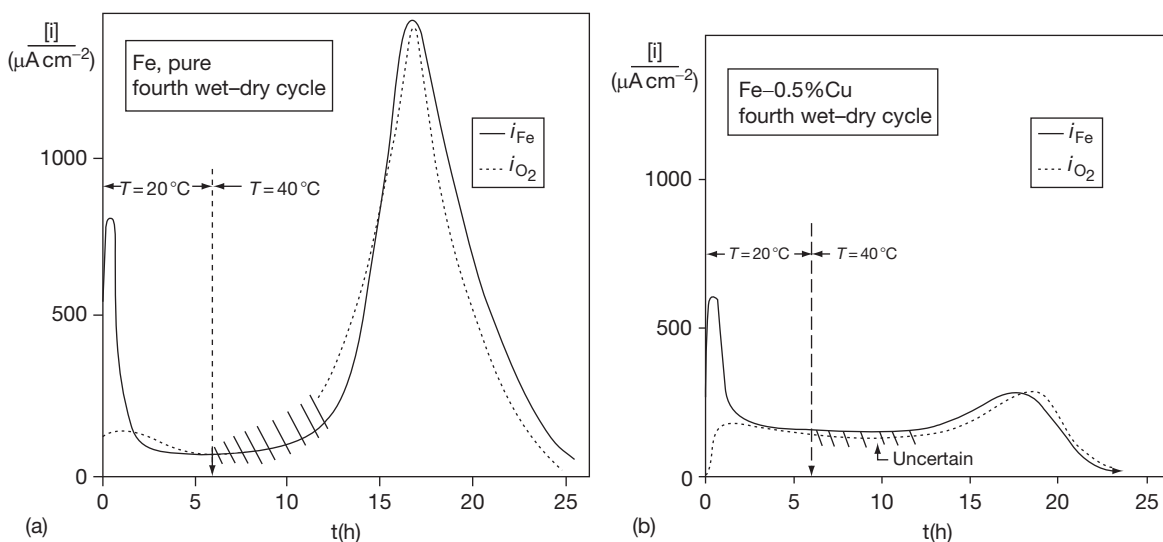


**Figure 15** Atmospheric corrosion rate of Fe and Fe-0.5%Cu alloy over the 4th cycle of wetting ( $20^\circ\text{C}$ ) and drying ( $40^\circ\text{C}$ ), after. Reproduced from Stratmann, M.; Bohnenkamp, K.; Ramchandran, T. *Corros. Sci.* **1987**, 27(9), 905–926.

bimodal, with more than 80% larger than 12 nm but the remaining fraction smaller than 9 nm. In laboratory experiments, the composition of adherent and nonadherent rusts formed by artificially corroded steel at varying chloride concentrations were also studied by Mössbauer analysis. Nonadherent rust was found to consist of lepidocrocite, goethite, with traces of akaganeite and magnetite.<sup>117</sup> The composition of the corrosion products was essentially independent of the exposure times and chloride concentration. Studies of steels exposed over 16 years in various industrial locations in the United States found similar compounds with the difference that maghemite was identified rather than the isostructural magnetite.<sup>118</sup>

In summary, the corrosion product (rust) layer that is developed on steel after long-term exposure in the atmosphere contains species that may be expected from thermodynamic considerations. Thus, the majority component is the most stable phase (goethite), which appears as the outer, and thickest, layer. Depending on the environment and conditions of exposure, an intermediate layer of corrosion product contains lepidocrocite while magnetite and maghemite are concentrated in a region adjacent to the steel substrate, although they may also be present as isolated crystallites within the intermediate layer. In marine environments, minor amounts of akaganeite are also commonly present. The phases are all finely grained (and commonly nano-crystalline) with a decrease in grain size and an increase in the volume fraction of goethite associated with improved corrosion resistance.

### 3.01.4.4 Atmospheric Corrosion Kinetics

#### 3.01.4.4.1 Climatic variation

Some representative figures to show how the rate of corrosion of carbon steel in the open air varies in different parts of the world are given in Table 10. They relate to  $100 \times 50 \times 3.2$  mm pieces of ingot iron freely exposed in a vertical position for 1 year and derive from historic data from the former BISRA.<sup>8</sup>

The results follow an expected pattern with by far the highest rate of corrosion being observed on a surf beach at Lagos, Nigeria. Indeed, this environment is so aggressive that the measured corrosion rate is several times that expected under immersed conditions. Conversely, the low rates of corrosion observed at Khartoum, Abisko, Delhi, Basrah, and Singapore are primarily associated with the absence of serious pollution. Moreover, at most of these locations the RH is low, for example, at Khartoum the RH lies below the critical value for rusting throughout the whole year.

Despite these results, it should not be assumed that corrosion rates of steel will necessarily be low in all comparatively nonpolluted desert environments. In regions such as the Arabian Gulf, considerable variations in corrosion rates may occur between inland and coastal sites. This arises not only from the salt content of the air but also from sand which is blown on to the steel. Although temperatures are high during the day, condensation occurs at night. The effects of different types of sand on the corrosion of mild steel have been studied.<sup>119</sup> It was concluded



**Table 10** Atmospheric corrosion rates of mild steel exposed outdoors in different climates

Type of atmosphere	Site	Corrosion rate ( $\text{mm year}^{-1}$ )
<i>Great Britain</i>		
Rural or suburban	Godalming	0.048
	Llanwrtyd Wells	0.069
	Teddington	0.070
Marine	Brixham	0.053
	Calshot	0.079
Industrial	Motherwell	0.095
	Woolwich	0.102
	Sheffield	0.135
	Frodingham	0.160
	Derby	0.170
<i>Overseas</i>		
Rural or suburban	Khartoum	0.003
	Abisko, North Sweden	0.005
	Delhi	0.008
	Basrah	0.015
	State College, PA, USA	0.043
Marine	Berlin-Dahlem	0.053
	Singapore	0.015
	Apapa, Nigeria	0.028
	Sandy Hook, NJ, USA	0.084
	Congella, South Africa	0.114
Marine/industrial	Pittsburgh, PA, USA	0.108
Industrial	Lagos	0.615
Marine, surf beach		

that fine sand has a higher salt content and is more corrosive than coarse sand within the size range  $<0.25\text{--}2.4\text{ mm}$ . Similarly in Canadian arctic and sub-arctic conditions corrosion rates as low as  $2\text{--}5\text{ }\mu\text{m year}^{-1}$  were recorded at inland sites while within 1 km of the sea much higher rates ( $21\text{--}34\text{ }\mu\text{m year}^{-1}$ ) were measured.<sup>120</sup> Thus, the rate of atmospheric corrosion is, as expected, dependent upon the local pollutant concentrations (e.g., affecting the surface chemistry and electrochemistry) as well as the local climatic conditions (e.g., controlling the total duration of corrosion, or time of wetness). It is important to remember that all quoted corrosion rates relate to average general penetration and take no account of pitting. Serious pitting of steel exposed to atmospheric corrosion is uncommon on simple test plates. However, it may be necessary to allow for this in some practical cases, where local attack may be occasioned by faulty design and other factors.

In reviewing this data, despite its historic nature, there is no reason to doubt the validity of the results in similar conditions. Thus, rates for the

atmospheric corrosion of steel can be expected to vary from exceptionally high  $>600\text{ }\mu\text{m year}^{-1}$ , to very low  $<5\text{ }\mu\text{m year}^{-1}$ . What has changed, and this is an important consideration, is that the industrial pollutant concentrations have decreased dramatically over the last 20–40 years and that rate data for a particular location (especially if it is inland and was close to industry) may no longer be valid.

#### 3.01.4.4.2 Conditions of exposure

It has long been known that sheltering and orientation of exposed steel during atmospheric corrosion testing influences significantly the measured corrosion rates. For example, the results of tests at Derby in the 1940s<sup>121</sup> show that specimens exposed at  $45^\circ$  to the horizontal corroded 10–20% more than specimens exposed vertically and that 54% of the total loss was on the underside. Likewise, for similar American tests<sup>122</sup> on specimens exposed at  $30^\circ$  to the horizontal, 62% of the total corrosion loss was on the underside. This influence is further demonstrated in experiments carried out 228 m from the sea at Kure Beach, North Carolina.<sup>123</sup> In these tests, the corrosion rates over a 4-year period varied by a factor of five depending on the orientation and degree of sheltering. Generally, east (sea) facing specimens exposed at  $30^\circ$  from the horizontal corroded at the highest rate while west (land) facing specimens exposed at the same angle corroded at the lowest rate. This can be ascribed to the prevailing wind direction driving sea salt aerosols onto the specimens.

The orientation of steel during atmospheric exposure tests is therefore found to have great influence on the final corrosion rates measured. This is because the amount of moisture and pollutants that can reach, and remain on, surfaces vary with compass direction, prevailing wind, sun, etc. In particular, the ground-facing side of a horizontal surface is protected from rain but it is also shielded from the drying action of the sun and often of the wind. Thus, condensation tends to remain in contact with the steel there for longer periods; moreover, harmful solid particles and soluble salts are not washed away by rain events. Consequently, and possibly counter intuitively, the ground-facing side is often found to corrode more rapidly than the sky-facing side. The same considerations apply to steel exposed obliquely. The relative corrosion of the opposite faces of a vertical steel plate will largely depend on the direction of the prevailing winds, pollution, rain and sun (i.e., whether the face is oriented towards the south (in the north of the equator) or the north (in the south of the equator).

### 3.01.4.4.3 Damage functions

Generally, in the majority of environments, except those that have exceptionally high levels of pollutant or salt aerosol, the corrosion rate of steel tends to decrease with time. This is a common observation, for example in recent work by Zhang *et al.*<sup>124</sup> for two different types of steel in a marine environment, **Figure 16**.

As may be seen in **Figure 16**, the tendency is for corrosion rates to decrease with time. Such behavior may be modeled simplistically by an exponential expression such as:

$$\text{Rate} = A t^n \quad [33]$$

where  $A$  is a constant,  $t$  is time and  $n$  is the kinetic rate order (or exponent). For  $n$  equal to 1, linear kinetics ensue and the reaction rate is likely to be chemical reaction controlled however, for diffusion-controlled parabolic kinetics,  $n$  is equal to 0.5. Any other value for  $n$  implies a mixed control process. For atmospheric corrosion of steel, the value of  $n$  commonly lies between 0.5 (more typical of weathering steel) and 0.8 (more common for carbon steel).

Traditionally field exposures have been used to determine the corrosion rates of materials at particular environments. Initially, just corrosion rate data were collected but gradually such work was extended to include simultaneous collection of an increasing range of other atmospheric data, including: RH, air and metal temperature, precipitation, sunlight, as well as deposition of chloride, sulfate, nitrate, and analysis of rain water. The concept behind this considerable amount of effort is to develop damage functions (or dose–response relationships) for atmospheric corrosion

so that predictive models may be developed. This approach culminated with an international program run under the auspices of the International Standards Organisation Technical Committee 156, Working Group 4 (ISO TC156/WG4) and the collaboration of 12 nations (Canada, Czechoslovakia, Finland, France, Germany, Japan, Norway, Spain, Sweden, UK, USA, and Russia) that commenced in 1986. The primary purpose of this was to verify the ISO 9223–9225 classification standards for the aggressiveness of atmospheres. A secondary, arguably more scientific, purpose was to collate the results across numerous and widely geographically separated locations in order to determine the best fit to the data by multivariate least squares regression analysis.

Results from the ISO-CORRAG program were published gradually over a number of years for example by Dean *et al.*<sup>125–127</sup> Generally, the data show strong correlation between the corrosion rates for steel with the corrosion rates of the other tested materials (zinc, copper, aluminum) as might be expected. However, the scientific aim, which was to describe the corrosion rate of materials effectively as a regression equation over the main variables, was not completely successful. Thus, the use of the exponential rate expression alone was found to account for ~75% of the observed corrosion rate variation for steel. Regression of the time exponent against time of wetness and chloride deposition rate improved the regression fit only slightly. A more complete analysis of the data by Mikhailov, Tidblad, and Kucera<sup>128</sup> resulted in two rate expressions that reflect the observed increase in corrosion rate with temperature to 10 °C, thereafter decreasing:

Below 10 °C:

$$C = 1.77[\text{SO}_2]^{0.52} \exp(0.020RH) \exp\{0.150(T - 10)\} \\ + 0.102[\text{Cl}^-]^{0.62} \exp(0.033RH + 0.040T)$$

Above 10 °C:

$$C = 1.77[\text{SO}_2]^{0.52} \exp(0.020RH) \exp\{-0.054 \\ (T - 10)\} + 0.102[\text{Cl}^-]^{0.62} \\ \exp(0.033RH + 0.040T)$$

where:  $C$  is the corrosion rate of steel ( $\mu\text{m year}^{-1}$ ),  $RH$  is relative humidity (%),  $T$  is temperature (°C),  $[\text{SO}_2]$  is the concentration of sulfur dioxide ( $\mu\text{g m}^{-3}$ ) and  $[\text{Cl}^-]$  is the chloride deposition rate ( $\text{mg m}^{-2} \text{day}^{-1}$ ). These expressions, regressed over 128 datasets, provide a correlation coefficient ( $R^2$ ) of 0.85. Dean commented on the overall results of the ISO-CORRAG program:

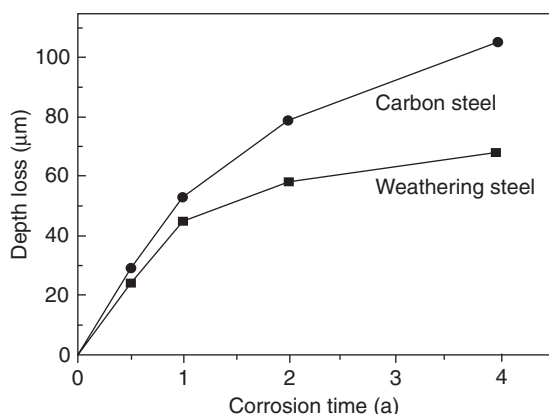


**Figure 16** Thickness loss of weathering steel and mild steel versus exposure time. Reproduced from Zhang, Q. C.; Wua, J. S.; Wang, J. J.; Zheng, W. L.; Chen, J. G.; Li, A. B. *Mater. Chem. Phys.* **2003**, 77(2), 603–608.

**Table 11** Kinetic parameters for the early stages of atmospheric corrosion of iron

Activation energy at 90% RH:	20 h	60 h	100 h
$\Delta E_{\text{act}}$ for 0.8 ppm $\text{SO}_2$	170 kJ mol <sup>-1</sup>	140 kJ mol <sup>-1</sup>	115 kJ mol <sup>-1</sup>
$\Delta E_{\text{act}}$ for 20 $\mu\text{g cm}^{-2}$ of NaCl;	70 kJ mol <sup>-1</sup>	45 kJ mol <sup>-1</sup>	35 kJ mol <sup>-1</sup>
Chemical reaction orders at 90% RH:	20 h	60 h	100 h
f [ $\text{SO}_2$ ]	1.56	1.46	1.40
f [NaCl]	0.70	0.60	0.61
Kinetic order (i.e., $n$ in $t^n$ ) at 90% RH	0.1 ppm	0.4 ppm	0.8 ppm
$n$ for the indicated p $\text{SO}_2$	0.78	0.76	0.68
$n$ for the indicated [NaCl]	10 $\mu\text{g cm}^{-2}$	20 $\mu\text{g cm}^{-2}$	40 $\mu\text{g cm}^{-2}$
	0.89	0.84	0.64

Source: Cai, J.-P.; Lyon, S. B. *Corros. Sci.* **2005**, 47(12), 2956–2973.

“Some other environmental variables will need to be found to improve this approach to predicting atmospheric corrosion.” Nevertheless, the fact that comparatively simple rate expressions may be used to provide a guide to atmospheric corrosion prediction is helpful.

Kinetic rate parameters can be measured with more control in the laboratory. For example, activation energies and reaction rate orders as a function of chloride contamination and gas-phase  $\text{SO}_2$  concentration have been determined in the laboratory for the early stages of the atmospheric corrosion of iron (i.e., between 0 and 120 h).<sup>129</sup> From the data in [Table 11](#) it can be noted that for exposure in gas-phase  $\text{SO}_2$ , activation energies, and kinetic and chemical rate orders, are consistent with the controlling mechanism for atmospheric corrosion of iron being slow solution-phase oxidation of sulfite to sulfate ion. Conversely, the corrosion process with surface chloride contamination is evidently much easier. These data provide input into corrosion models that may be extended out to longer exposure times in order to generate predictive corrosion models.

### 3.01.4.5 Weathering Steel

#### 3.01.4.5.1 Alloying effects

Historically, from the 1940s, a large degree of effort was put into the development of low alloy steels that had improved overall corrosion resistance. By the early 1960s and into the 1970s, this program of testing had largely been completed with the development of a generation of optimized weathering steels based on steel compositions containing at least 0.2% Cu with small additional amounts of P and Cr. The beneficial effect of copper additions to steel has been referred to already in [Figure 15](#) and [Figure 16](#). In turn, [Figure 17](#) refers to trials of 9 years duration at Rotherham in the

United Kingdom<sup>130</sup> while similar curves based on American tests,<sup>131</sup> in [Figure 18](#), show substantially the same features. The fact that the rates of corrosion are markedly slower in the American than in the British tests is mainly due to differences in the corrosiveness of the respective atmospheres.

The effects of the various alloying elements are not necessarily directly additive although same additions are synergistic (e.g., Cu+P is better than Cu on its own). Bearing this in mind, the practical effect of individual elements can be summarized as follows.

- Copper additions up to ~0.4% give a marked improvement, but further additions make little difference.
- Phosphorus, at least when combined with copper, is also highly beneficial. However, in practice, levels above ~0.10% adversely affect mechanical properties.
- Chromium, in fractional percentages, has a significant influence on corrosion rates.
- Nickel, while reducing corrosion rates a little, is not as important in its effect as the aforementioned elements.
- Manganese may have a particular value in chloride-contaminated environments, but its contribution is little understood.
- Silicon is in a similar position to manganese, with conflicting evidence as to its value.

#### 3.01.4.5.2 Wetting and drying

The improvement in corrosion resistance for weathering steels compared with carbon steel is found to depend on the nature and amounts of the alloying elements and the corrosive environment. Thus, weathering steels show greatest advantage when they are freely exposed to the open air in industrial environments, that is, where they are subjected to atmospheric

wetting and drying. The effect of variations in surface wetting is illustrated in **Figure 19**, which compares the relative rates of corrosion of a weathering steel and a carbon steel at a UK industrial location after 9 years exposure.<sup>132</sup> The greatest rate of corrosion was on panels facing the north-westerly direction, which is wettest for the longest period of time.

Initially, weathering steel appears to corrode like mild steel. However, unlike mild steel whose oxide repeatedly spalls off, the surface rust layer on weathering steel stabilizes with time, provided that the exposure conditions allow the steel to dry out periodically. The rust then becomes darker, granular, and tightly adherent whilst any pores or cracks

become filled. This protects the underlying steel by reducing the permeability of the oxide layer to water and air both of which must be present simultaneously at the metal surface for rusting to continue.

The distinguishing feature of the behavior of the slow-rusting low-alloy steels is the formation of this protective rust layer, which generally contains a finer grained (nano-crystalline) oxide particles and a higher proportion of the stable goethite phase compared with the rust layers formed on carbon steel. The first mechanistic evidence for this improvement in performance was made by Stratmann and is shown in **Figure 15**. In copper-free steel, a large fraction of the total corrosion process occurs during the drying phase of the wet-dry cycle. However, for copper-containing steel, the large increase in corrosion rate towards the end of the drying cycle is absent.<sup>112</sup> The precise reason for this suppression is not yet wholly clear however, it may be interpreted in terms either of a stabilization of iron oxy-hydroxide (rust) to reduction or in terms of the cathodic reduction of oxygen being inhibited.<sup>133</sup> Either way, the redox cycling (and associated volume changes) is suppressed resulting in a more compact and more protective rust layer.

### 3.01.4.5.3 Applications

The most widespread use of weathering steels has been for structural steelwork in buildings, bridges, roadside furniture, etc. especially where maintenance painting is particularly difficult, dangerous, inconvenient, or expensive. Bridges over land, rivers, railways, roads and estuaries fall into this category, although in the last two cases care should be taken with respect to airborne salinity and ensuring adequate drainage to

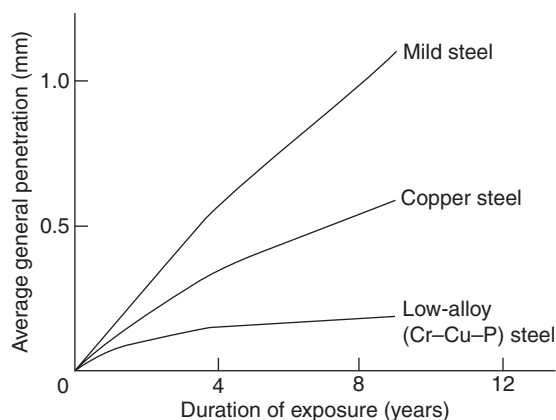


**Figure 17** Effect of low-alloy additions on the corrosion of steel in Rotherham, UK. Reproduced from Edwards, A. M. *Proc. Symp. on Developments in Methods of Prevention and Control of Corrosion in Buildings*, British Iron and Steel Federation, London, 1966.

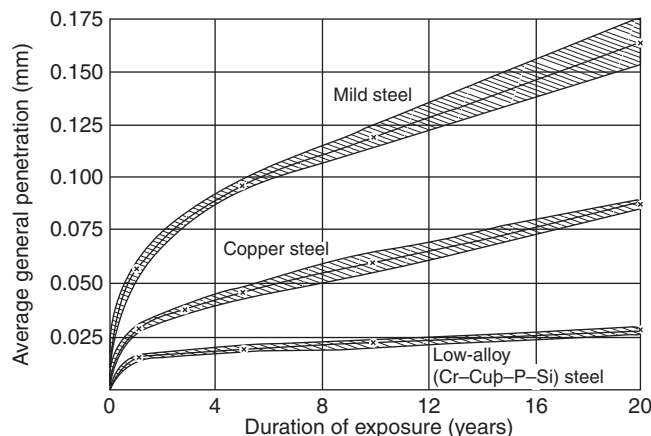


**Figure 18** Effect of low-alloy additions on the corrosion of steel outdoors at Kearny, NJ, USA. Reproduced from Larrabee, C. P.; Coburn, S. K. *Proc. First International Congress on Metallic Corrosion*, 1962; Butterworths: London, pp 276.

avoid the possibility of continuous wetting. Road bridges can be affected by salt-laden atmospheres or water, produced as a consequence of winter ice and snow clearing with deicing salt and grit. Chloride can be in the form of an airborne spray thrown up by passing vehicles or as a result of leaks in the bridge deck. In the presence of salt-water many materials, including steel, paint, reinforced concrete, aluminum, etc. deteriorate at an accelerated rate. Weathering steels are no exception, and higher than normal corrosion rates should be expected if they are exposed to saline waters or frequent spraying with salt. Albrecht has described the applications and pitfalls of using weathering steel in US highway bridges in an informative paper that is well worth consultation.<sup>134</sup>

#### 3.01.4.5.4 Next generation weathering steels

Recent research has been aimed at further optimization of the performance of weathering steels, partly by more detailed understanding of the nature of the rusts that are formed during exposures. Thus, X-ray diffraction, vibrational spectroscopy, and elemental analysis have all been applied to the analysis of various rusts on the micrometer scale. This has provided evidence of doping of the rust layers by  $\text{Cr}^{3+}$  and

$\text{Ni}^{2+}$ , which, in turn, limits cathodic oxygen reduction and promotes the stabilization of the goethite phase.<sup>135,136</sup> In the light of these results, more advanced weathering steels, based on modern high-strength, low-alloy compositions, have been developed,<sup>137</sup> Table 12.

The substitution of nickel for chromium, and the slightly increased level of copper, results in a considerably improved performance particularly in those atmospheres where the importance of chloride has increased due to the reduction in sulfur dioxide levels. The amount of corrosion on the novel material was less than 1/20 that of conventional weathering steel after 9 year exposure to a marine atmosphere in Japan.<sup>136</sup> It was suggested that this improved performance was due to nickel doping of the rust that resulted in an ion exchange process leaving a net negative charge at the inner rust layer, hence 'repelling' chloride ions.

#### 3.01.4.6 Classification of Atmospheres

Classification of the atmosphere into various corrosivity (i.e., severity of corrosion) categories depending on local environment has been the work of a

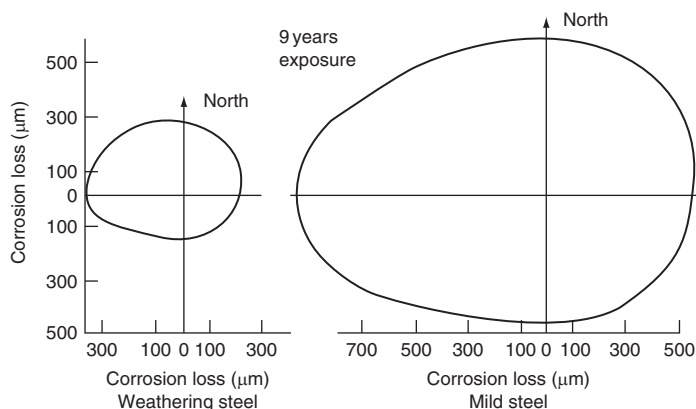


**Figure 19** Corrosion losses of steels exposed vertically, facing different compass directions. Reproduced from Hooper, R. A. E.; Lee, B. V. Proc. 12th International COR-TEN Conference, Florida, 1985, United States Steel, Pittsburgh, 1985.

**Table 12** Compositions of conventional and 'advanced' weathering steel

Material	Chemical composition (mass %)						
	C	Si	Mn	P	Cr	Cu	Ni
'Advanced' weathering steel	0.05	0.04	1.02	0.008	–	0.40	3.03
Conventional weathering steel	0.10	0.42	1.54	0.004	0.52	0.30	0.32

Source: Kimura, M.; Kihira, H.; Ohta, N.; Hashimoto, M.; Senuma, T. *Corros. Sci.* **2005**, *47*, 2499–2509.



number of national standards bodies. In the EU, this standardization is encompassed within BS EN 12500,<sup>138</sup> and consistent with ISO 9223–9226. The standard atmospheric corrosivity classifications are reproduced in **Table 13** with the corresponding expected corrosion rates for carbon steel in **Table 14**.

An example of this approach is given in **Table 15** where corrosion rates in various European (mainly Scandinavian) locations are matched to **Table 14** to derive an atmospheric corrosivity classification for that location.

### 3.01.5 Corrosion in Water

#### 3.01.5.1 Water Composition

The composition of water is clearly of importance in determining the rate of corrosion of steel exposed to it. Some of the more important factors that contribute to corrosion are the dissolved gas content (primarily

oxygen and carbon dioxide), the nature and amount of dissolved solids (which influences the electrical conductivity, pH and hardness of the water), the presence of organic matter (such as detergents, oils, wastes, etc.) and the presence or absence of microbial species such as bacteria, algae, or fungi.

##### 3.01.5.1.1 Dissolved gases

Oxygen is the most important dissolved gas in water and, at  $\text{pH} > 3$ , is generally the main cathodic reactant for the corrosion of steel. Thus, in neutral or near-neutral water, dissolved oxygen is necessary for any appreciable corrosion of steel. Increasing the oxygen availability for reaction either by increasing the dissolved oxygen concentration or by increasing its mass transfer rate (i.e., in a flowing system) will, in almost every case, result in an increase in corrosion rate. In view of this, the control of oxygen concentration in solution is one of the primary methods for

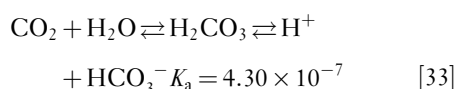
**Table 13** ISO standard classifications for atmospheric corrosivity

Corrosivity category	Corrosivity	Examples of typical environments	
		Indoor	Outdoor
C1	Very low	Heated spaces with low RH and insignificant pollution: schools, museums, etc.	Dry or cold zonesatmospheric environment with very low pollution and time of wetness for example, certain deserts, central Antarctica
C2	Low	Unheated spaces with varying temperature and RH. Low frequency of condensation and low pollution, for example, storage, rooms, sports halls	Temperate zones: environment with low pollution ( $\text{SO}_2 < 12 \text{ mg m}^{-3}$ ), for example, rural areas, small towns. Dry or cold zones: environment with short time of wetness, for example, deserts, subarctic areas
C3	Medium	Spaces with moderate frequency of condensation and moderate pollution from production process, for example, food-processing plants, laundries, breweries, dairies	Temperate zone: environment with medium pollution ( $\text{SO}_2: 12\text{--}40 \text{ mg m}^{-3}$ ) or some effect of chlorides, for example, urban areas, coastal areas with low deposition of chlorides
C4	High	Spaces with high frequency of condensation and high pollution from production process, for example, industrial processing plants, swimming pools	Tropical zone: atmosphere with low pollution Temperate zone: environment with high pollution, ( $\text{SO}_2: 40\text{--}80 \text{ mg m}^{-3}$ ) or substantial effect of chlorides, for example, polluted urban areas, industrial areas, coastal areas, without spray of salt water, strong effect of deicing salts. Tropical zone: environment with medium pollution
C5	Very high	Spaces with almost permanent condensation and/or with high pollution from production process, for example, mines, caverns for industrial purposes, unventilated sheds in humid tropical zones	Temperate zone: environment with very high pollution ( $\text{SO}_2: 80\text{--}250 \text{ mg m}^{-3}$ ) and/or strong effect of chlorides, for example, industrial areas, coastal and off shore areas, with salt spray. Tropical zone: environment with high pollution and/or strong effect of chlorides

Source: BS EN 12500: Protection of metallic materials against corrosion: Corrosion likelihood in atmospheric environment, classification, determination and estimation of corrosivity of atmospheric environments.

corrosion control of carbon steel (and indeed many other materials).

The presence of dissolved ambient carbon dioxide from the atmosphere ( $p\text{CO}_2 \sim 385$  ppm in 2008) alters the pH of water by the reaction:



Indeed, the pH of most natural (nonsaline) water exposed to the atmosphere is acidic due to the above equilibrium. Thus, changes in the dissolved  $\text{CO}_2$  level will tend to change the pH and, consequently, any process that depends upon pH. In near-neutral solutions, this will not affect the corrosion rate of steel directly. However, a change in pH may affect the stability of protective deposits and scales on the steel, particularly those containing calcium carbonate, which will tend to dissolve as the pH falls.

At higher  $\text{CO}_2$  pressures the situation changes significantly. Thus, in 3% sodium chloride solution at 1 atm. of carbon dioxide the corrosion rate of steel is increased substantially above what might be expected at the equilibrium pH of  $\sim 3$  with hydrogen

evolution as the cathodic reaction. Although the concentration of hydrogen ions in solution is relatively low at pH 3 (i.e.,  $10^{-3}$ ), carbonic acid dissociates as shown in eqn [34] to produce hydrogen ions immediately adjacent to the cathode. Thus, under these conditions, the hydrogen evolution reaction is controlled by mass transfer of carbonic acid to the cathode.<sup>139</sup>

This mechanism largely explains the phenomenon of 'sweet' corrosion, due to  $\text{CO}_2$  in oil and gas recovery and petrochemical production.

### 3.01.5.1.2 Dissolved solids

The effect of dissolved solids is complex. The presence of inorganic salts, notably of chlorides and sulfates, should promote corrosion, because they increase the conductivity of the water, thereby facilitating the electrochemical reactions via improved ion transport in solution. Alkaline waters tend to be less aggressive than acid or near-neutral waters, and corrosion can be well-controlled in a closed system by appropriate water treatment; for example, addition of inhibitors and/or making the water alkaline and the metal passive. Unfortunately, at pH values just insufficient to give complete passivation, there is a high risk of severe pitting, even though the total corrosion rate is reduced, and this is a greater danger in many applications.

The most important property of dissolved solids in fresh waters is whether or not they lead to deposition of a protective film on the steel that will impede the corrosion process. This is determined mainly by the equilibrium between calcium carbonate, calcium bicarbonate, and carbon dioxide and is of fundamental significance and where an appropriate scaling index (e.g., the Langelier index) can provide guidance.<sup>140</sup> Since hard waters are more likely to deposit a protective calcareous scale than soft waters, the former tend to be considerably less aggressive than the latter; also, soft waters can often be rendered less

**Table 14** Correspondence between mass loss of carbon steel after 1 year of exposure and ISO standard atmospheric corrosivity classifications

Corrosivity category	Mass loss per unit area ( $\text{g m}^{-2}$ )	Thickness loss ( $\mu\text{m}$ )
C1	$\leq 10$	$\leq 1.3$
C2	$> 10\text{--}200$	$> 1.3\text{--}25$
C3	$> 200\text{--}400$	$> 25\text{--}50$
C4	$> 400\text{--}650$	$> 50\text{--}80$
C5	$> 650\text{--}1500$	$> 80\text{--}200$

Source: BS EN 12500: Protection of metallic materials against corrosion: Corrosion likelihood in atmospheric environment, classification, determination and estimation of corrosivity of atmospheric environments.

**Table 15** Corrosion rates of carbon steel in various European locations

Environment	Deposition rates ( $\text{mg m}^{-2} \text{day}^{-1}$ )		Corrosion rate ( $\mu\text{m year}^{-1}$ )	Atmospheric corrosivity classification
	$\text{SO}_2$	$\text{Cl}^-$		
Rural	$< 20$	$< 3$	5–10	C2
Urban	20–100	$< 3\text{--}50$	10–30	C2/C3
Industrial	110–200	–	30–60	C3/C4
Marine	$< 10$	$> 100$	10–40	C3
Arctic	$< 10$	$< 3$	4	C2

Source: Bardal, E. *Corrosion and Protection*, Table 8.1; Springer: Berlin, 2004.

corrosive by treating them with lime (calcium hydroxide). Carbonate scales are not the only type that may form in water and, depending on water chemistry, scales of calcium sulfate, magnesium silicate, magnesium hydroxide and iron or manganese oxy-hydroxides may also form.

### **3.01.5.1.3 Microbial effects**

Another important factor is that most natural waters are far from being sterile. They contain greater or lesser amounts of organic matter, both living and dead. Some of the dead organic matter, for example, peat residues, may render the water corrosive by making it acid, but in most cases, the living organisms probably exert the greater influence. In natural seawater, fouling occurs and in freshwaters, algae may grow. A more detailed discussion of microbial corrosion can be found elsewhere in this book.

## **3.01.5.2 Deposits and Scales**

### **3.01.5.2.1 Fouling of surfaces**

During service, the surface of steel in contact with the environment will inevitably tend to become covered with a deposit of some nature. Such deposits may arise from the water chemistry (i.e., carbonate scaling), from corrosion (i.e., the formation of a corrosion product), from bio-films (i.e., slimes from bacterial, algal and other origins), from sediments and silts (i.e., from suspended solids in the water), etc. In all cases, the fouling of surfaces will have an effect on corrosion rates of materials used and on the process or function of the system. These effects need to be understood and allowed for in the design of the system. However, if the anticipated effects are detrimental, the surface fouling must be controlled in some way depending on its origin.

In many systems or processes, fouling deposits tend to form preferentially in the hottest part of the system, often on heat transfer surfaces (e.g., boilers, heat exchangers, etc.), because the solubility of the depositing material is lowered; this is particularly prevalent for carbonate scaling. In other cases, deposits tend to form at the coolest part of the system (i.e., also in heat exchangers) for the same reason. The formation of bio-films is clearly not an issue where the system temperature is sufficient to ensure sterilization. Conversely, in chilled water and air conditioning systems, bio-film formation is a significant hazard.

In addition to a reduction in the efficiency of heat transfer due to the isolation of the metal surface from

the water by a film of low thermal conductivity, fouling deposits can additionally cause significant problems due to constriction of flow, blocking of valves, etc.

### **3.01.5.2.2 Under-deposit corrosion**

Fouling deposits, depending on their nature, often result in enhanced corrosion underneath the deposit. On heat transfer surfaces at sufficiently high temperature, local boiling of water can occur beneath deposits giving rise to concentration of the species in solution at this point and consequent localized corrosion under the deposit. In the absence of heat transfer, under-deposit corrosion may still occur due to the differential aeration mechanism where the anode is localized to an area of lower oxygen concentration under the deposit.

Where water treatment is used to provide corrosion control, then the presence of deposits in the system will result in poor availability of the inhibitor at these locations and, again, increased corrosion will result. This is particularly significant where passivating inhibitors are used as the inhibitor concentration may locally (i.e., under the deposit) fall below the critical concentration required for passivity and, hence, give rise to a significant risk of pitting corrosion.

In many systems, a bio-film of an aerobic species may first colonize the steel surface, which will result in local oxygen depletion under the bio-film. The effect of this is both to promote differential aeration cell corrosion but, more significantly, to create a beneficial environment for possible further colonization under the original film by an anaerobic species, including sulfate reducing bacteria. In this latter case, the metabolic products include reduced sulfur species, particularly sulfides and hydrogen sulfide, both of which are very likely to promote severe corrosion.

## **3.01.5.3 Natural Waters**

### **3.01.5.3.1 Corrosion rates**

As pointed out already, corrosion rates of carbon steel in water vary significantly depending, amongst other things, upon the specific water composition, oxygen concentration, and flow rate in the fluid (i.e., the mass transfer rate of oxygen to the corroding surface). In practice, some form of corrosion protection is generally used for carbon steel in aqueous environments. In a few situations however, unprotected bare steel may be used provided a corrosion allowance is provided for in the design. Such applications include: pipe internals on potable water systems and fire protection systems, where only minimal (or no) water treatment

**Table 16** Rates of corrosion of mild steel in natural waters (total immersion)

Type of water	Test authority	Test site	Test duration	Average corrosion rate ( $\mu\text{m year}^{-1}$ )
Sea water	Institution of Civil Engineers <sup>141</sup> BISRA <sup>142</sup>	Halifax, Nova Scotia	15	108
		Plymouth	15	65
		Emsworth	5	65
Fresh water	Institution of Civil Engineers <sup>141</sup>	Plymouth: reservoir water	15	43
River water	Office Technique pour l'Utilisation de l'Acier <sup>143</sup>	La Cadène: soft water	5	68
		Dôle: hard water	5	10

is possible, etc.; and steel piles for shoring work (e.g., on river banks, jetties, etc.).

For interest, some historic data for corrosion rates in a range of environments are given in Table 16; for low-carbon structural steel tested under the conditions stated. The figures are for the average general penetration over the whole test areas. As an indication of the maximum penetration depth, it may be noted that in the sea-water tests of the Institution of Civil Engineers<sup>141</sup> the maximum depth of pitting for descaled mild steel after 15 years immersion was  $\sim 2.3$  mm; when the steel had been immersed in the as-rolled condition with its millscale, a Figure as high as 7.6 mm was observed. Under half tide immersion conditions, the corrosion rate of steel may be increased by a factor of 2–5 compared with the results for total immersion.

The rates of corrosion quoted in Table 16 are sufficiently low that with a suitable corrosion allowance they can be used unprotected with an anticipated life for structures of 40–50 years. Traditionally, low-strength steel grades were used for pipes and structural elements (such as piling) and required a relatively thick section for strength. Increasingly, such steels are being replaced with higher strength materials of thinner section resulting, obviously, in a decreased lifetime. It is not clear that design engineers fully appreciate that the good lifetime previously achieved for steel in waters was often due to generous thickness allowances with respect to strength and corrosion.

### 3.01.5.3.2 Piped fresh water systems

It is not uncommon for unprotected ferrous materials (i.e., cast iron or carbon steel) to be used in potable (drinking) water systems (as pipes, pumps, valves, etc.), in fire protection systems, as foundation or shoring materials (i.e., steel piles) for support of riverside, or reservoir structures, etc. In fresh water distribution systems, cast iron (historically graphitic iron, recently nodular ductile iron) is more commonly used as a pipe

material as opposed to steel; increasingly polymeric materials are now being used for water systems.

Corrosion problems of ferrous materials in domestic waters are a continuing problem.<sup>144</sup> In 1975, Larson comprehensively surveyed corrosion of steel in fresh water with data gathered from over 30 years of research in Illinois.<sup>145</sup> He developed a classification of waters for corrosion of steel in terms of dissolved oxygen, pH, and dissolved salts, Table 17.

The classification in Table 17 assumes no significant effects from microbial corrosion. In practice, however, microbial effects are ubiquitous and it cannot be assumed that they will always be dealt with satisfactorily by disinfection (e.g., chlorination).<sup>146</sup> However, in potable water systems, where fluid flow is significant, microbial problems are more commonly considered in the industry to affect drinking water quality (e.g., odors and discolouration of the water) than corrosion. Fire protection systems (i.e., risers and sprinklers), on the other hand, in effect comprise a series of stagnant sections in which microbial growth can proliferate. Consequently, microbiologically influenced corrosion is a significant risk in these and similar systems. It is generally advisable to minimize the risk by thorough initial cleaning of new systems in order to remove internal debris as well as hydrocarbons that may comprise a food source. Following cleaning, appropriate (i.e., not too frequent) test schedules should be undertaken in order to reduce the ingress of fresh water. In severe cases, it may be necessary to dose the system with biocides in order to reduce the microbial load.<sup>147</sup>

### 3.01.5.3.3 Structural steel in waters

A major application for unprotected steel in water is in retaining walls (revetments) along river banks, in sea walls, docks and harbors, structural pilings, etc. Particularly in river systems with low salinity, unprotected revetments are traditionally used and have an adequate life. The higher conductivity of saline and sea water permits the option of applying cathodic

**Table 17** Classifications for corrosivity of fresh water

Type of water	Corrosivity
Distilled water, no oxygen	Corrosion is negligible
Mineral salts present, oxygen and carbonate absent	Similar to previous case provided oxygen is kept out of the system
Distilled water and oxygen present	Corrosion rate decreases with increase in pH but danger of severe pitting corrosion if the steel has marginal passivity; danger of localized corrosion in crevices, under deposits and at the water line
Mineral salts and oxygen present, carbonate absent	Increased corrosion compared with distilled water due to higher conductivity; increased tendency for localized corrosion where passivity is marginal
Carbonate, mineral salts and oxygen present, calcium absent	In the absence of $\text{Ca}^{2+}$ , carbonates act to inhibit corrosion with their maximum effect appeared at more than 5–10 times the concentration of other salts ( $\text{Cl}^-$ or $\text{SO}_4^{2-}$ , etc.) at $\text{pH}$ 6.5–7
Dissolved calcium and carbonate present, oxygen present or absent	Significant reduction in corrosion rate if a carbonate scale is deposited, however this does not generally happen unless there is significant supersaturation of $\text{CaCO}_3$ at the pH of the water

Source: Larson, T. E. *Corrosion by Domestic Waters*, Bulletin 59; Illinois State Water Survey, 1975.

protection. However, designs often still rely on a corrosion allowance for unprotected steel. As noted above, although this strategy has worked well in the past, increasingly the use of thinner and higher strength steels is reducing the overall time to perforation. Additionally, increasing corrosion problems are being observed worldwide where severe corrosion of steel piles, retaining walls, etc. occurs at and just below the waterline. This phenomenon was observed from the 1970s onwards in sea water installations<sup>148</sup> and termed ‘marine low-water corrosion’<sup>149</sup>; it also occurs in saline and estuarine locations as well as in fresh water at inland docks (e.g., on Lake Superior, USA).<sup>150</sup>

In marine locations, this corrosion is now called ‘accelerated low-water corrosion’ (ALWC). It manifests itself as severe attack leading to premature failure of steel structures with unusually high rates of corrosion (i.e.,  $0.3\text{--}1\text{ mm year}^{-1}$  compared with expected rates of  $50\text{--}100\text{ }\mu\text{m year}^{-1}$ ). ALWC occurs at or close to the lowest astronomical tide and, hence, is only visible a few times per year and easily missed. The corrosion typically affects only a small percentage of the exposed surface area with a characteristic damage pattern that depends on the particular geometry and pile design.<sup>70</sup> The causal agent for ALWC appears to be a characteristic microbial colonization of the steel surface resulting in biofilms that contain synergetic populations of sulfur reducing and sulfur oxidizing bacteria. Laboratory *in vitro* studies found that an approximate ten-fold increase in corrosion rate for such colonization, similar to that observed in practice.<sup>151</sup> Control of ALWC in existing installations is probably best carried out by a combination of

sterilization of the marine muds combined with cathodic protection. Future installations are recommended to employ cathodic protection in the design (possibly combined with coating) in order to avoid the problem in the future.

#### 3.01.5.3.4 Variation of corrosion with height

The corrosion rate of steel will vary as a function of height above and below the water as the environment changes from predominantly atmospheric, through the splash zone, into water-saturated mud and eventually to an underground condition. In addition to the variation in environment, the available oxygen concentration will also vary with depth. Consequently, differential aeration corrosion is possible where an enhanced zone of corrosion occurs at the location of lowest oxygen concentrations (i.e., the anode becomes localized away from areas of higher oxygen concentration. **Figure 20** shows the variation in remnant thickness as a function of height.<sup>149</sup> The maxima in the corrosion rate are seen to occur in the splash zone immediately above mean high water and at just below mean low water. The former is due to rapid corrosion in intermittently wetted areas (similar to atmospheric corrosion on a surf beach) while the latter is due differential aeration corrosion. Note that the corrosion rate decreases as the pile depth increases into the mud/soil below the water line.

#### 3.01.5.4 Process Waters

##### 3.01.5.4.1 Heating and cooling systems

Corrosion in water systems that are used for process heating/cooling or space heating/air-conditioning is



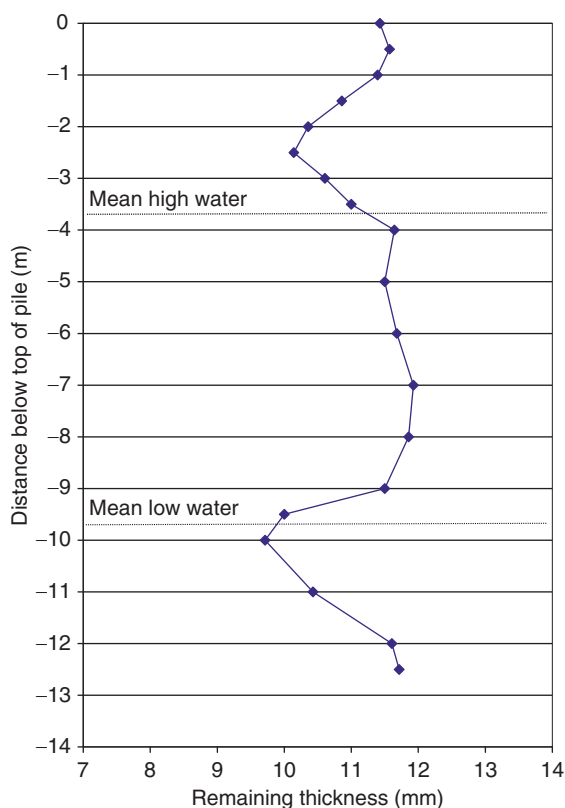


**Figure 20** Thickness loss as function of height in a piled steel dockside. Reproduced from Morley, J. *Struct. Survey* **1989**, 7(2), 138–151.

inevitable unless care is taken to condition the water environment. The principles for the control of corrosion, scaling and fouling in such systems are all well-known and summarized briefly in [Table 18](#). They are discussed in more detail in the relevant chapter in this book.

In cooler waters, control of the microbiology is essential in order to achieve an effective system. Where the oxygen concentration is controlled at a relatively low level in order to limit corrosion, then anaerobic species are of concern. These include the sulfur reducing bacteria that produce sulfides in solution, which can be of concern due to the formation of unstable sulfide films on steel resulting in pitting corrosion. The presence of nitrate/nitrite reducing bacteria is of concern where nitrite corrosion inhibitors are present since these species will metabolize nitrite and reduce its concentration. Iron oxidizing bacteria can also be problematic due to their oxidation of dissolved ferrous species to ferric, resulting in enhanced deposition of rust deposits throughout the systems.

**Table 18** Summary of main water treatments that are used to limit corrosion and related problems

Treatment	Effect
Water conditioning	Use of pH control, deaeration, softening and deionizing to pretreat the water supply and render it less likely to cause scaling and corrosion
Scale inhibition	Chemical addition made to prevent or modify the deposition of scales particularly on heat-transfer surfaces
Corrosion inhibition	Chemical addition made to reduce the rate of corrosion of metallic materials in the system
Microbial control	Chemical addition made to restrict microbial growth, essential where the water does not exceed sterilization temperatures (i.e., <60–70 °C)

#### 3.01.5.4.2 Boiler waters

The principles of water treatment for the control of corrosion in boilers and related equipment are rather similar to those for heating and cooling systems (except for the absence of microbial corrosion since the water should be sterile) and are also well-established.<sup>152</sup> Clearly the main purpose of boiler water treatment is to maintain the lowest practical corrosion rate at reasonable cost. Traditional water treatment commonly attempts to maintain the steel in the passive region where magnetite is the stable phase and this is achieved by a combination of controlled pH, dissolved oxygen concentration, dissolved salts and addition of inhibitors for corrosion control not just in the boiler but also in the steam lines and condensers. The interested reader is directed to the chapter on boiler corrosion and its control in this book.

### 3.01.6 Underground Corrosion

#### 3.01.6.1 Controlling Factors

In practice, bare carbon steel is rarely exposed underground without some form of functional corrosion protection system. Thus, cathodic protection is universally applied for the protection of buried metal underground almost always in combination with an effective protective coating system. Indeed, the performance of coating systems has been improved to such an extent that only a few milliamps of current per kilometer of buried pipeline might be required for adequate protection. Of course, the improvement in coatings (essentially a reduction in coating permeability to water and ions) leads to its own problems in

the shielding of protection currents where defects exist. The control of corrosion underground, including the influence of stray currents, is dealt with in more detail elsewhere and will not be considered further here.

Regarding the corrosion of buried steel, the seminal contributions from the 1950s and early 1960s of Romanoff in the USA<sup>153</sup> and Hudson in UK<sup>154</sup> for samples buried in some cases since the 1930s, still comprise the standard reference data for underground corrosion of bare, unprotected steel and other metals. Such data are of interest in situations where unprotected steel is used underground, which typically arise in construction applications where the use of steel for piles, revetments, shoring, etc. is not uncommon. More recent interest arises from the possible use of carbon steel as a cladding material for nuclear waste containers where knowledge of the long-term corrosion is essential for development of the relevant safety cases. In these cases, it is of merit to study the corrosion of buried archaeological artefacts as they are the only method for determining very long-term corrosion rates with any degree of certainty.

A detailed discussion of the effects of soil on corrosion of unprotected bare steel is beyond the scope of this article and the interested reader is directed to the relevant chapter on corrosion in soils in this book. In brief, soils vary greatly in corrosiveness according to their aeration, conductivity, composition, and microbial activity.<sup>155</sup> In general, dry, sandy, or calcareous soils, with a high electrical resistance, are the least corrosive. At the other end of the scale are the heavy clays and the highly saline soils, whose electrical conductivity is high. The depth of the water table is also important; much depends on whether the buried iron or steel is permanently above or below this, or even more perhaps on whether it is alternately 'wet' or 'dry.' The variation in corrosion rate with depth of burial is illustrated by the historic results quoted in **Table 19**, which also serve to indicate the rates of average general penetration in typical British soils.<sup>156</sup> It will be noted that the depth of burial had no consistent effect, which is not surprising since the average depth of the water table and the seasonal fluctuations in this varied from one site to another. Bacterial activity often plays a part in determining the corrosion of buried steel. This is particularly so in waterlogged clays and similar soils, where no atmospheric oxygen is present as such. If these soils contain sulfates, for example, gypsum and the necessary traces of nutrients, corrosion can occur under anaerobic conditions in the presence of sulfate-reducing bacteria. One of the final products is iron

**Table 19** Corrosion of mild steel in various soils and depths over 5 years

Site	Type of soil	Average general penetration ( $\text{mm year}^{-1}$ )	
		1.37 m	0.6 m
Benfleet	London clay	0.0185	0.0361
Gotham	Keuper marl	0.0132	0.0094
Pitsea	Alluvium	0.0353	0.0284
Rothamsted	Clay with flints	0.0201	0.0213

Source: Romanoff, M. Corrosion of steel piling in soils, National Bureau of Standards Monograph no. 58 (October 1962).

sulfide, and the presence of this is characteristic of attack by sulfate-reducing bacteria, which are frequently present.

The maximum corrosion rate reported in tests carried out in the USA was  $\sim 70 \mu\text{m year}^{-1}$ ,<sup>153,157</sup> while the maximum rates obtained in tests carried out in the UK were between 35 and  $50 \mu\text{m year}^{-1}$ .<sup>156</sup> However, the localized corrosion was much greater, with maximum rates of  $250 \mu\text{m year}^{-1}$  reported from American, and  $300 \mu\text{m year}^{-1}$  from British, tests.

### 3.01.6.2 Corrosion of Buried Steel

#### 3.01.6.2.1 Piling

Unprotected steel is frequently used in construction as pilings for foundations and soil retention. This is because any protective coating is almost certainly going to be removed by abrasion during the piling operations. Generally, undisturbed soil and earth should have relatively low oxygen content and, hence, steel should have a relatively low corrosion rate. As noted above, **Table 19**, corrosion rates in a variety of different undisturbed soil types are indeed generally quite low, from  $\sim 10$  to  $35 \mu\text{m year}^{-1}$ .

Examinations of steel pilings recovered after considerable times of exposure have confirmed that the average corrosion rate is indeed acceptably low. Romanoff's study in the USA found that the load-bearing capacity of the pilings was not compromised.<sup>158</sup> Studies in the UK on pilings removed from the ground after up to 85 years service found that they were in excellent condition with an estimated average corrosion rate of the order of  $10 \mu\text{m year}^{-1}$  with occasional rates up to  $30 \mu\text{m year}^{-1}$ .<sup>159</sup> On the land (fill) side of piled harbor walls (i.e., in disturbed soil) the corrosion rates were about twice those found for undisturbed soil, but this is still

relatively low. A systematic study in Japan over 10 years showed that the corrosion of piles was not linear with time but was initially high and tended to decrease after time to a long-term rate that was  $\sim 10 \mu\text{m year}^{-1}$ .<sup>160</sup> In Australia, 52 year-old piles from Port Adelaide were removed and the average corrosion rate below the mud line was found to be  $\sim 30 \mu\text{m year}^{-1}$ .<sup>161,162</sup> What also seems clear from this historic data is that microbial corrosion did not seem to be of a significant risk provided the soil was undisturbed.<sup>149</sup>

### 3.01.6.2.2 Pipelines

Buried pipe, whether of steel or cast iron, are invariably coated and additionally protected by a cathodic protection system. It is not proposed to discuss this topic further here except, for completeness, to note the occurrence, during cathodic protection, of intergranular stress corrosion cracking in carbonate–bicarbonate environments and transgranular stress corrosion cracking of higher strength pipeline steels at neutral pH.

### 3.01.6.2.3 Long-term burial

Research on the nature of corrosion product layers on historic buried artefacts is an important component in understanding the progress of corrosion and in the modeling of proposed nuclear waste repositories. Most repository designs comprise a multibarrier system that consists of immobilized (e.g., vitrified) nuclear waste packed into a metallic container that is, in turn, emplaced into a suitable geological repository and backfilled with clay buffer layer. This design is expected to be initially relatively oxidizing (aerated) but will eventually become anaerobic. Since the function of the metal container is to prevent contact between the groundwater and the radioactive wastes for as long as possible, knowledge of the corrosion processes, including the expected corrosion products likely to form, are essential in order to provide a credible model of long-term corrosion over hundreds to thousands of years.

In the United Kingdom, historic iron commonly arises from the period of Roman occupation and later, with the most frequent artefact comprising iron nails. In Europe, buried iron can be found from much earlier. Commonly identified corrosion products include all those that might be expected to form, **Table 4**. In most buried environments the corrosion sequence commences with the development of ‘green rusts,’ which are mixed oxy-hydroxides of iron containing Fe (+2/+3) species and incorporating typically, carbonate, chloride or sulfate depending on the

environment.<sup>163</sup> Generally, depending on local conditions of aeration and pH, this oxidizes further to form magnetite, maghemite, lepidocrocite or goethite; while in high chloride (e.g., marine) environments, akaganéite also forms. In anaerobic, waterlogged, conditions at higher pH (carbonated), siderite (iron carbonate) is a common corrosion product,<sup>164</sup> while at lower pH, vivianite (hydrated iron phosphate) has occasionally been observed.<sup>165</sup>

## References

1. Tylecote, R. F. *A History of Metallurgy*; Institute of Materials, 1992.
2. Micrographs appear by kind permission of R.F. Cochrane, University of Leeds and the DoITPoMS Micrograph Library, University of Cambridge.
3. Llewellyn, D. T.; Hudd, R. C. *Steels: Metallurgy and Applications*; Butterworth-Heinemann, 1998.
4. Bhadeshia, H. K. D. H.; Honeycomb, R. W. K. *Steels: Microstructure and Properties*, 2nd ed.; Edward Arnold, 1995.
5. *Steel Heat Treatment Handbook*; Totten, G. E., Howes, M. A. H.; CRC Press, 1997.
6. Hudson, J. C.; *The Corrosion of Iron & Steel*; Chapman and Hall: London, 1940; p 61.
7. Larrabee, C. P.; Coburn, S. K. Proceedings of the 1st International Congress on Metal Corrosion, 1961; pp 276, Butterworths: London, 1962.
8. Sixth Report of the Corrosion Committee, Spec. Rep. No. 66, Iron and Steel Institute: London, 1959.
9. Hudson, J. C. *J. Iron Steel Inst.* **1950**, 166, 123.
10. Mor, E. D.; Travesco, E.; Ventora, G. *Br. Corros. J.* **1976**, 11, 40.
11. Songa, T. International Conference on Steel in Marine Structures, Paris, ECSC: Luxembourg 1981.
12. Forgeson, B. W.; Southwell, C. R.; Alexander, A. L. *Corrosion* **1960**, 16, 105t.
13. Hudson, J. C.; Banfield, T. A.; Holden, H. A. *J. Iron Steel Inst.* **1942**, 146, 107.
14. Romanoff, M. *Underground Corrosion, National Bureau of Standards Circular 579*; US Government Printing Office: Washington, 1957.
15. Bockris, J. O'M.; Conway, B. E. *J. Phys. Colloid Chem.* **1949**, 53(4), 527–539.
16. Bockris, J. O. 'M.; Drazic, D. M. *Electrochim. Acta* **1962**, 7(3), 293–313.
17. Bockris, J. O. 'M.; Drazic, D. M.; Despic, A. R. *Electrochim. Acta* **1961**, 4(2–4), 325–361.
18. Despic, A. R.; Raicheff, R. G.; Bockris, J. O. 'M. *J. Chem. Phys.* **1968**, 49(2), 926–938.
19. Dražić, D. M.; Hao, C. S. *Electrochim. Acta* **1982**, 27(10), 1409–1415.
20. Dražić, D. M.; Zečević, S. K. *Corros. Sci.* **1985**, 25(3), 209–216.
21. El Miligy, A. A.; Geana, D.; Lorenz, W. J. *Electrochim. Acta* **1975**, 20(4), 273–281.
22. Lorbeer, P.; Lorenz, W. J. *Electrochim. Acta* **1980**, 25(4), 375–381.
23. Hackerman, N.; Stephens, S. J. *J. Phys. Chem.* **1954**, 58 (10), 904–908.
24. Drazic, D. M. In *Modern Aspects of Electrochemistry*; Conway, B. E., Bockris, J. O. M., White, R. E., Eds.; Plenum Press: New York, 1989; Vol. 19, p 69.

25. Walpert, G. Z. *Phys. Chem.* **1930**, A.151, 219.
26. Jeyaprabha, C.; Sathiyarayanan, S.; Muralidharan, S.; Venkatachari, G. *J. Braz. Chem. Soc.* **2006**, 17(1), 61–67.
27. Etzold, U.; Mohr, K. P.; Hulser, P. 38th Seminario de Laminacao Processos e Produtos Laminados e Revestidos; Florianopolis, SC; Brazil; 24–26 Oct. 2001, pp 210–223.
28. Keir, J. *Phil. Trans. R. Soc.* **1790**, 80, 359–384.
29. Schonbein, C. F.; Faraday, M. *Phil. Mag.* **1836**, 9, 53; 57; 122.
30. Kim, J. S.; Cho, E. A.; Kwon, H. S. *Corros. Sci.* **1989**, 29, 183.
31. Nagayama, M.; Cohen, M. J. *Electrochem. Soc.* **1962**, 109, 791.
32. Vetter, K. J.; Gorn, F. *Electrochim. Acta* **1973**, 18, 321–326.
33. O'Grady, W. E. *Electrochim. Acta* **1980**, 127, 555.
34. Eldridge, J.; Kordes, M. E.; Hoffman, R. W. *J. Vac. Sci. Technol.* **1982**, 20, 934.
35. Graham, M. J.; Bardwell, J. A.; Goetz, R.; Mitchell, D. F.; MacDougall, B. *Corros. Sci.* **1990**, 31, 139–148.
36. Davenport, A. J.; Sansone, M. J. *Electrochem. Soc.* **1995**, 142, 7254.
37. Ryan, M. P.; Newman, R. C.; Thompson, G. E. *J. Electrochem. Soc.* **1995**, 142, L177.
38. Toney, M. F.; Davenport, A. J.; Oblonsky, L. J.; Ryan, M. P.; Vitus, C. M. *Phys. Rev. Lett.* **1997**, 79, 4282–4285.
39. Hendy, S.; Walker, B.; Laycock, N.; Ryan, M. *Phys. Rev. B* **2003**, 67, 085407.
40. Vera, J.; Kapusta, S.; Hackerman, N. *J. Electrochem. Soc.* **1986**, 133(3), 461–467.
41. Froment, M.; Keddah, M.; Morel, P. *Compt. Rend.* **1961**, 253, 2529.
42. Dugstad, A. Proceedings CORROSION'98; Paper No. 31; NACE: Houston, TX, 1998.
43. Bockris, J. O. 'M.; Reddy, A. K. N.; Gamboa-Aldeco, M. *Modern Electrochemistry* Springer: Berlin, 2001; Vol. 2b, p 1670.
44. Jovancicevic, V.; Bockris, J. O. 'M. *J. Electrochem. Soc.* **1986**, 133, 1797–1807.
45. Levich, V. C. *Physicochemical Hydrodynamics*; Prentice-Hall: NJ, USA, 1962.
46. Udo Schwertmann; Cornell, Rochelle M. *The Iron Oxides: Structure, Properties, Reactions, Occurrences and Uses*; Wiley-VCH: London, 2003.
47. Wranglen, G. *Corros. Sci.* **1969**, 9(8), 585–592; 593–602.
48. Shifler, D. A.; Moran, P. J.; Kruger, J. *Electrochim. Acta* **1997**, 42(4), 567–577.
49. Reformatskaya, I. I.; Rodionova, I. G.; Beilin, Yu. A.; Nisel'son, L. A.; Podobaev, A. N. *Prot. Met.* **2004**, 40(5), 447–452.
50. Rothwell, G. P. *Corros. Prevention Control* **1979**, 26(3), 9–13.
51. Bardwell, J. A.; MacDougall, B. *J. Electrochem. Soc.* **1988**, 135, 2157.
52. Bardwell, J. A.; MacDougall, B.; Graham, M. J. *Corros. Sci.* **1991**, 32, 139.
53. Mitrovic-Scepanovic, V.; MacDougall, B.; Graham, M. J. *Corros. Sci.* **1984**, 24, 479.
54. Li, L. *Corrosion* **2001**, 57(1), 19–28.
55. Alonso, C.; Castellote, M.; Andrade, C. *Electrochim. Acta* **2002**, 47(21), 3469–3481.
56. Vera, J.; Kapusta, S.; Hackerman, N. *J. Electrochem. Soc.* **1986**, 133, 461–467.
57. Standard Guide for Development and Use of a Galvanic Series for Predicting Galvanic Corrosion Performance; ASTM G82–98, 2009.
58. Buecker, B. *Power Eng.* **2002**, 106(9), 32–34.
59. Buecker, B. *Power Eng.* **2007**, 111(7), 20–24.
60. Alan V. Levy *Solid Particle Erosion and Erosion–Corrosion of Materials*; ASM International, 1995.
61. Jones, D. D. *Corros. Technol. (Anti-Corros. Methods Mater.)* **1957**, 4(2), 56–59.
62. Huy, Ha Le; Ghali, E. *Corros. Sci.* **1993**, 35(1–4), 435–442.
63. Yeske, R. *Caustic Stress Corrosion Cracking Of Carbon Steels*, A Supplement To: Stress Corrosion Cracking Of Continuous Digesters, The Institute Of Paper Chemistry Appleton, Wisconsin, USA, Project 3589, October 17, 1986.
64. Parkins, R. N. *Fundamental Aspects of Stress Corrosion Cracking*, Proceedings of NACE Conference **1969**, p 361.
65. Zhagalya, N. N.; Marchak, I. I.; Melekhov, R. K. *Mater. Sci.* **1975**, 9, 342–344.
66. Bandyopadhyay, N.; Briant, C. L. *Scr. Metall.* **1982**, 16(8), 939–941.
67. Payer, J. H.; Berry, W. E.; Parkins, R. N. In *Stress Corrosion Cracking – The Slow Strain Rate Technique*; ASTM STP 665; Ugiansky, G. M., Payer, J. H., Eds.; American Society for Testing and Materials: Philadelphia, PA, 1979; pp 222–234.
68. Garverick, L. *Corrosion in the Petrochemical Industry*; ASM International, 1994; pp 212–213.
69. Farrow, K.; Hutchings, J.; Sanderson, G. *Br. Corros. J.* **1981**, 16(1), 11–19.
70. Little, B. J.; Lee, J. S. *Microbiologically Influenced Corrosion*; Wiley: London, 2007.
71. Mrowec, S.; Podgorecka, A. *J. Mater. Sci.* **1987**, 22, 4181–4189.
72. Chen, R. Y.; Yuen, W. Y. D. *Oxid. Met.* **2003**, 59(5–6), 433–468.
73. Picard, A.; Fang, H. *Metrologia* **2004**, 41, 333–339.
74. Schwartz, R. *Metrologia* **1994**, 31, 117–128.
75. Vernon, W. H. J. *Trans. Faraday Soc.* **1935**, 31(1), 668.
76. Gdowski, G. E.; Estill, J. C. Proceedings Materials Research Society Fall Meeting, Nov. 27, Dec. 1, 1995.
77. European Council Directive 1999/30/EC of 22 April 1999: Limit values for sulphur dioxide, nitrogen dioxide and oxides of nitrogen, particulate matter and lead in ambient air.
78. Smith, S. J.; Conception, E.; Andres, R.; Lurz, J. Historical Sulfur Dioxide Emissions 1850–2000: Methods and Results, U.S. Department of Energy, Contract DE-AC06-76RL01830.
79. Vannerberg, N. G. *Electrochem. Soc.* **1978**, Pittsburg 78–82, (Extended abstract p. 314).
80. Walton, J. R.; Johnson, J. B.; Wood, G. C. *Br. Corros. J.* **1982**, 17, 59.
81. Chandler, K. A.; Kilcullen, M. B. *Br. Corr. J.* **1968**, 3, 80–84.
82. Sydberger, T.; Vannerberg, N.-G. *Corros. Sci.* **1972**, 12, 775–784.
83. Chandler, K. A.; Stanners, J. F. *Proceedings of 2nd International Congress of Metallic Corrosion*; NACE: Houston, Tx, 1963; p 325.
84. Tanner, A. R. *Chem. Ind.* **1964**, 1, 027.
85. Schikorr, G. *Werkstoffe Korros.* **1963**, 14(2), 69.
86. Schwartz, H. *Werkstoffe Korros.* **1965**, 16(3), 208.
87. Schikorr, G. *Korros. Metall.* **1941**, 17, 305–313.
88. Chandler, K. A.; Stanners, J. F. *Proceedings of 2nd International Congress of Metallic Corrosion*; NACE: Houston, 1963; p 325.
89. Arroyave, C.; Morcillo, M. *Corros. Sci.* **1995**, 37(2), 293–305.
90. Katoh, K.; Yasukawa, S.; Nishimura, H.; Yasuda, M. *Boshoku Gijyutsu* **1981**, 30, 337.
91. Haynie, F. H.; Spence, J. W.; Upham, J. B. In *Atmospheric Factors Affecting the Corrosion of*

- Engineering Metals*; ASTM STP 646, 1978: Philadelphia, p. 30.
92. Eriksson, P.; Johansson, L.-G. Proceedings of 10th Scandinavian Corrosion Congress Stockholm 1986; p 43.
  93. Johansson, L.-G. In *Proceedings of Symposium: Corrosion Effects of Acid Deposition and Corrosion of Electronic Materials*; Mansfeld, F., Kucera, V., Haagenrud, S. E., Haynie, F. H., Sinclair, J. D., Eds.; The Electrochemical Society: Pennington, 1986; p 267.
  94. Oesch, S. *Corros. Sci.* **1996**, *38*, 1357–1368.
  95. Askey, A.; Lyon, S. B.; Thompson, G. E.; Johnson, J. B.; Wood, G. C.; Cooke, M.; Sage, P. *Corros. Sci.* **1993**, *34* (2), 233–247.
  96. Ross, T. K.; Callaghan, B. G. *Corros. Sci.* **1966**, *6*, 337.
  97. Chandler, K. A. *Br. Corros. J.* **1966**, *1*, 264–266.
  98. Evans, U. R.; Taylor, C. A. J. *Br. Corros. J.* **1974**, *9*(1), 26–28.
  99. Cole, I. S.; Ganther, W. D.; Paterson, D. A.; King, G. A.; Furman, S. A.; Lau, D. *Corros. Eng. Sci. Technol.* **2003**, *38*(4), 259–266.
  100. Cole, I. S.; Lau, D.; Paterson, D. A. *Corros. Eng. Sci. Technol.* **2004**, *39*(3), 209–218.
  101. Walton, J. R.; Johnson, J. B.; Wood, G. C. *Br. Corros. J.* **1982**, *17*(2), 59–64; 65–70.
  102. Ngai T. Lau; Chan K. Chak; Lap I. Chan; Ming Fang *Corros. Sci.* **2008**, *50*(10), 2927–2933.
  103. Askey, A.; Lyon, S. B.; Thompson, G. E.; Johnson, J. B.; Wood, G. C.; Sage, P. W.; Cooke, M. J. *Corros. Sci.* **1993**, *34*(7), 1055–1081.
  104. Schikorr, G. *Werkstoffe Korros.* **1963**, *14*, 69; **1964**, *15*, 457; **1967**, *18*, 514.
  105. Barton, K.; Kuchynka, D.; Beranek, E. *Werkstoffe Korros.* **1978**, *29*, 199–201.
  106. Weissenrieder, J.; Kleber, C.; Schreiner, M.; Leygraf, C. *J. Electrochem. Soc.* **2004**, *151*(9), B497–B504.
  107. Evans, U. R. *Trans. Inst. Met. Finish* **1960**, *37*, 1.
  108. Evans, U. R.; Taylor, C. A. J. *Corros. Sci.* **1972**, *12*(3), 227–246.
  109. Stratmann, M.; Bohnenkamp, K.; Engell, H.-J. *Corros. Sci.* **1983**, *23*(9), 969–985.
  110. Antony, H.; Perrin, S.; Dillmann, P.; Legrand, L.; Chaussé, A. *Electrochim. Acta* **2007**, *52*(27), 754–7759.
  111. Stratmann, M.; Bohnenkamp, K.; Engell, H.-J. *Werkstoffe Korros.* **1983**, *34*(12), 604–612.
  112. Stratmann, M.; Bohnenkamp, K.; Ramchandran, T. *Corros. Sci.* **1987**, *27*(9), 905–926.
  113. Stratmann, M. *Phys. Chem. Chem. Phys.* **1990**, *94*(6), 626–639.
  114. Stratmann, M.; Streckel, H. *Corros. Sci.* **1990**, *30*(6–7), 697–714.
  115. Shirkhanzadeh, M.; Thompson, G. E.; Lyon, S. B.; Johnson, J. B. *Br. Corros. J.* **1987**, *22*(4), 243–249.
  116. Okada, T.; Ishii, Y.; Mizoguchi, T.; Tamura, I.; Kobayashi, Y.; Takagi, Y.; Suzuki, S.; Kihira, H.; Itou, M.; Usami, A.; Tanabe, K.; Masuda, K. *Jpn. J. Appl. Phys.* **2000**, *39*, 3382.
  117. García, K. E.; Morales, A. L.; Barrero, C. A.; Greneche, J. M. *Hyperfine Interact.* **2005**, *161*(1–4), 127–137.
  118. Sei, J.; Oha, D. C.; Cook, H. E.; Townsend *Corros. Sci.* **1999**, *41*, 1687–1702.
  119. Awad, G. H.; Abdel Halim, F. M.; El Arabi, R. M. *Br. Corros. J.* **1980**, *15*, 140.
  120. Biefer, G. J. Exploratory corrosion tests in the Canadian Arctic, Canada Centre for Mineral and Energy Technology (CANMET), Ottawa Report, 1977, 77–45.
  121. Dearden, J. J. *Iron Steel Inst.* **1948**, *159*, 241.
  122. Larrabee, C. P. *Trans. Electrochem. Soc.* **1944**, *85*, 297.
  123. Laque, F. L. *Mater. Perf.* **1982**, *21*, 17.
  124. Zhang, Q. C.; Wua, J. S.; Wang, J. J.; Zheng, W. L.; Chen, J. G.; Li, A. B. *Mater. Chem. Phys.* **2003**, *77*(2), 603–608.
  125. Dean, S. W. In *Degradation of Materials in the Atmosphere*, ASTM STP 965; Dean, S. W., Lee, T. S., Eds.; American Society for Testing and Materials: Philadelphia, PA, 1988; pp 385–431.
  126. Dean, S. W. In *Atmospheric Corrosion*, STM STP 1239; Kirk, W. W., Lawson, H. H., Eds.; American Society for Testing and Materials, 2002; pp 3–18.
  127. Dean, S. W.; Reiser, D. B. In *Outdoor Atmospheric Corrosion*, ASTM STP 1421; Townsend, H., Ed.; American Society for Testing and Materials, 2002; pp 3–18.
  128. Mikhailov, A. A.; Tidblad, J.; Kucera, V. *Prot. Met.* **2004**, *40*(6), 541–550.
  129. Cai, J.-P.; Lyon, S. B. *Corros. Sci.* **2005**, *47*(12), 2956–2973.
  130. Edwards, A. M. Proceedings of Symposium on Developments in Methods of Prevention and Control of Corrosion in Buildings; British Iron and Steel Federation: London, 1966.
  131. Larrabee, C. P.; Coburn, S. K. Proceedings of First International Congress on Metallic Corrosion; Butterworths: London, 1962; p 276.
  132. Hooper, R. A. E.; Lee, B. V. Proceedings of 12th International COR-TEN Conference, Florida, 1985; United States Steel: Pittsburgh.
  133. Kamimura, T.; Nasu, S.; Segi, T.; Tazaki, T.; Morimoto, S.; Miyuki, H. *Corros. Sci.* **2003**, *45*(8), 1863–1879.
  134. Albrecht, P. In *Corrosion Forms and Control for Infrastructure* ASTM STP 1137; Chaker, V., Ed.; American Society for Testing and Materials: Philadelphia, PA, 1992; pp 108–125.
  135. Kamimura, T.; Stratmann, M. *Corros. Sci.* **2001**, *43*, 429–447.
  136. Kimura, M.; Kihira, H.; Ohta, N.; Hashimoto, M.; Senuma, T. *Corros. Sci.* **2005**, *47*, 2499–2509.
  137. Kihira, H.; Ito, S.; Mizoguchi, T.; Murata, T.; Usami, A.; Tanabe, K. *Zairyo-to-Kankyo* **2000**, *49*, 30.
  138. BS EN 12500: Protection of metallic materials against corrosion: Corrosion likelihood in atmospheric environment, classification, determination and estimation of corrosivity of atmospheric environments.
  139. de Waard, C.; Williams, D. E. *Corrosion* **1975**, *31*(5), 177.
  140. Langelier, W. F. *J. Am. Water Works Assoc.* **1946**, *38*, 169–178.
  141. Friend, J. N. *18th Report of the Committee of the Institution of Civil Engineers on the Deterioration of Structures of Timber*; Metal and Concrete Exposed to the Action of Sea Water: London, 1940.
  142. Hudson, J. C.; Stanners, J. F. *J. Iron Steel Inst.* **1955**, *180*, 271.
  143. Baudot, H.; Chaudron, G. *Rev. Met.* **1946**, *43*, 1.
  144. *Internal Corrosion of Water Distribution Systems*, 2nd ed.; American Water Works Association, 1996.
  145. Larson, T. E. *Corrosion by Domestic Waters*, Bulletin 59; Illinois State Water Survey, 1975.
  146. Hu, J. Y.; Yu1, B.; Feng, Y. Y.; Tan, X. L.; Ong, S. L.; Ng, W. J.; Hoe, W. C. *Biofilms* **2005**, *2*, 19–25.
  147. McReynolds, G. S. *Mater. Perf.* **1998**, *37*(7), 45–48.
  148. Martini, A.; Mennenoh, S. *Stahl und Eisen*; **1981**, *10*(1).
  149. Morley, J. *Struct. Survey* **1989**, *7*(2), 138–151.
  150. Marsh, C. P.; Bushman, J.; Beitelman, A. D.; Buchheit, R. G.; Little, B. J. Freshwater Corrosion in the Duluth-Superior Harbor-Summary of the Initial Workshop Findings, Special publication ERDC/CERL SR-05-3, U.S.; Army Corps of Engineers, 2005.



151. Beech, I. B.; Campbell, S. A. *Electrochim. Acta* **2008**, *54*, 14–21.
152. Buecker, B. *Power Plant Water Chemistry: A Practical Guide*; Pennwell Books: USA, 1997.
153. Romanoff, M. Underground Corrosion, National Bureau of Standards, Circular 579, Washington, 1957.
154. Hudson, J. C.; Acock, J. P. Symposium on the Corrosion of Buried Metals, The Iron & Steel Inst., Special Report No. 45, London, 1952.
155. Ismail, A. I. M.; El-Shamy, A. M. *Appl. Clay Sci.* **2009**, *42*, 356–362.
156. Hudson, J. C.; Watkins, K. O. BISRA Open Report No MG/B/3/68.
157. Romanoff, M. J. *Res. Natl. Bur. Stand* **1962**, *60*, 223–224.
158. Romanoff, M. Corrosion of steel piling in soils, National Bureau of Standards Monograph no. 58 (October 1962).
159. Morley, J. *Br. Corros. J.* **1986**, *21*, 177–183.
160. Ohsaki, Y. *Soils Found* **1982**, *22*(3).
161. Eadie, G. F. The Durability of Piles in Soils, Conference Paper 19, Australasian Corrosion Association, Perth, Western Australia (November 1979).
162. Eadie, G. R.; Kinson, K. Examination of Steel Piling Recovered from Port Adelaide after 52 Years' Service, Conference Paper 20, Australasian Corrosion Association, Adelaide, South Australia, (November 1980).
163. Neff, D.; Dillmann, P.; Bellot-Gurlet, L.; Beranger, G. *Corros. Sci.* **2005**, *47*, 515–535.
164. Matthiesen, H.; Hilbert, L. R.; Gregory, D. J. *Stud. Conservation* **2003**, *48*(3), 183–194.
165. Booth, G. H.; Tiller, A. K.; Wormwell, F. *Corros. Sci.* **1962**, *2*(3), 197–202.

## 3.02 Corrosion of Cast Irons

**A. Reynaud**

Centre Technique des Industries de la Fonderie, 44, av. de la Division Leclerc, F-92318 Sèvres Cedex, France

© 2010 Elsevier B.V. All rights reserved.

---

<b>3.02.1</b>	<b>General Introduction</b>	1739
3.02.1.1	White Cast Iron	1739
3.02.1.2	Gray Cast Iron	1739
3.02.1.3	Malleable Cast Iron	1740
3.02.1.4	Ductile Cast Iron	1740
3.02.1.5	Alloy Cast Irons	1740
<b>3.02.2</b>	<b>Production, Composition, and Microstructural Effects</b>	1740
3.02.2.1	Effect of Microstructure on Corrosion Resistance	1741
3.02.2.2	Influence of Galvanic Couples in the Microstructure	1743
<b>3.02.3</b>	<b>General Corrosion Behavior</b>	1743
3.02.3.1	Low-Alloy Lamellar or Spheroidal Graphite Cast Irons	1743
3.02.3.2	High-Alloy Cast Irons	1744
3.02.3.2.1	Austenitic nickel cast iron	1744
3.02.3.2.2	High chromium cast iron	1746
3.02.3.2.3	High silicon cast iron	1746
3.02.3.3	Typical Applications	1747
3.02.3.3.1	Unalloyed cast irons	1747
3.02.3.3.2	Alloyed ferritic cast irons	1748
3.02.3.3.3	Austenitic cast irons	1748
<b>3.02.4</b>	<b>Corrosion Environments</b>	1750
3.02.4.1	Atmospheric Corrosion	1750
3.02.4.1.1	Nickel cast irons	1750
3.02.4.2	Corrosion in Natural Water	1752
3.02.4.2.1	Introduction	1752
3.02.4.2.2	Aggressiveness and corrosiveness of water	1752
3.02.4.2.3	Influence of dissolved oxygen	1753
3.02.4.2.4	Corrosion of cast Iron in natural water	1754
3.02.4.2.5	Galvanic corrosion of cast iron in natural water	1756
3.02.4.2.6	Inhibition of corrosion in water	1757
3.02.4.3	Corrosion in Steam	1757
3.02.4.4	Corrosion in Seawater	1758
3.02.4.5	Soil Corrosion	1760
3.02.4.6	Methods of Protection	1762
<b>3.02.5</b>	<b>Corrosion in Industrial Environments</b>	1763
3.02.5.1	Sulfuric Acid	1763
3.02.5.2	Hydrochloric Acid	1765
3.02.5.3	Nitric Acid	1765
3.02.5.4	Phosphoric Acid	1765
3.02.5.5	Other Mineral Acids	1766
3.02.5.6	Organic Acids	1766
3.02.5.7	Corrosion by Alkalis	1767
3.02.5.8	Salt Solutions	1768
3.02.5.9	Corrosion–Fatigue	1768
3.02.5.10	Stress Corrosion Cracking	1770
3.02.5.11	Organic Compounds	1772

---

3.02.5.11.1	Alcohol and glycol	1772
3.02.5.11.2	Corrosion by food products	1773
<b>3.02.5.12</b>	<b>Corrosion by Molten Materials</b>	1773
3.02.5.12.1	Corrosion by liquid aluminum or aluminum alloys	1773
3.02.5.12.2	Corrosion by liquid zinc and zinc alloys	1774
3.02.5.12.3	Corrosion by other liquid metals	1774
3.02.5.12.4	Corrosion by liquid sulfur	1774
<b>3.02.5.13</b>	<b>Microbially Influenced Corrosion</b>	1774
3.02.5.13.1	Iron oxidizing bacteria	1775
3.02.5.13.2	Sulfate-metabolizing bacteria	1775
3.02.5.13.3	Mechanisms of action	1775
3.02.5.13.4	Microbial corrosion of cast iron	1775
3.02.5.13.5	Combating microbial corrosion	1776
<b>3.02.5.14</b>	<b>Flow-Induced Corrosion</b>	1777
3.02.5.14.1	Cavitation corrosion of cast iron	1777
3.02.5.14.2	Corrosion–erosion of cast iron	1778
<b>3.02.6</b>	<b>Corrosion by Gases</b>	1780
3.02.6.1	High Temperature Oxidation and Corrosion	1780
3.02.6.2	Corrosion by other Gas Atmospheres	1783
3.02.6.3	Corrosion in Gas Transport and Distribution Pipes	1784
<b>References</b>		1786

---

## Glossary

**Cast iron** An alloy of iron with >1.7% carbon and including appreciable amounts of silicon and other elements. Compared with carbon steel, cast iron has a relatively low melting point and high fluidity permitting it to be cast into complex shapes.

**Ductile or SG iron** A form of cast iron in which the carbon is present as nodular spheroids of graphite and, consequently the iron is ductile.

**Durichlor** A high-silicon iron containing a minimum of 14.5% silicon with additions of chromium and molybdenum and optimised for service in hydrochloric acid.

**Duriron** A high-silicon iron containing a minimum of 14.5% silicon exhibiting extreme abrasion resistance and chemical resistance in acids.

**Gray or LG iron** A form of cast iron with a relatively high silicon content (> ~2%) in which the carbon is present as lamellar graphitic (LG) flakes; generally gray iron is brittle and fails with little or no ductility.

**Hypersilid** A high silicon iron containing from 14–18% silicon and similar to Duriron in performance and usage.

**Malleable Iron** A form of white cast iron that is traditionally produced by subjecting a casting to extended periods of heat treatment, this results in the nucleation of graphite in a nonlamellar form and, consequently, the iron is ductile (malleable).

**Ni-Resist** A form of cast iron containing sufficient nickel such that the iron is able to retain the austenite phase structure at room temperature, consequently, Ni-Resist is heat-resistant and relatively corrosion resistant compared with LG or SG irons.

**White iron** A form of cast iron of relatively lower silicon content in which the carbon is present as carbides and, consequently, white iron is extremely hard and abrasion resistant.

## Abbreviations

**ASTM** American Society for Testing and Materials

**BCIRA** British Cast Iron Research Association (former body, no longer in operation)

**BS** British Standard

**EN** European Norm  
**ETIF** Editions Technique des Industrie de le  
 Fonderie  
**LG** Lamellar graphitic  
**LSI** Langelier saturation index  
**SG** Spheroidal graphitic

### 3.02.1 General Introduction

Cast iron is the term applied to a wide range of ferrous alloys, whose principal distinguishing feature is carbon content in excess of  $\sim 1.7\%$ . Cast iron can also be thought of as a composite material consisting of precipitated graphite or carbide particles in a metal matrix. The two major types of graphite morphology are flake, associated with gray iron and spherical (nodular), associated with ductile iron. While the properties of steel grades are determined (in addition to the composition) primarily by thermo-mechanical treatment, the properties of cast iron are controlled by inoculation, solidification, and cooling rate as well as alloy composition.

Four main types of iron are commonly encountered:

- white iron in which all the carbon is present in a metal carbide phase;
- gray iron in which most of the carbon is present as graphite flakes;
- nodular or ductile iron in which most of the carbon is present as graphite nodules, produced during solidification of the casting; and
- malleable iron in which most of the carbon is present as graphite nodules, produced subsequent to solidification by heat treatment of the casting.

Many properties of cast iron are first influenced by the form in which the carbon is present; that is, as graphite or as carbide and secondly by whether the matrix material is ferritic or pearlitic.

#### 3.02.1.1 White Cast Iron

In white iron, carbon is in the form of iron carbide in a matrix of pearlite, the amount of which depends on the carbon content of the iron; such materials are hard and brittle. Alloying of white iron is possible and results in the formation of alloy carbides that are even harder and ideal for hard and abrasion-resistant applications such as extrusion dies and cement mixer liners.

#### 3.02.1.2 Gray Cast Iron

Gray cast irons are by far the oldest and most common form of cast iron. Gray iron, named because of its characteristic fracture surface, has a gray appearance and consists of carbon in the form of flake graphite in a matrix consisting usually of pearlite or ferrite or a mixture of the two. The fluidity of liquid gray iron and its expansion during solidification due to the formation of graphite, has traditionally been ideal for the economical production of shrinkage-free, intricate castings such as motor blocks. These alloys are often known as lamellar graphitic (LG) cast irons; a sketch of the typical arrangement of lamellar graphite is shown in [Figure 1](#).

Gray iron exhibits essentially no elastic behavior, and fails under tension without significant plastic deformation. The mechanical properties of gray cast iron result from the effects of chemical composition and the cooling history. In general, as the combined equivalent of carbon and silicon is reduced the strength of the cast iron is increased. For thicker sections requiring tensile strengths above 350 MPa, additions of chromium, nickel or molybdenum alloys are required.

The presence of graphite flakes gives gray iron an excellent machinability, damping, and self-lubricating characteristics. Consequently, gray cast iron has an outstanding resistance to sliding wear and has been used very successfully for sliding surfaces including cylinder bores, piston rings, and machine tools. Due to the effect of the graphite flakes, gray cast iron has an excellent resistance to galling and seizing, and has a low coefficient of friction. Finally, gray cast irons have an excellent capacity for absorbing



**Figure 1** Sketch of lamellar (flake) graphite in cast iron.

vibration energy, and thus damping vibrations. This property is most evidenced with those materials with a high percentage of graphite flakes.

### 3.02.1.3 Malleable Cast Iron

Malleable irons are initially manufactured as white irons and subsequently heat treated in order to convert the carbide into graphite, which nucleates and grows from individual locations giving a more compact, nonlamellar form. Malleable irons are produced by two different processes, which result in either a ferrite or a pearlite matrix depending on the process adopted; however, even the pearlitic form is usually produced with a surface layer of ferrite. In malleable irons, the presence of graphite in a more compact or sphere-like form gives the material greatly increased ductility with tensile and yield strengths almost equal to cast, low-carbon steel.

### 3.02.1.4 Ductile Cast Iron

Ductile cast irons are similar to gray cast irons but have small amounts of alloying addition (e.g., magnesium) that promote the formation of carbon in a nodular form rather than as graphite flakes; they are often known as spheroidal graphitic (SG) irons or nodular graphitic irons; a schematic microstructure is shown in [Figure 2](#). Ductile iron generally solidifies with a pearlite matrix, but in order to develop the full ductility of the iron, the castings are often subsequently annealed to give a ferrite matrix. They have properties similar to that of gray irons with a relatively low melting point (compared with steels), good



**Figure 2** Sketch of spheroidal graphite in cast iron.

fluidity, castability, excellent machinability, and wear resistance. However, compared to gray cast iron they have improved strength, toughness, and hot workability. Moreover, the nodular forms of graphite result in greatly increased fracture toughness and offer the designer the option of choosing high ductility (with some grades guaranteeing more than 18% elongation), or high strength (with some tensile strengths exceeding 800 MPa).

### 3.02.1.5 Alloy Cast Irons

The properties of both white and gray cast irons can be altered and enhanced by the inclusion of alloying elements such as nickel, chromium, molybdenum, and silicon. For example, 4–5% nickel and 1.2% chromium additions are used to increase hardness and mechanical properties. Alloys containing over 14–25% nickel, are austenitic and have good heat and corrosion resistance. Alloys with 25–35% chromium result in a ‘stainless’ cast iron with good corrosion and high temperature properties, while irons containing up to 16% silicon offer enhanced hardness and excellent corrosion resistance at the expense of mechanical properties.

## 3.02.2 Production, Composition, and Microstructural Effects

A cast iron is an alloy of iron that contains 2–4% carbon, along with varying amounts of silicon and manganese and traces of impurities such as sulfur and phosphorus. The relatively low melting point of these alloys compared with that of steel and their tendency to expand slightly on solidification, which make them admirably suitable for the production of components by casting, result from this feature of their composition. The production of cast iron is relatively unsophisticated and mostly involves remelting charges consisting of pig iron (e.g., from a blast furnace), steel scrap, foundry scrap, and ferroalloys to give the appropriate composition. The composition figures quoted in [Table 1](#) provides a general guide for the range of compositions for the various types of iron. Due to this variation in composition, cast irons are usually specified in terms of their mechanical properties rather than on an analytical basis. Cast iron is used extensively to make machine parts, engine cylinder blocks, stoves, pipes, steam radiators, and many other products.



**Table 1** Composition ranges of cast iron alloys (nodular iron additionally: 0.04–0.1% Mg)

	Microstructure		Carbon (%)	Carbide (%)	Si (%)	Mn (%)	S (%)	P (%)
	Graphite	Matrix						
White iron	None	Pearlite	1.7–3.0	100%	0.8–1.3	0.4	<0.15	<0.5
Gray iron	Flake	Pearlite	2.7–4.0	<1	0.5–3.3	0.3–1.0	<0.15	<1.4
Nodular	Nodular	Pearlite/ferrite	3.3–3.9	<1	1.6–2.5	0.4	<0.01	<0.1
Malleable (blackheart)	Nodular	Ferrite	2.0–2.7	None	0.8–1.2	0.1–0.6	<0.15	<0.2
Malleable (whiteheart)	Nodular	Pearlite	3.3–3.9	0–1	0.3–0.8	0.1–0.5	<0.4	<0.1

### 3.02.2.1 Effect of Microstructure on Corrosion Resistance

The essential difference between the corrosion of cast iron and steel arises from the fact that cast iron contains in its microstructure several more or less corrosion-resistant phases that are largely or completely absent from steel. The most important of these corrosion-resistant phases are: graphite, phosphide eutectic, and, to a lesser extent, carbides, and carbide eutectic (i.e., pearlite). A close observation of the corrosion products of cast iron<sup>1</sup> can distinguish two distinct layers (see Figure 3).

The base layer, exactly occupying the place and volume of the original corroded metal and hence, sometimes called the 'topotaxial layer,' contains the inert, noncorroding elements of the cast iron, the graphite, in particular, possibly the phosphorous eutectic, and a few carbides for which the initial shape and distribution are preserved. The pores resulting from the selective attack of the ferrous matrix are generally filled by corrosion products of iron; additionally, the oxidation products of silicon (e.g., silicic acid) contribute to cohesion. This layer, which has no equivalent in steel, is often called the layer of 'graphitic corrosion residue.' This is because the species it contains, and which can most readily be identified (by X-rays), is graphite. This also explains terms such as graphitosis, graphitization, graphitic, or spongy corrosion, etc, that are often used to describe this form of corrosive attack.

The outer surface layer (epitaxial layer), which develops from the initial surface of the iron casting, results from the reaction of iron ions ( $\text{Fe}^{2+}$ ), migrating through the graphitic layer from the underlying residual metal. This layer often takes the form of a voluminous gangue (up to 3.7 times the volume of iron lost to corrosion). It may also contain elements from the corrosive environment, either by

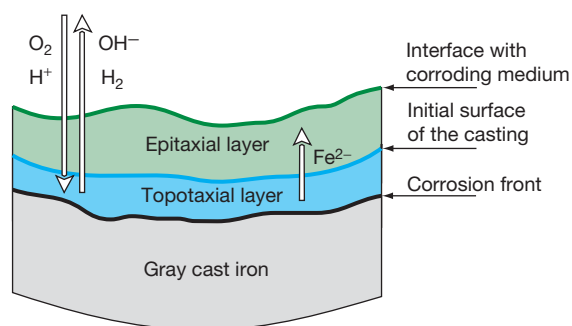


**Figure 3** Schematic diagram showing layers of corrosion on gray cast iron. Based on a diagram by Tsuda M.; Murata Y., *IMONO, 1982, 54, 605–611* and reproduced with permission from Reynaud, A. *Corrosion and Cast Iron*, ETIF, France, 2008.

incorporation, in the case of a solid aggressive medium (case of soils), or by precipitation, in the case of a liquid aggressive medium (e.g., calcareous rust). This layer (which has some protective capacity), thus, has variable density depending on the nature of the surrounding medium. Also, the layer may not even exist if the products of the reaction between the iron and the corrosive medium can be eliminated as they form, for example by an erosive action, or if they are immediately soluble.

These two layers are clearly distinct in both appearance and composition; one contains essential corrosion residues, while the other contains corrosion products. They can be separated more or less readily from one another (by scraping or as a result of an impact). Thus, after elimination of the outer layer of corrosion products, the casting most often appears in its initial form and may mask the actual extent of corrosion damage, which can be revealed only by sand blasting or by special measurements (ultrasound). The layer of corrosion products, consisting essentially of various hydrated iron oxides, is rather similar to the layer of

corrosion products that would form under the same conditions on steel.<sup>2</sup> However, it is anchored in a very different manner: in the case of steel, this layer develops from the evolving active corrosion front, while in the case of a cast iron, it develops on the unchanging inert surface of the layer of corrosion residues.

These layers, in particular the layer of corrosion residue, also act as a barrier that retard the progress of corrosion, as can be seen from the schematic representation (Figure 4) of the corrosion of a cast iron and of a steel in an acid medium: the graphite, highly cathodic with respect to the iron in an acid medium, at first speeds up the corrosion, then slows it by a barrier effect that limits the exchange between the acid medium and the corrosion front.

The amount of graphitic residue retained on a corroding surface depends partly on the morphology of the graphite and partly on the corrosivity of the medium. In general, coarse flake graphite tends to give a more permeable and less strong residue than finer graphite, while nodules produce an even weaker residue. However, these differences are only clear at very high corrosion rates. For example, while flake graphite iron retains virtually all the graphitic residue when corroded in 0.5% sulfuric acid, the residue from a nodular graphite iron is largely detached; in 0.05% sulfuric acid, however, there is little difference in the amounts retained by the two irons. Also, the effect of graphite on the corrosion of iron depends on the residue thickness – thus in 0.5% acid, graphite stimulates attack on the nodular graphite iron because of its ability to act as an efficient cathode for hydrogen evolution, however, in 0.05% acid, once the residue thickness reaches  $\sim 0.1$  mm, the attack tends to become stifled.<sup>3</sup>

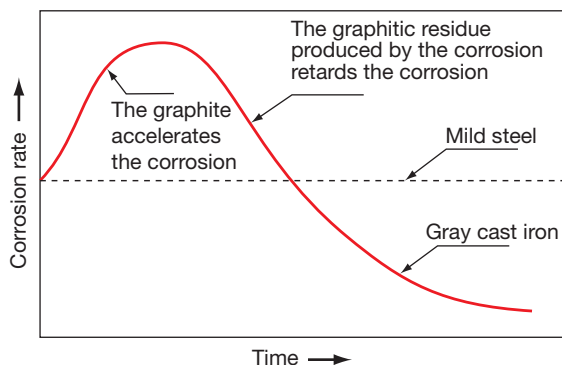


**Figure 4** Schematic representation of the corrosion of a cast iron and of a steel in an acid medium. Based on a diagram by Hasson, D.; Karmon, M. *World Water*, 1983 (November), 44–45 and reproduced with permission from Reynaud, A. *Corrosion and Cast Iron*, ETIF, France, 2008.

Also note, that the original geometry of the material is often preserved after graphitic corrosion, unless the corrosion products disintegrate, and that the mechanical strength of this graphitic residue is generally good (especially if the graphite is lamellar). For example, water pipes made of graphitic cast iron, although severely corroded after  $\sim 30$  years in service can still withstand high water pressures. However, ductile iron or steel pipes have burst under similar conditions. Similarly, some cast iron water pipes of the Château of Versailles are still functioning properly more than three centuries after they were installed (see Figure 5).

If the graphite form is spheroidal, the layer of graphitic residue is more friable and mechanically less strong because it receives less support from remaining graphite, which is distributed discretely, rather than continuously. On the other hand, the noncontinuity of graphite in SG cast irons also limits the penetration of the corrosion front, which occurs preferentially at the matrix–graphite interface. Otherwise, the often higher silicon content of spheroidal graphite cast iron implies, that the proportion of silica in the graphitic corrosion residue is slightly



**Figure 5** Length of lamellar graphite cast iron water pipe in Versailles (more than three centuries old). Reproduced with permission from Reynaud, A. *Corrosion and Cast Iron*, ETIF, France, 2008.

larger in these materials. Despite these factors, it is important to remember that the slight benefits given by improved mechanical strength of the graphitic residue in lamellar graphite iron must not lead us to overlook the considerable superiority of the mechanical properties of spheroidal graphite cast iron.

### 3.02.2.2 Influence of Galvanic Couples in the Microstructure

In the case of cast iron, an eminent heterogeneous alloy, there is apparently an involvement of the galvanic couples that exist between the various metallographic phases. In addition to the couples formed with graphite (which is inevitably the cathode), they include, for example, the iron carbide–ferrite and iron phosphide–ferrite couples, which lead to the selective preferential dissolution of the ferrite (because cementite and iron phosphide are relatively noble).

Residues of islands of pearlite and coalesced carbides, after a ferritizing heat treatment of SG cast irons, can also lead to the formation of very fine microcells. This can result in the complete removal of the ferrite matrix, leaving the carbides, the phosphorous eutectic, and in particular the graphite in the corrosion products. Research has shown that SG cast iron has a higher susceptibility to corrosion than LG cast iron because of the magnesium sulfide inclusions (magnesium is used to inoculate the casting to promote formation of graphite nodules).<sup>4,5</sup> A Japanese electrochemical study<sup>6</sup> showed that, in the case of spheroidal graphite cast irons, the resistance to corrosion decreases as the size of the spheroids decreases. In the special case of SG cast irons obtained by stepped quenching, a bainitic microstructure results. The effect of graphite morphology on the corrosion resistance of this type of iron, austempered ductile iron (ADI) as defined for example by European standard BS EN 1564:1997, has shown, by corrosion potential measurements and anodic polarization tests, that in a 0.01 M HCl, the size of the graphite spheroids has little effect on corrosion resistance. Otherwise, corrosion resistance is diminished as the duration of the stepped quenching increases.

Researchers<sup>6</sup> have also studied the corrosion behavior of ADI cast irons as a function of nickel content and of the chill effect. The corrosion tests, in a 1 N NaCl solution, lasted from 12 to 72 h. Mass loss experiments showed that increasing the nickel content increased the corrosion resistance (especially at the longest test duration). The specimens taken in the vicinity of the chill had a greater corrosion resistance, which was attributed to a particular

carbide content. Finally, this study reported that the corrosion resistance of ADI cast iron is superior to that of classical pearlitic cast iron.

## 3.02.3 General Corrosion Behavior

### 3.02.3.1 Low-Alloy Lamellar or Spheroidal Graphite Cast Irons

Apart from silicon, small variations in the composition of cast irons, or even the addition of minor amounts of alloying elements, generally have little effect on the corrosion resistance. This is illustrated by the work of Graham,<sup>7</sup> which related the corrosive wear of automobile cylinders and piston rings exposed to high sulfur fuels. Thus, iron exposed to 70% sulfuric acid at 130 °C is attacked at rates dependent on its silicon content, the rate being relatively low at below 1% Si but rising to a peak at ~2% Si (Figure 6).

Whittaker and Brandes<sup>8</sup> followed up this work, carrying out tests on iron containing small amounts of copper and nickel. The addition of 0.6% Cu to iron containing 2% Si improved the corrosion resistance significantly, but made little difference, or was detrimental, to iron containing less than 1.5% Si. Copper additions also appear to reduce the effect on corrosion of the sulfur content of an iron exposed to acid and the effect is thus lower in low sulfur irons. Since sulfur can stimulate corrosion in acidic

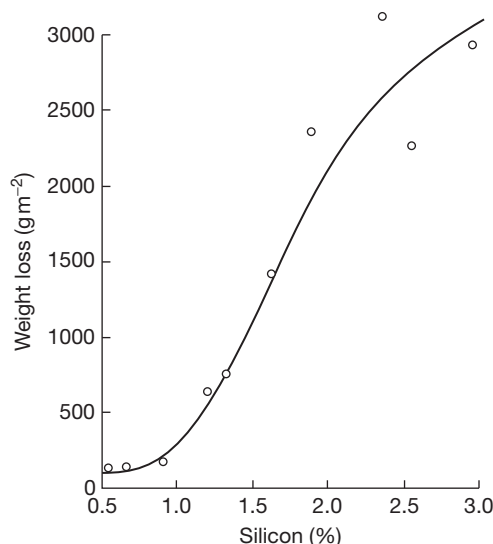


**Figure 6** Weight loss for cast iron exposed in 70% H<sub>2</sub>SO<sub>4</sub> at 130 °C for 16 h. Reproduced with permission from Graham, R.; Prado, O. S.; Collins, M. H.; Brandes, E. A.; Farmery, H. K. *Proc. Inst. Mech. Eng.* **1960**, 174, 617.

environments, it is usually kept as low as possible in irons to be used under these conditions; a low sulfur content, in any case, generally desirable.

### 3.02.3.2 High-Alloy Cast Irons

Significant additions of such alloy elements as nickel, chromium, and silicon have a great impact on the corrosion resistance of cast irons.<sup>9</sup> They modify the matrix, increasing its corrosion resistance and promote the formation of protective oxide (passive) films. The general outcomes of the most important additions are:

- nickel additions will tend to stabilize austenite;
- chromium cast irons, depending on the levels of chromium, carbon, and other added elements, including nickel, will be ferritic or austenitic;
- silicon cast irons will be ferritic.

#### 3.02.3.2.1 Austenitic nickel cast iron

The addition of ~20% nickel to cast iron produces materials with a stable austenitic structure; these materials are sometimes known as austenitic cast irons but are more often referred to commercially as 'Ni-Resist' cast irons. The austenitic matrix of these irons gives rise to very different mechanical and physical properties compared with those obtained with the nickel-free gray cast irons. The austenitic matrix is more noble than the matrix of unalloyed gray irons, and it was shown in the early work of Vanick and Merica<sup>10</sup> that the corrosion resistance of cast iron increases with increasing nickel content up to ~20% (Figure 7).

Although the Ni-Resist irons, due to their austenitic matrix, are tougher and more shock resistant than the nickel-free gray irons, those with carbon in the lamellar graphite form (LG irons) still exhibit certain disadvantages due to the graphite structure. Much better strength and impact properties can be obtained by treating the iron with a small quantity of magnesium sufficient to give a residual content of 0.05–0.1%, which converts the graphite to a spheroidal form (SG irons). The Ni-containing austenitic irons are thus available in both LG and SG forms. The matrix also contains small amounts of second phase carbides, the quantity of which increases with increasing chromium content.

The first alloys in the Ni-Resist series, containing ~20% nickel, were introduced in the 1930s and soon became established in both corrosion and heat resistant applications. The range of alloys has been

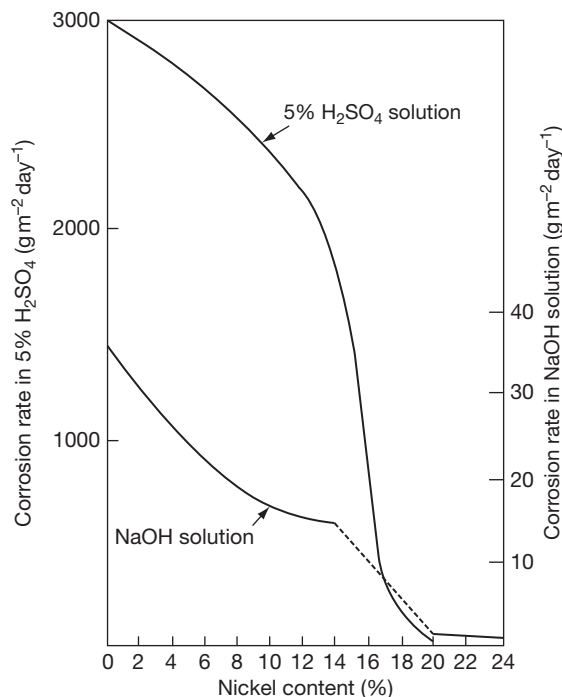


**Figure 7** Effect of nickel content on corrosion resistance of cast iron.

extended over the years with nickel contents varying from 13% to 35%. Each material has a somewhat different characteristic such that the most appropriate grade must be selected to obtain the most advantageous properties for any particular application. The compositions and mechanical properties of the principal grades of austenitic cast irons are summarized in Table 2. There is no spheroidal austenitic iron corresponding to Type 1 Ni-Resist, since it is difficult to obtain a good spheroidal graphite structure in an austenitic iron containing more than 2% copper. A considerable number of modified grades, differing in both composition and properties from the basic grades, also exist. Specifications for eight commonly used grades of austenitic cast irons are given in BS EN 13835:2002.

The tensile strengths of the spheroidal graphite iron are generally about twice as those of their flake graphite equivalents and can be further improved, by ~80 MPa, by quenching the iron in oil or water from temperatures of 925–1000 °C. This treatment is even more effective when applied to chill castings but the resulting ductility is reduced because of the increased amount of carbide formed as a result of chilling. The impact resistance of the spheroidal graphite grades is much better than that of the equivalent flake graphite

**Table 2** Composition and properties of principal grades of flake and spheroidal graphite austenitic case irons

BS 3468 designation	Ni-resist type	Composition (wt%)						Minimum tensile strength ( $\times 10^7 \text{ N m}^{-2}$ )	Brinell hardness
		C	Si	Mn	Ni	Cr	Cu		
AUS101A	Type 1	3.0	1–2.8	1–1.5	13.5–17.5	1.75–2.5	5.5–2.5	170	130–170
AUS102A	Type 2	3.0	1–2.8	0.8–1.5	18–22	1.75–2.5	0.5 max.	170	125–170
AUS105	Type 3	2.6	1–2	0.4–0.8	28–32	2.5–3.5	0.5 max.	170	120–160
—	Type 4	2.6	5–6	0.4–0.8	29–32	4.5–5.5	0.5 max.	170	150–210
—	Type 5	2.4	1–2	0.4–0.8	34–36	0.1 max.	0.5 max.	140	100–125
AUS104	—	1.6–2.2	4.5–5.5	1–1.5	18–22	1.8–4.5	0.5 max.	190	248 max.
AUS202A	Type D-2	3.0	1.75–3	0.7–1	18–22	1.75–2.5	—	370	140–200
AUS205	Type D-3	2.6	1.5–2.8	0.5 max.	28–32	2.5–3.5	—	370	140–200
—	Type D-4	2.6	5–6	0.5 max.	29–32	4.5–5.5	—	420	170–240
—	Type D-5	2.4	1.5–2.8	0.5 max.	34–36	0.1 max.	—	370	130–180
AUS204	—	3.0	4.5–5.5	1–1.5	18–22	1–2.5	—	370	230 max.



irons and elongation values as high as 40% can be obtained with the SG irons. The mechanical properties of the austenitic irons are also good at low temperatures and can be useful in a number of chemical plants and cryogenic applications.

The austenitic irons show excellent casting properties and good machinability, which, in combination with the good mechanical properties and good corrosion resistance, ensures wide use of these materials in many applications.

### **3.02.3.2.2 High chromium cast iron**

There is no clear demarcation between high-chromium steels and high-chromium cast irons other than the fact that components are fabricated from steels, and cast in the irons. In practice, however, irons are usually found to have carbon content varying between 0.6% and 3%, while most of the steels contain less than 0.3% carbon. Of the high-chromium irons, those used for components requiring a high degree of corrosion resistance, normally contain 25–35% chromium. It is established<sup>11</sup> that a useful formula to compute the minimum chromium content of a corrosion-resistant iron is:  $\%Cr = (\%Cr \times 10) + 12$ . That is, increased carbon content requires balancing with increased chromium content in the alloy. For example, a 1.5% carbon alloy should contain not less than 27% chromium.

The limitations imposed by this formula, together with the fact that the alloys in practice rarely contain more than 35% chromium, suggest that the maximum carbon content of the irons should be 2.3%, and that the irons normally contain between 1.0% and 2.0% carbon, unless some property other than corrosion resistance is of prime importance. Silicon may also be present in high-chromium irons in amounts varying between 0.5% and 2.5%; any value more than this has an embrittling effect. Silicon increases fluidity in the foundry and improve the surface quality of castings. Further effects are to refine the eutectic carbides in the iron, to produce a more uniform structure and to raise the temperature at which the matrix transforms from ferrite to austenite with consequent dimensional changes.

Irons with compositions discussed above have structures comprising a uniform dispersion of chromium–iron complex carbides in a matrix of chromium-containing ferrite. The chromium content of the ferrite is not known, although it is assumed to be ~10–13%. The carbides are probably mixtures of the types  $Cr_7C_3$  and  $Cr_{23}C_6$ , in which some of the chromium has been replaced by iron.<sup>12</sup>

In general, the high-chromium irons are hard but not completely unmachinable. Typically, chromium cast irons, of the compositions described above, have tensile strengths ~450–480 MPa and hardness ~350 Brinell. The hardness of these alloys makes them particularly useful in environments where abrasion or wear resistance may be as important as corrosion resistance. However, the principal difficulties in the production of castings in this alloy are its high shrinkage, which entails some tendency to develop porosity, and the ready formation of an oxide skin, which may cause cold laps in the casting. Castings must, in consequence, be produced by methods similar to those employed for steel castings and care must be taken to avoid the introduction of oxide into the mould.

The high-chromium irons undoubtedly owe their corrosion-resistant properties to the development on the surface of the alloys of an impervious and highly tenacious film, probably consisting of a complex mixture of chromium and iron oxides. Since chromium oxide is derived from the chromium present in the matrix and not from that combined with the carbide, it follows that a stainless iron will be produced only when chromium in excess of the amount required to form carbides is present.

High chromium-containing cast irons are most useful in environments containing an abundant supply of oxygen or oxidizing agents; anaerobic or reducing conditions may lead to rapid corrosion since this may detrimentally affect passivity. Physical effects such as abrasion or sudden dimensional changes induced by temperature fluctuations may rupture the film and allow corrosion to take place. The iron will also be subject to corrosion by solutions containing anions, such as those of the halides, leading to pitting corrosion. With respect to mineral acids, the most important characteristic of chromium cast irons is its resistance to nitric acid, especially in dilute solution. On the other hand, these cast irons do not resist alkaline hydroxides and concentrated mineral acids. Ferritic chromium cast irons turn out to have excellent resistance to high temperature oxidation up to 950–1000 °C.

### **3.02.3.2.3 High silicon cast iron**

Up to ~3%, increasing silicon content has little effect upon the corrosion resistance of the cast iron. In alloys containing much greater amounts of silicon, however, the silicon is responsible for the development of a marked increase in chemical resistance. These alloys can be divided into two types: those containing 4–10% silicon, which are used in

applications requiring an iron with good resistance to oxidation at high temperatures, and those containing 12–18% silicon, which are used in applications requiring an iron with very high resistance to acid attack. The latter are commonly referred to as the high-silicon irons. Compositions and mechanical properties of the high-silicon irons are given in Tables 3 and 4.

All these alloys are characterized by high values of hardness and low resistance to impact. Consequently, they are more similar to stoneware than to other metals but are superior to stoneware in thermal conductivity and in their resistance to thermal shock, which, however, is poor compared with that of other metals. Thus, high-silicon irons may be used at elevated temperatures if the process requires it. The principal limitation on their use is imposed by their relatively low thermal conductivities and susceptibility to cracking from thermal shock; this demands that the rate of application or removal of heat should not be rapid.

The microstructure of the high-silicon irons containing less than 15.2% silicon consists of a matrix of silico-ferrite<sup>13</sup> in which a majority of the carbon present in the alloy is distributed as fine graphite flakes. The addition of chromium or molybdenum in the alloy results in the formation of some alloy carbides. The hardness and brittleness of silicon-containing cast iron is predominantly due to the nature of the silico-ferrite, which is intrinsically brittle. Although attempts<sup>14</sup> have been made to produce high-silicon iron with a nodular graphite structure, because of the low strength of these alloys due to the matrix rather than to the graphite form, nodular graphite irons have little, if any, mechanical superiority.

Since the mechanical properties of high-silicon irons preclude any machining other than grinding, it is necessary to cast the materials essentially to net the final shape in such a way that subsequent treatment is kept to a minimum. Also, in view of their poor mechanical properties, the development of any stress in the castings during solidification is very dangerous, since they may cause the casting to crack in

subsequent service. To overcome this risk, it is often desirable to strip the castings from the moulds while they are still red hot and to anneal them at 850 °C for several hours, followed by slow cooling.<sup>15</sup>

### 3.02.3.3 Typical Applications

#### 3.02.3.3.1 Unalloyed cast irons

In spite of competition from other materials, cast iron has an extensive range of applications due to the improving number and variety of properties.<sup>16,17</sup> However, the adaptation of a type of cast iron to a given application calls for analysis and identification of the required properties, which are often very complex, among which the corrodibility and the cost price must in particular be considered. Austenitic cast irons and stainless steels cost roughly four and five times as much as unalloyed cast irons, respectively. These relative costs must be considered in the light of the respective service lives and replacement costs. Otherwise, the differences in properties between lamellar graphite unalloyed cast irons and austenitic cast irons are substantially of the same order as the differences between carbon steels and austenitic stainless steels.

When the service life of a unalloyed cast iron is mediocre, the addition of alloy elements (e.g., nickel, chromium, molybdenum, copper) can often extend it inexpensively. However, it must be borne in mind that possible casting defects (blowholes, porosities, inclusions of silica or slag, shrinkage cavities, irregularities of structure, segregation, undesirable constituents at grain boundaries, etc.) may be the locus of pitting or of local attack that may considerably shorten the life of the castings. Experience has shown that unalloyed iron castings of irreproachable quality and soundness, having a homogeneous structure, prepared using all the resources of the technique, can in some applications have longer service lives than parts made of special cast irons that are more delicate to work, more expensive, and not always free of defects.

**Table 3** Analysis of typical silicon-iron alloys

Name	Total carbon (%)	Si (%)	Mn (%)	S (%)	P (%)	Ni (%)	Cr (%)	Mo (%)
Grey cast iron	3.5	2.0	0.5	0.1	0.1	—	—	—
Hypersilid 14/16	0.65	14.5	0.5	0.02	0.15	—	—	—
Duriron	0.85	14.5	0.6	<0.05	<0.1	—	—	—
Durichlor 51	1.00	14.5	0.6	<0.05	<0.1	—	5.0	1.0
Hypersilid 16/18	0.35	17.0	0.5	0.02	0.1	—	—	—

**Table 4** Mechanical properties of silicon-iron alloys

Name	Ultimate tensile strength ( $\text{MN m}^{-2}$ )	Elongation 2 in (50 mm) gauge length	Brinell hardness no.
Gray cast iron	23	2%	180
14.5% silicon iron	129	Nil	540
Durichlor	108	Nil	450

**3.02.3.3.2 Alloyed ferritic cast irons**

The addition of chromium allows the use of cast iron in the chemical industry (retorts, tanks, heat exchangers, etc.) where gray iron would have an unacceptably high corrosion rate. The degree of corrosion resistance of a cast iron (with chromium, for example) depends first on the nature of the film or layer that forms on the surface. If this film is dissolved or broken up or is destroyed because of the agitation of the aggressive medium, corrosion continues and can reach unacceptable levels comparable to unalloyed cast iron.

For example, with chromium contents from 12% to 20%, cast iron is satisfactory for the retorts used in the synthesis of carbon disulfide, which are generally exposed continuously to temperatures between 850 °C and 900 °C; their average life is of the order of 6 months.<sup>16</sup> In pyrite furnaces, it is the best material for the production of certain parts, notably because of its good resistance to sour gas ( $\text{H}_2\text{S}$ ) at 1000 °C. The reaction between sodium chloride and concentrated sulfuric acid, producing gaseous hydrochloric acid at high temperature, requires ferritic chromium cast irons for the moving parts of the furnaces.<sup>16</sup> In aqueous corrosion conditions, chromium contents from 25% to 35% are often required to counter the removal of chromium from the matrix by the formation of carbides. If sufficient chromium is present, the cast iron has similar attributes to stainless steel and low corrosion rate when passive but is susceptible to pitting corrosion in chloride media and where oxidizing agents (e.g., cupric and ferric ion) are present in solution. The pitting corrosion of a high chromium cast iron in 4000  $\text{mg l}^{-1}$  chloride ion is shown in Figure 8.

Since the corrosion resistance of the high-silicon ferritic cast iron depends on the permanence and impermeability of a thin silica film on the surface of the metal, it is obvious that any reagent which can

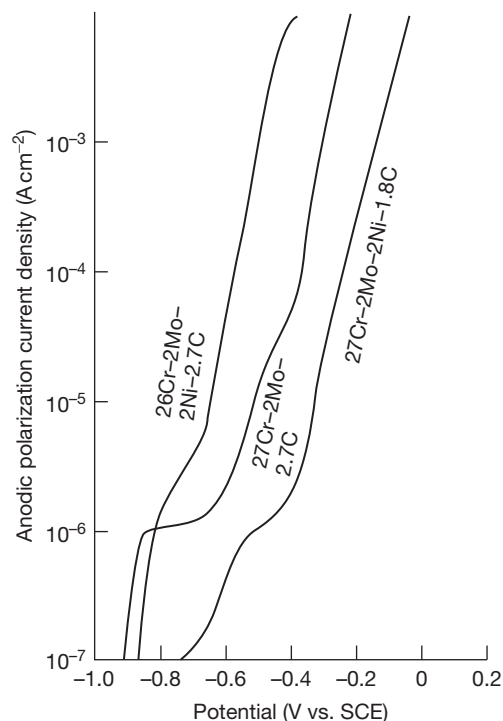


**Figure 8** Potentiodynamic polarization curves for high-chromium white irons in nitrogen-saturated solution containing 4000  $\text{mg l}^{-1}$  chloride at pH 7 and 25 °C. Reproduced with permission from Dodd, J. *J. Mater. Energy Sys.* **1980**, 2, 65–76.

damage the film will cause accelerated corrosion of the metal. For this reason all solutions containing hydrofluoric acid must be regarded as incompatible with the alloys.

Apart from this, high silicon iron offers an excellent resistance to attack by all concentrations of nitric and sulfuric acids and their mixtures. It also provides good performance in hydrochloric acid and in phosphoric acid that is relatively free of fluoride.

Ferritic silicon cast irons (14–18%) are routinely used in parts for contact with acids of all concentrations and for acid effluents. For example, the mixers used to prepare sulfuric acids containing less than 25% water, for the production of explosives and of nitrated derivatives that are themselves used in the production of dyestuffs, are made of silicon cast iron.<sup>16</sup> The thesis by Y. Cetre<sup>18</sup> is a useful source of information about this subject.

**3.02.3.3.3 Austenitic cast irons**

In addition to the ferritic structures produced by additions of silicon or chromium, there is another

major family of cast irons, produced by addition of large quantities of nickel, cast irons having an austenitic structure; their resistance to electrochemical corrosion is much better than that of unalloyed cast irons. Austenitic cast irons show lower corrosion rates than ferritic irons primarily due to the nickel content of the austenitic matrix. Thus, in deaerated sulfuric acid, active dissolution of the austenitic irons occurs at more noble potentials resulting in an intrinsically lower active corrosion rate. Similarly, the critical current density ( $i_{crit}$ ) for passivation of austenitic irons tends to decrease with increasing chromium and silicon content. Thus, austenitic irons, particularly those of higher chromium and silicon content, show superior corrosion resistance compared with ferritic irons.

In paper mills (installations processing pulp and paper), the standard practice is to use austenitic nickel cast irons for equipments operating in solutions of sulfites or sulfates or in caustic solutions. This type of cast iron is also used for parts of furnaces operating at high temperatures and for valves used in sulfuric, phosphoric, and concentrated brines. Spheroidal graphite austenitic cast irons, because of their good ductility and high impact energy, can be specified for vessels containing rather aggressive liquids at high pressures (see standard NF A 32-211 of January 1991)<sup>19</sup> and are also suitable for the production of pumps, valves, and turbo-expanders for low temperature duty in the petrochemical industry, and for the preparation, transport, and storage of liquefied gases.

The individual characteristics and uses of some of the basic grades of the austenitic irons are given in **Table 5**. The major uses of these materials occur in the handling of fluids in the chemical and petroleum industries and also in the power industry and in many marine applications. The austenitic irons are also used in the food, soap, and plastics industries where low corrosion rates are essential in order to avoid contamination of the product. Ni-Resist grades Type 2, 3, or 4 are generally used for such applications but the highly alloyed Type 4 Ni-Resist is preferred where low product contamination is of prime importance.

The modified grades of Ni-Resist are often different from the basic grades used in additional applications. Ni-Resist Types 1B, 2B, and D-2B have a higher chromium content than the corresponding basic grades which increases the erosion resistance of the materials; these grades are less expensive than the other grades with good erosion resistance, that is, Ni-Resist Types 3 and 4. A chromium-free grade of austenitic iron, Ni-Resist Type D-2C, has particularly good ductility and shows good mechanical properties below  $-100^{\circ}\text{C}$ . Even better low temperature properties are, however, obtained with Ni-Resist Type D-2M, a chromium-free 4% manganese grade, which was specially developed for cryogenic applications such as the separation of aromatic hydrocarbons and the production of ethylene. Ni-Resist Type D-4A is a recently developed grade of austenitic iron, which has particularly good resistance to high temperature oxidation and better ductility than the standard Type D-4 grade.

**Table 5** Characteristics and uses of basic grades of austenitic cast irons

<i>BS EN 13835 designation</i>	<i>Ni-Resist Type</i>	<i>Characteristics</i>	<i>Uses</i>
AUS101A	Type 1	Least expensive austenitic iron: good corrosion resistance particularly in acidic media	Pumps, valves, furnace components
AUS102A AUS202A	Type 2 Type D-2	Good corrosion resistance; better than Type 1 in alkaline environments	As for Type 1 but preferable for alkaline solutions; used in soap and plastic industries
AUS105 AUS205	Type 3 Type D-3	Good thermal shock resistance; high resistance to erosion particularly in alkaline media	Pumps, valves, pressure vessels, filter parts, exhaust gas manifolds
— —	Type 4 Type D-4	Best corrosion resistance and erosion resistance of the austenitic irons	Castings for industrial furnaces; used in food industry for low contamination of product
— —	Type 5 Type D-5	Very low thermal expansion; good dimensional stability	Scientific instruments, glass moulds
AUS104 AUS204	— —	Good resistance to high temperature oxidation; good corrosion resistance in sulphuric acid	Pumps and valves

One of the outstanding properties of the austenitic irons is their resistance to graphitic corrosion or 'graphitization.' In some environments, ferritic cast irons corrode in such a manner that the surface becomes covered with a layer of graphite. This compact graphite layer, being more noble than the matrix, markedly increases the rate of attack. The austenitic irons rarely form this graphite layer and consequently, in environments where graphitic corrosion is a problem, perform much better than low-alloy cast irons. Practical experience indicates that the corrosion resistance of the flake and spheroidal graphite irons is similar in many environments; however, the spheroidal graphite irons have shown superior corrosion resistance compared to the equivalent flake graphite grades in a number of cases.<sup>20</sup>

### 3.02.4 Corrosion Environments

#### 3.02.4.1 Atmospheric Corrosion

As cast iron components are normally very heavy in section, the relatively low rates of attack associated with atmospheric corrosion do not constitute a problem and little work has been carried out on the phenomenon. A summary of some data is given in [Table 6](#). The most extensive work in this field was initiated by the American Society for Testing and Materials (ASTM) in 1958 and some of the results produced by these studies are quoted in [Table 7](#).<sup>21</sup> It should be noted that there is a marked fall in corrosion rate with time for all the metals tested.

The atmospheric corrosion rate is generally determined by the atmospheric relative humidity (RH) and degree of air pollutants (i.e., gaseous, dust, and salt aerosols); at RH less than ~65%, atmospheric corrosion rates are usually relatively low. However, in areas of high humidity (above 70% for most of the year), unalloyed cast irons suffer generalized corrosion and results in the formation of rust similar to that in steel; that is, the corrosion product remains on the surface, [Figure 9](#). In such cases, the initial corrosion rates vary from below  $25 \mu\text{m year}^{-1}$  in a pollution-free rural atmosphere to over  $150 \mu\text{m year}^{-1}$  in a polluted atmosphere (i.e., containing  $\text{SO}_2$ ) or a marine atmosphere (i.e., containing sea-salt spray aerosol particles). However, this initial corrosion rate decreases as the duration of exposure increases due to the formation of an adherent and highly protective layer of corrosion product. The main characteristics of the two main types of atmospheric media (indoor and outdoor) are:

Indoors:

- partial pressure of water vapor generally less than the saturated vapor pressure at the same temperature (i.e.,  $\text{RH} < 70\%$ );
- no large variations of temperature;
- very thin films of water on the surfaces of metals;
- relatively low concentration of gaseous and solid pollutants.

Outdoors:

- presence of thick films of water on the surfaces of metals (e.g., rain, etc.);
- level of pollution by acid gases ( $\text{SO}_2$ ,  $\text{NO}_x$ ,  $\text{Cl}_2$ ) generally higher than indoors;
- large variations of temperature (e.g., periodic diurnal temperature variations);
- variation (cyclic or not) of sunshine and of exposure to wind.

The atmospheric corrosion of cast irons is not a very acute problem: in many cases, a simple coat of paint will provide adequate protection. Otherwise, there seems to be rather little difference between lamellar graphite cast irons and spheroidal graphite cast irons; the latter are slightly better in an industrial environment, where the medium is more aggressive, because there is so little corrosion that the differences of behavior are hardly significant. The presence of small amounts of copper tends to improve the resistance of lamellar graphite cast irons to atmospheric corrosion in an industrial environment.<sup>22</sup>

Specific consideration must be given to local industrial environments in a plant that might give rise to more extensive corrosion. Generally,  $\text{CO}_2$  in excess of the normal atmospheric level will not be a problem. However, acid gases or aerosols, such as  $\text{SO}_2$ , sulfuric acid and phosphoric acid (e.g., from industrial plant) and  $\text{H}_2\text{S}$  and  $\text{NH}_3$  (e.g., from sewage works) generally require a highly alloyed material or effective surface protection by an organic coating. Thus, in principle, the atmospheric corrosion of unalloyed or low-alloy irons is similar to steel.

##### 3.02.4.1.1 Nickel cast irons

Although the Ni-Resist irons will not remain rust-free when exposed to the atmosphere, their corrosion resistance is much better than that of plain cast iron or mild steel. The results of a 7.5 year exposure trial carried out in a marine environment at Kure Beach, North Carolina, USA are shown in [Figure 10](#). The corrosion rates derived from the curves after 7.5 years of exposure are given in [Table 8](#).



**Table 6** Corrosion rate of steels and irons in the atmosphere ( $\text{g m}^{-2}\text{day}^{-1}$ )

<i>Environment</i>	<i>Rural</i>			<i>Urban</i>			<i>Industrial</i>			<i>Marine</i>	
<i>Source</i>	<i>ASTM</i>	<i>Roll</i>	<i>Friend</i>	<i>Nekrytyi</i>	<i>Roll</i>	<i>ASTM</i>	<i>Dearden</i>	<i>Friend</i>	<i>Roll</i>	<i>LaQue</i>	<i>ASTM</i>
<i>Exposure period years</i>	12	2	6	1	2	12	1	6	2	–	12
<i>Material:</i>											
Steel	0.23			1.2		0.27	3.4	2.4–3.2		3.6	1.38
Grey iron			1.4–2.1				3.2	1.1–1.2		0.6	2.0
White iron			0.1–0.3				1.3				
Malleable iron											
(a) <0.1% S	0.11			2.1		0.14			3.3		0.43
(b) >0.1% S	0.15	3.3			4.9–6.0	0.20			3.6		0.75
Nodular iron											
(a) Pearlitic	0.10					0.15				0.9	0.37
(b) Ferritic	0.11					0.17					0.72

**Table 7** ASTM atmospheric corrosion data ( $\text{g m}^{-2}\text{day}^{-1}$ )

Location		State College, PA (rural)			Kure Beach, NC (marine)			Newark, NJ (industrial)		
Duration (years)		1	3	12	1	3	12	1	3	12
<i>Metal</i>	<i>Condition</i>									
Ferritic ductile iron	As cast	0.90	0.36	0.11	1.51	0.85	0.72	1.29	0.51	0.17
	Machined	0.56	0.31	0.09	0.90	0.63	0.60	0.88	0.36	0.12
Pearlitic ductile iron	As cast	0.62	0.30	0.10	0.96	0.53	0.37	0.15	0.43	0.15
	Machined	0.50	0.22	0.07	0.82	0.47	0.27	0.70	0.30	0.10
Malleable iron >0.1% S	As cast	0.75	0.40	0.15	1.41	1.11	0.75	1.53	0.70	0.20
Mild steel	Rolled	0.97	0.52	0.23	3.02	2.01	1.38	1.75	0.81	0.27

Source: Mannweiler, G. B. *Proc. Am. Soc. Test. Mater.* **1972**, 72, 42.



**Figure 9** Surface condition of a lamellar graphite iron casting exposed for several decades to atmospheric corrosion. Reproduced with permission from Reynaud, A. *Corrosion and Cast Iron*, ETIF, France, 2008.

### 3.02.4.2 Corrosion in Natural Water

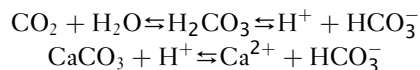
#### 3.02.4.2.1 Introduction

Water is a universal solvent for solids, liquids, and gases and, hence, water in its natural form is never chemically pure. It is likely to contain dissolved gases ( $\text{O}_2$ ,  $\text{CO}_2$ ,  $\text{N}_2$ ,  $\text{SO}_2$ ,  $\text{Cl}_2$ , etc.), organic or mineral matter (microorganisms, sand, etc.), and dissolved salts as ions ( $\text{Ca}^{2+}$ ,  $\text{Fe}^{3+}$ ,  $\text{Cl}^-$ ,  $\text{HCO}_3^-$ , etc.). In order to specify the properties of water, it is necessary to determine the following parameters: pH, color (due to mineral salts, colloidal organic matter), turbidity

(sands, etc.), temperature, total mineralization (or dry residue), total hardness, alkaline strength, total alkalinity, etc. and dissolved gases. For corrosion to occur an oxidizing agent must be present and, in most natural waters, this is usually dissolved oxygen. However, it is important to remember that other species (e.g.,  $\text{Cu}^{2+}$ , sulfur, etc.) can also act as oxidizers.

#### 3.02.4.2.2 Aggressiveness and corrosiveness of water

The aggressiveness of water is usually dependent on its acidity and this, in turn, depends on the presence of dissolved  $\text{CO}_2$ , which is in equilibrium with carbonate species and carbonic acid. Additional equilibria also exist with dissolved calcium and magnesium ions that result in these being undersaturated or supersaturated with respect to precipitation as the corresponding carbonate. For a given water chemistry, sufficient dissolved carbon dioxide must be present in order to prevent this precipitation. There is, therefore, a saturation equilibrium and pH for dissolved  $\text{CaCO}_3$ .<sup>23–26</sup> The governing equilibrium equations for this process are:



These equilibria control whether protective calcium carbonate films either deposit or not on the interior of the water pipe. In the absence of the carbonate film, the corrosion rate of the iron is increased and the water is therefore said to be aggressive (**Figure 11**).

Tillmans' formula gives the pH as a function of the free  $\text{CO}_2$  and the alkalinity in  $\text{CaCO}_3$  where the free  $\text{CO}_2$  and  $(\text{CaCO}_3)$  have units of  $\text{mg l}^{-1}$  (i.e., ppm)<sup>27</sup>:

$$\text{pH} = 7 - \log \frac{3 \times \text{freeCO}_2}{0.61 \times (\text{CaCO}_3)}$$

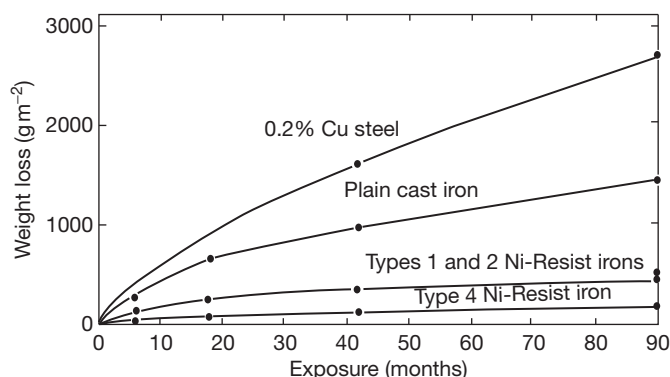


**Figure 10** Results of a 7.5-year exposure test program on 150 × 100-mm panels at Kure Beach, N.C. Reproduced from Mannweiler, G. B. *Proc. Am. Soc. Test. Mater.* **1972**, 72, 42.

**Table 8** Corrosion rates after exposure for 7.5 years at Kure beach

Alloy	Corrosion rate (mm year <sup>-1</sup> )
0.2% Cu steel	0.020
Cast iron	0.010
Types 1 and 2 Ni-Resist	<0.003
Type 4 Ni-Resist	<0.003

Langelier's formula can be used to determine an index of aggressiveness, Langelier saturation index (LSI):

$$\text{LSI} = \text{pH} - \text{pH}_s$$

where  $\text{pH}_s$  is the pH of saturation of  $\text{CaCO}_3$

- If LSI is negative, the water is aggressive;
- if LSI is zero, the water is inert;
- if LSI is positive, the water is scale-forming, calcareous.

To limit attack, the corrosion rate of the iron must be less than the rate of formation of the protective carbonate containing the deposit. Various conditions must then be satisfied: the water must not contain excessive  $\text{CO}_2$  and the pH must be above 7.4 for normally mineralized water, or 7.6 for soft water. To know whether water is calcareous or aggressive, it is also possible,<sup>28</sup> to refer to **Figure 12** and identify the water condition with respect to the carbonic acid equilibrium.

The corrosiveness of water in this context may be related to the presence of electrolytes in solution, mainly chlorides and sulfates, as measured by the conductivity. The point at which it starts to become significantly corrosive is also dependent on the dissolved oxygen concentration and other factors.

However, **Table 9** provides general indications for the limits of  $\text{Cl}^-$  ions and  $\text{SO}_4^{2-}$  ions before water can be thought of being significantly aggressive.

Importantly, it must be realized that the action of water on a pipe is also a dynamic phenomenon in which the flow velocity of water, its content of dissolved gases (e.g.,  $\text{O}_2$ ), matter in suspension, and microbiological phenomena must be taken into account. Potable water can dissolve  $\sim 40 \text{ cm}^3$  of air per liter of water, of which  $6 \text{ cm}^3$  is oxygen and  $14 \text{ cm}^3$  is nitrogen. A dissolved oxygen content of less than this value is a sign of the presence of organic matter; the presence of hydrogen sulfide suggests active sulfate reducing bacteria.

### 3.02.4.2.3 Influence of dissolved oxygen

Dissolved oxygen plays a critical role on the corrosion of iron (as it does for most metals). It is usually the primary cathodic reactant (oxidant) and its rate of influx at the metal surface influences the corrosion rate. Thus, the corrosion rates of many systems are controlled by the mass transport of dissolved oxygen to the reacting surface and this, in turn, is controlled by the concentration of dissolved oxygen, the fluid flow rate and the presence or absence of films (such as calcium carbonate or rust) on the surface. In the case of ferrous alloys (including iron and cast irons), the corrosion products (iron oxides) on the surface are more or less hydrated and have different crystallographic structures. Rust, therefore, often has several constituents, in particular: goethite ( $\alpha\text{-FeOOH}$ ); lepidocrocite ( $\gamma\text{-FeOOH}$ ) and magnetite ( $\text{Fe}_3\text{O}_4$ ).

In the absence of dissolved oxygen, the corrosion rate of iron and of low-alloy cast iron is low. However, once the  $\text{O}_2$  concentration increases, corrosion increases. In general, any process that modifies the

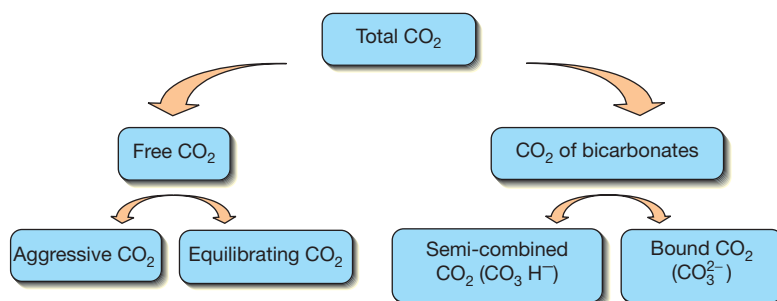


**Figure 11** Distribution of carbon dioxide in water. Reproduced with permission from Reynaud, A. *Corrosion and Cast Iron*, ETIF, France, 2008.

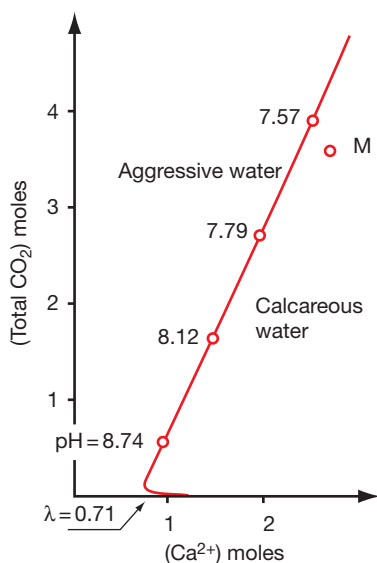


**Figure 12** Definition of water condition as a function of  $\text{CO}_2$  and  $\text{Ca}^{2+}$  contents. Based on a diagram by Lédion, J. *La corrosion par les eaux. La Revue des Laboratoires d'Essais*, no. 21, 1989, 9–13, and reproduced with permission from Reynaud, A. *Corrosion and Cast Iron*, ETIF, France, 2008.

**Table 9** Approximate limits for chloride and sulfate before water becomes significantly aggressive

Chloride ( $\text{Cl}^-$ )	Sulfate ( $\text{SO}_4^{2-}$ )	Reference
100 ppm	200 ppm	29
200 ppm	400 ppm	30
300 ppm	420 ppm	CEFRACOR

mass transport of oxygen to the metal surface for reaction (including the concentration of oxygen and the rate of agitation of the fluid) influences the corrosion rate. Note, however, that the presence of dissolved  $\text{O}_2$  can assist in the passivation of some alloy

cast irons. Moreover, the absence of oxygen, at least locally, can prevent the formation of a protective deposit or favor corrosion by differential aeration or crevice corrosion. This is the case, for example, of corrosion under deposits of scale, under joints, and on the plates of tube exchangers.

One interesting study has shown the influence of the concentration of dissolved oxygen on the mechanisms responsible for the corrosion of cast iron in water at  $50^\circ\text{C}$ .<sup>31</sup> The results of this study can be summed up using Figures 13 and 14.

#### 3.02.4.2.4 Corrosion of cast iron in natural water

Generally, cast irons provide excellent service in water following the formation of a protective layer on the inside wall of the pipe (layer of carbonate, most often). However, water that contains carbon dioxide in solution, acid effluents, chlorides, etc., is significantly more corrosive.

The presence of alloying elements of moderate composition has no great influence on the corrosion rate of cast irons in water. For example, a German study<sup>32</sup> has shown that the addition of 0–3% nickel does not improve the corrosion resistance of cast iron in artificial seawater, cooling water, or soft water. However, according to the same authors, the corrosion rate can be reduced by 50% in water containing dissolved  $\text{H}_2\text{S}$ , but the corrosion is still so high that this is not considered a cost-effective solution. In practice, the conditions that the castings are exposed to influences the corrosion rates. Typical corrosion rates for graphitic and 18% nickel (austenitic) cast iron in various environments are given in Table 10.

The use of Ni-Resist cast iron is recommended in the following cases: borehole water, fresh water with a brackish tendency ( $\text{pH} = 7.6$ ), water at  $80^\circ\text{C}$

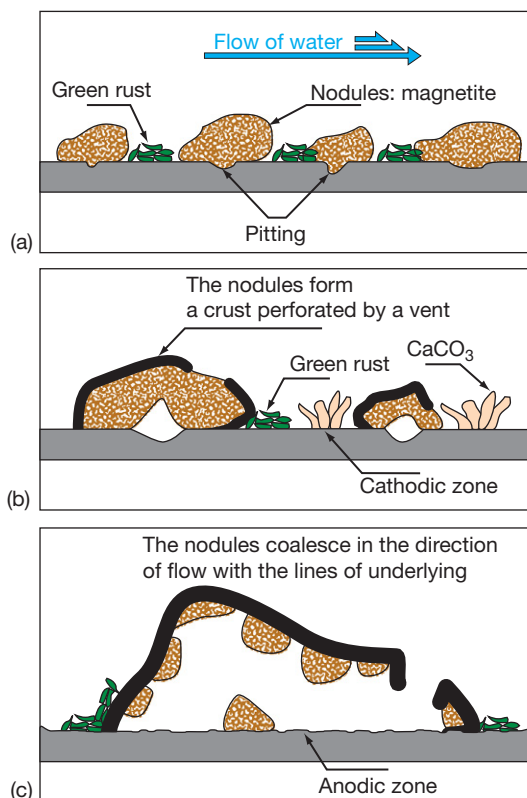


**Figure 13** Steps in the development of the layer of oxides that forms on lamellar graphite unalloyed cast iron immersed in water at 50 °C containing 0.44 ppm oxygen: (a) from 3 to 7 h (b) after 10 h (c) from 16 to 40 h. Reproduced with permission from Smith, D. C.; MacEnaney, B. *Corros. Sci.* **1979**, *19*, 379–394.

accompanied by ammonia vapors, and sulfite-rich water (pH = 3.5; e.g., from paper mills). On the other hand, low- or unalloyed cast irons can provide an adequate service life in the presence of more or less aerated water containing a large number of organic substances (low-alloy cast iron: 1.5% Ni + 0.5% Cr, for example). Small levels of copper and chromium also reduce the corrosion of lamellar graphite cast irons.

In certain cases, inhibitors may be used to protect cast irons against corrosion by water assuring that the materials are in a closed circulation system. The use of alkaline anodic inhibitors, such as 1% sodium silicate and 0.5% sodium nitrite, is effective. A mixture of phosphonocarboxylic acid and sodium nitrite also appears to be effective against the corrosion of cast irons by neutral solutions.<sup>22</sup> This results in the formation of a finer and more protective passive film than is formed in the presence of nitrite alone. A ranking of the inhibitors commonly used for closed

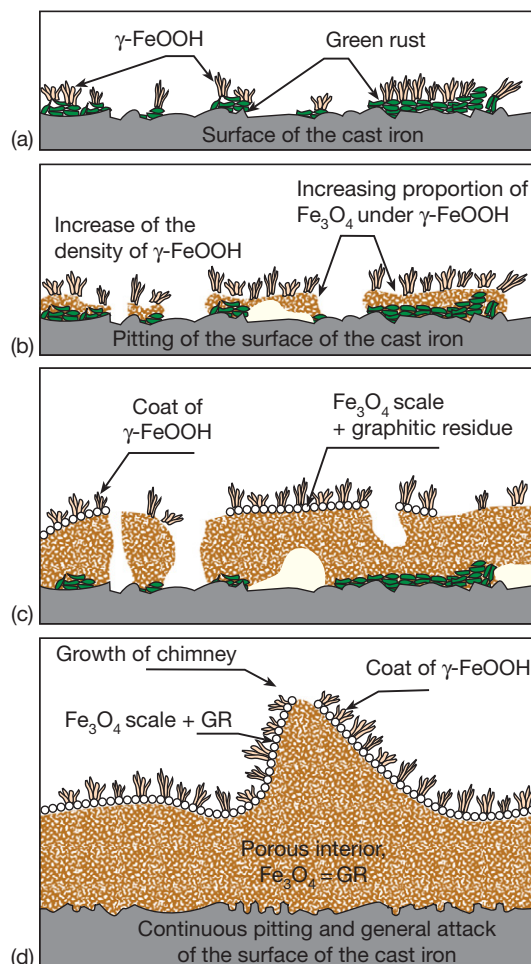


**Figure 14** The same as **Figure 13**, but in water at 50 °C containing 3 ppm oxygen: (a) after 10 min (b) after 3 h (c) after 6 h (d) after 27 h. Reproduced with permission from Smith, D. C.; MacEnaney, B. *Corros. Sci.* **1979**, *19*, 379–394.

cooling circuits has been proposed for cast irons although benzoates, known to be effective with steel, tend to aggravate the corrosion of cast irons:

- good protection: nitrites, phosphates;
- average protection: silicates, tannins;
- positive or negative effect according to conditions: borates.

Water containing sulfates generally has an electrochemical corrosive action on metals when the iron content exceeds 400–500 mg l<sup>-1</sup>. Note also the possible appearance of pitting corrosion, by differential aeration, under scales containing sulfates.<sup>33</sup> To forestall corrosion of cooling circuits, we must ensure that the sum (Cl<sup>-</sup> + SO<sub>4</sub><sup>2-</sup>) is less than 250 mg l<sup>-1</sup>;



corrosion becomes likelier when this sum exceeds 500 mg l<sup>-1</sup>.

In 2002, Indian researchers,<sup>34</sup> by means of electrochemical tests (measurements of Tafel slopes and of polarization resistance, for example), established a ranking for the aggressiveness of saline solutions at 28 °C on a cast iron. The concentrations tested were dilute (from a few ppm to a few hundred ppm), and likely to be encountered in drinking water. KCl and NaCl would seem to be more corrosive than MnSO<sub>4</sub>, Pb(NO<sub>3</sub>)<sub>2</sub>, KI, and KBr. The variation of the corrosion rates over time (up to 360 h) were also tracked: the results are given in Table 11.

**Table 10** Corrosion rates of unalloyed and austenitic cast irons in various waters

Types of water	Corrosion rate (mm year) <sup>-1</sup>	
	Unalloyed Cast iron	Austenitic Cast iron
Distilled water	0.25	0.015
CO <sub>2</sub> purifier water	4.06	3.05
Water (pH = 8) (+185 ppm CaCO <sub>3</sub> )	0.76	0.5
Brackish water in oil well	0.5	0.025
Seawater	0.25	0.06
Seawater (8 m s <sup>-1</sup> )	4.47	0.20
Sour bath (pH = 4) +0.05% CO <sub>2</sub>	1.78	0.5
Sour bath (pH = 4)+0.05% SO <sub>2</sub>	1.01	0.25
Sewage	0.45	0.127

**Table 11** Corrosion of gray cast iron in various saline electrolytes

Saline solution at 28 °C	Corrosion rate after 360 h immersion (mm year <sup>-1</sup> )
KCl	0.144
NaCl	0.141
Na <sub>2</sub> SO <sub>4</sub>	0.085
CaCO <sub>3</sub>	0.027
CaCl <sub>2</sub>	0.046
MgSO <sub>4</sub>	0.034
NaHCO <sub>3</sub>	0.038
NaNO <sub>3</sub>	0.019
MoSO <sub>4</sub>	0.004
Fb(NO <sub>3</sub> ) <sub>2</sub>	0.002
KBr	0.010
KI	0.010
Water	0.759

Data taken from Mehra and Soni.<sup>34</sup>

In early 2000, Japanese researchers<sup>35</sup> studied the effect of pH on the corrosion behavior of underground SG cast iron pipes immersed in simulated underground water (using polarization curves and immersion tests). The intended application was corrosion resistance in clay-rich marine mud. The study highlighted the effects of an intensive selective dissolution of the ferrite of the pearlite where phosphorus and sulfur seem to have segregated; spheroidal graphite and cementite favor the evolution of hydrogen. The schematic diagrams in Figure 15, sum up the mechanisms.

### 3.02.4.2.5 Galvanic corrosion of cast iron in natural water

Scandinavian authors<sup>36</sup> have reported interesting data on the corrosion by galvanic coupling of unalloyed cast iron with various alloys in town water at 25 °C and 75 °C (temperatures encountered in household sanitary installations); Table 12 groups these data.

These data show that the unalloyed cast iron is anodic, compared to the metals and alloys studied; only carbon steel and zinc are anodic with respect to

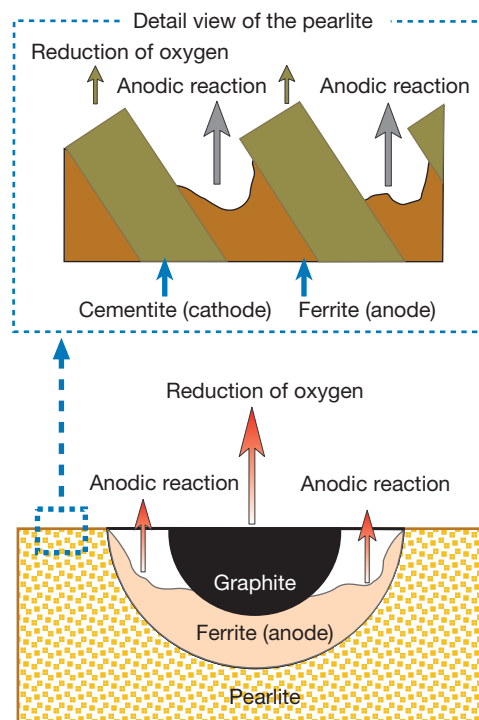


**Figure 15** Selective dissolution of the ferrite of the pearlite where phosphorus and sulfur have segregated. Reproduced with permission from Reynaud, A. *Corrosion and Cast Iron*, ETIF, France, 2008.

**Table 12** Corrosion potentials and galvanic currents for the listed materials coupled to LG iron

Alloys coupled to the cast iron	Town water at 25°C		Town water at 75°C	
	Current density ( $\mu\text{A cm}^{-2}$ )	Corrosion potential (mV/SHE)	Current density ( $\mu\text{A cm}^{-2}$ )	Corrosion potential (mV/SHE)
304 stainless steel	0.2	+250	1.0	+245
316 stainless steel	0.4	+250	0.9	+245
410 stainless steel	3.0	+250	1.0	+245
440 stainless steel	0.4	+250	1.0	+245
Carbon steel	-0.6	-470	-8.0	-390
Cu Zn39 TB3 brass	0.3	+190	0.7	+150
Cu Zn20 Al2 brass	0.4	+250	1.0	+245
Bronze	0.2	+250	3.0	+245
Cupro-nickel	0.2	+250	3.0	+245
Copper	0.09	+250	3.0	+245
Zinc	-0.6	-690	-4.0	-650
Cast iron alone	0.4	-90	-	-810

Data taken from Neumann *et al.*<sup>36</sup>

cast iron. On the subject of galvanic corrosion, reference to Bryant<sup>37</sup> will also be useful. Another type of 'galvanic' corrosion can occur on the same section of iron due to thermal-galvanic effects. Thus, the coexistence, in a single pipe, of hot zones and cold zones can create a chemical heterogeneity at the cast iron surface which leads to clearly separated anodic and cathodic regions. In this way a temperature difference of 20 °C can lead to a potential difference of 55 mV.<sup>38</sup>

Swedish work on the effects of galvanic coupling between SG cast iron and copper in water, published in 2005,<sup>39</sup> has shown that deaeration of water can diminish the galvanic corrosion of the cast iron, with the corrosion rate becoming equal to that observed in the absence of copper. The corrosion products formed on the surface of the cast iron under these conditions of deaeration have the appearance of a black film that consists of magnetite. However, if the temperature is raised from 30 °C to 50 °C, the galvanic corrosion current is multiplied by 10, even under conditions of deaeration.

#### 3.02.4.2.6 Inhibition of corrosion in water

Traditionally, a standard range of species can be used to inhibit the corrosion of cast irons. Chromates were previously used as anodic passivating inhibitors, however, this is no longer permitted due to the toxicity of hexavalent chromium. Alternative anodic inhibitors include nitrites, molybdates and phosphates. Film-forming organic inhibitors such as octadecylamine can be used commonly in boilers and refrigeration installations, etc. Tannins are often used as an

internal treatment for low-pressure steam boilers. Indian work in 2004, comparing the actions of different inhibitors of corrosion of cast irons in water,<sup>40</sup> showed that, among the products tested (molybdate, hydrogen phosphate, and nitrite), it is the molybdate ion that is the most effective. For potable water systems below 60 °C, sodium hexametaphosphate combines inhibition of scaling (at lower concentrations) and corrosion (at somewhat higher concentrations). It is one of the few chemicals that are permitted for use as a corrosion inhibitor for potable (drinking) water.

#### 3.02.4.3 Corrosion in Steam

Ordinary cast irons are acceptable up to a few bar wet steam pressure (120–130 °C) while silicon cast irons (>15%) resist steam up to 300 °C. Under more severe conditions of service, austenitic cast irons are recommended. For example, in saturated steam at 170 °C (8 bar pressure) the loss of thickness for Ni20Cr3 (LG1 grade) is 0.02 mm year<sup>-1</sup>. For steam at higher temperatures (up to 500 °C), castings must undergo a stabilization heat treatment (annealing at 760 °C for 4 h followed by cooling in the furnace down to ~500 °C). Generally, the high temperature corrosion of cast iron in steam is similar to steel. Thus, in the presence of superheated steam, from 450 °C to 600 °C, after 0.5–3 h of exposure, a film of magnetite (Fe<sub>3</sub>O<sub>4</sub>) forms on unalloyed cast irons, reinforced by wustite (FeO) if the temperature exceeds 575 °C. It is important to note that the relatively poor mechanical properties of cast iron compared with steel, constrain the application of cast irons to those at lower pressures.

### 3.02.4.4 Corrosion in Seawater

Evans,<sup>41</sup> in 1928, cites Hadfield, who describes various cases of cast iron foundations left in seawater for 25–50 years: they become extremely soft, to the point of consisting primarily of graphite and of the corrosion product. Evans points out that this ‘graphitic softening’ with no change of outward appearance is often found in cast iron objects that have remained immersed in the sea for a long time. He also recalls that cast iron objects from shipwrecks, found later, often seem at first glance not to have been affected, but are in fact constituted essentially of soft ferrous hydroxide held together by graphite lamellae; this ferrous hydroxide is subsequently oxidized when the objects are exposed to open air and akaganite ( $\beta$ -FeOOH).

Research has shown that the corrosion rate of cast iron in sodium chloride passes through a maximum at 3–3.5% NaCl,<sup>42</sup> a concentration that corresponds more or less to the composition of seawater (Figure 16). In short, seawater is an aggressive medium for cast irons, but their behavior is strongly influenced by the location and its specific conditions.

Tables 13 and 14 provide some examples. A corrosion rate of 50–100  $\mu\text{m year}^{-1}$  is often given for unalloyed cast irons in seawater. All tests were conducted on small plates taken from pipes, machined and ground to eliminate the protective action of the casting skin. They clearly show that the corrosion of cast iron in seawater is not excessive (2–3 times that in distilled water) and that there is no significant difference between lamellar graphite cast iron and spheroidal graphite cast iron.

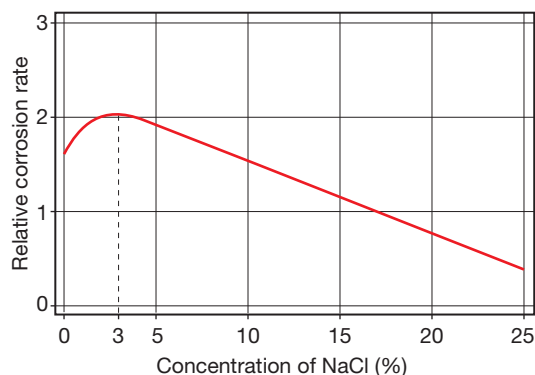


**Figure 16** Effect of the concentration of NaCl on the corrosion rate of iron in aerated solutions at ambient temperature. Reproduced with permission from ASM. Corrosion of cast irons. Metals Handbook, Corrosion, 1987, Vol. 13; pp 566–572.

Alloying additions of nickel or chromium greatly reduce corrosion. As shown in Figure 17, austenitic cast irons stand up much better than other cast irons to seawater, water contaminated by certain industrial pollutants, and water rich in  $\text{CO}_2$ . For the desalination of seawater, austenitic nickel cast iron is specified for many pumps and valves operating in the feed seawater and in the brine. Similarly, many cooling water pumps made up of this type of cast iron have been installed in conventional power stations, refineries, and steel mills.

Even though seawater is an aggressive medium for cast irons, a unalloyed cast iron can provide satisfactory service if the seawater is still and not polluted. Japanese authors have shown that the resistance of cast irons to seawater corrosion improves as the carbon content decreases and the silicon content increases. In addition, the nature of the matrix seems to have a large influence: white cast irons having an extensive carbide structure are the most resistant, followed, in order of decreasing corrosion resistance, by ferritic, ferrite–pearlitic, and finally pearlitic gray cast irons. Low contents of chromium improve the resistance of lamellar graphite cast iron to corrosion by seawater. Small additions of molybdenum, vanadium, and titanium increase corrosion resistance by refining the graphite and the matrix.

In flowing seawater, the commonest type of exposure, the corrosion rate varies with the velocity of water and increases rapidly as the velocity increases because more oxygen is available. It is also stated that the corrosion rate can be up to 15–25 times as great as in stagnant seawater; but it would seem that at still higher velocities, the level of corrosion can be decreased by the formation of a protective oxide deposit. Some authors<sup>43,44</sup> recommend using austenitic nickel cast irons for cases of corrosion–erosion in seawater, since these cast irons have an excellent resistance to such attack. The resistance of high-silicon cast irons in seawater has also been studied. However, it turns out that these are sensitive to pitting corrosion in stagnant seawater (and at low flow rates). Such pitting is initiated at the matrix/graphite lamellae and matrix/interdendritic carbide interfaces. Otherwise, in flowing water, their resistance to corrosion–erosion is excellent (Table 15).

The water temperature also plays a more or less marked role according to the grade of cast iron, as shown in Figure 18. Additionally, some British studies<sup>45</sup> have shown that there are practically no differences in corrosion behavior among the various unalloyed gray cast irons (lamellar or nodular

**Table 13** Corrosion rates of gray cast irons in various sea water environments

Type of Iron	Duration of exposure (years)	Corrosion ( $\text{g m}^{-2} \text{day}^{-1}$ )	Maximum pitting depth (mm)	Location
Continuous immersion				
Unalloyed gray cast iron, as-cast	4	2.0	6.4 <sup>a</sup>	Bristol Channel (Great Britain)
Unalloyed gray cast iron, as-cast	15	2.95	1.5	Halifax, Nova Scotia (Canada)
Unalloyed gray cast iron, as-cast	15	1.3	5.0 <sup>a</sup>	Plymouth (Great Britain)
Unalloyed gray cast iron, as-cast	15	4.25		Colombo (Sri Lanka)
Unalloyed gray cast iron, mean of S samples	3	2.4		Eastport, Maine (United States)
Austenitic gray cast iron, type L-NUC 15 6 2, as-cast	6	0.4	None	Kure Beach, North Carolina (United States)
Austenitic gray cast iron, type L-NO 20 2, as-cast	6	0.8	None	Kure Beach, North Carolina (United States)
Samples placed midway between high and low water				
Unalloyed gray cast iron, as-cast	15	0.75	1.3	Halifax, Nova Scotia (Canada)
Unalloyed gray cast iron, as-cast	15	1.0	4.6	Plymouth (Great Britain)
Unalloyed gray cast iron, mean of 9 machined samples	3	0.75		Eastport, Maine (United States)

<sup>a</sup>Extensive, graphic corrosion.Data taken from Reynaud, A. *Corrosion and Cast Iron*, ETIF, France, 2008.**Table 14** Corrosion rates ( $\text{mg dm}^{-2} \text{day}^{-1}$ ) of iron in various aqueous environments:  $1 \text{ mg dm}^{-2} \text{day}^{-1} \sim 5 \mu\text{m year}^{-1}$ 

Materials	Natural seawater	Natural seawater	Natural seawater	Synthetic seawater	Distilled water	Distilled water
	90 days, aerated	180 days, aerated	360 days, aerated	360 days, aerated	360 days, aerated	360 days, stagnant
Spheroidal (SG) iron	24	16.1	15.3	15.8	19.1	6.1
Lamellar (LG) iron	24.9	16.4	17	19.1	19.3	6.2

graphite, ferritic or pearlitic). According to the same authors, resistance of 'Ni-Resist' cast irons to seawater is better (2–3 times greater than that of unalloyed cast irons) even though it is the high-silicon and high-chromium grades that are generally thought to be the most resistant to corrosion in this medium.

This work also demonstrates the value of protection by coatings: examination of castings that had been metallized (by thermal spraying with aluminum) shows that the loss of mass is five times lower than for unprotected castings and significantly less than for austenitic cast irons. In the case of salt water mists at 100 °C, alloyed cast irons are generally recommended.

There is an interesting study<sup>46</sup> of the influence of ferrous sulfate (a corrosion inhibitor for copper alloy condenser tubes used in seawater) on the corrosion of

an austenitic cast iron of the Ni20Cr2 LGI type in seawater. It showed that the presence of  $\text{Fe}^{2+}$  ions could make seawater more corrosive if the concentration of these ions was not too high (less than or equal to 100 ppm). On the other hand, contents 10–25 times as high would tend to diminish the corrosion rates.

Dutch work<sup>47</sup> has shown that the corrosion products formed on spheroidal graphite cast iron immersed in water differed substantially according to whether the iron is exposed under static or flowing conditions. For example, it was shown that these corrosion products consisted of  $\alpha$ -FeOOH in a spongy form under static condition and of a hard mixture of  $\gamma$ - and  $\alpha$ -FeOOH under dynamic condition.

The austenitic irons have also been shown to exhibit better corrosion resistance than the ferritic irons in seawater. Tests over long periods of time have shown

that Ni-Resist irons of Types 1, 2, and 3 corrode at rates of 0.020–0.058 mm year<sup>-1</sup> in relatively quiet seawater. Under similar conditions low alloy cast irons have shown corrosion rates ranging from 0.066 to 0.53 mm year<sup>-1</sup>.<sup>22</sup> The Ni-Resist irons maintain this superiority over a wide variety of conditions (Figures 17 and 18), both in stationary and flowing seawater. In a test lasting 740 days in seawater moving at 1.5 m s<sup>-1</sup>, low-alloy cast iron showed a corrosion rate of 1.3 mm year<sup>-1</sup> compared to 0.050 mm year<sup>-1</sup> for Type 2 Ni-Resist. In tests carried out at controlled temperature at a higher

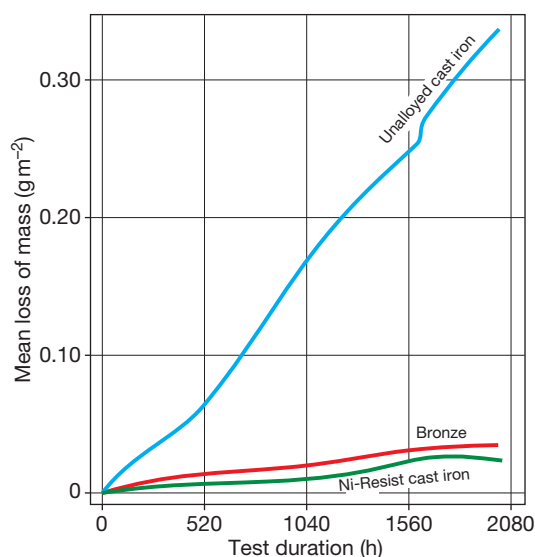


**Figure 17** Comparison of the corrosion rates of a unalloyed cast iron, a 'Ni-Resist' cast iron, and a bronze in seawater. Reproduced with permission from Berenson, J.; Wranglen, G. *Corros. Sci.* **1980**, *20*, 937–941.

velocity of 8 m s<sup>-1</sup> (Table 16), the Ni-Resist irons again showed better properties than low-alloy cast irons or mild steel.

### 3.02.4.5 Soil Corrosion

Since buried pipes for water, sewage, and gas are a major use of cast iron, the corrosion of buried iron structures needs special consideration in any study of the corrosion properties of cast iron. With gray iron pipes, leakage usually arises because the pipe fractures as a result of soil stresses or top-loads that exceed the hoop strength of the pipe. With ductile iron pipes, leakage is usually through small corrosion pits. For this reason gray iron pipes are susceptible to both uniform and pitting corrosion while ductile iron pipes are only seriously affected by pitting. A characteristic of corrosion on buried ferrous metals is that the attack is mostly in the form of pitting, especially with the cast irons. This causes a problem in measuring the extent of corrosion in burial trials. Usually both the weight loss, measuring the average loss of section, and the deepest pit, measuring the maximum loss of section, are reported. For assessing the severity of the attack on buried pipes, the second parameter is clearly the most important.

The rate of attack on buried iron depends on the corrosivity of the soil in question. A good guide, which is still valid, is the work carried out by the National Bureau of Standards in the United States between 1922 and 1955.<sup>48</sup> In this very detailed and extensive study, the chemical characteristics of more than 100 soils drawn from all over the United States were examined and compared in relation to the

**Table 15** Corrosion rates of cast irons in seawater

Source	Hudson's study	Kress's study	Parts and de la Bruniere's study	Speidel and Witmoser's study	LaQue's study
Location	Emsworth, England	Cuxhaven, Germany	laboratory, France	artificial seawater	Harber Island USA
Duration of test	2 years <sup>a</sup> (g m <sup>-2</sup> day <sup>-1</sup> )	6 months <sup>a</sup> (g m <sup>-2</sup> day <sup>-1</sup> )	380 days <sup>a</sup> (g m <sup>-2</sup> day <sup>-1</sup> )	220 days <sup>a</sup> (g m <sup>-2</sup> day <sup>-1</sup> )	3 years
Steel		4.4	2.4	1.6	
LGI	1.2	1.7	1.7	0.6	1.6 <sup>b</sup>
White cast iron				0.65	
Malleable cast iron	1.6			0.9	
Pearlitic SGI		1.0		1.4	5.6 <sup>b</sup>
Ferritic SGI		2.1	1.6	0.5	

<sup>a</sup>Results originally stated in mg cm<sup>-3</sup> day<sup>-1</sup> (based on loss of mass, with no indication of type of attack).

<sup>b</sup>Quantity measured: penetration depth of pitting.



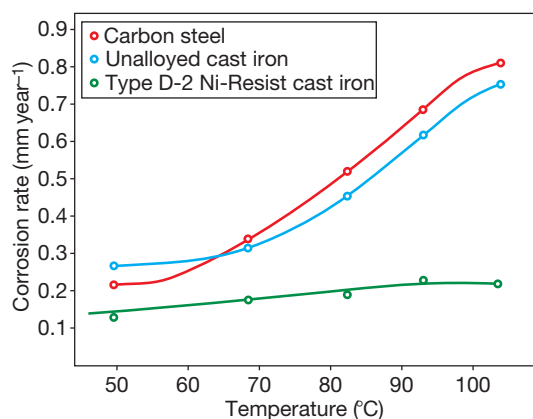


**Figure 18** Corrosion rate in deaerated seawater of a carbon steel, of a unalloyed cast iron, and of a 'Ni-Resist' cast iron as a function of temperature (test lasting 156 days).

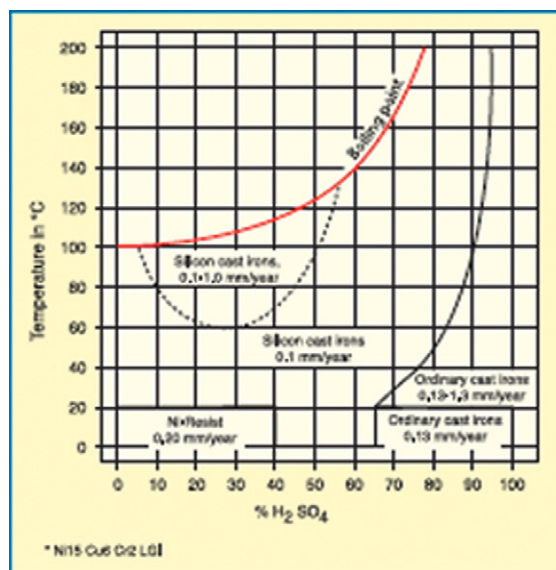


**Figure 19** Resistance of cast irons to sulfuric acid. Reproduced with permission from *Résistance des fontes à l'acide sulfurique concentré*. Fonderie no. 393, Nov. 1979, 339.

corrosion behavior of small steel and iron specimens that had been buried in them for up to  $\sim 17$  years. Detailed study of the published results suggests, however, that the only parameter to give any useful correlation with the severity of the corrosion is the electrical resistivity of the soil. Even this is only valid up to  $\sim 2000$  ohm cm with a correlation coefficient of  $\sim -0.5$ .<sup>49</sup> Currently, electrical resistivity is the factor used for dividing soils into corrosivity classes (Table 17).

Although resistivity surveys can decide which soils along a projected pipeline are probably aggressive to buried ferrous metals and which are not, it has been found that when unprotected pipes fail in service the local soil resistivity does not correlate to any significant extent with the corrosion rate at the pitted site. Indeed, Stokes<sup>50</sup> showed from a survey of statistics of ductile iron pipe failures in the United Kingdom, that the most likely pitting rate for an aggressive soil is  $\sim 1$  mm year<sup>-1</sup> with a range of  $\sim 0.3$ – $3$  mm year<sup>-1</sup>. Since the soil electrolyte is likely to be a dilute salt solution of low dissolved oxygen content and pH  $\sim 8.5$ , a consistent corrosion rate seems logical. Collins<sup>51</sup> has suggested that the tendency for low resistivity soils to be aggressive is due to the fact that for the most part they are poor in draining, and poorly aerated heavy clays are thus more liable to create differential concentration cells on the pipe surface than free-flowing soils such as sands. He argues that, as the soil resistivity falls, the probability of serious pitting increases but the pitting rate remains substantially constant. This would explain the poor correlation between the chemical parameters of the soil and its corrosivity. It also suggests that the physical characteristics of the soil should be better indicators of its corrosivity.

The results of tests on bare cast iron in soils that are relatively homogeneous on the scale of the size of the samples cannot be directly extrapolated to actual coated pipes; the latter, because of their length, will encounter a succession of soils (geological cells) that differ in their nature, their moisture content, their aeration – soils are sometimes made heterogeneous by borrowed materials or by differences of compaction. For example, in the case of a pipe passing in turn through a porous soil permeable to air, then a clay layer through which oxygen can pass only with great difficulty, a differential aeration cell may form, which results in the corrosion of the part of the pipe in the clay soil (which becomes the anode as it is in a region of oxygen restriction) while the part in the porous soil is only slightly corroded (since it is in a region with more easy oxygen access and is, hence, cathodic).<sup>52</sup> Additionally, corrosion of cast iron pipes in soils may also be affected by stray or induced currents: for example, from DC traction systems, induced AC current or from other cathodic protection systems.<sup>53,54</sup> Many of these conditions, which are difficult to circumvent, are likely to result in the formation of macrocells leading to a localized corrosion (pitting) that can be dangerous when the soil is highly corrosive.<sup>55</sup> Coupling with copper used for

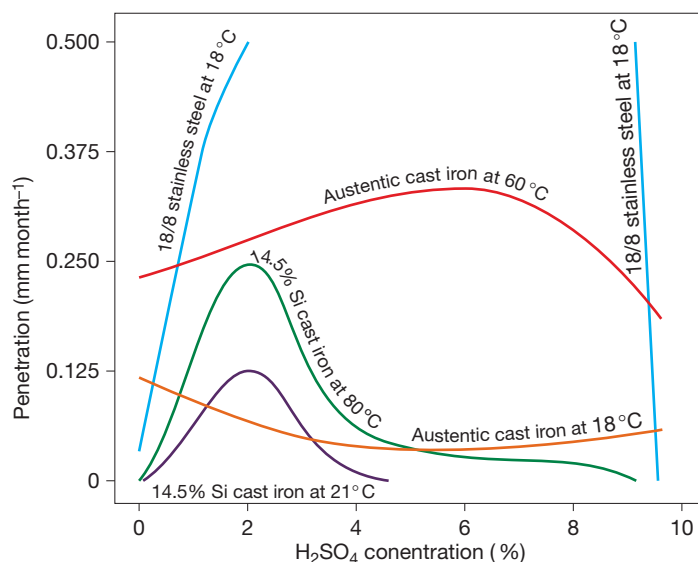


**Figure 20** Iso-corrosion curves of LCI cast iron containing 15% Ni, 6% Cu, and 2% Cr in  $\text{H}_2\text{SO}_4$ .

**Table 16** Seawater corrosion–erosion test carried out at  $8 \text{ m s}^{-1}$  at  $28^\circ\text{C}$  for 60 days

Alloy	Average corrosion rate ( $\text{mm year}^{-1}$ )
Cast iron	6.9
2% Ni cast iron	6.1
Type 1 Ni-Resist	0.74
Type 2 Ni-Resist	0.79
Type 3 Ni-Resist	0.53

Data taken from Berenson and Wranglen.<sup>22</sup>

**Table 17** Soil corrosion classes as a function of soil resistivity

	Aggressive	Nonaggressive
Resistivity:	$<2000 \Omega \text{ cm}$	$>2000 \Omega \text{ cm}$
Redox potential at pH 7	$<0.40 \text{ V SHE};$ ( $<0.43 \text{ V}$ in clay)	$>0.40 \text{ V SHE};$ ( $>0.43 \text{ V}$ in clay)
Borderline cases resolved by water content	$>20\%$ by mass	$<20\%$ by mass

water distribution pipes can also result in the functioning of macrocells.<sup>56</sup>

In early 2000, Japanese researchers<sup>57</sup> studied more particularly the corrosion resistance of SG cast iron pipes in clay marine muds. In 2003, Kubota (Japan) patented a spheroidal graphite cast iron having

improved corrosion resistance and high mechanical strength, for the production of pipes for underground applications.<sup>58</sup> Its composition is reported as: 3–4% C, 1–4% Si,  $<0.6\%$  Mn, 0.02–0.08% Mg, 0.05–0.5% Co,  $<1.5\%$  Ni, 0.2–0.8% Cr, and/or Cu.

It should be noted that it is extremely difficult to predict service lives of buried pipelines from the results of controlled trials with small specimens, whether in the laboratory or in the field. For example a study on the comparative corrosion resistances of ductile and gray iron pipes between 1964 and 1973<sup>59,60</sup> indicated a mean pitting rate of  $0.35 \text{ mm year}^{-1}$  for uncoated ductile iron pipe exposed in a typical heavy Essex clay of  $500\text{--}900 \Omega \text{ cm}$  resistivity for 9 years. This contradicts the rate of  $1 \text{ mm year}^{-1}$  normally found on a corroded service pipe from such a soil. The discrepancy appears to be due to the use of specimens that were only a third of a pipe length each and were buried separately. It may reflect the contribution of the total surface area of the pipe as a cathode to the corrosion current at the anodic area of the pitting site.

### 3.02.4.6 Methods of Protection

Experience and knowledge of the corrosion caused by local geological differences (macrocells) in the soil have led to the development not only of methods of evaluation of the corrosiveness of soils on a pipe alignment (e.g., by soil resistance survey), but also of methods of protection capable of disrupting the

macrocells. These methods include: ensuring that electrical continuity along the pipe is broken by use of insulating joints (also limiting stray currents), using active coatings that are self-healing (e.g., zinc), use of an inert backfill<sup>61</sup> and, for difficult cases, placing a flexible polyethylene sleeve around the pipe when it is laid to prevent direct contact with the local heterogeneities of the soil.

Note that cathodic protection is also an excellent remedy for corrosion of cast iron by soils (although it is most often applied to steel pipes).<sup>62,63</sup> For steels, cathodic protection is often combined with a protective organic coating<sup>64,65</sup>; this is rarely done in the case of cast irons. However, cathodic protection of the town water supply network of Scarborough, United Kingdom has been undertaken.<sup>62</sup> This network, made up primarily of ductile cast iron and lamellar graphite cast iron pipes, is protected by magnesium sacrificial anodes to overcome the problems due to the corrosiveness of soils (resistivity from 1000 to 3000  $\Omega$  cm), which is due partly to the use of deicing salts, and also to galvanic coupling with the copper used in distribution pipes. It must be borne in mind that the cathodic protection of a structure may also generate stray currents in the soil. It may then create, in an adjacent metallic structure, zones of current input and zones of current output at which corrosion will occur. In practice, even though there are many networks of cast iron pipes that coexist in the soil with networks of steel pipes with cathodic protection, there are very few cases of corrosion ascribable to the influence of cathodic protection, because a few simple rules<sup>66</sup> can be applied to solve most of the problems.

### 3.02.5 Corrosion in Industrial Environments

In general, unalloyed gray or white cast irons possess no resistance to dilute mineral acids. In very dilute acids, the presence of air, or other oxidizing agents such as ferric salts, appreciably increases the corrosion rate. If corrosion rates are to be held below 0.25 mm year<sup>-1</sup> in moderately aerated solutions, it is unwise to exceed a total acid concentration of 0.001 M (i.e., pH < 3), irrespective of the acid concerned.

#### 3.02.5.1 Sulfuric Acid

The use of unalloyed cast irons is generally impossible in the presence of dilute sulfuric acid since

the corrosion rates are very high (several millimeters a year).<sup>67</sup> By contrast, the same acid (sulfuric) in the concentrated state barely attacks unalloyed cast irons, even at high temperature. This is due to an iron sulfate salt film that forms at concentrations above  $\sim 70\%$  such that corrosion rates do not exceed 0.13 mm year<sup>-1</sup> at 20 °C.<sup>67,68</sup> In practice, thanks to this passivation effect, lamellar graphite cast irons, in the past, and spheroidal graphite cast irons, today, are used in coolers for concentrated sulfuric acid.

As for alloy cast irons, austenitic nickel grade can provide good corrosion resistance up to 20% sulfuric acid<sup>67</sup>; above this value, high-silicon cast irons must be used. For example, pumps used in the production of sulfuric acid are, in fact, often made of high-silicon cast irons. **Figure 19** shows the behavior of several cast irons under different conditions of service (temperature, concentration).<sup>68</sup> It can be seen that the resistance of these alloys to concentrated sulfuric acid is excellent up to its boiling temperature. Note that it is dangerous to use cast irons with oleum (concentrated sulfuric acid enriched with SO<sub>3</sub>) because of the risk of oxidation of the silicon they contain.

The austenitic irons can be used in handling very dilute solutions of sulfuric acid at ambient or moderately elevated temperatures under conditions corrosive to ordinary cast iron and carbon steel. Austenitic irons have also given satisfactory service in handling concentrated sulfuric acids, but although they show low corrosion rates in such environments they are not markedly superior to the unalloyed cast irons. Type 1 Ni-Resist and the high silicon grades AUS104 and AUS204 are the types most generally used in sulfuric acid environments. The iso-corrosion curves of an austenitic lamellar graphite cast iron containing 15% Ni, 6% Cu, and 2% Cr in sulfuric acid are given in **Figure 20**.

High-chromium irons have no useful resistance to sulfuric acid of more than 10% concentration at any temperature. At temperatures above 20 °C corrosion rates in excess of 1.27 mm year<sup>-1</sup> are probable even for acid of less than 10% concentration. The addition of 2% molybdenum increases the resistance to this acid at very low and very high concentrations (**Figure 21**).

Probably, the most useful characteristic of the high-silicon irons is their ability to withstand sulfuric acid at all temperatures and concentrations. The maximum rate of corrosion which can develop has been reported to be 0.482 mm year<sup>-1</sup> in 30% sulfuric acid at boiling point,<sup>3</sup> and this falls to a minimum rate of 0.025 mm

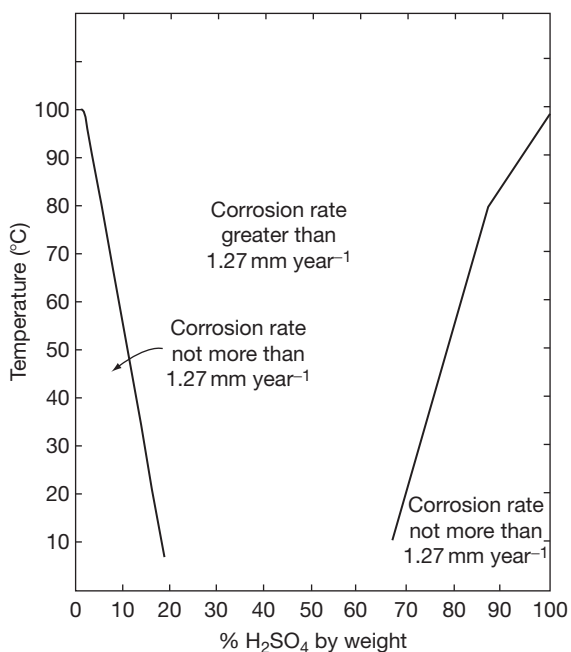


**Figure 21** Resistance of high-chromium iron containing 2% molybdenum to sulfuric acid solutions.

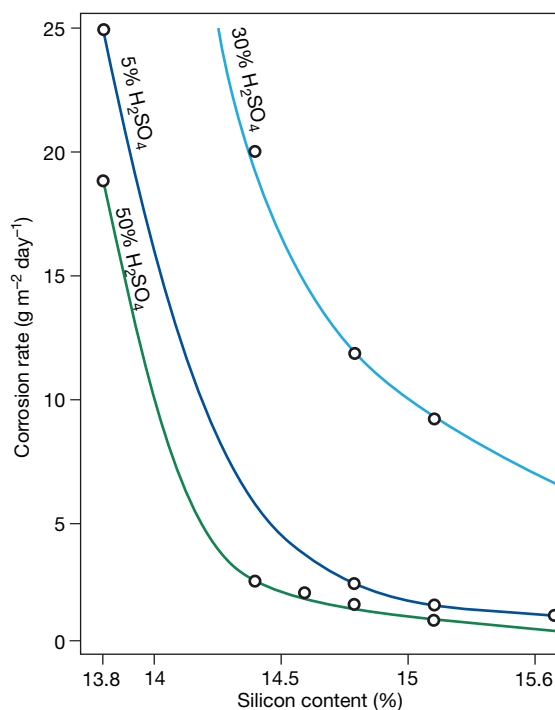


**Figure 23** Influence of Si content on the corrodibility of cast irons in  $\text{H}_2\text{SO}_4$  (5–30–50%).

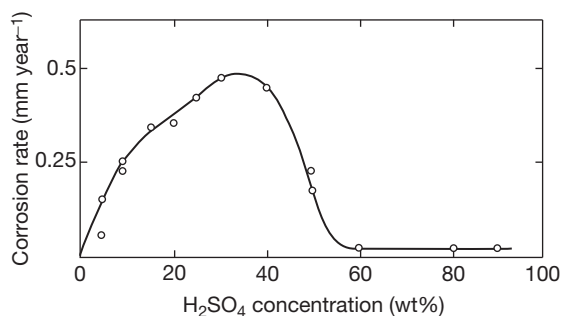


**Figure 22** Variation of corrosion rate with concentration of boiling sulfuric acid (Duriron Co. data).

year<sup>-1</sup> when the acid concentration exceeds 60% and the temperature is at boiling point (Figure 22).

In order to achieve optimum performance over the widest possible acid concentration range, it is essential to ensure that the alloy content of silicon is optimal. The corrosion rates of silicon iron are illustrated in Figure 23, which shows the influence of the silicon contents from 13.8% to 15.6%, on the resistance to corrosion by boiling sulfuric acid at different concentrations. From this data, it is clear that silicon contents in excess of 15% provide the best performance. Figure 24 illustrates an iso-corrosion chart for 15% silicon iron in sulfuric acid.

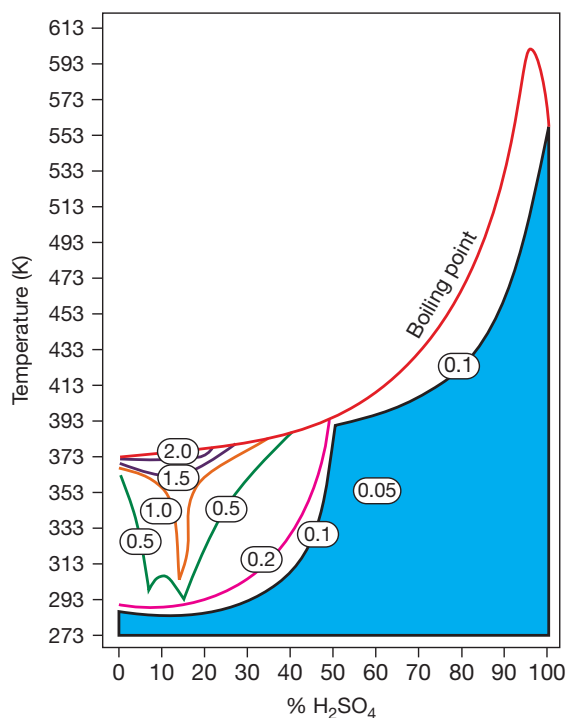


**Figure 24** Iso-corrosion curves in  $\text{H}_2\text{SO}_4$  of cast iron containing 15% Si.

### 3.02.5.2 Hydrochloric Acid

This commonly used acid attacks unalloyed cast irons very strongly, even in a dilute condition. High-chromium cast irons are only slightly better than unalloyed cast irons; the dissolution of these cast irons leaves a residue having a graphitic appearance and consisting of carbides.<sup>69</sup> Austenitic nickel cast irons are also attacked, especially by the cold concentrated acid and by boiling 20% acid. Attempts made to produce an alloy more resistant to hydrochloric acid have resulted in alloys containing 17–18% silicon or 14.5% silicon and chromium plus 3% molybdenum and both these alloys resist even concentrated hydrochloric acid relatively well. This is due to the protective layer of  $\text{SiO}_2$  that forms on the surface of the material. If the acid is boiling, the attack of such cast irons will be much more intensive and this is illustrated in Figure 25. For example, with a cast iron containing 15% Si and 3% Mo

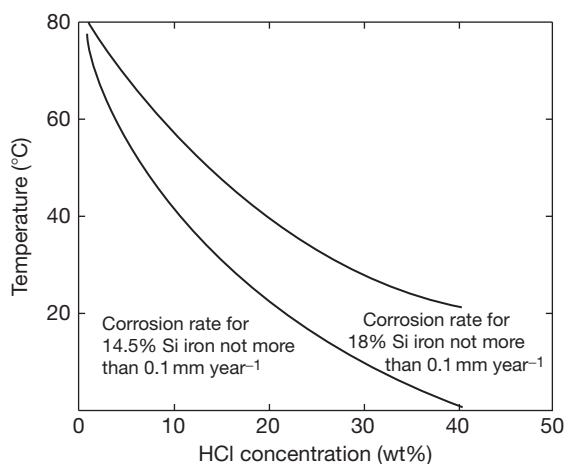


**Figure 25** Limits of use of silicon irons in HCl for Fe–18Si and Fe–14.5Si alloys.

**Table 18** Corrosion of Type 1 Ni-Resist, cast iron and carbon steel in deaerated HCl at room temperature

Acid concentration (%)	Corrosion rate (mm year <sup>-1</sup> )		
	Ni-Resist	Cast iron	Carbon steel
1.8	0.13	23	15
3.6	0.38	30	36
5.0	0.46	38	46
10.0	0.41	30	48
20.0	1.1	32	69
27.0	3.0	30	60
36.0	9.4	28	30

in the presence of boiling 20% HCl, the loss of mass is  $150 \text{ g m}^{-2} \text{ day}^{-1}$ .<sup>69</sup>

The austenitic irons are superior to ordinary cast iron in their resistance to corrosion in deaerated hydrochloric acid at room temperature (Table 18). However, for practical uses where such factors as velocity, aeration and elevated temperatures have to be considered, the austenitic irons are mostly used in environments where the hydrochloric acid concentration is low, generally less than 1% and preferably below 0.5%. Such environments occur in process streams encountered in the production and handling of chlorinated hydrocarbons, organic chlorides and chlorinated rubbers.

### 3.02.5.3 Nitric Acid

Unalloyed cast irons are not suitable for castings resistant to nitric acid, at any concentration. Nitric acid also attacks high-nickel cast irons at all concentrations, but more specifically in dilute solutions. Only high-silicon and high-chromium cast irons display good resistance to this acid, due to the formation of passive oxide films. However, there may be some corrosion in boiling concentrated solutions. This will, for example, be the case of cast irons containing 29% chromium, the chemical composition of which will be adjusted according to the concentration and temperature of the nitric solutions.<sup>69</sup>

Figure 26 has been derived from data<sup>2</sup> for corrosion by nitric acid solutions of an alloy containing 29% chromium and 0.8% carbon. It is interesting to note that the resistance by this alloy in these solutions is roughly complementary to that of the high-silicon irons, the high-chromium iron being more suitable for dilute solutions and the high-silicon iron for concentrated solutions.

Nitric acid is also withstood by high-silicon iron. The concentrated acid is believed to reinforce the silica film by the formation of a passive iron oxide film, and this assumption is supported by the fact that the highest rates of attack are associated with hot dilute solutions. The iso-corrosion rate data for 14% silicon iron in nitric acid is shown in Figure 27.

### 3.02.5.4 Phosphoric Acid

Phosphoric acid attacks unalloyed cast irons at all concentrations. Austenitic cast irons are satisfactory when used at ambient temperature in solutions having concentrations less than or equal to 30%; above this threshold, the attack is rapid. High-chromium cast irons are suitable in most cases. The corrosion rates



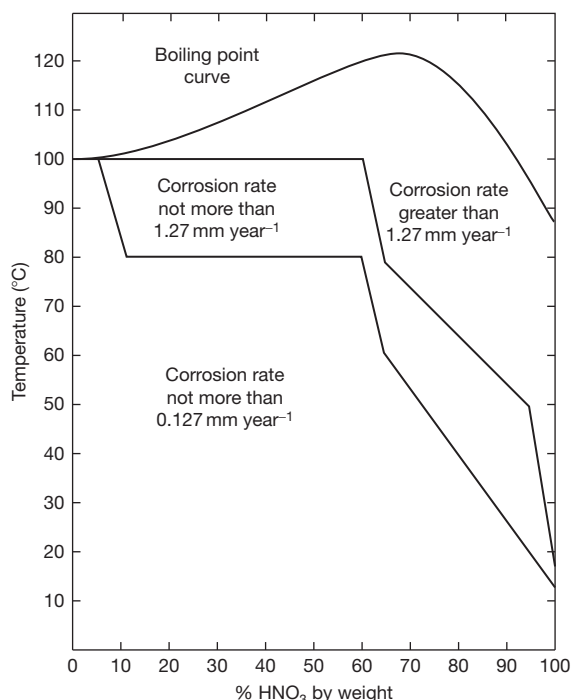


**Figure 26** Resistance of high-chromium iron to nitric acid solution.

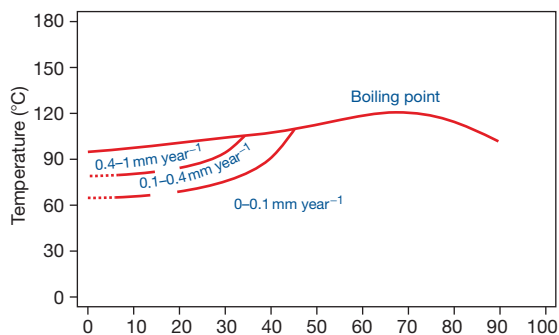


**Figure 27** Corrosion resistance in  $\text{HNO}_3$  of a cast iron containing 14% Si).

are  $\sim 0.12 \text{ mm year}^{-1}$  up to a concentration of 60%, at all temperatures up to boiling.<sup>69</sup> High-silicon cast irons best resist this acid, at all concentrations and almost all temperatures (see **Figure 28**). Note that most crude phosphoric acid contains appreciable amounts of fluoride which can lead to excessive corrosion rates.

The results published in the literature suggest that solutions of phosphoric acid at all concentrations and temperatures are not corrosive to high-silicon irons. Kosting and Heins<sup>70</sup> quote long-term results given by the Duriron Co, together with figures obtained in their own tests of 24 h duration (**Table 19**).

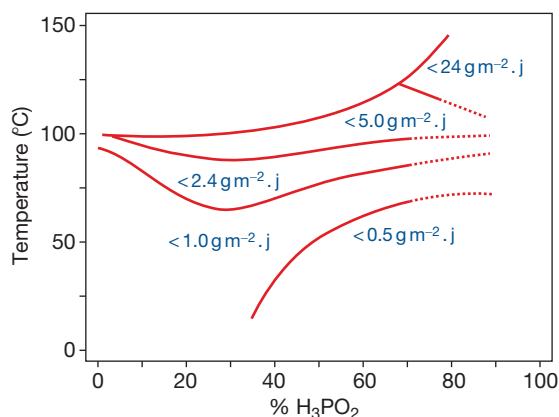


**Figure 28** Resistance to corrosion by phosphoric acid of a cast iron containing 14.5% silicon as a function of concentration and temperature. Reproduced with permission from Reynaud, A. *Corrosion and Cast Iron*, ETIF, France, 2008.

### 3.02.5.5 Other Mineral Acids

Most cast irons are resistant to chromic acid at all concentrations due to passivation of the material. However, 15–17% silicon irons are recommended at higher temperatures up to  $150^\circ\text{C}$ ; the corrosion of these cast irons is less than  $0.1 \text{ mm year}^{-1}$ . In dry hydro-halide acids (i.e.,  $\text{HBr}$ , etc.) unalloyed irons suffice, however, in wet acids high silicon iron is essential, preferably containing molybdenum. Hydrogen cyanide is generally noncorrosive except at higher temperatures in the gas phase if the humidity is sufficiently high.<sup>71</sup>

### 3.02.5.6 Organic Acids

The short-chain organic carboxylic acids attack unalloyed cast irons, especially in dilute solutions. Thus, unalloyed cast irons should not be used in formic or acetic acids, however, chromium cast irons are acceptable for both, with nickel austenitic iron acceptable for acetic acid. As the chain length of the acid increases, the acidity diminishes and the unalloyed irons may have acceptable corrosion rates. Thus, in palmitic (hexadecanoic) acid unalloyed cast irons should not be used while nickel cast irons are recommended, and in stearic (octadecanoic) acid unalloyed irons may be acceptable at lower concentrations and temperatures.<sup>71</sup>

Therefore, for most organic acids, the corrosion resistance of cast iron is essentially dependent on the strength of the acid. Thus, unalloyed cast irons should not be used in citric, lactic, or oxalic acids ( $3 \text{ mm year}^{-1}$  for unalloyed iron in citric acid) while for white chromium cast irons, the rate of attack is less than  $0.01 \text{ mm year}^{-1}$ .

**Table 19** Corrosion of high-silicon irons by phosphoric acid

Acid concentration (%)	Temperature (°C)	Corrosion rate (mm year <sup>-1</sup> )	Origin of data
10	82–88	0.007	Duriron Co.
	98	0.147	Kosting & Heins
25	82–88	0.010	Duriron Co.
	98	0.038	Kosting & Heins
50	98	0.185	Kosting & Heins
87	82–88	0.010	Duriron Co.

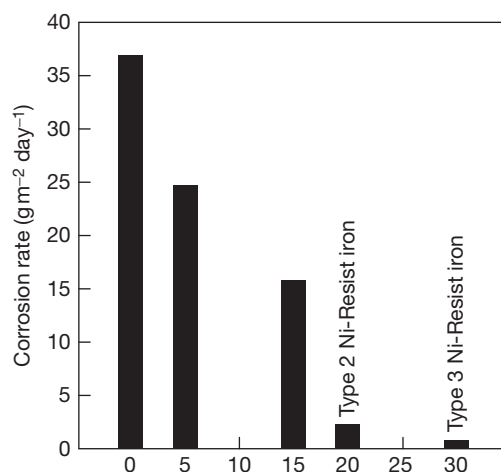
**Table 20** Corrosion of Type 1 Ni-Resist and ferritic cast iron in acetic acid at 15 °C

Acid concentration (%)	Corrosion rate (mm year <sup>-1</sup> )	
	Cast iron	Ni-resist
5	17	1.0
10	22	0.5
25	20	0.5
50	16	2.0

The austenitic irons are also useful in some circumstances for handling organic acids such as dilute acetic, formic and oxalic acids, fatty acids and tar acids. They are more resistant to organic acids than unalloyed cast irons, for example, in acetic acid the austenitic irons show corrosion rates 20–40 times lower than the ferritic iron (Table 20).

### 3.02.5.7 Corrosion by Alkalis

Dilute alkali solutions do not corrode cast iron at any temperature, but hot solutions exceeding ~30% concentration will attack it, with an accompanying evolution of hydrogen; this behavior is similar to that of steel. Broadly speaking, if the corrosion rates are to be held below 0.2 mm year<sup>-1</sup> the temperature should not exceed 80 °C; corrosion rates may range as high as 1.25–2.5 mm year<sup>-1</sup> in boiling solutions of more than 50% concentration. Molten caustic soda (650 °C) may attack cast iron initially at rates ~20 mm year<sup>-1</sup>, but this decreases significantly after some exposure. In spite of these high corrosion rates, caustic concentration and fusion pots are made from cast iron, since the material is relatively cheap, and the thick wall necessary for mechanical strength also gives the pot a long life. It is of utmost importance to ensure that concentration and fusion pots are cast in sound metal, as any unsoundness, particularly at the bottom of the pan, will lead to pitting attack and

**Figure 29** Effect of nickel additions to cast iron in reducing corrosion by caustic alkalis.

premature failure. On the other hand, high-silicon cast irons are less resistant to corrosion by alkalis than unalloyed cast irons and this is due to dissolution of the protective silicon oxide film by the alkali. Similarly, ferritic chromium cast irons should not be used in the presence of alkalis.

Austenitic cast irons show particularly good corrosion resistance in alkaline environments, even better than that shown by low alloy cast irons. The resistance to corrosion improves with increasing nickel content (Figure 29), and the irons containing ~30% nickel, such as Type 3 Ni-Resist, show the best resistance. An electrochemical study of the corrodibility of unalloyed SG cast irons in caustic soda has shown that some inhibition can be expected from the addition of thiourea<sup>72</sup>: 36% protection was found with the addition of 10<sup>-3</sup> moles of thiourea per liter of a molar solution of sodium hydroxide at 30 °C.

The addition of 3–5% nickel improves the resistance of both lamellar graphite and spheroidal graphite cast irons to alkali attack and, with increasing nickel content, the corrosion resistance of austenitic

cast irons in these media is much lower than that of non or low-alloy cast irons and alloys containing 30% nickel are the least vulnerable to corrosion by alkalis. For a 50% solution of caustic soda at 50 °C, the use of a Ni-Resist cast iron containing 20–30% nickel and 2–3% chromium is recommended. Figure 30 shows the corrosion rates of austenitic cast irons and of unalloyed cast irons in sodium hydroxide for various temperature–concentration domains.<sup>73</sup>

Test results cited by concerning the resistance of various cast irons in molten anhydrous caustic soda<sup>75</sup> at 510 °C (containing 0.5% NaCl, 0.5% Na<sub>2</sub>CO<sub>3</sub>, and 0.03% Na<sub>2</sub>SO<sub>4</sub>) are shown in Table 21. It can be seen here that the superiority of the austenitic grades

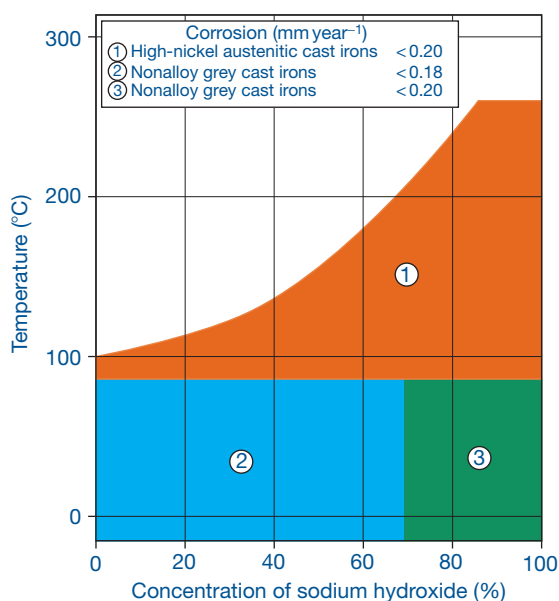


**Figure 30** Corrodibility of austenitic cast irons and unalloyed cast irons in NaOH. Reproduced with permission from Higgins, R. I. *J. Res. Bcira* 1956 6, 165–177.

**Table 21** Corrosion rate and pitting of cast iron in molten, anhydrous NaOH at 510 °C.

Cast iron	Corrosion rate (mm year <sup>-1</sup> )	Pitting depth (mm)
Unalloyed LGI	2.5–3.4	0.13
Unalloyed SGI	5.3	–
Unalloyed whise cast iron	3.8	0.5
3% Ni cast iron	1.8	–
Ni15 Cr8 Cr2 LGI	15.9	1.5
N2O Cr2 LGI	24.9	1.8
N2O Cr2 SGI	11.8	1.5
N3O Cr3 LGI	2.2	0
Ni3O Si5 Cr6 LGI	13.6	1.0

disappears in the case of concentrated caustic soda. This superiority exists only up to concentrations of 70% and temperatures approaching the boiling point. Finally, Table 22 confirms the favorable effect of nickel at lower concentrations<sup>65</sup> (81-day tests).

### 3.02.5.8 Salt Solutions

The corrosion rates of cast irons in salt solutions depend on the salt chemistry. Solutions which are alkaline or neutral in reaction are not generally so corrosive and even brines containing calcium and magnesium chloride can be safely handled by the austenitic irons (Table 23). Those salts which hydrolyze to give an acidic solution (e.g., divalent metal cations such as magnesium) are significantly more corrosive. The corrosion rates of Type 1 Ni-Resist and cast iron given in Table 24 demonstrate that the austenitic iron shows better resistance than the nickel-free cast iron in a wide range of salt solutions.

### 3.02.5.9 Corrosion–Fatigue

Cast iron, exposed under conditions of cyclic stress, is liable to corrosion fatigue. Some data on this effect have been given by Collins and Smith,<sup>75</sup> but a more extensive study has been reported by Palmer<sup>76</sup> who generated stress-cycle (S–N) data using rotating bend at a cycle frequency of 50 Hz and a duration of up to

**Table 22** Corrosion rate of cast iron as a function of nickel content in 30% NaOH solution

Nickel Content (%)	Corrosion rate (mm year <sup>-1</sup> )
0	1.9–2.3
3.5	1.2
5	1.24
15	0.8
20	0.08
20 (+2% Cr)	0.15
30	0.01

**Table 23** Corrosion of Type 1 Ni-Resist and cast iron in brine solutions

Environment	Temperature (°C)	Corrosion rate (mm year <sup>-1</sup> )	
		Ni-Resist	Cast iron
14% NaCl + 16.7% CaCl <sub>2</sub> + 3.4% MgCl <sub>2</sub> , pH = 6	69	0.08	0.53
Saturated NaCl	93	0.12	1.85

**Table 24** Corrosion of Type 1 Ni-Resist and cast iron in various inorganic salt solutions

Salt solution	Concentration (%)	Temperature (°C)	Corrosion rate (mm year <sup>-1</sup> )	
			Ni-Resist	Cast iron
Aluminum sulphate	5	16	0.41	1.0
Aluminum chloride	5	16	0.08	1.3
Aluminum chloride	5	93	0.15	4.8
Aluminum sulphate	5	16	0.15	0.76
Aluminum citrate	30	Room	1.5	550
Aluminum thiocyanate	50	27	0.38	3.3
Potassium aluminum sulphate	5	16	0.25	0.76
Zinc chloride	30	Boiling	2.0	16
Ammonium nitrate	5	Room	0.23	0.76
Manganese chloride	10	77	0.038	0.79
Ammonium chloride	20	93	0.25	5.8

10<sup>7</sup> cycles in demineralized water, 3% sodium chloride solution and demineralized water containing various inhibitors. The results for the uninhibited solutions are summarized in Table 25. Palmer found that corrosion fatigue due to water spray could be eliminated or mitigated by some of the inhibitor systems examined, but it was apparently easier to inhibit damage on gray irons than on ductile irons, which could only be inhibited by 0.25% potassium chromate solution. This was due to the inability of the other systems to maintain a continuous passive film on the iron; gray iron is less sensitive to a notch effect in fatigue so that the presence of local sites of attack would be less important to this metal provided that the overall corrosivity of the solution were depressed.

Various studies have also shown that it is possible to protect cast irons against corrosion fatigue by metallization with zinc or aluminum of thickness ~100–200 µm. The life of iron castings exposed to corrosion fatigue conditions in a saline medium is of the same order of magnitude as that of castings subjected to the same mechanical forces in air. Figure 31 clearly illustrates the effect of these coatings.

Another study emphasized, for different types of matrices, the low resistance of SG cast irons to corrosion fatigue in a 3% NaCl solution and the low aggressiveness of lubricating oils.<sup>77,78</sup> The results are shown in Table 26 and Figure 32. Fatigue resistance curves<sup>79</sup> in various media (air, water, salt water) are shown Figure 33. They concern a ferritic SG cast iron tested in rotary bending at 50 Hz. The influence of the aggressiveness of the medium is quite apparent.

An inhibitor consisting of 0.5% NaNO<sub>2</sub> plus 1% NaSiO<sub>4</sub> has been proposed<sup>80</sup> to prevent corrosion

**Table 25** Corrosion fatigue limiting strengths (MPa)

Environment	Air <sup>a</sup>	Water <sup>a</sup>	3% NaCl solution <sup>b</sup>
Pearlitic gray iron	126	100	39
Ferritic gray iron	93	77	23
Pearlitic ductile iron	270	224	46
Ferritic ductile iron	208	178	46

Data taken from Higgins.

<sup>a</sup>Fatigue strength based on 50 × 10<sup>6</sup> cycles.

<sup>b</sup>Fatigue strength based on 100 × 10<sup>6</sup> cycles.

fatigue of pearlitic SG cast irons in water as a replacement for the toxic chromate. Further data, reproduced below (Figure 34), concerning the corrosion fatigue resistance of SG cast irons shows the harmful effect of the marine medium and the value of a metallic coating (zinc or aluminum), which can increase the resistance of the material to that observed in a nonmarine atmosphere.<sup>81</sup>

The fatigue limit under reversing stress and corrosion in hot water at 70 °C in pipes has been studied by Japanese researchers<sup>82</sup> on an as-cast SG cast iron alloyed with copper and molybdenum, and compared to a carbon steel. In the static corrosion test of water containing sulfates and chlorides, the latter was found to be less resistant, and its resistance, unlike that of the former, could not be improved by adding sodium nitrite as an inhibitor. With the cast iron, the corrosive attack practically stopped with inhibitor contents in excess of 6000 ppm. The resistance of this cast iron to corrosion fatigue was also improved; at 260 MPa with 6000 ppm nitrite, it was better than that of the carbon steel.

Japanese researchers considered the question of the corrosion fatigue of ferritic and bainitic spheroidal

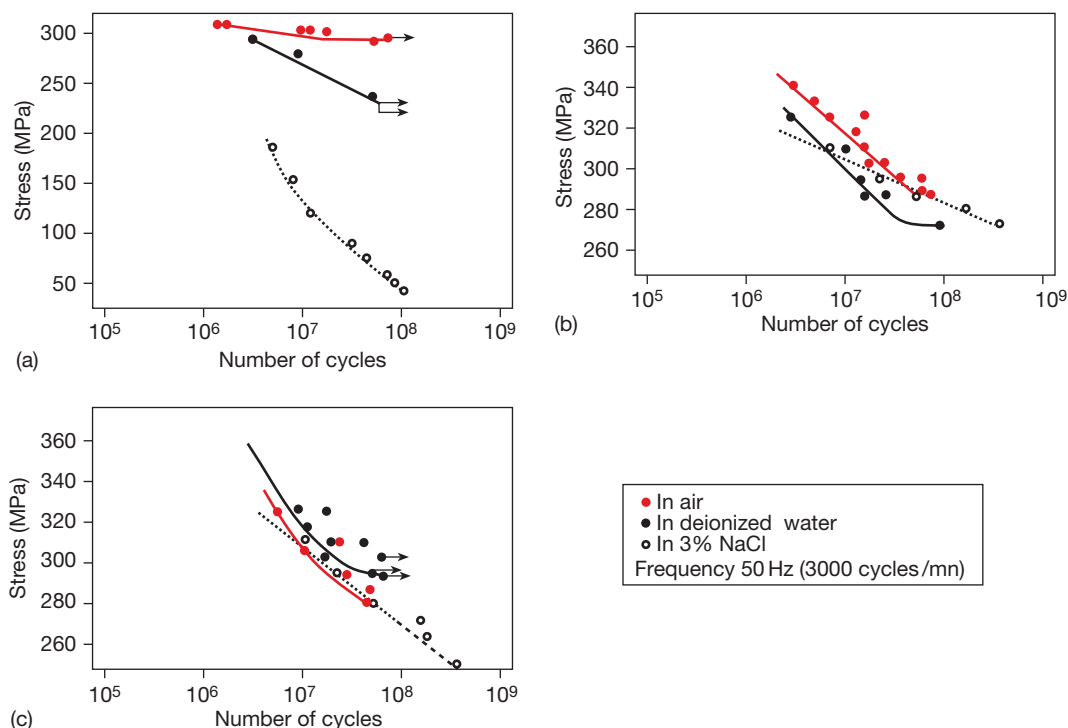


**Figure 31** Corrosion fatigue curves of pearlitic SG cast irons: (a) shot-blasted, (b) metallized with Zn, and (c) with Al. Reproduced with permission from Reynaud, A. *Corrosion and Cast Iron*, ETIF, France, 2008.

**Table 26** Fatigue resistance of some SG cast irons

Matrix	Fatigue resistance in air (MPa)	Resistance to corrosion fatigue	
		In 3% NaCl (MPa)	In lubricating oil (MPa)
Ferritic	240	100	225
Ferritic	350	75	330
Annealed	350	145	540
martensite			
Bainite	510	150	500

graphite cast irons (ADI) in water. They found that the fatigue limit of ADI cast irons declined in the course of time, apparently due to a selective dissolution of the acicular ferrite resulting from localized corrosion fatigue. It would seem that ferritic cast irons, in which the selective corrosion of ferrite does not occur, would perform better when exposed to water.

### 3.02.5.10 Stress Corrosion Cracking

In general, it can be said that cast irons are not liable to stress corrosion; however, in some particular media (concentrated sodium hydroxide solution for example),

stress corrosion, cracking of spheroidal graphite cast iron, can be observed.<sup>83</sup> The mechanisms of this type of damage have been studied<sup>84,85</sup> and is similar to steel at the same pH. Lamellar graphite cast irons seem to be less liable to this type of attack; additions of nickel (3–5%) improve the stress corrosion resistance of lamellar and spheroidal graphite cast irons.<sup>86</sup> Tests of the stress corrosion resistance of a ferritic SG cast iron in a medium containing sulfur, (saturated solution of  $H_2S$ )<sup>87</sup> have shown that this type of material is barely liable to this mode of attack – at least not more than a work-hardened carbon steel.

Unalloyed and low-alloyed cast irons are susceptible to varying degrees of stress corrosion cracking in high pH ( $>13$ ), in nitrite solutions, in  $H_2S$ , in acid (where a number of phenomena related to hydrogen occur), etc. These can be mitigated to a greater or lesser extent by alloying, as described elsewhere. Austenitic nickel cast irons are liable to stress corrosion in aerated sodium chloride solution<sup>85</sup> and this can be prevented by use of cathodic protection. Overall stress corrosion can be diminished or even eliminated by reducing the applied stress, by increasing the nickel content, and by reducing the dissolved oxygen content of the medium.



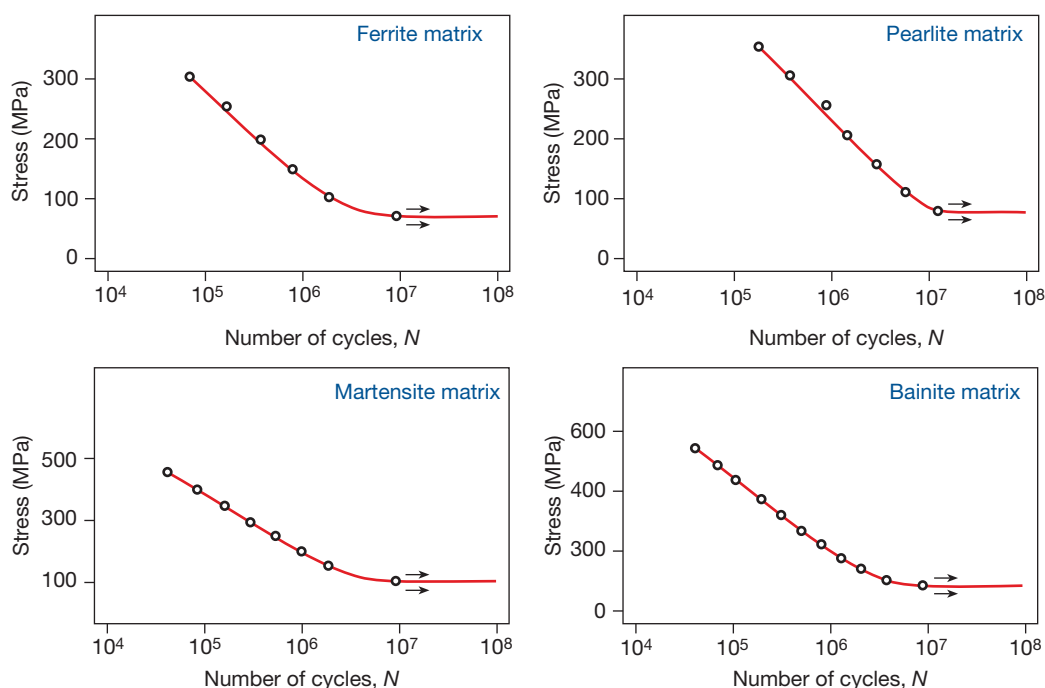


**Figure 32** Corrosion fatigue resistance of SG cast irons having different types of matrices (in 3% NaCl). Reproduced with permission from Reynaud, A. *Corrosion and Cast Iron*, ETIF, France, 2008.

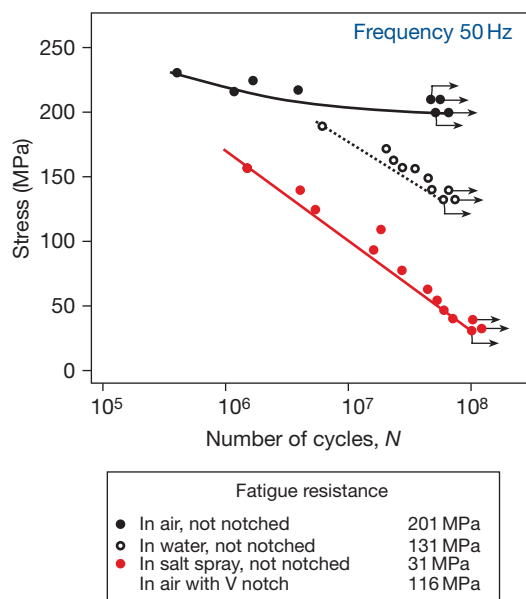


**Figure 33** Corrosion fatigue curves of a ferritic SG cast iron in rotary bending (50 Hz).

Unlike most stainless steels, austenitic cast iron, for example the EN-GJSA-XNiCr20-2 type, is not affected by crevice corrosion or by corrosion cracking, even in stagnant solution. Moreover, it provides

cathodic protection to any lower alloy cast steel or iron components. In many cases, however, cracks may occur by stress corrosion cracking in warm seawater, at temperatures above  $\sim 30^\circ\text{C}$ . The tensions that appear are not ascribable to the service loading; rather, they are due to internal stress. For this reason, a careful stress relieving annealing can reliably reduce the risk of stress corrosion cracking.<sup>88,89</sup>

The occurrence of stress corrosion cracking in EN-GJSA-XNiCr20-2 and EN-GJSA-XNiCr30-3 spheroidal graphite cast irons in magnesium chloride solutions containing 5–40%  $\text{MgCl}_2$ , at temperatures ranging from  $20^\circ\text{C}$  to the boiling point, was studied by German authors<sup>89,90</sup> on tensile test pieces and a diagram of the stability as a function of stress in % of yield strength for the two cast iron types is shown in **Figures 35 and 36**.

There exists, for both cast irons and for each temperature, a clear limiting stress below which corrosion cracking no longer occurs. Concerning the influence of the concentration of the solution, it turns out that the life is shortest in a 10% solution of  $\text{MgCl}_2$ . The life is reduced by anodic polarization, while stress corrosion cracking can be blocked by a weak cathodic polarization of 50–100 mV from the resting potential. This implies that the stress

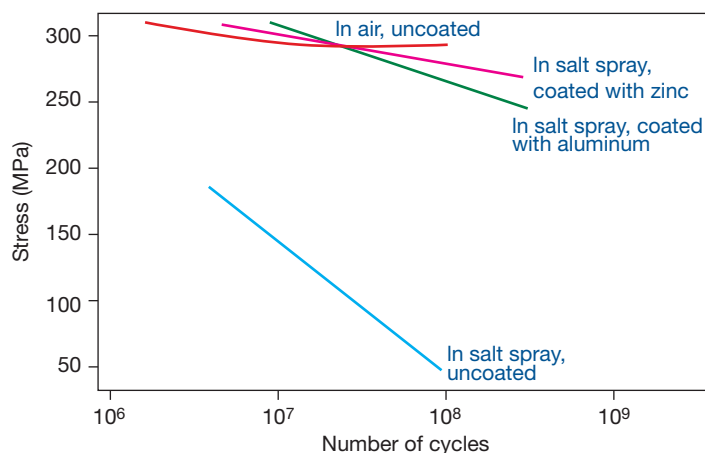


**Figure 34** Effect of Zn and Al coatings on the corrosion fatigue resistance of an SG cast iron in a salt spray (3% NaCl). Reproduced with permission from Forecast Progress in Metal Casting, no. 46, October 1983.

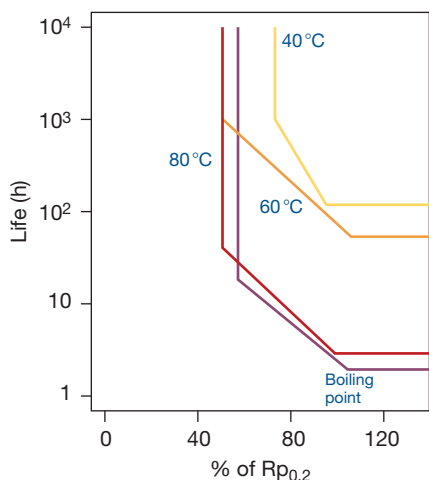


**Figure 35** Diagram of resistance of an ENGJSA-XNiCr20-2 cast iron. Relation between the stress in % of yield strength ( $R_{p0.2}$ ) and the temperature in 5–40% solutions of  $MgCl_2$ . Reproduced with permission from Baumel, A. *Werkstoffe Korros.* **1993**, 44, 107–108.

corrosion cracking of austenitic cast iron is favored by contact with an austenitic stainless steel, even in highly dilute solutions, containing for example 0.1%  $MgCl_2$ , where there is still a sensitivity to stress corrosion cracking at high stresses and temperatures. Also, EN-GJSA-XNiCr-30 cast iron is considerably more resistant than EN-GJSA-XNiCr20-2 cast iron. As the most effective remedy against corrosion cracking under load, a reduction of internal stress by a stress-relieving annealing is recommended. Acceptable residual stress levels of 100 MPa for EN-GJSA-XNiCr20-2 cast iron and 150 MPa for EN-GJSA-XNiCr-30-3 cast iron are allowed.

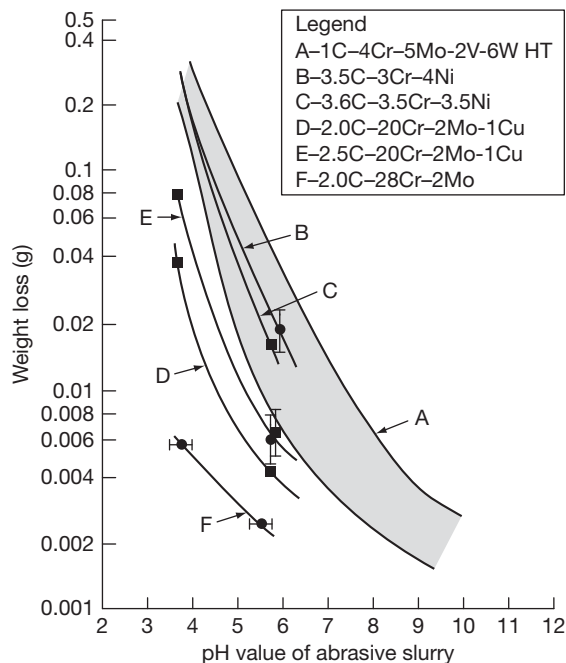


**Figure 36** Diagram of resistance of an ENGJSA-XNiCr-30 cast iron: relation between the stress in % of yield strength ( $R_{p0.2}$ ) and the temperature in 5–40% solutions of  $MgCl_2$ . Reproduced with permission from Baumel, A. *Werkstoffe Korros.* **1993**, 44, 107–108.

### 3.02.5.11 Organic Compounds

#### 3.02.5.11.1 Alcohol and glycol

Unalloyed cast irons and nickel cast irons can be used for ordinary applications in the presence of hydrocarbons, aldehydes, and amines although some slight attack occurs with the simultaneous presence of

water. Nickel cast irons have complete resistance at all concentrations of these species. On the other hand, alcohol–water mixtures will cause corrosion, the most common application occurring in the use of ethanediol and glycol compounds in automotive antifreeze and coolants. In order to combat this form of corrosion, one or more corrosion inhibitors, such as benzotriazoles and sodium benzoates, are often added, [Table 27](#).<sup>91</sup>

### 3.02.5.11.2 Corrosion by food products

Unalloyed cast irons and nickel cast irons must not be used with wine, vinegar, beer, cider, fruit juices, milk, maltose, and mustard. By contrast, unalloyed cast irons can be used with concentrated beverage, alcohols, and liqueurs. [Table 28](#) provides information about the corrosion resistance of two cast irons in the presence of a number of fruit juices and wine vinegar.

**Table 27** Corrosion rate of unalloyed gray iron in ethanediol–water mixtures in the presence of various inhibitors

Medium	Loss of mass after 50 days testing (mg cm <sup>-2</sup> )
50% Aqueous solution of ethanediol at 70°C (Medium A)	19–21
Medium A + 1% sodium benzoate	25–28
Medium A + 5% sodium benzoate	0.63
Medium A + 0.5% benzotriazole	11–13
Medium A + 1% benzotriazole	6–8
Medium A + 1% benzoate 0.1% benzotriazole	0.3–5
Medium A + 1% benzoate 0.5% benzotriazole	0.3
Medium A + 1% benzoate 1% benzotriazole	0.2

**Table 28** Corrosion rate of cast iron in various food products

Solution	Temperature (°C)	Corrosion rate (mm/year)	
		Unalloyed cast iron	Ni-Resist cast iron (≤ 20% Ni)
Pineapple juice	86	20	1.8
Pineapple juice	24	1.5	0.25
Grapefruit juice	Tb	59	0.5–1.5
Grapefruit juice	30	8.9	0.5–1.5
Tomato juice	50	2.8	0.5
Vinegar	15	3.3	–

### 3.02.5.12 Corrosion by Molten Materials

The resistance of cast iron furnace components, especially crucibles, to oxidation at elevated temperatures is important to ensuing dimensional stability and retaining a suitable wall thickness, especially in crucibles. The best material for crucibles from the standpoint of resistance to corrosion is a refractory alloy that can withstand a temperature of the order of 850 °C. According to Polish studies<sup>88,92</sup> a low-alloy chromium cast iron (1.5–3%) best meets this requirement: with such an alloy, the layers of oxides formed on the outside surfaces of the crucibles are relatively thin. The second problem for crucibles containing molten materials is their dissolution. First, a high, but nonuniform, dissolution of the crucible material can lead to the formation of deep local cavities, limiting the life of the crucible. Second, the crucible contents are polluted by iron, which can be a severe problem.

#### 3.02.5.12.1 Corrosion by liquid aluminum or aluminum alloys

Unfortunately, not much is known about the transfer mechanisms of iron from a ferrous crucible into a molten aluminum. However, it is known that the general rate of dissolution of iron into a light alloy increases as the temperature and the silicon content increase.<sup>64</sup> Baths containing magnesium are also highly corrosive, but aluminum alloys containing copper are less so. Among ferrous alloys, cast irons generally resist better than cast steel. According to the Polish work mentioned earlier,<sup>88,92</sup> the best corrosion resistance is found for lamellar graphite cast irons and blackheart malleable cast irons. Some work indicates that high-phosphorus (1.29%) lamellar graphite cast iron displays the best corrosion resistance in liquid aluminum alloys. But that it would be difficult to apply these results in industry, because cast irons having an extensive phosphorus eutectic distribution are not, in other respects, sufficiently resistant to oxidation. As for the influence of chromium, it has been shown that the rate of iron dissolution has a minimum of 2.9% chromium.

Generally, in cast iron crucibles containing molten aluminum, the aluminum diffuses into the crucible surface forming an intermetallic compound (FeAl<sub>3</sub>). This effect reduces the effective difference of aluminum content between the crucible and the liquid alloy, which is one of the drivers for the dissolution process. Some authors<sup>93</sup> have commented that since the FeAl<sub>3</sub> combination contains no carbon, there results an increase of the carbon content on

the perimeter of the ferrous sample, with a clear increase of the pearlite content. This local increase of the pearlite content favors the corrosion resistance of the metal. The same authors have also shown that ferritic white cast irons containing 32% chromium are among the materials that are least resistant to liquid aluminum.

Therefore, it appears that the optimum chemical composition for a cast iron that must resist corrosion by liquid aluminum and silicon alloys is: 3.4–3.5% C, 0.3% P, 2.5–3.0% Cr, 2.0–2.5% Si, 0.1% S, 4.0–5.0% Al, 0.4% Mn and a Polish patent (no. 55.549) was taken out for this grade of cast iron in 1968. In France, a similar cast iron, but containing no aluminum, is generally recommended. However, in practice, the problems of corrosion by liquid aluminum alloys are rarely solved at the metallurgical level; the recommendation most often made is to apply a good dye coating as the only way to ensure a satisfactory life.

### 3.02.5.12.2 Corrosion by liquid zinc and zinc alloys

A phenomenon of gradual dissolution also occurs in the cast iron crucibles used for melting zinc and its alloys. A detailed study at CTIF<sup>94</sup> of the corrosion of ferrous alloys by liquid zinc alloys found that ferrite is the most unfavorable constituent as regards resistance to this type of attack. Pearlite fairs better, even though there is a risk of progression of the corrosion between its lamellae, and a loosening of the latter. This last phenomenon is, however, rather rare: liquid surface tension generally prevents the molten zinc alloy from progressing between the lamellae when the pearlite is fine enough. Hence, it is preferable to avoid coarse structures. Since corrosion advances preferably along the graphite lamellae, it is also best to limit their size as much as is possible; spheroidal graphite once again seems preferable in this respect. As in the case of aluminum, corrosion by liquid zinc is chemical, not electrochemical. Thus, there is no reason to believe that the resistance of an austenitic cast iron of the 'Ni-Resist' type is better than that of a pearlitic cast iron.

### 3.02.5.12.3 Corrosion by other liquid metals

According to various sources, cast iron possesses good resistance ( $<0.025$  mm year<sup>-1</sup>) to dissolution in liquid magnesium, at its melting temperature (651 °C), liquid calcium up to 700 °C, liquid lead up to 500 °C and liquid cadmium at 600 °C. It has limited resistance (0.025–0.25 mm year<sup>-1</sup>) in liquid tin at its

melting point (322 °C), liquid magnesium from 700/800 °C and liquid sodium and potassium at 480 °C. However, cast iron has poor resistance ( $>0.25$  mm year<sup>-1</sup>) in liquid sodium and potassium at 600 °C, liquid tin at 600 °C, and liquid antimony at its melting point (630 °C).

Note that the dissolution of cast iron crucibles used for the melting of metals can sometimes be ascribed to other processes that may accompany the iron dissolution, such as the erosion–corrosion resulting from the flow of the liquid metals, cracking by thermal fatigue or by creep, and high temperature oxidation processes.

### 3.02.5.12.4 Corrosion by liquid sulfur

Table 29<sup>95</sup> indicates the rate of attack in liquid sulfur of a unalloyed lamellar graphite cast iron and of a type EN-GJLA-XNiCuCr15-6-2 austenitic cast iron, as a function of temperature.

It can be seen here that nickel cast irons behave like unalloyed cast irons up to 250–300 °C, and then more poorly at higher temperatures.<sup>96</sup> The addition of silicon (15%), possibly reinforced by an addition of molybdenum (or of chromium or copper), significantly reduces the rates of attack (Table 30).<sup>97</sup>

### 3.02.5.13 Microbially Influenced Corrosion

The role played by microbes in nature is well known. Numerous in the soil and in water, they decompose organic and mineral matter and participate in the

**Table 29** Dissolution rate of cast irons in liquid sulfur

Temperature (°C)	Corrosion rate (mm year <sup>-1</sup> )	
	Unalloyed LGI	EN-GJLA-XNiCuCr15-6-2
127	0.5	0.5
260	0.8	0.8
295	2.8	3.3
365	5.0	7.3
446	10.9	14.8

**Table 30** Dissolution rate of 15% silicon iron in liquid sulfur

Temperature (°C)	Corrosion rate (mm/year)
120	$<0.05$
200–300	$<0.1$
430	0.5–1.25

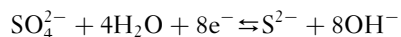
grand cycles of carbon, nitrogen, and sulfur. Most of the microorganisms responsible for microbially influenced corrosion can adapt to temperatures between  $-10$  and  $+99^{\circ}\text{C}$ , pH between 0 and 10.5 and concentration of oxygen between 0% and nearly 100%. Many bacterial species produce an extensive range of compounds and species capable of promoting corrosion, including organic acids, sulfuric acid, hydrogen sulfide, etc.

### 3.02.5.13.1 Iron oxidizing bacteria

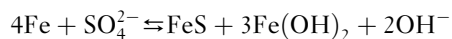
Iron oxidizing bacteria utilize the transformation of ferrous salts into ferric salts as part of their life cycle. The bacteria secrete enzymes that favor the oxidation of iron. Thus, at local anodes where ferrous hydroxide is formed, this quickly turns into ferric and carbonated hydroxide by dissolved oxygen and carbon dioxide. Generally, the microbial process ends there; however, the rapid transformation of the ferrous ions into ferric salts, results in the formation of a voluminous clump of 'rust' containing the bacterial bodies, sometimes known as a tubercule, followed by a continuing attack of the metal.<sup>98</sup> The local environment under the rust is likely to be depleted in oxygen and this can provide a microclimate for the proliferation of anaerobic microbial species.

### 3.02.5.13.2 Sulfate-metabolizing bacteria

Sulfate-reducing bacteria, being anaerobic in nature, are found under the layers of rust, in contact with the metal, where oxygen does not reach them. They generally transform sulfate into reduced sulfur species ending in hydrogen sulfide, which combines with the ferrous salts to produce a black sulfide for example:



With the overall reaction:



Sulfur oxidizing bacteria, for their part, metabolize sulfur from sulfur or sulfide compounds, resulting in the production of sulfite or sulfate species and acidification of the medium, causing severe corrosive attack. For example:



Historically, microbial oxidation of ferrous sulfide (e.g., in tin, lead, and coal mines) resulting in the formation of strongly acidic mine waters, provided the first industrial examples of this type of corrosion.

However, it is also found in many industrial water circuits (water sprinkler system, for example). In favorable circumstances, colonies of sulfate reducing and sulfate oxidizing bacteria may coexist giving rise to serious corrosion problem in water transport and in particular, the sewerage systems. The following conditions are generally favorable to biological corrosion by sulfur bacteria: an anaerobic medium, a pH of 5.5–8.5, the presence of sulfates, the presence of a food (carbon) source, the presence of essential nutrients such as phosphate, and an optimal development temperature (e.g.,  $30$ – $40^{\circ}\text{C}$ ).

### 3.02.5.13.3 Mechanisms of action

Together, microbiological knowledge of bacterial metabolisms and knowledge of corrosion on the chemistry of water in the presence of acid gases  $\text{CO}_2$  and  $\text{H}_2\text{S}$ , lead to the conclusion that sulfate-reducing bacteria can regulate the pH of their environment to favor their growth. Secondary reactions with traces of oxygen or of ferrous iron can modify this pH value.<sup>99</sup>

It is important as well to remember that corrosion that occurs in an anaerobic medium is not necessarily bacterial; it may well be just a sign of the activity of a macrocell of the differential aeration type at its anodic zones, located precisely in the anaerobic zone. In the case of extended structures, these two types of activity are often found superimposed. Also, bacterial corrosion may be observed in soils that are not strictly anaerobic, but in which, as a result of corrosion previously initiated by classical processes, conditions favorable to the spread of bacterial activity have been established, for example under the corrosion product layers.

### 3.02.5.13.4 Microbial corrosion of cast iron

Often, the formation of a gelatinous vesicle is an initial visible sign of bacterial attack. This vesicle takes the form of a brown mass with smooth contours containing a blackish liquid with a strong hydrogen sulfide odor. At this stage sulfur compounds such as S, FeS, and  $\text{FeS}_2$  are present in the gelatinous mass, which conceals corrosion, usually in the form of a crater that may perforate the metal. The craters contain pockets of bacteria, commonly with iron bacteria near the surface and sulfate-reducing bacteria in the interior, which is anaerobic. Generally, biological corrosion almost always follows as a result of electrochemical corrosion but can increase it substantially.

The process of development of corrosion vesicles on cast iron is shown schematically in **Figure 37**. From the outset, the ferrous ions that form at the



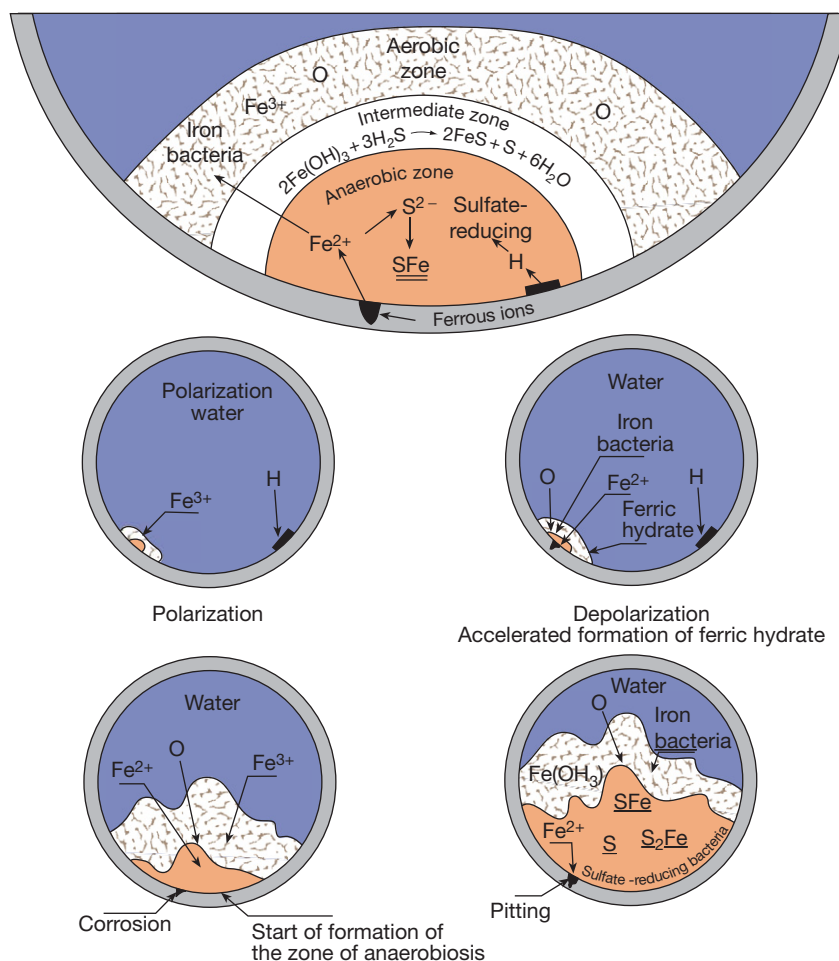


**Figure 37** Formation of a gelatinous vesicle during microbial corrosion. Based on a figure in Badan, B.; Magrini, M.; Ramous, E. *J. Mater. Sci.* **1991**, 26, 1951–1954, and reproduced with permission from Reynaud, A. *Corrosion and Cast Iron*, ETIF, France, 2008.

anode are transformed by oxidation into ferric hydroxide and hence, form a layer of rust, which gradually impregnates with ferrous salts that diffuse on the surface. These ferrous salts taken up by iron bacteria are quickly transformed into ferric hydroxide under aerobic conditions, and because of this the volume of the mass increases. It becomes more and more difficult for oxygen to diffuse to the interior. Aerobic development bacteria, therefore, can only thrive in the peripheral layers. This process creates, in the underlying layer, anaerobic conditions favorable to the development of sulfate-reducing bacteria, which reduce sulfates into hydrogen sulfide and iron sulfide. An Italian study<sup>100</sup> has confirmed the mechanisms stated above for microbial corrosion, in particular the formation of corrosion tubercles on the inside surface of cast iron pipes. In practice, in the

case of water delivery pipes, cement mortar linings have been used for nearly 50 years as a mechanism for controlling corrosion in new pipes and for renovation of old pipes.

### 3.02.5.13.5 Combating microbial corrosion

Many chemicals (biocides) can, in principle, be used to combat bacterially influenced corrosion. Among these include oxidizing agents (e.g., chlorine, bromine, potassium permanganate, etc.), toxic heavy metals (e.g., Ag, Cu, Zn, Hg), and their salts, detergents and amine derivatives, and aromatic alcohols (e.g., phenol and derivatives). These compounds are extremely varied, but often have high toxicity not only to the microbial species, but also to other lives. The use of many of these is controlled by legislation over the discharge of materials is the

environment. Chantereau's book<sup>98</sup> contains a list of the main products used in the fight against bacteria, with all their characteristics and domains of use. Note that chlorine, even though it is normally a corrosive substance, is beneficial in this context; its bactericidal action generally reduces corrosion by two thirds.

### 3.02.5.14 Flow-Induced Corrosion

#### 3.02.5.14.1 Cavitation corrosion of cast iron

When a liquid is subjected to a sudden fall of pressure, bubbles of vapor having a life of the order of a millisecond may form. This extremely brief existence ends when the local pressure increases in an implosion that, repeated thousands of times, can cause significant damage to some equipment. This is the phenomenon of cavitation. Some authors<sup>101</sup> have shown the impact of cavitation on corrosion damage: a ratio of 1–75 000 between 'simple' corrosion rates and cavitation corrosion rates. The interested reader may refer to Heuze<sup>102</sup> and for a theoretical examination of the phenomenon. In practice, two main types of cavitations are distinguished: 'flow' cavitation, which affects for example the vanes of turbines, and cavitation by vibrations. In cavitation by vibrations, the formation and implosion of bubbles result from the shock waves that a vibrating surface produces.

The apparently complex influence of temperature on the cavitation corrosion of cast irons has been the object of several studies.<sup>103–105</sup> It has, for example, been shown that the maximum attack occurs at a temperature approximately mid-way between the boiling and melting points of the corrosive medium (60 °C, in the case of water).<sup>104</sup> This critical temperature is assumed to be located differently according to the nature of the liquid and the ambient pressure.<sup>106</sup> It is found, in the case of water, that the deterioration of the material increases as the temperature rises from 0 to 50 °C. This seems to be explained by the concomitant lowering of the dissolved air content. Above 50 °C, the intensity of the cavitation decreases as the temperature increases; the lower air content of water is then offset by the higher vapor pressure. The nature of the fluid is also of some importance. Non-ionic liquids, such as toluene, are much less aggressive than water in the context of cavitation. The high vapor pressure of these liquids is invoked to explain this point. Otherwise, concerning the inhibition of this type of corrosion, in closed systems (cooling circuits), sodium nitrite or chromate and a few amines (triethanolamines, for example) have been proposed. The effectiveness of this protection by

inhibitors proves the importance of the electrochemical factor in cavitation corrosion.

Cast irons as a whole are said to be more sensitive to cavitation than steels. Certain authors<sup>107–110</sup> have shown that pearlitic cast irons are less vulnerable to cavitation than ferritic grades, and that the shape and size of the graphite inclusions also play a role on the spheroidal graphite cast irons being more resistant. Often surface hardening can improve the resistance to cavitation corrosion and studies have shown the utility of a superficial nitriding treatment.<sup>110,111</sup> Otherwise, austenitic spheroidal graphite cast irons from 20% Ni, 2% Cr to 30% Ni, 5% Cr display excellent resistance to cavitation corrosion under the most severe conditions. Thus, fishing-boat propellers and pump rotors made of these materials provide better service than a bronze or a stainless steel containing 18% chromium, **Table 31**.<sup>84</sup>

Some laboratory studies have simulated cavitation phenomena using sonic or ultrasonic vibrations.<sup>112</sup> In one of these studies, the vibrations were of 40 µm in amplitude at 15 kHz. In such operating conditions, the losses of mass of the four types of cast iron were as follows: ferritic lamellar graphite cast iron: 298 mg h<sup>-1</sup>; pearlitic lamellar graphite cast iron: 155 mg h<sup>-1</sup>; ferritic spheroidal graphite cast iron: 124 mg h<sup>-1</sup>; pearlitic spheroidal graphite cast iron: 67 mg h<sup>-1</sup>. It was found that the intensity of the corrosion cavitation was proportional to the square of the amplitude of the vibrations. However, the general rates of cavitation corrosion in this type of laboratory test are much larger than those in the field.

Cavitation is not an uncommon problem in internal combustion engines using cast iron cylinder liners. It has been shown<sup>113</sup> that the radial vibrations of the walls of the lining due to the running of an engine can lead to severe cavitation damage of the cast iron. Other work has shown that the superimposition of an external mechanical effect (tension or compression) does not appear to affect the intensity

**Table 31** Cavitation corrosion of various cast irons in seawater

<i>Material</i>	<i>Annual loss of thickness in seawater at 28 °C at a velocity of 8.2 m s<sup>-1</sup> (at mm)</i>
Unalloyed lamellar graphite cast iron	6.9
'Ni-Resist' cast iron (Ni20 Cr2 LGI)	0.75
88-10-2 Bronze	1.0

of the cavitation phenomenon (provided that it does not give rise to a significant stress phenomenon).

Some authors<sup>114</sup> have shown that the cavitation corrosion resistance of a lamellar graphite cast iron that has undergone superficial laser surface alloying by chromium (22%) in water (with or without 3% NaCl) at 50 °C is greatly increased. Similarly, other authors<sup>109</sup> have also shown the value of a surface hardening treatment. They found that a nitrided layer having the right hardness, thickness, and homogeneity is a good means of defence against cavitation corrosion.

An outline review of the literature on resistance of cast irons to cavitation<sup>109</sup> identified, or served to recall, a certain number of preliminary ideas. For example, it is known that the weakening effect of the graphite lamellae depends on their size, shape, and distribution in a given matrix. The spheroidal shape is optimal in this respect. Similarly, hard matrices (martensitic, bainitic, etc.) are preferable (the martensite must be tempered). Otherwise, note that saline solutions (3% NaCl) are much more aggressive than distilled water (up to seven times as corrosive). The use of inhibitors or of cathodic protection can be very effective. The presence of phosphorus (of phosphorus eutectic) has little effect other than a possible reduction of the incubation time of the phenomenon. Silicon, unlike chromium and molybdenum, increases cavitation resistance.

Kuwaiti researchers in 2001 studied the mechanisms of degradation of spheroidal graphite cast irons subjected to cavitation effects in seawater. They showed that the surfaces of iron castings, hollowed as wide craters, are prolonged in the cast iron by microcracks. The mechanism of initiation of the degradation seems to be related to the activity of a galvanic microcouple at the graphite–ferrite interface; the process is then prolonged by brittle fracture and ductile tearing of the material.<sup>97</sup>

### 3.02.5.14.2 Corrosion–erosion of cast iron

When the corrosive liquid also contains abrasive particles, there appears a phenomenon of erosion that strips away the corrosion products as they form, keeping the metal bare and therefore active. This mode of attack is commonly called ‘corrosion–erosion’ or ‘erosion–corrosion’ (the terms are often used interchangeably, but see below) or possibly ‘cavitation–erosion’ when the flow becomes highly turbulent.<sup>115,116</sup> The phenomenon of abrasion–corrosion (more correctly erosion–corrosion) is the result of mechanical damage by the action of solid

particles and electrochemical damage due to the presence of a corrosive medium. This type of situation is often found in industry, for example in treatment and transport of fluids in the oil and mining industries. Many parameters are influential on the damage: for example, the shape, hardness, size, and velocity of the particles, angles of incidence, characteristics of the medium, etc. Gray cast irons can be used, given their low cost price, if the erosion conditions are not too severe. However, significant performance benefits accrue using more resistance materials such as a ‘Ni-Hard’ grade. Lower alloyed materials have carbides predominantly as  $M_3C$  type and, in order to obtain increased resistance to erosion effects, the chromium and nickel contents must be increased to irons largely free of pearlite and containing harder carbides of the  $M_7C_3$  type.

Examination of the corrosion morphology of cast iron under erosion–corrosion conditions reveals that the erosion process generally begins with attack of the softer graphitic phase creating, in LG irons particularly, a network of voids that facilitates the penetration of the aggressive liquid. It follows that fine lamellar graphite is preferable to coarse lamellar graphite. After the preliminary stage, cracks form, essentially at the pearlite–phosphorus eutectic interfaces and at the boundaries between the various colonies of pearlite, leading to a gradual loss of cohesion of the cast iron. Ferrite seems to stand up better to this erosion process.

An ever-growing quantity of cast iron having high chromium and molybdenum contents is being used for the production of pumps that are harder and more resistant to abrasion. The results of tests on cast irons containing 15% Cr + 2% Mo or 25–27% Cr have, moreover, been published.<sup>117</sup> In this case, the advantages with respect to low-alloy white cast irons lie not only in their greater abrasion resistance and better fracture toughness, but also in their improved machinability. The housing and rotors of pumps transporting abrasive muds and of dredging pumps are manufactured by techniques that include annealing, machining, and quenching.<sup>118</sup> Elastic coatings to absorb impacts can also be considered.

High-chromium alloys with carbon contents in the range 0.5–2.0% afford a useful compromise between resistance to corrosion and resistance to abrasion. As the carbon content is increased, the resistance to abrasion improves, but corrosion resistance is reduced. The matrix structure of this range of high-chromium alloy irons can be largely austenitic or can be transformed to martensite by heat

treatment. There has been an increased interest in this series of alloy irons in recent years because they would seem to offer a cost-effective solution to problems encountered in handling abrasive slurries arising from gas scrubber installations in coal-fired power stations, **Figure 38**. They are also seen as candidate materials for the high-speed high-pressure pumps necessary in coal liquefaction projects, since they are able to resist abrasion at temperatures at which many abrasion-resistant steels would soften.

It is to be remembered that the hardness of the metal is not the only parameter to be considered in predicting resistance to corrosion-erosion. Allowance must also be made for factors related to the microstructure of the alloy, for example the size of the particles transported by the fluid relative to the size of the 'matrix' constituent. If the particle sizes are larger than the mean size of an 'island' of matrix in the microstructure, there will be less wear. There is a longstanding tendency to believe that, in these corrosion-erosion phenomena, the share of erosion prevails over the share of corrosion. In the light of certain tests, there seems to be less and less reason to believe this. Japanese authors<sup>119</sup> have shown that the erosion-corrosion of chromium cast irons is initiated at the matrix-carbide interface, and subsequently continues as corrosive and abrasive wear of the matrix

that can be reduced by increasing the chromium content. In general, additions of vanadium (5–8%), molybdenum (1–2%), and titanium (0.2%) seem to be effective ways to increase the resistance of grades containing 12–13% chromium.

Another Japanese study<sup>120</sup> has shown that the corrosion-erosion resistance of cast irons is often less than that of steels, because the preferential stripping of the graphite leads to the formation of craters, in which localized forms of corrosion are then initiated. These same authors have also shown that the deterioration of the material is inversely proportional to its hardness and that it can be prevented by cathodic protection. An electrochemical study of the corrosion-erosion resistance of white chromium cast irons has shown that the anodic corrosion current increases as the velocity of the abrasive substance increases and as the chromium content of the cast iron decreases.<sup>121</sup> Other work<sup>122</sup> has shown the value of austenitic-martensitic cast iron containing 5% manganese and 3% copper against corrosion-erosion, which would seem to have the same characteristics as a high-nickel alloyed grade. Finally, according to the same authors, a complementary addition of copper to chromium cast irons (5–6%) would seem to increase their resistance to this type of corrosion.

Many publications<sup>123,124</sup> report that laser surface hardening considerably increases erosion-corrosion resistance. Tests mentioned by American authors<sup>125</sup> have shown that, with gray cast irons (LG and SG), high power densities and long laser-cast iron interaction times result in very high hardness values (1200–1300 HV). The microstructures then observed correspond to fine carbide-ferrite aggregates. If the power density and interaction time are reduced, the hardness values are lower (600–800 HV) and the microstructure is found to be made up of dendrites of metastable austenite and films of interdendritic cementite. Depending on the values given to the various parameters of the laser treatment, the corrosion-erosion resistance can be improved by a factor of 2–5.

In the salt-rich and very polluted waters of the Persian Gulf, a comparative study of the corrosion-erosion resistance of a ferritic unalloyed SG cast iron, a silicon cast iron (14.5% Si), an austenitic lamellar graphite cast iron containing 20% Ni and 3% Si, and a duplex cast steel similar to a G-X 3 CrNiMo 26 6 3 cast steel with a reduced manganese content was carried out.<sup>126</sup> The objective was to test materials for ball valves. During these tests, the mechanism of corrosion and the formation of protective layers were also studied. The duplex cast steel suffered no measurable attack in the course of

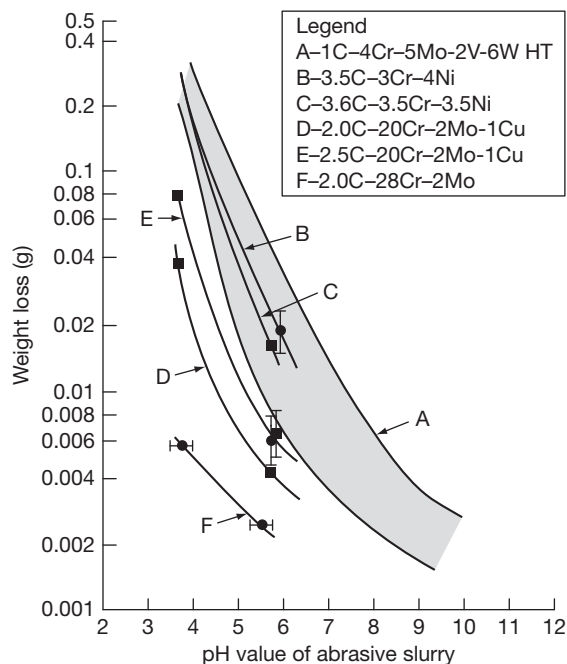


**Figure 38** Influence of pH value on weight loss in the slurry abrasion test.

25 days of tests. The corrosion losses of the three grades of cast iron are shown in **Figure 39**.

In stagnant water, only a small loss occurs, while in turbulent water the erosion increases significantly at first, except in the case of silicon cast iron where a coating made up of corrosion products forms.

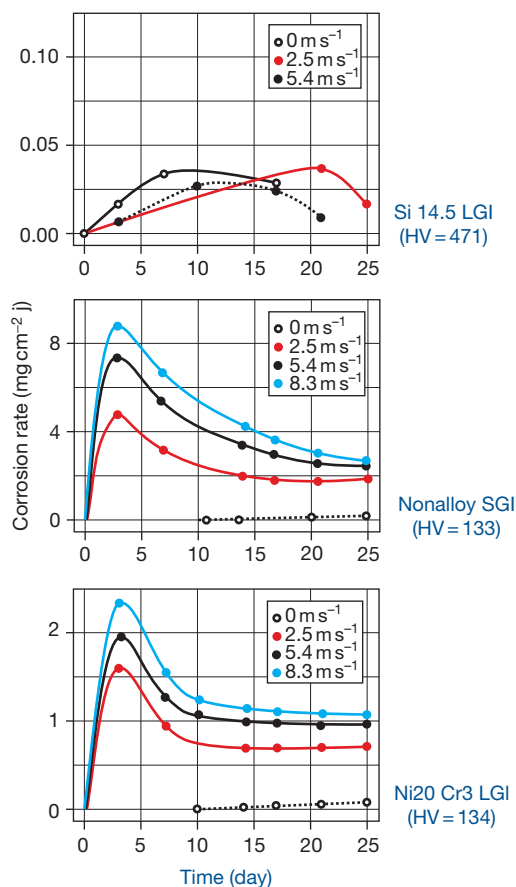


**Figure 39** Corrosion rates of three grades of cast iron in turbulent Persian Gulf seawater at 28 °C.

Gradually, the corrosion slows and the influence of the current velocity becomes weaker and weaker and forms, on the surface of the specimens, a thicker and thicker coating of corrosion products that slows the attack.

**Table 32** indicates the masses of the coating of corrosion products measured on the three grades of cast iron. On the silicon cast iron, the layer is very thin. At low current velocities and in still water, a phenomena similar to pitting or intergranular corrosion appeared on the cast irons; on the graphite lamellae and in the zones of segregation between the dendrites in particular. At higher current velocities, these phenomena disappear and the level of corrosion regresses to values too small to measure. The silicon cast iron suffered the least attack at all current velocities, thanks to its hardness, 470 HV, and to the thick coating of SiO<sub>2</sub>.

Some authors<sup>127</sup> have proposed two grades of white cast iron containing manganese (4–5%) and chromium (5–6%), with and without copper (0 and 2–3%), that seem to have the same corrosion–erosion resistance as an austenitic–martensitic white nickel–chromium cast iron of the ‘Ni-Hard’ type; the addition of copper seems to increase the corrosion resistance. Ageing these grades for 6 h at 800 °C is recommended, in order to precipitate very fine carbides in the austenitic matrix to increase the erosion resistance.

### 3.02.6 Corrosion by Gases

#### 3.02.6.1 High Temperature Oxidation and Corrosion

At temperatures above ~500 °C, unalloyed cast iron in an oxidizing atmosphere becomes covered with a

**Table 32** Mass of corrosion product on cast iron after exposure to seawater at different flow velocities

Duration of test (days)	Mass of corrosion product on surface (g)							
	Silicon cast iron (m s <sup>-1</sup> )		Unalloyed SGI iron (m s <sup>-1</sup> )			Ni20 Cr3 LGI		
	2.5	5.4	2.5	5.4	8.3	2.5	5.4	8.3
3	0.00	0.00	N.A	19.71	18.89	N.A	3.35	3.84
7	0.00	0.00	10.89	28.90	33.70	4.05	5.64	3.79
10	0.00	0.00	20.91	35.09	37.80	5.11	2.53	2.22
14	0.27	0.00	23.95	39.10	31.25	6.81	3.64	4.36
17	0.29	0.13	25.07	42.39	30.77	9.33	4.67	1.08
21	0.22	0.03	31.82	50.08	37.55	11.33	3.85	1.87
25	0.20	0.15	49.13	54.78	37.00	16.31	4.19	5.72



scale made up of several layers of oxides plus a layer consisting of ferrous oxide and oxides of the alloy element X:  $\text{FeO} + \text{Fe}_y\text{X}_z\text{O}$ . Thus, its behavior is very similar to steel under the same conditions. The effect of chromium, aluminum and silicon additions to cast iron alloys on oxidation at high temperature has long been known. Thus, alloyed irons preferentially form more protective oxide scales consisting of, respectively,  $\text{Cr}_2\text{O}_3$ ,  $\text{Al}_2\text{O}_3$ , and  $\text{SiO}_2$ . Reaction with  $\text{FeO}$  at the oxide-metal interface may additionally result in the formation of a spinel:  $\text{FeCr}_2\text{O}_4$  or  $\text{FeAl}_2\text{O}_4$ , or a silicate such as  $\text{Fe}_2\text{SiO}_4$ . At greater distances from the basic metal, the oxygen pressure increases and, at a certain level,  $\text{FeO}$  is transformed into  $\text{Fe}_3\text{O}_4$ , then  $\text{Fe}_2\text{O}_3$ . The diffusion velocity of the iron ions in the lower layer of compound oxides, highly adherent and more compact than the superficial layers of pure iron oxides, is very low and hence, protects alloys containing chromium, aluminum, and silicon. The presence of molybdenum also favors this oxidation resistance.

In this particular case of lamellar graphite cast irons,<sup>128</sup> oxidation at high temperature is not limited to the superficial layer, but progresses along the graphite-matrix interfaces in the interior of the casting. The oxygen first combines with carbon, which at the temperatures in question gives carbon dioxide,

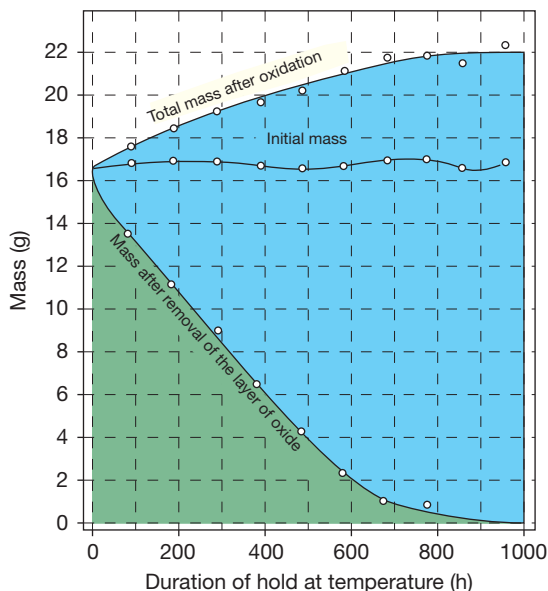
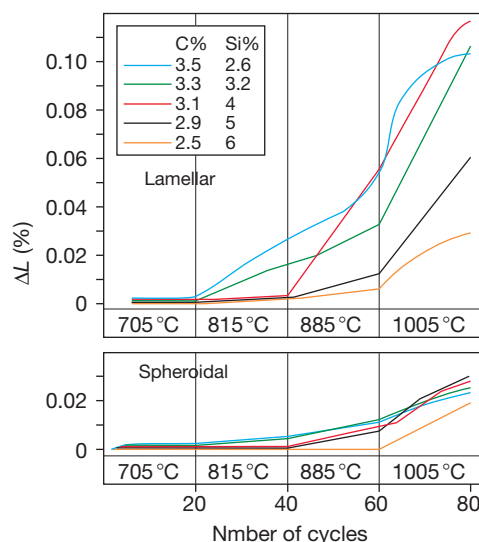


**Figure 40** Superficial oxidation of a unalloyed cast iron held in air at a temperature of 900 °C (the initial specimen was 10 mm in diameter and 30 mm long). Reproduced with permission from Sawamoto, A.; Usami, T.; Ogi, K.; Matsuda, K. *Imono* **1984**, 10, 597–601.

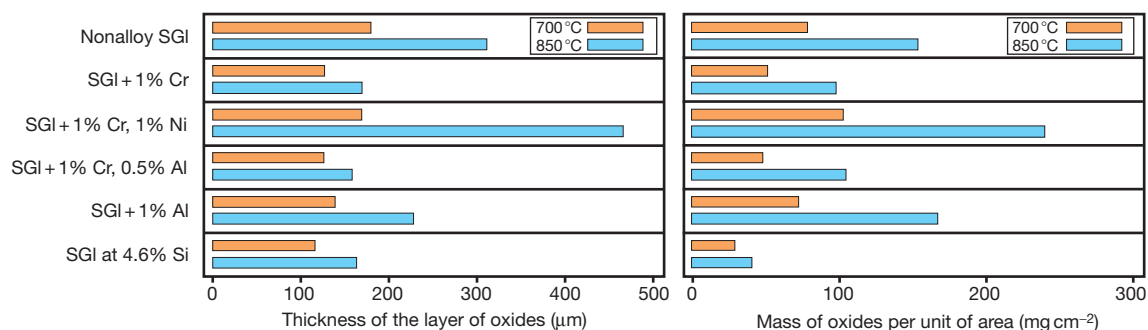
$\text{CO}_2$ , which in turn oxidizes the metal as it turns into  $\text{CO}$ . This gas tends to crack the protective oxide film, thereby facilitating the entry of oxygen. The formation of the oxidized compounds combines with the graphitization to cause a swelling of the cast iron. The progression of the oxidation, therefore, follows the path traced by the graphite; the layers of oxides are interposed between the matrix and the graphite lamellae.

Figure 40 below gives an idea of the intensity of the superficial oxidation that occurs when gray cast iron is held at 900 °C in air. Generally, the relative importance of the layer of oxides formed is measured using the change of mass of the sample. The absorption of oxygen is reflected by an increase of the mass due to the formation of the layer of oxides, while the removal of this layer causes a reduction of this mass. For specific graphite contents, the lamellar shape is therefore the most unfavorable; resistance to the penetration of the oxidation increases as the shape becomes more compact, with the spheroidal shape being the most favorable. Figure 41, which compares the swelling of five lamellar graphite cast irons having different silicon contents with the swelling of five spheroidal graphite cast irons having the same composition, shows the superiority of the latter very clearly.

A Japanese study of the effect of chromium, aluminum, nickel, and silicon on the oxidation rate of SG cast irons between 700 and 850 °C was



**Figure 41** Samples 10 cm long were subjected to cycles of heating (30 min at the temperature indicated) and cooling in air. Reproduced with permission from Bechet, S. *Hommes Fonderie* **1981**, 112, 15–28.



**Figure 42** Oxidation behavior at high temperature of various SG cast irons held for 100 h at 700 and 850 °C.

investigated<sup>129</sup> with the elements classified in order of decreasing effectiveness, as follows: Si–Cr–Al–Ni. Information on the influence of moderate additions of chromium, aluminum, nickel, and/or silicon on oxidation resistance at high temperature is shown in **Figure 42**.<sup>130</sup>

The beneficial effect of chromium on the oxidation resistance of cast irons is shown in **Figure 43**. This effect is very substantial from the first additions of chromium; this is a significant advantage, given that the chromium content of gray cast irons is always limited because of its strong tendency to produce carbides, which can for example result in machining difficulties.

In general, the types of cast iron used as a function of temperature are as follows:

- cast iron at 1–2% chromium for combustion gas with temperatures of not more than 850 °C or for preheating, up to a maximum of 350 °C, of gas having a high carbon monoxide content;
- cast iron at 30% chromium in the case of combustion gas of which the temperature is less than or equal to 1050 °C, or for the preheating of air to 650 °C.

The resistance of 30% chromium cast iron to destruction by gases having high carbon monoxide content is excellent in the temperature range from 400 to 600 °C.

The influence of the silicon content in conjunction with the carbon content shows that the oxidation resistance of hypoeutectic cast irons is better than that of hypereutectic cast irons. The harmful effect of carbon is also recognized. The influence of silicon content (between 2.4% and 6.4%) on the oxidation of five SG cast irons as a function of temperature is evident in **Figure 44**. This figure clearly shows that

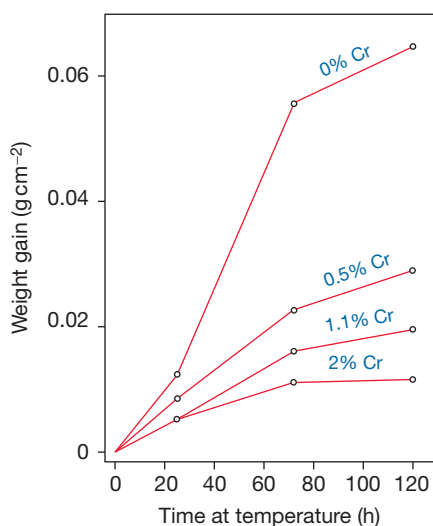


**Figure 43** Influence of chromium on the oxidation of cast irons at 800 °C. Reproduced with permission from Murakami, N.; Kobayashi, T. Owadano *Imono* **1986**, 58(7), 275–280.

the higher the temperature, the more important the role of silicon.

Certain American tests measured oxidation depths of 0.18 mm in a eutectic cast iron containing 4.7% silicon and 0.025 mm in a eutectic cast iron containing 5.9% Si, after exposure in air at 870 °C for 1000 h. It follows that increasing the silicon content very quickly reduces oxidation at high temperature.

Oxidation resistance is also greatly improved by the addition of aluminum. **Figure 45** illustrates the oxidation resistance of a cast iron containing 3% C and 0.8% Si as a function of its aluminum content (2.4, 4.3, and 6%), after 200 h exposure to temperatures up to 980 °C. **Figure 46** shows the influence of

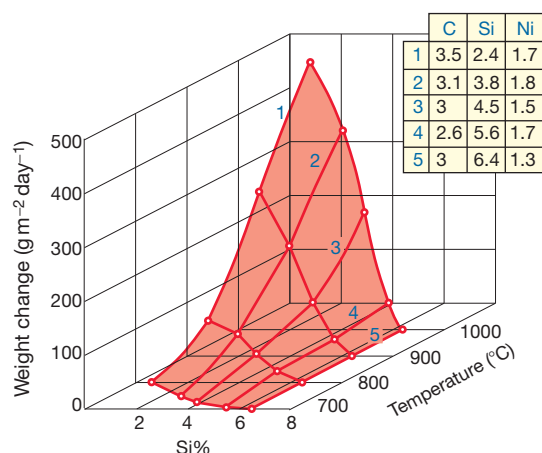


**Figure 44** Influence of silicon content on the oxidation resistance of SG cast irons as a function of temperature. Reproduced with permission from Murakami, N.; Kobayashi, T. Owadano *Imono* **1986**, 58(7), 275–280.

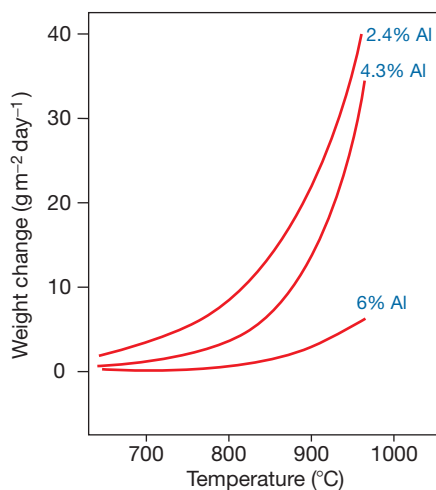


**Figure 45** Influence of aluminum content on oxidation resistance of cast irons containing 3% C, exposed for 200 h at the temperature indicated. Reproduced with permission from Murakami, N.; Kobayashi, T. Owadano *Imono* **1986**, 58(7), 275–280.

aluminum content on the oxidation resistance of gray cast irons as a function of temperature. Otherwise, with aluminum contents of the order of 20–25%, there is practically no oxidation:  $\sim 20 \text{ mg m}^{-2} \text{ day}^{-1}$  at  $1050^\circ\text{C}$ .

Combining silicon with aluminum provides significant improvement in oxidation resistance. The best resistance to oxidation at  $950^\circ\text{C}$  compatible with acceptable mechanical properties seems to be

obtained with fine graphite cast irons containing 6.5–7% Al and 5–6% Si; better performance occurs with a carbon content close to the eutectic, that is, close to 1.8% C. The addition of aluminum also increases the resistance of cast iron in a sulfurous atmosphere. There is literature evidence<sup>128</sup> that the lowest oxidation rate occurs in alloys having compositions close to 5% Al, 2% Mo, and 2–3% Si: the penetration of oxidation in a cast iron of this type, after 1000 h at  $925^\circ\text{C}$ , is  $8 \mu\text{m}$ . The resistance of some spheroidal graphite high-nickel high-alloy cast irons (e.g., 30% Ni, 5% Cr, 5% Si) to heat and to corrosion by hot gases, chlorine, and chlorides is excellent.<sup>131,132</sup> Their drawback is that they are very expensive. Otherwise, the resistance of ‘Ni-Resist’ cast irons to oxidation at high temperature is generally high. They are often used for certain applications, such as exhaust manifolds for extreme conditions and some turbocharger parts.<sup>133</sup>

### 3.02.6.2 Corrosion by other Gas Atmospheres

A precise, exhaustive treatment of this subject would greatly exceed the scope of this article. Thus, a few general remarks for a few of the most commonly encountered corrosive gases will be made.

Cast irons stand up rather well to hydrogen sulfide gas from  $-60$  to  $+20^\circ\text{C}$  provided it is dry; otherwise, there is risk of a form of hydrogen cracking.<sup>134</sup> The losses of thickness, in the case of a mixture of 98%  $\text{H}_2\text{S}$  and 2% air at  $32^\circ\text{C}$ , are  $0.075 \text{ mm year}^{-1}$  ( $1.75 \text{ mm year}^{-1}$  for damp  $\text{H}_2\text{S}$ ) for unalloyed cast irons and  $0.050 \text{ mm year}^{-1}$  for austenitic cast irons. At higher temperatures, cast irons perform satisfactorily (especially unalloyed cast irons); the losses of thickness are shown in Table 33. Silicon cast irons are also relatively resistant to hydrogen sulfide up to  $100^\circ\text{C}$ . The presence of chromium, even at moderate contents (2%), improves resistance to this gas; such cast irons in fact have acceptable performance up to  $300^\circ\text{C}$ .

In hot sulfur dioxide, the gas temperature significantly affects the corrodibility of cast iron. Thus, in roasting furnaces (8%  $\text{SO}_2$ ), an SG cast iron containing 0.5% Cr is acceptable provided the temperature remains below  $300^\circ\text{C}$ . At  $550^\circ\text{C}$ , it is still possible to use an ordinary cast iron provided that it is metallized by spraying with aluminum; at higher temperatures, at  $1000^\circ\text{C}$ , it becomes necessary to use a cast iron containing 30% chromium or 16% silicon and 3% molybdenum.

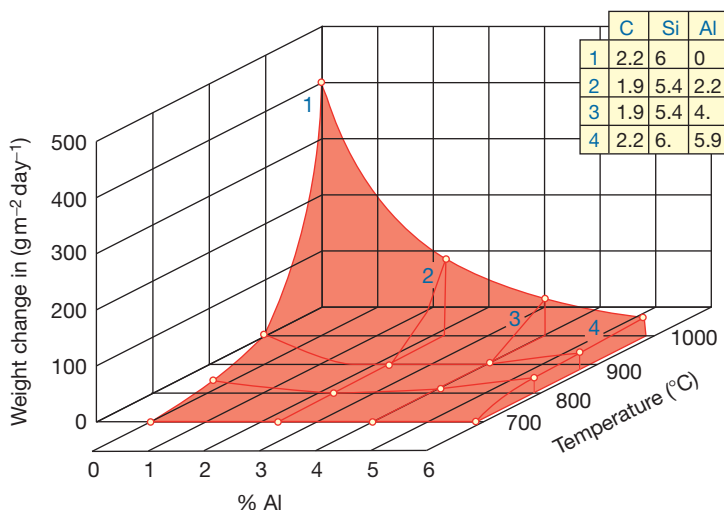


**Figure 46** Influence of aluminum content on the oxidation resistance of gray cast irons containing 6% Si and 2% C. Reproduced with permission from Murakami, N.; Kobayashi, T. Owoodano *Imono* **1986**, 58(7), 275–280.

**Table 33** Corrosion of cast iron in hydrogen sulphide

Medium	Loss of thickness (mm year <sup>-1</sup> )	
	Unalloyed cast irons	Austenitic cast irons
H <sub>2</sub> S at 80–85°C	0.64	0.21
H <sub>2</sub> S at 92°C	1.75	0.25

At ordinary temperatures (and at low temperatures), dry gaseous (or liquid) chlorine does not attack cast irons. Also, provided that the temperature is sufficient to avoid water condensation, chlorine containing some water vapor is not significantly aggressive. However, at higher temperatures, above ~350°C, chlorine reacts with water vapor to form hydrochloric acid and hypochlorite, which is highly aggressive and requires the use of high-alloy cast irons (e.g., containing 15% silicon and 3% molybdenum or Ni14Cu6Cr3 ‘Ni-Resist’ LGI cast irons or again cast irons containing 30% chromium). **Table 34** indicates the corrosion rates of a unalloyed cast iron and of carbon steel in chlorine as a function of temperature.<sup>135</sup>

Specific studies of corrosion risk are often performed for recuperators and heat exchangers for the cooling or heating of air that may contain chlorine traces. This is because, among the many causes of corrosion of heating installations, there is one that is especially insidious, namely corrosion by the action of halogens in air.<sup>136</sup> Note that any halogen present in

**Table 34** Corrosion of cast iron in chlorine gas as a function of temperature

Alloy	Temperature (°C)	Corrosion rate (mm year <sup>-1</sup> )
Unalloyed LGI	93	0.76
	120	1.52
	177	3.05
	232	30.00
	280	0.76
18–8	315	1.52
	400	15.20

a combustion atmosphere potentially react to produce aggressive products such as HCl. Halogen sources include chlorinated substances that have household, industrial, and recreational uses and, hence, incineration of wastes can produce a highly aggressive atmosphere.

Given the very large number of gases and mixtures of gases, an exhaustive study is impossible, so **Tables 35** and **36** indicate the cast irons recommended for given gas conditions.

### 3.02.6.3 Corrosion in Gas Transport and Distribution Pipes

The gas flowing in these pipes may, in the course of its travel, either remain at all times at a temperature above its dew point or occasionally cool to a temperature below this dew point. In the former case,

**Table 35** Recommended cast irons for use in the specified gas atmosphere

<i>Gaseous mixture</i>	<i>Recommended cast iron</i>
<b>Mixture</b>	
<i>Gas mixture with CO<sub>2</sub> or CO<sub>2</sub> + CO</i>	
+ CO <sub>2</sub> (95 %) + H <sub>2</sub> O (2,5 %) + NH <sub>3</sub> (1,5 %)	'Ni-Resist' cast iron
+ CO <sub>2</sub> (87 %) + H <sub>2</sub> O (2 %) + inert gases (11 %) NH <sub>3</sub> (traces)	'Ni-Resist' cast iron
+ CO <sub>2</sub> (70 %) + air (16 %) + H <sub>2</sub> O (10 %) + NH <sub>3</sub> (4 %)	'Ni-Resist' cast iron
+ CO <sub>2</sub> (17 %) + CO (25 %) + H <sub>2</sub> O (2 %) + H <sub>2</sub> (50 %) + N <sub>2</sub> (4 %) + CH <sub>4</sub> (52 %)	'Ni-Resist' cast iron or 15% Si cast iron
+ CO <sub>2</sub> (13 %) + CO (11 %) + H <sub>2</sub> (7 %) + O <sub>2</sub> (2 %)	15% Si cast iron or ferritic white Cr+Mo cast iron
+ CO <sub>2</sub> (11.6 %) + N <sub>2</sub> (77 %) + H <sub>2</sub> O (8 %)	'Ni-Resist' cast iron or 15% Si cast iron
+ CO <sub>2</sub> (5 %) + N <sub>2</sub> (74 %) + H (20 %) + O <sub>2</sub> + CH <sub>4</sub> + CO (1 %)	Unalloyed cast iron
+ CO <sub>2</sub> (4 %) + CO (70 %) + N <sub>2</sub> (18 %) + H <sub>2</sub> (6 %) + water and hydrocarbon vapours	1.5% Ni Pearlitic LGI
+ CO <sub>2</sub> (0.5 %) + H <sub>2</sub> O (6.6 %) + air (93 %)	Unalloyed cast iron
<i>Gas mixture with CO<sub>2</sub> and SO<sub>2</sub></i>	
+ CO <sub>2</sub> (10 %) + SO <sub>2</sub> (17 %) + O <sub>2</sub> (10 %) + N <sub>2</sub> (63 %)	Unalloyed cast iron
+ CO <sub>2</sub> (12 %) + SO <sub>2</sub> (0.1 %) + O <sub>2</sub> (3.4 %) + N <sub>2</sub> (74.5 %) + water vapour (10 %)	'Ni-Resist' cast iron
+ CO <sub>2</sub> + SO <sub>2</sub> (0.3 %) saturated with moisture	'Ni-Resist' cast iron
<i>Gas mixture with SO<sub>2</sub>, SO<sub>3</sub>, SO<sub>2</sub> + SO<sub>3</sub>, or SO<sub>2</sub> + NO<sub>2</sub></i>	
+ SO <sub>2</sub> (18 %) + N <sub>2</sub> (79 %) + O <sub>2</sub> (3 %)	Unalloyed cast iron
+ SO <sub>2</sub> (8 %) + N <sub>2</sub> (79 %) + O <sub>2</sub> (13 %) nearly dry (50 mg/m <sup>3</sup> H <sub>2</sub> O)	300 LGI, 1.8% Ni and 0.6% Cr
+ SO <sub>3</sub> (9 %) + N <sub>2</sub> (85 %) + O <sub>2</sub> (6 %) dry	Unalloyed cast iron
+ SO <sub>2</sub> + SO <sub>3</sub> (traces) dry (30°C)	2% Ni SGI
+ SO <sub>2</sub> (9.5 %) + NO <sub>2</sub> (84.7 %) + air (5.8 %) dry	Unalloyed cast iron
<i>Other gas mixtures</i>	
+ H <sub>2</sub> saturated with water + O <sub>2</sub> (3 %) + Cl <sub>2</sub> (2 ppm) (35°C)	'Ni-Resist' cast iron, Ni15 Cu5 Cr2 LGI
+ HCl (50 %) + N <sub>2</sub> (50 %) (dry)	Unalloyed cast iron
+ HCl (50 %) + N <sub>2</sub> (50 %) (dry) (damp)	15% Si cast iron
+ Vinyl chloride saturated with water vapour (36–100°C)	Unalloyed cast iron
+ O <sub>2</sub> Damp + CO <sub>2</sub>	'Ni-Resist' cast iron
+ Perchloric vapours	15% Si cast iron
+ CH <sub>4</sub> (62.5 %) + CO (12 %) + H <sub>2</sub> (5 %) + N <sub>2</sub> (10.4 %) + CNH <sub>2</sub> N (8.7 %) + O <sub>2</sub> (1.5 %)	Unalloyed cast iron
+ Dimethylether (38 %)/Methanol (27 %) + N <sub>2</sub> (28 %) + O <sub>2</sub> (3 %) + H <sub>2</sub> O (3 %) + CO <sub>2</sub> (1 %) + CO	Unalloyed cast iron
+ H <sub>2</sub> S (60–68 %) + CO <sub>2</sub> (22–28 %) + HCN (6–8 %) + water vapour (4 %)	None
+ H <sub>2</sub> S (13.4 %) + CO <sub>2</sub> (34 %) + HCN (1.5 %) + H <sub>2</sub> (24 %) + CO (22 %) + sodium aluminate (4.5 %) dry	Unalloyed cast iron
+ Air + heavy water (vapour)	'Ni-Resist' cast iron
+ Monochlorobenzene vapour saturated with water	15% Si cast iron

Data taken from Reynaud, A. *Corrosion and Cast Iron*, ETIF, France, 2008.

there is no condensation, while in the latter water is deposited. Such condensates are likely to form a thin film of moisture, continuous or not, which can lead to corrosion generally at the base of the pipes. For this reason, gas networks have traps, to be able to eliminate condensates. When this is done, centrifugal cast iron pipes only rarely suffer this type of internal corrosion due to the gas transported, even

if it contains water vapor. Industrial experience has in fact shown that the cast iron tubes used for natural gas distribution can survive for many decades without undergoing significant internal corrosion. In the case of oxygen-free natural gas, the principal aggressive constituents are sulfides. However, distributors will purify and condition gases so as to avoid these phenomena.



**Table 36** Recommended cast iron for use in specified gas atmosphere

Gaseous mixture	Recommended cast iron
Pure gases	
H <sub>2</sub> 100 % – 49°C	'N-Resist' cast iron (Ni23 Mn4 SGI)
HCl 100 %	32–34% Chromium cast iron
NH <sub>3</sub> 100 %	Unalloyed cast iron
Freon 113 – 50°C	Unalloyed cast iron
CCl <sub>4</sub> , dry, 40°C	Unalloyed cast iron
CCl <sub>4</sub> , damp, 40°C	'Ni-Resist' cast iron
Phenols (vapours)	Unalloyed cast iron
Acetone	Unalloyed cast iron
Toluene	Unalloyed cast iron
Ethanol	Unalloyed cast iron
Haptane	Unalloyed cast iron
NO, dry	Unalloyed cast iron
NO <sub>2</sub> dry	Unalloyed cast iron
Propane	Unalloyed cast iron
Bulane	Unalloyed cast iron
Ethane	Unalloyed cast iron
Mathane	Unalloyed cast iron
Ethylene	Unalloyed cast iron
Ethylene oxide	Unalloyed cast iron
Monochloroethylene, dry	Unalloyed cast iron
Dichloroethylene, dry	Unalloyed cast iron
Dichloroethylene, damp	15% Si cast iron
Oxygen	'Ni-Resist' cast iron

Data taken with permission from Reynaud, A. *Corrosion and Cast Iron*, ETIF, France, 2008.

## References

1. Tsuda, M.; Murata, Y. *IMONO*. **1982**, 54, 605–611.
2. Fontana, M. G.; Greene, N. D. *Corrosion Engineering*, 2nd ed.; McGraw-Hill.
3. Collins, H. H. *BCIRA J.* **1962**, 10, 543.
4. Landolt, D. *Corrosion et chimie de surfaces des métaux*. Traité des matériaux; Presses polytechniques et universitaires romandes, 1993; Vol. 2.
5. Ikenaga, A.; Nitta, Y.; Kavamoto, M. J. *Jpn. Foundry Eng. Soc.* **1996**, 68(7), 585–591.
6. Hemanth, J. J. *Mater. Process. Technol.* **2000**, 101(1/3), 159–166.
7. Graham, R.; Prado, O. S.; Collins, M. H.; Brandes, E. A.; Farmery, H. K. *Proc. Inst. Mech. Eng.* **1960**, 74, 617.
8. Whittaker, J. A.; Brandes, E. A. *Foundry* **1962**, 90, 70.
9. Wons, W. *Wasser Boden*. **1982**, 4, 138–144.
10. Vanick, J. S.; Merica, P. D. *Trans. Am. Soc. Steel Treat.* **1930**, 18, 923.
11. Kinzel, A. B.; Franks, R. Alloys of Iron and Chromium. In *High Chromium Alloys*; McGraw-Hill: New York, 1940; Vol. 2, pp 228–260.
12. Jackson, R. S. J. *I. S. I.* **1970**, 208, 163–167.
13. Hurst, J. E.; Riley, R. V. J. *Iron Steel Inst.* **1947**, 155, 172.
14. Dumitrescu, T.; Medeleanu, V.; Nicolaid, M.; Dinu, I. *Rev. Metall. (Roumania)* **1958**, 3(2), 19.
15. Hurst, J. E. *Proc. Inst. Brit. Foundrym.* **1944**, 37, B46.
16. Kulikov, V. I. *Chem. Pet. Eng.* **1981**, 16(7/8), 441–443.
17. CIFOM. Emploi des fontes dans l'industrie chimique. Supplément à l'Usine Nouvelle, June 1967, pp 1–8.
18. Cetre, Y. Etude du comportement à la corrosion de divers matériaux métalliques dans l'acide sulfurique concentré à chaud. Doctoral dissertation in engineering, INSA, Lyon, September, 1985.
19. Norme, N. F. A32–211, January 1991. Produits de fonderie – Fontes à graphite sphéroïdal pour robinetterie et appareils à pression.
20. Swales, G. L. *Ind. Chem. Chem. Manufacturer* **1963**, 39, 16–21, 79–83, 142–144.
21. Mannweiler, G. B. *Proc. Am. Soc. Test. Mater* **1972**, 72(1), 42.
22. Berenson, J.; Wranglen, G. *Corros. Sci.* **1980**, 20(7), 937–941.
23. Labbe, J. P. *L'agressivité des eaux dans les chauffe-eau électriques. Matériaux et techniques* 1983, pp. 126–130.
24. Jakobs, J. A.; Hewes, F. W. *Mater. Perf.* **1987**, 26(5), 42–49.
25. Smith, D. C. *Br. Corros. J.* **1980**, 15(4), 192–194.
26. Sontheimer, H.; Koelle, W.; Snoeyink, V. J. *AWWA*. **1981**, 73(11), 572–579.
27. Degremont *Mémento Technique de l'Eau*, 8th ed., 1978.
28. Lédion, J. *La Corrosion par les Eaux. La Revue des Laboratoires d'Essais*, no. 21, 1989, pp 9–13.
29. AFNOR standard, Protection électrochimique contre la corrosion, Recommandations concernant les traitements des influences du courant continu sur les structures métalliques enterrées. Standard NF A 05–615, July 1993.
30. Waanders, F. B.; Vorster, S. W. A Mössbauer Spectroscopy Study of the Corrosion of Nodular Cast Iron in Mine Waters. In *Hyperfine Interactions*; Springer: Netherlands; pp 1027–1033, Vol. 92, no. 1.
31. Smith, D. C.; Mac Enaney, B. *Corros. Sci.* **1979**, 19, 379–394.
32. Suery, P.; Hiltbrunner, K. *Archiv Für Das Eisenhuettenwesen* **1979**, 50(11), 493–498.
33. Degremont *Mémento Technique de l'Eau*, 8th éd. 1978.
34. Mehra, R.; Soni, A. *Bull. Mater. Sci.* **2002**, 25(1), 53–58.
35. Katz, W. *Giessen für die Chemie*; VDI-Verlag GmbH: Düsseldorf.
36. Neumann, E.; Behrendt, B.; Hecht, A. Nachweis von Korrosion (Spongiose) an den Innen Wänden von Orangußrohren mit Hilfe einer rechnergeführten Ultraschall prüfeinrichtung (Abakus) Materialprüfung. no.3, March 1987, pp 60–66.
37. Bryant, M. D. *BCIRA J.* **1972**, 20, 345–350.
38. Degremont *Mémento Technique de l'Eau*, 8th éd. 1978.
39. Smart, N. R.; Rance, A. P.; Fennell, P. A. H. Galvanic corrosion of copper–cast iron couples. Technical report TR-05-06, Svensk Kärnbränslehantering, January 2005.
40. Mehra, R.; Soni, A. Inhibition of corrosion of cast iron by nitrite, hydrogen phosphate, and molybdate ions in corrosive water. In *Chemical Engineering Communications*; Taylor & Francis: London, 2004; Vol. 191, no. 11, pp 1502–1524.
41. Evans, U. R. *La corrosion des Métaux*; Dunod: Paris, 1928.
42. *ASM Metals Handbook, Corrosion*; ASM International: Ohio, 1987; Vol. 13; pp 566–572.
43. Marshall, A. *Corros. Prevention Control* 1983, pp 177–181.
44. Une nouvelle nuance de fonte Ni-Resist à graphite sphéroïdal. INCO NICKEL, no. 33, 1971, pp 4.
45. Forecast Progress in Metal Casting; no. 46, 1983.

46. Daub, M. B.; Venkateswaran, G.; Venkateswarlu, K. S. *Br. Corros. J.* **1990**, 25(4), 303–307.
47. Waanders, F. B.; Vorster, S. W. *Hyperf. Interact.* **1994**, 92(1), 1027–1033.
48. Romanoff, M. Underground Corrosion US Nat. Bur. Std.: Washington DC, Circular No. 579, 1957.
49. Schwerdtfeger, W. J. J. *Res. Bur. Std.* **1985**, 69C, 71.
50. Stokes, R. F. *Chem. Ind.* **1983**, (17), 659–663.
51. Collins, H. H. Conference on Corrosion and the Water Industry, UMIST: Manchester, 1986.
52. Akimov, G. V. *Théorie et Méthodes d'Essai de la Corrosion des Métaux*, DUNOD: Paris, 1957.
53. Stadler, F. *AQUA* **1983**, 4, 183–187.
54. Heims, W. D. In *Gras Influence des Sources de Courant Électrique Extérieures sur la Corrosion et la Sécurité des Canalisations en Fonte Ductile Enterrées dans leur Voisinage*; FGR, Vol. 18, 1983; pp 17–31.
55. A.G.H.T.M. *Les canalisations d'eau et de gaz*, Editions Lavoisier: Paris, 1987.
56. Domerty, B. J. *Mater. Perf.* **1990**, 29(1), 22–28.
57. Katz, W. *Giessen für die Chemie*; VDI-Verlag GmbH: Düsseldorf.
58. Ductile cast iron having high strength and high corrosion resistance. Japanese patent, 09/04/2003, no. JP 2003105484.
59. Collins, H. H.; Fuller, A. G.; Harrison, J. T. In 12th World Gas Conference, Nice, Report 19 U/D 1973.
60. De Rosa, P. J.; Parkinson, R. W. Water Research Engineering Technical Report 241, 22, 1986.
61. Pont-à-Mousson. Les canalisations en fonte ductile. L'eau, l'industrie, les nuisances, no. 90, March 1985, pp 65–66.
62. Domerty, B. J. *Mater. Perf.* **1990**, 29(1), 22–28.
63. Garrity, K. C.; Jenkins, C. F.; Corbett, R. A. *Mater. Perf.* **1989**, 28(8), 25–29.
64. Jakobs, J. A.; Hewes, F. W. *Mater. Perf.* **1987**, 26(5), 42–49.
65. Schiff, M. J.; McCollom, B. *Mater. Perf.* **1993**, 32(8), 23–27.
66. AFNOR standard, Protection électrochimique contre la corrosion, recommandations concernant les traitements des influences du courant continu sur les structures métalliques enterrées. Standard NF A 05-615, July 1993.
67. Résistance des fontes à la corrosion de l'acide sulfurique. Fonderie-fondeur d'aujourd'hui, no. 61, January 1987, 19.
68. Résistance des fontes à l'acide sulfurique concentré. Fonderie no. 393, November 1979, 339.
69. Reynaud, A. Les fontes alliées au chrome et au silicium pour l'industrie chimique. Fonderie-fondeur d'aujourd'hui, no. 124, April 1993, pp 32–34.
70. Kosting, P. R.; Heins, C. *Ind. Eng. Chem.* **1931**, 23, 140–150.
71. Leconte, J. Protection contre la corrosion. Techniques de l'ingénieur métallurgie/génie industriel, pp A830.1–A835.4.
72. Lammia Al-Shama; Jalal Mohammed Saleh; Naema A. Hikmat, *Corros. Sci.* **1987**, 27(3), 221–228.
73. Higgins, R. I. *J. Res. Bcira* **1956**, 6, 165–177.
74. ASM. Corrosion of cast irons In *Metals Handbook, Corrosion*, 1987; Vol. 13, pp 566–572.
75. Collins, B. L.; Smith, J. O. *Proc. ASTM* **1942**, 42, 639.
76. Palmer, K. B. Proceedings of Conference on Engineering Properties and Performance of Modern Iron Castings, BCIRA, 1972, p 110.
77. Muthukumarasamy, S.; Seshan, S. *Bull. Electrochem.* **1991**, 7(1), 1–3.
78. Muthukumarasamy, S.; Seshan, S. *Transact. AFS* **1992**, 92(16), 873–879.
79. Dawson, J. V. *BCIRA J.* **1978**, 26, 135–144.
80. Palmer, K. B. *BCIRA J.* **1975**, 23, 40–43.
81. Forecast Progress in Metal Casting, no. 46, October 1983.
82. Yamamoto, S.; Ono, S.; Fukada, M. *Imono* **1993**, 65(9), 712; 717.
83. Smith, S. H. *BCIRA J. Res. Deterior.* 1957.
84. Morrison, J. C. *Anticorrosion* **1983**, 30(8), 8.
85. Miysaka, M.; Ogure, N. *Corrosion* **1987**, 43(10), 582–588.
86. Borel, P. Propriétés des fontes à graphite nodulaire. Techniques de l'ingénieur, métallurgie, p M392–19.
87. Diegle, R. B.; Treseder, R. S. *Mater. Perf.* **1978**, 17, 31–32.
88. Kosowski, A. *Przeglad Odlewnictwa* **1966**, 16, 362–367.
89. Baumel, A. *Werkstoffe Korros.* **1993**, 44, 107–108.
90. Atkinson, R. F. *Nickel*, 9(2), 10–11.
91. Mercer, A. D. *Br. Corros. J.* **1979**, 4(3), 179–182.
92. Podrucki, C. *Revue Métallurgie* **1968**, 65, 137–144.
93. Bastien, P.; Daeschner, S. Recherche sur la corrosion des fontes par l'aluminium et les alliages légers au silicium liquides. 21st ATF congress, October, 1947.
94. Charbonnier, J.; Parisien, J. Résistance des organes de machines à couler sous pression à la corrosion par les alliages de zinc liquides. Booklet CTIF, November, 1964.
95. Laque, F. L.; Uhlig, M. H. *Corrosion Handbook*; Wiley: London, 1978; p 197.
96. Eisensiliziumguss. Werkschrift der Rheinhütte: Wiesbaden, 1968.
97. Al-Hashem, A.; Abdullah, A.; Riad, W. *Mater. Charact.* **2001**, 47(5), 383–388.
98. Chantereau, J. *Tech. Documentation* 1980.
99. Crolet, J. L.; Daumas, S.; Magot, M. *Materiaux Tech.* **1992**, 9/10, 71–77.
100. Badan, B.; Magrini, M.; Ramous, E. *J. Mater. Sci.* **1991**, 26, 1951–1954.
101. Gouda, V. K.; Al-Hashem, A. H.; Abdullah, A. M.; Riad, W. T. *Br. Corros. J.* **1991**, 26(2), 109–116.
102. Heuze, J. L. Endommagement par érosion de cavitation de métaux et alliages de structure cubique à faces centrées. Thesis University of Paris 6, 27/10/1988.
103. Okada, T.; Iwai, Y.; Yamamoto, A. Division of Research Development and Administration University of Michigan, USA, Report UMICH 014571-43-I, March 1982.
104. Iwai, Y.; Okada, T.; Hammit, F. G. *Wear* **1983**, 88(3), 181–191.
105. Eisensiliziumguss. Werkschrift der Rheinhütte, Wiesbaden, 1968.
106. La cavitation par vibrations dans les fontes grises. Fonderie Fondeur d'Aujourd'hui no. 1, 1981, pp 35–37.
107. Okada, T.; Iwai, Y.; Yamamoto, A. *Wear* **1983**, 88(2), 167–179.
108. Tomlinson, W. J.; Talks, M. G. *Tribol. Int.* **1991**, 24(2), 67–75.
109. Berger, J.; Phol, M.; Sitnik, L. *Prakt. Metallograp.* **1986**, 23, 513–527.
110. La cavitation par vibrations dans les fontes grises. Fonderie Fondeur d'Aujourd'hui no. 1, 1981, pp 35–37.
111. Lopez Vazquez, L. B. *Colada* **1979**, 231–241.
112. Lopez Vasquez, L. B. Cavitation vibratoire dans les pièces en fonte. Fonderie Fondeur d'Aujourd'hui no. 1, January, 1981, pp 35–37.
113. Zhou, Y. K. L.; He, J. G.; Hammit, F. G. *Wear* **1982**, 76(3), 329–336.
114. Tomlinson, W. J.; Brandsen, A. S. *Surf. Eng.* **1988**, 4(4), 303–308.

115. Zhou, Y. K. L.; He, J. G.; Hammit, F. G. *Wear*. **1982**, 76(3), 329–336.
116. Tomlinson, W. J.; Brandsen, A. S. *Surf. Eng.* **1988**, 4(4), 303–308.
117. Koutny, A.; Nakladal, V.; Vogel, M. *Strojir.* **1982**, 32(11), 599–604.
118. Fairhurst, W.; Rohrig, K. *Foundry Trade J.* **1984**, 685–698.
119. Sawamoto, A.; Usami, T.; Ogi, K.; Matsuda, K. *Imono*. **1984**, 56, 597–601.
120. Murakami, N.; Kobayashi, T. *Owadano Imono*. **1986**, 58(7), 275–280.
121. Rajagopal, V.; Iwasaki, I. *Corrosion* **1992**, 48(2), 132–139.
122. Chakraborty, I.; Basak, A.; Chatterjee, U. K. *Wear* **1991**, 143, 203–220.
123. Vasil'ev, V. Y.; Edneral, N. V. *Zashchita Metallov*. **1982**, 18(3), 450–453.
124. Chen, C. H.; Alstetter, C. J.; Rigsbee, J. M. *Metallurg. Trans.* **1984**, 15A, 719–728.
125. Internal document Cavitation-érosion des fontes, 1985.
126. Shalaby, H. M.; Attari, S.; Riad, W. T.; Gouda, V. K. *Corrosion* **1992**, 48(3), 206–217.
127. Chakrabarty, I.; Basak, A. *Transact. AFS* **1990**, 98, 707–716.
128. Bevan, J. E. Climax Molybdenum Co, Report L-194-38, March 1974.
129. Komatsu, Y.; Sugimoto, S. *Imono*. **1978**, 50(12), 727–732.
130. Tomlinson, W. J.; Brandsen, A. S. *Surf. Eng.* **1988**, 4(4), 303–308.
131. Kurof, O. V.; Abramyan, E. S. *Fizko-Khimicheskaya Mekhanika Materialov*. **1973**, 9(2), 104.
132. CENTRE d'information du NICKEL. Fontes austénitiques au nickel, Ni-Resist, 1965.
133. Thouvenin, D. *Revue Française de Mécanique* **1990**, 1, 33–38.
134. Rabald, E. *Corrosion Guide*; Elsevier: Amsterdam, 1968.
135. Giessen für die Chemie. VDI-Düsseldorf.
136. Dugniolle, E.; Guillaume, M. La corrosion des chaudières et des cheminées métalliques par les halogènes PROCLIM, Tome 24, no. 7, December, 1993, pp 403–409.

## 3.03 Corrosion of Iron Nickel Alloys and Maraging Steel

**G. N. Flint**

Nickel Development Institute

**J. W. Oldfield**

Cortest Laboratories Ltd, Sheffield, UK

**D. P. Dautovich**

International Nickel Company

This article is a revision of the Third Edition articles 3.4 and 3.5 by D. P. Dautovich, G. N. Flint and J. W. Oldfield, volume 1, pp 3:78–3:100, © 2010 Elsevier B.V.

3.03.1	Introduction	1790
3.03.2	Iron–Nickel Alloys	1790
3.03.2.1	Electrochemistry	1790
3.03.2.2	Atmospheric Corrosion	1790
3.03.2.3	Corrosion in Natural Environments	1791
3.03.2.3.1	Seawater	1791
3.03.2.3.2	Freshwater	1791
3.03.2.4	Corrosion in Industrial Environments	1792
3.03.2.4.1	Acids	1792
3.03.2.4.2	Salt solutions	1792
3.03.2.4.3	Stress corrosion	1793
3.03.2.4.4	Galvanic corrosion	1793
3.03.3	Maraging Steels	1793
3.03.3.1	Composition	1793
3.03.3.2	Structural Features	1794
3.03.3.3	Physical and Mechanical Properties	1794
3.03.3.4	Fabrication	1794
3.03.3.5	Corrosion of Maraging Steels	1795
3.03.3.5.1	Natural environments	1795
3.03.3.5.2	Industrial environments	1795
3.03.3.6	Stress Corrosion Cracking	1796
3.03.3.6.1	Mechanisms	1796
3.03.3.6.2	Testing for SCC	1797
3.03.3.6.3	Cracking resistance in smooth materials	1798
3.03.3.6.4	Critical stress intensity factor	1798
3.03.3.6.5	Effect of metallurgical variables on SCC	1799
3.03.3.7	High Temperature Corrosion	1800
3.03.3.8	Applications	1800
References		1800

### Glossary

**Aging** A heat treatment process whereby an alloy, that has been previously quenched in order to retain alloying additions in solid solution, is reheated into a temperature range in which the rate of solid state diffusion is sufficient to permit the precipitation of strengthening second phase particles.

**Maraging steel** An ultrahigh strength low-carbon iron–nickel alloy that is strengthened by the precipitation of second phase intermetallic compounds rather than carbides.

**U-bend** A form of corrosion test specimen that is prepared in the shape of a ‘U’ and commonly used to determine the resistance of a material to SCC.

## Abbreviations

**AISI** American Iron and Steel Industry

## Symbols

$a_{cr}$  Critical crack length for propagation of stress corrosion crack

$K_{ISCC}$  Critical stress intensity threshold for the onset of stress corrosion cracking

### 3.03.1 Introduction

Alloys of iron with nickel have a number of important applications. The first class are of interest due to their unique magnetic characteristics and their abnormally low thermal expansion coefficients in the compositional region of Fe–36%Ni. Although not specifically used as corrosion-resistant materials, their high resistance to attack from many common environments is of benefit in their specialized applications. The second important class, ‘maraging steels,’ are ultra-high strength low-carbon iron–nickel alloys that derive their outstanding mechanical properties from the precipitation of second phase intermetallic compounds rather than carbides.

### 3.03.2 Iron–Nickel Alloys

#### 3.03.2.1 Electrochemistry

The potentiodynamic polarization curves of Beauchamp, [Figure 1](#), demonstrate the effect of increasing nickel content on the anodic behavior of iron–nickel alloys in 0.5 M H<sub>2</sub>SO<sub>4</sub>. The maximum current in the active region is reduced and the potentials moved to more noble values; the current in the passive region is increased and some evidence of secondary passivity appears. The greater nobility with increasing nickel content in the active region is of importance in acid environments where hydrogen evolution is the major cathodic reaction, and results in significantly lower rates of corrosion. In neutral environments, the protection provided by a layer of insoluble corrosion products is of greater significance.

#### 3.03.2.2 Atmospheric Corrosion

The addition of small amounts of nickel to iron improves its resistance to corrosion in industrial

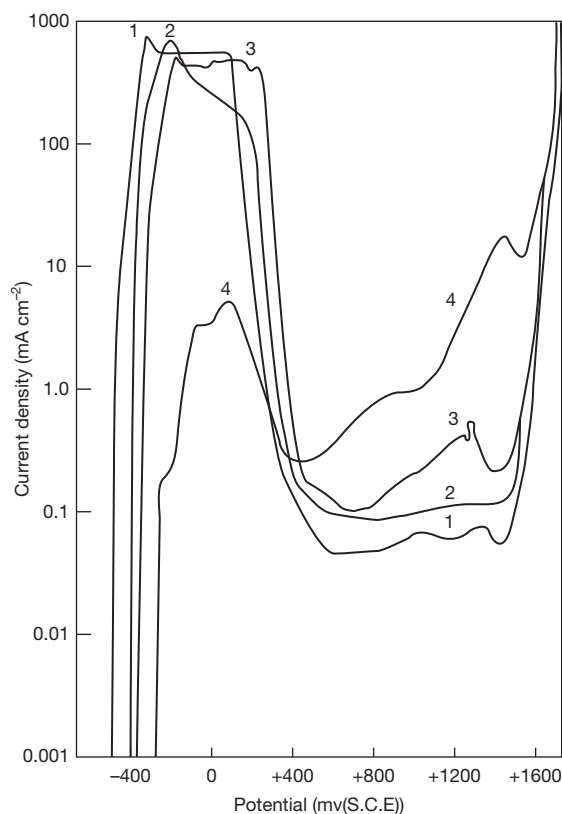


**Figure 1** Effect of nickel on the anodic behavior of iron alloys in 1 M H<sub>2</sub>SO<sub>4</sub> at 25 °C. Curve 1 – Fe; Curve 2 – Fe–10Ni; Curve 3 – Fe–36Ni; Curve 4 – Ni. Reproduced from Beauchamp, R. L. Dissertation, Ohio State University, 1966; Figure 27.

atmospheres due to the formation of a protective layer of corrosion products. Larger additions of nickel, for example, 36% or 42%, are not all that beneficial with respect to overall corrosion, since the rust formed is powdery, loose, and nonprotective, leading to a linear rate of attack as measured by weight loss. [Figure 2](#) of Pettibone<sup>2</sup> illustrates the results obtained.

With respect to resistance to pitting corrosion, there is an increasing advantage to be obtained by increasing the nickel content up to 50%. There is little distinction between the Fe–50Ni alloy and pure nickel. Data on the corrosion of Fe–36Ni alloy at an industrial site in the United States are reported by La Que and Copson<sup>3</sup> and at a European site by Evans.<sup>4</sup> In marine atmospheres, the overall rates of corrosion are reduced progressively with increase in nickel content up to 35%, but with small improvement thereafter. The rates of corrosion at various sites, reported by Friend,<sup>5</sup> show the superiority of Fe–36Ni over mild steel with respect to both average and localized corrosion ([Table 1](#)).



### 3.03.2.3 Corrosion in Natural Environments

#### 3.03.2.3.1 Seawater

The average rates of corrosion of Fe–36Ni alloy exposed to alternate immersion in seawater are appreciably greater than those that occur when the

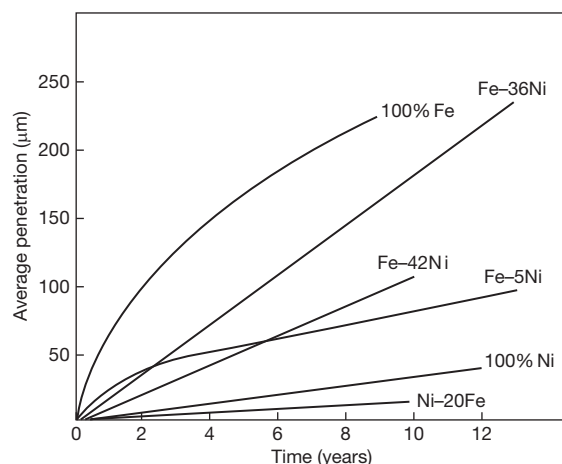


**Figure 2** Resistance of nickel–iron alloys to corrosion by an industrial atmosphere in Bayonne NJ, USA. Reproduced from La Que, F. L.; Copson, H. R., Ed. *Corrosion Resistance of Metals and Alloys*, 2nd ed.; Reinhold Publishing Corporation/Van Nostrand Reinhold Ltd: New York/London, 1963; p 458.

alloy is exposed to marine atmospheres. Although the rates of corrosion are significantly below those observed for mild steel (Table 2), the superiority over mild steel is not all that great with respect to pitting attack.

Nickel–iron alloys fully immersed in seawater may suffer localized corrosion, which can be severe under conditions where oxygen is constantly renewed at the surface and the formation of protective corrosion products is hindered, for example, in fully-aerated flowing seawater. In quieter, less oxygenated conditions, average corrosion rates of Fe–36Ni are low and well below those for mild steel, as exemplified in the data given in Table 3. However, the resistance to localized attack is not improved to the same extent.

#### 3.03.2.3.2 Freshwater

Nickel–iron alloys suffer significantly less corrosion than mild steel when exposed to a soft, freshwater, but Friend<sup>5</sup> found that the resistance to pitting is only slightly greater. For example, the average corrosion rate for mild steel after 15 years' exposure was  $0.94 \text{ g m}^{-2} \text{ day}^{-1}$  as against  $0.07 \text{ g m}^{-2} \text{ day}^{-1}$  for Fe–36Ni. On the other hand, the maximum pit depths were similar, 2.2 and 2.0 mm for mild steel and Fe–36Ni respectively.

**Table 1** Resistance of Fe–36Ni and mild steel to corrosion in marine atmospheres<sup>5</sup>

Location	Corrosion after exposure for 15 years			
	Average ( $\text{g m}^{-2} \text{ day}^{-1}$ )		Localized (max. pit depth, mm)	
	Fe–36Ni	Mild steel	Fe–36Ni	Mild steel
Colombo, Ceylon	0.08	5.5	0	–
Auckland, New Zealand	0.02	1.5	0	2.43
Halifax, Nova Scotia	0.03	0.65	0.1	1.64
Plymouth, England	0.08	3.5	0.19	1.09

**Table 2** Resistance of Fe–36Ni and mild steel to corrosion during alternate immersion in sea-water<sup>5</sup>

Location	Corrosion after exposure for 15 years			
	Average ( $\text{g m}^{-2} \text{ day}^{-1}$ )		Localized (max. pit depth, mm)	
	Fe–36Ni	Mild steel	Fe–36Ni	Mild steel
Colombo, Ceylon	0.64	3.4	1.0	2.55
Auckland, New Zealand	0.09	0.32	0.24	0.36
Halifax, Nova Scotia	0.24	1.5	2.59	2.15
Plymouth, England	0.36	1.4	0.25	1.58

### 3.03.2.4 Corrosion in Industrial Environments

#### 3.03.2.4.1 Acids

Much of the information available on the resistance of nickel-iron alloys to corrosion by mineral acids is summarized by Marsh.<sup>6</sup> In general, corrosion rates decrease sharply as the nickel content is increased from 0 to 30–40%, with little further improvement above this level. The value of the nickel addition is most pronounced in conditions where hydrogen evolution is the major cathodic reaction, that is, under conditions of low aeration and agitation. Results reported by Hatfield<sup>7,8</sup> show that the rates of attack of Fe–25Ni alloy in sulfuric and hydrochloric acid solutions, although much lower than those of mild steel, are still appreciable (Table 4). In solutions of nitric acid, nickel-iron alloys show very high rates of corrosion.

Bourelrier *et al.*<sup>9</sup> and Raicheff *et al.*<sup>10</sup> investigated the inhibitive effect of chloride ions on corrosion in sulfuric acid. The inhibition efficiency was found to depend on the alloy composition, alloy surface, and chloride concentration. The more aggressive the environment, the greater the inhibition efficiency. Yagupol'skaya *et al.*<sup>11</sup> studied the effect of iodine

additions to sulfuric acid on the corrosion resistance of Ni and Ni–Fe alloys. Again there was an inhibitive effect caused by the halide ion. Uto *et al.*<sup>12</sup> studied Ni–Fe–Si alloys, adding Si to improve the castability of the simple Ni–Fe materials. They found that alloys containing 0–70% Fe and 5–10% Si, with the balance being Ni, are usable in 0–85% sulfuric acid at temperatures of up to 80 °C and in 0–10% hydrochloric acid at temperatures of up to 40 °C.

Cid *et al.*<sup>23</sup> studied the corrosion resistance of Ni, 5% Fe–Ni and 10% Fe–Ni alloys in the transpassive region in sulfuric acid. For a given acid concentration, the addition of iron reduced the corrosion rate. It was concluded that the addition of small percentages of Fe was doubly beneficial, decreasing both general and intergranular corrosion.

#### 3.03.2.4.2 Salt solutions

Nickel-iron alloys are more resistant than iron to attack by solutions of various salts. In alternate immersion tests in 5% sodium chloride solution, Fink and De Croly<sup>13</sup> determined values of 2.8, 0.25, and 0.5 g m<sup>−2</sup> day<sup>−1</sup> for alloys containing 37%, 80%, and 100% nickel as against 46 g m<sup>−2</sup> day<sup>−1</sup> for iron. Corrosion rates of about 0.4 g m<sup>−2</sup> day<sup>−1</sup> are reported by Hatfield<sup>7</sup> for Fe–30Ni alloy exposed to solutions containing 5% magnesium

**Table 3** Resistance of Fe–36Ni alloy and mild steel to corrosion when fully immersed in seawater<sup>5</sup>

Location	Corrosion after exposure for 15 years			
	Average (g m <sup>−2</sup> day <sup>−1</sup> )		Localized (max. pit depth, mm)	
	Fe–36Ni	Mild steel	Fe–36Ni	Mild steel
Colombo, Ceylon	0.8	2.0	2.5	6.5
Auckland, New Zealand	0.5	2.0	1.08	2.59
Halifax, Nova Scotia	1.3	2.2	3.49	1.23
Plymouth, England	0.8	1.5	1.82	2.75

**Table 4** Resistance of Fe–25Ni and carbon steel to corrosion by sulfuric and hydrochloric acids

Alloy	Corrosion rate (mm year <sup>−1</sup> )					
	5% H <sub>2</sub> SO <sub>4</sub>		25% H <sub>2</sub> SO <sub>4</sub>		50% H <sub>2</sub> SO <sub>4</sub>	
	15 °C	40 °C	15 °C	40 °C	15 °C	40 °C
Carbon steel	62	183	93	378	0.95	2.8
Fe–25Ni	0.45	1.4	0.45	1.8	0.9	1.8
	5% HCl			25% HCl		
	15 °C	40 °C	60 °C	15 °C	40 °C	60 °C
Carbon steel	23	40	41	63	188	185
Fe–25Ni	0.45	2.3	5.4	0.9	0.9	19

sulfate, 10% magnesium chloride, and 10% sodium sulfate; the same alloy corroded at a rate of about  $1.2 \text{ g m}^{-2} \text{ day}^{-1}$  in 5% ammonium chloride.

In a study of the corrosion of 10 binary nickel–iron alloys in 3% sodium chloride solution, Schwerdtfeger<sup>14</sup> found the average corrosion rate to decrease from  $1.4\text{--}1.6 \text{ g m}^{-2} \text{ day}^{-1}$  for alloys containing 0–16% nickel alloy to  $0.1 \text{ g m}^{-2} \text{ day}^{-1}$  for a 57% nickel–iron alloy. There was little further reduction in the rate of weight loss for the higher-nickel alloys. However, the alloys showed an increasing tendency to suffer pitting and crevice corrosion with increasing nickel content.

### 3.03.2.4.3 Stress corrosion

In tests lasting for 14 days, Copson<sup>15</sup> found that the susceptibility of steel to stress corrosion cracking (SCC) in hot caustic soda solutions increased with increase in the nickel content up to at least 8.5%. Alloys containing 28% and more of nickel did not fail in this period. In boiling 42% magnesium chloride, the 9% nickel–iron alloy was the most susceptible of those tested to cracking (Table 5) with alloys containing 28 and 42% nickel not failing within 7 days. Couper<sup>16</sup> reports cracking of an Fe–36Ni alloy in 10–55 days in this medium. Radd *et al.*<sup>17</sup> have noted cracking of Fe–36Ni alloys at ambient temperatures in an unspecified environment, but this possibly may have been residual traces of acid copper chloride etching solution.

Marquez *et al.*<sup>18</sup> studied the effect of cold rolling on the resistance of Ni–Fe alloys to hydrogen cracking. It was found that low-carbon, 10–19% Ni–Fe alloys become considerably more resistant to hydrogen cracking after severe cold rolling. The observed resistance decreased with increasing carbon content and the improvement was directional, the optimum effect applying to specimens stressed in the longitudinal direction.

### 3.03.2.4.4 Galvanic corrosion

Galvanic corrosion of nickel–iron alloys may be of significance in welding operations. Ni–45Fe alloys are used as filler materials in the welding of cast irons but the favorable area relationship of weld metal to base plate mitigates the effect of the more noble characteristics of the nickel–iron alloy. Thus, their application in corrosive environments is rarely of concern.

Of more serious practical significance is iron contamination of nickel-clad steel welds. Tables 6 and 7 show the increase in corrosion of various nickel–iron alloys that may occur when coupled to nickel in calcium chloride or sodium hydroxide solutions. It is evident that in the calcium chloride solution, 5% iron contamination of weld metal can be tolerated, while in the sodium hydroxide solution bimetallic corrosion will not become significant until contamination exceeds 20%.

## 3.03.3 Maraging Steels

### 3.03.3.1 Composition

Notwithstanding their name, maraging steels are a class of high-strength iron alloys of very low carbon content. Strengthening is achieved by the use of substitutional alloying additions that result in the precipitation of secondary phases during age hardening of a quenched martensitic iron–nickel matrix. The term maraging was thus coined from the words ‘martensite’ and ‘age hardening.’

The development of maraging steels began in the late 1950s, on steels containing 20 and 25% Ni using a combination of aluminum, titanium, and niobium as age-hardening elements.<sup>19</sup> Later work<sup>20</sup> revealed the important synergistic age-hardening effect of cobalt plus molybdenum and led to the development of the 18% Ni maraging steels. Using titanium as a

**Table 5** Resistance of iron–nickel alloys to SCC in boiling 42% magnesium chloride

Composition of alloy					Hardness	Time to cracking (days)	Comments
Ni	C	Mn	Si	Fe			
Nil	0.19	1.65	0.20	Bal.	89 Rb	No cracking after 11 days	
2.02	0.19	0.46	0.18	Bal.	77 Rb	7	Few shallow cracks
4.96	0.15	0.51	Nil	Bal.	96 Rb	<3	Profuse deep cracks
8.67	0.10	0.76	0.23	Bal.	24 Rc	<3	Cracked in two
27.88	0.03	0.18	0.06	Bal.	81 Rb	No cracking after 7 days	
41.79	0.02	0.18	0.08	Bal.	77 Rb	No cracking after 7 days	
99.41	0.10	0.24	0.02	0.13	20 Rc	No cracking after 7 days	

Source: Rhodin, T. H. Ed. *Physical Metallurgy of Stress Corrosion Fracture*; Interscience: New York, 1959; pp 259–262.

supplementary hardening element, and with appropriate balancing of cobalt and molybdenum, nominal yield strengths in the range of 1370–2400 MPa can readily be achieved. **Table 8** lists the nominal composition of the 18% Ni maraging steels. Other types of maraging steel include an alloy (17% Ni) developed for use as a casting,<sup>21</sup> and a 12Ni–5Cr–3Mo alloy. Stainless-type alloys have also been developed<sup>22</sup> but are outside the scope of this section.

During the 1970s, the price of cobalt increased enormously and then declined. These price fluctuations plus the concern about the future supply of cobalt caused serious declines in the use of the cobalt-containing grades of maraging steel. In response to this market change, a new cobalt-free grade of maraging steel was developed.<sup>23</sup> The composition of this steel is given as 18.5Ni, 3.0Mo, 1.4Ti, and 0.1Al. Its strength is 1720 MPa and its mechanical properties approximate those of the 18% Ni 240 maraging steel. Discussion in this chapter is restricted to the 18% Ni maraging steels.

**Table 6** Bimetallic corrosion between nickel and nickel–iron alloys in 16% calcium chloride solution<sup>2</sup>

Alloy	Corrosion rate <sup>a</sup> (mm year <sup>-1</sup> )	
	Coupled	Uncoupled
100 Ni	–	0.02
Ni–5Fe	0.045	0.045
Ni–10Fe	0.7	0.055
Ni–20Fe	1.0	0.044

<sup>a</sup>Room temperature test of duration 120 days, solution agitated. Cathode:anode area = 100:1.

### 3.03.3.2 Structural Features

On cooling to room temperature after annealing, maraging steels transform completely to martensite. The as-annealed structure consists of packets of parallel lath-like martensite platelets arranged within a network of prior austenite grain boundaries. The platelets have a high dislocation density but are not twinned.

On heat treating at 485 °C, a very rapid age-hardening reaction takes place and greatly strengthens the material. Although the nature of the precipitates formed is still uncertain, the consensus of opinion is that ageing for several hours at 485 °C results in a Ni<sub>3</sub>Mo phase, while longer times produce the Fe<sub>2</sub>Mo phase. There may also be a titanium precipitate, η-Ni<sub>3</sub>Ti or Ni<sub>3</sub>(Mo,Ti)<sub>3</sub>. Ageing at higher temperatures or longer times results in some reversion to austenite, which may be stable at room temperature (depending on time and temperature of ageing), and to a lower strength.

### 3.03.3.3 Physical and Mechanical Properties

Summaries of the physical and mechanical properties of the 18% Ni maraging steels are given in **Tables 9** and **10**. The mechanical properties are highlighted by good ductility, toughness, and a lack of notch sensitivity. The plane strain fracture toughness of maraging steels is superior to other alloys at comparable strength levels (**Table 11**).

### 3.03.3.4 Fabrication

Maraging steels have been produced by both air and vacuum melting. Small amounts of impurities can

**Table 7** Bimetallic corrosion between nickel–iron alloys in sodium hydroxide<sup>2</sup>

Galvanic couple	Corrosion rate <sup>a</sup> (mm year <sup>-1</sup> )				
	23% NaOH		50% NaOH	75% NaOH	
	Coupled	Uncoupled	Coupled	Coupled	Uncoupled
{ Ni–5Fe	0.04	0.035	0.06	0.0250	0.02
{ Nickel	0.015	0.01	0.02	0.04	0.04
{ Ni–10Fe	0.07	0.03	0.48	0.38	0.035
{ Nickel	0.01	0.01	0.015	0.02	0.04
{ Ni–20Fe	0.095		0.04	0.05	0.015
{ Nickel	0.015		0.01	0.03	0.04
{ Ni–30Fe	0.04	–	0.2	0.31	–
{ Nickel	0.02	0.01	0.01	0.02	0.04
{ Ni–40Fe	0.04	–	0.21	0.34	–
{ Nickel	0.02	0.01	0.01	0.02	0.04

<sup>a</sup>Area ratio Ni:Ni–Fe = 10:1.

**Table 8** Nominal composition of 18% Ni maraging steels<sup>24</sup>

Maraging steel type	Nominal composition (%)					Nominal yield strength (MN m <sup>-2</sup> )
	Ni	Co	Mo	Ti	Fe	
18% Ni 200	18	8.5	3	0.2	Balance	1380
18% Ni 250	18	8	5	0.4	Balance	1720
18% Ni 300	18	9	5	0.6	Balance	2050
18% Ni 350	17.5	12.5	3.75	1.7	Balance	2390
Cast alloy	17	10	4.6	0.3	Balance	1580

**Table 9** Summary of physical properties for the 18% Ni 200 to 18% Ni 350 alloys

Density	8.0–8.1 g cm <sup>-3</sup>
Crystal structure	Martensite (body-centered cubic); austenite (face-centered cubic)
Lattice parameter	Martensite 2.856–2.862 Å at room temperature; austenite (retained) 3.58 Å
Thermal conductivity	19.68–20.93 kW m <sup>-2</sup> °C (20–100 °C)
Electrical resistivity	60–70 μΩ cm when solution annealed at 815 °C; 35–50 μΩ cm when maraged at 485 °C for 3 h
Melting temperature	1430–1445 °C
Transformation temperature	M 145–200 °C; M 77–145 °C; A 445 °C
Nominal length change	–0.06% to –0.10% during maraging

decrease toughness significantly. Sulfur in particular is detrimental and should be kept as low as possible. Silicon and manganese also have a detrimental effect on toughness and should be maintained below a combined level of 0.20%. Such elements as C, P, Bi, O, N, and H should be kept to the lowest levels practicable.

The maraging steels are readily hot worked by conventional rolling and forging operations. A preliminary homogenization at 1210–1260 °C is normally used prior to hot working at that temperature. During subsequent hot working, extended times at, or slow cooling through, temperatures from 760 to 1100 °C should be avoided, since they produce embrittlement.<sup>25</sup> Maraging steels can be cold worked up to 85% before requiring intermediate annealing (because of low work-hardening characteristics) but are usually annealed after smaller reductions.

Heat treatments are relatively simple and normally consist of annealing for 1 h at 815 °C followed by ageing for 3 h at 485 °C. Recently, double annealing treatments have grown in favor. Machining or fabrication is easily performed in the as-annealed condition. Subsequent age hardening generally introduces small and predictable dimensional changes.

### 3.03.3.5 Corrosion of Maraging Steels

#### 3.03.3.5.1 Natural environments

In atmospheric exposure, 18% Ni maraging steel corrodes in a uniform manner<sup>22</sup> and becomes completely rust covered. Pit depths tend to be less deep than for low-alloy high-strength steels.<sup>26</sup> Atmospheric corrosion rates<sup>27</sup> in industrial (Bayonne, NJ) and marine (Kure Beach, NC) atmospheres are compared with those for low-alloy steel in **Figures 3** and **4** respectively. The corrosion rates drop substantially after the first year or two, and in all cases, the rates for maraging steel are about half the corrosion rate for HY80 and AISI 4340 steels.

The corrosion rates for both maraging steel and the low-alloy steels in seawater are similar initially, but from about 1 year onwards, the maraging steels tend to corrode more slowly as indicated in **Figure 5**. The corrosion rates for both low alloy and maraging steel increase with water velocity.<sup>5</sup> During seawater exposure, the initial attack was confined to local anodic areas, whereas other areas (cathodic) remained almost free from attack; the latter were covered with a calcareous deposit typical of cathodic areas in seawater exposure. In time, the anodic rust areas covered the entire surface.<sup>6</sup>

Polarization tests<sup>27</sup> indicate that maraging steel does not exhibit passive behavior in 3% NaCl, and that the polarization curves are unaffected by changes in heat treatment.

#### 3.03.3.5.2 Industrial environments

The corrosion rates of maraging steels in acid solutions such as sulfuric, hydrochloric, formic, and stearic acids are substantial, although lower than those of the low-alloy high-strength steels.<sup>28</sup> Polarization studies<sup>29</sup> indicate that maraging steels exhibit active-passive behavior in 1 and 0.1 M sulfuric acid. The corrosion potential, critical current density, primary passivation potential, and passive current density are all affected by variations in ageing treatment.

**Table 10** Summary of nominal mechanical properties for the 18% Ni maraging alloys

Property	18% Ni 200	18% Ni 250	18% Ni 300	18% Ni 350
Yield strength –0.2% offset ( $\text{MN m}^{-2}$ )	1310–1550	1650–1820	1780–2060	2270–2480
Ultimate tensile strength ( $\text{MN m}^{-2}$ )	1340–1580	1680–1860	1820–2100	2300–2510
Elongation in 25.4 mm (1 in.), (%)	11–15	10–12	7–11	6–10
Reduction in area (%)	35–67	35–60	30–50	25–45
Modulus of elasticity $E$ ( $\text{kN m}^{-2}$ )	$18.0 \times 10^7$	$18.5 \times 10^7$	$18.9 \times 10^7$	$19.3 \times 10^7$
Hardness (Rockwell C)	44–48	48–50	51–55	56–59
Impact Charpy V-notch (J)	35–68	24–45	16–26	7–14
Notch tensile				
0.0128 m bar $K_1 = 10$ ( $\text{MN m}^{-2}$ )	2390	2350–2510	2900–3100	–
0.00762 m bar $K_1 = 10$ ( $\text{MN m}^{-2}$ )	–	2560–2660	–	1360–1490
Fracture toughness ( $K_{Ic}$ ) ( $\text{MN m}^{-2}$ )	101–176	98–165	88–143	44–82
Endurance limit ( $\text{MN m}^{-2}$ )				
Smooth bar $10^8$ cycles	620–795	620–760	760–900	690
Notched bar $10^8$ cycles ( $K_t = 2.2$ )	275–345	275–380	275–415	–
( $K_t = 2.8$ )	–	–	–	352

In all cases treatment was for 1 h at 815 °C plus 3 h at 485 °C.

**Table 11** Comparison of toughness of maraging steels and other high strength alloys

Alloy	Yield strength ( $\text{MN m}^{-2}$ )	$K_{Ic}$ ( $\text{MN m}^{-2} \sqrt{\text{m}}$ )
18% Ni 200	1380	110–176
18% Ni 250	1720	98–165
18% Ni 300	1930	88–143
D6 AC	1380	88–99
H–11	1790	66–71
AISI 4340	1790	61–66
AMS 6430	1510	61–71
Ti–16V–2.5Al	1170	49–55
Aluminum	415–485	39–66
7075.T6		

Source:  $K_{Ic}$  is the plane strain fracture toughness (see Section 8.9). Bourelle, F., Vu Quang, K. In Proceedings of the Conference, 10th International Congress Metallic Corrosion, Madras, India, November 1987, 1988; p 2813.

Data Bulletin on 18% Ni Maraging Steels, The International Nickel Company, Inc. 1964.

The critical and passive current densities increase as the structure is varied from fully annealed to fully aged. The normal heat treatment produces critical and passive current densities of 0.4 and 0.2  $\text{mA cm}^{-2}$  respectively ( $0.1 \text{ mA cm}^{-2} \sim 1.2 \text{ mm year}^{-1}$ ).<sup>30</sup>

### 3.03.3.6 Stress Corrosion Cracking

#### 3.03.3.6.1 Mechanisms

The 18% Ni maraging steels do not display passivity and normally undergo uniform surface attack.

Of more serious consequence, however, for all high strength steels, is the degree of susceptibility to SCC. For high-strength steels in general, the stress corrosion process in aqueous media is characterized by delayed failure, which consists of an incubation period followed by slow, and at times, intermittent crack growth. Failure can occur on loading to some fraction of the yield stress or through the action of residual stresses, often in environments as mild as humid air.<sup>31</sup> The degree of susceptibility depends on the mode of loading and is highest in cases of plane strain loading (triaxial stresses), with tensile loading and plane stress bending, in that order, representing less severe loading conditions<sup>32</sup> (tensile stresses of course are present in all these modes of loading). In general, susceptibility to SCC increases with increasing yield strength. Different alloy types, however, vary in their degree of resistance, and at comparable strength levels, maraging steels compare favorably in cracking resistance with other high-strength steels.

For a variety of steels, including maraging steels, it was found that under freely corroding conditions, the pH of the solution near the crack tip was about 3.8 for the materials studied.<sup>33</sup> Furthermore, potential measurements indicated that thermodynamic conditions were satisfied for hydrogen ion reduction. Further potential–pH measurements were made on AISI 4340 steel exposed to 0.6 N NaCl solutions of different pH and polarized to potentials both negative and positive with respect to the corrosion potential.<sup>34</sup> It was found that the pH of the solution in the crack was determined



solely by electrochemical reactions at the crack tip irrespective of starting pH. It was also apparent that, regardless of the impressed potential, the electrochemical conditions in the crack satisfied the thermodynamic requirements for the production of hydrogen. These results indicate that it is not necessary to invoke an active path mechanism and that hydrogen is available even during anodic polarization of AISI 4340 steel.

Activation energy measurements for SCC of H-11 steel and AISI 4340 in water and moist air are

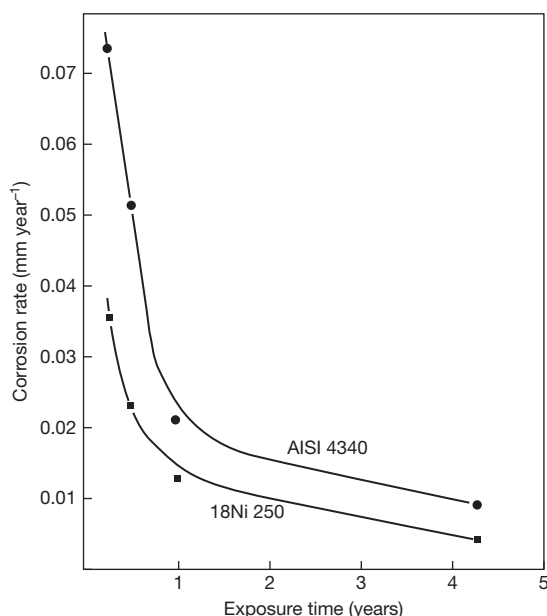


**Figure 3** Corrosion rates of maraging and low alloy steels in an industrial atmosphere at Bayonne NJ, USA. Reproduced from Kenyon, N.; Kirk, W. W.; van Rooyen, D. *Corrosion* **1971**, 27, 390.

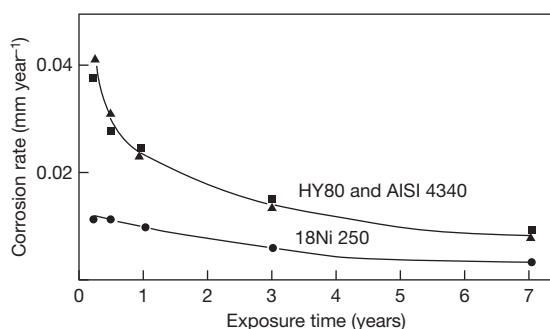


**Figure 4** Corrosion rates of maraging and low alloy steels 244 m from the sea at Kure Beach NC, USA. Reproduced from Kenyon, N.; Kirk, W. W.; van Rooyen, D. *Corrosion* **1971**, 27, 390.

similar<sup>34,35</sup> and suggest that the cracking rate in these alloys is controlled by the diffusion of hydrogen, since these are in close agreement with the value for the diffusion of hydrogen through AISI 4340 membranes.<sup>36</sup> There is little question that at strongly negative potentials, cracking occurs by hydrogen embrittlement. For all other cases, there does not appear to be a strong basis for favoring one mechanism over the other or to discard the possibility that each mechanism shares in the control of the cracking process. The latter possibility for maraging steel has been supported by a study of cracking response to polarization, fractographic studies, and pH determinations of the corrodent at the tip of the crack.<sup>37</sup> Craig and Parkins<sup>38</sup> have shown good evidence that cracking can proceed by hydrogen embrittlement at more negative potentials, by anodic dissolution at more positive potentials, and possibly by combinations of both mechanisms at intermediate potentials. The effects of precracking or pitting of smooth specimens was also examined. In many instances, the local changes in chemistry of the test solution in the cracks or pits was more important than the stress concentrations at these locations.

### 3.03.3.6.2 Testing for SCC

The stress corrosion resistance of maraging steel has been evaluated both by the use of smooth specimens loaded to some fraction of the yield strength and taking the time to failure as an indication of resistance, and by the fracture mechanics approach,<sup>39</sup> which involves the use of specimens with a preexisting crack. Using the latter approach, it is possible to obtain crack propagation rates at known stress intensity factors ( $K$ ) and to

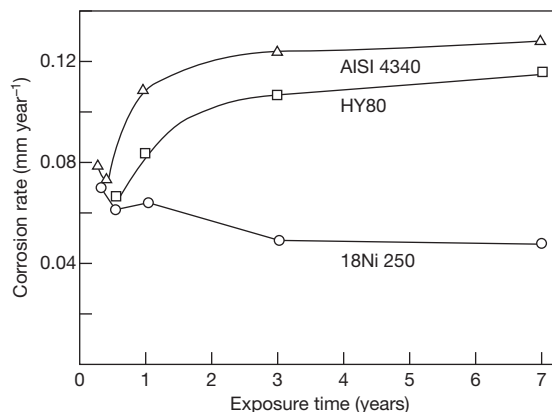


**Figure 5** Corrosion rates of maraging and low alloy steels in seawater flowing at  $0.6 \text{ m s}^{-1}$ . Reproduced from Kenyon, N.; Kirk, W. W.; van Rooyen, D. *Corrosion* **1971**, 27, 390.

determine critical stress intensity factors ( $K_{ISCC}$ ) below which a crack will not propagate.

Any test in which time to failure of smooth specimens is determined is an overall measure of the incubation period to initiate a crack, the ability to resist the propagation of a stress corrosion crack, and the ability to resist final mechanical fracture. Since this test does not indicate the relative merits of an alloy in each individual aspect of the cracking process, it is probably of less benefit to a design engineer. The use of precracked specimens in the fracture mechanics approach follows from the philosophy that structures are likely to contain crack-like defects. The use of precracked specimens promotes a rapid change in the chemistry of the solution at the crack tip and shortens or eliminates the initiation time for crack propagation.

### 3.03.3.6.3 Cracking resistance in smooth materials

Maraging steel in the strength range 1240–1720 MPa tested as U-bends in seawater displayed good resistance, as it did not fracture in periods of up to 2–3 years although there was considerable general corrosion and fouling. However, microcracks were observed after 6 months. Similar behavior<sup>22,26</sup> of U-bend and bent beam specimens can be expected in industrial or marine atmospheres, although general corrosion is less severe. By comparison, AISI 4340 at strength levels of 1660 MPa failed in about 1 week in both seawater and atmospheric tests. Maraging steel of yield strength at or above 2060 MPa was not resistant and failed rapidly. Welds in maraging steel are somewhat less resistant than base plate. U-bend exposure of 1240 MPa strength welds survived for up to 2 years in seawater, while at 1380 MPa, failures occurred in 2–18 months.<sup>28</sup>

It is possible to provide cathodic protection to materials of up to 1720 MPa yield strength, by coupling to mild steel or possibly to zinc.<sup>22,26</sup> However, zinc and metals more active than zinc tend to induce hydrogen embrittlement. Welds up to 1380 MPa may be cathodically protected by zinc, but at impressed potentials of  $-1.25$  V (vs. the standard calomel electrode), both 1240 and 1380 MPa welds fail rapidly due to hydrogen embrittlement.<sup>28</sup> Hence, although tests on smooth specimens indicate that cathodic protection of maraging steel is possible, tests on specimens with preexisting cracks indicate a greater sensitivity to hydrogen embrittlement during cathodic polarization.<sup>28</sup> The use of cathodic protection on actual structures must therefore be applied with caution, and the application of less negative potentials than are

indicated to be feasible in smooth specimen tests is to be recommended if it is assumed that structures contain crack-like defects. Further evidence of the relative resistance of maraging steel is reproduced in Figure 6. Also shown is the beneficial effect in smooth surface tests of cold rolling; shot peening has a similar beneficial effect.<sup>28</sup>

### 3.03.3.6.4 Critical stress intensity factor

It has become common to use  $K_{ISCC}$ , the critical stress intensity factor, as a measure of the resistance of an alloy to SCC. Tests are performed on specimens that are precracked by a fatigue machine and must be of sufficient dimensions to ensure plane strain conditions. Figure 7 presents a summary comparing the  $K_{ISCC}$  values of maraging steel, with values for H-11, AISI 4340, AM 355, AISI410, 17–4 PH, 13–8 Mo PH, D6AC, and 9Ni–4Co–C steels. The data have been taken from a number of sources<sup>28,40–43</sup> and are for exposures in aqueous environments, with and without NaCl. No attempt has been made to distinguish between different environments, since they do not affect the results appreciably.

Plotted points marked W in Figure 7 refer to data for welds; also included are lines of critical crack depth  $a_{cr}$ . The region below a line of specified critical crack depth corresponds to combinations of strength and  $K_{ISCC}$  for which a long crack of the specified depth will propagate when stressed to the yield point, whereas the region above the line corresponds

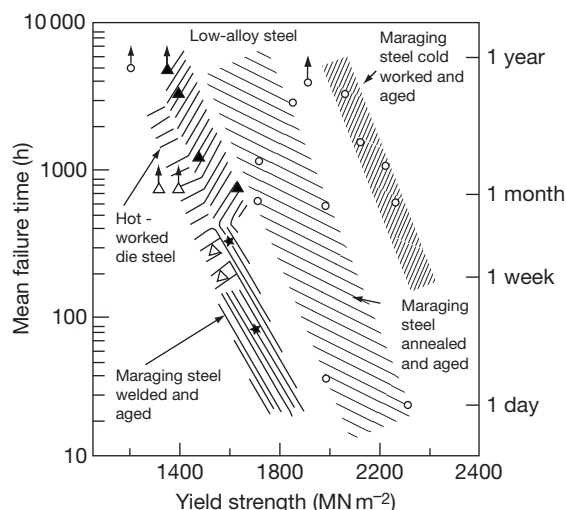


**Figure 6** Bent-beam test results in aerated distilled water. These specimens were exposed to the environment at a stress of 70% of yield. Reproduced from Setterlund, R. B. *Mater. Protect.* **1965**, 4(12), 27.

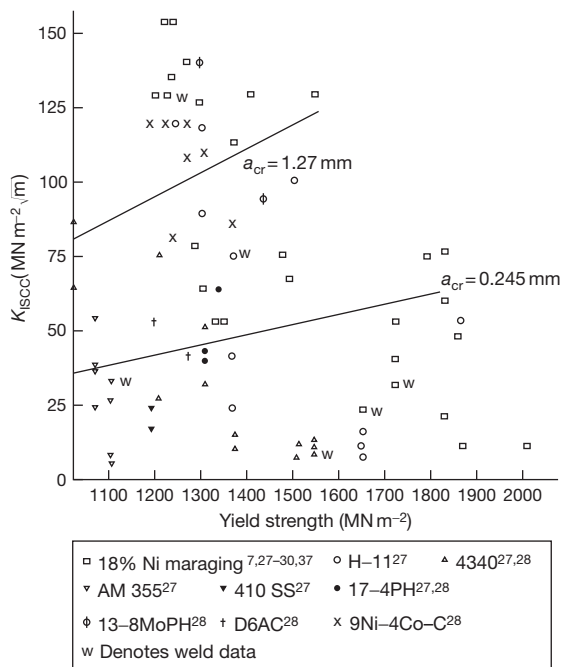


**Figure 7** Comparison of  $K_{ISCC}$  as a function of yield strength of 18% Ni maraging and other high strength steels.

to the strength and  $K_{ISCC}$  combinations for which the crack will not propagate. The critical crack depth (assuming yield point stresses) for cracks the length of which greatly exceeds their depth is given by:

$$a_{cr} = 0.2 \left( \frac{K_{ISCC}}{\sigma_y} \right)^2$$

where  $\sigma_y$  is the yield stress.<sup>44</sup>

In general, it is clear that maraging steels compare favorably with other high-strength steels and offer comparatively high  $K_{ISCC}$  values over a wide range of strength. It is also clear that maraging steels can withstand a greater crack depth without crack propagation.

A further estimation of the corrosion resistance of maraging steel can be obtained from data on the rate of crack propagation. Although the rate of crack propagation has been found to be a function of stress intensity in some alloys, for many alloys and heat treatments, there is a range of stress intensity above  $K_{ISCC}$  and approaching  $K_{IC}$  at which the rate of crack propagation is independent of stress intensity (Table 12).<sup>45</sup> The cracking rate for maraging steel is seen to be slower than for 4340 and D6AC and equivalent to H-11 and HP 9Ni-Co-C steels, at a strain rate of  $10^{-5} \text{ mm s}^{-1}$ . The fact that cracks propagate very slowly in maraging steels has an important consequence related to their stress corrosion testing.

**Table 12** Crack propagation rates for a number of high strength steels

Alloy	Yield strength ( $\text{MN m}^{-2}$ )	Crack velocity ( $\text{mm s}^{-1}$ )
Maraging 250	1570	$1.31 \times 10^{-5}$
Maraging 250	1690	$1.40 \times 10^{-5}$
Maraging 300	1950	$2.75 \times 10^{-4}$
Modified maraging 300 <sup>a</sup>	2180	$1.18 \times 10^{-4}$
Modified maraging 300 <sup>a</sup> (underaged)	1810	$0.72 \times 10^{-3}$
Modified maraging 300 <sup>a</sup> (overaged)	1760	$2.88 \times 10^{-5}$
4340	1430	$1.65 \times 10^{-3}$
D6AC	1540	$1.74 \times 10^{-4}$
H-11	1420	$1.19 \times 10^{-5}$
HP 9-4-25	1330	$2.54 \times 10^{-5}$
HP 9-4-45 (bainitic)	1460	$1.06 \times 10^{-5}$

Source: Carter, C. S. *Met. Trans.* 1970, 1, 1551.

<sup>a</sup>No details on the modification were available.

In determining  $K_{ISCC}$  by dead-weight loaded cantilever beam tests, it has been recommended<sup>46</sup> that maraging steel should withstand 1000 h without failure to ensure that the applied stress intensity is at, or lower than,  $K_{ISCC}$ .

### 3.03.3.6.5 Effect of metallurgical variables on SCC

It is notable that while it is possible to produce maraging steels with consistently uniform mechanical properties, the stress corrosion properties are subject to scatter, as indicated in Figure 7. To a large extent, this scatter is an indication of the greater sensitivity of SCC to metallurgical variables. Although the variation in cracking resistance is not well understood, and the reaction to certain treatments not always consistent, certain observations may be used to indicate guidelines for improved properties. Cracking in maraging steels has generally been observed to be intergranular with isolated cases of transgranular cracking.<sup>26,47,48</sup> Both  $\text{Ti}_2\text{S}$  and  $\text{Ti}(\text{C},\text{N})$  on prior austenite boundaries have been suggested to be related to greater susceptibility. Thus, since prolonged time in the temperature range 760–1100 °C favors the precipitation of  $\text{Ti}_2\text{S}$  and  $\text{Ti}(\text{C},\text{N})$  on prior austenite boundaries, such exposures should be avoided both in processing and in annealing.

Studies of the effect of ageing temperature on cracking behavior have shown rather marked effects. Under-ageing at temperatures of 455 °C or lower was found to increase greatly the rate of crack propagation without affecting the mode of crack propagation

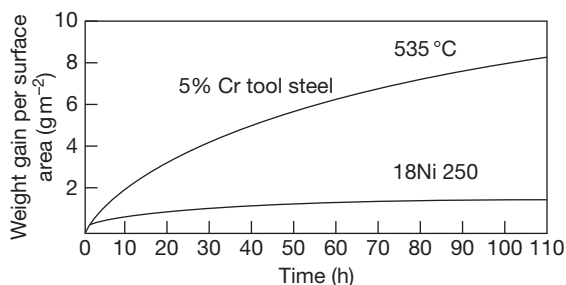


**Figure 8** Oxidation rate at 535 °C of 18Ni250 maraging steel compared with a generally-available tool steel. These tests were performed on 6.35 mm cubes exposed to still air for 5, 25, and 100 h. The weight gain includes the scale formed during heating and cooling. Reproduced from Data Bulletin on 18% Ni Maraging Steels, The International Nickel Company, Inc. 1964.

(intergranular) or  $K_{\text{ISCC}}$ .<sup>45,47,49</sup> However, over-ageing appears to offer slightly slower crack growth rates (Table 12), but it did not significantly improve  $K_{\text{ISCC}}$ .<sup>29</sup> The best combination of properties is obtained with the normal ageing treatment at 485 °C.

Studies on welds showed that cracking resistance as indicated in U-bend tests<sup>28</sup> was substantially increased by a postweld anneal (1 h at 815 °C) prior to the normal ageing treatment. Material aged in the as-welded condition was less resistant. The most significant structural difference resulting from the two heat treatments was a finer dispersion of austenite ribbons in material annealed before ageing.

### 3.03.3.7 High Temperature Corrosion

Little data are available on hot corrosion behavior. Figure 8 indicates maraging steel to have better resistance to air exposure at 535 °C than a 5% Cr tool steel.<sup>24</sup> Metallographic examination indicates that exposure to air at elevated temperatures results in reaction with both oxygen and nitrogen, forming both oxides and titanium carbonitrides. Under some conditions of reduced oxygen partial pressure, selective subsurface oxidation of iron can occur.

### 3.03.3.8 Applications

Maraging steels have found varied uses in the aerospace and aircraft industries. These uses have included rocket motor cases, landing gear components, aircraft forgings and fasteners. Other areas of usage include machine tool and die applications, and extrusion hardware. Marine uses include hydrofoil foil systems and aircraft arrester hooks.

## References

1. Beauchamp, R. L. Dissertation Ohio State University, 1966; Figure 27.
2. La Que, F. L.; Copson, H. R. Eds. *Corrosion Resistance of Metals and Alloys*, 2nd ed.; Reinhold Publishing Corporation/Van Nostrand Reinhold Ltd: New York/London, 1963; p 458.
3. Symposium on Atmospheric Corrosion of Non-Ferrous Metals, American Society for Testing and Materials, 58th Annual Meeting. June 29, 1955, Special Technical Publication No. 175, pp 141–158.
4. Evans, T. E. In 4th International Congress on Corrosion Amsterdam, 1969.
5. Friend, J. N. In 18th Report of the Committee of the Institution of Civil Engineers 1940.
6. Marsh, J. S. *The Alloys of Iron and Nickel: Vol. I Special-Purpose Alloys*; McGraw-Hill: New York, London, 1938; p 495 et seq.
7. Hatfield, W. H. *Engineer* **1922**, 134, 639.
8. Hatfield, W. H. *J. Iron Steel Inst.* **1923**, 108, 103.
9. Bourelle, F.; Vu Quang, K. In Proceedings of the Conference, 10th International Congress Metallic Corrosion, Madras, India, November 1987, 1988; p 2813.
10. Raicheff, R.; Aroyo, M.; Aropadjan, S. *Werkst. Korr.* **1982**, 33, 25.
11. Yagupol'skaya, L. N.; Lavrenko, V. A.; Kozachenko, E. V. *Zasch. Metal.* **1974**, 109, 291.
12. Uto, Y.; Kitajima, H.; Kai, T. *Nippon Kinzoku Gakkaishi* **1963**, 27, 18.
13. Fink, C. G.; De Croly, C. M. *Trans. Am. Electrochem. Soc.* **1929**, 56, 239.
14. Schwerdtfeger, W. J. *J. Res.* **1966**, 70C, 187.
15. Rhodin, T. H. Ed. *Physical Metallurgy of Stress Corrosion Fracture*; Interscience: New York, 1959; pp 259–262.
16. Couper, A. S. *Mater. Product.* **1969**, 8(10), 17.
17. Radd, F. J.; Wolfe, L. H.; Crowder, L. H.; Crowder, L. H. In *The World Petroleum Conference* 1967.
18. Marquez, J. A.; Matshushima, I.; Unlig, H. H. *Corrosion* **1970**, 26, 216.
19. Bieber, C. G. *Met. Prog.* **1960**, 78, 99.
20. Decker, R. F.; Eash, J. T.; Goldman, A. J. *Trans. Quart. ASM* **1962**, 55, 58.
21. Sadowski, E. P.; Koppi, W. A. *Trans. Am. Foundrymen's Soc.* **1967**, 75, 294.
22. Kirk, W. W.; Covert, R. A.; May, T. P. *Met. Eng. Quart.* **1968**, 8, 31.
23. Floreen, S. *U.S. Patent* **4 1984**, 443, 254.
24. Data Bulletin on 18% Ni Maraging Steels, The International Nickel Company, Inc. 1964.
25. Novak, C. J. D.M.I.C. Memo 1964; p 196.
26. Dean, S. W.; Copson, H. R. *Corrosion* **1965**, 21, 95.
27. Stavros, A. J.; Paxton, H. W. Paper presented at NACE Meeting, Chicago, Illinois 1971.
28. Kenyon, N.; Kirk, W. W.; van Rooyen, D. *Corrosion* **1971**, 27, 390.
29. Bui, N.; Pieraggi, B.; Dabosi, F. *Mem. Sci. Rev. Met.* **1971**, 68, 223.
30. France, W. D., Jr.; Mazzatenta, E. D. *Mater. Eng.* **1970**, 62.
31. Johnson, H. H. In Proceedings of Conference of Fundamental Aspects of Stress Corrosion Cracking, National Association of Corrosion Engineers 1969; p 439.
32. Hayden, H. W.; Floreen, S. *Corrosion* **1971**, 27, 429.
33. Brown, B. F. In Extended Abstract of paper presented at Fourth International Congress on Metallic Corrosion, Amsterdam, Netherlands, 1969.
34. Smith, J. A.; Peterson, M. H.; Brown, B. F. *Corrosion* **1970**, 26, 539.

35. Johnson, H. H.; Willner, A. M. *Appl. Mater. Res.* **1965**, 4, 34.
36. Beck, W.; Bockris, J. O'M.; McBreen, J.; Nanis, L. *Proc. Roy. Soc. London A* **1966**, 290, 221.
37. Syrett, B. C. *Corrosion* **1971**, 27, 270.
38. Craig, I. H.; Parkins, R. N. *Br. Corros. J.* **1984**, 19, 3–16.
39. Setterlund, R. B. *Mater. Protect.* **1965**, 4(12), 27.
40. Freedman, A. H. *J. Mater.* **1970**, 5(12), 431.
41. Brown, B. F. Naval Research Laboratory Report 7168, 1970.
42. Steigerwald, E. A. Presented at ASM Conference on Stress Corrosion Cracking, Philadelphia, PA, August 1970. Original work by Carter, C. S., Boeing Co. Report D6–19770 November 1967.
43. Dautovich, D. P.; Floreen, S. Paper presented at the International Conference on Stress Corrosion Cracking and Hydrogen Embrittlement of Iron Base Alloys, Unieux-Firminy, France, June, 1973.
44. Brown, B. F. *Met. Rev.* **1968**, 13, 171.
45. Carter, C. S. *Corrosion* **1971**, 27, 471.
46. Brown, B. F. Paper presented at ASM Conference on Fracture Control, Philadelphia, PA, January 1970.
47. Carter, C. S. *Met. Trans.* **1970**, 1, 1551.
48. Parkins, R. N.; Haney, E. G. *Trans. Met. Soc.* **1968**, 242, 1943.
49. Stavros, A. J.; Paxton, H. W. *Met. Trans.* **1970**, 1, 3049.

## 3.04 Aqueous Corrosion of Stainless Steels

### A. Iversen

Outokumpu Stainless AB, PO Box 74, SE 774 22 Avesta, Sweden

### B. Leffler

Outokumpu Stainless, Hot Rolled Plate, SE 693 81 Degerfors, Sweden

© 2010 Elsevier B.V. All rights reserved.

---

<b>3.04.1</b>	<b>Introduction</b>	1806
<b>3.04.2</b>	<b>The use of Stainless Steels</b>	1807
<b>3.04.3</b>	<b>Definition of Stainless Steels, Alloying Elements, and Microstructure</b>	1808
3.04.3.1	Classification of Stainless Steels	1808
3.04.3.2	Alloying Elements and Microstructure	1809
3.04.3.2.1	Chromium (Cr)	1809
3.04.3.2.2	Nickel (Ni)	1809
3.04.3.2.3	Molybdenum (Mo)	1809
3.04.3.2.4	Copper (Cu)	1809
3.04.3.2.5	Manganese (Mn)	1810
3.04.3.2.6	Silicon (Si)	1810
3.04.3.2.7	Carbon (C)	1810
3.04.3.2.8	Nitrogen (N)	1810
3.04.3.2.9	Titanium (Ti)	1810
3.04.3.2.10	Niobium (Nb)	1811
3.04.3.2.11	Aluminum (Al)	1811
3.04.3.2.12	Cobalt (Co)	1811
3.04.3.2.13	Vanadium (V)	1811
3.04.3.2.14	Sulfur (S)	1811
3.04.3.2.15	Cerium (Ce)	1811
<b>3.04.4</b>	<b>Mechanical Properties</b>	1812
3.04.4.1	Mechanical Properties at Room Temperature	1812
3.04.4.2	The Effect of Cold Work	1815
3.04.4.3	Toughness	1815
3.04.4.4	Fatigue Properties	1816
<b>3.04.5</b>	<b>Precipitation and Embrittlement</b>	1817
3.04.5.1	Embrittlement at 475°C	1817
3.04.5.2	Carbide and Nitride Precipitation	1817
3.04.5.3	Intermetallic Phases	1817
3.04.5.4	Carburization	1818
3.04.5.5	Heat Treatment	1818
3.04.5.5.1	Solution annealing	1818
3.04.5.5.2	Quenching, tempering, and ageing	1818
3.04.5.5.3	Stabilization annealing	1819
<b>3.04.6</b>	<b>Physical Properties</b>	1819
<b>3.04.7</b>	<b>Property Relationships for Stainless Steels</b>	1820
<b>3.04.8</b>	<b>Corrosion Properties of Stainless Steels</b>	1821
3.04.8.1	Passivity	1822
3.04.8.2	Contribution of Main Alloy Elements to Passivation	1822
3.04.8.3	General Electrochemical Considerations in Corrosion of Stainless Steels	1823
3.04.8.4	Breakdown of Passivity	1824
3.04.8.5	Localized Corrosion – Pitting and Crevice Corrosion	1824
3.04.8.5.1	Influence of alloy composition on localized corrosion	1825
3.04.8.5.2	Pitting corrosion	1826
3.04.8.5.3	Crevice corrosion	1829

---



<b>3.04.8.6</b>	<b>Stress Corrosion Cracking</b>	1830
3.04.8.6.1	SCC mechanisms	1831
3.04.8.6.2	Impact of mechanical stress on corrosion: stress intensity factor and crack rate	1832
3.04.8.6.3	Chloride-induced SCC	1832
3.04.8.6.4	Caustic SCC	1833
3.04.8.6.5	Sulfide stress cracking (SSC) by hydrogen sulfide	1833
3.04.8.6.6	Hydrogen-induced stress cracking (HISC) using cathodic protection	1833
3.04.8.6.7	SCC in atmospheric environments	1834
3.04.8.6.8	SCC of martensitic stainless steels	1835
3.04.8.6.9	SCC of ferritic stainless steels	1835
3.04.8.6.10	SCC of austenitic stainless steels	1835
3.04.8.6.11	SCC of duplex stainless steels	1836
<b>3.04.8.7</b>	<b>Corrosion Fatigue</b>	1836
<b>3.04.8.8</b>	<b>Corrosion on Stainless Steels Related to Welding Procedures</b>	1836
3.04.8.8.1	Ferritic stainless steels	1837
3.04.8.8.2	Duplex stainless steels	1837
3.04.8.8.3	Austenitic stainless steels	1837
3.04.8.8.4	Postweld treatment	1837
<b>3.04.8.9</b>	<b>General Corrosion</b>	1838
3.04.8.9.1	Sulfuric acid	1838
3.04.8.9.2	Hydrochloric acid	1840
3.04.8.9.3	Phosphoric acid	1841
3.04.8.9.4	Nitric acid	1842
3.04.8.9.5	Organic acids	1842
3.04.8.9.6	Alkaline solutions	1843
<b>3.04.8.10</b>	<b>Galvanic Corrosion</b>	1844
<b>3.04.8.11</b>	<b>Intergranular Corrosion</b>	1845
<b>3.04.8.12</b>	<b>Erosion Corrosion</b>	1846
<b>3.04.8.13</b>	<b>Common Test Procedures and Standards for Stainless Steels</b>	1846
<b>3.04.8.14</b>	<b>Localized Corrosion Testing of Stainless Steels using Electrochemical Methods</b>	1846
<b>3.04.8.15</b>	<b>Different Stainless Steel Grades and their Resistance to Pitting and Crevice Corrosion</b>	1847
3.04.8.16	Screening of General Corrosion Properties of Stainless Steel Grades	1849
3.04.8.17	Testing Stress Corrosion Cracking of Stainless Steels in Environments Containing Hydrogen Sulfide Under Acidic Conditions	1849
3.04.8.18	Laboratory Tests of SCC	1850
<b>3.04.9</b>	<b>Stainless Steels in Natural Wet Environments</b>	1851
<b>3.04.9.1</b>	<b>Microbially Influenced Corrosion</b>	1851
3.04.9.1.1	Chlorination	1852
<b>3.04.9.2</b>	<b>River Waters and Freshwater</b>	1853
3.04.9.2.1	Drinking water <sup>32</sup>	1853
3.04.9.2.2	Freshwater	1853
<b>3.04.9.3</b>	<b>Seawater</b>	1854
3.04.9.3.1	Material selection	1854
3.04.9.3.2	Polluted seawater	1855
3.04.9.3.3	Cathodic protection and hydrogen embrittlement	1856
3.04.9.3.4	Seawater exposures	1856
3.04.9.3.5	Anaerobic seawater environments	1857
<b>3.04.10</b>	<b>Stainless Steels Performance in Atmospheric Environments<sup>32</sup></b>	1858
<b>3.04.10.1</b>	<b>Types of Atmosphere, Corrosivity, and Material Selection</b>	1858
3.04.10.1.1	Indoor, heated, nonheated. Outdoor, arid, low pollution, deserts and arctic areas (Rural), C1–C2	1859

3.04.10.1.2	Indoor, humid, low pollution. Coastal areas with low deposits of salt. Urban and industrialized areas with moderate pollution, C3	1859
3.04.10.1.3	Indoor with volatile aggressive chemical compounds, roof parts with mechanical load in swimming pool buildings. Polluted urban and industrialized atmosphere. Coastal areas with moderate salt deposits, C4–C5	1859
3.04.10.2	Factors Influencing Atmospheric Corrosion on Stainless Steels	1860
<b>3.04.11</b>	<b>Application Areas of Commercial Significance</b>	1860
3.04.11.1	Domestic – Kitchenware	1860
3.04.11.2	Process Industry	1861
3.04.11.2.1	Hydrometallurgy <sup>32</sup>	1861
3.04.11.2.2	Desalination <sup>32</sup>	1863
3.04.11.2.3	Stainless steel within the pulp and paper industry	1865
3.04.11.2.4	Architecture – Art <sup>32</sup>	1866
3.04.11.2.5	Stainless steel in oil and gas production <sup>32</sup>	1867
3.04.11.2.6	Stainless steel in wastewater treatment <sup>32,49</sup>	1870
<b>3.04.12</b>	<b>High Temperature Corrosion<sup>32</sup></b>	1873
3.04.12.1	Oxidation	1875
3.04.12.2	Sulfur Attack	1876
3.04.12.3	Halogen Gas Corrosion	1876
3.04.12.4	Molten Salt corrosion	1876
3.04.12.5	Molten Metal Corrosion	1877
<b>References</b>		1877

## Glossary

**Active** Describes a metal which corrodes in the negative direction of electrode potential.

**Activation polarization** Corrosion reaction determined kinetically by the participating electrode reactions.

**Anaerobic** Free of air or oxygen.

**Anode** The electrode of an electrolyte cell at which oxidation occurs.

**Anodic polarization** The change in the electrode potential in the noble positive direction.

**Austenite** A face-centered cubic crystalline phase of iron-base alloy.

**Cathode** The electrode of an electrolytic cell at which reduction is the principal reaction.

**Cathodic polarization** The change of the electrode potential in the active negative direction.

**Cathodic protection** Reduction of corrosion rate by shifting the corrosion potential of the electrode towards a less oxidizing potential by applying an external electromotive force.

**Cold work** The operation of shaping metals at temperatures below their recrystallization temperatures so as to produce strain-hardening.

**Corrosion – fatigue** Fatigue type cracking of metal caused by repeated or fluctuating stresses in a corrosive environment.

**Corrosion potential,  $E_{\text{corr}}$**  The potential of a corroding surface in an electrolyte, relative to a reference electrode, also called open circuit potential.

**Double layer** The interface between an electrode or a suspended particle and an electrolyte created by charge-charge interaction leading to an alignment of oppositely charged ions at the surface of the electrode or particle.

**Ductility** Ability of materials to be deformed by working process and to retain strength and freedom from cracks when their shape is altered.

**Electrolyte** A chemical substance or mixture, usually liquid, containing ions that migrate in an electric field.

**Elongation** The percentage plastic extension produced in a tensile test.

**Embrittlement** Loss of ductility of a material resulting from a chemical or physical change.

**Equilibrium potential** The potential of an electrode in an electrolytic solution when the forward

rate of a given reaction is exactly equal to the reverse rate.

**Erosion** Destruction of materials by abrasive action of moving fluids, usually accelerated by the presence of solid particles.

**Fatigue** The phenomenon leading to fracture under repeated or fluctuating stresses having a maximum value less than the tensile strength of the material.

**Ferrite** A body-centered cubic crystalline phase of iron-base alloys.

**Galvanic corrosion** Corrosion associated with the current resulting from the electrical coupling of dissimilar electrodes in an electrolyte.

**General corrosion** A form of deterioration that is distributed more or less uniformly over a surface.

**Hardening** The process of making steel hard by cooling from above the critical range at a rate that prevents the formation of ferrite and pearlite and results in the formation of martensite.

**Heat affected zone (HAZ)** That portion of the base metal that was not melted by welding but whose microstructure and properties were altered by the heat of the welding process.

**Inclusion** A nonmetallic phase such as an oxide, sulfide or silicate particle in a metal.

**Martensite** Metastable body-centered phase of iron super-saturated with carbon, produced from austenite by shear transformation during quenching or deformation.

**Mixed potential** A potential resulting from two or more electrochemical reactions occurring simultaneously on one metal surface.

**Noble** The positive direction of electrode potential.

**Open circuit potential** The potential of an electrode measured with respect to a reference electrode when no current flows to or from it (see also corrosion potential).

**Passivation** A reduction of the anodic reaction rate of a metal.

**Passive** A metal corroding under the control of a surface reaction product.

**Passivity** The state of being passive.

**Pits, pitting** Localized corrosion of a metal surface that is confined to a small area and takes the form of cavities.

**Polarization** The deviation from the open circuit potential of an electrode.

**Polarization curve or polarization diagram** A plot of current density versus electrode potential for a specific electrode-electrolyte combination.

**Potentiodynamic** The technique for varying the potential of an electrode in a continuous manner at a present rate.

**Potentiostat** An instrument for automatically maintaining an electrode at a constant potential or controlled potential with respect to a reference electrode.

**Potentiostatic** The technique for maintaining a constant electrode potential.

**Precipitation hardening** Improving the strength of solid solution alloys by controlling the formation of precipitates on a crystal lattice scale.

**Reference electrode** A reversible electrode used for measuring the potentials of other electrodes.

**Relative humidity, RH** The ratio, expressed as a percentage, of the amount of water vapor present in a given volume of air at a given temperature to the amount required to saturate the air at that temperature.

**Scanning electron microscope (SEM)** An electron optical device that images topographical details with maximum contrast and depth of field by the detection, amplification and display of secondary electrons.

**Sensitizing heat treatment** A heat treatment, which causes precipitation of constituents at grain boundaries.

**Solution heat treatment** Heating a metal to a suitable temperature and holding at that temperature long enough for one or more constituents to enter into solid solution, then cooling rapidly enough to retain the constituents in solution.

**Tempering** The reheating of hardened steel at any temperature below the critical range, in order to decrease the hardness. Sometimes drawing.

**Toughness** Condition intermediate between brittleness and softness, as indicated in tensile tests by high ultimate tensile stress and low to moderate elongation and reduction in area, or by high values of energy absorbed by impact tests. More precisely it

is the value of the critical strain energy release rate.

**Transpassive** The noble region of potential where an electrode exhibits a current density higher than passive current density.

## Abbreviations

**BCC** Body centered cubic structure  
**CCT** Critical crevice corrosion temperature ( $^{\circ}\text{C}$ )  
**CPT** Critical pitting temperature ( $^{\circ}\text{C}$ )  
**FCC** Face centered cubic structure  
**GS** Grain size  
**HISC** Hydrogen-induced stress cracking  
**LT-MED** Low temperature multi effect, desalination plant  
**Me** Metal  
**MIC** Microbially influenced corrosion  
**MIG** Gas metal arc welding  
**MSF** Multistage flash  
**OCP** Open circuit potential (V)  
**PRE** Pitting resistance equivalent  
**REM** Rare earth metals  
**RH** Relative humidity (%)  
**RO** Reverse osmosis  
**RT** Room temperature  
**SCC** Stress corrosion cracking  
**SCE** Saturated calomel electrode  
**SEM** Scanning electron microscope  
**SHE** Standard hydrogen electrode  
**SSC** Sulfide stress cracking  
**SWRO** Seawater reverse osmosis  
**TIG** Gas tungsten welding  
**TTS** Time temperature sensitization  
**WPA** Wet process phosphoric acid

## Symbols

$\alpha$  Body centered cubic ferrite rich in iron  
 $\alpha'$  Body centered cubic ferrite rich in chromium  
 $A_5$  Elongation or permanent extension of the gauge length after fracture, as expressed as a percentage of the original gauge length.  
 $b_a$  Anodic Tafel slope  
 $C_s$  Concentration of metal ion  
 $\delta$  Diffusion length (m)  
 $D$  Diffusion coefficient of component  $i$  ( $\text{m}^2 \text{s}^{-1}$ )  
 $E$  Potential (V)  
 $E_r$  Transition potential (V)

$E_{\text{corr}}$  Corrosion potential (V)  
 $E_p$  Pitting Potential (V)  
 $E_{pp}$  Passivation Potential (V)  
 $E_{rp}$  Repassivation Potential (V)  
 $E_{tr}$  Transpassive Potential (V)  
 $F$  Faraday's constant ( $\text{A s mol}^{-1}$ )  
 $I$  Current (A)  
 $I_{\text{crit}}$  Critical current density for passivation ( $\text{A cm}^{-2}$ )  
 $i_L$  Anodic limiting current density ( $\text{A cm}^{-2}$ )  
 $K$  Equilibrium constant  
 $K_{\text{ISCC}}$  Threshold stress intensity factor ( $\text{MPa m}^{1/2}$ )  
 $M_{d30}$  The temperature at which martensite will form at a strain of 30%  
 $M_d$  The temperature below where martensite will form  
 $M_s$  Martensite temperature, the starting temperature for martensite transformation  
 $n$  Charge number  
 $N$  Number of cycles  
 $\varphi_s$  Ohmic potential drop in a pit cavity  
 $R$  Stress ratio  
 $R_m$  Tensile strength (MPa)  
 $R_{p0.2}$  Proof strength at which the material undergoes a 0.2% nonproportional (permanent) extension during a tensile test (MPa)  
 $R_{p1.0}$  Proof Strength at which the material undergoes a 1.0% nonproportional (permanent) extension during a tensile test (MPa)  
 $S$  Stress amplitude (MPa)

## 3.04.1 Introduction

The corrosion resistance of stainless steels, in combination with their good mechanical properties and manufacturing characteristics, makes them an extremely valuable and flexible material for designers. Although the usage of stainless steel may have traditionally been relatively low compared with that of carbon steels, growth has been steady, in contrast to the growth of structural steels. The most dominant product form for stainless steels is cold rolled sheet and the major application areas include consumer products and plant and equipment for the oil and gas, chemical process, and food and beverage industries. The most widely used stainless steels are the austenitic grade S30400 and ferritic grades such as S41000, followed by the molybdenum-alloyed austenitic grades, notably S31600.

In terms of their durability and corrosion resistance, iron and most iron-alloyed steels are relatively poor materials, since they easily corrode in air and acid environments unless protected by some external coating and scale in furnace atmospheres. Stainless steels, however, although also belonging to the category of iron-base alloys, offer superior corrosion resistance properties and durability in such diverse environments as seawater, diluted and concentrated acids, and high temperature environments up to 1100°C.

It was the discovery, made about 100 years ago, of the effect of chromium on the resistance of iron in many environments that triggered the development of what is currently the most common group of corrosion-resistant alloys. The first patent for stainless steel was registered in the United Kingdom in 1912 and the development of stainless steels was then sparked off simultaneously in the United Kingdom, the United States, and Germany. Even if most of the stainless steel types currently in use had been available in the 1930s, it was not until the 1960s that developments in process metallurgy gave rise to the growth and widespread use of modern stainless steels.

Early research found that increasing the chromium content of iron to about 10–14% produced a massive drop in corrosion rate in many diverse environments. In time it was also realized that increasing the chromium content above 18–20% improved the corrosion resistance by decreasing the corrosion rate even further. This is the reason that even today many common stainless steel grades contain about 18% chromium. It is the resistance to many common corrosive environments, in combination with good mechanical and fabrication properties, that makes stainless steels universally useful whenever corrosion resistance and long-lasting endurance are required.

### 3.04.2 The use of Stainless Steels

Steel is the predominant metal used in industry. The global production of steel is around 1 billion metric tons a year, of which stainless steel accounts for about 2.5%.

The use and production of stainless steels have for many years been dominated by the industrialized Western nations and Japan, but in recent years, Asian countries, such as India and China, as well as some South American countries, have emerged as important producers and consumers of stainless steels.

The most common product form for stainless steels is cold rolled sheet. Other products, such as

hot rolled plate and sheet, bar, tube and pipe, individually account for only a third or less of the total volumes of cold rolled sheet produced.

The use of stainless steels can be divided into a few major areas, with consumer products, industrial equipment, transport, and construction being the biggest. **Table 1** gives a breakdown of the use of stainless steel by end-user segment.

The most widely used stainless grades are austenitic steels, which typically contain 18% chromium and 8% nickel, that is, S30400/304L. These steels account for more than 50% of the global production of stainless steel. The next most widely used grades are ferritic steels, for example, S41000 (EN 1.4000), followed by molybdenum-alloyed austenitic steels, for example, S31600/316L (EN 1.4401/1.4404). Together, these grades account for over 70% of the total tonnage of stainless steels. However, the use of duplex stainless steels, such as UNS S32205 (EN 1.4462), has been growing considerably recently and this group of stainless steels now accounts for a considerable proportion of the stainless market. The use of duplex grades will certainly increase in future. **Figure 1** shows an

**Table 1** Use of stainless steel divided into application categories

<i>End-user segment</i>	<i>%</i>
Catering & household	32
Industrial equipment	26
Transport	16
Construction	15
Tubular products	5
Other	6



**Figure 1** White liquor tank from the pulp and paper industry built in a recently developed stainless steel grade, S32101 (1.4162).

example of the use of a recently developed duplex stainless steel grade, S32101 (1.4162), in a white liquor tank for the pulp- and paper industry.

### 3.04.3 Definition of Stainless Steels, Alloying Elements, and Microstructure

#### 3.04.3.1 Classification of Stainless Steels

Stainless steels are generally defined as iron-based alloys containing at least 10.5% chromium (by weight) and a maximum of 1.2% carbon (by weight). This is the definition given in the European standards. Other definitions may vary slightly, for example, requiring minimum chromium content of 12%, but all definitions agree that stainless steels are iron-based alloys with a substantial amount of chromium, usually in the range of 10.5–12%.

Stainless steels are normally subdivided into five major families or categories based on their crystalline structure and microstructure or hardening mechanism. Each category or family shares a distinct set of general properties, including chemical composition, mechanical properties, fabrication properties, and resistance to certain types of corrosion. Within each of the stainless families there is a considerable range of chemical compositions, and therefore each family consists of several steel grades with variations within the general property profile of the specific category/family.

Stainless steels are divided into different categories according to the three basic microstructures: ferrite, austenite, and martensite. The first two are phases with distinct crystalline structures; ferrite has a body-centered cubic structure and austenite has a face-centered cubic structure. Martensite, on the other hand, is a microstructure that is formed by a complex transformation of an austenitic microstructure under certain conditions. The different

categories of stainless steel are refined further from these basic criteria, either as a single-phase microstructure or as combinations of these structures, to result in five categories of stainless steel, as follows:

- ferritic stainless steels
- austenitic stainless steels
- ferritic–austenitic (duplex) stainless steels
- martensitic stainless steels
- precipitation-hardening (PH) steels

The most common alloying elements used in stainless steels are chromium, nickel, molybdenum, carbon, nitrogen, silicon, and manganese. Silicon and manganese are present in almost all stainless steels in concentrations of 0.2–0.7% and 1–2%, respectively. Other elements are also used for various purposes, but the first five named earlier are the most common alloying elements used to influence the composition of the steel in such a way that the grade falls into a specific category. Different typical combinations of these basic alloying elements are thus characteristic of the different categories of stainless steel, and in [Table 2](#), the typical ranges of the main alloying elements for the different categories of stainless steel are shown.

As can be seen from [Table 2](#), relatively low alloy content characterizes martensitic steels, whereas ferritic steels have high chromium content and no – or virtually no – nickel. This is in contrast to austenitic steels, which always contain nickel and have comparatively high chromium content. Duplex steels fall somewhere in between ferritic and austenitic steels as they typically have high chromium content but less nickel than standard austenitic grades. The use of nitrogen as an alloying element is restricted almost exclusively to austenitic and duplex steels. In some austenitic steel grades, nickel may, to some extent, be replaced by manganese.

**Table 2** Typical ranges for alloying elements in different stainless steel categories

Category	Composition (wt%)					Others
	C	N	Cr	Ni	Mo	
Martensitic	>0.10	–	11–14	0–1	–	
	>0.15	–	16–18	0–2	0–2	
	<0.10	0.05	12–18	4–6	0–2	
Precipitation hardening	0.03–0.20	–	12–17	4–8	0–2	Al, Cu, Ti, Nb, V
	0.05–0.15	–	15–18	4–8	1–3	
Ferritic	<0.08	–	12–27	0–5	0–5	Ti
	<0.25	–	24–28	–	–	
Austenitic	<0.08	0.03–0.7	16–30	8–35	0–7	Cu, Ti, Nb, Mn
Duplex	<0.05	0.05–0.4	18–33	0–7	1–5	Mn



Figures 2 and 3 show examples of a normal microstructure for austenitic and duplex stainless steel.

For commercial stainless steel grades, several international and national standards describe and specify the composition and required properties of stainless steel products. One of the most comprehensive catalogs of steel grades is the Unified Numbering System (UNS). This system does not contain specifications but provides a unified list of alloys that have compositions specified in standards or elsewhere. All stainless steels have the letter 'S' as a prefix in the UNS number. European stainless steel grades are listed along with their compositions in EN 10088-1.<sup>1</sup> American steel grades and their compositions are normally listed in the material and product standards published by ASTM or ASME, for example, ASTM A 240 or ASME SA 240. Table 3 shows the typical chemical composition for a number of commercial stainless steels of various types based mainly on American and European standards.

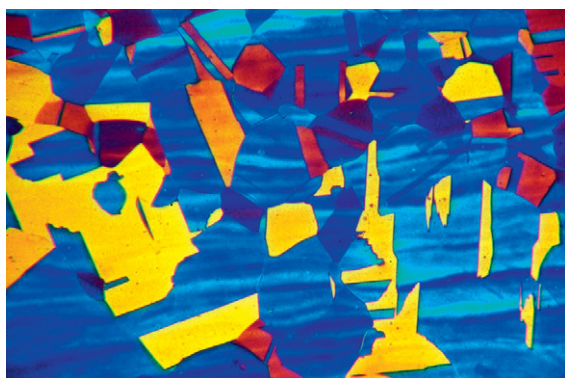


**Figure 2** Typical microstructure of an austenitic stainless steel.

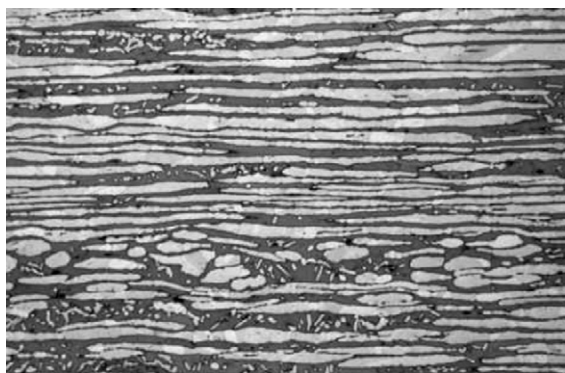


**Figure 3** Typical microstructure of a duplex stainless steel.

### 3.04.3.2 Alloying Elements and Microstructure

Stainless steels contain a number of different alloying elements, each of which has a specific effect on the properties of the steel. The properties of a specific steel grade will thus be determined by the combined effect of the alloying and trace elements in that specific grade. A brief overview of the alloying elements and their effects on the structure and properties of the steel are given in the following sections together with an explanation of why various elements are added to certain grades.<sup>2</sup> It should also be noted that the effect of the alloying elements differs in some aspects between the hardenable and the nonhardenable stainless steels.

#### 3.04.3.2.1 Chromium (Cr)

This is the most important alloying element as it provides stainless steels with their basic corrosion resistance. Generally speaking, the higher the chromium content, the better the corrosion resistance. Chromium also enhances the steel's resistance to oxidation at high temperatures and promotes a ferritic structure.

#### 3.04.3.2.2 Nickel (Ni)

The main reason for adding nickel is to promote an austenitic structure. Nickel generally increases ductility and toughness. It also lowers the corrosion rate and can thus be used to good effect in acid environments. In precipitation-hardening steels, nickel is also used to form the intermetallic compounds to increase the strength of the steel.

#### 3.04.3.2.3 Molybdenum (Mo)

Molybdenum substantially enhances the resistance to both general and localized corrosion and increases the mechanical strength of steels. In addition to promoting a ferritic structure, molybdenum promotes the formation of secondary phases in ferritic, duplex, and austenitic steels. In martensitic steels, it will increase the hardness at higher tempering temperatures because of its effect on carbide precipitation.

#### 3.04.3.2.4 Copper (Cu)

Copper enhances the corrosion resistance of steels in certain acid environments and promotes an austenitic structure. In precipitation-hardening steels, copper is used to form the intermetallic compounds to increase the strength of the steel.

**Table 3** Typical chemical compositions for some commercial stainless steel grades

<i>Steel grade</i>			<i>Microstructure</i>	<i>Typical chemical composition (wt%)</i>				
<i>UNS</i>	<i>ASTM</i>	<i>EN</i>		<i>Cr</i>	<i>Ni</i>	<i>Mo</i>	<i>N</i>	<i>Other</i>
S41000	410	1.4006	Martensitic	12			0.04	
S41600	416	1.4005	Martensitic	13			0.04	S
S42000	420	1.4021	Martensitic	13				
S43000	430	1.4016	Ferritic	16				
S43400	434	1.4113	Ferritic	17		1		
S44400	444	1.4521	Ferritic	17		2		
S20100	201	1.4372	Austenitic	17	5		0.15	Mn(7.08)
S20400	204		Austenitic	16	2.2		0.17	Mn(9.07)
S30100	301	1.4310	Austenitic	17	7			
S30100	301LN	1.4318	Austenitic	17.7	6.5		0.14	
S30300	303	1.4305	Austenitic	17.3	8.2			
S30400	304	1.4301	Austenitic	18.1	8.3			
S30403	304L	1.4307	Austenitic	17.5	8			
S30500	305	1.4303	Austenitic	17.7	12.5			
S34700	347	1.4550	Austenitic	18	9.5		0.04	Nb,Mn(2.0)
S31600	316	1.4401	Austenitic	17.2	10.2	2.1		
S31603	316L	1.4404	Austenitic	17.2	10.2	2.1		
S31635	316Ti	1.4571	Austenitic	16.8	10.9	2.1		Ti
S31653	316LN	1.4406	Austenitic	17.2	10.3	2.1	0.14	
S31600	316	1.4436	Austenitic	16.9	10.7	2.6		
S31703	S31703	1.4438	Austenitic	18.2	13.7	3.1		
N08904	N08904	1.4539	Austenitic	20	25	4.5		Cu(1.5)
S31254	S31254	1.4547	Austenitic	20	18	6.1	0.20	Cu
S34565	S34565	1.4565	Austenitic	24	17	4.5	0.45	5Mn(5.5)
S32101	S32101	1.4162	Duplex	21.5	1.5	0.3	0.22	
S32304	S32304	1.4362	Duplex	22	3.5	0.1	0.10	
S32205	S32205	1.4462	Duplex	22	5.5	3	0.17	
S32750	S32750	1.4410	Duplex	24	6	3	0.27	

**3.04.3.2.5 Manganese (Mn)**

Manganese is generally used in stainless steels to improve hot ductility. Its effect on the ferrite/austenite balance varies with temperature; at low temperatures, manganese is an austenite stabilizer, whereas at high temperatures, it will stabilize ferrite. Manganese increases the solubility of nitrogen and is used to obtain high nitrogen contents in austenitic steels.

**3.04.3.2.6 Silicon (Si)**

Silicon increases the resistance to oxidation, both at high temperatures and in strongly oxidizing solutions at lower temperatures. It promotes a ferritic structure.

**3.04.3.2.7 Carbon (C)**

Carbon is a strong austenite former and strongly promotes an austenitic structure. It also substantially increases the mechanical strength. Increasing carbon content reduces the resistance to intergranular corrosion. In ferritic stainless steels carbon will strongly reduce both toughness and corrosion resistance.

In the martensitic and martensitic–austenitic steels, carbon increases hardness and strength. In the martensitic steels, an increase in hardness and strength is generally accompanied by a decrease in toughness and in this way carbon reduces the toughness of these steels.

**3.04.3.2.8 Nitrogen (N)**

Nitrogen is a very strong austenite former and promotes an austenitic structure. It also substantially increases the mechanical strength of steel and enhances its resistance to localized corrosion, especially when used in combination with molybdenum. In ferritic stainless steels, nitrogen will lead to a significant reduction in toughness and corrosion resistance. In martensitic and martensitic–austenitic steels, the addition of nitrogen will increase hardness and strength but reduce the toughness of the steel.

**3.04.3.2.9 Titanium (Ti)**

Titanium is a strong ferrite former and a strong carbide former, and, as such, helps lower the effective

carbon content and promote a ferritic structure in two ways. In austenitic steels, it is added to improve the resistance to intergranular corrosion, but it also enhances the mechanical properties of the steel at high temperatures. In ferritic stainless steels, titanium is added to improve toughness and corrosion resistance by lowering the amount of interstitials in solid solution. In martensitic steels, titanium reduces the martensite hardness and increases the tempering resistance. In precipitation-hardening steels titanium is used to form the intermetallic compounds used to increase the strength of the steel.

#### 3.04.3.2.10 Niobium (Nb)

Niobium is both a strong ferrite and carbide former. Like titanium, it promotes a ferritic structure. In austenitic steels, it is added to improve the resistance to intergranular corrosion, but it also enhances mechanical properties at high temperatures. In martensitic steels, niobium reduces the hardness and increases the tempering resistance. It is also referred to as columbium (Cb).

#### 3.04.3.2.11 Aluminum (Al)

Aluminum improves the oxidation resistance, if added in substantial amounts. It is used in certain heat resistant alloys for this purpose. In precipitation-hardening steels, aluminum is used to form the intermetallic compounds that increase the strength in the aged condition.

#### 3.04.3.2.12 Cobalt (Co)

Cobalt is only used as an alloying element in martensitic steels in which it increases the hardness and tempering resistance, especially at higher temperatures.

#### 3.04.3.2.13 Vanadium (V)

Vanadium increases the hardness of martensitic steels due to its effect on the type of carbide present. It also increases tempering resistance. Vanadium stabilizes ferrite and will, at high contents, promote ferrite in the structure. It is only used in hardenable stainless steels.

#### 3.04.3.2.14 Sulfur (S)

Sulfur is added to certain stainless steels in order to increase the machinability. At the levels present in these grades, sulfur will substantially reduce corrosion resistance, ductility, and fabrication properties, such as weldability and formability.

#### 3.04.3.2.15 Cerium (Ce)

Cerium is one of the rare earth metals (REMs) and is added in small amounts to certain heat-resistant,

high temperature steels and alloys in order to increase the resistance to oxidation and high temperature corrosion.

Since it is the combined effect of the alloying elements that decide both the microstructure and the properties of a certain grade, the effect of the alloying elements can be summarized in various ways. One such summary of the effect of alloying elements on the microstructure is the Schaeffler–Delong diagram presented in [Figure 4](#). A guide to the composition of the stainless steels presented in [Figure 4](#) is given in [Table 4](#).

The diagram is based on the fact that the alloying elements can be divided into ferrite-stabilizers and austenite-stabilizers. This means that they favor the formation of either ferrite or austenite in the microstructure of the steel. Assuming that the ability of austenite-stabilizers to promote the formation of austenite is related to the nickel content, and that the ability of ferrite-stabilizers is related to the chromium content, it becomes possible to calculate the total ferrite and austenite stabilizing effect of the alloying elements in the steel, and thereby obtain the

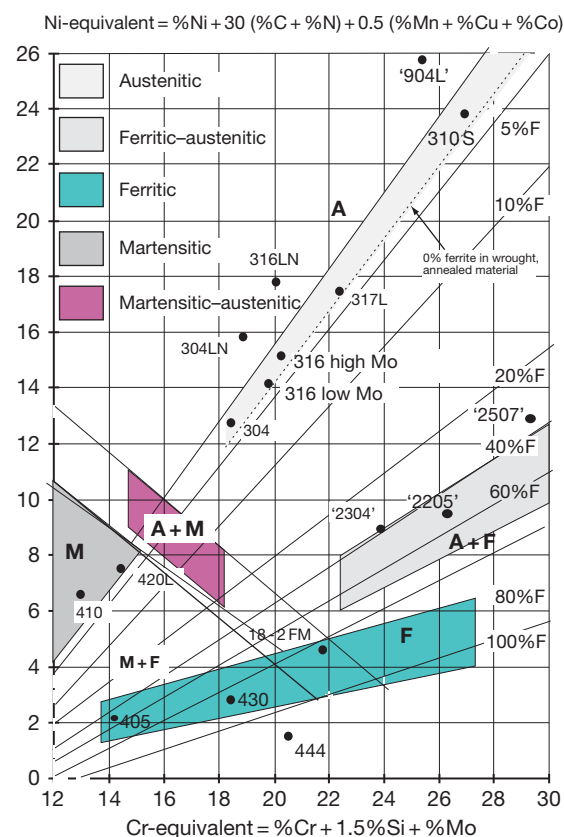


**Figure 4** The Schaeffler–Delong diagram. A guideline to the steel grades is presented in [Table 4](#).

**Table 4** Guide to the compositions of the stainless steels presented in **Figure 4**

Note in <b>Figure 4</b>	Steel grade			Typical chemical composition (wt%)				
	UNS	ASTM	EN	Cr	Ni	Mo	N	Other
410	S41000	410	1.4006	12			0.04	
420L	S42000	420	1.4021	13				
430	S43000	430	1.4016	16				
444	S44400	444	1.4521	17		2		
304	S30400	304	1.4301	18.1	8.3			
304LN	S30451	304LN	1.4311	18.5	10.5		0.14	
316LowMo	S31600	316	1.4401	17.2	10.2	2.1		
316LN	S31653	316LN	1.4406	17.2	10.3	2.1	0.14	
316HiMo	S31600	316	1.4436	16.9	10.7	2.6		
317L	S31703	317L	1.4438	18.2	13.7	3.1		
904L	N08904	N08904	1.4539	20	25	4.5		Cu(1.5)
2304	S32304	S32304	1.4362	22	3.5	0.1	0.10	
2205	S32205	S32205	1.4462	22	5.5	3	0.17	
2507	S32750	S32750	1.4410	24	6	3	0.27	
310S	S31008	310S	1.4845	25	20			

chromium and nickel equivalents in the Schaeffler–Delong diagram. It is thus possible to take into account the combined effect of alloying elements on the microstructure of a steel grade.

The Schaeffler–Delong diagram was originally developed for weld metal, that is, it describes the structure after melting and rapid cooling, but the diagram has also been found to give a useful picture of the effect of the alloying elements for wrought and heat-treated material. However, in practice, wrought or heat-treated steels with ferrite contents in the range 0–5% according to the diagram in fact contain smaller amounts of ferrite than that predicted by the diagram. It should be noted that the Schaeffler–Delong diagram is not the only diagram for assessing the ferrite content and microstructure of stainless steels. Several other diagrams have been published, all with slightly different equivalents, phase limits, or general layout.

Precipitation-hardening stainless steels can be divided into three subcategories: martensitic, semiaustenitic, and austenitic grades. The common denominator here is not the microstructure but the hardening mechanism, precipitation hardening. This involves the formation of second-phase particles from a supersaturated solution which induces an internal strain in the microstructure and thus increases the strength of the material. The elements most commonly used to induce precipitation hardening, either individually or in combination, are aluminum, titanium, and copper.

### 3.04.4 Mechanical Properties

The difference in the mechanical properties of different stainless steels is perhaps seen most clearly in the stress–strain curves in **Figure 5**. The high yield and tensile strengths but low ductility of the martensitic steels are apparent, as are the low yield strength and excellent ductility of the austenitic grades. Duplex and ferritic steels both lie somewhere between these two extremes. Ferritic steels generally have a slightly higher yield strength than austenitic steels, whereas duplex steels have an appreciably higher yield strength than both austenitic and ferritic steels. The ductility of ferritic and duplex steels is of the same order of magnitude, even if the latter are somewhat superior in this respect.

#### 3.04.4.1 Mechanical Properties at Room Temperature

In terms of their mechanical properties, stainless steels can be roughly divided into four groups: martensitic, ferritic, duplex, and austenitic, and the properties within each group are relatively similar. **Table 5** shows the typical mechanical properties at room temperature for a number of stainless steels.

Stress values are given as the nearest 10 MPa. Standard deviations are normally about 20 MPa for proof strengths,  $R_{p0.2}$ ,  $R_{p1.0}$  and tensile strength,  $R_m$ ; and 3 wt% for the elongation,  $A_5$ . More detailed information can be found in Nordberg *et al.*<sup>4</sup>

Martensitic steels are characterized by their high strength and the fact that this strength is strongly affected by heat treatment. Martensitic steels are usually used in the hardened and tempered condition.

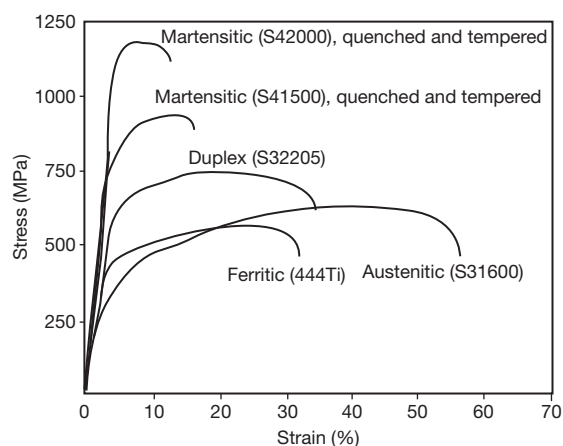


**Figure 5** Stress-strain curves for some stainless steels. Reproduced from Leffler, B. *Stainless – Stainless Steels and Their Properties*; Avesta Sheffield AB Research Foundation, Stockholm, Sweden, 1996.

In this condition, the strength of the steel improves in relation to the carbon content. Steels with more than 13 wt% chromium and a carbon content above 0.15 wt% are completely martensitic after hardening. A reduction in the carbon content causes an increase in the ferrite content and thus has an adverse effect on the strength of the steel. The ductility of martensitic steels is relatively low. Low carbon martensitic grades, often alloyed with nickel, have high strength in the hardened and tempered condition and good ductility. The mechanical properties of martensitic stainless steels are heavily influenced by the heat treatments to which the steels are subjected. A brief description of the general heat treatment of martensitic stainless steels and the effect on the mechanical properties is given as follows.<sup>5,6</sup>

To obtain useful properties, martensitic stainless steels are normally used in the hardened and tempered condition. The hardening treatment consists of heating to a high temperature in order to produce an austenitic structure with carbon in solid solution followed by quenching. The austenitizing temperature is generally in the range 925–1070°C. The effect of

**Table 5** Typical mechanical properties for stainless steels at room temperature for hot rolled plate

Micro structure	Steel grade		$R_{p0.2}$ (MPa)	$R_{p1.0}$ (MPa)	$R_m$ (MPa)	$A_5$ (%)
	EN	UNS(ASTM)				
Martensitic	1.4006	S41008	540		690	20
	1.4021	S42003	780		980	16
		S43100	690		900	16
		ASTM 248 SV	790	840	930	18
Ferritic		ASTM446	340		540	25
	1.4521	S44400	390		560	30
	1.4162	S32101	450		650	30
Duplex (ferritic-austenitic)	1.4362	S32304	470	540	730	36
	1.4462	S31803	500	590	770	36
	1.4410	S32750	600	670	850	35
	1.4301	S30400	310	350	620	57
Austenitic	1.4307	S30403	290	340	590	56
	1.4311	S30453	340	380	650	52
		S30451	350	400	670	54
		S32100	280	320	590	54
	1.4404	S31603	310	350	600	54
	1.4571	S31635	290	330	580	54
	1.4401	S31600	320	360	620	54
	1.4432	S31603	300	340	590	54
	1.4438	S31703	300	350	610	53
	1.4439	S31726	320	360	650	52
	1.4529	N08904	260	310	600	49
	1.4547	S31254	340	380	690	50
	1.4845	S31008	290	330	620	50
		S30415	380	410	700	50
Austenitic (heat-resistant steels)	1.4835	S30815	410	440	720	52
	1.4854	S35315	360	400	720	50

austenitizing temperature and time on hardness and strength varies with the composition of the steel, especially the carbon content. In general, the hardness will increase in relation to the austenitizing temperature up to a maximum and then decrease. The effect of increased time at the austenitizing temperature is normally a slow reduction in hardness with increased time. Quenching, after austenitizing, is done in air, oil, or water depending on the steel grade. On cooling below the  $M_s$  temperature, the starting temperature for the martensite transformation, the austenite transforms to martensite. The  $M_s$  temperature lies in the range 70–300°C and the transformation is usually completed at about 150–(200–248)°C below the  $M_s$  temperature. Almost all alloying elements will lower the  $M_s$  temperature, with carbon having the greatest effect. This means that in higher alloyed martensitic grades, the microstructure will contain retained austenite due to the low temperature (below ambient) needed to finish the transformation of the austenite into martensite.

In the hardened condition, the strength and hardness are high but the ductility and toughness is low. To obtain useful engineering properties, martensitic stainless steels are normally tempered. The tempering temperature used has a large influence on the final properties of the steel. The effect of tempering temperature on the mechanical properties of a martensitic stainless steel (Type 431) is shown in Figure 6. Normally, increasing tempering temperatures above 400°C will lead to a small decrease in tensile strength and an increase in reduction of area while hardness,

elongation, and yield strength are more or less unaffected. Above this temperature, there will be a more or less pronounced increase in yield strength, tensile strength, and hardness because of the secondary hardening peak, around 450–500°C. In the temperature range around the secondary hardening peak, there is generally a dip in the impact toughness curve. Above about 500°C, there is a rapid reduction in strength and hardness, and a corresponding increase in ductility and toughness. Tempering at temperatures above the AC1 temperature (780°C for the steel in Figure 6) will result in partial austenitizing and the possible presence of nontempered martensite after cooling to room temperature.<sup>7</sup>

Ferritic steels have relatively low yield strength and the work hardening is limited. The strength increases as the carbon content is increased, but the effect of increased chromium content is negligible. However, ductility decreases at high chromium levels and good ductility requires very low levels of carbon and nitrogen.

Duplex (ferritic–austenitic) steels have a high yield strength, which increases with higher carbon and nitrogen levels. Increased ferrite content will, within limits, also increase the strength of duplex steels. Their ductility is good and they exhibit strong work hardening properties.

Austenitic steels generally have a relatively low yield strength and are characterized by strong work hardening properties. The strength of austenitic steels increases with higher levels of carbon, nitrogen, and, to a certain extent, also molybdenum. The detrimental effect of carbon on corrosion resistance

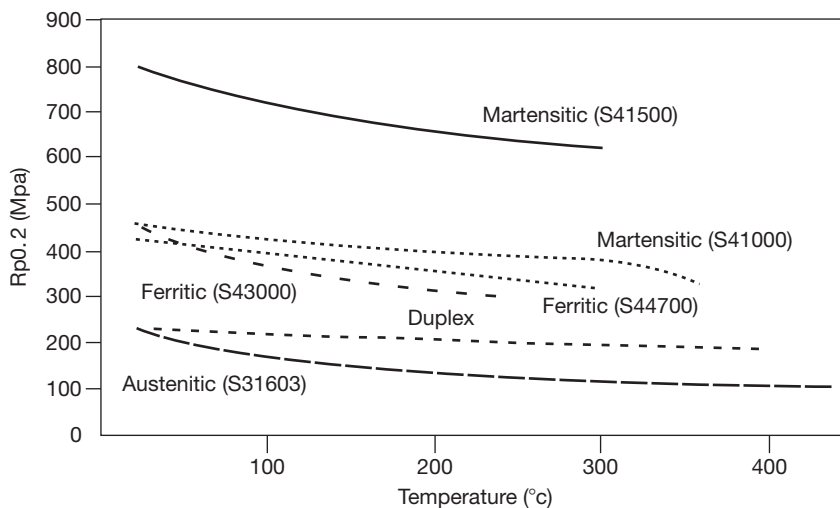


**Figure 6** Effect of tempering temperature on the mechanical properties ( $R_{p0.2}$  – 0.2% proof strength).



means that this element cannot be used for increasing strength. Austenitic steels exhibit very high ductility; they have a high elongation and are very tough.

Some austenitic stainless steels with a low overall content of alloying elements, for example, type 301 and 304 steels, can be metastable and may form martensite, either due to cooling below ambient temperatures or through cold deformation, or a combination of both. The formation of martensite will cause a considerable increase in strength, as illustrated in **Figure 7**. The  $M_d$  temperature is defined as the temperature below which martensite will form. The stability of the austenite depends on the composition of the steel; the higher the content of alloying elements, the more stable the austenite. A common equation for relating austenite stability to alloy composition is the  $M_{d30}$ , which is defined as the temperature at which martensite will form at a strain of 30%:

$$M_{d30} = 551 - 462(C + N) - 9.2Si - 8.1Mn - 13.7Cr - 29(Ni + Cu) - 18.5Mo - 68Nb - 1.42(GS - 8.0)(^{\circ}C)$$

where GS is the grain size, ASTM grain size number.

This type of equation gives a good idea of the behavior of lean austenitic stainless steels, but it must be noted that it is only approximate as interactions between the alloying elements are not taken into account.

The effects of alloying elements and structure on the strength of austenitic and duplex steels have been discussed over the years and several regression equations have been proposed for identifying the effects of the various alloying elements in stainless steels. Most of the regression equations proposed apply to austenitic stainless steels but some have also included duplex stainless steels in the equations.<sup>8,9,10</sup> These

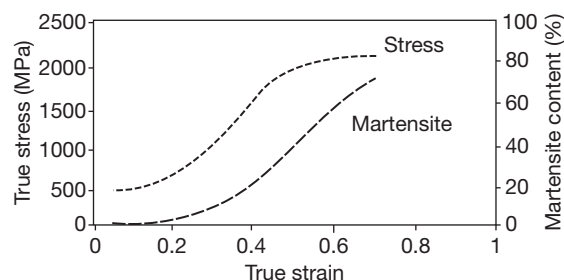


**Figure 7** The effect of strain on martensite and yield strength of AISI 301. Reproduced from Peckner, B. *Handbook of Stainless Steel*; McGraw-Hill, 1977.

equations may be used to estimate the strength of austenitic and duplex steel.

In contrast to the constructional steels, austenitic steels do not exhibit a clear yield stress but begin to deform plastically at a stress around 40% of the tensile strength,  $R_{p0.2}$ .

It should be noted that although the different elements are included in the equation through rather simple expressions, the actual strengthening mechanism might be more complex. At chromium contents over 20%, austenitic steel with 10% Ni will contain  $\delta$ -ferrite, which in turn causes a smaller grain size, and this will enhance both yield strength and tensile strength. Nitrogen has a strong strengthening effect but is also a powerful austenite stabilizer. In duplex stainless steels, the strengthening effect of nitrogen is, to a certain extent, countered by the increased austenite content caused by the addition of nitrogen.

#### 3.04.4.2 The Effect of Cold Work

Stainless steels will harden during deformation and the mechanical properties of stainless steels are strongly influenced by cold deformation. The amount of hardening depends on both the composition and the type of steel. The work hardening of austenitic and duplex steels in particular causes considerable changes in properties after cold forming operations. The general effect of cold work is to increase the yield and tensile strengths and at the same time decrease the elongation. **Figure 8** shows cold hardening curves for some stainless steels.

The work hardening is greater for austenitic steels than for ferritic steels. The addition of nitrogen in austenitic steels makes these grades particularly hard and strong: compare S31603 and S31653. The strong work hardening of the austenitic steels means that large forces are required for forming operations even though the yield strength is low. Work hardening can, however, also be deliberately used to increase the strength of a component.

#### 3.04.4.3 Toughness

The toughness of the different types of stainless steel shows considerable variation, ranging from excellent toughness at all temperatures for austenitic steels to the relative brittleness of martensitic steels.

Toughness is dependent on temperature and generally increases with increasing temperature. One measure of toughness is impact toughness, that

is, the toughness measured on rapid loading. **Figure 9** shows the impact toughness for different categories of stainless steel at temperatures ranging from  $-200$  to  $+100^{\circ}\text{C}$ . It is apparent from the diagram that there is a fundamental difference at low temperatures between austenitic steels on the one hand and martensitic, ferritic, and duplex steels on the other.

The martensitic, ferritic, and duplex steels are characterized by a transition in toughness, from tough to brittle behavior, at a certain temperature, the transition temperature. For the ferritic steel, the transition temperature increases with increasing carbon and nitrogen content, that is, the steel becomes brittle at successively higher temperatures. For the duplex steels, increased ferrite content gives a higher transition temperature,

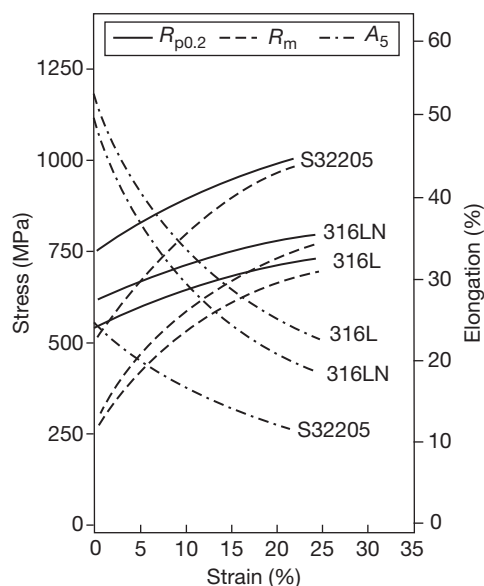


**Figure 8** Effect of cold work on some stainless steels. Reproduced from Leffler, B. *Stainless Steels and Their Properties*, 2nd revised ed.; Outokumpu Stainless Research Foundation, Stockholm, 1998.

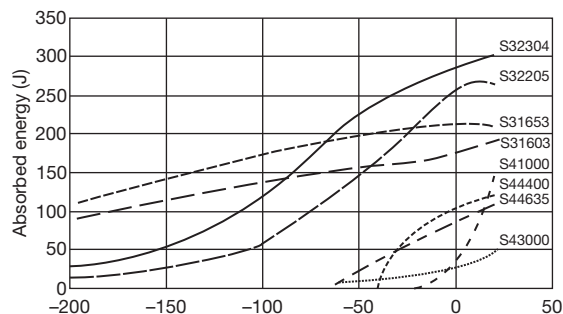


**Figure 9** Impact toughness for different types of stainless steels.

that is, more brittle behavior. Martensitic stainless steels have transition temperatures around or slightly below room temperature, while those for the ferritic and duplex steels are in the range  $0$ – $60^{\circ}\text{C}$ , with the ferritic steels in the upper part of this range.

The austenitic steels do not exhibit a toughness transition as the other steel types but have excellent toughness at all temperatures. Austenitic steels are thus preferable for low-temperature applications.

### 3.04.4.4 Fatigue Properties

During cyclic loading, stainless steels, like other materials, will fail at stress levels considerably lower than the tensile strength measured during tensile testing. The number of load cycles the material can withstand is dependent on the stress amplitude. **Figure 10** shows how the lifetime, that is, the number of cycles to failure, increases with decreasing load amplitude until a certain amplitude is reached, below which no failure occurs. This stress level is called the fatigue limit. In many cases, there is no fatigue limit, but the stress amplitude shows a slow decrease with an increasing number of cycles. In these cases, the fatigue strength, that is, the maximum stress amplitude for a certain time to failure (number of cycles) is called the fatigue strength and it is always given in relation to a certain number of cycles.

The fatigue properties of ferritic–austenitic and austenitic stainless steels with a fatigue limit at a lifetime of  $10^6$ – $10^7$  load cycles can be described by the Wohler curve or  $S$ – $N$  curve and related to their tensile strength, as shown in **Table 6**. The relation between the fatigue limit and tensile strength is also

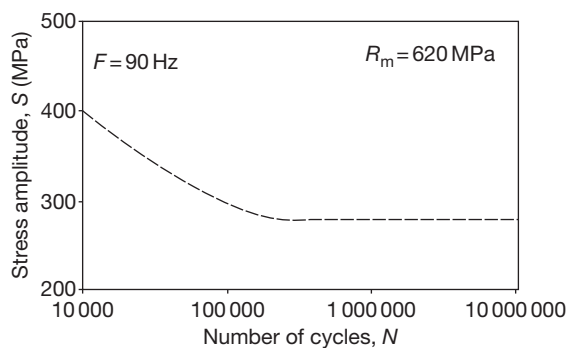


**Figure 10**  $S$ – $N$  curve (Wohler curve) for an austenitic stainless steel of Type S31600 (hMo) in air.  $S$  – stress amplitude,  $N$  – number of cycles. Reproduced from Leffler, B. *Stainless Steels and Their Properties*, 2nd revised ed.; Outokumpu Stainless Research Foundation, Stockholm, 1998.

**Table 6** Fatigue properties of stainless steels, relation between tensile strength and fatigue strength

Microstructure	$S_o/R_m$ , Stress ratio		Maximum stress
	$R=-1$	$R=0$	
Ferritic	0.7	0.47	Yield strength
Austenitic	0.45	0.3	Yield strength
Duplex	0.55	0.35	Yield strength

dependent on the type of load, which is the stress ratio ( $R$ ). The stress ratio is the ratio of the minimum stress to the maximum stress during the loading cycle. The compressive stresses are defined as negative.

### 3.04.5 Precipitation and Embrittlement

Under various circumstances, the different stainless steel types can suffer undesirable precipitation reactions, which can cause a decrease in both corrosion resistance and toughness.

#### 3.04.5.1 Embrittlement at 475°C

If martensitic, ferritic, or duplex steels are exposed to temperatures in the range 350–550°C, a serious decrease in toughness will occur after some time. The phenomenon is encountered in grades containing more than 15–18% chromium and the origin of this embrittlement is the decomposition of the ferrite into two phases of body-centered cubic, bcc, structure,  $\alpha$  and  $\alpha'$ . The former is very rich in iron and the latter very rich in chromium. This type of embrittlement is usually called 475°C embrittlement after the midpoint of the temperature range.

#### 3.04.5.2 Carbide and Nitride Precipitation

If ferritic steels are heated to temperatures above approximately 950°C, they suffer precipitation of chromium carbides and chromium nitrides during the subsequent cooling, which cause a decrease in both toughness and corrosion resistance. This type of precipitation can be reduced or eliminated by decreasing the levels of carbon and nitrogen to very low levels and/or stabilizing the steel by additions of titanium as in 18Cr–2Mo–Ti.

Carbide and nitride precipitation in austenitic and duplex steels occurs in the temperature range 550–800°C. Chromium-rich precipitates form in the grain boundaries and can cause intergranular

corrosion and, in extreme cases, even a decrease in toughness. However, during the short times in the critical temperature range experienced in the heat-affected zone adjacent to welds, the risk of deleterious precipitation is very small for the low-carbon steels.

#### 3.04.5.3 Intermetallic Phases

In the temperature range 700–900°C, iron alloys with a chromium content above about 17% form intermetallic phases such as  $\sigma$  phase,  $\chi$  phase, and Laves phase. These phases all have high chromium content and are brittle and consequently large amounts of these phases in the microstructure will lead to a drop in toughness and a decrease in resistance to certain types of corrosion.

Chromium, molybdenum, and silicon promote the formation of intermetallic phases, so the majority of ferritic, duplex, and austenitic steels show some propensity to form these phases. Intermetallic phases form most readily from highly alloyed ferrite. In ferritic and duplex steels, intermetallic phases therefore form readily but are, on the other hand, relatively easy to dissolve on annealing. In the austenitic steels, it is the highly alloyed grades that are particularly susceptible to intermetallic phase formation. The low chromium content and low molybdenum grades are considerably less sensitive to the precipitation of these phases.

Heat treatment may remove all types of precipitates by redissolving them. Renewed heat treatment of martensitic steels and solution annealing and quenching ferritic, duplex, or austenitic steels restore the microstructure. Relatively long times or high temperatures may be required for the dissolution of intermetallic phases in highly alloyed grades.

Stainless steels can pick up nitrogen if exposed to nitrogen-containing atmospheres such as nitrogen, nitrogen mixtures, and cracked ammonia. During nitrogen pick-up, nitrides and other brittle compounds of chromium, molybdenum, titanium, vanadium, and aluminum can form. Atmospheric oxygen, even at relatively low levels, reduces the risk for nitridation. At temperatures between 400 and 600°C, a layer of nitrides is formed at the steel surface; at higher temperatures, nitrogen uptake and nitride formation occur throughout the material. Nitridation, that is, nitride formation, causes chromium depletion and reduced oxidation resistance in the same way as carburization. This can lead to catastrophically high oxidation rates on the outer surface of equipment, which is subjected to a nitriding atmosphere on the inside – for example, the muffles in annealing

furnaces. Nitrogen pick-up can also cause embrittlement because of to surface or internal nitride formation. Nickel is the alloying element, which provides the greatest protection against nitridation, as nickel does not form stable nitrides.

#### 3.04.5.4 Carburization

If a material is exposed to gases containing carbon, for example, in the form of CO, CO<sub>2</sub>, or CH<sub>4</sub>, it can pick up carbon. The degree of carburization is governed by the levels of carbon and oxygen in the gas, also the temperature and steel composition. The carbon, which is picked up by the steel will largely form carbides, primarily chromium carbides.

The formation of a large amount of chromium carbides causes chromium depletion and thus a reduced resistance to oxidization, because carbides, or even a network of carbides, form in the grain boundaries as well as within the grains. The resistance to thermal cycling is reduced and, since carburization leads to an increase in volume, there is a danger of cracks developing in the material. Carbon pick-up can occur even at relatively low temperatures (400–800°C) in purely reducing–carburizing atmospheres and gives rise to catastrophic carburization or metal dusting. Attack is severe and characterized by ‘powdering’ of the steel surface because of the breakdown of the protective oxide layer and inward diffusion of carbon, which forms grain boundary carbides. The increase in volume on carbide formation means that grains are rapidly broken away from the steel surface, giving rapid and serious attack.

Chromium, nickel, and silicon are the alloying elements, which most improve resistance to carburization.

#### 3.04.5.5 Heat Treatment

The aim of heat treatment of stainless steels is to restore the microstructure after forming or other fabrication and production operations thereby removing or at least minimizing any possible negative effects. However, in the case of the hardenable stainless steels, that is, martensitic and precipitation-hardening grades, heat treatment is used to set the mechanical properties at the required level. In other cases, that is, stress relief heat treatment, the aim is to reduce the level of residual stresses caused by fabrication operations such as cold forming and welding.

##### 3.04.5.5.1 Solution annealing

Solution annealing is the most common heat treatment for ferritic, austenitic, and duplex stainless

steels, that is, the types of stainless steel in which the mechanical properties cannot be set by heat treatment. Instead the aim of the heat treatment is to restore the microstructure by allowing recrystallization to occur and deleterious phases, such as carbides and intermetallic phases, to be dissolved.

During solution annealing the material is heated to a temperature where detrimental phases will be dissolved, held at temperature for a time long enough to allow the unwanted phases to dissolve, and then rapidly cooled or quenched. Solution annealing is normally performed on austenitic and duplex stainless steels at temperatures above 1020°C. A higher alloying content will normally require a higher solution annealing temperature in order to produce a precipitate-free microstructure. For the stabilized austenitic grades, the temperature used should allow chromium carbides and other unwanted phases to dissolve but should be low enough to retain the titanium or niobium carbides used to stabilize the steel. Ferritic stainless steels are normally only annealed using temperatures below 1000°C. **Table 7** presents typical heat treatment as solution annealing or annealing temperatures for stainless steels.

Rapid cooling after heat treatment is normally required to ensure that unwanted reactions in the microstructure do not occur. Whether air- or water-cooling is required depends on parameters such as section thickness and the type of steel. It is not the cooling rate *per se* that is important, but the time spent in the temperature range in which precipitation or other unwanted reactions may occur. Higher alloyed grades and thicker sections will thus generally require water quenching rather than air-cooling.

##### 3.04.5.5.2 Quenching, tempering, and ageing

##### Martensitic grades

Heat treatment of the martensitic stainless steels is essentially the same as the heat treatment of other hardenable steels. The difference is that the high

**Table 7** Heat treatment temperatures for ferritic, austenitic and duplex stainless steels

Category	Temperature (°C)	Quenching
Ferritic	700–850	Water/forced air
Ferritic (high alloyed)	750–950	Water/forced air
Austenitic	1020–1100	Water/forced air
Austenitic (high alloyed)	1080–1200	Water
Duplex	1020–1150	Water

alloy content slows the transformation reactions and increases hardenability.

The normal heat treatment cycle of martensitic stainless steels is

1. hardening by austenitizing at temperatures of 950–1050°C followed by quenching in oil or water, and
2. tempering at temperatures of 300–700°C to set final properties.

Quenched hardness will increase with increasing austenitizing temperature in the lower end of the temperature range, but austenitizing in the high end of the temperature range will lower the as-hardened hardness.

Tempering is designed to allow the material to reach an optimum between strength and ductility. The tempering temperature is thus dependent on the strength level specified and these may normally be found in the appropriate product standards.

#### **Precipitation hardening Grades**

These steels can be divided into three subcategories: martensitic, semiaustenitic, and austenitic grades. All of the precipitations hardening grades depend on a precipitation reaction to induce the strengthening during aging. The precipitates may differ from grade to grade, but the principle is that a solution anneal is used to put some alloying elements into solution at high temperature followed by quenching to low temperature at which a supersaturated solution is obtained. Ageing at an elevated temperature will then cause the precipitation and hardening resulting in an increased strength. The heat treatment cycles of the different types of precipitation-hardening steels can be summarized as follows:

1. Martensitic grades
  - a. solution anneal in the austenite region (1020–1050°C)
  - b. quench to room temperature
  - c. age at 470–630°C to produce precipitation and hardening
2. Semiaustenitic grades
  - a. solution anneal in the austenite region (1020–1050°C)
  - b. quench to room temperature followed by sub-zero cooling or tempering at about 750°C
  - c. age at 470–570°C to produce precipitation and hardening
3. Austenitic grades
  - a. solution anneal (1000–1100°C)
  - b. quench to room temperature
  - c. age at 700–800°C to produce precipitation and hardening

#### **3.04.5.5.3 Stabilization annealing**

A stabilization heat treatment is applied to titanium- or niobium-stabilized grades in order to enhance the resistance to intergranular corrosion, that is, to make sensitization more difficult. The aim of this treatment is to ensure that the carbon dissolved in the matrix is forced to combine with the stabilizing element, for example, titanium or niobium, thus becoming securely locked up in as titanium or niobium carbides and therefore not unavailable for chromium carbide formation.

Titanium and niobium both form more stable carbides than do chromium and these carbides precipitate at higher temperatures than do chromium carbides. The stabilizing treatment therefore consists of heat treatment at a temperature slightly above the temperature range for chromium carbide precipitation. The temperature selected is normally in the range as low as possible in order to obtain maximum driving force for the precipitation. Stabilization heat treatment is usually performed at temperatures in the range 850–980°C on material that has previously been solution annealed. The lower part of the temperature range should be used with some caution, as this type of treatment is not equally effective in all environments.

### **3.04.6 Physical Properties**

The physical properties of the different stainless steels are dependent on both the microstructure (crystal structure) and the amount of alloying elements added. In many cases the physical properties cannot be manipulated by heat treatment or fabrication practices and are more or less 'locked' in the atomic arrangement of the steel. Again, the grouping of the property values follows the division of steel grades into the main stainless categories.

Ferromagnetism is a characteristic property of ferrite and martensite while austenite is not ferromagnetic. This means the ferritic and martensitic stainless steels are strongly magnetic while the fully austenitic stainless steels are nonmagnetic. However, since many of the more common and lower alloyed austenitic grades contain small amounts of ferrite they might show a weak magnetic behavior. The duplex steels containing about 40–60% ferrite will naturally be magnetic even if their magnetism is weaker than that of the ferritic or martensitic stainless steels.

Regarding the other physical properties it may be noted that the thermal expansion is strongly related to

the microstructure and this gives the austenitic steels a thermal expansion that is about 50% higher than that of the ferritic and martensitic stainless steels. The thermal conductivity is lower for austenitic steels compared with that of the ferritic or martensitic steels and within each category the thermal conductivity decreases with increasing alloying content. Other properties such as thermal capacity and the modulus of elasticity show relatively little variation across the different stainless steel categories. The most highly alloyed austenitic grades have a somewhat lower modulus compared with other stainless steels.

Typical values of the physical properties for the some stainless steels from the different categories are shown in [Table 8](#).<sup>11,12</sup>

### 3.04.7 Property Relationships for Stainless Steels

Martensitic and martensitic–austenitic stainless steels are characterized by their high strength but limited corrosion resistance. An increased carbon content increases strength, but at the expense of lower toughness and considerable degradation of weldability. The martensitic 13% chromium steels, with higher carbon contents, are not designed to be welded, even though it is possible under special circumstances. In order to increase high temperature strength, alloying with strong carbide formers such as vanadium and tungsten are used. An increase in

the nickel content also increases toughness. In contrast to the martensitic steels, the martensitic–austenitic steels do not have to be welded at elevated temperatures except in thick sections; even then only limited preheating is required.

The areas of use of martensitic and martensitic–austenitic steels are naturally those in which the high strength is an advantage and the corrosion requirements are relatively low. The martensitic steels with low carbon contents and the martensitic–austenitic steels are often used as stainless constructional materials. The martensitic steels with high carbon content are used for springs, surgical instruments, and for sharp-edged tools such as knives and scissors.

The ferritic steels are characterized by good corrosion properties, very good resistance to chloride-induced stress corrosion cracking (SCC), and moderate toughness. The toughness of ferritic stainless steels is generally not particularly high. Lower carbon and nitrogen levels give a considerable improvement in both toughness and weldability, although toughness is limited for thicker dimensions. Consequently ferritic steels are usually only produced and used in thinner dimensions. Ferritic stainless steels are used in household products and in applications with fairly low demands of the corrosion resistance of the material in combination with aesthetic reasons. Examples of such application areas are cookware lids, washing machine drums, refrigerator doors etc. They have stress–strain data similar to carbon steel; generally have higher yield strength than the austenitic stainless steels. Their

**Table 8** Typical physical properties of some stainless steels<sup>1</sup>

<i>Stainless steel grade</i>	<i>Density (kg dm<sup>-3</sup>)</i>	<i>Modulus (GPa)</i>	<i>Thermal expansion (10<sup>-6</sup> °C<sup>-1</sup>)</i>	<i>Thermal conductivity (W m<sup>-1</sup> °C<sup>-1</sup>)</i>	<i>Thermal capacity (J kg<sup>-1</sup> °C<sup>-1</sup>)</i>	<i>Electrical resistivity ( m)</i>
	<i>RT</i>	<i>RT</i>	<i>RT–400 °C</i>	<i>RT</i>	<i>RT</i>	<i>RT</i>
Ferritic						
S43000	7.7	220	10.5	25	460	0.60
Martensitic						
S42000	7.7	215	12.0	30	460	0.65
Duplex						
S32205	7.8	200	14.5	15	500	0.80
Austenitic						
S30100	7.9	200	18.0	15	500	0.73
S20100	7.8	200	17.5	15	500	0.70
S30403	7.9	200	18.0	15	500	0.73
S31603	8.0	200	17.5	15	500	0.75
N08904	8.0	195	16.9	12	450	1.00
S31254	8.0	195	18.0	14	500	0.85
S34565	8.0	190	16.8	12	450	0.92

RT, room temperature.



thermal conductivity is high and they transmit heat efficiently, which is one of the reasons to frequent use in electric irons and heat exchangers. They have further a low thermal expansion coefficient, lower than for the austenitic stainless steels, which give them less distortion when heated. Ferritic stainless steels are widely used in large tonnage all over the world.

The modern duplex steels span the same wide range of corrosion resistance as the austenitic steels depending on the alloy composition. Duplex equivalents can be found to both the ordinary austenitic grades, such as S31600 (1.4401), and to the high-alloyed austenitic grades, such as S31254 (1.4547). The corrosion resistance of S32304 (1.4362) type duplex is similar to that of S31600 (1.4401) while S32205 (1.4462) is similar to N08904L (1.4539) and S32750 (1.4410) is similar to the high-alloyed austenitic grades with 6% molybdenum, such as S31254 (1.4547). High strength, good toughness, and very good corrosion resistance characterize the duplex steels in general and excellent resistance to chloride-induced SCC and corrosion fatigue in particular. An increased level of chromium, molybdenum, and nitrogen increases corrosion resistance, while the higher nitrogen level also contributes to a further increase in strength above that associated with the duplex structure. Applications of duplex steels are typically those requiring high strength, good corrosion resistance and low susceptibility to SCC or combinations of these properties. The lower alloyed S32304 (1.4362) is used for applications requiring corrosion resistance similar to S31600 (1.4401) or lower and where strength is an advantage. Some examples of such applications are: hot water tanks in the breweries, pulp storage towers in the pulp and paper industry, tanks for storage of chemicals in the chemical process industry, and tank farms in tank terminals in the transportation industry. The higher alloyed S32205 (1.4462) is, for example, used in pulp digesters and storage towers in the pulp and paper industry where it is rapidly becoming a standard grade. It is also used in piping systems, heat exchangers, tanks and vessels for chloride-containing media in the chemical industry, in piping and process equipment for the oil and gas industry, in cargo tanks in ships for transport of chemicals, and in shafts, fans, and other equipment which require resistance to corrosion fatigue. High alloyed grades, for example, S32750 (1.4410), are used in piping and process equipment for the offshore industry, that is, oil and gas and in equipment for environments containing high chloride concentrations, such as seawater.

Very good corrosion resistance, very good toughness, and very good weldability characterize the austenitic steels. They are also the most utilized stainless steels. Resistance to general corrosion, pitting, and crevice corrosion generally increases with increasing levels of chromium and molybdenum. The low-carbon grades exhibit good resistance to intergranular corrosion and consequently the higher alloyed steels are only available with low carbon contents. Austenitic steels are generally susceptible to chloride-induced SCC; only the highly alloyed steels such as N08904 (1.4529), and S31254 (1.4547) exhibit good resistance to this type of corrosion.

The austenitic stainless steels are used in almost all types of applications and industries. Typical areas of use include piping systems, heat exchangers, tanks and process vessels for the food, chemical, pharmaceutical, pulp and paper, and other process industries. Nonmolybdenum alloyed grades, for example, S30400, are normally not used in chloride-containing media but are often used where demands are placed on cleanliness or in applications in which equipment must not contaminate the product. The molybdenum-alloyed steels are used in chloride-containing environment with the higher alloyed steels, N08904, S31254, being chosen for higher chloride contents and temperatures. S31254 is used to handle seawater at moderate or elevated temperatures. Applications include heat exchangers, piping, tanks, process vessels, etc. within the offshore, power, chemical and pulp- and paper industries. The low-alloyed grades, especially S30400 and S31600, are used in equipment for cryogenic applications. Examples are tanks, heaters, evaporator, and other equipment for the handling of condensed gases such as liquid nitrogen. Finally it is worth mentioning that austenitic stainless steels are often used in applications requiring non-magnetic materials since they are the only nonmagnetic steels.

### 3.04.8 Corrosion Properties of Stainless Steels

Stainless steels are widely used throughout the world in a variety of applications in both industrial and domestic environments, for example, as a construction material, in the manufacture of everyday utensils. The use of stainless steels has been growing steadily and new areas of application, often in demanding service environments, are constantly being developed. The serviceability of stainless steels

in many of these applications is determined by the material properties of the steels and how they perform when exposed to different service environments. Historically, the success stories of stainless steel usage have been widely accounted for in corrosion engineering. Extensive research has been carried out with the aim of reducing further the risk of various types of corrosion by choosing appropriate stainless steel grades for specific service environments. The following chapter is intended as a guide for explaining the different types of corrosion mechanisms that can affect stainless steel and their causes. This section also aims to increase the knowledge of stainless steels and their corrosion resistance in different service environments. Depending on the service environment involved, several types of corrosion may affect stainless steels.

**Figure 11** shows part of a stainless steel pipe after service in a very severe corrosive environment consisting of high amounts of chlorides, water, and oxygen in combination with high temperatures under evaporative conditions. The pipe suffered from several corrosion forms that affect stainless steels, notably pitting corrosion, crevice corrosion and SCC.

#### 3.04.8.1 Passivity

The reason for the good corrosion resistance of stainless steels is that they form a very thin, invisible



**Figure 11** SCC, crevice corrosion, and pitting corrosion on a stainless steel pipe, after service in a very aggressive environment consisting of high amounts of chlorides, water, and oxygen in combination with high temperatures under evaporative conditions. Photo: Outokumpu Stainless.

surface film, so called passive film or passive layer in oxygen containing environments. The passive film is mainly a chromium oxide, which protects the steel from corrosion attack in an aggressive environment. For a passive film to form on a stainless steel surface, a certain amount of chromium is required in the steel as an alloying element. As chromium is added to steel, a rapid reduction in corrosion rate is observed around 10 wt% because of the formation of this protective layer or passive film, as illustrated in **Figure 12**.

The commercial alloys of austenitic stainless steels typically contain between 16 and 28 wt% of chromium, while the chromium content of ferritic stainless steels ranges from 10.5 to 30 wt%. The chromium content varies in martensitic stainless steels, from 11.5 to 18 wt% and in duplex stainless steels; it is usually between 21 and 29 wt%. A passive film on a stainless steel surface consists of an inner layer of mixed iron/chromium oxides and an outer layer of chromium hydroxide. This film has self-healing properties when damaged in the presence of oxygen and a repair of the passive film can easily form after a scratch or other surface damage.

The thickness of a passive film is commonly considered to be in the range of 1–3 nm, depending on the service environment and the steel grade, but it also depends on pH values and the electrochemical properties in contact with a surrounding solution.

#### 3.04.8.2 Contribution of Main Alloy Elements to Passivation

As already indicated, chromium is the most important alloying element for corrosion resistance in stainless steels as it helps to form a passive film on

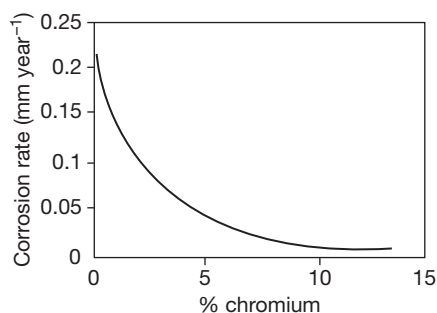


**Figure 12** The effect of chromium content on passivity. Reproduced from Design Guidelines for the selection and use of stainless steel, specialty steel industry of the United States, Washington, DC, USA.

the surface. The spontaneous formation of intact chromium oxide on the surface acts as a barrier layer and the surface electrochemistry is changed as a result of equilibrium reactions between the passive film and any surrounding solution.

It is also well-accepted and proved that the addition of molybdenum, as an alloying element, offers an efficient method for preventing corrosion in stainless steel by improving the passive film properties. The molybdenum content in stainless steels can be as much as 8%. However, the exact mechanism of detailed chemistry of molybdenum in a passive film with respect to passivity, interaction, and formation of compounds is the subject of extensive discussion, since molybdenum as an alloying element shows a complex oxide chemistry in the passive film with many oxidation stages.

The addition of nitrogen contributes to enhancing the resistance to pitting and crevice corrosion on austenitic stainless steels.<sup>14</sup> As the nitrogen stays soluble in the stainless steel, without any precipitation, the localized corrosion resistance is improved for rather high amounts. However, if nitrides are formed in the stainless steel the corrosion resistance is drastically decreased. More about nitride precipitation can be read in [Section 3.04.5](#).

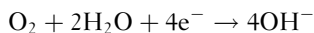
Nickel contributes to improved corrosion properties by assisting the repassivation process and helping reduce the rate of corrosion, for example, in strong acid solutions.

### 3.04.8.3 General Electrochemical Considerations in Corrosion of Stainless Steels

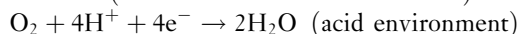
The basic electrochemical reactions for corrosion are that the metal, Me, is defined as the anode and balances the oxygen reduction attributed to the cathode.



In the classical electrochemical oxygen cathodic reaction there are two pathways accepted for the reduction according to.

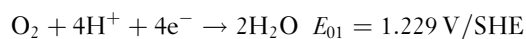


(neutral or alkaline environment)

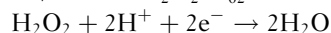
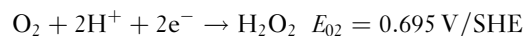


The oxygen reduction is, however, a known complex process with many proposed pathway, for example:

Four electron pathway:

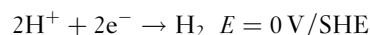


Two electron pathway:



The reduction pathway is influenced by many factors, for example, the surface composition of the electrodes.

In strongly reducing environments, reduction of hydrogen ions is often the cathodic reaction to balance the metal dissolution:



The oxidation of a metal, that is, corrosion, requires always a counter balance by a reduction.

A common test procedure for the investigation of stainless steel's resistance to corrosion in wet environments is to perform dynamic anodic polarization measurements in a conductive solution to obtain a polarization curve. [Figure 13](#) shows a schematic polarization curve undertaken for a stainless steel presenting the different potential area and the current density response.

The high current densities shown in [Figure 13](#) represent a corrosion process and the very low current response represents the passivity of a stainless steel. At low cathodic potentials, a line of high current densities represents the cathodic reaction. At the potential, when the cathodic reaction and the anodic reaction meet in the active area on occurring corrosion is denoted the corrosion potential,  $E_{\text{corr}}$ .

At the higher anodic potential, the passivity is represented by a decrease in current densities corresponding to the passivation current to stabilize in the passive potential area to a very low current density, the passive current density. Pitting corrosion or crevice corrosion is typically represented by a steep increase in the current response at an even higher potential, the pitting potential,  $E_p$ . Transpassive corrosion is represented by an increase in current density response in a rather extended potential area at even higher anodic potentials, associated with the transpassive potential,  $E_{\text{tr}}$ . In order to investigate the ability of a stainless steel to repassivate in, for example, chloride environment, a reverse scan is commonly performed while performing polarization measurements. The current response on the repassivation process is a clear decrease in the passive current and the potential for the steep decrease is noted repassivation potential,  $E_{\text{rp}}$ .

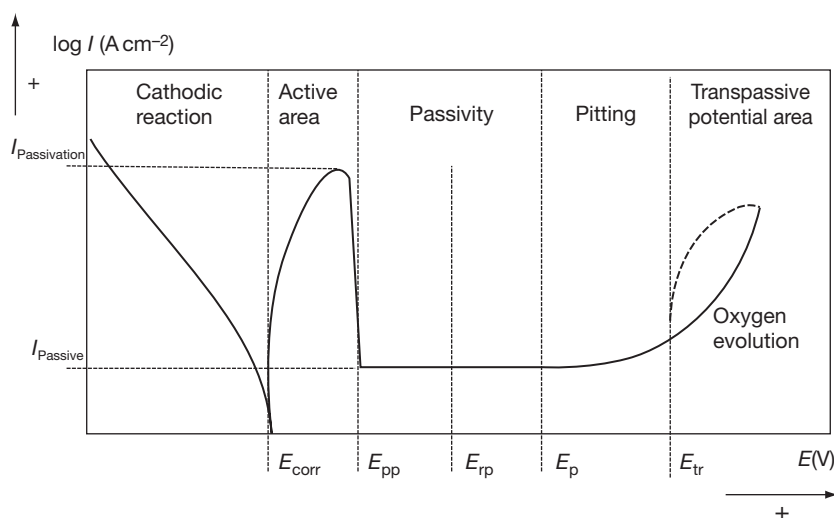


**Figure 13** Schematic polarization curve for a stainless steel.

#### 3.04.8.4 Breakdown of Passivity

All corrosion forms on stainless steels are related to any permanent damage of the passive film, either as a complete breakdown of the film causing uniform corrosion or locally as in pitting and crevice corrosion. Intergranular corrosion occurs along grain boundaries due to local breakdown of the passive film where chromium has been depleted. Once the passivity of stainless steel is broken down, completely or locally, and repassivation is not promoted by the aggressiveness of the surrounding solution, active corrosion occurs.

Local breakdown such as pitting and crevice corrosion is commonly initiated in neutral solutions, but can also occur in solutions with a low pH. The general aspect to consider in pitting and crevice corrosion is the very fast corrosion rate that can cause penetration through the steel in a short time and may lead to catastrophic failure.

Complete breakdown of the passive film causing uniform corrosion may occur in solutions of either low or high pH. Uniform corrosion or general corrosion occurs when the passive layer on a stainless steel surface breaks down partly or completely. The corrosion then propagates at a rate determined by a corrosive environment and the alloy composition in combination. Uniform corrosion causes a corrosion rate that can be expressed as a mean value of the attacked surface, making it possible to calculate a material loss, from weight loss determinations.

An even worse type of corrosion from the construction service point of view is SCC, which is characterized by the cracking of materials that are subjected to both a tensile stress and a corrosive environment. Most reported failures due to SCC occur in the standard stainless steel grades S30400 and S31600 with tensile stress in aqueous solutions containing chlorides at elevated temperatures,  $>60^{\circ}\text{C}$ . However, solutions containing chlorides are not the only environments that cause SCC in stainless steels. Similar cracking can also occur in hot caustic solutions and in environments containing impurities such as hydrogen sulfide.

#### 3.04.8.5 Localized Corrosion – Pitting and Crevice Corrosion

Smialowska recently reviewed the tremendous work performed on pitting and crevice corrosion and the use of electrochemistry to characterize stainless steel regarding pitting and crevice corrosion.<sup>15</sup> Detailed information about pitting and crevice corrosion and the historical research can be read in this review.

Defects in the passive film enhance the risk of pitting and crevice corrosion. Manganese sulfides are identified to be initiation points to pitting and crevice corrosion. However, in modern commercial stainless steels, the sulfur content is normally so low that there are only few recent reports about sulfur causing pitting corrosion.

Environments, which represent the greatest risk of pitting and crevice corrosion of stainless steels,

include seawater and process solutions in which there is a high concentration of chlorides sometimes also in combination with an increased temperature. High halide concentration, commonly chlorides, low pH, and high temperature increase the probability of pitting and crevice corrosion on stainless steels. Pitting corrosion may also be caused by the presence of thiosulphate in combination with chloride ions. The risk of pitting corrosion increases when the relative levels of thiosulfate, sulfate, and chloride reach a certain amount, but can be avoided by controlling the amount of thiosulfate.

Different types of formulas have been proposed to rank the resistance of stainless steels to pitting corrosion and to compare a steel grade among other grades by the influence of main alloying elements. The pitting resistance equivalent (PRE) of a specific steel grade can be estimated by formulas in which the relative influence of a few elements, that is, chromium, molybdenum, and nitrogen, are considered. The higher the PRE value of a stainless steel, the better the resistance to pitting corrosion in neutral chloride containing solutions. Table 9 shows the compositions of some commercial stainless steels and calculated PRE, indicating their relative pitting corrosion resistance.

One frequently used expression is:

$$\text{PRE} = \% \text{Cr} + 3.3\% \text{Mo} + 16\% \text{N}$$

There are also other formulas with different alloying elements included, such as manganese, wolfram, sulfur, and carbon.

Alfonsson and Qvarfort investigated some formulas for PRE, based on the chromium, molybdenum, and nitrogen content and compared the PRE values with critical pitting temperatures (CPT) measured potentiodynamically, using the Avesta cell.<sup>16</sup> They found an acceptable linearity between the CPT and PRE values for any of the PRE formulas studied.

### 3.04.8.5.1 Influence of alloy composition on localized corrosion

The increase in the chromium content and molybdenum content enhances the passive potential area to more anodic potentials and consequently increases the stainless steel's ability to passivate in more aggressive solutions. The higher alloyed stainless steel grades, for example, those containing 6% of molybdenum, do not often show any pitting potential due to pitting corrosion in polarization measurements at room temperature, and elevated temperatures are often required to break down the passivity in high amounts of chlorides.

Horvath and Uhlig investigated the influence of chromium, nickel, and molybdenum on the pitting potential in sodium chloride, NaCl, and sodium bromide, NaBr. They showed that the alloying elements, which had the greatest influence on the pitting

**Table 9** Typical chemical compositions and PRE numbers for some commercial stainless steel grades

Steel grade			Typical chemical composition (wt%)					PRE
UNS	EN	Microstructure	Cr	Ni	Mo	N	Other	
S41000	1.4006	Martensitic	11.5			0.04		11.5
S42000	1.4021	Martensitic	12					12
S43000	1.4016	Ferritic	16					16
S44400	1.4521	Ferritic	17		1			20
S20100	1.4372	Austenitic	17	5		0.15	Mn (7.08)	19
S20400		Austenitic	16	2.2		0.17	Mn (9.07)	19
S30100	1.4310	Austenitic	17	7				17
S30100	1.4318	Austenitic	17.7	6.5		0.13		20
S34700	1.4550	Austenitic	18	9.5		0.04	Nb, Mn(2.0)	18
S30400	1.4307	Austenitic	17.5	8				17.5
S31600	1.4404	Austenitic	17.2	10.2	2.1			25
S31600	1.4571	Austenitic	16.5	10.5	2		Ti	23
N08904	1.4539	Austenitic	20	25	4.5		Cu (1.5)	36
S31254	1.4547	Austenitic	20	18	6.1	0.20	Cu	43
S32101	1.4162	Duplex	21.5	1.5	0.3	0.22		26
S32304	1.4362	Duplex	22	3.5	0.1	0.10		23
S32205	1.4462	Duplex	22	5.5	3	0.17		35
S32750	1.4410	Duplex	24	6	3	0.27		38



potential, were chromium and molybdenum. The addition of nickel resulted in a minor increase of the pitting potential compared with the results obtained by the addition of chromium and molybdenum.<sup>17</sup> **Figure 14** shows the influence of alloying elements on pitting potentials in NaCl extracted from Horvath and Uhlig.<sup>17</sup> Comparing the data with an increasing addition of chromium in a Cr–Fe alloy, the pitting potential was around 0.2 V/SHE for 20 wt% chromium, which rose to around 0.9 V/SHE at 38 wt% of chromium. For nickel in a 15% Cr–Fe alloy, the pitting potential was at 20% Ni, 0.28 V/SHE, which at 40 wt% Ni increased to only 0.35 V/SHE. In contrast to the low increase in the pitting potential produced by the addition of nickel, the addition of molybdenum produced a significant influence, even at very low amounts. The pitting potential increased from 0.3 V/SHE for 0.48 wt% up to 0.76 for 2.4 wt% in a 15%Cr–13%Ni stainless steel.

As previously mentioned the presence of nitrogen increases the resistance of pitting and crevice corrosion on stainless steels. Jargelius-Pettersson showed that the effect of nitrogen was depressing both the active dissolution and passive current. The author also showed that the positive effect was pronounced in combination with molybdenum.<sup>18</sup> There are further methods to increase the surface content of nitrogen to enhance the pitting and crevice corrosion resistance of a stainless steel.

#### 3.04.8.5.2 Pitting corrosion

Pitting is a type of localized corrosion that is characterized by attacks at small discrete spots on the stainless steel surface. The pits often appear to be

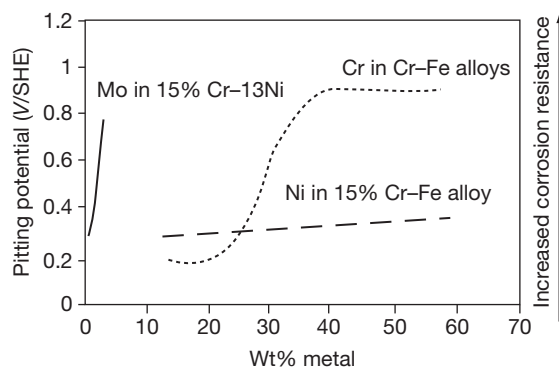


**Figure 14** Dependence of chromium, nickel and molybdenum in 0.1 M NaCl at 25 °C. Reproduced from Horvath, J.; Uhlig, H. H. *J. Electrochem. Soc.* **1968**, *115*(8), 791.

rather small on the surface, but may have larger cross section areas deeper inside the metal as indicated in **Figure 15**. When the metal corrodes inside the pit, dissolved metal ions generate an environment with a low pH and chloride ions migrate into the pit to balance the positive charge of the metal ions. The environment inside a growing pit gradually becomes more aggressive by the generation of hydrogen ions contributing to the ingress of chloride ions through a lacy cover to maintain the electroneutrality in the pit solution. The repassivation becomes less likely due to the increased aggressiveness in the pit solution and also by the restriction to mix the pit solution to the surroundings by the diffusion barrier of the lacy cover on top of the pit. **Figure 16** shows schematically the

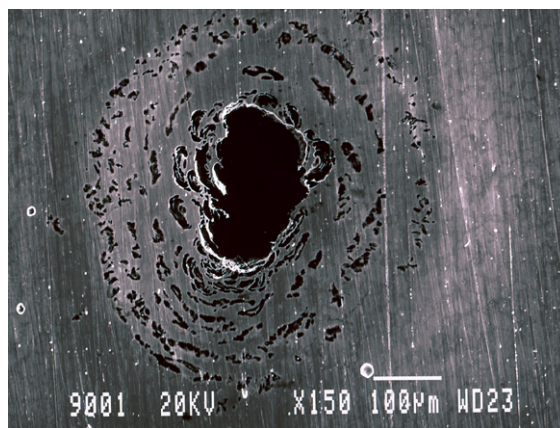


**Figure 15** Pitting corrosion on stainless steel, image from scanning electron microscope, SEM, Outokumpu Stainless, R. Qvarfort.

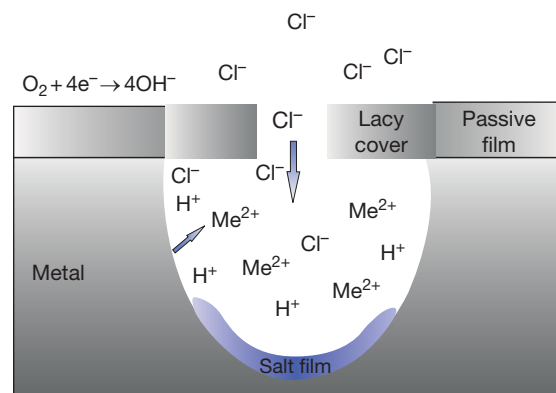
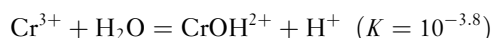


**Figure 16** Schematic presentation of the pit chemistry and the diffusion restriction due to corrosion product formation and the lacy cover of a stainless steel suffering from pitting corrosion.



pit chemistry and the diffusion restriction due to corrosion product formation and the lack of a protective layer on a stainless steel suffering from pitting corrosion. Since pitting may not be immediately visible from a surface inspection and may indeed be concealed altogether if the propagation occurs inside the pit rather than close to the surface, a pitting attack often remains undiscovered until it causes perforation and leakage.

In order for pitting corrosion to propagate and thrive in stainless steels, a concentrated pit solution is needed, else passivation processes would interrupt active corrosion. This solution is produced inside the pit as a result of the increase in the concentration of the dissolved metal. However, the exact chemistry of the solution inside an active pit is not yet determined. Newman has reviewed the research undertaken in recent years to explain the concept of pitting corrosion in stainless steels.<sup>19</sup> The author simplifies the complexity in the chemical reactions inside the pit by indicating that the low pH level results from a large ionic activity coefficient superimposed on hydrolysis reaction such as



Newman also describes the dependence of active dissolution rate on the concentration of dissolved products inside the pit.<sup>19</sup> Tester and Isaacs associated this anodic dissolution process in the pit by anodic diffusion control across an iron-rich salt film formed in the bottom of the pit.<sup>20</sup> The salt film stabilizes the dissolution process by providing a reservoir of acid but at the same time, it consumes acidity in the interface, leading to passivation when the aggressive solution inside the pit is not maintained. Landolt and Grimm showed further that this diffusion-controlled anodic dissolution process reaction was hindered when the amount of chromium in the steel increased to about 25%.<sup>21</sup>

Donker and Degg showed already in 1927 that, by applying an external potential to an iron anode, a pitting potential corresponds to a large increase in the current passing through an electrochemical cell using a cathode of silver and solutions of various salts.<sup>22</sup> The technique was then used by Brenner to study the passivity of stainless steels.<sup>23</sup> Streicher showed in 1956 that by applying a constant current instead of a potential the number of pits per unit of area found for a specific combination of steel and corrosive solution depends directly on the density of the current passing through the surface of a specimen. He also demonstrated the differences in the extent of pitting at increasing current densities and that the pitting data obtained for a certain stainless steel at one temperature cannot be used to predict the

behavior of other stainless steels or for the same steel at other temperatures.<sup>24</sup>

The pitting potential is characterized by the susceptibility of alloys to a defined environment and has been used extensively to rank different steel grades regarding pitting corrosion resistance in various environments containing halides such as chlorides. Laycock *et al.* recently stated that there was an obvious similarity between the pitting potentials of pits and crevices and related the pitting potential to the transition potential between the two regimes to activation control at lower potentials for metastable pitting, where crevice corrosion commonly occurs and diffusion control at higher potentials, where pitting corrosion occurs.<sup>25</sup>

In Smialowska's review of pitting corrosion, the induction time for pit initiation is referred to as the time required to form the first pit on a passive metal exposed to a solution containing aggressive anions (e.g.,  $\text{Cl}^-$ ).<sup>26</sup> Schwenk showed that this induction time at constant chloride content varies as a function of applied potential.<sup>27</sup> The induction time is shorter at a higher applied potential than at a lower potential.

### Critical pitting temperature (CPT)

Brigham and Tozer introduced the postulation of temperature dependence in pitting corrosion in 1973 to use for comparison of a large range of stainless steels with varying pitting corrosion resistance.<sup>28</sup> The authors introduced a method to test pitting corrosion properties in a potential area where temperature showed the main influence on pitting corrosion regardless of the potential. However, later the method was further developed by the introduction of a crevice-free cell by Qvarfort and he showed by polarization measurements that there is a temperature, above which the corrosion is pitting corrosion, but below this temperature pitting corrosion is impossible. This critical pitting temperature was illustrated in dynamic anodic polarization measurements showing a pitting potential above the CPT and transpassive corrosion at higher anodic potentials at a temperature below the CPT. He also showed that the transition between the transpassive corrosion and pitting corrosion was very abrupt at a temperature range  $\pm 1^\circ\text{C}$ .<sup>29</sup> The concept of critical pitting temperature was thereafter developed to measure potentiostatically at 700 mV/SCE in 1 M sodium chloride and it is, at present, widely used as standard (ASTM G 150). The method is used for ranking purposes of higher alloyed stainless steel grades

containing high levels of molybdenum and chromium. Figure 17 illustrates the potential dependence and independency of the CPT.

Newman has summarized the concept of CPT for stainless steel to understand the corrosion of stainless steel by the emphasis on the temperature as the main parameter for pitting corrosion.<sup>19</sup> The CPT is suggested to be the temperature at which passivation occurs simultaneously as the precipitation of an anodic salt film in the pit. The CPT for a specific stainless steel currently refers to the temperature at which passivation reactions intervene in active corrosion. Newman suggests further that two regimes of pit growth can be identified one under mixed activation/ohmic control, which is usually found at lower potentials, and the second under diffusion control, generally at higher potentials with a salt film in the pit bottom.<sup>19</sup> As a lacy cover at the pit mouth develops, it stabilizes the dissolution of the pit, but the dissolution is still metastable at this stage and as pitting corrosion is established, the cover will finally collapse. Repassivation occurs either because of the absence of the salt film or as the lacy cover ruptures. As long as the pit is growing and the salt film is present, the pitting corrosion is under diffusion control. The transition between those two domains is characterized by a transition potential,  $E_T$ . In general, the pitting potential  $E_p$  is the lowest transition potential  $E_T$ , the potential at which stable pitting can be distinguished for a specific stainless alloy and aggressive environment.

Nyman suggests that in order to compare two different stainless steels, for example, S30400 and

S31600 the following relation has to be considered<sup>19</sup>:

$$E_T = E_{\text{corr}} + b_a \log(i_L/i_{\text{corr}}) + \varphi_s$$

where  $E_{\text{corr}}$  and  $i_{\text{corr}}$  are the corrosion potential and corrosion current density, respectively, in the saturated pit solution;  $b_a$  is the anodic Tafel slope;  $i_L$  is the anodic limiting current density; and  $\varphi_s$  is the ohmic potential drop in the pit cavity, which is constant.

When the concentration of the metal cations is at, or slightly above the saturation concentration of metal cations, precipitation of the salt film occurs. In order to precipitate, an anodic current density greater than or equal to the limiting current density, has to flow in the cavity where pitting initiates. The anodic current density required to maintain the local chemistry is then compared with the critical current density for passivation  $i_{\text{crit}}$  from Salinas-Bravo and Newman<sup>30</sup>. For relatively concentrated solutions very clean linear plots of  $E_T$  vs  $\log i_L$  can be generated using artificial pits.

$$I_{\text{crit}}(T, C_s) = nFDC_s/\delta$$

where  $i_{\text{crit}}$  is the critical current density for passivation,  $D$  is the diffusivity of metal ions,  $\delta$  the diffusion length (pit depth),  $C_s$  is the metal ion concentration at the pit surface,  $n$  the charge number, and  $F$  the Faraday's constant.

Salinas-Bravo and Newman also considered that this critical current density exists in the most aggressive pit environment and also considered it to be a steeper function of the temperature than the anodic limiting current density. The concept of CPT was

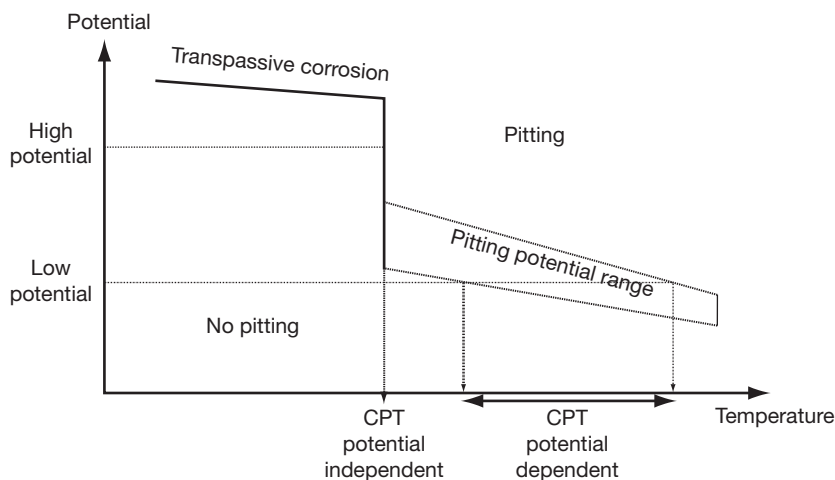


Figure 17 Potential dependence in transpassive and pitting corrosion.

then concluded to be when the critical current density equals the anodic limiting current density and the temperature at which the salt precipitation is possible.<sup>30</sup> Newman concludes recently, however, that the steeper function of the temperature is trivially true for experiments carried out in strong HCl solution mimicking the pit environment but that there are no precise data available for real pit environments at present.<sup>19</sup>

Moreover, the diffusion length is included in the concept of temperature dependence, which can explain why crevice corrosion appears at lower temperatures than pitting corrosion. Notable is, that the diffusion length in a crevice is generally longer and consequently any CCT, critical crevice corrosion temperature, is lower than CPT for a defined stainless alloy.

**Figure 18** shows a photograph of a stainless steel surface with pitting corrosion after CPT measurement using a crevice-free flush port cell.

Even if the CPT has proved to be a useful value for ranking a wide range of stainless steels with regard to their pitting resistance, it does not necessarily accurately reflect their performance and properties in actual environments. **Figure 19** shows examples of CPT for increasing chromium and molybdenum contents in various stainless steel grades represented by their PRE values. The figure indicates the very strong dependence of corrosion properties on the alloy composition of stainless steels. The difficulties associated with obtaining CPT values for lower

alloyed stainless steels are obvious. Lower alloyed stainless steels such as ferritic stainless steels containing 12% of chromium seem to have CPT values well below room temperature and these steel grades commonly corrode at temperatures of only a few or even below 0°C under these very aggressive conditions.

### 3.04.8.5.3 Crevice corrosion

Crevice corrosion attacks start in a narrow crevice or under a deposit on the stainless steel surface. Cavities, such as those found at flange joints or at threaded connections, are thus often the most critical sites for corrosion of stainless steels.

In narrow crevices, it is possible for a liquid to penetrate into the crevice and cause stagnant conditions by capillary forces. Oxygen and other oxidants are then consumed for the maintenance of the passive layer inside the crevice, the supply of oxygen is after some time restricted, causing a weakened passive layer. Small amounts of dissolved metal ions inside the crevice cause a further decrease of the solution's pH levels and finally, the presence of chlorides facilitates the breakdown of the passive layer. Thus the environment inside the crevice gradually becomes more aggressive and repassivation becomes less likely. As a result, crevice corrosion attacks often propagate at a high rate, thereby causing corrosion failure in a relatively short time.

The mechanisms for under deposit corrosion or crevice corrosion bear several similarities to pitting. However, one of the differences between pitting and crevice corrosion is that pitting initiates at points which are susceptible to corrosion and to which the

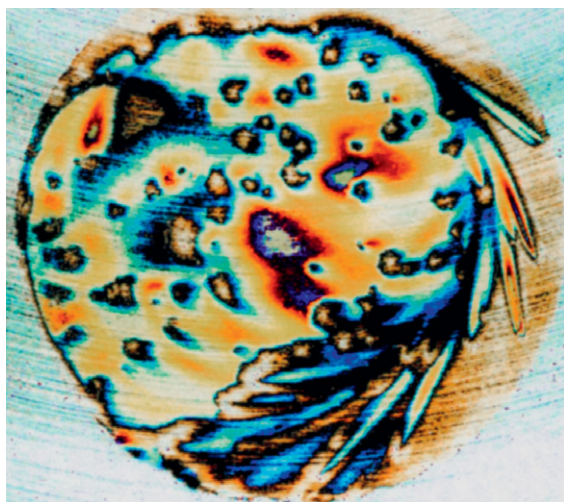


**Figure 18** Stainless steel surface with pitting corrosion after CPT measurement in a crevice-free flush port cell.

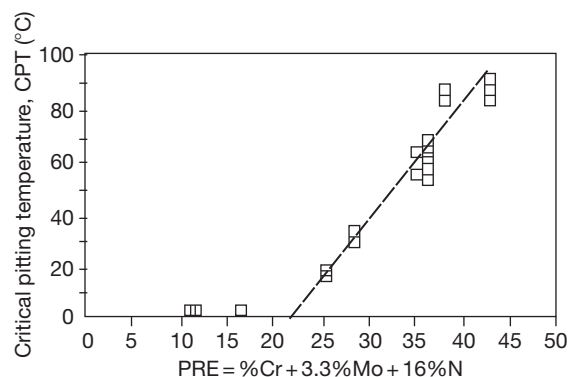


**Figure 19** Critical pitting temperatures (CPT) measured according to ASTM G 150 for stainless steels with different PRE. All data from surfaces of 320 mesh (Outokumpu Stainless data).

environment has free access. Crevice corrosion, on the other hand, is initiated on the metallic surface where the surrounding solution has restricted access.<sup>15</sup> The rate determining factors in this stage are proposed by Valen to be that the large current density consumes high amounts of oxygen and the narrow crevice, contains less amounts oxygen.<sup>31</sup> Both factors lead to more rapid oxygen depletion inside the crevice. Since oxygen depletion occurs in the crevice or under the deposit the oxygen reduction occurs as cathodic on the outside of the crevice. This causes a potential difference between the inside and the outside of a crevice, which causes the corrosion process to thrive.

Crevice corrosion can be unpredictable and one reason for this is that the critical potential, for crevice corrosion to occur, is dependent on the type of crevice. It is further experimentally more difficult to find universal crevice formers to predict all types of crevice corrosion since the type of crevice found in actual structures may come in many different shapes and forms. Examples of crevice formers are gaskets, flanges joining stainless steel structures, or almost any partial blocking of the stainless surface. It is almost impossible to avoid crevices completely in practical operations, but the principles of good design emphasize that crevices should be kept to a minimum.<sup>32</sup> Figure 20, shows crevice corrosion in a flange after exposure in high temperature and high amounts of chlorides exceeding the corrosion resistance of the steel grade.

One important parameter, which influences the risk of crevice corrosion, is the geometry of the crevice. A narrow crevice of a few micrometers in width is typically more prone to crevice corrosion than a

wider crevice, due to the influence of capillary forces in a narrow gap. The practice of draining the crevice area from the stagnant chloride containing solution may further decrease the risk of crevice corrosion.

In the case of deposits, it can be difficult to measure the crevice area, the degree of porosity and consequently the exact influence of this parameter. Dense deposits will cause more severe corrosion attacks compared with a porous deposit, which allows the solution to diffuse from the narrow area between the stainless surface and the deposit.

There are several ways to prevent crevice corrosion and several courses of action may be taken to minimize the risk, for example, selecting gasket materials that are nonporous and do not contain chlorides, since the chlorides can be released to the surrounding solution. However, in areas where crevices cannot be avoided weld-overlaying the sealing surface can be performed using a filler material that is higher alloyed and thus more corrosion resistant than the flange itself. Sharp corners or angles can be sites for collecting dirt or other solids that act like deposits and consequently increase the risk of corrosion under deposits. As regards other types of corrosion, the risk of crevice corrosion attacks decreases as the alloy content increases in the stainless steel, particularly with regard to chromium, molybdenum, and nitrogen. One stainless steel grade can be resistant to localized corrosion on open surfaces but another higher alloyed stainless steel might be used for creviced conditions.

In some cases when crevices cannot be avoided, there are ways of positioning beams, channels, and stiffeners to encourage smooth flow and to avoid the trapping of solids or deposits. If crevice corrosion occurs on a certain steel grade, the material selection process should take this into account and specify a better and more corrosion-resistant stainless steel grade.

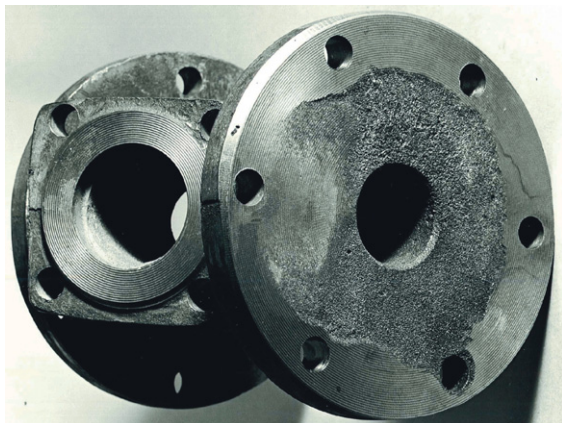


**Figure 20** Example of crevice corrosion in a flange.

#### **3.04.8.6 Stress Corrosion Cracking**

A material failure may be accelerated by the combined effect of a corrosion process and mechanical tensile stress. Two examples of such processes are SCC and corrosion fatigue. SCC does not occur if only one of the two conditions is present. For example, tensile stress present in a stainless steel in a noncorrosive environment is unable to cause SCC.

Different manufacturing processes can introduce stresses in the material. Examples of such processes are coarse grinding, forming, and welding. Any machining on the stainless steel surface that

introduces residual stresses, hardening or martensitic transformation can influence the resistance to SCC. Examples of machining operations of this kind are abrasion or machining techniques that involve deep grooves or notches.<sup>33</sup> However, the degree of the impact from machining on SCC properties is not easily evaluated and ranking methods are most commonly used to test any deterioration or improvement in SCC resistance.

The electrochemical potential of the stainless steel in solution has some effect on the risk for SCC. The susceptible potential zones at which SCC can occur for a given alloy/solution with a typical active-passive behavior are shown in **Figure 21**.

Two zones of susceptibility appear at the potential boundaries where the passive film is less stable. In the active-passive potential zone, SCC occurs where the passive film is relatively weak at active potentials almost inadequate forming the film A, and B in **Figure 28**. In the other potential zone C, in the passive potential area, SCC and pitting corrosion are associated in adjacent or overlapping potential ranges. The common example of SCC in the active-passive potential zone (B) is austenitic stainless steel in hot  $\text{MgCl}_2$  solutions. However, a material, which is not susceptible to SCC, will not crack in despite being in the susceptible zones. SCC in the active-potential area is commonly associated with a low pH contributing to the corrosion mechanism and the cracking in the passive-potential area is associated with high amounts of chlorides contributing to localized breakdown of the passive film.

#### 3.04.8.6.1 SCC mechanisms

There are many attempts to explain the SCC by mechanism taking into consideration both the corrosion process and the role of stresses in the material. Sedriks summarizes some of the numerous

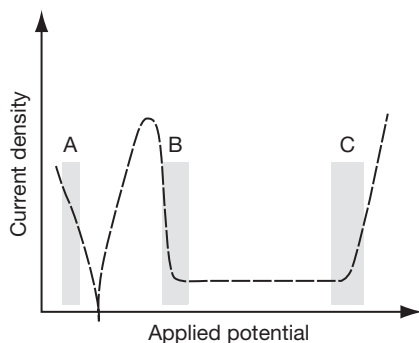


**Figure 21** Susceptible zones in the potential area for stainless steels and SCC.

mechanisms and concludes that the lack of agreement as to which mechanisms are operative have lead to a simplistic nomenclature to describe SCC in terms of the environments that cause it. For example, chloride SCC and caustic SCC describe SCC in chloride environment and in caustics respectively. Hydrogen embrittlement describes cracking in environments in which the cracking process is facilitated by the entrance of hydrogen into the metal.<sup>34</sup>

Some general processes were, however, concluded by Sedriks to provide a basis for a classification of SCC mechanisms based on either removal of material by dissolution or by film formation for separation of the material.<sup>34</sup> In the following section are some mechanisms summarized briefly that were chosen by Newman as three testable cracking models that may account for most known cases of SCC in metals: Slip-dissolution, film-induced cleavage, and hydrogen embrittlement.<sup>35</sup>

#### Slip dissolution

This mechanism is mainly used to explain intergranular cracking in ferritic stainless steels in environments where the stainless steel is passive and in sensitized stainless steels. The crack growth in the slip dissolution model is the result of an extremely localized anodic dissolution. Propagation of the cracks occurs as a result of film rupture, dissolution, and repair. The sides of the crack are considered to be protected by a film, an oxide, which is fractured as a result of plastic strain in the metal at the crack tip.

#### Film-induced cleavage

Film-induced cleavage occurs when the crack is going through a face cubic centre metal, fcc, as an austenitic stainless steel, with a very high velocity in a very short time. The stress corrosion crack introduces a brittle crack in the propagation direction, which is then widened by plastic arrests in the metal. The crack propagates in steps by a brittle crack, which is then widened in steps. As the crack goes further into the material the outer cracks get wider and wider.

#### Hydrogen embrittlement model

Hydrogen embrittlement is assisted by the absorption of hydrogen into the material from an aqueous environment. If the acidification from the hydrogen contributes to passive film breakdown in a crack, the absorbed hydrogen can promote cleavage, intergranular separation or a highly localized plastic fracture.<sup>35</sup> Microstructure plays an important role in



hydrogen embrittlement as in the other mechanistic approaches for SCC. In susceptible steel hydrogen enters under both anodic and cathodic conditions.

Hydrogen embrittlement is accounted for in the presence of hydrogen sulfide  $H_2S$  as in oil wells and releasing hydrogen is also commonly assisted with an acid environment in the presence of sulfur adsorption.

#### 3.04.8.6.2 Impact of mechanical stress on corrosion: stress intensity factor and crack rate

Generally, it is considered that decreasing the applied stress on the material increases the time to failure. Threshold stress intensities ( $K_{ISCC}$ ) are often referred to as stress intensity factors below which the rate of cracking in a given environment is very low. The threshold stress intensity factor indicates a level below which stress corrosion cracks will not propagate. Increasing the stress factor above  $K_{ISCC}$  failure will occur.<sup>34</sup> Stress intensity factors are usually derived from laboratory measurements in environments such as boiling magnesium chloride and care has to be taken since these environments do not coincide with real service in different applications. Pre-cracked specimens are used for measurements of the rate of growth as a function of the stress intensity factor at the tip of the crack. The presence of different microstructure phases, for example, in duplex stainless steels, can result in different stress intensity factor, depending on the microstructure. It is also generally considered that the duplex stainless steels have better SCC resistance than the corresponding austenitic stainless steels. Newman attributes these properties to the differences in the stress intensity factor in the different phases as ferritic and austenite in the microstructure. The effect seems to be that one phase is considered to assist to arresting the crack propagation.<sup>35</sup>

Figure 22 shows a schematic representation of the stress intensity factor and crack rate for S31600 cold worked at 25 and 50% in a hot chloride solution.

The plateau in the schematic representation of the stress intensity factor is proposed by Newman to occur due to chemical reactions controlling the crack rate, rather than mechanical properties. These chemical reactions might be dissolution, diffusion or adsorption.

#### 3.04.8.6.3 Chloride-induced SCC

Circumstances where there is a pronounced risk of SCC include evaporative conditions in chloride

solutions on stainless steel grades with low resistance to SCC, such as the austenitic grade S30400 subjected to stresses by manufacturing processes. The chloride content on the surface increases to very high values as a result of the evaporative conditions, causing corrosion to occur. Failure from SCC is very rapid; there are no warning signs before the failure and the corrosion propagates very rapidly, causing the construction to fail in a short time.

The most common type of SCC on austenitic stainless steel is transgranular SCC, which may develop in concentrated chloride-containing environments at elevated temperatures at around or above 50–60°C. The crack propagation is in many cases perpendicular to the introduced tensile stresses and in transgranular stress corrosion, the cracks run across the grains – to be compared with intergranular SCC, where the cracks run in the grain boundaries. Figure 23 shows typical transgranular SCC in austenitic stainless steel.

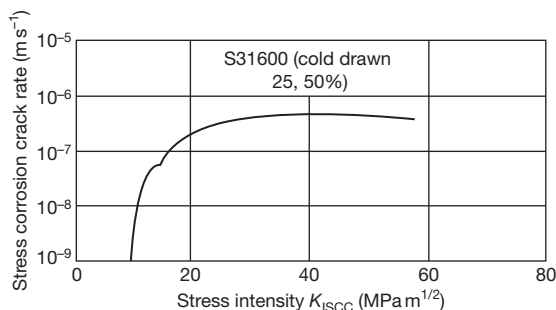


**Figure 22** Schematic representation of the Stress Intensity factor and crack propagation rate for S31600 cold worked 25 and 50% in a hot chloride solution. Reproduced from Extracted from Dickson, J. I.; Russel, A. J.; Tromans, D. *Can. Met. Q* **1980**, 19, 161.

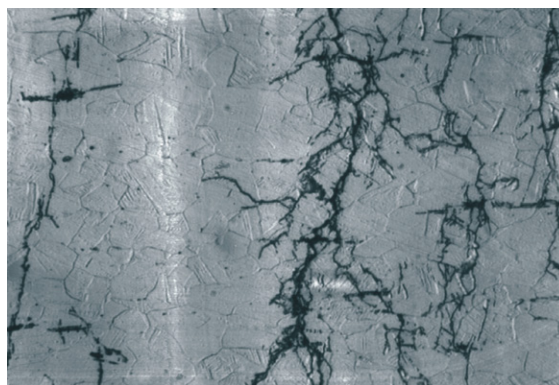


**Figure 23** Transgranular SCC in an austenitic microstructure.



Another frequently mentioned cause to SCC of stainless steels is the sensitization of the material. Sensitization occurs when stainless steel is submitted to a high temperature treatment for too long a time, which can cause carbide precipitation to occur if the steel's carbon content is too high. By avoiding sensitization and carbide precipitation, the risk of SCC can in many cases be eliminated. Most commercially available modern stainless steels have low carbon content and amounts below 0.05 wt% are seldom sensitized, even in welding operations. For use in hot concentrated nitric acid, the maximum carbon content is proposed not to exceed more than 0.03 wt%. These improved properties not only contribute to higher resistance to cracking but also enhance the steel's intergranular corrosion properties.

Solutions containing chlorides are not the only environments that can cause SCC of stainless steels. Solutions of other halides may also cause cracking. Sensitized 1.4301 (30400) stainless steels are also susceptible to intergranular SCC in steam and water environments, for example, in boiling water reactors if the stress level is sufficiently high.

#### **3.04.8.6.4 Caustic SCC**

Another risk scenario that may give rise to SCC, particularly in low alloy steels, is very alkaline solutions at high temperatures, where the pH values are above 14 at concentrations between 20 and 70 wt% and temperatures above 120°C. Caustic SCC has been of particular interest to some industries, such as chemicals, petrochemicals, and pulp and paper. Sedriks concludes that any heat treatment or sensitization to produce 475°C embrittlement in duplex stainless steels will promote caustic cracking but also that duplex stainless steels generally offer better resistance to cracking in hot caustic solutions.<sup>33</sup>

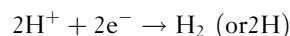
The alloy compositions of stainless steels influence the cracking of the material and it would appear that alloys including molybdenum have a different ranking in hot alkaline solutions compared with that obtained for other wet chloride-induced corrosion in stainless steels.

#### **3.04.8.6.5 Sulfide stress cracking (SSC) by hydrogen sulfide**

Contaminants, such as hydrogen sulfide, H<sub>2</sub>S, may increase the risk of SCC in stainless steels in chloride containing environments. Hydrogen sulfide exists in oil and gas wells and stainless steels intended for applications in the oil and gas industry are typically

tested for use under these circumstances. The most important environmental aspects of SCC in the sour service environments common in oil and gas production are hydrogen sulfide, H<sub>2</sub>S partial pressure, pH, and the chloride concentrations.

The cathodic reaction in chloride containing hydrogen sulfide solutions is mainly the reduction of hydrogen ions to hydrogen, which may form either as hydrogen gas or dissolve in the metal as hydrogen atoms:



The adsorption of hydrogen sulfide on the surface promotes the hydrogen absorption in iron alloys. The cathodic rate depends on several parameters such as temperature, pH, concentration of weak acids, and the electrochemical potential of the material. The role of the weak acid is to donate hydrogen ions.

Duplex stainless steels are frequently used in the oil and gas industry because of their mechanical properties and corrosion resistance in chloride environments, for example, in subsea components working at high pressures and high temperatures. Some examples are pipelines, flow lines, and pipe work.

#### **3.04.8.6.6 Hydrogen-induced stress cracking (HISC) using cathodic protection**

Martensitic and ferritic microstructures are susceptible to hydrogen embrittlement whereas austenitic stainless steels are much less likely to suffer from this type of cracking. The resistance to SCC can be influenced by cathodic currents applied to stainless steel in wet environments. For example, the super ferritic grade, UNSS44735, is prone to hydrogen embrittlement when polarized to potentials in the range of 0.9–1.4 V/SCE, caused by overprotection at potentials more negative than –0.8 V/SCE, so potential in this range should be avoided.

High strength steels, including many martensitic grades, are susceptible to hydrogen embrittlement. Yield strength seems to be an important factor and cause of hydrogen embrittlement along with the tempering and precipitation hardening of the material.<sup>33</sup>

Subsea duplex stainless steels are usually subjected to cathodic protection since these steels are typically connected to other carbon and low alloy steel structures that are already protected. Overall, duplex stainless steels have an excellent track record in subsea conditions but hydrogen-induced stress cracking is a risk if cathodic protection is applied in sour environments, containing H<sub>2</sub>S. The reported failures under

cathodic protection have been associated with unusually high mechanical loads, an unfavorable microstructure in the base metal, characterized by large grains, intermetallic phases, etc. or a high ferrite content in welds. Lowering the hydrogen sulfide concentration to below  $0.1 \text{ g l}^{-1}$  can reduce the susceptibility to SCC or by reducing the applied stress level to below 60% of the yield stress.

Many tests on hydrogen embrittlement are carried out using cathodic charging in sulfuric acid solutions that contain arsenic. Hydrogen embrittlement occurs if the applied stress is higher than the yield stress and the presence of hydrogen ions recombines in the presence of the poison arsenic compound in sulfuric acid. The presence of molybdenum in ferritic stainless steel can reduce the steel's resistance to hydrogen embrittlement.

#### **3.04.8.6.7 SCC in atmospheric environments**

A number of accidents have occurred where ceilings in swimming pool houses have collapsed due to corrosion, mainly involving 304 type steel grades. For example, in Steenswijk in the Netherlands in 2001, suspended air channels were collapsed due to corrosion. Analysis revealed that the reason for the collapses was SCC and also that it occurred at lower temperatures than expected based on previous experience. Most other reports of SCC related to atmospheric environments have been at temperatures above  $50^\circ\text{C}$  in combination with chlorides under evaporative conditions and not typically at room temperature.

In recent decades, the atmospheric environment in swimming pool houses has changed as modern pool houses use higher water and atmospheric temperatures for convenience. Furthermore, in many cases, dehumidifiers are installed and the pools have higher water agitation and heavier bather loadings. The swimming pool house atmosphere may also be subjected to changes in humidity and temperature during both day and night.

Experience has shown that items of stainless steel furniture and equipment immersed in or washed by pool water do not suffer from corrosion problems.

Chlorine-based disinfectants are used in most swimming pool water in a form of hypochlorous acid,  $\text{HClO}$ , hypochlorite,  $\text{ClO}^-$ , and chlorine,  $\text{Cl}_2$ , independent of the particular disinfection procedure. Assuming the most typical pH level for swimming pools, that is, between 7.2 and 7.4, the concentration of hypochlorite and hypochlorous acid in the pool water is approximately equal and the concentration of chlorine gas is negligible. The amount of free

chlorine in the pool water, that is, the total concentration of hypochlorite, hypochlorous acid, and chlorine, is usually kept at  $0.5\text{--}2 \text{ mg l}^{-1}$ .

Free chlorine reacts with ammonia and amine compounds introduced to the pool water by bathers forming relatively stable intermediate products, chloramines. Chloramines are volatile substances responsible for 'swimming pool smell' and causing most of the eye and nose irritations to pool users. Chlorine seems to be transported to the metal surface from the pool water in the form of volatile chlorine-based chemicals, probably mainly as trichloramines. Chloramines are sufficiently stable to be carried to relatively distant locations and dissolve in condensed water on a metal surface. However, the deposition of chlorine-based chemicals in the form of water aerosol has also to be considered. Regular maintenance, such as routine cleaning with clean water, reduces the risk of corrosion in these environments significantly.<sup>37</sup>

Iversen and Prosek simulated the worst possible conditions in a swimming pool atmospheric environment by exaggerating the concentration of chloride in the surface electrolyte, the level of tensile stress, the temperature, and the relative humidity of the atmosphere in comparison with values reported from real swimming pool environments to simulate extremely severe conditions.<sup>37</sup> The test method they used consisted in applying droplets of saturated magnesium and calcium chloride spots on the top of U-bent samples of eight grades of stainless steel. A part of each of the samples was exposed at  $50^\circ\text{C}$  over saturated water solutions of respective chloride salts to keep the relative humidity at the deliquescence point. The stainless steel grades S30400 (1.4301) and S31600 (1.4404) were susceptible to SCC in the presence of magnesium and calcium chloride deposits at  $50^\circ\text{C}$  and at the deliquescence point. Transgranular cracks were initiated rapidly, probably within the first week of exposure.

No SCC was found on samples of the higher alloyed austenitic stainless steel grades N08904 (1.4539) and S31254 (1.4547). These were completely free of corrosion or suffered from pitting corrosion. **Figure 24** shows SCC on S31600 from laboratory tests exposed with  $\text{MgCl}_2$  spots at  $50^\circ\text{C}$  and at 31% RH for 22 weeks.

Common austenitic stainless steel grades without molybdenum or with a maximum of 3% molybdenum have been recognized to suffer from SCC under the specific conditions that can occur in swimming pool atmospheres. Therefore, these stainless steels should be excluded from being used as safety-relevant fastening components in swimming pool buildings.

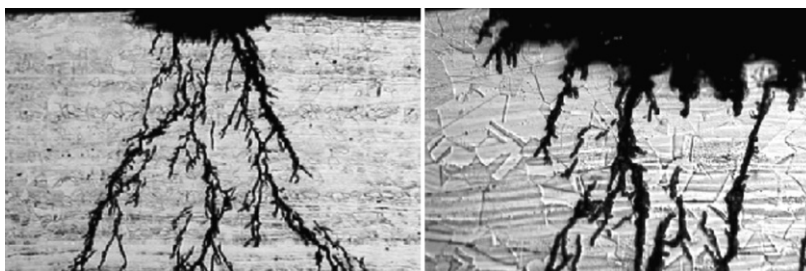


**Figure 24** SCC on S31600 (1.4404) from laboratory tests exposed with  $\text{MgCl}_2$  spots at 50 °C and at 31 % RH for 22 weeks. Reproduced from Iversen, A.; Prosek, T. Eurocorr 2007, Freiburg im Breisgau, Germany, 9–13 September, 2007.

It seems that highly corrosion-resistant stainless steels are necessary for the successful and safe application of stainless steels in swimming pool atmospheres in combination with maintenance such as regular cleaning of the stainless steel surfaces.

#### 3.04.8.6.8 SCC of martensitic stainless steels

Martensitic stainless steels such as S41000 are very susceptible to both SCC and hydrogen embrittlement. Martensitic grades are especially susceptible to hydrogen embrittlement in tempered conditions. This susceptibility to hydrogen embrittlement can have an adverse effect on any cathodic protection of martensitic stainless steels in applications such as in seawater. The cathodic protection sets the potential in a risk area, at low negative potentials, for hydrogen embrittlement to occur. Another risk scenario for martensitic stainless steels is grain boundary precipitation caused by tempering, which leads to an increased risk of intergranular SCC. The hardness of the material is often an important factor in the selection of martensitic stainless steels, but comes at a cost, since the mechanical toughness decreases with increasing hardness. This will also influence the stress levels in the material, particularly in welded components.

#### 3.04.8.6.9 SCC of ferritic stainless steels

Ferritic stainless steels are highly resistant to chloride-induced SCC, but even if ferritic grades do not crack under such conditions, their resistance to other types of corrosion, such as localized corrosion and uniform corrosion, is determined by a combination of the alloy composition and the service environment.

High chromium ferritic alloys can suffer from embrittlement under incorrect and prolonged heat treatment often referred to as 475 °C embrittlement. Even though ferritic stainless steels exhibit excellent resistance to stress corrosion in chloride solutions, sensitization or high temperature embrittlement at 475 °C leads to cracking of these grades in a chloride or caustic

solution. Another operation that increases the susceptibility to cracking in ferritic grades is cold work. Alloying elements in ferritic grades identified as causes of SCC include nitrogen, copper, nickel, and carbon. Microstructure effects on increasing cracking properties, are probably related to the reduction of ductility, which occurs where precipitation of carbides and nitrides occur in high temperature embrittlement at 475 °C.<sup>33</sup>

The most common reported cause of sensitization in ferritic stainless steels is high carbon content. Low carbon and nitrogen levels in ferritic stainless steels are beneficial as they improve the toughness of the material and also help prevent the precipitation of carbides and nitrides. Alloying elements that improve the resistance to cracking of ferritic stainless steels are titanium (Ti) and niobium (Nb).

#### 3.04.8.6.10 SCC of austenitic stainless steels

The alloying element nickel has been widely discussed in terms of its contribution to resistance to chloride-induced SCC of austenitic stainless steels in sodium chloride solutions. Copson showed that for low and high levels of nickel in austenitic stainless steels no SCC occurred in boiling magnesium chloride at 154 °C.<sup>38</sup> However, it should be pointed out that these measurements were carried out under conditions that cannot be transferred to any real environment. Nevertheless, Nickel has a beneficial effect and is known to prevent SCC when the nickel content exceeds 30–40 wt%. Very high amounts of nickel as an alloying element are accounted for in nickel-based materials. Any beneficial effect attributable to nickel only is excluded in the ferritic stainless steels as they normally do not contain nickel and are anyway highly resistant to chloride-induced SCC. An increase in the molybdenum content in austenitic stainless steels has produced a significant improvement in the resistance to SCC in sodium chloride solutions. The resistance to SCC generally increases

in line with the PRE number, as the chromium, molybdenum, and nitrogen content is increased in austenitic stainless steels. The super austenitic stainless steels are highly resistant to chloride-induced SCC. One of the reasons for this is that the assisting corrosion reaction to SCC does not initiate as easily in super stainless steels with a high PRE number as in the standard grades S30400 (1.4301) and S31600 (1.4401).

#### **3.04.8.6.11 SCC of duplex stainless steels**

Generally, duplex stainless steels are more resistant to SCC compared with austenitic stainless steels with corresponding PRE values and alloy composition. This is because duplex stainless steels have a two-phase microstructure. An austenite stabilizing alloying element such as nitrogen and nickel does not dissolve easily in the ferritic phase. The effect of the duplex microstructure on the overall material is a two-phase system and a possible reason mentioned in the literature is different stress intensity factors for the two phases.<sup>35</sup> There are also some theoretical considerations suggesting that the SCC process can be arrested by the differences between the two phases and that propagation is, to some extent, hindered between the two phases. However, occurrences of SCC in duplex stainless steels have been reported in strong alkaline solutions at very high temperatures.

#### **3.04.8.7 Corrosion Fatigue**

It is well-documented that material subjected to a cyclic load far below the ultimate tensile stress can fail, due to fatigue. If the metal is simultaneously exposed to a corrosive environment, the failure can take place at low loads and after a short period of time. Contrary to pure mechanical fatigue, there is no fatigue limit in corrosion-assisted fatigue. The fatigue fracture is brittle and the cracks are typically transgranular, as in SCC, but not branched. Fatigue properties of stainless steels can be read in [Section 3.04.4.4](#).

The fatigue strength is sensitive to the service environment and under both cyclic loading and corrosive conditions; the fatigue strength will generally decrease. In many cases there is no pronounced fatigue limit, as observed in air, but a gradual lowering of the fatigue strength with increasing number of load cycles. The more aggressive the corrosive conditions and the lower the loading frequency, the higher the effect of the environment. During very high frequency loads there is little time for the corrosion to act and the fatigue properties of the

material will mostly determine the service life. At lower frequencies the corrosive action is more pronounced and an aggressive environment may also cause corrosion attacks that will act as stress concentrations and thus contribute to a shorter life. There is a clear tendency that duplex stainless steels resist fatigue and corrosion fatigue better than austenitic stainless steels. The reason is a high strength combined with good corrosion resistance.

#### **3.04.8.8 Corrosion on Stainless Steels Related to Welding Procedures**

The procedure of welding changes mechanical properties, the surface geometry, surface appearance, and microstructure in the weld compared with the base material. These changes have an impact on the corrosion properties of the steel grades and have to be accounted for in a construction, welding procedure, the choice of filler material but also by the postweld treatment.

Welding defects, which occur in connection with the welding procedure, can in some cases have an adverse effect on corrosion resistance. The effects of weld defects will depend on the service environment in which the construction or application is placed. Weld defects in mild environments, for example, clean and moist air, do not normally cause any severe corrosion damage, whereas in more aggressive environments, such as those, which might occur in process industry, could lead to more severe damage. One good rule is to aim to eliminate defects and if they occur, to remove them to ensure optimum corrosion resistance of the welded construction.

In most cases where weld defects cause corrosion attacks, the types of corrosion typically seen are localized corrosion, such as pitting and crevice corrosion. Other types of corrosion attacks might be caused by nonproper welding procedures, as previously mentioned. The combination of unsuitable welding procedures and an aggressive environment can give rise to general corrosion, SCC and/or intergranular corrosion.

Defects possibly causing pitting corrosion are local areas of holes, microcrevices, surface pores, crater pores, spatter, slag or any other surface defect, which naturally can be a location for the initiation of pitting corrosion attacks. Crevice corrosion resistance is decreased by any defect that forms a crevice. Examples of such defects are all types of cracks, incomplete penetration or lack of fusion. Service environments causing deposits under service are also a trigger to the initiation of crevice corrosion.

Uniform corrosion may occur in strong acid environments in connection to oxides or defects caused by ignition spark. If a weld is underalloyed compared with the parent metal, the weld could corrode uniformly leaving the parent metal as if the service environment is too aggressive for the filler material used.

SCC is caused by a combination of factors. These include an aggressive environment as well as an elevated temperature in combination with tensile stresses in the surface. Welding can introduce tensile stresses in the material that can initiate SCC if the other two requirements are present. All types of defects known to cause SCC must be avoided, for example, cracks, or heavy undercuts. The presence of oxygen on the root side during gas tungsten welding, TIG or gas metal arc welding, MIG can, if present in the same concentrations as in the service atmosphere, lead to excessive oxidation of the melted metal during welding. The result is a weld with a totally unacceptable geometry combined with an excessive heat tint – thereby leaving the root side with an unacceptably low corrosion resistance. To avoid excessive oxidation, an inert root gas must always be used during welding.

All types of stainless steels ferritic, duplex, and austenitic must be thoroughly cleaned after welding to accomplish sufficient and acceptable corrosion resistance of the weld.

#### **3.04.8.8.1 Ferritic stainless steels**

The weldability of ferritic stainless steels depends on the chemical composition and more specifically on the ratio of alloying elements such as carbon and nitrogen in relation to the chromium content. Precipitation of chromium carbides along grain boundaries should be avoided since this increases the risk of intergranular corrosion. After welding, heat treatment may be necessary to restore the corrosion resistance of these steels. However, a low ratio of  $(C+N)/Cr$  reduces the risk of chromium carbide/nitride precipitation and any intergranular corrosion in connection with welding.<sup>32</sup>

If insufficient gas protection is used during welding, chromium nitrides may form, caused by an uptake of nitrogen from the atmosphere. These precipitates can cause embrittlement and lower the corrosion resistance.

#### **3.04.8.8.2 Duplex stainless steels**

The modern duplex stainless steels have much better welding characteristics than the ferritic stainless steels and require in general no preheating or postweld heat

treatment. However, duplex stainless steels show ferritic microstructure at very high temperatures and too rapid a cooling can conserve this structure. This could lead to the precipitation of nitride or carbide and consequently increase the risk of intergranular corrosion. However, modern duplex stainless steels contain high nitrogen content and low carbon contents, favoring a two-phase structure free from precipitates. The use of fillers with higher Ni-content ensures a weld metal with sufficient austenite level.

#### **3.04.8.8.3 Austenitic stainless steels**

Austenitic stainless steels are generally easy to weld and do normally not require any preheating or postweld heat treatment. Highly alloyed austenitic stainless steels – also known as super austenitic grades – generally have good weldability, but the micro segregation of molybdenum reduces the pitting resistance in the weld deposit. To counter the reduction in pitting resistance, these grades are welded with a nickel-based filler that has been overalloyed with molybdenum. Super austenitic steels should be welded with a minimum of heating. The presence of ferrite might influence the corrosion resistance in the ferrite phase in some specific environments as nitric acid. To rectify this, the use of fully austenitic electrodes and filler are used in some applications, such as the production of urea and acetic acid.

Intergranular corrosion was previously a problem for stainless steels with high carbon content. Nowadays, modern stainless steel manufacturers have no difficulties in maintaining a low carbon content so intergranular corrosion caused by chromium carbide precipitation after the welding of austenitic and duplex stainless steels is no longer a problem.

#### **3.04.8.8.4 Postweld treatment**

The presence of weld oxides can also cause decreased resistance to pitting corrosion.

Heat tint seen on stainless steels after welding is caused by an oxidation of even fairly minor amounts of oxygen at the high welding temperature during welding. The heat tint influences the passive film and the corrosion properties of the passive film negatively adjacent to the weld. Any oxides, tarnish or scale, should be removed by grinding and/or pickling to maintain the localized corrosion resistance of stainless steels. However, in some cases where the environment will lead to general corrosion such as in strong acids, the service environment will remove the oxide scale.

Grinding of the surface produces a more or less rough surface depending on the grit used. Generally,



the finer the surface finish, the better the corrosion resistance, and grinding coarser than grit 80 very often produces a surface with an unacceptably low pitting resistance compared with the pitting resistance actually inherent in the alloy composition. Coarse grinding can introduce tensile stresses in the surface, which increases the risk of SCC if the environment is too corrosive.

#### **3.04.8.9 General Corrosion**

General corrosion occurs uniformly over the stainless steel surface when the passive layer is completely broken down. Anodic and cathodic reactions occur on the same surface and the corrosion rate is similar over the entire surface.

General corrosion is easier to predict from corrosion rates and thinning of the material over time compared with localized corrosion such as pitting, crevice, and SCC. The corrosion rate can be used for lifetime predictions and in material selection, a stainless steel grade is generally chosen for its low corrosion rate. Material with a corrosion rate of less than  $0.1 \text{ mm year}^{-1}$  is generally regarded as being corrosion-proof, whereas a corrosion rate that exceeds  $1.0 \text{ mm year}^{-1}$  means that the material is regarded as unusable in terms of its corrosion resistance. Extensive data are available on the uniform corrosion properties of commercial stainless steels.<sup>32</sup> However, laboratory tests are not strictly comparable with actual service conditions, where the corroding medium often contains impurities. These may in some cases increase corrosion, in others, decrease it. In unfavorable cases, the increase can be very high. The best material advice is based on results obtained from the actual process or service environment concerned.

The uniform corrosion rate is also affected if the acid contains chemicals that are oxidizing or reducing. Reducing impurities, for example, hydrogen sulfide may increase the corrosion rate. An oxidizing acid that has a positive effect at a lower concentration is nitric acid, since this promotes passivation of the stainless steel surface at some concentrations rather than initiating uniform corrosion. Nevertheless, there is a limit to how oxidizing the environment may be from a corrosion point of view. Some exceptions occur in strongly oxidizing solutions such as in hot concentrated nitric acid or in chromic acid. In these environments, molybdenum is an undesirable alloy addition. A hot concentrated nitric acid can dissolve the passive layer and transpassive corrosion may

occur. The mechanism of transpassive corrosion is not similar to uniform corrosion as the passive layer will be oxidized to more soluble species but the consequence is the same, the passive layer breaks down partly or completely and uniform corrosion occurs. As for many other environments, in common mineral acids and organic acids the higher alloyed stainless steel grades containing higher amounts of chromium, nitrogen, and molybdenum are more resistant to uniform corrosion than the lower alloyed stainless steel grades. Severe environments from a general corrosion point of view are high concentrations of hydrochloric or hydrofluoric acid in which the corrosion may propagate at a rate that can be detrimental to a construction.

Severe environments from a general corrosion point of view are those with high concentrations of hydrochloric or hydrofluoric acid in which the corrosion may propagate at a rate that can be detrimental to a construction.

Engineering with stainless steels relies, in many cases, on test results obtained in laboratory measurements. As with other types of corrosion, a number of different methods are used to describe the susceptibility to uniform corrosion. Isocorrosion diagrams are available for a number of stainless steel grades tested in pure chemicals.<sup>32</sup> The test methods introduce activation of the stainless steel to corrosion in between test periods to forward either propagating uniform corrosion or repassivation.

##### **3.04.8.9.1 Sulfuric acid**

When stainless steels are exposed to acids, the aggressivity of the solution is generally related to the level of concentration and general corrosion increases with temperature, but as far as sulfuric acid is concerned, there are some exceptions to this rule, even with regard to the increase in the concentration. At low concentrations and in concentrated sulfuric acid, the aggressiveness towards stainless steels is low and at intermediate concentrations, sulfuric acid causes high uniform corrosion rates.

The isocorrosion line in the diagram shows the limit for use of the specific stainless steel grade. The line, one for each alloy, represents a corrosion rate of  $0.1 \text{ mm year}^{-1}$ . At concentrations or temperatures above this line the corrosion rate is unacceptably high. In other words, above the isocorrosion line, the corrosion rate is too high and below the line, the material is regarded as corrosion-proof. A safety limit is typically adopted to provide materials selection advice well below the line and not on the line.



As can be seen from the isocorrosion diagrams in **Figures 25** and **26** the steel grade N08904 (1.4539) performs better in sulfuric acid at intermediate concentrations than some other stainless steel grades. Increased nickel, molybdenum, and copper content in the steel sustain the uniform corrosion rate in sulfuric acid.

Comparing the corrosion resistance of N08904 in aerated and deaerated sulfuric acid, **Figures 25–27**, show that in the aerated sulfuric acid some increase in the corrosion rates were observed at intermediate concentrations.

**Figure 25** shows, at very high concentrations of sulfuric acid, above 90 wt% and, at temperatures below 30°C, that there is a possibility of using the standard grade of S31600, since the aggressiveness of the highly concentrated sulfuric acid is less for stainless steel compared to intermediate concentrations of sulfuric acid.

To understand the change in the corrosiveness of sulfuric acid solutions, which is higher at intermediate concentrations than at high concentrations, we must look to the hydrogen ion concentration in the sulfuric acid. At intermediate concentrations, the

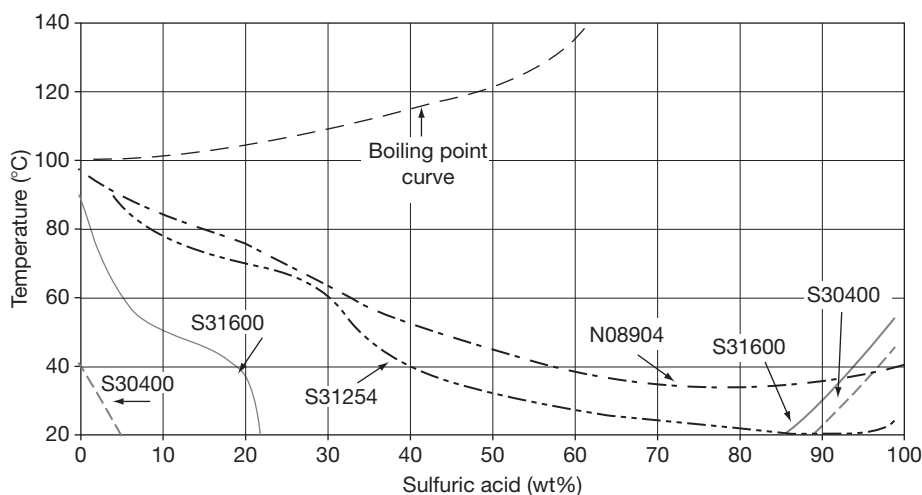


**Figure 25** Isocorrosion diagram at  $0.1 \text{ mm year}^{-1}$  for some austenitic stainless steels in aerated sulfuric acid. Reproduced from Alfonsso, E.; Arnvig, P.E.; Bergquist, A.; Ivarsson, B.; Iversen, A.; Leffler, B.; Nordström, J.; Olsson, J.; Stenvall, P.; Wallén, B.; Vangeli, P.; Outokumpu Stainless Corrosion Handbook, 9th ed.; Outokumpu Stainless Oy, Sandviken 2004, pp 1:8–1:103.

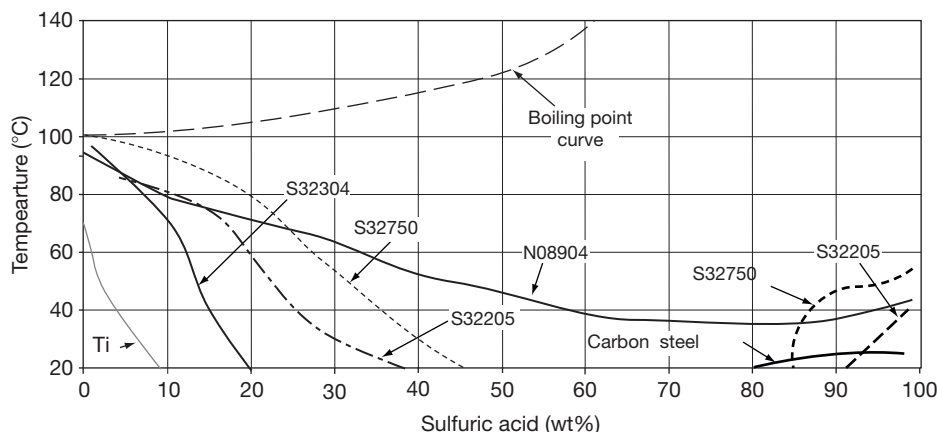


**Figure 26** Iso corrosion diagram at  $0.1 \text{ mm year}^{-1}$  for some duplex stainless steels in aerated sulfuric acid. Reproduced from Alfonsso, E.; Arnvig, P.E.; Bergquist, A.; Ivarsson, B.; Iversen, A.; Leffler, B.; Nordström, J.; Olsson, J.; Stenvall, P.; Wallén, B.; Vangeli, P.; Outokumpu Stainless Corrosion Handbook, 9th ed.; Outokumpu Stainless Oy, Sandviken 2004, pp 1:8–1:103.

hydrogen ions are able to dissolve into the water more easily than in the higher concentrations since there are minor amounts of water present in the higher concentrations. The ability of sulfuric acid to be either reductive or oxidizing is also affected by the concentration.

#### 3.04.8.9.2 Hydrochloric acid

Hydrochloric acid is one of the most severe mineral acids for stainless steels. Generally, the corrosion resistance in this type of environment increases with increasing alloy content of chromium, molybdenum, and nitrogen. However, stainless steels are only used at low concentrations of this acid and at low temperatures. The isocorrosion diagram, **Figure 28**,

shows that the corrosion rate increases rapidly when the steel is exposed to hydrochloric acid. Care must also be taken in chemicals where the risk of hydrochloric acid production is possible.

The beneficial effect from molybdenum as an alloying element in stainless steel can be seen from the results in the isocorrosion diagram, where S32654, containing approximately 7 wt% of molybdenum, performs better than the other stainless steels containing lower amounts of molybdenum. It should also be pointed out that even if a low general corrosion rate is obtained for a stainless steel in hydrochloric acid, there would still be an increased risk of pitting at moderate temperatures, as well as a risk of SCC at higher temperatures. Hydrochloric acid is the most

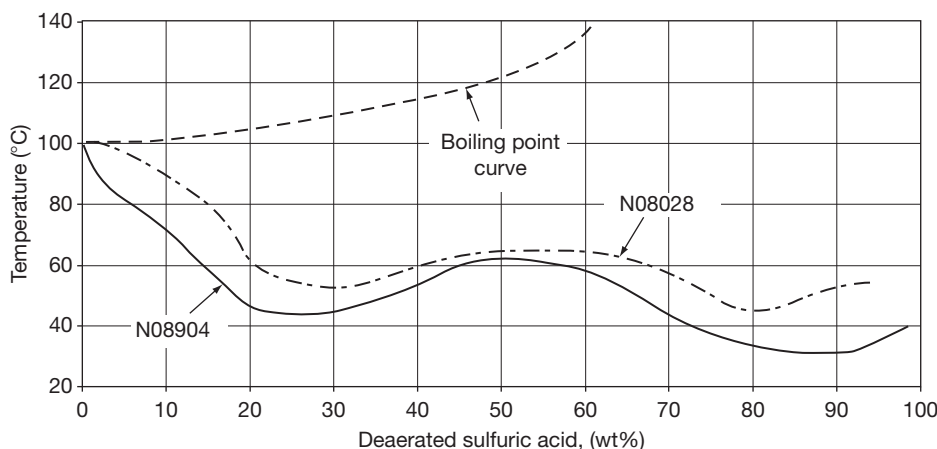


**Figure 27** Isocorrosion diagram at  $0.1 \text{ mm year}^{-1}$  for deaerated sulfuric acid. Reproduced from Alfonsson, E.; Arnvig, P.E.; Bergquist, A.; Ivarsson, B.; Iversen, A.; Leffler, B.; Nordström, J.; Olsson, J.; Stenvall, P.; Wallén, B.; Vangeli, P.; Outokumpu Stainless Corrosion Handbook, 9th ed.; Outokumpu Stainless Oy, Sandviken 2004, pp I:8-I:103.

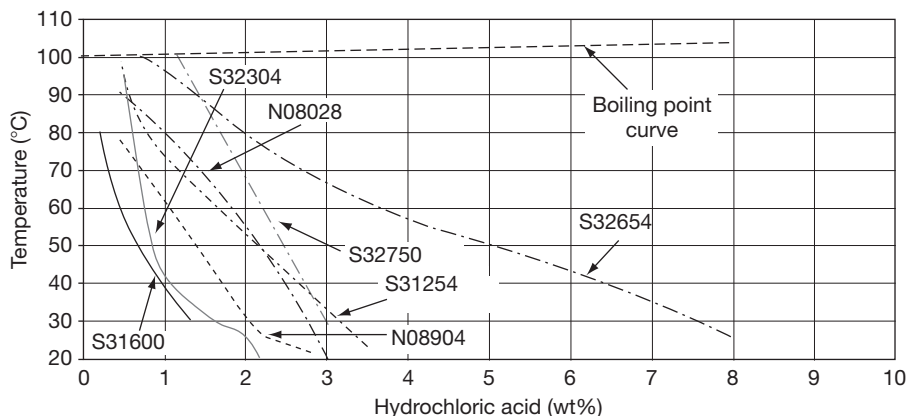


**Figure 28** Isocorrosion diagram at  $0.1 \text{ mm year}^{-1}$  for hydrochloric acid. Reproduced from Alfonsson, E.; Arnvig, P.E.; Bergquist, A.; Ivarsson, B.; Iversen, A.; Leffler, B.; Nordström, J.; Olsson, J.; Stenvall, P.; Wallén, B.; Vangeli, P.; Outokumpu Stainless Corrosion Handbook, 9th ed.; Outokumpu Stainless Oy, Sandviken 2004, pp I:8-I:103.

corrosive mineral acid and when a stainless steel is activated there is little or no chance of repassivation of the material.

### 3.04.8.9.3 Phosphoric acid

Phosphoric acid is used in many industrial processes and the quality of the acid varies in many cases depending on impurities. If oxidizing chemicals are present, passivity can be obtained, and in pure phosphoric acid, many stainless steel grades are capable of existing without any severe corrosion, as shown in the isocorrosion diagram for pure phosphoric acid (see [Figure 29](#)).

Many types of phosphoric acids are used in industrial applications. The common classification of these

is wet-process phosphoric acids (WPA) and usually means that the acid contains impurities in combination with phosphoric acid. Some triggers to increased corrosiveness in technical phosphoric acids are fluorides, chlorides, and bromides. Care has to be taken while using phosphoric acids containing chlorides and at increased temperatures. A temperature change of 50–100°C would cause the corrosion rate to increase more than 10-fold on a typical stainless steel grade such as S31600, even where only low amounts of chlorides are present in the acid. If the chloride content were to increase to values exceeding 500 mg l<sup>-1</sup> (ppm), even the S31600 grade would be unsuitable due to the high corrosion rate at this temperature range (see [Figure 30](#)).

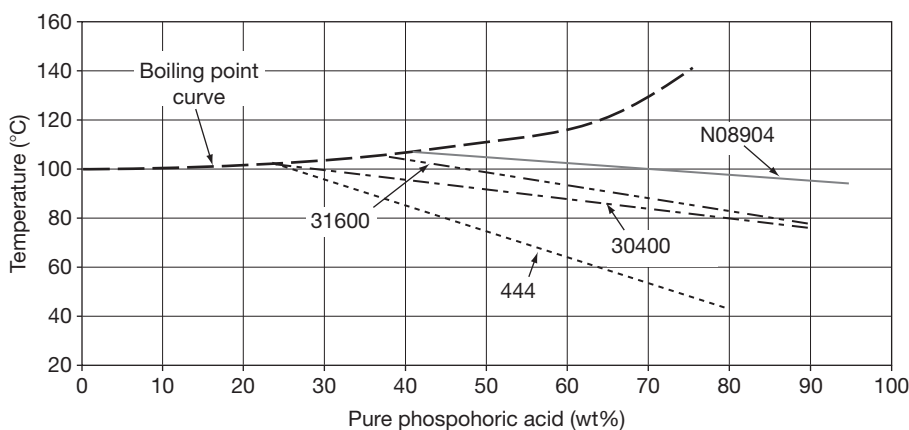


**Figure 29** Isocorrosion diagram at 0.1 mm year<sup>-1</sup> for pure phosphoric acid. Reproduced from Alfonsson, E.; Arnvig, P.E.; Bergquist, A.; Ivarsson, B.; Iversen, A.; Leffler, B.; Nordström, J.; Olsson, J.; Stenvall, P.; Wallén, B.; Vangeli, P.; Outokumpu Stainless Corrosion Handbook, 9th ed.; Outokumpu Stainless Oy, Sandviken 2004, pp 1:8–1:103.

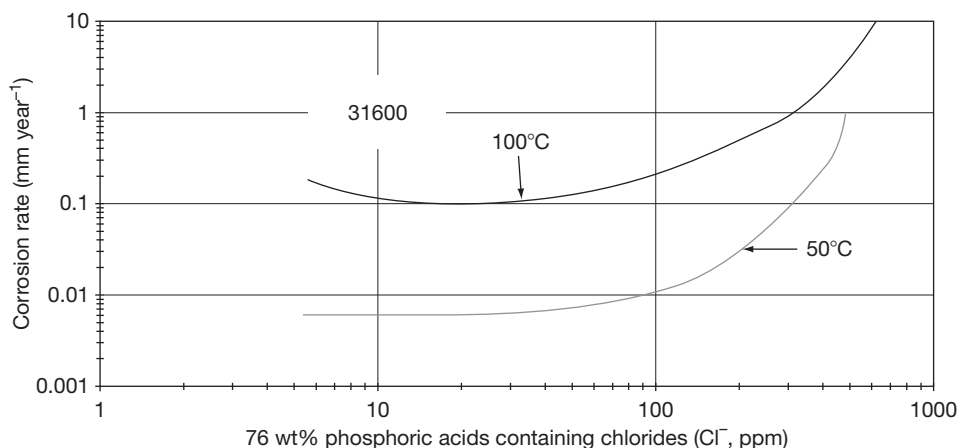


**Figure 30** Corrosion rate for the stainless steel grade S31600 in phosphoric acid containing chlorides. Reproduced from Alfonsson, E.; Arnvig, P.E.; Bergquist, A.; Ivarsson, B.; Iversen, A.; Leffler, B.; Nordström, J.; Olsson, J.; Stenvall, P.; Wallén, B.; Vangeli, P.; Outokumpu Stainless Corrosion Handbook, 9th ed.; Outokumpu Stainless Oy, Sandviken 2004, pp 1:8–1:103.

Fluorides in phosphoric acids may also have an adverse effect on corrosion resistance if the amounts are too high in combination with temperature increase, see [Figure 31](#). The worse conditions, however, are those where there are synergetic effects between chlorides and fluorides in combination with other impurities. In complex WPA that contains different impurities, it is usually advisable to seek additional information and advice from corrosion experts. Examples of WPA can be found in the literature, however, only as examples and in real applications, the amounts of impurities are typically not the same as published.<sup>32</sup>

#### 3.04.8.9.4 Nitric acid

Nitric acid is generally a passivation acid for common austenitic and duplex stainless steels containing 18 wt% chromium at concentrations of 20 wt% and below 100°C. It is used for cleaning and passivation after any alterations in the stainless steel surfaces in different applications. Nitric acid is also one of the chemicals in pickling acids used in the manufacturing of stainless steels. The use of the stainless steel grade S30400 in nitric acid of different concentrations up to 60 wt% and below 100°C is widely adopted. Even ferritic grades containing 13 wt% chromium are resistant to corrosion in nitric acid at concentrations of 20–60 wt% below 40°C.<sup>32</sup> However, in hot nitric acid there is a risk of intergranular corrosion in most stainless steel grades due to the oxidizing power of the solution. Sedrik reviewed that high silicon alloys have been used

for service in concentrated nitric acid solutions and the stainless steel grade 310L has been used for very hot concentrated nitric acid.<sup>34</sup>

#### 3.04.8.9.5 Organic acids

Most organic acids are less aggressive than the mineral acids. However, formic acid is one exception, as this is aggressive to S30400 at intermediate temperatures and concentrations. The temperature plays a significant role in determining the corrosiveness of formic acid and at intermediate concentrations ranging from 25–85 wt% in combination with a high temperature, that is, 100°C, most stainless steels corrode. However, at lower temperatures, most of the stainless steels containing higher amounts of chromium, nitrogen, and molybdenum are resistant to corrosion in formic acid, see [Figure 32](#). Other organic acids such as acetic and lactic acid are less corrosive and the stainless steel grades S30400 and S31600 are resistant to corrosion at most temperatures and concentrations. However, the stainless steel grades S30400 and S31600 corrode at higher temperatures and concentrations close to boiling point in lactic acid solutions, so higher-alloyed stainless steel must be used in such service environments. In acetic acid, S30400 is prone to corrosion at temperatures above 90°C at concentrations above 10 wt% and even to localized corrosion above 70°C at concentrations above 80 wt%. There are many organic chemicals in pure conditions, many of which are not at all corrosive to stainless steels such as S30400 and S31600. Some examples are fatty acids, such as oleic acid, stearic acid

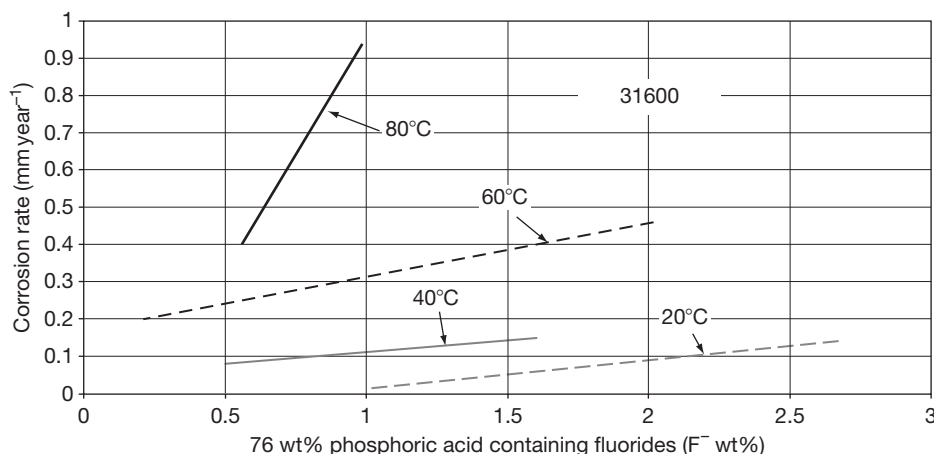


**Figure 31** Corrosion rate for the stainless steel grade S31600 in phosphoric acid containing fluorides. Reproduced from Alfonsson, E.; Arnvig, P.E.; Bergquist, A.; Ivarsson, B.; Iversen, A.; Leffler, B.; Nordström, J.; Olsson, J.; Stenvall, P.; Wallén, B.; Vangeli, P.; Outokumpu Stainless Corrosion Handbook, 9th ed.; Outokumpu Stainless Oy, Sandviken 2004, pp 1:8–1:103.

or ethanol. The S31600 grade can also cope with most concentrations and temperatures of citric acid.

Oxalic acid has two organic acid functional groups and can release two protons per molecule. This acid is more corrosive for standard stainless steel grades such as S30400 and S31600 and is further highly corrosive to titanium, see [Figure 33](#).

#### 3.04.8.9.6 Alkaline solutions

Stainless steels such as S30400 and S31600 are highly resistant in alkaline environments such as sodium hydroxide and potassium hydroxide at lower and

intermediate temperatures at all concentrations, see [Figure 34](#). The tolerance to chloride contamination in sodium and potassium hydroxide is also much higher compared with neutral water solutions. Uniform corrosion tests have shown that resistance was obtained in solutions containing 1–20 wt% sodium chloride in 40 wt% sodium hydroxide solution using activation and at a temperature as high as 80°C.<sup>32</sup> However, at high temperatures above 115°C and at intermediate concentrations above 20 and 70 wt%, stainless steels are prone to SCC in sodium and potassium hydroxide.

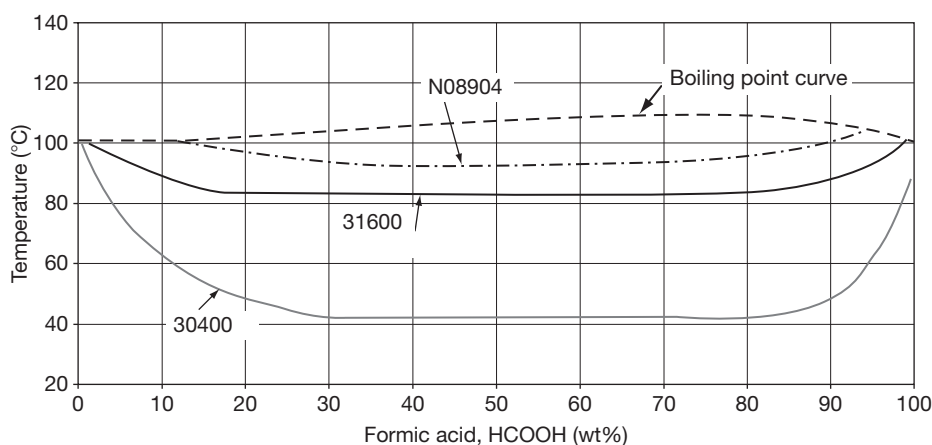


**Figure 32** Isocorrosion diagram at  $0.1 \text{ mm year}^{-1}$  for formic acid. Reproduced from Alfonsson, E.; Arnvig, P.E.; Bergquist, A.; Ivarsson, B.; Iversen, A.; Leffler, B.; Nordström, J.; Olsson, J.; Stenvall, P.; Wallén, B.; Vangeli, P.; Outokumpu Stainless Corrosion Handbook, 9th ed.; Outokumpu Stainless Oy, Sandviken 2004, pp I:8–I:103.

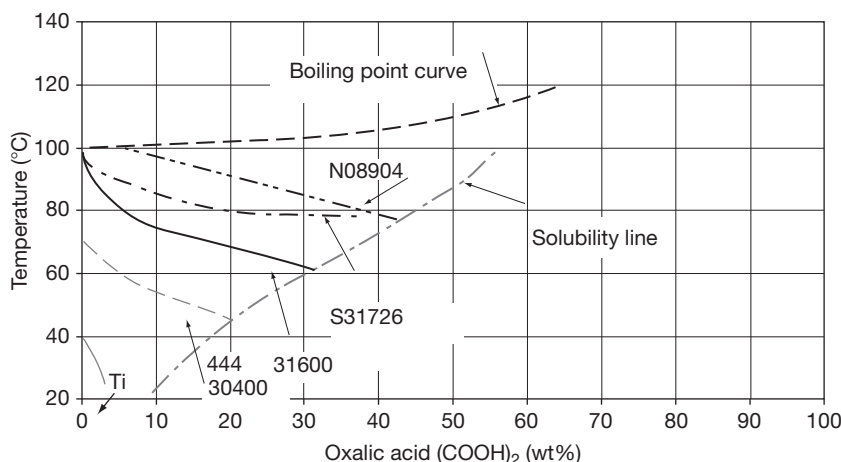


**Figure 33** Isocorrosion diagram at  $0.1 \text{ mm year}^{-1}$  for pure oxalic acid. Reproduced from Alfonsson, E.; Arnvig, P.E.; Bergquist, A.; Ivarsson, B.; Iversen, A.; Leffler, B.; Nordström, J.; Olsson, J.; Stenvall, P.; Wallén, B.; Vangeli, P.; Outokumpu Stainless Corrosion Handbook, 9th ed.; Outokumpu Stainless Oy, Sandviken 2004, pp I:8–I:103.

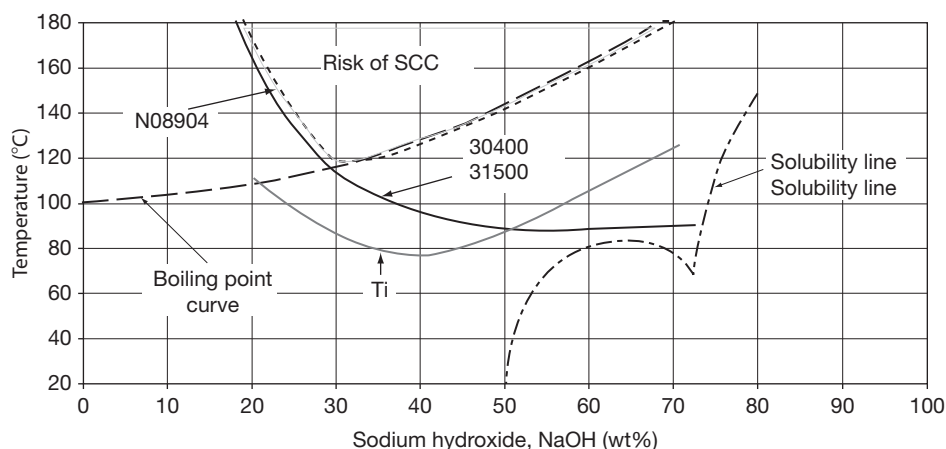


**Figure 34** Isocorrosion diagram at  $0.1 \text{ mm year}^{-1}$  for sodium hydroxide. Reproduced from Alfonsson, E.; Arnvig, P.E.; Bergquist, A.; Ivarsson, B.; Iversen, A.; Leffler, B.; Nordström, J.; Olsson, J.; Stenvall, P.; Wallén, B.; Vangeli, P.; Outokumpu Stainless Corrosion Handbook, 9th ed.; Outokumpu Stainless Oy, Sandviken 2004, pp 1:8–1:103.

### 3.04.8.10 Galvanic Corrosion

Galvanic corrosion may occur when two dissimilar metals are in electrical contact in a conductive solution, an electrolyte. The corrosion rate is dependent on the conductivity of the electrolyte, on the difference in the galvanic series between the metals and also on the surface ratio between the metals. The position of a metal in the galvanic series, at a specific temperature, in a specific electrolyte can be represented as the corrosion potential of the metal,  $E_{\text{corr}}$  or open circuit potential, OCP. For example, in seawater at  $10^\circ\text{C}$ , passive stainless steel is a more noble metal and has a higher corrosion potential in the galvanic series than the less noble mild steel. If a stainless steel construction is in conductive electrical contact with a less noble metal, the less noble metal will corrode at a higher corrosion rate. Furthermore, if the less noble metal has a small surface ratio compared with the more noble metal, the corrosion rate will increase even more.

Two different stainless steel grades in the passive state, coupled in an electrolyte, are quite close in the galvanic series and the risk of galvanic corrosion is less as long as the stainless steels remain in the passive state. If the passivity of one of the steel grades breaks down and corrosion occurs, the corrosion potential thus changes to the stainless steel active corrosion potential and the corrosion rate is influenced by this change between the two materials. Knowledge about the series in the specific environment is necessary to predict galvanic corrosion. The corrosion potential for a stainless steel can vary as the pH level of the

solution changes and if oxidizing or reductive chemicals are present in the solution.

In summary, the following circumstances influence the extent of galvanic corrosion:

- The relative area between the dissimilar metals. A smaller area of the less noble metal suffers from more aggressive corrosion attack. This relation is often referred to as a small anode to a large cathode.
- The magnitude in variation of nobility of the metals. The higher the potential difference between the dissimilar metals in the galvanic series, the higher the galvanic corrosion rates under wet conductive conditions. The solution's electrical conductivity. The worse leading ability of a solution contribute to limited corrosion attack close to the contact area between the two dissimilar metals.
- The corrosion rate of galvanic corrosion is further decreased by the decrease in temperature of the electrolyte.
- The solution's electrical conductivity. A high conductivity, that is, a high leading ability of a solution contributes to increased electron flow from the corrosion reactions and thereby a higher corrosion rate at the contact area between the two dissimilar metals.
- The rate of galvanic corrosion may be decreased by a reduction in the temperature of the electrolyte.

All passive stainless steels are relatively high up in electrochemical potential, compared with other material, whereas, for example, zinc is relatively low down in potential in the galvanic series, see [Figure 35](#).



There are several ways of preventing galvanic corrosion. Painting operations prevent the electrolyte from reaching the contact area. The use of wax or adhesives in narrow crevices prevents the electrolyte from reaching any contact area and thus prevents corrosion. The use of electrochemical knowledge between metals in construction can also prevent the occurrence of galvanic corrosion as well as being used in corrosion protection.

The risk of galvanic corrosion is severe in seawater applications. To predict the risk of galvanic corrosion the comparison of the different corrosion potentials can be utilized. The larger the difference the greater the risk of attack of the less noble component.

### 3.04.8.11 Intergranular Corrosion

Intergranular corrosion occurs as the name indicates along grain boundaries on. This corrosion form is sensitive to high carbon contents in the stainless steel and occurs if chromium carbides are precipitated in between the grains. Precipitation reactions in stainless steels can be read about in [Section 3.04.5](#). A stainless steel, which was heat-treated to conditions for grain boundary precipitations to occur, is referred to as sensitized. Other circumstances for intergranular corrosion to occur are when carbon is diffusing into the surface layer of the solid stainless steel as in carburization. If the stainless steel components are heat treated with oil, plastic tape or other organic substances on the surface or in atmosphere containing carbon monoxide or hydrocarbons there is a risk of carburization and intergranular corrosion as a result.<sup>32</sup> More about carburization can be read in [Section 3.04.5.4](#).

Intergranular corrosion occurs in solutions where the grain boundaries of chromium carbide are activated and the rest of the material is in a passive

condition, which means under strong oxidizing conditions. But it should also be pointed out that a sensitized stainless steel is vulnerable to other forms of corrosion as pitting, crevice corrosion, and SCC.

Measures to increase the resistance of stainless steels to intergranular corrosion caused by chromium carbide precipitations are to perform solution annealing or lowering the carbon content by stabilizing with titanium and niobium.

The addition of titanium or niobium to the steel, so-called stabilization, means that the carbon is bound as titanium or niobium carbides. Since titanium and niobium have a greater tendency to combine with carbon than chromium, this means that carbon is not available to form chromium carbides. The risk of intergranular corrosion is therefore appreciably reduced. There is, however, a disadvantage associated with stabilization. In the area closest to a weld, the temperature during welding can be so high that titanium or niobium carbides are dissolved. There is then a danger that they do not have time to re-precipitate before the material has cooled sufficiently to allow the formation of chromium carbides in the grain boundaries. This leads to so-called knife line attack in which a narrow zone of material very close to the weld suffers intergranular corrosion. Since the carbon level in stabilized steels is often quite high (0.05–0.08 wt%) this can give serious attack.

Nevertheless, a low carbon content in the stainless steel extends the time required for sensitization to occur and modern steel manufacturing methods enable lower carbon contents to provide a considerable decrease of the risk of intergranular corrosion to occur.

The effect of a decrease in the carbon content is most easily illustrated by a time–temperature–sensitization, TTS-diagram, an example of which is shown in [Figure 36](#). The curves in the diagram show the longest time an austenitic steel of type 18Cr–8Ni can be maintained at a given temperature before there is a danger of corrosion. This means that for

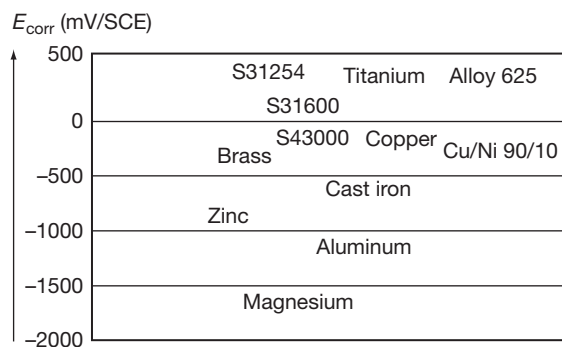


**Figure 35** The corrosion potential,  $E_{\text{corr}}$  of stainless steels in flowing seawater at 10°C.<sup>32,39</sup>

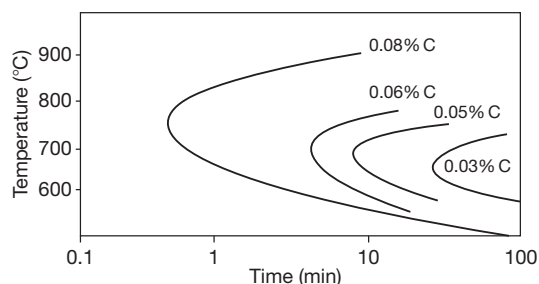


**Figure 36** TTS diagram for S30400 steels with different carbon contents. The curves are based on the Strauss test.<sup>40</sup>

standard low-carbon austenitic steels (L-grades) the risk of intergranular corrosion cracking is, from a practical point of view, eliminated. All high-alloyed austenitic and all duplex grades intended for aqueous corrosion service have carbon contents below 0.03 wt % and are consequently 'L-grades.' Due to the low solubility of carbon in ferrite, the carbon content will have to be extremely low in ferritic stainless steels if the risk of intergranular corrosion is to be eliminated. In ferritic stainless steels, stabilizing element and extra low carbon contents are often used to eliminate the risk of intergranular attack after welding or other potentially sensitizing treatments.

The stainless steels are usually delivered in the solution-annealed conditions which is a heating process causing the chromium carbides to dissolve, followed by rapid cooling. Such an operation leaves the carbon in solid solution in the steel. Even if a sensitized structure occurs, solution annealing recovers the stainless steel microstructure.

#### **3.04.8.12 Erosion Corrosion**

In construction systems where a flow of the solution is a part of the process, a sufficiently high rate to avoid deposits or marine growth is of preference. The mechanical impact from a flowing solution in combination of corrosion reaction might raise the risk of erosion corrosion in tubular systems. However, stainless steels commonly provide high tolerance against erosion corrosion in neutral chloride solutions and an optimum of flow rate avoiding erosion corrosion but mitigate deposits beneficial for both corrosion performance and economics of operation.

Erosion corrosion is a form of corrosion, which occurs at high relative metal-liquid velocities. This form of corrosion includes a mechanical wear of corrosion products. In a solution containing solid particles, for example, sand, the corrosion rate is higher. Stainless steels can be attacked if the composition of the steel grade provides unstable passivity in an aggressive solution. Attacks can occur on, for example, pump impellers. The resistance of stainless steels to erosion corrosion is generally increased by the same alloying elements as those, which increase resistance to general corrosion in the solution in question.<sup>40</sup>

#### **3.04.8.13 Common Test Procedures and Standards for Stainless Steels**

The most reliable test method for stainless steel's performance in an environment is the field-testing procedure. A number of stainless steel grades are

then tested in the service environment for a long period of time, a year or longer. However, there are a number of good test methods for ranking purposes of different stainless steel grades and also in some cases used for control purposes of the steel grades. Below are some of the most common test methods presented, used in the laboratory for research purposes and also for the screening of different stainless steel grades. The test methods are commonly based on the type of corrosion expected to occur.

Laboratory methods offer the most efficient way of ranking different stainless steel grades and their resistance to pitting and crevice corrosion. However, care has to be taken while using laboratory results in real environments, and field tests should, in some cases, be carried out to provide information about the optimum stainless steel grade to use. Laboratory tests can, nevertheless, still be very informative since some of the parameters that have the greatest influence on the corrosion properties of stainless steels may be used to simulate the most aggressive conditions, such as the amount of chlorides, temperature, pH levels, type of acid, any oxidizing chemicals, etc. Advice on material selection can then be formulated on the basis of these results.

#### **3.04.8.14 Localized Corrosion Testing of Stainless Steels using Electrochemical Methods**

The most common electrochemical method currently used to demonstrate the passivity and corrosion of standard alloy stainless steels in different solutions is to perform polarization measurements. **Figure 37** shows a schematic polarization curve for a stainless steel suffering from pitting corrosion at anodic potentials where the electrochemical response of active corrosion is a high current density.

The characteristic of pitting and crevice corrosion is the breakdown of the passive film, represented in polarization measurements by the pitting potential,  $E_p$ . The pitting potential can be defined as the potential at which the current density exceeds  $100 \mu\text{A cm}^{-2}$  for more than a minute. The most common polarization measurements show typically spikes in the current density before the breakdown to corrosion, which are referred to as metastable pitting corrosion.

Both the pitting potential  $E_{pr}$  and the repassivation potential,  $E_r$  are dependent on the scan rate. A higher scan rate will influence the chemical equilibrium reactions at the metal surface. If the scan rate is too high the pitting potential increases and the

repassivation potential,  $E_r$ , will typically decrease.<sup>15</sup> The effect of too high a scan rate is independent of the steel grade.<sup>41</sup>

The distinction between localized corrosion, such as pitting and crevice corrosion, and transpassive corrosion in the polarization measurements, is shown by the slope in the polarization measurements in the higher potential area, shown in **Figure 38**. In the case of pitting the increase in current density is much steeper than in the case of transpassive corrosion. Even more pronounced is the difference in the repassivation potential, where in transpassive corrosion this is closer to the transpassive potential,  $E_{tr}$  than for pitting corrosion.

**Figure 38** shows the polarization measurements illustrating transpassive corrosion at higher anodic potentials.

Comparing the pitting potentials, in solutions containing sufficient amounts of sodium chloride can successfully provide a ranking of the standard stainless steel grades S30400, S31600 and low alloy stainless steel grades. However, the test temperature in combination with the aggressiveness of the solution must exceed the critical pitting temperature (CPT) of the tested steel grade for pitting corrosion to occur.

### 3.04.8.15 Different Stainless Steel Grades and their Resistance to Pitting and Crevice Corrosion

Two common methods for determining the critical pitting temperature, CPT, are prescribed in ASTM G 150 and ASTM G 48. The former is an electrochemical method that uses a set potential at 700 mV/

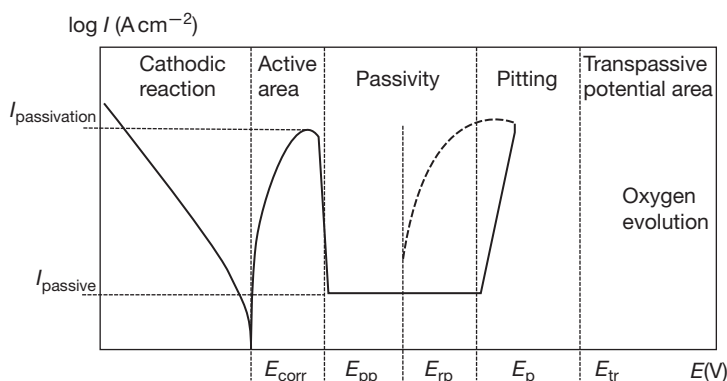


**Figure 37** Schematic polarization diagram of pitting potential,  $E_p$  and repassivation potential,  $E_r$  in a solution containing chlorides.

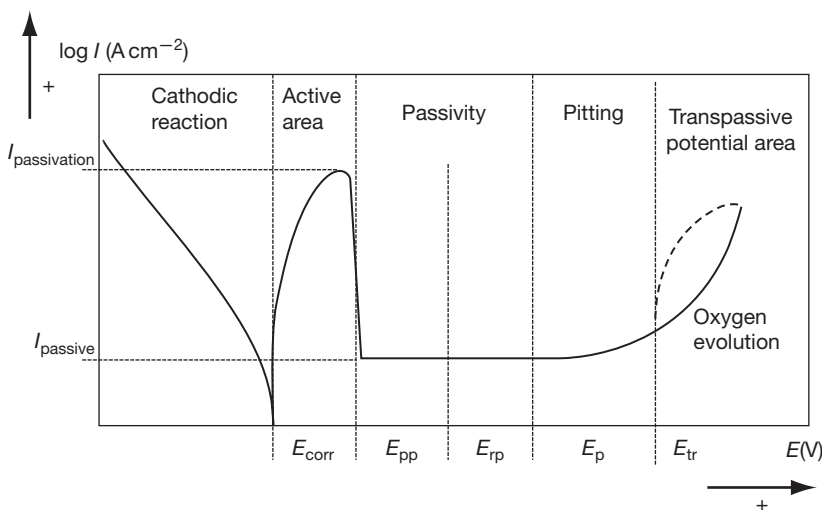


**Figure 38** Polarization measurements illustrating transpassive corrosion.

SCE in 1 M NaCl as the electrolyte and then screens the temperature from 0°C to the CPT where pitting corrosion of the steel grade propagates in a crevice-free electrochemical cell. This method provides a different CPT than ASTM G 48, which is an immersion test for 24 h in a 6% FeCl<sub>3</sub> solution that produces an oxidizing effect from the chemical solution instead of from a potentiostat. The temperature is then increased in intervals of 2.5°C until pitting corrosion occurs. Both methods show similar ranking properties with regard to the resistance to pitting corrosion among stainless steel grades, but ASTM G 150 offers better reproducibility than ASTM G 48. **Figure 39** shows critical pitting temperatures for higher-alloyed stainless steel grades according to ASTM G150 and **Figure 40** shows CPT according to ASTM G 48. It should be pointed out that these values do not represent exact values for each steel grade but may deviate due to effects from corrosion kinetics for various surfaces, welding or other mechanical treatments, etc.

The drawback of these methods is that it is extremely difficult to measure lower-alloyed stainless steels, such as 12% chromium ferritic stainless steels or austenitic S30400 (1.4301) grades, due to the aggressiveness of the methods. Both environments cause these types of stainless steel grades to corrode almost immediately when exposed. Today, pitting potentials are typically used for ranking lower-alloyed stainless steels in solutions with different

chloride contents. For comparison, pitting potentials are presented for some standard stainless grades, S30400 (1.4301) and S31600 (1.4401), in **Figure 41**.

There are several standardized methods for measuring stainless steels' susceptibility to crevice corrosion. One concept is to measure the critical crevice temperature CCT, using standard crevice formers of the MTI-2 type in a ferric chloride solution, according to a modified ASTM G 48 method, which is very aggressive to crevice corrosion in stainless steels due to the combination of acidity and oxidizing power. The higher-alloyed, more resistant stainless steel grades provide a higher CCT than the lower-alloyed stainless steels, but this method also has the disadvantage of being too aggressive for the lowest-alloyed stainless steel grades, such as the 12% ferritic stainless steels and S30400. This measure is similar to the CPT measurements only if used for ranking purposes and do not really provide data about the actual service environment. **Figure 42** presents some CCT values for higher-alloyed stainless steels. In testing crevice corrosion resistance of stainless steels a crevice former is used. Depending on the type of crevice former different results can be obtained. It can, in many real environments, be very difficult to translate the type of crevice to the laboratory since crevice corrosion is dependent on the pressure from the crevice former, the ability to drainage the solution out from the crevice and also the crevice area. Generally

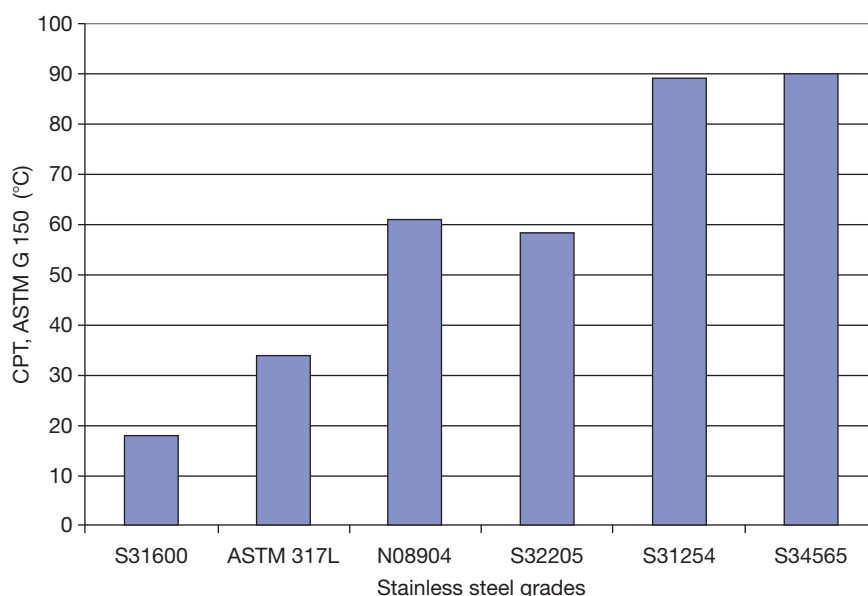


**Figure 39** CPT according to ASTM G 150; some examples of single measurements for surface 320 grit, for higher alloyed stainless steels.

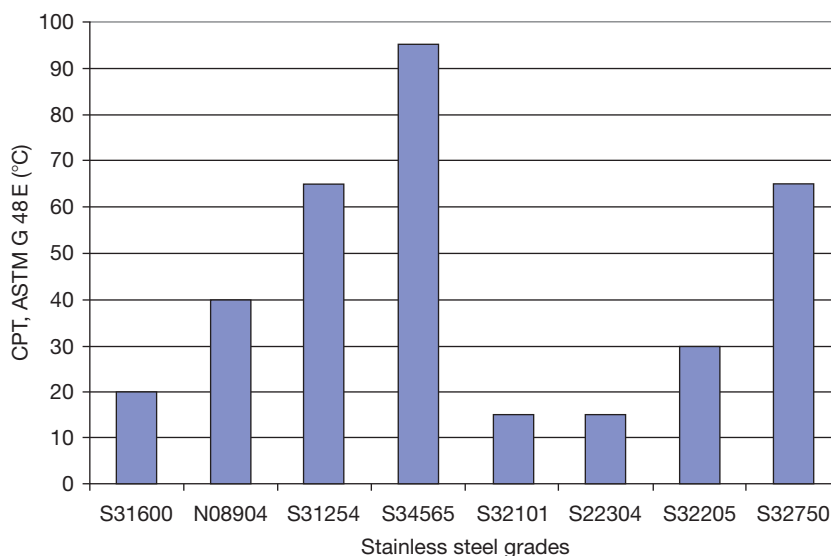


**Figure 40** CPT according to ASTM G 48E for some stainless steels.

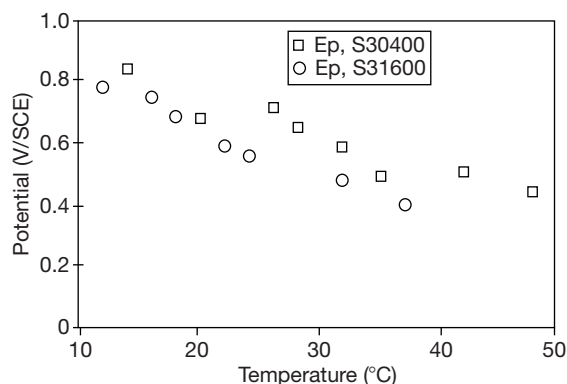


**Figure 41** Pitting potentials,  $E_p$ , for some standard stainless steels, S30400 and S31600, at different temperatures in 0.1 M NaCl. Scan rate  $20 \text{ mV min}^{-1}$  and defined at  $100 \mu\text{A cm}^{-2}$ .

standardized types of crevices are used for comparison of laboratory purposes. [Figure 43](#) shows an example of a crevice former of MTI type with heels.

#### 3.04.8.16 Screening of General Corrosion Properties of Stainless Steel Grades

One frequently used method to screen a stainless steel grade for many acids and to use for ranking purposes is ASTM G 157-98. The original test method was developed by MTI that has issued a number of strictly specified laboratory tests, which

facilitate direct comparison between stainless steel grades. Control alloys supplied by MTI are included in the tests. The stainless steel is considered to be passive and unaffected by corrosion when the corrosion rate is lower than  $0.127 \text{ mm year}^{-1}$  (5 mpy) and in ASTM G157-98 the lowest temperature at this measure is referred to as the critical temperature  $T_c$ .

A screening of the different stainless steel grades shows a clear influence of the alloy composition on the uniform corrosion properties. The super austenitic stainless steel grades S32654, S31254, and N08904 and the super duplex stainless steel grades S32750 and S32205 provide much better resistance to general corrosion compared with the standard grades of type S30400 and S31600, as can be seen in [Figure 44](#).

#### 3.04.8.17 Testing Stress Corrosion Cracking of Stainless Steels in Environments Containing Hydrogen Sulfide Under Acidic Conditions

Tests are adopted for material selection in environments containing hydrogen sulfide under acid conditions. The most internationally prevalent standardized method used for testing in these environments is NACE TM 0177, which employs a 5% NaCl + 0.5%  $\text{CH}_3\text{COOH}$  solution, saturated with  $\text{H}_2\text{S}$  by continuous bubbling after nitrogen de-aeration and a pH of 2.7–2.8. The test specimens are immersed in acidified solutions by the addition of acetic acid

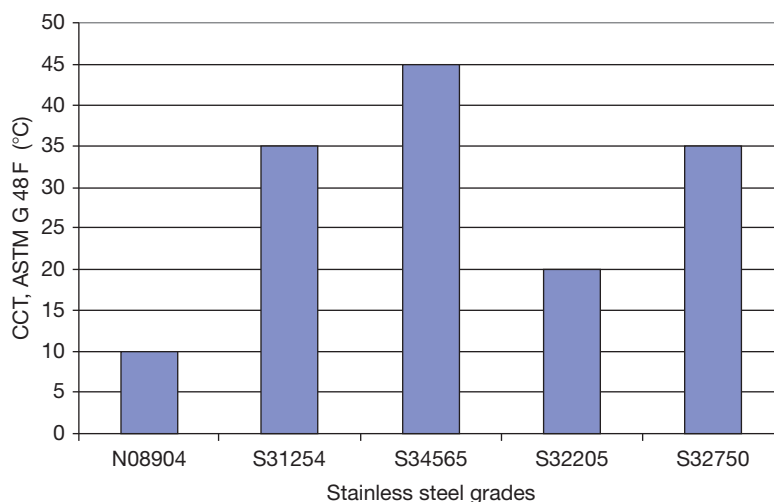


**Figure 42** CCT for higher alloyed stainless steel grades.

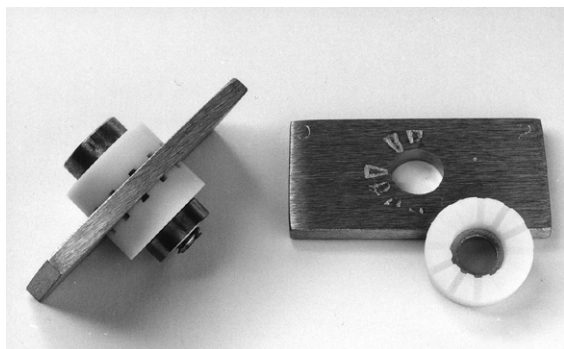


**Figure 43** Example of a MTI crevice former with heaters.

containing sodium chloride, which is saturated with hydrogen sulfide at room temperature prior to the test. The solution is also deaerated with nitrogen gas. Some test results obtained for duplex stainless steels tested according to NACE TM 0177 for 720 h are presented in [Table 10](#). Material selections based on this standardized method are included in NACE MR-0175.

#### 3.04.8.18 Laboratory Tests of SCC

Several methods can be used to test resistance to SCC. However, it can be very difficult to translate

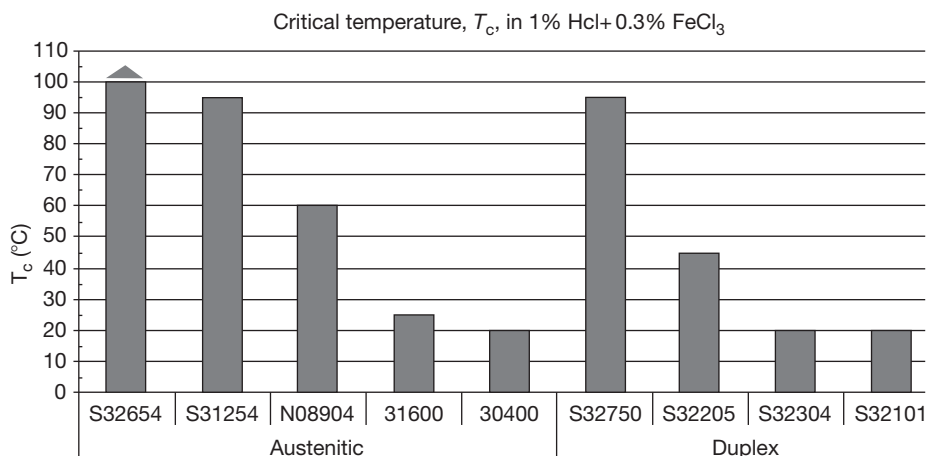


**Figure 44** Critical temperatures,  $T_c$ , at  $0.127 \text{ mm year}^{-1}$  for different stainless steel grades in 1% hydrochloric acid containing 0.3%  $\text{FeCl}_3$  additions.



the results of many of these more or less accelerated tests to reflect performance in an actual service environment, particularly in terms of the tensile stresses that can occur in the material. U-bent samples are used for many tests but can lose the introduced stress level in the test sample by test time. Nevertheless, the practice of ranking the results for different stainless steels can, in combination with experience, provide valuable data for the material selection process. One test method used for testing evaporative conditions is the 'Wick-test,' ASTM G-692-71, which was developed to simulate evaporative conditions at  $\sim 100^\circ\text{C}$  in an insulation material wetted with dilute chloride solution. The results obtained from this test for different stainless steel grades after 600 h of exposure are presented in [Table 11](#).

Austenitic stainless steels seems much more prone to SCC in this test compared with the duplex corresponding duplex stainless steel grades.

### 3.04.9 Stainless Steels in Natural Wet Environments

Experience has shown that natural water is considerably more corrosive for stainless steel than artificial water. Nevertheless, to understand the interactions between metal surfaces and microbial life in water, in terms of degradation and corrosion, a multidisciplinary view has to be adopted and there are several definitions used in the field of investigation of the interactions

between microbial life and materials resulting in corrosion and/or deterioration of materials.

Microbially influenced corrosion (MIC) can be referred to as the influence of microorganisms on the kinetics of corrosion processes of metals, caused by microorganisms adhering to the interfaces. A prerequisite for MIC is the presence of microorganisms.

#### 3.04.9.1 Microbially Influenced Corrosion

MIC on stainless steels in natural water is commonly related to an attached biofilm growth on a stainless steel surface. If the conditions favor microbial activity in the water, one of the effects of the adhesion of a biofilm to the stainless steel surface is ennoblement of the open circuit potential OCP or corrosion potential  $E_{\text{corr}}$ . The increase in the potential may cause localized corrosion on stainless steel if it reaches a value exceeding the pitting potential of the steel grade. Cases of MIC on stainless steels have been reported for alloys with relatively low molybdenum content as localized corrosion and deposits were often found at or close to the corrosion sites.<sup>41</sup>

[Figure 45](#) shows typical ennoblement on stainless steels S30400 (1.4301) and S31600 (1.4401) in a natural water containing microorganisms.

Parameters that influence microbial activity on metal surfaces are considered to be:

- temperature
- availability of nutrients

**Table 10** Some test results obtained for duplex stainless steels tested according to NACE TM 0177 for 720 h

Material	$H_2S$ (bar)	Load (% $R_{p0.2}$ )		
		70	95	100
S32205	0.01	No cracking	Not tested	No cracking
S32205	0.1	SCC	Not tested	SCC
S32750, welded tube	0.1	Not tested	No cracking	Not tested
S31254	1	No cracking	Not tested	No cracking

**Table 11** Results from the Wick-test, ASTM G-692-71 for some duplex and austenitic stainless steels after 600 h

Microstructure	Material	Number of tested specimens	Failed due to SCC	PRE
Duplex	S32101	6	0	26
	S32304	6	0	23
	S32205	2	0	35
	S31803	4	1	35
Austenitic	S30400	5	5	17.5
	S31603	4	4	24
	N08904	4	1	36
	S31254	3	0	43

- flow velocity
- pH
- oxygen level
- cleanliness
- toxic effects from chemicals

Biofilms may grow under favorable conditions to such proportions that they can be regarded as deposits and the risk of under deposit corrosion or crevice corrosion increases with the density of the deposits.

From early investigations by Mollica and Trevis of stainless steels immersed in seawater, an increase of the open circuit potential or corrosion potential, to high values ranging from 350 to 450 mV/SCE was observed and attributed to the formation of a biofilm on stainless steel surfaces.<sup>42</sup> These values were also reported by many other investigations and the results appeared to be similar and independent of geographical location or hydrological properties, but sensitive to temperature changes. Mollica and Trevis attributed the ennoblement to an increased rate of the cathodic reaction, which has an effect on the corrosion rate in the propagation stage. Feron investigated the temperature effect and the ennobled potential fell above 40°C.<sup>43</sup>

Another explanation for the mechanism of ennoblement is the action of manganese oxidizing bacteria. Tverberg, Pinnow, and Redmerski reported manganese-rich deposits in combination with corrosion in standard stainless steel grades.<sup>44</sup>

While evaluating and predicting MIC in stainless steels, several parameters that influence local corrosion have to be considered. The ennoblement from

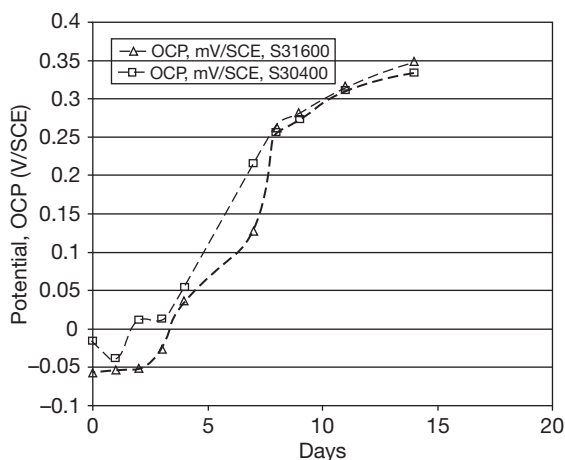
active microorganisms increases the risk of exceeding the pitting potential of the passive layer. However, the pitting potential is dependent on factors such as the alloying elements used in the steel grade, welding procedures, chloride content, nitrate content, and deposits. In addition, while considering the risk of MIC in water passing through different industrial water systems, one must also take into account the fact that the water quality varies with respect to factors such as oxygen content and chloride content.

#### 3.04.9.1.1 Chlorination

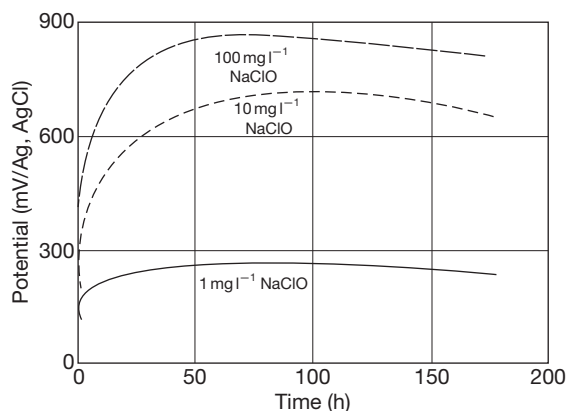
The conventional way to prevent biofouling or to reduce its effects is to chlorinate the water. This is normally done by continuously or intermittently, adding a strong hypochlorite solution. High chlorine concentrations may increase the corrosivity of water due to the oxidizing effect imposed on the stainless steel. For this reason, the chlorine addition should be restricted to a minimum. The addition of free chlorine in quantities as low as 0.1 mg l<sup>-1</sup> is just sufficient to prevent the formation of an active biofilm but not enough to increase the potential.

Figure 46 shows an example of the time dependence of the open circuit potential on addition of sodium hypochlorite for stainless steel grade S32205 (1.4462). The efficiency of the hypochlorite addition releasing chlorine in this case is approximately ~14%.

By intermittent chlorination, high potentials are reached during a short chlorination period. After chlorination, the potentials decrease to low values



**Figure 45** Ennoblement of the open circuit potential (OCP) on stainless steel in natural water containing microorganisms.



**Figure 46** Time dependence of the open circuit potential for S32205 at different additions of sodium hypochlorite (NaClO) in 1000 mg l<sup>-1</sup> chloride solution. Reproduced from Tverberg, J.; Pinnow, K.; Redmerski, L. NACE Corrosion, Paper 151, April 23–27, Nevada, 1990.

similar to sterile chloride solutions, before the next chlorination period. If the interval between two chlorination periods is very long, an active biofilm will be formed and the potentials will increase once again after a couple of weeks.

The risk of crevice corrosion initiation is increased by the chlorination but the propagation rate of the crevice attack is reduced if intermittent chlorination is used. Crevice corrosion on type S31600 (1.4401) specimens exposed to, for example, nonchlorinated and chlorinated seawater showed the strongest attack in the nonchlorinated water while intermittent chlorination causes only a minor shallow attack.<sup>32</sup>

### 3.04.9.2 River Waters and Freshwater

#### 3.04.9.2.1 Drinking water<sup>32</sup>

Drinking water may seem a relatively harmless environment from a corrosion point of view, and the common austenitic stainless steels, that is, S30400 (1.4301), S31600 (1.4401), and similar grades are suitable for most equipment used in the production and distribution of potable water, but may in rare circumstances suffer corrosion. Standard grade stainless steels such as S30400 and S31600 are widely used in the manufacture of vessels, piping, and heat exchanger tubing for handling all kinds of freshwater. Four primary environmental parameters must be defined for the serviceability of S30400 and S31600 in freshwater. These are the chloride content of the water, the presence of oxygen or any other strong oxidant, the temperature, and the presence of crevices. If one or more of these environmental parameters exceeds these empirical limits, the possibility of localized corrosion is introduced. In most countries, the chloride concentration is limited in potable water, often to a maximum of 0.250–0.300 g l<sup>-1</sup>. However, chemicals added at various stages in the water plant may contain chlorides, with the result that higher chloride concentrations than those specified for drinking water may occur close to the dosage points of such chemicals.

The corrosiveness of the water increases as its temperature rises. Most countries require the temperature of drinking water to be less than 25°C. In consumer applications, stainless steels may also be used in water heaters and hot water tubing, where the water temperature usually exceeds 60°C. In hot water systems, heat transfer may occur through the wall of a tube or a vessel. In such situations, the corrosion risk will also be influenced by the direction of the heat flux. In systems handling hot water, the risk of SCC must sometimes be considered. In the

case of a hot water tube, where the heat flux direction is from the water to the tube wall, the maximum temperature of the stainless steel wall will be that of the water. For the outside of the tube, there should be no risk of corrosion as long as the surface is dry or just wetted by water without chlorides. However, if the outside is wetted by water containing an appreciable amount of chloride ions, evaporation of the water may result in a concentrated solution that promotes pitting and crevice corrosion that, in turn, may act as starting points for SCC. Examples of this situation are water leaking through a chloride containing thermal isolation, or water leaking to the surface of a tube embedded in wall plaster containing a chloride-rich antifreeze agent. The 1.4301 grade (S30400) is sensitive to this type of SCC even after a short wet period whereas type 1.4401 (S31600) can tolerate such conditions for a longer period than 1.4301 (S30400). However, if the wall temperature is less than 50°C, SCC is not likely to occur in ordinary drinking water systems. Duplex stainless steels such as 1.4361 (S32304) and 2205 (S32205) offer better resistance to SCC than the 1.4301 and 1.4401 grades and should be considered for hot water tubing that might be subject to wetting from the outside.

Several oxidizing chemicals may be added at a water treatment plant and in the distribution system, for example, potassium permanganate for the precipitation of metal ions, iron (III) ions for coagulation, and various chlorine compounds and ozone for disinfection purposes. In the presence of strong oxidants, the corrosion potential of the steel will be polarized in the positive anodic direction and the pitting or crevice corrosion potential may be exceeded. Accordingly, there may be a greater risk of localized corrosion attack close to the points where oxidants are added to the water.

#### 3.04.9.2.2 Freshwater

Freshwaters such as lakes and rivers contain much less amounts of chlorides compared with seawater. The material choice of stainless steels relies, in many cases, on the chemical analysis of the water and the temperature. For example, the stainless steel grade chosen should rely on the chloride content of the water but in some cases there are beneficial effects of, for example, sulfates and nitrates solved in the water. However, no systematic studies are available on how beneficial those effects are but in some cases tentative engineering diagrams are used for the determination of a useful stainless steel. There are, however, circumstances when unexpected pitting

or crevice corrosion occurs in freshwater systems and experiences from real systems can be a guide to material advice. One example of tentative engineering diagrams is presented in [Figure 47](#). A significant decrease in the tolerance to chlorides and temperatures is seen from the tentative engineering diagram when crevice corrosion is a risk compared with a base material without any crevices.

Data from tentative engineering diagrams should be a guidance and also taken with care, since there are a number of factors not included such as the impact of different crevices, other impurities, etc.

### 3.04.9.3 Seawater

As seawater contains high amounts of chlorides (~21 000 ppm), standard stainless steels such as 30400 and 31600 are susceptible to localized corrosion such as pitting and crevice corrosion. In addition, natural seawater contains microorganisms, which under beneficial conditions are able to cause ennoblement of the open circuit potential and thereby impose an oxidizing effect. Typical values found in seawater are 300–350 mV/SCE, reached within 10–20 days of exposure. The ennoblement caused by active microorganisms is independent of stainless steel grade. Where ennoblement occurs in combination with biofouling by microorganisms or barnacles on a stainless steel surface, super austenitic or super duplex stainless steels are often

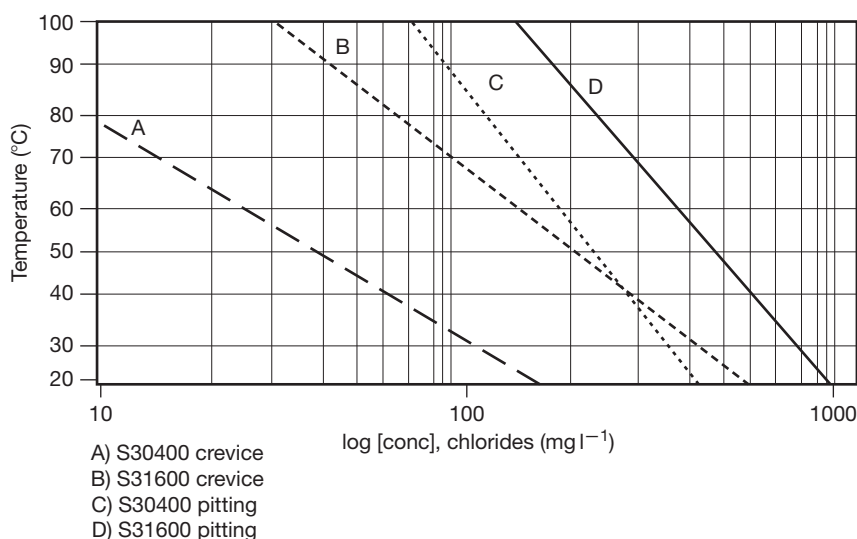
required to ensure corrosion resistance in seawater, even at low temperatures.

Also in seawater as in other natural waters, the ennoblement is sensitive to temperature and imposes a catalytic effect of the cathode reaction, which causes a high current density in corrosion reactions. Practical experience and numerous corrosion tests have shown that conventional stainless steels are prone to localized corrosion in seawater. Over the last decades a number of highly alloyed steels with excellent corrosion resistance have been introduced into the market. Some of the new steels are being used extensively in seawater applications, especially in the seawater systems on offshore platforms.

A common factor of the super austenitic and super duplex stainless steels is a high content of the alloying elements chromium, molybdenum and, in most cases, nitrogen. Typical compositions of seawater-resistant stainless steels, S31254 (1.4547) and S32750 (1.4410) with different structures are shown in [Table 12](#). The two stainless steels, S31254 (1.4547) and S32750 (1.4410) have approximately the same resistance to crevice and pitting corrosion.

#### 3.04.9.3.1 Material selection

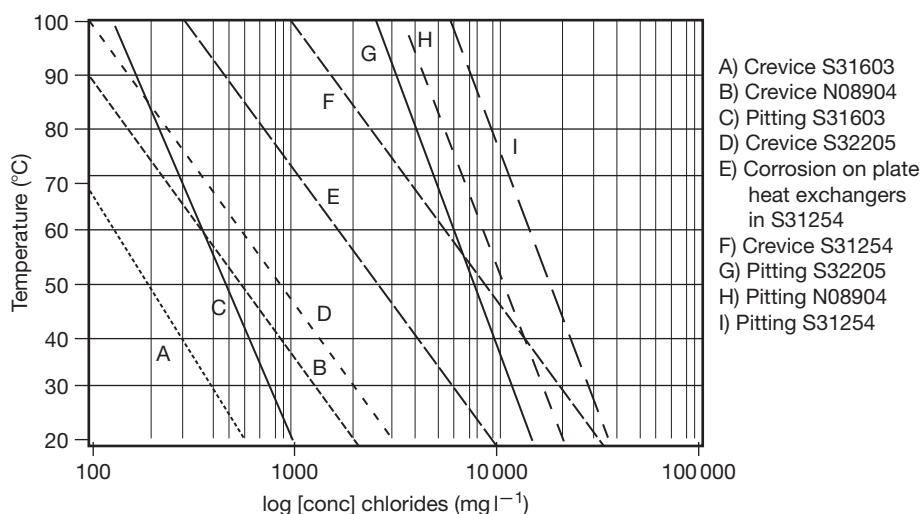
[Figure 48](#) shows up to which approximate temperatures stainless steel can be used in oxygen-saturated, slightly chlorinated water of varying chloride content. The diagram is based on studies of literature,



**Figure 47** Tentative engineering diagram for S30400 and S31600 for different chloride contents and temperatures extracted from Outokumpu Corrosion handbook. Reproduced from Alfonsson, E.; Arnvig, P.E.; Bergquist, A.; Ivarsson, B.; Iversen, A.; Leffler, B.; Nordström, J.; Olsson, J.; Stenvall, P.; Wallén, B.; Vangeli, P.; Outokumpu Stainless Corrosion Handbook, 9th ed.; Outokumpu Stainless Oy, Sandviken 2004, pp 1:8–1:103.

**Table 12** Chemical composition and mechanical strength (min. values) of some seawater-resistant and conventional stainless steels

EN	ASTM	Typical composition (%)						Mechanical properties $N\ mm^{-2}$ (20 °C)		Microstructure
		$C_{max}$	Cr	Ni	Mo	Cu	N	$R_{p0.2}$	$R_m$	
1.4547	S31254	0.020	20	18	6.1	0.7	0.2	300	650	Austenite
1.4410	S32750	0.030	25	7	4	–	0.3	550	800	Duplex
1.4436	S31600	0.050	17.5	11	2.6	–	–	220	510	Austenite
1.4539	N08904	0.020	20	25	4.5	1.5	–	220	500	Austenite
1.4462	S31803	0.030	22	5.7	3.1	–	0.17	480	680	Duplex

**Figure 48** Risk of pitting and crevice corrosion on high alloyed stainless steel in water of different chloride contents or temperatures. Reproduced from Alfonsson, E.; Arnvig, P.E.; Bergquist, A.; Ivarsson, B.; Iversen, A.; Leffler, B.; Nordström, J.; Olsson, J.; Stenvall, P.; Wallén, B.; Vangeli, P.; Outokumpu Stainless Corrosion Handbook, 9th ed.; Outokumpu Stainless Oy, Sandviken 2004, pp 1:8–1:103.

combined with practical experience, but it must be underlined that the resistance of a material is also influenced by factors other than temperature and chloride content. Examples of such factors are weld defects, presence of oxide from welding or other heat treatment, contamination of the steel surface by particles of nonalloyed or low-alloyed steel, pH, microbial activity, and the degree of chlorination. The crevice geometry is normally more difficult in a plate heat exchanger than for flange joints, a deeper and more effective crevice due to the curved contact surface, thereof two boundary lines for crevice corrosion on S31254 (1.4547). It should, however, be noted that the crevice geometry of a flange joint is dependent on the pressure that is obtained while tightening screws and bolts. Therefore, the boundary line for crevice corrosion under ‘normal’ conditions can, in

practice, be similar to that which applies to crevice corrosion for plate heat exchangers.<sup>32</sup>

Data from tentative engineering diagrams should be used as a guidance and also taken with care since there are a number of factors not included such as the impact of different crevices, other impurities etc.

### 3.04.9.3.2 Polluted seawater

In practice, the organisms most dangerous to stainless steels are the sulfate reducing bacteria, which receive their energy, by reducing sulfate ions to hydrogen sulfide while simultaneously oxidizing organic substances. The growth of these bacteria is promoted by anaerobic conditions, which, for instance, exist in bottom sediments containing decomposing organic matter.

Several investigations show that hydrogen sulfide stimulates the anodic reaction in the corrosion process

of stainless steels and consequently increases the corrosion rate. Accordingly, very high levels of hydrogen sulfide lower the pitting potential of a stainless steel and increase the rate of the active corrosion existing in the pit. However, hydrogen sulfide acts reducing on the potential, which lowers the corrosion potential. These low potentials mean that the risk of initiation of crevice and pitting corrosion will decrease.

### 3.04.9.3.3 Cathodic protection and hydrogen embrittlement

Naturally, cathodic protection of seawater-resistant stainless steels is not necessary. However, such steels might be included in a protection system if they are parts of a construction in which other components have to be protected, one example being subsea templates in the offshore industry. Another example can be found in power plant condensers when stainless steel tubes have been roller-expanded into tube sheets made of bronze and brass.

However, examples of intentional protection of stainless steel can be found in offshore flow lines, which are placed on the bottom of the sea to transport corrosive oil and gas from satellite platforms to the main platform. In this case, the environment inside the flow line determines the choice of material and this seldom justifies seawater-resistant steel. Therefore, cathodic protection of the outside of the flow line is often necessary in spite of extensive passive corrosion protection.

In cathodic protection with sacrificial anodes, there are always parts of the object where the potential is more negative than the reversible potential of hydrogen evolution, so significant hydrogen evolution always takes place. Under such circumstances certain alloys may pick up hydrogen and thus suffer embrittlement and cracking. The risk is particularly

high if the material is cold worked and subjected to high mechanical stresses and fatigue loading. The austenitic steel is not influenced by seawater and cathodic protection despite being cold worked to 30%. However, embrittle effect on the duplex steel is under debate. The phenomenon needs further investigation, but caution is recommended if severely cold-worked duplex stainless steels are used in seawater constructions equipped with cathodic protection.

### 3.04.9.3.4 Seawater exposures

One of the largest exposure programme run in Europe, the MAST II programme, studied the effects of biofilm growth and the impact of chloride concentrations from different locations in Europe.<sup>46</sup> In this programme, several commercial stainless steels for marine application were chosen and the electrochemical effects induced by biofilm growth were measured and collected on samples exposed in all European seas, from the Mediterranean to the North Sea. **Table 13** presents a list of the stainless steel grades tested. Potential ennoblement of the stainless steels in the passive state occurred at all marine stations and in all four seasons. The initial corrosion potential and the rate of ennoblement showed significant differences between the sites but the reasons for the varying rates were not explained. The ennoblement was related to the seasons of the year and was strongly dependent on the temperature being less rapid in winter than in the summer for all stations.

The samples were immersed in coastal seawaters adjacent to Trondheim (Norway), Kristineberg (Sweden), Cherbourg (France), Brest (France) and Genoa (Italy).

The main risk of corrosion attack for stainless steels in seawater where there is heavy biofouling is crevice corrosion. **Table 14** illustrates the risk of

**Table 13** Stainless steel grades exposed in the MAST II Programme<sup>46</sup>

EN	Trade name	Chemical composition (wt%)				
		Cr	Ni	Mo	Cu	N
1.4435	316L	17.2	12.6	2.6		
1.4462	2205	22	5.5	3.2		0.17
1.4460	UR47N	24.7	6.6	2.9		0.18
1.4507	UR52N+	25	6.3	3.6	1.5	0.25
1.4410	SAF 2507	24.9	6.9	3.8		0.28
1.4547	254SMO	19.9	17.8	6	0.69	0.2
1.4652	654SMO	24.5	21.8	7.3	0.43	0.48
1.4563	SAN28	26.7	30.3	3.4	0.9	0.07
1.4537	URSB8	24.9	25	4.72	1.4	0.21
1.4529	URB26	20	24.7	6.3	0.8	0.19



**Table 14** Results from crevice corrosion tests carried out at five marine stations<sup>46</sup>

EN	Trade Name	Genoa, Italy	Cherbourg, France	Brest France	Kristineberg Sweden	Trondheim Norway
1.4435	316L	5/5	0/4	0/4	0/4	4/4
1.4462	2205	++	+	+	0/5	+
1.4460	UR47N	++	+	0/4	0/4	0/4
1.4507	UR52N+	+	+	0/5	0/5	+
1.4410	SAF 2507	0/4	+	0/5	+	+
1.4547	254SMO	+	+	0/5	0/5	0/5
1.4652	654SMO	+	0/5	0/5	+	0/4
1.4563	SAN28	+	+	+	0/5	+
1.4537	URSB8	+	+	0/5	0/5	0/5
1.4529	URB26	0/5	0/5	0/5	+	0/5

+ / ++, one/several depassivated areas, no weight loss; 5/5 crevice corrosion on 5 coupons out of 5.

crevice corrosion for different stainless steels exposed to seawater.

The more-alloyed stainless steel grades either austenitic or duplex grades, appeared to be resistant to crevice corrosion in all marine stations after at least a 6000 h of immersion at ambient temperature. The winter and summer tests lasted 3000 h respectively. Some depassivation as discoloration was observed under the crevice washers on many of the samples but no weight losses were observed.

#### 3.04.9.3.5 Anaerobic seawater environments

The presence or absence of a cathodic reaction can determine the extent of corrosion. Oxygen reduction is not the most natural cathodic reaction in natural waters and by the absence of such a reaction may have a beneficial effect in terms of low or virtually zero oxygen content. Mollica, Montini, Scotto, and Marcenaro investigated three stainless steel grades, EN 1.4016(S43000), 1.4301(S30400), and 1.4401 (S31600) that were exposed in an anaerobic clay environment in seawater at the harbor in Genoa, Italy. The exposure time was six months and the coupons were exposed at six various levels of depth to the waterline, where the first level was just under the waterline. During exposure, the open circuit potentials were measured and weight loss measurements were performed after the test. Analysis of free sulfur and pH was carried out at the different levels of exposure. The pH was 7.6 and the sulfur content varied from 2.65 to 3.15 mol l<sup>-1</sup> in the clay. The OCP for EN 1.4301(304) and 1.4401(S31603) was after 40 days at the potential of  $-500 \pm 10$  mV/SCE without any initiation of local corrosion. The stainless steel grades EN 1.4301 and 1.4401 remained corrosion resistant under anaerobic conditions and their

corrosion potential coincided with the redox potential of the medium, indicating that the level of oxygen determined the open circuit potential, or corrosion potential. However, the less noble grade EN 1.4016 suffered local corrosion at potential levels ranging from  $-500$  and  $-600$  mV/SCE.<sup>47</sup>

These results indicate that in a completely oxygen-free environment, even where there are high amounts of chlorides, there is an electrochemical effect of the oxygen removal that coincides with the cathodic protection of the stainless steel. However, in an anaerobic clay or similar environment, any oxidizing coupling effect of the steel, that is, an oxidizing chemical is added or oxygen is present from another source, causes an increase in the potential which can have an adverse effect on the corrosion resistance of stainless steels.

Mollica and Ventura tested crevice samples of the following stainless steel grades: EN 1.4652 (S31654), EN S31254 (1.4547), EN N08904 (1.4539), ENS31600 (1.4404), and EN S32205 (1.4462) in an anaerobic marine environment and simulated a coupling effect between anaerobic and aerobic environments potentiostatically to simulate the rate of ennoblement found in aerobic conditions.<sup>48</sup> They found that the stainless steels were in the passive state at an open circuit potential close to  $-450$  to  $-500$  mV/SCE, almost independent of the alloy composition. However, the passivity was destroyed by a cathodic polarization at a potential below  $-700$  mV/SCE. An activity peak was observed at the potential range  $-600$  to  $-700$  mV/SCE, independently of alloy composition and tested temperatures. Nevertheless, spontaneous repassivation of activated stainless steels was also observed. The spontaneous initiation of crevice

corrosion attacks in stainless steels in totally anaerobic seawater seemed impossible. However, under oxidizing conditions, localized corrosion such as crevice corrosion was initiated.<sup>48</sup>

### 3.04.10 Stainless Steels Performance in Atmospheric Environments<sup>32</sup>

In architectural applications, that is, wall claddings and decorations, stainless steel is often chosen for its aesthetic qualities, since it can be supplied with a variety of surface finishes, and because of its cost benefits – it is virtually maintenance-free.

In structural applications, stainless steel is used for components within the building and construction industry where the emphasis is more on the strength and ductility of the material. In such cases, superficial staining and minor shallow corrosion are not necessarily a cause for concern as there is seldom any risk of structural or mechanical failure of the component. However, for stainless steel roofing, some superficial staining need not be critical, but any penetrating pitting attack will mean that the material chosen will have failed to serve its purpose.

Whatever the reason for choosing stainless steel for architectural applications, material selection must be based on experience and knowledge of the performance of specific grades in specific circumstances. Figure 49 shows the Sickla bridge constructed in duplex stainless steel. The bridge is located close to Stockholm in Sweden.



**Figure 49** The Sickla bridge, constructed in duplex stainless steel.

#### 3.04.10.1 Types of Atmosphere, Corrosivity, and Material Selection

Outdoor atmospheres were previously divided into four categories:

- rural
- urban
- industrial
- marine

Revisions of standards from the international standardization organization, for example, ISO define corrosivity classes rather than atmospheres. The corrosivity of the different atmospheres are calculated and evaluated by pure metals such as carbon, steel, and zinc. The results and corrosivity of environment have been compared with the performance of stainless steels and Table 15 shows stainless steels performing with corrosion resistance in the different corrosivity classes.

**Table 15** A comparison between corrosivity classes according to ISO 9223 and ISO 12944–2, including appropriate stainless steel grades

ISO	Typical environments	Grades
C 1	Indoor, heated. Outdoor, deserts and arctic areas (rural)	S43000, S30400
C 2	Indoor, nonheated. Outdoor, arid and low pollution (rural)	S43000, S30400
C 3	Indoor, humid, low pollution. Coastal areas with low deposits of salt. Urban and industrialized areas with moderate pollution	S30400, S31600
C 4	Indoor with volatile aggressive chemical compounds, swimming pool buildings. <sup>a</sup> Polluted urban and industrialized atmosphere. Coastal areas with moderate salt deposits	S31600, S32205, N08904, S32750, S31254
C 5	Severely polluted industrial atmospheres with high humidity and marine atmosphere with high degree of salt deposits, splashes	N08904, S31254

<sup>a</sup>Attention must be paid to cold stainless steel surfaces well above the water level where volatile compounds, especially chloramines, can condense and cause a special type of SCC. It has been found that only the most resistant grades, that is, N08904 (1.4539) and S31254 (1.4547), are capable of withstanding such conditions. See the previous section on SCC.

**3.04.10.1.1 Indoor, heated, nonheated. Outdoor, arid, low pollution, deserts and arctic areas (Rural), C1–C2**

A rural atmosphere is characterized by clean air, that is, a low level of pollutants, including airborne chlorides from the sea. Acid rain resulting from emissions of sulfur oxides due to the combustion of fossil fuels at remote power stations does not normally cause any problems for stainless steel as long as there are no chlorides present.

Ferritic grades with 17% chromium, for example, 1.4016 (S43000), can normally be used in this type of atmosphere.

Austenitic steels such as S30400 (1.4301) and similar grades are still very common, but these are often selected for their availability and fabrication aspects rather than for their corrosion resistance. Certain forming operations can be facilitated by the use of austenitic grades.

Ferritic grades have a transition temperature, that is, a temperature below which the material becomes brittle. This does not normally create any problems for thin gauges since the transition occurs at temperatures well below zero (°C). However, this phenomenon cannot be totally neglected in countries with cold winters. Austenitic grades are safer in that respect.

**3.04.10.1.2 Indoor, humid, low pollution. Coastal areas with low deposits of salt. Urban and industrialized areas with moderate pollution, C3**

The use of 1.4301 (304) should be limited to indoor nonpolluted atmospheres as described in [Table 1](#).

Urban and industrial atmospheres normally contain oily exhaust fumes from engines and soot and dust, including metal dust. A fall in temperature during the night may expose the stainless steel surface to a slightly acidic condensate, which in turn may cause staining. However, serious corrosion will never occur provided that the atmosphere is free from chlorides. Metal dust, especially if the source is a steel plant or a mechanical workshop fabricating steel items, can attach itself to stainless steel surfaces and affect both the aesthetic and corrosion resistance properties of the stainless steel surface unless it is cleaned regularly.

Stainless steel is commonly used for architectural applications in major cities, and in such an environment, regular cleaning is recommended if the material has been selected for its aesthetic qualities, particularly if the surface is close to street level.

Grades containing 2–2.5% molybdenum, that is, type S31600 (1.4401) and similar, normally offer adequate corrosion resistance even when used for applications in cities situated close to the sea.

The principles of material selection for industrial areas are virtually the same as those, which apply for major cities. However, in an industrial environment, the staining from nearby metal industries can sometimes be so severe that it is almost impossible to maintain a shiny surface appearance. In such cases, if the aesthetic aspects are a prime consideration in material selection, other materials are to be preferred. If the integrity of a structural component is more important, stainless steel is still an excellent material.

**3.04.10.1.3 Indoor with volatile aggressive chemical compounds, roof parts with mechanical load in swimming pool buildings. Polluted urban and industrialized atmosphere. Coastal areas with moderate salt deposits, C4–C5**

A marine atmosphere is characterized by its location to the sea resulting in airborne and depositing chlorides, either as salt crystals or close to water spray. The distance from the sea is important, as is the geographical location. Temperature and humidity are almost as important as the presence of chloride ions.

Molybdenum alloyed grades of type S31600 (1.4401) or comparable grades are normally specified for a marine atmosphere, regardless of whether the application is a prestigious building in a coastal city or an offshore platform. However, this material has inadequate resistance if used close to the sea in tropical countries with high levels of humidity and high daytime temperatures. Examples include cases of SCC reported from industrial installations along the Arabian Gulf coast and in South East Asia. A duplex grade such as 1.4462 (S32205) is a good alternative in those conditions. This grade has also been used for hand railings along beach promenades in the Canary Islands. For high prestigious buildings situated very close to the sea in such countries, it may be necessary to select a very highly alloyed grade such as 1.4547, S31254 or S32750 (1.4410).

Indoor atmospheres are often, to a certain extent justifiably, neglected. They do not normally contain chlorides and the low relative humidity and high temperature make the risk of condensation almost negligible. The criteria for material selection will, in such circumstances, be the same as for rural atmospheres, that is, either a ferritic grade or S30400

(1.4301) or similar as described earlier. This is also what we face while entering a modern office building, an elevator, or a hamburger bar.

However, there are indoor atmospheres for which serious consideration is warranted prior to the installation of stainless steel, whether stainless steel is chosen for its aesthetic properties or for load carrying structural components.

One such case is swimming pool buildings. In such an environment, the combination of high humidity, relatively high temperatures, and the evaporation of volatile chloramines can create very harsh conditions for stainless steel. Chloramines are formed from nitrogenous compounds such as sweat and urine from bathers, and from chlorine, which is used as a disinfectant. Grade S31600 (1.4401) can normally be used for components intended for use or installation below or just above the water surface, for example, handrails, ladders, stairs, etc., whether they are actually immersed in the water or merely exposed to it in the form of splashes. For weight-bearing structural components installed well above the surface of the water, sometimes towards the ceiling, more highly alloyed grades such as 1.4439 (N08904) and S31254 (1.4547) should be selected, for example, ceiling wires and wire ropes, strapping and hose clips, and various types of fasteners.

Another harsh indoor atmosphere can be found on industrial sites which handle acids or chlorinated hydrocarbons. These chemicals can evaporate and later condense on cold metal surfaces. Material selection must be based on actual conditions but grades lower alloyed than S31600 (1.4401) should not be considered. It might sometimes be necessary to use grades as highly alloyed as S32205 (1.4462) or, on rare occasions, even S31254 (1.4547).

### **3.04.10.2 Factors Influencing Atmospheric Corrosion on Stainless Steels**

The importance of keeping the surface clean cannot be stressed enough. 'Cleanliness' in this context can either be achieved by regular washing to avoid staining by soot and dust, or by a carefully prepared postweld cleaning procedure to restore the surface after welding.

The surface finish of the steel is another very important parameter, as it not only has a direct influence on the corrosion resistance, but can also determine the efficiency of cleaning operations.

Narrow crevices always involve a potential risk of crevice corrosion but pockets that collect dirt and moisture should also be avoided.

In some cases, when a design prevents postweld cleaning operations or contains crevices that cannot be avoided, it may be advisable to use a more highly alloyed grade than would otherwise have been chosen in normal service conditions.

## **3.04.11 Application Areas of Commercial Significance**

### **3.04.11.1 Domestic – Kitchenware**

The corrosion resistance of stainless steel is an appealing property of items used in domestic cutlery and kitchenware. The stainless steel grade S30400 (1.4301) or similar grades are frequently used and widespread in these applications. It is used in a wide variety of applications, ranging from brewing vessels to kitchen sinks and milk tankers. The deep drawing properties required to produce beer kegs are good for this steel grade. Stainless steels are tolerant to the wide range of temperatures common in cooking and resist thermal shock very well. A stainless steel surface is also easy to clean. The surface finish is important in applications such as domestic cutlery and kitchenware. A rough surface attracts food deposits, promoting an environment in which microorganisms can proliferate, whereas a smooth and easily cleaned surface will prevent this. The European Hygienic Engineering & Design Group provides guidelines on surface finish, recommending  $R_a$  0.8 mm or better, which can easily be achieved with cold-rolled stainless steels. The  $R_a$  value alone, however, is not a reliable indicator of whether the surface will attract solids or deposits. The cleaning procedure becomes even more important on rough surfaces than on smooth surfaces and it is important to establish how easy it is to clean the surface in actual service conditions.

The environments to which domestic cutlery and kitchenware are exposed often vary from very mild, indoor, dry, and less corrosive environments in the living room to warm, wet environments such as those found in kitchens, in which chloride may be present, or even to outdoor environments such as a patio close to the sea or coastal areas. The dry/wet environment in households varies depending on the chloride content in the water, the temperature and, to a large extent, the humidity and the stainless steel chosen must be capable of withstanding such environments. Typical variations are

- chloride contents: 0.020–0.250 g l<sup>-1</sup>
- temperatures: 20–100°C
- relative humidity: 20–100% RH
- cyclic drying and wet variations, as in flush shower, bath etc.

Some examples of corrosive parameters for using table salts and cooking in kitchenware are:

- food deposits in boiling chloride solution (table salt).
- long-term exposure to chloride water, for example, leaving the pasta in the saucepan.
- partly heated water with table salt for a long time
- acids in the food, for example, in jam, juice, rhubarb.

Examples of stainless steel grades used in cutlery blades and kitchens utensils are presented in [Table 16](#). The use of lower-alloyed and standard grade of S30400 (1.4301) are the most common in these applications. It is important to remember that, for certain application areas in a kitchen environment, corrosion might occur if stainless steel grades at the lower end of the scale are selected. An example is the use of the martensitic grade 1.4006 (410), which provides a sharp edge but is not really a suitably corrosion-resistant steel grade for use in hot chloride water environments.

The main source of corrosion resistance in the stainless steel grades presented in [Table 12](#) is chromium. The lower the chromium content, the lower the corrosion resistance. To test the corrosion resistance of stainless steels used for cutlery, there is an easy and useful test described in EN-ISO8442 – Material and articles in contact with foodstuff. A mild test for the lower end martensitic stainless steels is an immersion test in  $0.050 \text{ g l}^{-1}$  sodium chloride for 6 hours at room temperature, between 18 and  $26^\circ\text{C}$ . Another more aggressive test is EN-ISO8442 – Annex A, part 1 and Annex C part 2, where 1.0 wt% NaCl at  $60^\circ\text{C}$  of cyclic immersion 2–3 times per minutes for 6 h.

### 3.04.11.2 Process Industry

#### 3.04.11.2.1 Hydrometallurgy<sup>32</sup>

Many metals are extracted from mined ores and subsequently refined by hydrometallurgical processes,

which usually involve dissolving of the metals in an acid. Some examples of common hydrometallurgical processes are recovery of zinc, copper, and nickel. These processes vary not only in the sense of corrosive environments but also in process routes. Nevertheless, there are some general operations in the hydrometallurgy processes to recover the desired metals. These stages can include pressure or atmospheric leaching, separation by, for example, solvent extraction or ion exchange. Depending on the desired product the downstream process stages can include purification of solution, product recovery by electrorefining, electrowinning and/or thereafter casting to slabs as, for example, in the zinc production.

Because of its relatively low cost, sulfuric acid is the most important acid used in these processes and it is often produced on-site. Stainless steels are usually the basic materials of construction used for withstanding the acid environment and have several advantages from design and process flexibility point of view. Under the most severe conditions, there are possibilities to identify applications for the super duplex or super austenitic stainless steel grades as well as other steel grades for less severe environments.

The leaching stages have the most demanding environments for stainless steels, since these stages contain not only acid, but also chlorides and metal ions from the ores, concentrate or matte. The presence of metallic ions in combination with chlorides and sulfuric acid complicates the prediction of corrosion of stainless steels in hydrometallurgical process environments. The metal ions, that is,  $\text{Fe}^{2+}/\text{Fe}^{3+}$  and  $\text{Cu}^{2+}$ , have, due to the oxidizing influence, an inhibitive effect on uniform corrosion of stainless steels, when added to sulfuric acid. Conversely, in combination with chlorides this oxidizing effect increases the risk for localized corrosion and too high amounts of chlorides can also lead to increased uniform corrosion. In summary, the combination of sulfuric acid, chloride ions, oxidizing metal ions, and the elevated temperature creates harsh conditions for stainless steels.

**Table 16** Stainless steel grades used in cutlery blades and kitchen utensils

<i>Material</i>		<i>Microstructure</i>	<i>Typical composition (wt%)</i>			<i>PRE</i>
<i>EN</i>	<i>UNS</i>		<i>Cr</i>	<i>Ni</i>	<i>N</i>	
1.4006	S41000	Martensitic	11.5–13.			11.5–13.5
1.4028	S42000	Martensitic	12.0–14.			12–14
1.4016	S43000	Ferritic	16.0–18.0			18–18
1.4301	S30400	Austenitic	17.0–19.5	8.00–10.5	<0.11	17–19.5



**Zinc production**

One of the hydrometallurgical processes used for zinc production is the Jarosite process. This process can be divided into several stages. Neutral leaching is performed in sulfuric acid at a concentration of  $\sim 50\text{--}60\text{ g l}^{-1}$ , that is, at a low pH and a temperature of  $60^\circ\text{C}$ . Oxygen is blown into the process stage from below for further oxidation of the product stream. One stream of the outlets from the neutral leaching stage continues to purification and a separation stage where cadmium, copper, and cobalt are reduced from the product. The other product stream from the neutral leaching stage proceeds to the Jarosite process. The pH in the Jarosite stage is 1.5, containing  $\sim 7\text{--}10\text{ g l}^{-1}$  sulfuric acid. From the Jarosite stage a part of the process solution is recycled to the neutral leaching stage.

A large part of the product stream continues to the hot leaching stage, or concentrate leaching, where Jarosite  $\text{NaFe}_3(\text{SO}_4)_2(\text{OH})_6$  is precipitated. The hot leaching is carried out in tanks made of super-austenitic or super-duplex stainless steels at elevated temperatures of  $\sim 95^\circ\text{C}$ , at chloride contents of  $300\text{--}400\text{ mg l}^{-1}$  and sulfuric acid concentrations of  $60\text{--}80\text{ g l}^{-1}$ . In the hot leaching stage manganese oxide is partly circulated as an oxidizing agent and it can cause deposits on the tanks. Corrosion can occur on grade 1.4539 (N080904) in this very hostile environment while S32750 (1.4410) or S31254 (1.4547) are examples of more corrosion-resistant grades. **Figure 50** shows a tank on the road in S32750 (1.4410) manufactured for a hydrometallurgy process solution.

When cadmium, copper, and cobalt have been removed from the neutral leaching process solution,



**Figure 50** A tank on the road in stainless steel grade S2750 (1.4410).

it continues to the product recovery, the electrowinning stage, where pure zinc is precipitated electrochemically on large cathodes. In this stage manganese dioxide can precipitate on the anode surfaces (lead) causing efficiency loss in due time. For this reason, the manganese dioxide has to be removed. Chlorine can be used, solving the manganese dioxide by oxidation. However, there is an increased risk of localized corrosion on stainless steels, due to the oxidizing effect of chlorine.

The leaching processes in zinc production are under continuous development to increase production efficiency and new processes operate commonly with direct leaching. Zinc concentrate is in the direct leaching process leached in acid slurry at atmospheric conditions by the use of oxygen.

In addition to the hydrometallurgical production of zinc, sulfuric acid is also commonly produced on the site. Before entering the sulfuric acid production, the product stream is filtered electrostatically to remove mercury in a corrosive environment. An example of a steel grade used in the electrostatic precipitator is the super austenitic EN S31254 (1.4547).

**Copper production**

Copper refining is an electrolytic production process using direct current for transporting copper in an electrolyte to large cathodes. The electrolyte has a low pH and contains, for example, copper ions, sulfuric acid, and chlorides.

Copper is precipitated on large cathodes of stainless steels in the electrolytic process. The steel grade used is EN S31600 (1.4404). The high purity copper on the cathodes is then stripped mechanically from the cathodes. The electrolyte might be corrosive for EN 1.4404 when the cathodes are exposed in the solution for longer periods of time when the current is shut off, for example, at maintenance stops, but during operation the cathodes are cathodically protected at low potentials.

**Nickel production**

A very harsh environment for stainless steels can be found in solutions in nickel production using autoclaves at elevated temperatures in combination with chlorides and sulfuric acid. An example of the hostile conditions is the processes operating at a temperature as high as  $250^\circ\text{C}$  and under high pressure. In some of the more demanding environments, metals such as titanium and titanium alloys, zirconium, or even tantalum must be used in the leaching tanks to withstand



the severe conditions. Nonmetallic materials may also be suitable for certain applications in these environments.

#### **Corrosion resistance of stainless steels in simulated hydrometallurgical solutions**

Hydrometallurgical solutions are indeed very complex and in order to document the corrosion properties of stainless steels systematically, the most corrosive parameters have to be considered such as the sulfuric acid, oxidizing chemicals  $\text{Fe}^{2+}/\text{Fe}^{3+}$ ,  $\text{Cu}^{2+}$ , and chlorides and any synergistic effects in between. Laboratory tests have been performed in environments simulating some conditions in hydrometallurgy plants, that is, including chloride ions, ferric ions, cupric ions, and sulfuric acid. Selected temperature was  $98^\circ\text{C}$  and immersion time 30 days. Cold-rolled sheets were used for the preparation of samples, which also were equipped with crevice washers.

Table 17 shows typical compositions of tested stainless grades and Table 18 show the test compounds. Table 19 presents the indications of corrosion resistance in stainless steel grades in these compounds.

Both localized and uniform corrosion occurred simultaneously on the test coupons. In some cases the uniform corrosion was dominating, at very high corrosion rates.

At intermediate chloride contents, between 0.1 and  $0.5 \text{ g l}^{-1}$ , only the super duplex S32750 (1.4410), and super austenitic S31254 (1.4547) were resistant. Severe corrosion occurred while increasing the chloride content above the  $0.5 \text{ g l}^{-1}$  and the temperature was close to the boiling point. Table 20 shows the test results in compounds C and D. Increasing the sulfuric acid content to  $100 \text{ g l}^{-1}$ , but maintaining the low chloride amounts ( $0.1 \text{ g l}^{-1}$ ) did not seem to initiate any corrosion on any of the steel grades, Table 21. These results emphasize the importance on maintaining the chloride levels very low in these very harsh environments.

The corrosion tests were carried out without any activation of the samples during the tests which can have an impact on direct comparison with real service conditions as also other impurities most commonly included in hydrometallurgical service environments.

#### **3.04.11.2.2 Desalination<sup>32</sup>**

Water management will be one of the most important infrastructural tasks for the future to solve all over the world. Desalination, that is, the production of potable water or industrial boiler feed water by removing salt from brackish water, seawater or salty aquifers, involves several stages, each of which places different demands on the construction materials. Figure 51 shows an example of a desalination plant, Melitha.

#### **Multistage flash**

The oldest distillation process, and also the most common for the larger desalination plants, is multistage flash (MSF). In this process, hot deaerated seawater or a seawater/brine mixture at a temperature of around  $110\text{--}115^\circ\text{C}$ , occasionally with some residual chlorine, enters the first stage flash chamber, where some of it evaporates and also condenses. During each stage, the seawater/brine mixture loses some of its energy and the temperature drops far below  $100^\circ\text{C}$  towards the end of the process. However, creating a vacuum, which enables boiling to take place at these low temperatures, counterbalances this. The distillate is achieved by cooling the steam down via numerous condenser tubes running above the flashing seawater.

The most common stainless steel found in MSF plants is S31600 (1.4404), which in the past has been used for the lining of evaporator vessels and for a number of internal components, for example, orifice plates, distillate trays, demisters, and condenser tube support plates. More modern design calls for clad plates in the evaporator vessels, sometimes using S31700 (1.4438). The condenser tubes are mostly

**Table 17** Typical chemical compositions of tested stainless steel grades in weight %

Steel grade, EN	UNS	Cr	Ni	Mo	N	Others
1.4435	31600	17.1	12.7	2.64	0.060	1.5 Cu
1.4539	N08904	19.8	24.0	4.30	0.060	
1.4462	S32205	21.9	5.67	2.99	0.190	
1.4410	S32750	24.7	7.11	3.82	0.280	
1.4547	S31254	20.1	18.1	6.28	0.210	Cu
Hastelloy, C-276		15.3	REM	15.6		
ATi-24						

made of copper alloys, but titanium has also been used. Highly alloyed stainless steel grades, such as S31254 (1.4547) and 1.4565 (S34565) could be an option for the tubes, but neither grade has yet been used for this particular application in MSF plants. However, stainless steel tubes in the S31254 (1.4547) grade have successfully been used for condensers in ventilation systems.

The latest concept for evaporator vessels is solid stainless steel, which has been successfully used for recycling and also once-through plants. Hidd, a 135 000 m<sup>3</sup> day<sup>-1</sup> MSF recycling plant in Bahrain, was commissioned in February 2000 and Melittah, a 15 800 m<sup>3</sup> day<sup>-1</sup> recycling plant in Libya, will start

water production during 2004. The evaporator vessels were made of S31600 (1.4404) and S32205 (1.4462) respectively, and in the latter case the higher strength of 1.4462 (S32205) was used for redesigning the shells, making them around 30% thinner and less costly than if made of S31600 (1.4404).

Solid stainless steel has also been used for once-through plants, that is, MSF with no recycling of brine. The material used for the evaporator vessels must thus resist a very hostile internal environment and also a potentially aggressive external environment, which may include exposure to boiling seawater on a hot wall. Once through implies no deaeration, that is, the water entering the first stage is air saturated with an oxygen level of a few milligrams per liter, and it may contain some residual chlorine.

There are three MSF once-through plants in service in Chile, the oldest was commissioned in 1996, and solid 254 SMO has been used for the first six stages while ASTM 317LMN (1.4439) was used for the remaining six. However, plant tests have shown that 2205 would be a more cost effective alternative than ASTM 317LMN (1.4439) for stages downstream the first six stages. The total capacity of these plants is 10 400 m<sup>3</sup> day<sup>-1</sup>.

**Table 18** Test compounds for immersion tests at 98 °C

Test compound	$Me^{n+}$		$H_2SO_4$ (g l <sup>-1</sup> )	$Cl^-$ (g l <sup>-1</sup> )
	$Fe^{3+}$	$Cu^{2+}$		
A	5	4	10	0.1
B	5	4	10	0.5
C	5	4	100	0.1
D	25	4	100	0.1

**Table 19** Summary of test results at 98 °C in test compounds A and B, containing 5 g l<sup>-1</sup> Fe<sup>3+</sup>, 4 g l<sup>-1</sup> Cu<sup>2+</sup>, 10 g l<sup>-1</sup> H<sub>2</sub>SO<sub>4</sub> and two levels of chloride amounts according to the table

Chloride content, $Cl^-$ (g l <sup>-1</sup> )	S31600 (1.4435)	N80904 (1.4539)	S32205 (1.4462)	S32750 (1.4410)	S31254 (1.4547)	C-276
0.1	No corrosion	No corrosion	No corrosion	No corrosion	No corrosion	No corrosion
0.5	Corrosion	Corrosion	Corrosion	No corrosion	No corrosion	No corrosion

**Table 20** Summary of test results in test compound C containing 4 g l<sup>-1</sup> Cu<sup>2+</sup>, 100 g l<sup>-1</sup> H<sub>2</sub>SO<sub>4</sub> 0.1 g l<sup>-1</sup> chlorides, and 5 g l<sup>-1</sup> Fe<sup>3+</sup> and D with the same composition but with an increase in the amount of Fe<sup>3+</sup> to 25 g l<sup>-1</sup>

Fe(III) content Fe <sup>3+</sup> (g l <sup>-1</sup> )	S31600 (1.4435)	S32205 (1.4462)	S2750 (1.4410)	S31254 (1.4547)	C-276
5	No Corrosion	No Corrosion	No Corrosion	No Corrosion	Corrosion
25	No Corrosion	No Corrosion	No Corrosion	No Corrosion	Corrosion

**Table 21** Steel grades used in field and laboratory tests

UNS	EN	ASTM	CPT (°C)	PRE	Cr	Ni	Mo	N
S30400	1.4301	304	–	19	18	8.7	–	0.06
S31600	1.4436	316	27	27	17	11	2.7	0.06
S32205	1.4462	2205	52	35	22	5.5	3	0.17



**Figure 51** An example of a desalination plant, Melitha.

#### **Low-temperature multieffect, desalination plants (LT-MED)**

One major operational drawback of MSF plants is the formation of scale, calcareous deposits, created by the high temperatures. This has led to the development of LT-MED, where the main deviation is a maximum brine temperature of 55–60°C, as opposed to 110–120°C, resulting in reduced corrosivity towards metallic materials. The physics behind this process are the same as in MSF plants, that is, an applied vacuum causes boiling and evaporation of the incoming seawater at a temperature far below 100°C, but the design of the evaporators and condenser tubes is totally different. There is no flashing but evaporation due to a falling film on tubes where the internal side acts as a condenser while the external side causes boiling.

Different types of material have been used for the evaporator shells; epoxy coated mild steel, clad steel, solid S31600 (1.4404), and even S31254 (1.4547). A duplex grade, such as 1.4462 (S32205), would be an appropriate alternative. A pronounced advantage for a high strength grade such as 1.4462 (S32205) is the cylindrical shape of the LT-MED evaporators making an even more cost-effective design possible than in the case for MSF shells.

There is one LT-MED plant in service with highly alloyed stainless steel condenser tubes, AVR's Demi Water Plant, a 24 000 m<sup>3</sup> day<sup>-1</sup> plant in the Netherlands, where 1.4 million meters of 1.4565 (S34565) tubes were installed.

#### **Reverse osmosis and seawater reverse osmosis**

The reverse osmosis (RO) process is performed at ambient temperature but at a high pressure, for an seawater reverse osmosis (SWRO) plant it is often in

the range 70–80 bar. The feed, seawater or brackish water, is first pretreated, which implies mechanical filtering, chlorination to avoid biofouling, and the addition of chemicals to adjust pH values, etc.

However, the membranes used in RO plants do not tolerate chlorine, so also if the feed has been chlorinated as part of the water treatment, any residual chlorine must be removed prior to the membrane passage, often by an addition of sodium bisulfite or similar. The feed is still air saturated and as the design contains a number of crevices, there is an obvious risk of pitting and, above all, crevice corrosion in these plants.

Highly alloyed austenitic stainless steels, such as S31254 (1.4547), have frequently been used, very successfully, in a number of SWRO plants in the Middle East, on Mediterranean islands, on the Canary Islands, in the West Indies and in the USA. Most of the 'biggest in the world' plants are equipped with high-pressure piping made of S31254 (1.4547) or similar. Materials of type N08904 (1.4539), S32205 (1.4462), 1.4438 (S31700), and 1.4404 (S31600) have previously been used, but the failures have been numerous, not least for 1.4404 (S31600) and 1.4438 (S31700).

Highly alloyed grades have also been used for high-pressure pumps and the super duplex S32750 (1.4410) can be an extremely attractive option for energy recovery systems. The first plant to utilize the properties, that is, strength and corrosion resistance, for the energy recovery system of this grade will be Ashkelon, a 275 000 m<sup>3</sup> day<sup>-1</sup> plant in Israel.

Highly alloyed stainless steels, for example, S31254 (1.4547), can also be used for different filters upstream the high pressure pumps although other materials are often preferred for cost reasons.

#### **3.04.11.2.3 Stainless steel within the pulp and paper industry**

The stainless steel manufacturers have been developing specific stainless steel grades optimized in pulp- and paper process environments. Cost efficiency and sustainability of stainless steels in the pulp- and paper solve corrosion problems. One of the first fields of application for duplex grades was the pulp and paper industry, where the first digesters were mounted in New Zealand in 1988.

Apart from economic factors, a growing concern for the environment has led to a number of new processes being introduced and existing processes being modified. Effluent recycling has also become more common in modern plants. The positive environmental benefits of 'closing-up' the mills have been accompanied by a rise in the concentrations of

chemicals used in process streams, and in operating temperatures. These factors have drastically increased the demands made on the corrosion resistance of the structural materials used in such plants.

Process environments and their impact on corrosion varies in a great extent in different pulp- and paper processes, which also leads to that advice concerning material selection require modification while considering a particular environment at a particular mill.

The duplex alternative, for example, 1.4462 (S32205), is constantly gaining ground at the expense of the other alternatives and many duplex vessels have been started up. The selection of an appropriate duplex grade will, among other things, depend on the process environment in service.

#### 3.04.11.2.4 Architecture – Art <sup>32</sup>

The most visible and perhaps also the most common outdoor applications of stainless steel are for facades, wall claddings, and roofs. The surface finish is selected according to the aesthetic impression required by the architect, whilst the surrounding atmosphere determines the steel grade.

One of the oldest examples of this is the Chrysler Tower in New York, which was crowned with an Art Deco cap of stainless steel as early as 1929. It is still in perfect condition and the extra sheets shipped from Germany during the building's construction and intended for use in future maintenance were still held in storage as recently as 1995. This means that the stainless steel has stood the test of time for more than 70 years without any mass loss or localized corrosion. The steel grade selected was of type 1.4301 (S30200), which would today be regarded as a borderline steel grade in terms of its alloy composition, considering the previous discussion on corrosion hazards. Another equally old landmark is the canopy at London's Savoy Hotel. Both are clearly excellent examples of the understated elegance of stainless steel.

More recent installations that are equally well known are the Court of Human Rights in Strasbourg in France, Canary Wharf in London, and Petronas' 450 m high Twin Towers in Kuala Lumpur, that are all clad with stainless steel of type S31600 (1.4401). The same material was also used for the roof of the new departure terminal at Stockholm's central railway station, built in the late 1980s.

Another recent installation is the Tsing Ma Bridge along the highway to Chep Lap Kok, the new airport of Hong Kong. Whilst this construction is, in some respects, similar to those named earlier, there is an

important difference. In this case, the stainless wind deflectors were not only installed for aesthetic reasons; they are also intended to protect the traffic from strong side winds during the hurricane season.

The elegance of stainless steel can be seen in a number of monuments all over the world. **Figure 52** shows a bridge constructed in stainless steel located at the island Menorca.

The famous Finnish composer Jean Sibelius has been honored with a monument in Helsinki, a stainless steel 'organ,' created by Eila Hiltunen. The same sculptress also created 'The Sun Flower Field,' which was raised in a man-made seawater lagoon outside Jeddah. The selection of steel grade was in both cases based on the respective atmospheres, with type S31600 (1.4436) being selected for the urban atmosphere of the Finnish capital and S31254 (1.4547) for the harsh marine conditions of the Red Sea.

The steel grade S31254 (1.4547) was also used for Carl Milles' sculpture "God and the Rainbow", seen in **Figure 53**, which was inaugurated in 1995 by HRH King Carl XVI Gustaf of Sweden. Its location means that the rainbow is sprayed with water from the Baltic Sea and such conditions would be too harsh for a conventional grade such as S31600 (1.4401).

Maintenance-free structural components can be found in a number of industries, but in selecting a grade for a specific application, it is always important to consider the intended operating environment.

The cable ladders on the Norwegian platform Statfjord A were originally made of painted mild steel, which lasted four years. The replacement ladders made of zinc coated (galvanized) steel lasted another 7 years but were then replaced by stainless steel ladders made of S31600 (1.4401) in 1990.



**Figure 52** Bridge constructed in stainless steel, located at Menorca.





**Figure 53** S31254 (1.4547), used for Carl Milles' sculpture 'God and the Rainbow', seen in [Figure 53](#), which was inaugurated in 1995.

Another example is the internal wall lining of a building for the pickling of steel at a Swedish carbon steel producer. The original lining was made of stainless steel, 1.4436hMo (S31600), which, from an aesthetic point of view, offered inadequate corrosion resistance to the acid condensate precipitated on the walls. The result was heavy rusting and a thorough evaluation of several highly alloyed grades was performed prior to the selection of the wall lining for an expansion in 1998. However, despite the heavy rusting, it was eventually concluded that type 1.4436 was good enough from a functional point of view and this grade was also selected for the expansion.

If similar problems occur at other plants, it is recommended that an exposure test be performed prior to the selection of steel grade.

#### 3.04.11.2.5 *Stainless steel in oil and gas production*<sup>32</sup>

Although oil is not corrosive in itself, production of oil can involve highly corrosive environments because of the simultaneous presence of water and dissolved aggressive species such as oxygen, chlorides, carbon dioxide, and hydrogen sulfide. To a certain degree oil can in fact act as an inhibitor, though it is somewhat unreliable with regard to stainless steels when only a thin oil film is 'isolating' the metal from the corrosive water. Thick films of oil may totally inhibit corrosion.

Initially, mainly carbon steels were used in oil and gas production. However, because of the often increasing amounts of corrosive agents after years of production in old wells and the exploitation of more and more corrosive wells, stainless steels are used increasingly in this industry. Furthermore, environmental considerations have also led to the increased use of stainless steels, since carbon steel demands the addition of vast amounts of various artificial corrosion inhibitors, even under fairly mild corrosive conditions, and most of these inhibitors are more or less hazardous to the environment.

Looking at long term economics, by means of life cycle cost calculations, the use of a stainless steel can often repay the initial extra investment cost, mainly through low maintenance costs and weight savings since stainless steel components do not need to be over dimensioned to compensate for general corrosion, as do carbon steel components. Finally, much longer lifetimes can be achieved with stainless steels than with carbon steels.

#### *Environmental factors*

**'Sweet' or 'sour' environments** Production fluids and gases in the oil and gas industry are traditionally classified as 'sweet' or 'sour' environments, depending on whether hydrogen sulfide is absent or present in significant amounts respectively.

Sweet environments are those containing no or negligible amounts of hydrogen sulfide. High amounts of carbon dioxide may be present in sweet environments, causing accelerated corrosion on carbon steel. Sour environments are those containing significant amounts of hydrogen sulfide. The main concern regarding H<sub>2</sub>S is its ability to embrittle metals thereby causing cracking, 'sulfide stress cracking (SSC),' under certain conditions.

**Hydrogen sulfide** Hydrogen sulfide is one of the main factors to consider, while choosing a material for oil and gas production equipment, because of the risk of SSC.

Sulfides, S<sub>2</sub>, HS or H<sub>2</sub>S adsorbed to the metal surface, catalyze the absorption of hydrogen atoms by the metal, which may subsequently crack due to hydrogen, induced stress cracking (HISC) depending among other factors on the amount of hydrogen absorbed. It is this cracking that is usually termed 'SSC.' The full mechanism of hydrogen embrittlement by H<sub>2</sub>S is still under debate.

The hydrogen absorption caused by H<sub>2</sub>S may work synergistically with the factors involved in

chloride SCC, thereby increasing the risk of environmentally induced cracking.

Hydrogen embrittlement seems to be the most active cracking mode at low temperatures, whereas chloride SCC predominates at high temperatures. Consequently, the combined risk of cracking due to  $H_2S$  and chlorides tends to be most severe for the nonferritic stainless grades at intermediate temperatures, approximately in the range 80–100°C.

When  $H_2S$  is present, it is generally the risk of cracking that is of concern. However, very small amounts of  $H_2S$  should not necessarily be seen as a negative factor since the presence of  $H_2S$  guarantees a low redox potential in the environment and thereby lowers the risk of chloride-induced localized corrosion, for example, SCC, pitting and crevice corrosion.

Actual limiting critical values of  $H_2S$  partial pressures are difficult to give, due to several other factors temperature, pH, and chloride concentration probably being the dominating ones.

**Carbon dioxide** Stainless steels are not susceptible to the general  $CO_2$  corrosion as are carbon steels. For example, pipelines in carbon steel suffering  $CO_2$  corrosion have been replaced with stainless steel and have given very long service lives. However,  $CO_2$  can indirectly affect the performance of stainless steels by dissociation of carbonic acid, which leads to a lowering of pH.



It is not surprising that a higher hydrogen ion activity will increase the driving force for hydrogen being absorbed into the metal, so that the metal becomes more prone to cracking (SSC). A significant hydrogen uptake is, however, still only possible when  $H_2S$  above a certain concentration is present.

It should be borne in mind that most actual systems have natural pH buffering systems such as from bicarbonate present initially. Therefore the full pH lowering effect caused by  $CO_2$  may not be felt because of buffering action. So, in many practical situations, the system may not be as aggressive as expected from the knowledge only of the partial pressures of  $CO_2$  and  $H_2S$ .

**Chlorides** Chlorides are very often present in high concentrations in water associated with oil and gas formations. Localized corrosion on stainless steels induced by chlorides is well-known. However, the

oxygen content of these fluids is mostly extremely low and significantly higher chloride levels are therefore acceptable than under oxygen-saturated conditions. The main cathodic reaction in these systems is the reduction of hydrogen ions.

**Temperature** As is well-known, normally the higher the temperature the more aggressive the environment with regard to localized corrosion induced by chlorides. However, as mentioned earlier, nonferritic stainless steels seem to show their greatest sensitivity to SSC at around 80–100°C in terms of critical partial pressure of  $H_2S$ . This effect is most pronounced in the duplex stainless steels and lower-alloyed austenitic stainless steels. This phenomenon is thought to be explained by the reverse temperature dependency of sulfide-induced SSC and chloride-induced SCC.

**Sulfur** The presence of elemental sulfur has shown to be highly deleterious for stainless steels and may reduce the critical partial pressure of  $H_2S$  appreciably. One possible explanation for the deleterious effect of elemental sulfur is that it can be reduced by hydrogen ions to form  $H_2S$ . However, elemental sulfur does not seem to be present in most wells.

#### **Galvanic effects**

Creating a galvanic contact between stainless steels and carbon steels will often result in full cathodic protection of the stainless steel with regard to chloride-induced localized corrosion. However, ferritic and duplex stainless steels may, during long periods of exposure, develop hydrogen embrittlement from the increase in the cathodic reaction (hydrogen ion reduction) on the stainless steel surface. Obviously this effect is most pronounced at a low pH.

#### **Artificial environments**

In many cases the limiting environment with regard to corrosion may not be the gas or formation water present in the well. A number of chemicals are frequently added to the well in order to optimize the productivity or as part of the initial drilling and set-up procedures.

Stimulation acids are widely used to increase formation permeability. These acids are most often inhibited, however many of these inhibitors have been developed for carbon steel, and there is no guarantee that the inhibition is effective on stainless steels without prior testing.



In general, the use of organic acids is recommended. Excessively large injections should be avoided. This will minimize the risk of creating an unnecessarily aggressive local environment with a low pH. It should be recognized that even though the pH is lowered during acidifying, the concentration of dissolved sulfides is also lowered by general dilution in the near vicinity of the metal.

Completion fluids are sometimes used to counter balance the formation pressure. These fluids may contain high concentrations of chlorides or bromides that inherently introduce an enhanced risk of chloride (halide)-induced localized corrosion.

Injected waters to help secondary recovery may be seawater in the case of offshore production, or produced water in either onshore or offshore production. These waters can be treated in various ways, which influence their corrosivity like dc aeration (less aggressive) or chlorination (more aggressive).

#### **Offshore production – seawater**

Topside equipment may be exposed to seawater internally in the case of seawater being used as a cooling liquid or used for the production of freshwater. The unavoidable splashing from the marine environment causes external exposure of topside equipment to seawater.

In these cases, the selection of a stainless steel grade should be based on the maximum temperature and the condition (aerated and untreated, chlorinated, deaerated, etc.) of the seawater. In the case of splashing from the marine environment, possible evaporative conditions should be considered. The super austenitic 6Mo stainless steel grade S31254 (1.4547) has shown excellent performance in many seawater environments.

Submerged pipelines are another example where the outside environment is sometimes potentially more aggressive than that on the inside.

#### **Metallurgical factors**

It is generally accepted that the sensitivity to hydrogen embrittlement increases with increasing strength. This has led to the practice of specifying a maximum hardness of the material when used in sour service, as in NACE standard MR0175, which is discussed as follows.

It should be recognized that the traditional correlation between strength, hardness, and SSC sensitivity was based on industry experience with carbon steels. The application of this rule is not so straightforward for stainless steels, where the strength in the

annealed condition can vary greatly depending on a number of different metallurgical factors. For example, a high nitrogen content in the fully austenitic stainless steel S31254 (1.4547) or in the super duplex stainless steel S32750 (1.4410) introduces a high strength in the annealed condition, but these steel grades are in general less sensitive to SSC compared with the similar stainless steels containing lower amounts of nitrogen and having lower annealed strength.

Certain stainless steels do, however, become more susceptible to SSC, when they have been cold worked.

**Ferritic and martensitic stainless steels** Ferritic stainless steels are fairly susceptible to SSC, especially in the cold-worked condition. For common ferritic grades the resistance to chloride-induced pitting and crevice corrosion is also limited. Ferritic stainless steels have therefore found limited use in sour production environments.

Martensitic stainless steels are used mainly when high strength is needed in sweet environments, where they have shown to be cost effective in replacing carbon steel suffering from CO<sub>2</sub> corrosion.

Martensitic stainless steels have a fairly limited chloride-induced localized corrosion resistance, and they show a high susceptibility to SSC.

**Austenitic stainless steels** Low-alloyed austenitic stainless steels, types S30400 (1.4301) and S31600 (1.4401), are being used for a large number of components. These alloys are far less prone to SSC than ferritic and martensitic alloys as long as they are in the annealed condition. However, heavy cold work of these alloys does increase their susceptibility to SSC even at ambient temperature. Stainless steel S30400 (1.4301) cold worked 30% exhibits susceptibility to SSC even at very low chloride concentrations.<sup>37</sup>

The super austenitic 6Mo stainless steel grade, S31254 (1.4547) has shown excellent resistance to SSC and SCC. Even after cold work up to 80% and coupled to carbon steel, S31254 (1.4547) is highly resistant to SSC. The carbon steel coupling increases the driving force for hydrogen-induced cracking as discussed earlier.

At high temperatures the high chloride-induced SCC resistance is a further argument for the wide spread use of S31254 (1.4547) in oil and gas production.

**Duplex stainless steels** The high strength of duplex stainless steels together with their high resistance to chloride-induced localized corrosion is

important reasons for their popularity in oil and gas production.

However, it is necessary to observe some restrictions on their use in severe sour environments, since laboratory investigations have indicated moderate SSC susceptibility. It should be borne in mind that pH and stresses in practical applications try tests. This is clearly illustrated by a number of successful applications of duplex steels at far higher partial pressures of  $H_2S$  than a number of laboratory investigations have indicated should be possible.

**SSC test method NACE MR0175** NACE standard MR0175 presents material requirements for resistance to SSC in oil and gas production equipment and related equipment. The document is a broadly written document. Certainly not all materials listed in MR0175 are satisfactory for all practical sour service applications. However, MR0175 is frequently used as a minimum requirement for the selection of materials for sour service.

In this standard a sour gas environment is defined as containing water as a liquid and hydrogen sulfide in the gas at a partial pressure exceeding 3 mbar (0.05 psi), and with total pressures greater than 4.5 bar (65 psi).

In the case of multiphase systems (gas/'oil'/water) MR0175 defines sour environments as systems with  $H_2S$  partial pressure exceeding 3 mbar (0.05 psi) at a total pressure above 18.3 bar (265 psi). At total pressures below 18.3 bar, the partial pressure of  $H_2S$  above 0.7 bar (10 psi) or more than 15%  $H_2S$  also defines a sour environment. Sour multiphase systems that have operated satisfactorily with standard equipment are outside the scope of MR0175.

MR0175 lists a wide range of metallic materials and product forms that under certain conditions are found to be acceptable for use in sour service. In general the main restriction put on the materials is a maximum hardness level. Requirements for welds are generally the same as for the annealed

wrought material with regard to the maximum hardness level.

It should be remembered that MR0175 only addresses SSC in the context of the  $H_2S$  partial pressure, whereas effects of pH and chloride-induced localized corrosion are not taken into account.

### 3.04.11.2.6 *Stainless steel in wastewater treatment* <sup>32,49</sup>

The first methods used to treat wastewater involved reducing the amount of suspended matter in rivers. Biological treatment for further reduction of suspended matter and phosphorus reduction was added as a cleaning process in the 1970s followed by methods for nitrogen removal. During the 1990s, the use of an activated sludge process in the biological treatment of wastewater has increased. New biological purification treatments have been introduced in wastewater treatment plants worldwide, which efficiently reduce nitrates from the water.

#### *Methods of purification*

The design of a wastewater treatment plant will usually depend on what methods are required for purification of the wastewater. Both chemical and biological cleaning processes are used to clean the incoming wastewater.

Wastewater treatment plants may contain several stages involving different processes of purification. Main purification processes are mechanical treatment, chemical treatment with removal of phosphorous, biological treatment (including nitrogen reduction), and removal of organic matter. [Figure 54](#) shows a schematic representation of the main stages in a wastewater treatment plant.

**Mechanical treatment** The sewage enters a wastewater treatment plant through screens that remove

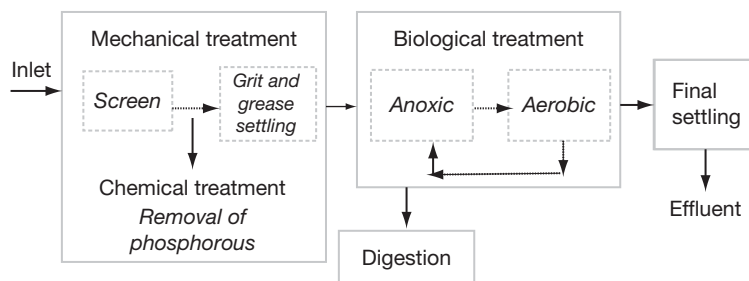


**Figure 54** Schematic view of the main processes in a wastewater treatment plant.

large particles. It then continues to a grit chamber, where grit, gravel, oil, and fat are removed from the wastewater, and thereafter to the primary settling stage.

**Chemical treatment** Phosphorus in wastewater consists of several compounds such as phosphorus in organic compounds and phosphates. However, the organic phosphorus compounds undergo hydrolysis in water and orthophosphate, which is the main compound, is usually removed from the sewage water by precipitation. A variety of precipitation chemicals can be used for this purpose and different plants may have different preferences.

Some examples of precipitation chemicals are ferrous sulfate, aluminum sulfate or iron (III) chloride. In Sweden, the use of poly aluminum chlorides and poly aluminum sulfates in wastewater treatment is a relatively recent development. The dosage point may be prior to the primary settling stage and/or, in some plants, before the final settling tank to ensure low phosphorus content in the effluent.

**Biological treatment** The biological treatment involves both the removal of nitrogen and the removal of biological carbons. In some plants, it may also involve the reduction of phosphorus. This purification process can be divided into several stages. The biological treatment can alternate between anaerobic (anoxic) conditions and aerobic conditions where air is blown into the water. Biological nitrogen is removed in the processes of nitrification and denitrification. An anaerobic environment assists the denitrification process and an aerobic environment assists the nitrification process. During nitrification, ammonia is converted to nitrate, whilst during denitrification, nitrate is converted to free nitrogen. The end product, nitrogen gas, is then released into the atmosphere.

The internal position of the aerobic nitrification and the anaerobic denitrification stages in the biological treatment may vary from plant to plant. In some plants, the aerobic stage may come first, whereas in others, it may occur at the end, followed by recycling to the anaerobic process. Biological carbons are removed during the aerobic stage where nitrification also occurs. During this process, the biological carbons are converted to carbon dioxide and water.

**Final settling** After the biological treatment the wastewater passes on to the final settling tanks where the remaining active sludge settles. The sludge may thereafter be passed back and recycled into the biological treatment or transferred into the

process of digestion. The temperature of the flowing water in the final settling tanks varies commonly between 10 and 15°C. After the final settling stage, the effluent can be released into the sea, lakes, or rivers.

**Digestion** Sludge is removed during the biological treatment and later transferred to large digesters where it undergoes a process of digestion. The active digestion of the sludge is oxygen consuming and the process is considered to be anaerobic. The temperature during the digestion process remains relatively constant at 38°C while the pH level of the sludge can vary between 6 and 8. During biological digestion, biogas containing hydrogen sulfide gas is produced.

The sludge may be dewatered after digestion by centrifugation. If it contains no heavy metals, the dried sludge may be used as fertilizer.

#### ***Corrosion conditions in waste water treatment plants***

**Chloride Content** The chloride ions present in the water promote local corrosion such as crevice corrosion and pitting, and the higher the chloride content, the more corrosive the water. The chloride concentration of the water that passes through sewage treatment plants is usually lower than the chloride concentration of seawater. In Sweden, where the use of de icing salt on the roads is common during the winter period, the chloride content passing through a plant may vary according to season. High values of chloride may be recorded during a few days in the winter season.

**MIC and requirements for localized Corrosion on Stainless Steels** Ennoblement from microbial activity such as, for example, after the biological cleaning stages, that is, in the final settling of a wastewater treatment plant might provide a high potential closer to, or in the vicinity of, the pitting potential for standard stainless steel grades of type S30400 (1.4301) and S31600 (1.4401) under certain conditions such as in the presence of chlorides, crevices, and deposits. In these environments, localized corrosion can be initiated and propagated with an increased corrosion rate due to the enhanced cathodic reaction caused by the microbial activity.

**Addition of Chemicals** The most common chemicals used in Scandinavian wastewater treatment plants to precipitate phosphates are aluminum

sulfate, iron (III) chloride, and iron sulfate. At the point where the dosage is in the plant, there is an increased risk of local corrosion using iron (III) chloride. However, the risk of corrosion on stainless steels declines very fast with the distance to this dosage point since the chemicals are diluted in the flowing water. Less corrosive chemicals with no chloride content are iron sulfate and aluminum sulfate.

If, at any stage of the purification process, any other chemicals are added, for example, strong oxidizing agents such as chlorine as a disinfectant, or potassium permanganate for precipitation reactions, care must be taken with the dosage. The dosage must be low enough to ensure that the effect on stainless steels does not promote any increase in the free corrosion potential. This is essential in both the aerobic and anaerobic stages. The effects of strong oxidizing agents such as chlorine and potassium permanganate are well-documented in [Section 3.04.9](#).

#### **Corrosion results from field tests in wastewater treatment plants**

Field exposures were carried out at different wastewater treatment plants at various locations in Sweden and Denmark to evaluate the risk of corrosion in wastewater treatment plants. The most corrosive part of the plants based on the processes was considered to be the final stages, the settling tanks where chlorides in combination with grown biofilm on the surfaces have to be taken into account. The test materials were welded standard austenitic stainless steel grades S30400, S31600 (1.4301, 1.4436), and a welded duplex stainless steel grade S32205 (1.4462). The chemical compositions of these steels are shown in [Table 21](#). The pitting resistance equivalent (PRE) numbers and the critical pitting temperatures CPT

according to ASTM G 150 for the steel grades are also presented in [Table 22](#).

Field tests were carried out over a 12-month period several wastewater treatment plants in Sweden and Denmark, where the samples were exposed in the final settling tanks. The chemical compositions of the water from three of the exposure sites in the plants are shown in [Table 22](#).

The open circuit potentials were measured in for the test coupons exposed in the plants. From these results it was shown that in aerobic conditions the potential increased to a maximum of 340 mV/SCE, schematically shown in [Figure 55](#), whereas, in more anaerobic conditions the OCP increase was low and even decreased as schematically shown in [Figures 56](#).

At plant 1, corrosion was found on stainless steel grades S30400 (1.4301), and S31600 (1.4436) in combination with heavy deposits, a high chloride content and ennoblement. [Figure 57](#) shows the extent of corrosion on the base material and on the welds of steel grade S31600 after the removal of the deposits containing both sulfur and manganese.

#### **Base material welds**

[Table 23](#) shows the potential values obtained in the field tests in combination with the chloride content and visual observations after the field tests. Biofilms or biological deposits were observed on all samples after the exposure at the plants, but ennoblement was only observed at some plants.

The combination of a high OCP value generated by microbial activity in a biofilm and high chloride content will lead to a higher susceptibility of localized corrosion for steel grade S30400 (1.4301), and S31600 (1.4436). The Localized corrosion was observed in plant 1 for S30400 (1.4301), and S31600

**Table 22** Chemical compositions of treated wastewater from the field-test locations

Compound	Plant 1	Plant 3	Plant 5 (anaerobic)
Nitrate-N ( $\text{mg l}^{-1}$ )	10.2	1.5	4.1
Sulphate ( $\text{mg l}^{-1}$ )	129	150	69
Chloride ( $\text{mg l}^{-1}$ )	515	585	78
Iron ( $\text{mg l}^{-1}$ )	0.16	0.083	0.98
Manganese ( $\text{mg l}^{-1}$ )	0.18	0.045	0.069
Aluminium ( $\text{mg l}^{-1}$ )	<0.01	<0.01	0.06
pH	6.8	7.1	7.6
Conductivity ( $\text{mS m}^{-1}$ )	208	263	60.2
COD <sup>a</sup> ( $\text{mg l}^{-1}$ )	4.3	6.6	16 <sup>b</sup>

<sup>a</sup>Oxygen consumption measured as chemical oxygen demand (COD).

<sup>b</sup>Higher value than expected from the anaerobic process.

(1.4436) because of a high OCP and high chloride content in combination with heavy deposits. On the other hand, for plants with a low chloride content in the water, no corrosion was observed.

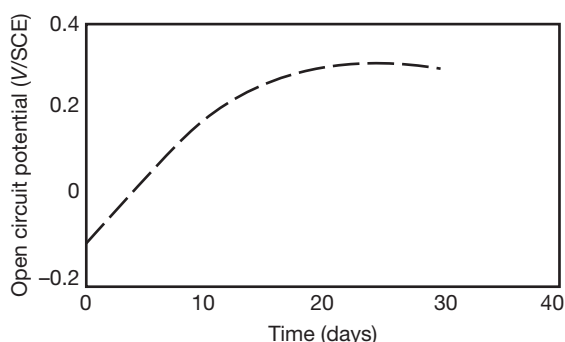


**Figure 55** Time dependence of OCP during exposure of stainless steels in the final stage of a wastewater treatment plant in Sweden (aerobic biodegradation of wastes in plant 1).

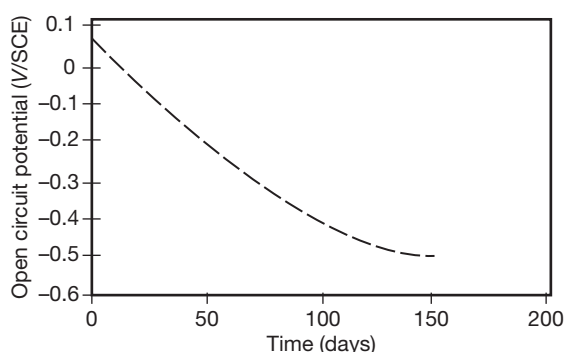


**Figure 56** Time dependence of OCP during exposure of stainless steels in the final stage of a wastewater treatment plant in Sweden (anaerobic biodegradation of wastes in plant 3).

### 3.04.12 High Temperature Corrosion<sup>32</sup>

When stainless steels are exposed to hot gases, chemical reactions take place between the steels, or rather between their alloying elements, and elements or compounds in the gases. As a rule, these reactions will lead to the formation of gas-metal interface layers of reaction products. The chemical compositions and morphologies of these products are determined by, among other factors, the steel and gas compositions and temperatures. These surface layers are more or less protective against further attacks from the gas.

The chemical composition and various standards' designations for some high temperature steels are given in [Table 24](#).

In practice, all stainless steels rely on the formation of an oxide layer. All other reaction products either form a porous, less adherent, and hence nonprotective scale, or are liquid or even volatile and will flux off any existing scale or evaporate. Thus, one condition that must be fulfilled for good high temperature corrosion resistance is that the gas must be oxidizing, that is, it must contain enough oxygen for the formation of a protective layer, consisting of oxides of one or several of the alloying elements. Even so, all oxide scales will eventually experience a breakdown due to growth stresses in the scale. Any measure taken to reduce the scale growth rate will therefore increase the time to breakdown. A low growth rate will also reduce the subscale depletion of the oxide forming element(s), thus improving the ability of the alloy to heal any cracks or other damage to the scale.

The terms oxidizing and reducing are common in the context of high temperature environments, but are not very well-defined and should be used with care. A gas may, for example, be reducing to some of

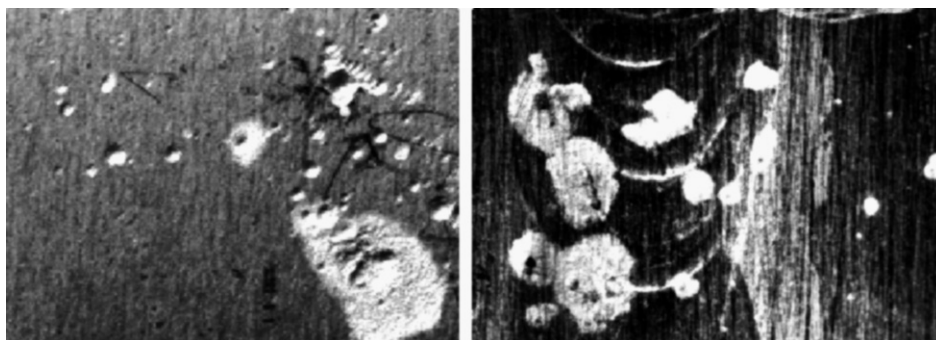


**Figure 57** Localized corrosion found on S31600 (1.4436) under heavy deposits after a field test at plant 1. (Magnification  $\times 3$ ).

**Table 23** Results from visual inspections made after the field tests in the final stages of six treated wastewater treatment plants

<i>Plant</i>	<i>S30400 weld</i>	<i>S31600 base</i>	<i>S31600 weld</i>	<i>S32205 weld</i>	<i>Max OCP (mV/SCE)</i>	<i>Chloride content (mg l<sup>-1</sup>)</i>
1	Corrosion	Corrosion	Corrosion	No corrosion	337	515
2	Corrosion	No corrosion	No corrosion	No corrosion	219	585
3	No corrosion	No corrosion	No corrosion	No corrosion	50	78

**Table 24** Typical chemical composition for some examples of high temperature stainless steels

<i>Steel grade</i>		<i>Typical chemical composition (wt%)</i>					
<i>EN</i>	<i>ASTM, UNS</i>	<i>C</i>	<i>N</i>	<i>Cr</i>	<i>Ni</i>	<i>Si</i>	<i>Others</i>
1.4948	304H	0.05	–	18.3	8.7	0.5	–
1.4878	321H	0.05	–	17.5	9.5	0.5	Ti
1.4818	S30415	0.05	0.15	18.5	9.5	1.3	Ce
1.4828		0.04	–	20	12	2.0	–
1.4833	309S	0.06	–	22.5	12.5	0.5	–
1.4835	S30815	0.09	0.17	21	11	1.7	Ce
1.4841	314	0.10	–	24	19	1.5	–
1.4845	310S	0.05	–	25	20	1.0	–
1.4854	S35315	0.05	0.15	25	35	1.5	Ce

the alloying elements but oxidizing to others. Another gas may contain enough oxygen for the formation of a protective layer; yet at the same time contain other elements that form other, faster growing but less protective compounds.

Gases and/or construction materials are generally chosen to ensure that such a protective layer is in fact formed on the material. For example, the type of gas chosen for heat treatment applications, where oxidation of the treated material is undesired, will generally be reducing, or at least nonoxidizing, to the treated material, but oxidizing to the higher-alloyed furnace construction materials.

In certain processes, however, truly reducing gases are used or produced, and in such circumstances, no oxide layer will form and any existing layer will, as a rule, dissolve. Preoxidation is often used to increase the corrosion resistance in such atmospheres. However, the resulting oxide layer has a limited lifetime and the process of preoxidation has to be repeated at certain intervals.

Heat resistant stainless steels are mainly developed for strength and corrosion resistance at elevated temperatures. As the technical requirements are different, the resistance of these alloys to room temperature 'wet' corrosion may be less satisfactory. The risk of condensation or deposition of aggressive compounds during temporary disturbances or shutdowns

must therefore be considered while selecting the construction material. Alternatively, removal of the aggressive gas may be specified in the service instructions for such events.

Several common corrosion types are described as follows. Since some of these corrosion types are generally active, simultaneously or in sequence, in practical cases, one often has to choose between fulfilling contradictory demands for the material's corrosion resistance. Whilst the mechanical or physical properties of the material may sometimes be paramount, this can to some extent be overcome by design.

The very complex nature of high temperature corrosion and the lack of standardized testing practices make it virtually impossible to present corrosion data in tables.

While choosing material for high temperature applications, one must have an extensive knowledge of existing or expected service conditions, such as gas temperature, gas composition and the temperature of the material. Knowledge of previously used materials, their service performance, and of the cause(s) of previous failures are usually of great support in the process of material selection to identify an optimum high temperature grade.

The demands on the corrosion resistance vary depending on the processes and constructions involved. In some plants, components can be maintained,



repaired, or replaced with minor if any interference to normal service, but in other applications, maintenance and repair must be carefully planned and can only be performed during annual or semiannual shut-downs. Obviously, a more careful choice of materials must be made in those cases.

### 3.04.12.1 Oxidation

When steel is heated in air or another oxygen containing gas, an oxide layer is formed on the surface, acting as a barrier between the steel and the gas. A dense and adherent layer will retard further oxidation, whilst a porous and crack-prone layer will be less protective. Chromium alloyed steels have a better resistance to oxidation than carbon steels since the presence of chromium and mixed chromium-iron oxides in an oxide layer makes it more protective than a pure iron oxides layer. When the chromium content is increased from 0 to 27 wt%, the scaling temperature increases from around 500 to 1125 °C. At temperatures above 1000 °C, aluminum oxides are more protective than chromium oxides. The amount of aluminum required for the formation of a protective layer will, however, make the alloy rather brittle and hence the fabrication difficult and costly.

The scaling temperature is a common measure of the oxidation resistance and is defined as the temperature above which the oxidation rate exceeds a certain value, and is usually determined in different short time cyclic tests, which differ between testing laboratories.

The scaling temperature is primarily used for ranking different alloys. The maximum service temperature in air is usually set some 50 °C lower.

Additions of silicon and rare earth metals (REM) improve the oxidation resistance of steels by reducing the oxide layer growth rate further. The protectiveness of the oxide layer also depends on the oxygen activity of the oxidizing gas, as this affects the morphology and composition of the scale.

Rapid temperature changes are detrimental, since thermal stresses will be induced in the oxide layer due to lower thermal expansion of the oxide relative to that of the base metal. This will eventually lead to cracking and spalling of the layer. Ferritic stainless steels have lower thermal expansion coefficients than austenitic high temperature stainless alloys and are therefore more resistant to oxidation under varying temperature conditions. Unfortunately, this advantage cannot generally be fully exploited at higher temperatures due to the poor mechanical strength and the greater tendency for embrittlement of the ferritic stainless steels. The negative effect of temperature variations on the performance of austenitic alloys can be reduced by several means, for example, by increasing the nickel content. Thereby, satisfactory oxidation resistance up to 1150 °C can be reached. REM additions will lead to the formation of a thinner, more ductile, and hence more adherent oxide layer.

In [Figure 58](#), the oxidation behavior of some common austenitic high temperature stainless steels is compared.

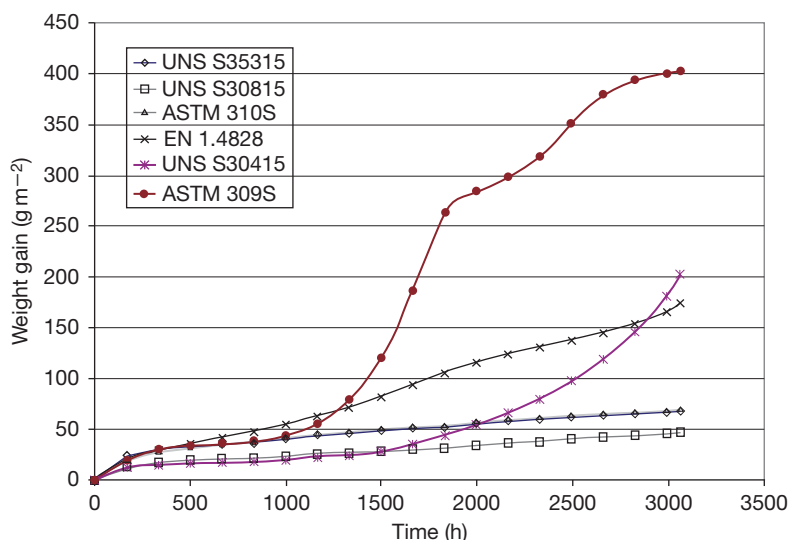


**Figure 58** Comparison between common high temperature steels in oxidation behavior at 1000 °C, 165 h cycles.

Although oxides as a rule are beneficial, there are a few elements which tend to form liquid or even gaseous oxides – especially in stagnant atmospheres – which may lead to “catastrophic oxidation,” that is, fluxing of the scale by the liquid oxide. Molybdenum (Mo), known to be one of these elements, however, is often used to increase wet corrosion resistance, but should be avoided in materials for service at temperatures above 750°C. A similar behavior is reported for tungsten (W). For niobium (Nb), even worse behavior than for Mo and W has been reported, although some sources claim that it can have a positive effect on the oxidation resistance, at least at lower temperatures.

Two other elements, which form liquid oxides, are vanadium and lead. Their concentration in alloys as either alloying or trace elements is too low to be harmful, but they are sometimes present as contaminants in the environment.

### 3.04.12.2 Sulfur Attack

Different sulfur compounds are often present as contaminants in flue gases and some process gases. Chemically, sulfidation is similar to oxidation. However, as a rule, sulfides have lower melting points than the corresponding oxide, so the risk for a fluxing of the scale is greater. Especially nickel is a nonfavorable alloying element in that respect. Moreover, the diffusion rates in sulfide scales are generally much higher than in the corresponding oxides, making the scale growth rate higher and the time to scale breakdown shorter.

In oxidizing gases, that is, when a protective oxide layer can be formed, the corrosion resistance is determined by the properties of that layer. Sulfur attacks generally start at cracks in the layer. A ranking of the corrosion resistance of different materials in oxidizing sulfur-containing environments is often equivalent to the oxidation resistance ranking. On the other hand, under conditions where it is difficult to form a protective oxide layer, the corrosion resistance is considerably lower and directly dependent on the bulk chemical composition of the tested alloys. Under these conditions, steels with high chromium content and little or no nickel are superior.

### 3.04.12.3 Halogen Gas Corrosion

Gases containing halogens, that is, F, Cl, Br, and I or hydrohalides are very aggressive against all metallic materials. Under reducing conditions, nickel and

chromium additions generally improve the corrosion resistance. In oxidizing environments, chromium and especially molybdenum and tungsten are very detrimental due to their tendency to form highly volatile oxychlorides and fluorides.

The halogens of practical interest are fluorine and chlorine. Fluorine is considered to be more corrosive than chlorine, which, on the other hand, is more common and more concentrated in most applications. Although theoretical considerations and laboratory tests yield very low maximum service temperatures (<300°C), in practice, stainless steels can often be used up to 600°C.

Other halogen compounds may be equally corrosive, but only after deposition or condensation, see molten salt corrosion in the following section.

### 3.04.12.4 Molten Salt corrosion

There are several industrial applications in which molten salts are intentionally used, the most important areas being heat treatment, metal extraction, and energy conversion. However, there are also many cases in which the presence of molten salts is far from intentional.

Mixtures of chloride salts are frequently used in salt pots for heat treatment. These ‘neutral salts’ will neither oxidize nor decarburize heat-treated or construction materials when they are pure, but their corrosivity can increase dramatically if they become oxidized or otherwise contaminated. The salt pots often experience localized attacks at the salt–air interface. Salt pot life can be extended by using special inserts at this transition zone, by using an inert gas instead of air, and/or by rectification (deoxidation) of the salt bath. As for chlorine gas corrosion, low-chromium, high- or medium-nickel alloys are the best material choices. Some recent tests have also shown a good performance for low-nickel, high-silicon alloys. In general, however, salt pot failures are due to poor manufacturing, operational, or maintenance procedures, rather than to poor alloy selection.

Fluoride salts have been suggested for use in nuclear power systems. Those mentioned earlier also apply to them.

In the case of hardening salt pots, cyanides are added to the common chloride mixture. The pot material should then be able to withstand carburization and nitridation, that is, high nickel content is beneficial. Since the cyanide keeps the oxygen content at a low level, these salt pots often show longer service lives than ‘neutral salt’ pots.

### 3.04.12.5 Molten Metal Corrosion

Construction materials are deliberately exposed to liquid metals in several applications, for example, heat treatment, energy conversion, and the actual production of those metals. The main corrosion mechanisms in those cases are massive or selective material dissolution, or possibly mass transfer.

Some general observations can be made. With respect to austenitic Ni–Cr–Fe alloys, the higher the nickel content, the more rapidly the alloy dissolves in liquid metal. Ferritic Fe–Cr stainless steels tend to be more resistant, and are not as likely to suffer intergranular attack, as are austenitic alloys.

Specific metals and alloys will not be treated separately in this article. The reader is referred to specialist literature on this subject.

A more unpredictable and hence more dangerous threat is liquid metal embrittlement – a phenomenon caused by local contamination by metals such as Ag, Cu, and Zn. When molten, these metals, or alloys of them, will penetrate austenitic alloys' intergranular and may cause rupture within seconds. Examples where this has been reported to occur are:

- Welding stainless steels to galvanized carbon steels or other zinc contaminated steels, for example, from melting off galvanized steel (e.g., during fire) or from zinc containing paint;
- Weld cracking due to copper contamination, for example, from cold forming tools or back-up bars;
- Cracking caused by copper containing antiseize compounds;
- Cracking from manual, and hence less well-controlled, silver brazing.

## References

1. European Committee for Standardization, Brussels, Belgium, EN 10088-1.
2. Leffler, B. *Stainless – Stainless Steels and Their Properties*; Avesta Sheffield AB Research Foundation, Stockholm, Sweden, 1996.
3. MNC Handbok nr 4, Rostfria stål, Metallnormcentralen, Stockholm, Sweden, 1983.
4. Nordberg, H.; Fernheden, K. Nordic Symposium on Mechanical Properties of Stainless Steels. Avesta Research Foundation, 1990.
5. Peckner, B. *Handbook of Stainless Steel*; McGraw-Hill, 1977.
6. *Metals Handbook*, 9th ed.; American Society for Metals, 1981; Vol 4.
7. Leffler, B. *Stainless Steels and Their Properties*, 2nd revised ed.; Outokumpu Stainless Research Foundation, Stockholm, 1998.
8. Nordberg, H. *La Metallurgia Italiana* **1994**, 85(3), 147–154.
9. Skuin, K. *Neue Hütte*, **1970**, 15(8), 477–479.
10. Sieurin, H.; Zander, J.; Sandström, R. *Mater. Sci. Eng.* **2006**, 415(1–2), 66.
11. Richter, F. *StahlEisen-Sonderberichte*; Verlag StahlEisen, 1973; Heft 8.
12. Richter, F. *StahlEisen-Sonderberichte*; Verlag StahlEisen, 1983; Heft 10.
13. Design Guidelines for the selection and use of stainless steel, specialty steel Industry of the United States, Washington, DC, USA.
14. Truman, J. E.; Coleman, M. J.; Pirt, K. R. *Br. Corros. J.* **1977**, 12(4), 236.
15. Szklarska-Smialowska, Z. *Pitting and Crevice Corrosion*, NACE International, Houston, TX, 2005.
16. Alfonsson, E.; Qvarfort, R. Investigation of the applicability of some PRE expressions for austenitic stainless steels, ACOM 1-1992, Avesta, 1992.
17. Horvath, J.; Uhlig, H. H. *J. Electrochem. Soc.* **1968**, 115(8), 791.
18. Jargelius-Pettersson, R. F. A. *Corros. Sci.* **1999**, 41, 1639.
19. Newman, R. C. *Corrosion* **2001**, 57(12), 1030–1041.
20. Tester, J. W.; Isaacs, H. S. *J. Electrochem. Soc.*, **1975**, 122(11), 1438.
21. Grimm, R. D.; Landolt, D. *Corros. Sci.* **1994**, 36, 1847.
22. Donker, H. J.; Dengg, R. A. *Korrosion Metallschutz* **1927**, 3, 217.
23. Brenner, S. J. *Korrosion Metallschutz* **1937**, 13, 379.
24. Streicher, M. A. *J. Electrochem. Soc.* **1956**, 103(7), 375.
25. Laycock, N. J.; Stewart, J.; Newman, R. C. *Corros. Sci.*, **1997**, 29(10–11), 1791–1809.
26. Szlarka-Smialowska, Z. *Pitting Corrosion of Metals*, NACE, Houston, 1986; p 103.
27. Schwenk, W. *Corrosion* **1964**, 20(4), 129t.
28. Brigham, R. J.; Tozer, E. W. *Corrosion* **1973**, 29(1), 33.
29. Qvarfort, R. *Corros. Sci.* **1988**, 28, 135 (ACOM, No 2–3).
30. Salinas-Bravo, V. M.; Newman, R. C. *Corros. Sci.* **1964**, 36, 67.
31. Valen, S. I. PhD thesis, University of Trondheim, 1991.
32. Alfonsson, E.; Arnvig, P. E.; Bergquist, A.; Ivarsson, B.; Iversen, A.; Leffler, B.; Nordström, J.; Olsson, J.; Stenvall, P.; Wallén, B.; Vangeli, P. *Outokumpu Stainless Corrosion Handbook*, 9th ed.; Outokumpu Stainless Oy, Sandviken, 2004, pp 1:8–1:103.
33. Sedriks, A. J. *SCC of Stainless Steels*; ASM International: Materials Park, OH, 1992; pp 91–130.
34. Sedriks, A. J. *Corrosion of Stainless Steels*, 2nd ed.; John Wiley, 1996.
35. Newman, R. C. In *Corrosion Mechanisms in Theory and Practice*; Marcus, P., Oudar, J., Eds.; Marcel Dekker, 1995; pp 311, 372.
36. Extracted from Dickson, J. I.; Russel, A. J.; Tromans, D. *Can. Met. Q* **1980**, 19, 161.
37. Iversen, A.; Prosek, T. Eurocorr 2007, Freiburg im Breisgau, Germany, 9–13 September, 2007.
38. Copson, H. R. *Physical Metallurgy of Stress Corrosion Fracture*; Interscience, New York, 1959; p 247.
39. Extracted from Valen, S. I. Proceedings 11th Scandinavian Corrosion Congress, Stavanger, Norway, June 19–21, 1989 and from reference 32.
40. Wallén, B.; Olsson, J. In *Handbook of Stainless Steel*; Peckner, D., Bernstein, I. M., Eds.; McGraw-Hill, 1977; pp 16.1–16.89.
41. Leckie, P. J. *Electrochem. Soc.* **1970**, 117, 1152.
42. Thierry, D.; Sand, W. *Microbially Influenced Corrosion, Corrosion Mechanisms in Theory and Practice*; Marcel Dekker, 199; pp. 457–499.

43. Mollica, A.; Trevis, E. Proceedings 4th International Congress on Marine Corrosion and Fouling, Juan les Pins, France, 1976, p 351.
44. Feron, D.; Dupont, I.; Novel, G. Eurocorr 96 (1996), European Federation of Corrosion, Publications No 22. Aspects of microbially induced corrosion, 1997.
45. Tverberg, J.; Pinnow, K.; Redmerski, L. NACE Corrosion, Paper 151, April 23–27, Nevada, 1990.
46. Mameng, S. Amase master thesis, EEIGM Nancy, École Européenne d'ingénieurs en Génie des Matériaux, Institut Nation Polytechnique de Lorraine, France, 2007.
47. MAST II Program. Biofilm Project Contract No MAS2 CT92 001.1, CNR-ICMM: Scotto, V. (coordinator), Mollica, A., Ventura, G., Traverso, E., Trentin, I., Marcenaro, G., Piccarolo, C., Martinoli, O., Andrei, E., Lai, E., Dellepiane, R., Decarolis, G., CEA: Féron, D., Dupont, I., Delepine, J., Blanchard, D., Letouze, J. M., Bourneuf, F., Laniece, V., Massilian, R., Lefevre, Y. ENRICERCHE: Carrera, P., Camilli, M., Pietrangeli, B., Gianna, R., IFREMER: Compère, C., Festy, D., Mazeas, F., Leroux, J. P., Riou, L., IRSID: Audouard, J. P., Dowling, N. J., Bonnet, C., SCl: Thierry, D., Taxen, C., Kivisäkk, U., Aronsson, C., Linder, M., SINTEF: Rogne, T., Steinsmo, U., Drugli, J. M., Solem, T., Bjordal, M., Final report Marine Biofilms on Stainless Steels: Effects, Monitoring and Prevention, European Commission, 1996.
48. Mollica, A.; Montini, U.; Scotto, V.; Marcenaro, G. Comportement face a la corrosion d'alliages ferreux en sediments anaerobies portuaires, Communication par affice à "Biocorrosion prevention et maintenance" Strasbourg (France), Octobre 1989.
49. Mollica, A.; Ventura, G. Crevice corrosion resistance of Stainless Steels in anaerobic seawater enriched by sulfides produced by SRB's activity, Technical Report, CNR-ICMM-BC-1/97.
50. Iversen, A. *Br. Corros. J.* **2001**, 36(4), 277–291.

## 3.05 Aqueous Corrosion of Nickel and its Alloys

**H. Alves**

ThyssenKrupp VDM GmbH, Plettenberger Str. 2, D-58791 Werdohl, Germany

**U. Heubner**

Consultant, Borgheller Str. 28, D-58791 Werdohl, Germany

© 2010 Elsevier B.V. All rights reserved.

<b>3.05.1</b>	<b>Introduction</b>	1880
<b>3.05.2</b>	<b>Brief Survey of Nickel and Nickel Alloy Groups for Aqueous Corrosive Applications</b>	1881
<b>3.05.3</b>	<b>Nickel and Nickel Alloy Groups for Aqueous Corrosive Applications</b>	1882
3.05.3.1	Nickel	1882
3.05.3.2	Nickel–Copper Alloys	1883
3.05.3.3	Nickel–Molybdenum Alloys	1884
3.05.3.4	Nickel–Chromium Alloys	1885
3.05.3.5	Nickel–Chromium–Molybdenum Alloys	1886
3.05.3.5.1	General	1886
3.05.3.5.2	Alloy C-276	1886
3.05.3.5.3	Alloy C-4	1887
3.05.3.5.4	Alloy 22	1887
3.05.3.5.5	Alloy 59	1887
3.05.3.5.6	Additional C-alloys and thermal stability as a criterion for alloy selection	1889
3.05.3.5.7	Alloy 625	1890
3.05.3.6	Nickel–Chromium–Iron–Molybdenum–Copper Alloys	1891
3.05.3.6.1	General	1891
3.05.3.6.2	Traditional materials: Alloys 20, 825, G-3, and G-30	1891
3.05.3.6.3	Advanced materials: Alloys 31 and 33	1892
3.05.3.7	Age-Hardenable Nickel–Chromium–Iron–Molybdenum (–Copper) Alloys	1898
<b>3.05.4</b>	<b>Corrosion Behavior of Nickel Alloys in the Welded State</b>	1898
3.05.4.1	The Specific Surface and Structural Condition of the Weld Metal and the HAZ	1898
3.05.4.2	Surface Condition and Necessary Surface Treatment after Welding	1899
3.05.4.3	IC in the HAZ	1900
3.05.4.4	Resistance of Weld Metal and Heat Affected Zone to Pitting	1900
<b>3.05.5</b>	<b>Application of Nickel and Nickel Alloys as Materials Resistant to Aqueous Corrosion in the CPI and in Environmental Technology</b>	1901
3.05.5.1	General	1901
3.05.5.2	Production of Caustic Soda	1902
3.05.5.3	Production and Handling of Sulfuric Acid	1903
3.05.5.4	Production of Phosphoric Acid	1905
3.05.5.5	Production of Hydrofluoric Acid and Aluminum Fluoride	1907
3.05.5.6	Production of Acetic Acid	1907
3.05.5.7	Production of VCM	1908
3.05.5.8	Production of Styrene	1908
3.05.5.9	Production of Acrylic Acid and Acrylate Esters	1909
3.05.5.10	Production of MDI and TDI as Feedstocks for Polyurethanes	1909
3.05.5.11	Production of Fine and Specialty Chemicals	1910
3.05.5.12	Transport of Corrosive Dangerous Goods in Tanks	1912
3.05.5.13	Environmental Technology	1912
<b>References</b>		1914

**Abbreviations**

<b>ABS</b>	Acrylonitrile butadiene styrene (copolymer)
<b>AOD</b>	Argon-oxygen-decarburization
<b>ASTM</b>	American Society for Testing and Materials
<b>BAM</b>	Bundesanstalt fuer Materialforschung und-pruefung (Germany)
<b>CCT</b>	Critical crevice corrosion temperature
<b>CPI</b>	Chemical process industry
<b>CPT</b>	Critical pitting temperature
<b>EDC</b>	Ethylene dichloride
<b>EN</b>	European standardization
<b>FGD</b>	Flue gas desulfurization
<b>FM</b>	Filler metal
<b>HAZ</b>	Heat affected zone
<b>IC</b>	Intercrystalline corrosion
<b>LC</b>	Low carbon
<b>MDI</b>	Methylene di-paraphenylene
<b>NACE</b>	National Association of Corrosion Engineers
<b>PRE</b>	Pitting resistance equivalent
<b>PVC</b>	Polyvinyl chloride
<b>SAN</b>	Styrene acrylonitrile (plastic resin)
<b>SBR</b>	Styrene butadiene rubber
<b>SEP</b>	Stahl-Eisen-Pruefblaetter (Germany)
<b>TDI</b>	Toluene di-isocyanate
<b>TIG</b>	Tungsten inert gas welding process
<b>UNS</b>	Unified numbering system (North America)
<b>VCM</b>	Vinyl chloride monomer
<b>VOD</b>	Vacuum-oxygen-decarburization

**Symbols**

<b>A<sub>v</sub></b>	Notch impact energy (J)
<b>mV<sub>NHE</sub></b>	Potential versus a normal hydrogen electrode (mV)
<b>M<sub>6</sub>C</b>	Metal carbide
<b>p.a.</b>	Analytical grade purity
<b>pH</b>	Negative logarithm of the concentration of dissolved hydrogen ions (H <sup>+</sup> )
<b>V<sub>SCE</sub></b>	Potential versus a saturated calomel electrode (V)

**3.05.1 Introduction**

Within the chemical process industry (CPI), as well as other industries, the austenitic corrosion-resistant stainless steels have been, and will continue to be, the most widely used tonnage material after carbon steel. Materials of construction for the modern chemical

process and petrochemical industries must not only resist uniform corrosion caused by various aqueous media, but must also have sufficient resistance to localized corrosion as pitting, crevice corrosion and stress-corrosion cracking. Chemical process and petrochemical industries have to cope with the technical and commercial challenges of rigid environmental regulations, the need to increase the production efficiency by utilizing higher temperatures and pressures and more corrosive catalysts and, at the same time, possess the necessary versatility to handle varied feedstock and upset conditions. Over the past 50 years, improvements in alloy metallurgy, melting technology, and thermomechanical processing, along with a better fundamental understanding of the role of various alloying elements, have led to new nickel alloys that not only extend the range of usefulness of the existing alloys by overcoming their limitations, but are also reliable and cost-effective, and have opened new areas of applications.

Nickel and nickel alloys have useful resistance to a wide variety of aqueous corrosive environments typically encountered in various industrial processes. In many instances, the corrosive conditions are too severe to be handled by other commercially available materials, including stainless and super stainless steels. Nickel by itself is a very versatile corrosion-resistant metal finding many useful applications in industry. More importantly, its metallurgical compatibility over a considerable composition range with a number of other metals as alloying elements has become the basis for many binary, ternary, and other complex nickel alloy systems having unique and specific corrosion-resistant behavior for handling the modern-day corrosive environments of chemical processing, petrochemical, marine, pulp and paper, agrichemicals, oil and gas, energy conversion, and many other industries. These alloys are more expensive than are the standard austenitic corrosion-resistant stainless steels because of their higher alloy content and more involved thermomechanical processing, and hence, are used only when stainless steels are not suitable or when product purity and/or safety considerations are of critical importance. Corrosion resistance depends on the chemical composition of the alloy, the alloy's microstructural features developed during thermomechanical processing, the chemical nature of the environment, and the various reactions occurring at the alloy–environment interface.

In this chapter, the major nickel alloy systems are discussed, including their major characteristics, the effects of alloying elements, and most



importantly, the strengths, weaknesses, and applications of these systems. A few words on fabrication are also included, because an improper fabrication may destroy the corrosion resistance of an otherwise fully satisfactory nickel alloy.

### 3.05.2 Brief Survey of Nickel and Nickel Alloy Groups for Aqueous Corrosive Applications

Nickel and nickel alloy systems for aqueous corrosive applications can be divided into various groups according to their composition as shown in Table 1.

Table 1 gives, in its first column, the internationally used, but not standardized, alloy designation, followed in the second column by the materials' number in use for European standardization (EN). In the third column, the designation according to the unified numbering system (UNS) of the Unified States is indicated. The following columns describe nickel

and the various nickel alloys by means of their main alloying elements, indicating typical values only.

With reference to Table 1 from top to bottom, the first alloy group is unalloyed nickel in its high-carbon (maximum 0.05 mass%) and special low-carbon (maximum 0.02 mass%) forms, designated as alloys 200 and 201, respectively. Second are the nickel–copper alloy 400 and its age-hardenable version alloy K-500, which are widely used. Third is the nickel–molybdenum group, where only one of its members, the quasibinary nickel–molybdenum alloy B-2 is mentioned, due to the very limited use of this type of alloy in special applications. The nickel–chromium alloy group can be considered to be an extension of the austenitic nickel–chromium stainless steels up to very high nickel and to rather low iron content.

The group of nickel–chromium–molybdenum alloys has restricted iron content only and may contain tungsten besides some other elements like niobium, copper, and tantalum. Since the corrosion behavior of these alloys is largely dependent on the amounts of

**Table 1** Principal nickel alloy groups for aqueous corrosive applications

Designation			Main alloying elements, typical values (mass%)					
Alloy	EN	UNS	Ni	Cr	Mo	Cu	Fe	Other elements/remarks
<i>Nickel</i>								
200	2.4066	N02200	99.5					Ni >99.2
201	2.4068	N02201	99.5					Ni >99, C ≤0.02
<i>Nickel–copper</i>								
400	2.4360	N04400	64			32	1.8	1.0 Mn
K-500	2.4375	N05500	65			30	1.0	0.6 Mn, 2.8 Al, 0.45 Ti
<i>Nickel–molybdenum</i>								
B-2	2.4617	N10665	69	0.7	28		1.7	
<i>Nickel–chromium</i>								
600 L	2.4817	N06600	73	16			9	0.25 Ti, C ≤0.025
690	2.4642	N06690	61	29			9	0.25 Ti
<i>Nickel–chromium–molybdenum with (Cr + Mo) in ascending order</i>								
625	2.4856	N06625	62	22	9		3	3.4 Nb
C-4	2.4610	N06455	66	16	16		1	
C-276	2.4819	N10276	57	16	16		6	3.5 W
22	2.4602	N06022	56	22	13		4	3 W
686	2.4606	N06686	58	21	16		1.5	3.8 W
MAT 21		N06210	58	19	19		<1	1.8 Ta
2000	2.4675	N06200	57	23	16	1.6	1.5	
59	2.4605	N06059	59	23	16		1	
<i>Nickel–chromium–iron–molybdenum–copper with (Cr + Mo) in ascending order</i>								
20	2.4660	N08020	38	20	2.4	3.4	34	0.2 Nb
825	2.4858	N08825	40	23	3.2	2.2	31	0.8 Ti
G-3	2.4619	N06985	48	23	7	2.0	19	0.3 Nb
31	1.4562	N08031	31	27	6.5	0.9	45	0.20 N
33	1.4591	R20033	31	33	1.6	0.6	32	0.40 N
G-30	2.4603	N06030	43	30	5	1.7	15	2.5 W, 0.7 Nb
<i>Age-hardenable nickel–chromium–iron–molybdenum–(Copper)</i>								
718	2.4668	N07718	53	19	3		18	5.2 Nb, 0.9 Ti, 0.6 Al
925	2.4852	N09925	44	21	3	2	27	2.1 Ti, 0.3 Al

chromium and molybdenum being added as alloying elements, the alloys are arranged in **Table 1** according to the sum of these elements in ascending order.

For the same reason, the members of the following nickel–chromium–iron–molybdenum–copper alloy group are arranged according to the sum of their alloying elements chromium and molybdenum in ascending order. However, other alloying elements like copper and nitrogen, and last but not least, nickel, exert an influence on the corrosion behavior too. This will be pointed out more in detail in the following subsection devoted to this alloy group. The alloys of this group are higher in iron than are the alloys of the nickel–chromium–molybdenum alloy group, and are, in this way, closely related to or – depending on the formalities of classification – at the same time part of the corrosion-resistant high-alloy special stainless steels.

At the bottom of the table is the age-hardenable nickel–chromium–iron–molybdenum (–copper) alloy group that is of great importance in the special application of oil and gas extraction.

Although the list of the principal nickel alloy groups for aqueous corrosive applications presented in **Table 1** seems to be quite large, it shows a selection of the most important alloys only. The great number of nickel alloys for aqueous corrosive applications that are available today is the result of a phenomenal recent growth in the development of new nickel alloys, with special emphasis on the high-performance nickel–chromium–molybdenum alloy group. This development of new alloys has become possible by the introduction of new metallurgical techniques like argon–oxygen–decarburization (AOD) and vacuum–oxygen–decarburization (VOD) in the 1960s. These new metallurgical techniques allow easy decarburization of large volumes of molten alloys down to very low carbon contents as, for instance, 0.005 mass%. **Table 2** gives a brief listing of developments of some nickel alloys during the pre-1950s and since the 1950s.<sup>1</sup> As is evident from this listing, today's corrosion and material engineers

have a much wider selection of alloys to meet their specific needs than had been the case prior to the 1950s when the alloy choices available for combating aqueous corrosion were very limited. This historical development has to be kept in mind when reading older literature on corrosion-resistant materials. New alloys and refinements of old ones are constantly under way.

### 3.05.3 Nickel and Nickel Alloy Groups for Aqueous Corrosive Applications

#### 3.05.3.1 Nickel

As Friend<sup>2</sup> points out, the standard reduction potential of nickel that is shown in the electrochemical series of metals is nobler than that of iron and less noble than that of copper. Owing to nickel's marked hydrogen overpotential, hydrogen is not so easily liberated from the usual nonoxidizing acids, and the presence of oxygen, for example, from dissolved air is generally necessary here in order to allow corrosion to proceed. The general rule is that oxidizing conditions promote the corrosion of nickel in chemical solutions, whereas reducing conditions retard it. However, nickel has the ability to protect itself against certain forms of corrosive attack by forming a passive layer of oxide or hydrated oxide, and in practice often exhibits a more noble behavior than does copper. Therefore, corrosion is not always accelerated by oxidizing conditions. A certain amount of pitting may occur if the passive layer is locally destroyed, for example, in hot chloride solutions. The results of the studies of the mechanism of passivation of nickel have been reviewed extensively by Friend.<sup>2</sup>

If the temperature is not excessively high, nickel has a useful measure of resistance to corrosive attack by dilute nonaerated solutions of most of the nonoxidizing mineral acids, for example, sulfuric, hydrochloric, and phosphoric acid. This also applies to the nonoxidizing salts of such acids, which can hydrolyze with the formation of dilute solutions of these

**Table 2**      Historical development and introduction to the market of selected nickel alloys

Alloy	Period					
	Pre-1950s	1950s	1960s	1970s	1980s	1990s
Ni, Ni–Cu, Ni–Cr	200, 400, 600					
Ni–Mo	B			B-2		B-2 'controlled composition'
Ni–Fe–Cr–Mo–Cu		825	20, G	G-3	G-30	31, 33
Ni–Cr–Mo	C		C-276, 625	C-4	22	59, 686, 2000, MAT 21

acids. Nickel may corrode rapidly in oxidizing acids, for example, nitric acid, or in other mineral acids containing significant amounts of oxidants.

Nickel has a useful measure of corrosion resistance to most nonaerated organic acids and other organic compounds. This enables it to be used in the plastics industry. When being used in the food industry, nickel itself might exhibit a sufficient level of corrosion resistance in the medium under consideration, nevertheless attention has to be paid to the amount of nickel ions that might migrate into the food, and for this reason, nickel-plated food contact materials should not be used.<sup>3</sup>

Nickel is very resistant to corrosion by most kinds of natural and highly purified water. However, if water intended for human consumption is considered, the size of the surface of the nickel-plated parts being exposed to the water should be limited and a sufficient amount of flow maintained as well, in order to avoid an excessive uptake of nickel by the drinking water, and in this way, meet the requirements of the European Council Directive 98/83/EC on the quality of drinking water.<sup>4</sup>

Nickel is also resistant to fast-flowing seawater. Under stationary conditions, however, it is susceptible to substantial growth of organisms, with the result that severe local attack may occur under this and other deposits.

Nickel is outstandingly resistant to alkalis such as sodium and potassium hydroxide, even at high concentrations and temperatures, with the exception of more highly concentrated ammonium hydroxide solutions, and to nonoxidizing alkaline and neutral salts. This property is the reason for nickel's use in chemical process equipment manufacturing for the production and processing of caustic soda and caustic potash. **Figure 1** shows an isocorrosion diagram of nickel in caustic soda solution originally established more than 30 years ago<sup>5</sup> and redrawn more recently,<sup>6</sup> due to its unique importance for the industrial application of metallic nickel. Obviously, in practice, this diagram can only be used as an initial guide, because admixtures and impurities that may be present in the caustic soda influence the metal's corrosion behavior.

More detailed information on nickel's corrosion behavior is provided by Friend.<sup>2</sup> In traditional parlance, unalloyed nickel in wet-corrosion applications is referred to as 'pure nickel.' The most popular grades for wet-corrosion service are the standard grade alloy 200 (EN 2.4066/UNS N02200) and the low-carbon grade alloy 201 (EN 2.4068/UNS N02201) shown in **Table 1**. The low-carbon grade must be used at temperatures in excess of 315 °C (600 °F) in order to

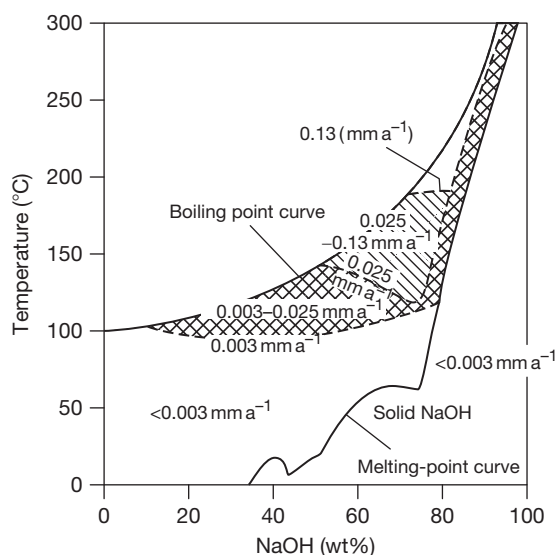


**Figure 1** Corrosion resistance of unalloyed nickel in sodium hydroxide, related to concentration and temperature. Reproduced from Heubner, U. In *Nickel Alloys and Special Stainless Steels*; 3rd ed.; Heubner/Klöwer, et al., Ed.; Expert Verlag: Renningen, 2003; Chapter 2, pp 47–93.

avoid loss of ductility because of the precipitation of graphite at the grain boundaries within the metal's microstructure.<sup>2</sup> In addition, unalloyed nickel when used in electroplated form, mainly on steel and brass, may be exposed to wet-corrosive attack too.

### 3.05.3.2 Nickel–Copper Alloys

Copper is reasonably corrosion-resistant in dilute, nonoxidizing, nonaerated solutions of mineral acids such as sulfuric, hydrochloric, phosphoric, or hydrofluoric acid, and also of most organic acids, for example, acetic and formic acid, even at quite high temperatures. It is attacked by hot concentrated solutions of these acids. When nickel and nickel alloys are alloyed with copper, their resistance to these nonoxidizing acid solutions is generally improved. In particular, copper is often added to increase the corrosion resistance of nickel alloys and high-alloy special stainless steels in sulfuric acid.

Nickel–copper alloys containing, for instance, 27–34 mass% copper may have a useful measure of corrosion resistance in nonaerated sulfuric acid at concentrations of up to 80% at room temperature, 60% at 70 °C, and 20% at boiling temperature (Craig and Anderson<sup>7</sup> indicate data that are at variance with this).

Nickel–copper alloys are reasonably resistant to dilute hydrochloric acid solutions, provided that, like

the aforementioned sulfuric acid solutions, they are kept free of air. These alloys can then be used at hydrochloric acid concentrations of up to ~15% at room temperature and ~5% at ~70 °C. Therefore, they can be used for handling nonoxidizing chlorides, which form hydrochloric acid in low concentrations by hydrolysis in the presence of water.

Nickel–copper alloys are one of the few types of metallic materials that exhibit good corrosion resistance in nonaerated hydrofluoric acid of all concentrations. In aerated solutions, on the other hand, severe metal dissolution and stress-corrosion cracking may occur. The corrosion rates are shown in detail in the isocorrosion diagram for nonaerated and aerated solutions.

Nickel–copper alloys are resistant to most kinds of water; their resistance to seawater with a high flow-velocity is particularly relevant for their use in actual service. They can therefore be used for, among other things, heat exchanger tubes and for shielding in seawater spray and tidal zones. The age-hardenable variant is used in places where not only resistance to seawater but also high strength are important, for example, for ship propeller shafts, valve seats, studs, bolts, and pump components. Under stationary conditions, incrustation by marine organisms can occur, causing concentration cells to form, which result in pitting. This, however, tends to slow down with time and even, in tropical waters, seldom exceeds penetration depths of ~0.75 mm (30 mils) after a few years.

Thanks to their high nickel content, nickel–copper alloys are resistant to most alkalis (except ammonium hydroxide) and most nonoxidizing alkaline and neutral salts. They have good resistance in caustic soda and caustic potash, similar to that of unalloyed nickel. Rates of corrosion of less than 0.05 mm year<sup>-1</sup> were found up to a concentration of 75% NaOH and a temperature of 130 °C. When 75% NaOH is evaporated to anhydrous NaOH, the corrosion rates are higher than with unalloyed nickel, and in molten NaOH, stress-corrosion cracking was observed in equipment items subjected to high mechanical stress. Under such conditions, therefore, the components must undergo stress-relief annealing.

Neutral and alkaline salt solutions such as chlorides, carbonates, sulfates, nitrates, and acetates have only a minimal corrosive effect on nickel–copper alloys, even at high concentrations and temperatures up to the boiling point; consequently, corrosion rates are generally less than 0.025 mm year<sup>-1</sup>. Nickel–copper alloys are, therefore, used in plants in which salts are crystallized from saturated brines.

Nickel–copper alloys are not resistant to highly oxidizing solutions such as nitric and chromic acid, moist chlorine, and hypochlorites.

The most important nickel–copper alloys for engineering purposes are alloy 400 (EN 2.4360/UNS N04400) and the age-hardenable variant alloy K-500 (EN 2.4375/UNS N05500) as mentioned in [Table 1](#).

Related, in the broader sense, to the nickel–copper alloys are the copper–nickel alloys, which are dealt with in [Chapter 3.07, Corrosion of Copper and its Alloys](#).

### 3.05.3.3 Nickel–Molybdenum Alloys

Molybdenum exhibits a very good corrosion resistance to nonoxidizing solutions of hydrochloric, phosphoric, and hydrofluoric acid at most concentrations and temperatures and to boiling sulfuric acid up to a concentration of ~60%. The alloying of nickel and nickel alloys with molybdenum improves their corrosion resistance in these media approximately in proportion to the percentage of added molybdenum. Nickel–molybdenum alloys, which typically contain 26–30 mass% molybdenum, are among the few metallic materials that are resistant to nonaerated hydrochloric acid at all concentrations and temperatures.<sup>6</sup> The prerequisite is the absence of oxidizing additions such as dissolved oxygen and heavy metal ions. Otherwise, the corrosion rates can increase significantly, as the isocorrosion diagrams shown by Craig and Anderson<sup>7</sup> for the alloy type B-2 make clear by way of example.

In nickel–molybdenum alloys, the practicable molybdenum content is subject to an upper limit owing to the constitutional situation.<sup>8–10</sup> As shown in [Table 1](#), the commercial alloy B-2 typically contains 28 mass% molybdenum. As [Figure 2](#) makes clear,<sup>6,11</sup> at this molybdenum content, a minimal rate of corrosion, which depends only to a slight extent on variations in the molybdenum content, can be anticipated in tests in boiling 10% hydrochloric acid as a test method, which is widely used in such circumstances.

Up to the mid-1990s, problems were frequently encountered when working and using the technologically established alloy B-2 (EN 2.4617/UNS N10665) because of fractures during working and stress-corrosion cracking while in service. The cause of both the fall in ductility and the stress-corrosion cracking is considered to be the formation of the ordered Ni<sub>4</sub>Mo phase,<sup>9,10</sup> a phenomenon that is accelerated by cold deformation.<sup>12</sup> A thorough

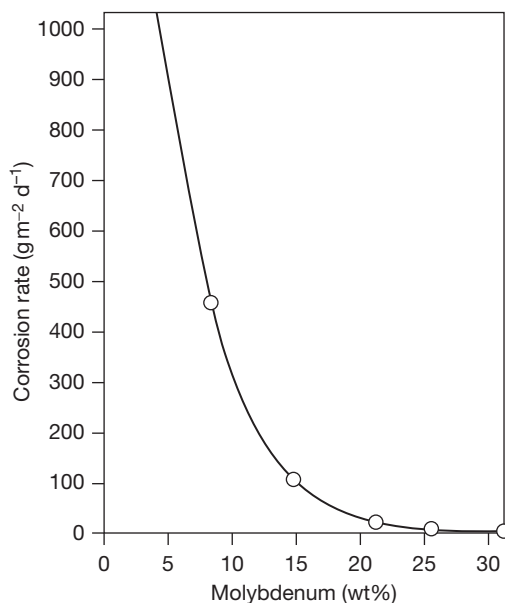


**Figure 2** Influence of the molybdenum content on the corrosion resistance of nickel-molybdenum alloys in boiling 10% hydrochloric acid.<sup>6,11</sup>

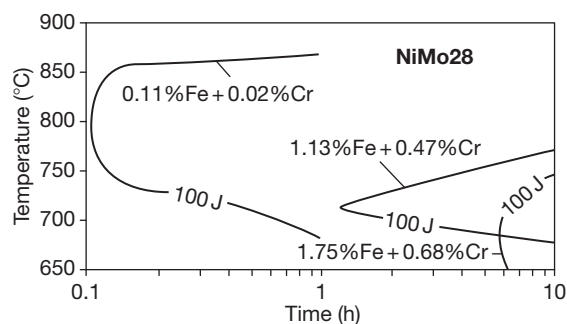


**Figure 3** Time-temperature-notch impact energy diagrams for the alloy NiMo28 – alloy B-2 (EN 2.4617/UNS N10665), established using three melts with different iron and chromium contents.<sup>6,8</sup>

analysis showed that the risk of such damage can be greatly reduced if the iron and chromium contents of this type of alloy are set close to the upper limit of what is acceptable according to the specification.<sup>10</sup>

**Figure 3** reveals by way of example how with this material the decrease in ductility during a working-related input of heat in the medium temperature range is delayed with increasing iron and chromium contents. It is due to these findings that a new alloy B-2 ‘controlled composition’ with Fe at 1.7 and Cr at 0.7 mass% as typical values, as shown in **Table 1**, had been introduced to the market in the 1990s (cf. **Table 2**). Nevertheless, solution annealing

of cold-formed parts, for example, heads, may be necessary when deformation is greater than 7% outer fiber elongation of cold work in order to avoid susceptibility to cracking at welds and heat affected zones during subsequent fabrication or later service.

The isocorrosion diagram plotted for alloy B-2 (EN 2.4617/UNS N10665) in nonaerated sulfuric acid shows interesting areas of resistance, for example, at concentrations between 60% and 80% and at temperatures above 120 °C. This too is subject to the prerequisite that clearly reducing conditions must be present; oxygen inputs due to aeration, heavy metal ions, and other oxidants accelerate corrosion.<sup>6,7</sup>

The corrosion resistance of alloy B-2 (EN 2.4617/UNS N10665) in organic acids, especially acetic acid, is tied to similar conditions.<sup>2</sup>

Thanks to its extremely low carbon and silicon contents, the NiMo28 alloy B-2 (EN 2.4617/UNS N10665) has good resistance to knife-line corrosion and selective corrosion in the heat-affected zone (HAZ) and can therefore usually be used in the welded state without further heat treatment.

### 3.05.3.4 Nickel–Chromium Alloys

Nickel and nickel alloys are alloyed with chromium to improve their resistance to strongly oxidizing media. Substances of this kind include nitric acid, chromic acid, and some acidic solutions containing oxidizing salts, with the exception of chlorides. In this case, corrosion resistance increases approximately in proportion to the chromium content, provided that it is more than 10 wt%. In the case of aerated acidic solutions, especially at elevated temperatures, chromium contents of more than 18% are preferable.<sup>2</sup>

**Figure 4** serves as a typical example of the effect of chromium on the reduction of the corrosion rate in strongly oxidizing solutions, referring as much to iron–chromium–nickel alloys as to nickel–chromium–iron alloys as shown by the example of alloy 690 (cf. **Table 1**). The difference between the older data and the newer data reflects the introduction of the melting technologies AOD and VOD, which occurred in the 1960s and resulted in cleaner alloys. Internal cleanness of the metallic grain structure is an often overlooked prerequisite for an enduring resistance to corrosive attack in the passive/transpassive and in the transpassive area, as may happen in strongly oxidizing solutions such as boiling azeotropic nitric acid as in **Figure 4**.

Since nickel–chromium alloys require the presence of further alloying elements in order for them



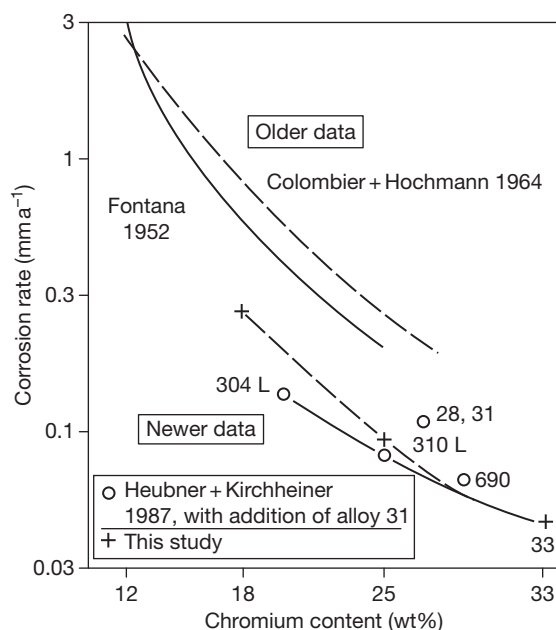


**Figure 4** Corrosion of iron–chromium–nickel and nickel–chromium–iron alloys in boiling azeotropic nitric acid.<sup>13,14</sup>

to be universally suitable for wet-corrosion service, they are few in number and their use tends to be limited to special cases. In current engineering practice, there are only two that are commonly used: alloy 600 L (EN 24817/UNS N 06600) and alloy 690 (EN 24642/UNS N 06690). As shown in [Table 1](#), these alloys also have a nominal iron content of 9 mass%. This means that, strictly speaking, they are nickel–chromium–iron alloys. Owing to their high nickel content, both can be considered for corrosive attack by hot alkaline solutions if they contain oxidants; examples are chlorates from diaphragm cells or sulfur compounds. These types of alloy are also used for steam generators in nuclear power stations. Owing to its high chromium content, alloy 690 has also been considered for corrosive attack by strongly oxidizing media. Nowadays, however, as is evident from [Figure 4](#), the more recently developed alloy 33 (EN 1.4591/UNS R20033) is probably a better alternative.<sup>13,14</sup>

### 3.05.3.5 Nickel–Chromium–Molybdenum Alloys

#### 3.05.3.5.1 General

As is to be expected, nickel–chromium–molybdenum alloys combine the good resistance to corrosion of nickel–molybdenum alloys under reducing conditions

with the good resistance to corrosion exhibited by nickel–chromium alloys under oxidizing conditions. The most important for engineering purposes are the so-called C-type alloys, the first of which was introduced as long ago as the 1930s. This was a nickel alloy with typically (figures in mass%) 16% chromium and 16% molybdenum, which also contained 4% tungsten and 6% iron together with 0.7% silicon and 0.05% carbon; this alloy is no longer in common use.<sup>15</sup> With the discovery that to reduce precipitation-readiness, it is important to reduce both the carbon and the silicon content of such materials to very low levels, it was developed into the alloy C-276 (EN 24819/UNS N10276), which is in use today, as shown in [Table 1](#). Since the 1960s, this has also been possible on a large scale without major problems, thanks to the new AOD and VOD production processes, which were introduced from that date onwards (cf. [Section 3.05.3.4](#)). Low silicon contents of typically 0.04 mass% and very low carbon contents of typically 0.005 mass% are nowadays characteristic of all the commonly used C-type nickel–chromium–molybdenum alloys,<sup>15</sup> which also include the alloys C-4 (EN 24610/UNS N06455), 22 (EN 24602/UNS N06022), and 59 (EN 24605/UNS N06059) in [Table 1](#).

#### 3.05.3.5.2 Alloy C-276

Alloy C-276 (EN 24819/UNS N10276) has its main areas of use for prevailing corrosive attack by reducing acids such as sulfuric acid, phosphoric acid, hydrochloric acid, and organic acids. Its isocorrosion diagram in technical grade sulfuric acid is reproduced in [Figure 5](#).

Owing to its good corrosion resistance in predominantly reducing media, even in the presence of halogens, it has succeeded in conquering a wide range of applications in the chemical industry; today, however, these are increasingly being taken over by the subsequently developed alloy 59 (see later text), which can be used on a more universal scale. This applies, for example, to plate-type heat exchangers in sulfuric acid production, which operate at reduced temperatures. Alloy C-276 is also used in applications where its resistance to hydrochloric acid solutions comes to the fore, for example, in the production of vinyl chloride monomer (VCM), methylene di-*para*-phenylene isocyanate (MDI), and toluene diisocyanate (TDI). Moreover, this type of alloy has good resistance to acetic acid at all concentrations and temperatures,<sup>7</sup> and is used for handling oxidizing acetic acid solutions and in places where acetic acid occurs in combination with inorganic acids and salts,



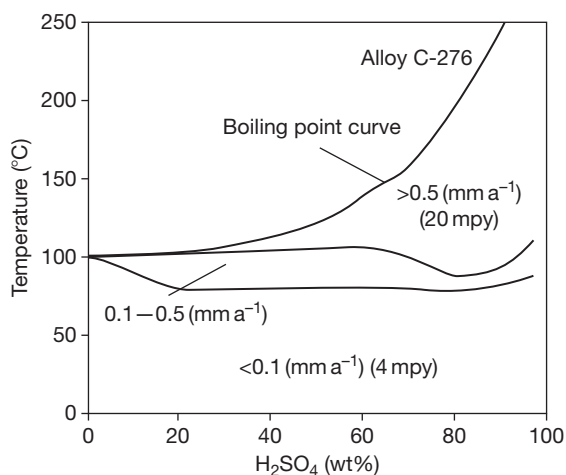


**Figure 5** Isocorrosion diagram of alloy C-276 (EN 2.4819/UNS N10267) in slightly aerated technical grade sulfuric acid, determined by immersion tests over at least 120 h. Reproduced from Kirchheiner, R.; Wahl, V. In *Nickel Alloys and Special Stainless Steels*; 3rd ed.; Heubner/Klöwer, et al., Ed.; Expert Verlag: Renningen, 2003; Chapter 8, pp 255–294.

which restrict the use of stainless steels.<sup>7</sup> Alloy C-276 has proved to be resistant to chloride-induced stress-corrosion cracking under very aggressive sour-gas conditions, even in the presence of elemental sulfur, but is susceptible to hydrogen-induced stress-corrosion cracking in such media below a temperature of 100 °C.<sup>16</sup> The material's capabilities are also well proven in environmental technology where it has a broad area of use in flue gas desulfurization (FGD).<sup>17</sup> Other important industries in which this type of alloy has become established together with its C-4 variant, which is described in the following section, are listed by Agarwal *et al.*<sup>15</sup> Some details of this material and its corrosion behavior are discussed in the following section in comparison with the other C-alloys.

### 3.05.3.5.3 Alloy C-4

Alloy C-4 (EN 2.4610/UNS N06455) is a variant of alloy C-276, which is in common use in the European chemical industry in particular. As shown in [Table 1](#), it differs from the latter material in the absence of tungsten as an alloying element and greatly reduced iron content. Consequently, the alloy is less resistant in predominantly reducing media, but is much less prone to precipitation and very much easier to work, with the result that, on its commercial launch in the 1970s, it rapidly gained acceptance in the chemical industry. The important chemical industry applications include fertilizer and pesticide production processes and the production of pharmaceutical

intermediates, acetic acid, and inorganic chemicals. In the version without the addition of titanium that is supplied by ThyssenKrupp VDM GmbH, it is free from titanium nitrides. This enables a uniformly smooth surface, which remains smooth, to be obtained in electropolishing and comparable conditions, for example, current feeding rollers in electrolytic plating.

### 3.05.3.5.4 Alloy 22

With alloy 22 (EN 2.4602/UNS 06022), a nickel–chromium–molybdenum alloy typically containing 22 mass% chromium and 13 mass% molybdenum together with 3 mass% tungsten and 3 mass% iron, which was brought into the market in the mid 1980s,<sup>15</sup> a material became available which, owing to the increased chromium content, has better corrosion resistance than do alloy C-276 and alloy C-4 in oxidizing media. However, owing to the reduced molybdenum content, the effect of which can only be partly compensated for by the tungsten addition, it is inferior to alloy C-276 in strongly reducing media and in conditions of extreme crevice corrosion attack.<sup>15</sup> The subsequently developed alloy 59 also exhibits, according to Heubner<sup>6</sup> and the following remarks, a more favorable behavior than does alloy 22 in many respects.

### 3.05.3.5.5 Alloy 59

Alloy 59 (EN 2.4605/UNS N06059), with its composition of 23 mass% chromium and 16 mass% molybdenum, is a considerable advance on alloy 22. This material,<sup>15</sup> which was introduced into engineering practice in the early 1990s, is not only far superior to the other nickel–chromium–molybdenum alloys listed in [Table 1](#) in handling reducing acids, even if contaminated, their main area of application, but has also been successfully qualified for further duties such as the handling of highly corrosive salt solutions resulting from waste water treatment in FGD<sup>18</sup> and control of critical crevice corrosion problems in seawater,<sup>15</sup> including those occurring in plate-type heat exchangers cooled with chlorinated seawater.<sup>19</sup>

Its isocorrosion diagram in aerated technical grade sulfuric acid, plotted using results from immersion tests, is depicted in [Figure 6](#). It shows a broad range of resistance, which, in these test series, falls only slightly below 100 °C up to a concentration of ~60% H<sub>2</sub>SO<sub>4</sub>. The corrosion behavior of alloy 59 in sulfuric acid is not influenced greatly by the amounts of oxidants present in the acid and is also less impaired by the presence of chlorides than is the

corrosion behavior of alloys that are more difficult to passivate.<sup>20</sup>

**Figure 7** depicts the isocorrosion diagram for alloy 59 in hydrochloric acid, also plotted using results from immersion tests. It shows that this material is resistant at all HCl concentrations up to at least 40 °C. This, however, means among other things, that it is corrosion resistant in many organic process media in which hydrochloric acid is formed, which with other materials would lead to corrosion damage.

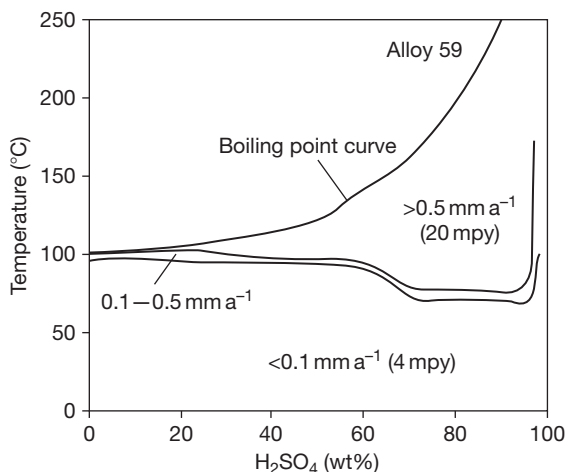


**Figure 6** Isocorrosion diagram of alloy 59 (EN 2.4605/UNS N06059) in slightly aerated technical grade sulfuric acid, determined by immersion tests over at least 120 h. Reproduced from Kirchheiner, R.; Wahl, V. In *Nickel Alloys and Special Stainless Steels*; 3rd ed.; Heubner/Klöwer, et al., Ed.; Expert Verlag: Renningen, 2003; Chapter 8, pp 255–294.

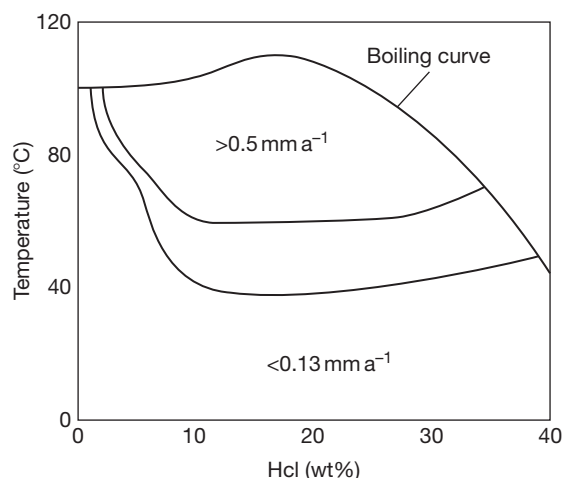


**Figure 7** Isocorrosion diagram for alloy 59 (EN 2.4605/UNS N06059) in hydrochloric acid, determined by static immersion tests.<sup>14,21</sup>

Alloy 59 should also be considered as a very attractive material for handling aerated hydrofluoric acid.<sup>15</sup> Finally, as shown in **Figure 8**, the results of testing in an oxidizing sulfuric acid solution in accordance with ASTM G-28 method A are also of interest. Even though they are not directly relevant to practical use, they illustrate, by way of example, the influence of the chromium to molybdenum plus tungsten ratio on the corrosion behavior of nickel–chromium–molybdenum alloys under oxidizing conditions.<sup>6,21</sup>

The ‘Green Death’ solution (11.5% H<sub>2</sub>SO<sub>4</sub> + 1.2% HCl + 1% FeCl<sub>3</sub> + 1% CuCl<sub>2</sub>), which is widely used for testing the pitting resistance of nickel–chromium–molybdenum alloys and which simulates acidic condensates of the kind that can occur in the flue gas ducts of coal-fired power stations, shows a critical pitting temperature (CPT) of >120 °C for alloy 59, compared with 120 °C for alloy 22, 115–120 °C for alloy C-276, and 100 °C for alloy C-4.<sup>22</sup> The Green Death solution decomposes at temperatures above 120 °C, which means that there is no point in measuring temperatures in excess of 120 °C. However, a further differentiation of the pitting behavior of very high-alloyed materials is enabled by the CaCl<sub>2</sub> test,<sup>23</sup> a potentiostatic holding test at

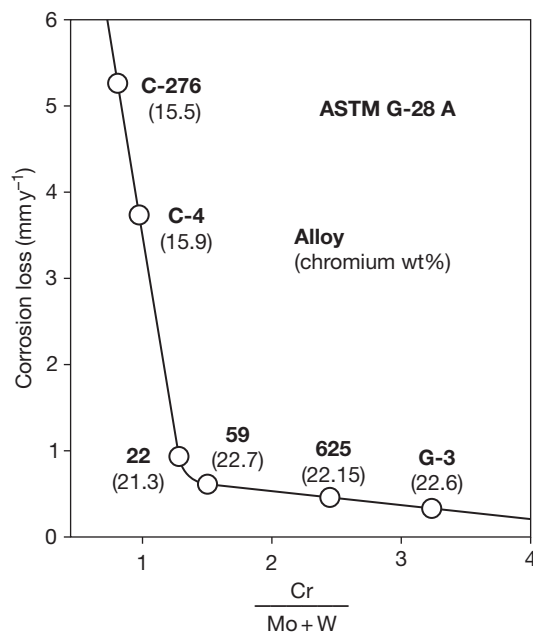


**Figure 8** Corrosion loss of nickel–chromium–molybdenum alloys in boiling 50% H<sub>2</sub>SO<sub>4</sub> with 42 g l<sup>−1</sup> Fe<sub>2</sub>(SO<sub>4</sub>)<sub>3</sub>·9H<sub>2</sub>O in accordance with ASTM G-28 A as a function of their ratio of chromium to molybdenum plus tungsten.<sup>6,21</sup>

0.2  $V_{\text{SCE}}$  in a 4.5 mol  $\text{l}^{-1}$  (500 g  $\text{l}^{-1}$ )  $\text{CaCl}_2$  solution boiling at 115 °C, which for alloy 59 gives a CPT of 100 °C, compared with 83 °C for alloy C-276. A realistic pitting test for FGD is the testing of unwelded and welded specimens at the chloride–pH–temperature matrix intersection  $\text{Cl}^-$  7%/pH 1/ $T$  105 °C, which is described with results in Figure 9 and which likewise shows that the performance of alloy 59 is superior to that of other nickel–chromium–molybdenum alloys.<sup>17</sup>

The time–temperature–sensitization diagram, which is discussed in the following section, shows that alloy 59 is supremely resistant to thermal influences. The harmonious relationship of outstanding corrosion behavior accompanied by good workability is the special distinguishing feature of alloy 59. This alloy is therefore used in many areas of chemical process technology and other process industries,<sup>24</sup> in marine technology,<sup>25</sup> as well as in environmental engineering on a very large scale.<sup>17,26</sup>

### 3.05.3.5.6 Additional C-alloys and thermal stability as a criterion for alloy selection

The additional alloy C variants, which have been brought onto the market since the introduction of alloy 59 are alloy 2000 (EN 2.4675/UNS N06200), which typically contains 23 mass% chromium and 16 mass% molybdenum plus 1.6 mass% copper and 1.5 mass% iron, alloy MAT 21 (UNS N06210) which, as shown in Table 1, typically contains both 19 mass% chromium and molybdenum and 1.8 mass% tantalum in addition, and alloy 686 (EN 2.4606/UNS N06686), which, as shown in Table 1, typically contains 21 mass% chromium, 16 mass% molybdenum and also 3.8 mass% tungsten and 1.5 mass% iron. With respect to alloy MAT 21, insufficient data are available to discuss its localized corrosion behavior and thermal stability. Alloy 2000 clearly attempts to take advantage of the well known influence of copper on the corrosion resistance of

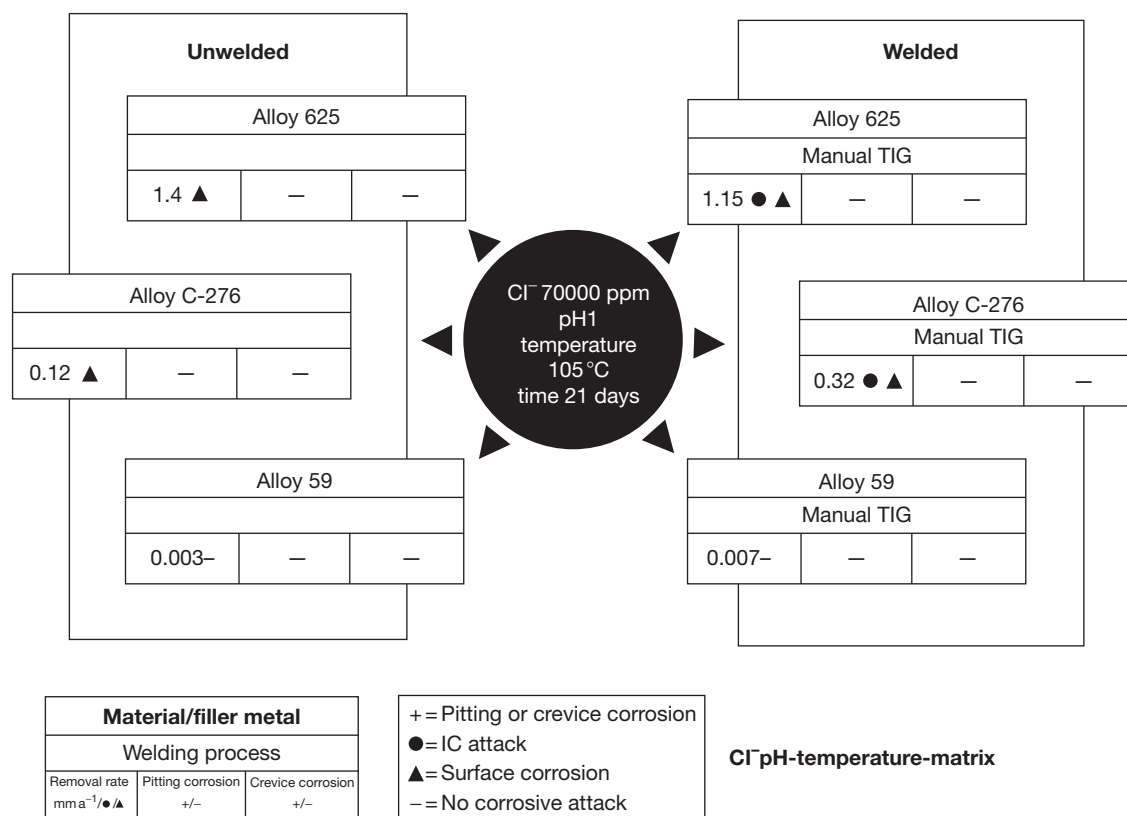


**Figure 9** Comparison of the corrosion behavior of NiCrMo materials in a diluted sulfuric acid-containing solution with 7% chloride addition; base materials unwelded and base materials welded with matching filler metal using the tungsten inert gas (TIG) process; corrosion rate given in  $\text{mm year}^{-1}$ , see legend for local corrosion assessment. Reproduced from Kirchheiner, R.; Wahl, V. In *Nickel Alloys and Special Stainless Steels*; 3rd ed.; Heubner/Klöwer, et al., Ed.; Expert Verlag: Renningen, 2003; Chapter 8, pp 255–294.

nickel alloys and high-alloyed special stainless steels in sulfuric acid.<sup>27</sup> In case of alloy 686, it is evident from the composition that the intention was to shift the best available corrosion resistance more toward reducing conditions. Both alloys achieve their special corrosion behavior at the expense of a thermal stability that is markedly inferior to that of alloy 59, as shown in **Table 3** by reference to the corrosive attack after sensitizing annealing treatment.<sup>15</sup>

The thermal stability of nickel–chromium–molybdenum alloys is an important criterion for their use, for example, in welding of thick-walled vessels where multipass welding is necessary, or in hot deformation of thick cross-sections. A fuller idea of the outstanding thermal stability of alloy 59 compared with alloy 686 and alloy 2000 with reference to the corrosive attack after sensitizing annealing treatment for periods ranging from 0.3 to 10 h at temperatures between 650 and 1000 °C is given<sup>6</sup> in **Figure 10**.

A further comparison is given by the time–temperature–sensitization diagrams<sup>26</sup> as shown in **Figure 11**. It is evident that alloy C-276 is very susceptible to intercrystalline corrosion (IC) under such criteria. In fact, this alloy is neither intended nor suitable for use under the kind of oxidizing conditions that are specified by the test in accordance with ASTM G-28 A. By contrast, alloy 59 performs significantly better under these oxidizing conditions, also in comparison with the other two nickel–chromium–molybdenum alloys C-4 and 22. Sensitization in the sense of an intercrystalline 50 µm depth of penetration IC criterion only begins after 2 h at the earliest. This is an adequate time in practice for avoiding IC after hot-forming, heat treatment, and welding even of thick dimensions.

### 3.05.3.5.7 Alloy 625

Alloy 625 (EN 2.4856/UNS N06625) is listed in **Table 1** as the leanest of the nickel–chromium–molybdenum alloy group. As is evident, it differs from the previously described C-type nickel–chromium–molybdenum alloys in that it is stabilized with niobium. Also, it has the lowest molybdenum content of 9 mass%, and hence the lowest pitting resistance of this group of alloys, but owing to its niobium content, the effect of which is similar to that of molybdenum, it gives the appearance, in terms of its corrosion behavior, of having a somewhat higher alloying content of molybdenum. This alloy was originally developed for high temperature applications, but is now widely used in wet-corrosion service. The isocorrosion diagram for this type of material in sulfuric acid is shown in Craig and Anderson.<sup>7</sup> Its high mechanical strength and good resistance to acids<sup>7</sup> enable the fabrication of thin-walled components with good heat transmission. As can be inferred from the chromium-to-molybdenum ratio and is confirmed by **Figure 8**, its preferred area of use is more on the oxidizing side. It is used in the processing of phosphate ores with fairly high impurity content because of its corrosion and erosion resistance to the phosphate slurries in the digestion reactor and in the evaporation equipment of the final stage.<sup>7</sup> However, in the processing of phosphate ores, alloy 625 is increasingly replaced by alloy 31 (EN 1.4562/UNS N08031), which, due to its higher chromium content, performs much better, and is more cost-effective in addition (cf. **Section 3.05.5.4**). Alloy 31 has increasingly taken the place of alloy 625 in flue gas cleaning too, where alloy 625 was typically used under less aggressive conditions not requiring the use of alloy 59. Also, worthy of mention is the use of alloy 625 for borehole equipment and flow lines under sour-gas conditions.

**Table 3** Thermal stability, stated as corrosion loss in millimeter per year after a sensitizing heat treatment for 1, 3, and 5 h at 87 °C (1600 °F) in tests in accordance with ASTM G-28 A and with ASTM G-28 B, according to data from Agarwal and Herda<sup>15</sup>

Test	Sensitization (h)	Alloy				
		C-276	22	686	C-2000	59
ASTM G-28 A	1	>12.5 <sup>a</sup>	>12.5 <sup>a</sup>	22.2 <sup>a</sup>	3.0 <sup>a</sup>	1.0 <sup>b</sup>
	3	>12.5 <sup>a</sup>	>12.5 <sup>a</sup>	>25.4 <sup>a</sup>	4.5 <sup>a</sup>	1.3 <sup>b</sup>
	5	>12.5 <sup>a</sup>	>12.5 <sup>a</sup>	>25.4 <sup>a</sup>	5.3 <sup>a</sup>	–
ASTM G-28 B	1	>12.5 <sup>a</sup>	8.6 <sup>a</sup>	0.4 <sup>a</sup>	>12.5 <sup>a</sup>	0.1 <sup>b</sup>
	3	>12.5 <sup>a</sup>	8.0 <sup>a</sup>	2.2 <sup>a</sup>	>12.5 <sup>a</sup>	0.1 <sup>b</sup>
	5	>12.5 <sup>a</sup>	>12.5 <sup>a</sup>	>12.5 <sup>a</sup>	>12.5 <sup>a</sup>	0.4 <sup>b</sup>

<sup>a</sup>The alloys C-276, 22, C-2000, and 686 exhibit severe pitting and intercrystalline corrosion with grains dropping out.

<sup>b</sup>Alloy 59 exhibits no pitting.

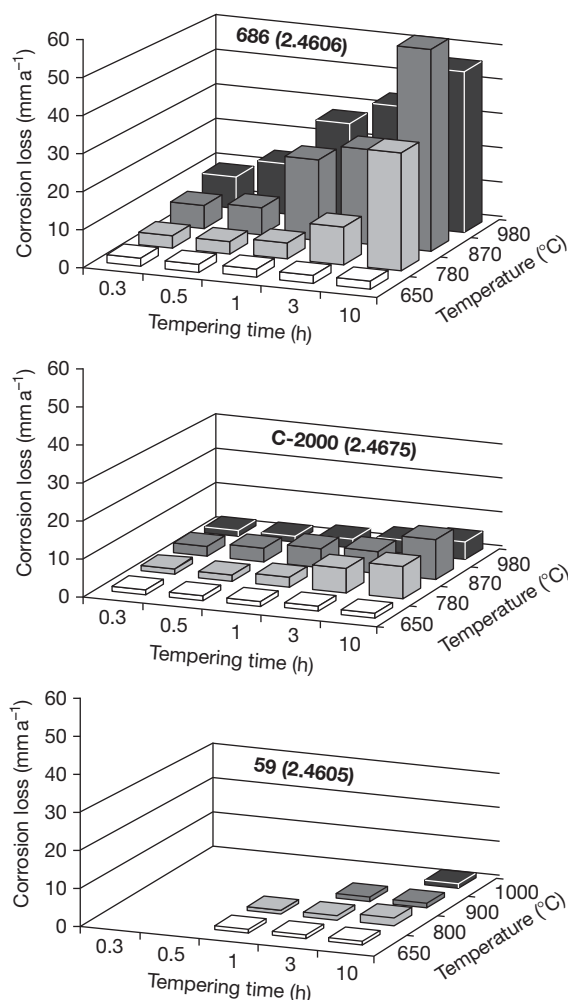


**Figure 10** Thermal stability of alloy 59 (EN 2.4605/UNS N06059) compared with alloys 686 (EN 2.4606/UNS N06686) and 2000 (EN 2.4675/UNS N06200), measured as corrosive attack in tests in accordance with ASTM G-28 A after sensitizing heat treatments for 0.3–10 h at between 650 and 1000 °C. Reproduced from Heubner, U. In *Nickel Alloys and Special Stainless Steels*; 3rd ed.; Heubner/Klöwer, et al., Ed.; Expert Verlag: Renningen, 2003; Chapter 2, pp 47–93.

### 3.05.3.6 Nickel–Chromium–Iron–Molybdenum–Copper Alloys

#### 3.05.3.6.1 General

Nickel–chromium–iron–molybdenum–copper alloys occupy a position between the nickel–chromium–molybdenum alloys and the high-alloy steels. Consequently, they are more limited in their application than the nickel–chromium–molybdenum alloys, but are significantly more corrosion resistant than the popular stainless steels in a large number of industrial

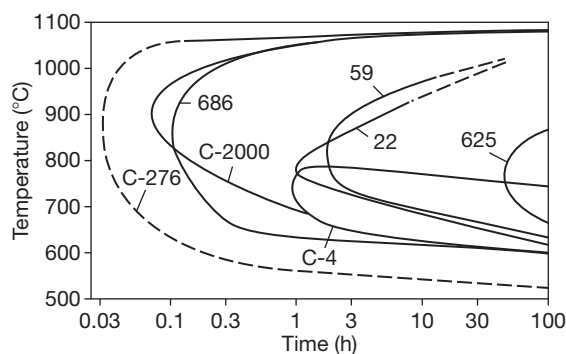


**Figure 11** Time–temperature–sensitization diagrams of various nickel–chromium–molybdenum alloys,<sup>26</sup> established in tests in accordance with ASTM G-28 A.

media. One of their characteristics is that, due to their still relatively high nickel content, they have excellent resistance to stress-corrosion cracking in aqueous and acidic media containing chloride ions. With the exception of alloy 33, these alloys are particularly intended for use in the reducing acids sulfuric acid and phosphoric acid. The alloys in question with their chromium, molybdenum, and tungsten contents in ascending order (cf. Table 1) are alloy 20 (EN 2.4660/UNS N08020), alloy 825 (EN 2.4858/UNS N08825), alloy G-3 (EN 2.4619/UNS N06985), alloy 31 (EN 1.4562/UNS N08031), alloy 33 (EN 1.4591/UNS R20033), and alloy G-30 (EN 2.4603/UNS N06030). Their resistance in sulfuric acid is significantly improved by the alloying addition of copper.<sup>27</sup>

#### 3.05.3.6.2 Traditional materials: Alloys 20, 825, G-3, and G-30

The alloys 20, 825, G-3, and G-30 can be considered traditional materials in that they are making use of titanium or niobium as stabilizing additions in combination with rather high nickel contents. Alloy 825's high stabilization with titanium marks it out as a veteran of material technology, which was developed before the 1960s (cf. Table 2). According to the isocorrosion diagram reproduced in Craig and Anderson,<sup>7</sup> it can be considered resistant to sulfuric acid of all concentrations up to a temperature of at least 50 °C with a corrosion rate of <0.13 mm year<sup>-1</sup>. Its corrosion resistance is further improved by the presence of nitric acid and oxidizing salts.<sup>7</sup> If the requirements are not too stringent, this very traditional yet versatile material can also be used for handling nitric acid and caustic soda solutions.<sup>7</sup> Alloy 20 can be regarded as a variant of alloy 825 with reduced nickel, chromium, and molybdenum



contents but an enhanced copper content. According to the comparative isocorrosion diagram,<sup>7</sup> its corrosion resistance in sulfuric acid is predominantly somewhat lower than that of alloy 825. Alloy 20 is a material of construction for sulfuric and phosphoric acid heat exchangers and pipes, which is in common and widespread use in the United States in particular. Alloy 825, on the other hand, is also used in the offshore sector as a preferred material for heat exchangers, product piping, and conveying pipes. Both the alloys are resistant to hydrofluoric acid of all concentrations at room temperature and at concentrations up to 10% HF at 70 °C.<sup>7</sup>

In view of the pitting resistance equivalent (PRE) relationship, which plays a dominant role here, both alloy 825 and alloy 20 can be expected to exhibit comparatively low resistance to pitting and crevice corrosion in chloride-containing media, including seawater. However, alloy 825 has a remarkably high resistance to chloride-induced stress-corrosion cracking with preceding pitting corrosion in aggressive sour-gas media.<sup>28</sup> Therefore, for this kind of attack, a parameter  $\Sigma = \text{Ni} + 2\text{Mo} + 0.5\text{Cr}$  (for  $\text{Mo} \geq 2.5$ ) calculated as mass% has been tentatively proposed by Rhodes<sup>16</sup> as a measure of alloy resistance in place of the commonly used PRE written for instance<sup>16</sup> as  $\text{PRE} = \text{Cr} + 3.3\text{Mo} + 30\text{N}$ . However, as the PRE shows very clearly, in the case of alloy 825, the fixing of all the available nitrogen by the titanium is not an advantage, and in the case of alloy 20, the high copper content is more likely to have a detrimental effect on its crevice corrosion resistance.<sup>6</sup> This weakness is counteracted by the higher molybdenum content of the variant alloy G-3, which is increased to 7 mass % nominal as shown in **Table 1**. Besides the handling of sulfuric and phosphoric acid, this type of alloy can also be used in acetic acid production<sup>7</sup> and for tubular products in oil and gas extraction. However, there are applications where more advanced materials such as alloy 31 (EN 1.4562/UNS N08031) have been substituted successfully for the traditional alloy G-3, and this change is expected to continue.

Alloy G-30 is a modification of alloy G-3, with increased chromium content and lower molybdenum content. Alloy G-30 has excellent corrosion resistance in commercial phosphoric acids as well as in many complex and mixed acid environments of nitric/hydrochloric and nitric/hydrofluoric acids. The alloy also shows good corrosion resistance to sulfuric acid. Typical applications of alloy G-30 are

in phosphoric acid service, mixed acid service, nuclear fuel reprocessing, components in pickling operations, agrichemicals manufacture, and mining industries.<sup>1</sup>

### 3.05.3.6.3 Advanced materials: Alloys 31 and 33

As shown in **Table 1** the alloys 31 and 33 are a new type of nickel–chromium–iron–molybdenum–copper materials characterized by lower content of nickel in order to save on the cost of raw materials, and instead of stabilizing alloying additions they contain appreciable amounts of nitrogen, which provides increased resistance to pitting corrosion and increased strength. It is for these reasons that they deserve a more detailed presentation.

According to **Table 1**, alloy 31 (EN 1.4562/UNS N08031) with the sum of its alloying elements chromium, molybdenum, and copper is higher than alloy G-3, whereas it is remarkably lower in nickel. In view that the amount of the alloying elements chromium, molybdenum, and copper, to a large extent, determines the corrosion behavior, alloy 31 can be taken as an excellent example for what can be done more with respect to corrosion resistance with less cost of raw materials. The isocorrosion diagram established by means of immersion tests in aerated technical grade sulfuric acid is reproduced in **Figure 12**. However, the presence of oxidants is important for the corrosion resistance of alloy 31 in sulfuric acid at concentrations above ~10%. Therefore, when testing in analytical grade sulfuric acid instead of aerated technical grade sulfuric acid, the 0.1 mm year<sup>−1</sup> isocorrosion line will be shifted to lower temperatures as shown in **Figure 13**, which results from detailed studies.<sup>20</sup> The presence of chlorides will shift the 0.1 mm year<sup>−1</sup> isocorrosion line of alloy 31 to lower temperatures too.<sup>20</sup>

In the production of phosphoric acid, the presence of chlorides, fluorides, oxidizing metal ions, and possibly further corrosion-accelerating impurities such as an influence of erosion or deposit formation should be anticipated depending on the composition of the phosphate ores. This means that for the concentration stage (>50% H<sub>3</sub>PO<sub>4</sub>), only special stainless steels or nickel alloys with very high alloying contents of chromium and molybdenum are suitable. Alloy 31 has been tested for such applications, both in the laboratory and directly in the plant, *inter alia* with specimens that were fixed to the agitating arms of acid digestion tanks as well as with tube specimens that were installed in the concentration units. As is evident from the results reproduced in **Table 4**, alloy



31 exhibits an attractive behavior in comparison with other materials that are commonly used for the production and processing of phosphoric acid. In fact, alloy 31 has proved its capabilities superbly under the particularly aggressive conditions of phosphoric acid production,<sup>29</sup> being probably the most cost-effective alloy to meet these harsh requirements<sup>30</sup> and having thus successfully replaced the higher-alloyed material alloy G-30 (cf. [Table 1](#)) in this application too.<sup>31</sup>

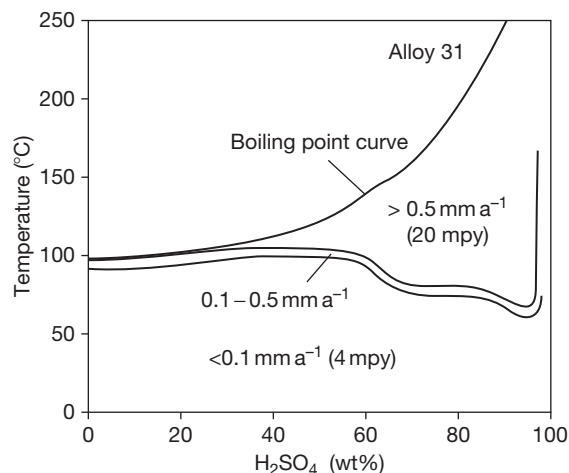


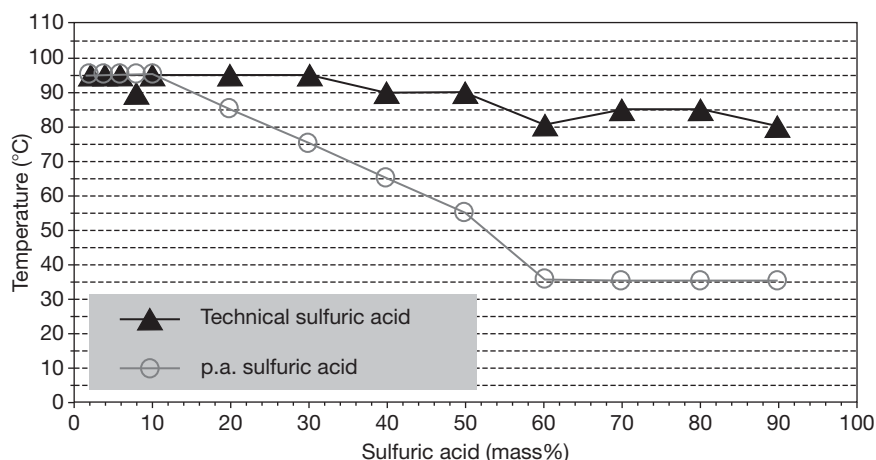
**Figure 12** Isocorrosion diagram of alloy 31 (EN 1.4562/UNS N08031) in slightly aerated technical grade sulfuric acid, determined by immersion tests over at least 120 h. Reproduced from Kirchheiner, R.; Wahl, V. In *Nickel Alloys and Special Stainless Steels*; 3rd ed.; Heubner/Klöwer, et al., Ed.; Expert Verlag: Renningen, 2003; Chapter 8, pp 255–294.

According to the isocorrosion diagram in hydrochloric acid shown in [Figure 14](#), which was established on the basis of immersion tests,<sup>32</sup> alloy 31 is resistant at room temperature up to a concentration of 8% and at 80 °C up to a concentration of ~3% HCl. It may be inferred from this that alloy 31 should have good resistance in chemical processes in which traces of HCl can form.<sup>6</sup>

Alloy 31 (EN 1.4562/UNS N08031) has been tested in 67% boiling HNO<sub>3</sub> solution (Huey test). Even after 10 boiling periods of 48 h each, alloy 31 base material exhibits exceptionally low corrosion rates of 0.11 mm year<sup>-1</sup>, as shown by its position in [Figure 4](#). Notwithstanding its high Mo content, alloy 31 is therefore also outstandingly resistant in strongly oxidizing media.

Alloy 31 (EN 1.4562/UNS N08031) has also been tested under sour-gas conditions (10 bar H<sub>2</sub>S at 232 °C). In this test, the rate of uniform corrosion after 35 days was 0.01 mm year<sup>-1</sup> with no signs of pitting and stress-corrosion cracking at a load of 95% R<sub>p0.2</sub>. Alloy 31 complies with NACE specification MR-0175 (Level VI) and the requirements of the Exxon Slow Strain Rate Test (177 °C, 7 bar H<sub>2</sub>S, 980 MPa).<sup>33</sup>

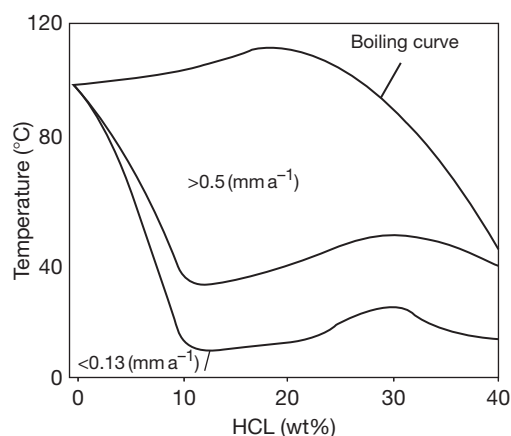
The critical pitting corrosion temperature of alloy 31 is close to the upper 85 °C limit of the of the widely used FeCl<sub>3</sub> test.<sup>17</sup> Therefore, a direct comparison of the pitting corrosion resistance of alloy 31 with the pitting corrosion resistance of higher-alloyed nickel-base materials is better done by testing in a CaCl<sub>2</sub> test solution.<sup>34</sup> The results are demonstrated in [Figure 15](#). In this test, the critical pitting corrosion temperature



**Figure 13** Corrosion resistance of alloy 31 (EN 1.4562/UNS N08031) in sulfuric acid and its dependence on the presence of oxidants in the acid as shown by the position of the 0.1 mm year<sup>-1</sup> isocorrosion lines in aerated technical grade sulfuric acid and in analytical-grade (p.a.) sulfuric acid, as published by Alves *et al.* Reproduced from Alves, H.; Werner, H.; Agarwal, D. C. CORROSION 2006; NACE International: Houston, TX, 2006, Paper No. 06222.

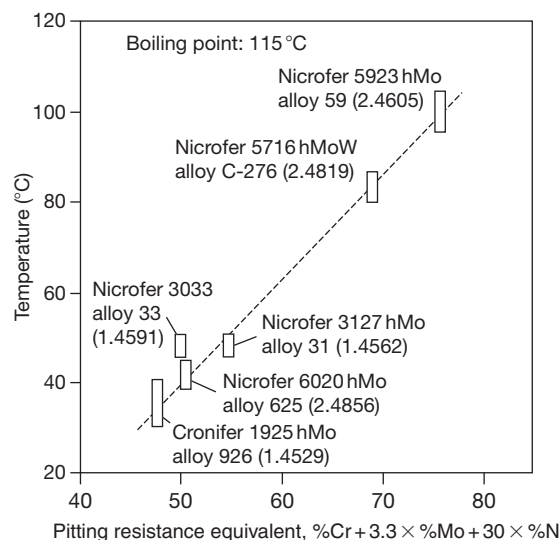
**Table 4** Corrosion loss in millimeters per year of alloy 31 (EN 1.4562/UNS N08031) and other alloys in technologically relevant phosphoric acid solutions,<sup>6</sup> according to data from White *et al.*<sup>29</sup>

Test – Medium	Temperature (°C)	Alloy			
		Alloy 31 (EN 1.4562)	Alloy 926 (EN 1.4529)	Alloy 28 (EN 1.4563)	Alloy G-3 (EN 2.4619)
72% H <sub>3</sub> PO <sub>4</sub> + 4.5% H <sub>2</sub> SO <sub>4</sub> + 0.9% H <sub>2</sub> SiF <sub>6</sub> + 1.5% Fe <sub>2</sub> O <sub>3</sub> + 400 ppm Cl <sup>−</sup>	80	0.02	0.06	0.075	
	120	0.78			
52% P <sub>2</sub> O <sub>5</sub>	116	0.08 <sup>a</sup>		1.2	0.28
42% H <sub>3</sub> PO <sub>4</sub> + 2.4% H <sub>2</sub> SO <sub>4</sub> + 2.3% H <sub>2</sub> SiF <sub>6</sub> + 1% Fe <sub>2</sub> O <sub>3</sub> + 1000 ppm Cl <sup>−</sup>	80	0.015	0.03		
54% P <sub>2</sub> O <sub>5</sub>	116	0.05 <sup>a</sup>		1.4	0.40
54% P <sub>2</sub> O <sub>5</sub> + 2000 ppm Cl <sup>−</sup>	116	2.35 <sup>a</sup>		2.3	0.40
	100	1.30			

<sup>a</sup>Temperature: 120 °C.**Figure 14** Isocorrosion diagram for alloy 31 (EN 2.4605/UNS N08031) in hydrochloric acid, determined by static immersion tests.<sup>14,32</sup>

of alloy 31 (EN 1.4562/UNS N08031) is at ~48 °C, well above the critical pitting corrosion temperature of alloy 625 (EN 2.4856/UNS N06625).

To obtain an initial indication of the relationship between temperature and pitting resistance in chloride-contaminated aqueous media, the pitting potential of alloy 31 (1.4562) was measured in ASTM artificial seawater.<sup>6</sup> The pitting potential is plotted against the temperature in **Figure 16** in comparison with the other two high-alloy materials, alloy 28 (EN 1.4563) and alloy 926 (EN 1.4529). Obviously, the potentials for the two reference materials fall sharply as the temperature rises, whereas for alloy 31 the pitting potential remains almost constantly high, even at temperatures up to 90 °C. This indicates outstanding resistance to pitting in actual media such as seawater, brackish water, and chloride-contaminated cooling water.

**Figure 15** Critical pitting temperatures (CPTs) in the CaCl<sub>2</sub> test as a function of the pitting resistance equivalent (PRE), according to Voigt *et al.*<sup>34</sup>

Besides its pitting resistance, the crevice corrosion resistance of alloy 31 in actual seawater service is also superior to that of the conventional 6% molybdenum steels such as EN 1.4529. As **Figure 17** shows,<sup>14</sup> when used as a flange material, the resistance limits are correspondingly broadened in the direction of higher temperatures and chlorine contents.

With regard to resistance to IC, the time–temperature–sensitization diagram plotted in the test according to ASTM G-28 Method A shows that sensitization in the sense of an intercrystalline 50 μm depth of penetration IC criterion only occurs after 2 h in the temperature range between ~650 and 700 °C.<sup>6</sup> To complement this, individual tests were also carried out on welded specimens (plate thickness

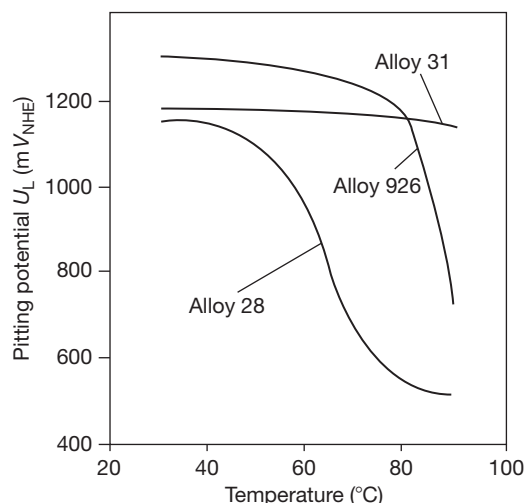


**Figure 16** Pitting potential of three high-alloy corrosion-resistant steels in ASTM seawater, agitated and air-saturated. Reproduced from Heubner, U. In *Nickel Alloys and Special Stainless Steels*; 3rd ed.; Heubner/Klöwer, et al., Eds.; Expert Verlag: Renningen, 2003; Chapter 2, pp 47–93.

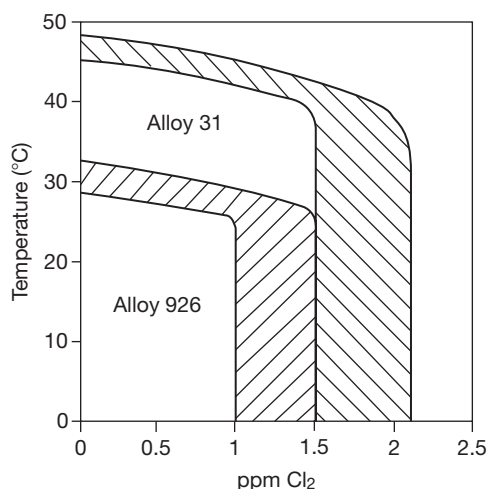


**Figure 17** Stability limits of alloy 926 (EN 1.4529/UNS N08926) when used as a flange material in chlorinated seawater up to the onset of crevice corrosion and their extension when using alloy 31 (EN 1.4562/UNS N08031), determined in tests in realistic conditions (North Sea, Norway), from Heubner. Reproduced from Heubner, U. In *Nickel Alloys and Special Stainless Steels*; 3rd ed.; Heubner/Klöwer, et al., Eds.; Expert Verlag: Renningen, 2003; Chapter 1, pp 1–46.

6 mm) according to both ASTM G-28 Method A (120 h) and SEP 1877 Method II (24 h). The results are compared with those obtained for the two high-alloy special steels EN 1.4529 and EN 1.4563 in

**Table 5** Results of testing of TIG-welded alloy 31 (EN 1.4562/UNS N08031) specimens and reference materials in accordance with (a) ASTM G-28, Method A, 120 h, (b) testing in accordance with SEP 1877, Method II, 24 h. Surface ratio weld metal/base material of the corrosion specimens as 1:6, corrosion loss in millimeters per year, according to data taken from Heubner<sup>6</sup>

(a) ASTM G 28 A	Base material	Welded specimen
Alloy 926 (EN 1.4529)	0.43; 0.37	0.45; 0.58
Alloy 28 (EN 1.4563)	0.18; 0.14	0.20; 0.23
Alloy 31(EN 1.4562/UNS N08031)	0.18; 0.13	0.17; 0.20
(b) SEP 1877 II	Base material	Welded specimen
Alloy 926 (EN 1.4529)	0.13	0.24
Alloy 28 (EN 1.4563)	0.03	0.08
Alloy 31(EN 1.4562/UNS N08031)	0.04	0.05

**Table 5.** In both the tests, alloy 31 (1.4562) exhibits the lowest corrosion rates. The weld metal, HAZ and base metal are all free from IC. Hence, the IC resistance after welding that is required in actual service is guaranteed. It should be noted, however, that in the case of alloy 31 only the carbides that are precipitated at low temperatures manifest themselves in the form of sensitization; this is not the case with the sigma phase, which can form at high temperatures. Particularly after hot-forming work, which is critical for this, such as pressing of heads, a test for pitting resistance and notch impact toughness can indicate more readily than can an IC test whether the material is in perfect condition. This applies to welding as well.

The results of the corrosion tests and service experience to date indicate the following typical areas of application for alloy 31 (EN 1.4562/UNS N08031): equipment for production and the handling of phosphoric acid, pipes, and heat exchangers in contact with sulfuric acid and seawater, components for oil and natural gas extraction under sour-gas conditions, components for the pulp and paper industry, salt manufacturing industry, and, last but not least, flue gas desulphurization, where the use of alloy 31 is preferred especially for regulating and shut-off systems operating under extremely demanding conditions in modern coal-fired power stations. It is also qualified for the evaporation of effluents from flue gas cleaning (first evaporation stage).<sup>18</sup>

While alloy 31 (EN 1.4562/UNS N08031) has a wide-ranging scope for application, alloy 33

(EN 1.4591/UNS R20033) is suitable for specific applications. Although it was originally intended chiefly for use in oxidizing media in view of its high chromium content, it has also proven to be an attractive material for the handling of nonoxidizing acids and alkaline media and for use in chloride-containing aqueous solutions, for instance, seawater.

Alloy 33 exhibits lower corrosion rates in the passive state and a greater ease of passivation in 15–80% sulfuric acid at temperatures between 50 and 90 °C than do the traditional materials alloy 825 (EN 2.4858/UNS N08825) and alloy 20 (EN 2.4660/UNS N08020) that are well established for such applications. As a result, its range of use in the passive condition is broadened in comparison with these materials. Low oxidant contents enable the range of application to be extended to higher acid concentrations and temperatures. For example, as can

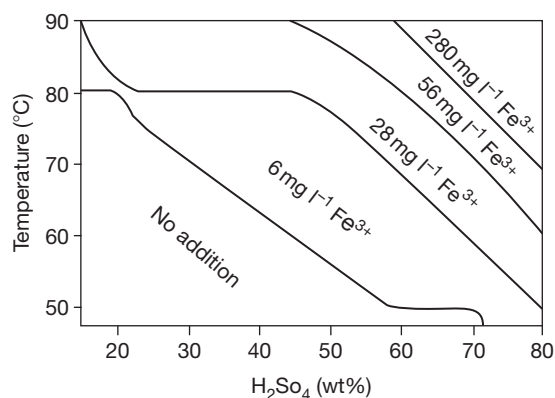


**Figure 18** Corrosion resistance of alloy 33 (EN 1.4591/UNS R20033) in stationary analysis-grade sulfuric acid of medium concentration for corrosion rates  $<0.13 \text{ mm year}^{-1}$  and various additions of  $\text{Fe}^{3+}$  as oxidant, added in the form of  $\text{Fe}_2(\text{SO}_4)_3$ , established using three parallel specimens in each case over a test period of 7 days. Reproduced from Heubner, U. In *Nickel Alloys and Special Stainless Steels*; 3rd ed.; Heubner/Klöwer, et al., Ed.; Expert Verlag: Renningen, 2003; Chapter 2, pp 47–93.

be seen from the corrosion resistance diagram in **Figure 18**,  $\sim 6 \text{ mg l}^{-1} \text{Fe}^{3+}$  is sufficient to allow it to be used in conditions of up to 45%  $\text{H}_2\text{SO}_4$  and 80 °C, and  $\sim 28 \text{ mg l}^{-1} \text{Fe}^{3+}$  is sufficient in order to extend the range of application to 45%  $\text{H}_2\text{SO}_4$  and 90 °C.

In boiling 67% nitric acid (Huey test), alloy 33 exhibits a corrosion loss of only  $0.04 \text{ g m}^{-2} \text{ h}^{-1}$  in tests over  $15 \times 48 \text{ h}$ , and hence has the lowest level of corrosive attack of all known iron–nickel–chromium alloys under these corrosive conditions, as shown in **Figure 4**. On the basis of the results of extensive corrosion testing for up to 100 days, the alloy can be regarded as corrosion resistant, even in the welded state, at a  $\text{HNO}_3$  concentration of up to 95% at 25 °C, up to 90%  $\text{HNO}_3$  at 50 °C, up to slightly below 85%  $\text{HNO}_3$  at 75 °C, and in 67%  $\text{HNO}_3$  up to boiling point.<sup>13</sup> Alloy 33 is also of interest for handling nitric–hydrofluoric acid mixtures, as shown by the test results in **Tables 6** and **7**. It is therefore an attractive material not only for nuclear fuel reprocessing, but in particular for lining of pickling tanks for stainless steels.

The corrosion behavior of alloy 33 in highly concentrated sulfuric acid has been comprehensively tested.<sup>35–37</sup> **Figure 19** reproduces the isocorrosion diagram of alloy 33 for corrosion losses of 0.1 and 0.5 mm  $\text{year}^{-1}$  in stationary highly concentrated industrial-grade sulfuric acid according to the data given in Renner and Michalski-Vollmer.<sup>36</sup> It is evident that toward lower sulfuric acid concentrations, there are obviously two different corrosion mechanisms at work, depending on the temperature, which have their maximum reaction rates at  $\sim 110$  and  $\sim 190$  °C, respectively. However, under different test conditions and especially with a different test period, the situation may differ<sup>37</sup> from that shown in **Figure 19**, making the small window of corrosion resistance even narrower. Therefore, for practical applications, prior corrosion tests under the specific operating conditions are strongly advised.

It is not only in oxidizing acids and in reducing acids, whose composition has been sufficiently adjusted

**Table 6** Results of corrosion testing of alloy 33 (EN 1.4591/UNS R20033) and other materials for comparison in nitric/hydrofluoric acid solutions, immersion tests over 21 days at 90 °C, corrosion loss in grams per square meter per hour, according to data taken from Heubner<sup>6</sup>

Alloy	12% $\text{HNO}_3$			0.4% $\text{HF}$			
	+0% $\text{HF}$	+0.9% $\text{HF}$	+3.5% $\text{HF}$	+32% $\text{HNO}_3$	+44.5% $\text{HNO}_3$	+56% $\text{HNO}_3$	+67.5% $\text{HNO}_3$
28 (EN 1.4563)	<0.01	5.74	20.74	0.96	1.78	3.38	5.46
690 (EN 2.4642)	<0.01	0.61	6.34	1.46	1.97	4.69	7.42
G-30 (EN 2.4603)	<0.01	0.28	1.21	0.49	1.45	2.39	4.49
33 (EN 1.4591)	<0.01	0.24	1.19	0.27	0.67	1.66	3.08

**Table 7** Results of corrosion testing of alloy 33 (EN 1.4591/UNS R20033) and other materials for comparison in 20% nitric acid solutions with additions of 3, 5, and 7% hydrofluoric acid, immersion tests over 21 days at 25 and 50 °C, corrosion loss in grams per square meter per hour, according to data taken from Heubner<sup>6</sup>

Alloy	25 °C			50 °C		
	+3% HF	+5% HF	+7% HF	+3% HF	+5% HF	+7% HF
316 Ti (EN 1.4571)	3.33	6.20	5.68	17.3 <sup>a</sup>	24.4 <sup>a</sup>	33.45 <sup>a</sup>
28 (EN 1.4563)	0.03	0.04	0.06	0.18	0.29	0.41
33 (EN 1.4591)	0.01	0.01	0.02	0.08	0.11	0.17

<sup>a</sup>Duration of test: 7 days.

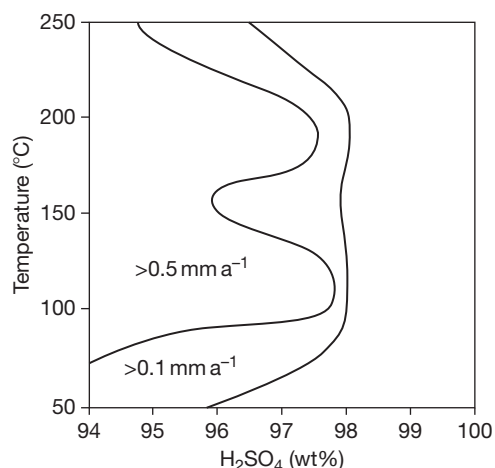


**Figure 19** Isocorrosion diagram for alloy 33 (EN 1.4591/UNS R20033) in stationary highly concentrated industrial grade sulfuric acid,<sup>6</sup> based on the data established by Renner *et al.*<sup>36</sup> over a test period of 21 days.

to oxidizing, that alloy 33 exhibits a corrosion behavior that is attractive for practical applications of many kinds; this also applies to alkaline media. For example, a corrosion loss of  $<0.01 \text{ mm year}^{-1}$  was measured in 25% and 50% caustic soda solution up to the boiling point.<sup>35</sup> Even for 70% caustic soda at 170 °C, a corrosion loss of only  $0.03 \text{ mm year}^{-1}$  is stated.<sup>38</sup> To complement this, field tests were carried out in NaOH tanks with added chlorine, the specimens therefore being exposed to both the liquid and the vapor phase. The material performed faultlessly, with only slight signs of crevice corrosion.<sup>6</sup> In a further field test with chloride- and chlorate-contaminated caustic soda from the diaphragm cell process, an outstanding resistance was measured,<sup>39</sup> as reported in Section 3.05.5.2.

The resistance of alloy 33 to pitting, which has been comprehensively tested<sup>34</sup> with regard to the handling of chloride-containing cooling water and use in seawater, is comparable with that of alloy 31 (EN 1.4562/UNS N08031), alloy 31 tending to

**Table 8** Critical pitting temperatures (CPT) and crevice corrosion temperatures (CCT), established in  $\text{FeCl}_3$  tests,<sup>34</sup> indicating the pitting resistance equivalent (PRE) as  $\% \text{ Cr} + 3.3 \times \% \text{ Mo} + 30 \times \% \text{ N}$

Alloy	EN	UNS	PRE	CPT (°C)	CCT (°C)
20	2.4660	N08020	28.3	15	<5
825	2.4858	N08825	33	30	<5
904L	1.4539	N08904	37	45	25
926	1.4529	N08926	47	70	40
33	1.4591	R20033	50	85	40
31	1.4562	N08031	54	>85	65

perform somewhat better. This is made clear by the results of the  $\text{FeCl}_3$  test shown in Table 8. In the  $\text{CaCl}_2$  test, on the other hand, both alloys have practically the same CPT, as is evident from Figure 15.

In terms of crevice corrosion resistance, on the other hand, alloy 33 (EN 1.4591/UNS R20033) is comparable with alloy 926 (1.4529/UNS N08926), as is again evident from Table 8. This confirms that higher nitrogen contents have a lesser effect on the crevice corrosion resistance than on the pitting resistance, in accordance with the data in Kirchheiner and Wahl<sup>17</sup> for the material EN 1.4565. Alloy 33 and alloy 926 can also be rated equally with regard to their repassivation potential in the case of crevice corrosion in seawater according to Voigt *et al.*<sup>34</sup> Combined with its high strength, excellent ductility, and high resistance to stress-corrosion cracking, even under sour-gas conditions,<sup>40</sup> possibilities for application in seawater and offshore service are therefore open to alloy 33.

In conclusion, it should be noted that alloy 33 (EN 1.4591/UNS R20033) exhibits a high degree of thermal stability. During ageing between 700 and 900 °C, its notch impact toughness decreases slightly because of precipitation of sigma phase, but nevertheless still exceeds 100 J even after a tempering time of 8 h. When tested for sensitization in boiling azeotropic nitric acid (Huey test), there are no signs of

either grain boundary attack or an increase in the rate of uniform corrosion even after tempering for up to 1000 h.<sup>35</sup>

### 3.05.3.7 Age-Hardenable Nickel–Chromium–Iron–Molybdenum (–Copper) Alloys

Positioned at the bottom of **Table 1** is an alloy group consisting of two important age-hardenable nickel–chromium–iron–molybdenum (–copper) alloys. They are used for bars, tools, pump shafts, valves, and forgings in oil and gas production where low weight and hence high strength is a requirement. Their high mechanical strength is achieved by so-called age-hardening in an intermediate range of temperatures where intermetallic phases are precipitating within the metallic matrix, causing an increase of strength. Alloy 925 (EN 2.4852/UNS N09925) is the age-hardenable version of alloy 825 (EN 2.4858/UNS N08825), with an almost identical corrosion behavior (cf. **Section 3.05.3.6.2**). Alloy 718 (EN 2.4668/UNS N07718), however, has its origin in high temperature/high-strength applications and has been adapted very successfully for the wet corrosive requirements of oil and gas extraction.

## 3.05.4 Corrosion Behavior of Nickel Alloys in the Welded State

### 3.05.4.1 The Specific Surface and Structural Condition of the Weld Metal and the HAZ

In chemical, environmental, power, and marine engineering, welding is the most popular joining method. In these fields, there are very few material applications where welding is not required. The corrosion resistance that is determined for a material in its various mill product forms should therefore generally apply to this material in the welded state as well, that is, to the weld metal and the whole area of the weld. The weld area of a construction may well be the location of preferential corrosive attack, because here – in contrast to the homogeneous solution-annealed or stabilized and subsequently (if necessary) shot-blasted and pickled state – a clean, bright metal surface may not be obtained easily. Instead, the weld may have slag residues or may be oxidized depending on the welding process used. The adjacent HAZ is also likely to be coated with surface oxides to varying extents, which are generally recognizable as temper colors. A lookout should also be kept for spatter and contamination away from the weld, which are usually

detrimental to corrosion resistance. Moreover, in the weld area the microstructure is heterogeneous not only in the weld metal with its cast structure, but often also in the HAZ directly adjoining the weld. The extent of the structural changes caused by the welding operation in the HAZ depends on the material and its susceptibility to precipitation of carbides and intermetallic phases at medium temperatures, as well as on the heat input and the rate of cooling during welding. Problem-free welding of a material by means of the particular welding process is only possible if welding techniques and welding parameters can be used to keep the heat input so low that the agreed testing methods fail to discover any intolerable structure-related impairment of the corrosion behavior and the mechanical properties in the HAZ. Moreover, care should be taken where necessary to ensure, by appropriate posttreatment of the surface, that any scale and any surface oxides manifesting themselves as temper colors do not adversely affect the material's corrosion behavior.

Some possible defects in the weld area are depicted schematically in **Figure 20**. Slag residues

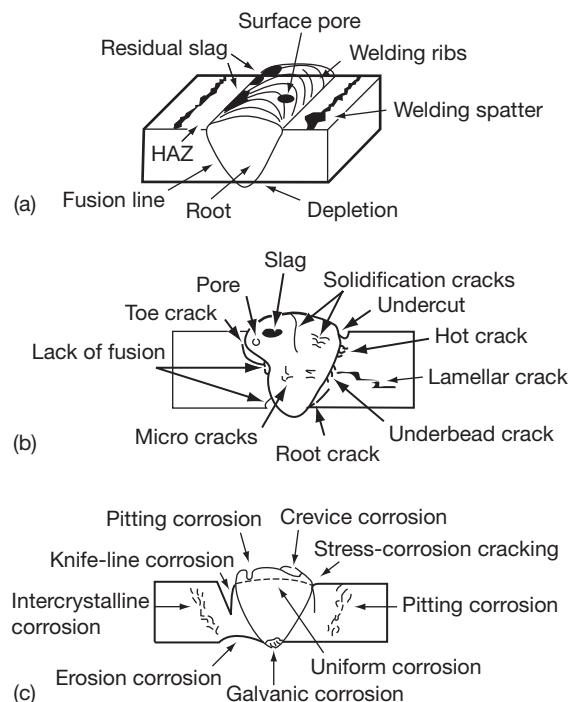


**Figure 20** Possible defects in the weld area and their effects on corrosion behavior, from Heubner. Reproduced from Heubner, U. In *Nickel Alloys and Special Stainless Steels*; 3rd ed.; Heubner/Klöwer, et al., Ed.; Expert Verlag: Renningen, 2003; Chapter 2, pp 47–93.



on the surface of the weld are sites of preferential attack, because they offer ideal conditions for crevice corrosion and pitting. The same applies to pores, which, in the form of solidification porosity, cannot be ruled out for nickel alloys, but can be controlled by alloying techniques with respect to the filler metal or by other welding engineering measures. An excessively rough material surface (ribbed texture), edge misalignment, or severe cases of drop-through chiefly allow room for the formation of sediments, deposits, and incrustations, which, acting like a sponge, result in local concentrations of corrosive media constituents such as chloride ions that can lead to localized corrosion. Solidification cracks, hot cracks, weld undercuts, weld interface, and root cracks and incomplete root fusion are ideal locations for crevice corrosion attack. With materials that require a higher-alloyed filler metal, unmixed fusion zones in the root area, but also on the capping pass side, can be sites of preferential corrosive attack. High mechanical stresses in the weld area, including thermally caused stresses, may result in an increased likelihood of stress-corrosion cracking, depending on the material and the surrounding medium. A rough-ribbed structure of the weld metal can also contribute to this on account of the stress peaks, which then arise.

#### 3.05.4.2 Surface Condition and Necessary Surface Treatment after Welding

Oxide layers on the weld metal and oxides over the HAZ, which manifest themselves as temper colors, weaken the resistance of nickel alloys to pitting. As known from stainless steels,<sup>6</sup> the differences in corrosion resistance may be greatest between pickled surfaces and those with 'light,' that is, straw-yellow temper colors. As temper colors become darker, corrosion resistance further decreases. The surface oxide layers either consist almost exclusively of chromium oxide,  $\text{Cr}_2\text{O}_3$  (spinel type)<sup>41</sup> or are, at any rate, generally significantly enriched with chromium.<sup>42</sup> The chromium required for oxide formation is extracted from the matrix of the material, which consequently becomes depleted in chromium. As the resistance of nickel–chromium–molybdenum alloys to pitting is almost exclusively determined by their chromium and molybdenum contents, a decrease in the chromium content is synonymous with reduced resistance to this type of corrosion.<sup>41</sup> There is even a strong possibility that immediately beneath the oxide coating, there is a thin metallic surface layer, which no

longer corresponds to the intended material grade at all. Therefore, it is understandable that in such a case, simply removing the temper colors may not be sufficient to restore the resistance of the unwelded base material; it may in fact be necessary to remove the chromium-depleted metallic surface layer lying immediately beneath them at the same time. In practice, the situation may become really problematic, for the technical corrosion resistance of a material depends less on the pitting potential than on the lower repassivation potential, because it is only below this repassivation potential that pitting, once begun, can be stopped again.

In industrial engineering practice, therefore, full-immersion pickling of welded components is recommended for critical situations. This, however, is feasible only in certain cases and to a limited extent. Moreover, its success depends on the material and on the pickling method employed. As a rule, it is necessary to use a different means for removing the surface oxides. In modern fabrication practice, the methods of *in situ* pickling of the component, abrasive blasting, and grinding are mainly used. The effectiveness of each of these measures was investigated by, among other things, measuring the critical pitting potential in artificial seawater.<sup>43,44</sup> It turned out that, among the methods of grinding with disc wheels, blasting with glass beads and pickling with  $\text{HNO}_3/\text{HF}$  pickling pastes, grinding was the least effective – at least with a very rough finish – and the best results were obtained with the pickling pastes. For the some types of stainless steels, the results of the investigation show that when using the pickling pastes, it is at best possible to obtain a corrosion resistance that is virtually equivalent to that of the metal in the bright, unwelded state. On the other hand, in the case of higher-alloyed materials such as alloy 625 (EN 2.4856/UNS N06625), there was only a slight dependence of the corrosion resistance on the method of surface treatment. With this material, the pickling action achieved was insufficient to remove not only the oxide coating but also an adequate amount of the chromium-depleted metallic surface layer beneath it, because even in a chromium-depleted surface condition, this material is too corrosion-resistant in relation to the pickling agent for this to be achieved within the treatment time. This is true not only of treatment with pickling paste, but has also been observed with nickel–chromium–molybdenum alloys in the case of post-treatment by immersion or spray pickling.

Consequently, brushing of welds with a stainless steel wire brush immediately after welding while

the metal is still hot, at the least, is vital in order to remove surface contamination, slag residues, and temper colors to the greatest possible extent. Subsequent pickling is then likely to produce a further marked improvement in corrosion resistance, but mechanical removal of the chromium and molybdenum-depleted metallic surface might be an additional requirement in case of very corrosion-resistant materials when used near to the limit of their corrosion resistance. The highest resistance to pitting is obtained with electrochemical polishing. If there are doubts regarding the nature and extent of postweld treatment, the testing of expertly executed and experimentally posttreated welded joints in a manner which corresponds or at least approximates to the level of corrosive attack in practice is essential.

### 3.05.4.3 IC in the HAZ

In chromium-alloyed nickel-base materials, with a sufficiently high carbon content of the HAZ adjacent to a welded joint, preferential precipitation of chromium carbides at the grain boundaries may occur, with the consequence of chromium depletion in the region near the grain boundaries. This may go so far that under corrosive attack, adequate corrosion resistance no longer exists in this region, and IC occurs. This can also take the form of pitting along the grain boundaries; it is then referred to as sensitization. In the case of the chromium-alloyed nickel-base materials for wet-corrosion service that are the focus of interest here, only LC grades or stabilized materials are in use today; as a result, IC, owing to simple precipitation of chromium carbide, only rarely comes up for discussion in the case of these materials—for instance, if it is necessary to consider a high temperature material with a high carbon content, such as the nickel–chromium alloy 600 (EN 2.4816/UNS N06600) with regard to temporary service under wet-corrosion conditions (e.g., shutdown dew point corrosion and during cleaning) among other factors.

However, in the case of the chromium-alloyed nickel-base materials, IC in the HAZ of welded joints may well be a matter, which requires consideration owing to the precipitation of intermetallic phases, including the  $M_6C$  type of carbide. On the other hand, the sigma phase, which is precipitated in, for example, the nickel–chromium–iron–molybdenum–copper alloy 31 (EN 1.4562/UNS N08031) in the medium temperature range<sup>45</sup> leads, when tested in the conventional tests according to ASTM G 28 A or SEP 1877 II, not to IC but to an increased

susceptibility to pitting;<sup>46</sup> however, this does not usually cause problems in fabrication by welding.

Figure 11 shows a summary of the time–temperature–sensitization diagrams that have been plotted for nickel–chromium–molybdenum alloys.

Leaving aside the more stringent Strauss test, which is little used, the test methods employed for IC testing of high-alloyed materials range from the Huey test, which specifies very strongly oxidizing conditions, *via* the Streicher test in accordance with ASTM G 28 A, which likewise specifies oxidizing conditions, to – with decreasing aggressiveness – the testing of nickel–molybdenum alloys in hydrochloric acid. However, there is no standardized method of IC testing for slightly oxidizing conditions, which would be typical of the corrosive conditions to which nickel–chromium–molybdenum alloys are frequently exposed, for example, in the aqueous media encountered in FGD plants of fossil-fired power stations. To fill this gap, the anodic polarization behavior of welded nickel–chromium–molybdenum alloys in solutions containing sulfuric acid with the addition of anions with a structure-specific effect, such as  $SCN^-$  and  $Cl^-$ , was investigated.<sup>47</sup> The results showed that in the transitional active/passive range of the materials, it is actually possible to distinguish between the behavior of different heat treatment states with regard to IC of the HAZ and pitting-like selective corrosion of the weld metal, which also occurs under these test conditions. In such a test, after welding with a heat input in excess of  $8 \text{ kJ cm}^{-1}$ , the tendency for increased IC within the HAZ and for selective corrosion of the weld metal is most marked in the case of alloy C-276, followed by alloy C-4. With the alloy 59 (2.4605), any influence of the heat input during welding only becomes noticeable if the values for the energy inputs per unit length of weld are as extreme as  $6.2 \text{ kJ cm}^{-1}$  on the one hand, or  $15.1 \text{ kJ cm}^{-1}$  on the other. In this respect too, therefore, alloy 59 (EN 2.4605/UNS N06059) proves to be the least susceptible nickel–chromium–molybdenum alloy.

### 3.05.4.4 Resistance of Weld Metal and Heat Affected Zone to Pitting

The cast structure of the weld metal and the associated segregations have widely differing effects on corrosion resistance, depending on the material and the surrounding medium. Because of this, unalloyed nickel and the nickel–copper, nickel–molybdenum, and nickel–chromium alloys are welded with fillers of identical or at least similar composition to the base

metal; here, peculiarities in the chemical composition of the filler metals have more to do with the technical requirements of the welding operation than with the demands of corrosion resistance.

If nickel–chromium–molybdenum alloys are welded with filler of identical composition to the base metal, practical experience clearly shows that the identical-composition weld metal generally has the same high corrosion resistance, in spite of its heterogeneous nature,<sup>22</sup> as the homogeneous austenitic base metals, at least below certain threshold conditions of attack. Electrochemical tests in oxidizing ASTM G-28 A solution have revealed only minor differences, the weld metal, in fact, having a more noble corrosion and passivation potential.<sup>48</sup> Potential profiles relating to joint welding of nickel–chromium–molybdenum alloys with filler of the same composition as the base metal show no or only slight differences between the wrought alloy and the weld metal.<sup>49</sup> However, marked differences arise in the testing of the pitting resistance. For instance, in the ‘Green Death’ test<sup>23</sup> the CPT established for the weld metal of FM 625 (EN 2.4831/UNS N06625) was on average  $\sim 12$  K lower than that established for the corresponding homogeneous austenitic material alloy 625 (EN 2.4856/UNS N06625), and for the weld metal of FM C-276 (EN 2.4886/UNS N10276) the CPT was on average  $\sim 18$  K lower than that of the corresponding homogeneous austenitic material alloy C-276 (EN 2.4819/UNS N10267).<sup>23</sup> In the  $\text{CaCl}_2$  test,<sup>23</sup> which is more sensitive and can be used over a wider range of alloys, this difference is on average c. 25 K for alloy C-276 (EN 2.4819/UNS N10267).<sup>23,50</sup> If the actual conditions of service make it necessary to do so, for example, as a result of realistic tests in the chloride/pH/temperature matrix (cf. Figure 9), it is probable, based on the test results available so far,<sup>22,23</sup> that the reduced corrosion resistance of the weld metal of FM 625 and FM C-276, as shown by the ‘Green

Death’ test,<sup>23</sup> can be avoided by instead using FM 59 (EN 2.4607/UNS N06059) as filler metal.

A good guide to the anticipated behavior of materials on welding is also given by cooling tests at different rates from the solution-annealing temperature.<sup>46</sup> Table 9 shows the results obtained from tests with alloy 31 (EN 1.4562/UNS N08031). This alloy should preferably be solution-annealed at 1150–1180 °C. If the CPT in the HAZ, to be measured in the  $\text{FeCl}_3$  test, must not fall below 75 °C, the cooling rate in the range between the solution-annealing temperature and 600 °C should, according to these test results, be at least 150 °C  $\text{min}^{-1}$ . The associated notch impact energy values, which are often of interest to the design engineer, are also shown in Table 9 for comparison. It is interesting to note that in this case the notch impact energy does not fall in parallel with the pitting resistance, but initially rises; this has been observed, to a far greater extent, with alloy 926 (EN 1.4529/UNS N08926) as well in the case of isothermal ageing.<sup>51</sup>

### 3.05.5 Application of Nickel and Nickel Alloys as Materials Resistant to Aqueous Corrosion in the CPI and in Environmental Technology

#### 3.05.5.1 General

The CPI and environmental technology have to cope with a large variety of adverse operating conditions, including a wide range of temperatures, all kinds of static and dynamic loads, as well as numerous solid, liquid, and gaseous products and product mixtures. Safety, cost-efficiency, and even the feasibility of a process depend on whether the materials envisaged for the plant and its components can handle the required range of different operating conditions.

Nickel and nickel alloys are needed in all areas of halogen chemistry/chlorine chemistry to withstand both general and localized forms of corrosion. Further applications can be found in chemical processes involving alkalis (e.g., caustic soda) or acids (e.g., sulfuric acid and acetic acid) at different concentrations and temperatures. These high corrosion-resistant materials are well established in wide areas of chemical processing, and in the following section, some selected examples of their application are presented.

Beyond the scope of the CPI and environmental technology, nickel alloys are finding wet corrosive applications in many other industrial sectors, for example, marine technology<sup>14</sup> and oil and gas extraction.<sup>28,33</sup>

**Table 9** Influence of the cooling rate from the solution-annealing temperature down to 600 °C on the CPT to be measured in the  $\text{FeCl}_3$  test and the notch impact energy ( $A_v$ ) of alloy 31 (EN 1.4562/UNS N08031)<sup>6,46</sup>

Condition	CPT (°C)	$A_v$ (J)
Solution-annealed	85	266
At 150 °C $\text{min}^{-1}$ to 600 °C	75	270
At 50 °C $\text{min}^{-1}$ to 600 °C	70	280
At 25 °C $\text{min}^{-1}$ to 600 °C	55	240

### 3.05.5.2 Production of Caustic Soda

Caustic soda (NaOH) is one of the most important chemical feedstocks, with a total annual production of  $10^6$  tons. NaOH is used in organic chemistry, in the production of aluminum, in the paper industry, in the food processing industry, in the manufacture of detergents, etc. Caustic soda is a coproduct in the production of chlorine, 97% of which takes place by the electrolysis of sodium chloride.

Caustic soda has an aggressive impact on most metallic materials, especially at high temperatures and concentrations. It has been known for a long time, however, that nickel exhibits excellent corrosion resistance to caustic soda at all concentrations and temperatures, as shown by **Figure 1**. In addition, except at very high concentrations and temperatures, nickel is immune to caustic-induced stress-corrosion cracking. The nickel standard grades alloy 200 (EN 2.4066/UNS N02200) and alloy 201 (EN 2.4068/UNS N02201) are therefore used at these stages of caustic soda production, which require the highest corrosion resistance. The cathodes in the electrolysis cell used in the membrane process are made of nickel sheets as well. The downstream units for concentrating the liquor are also made of nickel. They operate according to the multistage evaporation principle mostly with falling-film evaporators. In these units, nickel is used in the form of tubes or tube sheets for the preevaporation heat exchangers, as sheets or clad plates for the preevaporation units, and in the pipes for transporting the caustic soda solution. Depending

on the flow rate, the caustic soda crystals (super-saturated solution) can cause erosion on the heat exchanger tubes, which makes it necessary to replace them after an operating period of 2–5 years. The falling-film evaporator process is used to produce highly concentrated, anhydrous caustic soda. In the falling-film process developed by Bertrams, molten salt at a temperature of  $\sim 400^\circ\text{C}$  is used as the heating medium. Here, tubes made of low-carbon nickel alloy 201 (EN 2.4068/UNS N02201) should be used, because at temperatures higher than  $\sim 315^\circ\text{C}$  ( $600^\circ\text{F}$ ), the higher carbon content of the standard nickel grade alloy 200 (EN 2.4066/UNS N02200) can lead to graphite precipitation at the grain boundaries. Nickel is the preferred material of construction for caustic soda evaporators where the austenitic steels cannot be used. In the presence of impurities such as chlorates or sulfur compounds – or when higher strengths are required – chromium-containing materials such as alloy 600 L (EN 2.4817/UNS N06600) are used in some cases. Also of great interest for caustic environments is the high-chromium-containing alloy 33 (EN 1.4591/UNS R20033). If these materials are to be used, it must be ensured that the operating conditions are not likely to cause stress-corrosion cracking. Alloy 33 (EN 1.4591/UNS R20033) exhibits excellent corrosion resistance in 25% and 50% NaOH up to boiling point and in 70% NaOH at  $170^\circ\text{C}$ . This alloy also showed excellent performance in field tests in a plant exposed to caustic soda from the diaphragm process.<sup>39</sup> **Figure 21**

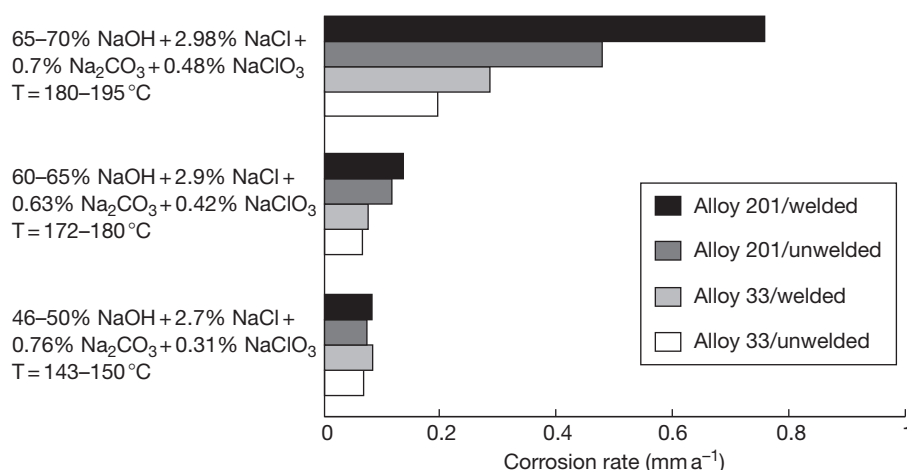


**Figure 21** Corrosion rates of alloy 33 (EN 1.4591/UNS R20033) and low carbon nickel alloy 201 (EN 2.4068/UNS N02201) after almost 3 months of exposure to diaphragm caustic soda contaminated with NaCl, Na<sub>2</sub>CO<sub>3</sub>, and NaClO<sub>3</sub> in various ranges of concentrations and temperatures. Reproduced from Alves, H.; Horn, E. M.; Klöwer, J. In *Nickel Alloys and Special Stainless Steels*; 3rd ed.; Heubner/Klöwer, *et al.*, Ed.; Expert Verlag: Renningen, 2003; Chapter 7, pp 226–254.

shows some results regarding the concentration of this diaphragm caustic liquor, which was contaminated with chlorides and chlorates. Up to a concentration of 45% NaOH, the materials alloy 33 (EN 1.4591/UNS R20033) and nickel alloy 201 (EN 2.4068/UNS N02201) show a comparable outstanding resistance. With increasing temperature and concentration, alloy 33 becomes even more resistant than nickel. Thus, as a result of its high chromium content, alloy 33 seems to be advantageous to handle caustic solutions with chlorides and hypochlorite from the diaphragm or mercury cell process.

### 3.05.5.3 Production and Handling of Sulfuric Acid

Sulfuric acid ( $\text{H}_2\text{SO}_4$ ) is one of the basic raw materials for the chemical industry. It is used in numerous processes as a reagent, as a catalyst, and as a drying agent. Examples of the wide-ranging applications of this acid include the treatment of raw phosphates in the fertilizer industry, the treatment of titanium ores for the production of titanium dioxide, the manufacture of phosphoric and hydrofluoric acid, and the wide field of organic chemical synthesis, for example, in sulfonation and nitration.

Today, primarily elemental sulfur but also pyrite is used as raw material for the production of sulfuric acid. Combustion produces sulfur dioxide ( $\text{SO}_2$ ) which is subsequently converted catalytically to form sulfur trioxide ( $\text{SO}_3$ ) and thereafter is absorbed in concentrated sulfuric acid, usually in several stages. The absorption of  $\text{SO}_3$  in concentrated sulfuric acid takes place in packed towers. Absorption occurs in a counter-current system, the  $\text{SO}_3$  gas flowing upwards and the concentrated sulfuric acid flowing downwards. This process is highly exothermic.

So far, only a few materials were available which offer adequate corrosion resistance to highly concentrated sulfuric acid at high temperatures. As a result, the operating temperatures for the downstream equipment such as heat exchangers, pumps, and piping had to be reduced. For components operating at these lower sulfuric acid temperatures, various special materials are used. The nickel alloy C-276 (EN 2.4819/UNS N10276) is used for plate-type heat exchangers serving as acid coolers. Alloy 59 may also be used for this purpose. The isocorrosion diagram of alloy C-276 in technical grade sulfuric acid (Figure 5) at its extreme high concentration side on the right shows a large horizontal distance between the 0.1 and the 0.5 mm year<sup>-1</sup> isocorrosion

line, indeed. This represents an excellent safety margin in case of temporary excursions of the sulfuric acid to lower concentrations.

Alloy 33 (EN 1.4591/UNS R20033) had been developed with the aim to use it, for example, for large acid distribution systems and plate heat exchangers.<sup>36</sup> Figure 19 shows the isocorrosion diagram for this material in highly concentrated sulfuric acid. However, it must be emphasized that sulfuric acid can exhibit very complex behavior toward materials. For example, the temperature dependence of the corrosion rate of alloy 33 in highly concentrated sulfuric acid is not monotonous.<sup>36,37</sup> For certain acid concentrations, it is possible to cause the corrosion rate to rise by decreasing the temperature, an effect which can be observed in the isocorrosion diagram of Figure 19. Furthermore, traces of impurities, changes in the rate of flow, slight changes in concentration and/or slight increases in temperature can cause markedly higher rates of corrosion. In view of this, the isocorrosion diagram presented in Figure 19 can only serve to provide an initial orientation and extensive testing in the actual plant acid and environment is necessary when selecting alloy 33 (EN 1.4591/UNS R20033).

Depending on the actual operating conditions, deviations can be expected to occur to a lesser or greater extent. This is true not only for the highly concentrated sulfuric acid discussed here in detail but for the whole range of sulfuric acid concentrations as shown in Figures 5, 6, and 12, in particular for those temperatures under which materials are near their limits of resistance. If the operating parameters cannot be closely controlled, it may, in some cases, be necessary to select a material not as a function of its resistance to the theoretical operating conditions, but rather because of its ability to absorb variations in these conditions. As is so often the case, only plant testing under true service conditions is likely to give a reliable indication on the suitability of materials in most circumstances.

With these considerations in mind, the handling of sulfuric acid and sulfuric acid-based aqueous solutions constitutes a very broad field of application for nickel alloys. Standard stainless steel grades can be used only to handle much diluted acid at low temperatures. At higher concentrations and temperatures, the use of materials like high-alloy stainless steels and nickel alloys becomes necessary. Alloy 20 (EN 2.4660/UNS N08020), alloy 825 (EN 2.4858/UNS N08825), alloy 31 (EN 1.4562/UNS N08031), alloy 59 (EN 2.4605/UNS N06059), and alloy B-2 (EN 2.4617/UNS N10665) are some examples.



As pointed out in [Section 3.05.3.3](#), the use of alloy B-2 may become necessary at sulfuric acid concentrations between 60% and 80% and temperatures even above 120 °C, but clearly reducing conditions must be present.

The use of the alloys 825 and 20, on the other hand, is restricted to the lower temperature range, but is facilitated by the presence of oxidants, as mentioned in [Section 3.05.3.6.2](#). The newer alloys 31 (EN 1.4562/UNS N08031) and 59 show a more extended suitability. This is obvious from their isocorrosion diagrams in technical grade aerated sulfuric acid shown in [Figure 6](#) for alloy 59 (EN 2.4605/UNS N06059) and in [Figure 12](#) for alloy 31 (EN 1.4562/UNS N08031). However, it has to be kept in mind that the 0.1 mm year<sup>-1</sup> isocorrosion line of alloy 31 in sulfuric acid is shifted to lower temperatures if no oxidants are present as demonstrated in [Figure 13](#) with the comparison of the corrosion behavior in technical grade sulfuric acid and in a p.a. sulfuric acid, established by Alves *et al.*<sup>20</sup> Although oxidants can extend the region of passivity of alloy 31, the corrosion behavior of alloy 59 is not influenced greatly by the amounts of oxidants present in the acid.<sup>20</sup>

Besides the influence of oxidants, the influence of the temperature deserves a closer look, too. Near the isocorrosion line, temperature is an extremely important variable influencing the corrosion rate, since above that line corrosion rate rises above 0.1 mm year<sup>-1</sup> and materials may become unsuitable for service. Alloy 31 (EN 1.4562/UNS N08031) and alloy 59 (EN 2.4605/UNS N06059) behave differently in this respect. While for alloy 31, a small temperature

increase above the isocorrosion line can cause a jump in corrosion rate, for alloy 59 the corrosion rate also increases but more moderately, as shown in [Figure 22](#). This is because the corrosion rate in active state, which depends directly on the test temperature and on the alloy composition, is significantly higher for alloy 31 than for alloy 59. Particularly, high Ni and Mo contents are known to reduce the rate of active current density giving rise to the lower active corrosion rates of alloy 59.<sup>20</sup> Anodic polarization curves, which had been established in this context by Alves *et al.*,<sup>20</sup> indicate that alloy 31 is not so easy to passivate as alloy 59, but once passive, it exhibits lower passive current density than does alloy 59. This is probably related to the copper content of alloy 31 (EN 1.4562/UNS N08031), since copper is known to influence the passive current density in sulfuric acid.<sup>20</sup>

In many sulfuric acid applications, chlorides are also present, for example, in wall condensate in FGD units. Chlorides impair the corrosion resistance in sulfuric acid in shifting the anodic curve to higher current densities, making passivation more difficult, increasing the corrosion rates and may produce pitting corrosion. Indeed, as shown by Alves *et al.*,<sup>20</sup> the 0.1 mm year<sup>-1</sup> isocorrosion line of alloy 31 (EN 1.4562/UNS N08031) is shifted to significantly lower temperatures when 1 g l<sup>-1</sup> chloride is added to the sulfuric acid. However, in sulfuric acid contaminated with chlorides, alloy 59 (EN 2.4605/UNS N06059) has advantages over alloy 31, as exemplified in [Figure 23](#), and its resistance to pitting is higher.

Many chemical processes use 98–99% sulfuric acid. After reaction is completed, the acid is not totally consumed, but is discharged in a diluted and

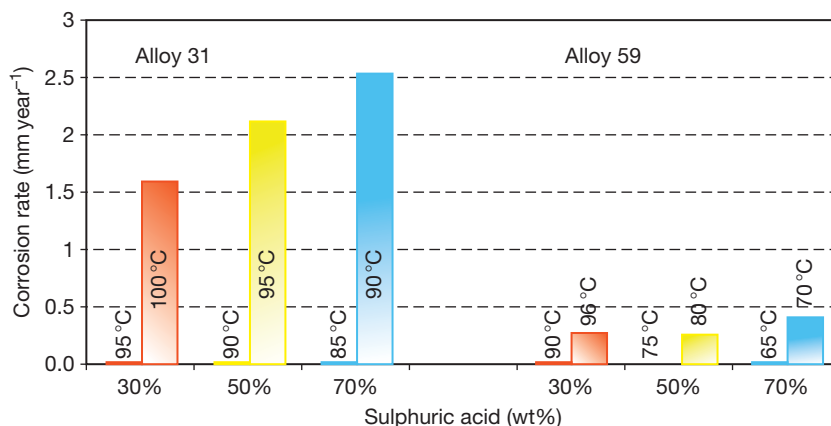


**Figure 22** Corrosion rates of alloy 31 (EN 1.4562/UNS N08031) and of alloy 59 (EN 2.4605/UNS N06059) in aerated technical grade sulfuric acid closely below and above the 0.1 mm year<sup>-1</sup> isocorrosion line, 24 h immersion test, according to Alves *et al.*<sup>20</sup>



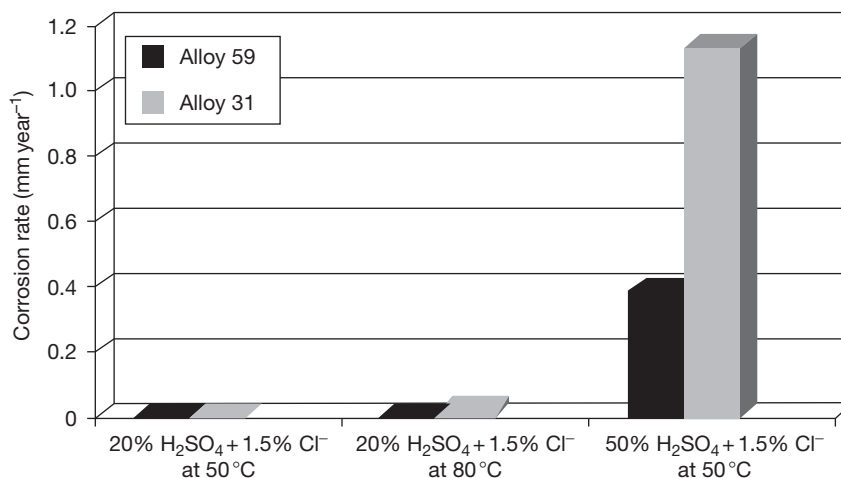


**Figure 23** Corrosion rates of alloy 31 (EN 1.4562/UNS N08031) and of alloy 59 (EN 2.4605/UNS N06059) in aerated technical grade sulfuric acid with addition of 1.5% chloride, graph published by Alves *et al.*<sup>20</sup>

contaminated form. This waste acid is totally useless unless it can be concentrated (e.g., up to 75–80%) and purified for further use in chemical process reactions. Both alloy 31 (EN 1.4562/UNS N08031) and alloy 59 (EN 2.4605/UNS N06059) are in use in the regeneration of waste sulfuric acid.

For example, in viscose Rayon plants, alloy 31 (EN 1.4562/UNS N08031) is used in the regeneration of sulfuric acid. In the spinning step, the viscose is forced through a spinneret to produce the fine filaments and then comes into contact with a solution of sulfuric acid, sodium sulfate, and usually  $\text{Zn}^{2+}$  ions. The waste sulfuric acid from this step is regenerated by condensation under vacuum at temperatures between 30 and 40 °C and further adjusted with highly concentrated sulfuric acid, the dissociation heat of which can raise the temperature to up to 60 °C. The resulting 80–85% acid can be used for further processes.

In the production of titanium dioxide by the sulfate process, finely ground ilmenite ( $\text{FeTiO}_3$ ) or ilmenite slag is digested with sulfuric acid in a concentration of ~90% and the cleaned titanium oxide sulfate is hydrolyzed to form titanium oxide hydrate, which is then calcined to form  $\text{TiO}_2$ . Modern plants incorporate a downstream dilute sulfuric acid processing facility. Alloy 31 (EN 1.4562/UNS N08031) is used in this application.

Further examples of waste acid recovery systems can be found in the metal-producing industry. In the copper production, alloy 31 (EN 1.4562/UNS N08031) is used in autoclaves to concentrate spent waste-contaminated sulfuric acid from 25% to ~75–80% in evaporators under vacuum. The

presence of oxidizing metal ions in the contaminated acid helps maintain the passivity of alloy 31 (EN 1.4562/UNS N08031).

### 3.05.5.4 Production of Phosphoric Acid

A large amount of the world's fertilizer production is based on phosphoric acid ( $\text{H}_3\text{PO}_4$ ). Two principal production methods are used. Thermal phosphoric acid is produced by the combustion of phosphorus with atmospheric oxygen, followed by the hydration of the oxide obtained. Owing to its high purity, this acid is primarily used as a food additive. Because of the high energy requirement, this method is of secondary importance. In the wet process, phosphoric acid is produced by digesting phosphate rock (apatite), usually with sulfuric acid. The by-products of this process are calcium sulfate, in the form of dihydrate (gypsum), and fluosilicic acid. About 95% of the global demand for phosphoric acid is met by the wet process. After filtration, the phosphoric acid, usually at a concentration of ~28%  $\text{P}_2\text{O}_5$ , is concentrated either to the standard commercial grade of 54%  $\text{P}_2\text{O}_5$  or to super phosphoric acid with 70%  $\text{P}_2\text{O}_5$ .

The action of phosphoric acid on most metals is not particularly aggressive. However, the sulfuric acid and the presence of fluorine, chloride, and silica in the phosphate ores, which leads to the formation of hydrofluoric acid, fluosilicic acid, and also hydrochloric acid, give rise to very complex corrosion conditions. Silica and aluminum are used to complex with fluorine and reduce its corrosive effect. The chloride concentration strongly depends on the origin of the apatite and increases if the ores are washed using

seawater. Corrosiveness is further increased by the presence of sulfides. In addition, the degree of corrosive attack is aggravated by erosion resulting from the presence of abrasive solids such as phosphate rock particles and gypsum crystals, by turbulence and high velocity fluid flow, by deposit formation and by increases in temperature. From literature and plant experience, it is known that high chromium levels in the alloys used are required for sufficient corrosion resistance to phosphoric acid under those conditions.

In the wet process, the first stage for which corrosion-resistant materials are required is the reactor for digesting the ore. The reactor vessel is made of carbon steel throughout with a nonmetallic lining, sometimes augmented with acid-resisting bricks, particularly in locations of impingement and abrasion. The agitators are often made of special stainless steels. The application of these alloys, however, is limited by the increasing impurities in the phosphate ores and higher temperatures for digesting the ore. Experience gained under real service conditions proved that the materials alloy 31 (EN 1.4562/UNS N08031) and alloy 625 (EN 2.4856/UNS N06625) are particularly resistant to erosion and corrosion in phosphoric acid slurries.<sup>29</sup>

The filtration equipment requires special materials, in particular, with good resistance to pitting and crevice corrosion. The materials used for this equipment item are high-alloy stainless steels, but higher resistance to pitting and crevice corrosion can be achieved with alloy 31 (EN 1.4562/UNS N08031).

After filtration, the raw phosphoric acid, which may be contaminated with sulfuric acid, chlorides, fluorides, and fluosilicic acid, is concentrated to 54%  $P_2O_5$ . This takes place in an evaporator that is either equipped with metal tubes or is made of graphite. It has been shown that metallic heat exchangers

operate satisfactorily when hot water is used as the heating medium. The solids settling on the tube walls, mainly gypsum, are easily removed by routine cleaning, which prevents corrosion under the deposits. Alloy 28 (EN 1.4563/UNS N08028) and alloy 31 (EN 1.4562/UNS N08031) are used for the heat exchangers.

In the further processing to produce super phosphoric acid (70–72%  $P_2O_5$ ), usually no particular corrosion problems arise, because most of the fluorine contaminants have been removed in the upstream stages. The nickel–chromium–molybdenum alloy 625 (EN 2.4856/UNS N06625) is the standard material here. Nickel alloys are also used for further equipment in the phosphoric acid production, such as plate heat exchangers, equipment for the removal of gaseous fluorine compounds, pumps, and fans.

According to [Table 4](#), alloy 31 (EN 1.4562/UNS N08031) exhibits high resistance to uniform and localized corrosion in industrial phosphoric acid under diverse conditions.<sup>29</sup> In phosphoric acid contaminated with sulfuric acid, fluosilicic acid, oxidizing metallic ions, and high amount of chlorides at 80 °C, this alloy shows outstanding corrosion resistance. At 120 °C, the corrosion rate becomes considerably higher. At these high temperatures, contamination is extremely important and must be well defined and controlled. In the example of [Table 4](#), the contaminated 52% phosphoric acid at 120 °C is ~10 times more corrosive than is the technical pure one.

It should be emphasized that the performance of alloy 31 (EN 1.4562/UNS N08031), which combines a high chromium content with a sufficient molybdenum level is comparable or even many times superior to higher-alloyed materials of significantly higher price. As an example, [Figure 24](#) shows the corrosion rate of various alloys in attack acid with different

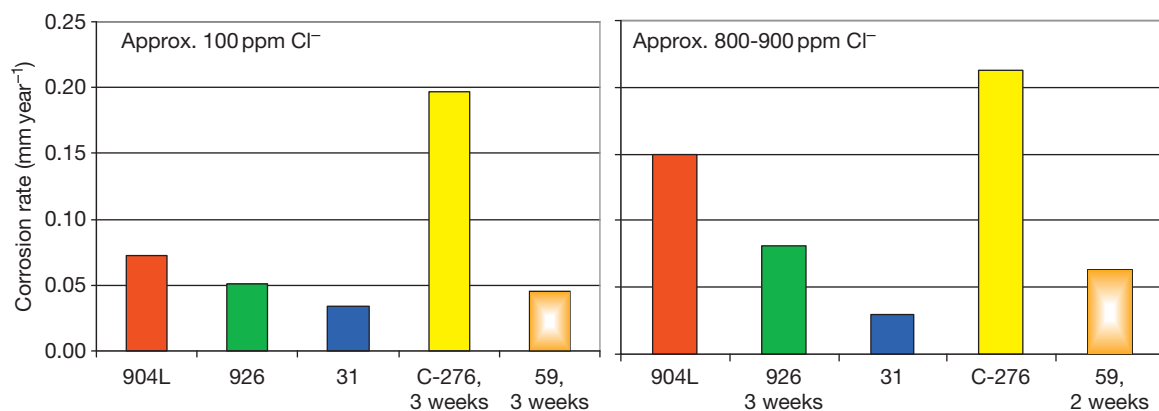


**Figure 24** Corrosion rate of various alloys upon immersion in attack acid with (mass%) 33  $P_2O_5$ , 1.6  $SO_3$ , 1.8 F, and different chloride content at 90 °C.

chloride content at 90 °C, demonstrating that alloy 31 excels with the lowest corrosion rate.<sup>30,52</sup> This alloy also resists well to erosion–corrosion conditions,<sup>29</sup> which is in accordance with studies suggesting that under the mixed erosion–corrosion conditions found in the phosphoric acid industry, it is primarily corrosion resistance rather than hardness that determines the performance of the material. Typical applications for alloy 31 (EN 1.4562/UNS N08031) in phosphoric acid production include mixers, filter components, piping systems, heat exchanger tubes in concentration units, sulfuric acid coolers, vapor systems in concentration plant, flash coolers, and others. In particular, the use of alloy 31 (EN 1.4562/UNS N08031) in phosphoric acid production increases feedstock flexibility by contributing in a cost-effective manner to the solution of corrosion problems in the processing of, for example, phosphate ores containing high levels of chlorides.<sup>30,31</sup> Additional information on suitable alloys for application in phosphoric acid and on tackling chloride corrosion in phosphoric acid production is provided by Alves *et al.*<sup>52</sup> and by Hoxha *et al.*<sup>53</sup>

### 3.05.5.5 Production of Hydrofluoric Acid and Aluminum Fluoride

Hydrofluoric acid (HF) is produced by the reaction of concentrated sulfuric acid with fluorspar (calcium fluoride):  $\text{CaF}_2 + \text{H}_2\text{SO}_4 \rightarrow 2 \text{HF} + \text{CaSO}_4$ . The reaction can take place in two stages. In the first stage, preheated fluorspar and preheated sulfuric acid are mixed together. The reaction is exothermic and the temperatures can reach 150 °C. The materials used here must therefore be able to resist hot concentrated sulfuric acid as well as hydrofluoric acid and possess adequate erosion resistance to fluorspar and calcium sulfate crystals. Depending on concentration and temperature, the materials alloy 20 (EN 2.4660/UNS N08020), alloy C-276 (EN 2.4819/UNS N10276), and alloy 59 (EN 2.4605/UNS N06059) are successfully used for these equipment items.

The second stage is a rotary kiln, in which the reaction is taken to completion. Some kilns, or their linings, are made of alloy 20 (EN 2.4660/UNS N08020), while in others, special stainless steels are used. Recently, good experience has been achieved with alloy 59 (EN 2.4605/UNS N06059) as a material for the rotary kiln. The gaseous hydrogen fluoride leaving the kiln is contaminated with entrained sulfuric acid and silicon tetrafluoride; these contaminants are removed in a sulfuric acid scrubber. The material for

the scrubber will be determined by the concentration of sulfuric acid in the scrubber liquid. In some plants, the high-alloyed stainless steel alloy 926 (EN 1.4529/UNS N08926) is successfully used; depending on the sulfuric acid concentration, alloy 31 (EN 1.4562/UNS N08031) or alloy 59 (EN 2.4605/UNS N 06059) may also be considered.

The HF gas is liquefied at ambient temperature in condensers made of carbon steel and then distilled in two stages to remove impurities. The volatile constituents are first removed in a carbon steel column. In the second stage, the less volatile impurities are removed. The residue is an aqueous mixture of hydrofluoric acid and sulfuric acid. In the upper part of the distillation column, carbon steel can be used, while alloy 400 (EN 2.4360/UNS N04400) is generally used for the lower part and the reboiler.<sup>39</sup>

Only a few special stainless steels and nickel alloys can be used for handling aqueous hydrofluoric acid solutions; alloy G-3 (EN 2.4619/UNS N06985), alloy 31 (EN 1.4562/UNS N08031), and alloy 59 (EN 2.4605/UNS N06059) are suitable within very narrow temperature and concentration limits.<sup>39</sup> If alloy 400 (EN 2.4360/UNS N04400) is used, it must be kept in mind that stress corrosion cracking can occur in air containing hydrofluoric acid vapors, and to a lesser extent also in the liquid phase.

Aluminum fluoride is produced in fluidized beds of aluminum oxide and hydrogen fluoride at a temperature of 650 °C. Owing to the excellent corrosion resistance of alloy 600 L (EN 2.4617/UNS N06600) at high temperatures in the presence of gaseous HF, this alloy is used to make the reactors and the tubes for the product coolers.<sup>39</sup>

### 3.05.5.6 Production of Acetic Acid

Acetic acid ( $\text{CH}_3\text{COOH}$ ) is the most important of the organic acids. It is used as a raw material in a large number of chemical processes. For example, acetic acid is used for the production of cellulose acetate, vinyl acetate monomer, acetic ester, pharmaceuticals, plastics, dyes, and insecticides. Acetic acid can be produced by fermentative oxidation of methanol. More common is the catalytic oxidation of hydrocarbons (e.g., butane) or the catalytic reaction of methanol and carbon monoxide:  $\text{CH}_3\text{OH} + \text{CO} \rightarrow \text{CH}_3\text{COOH}$ .

The most well known process using this route was developed by Monsanto, the license now being held by BP Chemicals. Rhodium activated with iodide acts as the catalyst. From carbon monoxide and the methyl groups, a complex compound is produced,

which is converted into acetic acid by hydrolysis, carbon dioxide and water arising as by-products. The exothermic reaction takes place at temperatures of 180–200 °C and a pressure of 15 bars in a special reactor. The acetic acid formed is then collected in an overhead condenser from where the iodine compounds are recycled to the reactor. The raw acetic acid is then distilled in two stages, with the unconverted methanol also being returned to the reactor.

The combination of hydroiodic acid, acetic acid, and water in the reactor, scrubber, and distillation columns produces extremely corrosive, reducing conditions. The materials in use for these items are alloy B-2 (EN 2.4617/UNS N10665), which is particularly corrosion resistant under reducing conditions, or alternatively zirconium.

After separation of the halogen ions, the acetic acid is less corrosive, so that the materials alloy C-276 (EN 2.4819/UNS N10276), alloy 59 (EN 2.4605/UNS N06059), alloy G-3 (EN 2.4619/UNS N06985), or alloy 31 (EN 1.4562/UNS N08031) can then be used in the downstream process equipment.

In other acetic acid processes like the Eastman process, in which no iodine is used, nickel–chromium–molybdenum alloys such as alloy C-276 (EN 2.4819/UNS N10276) and alloy 59 (EN 2.4605/UNS N06059) are likewise used.

### 3.05.5.7 Production of VCM

VCM is a feedstock for the manufacture of PVC and is nowadays produced from ethylene and chlorine. Ethylene is either converted directly with chlorine to form ethylene dichloride (EDC), which is then thermally cracked to produce VCM or ethylene is subjected to oxychlorination followed by pyrolysis.

As would be expected in pyrolysis processes, many equipment items are exposed to high temperatures and severe corrosive attack. The highly corrosive nature of dissolved chlorine and hydrogen chloride comes to the fore at elevated temperatures and, to a particularly strong extent, in the presence of moisture. Priority therefore attaches to the operation of a dry process. Any introduction of moisture or water would lead to the formation of hydrochloric acid and other corrosive media. As the demand for absolute dryness cannot be fulfilled in actual practice (start-up and shutdown, downtimes, leaks, decoking with steam), suitable measures must be found to prevent premature material failure as a result of corrosion. Where the process temperature permits, such measures include coatings (in most cases organic-based)

and the use of corrosion-resistant materials. According to Alves *et al.*,<sup>39</sup> here it is mainly nickel alloys that have proved successful in the relevant operating conditions. Thus, alloy 825 (EN 2.4858/UNS N08825) is used for gas inlet tubes and alloy 59 (EN 2.4605/UNS N06059) or alloy C-276 (EN 2.4819/UNS N10276) for tube sheets and as cladding material in the catalysis section of fluidized bed reactors. The fixed-bed reactors are equipped with vertical tubes that are usually made of the nickel standard grade alloy 200 (EN 2.4066/UNS N02200), alloy 600 (EN 2.4816/UNS N06600), or alloy 625 (EN 2.4856/UNS N06625).

Thermal cracking of the EDC to form VCM and hydrochloric acid takes place in a pyrolysis kiln at 425–550 °C. Alloy 800 H (EN 1.4958/UNS N08810) is the standard material for this application. A few facilities are also constructed in alloy 600 (EN 2.4816/UNS N06600). In the EDC purification section, the main corrosion problem is created by hydrochloric acid. Here, various nickel materials such as alloy 400 (EN 2.4360/UNS N04400), alloy B-2 (EN 2.4617/UNS N10665), and 6Mo stainless steels such as alloy 926 (EN 1.4529/UNS N08926) are used for columns, heat exchangers, pumps, and valves. The use of standard chromium–nickel steel grades cannot be recommended owing to their high susceptibility to pitting corrosion and stress-corrosion cracking in the special conditions of VCM production.

A characteristic feature of some older VCM plants is the flare stack used to burn off waste gases. Alloy 59 (EN 2.4605/UNS N06059) is suitable for the stack head, which is subject to heavy corrosive attack. For environmental reasons, in new facilities, this gas is no longer burnt off but recycled to the process. The same materials can be used for the recycling process as for the VCM process itself, because their corrosion behavior has to meet similar requirements.

### 3.05.5.8 Production of Styrene

Styrene ( $C_6H_5CH:CH_2$ ) is an important chemical for the production of a range of plastics, including polystyrene, SBR, ABS, and SAN resins, synthetic latexes, and polyesters. The main process used to produce styrene is the production of ethylbenzene in a first step by catalytic reaction of benzene and ethylene followed by the dehydrogenation of ethylbenzene.

In the first reaction stage, in which the ethylbenzene is produced, it is the corrosiveness of the catalyst that determines the type of material required. The Union Carbide/Badger process employs aluminum chloride as catalyst. Aluminum chloride is extremely

corrosive, meaning that only acid-resistant glass or ceramic linings come into consideration here. For metal linings, heating coils, and other internals, alloy B-2 (EN 2.4617/UNS N10665) and alloy C-276 (EN 2.4819/UNS N10276) can be used. The same alloys are also used in the downstream heat exchangers and piping systems. Columns and heat exchangers that come into contact with traces of chlorides are often made of the nickel–copper alloy 400 (EN 2.4360/UNS N04400). Special stainless steels such as the 6Mo grade alloy 926 (EN 1.4529/UNS N08926) can also be considered.

Other ethylbenzene processes use noncorrosive catalysts, and therefore, only low-alloy materials are required in the first stage.

The second process stage, in which hydrogen is split off, runs at high temperatures (950–1000 °C) in the presence of superheated steam. The steam is produced in furnaces in which the tubes and the manifolds are generally made of alloy 800 H (EN 1.4958/UNS N08810). The connection line from the superheater to the reactor may also be made of the same material. High temperature materials are also used for the reactor in which dehydrogenation takes place. These are mainly heat-resistant steels such as alloy 800 H (EN 1.4958/UNS N08810) or nickel alloys such as alloy 617 (EN 2.4663/UNS N06617). The exact choice of material depends on the design and the degree of attack.

### 3.05.5.9 Production of Acrylic Acid and Acrylate Esters

Acrylic acid ( $\text{C}_2\text{H}_3\text{COOH}$ ) is a feedstock for the production of polyacrylic acid and acrylic esters. Acrylate esters (such as methyl acrylate, ethyl acrylate, butyl acrylate, etc.) are used in polymerized form for the production of dyes and paints, adhesives, textiles, and plastics. Polyacrylic acid is used in the production of hygiene products, cleaning products, and water treatment agents.

The most important process for the production of acrylic acid is the partial oxidation of propylene. In general, this process is regarded as ‘noncorrosive,’ enabling low-alloy steels to be used. Recently, however, a number of cases of corrosion damage have occurred in the extraction column. These problems have been attributed to traces of formic acid in the plant. Field tests have led to the selection of different materials according to the corrosiveness of the medium. Thus, in one plant, the 6Mo stainless steel grade alloy 926 (EN 1.4529/UNS N08926) was selected, in another plant

the nickel alloy C-276 (EN 2.4819/UNS N10276), and in a third plant alloy 31 (EN 1.4562/UNS N08031).

Acrylate esters are produced by reacting acrylic acid with the corresponding alcohol in the presence of a catalyst. The catalyst can, for example, be sulfuric acid or sulfonic acid; the reaction temperature is in the order of 130 °C. An oxidizing or reducing stabilizer is added to prevent polymerization. The corrosiveness of the process is determined by the type of catalyst. Therefore, the choice of material for the reactor, heating tubes, and mixer will be determined by its corrosion resistance to sulfuric or sulfonic acids under either oxidizing or reducing conditions.

When reducing conditions are encountered, the copper–nickel alloy 400 (EN 2.4360/UNS N04400) can be successfully employed. It should be kept in mind, however, that alloy 400 loses its resistance to corrosion under oxidizing conditions. In one plant, severe corrosive attack was observed when the stabilizer was converted from reducing to oxidizing. Extensive exposure tests as much with high-alloy stainless steel grades as with the nickel alloy grades alloy G-3 (EN 2.4619/UNS N06985), alloy 625 (EN 2.4856/UNS N06625), alloy 31 (EN 1.4562/UNS N08031), alloy C-276 (EN 2.4819/UNS N10276), alloy 59 (EN 2.4605/UNS N06059), etc. showed that alloy 59 was the only material exhibiting an overall corrosion rate below  $0.01 \text{ mm year}^{-1}$  and no pitting or crevice corrosion. For this reason, alloy 59 (EN 2.4605/UNS N06059) was selected for the particularly critical part of the plant, the heating tubes. As Alves *et al.*<sup>39</sup> report, after 3 years in use without any problems, the entire reactor was constructed in alloy 59.

### 3.05.5.10 Production of MDI and TDI as Feedstocks for Polyurethanes

Polyurethanes are produced by the polyaddition of isocyanates and alcohol. The most common processes use MDI and TDI as feedstocks. MDI and TDI are synthesized by conversion of diamines in the presence of carbonyl chloride (phosgene).

In the synthesis of both MDI and TDI, hydrogen chloride is generated as a by-product. Owing to the corrosiveness of HCl it is generally necessary to use corrosion-resistant materials. The heat exchangers downstream of the reactor are exposed to corrosive attack from a mixture of TDI, HCl, and phosgene (in traces) at temperatures of  $\sim 200^\circ\text{C}$ . The nickel–chromium alloy 600 L (EN 2.4817/UNS N06600) is generally used for these heat exchangers. Under normal conditions, this material lasts  $\sim 10$  years. Under



particularly critical conditions, alloy 59 (EN 2.4605/UNS N06059) has been successfully selected.

In other areas of the plant, materials are required that are resistant to hydrochloric acid in aqueous solution. Depending on the overall process, the process stage and the precise composition of the medium, the nickel alloy grades alloy B-2 (EN 2.4617/UNS N10665), alloy 400 (EN 2.4360/UNS N04400), alloy C-276 (EN 2.4819/UNS N10276), or alloy 59 (EN 2.4605/UNS N06059) are used.<sup>39</sup>

Recently, a new gas phase technology has emerged whereby alloy C-4 and alloy 59 have proved to withstand corrosion in key equipment parts. In the reactor sump vessel, the mixture of TDI, hydrogen chloride, and phosgene at high temperature leads to strong pitting on standard stainless steel. In field tests and long-term pilot plant operation, alloy C-4 (EN 2.4610/UNS N06455) and alloy 59 (EN 2.4605/UNS N06059) have proved to be the material of choice.

### 3.05.5.11 Production of Fine and Specialty Chemicals

The fine and specialty chemicals industry produces a wide variety of chemical ingredients and active intermediates to be used, for example, in the pharmaceutical, food, agrochemical, and home and care industries. The selection of materials for the production of fine chemicals is made more difficult by the fact that the chemical plants involved are increasingly used to produce different types of substances to satisfy fast-changing market demands, so that reactors, vessels, piping systems, and heat exchangers are frequently exposed to changing corrosive media requiring the use of equally versatile multipurpose materials.

In addition, metallic contamination of the final product is not tolerable in many cases. Dissolved metallic ions may either lead to a discoloration of the products or trigger undesired catalytic reactions within the products or their amount may be limited by legal requirements. For this reason, specifications have to be met in many cases where tolerable mass loss is far below the corrosion rate of  $\leq 0.1 \text{ mm year}^{-1}$ , which is usually considered the limit for the technical corrosion resistance in case of metallic alloys.<sup>54</sup> The requirement for resistance to a broad spectrum of different media, which is given in most cases leads to the selection of either nonmetallic materials, like glass-linings and polymers, or special metallic materials. Such special metallic materials are alloys belonging to the family of C-type nickel–chromium–molybdenum alloys, titanium, zirconium, and

tantalum. Lower-alloyed materials like alloy 31 (EN 1.4562/UNS N08031) are useful to a certain extent.

C-type nickel–chromium–molybdenum alloys, particularly alloy 59 (EN 2.4605/UNS N06059) can be considered for critical equipment as synthesis reactors and distillation columns. In the case of centrifuges, fittings, agitators, and valves, the material selection is mainly restricted to metals due to mechanical and design requirements.

Furthermore, cleanability is an important issue in multipurpose plants. In the case of nickel alloys, a high degree of cleanability can be achieved by electropolishing. Electropolishing of nickel alloys allows obtaining extremely smooth surface structures to which it is difficult for the products to adhere. In addition, the true surface area of an extremely smooth surface is considerably reduced compared with a surface of greater roughness, which results in a lower corrosion rate of the alloy and less migration of alloying constituents to the product. However, obtaining smooth surfaces by electropolishing requires a high degree of homogeneity of the alloy that has to be part of the material specification for this reason.

The wide variety of service media encountered in this industry is outside the scope of this work. As an example, reactions involving organic acid or solvents and catalyzed by small amounts mineral acids like sulfuric acid or hydrochloric acid can be found in the production of fine chemicals. Although more corrosive than the sulfuric acid, the hydrochloric acid is sometimes preferred owing to its higher catalytic activity. Oxidizing contaminants like oxygen, ferric, or cupric ions should also be considered, because they tend to shift the redox potential.

Figures 25 and 26 present data from laboratory tests intended to simulate in a simplified manner such type of environments.<sup>55</sup> Distinct levels of dissolved oxygen were achieved by bubbling nitrogen or oxygen into the solution and different concentrations of ferric ions were added in the form of sulfate. As indicated by the results, alloy 31 (EN 1.4562/UNS N08031) may sometimes require a shift of the free corrosion potential to more oxidizing conditions in order to make it corrosion resistant in these media. Alloy 59 (EN 2.4605/UNS N06059), however, exhibits very low corrosion rates under all conditions tested. Nickel–molybdenum alloys of the B-type are not considered for changing conditions in multipurpose plants, as they are resistant to few specific media only. In addition, their corrosion rate is increasing strongly with increasing amounts of accompanying oxidizing substances.



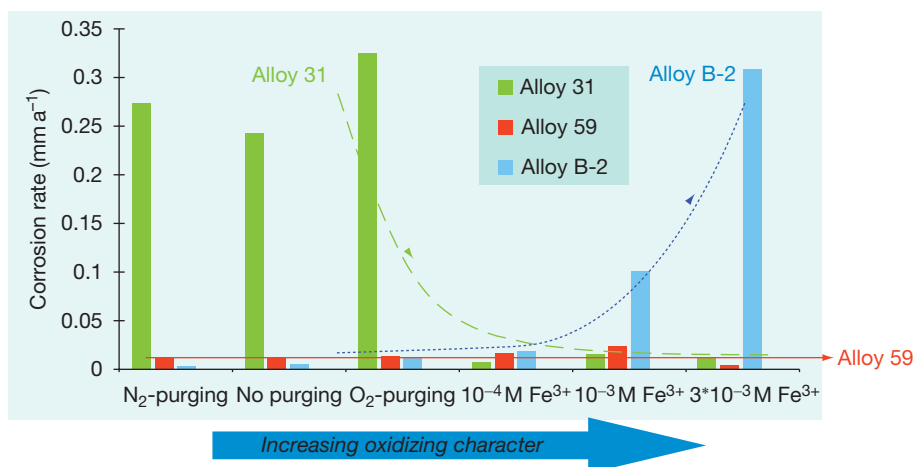


**Figure 25** Corrosion behavior of alloy 31 (EN 1.4562/UNS N08031), alloy 59 (EN 2.4605/UNS N06059), and alloy B-2 (EN 2.4617/UNS N10665) in 50% CH<sub>3</sub>COOH + 40% HCOOH + 5% H<sub>2</sub>SO<sub>4</sub> + 5% H<sub>2</sub>O under different oxidizing conditions at 95 °C, graph made from data (Table 3 in Alves and Werner<sup>55</sup>) determined by Alves *et al.* in a 24 h immersion tests.

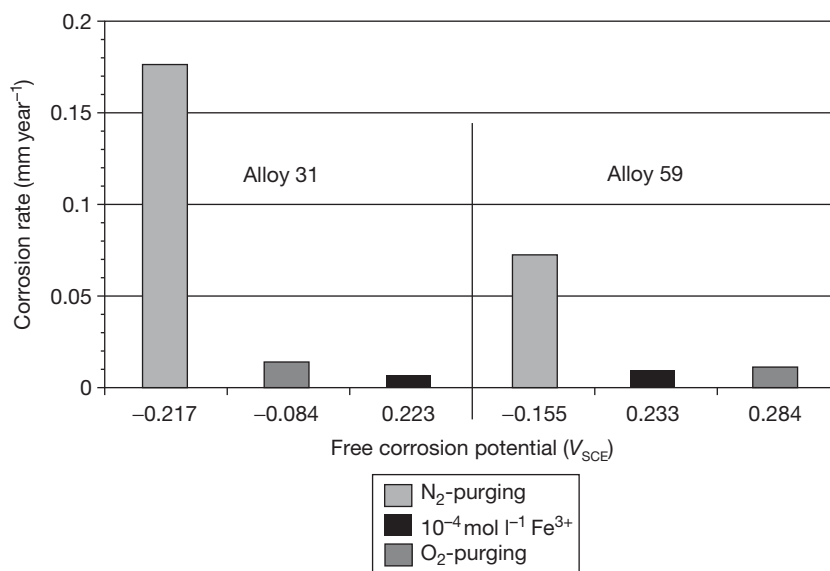


**Figure 26** Dependence of corrosion rate on the free corrosion potential of alloy 31 (EN 1.4562/UNS N08031) and alloy 59 (EN 2.4605/UNS N06059) in 94% C<sub>2</sub>H<sub>5</sub>OH + 2% HCl + 4% H<sub>2</sub>O at 60 °C, determined by Alves *et al.* in a 24 h immersion tests. Reproduced from Alves, H.; Werner, H. *CORROSION* 2004; NACE International: Houston, TX, 2004, Paper No. 04235.

An additional study by Alves *et al.*<sup>56</sup> on the corrosion resistance in organic solvents with small amounts of sulfuric acid or hydrochloric acid showed again that alloy 31 (EN 1.4562/UNS N08031) requires a threshold oxidizing capacity to passivate, being preferred for the more oxidizing conditions. Alloy 59 (EN 2.4605/UNS N06059), however, revealed to be the more versatile alloy, having good resistance in the most environments studied. Alloy 59 (EN 2.4605/UNS N06059) shows higher ability to

passivate and little susceptibility to variations on the content of oxidants or chlorides. Another interesting conclusion of the same study is that the corrosive impact of the small additions of HCl (2%) depends on the solvent and decreases in the sequence: methanolic solution > ethanolic solution > aqueous solution as a result of the different protonic activity. If methanol is used as a solvent, a certain threshold of water is required to maintain the passivity of nickel alloys. The water contents required to maintain

passivity and the corrosion rate  $<0.1 \text{ mm year}^{-1}$  were found to be 8% at 40 and 50 °C for the unwelded alloy 31 (EN 1.4562/UNS N08031), and 12% at 40 °C and 18% at 50 °C for the welded alloy 31. Alloy 59 (EN 2.4605/UNS N06059) requires significantly lower amounts of water to maintain passivity (2% at 40 °C and 4% at 50 °C) and is not influenced by the welding conditions.

The C-type family of nickel–chromium–molybdenum alloys, in particular, alloy 59 (EN 2.4605/UNS N06059), offers a high level of reliability when equipment items are exposed to a variety of corrosive media. Indeed, this versatile alloy is suitable for a wide variety of corrosive environments, including mineral and organic acids, acid mixtures, halides, etc., and resists high levels of chlorides, oxidizing and reducing contaminants, and stress-corrosion cracking. Thus, alloy 59 (EN 2.4605/UNS N06059) can often be considered to replace more expensive materials like zirconium and tantalum or the mechanically fragile enamel.

### 3.05.5.12 Transport of Corrosive Dangerous Goods in Tanks

In Germany, the “BAM – List Requirements for Tanks for the Transport of Dangerous Goods” with compatibility evaluations of selected metallic material groups as well as of polymeric gasket and lining materials under the influence of dangerous goods and water-polluting substances is the basis for substance-related prototype approvals for tank containers designed for the carriage of dangerous goods.<sup>57</sup> Such information is applicable also to tanks, trucks, and rail cars. There are a large number of dangerous goods with high corrosivity to metals where the standard steels are not corrosion resistant. One possibility to solve corrosion problems is to line the tank with a polymeric material. An alternative possibility is the application of high-alloyed stainless steels and nickel alloys as there are alloy 31 (EN 1.4562/UNS N08031) and alloy 59 (EN 2.4605/UNS N06059). For lack of corrosion test results with welded test samples of these high-alloyed materials under the influence of corrosive dangerous goods, a comprehensive test program was performed in 14 relevant groups of media at 55 °C.<sup>58,59</sup>

The results obtained indicate that alloy 59 (EN 2.4605/UNS N06059) showed the most universal corrosion resistance of the materials tested. This alloy is suitable as material for tanks transporting almost all corrosive substances having been included in the test series. One exception is the limitation of temperature during the transport of hydrochloric acid.

Alloy 31 (EN 1.4562/UNS N08031) is very corrosion resistant, but more restricted in its use than alloy 59. Exceptions for the use of this material are hydrochloric acid, perchloric acid, and molten monochloroacetic acid at 110 °C. Limitations for the use exist in the concentration range of aqueous solutions of aluminum chloride, copper (II) chloride, ferric chloride, and 2-chloropropionic acid. Alloy 31 can be considered corrosion-resistant tank material for the transport of mixtures of concentrated nitric acid and 96% sulfuric acid if the content of the nitric acid does not exceed 50% or the temperature does not exceed 30 °C. Alloy 31 has excellent prospects for application in transportation tanks because of the multipurpose corrosion resistance characteristics in combination with the beneficial cost ratio in comparison with the standard stainless steel grade AISI 316L.

All details of those and future test results will be included in the most recent edition of the BAM-List – Requirements for Tanks for the Transport of Dangerous Goods.

### 3.05.5.13 Environmental Technology

Air pollution control occupies a leading position in the market for environmental technology. Therefore, the subject of this section<sup>16</sup> is the removal of oxidation products of the sulfur and of the accompanying HCl/HF gases from the combustion processes of organic materials (coal, lignite, oil) by chemical gas scrubbing. This process is generally known as ‘FGD’ and the associated plants as ‘FGD plants.’

The wide range of scrubbing processes developed can be divided into scrubbing processes with regeneration of the scrubbing solution, spray absorption processes, and scrubbing processes without regeneration of the scrubbing solution. The scrubbing processes without regeneration, the so-called limestone processes are used throughout the world in ~90% of all FGD plants.

In a typical single-circuit process limestone FGD plant, the flue gas passes through an electrostatic precipitator; subsequently, the dust-free raw gas is sprayed with a scrubbing suspension in a quencher, whereby it is cooled and saturated with water vapor. In plants with a heat recovery system, the raw gas is cooled from ~200 to 300 °C (with/without NO<sub>x</sub> reduction) to 150 °C by means of a so-called clean gas preheater before entering the scrubber. The gas flow and the circulation of the scrubbing suspension are adjusted so that the temperature of the scrubbing suspension is ~60 °C. The pH is adjusted to between

4.5 and 6. In the scrubber sulfur dioxide/sulfur trioxide ( $\text{SO}_2/\text{SO}_3$ ) are transformed by the addition of limestone into calcium sulfite ( $\text{CaSO}_3$ ) and subsequently transformed by the injection of air or oxygen into essentially insoluble  $\text{CaSO}_4 \times 2 \text{H}_2\text{O}$ , that is, gypsum. This essentially insoluble gypsum precipitates out, and thus promotes the very high  $\text{SO}_2/\text{SO}_3$  conversion rate of over 90%. A suspension of quicklime ( $\text{CaO}$ ), hydrated lime ( $\text{Ca(OH)}_2$ ), or limestone ( $\text{CaCO}_3$ ) is used as the scrubbing solution. Chemical buffer reactions provide a constant pH in the absorber after the start-up phase of a FGD plant. Secondary reactions that take place after entry into the quencher or the bottom section of the integrated absorber are the almost 100% removal of hydrogen chloride ( $\text{HCl}$ ) and hydrogen fluoride ( $\text{HF}$ ), which are produced in the combustion process by chemical reactions and carried over with the flue gas. In counter-current systems, the flue gas is again sprayed with the scrubbing suspension in the upper region of the scrubber, the limestone excess in the added suspension resulting in a further increase in the degree of desulphurization. A pH shift toward a pH of  $\sim 6$  is obtained by the buffer reaction of hydrogen carbonate. The main reaction in the FGD therefore consists in the transformation of sulfur oxides into inert insoluble end products (gypsum) in a weakly acidic medium. The resultant attack of the material arising from this process is in principle not critical. Practice shows, however, that particular zones within the plant are more sensitive with regard to materials than others, apparently because of secondary reactions or nonequilibrium conditions. Effects such as local temperature variations, catalytically acting surface conditions, and the tendency toward formations of incrustations and concentrations of individual harmful ions contribute to this. This results in zones ranking in their aggressiveness from slight to very severe requiring a whole spectrum of corrosion-resistant materials, from high-alloy stainless steels to nickel alloys.

The lower-alloyed stainless steels can – as a simplification – only be used in the area of the FGD absorber in very mild conditions, at low temperatures and if the development of concentrations under incrustations or deposits can definitely be ruled out, that is to say, in the neutral to weakly acidic region, if the chloride ion concentration is adjusted to  $\leq 0.5\%$ . The operating range of the alloys mentioned in [Table 1](#), for example, alloy 31 (EN 1.4562/UNS N08031) commences in weakly acidic solutions and extends to strongly acidic solutions with moderate chloride ion attack. Higher-alloyed nickel alloys are

usually used at chloride concentrations  $>0.5\%$  and in acidic to very strongly acidic conditions as well as where temperature increases to well over  $70^\circ\text{C}$  are expected. At temperatures over  $100^\circ\text{C}$ , with large fractions of chloride in the flue gas and much incrustation with dust or gypsum deposits, only the highest-alloyed materials such as alloy C-276 (EN 2.4819/UNS N10276) and alloy 59 (EN 2.4605/UNS N06059) turned out to have long-term resistance, but even these two broadly similar materials in practice exhibited marked differences in resistance to the most aggressive FGD conditions. In the past, countless reference plants have shown that alloy 59 (EN 2.4605/UNS N06059) is the only material that is still in use in an undamaged condition, even after many years of operation, in areas that are at greatest risk of corrosion such as the raw gas inlet of an FGD plant in a lignite-fired power station, and can also guarantee safe operation of the plant for its entire service life.

With this simplified representation of the areas of application of the special steels and nickel alloys, it is, however, vital to bear in mind that the actual material specification is only possible with reference to the specific project and by the material manufacturer, the equipment fabricator, the engineering consultant, and the plant operator working together. In doing so, a large number of other parameters such as processing, fuels, mode of plant operation, operating temperatures, magnitude, and frequency of deviations from the state of equilibrium, proportion of particulates, incrustations, design, and geometry of the components have to be taken into account.

It is economically sensible to produce in metal all the components of the heat recovery system, the quencher with the raw gas inlet, the absorber, the ducting, the second heat exchanger, and the stack. Nickel alloys are to be used for the components that will be subjected to the most aggressive media. Heat recovery systems, raw gas inlet areas, as well as fixing and sealing elements of dampers, are as a rule the components that are usually subjected to high condensate attack, and must therefore be made from the most-resistant materials. In recent years, alloy 59 (EN 2.4605/UNS N06059) has been used to a large extent for this application. Alloy C-276 (EN 2.4819/UNS N10276) may also be selected for these components; however, with this, the reserve capacity of alloy 59 is not quite attained. Since failure of fastening components could be disastrous and because of the extreme crevice conditions encountered there, alloy 59 (EN 2.4605/UNS N06059) is recommended for any fastening components too.

Alloy 59 is also recommended as a universal filler metal in welding, taking advantage of its high corrosion resistance combined with its high thermal stability.

If a stable chemical system with pH values in the range 4.5–6.5 is formed in the absorber sump and thus the aggressiveness can be calculated, and also as long as the chloride content is not too high, even alloy 31 (EN 1.4562/UNS N08031) can be used, given an exact knowledge of the operating conditions. The condition for the use of the latter material, however, is the avoidance of gypsum deposits by designing the agitating units accordingly. If there are any doubts, it is better to manufacture the absorber sump region in alloy 59 (EN 2.4065/UNS 06059), for example, in clad form (10 + 4 mm). In the transition zone from the raw gas inlet to the wet–dry interface of the sump, certain areas have to be constructed with a greater amount of alloy 59 or alloy C-276.

This also applies to the quencher nozzle system up to the process-specific transition into the absorber region (bowl in the dual-circuit scrubber). The first absorption planes, that is, the first spray pipe layers above the quencher nozzle system, can be made from alloy 31 (EN 1.4562/UNS N08031). The head of a dual-circuit absorber may be made from a high-alloy stainless steel, depending on the effectiveness of the mist eliminator. The heat recovery system, which is coupled with the raw gas inlet must, even in the parts where the gas is clean, be fabricated from nickel alloys of the type alloy 59 (EN 2.4605/UNS N06059).

It is necessary to make a distinction between coal-fired and lignite-fired power stations where the clean-gas connections to the stack are concerned. While, as a rule, in lignite-fired power stations with heat recovery systems, very clean treated gas duct conditions usually occur and thus limited deposits form, the situation in coal-fired power stations is the opposite. In particular, if there is no heat recovery system and the mist eliminator system is not working effectively or is not rinsed out frequently, thick deposits form in coal-fired power stations, which can give rise to an extremely high risk of corrosion with simultaneous condensate formation, particularly in the 6 o'clock position and in the flow deviation areas, and at design-related flow interruption points. Clean-operating treated gas ducts can, in some cases, even be fabricated from alloy 31 (EN 1.4562/UNS N08031) or even from a 6Mo stainless steel such as alloy 926 (EN 1.4529/UNS N08926). With all other methods of operation, higher-alloyed nickel alloys must be used, particularly in the 6 o'clock position and at the other flow interruption points, to achieve a

corresponding increase in corrosion resistance. Stack inlet pipes or stacks built of solid metal usually require the materials alloy C-276 (EN 2.4819/UNS N10276) and alloy 59 (EN 2.4605/UNS N06059), since it is not possible to calculate accurately over the stack height and cross-section where the condensation zone occurs as a function of the external climate. Massive damages to coating systems (resin coatings with flake filling) as well as serious rotting of unprotected concrete stacks have recently increased the use of metallic nickel–chromium–molybdenum materials in stack construction.

Despite some fluid mechanics-related requirements, materials for shut-off fittings, for example, dampers and gates, must naturally be assessed according to their location in the gas stream. The material selection is obviously based on the aforementioned remarks.

On the basis of past experience, the selection of suitable materials specific to the component can guarantee a better long-term reliability and thus higher plant availability. If costs dictate thin-walled application of highly corrosion-resistant materials, this can be produced by the cladding of existing or new carbon steel structures with thin large sheets of nickel–chromium–molybdenum materials (wallpapering), or by the use of explosively or roll-bond clad composites with highly corrosion-resistant cladding materials.

## References

1. Agarwal, D. C. Nickel and Nickel Alloys In *Uhlig's Corrosion Handbook*; 2nd ed.; Winston Revie, R., Ed.; John Wiley & Sons, 2000; Chapter 45, pp 831–851.
2. Friend, W. Z. *Corrosion of Nickel and Nickel-Base Alloys*; John Wiley & Sons: New York, 1980.
3. Council of Europe's Policy Statements Concerning Materials and Articles Intended to Come into Contact with Foodstuffs – Policy Statement Concerning Metals and Alloys – Technical Document – Guidelines on Metals and Alloys Used as Food Contact Materials – 13.02.2002, – [www.coe.fr/soc-sp](http://www.coe.fr/soc-sp), Partial Agreement Department in the Social and Public Health Field, Council of Europe, Avenue de l'Europe, F-67000, Strasbourg.
4. Council Directive 98/83/EC of November 1998 on the quality of water intended for human consumption, Official Journal of the European Communities, 5.12.98, L 330/32–54.
5. International Nickel Co., Inc., Corrosion Resistance of Nickel and Nickel Containing Alloys in Caustic Soda and Alkalis, Corrosion Engineering Bull. CEB-2, 1973.
6. Heubner, U. In *Nickel Alloys and Special Stainless Steels*; 3rd ed.; Heubner/Klöwer, et al., Ed.; Expert Verlag: Renningen, 2003; Chapter 2, pp 47–93.
7. Craig, B. D.; Anderson, D. S. Eds.; *Handbook of Corrosion Data*, 2nd ed.; ASM International: Materials Park, OH, 1995.

8. Büth, H. J.; Köhler, M. *Werkstoffe Korrosion* **1992**, *43*, 421–425.
9. Köhler, M.; Heubner, U. CORROSION 94; NACE International: Houston, TX, 1994, Paper No. 230.
10. Agarwal, D. C.; Heubner, U.; Köhler, M.; Herda, W., *Mater. Perform.* **1994**, *33*(10), 64–68.
11. LaQue, F. L.; Flint, G. N. *Nickel und Nickellegierungen*; Springer: New York, 1970; Chapter H, pp 356–398.
12. Alves, H.; Godinho, V.; Köster, U.; Ferreira, M. G. Proceedings EUROCORR. 2005, Lisbon, Sept. 2005.
13. Köhler, M.; Heubner, U.; Eichenhofer, K.-W.; Renner, M. CORROSION 97; NACE International: Houston, TX, 1997, Paper No. 115.
14. Heubner, U. In *Nickel Alloys and Special Stainless Steels*; 3rd ed.; Heubner/Klöwer, et al., Eds.; Expert Verlag: Renningen, 2003; Chapter 1, pp 1–46.
15. Agarwal, D. C.; Herda, W. *Mater. Corros.* **1997**, *48*, 542–548.
16. Rhodes, P. R. *Corrosion* **2001**, *57*(11), 923–966.
17. Kirchheiner, R.; Wahl, V. In *Nickel Alloys and Special Stainless Steels*; 3rd ed.; Heubner/Klöwer, et al., Eds.; Expert Verlag: Renningen, 2003; Chapter 8, pp 255–294.
18. Riedel, G.; Voigt, C.; Werner, H.; Heubner, U. *Mater. Corros.* **1999**, *50*, 452–462.
19. Alves, H.; Aberle, D.; Stenner, F. CORROSION 2007; NACE International: Houston, TX, 2007, Paper No. 07215.
20. Alves, H.; Werner, H.; Agarwal, D. C. CORROSION 2006; NACE International: Houston, TX, 2006, Paper No. 06222.
21. Heubner, U.; Köhler, M. *Werkstoffe Korrosion* **1992**, *43*, 181–190.
22. Kirchheiner, R.; Köhler, M.; Heubner, U. *Werkstoffe Korrosion* **1992**, *43*, 388–395.
23. Riedel, G.; Voigt, C.; Werner, H. *Mater. Corros.* **1997**, *48*, 518–527.
24. Agarwal, D. C.; Herda, W. R.; Klöwer, J. CORROSION 2000; NACE International: Houston, TX, 2000, Paper No. 501.
25. Agarwal, D. C.; Brill, U.; Behrens, R. CORROSION 2004; NACE International: Houston, TX, 2004, Paper No. 04281.
26. Butts, M. D.; Cripps, P. R.; Gilbertson, O.; Agarwal, D. C. In AIRPOL Symposium 2004, August 29, 2004, Washington, DC; NACE International: Houston, TX, 2004.
27. Heubner, U.; Rockel, M. B.; Wallis, E. *ATB Metall.* **1985**, *XXV*(3), 235–241.
28. Hibner, E. L.; Pucket, B. C.; Patchell, J. K. CORROSION 2004; NACE International: Houston, TX, 2004, Paper No. 04110.
29. White, F. E.; Jallouli, E. M.; Moustaqssa, A.; Agarwal, D. C. In AIChE Central Florida Section, 23rd Annual Memorial Weekend Conference on Phosphate Technology, Clearwater, Florida, May 28–30, 1999.
30. Alves, H.; Stenner, F.; Agarwal, D. C.; Hoxha, A. CORROSION 2006; NACE International: Houston, TX, 2006, Paper No. 06221.
31. Thomas, B.; Agarwal, D. C. CORROSION 2007; NACE International: Houston, TX, 2007, Paper No. 07216.
32. Heubner, U.; Kirchheiner, R.; Rockel, M. CORROSION 91; NACE International: Houston, TX, 1991, Paper No. 321.
33. Klöwer, J.; Schlerkmann, H.; Pöpperling, R. CORROSION 2001; NACE International: Houston, TX, 2001, Paper No. 01004.
34. Voigt, C.; Riedel, G.; Werner, H.; Köhler, M. *Mater. Corros.* **1998**, *49*, 489–495.
35. Köhler, M.; Heubner, U.; Eichenhofer, K. W.; Renner, M. *Stainless Steel World* **1999**, *11*(4), 38–49.
36. Renner, M. H.; Michalski-Vollmer, D. In Proceedings of Stainless Steel World 99 Conference, KCI Publishing BV, Zutphen, 1999; Book 2, pp. 443–452.
37. Werner, H.; Riedel, G.; Brill, U. *Mater. Corros.* **2002**, *53*, 893–897.
38. Gramberg, U. *Stainless Steel World* **1996**, *8*, 24–29.
39. Alves, H.; Horn, E. M.; Klöwer, J. In *Nickel Alloys and Special Stainless Steels*; 3rd ed.; Heubner/Klöwer, et al., Eds.; Expert Verlag: Renningen, 2003; Chapter 7, pp 226–254.
40. Klöwer, J.; Rommerskirchen, I.; Kolb-Telieps, A.; Köhler, M. CORROSION 2000; NACE International: Houston, TX, 2000, Paper No. 636.
41. Herbsleb, G. *BBR* **1989**, *40*, 554–559.
42. Koppe, J.; Lausch, H.; Heubner, U.; Brill, U. *Chem. Ingenieur Technik* **1999**, *71*, 609–612.
43. Vollmer, T.; Gümpel, P.; Blaise, M.; Racky, W. *Mater. Corros.* **1995**, *46*, 92–97.
44. Gümpel, P.; Vollmer, T.; Blaise, M.; Racky, W. *Stainless Steel Eur.* **1995**, 47–51.
45. Heubner, U.; Hoffmann, T.; Köhler, M. *Mater. Corros.* **1997**, *48*, 785–790.
46. Köhler, M. *Mater. Corros.* **1997**, *48*, 528–534.
47. Riedel, G.; Kirchheiner, R.; Heubner, U. *Mater. Corros.* **1997**, *48*, 113–124.
48. Heubner, U. L.; Altpeter, E.; Rockel, M. B.; Wallis, E. *Corrosion* **1989**, *45*, 249–259.
49. Altpeter, E.; Heubner, U.; Rockel, M. *Werkstoffe und Korrosion* **1992**, *43*, 96–105.
50. Riedel, G.; Werner, H.; Voigt, C. *Werkstoffwoche*; Wiley VCH, 1999; Vol. 3, pp 275–280.
51. Heubner, U.; Rockel, M.; Wallis, E. *Werkstoffe Korrosion* **1989**, *40*, 459–466.
52. Alves, H.; Hoxha, A.; Stenner, F.; Coppe, P. Proceedings COVAPHOS II Conference, Marrakech, 9–11 November 2006.
53. Hoxha, A.; Stenner, F.; Alves, H.; Novello, F. Proceedings IFA 2006, Vilnius, 25–28 April 2006.
54. Korkhaus, J. Materials for Future Chemical Plant Concepts, Achema Conference, Workshop Nickel Alloys Selection in the Chemical Process Industry, Frankfurt/Main, 15–19 May 2006.
55. Alves, H.; Werner, H. CORROSION 2004; NACE International: Houston, TX, 2004, Paper No. 04235.
56. Alves, H.; Werner, H. Proceedings of the 16th International Corrosion Congress, Beijing, 19–24 September 2005.
57. BAM – List – Requirements for Tanks for the Carriage of Dangerous Goods – 8th edition, Federal Institute for Materials Research and Testing (BAM), Berlin 2005.
58. Weltchev, M.; Baessler, R.; Werner, H.; Alves, H.; Behrens, R. CORROSION 2006; NACE International: Houston, TX, 2006, Paper No. 06688.
59. Weltchev, M.; Baessler, R.; Werner, H.; Alves, H. CORROSION 2008; NACE International: Houston, TX, 2008, Paper No. 08180.

## 3.06 Aqueous Corrosion of Cobalt and its Alloys

### A. Neville

Institute of Engineering Thermofluids, Surfaces and Interfaces, School of Mechanical Engineering, University of Leeds, Leeds LS2 9JT, UK

### U. Malayoglu

Faculty of Engineering, Dokuz Eylul University, Bornovo, Izmir, Turkey

© 2010 Elsevier B.V. All rights reserved.

<b>3.06.1</b>	<b>Metallurgy</b>	1916
3.06.1.1	Introduction	1916
3.06.1.2	Alloying	1917
3.06.1.3	Microstructure and Microstructural Influences	1918
3.06.1.4	Alloy Systems	1920
3.06.1.5	Processing	1920
3.06.1.6	Strengthening Mechanisms	1922
<b>3.06.2</b>	<b>Corrosion</b>	1923
3.06.2.1	Electrochemistry	1923
3.06.2.2	Passive Films on Co-Base Alloys	1923
3.06.2.3	Corrosion of Cobalt-Based Alloys	1924
3.06.2.4	Oxidation	1926
3.06.2.5	Corrosion in Biomedical Applications	1927
3.06.2.5.1	Joints	1927
3.06.2.5.2	Galvanic corrosion	1928
3.06.2.6	Erosion-Corrosion	1929
3.06.2.7	Wear and Wear-Corrosion of Cobalt-Base Alloys	1931
<b>References</b>		1934

### Glossary

**Stellite** A family of cobalt–chromium based alloys typically containing additions of carbon, tungsten, and molybdenum and notable for their extreme hardness and good corrosion resistance.

### Abbreviations

**Bcc** Body centred cubic  
**Fcc** Face centred cubic  
**GTAW** Gas tungsten arc welding  
**Hcp** Hexagonal close packed  
**HIP** Hot isostatic pressing  
**MoM** Metal-on-metal  
**SFE** Stacking fault energy  
**TCP** Topologically close packed  
**THR** Total hip replacement  
**TJR** Total joint replacement  
**TWL** Total weight loss

### Symbols

$E_{\text{corr}}$  Corrosion potential  
 $i_{\text{corr}}$  Corrosion current density

## 3.06.1 Metallurgy

### 3.06.1.1 Introduction

Cobalt is one of the transition metals appearing between iron and nickel; it was discovered by Brandt in 1735. Depending on temperature, there are two allotropic modifications of cobalt: face centered cubic (fcc), which is stable above 690 K and hexagonal close packed (hcp), stable below 690 K. Pure cobalt is soft and it has poorer oxidation resistance than nickel and iron. However, the alloying of cobalt with chromium and various quantities of carbon and tungsten results in the family of Stellite alloys, which have excellent corrosion and wear resistance. Cobalt is generally obtained as a secondary product from the mining of other elements, particularly copper and



nickel; relatively minor quantities (15%) derive from primary cobalt mining.<sup>1</sup> Current production is around ~50 000 tonnes per annum at a producer cost generally from three to five times that of nickel.

The cobalt-base alloys are extremely resistant to many forms of wear and moderately resistant to many forms of corrosion. For example, alloys optimized for wear resistance generally include significant carbon addition, which results in the formation of carbides in the microstructure during alloy solidification. These carbides increase the hardness of the alloys and their resistance to low-stress abrasion. Key applications are in wear and erosion-resistant alloys (e.g., the Stellite family and cemented carbides) and in high temperature oxidation-resistant alloys: these comprise ~40% of cobalt use. The balance of production is used in batteries (25%), magnetic alloys (6%), colors and pigments (10%), catalysts (9%), etc.

Alloys designed for service in severely corrosive environments typically contain low carbon levels. Not only does this markedly improve resistance to corrosion, but also it increases ductility. The chief benefits of high carbon content are increased hardness and enhanced resistance to low-stress abrasion, both of which increase with increasing carbon content. Aspects of the corrosion resistance are discussed in detail later in the chapter.

In forming carbides, the carbon ties up a portion of vital alloying elements, such as chromium. The effective chromium content from a corrosion standpoint (the chromium remaining in the solid solution) is therefore considerably lower than indicated by the nominal composition. Carbide forming elements such as tungsten (which forms  $W_6C$  type carbides) may reduce the amount of carbon required to reach the eutectic composition.

### 3.06.1.2 Alloying

Historically, many of the commercial cobalt-base alloys are derived from the cobalt–chromium–tungsten and cobalt–chromium–molybdenum ternaries first investigated by Elwood Haynes in the beginning of the twentieth century.<sup>2</sup> He discovered the high strength and stainless nature of the binary cobalt–chromium alloy, and he later identified tungsten and molybdenum as powerful strengthening agents within the cobalt–chromium system. When he discovered these alloys, Haynes named them the Stellite alloys after the Latin ‘stella’ (star), because of their star-like microstructure. Having discovered their high strength at elevated temperatures, Haynes also promoted the use of Stellite alloys as cutting tool materials. In [Figure 1](#) a typical microstructure of the Stellite 6 alloy is shown and the

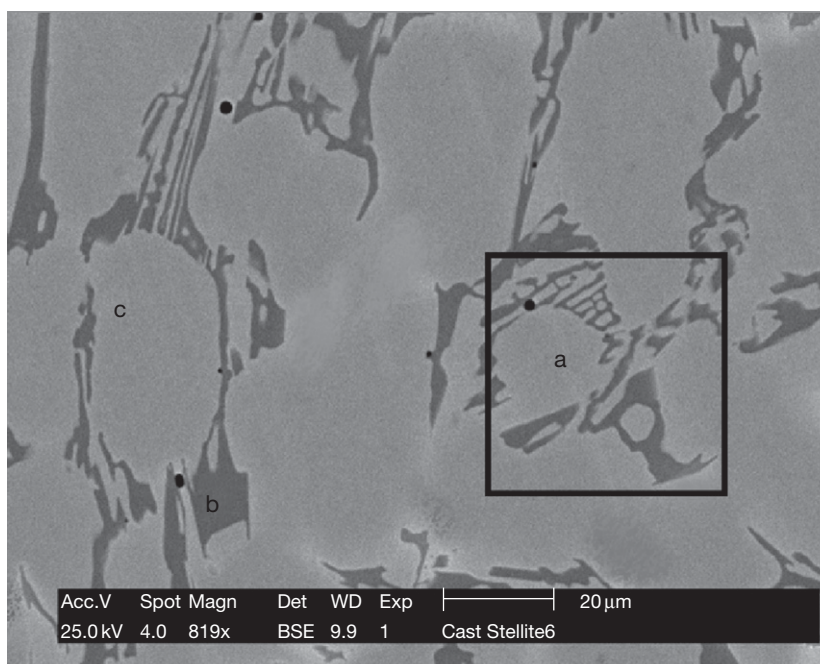


**Figure 1** Typical microstructure of Stellite 6 alloy: (a) analysis area composition in wt% is 60.8% Co, 29.8% Cr, 6.2% W, 1.7% C, 1.4% Fe (b) is eutectic Cr-rich carbide, and (c) is the Co rich matrix. Reproduced from Malayoglu, U. PhD Thesis, Heriot-Watt University, 2005.<sup>3</sup>

complex structure of eutectic carbides and the Co-rich matrix is clear.

The chemical constitution of cobalt alloys is analogous to the general family of stainless steels and the role of major and minor alloying elements is virtually identical throughout these austenitic alloy systems. The addition of alloying elements alters the thermodynamic stability of the fcc compared with the hcp phases by either enlarging or constricting their fields. These alloys also effect the martensitic transformation by influencing the  $M_s$  (martensitic start) and  $A_s$  (austenite start) temperatures.

In cobalt-base alloys, the key element, chromium, is added in the range of 20–30 wt% to improve corrosion and wear resistance and for some measure of solid-solution strengthening. Where carbide precipitation strengthening is a desirable feature, chromium also plays a strong role through the formation of a series of varying chromium-carbon ratio carbides such as  $M_7C_3$  and  $M_{23}C_6$ .  $M_7C_3$  carbides, which have a hexagonal crystal structure and contain ~70 wt% Cr, ~12 wt% Co, and small amounts of other metallic elements in the alloy.

The refractory elements, tungsten and molybdenum, are utilized as the major solid-solution strengtheners for both wrought and cast cobalt alloys, while those of lower solubility such as tantalum, columbium, zirconium, and hafnium are generally more effective in their carbide forming role. Molybdenum and tungsten produce strengthening by formation of intermetallic compounds of  $Co_3M$  and MC carbides and the formation of  $M_6C$  carbides

For cast alloys, Morrow *et al.*<sup>4</sup> demonstrated that replacing tungsten with an atomic equivalent addition of molybdenum improves elevated tensile and rupture ductility without decreasing strength in alloys such as FSX 414 and MM 509. Additionally, alloy cost and density decreases with little change in expansion coefficient or microstructural characteristics. However, molybdenum addition slightly decreases the solidus and liquidus temperatures and increases the total solidification range, which somewhat alters the carbide morphology and produces additional eutectic carbides.

The refractory element rhenium has been successfully utilized in nickel alloys for solid solution strengthening; however, its potential in cobalt alloys has not fully been explored. Like tungsten, it exhibits extensive solubility in the matrix and increases the solidus and liquidus temperatures. Of the alloying elements, tungsten produces a favorable increase in melting temperature. Tantalum has been successfully utilized as a replacement for tungsten in high temperature sheet alloys MM-918 and S-57, where

**Table 1** The effect of several elements in cobalt-base superalloys

<i>Element</i>	<i>Effect</i>
Chromium	Improves oxidation and hot-corrosion resistance; produces strengthening by formation of $M_7C_3$ and $M_{23}C_6$ carbides
Molybdenum	Solid-solution strengtheners; produce strengthening by formation of intermetallic compound $Co_3M$ ; formation of $M_6C$ carbide
Tungsten	Solid-solution strengtheners; produce strengthening by formation of intermetallic compound $Co_3M$ and MC carbide; formation of $M_6C$ carbide
Tantalum	
Columbium	Improves oxidation resistance; formation of intermetallic compound CoAl
Aluminum	
Titanium	Produces strengthening by formation of MC carbide and intermetallic compound $Co_3Ti$ ; with sufficient nickel produces strengthening by formation of intermetallic compound $Ni_3Ti$
Nickel	Stabilizes fcc form of matrix; produces strengthening by formation of intermetallic compound $Ni_3Ti$ ; improves forgeability
Boron	Produce strengthening by effect on grain boundaries and by precipitate formation; zirconium produces strengthening by formation of MC carbide
Zirconium	Produces strengthening by formation of carbides MC, $M_7C_3$ , $M_{23}C_6$ , and possibly $M_6C$
Carbon	
Yttrium	Increases oxidation resistance
Lanthanum	

Source: Anon, Cobalt Monograph, Centre d'Information du Cobalt/Battelle, 1958.

some improvement in oxidation resistance was also demonstrated. The effect of different alloying elements is summarized in [Table 1](#).

### 3.06.1.3 Microstructure and Microstructural Influences

The microstructure of Stellite alloys varies considerably with composition. They may either be in the form of hypoeutectic structure consisting of primary dendrites of a cobalt-rich solid solution surrounded by eutectic carbides, or of hypereutectic type containing large idiomorphic primary chromium rich carbides and eutectic.

Among the alloying elements, carbon is found to have a large influence on the microstructure, causing a change from a hypoeutectic to hypereutectic alloy. [Figure 2](#) shows the phase diagram for the

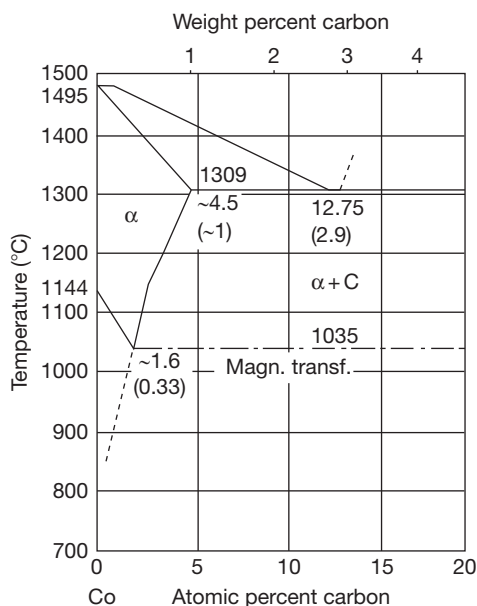


**Figure 2** Cobalt-carbon binary system. Reproduced from Atamert, S. Stability, wear resistance and microstructure of iron, cobalt and nickel-based hardfacing alloys, PhD thesis, University of Cambridge UK, 1989.<sup>5</sup>

carbon-cobalt alloy system. As can be seen in the hypoeutectic side of the system (<1.6at% of C) the liquidus temperature of the alloy decreases by  $\sim 14^\circ\text{C}$  for each 1% increase in carbon content. Carbon is clearly critical to those casting alloys formulated for the highest creep rupture strength levels, since carbide strengthening is the primary precipitation hardening mechanism utilized in the cobalt alloy system. The control of carbon is critical for tensile and rupture strength and ductility since it has been shown that a nonlinear increase in strength occurs over a range of  $\sim 0.3\text{--}0.6\%$  carbon.

The strength of most cobalt base superalloys is derived from the carbide phases present in the matrix and distributed around the grain boundaries. The carbides that form depend on the composition and thermal history of the material. The carbide former elements are from group IV (Ti, Zr, Hf), group V (Cb, Ta), and group VI (Cr, Mo, W). The types of carbides that are formed are as follows (M and C represents metal and carbon atoms respectively):

$\text{M}_3\text{C}_2$ : rhombic, a high chromium content carbide which forms at low Cr/C ratio;

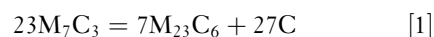
$\text{M}_7\text{C}_3$ : trigonal, a high chromium content carbide which forms at a slightly higher Cr/C ratio;

$\text{M}_{23}\text{C}_6$ : cubic, a high chromium content carbide which forms at an higher Cr/C ratio, when the Cr is greater than 5 wt% of the alloy;

$\text{M}_6\text{C}$ : complex cubic, a carbide phase whose volume fraction increases as refractory metals are introduced;

MC: fcc NaCl structure, a carbide comprising metal groups IV and VI.

These carbides are listed above in the order of increasing stability, or free energy of formation. The stronger the carbide formers used, the greater is the tendency to form  $\text{M}_6\text{C}$  and MC carbides. The type of carbides that form is dependent upon both thermal history and composition. Lane and Grant<sup>6</sup> suggested a transformation of  $\text{M}_7\text{C}_3\text{--M}_{23}\text{C}_6$  during aging in an X-40 casting, which is described by the reaction



This demonstrates that a nonequilibrium structure exists in Co castings at high temperatures.

The microstructure of cobalt base superalloys is thus a combination of MC,  $\text{M}_7\text{C}_3$ ,  $\text{M}_{23}\text{C}_6$ , and  $\text{M}_6\text{C}$  carbides. In the cast structures, both composition and shape help to distinguish one carbide from another. The MC carbides have two characteristic shapes, a Chinese script and a block-like angular particles. The differences are believed to be the result of formation at various times during solidification. Block-like angular MC carbides may form initially before the bulk of the melt has started to solidify, whereas in the Chinese script, MC carbide is formed within the eutectic composition.<sup>7</sup>

$\text{M}_{23}\text{C}_6$  carbides are found mostly as fine plates interlayered with the cobalt matrix. This eutectic structure has a block-like shape. Subsequent heating of the cast structure can dissolve the  $\text{M}_{23}\text{C}_6$  carbides. Upon aging, the carbides are precipitated as fine particles, usually near the eutectic  $\text{M}_{23}\text{C}_6$  islands. In contrast to other carbides, the  $\text{M}_6\text{C}$  carbides do not have a characteristic morphology. Other important microstructural features of cobalt base superalloys are stacking faults, which have been reported to be present on all  $\{111\}$  planes.<sup>8</sup> Stacking faults appear to be related to the tendency to form hcp. Since stacking faults in fcc materials have an hcp structure, this is not surprising.

Many of the chemical attributes of the cobalt-based alloys derive from their crystallographic characteristics, which are summarized in Figure 3. The influence of alloying elements such as iron and nickel is explained through their effect on the stacking fault energy (SFE). Ni, Mn, and Fe have a strong effect on the SFE stabilizing the fcc allotrope, but Mo, W and Cr tend to stabilize the hcp allotrope and decrease the SFE. The excellent erosion resistance of cobalt-based

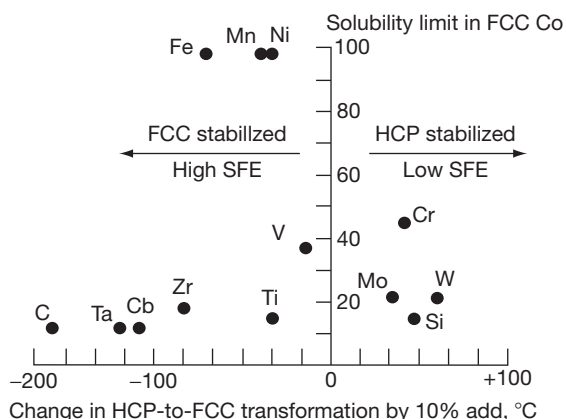


**Figure 3** Effect of alloying elements on the fcc-hcp transformation in cobalt as a function of solubility. Reproduced from Sims Chester, T.; Stoloff, N. S.; Hagel, W. C. *Super Alloys II*; John Wiley & Sons: London, 1987.<sup>9</sup>

Stellite alloy is greatly attributed to the low SFE, which in turn means higher stacking fault probability and a greater chance for the formation of  $\epsilon$  hcp platelets. The lower the SFE (the greater the width of stacking fault), the more difficult cross-slip is and the higher the work hardening and the strain to fracture. The materials with low SFE tend to strain harden rapidly, and show the highest galling resistance.

The effect of stacking faults may be detrimental to overall mechanical properties of cobalt base superalloys. Stacking faults have been shown to contribute to the strength of materials by inhibiting dislocation flow.<sup>5</sup> They also serve as sites for precipitation of second phases in cobalt base superalloys, which can likewise increase strength.<sup>10</sup> In contrast, it has been suggested that excessive stacking faults decrease the ductility of cobalt base superalloys to a value unacceptable for commercial use.

Stellite 6B is more likely to transform to hcp phase than most cobalt-base alloys since the fcc stabilizing elements iron and manganese are present in small amounts. Although carbon has a strong stabilizing effect in solution, most of it is tied as carbides. In fact, by suitable heat treatment, partial transformation may be achieved by thermal exposure alone.

Addition of iron and nickel are known to increase the stability of the fcc phase (and therefore, the SFE) of cobalt-base alloy. Furthermore, an increase in the SFE results in a change in the mode of deformation. The  $\alpha \rightarrow \epsilon$  transformation occurs to a lesser extent and there is a greater tendency towards slip of undissociated dislocations  $\{111\}$  phase. The  $\alpha \rightarrow \epsilon$  phase transformation and the formation of mechanical twins have

been found to cause rapid increase in the work hardening rate while also producing a maximum in the strain to fracture. These two phases are considered necessary for erosion resistance and therefore, any factor suppressing these structural changes must lead to a decrease in resistance.

### 3.06.1.4 Alloy Systems

The cobalt-chromium-carbon system is characterized by the affinity of chromium for the formation of carbides of various types in which cobalt can replace some of the chromium. Wever and Haschimoto<sup>11</sup> carried out extensive studies on the solidification behavior of cobalt-chromium-carbon alloys of various compositions by thermal analysis. According to their findings the 30% Cr, 1% C alloy has a solidification range (the temperature difference between the solidus and liquidus temperatures) of  $\sim 150^\circ\text{C}$ . In the carbon content range of 1.0% to 1.7%, the solidification range decreases by  $\sim 5.5^\circ\text{C}$  with each 0.1% increase in carbon content. Also, they showed that at 1% carbon, an increase in chromium from 20% to 30% results in reduction of the solidification range by  $\sim 50^\circ\text{C}$ .

Koster and Spencer<sup>12</sup> studied the constitution of the cobalt-chromium-tungsten alloy system and their work showed for up to  $\sim 30\%$  chromium and 15% tungsten the microstructure at room temperature consists of only the cobalt base solid solution. At higher chromium and tungsten contents various intermetallic phase would form in addition to the solid solution.

The carbon-tungsten-carbon system has been the subject of many investigations concerning cemented tungsten carbides (WC and  $\text{W}_2\text{C}$ ), dealing mainly with alloys containing less than 25% cobalt. However, Rautala and Norton<sup>13</sup> covered most of the alloy system and produced diagrams showing phase equilibria at  $1400^\circ\text{C}$ . These studies show that if the carbon content is maintained close to that required for stoichiometric formation of WC there will be a stable two-phase region of Co + WC below  $1400^\circ\text{C}$ . Carbon deficiencies lead to formation of  $\text{Co}_3\text{W}_3\text{C}$  while carbon excess leads to the formation of graphite. However, it has to be mentioned that up to  $\sim 7.5\%$  WC is soluble in cobalt.<sup>13</sup> Thus in alloys containing small quantities of carbon and tungsten, the formation of WC phase would not be expected.

### 3.06.1.5 Processing

There are numerous processing techniques depending on the application and the environment available to provide good wear and corrosion resistance parts from



cobalt base alloys. The effect of different processing techniques on the microstructure and the mechanical properties has been studied by different researchers and a short review is presented later in the chapter.

Wrought cobalt–tungsten base alloys were studied by Adkins *et al.*<sup>14</sup> In the binary alloys, the room temperature hardness increased with increasing tungsten content up to 15%. There was a slight drop in hardness for alloys containing over 15% tungsten. Solution-treated and quenched alloys showed a martensitic  $\text{Co}_3\text{W}$  phase.

Stellite alloys are often used as a coating for hard-facing applications or as castings. The casting and hard-facing of Stellite is, however, difficult and leads to an inhomogeneous coarse grain structure and also to excess dilution and improper adherence when there is overlaying.

Mohamed *et al.* studied the localized corrosion behavior of alloy Stellite 6 produced by hot isostatic pressing (HIP) and by wet powder pouring using electrochemical techniques.<sup>15</sup> In another work Wong-Kian *et al.* compared the erosion corrosion behavior of HIPed and welded Stellite coatings<sup>16</sup> and showed that HIPed alloys have lower mass loss due to finer microstructure. Malayoglu also confirmed the superior resistance of HIPed Stellite 6 and attributed this to the different microstructure with spherical carbides and the enriched Cr in solid solution in the matrix.<sup>3</sup> Figure 4 shows the HIPed microstructure of Stellite 6.

Frenk and Kurz<sup>17</sup> investigated the solidification conditions and microstructure of a cobalt base alloy.

They concluded that different processing conditions can be achieved using laser surface cladding. For example, a variation in the laser scanning rate over two orders of magnitude from  $1.67$  up to  $167 \text{ mm s}^{-1}$  led to a considerable refinement of the microstructure. Antony<sup>18</sup> compared the wear performance of various forms of Stellite alloy 6B. He showed that gas tungsten arc welded (GTAW) alloy had better cavitation resistance compared to investment cast, wrought and oxyacetylene Stellite 6B deposit. Berns and Wendl analyzed the microstructure of the alloy Stellite 6 in the cast, forged and powder metallurgy state and compared them to the mechanical and wear properties.<sup>19</sup>

Weld overlays are used for economic and technical reasons. From an economic standpoint, it is sensible to use relatively expensive wear and corrosion resistant alloys only where their properties are necessary. From a technical standpoint, many wear-resistant alloys are brittle by nature and thus unsuitable for use in bulk form. The largest problem associated with the use of weld overlay material is dilution that is, the intermixing which occurs with the substrate material, generally stainless steel. It has been reported that dilution of iron into the cobalt-base alloy is detrimental to the corrosion and cavitation resistance of cobalt-base alloys.<sup>20</sup>

Cobalt and cobalt–molybdenum binary alloys have been the subject of work by Bibring and coauthors.<sup>21</sup> In alloys containing 8% or 10% molybdenum, quenching results in a structure that consists primarily of the hcp low temperature phase, and a significant proportion of the fcc nonequilibrium high temperature phase. When aged at a temperature below the solubility limit, the supersaturated hcp phase increases rapidly in hardness, while the fcc phase remains unchanged. This selective hardening of the hcp phase is due to the appearance of a phase with a composition corresponding to  $\text{Co}_3\text{Mo}$ . Darby and Beck<sup>22</sup> investigated the cobalt–chromium–molybdenum alloys and they reported an existence of  $\text{Co}_{13}\text{Cr}_{17}$ , which had a beneficial effect on the mechanical properties of the alloy. Silverman *et al.*<sup>23</sup> increased the proportion of chromium and molybdenum in commercial alloy Stellite 21. They found that room temperature hardness increased with increasing proportion of chromium and molybdenum.

Precipitation of an intermetallic compound in cobalt–chromium–molybdenum alloys was found to increase the room-temperature hardness in alloys containing 20% chromium and up to 16% molybdenum. A study of precipitation hardening in alloys containing 12.0% to 17.5% chromium and from 15% to 20% molybdenum was made by Lux and

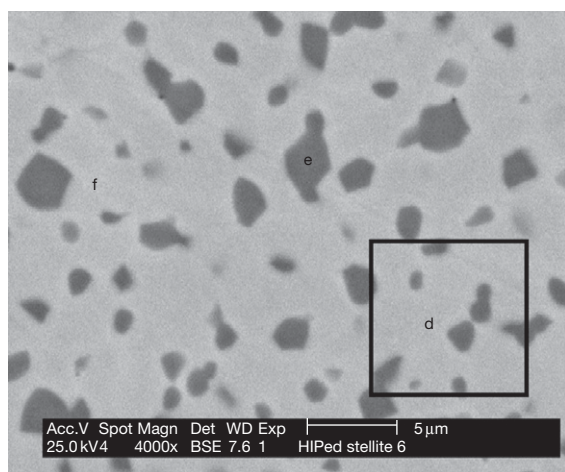


**Figure 4** Microstructure of HIPed Stellite 6 (e) Cr-rich carbides, (f) Co-rich matrix. Reproduced from Malayoglu, U. PhD Thesis, Heriot-Watt University, 2005.

Bollmann.<sup>24</sup> The alloys as-cast all contained a coarse precipitate of  $\text{Co}_7\text{Mo}_6$ . Some of the alloys in the cast condition showed Widmanstätten structure. It was suggested that this structure was associated with the formation of a  $\text{Co}_3\text{Mo}$  super lattice. Generally speaking, the precipitate observed in cast specimens that had been aged for 100 h at  $1000^\circ\text{C}$  gave an X-ray pattern that corresponded to  $\text{Co}_7\text{Mo}_6$ , but chemical analysis of precipitates indicated a partial replacement of the molybdenum by chromium. The amount of chromium in the precipitate increased with aging temperature. At room temperature, the data offered three possible relationships between the precipitate and the matrix: a  $\text{Co}_3\text{Mo}$  super lattice, a coherent  $\text{Co}_3\text{Mo}$  precipitate, or a coherent  $\text{Co}_7\text{Mo}_6$  precipitate.

### 3.06.1.6 Strengthening Mechanisms

Intermetallic compounds play an important role in the microstructure of Co-base alloys and the next few paragraphs discuss the nature of these and their role in affecting the properties of Co-base alloys.

Geometrically close-packed (GCP) phases are usually designated by the chemical formula  $\text{A}_3\text{B}$ , where A is the larger atom. For example, in nickel base superalloys a fine precipitate  $\text{Ni}_3(\text{Al},\text{Ti})$  contributes greatly to high temperature strength. Because of its strengthening characteristics and high solution temperature, this phase has improved tremendously the high temperature properties of nickel superalloys, and even surpassed the properties of the cobalt systems. The generation of GCP phases within cobalt alloys is substantially more difficult since the chemical and crystallographic stability is affected by a lattice mismatch that is rarely less than 1%. In contrast, topologically close-packed phases (TCP) are usually detrimental to high temperature mechanical properties of cobalt superalloys. These phases are made up of close-packed layers of atoms separated from one another by relatively large interatomic distances forming a characteristic topology. By contrast, GCP phases are characterized as close-packed in all directions. The most common TCP phases are  $\sigma$ ,  $\mu$ , and R which are electron compounds. The general formula for a TCP phase is:  $(\text{Co},\text{Ni})_x(\text{Cr},\text{Mo},\text{W})_y$ , where  $x$  and  $y = 1-7$ . The structure of the TCP-type phases ( $\sigma$ ,  $\mu$  and R) are as follows:

$\sigma$ = complex body centre tetragonal	30 atoms/unit cell
$\mu$ = rhombohedral	13 atoms/unit cell
R = rhombohedral	53 atoms/unit cell

Laves phases are the most common intermetallic compounds of the TCP type. The chemical formula for Laves phase is  $\text{A}_2\text{B}$ , where A and B are two different metallic elements and occur in high temperature superalloys when excessive amounts of refractory metals are added. These phases precipitate as both plate and block structures and are generally detrimental to mechanical properties.

The primary strengthening mechanism in cobalt base alloys is precipitation hardening; principally by the presence of carbides in the matrix and grain boundaries. The carbides, especially  $\text{M}_{23}\text{C}_6$ , precipitate at the grain boundaries, pin the grain boundaries preventing grain boundary sliding, or in the case of higher carbon content, the carbide network may support some of the load. The large carbide particles can act as dislocation generators under the influence of a stress and the subsequent dislocation interaction can give rise to an increase in the flow stress of the metal. Regarding carbides, another important mode of strengthening arises from precipitation of fine  $\text{M}_{23}\text{C}_6$  particles on stacking faults. This provides a rather uniform dispersion of interlocking structural effects caused by the hard carbide particles at stacking faults and stacking fault intersections.

Beside carbides, another form of second phase particles in cobalt-based alloys are intermetallic compounds as mentioned earlier. These phases have to be considered as they can cause a significant loss of both strength and ductility. Their deleterious effect is due primarily to the chemical partitioning effect caused by the mass presence of the phase itself, thus depleting the matrix of solute-strengthening atoms. As mentioned earlier, solid solution strengtheners include mainly the refractory elements such as chromium, molybdenum and tungsten. These atoms contribute to strengthening in a number of ways: they inhibit recovery by binding vacancies; and also they impede dislocation glide through the existence of interstitial complex around the refractory atoms. The fcc-hcp transformation in cobalt alloys has not been fully utilized in the development of desired mechanical properties. This is primarily due to the fact that the details of the allotropic transformation have not been well understood. The first detailed examination using transmission electron microscopy of the fcc-hcp transformation in the Co-Cr-Mo-C system was carried out by Vander Sande *et al.*<sup>25</sup> Their work was initiated by earlier findings of property modifications in response to heat treatment and processing variables and associated microstructural changes.



### 3.06.2 Corrosion

#### 3.06.2.1 Electrochemistry

Compared with iron, cobalt is significantly more noble and part of its domain of stability lies above the hydrogen stability line for water. Compared with nickel, it is slightly less noble; the main difference in chemistry being a considerably larger stability for the Co(III) oxidation state compared to the corresponding nickel species. Cobalt is passive in neutral to alkaline pH but dissolves in aerated and deaerated acids below pH 7. The Pourbaix diagram for cobalt is shown in Figure 5.

#### 3.06.2.2 Passive Films on Co-Base Alloys

It is generally acknowledged that the susceptibility of passive metals to localized corrosion (including pitting) and the rate at which this corrosion process occurs are closely related to the ability of the passive film to resist breakdown and to repassivate once corrosion has initiated.<sup>26</sup> The chemical composition of the passive film, its structure, physical properties, coherence and thickness are of paramount importance in the nucleation and propagation of localized corrosion.

Investigations into the composition and structure of passive oxide films on stainless steels and other related passive alloys, of which the Co-base superalloys are one class, are much more difficult than in

the case of analysis of oxide films on iron because the films are thinner, their chemical composition is complicated, and they cannot be reduced cathodically. A major part of the information available on composition and structure of passive films on stainless steels has been obtained with spectroscopic techniques, particularly X-ray photoelectron spectroscopy (XPS) and Auger electron spectroscopy (AES). Other methods such as ion scattering spectroscopy (ISS) and secondary ion mass spectrometry (SIMS) also provide valuable data.

The XPS method was used to study the composition and structure of oxide films on iron-chromium alloys. Li *et al.*<sup>27</sup> used this method to compare the film formed on Fe–30Cr and Fe–30Cr–2Mo alloys during passivation in 1 M KCl. They did not find any substantial differences in the film composition, which was primarily hydrated chromium oxyhydroxide. XPS and AES methods were also used by Olefjord and Elfstrom to study oxide films on austenitic stainless steels passivated in 0.1 M HCl + 0.4 M NaCl solution.<sup>28</sup> The passive film consisted primarily of chromium oxide. Iron was preferentially dissolved even during passivation. Mo enrichment was observed in high Mo alloyed (6%) steel. Ni was present only to a small extent in the film.

Compared to the extensive literature on Fe-based alloys (especially stainless steels) there is very little information available on other alloys which exhibit

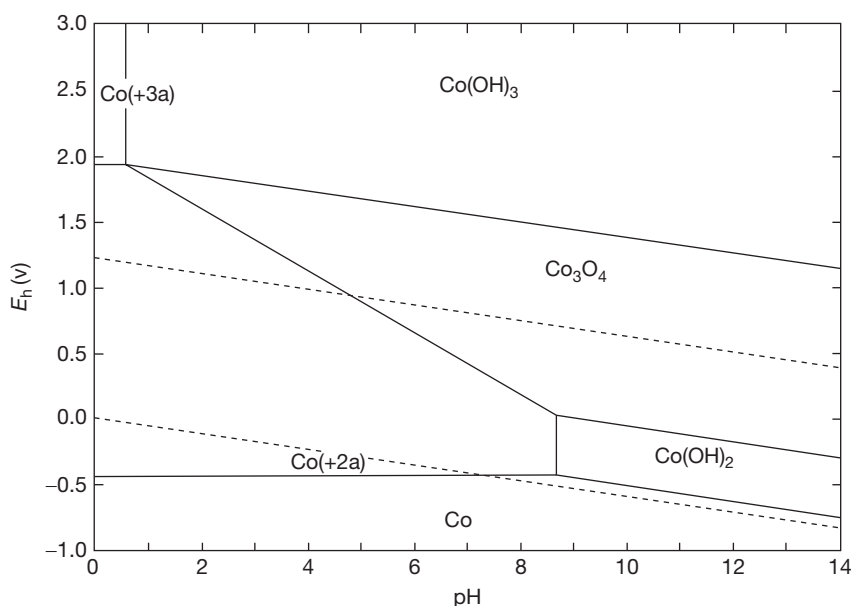


**Figure 5** Pourbaix diagram for cobalt at a metal ion concentration of  $10^{-5}$  M.

passivity (e.g., Ni and Co-based alloys). Hocking *et al.*<sup>29</sup> studied the corrosion of Stellite 6 in lithiated high temperature water used in pressurized water reactors (PWR) coolant circuits. By using XPS, they determined the chemical composition at the outer surface of the corrosion layer and concluded that oxidation of Stellite 6 alloy is believed to occur by preferential dissolution of Co at the solution interface, leaving a Cr-rich oxide. An increase in oxygen activity leads to a change in the mechanism from diffusion controlled to solution transport, dissolution-precipitation process and the corrosion rate increases.

McIntyre *et al.* also studied on the formation of the corrosion film on Stellite 6 alloy<sup>30</sup> According to their work there are two major mechanisms controlling the corrosion behavior of the alloy during aqueous oxidation. One is migration via solid-state processes, while a second results from dissolution of the cation and its subsequent reprecipitation on the oxide surface. As a result of their work, they concluded that during aqueous exposure in either reducing or mildly oxidizing conditions, a depletion of the cobalt surface composition was observed. This implies that there is a preferential dissolution of cobalt, which had already migrated preferentially to the interface.

It is also known for passive alloys that there is generally an inverse relationship between the thickness of the film and its protective property. This was seen in work by Malayoglu *et al.*<sup>3</sup> where the breakdown potential in anodic polarization tests was shown to be reduced aligned with a thinning of the passive film detected by XPS on HIPed Stellite 6 in 3.5% NaCl.

For the as-polished sample of Stellite 6, the C 1s spectrum revealed the presence of an overlay of carbonaceous contamination, and the O 1s spectrum the presence of oxide/hydroxide species at the surface. The carbon contamination and oxygen-containing species are readily removed by argon etching. The C 1s spectrum also reveals the presence of metal carbide species below the contamination over layer. The Cr 2p spectrum comprises the presence of Cr metal, carbide and oxide/hydroxide species and the W 4f spectrum is consistent with the metal but not W oxides. The Co 2p spectrum is consistent with the presence of Co metal and oxide/hydroxide species. The XPS signals of the metal oxide/hydroxide species decrease with argon ion etching, hence the model for the as-polished surface is of a matrix of metal and metal carbide species with an over layer of Cr and Co oxide/hydroxide and carbonaceous contamination.

The analysis of the spectra after anodic polarization on HIPed Stellite 6 indicates a multilayer duplex structure, where the composition changes continually with depth. At the outer surface, the film contains no metallic Co, Cr or W and consists of  $\text{Cr}(\text{OH})_3/\text{Cr}_2\text{O}_3$  and  $\text{WO}_2$ . Immediately beneath this layer, depending on the test temperature, the film is composed of Cr  $(\text{OH})_3/\text{Cr}_2\text{O}_3$  and metallic Cr, from the bulk material can be observed. Similarly, W was detected in the form of  $\text{WO}_3$  and metallic W. A schematic representation of the key components of the air-formed film and corroded surface was presented as shown in Figure 6.

Maffiotte *et al.*<sup>31</sup> confirmed the qualitative similarity in oxide film composition on a 30%Cr, 4.5%W, 2.5% Ni alloy when exposed to different environments representative of operating conditions in PWR. The film in both solutions was Cr-enriched and Co-depleted but the depth profile of the oxide film composition was dependent on the solution composition. Longer exposure to the solution further enriched the oxide with Cr as shown in Figure 7.

### 3.06.2.3 Corrosion of Cobalt-Based Alloys

Co-base alloys have seen extensive use in wear environments mainly due to their high strength, corrosion resistance and hardness. Application of cobalt-based superalloys was traditionally most prevalent in the nuclear industry in the 1960s and 1970s and, for this reason, much research into corrosion of Stellite was focused in conditions relevant to nuclear power applications such as simulated pressurized water reactor and primary heat transfer conditions, for example.<sup>32</sup>

Currently, use of Stellite alloys has extended into various industrial sectors (e.g., pulp and paper processing, oil and gas processing, pharmaceuticals, chemical processing) and the need for improved

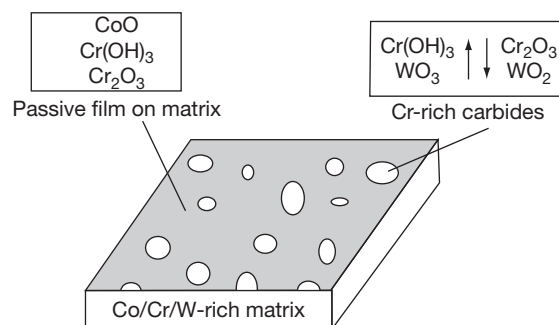


**Figure 6** Key components of the air-formed passive film. Reproduced from Malayoglu, U. PhD Thesis, Heriot-Watt University, 2005.

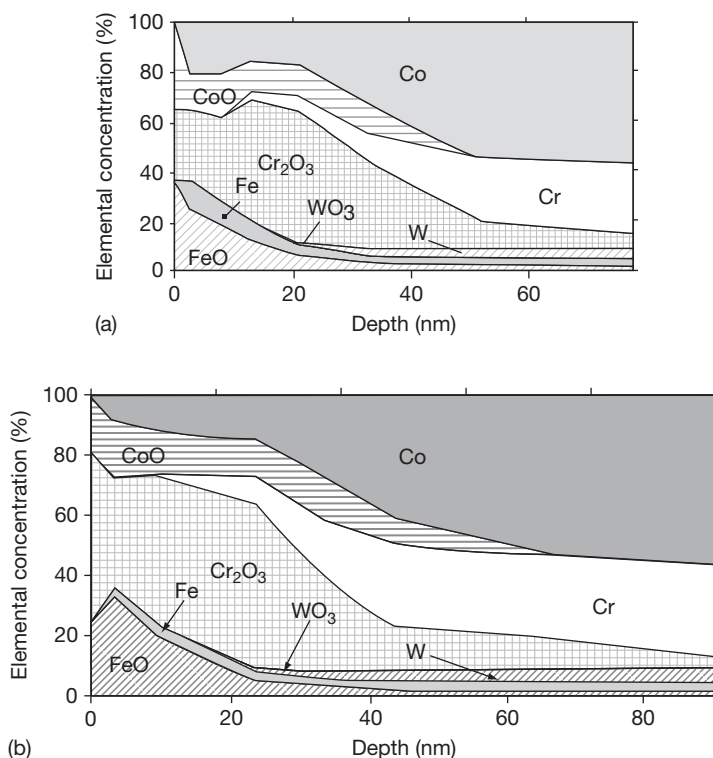


**Figure 7** XPS composition depth profiles from Stellite 6 immersed in 300 ppm  $\text{H}_2\text{BO}_3$ , 2.65 ppm  $\text{LiOH}$ , 2 ppm  $\text{H}_2$  for 250 h (a) and 2000 h (b). Reproduced from Maffiotte, C.; Navas, M.; Castaño, M. L.; Lancha, A. M. *Surf. Interface Anal.* **2000**, 30(1), 161–166.

information regarding corrosion (and often tribo-corrosion) of Stellite alloys has increased. It has been recognized that processing changes, which affect the microstructure of Stellite alloys, affect the corrosion behavior. Stellite alloys have been used as surface engineering systems as weld overlays, laser-clad overlays and HVOF coatings, and because of the very different microstructures as a result of the thermal cycling, the corrosion properties can vary. In a study by Kim and Kim<sup>33</sup> the corrosion resistance of Stellite 6 resulting from the plasma transferred arc (PTA) welded surfaces was compared to spray-fused and open arc-welded surfaces. Their corrosion results showed that the corrosion resistance of PTA weld surfaced Stellite 6 is better than that of the open arc weld surfaced Stellite 6 because dilution ( $\sim 15\%$ ) with the iron substrate for the open arc weld surfaced Stellite 6 is higher than that ( $\sim 5\%$ ) of the PTA weld surface Stellite 6. **Figure 8** shows the increase in corrosion current density ( $i_{\text{corr}}$ ) for the alloys experiencing higher dilution.

Mohamed *et al.*<sup>15</sup> studied the localized corrosion behavior of powder metallurgy processed cobalt-base

alloy Stellite 6 in a chloride environment. They showed that the Stellite 6 alloys produced by the HIP technique had the highest pitting and crevice corrosion resistance compared with identical alloys manufactured by the rolling or wet powder process. They discussed how the Oldfield–Sutton model of acidification was more appropriate for crevice corrosion in HIPed alloys than the models used to describe  $\text{Cl}^-$  accumulation. The finer microstructure for the HIPed alloy was thought to be the main reason for the improved resistance.

Human *et al.*<sup>34</sup> studied the electrochemical polarization and corrosion behavior of a cobalt–tungsten–carbon alloy in 0.5 M sulfuric acid. They showed that tungsten and carbon additions influence the corrosion behavior of the alloy. With increasing tungsten and carbon additions, the corrosion current density and the critical current density were reduced. The corrosion potential shifted to more positive values with increasing additions. As the corrosion studies have not necessarily been made with high purity elements, the effect of small amounts of impurity or alloying elements and the synergistic

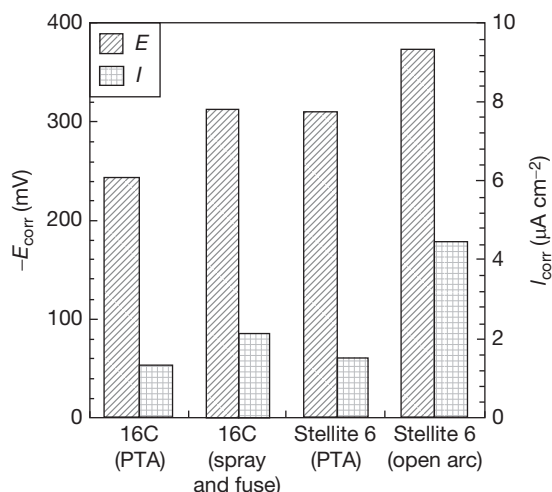


**Figure 8** Comparisons of free corrosion potential and corrosion current density for surface engineered Stellite alloys in 3%NaCl. Reproduced from Kim, H. J.; Kim, Y. J. *Surf. Eng.* **1999**, 15, 495–501.

effects of them on the corrosion performance of the metals and alloys is difficult to determine and understand.

In this work empirical relationships were developed for the alloys of the form

$$E_{\text{corr}} = -372 + 70V_v^{\text{fcc}}(C, W)[\text{mV}]$$

where  $V_v^{\text{fcc}}$  is the volume fraction of fcc phase. In this nonpassivating system, the cracks and pores in the surface layer are clearly visible (**Figure 9**).

Malayoglu assessed the corrosion resistance of three Stellite alloys in the cast and HIPed form. The Stellite 12 has a similar composition to Stellite 6 but with a much higher content of W of 9%. In Stellite 706, the W in Stellite 6 is replaced with Mo. As shown in **Figures 10a and 10b** the resistance to passivity breakdown ( $E_b$ ) is affected by temperature and the alloys are affected to a different extent. At low temperature for the cast alloy Stellite 12 and Stellite 706 are comparable and more resistant than Stellite 6. Between 30 and 40 °C, there is a significant loss of resistance for Stellite 6. In potentiostatic tests on HIPed alloys, it was shown that the critical temperature was higher for Stellite 12 and Stellite 706. However, severe tunneling pitting was seen on Stellite 12 – not seen on Stellite 6.

#### 3.06.2.4 Oxidation

The effect of alloying elements on the high temperature corrosion performance of the metals and

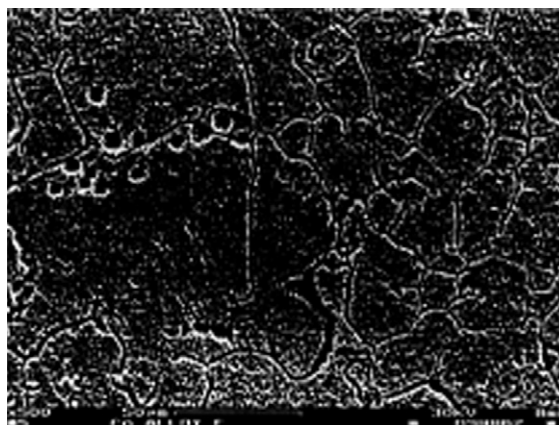


**Figure 9** Cracks and pores in the surface layer of Co—WC alloy in sulfuric acid. Reproduced from Human, A. M.; Roebuck, B.; Exner H. E. *Mater. Sci. Eng.* **1981**, A241, 202–210.

alloys, and the corrosion resistance of films and scales have been summarized by Frantsevich<sup>35</sup> who stated that;

- Small amounts of alloying elements will affect the parent metal oxide by changing its conductance. Factors influencing this will be the alloying element's valence, ion radius, and the heat of formation of the oxide.
- Large amounts of alloying elements will affect, more significantly, the properties, such as: electrical conductivity, mechanical and thermodynamic stability, and mutual solubility of the oxide phase. Changes in the dissolution pressure, concentration defects in the lattice, appearance of physical defects in the scale owing to stresses originating in the oxide film can be expected.

The effects of the alloying elements on improving the oxidation resistance of an alloy may be due to one or more of the following main factors:

- Reduction of the diffusion rate of reaction components in the oxide layer and metal through the decreased concentration of lattice defects and the formation of new phases of combined oxides.
- An increase of the ion mobility in the oxide may improve the mechanical properties of the scale phase and permit some plastic deformation.
- The decrease of the metal/oxide volume ratio, due to the change of parameters of the oxide and metal lattices, occurs when the cations are replaced with ions of smaller radii.

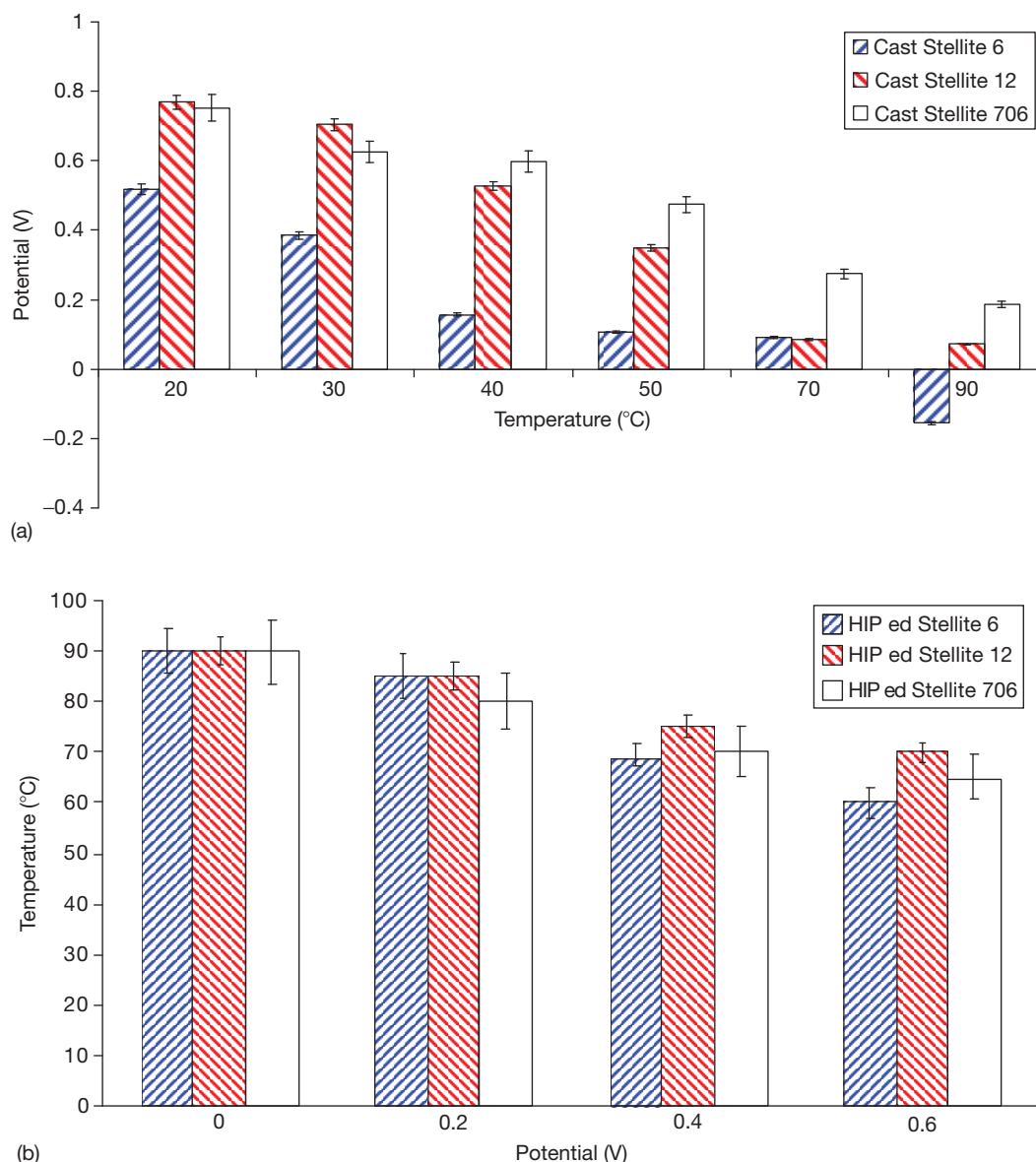


**Figure 10** (a) Breakdown potential of cast 6, 12 and 706 Stellite alloys as a function of temperature in 3.5% NaCl. Reproduced from Malayoglu, U. PhD Thesis, Heriot-Watt University, 2005. (b) Breakdown temperature from potentiostatic tests on HIPed 6, 12 AND 706 Stellite alloys in 3.5% NaCl. Reproduced from Malayoglu, U. PhD Thesis, Heriot-Watt University, 2005.

### 3.06.2.5 Corrosion in Biomedical Applications

#### 3.06.2.5.1 Joints

CoCrMo alloys have been widely and successfully used in hip joints due to their high corrosion resistance and good mechanical properties. Many authors have studied effects of the microstructure and elemental content on the joint-bearing performance. It has been shown that many factors influence their performance.<sup>36–39</sup> However, one major concern

about the use of CoCrMo alloys is the toxicity of the released Co and Cr ions. From clinical examinations, released metal ions lead to various phenomena: transportation, metabolism, accumulation in organs, allergic reactions, and carcinoma. If a large amount of metal ions are released, it is generally thought to be harmful to human health.<sup>40–42</sup> Some researchers have found Co, Cr, and Ni ions can be eliminated through urine.<sup>43</sup> Nevertheless, how they affect different organs, and the safe level of metal ions, are still

under investigation. Their effects are thought to be also dependent on the individual. Since the release of metal ions depends on the electrochemical reactions or on tribocorrosion processes, a full understanding of how corrosion and wear processes lead to the loss of ions from the surface is necessary.

Many authors have been studying metal on metal wear behavior *in vivo* and *in vitro*. A running-in (or bedding-in, wearing-in) stage is found for most cases, followed by a lower wear rate steady-state.<sup>44</sup> The length of running-in varies depending on the different simulators and geometry of contacts (pin-on-plate, ball-on-plate, etc.) from thousands of cycles to one million cycles.<sup>44–46</sup> Small wear debris particles are created in the running-in phase and cause abrasive wear. From clinical examinations, for the first few days after implantation of metal-on-metal joints, metal ions were found to increase dramatically. The metal ion level then stabilized,<sup>47–49</sup> which is possibly related to differences between the running-in and the steady-state phases phenomena and the saturation of metal ions in the body.

Corrosion has been considered as one of the major problems for metallic biomaterials. When devices are implanted into the human body, they are immediately surrounded by biological fluids. Even though corrosion can occur on plastics, ceramics, and glasses, the term is often associated with metals. In this section, corrosion of metallic bio-implant materials is the focus. From a corrosion engineering point of view, these liquids are not as aggressive as some industrial process fluids, but the body is still a harsh environment due to the oxygenated saline solution and the involvement of organic species. Ever since metallic biomaterials were adapted for surgical use, studies have been done to assess corrosion resistance of those materials. Three major metallic materials; stainless steel, cobalt chromium alloys, and titanium/titanium alloys are normally used and the understanding of their performance and improvement has been under investigation for several years.

Corrosion can severely limit the fatigue life and ultimate strength of materials, leading to the mechanical failure of implants. Corrosion has been implicated in causing local pain and swelling in the region of the implant and affect the performance of those implants resulting in failure and revision. The release of ions from implanted metallic biomaterials to the local host environment is also a great concern. Ions are released by chemical and electrochemical processes (corrosion).

One point which should not be ignored is the corrosion of wear debris. Even though nano-size

metal debris is very difficult to be collected and analyzed, it is still a potentially important source of the metal ion release which has not largely been studied until now.

The corrosion mechanisms of these metallic materials for surgical use have been extensively investigated, from both *in vitro* experiments and *in vivo* observations.

**Pitting corrosion:** Pitting corrosion is the most common type of localized corrosion. It was found on stainless steel implant materials resulting in extensive damage and causing release of significant amounts of metal ions.<sup>50</sup>

**Crevice corrosion:** Compared to the other types of metallic implant materials, Type 316L stainless steel is highly susceptible to this corrosion attack. In the area of contact between stainless steel screw heads and the bone plate, the occurrence of corrosion was found. It also induced crack propagation of bone plate.<sup>51</sup>

**Fretting corrosion:** Fretting corrosion phenomena are associated with micromotions between components.<sup>52</sup> When an oscillating rubbing action is continuously applied on two opposing surfaces such as bone plates and the screw heads of the prosthetic devices, fretting corrosion can occur.<sup>53</sup> It is the major factor to cause the initiation of cracks and fracture failures for surgical screws.

### 3.06.2.5.2 Galvanic corrosion

When metals of different types from different devices are in physical contact in body fluid, galvanic corrosion can occur. For example, a bone screw and a bone plate made of dissimilar metals and alloys can form a galvanic couple.

**Wear-corrosion:** When implant materials are under cyclic loading, wear-corrosion is always present.<sup>54</sup> Wear-corrosion resistance is an important factor of consideration for load-bearing surgical implants such as hip and knee replacement implants.

Metallic materials used for bearing surfaces in hip arthroplasties normally rely on a stable passive film, which forms spontaneously in air, for their biocompatibility. The passive film can form a barrier, which can efficiently separate the metal from the corrosive environment and protect it from further corrosion processes. The passive film inhibits corrosion and keeps current flow and the release of corrosion products at a very low level. Nonetheless, the release of metal into the body is a well-documented fact. Uniform passive dissolution resulting from the slow diffusion of metal ions through the passive film, trans-passive dissolution under high oxidizing conditions,



or the local breakdown of passivity as a consequence of localized forms of corrosion such as pitting or crevice corrosion, or as a consequence of mechanical events, such as fretting and wear corrosion, are all possible mechanisms.

XPS and other surface analysis techniques have been used to determine the nature of passive films on Co-base alloys. Primarily  $\text{Cr}_2\text{O}_3$ ,  $\text{CoO}$ , and  $\text{MoO}_3$  are found in the top layer (1.6 nm) of the spontaneously formed passive film in air for CoCrMo alloys. The inner layer of the passive film contains  $\text{Cr}_2\text{O}_3$  and Co and Mo metal species.<sup>55</sup> The total thickness of the passive film on CoCrMo alloys in the atmosphere is  $\sim 4\text{--}5$  nm.

Hanawa *et al.*<sup>56</sup> examined the surfaces of metallic stainless steel, CoCrMo alloys, and titanium. A preferential release of Co ion for CoCrMo alloys and Fe ion for stainless steel 316L were obtained. The release of Mo in CoCrMo was reported to be insignificant. A ratio of approximately 2.9:1 of Co/Cr for pin-on-disk tests on CoCrMo was reported.<sup>57</sup> However, the amount of Co released from cast CoCrMo alloys was found to be very small in the biological solution.<sup>58</sup> In addition it was found that the amount of Ni released from 316L gradually decreased with increasing pH; similarly, the amount of Cr and Mo ions released from CoCrMo decreased at pH 4 and higher. One thing which should be noticed is that, in the natural body serum condition, the pH is  $\sim 7.4$ . Calcium phosphate was found as precipitates on implant metals and alloys surfaces. They also suggested that the formation of oxide or hydroxides of metal ions was less toxic than the complex of protein-bond-metal.<sup>59</sup>

The CoCrMo alloys are highly corrosion resistant with only a minimal susceptibility whilst stainless steel quite readily suffers crevice and pitting corrosion. CoCrMo alloys are considered biocompatible. However, very high levels (20–30 times as reference normal serum cobalt value ( $0.15\text{ }\mu\text{g l}^{-1}$ ) and serum chromium value ( $0.26\text{ }\mu\text{g l}^{-1}$ )) of metal ions are reported cytotoxic with increasing concern over the biocompatibility of implant materials and especially in terms of the significance of corrosion, wear, hypersensitivity and carcinogenicity.<sup>60</sup> The quantity of organometallic production over longer periods after total joint replacement (TJR), correlation with patient health medication and activity levels remain the objective of many studies.<sup>61</sup> There can be no doubt, therefore, that patients with metal-on-metal (MoM) implants will be exposed to elevated levels of metal ions locally. The outstanding question is the clinical impact of these elevated ion levels. Brondner *et al.*<sup>62</sup> examined patients with CoCrMo MoM total hip

replacement (THR) and found that the Co and Cr concentration in blood serum and urine are high. They seem to fall after the initial one-year running-in phase. Average preparative blood serum cobalt levels of  $0.15\text{ }\mu\text{g l}^{-1}$  were cited as reference values for patients who had MoM hip implants from Muniz's studies on elements trace<sup>63</sup> and it is generally in line with the others. Black *et al.*<sup>64</sup> showed a disagreement concerning 'normal' levels for these elements in serum. Because it is still unclear what constitutes a normal level for an individual patient and what the consequences are of transient or chronic deviations from that level, a question mark still exists over MoM implantation.

Visuri and Koskenvuo<sup>65</sup> showed that there was no increase in the risk of cancer in patients with McKee-Farrar type CoCrMo MoM THR and Willert<sup>66</sup> found no proof that the release of metal is teratogenic but did show the possibility of hypersensitivity to metals. Koegel and Black<sup>67</sup> and others disagreed. An increased incidence in cardiomyopathy (a disease or disorder of the heart muscle) and tumors was found from animal tests. Because the number of patients with a MoM TJR for 10, 20, or more, years increases, it suggested that long-term studies are still required to fully address the issue of metal-ion associated diseases. Investigations to clarify the importance of toxicology are currently being undertaken by many researchers and clinicians.

Electrochemical methods have been employed to understand corrosion behavior for implant materials and then to assess their biocompatibility. Many authors have been trying to monitor the performance of TJR by measuring metal levels.<sup>68–69</sup>

At this stage, it is important that a more detailed understanding of the effects of implanted metals must be gained.<sup>69</sup> A wide variety of serum proteins exists *in vivo* and it is reasonable to assume that many of these become rapidly adsorbed onto the metal surfaces upon implantation. It is suggested that the adsorbed proteins influence the material corrosion rate.

### 3.06.2.6 Erosion-Corrosion

In certain environments, either where two moving surfaces come into contact or where there is impingement of a slurry onto a surface, wear is unavoidable. There is usually progressive deterioration of the surface resulting from the removal of material by at least one of the following mechanisms, abrasion, erosion, and erosion-corrosion. Additionally, forms of corrosion may occur locally to exacerbate the damage.

Neville *et al.*<sup>70</sup> discussed the effect of temperature on the erosion rate of Stellite X40 and BS 3468 cast

iron in the slurry erosion conditions. The focus of this work was to validate the use of Stellite X40 as an optimum material for subsea drill bit castings (Figure 11). Drill bits for subsea use have to be able to tolerate the impingement of the drilling fluid injected through the nozzle onto the faces of the bit which contain the diamond cutters. Material loss in this region is serious as the support for the cutters is lost, as seen in Figure 11(b). In their work, it was shown that the damage on the face is a complex mix of erosion and corrosion processes and that Stellite X40, is in fact the optimum material when compared with a variety of Fe and Ni base materials.

The synergistic effect between erosion and corrosion has received more and more attention in recent years because of the widespread occurrence of such problems in material processing industries. In such conditions, material selection can be a problem and, in many cases, is only carried out on the basis of empirical evidence. Erosion-corrosion can cause high material degradation rates because the action of the erodent particles can remove a stable passive film on the surface of the material. Hence, the wastage rates of the material can be significantly higher than the combined effects of erosion and corrosion acting separately.

The literature has not been consistent in the use and meaning of the synergistic effect in aqueous erosion-corrosion. Some authors describe it as the sum of the enhancement of erosion due to corrosion and vice versa ( $dE_C$  and  $dC_E$ ).<sup>71</sup> Some authors used the term

‘additive effect’ to refer to an enhancement, but there is a difference between these two terms. Often an ‘additive effect’<sup>72</sup> is when the sum of pure erosion in the absence of corrosion ( $E$ ), the pure corrosion in the absence of erosion ( $C$ ) and the change of corrosion rate due to erosion ( $dC_E$ ) is equal to the total weight loss (TWL). If this is not the case the ‘synergistic effect’ is observed. In other words, the term synergism is restricted to the erosion enhancement due to corrosion ( $S$  or  $dE_C$ ). The following equations [2] and [3] show the differences between the additive effect and the synergy ( $S$ ) effect from on which this work is based.

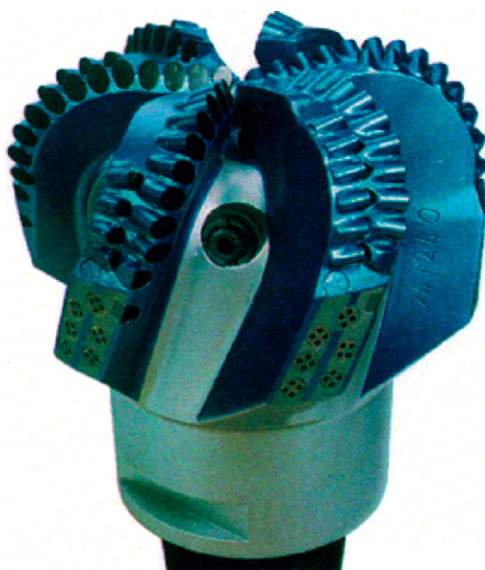
$$\text{TWL} = E + C + dC_E + dE_C \quad [2]$$

$$\text{TWL} = E + C + S \quad [3]$$

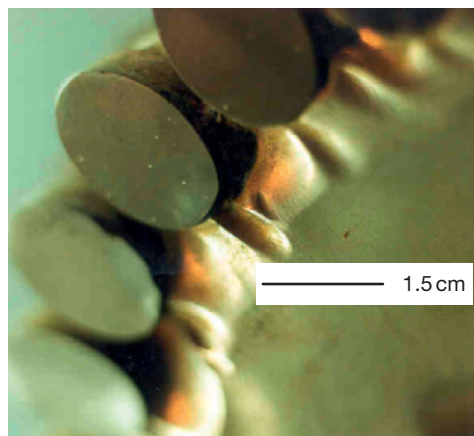
In order to define the synergistic effect, both erosion and corrosion must be studied independently of each other under controlled conditions. To obtain the corrosion rate, a potentiostat or galvanostat is used to control the electrical potential or current of the erosion sample.

Neville *et al.*<sup>70,73,74</sup> used a range of engineering alloys ranging from low grade C-Mn steel to super alloys, Stellite X40, to calculate the percentage damage caused by synergy.

They measured the TWL at the free corrosion potential; anodic polarization with presence of liquid–solid impingement and by using Tafel extrapolation *in situ* pure corrosion component of TWL ( $C$ )



(a)



(b)

**Figure 11** New subsea drill bit (a) and erosion-corrosion of the Stellite X40 around the polycrystalline diamond cutters (b).

is calculated. By applying a cathodic potential to the sample the pure erosion component ( $E$ ) of the TWL was obtained.

The TWL of the material was identified as pure erosion, corrosion and synergistic effects. In the literature, the effect of temperature, salinity, and solid particles content in the impingement jet was analyzed and their effect on the different mechanisms were quantified. Das *et al.*<sup>75</sup> showed that the corrosive wear rate increases with increasing angle of inclination and a higher wear rate was obtained for the impingement angle  $90^\circ$  and, the lowest weight loss was obtained at  $30^\circ$ . Similar findings were reported by Fan *et al.*<sup>76,77</sup> where they related these findings to the properties of the passive film. They showed that in the areas where the tangential component of impact velocity is large, the main mechanism is a cutting mode. On the contrary, in the areas where the normal component of impact velocity is larger, the failure mode consists of the formation of micro-cracks and the removal of second phases.

The performance of the different alloys under erosion-corrosion conditions has been studied with various techniques. Important variables relating to erosion such as load, fluid velocity, impact angle and solid loading have been studied to determine the erosion-corrosion behavior of materials. However, there is virtually no information available on cobalt-based superalloys under erosion-corrosion conditions and in particular, the effect of alloying elements on the mechanical and electrochemical damage, which is one of the main objectives of the current project.

### 3.06.2.7 Wear and Wear-Corrosion of Cobalt-Base Alloys

Cobalt-base alloys have enjoyed extensive use in wear-related engineering applications for well over 50 years because of their inherent high-strength corrosion resistance and ability to retain hardness at elevated temperatures. In recent years, a concentrated effort has been made to understand the deformation characteristics of cobalt-base alloys exposed to erosive environments in order to optimize those factors contributing to their erosion resistance.

In Stellite alloys the cobalt-rich solid solution incorporating elements such as chromium, tungsten and molybdenum, is highly resistant to erosion. This is due to rapid increase in the work hardening rate and the strain to fracture, which are caused by deformation

twinning and presence of a small amount of strain-induced  $\epsilon$  phase.

The wear properties of the cobalt-based alloys are believed to be influenced by:

- the limited mobility of the stacking faults generated by mechanical stress, which limits plastic deformation;
- interaction between stacking faults (this results rapid hardening);
- mechanical twinning which occurs extensively in certain alloys and absorbs energy;
- the formation of hcp platelets, which are believed to absorb energy; and
- the characteristics of this hcp phase once formed.

Most cobalt-based alloys possess good cavitation resistance and moderate abrasion and slurry erosion resistance. The last two features are independent of the carbon content, and have been attributed by Crook<sup>78</sup> to crystallographic transformation, under stress, from the fcc to hcp structure by twinning. During deformation, energy is absorbed and the effect of the stress is decreased.

Cobalt-based superalloys have been recognized as an alloy type one of the most resistant to both cavitation and liquid impact erosion.<sup>79</sup> The underlying reason for their superior erosion resistance behavior however, is not yet clear. Investigations have attempted to obtain universal correlation between the erosion resistance of the materials and the mechanical properties such as hardness and strain energy to fracture but all such attempts have been unfortunately unsuccessful. For example, austenitic stainless steel had higher erosion resistance than martensitic stainless steel of the same hardness and cobalt-base alloys had much higher resistance in relation to hardness.<sup>80</sup>

Lee *et al.*<sup>80</sup> compared the liquid impact erosion resistance of 12 Cr steel with a Vickers hardness of  $380 \text{ kg mm}^{-2}$  and Stellite 6B with a hardness value of  $420 \text{ kg mm}^{-2}$ . The liquid impact erosion resistance of Stellite 6B was at least six times greater than that of 12 Cr steel, implying that hardness is not the governing factor for liquid erosion. Stellite 6B also showed very different behavior in liquid impact erosion in comparison with 12 Cr steel (Figure 12). They concluded that the superior erosion resistance of Stellite 6B results from the cobalt matrix whose deformation appeared as mechanical twins. Other studies showed a trend of increasing erosion resistance with decreasing grain size. The twins are produced by the passage of partial dislocations, which had a Burgers vector equal to a fraction of the lattice vector, giving twinned

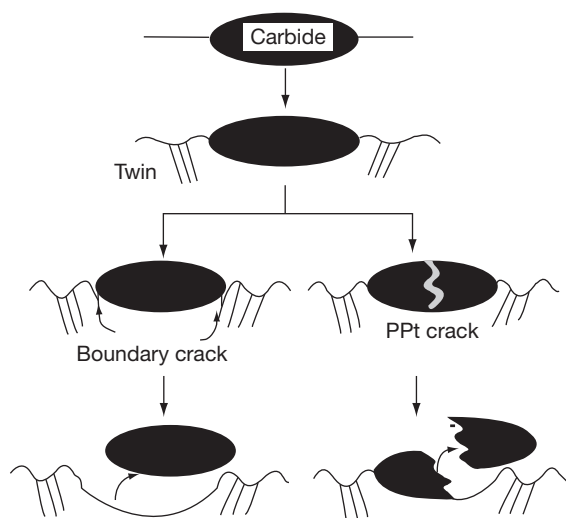


**Figure 12** Liquid impact erosion mechanisms of Stellite No. 6B.

regions and untwinned regions of different orientations. Therefore, the increase in density of twins with a number of impacts would play the role of fragmentation of the grains in the cobalt matrix into a submicrometer level. This would decrease the mean free path of dislocations to a limit surface distortion severely and given a much higher erosion resistance.

In the case of cavitation erosion, it is observed that the dynamic and localized nature of the stresses generated by the imploding cavities produce a material response which is quite different from that obtained under bulk quasi-static loading. A striking example of this is that cobalt and its alloys exhibit far greater erosion resistance than other metals and alloys comparable strength.<sup>81</sup> In fact pure cobalt is the most erosion resistant of comparable pure metals known.

Wong-Kian *et al.*<sup>16</sup> showed that under erosion-corrosion conditions HIPed Stellite alloys 1, 6, and 21 had lower mass loss than the welded specimens of the same Stellites. They related their finding to the finer and homogeneous microstructure, which was obtained after HIPing. They also showed that wear resistance of the cobalt-based alloys is promoted by the harder complex carbides of chromium and tungsten, while corrosion resistance is enhanced by the presence of cobalt in the matrix.

From almost all of the work done on the wear properties of Stellite alloys it has been concluded that the exceptional erosion resistance of the Stellite alloys can be ascribed to the drastic change in mechanical properties brought about by the formation of mechanical twins and by the presence of platelets of

the  $\epsilon$  hcp phase. It has been shown that the formation of twins and  $\epsilon$  phase is controlled by the SFE.

Strain hardening occurs as a result of interactions of dislocations with each other, and with barriers, which impede dislocation motion. One of the earliest explanations for strain hardening is that dislocations pile up on slip planes at barriers in the crystal, and produce a back stress, which opposes the applied stress on the slip plane.<sup>82</sup> Possible dislocation interactions and intersection of the active slip planes were suggested as another dominating mechanism for strain hardening. Mechanical twinning, and the presence of hcp platelets may also contribute to the work-hardening in cobalt base alloys. The effectiveness of each mechanism in terms of work-hardening depends upon the strain increment characteristics of each process. This concept was studied by Roebuck *et al.*,<sup>83</sup> who found the best strengths and ductilities in extruded Co-C-W alloys correspond with the highest fcc content. They suggested that when the fcc phase is stabilized deformation occurs by twinning or slip rather than by fcc-hcp martensitic transformation.

The strength of the matrix is considered in detail here. Kosel *et al.*<sup>84</sup> showed the effect of the matrix strength can affect the wear rate. They used the normalized alloy content (NAC) as a measure of the matrix strength. They defined the NAC as the sum of the weight percentages of Ni, V, W, Mo and in Table 2 they are normalized with respect to Stellite 6 alloy. The alloys that are used as solid-solution strengtheners give an approximate measure of the degree of solid-solution strengthening.

By using the same approach the NAC of the alloys Stellite 6, Stellite 12, and Stellite 706 were calculated and normalized against cast Stellite 6 as shown in Table 2.

Figures 13 and 14 show the change in the weight loss as a function of NAC. In Figure 12, only Stellite 6 and Stellite 12 are compared to assess the effect of increased tungsten on the NAC and the resistance to wear. Figure 13 is a comparison of Stellite 6 and Stellite 706 and the factor being considered here is replacing tungsten and molybdenum. From Figure 12 it can be clearly seen that an increase in the tungsten amount increases the NAC and the weight loss at both test temperatures and both solid loadings is not affected by the increase in NAC. However, as shown in Figure 13, there is a linear relationship between the NAC and the erosion-corrosion resistance of the alloys. The alloys with high NAC gave a lower weight loss in all test conditions. These two results show that molybdenum as a solid-solution strengthener is much more

effective in providing erosion-corrosion resistance than tungsten.

It is apparent that SFE has a significant influence in changing the deformation mode. The excellent erosion resistance of cobalt-based Stellite alloys is generally attributed to the low SFE,<sup>85</sup> which, in turn, means higher stacking fault probability and a greater chance for the formation of  $\varepsilon$  hcp platelets. The lower the SFE (the greater the width of the stacking fault) the more difficult is cross-slip, and the higher is the rate of work-hardening and the strain to fracture. Bhansali and Miller<sup>86</sup> examined the role of SFE on the galling and wear behavior of Stellite 6 modified by the addition of Ni, which in turn increases SFE and stabilizes the fcc matrix. Their results showed that materials with low SFE tend to strain harden rapidly, and to show the highest galling resistance.

Remy and Pineau<sup>87</sup> found that in Co–Cr–Ni–Mo alloys an SFE of  $\sim 20 \text{ mJ m}^{-2}$  resulted in an Md temperature (i.e., the maximum temperature at which the

fcc–hcp reaction can be stress induced of  $\sim 25^\circ \text{C}$ ). This low value of the SFE also gives rise to the optimum mechanical properties, that is, the highest work-hardening rate and the maximum strain to fracture.

Heathcock and Ball,<sup>79</sup> compared the cavitation erosion resistance of a number of Stellite alloys, (3, 4, 6, 8, 20, and 2006), cemented carbides and surface-treated alloy steels. They showed that among the Stellite alloys, Stellite 3 has the highest resistance to cavitation erosion. Stellite 4, 6, 8, and 20 have similar resistance and Stellite 2006 is a little less resistant than all the Stellite alloys. They considered this difference to be a consequence of the microstructure. Stellite 3 has carbides  $\text{Cr}_7\text{C}_3$  and  $\text{W}_6\text{C}$  which form a fine interdendritic network in a cobalt-rich matrix whereas in Stellite 20 acicular  $\text{Cr}_7\text{C}_3$  carbide formation and islands of cobalt-rich solid solution were observed. They also showed that acicular carbides in Stellite 20 are much harder than those in Stellite 3 (1860 HDP compared with 1100 HDP), which also showed the inverse relation between the hardness and the cavitation erosion resistance of the alloys. They concluded that in Stellite alloys the cobalt-rich solid solution, incorporating elements such as chromium, tungsten, and molybdenum is highly resistant to erosion, due to a rapid increase in the work-hardening rate and the strain to fracture which is caused by deformation twinning and the presence of a small amount of strain-induced  $\varepsilon$  phase.

Although some attempts have been made to correlate hardness with erosion resistance, a good

**Table 2** Normalized alloy content of Stellite 6, Stellite 12, and Stellite 706 (both cast and HIPed)

Alloy	Normalized alloy content (NAC)
Stellite 6 Cast	1
Stellite 6 HIPed	1.2
Stellite 12 Cast	2.5
Stellite 12 HIPed	2.4
Stellite 706 Cast	1.36
Stellite 706 HIPed	1.39

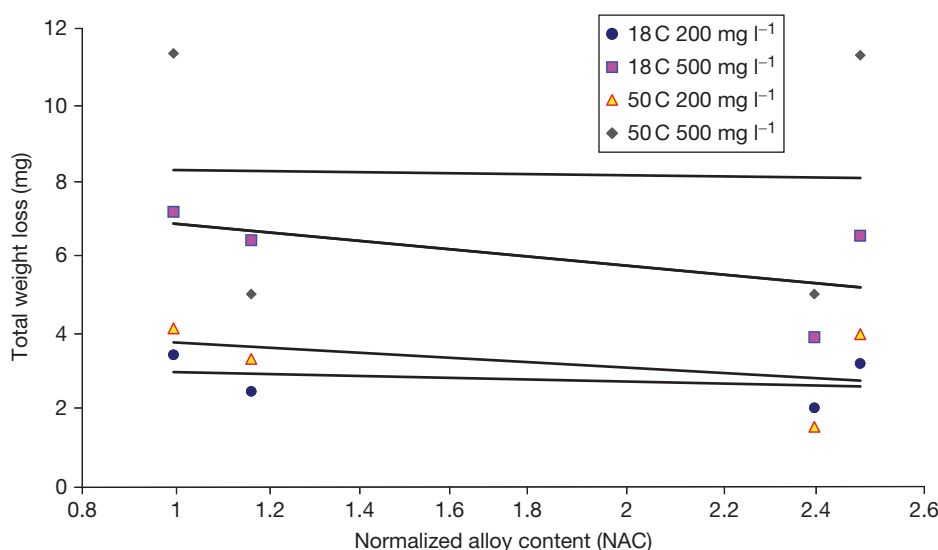


**Figure 13** Total Weight Loss (TWL) test results plotted versus normalized alloy content for Stellite 6 and Stellite 12. Reproduced from Malayoglu, U. PhD Thesis, Heriot-Watt University, 2005.



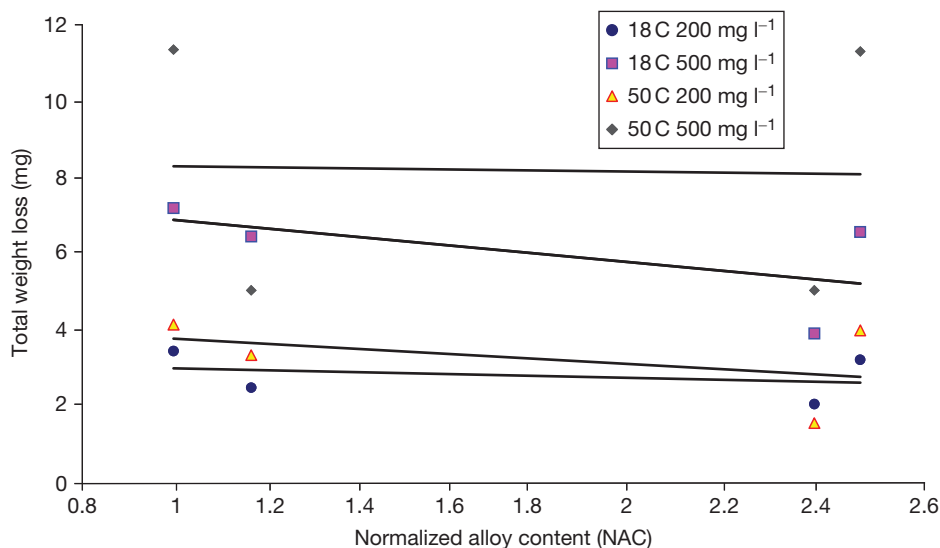


**Figure 14** Total Weight Loss (TWL) test results plotted versus normalized alloy content for Stellite 6 and Stellite 706. Reproduced from Malayoglu, U. PhD Thesis, Heriot-Watt University, 2005.

correlation generally has been recognized only for pure metals or alloys with the same compositional system. For example, Finnie *et al.*<sup>88</sup> showed that a good relationship between material hardness and erosion resistance existed for pure metals but not for heat-treated carbon steel (the erosion resistance was nearly constant, independent of the heat treatment). In another study, the cobalt alloy Stellite 6 B was shown to have a steady-state rate of volume loss, an order of magnitude less than many titanium- and iron-base alloys of comparable hardness.<sup>89</sup> These results may suggest that it is not possible to use material hardness as the sole parameter in evaluation of erosion resistance for all materials.

Frenk and Kurz<sup>81</sup> investigated the influence of the microstructure on the dry sliding wear resistance of a hypoeutectic Stellite 6 alloys. They showed that the hardness is dependent on the microstructure and in particular, on the size of the dendrites and the chemical composition of the matrix, in particular elements modifying the SFE. They reported a severe delamination wear of the Stellite under the sliding conditions investigated. During the stationary wear regime, no dependence of the wear rate on the as-solidified microstructure was determined. They suggested addition of alloying elements which decreases the SFE, which could improve the dry sliding wear resistance.

Desai *et al.*<sup>90</sup> studied the effect of carbide size on the abrasion resistance of two cobalt-based powder metallurgy alloys 6 and 19. As a result of their SEM investigation they divided the wear scar into three

parts, entrance, central, and exit regions. In the entrance region, many of the abrasive particles move at angles to the length of the wear scar, while in the central and exit regions the particles create long straight grooves. Stellite 6 gave a greater mass loss than alloy 19 at any given carbide size. They attributed this to the combined effect of the higher matrix microhardness of alloy 19. They also concluded that the wear rate decreased monotonically with increasing carbide size. The effect of carbide size is attributed primarily to the fact that the smaller carbides are often found to be contained wholly within micromachining chips, indicating that these carbides contribute little to wear resistance.

## References

1. Cobalt Development Institute, Facts About Cobalt ([www.theecdi.com](http://www.theecdi.com))
2. Anon, Cobalt Monograph, Centre d'Information du Cobalt/Battelle, 1958
3. Malayoglu, U. PhD Thesis, Heriot-Watt University, 2005
4. Morrow, H.; Danes, W. P.; Sponseller, D. L. *Cobalt* **1973**, 4, 93–102.
5. Atamert, S. Stability, wear resistance and microstructure of iron, cobalt and nickel-based hardfacing alloys, PhD thesis, University of Cambridge: UK, 1989.
6. Lane, J. R.; Grant, N. J. *Trans. Am. Soc. Met.* **1952**, 44, 113–121.
7. Wagner, H. J.; Hall, A. M. The physical metallurgy of cobalt-base superalloys, Defence Metals Information Centre, 1962.
8. Woodfor, D. A. *Metall. Transac* **1972**, 3, 1137–1145.



9. Sims Chester, T.; Stoloff, N. S.; Hagel, W. C. *Super Alloys II*; John Wiley & Sons: London, 1987.
10. Kuzucu, V.; Ceylan, M.; Celik, H.; Aksoy, I. *J. Process. Technol.* **1997**, 69, 257–263.
11. Wever, F.; Haschimoto, U. *Mitt. Kaiser Wilhelm Inst. Eisenforsch* **1929**, 11, 293–301.
12. Koster, W.; Spencer, F. *Arch. Eisenhüttenwesen* **1955**, 29, 555–565.
13. Rautala, P.; Norton, J. T. *J. Met.* **1952**, 4, 1045–1050.
14. Adkins, E. F.; Williams, D. N.; Jaffe, R. I. *Cobalt* **1960**, 8, 16–25.
15. Mohamed, K. E.; Gad, M. M. A.; Nassef, A. E.; El-Sayed, A. W. A. *Z. Metallkd.* **1990**, 90, 195–201.
16. Wong-Kian, M.; Cornish, L. A.; Van Bennekom, A. J. *South African Inst. Mining Metall.* **1995**, 319–335.
17. Frenk, A.; Kurz, W. *Wear* **1994**, 174, 81–91.
18. Antony, K. C. *J. Met.* **1983**, 35, 52–60.
19. Berns, H.; Wendl, F. Microstructure and properties of CoCr29W (Stellite 6) in the as-cast, forged and powder metallurgical conditions, 2nd International Conference on Cobalt, Venice **1985**; pp 292–305.
20. Crook, P. *Corros. Sci.* **1993**, 35, 647–653.
21. Bibring, H.; Seibel, G. *Comptes Rendus Hebdomadaires Des Seances De L Academie Des Sciences Serie C* **1969**, 268(2), 144.
22. Darby, J. B., Jr.; Beck, P. A. *J. Met.* **1955**, 7(203), 765–766.
23. Silverman, R.; Arbitr, R.; Hodi, F. *Trans. Amer. Soc. Met.* **1957**, 49, 805–815.
24. Lux, B.; Bollmann, W. *Cobalt* **1961**, 11, 4–12.
25. Vander Sande, J. B.; Coke, J. R.; Wulff, J. *Metall. Trans. A* **1976**, 7A, 389–397.
26. Morral, F. R. *Corros. NACE* **1969**, 25, 307–322.
27. Li, X. Y.; Akiyama, E.; Habazaki, H.; Kawashima, A.; Asami, K.; Hashimoto, K. *Corros. Sci.* **1997**, 39, 1365–1375.
28. Oleford, I.; Elfstron, B. O. *Corrosion* **1982**, 38(1), 46–52.
29. Hocking, W. H.; Stanchell, F. W.; McAlpine, E.; Lister, D. H. *Corros. Sci.* **1985**, 25(7), 531–557.
30. McIntyre, N. S.; Zetaruk, D.; Murphy, E. V. *Surf. Interface Anal.* **1979**, 1(4), 105–110.
31. Maffiotte, C.; Navas, M.; Castaño, M. L.; Lancha, A. M. *Surf. Interface Anal.* **2000**, 30(1), 161–166.
32. Mirza, N. M.; Rafique, M.; Hyder, M. J.; Mirza, S. M. *Ann. Nucl. Energy* **2003**, 30(7), 831–851.
33. Kim, H. J.; Kim, Y. J. *Surf. Eng.* **1999**, 15, 495–501.
34. Human, A. M.; Roebuck, B.; Exner, H. E. *Mater. Sci. Eng.* **1981**, A241, 202–210.
35. Frantsevich, I. N. *Poroshkovaya Metall.* **2002**, 9–10, 11–29.
36. Zhu, J.; Xu, N.; Zhang, C. *Adv. Contracept* **1999**, 15, 179.
37. Khan, M. A.; Williams, R. L.; Williams, D. F. *Biomaterials* **1999**, 20, 631.
38. Goldberg, R. J.; Gilbert, L. J. *Biomaterials* **2004**, 25, 85.
39. Lewis, A. C.; Kilburn, M. R.; Papageorgiou, I.; Allen, G. C.; Case, C. P. *J. Biomed. Mater. Res. A* **2005**, 73, 456.
40. Hanawa, T.; Ota, M. *Biomaterials* **1991**, 12, 767.
41. Hallab, N. J.; Bundy, K.; O'Connor, K.; Moses, R.; Jacobs, J. *Tissue Eng.* **2001**, 7, 55.
42. Yan, Y.; Neville, A.; Dowson, D. *J. Phys. D: Appl. Phys.* **2006**, 39, 3200.
43. Beamson, G.; Briggs, D.; Davies, S. F.; Fletcher, I. W.; Clark, D. T.; Howard, J.; Gelius, U.; Wannberg, B.; Balzer, P. *Surf. Interface Anal.* **1990**, 15, 541.
44. Walker, P. S. *Acta Orthop. Belg.* **1973**, 39, 43.
45. Lebugle, A.; Subirade, M.; Gueguen, J. *Biochem. Biophys. Acta* **1995**, 1248, 107.
46. Franks, F. *Biophys. Chem.* **2002**, 96, 117.
47. Contu, F.; Elsener, B.; Bohni, H. *Biomed. Mater.* **2002**, 62, 412.
48. Hanawa, T.; Hiromoto, S. *Corros. Eng.* **1998**, 47, 895.
49. Adelina, B. Synopses of International Tribology Conference (Kobe) **2005**; p 21 Vol C-04.
50. Contu, F.; Elsener, B.; Bohni, H. *Corros. Sci.* **2004**, 47, 1863–1875.
51. Roberge, P. R. *Handbook of Corrosion Engineering*; McGraw Hill: New York, 2000.
52. Kuhn, A. T. *Biomaterials* **1981**, 2, 68–77.
53. Yang, J.; Meritt, K. J. *Biomed. Mater. Res.* **1994**, 28, 1249–1258.
54. Khan, M. A.; Williams, R. L.; Williams, D. F. *Biomaterials* **1999**, 20, 762–772.
55. Jacobs, J. J.; Skipor, A. K.; Campbell, P. A.; Hallab, N. J.; Urban, R. M.; Amstutz, H. C. *J. Arthroplasty* **2004**, 19, 59–65.
56. Hanawa, T. *Corros. Eng.* **2000**, 49, 687–699.
57. Stemp, M.; Mischler, S.; Landolt, D. *Wear* **2003**, 255, 466–475.
58. Jacobs, J. J.; Skipor, A. K.; Patterson, L. M.; Hallab, N. J.; Paprosky, W. G.; Black, J.; Galante, J. O. *J. Bone Joint Surg.* **1998**, 80, 1447–1458.
59. Lindsley, B. A.; Marder, A. R. *Wear* **1999**, 225–229, 510–516.
60. Hensten-Pettersen, A.; Jacobsen, N. *Systemic Toxicity and Hypersensitivity, Biomaterials Science*; Elsevier Academic Press: London, 2004.
61. Barril, S.; Mischler, S.; Landolt, D. *Wear* **2004**, 256, 963–972.
62. Brodner, W.; Bizan, P.; Meisinger, V.; Kaider, A.; et al. *J. Bone Joint. Surg.* **1997**, 79, 316–321.
63. Muniz, C. S.; Fernandez-Martin, J. L. *Biol. Trace Elem. Res.* **2001**, 82, 259–269.
64. Black, J.; Maitin, E. C.; Gelman, H.; Morris, D. M. *Biomaterials* **1983**, 4, 160–164.
65. Visuri, T.; Koskenvuo, M. *Orthopedics* **1991**, 14, 137–142.
66. Willert, H. G.; Buchhorn, G. H.; Gobel, D. *Clin. Orthop. Relat. Res.* **1996**, 329, 160–186.
67. Koegel, A.; Black, J. *Soc. Biomater.* **1983**.
68. Rossi, S.; Fedrizzi, L.; Deflorian, F.; Zen, M. *Mater. Corros.* **2000**, 51, 552–556.
69. Micheli, S. M. d. D.; Riesgo, O. *Biomaterials* **1982**, 3, 209–212.
70. Neville, A.; Reyes, M.; Xu, H. *Tribol. Int.* **2002**, 35, 643–650.
71. Stack, M. M.; Corlett, N.; Zhoi, S. *Wear* **1997**, 215, 67–76.
72. Stack, M. M.; Stott, F. H. *Corros. Sci.* **1993**, 35, 1027–1034.
73. Neville, A.; Hodgkiess, T. *Br. Corros. J.* **1997**, 32, 197–205.
74. Neville, A.; Hodgkiess, T.; Dallas, J. T. *Wear* **1995**, 186–187, 497–507.
75. Das, S.; Mondal, D. P.; Dasgupta, R.; Prasad, B. K. *Wear* **1999**, 236, 295–302.
76. Fan, A.; Long, J.; Tao, Z. *Wear* **1995**, 181–183, 876–882.
77. Fan, A.; Long, J.; Tao, Z. *Wear* **1996**, 193, 73–77.
78. Crook, P. *Cobalt and Cobalt Alloys*, 10th ed.; ASM International: Materials Park, OH; 447–454, Vol. 2
79. Heathcock, C. J.; Ball, A. *Wear* **1982**, 74, 11–26.
80. Lee, M. K.; Kim, W. W.; Rhee, K. C.; Lee, J. W. *J. Nucl. Mater.* **1998**, 257, 134–144.
81. Vaidya, S.; Mahajan, S.; Preece, C. M. *Metall. Transac. A* **1980**, 11A, 1139–1150.
82. Honeycombe, R. W. K. *Steel, Microstructure and Properties*, E Arnold: London, 1981.
83. Roebuck, B.; Almond, E. A. *Mater. Sci. Eng.* **1984**, 66, 179–194.
84. Kosel, T. H.; Fiore, N. F. *J. Mater. Energy Sys.* **1981**, 3, 7–27.
85. Remy, T. L.; Pineau, A. *Mater. Sci. Eng.* **1976**, 26, 123–132.

86. Bhansal, K. J.; Miller, A. E. *Wear* **1982**, 75, 241–251.
87. Remy, L. *Metall. Transac. A* **1981**, 12A, 387–407.
88. Finnie, I.; Stevick, Gr; Ridgely, Jr. *Wear* **1992**, 152, 91–98.
89. Hansen, J. S. *Am. Soc. Test. Mater*; 1979, 148–162.
90. Desai, V. M.; Rao, C. M.; Kosel, T. H.; Fioren, F. *Wear* **1984**, 94, 89–101.

## Further Reading

Cobalt Development Institute, 167 High Street, Guildford, Surrey, GU1 3AJ: <http://www.thecdi.com/>  
Cobalt News – published, and available for free download, by the Cobalt Development Institute.

## 3.07 Corrosion of Copper and its Alloys

### C. D. S. Tuck

Lloyd's Register EMEA, London, UK

### C. A. Powell

Copper Development Association, Hemel Hemstead, UK

### J. Nuttall

European Copper Institute, Belgium

© 2010 Elsevier B.V. All rights reserved.

<b>3.07.1</b>	<b>Introduction</b>	1938
<b>3.07.1.1</b>	<b>Alloy Compositions and Properties</b>	1938
3.07.1.1.1	Coppers	1938
3.07.1.1.2	High conductivity coppers	1942
3.07.1.1.3	Heat treatable copper alloys	1942
3.07.1.1.4	Brasses	1942
3.07.1.1.5	Cupronickel alloys	1942
3.07.1.1.6	Tin bronze	1943
3.07.1.1.7	Aluminum-bronzes	1943
3.07.1.1.8	Silicon-bronzes	1943
3.07.1.1.9	Nickel silvers	1943
3.07.1.1.10	Copper-nickel-chromium	1943
<b>3.07.2</b>	<b>Theoretical Aspects of Copper Corrosion</b>	1943
3.07.2.1	Electrode Potential Relationships	1944
3.07.2.2	Behavior of Copper Electrodes	1944
<b>3.07.3</b>	<b>Corrosive Environments Experienced</b>	1946
3.07.3.1	Atmospheric Corrosion	1946
3.07.3.2	Soil Corrosion	1949
3.07.3.3	Corrosion in Natural Waters	1950
3.07.3.3.1	Impingement attack	1950
3.07.3.3.2	Dezincification of brasses	1952
3.07.3.3.3	Selective attack in other alloys	1954
3.07.3.3.4	Deposit attack and pitting	1954
3.07.3.4	Corrosion in Freshwater	1954
3.07.3.4.1	Pitting	1954
3.07.3.4.2	Chemical attack	1956
3.07.3.4.3	Microbiologically influenced corrosion	1956
3.07.3.4.4	Stress corrosion cracking	1957
3.07.3.4.5	Dissolution	1957
3.07.3.5	Corrosion in Seawater	1958
3.07.3.6	Effect of Exposure to Contaminated Environments	1960
3.07.3.6.1	Stress corrosion of brasses	1961
3.07.3.6.2	Stress corrosion of other copper alloys	1962
3.07.3.7	Corrosion in Industrial Chemicals	1962
3.07.3.7.1	Acid solutions	1963
3.07.3.7.2	Neutral and alkaline solutions	1963
3.07.3.7.3	Hydrogen sulfide pollution	1963
3.07.3.7.4	Other chemicals	1964
3.07.3.8	High Temperature Oxidation and Scaling	1965
3.07.3.8.1	High temperature oxidation of copper	1965
3.07.3.8.2	High temperature oxidation of copper alloys	1966
<b>3.07.4</b>	<b>Protective Measures</b>	1966

3.07.5	Areas of Future Development	1967
3.07.5.1	Antimicrobial Benefits of Copper Corrosion	1967
3.07.5.2	Alloy Developments	1967
References		1968

## Glossary

**Antimicrobial** Capable of destroying or inhibiting the growth of microorganisms.

**Dealloying** A corrosion process whereby one constituent of a metal alloy is preferentially removed from the alloy, leaving an altered residual microstructure.

**Dezincification** A corrosion process specific to brasses (copper–zinc alloys) whereby zinc is preferentially removed from the alloy, resulting in a porous residual microstructure.

**Shape memory alloy** An alloy which, after it is deformed, will automatically regain its original geometry when it is heated.

## Abbreviations

**BTAH** Benzotriazole

**FPSO** Floating production, storage and offloading vessel

**MIC** Microbiologically influenced corrosion

**MRSA** Meticillin-resistant *Staphylococcus aureus*

**SCC** Stress corrosion cracking

**SEM** Scanning electron microscopy

**STEM** Scanning transmission electron microscopy

**WHO** World Health Organization

## Symbols

**$A_i$**  Activity of species *i*

**$K$**  Equilibrium constant and rate constant

**$Q$**  Activation energy

**$R$**  Copper run-off rate

**$R$**  Gas constant

**$T$**  Temperature (K)

## 3.07.1 Introduction

Copper and copper alloys are among the earliest metals known to man, as they have been used from

prehistoric times, and their present-day importance is greater than ever before. Their widespread use depends on a combination of good corrosion resistance in a variety of environments, excellent workability, high thermal and electrical conductivity, and attractive mechanical properties at low, normal, and moderately elevated temperatures.

A wide range of cast and wrought alloys is available. For detailed expositions of properties and uses, the reader is referred to publications of many specialized aspects obtainable from the Copper Development Association offices in various countries. Relevant publications of the British Standards Institution include BSEN1982, *Copper Alloy Ingots and Castings*,<sup>1</sup> and those covering wrought products.<sup>2,3</sup> All ASTM standards relating to copper and copper alloys are included in a volume published annually.<sup>4</sup>

### 3.07.1.1 Alloy Compositions and Properties

The mechanical properties of wrought alloys<sup>5,6</sup> depend on composition and metallurgical condition. At the extremes, annealed pure copper has a tensile strength of  $220 \text{ MN m}^{-2}$  and a hardness of 40 HV, and heat-treated beryllium copper can have a tensile strength of  $1450 \text{ MN m}^{-2}$  and a hardness of 400 HV. Summaries of typical properties of some of the more important wrought and cast copper alloys are given in [Tables 1–4](#).

#### 3.07.1.1.1 Coppers

The purest grade of copper commercially available, and that with the highest electrical conductivity, is oxygen-free high-conductivity copper. The minimum copper content required by some specifications is 99.99% and the method of manufacture is such that no residual deoxidant is present. Oxygen itself has very little effect on conductivity, and the ‘tough pitch’ coppers (either electrolytic or fire-refined), containing ~0.04% oxygen are high-conductivity materials.

One disadvantage of tough pitch coppers is embrittlement, which is liable to occur when they are heated in atmospheres containing hydrogen. Therefore, for many purposes (and particularly where fabrication is involved) deoxidized coppers are preferred. The usual

**Table 1** Compositions of wrought copper alloys.<sup>2</sup>

<i>Alloy</i>												
<i>Description</i>	<i>EN No.</i>	<i>Cu</i>	<i>Al</i>	<i>Fe</i>	<i>Mn</i>	<i>Ni</i>	<i>P</i>	<i>Pb</i>	<i>Si</i>	<i>Sn</i>	<i>Zn</i>	<i>Other</i>
HC copper Cu–ETP	CW004A	99.90Min						0.005				0.0005Bi 0.040 O
Deoxidized nonarsenical copper Cu–DHP	CW024A	99.90Min					0.015–0.040					
Oxygen-free copper, Cu–OF	CW008A	99.95Min						0.005				0.0005Bi
Silver-alloyed copper, Cu–EPT	CW012A	Rem										0.06–0.08Ag 0.0005Bi 0.040 O
Tellurium copper	CW118C	Rem					0.003–0.012					0.4–0.7Te
Beryllium copper	CW100C	Rem		0.2		0.3						1.6–1.8Be 0.3Co
85/15 brass	CW502L	84.0–86.0	0.02	0.05		0.3		0.05		0.1	Rem	
70–30 brass	CW505L	69.0–71.0	0.02	0.05		0.3		0.05		0.1	Rem	
60/40 brass	CW509L	59.5–61.5	0.05	0.02		0.3		0.3		0.2	Rem	
Dezincification resistant brass	CW602N	61.0–63.0	0.05	0.1	0.1	0.3		1.7–2.8		0.1	Rem	0.02–0.15 As
Free machining brass	CW614N	57.0–59.0	0.05	0.3		0.3		2.5–3.5		0.3	Rem	
Aluminum brass	CW702R	76.0–79.0	1.8–2.3	0.07	0.1	0.1	0.01	0.05			Rem	0.02–0.06As
Naval brass	CW712R	61.0–63.0		0.1		0.2		0.2–0.6		1.0–1.5	Rem	
High tensile brass	CW705R	65.0–68.0	4.0–5.0	0.5–3.0	0.5–3.0	1.0		0.2–0.8		0.2	Rem	
18% Nickel silver	CW409J	60.0–63.0		0.3	0.5	17.0–19.0		0.03		0.03	Rem	
5% Tin bronze	CW451K	Rem		0.1		0.2	0.01–0.4	0.02		4.5–5.5	0.2	
Silicon bronze	CW116C	Rem	0.05	0.2	0.7–1.3		0.05	0.05	2.7–3.2		0.4	
High strength bronze	CW111C	Rem		0.2	0.1	1.6–2.5	0.02		0.4–0.8			Additions of Co, Mg, Cr
10% Aluminum bronze	CW307G	Rem	8.5–11.0	3.0–5.0	1.0	4.0–6.0		0.05	0.2	0.1	0.4	
90–10 Cupronickel	CW352H	Rem		1.0–2.0	0.5–1.0	9–11	0.02	0.02		0.03	0.5	
70–30 Cupronickel	CW354H	Rem		0.4–1.0	0.5–1.5	30–32	0.02	0.02		0.05	0.5	

Values are given in % mass fraction and are maximum values unless indicated otherwise.

**Table 2** Typical properties of wrought alloys

<i>Alloy</i>		<i>Melting</i>	<i>Density</i>	<i>Coeff of expansion</i>	<i>Electrical</i>	<i>Thermal</i>	<i>Tensile</i>	<i>Elongation</i>	<i>Hardness</i>
<i>Description</i>	<i>EN No.</i>	<i>point (°C)</i>	<i>(g cm<sup>-3</sup>)</i>	<i>(× 10<sup>-6</sup> °C<sup>-1</sup>)</i>	<i>Cond (% IACS)</i>	<i>conductivity (W mK<sup>-1</sup>)</i>	<i>Strength (MN m<sup>-2</sup>)</i>	<i>(%)</i>	<i>(HV)</i>
HC copper Cu-ETP	CW004A	1083	8.94	18	103	390	220–385	4–55	40–110
Deoxidized nonarsenical copper	CW024A	1082	8.93	18	80	340	220–385	4–60	40–120
Cu-DHP									
Oxygen-free copper, Cu-OF	CW008A	1083	8.94	18	100	395	220–385	4–60	40–110
Silver-alloyed copper, Cu-EPT	CW012A	1083	8.94	18	102	390	220–385	4–55	40–110
Tellurium copper	CW118C	1075	8.93	18	96	360	250–360	2–7	90–110
Beryllium copper	CW100C	955	8.2	18	23	85	680–1450	3–35	100–400
85/15 Brass	CW502L	1025	8.74	19	35	155	260–420	4–50	55–135
70–30 Brass	CW505L	955	8.53	20	27	125	270–490	9–50	55–150
60/40 Brass	CW509L	905	8.38	21	29	125	340–480	6–43	85–140
Dezincification resistant brass	CW602N		8.43	21	26	117	280–520	15–45	70–140
Free machining brass	CW614N		8.47	21	27	120	350–450	20–30	100–150
Aluminum brass	CW702R	980	8.33	19	23	100	300–390	25–35	70–110
Naval brass	CW712R	890	8.41	21	25	110	340–460	10–30	85–140
High tensile brass	CW705R	890	8.35	21	23	105	550–650	8–12	150–200
18% Nickel silver	CW409J		8.69	16	7	35	380–900	2–40	85–230
5% Tin bronze	CW451K	1050	8.89	18	17	80	340–740	1–60	70–220
Silicon bronze	CW116C	1030	8.52	18	8	40	380–900	3–50	90–220
High strength bronze	CW111C	1060	8.86	17	50	220	600–800	5–15	100–250
10% Aluminum bronze	CW 307G	1075	7.5	18	8	40	430–770	15–25	200–240
90–10 cupronickel	CW352H	1150	8.91	16	10	50	290–520	8–35	80–160
70–30 cupronickel	CW354H	1240	8.94	16	5	30	350–520	12–35	90–130



**Table 3** Compositions of cast copper alloys<sup>1</sup>

<i>Alloy</i>														
<i>Description</i>	<i>EN No.</i>	<i>Cu</i>	<i>Al</i>	<i>Fe</i>	<i>Mn</i>	<i>Ni</i>	<i>P</i>	<i>Pb</i>	<i>S</i>	<i>Sb</i>	<i>Si</i>	<i>Sn</i>	<i>Zn</i>	<i>Other</i>
High conductivity copper	CC040	Not specified												
Dezinification resistant brass	CC752S	61.5–64.5	0.3–0.70	0.35	0.15	0.25		1.5–2.5		0.15	0.02	0.4	Rem	0.15As
High tensile brass	CC765S	57.0–65.0	0.5–2.5	0.5–2.0	0.5–3.0	6.0	0.03	0.5		0.08	0.1	0.1	Rem	
Tin bronze	CC481K	87.0–89.5	0.1	0.1	0.05	0.1	0.5–1.0	0.25	0.05	0.05	0.01	10.0–11.5	0.05	
Leaded gunmetal	CC491K	83.0–87.0	0.1	0.3		2.0	0.10	4.0–6.0	0.1	0.25	0.01	4.0–6.0	4.0–6.0	
Aluminum bronze	CC331G	83.0–89.5	8.5–10.5	1.5–3.5	1.0	1.5		0.1			0.2	0.2	0.5	0.05Mg
Copper nickel chrome	CC382H	Rem	0.01	0.5–1.0	0.5–1.0	29.0–31.0	0.01	0.005	0.01		0.15–0.50		0.2	1.5–2.0Cr, 0.15Zr 0.25Ti
Copper chromium	CC140C	Rem												0.4–1.2Cr

Values are given in % mass fraction and are maximum values unless indicated otherwise.

**Table 4** Properties of cast copper alloys<sup>1</sup>

<i>Alloy</i>		<i>Tensile strength, minimum (MN m<sup>-2</sup>)</i>	<i>Elongation, minimum (%)</i>	<i>Brinell hardness HB, minimum</i>
<i>Description</i>	<i>EN No.</i>			
High conductivity copper	CC040A	150	25	40
Dezincification resistant brass	CC752S	280	10	70
High tensile brass	CC765S	500	18	120
Tin bronze	CC481K	350	4	85
Leaded gunmetal	CC491K	230	10	65
Aluminum bronze	CC331G	550	18	130
Copper nickel chrome	CC382H	440	18	115
Copper–chromium	CC140C	300	10	95

deoxidizing agent is phosphorus, and specifications require residual phosphorus contents of between 0.004% and 0.06%. Phosphorus-deoxidized coppers with lower phosphorus content have electrical conductivities  $\sim 98\%$  of that of pure copper.

### 3.07.1.1.2 High conductivity coppers

Pure copper has the highest electrical conductivity of any metal apart from silver. However, it has poor strength and suffers from creep at temperatures above  $\sim 150^\circ\text{C}$ . A small addition of silver (0.03–0.12%) gives an increase in creep strength and resistance to softening up to  $250^\circ\text{C}$  (up to  $350^\circ\text{C}$  for short times). Copper–silver alloys are widely used in electrical motors and for contact and catenary wires for electric railways and tramways. They have a nominal conductivity of 100% IACS. In the past, copper–cadmium alloys (0.5–1.2% Cd), which have an excellent combination of strength and electrical conductivity, were widely used for such applications. However, due to health concerns regarding cadmium when the alloy is molten, the use of copper–cadmium alloys is declining. Other high conductivity alloys such as copper–magnesium and copper–tin (0.1–0.5%) have been developed. For all of these high conductivity alloys, a compromise has to be made between high strength and electrical conductivity.

### 3.07.1.1.3 Heat treatable copper alloys

Copper alloyed with 0.5–1.2% chromium with or without 0.03–0.3% zirconium gives precipitation hardening alloys with strengths up to  $450\text{ MN m}^{-2}$ . Such alloys have electrical conductivities of 80% IACS together with good thermal conductivity properties.

Precipitation hardening Cu–Ni–Si alloys are also available. One type is based on copper, nickel, and silicon (described as ‘High strength bronze’ in [Table 3](#)), which, with further alloy additions, can

reach tensile strengths of around  $800\text{ MN m}^{-2}$  while retaining its high conductivity. For this material, which is widely used for plastic moulding equipment, the main precipitating phase is  $\text{Ni}_2\text{Si}$ . Stress relaxation and the ability to withstand high temperatures under stress without losing spring properties or ease of bending are importance for this material.

The highest strength of any copper alloy (up to  $1450\text{ MN m}^{-2}$ ) is obtained by precipitation hardening and cold working copper–beryllium (1.8–2.0% Be). However, due to the toxic nature of beryllium, care must be exercised in melting and machining this alloy.

### 3.07.1.1.4 Brasses

Brasses are basically alloys of copper and zinc, containing between  $\sim 10\%$  and 45% Zn, but many other additions can be made.<sup>7</sup> The single-phase ( $\alpha$ ) brasses, containing up to  $\sim 37\%$  Zn in the binary alloys, may have additions of 1% Sn (Admiralty brass), 2% Al (aluminum brass), or 1–3.5% Pb for ease of machining. Duplex ( $\alpha$ – $\beta$ ) brasses containing more than 37% Zn, may have additions of 1% Sn (Naval brass), or 1–3% Pb to assist machining. Both  $\alpha$  and  $\alpha$ – $\beta$  brasses, with and without lead, are used in the cast as well as the wrought form. High-tensile brasses are  $\alpha$ – $\beta$  alloys containing up to 5% Al and 1–2% of one or more of the following: Sn, Pb, Fe, or Mn. These alloys also are used in both wrought and cast form.

### 3.07.1.1.5 Cupronickel alloys

Cupronickel alloys contain between 5% and 30% Ni and are mainly used in the wrought condition.<sup>8</sup> The more popular grades have 10% and 30% Ni and are recognized for their very good corrosion and biofouling resistance in marine applications.<sup>9,10</sup> Small controlled alloying additions of iron and manganese are essential to optimize their resistance to localized corrosion and seawater flow. The addition of chromium has also been shown to improve resistance to flow

velocity and a cast (30Ni–1.6Cr)<sup>11</sup> as well as a wrought version (16Ni–0.5Cr)<sup>12</sup> have been developed. The cast version has been predominantly used by the British Navy and is covered by DEF STAN 02-824.<sup>11</sup>

Other higher strength cupronickels have additions of aluminum or tin, producing two ranges of products. The Cu–Ni–Al alloys<sup>13</sup> are thermally age-hardened to form Ni<sub>3</sub>Al precipitates in the matrix whereas Cu–Ni–Sn alloys display spinodal strengthening through the development of submicroscopic chemical composition fluctuations.<sup>14</sup>

#### 3.07.1.1.6 Tin bronze

Copper alloys with 1.5–9% Sn and 0.01–0.4% P are wrought alloys known as phosphor bronzes. They have good elastic properties combined with good resistance to corrosion and corrosion fatigue.

Cast copper alloys with between 2% and 11% Sn and 1–10% Zn are termed gunmetals. Modified forms may contain lead (up to 7%) giving leaded gunmetal or nickel (up to 6%) giving a nickel gunmetal. Gunmetals are the most widely used copper casting alloys combining good corrosion resistance with modest strength and good castability.

#### 3.07.1.1.7 Aluminum-bronzes

Wrought aluminum bronzes contain between 4% and 12.5% Al. If less than 8% Al is present, the alloys are  $\alpha$ -phase and may be cold worked. The two phase ( $\alpha$ – $\beta$ ) alloys, which may be wrought or cast, contain 8–12.5% Al with possible additions of iron (0.5–7%), manganese (1.5–3.5%), nickel (2–7%), and silicon (2%). In terms of its influence on corrosion resistance, the addition of nickel is the most important, as it acts to reduce dealuminification (see [Section 3.07.3.3.3](#)).

Aluminum bronzes can be hardened by heat treatment and have an enhanced corrosion resistance due to the existence of a complex naturally-formed protective film which includes both aluminum oxide<sup>15</sup> and copper oxide. If damaged, the film is self healing and this gives aluminum bronzes good wear, cavitation, and antigalling characteristics.

#### 3.07.1.1.8 Silicon-bronzes

Silicon-bronzes usually contain 2.8–4.5% Si and 0.8–1.5% Mn. The wrought alloys combine high tensile strength (see [Table 2](#)) with good corrosion resistance and an attractive color. They are used in chemical equipment and marine hardware. The cast alloy has found application in statuary, art castings, and plaques.

#### 3.07.1.1.9 Nickel silvers

Nickel silvers do not contain silver but are essentially copper–zinc brasses with nickel in the range of 9–18%. The 18% nickel alloy polishes to a white color (like silver) and has good corrosion resistance. All have excellent ductility and are available as tube, wire, plate, sheet, and strip.

#### 3.07.1.1.10 Copper–nickel–chromium

Copper–nickel–chromium alloys have been developed chiefly as cast alloys, the most prominent of which is CC382H. A version of this is DEF STAN 02-824, which is commonly used by the British Navy.

### 3.07.2 Theoretical Aspects of Copper Corrosion

Copper is the first member of Group IB of the periodic table, having atomic number 29 and electronic configuration [Ar]3d<sup>10</sup>4s<sup>1</sup>. Loss of the outermost s electron gives the cuprous ion Cu<sup>+</sup> and a second electron may be lost from the filled d shell to form the cupric ion Cu<sup>2+</sup>. The availability of the d electrons for coordination allows copper to readily form complexes with such species as NH<sub>3</sub> and CN.

Copper occurs in the uncombined state in nature and is relatively easily obtained by the reduction of its compounds. It is not very active chemically and oxidizes very slowly in air at ordinary temperatures. In the electrochemical series of elements, copper is near the noble end and will not normally displace hydrogen, even from acid solutions. Indeed, if hydrogen is bubbled through a solution of copper salts, copper is slowly deposited, a process which occurs more rapidly if it is carried out under pressure.

As copper is not an inherently reactive element, it is not surprising that the rate of corrosion, even if unhindered by films of insoluble corrosion products, is usually low. Nevertheless, although the breakdown of a protective oxide film on copper is not likely to lead to such rapid attack as with a more reactive metal (e.g., aluminum), in practice the good behavior of copper, and, more particularly, of some of its alloys often depends to a considerable extent upon the maintenance of a protective film of oxide or other insoluble corrosion product.

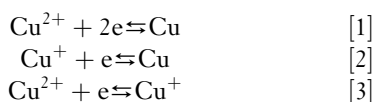
In many environments, alloys of copper can be more resistant to corrosion than is copper itself, owing to the incorporation either of relatively corrosion-resistant metals, such as nickel or tin, or of metals such as aluminum or beryllium which would

be expected to assist in the formation of protective oxide films. Several types of copper alloys are liable to undergo a selective type of corrosion in certain circumstances, the most notable example being the dezincification of brasses (see [Section 3.07.3.3.2](#)). Some alloys are liable to suffer stress corrosion by the combined effects of internal or applied stresses and the corrosive effects of certain specific environments. The most widely known example of this is the season cracking of brasses (see [Section 3.07.3.6](#)). In general, brasses are the least corrosion-resistant of the commonly used copper-based alloys.

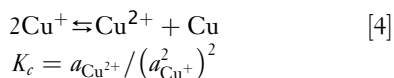
The various grades of commercial copper available do not differ to any marked extent in their corrosion resistance, and a choice between them is usually based on other grounds. Subsequent references to the corrosion behavior of copper may therefore be taken to apply broadly to all types of copper. The choice of alloy for any particular application is determined by the desired physical, mechanical, and metallurgical properties. Within these limits, however, a range of materials is usually available. It is essential that, at the very earliest stage, the choice of materials and the detail of design of the installation should be considered from the point of view of corrosion if the best performance is to be obtained in service. This is particularly true for copper alloys, where protective measures are not normally applied.

### 3.07.2.1 Electrode Potential Relationships

The electrode potentials for the equilibria:



are +0.34, +0.52, and + 0.17 V respectively, as measured against a standard hydrogen electrode. For the equilibrium



$K_c$  has the value of  $\sim 1 \times 10^6$  at 298 K, and in solutions of copper ions in equilibrium with metallic copper, cupric ions therefore greatly predominate over cuprous ions, except in very dilute solutions. Cupric ions are therefore normally stable and become unstable only when the cuprous ion concentration is very low. A very low concentration of cuprous ions may be produced in the presence of a suitable anion, by the formation of either an insoluble cuprous salt or a very

stable complex cuprous ion. Cuprous salts can therefore exist in contact with water only if they are very sparingly soluble (e.g., cuprous chloride) or are combined in a complex, for example,  $[\text{Cu}(\text{CN})_2]^{-}$  and  $[\text{Cu}(\text{NH}_3)_2]^{+}$ . Cuprous sulfate can be prepared in nonaqueous conditions, but because it is not sparingly soluble in water, it is immediately decomposed by water to copper and cupric sulfate. The equilibrium between copper and cuprous and cupric ion is disturbed by the presence of oxygen in solution, since the reaction shown in [eqn \[3\]](#) is facilitated, the oxygen acting as an electron acceptor.

### 3.07.2.2 Behavior of Copper Electrodes

The electrode potential behavior of copper in various solutions has been investigated in detail by Gatty and Spooner.<sup>16</sup> According to these workers a large part of the surface of copper electrodes in aerated aqueous solutions is normally covered with a film of cuprous oxide and the electrode potential is usually close to the potential of these film-covered areas. The filmed metal simulates a reversible oxygen electrode at the oxygen concentration and pH, less an overvoltage determined by the existing current density. The principal factors which affect the electrode potential are thus the nature of the solution, the way in which this influences the area of oxide film, and the supply of oxygen to the metal surface. In solutions containing chloride, there is a tendency for the establishment of the  $\text{Cu}/\text{CuCl}/\text{Cl}^{-}$  electrode potential, so that the activity of chloride ions is an important factor in determining the electrode behavior. From a knowledge of the solubility products of cuprous chloride and cuprous oxide, it is possible to predict under what conditions chloride or hydroxyl ions are the potential-determining ions. According to Gatty and Spooner, chloride determines the potential if  $a_{\text{OH}^{-}} < 10^{-8.1} \times a_{\text{Cl}^{-}}$  and hydroxyl determines the potential if  $a_{\text{OH}^{-}} > 10^{-8.1} \times a_{\text{Cl}^{-}}$ . However, this will not hold in concentrated solutions as complex  $[\text{CuCl}_2]^{-}$  ions as well as simple ions will be present. A further factor to be considered is the ready formation of insoluble basic compounds. In solutions which do not contain chloride (e.g., sulfate or nitrate solutions), corrosion rates are usually lower and the electrode potential is more steady over a wide range of conditions.

Gatty and Spooner consider that the rate of corrosion is probably determined by the rate at which metal ions can escape through pores in the protective oxide film, and this is supported by the results of

experiments on the anodic and cathodic polarization of copper.

One of the potential–pH equilibrium diagrams devised by Pourbaix<sup>17</sup> relating to the Cu–H<sub>2</sub>O system is shown in **Figure 1**. Such diagrams are of considerable assistance in discussing many problems associated with the chemistry, electrochemistry, electrodeposition, and corrosion of copper. It must be pointed out that the thermodynamic approach on which these are based has limitations, the most important being that, although predictions can be made about the possibility of a given reaction proceeding in certain circumstances, no information can be gained about the rate at which it will proceed.

A similar method of representing the behavior of copper in dilute aqueous solutions by means of corrosion-current/pH diagrams has been given by Rubinic and Markovic.<sup>18</sup> A study of the behavior of copper when anodically polarized has been made by

Hickling and Taylor<sup>19</sup> and, more recently, by Kuksina *et al.*<sup>20</sup> using electrochemical methods which record the variation of potential with the Faradaic charge passed. In alkaline solutions, the main stages of polarization have been found to be (1) the charging of the double layer, and (2) the formation of a film of cuprous oxide which was almost at once oxidized to cupric oxide. Mayer and Muller<sup>21</sup> report evidence that this converts to Cu<sub>2</sub>O<sub>3</sub> at potentials above –25 mV versus Hg/HgO in 1 M KOH. However, in 0.1 M NaOH,<sup>20</sup> the Cu<sub>2</sub>O film was found to be around four molecules thick when oxygen evolution first commenced. In buffer solutions of decreasing pH, the formation of sparingly soluble salts preceded or accompanied the formation of the oxide film. In acid solutions yielding soluble copper salts, no passivity developed, the anodic process being merely dissolution of copper. In nitrate solutions, the cathodic process has a significant effect on the

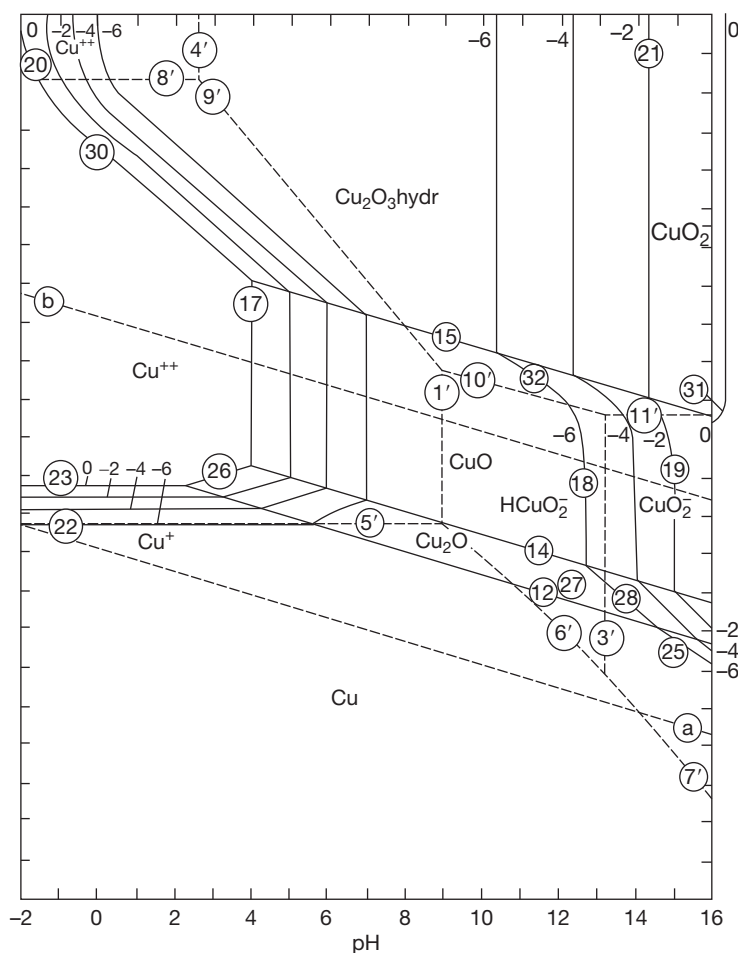


**Figure 1** Potential–pH equilibrium for the system copper–water at 25 °C.

anodic dissolution of copper. Low-frequency AC polarization techniques have shown<sup>22</sup> that  $\text{OH}^-$  ions adsorbed during the cathodic half-cycle facilitate copper dissolution in the anodic half-cycle through the production of an insoluble hydroxide layer. Other workers have also studied the anodic behavior of copper or copper alloys in alkaline<sup>23</sup> and in acid<sup>24,25</sup> solutions, using both static conditions and turbulent conditions, such as those generated by rotating cylinder electrodes<sup>26</sup> and the presence of light has been found to have an influence on the electrochemistry.<sup>21</sup> For instance, in Cu–Al–Sn anodically polarized in sodium sulfate solution,<sup>27</sup> an enrichment of the passive film with aluminum oxide can be detected as the photocurrent spectrum changes from a ‘copper-type’ to an ‘aluminum-type’ with time.

The excellent corrosion resistance of cupronickel alloys is related to the formation of a particularly effective protective film of corrosion products in the early stages of exposure. A number of studies have been carried out involving a wide range of analytical techniques.<sup>28</sup> The film formed is dark brown in color and there is general agreement that it contains an inner layer of  $\text{Cu}_2\text{O}$  which is enriched with nickel and iron. Recent electrochemical studies<sup>29</sup> have identified that over this layer, a thin outer layer of  $\text{CuO}$  develops and an increasing nickel content in the alloy produces a decrease in the overall corrosion rate. The corrosion rate also falls as the chloride ion concentration rises above 0.3 M due to an enhanced formation of the passive  $\text{Cu}_2\text{O}$  film.<sup>30</sup> On this subject, in a seawater context, see [Section 3.07.3.5](#).

### 3.07.3 Corrosive Environments Experienced

Copper and its alloys have a very diverse range of properties and their application exposes them to many types of environment. Artifacts dating back thousands of years are testimony to the resilience of copper alloys to atmospheric corrosion, waters, and soils. Also, they have been recognized for marine use for several decades and are still selected even though other noncopper alloy systems have been developed in the interim. The release of copper ions and the cuprous oxide film have antifouling properties and, in addition, recent work has proved their antimicrobial properties; investigations into the mechanisms for these beneficial effects are ongoing, as are their development into new applications. More traditional applications requiring corrosion resistance of copper

alloys involve roofing, plumbing, naval and commercial shipping, and desalination plant. The level of corrosion and corrosion mechanisms occurring in different environments depend on the alloy group chosen and can vary from mildly resistant to highly resistant. Various corrosion mechanisms exist and these have been found to be related to the type of alloy and to the environment to which it is exposed. The following sections give details of the effects seen in a range of different corrosive environments experienced.

#### 3.07.3.1 Atmospheric Corrosion

Copper has a high degree of resistance to atmospheric corrosion and is widely used for roofing sheets, flashings, gutters, and conductor wires as well as for statues and plaques. The corrosion resistance of copper and its alloys is due to the development of protective layers of corrosion products, which act to reduce the subsequent rate of attack. The formation, in course of time, of the typical green ‘patina’ gives copper roofs a pleasing appearance; indeed, methods are used to produce it artificially or to accelerate its formation.<sup>31</sup> The nature of the corrosion products formed on copper exposed to the atmosphere has been exhaustively studied by Vernon and Whitby.<sup>31–33</sup> A comprehensive review of the literature on atmospheric corrosion including copper and copper alloys up to 1995 has been produced by Dechema<sup>34</sup> It has been found that in the early periods of exposure, the corrosion deposit contains sulfide, oxide, and soot. By the action of sulfuric acid and by the oxidation of sulfide, copper sulfate is formed and this hydrolyzes and forms a coherent and adherent basic form of this compound. Initially, this approximates to  $\text{CuSO}_4\text{--Cu}(\text{OH})_2$  but it gradually increases in basicity until after 70 years or so it becomes  $\text{CuSO}_4\text{--}3\text{Cu}(\text{OH})_2$  and is identical with the mineral brochantite. In some cases, small quantities of basic carbonate,  $\text{CuCO}_3\text{--Cu}(\text{OH})_2$  (malachite), are also present, and, near the sea coast, basic chloride  $\text{CuCl}_2\text{--}3\text{Cu}(\text{OH})_2$  (atacamite) is produced. However, even very near the sea coast, sulfate usually predominates over chloride.

In laboratory tests, Vernon<sup>33</sup> showed that the relative humidity and the presence of sulfur dioxide have a profound effect on the rate of corrosion of copper, as they do with many other metals. He found that when the relative humidity was less than 63%, there was little attack even in the presence of much sulfur dioxide, but when the relative humidity was raised to



75%, corrosion became severe and increased with the concentration of sulfur dioxide present. By exposing specimens to the atmosphere at different times of the year, Vernon found that the rate of attack on copper was determined by the conditions prevailing at the time of first exposure. For specimens first exposed in winter, there was a linear relationship between increase in weight and time of exposure, indicating that the layer of corrosion product formed under these conditions was nonprotective. For specimens first exposed in summer, the square of the increase in weight was proportional to the time of exposure. This indicated that the coating formed in summer (when the atmospheric pollution was relatively low) was protective. It was found that the parabolic law holds when the corrosion product layer obstructs the access of the corrosive agent to the metal, the rate of attack then being inversely proportional to the thickness of the layer. It was apparent that the protective character of the layer persisted through subsequent periods when the pollution was relatively high.

Copper tarnishes rapidly when exposed to atmospheres containing hydrogen sulfide. Atmospheric corrosion tests on copper and several copper alloys were carried out by Hudson<sup>35</sup> at a number of sites in the United Kingdom. Corrosion damage was assessed by one or more of the following methods: gain in weight, loss of weight after cleaning, loss of electrical conductivity, and loss of tensile strength. Hudson found that the resistance to atmospheric corrosion was high and that the rate of attack tended to decrease with time of exposure. Little difference was found between the behavior of arsenical copper and high-conductivity copper, and most of the alloys

tested behaved very similarly except for the brasses, which deteriorated more rapidly owing to dezincification (see [Section 3.07.3.3.2](#)). Several series of atmospheric exposure tests have been carried out since Hudson's work, and the loss in weight data obtained in six of the most important investigations are summarized in [Table 5](#). In all cases, losses in tensile strength were also determined, and the results from the two methods were, in general, in good agreement. However, for alloys suffering selective attack (such as with the dezincification of brasses) change in mechanical properties usually provided a more reliable indication of deterioration than weight loss. Some other findings common to all the tests were that (1) corrosion rates decreased with time, (2) least attack occurred at rural sites and most in urban and industrial atmospheres, (3) corrosion was uniform, and (4) with a few exceptions, there was no significant pitting.

Tracy *et al.*<sup>36</sup> exposed specimens of 11 different grades of copper in the form of sheet and wire to rural, marine, and industrial atmospheres in the United States for periods up to 20 years. The differences in the behavior of the materials were small and of little, if any, practical significance. Very similar results for various types of copper were found by Mattsson and Holm<sup>37</sup> in Sweden and Scholes and Jacob<sup>38</sup> in the United Kingdom (see [Table 5](#)).

[Table 5](#) gives the results of tests on copper alloys by Tracy,<sup>36</sup> Thompson,<sup>40</sup> and Mattson and Holm,<sup>37</sup> Scholes and Jacob<sup>38</sup> and, more recently, Morcillo<sup>39</sup> together with their co-workers. The tests of Tracy and Scholes were for periods up to 20 years; in the work of Thompson and Mattson, specimens were

**Table 5** Atmospheric corrosion tests on copper and copper alloys

	No. of types of copper	No. of different alloys	No. of sites	Period of exposure (years)	Average rates of attack from weight losses ( $\text{mm year}^{-1} \times 10^4$ )		
					Rural sites	Marine sites	Urban/Industrial sites
Tracy, Thompson, and Freeman <sup>36</sup>	11	—	4	20	5.6–4.3	6.9–9.4	8.6–12
Tracy <sup>43</sup>	2	9	7	20	0.5–7.6	1.3–23 <sup>a</sup>	13–30 <sup>a</sup>
Thompson <sup>40</sup>	1	17	4	7	3.3–10	4.3–25	13–27
Mattson and Holm <sup>41</sup>	4	—	3	7	5–6	7–8	10–12
	—	18	3	7	2–5	6–11	9–22
Scholes and Jacob <sup>38</sup>	4	—	2	20	—	6–10	11–20
	—	17	2	20	—	8–26	14–38
Morcillo <i>et al.</i> <sup>39</sup>	1	—	66	4	0.1–0.2		

<sup>a</sup>Rates of attack for high tensile brass were  $(45\text{--}115) \times 10^{-4} \text{ mm year}^{-1}$ .

removed after 2 and 7 years and further specimens were removed after 16 years.<sup>41</sup> The average penetration during the 16-year period was found to be about the same as during the first 7 years, but considerably lower than during the initial 2 years. The materials tested included brass, nickel-silvers, cupronickels, copper-beryllium alloys, and various bronzes. Recent studies have involved the investigation of seasonal effects of industrial pollutants ( $\text{NO}_x$ ) and comparison of rural and marine locations in South America.<sup>42</sup>

In the tests described by Tracy,<sup>43</sup> a high-tensile brass suffered severe dezincification (see Table 5). The loss in tensile strength for this material was 100% and, for a non-arsenical 70–30 brass, 54%; no other material lost more than 23% during 20 years' exposure. In Mattsson and Holm's tests, the highest corrosion rates were also shown by some of the brasses. Dezincification caused losses of tensile strength of up to 32% for a  $\beta$  brass and up to 12% for some of the  $\alpha$ - $\beta$  brasses; no other materials lost more than 5% in 7 years. Dezincification also occurred, though to a lesser degree, in the  $\alpha$  brasses tested, even in a material with as high a copper content as 92%. Incorporation of arsenic in the  $\alpha$  brasses consistently prevented dezincification only in marine atmospheres.

In Thompson's reported work, the alloy showing the lowest rate of attack at all sites was a bronze containing 7Al–2Si. Relatively high corrosion rates were shown by Cu–5Sn–0.2P at a marine site and Cu–2.5Co–0.5Be in an industrial environment. The beryllium–copper alloys were the only materials to show measurable pitting, the deepest attack being 0.6 mm after 7 years. In Scholes and Jacob's tests pitting, intergranular (or transgranular) penetration, or selective attack occurred on some alloys. The maximum depth of attack exceeded 0.2 mm in 20 years on 6 of the 21 materials (three brasses, two nickel silvers, and Cu–20Ni–20Mn), but exceeded 0.5 mm in 20 years only on Cu–20Ni–20Mn and 60/40 brass. These two latter alloys lost up to 73% and 13% respectively of their tensile strength; no other alloys lost more than 10% in 20 years.

The work of Ramos *et al.*<sup>42</sup> has demonstrated a clear correlation between seasonal increases in  $\text{SO}_2$  and  $\text{NO}_x$  concentrations in urban atmospheres with higher corrosion rates and the presence of sulfates in the corrosion products. This broadly agreed with a previous study of comparative weight gains of copper over a 2-year period at 39 sites spread across Europe,<sup>44</sup> where a clear correlation was found between weight gain and  $\text{SO}_2$  content of the environment, although attempts to find mathematical

correlations of weight increase with other atmospheric species was not found to be possible. However, other works report that the corrosion of copper by sulfur dioxide is measurably accelerated by the presence of  $\text{NO}_2$ <sup>45</sup> or ozone.<sup>46</sup> The recent study conducted in South America, which involved the comparison of 21 unpolluted sites with 45 marine locations, showed that there is a threshold chloride concentration of  $20 \text{ mg m}^{-2} \text{ day}^{-1}$  in the environment above which the corrosion rate intensifies. Other recent studies have involved comparing the effects of different types of climates throughout four continents.<sup>47</sup>

From the work described and other investigations,<sup>48</sup> it is evident that copper and most copper alloys are highly resistant to atmospheric corrosion. The reported results indicate that copper itself is as good as, or better than, any of the alloys with regard to atmospheric corrosion. Some of the brasses are liable to suffer rather severe dezincification and it is unwise to expose these to the more corrosive atmospheres without applying some protection.

When unusually rapid corrosion of copper and its alloys occurs during atmospheric exposure, it is likely to be for one of the following reasons:

1. Extreme local pollution by products of combustion.
2. Bad design or construction, for example, the presence of crevices where moisture may lodge for long periods, including, for instance, coiled wire.<sup>49</sup>
3. Constant dripping of rain water contaminated by atmospheric pollution (e.g., from near-by chimney stacks) or by organic acids from lichens, etc.
4. Corrosion fatigue due to inadequate allowance for expansion and contraction with consequent buckling as the temperature fluctuates.

Most of these disorders can be avoided by attention to design.<sup>50</sup>

The discussions in recent years of the possibility of pollution occurring as a result of released copper due to atmospheric corrosion have resulted in studies of runoff from roofs and facades by several workers.<sup>51–54</sup> A number of research results have been published by the Royal Institute of Technology, Stockholm, Sweden<sup>55–61</sup> and the EMPA laboratories, Switzerland. It has been found that, after a short initiation period, the runoff rate of copper per year is constant over a long time.<sup>55,56,58,62</sup> This makes it possible to model the copper runoff rate,  $R$ ,<sup>57</sup> based on  $\text{SO}_2$  concentration, the pH of the rainwater, and its quantity. The roof surface angle of inclination  $\theta$  has

also been taken into account,<sup>61</sup> according to the following equation:

$$R = (0.37[\text{SO}_2]^{0.5} + 0.95[\text{Rain}]10^{-0.62\text{pH}}) \frac{(\cos \Theta)}{(\cos 45^\circ)} \quad [5]$$

The seasonal variation of copper corrosion rate and the runoff rate have also been studied.<sup>60</sup>

Some workers note that the released metal from the corrosion reaction is in ionic form directly on the roof and the environmental impact of these released ions has been determined. Other workers state that the run-off is mainly in particulate form. However, the interaction with solid surfaces in the near vicinity of buildings has been looked at together with the changes of transport which occur from the source to the end product. Investigations of reactivity have been made toward various natural and manmade surfaces, such as different soil systems, limestone, and concrete. The results illustrate that, for scenarios where copper ions come in extensive contact with solid surfaces, a large fraction of released copper is retained in the immediate vicinity of the building.<sup>56</sup> The potential ecotoxic effects from released copper have also been investigated. Copper biosensor testing with a bacteria and growth inhibition testing with green algae have been used. The runoff water directly after release was found to cause significant reduction of the green algae growth rate, indicating that the copper is bioavailable. However, it was found that contact with solid surfaces effectively reduces this bioavailable copper.

The fate of released copper in runoff has also been studied in the United States.<sup>62–64</sup> The results obtained also show that the bioavailable copper fraction is low after contact with solid surfaces.

Sundberg<sup>62</sup> followed the runoff from a new copper roof for 3.5 years. A relatively stable runoff rate per year was found after 0.5 years. The result was

compared with the runoff from a roof prepatinated 40 years ago, which was found to have a copper runoff rate which was 10% lower.

### 3.07.3.2 Soil Corrosion

Several extensive series of soil-corrosion tests have been carried out by the National Bureau of Standards in the United States, and the results summarized by Romanoff.<sup>65</sup> In one series, 2 types of copper and 10 copper alloys were exposed in 14 different soils for periods up to 14 years. The results for the copper specimens are summarized in Table 6.

The behavior of the phosphorus-deoxidized and tough-pitch coppers was, in general, very similar. At the less corrosive sites, with a few exceptions, copper was the best material. Most of the alloys lost weight ranging up to twice that of copper, with maximum depths of attack up to three times greater. At the other sites, although the coppers were usually rather better than the alloys, some of the alloys were occasionally superior.

The three most corrosive sites were rifle peat (pH 2.6), cinders (pH 7.6), and tidal marsh (pH 6–9). Corrosion of some of the alloys was particularly severe in the cinders. The behavior of the brasses tested, particularly those high in zinc, was rather different from that of the other materials. In most cases dezincification occurred and the brasses were the worst behaved materials; in the cinders, for instance, several brass specimens were completely destroyed by dezincification. However, in some of the soils rich in sulfides, the brasses were the best materials.

The British NonFerrous Metals Research Association carried out two series of tests, the results of which have been given by Gilbert<sup>66</sup> and Gilbert and Porter<sup>67</sup>; these are summarized in Table 6. In the first series,<sup>66</sup> tough pitch copper tubes were exposed at

**Table 6** Soil-corrosion tests on copper by National Bureau of Standards and British Nonferrous Metals Research Association (BNFMRA)

	<i>Period of exposure (years)</i>	<i>Average rate of attack from loss in weight (mm year<sup>-1</sup> × 10<sup>-4</sup>)</i>	<i>Maximum rate of pitting (mm year<sup>-1</sup>)</i>
BNFMRA first series five least corrosive soils	10	0.5–2.5	Nil
BNFMRA second series four least corrosive soils	5	5.0–25	0.140
Nat. Bur. Standards nine least corrosive soils	14	4.0–25	0.043
Nat. Bur. Standards two next most corrosive soils	14	23–130	0.033
BNFMRA first series acid clay and acid peat	10	53–66	0.046
BNFMRA second series cinders	5	66	0.32
Nat. Bur. Standards three most corrosive soils: rifle peat, cinders, tidal marsh	14	160–355	0.115

seven sites for periods of up to 10 years. The two most corrosive soils were a wet acid peat (pH 4.2) and a moist acid clay (pH 4.6). In these two soils, there was no evidence that the rate of corrosion was decreasing with duration of exposure. In the second series,<sup>67</sup> phosphorus deoxidized copper tube and sheet were exposed at five sites for 5 years. Severe corrosion occurred only in cinders (pH 7.1). In these tests, sulfides were found in the corrosion products on some specimens and the presence of sulfate-reducing bacteria at some sites was proved. However, it was not clear to what extent the activity of these bacteria was a factor accelerating the corrosion of copper.

Cinders and acid peaty soils are obviously among the soils most corrosive toward copper. There is, however, no direct relationship between the rate of corrosion and any single feature of the soil composition or constitution.<sup>68</sup> For instance, in the American tests, corrosion in several soils with either low pH or high conductivity was not particularly severe, while the British tests show that chloride or sulfate contents are not necessarily harmful. The latter tests showed that bare copper can safely be buried in a wide range of soils without fear of excessive corrosion. Experience of the behavior of copper water service pipes, which are used widely, confirms this. Difficulties are generally confined to 'made-up' ground containing cinders, etc. and a few other aggressive soils, and in these circumstances it is necessary to apply protection such as bitumen-impregnated wrappings or plastic coatings. Tin coatings cannot be recommended as experience shows that accelerated attack is liable to occur at pores and scratches in the coating, leading to premature failure. Copper water pipes have been known to fail by the action of stray electric currents, but this is not a common occurrence.

There is agreement between the soil-corrosion tests carried out by National Bureau of Standards and practical experience of the behavior of hot-pressed brass fittings used for joining copper water service pipes. These duplex-structure brass fittings are liable to suffer attack by dezincification in many soils in which copper behaves satisfactorily, and, for burial underground, fittings of copper, gunmetal, or dezincification-resistant brass are to be preferred. In general, it may be said that, unless there is some special reason for using a copper alloy, it is preferable to choose copper for applications involving subterranean service. A comparison of the corrosion produced through the influence of possible ionic species present around buried copper has shown<sup>69</sup> that the major damage is caused by chloride ions.

Ammonium and sulfide species appear to be relatively benign. The corrosion products which result are cuprite and malachite, the latter being favored for soils with higher water content.<sup>70</sup>

### **3.07.3.3 Corrosion in Natural Waters**

Copper and copper alloy pipes and tubes are used in large quantities both for conveying fresh and salt water and in condensers and heat exchangers where fresh or salt water is used for cooling. Pumps, screens, valves, and other ancillary equipment may also be largely constructed of copper alloys. Large tonnages of these materials are therefore used on offshore structures, multistage flash desalination plants, power stations, on board ships, in sugar factories, and in oil refineries, as well as in hot and cold water circuits and heating and cooling systems in hospitals, factories, hotels, and homes.

Corrosion problems that arise frequently are discussed under separate headings, depending on whether the environment is seawater or freshwater. In fact, there is no sharp dividing line between these environments, since some harbor, estuarine, and brackish well waters are mixtures of seawater and freshwater and are often variable in composition. Corrosion has been found to occur in all these media, particularly in seawater, but this is more frequently seen as a result of poor design or operation than as a result of lack of materials suitable for the application. This section will deal with the types of corrosion which can be seen in all types of natural water; seawater, brackish water, or freshwater. Separate sections will follow which deal with corrosion types seen almost entirely solely in freshwater and with the behavior of copper alloys specifically in seawater.

#### **3.07.3.3.1 Impingement attack**

Copper alloys have good corrosion resistance under moderate fluid flow rates. However, above a certain flow velocity, called the breakaway velocity, the shear stress of the liquid on the alloy protective surface film is sufficient to damage it and much higher corrosion rates occur. This phenomenon is called impingement attack or erosion-corrosion. Therefore, tube and piping systems are designed to operate satisfactorily up to a maximum velocity and it is important that this is not exceeded in service. Breakaway velocity can be influenced by many factors, including the alloy being used, the resilience of the surface film, the geometry of the product and system, the corrosive nature of the

fluid being handled, pollution, solids (e.g., sand in seawater), and turbulence.<sup>71</sup>

Copper tubes have been found to suffer from impingement attack in systems where the speed of water flow is unusually high. The phenomenon has been discovered to be dependent in some degree on the quality of the water, for instance where no protective scale is able to form, for example, in a soft water containing appreciable quantities of free carbon dioxide.<sup>72</sup> Impingement attack is most often seen downstream of poorly installed fittings or sharp bends in pipework systems. Such obstructions to flow and sharp changes in direction where the speed of the water is high can lead to eddy currents concentrating the flow on specific parts of the tube, the creation of bubbles at areas of low pressure (which subsequently collapse), and the streaming of particulate matter. The latter can act alone or in concert to remove any protective scale that has formed on the copper surface, thus exposing the metal to further corrosion and subsequent removal of corrosion product. In such a way, severe metal loss can occur, leading eventually to failure of the tube. Impingement attack is characterized by areas of bright metal and horseshoe-shaped undercut areas, their direction being as though the horse was walking upstream. In the middle of such undercut areas, there may be islands of bright metal or metal still retaining some protective corrosion product. An example of this phenomenon is shown in [Figure 2](#). Ball valve seatings may also suffer an erosive type of attack. The corrosion of ball valves, including the effect when the water is chlorinated, has been studied by several workers.<sup>73</sup> Avoidance of impingement attack is usually achieved by reducing the flow velocities by one

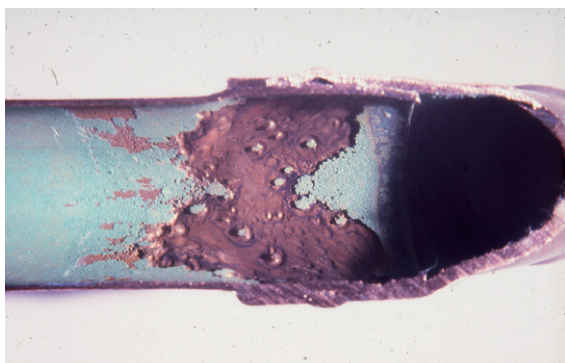


**Figure 2** Photograph showing typical impingement attack caused by eddy currents which were present as a result of burrs on the internal wall. The tube type is 15 mm diameter copper tube to EN 1057, R250 (half-hard condition).

or a combination of the following: reducing the pump output, increasing the pipe size, modification of the change of direction to one which is less abrupt, opening partially closed valves, etc. The maximum flow velocity quoted in European Standard EN806 part 3 is  $2.0 \text{ m s}^{-1}$  for header, riser, and floor service pipes and  $4.0 \text{ m s}^{-1}$  for (replaceable) connection pipes to one fitting. The Swedish Building Standard 2522 recommends a reduction in velocity as the design operating water temperature increases viz,  $2 \text{ m s}^{-1}$  at  $10^\circ\text{C}$ ,  $1.5 \text{ m s}^{-1}$  at  $50^\circ\text{C}$ ,  $1.3 \text{ m s}^{-1}$  at  $70^\circ\text{C}$ , and  $1.0 \text{ m s}^{-1}$  at  $90^\circ\text{C}$ .

The actual velocity at which impingement commences depends on the fluid and varies from alloy to alloy.<sup>74</sup> In general, the nickel aluminum bronzes and copper–nickel alloys have the highest velocity tolerances in seawater and are somewhat better than gunmetals, brasses and tin bronzes<sup>75</sup> (see [Table 7](#) and [Section 3.07.3.5](#)). The cupronickel 90–10 and 70–30 alloys are commonly used for seawater condensers, heat exchangers, and pipework in naval vessels as well as merchant shipping. For tube sizes used in heat exchangers and condensers, the velocity is limited to  $\sim 2\text{--}2.5 \text{ m s}^{-1}$ . For seawater pipework of internal diameter 100 mm and with bends of long radius, the recommended maximum seawater flow velocities are  $3.5 \text{ m s}^{-1}$  for the 90–10 alloy and  $4 \text{ m s}^{-1}$  for the 70–30 alloy<sup>76</sup>. This has worked well in practice although it is now believed to be a little on the conservative side.<sup>77,78</sup> Areas causing high turbulence such as bends with tight radii, partially throttled valves, and partial obstructions need to be avoided.

Other cupronickel alloys have been developed and have been found to offer even better resistance to impingement attack. In particular, a 16.5% Ni–0.5% Cr alloy first developed by INCO in the 1970s has a much higher, critical shear stress than the 70–30 alloy.<sup>12</sup> Also a 2% Mn–2% Fe–30% Ni alloy, developed for extra impingement resistance in situations where entrained sand is present in seawater, is now successfully used in the more demanding areas of desalination plants.<sup>9</sup>

Gunmetals and aluminum bronzes have good resistance to impingement attack but these alloys are not normally used for heat exchange tubing, the former because they are casting alloys and the latter because it may pit in quiescent conditions. However, both groups are used for components such as pumps and valve bodies. The nickel aluminum bronze alloy is used for propellers and pump components as it has excellent resistance to cavitation compared to many other copper based alloys.



**Table 7** Comparative results showing corrosion and erosion/corrosion performance of a number of copper alloys<sup>a</sup>

<i>Alloy</i>	<i>General corrosion rate (mm year<sup>-1</sup>)<sup>b</sup></i>	<i>Crevice corrosion rate (mm year<sup>-1</sup>)<sup>b</sup></i>	<i>Minimum flow rate to produce erosion/corrosion (m s<sup>-1</sup>)<sup>c</sup></i>
<i>Wrought Alloys:</i>			
Phosphorus deoxidized copper, CW024A	0.04	<0.025	1.8
Admiralty brass, CW706R	0.05	<0.05	3
Aluminum brass, CW702R	0.05	0.05	4
Naval brass, CW712R	0.05	0.15	3
HT brass, CW705R	0.18	0.75	3
90–10 cupronickel	0.04	<0.04	3.6
70–30 cupronickel	0.025	<0.025	4.5
5% Al-bronze	0.06	<0.06	4.3
8% Al-bronze	0.05	<0.05	4.3
9% Al-bronze	0.06	0.075	4.5
Nickel aluminum bronze	0.075	<0.30	4.3
Aluminum silicon bronze	0.06	<0.075	2.5
High strength cupronickel (Cu–Ni–Al–Mn–Fe)	0.02	<0.02	4.8
<i>Cast alloys:</i>			
Gunmetal, CC491K	0.04	<0.04	3.6
Gunmetal, CuSn10Zn2	0.025	<0.025	6
High tensile brass, CC765S	0.18	0.25	2.5
Aluminum bronze, CC331G	0.06	<0.06	4.5
Nickel aluminum bronze, CC333G	0.06	<0.5	4.3
Manganese aluminum bronze, CC212E	0.04	3.8	4.3

<sup>a</sup>Due to difficulties of achieving consistent results for tests in seawater, data should be used for comparing relative performance rather than being taken as absolute.<sup>75</sup>

<sup>b</sup>The figures for general corrosion rate and crevice corrosion rate were determined using samples fully immersed beneath rafts in Langstone Harbour, Portsmouth, UK, for 1 year.<sup>75</sup>

<sup>c</sup>The corrosion/erosion resistance tests were carried out using the following method (known as the Brownsdon and Bannister method): the specimens were fully immersed in natural sea water and supported at 60 °C to a submerged jet, 0.4 mm diameter placed 1–2 mm away, through which air was forced at high velocity. From the minimum air jet velocity required to produce corrosion/erosion in a fourteen-day test, the minimum sea water velocity required to produce corrosion/erosion under service conditions was estimated on the basis of known service behavior of some of the materials.

A number of studies have evaluated the impingement resistance for marine condensers and piping involving several types of test apparatus, including rotating discs, rotating spindles, model condensers, multivelocity jet tests, and jet impingement tests.<sup>79</sup> This work has proved reliable in ranking materials as a function of impingement resistance and has been an important factor in the development of alloys resistant to impingement attack.

Experience has shown that for intermittent flow (as might be the case of firewater systems used on offshore platforms which are tested periodically), short-term high velocities in the order of 7–15 m s<sup>-1</sup> for cupronickels are not detrimental. Also open geometries need not have the velocity restrictions of pipe and tubing; for example, 90–10 cupronickel has been successfully used on ship hulls operating at 24 knots (12 m s<sup>-1</sup>) with little thinning experienced.<sup>9</sup>

### 3.07.3.3.2 Dezincification of brasses

Historically, the most common dealloying phenomenon seen in copper alloys has been the dezincification of brasses. In recent years, the development of dezincification-resistant brasses and a greater understanding of the required conditions under which dezincification manifests itself have lessened its occurrence, but it retains a high degree of scientific interest. Dezincification is characterized by regions of the brass becoming replaced by a porous mass of copper which, though retaining the shape of the original article, has virtually no strength. There has long been discussion as to whether there is selective corrosion of the zinc in the brass, which leaves the copper behind, or whether complete dissolution of the brass occurs, followed by redeposition of copper. Possibly both processes occur under different circumstances.



The mechanism of dezincification of brass has been investigated and discussed by Evans,<sup>80</sup> Fink,<sup>80</sup> Lucey,<sup>81</sup> Feller,<sup>82</sup> and Heidersbach,<sup>83</sup> and is referred to in many other papers.<sup>84–92</sup> Recent extensive studies<sup>93,94</sup> which have investigated the distribution of copper isotopes and the effects of specimen rotation during testing, show that redeposition of copper is a major mechanism.

With a single-phase brass, the whole of the metal in the corroded areas is affected. Dezincification may proceed fairly uniformly over the surface, and this 'layer type' takes much longer to cause perforation than the more localized 'plug type' which more often occurs.<sup>95</sup> With a two-phase brass, the zinc-rich  $\beta$  phase is preferentially attacked and eventually the  $\alpha$  phase may be attacked as well. The zinc corrosion products which accompany dezincification may be swept away, or, in some conditions, may form voluminous deposits on the surface. These may in turn lead to blockages, for example, in fittings. In general, the rate of dezincification increases as the zinc content rises, and great care needs to be exercised in making brazed joints with copper/zinc brazing alloys, particularly if they are to be exposed to seawater. Under these conditions, a properly designed capillary joint may last for some time, but it is preferable to use corrosion-resistant jointing alloys such as silver solders<sup>96</sup>, as specified in BS EN 1044:1999.

Factors which cause increased rates of dezincification are high temperature, high chloride content of water, and low water speed.<sup>97–100</sup> Dezincification is also likely to occur preferentially beneath deposits of sand or silt on the metal surface, or in crevices where there is a low degree of aeration.

Addition of  $\sim 0.04\%$  arsenic will inhibit dezincification of  $\alpha$  brasses in most circumstances and arsenical  $\alpha$  brasses can be considered to be immune to dezincification for most practical purposes.<sup>101</sup> There are conditions of exposure in which dezincification of these materials has been observed, for example, when exposed outdoors well away from the sea<sup>37</sup> or when immersed in pure water at high temperature and pressure, but instances are rare. In other conditions, for example, in polluted seawater, corrosion can occur with copper redeposition away from the site of initial attack, but this is not truly dezincification, which, by definition, requires the metallic copper to be produced *in situ*. The work of Lucey<sup>81</sup> goes far in explaining the mechanism by which arsenic prevents dezincification in  $\alpha$  brasses

but not in  $\alpha$ – $\beta$  brasses. An interesting observation is that the presence of a small impurity content of magnesium will prevent arsenic in  $\alpha$  brass from having its usual inhibiting effect.<sup>102</sup>

The addition of antimony or phosphorus, in amounts similar to arsenic, are claimed to be also capable of preventing dezincification of  $\alpha$  brasses. However, most manufacturers use arsenic. It appears desirable to avoid using phosphorus, as Bem<sup>103</sup> has shown that this element can, in some circumstances, lead to an undesirable susceptibility to intergranular corrosion. The same can be true for arsenic additions over  $\sim 0.05\%$ .

A dezincification resistant alloy, CW602N, was first introduced in 1980. This alloy is a leaded brass with a zinc content sufficiently high to permit hot forging and extrusion in the  $\beta$  range without cracking. After hot working, a heat treatment of up to 6 h at 500 °C followed by slow cooling transforms any residual  $\beta$  phase to  $\alpha$  so that the finished component is essentially  $\alpha$  brass. Dezincification is inhibited by adding arsenic (0.02–0.15%) which protects the  $\alpha$  phase, and good machinability is assured by adding lead (1.7–2.8%). The impurities iron and manganese, which combine with arsenic, must be carefully controlled for the arsenic to be effective. A rule of thumb is that the percentage of arsenic must be greater than the combined percentage of iron and manganese to provide resistance to dezincification. There is practical evidence that the maximum limits for iron and manganese allowed in the specification (0.1% each) are too high as, at these levels, the arsenic may be rendered ineffective.

Newer studies of intergranular corrosion attack (IGA) of arsenic-containing dezincification resistant brass<sup>93,104</sup> show that there is a close relationship with the degree of precipitation of iron–arsenic compounds in the grain boundaries. The precipitates are formed during low temperature heat treatment or slow cooling after hot forging or a prior heat treatment. Sulfide corrosion and dezincification in the grain boundary appear to be the result as the arsenic is bound to impurities like iron. IGA has also been reported for aluminum brass (CW 702R) and Mazza and Torchio<sup>105</sup> have presented a laboratory test method to reveal IGA in this material. The method has also been used successfully for dezincification resistant brass<sup>104</sup> and correlation with field tests in seawater is good.

The addition of 1% tin can markedly reduce the rate of dezincification in two phase brasses, and naval

brass (61Cu–38Zn–1Sn) is attacked considerably more slowly than 60/40 brass in seawater, although there may be virtually no difference between them in most freshwaters. Some of the cast complex high-strength two-phase brasses containing tin, aluminum, iron, and manganese appear to have relatively good resistance to dezincification, but they are by no means immune to it.

Dezincification of brasses in drinking water may occur, particularly in stagnant or slowly-moving warm or hot waters relatively high in chloride and containing little carbonate hardness.<sup>106</sup> Dezincification of  $\alpha$  brasses is inhibited by the usual arsenic addition, but two-phase brasses are liable to severe attack in some waters. In such cases, dezincification-resistant brass or gunmetal fittings should be used. If copper/zinc brazing alloys are used, these may dezincify in water known to support this type of corrosion and may consequently give rise to leaks.<sup>106</sup>

#### 3.07.3.3.3 Selective attack in other alloys

Selective attack analogous to dezincification can occur in other copper alloys, particularly in aluminum bronzes and, less frequently, in tin bronzes,<sup>107</sup> cupronickels,<sup>108</sup> and other alloys. Dealuminification of aluminum bronzes has been studied extensively<sup>109</sup> and the results indicate that, while  $\alpha$ -phase alloys suffer such attack comparatively rarely, alloys of higher aluminum content can be more susceptible. The electrochemical relationships are such that preferential corrosion of the second phase is liable to occur in  $\alpha$ - $\gamma_2$  alloys, but  $\alpha$ - $\beta$  alloys are relatively resistant to attack. Retention of  $\beta$  phase is favored by rapid cooling after casting or after high temperature heat treatment, and also by incorporating manganese in the alloy. A tempering heat treatment in the temperature range of 650–740 °C has been found to hinder the occurrence of dealuminification due to the transformation of the more corrosion-prone  $\beta$  phase to a combination of  $\alpha$  phase and comparatively benign  $\kappa$  phases.<sup>110</sup>

The addition of nickel to aluminum bronze has been found useful in controlling the occurrence of the  $\gamma_2$  phase, which has a corrosion potential  $\sim 100$  mV less noble than the  $\alpha$  phase, thereby undergoing selective attack in seawater. Weill-Couly and Arnauld<sup>111</sup> have determined an empirical relationship, eqn [6] shown below, which denotes the aluminum content of nickel–aluminum bronze castings below which a resistance to dealuminification is found.

$$\text{Al} \leq 8.2 + \frac{\text{Ni}}{2} \quad [6]$$

#### 3.07.3.3.4 Deposit attack and pitting

When water speeds are low and deposits settle on the surface, pitting in copper and copper alloys is liable to occur by differential aeration effects. This is particularly so at water speeds below  $\sim 1 \text{ m s}^{-1}$ . In seawater systems, such attack may occur under dead barnacles or shellfish, the decomposing organic matter assisting the corrosion process. Pitting is most likely to occur in polluted in-shore waters, particularly when hydrogen sulfide is present. In such contaminated waters, non-protective sulfide scales are formed and these tend to stimulate attack. It has been found possible to develop a mathematical model which can be successfully used to calculate the electrode potential below which copper is immune to pitting in tap water or seawater in the temperature range 25–75 °C.<sup>112</sup> Of the 26 ionic species which have been included in the calculation,  $\text{CO}_3^{2-}$  and  $\text{SO}_4^{2-}$  were found to be the most aggressive.

#### 3.07.3.4 Corrosion in Freshwater

Freshwaters are, in general, less corrosive toward copper than is seawater and copper is widely and satisfactorily used for distributing cold and hot waters in domestic and industrial installations.<sup>113–116</sup> Copper and copper alloys are used for pipes, hot-water cylinders, ball valves, taps, fittings and heater sheaths. In condensers and heat exchangers using freshwater for cooling, tubes of 70/30 brass or Admiralty brass are usually used, and corrosion is rarely a problem. Nevertheless, the widespread use of copper and copper alloys since the early part of last century especially in domestic water systems has meant that all adverse situations have been experienced and the following are rare but notable corrosion issues. Two British Standards give guidance on the likelihood of corrosion in water distribution and storage systems and in water recirculating systems. These are BSEN 12502:2004 and BSEN14868:2005.

##### 3.07.3.4.1 Pitting

Occasionally copper water pipes fail prematurely by pitting. This a general term and is used for any failure of the pipework system leading to a leak. Pitting corrosion of copper in drinking water systems is often categorized as Type I, II, or III but other types of localized corrosion are also known. However, there may be no strict limits between Type I and Type II pits; in relatively saline tap waters, corrosion pits showing traits of both types have been found. Only through proper investigation can the cause of pitting be identified, such as in the following sections.

#### 3.07.3.4.1.1 Carbon film pitting

Carbon film pitting, also known as "Type I" pitting, has been a frequent problem. An example of this in a copper tube from a domestic water supply is shown in **Figure 3** with the corrosion products removed from the main pit. The characteristics of the pits are hemispherical cavities with large crusts of corrosion products outside. The composition of the crusts is mainly basic cupric carbonates for example, malachite. Cuprous chloride and reddish cuprous oxide crystals may be found inside the cavity. The presence of  $\text{CaCO}_3$  in the crust outside the cavity led Lucey<sup>117</sup> to propose a particular mechanism for this type of pitting. Contrary to conventional descriptions of the pitting processes, Lucey postulated that the cathodic reaction that is, the oxygen reduction, takes place at the crust of corrosion products which cover the cavity. The phenomenon was found to occur in organically pure, cold waters originating from deep wells and boreholes and was shown by Campbell<sup>118</sup> to be associated with residual films of carbon on the bore of the tubes. This carbon was caused by decomposition of residual drawing lubricant during bright (reducing atmosphere) annealing. It is therefore necessary for manufacturers to take steps to avoid these harmful residues. This type of pitting attack has been identified in many different countries<sup>119</sup> and may be assisted by iron-rich precipitates which can be present at the grain boundaries.<sup>120,121</sup> There is evidence that it could be inhibited by the presence of organic species in the water.<sup>122</sup>

This evidence has been corroborated in the United Kingdom by Campbell, who found failures due to this effect were confined to certain districts that is, supply waters. He showed that for many supply waters this

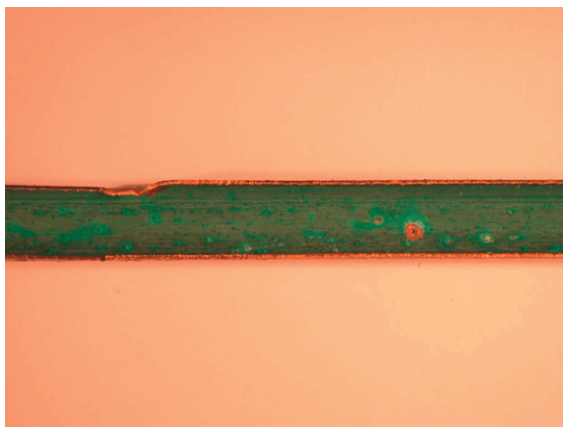


**Figure 3** Photograph showing carbon film pitting on a copper tube.

pitting cannot proceed even in tubes containing carbonaceous cathodic films. He proposed that this is most probably due to the presence of small amounts of a naturally-occurring inhibitor in the water, probably an organic colloidal material, which stifles pitting of copper. Pipe failures therefore only occur in waters which contain little or none of this inhibitor.

Pitting problems also occasionally occur in copper water cylinders<sup>123</sup> and, as a result of a study of this problem, Lucey<sup>117</sup> has made suggestions about the mechanism of pitting of copper in potable water supplies. Several suggested methods of avoiding pitting failures in copper cold-water tubes have been evaluated.<sup>124–126</sup>

#### 3.07.3.4.1.2 Hot soft water pitting and Type II pitting

In hot water pipes, failures sometimes occur in certain areas supplied with soft waters from moorland gathering grounds. The waters concerned contain a few hundredths of a part per million of manganese, and in the course of several years' exposure, a deposit rich in manganese dioxide is laid down in the hottest parts of the system. This may cause pitting which could eventually lead to failure.

Hot-water pitting of another type, often referred to as "Type II" pitting, is sometimes experienced in soft waters having high sulfate content in relation to the carbonate hardness and a relatively low pH value and it has been described by Mattson and Fredriksson.<sup>127</sup> The crusts covering these pits are less voluminous than Type I pits, the cavities are branching and they may be almost completely filled with black cuprous oxide. The occurrence of Type II pitting is associated with waters with  $\text{pH} \leq 7$  and low carbonate contents. A successful remedy has been to increase pH, introduce carbonate dosing to give a minimum of  $70 \text{ mg HCO}_3^-$  per liter, or reduce the water temperature to less than  $60^\circ\text{C}$ .

#### 3.07.3.4.1.3 Type III pitting

This type of pitting occurs in cold soft waters with a pH above 8.0 and it is geographically localized, being mainly confined to Sweden. It is a generalized form of pitting where the pits are sparse<sup>128,129</sup>. Mattson<sup>128</sup> describes the phenomenon, noting its morphology and means of avoidance through a method involving bicarbonate dosing of the drinking water.

#### 3.07.3.4.1.4 Electrochemistry of pitting

Drogowska *et al.*<sup>130</sup> have used solutions designed to mimic natural waters containing bicarbonate and chloride ions to study the anodic oxidation of copper and onset of pitting corrosion. They have found that,

as the anodic polarization of copper increases in this environment, a porous layer of  $\text{Cu}_2\text{O}$  initially forms on the metal surface. This is found to convert to basic  $\text{CuCO}_3$  at more positive anodic potentials or in higher concentrations of  $\text{HCO}_3^-$  ions. A passivity breakdown potential is recorded at which pitting initiates, and this becomes more positive when  $\text{HCO}_3^-$  ions are present. The presence of  $\text{Cl}^-$  ions shifts the pitting potential to lower values, but the  $\text{HCO}_3^-$  ions are found to act to prevent this effect. Sulfate ions are found to have a very similar effect to chloride ions in lowering the breakdown potential<sup>131</sup> and pitting is found to be avoided if the  $\text{pH} \geq 7.4$  and the  $[\text{HCO}_3^-]/[\text{SO}_4^{2-}]$  ratio is  $\geq 1$ . The effect of increasing the solution temperature to  $60^\circ\text{C}$  is found to give improvement to the passivity of the oxide film.<sup>132</sup> Two new international standards have been produced which give guidance on corrosion prevention in water distribution and storage systems.<sup>133</sup>

#### 3.07.3.4.2 Chemical attack

Joining copper should be accomplished according to recommended practice to avoid corrosion issues. Copper pipework installations are joined using capillary attraction of solder or braze material or by mechanical means.

In the case of capillary joints, fittings, or in some cases specifically formed tube ends, are used to form an annular capillary gap into which molten solder or braze is run. Fluxes containing chlorides have to be used when soldering. The chlorides act to remove surface oxide and reduce the surface tension, allowing the solder to be drawn into the capillary gap. Excessive use of flux can lead to its retention in the pipework and attack by the chloride ions present.

This will normally take place in the first few months after installation. An example of this is shown in **Figure 4**. Over longer periods when the active elements of the flux are exhausted, the presence of residue can lead to deposit attack. In both of these cases, pitting corrosion and failure of the tube can result. Good installation practice which ensures complete removal of any flux residue by washing (as given by BS 6700:1997) will prevent this type of corrosion. Capillary joints formed using copper/phosphorus, copper/silver/phosphorus, or silver brazing alloys do not need flux and therefore cannot suffer this type of attack.

#### 3.07.3.4.3 Microbiologically influenced corrosion

Microbiologically influenced corrosion (MIC), describes a form of pitting considered to be due to the action of microbes. This form of corrosion of metals has been known for many years, for instance in the oil industry, and an early description of its occurrence with copper alloys was given by Rogers in 1948.<sup>134</sup> In some instances, MIC has been associated with soft water which is high in organic content which has been allowed to maintain temperatures in the region of  $20\text{--}30^\circ\text{C}$  under low velocity conditions. In such circumstances, the resulting warm high concentration of organic material at the bottom of horizontal tubes provides ideal conditions for MIC to take place.<sup>135</sup> Other circumstances with a different water quality have been described by Wagner *et al.*<sup>136</sup> However, the exact MIC mechanism has not been elaborated. The general view is that a region of low pH is created under a biofilm containing polysaccharides and that the organic materials present provide transport for the metal ions to the liquid phase.<sup>137</sup>

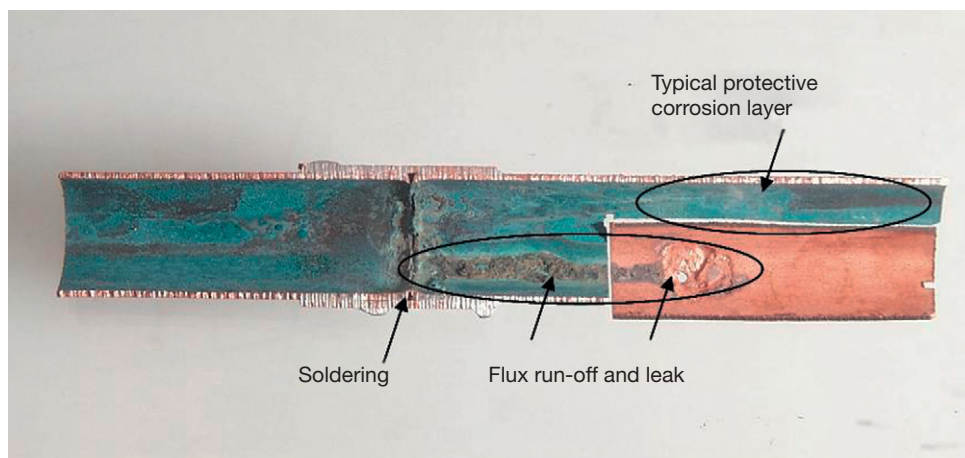


**Figure 4** Photograph showing flux attack on a soldered copper tube.



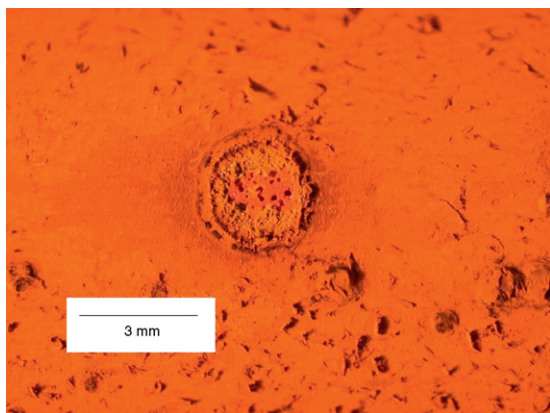


**Figure 5** Optical micrograph showing an example of the typical pit morphology found in MIC.

MIC of copper water pipes in institutional buildings has been reported in several countries. The results of research, leading to remedial measures, have been summarized by Geesey.<sup>138</sup>

An example of this type of corrosion associated with soft high organic content water is shown in **Figure 5**. Avoidance entails operating the system at correct temperatures and flow rates as well as providing water with a low organic burden and with the implementation of appropriate disinfection measures.

#### 3.07.3.4.4 Stress corrosion cracking

Stress corrosion cracking (SCC) may occur with brass fittings (see **Section 3.07.3.6.1**) due to traces of ammonia in the environment or arising from nitrates in the water. In certain rare instances, copper tubes are known to suffer SCC, an example of which is shown in **Figure 6**. In the great majority of cases of stress corrosion encountered, traces of ammonia have been found in the cracks.

#### 3.07.3.4.5 Dissolution

The corrosion of copper in contact with drinking water soon reduces to a very low rate due to the formation of stable scale. However, some waters continuously dissolve appreciable amounts of copper.<sup>139–141</sup> Factors which favor this action are waters with low pH and low total dissolved solids. Therefore, most dissolution is found in hot, soft, acid waters. Desalination plants will produce such an aggressive water and unless treated to increase its mineral content this water should not be used with copper. This type of corrosion is general and the resulting pipe wall thinning is so slight that the useful life of the pipe or component is virtually unaffected unless



**Figure 6** Photograph showing longitudinal stress corrosion cracking of a 15 mm diameter copper tube (EN 1057, R250, half-hard condition).

impingement attack occurs. A few very hard waters can also give rise to copper dissolution. Research has indicated that the difference between a scale forming water (with a resulting low copper dissolution rate) and a ‘dissolving’ hard water appears to be organic content.<sup>142</sup>

High levels of copper complexed with organic material gives the water a distinctive blue color, and is hence given the term ‘blue water corrosion.’ It tends to be confined to soft, unstable water types and, to date, appears to be confined to Australia and New Zealand. This form of dissolution has been found to be due to microorganisms<sup>143</sup> and restoring the disinfection agent (e.g., free chlorine) to its desired level will stop the effect and prevent the occurrence of further episodes.

A review of the current state of knowledge on dissolution in drinking water has been prepared by Merkel and Pehkonen.<sup>144</sup> In considering copper dissolution, this paper subdivides general copper corrosion into the subprocesses (oxidation, scale formation, and scale dissolution) enabling a better understanding of the influence of water quality parameters and operating conditions on copper release. This work also considers that research needs to be carried out to distinguish between organic components which promote or reduce the dissolution process.

Once copper has been dissolved, it may then lead to problems downstream. For instance, the dissolved copper can (1) plate out and cause galvanic corrosion on other products such as zinc-coated steel,<sup>145</sup> light alloys,<sup>146</sup> or bare steel and (2) cause blue–green staining in baths, sinks, and sometimes clothes or hair due

to the combination of copper with stearates in soaps and shampoos.

The World Health Organization (WHO) Guidelines for Drinking Water Quality 1993<sup>147</sup> notes that copper is an essential element necessary for human health and that in most parts of the world deficiency was a problem. However, it was decided that setting an upper limit for the allowable concentration was necessary. Following this guideline, many countries have regulated the maximum weekly average of drinking water to 2 mg Cu per liter. Araya *et al.*<sup>148</sup> showed that the likely taste level for copper in drinking water was 4 mg l<sup>-1</sup> or above for 95% of the population.

In deaerated conditions, for instance, in most central heating systems, little attack on copper occurs.<sup>149–151</sup> Further reference to the subject of copper in water can be found in an extensive review by Grunau.<sup>152</sup>

### 3.07.3.5 Corrosion in Seawater

Copper alloys have had an extensive history of use in a wide range of marine applications<sup>9,153</sup> due to their advantageous properties with respect to corrosion and biofouling resistance, conductivity, and ease of fabrication.

Exposure tests of various copper alloys have been carried out in natural seawater by the UK Ministry of Defence laboratories.<sup>154</sup> Weight loss measurements were used to measure general corrosion rates, crevice corrosion rates, and erosion/corrosion flow velocity limits. The results are shown in **Table 7**, although some anomalies have been reported for the data as presented<sup>75</sup>. It was found that the brasses exhibited the highest corrosion rates and the alloys most resistant to corrosion and erosion/corrosion were the cupronickels.

Regarding practical applications of copper alloys in seawater, a major example is their use for condensers and heat exchangers, which has been long established. Recent reviews have considered potential corrosion in this application, the likely causes and remediation procedures.<sup>76,155–157</sup> Specific aspects covered include the effects of surface films, the commissioning process, stagnant conditions, flow velocity, ferrous sulfate treatment, and cleaning techniques. The latter may lead to greater corrosion, though ferrous sulfate treatment can offset the effect. Chlorination can cause increased attack in some circumstances, aluminum brass being more susceptible to attack than cupronickels. The presence of sulfide

contamination causes serious corrosion if polluted and aerated conditions alternate, or if oxygen and sulfide are simultaneously present.

Corrosion of condenser tubes was a problem of great magnitude during the first quarter of the twentieth century. In those times, 70–30 brass condenser tubes failed by dezincification and Admiralty brass (70Cu–29Zn–1Sn) was brought into use. This proved little better, but some time later the addition of arsenic was found to inhibit dezincification. Failures of Admiralty brass by impingement attack became a serious problem, particularly as cooling water speeds increased with the development of the steam turbine. The introduction of alloys resistant to impingement attack was a great step forward and immediately reduced the incidences of failure. A history of condenser tubes up to 1950 has been published by Gilbert.<sup>158</sup>

The alloys most commonly employed today are cupronickels,<sup>159</sup> containing appropriate iron and manganese levels and aluminum brass (76Cu–22Zn–2Al–0.04As). Three cupronickel alloys are in widespread use and these are: (1) 30Ni–0.7Fe–0.7Mn, (2) 30Ni–2Fe–2Mn, and (3) 10Ni–1.5Fe–1 Mn. These materials are extensively and successfully applied in ships, power stations, oil refineries, desalination plants, etc., in condensers and heat exchangers, with limitations on water flow velocities, sometimes with much entrained air present. At the highest water flow velocities, there is a rather greater factor of safety with 70–30 cupronickel. The 30Ni–0.7Fe–0.7Mn variant is usually to be preferred under most polluted water conditions.

A number of studies have been carried out on the reasons for the high seawater corrosion resistance of cupronickels. In 70–30, a nickel-rich zone is formed in the oxide layer at the metal surface.<sup>160</sup> This acts to anodically protect the matrix from further corrosion. If the film develops defects, which may be caused by prior deformation of the metal,<sup>161</sup> then corrosion initially accelerates in those areas, but quickly diminishes, resulting in a smooth overall surface.

The occasional failures which still occur in condenser tubes are usually due to one (or sometimes several) of the following factors:

1. Localized attack or pitting in badly contaminated waters.
2. Pitting under decaying barnacles, shell fish, or other deposits.
3. Impingement attack due to high local water velocities, e.g., at partial obstructions in a tube such as barnacles or *Hydra*.



4. Erosion due to sand or other abrasive particles suspended in the water.
5. Use of tubes of the wrong alloy, or of incorrect composition or which contain manufacturing defects.
6. Poor welding techniques causing welds to protrude into the flow.

The material most commonly used when suspended abrasive matter is a problem is the 30% Ni alloy containing 2% each of Fe and Mn.<sup>156,157</sup>

A difficult condenser-tube corrosion problem arises from the use of polluted cooling waters from harbors and estuaries, which may be severely contaminated, particularly when warmer climates are involved.<sup>162</sup> Many condenser-tube materials are liable to suffer corrosion in these circumstances, and the choice of materials is made difficult by the fact that different orders of merit apply at different locations and even at the same location at different times. The state of the water when the tubes are commissioned and first enter service, which influences the type of surface film formed, may well determine whether or not a satisfactory service life will be obtained.<sup>159,163</sup> Full salinity seawater, free from sulfides, is reported to be the most effective passivating medium<sup>162</sup> although the 14–60 days which this takes to complete may put it at a lower ranking than other methods, particularly those involving dosing with ferrous sulfate<sup>76</sup>.

In power plants, the condenser tubes must be able to withstand corrosive cooling waters and complex boiler water treatments. Also, the use of recirculating water can cause dissolved salts to concentrate between twice and eight times the initial concentration, making the water significantly more aggressive.<sup>164</sup> Corrosion of power-station condenser tubes by polluted waters was at one time particularly troublesome in Japan. Improved results have been reported using tin brasses or special tin bronzes.<sup>165</sup> Elsewhere, pretreatments have been investigated with mixed success<sup>76,166</sup> and sodium dimethyldithiocarbamate is reported to give protective films which will withstand the action of polluted waters<sup>167</sup> and has had some naval use.<sup>76</sup>

Methods of maintaining tube cleanliness include chlorination and mechanical methods such as water lancing and the use of the Taprogge system of circulating sponge-rubber balls.<sup>157</sup> Hot acid is now not environmentally acceptable and the use of commercial descaling agents invariably results in the near complete loss of the passive surface layers on the material.<sup>168</sup> Thus, it is recommended that, after

their use, a period of 3 weeks or more should be imposed during which natural seawater is allowed to flow through the system to restore passivity.

Condenser tube-plates of naval brass usually undergo some dezincification in seawater service, but this is normally not serious in view of the thickness of the metal involved. Use has been made of tube-plates of more resistant materials such as aluminum bronze, or cupronickel. Plates that are too large to be rolled in one piece can be fabricated by welding together two or more items. In some special applications, the tubes are fusion welded or explosively welded to the tube plates. Fusion welding operations are rather more difficult with brasses than with other copper alloys due to the evolution of zinc fume during the process.

Condenser water-boxes were at one time made of unprotected (or poorly protected) cast iron and these afforded a measure of cathodic protection to the tube plates and tube ends. This beneficial effect has been lost with the general adoption of water-boxes which are completely coated with rubber or some other impervious layer, or which are made from resistant materials such as gunmetal, aluminum-bronze, or cupronickel. Steel water-boxes which are clad with cupronickel are also used. To prevent attack on tube-plates and tube-ends in these circumstances, either a suitable applied-current cathodic protection system can be applied or sacrificial soft-iron or mild-steel anodes can be installed, the required protection voltage being fairly low (50 mV minimum).<sup>169</sup> Ferrous wastage plates have the additional advantage that the iron corrosion products introduced into the cooling water assist in the development of good protective films throughout the length of the tubes. This is particularly important in the case of aluminum-brass tubes; indeed, with such tubes it may be desirable, as an additional preventative measure, to add a suitable soluble iron salt (such as ferrous sulfate) regularly to the cooling water.

As it has become increasingly necessary to supplement natural sources of freshwater in various parts of the world, processes for producing freshwater from seawater have been intensively studied. Distillation is one method widely used and, during recent years, large numbers of multistage flash-distillation plants have been installed in various countries particularly in the Middle East. Many of the larger flash-distillation units are capable of producing several millions of gallons of freshwater per day. In these plants, seawater passes through horizontally disposed tubes and steam, which is 'flashed' from the brine, condenses

on the outside. In some parts of the plant, the conditions are similar to those in steam condensers, but in other parts the seawater has been treated to remove dissolved gases and is at much higher temperatures. Copper alloy tubes are used in large numbers for the heat exchange units in this type of desalination plant,<sup>170,171</sup> these being mainly aluminum-brass and the various cupronickel alloys.

For cooling-water trunking and saltwater services in the engine room and elsewhere, including fire mains, plumbing, and air-conditioning systems in ships, more resistant alloys are taking the place of copper or galvanized steel. The latter were formerly extensively employed, but they do not have adequate resistance to attack by seawater. Cu-10Ni-1.5Fe alloy has been widely utilized and normally gives excellent service. In some special naval applications, pipelines of 70-30 cupronickel are used and it has been found that adequate attention must be given to correct fabrication and installation techniques. Carbonaceous residues from fillers used in bending operations must be avoided or pitting corrosion may occur in service. Jointing materials of low corrosion resistance should not be used, silver brazing or appropriate welding methods being the correct techniques. Residual stresses, if present, can cause stress-corrosion failures of aluminum-brass pipelines in service.

Copper alloys in wrought or cast form are employed for other purposes in ships and marine installations, such as for propellers, bearings, valves, and pumps. For instance, aluminum-brass is used for heating coils in tankers carrying crude oil or petroleum products. However, some corrosion problems encountered in this and other applications on board ship have been described by Gilbert and Jenner.<sup>172</sup>

Cupronickels have been shown to possess extremely low long-term corrosion rates in quiet or slowly-moving seawater. The 90-10 alloy is of particular interest<sup>28,163</sup>; this alloy is now well established for use for pipelines on ships and it has become widely used for piping systems on floating production, storage and offloading vessels (FPSO's), and offshore platforms. In addition to its good corrosion resistance, 90-10 cupronickel has a high resistance to marine macrofouling providing that it is not cathodically protected. This has led to applications such as the construction or sheathing of ships' hulls, fish cages for aquaculture and cladding of steel offshore structures in the tidal/splash zones.<sup>9</sup>

Investigations into the effects of arsenic and phosphorus in single phase brasses on their susceptibility to intergranular attack and SCC in seawater have

shown that the normal additions of arsenic to inhibit dezincification ( $\sim 0.04\%$ ) have no significant adverse effect. Other possible consequences of exposing copper alloys to seawater which have been investigated included dealloying of aluminum bronzes<sup>109</sup> and the effects at bimetallic contacts.

Major efforts have been made to understand the nature of films formed on copper alloys in natural seawater. These films have quite different characteristics to those formed in sodium chloride solution, the differences being associated with the presence of organic material in the natural environment. However, the structure of the films is affected by variables such as water velocity, temperature, and oxygen content. Protective films often have a multilayered structure,<sup>157</sup> with an outer layer rich in iron providing impingement resistance and an inner layer giving chemical/electrochemical protection. With aluminum brass, a colloidal mixed hydroxide inner layer provides a buffering action, with tin-containing brass there is a tin-rich layer near the copper surface<sup>173</sup> and, with cupronickel, there is a chloride-rich layer which strongly inhibits the cathodic reaction. A study on Cu-Si alloys in seawater has found that the formation of copper silicide at the alloy surface acts to prevent corrosion.<sup>174</sup>

### 3.07.3.6 Effect of Exposure to Contaminated Environments

As with many metallic materials, failure of copper alloys may occur by cracking due to the combined influence of tensile stress and exposure to a debilitating environment due to the presence of a contaminant. Failures of brass components due to this form of stress corrosion cracking have been known for many years<sup>175</sup> and has been termed *season cracking*. In this case, the stresses in the material are produced in components during their manufacture and the contaminant is ammonia vapor produced by the natural decay of organic matter.

Only certain specific environments appear to produce stress corrosion of copper alloys, most notably ammonia,<sup>176-178</sup> ammonium compounds, or amines. Interestingly, pure copper does not suffer from ammonia-induced stress corrosion but will display the phenomenon in the presence of nitrites.<sup>179</sup> Stress corrosion can also occur with moist sulfur dioxide, sulfites, and some organic acids.<sup>180</sup> Mercury or solutions of mercury salts (which cause deposition of mercury), or other molten metals will also cause cracking, but the mechanism is undoubtedly

different.<sup>181</sup> Cracks produced by mercury are always intergranular, but ammonia, according to the exact conditions, may produce cracks which are fully transgranular, fully intergranular, or a mixture of both. As an illustration of this, Edmunds<sup>182</sup> found that mercury would not produce cracking in a stressed single crystal of brass, whereas ammonia could do so.

In certain circumstances, corrosion of copper alloys can occur through seemingly random interconnected microtunnels which spread out into the metal from what appears to be only a discoloration of the surface film. As a result of this phenomenon, through-thickness perforation of tube can result in weeks or months. This type of corrosion has been termed formicary corrosion due to its morphological similarity to an ants nest. Elliott<sup>183</sup> has produced a summary of knowledge of formicary corrosion up to 1999. The cause has been ascribed to contamination of the outside of the tube by carboxylic acids.

#### 3.07.3.6.1 Stress corrosion of brasses

Brasses containing only a few percent of zinc may crack under load if the stresses are high and the environment is sufficiently corrosive and most types of brass appear to be susceptible to the occurrence of this phenomenon of stress corrosion. An investigation of the effect of additions to 70–30 brass has been carried out by Wilson *et al.*,<sup>184</sup> who found that an addition of ~1% Si was markedly beneficial. Other additions were beneficial under some circumstances but none of the 36 additions tested accelerated stress-corrosion cracking. Further results have been given in later papers.<sup>185,186</sup>

In general, the susceptibility to stress corrosion in brasses appears to rise with an increase of zinc content, but in some circumstances alloys containing 64–65% Cu were found to be rather more affected than those containing 60% Cu.<sup>187</sup>

Many workers<sup>188–193</sup> have investigated the residual stresses introduced by different working processes in brasses of various compositions and the annealing treatments necessary to remove these stresses or reduce them to a safe level. A 'stress-relief anneal' at ~300 °C will usually lower internal stresses to comparatively small values without much effect on hardness of the material.

Specifications for brass products customarily include the provision for carrying out a mercurous nitrate test<sup>194,195</sup> (EN ISO 196:1995) to ensure that unduly high residual tensile stresses are not present, but a satisfactory result in this test does not

guarantee freedom from cracking in environments containing ammonia. More searching tests involving exposure to ammonia have therefore been devised, such as ISO 6957:1988. The standardization of stress-corrosion cracking tests and their correlation with service experience have been the subject of several papers.<sup>196–200</sup> A European standard for the assessment of susceptibility to SCC was published in 2006: EN 14977, Copper and copper alloys – detection of tensile stress – 5% ammonia test. Many authors<sup>201–205</sup> have described practical cases of stress-corrosion cracking usually involving tensile stresses applied in service. Two possible preventive measures are the use of coatings<sup>206–208</sup> or inhibitors.<sup>209</sup>

The behavior of a wide range of  $\alpha$ ,  $\alpha$ - $\beta$ , and  $\beta$  brasses in various corrosive environments was studied by Voce and Bailey and their results have been summarized by Whitaker.<sup>210</sup> Penetration by mercury and by molten solder was found to be intergranular in all three types of brass. In moist ammoniacal atmospheres, the penetration of unstressed brasses of all types was intergranular. Internal applied stresses accelerated the intergranular penetration of  $\alpha$  brasses and initiated some transgranular cracking. It also caused severe transgranular cracking of  $\beta$  alloys and transgranular cracking across the  $\beta$  regions in the two-phase brasses. Immersion in ammonia solution, however, caused intergranular cracking of stressed  $\beta$  brasses.  $\beta$  brasses containing 3% or more aluminum failed with an intergranular fracture when stressed at ~0.1% proof stress in air. The behavior of alloys of this type was subsequently studied by Perryman<sup>211</sup> and Bailey<sup>212</sup> who showed that cracking in air occurs only when moisture is present. It has been confirmed that  $\beta$  brasses are prone to crack in service.<sup>213</sup>

High-strength  $\alpha$ - $\beta$  brasses containing up to ~5% Al (with small amounts of Fe, Mn, Sn, etc.) used for propellers, parts of pumps, nuts and bolts, and similar applications usually give good service but occasionally suffer intergranular failure, for instance in contact with seawater. Examination of such failures usually reveals thin dezincified layers along the cracks, but it is often difficult to decide whether the crack or the dezincification occurred first.

The theoretical aspects of stress-corrosion cracking have attracted much attention in recent years. Among the copper alloys, the behavior of brasses in ammoniacal environments has been most studied. While cracking has been shown to be possible in contact with some other corrosive agents, ammonia has the most powerful effect. Evans<sup>214</sup> suggests that

this is because ammonia is a feeble corrodent which produces little attack except at regions such as grain boundaries or other lattice imperfections. Also, it prevents accumulation of copper ions in the crevices formed owing to the formation of stable complexes such as  $\text{Cu}[(\text{NH}_3)_4]^{2+}$ . The mode of cracking (intergranular or transgranular) can be affected by changes in composition of the brass or by changes in the nature of the environment.<sup>215</sup> Mattsson<sup>216</sup> found that, on immersion in ammoniacal solutions of different pH values, stressed brasses cracked most rapidly at pH 7.1–7.3 and that in this range black surface films formed on the metal. The role of tarnish films has been further studied subsequently.<sup>217–219</sup> Many authors have studied electrochemical<sup>220–235</sup> or metallurgical<sup>236–241</sup> aspects of the stress corrosion of copper alloys and discussed theories of the mechanism. Papers on the subject have been included in several symposia or conferences on stress corrosion of metals.<sup>242–244</sup> The stress cracking of brasses has been reviewed by Bailey<sup>245</sup> and other workers<sup>246–254</sup> and reviews of stress corrosion as a general subject have also been published.<sup>255–257</sup>

### 3.07.3.6.2 Stress corrosion of other copper alloys

Evidence indicates that pure copper is not likely to be susceptible to stress corrosion<sup>258–260</sup> but instances of the failure of copper are known, when it contains 0.4% As<sup>261</sup> or 0.02% P.<sup>258</sup> SCC has also been found to occur in copper–beryllium,<sup>262</sup> copper–manganese,<sup>263–265</sup> aluminum–bronzes,<sup>266,267</sup> tin–bronzes, silicon–bronzes, nickel silvers,<sup>268</sup> and cupronickels.<sup>268,269</sup> Most of these alloys are much less susceptible to cracking than brasses,<sup>270</sup> although under some conditions aluminum–bronzes can be particularly prone to cracking.<sup>271</sup> In ammoniacal environments, the cracking tends to be transgranular, and in steam atmospheres, intergranular cracking is favored.<sup>272</sup> Additions of 0.35% Sn or Ag are claimed to be effective in preventing intergranular cracking.<sup>273,274</sup> Aluminum–bronzes containing 2% Ni and 0.5–0.75% Si are claimed to have good resistance to stress corrosion,<sup>273,275</sup> although there is evidence that silicon bronzes can show accelerated intergranular fracture in the presence of moist air.

Thompson and Tracy<sup>258</sup> carried out tests in a moist ammoniacal atmosphere on stressed binary copper alloys containing zinc, phosphorus, arsenic, silicon, nickel, or aluminum. All these elements gave alloys susceptibility to stress corrosion. In the case of zinc, the failure time decreased steadily with increase

of zinc content, but with most other elements there was a minimum in the curve of concentration of alloying elements against time to failure. In tests carried out under a static load of  $70 \text{ MN m}^{-2}$ , these minima were found to occur at concentration levels of  $\sim 0.2\%$  P,  $0.2\%$  As,  $1\%$  Si,  $5\%$  Ni, and  $1\%$  Al. In most cases, the cracking was observed to be intergranular.

A series of slow strain rate tests have been carried out on high strength Cu–Ni–Al alloys in environments which could be encountered by the offshore oil and gas industry<sup>276</sup> and these have found that the application of a cathodic potential (as applied in cathodic protection) gives protection against stress corrosion. However, molybdenum disulfide greases mixed with seawater and greases containing bentone were found to promote stress corrosion as did the more well known debilitating species such as amines. Work on relating the microstructural aspects of these alloys to their possible susceptibility to stress corrosion has identified<sup>277</sup> that the production process should be undertaken in such a way that the presence of iron-rich phases on the grain boundaries is restricted, the material has a fine grain size and that it is supplied in an under-aged condition.

Cupronickels (90–10 and 70–30) have generally been considered immune to sulfide stress corrosion in most seawater environments.<sup>9</sup> However, there have been recent trials<sup>278</sup> in seawater containing severe sulfide levels of 100–1000 ppm which indicate a cracking possibility for the 90–10 alloy.

A related debilitating effect to stress corrosion cracking is hydrogen embrittlement, and it is interesting to note that copper alloys have not been reported to suffer from this phenomenon. In particular, testing has demonstrated that high strength Cu–Ni–Al and Cu–Ni–Sn alloys do not embrittle under hydrogen charging conditions<sup>277</sup> whereas nickel alloys containing copper and aluminum (Ni–Cu–Al) lose ductility under the same conditions. Detailed electrochemical work carried out by Pound<sup>279</sup> allowed him to suggest that this is because the internal hydrogen becomes associated with both reversible and irreversible trap sites. He postulates that the trap sites in a Cu–Ni–Al alloy are measurably more reversible than those in Ni–Cu–Al, preventing the former from being susceptible to hydrogen embrittlement.

### 3.07.3.7 Corrosion in Industrial Chemicals

A number of publications are available which give detailed information on the action of a wide range of chemicals on copper and copper alloys.<sup>280–285</sup>

When contemplating the use of copper-based materials for industrial purposes it is necessary to bear in mind that, even though a satisfactory life of the component may be obtained, possible difficulties may arise from the following other causes:

1. Copper compounds can be tolerated only in small amounts in potable waters or food substances. The WHO current safe concentration limit for copper in drinking water of  $2.0 \text{ mg l}^{-1}$ .
2. Copper compounds are highly colored, and a very small amount of corrosion may lead to staining and discoloration of products.
3. Stimulation of the corrosion of vital parts made of more anodic metals may occur if they are connected to copper.
4. Very small amounts of copper taken into solution may cause considerable corrosion of more anodic metals elsewhere in the system, particularly zinc,<sup>145</sup> aluminum,<sup>146</sup> and sometimes steel.<sup>286</sup> Small particles of copper deposited from solution set up local cells which can cause rapid pitting.

Despite these qualifications, copper and its alloys are used extensively and successfully in many types of chemical production equipment. Uses include condensers and evaporators, pipelines, pumps, fans, vacuum pans, and fractionating columns. Tin-bronzes, aluminum-bronzes, silicon-bronzes, and cupronickels are used in some circumstances because they present better corrosion resistance than copper or brasses.

#### 3.07.3.7.1 Acid solutions

Copper does not normally displace hydrogen, even from acid solutions, and it is therefore virtually unattacked in nonoxidizing conditions. For strongly reducing conditions in the temperature range 300–400 °C, corrosion resistance is comparable, if not better, than stainless steel. However, when copper alloys come into contact with most solutions, which invariably contain dissolved air, cathodic depolarization can occur which increases the chances that corrosion will take place.<sup>287</sup> Therefore, it is difficult to lay down any general recommendations for the use of copper in acid solutions, since the rate of attack significantly depends on the particular circumstances. Under fairly mild conditions copper or copper alloys are successfully used for handling solutions of hydrofluoric,<sup>280,288,289</sup> hydrochloric,<sup>280,290</sup> sulfuric,<sup>291</sup> phosphoric,<sup>280,292</sup> acetic, and other fatty acids.<sup>280,293</sup> Rates of corrosion, in general, increase with concentration of acid, temperature, amount of aeration,<sup>294,295</sup> and speed

of flow.<sup>296</sup> Tin-bronzes, aluminum-bronzes,<sup>297–299</sup> silicon-bronzes, and cupronickels are among the copper alloys most resistant to acids. For instance, aluminum bronze will withstand 50% sulfuric acid at 120 °C and 60% sulfuric acid at 30 °C. Silicon bronze is resistant to hydrochloric acid over the range 10% HCl at 70 °C/20% HCl at 50 °C/35% HCl at 15 °C. Brasses should not normally be used in acids. All copper-based materials are attacked rapidly by oxidizing acids such as nitric acid, strong sulfuric acid, or chromic acid (including dichromates) and also by hydrocyanic acid. The maximum temperature of operation of copper in dry HCl is 93 °C and in dry chlorine it is 200 °C.

The dissolution of copper and brasses in acid solutions has been studied by several authors.<sup>300–305</sup> In sulfuric acid, pitting attack has been found to occur in 95% sulfuric acid at 50 °C, in 80% sulfuric acid at 70 °C, and in 60% sulfuric acid at 100 °C. Various substances have been found to have an inhibiting effect on the rate of attack of copper or brasses in nitric acid<sup>306–310</sup> and in hydrochloric acid.<sup>311</sup>

#### 3.07.3.7.2 Neutral and alkaline solutions

Copper-based materials are resistant to alkaline solutions over a wide range of conditions,<sup>312</sup> but may be appreciably attacked by strong solutions, particularly if hot. Cupronickel alloys usually give the best results in alkaline solutions. Copper and its alloys should be avoided if ammonia, ammonium compounds, or organic amines are present<sup>313–317</sup> owing to the danger of both general corrosion and stress corrosion.

Copper is satisfactory for handling solutions of most neutral salts<sup>280,318</sup> unless aeration and turbulence are excessive. All exception is provided by those salts that form complexes with copper, such as cyanides, and solutions containing oxidizing agents, such as ferric or stannic compounds.

#### 3.07.3.7.3 Hydrogen sulfide pollution

Polluted and stagnant waters can be a source of corrosion to copper alloys because of the metal reaction with hydrogen sulfide to form sulfide surface films. Higher corrosion rates and pitting corrosion can result because the films do not provide the same protection as those normally formed. Sources of hydrogen sulfide include industrial waste, decomposition of organic matter, and sulfate reducing bacteria.

When there is little or no oxygen present in the system, then the corrosion rate of copper alloys with a sulfide film is only slightly higher than in aerated seawater.<sup>319</sup> However, when aerated seawater mixes with sulfide-containing seawater, higher rates of



corrosion can occur. Such corrosion is also velocity sensitive and is found to be more pronounced in regions of highest flow velocity.

A sulfide film can gradually be replaced by an oxide film in seawater during subsequent exposure to aerated conditions,<sup>9,162</sup> although this may take several days and high corrosion rates can be expected in the interim. However, if an established cuprous oxide film is already present, then periodic exposure to polluted water can be tolerated without damage to the film. Therefore, exposure to sulfides should be restricted wherever possible and this should be particularly so during commissioning and during the first few months of exposure to seawater, during which time the oxide film is maturing. Typical guidelines for commissioning or shut down/standby of copper alloy piping systems are given in **Table 8**.

The addition of ferrous ions to seawater systems, usually as a result of dosing with ferrous sulfate or by the use of a stimulated iron anode, has been found to improve the corrosion resistance of aluminum brass and cupronickels when exposure to polluted conditions are anticipated.<sup>76</sup> Other pretreatments have been investigated with variable success.<sup>76,166</sup>

The common cast alloys used for seawater systems are gunmetals, high tin bronzes, and nickel aluminum bronze. In clean water, nickel aluminum bronze is the favored alloy for pumps and valves<sup>319</sup> but 10% tin bronzes can be better in mildly polluted conditions, particularly for erosion resistance.

Francis has reported<sup>319</sup> that the presence of sulfides can reduce the temperature above which hot

spot corrosion can be found in heat exchangers from  $\sim 130^\circ\text{C}$  down to  $80^\circ\text{C}$ . This type of attack is caused by thermogalvanic effects under slow flow or stagnant conditions. Cupronickel (70–30) is the most susceptible alloy for hot spot corrosion and aluminum brass is the most resistant. Again, ferrous sulfate dosing, or higher flow rates, can provide improved resistance.

A microstructural study of the behavior of high strength Cu–Ni–Al alloy toward aqueous  $\text{H}_2\text{S}$  has been carried out using STEM and SEM surface analysis.<sup>320</sup> The morphology of the surface is shown in **Figure 7** together with a schematic diagram derived from microanalysis explaining the chemical composition of the various corrosion product layers formed. It was concluded that the large copper sulfide crystals were deposited on the surface following preferential corrosion of copper from the alloy surface. The general corrosion rate was about three times lower than that of 70–30 cupronickel as a result of the formation of an aluminum-rich oxide layer directly at the solid/solution interface.

#### 3.07.3.7.4 Other chemicals

Copper and copper alloys are unsuitable in hydrogen peroxide<sup>279,321</sup> or molten sulfur.<sup>279,322</sup> Halogens have little action on copper at room temperature when dry, but are corrosive when wet. Hypochlorite solutions are corrosive.<sup>323</sup> Most organic compounds are without appreciable action,<sup>279</sup> although contact with moist acetylene should be avoided, as explosive compounds are formed. Moisture also accelerates

**Table 8** Guidelines for shutdown and standby conditions of a copper alloy piping system in order to avoid possible problems caused by the presence of sulfides

<i>Conditions in the system</i>		
<i>Duration</i>	<i>Clean seawater or freshwater without deposits</i>	<i>Polluted seawater or freshwater where deposits are present</i>
4–6 days	Keep the system filled	Commissioned system: <ul style="list-style-type: none"> <li>● Avoid high flow rates</li> <li>● If possible, drain the system and fill with clean seawater or freshwater</li> </ul> New system: <ul style="list-style-type: none"> <li>● Clean the system and fill with clean seawater or freshwater.</li> </ul>
>4–6 days	Keep the system filled and replace the water by oxygenated water every 2–3 days	Possibility I: <ul style="list-style-type: none"> <li>● Clean the system and fill with clean seawater or freshwater</li> <li>● Replace the water by oxygenated clean water every 2–3 days.</li> </ul> Possibility II: <ul style="list-style-type: none"> <li>● Clean the system and keep it dry.</li> </ul>



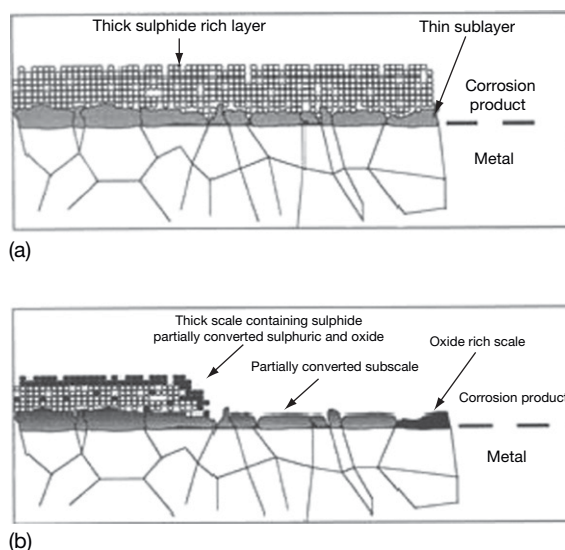
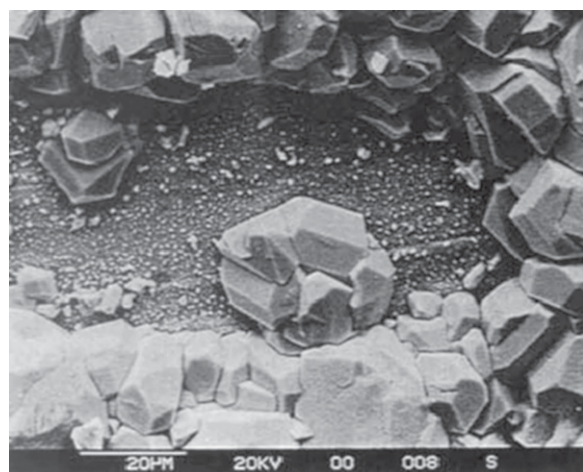


**Figure 7** Scanning electron image and schematic diagram of Cu-Ni-Al surface after exposure to saturated aqueous  $\text{H}_2\text{S}$  at 25 °C.

attack by halogenated organic compounds, particularly carbon tetrachloride and trichloroethylene, which hydrolyze to give traces of hydrochloric acid. Cupronickels show most resistance to these chemicals.

Copper alloys are widely used for handling hydrocarbon oils, although, if sulfur compounds are present, attack can be serious. The effects of synthetic detergents on copper have been investigated<sup>324,325</sup> and several authors<sup>279,326–328</sup> have discussed various aspects of the behavior of copper and its alloys in the food-processing industry, where direct contact with copper alloys can result in the alteration of taste or color.

### 3.07.3.8 High Temperature Oxidation and Scaling

Several authors have reviewed the literature on the oxidation and scaling of metals, including copper.<sup>329–332</sup>

#### 3.07.3.8.1 High temperature oxidation of copper

The volume ratio for cuprous oxide on copper is 1.7, so that an initially protective film is to be expected. Such a film must grow by a diffusion process and should obey a parabolic law. This has been found to apply for copper in many conditions, but other relationships have been noted. For instance, in the very early stages of oxidation, a linear growth law is found (e.g., at 1000 °C).<sup>333</sup>

At 180–290 °C, it has been determined<sup>334</sup> that the parabolic law first applies but, subsequently, this changes to a logarithmic relationship of the type shown in eqn [7]:

$$Y = K \log B(t + 1/B) \quad [7]$$

$B$  being a constant. However, other workers have reported a cubic relationship under some conditions. Evans<sup>335,336</sup> has shown how the effect of internal stresses in growing films may have various effects which can lead to any one of the three growth laws referred to above.

At medium and high temperatures<sup>337–345</sup> copper ultimately follows the parabolic law.<sup>346</sup> It has been shown using radioactive tracers<sup>347,348</sup> that the diffusion of copper ions in cuprous oxide is the rate-determining step at 800–1000 °C, and there is considerable evidence in favor of the view that metal ions move outwards through the film by means of vacant sites in the oxide lattice.<sup>133</sup>

When oxidation is a diffusion-controlled process, the oxidation rate should be related to the temperature by the Arrhenius relationship, eqn [8]:

$$K = A \exp(-Q/RT) \quad [8]$$

where  $K$  is the rate constant,  $A$  a constant,  $R$  the gas constant,  $T$  the absolute temperature, and  $Q$  the activation energy. Values which have been obtained for  $A$  and  $Q$  are summarized by Tylecote,<sup>349</sup> Pilling and Bedworth,<sup>350</sup> Feitknecht,<sup>351</sup> and others

and give values of  $Q$  of  $\sim 0.17$  MJ for temperatures of 700–1000 °C, while at lower temperatures (up to 500 °C) Vernon<sup>352</sup> and others have obtained values of about 85 kJ. These values are in agreement with calculations by Valensi,<sup>353</sup> based on the assumption that, at high temperatures, the oxidation proceeds by the reaction of oxygen with metallic copper to produce cuprous oxide while at lower temperatures the rate is determined by the reaction between oxygen and cuprous oxide to form cupric oxide.

At low temperatures (e.g., 300 °C) the film consists almost entirely of CuO. As the temperature increases, the film consists of a layer of Cu<sub>2</sub>O beneath a layer of CuO, the proportion of Cu<sub>2</sub>O increasing until, at high temperature, the film is almost entirely Cu<sub>2</sub>O. The precise composition of the film depends, however, on a number of factors, including temperature, time, and oxygen concentration in the atmosphere. Tylecote<sup>346</sup> has investigated the composition, properties, and adherence of scales formed on various types of copper at temperatures between 400 and 900 °C. At the higher temperatures, the scales formed on copper containing phosphorus were more brittle and less adherent than those formed on copper containing no phosphorus.

Studies have been carried out on the effects at high temperature of sulfur<sup>349</sup> and of atmospheres containing hydrogen sulfide,<sup>354–356</sup> steam,<sup>357,358</sup> sulfur dioxide,<sup>358</sup> and hydrogen chloride.<sup>358</sup>

### 3.07.3.8.2 High temperature oxidation of copper alloys

In the case of copper alloys which contain elements which are more noble than copper, the resulting surface oxide will be substantially pure copper oxide as the oxides of the noble metals have higher dissociation pressures than the copper oxides. Conversely, for alloys containing baser metals, the alloying element will appear as an oxide in the scale often in greater concentration than in the alloy itself, and sometimes to the exclusion of copper oxides. The dissociation pressures of many oxides have been calculated by Lustman.<sup>359</sup>

Whether the rate of oxidation of an alloy of copper with a base metal is less or more than that of copper will depend on the concentration of the alloying element and the relative diffusion velocities of metal atoms or ions in the oxide layers. There is extensive literature on the oxidation behavior of copper alloys.<sup>346,347,360–367</sup> According to Wagner's theory<sup>368–371</sup> the rate of oxidation will be largely influenced by the electrical conductivity of the film

and this theory is supported by the fact that the alloying elements giving maximum oxidation resistance to copper, that is, beryllium, aluminum, and magnesium, form oxides having very low conductivities, as shown by Price and Thomas.<sup>372</sup> Wagner calculated that when sufficient aluminum was present in copper to cause the formation of an alumina film, the oxidation rate should be decreased by a factor of more than 80 000. Experiment showed the factor to be only 36, but when Price and Thomas carried out initial oxidation under only slightly oxidizing conditions, producing only a film of alumina, the oxidation rate on subsequent exposure to full oxidizing conditions was decreased by a factor of  $\sim 240$  000. Hallowes and Voce<sup>358</sup> found that selective oxidation of a 95Cu–5Al alloy by this method gave protection from atmospheric oxidation up to 800 °C unless the film was scratched or otherwise damaged, or the atmosphere contained sulfur dioxide or hydrogen chloride.

The effects on oxidation resistance of copper as a result of adding varying amounts of one or more of aluminum, beryllium, chromium, manganese, silicon, and zirconium are described in a number of papers.<sup>360–367</sup> Other authors have investigated the oxidation of copper–zinc<sup>373,374</sup> and cupronickel alloys,<sup>374,375</sup> the oxidation of copper and copper–gold alloys in carbon dioxide at 1000 °C<sup>376</sup> and the internal oxidation of various alloys.<sup>377–379</sup>

Copper alloys have been used extensively in high-pressure feed-water heaters in power generating plant.<sup>380</sup> Experience has shown that when such heaters are operated intermittently, 70Cu–30Ni or 80Cu–20Ni alloy tubes suffer fairly rapid and severe steam-side (external) oxidation with the formation of exfoliating scales. This corrosion, which may be associated with ingress of air during shutdowns, has been the subject of several published papers.<sup>381–385</sup> The behavior of other alloys for feed-water heater service has also been discussed.<sup>380,386–388</sup>

## 3.07.4 Protective Measures

The good corrosion behavior of copper and copper alloys is dependent upon correct choice of material, good design of equipment, and proper methods of operation. Brasses and bronzes may often be effectively protected by polishing followed by periodic waxing. If proper attention is given to these factors, there will usually be no need for protective measures. In special cases, however, for example, to prevent the dissolution of small amounts of copper or to maintain

a high-grade finish, metallic coatings of one or more of the following metals may be applied: tin, lead, nickel, silver, chromium, rhodium, or gold. In other cases painting, varnishing, or lacquering may be desirable, or if the conditions are very severe (as in some corrosive soils) heavier protection such as bituminous or plastic coatings may be necessary. Brasses that are liable to suffer dezincification or stress corrosion may need protection where other copper alloys would be satisfactory in an unprotected condition. Sometimes use is made of the principles of cathodic protection, for example, steel 'protector blocks' in condenser water-boxes.

In some circumstances, use of inhibitors may be a desirable remedial measure. For instance, benzotriazole (BTAH) has been found of considerable value for preventing staining and tarnishing of copper products.<sup>389</sup> The characteristics of the behavior seen indicate that an inhibiting film is formed by adsorption of neutral BTAH molecules on the copper surface followed by adsorption of a thin layer of copper BTAH in polymeric form. Also, a synergistic effect has been found when BTAH and iodide ions are used together to prevent copper corrosion in sulfuric acid.<sup>390</sup> Sodium diethyldithiocarbamate also has useful inhibiting properties.<sup>391</sup> Other types of inhibitors can be of value in condensate systems<sup>392,393</sup> and in acid solutions.<sup>305–310</sup> Reviews have been given of corrosion inhibitors for copper<sup>394</sup> and brasses.<sup>395,396</sup> The effects and efficiencies of various inhibitors continues to be the subject of much research.<sup>397–400</sup> Low concentrations (0.1 mM) of amino acids (glycine and cysteine) have been demonstrated to provide over 95% inhibition efficiency for 95–5 cupronickel corrosion.<sup>401</sup>

The danger of accelerated attack on copper-base materials due to coupling with other metals is small in many environments since copper is usually the cathodic member of the couple, but precautions are often necessary to prevent excessive corrosion of the anodic member. Surveys of the behavior of couples involving copper and copper alloys have been given.<sup>319</sup> Titanium, high nickel alloys, and super stainless steels can be sufficiently more noble than copper alloys in seawater environments to cause galvanic attack of the copper alloy and electrical isolation or insulated spool pieces may be required. This is less of a problem in chlorinated systems as prevention of the biofilm can reduce the efficiency of the cathode.<sup>319,402</sup> Another material that has been found capable of accelerating attack on copper in practice is graphite; hence graphitic paints or graphite in

gasketing, etc., are undesirable. Occasionally the action between different copper-based materials may be appreciable particularly if the relative surface areas are unfavorable, for example, gunmetal may stimulate the corrosion of copper or brass in seawater and due care should be taken.

### 3.07.5 Areas of Future Development

#### 3.07.5.1 Antimicrobial Benefits of Copper Corrosion

The formation of cuprous  $\text{Cu}^+$  and cupric ions  $\text{Cu}^{2+}$  has been described earlier. The ability of copper to gain and lose outer electrons is the source of many of copper's important physical properties such as high electrical and thermal conductivity, chemical stability, and its reddish color. Copper ions also play a crucial role in copper's antimicrobial action and the main hypotheses for the mode of actions in damaging the functionality of a cell of a microorganism are:

1. Their competing with and hindering uptake of major minerals such as sodium and potassium. This causes serious imbalances in the mineral composition of the cell of the microorganism.<sup>403</sup>
2. Their binding to proteins inside the cell which do not require copper, creating a dysfunction of that protein.<sup>404,405</sup>
3. Their causing oxidative damage, thereby damaging the cell wall and other cellular structures and finally causing bacterial cell death.<sup>406</sup>

Recent work<sup>407–409</sup> has shown the effectiveness of copper in inactivating pathogens such as *Escherichia coli*, Meticillin-resistant *Staphylococcus aureus* (MRSA), and *Influenza A* and in reducing environmental contamination in a clinical setting.<sup>410,411</sup>

#### 3.07.5.2 Alloy Developments

Cupronickel alloys in particular are being developed for applications in seawater and oil and gas well environments. Copper nickel chrome (DEF STAN 02-824) cast components are beginning to replace those made from nickel aluminum bronze when long-term seawater corrosion resistance is required. This is due to the fact that, after 10 years of seawater service, only such components have been found to have lost only  $\sim 0.15$  mm from their original thickness through corrosion, performing significantly better than cast nickel aluminum bronze under the same conditions.<sup>412</sup> Cu–Ni–Al and Cu–Ni–Sn alloys are

being developed as high strength corrosion resistant alloys for seawater applications requiring hydrogen-embrittlement-free, antigalling properties, and as alternative corrosion resistant, nonmagnetic bearing alloy to Be–Cu in directional oilfield drilling equipment.

Shape memory effect alloys have recently been under development for use in electronics and dentistry. Those based on Cu–Al and Cu–Ag–Al have been found to exhibit curious electrochemical effects during dissolution in alkali media if oxygen is present.<sup>413</sup> This has been explained in terms of fast preferential dissolution of aluminum followed by the slow transport of aluminate ions from the surface. This influences the formation of Cu<sub>2</sub>O, which is the main corrosion reaction, such that an unusual oscillatory electro-potential effect is produced.

## Acknowledgements

This section is comprised of a revised version of the chapter by P.T. Gilbert, which appeared in the previous edition. This, in turn, was based on ‘Chemical Properties and Corrosion Resistance of Copper and Copper Alloys,’ which formed Chapter XVIII of the American Chemical Society Monograph No. 122, ‘*The Science and Technology of the Metal its Alloys and Compounds*,’ edited by Professor Allison Butts, and published by the Reinhold Publishing Corporation, New York, in 1954. Acknowledgement is hereby made to the Reinhold Publishing Corporation for permission to make derivations from this work. The revisions of the current chapter have also been contributed to by Peter Webster, Technical Consultant, and Angela Vessey, Director, Copper Development Association UK, Claes Taxén of KIMAB, Sweden and Rolf Sundberg of Västerås, Sweden, to whom further acknowledgements are given.

## References

1. BSEN. *Copper and Copper Alloys – Ingots and Castings*, BSI: London, 1982.
2. CEN TC 133. CR 13388. *Copper and Copper Alloys – Compendium of composition and products*, BSI: London.
3. EN1652. *Specifications for Copper and Copper Alloys: Plate, sheet, strip and circles for general purposes*, EN 12163 Rod, EN12166 Wire, EN 12449 Tubes, EN12420 Forgings, BSI, London.
4. *Copper and Copper Alloys*; ASTM: Pittsburgh, 2006.
5. A1322. *Standards Handbook for Wrought and Cast Copper and Copper Alloy Products*; Copper Development Association Inc., New York, 2003.
6. *Copper and Copper Alloys Compositions, Application and Properties*; Publication 120, Copper Development Association: UK, 2004.
7. *The Brasses-Properties and Applications*; Publication 117, Copper Development Association: UK, 2005.
8. DKI German Copper Institute Booklet: Copper nickel alloys; Properties, Processing, Application, DKI: Germany, 2000.
9. Powell, C. A.; Michels, H. T. *Cupronickel Alloys for seawater corrosion resistance and antifouling – a state of the art review*; Corrosion, NACE: Houston, 2000.
10. Powell, C. *Corr. Management*. **2005**, 63, 8.
11. DEF-STAN 02-824. *Copper Nickel Chromium Sand Castings and Ingots*; UK Ministry of Defence, Abbey Wood: UK, 2002.
12. Gaffoglio, C. J. *Power Eng.* **1982**, 60.
13. Tuck, C. D. S.; Bendall, K. C.; Radford, G. W. J.; Campbell, S. A.; Grylls, R. J. Paper No. 78, *Corrosion/96*, NACE: Houston, 1996.
14. Ratka, J. O.; Maligas, M. N. Paper No. 04298, *Corrosion 2004*, NACE: Houston, 2004.
15. Ateya, B. G.; Elsayed, A. A.; Sayed, M. S. *J. Electrochem. Soc.* **1993**, 141(1), 71–78.
16. Gatty, O.; Spooner, E. C. R. *Electrode Potential Behaviour of Corroding Metals in Aqueous Solutions*; Clarendon Press: Oxford, 1938.
17. Pourbaix, M. J. N. *Atlas of Electrochemical Equilibria in Aqueous Solutions*; Pergamon: Oxford, 1966.
18. Rubinic, L.; Markovic, T. *Werkst. Korrosion* **1959**, 16, 666.
19. Hickling, A.; Taylor, D. *Trans. Faraday Soc.* **1948**.
20. Kuksina, O. Y.; Kondrashin, V. Y.; Mashakov, I. K. *Protec. Met. (Russia)* **2006**, 42(2), 144.
21. Mayer, S. T.; Muller, R. H. *J. Electrochem. Soc.* **1992**, 139(2), 426–434.
22. Kusina, O. Y.; Kondrashin, V. Y.; Marshakov, I. K. *Protect. Met. (Russia)* **2004**, 40(6), 581.
23. Wilde, B. E.; Teterin, G. A. *Br. Corros. J.* **1967**, 2, 125.
24. Mansfield, F.; Uhlig, H. H. *J. Electrochem. Soc.* **1970**, 117, 427.
25. Varenko, E. S.; Galushko, V. P.; Kovtan, V. N.; Fedash, P. M.; Loshkarev, Y. M. *Zashchita Metallov* **1970**, 6, 103.
26. Gavgahi, M.; Kaymaz, I.; Totik, Y.; Sadeler, R. *Corr. Rev.* **2002**, 20(4–5), 403.
27. Virtanen, S.; Wojtas, H.; Schmuki, P.; Böhni, H. *J. Electrochem. Soc.* **1993**, 140(10), 2786–2790.
28. Parvizi, M. S.; Aladjem, A.; Castle, J. E. *Int. Mater. Rev.* **1988**, 33(4), 169.
29. Mathiyarasu, J.; Palaniswamy, N.; Muralidharan, V. S. *Corr. Rev.* **2000**, 18(1), 65.
30. Badawy, W. A.; Ismail, K. M.; Fathi, A. M. *Electrochimica Acta* **2005**, 50(18), 3603.
31. Vernon, W. H. J. *J. Inst. Met.* **1932**, 49, 153.
32. Vernon, W. H. J.; Whitby, L. J. *Inst. Met.* **1929**, 42, 181; **1932**, 44, 389.
33. Vernon, W. H. J. *Trans. Faraday Soc.* **1931**, 27, 255, 582.
34. Baumann, K.; Ruhrberg, U.; Kreysa, G. DECHEMA-Werkstoffe-Tabelle, 37th Supplement (Atmosphere), DECHEMA: Frankfurt, 1995.
35. Hudson, J. C. *Trans. Faraday Soc.* **1929**, 25, 177; *J. Inst. Met.* **1930**, 44, 409; *J. Birmingham Met. Soc.* **1934**, 14, 331; *Met. Ind.* **1934**, 44, 415; *J. Inst. Met.* **1935**, 56, 91.
36. Tracy, A. W.; Thompson, D. H.; Freeman, J. R. *Special Technical Publication No. 175*; ASTM: Pittsburgh, 1955; pp 77–87.
37. Mattsson, E.; Holm, R. *Metal Corrosion in the Atmosphere*; STP 435; ASTM: Pittsburgh, 1968; p 187.
38. Scholes, I. R.; Jacob, W. R. *J. Inst. Met.* **1970**, 99, 272.
39. Morcillo, M.; Almeida, E.; Marmcos, M.; Rosales, B. *Corrosion* **2001**, 57(11), 967.

40. Thompson, D. H. *Metal Corrosion in the Atmosphere*; STP 435; ASTM: Pittsburgh, 1968; p 129, 199.
41. Holm, R.; Mattsson, E. *Atmospheric Corrosion of Metals*; STP 767; ASTM: Pittsburgh, 1982; p 85.
42. Ramos, A. C.; Camoes, M. F.; Mendonca, M. H.; Foneca, I. I. E. *Corr. Prot. Mater.* **2001**, 20(4), 16.
43. Tracy, A. W. STP No. 175; ASTM: Pittsburgh, 1955; pp 67–76.
44. Tidblad, J.; Leygraf, C.; Kucera, V. *J. Electrochem. Soc.* **1991**, 138(12), 3592–3598.
45. Eriksson, P.; Johansson, L.-G.; Strandberg, H. *J. Electrochem. Soc.* **1993**, 140(1), 53–59.
46. Strandberg, H.; Johansson, L.-G. *J. Electrochem. Soc.* **1998**, 145(4), 1093.
47. Knotkova, D. Proceedings of 12th International Corrosion Congress, Houston; NACE: Houston; Sept 1993; Vol. 2, p 51.
48. Laub, H. *Metallurgy* **1968**, 22, 1116.
49. Veleve, L.; Luja, M. *Br. Corr. J.* **1999**, 34(1), 34.
50. Hullman, H. Proceedings of UN ECE Workshop, Munich, May 2003; Swedish Corrosion Institute, Stockholm, 2003.
51. Priggemeyer, S. Report AZ 10730, *Deutsche Bundesstiftung Umwelt*; 1998.
52. Priggemeyer, S.; Priggemeyer, S. *Metallurgy* **1999**, 53, 204.
53. Leuenberger-Minger, A. U.; Faller, M.; Richner, P. *Mat. Corr.* **2002**, 54(3), 157.
54. UN ECE-Report. *Investigation of the Metal Run-off from Copper Surfaces exposed to Atmosphere*; Bulletin – Korrosions Institutet, 2003, ISSU 109E.
55. Odnevall Wallinder, I.; Leygraf, C. *J. Corr. Sci.* **1997**, 39, 2039.
56. Bertling, S.; Odnevall Wallinder, I.; Berggren Kleja, D.; Leygraf, C. *Environ. Toxicol. Chem.* **2006**, 25, 891.
57. Odnevall Wallinder, I.; Bahar, B.; Leygraf, C.; Tidblad, J. *J. Environ. Monit.* **2007**, 9, 66.
58. Sandberg, I.; Odnevall Wallinder, I.; Leygraf, C.; Le Bozec, N. *J. Corr. Sci.* **2006**, 39, 4316.
59. Karlén, C.; Odnevall Wallinder, I.; Heijerick; Leygraf, C. *Environ. Pollut.* **2002**, 120, 691.
60. Odnevall Wallinder, I.; Leygraf, C. *J. Corr. Sci.* **2001**, 43, 2379.
61. Odnevall Wallinder, I.; Verbiest, P.; He, W.; Leygraf, C. *J. Corr. Sci.* **2000**, 42, 1471.
62. Sundberg, R. *Metallurgy* **2005**, 59, 10.
63. Arnold, R. *Integrat. Environ. Assess. Mgmt.* **2005**, 1, 333.
64. Boulanger, B.; Nikolaidis, N. P. *J. Am. Water Resources Assn.* **2003**, 39, 325.
65. Romanoff, M. *Underground Corrosion*; Nat. Bur. Stand. Circ. 579; Supt. of Documents: Washington, D.C., 1957.
66. Gilbert, P. T. *J. Inst. Met.* **1947**, 7, 139.
67. Gilbert, P. T.; Porter, F. C. *Iron and Steel Institute Special Report No. 45*, 1952, pp 55–74, pp 127–134.
68. Markovic, T.; Sevic, M.; Rubinic, L. *Werkst. Korrosion* **1960**, 11, 87.
69. Maeda, M.; Tenyama, K.; Shibayanagi, T.; Naka, M. *Mater. Charac.* **2005**, 55(2), 127.
70. Angelini, E.; Mongiatti, A.; Grassini, S.; Rosalbino, F.; Ingo, G. M.; De Caro, T. EUROCORR 2004, Nice, Sept 2004. Published CEFRACOR: Paris, 2004.
71. Efird, K. D. *Corrosion* **1977**, 33(1), 347.
72. Obrecht, M. F. *Corrosion* **1962**, 18, 189t.
73. Solelev, A. *J. Inst. Wat. Engrs.* **1955**, 9, 208.
74. Gilbert, P. T. *Br. Corr. J.* **1979**, 14, 20.
75. *Aluminium Bronze Alloys Corrosion Resistance Guide*; Publication 80, Copper Development Association, UK, 1981.
76. Defence Standard 01-782. *Protection of Seawater System Pipework and Heat Exchanger Tubes in HM Surface Ships and Submarines*; UK Ministry of Defence, Abbey Wood, 2009.
77. Kirk, W. Evaluation of Critical Seawater Hydrodynamic Effects of Erosion Corrosion of CuNi, INCRA Report 396 1987.
78. Beckmann, W.; Hecht, M.; Jasner, M.; Steinkemp, K. Kuala Lumpur Fabrication Technology Corrosion 2001, Kuala Lumpur; Institute of Materials: London, 2000.
79. LaQue, F. L. *Proc. Am. Soc. Test. Mater.* **1952**, 52, 1.
80. Evans, U. R. *J. Electrochem. Soc.* **1939**, 75, 446; Fink, F. W. *J. Electrochem. Soc.* **1939**, 75, 446, 441.
81. Lucey, V. F. *Br. Corr. J.* **1965**, 1(9), 53.
82. Feller, H.-G. *Z. Metallkunde* **1967**, 58, 875.
83. Heidersbach, R. *Corrosion* **1968**, 24, 38.
84. Kenworthy, L.; O'Driscoll, W. G. *Corr. Technol.* **1955**, 2, 247.
85. Piatti, L.; Grauer, R. *Werkst. Korrosion* **1963**, 14, 551.
86. Hashimoto, K.; Ogawa, S.; Shimodaira, S. *Trans. Jpn. Inst. Met.* **1963**, 4, 42.
87. Sugawara, H.; Ebiko, H. *Corr. Sci.* **1967**, 7, 513.
88. Joseph, G.; Arce, M. T. *Corr. Sci.* **1967**, 7, 597.
89. Langenegger, E. E.; Robinson, F. P. A. *Corrosion* **1968**, 24, 411; **1969**, 25, 59.
90. Horton, R. M. *Corrosion* **1970**, 26, 160.
91. Rothenbacher, P. *Corr. Sci.* **1970**, 10, 391.
92. Pötl, A.; Lieser, K. H. *Z. Metallkunde* **1970**, 61, 527.
93. Sundberg, R.; Holm, R.; Hertzman, S.; Hutchinson, B.; Lindh-Ulmgren, E. *Metallurgy* **2003**, 57, 721.
94. Hutchinson, B.; Oliver, J.; Lindh-Ulmgren, E.; Symiotis, E. In *Investigation into the Dezincification of  $\alpha$ -Brass*; Proceedings of the International Conference Copper 2006; Welter, J.-M. Ed.; Wiley-VHC, 2006.
95. Bengough, G. D.; Jones, R. M.; Pirret, R. *J. Inst. Met.* **1920**, 23, 65.
96. Upton, B. *Br. Corros. J.* **1966**, 1, 134.
97. Baldwin, A. B.; Campbell, H. S. *Brit. Waterworks Assoc. J.* **1961**, 43, 13.
98. Schafer, G. J.; Dall, R. A. *Aust. Corr. Eng.* **1966**, 10, 39.
99. Ladeburg, H. *Metallurgy* **1966**, 20, 33.
100. Simmonds, M. A.; Huxley, W. G. S. *Aust. Corr. Eng.* **1967**, 11, 9.
101. Bengough, G. D.; May, R. J. *Inst. Met.* **1924**, 32, 81; Discussion of Bradbury, E. J.; Johnson, L. W. *Trans. Inst. Mar. Engrs.* **1951**, 63, 59.
102. Breckon, C.; Gilbert, P. T. *Chem. Ind.* **1964**, 4, 35.
103. Bem, R. S. *The Engineer* **1958**, 206, 756.
104. Sundberg, R.; Hertzman, S.; Linder, M. In *Intergranular Corrosion (IGA) of Brass*; Proceedings of the International Conference Copper 2006 Welter, J.-M. Ed.; Wiley-VHC, 2006.
105. Mazza, F.; Torchio, S. *J. Corr. Sci.* **1983**, 23, 1053.
106. Turner, M. E. D. *Proc. Soc. Water Treatm. Exam.* **1961**, 10, 162; **1965**, 14, 81.
107. Clark, W. D. *J. Inst. Met.* **1947**, 73, 263.
108. Breckon, C.; Gilbert, P. T. Proceedings of the first International Congress on Metal Corrosion, London; Butterworths: London, 1962; p 624.
109. Meigh, H. *Cast and Wrought Aluminum Bronzes – Properties, Processes and Structure*; IOM Communications, 2000.
110. Brezina, P. *Int. Met. Rev.* **1982**, 27(2), 1.
111. Weill-Couly, P.; Arnoud, D. *Fonderie* **1973**, 322.
112. Taxen, C. *Korrosionsinstitutet Rapport* **1996**, 8, 1.
113. Campbell, H. S. *Chem. Ind.* **1955**, 692.
114. Hatch, G. B. *J. Am. Waterworks Assn.* **1961**, 53, 1417.
115. Hatch, G. B. NACE Tech. Rep. 60–11; *Corrosion* **1960**, 16, 453t.
116. Schafer, G. J. *New Zealand J. Sci.* **1962**, 5, 475.



117. Lucey, V. F. *Br. Corr. J.* **1967**, 2, 175.
118. Campbell, H. S. Proceedings of the second International Congress on Metal Corrosion, New York (1963); NACE: Houston, 1966; p 237.
119. Gilbert, P. T. *Aust. Corr. Eng.* **1969**, 13, 513.
120. Zhu, X.; Lei, T. *J. Mat. Sci. Technol. (China)* **1998**, 14(1), 57.
121. Lin, L.; Lui, S.; Lui, Z.; Xu, J. *Corr. Sci. Protect. Technol.* **1999**, 11(1), 37.
122. Sundberg, R. *Metallurgy* **2002**, 56(11), 714.
123. Schafer, G. J.; Dall, R. A. *Aust. Corr. Eng.* **1963**, 7(10), 33.
124. Proceedings of the International Corrosion of Copper & Copper Alloys in Building; Tokyo, Japanese Copper Development Association, 1982.
125. Cornwall, F. J.; Wildsmith, G.; Gilbert, P. T. *Br. Corr. J.* **1973**, 8, 202.
126. Oliphant, R. J. *Causes of Copper Corrosion in Plumbing Systems*; Foundation for Water Research, 2003.
127. Mattson, E.; Fredriksson, A.-M. *Br. Corr. J.* **1968**, 3, 246.
128. Mattson, E., *Werkst. U Korros.* **1988**, 39, 499.
129. Linder, M. *Proceedings of the 9th Scandinavian Corrosion Congress, Copenhagen*, 1983, pp 569–581.
130. Drogowska, M.; Brossard, L.; Menard, H. *J. Electrochem. Soc.* **1992**, 139(1), 39–47.
131. Milosev, I.; Metikos-Hukovic, M.; Drogowska, M.; Menard, H.; Brossard, L. *J. Electrochem. Soc.* **1992**, 139(9), 2409–2418.
132. Drogowska, M.; Brossard, L.; Menard, H. *J. Electrochem. Soc.* **1993**, 140(5), 1247–1251.
133. BSEN 12502:2004. Protection of metallic materials against corrosion. *Guidance on the assessment of corrosion likelihood in water distribution and storage systems. Influencing factors for cast iron, unalloyed and low alloyed steels* and BSEN 14868:2005, *Protection of Metallic Materials against Corrosion. Guidelines on the assessment of corrosion likelihood in closed water circulation systems*, BSI, UK, 2005.
134. Rogers, T. H. *J. Inst. Met.* **1948**, 75, 19–38.
135. Keevil, C. W.; Walker, J. T.; McAvoy, J.; Colbourne, J. S. In *Biocorrosion*; Gaylarde, C. C., Moreton, L. H. G., Eds.; Biodeterioration Society: Kew, 1988.
136. Wagner, D.; Fischer, W.; Tuschewitzki, G. J. Microbiologically influenced corrosion of copper pipes Final report, ICA project number 453, 1992.
137. Geesey, G. G.; Mittleman, M. W.; Iwaoka, T.; Griffiths, P. R. *Materials Performance* **1986**, 37–40.
138. Geesey, G. C.; Lewandowski, Z.; Fleming, H.-C. *Biofouling/Biocorrosion in Industrial Water Systems*; Lewis Publishers: Chelsea, MI, 1993.
139. Tronstad, R.; Veimo, R. *J. Inst. Met.* **1940**, 66, 17.
140. Kenworthy, L. *J. Inst. Heat. Vent. Engst.* **1940**, 8, 15.
141. Gilbert, P.T. *Proc. Soc. Water Treatm. Exam.* **1966**, 15, 165.
142. Priggemeyer, St.; Priggemeyer, S.; Meyer, E.; Sauter, W.; Breu, M.; Schütz, G.; Arens, P.; Baukloh, A. In *Copper Release of Copper Tubes in Contact with Hard Drinking Waters*, Conference Proceedings of CEOCOR Plenary Meeting 2001; Biarritz.
143. Critchley, M.; Taylor, R.; O'Halloran, R. *Mater. Perform.* **2005**, 44(6), 56.
144. Merkel, T. H.; Pehkonen, S. O. *Corr. Eng. Sci. Technol.* **2006**, 41(1), 21–37.
145. Kenworthy, L. *J. Inst. Met.* **1943**, 69, 67.
146. Porter, F. C.; Hadden, S. E. *J. Appl. Chem.* **1953**, 3, 385.
147. Guidelines for Drinking Water Quality, 3rd ed.; WHO: Geneva, 2008.
148. Araya, M.; McGoldrick, M. C.; Klevay, L. M.; Strain, J. J.; Robson, P.; Nielsen, F.; Olivares, M.; Pizarro, F.; Johnson, L.; Poirier, K. A. *Regulat. Toxicol. Pharmacol.* **2001**, 34, 137–145.
149. Davenport, W. H.; Nole, V. F.; Robertson, W. D. *J. Electrochem. Soc.* **1959**, 106, 1005.
150. Ives, D. J. G.; Rawson, A. E. *J. Electrochem. Soc.* **1962**, 109, 447.
151. Obrecht, M. F.; Pourbaix, M. *J. Am. Waterworks Assoc.* **1967**, 59, 977.
152. Grunau, E. B. *Städtehygiene* **1967**, 7, 153.
153. Tuthill, A. H. *Mater. Perfor.* **1987**, 26(9), 12.
154. Defence Standard 01/2 and Angell, B.; Tuck, C. D. S., private communications, UK Ministry of Defence, Bristol, UK.
155. Shone, E.; Grim, G. *Trans I. Mar. Eng.* **1976**, 98, Paper 11.
156. Kirk, W.; Tuthill, A. The Application of Copper Nickel Alloys in Marine Systems. Copper Nickel Condenser and Heat Exchanger System, CDA Inc Seminar Technical Report 7044–1919, CDA, Inc: New York, 1992.
157. Jasner, M.; Hecht, M.; Beckman, W. *Heat Exchangers and Piping Systems from Copper Alloys – Commissioning, Operating and Shutdown*; KME: Osnabruck, 1998.
158. Gilbert, P. T. Conference of Historical Metallurgy Society, Birmingham, Paper Copper 4, 1984.
159. Powell, C. A.; Michels, H. T. *Cupronickel Alloys for seawater corrosion resistance and antifouling – A State of the Art review*; Corrosion 2000; NACE: Houston, 2000.
160. Zhu, X.; Lin, L.; Lei, T. *Acta Metall. Sinica (China)* **1997**, 33(12), 1256.
161. Zhu, X.; Lin, L.; Xu, J.; Lei, T. *Chin. J. Non-ferrous Met.* **1997**, 7(2), 79.
162. Nicklin, G. J. E. *Living with the threat of microbiologically influenced corrosion in submarine seawater systems-the Royal Navy's perspective*. Proceedings of 9th International Naval Engineering Conference (INEC 2008), Hamburg, IMarEST, London, 2008.
163. Schleich, W. Corrosion 2005; NACE: Houston, 2005, Paper No. 5222.
164. Theile, E. W. Proceedings of CDA Heat Exchanger Seminar; New York, April; Copper Development Association: New York, 1981.
165. Sato, S. Proceedings of the fourth International Congress of Metal Corrosion Amsterdam, 1969; NACE: Houston, 1975, 792.
166. i,s Lee, T. S. *Pre-treatment of Condenser Tubing for Enhanced Corrosion Resistance*; INCRA Project 284 Final Report, NiDI, 1985.
167. Rowlands, J. C. *J. Appl. Chem.* **1965**, 15, 57.
168. Lemieux, E.; Wolejsza, T. M.; Grolleau, A. M. *Corrosion* **2002**; Denver; NACE: Houston, 2002, Paper No. 02210.
169. Berthagen, L. *The use of Cathodic Protection for Copper Alloys in Seawater Cooling Systems*, EFC Working Party Report, EuroCorr 2001, Maney Publishing: London, 2001.
170. Tuthill, A. H.; Todd, B.; Oldfield, J. *IDA World Congress on Desalination and Water Reuse; Madrid* **1997**; Vol. IIIp 251p 25, paper No. 73.
171. Oldfield, J. W.; Todd, B. *A Review of Materials and Corrosion in Desalination-Key Factors for Plant Reliability*; IDA World Congress on Desalination and Water Science: Abu Dhabi, 1995.
172. Gilbert, P. T.; Jenner, B. J. *International Marine and Shipping Conference*; Institute of Marine Engineers: London, 1969.
173. Li, W.; Lui, D.; Wei, K. *Corr. Sci. Protect. Technol.* **1995**, 7(3), 232.
174. Singh, I.; Basu, D. K.; Singh, M. N.; Battamishra, A. K. *Anti-Corrosion Meth. Mat.* **1993**, 44(3), 195.
175. Nelson, G. A. *Bull. Am. Soc. Test. Mat.* **1959**, 240, 39.
176. Agarwal, D. C. *Br. Corr. J.* **2002**, 37(2), 105.
177. Agarwal, D. C. *Corr. Eng. Sci. Technol.* **2003**, 38(4), 275.



178. Agarwal, D. C.; Sarin, S.; Wadhura, R.; Vishwakarma, R.; Deshmukh, M. B.; Kurian, S. J. *Failure Anal. Prev.* **2005**, 5, 70.
179. Slusser, J. W.; Dean, S. W.; Drummer, D. M. Corrosion '86 NACE: Houston, 1986, Paper 330.
180. Parkins, R. N.; Holroyd, N. J. H. *Corrosion* **1982**, 38, 245.
181. Robertson, W. D. *Trans. Amer. Inst. Min. (Metall.) Engrs.* **1951**, 191, 1190.
182. Edmunds, G. *Symposium on Stress-corrosion Cracking in Metals*; ASTM: Philadelphia, 1944; pp 67–89.
183. Elliot, P.; Corbett, R. A. In Corrosion/1999 NACE: Houston, 1999, Paper No. 342.
184. Wilson, T. C.; Edmunds, G.; Anderson, E. A.; Peirce, W. M. *Symposium on Stress-corrosion Cracking in Metals*; ASTM: Philadelphia, 1944; pp 173–193.
185. Sato, S.; Nosetani, T. *Sumitomo Light Metal Tech. Rep.* **1969**, 10(2), 83.
186. Syrett, B. C.; Parkins, R. N. *Corr. Sci.* **1970**, 10, 197.
187. Uhlig, H. H. Ed. *Corrosion Handbook*; Wiley: New York, 1948; pp 78–79.
188. Sato, S. *Sumitomo Light Met. Tech. Rep.* **1960**, 1(3), 45.
189. Kamath, K. V.; Erdmann-Jesnitzer, F. *Metallurgy* **1960**, 14, 1061.
190. Thompson, D. H. *Chem. Eng.* **1961**, 68(3), 130.
191. Laub, H. *Metallurgy* **1966**, 20, 1174.
192. Adamson, K. *Corr. Sci.* **1967**, 7, 537.
193. Erdmann-Jesnitzer, F.; Kacslingk, N. *Werkst. Korrosion* **1969**, 20, 493.
194. Copper Alloys-ammonia test for stress corrosion resistance, ISO 6957; BSI: London, 1988.
195. Wrought copper and copper alloys. Detection of residual stress. Mercurous nitrate test, ISO 196; BSI: London, 1995.
196. Helling, S.; Lissner, O.; Rask, S.; Ström, B. *Werkst. Korrosion* **1957**, 8, 569.
197. Aebi, F. Z. *Metallk.* **1958**, 49, 63.
198. Thompson, D. H. *Mater. Res. Standards* **1961**, 1, 108.
199. Szabo, E. *Werkst. Korrosion* **1963**, 14, 162.
200. Mattsson, E.; Lindgren, Rask, S.; Wennström, G. *Current Corrosion Research in Scandinavia*; Kemian Keskusliitto: Helsinki, 1965; p 171.
201. Baumann, G. *Werkst. Korrosion* **1962**, 13, 737.
202. Sato, S. *Sumitomo Light Metal Tech. Rep.* **1963**, 4(1), 48.
203. Uhlig, H. H.; Sansone, J. *Mater. Protection* **1964**, 3(2), 21.
204. Peters, B. F.; Carson, J. A. H.; Barer, R. D. *Mater. Protect.* **1965**, 4(5), 24.
205. Logan, H. L.; Ugiansky, G. M. *Mater. Protect.* **1965**, 4(5), 79.
206. Laub, H. *Metallurgy* **1966**, 20, 597.
207. Laub, H. *Metallurgy* **1967**, 21, 173.
208. Laub, H. *Metallüberfläche* **1966**, 20, 413, 453, 493.
209. Sato, S.; Nosetani, T. *Sumitomo Light Metal Tech. Rep.* **1969**, 10(3), 175.
210. Whitaker, M. E. *Metal. Manchr.* **1948**, 39, 21, 66.
211. Perryman, E. C. W.; Goodwin, R. J. *J. Inst. Met.* **1954**, 13, 378.
212. Bailey, A. R. *J. Inst. Met.* **1959**, 87, 380.
213. Sheehan, T. L.; Dickerman, H. E. *J. Am. Soc. Nav. Engrs.* **1946**, 58, 586.
214. Evans, U. R. *Symposium on Internal Stresses in Metals and Alloys*; Institute of Metals: London, 1947; pp 291–310.
215. Pugh, E. N.; Craig, J. V.; Montague, W. G. *ASM. Trans. Quart.* **1968**, 61, 468.
216. Mattsson, E. *Electrochim. Acta* **1961**, 3, 279.
217. Forty, A. J.; Humble, P. *Philos. Mag.* **1963**, 8(86), 247.
218. Proceedings of the Second International Conference of Metal Corrosion, New York (1963); NACE: Houston, 1966; p 80.
219. McEvily, A. J., Jr.; Bond, A. P. *J. Electrochem. Soc.* **1965**, 112, 131.
220. Forty, A. J. *Met. Progr.* **1959**, 75, 154.
221. Graf, L.; Lacour, H. R. Z. *Metallk.* **1960**, 51, 152; **1962**, 53, 764.
222. Graf, L.; Richter, W. Z. *Metallk.* **1961**, 52, 834.
223. Aebi, F. Z. *Metallk.* **1955**, 46, 547; **1956**, 47, 421.
224. Bakish, R.; Robertson, W. D. *J. Electrochem. Soc.* **1956**, 103, 320.
225. Edeleanu, C.; Forty, A. J. *Philos. Mag.* **1960**, 5(58), 1029.
226. Graf, L. *Metallurgy* **1964**, 18, 1163, 17.
227. Lynes, W. *Corrosion* **1965**, 21, 125.
228. Pugh, E. N.; Westwood, A. R. C. *Philos. Mag.* **1966**, 13, 167.
229. Pugh, E. N.; Montague, W. G.; Westwood, A. R. C. *ASM. Trans. Quart.* **1965**, 58, 665.
230. Hoar, T. P.; Booker, C. J. L. *Corr. Sci.* **1965**, 5, 821.
231. Fairman, M. *Corr. Sci.* **1966**, 6, 37.
232. Takano, M.; Shimodaira, S. *Corr. Sci.* **1968**, 8, 55.
233. Lahiri, A. K. *Br. Corr. J.* **1968**, 3, 289.
234. Lahiri, A. K.; Banerjee, T. J. *Corr. Sci.* **1968**, 8, 895.
235. Hoar, T. P.; Rothwell, G. P. *Electrochim. Acta* **1970**, 15, 1037.
236. Swann, P. R.; Nutting, J. J. *Inst. Met.* **1960**, 88, 478.
237. Swann, P. R. *Corrosion* **1963**, 19, 102t.
238. Swann, P. R.; Pickering, H. W. *Corrosion* **1963**, 19, 369t, 373t.
239. Tromans, D.; Nutting, J. *Corrosion* **1965**, 21, 143.
240. Brown, B. F. *Met. Mater.* **1968**, 2(12), 171.
241. Graf, L. *Werkst. Korrosion* **1969**, 20, 408.
242. Robertson, W. D. Ed. *Stress Corrosion Cracking and Embrittlement (Electrochem. Soc. Symposium)*; Wiley: New York, 1956.
243. Rhodin, T. N. Ed. *Physical Metallurgy of Stress-Corrosion Fracture (AIME Symposium)*; Interscience: New York, 1959.
244. Conference on Fundamental Aspects of Stress Corrosion Cracking, Ohio State University, 1967; NACE: Houston, 1969.
245. Bailey, A. R. *Metall. Rev.* **1961**, 6(21), 101.
246. Sparks, J. M.; Scully, J. C. *J. Corr. Sci.* **1974**, 16, 619.
247. Kermani, M.; Scully, J. C. *J. Corr. Sci.* **1978**, 18, 833; **1979**, 89, 489.
248. Scully, J. C. *Met. Sci.* **1978**, 12, 290; *J. Corr. Sci.* **1980**, 20, 297.
249. Takano, M.; Staehle, R. W. *Trans. Jpn. Inst. Met.* **1978**, 19, 1.
250. Takano, M. *Trans. Jpn. Inst. Met.* **1977**, 18, 787.
251. Takano, M. *Corrosion* **1974**, 30, 441.
252. Kawashima, A.; Agrawal, A. K.; Staehle, R. W. *Spec. Tech. Pub.* **1979**, 665, 266.
253. Uhlig, H.; Gupta, K.; Liang, W. J. *Electrochem. Soc.* **1975**, 122, 343.
254. Holroyd, N. J. H.; Hardie, D.; Pollock, W. J. *Br. Corr. J.* **1982**, 17, 103.
255. Logan, H. L. *Meta. Eng. Quart.* **1965**, 5, 32.
256. Parkins, R. N. *Metall. Rev.* **1964**, 9(35), 201.
257. Engel, H.-J.; Speidel, M. O. *Werkst. Korrosion* **1969**, 20, 281.
258. Thompson, D. H.; Tracy, A. W. *J. Met. N.Y.* **1949**, 1, 100.
259. Pugh, E. N.; Montague, W. G.; Westwood, A. R. C. *Corr. Sci.* **1966**, 6, 345.
260. Uhlig, H. H.; Duquette, D. J. *J. Corr. Sci.* **1969**, 9, 557.
261. White, L. F.; Blazey, C. *Met. Ind.* **1949**, 75, 92.
262. Sylwestrowicz, W. D. *Corrosion* **1969**, 25, 168, 405; **1970**, 26, 160.
263. Lahiri, A. K.; Banerjee, T. *Corr. Sci.* **1965**, 5, 731.

264. Chatterjee, U. K.; Sircar, S. C.; Banerjee, T. *Corrosion* **1970**, 26, 141.
265. Chatterjee, U. K.; Sircar, S. C. *Br. Corros. J.* **1970**, 5, 128.
266. Blackwood, A. W.; Stoloff, N. S. *ASM. Trans. Quart.* **1969**, 62, 677.
267. Harry Meigh. *Cast and Wrought Aluminum Bronzes-Properties, Processes and Structure*; IOM Communications, 2000.
268. Helliwell, B. J.; Williams, K. J. *Metallurgia* **1970**, 81, 131.
269. Nishimara, R.; Yoshida, T. *Corr. Sci.* **2008**, 50(4), 1205.
270. Thompson, D. H. *Corrosion* **1959**, 15, 433t.
271. Marshall, T.; Hugil, A. J. *Corrosion* **1957**, 13, 329t.
272. Klement, J. F.; Maersch, R. E.; Tully, P. A. *Corrosion* **1959**; 15p 295t.
273. Norden, R. B. *Chem. Eng.* **1958**, 65, 194, 196.
274. Klement, J. F.; Maersch, R. E.; Tully, P. A. *Met. Prog.* **1959**, 75, 82; *Corrosion*, **1960**, 16, 519t; U.S. Pat. 2 829 972.
275. Robertson, W. D.; Grenier, E. G.; Davenport, W. H.; Nole, V. F. *Met. Prog.* **1959**, 75, 152; U.K. Pat. 802 044.
276. Andersen, M. W.; Joosten, M.; Murali, J.; Milliams, D. E. *Corrosion/96*; NACE: Houston, 1996, Paper No. 78.
277. Tuck, C. D. S. *Corrosion 2005*; NACE: Houston, 2005, Paper No. 5462.
278. El Domiaty, A.; Alhajji, J. N. *J. Mat. Eng. Perform.* **1997**, 6(4), 534.
279. Pound, B. G. *Corrosion* **1994**, 50(4), 301.
280. Lee, J. A. *Materials of Construction for Chemical Process Industries*; McGraw-Hill: New York, 1950.
281. Rabald, E. *Corrosion Guide*; Elsevier: New York, 1951.
282. LaQue, F. L. *Corrosion* **1954**; 10p 391.
283. Heim, A. T. *Ind. Eng. Chem.* **1957**, 49, 63A, 64A, 66A.
284. Baker, S. *Corr. Technol.* **1961**, 8, 8.
285. Tracy, A. W. *Chem. Eng.* **1962**, 69, 130, 152.
286. Gould, A. J.; Evans, U. R. *J. Iron Steel Inst.* **1947**, 155, 195.
287. Lacan, M.; Markovic, T.; Rubinic, L. *Werkst. Korrosion* **1959**, 10, 767.
288. Holmberg, M. E.; Prange, F. A. *Ind. Eng. Chem.* **1945**, 37, 1030.
289. Lingnau, E. *Werkst. Korrosion* **1957**, 8, 216.
290. Fontana, M. G. *Ind. Eng. Chem.* **1950**, 42, 69A.
291. Groth, V. J.; Hafsten, R. J. *Corrosion* **1954**, 10, 368.
292. Bulow, C. L. *Chem. Eng.* **1946**, 53, 210.
293. Friend, W. Z.; Mason, J. F. *Corrosion* **1949**, 5, 355; NACE, Report; *Corrosion* **1957**, 13, 757t.
294. Russell, R. P.; White, A. *Ind. Eng. Chem.* **1927**, 19, 116.
295. Damon, G. H.; Cross, R. C. *Ind. Eng. Chem.* **1936**, 29, 231.
296. Cornet, I.; Barrington, E. A.; Behrsing, G. U. *J. Electrochem. Soc.* **1961**, 108, 947.
297. Caney, R. J. T. *Aust. Eng.* **1954**, 64, 54; U.K. Pat 718,987.
298. Zitter, H.; Kraxner, G. *Werkst. Korrosion* **1963**, 14, 80.
299. Piatti, L.; Fot, E. *Werkst. Korrosion* **1964**, 15, 27.
300. Gregory, D. P.; Riddiford, A. C. *J. Electrochem. Soc.* **1960**, 107, 950.
301. Talati, J. D.; Desai, M. N.; Trivedi, A. M. *Werkst. Korrosion* **1961**, 12, 422.
302. Graydon, W. F. *J. Electrochem. Soc.* **1962**, 109, 1130.
303. Kagetsu, T. J.; Gradon, W. F. *J. Electrochem. Soc.* **1963**, 110, 856.
304. Feller, H.-G. *Corr. Sci.* **1968**, 8, 259.
305. Otsuka, R.; Uda, M. *Corr. Sci.* **1969**, 9, 703.
306. Rana, S. S.; Desai, M. N. *Indian J. Technol. S* **1967**, 393.
307. Desai, M. N.; Shah, Y. C. *Anti-Corr. Meth. Mater.* **1968**, 15(12), 9.
308. Desai, U.; Gandhi, M. H. *Corr. Sci.* **1969**, 9, 65.
309. Padma, D. K. *Anti-Corr. Meth. Mater.* **1969**, 16, 4.
310. Desai, M. N.; Shah, Y. C.; Punjani, B. K. *Br. Corr. J.* **1969**, 4, 309.
311. Ammar, I. A.; Riad, S. *Corr. Sci.* **1969**, 9, 423.
312. Desai, M. N.; Rana, S. S. *Werkst. Korrosion* **1966**, 17, 870.
313. Radley, J. A.; Stanley, J. S.; Moss, G. E. *Corr. Technol.* **1959**, 6, 229.
314. Schaefer, B. A. *Corr. Sci.* **1968**, 8, 623.
315. Bartoniček, R.; Holinka, M.; Lukašová, M. *Werkst. Korrosion* **1968**, 19, 1032.
316. Green, J. A. S.; Mengelberg, H. D.; Yolken, H. T. *J. Electrochem. Soc.* **1970**, 117, 433.
317. Jenkins, L. H.; Durham, R. B. *J. Electrochem. Soc.* **1970**, 117, 768.
318. Dubrisay, R.; Chesse, G. *Comp. Rend. Acad. Sci. Paris* **1945**, 220, 707.
319. Francis, R. *The Selection of Materials for Seawater Cooling Systems – A Practical Guide for Engineers*; NACE Publication, 2006.
320. Campbell, S. A.; Radford, G. J. W.; Tuck, C. D. S.; Barker, B. D. *Corrosion* **2002**, 58(1), 57.
321. Reichert, J. S.; Pete, R. H. *Chem. Eng.* **1947**, 54, 218.
322. West, J. R. *Chem. Eng.* **1951**, 58, 281.
323. Botham, G. H.; Dummett, G. A. *J. Dairy Res.* **1949**, 16, 23.
324. Holness, H.; Ross, T. K. *J. Appl. Chem.* **1951**, 1, 158.
325. Bukowiecki, A. *Schweizer Archiv. Angew. Wiss.* **1958**, 24, 355.
326. Mason, J. F. *Corrosion* **1948**, 4, 305.
327. Inglesent, H.; Storrow, J. A. *J. Soc. Chem. Ind.* **1945**, 64, 233.
328. Clendenning, K. A. *Canad. J. Res. F (Technol.)* **1948**, 26, 277.
329. Mimura, K.; Lim, J.-W.; Isshika, M.; Zhu, Y.; Jiang, Q. *Met. Mat. Trans. A* **2006**, 37(4), 1231.
330. Vernon, W. H. *J. Chem. Ind. (Rev.)* **1940**, 59, 87.
331. Kubaschewski, O.; Hopkins, B. E. *Oxidation of Metals and Alloys*; Butterworths: London, 1953.
332. Hauffe, K. *Oxydation von Metallen und Legierungen*; Springer-Verlag: Berlin, 1956.
333. Wagner, C.; Grunewald, K. Z. *Phys. Chem.* **1938**, 40, 455.
334. Dighton, A. L.; Miley, H. A. *Trans. Electrochem. Soc.* **1942**, 81, 321.
335. Evans, U. R. *Trans. Electrochem. Soc.* **1947**, 91, 547.
336. Evans, U. R. *Res. Lond.* **1953**, 6, 130.
337. Mott, N. F. *Trans. Faraday Soc.* **1939**, 35, 1175; **1940**, 36, 472; **1947**, 43, 429.
338. McKewan, W.; Fassell, W. M. *J. Met. M. Y.* **1953**, 51, 1127.
339. Paidassi, J. *Acta Metall.* **1958**, 6, 216.
340. Lohberg, K.; Wolstein, P. Z. *Metallk.* **1955**, 46, 734.
341. Baur, J. P.; Bridges, D. W.; Fassell, W. M. *J. Electrochem. Soc.* **1956**, 103, 273.
342. Gulbrausen, E. A.; Copan, T. P.; Andrew, K. F. *J. Electrochem. Soc.* **1961**, 108, 119.
343. Ro'nquist, A. *J. Inst. Met.* **1962**, 91, 89.
344. Yoda, E.; Siegel, B. M. *J. Appl. Phys.* **1963**, 34, 1512.
345. Wallwork, G. R.; Smeltzer, W. W. *Corr. Sci.* **1969**, 9, 561.
346. Tylecote, R. F. *J. Inst. Met.* **1950**, 78, 327; **1952**, 81, 681.
347. Bardeen, J.; Brattain, W. H.; Shockley, W. *J. Chem. Phys.* **1946**, 14, 714.
348. Castellan, G. W.; Moore, W. J. *J. Chem. Phys.* **1949**, 17, 41.
349. Tylecote, R. F. *J. Inst. Met.* **1950**, 78, 301.
350. Pilling, N. B.; Bedworth, R. E. *J. Inst. Met.* **1923**, 19, 529.
351. Feitknecht, W. Z. *Elektrochem.* **1929**, 35, 142, 500.
352. Vernon, W. H. *J. Chem. Soc.* **1926**, 2273.
353. Valensi, G. *Pittsburgh International Conference on Surface Reactions*; Corrosion Publishing: Pittsburgh, 1948; pp 156–165.

354. Oudar, J. *Metaux* **1960**, 35, 397, 445.
355. Dyess, J. B.; Miley, H. A. *Trans. Am. Inst. Min. (Metall.) Eng.* **1939**, 133, 239.
356. Vernon, W. H. J. *Trans. Faraday Soc.* **1924**, 19, 839.
357. Preston, G. D.; Bircumshaw, L. L. *Philos. Mag.* **1935**, 20, 706.
358. Hallows, A. P. C.; Voce, E. *Metal. Manchr.* **1946**, 34, 95.
359. Lustman, B. *Met. Prog.* **1946**, 50, 850.
360. Dennison, J. P.; Preece, A. J. *Inst. Met.* **1952**, 81, 229.
361. Blade, J. C.; Preece, A. J. *Inst. Met.* **1959**, 88, 427.
362. Maak, F.; Wagner, C. *Werkst. Korrosion* **1961**, 12, 273.
363. Wallbaum, H. J. *Werkst. Korrosion* **1961**, 12, 417.
364. Maak, F. Z. *Metallkunde* **1961**, 52, 538.
365. Zwicker, U. *Metallurgy* **1962**, 16, 1110.
366. Kapteijn, J.; Couperus, S. A.; Meijering, J. L. *Acta Metall.* **1969**, 17, 1311.
367. Sanderson, M. D.; Scully, J. C. *Corr. Sci.* **1970**, 10, 165.
368. Dunwald, H.; Wagner, C. Z. *Phys. Chem.* **1933**, 22, 212.
369. Wagner, C. Z. *Phys. Chem.* **1933**, 21, 25.
370. Wagner, C. *Pittsburgh International Conference on Surface Reactions*; Corrosion Publishing: Pittsburgh, 1948; pp 77–82.
371. Hoar, T. P.; Price, L. E. *Trans. Faraday Soc.* **1938**, 34, 867.
372. Price, L. E.; Thomas, G. J. *Inst. Met.* **1938**, 63, 21.
373. Schu'ckher, F.; Lampe, V. *Prog. Met.* **1965**, 105, 192.
374. Wood, G. C.; Chattopadhyay, B. *Inst. Met.* **1970**, 98, 117.
375. Whittle, D. P.; Wood, G. C. *Inst. Met.* **1968**, 96, 115, *J. Corr. Sci.* **1968**, 8, 295.
376. Swaroop, B.; Wagner, J. B., Jr. *J. Electrochem. Soc.* **1967**, 114, 685.
377. Ashby, M. F.; Smith, G. C. *Inst. Met.* **1963**, 91, 182.
378. Bolsaitis, P.; Kahlweit, M. *Acta Metall.* **1967**, 15, 765.
379. Pötschke, J.; Mathew, P. M.; Froberg, M. G. Z. *Metallkunde* **1970**, 61, 152.
380. *Alloy 400 for use in High Pressure Feedwater Heaters*; Nickel Institute Publication 14021, Nickel Institute: Alvechurch, UK, 1993.
381. Moore, C.; Bindley, D. *Proceedings of the Second International Congress on Metal Corrosion*, New York, 1963; NACE: Houston, 1966; p 391.
382. Castle, J. E.; Harrison, J. T.; Masterson, H. C. *Proceedings of the Second International Congress on Metal Corrosion*, New York (1963) NACE: Houston, 1966; p 822.
383. Hopkinson, B. E. ASME 1962, Paper No. 62-WA.
384. Wiedersum, G. C.; Tice, E. A. ASME WA/CT-3, ASME, 1964, Paper No.64.
385. Castle, J. E.; Harrison, J. T.; Masterson, H. G. *Br. Corros. J.* **1966**, 1, 143.
386. Otsu, T.; Sato, S. *Trans. Jpn. Inst. Met.* **1961**, 2, 153.
387. Sato, S. *Sumitomo Light Metal Tech. Rep.* **1964**, 5(1), 2; **1964**, 5(2), 27; **1964**, 5(3), 231; **1964**, 5(4), 290.
388. Brush, E. G.; Pearl, W. L. *Corrosion* **1969**, 25, 99.
389. Tromans, D.; Sun, R. *J. Electrochem. Soc.* **1991**, 138(11), 3235–3244.
390. Wu, Y. C.; Zhang, P.; Pickering, H. W.; Allara, D. L. *J. Electrochem. Soc.* **1993**, 140(10), 2791–2800.
391. Bhatt, I. M.; Soni, K. P.; Trivedi, A. M. *Werkst. Korrosion* **1967**, 18, 968.
392. Tinley, W. H. *Chem. Ind.* **1964**, 12, 2036.
393. Obrecht, M. F. *Proceedings of the Second International Congress on Metal Corrosion*, New York (1963); NACE: Houston, 1966; p 624.
394. Desai, M. N.; Rana, S. S.; Gandhi, M. H. *Anti-Corr. Methods Mater.* **1970**, 17(6), 17.
395. Desai, M. N.; Shah, Y. C.; Gandhi, M. H. *Aust. Corros. Eng.* **1968**, 12(3), 3.
396. Desai, M. N.; Shah, Y. C. *Werkst. Korrosion* **1970**, 21, 712.
397. Gupta, P.; Chaudhary, R. S.; Prakash, B. *Br. Corr. J.* **1983**, 18, 98.
398. Walker, R. *Corrosion* **1973**, 20, 290.
399. Lewis, G. *Br. Corr. J.* **1981**, 16, 169.
400. Subramanyan, N. C.; Sheshadri, B. S.; Mayanna, S. M. *Br. Corr. J.* **1984**, 19(4), 177.
401. Badawy, W. A.; Ismail, K. M.; Fathi, A. M. *Electrochim. Acta* **2006**, 51(20), 4182.
402. Francis, R. *The Selection of Materials for Seawater Cooling Systems: A Practical Guide for Engineers*; NACE: Houston, 2003.
403. Avery, S. V.; Howlett, N. G.; Radice, S. *Appl. Environ. Microbiol.* **1996**, 62(11), 3960.
404. Kim, J. H.; Cho, H.; Ryu, S. E.; Choi, M. U. *Arch. Biochem. Biophys.* **2000**, 382(1), 72.
405. Karlstrom, A. R.; Levine, R. L. *Proc. Natl. Acad. Sci. USA* **1991**, 88(13), 5552.
406. Pena, M. M.; Lee, J.; Thiele, D. J. *J. Nutr.* **1999**, 129(7), 1251.
407. Noyce, J. O.; Michels, H.; Keevil, C. W. *J. Hosp. Infect.* **2006**, 63, 289.
408. Noyce, J. O.; Michels, H.; Keevil, C. W. *Appl. Environ. Microbiol.* **2006**, 72, 4239.
409. Noyce, J. O.; Michels, H.; Keevil, C. W. *Appl. Environ. Microbiol.* **2007**, 73, 2748.
410. Casey, A. L.; Lambert, P. A.; Miruszenko, L.; Elliott, T. S. J. *Copper for preventing microbial environmental contamination*; Interscience Conference on Antimicrobial Agents and Chemotherapy (ICAAC) ASM, Washington, 2008.
411. Casey, A. L.; Adams, D.; Karpanen, T. J.; Lambert, P. A.; Cookson, B. D.; Nightingale, P.; Miruszenko, L.; Shillam, R.; Christian, P.; Elliott, T. S. J. *The role of copper in the reduction of contamination of the hospital environment*, submitted to J. Hospital Infection, March 2009.
412. Mawella, J. UK Ministry of Defence, Abbey Wood, Bristol, Communication on Corrosion performance of NES 824 copper-nickel chrome [www.marinecorrosionforum.org](http://www.marinecorrosionforum.org), 2005.
413. Hurtado, M. R. F.; Sumodjo, P. T. A.; Benedetti, A. V. *J. Electrochem. Soc.* **1993**, 140(6), 1567–1571.

## 3.08 Corrosion of Aluminum and its Alloys

### G. M. Scamans

Innoval Technology Limited, Beaumont Close, Banbury, Oxon OX16 1TQ, UK; Brunel Centre for Advanced Solidification Technology, Brunel University, Uxbridge, Middlesex UB8 3PH, UK

### N. Birbilis

Department of Materials Engineering, Monash University, Clayton VIC 3800, Australia

### R. G. Buchheit

Department of Materials Science and Engineering, The Ohio State University, Columbus, OH 43210, USA

© 2010 Elsevier B.V. All rights reserved.

3.08.1	Introduction	1975
3.08.2	Historical Perspective	1975
3.08.3	Production and Types of Aluminum Alloys	1976
3.08.3.1	Aluminum Production	1976
3.08.3.2	Physical Metallurgy	1977
3.08.3.3	Description of Alloys and Tempers	1979
3.08.3.3.1	Pure aluminum	1979
3.08.3.3.2	Manganese-containing alloys	1979
3.08.3.3.3	Magnesium-containing alloys	1980
3.08.3.3.4	Silicon- and magnesium-silicon-containing alloys	1981
3.08.3.3.5	Copper- and copper-magnesium-containing alloys	1981
3.08.3.3.6	Zinc- and zinc-magnesium-containing alloys	1981
3.08.3.3.7	Lithium-containing alloys	1981
3.08.3.3.8	Other alloys classified as 8xxx alloys	1982
3.08.3.4	Properties of Aluminum Alloys	1982
3.08.3.4.1	Wrought aluminum alloys	1982
3.08.3.4.2	Cast aluminum alloys	1983
3.08.4	Processing of Aluminum Alloys	1983
3.08.4.1	Shape Casting	1983
3.08.4.2	Direct Chill Casting	1984
3.08.4.3	Hot and Cold Rolling	1985
3.08.4.4	Extrusion	1985
3.08.4.5	Continuous Casting	1985
3.08.5	Corrosion of Aluminum Alloys	1986
3.08.5.1	Forms and Causes of Corrosion	1986
3.08.5.1.1	General dissolution	1986
3.08.5.1.2	Pitting and localized corrosion	1986
3.08.5.1.3	Bimetallic or galvanic corrosion	1988
3.08.5.1.4	Crevice corrosion	1989
3.08.5.1.5	Filiform corrosion	1990
3.08.5.2	Effects of Microstructure on Corrosion	1990
3.08.5.3	Intergranular Forms of Corrosion	1992
3.08.5.4	Environmentally Assisted Cracking	1993
3.08.5.4.1	Stress-corrosion cracking	1993
3.08.5.4.2	Liquid metal embrittlement	1995
3.08.5.4.3	Corrosion fatigue	1995
3.08.5.4.4	Hydrogen embrittlement	1996
3.08.5.5	Influence of Environment and Processing	1996
3.08.5.5.1	Influence of alloy processing	1996
3.08.5.5.2	Atmospheric corrosion	1996
3.08.5.5.3	Natural waters	1997

3.08.5.5.4	Underground corrosion by soils	1998
3.08.5.5.5	Corrosion in chemical environments	1998
3.08.5.5.6	High temperature corrosion	2000
3.08.5.5.7	Aluminum in contact with other materials	2000
3.08.5.5.8	Applied stress	2001
<b>3.08.6</b>	<b>Corrosion Prevention Strategies</b>	2001
3.08.6.1	Inhibitors	2001
3.08.6.2	Conversion Coatings	2002
3.08.6.3	Anodizing	2005
3.08.6.4	Organic Coatings	2006
<b>3.08.7</b>	<b>Applications of Aluminum Alloys</b>	2007
<b>References</b>		2008

### 3.08.1 Introduction

Having been discovered some 180 years ago, aluminum has a relatively short history and only recently completed its first century of commercial manufacture. The key to its extensive use today is its corrosion resistance and its extreme versatility that make it suitable for a wide range of products from household foil to armor plate and the essential construction material for generations of aircraft and space vehicles. Aerospace applications, which demand strength, toughness, corrosion resistance and light weight, have provided the greatest stimulus for alloy development and corrosion research, which continues even today.<sup>1</sup> Durable aluminum has provided a vast web of power transmission cables, cladding for all types of buildings and the versatile extruded section for glass house construction. It is increasingly the metal chosen for reducing the weight, thereby reducing emissions from the world's vast and rapidly expanding population of cars and trucks.

Aluminum and its alloys offer a diverse range of desirable properties that can be matched precisely to the demands of each application by the appropriate choice of composition, temper and fabrication mode. Aluminum can be rolled, forged, slit and sheared and shaped by extrusion through dies of a multiplicity of shape or can be cast directly into shaped products. In addition to its low density and high corrosion resistance, its other major attributes are its high thermal and electrical conductivity, heat and light reflectivity, cryogenic compatibility, nonferromagnetic property as well as its hygienic and nontoxic qualities for food contact applications.<sup>2</sup>

Aluminum as an engineering material ranks in tonnage use only behind iron and steel, and its growth in production has been continually increasing year by

year. The global tonnage shipped in 2007 was 60 Mt, of which 37 Mt was provided by primary production and 23 Mt by recycled scrap.<sup>3</sup> Aluminum is unique in its high level of recyclability, which can compensate for the high energy cost of its primary production.

Aluminum is an essential material for modern economies and often substitutes as the preferred material for steel and plastics in automotive and building applications; copper in electricity production and transmission; magnesium, titanium, composites and plastics in aerospace and defense applications; steel, plastics and glass in packaging applications; and wood and vinyl for building and construction applications.

This chapter provides a general, yet concise, account of the corrosion behavior of aluminum and its alloys with reference to their classification, processing and surface treatment.

### 3.08.2 Historical Perspective

Aluminum was first produced in impure form in 1825 by Hans Christian Ørsted and in pure form in 1827 by Friedrich Wöhler. The first commercial preparation of aluminum was in 1855 in France when Henry Etienne Sainte-Claire Deville reduced aluminum chloride with sodium. He also, most likely, conceived the idea of the electrolysis of aluminum oxide dissolved in cryolite, which in 1886 was used independently by Charles Martin Hall in the United States and Paul Héroult in France for the development of electrolytic extraction of high-purity aluminum in an economical manner and remains the basis for production even today.<sup>4,5</sup> Before the Hall-Héroult process was developed, aluminum was more valuable than gold and was used for dinner plates by Napoleon

III and the apex of the Washington Monument in 1884. Commercial production started in 1888 at the Pittsburgh Reduction Company, today known as Alcoa, and in 1889 in Switzerland at Aluminium Industrie, now part of Alcan.

Aluminum is the most abundant metal and comprises about 8% of the earth's crust. It occurs naturally as bauxite, the name given to its ore containing 30–50% hydrated alumina (along with impurities including iron oxide, titania and silica). The processing of bauxite is carried out by the chemical process invented by Karl Joseph Bayer in 1888,<sup>6</sup> which converts bauxite to alumina by digestion in caustic soda followed by precipitation and calcination. Impurities from bauxite and from the steel vessels and pipe-work of the alumina plants have a significant influence on the corrosion behavior of aluminum and its alloys.

The Hall–Héroult process is carried out in aluminum primary production plants, known as smelters, where the alumina from the Bayer plant is dissolved in molten cryolite, and electrolysis is carried out in an electrolytic reduction cell (or ‘pot’) consisting of baked carbon anode rods (which are consumed), a carbon-lined vessel to hold the electrolyte and a molten pool of liquid aluminum (the cathode).<sup>4,5</sup> The reduction cell is operated at about 950 °C. The anodes are consumed during the process as they react with the oxygen coming from the alumina. A typical smelter has hundreds of cells arranged in potlines operating at currents up to 500 kA. All potlines built since the early 1970s use prebake anode technology, where the anodes, manufactured from a mixture of petroleum coke with coal tar pitch binder, are prebaked in separate anode plants. In the earlier Soederberg technology, the carbonaceous mixture is fed directly into the top part of the pot, where self-baking anodes are produced using the heat released by the electrolytic process. Potlines of this type are being progressively phased out.

At regular intervals, molten aluminum is tapped from the pots and is transported to the cast house where it is alloyed in holding furnaces by the addition of other metals, cleaned of oxides and gases and then cast into ingots. These can take the form of extrusion billets for extruded products, or rolling ingots for plate, sheet and strip products, depending on the way they are to be further processed. Aluminum castings are produced by foundries using a number of molding techniques to manufacture shaped components.

Generally, the purity of aluminum from electrolysis cells is adequate (i.e., 99.7–99.9%) for alloying,

the main impurities being iron and silicon together with lower levels of zinc, magnesium, manganese and titanium; however, if high- or super-purity aluminum is required, a second stage of refining is carried out in a three-layer Hoopes cell producing purities between 99.99% and 99.999%. Higher purities can be achieved by zone-refining super-purity aluminum. World aluminum production grew rapidly from 180 kt in 1918 to 2 Mt in 1952 to 20 Mt in 1989. Since that time, the rate of increase has been more modest, rising steadily to 24 Mt in 2000 and recently, more rapidly to 37 Mt in 2007. Aluminum has been traded on the London Metal Exchange (LME) since 1978, and from 1985, the LME price was adopted as the market price. Over the past 30 years, the average LME quoted price of aluminum has been \$1.5 per kilogram but has ranged between \$1.00 and \$3.00 per kilogram depending on the variation in supply and demand.<sup>7,8</sup>

From a corrosion perspective, aluminum has been a remarkably successful metal, and many of the earliest artifacts remain like the mill-finished roof of the church of St. James in Rome built in 1897 and the statue of Eros by Albert Gilbert unveiled in London in 1893. The aluminum industry maintained strong corrosion technology support groups for many years as aluminum production and its range of applications expanded. The major corrosion issues addressed during this time were the tropicalization of aluminum alloys containing magnesium, the stress corrosion cracking of alloys used in aerospace applications, the galvanic corrosion of aluminum in architectural and automotive applications and, most recently, the filiform corrosion of painted aluminum sheet in both architectural and automotive applications. The most significant aluminum corrosion challenges at present are the ramifications from the elimination of chromates and the tolerance of increased impurity levels due to the increased use of recycled metal.

### **3.08.3 Production and Types of Aluminum Alloys**

#### **3.08.3.1 Aluminum Production**

Bauxite production has increased from 144 Mt worldwide in 2002 to 178 Mt in 2006. Most of this is mined from open cast mines in Australia (62 Mt), Brazil and China (both 20 Mt) followed by Guinea (15 Mt), Jamaica (15 Mt), and India (13 Mt). In 2006, Alcoa, Chinalco, Alcan, Rusal and BHP Billiton accounted for or controlled almost 60% of the



69 Mt of worldwide alumina production from the 178 Mt of bauxite.<sup>9</sup> The largest alumina producers in 2006 were Australia (18 Mt) and China (14 Mt). Like many commodities, alumina is sold both on spot prices and contract terms, for which it is typically priced between 11.5% and 13.5% of the aluminum price quoted on the LME. The recent rapid growth in Chinese demand for aluminum has led to a predicted increase in annual demand from 69 Mt per year in 2006 to 88 Mt per year by 2011. The largest producers of primary aluminum in 2003 were China (5.5 Mt), Russia (3.5 Mt), Canada (2.8 Mt), United States (2.7 Mt), Australia (1.8 Mt) and Norway (1.1 Mt). By 2007, Chinese production had increased to 12.6 Mt out of the total world primary production of 34 Mt.<sup>9</sup> The amount of electrical energy to produce aluminum has been reduced from more than 50 kWh kg<sup>-1</sup> in 1890 to 16.1 kWh kg<sup>-1</sup> in 1990 and to 15.2 kWh kg<sup>-1</sup> in 2006.

Four tons of bauxite is used to produce 2 tons of alumina, which then produces 1 ton of aluminum. The industry average emissions associated with primary aluminum production is 9.73 kg CO<sub>2</sub>e per kilogram, 55% of this from electricity generation, so this varies considerably depending on how the electricity is generated.<sup>3</sup> Historically, over 50% of the electricity used to produce aluminum has been hydroelectrically generated, and although it is expected that this trend will continue, recently significant smelter capacity has been installed, particularly in the Middle East, using gas. Aluminum production consumes 3% of the world's electricity and about 10% of its hydropower.

The aluminum industry maintains a close watch on the composition of primary aluminum by regular chemical analysis of samples from each individual electrolysis cell. Purity is calculated by subtracting all the trace element concentrations from 100%. Trends are noted with respect to age of the cell, anode technology and alumina source, as well as the use of recycled alumina from the environmental control systems (scrubbers) used in smelters that are used to trap elements that volatilize from reduction cells. Use of this scrubber alumina results in higher levels of nickel, lead, gallium and vanadium. From the corrosion perspective, the most significant impurities are iron (typically 0.03–0.2 wt %) and silicon (0.03–0.1 wt%) and the lower levels of elements such as copper, manganese, nickel, titanium, zinc, vanadium and gallium. Volatile elements such as sodium, calcium and phosphorous are removed by flux treatments prior to ingot casting.

Aluminum and its alloys are readily recyclable, with recycled scrap providing an increasingly important and growing contribution of 23 Mt per year to the more than 60 Mt total annual metal supply.<sup>3,10</sup> The ever-growing environmental concerns over raw material processing and primary aluminum production as well as the favorable economics of recycling have led to a strong secondary aluminum production industry based on reclaimed scrap accounting for about 30–35% of total aluminum production since the early 1990s. The recycling of aluminum requires 95% less energy than that is required for primary aluminum production, and recycling of used aluminum products generates only 0.5 kg of CO<sub>2</sub>e per kilogram of aluminum produced.

However, in order to meet the mechanical and corrosion performance requirements of many alloy and product specifications, much of the recycled metal must be 'sweetened' with primary metal to reduce impurity levels. The result is that in many cases (except beverage cans) recycled metal tends to be used primarily for lower grade casting alloys and products. While a certain amount of this is acceptable, the recycle-friendly world will be truly optimized only when the recycle loop is closer to a closed loop within a number of product lines. Elements that increase in the recycled metal are mainly iron and silicon, and other elements such as magnesium, nickel and vanadium.<sup>11</sup> It is generally advisable to separate wrought alloys from cast alloys.

The total weight of aluminum products in use in 2006 was estimated to be 584 Mt, of which 32% is in building products, 28% in transport applications, 28% in engineering and cable, 1% in packaging and 11% in other products. Since the 1880s, close to 800 Mt of aluminum have been produced, and about three-quarters of this metal, more than 580 Mt, is still in productive use. This is a testament to the excellent corrosion resistance and recyclability of aluminum in almost all its applications. Recycling the metal currently in use would equal 17 years' primary aluminum output.<sup>3</sup>

### 3.08.3.2 Physical Metallurgy

The properties of aluminum alloys (mechanical, physical and chemical) depend on both alloy composition and alloy microstructure as determined by casting conditions and the thermomechanical processing history. While certain metals alloy with aluminum rather readily,<sup>12</sup> comparatively few have sufficient solubility to serve as major alloying elements. Of the commonly

used alloying elements, magnesium, zinc, copper and silicon have significant solubility, while a number of additional elements (with <1% total solubility) are also used because of the important improvements to alloy properties they confer. Such elements include manganese, chromium, zirconium and titanium.<sup>1,13</sup>

The low yield strength of pure aluminum (~10 MPa) mandates strength increase by alloying for subsequent engineering applications. The simplest strengthening technique is 'solution hardening,' whereby alloying additions as solute must have appreciable solid solubility over a wide range of temperatures and must remain in solution after any heating/cooling cycles, ultimately not being removed from solution by reacting with elements to form insoluble phases. Solid solution strengthening can lead to strength increases of about a factor of 2–4.

However, the most significant increase in strength for aluminum alloys is derived from age-hardening, and in the extreme, this can result in strengths up to 800 MPa. Age-hardening requires a decrease in solid solubility of one (or more) alloying elements with decreasing temperature. The age-hardening process can be summarized by the following stages

- solution treatment at a temperature within a single-phase region to dissolve the alloying element(s);
- quenching or rapid cooling of the alloy to obtain what is termed a supersaturated solid solution;
- decomposition of the supersaturated solid solution at ambient or moderately elevated temperature to form finely dispersed (nanoscale) precipitates.

The fundamental aspects of decomposition of a supersaturated solid solution are complex and still under debate.<sup>14–16</sup> Typically, however, Guinier–Preston (GP) zones and intermediate phase (as shown in **Figure 1**) are formed as precursors to the equilibrium precipitate phase.<sup>13</sup>

In addition, increases in yield strength may also be achieved by grain refinement by exploiting the Hall–Petch relationship.<sup>1</sup> Grain refinement in aluminum alloys is achieved at the casting stage (by additions of small amounts of low-solubility additions such as Ti and B to provide grain nuclei) or by recrystallization control using dispersoids (formed by making trace alloying additions of Cr, Zr or Mn to promote submicron-sized insoluble particles which subsequently restrict or pin grain growth).

Strength development can be further enhanced or modified by careful thermomechanical processing which may include heat treatments such as duplex

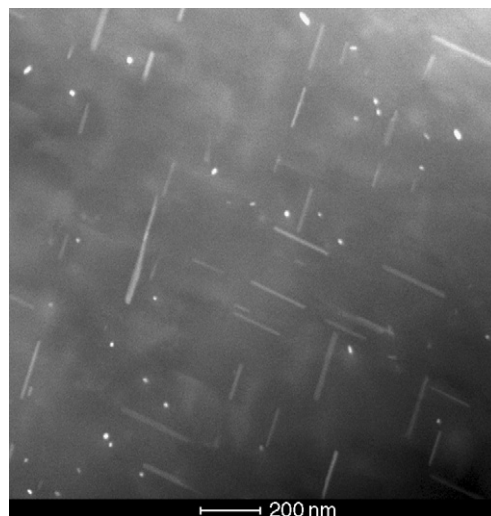


**Figure 1** Dark field scanning transmission electron micrograph of fine precipitate  $\text{Al}_2\text{CuMg}$  particles in an Al–Mg–Cu–Si alloy – imaged down the <100> zone axis. Courtesy of Nick Birbilis.

aging and retrogression and reaging. Maximum hardening in commercial alloys is often achieved when the alloy is cold-worked by stretching after quenching and before aging, increasing dislocation density and providing more heterogeneous nucleation sites for precipitation.<sup>14</sup>

In reality, the microstructures developed in aluminum alloys are complex and incorporate a combination of equilibrium and nonequilibrium phases. Typically, commercial alloys have a chemical composition incorporating up to 10 deliberately made alloying additions. It is prudent, from a corrosion point of view, to understand the role that impurity elements have on the microstructure. While not of paramount significance to alloy designers, impurity elements such as Fe and Si with additional elements form insoluble/high-melting-point compounds that form constituent particles at the alloy casting stage. These constituent particles are comparatively large and irregularly shaped, with characteristic dimensions ranging from 1 to 10  $\mu\text{m}$ . These particles are formed during alloy solidification and are not appreciably dissolved during subsequent thermomechanical processing. Rolling and extrusion tend to break up and align constituent particles into bands within the alloy as shown in **Figure 2**. Often, constituents are found in colonies made up of several different intermetallic compound types. Because these particles are rich in alloying elements, their electrochemical behavior is often significantly different from that

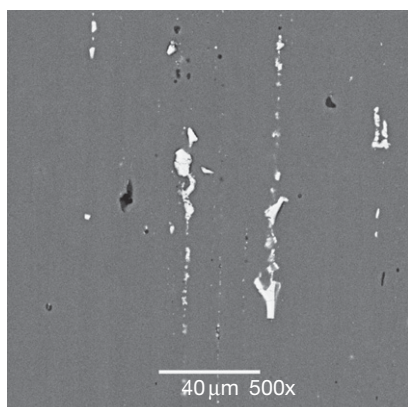


**Figure 2** Scanning electron micrograph of constituent particles in AA7075-T651 imaged in the backscattered electron mode. Courtesy of Katja Meyer.

of the surrounding matrix phase. In most alloys, pitting is associated with specific constituent particles present in the alloy.<sup>17,18</sup> A range of alloying elements are found in constituent particles: examples include  $\text{Al}_3\text{Fe}$ ,  $\text{Al}_6\text{Mn}$  and  $\text{Al}_7\text{Cu}_2\text{Fe}$ .

### 3.08.3.3 Description of Alloys and Tempers

Traditionally, the global prescription of aluminum alloys for use in engineering was difficult owing to the alloy designations differing from country to country.<sup>1</sup> For this reason, the introduction of an International Alloy Designation System (IADS) introduced in the 1970s was a welcome rationalization and advance. The IADS, and its European Standard equivalent (EN 573), give each wrought alloy a four-digit number of which the first digit is assigned on the basis of the major alloying element(s), as is summarized in [Table 1](#), along with the associated temper description.

In the case of cast aluminum alloys, the alloy designations used in a global sense principally adopt the notation of the Aluminium Association system summarized in [Table 2](#). The casting compositions are described by a four-digit system which incorporates three digits followed by a decimal. The .0 decimal indicates the chemistry limits applied to an alloy casting; the .1 decimal indicates the chemistry limits for ingot used to make the alloy casting; and the .2 decimal indicates ingot composition but with somewhat different chemical limits (typically tighter, but still within the limits for ingot).<sup>19</sup> Generally, the XXX.1 ingot version can be supplied as a secondary product (remelted from scrap, etc.), whereas the XXX.2 ingot version is made from primary aluminum. Some alloy designations include a letter. Such

letters, which precede an alloy number, distinguish between alloys that differ only slightly in percentages of impurities or minor alloying elements (e.g., 356.0, A356.0, B356.0 and F356.0).

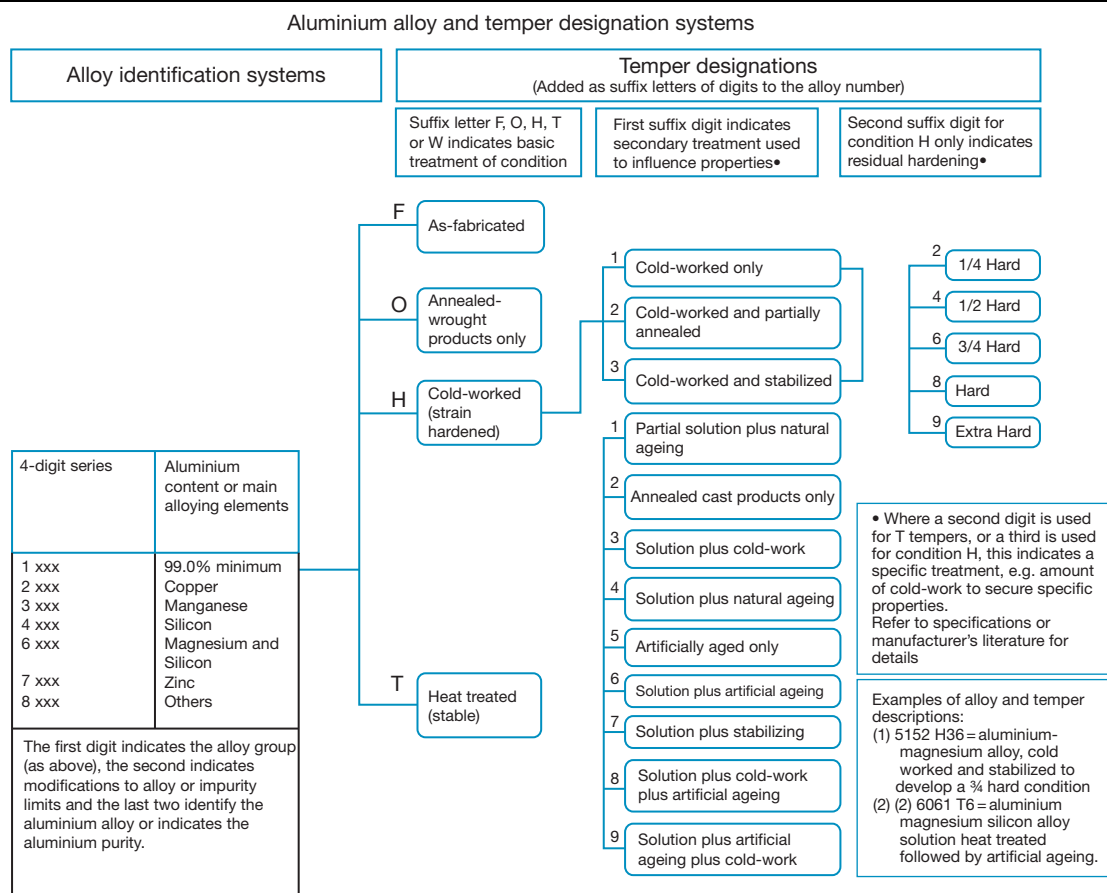
The temper designation system adopted by the Aluminium Association is similar for both wrought and cast aluminum alloys. Comprehensive details of alloy properties and characteristics are provided in the publications of the major aluminum companies and independent organizations.<sup>19</sup> Aluminum alloys tend to fall into several distinct groups, sometimes with apparently small differences within the group. Characteristics that could influence the selection of the most appropriate wrought products for a specific application are tabulated (in [Table 4](#)), but further details are provided as successful utilization of aluminum begin with the selection of alloy.

#### 3.08.3.3.1 Pure aluminum

Corrosion resistance of unalloyed aluminum increases with increasing metal purity. The use of the 99.8% and 99.9% grades is usually confined to those applications in which very high corrosion resistance or ductility is required. The chemical industry can advantageously use these purities for handling some products, but because of their low mechanical strength, they are sometimes used as a cladding material for a stronger substrate. Decreasing the purity results in modestly increased strength for the 99% and 99.5% grades, which still retain a high resistance to corrosion. The 99% pure metal may be considered the more useful general-purpose metal for lightly stressed applications such as cooking utensils. These alloys are known as the 1xxx series alloys, and the last two of the four digits indicate the minimum aluminum percentage. For example, 1050 is aluminum with a minimum purity of 99.5%. Alloys for electrical use are of special composition (i.e., AA1350 conductor alloys).

#### 3.08.3.3.2 Manganese-containing alloys

Manganese has a relatively low solubility in aluminum but improves its corrosion resistance in solid solution and can moderate the harmful influence of iron-bearing primary intermetallic phases. Additions of manganese of up to 1% form the basis for an important series of non-heat-treatable (3xxx series) wrought alloys, which have good corrosion resistance, moderate strength and high formability. For example, AA3003 displays a tensile strength of  $\sim 110$  MPa. In sheet form, its attractive combination of properties has resulted in large tonnages being used in buildings cooking utensils, and many general engineering

**Table 1**      Wrought aluminum alloy and temper designations

Source: Polmear, I. J. *Light Alloys: Metallurgy of the Light Metals*, 3rd ed.; Arnold: London, 1995.  
 Schlesinger, M. *Aluminium Recycling*; CRC Press: Boca Raton, FL, 2006.

**Table 2**      Four digit system for cast aluminum alloy designations

Alloy class	Designation
Aluminum of $\geq 99.0\%$	1xxx.x
Al + Copper	2xxx.x
+ Silicon (with copper and/or magnesium)	3xxx.x
+ Silicon	4xxx.x
+ Magnesium	5xxx.x
(Series is unused)	6xxx.x
+ Zinc	7xxx.x
+ Tin	8xxx.x
+ Other elements	9xxx.x

Source: Polmear, I. J. *Light Alloys: Metallurgy of the Light Metals*, 3rd ed.; Arnold: London, 1995.  
 Schlesinger, M. *Aluminium Recycling*; CRC Press: Boca Raton, FL, 2006.

applications. The predominant architectural sheet alloys are AA3005 and AA3105, and alloys such as AA3104 are used for beverage cans because of their deep-drawing capability.

### 3.08.3.3.3 Magnesium-containing alloys

Magnesium that has a relatively high solubility in aluminum can impart substantial solid solution strengthening and improvement of work-hardening characteristics. The 5xxx series alloys (containing  $<7\%$  Mg) do not age-harden. Nominally, the corrosion resistance of these weldable alloys is good, and their mechanical properties make them ideally suited for structural use in aggressive conditions. These alloys are used both for boat and shipbuilding, for which a long history of satisfactory corrosion

performance is on record, and for automotive structural applications. However, elevated temperatures should be avoided, since for alloys containing more than 3 wt% Mg, the precipitation of  $\beta$ -type phase ( $\text{Mg}_2\text{Al}_3$ ,  $\text{Mg}_5\text{Al}_8$ ) over a period of time can lead to serious corrosion in the form of intergranular attack or stress corrosion cracking. Fully work-hardened AA5456 (Al–4.7Mg–0.7Mn–0.12Cr) has a tensile strength of 385 MPa.

#### **3.08.3.3.4 Silicon- and magnesium–silicon-containing alloys**

Silicon additions alone can lower the melting point of aluminum while simultaneously increasing fluidity, which is very important and is largely the basis of aluminum casting alloys and the associated shape-casting industry. These alloys are making an increasingly important contribution in automotive applications for engine and drive train components. Generally, corrosion issues with aluminum casting alloys are rare or at least under-reported unless they are in contact with other metals, fasteners or fixtures that promote galvanic corrosion. Wrought 4xxx series aluminum–silicon alloys are used extensively as cladding materials for brazing alloys. Where free machining characteristics are required, this may be achieved by additions of cadmium, antimony, tin or lead.

The heat-treatable Al–Mg–Si alloys are predominantly structural materials, all of which have a high resistance to corrosion, immunity to stress corrosion cracking (SCC) and a satisfactory degree of weldability. These 6xxx series alloys are mainly used in extruded form, although increasing tonnages of automotive closure sheet are being produced. Magnesium and silicon additions are made in balanced amounts to form quasibinary Al– $\text{Mg}_2\text{Si}$  alloys, or excess silicon additions are made beyond the level required to form  $\text{Mg}_2\text{Si}$ . Alloys containing magnesium and silicon in excess of 1.4% develop higher strength upon aging. AA6061 (Al–1Mg–0.6Si–0.25Cu–0.2Cr) in the United States and AA6063 (Al–0.6Mg–0.4Si–0.10Cu) in the EU are used as general-purpose building materials. Automotive closure sheet is made from AA6016 in the EU and AA6111 in North America.

#### **3.08.3.3.5 Copper- and copper–magnesium-containing alloys**

Copper is one of the most common alloying additions to aluminum since it has both good solubility and a significant strengthening effect by its promotion of age-hardening response. Copper is added as a major

alloying element in the 2xxx series of alloys. The copper–magnesium alloys led to the accidental discovery of age-hardening by Wilm in 1906.<sup>20</sup> These alloys were the foundation of the modern aerospace construction industry, and, for example, AA2024 (Al–4.4Cu–1.5Mg–0.8Mn) can achieve strengths of up to 520 MPa depending on temper. Such Al–Cu–Mg alloys develop their strength by precipitation of the S-phase ( $\text{Al}_2\text{CuMg}$ ).

#### **3.08.3.3.6 Zinc- and zinc–magnesium-containing alloys**

Zinc is added to certain types of casting alloys, and wrought binary aluminum–zinc alloys are used as clad layers to sacrificially protect aerospace and armor alloys. However, binary alloys show a limited age-hardening response, which is significantly increased by the addition of magnesium and copper. The Al–Zn–Mg alloy system provides a range of commercial compositions, primarily where strength is a major consideration along with weldability, although this requirement limits the maximum amount of copper that can be added to less than 0.3 wt%. Al–Zn–Mg–Cu alloys have traditionally offered the greatest potential for age-hardening, and as early as in 1917, a tensile strength of 580 MPa was achieved; however, such alloys were not suitable for commercial use until their high susceptibility to stress-corrosion cracking could be moderated. Military and commercial aerospace needs following World War II led to the introduction of a range of high-strength aerospace alloys of which AA7075 (Al–5.6Zn–2.5Mg–1.6Cu–0.4Si–0.5Fe–0.3Mn–0.2Cr–0.2Ti) is perhaps the most well known.

The high-strength 7xxx series alloys derive much of their strength from the precipitation of the  $\eta$ -phase ( $\text{MgZn}_2$ ) and its precursor forms. The heat treatment of the 7xxx series alloys is complex, involving a range of heat treatments that have been developed to balance strength and stress corrosion cracking performance.<sup>21</sup>

#### **3.08.3.3.7 Lithium-containing alloys**

Lithium is soluble in aluminum to a maximum level of about 4 wt%; however, as this is 16 at.%, it means that significant density improvements result from lithium additions. The strong response of these alloys to heat treatment has led to intense research and development on these alloys of high specific strength and stiffness for aerospace applications. Although research into Al–Li alloys dates back to the 1950s, there are continuing



concerns relating to low ductility and poor toughness and low corrosion resistance.

Recent studies have focused on Al–Cu–Li, Al–Li–Mg and Al–Li–Cu–Mg alloys (including the use of minor Ag additions). These alloys derive their strength from age-hardening, involving intermetallics such as  $\text{Al}_2\text{CuLi}$  and  $S'$  phase resulting in strengths in excess of 700 MPa.<sup>22</sup> Such alloys are very attractive for aerospace applications such as, for example, the launching of payloads into space orbit. The new Airbus A350XWB aircraft (expected 2013) is proposed to be predominantly comprised of Al–Li-based alloys. The corrosion challenge that remains to be resolved is the susceptibility to intergranular corrosion (IGC).

### 3.08.3.3.8 Other alloys classified as 8xxx alloys

Certain alloys high in lithium are classified as 8xxx alloys. This designation also includes alloys containing high levels of iron and manganese near the ternary eutectic content, such as 8006, that have useful combinations of strength and ductility at room temperature and retain their strength at elevated temperatures. These properties are due to the fine grain size stabilized by the finely dispersed iron-rich second phase. Alloys such as 8011 are based on Al–Fe–Si but with more than 1 wt% total alloying element present to give correspondingly higher strengths. Such alloys find application as foil and closures as well as heat exchanger finstock.

An Al–Ni–Fe alloy 8001 is used in nuclear power generation for applications demanding resistance to aqueous corrosion at elevated temperatures and pressures. Other alloys included in the 8xxx series are bearing alloys commonly used in cars and trucks which are based on the Al–Sn system (e.g., 8280 and 8081).

### 3.08.3.4 Properties of Aluminum Alloys

The basic physical properties of aluminum are given in Table 3.

The diverse and exacting technical demands made on aluminum alloys in different applications are met by the considerable range of alloys available for general and specific engineering purposes, each of which have been designed and tested to provide various combinations of useful properties. These include strength/weight ratio, corrosion resistance, workability, castability or high temperature properties, to mention a few. Some basic properties of these standard alloys are given in Table 4.

**Table 3** Properties of aluminum

<i>Physical</i>	
Atomic number	13
Atomic weight	10.0
Atomic volume	26.97
Valency	3
Crystal structure	Face-centered cubic
Interatomic distance	2.863 Å
Electrochemical equivalent	$0.3354 \text{ g A}^{-1} \text{ h}^{-1}$
Density at 293 K	$2700 \text{ kg m}^{-3}$
<i>Thermal</i>	
Melting point	931 K
Sp. heat at 293 K	$896 \text{ J kg}^{-1} \text{ K}^{-1}$
Mean sp. heat (293–931 K)	$1047 \text{ J kg}^{-1} \text{ K}^{-1}$
Latent heat of fusion	$387 \text{ kJ kg}^{-1}$
Coeff. of linear exp. (293–393 K)	$0.61 \times 10^{-6} \text{ m K}^{-1}$
Thermal conductivity at 273 K	$214 \text{ W m}^{-1} \text{ K}^{-1}$
<i>Electrical</i>	
Elec. vol. resistivity at 293 K	$2.7\text{--}3.0 \mu\Omega \cdot \text{cm}$
Elec. vol. conductivity at 293 K	63–57% IACS
Temp. coeff. of elec. resistance per K for 293 K	0.0041
Thermoelectric power vs. platinum	+0.41 mV/100 K

Wrought aluminum alloys are fabricated into the familiar semifabricated forms such as plates, sheets, extruded sections and drawn tubes from direct chill (DC) cast blocks or billets as appropriate. The largest DC cast rolling blocks are of the order of 20 tons, and most of these are made from primary metal alloyed and cast at smelters. These large rolling blocks are processed through a series of breakdown mills as well as hot and cold tandem mills to produce the wide range of plate and sheet products that represent the largest tonnage of aluminum alloy usage. Continuous casting (CC) of aluminum for sheet products has grown from its commercial inception in the early 1960s to more than 6 Mt per year capacity today. These CC alloys have both modified composition and microstructure when compared to their DC cast equivalents, and this results in modified corrosion behavior. Joining may be carried out by mechanical methods (such as riveting and bolting), brazing, soldering, adhesive bonding or welding. The argon-shielded arc welding methods (MIG and TIG), and more recently, friction stir welding are particularly appropriate where corrosion resistance of the welded joints is of importance.<sup>23</sup>

#### 3.08.3.4.1 Wrought aluminum alloys

The wrought aluminum alloys are often classified according to two major groups, which are the



**Table 4** Properties of selected aluminum alloys

<i>Alloy</i>	<i>Temper</i>	<i>Wrought/cast</i>	<i>Density (g cm<sup>-3</sup>)</i>	<i>Electrical conductivity (% IACS)</i>	<i>Thermal conductivity at 25 °C (W m<sup>-1</sup> K<sup>-1</sup>)</i>	<i>Yield strength (MPa)</i>	<i>Tensile strength (MPa)</i>	<i>Elongation (%)</i>
1199	O	W	2.71	60	237	10	45	50
1100	O	W	2.71	59	222	34	90	35
3003	H14	W	2.73	50	193	145	152	8
5005	H38	W	2.70	52	200	200	186	5
5052	H38	W	2.68	35	138	290	255	7
2024	T4	W	2.77	30	121	324	469	20
	T861					490	517	6
6061	T6	W	2.7	43	167	276	310	12
7075	T6	W	2.80	22	130	503	572	11
	T73					434	503	13
201.0	T4	C (sand cast)	2.80	30	121	215	365	20
356.0	T51	C (sand cast)	2.69	41	150	140	175	2
413.0	F	C (die cast)	2.66	39	154	140	300	2.5

Source: Polmear, I. J. *Light Alloys: Metallurgy of the Light Metals*, 3rd ed.; Arnold: London, 1995.

Grjotheim, K.; Welch, B. J. *Aluminium Smelting Technology*, 2nd ed.; Aluminium-Verlag: Dusseldorf, 1988.

Hatch, J. E. *Aluminium: Properties and Physical Metallurgy*; ASM International: Materials Park, OH, 1984; pp 424.

non-heat-treatable, and heat-treatable wrought alloys. Non-heat-treatable alloys derive their strength from a combination of solid solution or dispersion hardening. Such alloys can be further strengthened by strain-hardening and cold work.

In contrast, the heat-treatable alloys are strengthened by solutionizing and subsequent age-hardening. The designations, properties and applications of wrought alloys are covered elsewhere in this chapter.

#### 3.08.3.4.2 Cast aluminum alloys

Naturally, casting alloys may not be worked or strain-hardened; however, they may be heat-treated. It was estimated that in 1997 ingots for casting represented a total of ~26% of the total aluminum market in the United States. Of this amount, about 60% was die cast, with the remainder either sand cast, permanent mold cast, etc. The strength of the cast component is typically lower than that of wrought alloys; however, a tensile strength of up to 485 MPa may be realized with heat-treated 2xx.x series casting alloys, with a number of commercial casting displaying a good medium strength in the vicinity of 300 MPa.

### 3.08.4 Processing of Aluminum Alloys

#### 3.08.4.1 Shape Casting

Cast products are usually produced in foundries from prealloyed metal supplied from secondary smelters,

although certain high-performance castings are made from primary metal. The three most commonly used processes are sand casting, permanent mold casting and die casting. Sand molds are gravity fed, whereas the metal molds used in permanent mold casting are either gravity fed or by using air or gas pressure to force the metal into the mold. In high pressure, diecastings, parts up to 5 kg are made by injecting molten aluminum alloy into a metal mold under substantial pressure using a hydraulic ram. Sand castings and permanent mold castings are made from alloys that respond to heat treatment; however, because of their entrapped gas content, die castings are not easily welded or heat treated. Approximately, 85% of aluminum alloy die castings are produced in aluminum-silicon-copper alloys. Permanent mold castings are used for higher production runs than diecastings and, as the metal mold produces rapid solidification, such castings have excellent mechanical properties, low porosity and good dimensional tolerances. Sand casting is a versatile and low-cost process used for a wide range of alloy types although such castings do not have dimensional accuracy and have a relatively poor surface finish. Plaster molds have better surface finish than sand castings, allowing castings to be made with fine detail and close tolerances. Investment casting uses refractory molds formed over expendable wax or thermoplastic patterns. The molten aluminum is then cast into the fired mold to produce precision parts with thin walls, good

dimensional tolerance and a fine surface finish that require little further machining.

Aluminum castings are found in most of the vehicles in use today from cars, buses and trains, to ships, aircraft and spacecraft. The wide variety of aluminum casting alloys available allows the selection of materials with good strength, good corrosion resistance and other special properties. Approximately, 60% of aluminum castings are used in transport applications, 15% in domestic and office equipment, 6% in general engineering applications and 5% in the building and construction industry. Aluminum castings form parts used in cooking pots, washing machines, refrigerators, chairs and tables, and in offices castings are used in furniture, computers and other small, lightweight, high-technology equipment.

However, despite their wide use comparatively, little work has been carried out to date to understand the corrosion behavior of aluminum casting alloys. Because of their high content of alloying elements such as silicon, iron and magnesium, casting alloys have a higher density of intermetallic particles when compared to wrought aluminum alloys. Processing parameters such as cooling rate and pouring temperature and even minor alloying element content variation lead to significant changes in the microstructure of these alloys.

#### 3.08.4.2 Direct Chill Casting

This is a semicontinuous process used for the production of rectangular ingots or slabs for rolling into plate, sheet and foil and cylindrical ingots or billets for extruded rods, bars, shapes, hollow sections, tube, wires and rods. Most of the production is from primary aluminum and process scrap or selected post-consumer scrap. The shallow mold for a DC casting is made from an aluminum- or copper-based alloy with good thermal conductivity, and the walls of the mold are water cooled. The base of the mold is lowered hydraulically or mechanically at a speed that depends on the size and composition of the alloy being cast.

Casting starts by pouring molten metal into the mold which solidifies on contact with the water-cooled base of the mold. Before the mold is filled, it is lowered and the pouring rate is controlled to maintain a constant level of metal in the mold. The solidified shell holding the molten metal is directly chilled by water sprays directed onto the emerging ingot, and pouring is continued until the required ingot length is cast. For small diameter ingots, multiple ingots in lengths of 3 to 4 m may be cast in one

drop. This requires a high degree of automation and control for both quality and safety.

Before DC casting, the melt is degassed, filtered and grain-refined. The cast surface is often uneven, and the outermost 20 cm of the cast surface is often of a coarser grain structure than the interior and can contain higher levels of segregates. The outer cast surface is commonly scalped off.

An ideal structure for a DC cast ingot is a fine and uniform grain size, and this is achieved by using a grain refining master alloy in rod form that is fed into the molten alloy during casting at a rate of  $0.2-1 \text{ kg t}^{-1}$  of alloy. Grain refiner is usually an alloy that contains 5% titanium and 1% boron as intermetallic phases of titanium aluminide and titanium diboride. These provide the nuclei for solidification in the cooled melt. Cast ingots have a 5–20-mm-thick coarse-grained shell zone with fine grain and a coarse-grained center. DC cast ingots also suffer from macrosegregation and the middle of the ingot can have a significantly different composition.

The stress in the cast ingot depends on the alloy composition, the size and shape of the ingot, the casting speed and the cooling rate, but can be large enough to result in ingot splitting. Certain high-strength 7xxx alloys require stress relieving by heating to 450 °C and slow cooling to prevent splitting.

Thermodynamic considerations often fail to predict correctly the phase content and solid solution content of the as-cast microstructure because of the nonequilibrium nature of solidification during DC casting. This is important, as alloy corrosion properties are controlled by solid solution levels and intermetallic phase crystallography and morphology, which depend on complex kinetic competitions for nucleation and growth. An understanding of the factors that govern phase selection in aluminum alloys under conditions of nonequilibrium solidification is important since varying solidification conditions can lead to variations in secondary Al–Fe and ternary Al–Fe–Si phase contents at different positions in the casting, which in turn can lead to a degradation in the corrosion resistance of the fabricated products.<sup>24</sup>

Following DC casting, ingots are homogenized at high temperature between 450 and 630 °C prior to rolling or extrusion. Homogenization reduces segregation, encourages the transformation of metastable secondary and ternary phases into equilibrium phases and acts to equilibrate solid solution levels of soluble elements, resulting in certain cases in the precipitation of dispersoids. Homogenization can

therefore exert a significant influence on corrosion performance. The transformation of Al-Fe phases to Al-Fe-Si phases, known as beta to alpha transition, is particularly important in the processing of 6xxx extrusion alloys and 3104 can stock.<sup>25</sup> These transitions can exert a controlling influence on subsequent corrosion behavior.

### 3.08.4.3 Hot and Cold Rolling

Rolling blocks or slabs that are up to 30 tons in weight are scalped by milling away the cast surface and usually have their tops and bottoms sawn off. Slabs are heated to a temperature in the range 400–500 °C and passed through a reversing breakdown mill using heavy reductions per pass to reduce the slab gauge down to 15–35 mm. The surface of the slab undergoes intense shear deformation during this process, and a thin deformed layer is developed that can have a major influence on the subsequent corrosion performance of the rolled sheet if the layer is not removed by chemical or electrochemical cleaning.<sup>26</sup> The slab from the breakdown mill is then hot-rolled on a multi-stand tandem mill down to a gauge of 2.5–8 mm. Strip is coiled from the hot mill in tandem. Hot rolling deforms the original cast structure and the as-cast grains are elongated in the rolling direction. Depending on the alloy composition, temperature and rolling reduction, recovery processes and partial recrystallization can take place during hot rolling and the slow cooling of the hot-rolled coil. The elongated microstructure developed during hot rolling can have a profound effect on corrosion properties such as stress-corrosion cracking and exfoliation corrosion. For example, the exfoliation corrosion of 7xxx alloys was shown to be due to manganese segregation during DC casting, which developed into a banded microstructure during hot rolling, and exfoliation corrosion occurred as a result of preferential matrix attack adjacent to bands of manganese-containing intermetallic phases.<sup>27</sup>

Cold rolling is usually carried out continuously on multiple-stand tandem mills in which each stand has four rolls and the small diameter work rolls are prevented from bending by large diameter backup rolls. Surface roughness is controlled by the surface finish of the steel rolls. In cold rolling, there is still asperity contact between the roll and the aluminum surface and this can also produce a deformed surface layer with lower corrosion resistance than the underlying alloy. Removal of this surface has been shown to be important for the control of filiform corrosion of coil-coated aluminum architectural sheet.

### 3.08.4.4 Extrusion

In aluminum extrusion, a hydraulic ram forces a preheated billet held in a fixed container against a die and squeezes the metal through the die opening. The billet surface sticks to the container wall and a new surface is generated on the extrudate. However, this is not the case in backward or indirect extrusion, where the billet surface becomes the surface of the extrusion. Control of temperature and speed is important to avoid problems associated with overheating. However, most of these problems relate to surface defects seen during finishing operations such as anodizing rather than to direct corrosion issues. As with rolling corrosion of extruded sections is controlled largely by the distribution of primary intermetallic phases from DC casting and how these phases are broken up and elongated in the extrusion direction. Grain size and shape are important particularly if recrystallization does not occur and the as-cast grain structure is elongated in the extrusion direction. Partial recrystallization of an outer band of the extrusion can lead to a duplex structure with a predominately fibrous core and a thin, recrystallized outer zone.

### 3.08.4.5 Continuous Casting

Aluminum flat products can also be produced by twin roll casting or twin belt casting. This effectively removes the requirement for DC casting, formal homogenization and hot rolling. Molten aluminum is directly cast onto a water-cooled hollow steel roll or onto a cooled belt or block. Growth in continuous casting capacity has increased to more than 6 Mt per year from almost zero in 1960. Continuous casting has proven to be remarkably effective for the production of coiled strip suitable for coil coating for use as painted architectural sheet and for foilstock.

From a corrosion perspective, as solidification is more rapid in continuous casting, higher levels of supersaturation are achieved and the size of iron-bearing intermetallic phases is refined. This can be beneficial from a corrosion perspective. However, the surface quality is generally inferior to more conventionally cast and rolled strip, as the cast surface is not removed by scalping and variations in casting conditions can lead to surface streaks that persist at the final gauge after cold rolling. The range of alloys that can be made by continuous casting is more limited, and to date, only limited success has been achieved with automotive sheet alloys although belt

casting capacity for this purpose has been installed in Japan.

Continuous casting is particularly suitable for making strip from secondary metal sources such as recycled post-consumer scrap. This, together with the lower surface quality, has raised concerns about corrosion resistance, but service experience of painted architectural sheet has been positive provided that the sheet is properly cleaned prior to pretreatment and coating.

### 3.08.5 Corrosion of Aluminum Alloys

Aluminum is a very reactive metal with high affinity for oxygen. This is indicated from its position on the electromotive force series. The metal is nevertheless highly resistant to most atmospheres and to a great variety of chemical agents. This resistance is due to the inert and protective character of the aluminum oxide film which forms on the metal surface and reforms rapidly if damaged. In most environments, therefore, the rate of corrosion of aluminum decreases rapidly with time.

The protective oxide film on aluminum attains a thickness of about 1 nm on freshly exposed metal in seconds. Oxide growth is modified by impurities and alloying additions and is accelerated by increasing temperature and humidity and immersion in water. The protective oxide film inhibits corrosion because it is both resistant to dissolution and a good insulator that prevents electrons produced by oxidation of the metal from reaching the oxide/solution interface, where either the cathodic reduction of oxygen or water can take place. Restricting these cathodic reactions reduces the amount of aluminum oxidation that can occur.

The oxidation of aluminum at room temperature is reported to conform to an inverse logarithmic equation for growth periods up to 5 years.<sup>28</sup> At elevated temperatures, oxidation studies over shorter periods illustrate conformity to parabolic, linear and logarithmic relationships according to time and temperature. These kinetic variations are attributed to different mechanisms of film formation.<sup>29,30</sup>

Corrosion of aluminum is an electrochemical process that involves the dissolution of metal atoms; so it can take place only once the protective oxide film has been dissolved or damaged. Aluminum is amphoteric in nature, meaning its oxide film is stable in neutral conditions but soluble in acidic and alkaline environments. The thermodynamic stability of aluminum's oxide film is expressed by the potential versus pH (Pourbaix) diagram shown in [Figure 3](#).<sup>31</sup>

This diagram indicates the theoretical circumstances in which aluminum should show corrosion (forming  $\text{Al}^{3+}$  at low pH values and  $\text{AlO}_2^-$  at high pH values), passivity due to hydrargillite, that is,  $\text{Al}_2\text{O}_3 \cdot 3\text{H}_2\text{O}$  (at near-neutral pH values) and immunity (at high negative potentials). The nature of the oxide actually varies according to temperature, and above about 75 °C boehmite ( $\text{Al}_2\text{O}_3 \cdot \text{H}_2\text{O}$ ) is the stable form. It should be noted that the potential versus pH diagram does not indicate one of the most important properties of aluminum, that is, its ability to become passive in strongly acidic solutions of high redox potential such as concentrated nitric acid.

#### 3.08.5.1 Forms and Causes of Corrosion

Corrosion is an electrochemical process, and hence the corrosion potential of different aluminum alloys is of considerable importance. In addition, the difference between the potential of aluminum alloys and other metals is important, as is the relationship between the potential of microstructural constituents of a single alloy. As we discuss in the following, the compositions of solid solutions and additional phases, in addition to the spatial distribution and number density of additional phases, impact both the extent and the morphology of resultant corrosion. The major forms and causes of corrosion are covered individually below.

##### 3.08.5.1.1 General dissolution

As a general rule, general dissolution occurs spontaneously in strongly acidic or strongly alkaline solutions (as predicted by the Pourbaix diagram), but there are specific exceptions. Thus, in concentrated nitric acid, the metal is passive and the kinetics of the process is controlled by ionic transport through the oxide film, while inhibitors such as silicates permit the use of some alkaline solutions (up to pH 11.5) to be used with aluminum. Even where corrosion may occur to a 'limited' extent, aluminum is often preferred to other metals because its corrosion products are colorless.

##### 3.08.5.1.2 Pitting and localized corrosion

This is the most commonly encountered form of aluminum corrosion. In certain near-neutral aqueous solutions, a pit once initiated will continue to propagate as the solution within the pit becomes acidified and the alumina is no longer able to form a protective film to prevent pit growth.<sup>32</sup>

Pitting arises from the creation of a very localized and 'aggressive' environment that breaks down the

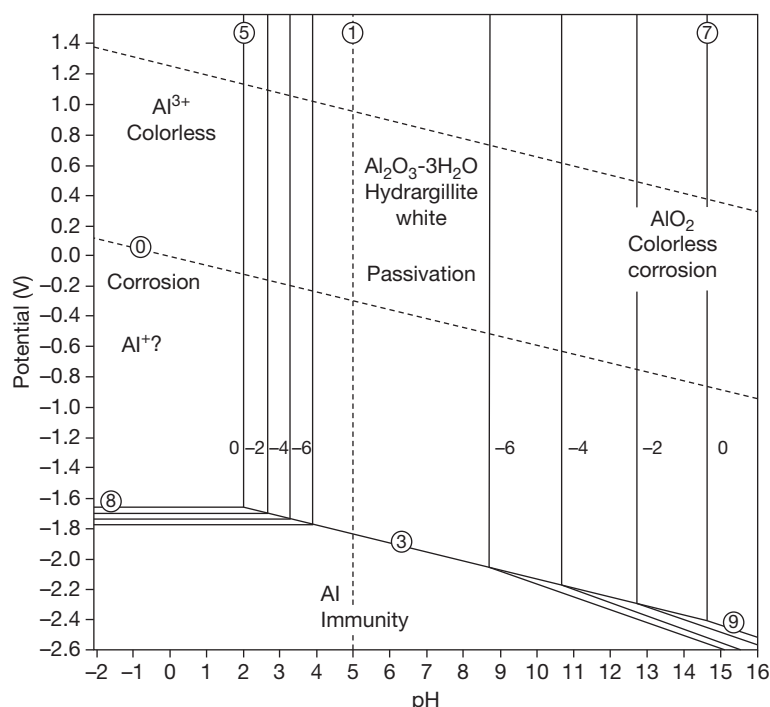


**Figure 3** Pourbaix diagram for aluminum.

nominally passive and corrosion-resistant film on the metal. Such an environment usually contains halide ions, of which chlorides are the most common. Solutions containing chlorides are very harmful, while the presence of chlorides can create local corrosion potential 'drops' between the metal surface and the occluded region at which the chloride is concentrated or accumulated. Pits may form at scratches, mechanical defects or stochastic local discontinuities in the oxide film. Pitting occurs only in the near-neutral pH range since the oxide is unstable in a bulk sense under acidic or alkaline conditions. Chlorides facilitate the breakdown of the film by forming  $\text{AlCl}_3$ , which is also usually present in the solution in the pits. When aluminum ions migrate away from the pits, alumina precipitates as a membrane, further isolating and intensifying local acidity, and sustained pitting of the metal results.

With increasing purity of aluminum, greater resistance to pitting corrosion is developed. On high-purity materials, however, any pits that develop are likely to be deeper though fewer in number than those formed in more impure metal. In some special applications, notably in contact with ammonia solutions or pure water at elevated temperatures and pressures, the iron and silicon present in commercial-purity metal

are beneficial and retard corrosion. Up to about 5% magnesium improves the corrosion resistance to seawater.

While the shape of the pits can vary rather significantly depending on the alloy type and environment, pit cavities are nominally hemispherical. This distinguishes pits from other forms of corrosion such as intergranular or exfoliation corrosion. Pitting is strongly influenced by the alloy type and microstructure, and [Section 3.08.5.2](#) covers the effect of microstructure on the corrosion mode in more detail.

The pitting potential defines the conditions under which metals in the passive state are subject to corrosion by pitting, and also serves as a means of discriminating the pitting propensity of alloys. However, the pitting potential yields no information regarding the number and size of pits which may form upon a given alloy, but it does give a measure of the driving force required for pitting to proliferate for a given alloy. There is a definite pitting potential for aluminum and its alloys in near-neutral pH environments, which has been readily and reproducibly measured by many investigators.<sup>33–35</sup>

A review of certain aspects of pitting corrosion of aluminum was given by Smialowska.<sup>18,36</sup> This review highlighted that from a detailed mechanistic point of view, the processes (at the atomic level) that lead

to breakdown of the film due to halide interaction are presently not understood in sufficient detail. However, different analytical techniques including selected ion monitoring (SIM), X-ray photoelectron spectroscopy (XPS) and autoradiography have revealed a clear adsorption of  $\text{Cl}^-$  on passive films of aluminum.<sup>36</sup>

In addition, since the 1980s, the work of Macdonald and coworkers has endeavored to explain the role of the film structure on pitting using the point defect model.<sup>37–41</sup> This model hypothesizes that chloride ions may be incorporated into the passive film by occupying anion vacancies resulting in a decrease of anion vacancies and an increase in cation vacancies. Cation vacancies are then posited to pile up at the metal interface leading a film breakdown.

More recently, certain researchers have observed current oscillations at a constant anodic potential below the pitting potential for different aluminum alloys.<sup>42–45</sup> The occurrence of these oscillations was explained by the formation and repassivation of nano/micropits termed ‘metastable’ pits. These investigations have been largely carried out to understand the processes that lead to the formation of stable pits. A typical current versus time record is shown below in Figure 4.

Recent studies have shown that the surface of rolled, ground or machined aluminum alloys have deformed surface layers that range in thickness from 100 to 200 nm up to several microns<sup>46,47</sup> and that the presence of these layers has a strong effect on the initiation of pitting corrosion. These deformed layers are characterized by ultrafine grains formed as a result of the high levels of shear strain locally experienced by the aluminum alloy surface. The

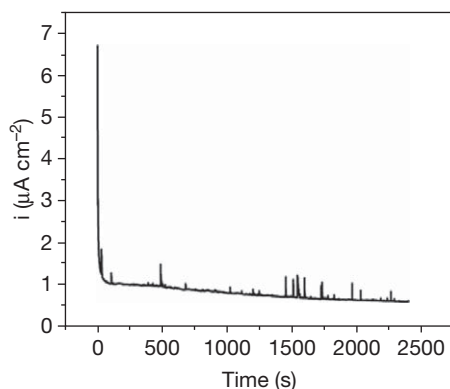


**Figure 4** Current vs. time record for AA7075-T651 in deaerated 0.1 M NaCl held potentiostatically at  $-0.755 V_{\text{SCE}}$ . Courtesy of Mary K. Cavanaugh.

surface layer grains are 50–100 nm in diameter, are stabilized by oxide particles on their boundaries and are more susceptible to corrosion than the underlying bulk alloy. Deformed layers on AA3005 and similar architectural alloys are activated by the preferential precipitation of manganese-containing dispersoids, whereas the similar layers on AA6016 and AA6111 automotive AA7075 aerospace alloys are more susceptible to pitting due to the preferential precipitation of the aging precipitate. High-shear processing of the surface of aged alloys results in the dissolution of the aging precipitate and this can lead to double breakdown potentials in polarization tests, as the surface is effectively in an underaged state and the pits are at a lower potential than the underlying bulk alloy.<sup>48</sup>

### 3.08.5.1.3 Bimetallic or galvanic corrosion

Aluminum is anodic to many other metals, and when it is joined to them in a suitable electrolyte which may even be a damp, porous solid, the resultant potential difference (see Table 5) causes a current to flow and result in considerable corrosion. Corrosion is most severe when the resistance of the electrolyte is low, for example, seawater. In some cases, surface moisture on structures exposed to an aggressive atmosphere can give rise to galvanic corrosion.

**Table 5** Comparison of measured corrosion potentials according to ASTM G-69

Alloy/material	Corrosion potential ( $V_{\text{SCE}}$ )
Al (99.999)	−0.75
Cr (99.9)	+0.23
Cu (99.999)	+0.00
Fe	−0.55
Mg	−1.64
Zn	−0.99
1100	−0.74
2014-T6	−0.69
2024-T3	−0.60
3003	−0.74
5052	−0.76
5154	−0.77
6061-T4	−0.71
6061-T6	−0.74
6063	−0.74
7039-T6	−0.84
7055-T77	−0.75
7075-T6	−0.74
7075-T7	−0.75
7079-T6	−0.78
8090-T7	−0.75



The corrosion potentials for a range of non-heat-treatable (wrought), heat-treatable (wrought), and cast aluminum alloys with some other standard corrosion potentials based on measurements made according to ASTM G 69 are shown in [Table 5](#).

In practice, copper, brasses and bronzes in marine conditions cause the most trouble. The danger from copper and its alloys is enhanced by the slight solubility of copper in many solutions and its subsequent redeposition on the aluminum to set up active local cells. This can occur even when the copper and aluminum are not originally in contact: for example, when water running over cuprous surfaces subsequently comes into contact with aluminum. Similarly, water washings from lead can cause pitting of aluminum. The controlling factor with lead and cuprous washings is the solvency of the water, so soft water is the most damaging in this respect. The successful utilization of these metals in close proximity to aluminum, for example, in plumbing and roofing, therefore requires careful design to avoid the transfer of a harmful solute to the aluminum.

Contact with steel, though less harmful, may accelerate attack on aluminum, but in some natural water and other special cases, aluminum can be protected at the expense of ferrous materials. Stainless steels may increase attack on aluminum, notably in seawater or marine atmosphere, but the high electrical resistance of the two surface oxide films minimizes bimetallic effects in less aggressive environments. Titanium appears to behave in a similar manner to steel. Aluminum–zinc alloys are used as sacrificial anodes for steel structures, usually with trace additions of tin, indium or mercury to enhance dissolution characteristics and to render the operating potential more electronegative. Aluminum–55% zinc alloys applied as hot dip coatings are also used extensively as a protective coating for steel for roofing and automotive applications.

Additions of elements such as zinc, tin, indium and mercury activate aluminum electrochemically and are 4 of the 10 elements that can enhance aluminum dissolution in aqueous electrolytes when contained as solute in the aluminum solid solution. The full list of these activators is antimony, zinc, lead, cadmium, thallium, bismuth, tin, indium, gallium and mercury in the order of increasingly negative potential. When these activators are mixed, the potential is controlled by the dominant activator which is the one with the highest melting point.<sup>49</sup> Aluminum alloys are similarly activated by additions of the activator elements to the electrolyte. These additions may be used to

turn aluminum into an anode plate for dry cells or metal–air batteries. The best addition for this purpose has been found to be tin together with an addition of magnesium. The magnesium addition is required to prevent a higher level of activation, and hydrogen production associated with the use of activators that can form hydrides.<sup>50</sup>

Aluminum in contact with galvanized steel may accelerate attack on the zinc coating and this is particularly noticeable when there is an unfavorable area ratio, as with galvanized fittings on aluminum sheets. In alkaline solutions, however, aluminum may be preferentially attacked. The copper-bearing aluminum alloys are nobler than most other aluminum alloys and this can accelerate galvanic attack on these, notably in seawater. Mercury and all the precious metals are harmful to aluminum.

Bimetallic corrosion of aluminum is a frequent cause of service-related corrosion failures, as the rate of attack can be rapid and corrosion can be severe and unexpected. In automotive applications, galvanic corrosion of aluminum is found in accelerated vehicle and component tests, particularly where aluminum is in direct electrical and electrolytic contact with a nobler metal. The solution is generally simple and involves providing sufficient protection using combinations of paints and barrier tapes to ensure that either electrical or electrolytic continuity is broken.

#### 3.08.5.1.4 Crevice corrosion

If a crevice is formed between two aluminum surfaces, or between the surfaces of aluminum and a nonmetallic material (i.e., a polymer) localized corrosion may occur within the crevice in the presence of electrolyte.

Crevice corrosion is due to the formation of a local cell, since at the mouth of the crevice (whether it is submerged or not) the concentration of oxygen is higher than that within the crevice. The difference in oxygen concentration leads to a difference in local corrosion potentials leading to corrosion in the ‘less noble’ area, which is the oxygen depleted zone. Concomitantly, the oxygen rich zone (i.e., the mouth) assumes the role of the cathode. This mode of attack is often termed ‘differential aeration cell corrosion’ or ‘concentration cell corrosion,’ which are terms that may be applied more generally to describe corrosion phenomena other than crevice corrosion.

Crevice corrosion can be a very problematic form of corrosion in an engineering sense, as the sites for crevice corrosion are often difficult to avoid in ‘real’ constructions which include welded lap joints,

rivetings, valve seats, or even deposits that arise in service.<sup>51</sup> Crevice geometry is the governing factor that determines the susceptibility, or conversely the resistance, to crevice corrosion. As a result, crevices are defined by their degree of tightness and their depth (distance from the mouth).

The general rules for the severity of crevice corrosion are presently under active research for several metal alloy systems, including aluminum.<sup>51–53</sup> Typically, in aluminum, tighter crevices lead to more rapid initiation of attack (owing to less electrolyte and a steeper oxygen concentration profile being achieved more rapidly). In addition, increasing crevice depth may also increase the likelihood of crevice initiation. Elimination of crevices should be done at the design stage where possible, and when unavoidable, they should be kept as open and shallow as possible or possibly even sealed with some type of appropriate non-crevice-forming sealant.

#### 3.08.5.1.5 Filiform corrosion

Filiform corrosion may be considered as a specific type of differential aeration cell corrosion that occurs from defects where the bare metal is exposed on painted or coated aluminum surfaces.<sup>2</sup> Filiform corrosion attack has a unique appearance that resembles fine filaments (worm-like threads) emanating from one or more defects in semirandom directions. Much like crevice corrosion, filiform attack is driven by a differential aeration cell with an anodic head growing under the coating and a cathodic tail where oxygen is reduced. The filiform filaments are filled with corrosion products that can include alumina gel and partially hydrated corrosion products. Typical filiform filament growth rates average about 100  $\mu\text{m}$  per day.<sup>2</sup> Filiform corrosion has been an issue for aluminum alloys in the aging aircraft sector. This is because aircraft are routinely painted for corrosion protection with polyurethanes and more complex coating systems.<sup>53–56</sup> Filiform corrosion, however, is not observed in cases where aluminum has been anodized or conversion-coated. More recently, filiform corrosion has also been observed in automobiles with aluminum closure sheet, in architectural sheet in Northern Europe and in packaging products.<sup>46,47</sup>

Recent work has shown that susceptibility to filiform corrosion in architectural and automotive applications in most if not all cases is due to the presence of a deformed layer on the surface of the sheet. For architectural applications, this is the residual surface layer from the high levels of surface shear induced by hot and cold rolling that becomes corrosion

susceptible as a result of the preferential precipitation of manganese-containing dispersoid particles. This type of deformed layer-induced filiform corrosion can be prevented by acid or alkaline etching to remove the deformed surface layer, by reducing the manganese level in the alloy or by heat treatment to precipitate the manganese from solid solution before rolling. In automotive applications, the susceptibility to filiform corrosion is induced by the grinding treatment that is used to rectify surface blemishes prior to painting. This type of corrosion is prevented by limiting the rectification grinding treatments in vehicle areas susceptible to stone chip damage in service or by providing additional protection to the painted surface to prevent stone chip damage.<sup>57</sup>

#### 3.08.5.2 Effects of Microstructure on Corrosion

The microstructure of aluminum alloys develop as a result of alloy composition, including impurities, casting practice and thermomechanical treatment. From the corrosion perspective, the dominant features of alloy microstructures are grain structure and the distribution of second phase (intermetallic) particles as constituent particles, dispersoids or precipitates. Such particles have electrochemical characteristics that differ from those of the surrounding alloy matrix, making the alloys susceptible to localized forms of galvanic attack, that has been termed microgalvanic corrosion.

Over the years, a number of studies have been carried out in order to assess the effect of specific intermetallic particles on the corrosion susceptibility of specific aluminum alloys.<sup>34,58–62</sup> In the mid-1990s, Buchheit collected the corrosion potential values for intermetallic phases common to aluminum alloy families mainly in chloride-containing solutions.<sup>18</sup> More recently, various groups have focused on the electrochemical properties of Fe-containing intermetallics<sup>63,64</sup> and Cu-containing intermetallics<sup>65–67</sup> and this has been expanded into a more comprehensive treatise covering a variety of common intermetallics present in commercial aluminum alloys (both wrought and cast).<sup>32</sup> A summary of the results of these studies is shown in Table 6.

The identification and structural characterization of intermetallic particles present in aluminum alloys have been quantified by particle extraction techniques combined with X-ray diffraction, by automated electron probe microanalysis and by scanning and transmission electron microscopy combined with X-ray microanalysis. For example, Buchheit *et al.*<sup>67</sup>

quantitatively determined the chemical composition of constituent particles in AA2024-T3 and were able to determine both their stoichiometry and relative surface area.

Intermetallic particles in aluminum alloys may be either anodic or cathodic relative to the matrix. As a

result, two main types of pit morphologies are typically observed.<sup>68,69</sup> The so-called circumferential pits appear as a ring of attack around a more or less intact particle or particle colony and the corrosion attack is mainly in the matrix phase. This type of morphology arises from localized galvanic attack of the more active matrix promoted by the more noble (cathodic) particle, as shown in **Figure 5**.

The second pit type of morphology is due to the selective dissolution of the constituent particle. Pits of this type are often deep and may have the remnants of the particle in them. This morphology has been interpreted as particle fallout, selective particle dissolution in the case of electrochemically active particles, or in the case of some Cu-bearing particles, particle dealloying and non-faradaic liberation of the Cu component.

Localized corrosion activity is, however, a complex phenomenon that is still under active research. Localized corrosion leads to local pH gradients, as recently studied by Scully *et al.*<sup>61</sup> Cathodic sites of enhanced oxygen reduction will naturally generate hydroxyl ions and promote local pH increases, which can then modify the subsequent rate and morphology of corrosion propagation. The precise morphology of particle-induced pitting is important for the emerging damage accumulation models. For these models to be predictive, it is necessary to develop a comprehensive,

**Table 6** Summary of corrosion potentials in NaCl at the given concentration for intermetallic particles common to Al alloys

Stoichiometry	Phase	Corrosion potential ( $mV_{SCE}$ )		
		0.01 M	0.1 M	0.6 M
Al <sub>3</sub> Fe	B	-493	-539	-566
Al <sub>2</sub> Cu	θ	-592	-665	-695
Al <sub>3</sub> Zr	β	-752	-776	-801
Al <sub>6</sub> Mn	-	-839	-779	-913
Al <sub>3</sub> Ti	β	-620	-603	-799
Al <sub>32</sub> Zn <sub>49</sub>	T'	-1009	-1004	-1063
Mg <sub>2</sub> Al <sub>3</sub>	β	-1124	-1013	-1162
MgZn <sub>2</sub>	M, η	-1001	-1029	-1095
Mg <sub>2</sub> Si	β	-1355	-1538	-1536
Al <sub>7</sub> Cu <sub>2</sub> Fe	-	-549	-551	-654
Mg(AlCu)	-	-898	-943	-936
Al <sub>2</sub> CuMg	S	-956	-883	-1061
Al <sub>20</sub> Cu <sub>2</sub> Mn <sub>3</sub>	-	-550	-565	-617
Al <sub>12</sub> Mn <sub>3</sub> Si	-	-890	-810	-858
Al-2%Cu	-	-813	-672	-744
Al-4%Cu	-	-750	-602	-642

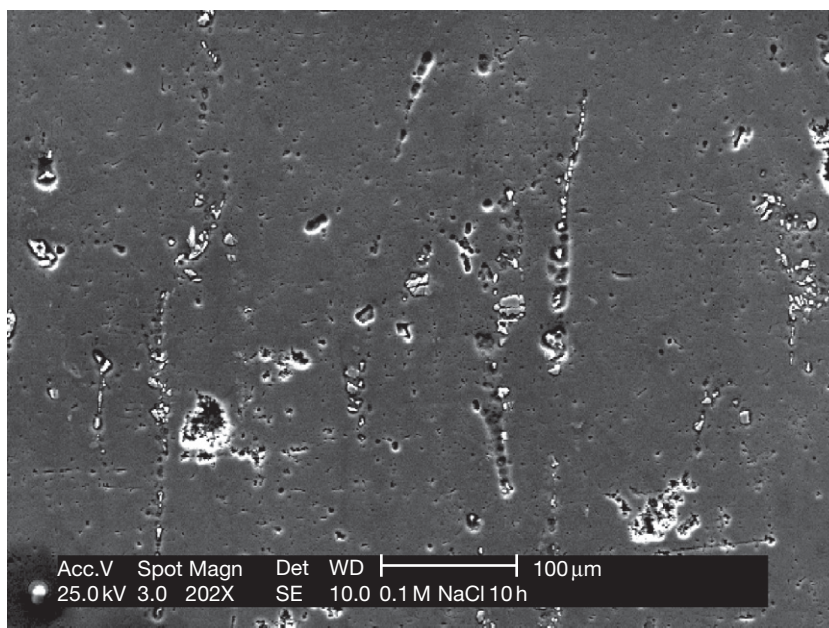


**Figure 5** Scanning electron micrograph of early stage corrosion development upon AA7075-T651 immersed in quiescent 0.1 M NaCl for 10 h. Courtesy of Mary K. Cavanaugh.

self-consistent account for this type of pitting. In cases where the electrochemical characteristics of constituent particles have been rigorously characterized, they have been found to have much more complicated behavior than that could be categorized by simple characterizations such as 'noble' or 'active.'

Generally, the constituent intermetallics of interest for a particular aluminum are those that appear in the greatest proportion either by size or by frequency. Variations in thermal treatments will have marked effects on the local chemistry (hence local electrochemistry) and hence the local corrosion resistance of the alloy. Similarly, the impact of mechanical working will influence the number of grain boundaries (hence grain boundary precipitates) and the distribution and size of constituent type particles (which tend to break up and align in the direction of working). Furthermore, directional solidification and segregation from casting will influence the resultant microstructure, all of which will impact the type and number of particles that form and their location within the material.

### 3.08.5.3 Intergranular Forms of Corrosion

IGC is a phenomenon of which the precise mechanisms have been under debate for almost half a century.<sup>70–76</sup> While in a global sense we can consider IGC as a special form of microstructurally influenced corrosion, in a generic sense, IGC can be summarized as a process whereby the grain boundary region of the alloy is anodic to the bulk or adjacent alloy microstructure.

Corrosion is often microgalvanic (or even nanogalvanic), with activity developing as a result of some heterogeneity in the grain boundary structure. In aluminum–copper alloys, precipitation of  $\text{Al}_2\text{Cu}$  particles at the grain boundaries leaves the adjacent solid solution anodic and more prone to corrosion.<sup>76</sup> With aluminum–magnesium alloys, the opposite situation occurs, since the precipitated  $\text{Mg}_2\text{Al}_3$  phase is less noble than the solid solution. However, serious intergranular attack in these two alloys may be avoided, provided correct manufacturing and heat treatment conditions are observed.

In the case of the aluminum–magnesium system, almost all commercial alloys are supersaturated as the magnesium solubility at ambient temperatures is less than 1 wt%. This effectively means that for alloys with more than 3 wt% magnesium elevated service temperatures can lead to grain boundary precipitation and sensitization of grain boundaries to corrosion as intercrystalline attack. The extent of this

sensitization may be approximately deduced from the continuity of  $\text{Mg}_2\text{Al}_3$  precipitation at the boundaries as determined by optical metallography of polished and etched cross sections. Apparently, continuous or nearly continuous etched boundaries correspond to high levels of sensitization to IGC.

Although the precipitation of  $\text{Mg}_2\text{Al}_3$  may appear continuous from examination of polished and etched sections in an optical microscope, examination of microstructures at higher resolution in a scanning or transmission electron microscope invariably reveals the precipitation to be discontinuous. Susceptibility of AA5xxx alloys is controlled in practice either by limiting the level of magnesium in the alloy to below 3 wt%, as such alloys can be sensitized to IGC only under extreme conditions or by the use of a deliberate stabilization treatment for a more magnesium-rich alloy. Stabilization of AA5xxx alloys with more than 3% magnesium is achieved by a deliberate heat treatment to promote intragranular precipitation of  $\text{Mg}_2\text{Al}_3$ . The temperature and time of this treatment depend on the precise magnesium level in the alloy. In production sometimes, this process is carried out by a specific formal heat treatment, and sometimes the rolling practice is modified so that the required level of intragranular precipitation is achieved during warm rolling. The level of sensitization to IGC of a fabricated sheet, plate or extrusion can be easily determined by measurement of the NAMLT value. This is a 24 h exposure to nitric acid and a measurement of weight loss due to IGC and loss of grains. A NAMLT value of more than  $30 \text{ g cm}^{-2}$  of surface is necessary before an alloy has become sensitized to IGC or cracking.

In the case of Al–Zn–Mg alloys, where the precipitated phase is the highly anodic  $\text{MgZn}_2$  phase, IGC can occur rather readily. However, susceptibility to IGC is strongly dependent on the heat-treated condition and its effect on grain boundary solute segregation and the morphology and composition of the grain boundary precipitate and the surrounding alloy matrix.<sup>77</sup> The most resistant heat treatments are based on the use of overaging to the T7 condition. More complex heat treatments that involve retrogression and reaging are also used to provide a high level of IGC resistance with a lower loss of strength.<sup>1,2</sup>

The images in **Figure 6** help rationalize the origins of IGC.

IGC differs from pitting corrosion. While IGC may initiate from a pit, propagation of IGC proceeds more rapidly than pitting corrosion, and while both may have a deleterious effect on corrosion fatigue,



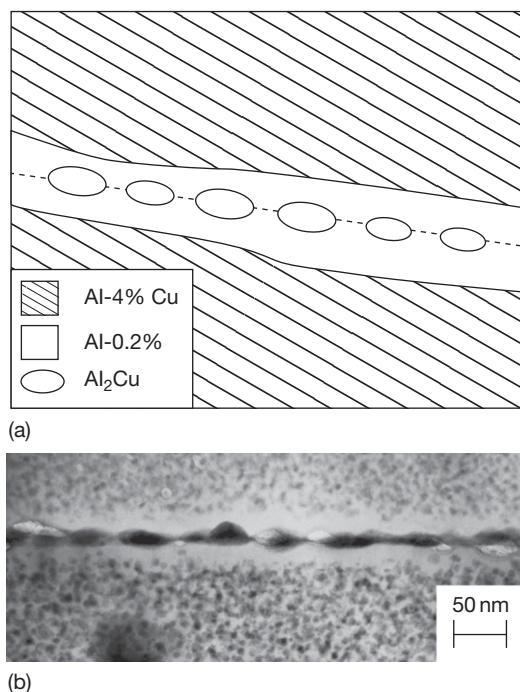


**Figure 6** (a) Schematic of hypothetical grain boundary in an Al-Cu alloy. This schematic indicates the different chemistry that exists in the grain interior, solute depleted zone (precipitate-free zone) and grain boundary precipitates – giving rise to electrochemical heterogeneity localized at the grain boundary region. (b) Conventional bright field TEM image of high-angle grain boundary in AA7022-T651, revealing grain boundary precipitates ( $\text{MgZn}_2$ ) and a distinguishable precipitate-free zone. Courtesy of Steven P. Knight.

IGC is more detrimental as the sharper corrosion front compared to a more rounded pit front is a higher stress concentrator that reduces the number of cycles to failure.

The test method used to evaluate susceptibility to IGC depends on the alloy type. For 5xxx series alloys, the NAMLT method (ASTM G 67) is adopted, whereas for 2xxx and 7xxx series alloys, ASTM G 110 is most common, employing testing in sodium chloride solutions containing hydrogen peroxide.

Exfoliation corrosion<sup>78</sup> of aluminum alloys is also frequently due to IGC. It generally occurs in cases where the alloy microstructure has been heavily deformed by rolling, extrusion or forging where the grain structure has been flattened and significantly extended in the direction of working. IGC attack from transverse edges and pits then runs along grain boundaries parallel to the alloy surface, and the resulting layers of corrosion attack are sometimes referred to as ‘layer corrosion.’ Exfoliation corrosion

is characterized by leafing off of layers of relatively uncorroded intragranular metal caused by the swelling of the corrosion product in the layers of IGC. Exfoliation corrosion is observed on aircraft components, for example, around riveted or bolted components or wing brackets. Testing for exfoliation corrosion is carried out by a number of ASTM tests, including the acidified salt spray test (ASTM G 85), the ASSET immersion test (ASTM G 66) and the EXCO immersion test (ASTM G 34).

### 3.08.5.4 Environmentally Assisted Cracking

Environmentally assisted cracking is a generic term that includes stress corrosion cracking (SCC), liquid metal embrittlement (LME), corrosion fatigue (CF) and hydrogen embrittlement (HE).

#### 3.08.5.4.1 Stress-corrosion cracking

Stress-corrosion cracking is a time-dependent, predominantly intergranular fracture mode in aluminum alloys that requires the simultaneous presence of a susceptible alloy, a sustained tensile stress and a corrosive environment.

The minimum tensile stress required to cause SCC in susceptible alloys is usually small and significantly less than the macroscopic yield stress.<sup>79,80</sup> Susceptibility to SCC has restricted the use of aluminum alloys, particularly the weldable 7xxx series alloys, to well-controlled and well-protected applications. There are several theories postulated for the mechanism of SCC. The main theories are either corrosion dominated where cracking is due to preferential corrosion along the grain boundaries by anodic dissolution (i.e., analogous to IGC) or hydrogen dominated where cracking along grain boundaries is enhanced by absorbed atomic hydrogen. The origin of this hydrogen is from IGC itself, and it is considered that the presence of absorbed hydrogen weakens grain boundaries.

While SCC is a very important corrosion-related phenomenon for aluminum alloys, in order to do justice to the topic, the reader is referred to specific monographs on the topic for a more detailed treatise of the SCC theories.<sup>81,82</sup> As previously mentioned, SCC in aluminum alloys is predominately intergranular, and this is seen in **Figure 7**.

Whether or not SCC develops will depend on both the duration and magnitude of the applied tensile stress. Fracture mechanics tools for the determination of crack growth rates are commonly used in the evaluation of SCC resistance for aluminum

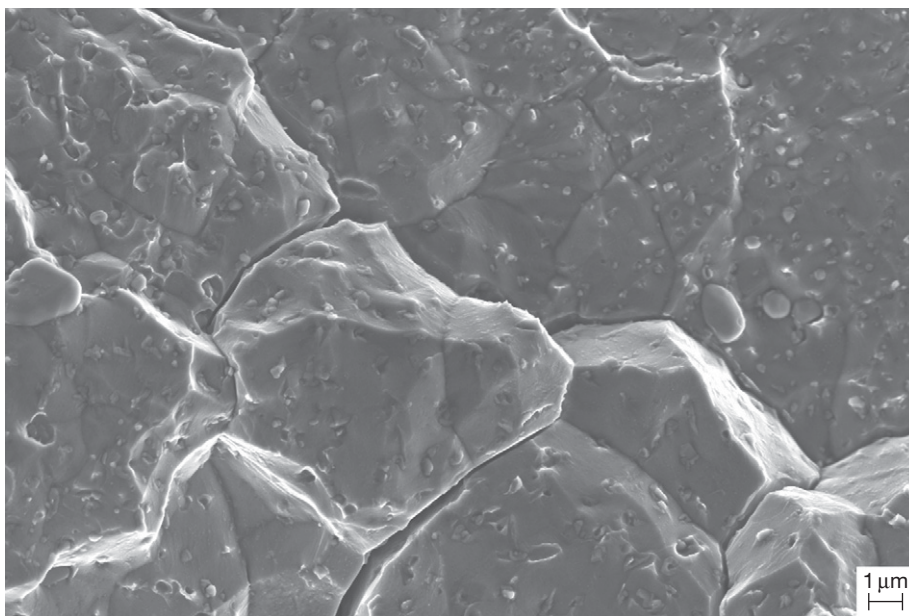


**Figure 7** High-resolution SEM micrograph of an SCC fracture surface taken from an AA7079-T651 DCB specimen exposed to 75% relative humidity (specimen was from the T/6 position from a 3-in.-thick rolled plate). Courtesy of Steven P. Knight.

alloys. Such tests suggest a minimum (threshold) stress intensity is required for cracks to develop. This empirical test is largely the basis on which susceptibility to SCC is compared between different alloys under the specific conditions of a particular test or environment.<sup>2</sup>

Residual stresses in aluminum products that may arise as a result of quenching following solution heat treatment and cold working may play an important role in SCC should the level of residual stress be significant. After solution heat treating and quenching of aluminum aerospace and defense plates, it is a common practice to ‘stress relieve’ the cold-rolled plate by controlled plastic deformation typically to 1.5% by tensile stretching using a plate stretcher. The stress-relieved temper is designated by the Tx5x designation following the temper designation: examples include AA7075-T651 or AA2124-T351.<sup>1</sup>

SCC of 7xxx alloys occurs in water and water vapor in addition to chloride-containing electrolytes. Most other susceptible alloys fail only because of exposure to environments containing chloride ions.

Grain structure has a major influence on SCC of thick section aluminum wrought products. Generally, these products, of which plate is the main example, are not recrystallized and have directional, highly anisotropic grain structures. This means that cracks can

grow only in directions parallel to the rolling direction along the flattened grain boundaries. This means that testing the plate in the short transverse direction determines the lowest SCC resistance, followed by the long transverse, and then the longitudinal direction where the intergranular crack path is the most tortuous. This is a very important consideration for the use of plates in the aerospace and defense sector, where thin sections need to be designed such that there is little or no stress in the short transverse direction, or that the most SCC-resistant tempers are used. For welded aluminum alloys in defense applications, exposed short transverse edges are protected by buttering with weld metal or by the use of flame-sprayed protective coatings of sacrificial alloys based on aluminum zinc alloys.

Generally speaking, the low-strength and relatively pure aluminum alloys are not susceptible to SCC. The alloys most prone to SCC are the 7xxx, 2xxx and the higher strength 5xxx series alloys. Most service failures involving SCC have occurred as a result of residual stresses acting in the short transverse direction.<sup>83</sup> The relative resistance of certain aluminum alloys to SCC is tabulated in [Table 7](#) (adapted from Davies).<sup>2</sup> As noted, progressively overaging beyond the peak (T6) condition generally improves SCC resistance (while lowering strength).



### 3.08.5.4.2 Liquid metal embrittlement

While LME is not commonly observed in the routine use of aluminum alloys, it can be defined as a mode of attack that results in a complete loss of alloy ductility of a solid metal, below the normal yield stress, as a result of the surface being wetted by a liquid metal. LME-induced fractures may be both intergranular and transgranular but are generally intergranular in aluminum alloys. A micrograph of intergranular fracture due to LME in mercury is shown in [Figure 8](#).

It is well known that gallium in contact with aluminum can result in the disintegration of aluminum (or aluminum alloy) into individual grains. In addition, mercury can also embrittle aluminum and

**Table 7** Qualitative SCC resistance of aluminum alloys (in the rolled plate form)

Alloy and temper	SCC resistance
2014-T3	Poor
2024-T3, T4	Poor
2024-T8	Good
2124-T851	Good
2219-T3, T4	Poor
2219-T6, T8	Excellent
6061-T6	Excellent
7049-T73	Good
7x75-T6	Poor
7x75-T73	Excellent
7x75-T76	Intermediate

Source: Davies, J. R., Ed. *Corrosion of Aluminium and Aluminium Alloys*; ASM International: Materials Park, OH, 1999.  
US Air Force Research Laboratory, Wright Patterson Air Force Base, OH.

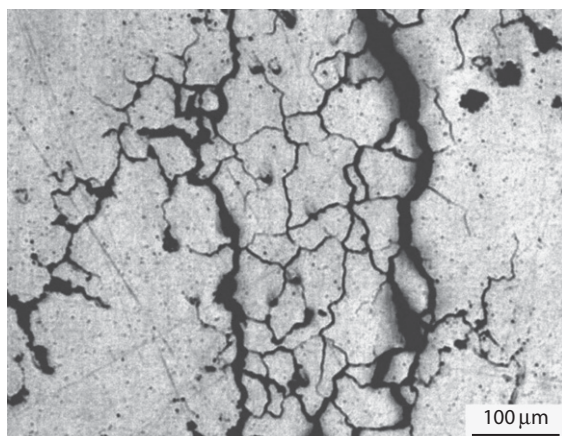


**Figure 8** Intergranular failure of an Al alloy pressure vessel in a natural-gas plant due to LME by Hg. Courtesy of Stan P. Lynch.

its alloys, though to a lesser extent. Aluminum has also been noted as being embrittled appreciably by tin–zinc and lead–tin alloys, indium and sodium.

### 3.08.5.4.3 Corrosion fatigue

Corrosion fatigue is the interaction of irreversible cyclic plastic deformation with localized corrosion (electrochemical) activity. The combination of each of the mechanisms, as well as the transition from initiation to propagation, is an issue under research currently and of considerable technological importance. However, corrosion pits have been observed to nucleate crack growth in structures subject to fatigue loading.<sup>84</sup>

Recent work has emphasized that in a fatigue study of aluminum alloy 7075-T6 all specimens in that study fractured from cracks associated with pitting.<sup>85</sup> Indeed, the numerous studies referenced with [Ref. 2](#) support the notion that pitting has a critical and detrimental effect on fatigue life.

Corrosion fatigue is an area that is of relevance to the aerospace sector and, indeed, a significant amount of work exists in the area, including several technical publications, dedicated monographs and handbooks.<sup>86,87</sup>

A fatigue crack can initiate from a corrosion pit or surface flaw when the flaw reaches a critical size at which the stress intensity factor reaches a threshold for fatigue cracking, or conversely when the rate of fatigue crack growth exceeds that of pit growth.<sup>88,89</sup>

A simple expression revealing the relationship between the critical pit size and the stress concentration can be given by:<sup>90</sup>

$$a_{p-c} = \pi \left( \frac{\Delta K_{th}}{2.2 K_t \Delta \sigma} \right)^2$$

where  $a_{p-c}$  is the pit–crack transition size and  $K_t$  is the stress concentration factor.

As noted in recent works,<sup>91</sup> aerostructures nominally experience corrosion between flights and fatigue loading during flight, suggesting the notion of ‘prior corrosion.’ This eludes to corrosion pits as precursors to fatigue cracking, a notion that can be seen elegantly in [Figure 9](#) as adapted from Harlow.<sup>92</sup>

Corrosion fatigue phenomena are diverse and specific to the environment and particular application at hand; however, certain variables that can influence corrosion fatigue crack growth propagation naturally include stress intensity, frequency of loading, stress ratio, alloy composition and microstructure (hence electrochemical potential) and the environment composition (and temperature).

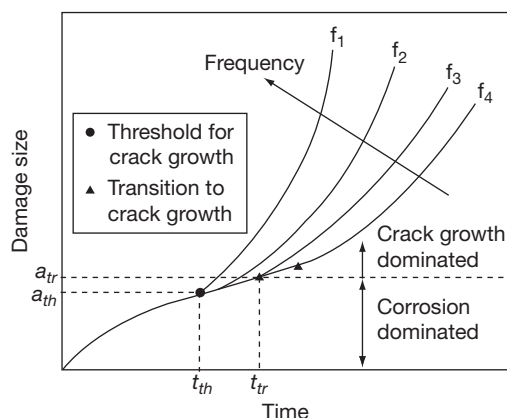


**Figure 9** Schematic diagram of the development of corrosion and corrosion fatigue crack growth, indicating the transition from one mode to another via some threshold pit depth.

#### 3.08.5.4.4 Hydrogen embrittlement

Hydrogen is capable of dissolving in aluminum and its alloys both in the molten state and during thermal treatments at temperatures close to the alloy melting temperature where the atmosphere may include water vapor or excessive hydrocarbons. Hydrogen from molten aluminum results in porosity in cast products but does not have an influence on corrosion performance or hydrogen embrittlement.

However, there is experimental evidence that hydrogen generated during corrosion can penetrate into the grain boundaries and lead to embrittlement, a factor in the initiation and propagation of cracking (in particular SCC).<sup>93–96</sup> The mechanism by which hydrogen causes the embrittlement is difficult to study and is posited to act by either facilitating enhanced dislocation emission ahead of an advancing crack or by bond weakening and enhanced plasticity ahead of an advancing crack. The strongest evidence for the involvement of hydrogen in the SCC of 5xxx and 7xxx aluminum alloys comes from the observations of recovery and hydrogen evolution, from the measurement of sufficiently rapid grain boundary hydrogen diffusion and the precise matching of intergranular fracture surfaces that are striated with crack arrest markings.

Understanding hydrogen embrittlement is important in unraveling the mechanism and modes of failure processes including SCC; however, this far it has not been a key factor that has restricted the usage of high-strength aluminum alloys. There are no specific and generally accepted tests for assessing hydrogen embrittlement susceptibility of aluminum alloys, as

embrittlement in hydrogen gas has not been observed irrespective of the test pressure.

### 3.08.5.5 Influence of Environment and Processing

#### 3.08.5.5.1 Influence of alloy processing

The bulk microstructure of aluminum alloys is determined by the complex interaction between the cast microstructure and any subsequent thermomechanical processing operation. The situation is then complicated by any forming, finishing or joining operations that may locally modify alloy microstructures. Any deformation or heat-treatment processes that modify the local or bulk microstructure of the alloy will have an attendant influence on alloy corrosion. This is mainly due to the modification of the size and distribution of intermetallic phases at the micron, sub-micron and nanoscale and the change in grain size and grain shape from the cast state.

Soldered or brazed joints will usually have lower corrosion resistance than the parent metal, but sound-welded joints with resistance to attack equal to that of the parent metal can be obtained in most alloys.<sup>97</sup> Many assemblies contain angles, pockets or crevices that attract moisture originating either from external sources or from condensation. The corrosion so caused could often be avoided by redesign of the assembly, the provision of drain holes if possible (of at least 5 mm diameter) and the avoidance of horizontal surfaces being among the more important features.

#### 3.08.5.5.2 Atmospheric corrosion

The aluminum alloys as a group present with a pleasant gray color outdoors, which may deepen to black in industrial atmospheres. Superficial pitting occurs initially but gradually ceases, being least marked on high-purity aluminum. With some alloys, including the copper-bearing alloys and the medium-strength Al–Zn–Mg alloys, additional protection, for example, painting, is desirable in the more aggressive atmospheres to avoid any risk of IGC.

Gases such as hydrogen sulfide and carbon dioxide do not typically increase the corrosivity of the atmosphere towards aluminum.<sup>98</sup> Service experience extends over 100 years and includes such well known examples as Eros, which is in an excellent condition although cast in a low purity (98%) aluminum, and the cupola of San Gioacchino (St. James), a church in Rome that was covered in 1897 with a sheet 1.25 mm thick and now shows attack to a depth of less than 0.13 mm. Twenty-year tests at selected marine,

industrial and rural sites in the United States<sup>99</sup> have shown that the greater part of the attack takes place in the first or second year and that thereafter the rate of attack maintains a low value.

The relatively high percentage strength losses are due to the extremely thin test specimens. After 20 years, the average measured depth of attack for an aluminum–copper alloy at a sea coast test site did not exceed 0.15 mm. The falling-off in the rate of pitting with time is in sharp contrast to the behavior of the older established structural metals that have a fairly uniform corrosion rate throughout their life, and indicates that the relative merit of aluminum increases with scheduled life.

Aggressive environments include marine conditions and particularly industrial atmospheres containing high concentrations of acid gases such as sulfur dioxide; rain washing is beneficial in both environments, while dampness and condensation alone can accentuate the rate of attack in the presence of chlorides and acidic sulfates. The relative severity of industrial, marine and rural conditions has been demonstrated by the results of 7-year tests in the United States and the United Kingdom,<sup>100</sup> and in this work the benefit from rain washing was especially manifest for the industrial sites in the United Kingdom. While the continual removal of atmospheric pollution by rain washing is beneficial, the removal of the protective corrosion product is obviously undesirable. The retention of the weathered surface is therefore usually preferred unless aesthetic considerations are of major importance, in which case abrasive or specialist chemical cleaning are effective.

Over many years Alcan used the CLIMAT test originally developed by Bell Laboratories<sup>101</sup> to “classify industrial and marine atmospheres.” The test that has been standardized<sup>102</sup> involves the exposure of wire-on-bolt samples to the atmosphere of interest for a period of 90 days. Following the exposure, the wire-on-bolt samples are disassembled, cleaned and weighed, and the CLIMAT indices are determined from the percentage weight losses. Generally, three wire-on-bolt samples are exposed with aluminum wires wound on to plastic, copper and mild steel bolts. The relative values of the weight loss indexes enable the corrosivity of different sites to be compared and ranked. By 1988, it was estimated that Alcan had carried out over 13 000 individual CLIMAT tests in locations all over the world, and summarized versions of the test results have been published.<sup>103–105</sup> More recently, the CLIMAT test has been used to monitor and compare the severity of outdoor exposure sites in

Europe and to assess the corrosivity of the automotive environment. The test has also begun to be used to compare the severity of different types of cabinet tests compared to outdoor exposure sites.

In urban areas, atmospheric fallout of carbon from partially burned fuel can cause severe localized pitting by galvanic action, although this is not commonly encountered. Indoors, aluminum retains its appearance well, and even after prolonged use may show no more than slight dulling, or on aluminum–magnesium alloys a slight bloom. This superficial deterioration can be accelerated by the presence of moist conditions and condensation which in extreme cases may lead to staining.

In order to enhance the durability of structural aluminum, anodizing provides a good level of protection. Anodized aluminum extrusions can survive even prolonged exposure in accelerated salt spray testing, indicating that the anodizing process where applicable is an industrially acceptable means of protection.

#### 3.08.5.5.3 *Natural waters*

Immersed aluminum and its alloys have excellent resistance to attack by distilled or pure condensate water, and are used in industry in condensing equipment and in containers for both distilled and deionized water, as well as in steam-heating systems.<sup>106</sup>

Of the commercial alloys, only those that contain copper as a major alloying element are likely to corrode in unpolluted seawater, but pollution of the seawater may cause localized pitting attack to occur on other aluminum alloys. The Al–Mg alloys containing up to about 4.5% magnesium offer particularly good combinations of corrosion resistance and strength. Fouling collects readily on aluminum alloys, as on other materials, and where it may be necessary to use paints containing cuprous oxide for antifouling purposes, the risk of bimetallic corrosion must be substantially inhibited by a chemical pretreatment. Nowadays, the use of chromate priming paint in addition to mercury-containing antifouling compositions is not considered as a best practice. The behavior of aluminum in natural fresh water and tap water may vary, as these types of water differ widely in their dissolved solid content. No corrosion occurs immediately on immersion of aluminum and its alloys in these kinds of near-neutral water, and aluminum gives satisfactory service with all types of tap water provided regular cleaning and drying takes place, as occurs with aluminum hollowware. In some types of water, black or brown stains, which are largely due to

optical effects associated with the oxide film on the metal surface, occur. Although somewhat unsightly, the film is quite harmless and can be removed by simple methods such as boiling of fruits (e.g., rhubarb). Alternatively, preliminary boiling with pure water provides some protection against the staining, but can hardly be considered justifiable in most of the cases.

The combination of carbonate, chloride and copper is more damaging than if they are present singly or if one of them is absent,<sup>107,108</sup> so that some kinds of supply water are naturally more aggressive than others. The role of copper is of particular relevance, since as little as 0.02 ppm can initiate pitting in hard waters,<sup>109</sup> although more is required in soft waters which are otherwise less aggressive. In this context, however, it must be remembered that soft waters are inherently more cupro-solvent than hard waters; consequently, the conjoint use of aluminum and copper fittings is rarely advisable irrespective of the necessity for avoiding galvanic interaction when the two metals are in direct contact. This latter point has traditionally stifled the usage of aluminum in more routine plumbing applications, although use of aluminum in such applications is likely to be considered again as the price of brass- and copper-based fittings and pipework increases relative to the price of aluminum.

Once pitting has started, it may continue in solutions which would themselves be incapable of initiating corrosion. In water of all types, the rate of increase in the depth of pitting falls off rapidly with time. Water movement (of the order of  $0.3 \text{ m s}^{-1}$  or more) will reduce pitting or prevent its initiation. A rise in temperature tends to lead to higher corrosion rates at existing pits, but even with the most aggressive hard waters, above about  $50^\circ\text{C}$  the oxide-forming mechanisms act to prevent the initiation of pitting as shown by the long and satisfactory service given by aluminum hollowware, which is assisted in some waters by scale formation.

Where aluminum is to be used in direct contact with cold, natural water with no possibility of regular cleaning, clad aluminum alloys are the preferred materials. Aluminum–zinc alloys are used for cladding that is anodic to the core alloy and corrosion is therefore restricted to the surface cladding, thereby obviating the risk of perforation. Cladding with super-purity aluminum is preferable where it is important to have the minimal degree of total corrosion, but in this case, the potential relationship with the core is more critical and in some circumstances the cladding can actually become cathodic. Sacrificial protection may also be obtained from sprayed

coatings of appropriate composition which can be applied to extrusions and castings as well as to sheets, rods, plates and tubes. In practice, unclad aluminum–manganese alloys have been used for piping soft water in the United Kingdom and, more widely, in the United States.

#### **3.08.5.5.4 Underground corrosion by soils**

This is largely related to the presence of moisture which can leach out soluble constituents from the soil. As it is the case with natural water, the nature of the corrosive environment is a more important factor than the alloy used, provided that copper-bearing alloys are avoided. At present, it is difficult to produce a satisfactory classification of soils with respect to their aggressive action on aluminum alloys. Made-up ground, particularly when it includes carbonaceous cinders, is usually extremely corrosive, while neutral clays are often the least corrosive. It is desirable that protection should be given to all aluminum materials buried in soils<sup>110</sup> except where there is previous experience of satisfactory service from aluminum in a given soil. Pipe wrappings based on bitumen (or the now legislated-against chromates) are effective, while for cable sheathing, a continuous plastic coating provides both electrical and corrosion protection. Cathodic protection has been utilized for pipelines<sup>111</sup> but is not widely practiced; close control is necessary since overprotection can result in alkali attack (from excessive accumulation of hydroxyl ions generated from the CP). Potentials in the region of  $-1.0 \text{ V}$  versus saturated  $\text{Cu}/\text{CuSO}_4$  are favored although some divergence of opinion exists in this respect.

#### **3.08.5.5.5 Corrosion in chemical environments**

Detailed information about the behavior of specific chemicals is given in several works of reference.<sup>112–115</sup>

##### **Acids**

Most acids are corrosive to aluminum-based materials. The oxidizing action of nitric acid at concentrations above about 80%, however, causes passivation of aluminum. Very dilute and concentrated sulfuric acid dissolves aluminum only slowly. This is seen graphically in **Figure 10**.

Boric acid also exerts little attack on aluminum, while a mixture of chromic and phosphoric acids can be used for the quantitative removal of corrosion products from aluminum without attacking the metal.

Organic acids usually have low rates of attack on aluminum, notable exceptions to this generalization

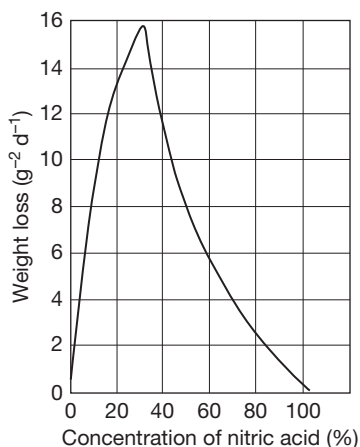


**Figure 10** Action of nitric acid of various concentrations on commercial-purity aluminum at 20 °C. Adapted from *Aluminium in the Chemical and Food Industries*; British Aluminium: London, 1959.

being formic acid, oxalic acid and some chloride-containing acids such as trichloroacetic acid. Glacial acetic acid (pH 3) has no significant corrosive effect on aluminum but the rate of attack increases rapidly with decreasing concentration or in the absence of the traces of water normally present. The rate of corrosion in an acid solution rises rapidly with temperature, often doubling or more with a 10 °C rise.

A summary of the effect of dilute inorganic acids on the corrosion of aluminum is seen in [Figure 11](#).

### Alkalies

Alkalies are generally corrosive to aluminum; caustic soda is in fact used for chemical milling of aluminum. Ninety-nine percent pure aluminum is, however, resistant to ammonium hydroxide, even at pH 13, while the action of more dilute caustic alkalis can be inhibited by the use of silicates. Mild alkalis such as sodium carbonate are moderately corrosive and are not recommended for washing aluminum hollowware. Synthetic detergents, in general, give satisfactory service in cleaning aluminum, but those containing uninhibited sodium carbonate may give some surface roughening. Inhibitors such as silicates can prevent attack by the more dilute solutions.

Alloys of aluminum with magnesium or magnesium and silicon are generally more resistant than other alloys to alkaline media. The corrosion rate in potassium and sodium hydroxide solutions decreases with increasing purity of the metal, but with ammonium hydroxide the reverse occurs.

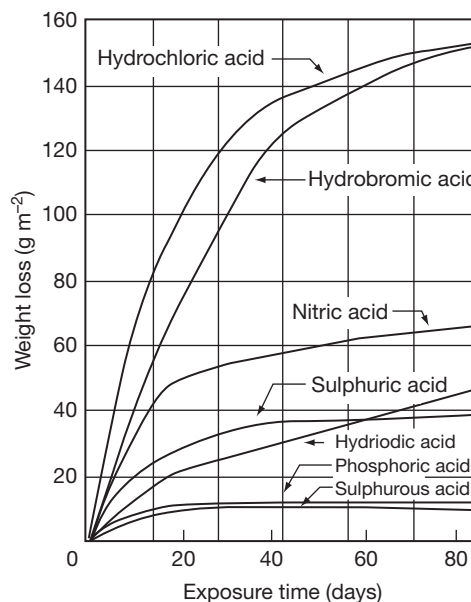


**Figure 11** Action of dilute (0.1 N) solutions of inorganic acids on commercial-purity aluminum at 25 °C. Adapted from *Aluminium in the Chemical and Food Industries*; British Aluminium: London, 1959.

### Inorganic salts

Most simple inorganic salt solutions cause virtually no attack on aluminum-based alloys unless they possess the qualities required for pitting corrosion, which have been considered previously, or hydrolyze in solution to give acid or alkaline reactions, as do, for example, aluminum, ferric and zinc chlorides. With salts of heavy metals, notably copper, silver and gold, the heavy metal deposits on the aluminum, where it subsequently causes serious bimetallic corrosion.

Some salts, notably chromates, dichromates, silicates, borates and cinnamates, have marked inhibitive power and are very effective in closed-circuit water systems. Care must be taken to ensure that a sufficient quantity of such anodic inhibitors as chromates is added, as otherwise attack, though occurring at fewer points, may be more severe at these points. Chromates and dichromates have little inhibitive power in strongly acidic solutions. It is emphasized that while chromates are mentioned herein for historical purpose, the toxicity of chromates has resulted in a dramatic decrease in their use in the past decade, and may result in a zero-usage policy on the global scene within the coming few years.

Aluminum is used in hydrogen peroxide processing and storage equipment partly because of its high corrosion resistance and also because it does not cause degradation of the peroxide.



**Organic compounds**

With many organic compounds, aluminum shows high corrosion resistance either in the presence or absence of water. The lower alcohols and phenols are corrosive when they are completely anhydrous, although this is rarely encountered in practice since repair of breaks in the natural protective oxide film on aluminum cannot take place in the absence of water. Amines generally cause little attack unless very alkaline.

Processing and storage equipment for many chemicals, including acetaldehyde, formaldehyde, nylon salt, methyl methacrylate, carbon tetrachloride, glycerol, triacetin, propionic acid, acetic acid and acetic anhydride, is manufactured from aluminum alloys, primarily because of their excellent corrosion resistance.

Aluminum has good resistance to petroleum products, and an Al–2Mg alloy is used for tank heating coils in crude-oil carriers. Caked-on deposits must be removed from the coils by hot seawater cleaning in order to maintain effective heat transfer and prevent corrosion. Aluminum is also used in the petroleum industry for sheathing for towers, heat exchangers, transport and storage tanks and scrubbers. Many industries use aluminum alloys for heat exchangers, clad alloys being used where pitting corrosion is liable to be initiated by one of the contacting materials. Heat exchangers in the gas industry have utilized duplex tubes, with aluminum on the water side and steel on the gas side in cases where aluminum is unsuitable owing to the presence of catechol which can attack it.

Aluminum does not become brittle at low temperatures and for this reason (and because of its corrosion resistance), it has been adopted for the carriage and storage of liquefied methane.

**3.08.5.5.6 High temperature corrosion****Dry atmospheres**

When exposed to high temperatures in dry atmospheres, aluminum is highly resistant to corrosion by most of the common gases, other than the halogens or their compounds.

**High temperature aqueous systems**

When aluminum corrodes at temperatures below 90 °C in aqueous systems, attack is usually by pitting. At temperatures between 90 and 250 °C (for the attainment of which considerable pressures are needed), uniform attack is the commonest form of aqueous corrosion. Above about 250 °C, uniform attack is merely the prelude to highly destructive

intergranular attack. The corrosion products from the uniform attack form a film which includes a barrier layer and a bulk film analogous to those formed during anodizing; it is the bulk film that controls the corrosion rate, which is not significantly affected by most common dissolved ions. The onset of intergranular attack occurs at about the same time as the crystallization of the amorphous barrier layer oxide. Kinetic studies indicate that over the temperature range from 100 to 363 °C the oxidation rate law is successively inverse logarithmic, parabolic and linear.<sup>116</sup>

The requirements of nuclear energy application fostered an interest in special alloys for service in high temperature aqueous environments, but their utilization has not been widespread. Encouraging results have been reported for alloys of 2Ni–0.5Fe and 1.2Ni–1.8Fe.<sup>117</sup>

Steam forms a protective white film at temperatures up to about 250 °C, but above this temperature steam can, under some conditions, react with aluminum progressively to form aluminum oxide and hydrogen. Sintered aluminum powder (SAP) has relatively good resistance to steam at 200 °C, but at about 300 °C an addition of 1% nickel to the SAP is needed to prevent rapid disintegration.

**Molten salts and metals**

Aluminum alloys resist the action of many molten salts which are nearly neutral in reaction. Molten sodium nitrate or mixtures of sodium nitrate and potassium nitrate are, even nowadays, most commonly used for salt-bath heat treatment of most aluminum alloys.

Molten metals generally attack aluminum alloys. Both zinc and tin form alloys by dissolution of aluminum, although the aluminum does not melt. Molten lead is inert to aluminum, and molten lead baths can be used for heating aluminum alloys.

**3.08.5.5.7 Aluminum in contact with other materials**

The aluminum alloys recommended for structural and architectural purposes (not including the high-strength alloys containing copper) have relatively good resistance to concretes, mortars, plasters and cement products. When freshly mixed, some of the materials release traces of alkaline products that are sufficient to stain aluminum (that is, to etch it). As soon as the mixture is set, the attack, however, is noted to cease, and even after many years' service attack on embedded aluminum is found – empirically – to be negligible.<sup>118</sup>



With cement and concrete under continuous wet conditions, there may, however, be surface attack. This decreases with time, and the strength of components is not significantly affected. Under embedment conditions, bituminous protection is advisable to avoid risk of cracking of the concrete due to stresses set up by the bulk of the voluminous aluminum corrosion product. Plasters are generally less aggressive than Portland cement. In damp environments, some corrosion of aluminum may arise in contact with the more open-grained building stones and brickwork, but the hard stones, such as granite, are inert. With building stone and brickwork, as with soils, it is the nature of the products that can be leached out which will determine whether aluminum corrodes. Unprotected aluminum, in the form of nails for example, can be satisfactorily used in contact with precast concrete blocks, which are usually noncorrosive to aluminum. Magnesium oxychloride compositions (used for flooring), on the other hand, stimulate corrosion of aluminum under moist conditions, as well as many insulation materials based on magnesium and calcium silicates.

Plastics generally do not react with aluminum and are widely used to provide insulation between other metals and aluminum. Rubber has no effect upon aluminum unless it is filled with carbon.

A few acid woods, such as oak, chestnut and Western red cedar, accelerate surface weathering of aluminum, but do not usually give rise to serious attack.<sup>119</sup> Timber preservatives containing soluble copper compounds should be avoided; creosote and zinc naphthenate are satisfactory preservatives for wood in contact with aluminum.

Common packaging materials are a potential source of aggressive substances,<sup>120,121</sup> and careful selection is recommended to avoid surface deterioration. Where paper is in contact with aluminum, the chloride content should be below 0.05%, sulfate content below 0.25% and copper content below 0.01%, and the pH of aqueous extracts in the range pH 5.5–7.5, in order to avoid corrosion in damp conditions. Papers and felts used in building applications should also conform to this specification as a minimum requirement and be of the highest quality, since metallic copper found in materials of inferior origin can result in severe local galvanic attack of aluminum. Tarpaulins are sometimes treated with copper-containing preservatives, and water leached from these has been found to cause corrosion of underlying aluminum sheets.

Fiberglass insulation produced from soda glass can cause pitting in conditions where leaching of

alkali occurs, for example, by condensation: the use of fiberglass produced from Pyrex glass is therefore preferred. Common putties of whiting/linseed oil composition do not attack aluminum; adhesion is obtained by allowing the metal surface to weather, or by applying an etch primer treatment to the metal. Both thermosetting adhesives (e.g., the phenolic types) and thermoplastic adhesives (such as paraffin and microcrystalline waxes or bitumen) are noncorrosive to aluminum. In general, adhesives applied to aluminum should not contain chlorides in excess of 0.05% (as NaCl) of the solid content, and should be free from copper- or mercury-containing fungicides. The presence in the adhesive of borax or sodium silicate is beneficial when one of the adhesive components is of an acidic character.

#### 3.08.5.5.8 Applied stress

Stress below the proof stress does not normally affect corrosion rates. Cyclic stresses in combination with a corrosive environment (corrosion fatigue) can produce failure at below the ordinary fatigue limit. Alloys susceptible to intergranular attack may corrode faster when stressed (see [Section 3.08.5.4](#)).

### 3.08.6 Corrosion Prevention Strategies

#### 3.08.6.1 Inhibitors

Corrosion of aluminum and aluminum alloys can be controlled by use of inhibitors added to aggressive aqueous environments. For the purpose of this discussion, an inhibitor is a chemical substance, soluble in water, that slows the corrosion cell process on aluminum. The range of inhibitors that slow corrosion of aluminum is large, and there are a number of useful ways to deliver chemical inhibitors when corrosion is a risk.

Soluble corrosion inhibitors act by slowing either the anodic reaction or the cathodic reaction or both. This gives rise to a useful scheme for classifying chemical inhibitors. Those that slow the anodic reaction are referred to as ‘anodic’ inhibitors, those that slow the cathodic reaction are ‘cathodic’ inhibitors, and those that slow both reactions are ‘mixed’ inhibitors.

For aluminum alloys, anodic inhibitors typically act to increase the pitting potential in electrochemical testing, or slow or suppress the onset of pitting in exposure testing. Even with good anodic inhibitors, pitting may occasionally occur if pre-existing defects

on the alloy surface are weak enough. Additionally, anodic inhibitors may have no effect on slowing the growth of existing pits.

Cathodic inhibitors are usually substances that slow the rate of the oxygen reduction reaction on aluminum alloy surfaces. By slowing down oxygen reduction, the companion aluminum oxidation reaction must also slow down. This results in an overall decrease in the corrosion cell kinetics, as well as a decrease in the free corrosion potential. For the best inhibitors, the decrease in the corrosion potential is usually to a value well below the alloy's pitting or repassivation potential. Cathodic inhibitors have the advantage of being able to improve corrosion resistance at very low concentrations. For example, chromate added at micromolar concentrations to an aerated dilute chloride solution is enough to significantly reduce the rate of oxygen reduction leading to significant corrosion protection.

Soluble corrosion inhibitors are usually ions in solution. Important inorganic anions that inhibit aluminum corrosion include chromate, phosphate, permanganate, nitrate, vanadate, molybdate, tungstate and silicate. Cations of strontium, cerium and the lanthanides as well as zinc are inorganic cationic inhibitors. Organic substances that are inhibitors of aluminum corrosion include phosphonates, sulfonates, benzoates, thiols, azoles, amines, fatty acids and natural compounds such as tannins. Among these, special attention must be given to chromates. Chromate is an exceptionally powerful inhibitor of oxygen reduction and an excellent inhibitor of aluminum corrosion. Chromates are used across all industries as aluminum corrosion inhibitors. However, their use is becoming increasingly restricted over concerns for work-place safety and environmental pollution because chromates are human carcinogens.

Inhibitors can be incorporated into coating systems in a variety of ways. Sparingly soluble inorganic compounds and ion exchange materials are used as corrosion inhibiting pigments in coating formulations. Inhibitor ions can be attached to reactive sites on coating resin polymers or directly applied to aluminum surfaces using an evaporable solvent.

### **3.08.6.2 Conversion Coatings**

Conversion coatings, which are frequently referred to as pretreatments or pretreatment coatings, are applied to aluminum and aluminum alloys to improve corrosion resistance or to improve adhesion of subsequently applied organic coatings and adhesives.

From a technological and processing perspective, conversion or pretreatment coating of aluminum is analogous in some ways to phosphating of steel and passivation of stainless steels. The conversion coating process involves contacting the surface to be coated with an aqueous solution containing surface activators and coating-forming ingredients. Contact times in commercial processes range from seconds on a continuous coil processing line to minutes for certain aerospace applications, and solution contact with the surface can be applied by immersion, spraying or rolling. Coating solutions are operated at or slightly above room temperature, and bath stability is maintained under careful control using guidelines from the pretreatment system supplier. Commercial conversion coating processes are well supported by suppliers, and methods for maintaining coating baths and ensuring coating quality are almost always provided.

Conversion coatings are not as protective as anodized coatings, and in most cases, conversion-coated surfaces are subsequently primed or painted. Conversion coatings are used for stand-alone corrosion protection when mild to moderate, occasionally condensing, atmospheric exposure conditions are expected, or for temporary corrosion protection.

Pretreatment of aluminum has relied extensively on chromate-based systems. There are two general classes of chromate conversion processes: the activated acidic formulations such as the chromium chromate processes that use a sodium fluoride–chromic acid chemistry, and alkaline oxide processes based on a sodium chromate–sodium hydroxide or carbonate chemistry. Activated acid processes have been the dominant process across many industry sectors for over 50 years. In finished form, conversion coatings produced are a light to deep yellow, continuous, and conformal across the surface with thicknesses ranging from 0.1 to 1.5  $\mu\text{m}$  depending on coating bath contact time. Freshly formed coatings are gelatinous and require at least a day to harden before handling. Such coatings can prevent pitting for several thousand hours of continuous salt spray exposure. Alkaline oxide coatings fell out of common use with the emergence of activated acidic formulations. Alkaline oxide coatings are thicker, less uniform and occasionally dusty. Coating baths produce much sludge and are difficult to maintain.

Chromate conversion coatings are noted for their ability to self-heal. Self-healing refers to the ability of the coating to resist corrosion from scribes or defects in the coating. This phenomenon is attributed to the release of labile hexavalent chromium in the coating

into an aggressive solution contacting the surface. Chromate ions are released by the coating, and can be transported to the site of damage to participate in repair of the film by reduction of the chromate to a chromic species that bond with the aluminum substrate and the existing conversion coating.

Chromate is a human carcinogen, and chromate-based coatings are banned in many countries. In response to this ban, trivalent chromium conversion coatings have been developed. These coatings provide useful levels of corrosion protection, but are not as protective as chromate conversion coatings. They are also observed to perform better on certain alloys than others.

There has been a major worldwide initiative to develop chrome-free pretreatment systems for aluminum alloys. Successful chrome-free pretreatment of aluminum alloys depends on a number of critical factors ranging from alloy and process route selection through to appropriate surface cleaning and how corrosion or durability testing is carried out to compare chrome-free and chrome-based systems.

Recent results have shown that the severity of corrosion of coil-coated aluminum architectural sheet is directly related to the manganese content of the alloy. This means that alloys such as AA3003, AA3103, AA3004, AA3104 and AA3005 are all potentially more susceptible to corrosion than alloys with a lower manganese level, such as AA3105, or AA5050, AA5251, AA5754, etc. It is quite difficult to make the low-manganese AA3xxx or AA5xxx alloys susceptible to corrosion under paint films.

Generally, the corrosion susceptibility of painted aluminum is due to an active surface layer.<sup>122–128</sup> This arises from the high level of surface shear induced during rolling, which transforms the near-surface microstructure. Deformed surfaces are characterized by an ultrafine grain size that can be stabilized by magnesium oxide pinning in magnesium-containing alloys.<sup>129</sup> A typical deformed surface layer on an AA3104 alloy after hot rolling is shown in **Figure 12**.

However, it is not the fine grain size that is responsible for the corrosion susceptibility of the surface layer. This susceptibility is promoted by the preferential precipitation of manganese-rich dispersoids during annealing treatments. Susceptibility is directly related to density of precipitated dispersoids, which, in turn, depends on the manganese solid solution level and the temperature and time of annealing. This is why manganese has such a strong influence on corrosion susceptibility.<sup>130–132</sup>

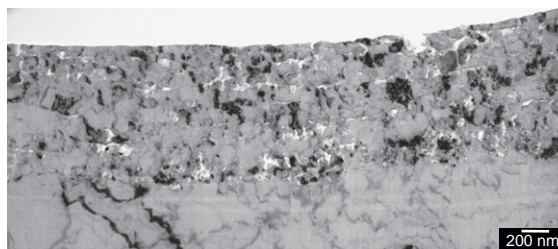


**Figure 12** TEM image of an ultramicroformed section of a hot-rolled AA3104 alloy after breakdown rolling showing the ultrafine grains pinned by magnesium oxide particles. Courtesy of Yanwen Liu.

Deformed surface layers on aluminum alloys are produced most readily by hot rolling, and generally the layer thickness of sheets and plates after hot rolling is of the order of a micrometer. The deformed layer thickness is progressively reduced by cold rolling, so alloys that have been extensively cold rolled have thinner deformed layers that can more readily be removed by conventional etch-cleaning operations. This means that resistance to corrosion can be improved by increasing the transfer gauge thickness so that after cold rolling the amount of surface to be removed at final gauge is 0.2  $\mu\text{m}$  or less.

Another route to reduce susceptibility is to homogenize rolling blocks before hot rolling to precipitate out the manganese from solid solution. This is equivalent to using a lower manganese-containing alloy. A further possibility is to eliminate hot rolling by using either roll-cast or thin belt-cast production routes. This is particularly effective when used in combination with appropriate alloy selection.

Cleaning is the most critical process step to provide alloy surfaces that can be successfully pretreated with a chrome-free pretreatment. Basically, the corrosion active surface layer must be removed using either an acidic or alkaline treatment. The amount of metal to be removed depends directly on the layer thickness, and this means that cleaning is facilitated where there has been significant cold rolling to reduce layer thickness. In low-magnesium alloys, the ultrafine grains are usually annealed out, but there is still a preferential precipitation of dispersoids compared to the bulk microstructure. The entire corrosion sensitive layer must be removed. For most AA5xxx alloys, the only requirement is to remove magnesium oxide from the surface, as this can reduce adhesion particularly for bonding applications. This means that cleaning of AA5xxx alloys is much more straightforward than cleaning AA3xxx alloys, particularly those with high manganese content.

Aluminum alloys generally become immune to underfilm corrosion following effective cleaning to remove any corrosion-susceptible layers. However, it is very important to avoid accumulation of copper on the alloy surface during the cleaning operation and/or to ensure that any copper enrichment is removed by a suitable desmutting treatment. Copper is readily enriched on the surface of aluminum alloys in both acid and alkaline etching solutions. Generally, it is important that surfaces are not overcleaned and that the cleaning operation is calibrated such that the end of cleaning coincides with active layer removal. Copper enrichment during cleaning can be measured on alloys where the nominal copper level in the alloy is less than 0.1%.

The principal function of pretreatment or conversion treatment after cleaning of architectural and automotive sheet alloys is to provide good adhesion. This can be achieved by using a treatment to enhance the natural oxide layer, such as anodizing or hydrothermal treatment in water or steam. Anodizing pretreatments have been used very effectively for many years, although they are not in widespread use as coil-line treatments. Coil-line treatments are based on fast anodizing in either sulfuric acid or phosphoric acid. These types of pretreatment have the advantages of speed, control and uniformity compared to most chemical conversion treatments. They are much underutilized as chrome-free pretreatments for aluminum alloys.

Fluorotitanic- and fluorozirconic-acid-based pretreatments are in widespread use as chrome-free alternatives. Such pretreatments are effective but are more difficult to monitor in production compared to traditional chrome-based systems. This is particularly an issue where polymeric additions are made to the formulation to improve performance. For such systems, good adhesion is achieved through good surface coverage of a uniform film of either zirconium and/or titanium oxide. However, adhesion is severely compromised if the film is too thick, and this can lead to coating failure in service that is unrelated to corrosion sensitivity.

Pretreatment systems based on the use of adhesion promoters such as silanes, phosphonates and polyacrylic acids have been extensively researched. These pretreatments can be very effective especially when applied as monolayers rather than thick films. They are probably most useful when used in combination with a thin anodizing treatment or similar treatment to increase barrier film thickness and to develop a micro-surface roughness to enhance adhesion.

There is very little systematic information on the field performance of painted aluminum products. Most useful information has come from the carefully monitored exposure of sets of test panels on exposure sites. The results of these studies correlate extremely well with filiform corrosion tests and with certain cyclic corrosion tests that are not overaccelerated by acidification or the use of additions of copper salts. There is generally poor correlation with the results of acidified salt spray tests either in terms of performance ranking or in the observed mode of corrosion. It is inappropriate to use corrosion tests designed for steel substrates for aluminum, as the conditions that promote corrosion are quite different. Corrosion of painted aluminum requires the presence of chloride and a high humidity. Corrosion of aluminum under conditions of total immersion or at humidity levels of more than 95% does not show the filamental corrosion mode that is seen on exposure sites or in service.<sup>133</sup>

Corrosion on painted panels occurs most readily on marine sites when panels are exposed vertically, facing north, and the panel is protected by an overhang so that accumulated chloride is not removed by rain. Such conditions are not reproduced in most cabinet-based corrosion tests.

Although the surface of wrought aluminum products can be made corrosion resistant by cleaning to remove active surface layers, it is important that such surfaces are not damaged by subsequent high shear processes such as grinding or machining operations. This is particularly important for aluminum automotive alloys, such as AA6111 and AA6016, which are used in external closure panel applications. Mechanical grinding during processes such as rectification can readily produce an ultrafine-grain-sized surface layer as shown in [Figure 13](#). This layer is not removed during cleaning and phosphating as part of the body-in-white finishing operation. The layer can become more corrosion-active than the underlying bulk metal following paint baking. This is due to preferential precipitation of the aging precipitate in the surface layers compared to the bulk microstructure.

The situation of aluminum external closure panels is similar to using galvanized steel, in that rectification must be minimized in the areas that are susceptible to stone chip damage. For galvanized steel, surface grinding removes the protective zinc layer, whereas for aluminum, a corrosion active layer is created by the grinding and finishing operation. However, corrosion in service can occur only if the paint film is damaged to expose the bare metal.

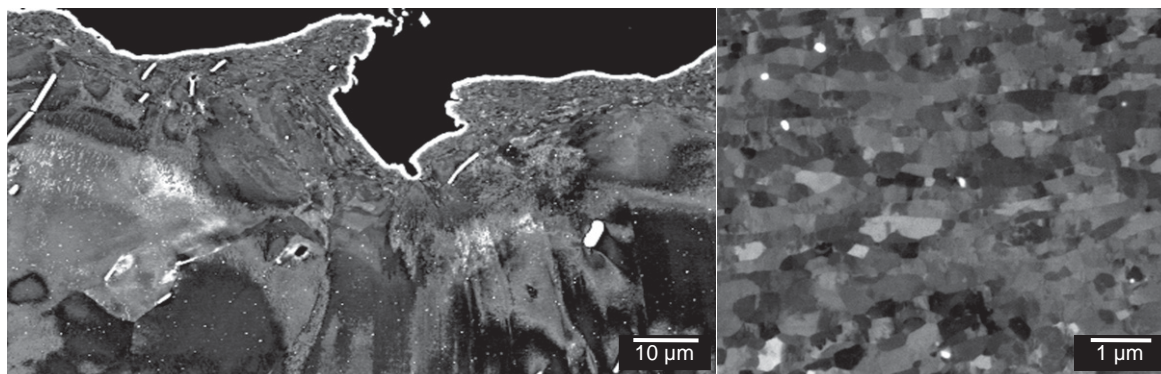


**Figure 13** Scanning electron micrographs of the surface of an AA6016 alloy after rectification by grinding. The higher magnification image shows the ultrafine grain size of the deformed layer. Courtesy of George Thompson.

Although as-cast surfaces have not been found to be susceptible to filiform corrosion, it is possible to develop active layers on castings by grinding or machining and subsequent thermal treatment. This is probably the main influence on the corrosion of cast aluminum wheels. The surface of extruded aluminum has been studied extensively, although ultrafine grain microstructures have not been reported. However, transformed surface microstructures, particularly those with coarse grain structures, have been well documented. Resistance to filiform corrosion is also significantly improved by deep surface etching. Cutting, grinding and machining operations, following cleaning and pretreatment either before or especially after painting, are probably highly significant in promoting corrosion in service.

Secondary metal generally contains higher levels of impurities compared to primary metal. This can lead to higher levels of elements such as iron, silicon and copper and also contamination by elements such as lead, bismuth, zinc and tin. Aluminum alloys made from secondary metal can be highly resistant to corrosion using chrome-free pretreatments, provided that alloy compositions are optimized. In addition, continuous casting production routes should be chosen to minimize active layer development by eliminating hot rolling. Effective cleaning is critical, and surface enrichment of elements such as copper, lead, bismuth, zinc and tin must be avoided or such enriched layers must be removed. After such cleaning, continuously cast alloys made from secondary metal can be shown to be highly resistant to corrosion using simple chrome-free pretreatments that promote good adhesion.

### 3.08.6.3 Anodizing

Aluminum and aluminum alloys can be anodized to enhance corrosion protection and improve adhesion of subsequently applied organic coatings, and improve a range of other surface properties. For this reason, it is a very widely used process. Anodized coatings are formed electrochemically in an aqueous solution that results in an aluminum oxide surface film (see [Figure 14](#)). Anodized coatings on aluminum alloys are on the order of 2–50 µm in thickness. Aluminum anodization is usually carried out in an acidic bath that contains ingredients which promote formation of an adherent oxide film. Anodization is most commonly carried out in chromic acid solutions and sulfuric acid solutions. To improve corrosion protection, anodized coatings can be sealed in a second step in the process.

Chromic acid anodization is carried out in solutions that are at or slightly above room temperature. Coating times range from 30 to 60 min, and result in a 2–5-µm-thick gray-colored coating. This process does not consume much of the base metal, making it suitable for applications where precise part dimensions must be maintained. Among various anodization processes, the chromic acid process causes the smallest fatigue strength debit. The chromic acid process is the process of choice for porous surfaces and complex shapes where rinsing of the anolyte may be difficult. The residual anolyte is rich in chromate, which is passivating and protective for aluminum alloys.

Sulfuric acid anodization is carried out at ambient temperatures in  $\text{H}_2\text{SO}_4$  solutions. Coating times range from 30 to 60 min. The process yields coatings that are 5–10 µm in thickness. These coatings possess



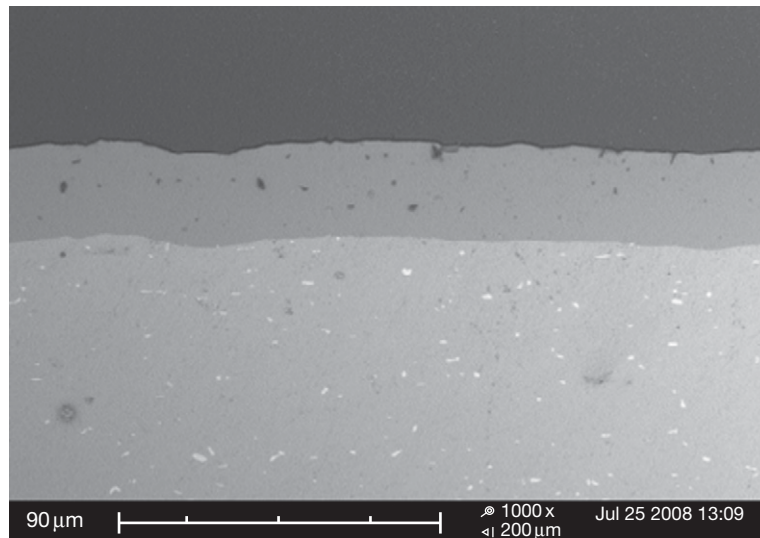


**Figure 14** Backscattered SEM image revealing the anodized coating upon a sectioned piece of extruded AA6060. Courtesy of Brendan Stafford.

good corrosion resistance, which can be improved by sealing the coating through subsequent immersion in the sodium chromate solution. Coatings produced by this process can be dyed to take on a range of colors.

Changes to the sulfuric acid anodization process can be made to produce anodized layers with high hardness. The so-called hard coat anodization processes are carried out in solutions chilled to near freezing (about 1 °C). Coating times range from 20 to 120 min. These coatings can be as much as 50 μm in thickness. Coatings are very hard and suitable for applications where wear resistance is needed. The intrinsic porosity of the coatings makes them well suited for adhesive bonding applications. Corrosion resistance of these coatings is excellent and can be further improved by sealing in boiling water or nickel-based sealing solutions.

The protectiveness of anodized coatings is commonly tested using accelerated exposure testing. When anodized coatings fail, the substrate is subjected to localized corrosion, which occurs mainly in the form of pitting. Electrochemical methods are appropriate for characterizing the corrosion resistance of anodized coatings. In particular, electrochemical impedance methods are useful for determining the effectiveness of sealing treatments as well as the overall protectiveness of the anodized layer.

#### 3.08.6.4 Organic Coatings

The natural passivity of aluminum is often insufficient to protect against corrosion in many common

service environments. Alloying aluminum further degrades protection conferred by passivity, and alloys are almost always coated when the application requires prolonged exposure to outdoor environments.<sup>134</sup> A broad range of organic coatings can be applied to aluminum alloys. For many engineering applications, and certainly the most demanding ones, a coating system consisting of multiple coating layers is used. Each layer contributes to the functionality of the overall coating system. Functions imparted may include adhesion to the underlying alloy, flexibility, impermeability, chemical resistance, abrasion resistance, electromagnetic signature control and, of course, corrosion protection.

There are two general strategies for imparting corrosion protection by organic coatings: barrier protection and active corrosion protection. The barrier protection strategy is based on the simple concept of preventing contact of the underlying aluminum substrate with the environment. The vast majority of protective coatings systems used today are based on this concept. While simple and straightforward, this concept is remarkably difficult to implement and sustain in practice in engineered systems. There are two reasons for this. First, coatings contain defects that are formed during the application process. These defects can serve as corrosion initiation sites when a coated component is placed in service. In modern coating operations, great effort is made to apply coatings on scrupulously clean surfaces under very well controlled conditions. This minimizes defect



formation and leads to higher quality, longer lasting coating systems. Second, coatings will sustain damage in service. Damage can arise from mechanical action at the surface that scrapes or scratches. Damage can also arise by exposure to aggressive chemical agents. This can degrade the organic component of the coating destroying the barrier properties. Exposure to thermal energy and ultraviolet radiation can also degrade the integrity of the organic component of the coating.

In the active corrosion protection strategy, barrier properties of the coating are not necessarily important. Coatings that protect by this mechanism contain a releasable corrosion inhibitor. As moisture from the environment penetrates the coating, the corrosion inhibitor is released. In well-designed coatings, any moisture that reaches the coating-metal interface will have enough inhibitor in it so that the natural passivity of the underlying alloy is preserved. This protection strategy is not as widely employed as barrier protection, but strontium chromate-pigmented organic primer coatings used widely in aerospace applications depend critically on this protection mechanism.

Corrosion of aluminum under organic coatings generally occurs as filiform corrosion, although blistering is observed on samples exposed to accelerated corrosion tests or where coating adhesion is entirely inadequate. In thick and opaque coating systems, corrosion under the coating may be difficult to detect until corrosion has progressed to a significant extent.

Corrosion of organically coated metals is typically characterized using outdoor exposure tests or simulated service testing. Overaccelerated corrosion tests should be avoided, as their relative ranking of corrosion susceptibility is usually erroneous and the observed mode of corrosion is not that found in service. The extent of corrosion damage accumulation is normally characterized visually. Early stages of coating degradation and undercoating substrate corrosion can be characterized by electrochemical methods including electrochemical noise and electrochemical impedance spectroscopy. The application of impedance spectroscopy for characterizing degradation of organically coated metal surfaces has been thoroughly reported in the scientific literature.

### 3.08.7 Applications of Aluminum Alloys

In recent years, the aluminum industry has become a global industry, just as the business interests of its

customers have become global. The world economy has integrated, and major industry consolidation has occurred. Today, Alcoa is the only independent major producer in North America, as Alcan has become part of Rio Tinto. Alcoa, Alcan (as Rio Tinto Alcan) and Rusal are the three largest aluminum companies.

Total global aluminum consumption (as measured as aluminum semis, castings and forgings) grows each year by about 5% on average. Rolled products are the largest product form at 35% (16.4 mt) followed by castings at 26% (12 mt), extrusions at 24% (11.3 mt), wire and cable at 10% (4.8 mt), and forgings and other forms at 5% (2.5 mt). In 2005, the geographical market was split among North America (24%), Western Europe (22%), China (22%), Asia (21%), Latin America (5%), Africa and Oceania (2%), Eastern Europe (2%) and CIS (2%).<sup>3</sup>

Presently, there are three main markets for the aluminum industry: packaging (cans and foil), transportation (automotive and light trucks) and building and construction. About 25 years ago, building and construction was the largest aluminum market, packaging was second and transportation was third. Then, 10 years ago, transportation became the largest market, followed by packaging and then construction. However, more recently in the emerging economies, building and construction has been the greatest source of growth and this is now the second largest market for aluminum after transportation. In terms of global consumption of the 43 Mt of aluminum produced in 2005, transportation was 27%, building and construction 20% and containers and packaging 16%. These main uses were followed by electrical (10%), machinery and equipment (8%), consumer durables (7%) and other uses (12%). In 2007 ~14.5 Mt of aluminum was used in transportation, 13 Mt in building and construction, and 4.5 Mt in beverage cans.<sup>3</sup>

In packaging, aluminum cans are in competition with plastic containers and, to a much lesser degree, glass, although this varies considerably from country to country. In North America, steel is not much of a factor, whereas in Europe it still is, and in certain markets like the United Kingdom, there is direct and sustained competition between aluminum and steel cans. Presently, the recycling rate of aluminum used beverage cans (UBCs) varies significantly from country to country and from state to state in the United States. Critical factors are legislation and the use of financial incentives (e.g., returnable deposits on cans) to promote collection and return. Corrosion concerns in packaging applications are not a major factor.

There is a direct relationship between the weight of a car and its fuel consumption, and although there are global legislative initiatives to reduce fuel consumption and carbon emissions, the weight of cars has in fact progressively increased since the 1970s. This is shown by the increase in weight of the VW Golf from the Mark 1 (750 kg) to the Mark 2 (770 kg), the Mark 3 (960 kg), the Mark 4 (1060 kg) and the Mark 5 (1200 kg). The main factors that have led to this weight increase are safety, both for crash and pedestrians, comfort and build quality. The weight of a car is mainly from its structure or 'body-in-white' (BIW) (34%), its drive train (25%) and its engine (17%), and the increase in BIW weight has been the most significant contributor to vehicle's weight increase. There is strong competition between high-strength steel, aluminum, magnesium high pressure die castings and plastics for BIW construction. The average aluminum content of European cars increased from 32 kg in 1978 to 120 kg in 2002 and is predicted to be 160 kg by 2010. This total use of 160 kg is split between BIW hang-on panels (50 kg), suspension and wheels (50 kg), engine and drive train (43 kg) and interior components (17 kg). Audi has led the way in making aluminum-intensive cars exemplified by the A2 1.2TDi introduced in 1999, which was the first mass-producible car with a fuel consumption of 3 l of fuel per 100 km traveled. The emissions from this car were only 80 g of CO<sub>2</sub> per kilometer. In North America, it is estimated that an average car or a light truck has about 160 kg of aluminum and the major applications are in hang-on panels (bonnets and deck lids) and engines, with aluminum engines representing about 90% of current production. The potential for increased use of aluminum in cars is enormous, particularly as number of vehicles on the road is predicted to increase from 800 million to more than 1450 million in 2030 with nearly all of this increase in developing economies like India and China.

Forming and joining issues associated with the use of aluminum in cars have been solved, and the only reported corrosion issues have been galvanic corrosion where protection systems were not in place and filiform corrosion associated with rectification by grinding prior to painting. The main barrier remains the relatively high cost of aluminum automotive sheet as compared to its steel equivalent. Just as aluminum beverage cans compete favorably with steel cans through their high level of recyclability, it is the same for aluminum in transportation applications. Aluminum automotives become both cost and energy competitive with steel if the aluminum sheet

is recycled back to the same sheet and this is maintained over repeated construction and end-of-vehicle life cycles. Aluminum-intensive vehicles also offer increased vehicle life. Durability and corrosion issues associated with the use of recycled sheet will need to be addressed.

Although aluminum has enjoyed a dominant position as the material of choice for airframe construction, it has become increasingly threatened by composite materials. However, the overall tonnage of aluminum aircraft plate required by major manufacturers such as Airbus and Boeing is predicted to increase. For example, Airbus have estimated that their plate demand, which was 20.2 kt in 2002 and was 88 kt in 2007, will be more than 100 kt from 2010 onwards. Airbus consider the latest generation of aluminum lithium alloys such as 2050 with less than 2 wt% lithium to be competitive with composites for fuselage applications, and that their corrosion resistance is such that they can be used without cladding for fuselage skin applications. They are also considering an increased use of weldable alloys (AlMgSc) and using joining procedures like laser welding and friction stir welding to decrease the buy-to-fly ratio. The competition between aluminum plate and sheet and composites for airframe construction has stimulated the development of 2xxx, 7xxx (7449 and 7140) and 6xxx (6056) alloys with improved mechanical performance in terms of both strength and toughness. The development of improved alloys and the use of new joining techniques have stimulated significant corrosion-testing activity.<sup>135,136</sup>

## Acknowledgements

The authors gratefully acknowledge Ms. Julie Fraser (Monash University) for the careful production of diagrams, figures and tables.

## References

1. Polmear, I. J. *Light Alloys: Metallurgy of the Light Metals*, 3rd ed.; Arnold: London, 1995.
2. Davies, J. R. Ed. *Corrosion of Aluminium and Aluminium Alloys*; ASM International: Materials Park, OH, 1999.
3. <http://www.world-aluminium.org> (accessed December 2008).
4. Grjotheim, K.; Kvande, H. Eds. *Introduction to Aluminium Electrolysis*, 2nd ed.; Aluminium-Verlag: Dusseldorf, 1993.
5. Grjotheim, K.; Welch, B. J. *Aluminium Smelting Technology*, 2nd ed.; Aluminium-Verlag: Dusseldorf, 1988.

6. Hetherington, L. E.; Brown, T. J.; Benham, A. J.; Lusty, P. A. J.; Idoine, N. E. *World Mineral Production 2001–05*; British Geological Survey: Keyworth, Nottingham, 2007.
7. <http://www.infomine.com/commodities/aluminium.asp> (accessed September 2008).
8. <http://www.lme.co.uk/aluminium.asp> (accessed October 2008).
9. [http://www.indexmundi.com/en/commodities/minerals/bauxite\\_and\\_alumina](http://www.indexmundi.com/en/commodities/minerals/bauxite_and_alumina) (accessed December 2008).
10. Schlesinger, M. *Aluminium Recycling*; CRC Press: Boca Raton, FL, 2006.
11. Das, S. K. *Light Metal Age*, June 2006, 26.
12. Van Horn, K. R. Ed. *Aluminium*, ASM International: Materials Park, OH, 1967; Vol. 1.
13. Hatch, J. E. *Aluminium: Properties and Physical Metallurgy*; ASM International: Materials Park, OH, 1984; pp 424.
14. Raviprasad, K.; Hutchinson, C. R.; Sakurai, T.; Ringer, S. P. *Acta Materialia* **2003**, 51(17), 5037–5050.
15. Kovarik, L.; Miller, M. K.; Court, S. A.; Mills, M. J. *Acta Materialia* **2006**, 54(7), 1731–1740.
16. Winkelman, G. B.; Raviprasad, K.; Muddle, B. C. *Acta Materialia* **2007**, 55(9), 3213–3228.
17. Szklarska-Smialowska, Z. *Pitting and Crevice Corrosion*; NACE International: Houston, 2005; pp 650.
18. Buchheit, R. G. *J. Electrochem. Soc.* **1995**, 142, 3994.
19. [www.aluminium.org](http://www.aluminium.org) (The Aluminium Association) (accessed October 2008).
20. Polmear, I. J. 100 years of Aluminium Alloys, ICAA 2004 Queensland Australia.
21. Sprowls, D. O. *Aluminum* **1978**, 54(3), 214–217.
22. Rao, K. T. V.; Ritchie, R. O. *Int. Mater. Rev.* **1992**, 37(4), 153–185.
23. *The Properties of Aluminium and its Alloys*, 6th ed.; The Aluminium Federation: Birmingham, 1968.
24. Allen, C. M.; O'Reilly, K. A. Q.; Cantor, B.; Evans, P. V. *Prog. Mater. Sci.* **1998**, 43, 89–170.
25. Alexander, D. T. L.; Greer, A. L. *Acta Mater.* **2002**, 50, 2571.
26. Fishkis, M.; Lin, J. C. *Wear* **1997**, 206, 156.
27. Evans, D. G.; Jeffrey, P. W. In *NACE 3, Localised Corrosion*, 1971, pp 614, 622.
28. Godard, H. P. *J. Electrochem. Soc.* **1967**, 114, 354.
29. Aylmore, D. W.; Gregg, S. J.; Jepson, W. B. *J. Inst. Met.* **1959–1960**, 88, 205.
30. Bartlett, R. W. *J. Electrochem. Soc.* **1964**, 111, 903.
31. Pourbaix, Atlas of Electrochemical Equilibria
32. Frankel, G. S. *J. Electrochem. Soc.* **1998**, 145(6), 2186–2198.
33. Kaesche, H. *Werkstoffe Korros.* **1963**, 14, 557.
34. Birbilis, N.; Buchheit, R. G. *J. Electrochem. Soc.* **2005**, 152, B140–B151.
35. Wall, F. D. *J. Electrochem. Soc.* **2003**, 150(4), B146–B157.
36. Szklarska-Smialowska, Z. *Corros. Sci.* **1999**, 41, 1743.
37. Chao, C. Y.; Lin, L. F.; Macdonald, D. D. *J. Electrochem. Soc.* **1981**, 128(6), 1187–1194.
38. Lin, L. F.; Chao, C. Y. *J. Electrochem. Soc.* **1981**, 128(6), 1194–1198.
39. Chao, C. Y.; Lin, L. F.; Macdonald, D. D. *J. Electrochem. Soc.* **1982**, 129(9), 1874–1879.
40. Macdonald, D. D. *J. Electrochem. Soc.* **1992**, 139(12), 3434–3449.
41. Macdonald, D. D. *J. Electrochem. Soc.* **2006**, 153(7), B213–B224.
42. Pride, S. T.; Scully, J. R.; Hudson, J. L. *J. Electrochem. Soc.* **1994**, 141(11), 3028–3040.
43. Kim, Y.; Buchheit, R. G. *Electrochimica Acta* **2007**, 52, 2437–2446.
44. Cavanaugh, M. K. ECS Transactions, 2008.
45. Trueman, A. R. *Corros. Sci.* **2005**, 47(9), 2240–2256.
46. Zhou, X.; Thompson, G. E.; Scamans, G. M. *Corros. Sci.* **2003**, 45(8), 1767–1777.
47. Scamans, G. M.; Afseth, A.; Thompson, G. E.; Zhou, X. Ultra-fine Grain Sized Mechanically Alloyed Surface Layers on Aluminium Alloys, 8th International Conference on Aluminium Alloys, Aluminium Alloys their Physical and Mechanical Properties 2002, pp 1461–1466.
48. Zhao, Z.; Frankel, G. S. *Corros. Sci.* **2007**, 49(7), 3089–3111.
49. Hunter, J. A.; Scamans, G. M.; Sykes, J. M. *J. Power Sources* **1990**, 13, 193–211.
50. Scamans, G. M.; Hunter, J. A.; Holroyd, N. J. H. *A Surface Engineering Approach to the Corrosion of Aluminum, Aluminium Alloys Contemporary Research and Applications*; Academic Press, 1989.
51. Burleigh, T. D. *Corrosion* **1991**, 47(2), 89–98.
52. Roberge, P. R. *Handbook of Corrosion Engineering*; McGraw-Hill Professional, 2000.
53. Chen, Z. Y.; Cui, F.; Kelly, R. G. *J. Electrochem. Soc.* **2008**, 155(7), C360–C368.
54. Schneider, O.; Ilievbare, G. O.; Kelly, R. G.; Scully, J. R. *J. Electrochem. Soc.* **2007**, 154(8), C397–C410.
55. McMurray, H. N.; Coleman, A. J.; Williams, G.; Afseth, A.; Scamans, G. M. *J. Electrochem. Soc.* **2007**, 154(7), C339–C348.
56. Coleman, A. J. *Electrochem. Solid State Lett.* **2007**, 10(5), C35–C38.
57. Scamans, G. M. International Conference on Environmental-friendly Pretreatment of Aluminium and Other Metals, ICEPAM 2004, Oslo, June 2004.
58. Zamin, M. *Corrosion* **1981**, 37, 627.
59. Mazurkiewicz, B.; Piotrowski, A. *Corros. Sci.* **1983**, 23, 697.
60. Seri, O. *Corros. Sci.* **1994**, 36, 1789.
61. Scully, J. R.; Knight, T. O.; Buchheit, R. G.; Peebles, D. E. *Corros. Sci.* **1993**, 35, 185.
62. Nişancioğlu, K. *J. Electrochem. Soc.* **1990**, 137, 69.
63. Pryor, M. J.; Fister, J. C. *J. Electrochem. Soc.* **1984**, 131, 1230.
64. Afseth, A.; Nordlien, J. H.; Scamans, G. M.; Nişancioğlu, K. *Corros. Sci.* **2002**, 44, 2543.
65. Searles, J. L.; Gouma, P. I.; Buchheit, R. G. *Met. Mat. Trans. A* **2001**, 32A, 2859.
66. Birbilis, N.; Buchheit, R. G. *J. Electrochem. Soc.* **2008**, 155(3), C117.
67. Birbilis, N.; Cavanaugh, M. K.; Buchheit, R. G. *Corros. Sci.* **2006**.
68. Park, J. O. *J. Electrochem. Soc.* **1999**, 146(2), 517.
69. Ramgopal, T.; Gouma, P. I.; Frankel, G. S. *Corrosion* **2002**, 58, 687.
70. Ilievbare, G. O. *J. Electrochem. Soc.* **2002**, 148(5), 687.
71. Liao, C. M.; Olive, J. M.; Gao, M.; Wei, R. P. *Corrosion* **1998**, 54, 451.
72. Buchheit, R. G.; Montes, L. P.; Martinez, M. A.; Michael, J.; Hlava, P. F. *J. Electrochem. Soc.* **1999**, 146, 4424.
73. Büchler, M.; Watari, T.; Smyrl, W. H. *Corros. Sci.* **2000**, 42, 1661.
74. Schneider, O.; Ilievbare, G. O.; Kelly, R. G.; Scully, J. R. *J. Electrochem. Soc.* **2004**, 151, 465.
75. Ilievbare, G. O.; Schneider, O.; Kelly, R. G.; Scully, J. R. *J. Electrochem. Soc.* **2004**, 151, 453.
76. Hunter, M. S.; Frank, G. R.; Robinson, D. L. 2nd International Congress on Metallic Corrosion 1963, 66.
77. Knight, S. P. A review of Heat Treatments, Australasian Corrosion Association 2003.
78. Zhao, X. Y.; Frankel, G. S. *Corros. Sci.* **2007**, 49(2), 920–938.

79. Scamans, G. M.; Holroyd, N. J. H.; Tuck, C. D. S. *Corros. Sci.* **1987**, 27(4), 329–347.
80. Scamans, G. M.; Holroyd, N. J. H. *J. Electrochem. Soc.* **1986**, 133(8), C308–C308.
81. Sedriks, A. J. *Stress Corrosion Cracking: Test Methods*; National Association of Corrosion Engineers: Houston, Texas, 1990.
82. Jones, R. H. Ed. *Stress-Corrosion Cracking*; ASM International: Materials Park, Ohio, 1992.
83. Summerson, T. J.; Sprowls, D. O. In *Corrosion Behavior of Aluminium Alloys*, International Conference of the Hall-Heroult Process, Conference Proceedings of Engineering Materials Advisory Services Ltd. (University of Virginia), 1986; Vol. 3, pp. 1576–1662.
84. van der Walde, K.; Brockenbrough, J. R.; Craig, B. A.; Hillberry, B. M. *Int. J. Fatigue*; **2005**, 27.
85. Jones, K.; Hoepfner, D. W. *Corros. Sci.*; **2005**, 47.
86. Suresh, S. *Fatigue of Materials*; Cambridge University Press: Cambridge; New York, 1998.
87. Hertzberg, R. W. *Deformation and Fracture Mechanics of Engineering Materials 1989–01*; John Wiley & Sons Inc.
88. Hoepfner, D. W. Model for Prediction of Fatigue Lives based upon a Pitting Corrosion Fatigue Process. In *Fatigue Mechanisms*; Fong, J. T., Ed.; Proceedings of ASMT-NBS-NSF Symposium, Kansas City, Mo. ASTM STP675, ASTM, 1979, pp 841.
89. Kondo, Y. *Corrosion* **1989**, 45, 7.
90. Wang, Y. Q.; Wang, X. S.; Liang, F.; Zeng, Y. P. *Acta Mech. Sin.*; **2003**, 19(3).
91. Sankaran, K. K.; Perez, R.; Jata, K. V. *Mater. Sci. Eng.* **2001**, A297, 223.
92. Harlow, D. G.; Wei, R. P. *Key Eng. Mater.* **2001**, 200, 119.
93. Thakur, A.; Raman, R.; Malhotra, S. N. *Mater. Chem. Phys.* **2007**, 101(2–3), 441–447.
94. Osaki, S.; Kondo, H.; Kinoshita, K. *Mater. Trans.* **2006**, 47(4), 1127–1134.
95. Kannan, M. B.; Raja, V. S. *J. Mater. Sci.* **2006**, 41(17), 5495–5499.
96. Lynch, S. P. Paper from Hydrogen Conference, Wyoming 2008.
97. Blewett, R. V.; Skerry, E. W. *Metallurgia* **1965**, 71, 73.
98. Aziz, P. M.; Godard, H. P. *Corrosion* **1959**, 15, 529t.
99. Symposium on Atmospheric Corrosion of Non-Ferrous Metals. American Society for Testing Materials Special Technical Publication No. 175, 1956.
100. Metal Corrosion in the Atmosphere, American Society for Testing Materials, Special Technical Publication No. 435 (1968). Papers by McGeary, et al., p. 141 and Ailor, J. R., p. 285
101. Compton, K. G.; Mendizza, A.; Bradley, W. W. *Corrosion* **1955**, 11, 383t.
102. Standard Practice for Conducting Wire-on-Bolt Test for Galvanic Corrosion. ASTM G116, 1993.
103. Doyle, D. P.; Godard, H. P. *Nature* **1963**, 200, 1167–1168.
104. Doyle, D. P.; Wright, T. E. In *Atmospheric Corrosion*; Ailor, W. H., Ed.; 1982, pp. 227–243.
105. King, G. A. *Assessment of the Corrosivity of the Atmospheres in an Intensive Piggery using CLIMAT Testers*; Corrosion Australasia, 1987; p 14.
106. Symposium on Corrosion by High Purity Water. *Corrosion* **1957**, 13, 151t.
107. Davies, D. E. *J. Appl. Chem.* **1959**, 9, 651.
108. Rowe, L. C.; Walker, M. S. *Corrosion* **1961**, 17, 353t.
109. Porter, F. C.; Hadden, S. E. *J. Appl. Chem.* **1953**, 3, 385.
110. Raine, P. A. *Chem. Ind. (Rev.)* **1956**, 1102, 1196.
111. Sprowls, D. O.; Carlisle, M. E. *Corrosion* **1961**, 17, 125t.
112. *Aluminium in the Chemical and Food Industries*; British Aluminium: London, 1959.
113. *Aluminium with Food and Chemicals*; Alcan Booth Industries, 1966.
114. Ritter, F. *Korrosionstabellen Metallischer Werkstoffe*; Springer-Verlag: Vienna, 1944.
115. *Aluminium with Food and Chemicals*; The Aluminium Association: New York, 1967.
116. Troutner, V. H. *Corrosion* **1959**, 15, 9t.
117. Dillon, R. L. *Corrosion* **1959**, 15, 13t.
118. Dillon, R. L.; Bowen, H. C. *Corrosion* **1962**, 18, 406t.
119. Porter, F. C. *Metallurgia* **1962**, 65, 65.
120. Farmer, R. H.; Porter, F. C. *Metallurgia* **1963**, 68, 161.
121. Scott, D. J.; Skerrey, E. W. *Br. Corros. J.* **1970**, 5, 239.
122. Leth-Olsen, H. Ph.D. thesis, NTNU, 1996.
123. Afseth, A. Ph.D. thesis, NTNU, 1999.
124. Scamans, G. M.; Amor, M. P.; Ellard, B. R.; Hunter, J. A. *Aluminium Surf. Sci. Technol.* **1997**, p 229, Antwerp.
125. Nisancioglu, K.; Nordlien, J. H.; Afseth, A.; Scamans, G. M. *Significance of Thermomechanical Processing in Determining Corrosion Behavior and Surface Quality of Aluminum Alloys* 7th International Conference on Aluminium Alloys their Physical and Mechanical Properties 2000, pp 111–125.
126. Scamans, G. M.; Afseth, A.; Thompson, G. E.; Zhou, X. Thermomechanical Processing Induced Corrosion of Aluminium Alloy Sheet, Aluminium Surface Science and Technology 2, Manchester, p9, May 2000.
127. Scamans, G. M.; Afseth, A.; Thompson, G. E.; Zhou, X. In *Control of the Filiform Corrosion Susceptibility of Aluminium Alloy Sheet DFO/DGO Conference on Light Alloys*, Munster, 2001.
128. Scamans, G. M.; Afseth, A.; Thompson, G. E.; Zhou, X. In *Ultra-fine Grain Sized Mechanically Alloyed Surface Layers on Aluminium Alloys*, 8th International Conference on Aluminium Alloys, Aluminium Alloys their Physical and Mechanical Properties 2002, pp 1461–1466.
129. Scamans, G. M.; Afseth, A.; Thompson, G. E.; Zhou, X. *Surface Microstructure and Corrosion Resistance of Aluminium-Manganese Alloy*, Aluminium Surface Science and Technology 3, Bonn, May 2003.
130. Zhou, X.; Thompson, G. E.; Scamans, G. M. *Corros. Sci.* **2003**, 45(8), 1767–1777.
131. Ambat, R.; Davenport, A. J.; Afseth, A.; Scamans, G. M. *J. Electrochem. Soc.* **2004**, 151(2), B53–B58.
132. Scamans, G. M.; Afseth, A.; Thompson, G. E.; Zhou, X. In *Control of the Cosmetic Corrosion of Aluminium Automotive Alloys*, DFO/DGO Conference on Light Alloy Applications, Dusseldorf, March 2004.
133. Scamans, G. M.; Afseth, A.; Remmers, U.; van der Meer, W.; Hallenstvet, M.; schauzier, F. E.; Katgerman, L.; Nisancioglu, K. In *Analysis of the Exposure Site and Accelerated Test Results of the FICARP (Filiform Corrosion of Aluminium Rolled Products) Project*, ECCA Conference, Budapest, May 2001.
134. Vilche, J. R.; Bucharsky, E. C.; Giudice, C. A. *Corros. Sci.* **2002**, 44, 1287.
135. Leque, P.; Lassince, P.; Warner, T.; Raynard, G. M. *Int. J. Aircraft Eng.* **2001**, 73(2), 147–159.
136. Dif, R.; Bes, B.; Warner, T.; Leque, P.; Ribes, H.; Lassince, P. Recent developments in AA6056 aluminum alloy used for aerospace. Presented at the ASM International Conference, 2001.

## 3.09 Corrosion of Magnesium and its Alloys

**K. U. Kainer, P. Bala Srinivasan, C. Blawert, and W. Dietzel**

Institute of Materials Research, GKSS-Forschungszentrum Geesthacht GmbH, D 21502 Geesthacht, Germany

© 2010 Elsevier B.V. All rights reserved.

<b>3.09.1</b>	<b>Introduction</b>	2011
<b>3.09.2</b>	<b>Historical Perspective</b>	2012
<b>3.09.3</b>	<b>Production and Types of Magnesium Alloys</b>	2013
3.09.3.1	Extraction of Magnesium	2013
3.09.3.2	Physical Metallurgy	2013
3.09.3.3	Alloying Elements	2013
3.09.3.4	Alloy Designations	2015
3.09.3.5	Cast Magnesium Alloys	2017
3.09.3.6	Wrought Magnesium Alloys	2019
3.09.3.7	Magnesium Matrix Composites	2020
<b>3.09.4</b>	<b>Processing of Magnesium Alloys</b>	2021
3.09.4.1	Casting Technologies	2021
3.09.4.2	Forming Technologies	2022
3.09.4.3	Joining Technologies	2023
<b>3.09.5</b>	<b>Corrosion of Magnesium Alloys</b>	2025
3.09.5.1	Forms and Mechanisms	2026
3.09.5.2	Environmentally Assisted Damages	2028
3.09.5.3	Influence of Alloying and Processes	2031
<b>3.09.6</b>	<b>Corrosion Prevention Strategies</b>	2033
3.09.6.1	Coatings	2033
3.09.6.1.1	Chemical conversion coatings	2033
3.09.6.1.2	Electrochemical conversion coatings	2034
3.09.6.1.3	Electro and electroless deposition	2034
3.09.6.1.4	Physical techniques	2036
3.09.6.1.5	Organic coatings	2036
3.09.6.2	Choice of Coating Systems and Design Aspects	2037
<b>3.09.7</b>	<b>Applications of Magnesium Alloys</b>	2037
<b>References</b>		2039

### Abbreviations

**CVD** Chemical vapor deposition  
**EB** Electron beam  
**EMF** Electromotive force  
**IG** Intergranular  
**LB** Laser beam  
**MAO** Micro arc oxidation  
**PEO** Plasma electrolytic oxidation  
**PVD** Physical vapor deposition  
**RA (%)** Percentage reduction in area  
**RE** Rare earth  
**SCC** Stress corrosion cracking  
**SCE** Saturated calomel electrode  
**SSRT test** Slow strain rate tensile test  
**TG** Transgranular

**UTS** Ultimate tensile strength  
**YS** Yield strength

### 3.09.1 Introduction

There is great concern about the weight of vehicles in automobile, aircraft, and aerospace sectors. With the existing rules of the European Commission on CO<sub>2</sub> emissions, the drive for a reduction in the consumption of petrol in automobiles has already be felt. A reduction in the weight of vehicles would not only help in minimizing the fuel consumption and emission levels, but would to a great extent enable the automobile and aviation industries to improve passenger and

transportation capacities, with considerable control of overall operating costs. However, it becomes essential to ensure passenger comfort and safety when such a design is being looked into.

So far, high-strength low alloy steels have a major share in the automobile industry, whereas age-hardenable aluminum alloys and titanium alloys mainly cater to the needs of the aircraft and aerospace sectors. With recent developments, the requirement for lightweight constructions can be fulfilled to a great extent by magnesium and its alloys. Magnesium alloys with lower density levels are destined to be the construction material in the aforementioned industries in the days to come. Weight savings of up to 30% could be achieved with magnesium in place of aluminum. This could be further improved by appropriate processing and additional treatments on magnesium alloys, and thus these alloys have a great potential for many applications. However, there are issues concerning magnesium alloys which limit their usage for critical applications. The low ductility of some of the alloys is one problem, and the galvanic corrosion of magnesium in contact with other materials is another big concern.

In this chapter, a comprehensive discussion of the magnesium alloys with reference to their classification, processing, and treatments is provided. The different forms of corrosion and their associated mechanisms, including environmentally assisted cracking, are dealt with in detail. The methods of combating the problems of corrosion, including some of the recent

advancements and modern practices, are addressed in the last segment.

### 3.09.2 Historical Perspective

Magnesium was discovered in 1808 by Sir Humphrey Davy. He achieved this by the electrolytic splitting of magnesium oxide with the help of cinnabar. Subsequently, different production techniques were developed by Bussy (1828), Liebig (1830), Bunsen (1852), and Sainte-Claire Deville (1857) for the extraction of magnesium, and magnesium found its first application as an explosive. Magnesium was first produced industrially by a procedure developed by Grätzel in an aluminum and magnesium factory at Hemelingen in 1886.

In 1896, magnesium was produced by molten bath electrolysis in a chemical factory in Bitterfeld. Until 1900, the global production of magnesium amounted to only 10 tons. With further developments, the production of magnesium rose steadily from 2200 tons in 1932 to about 14 000 tons in 1935. By 1939, this amount was doubled to 30 000 tons and then reached a level of 235 000 tons in 1943 owing to the high demand for materials during the Second World War. At the end of the war, the production dropped down again to 17 000 tons, with a more or less continuous increase in usage up to the present day. As of 2002, the global production of magnesium was around 400 000 tons per annum (Figure 1) and by the end of 2006 the

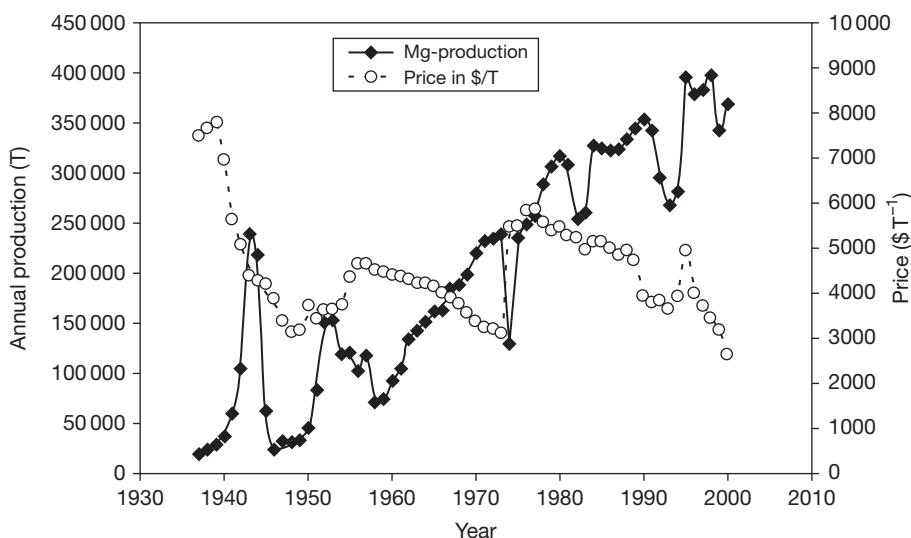


**Figure 1** Trend of global production and price of primary magnesium since 1937.

Source: <http://minerals.usgs.gov/minerals/pubs/commodity/magnesium/>



production of primary magnesium has been reported to be approximately 726 000 tons per annum.

In the early days, magnesium alloys were accepted by the automotive and aviation industry<sup>1</sup> owing to their light weight and good strength-to-weight ratio. In the 1970s, magnesium alloys were virtually forced out of applications owing to their poor corrosion properties and the low prices of aluminum alloys. Nevertheless, with increase in crude oil prices and stringent requirements from the environmental viewpoint (CO<sub>2</sub> emissions), magnesium alloys are experiencing a renaissance; they are popular today with wide acceptance and a large number of applications since the early 1990s.

### 3.09.3 Production and Types of Magnesium Alloys

#### 3.09.3.1 Extraction of Magnesium

Magnesium is the eighth most abundantly available element in the earth's crust, but it is not available in the metallic form in nature. **Table 1** shows the essential source materials for magnesium. Magnesite appears to be the most important ore of magnesium and is reported to be available with 95% purity level.

More than 50% of the global production of primary magnesium today is in China, and production installations are also found in Russia, Canada, Israel, Brazil, and the United States. In Australia and Congo, some projects are underway. Owing to the very high operating costs in the EU, no primary magnesium is produced there nowadays. Compared to the early stages in the 1980s when primary magnesium was sold at \$3.6 per kg, the prices touched \$2 per kg in 2002. However, with the increase in demand for raw materials, the prices have gone up again. Today, the primary production of magnesium is dominated by two routes *viz.*, (a) molten salt bath electrolysis and (b) thermal reduction. In the first case, MgCl<sub>2</sub> obtained from the source products is reduced by the electrolytic process, and in the thermal reduction process either dolomite or magnesite is processed with the addition of ferrosilicon. The composition and characteristics of some of the typical electrolytes used in the electrolytic reduction of MgCl<sub>2</sub> are provided in **Table 2**.

#### 3.09.3.2 Physical Metallurgy

While magnesium was primarily used as an alloying element for aluminum alloys in the early days, it took

**Table 1** Raw materials and their magnesium content<sup>2,6,7</sup>

		Percentage
Carnallite	MgCl <sub>2</sub> · KCl · 6H <sub>2</sub> O	8.7
Magnesite	MgCO <sub>3</sub>	28.8
Dolomite	MgCO <sub>3</sub> · CaCO <sub>3</sub>	13.2
Brucite	Mg(OH) <sub>2</sub>	41.7
Kieserite	MgSO <sub>4</sub> · H <sub>2</sub> O	17.6
Kainite	MgSO <sub>4</sub> · KCl · 3H <sub>2</sub> O	9.8
Forsterite	Mg <sub>2</sub> SiO <sub>4</sub>	17.3
Periclase	MgO	60.3
Sea water	MgCl <sub>2</sub>	0.5
Natural brines	MgCl <sub>2</sub>	3–10

until 2003 to reach the same level of use as a construction material (**Figure 2**). Other applications such as desulphurization of iron are also shown in the figure. The effect of alloying elements and important alloys of magnesium are introduced in the following sections. Most alloying elements form intermetallic phases with magnesium, resulting in either eutectic or peritectic systems. **Table 3** lists a group of binary alloys based on magnesium, indicating the solubility of alloying elements, the possible intermetallic phases, and also the melting point of each system.

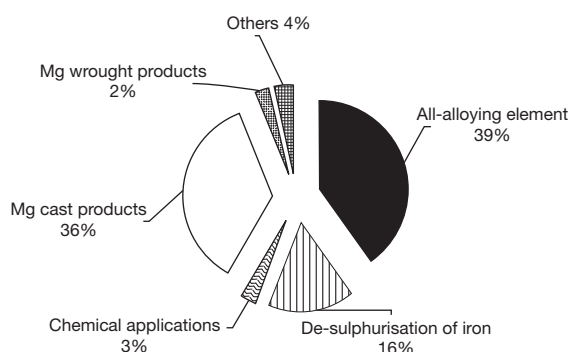
The first industrially useable magnesium alloys were developed at the beginning of the twentieth century. The basic works at that time showed very clearly the influence of essential alloying elements on the property profile and the workability of magnesium alloys. The effect of alloying elements on the properties of a variety of magnesium alloys has been addressed in the literature.<sup>1–5</sup> An overview concerning the effect of the alloying elements on the properties is given in **Table 4**. **Table 5** shows the essential physical properties of pure magnesium and a very popular alloy containing aluminum and zinc, called AZ91. Furthermore, the chemical compositions of some of the commonly used alloys are provided in **Table 6**.

#### 3.09.3.3 Alloying Elements

Aluminum is considered as one of the primary alloying elements for magnesium alloys. The addition of aluminum to magnesium improves the strength and corrosion resistance, reduces the melting point and increases the melting range. Aluminum is also known to cause microporosity. In alloys containing more than 6% (by weight) aluminum, the intermetallic phase Mg<sub>17</sub>Al<sub>12</sub> (**Figure 3**) is formed. These alloys are heat

**Table 2** Typical electrolyte composition for electrolytic reduction of magnesium<sup>3</sup>

<i>Electrolyte</i>	<i>Composition (wt%)</i>	<i>Melting point (°C)</i>	<i>Density (kg m<sup>-3</sup>)</i>	<i>Conductivity (S m mm<sup>-2</sup>)</i>	<i>Viscosity (mPa s)</i>	<i>Surface tension (mN m<sup>-1</sup>)</i>
Potassium Electrolyte	5–12 MgCl <sub>2</sub> 70–78 KCl 12–16 NaCl	650	1600	183	1.35	104
Sodium–Potassium Electrolyte	10 MgCl <sub>2</sub> 50 NaCl 12–16 NaCl	625	1625	200	1.58	108
Sodium–Calcium Electrolyte	8–16 MgCl <sub>2</sub> 30–40 CaCl <sub>2</sub> 35–45 NaCl	575	1780	200	2.22	110
Lithium–Potassium–Electrolyte	0–10 KCl 10 MgCl <sub>2</sub> 70 LiCl 20 KCl	550	1500	420	1.20	Data not available
Lithium–Sodium Electrolyte	10 MgCl <sub>2</sub> 70 LiCl 20 NaCl	560	1521	488	Data not available	Data not available
Sodium–Barium Electrolyte	10 MgCl <sub>2</sub> 20 BaCl <sub>2</sub> 50 NaCl 20 KCl	686	1800	217	1.70	110
Mg		650	1580	22.4	1.25	563

**Figure 2** Applications of magnesium (statistics as of 2002).

Source: <http://minerals.usgs.gov/minerals/pubs/commodity/magnesium/>  
<http://www.intlmag.org>

treatable and thus an improvement in mechanical properties is feasible. Aluminum has no adverse influence on the weldability of magnesium. Nevertheless, aluminum in excess of 1.5% has been reported to increase the stress corrosion cracking (SCC) susceptibility of magnesium alloys. An aluminum content of about 10% favors fine grained solidification and also weldability. With regard to high temperature mechanical properties and creep strength, aluminum shows no positive effect.

Zinc is used, very often in combination with aluminum, in magnesium alloys. Because of its low melting point, the addition of zinc lowers the melting range of Mg–Al alloys, which on the other hand causes problems in solidification. A zinc content of more than 1% in magnesium alloys can lead to hot cracking problems during solidification, and a content higher than 2% can cause cracking during welding. Nevertheless, in combination with zirconium and/or thorium, zinc positively influences the mechanical properties. In addition, zinc improves the corrosion behavior of magnesium alloys.

Zirconium is used as a grain refiner in magnesium alloys which do not contain Al, Mn, Sn, Sb, Ni, Fe, Co, or Si or contaminants such as C, N, O or H. Zirconium helps in the development of a fine grain structure in the welding of magnesium alloys and in addition Zr minimizes the loss of ductility in welded joints. Furthermore, the presence of zirconium prevents excessive grain growth during heat treatment.

Alloying elements of the group of rare earth (RE) elements as well as thorium results in eutectic systems with limited solubility. The level of porosity is reduced in the presence of RE elements. In general, these elements form stable precipitates/intermetallic phases which improve the elevated temperature strength and creep resistance. In addition, an improvement in the

**Table 3** List of selected binary magnesium alloy systems<sup>9</sup>

System	Max solubility		Phase	Melting point (°C)
	wt%	at. %		
Mg–Ag <sup>a</sup>	15.5	4.0	Mg <sub>3</sub> Ag	492
Mg–Al <sup>a</sup>	12.7	11.6	Mg <sub>17</sub> Al <sub>12</sub>	402
Mg–Bi <sup>a</sup>	8.85	1.12	Mg <sub>3</sub> Bi <sub>2</sub>	821
Mg–Ca <sup>a</sup>	0.95	0.58	Mg <sub>2</sub> Ca	714
Mg–Ce <sup>a</sup>	0.74	0.13	Mg <sub>12</sub> Ce	611
Mg–Dy <sup>a</sup>	25.8	4.83	Mg <sub>24</sub> Dy <sub>5</sub>	610
Mg–Ga <sup>a</sup>	8.5	3.1	Mg <sub>5</sub> Ga <sub>2</sub>	456
Mg–In <sup>b</sup>	53.2	19.4	Mg <sub>3</sub> In	484
Mg–Li <sup>a</sup>	17.0	5.5	–	–
Mg–Mn <sup>b</sup>	2.2	1.0	Mn	1245
Mg–Nd <sup>a</sup>	3.6	0.63	Mg <sub>41</sub> Nd <sub>5</sub>	560
Mg–Pb <sup>a</sup>	41.7	7.75	Mg <sub>2</sub> Pb	538
Mg–Sc <sup>b</sup>	25.9	15.9	MgSc	–
Mg–Sm <sup>a</sup>	5.8	0.99	Mg <sub>6.2</sub> Sm	–
Mg–Sn <sup>a</sup>	14.85	3.45	Mg <sub>2</sub> Sn	770
Mg–Tb <sup>a</sup>	24.0	4.57	Mg <sub>24</sub> Tb <sub>5</sub>	–
Mg–Th <sup>a</sup>	5.0	0.49	Mg <sub>23</sub> Th <sub>6</sub>	772
Mg–Ti <sup>a</sup>	60.5	15.4	Mg <sub>5</sub> Ti <sub>2</sub>	413
Mg–Tm <sup>a</sup>	31.8	6.26	Mg <sub>24</sub> Tm <sub>5</sub>	645
Mg–Y <sup>a</sup>	12.0	3.6	Mg <sub>24</sub> Y <sub>5</sub>	620
Mg–Yb <sup>a</sup>	3.3	0.48	Mg <sub>2</sub> Yb	718
Mg–Zn <sup>a</sup>	8.4	3.3	MgZn	347
Mg–Zr <sup>b</sup>	3.6	0.99	Zr	1855

<sup>a</sup>Eutectic.<sup>b</sup>Peritectic.

corrosion behavior is also observed with the addition of these elements. Yttrium is used as an alloying element along with RE elements. The other RE elements, *viz.*, Nd, Ce, La, and Pr, are often used in combinations. For example, the magnesium alloy designated as ‘QH21A,’ contains 2.5% Ag, 1.0% Th, 0.7% Zr, and 1.0% Di. Didymium (Di) consists basically of about 85% Nd and 15% Pr.

Beryllium has a very low solubility in magnesium; nevertheless, it has great potential to control the melt oxidation while melting or welding. However, the addition of beryllium needs to be done very carefully as it may cause grain coarsening. As a rule, the addition of beryllium should be restricted to a maximum of 30 ppm in magnesium alloys.

Additions of calcium in quantities >0.03% will increase the susceptibility to hot cracking. During solidification, the calcium-rich low melting eutectic mixture wets the grain boundaries, consequently leading to cracking assisted by the solidification stresses. In aluminum containing magnesium alloys, calcium additions lead to the formation of a stable intermetallic phase Al<sub>2</sub>Ca in preference to

Mg<sub>17</sub>Al<sub>12</sub>, which helps in improving the high temperature properties.

The addition of strontium in small quantities is reported to reduce the porosity during welding of high pressure die cast alloys, as it improves the solubility of hydrogen. Further, in conjunction with RE additions, strontium is found to improve the high temperature properties of magnesium alloys.

Silicon improves the castability if added in small quantities. With addition of up to 1% it forms the high-melting intermetallic phase magnesium silicide (Mg<sub>2</sub>Si) and thus improves the high temperature properties. However, in the presence of iron it deteriorates the corrosion resistance of magnesium to a great extent. Higher silicon content (>1%) in magnesium alloys decreases the castability drastically because of primary precipitation of Mg<sub>2</sub>Si in the melt.

Lithium can be used in large quantities in order to reduce the density of magnesium even further. Besides, an increase in Li content beyond 11%, leads to a change in the crystal structure from hexagonal close packed to body centered cubic structure. With the availability of more slip systems, the formability of the alloys is greatly improved, but the strength of Mg–Li alloys is generally reduced. Further, the problems of burning and vaporization arise while melting in presence of higher levels of lithium. In addition, the corrosion resistance of magnesium alloys in presence of lithium has been reported to be poor.

Manganese is found in most of the magnesium alloys. Primarily, manganese in magnesium alloys improves the ductility, and as it forms stable compounds with iron and other alloying elements, the corrosion resistance is improved on account of control of ‘free’ iron. Manganese also has a positive effect on the weldability and shows some grain refinement effect, too.

Copper has been reported to improve the high temperature properties of magnesium alloys. At the same time, Cu levels greater than 0.05% have been found to be highly detrimental for the corrosion resistance of the magnesium alloys. Other elements with similar adverse effect on the corrosion resistance of magnesium alloys are, Fe, Ni, Cr and Co. However, they are generally regarded as impurities in magnesium alloys.

### 3.09.3.4 Alloy Designations

As for ferrous systems, there are quite a number of alloy designation systems for magnesium alloys, too. An overview of the universally accepted alloy designation for magnesium systems, as recommended by the German Institute for Standardization (DIN) and

**Table 4** Selection of alloying elements and their effect on properties of magnesium alloys<sup>13</sup>

<i>Alloying element</i>											
	<i>Tensile strength</i>	<i>Ultimate strain</i>	<i>Compressive strength</i>	<i>Hardness</i>	<i>Ductility</i>	<i>Liability of cracks/notches</i>	<i>Creep resistance</i>	<i>Hot strength</i>	<i>Corrosion resistance</i>	<i>Grain refinement</i>	<i>Castability</i>
Aluminum	+	+		+					+	+	+
Copper	⊗	+	⊗						⊗⊗	⊗	
Chromium								+		+	
Yttrium	+					⊗			+	+	+
Cobalt		+							⊗⊗		
Strontium	+	+	+							+	
Zirconium	+	⊗			+			+		++	
Lithium	⊗		⊗		+				⊗		
Manganese	+				+	+	+		+	+	
Nickel									⊗⊗⊗		
Silicon		⊗	+	+							⊗
Zinc	+										
Calcium						⊗	+			+	+

+ Beneficial; ⊗ Deleterious.

**Table 5** Characteristic physical properties of pure magnesium and AZ91 alloy<sup>14</sup>

	Mg	AZ91
Density (g cm <sup>-3</sup> , RT)	1.74	1.81
Liquidus temperature (°C)	650	598
Thermal expansion coefficient (10 <sup>-6</sup> K <sup>-1</sup> , 20–100 °C)	24.8	26.0
Specific enthalpy (kJ kg <sup>-1</sup> )	382	370
Specific heat (kJ kg <sup>-1</sup> K <sup>-1</sup> , RT)	1.03	1.02
Thermal conductivity (W K <sup>-1</sup> m <sup>-1</sup> , RT)	156	51
Electrical conductivity (10 <sup>6</sup> Ω <sup>-1</sup> m <sup>-1</sup> , RT)	22.6	6.6

RT – room temperature.

the American Society for Testing of Materials (ASTM) is provided below.<sup>3,4,6</sup> As per the German Institute for Standardization (DIN) EN 1754 the materials receive a prefix EN M followed by the marking of the product form as below:

- A: Anodes (Ingots)
- B: Block metals
- C: Castings

After this marking, the chemical composition is provided. Therefore, the marking EN M C MgAl9Zn1 is the designation for a magnesium alloy casting with 9% Al and 1% Zn.

The identification of magnesium alloys is also standardized worldwide by the ASTM standards; each alloy is marked with letters indicating the main alloying elements, followed by the rounded figures of each element in weight percentage. Table 7 shows the key letters for each of the available alloying elements. The last letter in each identification number indicates the stage of development of the alloy (A, B, C, etc.). The alloy AZ91D, for example, is an alloy with a rated content of 9% aluminum (A) and 1% zinc (Z). Its development stage is 4 (D). The corresponding DIN specification would be MgAl9Zn1.

ASTM specifies the following composition for the above designation D (all values wt%): Al 8.3–9.7; Zn 0.35–1.0; Si (max.) 0.10; Mn (max.) 0.15; Cu (max.) 0.30; Fe (max.) 0.005; Ni (max.) 0.002; others (max.) 0.02.

Some of the alloy designations may also contain the history of heat treatment. The designation of heat treatment follows the rules of aluminum alloys.<sup>3</sup> The purpose of the heat treatments in the case of magnesium alloys would be to achieve the desired microstructural state and properties. The different temper designations concerning the heat treatment of magnesium alloys are presented in Table 8.

### 3.09.3.5 Cast Magnesium Alloys

The first commercial magnesium alloys, among them many AZ systems, were developed in the mid 1930s, and in recent times significant developments have taken place on alloy development. Even though new alloys have been developed with specific properties viz., high strength, creep and corrosion resistance etc., the AZ system of alloys still remains as the prime group. These alloys are of importance because of good casting properties, especially in high pressure die casting, and in general these alloys possess a good combination of properties. The main alloying elements are aluminum and zinc, with both the elements improving the castability. Alloys belonging to the category of AM designations, with Al and Mn as the major alloying elements, have relatively inferior castability. However, these alloys have better toughness and reasonable strength. Both these categories of alloys are suitable for both cold and hot chamber pressure die casting. Nevertheless, the properties of the AZ and AM series alloys are highly insufficient for applications at temperatures higher than 130 °C.<sup>7</sup>

For elevated temperature applications (>130 °C), AE and AS categories of alloys are preferred, in which the RE elements or silicon, respectively, are the essential alloying elements in addition to aluminum. These alloys have poor castability, and owing to the high melting points and formation of precipitates in the melt, the alloys are not suitable for hot chamber high pressure die casting. These alloys can successfully be employed at temperatures up to 180 °C.

Other alloys for high temperature applications are available in the WE, ZE, or QE systems. The WE group of alloys contains yttrium and RE elements as main constituents are currently used in the aviation industry, e.g. for gear cases in helicopters. They can be used up to temperatures of 300 °C.<sup>8–10</sup> While the alloys of the ZE system are based on zinc and RE elements, the QE alloys are based on silver and RE elements. These alloys are processed predominantly by sand casting and are not suitable for high pressure die casting. The processing capabilities of these alloys in the semisolid state have not yet been fully understood. Further, both the above systems are not used any more for major industrial applications. The newly developed alloys MRI, AJ, and ACM appear to be superior compared to the old ZE and QE type of alloys for the high temperature applications, as can be seen from Tables 9 and 10.

All aforementioned alloys are used nowadays in the form of high purity alloys. The level of impurities in

**Table 6** Nominal chemical compositions of standard magnesium alloys<sup>9,10,15,16</sup>

	<i>Al</i>	<i>Zn</i>	<i>Mn</i>	<i>Zr</i>	<i>RE</i>	<i>Ag</i>	<i>Th</i>	<i>Si</i>	<i>Y</i>	<i>Others</i>
High pressure die casting alloys										
AE42	4.0		0.10		2.5					
AJ52x	5.0									1.95 Sr
AJ62x	6.0									2.4 Sr
AJ62Lx	6.15									1.9
AM50A	4.9		0.26							
AM60A	6.0		0.13							
AS21	2.2		0.10					1.0		
AS41A	4.2		0.20					1.0		
AZ91D	8.7	0.7	0.13							
Sand and gravity die casting alloys										
AM100A	10.0		0.1							
AZ63A	6.0	3.0	0.15							
AZ81A	7.6	0.7	0.13							
AZ91E	8.7	0.7	0.13							
AZ92A	9.0	2.0	0.1							
EQ21A				0.7	2.1 Di					
EZ33A		2.7		0.6	3.3					
HK31A				0.7			3.3			
HZ32A		2.1		0.7			3.3			
K1A				0.7						
QE22A				0.7	2.1 Di	2.5				
QH21A				0.7	1.0 Di	2.5	1.0			
WE43A				0.7	3.4				4.0	
WE54A				0.7	3.0				5.2	
ZC63A		6.0	0.25							2.7 Cu
ZE41A		4.2		0.7	1.2					
ZE63A		5.8		0.7	2.6					
ZH62A		5.7		0.7			1.8			
ZK51A		4.6		0.7						
ZK61A		6.0		0.7						
Wrought alloys										
AZ10A	1.2	0.4	0.2							
AZ31B	3.0	1.0	0.2							
AZ61A	6.5	1.0	0.15							
AZ80A	8.5	0.5	0.12							
M1A			1.2							
ZC71		6.5	0.5							1.25 Cu
ZK21A		2.3		0.45						
ZK31		3.0		0.6						
ZK40A		4.0		0.45						
ZK60A		5.5		0.45						
ZK61A		6.0		0.7						
ZM21		2.0	0.5							

RE – Rare earth elements.

Di – Nd + Pr.

the magnesium alloys is of great importance from the viewpoint of corrosion resistance. Even small levels of nickel, iron or copper as impurities may adversely influence the corrosion behavior of magnesium alloys. These elements are controlled in the primary processing stages, for example, by the addition of elements like manganese to form an intermetallic compound with iron. The high purity magnesium alloys offer a

much superior corrosion resistance compared to those with intolerable levels of impurities.<sup>8</sup>

A new trend in alloy development is to check the current alloys on their ability to be processed in the semisolid state and to modify them for better semisolid processing. The modification is done by additions of calcium, strontium and also RE elements. These elements have been reported to improve the



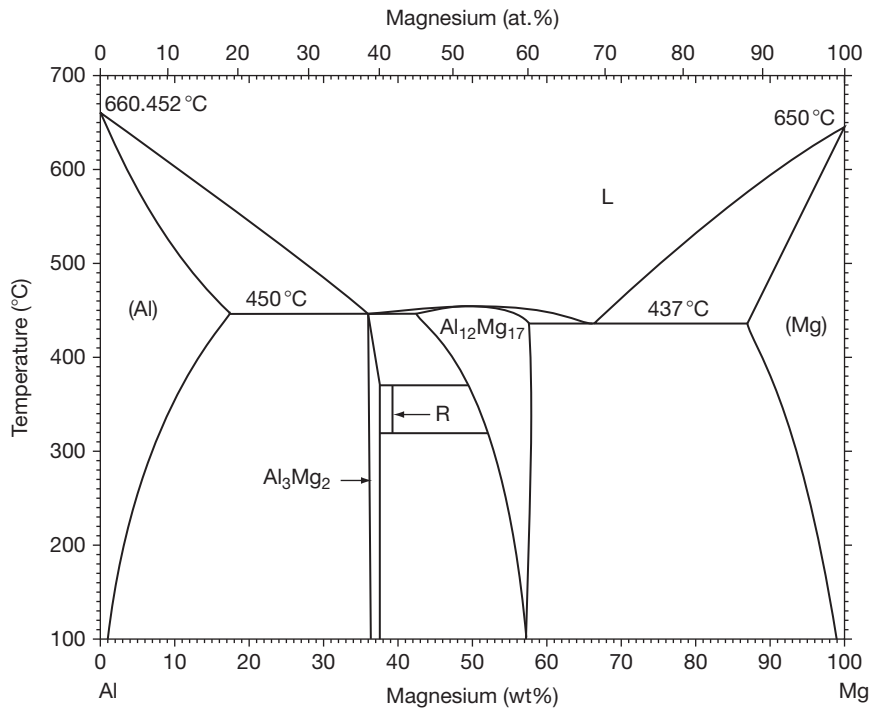


**Figure 3** Binary phase diagram of Mg–Al system.<sup>3</sup>

**Table 7** Codes for alloying elements in magnesium alloys<sup>9,10</sup>

Element	Letter	Element	Letter
Aluminum	A	Manganese	M
Bismut	B	Nickel	N
Copper	C	Phosphorous	P
Cadmium	D	Silver	Q
Rare earth	E	Chromium	R
Iron	F	Silicon	S
Thorium	H	Tin	T
Zirconium	K	Yttrium	W
Lithium	L	Antimony	Y
		Zinc	Z

mechanical properties and corrosion behavior as well.<sup>10,11</sup> The RE elements especially improve the mechanical properties at high temperatures due to formation of stable precipitates. Thus, the creep behavior is strongly improved.<sup>12–14</sup>

Unlike aluminum alloys, grain refiners for use with magnesium alloys are not well known. Only a few elements such as Zr, Sr, Si and C are known as effective grain refiners.<sup>1,3,15,17</sup> Zirconium works only in magnesium alloys which are free from Al, Si, Sn, Mn, Sb, Ni, Fe and Co. In such alloys Zr addition has been reported to provide finer grain size and this

contributes to better formability. Particles such as SiC can work as grain refining agents as well.<sup>17</sup> However, none of the mechanisms for the grain refinement of magnesium alloys is completely understood. Most of the grain refiners work only in certain alloys and combinations of them may influence the effectiveness or may even have an opposite effect.<sup>2,3,17</sup>

Magnesium castings are also produced by squeeze and thixocasting techniques. In the first case, the material is handled in a completely molten state and in the latter it is processed in a semisolid state. The squeeze cast magnesium alloys exhibit a good strength and ductility, owing to the fact that the squeeze casting develops fine grained structures.<sup>18</sup> Even though the squeeze cast alloys are expected to exhibit good fatigue behavior, their creep properties are poor, essentially because of the fine grains. Properties of semisolid processed alloys are still under investigation. As the main applications are housing for electronic components, the property requirements are not that stringent for these alloys.

### 3.09.3.6 Wrought Magnesium Alloys

Wrought magnesium alloys have a great potential for light weight construction, especially in the automobile

industry, owing to the excellent strength to weight ratio. For rolling into sheet alloys, low levels of alloying elements are generally used (e.g., AZ31), while for extrusion and forging, basically, all alloys can be used. The AZ family of alloys with low zinc content and different levels of aluminum is the dominant alloy system, as they exhibit an attractive combination of strength and ductility. The increase in aluminum content in the alloy leads to an increase in the secondary phase content ( $Mg_{17}Al_{12}$ ), which in turn results in increased strength levels with acceptable drop in ductility. In the wrought systems, the most commonly used alloys are AZ31, AZ61, and AZ80. Furthermore, Mg–Mn alloys (M1 and M2) are used for extrusions. The advantage is the high press rate; however, the

ductility is rather low, hence this alloy system is of less importance.<sup>19</sup> Other alloys used are based on the Zn system (ZK30, ZK60) in which Zr is working as grain refiner and providing an improved formability to the material. Furthermore, typical cast alloys of the AZ (AZ91) and AM (AM50, AM60) systems are used mainly for extrusions,<sup>20–22</sup> and also for forgings. The WE system (WE43, WE54) has also gained commercial importance in extrusions and forgings in recent times. The mechanical properties of typical wrought alloys are given in [Tables 11 and 12](#).

### 3.09.3.7 Magnesium Matrix Composites

In addition to conventional magnesium alloys, metal matrix composites (MMCs) based on magnesium are studied to extend the field of applications. MMCs, as they are defined, contain at least 5% of strengthening phases/constituents in the alloy matrix. The secondary strengthening constituents may be present in the form of long fibers, short fibers, whiskers or particles and in addition, a mixture of particles and fibers is also feasible. Generally, all magnesium alloys can be used as matrix material, but in view of the intended applications, the heat-resistant alloys are mostly used as matrix.

The MMCs have been reported to possess higher specific strength than the monolithic magnesium alloys. MMCs have shown better properties in terms of Young's modulus, thermal expansion coefficient, electrical and thermal conductivity and creep resistance.<sup>23,24</sup> The creep rates of the magnesium MMCs are reported to be about 10–100 times lower than those of the monolithic alloys, and in fact these MMCs are believed to compete with some class of steels in terms of creep properties. However, corrosion resistance is most of the time adversely affected because of galvanic effects between the reinforcement

**Table 8** Temper designations in magnesium alloys<sup>9</sup>

F	As-manufactured
O	Heat treated and recrystallized
H	Cold deformed
H1	Only cold deformed
H2	Cold deformed and partially annealed
H3	Cold deformed and stabilized
T	Heat treated to obtain conditions other than mentioned under F, O or H
T1	Cooled down and naturally aged
T2	Annealed (only cast alloys)
T3	Solution treated and cold deformed
T4	Solution treated
T5	Cooled down and artificially aged
T6	Solution treated and artificially aged
T7	Solution treated and stabilized
T8	Solution treated, cold deformed, and artificially aged
T9	Solution treated, artificially aged, and cold deformed
T10	Cooled down, artificially aged, and cold deformed t
W	Solution treated (unstable condition)

**Table 9** Comparison of typical properties of newly developed magnesium alloys and standard alloys<sup>15,39</sup>

	<i>MRI</i> 153 M	<i>MRI</i> 230D	<i>AJ62Lx</i>	<i>AJ62x</i>	<i>AJ52x</i>	<i>AZ91D</i>	<i>AE42</i>	<i>AS41</i>	<i>AS21</i>
$R_p$ (RT)	170	180	147	142	134	160	135	130	125
$R_p$ (150 °C)	135	150	116	108	110	105	100	–	87
$R_m$ (RT)	250	235	270	239	212	260	240	240	230
$R_m$ (150 °C)	190	205	166	163	163	160	160	–	120
A (% , RT)	6	5	11	8	6	6	12	10	16
A (% , 150 °C)	17	16	27	19	12	18	22	–	27
Corrosion rate (mg cm <sup>-2</sup> day <sup>-1</sup> )	0.09	0.10	0.04	0.08	0.09	0.10	0.21	–	0.34

Corrosion data: Based on salt spray tests, ASTM B117.

**Table 10** Mechanical properties of sand gravity and die cast magnesium alloys<sup>9,10</sup>

		UTS (MPa)	YS (MPa)	% RA
AM100A	T61	275	150	1
AZ63A	T6	275	130	5
AZ81A	T4	275	83	15
AZ91E	T6	275	145	6
AZ92A	T6	275	150	3
EQ21A	T6	235	195	2
EZ33A	T5	160	110	2
HK31A	T6	220	105	8
HZ32A	T5	185	90	4
K1A	F	180	55	1
QE22A	T6	260	195	3
QH21A	T6	275	205	4
WE43A	T6	250	165	2
WE54A	T6	250	172	2
ZC63A	T6	210	125	4
ZE41A	T5	205	140	3.5
ZE63A	T6	300	190	10
ZH62A	T5	240	170	4
ZK51A	T5	205	165	3.5
ZK61A	T5	310	185	—
ZK61A	T6	310	195	10

and the matrix. Nonconducting reinforcements are generally a better choice to minimize the galvanic corrosion attack.

### 3.09.4 Processing of Magnesium Alloys

#### 3.09.4.1 Casting Technologies

About 95% of the magnesium components are produced by liquid metallurgy route, and the processing temperatures are normally in the range of 600–800 °C. Magnesium and its alloys are extremely reactive in the molten state and extreme care is required for protecting the melt. In the early days, salt-fluxes were used to protect the melt, and in addition these are useful to clean the impurities in the melt, to some extent.<sup>1</sup> However, today, these fluxes are seldom used and the modern foundries, which process magnesium alloys mostly employ controlled atmospheres. In the beginning, a mixture of inert gases, e.g. N<sub>2</sub>, with SF<sub>6</sub>, was used for protection,<sup>25,26</sup> with SF<sub>6</sub> offering an efficient protection against oxidation to the molten baths up to temperatures of around 700 °C by forming a thick protective film. However, since 2007, the use of SF<sub>6</sub> has been restricted on account of environmental regulations. SO<sub>2</sub> has been recommended by the European Commission as an alternative to SF<sub>6</sub>. However, SO<sub>2</sub> is a toxic gas, and handling it is more

**Table 11** Mechanical properties of forged magnesium alloys<sup>9,10</sup>

		UTS (MPa)	YS (MPa)	% RA
AZ31B	F	260	170	15
AZ61A	F	295	180	12
AZ80A	T5	345	250	6
AZ80A	T6	345	250	11
M1A	F	250	160	7
ZK31	T5	290	210	7
ZK60A	T5	305	215	16
ZK61	T5	275	160	7
ZM21	F	200	125	9

difficult than SF<sub>6</sub>; thus, the magnesium producers are exploring the possibilities of employing SO<sub>2</sub> on the production scale.

Sand casting belongs to the traditional casting techniques and was already employed for magnesium in the early days, but the problems that were encountered are partly unsolved up to now. The exothermic reaction between the components of sand (silicon dioxide, iron oxide, and water) and molten magnesium can damage the mould and the surface of the component. In order to minimize this problem, sulfur, boric acid, calcium fluoroborate, ammonium fluorine silicate and urea (referred to as inhibitors) are used individually or in combination.<sup>1,4</sup>

For gravity die casting, moulds from steel are normally used. Even though the problem of reaction between the mould and the molten metal does not arise in this case, the steel moulds are expensive, and the surface finish is rather inferior. However, generally good quality casting can be produced by gravity die casting procedure, if the wall thickness is high enough. Thin walled parts are better produced by pressure assistance.

Magnesium components are produced predominantly by pressure die casting techniques and both the cold and hot chamber die casting procedures are adopted in the industry. Both techniques yield components with fine grain structure, excellent quality surface finish and a greater dimensional accuracy. The major disadvantage of these techniques, however, is the inevitable gas inclusions in the castings, preventing the use of heat treatments to fully utilise the potential of the alloys. Employment of either cold or hot chamber technique for the production of castings depends also on the type of alloys. AZ91, AM50 and AM60 alloys are most suitable for the production of castings by hot chamber pressure die casting technique. The AS and AE systems of magnesium alloys, which have relatively higher melting points than the

**Table 12** Mechanical properties of wrought magnesium alloys<sup>40</sup>

<i>Alloy</i>	<i>Tensile strength (MPa)</i>	<i>Yield strength <math>R_{p0.2}</math> (MPa)</i>	<i>Compressive strength (MPa)</i>	<i>Elongation (%)</i>
AZ31	250	180	110	14
AZ61	300	220	130	12
AZ80	340	240	145	10
M1A	260	170	–	10
M2A	250	180	110	4
ZK31	290	240	190	14
ZK60	320	290	230	12
WE34	260	170	165	12
WE54	280	190	180	10

AZ or AM alloys, are more suitable for casting in cold chamber pressure die casting machines. The latter can also be used for processing AZ and AM based alloys.

Squeeze-casting is a special process with a vertical arrangement of a slewable casting unit and molding direction. When the unit is filled, it closes and docks to the mould. Then, the piston rises up and the actual filling begins. In contrast to die-casting, the molding is done slowly (minimum turbulence and hence low porosity), though the final compression is the same. In squeeze-casting, however, the pressure is maintained until freezing is complete and even allows for further feeding in the semi-solid condition. Injection pressures are usually between 70 and 100 MPa, so as to obtain a compact and fine-grained microstructure. Squeeze-casting is an excellent method for producing pressure-sealed, low-porosity, weldable, heat-treatable parts with reproducible high quality. It is increasingly being used in place of classical gravity casting. Magnesium alloy casting can be made by employing both direct and indirect squeeze casting techniques and the same is applied for the production of MMCs, too.

Thixocasting is a fairly new method based on the thixotropic properties of semi liquid alloys. The material while processing would reach the liquidus temperature and would consist of a mixture of solid and liquid phases (also known as semi-solid metal forming). For example, intense stirring can be used to prevent the usual formation of dendritic grains, instead, globular grains form. This condition is characterized by thixotropic flow behavior; with increasing viscosity the shearing strain falls off. The actual procedure requires suitably manufactured raw material. Technically, it is carried out by electromagnetic stirring (rheocasting) within a slab-casting machine.

Recently, much effort has been directed towards shortening the time required for the electromagnetic

stirring so as to lower the processing costs. A first step towards this goal is the so-called NRC process (new rheo-casting process). This process tries to avoid dendritic growth by a customized melting-cooling process and simultaneous turning of the melting crucible. The advantages of this procedure compared to conventional casting are as follows: (a) complete automation of the production process, (b) high productivity, (c) cost savings due to low energy consumption, (d) higher tool lifecycles, (e) parts free from gas inclusions and hence weldable, (f) low cooling shrinkage and no blow holes, (g) parts with excellent mechanical properties, and (h) final parts with near-net-shape quality.<sup>27–30</sup> Even though all the three procedures, NRC, thixocasting, and thixomoulding can process the material in the partially liquid state, the source, state, pretreatment and realization of the process differ in each case.<sup>31</sup> Thixocasting, in general, promises improved mechanical properties and comparable wall strengths for magnesium alloy components compared to high pressure die castings.<sup>32,33</sup> Microstructures of some of the commercial alloys in the various cast conditions are presented in [Figure 4](#).

### 3.09.4.2 Forming Technologies

The three major metal forming processes that are widely employed for the processing of magnesium alloys are (a) rolling, (b) extrusion, and (c) forging. The deformation behavior of magnesium alloys is greatly influenced by a number of variables, *viz.*, crystal structure, initial microstructure, thermodynamic conditions, state of stress, method of deformation etc. At ambient temperatures, the formability of magnesium alloys is limited, owing to the hexagonal close packed structure. However, with increase in temperatures to about 225 °C a higher number of slip systems becomes active and an improved metal forming behavior is observed.

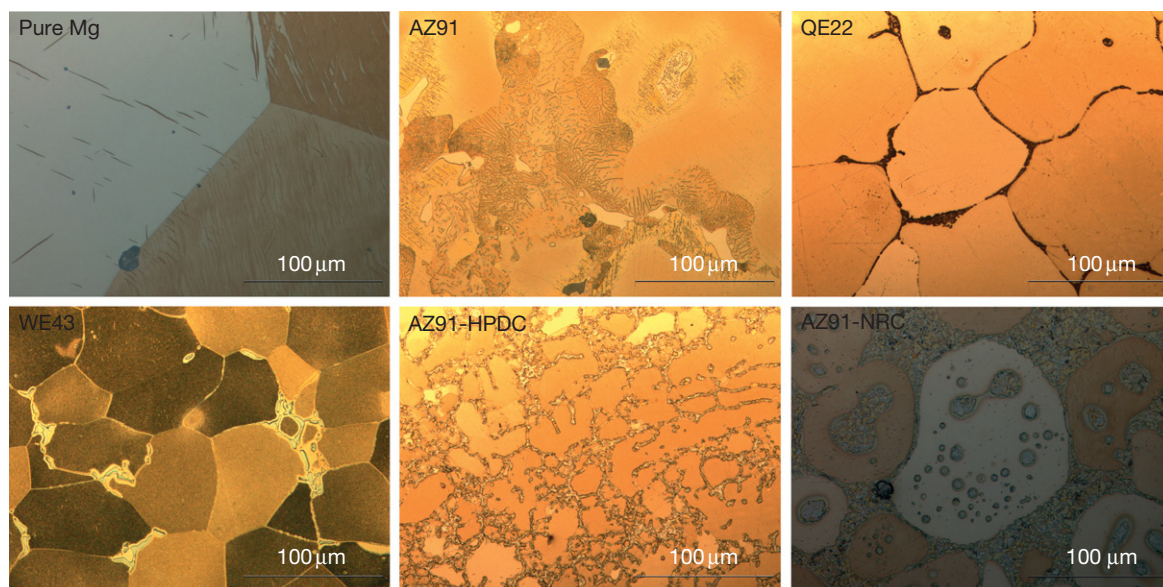


**Figure 4** Optical micrographs of some cast magnesium alloys.

Magnesium alloy sheets have to compete with aluminum and steel sheets for automotive applications, offering at least the same economical and technical benefits. For economic reasons, rolling is preferred to be done at temperatures as close as possible to ambient temperature. However, considerable optimization is required for obtaining sheets with acceptable mechanical, thermal and corrosion properties and surface finish.<sup>34</sup> The surface quality is controlled by the use of appropriate lubricants, either oil based or solid lubricants like molybdenum disulphide.<sup>35</sup> The anisotropy that is observed in the magnesium alloy sheets can be minimized by appropriate use of thermo-mechanical treatments and the choice of alloys.

The coarse grained structure of magnesium cast alloys can be readily converted into fine grained ones by hot working processes, such as extrusion. The mechanical properties of the extruded alloys depend on the chemical composition and the thermo mechanical pretreatment that is given to the alloys.<sup>36</sup> The extrusion processes have three variants, *viz.*, direct extrusion, indirect extrusion and hydrostatic extrusion, but most commonly used industrial processes are direct and indirect extrusion. Cylindrical ingots are heated to 300–400 °C depending on the alloy and pressed through matrices with manifold cross-sections. The maximum extrusion length is 50 m. Because of the required complexity, only AZ31 or M2 alloys with restrictions, and AZ61 alloys

as well, can be extruded with economical speed, the minimum wall thickness that could be achieved is determined by the alloy and the type of profile. For small to medium-sized AZ31 profiles, the minimum wall thickness that is achievable is 1.2 mm.<sup>37,38</sup> Hydrostatic extrusion is still under examination, but it seems to allow higher extrusion rates and lower extrusion temperatures. Representative micrographs of typical wrought alloys are shown in [Figure 5](#).

Magnesium alloy components can also be produced by forging. However, there are limitations in terms of availability of suitable alloy systems, formability and corrosion behavior of these alloys. Nevertheless, wheel rims have been successfully forged and used in commercial vehicles and racing cars.

### 3.09.4.3 Joining Technologies

The joining technologies for magnesium alloys can generally be classified into two broad categories, *viz.*, mechanical fastening and metallurgical bonding. Screwed connections, riveted joints and use of adhesives form the first group, and the second group is constituted by fusion or solid state joining processes, *viz.*, power beam welding, friction stir welding, diffusion bonding, etc.

An overview of the different aspects of preparing screwed connections for magnesium alloys was given by Weissert.<sup>39</sup> It is important to bear in mind the different thermal expansion coefficient values of



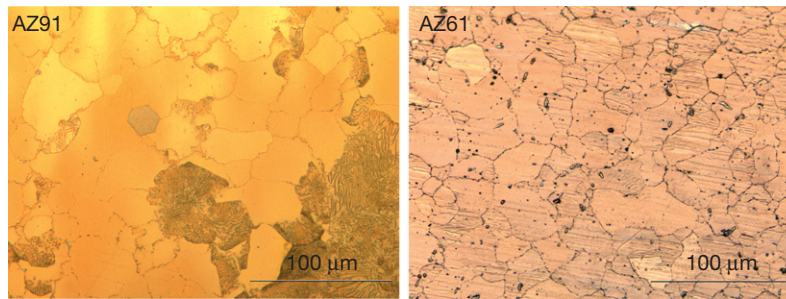


**Figure 5** Optical micrographs of wrought magnesium alloys (extruded).

magnesium and steel/aluminum when designing components for elevated temperature operation (especially above 100 °C) in a multi-material mix design. From the design and the material selection perspective, it is necessary to ensure that the screwed/bolted assemblies do not lose their pre-stress during application, and the materials chosen as screw do not foster galvanic corrosion. The latter can be minimized by the right choice of material combinations, appropriate coatings, and constructive measures.

Welding is one of the most widely used joining technologies for magnesium alloys. The weldability of magnesium alloys is influenced by (a) chemical and physical properties, (b) chemical composition, and (c) production process, and the quality of base material. The physical properties that are considered relevant for welding are the melting point, the boiling point, the thermal conductivity, and the coefficient of thermal expansion. A wide solidification range in the alloys, increases the possibility of hot cracking as well as the localized melting of some of the eutectic phases in the alloy.

Joining of magnesium alloys can be accomplished by different fusion welding processes *viz.*, gas tungsten arc welding, gas metal arc welding, plasma arc welding, laser beam welding and electron beam welding. Solid state joining processes *viz.*, friction welding, friction stir welding, and diffusion bonding are also employed for this purpose.<sup>40–42</sup>

Even though the gas tungsten arc (GTA) and gas metal arc (GMA) welding are still popular,<sup>43–45</sup> with the advent of power beam processes and friction stir welding, the trend moves towards the modern techniques for the joining of magnesium alloys.<sup>46,47</sup> The GTA and GMA welds suffer from the inherent drawbacks of large weld pool/heat affected zone, low welding speeds and higher degree of distortion and residual stress. In some cases, hybrid welding with laser and GTA/GMA combination has proved to be successful for achieving

deeper penetration welds in magnesium alloys,<sup>48</sup> also overcoming some of the issues mentioned above. Recently, the activated-GTA (popularly called as A-TIG) with flux addition was employed for the welding of AZ31B, and full penetration joints in 5 mm thick plates were claimed to have been realized with acceptable quality.<sup>49</sup>

The absorption of laser beam on the surface of materials being joined plays a crucial role in the case of magnesium alloys, and this has been treated extensively in literature.<sup>50,51</sup> Even though both CO<sub>2</sub> and Nd:YAG lasers are employed for welding of magnesium alloys, the weldability with Nd:YAG has been reported to be much superior due to shorter wave length and stable molten pool.<sup>52,53</sup> Quite a large number of researchers have investigated the evolution of microstructures and the mechanical properties of magnesium alloy laser beam welds.<sup>54,55</sup> The mechanical properties of the resultant weldments were observed to be dependent on the alloy composition, and a wide range of property variations have been reported for these weldments. However, in almost all the cases, a distinct reduction in the fracture strain values of the weldments was reported. Also, the electron beam welding of magnesium alloys is attempted by researchers, especially, for welding of higher section thickness magnesium alloys.<sup>47</sup>

The application of the friction stir welding process for joining of magnesium alloys is described in the literature.<sup>4,56</sup> The development of this modern solid state joining technique has given a new dimension to the joining of the so-called difficult to weld aluminum and magnesium alloys. However, in contrast to the aluminum alloys, the published literature on the characterization of friction stir welded joints of magnesium alloys is quite limited.<sup>57–59</sup> The investigations made and documented so far, suggest, that there exists a great potential for employing FSW for making not only similar, but dissimilar welds containing



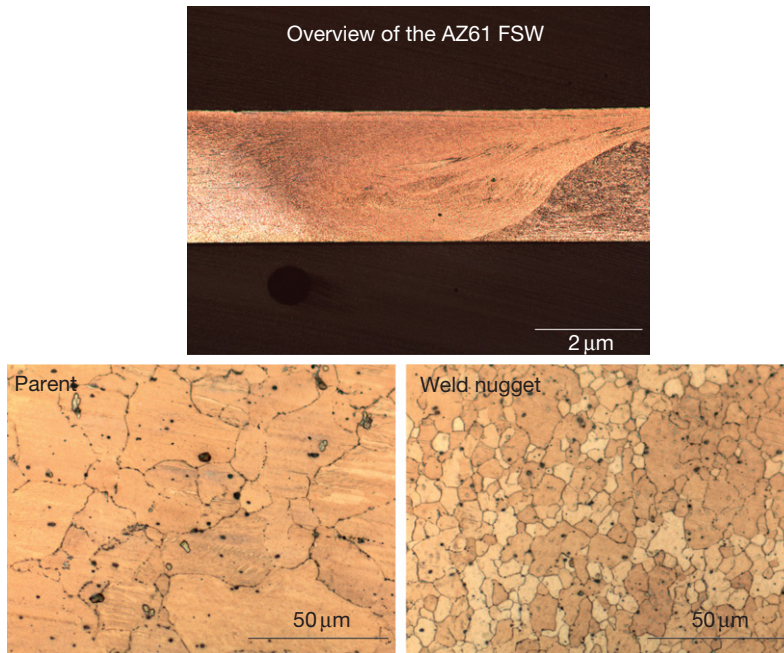


**Figure 6** Microstructural features of a friction stir weldment.

magnesium alloys, as well. The macrostructure and the microstructural features of the parent and weld nugget regions of the friction stir weldment of AZ61 alloy are depicted in [Figure 6](#).

### 3.09.5 Corrosion of Magnesium Alloys

Until recently, it was believed that magnesium has a poor corrosion resistance amidst the metals and alloys known to the engineering industry. This widespread view was essentially owing to a variety of reasons which include, but are not limited to: (a) poor alloy design (with higher levels of impurities like Fe, Ni, and Cu, and or inclusions of melting salts), (b) improper design of the components, or (c) none or a wrong or inadequate surface protection for the chosen application. But, today's magnesium alloys show corrosion properties similar to or better than some of the structural grade carbon steels and copper-containing high strength aluminum alloys ([Figure 7](#)). With the right choice of alloy and the developments in the field of surface engineering, the so-called 'susceptible magnesium' alloys are nowadays used for a variety of applications in the electronic, automobile and aircraft industry with appropriate surface protection.<sup>60–63</sup>

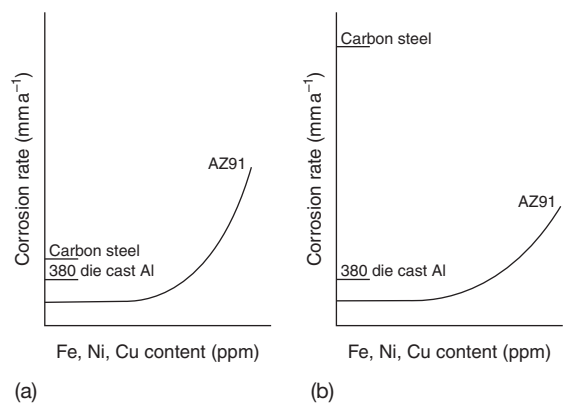


**Figure 7** Corrosion rates of AZ91 die cast alloy with different impurity levels. (a) In salt spray test and (b) atmospheric exposure at the Brazos River on the Texas Gulf Coast for 2 years.

On the one hand, the uniform or general corrosion of magnesium alloys in various environments is relatively well controllable, whereas on the other hand, the galvanic corrosion and the environmentally assisted cracking (SCC and corrosion fatigue) are the causes of failures of components made from these alloys. Other forms of corrosion such as pitting corrosion, filiform corrosion, and crevice corrosion apparently play an assisting role in the damage.

Intergranular corrosion of magnesium alloys does not seem to happen because of the fact that the grain boundaries outlined with secondary phases are nobler than the matrix/interior grains.

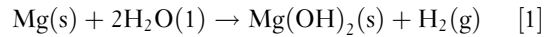
### 3.09.5.1 Forms and Mechanisms

Like all the metals which do not exist in the metal state in nature, magnesium has to be extracted from its ores, requiring considerable quantum of energy. Hence, magnesium also tends to return to its stable natural state by reactions with elements of the environment, that are mainly oxygen and water. Magnesium has a standard electrode potential of  $-2.37$  V for bare magnesium in contact with a solution containing Mg divalent ions, and is the most active construction material in the EMF series (Figure 8). Its free corrosion potential in neutral chloride solution is around  $-1.7$  V *versus* SCE, and is in the active end of the galvanic series (Figure 9). The shift of the potential is caused by the polarization due to passive film formation.

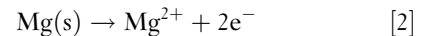
The fact that magnesium reacts instantaneously with air and water leads to the formation of corrosion products on the surface. The nature of the layer is determined by the surrounding environment, and in many instances, this leads to a reduction of the corrosion rate due to the effect of passivation, which by itself is an effective corrosion protection means. Thus, in normal atmospheres, the level of corrosion damage on magnesium alloys is insignificant. However, with increase in relative humidity of air the extent of corrosion damage in general increases. At low ambient humidity magnesium reacts with the oxygen of the air to form magnesium oxide ( $\text{MgO}$ ), which forms as a thin passive layer on the surface of the material. In more humid conditions ( $>93\%$  relative humidity) first, a surface layer of magnesium hydroxide ( $\text{Mg(OH)}_2$ ) develops, which subsequently

converts into magnesium carbonate ( $\text{MgCO}_3$ ) as a result of the reaction with the  $\text{CO}_2$  in the air. In marine and industrial atmospheres, chlorides, sulfates, and nitrates can destroy this protective layer and may induce corrosion damages.

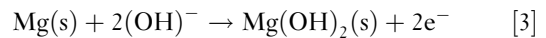
In aqueous solutions, the process of corrosion of magnesium, which is dependent on the pH and temperature, is described below:



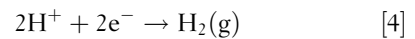
The dissolution of magnesium is the partial anodic reaction



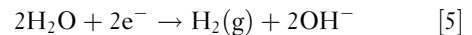
and/or



and the hydrogen evolution is the partial cathodic reaction



The following cathodic reaction can lead to the evolution of hydroxyl ions



The potential–pH diagram, known as the Pourbaix diagram, for the system magnesium–water is shown in Figure 10. It is obvious from this diagram that magnesium undergoes active dissolution in the pH range from 0 to 11, and magnesium hydroxide is stable only above pH 11. In contrast to aluminum, magnesium forms stable and self healing passive oxide/hydroxide layers in aqueous solutions without additional ions, only if the pH values are higher than 11. Immunity, the state in which corrosion cannot take place due to thermodynamic reasons, exists only below  $-2.5$  V, because of the very low negative standard potential of magnesium. Nevertheless, the corrosion rate is normally very low in small sealed off water volumes because of the low solubility of  $\text{Mg(OH)}_2$  (the saturation equilibrium is reached fast), and owing to the dissolution of magnesium, a pH value above 10 is quickly reached. However, if the exchange of water becomes constant, this equilibrium will not be reached and the corrosion progresses continuously. An increase in temperature also accelerates the corrosion rate.

In aqueous chloride solutions with heavy metal ions such as Ni, Fe, and Cu, the corrosion rate of magnesium alloys is generally very high. These metal ions will be deposited on the anodic magnesium surface and act as very active cathodes, thus driving

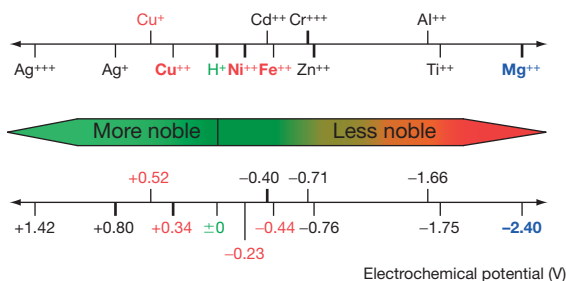
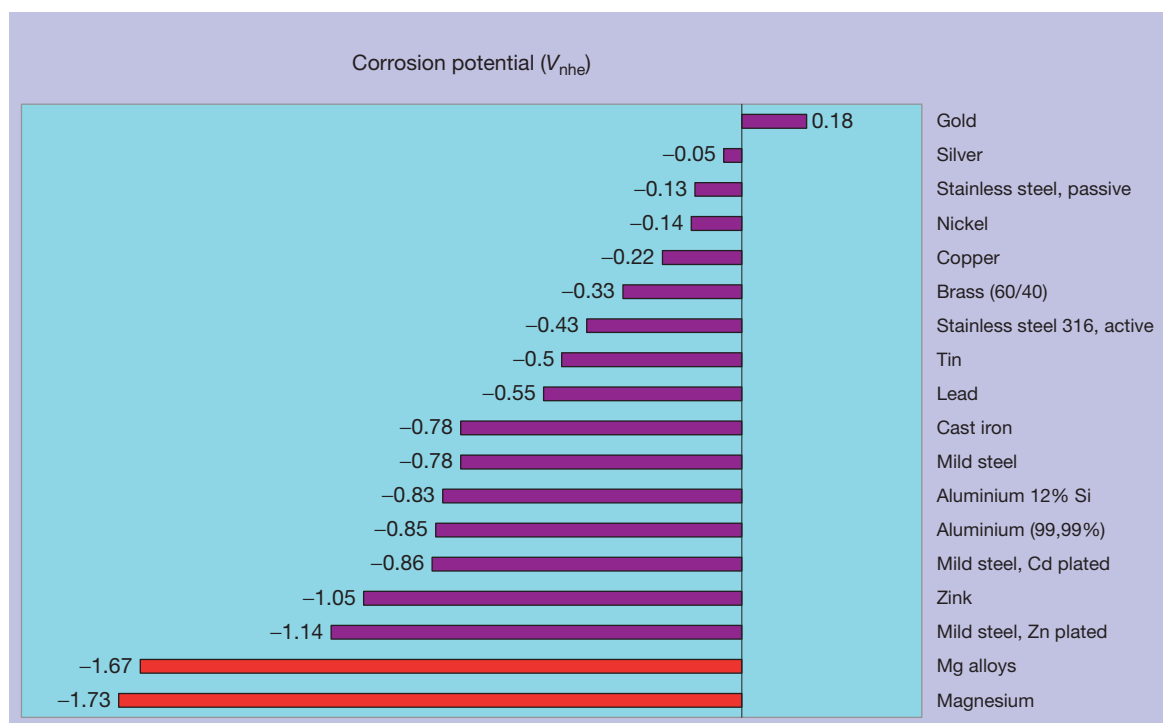
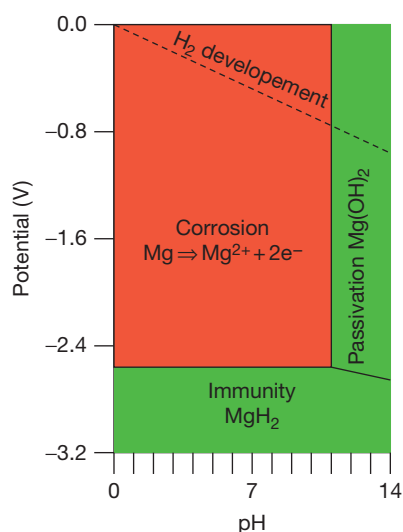


Figure 8 Electromotive force series (EMF series).



**Figure 9** Free corrosion potentials of metallic materials in neutral sodium chloride solution.



**Figure 10** Potential-pH diagram (Pourbaix diagram) of Mg-H<sub>2</sub>O system.

magnesium to dissolve at a rapid rate by galvanic action. Various anions, too, have an effect on the localized dissolution of magnesium hydroxide, and chlorides play a much more prominent role than sulfates and nitrates. However, there is a group of anions that help in the formation of a protective

layer on the surface, upon forming hardly soluble and adherent compounds with marginal dissolution of magnesium. Such salts are used in the electrochemical surface treatment of magnesium alloys (fluorides, chromates, vanadates, phosphates, etc.). Dissolved oxygen in water or salt solutions has no additional corrosive effect.

As magnesium is stable in solutions with pH > 11, due to a stable  $Mg(OH)_2$  layer, it does not corrode in alkaline solutions. All acids, except HF and  $H_2CrO_4$ , tend to attack and dissolve magnesium strongly. In the aforementioned exemptions, the formation of a stable film upon initial dissolution helps in preventing further dissolution. An aqueous chromic acid ( $180 \text{ g l}^{-1}$ ) solution is often used to clean magnesium alloys from corrosion products.

Most of the organic compounds (aliphatic and aromatic hydrocarbons, ketones, ether, glycol, etc.) have very little effect on the corrosion of magnesium alloys. The corrosion effect on magnesium alloys by ethanol is rather light, and anhydrous methanol inflicts a strong attack. Sour liquids like fruit juices, carbonated drinks, milk, etc., also cause measurable corrosion attack.

The resistance of magnesium alloys to almost all gases, including the aggressive chlorine, is very good

as long as the gases are dry. Even very small quantities of humidity lead to the formation of acids and hence, may result in a strong damage to the magnesium alloys, for example, in the presence of chlorine and sulfur dioxide. In contrast, the performance of magnesium alloys in ammonia containing atmosphere is good, regardless of whether the conditions are dry or humid. The oxidation of magnesium in the presence of oxygen increases with temperature; however, the applications at elevated temperatures are limited mostly by the creep resistance and not by the oxidation rates. As mentioned earlier, the corrosion performance is dependent on the pH value, and apparently the corrosion performance of magnesium alloys in soils depends on the pH value of the soil. Thus, the corrosion rate is higher in saline acidic soils than in neutral or alkaline soils.

Because of the basic nature of magnesium alloys with very active corrosion potentials, the corrosion is accelerated when in contact with other metals due to the galvanic effect. This is taken as an advantage for applications, wherein, magnesium alloys are used as sacrificial anodes for the cathodic protection of metals. However, for structural applications in aggressive media some additional coating and/or constructional measures are required on components to be protected.

The compatibility of magnesium (so-called anodes) and a second metal (cathodes) to be used as a couple in a given environment, is determined by the potential difference of the couple and the polarization resistance. In principle, these potential differences should be as low as possible and the resistance polarization (of the cathode material) should be as high as possible. Aluminum alloys belonging to the 5XXX and 6XXX series are the most compatible materials due to a relatively low potential difference with magnesium, compared to most other acceptable materials. Interestingly, despite a very large potential difference 80Sn/20Zn alloy coatings are also acceptable because of their high polarization resistance characteristics. The following materials are absolutely not acceptable to be used as a direct couple with magnesium alloys: practically all steels, nickel and aluminum alloys containing copper. However, in the case of steels, a coating of zinc plus a cataphoretic painting to the tune of 15  $\mu\text{m}$  would be helpful for making a couple with magnesium alloys.

Magnesium alloys are not only susceptible to galvanic corrosion when in contact with other metals, but also for a special kind of galvanic corrosion in the form of so-called ‘microgalvanic cells’. The potential differences between the anodic and cathodic regions

within the alloy is the reason for this type of corrosion that can occur in chloride-containing neutral as well as in alkaline media. Impurities such as iron, copper, and nickel, although mostly present as intermetallic compounds in the matrix, have very noble potentials compared to the matrix and thus, accelerate the corrosion damage of the matrix. The corrosion damage can at times be highly localized and lead to pits. The effect is similar in alloys containing the secondary phase  $\text{Mg}_{17}\text{Al}_{12}$ , wherein the regions with this intermetallic compound exhibit more noble potentials than the matrix in chloride solutions. The same effect can be observed for almost all intermetallics, formed between magnesium and alloying elements.

Even though the galvanic drive is expected to accelerate the dissolution of the surrounding matrix, it is feasible to tailor the properties of magnesium alloys with proper distribution of the secondary phase in the matrix. For example, in pressure die cast alloys with fine grained structure, the distribution of  $\text{Mg}_{17}\text{Al}_{12}$  secondary phase can be made more favorable, and this phase can form a coherent corrosion barrier network along the grain boundaries (Figure 11),<sup>65</sup> and thus, may lead to lowering of the corrosion rate.

### 3.09.5.2 Environmentally Assisted Damages

The term environmentally assisted cracking, in general, refers to failures under conditions of either static or dynamic loading with considerable assistance from

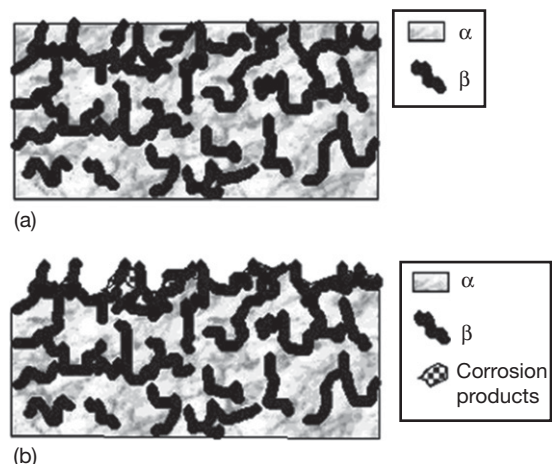


**Figure 11** Schematic representation of the change of surface conditions during corrosion of a magnesium alloy with nearly continuous  $\text{Mg}_{17}\text{Al}_{12}$  phase near to the surface.<sup>65</sup> (a) Initial surface and (b) final surface.

the environment. In the case of statically loaded components, this failure is influenced by the dissolution of the alloy, known as SCC, or induced by the entrapped/picked up/generated hydrogen at the tip of the crack, referred to as hydrogen induced cracking (HIC), or hydrogen embrittlement (HE). Under conditions of cyclic loading, the failures that happen with the influence of the environment are termed as corrosion fatigue (CF).

SCC is generally considered to be a dangerous form of damage, as it often leads to catastrophic failures. The mechanisms of SCC vary from one system to the other, and mechanistically SCC is quite subtle. The failure under these circumstances can be without any signs of visible deterioration of surfaces, but can happen due to highly localized damage. In fabricated components, apart from the external stresses, the residual stress in the components itself can lead to failures. The SCC susceptibility of wrought magnesium alloys has been widely looked at by researchers. Nevertheless, cast Mg alloys too, have been reported to be susceptible to SCC, especially when the stress levels are higher.

The SCC behavior of magnesium alloys is very similar to that experienced in the metals/alloys with a passive layer. There has always been a debate, as to whether pure magnesium is susceptible to SCC or not<sup>66–70</sup>; however, the alloys of magnesium are susceptible to this form of damage to a great extent. Stampella *et al.*<sup>70</sup> reported the susceptibility of 99.95% (high pure) magnesium to SCC in sulphate solutions based on slow strain rate tensile (SSRT) tests. The susceptibility of magnesium alloys to SCC was reported based on the laboratory tests performed by numerous researchers and compiled by Winzer *et al.*<sup>71</sup> SCC of a variety of magnesium alloys was observed in environments containing very low concentrations of (as low as 0.001 N) sulfates or chlorides or even in distilled water. Further, SCC has been observed in chromate containing solutions.

A fairly large amount of work has attempted to understand the effect of alloying elements on the SCC behavior of magnesium alloys. Aluminum, one of the major elements for strengthening, has been reported to adversely influence this behavior, with the threshold concentration level of around 2.5%.<sup>69,70</sup> Higher aluminum containing alloys have been found to fail by SCC, even in distilled water. Miller<sup>72</sup> reported that zinc increases the SCC susceptibility, which was contradicted by Fairman and Bray.<sup>73</sup> Surprisingly, the manganese containing magnesium alloys are generally considered to be immune in the atmosphere, chloride

solutions, and chloride–chromate solutions,<sup>72</sup> but have been reported to be susceptible in distilled water.<sup>74</sup> Addition of cadmium and neodymium to Mg–Zn–Zr alloy has been reported to improve the SCC resistance<sup>75</sup> and, conversely, the deleterious effect of Cd was also reported.<sup>69</sup> The presence of Fe as impurity plays a crucial role in SCC, especially in the impure alloys. The presence of intermetallic compounds such as FeAl is reported to influence the SCC,<sup>76</sup> the micro galvanic effect in these alloys leads to stronger hydrogen evolution, and the cracking is expected to be with the assistance of hydrogen.<sup>77,78</sup>

In a recent work, the SCC susceptibility of an extruded magnesium alloy (AZ31) in ASTM D 1384 test solution (Figure 12) was addressed.<sup>79</sup> The fracture was observed at a stress level of around 100 MPa with a strain of 2% compared to the strain level of about 45% in the tests in air. The fracture surfaces of SSRT tested AZ31 magnesium alloy (in air and in ASTM D 1384 solution) presented in Figure 13 show characteristic fine dimples in the specimen tested in air, and a distinct transgranular cleavage fracture in the specimen tested in ASTM D 1384 solution.

The documented literature on the SCC of magnesium alloys suggests that in a majority of the cases the failure was transgranular (TG) in nature. SCC of magnesium alloys in intergranular (IG) or mixed modes are also reported in literature.<sup>80,81</sup> The differences in fracture modes have been attributed to the heterogeneities at the grain boundaries, leading to the formation of micro galvanic cells and subsequent dissolution along the grain boundaries, thus resulting in IGC.

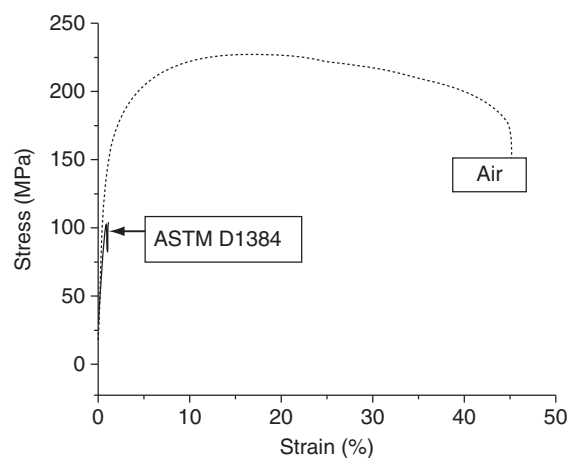


**Figure 12** Stress–strain plots of SSRT tested AZ31 magnesium alloy.<sup>79</sup>



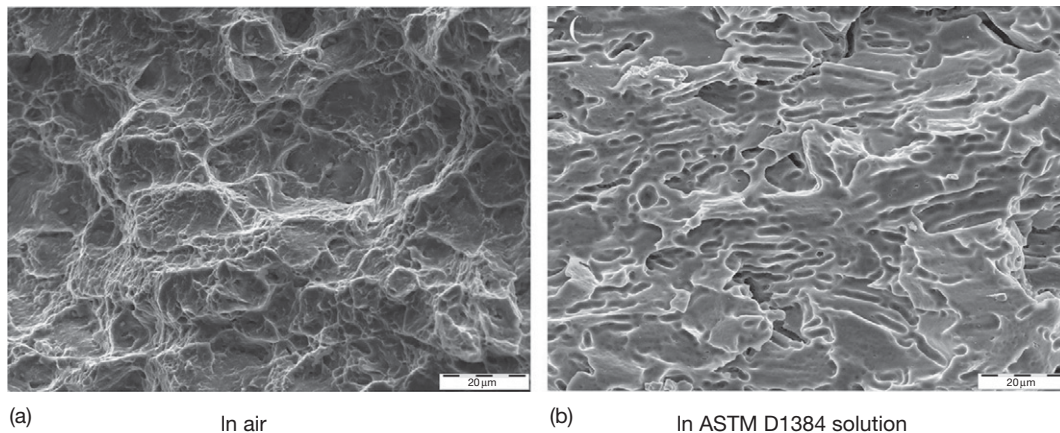


**Figure 13** Fracture surface appearance of SSRT tested AZ31 alloy ( $10^{-6} \text{ s}^{-1}$ )<sup>79</sup>: (a) in air and (b) in ASTM D 1384 solution.

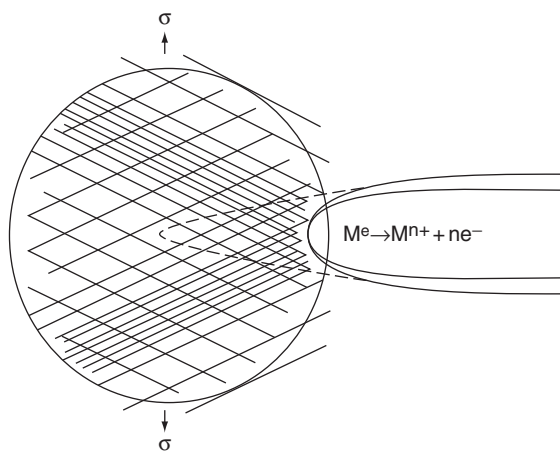


**Figure 14** Continuous crack propagation by dissolution following film rupture.<sup>82</sup>

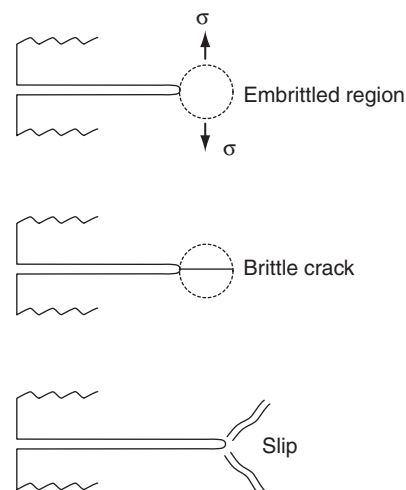


**Figure 15** Model for transgranular cracking in Mg-Al alloys.<sup>83</sup>

The SCC propagation mechanisms for magnesium alloys fall in one of the following two groups: (a) continuous crack propagation by anodic dissolution at the crack tip (Figure 14)<sup>82</sup> or (b) discontinuous crack propagation by a series of mechanical fractures at the crack tip (Figure 15).<sup>83</sup> The dissolution mechanisms could be (a) preferential attack, (b) galvanic attack by film rupture, or (c) tunneling. The mechanical fracture mechanisms are broadly either (a) cleavage fracture or (b) hydrogen embrittlement. A comprehensive description of the SCC mechanisms in magnesium alloys can be found in the review by Winzer *et al.*<sup>71</sup>

There is not much published information on the effect of processing conditions on the cracking susceptibility of magnesium alloys. The data presented in Figure 16<sup>84</sup> suggests that the processing

conditions have a definite influence on the mechanical properties of AZ31 alloy. However, it is interesting to note that the strain to failure of the specimens in chloride environment is nearly the same although the difference in air is quite large.

The information on the SCC behavior of welded magnesium alloys is also quite scarce. Welds produced by the modern joining technologies *viz.*, friction stir welding and laser beam welding, seem to have good mechanical properties. The SCC of laser and friction stir weldments addressed recently,<sup>79</sup> suggest that the fusion boundary region is susceptible to SCC. A mixed mode of fracture (transgranular + intergranular) has been reported in both these weldments subjected to SSRT tests in ASTM D1384 solution, and further, the



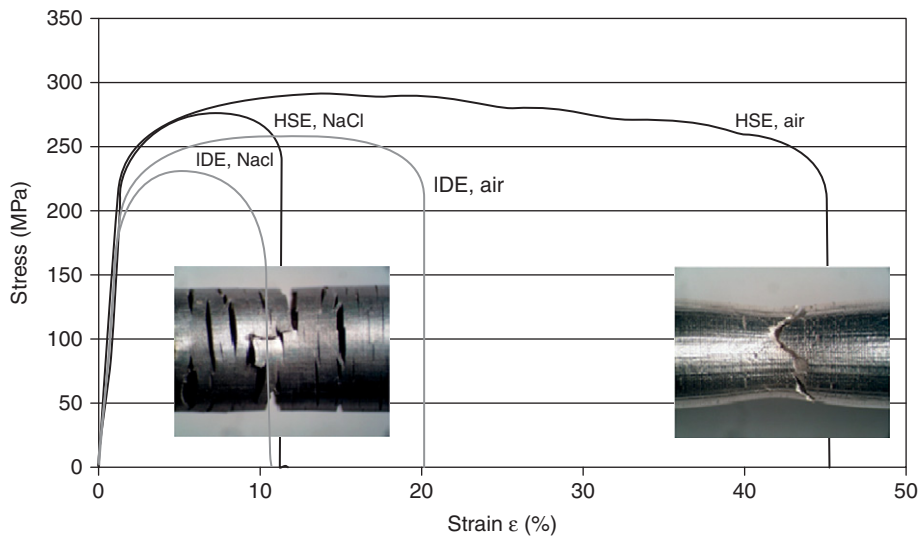


**Figure 16** Effect of processing conditions on the SCC of AZ31.<sup>84</sup> IDE – indirect extrusion; HSE – hydrostatic extrusion.

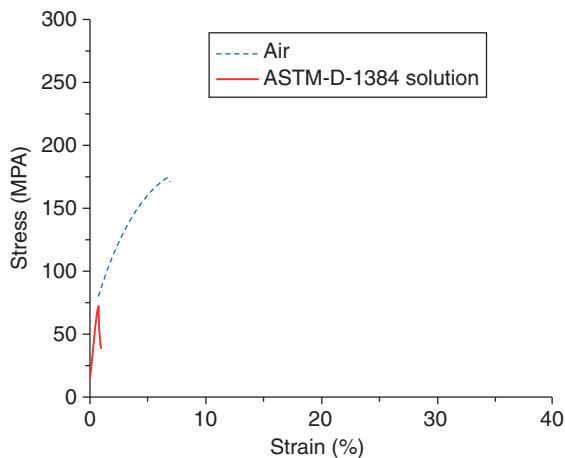


**Figure 17** Stress-strain plot of SSRT tested friction stir weldment of AZ31.<sup>79</sup>

weldments showed a higher susceptibility to SCC than the parent alloy (**Figures 17 and 18**).

Cathodic polarization of magnesium alloys is reported to reduce or even prevent SCC of magnesium alloys in aqueous solutions.<sup>66,70,72</sup> However, yet in another recent work,<sup>85</sup> it has been found that AZ80 alloys undergo SCC–HE under conditions of continuous charging under cathodically polarized conditions in distilled water. **Figure 19** shown below explains the effect of cathodic charging on the cracking behavior. The exact role of hydrogen and the precise underlying mechanisms of SCC under such conditions are still being debated.

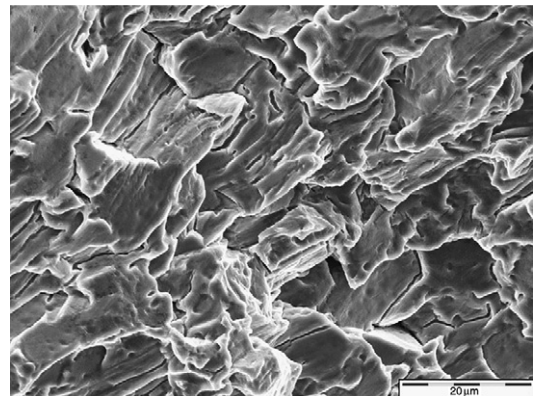


**Figure 18** Fracture surface appearance of FSW weldment of AZ31.<sup>79</sup>

### 3.09.5.3 Influence of Alloying and Processes

The corrosion behavior of magnesium alloys is influenced substantially by the impurities. The heavy metals contained as impurities (*viz.*, Fe, Cu, and Ni) form galvanic cells and enhance the corrosion rate, and the effect of these impurities on the corrosion rate is depicted in **Figure 20**.<sup>86</sup>

The tolerance limit depends on the alloy composition. For pure magnesium, the tolerable limits for Cu, Fe, and Ni are 0.1%, 0.005%, and 0.0005%, respectively. These impurities in magnesium alloys arise from various sources; the iron pick up is primarily from the melting crucibles and tools, copper comes from impure aluminum, while nickel gets in

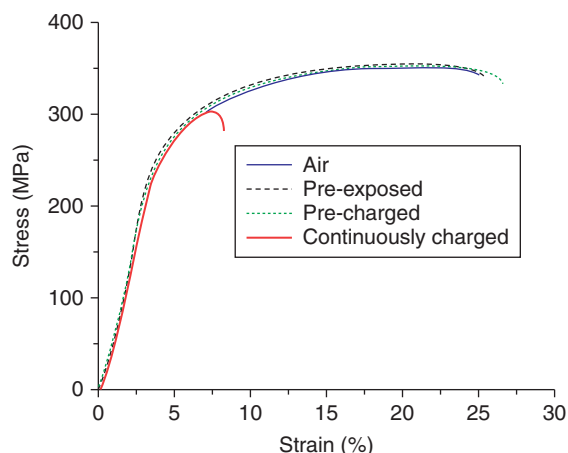


**Figure 19** Stress-strain curve of AZ80 alloy at a strain rate of  $10^{-6} \text{ s}^{-1}$ : in air; preexposed in distilled water for 24 h and then immediately strained in air; precharged at  $\sim 300 \text{ mV}$  cathodic to the open circuit potential (OCP) for 24 h in distilled water and then immediately strained in air; continuously charged at  $\sim 300 \text{ mV}$  cathodic to OCP in distilled water during the test.<sup>85</sup>

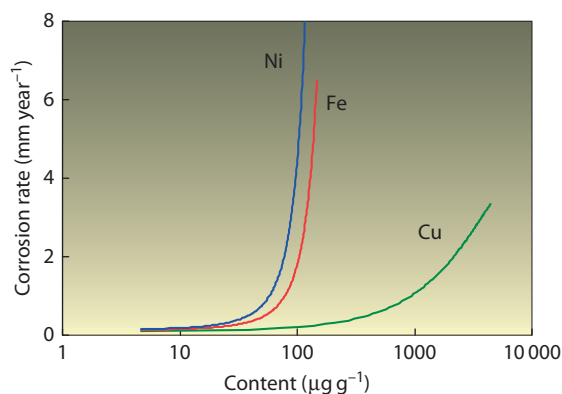


**Figure 20** Effect of impurities on the corrosion rate of magnesium alloy AZ91.<sup>86</sup>

from nickel containing stainless steel crucibles or at times very low levels of Ni may be contained in the raw magnesium itself.<sup>87</sup> If these impurities are restricted within tolerable limits, a substantial improvement in the corrosion resistance of magnesium alloys could be accomplished.

Magnesium alloys in which the total content of these impurities is restricted to 'ppm' levels are referred to as high purity (HP) alloys, and these alloys can virtually compete with aluminum alloys in terms of corrosion resistance.<sup>86</sup> In the salt spray tests performed as per ASTM B 117, the high purity magnesium alloys (with the exception of AM20) showed very low corrosion rates, (Figure 21)

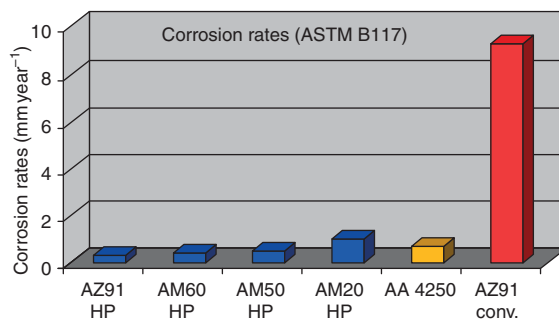


**Figure 21** Comparison of corrosion rates of HP magnesium alloys and  $\text{AlSi}_9\text{Cu}_3$ . (Note the corrosion rate of AZ91 with impurities beyond the tolerable limits.)

compared to a silicon and copper containing aluminum alloy (AA4250), which is used as a secondary alloy in the automobile industry.

The micro galvanic effects, as well as the formation of passive layers to minimize the corrosion can be influenced by addition of specific alloying elements. Besides the production of HP alloys, the susceptibility to corrosion of magnesium alloys can be controlled by the addition of RE elements. It is believed that these elements stabilize the passive film formed on the surface of magnesium alloys. In addition, the intermetallic phases formed in the magnesium alloys containing SE, show corrosion potentials similar to the aluminum containing matrix and thus, eliminate the galvanic effect. Additions of manganese to magnesium alloys help in reducing the galvanic corrosion, as manganese preferentially forms an intermetallic compound with aluminum, incorporating Fe and Ni, thus bringing down the effect of potential differences between free iron or nickel and the magnesium matrix in the alloys. The tolerance limits for impurities (especially Fe) in such alloys can be higher, without many of its problems. Aluminum improves the corrosion resistance in magnesium alloys when the alloying addition is increased from 2% to 9%. The benefit is two fold, first,  $\text{Mg}_{17}\text{Al}_{12}$  forms a favorable corrosion resistant network along the grain boundaries, and second, the incorporation of aluminum oxide in the  $\text{Mg}(\text{OH})_2$  layer improves the stability of the passive layer and thus enhances the corrosion resistance. Owing to the superior passive layer on the surface in aluminum containing magnesium alloys, a special form of corrosion, so-called filiform corrosion, is observed which is otherwise observed only underneath thin coatings. Zinc increases the corrosion potentials and thus reduces the corrosion rate. Also, the elements such as zirconium added as grain refiners to magnesium alloys can influence the corrosion behavior positively.

The microstructure with a given grain size and precipitate has a great influence on the corrosion resistance. Small grain size is often reported to be more corrosion resistant than larger grains. Thus, corrosion resistance can be optimized by the choice of the production process. So, the same alloy processed with HPDC has generally a better performance than sand or gravity die casting, and this can be explained by higher cooling rates resulting in a finer microstructure. Using special melt or powder metallurgical production processes or thermo mechanical treatments, even smaller grain size can be obtained. The new production processes, such as semi-solid processing, result in specific microstructures and thus have an influence on the corrosion performance. The globular microstructure with surrounding intermetallic phases is often reported to have good corrosion resistance. The best corrosion resistance, however, is often found with the products of rapid solidification processes. Precipitates and impurities are often finer and more uniformly distributed or the alloying elements remain in solid solution without forming precipitates. Passive films on supersaturated alloys are more easily formed and are more uniform and stable. In Mg–Al alloys, the  $\beta$ -phase ( $\text{Mg}_{17}\text{Al}_{12}$ ) formation can be suppressed by rapid solidification, and there is sufficient Al available to stabilize the passive layer by the formation of  $\text{MgAl}_2\text{O}_4$  spinels.<sup>88</sup>

Heat treatment of magnesium alloys influences the corrosion behavior, as the involved diffusion process has an effect on the distribution of alloying elements in the matrix and also influences the secondary phase formation. In general, magnesium alloys subjected to heat treatment (solution treatment, ageing, etc.) exhibit a higher corrosion rate when compared to the as-cast condition. The latter is especially the case if the precipitates have a barrier function in the as-cast condition, owing to the formation of a dense network along the grain boundaries.

### 3.09.6 Corrosion Prevention Strategies

#### 3.09.6.1 Coatings

Magnesium and magnesium alloys can hardly be protected by alloy development against general corrosion in acidic environments and against galvanic corrosion. Instead, for this purpose, a wide variety of coatings are available. The coatings are also used for improving the aesthetic appeal and for increasing the decorative finish. The following techniques are

available for the surface modification of magnesium and its alloys:

- Chemical conversion coatings  
Chromating, phosphating
- Electro-chemical coatings  
Anodizing  
Electroplating (Zn, Cu, Ni, Cr)  
Plasma electrolytic oxidation
- Physical techniques  
Physical vapor deposition  
Plasma/laser assisted vapor deposition  
Thermal spraying
- Nonmetallic coatings  
Varnish, wax, polymeric coatings, paints.

The physical techniques are still in the research stage, and only the other surface modification technologies are adopted in the industry to some extent as of today. A detailed overview, description of the processes, and information about the advantages and disadvantages of many surfaces treatments for magnesium alloys is given by Gray and Luan.<sup>89</sup> Before selecting a coating system for a given application, it is necessary to understand the corrosion behavior of the magnesium alloy in question in the service environment and the suitability of the material for processing, to deposit the coating. The surface preparation plays a crucial role in making the coating system perform well in the field of operation.

A number of problems are specific for coatings on magnesium alloys. No coating system polarizes magnesium in the cathodic direction, since all the coatings are more noble than the magnesium alloy matrix. Coating of magnesium, especially with a metallic coating, may lead to an accelerated galvanic attack in aqueous environments, if the deposited layers are not sufficiently thick enough or if there are any defects/damages in the coatings. However, magnesium surfaces can be modified and effectively protected by multilayered systems. For reasons of cost, the coating system is mostly decided, based on the aggressiveness of the environment and the application demand. Pickling, conversion coating, anodizing, plating, and organic coatings are available and multiple combinations of these are possible.

##### 3.09.6.1.1 Chemical conversion coatings

Chromating is a known surface treatment for aluminum, zinc, and magnesium for years and this treatment develops a very thin layer (to about 1  $\mu\text{m}$  maximum). The treatment can be used for the prevention of damage by corrosion of magnesium alloy

components during storage and transport. In addition to corrosion protection, these films offer an inhibitive effect inherent to the chromate film. The adhesion to organic coatings is also greatly improved by this treatment.<sup>90</sup> Nevertheless, the use of chromates is limited by the new environmental regulations in Europe since 2003, owing to growing health concerns associated with hexavalent chromium.<sup>91,92</sup>

New alternatives to the chromating process based on phosphate permanganate or fluoride zirconate have been proposed.<sup>90</sup> Alternate chrome-free conversion coatings based on alkali potassium permanganate solutions (MAGPASS-COAT<sup>®</sup>) and from solutions containing vanadates, molybdates and tungstates have also been attempted.<sup>93,94</sup> As these conversion coatings impart good adhesion properties, a few attempts have been made to produce chrome-free coatings in electrolytes based on stannates<sup>95</sup> and RE salts.<sup>96</sup> Effort was also made to produce conversion coatings based on zinc manganese phosphating electrolytes on magnesium alloys.<sup>97</sup> In general, all these conversion coatings need to be used in combination with an overlay coating for efficient corrosion protection, especially in aggressive environments.

#### 3.09.6.1.2 Electrochemical conversion coatings

The anodic oxidation of magnesium alloys result in a relatively thick and electrically insulating layer with good wear resistance. Like the chemical conversion coatings, the anodic oxide films also provide a good base for organic coatings, and in addition these can be impregnated as well. In particular, the newer processes are capable of developing very hard ceramic layers (ANOMAG<sup>®</sup>, KERONITE<sup>®</sup>, TAGNITE<sup>®</sup>, and MAGOXID<sup>®</sup>). These treatments are carried out in electrolytes at higher operating voltages with low current density levels leading to a plasma discharge.<sup>98</sup> The temperature of the bulk electrolyte tends to rise, typically to around 50 °C (depending on the degree of cooling provided to the system). The local temperature in the plasma zone would probably be in excess of 1000 °C, this results in the formation of 'glassy' or 'ceramic' anodic coatings. The process is called by various names, *viz.* plasma anodizing, micro arc oxidation (MAO), and plasma electrolytic oxidation (PEO).

The composition and the thickness of the conversion layers developed, depend on the processing conditions, *viz.* the chemical composition of the alloy, electrolyte composition, operating voltage, current density, temperature of electrolyte, duration, etc.

The thickness of the layers ranges from a few microns to as high as 150 µm. Electrolytes containing combinations of hydroxides, carbonates, silicates, phosphates, aluminates, and borates have been explored. The processing voltages are in general a function of the composition of electrolytes, and voltage levels as high as 600 V are achieved during this PEO processing. The current density for the PEO operation ranges generally from 5 to 50 mA cm<sup>-2</sup>, which is decided depending on the electrolyte/material combination. A few of the conventional and plasma anodizing processing electrolytes, processing conditions and resultant films are presented in Table 13.<sup>99</sup>

Figure 22 represents schematically a typical PEO coating obtained in an electrolyte based on silicate and hydroxide. The various zones that are observed in the PEO coatings are: Zone 1 (interface): The interface is very rough. It appears as if there were thin layers of less than 1 µm thickness with a finer and more dense structure in the interface region; Zone 2 (micro porosity): This has an extension from 20 to 80 µm. Here, the ceramic oxide film is denser, and only a small number of larger pores or cavities are visible; Zone 3 (pore band): This is observed in all specimens and can be identified by a pronounced band of cavities at a depth of 20–40 µm from the surface. Most of the visible surface pores (craters with discharge channels) seem to end in this band of cavities; Zone 4 (near surface): This is the outermost surface with the crater structure on the top. The ceramic layer is enforced by a large number of discharge channels reaching from the crater surface toward Zone 3. The porosity is the most striking feature of the anodized layers (Figure 23), and the size and distribution of pores strongly influence the properties of the layers. It should be noted that the other coatings can vary from this layered structure.

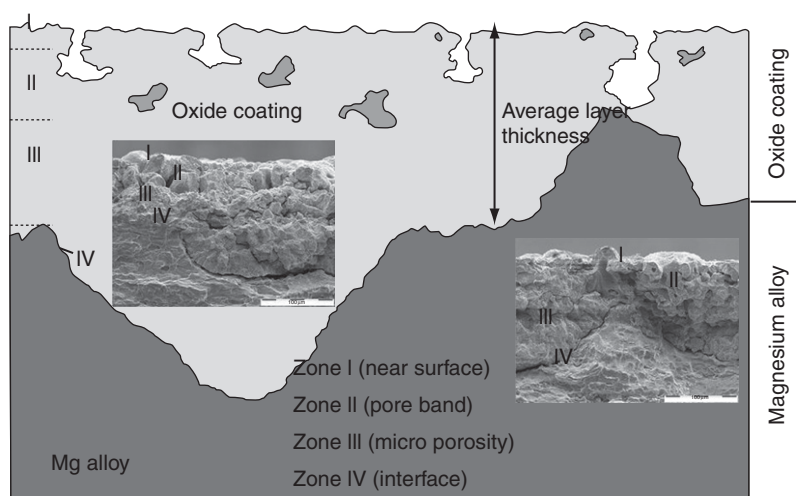
As almost all PEO layers are more or less porous, a secondary seal coat would be preferred for an enhanced corrosion protection, depending on the environment in which the components are to be used. However, their use in the commercial market as of date, is somewhat restricted owing to the high operating costs associated with the processing.

#### 3.09.6.1.3 Electro and electroless deposition

The deposition of metals and/or alloys from aqueous solutions containing the respective metal salts is practiced for many of the components made of both ferrous and nonferrous metallic substrates for imparting better surface finish, aesthetic appeal, corrosion resistance, electrical conductivity, solderability etc.

**Table 13** Some commonly used anodic oxidation processes for magnesium alloys<sup>99</sup>

Process	Electrolyte Components	Current density ( $A\ cm^{-2}$ )	Type of current	Electrolyte temperature ( $^{\circ}C$ )	Layer color
HAE	Potassium fluoride Sodium phosphate Potassium hydroxide Aluminum hydroxide Potassium permanganate	1.5–2.5	AC or DC	27	Brown
DOW 17	Ammonium difluoride Sodium dichromate o-Phosphoric acid	0.5–5.0	DC	70–80	Green
AHC Magoxid-Coat®	Mineral acid (fluoric, phosphoric, boracic acids)  Organic matters	1–5	Special types of signals with plasma-chemical reaction	15–20	White

**Figure 22** Schematic representation of a typical cross section of PEO-coated magnesium alloy.<sup>100</sup> (Typical features of the scanning electron micrographs inserted.)

There is not much older literature on the established practices for the deposition of metals/alloys on magnesium, but recently the interest manifested in the number of publications is increasing, especially in China.

There are lots of issues in the deposition of metals/alloys on magnesium alloys. First, magnesium is quite active and can react with oxygen to form a layer on the surface which very strongly inhibits effective deposition. Hence, it calls for a specific and careful preplating treatment procedure. Second, magnesium undergoes active dissolution in acidic or near neutral solutions upon immersion, and hence needs to be handled carefully while plating. Nevertheless, there have been a number of research attempts for the prevention of

corrosion of magnesium by plating techniques. Plating of nickel/gold has proved to be good for some space applications, while plating with silver was rated good from electrical conductivity. Plating of gold is reported to be done in stages with the first stage being zinc immersion plating, followed by nickel electro flash and finally the gold coating.<sup>101</sup> Recently, in an interesting work, plating of zinc from ionic solutions was demonstrated by Bakkar and Neubert and it is claimed that deposits were free from defects and showed corrosion behavior (Figure 24) similar to that of pure zinc in chloride solutions.<sup>102</sup>

Electroless nickel plating is also contemplated for magnesium alloys with a careful pretreatment of the substrates. In order to promote better coating



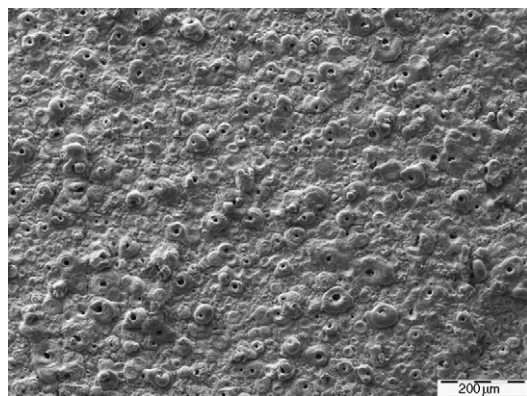


**Figure 23** SEM image showing the topography of the PEO-coated magnesium alloy.<sup>100</sup>

characteristics, magnesium surfaces may be given a zinc or copper flash coating over which nickel can be deposited by the electroless technique,<sup>98</sup> and the deposition of flash coating is similar to that performed for the deposition of gold. The electroless nickel deposits are harder than most of the magnesium alloys ( $\leq 80 \text{ HV}_{0.1}$ ), in general to about  $500 \text{ HV}_{0.1}$ . Such coated magnesium alloys find applications in electronics and telecommunications, guaranteeing a stable electrical contact with good resistance to adhesive wear and corrosion. It is mandatory to ensure that the deposits are free from pores and cracks as these defects can very adversely influence the corrosion behavior of the coated magnesium alloy (galvanic effect), despite the presence of a layer intended for protection. Further, recycling of such coated alloys is not feasible, especially if one looks at the production of high purity magnesium alloys. This is true despite the fact that there are quite a number of stripping solutions available for the removal of coatings from magnesium substrates.

#### 3.09.6.1.4 Physical techniques

Advanced techniques like laser beam (LB) and electron beam (EB) processing offer large scope for the modification of the surface of engineering alloys. Thus, magnesium alloys can be tailored by just heating to critical temperatures, or remelting with or without the addition of alloying elements, or by depositing coatings (cladding).

The thermal spray coatings often have a good amount of porosity, and this could be a major disadvantage from the corrosion point of view. The modern thermal spray techniques like high velocity oxy fuel or detonation gun spray process could produce effective coatings as the porosity levels are substantially low.

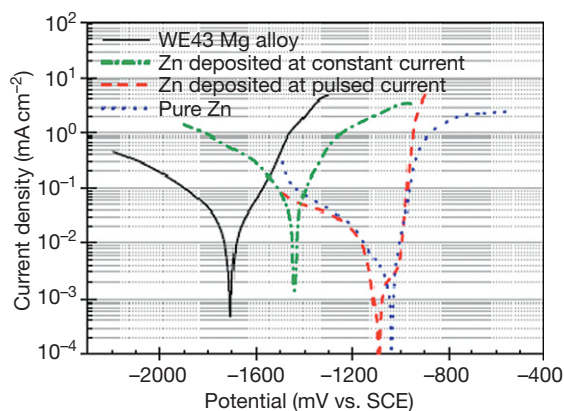


**Figure 24** Potentiodynamic polarization behavior of WE43 magnesium alloy with and without Zn electrodeposit in 0.1 M NaCl solution.<sup>102</sup>

Thermal spray coatings on magnesium alloys have been reported for space applications.<sup>103</sup>

With the LB, EB and thermal spray processing, surfaces resistant to wear and corrosion can be produced by means of alloying and diffusion and it is even feasible to develop functionally graded layers. The physical and chemical vapor deposition technologies can also be used for coating a number of metallic and ceramic layers on magnesium alloys. The advantage and disadvantage at the same time is that they can be used economically only for reinforcement of smaller local areas whereas large area coatings are normally too time consuming. The coatings that can be achieved by thermal sputtering in highly controlled atmospheres are free from oxidation, and it is possible to produce thin and thick corrosion resistant protective coatings depending on the requirement.

Laboratory scale experiments on chemical vapor deposition (CVD) of molybdenum are reported to improve the corrosion resistance significantly, by the formation of a stable thin film ( $<0.5 \mu\text{m}$ ) of molybdenum on magnesium alloy substrates.<sup>104</sup> Deposition of titanium nitride and zirconium nitride by plasma assisted CVD have also been attempted.<sup>105</sup> PVD coatings based on Mg alloys can be used for cathodic protection of conventional magnesium substrates.<sup>106–108</sup> However, the applicability of PVD and CVD coatings on large scale industrial components has not yet been fully explored.

#### 3.09.6.1.5 Organic coatings

The effect of organic coatings is generally to prevent or reduce the contact of water, oxygen, or other electrolytes with the metal surface. They are generally used in combination with conversion or anodized



coatings and offer in this combination an excellent corrosion protection (paint). If they are used alone, then normally only a temporary protection is intended, for example, the use of wax or oil for storage or shipping. The most important aspect for the selection is a resistance against alkaline corrosion products of magnesium alloys.

### 3.09.6.2 Choice of Coating Systems and Design Aspects

The damage caused by galvanic corrosion of the magnesium components in contact with other metallic materials can also be reduced or fully suppressed by employing appropriate constructive measures. The most effective method is to avoid the accumulation of electrolyte in the area of contact of materials, as this virtually eliminates the formation of a galvanic cell.

The other way of controlling the galvanic corrosion of magnesium alloys is to control the cathodic reaction so that the net anodic reaction (galvanic attack) on magnesium can be reduced correspondingly.<sup>109</sup> The galvanic current ( $I$ ) is expressed as

$$I = (E_C - E_A)/(R_C + R_E + R_M)$$

where  $E_C$  and  $E_A$  are the open circuit potentials of the cathode and anode, respectively,  $R_M$  and  $R_E$  are the resistances of the metal circuit and the electrolyte, respectively, and  $R_C$  is the cathodic polarization resistance.

Based on the above equation, the net galvanic current flow can be controlled by selecting an appropriate and compatible material as a couple, thus keeping the potential difference as low as possible. By using suitable coatings and insulation materials, the resistances  $R_C$  and  $R_M$  can be increased, resulting in lower galvanic current. As mentioned earlier, keeping the electrolyte away will result in an increased  $R_E$ , hence, in that case, too, a better galvanic corrosion resistance can be expected.

The choice of protective systems for magnesium alloys depends on the size, shape and geometry of the components and the joining technologies employed. Screwed and riveted joints offer the most varied possibilities to control, as one can alter the anode, cathode and the electric contact between these as well as the contact with the electrolyte. In some cases, by providing insulation between the magnesium and the other contacting material, the magnesium component can be left as such without any coating. There have been instances in which failure of a coating on

magnesium alloys led to accelerated form of damage by the galvanically driven corrosion.

Conventionally galvanized steel screws can be employed with a silicate sealing for fastening of magnesium alloys, and it has been proven to be successful for applications in commercial vehicles.<sup>110</sup> The steel screws can also be electroplated with an alloy deposit of 80%Sn–20%Zn for a better performance.<sup>111</sup> The steel fasteners can also be used with nylon or plastic caps as cover for the screw heads.<sup>109</sup> In addition, washers made of an aluminum alloy (6XXX series, anodized) or polymer can be used with steel screws to minimize the galvanic corrosion. The use of Al screws instead of steel, if the loading conditions are not that severe, is a good idea. Fiber reinforced plastic screws on PEEK base with carbon or polyamide fibers can also be used considering the fact that the polymers are free from galvanic corrosion.<sup>112</sup>

The surface treatment procedures described above can also be applied for the treatment of magnesium alloy weldments. In principle, these weldments can be treated as an individual component; however, it is well known that the heat affected zones could be the vulnerable region in the weldments.<sup>113</sup> Nevertheless, by appropriate selection of processing parameters, a good protection from corrosion damage can be offered to these weldments.

### 3.09.7 Applications of Magnesium Alloys

Magnesium alloys have had applications since the early 1930s, when they were first used in the cast form in automobiles. Since the start of its production in 1939, more and more parts, such as the crank case, camshaft sprocket, gearbox housing, several covers, and the arm of an electric generator, were added, until the total magnesium weight reached 17 kg in 1962, which meant a reduction of 50 kg in total mass compared to steel. The production of the VW Beetle used almost 21 000 tons of magnesium alloys in 1960,<sup>114</sup> and the Volkswagen Group reached a total consumption of 42 000 tons of magnesium alloys in 1972,<sup>115</sup> until the change from air-cooled to water-cooled engines reduced the use of magnesium alloys. Other manufacturers used magnesium in their technical applications as well as in complex parts such as tractor hoods made of die-castings (dimensions: 1250 mm × 725 mm × 480 mm; weight 7.6 kg), main gear boxes for helicopters (casting weight 400 kg, machined 200 kg), crank cases for zeppelin engines, air intake cases for propjet engines (weight 42 kg), frames,

rims, instrument panels, fan blades for cooling towers (weight 169 kg), etc.

The development of high purity (HP) alloys, with their much improved corrosion resistance, contributed to the rapidly expanding production. In the past, the corrosion behavior of the available alloys had often been the overriding factor preventing their application. The factor favoring the use of magnesium is that it counts as a substitute for polymers for which no satisfactory recycling solution has yet been found. Furthermore, it allows light-weight construction for reduced energy consumption or simply easier handling.

With regard to the processing of magnesium alloys, pressure die-casting is preferred in view of its advantages compared to the processing of aluminum and zinc, which are both amenable to this type of casting. Besides the specific properties of magnesium mentioned above, the other favorable factors

are its low casting temperature (650–680 °C, depending on the alloy) and the relatively low energy needed for melting. The energy needed for AZ91 ( $2 \text{ kJ cm}^{-3}$ ) is about 77% of that required to melt the aluminum alloy AlSi12CuFe.<sup>116</sup> The high price of magnesium usually refers to its mass not its volume, and the lower density coupled with other factors can actually make it cheaper in real terms. Thus, the low thermal heat content allows the casting process to be 50% faster than with aluminum; a high clock cycle of parts is possible, maintaining high precision and good surface quality.

Thus, magnesium can be found in a variety of applications today. The density, its shielding against electromagnetic radiation, and the possibility of producing thin-walled parts has led to furthering the use of magnesium die-cast parts in the computer industry, in mobile phones (Figures 25(a) and 25(b)), and in hand tools (e.g., chainsaws).

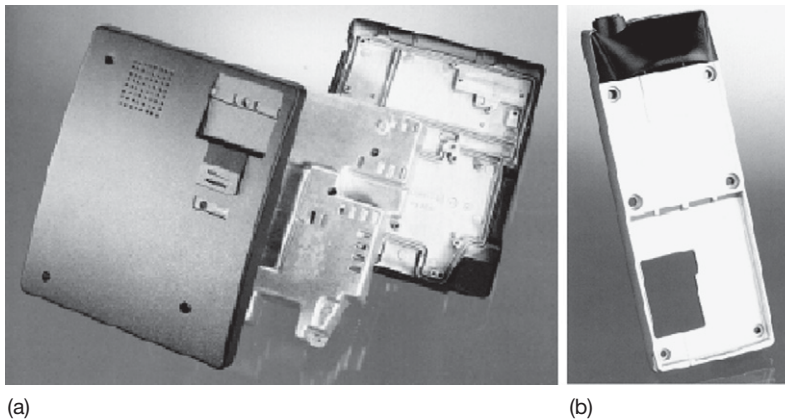


**Figure 25** Applications of magnesium alloys in the communications sector.<sup>122</sup> (a) Parts for a telephone switch board and (b) a mobile case.

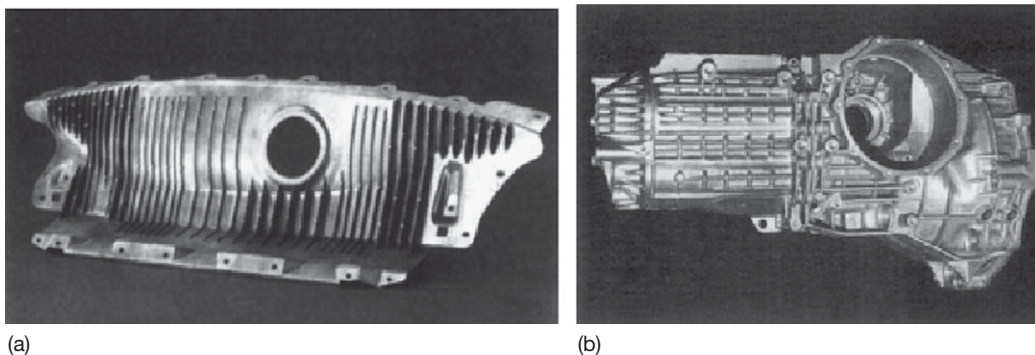


**Figure 26** Applications of magnesium alloys in automobiles.<sup>122</sup> (a) Fuel tank cover in Mercedes Benz and (b) gearbox housing in VW-Passat (Volkswagen AG).

Other examples of magnesium parts in vehicles include:

- gearbox housing, e.g., in the VW Passat, Audi A4
- the inner tailgate in the Lupo ('3-liter car'), which was made of AM50 (3.2 kg)
- tank cover in the Mercedes-Benz SLK
- cylinder head caps, for example, made of AZ91HP by cold-chamber high pressure die casting, and having a weight of 1.4 kg<sup>117</sup>
- dashboard, for example, in the Audi A8 and in the Buick Park Avenue/Le Sabre<sup>118</sup>
- seat-frames<sup>119</sup>
- steering wheels, for example, in the Toyota Lexus, Celica, Carina, and Corolla<sup>118</sup>
- rims, for example, in the Porsche Carrera RS (9.8 kg AM70 HP; low-pressure ingot casting).<sup>117</sup>

The list of magnesium parts in cars could be further continued<sup>120,121</sup> and new examples are constantly being added. Two recent applications of magnesium are illustrated in **Figures 26(a) and 26(b)**. The Mercedes-Benz SLK fuel tank cover is used as an example to show the advantages resulting from converting the construction from conventional materials to magnesium alloys. The part supports the car body and serves as a separation between the trunk and the back seats. Previous solutions consisted of a welded conduit frame. The first alternatives were steel and aluminum welding (7–8 kg each) and a magnesium cast part. The magnesium casting could be established as a serial part with a total weight of 3.2 kg, a decreased spatial requirement, and fewer components. Moreover, no post processing was necessary and the part could be used uncoated. The use of magnesium in the gearbox housing in the VW Passat is also primarily based on the weight savings achieved by replacing aluminum alloys. The use of the AZ91 alloy instead of aluminum led to a total weight reduction of almost 25%, and the geometry and production equipment remained identical.

## References

1. Beck, A. *Magnesium und seine Legierungen*; Julius Springer Verlag: Berlin, 1939.
2. Emley, E. F. *Principles of Magnesium Technology*; Pergamon Press: New York, USA, 1966.
3. Avedesian, M. M.; Baker, H. *ASM Specialty Handbook Magnesium*; ASM International: Materials Park, OH, USA, 1999.
4. Kammer, C. *Magnesium-Taschenbuch*; Alumiunverlag: Düsseldorf, 2000.
5. Neite, G.; Kubota, K.; Higashi, K.; Hehmann, F. In *Materials Science and Technology, Volume 8, Structure and Properties of Non-Ferrous Alloys*; Cahn, R. W., Haasen, P., Kramer, E. J., Eds.; VCH Weinheim, 1996.
6. Annual book of ASTM Standards. Nonferrous metal Products. Volume 02.02. Aluminium and Magnesium alloys. ASTM West Conshohocken, 1996.
7. Fink, R. In *Magnesium – Eigenschaften, Anwendungen, Potenziale*; Kainer, K. U. Ed.; Wiley-VCH, 2000; pp 26–49.
8. Zeumer, N.; Fuchs, H.; Betz, G. *Proc. Int. Conf. Magnesium Technology*; London 1987; pp 18–24.
9. Unsworth, W.; King, J. F. *Proc. Int. Conf. Magnesium Technology*; London 1987; pp 25–36.
10. King, J. F. In *Magnesium Alloys and their Applications*; Kainer, K. U., Ed.; Wiley-VCH, 2000; pp 14–22.
11. Alves, H.; Köster, U. In *Magnesium Alloys and their Applications*; Kainer, K. U., Ed.; Wiley-VCH, 2000; pp 439–444.
12. Mordike, B. L.; Buch, F. V. In *Magnesium Alloys and their Applications*; Kainer, K. U., Ed.; Wiley-VCH, 2000; pp 35–40.
13. Pettersen, K.; Westengen, H.; Skar, Y. I.; Videm, M.; Wei, L.-Y. In *Magnesium Alloys and their Applications*; Kainer, K. U., Ed.; Wiley-VCH, 2000; pp 29–34.
14. Pekguleryuz, M. O. *Mater. Sci. Forum* **2000**, 350–351, 131–140.
15. Du, W.; Sun, Y.; Min, X.; Xue, F.; Zhu, M.; Wu, D. *Mater. Sci. Eng. A* **2003**, 356, 1–7.
16. Yuan, G. Y.; Liu, L.; Wang, Q. D.; Ding, W. J. *Mater. Lett.* **2002**, 56, 53–58.
17. Lee, Y. *Grain Refinement of Magnesium*; PhD Thesis, University of Queensland: Australia, 2002.
18. Sillekens, W. H.; Bohlen, J. In *Magnesium, Proc. 6th Int. Conf. and Exhibition on Magnesium Alloys and their Applications*; Kainer, K. U., Ed.; Wiley VCH, 2003; pp 1046–1052.
19. Becker, J.; Fischer, G. In *Magnesium-Eigenschaften, Anwendungen, Potenziale*; Kainer, K. U., Ed.; Wiley-VCH Verlag, 2000; pp 95–110.
20. Mabuchi, M.; Yamada, Y.; Higashi, K. In *Magnesium Alloys and their Applications*; Wiley-VCH Verlag, 2000; pp 280–284.
21. Lin, H. K.; Huang, J. C. *Key Eng. Mater.* **2003**, 233–236, 875–880.
22. Kainer, K. U.; Doege, E.; Janssen, S.; Ebert, T. *Magnesium Alloys and their Applications*; Wiley-VCH Verlag, 2000; pp 596–601. (ISBN: 3-527-30282-2).
23. Everett, R. K.; Arsenault, R. J. *Metal Matrix Composites: Mechanisms and Properties*; Academic Press, 1991.
24. Clyne, T. W.; Withers, P. J. *An Introduction to Metal Matrix Composites*; Cambridge University Press, 1993.
25. Freuling, J. W.; Hanawalt, J. D. *Trans. AFS* **1969**, 77, 159–164.
26. King, J. F. *Proc. 60th Annual World Magnesium Conference*, Stuttgart, 2003; pp 10–15.
27. Kainer, K. U.; Benzler, T. U. In *Magnesium – Eigenschaften, Anwendungen, Potenziale*; Kainer, K. U., Ed.; Wiley-VCH, 2000; pp 59–75.
28. Wabusseg, H.; Kaufmann, H.; Uggowitzer, P. J. *Giesserei* **2000**, 87(3), 39–43.
29. Mundl, A.; Kaufmann, H. *Giesserei* **2001**, 88(8), 55–58.
30. Noll, T. R.; Friedrich, B.; Mueser, H.; Budak, I. *Giesserei* **2001**, 88(8), 60–66.
31. Gräf, T.; Hauer, H. *Giesserei* **2001**, 88(10), 38–41.
32. Czerwinski, F.; Zielinska-Lipiec, A.; Pinet, P. J.; Overbeeke, J. *Acta Mater.* **1991**, 49, 1225–1235.
33. Sasaki, H.; Adachi, M.; Sakamoto, T.; Takimoto, A. *Giesserei-Praxis* **1997**, 15/16, 341–246.
34. Kainer, K. U.; Dietzel, W.; Blawert, C. *Reaktionsfreudig – Korrosionsschutz von Magnesium-werkstoffen Maschinenmarkt – Das Industrie Magazin* **2003**, Vol. 14, 66.

35. Haferkamp, H.; Zilberg, J.; Rodman, M.; Nicmeyer, M.; Weber, J.; Holzham, U. *Theorie Praxis Metall.* **2000**, 19(5), 23–24.
36. Swiostek, J.; Bohlen, J.; Letzig, D.; Kainer, K. U. In *Proc. 6th Int. Conf. and Exhibition on Magnesium Alloys and their Applications*; Kainer, K. U., Ed.; Wiley VCH, 2003; pp 278–284. (ISBN: 3-527-30975-6).
37. Becker, J.; Fischer, G. In *Magnesium – Alloys and Technology*; Kainer, K. U., Ed.; Wiley-VCH Verlag GmbH: Weinheim, 2003. ISBN: 3-527-30570-X.
38. Müller, K. B. In *Magnesium Technology*; Kaplan, H. I., Ed.; 2002; pp 187–192.
39. Weissert, W. *Mat.-wiss. U. Werkstofftechn.* **2001**, 32, 81–83.
40. AWS, *Welding Handbook*, 8th ed.; American Welding Society: Miami, 1991; Vol. 2, pp 739–762.
41. *Welding of Magnesium Alloys*; In *ASM Handbook*; ASM international, 1990; pp 772–782.
42. Ryavov, V.; Ryazantsev, V. *Arc Welding of Aluminium and Magnesium Alloys*; Backbone Publishing: USA, 1998.
43. Rethmeier, M.; Wohlfahrt, H.; Wiesner, S. Joining of Lightweight Mg-Alloys by MIG Welding, IIW-Doc. IX-2042-02, 2002.
44. Liu, L.; Dong, C. *Mater. Let.* **2006**, 60, 2194–2197.
45. Munitz, A.; Cotler, C.; Stern, A.; Kohn, G. *Mater. Sci. Eng. A* **2001**, 302, 68–73.
46. Xunhong, W.; Kuaishe, W. *Mater. Sci. Eng. A* **2006**, 431, 114–117.
47. Chao-Ting, C.; Chuen-Guang, C. *J. Mater. Process. Technol.* **2007**, 182, 369–373.
48. Liming, L.; Jifeng, W.; Gang, S. *Mater. Sci. Eng. A* **2004**, 381, 129–133.
49. Liu, L. M.; Cai, D. H.; Zhang, Z. D. *Scripta Mat.* **2007**, 57, 695–698.
50. Haferkamp, H. H.; Niemeyr, M.; Schmid, C.; Kaese, V.; Cordini, P. Magnesium 2000: Proceedings of the Second Israeli International Conference on Magnesium Science & Technology, Dead Sea, Israel, MRI, 2000; pp 449–455.
51. Weisheit, A.; Galun, R.; Mordike, B. L. *Magnesium Alloys and Their Properties*; DGM: Wolfsburg, 1998.
52. Sanders, P. G.; Keske, J. S.; Leong, K. H.; Kornecki, G. *J. Laser Appl.* **1999**, 11(2), 96–103.
53. Leong, K.H.; Kornecki, G.; Sanders, P.G.; Keske, J.S. ICALEO 98: Laser Materials Processing Conference, Orlando, FL, 16–19 November 1998; pp 28–36.
54. Weisheit, Galun, R.; Mordike, B.L. Proceedings of the Conference: Magnesium Alloys and Their Applications, Wolfsburg, Germany, 28–30 April 1998; pp 619–624.
55. Coelho, R. S.; Kostka, A.; Pinto, H.; Riekehr, S.; Koçak, M.; Pyzalla, A. R. *Mater. Sci. Eng.* **2008**, 485, 20–30.
56. Schram, S.; Kettler, C.; Mazac, K.; Goldstein, C. *Schweißen Schneiden* **2000**, 52(6), 349–353.
57. Lackyer, S., Friction stir welds in magnesium alloys – Just how good are the mechanical properties, TWI: Bulletin March/April 2001.
58. Kato, K.; Tokisue, H. *Weld. Int.* **1994**, 8, 452–457.
59. Nagasawa, T.; Otsuka, M.; Yokota, T.; Ueki, T. Magnesium Technology 2000, TMS, Nashville, 12–17 March 2000, pp 383–387.
60. Hawke, D. L. In *ASM Speciality Handbook Magnesium and Magnesium Alloys*; ASM International, 1987; pp 194–210.
61. Song, G.; Atrons, A. *Adv. Eng. Mater.* **1999**, 1, 11–33.
62. Boese, E.; Göllner, J.; Hevn, A.; Strunz, A.; Baierl, C.; Schreckenberger, H. *Mater. Corros.* **2001**, 52, 247–256.
63. Makar, G. L.; Kruger, J. *Int. Mater. Rev.* **1993**, 38(3), 138–153.
64. Hillis, J. E.; Reichek, K. N. High purity magnesium AM60 alloy: The critical contaminant limits and the salt water corrosion performance, SAE Technical Paper Series #860 288, Detroit, 1986.
65. Song, G.; Atrons, A.; Dargusch, M. *Corros. Sci.* **1998**, 41, 249–273.
66. Ghali, E. In *Uhlig's Corrosion Handbook*; Revie, R. W., Ed.; John Wiley: New York, 2000; ch. 44, pp 793–830.
67. Lynch, S. P.; Trevena, P. *Corrosion* **1988**, 44, 113.
68. Meletis, E. I.; Hochman, R. F. *Corrosion* **1984**, 40, 39.
69. *ASM Speciality Handbook: Magnesium and Magnesium Alloys*; ASM International: USA, 1999; p 211.
70. Stampella, R. S.; Procter, R. P. M.; Ashworth, V. *Corros. Sci.* **1984**, 24, 325–341.
71. Winzer, N.; Atrons, A.; Song, G.; Ghali, E.; Dietzel, W.; Kainer, K. U.; Hort, N.; Blawert, C. *Adv. Eng. Mater.* **2005**, 7, 659–693.
72. Miller, W. K. In *Stress Corrosion Cracking: Materials Performance and Evaluation*; ASM International: USA, 1992; p 251.
73. Fairman, L.; Bray, H. J. *Corros. Sci.* **1971**, 11, 533–541.
74. Tomashov, N. D.; Modestova, V. N. Proceedings of the Inter-crystalline Corrosion and Corrosion of Metals Under Stress; Levin, I. A. Ed.; Consultants Bureau: New York, 1962; p 251.
75. Rokhlin, L. L. *Magnesium Alloys Containing Rare Earth Metals*; Taylor and Francis: UK, 2003; p 221.
76. Perryman, E. C. W. *J. Inst. Metals* **1951**, 78, 621.
77. Pelensky, M. A.; Gallaccio, A. Stress Corrosion Testing, STP 425, ASTM 1967; p 107.
78. Pardue, W. M.; Beck, F. H.; Fontana, M. G. *Trans. Am. Soc. Metals* **1961**, 54, 539.
79. Bobby Kannan, M.; Dietzel, W.; Zeng, R.; Zettler, R.; dos Santos, J. F. *Mater. Sci. Eng. A* **2007**, 460–461, 243–250.
80. Fairman, L.; Bray, H. J. *Br. Corros. J.* **1971**, 6, 170.
81. Priest, D. K.; Beck, F. H.; Fontana, M. G. *Trans. Am. Soc. Metals* **1955**, 47, 473.
82. Jones, R. H.; Ricker, R. E. *Stress Corrosion Cracking: Materials Performance and Evaluation*; ASM International: USA, 1992; p 1.
83. Bursle, A. J.; Pugh, E. N. *Mechanisms of Environment Sensitive Cracking of Materials*; Materials Society: London, 1977; p 471.
84. Blawert, C.; Swiostek, J.; Dietzel, W.; Letzig, D.; Atrons, A. Proceedings of the Inżynieria Powierzchni 2A, 2005, Corrosion 2005, Warsaw, Poland, 8–10 June 2005; pp 183–189.
85. Bobby Kannan, M.; Dietzel, W.; Singh Raman, R. K.; Lyon, P. *Scripta Mater.* **2007**, 57, 579–581.
86. Hillis, J. E. The effects of heavy metal contamination on magnesium corrosion performance, SAE Technical Paper No. 830523, Detroit, 1983.
87. Bühler, K. *Metall* **1990**, 8, 748–753.
88. Bray, D. J. Cast and rapidly solidified magnesium alloys – New light alloys. Advisory Group for Aerospace Research and Development, 92 – Neuilly sur Seine; NATO, Brussels; AGARD Conference on New Light Alloys 1990, Monterey, CA, USA 1990; pp 7.1–7.29.
89. Gray, J. D.; Luan, B. J. *Alloys Compounds* **2002**, 336, 88–113.
90. Schreckenberger, H. Proceedings of Fortschritte mit Magnesium im Automobilbau; Bad Nauheim 2000; pp 41–50.
91. Murray, R. W.; Hillis, J. E. Magnesium finishing – Chemical treatment and coating practices, SAE Technical Paper No. 900791, Detroit, 1990.
92. Kurze, P. Proceedings of Berichtsband 23, Ulmer Gespräch 2001, pp 82–88.

93. Zeng, A. P.; Xue, Y.; Qian, Y. R.; Want, Z. J. *Acta Metall. Sin.* **1999**, *12*, 946–951.
94. Gonzalez-Nunez, M. A.; Nunez-Lopez, C. A.; Skeldon, P.; Thompson, G. E.; Karimzadeh, H.; Lyon, P.; Wilks, T. E. *Corros. Sci.* **1995**, *37*, 1763–1772.
95. Rudd, A. L.; Breslin, C. B.; Mansfeld, F. *Corros. Sci.* **2000**, *42*, 275–288.
96. Reinhold, B. *OWT & WTK, Chemnitz* **2001**, 151–158.
97. Leyendecker, F. *DFO Leichtmetall-Anwendungen–Neue Entwicklungen in der Ober-flächentechnik* **2001**, *46*, 131–142.
98. Hillis, J. E. *Proc. of 40th Annual Conf. of Metallurgists of CIM* 2001; pp 3–26.
99. Kurze, P. In *Magnesium – Alloys and Technology*; Kainer, K. U. Ed.; Wiley-VCH Verlag GmbH: Weinheim, 2003. ISBN: 3-527-30570-X.
100. Blawert, C.; Heitmann, V.; Dietzel, W.; Nykyforchyn, H. M.; Klappiv, M. D. *Surf. Coat. Technol.* **2005**, *200*, 68–72.
101. Sharma, A. K. *Metal Finishing* **1991**, *89*(7), 16.
102. Bakkar, A.; Neubert, V. *Electrochem. Commun.* **2007**, *9*, 2428–2435.
103. Yoshinori, Y. Method for plating magnesium alloy, JP60024383, 1985.
104. Feurer, R.; Bui-Nam; Moranchio, R.; Larharfi, M.; Calsou, R. *Br. Corros. J.* **1989**, *24*, 126–130.
105. Rie, K. T.; Whole, J. *Surf. Coat. Technol.* **1999**, *112*, 226–233.
106. Seeger, D. M.; Blawert, C.; Dietzel, W.; Bohne, Y.; Maendl, S.; Rauschenbach, B. In *Magnesium Technology 2005, TMS 2005, 134th Annual Meeting and Exhibition*; San Francisco, CA (USA), 13–17, February; Neelameggham, N. R., Kaplan, H. I., Powel, B. R., Eds.; 2005; pp 323–328. ISBN:0-87339-582-4.
107. Bohne, Y.; Seeger, D. M.; Blawert, C.; Dietzel, W.; Maendl, S.; Rauschenbach, B. *Surf. Coat. Technol.* **2006**, *200*(22–23), 6527–6532.
108. Blawert, C.; Heitman, V.; Dietzel, W.; Stoermer, M.; Bohne, Y.; Gerlach, J. W.; Manowa, D.; Maendl, S. Proceedings of the Light Metals Technology Conference, Saint-Sauveur (CDN), 24–26 September 2007; pp 135–139.
109. Hydro Magnesium, Corrosion and Finishing of Magnesium Alloys, Technical Brochure.
110. Reinhold, B.; Kose, S. G.; Strobl, C. *Mater. Corros.* **1999**, *50*, 517–522.
111. Lehmkuhl, H.; Mehler, K.; Reinhold, B.; Bangard, H.; Tesche, B. *Adv. Eng. Mater.* **2001**, *3*, 412–417.
112. Skar, J. I.; Albright, D. *Magnesium Technology 2002*; TMS, 2002; pp 255, 261.
113. Lübbert, K.; Kopp, J.; Wendler-Kalsh, E. *Mater. Corros.* **1999**, *50*, 65–72.
114. Serwe, G. Magnesiumgußteile im Volkswagen, VDI-Berichte Nr. 58, VDI-Verlag, Düsseldorf, 1962.
115. Höllrigl-Rosta, F.; Just, E.; Köhler, J.; Melzer, H.-J. *Metall* **1980**, *34*, 12.
116. Cahn, R. W.; Hassen, P. In *Materials Science and Technology – A Comprehensive Treatment*; Kramer, E. J., Ed.; *Structure and Properties of Nonferrous Alloys* Matucha, K. H.; Ser Ed.; VCH Weinheim, 1996; Vol. 8.
117. Olsen, A. L. *Metall* **1992**, *46*, 570–574.
118. Magers, D. Einsatzmöglichkeiten von Magnesium im Automobilbau, Leichtmetalle im Automobilbau (Sonderausgabe der ATZ und MTZ 1995), Franckh-Kosmos Verlags-GmbH, Stuttgart, 1995.
119. Hector, B.; Heiss, W. Magnesium die-castings as structural members of the new Mercedes-Benz Roadster, SAE-Technical Paper Series No. 900798, 1990.
120. Müller, C. M. *Giesserei*; **1991**, 78(19).
121. Polmear, I. J. *Mater. Sci. Technol.* **1994**, *10*, 1–16.
122. Kainer, K. U.; Von Buch, F. In *Magnesium – Eigenschaften, Anwendungen, Potenziale*; Kainer, K. U., Ed.; Wiley-VCH, 2000; pp 1–26.



## 3.10 Corrosion of Titanium and its Alloys

**D. W. Shoesmith and J. J. Noël**

Department of Chemistry, The University of Western Ontario, London, ON, Canada N6A 5B7

© 2010 Elsevier B.V. All rights reserved.

3.10.1	Introduction	2043
3.10.2	General Physical Properties	2043
3.10.3	General Corrosion Properties	2044
3.10.3.1	Influence of pH	2045
3.10.3.2	Influence of Temperature	2045
3.10.3.3	Influence of Fluoride	2045
3.10.3.4	Hydrogen Absorption into Ti	2046
3.10.4	Localized Corrosion Processes	2046
3.10.4.1	Crevice Corrosion	2046
3.10.4.2	Environmentally-Assisted Cracking	2047
3.10.4.2.1	Stress corrosion cracking	2047
3.10.4.2.2	Hydrogen-induced cracking	2047
3.10.5	Specific Applications	2048
3.10.5.1	Aerospace	2048
3.10.5.2	Seawater and Brine	2048
3.10.5.3	Biomedical and Dental Implants	2049
3.10.5.4	Chemical Processing and Power Generation	2049
References		2049

### Glossary

**Adsorption** The surface retention of atoms, molecules, or ions by a solid or a liquid.

**Alloy** A metal product containing two or more elements as a solid solution, intermetallic compound, or mixture of metallic phases.

**Anatase** A tetragonal polymorph of titanium dioxide, also called octahedrite.

**Cathodic modification** Enhancement of cathodic kinetics by alloying additions leading to depolarization of the cathodic reaction and a shift of the corrosion potential to the passive region.

**Complexation** Formation of a coordination compound between a metal ion and a molecular or ionic entity known as a ligand.

**Corrosion allowance** An excess amount of metal included in a component, beyond that required for mechanical considerations, to compensate for expected corrosion losses.

**Creep** Slow, time-dependent strain of a solid caused by stress.

**Diffusion coefficient** The mass of a species, in grams, diffusing across an area of 1 cm<sup>2</sup> in

one second in a unit concentration gradient. Also known as diffusivity.

**Environmentally-assisted cracking** A cracking process driven by tensile stress in the presence of particular favorable environmental conditions (e.g., stress corrosion cracking, hydrogen-induced cracking).

**Film fracture events** Spontaneous and sudden rupture of the passive film on a metal, resulting in exposure of the underlying metal to the environment.

**Fretting** Wear and corrosion damage at the asperities of contact surfaces induced by repeated relative surface motion under load.

**Galvanic coupling** The joining of two dissimilar metals in an electrolyte, potentially leading to galvanic corrosion.

**Halide** The anion of an element belonging to the halogen group (F, Cl, Br, I, At).

**Hydriding** The formation of a covalent compound between hydrogen and a metal

**Hydrolysis** The reactions of metal cations with water to produce oxides or hydroxides and increase acidity.

**Initiation** The start of a localized corrosion process.

**Intermetallic compound** A covalent compound of two or more metals, or the alloy of two metals in which a progressive change in composition is accompanied by a progression of phases, differing in crystal structure.

**Lamination** A layered arrangement.

**Load** The mechanical force that is applied to a body.

**Metallosis** Infiltration of metal ions and/or particles into, and inflammation of, soft and/or bony tissues proximate to metallic biomedical implants as a result of wear, corrosion, and/or hypersensitivity reaction.

**n-Type** A semiconductor whose electrical conduction is associated with electrons (as opposed to holes) as the majority charge carrier.

**Nitinol** A TiNi shape-memory alloy.

**Propagation** The active stage of ongoing reaction and damage formation during a localized corrosion process.

**Repasivation** The cessation of corrosion and return to passivity of a surface after loss of passivity caused by localized corrosion or mechanical damage.

**Rolling** Reducing or changing the cross-sectional area of a workpiece by the compressive forces exerted by rotating rollers.

**Rutile** A tetragonal polymorph of titanium dioxide.

**Semiconductor** A solid material whose electrical conductivity is intermediate between that of a conductor and insulator, and is usually strongly temperature-dependent.

**Stress intensity factor** A measure of the stress at a point in a structure due to pressure resulting from combined tensile and compressive stresses.

**Texture** The anisotropic ordering of size, shape, and crystallographic orientation of grains in a polycrystalline solid.

**Toughness** A property of a material capable of absorbing energy by plastic deformation (see fracture toughness).

**Young's modulus** The ratio of a simple tensile stress applied to material to the resultant strain parallel to the tension.

## Abbreviations

**ASTM** American Society for Testing and Materials

**BCC** Body-centered cubic

**HCP** Hexagonal close-packed

**HIC** Hydrogen-induced cracking

**MIC** Microbiologically-influenced corrosion

**ppm** Parts per million (by weight)

**SCC** Stress corrosion cracking

**SCE** Saturated calomel electrode

**UNS No.** Unified Numbering System number

## Symbols

**H<sub>c</sub>** Critical hydrogen concentration for hydrogen-induced cracking [ppm]

**pH**  $-\log$  (hydrogen ion activity)

**pK<sub>a</sub>**  $-\log$  (acid dissociation constant)

**Ti<sub>x</sub>Fe** Intermetallic compound of titanium and iron with uncertain stoichiometry represented by *x*

**TiH<sub>x</sub>** Titanium hydride with uncertain stoichiometry represented by *x*

**α** The hexagonal phase of titanium

**β** The cubic phase of titanium

### 3.10.1 Introduction

The key attributes of titanium and its alloys are high strength-to-density ratios and corrosion resistance, making these materials attractive choices for aerospace applications and the chemical process industry, respectively.<sup>1–6</sup> More recently, improvements in the corrosion resistance of the higher strength alloys by minor alloying additions have led to their expanded usage as medical and dental implants.<sup>7</sup>

### 3.10.2 General Physical Properties

Titanium has two elemental crystalline structures, the hexagonal close-packed (HCP)  $\alpha$  structure and the body-centered cubic (BCC)  $\beta$  structure.<sup>8–11</sup> While commercially pure Ti has the  $\alpha$  structure, the impurity Fe and added alloying elements can produce a range of alloy microstructures. Depending on the predominant phase, Ti and its alloys are classified as  $\alpha$ , near- $\alpha$ ,  $\alpha$ - $\beta$ , or  $\beta$ .<sup>9</sup> The commercially

pure materials have the  $\alpha$  structure and vary in oxygen content depending on strength requirements. The already good corrosion resistance of these materials can be further improved by the addition of small amounts of Pd and Ru.<sup>7</sup> The near- $\alpha$  alloys retain the HCP structure, but the addition of metals such as Al, Sn, V, Mo, and Ni may stabilize small amounts of the  $\beta$ -phase. This leads to increases in strength and toughness. The addition of very small amounts (<1 wt%) of Mo and Ni, and especially Pd or Ru, improves their corrosion resistance. Further increases in alloy content, particularly V and Al, lead to a range of higher strength  $\alpha$ - $\beta$  alloys, whose corrosion resistance can again be enhanced by Pd or Ru additions. The  $\beta$  alloys, predominantly used in aerospace applications, contain additional alloying elements, such as Cr, Zr, and Nb.

When corrosion resistance is paramount,  $\alpha$  or near- $\alpha$  alloys are the appropriate choice, while  $\alpha$ - $\beta$  and  $\beta$  alloys are more appropriately selected for high-strength applications. Table 1 shows a representative selection of materials and properties. More extensive listings and a general description of mechanical properties are available elsewhere.<sup>2,5-7</sup>

Small variations in impurity Fe content (generally <0.2 wt%) and distribution influence the microstructure by inhibiting grain growth during fabrication. This leads to decreased  $\alpha$ -grain size and Fe-stabilized  $\beta$ -phase along grain boundaries. Fe contents ( $\geq 0.03$  wt%) can lead to the precipitation of  $\text{Ti}_x\text{Fe}$  particles on grain boundaries and at triple points.<sup>12-14</sup> The time spent in the temperature range 700–860 °C (during fabrication, welding, or heat treatments) enhances  $\beta$ -phase and  $\text{Ti}_x\text{Fe}$  formation.

Small microstructural changes also occur on addition of the slightly soluble Pt group metals.<sup>7</sup> Pd can form intermetallic compounds in the  $\alpha$ -matrix without affecting grain growth, while Ru additions stabilize  $\beta$ -phase and inhibit  $\alpha$  grain growth. For near- $\alpha$  Ti containing 0.15 wt% of Ru,  $\beta$ -phase Ru content can exceed 10 wt%.<sup>15</sup> In  $\alpha$ - $\beta$  alloys, both Pd and Ru are accommodated in the  $\beta$ -phase and the microstructure is unaffected.<sup>7</sup> Since both noble metals and Fe stabilize  $\beta$ -phase and intermetallics, their cosegregation can occur. For example,  $\beta$ -phase containing 12 wt% Ru and 5 wt% Fe is observed in Ti containing 0.15 wt% Ru,<sup>16</sup> and grain boundary phases containing 2.6–6.9 wt% Fe and 0.3–0.8 wt% Pd are observed in Grade-7 (0.15 wt% Pd).<sup>16</sup>

### 3.10.3 General Corrosion Properties

Titanium is highly reactive with oxygen, and its corrosion resistance is attributable to the presence of a chemically inert, adherent, oxide film. This film forms spontaneously in air and aqueous environments and can be amorphous or crystalline, depending on the mode and rate of formation, slow growth favoring crystallinity.<sup>17-19</sup> The crystalline oxide can be anatase or the more stable rutile.<sup>20-22</sup> The presence of oxygen vacancies and  $\text{Ti}^{\text{III}}$  interstitial ions makes the oxide an n-type semiconductor.<sup>23-25</sup> Its composition is close to  $\text{Ti}^{\text{IV}}\text{O}_2$  with  $\text{Ti}^{\text{III}}/\text{Ti}^{\text{II}}$  states at the metal-oxide interface.<sup>26,27</sup> The oxide-solution interface is commonly hydrated.<sup>20</sup>

For  $\alpha$  and near- $\alpha$  alloys, alloying elements (Pd, Ru, Ni) do not incorporate into the oxide, but, for  $\alpha$ - $\beta$

**Table 1** Composition and properties of selected ASTM grades of titanium

ASTM grade (UNS No.)	Alloy type	Nominal composition (wt%)	Minimum yield strength (MPa)	Minimum tensile strength (MPa)
1	$\alpha$	0.06 O	170	240
2	$\alpha$	0.12 O	275	345
4	$\alpha$	0.3 O	483	550
7	$\alpha$	0.12 O, 0.15 Pd	275	345
16	$\alpha$	0.12 O, 0.05 Pd	275	345
26	$\alpha$	0.12 O, 0.1 Ru	275	345
9	Near- $\alpha$	3 Al, 2.5 V	483	620
18	Near- $\alpha$	3 Al, 2.5 V, 0.05 Pd	483	620
12	Near- $\alpha$	0.3 Mo, 0.8 Ni	345	483
28	Near- $\alpha$	3 Al, 2.5 V, 0.1 Ru	483	620
5	$\alpha$ - $\beta$	6 Al, 4 V	828	895
24	$\alpha$ - $\beta$	6 Al, 4 V, 0.05 Pd	828	895
25	$\alpha$ - $\beta$	6 Al, 4 V, 0.5 Ni, 0.05 Pd	828	895
19	$\beta$	3 Al, 8 V, 6 Cr, 4 Zr, 4 Mo	759	793
20	$\beta$	3 Al, 8 V, 6 Cr, 4 Mo, 4 Zr, 0.05 Pd	759	793

alloys the oxide on the  $\beta$ -phase is slightly enriched in Al and V.<sup>28,29</sup> The oxide thickness and crystallinity may vary spatially.<sup>30</sup> The film at grain boundaries may be less protective than that on the grains when secondary phases are present.<sup>16,31</sup> The durability of this film is essential for corrosion protection, and the parameters most likely to influence its properties are (i) environmental redox conditions (i.e., corrosion potential), (ii) pH, and (iii) temperature.

### 3.10.3.1 Influence of pH

For  $\text{pH} < 4$ , the oxide can dissolve<sup>31</sup> and the Ti become active. An active to passive transition is observed over the potential range  $-0.7$  to  $-0.3$  V (vs. SCE).<sup>32</sup> Active corrosion can be rapid, leading to surface hydride ( $\text{TiH}_x$ ) formation,<sup>2</sup> but the rate is significantly suppressed on Pd- and Ru-containing alloys,<sup>7</sup> which become surface-enriched in Pd/Ru.<sup>33–38</sup> Even for hot, strongly reducing acidic conditions, enrichment can catalyze proton reduction and shift the corrosion potential into the passive region; this process is known as cathodic modification,<sup>39,40</sup> and is also observed with the Grade-12 alloy.<sup>41</sup>

In a sufficiently oxidizing environment, the corrosion potential will be  $> -0.3$  V (vs. SCE) and the alloy passive. Corrosion rates are negligible and insensitive to environment and to temperature well above  $100^\circ\text{C}$ .<sup>2,5</sup> An increase in potential thickens the oxide and makes it less defective.<sup>42</sup> For an applied potential  $> 1$  V (vs. SCE), a current for water oxidation to  $\text{O}_2$  is observed,<sup>43,44</sup> and often mistaken for the onset of pitting in  $\alpha$  and near- $\alpha$  alloys. Pitting only occurs in  $\text{Br}^-$  solutions, an effect which has been attributed to  $\text{Br}^-$  adsorption at sites associated with impurity inclusions containing either Al and Si or Fe.<sup>50–52</sup> In  $\text{Cl}^-$  solutions, polarization to  $> 5$  V (vs. SCE) is required to induce pitting,<sup>53,54</sup> and temperatures  $> 100^\circ\text{C}$  are required before pitting potentials decrease to  $\sim 2$  V (vs. SCE). Pitting requires high film stresses leading to film breakdown/recrystallization and the introduction of enhanced transport pathways for  $\text{Cl}^-$  ions.<sup>44,55–57</sup>

Since potentials  $> 1$  V (vs. SCE) are unattainable under natural corrosion conditions, pitting does not occur in Ti and its alloys, and protection against active corrosion is ensured at corrosion potentials  $> -0.3$  V (vs. SCE). Protection can be ensured by anodic protection<sup>58–60</sup> or by the addition of small concentrations of oxidants (e.g.,  $\text{O}_2$ ,  $\text{Fe}^{3+}$ ).<sup>2,5</sup> Anodic or thermal oxidations are also options,<sup>61,62</sup> but anodic oxidation produces only short term protection.

In dry environments (e.g.,  $\text{Cl}_2$  gas) and organic process streams, only small amounts of moisture or  $\text{O}_2$  are needed to maintain passivity.<sup>2,63</sup>

Corrosion rates increase in alkaline solutions as the protective oxide is more soluble, but, except at high temperatures, they remain low.<sup>2,5,64</sup> In peroxide solutions at  $\text{pH} > 12$ , commonly encountered in the pulp and paper industry, corrosion rates can be extremely high.<sup>65,66</sup> These high rates are attributed to the aggressive  $\text{HO}_2^-$  anion, the dominant form of peroxide above  $\text{pH} 10.6$  (the  $\text{pK}_a$  for  $\text{H}_2\text{O}_2$ ).<sup>67–69</sup> By contrast, peroxide, while modifying the passive oxide, does not cause rapid corrosion at lower pH values.<sup>70,71</sup>

### 3.10.3.2 Influence of Temperature

For active conditions (reducing acids and alkaline peroxide), increasing the temperature increases corrosion rates, but its influence under passive conditions is marginal. As the temperature is increased up to  $\sim 70^\circ\text{C}$ , the passive film becomes more crystalline and absorbs water,<sup>17,72,73</sup> and flaws begin to appear.<sup>57,74</sup> Although observable through the fluctuations in corrosion potential that they cause, these flaws rapidly self-repair and no significant loss of passivity is observed up to  $150^\circ\text{C}$  in  $\text{Cl}^-$  solutions.<sup>75,76</sup> In fact, extensive corrosion testing in extremely saline environments to temperatures well above  $200^\circ\text{C}$  shows that corrosion rates are not significantly enhanced.<sup>39,77–84</sup>

### 3.10.3.3 Influence of Fluoride

Fluoride appears to be the only ion in aqueous solution that is able to destroy passivity. Its influence has been studied widely for dental applications,<sup>85–101</sup> since dental gels and rinses can contain  $1000$ – $10\,000\ \mu\text{g g}^{-1}$  (ppm) of  $\text{F}^-$  in the pH range 3.5 to neutral, and in flue gas scrubber environments,<sup>102,103</sup> in which the liquors formed can contain up to  $\sim 1000\ \text{mg l}^{-1}$  of  $\text{F}^-$ . This aggressiveness is attributed to the solubilization of Ti as  $\text{TiF}_6^{2-}$  and  $\text{TiF}_6^{3-}$  aqueous complexes. It is generally recognized that a substantial  $\text{F}^-$  concentration and a low pH must coexist<sup>104,105</sup> for passivity to be lost. The pH threshold varies with  $\text{F}^-$  concentration and the Pd/Ru content of the alloy; for example, for a Pd content  $> 0.1\ \text{wt}\%$ , passivity in  $900\ \text{mg l}^{-1}$  of  $\text{F}^-$  is maintained at pH 4, while at  $9000\ \text{mg l}^{-1}$  no general corrosion was observed at pH 6.5 but shallow (up to  $\sim 2\ \mu\text{m}$  in cross section) pitting was observed.<sup>98</sup> The most likely location of these pits is at Fe impurity sites in grain boundaries. Their extensive propagation is unlikely because it will be limited by the cathodic modification process.<sup>98–101</sup>

Despite the much more aggressive environments, the influence of  $F^-$  in flue gas scrubbers is muted. These environments contain  $Cl^-$  up to  $15\,700\,\mu g\,g^{-1}$ ,  $SO_4^{2-}$  in the range  $9000\text{--}26\,000\,\mu g\,g^{-1}$ ,  $F^-$  up to  $12\,000\,\mu g\,g^{-1}$ , and the pH can be as low as 1 (at  $T \sim 170\text{--}180\,^{\circ}C$ ).<sup>102,103</sup> For Ti Grades-2 and-12,  $F^-$  led to a loss of passivity for  $pH \leq 3$  and  $<1.5$ , respectively. The relatively minor influence of  $F^-$  was attributed to its removal by complexation with cations (e.g.,  $NaF$ ,  $Na_2F^+$ ,  $CaF^+$ ) and its reaction with the silica in fly ash. The resilience of Pd/Ru-containing alloys in extreme environments has been demonstrated by testing of the Ti-6Al-4V-Ru alloy (Grade-29) in deep gas well environments.<sup>106</sup>

### 3.10.3.4 Hydrogen Absorption into Ti

Under active conditions (reducing acid and alkaline peroxide solutions) corrosion is driven by  $H^+$  reduction leading to H absorption.<sup>24</sup> Since the solubility of H in  $\alpha$ -Ti is low ( $20\text{--}100\,\mu g\,g^{-1}$  at room temperature, depending on alloy composition<sup>107</sup>), brittle hydrides then precipitate in  $\alpha$ - and near- $\alpha$  alloys, and embrittlement may be possible. Also, even relatively small H contents ( $>70\,\mu g\,g^{-1}$ ) can cause a loss of impact toughness.<sup>108</sup> However, at room temperature, the diffusion coefficient of H in the  $\alpha$ -phase is low,<sup>109,110</sup> and H is retained in a surface hydride layer<sup>2,5,111–113</sup> and material integrity is not challenged.

The rate and extent of absorption depend on alloy composition, microstructure, and temperature. On Pd/Ru alloys, catalysis of  $H^+$  reduction leads to enhanced absorption,<sup>40,114</sup> but this can be limited by solution aeration.<sup>115</sup> In the Grade-12 alloy,  $Ti_2Ni$  particles act as galvanically-coupled cathodes in the  $\alpha$ -matrix and form hydride readily.<sup>116</sup> Furthermore, the Ni-stabilized  $\beta$ -phase in the grain boundaries facilitates H transport into the bulk of the alloy, as the  $\beta$ -phase diffusion coefficient is  $\sim 10^5$  times that in the  $\alpha$ -phase.<sup>110,117</sup>

The passive oxide is generally impermeable to H, and the absorption efficiency approaches zero for  $pH > 3$ ,<sup>118</sup> unless the alloy is cathodically polarized to  $<-0.6\,V$  (vs. SCE) when redox transformations in the oxide are accompanied by H absorption ( $TiO_2 + H^+ + e^- \rightarrow TiOOH$ ).<sup>119–124</sup> Although the oxide is then rendered permeable, significant H transport through it requires a potential  $<-1.0\,V$  (vs. SCE).<sup>119,125</sup>

Polarization to these potentials requires either galvanic coupling to active metals (e.g., Zn or carbon steel) or the application of cathodic protection. To avoid significant hydrogen absorption, an operating

threshold of  $>-0.7\,V$  (vs. SCE) is recommended.<sup>2</sup> Although the potentials during galvanic coupling to carbon steel can be below this value (at temperatures in the range  $18\text{--}60\,^{\circ}C$ <sup>126</sup>), the H absorption rate (generally measured at  $-1.0\,V$  (vs. SCE)) decreases parabolically with time as H accumulates in a surface hydride layer<sup>127,128</sup> and absorption becomes controlled by diffusion into the alloy. For  $\alpha$ -alloys, the transport is slow and little damage is done. For Grade-12 Ti, however,  $\beta$ -phase transport accelerates diffusion and the overall absorption rate is higher.<sup>129</sup> Since diffusion coefficients are temperature-dependent, embrittlement below  $80\,^{\circ}C$  is not expected.<sup>2</sup> Generally, this is observed to be the case,<sup>130</sup> although high stress levels promote absorption and hydriding.<sup>131</sup>

Cathodic protection is common in marine applications, with relative absorption tendencies in the order  $Ti-12 > Ti-2 > Ti-5/Ti-9$ .<sup>132</sup> Noble metal additions to near- $\alpha$  and  $\alpha$ - $\beta$  alloys increase absorption only slightly (up to  $\sim 40\%$ ).<sup>128</sup> Thermal oxidation prior to exposure suppresses absorption (in 6% NaCl, up to  $120\,^{\circ}C$ ),<sup>135</sup> and H absorption in deaerated HCl ( $2 \leq pH \leq 4$ ) up to  $250\,^{\circ}C$  can be prevented by aeration.<sup>115</sup>

## 3.10.4 Localized Corrosion Processes

A major asset of Ti alloys is their apparent immunity to many localized corrosion processes, especially pitting and vapor phase corrosion<sup>2,5,134,135</sup> and microbially-influenced corrosion (MIC).<sup>134–143</sup> The two predominant localized corrosion failure modes are crevice corrosion and hydrogen-induced cracking (HIC).

### 3.10.4.1 Crevice Corrosion

Crevice corrosion is generally observed in hot oxidizing halide (or, less commonly, sulfate) environments, under tight gaskets, in metal-metal joints, and under adherent deposits produced in industrial process streams. Reviews summarizing industrial observations and laboratory studies have been published.<sup>2,5,144</sup> For the most commonly used Ti material, Grade-2, it is accepted that crevice corrosion will not occur for  $T < 70\,^{\circ}C$ , regardless of pH and  $Cl^-$  concentration, and for  $pH > 10$ , regardless of temperature.

The initiation of crevice corrosion requires a loss of passivity and the establishment of active corrosion



conditions within the creviced region. The importance of temperature shows that initiation is primarily dependent on the film breakdown events, which commence around 70 °C.<sup>57,74–76</sup> The rapid repair observed on open surfaces does not occur within a tight crevice, and the acidity developed by dissolved metal cation ( $\text{Ti}^{3+}/\text{Ti}^{4+}$ ) hydrolysis leads to the establishment of active conditions.<sup>145</sup> Once initiated, propagation is rapid and extensive, being supported both within the crevice by  $\text{H}^+$  reduction (70–80%) and outside the crevice by  $\text{O}_2$  reduction (30–20%).<sup>12,146</sup>

For Grade-2 Ti, the depth of crevice penetration is dependent on the amount and distribution of the impurity Fe. When Fe is present in grain boundaries, but not separated into  $\text{Ti}_x\text{Fe}$  precipitates, penetration (at 95 °C) is rapid (up to 2 mm) and limited only by the ohmic potential drop caused by corrosion product accumulated within the crevice.<sup>147</sup> When  $\text{Ti}_x\text{Fe}$  precipitates are present, the crevice is polarized to repassivation (by the cathodic modification mechanism), and penetration is limited to  $\leq 0.8$  mm.<sup>12,119</sup> For Grade-12, which contains a large number of  $\text{Ti}_2\text{Ni}$  precipitates, repassivation occurs more rapidly, and penetration is limited to  $< 0.4$  mm.<sup>148</sup> The inherent instability of this alloy is clear from the observation that  $> 95\%$  of the damage is due to proton reduction within the creviced site.<sup>148</sup>

The threat of crevice corrosion can be effectively eliminated by alloying Ti with Pd or Ru.<sup>7</sup> Despite the presence of film fracture events for  $T > 70$  °C,<sup>12</sup> no significant damage occurs up to 200 °C on near- $\alpha$  and  $\alpha$ - $\beta$  alloys, even in extremely aggressive environments such as 10%  $\text{FeCl}_3$  (pH 2) and  $\text{Cl}_2$ -saturated 20% NaCl.<sup>81</sup> Other methods of preventing, mitigating, or at least detecting, crevice corrosion have been discussed.<sup>5,149,150</sup>

### 3.10.4.2 Environmentally-Assisted Cracking

The primary factors influencing these processes, which include stress corrosion cracking (SCC), corrosion fatigue cracking, and HIC have recently been reviewed.<sup>5</sup> These processes can often occur simultaneously, and a case can be made that H absorption is a key feature of crack propagation in all three processes.

#### 3.10.4.2.1 Stress corrosion cracking

Since passivity is difficult to breach, the majority of Ti alloys do not suffer SCC except in aqueous halide

systems and in a few nonaqueous environments, such as dry methanol, where the addition of even small amounts of water is enough to ensure passivity and avoid cracking.<sup>5</sup> In aqueous halides, SCC is more likely at high concentrations, low pH, and high temperature, and appears to progress via oxide rupture and local acidification leading to H absorption and crack tip embrittlement.<sup>151,152</sup>

The ductility and passivity of Ti alloys means industrial failures are unusual and generally observed only for higher strength near- $\alpha$  alloys containing Al and Sn. When SCC is feared, susceptibility can be reduced by using alloys with low interstitial ion (O, C, N) contents. Generally, initiation requires the presence of stressed surface cracks or flaws. Recently, extensive testing of Grades-12 and -7 over a 4 year period in a range of saline environments (pH 2.7 to  $> 12$ ; 60–90 °C) confirmed the resistance of these materials to SCC,<sup>153</sup> although cracking could be forced to occur when low-frequency cyclic loading was applied.<sup>154</sup>

#### 3.10.4.2.2 Hydrogen-induced cracking

For HIC to occur, a considerable amount of H must be absorbed by the alloy, which is most likely to occur when cathodic protection is applied. The tolerance of an alloy for H will be a function of H solubility, and the material's microstructure and texture. The solubility of H is very different in the  $\alpha$  and  $\beta$  phases (20–100 and  $> 9000$   $\mu\text{g g}^{-1}$ , respectively), making  $\beta$ -alloys generally insensitive to HIC. However, this difference, and the more rapid transport of H through the  $\beta$ -phase than through the  $\alpha$ -phase, mean that the microstructure of near- $\alpha$  and  $\alpha$ - $\beta$  alloys has a strong influence on HIC.

Even H contents as low as 70  $\mu\text{g g}^{-1}$  can lead to a decrease in impact toughness,<sup>5,155</sup> although the resistance can be improved by increasing the Al content of the alloy.<sup>5</sup> However, under slow straining or sustained load conditions, tolerance for H is much higher. Slow strain rate tests on Ti Grades-2 and -12 indicate no influence on fracture toughness below a critical level ( $H_c$ ),<sup>156–158</sup> which is taken to be the concentration below which fast crack growth will not occur. The combinations of stress intensity factor and H concentration leading to either fast crack growth (brittle failure) or slow crack growth by either sustained load cracking or ductile rupture, or to no failure have been determined.<sup>156–158</sup>

The values of  $H_c$  were found to be very sensitive to material microstructure and texture with respect to the orientation of the crack and the applied stress.<sup>159</sup>

For Grade-2 Ti, depending on crack orientation with respect to the laminations introduced by rolling,  $H_c$  varied between  $\sim 400$  and  $1000 \mu\text{g g}^{-1}$ .<sup>157</sup> For Ti Grade-12,  $H_c$  for cracks aligned with the rolling direction was  $500 \mu\text{g g}^{-1}$  compared with  $2000 \mu\text{g g}^{-1}$  for cracks perpendicular to this direction. Values of  $H_c$  rose markedly with temperature, which was attributed to the prevention of stress concentration by enhanced creep deformation.<sup>157</sup> Similar measurements for the Grade-5  $\alpha$ - $\beta$  alloy yielded  $H_c = 200 \mu\text{g g}^{-1}$ .<sup>159</sup> On the basis of these measurements, models to predict HIC failures of Ti nuclear waste containers have been developed.<sup>160–163</sup>

### 3.10.5 Specific Applications

Because titanium is an expensive material, its practical use is limited to applications that require one or both of the material's particular performance advantages: superior corrosion resistance and high strength-to-density ratio. Alloying to improve these properties adds further expense. As a commercial material, Ti and its alloys have an established history of reliable long term performance in aggressive environments, including hot oxidizing acids, hot saline solutions, chlorine- and sulfur-bearing gases, and organic solvents. Its industrial and commercial usage continues to grow, and Ti is now the material of choice for many chemical, marine, biomedical, and energy systems applications. Two recent extensive reviews are available.<sup>164,165</sup>

#### 3.10.5.1 Aerospace

The emergence of Ti as an industrial material in the late 1940s and 1950s was driven primarily by the demands of military, and subsequently commercial, aircraft production. While corrosion resistance is important, the primary reasons to use Ti in aircraft and spacecraft are its high strength-to-density ratio and high temperature performance.<sup>165,166</sup> While maintaining the strength of steel, Ti is 45% lighter, and is twice as strong as Al, but only 60% heavier.<sup>164</sup> Ti is an effective replacement for Al alloys for temperatures above  $130^\circ\text{C}$ , the normal limit for conventional Al. The right choice of alloy permits Ti engine components to function at temperatures up to  $600^\circ\text{C}$ .<sup>166</sup>

The main, general-purpose aerospace alloy is Grade-5, although many others are adopted for specific situations. Ti comprises  $\sim 10 \text{ wt}\%$  of the airframe of a modern commercial aircraft<sup>167</sup> and up

to 95 wt% in military planes. Gas turbine engines have  $\sim 30 \text{ wt}\%$  Ti.<sup>165</sup> Ti bands are even wrapped around Al fuselages to prevent propagation of fatigue cracks.<sup>165</sup>

Except for hot hydraulic fluids, few media encountered in the aerospace environment can corrode Ti, allowing the use of unpainted/uncoated Ti throughout the aircraft. Paint is only necessary at Ti interfaces with Al or low-alloy steels to prevent galvanic corrosion.<sup>166</sup> The use of Ti alloys is mandated for lavatory and galley floors because of the corrosiveness of those environments to Al and steels.<sup>165,166</sup> Even the hydraulic fluid problem, in which organophosphoric acids produced by high temperature breakdown can cause severe etching of Ti alloys and H absorption to embrittlement, has been managed using the  $\beta$ -alloy Timetal 215. This alloy is immune to attack by hydraulic fluid, purportedly through the synergistic effects of its Nb and Mo contents.<sup>166</sup>

#### 3.10.5.2 Seawater and Brine

Ti alloys have supplanted cupronickel alloys, such as Monel, as the preferred materials for heat exchangers and condensers in brackish water, seawater, and polluted waters. Unlike the cupronickel alloys, Ti is immune to general corrosion up to  $260^\circ\text{C}$ , and resistant to localized corrosion processes, sulfide attack, and flow-accelerated forms of corrosion. Flow rates over  $36 \text{ m s}^{-1}$  do not cause erosion corrosion, cavitation corrosion, or impingement attack in the presence of abrasive particles such as sand.<sup>164,165,168</sup> This allows the use of thin-walled tubing (with good heat transfer properties), as a zero corrosion allowance can be specified. This reliability is demonstrated by the industrial use of millions of meters of tubing over many decades without corrosion failures.<sup>164,165,168</sup>

Other seawater and brine applications include submarine hulls, surface ships, oil and gas platforms, desalination and salt production evaporators, and water jet propulsion systems.<sup>165,166,168</sup> Wet-dry cycling, water line exposure, and salt spray have no effect on corrosion.<sup>167</sup> Since Ti does not suffer MIC, it can withstand biofouling. It is not biotoxic, nor does it suffer corrosion in the presence of biocides.<sup>136,164,165,168</sup> Although it may require the specification of Pd/Ru-containing alloys, crevice corrosion can be avoided. As discussed earlier, galvanic corrosion can be an issue for Ti in seawater environments. Since Ti is normally the cathode in the galvanic couple, it can accelerate attack of the active anodic material while absorbing H itself. While

embrittlement and HIC are not issues at low temperatures, they can be at higher temperatures (Sections 3.10.3.4 and 3.10.4.2.2).

### 3.10.5.3 Biomedical and Dental Implants

The oxygenated, warm (37 °C), neutral (pH ~ 7.4) saline conditions encountered in the human body are not aggressive towards Ti. Its corrosion resistance, including resistance towards processes involving stress and fatigue, and biocompatibility make Ti an ideal implant material.<sup>169</sup> Its major uses include cranial plates, orthopedic fracture plates, joint replacements, stents, catheters, pacemaker cases, dental implants and wires, and maxillofacial and orbit reconstruction plates.<sup>170</sup> The extremely low corrosion rates mean Ti dental implants have no taste.<sup>164</sup>

Nitinol shape-memory materials, often used in orthodontics and stents, have been known to undergo pitting and crevice corrosion *in vivo* if heat treatments leave a crystalline oxide on the surface. However, this can be avoided by applying surface treatments to produce an amorphous oxide.<sup>171</sup> Corrosion fatigue, though rare, has been observed on Ti-6Al-4V implants.<sup>172</sup> Some cases of metallosis involving this alloy have also been encountered, but these are primarily due to fretting and wear producing fine metal particulates, rather than to corrosion.<sup>173,174</sup> Care must also be taken to avoid galvanic corrosion, even between materials as similar as commercially pure Ti and Ti-6Al-4V implants.<sup>170</sup>

Although Ti alloys are corrosion resistant *in vivo*, and there have been no clinically substantiated reports of problems stemming from the presence of Al and V in the implants,<sup>174</sup> some concern over the long term impact of these alloying elements remains.<sup>174</sup> Studies on alternative materials to Ti-6Al-4V to avoid potentially toxic alloying compounds are underway.<sup>174-178</sup> In these new materials, V and Al are being replaced by various amounts of other less toxic elements, including Fe, Zr, Mo, Ta, and Sn. These materials possess similar corrosion properties to Ti-6Al-4V but have improved mechanical properties, such as a decreased Young's modulus.

### 3.10.5.4 Chemical Processing and Power Generation

The use of Ti and its alloys in the chemical process industry has been extensively reviewed<sup>2,5</sup> and will not be dealt with here, except to note that their usage is still expanding. The key corrosion issues, as

discussed earlier, are crevice corrosion and hydrogen absorption leading to embrittlement and cracking.

Titanium alloys have recently been extensively studied as candidate materials for the fabrication of high-level nuclear waste containers and container dripshields.<sup>134,135,153,160,179,180</sup> The critical requirement in these applications is the need to maintain corrosion resistance over tens of thousands of years. The ability of Ti alloys to maintain extremely low corrosion rates over extensive time periods and their lack of susceptibility to localized corrosion processes<sup>135,160</sup> make them ideal candidates for this application. A particularly attractive feature is their insensitivity to  $\gamma$ -radiation even at extremely high dose rates.<sup>181</sup>

## References

1. Schutz, R. W.; Grauman, J. S. Titanium for marine applications; Presented at the Second Corrosion Control Workshop, sponsored by The Colorado School of Mines, New Orleans, LA, February 1997.
2. Schutz, R. W.; Thomas, D. E. In *Metals Handbook*, 9th edn.; ASM: Metals Park, OH, 1987; Vol. 13, pp 669-706.
3. Schutz, R. W.; Grauman, J. S. In *Industrial Applications of Titanium and Zirconium*; ASTM: Philadelphia, PA, 1986; Vol. 4, STP 917, pp 130-143.
4. Schutz, R. W. *Beta Titanium Alloys in the 1990's*; The Minerals, Metals and Materials Society: Warrendale, PA, 1993; pp 75-91.
5. Been, J.; Grauman, J. S. In *Uhlig's Corrosion Handbook*, 2nd edn.; Revie, R. W., Ed.; John Wiley: New York, NY, 2000; pp 863-885.
6. Boyer, R. W.; Welsch, G.; Collins, E. W. Eds. *Titanium Alloys, Materials Properties Handbook*; ASM: Materials Park, OH, 1994.
7. Schutz, R. W. *Corrosion* **2003**, 59, 1043-1057.
8. Lide, D. R. Ed. *CRC Handbook of Chemistry and Physics*, 82nd edn.; CRC Press: Boca Raton, FL, 2002.
9. Donachie, M. J., Jr. Ed. *Titanium: A Technical Guide*, 2nd edn.; ASM International: Materials Park, OH, 2000.
10. Blackburn, M. *The Science, Technology and Application of Titanium*; Pergamon Press: New York, NY, 1970; pp 633.
11. Margolin, H.; Farrar, P. *Ocean Eng.* **1969**, 1, 329.
12. He, X.; Noel, J. J.; Shoesmith, D. W. *Corrosion* **2004**, 60, 378-386.
13. Watanabe, T.; Kondo, M.; Naito, H.; Sakai, K. In *Sixth World Conference on Titanium, Cannes, June 6-9, 1988*; Lacombe, P., Tricot, R., Beranger, G., Eds.; 1988; Vol. IV, pp 1735-1740.
14. Tsujikawa, S.; Kojima, Y. *Mat. Res. Soc. Symp. Proc.* **1990**, 212, 261.
15. van der Lingen, E.; Sandenbergh, R. F. *Corros. Sci.* **2001**, 43, 577-590.
16. Zhu, R.; Qin, Z.; Noel, J. J.; Shoesmith, D. W.; Ding, Z. *Anal. Chem.* **2008**, 80, 1437-1447.
17. Shibata, T.; Zhu, Y. C. *Corros. Sci.* **1995**, 37, 253-270.
18. Tyler, P. S.; Kozlowski, M. R.; Smyrl, W. H.; Atanasoski, R. T. *J. Electroanal. Chem.* **1987**, 237, 295-302.
19. McAleer, J. F.; Peter, L. M. *Faraday Discuss.* **1980**, 70, 67-80.

20. Noel, J. J. Ph.D. Thesis, University of Manitoba, Winnipeg, Manitoba, Canada, 1999.
21. Kim, Y. J.; Oriani, R. A. *Corrosion* **1987**, *43*, 92–97.
22. Kim, Y. J.; Oriani, R. A. *Corrosion* **1987**, *43*, 85–91.
23. Torresi, R. M.; Camara, O. R.; dePauli, C. P.; Giordano, M. C. *Electrochim. Acta* **1987**, *32*, 1291–1301.
24. Casillas, N. Ph.D. Thesis, University of Minnesota, St. Paul, MN, 1993.
25. da Fonseca, C.; Boudin, S.; da Cunha Belo, M. *J. Electroanal. Chem.* **1994**, *379*, 173–180.
26. Tomashov, N. D.; Al'touski, P. M. Corrosion and Protection of Titanium, Government Scientific-Technical Publication of Machine – Building Literature (Russian Translation), Moscow, Russia 1963.
27. Huang, Y. Z.; Blackwood, D. J. *Electrochim. Acta* **2005**, *51*, 1099–1107.
28. Ask, M.; Lausmaa, J.; Kasemo, B. *Appl. Surf. Sci.* **1988–1989**, *35*, 283–301.
29. Ask, M.; Rolander, U.; Lausmaa, J.; Kasemo, B. *J. Mater. Res.* **1990**, *5*, 1662–1667.
30. Kudelka, S.; Michaelis, A.; Schultze, J. W. *Ber. Bunsenges, Phys. Chem* **1995**, *99*, 1020–1027.
31. Blackwood, D. J.; Peter, L. H.; Williams, D. E. *Electrochim. Acta* **1988**, *33*, 1143–1149.
32. Kelly, E. J. *J. Electrochem. Soc.* **1979**, *126*, 2064–2075.
33. Sedriks, A. J. *Corrosion* **1975**, *31*, 60–65.
34. Kitayama, S.; Shida, Y.; Ueda, M.; Kudo, T. In *CORROSION92*; NACE: Houston, TX, 1992; Paper No. 52.
35. Cotton, J. B. *Platinum Met. Rev.* **1967**, *11*, 50–52.
36. Higginson, A. *Br. Corros. J.* **1989**, *24*, 297–302.
37. Brossia, C. S.; Cragnolino, G. A. In *Corrosion/2001*; NACE: Houston, TX, 2001; Paper No. 127.
38. Kornienko, L. P.; Tomashov, N. D.; Chernova, G. P. *Zasch. Met* **1993**, *29*, 359–367.
39. Satoh, K.; Shimogori, K.; Kamikubo, F. *Platinum Met. Rev.* **1987**, *31*, 115–121.
40. Schutz, R. W.; Xiao, M. In *Corrosion Control for Low-Cost Reliability, 12th International Corrosion Congress*; Houston, TX, Sept. 19–24 1993; Vol. 3A, pp 1213–1225.
41. Hall, J. A.; Banerjee, D.; Wardlaw, J. L. In *Titanium Science and Technology*; Proceedings of the Fifth International Conference on Titanium, Munich, Germany, Sept. 10–14, 1984; Lutjering, G., Zwicker, U., Bunk, W., Eds.; 1985; Vol. 4, pp 2603–2610.
42. Ohtsuka, T.; Masuda, M.; Sato, N. *J. Electrochem. Soc.* **1985**, *132*, 787–792.
43. Casillas, N.; Charlebois, S.; Smyrl, W. H.; White, H. S. *J. Electrochem. Soc.* **1994**, *141*, 636–642.
44. Kolman, D. G.; Scully, J. R. *J. Electrochem. Soc.* **1994**, *141*, 2633–2641.
45. Raetzer-Scheibe, H. *J. Corrosion* **1978**, *34*, 437–442.
46. Beck, T. R. *J. Electrochem. Soc.* **1973**, *120*, 1310–1316.
47. Beck, T. R. *J. Electrochem. Soc.* **1973**, *120*, 1317–1324.
48. Petit, J. A.; Kondro, B.; Dabosi, F. *Corrosion* **1980**, *36*, 145–151.
49. Basame, S. B.; White, H. S. *J. Electrochem. Soc.* **2000**, *147*, 1376–1381.
50. Garfias-Mesias, L. F.; Alodan, M.; James, P. I.; Smyrl, W. H. *J. Electrochem. Soc.* **1998**, *145*, 2005–2010.
51. Kamikubo, F.; Satoh, H.; Shimogori, K.; Fukuzuka, T. In *Proceedings of the Eighth International Congress on Metallic Corrosion, DECHEMA, Frankfurt/Main, Germany 1981*; pp 1378–1383.
52. Curty, C.; Virtanen, S. *Electrochem. Soc. Proc.* **1999**, *99–27*, 445–452.
53. Koizumi, T.; Furuya, S. In *Proceedings of the Second International Conference: Titanium, Science and Technology*; Jaffe, R. I., Burte, H. M., Eds.; Plenum Press: New York, NY, 1973; pp 2382–2393.
54. Posey, F. A.; Bohlman, E. G. *Desalination* **1967**, *3*, 269–279.
55. Leach, J. S. L.; Pearson, B. R. *Corros. Sci.* **1988**, *28*, 43–56.
56. Shibata, T.; Zhu, Y. C. *Corros. Sci.* **1995**, *37*, 253–270.
57. Dyer, C. K.; Leach, J. S. L. *J. Electrochem. Soc.* **1978**, *125*, 1032–1038.
58. Cotton, J. B. *Chem. Eng. Prog.* **1970**, *66*, 10, 57.
59. Cotton, J. B. *Br. Cor. J.* **1975**, *10*, 2, 66.
60. Tomashov, N. D.; Chernova, G. P.; Ruscol, Y. S.; Ayuyan, G. A. *Electrochim. Acta* **1974**, *19*, 159.
61. Schutz, R. W.; Covington, L. C. *Corrosion* **1981**, *37*, 585.
62. Fukuzuka, T.; Shimogori, K.; Satoh, H.; Kamikubo, F. In *Titanium 80, Science and Technology*; Kimura, H., Izumi, O., Eds.; 1980; Vol. 4, pp 2783–2787.
63. Millaway, E. E.; Kleinmann, M. H. *Corrosion* **1972**, *23*, 88.
64. Popa, M. V.; Vasilescu, E.; Mirza-Rosca, I.; Gonzalez, S.; Lorente, M. L.; Drob, P.; Anghel, M. In *Eurocorr'97*, Trondheim, Norway 1997; Vol. II, pp 687–692.
65. Been, J. Ph.D. Thesis, University of British Columbia, Vancouver, Canada, 1998.
66. Been, J.; Tromans, D. *Pulp Paper Can.* **1999**, *100*, 50.
67. Varjonen, O. I.; Hakkarainen, J. J. *Tappi J.* **1995**, *78*, 161–166.
68. Hyokivirta, O. A. *Mater. Corros.* **1997**, *48*, 376–387.
69. Wyllie, W. E., II; Brown, B. E.; Duquette, D. J. In *CORROSION94*; NACE International: Houston, TX, 1994, Paper No. 421.
70. Pan, J.; Thierry, D.; Leygraf, C. *J. Biomed. Mater. Res.* **1994**, *28*, 113.
71. Pan, J.; Thierry, D.; Leygraf, C. *Electrochim. Acta* **1996**, *41*, 1143.
72. Shibata, T.; Zhu, Y. C. *Corros. Sci.* **1994**, *36*, 1735–1749.
73. Noel, J. J.; Ikeda, B. M.; Miller, N. H.; Shoesmith, D. W.; Sunder, S.; Tun, Z. In *Proceedings Symposium on Surface Oxide Films*; Bardwell, J. A., Ed.; Electrochemical Society: Pennington, NJ, 1996; pp 246–257, 996–918.
74. Yahalom, J.; Zahavi, J. *Electrochim. Acta* **1970**, *15*, 1429–1435.
75. He, X.; Noel, J. J.; Shoesmith, D. W. *Corrosion* **2007**, *63*, 781–792.
76. Noel, J. J.; Yan, L.; Ofori, D.; Jakupi, P.; Shoesmith, D. W. In *Passivation of Metals and Semiconductors*; Marcus, P., Maurice, V., Eds.; Elsevier BV: Amsterdam, 2006; pp 199–204.
77. Smailos, E.; Koster, R. In *Materials Reliability in the Back End of the Nuclear Fuel Cycle*; Proceedings of a Technical Committee Meeting of the International Atomic Energy Agency (IAEA), Vienna, Austria, Sept. 2–5, 1986, IAEA-TECDOC-421, 1986.
78. Molecke, M. A.; Ruppen, J. A.; Diegle, R. B. Materials for high level waste canisters/overpacks in salt formations; Sandia National Laboratory Report, SAND82-0429, 1982.
79. Schutz, R. W. *Mater. Perform.* **1985**, *24*(1), 39–47.
80. Schutz, R. W.; Grauman, J. A. In *Corrosion 88*; NACE International: Houston, TX, 1988; Paper 162.
81. Schutz, R. W. *Platinum Met. Rev.* **1996**, *40*, 54–61.
82. Schutz, R. W. In *CORROSION97*; NACE International: Houston, TX, 1997; Paper No. 32.
83. Schutz, R. W.; Porter, R. L.; Horrigan, J. M. *Corrosion* **2000**, *56*, 1170–1179.
84. Schutz, R. W. In *CORROSION03*; NACE International: Houston, TX, 2003; Paper No. 03455.
85. Lausmaa, J.; Kasemo, B.; Hansson, S. *Biomaterials* **1985**, *6*, 23–27.
86. Boere, G. *J. Appl. Biomater.* **1995**, *6*, 283–288.

87. Oda, Y.; Kawada, E.; Yoshinari, M.; Hasegawa, K.; Okabe, T. *J. Dent. Mater. Dev.* **1996**, *15*, 317–322.
88. Mimura, H.; Miyagawa, Y. *Jpn. J. Dent. Mater. Dev.* **1996**, *15*, 283–295.
89. Toumelia-Chemla, F.; Rouelle, F.; Burdairon, G. *J. Dent.* **1996**, *24*, 109–115.
90. Probst, L.; Lin, W.; Hutteman, N. *Int. J. Oral Maxillofac. Implants* **1992**, *7*, 390–394.
91. Nakagawa, M.; Matsuya, S.; Shiraishi, T.; Ohta, M. *J. Dent. Res.* **1999**, *78*, 1568–1571.
92. Johansson, B. I.; Berengman, B. *Dent. Mater.* **1995**, *11*, 41–46.
93. Siirila, H. S.; Kokonen, M. *Int. J. Oral Maxillofac. Implants* **1991**, *5*, 50–54.
94. Nakagawa, M.; Matsuya, M.; Udoh, K. *J. Dent. Mater.* **2001**, *20*, 305–314.
95. Schiff, N.; Grosogogeat, B.; Lissac, M.; Dalard, F. *Biomaterials* **2002**, *23*, 1995–2002.
96. Huang, H. H. *Biomaterials* **2002**, *23*, 59–63.
97. Fernandez Lorenzo de Mele, M.; Cortizo, M. C. *J. Appl. Electrochem.* **2000**, *30*, 95–100.
98. Nakagawa, N.; Matono, Y.; Matsuya, S.; Udoh, K.; Ishikawa, K. *Biomaterials* **2005**, *26*, 2239–2246.
99. Yokoyama, K.; Ogawa, T.; Asaoka, K.; Sakai, J. *Mat. Sci. Eng. A* **2004**, *384*, 19–25.
100. Yokoyama, K.; Ogawa, T.; Asaoka, K.; Sakai, J. *J. Alloys Compds.* **2005**, *400*, 227–233.
101. Yokoyama, K.; Ogawa, T.; Asaoka, K.; Sakai, J. *Mat. Sci. Eng. A* **2006**, *419*, 122–130.
102. Schutz, R. W.; Grauman, J. S. *Mater. Perform.* **1986**, *25*(4), 35–42.
103. Thomas, D. E.; Bomberger, H. B. *Mater. Perform.* **1983**, *22*(11), 29–36.
104. Mandry, M. J.; Rosenblatt, G. J. *Electrochim. Soc.* **1972**, *119*, 20.
105. Wilhelmsen, W.; Grande, A. P. *Electrochim. Acta* **1987**, *32*, 1469–1474.
106. Schutz, R. W.; Porter, R. L.; Horrigan, J. M. *Corrosion* **2000**, *56*, 1170–1179.
107. Paton, N. E.; Williams, J. C. In *Hydrogen in Metals*; Bernstein, I. M., Thompson, A. W., Eds.; American Society for Metals: New York, NY, 1974; pp 409–431.
108. Wasz, M. L.; Ko, C. C.; Brotzen, F. R.; McLellan, R. B. *Scripta Metall.* **1990**, *24*, 2043.
109. Sundaram, P. A.; Wessel, E.; Clemens, H.; Kestler, H.; Ennis, P. J.; Quadackers, W. J.; Singheiser, L. *Acta Mater.* **2000**, *48*, 1005–1019.
110. Christ, H. J.; Decker, M.; Zeitler, S. *Metall. Mater. Trans. A* **2000**, *31*, 1507–1517.
111. Phillips, I. I.; Poole, P.; Shreir, L. L. *Corros. Sci.* **1972**, *12*, 855.
112. Phillips, I. I.; Poole, P.; Shreir, L. L. *Corros. Sci.* **1974**, *14*, 533.
113. Yan, L.; Ramamurthy, S.; Noel, J. J.; Shoesmith, D. W. *Electrochim. Acta* **2006**, *52*, 1169–1181.
114. Fukuzuka, T.; Shimogori, K.; Satoh, H. In *Titanium'80, Science and Technology*; Proceedings of the Fourth International Conference on Titanium Kyoto: Japan, May 19–20, 1980; pp 2695–2703.
115. Shimogori, K.; Satoh, H.; Kamikubo, F. In *Titanium, Science and Technology*; Proceedings of the Fifth International Conference on Titanium, Munich, Germany, Sept. 10–14, 1984; Lutjering, G., Zwicker, U., Bunk, W., Eds.; 1985; pp 1111–1118.
116. Glass, R. S. *Electrochim. Acta* **1983**, *28*, 1507–1513.
117. Prussner, K.; Decker, M.; Christ, H. J. *Adv. Eng. Mater.* **2002**, *4*, 308–312.
118. Okada, T. *Electrochim. Acta* **1983**, *28*, 1113–1120.
119. Yan, L. Ph.D. Thesis, University of Western Ontario, London, Ontario, Canada, 2007.
120. Dyer, C. K.; Leach, J. S. L. *Electrochim. Acta.* **1978**, *23*, 1387–1394.
121. Weber, M. F.; Shumacker, L. C.; Dignam, M. J. *J. Electrochem. Soc.* **1982**, *129*, 2022–2028.
122. Ohtsuka, T.; Masuda, M.; Sato, N. *J. Electrochem. Soc.* **1987**, *134*, 2406–2410.
123. Tun, Z.; Noel, J. J.; Shoesmith, D. W. *J. Electrochem. Soc.* **1999**, *146*, 988–994.
124. Murai, T.; Ishikawa, M.; Miura, C. *Corros. Eng.* **1977**, *26*, 177–183.
125. Noel, J. J.; Bailey, M. G.; Crosthwaite, J. P.; Ikeda, B. M.; Ryan, S. R.; Shoesmith, D. W. Hydrogen absorption by grade-2 titanium, Atomic Energy of Canada Limited Report, AECL-11608, 1996.
126. Hodgkiss, T.; McIver, A.; Chong, P. Y. *Desalination* **1987**, *66*, 147–170.
127. Tomari, H.; Masugata, T.; Shimogori, K.; Nishimura, T.; Wada, R.; Taniguchi, N. *Zairyo-to-Kankyo* **1999**, *48*, 807–814.
128. Seiersten, M.; Eggen, T. G.; Lunde, L.; Rogne, T. In Proceedings of the 21<sup>st</sup> International Conference on Offshore Mechanics and Arctic Engineering, June 23–28, Oslo, Norway 2002; pp 493–498.
129. Lunde, L.; Nyborg, R. In *Engineering Solutions to Industrial Corrosion Problems*; NACE International: Houston, TX, 1993; Paper No. 5.
130. Lee, J. I.; Chung, P.; Tsai, C. H. In *CORROSION86*; NACE International: Houston, TX, 1986; Paper No. 259.
131. Venkataraman, G.; Goolsby, A. D. In *CORROSION96*; NACE International: Houston, TX, 1996; Paper No. 554.
132. Gartland, P. O.; Bjornais, F.; Schutz, R. W. In *CORROSION97*; NACE International: Houston, TX, 1997; Paper No. 477.
133. Covington, L. C. *Corrosion* **1979**, *35*, 378–382.
134. Shoesmith, D. W.; Ikeda, B. M. The resistance of titanium to pitting, microbially induced corrosion and corrosion in unsaturated conditions, Atomic Energy of Canada Limited Report, AECL-11709, COG-96-557-I, 1997.
135. Hua, F.; Mon, K.; Pasupathi, P.; Gordon, G. M.; Shoesmith, D. W. In *CORROSION04*; NACE International: Houston, TX, 2004; Paper No. 04689.
136. Schutz, R. W. *Mater. Perform.* **1991**, *30*, 58–61.
137. Little, B. J.; Wagner, P. A.; Ray, R. I. In *CORROSION93*; NACE International: Houston, TX, 1993; Paper No. 308.
138. Dexter, S. C.; Zhang, H. J. In *Proceedings of the 11th International Corrosion Congress, Florence, Italy*; Associazione Italiana di Metallurgia: Milan, Italy, 1990; pp 333–340.
139. Mansfeld, F.; Tsai, R.; Shih, H.; Little, B. J.; Ray, R.; Wagner, P. In *CORROSION90*; NACE International: Houston, TX, 1990; Paper No. 109.
140. Mansfeld, F.; Tsai, R.; Shih, H.; Little, B. J.; Ray, R.; Wagner, P. *Corros. Sci.* **1992**, *33*, 445–446.
141. Mansfeld, F.; Liu, G.; Xiao, H.; Tsai, C. H.; Little, B. J. *Corros. Sci.* **1994**, *36*, 2063–2095.
142. Mansfeld, F.; Little, B. J. *Corros. Sci.* **1991**, *32*, 247–272.
143. Little, B. J.; Wagner, P. A.; Ray, R. I. In *CORROSION92*; NACE International: Houston, TX, 1992; Paper No. 173.
144. Noel, J. J.; Shoesmith, D. W. In *Proceedings of the NACE 2001 Research Topical Symposium, March 2001*; Frankel, G. S., Scully, J. R., Eds.; NACE International: Houston, TX, 2001; pp 65–102.
145. He, X.; Noel, J. J.; Shoesmith, D. W. *J. Electrochem. Soc.* **2002**, *149*, B440–B449.
146. He, X. Ph.D. Thesis, University of Western Ontario: London, Ontario, Canada, 2003.
147. He, X.; Noel, J. J.; Shoesmith, D. W. *Corros. Sci.* **2005**, *47*, 1177–1195.
148. He, X.; Noel, J. J.; Shoesmith, D. W. *J. ASTM Int.* **2008**, *5*(8). Available online at <http://www.astm.org>.



149. Schutz, R. W. In *CORROSION91*; NACE International: Houston, TX, 1991; Paper No. 162.
150. Bergman, D. D.; Grauman, J. S. In *Titanium'92, Science and Technology*; Froes, F. H., Caplan, I., Eds.; The Minerals, Metals, and Materials Society: Warrendale, PA, 1993; pp 2193–2200.
151. Hollis, A. C.; Scully, J. C. *Corros. Sci.* **1993**, *34*, 821.
152. Kolman, D. S.; Scully, J. R. *Metall. Mater. Trans. A* **1997**, *28A*(12), 2645–2656.
153. Gordon, G. M. *Corrosion* **2002**, *58*, 811–825.
154. Andresen, P. L.; Emigh, P. W.; Young, L. M.; Gordon, G. M. In *CORROSION01*; NACE International: Houston, TX, 2001; Paper No. 01130.
155. Wasz, M. L.; Ko, C. C.; Brotzen, F. R.; McLellan, R. B. *Scripta Metall.* **1990**, *24*, 2043.
156. Clarke, C. F.; Hardie, D.; Ikeda, B. M. *Corros. Sci.* **1994**, *36*, 487–509.
157. Clarke, C. F.; Hardie, D.; Ikeda, B. M. Hydrogen induced cracking of grade-2 titanium, Atomic Energy of Canada Limited Report, AECL-11284, 1995.
158. Shoesmith, D. W.; Noel, J. J.; Hardie, D.; Ikeda, B. M. *Corros. Rev.* **2000**, *18*, 331–359.
159. Hardie, D.; Ouyang, S. *Corros. Sci.* **1999**, *41*, 155–177.
160. Hua, F.; Mon, K.; Pasupathi, P.; Gordon, G. M.; Shoesmith, D. W. In *CORROSION05*; NACE International: Houston, TX, 2005; Paper No. 05582.
161. Hua, F.; Mon, K.; Pasupathi, P.; Gordon, G. M.; Shoesmith, D. W. *J. Metals* **2005**, *57*(1), 20–26.
162. Qin, Z.; Shoesmith, D. W. *Mater. Res. Soc. Symp. Proc.* **2007**, *985*, 467.
163. Qin, Z.; Shoesmith, D. W. *J. Nucl. Mater.* **2008**, *379*(1), 169–173.
164. Ikeda, B. M.; Shoesmith, D. W. Industrial experience with titanium, Atomic Energy of Canada Limited Report, AECL-11750, COG-97-4-I, 1997.
165. Leyens, C.; Peters, M. Eds. *Titanium and Titanium Alloys: Fundamentals and Applications*; Wiley-VCH: Weinheim, Germany, 2003; pp 233–497.
166. Boyer, R. R. *Mater. Sci. Eng. A* **1996**, *213*, 103–114.
167. Lütjering, G.; Williams, J. C. In *Engineering Materials and Processes*; Derby, B., Ed.; Springer: Berlin, 2007.
168. Titanium Metals Corporation (Timet) Corrosion resistance of titanium. Available online at <http://www.timet.can/pdfs/corrosion.pdf>.
169. Van Noort, R. *J. Mater. Sci.* **1987**, *22*, 3801–3811.
170. Hansen, D. C. *Interface* **2008**, *17*, 31–34.
171. Shih, C. C.; Lin, S. J.; Chung, K. B.; Chen, Y. L.; Su, Y. Y. *J. Biomed. Mater. Res.* **2000**, *52*, 323–332.
172. Schmutz, P.; Quach-Vu, N. C.; Gerber, I. *Interface* **2008**, *17*, 35–39.
173. Black, J.; Shenk, H.; Boninc; Rostocker, W. R.; Schajowicz, F.; Galante, J. O. *J. Bone Joint Surg.* **1990**, *72*, 126–130.
174. Jacobs, J. J.; L Gilbert, J.; Urban, R. M. *J. Bone Joint Surg.* **1998**, *80-A*, 268–282.
175. Wang, K. *Mater. Sci. Eng. A* **1996**, *213*, 134–137.
176. Okazaki, Y.; Ito, Y.; Kyo, K.; Tateishi, T. *Mater. Sci. Eng. A* **1996**, *213*, 138–147.
177. Niinomi, M.; Kuroda, D.; Fukunaga, K. I.; Morinaga, M.; Kato, Y.; Yashiro, Y.; Suzuki, A. *Mater. Sci. Eng. A* **1999**, *263*, 193–199.
178. Kuphasuk, C.; Oshida, Y.; Andres, C. J.; Hovijitra, S. T.; Barco, M. T.; Brown, D. T. *J. Prosthet. Dent.* **2001**, *85*, 195–202.
179. Johnson, L. H.; King, F. Canister options for the disposal of spent fuel, Nagra, Switzerland, Technical Report 02–11, 2002.
180. Johnson, L. H.; Tait, J. C.; Shoesmith, D. W.; Crosthwaite, J. L.; Gray, M. N. The disposal of Canada's nuclear fuel waste: Engineered barriers alternatives, Atomic Energy of Canada Limited Report, AECL-10718, COG-93-8, 1994.
181. Shoesmith, D. W.; King, F. The effects of gamma radiation on the corrosion of candidate materials for the fabrication of nuclear waste packages, Atomic Energy of Canada Limited Report, AECL-1199, 1999.

## 3.11 Corrosion of Lead and its Alloys

**S. B. Lyon**

Corrosion and Protection Center, School of Materials, University of Manchester, Manchester M13 9PL, UK

This article is a revision of the Third Edition article 4.3 by P. C. Frost, E. Littauer and H. C. Wesson, volume 1, pp 4:76–4:97, © 2010 Elsevier B.V.

<b>3.11.1</b>	<b>Introduction</b>	2053
3.11.1.1	History and Production	2053
3.11.1.2	Physical Properties	2054
3.11.1.3	Applications	2054
3.11.1.4	Alloying	2055
3.11.1.5	Mechanical Properties	2056
3.11.1.5.1	Lead	2056
3.11.1.5.2	Lead alloys	2056
<b>3.11.2</b>	<b>Electrochemistry</b>	2057
3.11.2.1	Thermodynamics	2057
3.11.2.2	Dissolution	2058
3.11.2.3	Oxidation and Passivation	2058
3.11.2.4	Corrosion Products	2059
3.11.2.5	Galvanic Corrosion	2060
<b>3.11.3</b>	<b>Corrosion</b>	2060
3.11.3.1	Atmospheric Corrosion	2060
3.11.3.2	Water	2061
3.11.3.2.1	Distilled and condensed water	2061
3.11.3.2.2	Natural waters	2061
3.11.3.3	Buried Structures	2062
3.11.3.3.1	Stray-current corrosion	2062
3.11.3.3.2	Underground corrosion	2062
3.11.3.4	Acids	2063
3.11.3.4.1	Mineral acids	2063
3.11.3.4.2	Organic acids	2063
3.11.3.5	Lubrication Oils	2064
3.11.3.6	Miscellaneous Environments	2064
<b>3.11.4</b>	<b>Specific Applications</b>	2064
3.11.4.1	Lead Anodes	2064
3.11.4.2	Lead–Acid Battery	2065
3.11.4.3	Reactor Coolants	2066
<b>References</b>		2066

### 3.11.1 Introduction

#### 3.11.1.1 History and Production

Lead was one of the metals known in antiquity; there is evidence of lead production dating back to before the early Bronze Age, with a lead figurine from Upper Egypt dated to approximately 3000 BC.<sup>1</sup> However, at that time lead does not appear to have been greatly prized as it is soft and easily tarnishes. Indeed, early lead ores seem to have been smelted mainly in order

to obtain the silver, with which it frequently occurs. However, lead production grew very significantly during the Roman period, where it was useful in its own right for a number of purposes, including plumbing (water transport, water tanks, etc.) and kitchenware and drinking vessels (despite the knowledge, even in antiquity, that lead is generally harmful to human health).

Lead ores comprise mainly sulfide mineralization with smaller amounts of carbonate and sulfate.

Historically, lead was mined on its own (in the United Kingdom, Derbyshire and Leadhills in Southern Scotland were historic sources). Modern ores frequently occur along with zinc, and other species (silver, copper, gold, antimony, bismuth, etc.) in considerably lesser amounts. Lead sulfide (galena) is easily smelted by roasting in air to produce lead oxide, then by carbothermic reduction, which traditionally used charcoal but now uses coke, in a blast furnace.

Lead is currently produced in Australia, China, the United States, Canada, Mexico, and Peru. Western Europe produces about 8% of the total world ore production of around 3 million tonnes (2007), mainly from Sweden, but also Ireland and Spain. Lead is amongst the most recyclable of all metals and has by far the highest recycling rate, primarily from batteries and also from usage in the building trade. Secondary (i.e., recycled) sources of lead generally account, in developed economies, for more than 70% of lead usage.

### 3.11.1.2 Physical Properties

Lead is characterized by its relatively high density (in comparison to other engineering materials), its extremely low hardness and strength, and its favorable electrochemical properties, including its good resistance to corrosion.<sup>1,2</sup> However, it should be noted that lead is by no means the most dense element; for example, tungsten and tantalum are significantly more dense. **Table 1** provides a summary of some physical properties in comparison with other materials.

The density of lead provides it with useful properties in respect of the attenuation of phonon vibrations and electromagnetic waves. Thus, the mass attenuation coefficient for lead is relatively high, and also the neutron absorption cross-section for lead is small, which makes lead effective for the radiation shielding

of X-rays,  $\gamma$ -rays, and neutrons. In addition, the softness and high mass of lead effectively damps the propagation of sound waves.

### 3.11.1.3 Applications

Traditionally, lead as a metal has a number of uses driven by its general resistance to corrosion, as well as its electrochemical properties in rechargeable lead–acid batteries. The main uses of metallic lead are<sup>2</sup>

1. *Lead–acid batteries*: this currently accounts for over 50% and up to 90% of use in certain countries; most lead used in this way is recovered and recycled into the secondary lead market.
2. *Construction*: the main application in construction is for waterproofing flashings and roofing of historic buildings, as well as architectural detailing; the traditional use in water pipes and water storage has now vanished; lead from construction also has a high recycling rate.
3. *Chemical industry*: lead lining of vessels was traditionally used in the chemical industry, particularly in the production of sulfuric acid; however, these uses have now almost vanished.
4. *Metal joining*: lead is (with tin) a key component of solder used to join copper (piping, heat exchangers, etc.) and steels, and for electrical contacts; however, lead-free solders are now widely used in the water and electronics industry.
5. *Munitions*: lead is traditionally used in the manufacture of ammunition, although depleted uranium and tungsten, which are both significantly more dense than lead, are used in high performance (e.g., armor piercing) rounds; however for sporting purposes nontoxic alternatives exist and are increasingly being used.
6. *Dense metals*: lead is used for radiation shielding, for sound dampening, and for balancing of machinery; weights used in sporting applications

**Table 1** Physical properties of lead compared with some other common metals

	<i>Pb</i>	<i>Sn</i>	<i>W</i>	<i>Cu</i>	<i>Fe</i>
Atomic number	82	50	74	29	26
Atomic weight (g)	207.19	118.69	183.84	63.55	55.85
Density (g cm <sup>−3</sup> )	11.34	7.3	19.3	8.96	7.87
UTS, 99.9% pure (MPa)	12–15	20–30	950–1000	120–170	100–200
Melting point (K)	601	505	3680	1358	1810
Boiling point (K)	2020	2540	5830	2816	3130
Electrical conductivity $\times 10^6$ ( $\Omega^{-1}$ cm <sup>−1</sup> )	0.048	0.079	0.189	0.596	0.099
Thermal conductivity (W cm <sup>−1</sup> K <sup>−1</sup> )	0.35	0.73	1.74	4.01	0.238
Linear expansion coefficient $\times 10^{-6}$	29.0	23.5	–	16.5	12.2
Crystal structure (room temperature)	fcc	bct	bcc	fcc	bcc

(such as fishing weights) are being phased out in favor of nontoxic alternatives.

7. *Cable sheathing*: the first electrical cables were sheathed with lead to protect the cable from moisture ingress. For undersea cables, especially high-voltage power transmission lines, there is still no adequate alternative; thus, properly applied lead sheathing has zero water and water vapor transmission.
8. *Alloying*: lead is used as an addition in a number of alloys, including solders, pewter, bearing alloys, etc.; it also may be added to other materials (such as copper alloys and steels) to improve machinability, although alternatives are now available.
9. *Anodes*: by virtue of its relative chemical stability and easy passivation, lead is used as an insoluble anode in many electroplating processes (e.g., for chromium); traditionally, it was also used as a nonconsumable anode in cathodic protection systems, but this application area is decreasing as alternatives now exist.
10. *Fusible alloys*: eutectic alloys containing lead with bismuth, tin, cadmium, and indium are used as low melting point fuses and plugs in certain applications such as sprinkler systems, etc.

### 3.11.1.4 Alloying

Apart from tin, indium, and bismuth, lead has extremely limited solid solubility for most elements at room temperature, although solubility can

increase somewhat at higher temperatures.<sup>3</sup> Thus, most lead alloys consist of primary lead grains either with second phase particles (which may be intermetallic compounds), or with a eutectic mixture, decorating the grain boundaries. Because of the very poor mechanical properties of high-purity lead, alloying is almost always essential in order to achieve acceptable performance. Most commercial lead alloys contain a few tenths of a percent of alloying elements, with strengthening caused by precipitation or by the presence of a eutectic; many alloys are age-hardenable. The main classes of alloy listed below with composition ranges presented in [Table 2](#):

1. *Lead–antimony (+ tin, arsenic)*: the traditional alloy used for batteries, ammunition, sheet, and chemical plant; still very widely used, but the battery application is increasingly being replaced with lead–calcium.
2. *Lead–calcium (+ tin, aluminum)*: increasingly replacing lead–antimony alloys, particularly in battery applications, as they have very low hydrogen evolution characteristics and can therefore be sealed. Lead–calcium–tin is used for electrowinning anodes.
3. *Lead–tin (+ silver, antimony)*: used for jointing alloys (solders) and bearings.
4. *Lead–copper*: used generally for sheet products and linings; also for cable sheathing and in chemical plant.
5. *Lead–silver*: used for anode materials and higher temperature solders.

**Table 2** Compositions of typical lead alloys

<i>Alloy type</i>	<i>Specification</i>	<i>Application</i>	<i>Composition</i>
Pb–Sb	BS EN 12548	Battery grids	1–3% Sb + 0.5–1% S, Se and Cu
		Ammunition	0.5–8% Sb + 0.02–3% As
		Cable sheaths	0.5–1% Sb
		Anodes	6–10% Sb + 0.5–1% As
	BS EN 12659	Chemical lead	<0.06% impurities
Pb–Ca	BS ISO 4381	Bearings	9–15% Sb + 1–20% Sn
		Battery grids	0.03–0.07% Ca; +0.03% Al and 0.3% Sn
		Cable sheath/splices	0.04% Ca
		Anodes	0.03–0.09% Ca; + up to 0.3% Sn
	BS EN ISO 9453	Solders	2–70% Sn; + up to 2% Sb
Pb–Sn	BS ISO 4999	Terne plate	15–20% Sn
Pb–Cu	BS EN 12588	Construction (sheet)	0.03–0.06% Cu
Pb–Ag		Battery grids	0.005–0.05% Ag
		Solder	1–6% Ag
		Anodes	0.25–2% Ag; + up to 1% Sn or up to 6% Sb
Pb–Te	BS 3909	Nuclear/radiation	0.06% Te
	BS EN 50307	Cable sheaths	0.035–0.1% Te; +0.03–0.08% Cu

Source: Pregaman, D. R. In *Ullman's Encyclopedia of Industrial Chemistry*; Wiley: New York, 2005.

6. *Lead–tellurium (+ copper)*: because of its low alloy content, used for radiation shielding and, with copper, is a cable sheathing alloy.

### 3.11.1.5 Mechanical Properties

#### 3.11.1.5.1 Lead

Unalloyed lead has relatively poor mechanical properties,<sup>2,4</sup> thus, in addition to a low ultimate tensile strength (<12 MPa), it has a very low yield stress (<4 MPa); these are considerably lower than tin, for example. The low melting point of lead means that, like tin, it undergoes recrystallization and grain growth at room temperature and is susceptible to creep at stresses above ~2 MPa (~15% of the UTS), which is very low indeed. Thus, while lead of purity in excess of 99.99% is commercially available (BS EN 12659), it is not specified unless its superior corrosion resistance is required. Lead is also susceptible to fatigue, particularly due to thermal cycling, and this is a key failure mechanism in pure and alloyed lead. Table 3 provides typical mechanical properties for pure lead as well as a range of common lead alloys.

#### 3.11.1.5.2 Lead alloys

Of the elements commonly found in lead alloys, zinc and bismuth aggravate corrosion in most circumstances, while additions of copper, tellurium, antimony, nickel, silver, tin, arsenic, and calcium affect corrosion resistance only slightly, or may even improve it depending on the service conditions. Alloying elements that are of increasing importance are calcium, especially in maintenance-free battery alloys and selenium or sulfur, together with copper as grain refiners (nucleants), in low antimony battery alloys. Other elements of interest are indium and silver in anodes,<sup>5</sup> aluminum in batteries (to control calcium losses),<sup>6</sup> and selenium in chemical lead as a grain refiner.<sup>7</sup>

In Europe, lead alloy designations are specified in ISO TR 7003, “Unified format for the designation of metals,” in the format PBnnnA. The designate ‘PB’ is the chemical symbol for lead, the three digits ‘nnn’ define specific alloy compositions, while the ‘A’ designates the application: ‘R’ for pure lead, ‘K’ for cable, ‘A’ for battery alloys, and ‘M’ for miscellaneous alloys.

Historically, lead for use in chemical plant was specified in BS 334, which defines compositions for five types of lead: A, B1, B2, B3, and C. This standard has now been superseded by BS EN 12659, “Lead and lead alloys,” which specifies the composition of effectively pure lead (formally type A). This is because satisfactory alternative materials exist such that lead is now rarely, if ever, specified in chemical plant. Type A lead should only be used in a vibration-free environment and where the superior corrosion resistance is of paramount importance. Historically, for general chemical plant use, type B1 (copper–lead) is to be preferred on account of its much greater structural stability, especially at elevated temperatures. Type B2 (copper–tellurium–lead) has extremely good fatigue resistance, which is retained to a greater extent at elevated temperatures, than does type B1. The main effect of tellurium is to form a fine-grained uniform grain structure, to enhance work hardening, and to delay recrystallization. The silver content in type B3 also delays recrystallization and promotes a large-grained stable structure, which is creep resistant. Type C (antimony–lead) is used for valves, pump bodies, and fatigue-resistant applications, but is not suitable for use at temperatures above 60 °C owing to a rapid increase in creep rate, or in sulfuric acid concentrations above 60%.

BS EN 12548, “Lead alloy ingots for electric cable sheathing and for sleeves,” gives compositional requirements for a range of lead alloys for this application.

**Table 3** Mechanical properties of selected lead and lead alloys

Material	Yield Stress (MPa)	UTS (MPa)	Elongation (%)	Fatigue limit (MPa)	Creep failure at 20 MPa (h)
99.99% Pb	3.5	12.2	55	2.7	–
0.06% Cu	9.0	17.5	55	4.9	–
0.06% Ca	24.3	27.9	30	9.0	10
0.5% Sn	27.9	41.8	15	–	30
0.08% Ca + 1% Sn	46.0	59.7	15	–	850
1% Sb	19.3	37.9	20	–	–
2% Sb	24.1	46.9	15	–	–
2.75% Sb	55.2	65.5	10	–	–
6% Sb	71.0	73.8	8	–	–



The main types are PB001K (formally type B), containing 0.85% antimony; PB021K (formally type E), containing 0.2% Sb and 0.4% Sn; and PB012K (formally 1/2C), containing 0.2% Sn and 0.07% Cd. Type B is suitable for use in environments where severe vibration is expected, while type E is relatively resistant to vibration compared with type 1/2C. The performance of these materials is generally adequate in underground or marine environments.

BS EN 12588, "Rolled sheet lead for building purposes," lays down requirements for composition, structure, thickness, freedom from defects, width and length, and marking. The specified copper content stabilizes the structure of the material, conferring resistance to thermal fatigue cracking caused by grain growth and thermal cycling.

Other UK, European, or worldwide specification standards exist for specific applications, for example, radiation shielding, soft solders, and bearing alloys. However, there are no standards for battery alloys as many of these are proprietary to specific battery manufacturers.

### 3.11.2 Electrochemistry

#### 3.11.2.1 Thermodynamics

Pourbaix *et al.*<sup>8</sup> studied the Pb–H<sub>2</sub>O and Pb–H<sub>2</sub>O–X systems, where X is a nonmetal, and have established

the domains of thermodynamic stability of lead, lead cations and anions, and insoluble compounds of lead. Figure 1 shows the Pb–H<sub>2</sub>O system in the absence of complexing agents such as acetic acid. Lead can be seen to be a relatively noble metal from pH > 5, but dissolves to form Pb<sup>2+</sup> species at lower pH and the plumbite oxyanion at pH > 10.5. This is due to the amphoteric nature of lead and is a significant factor in actual environments. Also, passivation at high potential, due to the formation of PbO<sub>2</sub>, is evident across the whole pH domain.

In regions where the dissolution of lead is possible, according to the thermodynamics, the rate of corrosion may be very slow. This is because the overpotential for hydrogen evolution on lead is very high in 1 M H<sub>2</sub>SO<sub>4</sub>, 10<sup>−12</sup> A cm<sup>−2</sup> with a Tafel slope of 0.125 mV per decade current, indicating that a 1-electron transfer reaction is rate controlling.<sup>9</sup> Corrosion in near-neutral environments generally results in passivation, with the development of insoluble salt film corrosion products. In strong alkali, the corrosion is more rapid with the formation of plumbite ions.<sup>10</sup> Consequently, in acidic or moderately alkaline solutions, free from complexing agents (particularly organic acids), the corrosion of lead is generally negligible.

In contrast with the Pb–H<sub>2</sub>O system, in the presence of significant concentration of sulfate ion, the

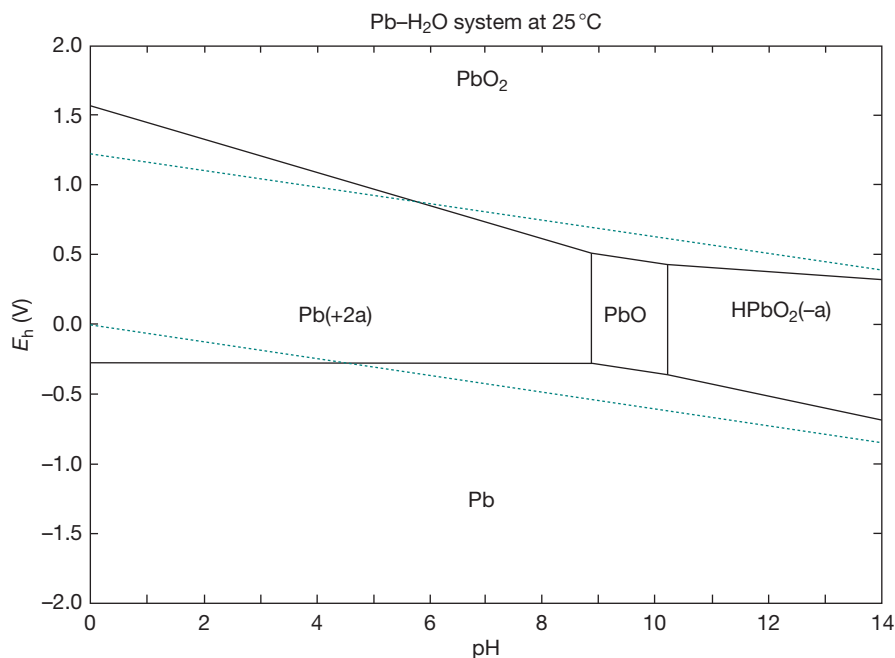


Figure 1 Pourbaix diagram for lead at a dissolved total metal ion concentration of 10<sup>−5</sup> M.

zone of thermodynamic stability of  $\text{PbSO}_4$  expands, and lead now passivates by the formation of a salt film of lead sulfate, which is the basis of lead's low corrosion rate in sulfuric acid (Figure 2).

In similar way, lead forms a series of relatively insoluble compounds, many of which are strongly adherent to the metal surface. Thus, in conditions where a stable continuous film can form, further reaction is often prevented or greatly reduced. The generally good corrosion resistance of lead results, therefore, from the formation of relatively thick protective films of corrosion product.

### 3.11.2.2 Dissolution

The standard electrode potential,  $E^0: \text{Pb}^{2+}/\text{Pb} = -0.126 \text{ V}$ ,<sup>11</sup> shows that lead is thermodynamically unstable in acid solutions, but stable in neutral solutions. In acid conditions, the exchange current density for the hydrogen evolution reaction on lead is very small ( $\sim 10^{-12} \text{ A cm}^{-2}$ ), but, at higher pH, control of corrosion is usually due to physical blocking of local anodes (from alloying additions and intermetallic compounds, which generally have higher exchange current densities) by virtue of insoluble lead salts that frequently form protective films. At  $\text{pH} > 11$ , lead will corrode freely at low anodic overpotentials dissolving

as the  $\text{HPbO}_2^-$  species. However, at higher potentials, it will passivate, again forming  $\text{PbO}_2$ . Lead may thus be used as an insoluble anode effectively throughout the entire pH range; an extremely useful characteristic. In summary, the corrosion rate of lead in an environment is frequently not controlled by the electrochemical processes but by the chemical dissolution rate of the corrosion product film.

Under strong cathodic polarization, disintegration can occur with lead, observable as a gray cloud of fine metal particles; this is a significant phenomenon in the application of lead to electrowinning (metal plating) anodes. Hydrogen evolved on the surface of the lead can be absorbed if the current density is sufficiently high,<sup>12</sup> and above this level, the formation of lead hydride may occur, which leads to severe disintegration.<sup>13</sup>

### 3.11.2.3 Oxidation and Passivation

Lead is characterized by a series of anodic corrosion products, which give a film or coating that effectively insulates the metal physically from the electrolyte, for example:  $\text{PbSO}_4$ ,  $\text{PbCl}_2$ ,  $\text{Pb}_3\text{O}_4$ ,  $\text{PbCrO}_4$ ,  $\text{PbO}$ ,  $\text{PbO}_2$ ,  $2\text{PbCO}_3 \cdot \text{Pb(OH)}_2$ ; of which  $\text{PbSO}_4$  and  $\text{PbO}_2$  are the most important, as they play a part in batteries and anodes. Lead carbonate and lead sulfate are

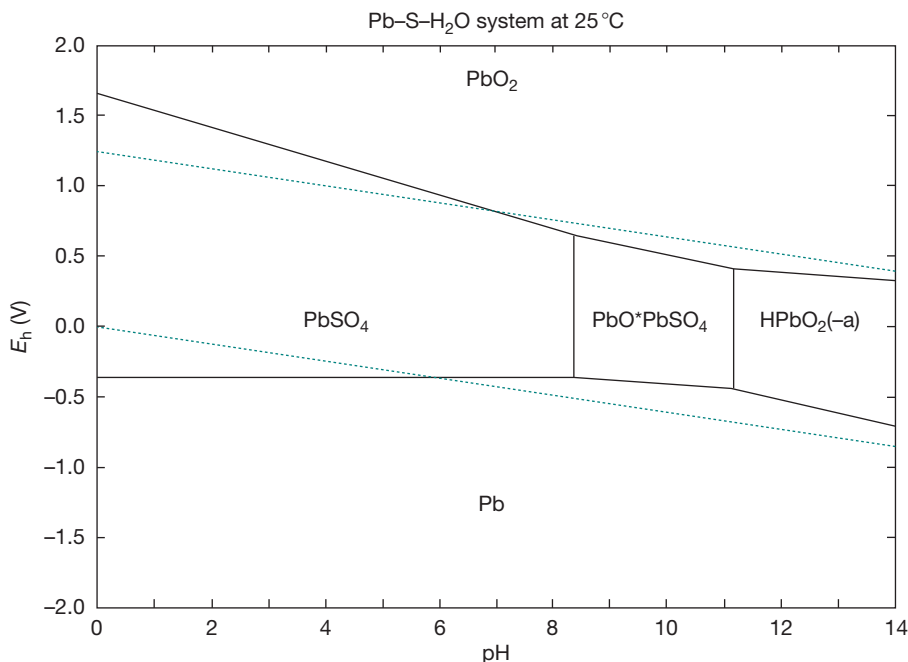


**Figure 2** Pourbaix diagram for lead-sulfur in 1 M sulfate ion concentration and a dissolved total metal ion concentration of  $10^{-5} \text{ M}$ .

particularly important also in atmospheric passivation and chemical industry applications.

In aqueous electrolytes, the anodic behavior of lead varies greatly, depending on the conditions prevailing. Extensive reviews of the aqueous electrochemistry of lead, including its anodic behavior, have been produced, for example, by Kuhn in 1979,<sup>14</sup> and much of this is still valid. The vast majority of historic and current research is concerned with the behavior of lead in sulfuric acid and this is understandable, given that the main application is still in lead-acid batteries. More recently, research has been concerned increasingly with environmental concerns, including lead removal from contaminated locations and the possible application of lead as a barrier material in nuclear waste disposal; these specific issues are dealt with in more detail later.

The dry oxidation of lead was studied in oxygen pressures from  $10^{-2}$  to 1000 torr and at temperatures between  $-90$  and  $150^{\circ}\text{C}$ .<sup>15</sup> Over several weeks, the oxide grew to a limiting thickness of about 10 nm. Ellipsometry and Auger electron spectroscopy confirmed that the oxide was PbO and that the growth law conformed to the Cabrera-Mott model (high-field ion conduction). X-ray diffraction data confirmed that the oxide was epitaxial to the lead, but that it was highly strained and that recrystallization of the lead substrate promoted oxide growth.

Passivation of lead in sulfuric acid is caused by the potential-dependent, and generally reversible, formation of PbO, PbSO<sub>4</sub>, and PbO<sub>2</sub>. However, the reactions and transformations are complex and difficult to characterize.<sup>16</sup> At potentials just above the reversible potential for lead oxidation, a dense layer of PbO can form together with porous PbSO<sub>4</sub>;<sup>17,18</sup> the growth of PbO formed in this way is controlled by the rate of oxygen anion transport through the oxide. At higher potentials, PbO and PbSO<sub>4</sub> transform to PbO<sub>2</sub>, which occurs in one of the two nonstoichiometric polymorphs, both with a slight oxygen deficiency. Lead anodic corrosion proceeds in two stages in sulfuric acid. Initially, Pb is oxidized to tetragonal PbO, as mentioned earlier; then, in the second stage, this is oxidized to PbO<sub>2</sub>. If this process is performed in solid state,  $\alpha$ -PbO<sub>2</sub> forms; however,  $\beta$ -PbO<sub>2</sub> can be formed by a dissolution-precipitation mechanism.<sup>19,20</sup> The oxide species are O<sup>2-</sup> anionic conductors; additionally, there is evidence from studies in batteries that PbSO<sub>4</sub> is a Pb<sup>2+</sup> cationic conductor.<sup>21</sup>

Passivation of lead also occurs in a range of other media, the most important of which is carbonate/bicarbonate as these equilibria are commonly

encountered in natural environments.<sup>22</sup> The passivation sequence on anodic polarization is similar to that in sulfuric acid except for the formation of lead carbonate instead of lead sulfate. Thus, Pb may be directly oxidized to PbO or Pb(OH)<sub>2</sub>, which then reacts with CO<sub>2</sub> (in the atmosphere) or bicarbonate/carbonate ions (in solution) to form protective PbCO<sub>3</sub>; at higher potentials, PbO<sub>2</sub> is formed. The rate of growth of the passive carbonate film is dependant on the concentration of carbonate in solution. However, unlike in sulfuric acid, the passivation process in carbonate media is essentially irreversible. Although pitting in sulfuric acid is possible (e.g., by perchlorate ions),<sup>23</sup> it is not the common degradation mechanism. However, in carbonate media, pitting is observed with a number of species in solution, including perchlorate<sup>24</sup> and nitrate.<sup>25</sup>

In summary, lead is passive at higher potentials at all pH, forming lead dioxide, which is a defect anion conductor. At intermediate potentials and in solutions of near-neutral to acid pH, lead generally passivates by formation of a salt film characteristic of the solution, for example, PbSO<sub>4</sub> in solutions of sulfuric acid. In such cases, the corrosion rate of lead tends to be controlled by the chemical dissolution of the corrosion product (salt film) and not by the potential. At intermediate potentials and high pH, lead will tend to dissolve forming the plumbite ion HPbO<sub>2</sub><sup>-</sup>. In strong alkali (1 M NaOH), formation of Pb(OH)<sub>2</sub> occurs at less positive potentials, which transforms to PbO according to a nucleation and growth mechanism under diffusion control.<sup>10</sup>

### 3.11.2.4 Corrosion Products

The nature (composition and morphology) of the corrosion product on lead will very frequently enable a good interpretation of the environment in which the material was exposed. However, note that lead dioxide cannot form under ordinary environmental conditions and that other metals cannot polarize lead sufficiently for it to form. Lead dioxide corrosion products can, therefore, only be produced by external polarization, either deliberately (as in a battery or anode) or accidentally (e.g., via stray currents).

From an inspection of the more common compounds of lead, it will be seen that, in many environments, the corrosion product will be relatively insoluble (Table 4). Often, however, compact protective films are prevented from forming on the surface of the metal. The nature of the film is influenced by the mode of crystallization, and in the case of the

**Table 4** Solubility of lead compounds

Compounds of lead	Formula	Solubility at 25 °C (g dm <sup>-3</sup> )
Acetate	(CH <sub>3</sub> COO) <sub>2</sub> Pb	550
Formate	(CHOO) <sub>2</sub> Pb	16
Nitrate	Pb(NO <sub>3</sub> ) <sub>2</sub>	600
Chloride	PbCl <sub>2</sub>	1 × 10 <sup>-4</sup>
Hydroxide	Pb(OH) <sub>2</sub>	4 × 10 <sup>-15</sup>
Carbonate	PbCO <sub>3</sub>	3.3 × 10 <sup>-14</sup>
Basic carbonate	2PbCO <sub>3</sub> Pb(OH) <sub>2</sub>	3.3 × 10 <sup>-14</sup>
Sulfate	PbSO <sub>4</sub>	1 × 10 <sup>-8</sup>
Sulfide	PbS	3.4 × 10 <sup>-28</sup>
Phosphate	Pb <sub>3</sub> (PO <sub>4</sub> ) <sub>2</sub>	10 <sup>-55</sup>
Oxide	PbO	Insoluble
Dioxide	PbO <sub>2</sub>	Insoluble

Source: Weast, R. C., Ed. *Handbook of Chemistry and Physics*, 57th ed.; CRC Press: Boca Raton, FL, 1989; pp B68–B146.

lower oxides, for example, frequently little protection is afforded. Lead dioxide often forms a good adherent film, especially when it is produced from a sulfate film or other adherent compounds during anodizing. Concentrated hydrochloric acid gradually dissolves it to form hexachloroplumbic acid, and with alkalis, plumbites are formed. With sparingly soluble salts of lead, the compactness of the deposits is likely to be strongly influenced by the concentration of the relevant anion; with low concentrations tending to result in imperfect coatings.

### 3.11.2.5 Galvanic Corrosion

Lead is relatively noble compared with most other metals in common use, apart from copper, and therefore, there is normally little concern about its galvanic corrosion as it will usually be the cathode in a coupled system. Where it is anodic, it will often not corrode significantly due to the formation of protective corrosion product films. However, increases in temperature may cause changes in the porosity of the protective film, or a phase change that, consequently, reduces its protective function. For example, at 75 °C, lead was found to be anodic to steel in seawater and groundwater because of a polarity reversal.<sup>26</sup> However, the expected order of potentials was restored if the water also contained a Bentonite clay suspension.

There are continuing concerns regarding galvanic corrosion involving lead in drinking water systems, where lead-containing solders are traditionally used (but are now being phased out). Particularly, in plumbo-solvent soft waters, lead is leached out from solders in measurable quantities that may be harmful to health.<sup>27</sup> Clearly, the best solution to this problem

is not to use lead; however, for the large numbers of historic properties where lead is still present in pipe-work, inhibition of this form of attack, for example, using silicates or phosphonates, is possible.<sup>28</sup> However, the ratio of chloride to sulfate is critical in controlling the leach rate of lead, and water utilities need to take note of this also in order to minimize the lead solubility of the water supply.<sup>29</sup>

## 3.11.3 Corrosion

### 3.11.3.1 Atmospheric Corrosion

Lead has been (and especially in historic and prestige properties, still is) used for roofing, gutters, flashings, downspouts, etc. and exhibits excellent resistance to air (dry or humid) and rain water, producing, after an initial period of time, an attractive patina. Initially, an oxide (PbO) is formed, which then converts by reaction with atmospheric carbon dioxide to plumbonacrite (Pb<sub>5</sub>O(OH)<sub>2</sub>(CO<sub>3</sub>)<sub>2</sub>) and hydrocerussite (Pb<sub>3</sub>(OH)<sub>2</sub>(CO<sub>3</sub>)<sub>2</sub>).<sup>30</sup> In atmospheres containing sulfur dioxide from industrial pollution, the general sequence of corrosion product (patina) formation is: lead oxide → basic lead carbonate → normal lead carbonate → normal lead sulfite → normal lead sulfate.<sup>31</sup> Lead is found to be reactive to common atmospheric gases, NO<sub>x</sub>, SO<sub>2</sub>, CO<sub>2</sub>, as well as the vapors of carboxylic acids.<sup>32</sup> As noted earlier, outdoor exposures were found to produce anglesite (PbSO<sub>4</sub>) and/or cerussite (PbCO<sub>3</sub>) while indoor exposures often produced lead carboxylates, due to higher levels of organic acid vapors from wood and wood products. Excluding the carboxylates, these corrosion products have a low solubility and are protective; however, they can produce a white flocculant 'run-off' in wet weather, which can stain surrounding surfaces in the very early stages of exposure.<sup>33</sup>

In marine environments, the initial oxide film reacts with sodium chloride when wet to produce basic lead chloride, which may result in corrosion of adjacent materials such as aluminum.<sup>34</sup> In such environments, the patina stabilizes, but takes approximately twice as long as in other atmospheric environments. A common treatment for new lead is a resin-based patination oil, which suppresses the formation of basic carbonates, allowing the slow controlled growth of a strongly adherent normal carbonate patina from the outset.<sup>35</sup>

Because of increasing concerns about lead in the environment, corresponding concerns regarding the release of lead from buildings are also evident. Thus,

lead ions can be introduced into the biosphere via corrosion and subsequent run-off of  $\text{Pb}^{2+}$  species, primarily from the solubility of cerussite (lead carbonate), hydrocerussite (lead hydroxy carbonate), and anglesite (lead sulfate) in rainwater. After an initial induction period, the measured release rate for lead ions was found to be  $10^{-5}$  moles of Pb per liter, or precipitation run-off per square meter of lead surface (i.e.,  $2.1 \text{ mg dm}^{-3}$ ) in both marine and rural locations,<sup>35</sup> which corresponds to a corrosion rate of about  $0.3 \mu\text{m year}^{-1}$  in these atmospheres.

It has been known for centuries that certain species of wood are 'more aggressive' to lead than are others, and this is now understood to be caused by the breakdown of cellulose species in the timber to volatile organic compounds (VOCs), especially acetic acid.<sup>36</sup> These can be liberated by new wood, especially oak, and also by varnishes, glues, urea formaldehyde, plastics, fabrics, and drying-oil paints, which can liberate fumes for a considerable time after application. Acetic acid in the 100–200 ppb range strongly accelerates the corrosion of lead, giving a corrosion product containing lead acetate–oxide–hydrate ( $\text{Pb}_3\text{O}_2(\text{CH}_3\text{COO})_2\text{H}_2\text{O}$ ) as well as cerussite and hydrocerussite.<sup>37</sup> The corrosion rate was found to be independent of relative humidity from 45% to 95% RH. This effect of VOCs on lead corrosion is significant not only in the context of buildings, but also in museums for display of historic artifacts.<sup>38</sup> However, the use of fatty acid soaps, such as sodium decanoate, successfully provides 99.9% inhibition to corrosion, by the formation of lead soaps, which are well known as corrosion inhibitors.<sup>39</sup>

### 3.11.3.2 Water

#### 3.11.3.2.1 Distilled and condensed water

In distilled water free from dissolved gases, corrosion is slight though significant; however, the rate of corrosion is increased by the presence of oxygen. Small amounts of dissolved oxygen and carbon dioxide cause rapid attack because the formation of a continuous protective film of lead carbonate does not occur. At moderate  $\text{CO}_2$  concentrations, passivation of the lead surface occurs because of  $\text{PbCO}_3$  formation, but in high- $\text{CO}_2$  contents, corrosion is increased because of the formation of soluble lead bicarbonate.<sup>40</sup>

Condensation corrosion is a common cause of failure in lead-work on buildings. Trapped water is evaporated from and condensed on the underside of the lead during thermal cycling in the environment. This repeated condensation causes the production of

lead oxide and lead hydroxide, which migrates away from the surface, leaving it unpassivated. Subsequent reaction with  $\text{CO}_2$  in the atmosphere produces copious quantities of basic lead carbonate, resulting in blistering, perforation, and finally, disintegration of the lead.<sup>41</sup> Adequate ventilation and adherence to codes of practice are essential to prevent this.<sup>42</sup> Lead sheet can also crack through thermal fatigue, and hence, admit water into a building structure. This is a consequence of over-fixing the lead, using sheets which are too large, or of using lead containing insufficient copper, and can be eliminated by correct installation.

#### 3.11.3.2.2 Natural waters

The European Union directive on the reduction of hazardous materials<sup>43</sup> stipulates that lead is no longer permitted for use in water supply, either as pipework or in solders. Where it is encountered in old buildings, its replacement is strongly recommended. However, because of the long life of existing installations, water may be conveyed through existing lead pipes, or pipes secured using lead-containing solders, for years to come. This may not be hazardous if the waters contain sufficient carbonate, sulfate, or silicate, and are alkaline. The current UK limit for lead in cold water drawn from a water supply tap is 25 ppb (the US limit is lower at 15 ppb); anything above these levels is actionable. Soft waters invariably dissolve lead to some extent, and raised levels of organic acids will render even harder supply waters plumbo-solvent.<sup>44</sup> Thus, water treatments to reduce lead solubility are required.

Lead corrodes slightly in most supply waters dependent primarily on the solution pH. The presence of oxygen and oxidizers in the aqueous medium affects the corrosion resistance of the metal more in acidic waters.<sup>45</sup> The most common treatments given to water are to increase the pH (reduce acidity) and remove organic acids; this is easily carried out by flocculation (e.g., with aluminum sulfate) and alkalinization (e.g., with calcium hydroxide or carbonate), which will encourage the formation of a protective carbonate scale.<sup>46</sup> Silicate and orthophosphate treatments reduce lead solubility; however, the common use of zinc orthophosphate to control corrosion of steel and cast iron water mains may increase lead corrosion rates.<sup>47,48</sup> In more saline waters, including seawater, lead usually has a good corrosion performance owing to the formation of the normal passive film of hydrocerussite ( $\text{Pb}_3(\text{OH})_2(\text{CO}_3)_2$ ) together with  $\text{Pb}(\text{OH})\text{Cl}$  and  $\text{PbCl}_2$  carbonate–chloride



double salts;<sup>49</sup> however, corrosion rates are linked to the activity of  $\text{Cl}^-$  ions, particularly in flowing solution.<sup>50</sup>

### 3.11.3.3 Buried Structures

#### 3.11.3.3.1 Stray-current corrosion

Stray currents are a source of damage to all buried metal structures, and lead pipes and cable sheaths are particularly susceptible. Although lead can corrode under cathodic (alkaline) conditions, it is generally the anodic sites on the pipe or cable sheath that are attacked. Lead is considered to be endangered if the current density is more than  $25 \text{ mA m}^{-2}$ . This is influenced by the conductivity of the soil, which is largely determined by the moisture content, but may be affected by salting of roads in winter. Non-metallic links in pipework may break electrical continuity. This will produce more numerous corrosion sites, but they are frequently less intense.<sup>51</sup> The surface will normally be covered with a mostly whitish corrosion deposit associated with either a smooth pitted surface or a more general rough etched appearance.<sup>40</sup> The corrosion product may comprise oxides, carbonates, hydroxides, and  $\text{PbCl}_2 \cdot \text{Pb(OH)}_2$  and  $\text{PbCl}_2 \cdot 6\text{PbO} \cdot 2\text{H}_2\text{O}$  have additionally been identified. Stray alternating current can also markedly increase corrosion rates,<sup>52</sup> and the use of lead pipes for electrical grounding has resulted in serious corrosion.<sup>51</sup> Electrolytic corrosion may also occur on the inside of cable sheaths by the passage of current from the cable sheath to the wire.<sup>51</sup> No protective coating is fully effective, but many give good protection with modern systems using polymers.<sup>53</sup>

#### 3.11.3.3.2 Underground corrosion

Lead has a long history of use underground in buried structures; historically for water supply, more recently for lead sheathed electrical cables. Corrosion is promoted by stray currents, local inhomogeneities in the lead, galvanic corrosion with another metal, and the environment of the soil.<sup>40</sup> Thus, soils may differ in water content, degree of aeration, or the presence of various chemicals or bacteria, and these can cause local or extensive corrosion of lead. Historically, extensive long-term tests have been conducted on lead in soils, and these data are still valid.<sup>54,55</sup> The worst combination of soils is wet clay and cinders (ashes from coal combustion). The carbon in the cinder acts as an efficient cathode and severe anodic corrosion takes place in the clay environment. Moisture held in the clay permits the passage of relatively

high currents. Anodic corrosion can occur when cables are in contact with dissimilar metals, such as steel support racks or copper bonding ribbon. A new (clean) section of cable may also become anodic to an old (passivated) cable and can then corrode.

Sandy soils and loams of high permeability are less aggressive because water tends to be mobile, thereby reducing concentration cells, and frequently drains readily to allow free movement of oxygen, thus reducing the effect of differential aeration cells. Where air circulates freely, a stable patina is often formed. Very large-grained soils are normally good for the reasons aforementioned, but under certain conditions, severe localized pitting can be caused by differential aeration (e.g., caused by differing degrees of soil density and compaction). Soils of low permeability, such as clays and silts, tend to be most corrosive; however, if the soil becomes deaerated the corrosion rate may fall; under such environments, microbial effects, due to sulfate reducing bacteria, often become important and corrosion can then become severe. Trenches are often lined before cable laying and backfilled after laying, with materials such as sand and crushed chalk, in order to encourage good drainage and ensure a consistent and benign local environment.

Sulfates, silicates, carbonates, colloids, and certain organic compounds in soils act as inhibitors if evenly distributed.<sup>40</sup> Nitrates tend to promote corrosion, especially in acid soil waters, due to cathodic depolarization and to the formation of soluble nitrates. Alkaline soils can cause serious corrosion with the formation of the plumbite anion, which decomposes to give  $\text{PbO}$ . Organic acids and carbon dioxide from rotting organic matter also have a strong corrosive action. Pitting corrosion in most groundwater/soil environments does not occur in the traditional meaning of the term; however, areas of nonuniform, general attack did occur, resulting in pitted surface morphologies.<sup>56</sup>

Calcium hydroxide leached from incompletely cured concrete causes serious corrosion of lead. This is because carbon dioxide reacts with the lime solution to form calcium carbonate, which is practically insoluble. Carbonate ions are therefore not available to form a passive film on the surface of the lead.<sup>40</sup> Typically, thick layers of  $\text{PbO}$  are formed, which may show seasonal rings of litharge (tetragonal  $\text{PbO}$ ) and massicot (orthorhombic  $\text{PbO}$ ).<sup>57</sup>

To prevent underground corrosion, lead was traditionally protected with coatings of tar, bitumen, resin, etc.; recently, however, polymeric materials (such as polyvinyl chloride, polypropylene, etc.) are

preferred. No coating is wholly effective unless they completely insulate the metal from corrosive agents and stray currents. The most successful method of protection for lead cables is cathodic protection. It is effective at a potential of  $E^\circ = -0.8\text{ V}$  or about 0.1 V more negative than its equilibrium potential in the soil in question;<sup>58</sup> both impressed currents or sacrificial anodes have been used. Excessively negative potentials can increase the pH of the environment, thus causing corrosion.

Sulfate-reducing bacteria in soils can produce metal sulfides and  $\text{H}_2\text{S}$ , which results in the formation of conductive lead sulfide and increased corrosion rates;<sup>59</sup> deep pits containing a black mass of lead sulfide have also been observed. Other microorganisms may also be involved in the corrosion of lead in soil, including other bacteria and fungi.<sup>60</sup>

Interest in lead as a possible barrier material for use in underground repositories for nuclear waste has prompted a number of studies. Repository environments with static groundwater would have very low oxygen contents and high ionic strengths and, under these conditions, lead would corrode at an unsuitably high rate. However, if the repository is flooded and oxygen levels increase, then lead might be acceptable.<sup>61</sup> Mass loss tests, supported by electrochemical polarization experiments, were carried out in natural and simulated groundwater, and in a range of specific salt solutions.<sup>62</sup> Corrosion rates in aerated conditions varied between  $1\text{--}3\text{ }\mu\text{m year}^{-1}$  in groundwater (which is acceptable) to over  $600\text{ }\mu\text{m year}^{-1}$  in sodium acetate and over  $380\text{ }\mu\text{m year}^{-1}$  in sodium nitrate (which is very high and unacceptable). Corrosion rates in bentonite clay suspensions likely to be used as repository backfill were  $10\text{--}15\text{ }\mu\text{m year}^{-1}$  and deemed to be acceptable.

### 3.11.3.4 Acids

#### 3.11.3.4.1 Mineral acids

Traditionally, sulfuric acid was made, stored, and conveyed in lead; this is because its corrosion resistance at moderate temperatures and over almost all the concentration range of the acid is excellent, provided that the protective sulfate film is not disrupted. Rupture of the sulfate film may be caused by erosion as a result of high-velocity liquids and gases containing acid spray. In such an environment, acid-resistant brick is often used with a liner of lead in between the brick and the (usually steel) vessel. Thermal cycling may also disrupt the film by thermal fatigue. The corrosion rate of lead is generally less

than  $125\text{ }\mu\text{m year}^{-1}$ , below about 55% concentration up to its boiling point ( $130^\circ\text{C}$ ), while acid concentrations to 80% have similar corrosion rates below  $100^\circ\text{C}$ . Above an acid concentration of 85%, the corrosion rate of lead increases to unacceptable values.<sup>62</sup> Lead is no longer used for this service in industry, its place having been taken by passive alloys such as tantalum, zirconium, specialist stainless steels, and nickel-based alloys.<sup>63</sup>

Nitric acid readily attacks lead if dilute, and the metal should not even be used for handling nitrate or nitrite species, except at extreme dilutions and preferably with a passivating reagent such as a sulfate, which will confer some protection. Corrosion decreases to a minimum at 65–70%  $\text{HNO}_3$ , and lead has been used for storage of nitric acid in the cold at this concentration.<sup>40</sup> Hydrochloric acid should generally be regarded as aggressive to lead and its use cannot be recommended, although a satisfactory life has been obtained with acid of up to 30% concentration at ambient temperature and 20% concentration at  $100^\circ\text{C}$ .<sup>40</sup> Resistance of lead to corrosion by HCl is presumably due to the formation of a protective film of lead chloride, which is only slightly soluble at these concentrations combined with its high overpotential for hydrogen evolution. In mixed hydrochloric and hydrofluoric acids (e.g., used for pickling steel) the behavior of lead is unreliable unless the lead is initially passivated in hydrofluoric acid first.

The remaining use of lead in industrial processes is as an anode in electrowinning and as an inert anode in electroplating, and for these applications, there are few economic alternatives. Lead has good resistance to phosphoric and chromic acids (e.g., in chromium plating), and at high current densities, will tend to passivate anyway with the formation of lead dioxide.

#### 3.11.3.4.2 Organic acids

Lead is attacked by most organic acids, which produce soluble lead salts, particularly in the presence of air or other organic oxidants. Aqueous acetic acid, solutions containing acetates, and acetic acid vapor all rapidly corrode lead and should be avoided if possible. During corrosion, the protective film is dissolved yielding lead salts of the organic acid. These are susceptible to rapid carbonation in the presence of  $\text{CO}_2$  and water, forming basic lead carbonate, which, in these circumstances, does not form a passive film.

Studies of the electrochemical behavior of lead at  $25^\circ\text{C}$  in acetic, lactic (0.01–1.0 M), oxalic, and tartaric (0.01–0.15 M) acid solutions demonstrated that

lead is readily soluble both in acetic and lactic acid solutions up to 2000 mV.<sup>64</sup> In these acids, anodic dissolution appears to be under charge transfer control, with lactic acid more aggressive than acetic acid with lead passivating at higher potentials. However, in oxalic and tartaric acid solutions a dependence on the acid concentration is evident. Thus, above a certain specific concentration, an anodic current peak is followed by a reduction in current associated with the formation of a passivation salt film that consisting of the oxalate or tartrate species, respectively. As noted above, corrosion by organic acids is important in the construction sector and also in the conservation of historic artifacts.

### 3.11.3.5 Lubrication Oils

White metal (tin–lead) bearings do not normally fail due to corrosion, but where this has occurred, it has been associated with the generation of acidity in the lubricant, the production of peroxides, and the presence of air. Peroxides appear to be the controlling factor, but corrosion is also reduced in the absence of air. The corrosion product generally consists of basic lead salts of organic acids.<sup>65</sup> The presence of residual organic acids is thought to be the main cause of the corrosion of terne (lead) plated steel when used as fuel tanks.

### 3.11.3.6 Miscellaneous Environments

As can be seen from the Pourbaix diagram, lead has no stable passive species at  $\text{pH} > 10$ –11, and hence, lead is not particularly resistant to dilute alkalis, and will dissolve freely as the plumbite oxyanion. Where free access to carbon dioxide is available, a passivating salt film of lead carbonate may form. However, lead is susceptible to lime drips from fresh concrete and cement mortar, which will tend to disrupt the lead carbonate film formation. Lead can tolerate concentrated alkalis such as KOH to 50% and up to 60 °C and NaOH to 30% and 25 °C, although it is explicitly not used for this purpose.

Lead is not generally attacked rapidly by solutions that contain anions, where the lead salt is sparingly soluble, and hence, where lead can passivate by the formation of a salt film. Thus, only nitrates and, to a lesser extent chlorides, are corrosive. The presence of nitrate tends to pit lead, for example, in carbonate solution.<sup>22</sup> In sodium chloride, the corrosion rate increases with concentration to a maximum in 0.05 M solution, then decreases because of the

formation of a relatively porous film  $\text{PbCl}_2$ . Control of the cyclic voltammetry conditions allowed the development of a relatively thick and more protective layer.<sup>66</sup> In potassium bromide, adherent deposits are formed, and the corrosion rate increases with concentration. The attack in potassium iodide is slow in concentrations up to 0.1 M, but in concentrated solutions rapid attack occurs, probably owing to the formation of soluble  $\text{KPI}_3$ . In dilute potassium nitrate solutions (0.001 M and below) the corrosion product is yellow and is probably a mixture of  $\text{Pb}(\text{OH})_2$  and  $\text{PbO}$ , which is poorly adherent. At higher concentrations, the corrosion product is more adherent and corrosion is somewhat reduced.<sup>67</sup>

## 3.11.4 Specific Applications

### 3.11.4.1 Lead Anodes

Anodes for electroplating and for electrolysis of brine are frequently made of lead and lead alloys. This is because the formation of a passive film of lead dioxide at high anodic potentials where conventional passive alloys, such as chromium containing materials, would be destroyed by transpassive dissolution. Nevertheless, there is generally a very slow continued corrosion, which leads to thickening of the  $\text{PbO}_2$  film. The resulting stresses caused by growth of the oxide layer can cause it to crack and disbond, releasing  $\text{PbO}_2$  particles into the electrolyte. Alloying elements are frequently added for strength and to stabilize the film; rolled or extruded alloys are generally found to be more resistant to this form of degradation than are cast alloys.

Lead–silver (1–2% Ag) anodes for cathodic protection may be used in brine and seawater applications for cathodic protection of ships and dockside structures<sup>68,69</sup> at current densities of up to  $120 \text{ A m}^{-2}$ , although in many applications these have now been superseded with platinum-doped titanium or niobium alloys, which can operate at still higher current densities.

Lead–silver, lead–tin, lead–calcium–tin, lead–calcium–silver, and lead–tin–silver are all used for electrowinning, which is generally carried out using sulfuric-acid-based electrolytes. These alloys have replaced the more traditional lead–antimony compositions due to requirements of higher purity in the deposits. In all electrowinning applications, it is essential to keep the potential of the anode well above the  $\text{PbO}_2/\text{PbSO}_4$  equilibrium potential, otherwise rapid corrosion will occur.<sup>69</sup> Electrochemical

studies of electrowinning anodes have been extensively studied and are focused on (a) reduction of anode corrosion rate, (b) reduction of (lead and other metal) contamination in the deposit, and (c) improved current efficiency.

For example, the efficiency and corrosion resistance of calcium- and silver-containing alloys appears to depend on the nature of the  $\text{PbO}_2$  passive layer and its electronic and ionic conductivity.<sup>70</sup> The corrosion rate and current efficiency of anodes can be improved significantly by the incorporation of minor amounts of foreign species in the electrolyte. Thus, preconditioning of anodes in a fluoride solution prior to use can result in a compact and more protective  $\text{PbF}_2/\text{PbO}_2$  bilayer that is more corrosion resistant.<sup>71</sup>

The corrosion rates for lead-silver anode corrosion rates in zinc electrowinning solutions were studied at a range of current densities from 2500 to 10 000  $\text{A m}^{-2}$ . Increases in acid concentration and temperature caused increases in corrosion rate, whereas in the absence of bath additions, the rate was independent of current density.<sup>72</sup> Chloride ions increased the corrosion rate, while fluoride preconditioning reduced it, but only in the presence of manganese. The presence of small concentrations of cobalt and manganese ions can reduce the corrosion rate of electrowinning anodes considerably. The effect appears to be related to an increase in the oxygen evolution kinetics that reduces cell overvoltage and causes less disruption of the  $\text{PbO}_2$  passive layer.<sup>73</sup>

Traditional chromium plating uses lead-tin or lead-antimony alloys as the anode material, although coated passive metal anodes (e.g., platinized Ti, Zr, Nb, and Ta) have recently been advocated.<sup>74</sup> Lead anodes offer processing advantages in that they can be formed or cast to conform to the surface to be plated, and hence give an even current density and uniform coverage of coating. The electrochemistry of anodes containing tin, antimony, and silver have been studied in electrolytes similar to chrome plating baths. In chromic acid, a passive film of  $\text{PbCrO}_4$  forms at very low overpotentials, and the subsequent formation of  $\text{PbO}_2$  is masked by oxygen evolution. The effects of alloying additions were found to be minor, although antimony raises the passive current substantially and silver reduces the overpotential of oxygen evolution by about 0.2 V.<sup>75</sup> As for electrowinning anodes, the quiescent (nonpolarized) corrosion rate can be very high and it is recommended that anodes are connected at all times. It has been found that 0.5  $\text{g l}^{-1}$  of magnesium fluosilicate suppresses corrosion without affecting the plating process.<sup>76</sup>

### 3.11.4.2 Lead-Acid Battery

Lead-acid batteries comprise by far the single most important worldwide application for lead. The technology of lead-acid batteries is still under constant improvement and is technically still very much relevant;<sup>77</sup> this section briefly discusses very general aspects of the technology. Lead-acid batteries typically consist of lead alloy supports, which carry an electrochemically active mass, the composition of which differs between positive and negative plates, and with the state of charge of the battery. Failure normally occurs in the positive grids of a battery. The main cause of failure is loss of contact between the grid and the active mass because of 'grid growth,' which is caused by the change in volume of the active material during the charge/discharge cycle, and by corrosion of the metal surface, which can be accelerated by stress. Batteries for automotive, electric vehicle, standby services, etc., all have different characteristics and requirements, which are met by battery grid design and choice of alloy.<sup>78,79</sup>

Traditionally, battery grids have been made from lead with 6–14% antimony, with a small amount of arsenic. High antimony alloys have a significant electrochemical disadvantage, that is, they reduce the overpotential for hydrogen evolution on the lead, leading to electrolysis of the electrolyte (to hydrogen and oxygen). Thus, batteries using traditional materials require regular maintenance (topping-up) via additions of distilled water. While alloys in the region of 5–6% antimony are still used in some industrial, deep discharge, and traction applications, high antimony contents have been largely replaced in automotive batteries by complex low antimony or antimony-free lead-calcium-(tin) alloys. Modern automotive batteries now use lead-calcium-based alloys that do not require topping up (provided they are operated within their electrical design parameters). This reduction in antimony content has been made possible by the introduction of additions of solidification nucleants, such as selenium and sulfur, which promote fine-grain structure. It is also increasingly common to find different alloys used in the positive and negative grids and optimized for these applications.

High antimony alloys exhibit high strength, good castability, and give good deep cycling performance. The latter requires that the active mass has good adhesion to the metal, is structurally stable during cycling, and does not passivate. Antimony reduces shedding of active material from the cells, produces a surface film of greater porosity, which becomes more

porous during cycling, promoting stability of the active mass. It has also been shown that  $\text{PbSO}_4$  is more reluctant to nucleate on antimonial lead.<sup>80</sup> Although corrosion rates may appear quite high, attack is normally of a general nature, which allows a satisfactory service life. This is because the eutectic is preferentially corroded, which reduces intergranular corrosion. Antimony reduces the oxygen overpotential on the positive grid, while  $\text{Sb}^{5+}$  ions migrate from the positive grid to the negative and be reduced to metallic antimony.<sup>81</sup> This reduces the hydrogen overpotential, leading to excessive gassing, consuming water from the electrolyte, reducing charge efficiency, and liberating stibine ( $\text{SbH}_3$ ). During overcharge, antimony increases the rate of formation of the inner corrosion layer on the positive grid.

Low maintenance batteries, which only require the addition of water infrequently in the second half of their service life, use low antimony alloys that typically contain less than 3% antimony, with some alloys containing as little as 0.6%. The most commonly used alloys have 1.3–1.8% Sb. They always contain As to assist hardening, and a nucleating agent such as Se or S with Cu. These are necessary because the coarse dendritic structure is prone to porosity and hot cracking during casting. The addition of nucleating agents gives a fine-grained structure with good corrosion resistance. Tin is often added to increase fluidity in casting alloys.

Lead–calcium–(tin) alloys are used in maintenance-free automotive starting, lighting, ignition (SLI) batteries, in stationary batteries, and some traction batteries. It is essential that the correct calcium content and a suitable calcium–tin ratio is used. In the binary lead–calcium alloys, a fine-grained structure with serrated grain boundaries is produced by a discontinuous precipitation reaction.<sup>82</sup> The addition of tin changes the nature of the precipitation reactions to give two areas of stability. One is with high calcium–low tin and the other is in the region below 1.8% tin and less than 0.07% calcium. Batteries made from these alloys have a much reduced rate of self-discharge compared with antimonial alloys, thus giving a longer shelf-life, and maintain a high discharge voltage throughout their life.

### 3.11.4.3 Reactor Coolants

Lead-based liquid metal coolants (using either liquid lead or liquid lead–bismuth eutectic) were first used in a nuclear reactor in the 1960s by the Soviets as an advanced, high power density, submarine propulsion

plant. Reactors designed using such coolants have some compelling advantages (e.g., operation at atmospheric pressure, boiling point greatly in excess of the reactor operating temperature, relative nonreactivity to water and air compared with liquid sodium) and comprise a candidate ‘Generation IV’ fast neutron reactor system as well as a candidate coolant system for fusion reactors. However, lead alloys are significantly more corrosive to constructional materials (e.g., steels) than is liquid sodium. This is due to dissolved oxygen in the lead that reacts with the containing material, as well as liquid metal embrittlement.<sup>83,84</sup> To avoid excessive oxidation of structural alloys, such as martensitic steels, it is necessary to control the oxygen activity to below  $10^{-24}$  atm, and this can be monitored by the use of electrochemical probes.<sup>85</sup>

## References

1. Thornton, I.; Rautiu, R.; Brush, S. *Lead – The Facts*; International Lead Association, 2001.
2. Blasket, D. R.; Boxall, D. *Lead and Its Alloys*; Ellis Horwood, 1990.
3. *Smithell's Metal Handbook*, 7th ed.
4. Guruswamy, S. *Engineering Properties and Applications of Lead Alloys*; CRC Press, 1999.
5. Hine, F.; Ogata, Y.; Yasuda, M. *Bull. Electrochem.* **1988**, *4*, 61–65.
6. Prengaman, R. E. In *Structure Control of Non-antimonial Lead Alloys via Alloy Additions, Heat Treatment and Cold Working*; Proceedings of the 7th International Lead Conference, Lead Development Association: Madrid, 1983.
7. Heubner, U.; Reinert, M. In *Development of Improved Lead Materials for Chemical Plant*; Proceedings of the 7th International Lead Conference, Lead Development Association: Madrid, London, 1983.
8. Delahay, P.; Pourbaix, M.; Van Rysselbergh, P. *J. Electrochem. Soc.* **1951**, *98*, 57.
9. O'M Bockris, J.; Reddy, A. K. *Modern Electrochemistry*; Plenum, 1986; Vol. 2, Table 10.12.
10. Birss, V. I.; Seralier, M. T. *J. Electrochem. Soc.* **1987**, *134*, 802–808, 1594–1600.
11. Lingane, J. J. *Am. Chem. Soc.* **1938**, *60*, 724–725.
12. Ives, D. J. G.; Smith, F. R. *Trans. Faraday Soc.* **1967**, *63*(1), 217–233.
13. Salzberg, H. W. *J. Electrochem. Soc.* **1953**, *100*, 146–151.
14. Kuhn, A. T. Ed. *The Electrochemistry of Lead*; Academic Press: London, 1979.
15. Eldridge, J. M.; Dong, D. W. *Surf. Sci.* **1973**, *40*, 512–530, 531–544.
16. Bullock, K. R. *J. Electroanal. Chem.* **1987**, *222*, 347–366.
17. Ruetschi, P. *J. Electrochem. Soc.* **1973**, *120*, 331–336.
18. Pavlov, D. *Electrochim. Acta* **1978**, *23*, 845–854.
19. Pavlov, D.; Rogachev, T. *Electrochim. Acta* **1978**, *23*, 1237–1242.
20. Fletcher, S.; Matthews, O. B. *J. Electroanal. Chem.* **1981**, *126*, 131–144.
21. Hall, S. B.; Wright, G. A. *Corros. Sci.* **1990**, *31*, 709–714.
22. Abd El Aal, E. E.; Abd El Wanees, S.; Abd El Aal, A. J. *Mater. Sci.* **1993**, *28*, 2607–2614.



23. Ahlberg, E.; Berghult, B. *Electrochim. Acta* **1991**, *36*, 197–201.
24. Abd El Aal, E. E. *Anti-Corros. Meth. Mater.* **2001**, *48*, 116–125.
25. Amin, M. A.; Rehim, S. S. A. *Electrochim. Acta* **2003**, *49*, 2415–2424.
26. Semino, C. J.; Burkart, A. L.; García, M. E.; Cassibba, R. *J. Nucl. Mater.* **1996**, *238*, 198–204.
27. Subramanian, K. S.; Sastri, V. S.; Elboudjaini, M.; Connor, J. W.; Davey, A. B. C. *Water Res.* **1995**, *29*, 1827–1836.
28. Sastri, V. S.; Subramanian, K. S.; Elboudjaini, M.; Perumareddi, J. R. *Corros. Eng. Sci. Technol.* **2006**, *41*, 249–254.
29. Edwards, M.; Triantafyllidou, S. J. *Am. Water Works Assoc.* **2007**, *99*, 96–109.
30. Olby, J. K. J. *Inorg. Nucl. Chemist* **1966**, *28*, 2507.
31. Tranter, G. C. *Br. Corros. J.* **1976**, *11*, 222.
32. Graedel, T. E. *J. Electrochem. Soc.* **1994**, *141*, 922–927.
33. Cook, A. R.; Smith, R. In *Atmospheric Corrosion*; Ailor, W. H., Ed.; Wiley: New York, 1982.
34. Hill, R. H.; Frost, P. C.; Smith, R. In *Corrosion of Aluminium in Contact with Lead in Atmospheric Environments*; Proceedings of the 7th International Lead Conference, Lead Development Association: London, 1983.
35. Matthes, S. A.; Cramer, S. D.; Covino, B. S., Jr.; Bullard, S. J.; Holcomb, G. R. In *Outdoor Atmospheric Corrosion*; Townsend, H. E., Ed.; ASTM Special Technical Publication, 2002, Vol. 1421, pp 265–274.
36. Echavarría, A. V.; Echeverría, F. E.; Arroyave, C.; Cano, E.; Bastidas, J. M. *Corros. Rev.* **2003**, *21*, 395–413.
37. Niklasson, A.; Johansson, L.-G.; Svensson, J.-E. *Corros. Sci.* **2008**, *50*, 3031–3037.
38. Tétreault, J.; Sirois, J.; Stamatopoulou, E. *Stud. Conservat.* **1998**, *43*, 17–32.
39. Rocca, E.; Rapin, C.; Mirambet, F. *Corros. Sci.* **2004**, *46*, 653–665.
40. Hofmann, W. *Lead and Lead Alloys Properties and Technology*; Springer-Verlag: London, 1970; English Translation by Lead Development Association.
41. Hill, R. H.; Frost, P. C.; Smith, R. In *Various Aspects of Weathering and Corrosion of Lead in Building Applications*; Proceedings of the 8th International Lead Conference Lead Development Association: London, 1985.
42. *Rolled Lead Sheet – The Complete Manual*; Lead Sheet Association, 2007.
43. *Reduction of Hazardous Substances*; European Commission Directive, 2002/95/EC.
44. Miles, G. J. *Soc. Chem. Indust.* **1948**, *67*, 10–13.
45. Badawy, W. A.; Al-Kharafi, F. M. *Corros. Prevent. Contr.* **1999**, *46*, 13–22.
46. Boffardi, B. P.; Sherbondi, A. M. In *Control of Lead Corrosion by Chemical Treatment*; Proceedings of 'Corrosion 1991' NACE: USA, 1991; Paper 445.
47. Patterson, J. W.; O'Brien, J. E. *J. Am. Water Works Assoc.* **1979**, *71*, 264–271.
48. Edwards, M.; McNeill, L. S. *J. Am. Water Works Assoc.* **2002**, *94*, 79–90.
49. Beccaria, A. M.; Mor, E. D.; Bruno, G.; Poggi, G. *Werkstoffe Korros.* **1982**, *33*, 416–420.
50. Beccaria, A. M.; Mor, E. D.; Bruno, G.; Poggi, G. *Br. Corros. J.* **1982**, *17*(2), 87–91.
51. Glander, F.; Glander, W. *Zeitschrift Metallkunde* **1953**, *44*, 97–101.
52. Costa, J. M.; Hoar, T. P. *Corros. Sci.* **1962**, *2*, 269–274.
53. Dyba, J.; Goodwin, F. In *New Developments in Lead-Sheathed Cables*; Proceedings IEEE International Symposium on Electrical Insulation, USA, 1998.
54. Romanoff, M. *Underground Corrosion*; National Bureau of Standards, 1957; publication #579.
55. Robson, W. W.; Taylor, A. R. Some experiments in the mechanism of corrosion of lead pipes in soils. Report MM/19/54. Associated Lead Manufacturers Ltd., 1954.
56. Joerg, E. A.; Devereux, O. F. *Corrosion* **1996**, *52*, 953–957.
57. Wolf, E. F.; Bonilla, C. F. *Trans. Electrochem. Soc.* **1941**, *79*, 307.
58. Compton, K. G. *Corrosion*; **1956**, *12*, 553–60.
59. Schmeling, E. L.; Roschenbleck, B. *Werkstoffe Korros.* **1961**, *12*, 215–23.
60. Pintado, J. L.; Montero, F. *Int. Biodeter. Biodegrad.* **1992**, *29*, 357–365.
61. Goodwin, F. E. *Corros. Prev. Contr.* **1985**, *32*(2), 21–24.
62. Cassibba, R. O.; Fernandez, S. J. *Nucl. Mater.* **1989**, *161*, 93–101.
63. Gaverick, L. Ed. *Corrosion in the Petroleum Industry*; ASM International, 1994.
64. Abd-El Rehim, S. S.; Amin, N. H.; Ali, L. I.; Mohamed, N. F. *J. Chem. Tech. Biotechnol.* **1998**, *72*, 197–201.
65. Wilson, B. S.; Garner, F. H. *J. Inst. Petroleum*; **1951**, *37*, 225–38.
66. El-Halim, A. M. A.; Fawzy, M. H.; Saty, A. *J. Electroanal. Chem.* **1991**, *316*, 275–292.
67. Vaivads, A.; Liepina, L. *Latvijas PSR Zinatnu Akademijas Vestis* **1954**, *8*, 119–129.
68. Barnard, K. N.; Christie, G. L.; Gage, D. G. *Corrosion* **1959**, *15*, 581–586.
69. Lander, J. J. *J. Electrochem. Soc.* **1956**, *103*, 1–8.
70. Kozin, L. F.; Kozin, V. F. *Protection Metals* **1997**, *33*, 131–136, 549–555.
71. Ramachandran, P.; Balakrishnan, K. *Bull. Electrochem.* **1996**, *12*, 352–354.
72. Newnham, R. H. *J. Appl. Electrochem.* **1992**, *22*, 116–124.
73. Cachet, C.; Le Pape-Rérolle, C.; Wiat, R. *J. Appl. Electrochem.* **1999**, *29*, 813–820.
74. Pavlović, M. G.; Dekanski, G. *J. Solid State Electrochem.* **1997**, *1*, 208–214.
75. McBurney, M. J. P.; Gabe, D. R. *Surf. Technol.* **1979**, *9*, 253–266.
76. Carter, V. E.; Campbell, H. S. *Metal Finishing J.*; **1962**, *8*, 103–7.
77. Kiehne, H. A., Ed. *Battery Technology Handbook*; CRC Press, 2003.
78. Berndt, D. INTELEC, Proceedings of the International Telecommunications Energy Conference **2005**; pp 269–275.
79. Garche, J. *Phys. Chem. Chem. Phys.* **2001**, *3*, 356–367.
80. Webster, S.; Mitchell, P. J.; Hampson, N. A.; Dyson, J. I. *J. Electrochem. Soc.* **1986**, *133*, 133–137, 137–139.
81. Dawson, J. L.; Wilkinson, J.; Gillibrand, M. I. In *Power Sources 3*, Proceedings of the 7th International Symposium in Non-mechanical Electrical Power Sources; Brighton, UK, Collins, D. H., Ed., Oriel Press: Newcastle-upon-Tyne, 1970; pp 1–9.
82. Caillerie, J. L.; Albert, L. *J. Power Sources* **1997**, *67*, 279–281.
83. Tortorelli, P. F.; Chopra, O. K. *J. Nucl. Mater.* **1981**, *103*, 621–632.
84. Fazio, C.; Benamati, G.; Martini, C.; Palombarini, G. *J. Nucl. Mater.* **2001**, *296*, 243–248.
85. Li, N. *J. Nucl. Mater.* **2002**, *300*, 73–81.

## Relevant Websites

[www.ilzro.org](http://www.ilzro.org) – International Lead-Zinc Research Organisation.  
[www.ila-lead.org](http://www.ila-lead.org) – International Lead Association.

## 3.12 Corrosion of Tin and its Alloys

**S. B. Lyon**

Corrosion and Protection Centre, School of Materials, The University of Manchester, Oxford Road, Manchester, M13 9PL, UK

This article is a revision of the Third Edition article 4.6 by S. C. Britton, volume 1, pp 4:157–4:167,

© 2010 Elsevier B.V.

<b>3.12.1</b>	<b>Introduction</b>	2068
3.12.1.1	Physical Properties	2068
3.12.1.2	Applications	2069
<b>3.12.2</b>	<b>Electrochemistry</b>	2070
3.12.2.1	Thermodynamics	2070
3.12.2.2	Dissolution	2071
3.12.2.3	Passivation	2071
<b>3.12.3</b>	<b>Corrosion and Oxidation</b>	2072
3.12.3.1	Atmospheric Corrosion	2072
3.12.3.1.1	Oxidation in dry air	2072
3.12.3.1.2	Corrosion in humid air	2072
3.12.3.1.3	Atmospheric corrosion products	2072
3.12.3.2	Corrosion in Acid	2073
3.12.3.2.1	Mineral acids	2073
3.12.3.2.2	Organic acids	2073
3.12.3.3	Corrosion in Near-neutral Conditions	2073
3.12.3.4	Corrosion by Alkalis	2073
3.12.3.5	Corrosion in Foodstuffs	2074
3.12.3.6	Galvanic Corrosion	2074
<b>3.12.4</b>	<b>Applications</b>	2074
3.12.4.1	Tin Coatings	2074
3.12.4.2	Solders	2075
3.12.4.3	Tin Interconnections	2076
3.12.4.4	Bearing Metals	2076
<b>References</b>		2077

### Glossary

**Allotropy** The existence of two or more different forms (allotropes) of the same element that are bonded in a different manner; allotropes are thus different structural modifications of an element.

**Gray tin** The low-temperature allotrope of tin having a cubic structure that is stable below  $\sim 13^{\circ}\text{C}$ . Note that the transformation from white tin to gray tin is sluggish and generally does not proceed significantly until the temperature is well below  $0^{\circ}\text{C}$ .

**White tin** The high temperature allotrope of tin having a body centered tetragonal structure that is stable above  $\sim 13^{\circ}\text{C}$ .

### Abbreviations

**AES** Auger electron spectroscopy

**SHE** Standard hydrogen electrode

**XPS** X-ray photoelectron spectroscopy

### 3.12.1 Introduction

#### 3.12.1.1 Physical Properties

The element tin is located in Group VI of the periodic table, lying above lead, with which it shares many properties. Tin, like lead, is one of the metals known from antiquity and highly prized for its ability to harden copper, forming bronze. There is evidence that tin was mined in the United Kingdom in

Cornwall from the early bronze age (2100–1500 BC). Certainly, by Roman times, tin from the western edge of Europe (mainly Cornwall and Spain) was traded widely throughout the known world. Tin ore resources are not widely distributed and production is mainly from two forms: (1) hard rock, typified by the Cornish deposits and similar ore bodies in Bolivia and Queensland; and (2) alluvial (placer) deposits, typified by the southeast Asian ore field stretching from Indonesia and Malaysia to Thailand.

Tin is allotropic with the normal, metallic ( $\beta$ ) form being body-centered tetragonal above the transformation temperature, that is,  $\sim 13.2^\circ\text{C}$ .<sup>1</sup> The lower temperature allotrope,  $\alpha$  or 'gray' tin, is cubic and forms with a significant volume change that tends to result in the disintegration of the material. However, the transformation is kinetically sluggish, although it can be encouraged by mechanical deformation and delayed, or effectively suppressed to lower temperatures, by impurities such as antimony, lead, and bismuth.<sup>2</sup> Gray tin normally appears as nodules of a friable material on the surface of the metallic form and resembles a corrosion product. Thus, the transformation is often not readily distinguishable from corrosion.<sup>3</sup> The transformation mechanism has been studied by high-resolution electron microscopy in order to obtain the lattice orientation relationship between the two allotropes.<sup>4</sup> Thus, the (011) plane of gray tin is parallel to the (001) plane of white tin, and the [211] direction of gray tin is nearly parallel to the [010] direction of white tin. This evidence supports a model for the  $\alpha$ -to- $\beta$  transformation that is partly martensitic and partly diffusional.

The use of unalloyed tin is restricted by its low melting point ( $232^\circ\text{C}$ ) and by its low tensile strength (15 MPa). On the other hand, its melting point, and its ability to 'wet' other metals (often by the formation of intermetallic compounds), facilitates its use as solder (for metal joining) and as a coating (for corrosion protection), while its softness and high ductility make it suitable for cold working and for bearing applications. Given its relatively low melting point, tin recrystallizes readily at room temperatures, and therefore, the effects of mechanical working are slight and arise from the differences in grain size and not from the effects of work hardening. The formation of tin whiskers is also thought to be a consequence of its low melting point, which results in the growth of fine threadlike structures, typically  $\sim 1\text{--}2\text{ }\mu\text{m}$  in diameter, with growth rates of up to millimeters per month under appropriate conditions.<sup>5,6</sup>

Given increasing health and safety concerns that lay severe limits on the use of lead in materials, there has been, for some time, a legislative driver for the development of essentially lead-free tin alloys. This has reintroduced problems relating to the formation of gray tin (at lower temperatures) and tin whiskers that were generally absent in lead-containing materials. For example, in the electronic industry, where tin-based solders are now widely used, whisker growth, in particular, can cause problems such as short-circuiting.<sup>7</sup>

### 3.12.1.2 Applications

The industrial use of tin is limited by its low strength and very limited solubility for most elements at room temperature. However, tin is essential in a number of alloys where it is a minor constituent (e.g., in copper–tin bronzes) and also where it is the major component (e.g., in pewter). The most important forms in which tin is used are

1. tin of more than 99% purity for specialist applications;
2. tin hardened by additions of 1–2% Cu or Sb;
3. pewter with 90–95% Sn, 4–8% Sb, and 1–2% Cu;
4. coatings for other metals, which may be pure tin or tin plus a codeposited species;
5. soft solders with tin and lead in all proportions;
6. lead-free soft solders with  $>90\%$  Sn and additions of silver, copper, bismuth, indium, or zinc;
7. bearing metals 'high tin' and 'head lead' with a wide range of proportions of tin, antimony, copper, and lead, or with tin (5–30%) in aluminum;
8. diecasting alloys containing 70–80% Sn with antimony, copper, and lead, either one of them or a combination.

The corrosion behavior of tin and tin alloys, whatever their form, is basically similar, except in the case of solders and bearing metals where the wide composition range and special duties of the materials give particular issues. The impurities likely to be present in nominally pure tin are unlikely to affect its corrosion resistance, except for minor effects on the rate of oxidation in air. Low aluminum contents, however, may result in a severe intergranular attack by water; the addition of antimony counteracts this effect. Although 0.1% magnesium appears to be tolerable, larger amounts produce effects similar to those of aluminum.<sup>8</sup>

Apart from the special uses in solders and bearings metal already referred to, and as coatings, tin and its alloys find employment where we can take advantage

of their physical properties and their fair resistance to tarnish and corrosion in near-neutral environments. Tin has traditionally been used in many food-grade applications, although such applications nowadays increasingly use cheaper materials, such as stainless steels and polymers. Tin pipe can be used to condense steam for high-purity distilled water, as a conveyor of beer and soft drinks, especially in coils through cooling media, and, in a larger size, as organ pipes. Some pharmaceutical and food products are packed in collapsible tin tubes, and tinfoil coverings are used on cork wads for jar and bottle closures. The tin alloy pewter is most valued for the decorative forms into which it is easily worked or cast, but it is also used for making drinking vessels and dishes.

### 3.12.2 Electrochemistry

#### 3.12.2.1 Thermodynamics

The Pourbaix diagram for tin, **Figure 1**, refers only to solutions in which the formation of soluble tin complexes (e.g., with citric acid) does not occur. Tin is a slightly active metal with its domain of stability below that of the hydrogen equilibrium; in theory, it will corrode in acid, evolving hydrogen gas. It is more noble than iron and nickel, but slightly less noble than lead, although in practice, passivity will alter this sequence. Tin shows a wide range of passivity

because of the stability of tin (IV) oxide,  $\text{SnO}_2$ , which is stable at a lower pH than is  $\text{PbO}$ . However, tin will dissolve as  $\text{Sn}^{2+}$  ions at  $\text{pH} < 2$  and as the corresponding (II)- or (IV)-valent oxy-anion species at  $\text{pH} > 11$ . Note, however, that in regions where, as shown in the diagram, the dissolution of tin is possible, the rate of corrosion may be very low. This is because the overpotential for hydrogen evolution on tin is high, particularly in acid solution. Thus, in a range of concentrations of  $\text{H}_2\text{SO}_4$ ,<sup>9</sup> the exchange current for the hydrogen evolution reaction was found to be  $10^{-11} \text{ A cm}^{-2}$  with a Tafel slope of 0.118 mV per decade current, indicating that a one-electron transfer reaction was rate controlling. In KOH solutions,<sup>10</sup> the exchange current was higher,  $3 \times 10^{-6} \text{ A cm}^{-2}$ , while the Tafel slope was similar to that in acid, 0.120 mV per decade current. Consequently, in alkaline or moderately acid solutions free from oxygen or oxidizing agents, the corrosion of pure tin may be barely detectable unless the tin is in contact with another metal that has a lower overpotential (higher exchange current density) for hydrogen evolution.

The passivity of tin in the middle pH range (i.e., between 3 and 10), its solubility in acids or alkalis (modified by the high hydrogen overpotential), and the formation of complex ions (especially with organic acids) are the bases of its general corrosion behavior. Other properties that have influenced the selection of tin for particular purposes are the

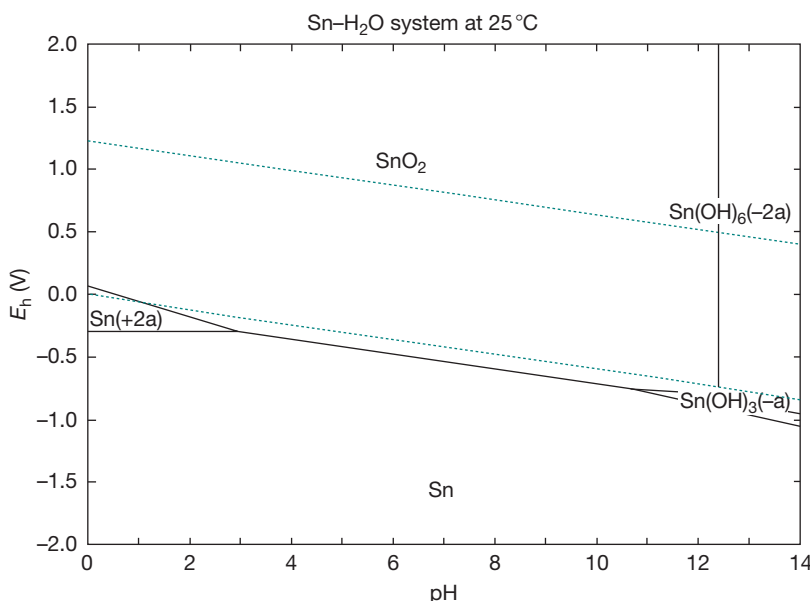


**Figure 1** Pourbaix ( $E$ -pH) diagram for tin in water at a dissolved concentration of  $10^{-5} \text{ M}$  tin species. Reproduced from HSC: Chemistry, version 6.12, Outotec Research Oy, Finland, 2007.

low toxicity of tin salts (that permit the use of tin in food-grade applications) and the absence of catalytic promotion of oxidation processes that may cause changes in oils or other neutral media affecting their quality or producing corrosive acids.

### 3.12.2.2 Dissolution

The electrochemistry of tin was extensively reviewed by Stirrup and Hampson in 1977.<sup>11</sup> As can be seen from the Pourbaix diagram, tin shows passivity by virtue of the formation of Sn(IV) oxide ( $\text{SnO}_2$ ), over an extended pH range from about 3 to above 10. Also, as previously indicated, the dissolution kinetics are slow, especially in acid, by virtue of a low exchange current density for hydrogen evolution.

At potentials just above its reversible value, tin dissolves under anodic polarization in acids initially as stannous ion ( $\text{Sn}^{2+}$ ). In 4–8 M sulfuric acid, this reaction has a Tafel slope of close to 40 mV per decade current, indicating a two-electron transfer reaction with a probable bisulfate ion intermediate.<sup>12</sup> The stannous ion is unstable in water at most values of pH (except in acid concentrations typically  $>1$  M), and at low concentrations, is hydrolyzed giving a number of species, depending on pH:  $\text{SnOH}^+$ ,  $\text{Sn(OH)}_2$ ,  $\text{Sn(OH)}_3^-$ , etc.; at higher tin concentrations, the complex species  $\text{Sn}_2(\text{OH})_2^{2+}$  and  $\text{Sn(OH)}_4^{2+}$  are prevalent.<sup>13</sup> The hydroxide complexes are well known to react with halides to give a number of Sn(II) hydroxy-halide complexes; however, these are only present in solution when the halide concentration is  $>10^{-3}$  M and at pH values  $<4$ . In alkaline conditions, tin initially dissolves as stannite ion,  $\text{Sn(OH)}_3^-$ , which is subject to the same speciation as a function of pH, as indicated earlier.

At higher potentials, Sn(II) is universally oxidized to Sn(IV) species. There are very little experimental data on this reaction; however, Sn(II) to Sn(IV) oxidation was studied in strong sulfuric acid and found to have first-order kinetics with respect to the dissolved species; an increase in  $\text{H}^+$  ion concentration decreased the reaction rate, while an increase in  $\text{SO}_4^{2-}$  had the opposite effect.

### 3.12.2.3 Passivation

Over the majority of the pH range, the passive film is generally assumed to consist of  $\text{Sn(OH)}_4$  or  $\text{SnO}_2$ ; however, in view of its very low solubility, data for the speciation of tin (IV) oxides and hydroxides in aqueous environments are very sparse. Indeed,

the formation of  $\text{SnO}_2$  as a passive film is one of the reasons for the excellent corrosion resistance of tin in noncomplexing aqueous environments.

In 4–8 M sulfuric acid, passivity is consistent with thin films of stannous oxide ( $\text{SnO}$ );  $\text{SnO}_2$  only formed at significantly more positive potentials.<sup>12</sup> Passive films on tin corroded at the open circuit potentials in 6.7 M nitric acid, 5.7 M hydrochloric acid, and 9 M sulfuric acid were analyzed using Mössbauer spectroscopy and found to consist of hydrated  $\text{SnO}_2$ ,  $\text{Sn}_4(\text{OH})_6\text{Cl}_2$ , and  $\text{SnSO}_4$ , respectively.<sup>14</sup>

Passive films on tin were studied using infrared and surface-enhanced Raman spectroscopy.<sup>15</sup> In 0.1 M NaOH solution,  $\text{Sn(OH)}_4$  was found to dominate, and further exposure to dry air was found to dehydrate the film to  $\text{SnO}_2$ , with the evidence of only a small amount of  $\text{SnO}$ . The passive film on 0.15 M NaCl solution (near-neutral) was found to consist only of  $\text{Sn(OH)}_4$ . However, angle-resolved X-ray photoelectron spectroscopy (XPS) was used to develop a model for the passive film on tin in 0.1 M KOH, and it was found that tin hydroxide was present only in the outer layers of the film. The inner layer consisted of  $\text{SnO}_2$ , with the evidence of  $\text{SnO}$  adjacent to the metal-oxide interface.<sup>16</sup> This appears to be consistent with results from phosphate buffer solutions (pH 4.3) where  $\text{Sn(OH)}_4$  was found along with a reduced species, either  $\text{Sn(OH)}_2$  or  $\text{SnO}$ , at the metal-oxide interface.<sup>15</sup> An electrochemical study of the anodic oxidation of tin was performed in carbonate-bicarbonate buffer solution at pH 8.9. From  $-0.1$  to  $1.2$  V (SCE), tin exhibited an essentially potential-independent, steady-state, passive current, which was found to be independent of flow conditions.<sup>17</sup> The results indicate that the anodic film grows according to the Mott-Cabrera model and is an oxygen ion conductor. Finally, the electrochemical passivation of tin was studied in citric acid buffer at pH 6.<sup>18</sup> Prepassivation was found to occur along with Sn(II) and Sn(IV) species, while full passivation was associated with Sn(IV) species only. The results indicated that, although the initial film formed coincided mainly with  $\text{Sn(OH)}_4$ , this transformed at longer periods of time to the more thermodynamically stable  $\text{SnO}_2$  species.

In summary, tin is found to passivate in aqueous environments from below pH 1 to above pH 12, forming an oxide film that consists of  $\text{Sn(OH)}_4$  or  $\text{SnO}_2$ . The latter oxide, which is more stable, may form either initially or transform gradually with time from the hydroxide. It is likely that a thin layer of Sn(II) species is stable at the interface between the passive film and the metal, although films consisting



predominantly of Sn(II) species are not observed except in high concentrations of the reducing acid.

### 3.12.3 Corrosion and Oxidation

#### 3.12.3.1 Atmospheric Corrosion

##### 3.12.3.1.1 Oxidation in dry air

Oxidation of tin in dry air is slow; the metal remains bright and interference colors are not developed below  $\sim 180^\circ\text{C}$ . On a rolled tin surface heated in air,<sup>19,20</sup> the thickness of the oxide grew according to the logarithmic law at temperatures of up to  $\sim 160^\circ\text{C}$  and according to the parabolic law at higher temperatures, for which the oxide was identified as SnO. For electropolished tin heated in oxygen at pressures of  $130\text{ N m}^{-2}$  and above, three stages of oxidation were observed at temperatures of up to  $220^\circ\text{C}$ :<sup>21–24</sup>

1. an initial sigmoid growth curve during nucleation;
2. a logarithmic growth curve when cavities acted as diffusion barriers;
3. erratic behavior caused by random film rupture.

The oxide formed was identified as SnO at temperatures down to  $75^\circ\text{C}$ . However, a mixture of SnO and SnO<sub>2</sub> is formed in dry air at lower temperatures, and in humid air, at temperatures of at least  $100^\circ\text{C}$ .<sup>25</sup> The electrochemical reduction analysis on tin oxidized in dry air at 125 and  $150^\circ\text{C}$  confirmed the presence of SnO with a thin surface layer of SnO<sub>2</sub>.<sup>26,27</sup> Small additions, for example, 0.1%, of indium, zinc, or phosphorus reduce the rate of oxidation, and the addition of antimony, thallium, or bismuth accelerates it.<sup>24</sup>

##### 3.12.3.1.2 Corrosion in humid air

In the absence of polluting gases or dusts, increasing relative humidity tends to increase the rate of oxidation<sup>28</sup> and may cause the development of interference colors. In an ordinary atmosphere, some corrosion product may be formed over time. However, tin products are not hygroscopic, and tin is not attacked at relative humidities of below 100% unless the dust falling on the surface is hygroscopic, or impurities in the metal are able to form a hygroscopic product. Indoors, in an unpolluted laboratory atmosphere, a gray film, increasing in weight linearly with time ( $4\text{ mg m}^{-2}\text{ day}^{-1}$ ), is formed, while in sheltered exposure (no rain) outdoors, the corrosion rate declined with time. The reflectivity of the surface is slowly lost if it is left untouched, but may be preserved by regular washing; in one experiment, when the surface was washed at intervals of 3 weeks, a water wash was adequate for

6 weeks, and although the use of soap was necessary thereafter, almost a complete preservation of reflectivity was achieved.

The impurities ordinarily present in the atmosphere do not appreciably affect the character of corrosion. No tarnishing effect is exerted by hydrogen sulfide, sulfur dioxide, and other acids in low concentrations, including formic, acetic, and other organic acids, which, when evolved from wood or insulating materials, are very often destructive to metals other than tin, in the confined spaces of electrical equipment or of packages. Chlorides accelerate corrosion and tend to form a white corrosion product containing oxychloride. The presence of some impurities, notably zinc, in the metal may cause tarnishing and a loss of brightness in atmospheres containing SO<sub>2</sub>.<sup>29</sup> The corrosion rate of electroplated tin on nickel in the presence of sub-ppm amounts of either SO<sub>2</sub> or NO<sub>x</sub> did not increase. However, a synergetic effect was found with both pollutants where the corrosion rate was increased significantly.

The atmospheric pollution prevailing in special industrial or laboratory locations may induce more severe corrosion, for example, the vapors from concentrated hydrochloric or acetic acid will etch tin, and moist sulfur dioxide will produce a sulfide tarnish, as will hydrogen sulfide at temperatures of above  $\sim 100^\circ\text{C}$ , and halogens attack tin readily.

When tin is fully exposed out of doors, corrosion is uniform, and the rate falls only slightly with time. The metal becomes dull and accumulates a compact layer of pale gray product, mainly stannous oxide. Rates observed during exposures in the United States for periods of up to 20 years were  $1.3\text{--}1.8\text{ }\mu\text{m year}^{-1}$  in industrial atmospheres (i.e., mainly polluted with sulfur dioxide),  $1.8\text{--}2.8\text{ }\mu\text{m year}^{-1}$  in marine atmospheres (i.e., mainly polluted with sea-salt), and less than  $0.5\text{ }\mu\text{m year}^{-1}$  in rural atmospheres (i.e., relatively unpolluted).<sup>30</sup>

##### 3.12.3.1.3 Atmospheric corrosion products

The corrosion of tin in various humid atmospheres has been examined using a number of surface analytical techniques, including XPS and Auger electron spectroscopy (AES).<sup>25,31,32</sup> While it is difficult to resolve the peaks of the oxide from those of the hydroxide, and hence, to establish their degree of surface hydration, there is a general agreement that both SnO and SnO<sub>2</sub> may be present depending on the temperature of exposure.

In atmospheres polluted with  $>100$  ppm nitrogen dioxide, tin nitrate was reported to form at 30–35%

RH.<sup>33</sup> In a mixed atmosphere containing more representative atmospheric conditions (40 ppb  $\text{H}_2\text{S}$ , 350 ppb  $\text{SO}_2$ , 500 ppb  $\text{NO}_2$ , and 3 ppb  $\text{Cl}_2$ ) at 81% RH, only tin oxides were found.<sup>34</sup> An XPS study on the films formed in  $\text{SO}_2$  and  $\text{NO}_x$  found only oxide species in  $\text{SO}_2$ , but a mixture of oxides and nitrates with  $\text{NO}_x$ . No synergy was noted between at-ppm concentrations of  $\text{SO}_2$  and  $\text{NO}_x$  at 85% RH.<sup>35</sup>

### 3.12.3.2 Corrosion in Acid

#### 3.12.3.2.1 Mineral acids

As the high overvoltage restricts hydrogen evolution, corrosion in organic acids or dilute nonoxidizing mineral acids is generally controlled by the rate of supply of oxygen.<sup>2,3</sup> In solutions of acid open to air, with specimens of size  $50 \times 20$  mm completely immersed, corrosion rates were, in a range of 0.1 M organic acids,  $400\text{--}500 \text{ g m}^{-2} \text{ day}^{-1}$ , and in 0.1 M hydrochloric or sulfuric acids,  $600 \text{ g m}^{-2} \text{ day}^{-1}$ . In the absence of oxygen, the rates in the two mineral acids were  $100\text{--}150 \text{ g m}^{-2} \text{ day}^{-1}$ , while they were negligible in the organic acids. Phosphoric acid forms a protective layer, and even in the presence of air, the corrosion rate is only  $\sim 20 \text{ g m}^{-2} \text{ day}^{-1}$ . Nitric acid corrodes tin freely even in the absence of oxygen; however, chromic acid forms a protective film. This film, which contains chromic oxide and tin oxides, will, after withdrawal from the acid, give some degree of protection against mildly corrosive conditions. Thus, hot solutions of chromic acid, alone or mixed with phosphoric acid, may be used as passivating media.

#### 3.12.3.2.2 Organic acids

Tin forms complex ions with many organic acids, including those commonly found in fruits (citric, oxalic, malic). This action has important effects on the galvanic behavior of tin. The normal electrode potential of tin is  $-0.136 \text{ V}$ , but the reduction of stannous ion activity resulting from the formation of complexes may depress the corrosion potential to make tin anodic to iron.<sup>36</sup>

The attack of tin by oxalic, citric, and tartaric acids was found to be under the anodic control of the  $\text{Sn}^{2+}$  salts in solution in oxygen-free conditions.<sup>37</sup> In a study of tin contaminated by up to 1200 ppm Sb, it was demonstrated<sup>38</sup> that the modified surface chemistry catalyzed the hydrogen evolution reaction in deaerated citric acid solution. Tin was found to corrode more rapidly in tartaric acid because of the reduction in the hydrogen overpotential; passivation was caused by a film of tin hydroxide or oxide.<sup>39</sup>

### 3.12.3.3 Corrosion in Near-neutral Conditions

Pure tin is completely resistant to distilled water, hot or cold. Local corrosion occurs in salt solutions that do not form insoluble compounds with stannous ions (e.g., chloride, bromide, sulfate, nitrate), but is unlikely in solutions giving stable precipitates (e.g., borate, monohydrogen phosphate, bicarbonate, iodide).<sup>40</sup> In all solutions, oxide film growth occurs and the potential of the metal rises. Any local dissolution may not begin for several days, but once it has begun, it will continue, its presence being manifested at first by small black spots and later by small pits. The movement of the solution tends to prevent pitting; stagnation, especially in crevices where the tin touches another solid surface, favors its progress. Contact with a more noble metal such as copper or nickel increases the number and intensity of pits; contact with metals such as aluminum and zinc gives cathodic protection.

As indicated earlier, the bicarbonate ion inhibits the process, which does not occur, therefore, in many supply waters; attack is most likely in waters that, by nature or as a result of treatment, have a low bicarbonate content and relatively high chloride, sulfate, or nitrate content. The number of points of attack increases with the concentration of aggressive anions, and ultimately, slow general corrosion may occur.

During the exposure of 99.75% tin to seawater for 4 years, a corrosion rate of  $0.0023 \text{ mm year}^{-1}$  was observed.<sup>41</sup> Corrosion in soil usually produces slow general corrosion with the production of crusts of oxides and basic salts. For example, the production of the significant quantities of the metastable corrosion product romarchite ( $\text{SnO}$ ) is commonly seen when studying pewter corrosion products from marine archaeological sites,<sup>42</sup> but is never seen, except transiently or as a thin interfacial phase, in passive films and atmospheric corrosion products.

### 3.12.3.4 Corrosion by Alkalis

The Pourbaix diagram indicates the possibility of attack by solutions of pH values above  $\sim 10.5$ , but the position of this limit is influenced by temperature, by the constitution of the solution, and by the surface condition of the metal. Corrosion will ensue if the surface oxide is significantly soluble, which will occur increasingly beyond pH 12.

Once corrosion begins, its rate is governed by the oxygen supply and temperature and is not greatly affected by the character of the alkali. Rates of attack

for specimens completely immersed in still solutions open to air are  $\sim 600 \text{ g m}^{-2} \text{ day}^{-1}$  at  $30^\circ\text{C}$  and  $1000 \text{ g m}^{-2} \text{ day}^{-1}$  at  $70^\circ\text{C}$ . In intermittent immersion such as is experienced in the cleaning of tinned ware by alkaline detergents, however, the rate of corrosion is affected by the nature and concentration of the solution, as these affect the time required for the removal of the oxide film at each fresh immersion.<sup>43</sup> Saturated ammonia solutions do not attack tin, possibly because of the negligible oxygen content, but more dilute solutions behave like those of other alkalis of comparable pH. In aerated alkaline conditions, 0.01–1 M NaOH, corrosion of tin was confirmed to be under cathodic control, and additions of other species, apart from chromate, were found to make little difference to the corrosion rate.<sup>44</sup>

The removal of oxygen from an alkaline solution, as by the addition of sodium sulfite, can prevent corrosion unless the tin is in contact with another metal, such as steel, from which hydrogen can be evolved. Additions of oxidizing agents in small amounts stimulate corrosion, but sufficiently large additions produce passivity. Alkaline chromate solutions in the passivating range produce a film containing chromium oxide, which has some protective value.<sup>19,45</sup>

### 3.12.3.5 Corrosion in Foodstuffs

Sulfide solutions, sulfurous acid, and some foodstuffs containing organic sulfur compounds produce stains of sulfide, but the rate of loss of metal is low.<sup>2,3</sup> Milk and milk products are usually without action, although local corrosion has been known to occur in dairy equipment. Beer initially dissolves a trace of tin and this may be sufficient to cause a haze in the liquor, but any corrosion usually slows to an insignificant rate after some time.

In general, near-neutral aqueous products are without action except for possible sulfide staining, or when there are dissolved salts present, some local corrosion. The slight acidity, which may develop in solutions of some organic compounds such as formaldehyde or alcohols can be tolerated. Many organic liquids, including oils (essential, animal, vegetable, or mineral), alcohols, fatty acids, chlorinated hydrocarbons, and aliphatic esters, are without action. The absence of any catalytic action of tin on oxidative changes is helpful in this respect. When, however, mineral acidity can arise, as with the chlorinated hydrocarbons containing water, there may be some corrosion, especially at elevated temperature.

**Table 1** Standard reduction potentials and galvanic series compared with tin

<i>Standard reduction potentials (vs. SHE)</i>	<i>Practical galvanic series in sea water</i>
$\text{Cu}^{2+} + 2\text{e}^- \Rightarrow \text{Cu}: +0.34 \text{ V}$	Graphite
$\text{Pb}^{2+} + 2\text{e}^- \Rightarrow \text{Pb}: -0.12 \text{ V}$	Passive stainless steels
$\text{Sn}^{2+} + 2\text{e}^- \Rightarrow \text{Sn}: -0.14 \text{ V}$	Copper alloys
$\text{Ni}^{2+} + 2\text{e}^- \Rightarrow \text{Ni}: -0.25 \text{ V}$	Tin (and tin-rich solders)
$\text{Fe}^{2+} + 2\text{e}^- \Rightarrow \text{Fe}: -0.44 \text{ V}$	Lead (and lead–tin solders)
$\text{Zn}^{2+} + 2\text{e}^- \Rightarrow \text{Zn}: -0.76 \text{ V}$	Steel and cast iron
$\text{Al}^{3+} + 3\text{e}^- \Rightarrow \text{Al}: -1.67 \text{ V}$	Aluminum
$\text{Mg}^{2+} + 2\text{e}^- \Rightarrow \text{Mg}: -2.37 \text{ V}$	Zinc
	Magnesium

### 3.12.3.6 Galvanic Corrosion

As indicated from the galvanic series, tin is less noble than copper and stainless steels, but more noble than most other elements in common use (Table 1). However, tin is usually ineffective as a sacrificial anode because of its very low self-corrosion rate, and generally, may be safely used in contact with most materials.<sup>46</sup> However, in the presence of species such as citric acid, which can form complex ions, tin will activate with its equilibrium potential moving to more negative values. This effect is important in the corrosion protection of steel cans with tinplate.

## 3.12.4 Applications

### 3.12.4.1 Tin Coatings

Interested readers are directed to the dedicated section on tin coatings elsewhere in this volume; only brief comments are provided here. Tin coatings may be applied either by hot-dipping from molten metal or by electroplating from either acid or alkaline solutions<sup>2,3</sup> or by metal spraying.<sup>47</sup> Also, tin may be codeposited during electroplating with a range of other elements such as nickel, cobalt, copper, and zinc, each of which gives rise to a particular property. Tin-plated steel is extremely widely used in the food and beverage canning industry as a container and relies on both the low corrosion rate of tin (can exterior) and the common potential reversal to steel in the presence of natural complexing agents (can interior). In practice, because of the high cost of tin, it is essential to use as thin a layer as possible. Thus, the corrosion protection afforded by the tin is usually supported by internal and external lacquering (organic coating) of the can, and it is therefore, the

organically coated tin that provides the full corrosion protection system for the steel substrate.

The thinnest tin coatings are most efficiently applied by electroplating; where this is likely to give pinholes, surface melt reflowing may be used to improve the performance. Where thicker coatings are required, usually for specialist applications, for example, hot dipping or metal spraying can be used. For example, traditional copper cooking utensils are frequently internally coated with tin to several tens of microns in thickness to prevent the interaction of copper with foods that can lead to the development of taints. The advantage of this process is that when the tin wears off, it can be easily replaced by redipping. Hot-dipped (and sprayed) coatings take advantage of the formation of tin-iron or tin-copper intermetallic species for excellent adhesion of the coating.

### 3.12.4.2 Solders

Alloys of tin with lead and/or a number of other elements comprise a class of jointing materials known as solders. Solders are used for cost-effective and efficient jointing of many materials, most commonly for copper alloys (e.g., heat exchangers) and steels (e.g., cans). Solders are generally characterized by their ability to flow across or 'wet' the metal to be jointed; such wetting is usually accomplished by the formation of intermetallic compounds between the solder and the substrate. Thus, tin forms  $\text{Cu}_6\text{Sn}_5$  and  $\text{Cu}_3\text{Sn}$  with copper alloys<sup>48</sup> and  $\text{FeSn}$ ,  $\text{Fe}_3\text{Sn}$ , and  $\text{FeSn}_2$  with steel.<sup>49</sup> The mechanical properties of these intermetallic species are critical; thus, they provide a metallurgical bonding between the jointed materials, but must not form brittle phases. Many types of tin-based solders are available, for example, Sn-Pb (traditional solders with compositions from 60/40, 50/50, 40/60 depending on use), Sn-Zn (for jointing aluminum), and Sn-Ag (lead-free solder for general use). In particular, for health reasons, there is an increasing use of low-lead, or lead-free solders, especially for joints in water supply systems and in food canning. These environmental concerns are now making the electronics industry also move to lead-free formulations.

Effective soldering requires a clean surface, free of contamination such as greases, oils, and water and the removal of the normal air-formed oxide on the material that is to be jointed. Typically, this is carried out initially by mechanical abrasion or solvent cleaning with the final removal of the tenacious surface oxide via a 'flux'. A flux is, by its nature, corrosive, and

hence, careful selection of the flux material is necessary. Otherwise, corrosion in service will be promoted locally.<sup>50</sup> It is, however, possible to select fluxes that are active when hot, but give noncorrosive residues when cold, for example, solid organic acids. If it is necessary to use more vigorous materials, such as zinc chloride, any residues must be fully removed. By the nature of their use as a jointing material, solders are usually presented to a corrosive environment as a small area within a much larger area of another metal. Thus, if the solder is anodic to the metal it joins, and if the corroding medium has good electrical conductivity, damaging corrosion is possible due to the unfavorable (small anode versus large cathode) anode-to-cathode area ratio.

Traditional lead-tin solders are anodic to copper, but soldered joints in copper pipes have been widely used without trouble for cold supply waters; possibly, corrosion is restricted by the deposition of cathodic carbonate scales and the formation of insoluble lead compounds. Hot supply waters tend to be more aggressive, but are likely to still give satisfactory service. However, electrolytes of sufficiently high conductivity, such as seawater, will cause corrosion of soldered joints in copper and copper alloys. In automotive radiators, antifreeze solutions have been alleged to cause corrosion, possibly because materials such as ethylene glycol sometimes detach protective deposits. Sodium nitrite, valuable as a corrosion inhibitor for other metals in a radiator, tends to attack solders, but sodium benzoate is safe, and in addition, protects the soldered joint against the action of nitrites.<sup>51</sup>

In environments in which tin is less readily corroded than lead, corrosion resistance of the alloy decreases as the lead content increases; the decrease may, in some circumstances, be sharp at a particular composition. In the more corrosive media, a sharp increase of corrosion rate is observed as the lead content increases beyond 30%. However, in waters with low contents of dissolved salts, the corrosion rate increases slowly with lead content up to ~70% and then rises more steeply. Selective dissolution of tin has been reported to occur in prolonged contact of solders with solutions of anionic surface active agents.<sup>52</sup>

In view of the known tendency for lead to be released in supply waters from conventional soldered joints,<sup>53</sup> there is an accelerating trend away from the use of lead-containing solders in contact with potable water, which is also being driven by legislation.<sup>54</sup> The effects of galvanic corrosion of one of the substitute alloys (Sn-3Ag) in contact with a number of other metals, including copper, have therefore been studied.<sup>55</sup>

### 3.12.4.3 Tin Interconnections

Tin-based jointing alloys (solders) are the materials of choice for connections and interconnections in the electronics industry. Traditionally, a eutectic tin-lead (67Sn–33Pb) alloy has been used, but the legislative driver for the removal of lead has also affected this sector, which has now effectively moved to encompass the use of lead-free solders. The performance characteristics of electronic connectors is dominated by (1) local galvanic corrosion between different metals, either in contact or as a coating and influenced by applied direct currents; (2) the corrosion of the soldering alloy, which is controlled largely by the presence of residues from various manufacturing and assembly operations; (3) fretting forms of corrosion damage induced by repeated making and breaking of electrical contacts; and (4) the formation of metal whiskers of tin that tend to be produced as a result of applied stress and voltage. All of these phenomena can lead to either a reduction of performance or an outright failure via a variety of mechanisms,<sup>55</sup> the most important of which are increases in the contact resistance with time and short-circuit current paths between contacts because of corrosion products, soldering residues (i.e., fluxes), and whiskers of tin.

Many lead-free solders are based on Sn–Ag–Cu formulations, with Sn–3.5Ag, Sn–0.7Cu, and Sn–3.8Ag–0.7Cu widely in use because of their good mechanical and wetting properties. In 3.5% sodium chloride solution, lead-free solders show an improved corrosion resistance compared with Sn–Pb solder because of lower active currents and lower passive current densities and that the Sn–Ag material was the most resistant.<sup>56</sup> The contact resistance and fretting corrosion resistance of lead-free solders were measured as a function of time.<sup>57</sup> In this case, the contact resistance of the conventional eutectic solder fell more quickly than the lead-free solder; however, the fretting corrosion resistance of Sn–Ag materials was generally improved. The lead-free solders performed significantly better than did the lead-containing solders after steam aging at 93 °C, 100% RH and after mixed flowing gas testing (in 200 ppb NO<sub>2</sub>, 10 ppb H<sub>2</sub>S, 10 ppb Cl<sub>2</sub>) at 30 °C and 70% RH.

There is, therefore, good evidence that the general and fretting corrosion behavior, and consequent contact resistance changes with time, of lead-free solders is at least as good as, and often better than, traditional tin-lead eutectic solders. However, lead-free solders have a greatly increased tendency for the formation of thin filamentary whiskers of tin, which may lead to

failure by short-circuit. Tin whisker formation has been known for many years and was originally thought to be driven primarily by electromigration between two contacts or conductive tracks.<sup>58,59</sup> More recently, however, it has become clear that most whisker growth is a process driven by relief of stresses<sup>60</sup> (i.e., from plating or from contact forces), although electromigration may play a role in more extreme conditions.<sup>61</sup>

### 3.12.4.4 Bearing Metals

There are several classes of tin-containing bearing alloys for use in lubricating conditions: high-tin alloys (substantially lead-free), bearing alloys containing increasing amounts of lead, and aluminum tin alloys; each class may have minor elements (e.g., antimony, indium) added to promote, for example, intermetallic formation. The corrosion of tin-rich white metal bearings is rare, and consequently, detailed studies of the phenomenon are not extensive in the literature. High-tin alloys are relatively resistant to corrosion in the organic acids that tend to be formed during the degradation of lubricating fluids and the tin salts that form have antioxidant capability. Where corrosion of tin-rich bearings has occurred, it is invariably associated with water ingress.<sup>62</sup> For example, 500 ppm water has been shown to be sufficient to cause corrosion, especially in conjunction with chlorine-based high-pressure additives in the oil.<sup>63</sup>

When free access of salt water to a bearing is possible, the tin-lead ‘Babbitt’ alloys are not suitable, since they are cathodic to steel shafts. For underwater bearings, alloys with 70% Sn, 1.5% Cu, and the balance Zn, are traditionally used; the possible dissolution of zinc gives cathodic protection to the shaft, although the more easily replaced bearing suffers some corrosion.

## References

1. Raynor, G. V.; Smith, R. W. *Proc. R. Soc.* **1958**, *244*, 101–109.
2. Britton, S. C. International Tin Research Institute, Report no. 501, 1975.
3. Hedges, E. S. *Tin and Its Alloys*; Edward Arnold: London, 1960.
4. Ojima, K.; Takasaki, A. *Philos. Mag. Lett.* **1993**, *68*(4), 237–244.
5. Britton, S. C.; Clarke, M. *Trans. Inst. Met. Finish.* **1963**, *40*, 205.
6. Britton, S. C. *Trans. Inst. Met. Finish.* **1974**, *52*(3), 95–102.
7. Langan, J. P. Proceedings of the AESF Annual Technical Conference **1993**; pp 689–691.



8. HSC: Chemistry, version 6.12, Outotec Research Oy, Finland, 2007.
9. Quintin, M.; Hagymas, G. J. *J. Chim. Phys.* **1964**, 61(4), 541–547.
10. Ross, T. K.; Firoiu, C. *Electrochim. Acta* **1963**, 8, 877.
11. Stirrup, B. N.; Hampson, N. A. *Surf. Technol.* **1977**, 5, 429–462.
12. Laitinen, T.; Salmi, K.; Sundholm, G.; Viinikka, P.; Yli-Pentti, A. *Electrochim. Acta* **1992**, 37(10), 1797–1803.
13. Séby, F.; Potin-Gautier, M.; Giffault, E.; Donard, O. F. X. *Geochim. Cosmochim. Acta* **2001**, 65, 3041–3053.
14. Shibuya, M.; Endo, K.; Sano, H. *Bull. Chem. Soc. Jpn.* **1978**, 51(5), 1363–1367.
15. Huang, B. X.; Tornatore, P.; Ying-Sing Li. *Electrochim. Acta* **2000**, 46, 671–679.
16. Keller, P.; Strehblow, H. H. *Z. Phys. Chem.* **2005**, 219(11), 1481–1488.
17. Gervasi, C. A.; Alvarez, P. E. *Corros. Sci.* **2005**, 47, 69–78.
18. Seruga, M.; Metiko-Hukovi, M.; Valla, T.; Milun, M.; Hoffschultz, H.; Wandelt, K. *J. Electroanal. Chem.* **1996**, 407, 83–89.
19. Britton, S. C.; Bright, K. *Metallurgia* **1957**, 56, 163–168.
20. Trillat, J. J.; Tertian, L.; Britton, S. C. *Métaux Corros. Ind.* **1957**, 32, 475–481.
21. Boggs, W. E.; Kachik, R. H.; Pellissier, G. E. *J. Electrochem. Soc.* **1961**, 108, 6–12.
22. Boggs, W. E.; Trozzo, P. S.; Pellissier, G. E. *J. Electrochem. Soc.* **1961**, 108, 13–24.
23. Boggs, W. E. *J. Electrochem. Soc.* **1961**, 108, 124–129.
24. Boggs, W. E.; Kachik, R. H.; Pellissier, G. E. *J. Electrochem. Soc.* **1963**, 110, 4–11.
25. Okamoto, Y.; Carter, W. J.; Hercules, D. M. *Appl. Spectrosc.* **1979**, 33(3), 287.
26. Hillman, D. D.; Chumbley, L. S. *Sold. Surf. Mount. Technol.* **2006**, 18, 31–41.
27. Britton, S. C.; Sherlock, J. C. *Br. Corros. J.* **1974**, 9, 96–102.
28. Kenworthy, L. *Trans. Faraday Soc.* **1935**, 31, 1331.
29. Zakipour, S.; Leygraf, C.; Portnoff, G. *J. Electrochem. Soc.* **1986**, 133, 873–876.
30. Hiers, G. O.; Minarcik, E. J. Symposium on the Atmospheric Corrosion of Non-ferrous Metals, American Society for Testing and Materials, Special Technical Publication #175, 1956, 135.
31. Ansell, R. O.; Dickinson, T.; Povey, A. F.; Sherwood, P. M. A. *J. Electrochem. Soc.* **1977**, 124, 1360–1364.
32. Lau, C. L.; Wertheim, J. *Vac. Sci. Technol.* **1978**, 15, 622–624.
33. Tompkins, H. G. *Surf. Sci.* **1973**, 39, 143.
34. Brusic, V.; DiMilia, D. D.; MacInnes, R. *Corrosion* **1991**, 47, 509–518.
35. Sasaki, T.; Kanagawa, R.; Ohtsuka, T.; Miura, K. *Corros. Sci.* **2003**, 45, 847–854.
36. Willey, A. R. *Br. Corros. J.* **1972**, 7, 29–35.
37. Gouda, V. K.; Rizkalla, E. N.; Abd-el-Wahab, S.; Ibrahim, E. M. *Corros. Sci.* **1981**, 21, 1–15.
38. Leidheiser, H.; Rauch, A. F.; Ibrahim, E. M.; Granata, R. D. *J. Electrochem. Soc.* **1982**, 129, 1651–1658.
39. Abd El Rehim, S. S.; Zaky, A. M.; Mohamed, N. F. *J. Alloys Compd.* **2006**, 424, 88–92.
40. Hoar, T. P. *Trans. Faraday Soc.* **1937**, 33, 1152–1167.
41. Friends, J. N. *J. Inst. Met.* **1928**, 32, 449–454.
42. Dunkie, S. E.; Craig, J. R.; Lusardi, W. R. *Geoarchaeology* **2004**, 19, 531–552.
43. Britton, S. C.; Michael, D. G. *J. Appl. Chem.* **1955**, 5, 402–413.
44. Costa, J. M.; Culler, J. R. *Corros. Sci.* **1976**, 16, 587–590.
45. Britton, S. C.; Angles, R. M. *J. Appl. Chem.* **1954**, 4, 351–364.
46. Hoar, T. P. *Trans. Faraday Soc.* **1934**, 30, 472–482.
47. Vourlias, G.; Pistofidis, N.; Stergioudis, G.; Polychroniadis, E. K. *J. Alloys Compd.* **2006**, 416, 183–187.
48. Parent, J. O. G.; Chung, D. D. L.; Bernstein, I. M. *J. Mater. Sci.* **1988**, 23, 2564–2572.
49. Crichton, T. J.; Farr, J. P. G. *Trans. Inst. Met. Finish.* **2004**, 82, 169–173.
50. Costas, L. P. *Weld. J.* **1982**, 61, 320–326.
51. Wormwell, F.; Mercer, A. D.; Ison, H. C. K. *J. Appl. Chem.* **1953**, 3, 22–27, 133–144.
52. Watts, C. *Eng. Mater. Des.* **1961**, 4(11), 740.
53. Subramanian, K. S.; Sastri, V. S.; Elboudjaini, M.; Connor, J. W.; Davey, A. B. C. *Water Res.* **1995**, 29, 1827–1836.
54. Linder, M.; Mattson, E. Proceedings of the 7th Scandinavian Corrosion Congress, Trondheim **1975**; pp 19–35.
55. Guttenplan, J. D.; Violette, D. R. *Mater. Perform.* **1980**, 29(4), 76–81.
56. Li, D.; Conway, P. P.; Liu, C. *Corros. Sci.* **2008**, 50(4), 995–1004.
57. Wu Ji; Pecht, M. G. *IEEE Trans. Compon. Packag. Technol.* **2006**, 29, 402–410.
58. Berry, R. W.; Bouton, G. M.; Ellis, W. C.; Engling, D. E. *Appl. Phys. Lett.* **1966**, 9, 263–265.
59. Vardaman, E. J. *Circ. Assemb.* **2004**, 15, 22–23.
60. Galyon, G. T.; Palmer, L. *IEEE Trans. Electron. Packag. Manuf.* **2005**, 28, 17–30.
61. Liu, S. H.; Chen, C.; Liu, P. C.; Chou, T. *J. Appl. Phys.* **2004**, 95, 7742–7747.
62. Bryce, J. G.; Roehner, T. G. *Trans. Inst. Mar. Eng.* **1961**, 73, 377.
63. Hiley, R. W. *Trans. Inst. Mar. Eng.* **1979**, 91(2), 52–66.

## Relevant Websites

[www.itri.co.uk](http://www.itri.co.uk) – The International Tin Research Institute.

## 3.13 Corrosion of Zinc and its Alloys

**F. E. Goodwin**

International Lead Zinc Research Organization, Inc., 1822 East NC Highway 54, Suite 120, Durham, NC, USA

This article is a revision of the Third Edition article 4.7 by A. R. L. Chivers and F. C. Porter, volume 1, pp 4:168–4:183, © 2010 Elsevier B.V.

<b>3.13.1</b>	<b>Introduction</b>	2078
3.13.1.1	History	2078
3.13.1.2	Production and Usage	2079
<b>3.13.2</b>	<b>Physical and Mechanical Properties</b>	2079
<b>3.13.3</b>	<b>Corrosion Properties</b>	2080
3.13.3.1	Protective Layers on Zinc	2080
3.13.3.2	Atmospheric Corrosion	2081
3.13.3.2.1	General properties	2081
3.13.3.2.2	White rust	2083
3.13.3.3	Aqueous Corrosion	2083
3.13.3.3.1	Corrosion of zinc in natural waters	2083
3.13.3.3.2	Corrosion in seawater	2085
3.13.3.3.3	The effect of temperature	2085
3.13.3.4	Soil Corrosion	2085
3.13.3.5	Corrosion Resistance of Zinc in Chemical Environments	2086
3.13.3.5.1	Acids and alkalis	2086
3.13.3.5.2	Salt solutions	2089
3.13.3.5.3	Organic chemicals	2089
3.13.3.6	Cathodic Protection by Zinc Anodes	2089
3.13.3.7	Zinc–Aluminum (ZA) Casting Alloy Corrosion	2090
3.13.3.7.1	Behavior of the ZA alloys in aerated water from pH 2.0 to 13.0	2090
3.13.3.7.2	Behavior of ZA alloys in neutral salt spray	2091
3.13.3.7.3	Behavior of the ZA alloys at a waste water plant	2091
3.13.3.8	Intergranular Corrosion	2091
<b>3.13.4</b>	<b>Recent Developments</b>	2091
<b>References</b>		2092

### Glossary

**White rust** A porous layer of zinc oxide and hydroxide build up on zinc coatings after storage in poorly ventilated conditions.

**ISO CORRAG** International organization for standardization-collaborative atmospheric exposure program

**SHG** Special high grade (reference to zinc purity)

**ZA** Zinc aluminum

### Abbreviations

**ASTM** American Society for Testing and Materials

**BISRA** British Iron and Steel Research Association

**GOB** Good ordinary brand (reference to zinc purity)

**HG** High grade (reference to zinc purity)

**ISO** International organization for standardization

### 3.13.1 Introduction

#### 3.13.1.1 History

Despite its frequent occurrence with lead, zinc (boiling point 907 °C) was not known to the ancient world as it was generally lost during smelting by evaporation. Thus, the earliest reports of metallic zinc date only from the fifteenth century in China, while in

Europe zinc was not recognized as a separate element until the eighteenth century when small smelting works were first set up for its production. Its earliest use was in alloying, especially with copper (to produce brass), although its compounds were also used for medicinal purposes (e.g., calamine,  $\text{ZnCO}_3$ ) and as pigments. Significant European production of zinc commenced from the early eighteenth century. Prior to the discovery of significant lead–zinc sulfide mineralization (e.g., at Broken Hill in Australia), the principal ore source was zinc carbonate (calamine) found throughout Europe and also in the United Kingdom. Final stimulus for the mass production of zinc did not arrive until the dual discoveries of galvanizing for steel and zinc sheet production in the mid-nineteenth century.

### 3.13.1.2 Production and Usage

The excellent resistance of zinc to corrosion under natural conditions is largely responsible for the many and varied applications of the metal. In fact, half of the world consumption of zinc is in the form of coatings for the protection of steel from corrosion. Zinc is produced and sold according to standard specifications. Three principal grades are recognized by international standards organizations such as ISO, where the zinc specifications are set forth in ISO 752, and the various national standards organizations such as ASTM (Standard Specification B6). The great majority of zinc sold today is made by the electrolytic process, to a purity of 99.99% zinc, and is commonly referred to as special high grade (SHG) zinc. A lower purity grade termed high grade (HG) has a minimum zinc content of 99.9%; the old standard grade, containing 98.0% minimum zinc, is commonly termed Prime Western or good ordinary brand (GOB) zinc. Common impurities in all three grades are lead, cadmium, and iron. Grades with higher purities than SHG are available but are not referred to in the national or international standard specifications.

Zinc in coatings used to protect steel articles coated after fabrication is generally SHG or GOB zinc, although coatings with minor additions of nickel and tin (added during the galvanizing process) can be used to control the reactivity of the steel. Zinc coatings used in continuous coating of sheet and wire are almost always SHG alloyed with aluminum at various levels around 0.15%, 5%, and 55% Al. Additions of magnesium up to 3% can also be made. Further details on zinc coatings and their performance are described elsewhere.

Zinc casting alloys account for about 20% of annual zinc usage. These alloys are commonly alloyed with 4% aluminum to improve castability and strength. Smaller quantities of zinc alloys containing 8, 12, or 27% aluminum, termed ZA alloys, are also utilized. Die castings can be made readily on account of the low melting points and the good flow properties of zinc alloys. Continuous casting is also used, mainly for production of hollow cylinders for bearing materials but also as stock for machining of zinc shapes.

Another 6% of zinc production is sold in semi-manufactured form including rolled zinc roofing, anodes, and dry cell battery cans. Its malleability and ductility make it possible to produce zinc in sheet, strip, and plate form by rolling and as rod and wire by extrusion. Rolled zinc in sheet and strip form is a well-established roofing material, particularly in parts of France and northern Europe. A small amount of copper, up to 1.5%, is added to these alloys to improve creep strength. Brass (discussed in the section on copper alloys) and zinc chemicals (chiefly oxide) make up the balance of major zinc uses.

### 3.13.2 Physical and Mechanical Properties

The bluish-white form of the unalloyed metal is familiar. It is moderately hard and quite malleable at normal temperatures. The tensile strength and impact resistance of the unalloyed metal, although greater than that of tin or lead, are low, so unalloyed zinc is not to be regarded as a structural metal. The main consequence of using unalloyed zinc in applications subject to prolonged loading is the occurrence of creep deformation. Although brittle at room temperature, pure zinc can be rolled and otherwise formed at about 100 °C.

The physical and mechanical properties of pure zinc are given in [Table 1](#). A detailed description of the physical and mechanical properties of zinc alloys for cast and wrought zinc products is given in [Table 1](#).<sup>1</sup>

Factors influencing the physical and mechanical properties of zinc pressure diecasting alloys are their composition and the cooling rate after casting. Modern zinc pressure diecastings are made with wall thickness between about 0.75 and 3 mm. Such thin sections, coupled with the high cooling rate of the metal die, results in very uniform microstructures. A very fine distribution of zinc-rich and aluminum rich phases is observed regardless of composition.

**Table 1** Mechanical and physical properties of pure zinc

<i>Property</i>	
Tensile strength (cast)	28 MN m <sup>-2</sup> (4000 psi)
(rolled – with grain)	
(99.95% zinc soft temper)	126 MN m <sup>-2</sup> (18 000 psi)
(98.0% zinc hard temper)	246 MN m <sup>-2</sup> (35 000 psi)
Elongation (rolled – with grain)	
(99.95% zinc soft temper)	6%
(98.0% zinc hard temper)	5%
Modulus of elasticity	7 × 10 <sup>4</sup> MN m <sup>-2</sup> (1 × 10 <sup>7</sup> psi)
Brinell hardness, 500 kg load for 30 s	30
Impact resistance	
(pressed zinc, elongation = 30%)	6.5–9 J cm <sup>-2</sup> (26–35 ft-lbs in <sup>-2</sup> )
Surface tension – liquid (450 °C)	0.755 N m <sup>-1</sup>
Surface tension – liquid (419.5 °C)	0.782 N m <sup>-1</sup>
Viscosity-liquid (419.5 °C)	0.00385 N m <sup>-1</sup>
Velocity of sound (20 °C)	3.67 km s <sup>-1</sup>
Coefficient of friction	
(rolled zinc v rolled zinc)	0.21
Hardness	2.5 mohs

Source: Porter, F. C. *Zinc Handbook*; Marcel Dekker: New York, 1991.

Gravity cast zinc–aluminum alloys cool at slower rates, allowing coarser microstructures to be produced. However, the average grain size is still of the order of 1 μm, meaning that galvanic effects between the zinc-rich and aluminum-rich constituents of the microstructure are not observed in practice.

Rolled zinc for architecture and other outdoor uses is generally on the basis of the use of zinc–copper–titanium alloys, where the maximum levels of copper and titanium are 1.5% and 0.15%, respectively. However, the relatively high creep strength attainable in this family of alloys can be realized only if the correct mechanical and thermal treatments have been used. A fine-grained, uniformly corroding sheet product can be obtained.

### 3.13.3 Corrosion Properties

Both zinc and zinc alloys have excellent resistance to corrosion in the atmosphere and in most natural waters, particularly if the waters are scale-forming. The property which gives zinc this valuable corrosion resistance is its ability to form a protective layer consisting of zinc oxide and hydroxide, or of various

basic salts, depending on the nature of the environment. When the protective layers have formed and completely covered the surface of the metal, the corrosion proceeds at a greatly reduced rate.

#### 3.13.3.1 Protective Layers on Zinc

In dry air, a film of zinc oxide is initially formed by the influence of atmospheric oxygen, but this is soon converted to zinc hydroxide, basic zinc carbonate, and other basic salts by water, carbon dioxide and chemical impurities present in the atmosphere. It is possible to form many zinc compounds during the process of corrosion of zinc, particularly in tap water. In atmospheric exposures also, the reactions are complex, but a simplified summary is given in [Table 2](#).

Below about 200 °C, the initially formed thin film grows very slowly, is invisible and very adherent. This initially formed layer influences the corrosion resistance of the zinc throughout its life. If the film becomes too thick, it is liable to break away or become porous, when, of course, it ceases to provide protection. Moreover, zinc corrosion products occupy a larger volume than the zinc from which they originated and, as the layer thickens, strains are set up which lead to the production of fissures and cracks.

Factors influencing the formation of protective layers are the local pH and the presence of acidic pollutants in the environment. Zinc forms an amphoteric oxide and therefore, the formation of protective layers is slowed by both acidic and alkaline conditions.

Vernon<sup>2</sup> claims that in outdoor atmospheres the corrosion products consist largely of zinc oxide, hydroxide and combined water, but they also contain zinc sulfide, zinc sulfate, and zinc carbonate. The corrosion products can be complex and the manner in which they develop into passive films is described in great detail by Zhang.<sup>3</sup> [Figure 1](#) shows how the corrosion rate of zinc varies with the pH<sup>4</sup> and it will be seen from this that the attack is most severe at pH values below 6 and above 12.5, while within this range the corrosion is very slow. The actual rates of corrosion shown in [Figure 1](#) are not of direct relevance, being from aqueous solutions; however the general shape of the curve has been confirmed for many environments.<sup>5</sup>

The electrochemical properties of zinc also have a large bearing on its corrosion behavior. Zinc is more active than the hydrogen equilibrium potential and most other metals commonly encountered, except magnesium and aluminum, but including those found

**Table 2** Zinc corrosion reactions in different atmospheres (schematic)

Type of atmosphere	Attacking substances	Corrosion products		
		composition	Relative solubility in water	Corrosion rate
Rural	$O_2 + H_2O + CO_2$	$ZnO \rightarrow Zn(OH)_2$ $\rightarrow 2ZnCO_3 \cdot 3Zn(OH)_2$	Very low	Very low
Marine	$O_2 + H_2O + CO_2 +$	$ZnO \rightarrow Zn(OH)_2$ $\rightarrow 2ZnCO_3 \cdot 3Zn(OH)_2 \rightarrow$	Moderate	Low
	+ Cl	$\left\{ \begin{array}{l} ZnCl_2 \cdot 4Zn(OH)_2 \\ ZnCl_2 \cdot 6Zn(OH)_2 \end{array} \right\} + \left\{ \begin{array}{l} Zn_3OCl_4 \\ Zn_4OCl_6 \end{array} \right\}$		
Urban and Industrial	$O_2 + H_2O +$ + $CO_2 +$ + $SO_2$	$ZnO \rightarrow Zn(OH)_2$ $\rightarrow 2ZnCO_3 \cdot 3Zn(OH)_2 \rightarrow$ $\rightarrow ZnS + ZnSO_3 + ZnSO_4$	Good	High

$CO_2$  has been included as an attacking substance because it participates in the formation of corrosion products. However,  $CO_2$  is also necessary to form stable films.

Source: Thomas, R. *Rust Prevention by Hot Dip Galvanizing*; Nordic Galv. Assoc.: Stockholm, Sweden, 1980; 32 pp.

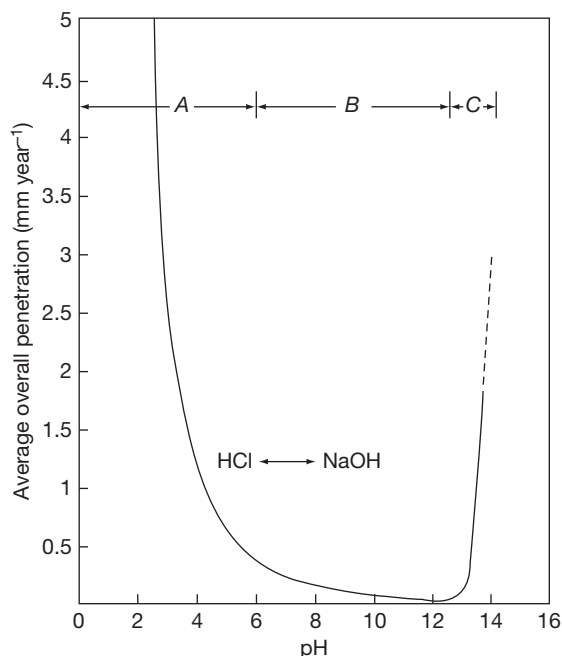


**Figure 1** Effect of pH on the rate of corrosion of zinc: (a) rapid corrosion, (b) stable film – low corrosion rate, (c) rapid corrosion. Reproduced from Roetheli, B. E., Cox, G. L.; Littreal, W. B. *Metals and Alloys* **1932**, 3, 73.

in the less pure forms of zinc. This means that when zinc is in contact with these metals sacrificial electrochemical action (galvanic corrosion) can take place, with zinc forming the anode. Contact with other metals and impurities can therefore cause zinc to corrode rapidly and it is important to avoid intermetallic contacts with metals such as copper, tin, iron or nickel,

under immersion in water. On the other hand, the overvoltage for hydrogen evolution on zinc is high, and this can, in some circumstances, lead to a reduction in the corrosion rate, although under normal atmospheric conditions oxygen is generally present in sufficient concentration to act as a cathode reactant.

The severity of bimetallic corrosion is dependent on the ratio of the areas of metals in contact, the duration of wetness, and the conductivity of the electrolyte. For example, other things being equal, seawater, a highly conducting solution, gives rise to more severe bimetallic corrosion than most fresh waters that are of lower conductivity. A film of moisture condensed from the air or rainwater can dissolve contaminants and provide conditions conducive to bimetallic corrosion. Moreover, contaminants already present on the metal surface, such as fingerprints or residues of processing solutions, may absorb moisture from the atmosphere that, although humid, has not actually reached the dew point.

### 3.13.3.2 Atmospheric Corrosion

#### 3.13.3.2.1 General properties

In dry air, the stability of zinc is remarkable and is conferred by the development of insoluble basic carbonate films after the initially formed oxide layer is exposed to the usual carbon dioxide-containing atmosphere. Once this protective layer of zinc is complete, further attack is negligible. Even under normal urban conditions, such as those in London, zinc sheet, 0.8 mm thick, has been found to have an



effective life of 40 years or more when used as a roof covering and no repair has been needed except for mechanical damage.

Two factors accelerate zinc corrosion in the atmosphere: the duration and frequency of moisture contact and the extent of atmospheric pollution. When moisture is present the initial corrosion product is zinc hydroxide, which is then converted by the action of carbon dioxide to a basic zinc carbonate of composition similar to  $\text{ZnCO}_3 \cdot 3\text{Zn(OH)}_2$ .<sup>6</sup> In very damp conditions, unprotected zinc sometimes forms a loose and more conspicuous form of corrosion product known as 'wet storage stain' or 'white rust.'

Industrial atmospheres usually accelerate the corrosion of zinc. When heavy mists and dews occur in these atmospheres, they are contaminated with considerable amounts of acidic substances such as sulfur dioxide and the film of moisture covering the metal can be quite acidic and can have a pH as low as 3. The formation of basic protective films is prevented when zinc is attacked by acidic moisture. Under these conditions the zinc is dissolved but, as the corrosion proceeds, the pH rises, and when it has reached a sufficiently high level basic salts are once more formed and provide further protection for the metal. These usually contain the basic carbonate but may sometimes contain a basic sulfate. As soon as the pH of the moisture film falls again, owing to the dissolution of acidic gases, the protective film dissolves and renewed attack on the metal occurs. Hudson and Stanners<sup>7</sup> conducted tests at various locations in order to determine the effect of atmospheric pollution on the rate of corrosion of steel and zinc. Their figures for zinc are given in Table 3 and clearly show the effect which industrial contamination has on the corrosion rate. The effect can vary with the direction of

the prevailing wind or the ease with which deposits can remain on the surface. Goodwin<sup>8</sup> reported that in acidic atmospheres the increase in corrosion is principally caused by dry deposition of sulfur dioxide and to a lesser extent by acid rain.

In areas near the sea coast, the rates of corrosion may be increased somewhat by the sea spray containing soluble chlorides, but the rates are still much lower than those prevailing in heavily polluted industrial areas. The white corrosion product which is sometimes found under these conditions probably consists of the basic chloride  $4\text{Zn(OH)}_2 \cdot \text{ZnCl}_2$ .<sup>6</sup> Chlorides have far less effect than sulfur compounds on the corrosion rate of zinc, but removal of salt deposits by washing is highly beneficial. The effect of chlorides is most harmful when it is combined with sulfurous contamination such as in coastal industrial areas. The effect of sea spray is very different in temperate and tropical areas, in addition to any temperature or humidity effects. Temperate seawater and spray contain higher portions of magnesium salts than those in tropical conditions; these salts help inhibit the corrosion of zinc.

Anderson,<sup>9</sup> reporting on a series of 20-year exposure tests carried out by the ASTM, quotes the average rates of corrosion for various types of environment which are given in Table 4.

These results clearly demonstrate; (a) the effect of moisture in increasing the corrosion rate six times in the rural areas compared with the arid areas, and (b) the considerable increase of attack in the industrial areas. Anderson considers that the principal features that control the rate of corrosion of zinc are; (a) the frequency of rainfall and dew fall, (b) the acidity of the atmosphere, and (c) the rate of drying. In situations where the drying of zinc is retarded, corrosion is found to be most severe, for example,

**Table 3** Atmospheric corrosion of zinc in various parts of the United Kingdom

Site	Degree of pollution	Standard pollution <sup>a</sup>	Corrosion rate (mm year <sup>-1</sup> )	
			Zinc	Steel
Godalming	Slight	0.23	0.001 07	0.042 5
Teddington		0.82	0.002 11	0.063 3
Hornchurch		0.92	0.003 24	0.062 7
London (Victoria Park)	Moderate	1.28	0.004 45	0.075 6
Barking (Greatfield Park)		1.60	0.008 43	0.075 0
Salford (Ladywell)		2.31	0.008 43	0.105
Sheffield (Hunshelf Bank)	Severe	3.58	0.012 9	0.107
Billingham (Council Offices)		5.24	0.012 5	0.180

<sup>a</sup>Calculated on weight (mg) of  $\text{SO}_3$  absorbed per day by 1 dm<sup>2</sup> on lead dioxide.

the bottom strand of a galvanized wire fence, which is shielded from the sun by grass and weeds.

Ambler<sup>10</sup> has attempted to find a relationship between the corrosion of zinc and iron and atmospheric salinity in the United Kingdom. This followed previous tests in Nigeria,<sup>11</sup> when it was concluded that the governing factor in the corrosion of steel and zinc was airborne salt and that there was a relationship between corrosion and the distance from the sea. In the United Kingdom, however, no such relationship was found to exist and the governing factor in the corrosion of zinc in the atmosphere is confirmed to be the amount of sulfur dioxide pollution.

Environmental concerns have led to studies that have measured the release rate of zinc from rolled zinc sheet during atmospheric exposure. These sheets were exposed either in new conditions or after prior outdoor exposure for durations up to 62 years, at three locations, Stockholm (urban), Olen, Belgium (industrial), and Hoboken, Belgium (urban-highly industrial), for 1 year. Figure 2 shows both the corrosion rates and the zinc runoff rates as a function of atmospheric sulfur dioxide concentration. The runoff

rate is observed to be considerably lower than the corrosion rate, and the corrosion rate was independent of the age of the preweathered panel, depending only upon the sulfur dioxide concentration of the atmosphere.<sup>12</sup> After release from the panel, most dissolved zinc quickly combines with the cations in the soil or water, leaving very little available for interaction with living forms.<sup>13</sup>

### 3.13.3.2 White rust

When condensation occurs on a fresh zinc surface, as may easily happen during storage in an environment with restricted circulation in which the temperature varies periodically, zinc is generally attacked by the oxygen dissolved in the water, owing to differential aeration between the edges and the centers of the drops. In this form of corrosion, a porous layer of zinc oxide and zinc hydroxide builds up. If the supply of air to the surface is restricted, insufficient carbon dioxide is supplied for the normal formation of a protective zinc carbonate layer. The resulting corrosion product, termed white rust or wet storage stain, is voluminous and porous, and adheres only loosely to the zinc surface. Consequently, it does not protect the zinc against corrosion, which can therefore proceed so long as there is moisture on the zinc surface.

This type of corrosion can take place on any new surface of zinc and is best prevented by storing the metal in a dry, airy place until a protective layer has been formed. Zinc, which has been properly aged in this way, is safe against white-rust formation. Various methods are employed to prevent white rust. Passivation treatments (e.g., chromate or phosphate) are widely used for zinc-plated articles and for galvanized sheet, and occasionally for zinc die castings. Fatty substances, such as oils or lanolin, are sometimes used to protect larger items. Light build-up of white rust can be removed by swabbing with dilute ammonia solution, for example: 19 ml ammonia, 6 g ammonium chloride, 6 g ammonium carbonate, and 71 ml tap water. The area should be well-ventilated and protective goggles should be worn by the operator.

### 3.13.3.3 Aqueous Corrosion

#### 3.13.3.3.1 Corrosion of zinc in natural waters

Fundamentally, the rate of zinc corrosion depends upon the type, quantity and mode of corrosion products. When zinc is immersed in distilled water containing dissolved oxygen, a protective film, probably

**Table 4** Further examples of atmospheric corrosion rates for zinc

Atmosphere	Corrosion rate ( $\text{mm year}^{-1}$ )
Industrial	0.006 4
Sea Coast	0.001 5
Rural	0.001 1
Arid	0.000 18

Source: Anderson, E. A. Am. Soc. Test. Mater. Special Publication No. 175, June 1955.

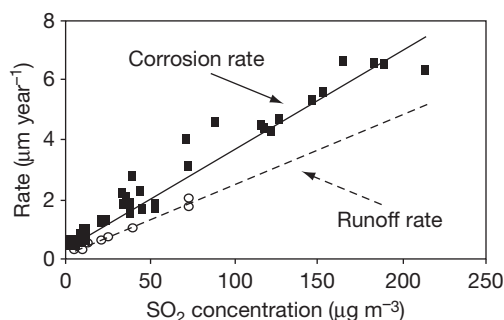


**Figure 2** Experimental values and regressions (lines) for corrosion rates (squares) and runoff rates (circles) of zinc. Reproduced from Odneval Wallinder, I., et al. *Corros. Sci.* **1988**, 40(11), 1977–1982.

consisting of zinc hydroxide, is slowly formed and this extends over nearly the whole surface. At certain points the metal seems to remain uncovered and local attack continues, resulting in pitting. This may be quite serious and can lead to the rapid penetration of a zinc sheet. The attack does not spread over the whole surface of the zinc but is confined to these small local areas, although similar pits are liable to appear at points in a vertical line directly below the seat of the original corrosion. It has been suggested that the areas attacked occur where particles of corrosion product have fallen and are resting on the surface, shielding it from oxygen. The point thus shielded becomes anodic and suffers corrosion. If oxygen replenishment is made uniform over the whole surface, for example, by 'whirling'<sup>9</sup> a zinc plate, pitting is avoided and the protective film of zinc hydroxide is found over the entire surface. However, too much agitation can sweep away corrosion products before they can become protective. The corrosion rate of zinc in distilled water ranges between 15 and 150  $\mu\text{m year}^{-1}$  and depends strongly on the amount of dissolved oxygen and carbon dioxide.<sup>3</sup> Corrosion data are shown in Table 5.

The factors affecting zinc corrosion in distilled water – oxygen, carbon dioxide content, and agitation – also affect corrosion of zinc by natural waters.

**Table 5** Effect of oxygen on the corrosion of zinc in distilled water

Test condition <sup>a</sup>	Temperature (°C)	Corrosion rate <sup>b</sup> ( $\mu\text{m year}^{-1}$ )
Boiled distilled water; specimens immersed in sealed flasks	Room	25.4
Boiled distilled water; specimens immersed in sealed flasks	40	48.3
Boiled distilled water; specimens immersed in sealed flasks	65	83.8
Oxygen bubbled slowly through the water	Room	218.4
Oxygen bubbled slowly through the water	40	348.0
Oxygen bubbled slowly through the water	65	315.0

<sup>a</sup>High grade zinc specimens, in duplicate, immersed for 7 days.

<sup>b</sup>The corrosion rate was calculated after removal of corrosion products.

Source: Anderson, E. A.; Reinhard, C. E. In *Corrosion Handbook*; Uhlig, H. H., Ed.; Wiley: New York, 1948.

Natural waters all contain dissolved salts to a certain extent and these tend to form a scale on the surface of the metal. As such scales have a protective affect it is to be expected that corrosion will be less severe in natural, particularly hard, water. This is in fact true and it is often found that distilled water is more corrosive than natural waters. Whether the water is scale forming or not is determined by calculating the Langlier saturation index, a relationship involving concentrations of carbon dioxide, calcium bicarbonate and calcium carbonate together with pH described elsewhere in this handbook. The effect of free carbon dioxide in a hard tap water and in equal mixtures of hard water and low conductivity water is shown in Figure 3.

The effect of pH on the corrosion of zinc has already been mentioned. In the range of pH values from 5.5 to 12, zinc is quite stable and as most natural waters come within this range, little difficulty is encountered in respect of pH. If the pH is below the value at which the water is in equilibrium with calcium carbonate, the calcium carbonate will tend to dissolve rather than form a scale. The same effect is produced in the presence of considerable amounts of carbon dioxide, which also favors the dissolution of

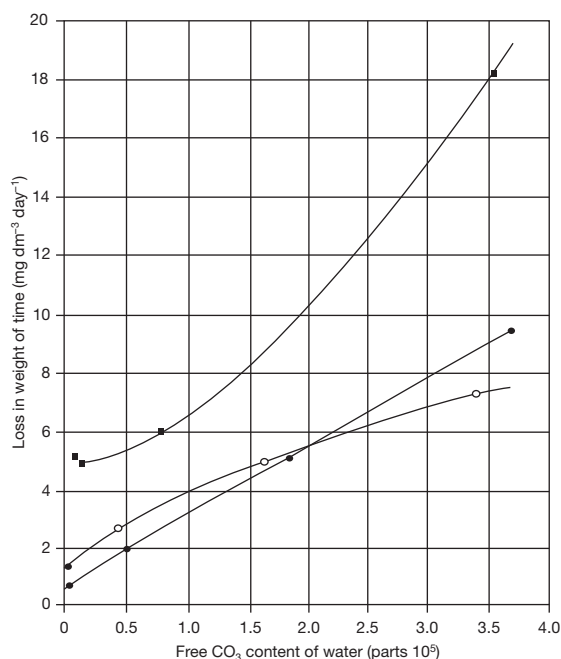


**Figure 3** Effect of free carbon dioxide on the corrosion of zinc in different waters: (■) conductivity water; (○) hard water; (●) equal mixture of hard and conductivity water. Reproduced from Kenworthy, L.; Sith, M. D. *J. Inst. Met.* **1944**, *70*, 463–489, with permission from Maney Publishing.

calcium carbonate. In addition, it is important to note that small amounts of metallic impurities (particularly copper) in the water can cause quite severe corrosion and as little as 0.05 ppm of copper in a domestic water system can be a source of considerable trouble with galvanized tanks and pipes. The copper deposits as small cathodic particles on the zinc surface and thereby accelerates localized pitting corrosion.

### 3.13.3.3.2 Corrosion in seawater

Seawater contains considerable amounts of soluble salts, particularly sodium chloride, which is present in concentrations from 1 to 25%. The North Sea, for example, contains about 3% sodium chloride, 0.47% magnesium sulfate, 0.2% magnesium chloride, and 0.1% calcium chloride. The carbon dioxide content is about 0.0005–0.01% and the pH is between 7.6 and 8.1. The high chloride content would tend to increase the rate of corrosion and this usually takes the form of pitting under these conditions. The corrosive influence of the chloride ions is, however, inhibited by the presence of magnesium and calcium ions by virtue of the formation of a protective layer of magnesium and calcium salts (calcareous scale). Typical corrosion rates of zinc range from  $25 \mu\text{m year}^{-1}$  in the tropics to half that in temperate seas such as the North Atlantic. In tidal areas, where zinc surfaces are immersed twice daily, or areas washed by waves, the corrosion rate is typically twice that of completely immersed zinc.

The effect of the magnesium salts has been clearly demonstrated by Schikorr.<sup>14</sup> Zinc immersed in a solution containing  $30 \text{ g dm}^{-3}$  of sodium chloride showed a weight loss of  $198 \text{ g m}^{-2}$  after 14 days. When the solution contained in addition  $12 \text{ g dm}^{-3}$  of magnesium chloride, the loss in weight was only  $4 \text{ g m}^{-2}$  after the same period. Artificial seawater was also tested and gave a weight loss of  $5 \text{ g m}^{-2}$ .

Zinc roofs are quite satisfactory at the coast, where they receive a large amount of saltwater spray, and many British piers have been covered with sheet zinc, which has lasted 50 years and more. Most of the zinc actually immersed in seawater is in the form of zinc coatings, the behavior of which is discussed elsewhere. Experience with these coatings has proved the value of zinc in seawater compared with many other metals in this environment.<sup>15</sup>

### 3.13.3.3.3 The effect of temperature

It is found that temperature has a marked effect on the rate at which zinc corrodes in water. The

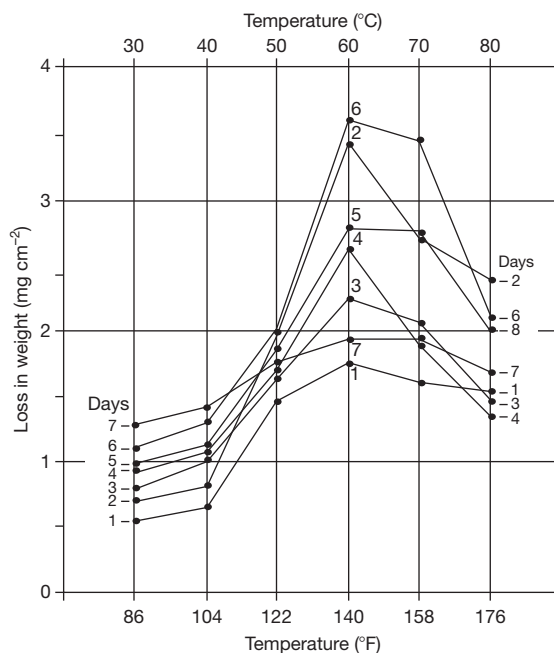


**Figure 4** Effect of temperature on the corrosion rate of zinc sheet in distilled water. Reproduced from Maconachie, J. E. *Trans. Electrochem. Soc.* **1934**, 66, 213–221.

corrosion rate in distilled water reaches a maximum in the temperature range 65–75 °C, **Figure 4**.

This variation in the corrosion rate with temperature is attributed to changes in the nature of the protective film. At lower temperatures the film is found to be very adherent and gelatinous, while at temperatures around 50 °C it becomes distinctly granular in character and much less adherent. Above 75 °C it again tends to become more adherent and assumes a very compact and dense form. It is believed that the granular coating formed at temperatures around 70 °C is more porous than the others and permits greater access of the dissolved oxygen to the metal. Casting alloys are considerably more corrosion resistant in water than pure zinc because they contain aluminum. **Figure 5** shows the effect of temperature on corrosion of three casting alloys with 8%, 12%, and 27% aluminum. The temperature where maximum corrosion rates are observed is 60 °C.

### 3.13.3.4 Soil Corrosion

The factors influencing the corrosion of metals in soil are more numerous than those prevailing in air or water and the electrochemical effects are more pronounced. Moreover, soils vary widely in their composition and

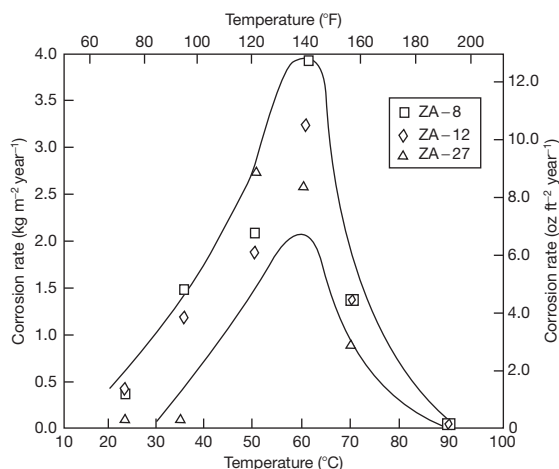


**Figure 5** Effect of temperature on the corrosion rate of ZA alloys in tap water, 30–45 day tests. Reproduced from Belisle, S.; Dufresne, R. In *International Symposium on Zinc–Aluminum (ZA) Casting Alloys*, Toronto, Canada; Canadian Institute of Mining and Metallurgy: Montreal, 1987; pp 109–126.

behavior even over very short distances. Many chemical elements are present in soils, but the ones influencing zinc corrosion behavior are those which are soluble in water, notably base-forming elements such as sodium, potassium, calcium and magnesium. Acid-forming groups such as carbonate, bicarbonate, chloride, nitrate, and sulfate are equally important to consider. The electrical resistivity of soils also strongly influences zinc corrosion rates and is determined by the nature and concentration of the ions formed by chemical salts dissolved in the soil moisture. Moreover, zinc corrosion rates are influenced by physical properties of soils that determine their permeability to air and water. Because of the wide variety of possible soil conditions, it is difficult to obtain reliable data. It is evident, however, that zinc has considerable resistance to corrosion when buried and the severest attack is caused by soils, which are acidic or contain large amounts of soluble salts. A general guideline is that a  $600 \text{ g m}^{-2}$  galvanized coating on steel will provide protection for 10–20 years in inorganic oxidizing soils but half of this time in inorganic reducing soils.

In tests carried out by the National Bureau of Standards in the United States (now the National Institute of Standards and Technology)<sup>16</sup> specimens of copper alloys, lead, zinc, and zinc alloys were buried at a number of different sites for periods varying from 11 to 14 years. The soils tested covered a pH range from 2.6 to 9.4 and resistivities ranged

from 60 to  $17\,800 \Omega \text{ cm}$ . The weight losses and maximum depths of pitting were recorded and the results indicated that the most severe corrosion occurred in soils of poor aeration having high acid and soluble-salt contents. Details are shown in [Table 6](#).

Although there was no significant difference in weight loss between rolled zinc and zinc alloys, the maximum penetration of the alloys definitely appeared to be greater than that of rolled zinc. BISRA tests on galvanized steel pipe buried for five years at five different sites are described by Hudson and Acock.<sup>17</sup> The galvanized pipes resisted corrosion rather better than steel at all sites. Galvanized pipes of small diameter are frequently used to provide underground water services in farms and similar establishments, and little trouble is experienced.

### 3.13.3.5 Corrosion Resistance of Zinc in Chemical Environments

#### 3.13.3.5.1 Acids and alkalis

Zinc dissolves in liquids whose pH is below about 5 and above 12.5. Many acids have pH levels below 5 and therefore will attack zinc, while only the stronger solutions of most alkalis would cause any corrosion. Zinc dissolves in caustic soda solution to form zincate ions, that is,  $\text{ZnO}_2^{2-}$ . Many other factors including agitation, aeration, temperature, polarization, and in some cases the presence of inhibitors may considerably influence the corrosion rate of zinc.

Owing to the high overpotential for hydrogen evolution pure zinc is attacked only very slowly by dilute sulfuric and hydrochloric acids, but impure zinc dissolves quite readily, evolving hydrogen. Thus, when ordinary commercial zinc is placed in a dilute acid it immediately starts to corrode, at first relatively slowly. As corrosion proceeds the impurities present are reprecipitated as a black metallic sponge which may further accelerate the reaction owing to the increased surface area of low overpotential cathodic sites, for example, copper. Some metallic impurities, notably aluminum, retard the corrosion of zinc by acids. This is due to the production of highly protective films. Other metals, such as tin and lead, retard the corrosion initially but after a few hours they are deposited as a metallic sponge, resulting in corrosion as rapid as with ordinary zinc.

Zinc is widely used in contact with many milder chemicals such as detergents and agricultural chemicals. In most cases, zinc or zinc-coated steel comes in contact with these chemicals during handling, packaging and storage.



**Table 6** Corrosion of rolled zinc in various soils in the United States

		<i>Average metal loss (<math>\mu\text{m year}^{-1}</math>) and maximum pit depth (mm) after burial for years stated<sup>b</sup></i>							
<i>Soil type</i>	<i>Metal<sup>a</sup></i>	<i>Loss after 2.1 years</i>	<i>Maximum pit depth</i>	<i>Loss after 4 years</i>	<i>Maximum pit depth</i>	<i>Loss after 9 years</i>	<i>Maximum pit depth</i>	<i>Loss after 12.7 years</i>	<i>Maximum pit depth</i>
Inorganic oxidizing acid soils									
Cecil clay loam	P	4	0.25	6	0.25	5	0.33	7	0.43
	A	7	0.38	6	0.56	5	0.66	10	0.79
Hagerstown loam	P	8	0.81	6	0.64	3	0.33	4	0.41
	A	9	0.89	7	0.69	4	0.40	5	0.51
Susquehanna Clay	P	12	0.23	13	0.23	6	0.30	6	0.23
	A	9	0.30	7	0.41	4	0.48	6	0.81
Inorganic oxidizing alkaline soils									
Chino silt loam	P	10	0.76	8	0.91	7	1.42	6	1.42
	A	26	0.56	9	0.41	10	0.84	9	1.29
Mojave fine – gravelly loam	P	34	0.64	28	0.71	4	1.12	18	0.86
	A	79	2.41	54	P	7	0.91	17	P
Inorganic reducing acid soils									
Sharkey clay	P	10	0.30	11	0.20	5	0.36	7	0.36
	A	11	0.36	13	0.71	6	0.91	9	0.94
Acadia Clay	P	40	0.76			22	0.71		
	A	57	0.84			26	1.32		
Inorganic reducing alkaline soils									
Docas clay	P	14	0.41	6	0.46	7	2.01	7	0.53
	A	28	0.46	29	0.51	13	1.14	13	1.32

Continued

**Table 6** Continued

<i>Average metal loss (<math>\mu\text{m year}^{-1}</math>) and maximum pit depth (mm) after burial for years stated<sup>b</sup></i>									
<i>Soil type</i>	<i>Metal<sup>a</sup></i>	<i>Loss after 2.1 years</i>	<i>Maximum pit depth</i>	<i>Loss after 4 years</i>	<i>Maximum pit depth</i>	<i>Loss after 9 years</i>	<i>Maximum pit depth</i>	<i>Loss after 12.7 years</i>	<i>Maximum pit depth</i>
Merced silt loam	P	34	1.42	17	2.59+	17	2.13	D	P
	A	44	0.86	25	2.03+	9	0.97	D	P
Lake Charles clay	P	22	0.25	36	0.66	21	0.74	30	1.35
	A	48	0.64	57	0.76	32	1.42	33	2.21
Organic reducing acid soils									
Carlisle muck	P	14	<0.15	18	0.25	22	0.56	15	0.46
	A	20	0.30	18	0.91	20	2.44	18	2.51
Tidal marsh	P	24	0.66	24	0.86	9	0.64	14	1.09
	A	20	0.30	16	0.61	16	0.86	15	1.19
Muck	P	67	0.97	54	1.68	35	1.47	25	1.27
	A	81	2.74+	72	P	38	P	35	P
Rifle peat	P	93	1.35	110	2.54	D	P	D	P
	A	164	1.88	172	P	D	P	D	P
Cinders									
Cinders	P	93	2.72+	130	2.99+	D	P	D	P
	A	232	1.48	150	P	D	P	D	P

<sup>a</sup>P = High Grade zinc (58 × 300 × 4 mm) sheet; A = Alloy (4.0%Al + 1.0%Cu) sheet (112 C 170 × 3 mm).

<sup>b</sup>P, perforated; D, specimen destroyed; +, one specimen perforated. Results are usually averaged of two specimens.

Source

Romanoff, M. Underground Corrosion, U.S. Government Printing Office, for National Bureau of Standards, Washington, DC, Circular 579, 1957; 227 pp.

### 3.13.3.5.2 Salt solutions

When a zinc sheet is immersed in a solution of a salt, such as potassium chloride or potassium sulfate, corrosion usually starts at a number of points on the surface of the metal, probably where there are defects or impurities present. From these it spreads downwards in streams, if the plate is vertical. Corrosion will start at a scratch or abrasion made on the surface but it is observed that it does not necessarily occur at all such places. In the case of potassium chloride (or sodium chloride) the corrosion spreads downwards and outwards to cover a parabolic area. Evans<sup>18</sup> explains this in terms of the dissolution of the protective layer of zinc oxide by zinc chloride to form a basic zinc chloride, which remains in solution.

Feitknecht<sup>19</sup> has examined the corrosion products of zinc in sodium chloride solutions in detail. The compound on the inactive areas was found to be mainly zinc oxide. When the concentration of sodium chloride was greater than 0.1 M, basic zinc chlorides were found on the corroded parts. At lower concentrations a loose powdery form of a crystalline zinc hydroxide appeared. A close examination of the corroded areas revealed craters, which appeared to contain alternate layers and concentric rings of basic chlorides and hydroxides. Two basic zinc chlorides were identified, namely  $6\text{Zn}(\text{OH})_2 \cdot \text{ZnCl}_2$  and  $4\text{Zn}(\text{OH})_2 \cdot \text{ZnCl}_2$ . These basic salts and the crystalline zinc hydroxides were found to have layer structures similar in general to the layer structure attributed to the basic zinc carbonate which forms dense adherent films and appears to play such an important role in the corrosion resistance of zinc against the atmosphere. The presence of different reaction products in the actual corroded areas leads to the view that, in addition to action between the major anodic and cathodic areas as a whole, there is also a local interaction between smaller anodic and cathodic elements.

### 3.13.3.5.3 Organic chemicals

Most organic liquids, other than the stronger acids, attack zinc only slowly. Zinc is therefore suitable for storage tanks for liquid hydrocarbons such as motor fuels, for phenols and for trichlorethylene degreasers. Particular care must be taken to exclude moisture, because corrosion at the interface between moisture and hydrocarbon fuels may be considerable. Zinc or zinc-coated vessels are not recommended for use in contact with acid foodstuffs, but are regularly used for dry foods. Zinc is essential in the human diet; the typical recommended daily allowance is 15 mg.

### 3.13.3.6 Cathodic Protection by Zinc Anodes

Zinc should give a potential of  $-1.05\text{ V}$  versus  $\text{Cu}/\text{CuSO}_4$  and should have a driving potential of about  $-0.25\text{ V}$  with respect to cathodically protected steel. Zinc is therefore sufficiently negative to act as a sacrificial anode and its first use for such purposes was on the copper-sheathed hulls of warships more than a century ago. The first attempts to fit zinc anodes to steel hulls, however, were a complete failure, for the sole reason that it had not been realized that the purity of the zinc was of paramount importance. The presence of even small amounts of certain impurities leads to the formation of dense adherent films, which cause the anodes to become inactive.

The major harmful impurity is iron and by keeping the iron content to less than 15 ppm it became possible to produce perfectly satisfactory anodes of zinc.<sup>20,21</sup> Alternatively the effect of the iron can be neutralized by alloying the zinc with certain metals, among which aluminum and silicon or cadmium have been found to be particularly effective. However such alloyed anodes are susceptible to intercrystalline corrosion particularly above  $50^\circ\text{C}$  and for such temperatures the purer anodes are preferable. The presence of cadmium causes the corrosion product to fall away evenly, leaving an active surface.

Zinc alloy anodes are generally very efficient, owing to their nonpolarizing characteristics and to the absence of parasitic reactions when buried or immersed. Therefore, as zinc's 'self-corrosion' is very small, the anode's high efficiency of 85–95% holds throughout the current-density range, whereas the efficiency of magnesium, about 50–55% at high current densities, may fall to only 30% at low current densities. The use of these zinc alloys for reference electrodes to monitor some hull-protection schemes or as permanent reference cells located along pipelines, underlines their nonpolarizing characteristics. The electrochemical equivalent of zinc indicates that  $10.5\text{ kg}$  should give  $1\text{ A year}^{-1}$ , but in practice this amount of charge is given by about  $11\text{--}12\text{ kg}$  of zinc compared with  $7.7\text{--}9\text{ kg}$  of magnesium. As the cost of zinc is relatively low, zinc anodes are found to be very economical. Moreover, as zinc is fairly dense, the volume consumption is about three times lower than that for magnesium and the dimensions of the zinc anode are correspondingly smaller.

The driving potential of zinc to cathodically protected steel is  $200\text{--}250\text{ mV}$  and this is considerably lower than the  $700\text{ mV}$  given by magnesium. While

this value is ideal in seawater or other electrolytes of low resistivity, the use of zinc is not always practicable in environments of higher electrical resistance. For example, it is not likely to be of much use for protecting large underground systems in a high resistivity soil, but on the other hand it proves to be of value for smaller underground units, such as storage tanks, situated in soils of resistivity below about  $3000 \Omega \text{ cm}$ . Olive,<sup>22</sup> for instance, in the United States, discussed the application of zinc anodes for protecting underground equipment at gasoline filling stations. Larger installations, which employ a considerable number of zinc anodes, are the protective schemes for the steel gas mains in Houston and New Orleans.<sup>23</sup> Of a total of some 1200 galvanic anodes in New Orleans about 1000 are of zinc. This is a good example of a case where a system of zinc anodes can be used to protect a large underground installation under the right soil conditions. Zinc is used quite widely for the protection of bare service pipes of small diameter and is receiving increased acceptance for the protection of large-diameter coated pipes in built-up areas in order to minimize interference on adjacent mains. It is also used for protecting galvanized cold-water tanks.

Where the use of zinc anodes is practicable, the low driving potential is a great advantage as the resistance of the steel to be cathodically protected is the controlling resistance and the current output of the anode varies with the requirements of the cathode. Thus it can be said that zinc anodes are largely self-governing.

By far the largest use of zinc anodes is in seawater for the protection of ships' hulls and of North Sea pipelines and drilling rigs. The high conductivity of the seawater and the excellent natural resistance of zinc to corrosion make it very effective in this application. Many examples of trials with zinc anodes on ships can be quoted and the US Navy has done much work in this respect. One example is a paper by Carson,<sup>21</sup> describing zinc anodes attached directly to the hull, which were found to have a life of 8–10 years. This paper also gives the results of tests carried out at the Pacific Naval Laboratory, showing the effect of various impurities in the zinc. Carson looks into the economics of zinc alloy anodes and concludes that for small and medium hull sizes, for example,  $1400 \text{ m}^2$  wetted hull area, zinc alloy anodes are more economical than the most competitive alternative systems available and have the additional advantages of more even current distribution, minimum risk of paint-stripping, and maintenance-free

long life. For larger hull areas zinc alloy anodes are at least as economic as many alternative systems.

Zinc anodes are made in a variety of shapes and sizes, ranging in weight from 2.25 to 11 kg and in shape from cylindrical rods to rectangular bars. When used underground they are usually placed in a backfill, consisting of gypsum, sodium sulfate and clay, which may be added loose, shipped in a bag around the anode, or obtained in cast form.

The use of zinc anodes together with protection of steel by paint or polymer coatings has been found to confer great advantages of longevity. Even the best types of paint or polymer coatings are porous, so corrosion of the underlying metals must ultimately occur. This may take several years with the best coatings, but the corrosion ultimately destroys the adhesion between the metal and coating so that rapid deterioration takes place. The use of zinc anodes in conjunction with a protective coating greatly improves service life. The corrosion which undermines the coating is prevented and the coating remains firmly attached to give its maximum life. At the same time, the consumption of zinc is reduced dramatically, typically by a factor of 10, because much less steel is exposed and needs protection; a zinc consumption of less than  $1.2 \text{ kg A}^{-1} \text{ year}^{-1}$  (i.e., about  $0.12 \text{ kg year}^{-1} \text{ m}^{-2}$  of surface to be protected) is a reasonable estimate. The combination of coating and cathodic protection can therefore prove most economical.

### 3.13.3.7 Zinc–Aluminum (ZA) Casting Alloy Corrosion

#### 3.13.3.7.1 Behavior of the ZA alloys in aerated water from pH 2.0 to 13.0

As part of an International Lead Zinc Research Organization Programme, the corrosion behavior of the ZA casting alloys has been studied at the Noranda Research Center in Canada.<sup>24</sup> Air was bubbled continuously through distilled water flowing through the corrosion cells, its pH being controlled by additions of hydrochloric acid or sodium hydroxide. The temperature was  $22 \pm 2^\circ \text{C}$ . Pure zinc sheet was included for comparison. The results are on the basis of immersion times of 4–15 days and show that ZA27 undergoes little attack between pH 6 and 11.5, as does pure zinc. At pH 4.0 there was preferential attack of the decomposed  $\beta$ -phase, whereas at pH 12.8 there was selective dissolution of the aluminum-rich primary dendrites leaving a sponge-like surface. The samples were gravity cast plates.

### 3.13.3.7.2 Behavior of ZA alloys in neutral salt spray

The ASTM B 117 neutral salt spray test was used with pure zinc and the 4% aluminum diecasting alloy. They were observed to be corroded slightly more than ZA8 and ZA12 during up to 600 h exposure; after longer periods the difference diminished. ZA27 corroded at about one-third the rate of the other alloys, probably because attack occurs on the zinc rich matrix, while ZA27 contains a significantly larger amount of the aluminum-rich phase and behaves like the aluminum die-casting alloy 380 also included in the test.<sup>24</sup>

### 3.13.3.7.3 Behavior of the ZA alloys at a waste water plant

Gravity die cast ZA alloy test plates and 99.99% pure rolled zinc samples were exposed at a waste water treatment plant in Detroit, MI, USA. The results after one year are summarized in Table 7.<sup>20</sup> High corrosion rates were observed in these sedimentation tanks; by contrast steels with a zinc coating thickness of 85  $\mu\text{m}$  in similar locations in the United Kingdom were found to have substantial residual zinc after 7 years exposure.<sup>20</sup> The Michigan experience showed that the ZA alloys may be better than pure zinc in, for example, the secondary sedimentation tank, but additional protection should be provided unless there is satisfactory performance in a comparable water sample.

### 3.13.3.8 Intergranular Corrosion

Zinc of high purity is not susceptible to intergranular corrosion. However, this type of corrosion has been observed on zinc alloys in all common environments; the presence of alloying elements, aluminum in particular, is required to cause intergranular corrosion. With aluminum, intergranular corrosion is observed in the composition range 0.03–50% and is most severe at 0.2% because of the precipitation of aluminum-rich precipitates at zinc grain boundaries. The presence of other impurities, especially lead, cadmium and tin, greatly accelerates intergranular corrosion rates in zinc-aluminum alloys; however, maintaining the limits of these impurities within the SHG zinc specification prevents this. Heat treatment tends to increase grain boundary segregation in zinc casting alloys and therefore increases susceptibility to intergranular corrosion. Intergranular corrosion is most severe at higher temperatures and in moist, alkaline environments, especially above a pH level of 10.

**Table 7** Corrosion results from 1 year at Detroit, USA Wastewater Treatment Plant

<i>Exposure site</i>	<i>Sample</i>	<i>Corrosion rate (<math>\text{g m}^{-2} \text{year}^{-1}</math>)</i>
Atmospheric – Indoor		
Bar screen (high $\text{H}_2\text{S}$ concentration and humidity)	Zinc	1
	ZA8	2
	ZA12	1
	ZA27	1
Atmospheric – Outdoor		
Primary sedimentation tank (relatively high $\text{H}_2\text{S}$ and humidity)	Zinc	8–12
	ZA8	9
	ZA12	9
	ZA27	4
Secondary sedimentation tank (relatively high $\text{H}_2\text{S}$ and humidity)	Zinc	9
	ZA8	10
	ZA12	10
	ZA27	9
Immersed		
Primary sedimentation tank (wastewater with low $\text{O}_2$ containing phosphorus precipitants and coagulants)	Zinc	1239–1601
	ZA8	625
	ZA12	2181
	ZA27	1209
Secondary sedimentation tank (oxygenated wastewater containing microorganisms)	Zinc	857–1174
	ZA8	324
	ZA12	352
	ZA27	253

A corrosion rate of  $\text{g m}^{-2} \text{year}^{-1}$  corresponds to a uniform depth of penetration between 50 and 60  $\mu\text{m}$  for the ZA alloys. Visual examination of the immersed samples showed that ZA8 suffered moderate, uniform corrosion in both tanks. ZA12 showed extensive localized corrosion in the primary tank but slight uniform corrosion with localized corrosion at several spots in the secondary tank. ZA27 suffered extensive localized corrosion over most of the surface in the primary tank but only slight uniform corrosion with several very small pits dispersed all over the surface in the secondary tank.

Source: Progress reports Nos. 9 and 10, Project ZM-287 International Lead Zinc Research Organization, Durham, NC 27713-3210, USA.

### 3.13.4 Recent Developments

The most important recent development is the availability of computer-based prediction methods for zinc corrosion rates, particularly in atmospheric exposures. Traditionally, corrosion rates, and therefore service lives, have been estimated by using a generalized value for each type of atmosphere: rural, industrial, urban and marine. The certainty of prediction has recently been greatly improved by development of a prediction technique based on neural network modeling and assembly of a database relating zinc corrosion rate to the most important primary variables: annual average rainfall, temperature, relative humidity, sulfur dioxide deposition, sea salt deposition and time of



exposure<sup>25</sup>; 47 sets of data, representing different environments, were used to train the model. The correlation coefficient was greatly improved in comparison with past models; the average error of prediction is  $(36 \pm 13)\%$  at 95% confidence interval. The major source of error is believed to be factors other than the six that contribute to corrosion performance in this model. Nevertheless, the accuracy is improved in comparison to the ISO CORRAG model<sup>26,27</sup> and various published regression models.<sup>28–31</sup> The model is available at the internet site <http://www.galvininfo.com>

Alloys with higher contents of aluminum continue to grow in importance, especially for casting using metal or graphite moulds. Up to about 15% aluminum, the materials are non-sparking and can be used in mines. The corrosion behavior of the zinc–aluminum casting alloys can, for practical purposes, be considered as similar to that of pure zinc, even a factor of two in corrosion rate would be of little significance in a solid product. This is to be contrasted with both the behavior and significance of zinc–aluminum alloys when produced as coatings. In this latter case, the production process is designed to give inherently corrosion-resistant structures and only limited corrosion attack can be tolerated because the coating is thin. With castings, the only corrosion criterion is that harmful impurities such as lead, tin and cadmium, which could cause intercrystalline corrosion, should be below specified and low levels; the difference in levels of general corrosion is unlikely to affect the choice of alloy.

The general corrosion rates of zinc and zinc alloys in practice often have been shown to be much less than in simulated conditions; this is because many naturally occurring substances act as inhibitors. **Figure 1** is a good example of this. The diagram is valuable for the qualitative relationship among acid, neutral and alkaline conditions but, in practice, the corrosion rates are usually very much lower than that indicated by the pH because of the effect of other dissolved constituents and the barrier effect of corrosion products. Seawater around the British Isles is much less corrosive to zinc than tropical seawater.

It should be noted that the atmospheric corrosion data in **Table 3** are related to historic environments. Current use in the industrial areas listed with acidic pollution would show much lower corrosion rates as the corrosion of zinc in the atmosphere is essentially related to the SO<sub>2</sub> content (and the time of wetness) and in many countries the sulfurous pollution has been greatly reduced in the past 30 years. Zinc also benefits from rainwater washing to remove corrosive pollutants; therefore, although initial corrosion rates are usually not very

different on upper and lower surfaces, the latter tend, with time, to become encrusted with corrosion products and deposits, and these are not always protective.

## References

- Porter, F. C. *Zinc Handbook*; Marcel Dekker: New York, 1991.
- Vernon, W. H. J. *Trans. Faraday Soc.* **1927**, 22, 113.
- Zhang, X. G. *Corrosion and Electrochemistry of Zinc*; Plenum: New York, 1996.
- Roetheli, B. E.; Cox, G. L.; Littreal, W. B. *Metals and Alloys* **1932**, 3, 73.
- Belisle, S.; Dufresne, R. In International Symposium on Zinc–Aluminum (ZA) Casting Alloys, Toronto, Canada; Canadian Institute of Mining and Metallurgy: Montreal, 1987; pp 109–126.
- Morriset, P. *Zinc Alliances* **1959**, 20, 15.
- Hudson, J. C.; Stanners, J. F. J. *Appl. Chem.* **1953**, 3, 86.
- Goodwin, F. E. In Proceedings of the 16th International General Galvanizing Conference; European General Galvanizing Association: Caterham UK.
- Anderson, E. A. Am. Soc. Test. Mater. Special Publication No. 175, June 1955.
- Ambler, H. R. J. *Appl. Chem.* **1960**, 10, 213.
- Ambler, H. R.; Bain, A. A. J. *Appl. Chem.* **1955**, 5, 437.
- Odneval Wallinder, I.; Verbiest, P.; He, W.; Leygraf, C. *Corros. Sci.* **1988**, 40(11), 1977–1982.
- Brix, K. V. In Proceedings of the 6th International Conference on Zinc and Zinc Alloy Coated Steel Sheets (Galvatech'04), Chicago, USA; AIST: Warrendale, PA, 2004; pp 815–827.
- Schikorr, G. Z. *Metallk.* **1940**, 32, 314.
- Hudson, J. C.; Banfield, T. A. J. *Iron Steel Inst.* **1946**, 154, 229.
- Denison, I. A.; Romanoff, M. J. *Res. Nat. Bur. Stand.* **1950**, 44, 259.
- Hudson, J. C.; Acock, G. P. Tests on the Corrosion of Buried Iron and Steel Pipes, Iron and Steel Inst. Special Report No. 45, 1953.
- Evans, U. R. *The Corrosion and Oxidation of Metals*; Edward Arnold: London, 1960.
- Feitknecht, W. *Chem. Ind. (Rev.)* **1959**, 36, 1102.
- Crennell, J. J.; Wheeler, W. C. G. J. *Appl. Chem.* **1958**, 8, 571; **1956**, 6, 415.
- Carson, J. A. H. *Corrosion* **1960**, 16, 99.
- Olive, M. J. *Corrosion* **1960**, 16, 9.
- Trouard, S. E. *Corrosion* **1957**, 13, 21.
- Progress reports Nos. 9 and 10, Project ZM-287 International Lead Zinc Research Organization, Durham, NC 27713-3210, USA.
- Zhang, X. G.; Goodwin, F. E. In Proceedings of the 5th International Conference on Zinc and Zinc Alloy Coated Steel Sheets (Galvatech'01), Brussels; Belgium Verlag Stahleisen: Dusseldorf, Germany, 2001; pp 311–316.
- International Standard, ISO 9223, 1992, International Standards Organization, Geneva, Switzerland.
- King, G. A. *Corros. Mater.* **1998**, 23, 88.
- Knotkova, D.; Boschek, P.; Kreislova, K. *ASTM STP 39*; ASTM: Conshohocken, PA, 1995; p 38.
- Feliu, S.; Morcillo, M.; Feliu, S., Jr. *Corros. Sci.* **1993**, 34, 403.
- Feliu, S.; Morcillo, M.; Feliu, S., Jr. *Corros. Sci.* **1993**, 34, 415.
- NeuralShell 2, 4th ed.; Ward System Group Inc.: Frederick, MD, 1996.

## Further Reading

Revie, R. W. *Uhlig's Corrosion Handbook*; 2th ed.; Wiley: New York, 2000.

Porter, F. C. *Corrosion Resistance of Zinc and Zinc Alloys*; Marcel Dekker: New York, 1994.

Zhang, X. G. *Corrosion and Electrochemistry of Zinc*; Plenum: New York, 1996.

*ASM Handbook: Corrosion*; ASM International: Materials Park, OH, 2005; Vol. 13B.

Baboian, R. *Corrosion Tests and Standards – Application and Interpretation*, ASTM Manual Series MNL 201995; ASTM: Conshohocken, PA, 2004.

Townsend, H. E. *Outdoor Atmospheric Corrosion*, ASTM STP 1421; ASTM: Conshohocken, PA, 2002.

*ILZRO Engineering Properties of Zinc Alloys*, 3rd ed.; ILZRO: Durham, NC, 1989; revised, p 116.

ASTM Symposia on Corrosion Behaviour, ASTM STP 175, 290, 435, 646; ASTM: Philadelphia, 1956, 1959, 1968, 1978.

Slunder, C. J.; Boyd, W. K. *Zinc: Its Corrosion Resistance*, 2nd ed., ILZRO: Durham, NC, 1983.

## Relevant Websites

[www.zincinfocentre.org](http://www.zincinfocentre.org) – Zinc Development Association/Zinc Information Centre.

[www.zincworld.org](http://www.zincworld.org) – International Zinc Association.

## 3.15 Corrosion of Tantalum and Niobium and their Alloys

**S. B. Lyon**

Corrosion and Protection Centre, School of Materials, The University of Manchester, Oxford Road, Manchester M13 9PL, UK

© 2010 Elsevier B.V. All rights reserved.

<b>3.15.1</b>	<b>Introduction</b>	2135
3.15.1.1	Historical Information	2135
3.15.1.2	Occurrence and Production	2136
3.15.1.3	Physical Properties	2136
3.15.1.4	Mechanical Properties and Alloying	2136
3.15.1.5	Fabrication	2137
3.15.1.6	Applications	2138
3.15.1.7	Economics and Availability	2138
<b>3.15.2</b>	<b>Electrochemistry</b>	2139
3.15.2.1	Thermodynamics	2139
3.15.2.2	Hydride Formation	2139
<b>3.15.3</b>	<b>Corrosion Processes</b>	2141
3.15.3.1	Anodizing	2141
3.15.3.2	Passivity, Corrosion, and Localized Corrosion	2142
3.15.3.3	Gaseous Environments	2143
3.15.3.3.1	Oxidation in air	2143
3.15.3.3.2	Other gaseous environments	2144
3.15.3.4	Aqueous Environments	2144
3.15.3.4.1	Mineral acids	2144
3.15.3.4.2	Alkalis	2145
3.15.3.4.3	Hydrogen embrittlement and galvanic interactions	2146
3.15.3.4.4	Fluorides	2146
3.15.3.4.5	Aqueous salts	2147
3.15.3.5	Liquid Metals	2147
3.15.3.6	Organic Compounds	2148
<b>3.15.4</b>	<b>Industrial Applications</b>	2148
3.15.4.1	Chemical Process Equipment	2148
3.15.4.2	Anodes	2148
3.15.4.3	Medical and <i>In Vivo</i> Applications	2148
<b>References</b>		2149

### 3.15.1 Introduction

#### 3.15.1.1 Historical Information

Niobium was the first of this pair of elements to be discovered in 1801 when an English chemist, Charles Hatchett, analyzed a specimen of an unknown mineral that had been brought back from America to London.<sup>1</sup> He found evidence that it contained a new element and named it 'columbium' in homage to its original source. A year later, Anders Ekeberg of the University of Uppsala, analyzed a different mineral, this time originating from Ytterby in Sweden and isolated another previously unknown element.

He called his discovery 'tantalum' (after Tantalus, son of the Greek god Jupiter, who was sentenced to eternal frustration); isolating the element had obviously been an extremely difficult task.

Columbium and tantalum were assumed to be the same element for over 35 years until, in 1844, their individual valence states were uniquely identified; columbium had both +3 and +5 states while tantalum exhibited only a +5 state. In order to avoid misunderstanding, columbium was renamed 'niobium' (after Niobe, daughter of Tantalus) inadvertently creating over 100 years of dispute between metallurgists (who stuck to the name columbium) and chemists (who

preferred niobium). However, in 1949, the International Union of Pure and Applied Chemistry ruled that niobium was the official usage, although it is still sometimes referred to by its original name, especially in North America.

### 3.15.1.2 Occurrence and Production

Current primary sources of tantalum and niobium occur separately with the largest single source of tantalum in the world found in West Australia with additional resources in Canada, China, Brazil, and central Africa; it also occurs in small but significant quantities as a by-product of alluvial tin operations, for example, from southeast Asia.<sup>1</sup> The primary ore 'tantalite' is similar in composition to columbite and is an iron-manganese tantalum oxide ( $\text{Fe} + \text{MnTa}_2\text{O}_6$ ). Regarding niobium, the world's largest deposit is in Brazil with a pyrochlore mineralization ( $\text{Na} + \text{CaNb}_2\text{O}_6$ ); reserves here are sufficient to last over 400 years at current production rates. Columbite-tantalite ('coltan'), a mineral with a ratio of  $\text{Nb}_2\text{O}_5:\text{Ta}_2\text{O}_5$  ranging from 10:1 to 13:1, occurs in Brazil, Nigeria, and Australia as well as other countries in central Africa.

The extraction and refining of both the metals is determined by the need to separate the elements from each other. The final product is generally the oxide ( $\text{Ta}_2\text{O}_5$  or  $\text{Nb}_2\text{O}_5$ ) but the extraction and refining process involves mineral concentration, dissolution as complex fluorides and solvent extraction or liquid ion exchange. Tantalum and niobium industrial chemicals are generally produced from the oxides, or occasionally from an intermediary fluoride while the metals are derived from their corresponding precursors by thermal reduction using a reactive metal such as sodium or aluminum. The metallic powders can then be used directly for electronic applications (e.g., capacitors), which, in the case of tantalum, amounts to a significant volume (>50%) of the market. Metal powders are processed further under vacuum using electric-arc or

electron-beam melting into ingots for the production of pure material or alloys. Multiple remelting may be required to provide the desired level of metallic purity.

### 3.15.1.3 Physical Properties

Tantalum and niobium are immediately below vanadium in the same group of the periodic table and, hence, share many general properties. They are characterized by their exceptionally high melting points (respectively the fourth and sixth highest melting points of all the elements) and extremely high corrosion resistance due to very stable passive oxide films.<sup>2,3</sup> Like molybdenum and tungsten, they have body-centered cubic structures but, unlike them, their ductile to brittle transitions are well below room temperature ( $-150^\circ\text{C}$  for niobium,  $-200^\circ\text{C}$  for tantalum; both influenced by impurity content) and they have considerably lower strengths. Consequently, they have excellent ductility and can be easily formed and worked. However, both materials start to oxidize at significant rates above around  $200\text{--}300^\circ\text{C}$  and thus require protection at high temperatures, either by the use of coatings, or by keeping them in a protective atmosphere. Niobium has very similar properties, in general, to tantalum but has the advantage of being about half the density (i.e., twice the volume for the same mass) as well as cheaper. The physical properties of tantalum and niobium are similar to their adjacent colleagues in the periodic table, tungsten and molybdenum, respectively (Table 1).

### 3.15.1.4 Mechanical Properties and Alloying

Commercially pure annealed niobium and tantalum have relatively good mechanical properties with, depending on the level of impurities, strengths similar to, or somewhat less than, annealed austenitic stainless steel (Table 2). However, they have low

**Table 1** Selected physical properties of tantalum, niobium, molybdenum, and tantalum<sup>3</sup>

	<i>Tantalum (Ta)</i>	<i>Tungsten (W)</i>	<i>Niobium (Nb)</i>	<i>Molybdenum (Mo)</i>
Atomic number	73	74	41	42
Atomic weight (g)	180.95	183.84	92.91	95.95
Density ( $\text{g cm}^{-3}$ )	16.6	19.3	8.55	10.2
Melting point (K)	3287	3680	2740	2890
Boiling point (K)	5731	5830	5017	4920
Electrical conductivity ( $\times 10^6 \Omega^{-1} \text{cm}^{-1}$ )	0.0761	0.189	0.0693	0.187
Thermal conductivity ( $\text{W cm}^{-1} \text{K}^{-1}$ )	0.575	1.74	0.537	1.38
Crystal structure	bcc	bcc	bcc	bcc

**Table 2** Room temperature mechanical properties of annealed tantalum and niobium compared with molybdenum and stainless steel<sup>4,5</sup>

Property	Tantalum	Niobium	Molybdenum	Austenitic steel (321)
Density (g cm <sup>-3</sup> )	16.6	8.55	10.2	8.0
Ultimate tensile strength (MPa)	280	125	415	620
Yield stress (MPa)	170	75	300	210
Elongation (%)	50	25	35	45
Young's modulus (GPa)	180	100	330	200
Shear modulus (GPa)	69	37.5	120	86
Poisson's ratio	0.35	0.38	0.32	0.29
Specific strength (MPa g <sup>-1</sup> cm <sup>-3</sup> )	16.9	14.6	40.7	77.5
Specific modulus (GPa g <sup>-1</sup> cm <sup>-3</sup> )	10.8	11.7	32.3	25

work-hardening rates (so, the yield stress does not increase to particularly high values after work hardening) and relatively low specific modulus. Despite being refractory metals, they have somewhat disappointing strengths at high temperatures compared with, for example, molybdenum and tungsten and, without alloying, the room temperature values are not maintained much beyond about 500–600 °C. This is not a practical constraint for aqueous corrosion applications. Both metals (and their alloys) are increasingly susceptible to oxidation above around 300 °C and must be protected in some way. Alloying (e.g., with tungsten, zirconium, etc.) increases the room- and high temperature strengths considerably but at the expense of ductility.

Both metals form a full range of solid solutions with each other resulting in properties that are generally intermediate between the two metals alone. The main commercial solid solution alloy is Ta–40Nb, which has mechanical and corrosion properties slightly lower than unalloyed tantalum but at lower cost. Tantalum may also be alloyed with tungsten ('Tantaloy'); Ta–2.5W, Ta–7.5W, and Ta–10W being the most common commercial alloys (Table 3). More complex systems are based on Ta–8W compositions; for example, T-111: Ta–8W–2Hf, and ASTAR 811C: Ta–8W–1Re–0.7Hf–0.025C (which is precipitation hardened). These alloys are designed principally for high strength maintained to reasonably high temperatures; oxidation protection is required and they are not generally used for corrosion applications. Other alloys include those with molybdenum and titanium (Ta–10Ti); the latter being useful for anode applications, as it is less dense (and cheaper) than unalloyed tantalum.

The mechanical properties and corrosion resistance of niobium are somewhat less than tantalum; however, the material is considerably cheaper. Many

**Table 3** Room temperature mechanical properties of some tantalum and niobium alloys<sup>4,5</sup>

Alloy	UTS (MPa)	YS (MPa)	Elongation (%)
Ta–2.5W	380	240	30
Ta–10W	620	480	30
Ta–40Nb	310	210	40
Nb–1Zr	195	125	20
Nb–10W–2.5Zr (Cb-752)	510	380	20
Nb–10Hf–1Ti (C103)	380	260	20
Nb–10Hf–10W–0.1Y (C129Y)	550	410	20

niobium alloys were developed to optimize their high temperature properties and these include Nb–10Hf–1Ti (C103), Nb–10W–2.5Zr (Cb-752), and Nb–10W–10Hf–0.1Y (C129Y); these alloys also require protection from high temperature oxidation when in use. However, unalloyed niobium is often specified for corrosion-resistant applications; where a higher strength material is required, Nb–1Zr can be substituted with little or no loss of corrosion resistance.

### 3.15.1.5 Fabrication

Owing to the high melting point and reactivity of tantalum and niobium with oxygen and nitrogen at high temperatures, which prevents conventional consolidation by melting and casting in air, the materials are normally vacuum-sintered, vacuum-arc melted, or electron-beam melted from compacted powder.<sup>4,5</sup> Vacuum sintering yields metal of fine grain, whereas electron-beam melting yields softer coarse-grained metal which requires cold forging prior to rolling. Metal produced by all three techniques will absorb considerable cold work (up to 90% reduction in area) before annealing is necessary; typically 1 h at 1200 °C



(in a vacuum or inert gas shielded furnace) gives full recrystallization. Both tantalum and niobium are weldable using tungsten-electrode inert gas (TIG), resistance, electron-beam (EB) and plasma-arc welding. However, welding is ideally carried out in an inert-gas chamber to avoid reaction with the atmosphere. Material thinner than 0.5 mm cannot readily be TIG or plasma-arc welded and resistance welding may be used, either in air or under water. EB welding gives the best results and generally produces a contamination-free narrow weld and heat affected zone, irrespective of material thickness.

Niobium and tantalum possess excellent room-temperature fabrication characteristics, similar to copper, and compatible with all conventional production practices. Large reductions (up to 90%) in recrystallized material can be achieved without intermediate process annealing. Secondary fabrication operations such as stamping, drawing, spinning, or forming into complex shapes can be performed at room temperature. Intermediate anneals are dependent on the amount of work involved. In tube drawing or deep drawing, annealed material should be used initially with reductions of up to 60–80%, and multiple draws possible, before reannealing.

All conventional machining techniques may be used with the proviso that niobium and tantalum have strong tendencies to gall, tear, and adhere (weld) to the cutting tool. This makes tool design and selection of machining lubricant very important. Carbide, coated carbide, and high-speed tools may all be successfully used with water-soluble cutting oils; lathe operations can also use soluble oil emulsions.

Tools should be kept sharp with steep rake angles and fast deep cuts preferred. In practice, most machining procedures that give a satisfactory result with soft copper will generally also give good results with tantalum and niobium.

### 3.15.1.6 Applications

The majority of tantalum is used in electronic applications (capacitors, etc.) with another large percentage utilized in fine chemicals for a variety of purposes. Likewise, the vast majority of niobium is used as alloying additions to steels. However, although only a small minority of either element is used as a primary metal or alloy in its own right, they are generally used in critical applications in corrosion control where few other choices exist (Tables 4 and 5).

### 3.15.1.7 Economics and Availability

There are sufficient worldwide reserves of both tantalum and niobium to last several hundred years at the current consumption rates. The price of these materials is subject to significant market fluctuation depending upon market demand and mine supply. However, tantalum is significantly more costly than niobium with a traditional spread of about 4–5 times. For example, at the end of 2008, the consumer price for recycled niobium was US\$ 55–60 kg<sup>-1</sup>, and for tantalum US\$ 250–260 kg<sup>-1</sup> (by contrast, for molybdenum it was US\$ 35–40 kg<sup>-1</sup> and for platinum \$30 000–40 000 kg<sup>-1</sup>).

**Table 4** Applications for tantalum<sup>6</sup>

<i>Tantalum product</i>	<i>Application</i>	<i>Technical attributes/benefits</i>
Tantalum carbide and nitride	Cutting tools and tool coatings	Increased high temperature deformation, control of grain growth, high hardness
Tantalum oxide	Optical lenses	High index of refraction
Tantalum powder	Capacitors	High dielectric constant, excellent temperature stability, small size
Tantalum and tantalum alloy fabricated products	Sputtering targets	Thin coatings of tantalum, tantalum oxide or nitride coatings to semi-conductors
	Chemical process equipment	Superior corrosion resistance, passivity at high anodic potentials
	Cathodic protection anodes	Attack by body fluids is non-existent.
	Prosthetic devices, hips, plates in the skull	
Tantalum alloy additions	Suture clips, fasteners, fixings	Melting point is 2996 °C, but protective atmosphere or high vacuum required.
	High temperature applications	
	High temperature alloys for air- and land-based turbines (e.g., jet engines)	High temperature reliability and strength, resistance to corrosion by hot gases.

**Table 5** Applications for niobium<sup>6</sup>

<i>Niobium product</i>	<i>Application</i>	<i>Technical attributes/benefits</i>
Ferro-niobium (~60%Nb)	Niobium additive to 'high strength low alloy' steel	Imparts a doubling of strength and toughness because of grain refining
Niobium oxide	Optical lenses, non-reflective coatings	High index of refraction, high dielectric constant
Niobium powder	Capacitors for electronic circuits	High dielectric constant, stability of oxide dielectric
Niobium carbide and nitride	Cutting tools and tool coatings	High temperature deformation, controls grain growth, high hardness
Niobium and niobium alloy fabricated products	Sputtering targets for coatings Cathode protection anodes Chemical processing equipment	Superior corrosion resistance, passivity at high anodic potentials
Niobium–1% zirconium alloy	Sodium vapor lamps Chemical-processing equipment	Corrosion resistance, gettering of oxygen, resistance to embrittlement
Ferro-niobium and nickel–niobium	Additions to turbine blade alloys for air- and land-based gas turbines	Increase in high temperature resistance and corrosion resistance, oxidation resistance, improved creep resistance, reduced erosion at high temperatures
Niobium–titanium; Niobium–tin	Superconducting wires for high-field magnets and resulting applications	Superconductivity at cryogenic temperatures

The relatively high cost of tantalum is a significant limiting factor in its use, especially since much of the corrosion performance can be obtained from niobium. Nevertheless, its mechanical properties, which are typically more than twice that of niobium, can compensate to a large extent for the cost difference and are critical in some applications. Where thin linings are used, the long life and high reliability of tantalum equipment can more than offset its higher initial cost. In many applications, tantalum and niobium (or their alloys) are increasingly specified as either complete replacements for noble metals, or as stable substrates for noble metal coatings, at considerably lower cost for essentially equivalent performance.

### 3.15.2 Electrochemistry

#### 3.15.2.1 Thermodynamics

Tantalum and niobium have remarkably similar electrochemistry that is characterized by their passivity over almost the entire range of pH and potential. Thus, although both metals are more active than zinc, for example, the stability of the passive oxide film against almost all corrosive agents (except fluoride) is remarkable. The only significant difference between the elements, which forms the industrial basis for their separation, is that tantalum displays generally only one oxidation state (+5), while niobium has multiple oxidation states (+2, +4, and +5). This difference is reflected in the *E*–pH (Pourbaix)

diagrams shown in **Figures 1** and **2**, which are otherwise notable for their lack of complexity. Thus, niobium should theoretically passivate at intermediate potentials with, successively, NbO, NbO<sub>2</sub>, and Nb<sub>2</sub>O<sub>5</sub> while tantalum forms just Ta<sub>2</sub>O<sub>5</sub>.

As mentioned above, the metals are relatively susceptible to fluoride which destroys oxide passivity and must therefore be avoided. Also, although not shown on these diagrams, the +5 oxyanions, niobate (NbO<sub>3</sub><sup>–</sup>) and tantalate (TaO<sub>3</sub><sup>–</sup>), are stable in strong alkali, which can lead to dissolution of the passive film and activation of the metals under these conditions.

#### 3.15.2.2 Hydride Formation

Both tantalum and niobium have high solubility and diffusivity for hydrogen. Thus, reducing conditions (i.e., under either a significant partial pressure of hydrogen gas or electrochemical cathodic polarization) will inevitably cause hydrogen embrittlement of Nb/Ta metals and their alloys; predominantly because of hydride formation.<sup>7</sup> Significant amount of hydrogen can be absorbed into solid solution, up to several percent<sup>8</sup> and two hydride phases are known, Ta/NbH (β-hydride, generally substoichiometric) and Ta/NbH<sub>2</sub> (γ-hydride, close to stoichiometric); thermochemical phase diagrams have been constructed to demonstrate their regions of phase stability as a function of temperature and hydrogen pressure.<sup>9</sup> Hydride formation from solid solution is accompanied

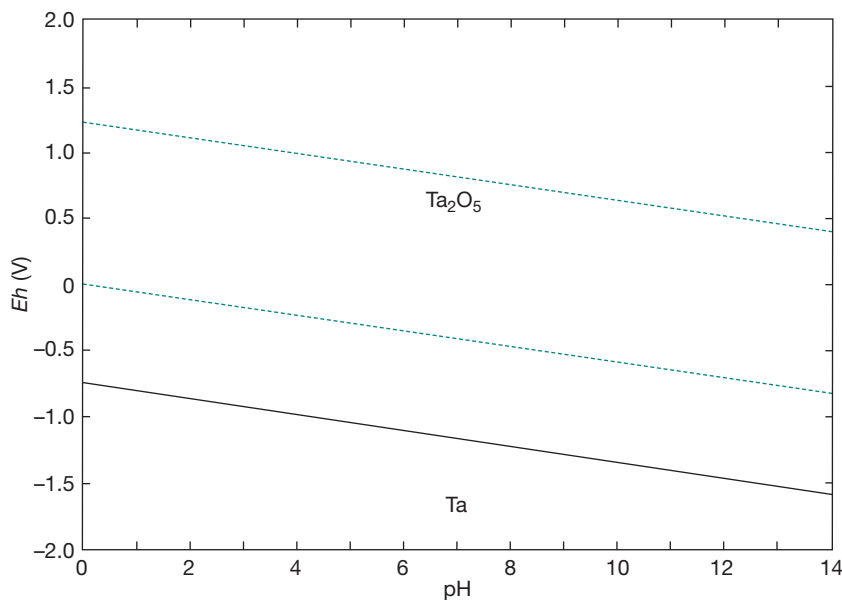


**Figure 1**  $E$ -pH diagram for tantalum at a dissolved metal ion concentration of  $10^{-5}$  M.<sup>3</sup>

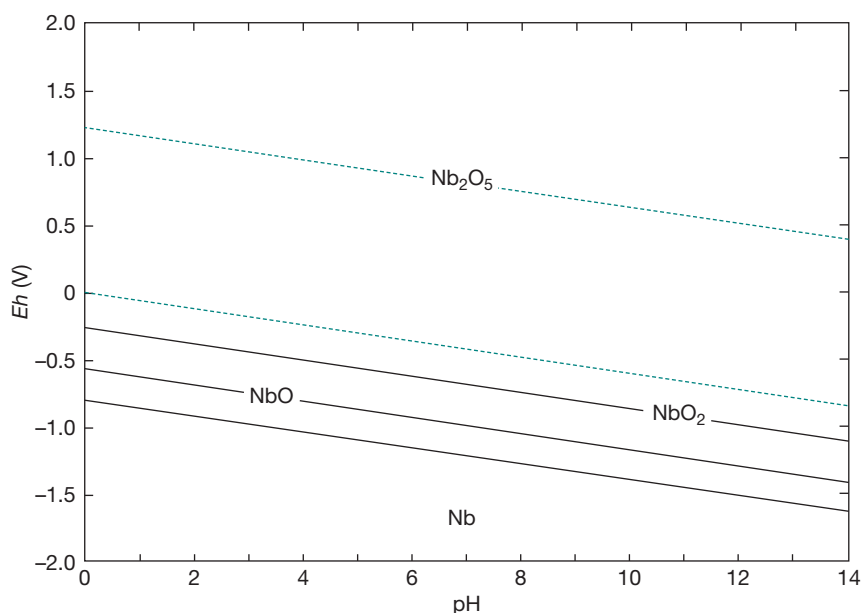


**Figure 2**  $E$ -pH diagram for niobium at a dissolved metal ion concentration of  $10^{-5}$  M.<sup>3</sup>

by significant local strain that causes cracking of the hydride phases and, hence, generation of a population of defects thus lowering the fracture toughness;<sup>10,11</sup> this comprises the main mechanism for embrittlement.

Despite the rapid diffusion rate of hydrogen in the bcc metals ( $\approx 10^{-9}$  m<sup>2</sup> s<sup>-1</sup> at 298 K,<sup>12</sup>) the observed rate of hydride formation is sluggish. The kinetics of

hydride formation appears to be limited by the presence of the passive oxide film, which acts as a barrier to hydrogen entry. Alloying significantly increases the rate of hydrogen entry (presumably by disrupting the passive film in some way) and this effect can be utilized for hydrogen storage or for hydrogen permeation membranes.<sup>13</sup> Mechanical deformation of the

alloy (presumably with local cracking of the passive film) can also lead to enhanced hydrogen uptake.<sup>14</sup> Both tantalum and niobium act as cathodes when in contact with almost all other metallic conductors and will, in appropriate environments, become severely embrittled because of hydrogen generation, a situation that should definitely be avoided.

### 3.15.3 Corrosion Processes

#### 3.15.3.1 Anodizing

The formation of oxide films on tantalum and niobium can be accomplished by direct electrochemical oxidation, generally, either at constant voltage or at constant current. Thus, tantalum and niobium are part of the family of 'valve metals' (including aluminum, tungsten, titanium, zirconium, and hafnium) that form oxides of increasing thickness under increasing anodic polarization. This process is possible because of the thermodynamic stability of the relevant oxides,  $\text{Ta}_2\text{O}_5$  and  $\text{Nb}_2\text{O}_5$  (in particular, their insolubility in the electrolytes used and their lack of higher oxidation states). Like all other anodic oxides, they tend to be noncrystalline and incorporate species from the electrolyte into the films during their growth. Indeed, the properties of the formed oxide films can vary considerably as a function of electrolyte used in the anodizing process.

There is great interest in (and indeed applications for) the use of tantalum and niobium in electronic capacitors. This is because the dielectric constants of tantalum and niobium oxides are, respectively, about three and six times higher than anodic alumina, which is the traditional material used for electrolytic capacitors (Table 6). This implies that capacitors of equivalent values (in farads) can be made with smaller volumes, a critical factor in miniaturization of electronic circuitry. Traditionally, it is anodized tantalum that has been used for capacitor applications, predominantly because it has the required electrical properties (thermal stability and low loss at high frequencies). Anodized niobium shows considerably poorer electrical properties despite the favorable factors of its dielectric constant, greater availability and lower cost. This is because, during anodizing, as well as forming the preferred  $\text{Nb}_2\text{O}_5$ , suboxides of  $\text{NbO}$  and  $\text{NbO}_2$  may also form, and these are, respectively, conducting and semiconducting.<sup>15</sup> In recent years, however, there has been a greater understanding of the formation of the anodic film on niobium, as well as novel methods of forming dielectric materials, for

**Table 6** Electrical properties of various anodic oxides<sup>17,18</sup>

<i>Metal</i>	<i>Oxide growth ratio (nm V<sup>-1</sup>)</i>	<i>Dielectric constant (at 1 kHz)</i>	<i>Electrolyte</i>
Tantalum	3.65	33	0.26M borate + glycol
Niobium	2.33	60	glycol
Tantalum	3.87	29	0.7M sulphuric acid
Niobium	2.56	65	0.5M boric acid +
Aluminium	1.2	9	0.05M sodium borate

example, by atomic layer epitaxy.<sup>16</sup> Consequently, reliable niobium-based capacitors are now becoming available in the market.

The oxide growth ratio as a function of voltage for anodic film formation is also shown in Table 6. As can be seen, these values can vary considerably from metal to metal and depend on anodizing solution and electrical conditions. The oxide growth ratio derives from a complex interaction of parameters and is principally governed by the densities of metal and oxide, the electric field that is required for the species in the oxide film to migrate, and the efficiency of the film-forming process.

In general, for an anodic oxide film to grow, ions must migrate within the oxide under the influence of the applied voltage (i.e., at a field strength  $\approx 100 \text{ MV m}^{-1}$ ). The current is carried both by anions (e.g.,  $\text{O}^{2-}$ ) that migrate inwards and by cations (e.g.,  $\text{Nb}^{3+}$ ) that migrate outwards.<sup>19</sup> When outwardly migrating cations reach the oxide-solution interface either they may react with the electrolyte, forming more oxide and thus thickening the film, or they may dissolve in the electrolyte, contributing to loss of current efficiency in film formation. Thus, an electrolyte in which the cations have a high solubility is likely to result in lowered film-formation efficiency. At the oxide-solution interface, the electrolyte may generate oxygen gas, further reducing current efficiency. Finally, the field at the oxide-solution interface encourages incorporation of anions from the solution into the film. Thus, anodic films on niobium and tantalum inevitably incorporate a greater or lesser quantity of anion species from the electrolyte concentrated in the film at the oxide-electrolyte interface.<sup>20</sup>

Generally, anodic films on tantalum are of the barrier type, relatively featureless and reminiscent of barrier films on aluminum.<sup>21</sup> The ionic transport

numbers of tantalum and aluminum have been studied in mixed oxides spanning the composition range. Tantalum ions ( $\text{Ta}^{5+}$ ) are shown to migrate more slowly than  $\text{Al}^{3+}$  ions, which is consistent with the respective metal–oxygen bond energies,  $\text{Ta}^{5+}\text{—O}$  being higher than  $\text{Al}^{3+}\text{—O}$ . In addition, the cation transport number for tantalum is lower (0.24)<sup>22</sup> than that for aluminum (0.41).<sup>19</sup> The situation of niobium is complicated by the presence (depending on the formation conditions) of additional  $\text{Nb}^{2+}$  and  $\text{Nb}^{4+}$  species in the oxide,<sup>23</sup> which are detrimental to its performance in capacitor applications. Nevertheless, the general overview is very similar. Thus, electrolyte species (including phosphate but not chloride) incorporate into the film during anodizing.<sup>24</sup> However, recent work has demonstrated a profound difference with niobium in alkaline electrolytes. Thus, in phosphoric acid at pH 2 the transport number for  $\text{Nb}^{5+}$  ions is 0.26 which is similar to that for tantalum.<sup>25</sup> However, when the pH is adjusted with ammonium hydroxide to pH 10, the transport number falls to 0.02 and the dielectric constant rises to more than 80 (from 44 at pH 2). It is thought that this change is due to the relative changes in the incorporation of anionic species into the film, specifically phosphate at low pH and a nitrogen species at high pH.

### 3.15.3.2 Passivity, Corrosion, and Localized Corrosion

As predicted from the Pourbaix diagram, the excellent corrosion resistance of tantalum and niobium is due to the presence of tenacious passive oxide films on the respective metals. Indeed, unalloyed tantalum is indubitably the ‘most passive’ of all metals just below rhodium and above gold in the Pourbaix practical nobility table. Compared with tantalum, niobium is significantly less passive; however, this is merely relative as niobium is still considerably more corrosion resistant than most other materials. Both the metals spontaneously passivate in almost all environments below 100 °C at atmospheric pressure, except those of low water activity and those containing fluoride, the latter being the metals’ (almost only) Achilles heel.

It is extremely difficult to locate literature data on the electrochemistry of dissolution for tantalum or niobium other than in extreme conditions; one must therefore presume that the metals are passive (with consequently low corrosion rates) in most environments. Tantalum is spontaneously passive, with an

extremely low corrosion rate in all mineral acids (except HF), at all concentrations and at all temperatures below 100 °C. It is used to condense and concentrate sulfuric acid and exhibits passivity in this medium at a much higher temperature. The corrosion resistance of niobium is generally inferior to that of tantalum, with alloys of niobium and tantalum being intermediate in performance.<sup>26,27</sup>

Recently, the corrosion of niobium has been re-evaluated in sulfuric (20, 40, and 80%) and hydrochloric (20 and 38%) acids at room temperature, 75 and 95 °C.<sup>28</sup> The metal was found to remain passive under all conditions, but with variations in the passive current density corresponding to changes in the mass-loss (corrosion) rate. Minor pitting was observed only in sulfuric acid at concentrations of 20% and 40%. It was suggested that dissolution of the passive oxide was via a  $\text{Nb}(\text{OH})_4^+$  species, for which species thermodynamic data had recently been obtained.

The pitting (breakdown) potentials of niobium have been investigated in 0.1 M halide solutions.<sup>29</sup> In chloride and iodide up to about 150 V, no pitting or breakdown was observed, and the metal formed an anodic film. In bromide, the breakdown voltage was only 42 V with some slight pitting observed. Likewise, the corrosion behavior of tantalum and niobium was studied in concentrated HBr solution at 25 and 100 °C and, under oxidizing conditions (with added bromine) or reducing conditions (with bubbled hydrogen gas).<sup>30</sup> Tantalum was found to passivate under all conditions studied while niobium corroded slowly at 100 °C with pits of around 5  $\mu\text{m}$  evident. Under reducing conditions, niobium gradually began to corrode actively with hydrogen evolution, while under oxidizing conditions it passivated. Tantalum is thus remarkable in its resistance to pitting corrosion by chloride, bromide and iodide species, and niobium is scarcely far behind.

In contrast to their corrosion resistance in acids, niobium and tantalum corrode at significant rates in strong alkali. Thus, niobium is spontaneously active in NaOH at concentrations greater than 10% and at temperatures above 25 °C.<sup>31</sup> Corrosion leads to the formation of the niobate species,  $\text{NbO}_3^-$ , with the corrosion rate increasing with concentration and time. Tantalum was found to be significantly more resistant than niobium and remained passive in 10% NaOH up to 75 °C and in 15% NaOH up to 50 °C.<sup>32</sup> At higher concentrations and temperatures, the passive film on tantalum dissolved slowly, forming a



polytantalate species. Tantalum–niobium alloys were found to be intermediate in behavior.<sup>33</sup>

### 3.15.3.3 Gaseous Environments

#### 3.15.3.3.1 Oxidation in air

Tantalum and niobium are not resistant to oxidation at high temperatures in air. Reaction with both oxygen and nitrogen occurs; in air, reaction is increasingly rapid for both materials above about 500 °C, leading to catastrophic failure. Thus, these metals and their dilute alloys can only be used in high temperature conditions either in a protective (or nonaggressive) environment, or if coated to prevent reaction with the gaseous environment.

Both metals have significant solubility for oxygen and were found to obey Henry's Law for oxygen solubility between 600 and 1100 °C. At 850 °C, oxygen dissolved at up to 2.3 at.% in pure tantalum and 1.3 at.% in niobium; an alloy of Ta–25% Nb dissolved up to 3.4 at.%.<sup>34</sup> The volumetric expansion on proceeding from metal to oxide (Pilling–Bedworth ratio) is among the largest of the engineering alloys: 2.5 and 2.7 for tantalum oxide and niobium oxide, respectively. This can be compared with 2.1 for chromium oxide, 1.65 for nickel oxide and 1.3 for aluminum oxide. This implies that the oxides form under a considerable compressive stress and, indeed, the oxide scales are generally poorly adherent and greatly influenced by specimen geometry.<sup>35</sup> Oxidation rates at even modest temperatures are high and neither alloy is recommended for use in air above 250–300 °C.

For tantalum, initial oxidation is delayed until the equilibrium solubility for oxygen in the metal has been achieved (which is usually rapid). Afterwards, the oxidation process at temperatures below around 400 °C follows a parabolic rate law, thus indicating diffusion-controlled kinetics across the growing oxide film. For thin oxides, in this regime the oxide is relatively protective. Above 500 °C, oxidation proceeds following a linear rate law; in this regime, the oxide is clearly not protective and indeed oxidation will inevitably become catastrophically rapid as the temperature increases. At temperatures in excess of 1000 °C, the metal will effectively burn in pure oxygen.<sup>36</sup> The scale formed in tantalum consists of pure Ta<sub>2</sub>O<sub>5</sub>; as there is no stable lower oxidation state, there is no other stable oxide. Thicker scales on tantalum tend to comprise parallel layers interspaced with lines of small voids. There is strong evidence

that these voids nucleate over metastable suboxide platelets within a thin, oxygen-saturated layer in the metal immediately under the scale.<sup>37</sup>

Niobium, like tantalum, reacts measurably with oxygen at relatively low temperatures (200 °C) although reaction does not become rapid until above about 400 °C. Niobium is influenced, like tantalum, by the dissolution of oxygen in the metal and by the formation of large compressive stresses in the oxide during scale growth. Again, like tantalum, the oxidation kinetics below about 350 °C are parabolic with thinner oxides relatively protective. Above 400 °C, oxidation is initially linear or parabolic and proceeds at a relatively slow rate; however, after a period of time (decreasing with increasing temperature) breakaway oxidation sets in and the oxidation rate increases markedly up to about 600 °C, then decreases substantially.<sup>38</sup> The scale formed mainly comprises Nb<sub>2</sub>O<sub>5</sub> with the metastable suboxide also present in the metal just beneath the metal–scale interface (as for tantalum). However, unlike tantalum, Nb<sub>2</sub>O<sub>5</sub> increasingly intrudes into the metal from the scale disrupting the formation of the suboxides and causing the rapid breakaway oxidation evident in niobium (and absent in tantalum).<sup>39</sup> The formation of NbO<sub>2</sub> beneath the main scale of Nb<sub>2</sub>O<sub>5</sub> at temperatures above around 600 °C is thought to be the major mechanism behind the decrease in the oxidation rate at this temperature.

Wider application of both alloys would result from improving their oxidation resistance. However, owing to the high cost and density of tantalum, much of the research and industrial effort in improving high temperature oxidation resistance focuses on niobium. There are basically two possible methods for achieving this goal: alloying and application of a protective coating. Extensive early work on binary, ternary, and quaternary alloys of niobium with tantalum, tungsten, titanium, and zirconium was performed and it is indeed possible to reduce considerably the oxidation rate of niobium; for example, in Nb–W–Ti alloys.<sup>40</sup> However, in nonoptimized alloys the oxidation rate is still too rapid to be useful and, furthermore, the alloys are required to have satisfactory high temperature mechanical properties (strength and creep resistance).

More recent alloy developments have involved complex alloys containing titanium, aluminum, chromium, silicon, and hafnium (with other minor elements).<sup>41</sup> Although such alloys have somewhat poorer oxidation resistance at lower temperatures,

at temperatures above 1000 °C the oxidation resistance is comparable to or better than nickel-based superalloys. The requirement of good strength and creep resistance is obtained by alloying to promote the formation of intermetallics; either aluminides (up to 1200 °C) or silicides (up to 1500 °C). Thus, alloys such as Nb–30Ti–9Cr–11Al–11Si show an oxidation rate at 1200 °C of 2–3  $\mu\text{m h}^{-1}$ , compared with unalloyed Nb ( $\gg 125 \mu\text{m h}^{-1}$ ) and nickel superalloys (20  $\mu\text{m h}^{-1}$ ), while having acceptable strength and creep resistance<sup>42</sup>; room temperature fracture toughness, however, remains low.

The alternative method for improving high temperature oxidation resistance is to form adherent, dense and protective coatings on the metal surface. They also need to have excellent oxidation resistance as well as providing an effective diffusion barrier for oxygen (and other species) from the coating into the alloy. Coatings based on the development of single or multiple layers of aluminum, molybdenum and niobium silicide have successfully demonstrated oxidation resistance at temperatures of 1300 °C.<sup>43–45</sup> Such coatings may be applied by pack cementation, chemical or physical vapor deposition and thermal spraying.

### 3.15.3.3.2 Other gaseous environments

The reaction of tantalum and niobium with hydrogen to form hydrides has been discussed above and can occur both electrochemically and from the gas phase. Both materials can react with hydrogen at significant rates even at room temperature, for example, by mechanical action.<sup>46</sup> There has, indeed, been considerable interest in the properties of tantalum and, particularly, niobium for hydrogen storage applications. Thermodynamic data predicts the formation of both the mono- and di-hydride phases, which have been confirmed by observation.<sup>47</sup> Hydriding is used commercially as a method to produce powders of niobium and tantalum and their alloys.<sup>48</sup> Since the metals are generally cathodic to other metals, galvanic coupling must be avoided to restrict the possibility of hydrogen embrittlement.

Although tantalum and niobium also react to form nitrides, in air the dominant reaction will be the formation of the oxide. This is because, first, the kinetics of oxidation are much more rapid and, secondly, the nitrides are themselves thermodynamically unstable with respect to oxidation.<sup>49</sup> However, in a predominantly nitrogen atmospheric, both tantalum and niobium will nitride at temperatures above about 400 °C with parabolic kinetics forming a scale of, respectively, TaN or NbN; in some circumstances

the sub-nitride Ta<sub>2</sub>N or Nb<sub>2</sub>N may also form.<sup>50</sup> Interest in nitriding derives from the extreme hardness of the materials and their potential use as hard finishes for cutting tools, etc, using physical vapor deposition.

Neither tantalum nor niobium are attacked to any great extent by dry or wet chlorine, bromine or iodine liquids or vapors below about 200–250 °C. Tantalum is also virtually uncorroded by HBr and HCl below 370 °C, attack starting at about 375 and 410 °C, respectively. However, as mentioned previously, neither metal has any significant resistance to fluorine or HF.

## 3.15.3.4 Aqueous Environments

### 3.15.3.4.1 Mineral acids

Extensive tests were carried out on the corrosion rates of tantalum and niobium in various highly aggressive media by Bishop in the early 1960s<sup>51</sup> and there is no reason to doubt the data today. Tantalum is essentially resistant to corrosion in nitric acid at all concentrations and temperatures. The corrosion rate in 70% acid at 270 °C is only about 100  $\mu\text{m year}^{-1}$ , which is lower than zirconium and it does not have the latter's sensitivity to halide or metal ion contamination. Niobium is only marginally less resistant to tantalum in nitric acid. Corrosion in other oxidizing acids (e.g., chromic, perchloric) is minimal at all concentrations and temperatures.

Tantalum resists hydrochloric acid at all concentrations up to 190 °C. However, above 25% HCl at 190 °C, the corrosion rate of tantalum (and niobium) rises rapidly (Figure 3) and entry of hydrogen will cause embrittlement. Tantalum is also resistant to hydrochloric acid mixtures even in the presence of sulfuric acid and its salts in all proportions and at concentrations up to boiling point. It is not corroded by phosphoric acid at concentrations up to 85% and temperatures up to 200 °C, provided fluoride ion contamination often found in commercial acid does not exceed 5 ppm. It is essentially completely resistant to perchloric acid, chromic acid, hypochlorous acid, hydrobromic acid, hydriodic acid and most organic acids provided they do not contain fluorides, fluorine or free sulfur trioxide.

Tantalum is resistant to 98% sulfuric acid up to at least 160 °C and even higher temperatures at lower concentrations. Practically, it may be used up to 200 °C in all concentrations and 225–250 °C at concentrations between 80 and 90%. Tantalum is attacked by sulfur trioxide at ambient conditions at

rates higher than  $1 \text{ mm year}^{-1}$  and fuming sulfuric acid, containing sulfur trioxide, attacks tantalum at room temperature as do hydrofluoric and fluorosilicic acids.

Niobium is resistant to mineral acids at lower concentrations and temperatures, especially under oxidizing conditions. **Figures 3** and **4** show the corrosion behavior of niobium and tantalum in laboratory tests in various concentrations of sulfuric, hydrochloric acids and phosphoric acid. It has excellent

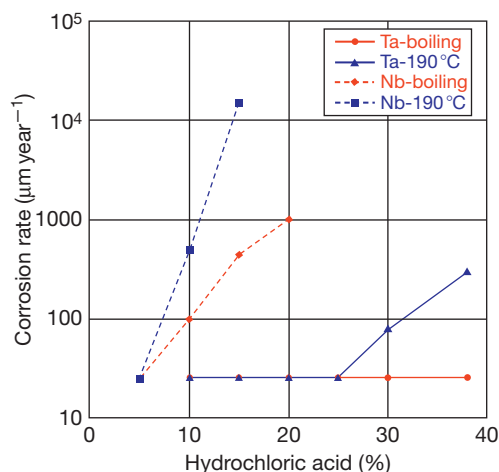


**Figure 3** Corrosion rates for tantalum and niobium in HCl ( $25 \mu\text{m year}^{-1}$  was the lower limit of measurement and, where this value is indicated, corrosion rates were generally less than this value; in most cases, considerably so).<sup>53</sup>

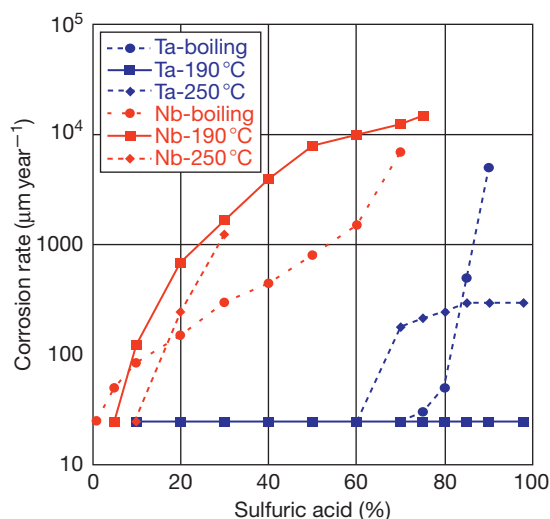


**Figure 4** Corrosion rates of tantalum and niobium in  $\text{H}_2\text{SO}_4$  ( $25 \mu\text{m year}^{-1}$  was the lower limit of measurement and, where this value is indicated, corrosion rates were generally less than this value; in most cases, considerably so).<sup>53</sup>

resistance to nitric acid, the rate of attack in 70% acid at  $250^\circ\text{C}$  being only  $250 \mu\text{m year}^{-1}$ . In dilute sulfurous acid at  $100^\circ\text{C}$ , the corrosion rate is below  $15 \mu\text{m year}^{-1}$ , but in concentrated acid at the same temperature it is greater than  $250 \mu\text{m year}^{-1}$ .

In view of the cost of tantalum, and the overall inferior corrosion resistance for critical applications offered by niobium, there is interest in exploring the performance of alloys of tantalum with other elements. The most commercially developed alloys are Ta–Nb materials although Ta–W, Ta–Mo as well as ternary and quaternary alloys of titanium and zirconium where tantalum or niobium ( $\beta$ -phase stabilizers) are significant components. Robin and coworkers have extensively investigated the entire composition range of Ta–Nb alloys in sulfuric, hydrochloric and phosphoric acids,<sup>52,53</sup> and confirmed the earlier results of Bishop while generating isocorrosion curves for the range of alloys in these environments.

In sulfuric acid, the corrosion rates increase with temperature and acid concentration but decrease with time because of slow oxide growth. The addition of tantalum improves the corrosion resistance of niobium with corrosion rates of Ta–Nb alloys intermediate between niobium and tantalum; the corrosion mechanism in the alloys included selective dealloying of niobium. Anodizing of the alloys reduced the short-term corrosion rates but made no difference to the long-term rates. Similar comments apply to exposures in hydrochloric and phosphoric acid except that the alloy with composition Ta–40Nb was confirmed as extremely corrosion resistant with performance similar to tantalum and Ta–W alloys show increased resistance to hydrogen embrittlement.

### 3.15.3.4.2 Alkalis

Neither tantalum nor niobium has satisfactory corrosion resistance in alkaline solution with the passive oxide films dissolving at varying rates depending on the concentration and temperature of the environment (**Table 7**). Corrosion thus occurs by continuous reformation of the passive film; no pitting is seen. Damage to tantalum equipment has been experienced unexpectedly when strong alkaline solutions are used during cleaning and maintenance.

Tantalum is attacked, even at room temperature, by concentrated alkaline solutions. However, tantalum is fairly resistant to dilute alkaline solutions. In one long-term exposure test in a paper mill, tantalum suffered no attack in a solution with a pH of 10. In contrast, niobium is not resistant to alkalis even

**Table 7** Corrosion rates of tantalum and niobium in some alkaline media<sup>54</sup>

<i>Material</i>	<i>Alkali</i>	<i>Temperature (°C)</i>	<i>Corrosion rate (<math>\mu\text{m year}^{-1}</math>)</i>	<i>Embrittlement</i>
Tantalum	NaOH (5%)	98	3–4	No
	NaOH (10%)	20	0.25	No
	NaOH (10%)	98	8–10	No
	NaOH (50%)	38–57	>1000	Yes
	NaOH (50%)	120	>1000	Yes
Niobium	NaOH (73%)	113–129	>1000	Yes
	NaOH (1%)	98	>750	Yes
	NaOH (5%)	98	>1200	Yes
	NaOH (10%)	98	>2000	Yes
Tantalum	KOH (5%)	100	<80	Yes
	KOH (10%)	Boiling	<120	Yes
	KOH (40%)	27	>1000	Yes
	KOH (50%)	100	>1000	Yes
Niobium	KOH (1%)	98	600	Slightly
	KOH (5%)	98	>2500	Yes
	Na <sub>2</sub> CO <sub>3</sub> (10%)	98	>1500	Yes
	K <sub>2</sub> CO <sub>3</sub> (10%)	98	>1500	Yes
	Na <sub>2</sub> PO <sub>4</sub> (25%)	98	>1300	Yes
	Na <sub>2</sub> S (10%)	98	90	No

in dilute solution or in weak alkali (e.g., Na<sub>2</sub>CO<sub>3</sub>) and suffers rapid attack with severe hydrogen embrittlement occurring at higher temperatures of exposure.

#### 3.15.3.4.3 Hydrogen embrittlement and galvanic interactions

As indicated previously, a galvanic couple in which tantalum or niobium is the cathode can prove disastrous because of embrittlement. On the other hand, if either material is the anode they generally passivate so readily in most environments that no damage occurs, and the galvanic current drops to a very low value. Haissinsky<sup>55</sup> studied couples of tantalum with platinum, silver, copper, bismuth, antimony, molybdenum, nickel, lead, tin, zinc, and aluminum in 0.1 N H<sub>2</sub>SO<sub>4</sub>. Except when tantalum was coupled to zinc or aluminum, it was the more negative member (anode) of the couple. However, the galvanic current rapidly decreased as the tantalum passivated. In hydrofluoric acid, tantalum was again more positive than zinc and aluminum, but more negative than platinum, silver, copper, antimony, nickel, and lead. However, in this environment high steady-state currents were observed because tantalum corrodes rather than passivates in fluoride solutions.

Time is an important factor in determining whether tantalum will be damaged by galvanic effects<sup>56</sup> as illustrated in Table 8. However, such data provides only guidance. In practice, it would be dangerous to depend on laboratory tests only to provide information as to whether tantalum is negative in a

given galvanic couple situation. Niobium behaves similarly and if it is cathodic in a galvanic couple the results can prove disastrous because of hydrogen embrittlement. If niobium is the anode in such a couple, it anodizes so readily that no damage occurs and the galvanic current drops to a very low value because of the formation of an anodic oxide film.

Hydrogen embrittlement of these materials may be avoided completely by polarizing the metals anodically (anodic protection). In such cases, the passive film will thicken or at least be maintained. An effective technique is to couple the metal to a material with a very high exchange current density for hydrogen evolution; essentially, a platinum group metal (e.g., platinum, palladium, ruthenium, etc.). This method can also work by surface ion implantation, for example, with platinum,<sup>57</sup> or by the introduction of some platinum species into the environment, where it will deposit onto the exposed surfaces. Another method is to use alloying, typically with rhenium, tungsten or molybdenum.<sup>58</sup> These are believed to function either by doping the passive film and so favorably changing the charge carrier density (so, it is less conductive), or by changing the hydrogen solubility and hydride nucleation mechanism in the alloy.

#### 3.15.3.4.4 Fluorides

Neither tantalum nor niobium has any significant corrosion resistance to fluorine, hydrofluoric acid or indeed environments containing even relatively low concentrations of fluoride. For example, in

**Table 8** Electrochemical potential of tantalum in the indicated solution with respect to various metals<sup>56</sup>

Time after immersion (s)	Coupled metal	Potential of tantalum (mV)		
		3% NaCl	1% HCl	1% NaOH
30	Hastelloy B	−34	−30	−105
3600	Hastelloy B	+3	+1	−5
30	Hastelloy C	−50	−70	−135
3600	Hastelloy C	−3	−3	−5
30	Nickel	−65	−35	−180
3600	Nickel	−3	0	−5
30	Lead	−2	+50	−10
3600	Lead	+60	+55	+30
30	Aluminum	+130	+275	+620
3600	Aluminum	+230	+210	+510
30	304 stainless	−50		
3600	304 stainless	−3		

concentrated nitric acid at 50 °C no significant increase in the corrosion rate for tantalum was observed.<sup>59</sup> However, at 13 ppm fluoride the corrosion rate increased 2–3 times, and above this level increasingly so. Ta–40Nb alloy corroded about 10 times faster than unalloyed tantalum under all conditions studied. Apart from strong alkali, fluoride-containing environments are the only conditions where tantalum and niobium would be expected to corrode at significant rates at ambient temperatures. This is because the passive oxide films are dissolved to form fluoro and oxyfluoro complexes. It is perhaps not surprising that this would occur, since reaction with fluoride forms the basis of the industrial process for purification and separation of the elements.

#### 3.15.3.4.5 Aqueous salts

Tantalum and niobium have excellent resistance to virtually all salt solutions under virtually all conditions of concentration and temperature, including: chlorides, sulfates, nitrates and salts of organic acids, provided (a) they do not contain fluorides, fluorine, and free sulfur trioxide, or (b) hydrolyze to produce strong alkalis.

#### 3.15.3.5 Liquid Metals

Significant interest lies in the use of refractory metals for two main applications: as a constructional material for molten metal die casting and in applications (particularly relating to nuclear) where molten metal coolants might be used. The high cost of niobium and tantalum precludes their use as die materials and, in any case, (unlike molybdenum, which is the preferred die material) they have limited resistance to molten zinc above 450 °C.<sup>60</sup>

Molten metals have many advantages as nuclear reactor coolants. Thus, they have very high heat transfer capability with no change in phase and can operate at atmospheric pressure (unlike water–steam systems, for example). Applications that have been considered (and even implemented in some cases) include: fission reactor coolants, fusion reactor coolants/deuterium breeder blankets and spallation neutron targets (where a high-intensity particle beam from an accelerator impacts upon a heavy metal target, generating a high-intensity neutron source. The liquid metal systems that have been considered include: mercury, gallium, lead, lead–bismuth eutectic, sodium, sodium–potassium eutectic, and lithium.

The degradation of a metallic container material in a liquid metal environment depends upon a number of factors and can manifest in two main ways: dissolution of the container material (or its protective oxide) into the molten environment, embrittlement (liquid metal embrittlement) of the container material with the environment. The mechanisms for liquid metal embrittlement remain complex and unclear, and often depend upon the container–environment combination; however, reaction of the container material with impurities (e.g., dissolved oxygen) in the molten metal and formation of destructive or protective intermetallic compounds between the container material and the environment appear to be among the important factors.<sup>61</sup>

Considerable research was carried out in the 1950s by the then US Atomic Energy Commission<sup>62</sup> on the corrosion resistance of materials in liquid metals, particularly in regard to fast fission reactor coolants and this work is summarized as follows. Liquid bismuth was found to have little action on



tantalum at temperatures below 1000 °C but caused some intergranular attack above this temperature; with no detrimental effects on stress rupture properties up to 815 °C. Niobium was also resistant to bismuth at lower temperatures (up to 560 °C) and it suffered some degree of embrittlement at 815 °C. In molten gallium, tantalum was resistant up to 450 °C, but poor above 600 °C. Niobium was slightly less resistant than tantalum, showing good resistance at 400 °C but poor resistance above 450 °C. Both tantalum and niobium were resistant to liquid lead at least up to 815 °C, possessed good resistance to molten lithium up to 1000 °C and in mercury vapor up to 600 °C. Liquid sodium, potassium or their alloys had little effect on either tantalum or niobium up to 1000 °C if oxygen free. However, in the presence of significant dissolved oxygen, the liquid metals could become corrosive at lower temperatures.

More recent work has shed light on the critical importance of the dissolved impurity levels (particularly oxygen) in the molten metal and also the proposed containment materials. Tantalum exhibited essentially no reaction in liquid lead under oxidizing conditions at 600 °C for 100 h.<sup>63</sup> In liquid sodium or potassium, reaction with the passive oxide layers on niobium and tantalum form ternary oxides whose solubility contribute to the overall corrosion rates. Nitride, carbide and hydride formation is also seen with the corresponding dissolved species.<sup>64</sup> In liquid lithium, however, the oxides on tantalum and niobium are unstable and are reduced to the metal. Additionally, liquid metal embrittlement by lithium, in the form of metal penetration along grain boundaries, occurs when the oxygen levels exceed 400 or 100 ppm in niobium or tantalum respectively.<sup>65</sup>

### 3.15.3.6 Organic Compounds

In general, tantalum is completely resistant to organic compounds and may be used in almost all conditions. However, in environments of low water activity niobium and tantalum show evidence of pitting corrosion (in methanol)<sup>66</sup> and even dissolution (bromine in acetone).<sup>67</sup>

## 3.15.4 Industrial Applications

### 3.15.4.1 Chemical Process Equipment

Tantalum and niobium and their alloys find significant use in process equipment in very corrosive duties that arise in metal pickling, chemicals/petrochemicals manufacture, oil refining and other

operations or in processes that can tolerate only limited metal ion contamination such as pharmaceuticals manufacture. Typical applications include reaction and separation equipment, heaters and heat exchangers, piping and valves, thermowells and rupture discs. The relatively high costs and excellent corrosion resistances of the alloys dictate/permit the use of relatively thin, typically 0.5–1.00 mm sections for heat exchange or as clad/loose linings on cheaper substrates, usually steels, for pressure containment. A common application is in heat exchangers (evaporators and coolers) for the concentration, handling and reconcentration of sulfuric, nitric, hydrohalide and mixed acids. However, the alloys cannot be used in HF or HF-containing fluids, which include commercial, pure phosphoric acid.

### 3.15.4.2 Anodes

Both tantalum and niobium have exceptionally high positive breakdown potentials for pitting corrosion and significant oxygen evolution in chloride environments (>150 V for tantalum and >100 V for niobium in seawater). Thus, they are both ideal substrates either on their own, or as substrates for platinum group metals as nonconsumable anodes and are used in all fluoride-free environments, although niobium is preferred because of its lower cost.

Applications for impressed current anodes include all those where nonconsumable impressed current anode might be specified, for example, in sea and brackish water, brines, concrete and soils. However, platinized niobium anodes are particularly suitable (compared with platinized titanium) for use in high-resistance environments where large positive driving voltages are required to deliver reasonable currents. They are often used, therefore, in deep well ground beds in order to protect long lengths of buried pipe. Although driving potentials up to about 100 V may be used, crevice corrosion can occur at lower driving voltages in the range 20–40 V especially in the presence of impurities such as copper and iron, and under deposits or in mud.<sup>68</sup>

In similar manner, both tantalum and niobium have been explored for use as nonconsumable long-life anodes for electrowinning, electroplating, and oxygen evolution applications.<sup>69,70</sup>

### 3.15.4.3 Medical and *In Vivo* Applications

Tantalum and niobium are very stable passive metals and are completely inert to body fluids and tissues.

In particular, bone and tissue do not recede from tantalum, which makes it attractive as an implant material for the human body. Tantalum's comparatively low strength precludes its use as a structural (i.e., joint) implant although it is, for example, used for bone-support plates. However, its electrical properties are such that tantalum (or anodized tantalum) is used extensively for capacitively coupled electrodes for muscle or nerve stimulation.<sup>71</sup> Its high density provides radioopacity and it has uses as a marker on other larger implant components, where tantalum is usually deposited as a surface layer.

## References

1. Tantalum and Niobium International Study Center. Historical information, occurrence and production Available at [www.tanb.org](http://www.tanb.org).
2. Smallwood, R. E. Ed. *Refractory Metals and their Industrial Applications*; ASTM Special Technical Publication, 1982; Vol. 849.
3. *HSC: Chemistry – V6.12 (Thermochemical Database)*; Outotec Research Oy: Finland, 2007.
4. Allegheny Technologies. Niobium technical data sheet from ATI Wah Chung. Available at [www.wahchang.com](http://www.wahchang.com).
5. Cabot Corporation. Tantalum and niobium technical data sheets. Available at [www.cabot.com](http://www.cabot.com).
6. Tantalum and Niobium International Study Center. Applications of niobium and tantalum. Available at [www.tanb.org](http://www.tanb.org).
7. Maeland, A. J.; Libowitz, G. G.; Lynch, J. F.; Rak, G. *J. Less-common Metals* **1984**, *104*, 133–139.
8. Westlake, D. G.; Miller, J. F. *J. Less-common Metals* **1979**, *65*, 139–154.
9. Oates, W. A.; Kuji, T.; Flangan, T. B. *J. Less-common Metals* **1985**, *105*, 333–338.
10. Matsui, H.; Yoshikawa, N.; Koiwa, M. *Acta Metall.* **1987**, *35*, 413–426.
11. Gahr, S.; Grossbeck, M. L.; Birnbaum, H. K. *Acta Metall.* **1977**, *25*, 125–134, 135–147.
12. Viikil, J.; Alefeld, G. In *Diffusion in Solids: Recent Developments*; Nowick, A. S., Burton, J. J., Eds.; Academic Press: New York, 1974.
13. Rothenberger, K. S.; Howard, B. H.; Killmeyer, R. P.; Cugini, A. V.; Enick, R. M.; Bustamante, F.; Ciocco, M. V.; Buxbaum, R. E. *J. Membr. Sci.* **2003**, *218*, 19–37.
14. Clauss, A.; Forestier, H. *Les Compt. Rendus l'Académie Sci. Paris* **1958**, *246*, 3241–3243.
15. Olszta, M. J.; Dickey, E. C. *Microsc. Microanal.* **2008**, *14*, 451–458.
16. Kukli, K.; Ritala, M.; Leskelä, M. *J. Electrochem. Soc.* **2001**, *148*, F35–F41.
17. Kover, F.; Musselin, M. *J. Thin Solid Films* **1968**, *2*, 211–238.
18. Skeldon, P.; Shimizu, K.; Thompson, G. E.; Wood, G. C. *Surf. Interf. Anal.* **1983**, *5*, 252–263.
19. Brown, F.; Mackintosh, W. D. *J. Electrochem. Soc.* **1973**, *120*, 1096–1120.
20. Randall, J. J., Jr.; Bernard, W. J.; Wilkinson, R. R. *Electrochim. Acta* **1965**, *10*, 183–201.
21. Chung, S.; Thompson, G. E.; Wood, G. C.; Drake, M. P. *Chemtronics* **1987**, *2*, 98–100.
22. Pringle, J. P. S. *J. Electrochem. Soc.* **1974**, *120*, 1391–1400.
23. Magnussen, N.; Quinones, L.; Dufner, D. C.; Cocke, D. L.; Schweikert, E. A.; Patnaik, B. K.; Barros Leite, C. V.; Baptista, G. B. *Chem. Mater.* **1989**, *1*, 220–225.
24. Li, Y.-M.; Young, L. *J. Electrochem. Soc.* **2000**, *147*, 1344–1348.
25. Ono, S.; Kuramochi, K.; Asoh, H. *Corros. Sci.* **2009**, doi: 10.1016/j.corsci.2008.11.027.
26. Robin, A. *Int. J. Refract. Metals Hard Mater.* **1997**, *15*, 317–323.
27. Robin, A.; Rosa, J. L. *Int. J. Refract. Metals Hard Mater.* **2000**, *18*, 13–21.
28. Asselin, E.; Ahmed, T. M.; Alfantazi, A. *Corros. Sci.* **2003**, *49*, 694–710.
29. Lavanya, A.; Anjaneyulu, Ch. *Bull. Electrochem.* **2002**, *18*, 317–320.
30. Uehara, I.; Sakai, T.; Ishikawa, H.; Takenaka, H. *Corrosion* **1989**, *45*, 548–553.
31. Robin, A. *J. Appl. Electrochem.* **2004**, *34*, 623–629.
32. Robin, A. *J. Appl. Electrochem.* **2003**, *33*, 37–42.
33. Robin, A. *Corros. Eng. Sci. Technol.* **2003**, *40*, 51–56.
34. Lauf, R.; Altstetter, C. *Scr. Metall.* **1977**, *11*, 983–985.
35. Stringer, J. *J. Less-common Met.* **1968**, *16*, 55–64.
36. Cowgill, M. G.; Stringer, J. *J. Less-common Met.* **1960**, *2*, 233–240.
37. Stringer, J. *J. Less-common Met.* **1966**, *11*, 111–118.
38. McLintock, C. H.; Stringer, J. *J. Less-common Met.* **1963**, *5*, 278–294.
39. Taylor, A.; Stringer, J. *J. Less-common Met.* **1975**, *39*, 143–159.
40. Miller, G. L.; Cox, F. G. *J. Less-common Met.* **1960**, *2*, 207–222.
41. Briant, C. L. *J. Eng. Mater. Technol.* **2000**, *122*, 338–341.
42. Subramanian, P. R.; Mindiratta, M. G.; Demiduk, D. M. *J. Met.* **1996**, *48*, 33–38.
43. Dzyadykevich, Yu. V. *Powder Metall. Met. Ceram.* **1986**, *25*, 38–43.
44. Majumdar, S.; Sengupta, P.; Kale, G. B.; Sharma, I. G. *Surf. Coat. Technol.* **2006**, *200*, 3713–3718.
45. Vilasi, M.; Francois, M.; Podor, R.; Steinmetz, J. *J. Alloys Compd.* **1998**, *264*, 244–251.
46. Dunlap, R. A.; Small, D. A.; Mackay, G. R. *J. Mater. Sci. Lett.* **1999**, *18*, 881–883.
47. Esayed, A. Y.; Northwood, D. O. *Int. J. Hydrogen Energy* **1992**, *17*, 41–52.
48. Candioto, K. C. G.; Nunes, C. A. *Int. J. Refract. Metals Hard Mater.* **2006**, *24*, 413–417.
49. Strafford, K. N. *Corros. Sci.* **1979**, *19*, 49–62.
50. Prokoshkin, D. A.; Voronova, T. A.; Gorbova, A. S.; Kashirtsev, V. N. *Met. Sci. Heat Treat.* **1984**, *26*, 357–360.
51. Bishop, C. R. *Corrosion* **1963**, *19*, 308t–314t.
52. Robin, A. *Int. J. Refract. Metals Hard Mater.* **1997**, *15*, 317–323.
53. Robin, A.; Rosa, J. L. *Int. J. Refract. Metals Hard Mater.* **2000**, *18*, 13–21.
54. Tingley, I. I.; Rogers, R. R. *Corrosion* **1965**, *21*, 132.
55. Haissinsky, M. *Metaux Corros.* **1948**, *23*, 15–18.
56. Wehrmann, R. *Corrosionomics*; Fansteel Metallurgical Corp., Sept. 1956.
57. Ensinger, W.; Wolf, G. K. *Surf. Coat. Technol.* **1992**, *51*, 41–44.
58. Gypen, L. A.; Brabers, M.; Deruyttere, A. *Werkstoffe Korrosion* **1984**, *35*, 37–46.
59. Klas, W.; Herpers, U.; Michel, R.; Reich, M.; Droste, R.; Holm, R.; Horn, E.-M.; Mueller, G. *Werkstoffe Korrosion* **1991**, *42*, 570–575.
60. Hodge, W.; Evans, R. M.; Haskins, F. *J. Met.* **1955**, *7*, 824–832.

61. Joseph, B.; Picat, M.; Barbiera, F. *Eur. J. Appl. Phys.* **1999**, 5, 19–31.
62. Miller, E. C. *Liquid Metals Handbook*; Atomic Energy Commission, Navy Department: Washington, DC, 1952; Chapter 4, pp 144–183.
63. Loewen, E. P.; Ballinger, R. G.; Lim, J. *Nucl. Technol.* **2004**, 147, 436–456.
64. Barker, M. G. *Revue Int. Hautes Temperatures Refractaires* **1979**, 16, 237–243.
65. Klueh, R. L. *Metall. Trans.* **1974**, 5, 875–879.
66. Ramgopal, T. *Corrosion* **2005**, 61, 757–765.
67. Kamada, K.; Mukai, M.; Matsumoto, Y. *Electrochim. Acta* **2004**, 49, 321–327.
68. Hayfield, P. C. S. *Mater. Perform.* **1981**, 20, 9–15.
69. Skomoroski, R. M.; Baboian, R.; Zobbi, R. G.; Camp, E. K. *Plating* **1973**, 60, 1115–1119.
70. Cardarelli, F.; Taxil, P.; Savall, A.; Comninellis, Ch.; Manoli, G.; Leclerc, O. *J. Appl. Electrochem.* **1998**, 28, 245–250.
71. Donaldson, P. E. K. *Med. Biol. Eng.* **1974**, 12, 131–135.

## Further Reading

*Corrosion Handbook*; ASM International, 2008; Vol. 13B.

## 3.16 Corrosion of Tungsten and its Alloys

**S. B. Lyon**

Corrosion and Protection Centre, School of Materials, The University of Manchester, Oxford Road, Manchester M13 9PL, UK

© 2010 Elsevier B.V. All rights reserved.

<b>3.16.1</b>	<b>Occurrence and Production</b>	2151
3.16.1.1	General Properties	2151
3.16.1.2	Fabrication	2152
3.16.1.3	Applications	2152
3.16.1.4	Alloys	2153
<b>3.16.2</b>	<b>Corrosion</b>	2153
3.16.2.1	Electrochemistry	2153
3.16.2.1.1	Thermodynamics	2153
3.16.2.1.2	Anodic dissolution of tungsten	2154
3.16.2.2	Corrosion Processes	2154
3.16.2.2.1	Oxide removal/cleaning	2154
3.16.2.2.2	Aqueous corrosion of tungsten and its alloys	2155
3.16.2.2.3	Electrochemical planarization of electronic interconnects	2155
3.16.2.2.4	Dissolvable implants	2155
3.16.2.2.5	High temperature oxidation and corrosion	2155
3.16.2.2.6	Corrosion in liquid metals	2156
<b>References</b>		2156

### Glossary

**Oxide dispersion strengthened** A method of strengthening or hardening alloys by dispersing a fine (micron-size) oxide throughout the structure usually by processing the material via powder route. This acts both to pin dislocations (and hence harden the material) and also to pin grain boundaries (and hence limit grain growth and reduce creep at high temperatures).

### 3.16.1 Occurrence and Production

Tungsten is a relatively rare element in nature with soil abundance similar to molybdenum. It is mined predominantly as wolframite (iron manganese tungstate) or scheelite (calcium tungstate) both containing above 70% of tungsten. Due to the high melting point of tungsten, routes to the production of tungsten powder are essential. Thus in processing, and after gravity concentration, most ores are converted to a form in which they can be reduced to the metal. This is generally carried out by initial leaching of the

ore to produce tungstic acid followed by conversion to ammonium paratungstate, calcining to tungsten oxide ( $\text{WO}_3$ ) and then reduction in hydrogen at 800–1000°C to produce commercially pure tungsten powder.<sup>1</sup>

#### 3.16.1.1 General Properties

Tungsten is a transition element in the third row of the periodic table, the elements immediately above tungsten (in Group 6B) being molybdenum and chromium with which tungsten shares many similarities in chemistry (oxidation states from 2 to 6) and metallurgy (body-centered cubic lattice). Tungsten has the highest melting point (3410°C) – more than any metal – while its vaporization point (5550°C) is second only to that of rhenium. Excluding actinides, its density ( $19.3 \text{ Mg m}^{-3}$ ) is the fifth greatest of the elements, being equivalent to gold and only slightly less than the adjacent elements rhenium, osmium, iridium, and platinum.<sup>2</sup>

Commercially pure tungsten has relatively high ultimate tensile strength (1000 MPa at 25°C dropping to 250 MPa at 1500°C) and elastic modulus (410 GPa at 25°C, dropping to 360 GPa at 1500°C).

Thus, a significant fraction of the room temperature mechanical properties are retained at high temperatures.<sup>3</sup> Tungsten also has relatively high thermal and electrical conductivity (about one-third of copper).<sup>2</sup> Tungsten oxidizes relatively easily at elevated temperatures, reacting with both oxygen and nitrogen to form oxides and nitrides; these are generally nonprotective above 300°C. Thus, the processing of and the applications for tungsten must take care to avoid reaction, for example, by use of inert gas or reducing gas blanketing, or necessarily must remove oxides that form after processing.<sup>1</sup> Electrochemically, tungsten is rather similar to molybdenum, dissolving as tungstate ions at pH greater than about 5. However, it does have an extended stability regime for  $\text{WO}_3$  (compared with  $\text{MoO}_3$ ) and therefore tungsten has reasonable stability (is passive) in acidic solutions. Indeed, tungsten, as one of the so-called ‘valve metals,’ may be anodized (e.g., in sulfuric acid) to form a stable, relatively protective film of tungsten oxide.<sup>4</sup>

### 3.16.1.2 Fabrication

There are no refractory materials that can contain molten tungsten; consequently powder metallurgical routes are invariably used in the initial processing of tungsten. Thus, tungsten (and any alloying components) in powder form are generally hydrostatically pressed into billets to a green density of 55–60%. Such billets are then sintered by direct resistance electric arc or electron beam heating to 2500–3000°C in order to increase the density to above 90% and preferably above 93%, in order to permit further mechanical processing.

During processing, care must be taken to avoid pick-up of oxygen, nitrogen, and carbon from the environment. These elements will form, respectively, oxides, nitrides, and carbides generally residing at grain boundaries, which will cause embrittlement of the material and importantly, reduce ductility and limit mechanical working. Typical impurities after powder processing are: carbon – 0.04%, oxygen – 0.023%, and nitrogen – 0.002%. Vacuum arc remelting can significantly lower these values to 0.03%, 0.004%, and 0.001%, respectively.<sup>3</sup>

Tungsten, as a body-centered cubic metal, undergoes a ductile–brittle transition that is a function of temperature, sample dimensions and also impurity levels and alloying content. Generally, this occurs well above room temperature and for commercially pure tungsten (99.95%) the transition temperature is 300–500°C. However, this transition temperature can be

reduced by prior mechanical deformation such that at small section sizes it is possible to successfully undertake wire drawing, extrusion, etc. at room or slightly elevated temperatures. Typically, sintered tungsten billets are initially forged or swaged above the recrystallization temperature at 1600–1700°C in a reducing atmosphere in order to densify them and, by this way, the ductile-to-brittle transition temperature can be reduced to below 100°C. The lowered processing temperature permits easier operation of sheet rolling and wire drawing, although, due to the high intrinsic yield stress of tungsten, working forces are necessarily significantly larger than for other materials. The ductility of tungsten is significant above its ductile-to-brittle transition temperature with a reduction of area of about 20% at 100°C and over 60% at 1000°C.<sup>1</sup>

### 3.16.1.3 Applications

The greatest use (50–55%) of tungsten is as tungsten carbide ( $\text{WC}$  and  $\text{W}_2\text{C}$ ) in the form of metal matrix composite materials such as ‘cemented’ carbide machine tools, hard coatings, etc. Corrosion of cemented carbides, of course, does not involve corrosion of the  $\text{WC}$  particles themselves, but of the cobalt or cobalt–chromium metallic binder. Other uses are in alloying of carbon steel (15–20%) for various purposes, in particular for ‘high-speed’ tool steels, also containing  $\text{WC}$ . Tungsten is also used as an alloying addition to stainless steels (e.g., for enhanced resistance to chloride) and in high temperature nickel-based superalloys. A further quantity is used in the fine chemicals and electronics industry. Only about 15% of tungsten is used in the metallic form.<sup>5</sup>

The main uses of tungsten metal invoke its unique properties of high melting point, high density and intrinsically high strength, and elastic modulus at high temperature. The classical high melting point application is, of course, as incandescent filaments in lighting with other common uses including electric arc electrodes (in welding, arc lamps, etc.), electrical contact materials for relays, etc., and in electron-emitting (thermionic) materials for vacuum valves, etc. An unusual application where the high strength and high melting point of tungsten are both useful is in rocketry components. Regarding high density materials, the main civil applications include yacht keels, moveable ballast in racing cars and aircraft (where the competitive material in both cases is depleted uranium), in sports materials for weight trimming (e.g., professional darts, golf clubs, etc.),



and for radiation shielding where it can be used in significantly thinner sections than the traditional lead materials and is effectively nontoxic in handling.

A new application that is being developed is for military materiel (i.e., high kinetic energy projectiles) where the current use of depleted uranium on the battlefield has, self-evidently, been found to cause serious, and lingering, toxicological and radiation hazards. Although the use of tungsten in this application is not without its own toxicological problems, the immediate and long-term health risks are of a significantly lower order of magnitude compared to uranium. Tungsten also has a generally very low solid solubility with most metallic elements and it has been proposed that this property may be exploited in future (Generation IV) liquid metal fast neutron reactors for power generation.

### 3.16.1.4 Alloys

Tungsten is commonly alloyed to reduce the inevitable decrease in mechanical properties as the temperature is raised, to limit grain growth at high temperatures, and to control thermionic electron emissivity. Alloying is invariably undertaken by powder metallurgical routes and, by this method, it is also easy to incorporate ceramic powders, for example, as oxide dispersion strengthened (ODS) materials.<sup>1</sup>

Tungsten has significant solid solution miscibility only with a few other elements, the most important of which are molybdenum (where a series of alloys up to 50% Mo are in use) and rhenium, which is totally miscible with tungsten and where alloys of up to 25% are useful (Table 1). Interestingly, solid solution alloying with molybdenum reduces the mechanical properties while alloying with rhenium increases the yield stress by up to 15% and significantly increases the alloy recrystallization temperature; it also lowers the ductile-to-brittle transition temperature such that the alloy with 25% Re is fully ductile at room temperature. Unfortunately, the very high cost and limited availability of rhenium limits the significant use of these latter materials.

The high temperature mechanical properties of tungsten and solid solution tungsten alloys may be improved by oxide dispersion hardening. Typically, thorium (especially for electrical applications due to increased electron emissivity) is preferred as it has the best high temperature stability. For incandescent lamp filaments, potassium oxide is frequently used as a dispersant. On processing, this decomposes to produce numerous tiny bubbles in the structure that pin

**Table 1** Chemical composition of selected tungsten alloys<sup>7</sup>

<i>Alloy</i>	<i>Composition (wt)</i>
<i>Commercial purity alloys</i>	
W – powder processed	0.04% C, 0.023% O, 0.002% N
W – vacuum arc remelted	0.03% C, 0.004% O, 0.001% N
<i>Oxide dispersed alloys</i>	
Thorium dispersed tungsten	As above+1–2% ThO <sub>2</sub>
<i>Solid solution alloys</i>	
W–Mo	10–50% Mo
W–Re	3–5% and 25% Re
<i>Binder phase alloys</i>	
W–Ni–Cu and W–Ni–Fe	Usually in grades of 90%, 93%, 95%, and 97% W, balance of Ni+Cu or Ni+Fe

grain boundaries thus restricting grain growth.<sup>6</sup> The final class of alloys essentially comprises tungsten grains embedded within a binder phase (e.g., W with Ni/Cu/Fe/Mo as binder).

## 3.16.2 Corrosion

### 3.16.2.1 Electrochemistry

#### 3.16.2.1.1 Thermodynamics

Tungsten is a base metal with its domain of thermodynamic stability lying completely below that of water (Figure 1). However, it is significantly more noble than molybdenum and particularly chromium, elements that are above tungsten in the same group (VI) of the periodic table. Tungsten tends to dissolve in near neutral to alkaline solutions to tungstate species in association with an alkali metal cation; other cations tend to produce insoluble tungstates. Tungsten has domains of passivity associated with WO<sub>2</sub> and WO<sub>3</sub> with the latter material having low solubility and being stable to further oxidation. This characteristic allows tungsten to be anodized successfully, for example in sulfuric acid, and hence the metal belongs to the family of ‘valve metals.’ Tungsten forms many relatively insoluble complexes, including chloride ions. Its alloying effects are similar to that of molybdenum in that it is added to stainless steels and other alloys to increase the resistance to chloride-induced localized corrosion.<sup>5</sup>

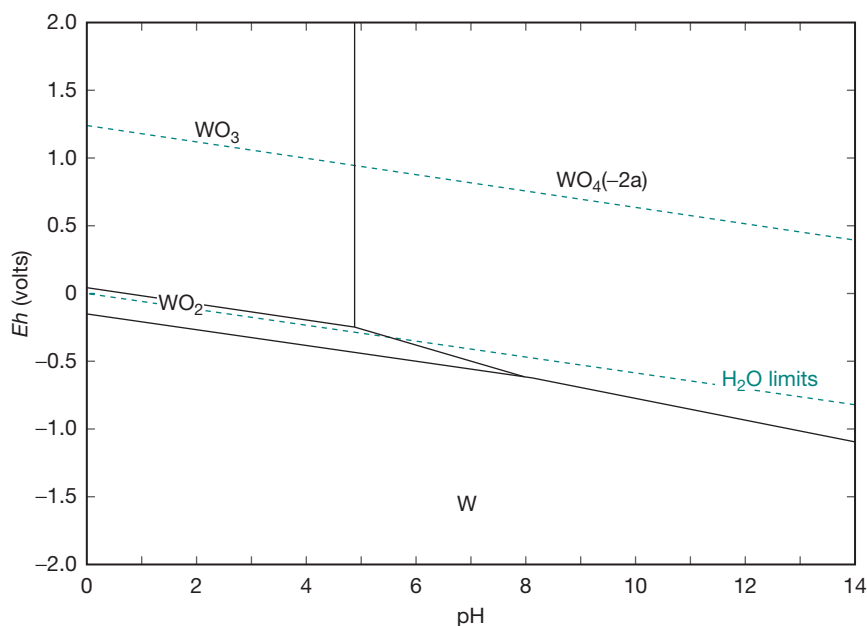


**Figure 1** Pourbaix diagram for tungsten at a metal ion concentration of  $10^{-5}$  M. Reproduced from *HSC: Chemistry*, version 6.12, Outotec Research Oy: Finland, 2007.

### 3.16.2.1.2 Anodic dissolution of tungsten

As implied by the Pourbaix diagram, there are no simple aquo-cations of tungsten; rather tungsten dissolves generally as a tungstate ( $\text{WO}_4^{2-}$ ) above about pH 5, or as tungstic acid ( $\text{H}_2\text{WO}_4$ ) at very low pH. In alkaline solutions above about pH 12, the dissolution kinetics have been found to be Tafel in nature with smooth dissolution to dissolved tungstate anion. The rate limiting step apparently involves a one-electron transfer process (Tafel slope  $\approx 120\text{mV}$  per decade) and has first order kinetics with respect to hydroxide ion concentration.<sup>8</sup> This no doubt masks a complex, step-wise, dissolution mechanism. Controlled dissolution of tungsten is an important process in the semiconductor industry where efficient planarization of tungsten chip layer interconnects is required.<sup>9</sup>

In contrast, below pH 5, tungsten forms a passive anodic oxide film of  $\text{WO}_2$  (at intermediate voltages) or  $\text{WO}_3$  (more commonly). Under galvanostatic anodization, voltages can reach up to 120–150 V at currents between 2 and  $16\text{A m}^{-2}$ . However, the resultant anodic film requires a relatively high (compared with other valve metals) current density to maintain it and this is thought to be due to the significantly higher solubility of the amorphous film compared to crystalline  $\text{WO}_3$ .<sup>10</sup> The dissolution of anodically-formed tungsten oxide in 0.1 M sulfuric acid occurs

under first-order reaction kinetics via hydration to tungstic acid and is significantly more soluble if higher formation currents are used initially.<sup>11</sup>

### 3.16.2.2 Corrosion Processes

#### 3.16.2.2.1 Oxide removal/cleaning

As noted above, it is necessary to carry out many fabrication operations, especially of heavy sectioned material, at temperatures in excess of  $1000^\circ\text{C}$ . Under these conditions, and unless a protective atmosphere is used, the surface of the tungsten will become covered in an oxide scale. The thickness and tenacity of the oxide depends on the temperature used for the fabrication operation. Thick oxide scales may be removed in a molten mixture of 90% sodium hydroxide and 10% sodium nitrite at  $400^\circ\text{C}$  for a few seconds. This attacks tungsten oxide rapidly and care should be taken during this process, in particular the material must be dry, otherwise splashing could occur. On removal the component should be allowed to cool in air before washing the retained salt in hot water. Alternatively, thick oxide layers may be removed by a mechanical abrasion, for example abrasive blasting. Thinner tungsten oxide scales may be removed by immersion in mixed acid etch solutions, for example: nitric acid+HF+water at 1:1:1 ratio.

Lightly oxidized tungsten can be cleaned by heating in 10% caustic soda solution at about 80°C followed by rinsing in water and then dilute hydrochloric acid solution (10%) to neutralize the remaining caustic before finally rinsing in water and drying.<sup>1</sup>

### 3.16.2.2.2 Aqueous corrosion of tungsten and its alloys

Generally, the aqueous corrosion of commercially pure (and oxide dispersed) tungsten depends upon the pH, with passivity expected below pH 5 and active dissolution above pH 5. In practice, the air-formed film on tungsten oxide provides significant protection against dissolution to mildly alkaline conditions (pH  $\approx$  8) while the dissolution kinetics at pH 12 imply a corrosion rate of about 20–30  $\mu\text{m year}^{-1}$ , that is, about one-tenth of iron. Thus, commercially pure tungsten is passive or corrodes relatively slowly in most aqueous conditions except in strong alkali at pH > 12.<sup>12</sup>

Tungsten is generally more active than most common alloying additions except iron, against which it is slightly noble under alkaline conditions. Thus, tungsten might be expected to act sacrificially under immersed aqueous conditions and this has been confirmed in the corrosion of alloys containing copper in the binder phase which suffer from preferential corrosion of the tungsten grains. However, metal bonded tungsten alloys using a Ni–Fe binder phase are generally found to be somewhat more active than tungsten. This may be due to the solubility of tungsten into this phase (in contrast tungsten has negligible miscibility in copper-containing binder phases) and also due to the protective nature of the air-formed passive film on tungsten.<sup>12</sup>

Amorphous alloys of tungsten with niobium, tantalum, zirconium, and chromium, at concentrations from 15 to 50%, have been prepared by DC magnetron sputtering and the corrosion of these materials has been studied in hydrochloric acid at 1–12M. Under these conditions, the deposited films are non-equilibrium, amorphous, and spontaneously passive. Also, generally such alloys have exceptionally low passive current densities.<sup>13</sup>

### 3.16.2.2.3 Electrochemical planarization of electronic interconnects

Electronic integrated circuits frequently comprise deposition of electronic components on multiple layers. Thus, current microprocessors have 7–9 layers and it seems likely that this figure will increase. Copper is used as the electrical connection strips within

each layer while tungsten plugs are used as the inter-layer connections. A critical process after tungsten deposition is ‘planarization,’ which is designed to reflaten the wafer prior to formation of the next semiconductor layer. The process, more properly known as chemomechanical polishing, is essentially a controlled erosion–corrosion process. There are many proprietary solution mixtures that are used but their common feature is that they contain a mild oxidizing agent designed to dissolve the tungsten while leaving the silicon wafer untouched.<sup>9</sup>

### 3.16.2.2.4 Dissolvable implants

There is a significant application for dissolvable body implants in certain applications. For example, stents are often used to secure blood vessels, etc. in the body from, for example, embolisms. While most of such stents are permanent, some are temporary and there is an advantage if they gradually dissolve (i.e., corrode) in the body. Clearly, such materials need to be nontoxic and magnesium alloys are a clear material of choice in such an application. Unfortunately, the corrosion rate of magnesium alloys is generally rather high, they corrode with release of hydrogen gas and they are difficult to locate in X-rays. In view of this, research is currently underway on the use of tungsten stents which are thought to be relatively or completely nontoxic.<sup>14</sup>

### 3.16.2.2.5 High temperature oxidation and corrosion

Tungsten begins to oxidize significantly above about 300°C in dry air forming a  $\text{WO}_3$  scale that grows under parabolic kinetics. Marker studies demonstrate that the growth kinetics are by inwards diffusion of oxygen anions through the anion vacancies in a scale with distinct oxygen sub-stoichiometry (i.e.,  $\text{WO}_{3-x}$ ). The Pilling–Bedworth ratio for  $\text{WO}_3$  is 3.3, which implies that a protective scale is expected but that the growth stresses are relatively large. In view of this, oxide spallation might be expected and, indeed, this occurs rather readily under thermal cycling.<sup>15,16</sup> In contrast to its behavior in dry air, the oxidation of tungsten in steam is characterized by the formation, above about 800°C, of relatively volatile tungstic acid ( $\text{H}_2\text{WO}_4$ ) – or more accurately hydrated tungsten oxide ( $\text{WO}_3 \cdot \text{H}_2\text{O}$ ). Under these conditions, oxidation occurs by linear kinetics and the metal ‘evaporates’ at a rate controlled by the mass transport of water vapor. This process is rapid with rates of up to 1–2  $\text{mg cm}^{-2} \text{h}^{-1}$  at 800°C.<sup>17</sup>

Compared with air, tungsten corrodes more rapidly in carburizing and sulfidizing environments at

high temperature, however, its performance in a chloridizing environment is considerably better than most other high temperature materials and significantly improved molybdenum.<sup>18</sup> In view of this tungsten is added to several alloys to improve the resistance to environments containing chlorine. The chlorination kinetics are similar to those of molybdenum, but considerably slower. Mass changes are linear with time implying that a protective scale does not form. Also, the reaction rate order with respect to the partial pressure of chlorine is about one-half, which implies that the reaction is under chemical rate control with respect to dissociation of chlorine molecules.<sup>19</sup>

### 3.16.2.2.6 Corrosion in liquid metals

Several next generation (Generation IV) nuclear reactor concepts include fast neutron reactor technologies based on liquid metal coolants. These include, for example, the sodium-cooled fast reactor and the lead–bismuth cooled fast reactor. Further, fusion reactor concepts include deuterium fuel breeding using molten lithium or lead–lithium alloys. Finally, specialist applications in nuclear science (e.g., spallation neutron targets, liquid metal ion sources) require the use of molten metals and, hence, containment of such materials is critical.

In view of the limited or zero miscibility of tungsten with many other materials its corrosion performance has been studied in most of these applications. Thus, the corrosion of tungsten in lead and lead–bismuth eutectic was excellent at 600°C with no apparent wetting of the metal and no degradation detected after 100h exposure.<sup>20</sup> Likewise, no degradation of tungsten was evident in liquid lead–lithium eutectic at 800°C. Finally, in liquid sodium minimal signs of corrosion were evident on polished tungsten at 600°C after 1500h of exposure.<sup>21</sup> These results indicate that tungsten clearly has excellent resistance at a wide range of liquid metals and, although it cannot be used as a structural material due to cost and resource limitations, it will find application in critical niche areas.

## References

1. Yih, S. W. H.; Wang, C. T. *Tungsten Sources, Metallurgy, Properties, and Applications*; Plenum Press: New York, 1979.
2. Lide, D. R. Ed. *CRC Handbook of Chemistry and Physics*, 86th ed.; Taylor & Francis: USA, 2005.
3. Gregor, M.; Čížek, L.; Widomska, M. *J. Mater. Process. Technol.* **2004**, *157–158*, 683–687.
4. Pourbaix, M. *NACE* **1974**, 281–285.
5. International Tungsten Industry Association, Rue Père Eudore Devroye 245, 1150 Brussels, Belgium. <http://www.itia.org.uk/>.
6. Matweb: Online materials information resource. <http://www.matweb.com/>.
7. Schade, P. *Int. J. Refract. Met. Hard Mater.* **2002**, *20*, 301–309.
8. Kelsey, G. S. *J. Electrochem. Soc.* **1977**, *124*, 814–819.
9. Seo, Y.-J.; Kim, N.-H.; Lee, W.-S. *Mater. Lett.* **2006**, *60*, 1192–1197.
10. Ammar, I. A.; Salim, R. *Corros. Sci.* **1971**, *11*, 591–609.
11. El-Basouny, M. S.; Hassan, S. A.; Hefny, M. M. *Corros. Sci.* **1980**, *20*, 909–917.
12. Ogundipe, A.; Greenberg, B.; Braida, W.; Christodoulatos, C.; Dermatas, D. *Corros. Sci.* **2006**, *48*, 3281–3297.
13. Bhattarai, J.; Akiyama, E.; Habazaki, H.; Kawashima, A.; Asami, K.; Hashimoto, K. *Corros. Sci.* **1998**, *40*, 1897–1914.
14. Peuster, M.; Fink, C.; von Schakenburg, C. *Biomaterials* **2003**, *24*, 4057–4061.
15. Royce, R. E.; Roberts, E. F. I. *Corros. Sci.* **1969**, *9*, 357–361.
16. Sikka, V. K.; Rose, C. J. *Corros. Sci.* **1980**, *20*, 1201–1209.
17. Greene, G. A.; Finfrock, C. C. *Exp. Therm. Fluid Sci.* **2001**, *25*, 87–99.
18. Prescott, R.; Stott, F. H.; Elliott, P. *Corros. Sci.* **1981**, *29*, 465–475.
19. Landsberg, A.; Hoatson, C. L.; Block, F. E. *J. Electrochem. Soc.* **1971**, *118*, 1331–1336.
20. Loewen, E. P.; Ballinger, R. G.; Lim, J. *Nucl. Technol.* **2004**, *147*, 436–456.
21. Xu, Y.-L.; Long, B.; Xu, Y.-C.; Li, H.-Q. *J. Nucl. Mater.* **2005**, *343*, 360–365.
22. *HSC: Chemistry*, version 6.12, Outotec Research Oy: Finland, 2007.

## Further Reading

Lassner, E.; Schubert, W.-D. *Tungsten: Properties, Chemistry, Technology of the Element, Alloys, and Chemical Compounds*; Kluwer Academic/Plenum: New York, 1999.

## 3.17 Corrosion of Molybdenum and its Alloys

**S. B. Lyon**

Corrosion and Protection Centre, School of Materials, The University of Manchester, Oxford Road, Manchester M13 9PL, UK

© 2010 Elsevier B.V. All rights reserved.

<b>3.17.1</b>	<b>Occurrence and Production</b>	2157
<b>3.17.2</b>	<b>General</b>	2158
3.17.2.1	Physical Properties	2158
3.17.2.2	Mechanical Properties	2158
3.17.2.3	Applications	2159
3.17.2.4	Fabrication	2159
3.17.2.5	Alloys	2161
<b>3.17.3</b>	<b>Aqueous Corrosion</b>	2161
3.17.3.1	Electrochemistry	2161
3.17.3.1.1	Thermodynamics	2161
3.17.3.1.2	Anodic behavior and passivation	2161
3.17.3.2	Corrosion Processes	2163
3.17.3.2.1	General corrosion	2163
3.17.3.2.2	Galvanic corrosion	2163
3.17.3.2.3	High temperature water	2163
3.17.3.2.4	Corrosion of molybdenum alloys	2163
<b>3.17.4</b>	<b>High Temperature Corrosion</b>	2164
3.17.4.1	Gaseous Environments	2164
3.17.4.1.1	Oxidation	2164
3.17.4.1.2	Sulphidation	2164
3.17.4.1.3	Other environments	2165
3.17.4.2	Fused Materials	2165
3.17.4.2.1	Liquid metals	2165
3.17.4.2.2	Molten glasses	2165
3.17.4.3	Protection	2166
<b>References</b>		2166

### 3.17.1 Occurrence and Production

Molybdenum, which with tungsten is below chromium in Group VI of the periodic table, was not discovered as an element until the latter part of the eighteenth century, around the same time as tungsten. Molybdenum and tungsten are relatively rare elements in nature with similar soil abundances and many chemical similarities. Molybdenum assumed industrial significance during the First World War when a shortage of tungsten caused molybdenum to be used as a substitute in alloy steels.

Molybdenum occurs as the primary ore molybdenite ( $\text{MoS}_2$ ) and also in association with other sulfide mineralizations, particularly copper. The original resources for the primary ore are in the United States, China, and in the Russian Federation, while the

majority of molybdenum is now produced as a by-product of copper mining in Chile, Canada, and elsewhere. The current (2006) production of molybdenum amounts to 195 000 tonnes while the estimated global reserves amount to 19 million tonnes giving about 100 years supply at current consumption rates.<sup>1</sup>

Molybdenite is concentrated, from either primary or by-product sources, by froth floatation and then roasted to produce technical grades of molybdenum oxide ( $\text{MoO}_3$ ), from which ferro-molybdenum (for alloying with steel) is produced using an iron thermite reaction. Further purification of  $\text{MoO}_3$  is carried out in a similar manner to tungsten, that is, by chemical purification via an ammonium molybdate intermediate and then reprecipitation of purified  $\text{MoO}_3$ . Pure molybdenum metal and its alloys are

produced via powder metallurgy routes and the metal powder is obtained by direct reduction of purified  $\text{MoO}_3$  using hydrogen.  $\text{MoS}_2$ , which is used as a lubricious additive, is usually obtained directly by purification of molybdenite.<sup>2</sup>

### 3.17.2 General

#### 3.17.2.1 Physical Properties

Molybdenum shares many of its industrially useful properties with tungsten, but it has the advantage of being more readily available and can be much more easily processed due to its lower melting point. **Table 1** compares its physical properties with other selected materials. It has excellent electrical and thermal conductivity, only slightly less than tungsten, but has the advantage of being about half the density. Molybdenum has also one of the lowest linear expansion coefficients of any metal from room temperature to above  $1000^\circ\text{C}$ , which makes its use in glass-to-metal seals and in electronic components important. In addition, its thermal conductivity and linear expansion coefficient are quite close to silicon and also, given its

relatively good electrical conductivity (31% of copper), molybdenum finds use as a chip packaging and interconnect material.

#### 3.17.2.2 Mechanical Properties

Like tungsten, molybdenum retains significant mechanical properties at high temperatures and, hence, is useful in a number of specialist applications although it needs to be protected from significant oxidation above about  $300\text{--}400^\circ\text{C}$ . Like all body centred cubic metals, molybdenum has a ductile-to-brittle transition which is usually at or slightly above room temperature. However, thin sections are generally sufficiently ductile to be formed at ambient temperatures; thicker sections require an increased temperature to avoid cracking. Commercially pure molybdenum has a relatively high yield and the ultimate tensile strength, the values of which are affected by the presence of impurities such as carbon or oxygen. **Table 2** compares some typical mechanical properties for tungsten and molybdenum where it is evident that molybdenum has a further significant advantage in terms of its relatively high specific modulus (stiffness).

**Table 1** Physical properties of molybdenum compared with other elements<sup>3</sup>

	<i>Mo</i>	<i>W</i>	<i>Re</i>	<i>Cu</i>
Atomic number	42	74	75	29
Atomic weight (g)	95.95	183.84	186.21	63.55
Density ( $\text{g cm}^{-3}$ )	10.2	19.3	21.1	8.96
Melting point (K)	2890	3680	3450	1358
Boiling point (K)	4920	5830	5870	2816
Electrical conductivity ( $\times 10^6 \Omega^{-1} \text{cm}^{-1}$ )	0.187	0.189	0.054	0.596
Thermal conductivity ( $\text{W cm}^{-1} \text{K}^{-1}$ )	1.38	1.74	0.479	4.01
Linear expansion coefficient ( $\times 10^{-6}$ )	4.8	—	4.5	16.5
Crystal structure	bcc	bcc	hcp	fcc

**Table 2** Typical mechanical properties of commercially pure annealed molybdenum compared with other annealed high temperature materials<sup>4–6</sup>

	<i>Molybdenum</i> (at $25^\circ\text{C}/1200^\circ\text{C}$ )	<i>Tungsten</i> (at $25^\circ\text{C}$ )	<i>AISI-321</i> (at $25^\circ\text{C}$ )	<i>Waspalloy</i> (at $25^\circ\text{C}$ )
Density ( $\text{g cm}^{-3}$ )	10.2/10.1	19.3	8.0	8.2
Elastic modulus (GPa)	330/240	420	200	230
Ultimate tensile strength (MPa)	550/140	980	620	1330
Yield stress (MPa)	350/—	750	210	910
Elongation at failure	35%/—	<5%	45%	27%
Specific modulus ( $\text{GPa g}^{-1} \text{cm}^{-3}$ )	31.4/23.7	21.8	25.0	28.0
Specific strength ( $\text{MPa g}^{-1} \text{cm}^{-3}$ )	53.9/13.9	51.8	27.5	162.8



At ambient temperatures the yield strength of molybdenum is similar to normalized low-alloy steel and significantly higher than that of austenitic stainless steel. However, while the low-alloy steels are limited to use at service temperatures of about 550 °C and stainless steels to about 870 °C, unalloyed molybdenum retains useful strength up to 1200 °C (in appropriate protective atmospheres).

### 3.17.2.3 Applications

Molybdenum has a wide variety of industrial applications: as an alloying ingredient in low alloy and stainless steels, in combined forms as an industrial chemical or catalyst, and as a functional metal or alloy. In aqueous environments, molybdenum corrodes at a relatively low rate, generally considerably slower than iron. It is also relatively resistant to acid corrosion and has exceptional resistance to corrosion in hydrochloric acid. Although normally it shows passivity, molybdenum is subject to transpassive oxidation at most pH to a soluble (molybdate) species in aqueous conditions. However, molybdenum is useful in many specialist industry applications especially under mildly oxidizing to reducing conditions. In gaseous atmospheres, molybdenum oxidizes at modestly elevated temperatures in oxidizing environments to form the volatile species  $\text{MoO}_3$ . Thus, the metal is thermodynamically unstable under oxidizing conditions, both aqueous and at high temperature. Without adequate protection, care must therefore be taken to avoid temperatures above about 400 °C in oxidizing gaseous environments.

About one-half of the demand for metallic molybdenum (usually as ferro-molybdenum) is as an alloying addition to carbon steels where it delays the onset of the pearlite transformation and forms strengthening carbide phases in preference to iron.<sup>1</sup> Thus, molybdenum, in concentrations in the range 0.1–1%, is part of the portfolio of alloying additions to steels (e.g., including chromium, molybdenum, vanadium, tungsten, and nickel) that perform this general function. Compared with plain carbon–manganese steels, molybdenum-containing steels have increased strength and creep resistance, at elevated working temperatures.<sup>7</sup> At higher concentrations, that is, above 1% and up to 8%, molybdenum is a critical addition to many grades of steel tool, steel grades that resist softening at high temperatures where it functions by precipitation of alloy carbides ‘high speed steels.’<sup>7</sup> However, the presence of molybdenum (in quantities up to several percent) has relatively minor effects on the corrosion resistance of the ferrous based alloy.

An important secondary use is that about one-quarter of the demand<sup>1</sup> is used as an alloying addition to corrosion resistant alloys such as stainless steels and nickel–chromium alloys. In these applications, molybdenum strongly influences the localized corrosion resistance. Thus, modification of 18Cr–10Ni austenitic stainless steel (i.e., AISI304L) by the addition of at least 2% Mo, results in an alloy (AISI316L) that has substantially improved pitting and crevice corrosion resistance (and lower critical current density for passivation). Further additions of molybdenum (with appropriate metallurgical balancing) give additional improvements.

Molybdenum is also used in much smaller quantities as an alloying addition to titanium (as a beta phase stabilizer) and in high temperature nickel-based superalloys. However, the main applications for unalloyed molybdenum (or molybdenum-based alloys), about 20–25% of the demand, take advantage of its good retention of strength at elevated temperature (up to 1800 °C), its relatively high thermal and electrical conductivity, its low thermal expansion coefficient, its high melting point, its generally good compatibility with molten glasses and ceramics, and its generally low wettability for molten metals. Thus, key applications for molybdenum metal and its alloys include:

- electrical industry (i.e., high current switch contacts, etc.),
- electronic industry (i.e., chip-level interconnects, etc.),
- hot working tools for metal forming,
- dies for molten metal casting especially of zinc (Mo–30W),
- corrosion resistant coatings (for specific chemical processes),
- corrosion resistant equipment for specialist chemical manufacture,
- seals and plugs in glass-lined vessels,
- equipment for glass manufacture: furnaces, crucibles, and stirrers,
- high temperature furnaces and associated components,
- glass-to-metal seals,
- heat shielding in engine parts and in rocketry,
- halide processes for metal purification (e.g., Van Aarke process for Ti and Zr).

### 3.17.2.4 Fabrication

Due to the high melting point of molybdenum, powder processing methods are normally applied whereby

the metal powder is sintered after isostatic pressing typically in the temperature range 1650–1900 °C. Additional arc or electron-beam remelting may then be used to further consolidate ingots; however, care must be taken to avoid excessive grain growth. As implied above, the fabrication of molybdenum and its alloys is largely dictated by its ductile–brittle transition temperature. Although many metal forming operations, for example, on thin sheet and wire less than about 0.5 mm in thickness, can be carried out at room temperature it is cautionary to raise the working temperature of the work piece and die slightly (e.g., 50–200 °C). Thicker sections will require commensurately higher working temperatures; however, above about 550 °C molybdenum starts to oxidize at a considerable rate thus protective atmospheres of hydrogen (e.g., cracked ammonia) are required for significant metal-working of sections above about 650 °C.<sup>2</sup>

All normal fabrication routes can be used to produce molybdenum components, such as metal spinning, flow turning, deep drawing, and pressing. Specific fabrication temperatures are given<sup>8</sup> for various forming processes, including roll forming. Ingots of molybdenum produced either by sintering or by arc-melting are readily forged after heating to about 1500 °C (with appropriate protection against oxidation). Swaging or hot rolling to reduce the ingot size is performed while it is hot, commencing at about 1300 °C and falling as the ductility of the metal

improves to about 700 °C. As the metal thickness decreases, the rolling temperature can also be decreased. Sheet rolling is generally performed at room temperature (or slightly warm) with intermediate anneals at 700–1000 °C. The typical annealing temperature range for full stress-relief of cold worked material lies in the range 870–980 °C. Commercially pure molybdenum may be recrystallised at around 1150–1200 °C; for alloyed molybdenum this temperature generally is increased.

Molybdenum alloys may be machined by any of the standard methods such as milling, turning, drilling, boring, grinding, shaping, threading, and tapping (Table 3). However, the low coefficient of expansion of molybdenum makes it necessary to keep the tool cool when drilling in order to prevent seizure or possible cracking of the metal or tool. Drilling is normally carried out dry but swarf can be carried out with suitable cutting oils. When milling, cutters must be kept sharp and a copious amount of coolant be provided.

It is possible to weld molybdenum using a TIG inert gas-shielded arc-welding process although this is generally more successful on vacuum arc remelted material. When welding, a heat-affected zone is unavoidable and grain growth must be anticipated. These characteristics always give a weld with less ductility than the parent material and no method of welding is entirely satisfactory particularly if the joint is to be stressed. Resistance spot and seam welding is

**Table 3** Some commercially produced molybdenum alloys<sup>2</sup>

<i>Material</i>	<i>Composition</i>	<i>Recrystallization temperature</i>	<i>Applications</i>
<i>Commercial purity: Mo</i>	0.01–0.04% C, <0.02 Fe, <0.01% Ni, Si, <0.003% O, N	1100 °C	Furnace components, windings, etc., glass-metal seals
<i>Clad alloys:</i>			Electrical switch, contact materials, electronic packaging
Mo–Cu	15, 30% Cu	–	
Mo–Ag	35, 50% Ag	–	
<i>Substitutional:</i>			
Mo–W	20–30% W	1200 °C	Molten metal casting
Mo–Re	25–45% Re	1300 °C	Cryogenic ductility
<i>Carbide strengthened:</i>			
TZM	0.5% Ti, 0.08% Zr, 0.03% C	1400 °C	Hot work tooling, dies, glass
TZC	1.2% Ti, 0.3% Zr, 0.1% C	1550 °C	manufacture, spinnerets,
MHC	1.2% Zr, 0.05% C	1550 °C	heating electrodes, etc.
ZHM	0.4% Zr, 1.2% Hf, 0.12% C	1550 °C	
HWM-25	25%W, 1.0% Hf, 0.07% C	1650 °C	
<i>Oxide dispersed:</i>			
PSZ	0.5% ZrO <sub>2</sub>	1250 °C	Furnace components and
MH	0.015% K, 0.03% Si	1800 °C	elements from 1800 to 2000 °C
KW	0.02% K, 0.03% Si, 0.1% Al	1800 °C	
MLR	0.7% La <sub>2</sub> O <sub>3</sub>	1800 °C	
MY	0.55% Y <sub>2</sub> O <sub>3</sub>	1300 °C	

used to join thin sections particularly for electrical and electronic applications. Molybdenum may be brazed using a flame torch and furnace brazing techniques. Small components may also be soldered although they require preplating, usually with nickel.

### 3.17.2.5 Alloys

Molybdenum has sufficient strength to be useful in its commercially pure form. However, as it is not possible to strengthen molybdenum by heat treatment, work hardening is the only viable method of increasing strength in commercially pure material. Like tungsten, molybdenum has poor solubility for most other elements (which is useful for applications involving molten metals); however, solid solution alloys with up to 30% tungsten and 45% rhenium are successfully used. Carbide precipitate and oxide dispersion hardened alloys are also effective with the second phase particles effective in preventing excessive grain growth at very high temperatures.

## 3.17.3 Aqueous Corrosion

### 3.17.3.1 Electrochemistry

#### 3.17.3.1.1 Thermodynamics

Molybdenum is a relatively base metal, similar to iron, with its domain of thermodynamic stability lying

completely below that of water (**Figure 1**). However, it is significantly more noble than chromium and slightly more so than tungsten. Molybdenum has a partial domain of passivity associated with the formation of  $\text{MoO}_2$  across the whole pH range, but is unstable to oxidation from the Mo(IV) to the Mo(VI) state (i.e., it is transpassive) at higher potentials. Thus, molybdenum dissolves at more positive potentials as an oxyanion of molybdic acid depending upon the pH; that is, as  $\text{MoO}_3 \cdot \text{H}_2\text{O}$  (more properly molybdic acid  $\text{H}_2\text{MoO}_4$ ) at low pH, as the hydrogen molybdate anion between pH 3 and 5, and as the molybdate anion above about pH 5–6. Molybdenum tends to form less soluble compounds with species such as sulfur and chlorine. For example, the  $E$ -pH diagram containing 0.1 M sulfur species shows a large domain of stability for  $\text{MoS}_2$  at more negative potentials (**Figure 2**).

Generally, in aqueous conditions, molybdenum and its alloys are effectively passive and show considerably lower corrosion rates than iron (e.g., see **Table 4**).

#### 3.17.3.1.2 Anodic behavior and passivation

The main electrochemical interest in molybdenum arises because of its profound influence on the localized corrosion of stainless steels. Several theories exist for this effect. For example, it has been proposed that the presence of high valency Mo in the chromia passive film reduces the density of cationic charge carriers thus increasing the breakdown potential.<sup>9</sup>

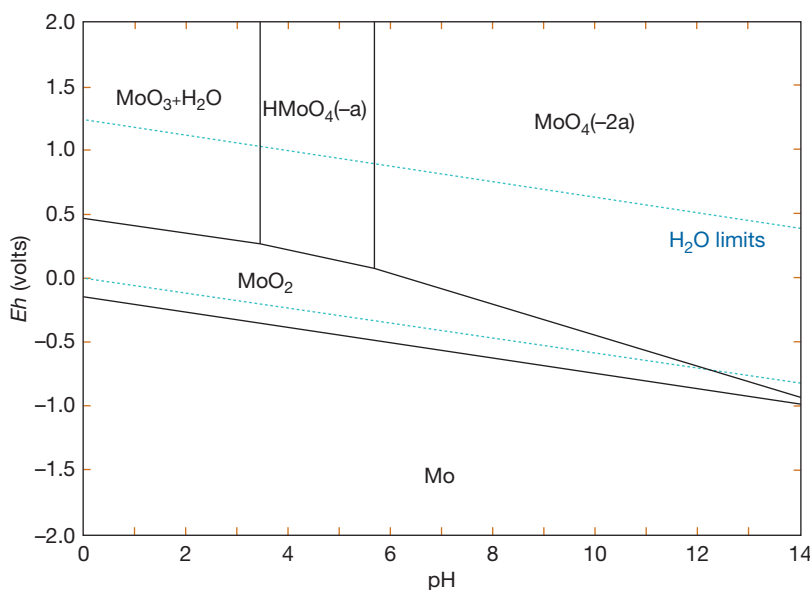


**Figure 1**  $E$ -pH diagram at 25 °C and at a molybdenum ion concentration of  $10^{-5}$  M.<sup>3</sup>

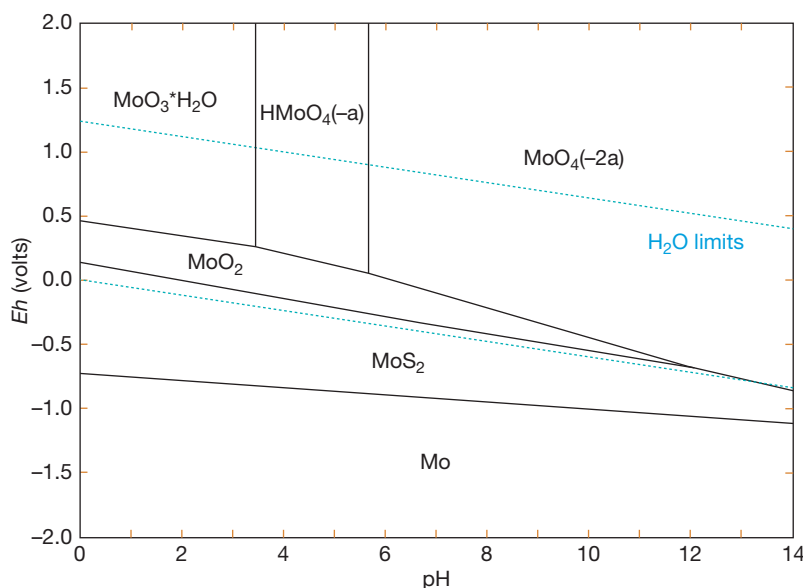


**Figure 2**  $E$ -pH diagram at 25 °C and at Mo ion and S ion concentrations of  $10^{-5}$  and 0.1 M respectively.<sup>3</sup>

**Table 4** Corrosion rates in selected aqueous solutions – 6 day tests<sup>20,21</sup>

Environment (25–35 °C)	Corrosion rate: aerated (mm year <sup>-1</sup> )	Corrosion rate: deaerated (mm year <sup>-1</sup> )
<b>Acids</b>		
HCl: 1–35%	0.03–0.06	–
H <sub>2</sub> SO <sub>4</sub> : 1–30%	0.5–10	–
H <sub>3</sub> PO <sub>4</sub> : 1–30%	0.5–0.3	–
<b>Salts</b>		
NaCl (3%)	0.01	0
NH <sub>4</sub> Cl (20%)	0.005	0
FeCl <sub>3</sub> (20%)	41	34
CuCl <sub>2</sub> (20%)	19	6.5
<b>Alkalis</b>		
NH <sub>3</sub> (0.35%)	0.14	0
NH <sub>3</sub> (29%)	0.02	0
NaOCl (10%)	11	–
NaOH (1%)	0.4	0
NaOH (10%)	0.1	0.025

Other notable theories include: adsorption of molybdate in the outer reaches of the film producing a cation-selective membrane (i.e., reducing chloride ion penetration),<sup>10</sup> local enrichment at actively dissolving sites reducing the local dissolution kinetics,<sup>11</sup> and the reduced solubility of molybdenum chloride and sulphate species affecting pit solution chemistry.<sup>12</sup> However, no general consensus is evident from this data and it is possible that a variety of mechanisms may operate in synergy.

Regarding the anodic behavior of pure molybdenum metal, the Pourbaix diagram implies that molybdenum is passive at intermediate potentials, with the formation of molybdenum dioxide, and that it is subject to transpassive dissolution at more positive potentials. It is generally accepted that molybdenum exhibits passivity over the majority of the pH range; however, the exact nature of this passivity is still in some doubt. The most generally accepted model, consistent with the thermodynamic diagram, is that the passive film consists of MoO<sub>2</sub> which dissolves to a higher valency species at more positive potentials with a higher valence oxide, MoO<sub>3</sub>, present under alkaline conditions.<sup>13</sup> For example, in 0.1 M HCl, X-ray photoelectron spectroscopy (XPS) evidence shows that a film is present on molybdenum that consists of an inner MoO<sub>2</sub> region and an outer layer of MoO(OH)<sub>2</sub>.<sup>8,14</sup> Also, electrochemical impedance spectroscopy (EIS) evidence is consistent with the presence of a passive film at all pH between 1 and 13.<sup>15–17</sup> However, since the anodic polarization curve, for example in sulfuric acid, shows no anodic peak but rather progresses immediately to a potential independent region, some workers have argued that at low pH there is no macroscopic passive film but rather a chemisorbed, strongly-bound oxygen layer.<sup>18</sup> There is general agreement, however, that molybdenum corrodes by transpassive dissolution at all pH at relatively higher potentials, dissolving, most probably via a Mo(V) intermediate state.<sup>19</sup>

### 3.17.3.2 Corrosion Processes

#### 3.17.3.2.1 General corrosion

Arc cast (or arc remelted) molybdenum has greater corrosion resistance than the powder metallurgical product, especially in large sections, which is probably due to the decreased porosity of the cast variety. Components that have been metal sprayed (clad) with molybdenum have considerably worse corrosion resistance than the bulk material, again due to the porosity of the coating. However, where techniques (such as high velocity oxy fuel (HVOF)) can produce dense coatings, the corrosion resistance should improve and cladding of materials such as steel should then become viable. **Table 4** gives corrosion rates in a selection of environments.

In contrast to most other passive metals, molybdenum is relatively unaffected by the presence of halide ions and is consequently relatively resistant to most localized corrosion processes. Molybdenum thus has generally excellent performance in nonoxidizing acid to near-neutral environments (containing halides or otherwise) and particularly in hydrohalide acids (e.g., HCl). However, in neutral-to-alkaline conditions, where molybdenum oxyanions become more stable, dissolution of molybdenum increases. Thus, it is only moderately resistant to aerated solutions of ammonium hydroxide and has fair resistance in 1–10% sodium hydroxide. Molybdenum is significantly less resistant to corrosion in organic acids such as acetic and formic (at 10%, the corrosion rate being 0.2–0.3 mm year<sup>-1</sup>), and in 0.25% benzoic acid (0.25 mm year<sup>-1</sup>) at 100 °C. Combinations of inorganic and organic acids generally lead to increased corrosion rates, for example, addition of 5% sulfuric to 10% acetic acid triples the corrosion rate from 0.33 to about 1 mm year<sup>-1</sup>.<sup>20</sup>

Oxidizing conditions severely reduce molybdenum's corrosion resistance, and aeration causes a significant increase in corrosion. It is therefore rapidly attacked by oxidizing acids such as nitric acid, and by reducing acids containing oxidizers such as HNO<sub>3</sub>, FeCl<sub>3</sub>, CuCl<sub>2</sub>, etc. Also, mercuric chloride causes an intense form of pitting corrosion. It is severely corroded in sodium hypochlorite solutions.

#### 3.17.3.2.2 Galvanic corrosion

In seawater (and presumably most other environments) molybdenum is found to be effectively protected by coupling to aluminum, steel, and magnesium.<sup>19</sup> However, contact with copper is more problematic and may slightly increase or decrease its corrosion

rate in neutral chloride media, but act protectively in acid reducing media. In sodium hydroxide solution, molybdenum acts sacrificially to protect steel and, hence, Mo coatings on steel or cast iron are not always effective in alkaline conditions, especially when significantly porous. Coupling of molybdenum to stainless steels in most environments has no effect on the corrosion rate of either material.

#### 3.17.3.2.3 High temperature water

Refractory and dense materials such as molybdenum, tungsten, and rhenium, are candidates for use in nuclear applications. For nuclear fusion reactor concepts in particular, dense refractory alloys that are resistant to liquid metals and that have good thermal conductivity are essential for efficient heat transfer. Similar requirements are evident in nuclear science applications such as spallation neutron sources. In all such cases, water cooling is likely to be important. To this end, a study of the corrosion of various candidate alloys was undertaken in high temperature pressurized water up to 320 °C.<sup>22</sup>

In flowing, high temperature water containing 400 ppb dissolved oxygen at pH 6–7, molybdenum and its alloys were found to have significantly better corrosion resistance than tungsten and its alloys. Up to 260 °C, neither material is corroded significantly (<50 μm year<sup>-1</sup> for tungsten and ~25 μm year<sup>-1</sup> for molybdenum). However, at 320 °C the corrosion rate of tungsten increased significantly to over 200 μm year<sup>-1</sup> while that of molybdenum was about 4 times lower (~50 μm year<sup>-1</sup>). Alloying with rhenium had a detrimental effect on the high temperature corrosion resistance for both alloys, resulting in grain boundary attack with corrosion rates rising to over 1 mm year<sup>-1</sup> in the case of W–Re alloys.<sup>22</sup>

#### 3.17.3.2.4 Corrosion of molybdenum alloys

The general and galvanic corrosion behavior of both the TZM and Mo–30W alloy are generally at least equal or sometimes superior to that of unalloyed molybdenum in many aqueous solutions of acids, bases and salts apart from strongly oxidizing environments such as in nitric acid.<sup>23</sup>

Sintered and amorphous molybdenum alloys containing significant amounts of tantalum, titanium, chromium and niobium have all been found to offer excellent resistance to strong reducing acids such as hot concentrated hydrochloric, sulfuric, phosphoric, oxalic and formic. For example, a sintered Ti–40Mo alloy corrodes between 1000 and 10 000 times more

slowly than Ti in boiling 35% hydrochloric acid although the corrosion rate in neutral conditions was unaffected.<sup>24</sup> Likewise, binary amorphous Mo–Cr, Mo–Nb, and Mo–Ta alloys all show spontaneous passivity in 12 M HCl with overall corrosion rates, in all cases, significantly less than the individual alloy components.<sup>25</sup>

Ti–15Mo alloys are of interest for prosthetic and replacement body implants (e.g., joints replacements and dental implants) because their relatively low elastic modulus matches better than that of bone. Further advantages include the excellent corrosion resistance of the alloy in body fluids, the relatively low toxicity of molybdenum and, for dental implants, resistance to fluoride.<sup>26,27</sup>

### 3.17.4 High Temperature Corrosion

#### 3.17.4.1 Gaseous Environments

##### 3.17.4.1.1 Oxidation

Molybdenum begins to oxidize significantly in air at about 300 °C. Oxidation becomes rapid at 500 °C and the rate of attack is very rapid by 1200 °C.<sup>28</sup> Below about 400 °C an adherent relatively stable MoO<sub>2</sub> scale is formed and oxidation proceeds according to the parabolic law under diffusion controlled transport through the growing scale. However, MoO<sub>2</sub> is unstable to further oxidation to MoO<sub>3</sub>, which has a significant vapor pressure. Above 500 °C, the vapor pressure of MoO<sub>3</sub> becomes increasingly significant and at some higher temperature, depending on the total partial pressure of oxygen, the rate of evaporation of MoO<sub>3</sub> equals its rate of formation. At this point the volatilization rate becomes extremely rapid following linear kinetics. This sequence is summarized in Table 5.

The formation of molten MoO<sub>3</sub> above 802 °C results in a sudden increase in the oxidation rate because the rate of diffusion of oxygen through a liquid phase is considerably higher than through the solid phases present at lower temperatures. Also, for molybdenum-containing alloys where Mo is less than 50 wt%, the molten oxide can act as a flux for other potentially protective oxide species.<sup>29</sup> Note that the sequence of oxidation is consistent with the thermodynamic properties of the oxides. The activation energy for molybdenum oxidation to MoO<sub>3</sub> in the chemical rate-controlled region was found to be 82 kJ mol<sup>−1</sup> at all temperatures above about 550 °C. At temperatures above around 1100 °C, samples were required to be as small as possible in order to provide enhanced diffusion and, hence, eliminate gas-phase effects. The reaction rate between molybdenum and oxygen in this regime is among the highest measured of all elements and significantly greater than that for tungsten.<sup>27</sup> At exceptionally high temperatures, typically less than 1900 °C and depending on pressure, MoO<sub>3</sub> dissociates to MoO<sub>2</sub>, which then immediately combusts producing a flame.<sup>30</sup>

Secondary ion mass spectrometry (SIMS) has been performed on molybdenum oxide scales of thickness 10–12 μm after oxidation at 500 °C in order to analyze the distribution of MoO<sub>2</sub> and MoO<sub>3</sub>, and the thicknesses of these layers, in the scale.<sup>31</sup> The majority of the scale (>90%) was found to consist of MoO<sub>2</sub> with only a comparatively thin region, less than 0.5 μm in thickness, corresponding to MoO<sub>3</sub> and located at the oxide–gas interface

##### 3.17.4.1.2 Sulphidation

There is considerable interest in the corrosion of molybdenum in sulfidizing environments containing H<sub>2</sub>S or SO<sub>2</sub>/SO<sub>3</sub>. This is in part due to the beneficial

**Table 5** Oxidation sequence for molybdenum as a function of temperature<sup>27</sup>

Oxidation class	Reaction conditions	Oxidation phenomena	Rate-controlling process
1	Below 450 °C	Adherent solid oxide films or scales form	Diffusion control of metal or oxygen through oxide
2	450–800 °C	Solid oxide scales form but MoO <sub>3</sub> volatilizes with lower pressures favoring evaporation	Oxide scales not protective – chemical control via interfacial reaction.
3	802 °C – a transition temperature governed by gas-phase mass transport	Liquid MoO <sub>3</sub> is stable, but volatilizes as soon as oxide forms	Chemical reaction at metal interface with liquid oxide/gas.
4	Above transition temperature	Oxide volatilizes as fast as it forms	Gas-phase transport of oxygen to metal interface.



effect of molybdenum alloying additions for some alloys in reducing hot corrosion in these environments<sup>32</sup> and in part due to the manufacture of MoS<sub>2</sub> catalysts, for example by sulfidation of Mo-containing alloys, which are used in the hydrodesulfurization of petroleum fuels.<sup>33</sup>

Below about 600–700 °C, molybdenum undergoes relatively slow sulfidation, forming MoS<sub>2</sub>. Appreciable reaction rates commence only above about 700 °C where an adherent and generally protective scale of MoS<sub>2</sub> forms by inwards diffusion of sulfur with parabolic reaction kinetics.<sup>34</sup> A change in the sulfidation rate after an initial period has been found to be the result of the formation of an inner layer of Mo<sub>2</sub>S<sub>3</sub>.<sup>35</sup> Sulfidation occurs in any environment containing significant partial pressure of sulfur, such as sulfur vapor, and also in gas mixtures containing sulfur species such as H<sub>2</sub>S or SO<sub>2</sub>.

The extremely low defect density of MoS<sub>2</sub>, coupled with its relatively high melting point, is the main reason why molybdenum is resistant to sulfidation. In contrast, the sulfides of most other functional metals are highly defective and have low melting points (e.g., Fe<sub>1-x</sub>S) and thus offer effectively no protective barrier. In view of this, doping of the sulfide scale is important and controls the sulfidation rate. Thus, in H<sub>2</sub>/H<sub>2</sub>S gas mixtures the sulfidation rate of molybdenum is increased with increasing hydrogen partial pressure and this may be explained by hydride doping of MoS<sub>2</sub>.<sup>36</sup> Likewise, doping of lithium into the scale can increase the sulfidation rate by up to 10<sup>4</sup> times.<sup>37</sup>

#### 3.17.4.1.3 Other environments

Carburization of molybdenum proceeds at high temperatures in vacuum when in contact with graphite components. Reaction only becomes significant above about 1200 °C when a layer of Mo<sub>2</sub>C is formed on the metal surface. This is thought to grow by diffusion of carbon across the layer and is found to thicken with parabolic kinetics. This behavior is similar to that of tungsten but the molybdenum carbide layer grows faster than that for tungsten carbide. The formation of the continuous surface carbide layer in these materials slows their whole-scale carburization and embrittlement under these conditions.<sup>38</sup>

Molybdenum is nitrided in environments containing nitrogen (such as cracked ammonia) at temperatures 800–1200 °C with the formation of a continuous Mo<sub>2</sub>N layer under approximate parabolic growth kinetics. Below 800 °C, the reaction is too slow to measure while above 1200 °C Mo<sub>2</sub>N starts to decompose.

Unlike with carburization, the reaction layer does not appear to provide protection against nitriding of the underlying material, which is likely to become extensively embrittled above around 1000 °C.<sup>39</sup>

In halogenating environments, molybdenum has significantly worse corrosion performance compared with tungsten<sup>40</sup> and the latter is a preferred alloying addition to improve the resistance to environments containing chlorine. The chlorination kinetics are similar to tungsten but considerably faster and no protective scale forms.<sup>41</sup>

### 3.17.4.2 Fused Materials

#### 3.17.4.2.1 Liquid metals

Like tungsten, molybdenum has a relatively low solubility in many molten metals and this has inspired research on the use of molybdenum as a container, or as a process component, in liquid metal environments, particularly in molten metal die casting, and for the nuclear industry (liquid metal cooled fission reactors and fusion reactor concepts). Thus, like tungsten, molybdenum has excellent resistance to molten lead and lead–bismuth alloys.<sup>42</sup> In liquid sodium, molybdenum appears to be unaffected by the dissolved oxygen content but is dependent on dissolved carbon resulting in the formation of a Mo<sub>2</sub>C corrosion product layer. This compares with tungsten, which is dependent on the mass transport of dissolved oxygen in forming ternary layers of oxide.<sup>43</sup> Molybdenum has significant advantages (high temperature strength, etc) in dies for hot metal working and for molten metal dies. In particular, the Mo–30W alloy is extremely resistant to molten zinc and this material is used extensively for zinc dies and as a container/crucible for molten zinc.<sup>44</sup>

#### 3.17.4.2.2 Molten glasses

Molybdenum has good resistance to corrosion/degradation in most molten glasses except those containing lead oxide, which acts as an effective flux. Of course, molybdenum is still susceptible to oxidation above about 400 °C, unless protected by an appropriate gas atmosphere or by a coating. Further information on protective coatings is given below, however, traditionally physical cladding with platinum, or electrodeposition of dense, protective platinum coatings have been used and are effective. The corrosion resistance of molybdenum disilicide in molten glass is also of interest as this material is frequently used as a heating element for temperatures up to 1800 °C in air (due to the formation of protective layers of silica).

Additionally, direct electrical resistance heating of molten glass using molybdenum electrodes is often used (molten glass is an ionic conductor).

The corrosion resistance of molybdenum and molybdenum disilicide in molten soda-glass was studied at 1565 °C over a period of 48 h.<sup>45</sup> Molybdenum was found to have the best corrosion resistance forming a film of MoO<sub>2</sub> that was about 15 µm thick with a total recession loss over the testing period equivalent to about 110 µm. The oxide film on molybdenum was found to be cracked and this clearly allowed additional reaction beneath the film and further corrosion. On MoSi<sub>2</sub>, no protective layer was formed with a loss of recession equivalent to over 315 µm. In all cases the corrosion rate was found to be related to the amount of dissolved oxygen in the glass. In contrast, molten borosilicate (E) glass under similar conditions is a much less aggressive environment, with no significant corrosion of molybdenum noted and considerably less attack on MoSi<sub>2</sub>.<sup>46</sup>

### 3.17.4.3 Protection

The inability of molybdenum to withstand oxidizing conditions at even moderate temperatures has led to many investigations of the means of reducing the oxidation rate. Alloying has not been successful since the loss of key high temperature mechanical properties are unacceptable. Thus, protective coatings appear to be the most effective option. A number of coatings have been developed for molybdenum. At intermediate temperatures, up to about 900–1000 °C, molybdenum can effectively be protected against oxidation by cladding, by thermal sprayed coatings or by electroplating, for example with chromium–nickel.<sup>47</sup>

At higher temperatures, most protective strategies are based on siliconizing, that is, the formation of a coating of molybdenum disilicide. Such coatings generally have similar oxidation resistance to MoSi<sub>2</sub> heating elements up to about 1700 °C. Simple silicide coatings may be formed on molybdenum using a variety of methods, for example using gas-phase diffusion (i.e., cementation) processes. This predominantly forms the favored phase MoSi<sub>2</sub>, however, after the cementation process is completed and during high temperature service, silicon can further diffuse into the molybdenum substrate forming the less protective Mo<sub>5</sub>Si<sub>3</sub> phase. The service life of the coated alloy depends on the initial thickness of the MoSi<sub>2</sub> layer, whether it remains uncracked as also the temperature of operation, as the coating is slowly consumed by

oxidation to silica.<sup>48</sup> More sophisticated coatings, used especially in the glass industry, are based on Si–B–C formulations and these can give more reliable operation to about 1450 °C.<sup>49</sup>

## References

1. Imgrund, H.; Kinsman, N. *Stainless Steel World*, 20–31 September 2007.
2. International Molybdenum Association, Molybdenum and Applications of Molybdenum and Its Alloys. Available at <http://www.imoa.info/>.
3. *HSC: Chemistry*, V6.12 (*Thermochemical Database*); Outotec Research Oy: Finland, 2007.
4. Suppliers data via MATWEB. Available at <http://www.matweb.com/>.
5. Stoloff, N. S. In *Superalloys II: High Temperature Materials for Aerospace and Industrial Power*; Sims, C. T., Stoloff, N. S., Hagel, W. C., Eds.; Wiley: USA, 1987; pp 61–96.
6. Gupta, C. K. In *Extractive Metallurgy of Molybdenum*; CRC Press, 1992; Chapter 1.
7. Brandes, E. A.; Brook, G. B. *Smithells Metals Reference Book*, 7th ed. Butterworth-Heinemann, 1994; Table 22–47.
8. Czarnecki, E. G.; Stacey, J. T.; Zimmerman, D. K. In *Refractory Metals and Alloys*; Semchyshen, M., Perlmutter, I., Eds.; Interscience Publishers: New York, 1963; Vol. 2.
9. Urquidi-Macdonald, M.; Macdonald, D. D. *J. Electrochem. Soc.* **1989**, *136*, 961–967.
10. Clayton, C. C.; Lu, Y. C. *J. Electrochem. Soc.* **1986**, *133*, 2465.
11. Newman, R. C. *Corros. Sci.* **1985**, *25*, 331–350.
12. Schneider, A.; Kuron, D.; Hofman, S.; Kirchheim, R. *Corros. Sci.* **1990**, *31*, 191.
13. Hull, M. N. *Electroanal. Chem. Interf. Electrochem.* **1972**, *38*, 143–157.
14. Halada, G. P.; Clayton, C. R.; Herman, H.; Sampath, S.; Tiwari, R. *J. Electrochem. Soc.* **1995**, *142*, 74.
15. Badawy, W. A.; Al-Khara, F. M. *Electrochim. Acta* **1998**, *44*, 693–702.
16. Gad-Allah, A. G.; Abd El-Rahman, H. A. *J. Appl. Electrochem.* **1988**, *18*, 441–446.
17. De Rosa, L.; Tomachuk, C. R.; Springer, J.; Mitton, D. B.; Saiello, S.; Bellucci, F. *Mater. Corros.* **2004**, *55*, 602–609.
18. Pozdeeva, A. A.; Antonovskaya, E. I.; Sukhotin, A. M. *Corros. Sci.* **1966**, *6*, 149–158.
19. Itagaki, M.; Suzuki, T.; Watanabe, K. *Electrochim. Acta* **1997**, *42*, 1081.
20. Acherman, W. L.; Carter, J. P.; Kenahan, C. B.; Schlain, D. *Corrosion properties of molybdenum, tungsten, vanadium and their alloys, Report Investigations No. 6, US Bureau of Mines* **1966**, p 715.
21. Bishop, C. R. *Corrosion* **1963**, *19*, 308t–314t.
22. Ishijima, Y.; Kakiuchi, K.; Furuya, T.; Kurishita, H.; Hasegawa, M.; Igarashi, T.; Kawai, M. *J. Nucl. Mater.* **2002**, *307–311*, 1369–1374.
23. Ackerman, W. L.; Carter, J. P.; Schlain, D. *Corrosion properties of the TZM and Mo–30W alloy, US Bureau of Mines Report No. 7* **1969**, p 196.
24. Nakahara, K.; Tokumoto, K.; Sakaguchi, S.; Hayashi, Y. *J. Jpn. Soc. Powder Powder Metall.* **1997**, *44*, 241–246.
25. Park, P. Y.; Akiyama, E.; Habazaki, H.; Kawashima, A.; Asami, K.; Hashimoto, K. *Corros. Sci.* **1996**, *38*, 1731–1750.
26. Kumar, S.; Narayanan, T. S. N. *S. J. Dent.* **2008**, *36*, 500–507.

27. Karthega, M.; Raman, V.; Rajendran, N. *Acta Biomater.* **2007**, *3*, 1019–1023.
28. Gulbranson, E. A.; Andrew, K. F.; Brassart, F. A. *J. Electrochem. Soc.* **1962**, *110*, 952–959.
29. Brenner, S. S. *J. Electrochem. Soc.* **1955**, *102*, 16–21.
30. Bartlett, R. W. *J. Electrochem. Soc.* **1964**, *113*, 744–746.
31. Gritscha, M.; Piplitsa, K.; Hutter, H.; Wilhartitz, P.; Wildner, H.; Martinz, H. P. *Surf. Sci.* **2000**, *454–456*, 284–288.
32. Strafford, K. N.; Winstanley, G. R.; Harrison, J. M. *Werkstoffe Korrosion* **1974**, *25*, 487.
33. Vissers, J. P. R.; De Beer, V. H. J.; Prins, R. *J. Chem. Soc., Faraday Trans. 1: Phys. Chem. Cond. Phases* **1987**, *83*, 2145–2155.
34. Gerlach, J.; Hamell, H. J. *Metall* **1969**, *23*, 1006–1011.
35. Lee, B. S.; Rapp, R. J. *J. Electrochem. Soc.* **1984**, *131*, 2998–3006.
36. Cheung, W. H.; Young, D. J. *Oxid. Met.* **1991**, *36*, 15–25.
37. Grzesik, Z.; Migdalska, M.; Mrowec, S. *High Temp. Mater. Processes* **2007**, *26*, 355–363.
38. Martinz, H. P.; Prandini, K.; Kock, W.; Sporer, D. *Mater. Corros.* **1998**, *49*, 246–251.
39. Martinz, H. P.; Prandini, K. *Int. J. Refract. Met. Hard Mater.* **1993/1994**, *12*, 179–186.
40. Prescott, R.; Stott, F. H.; Elliott, P. *Corros. Sci.* **1981**, *29*, 465–475.
41. Landsberg, A.; Hoatson, C. L.; Block, F. E. *J. Electrochem. Soc.* **1971**, *118*, 1331–1336.
42. Loewen, E. P.; Ballinger, R. G.; Lim, J. *Nucl. Technol.* **2004**, *147*, 436–456.
43. Barker, M. G.; Morris, C. W. *J. Less-Common Met.* **1976**, *44*, 169–176.
44. Burman, R. In *Refractory Metals and Their Industrial Applications*; Smallwood, R. E., Ed.; ASTM STP, 1982; Vol. 849, pp 3–17.
45. Kamakshi Sundamn, S.; Hsu, J.-Y.; Speyer, R. F. *J. Am. Ceram. Soc.* **1994**, *77*, 1613–1623.
46. Kamakshi Sundamn, S.; Hsu, J.-Y.; Speyer, R. F. *J. Am. Ceram. Soc.* **1995**, *78*, 1940–1946.
47. Couch, D. E.; Shapiro, H.; Taylor, J. K.; Brenner, A. *J. Electrochem. Soc.* **1958**, *105*, 450–456.
48. Wang, Y.; Li, Y.; Hu, X. *J. Mater. Sci. Technol.* **2001**, *17*, 479–481.
49. Martinz, H. P.; Nigg, B.; Matej, J.; Sulik, M.; Larcher, H.; Hoffmann, A. *Int. J. Refract. Met. Hard Mater.* **2006**, *24*, 283–291.

## 3.14 Corrosion of Zirconium and its Alloys

**T.-L. Yau**

12103 SE High Creek Road, Happy Valley, OR 97086-4729, USA

© 2010 Elsevier B.V. All rights reserved.

---

<b>3.14.1</b>	<b>Introduction</b>	2095
<b>3.14.1.1</b>	<b>General Characteristics</b>	2096
3.14.1.1.1	Alloy categories	2096
3.14.1.1.2	Physical and mechanical properties	2096
3.14.1.1.3	Microstructure	2099
<b>3.14.1.2</b>	<b>Chemical and Corrosion Properties</b>	2100
<b>3.14.1.3</b>	<b>Manufacture</b>	2101
3.14.1.3.1	Fabrication	2101
3.14.1.3.2	Problems arising from handling	2102
3.14.1.3.3	Welding	2103
3.14.1.3.4	Heat treatment	2103
3.14.1.3.5	Chemical cleaning	2103
<b>3.14.2</b>	<b>Corrosion</b>	2103
<b>3.14.2.1</b>	<b>Oxide Films</b>	2103
<b>3.14.2.2</b>	<b>Effects of Water</b>	2104
<b>3.14.2.3</b>	<b>Effects of Temperature</b>	2104
<b>3.14.2.4</b>	<b>Effects of pH</b>	2105
<b>3.14.2.5</b>	<b>Localized Corrosion</b>	2106
3.14.2.5.1	Pitting corrosion	2106
3.14.2.5.2	Crevice corrosion	2106
3.14.2.5.3	Intergranular corrosion	2107
3.14.2.5.4	Stress corrosion cracking	2108
3.14.2.5.5	Delayed hydride cracking	2109
<b>3.14.2.6</b>	<b>Galvanic Corrosion</b>	2109
<b>3.14.2.7</b>	<b>Microbiologically Influenced Corrosion</b>	2110
<b>3.14.2.8</b>	<b>Erosion–Corrosion</b>	2110
<b>3.14.2.9</b>	<b>Fretting Corrosion</b>	2110
<b>3.14.2.10</b>	<b>Surface Condition</b>	2111
<b>3.14.2.11</b>	<b>Tin in zirconium</b>	2111
<b>3.14.3</b>	<b>Corrosive Environments</b>	2112
<b>3.14.3.1</b>	<b>Pressurized Water and Steam</b>	2112
<b>3.14.3.2</b>	<b>Other Aqueous Systems</b>	2112
3.14.3.2.1	Cooling waters	2112
3.14.3.2.2	Salt solutions	2113
3.14.3.2.3	Sulfur compounds	2113
<b>3.14.3.3</b>	<b>Inorganic Acids</b>	2113
3.14.3.3.1	Sulfuric acid	2113
3.14.3.3.2	Halogen acids	2116
3.14.3.3.3	Nitric acid	2119
3.14.3.3.4	Phosphoric acid	2121
3.14.3.3.5	Other inorganic acids	2122
<b>3.14.3.4</b>	<b>Other Aqueous Environments</b>	2124
3.14.3.4.1	Hydrogen peroxide	2124
3.14.3.4.2	Alkaline solutions	2124
3.14.3.4.3	Urea	2125
<b>3.14.3.5</b>	<b>Organic Acids</b>	2125

---

3.14.3.5.1	Acetic acid	2125
3.14.3.5.2	Formic acid	2125
3.14.3.6	Other Organic Environments	2126
<b>3.14.4</b>	<b>High Temperature Degradation</b>	2126
3.14.4.1	Oxidation and Hot Corrosion	2126
3.14.4.2	Molten Salts and Metals	2127
<b>3.14.5</b>	<b>Corrosion Protection</b>	2127
3.14.5.1	Protective Film Formation	2127
3.14.5.2	Surface Conditioning	2128
3.14.5.3	Electrochemical Protection	2128
3.14.5.4	Other Measures	2128
<b>3.14.6</b>	<b>Industrial Applications</b>	2130
3.14.6.1	Processes Using Sulfuric Acid	2130
3.14.6.2	Processes Using Halogen Acids	2130
3.14.6.3	Processes Using Nitric Acid	2131
<b>3.14.7</b>	<b>Safety</b>	2132
<b>3.14.8</b>	<b>Future Possibilities</b>	2132
<b>References</b>		2133

## Glossary

**Widmanstätten** A metallurgical structure showing a characteristic cross-hatched appearance due to the grains is formed along the preferred crystallographic planes.

**Zircaloy** One of a group of alloys used as a nuclear fuel cladding material in light water reactors, thus taking advantage of the relatively low neutron capture cross section and relatively high corrosion resistance of zirconium.

## Abbreviations

**CPI** Chemical process industry  
**DHC** Delayed hydride cracking  
**HAZ** Heat affected zone  
**NHE** Normal hydrogen electrode  
**SCC** Stress corrosion cracking

### 3.14.1 Introduction

Zirconium belongs to Group IVb of the period table being in the second row, beneath titanium and above hafnium. It has similar (but not identical) metallurgical and chemical properties to titanium and may be described as refractory (since their melting points are above the range of iron, cobalt, and nickel), reactive (since they are highly active and have, consequently,

extremely negative equilibrium potentials), and corrosion resistant (since, by virtue of their passivity, they resist attack in many highly corrosive environments). Zirconium and titanium have similar corrosion properties; thus, both metals are excellent for handling seawater, while chromium-containing passive alloys (i.e., stainless steels) are susceptible to localized corrosion in seawater.<sup>1</sup> Moreover, both metals are susceptible to environments of low water activity and are attacked, for example, by halide-containing methanolic solutions; such attack being preventable by the addition of small quantities of water as an inhibitor.<sup>2,3</sup>

Zirconium and titanium are also sister metals of distinctive contrast.<sup>4</sup> The common perception is that zirconium is more suitable than titanium in handling reducing environments (such as hydrochloric and dilute sulfuric acids) than oxidizing environments (such as ferric chloride). Although there is some truth to this perception, it is not always true. Thus, in chloride-free and highly oxidizing environments (e.g., nitric acid), zirconium is often more corrosion resistant than titanium; mistakes can be made when such differences are ignored.

Historically, while the development of titanium resulted from the ever-increasing demands of the aerospace industry, the demand for zirconium arose from the nuclear industry.<sup>5</sup> For this latter application, a suitable structural material to clad nuclear fuel must have good corrosion–oxidation resistance, resistance to irradiation damage, adequate mechanical properties, and

transparency to thermal neutrons. Properly alloyed zirconium meets these requirements. After zirconium became available outside nuclear submarine programs in 1958, research on developing additional applications for zirconium has grown. So, in addition to fuel cladding material for water-cooled nuclear reactors, zirconium began to find uses in the chemical process industry because of its excellent resistance to a broad range of corrosives. Zirconium is also used in specialist surgical tools and instruments and is a highly beneficial alloying addition to iron-, copper-, magnesium-, aluminum-, molybdenum-, and titanium-based alloys. Zirconium is useful as a getter because of its ability to combine with gases at elevated temperatures. Along with niobium, zirconium is superconductive at low temperatures and is used to make superconductive magnets.

### 3.14.1.1 General Characteristics

#### 3.14.1.1.1 Alloy categories

There are two major applications for zirconium and its alloys: nuclear and nonnuclear. Both of these use alloys with low levels of alloying additions and are, thus, based on the alpha microstructure (i.e., the hexagonal close packed lattice) with dilute additions of solid solution strengthening and alpha stabilizing elements like oxygen and tin. However, in niobium-containing alloys, there is the presence of some niobium-rich second phase particles of the body-centered cubic (beta) lattice.

One of the major differences between nuclear and nonnuclear zirconium alloys is in hafnium content. Nuclear grades of zirconium alloys are virtually free of hafnium (not greater than 100 ppm). Hafnium has an enormous effect on absorbing thermal neutrons,

which is critical for nuclear applications and is, therefore, suitable for nuclear reactor control rods that are required to absorb excess neutrons in order to control the uranium fission process. On the other hand, non-nuclear grades of zirconium may contain up to 4.5% hafnium. Hafnium has only a minor effect on zirconium's mechanical and chemical properties.

#### 3.14.1.1.2 Physical and mechanical properties

Zirconium is a lustrous, grayish white, ductile metal whose typical physical and mechanical properties are listed in **Tables 1 and 2**, respectively. For engineering purposes, there are three interesting features of zirconium. First, the density of zirconium is lower than those of iron- and nickel-based stainless alloys. Second, zirconium has a low coefficient of thermal expansion (the coefficient of thermal expansion of zirconium is about two-thirds that of titanium, about one-third that of type 316 stainless steel, and about one-half that of nickel-copper alloys). Third, zirconium has a thermal conductivity ( $22 \text{ W m}^{-1} \text{ K}^{-1}$ ), which is about 30% greater than that of stainless alloys ( $16 \text{ W m}^{-1} \text{ K}^{-1}$ ). These features allow zirconium to be fabricated into compact, efficient equipment, for example as heat exchangers in aggressive environments.

Zircaloy-2, Zircaloy-4, and the niobium-containing alloys are nuclear grades. Zircaloy-2 and Zircaloy-4 contain about 1.5% tin but are different in iron and nickel contents. Thus, Zircaloy-4 has more iron but no nickel in order to minimize hydrogen pick-up. Both alloys are popular in water-moderated reactors, such as boiling water and pressurized water reactors. The Zr-2.5Nb alloy is used in heavy water moderated reactors, such as Canada Deuterium Uranium (CANDU) reactors.

**Table 1** Physical properties of zirconium, titanium, hafnium, and iron

	<i>Zirconium</i>	<i>Titanium</i>	<i>Hafnium</i>	<i>304L</i>
Atomic number	40	22	72	26
Relative atomic mass	91.22	47.87	178.49	55.85
Lattice structure	hcp < 1140 K bcc > 1140 K	hcp < 1060 K bcc > 1060 K	hcp < 2050 K bcc > 2050 K	bcc < 1180 K fcc > 1180 K
Melting point (K)	2125	1943	4876	1809
Density ( $\text{Mg m}^{-3}$ )	6.49	4.5	13.1	7.86
Young's modulus (GPa)	68	116	78	211
Electrical conductivity ( $\Omega \text{ cm}$ ) <sup>-1</sup>	$0.0236 \times 10^{-6}$	$0.0234 \times 10^{-6}$	$0.0312 \times 10^{-6}$	$0.0993 \times 10^{-6}$
Thermal conductivity ( $\text{W m}^{-1} \text{ K}^{-1}$ )	22.7	21.9	23	80.2
Thermal expansion ( $\text{K}^{-1}$ )	$5.7 \times 10^{-6}$	$8.6 \times 10^{-6}$	$5.9 \times 10^{-6}$	$11.8 \times 10^{-6}$
Thermal neutron capture cross-section ( $\text{m}^2$ )	$1.8 \times 10^{-29}$	–	$1.05 \times 10^{-26}$	–

hcp, hexagonal close packed; bcc, body centered cubic; fcc, face centred cubic.



**Table 2** Nuclear and nonnuclear grades of zirconium alloys

Alloy design (UNS #)	Composition (wt%)									
	Zr + Hf (min)	Hf (max)	Sn	Nb	Fe	Cr	Ni	Fe + Cr	Fe + Cr + Ni	O (max)
Nuclear grades										
Zircaloy-2 (R60802)	–	0.01	1.20–1.70	–	0.07–0.2	0.05–0.15	0.03–0.08	–	0.18–0.38	–
Zircaloy-4 (R60804)	–	0.01	1.20–1.70	–	0.18–0.24	0.07–0.13	–	0.28–0.37	–	–
Zr-2.5Nb (R60901)	–	0.01	–	2.40–2.80	–	–	–	–	–	–
Nonnuclear wrought grades										
Zr700 (R60700)	99.2	4.5	–	–	–	–	–	0.2 (max)	–	0.10
Zr702 (R60702)	99.2	4.5	–	–	–	–	–	0.2 (max)	–	0.16
Zr704 (R60704)	97.5	4.5	1.0–2.0	–	–	–	–	0.2–0.4	–	0.18
Zr705 (R60705)	95.5	4.5	–	2.0–3.0	–	–	–	0.2 (max)	–	0.18
Zr706 (R60706)	95.5	4.5	–	2.0–3.0	–	–	–	0.2 (max)	–	0.16
Nonnuclear casting grades										
Zr702C	98.8	4.5	–	–	–	–	–	0.3 (max)	–	0.25
Zr704C	97.1	4.5	1.0–2.0	–	–	–	–	0.3 (max)	–	0.3
Zr705C	95.1	4.5	–	2.0–3.0	–	–	–	0.3 (max)	–	0.3

Zr700, Zr702, Zr704, Zr705, and Zr706 are non-nuclear grades for wrought materials. Zr702C, Zr704C, and Zr705C are nonnuclear grades for casting materials. Zr700 is an alloy with an oxygen content of less than 1000 ppm which has improved bondability in explosive cladding applications and deep drawing applications. Zr702 is commercially pure zirconium and is most popular for corrosion resistant applications. Zr705 is preferred when strength is an important factor.

Moreover, because recyclable material is generated from fabrication of nuclear fuel cladding, a major impurity in nonnuclear alloys is tin, which is not shown in Table 2. The use of recycled materials lowers the cost of nonnuclear alloys and keeps mechanical properties consistent. The elevated tin

content may affect zirconium's corrosion properties in certain environments. Also, since there is not enough demand in nonnuclear applications to support the production of Zr704, in nonnuclear applications, Zr704 may be effectively Zircaloy-2 or Zircaloy-4.

Zirconium and hafnium form a solid solution at all concentrations. However, the presence of small amounts of hafnium in zirconium does not significantly affect mechanical or chemical properties other than the thermal neutron cross-section. The counterparts of nuclear and nonnuclear grades of zirconium alloys are interchangeable in mechanical properties. However, specification requirements for nuclear materials are more extensive than those for nonnuclear materials. Mechanical requirements only for nonnuclear alloys are given in Tables 3 and 4. It can be seen that Zr705 is the strongest alloy with improved formability.

Additional typical property data are given in Table 5 and in Figures 1 and 2. Table 5 shows that the fatigue limits of zirconium alloys are very notch sensitive. Figure 1 shows that the tensile strengths of zirconium alloys decrease quickly with increasing temperature. Figure 2 indicates that Zr702 and Zr705 creep at low temperatures and stresses. These are important factors to consider in the application of zirconium equipment, particularly at elevated temperatures.

**Table 3** ASTM requirements for the room temperature mechanical properties of zirconium alloys

Alloy	UTS (MPa)	YS (MPa)	Elongation (%)	Bend test radius
Zr700	380 (max.)	305 (max.)	20	5T
Zr702	380	205	16	5T
Zr704	415	240	14	5T
Zr705	550	380	16	3T
Zr706	510	345	20	2.5T

Bend tests are not applicable to material more than 4.75-mm thick. T is the thickness of the bend test specimen.

**Table 4** ASME mechanical requirements for Zr702 and Zr705 used for unfired pressure vessels

Material form and condition	ASME number	Alloy grade	UTS (min) (MPa)	YS (min) (MPa)	Maximum allowable stress in tension for metal temperatures not exceeding °C (MPa)							
					–30 to 40	65	125	175	225	275	325	375
Plate, sheet, strip	SB 551	702	380	205	108	104	84.3	70.1	58.7	47.9	40.3	35.5
		705	550	380	158	144	119	105	94.7	86.8	81.2	77.6
Seamless tubing	SB 523	702	380	205	108	104	84.3	70.1	58.7	47.9	40.3	35.5
		705	550	380	158	144	119	105	94.7	86.8	81.2	77.6
Welded tubing <sup>a</sup>	SB 523	702	380	205	92.4	122	71.4	59.7	49.4	40.7	34.1	30.9
		705	550	380	134	88.4	101	89.5	80.8	73.9	68.9	66
Forgings	SB 493	702	380	205	108	104	84.3	70.1	58.7	47.9	40.3	35.5
		705	550	380	158	144	119	105	94.7	69.4	81.2	77.6
Bar	SB 550	702	380	205	108	104	84.3	70.1	58.7	47.9	40.3	35.5
		705	550	380	158	144	119	105	94.7	86.8	81.2	77.6
Seamless pipe	SB 658	702	380	205	108	104	104	70.1	58.7	47.9	40.3	35.5
		705	550	380	158	144	119	105	94.7	86.8	81.2	77.6
Welded pipe <sup>a</sup>	SB 658	702	380	205	92.4	122	71.4	59.7	49.4	40.7	34.1	30.9
		705	550	380	134	88.4	101	89.5	80.8	73.9	68.9	66

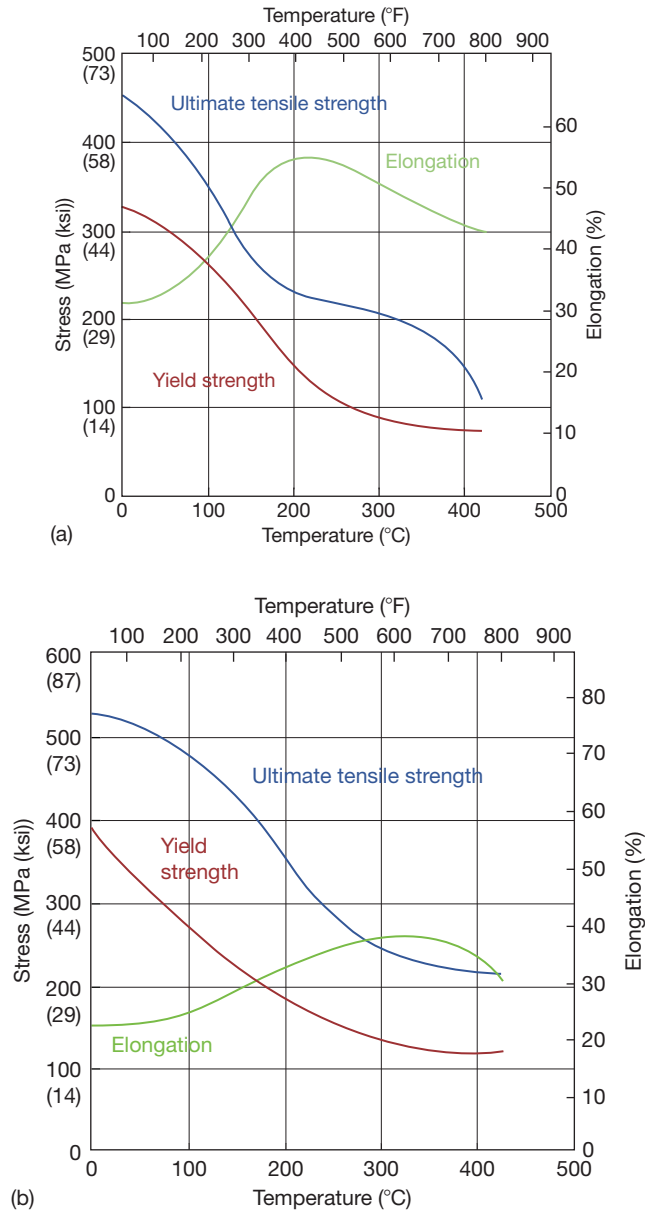
<sup>a</sup>0.85 factor used for welded product.

**Table 5** The  $10^7$  fatigue limits for zirconium alloys

Alloy	Fatigue limit (MPa)	
	Smooth	Notched
Iodide Zr	145	55
Zircaloy or Zr 705 (annealed 2 h at 732 °C)	283	55
Zr-2.5% Nb (Aged 4 h at 566 °C)	290	55

**3.14.1.1.3 Microstructure**

Typical microstructures for the parent metal, heat-affected zone (HAZ), and weld metal of annealed zirconium alloys are shown in **Figures 3–5**. Zr702 is effectively an unalloyed grade (apart from some oxygen) and exhibits an equiaxed alpha structure as shown in **Figure 3(a)**. Most elements have very low solubility in zirconium with oxygen, titanium, hafnium, and scandium the few exceptions. Zirconium

**Figure 1** (Continued)

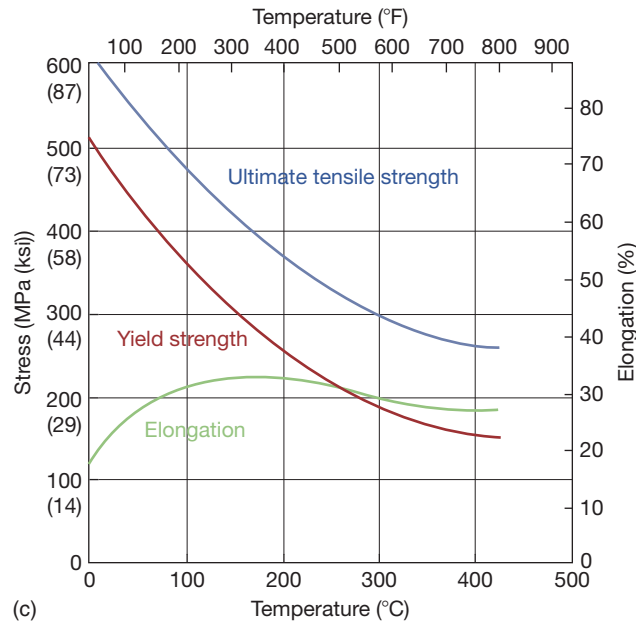


**Figure 1** Tensile properties vs. temperature curves for zirconium alloys: (a) Zr702, (b) Zr704, and (c) Zr705.

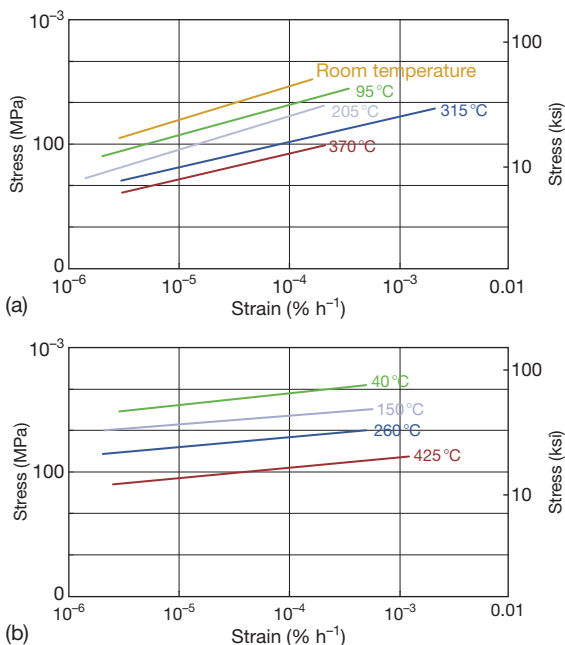


**Figure 2** Minimum creep rate vs. stress curve for zirconium alloys: (a) Zr702 and (b) Zr705.

tends to react with many elements to form intermetallic compounds during the production stage, and one of these (and also a major impurity) is iron. Consequently, the most visible second-phase particles in [Figure 3\(a\)](#) are Zr–Fe compounds. There may

also be fine chromium and nickel particles incorporated into these compounds that are well distributed in the alpha structure.

With few grain-boundary pinning precipitates in Zr702, grains in the HAZ grow to much larger sizes generally with an acicular structure ([Figure 3\(b\)](#)) while the weld metal itself exhibits a Widmanstätten structure as shown in [Figure 3\(c\)](#). Welding has a great effect on the morphology of second-phase particles, and this affects the corrosion of zirconium in certain conditions. Like Zr702, Zircalloys or Zr704 exhibit an equiaxed alpha structure in the parent metal ([Figure 4\(a\)](#)), a pronounced acicular alpha structure in the HAZ ([Figure 4\(b\)](#)), and a Widmanstätten structure in the weld metal ([Figure 4\(c\)](#)).

Zr705 exhibits a two-phase structure. It has much finer grain than that of the alpha alloys as shown in [Figure 5](#). It contains both the alpha zirconium phase and the beta niobium phase in the parent metal ([Figure 5\(a\)](#)). The HAZ has a mild change in structure as shown in [Figure 5\(b\)](#). The weld metal has a fine acicular structure of alpha zirconium and beta niobium ([Figure 5\(c\)](#)).

### 3.14.1.2 Chemical and Corrosion Properties

Zirconium is a highly reactive metal, as evidenced by its standard potential of  $-1.53$  V versus the normal hydrogen electrode (NHE) at  $25^\circ\text{C}$ . For comparison,

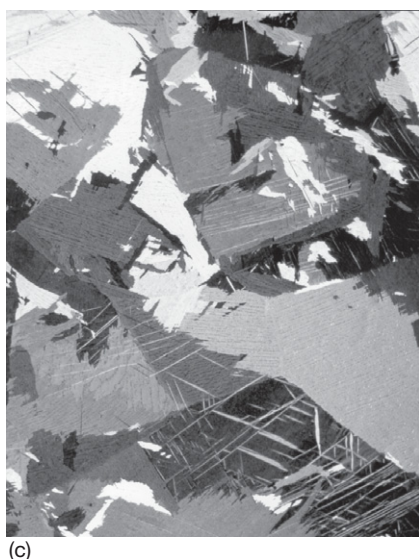
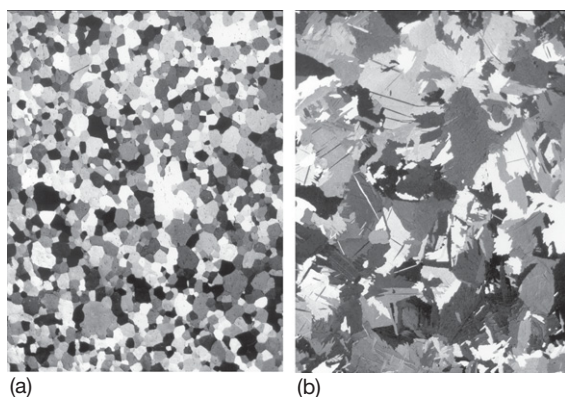


**Figure 3** Microstructure of Zr702: (a) parent metal of Zr702, (b) HAZ of Zr702, and (c) weld metal of Zr702.

the potentials for titanium, chromium, iron, and nickel are  $-1.53$ ,  $-0.74$ ,  $-0.44$ , and  $-0.25$  V, respectively. Zirconium owes its high corrosion resistance to its strong affinity for oxygen. In an oxygen-containing medium such as air, water, or carbon dioxide, zirconium spontaneously reacts with oxygen at ambient temperature and below to form an adherent, protective oxide film on its surface. This film is self-healing and protects the base metal from chemical and mechanical attack at temperatures up to about  $350^{\circ}\text{C}$ . As a result, zirconium resists attack in most acids, salt solutions, alkaline solutions, and organic media. Zirconium is particularly suitable for handling reducing acids in which most passive alloys have great difficulty in forming passive films. However, in more extreme conditions, such as hydrofluoric acid, hot concentrated sulfuric acid, and certain dry organic halides, a passive

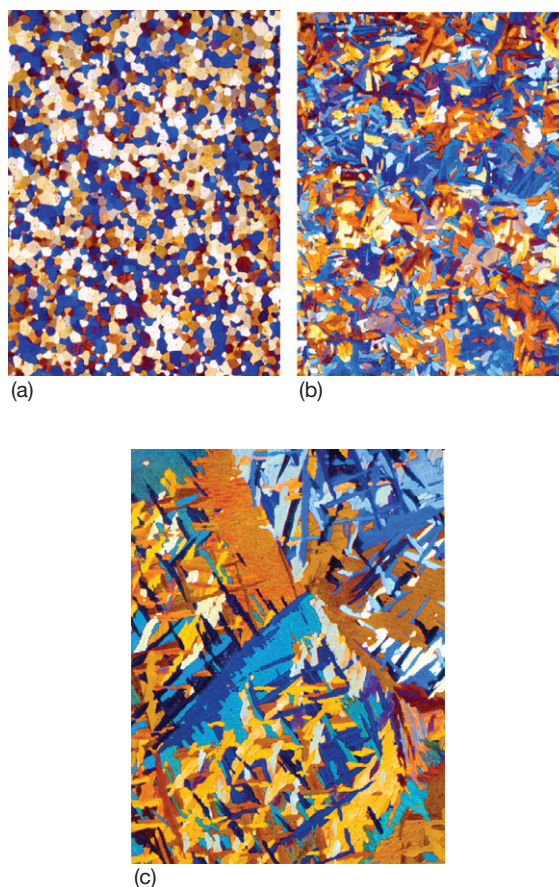


**Figure 4** Microstructure of zircaloy-4 or Zr704: (a) parent metal of zircaloy-4 or Zr704, (b) HAZ of zircaloy-4 or Zr704, and (c) weld metal of zircaloy-4 or Zr704.

oxide cannot readily form and, hence, zirconium is not suitable for handling these media.

In addition, zirconium is susceptible to localized corrosion, such as pitting and SCC in chloride solutions under oxidizing conditions. However, zirconium is not susceptible to crevice corrosion in chloride solutions since the condition in a crevice is often reducing. However, zirconium is susceptible to crevice corrosion in fluoride solutions and sulfuric acid. Examples of review articles on the corrosion of zirconium are given.<sup>6,7</sup>

### 3.14.1.3 Manufacture

#### 3.14.1.3.1 Fabrication

Corrosion failures of zirconium equipment can often be prevented by using alternate choices or methods of design, fabrication (including welding), or by specific heat treatment processes and techniques. Final



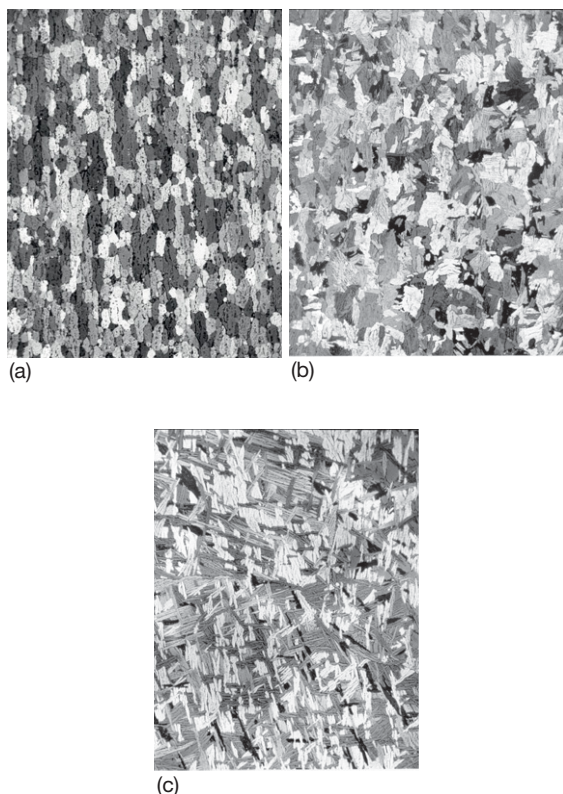


**Figure 5** Microstructure of the Zr-2.5Nb alloy or Zr705: (a) parent metal of the Zr-2.5Nb alloy or Zr705, (b) HAZ of the Zr-2.5Nb alloy or Zr705, and (c) weld metal of the Zr-2.5Nb alloy or Zr705.

surface treatment methods can also be applied to modify a surface finish or remove impurities from a surface for improved corrosion resistance. During standard fabrication processes, the surface of the material can become embedded with particles that may affect the corrosion resistance of the zirconium. Since zirconium is relatively a soft metal, abrasive grinding stones may embed aluminum oxide or silicon carbide particles in the material surface causing preferred sites for the initiation of localized corrosion. Abrasive grinding operations performed on zirconium should, therefore, be followed by conditioning with a clean stainless steel brush, clean draw file, or rotary carbide burr to remove any abrasive particles embedded on the surface. If the final part is blasted for a cosmetic appearance, steel shot blast should not be used because the shot will embed into the material surface causing potential localized corrosion failures, especially if used in an acidic chloride environment. However, if the use of steel shot cannot be avoided, then it must be followed by acid pickling or chemical cleaning to remove embedded iron particles.

If other alloys are fabricated near the zirconium vessel, potential sources for embedded particles include grinding and weld spatter of foreign material. For this reason, it is recommended that the zirconium equipment not be welded and fabricated in an area where other materials are being ground, welded, or torch cut. If a zirconium vessel is fabricated in a bay where other materials are being fabricated, then the area should be surrounded by protective barriers and kept clean. Any weld spatter should be removed by stainless steel brushing, grit or glass bead blasting, or light grinding.

It is recommended that hydrostatic expansion be performed when zirconium tubes are expanded into a tubesheet prior to welding. This minimizes the potential for embedded particles on the ID of the tube surface caused during roller expansion as a result of improperly cleaned roller expansion tooling. Corrosion failures in halogen acid environments have been identified where roller expansion of tubes was used. Embedded particles may cause localized pitting attack of the tubes and eventual penetration of the tube wall. For halogen acid applications, all final equipment surfaces exposed to the corrosive environment should be free of iron contamination.

Any tooling used for the fabrication of zirconium should be thoroughly cleaned to remove any contamination left by previous materials. Tooling used for welding or conditioning, such as grinding stones, wire brushes, draw files, etc., should be dedicated for zirconium only. If this tooling has been used previously on other materials, the materials may contaminate the zirconium surface. It is recommended that color coding of the ancillary tooling (files, grinding stones, wire brushes, etc.) be implemented to minimize the potential for cross contamination.

#### 3.14.1.3.2 Problems arising from handling

When zirconium is handled or moved using a forklift and/or lifting straps, protective coverings should be used to prevent the steel from being smeared into the zirconium metal surface. Forklift blades and steel straps will also cause scratches, scrapes, and surface defects that could be detrimental when it is exposed to subsequent forming operations and to certain corrosive environments. To minimize pickup of steel and other metal particles, it is recommended whenever possible to cover the forming dies with a protective covering such as leather, rubber, or some other types of noncontaminating material. This will also minimize the potential for surface damage caused by the steel tooling.



### 3.14.1.3.3 Welding

Generally, zirconium welds exhibit similar corrosion resistance to nonwelded areas except when used at the higher concentrations of sulfuric acid (see corrosion resistance of Zr in [Section 3.14.3.3.1](#)). Improper welding processes, however, can affect the mechanical and corrosion properties of zirconium. Interstitial element pickup, such as hydrogen, nitrogen, oxygen, and carbon in welds will generally not increase the corrosion rate of zirconium. These interstitials may, however, reduce the ductility of the metal and cause premature mechanical failures. Nitrogen contamination caused by plasma cutting with nitrogen gas may increase the corrosion rate of zirconium in nitric acid environments. If any type of cutting operation performed (e.g., oxyacetylene, plasma, laser, etc.) is used, the HAZ should be removed by grinding or machining prior to welding. Water jet cutting should be used for the cutting of zirconium, where possible, to avoid the potential for contamination caused by the heat input. The water jet cut should also be conditioned because this process utilizes an abrasive (i.e., garnet, etc.), which will embed into the zirconium surface.

### 3.14.1.3.4 Heat treatment

Improper heat treatment can result in damage to zirconium in a way which could be deleterious to corrosion resistance. Zirconium can be damaged during heat treatment if the material is placed in a nonoxidizing (i.e., reducing) atmosphere. An atmosphere with excess hydrogen (or with sufficient cathodic polarization) will cause the zirconium to absorb hydrogen and may affect the corrosion resistance of the zirconium. Before heat treatment, the zirconium vessel must be thoroughly cleaned of any surface impurities to prevent contamination during elevated temperature annealing.

When zirconium is cold formed and then heated into the full annealing temperature range, critical grain growth may occur. The grain structure will enlarge in the areas where 2–10% strain energy or cold work has been placed. Cold work of this degree can occur in some cases where plate has been brake press formed into pipe or elbows. On many occasions, formed pipe should be stress relieved at 550 °C for 30 min per 25 mm of thickness. This heat treatment will relieve the stresses caused by forming and welding. If the material is heated to the annealing range of 650–790 °C, the cold worked areas with 2–10% work will recrystallize forming very large grains surrounded by fine grains (i.e., unworked areas). These areas can be either on the outer metal surface, which

is in tension, or on the inner surface, which is in compression and will have large grains with large grain boundaries. These very large areas of accelerated grain growth may be more susceptible to intergranular attack in the higher concentrations of sulfuric acid and should be avoided.

### 3.14.1.3.5 Chemical cleaning

If zirconium equipment is to be used in halogen acids, it is recommended that it has to be cleaned chemically to remove any embedded iron during fabrication. This process should be done by a company experienced in the cleaning of a reactive metal. Smooth and clean surfaces will have the optimum corrosion resistance where rough surfaces are more likely to have surface imperfections, which could initiate premature corrosion attack, especially in the more severe environments. Before any equipment is placed in any corrosive media, it should be cleaned thoroughly to remove oils, grease, paint, and other surface debris.

## 3.14.2 Corrosion

### 3.14.2.1 Oxide Films

Zirconium behaves much like other passive metals, such as titanium, iron, and chromium, relying on passive oxide films for corrosion resistance. However, zirconium is unique in several aspects in the formation and properties of its oxide film. First, the growth of the zirconium oxide film entirely results from the migration of the  $O^{2-}$  ion.<sup>8</sup> That is, a new layer of oxide film continues to form at the metal–oxide interface. The first layer will form spontaneously because of the reactive nature of zirconium and its strong affinity (reactivity and solubility) for oxygen. Additional layers will form at much reduced and decreasing rates resulting from the protective power of the first and additional layers. This also implies that zirconium can conveniently heal any damage done at the metal–oxide interface, provided that the damage is done in an oxygen-containing environment. Very often, there is a thin layer of protective oxide film at the interface even if or when the outer layer is porous and not so protective.

Second, the oxide film on zirconium is most likely  $ZrO_2$ . The existence of oxygen derivatives of zirconium in valence states other than four may be possible but is doubtful.<sup>9</sup> However, the passive films on most passive metals can be oxides in valency of various states. For example, the oxide film on titanium

can be the most protective  $\text{TiO}_2$  film formed in oxidizing media, or a much less protective film as  $\text{TiO}$ ,  $\text{Ti}_2\text{O}_3$ , and their mixture formed in reducing media. Third,  $\text{ZrO}_2$  is a compound that is closer to insulators than to semiconductors. The chemical bonding between zirconium and oxygen is very strong and the transport of current through the film becomes increasingly difficult as the film grows. However, as for many passive alloys, the protective film is unreliable in the presence of flaws on the surface.

Accepting  $\text{ZrO}_2$  as the compound for the passive film on zirconium does not lead to a total agreement among researchers. After all,  $\text{ZrO}_2$  has three different crystalline structures: cubic (c), tetragonal (t), and monoclinic (m). Normally, c, t, and m  $\text{ZrO}_2$  are stable at temperatures between 2680 and 2370 °C, between 2370 and 1240 °C, and below 1240 °C, respectively. Burgers *et al.*<sup>10</sup> reports the film formed on zirconium during anodic polarization in a phosphoric solution to be monoclinic (m)  $\text{ZrO}_2$ , identical to the natural zirconium ore 'baddeleyite'. However, according to Charlesby,<sup>11</sup> the anodic film is cubic (c)  $\text{ZrO}_2$  in the case of polarization in 0.1 N  $\text{HNO}_3$ ; in dilute  $\text{H}_2\text{SO}_4$  or a borate solution, the film is primarily amorphous, but contains some cubic  $\text{ZrO}_2$ . Cox<sup>12</sup> has stated that the passive film formed on  $\text{H}_2\text{SO}_4$  is predominantly the cubic structure with traces of the monoclinic structure.

The oxide film formed on zirconium alloys in water and steam is just as complicated. The oxide scales are known to be predominately monoclinic  $\text{ZrO}_2$ ; however, it has been shown that the oxide layer is under high compressive stress, which may stabilize the oxide in its tetragonal form.<sup>13,14</sup> Studies by Raman spectroscopy and X-ray diffraction have shown that the oxide is a mixture of both (t) and (m)  $\text{ZrO}_2$  structures.<sup>15,16</sup> Godlewski *et al.*,<sup>15</sup> using tapered samples, have shown that in Zircaloy-4 and Zr-1% Nb alloys, ~40% of the oxide film near the oxide-metal interface has (t) structure and the proportion of (t) decreases to ~15% as the distance from the interface increases beyond ~600 nm. Using the reflection high energy electron diffraction technique on the Zr-2.5% Nb alloy, Khatamian and Lalonde<sup>17</sup> detected a mixture of nearly (c), (t), and (m) structures for films of 200-nm thick or less and the (m) structure for the outer layers of films thicker than 800 nm.

It appears that protective oxide films can, therefore, be (m), (t), (c), or their mixtures. It would be incorrect to assume that zirconium and its alloys have, for example, (t)  $\text{ZrO}_2$  to be corrosion and oxidation resistant. After all, to form, for example, (t)  $\text{ZrO}_2$  at a temperature between 1240 and 2370 °C

cannot protect zirconium. All three forms of zirconium oxide are about equally inert. Which one forms on zirconium's surface depends on temperature, alloying elements, environmental composition, and the state of stress in the film. Regardless of its structure, as long as the film is compact and adherent, it is protective.

### 3.14.2.2 Effects of Water

Water is the essential ingredient in aqueous corrosion of most metals and alloys. The presence of water in many environments makes them much more corrosive to common metals. However, with few exceptions, water is zirconium's best friend. For example, a major reason for using zirconium in the nuclear industry (apart from its low neutron capture cross section) is its excellent resistance to water and steam. This capability even extends into highly reducing conditions such as hydrochloric and dilute sulfuric acids. However, zirconium may become vulnerable in certain water-free environments, for example, organic solutions. Without water, zirconium is not able to repair any damage made to the protective film. Hence, the reactive nature of zirconium will be exposed to corrosive attack; the addition of small amounts of water may stop this.

Exceptions include the presence of water in chlorine and fluorine that makes them corrosive to zirconium. Unlike titanium, zirconium resists attack by dry chlorine (titanium may even ignite in dry chlorine). However, zirconium is susceptible to local attack in wet chlorine, which can be regarded as an oxidizing chloride solution (i.e., containing chloride and hypochlorite). Water-containing fluorine is corrosive to both titanium and zirconium.

### 3.14.2.3 Effects of Temperature

Zirconium is regarded as both a reactive and refractory metal because of its high melting point of 1852 °C. However, zirconium is not suitable for high temperature applications because of its reactivity. Zirconium reacts with many metallic and nonmetallic elements at elevated temperatures, that is why zirconium needs a clean surface and argon shielding in welding. Heat treatments may be done in air, but only with a clean surface. For example, to leave a fingerprint on zirconium's surface, this may result in local break-away oxidation as demonstrated in [Figure 6](#).

Zirconium may be used for long-term service generally only when the temperature is 350 °C or lower. For example, the corrosion rate of zirconium changes

little in nitric acid and dilute sulfuric acid as the temperature increases within zirconium's limit. With increasing temperature, the corrosion rate of zirconium may increase but so does the film formation rate. The net change remains small. Of course, in noncompatible media, such as hydrofluoric acid and concentrated sulfuric acid, the corrosion rate of zirconium increases rapidly with increasing temperature.

### 3.14.2.4 Effects of pH

Thermodynamically, zirconium behaves like most passive metals in acidic and alkaline solutions as

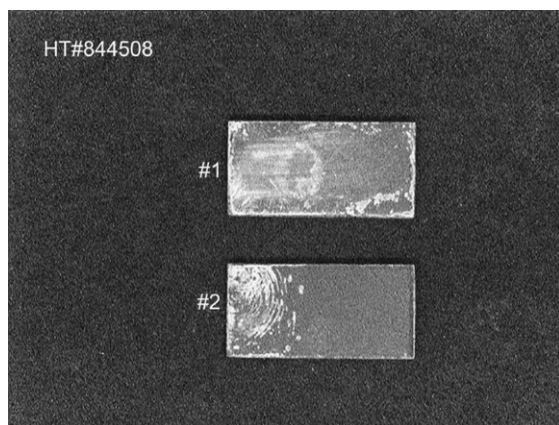


**Figure 6** Effect of finger print on zirconium after heating at 760 °C for 30 min.

shown in [Figure 7](#).<sup>9</sup> Zirconium dioxide or hydrated zirconium dioxide dissolves as  $\text{ZrO}^{2+}$  when the pH is less than or equal to 3.5 and as  $\text{Zr}^{4+}$  when the pH is less than about 1. Dissolution as  $\text{ZrO}^{2+}$  is expected to be much slower than as  $\text{Zr}^{4+}$ . Zirconium dioxide retains most of its protective capability until the pH is less than 1 and above 13. In fact, zirconium is one of the few metals that exhibit excellent corrosion resistance over such a wide range of pH and, hence, zirconium equipment can be used in processes that cycle between strong acids and strong alkalis. In this aspect, zirconium is better than other high-performance materials, such as titanium, tantalum, glass, and polytetrafluoroethylene (PTFE), which are generally poor in strong alkalis.

The pH has some effect on the solubility of the oxide film on zirconium, but the effect is not dramatic. Practically, the corrosion resistance of zirconium has little dependence on pH over a wide range.<sup>18</sup> Zirconium dioxide is virtually insoluble in neutral water. It dissolves slightly as the pH increases or decreases as long as pH is not extreme. Slight dissolution conditions for zirconium oxides may have some beneficial effects that are discussed later.

However, pH change may alter the corrosive nature of impurities in a solution. Two important impurities to be considered are ferric ion and fluoride ion. Ferric ion is a common, well-known oxidizing ion that induces pitting on metals and alloys in halide

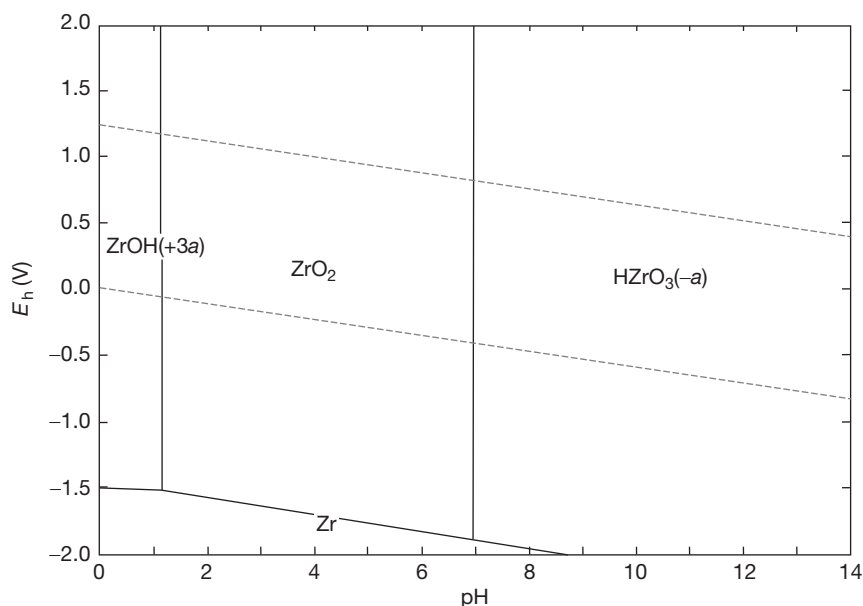


**Figure 7** The potential–pH diagram of zirconium in water at 25 °C for a dissolved metal ion concentration of  $10^{-5}$  M.

solutions. Fluoride ion has the capability to interfere with oxide formation even at low temperatures. Normally, ferric ion exists in solutions when the pH is less than or equal to 2.5 and when the solution potential exceeds 0.771 V versus NHE.<sup>9</sup> In a nonaerated acid, iron corrodes to yield ferrous ions that are too reducing to induce pitting on most metals and alloys. Ferrous ion tends to become ferric ion in the presence of oxygen. Zirconium resists pitting in iron-containing chloride solutions when the pH is 3 or greater.<sup>19</sup> To control the pitting of zirconium in copper-containing chloride solutions, the pH needs to be 5 or greater.<sup>20</sup>

Furthermore, the corrosivity of fluoride solutions may change dramatically with changing pH. Zirconium is totally defenseless in hydrofluoric acid (HF) at all concentration and temperature as it forms soluble zirconium complex ions in the acid. Although zirconium is not suitable for handling HF solutions, it has some resistance to certain fluoride solutions, such as calcium and sodium fluorides, provided the pH is sufficiently high and the temperature is sufficiently low. The corrosion rate of zirconium in saturated calcium fluoride at pH 5 and 90 °C is close to zero ( $<0.025 \text{ mm year}^{-1}$ ). However, although the corrosion rate of zirconium in saturated sodium fluoride (at pH 7.4) is also effectively zero at 28 °C, it is more than  $1270 \mu\text{m year}^{-1}$  at 90 °C. One major difference between calcium and sodium fluorides is their solubility in water. At room temperature, the solubility of calcium and sodium fluorides are 2 and 4300 ppm, respectively. Hot solutions with a lot of dissolved fluoride ions are potentially corrosive to zirconium. However, the concentration of dissolved fluoride ions is not always proportional to the concentration of the added fluoride salt.

Thermodynamically, hydrofluoric acid exists when the pH is less than or equal to about 3.2.<sup>9</sup> The solution then becomes increasingly corrosive to zirconium, regardless of temperature, with decreasing pH. Therefore, zirconium is not recommended for handling fluoride-containing acids, unless the fluoride ions are effectively removed by complexing.<sup>21</sup> It is important to be aware that there may be overlooked sources of fluoride in particular processes.<sup>22</sup> For example, technical grade phosphoric acid can contain over 1000 ppm of fluoride ion (not necessarily indicated in the specification). Food grade phosphoric acid clearly gives the minimum fluoride content, typically,  $<5 \text{ ppm}$ . Other overlooked sources include contaminated waters, recycled acids, fluxes, and fluorinated compounds.

### 3.14.2.5 Localized Corrosion

#### 3.14.2.5.1 Pitting corrosion

Like most passive metals and alloys, zirconium is susceptible to pitting in all halide solutions except fluoride solutions<sup>23</sup> where it is vulnerable to general corrosion. For zirconium, the susceptibility to pitting is greatest in chloride solutions and decreases as the halide ion becomes heavier. This is the reverse order in the case for titanium, which is highly resistant to pitting in chloride solution but is vulnerable to pitting in iodide solutions.

The pitting potentials of zirconium in 1 N solutions of  $\text{Cl}^-$ ,  $\text{Br}^-$ , and  $\text{I}^-$  are +380, +660, and +910 mV NHE, respectively. These potentials decrease gradually with increasing concentration and decrease rapidly in concentrated halide solutions.<sup>24</sup> Other factors, such as pH,<sup>24</sup> temperature,<sup>24</sup> alloying element,<sup>25</sup> and film quality,<sup>26</sup> also affect pitting potential under certain conditions. The major concern for zirconium is pitting in chloride solutions. Figure 8 illustrates the electrochemical behavior of zirconium and stainless steel. In chloride-free solutions, zirconium is more corrosion resistant than stainless steel and most other passive alloys. However, in chloride-containing solutions, zirconium's advantage disappears in oxidizing conditions. Thus, although zirconium may have a slightly higher pitting potential than stainless steel in chloride solutions, it pits at a much higher rate than stainless steel under a constant potential condition.

Zirconium does not pit in most chloride solutions, such as seawater and underground fluids, because its corrosion potential is often lower than the pitting potential.<sup>27,28</sup> The presence of oxidizing ions, such as ferric and cupric ions, in acidic chloride solutions may increase the corrosion potential to exceed the pitting potential, therefore, pitting may occur. Pitting may also occur when there is an applied anodic potential or when zirconium is coupled with a more noble material, such as graphite or platinum. Nitrate and sulfate ion can inhibit the pitting of zirconium under certain conditions.<sup>20,29,30</sup> Corrosion control measures for pitting and other types of corrosion will be discussed in a later section.

#### 3.14.2.5.2 Crevice corrosion

In chloride solutions, zirconium is among the most resistant of metals to crevice corrosion. Zirconium is not subject to crevice corrosion even in low-pH chloride solutions or chlorine gas. This can be rationalized by the common model proposed for

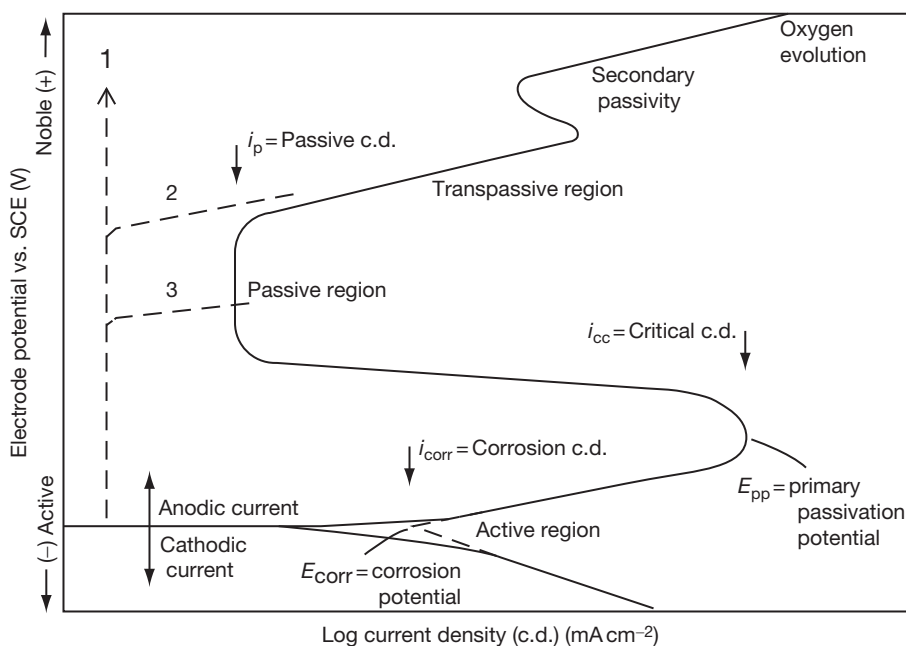


**Figure 8** The electrochemical behavior of stainless steel and zirconium in (1) chloride-free dilute solutions, (2) chloride-free concentrated solutions, and (3) chloride-containing solutions. Solid line: Common features found in stainless. Dotted line: Common features found in zirconium.

crevice corrosion. In the initial stage of crevice corrosion, metal dissolution and oxygen reduction occur uniformly over the entire surface, including the interior of the crevice. After a short interval, the oxygen within the crevice is depleted because of its confinement, so oxygen reduction ceases within the crevice while metal dissolution continues. This tends to produce an excess of positive charge in the solution, which is necessarily balanced by the migration of negative chloride ions into the crevice. At the same time, positively charged ions, such as  $\text{Fe}^{3+}$ , stay outside the crevice. Similar to the pitting process, metal chloride dissociates into an insoluble hydroxide and a free acid ( $\text{H}^+ + \text{Cl}^-$ ). In addition, the condition within crevices is too reducing to have ferric ions. These changes are actually favorable for zirconium. Consequently, zirconium is not susceptible to crevice corrosion in chloride solutions.

To follow the same model, zirconium would be susceptible to crevice corrosion in fluoride solutions. Crevice corrosion at the contact between zirconium and PTFE would be a special case. PTFE is an inert material and releases few fluoride ions when it is produced by the pressurized process for making virgin materials. It can also be produced from recycled materials by remelting. Recycled PTFE is not as stable as virgin PTFE and may release large amounts

of fluorides. Crevice corrosion of zirconium under PTFE gaskets has occurred several times in acids when recycled PTFE or a less stable type of fluoropolymer had been used.

Furthermore, zirconium is susceptible to crevice corrosion in dilute sulfuric acid when the acid is allowed to concentrate within the crevice.

### 3.14.2.5.3 Intergranular corrosion

Zirconium alloys poorly with most elements and is miscible only with titanium, hafnium, and scandium. Thus, most elements have very low solubility in zirconium and form intermetallic compounds as second phase precipitates. Iron is the major, most visible impurity in zirconium, and zirconium-iron compounds are the most important to consider. Depending on thermomechanical history, zirconium-iron compounds distribute in zirconium in several ways.<sup>31</sup> Mill products typically have the uniform distribution of fine particles. Grain boundaries also are favorite sites for these particles to precipitate. More importantly, these particles tend to be spheroidal under the annealed condition. These particles can become elongated in the HAZ and the weld metal under the as-welded condition as shown in **Figure 9(a)** and **9(b)**. When there are sufficient elongated particles, they tend to form interconnected networks and are,



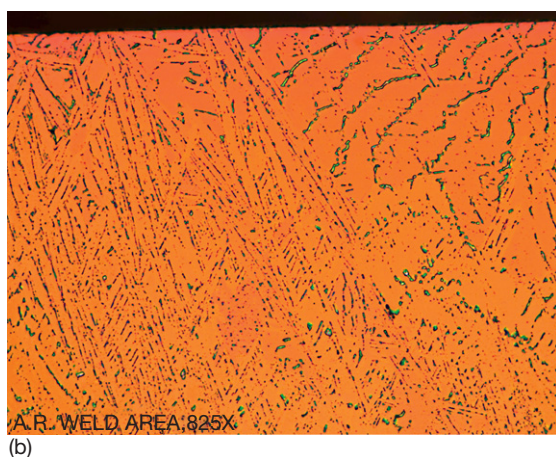
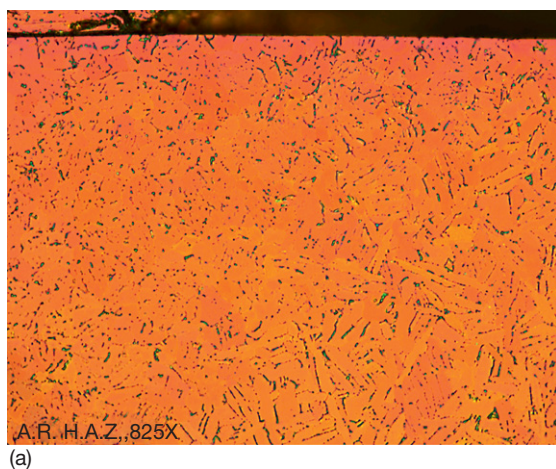


**Figure 9** (a) The HAZ of as-welded Zr702 and (b) the weld metal of as-welded Zr702.

therefore, not as corrosion resistant as zirconium in most environments. Consequently, the HAZ and the weld metal are susceptible to intergranular corrosion in media such as concentrated sulfuric and hydrochloric acids.

Heat treatment can be used to modify the morphology of the second-phase particles in the HAZ and the weld metal. Heating at 770 °C is effective as shown in [Figure 10](#). After heat treatment, elongated particles become spheroidal similar to those in the parent metal. The resistance of zirconium to intergranular corrosion is, therefore, greatly improved.

#### 3.14.2.5.4 Stress corrosion cracking

Zirconium and its alloys resist stress-corrosion cracking (SCC) in many environments, such as NaCl, MgCl<sub>2</sub>, NaOH, and H<sub>2</sub>S, which are strong

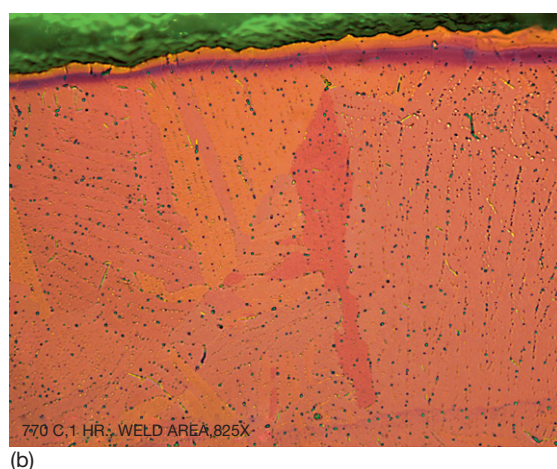
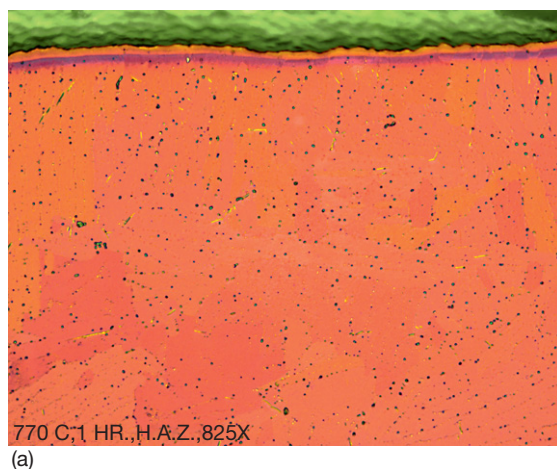


**Figure 10** (a) The HAZ of heat-treated Zr702 and (b) the weld metal of heat-treated Zr702.

SCC-inducing agents on common metals and alloys. Thus, zirconium service failures resulting from SCC are few in chemical applications. The high SCC resistance of zirconium can be attributed to its high repassivation rate. In the presence of water or oxygen, any breakdown in the surface oxide film is quickly healed. The environments known to cause SCC of zirconium include FeCl<sub>3</sub>, CuCl<sub>2</sub>, halogen, or halide-containing methanol and certain other organics, concentrated HNO<sub>3</sub>, liquid mercury or caesium,<sup>32</sup> and 64–69% H<sub>2</sub>SO<sub>4</sub>.<sup>33</sup> Control measures for the SCC of zirconium include:

- avoiding high sustained tensile stresses;
- modifying the environment, for example, changing pH, concentration, or adding an inhibitor;
- maintaining a high-quality surface film, that is, one low in impurities, defects, and mechanical damage;



- applying a small cathodic potential or coupling with a more active material;
- insulating the contact between zirconium and a noble material, such as graphite and platinum;
- shot peening.

### 3.14.2.5.5 Delayed hydride cracking

Hydrogen is well known for its capability to cause damage in many metals and alloys. In titanium and zirconium, which form brittle hydrides, failure can occur by two embrittlement processes. One process is a reduction in the fracture toughness of the metal due to the presence of a high concentration of hydride platelets that have their in-plane dimensions in the crack growth direction. The second process is delayed hydrided cracking (DHC), which is the result of a mechanism of crack initiation and slow propagation.<sup>34</sup>

In DHC, hydrogen diffusion in the metal is required. Gradients of concentration, temperature, and stress are all important factors in controlling diffusivity as given in the general diffusion equation:

$$\mathcal{J} = \frac{DC_x}{RT} \left[ RT \frac{d \ln C_x}{dx} + \frac{Q^* dT}{T dx} - \frac{V^* d\sigma}{3 dx} \right]$$

where  $\mathcal{J}$  is the hydrogen flux;  $D$ , the diffusivity of hydrogen at any point  $x$ ;  $C_x$ , the concentration of hydrogen at any point  $x$ ;  $R$ , the gas constant;  $T$ , the temperature;  $Q^*$ , the heat of transport of hydrogen in metal;  $V^*$ , the volume of transport of hydrogen in metal; and  $\sigma$  is the tensile stress (a compressive stress would have a negative value).

That is, hydrogen is driven by three forces to an area of lower concentration, colder temperature, and higher tensile stresses. Since DHC may occur at low temperatures in a matrix of uniformly distributed hydrogen, its mechanism is believed to be as follows: stress gradients at stress concentration sites attract hydrogen, resulting in local hydride precipitation, growth, and reorientation. When the growing hydride reaches some critical size, the hydride either cleaves or the hydride–matrix interface opens up to nucleate a crack. Once a crack has nucleated, propagation occurs by repeating the same process at the crack tip and, as such, is a discontinuous process. It should be noted that the formation of hydrides is not a necessary requirement for this mechanism to operate, as is the case in delayed hydrogen embrittlement in high-strength steels.

Stress and stress gradient are two necessary requirements for DHC to occur and, fortunately, they are controllable. High stresses without gradients

will not induce DHC. Hydrogen cannot move when high stresses are uniformly distributed in the structure. High-stress gradients are needed to move hydrogen but cannot be created without high stresses. High stresses are also required in fracturing hydride.

Stress relieving is one of the most effective measures in preventing DHC. It takes considerable time for hydrogen to reach the highly stressed area and to precipitate out as hydride platelets. Furthermore, the platelets must grow large enough for cracking to occur. Depending on many factors, it sometimes takes 2 years for DHC to happen, but 5 weeks after welding is the shortest known period for Zr705 to suffer DHC at room temperature. This provides a base for the Boiler and Pressure Vessel Code of the ASME (Section VIII, Division 1, Subsection C, UNF-56, (d), 1992, p.183) to add the following guideline:

Within 14 days after welding, all products of zirconium Grade R60705 shall be heat-treated at (538–593 °C) for a minimum of 1 h for thicknesses up to 1 in. (25.4 mm) plus ½ h for each additional inch of thickness. Above 800 °F (427 °C), cooling shall be done in a closed furnace or cooling chamber at a rate not greater than 500 °F h<sup>-1</sup> (260 °C h<sup>-1</sup>) divided by the maximum metal thickness of the shell or head plate in inches but in no case more than 500 °F h<sup>-1</sup>. From 800 °F, the vessel may be cooled in still air.

### 3.14.2.6 Galvanic Corrosion

With the naturally occurring oxide film, zirconium often assumes a noble potential in most environments. As an example, the galvanic series in seawater is close to the nobility of noble materials. Since zirconium is more corrosion resistant than most materials in a wide range of corrosives, zirconium is likely the cathode in most cases. The material in contact with zirconium could corrode at a much faster rate. The risk for zirconium is absorption (as cathode) and, hence, hydrogen embrittlement.

However, in incompatible environments, such as hydrofluoric acid and concentrated sulfuric acid, zirconium may assume an active potential. Moreover, zirconium may be activated at vulnerable sites when it is in contact with a noble material in chloride solutions. Graphite and carbides in the powder form can be very effective in promoting galvanic corrosion on zirconium since a small amount of powder may produce a very large cathodic area. The effect of coupling with graphite on the corrosion of zirconium in boiling 20% HCl is shown in Table 6.<sup>20</sup> It is

**Table 6** Effect of graphite-coupling on the corrosion of zirconium in boiling 20% HCl after 4 weeks of exposure

Specimen area (cm <sup>2</sup> )		Area ratio graphite/ zirconium	Corrosion rate, mm year <sup>-1</sup> (mpy)
Graphite	Zirconium		
–	31.0	0	0.013 (0.51)
5.9	31.0	0.19	0.013 (0.51)
24.8	5.0	4.96	0.0173 (0.68) <sup>a</sup>
27.0	2.5	10.8	0.239 (9.4) <sup>a</sup>

<sup>a</sup>Localized corrosion.

evident that the effect can be dramatic when the surface area of graphite is significantly larger than that of zirconium.

The effect of galvanic coupling to carbon-based materials is common in chemical equipment due to their popularity and the availability of various forms. Carbon-based materials are used as structural materials, gaskets, additives to lubricants, etc. Galvanic effects induced by carbon-based materials should be appraised not just for zirconium but also for other common metals and alloys.

### 3.14.2.7 Microbiologically Influenced Corrosion

Microbiologically induced or influenced corrosion (MIC) occurs as a result of the presence and metabolism of living organisms in the corrosion environment or on the corroded material. Regardless of the mechanism, MIC can cause large damage to process equipment when natural waters are used in hydrostatic tests or as cooling fluids. However, results of long-term tests in natural waters indicate that zirconium is immune to MIC.

The organisms of greatest concern are sulfate-reducing bacteria. Metabolic processes may produce corrosives, such as sulfuric acid, inorganic or organic sulfides, and organic acids. Common metals and alloys have a high affinity for sulfur and its compounds. As a result, metabolic products simply make it too corrosive for common metals and alloys. Conversely, zirconium has little affinity for sulfur and its compounds. Zirconium resists attack by most inorganic and organic acids as well. Metabolic products are not corrosive to zirconium. In addition, changes in oxygen potential, salt concentration, pH, etc. from organisms do not degrade zirconium's corrosion resistance. Cathodic depolarization associated with anaerobic growth is unfavorable to certain metals and alloys but not to zirconium.

### 3.14.2.8 Erosion–Corrosion

Erosion is defined as accelerated corrosion resulting from the conjoint action of corrosion and erosion in the presence of a moving corrosive fluid. This type of attack is highly dependent on fluid flow-rate and corrosivity. It is particularly prevalent in areas where high local turbulence, impingement, or cavitation of the fluid may occur on metal surfaces. Solids that are suspended in fluid may result in abrasion, which may also drastically accelerate metal removal.

In compatible environments, zirconium forms a hard, tenacious ZrO<sub>2</sub> surface film that provides an excellent barrier to erosion–corrosion. Also, zirconium can quickly repair damage done to the film in environments containing oxygen. Consequently, zirconium can withstand many corrosives at high flow rates. To study this, a corrosion test loop was constructed to investigate the effects of flow rate and heat flux on the corrosion of zirconium tube specimens.<sup>35</sup> No effect was detected when the test conditions were 50% sulfuric acid at 166 °C flowing at 2.1 m s<sup>-1</sup>.

Many passive alloys have the difficulty of forming protective films on their surfaces in sulfuric acid, and they are, therefore, vulnerable to erosion–corrosion in the acid. This is demonstrated in Figure 11.<sup>36</sup> In a sulfuric acid-based mixture, the corrosion of zirconium is insensitive to increasing rotation speed up to 10 000 rpm. On the other hand, corrosion of Alloy C-276 increases continuously from low speed to high speed under the same test conditions.

### 3.14.2.9 Fretting Corrosion

Fretting corrosion results from the combined effects of wear and corrosion and takes place when vibration contact is made at the interface of tight-fitting, highly loaded surfaces, such as between the leaves of a spring or in rolling contact bearings. Factors affecting fretting corrosion include contact load, amplitude, frequency, temperature, and corrosivity of the environment.

Fretting corrosion is a concern for zirconium, since zirconium is a soft and reactive metal. It occurs when zirconium's protective oxide film is mechanically damaged or removed. Measures should be taken to control fretting corrosion. Fretting corrosion on zirconium may be avoided by proper design and fabrication, or through the addition of a heavy oxide coating to combat mechanical effects. This coating drastically reduces friction and prevents the removal of the protective oxide layer.

### 3.14.2.10 Surface Condition

Corrosion is a surface phenomenon, so surface condition is an important factor in the corrosion of metals and alloys. It plays an important role not just in the initiation but also in the propagation of localized corrosion. The corrosion resistance of zirconium is not affected by common surface features such as scratch and heat tint, but may be degraded by embedded particles such as iron and silicon carbide in oxidizing chloride solutions. As indicated in [Figure 12](#), zirconium with different surface conditions has a wide range of rest potential in a hydrochloric acid solution.<sup>20</sup> The potential of pickled zirconium is low and stays low. The potential

of zirconium with SiC abraded surface increases quickly to reach the breakdown potential. In chloride solutions, it is preferred for zirconium to have a low potential that is below the breakdown potential. Pitting is therefore avoided. Zirconium with a clean, smooth surface is expected to have the optimum resistance to localized corrosion including pitting, SCC, and DHC.

### 3.14.2.11 Tin in zirconium

Zircaloy recycling is a major source for zirconium in making zirconium alloys and it can be noted that there may be more than 2000 ppm tin in Zr702 without violating the chemical requirements given in [Table 2](#).

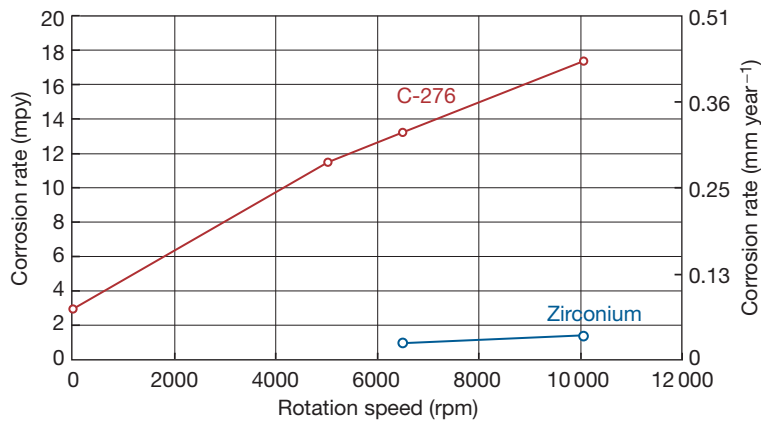


**Figure 11** Results of rotating cylinder electrode tests in a mixture of sulfuric acid, organic acids, and water at 100°C.

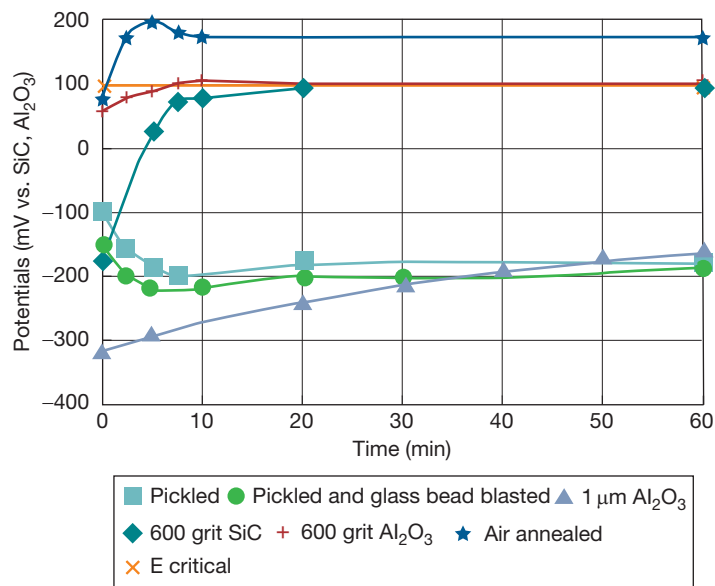


**Figure 12** Surface effect on the rest potential of Zr702 in 10% HCl + 500 ppm ferric ion at 30°C.

Advantages of utilizing Zircaloy recycle include consistent mechanical properties, improved corrosion-oxidation resistance in water and steam, and reduction in cost and material conservation. Small amounts of tin may be beneficial or acceptable for Zr702. However, there are cases to implicate that zirconium with a sufficiently high tin content has degraded corrosion resistance in certain environments. Zircaloys have a mechanical strength advantage over Zr702 and, hence, have been used in the manufacture of fittings for corrosive applications. Zircaloy fittings have failed in hot glacial acetic acid after 3 weeks to 5 months of service.<sup>37</sup> Zr702 and Zr705 are known to be highly compatible with acetic acid. Thus, the failures of Zircaloy can be attributed to the high tin content ( $\sim 1.4\%$ ) in the alloys.

The zircaloy family of materials was developed for improved corrosion properties in high pressure water and steam primarily as a cladding material for nuclear fuel. Tin additions to zirconium were originally intended to offset the harmful effects of impurities like nitrogen where they were often higher than 40 ppm. However, the nitrogen content of the present zircaloy materials is much lower, and higher levels of tin can be more harmful than beneficial in this circumstance. Thus, the corrosion resistance of zircaloy-4 in 400 °C steam improves with decreasing tin content from 1.41 to 0.09%.<sup>38</sup> It should be noted that the test temperature was much higher than the operating temperature of zirconium equipment in nuclear reactor (pressurized water) environments (285–350 °C). This effect of tin is expected to decrease with decreasing temperature.

Results of 28-day tests show that the presence of greater than 3000 ppm tin is much more critical to zirconium in boiling sulfuric acid than in boiling acetic, hydrochloric, and nitric acids. The critical tin content in zirconium for sulfuric acid service seems to be between 2000 and 3000 ppm.<sup>39</sup> However, the distribution of tin in zirconium is not uniform. To take the fluctuation into consideration, the target point for the tin content in Zr702 should be set at 1500 ppm, if 2000 ppm proves to be the limit for the alloy in sulfuric acid service.<sup>39</sup> Recently generated data seem to support this recommendation.<sup>40</sup>

### 3.14.3 Corrosive Environments

#### 3.14.3.1 Pressurized Water and Steam

Due to its passivity, zirconium is suitable for nuclear applications since water-cooled reactors operate with oxygen or hydrogen charged coolant at temperatures

from 286 to 350 °C. The corrosion and oxidation of unalloyed zirconium in high temperature water and steam are irregular; that is, oxide growth is not generally self-limiting. This behavior is related to variations in the impurity content of the metal with nitrogen and carbon impurities particularly harmful. The oxidation rate of unalloyed zirconium increases markedly when nitrogen and carbon concentrations exceed 40 and 300 ppm, respectively.<sup>41,42</sup> The irregular behavior of unalloyed zirconium has stimulated alloy development programs. Zircaloy-2, zircaloy-4, Zr-2.5Nb, and Zr-1Nb ('Zirlo') are the most important alloys developed for nuclear applications because they are more reliable and predictable for use in hot water and steam, in addition to being stronger.

During oxidation at elevated temperatures, zirconium alloys initially form a tightly adherent oxide film at a rate that is at first quasicubic but, after an initial period, undergoes a transition to linear behavior. Unlike the white, porous oxide films on unalloyed zirconium, the oxide film on zircaloy-2 remains dark and adherent throughout transition and in the post-transition region. Zircaloy-4 differs in composition from zircaloy-2 by having a slightly higher iron content but no nickel. Both variations are intended for reducing hydrogen pickup during corrosion but with minimal effect on overall corrosion resistance during reactor operation. Hydrogen pickup detrimentally influences fuel cladding performance with regard to hydride formation. For example, in water at 360 °C, the hydrogen pickup for zircaloy-4 is about 25% of the theoretical quantity, or less than half of that for zircaloy-2. In addition, hydrogen pickup for zircaloy-4 is less sensitive to hydrogen overpressure than that for zircaloy-2. For both alloys, hydrogen pickup is greatly reduced when dissolved oxygen is present in the medium.<sup>41</sup>

The Zr-2.5Nb alloy is considered somewhat less resistant to corrosion than the zircaloys with exceptions. Nevertheless, the Zr-2.5Nb alloy is suitable for many applications, such as pressure tubes in the primary loops of some reactors. Furthermore, the corrosion resistance of the Zr-2.5Nb alloy can be substantially improved by heat treatments.<sup>42,43</sup> In addition, the Zr-2.5Nb alloy is superior to Zircaloys in steam at temperatures above 400 °C.<sup>43</sup>

#### 3.14.3.2 Other Aqueous Systems

##### 3.14.3.2.1 Cooling waters

Unalloyed zirconium does not seem to have irregular behavior in cooling waters, such as the towns water, river water, or potable water, that are used as the

cooling media in the chemical process industry. Such waters have much higher levels of impurities than water used in the nuclear reactors. The highest temperature in such heat exchangers is around 300 °C, and the longest lifetime is more than 20 years; zirconium has generally performed well in these waters.

The major difference between pure water in nuclear reactors and common cooling waters is their corrosivity. There is also the important factor of the effect of neutron flux on the oxidation process, which is likely to accelerate corrosion by increasing lattice diffusion. However, in the chemical process industry zirconium heat exchangers can have a long and satisfactory life. For example, two zirconium heat exchangers were retired from a urea plant after continual service for 20 years. The tubes looked like new and were used to build yet another heat exchanger. The watersides of the tubes were covered with very thin oxide films without any sign of breakaway oxidation after 20 year's use.

### 3.14.3.2.2 Salt solutions

Zirconium has excellent corrosion resistance to seawater, brackish water, and polluted water. Zirconium's advantages in salt waters include its insensitivity to variation in factors like chloride concentration, pH, temperature, velocity, crevice, and sulfur-containing organisms. The effects of pH on iron-ions-containing salt water were discussed earlier. Results of certain field and laboratory tests are summarized as follows.<sup>28</sup>

Zr702 specimens with or without a crevice attachment were placed in the Pacific Ocean at Newport, OR, for up to 129 days. All welded and nonwelded specimens exhibited nil corrosion rates. Marine biofouling was observed; however, no attack was found beneath the marine organisms or within the crevices. Laboratory tests were performed on specimens of Zr702 and Zr704 in boiling seawater for 275 days and in 200 °C pressurized seawater for 29 days. Both alloys resisted general corrosion, pitting, and crevice corrosion.

U-bend specimens, with or without steel coupling, of Zr702, nickel-containing Zr704 or zircaloy-2, and nickel-free Zr704 or zircaloy-4, were tested in boiling seawater for 365 days as shown in Table 7. No cracking was observed during the test period. Overstressing of the tested U-bends indicated that all specimens, except one, remained ductile. The exception was the welded nickel-containing Zr704 with steel coupling which showed some hydrogen and oxygen absorption. Chemical analyses and metallographic examinations on other U-bends did not reveal any evidence of hydrogen absorption and

**Table 7** Chemical analyses for hydrogen and oxygen (ppm) of tested U-bends in boiling seawater for 365 days

<i>Metal</i>	<i>Hydrogen</i>	<i>Oxygen</i>
Nonwelded Zr702 U bend with steel coupling	6	1350
Nonwelded Zr704 (Ni-containing) U bend with steel coupling	8	1480
Nonwelded Zr704 (Ni-free) U bend with steel coupling	9	1440
Welded Zr702 U bend with steel coupling	8	1250
Welded Zr704 U bend (Ni-containing) with steel coupling	450	5000
Welded Zr704 (Ni-free) U bend with steel coupling	5	1480

hydride formation. Results of chemical analyses are given in. These results support that the presence of nickel in zirconium promotes hydrogen pick-up.

Zirconium resists most salt solutions, which include halogen, nitrate, carbonate, and sulfate.<sup>59,60</sup> Corrosion rates are typically very low at temperatures at least up to the boiling point. Solutions of strong oxidizing chloride salts, such as ferric and cupric chlorides, are examples of the few exceptions. Zirconium is considerably more resistant to chloride SCC than are stainless steels.<sup>32</sup> For example, U-bends of Zr702 do not fail in boiling 42% magnesium chloride. Another attractive property of zirconium is its high resistance to crevice corrosion. Zirconium is not subject to crevice corrosion even in acidic chloride solutions at elevated temperatures. No attack was observed on zirconium in a salt spray environment.<sup>67</sup>

### 3.14.3.2.3 Sulfur compounds

Sulfur and its compounds are highly corrosive to common metals. They are often present in underground fluids, such as oil, natural gas, and geothermal fluids. Though zirconium is a reactive metal, it has little affinity for sulfur. Consequently, zirconium has excellent corrosion resistance to sulfur and its compounds. It requires a high temperature, around 700–900 °C, for zirconium to react with sulfur vapor or hydrogen sulfide to yield a number of sulfides. Moreover, there is no instance of zirconium–sulfur bonds forming in aqueous systems.<sup>44,45</sup> Practically, therefore, zirconium is immune to sulfide stress cracking (SSC).

### 3.14.3.3 Inorganic Acids

#### 3.14.3.3.1 Sulfuric acid

Sulfuric acid is the most important acid for use in the manufacture of many chemicals. For example, the



acid is used as a dehydrating agent, an oxidizing agent, an absorbent, a catalyst, a reagent in chemical syntheses, and much more. These highly versatile capabilities can be attributed to the complicated nature of this acid. Sulfuric acid is a corrosive with a continuously changing character. It changes from the reducing nature of dilute acid to the oxidizing nature of concentrated acid. The reactivity of sulfur compounds and the difficulty of forming protective oxide films under reducing condition make common passive metals vulnerable to corrosion in dilute acid. In fact, hot, dilute acid is a pickling solution for steel and stainless steel. Solutions become increasingly oxidizing at or above 65%. The usefulness of passive metals and alloys depends strongly on acid concentration, temperature, aeration, and other impurities.

Zirconium and its alloys are straightforward in their corrosion resistance to sulfuric acid as shown in **Figures 13–15**.<sup>48</sup> Published data for zirconium before the establishment of Zr702 were collected to construct **Figure 13(a)**. Corrosion data generated at the Wah Chang company were used to construct **Figures 13(b), 14, and 15** for ASTM grades. It should be noted that isocorrosion curves are normally constructed based on short-term results of laboratory tests conducted under well-controlled conditions. The curves should be used to understand the corrosion behavior of the alloys rather than to predict the performance of the alloys in actual service. There are many factors affecting the performance of the alloys. The factors include impurities in the alloys and environments, equipment design and fabrication, operating conditions, and maintenance.

Zirconium and its alloys resist attack by sulfuric acid at all concentrations up to 70%. The major difference among these grades is in the near boiling region when the acid concentration is greater than 60%. In this region, Zr702 outperforms Zr704 and Zr705. In 70–80% sulfuric acid, the corrosion resistance of zirconium and its alloys depends strongly on temperature. In higher concentrations, the corrosion rate of zirconium and its alloys increases rapidly with concentration due to the formation of nonprotective zirconium sulfate film.

There are three regions in **Figure 13(a)** that are attractive for using zirconium in sulfuric acid services. The first region is dilute sulfuric acid,  $\leq 10\%$ , at elevated temperatures. In this region, the temperature limit for zirconium is well above 200 °C. The second region is hot 10–45% sulfuric acid, where zirconium is highly stable in the passive state. Zirconium can tolerate lots of oxidizing impurities and some chlorides. The third region is 45–70% sulfuric acid where

zirconium stays corrosion resistant when factors like acid concentration and impurities are controlled within zirconium's limitations.

The corrosion behavior of zirconium can be further examined from electrochemical measurements. The anodic polarization curves of zirconium in 4.9–72.5% sulfuric acid at near-boiling temperatures are shown in **Figure 16**. As indicated in **Figure 16**, zirconium experiences a passive-to-transpassive transition in sulfuric acid with an increasing potential. Zirconium does not have the active region in sulfuric acid as is the case with common metals and alloys.

As indicated in **Figure 16**, zirconium has very high transpassive (breakdown) potentials in dilute sulfuric acid. This indicates that zirconium can tolerate large amounts of oxidizing agents, such as ferric and nitrate ions in dilute sulfuric acid. For example, there is no effect on zirconium in steel pickling application even after a few percent of iron dissolves in dilute sulfuric acid, provided that chlorides are not present in significant amounts.

In  $>20\%$  sulfuric acid, the breakdown potential of zirconium decreases noticeably with increasing concentration. Looking at **Figure 16** closely, still there is a visible passive region for zirconium in 65% sulfuric acid. This means zirconium can tolerate some amounts of strong oxidizing agents in  $\leq 65\%$  sulfuric acid.<sup>47</sup> In  $>65\%$  sulfuric acid, zirconium becomes sensitive to the presence of oxidizing agents. **Figure 17** illustrates the effect of the presence of 200 ppm of various oxidizing agents on zirconium in  $>65\%$  sulfuric acid.

The acid concentration limit is very important when zirconium is used to process sulfuric acid in the marginal concentration region, such as 60% or more. In less than 65% sulfuric acid, although the vapor is almost entirely water, the concentration shows little change in a pressurized system. However, acid concentration can change significantly because, for example, of the imperfect sealing of a system. Acid concentration can easily change in a vacuum system because the water vapor is continuously removed.

When the acid concentration limit is exceeded, zirconium may corrode rapidly. Under certain conditions, a pyrophoric surface layer may be formed on zirconium. The pyrophoric surface layer on zirconium formed in 77.5% sulfuric acid + 200 ppm ferric ion at 80 °C consisted of  $\gamma$ -hydride, zirconium sulfate, and fine metallic particles. The combination of  $\gamma$ -hydride and metallic particles is suggested to be responsible for the pyrophoricity.<sup>48</sup> Treating in hot steam can be used to eliminate this tendency.

As shown in **Figures 13(b), 14, and 15**, the resistance of zirconium in  $>55\%$  sulfuric acid is



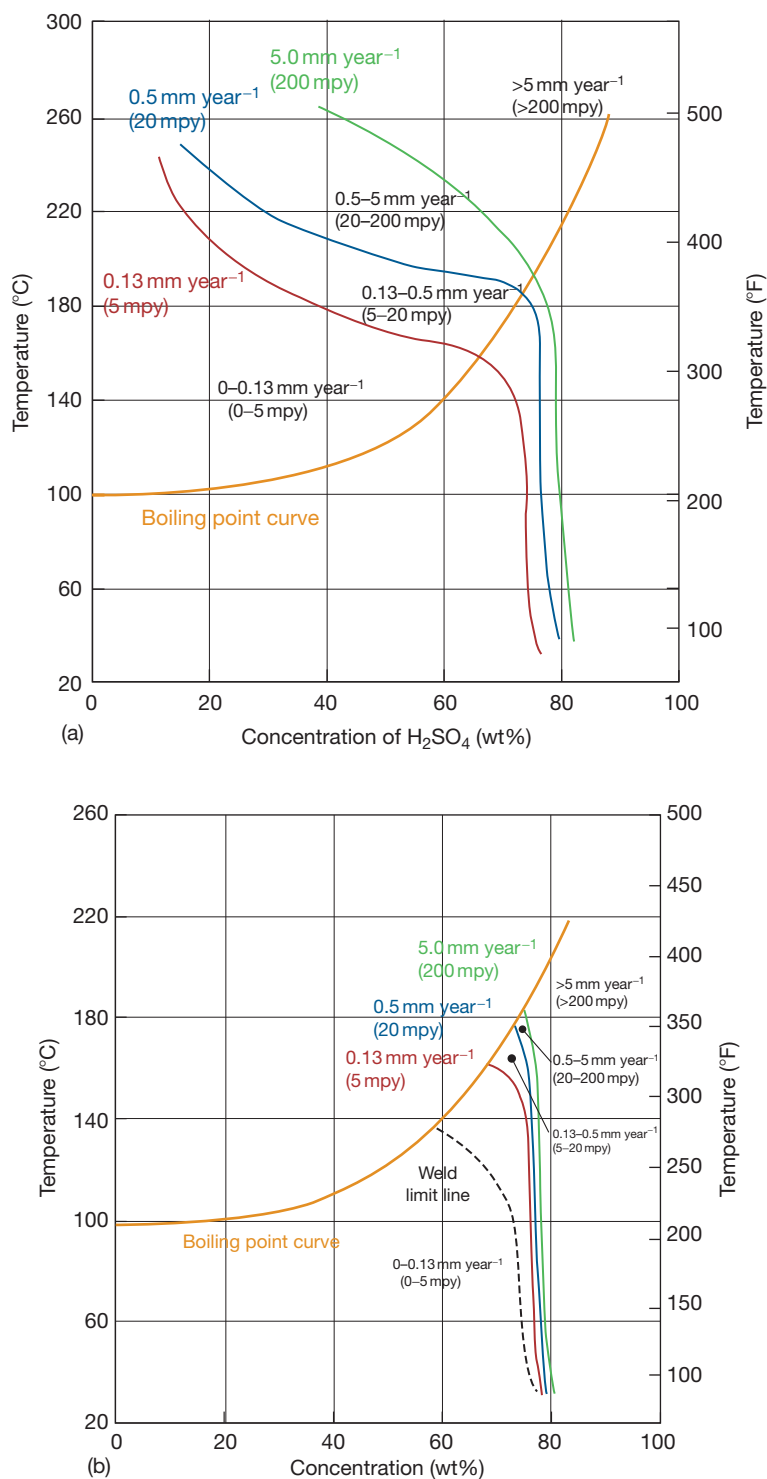


**Figure 13** The isocorrosion diagram of (a) zirconium in sulfuric acid and (b) Zr702 in sulfuric acid.

somewhat degraded resulting from welding. Zirconium weld metal may corrode preferentially and can be attributed to the morphology of the second-phase particles as previously discussed. Heat treatment at

$775 \pm 15^\circ\text{C}$  for 1 h per 25 mm of thickness can be used to restore the corrosion resistance of weld metal.

The presence of chlorides in sulfuric acid does not degrade zirconium's resistance unless oxidizing ions

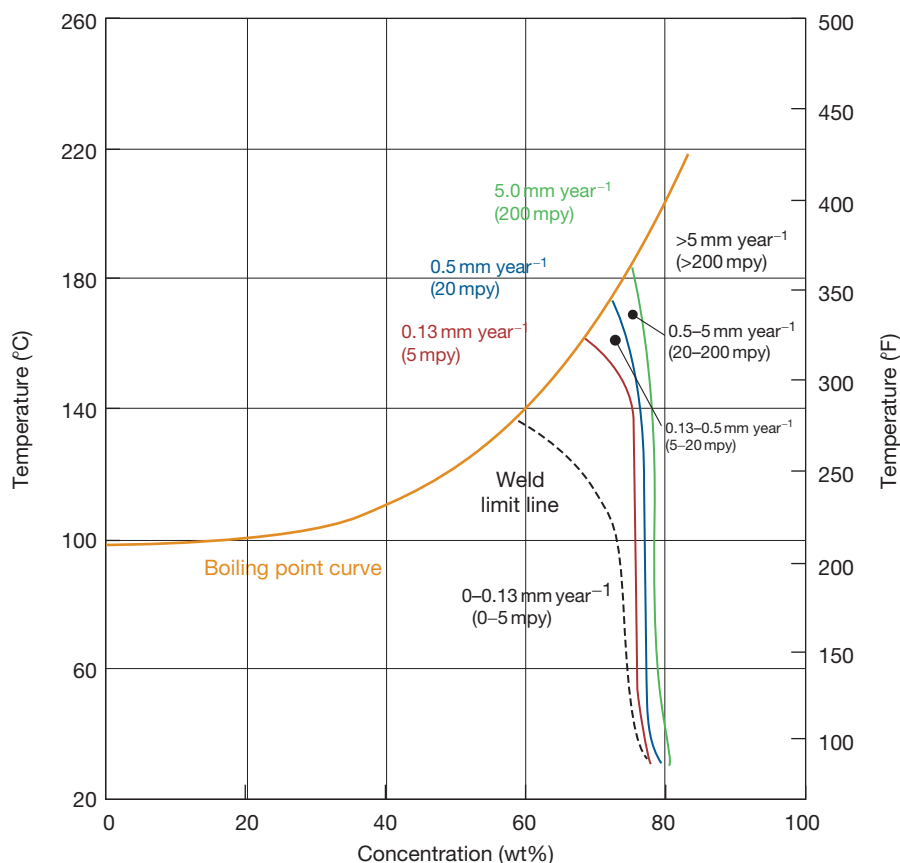


**Figure 14** The isocorrosion diagram of Zr704 in sulfuric acid.

are also present. When heavy metal ions and halide ions coexist in sulfuric acid, the optimum acid concentration range for zirconium is 60–65%. Sulfate ion possesses a mild inhibitive effect on the pitting of zirconium in chloride solutions. In  $\leq 1\%$  chloride solution, a minimum  $[\text{SO}_4^{2-}]/[\text{Cl}^-]$  ratio of  $\geq 42$  is needed for inhibition.<sup>20</sup> The more sulfate ions in the solution, the more oxidizing ion zirconium can tolerate before pitting occurs. **Figure 18** can be used as a guide when chloride ions and oxidizing ions coexist.

#### 3.14.3.3.2 Halogen acids

Zirconium resists attack by most halides, including halogen acids. Exceptions include hydrofluoric acid and oxidizing chloride solutions. It has been discussed that surface condition greatly affects the corrosion of zirconium in oxidizing chloride solutions. Zirconium has some corrosion resistance in certain fluorides when the pH is high enough. For example, small amounts of fluorides in city or ground water have little effect on zirconium's corrosion resistance. However, a few ppm hydrofluoric acid will noticeably increase the general

corrosion of zirconium. Nevertheless, zirconium and its alloys have very limited usefulness in fluoride-containing solutions. The concern is general corrosion but not pitting. Zirconium and its alloys exhibit low corrosion rates in fluoride solutions only when the temperature is low enough, and the pH is high enough. They are totally defenseless in HF-containing solutions. At room temperature, hydrofluoric acid exists when the pH is less than 3.18. The effect of pH on the corrosion of zirconium in fluoride-containing solutions is shown in **Table 8**.<sup>49</sup>

It should be noted that there are overlooked sources for fluorides.<sup>21,22</sup> Overlooked sources include recycled chemicals and PTFE. For example, recycled sulfuric acid may contain more than 100 ppm fluoride ions.<sup>21</sup> When zirconium equipment faces fluoride-containing acids, inhibitors that form strong fluoride complexes should be added for protection.<sup>21</sup> Useful inhibitors include zirconium sponge, soluble zirconium chemicals, and phosphorous pentoxide. **Table 9** gives results of the effects of certain inhibitors on zirconium's corrosion in fluoride-containing solutions.

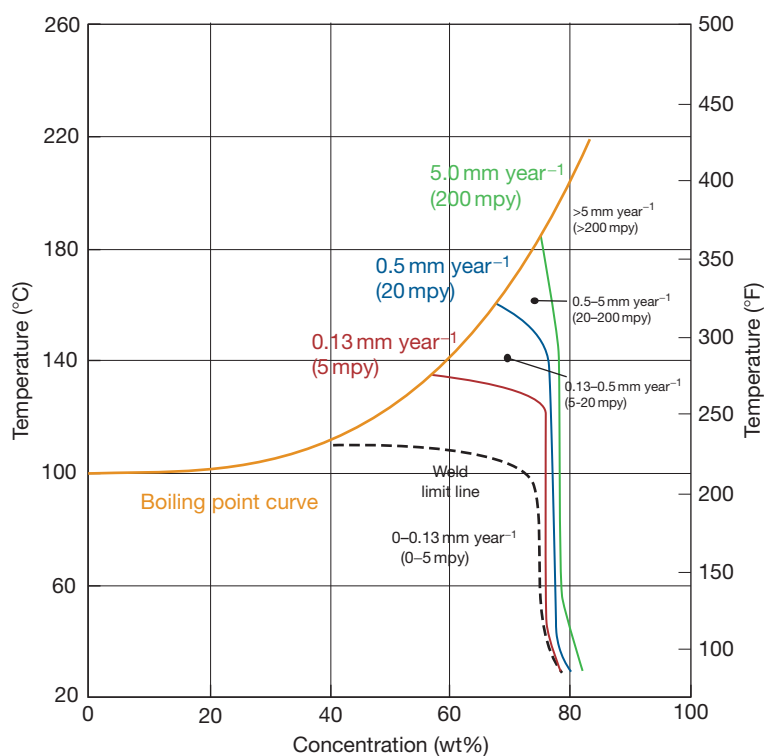


**Figure 15** The isocorrosion diagram of Zr705 in sulfuric acid.

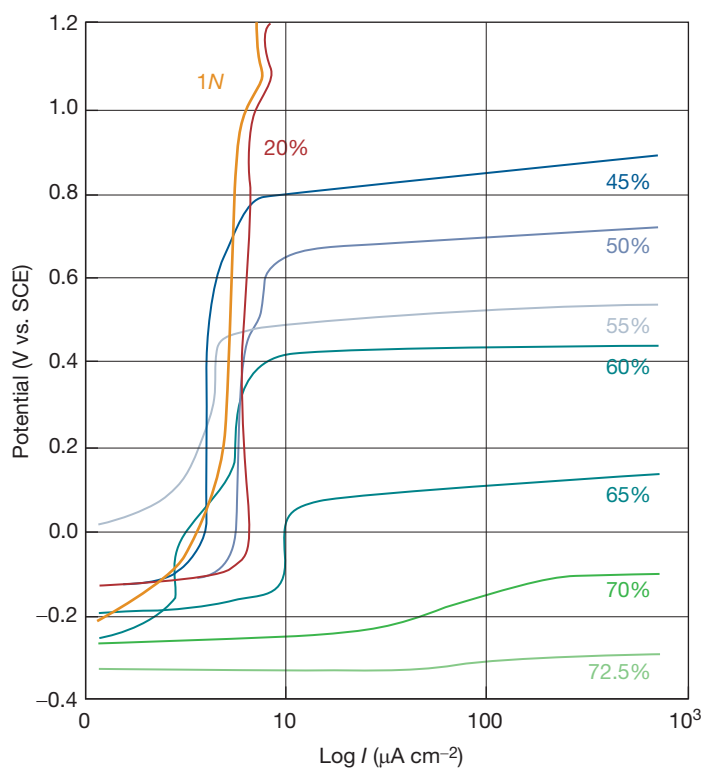


**Figure 16** Anodic polarization curves for Zr702 in sulfuric acid at near boiling temperature.

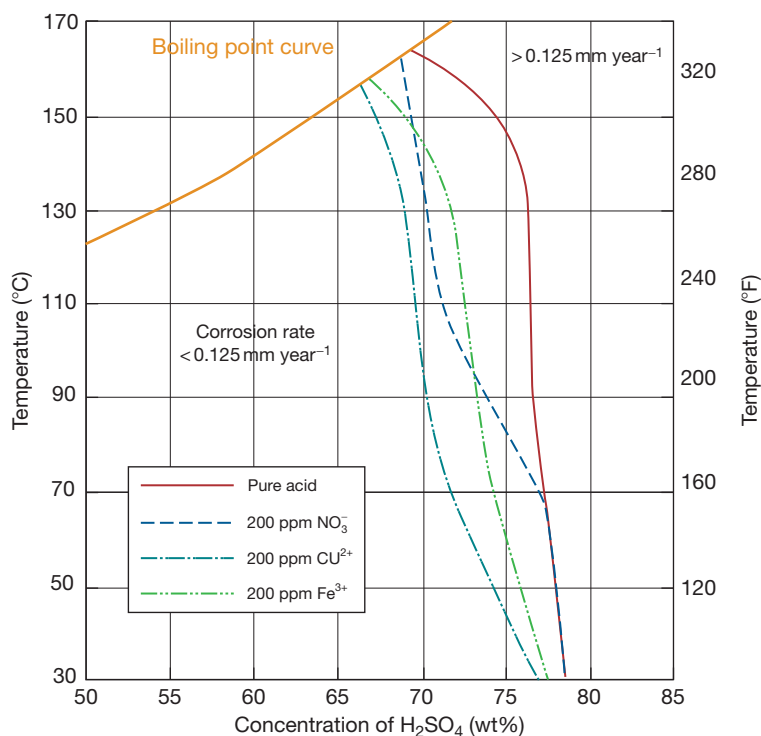


**Figure 17** Effect of various oxidizing ions on the 0.125-mm year<sup>-1</sup> isocorrosion line for Zr702 in sulfuric acid.

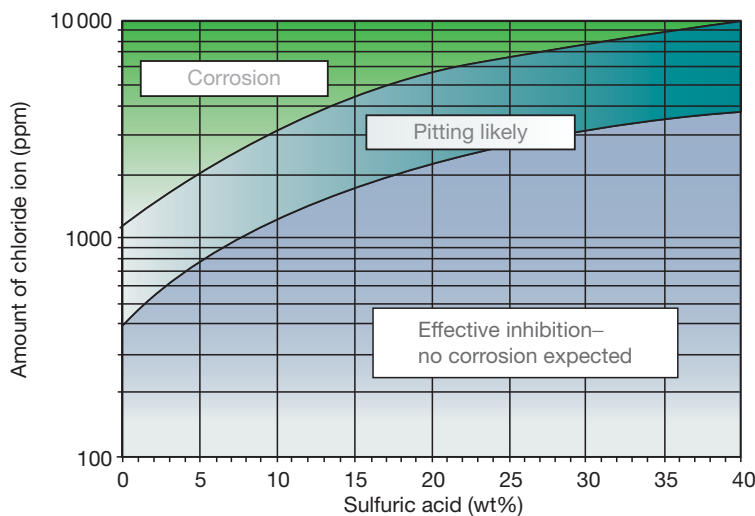


**Figure 18** Chloride allowable for Zr702 in sulfuric acid in oxidizing condition.

Unlike titanium and tantalum, the corrosion resistance of zirconium in halides increases in the order of chloride, bromide, and iodide. Unless the condition is oxidizing, zirconium is very corrosion resistant in chloride solutions, including strong hydrochloric acid. Oxidizing conditions include the presence of oxidizing agents, coupling with a noble material,

and applied anodic potential. In the absence of oxidizing conditions, zirconium is one of the most corrosion resistant metals to hydrochloric acid. As shown in [Figure 19](#), zirconium is totally resistant to attack in all concentrations of hydrochloric acid. Normally, stainless alloys can be considered only for handling very dilute and/or low-temperature hydrochloric

**Table 8** Corrosion of Zr702 in fluoride-containing solutions at 80 °C after four 1-day cycles

<i>Solution (ppm)</i>						
<i>CaCl<sub>2</sub> (%)</i>	<i>MgCl<sub>2</sub> (%)</i>	<i>F (as NaF)</i>	<i>F (as CaF<sub>2</sub>)</i>	<i>P<sub>2</sub>O<sub>5</sub></i>	<i>pH</i>	<i>Corrosion rate, mm year<sup>-1</sup> (mpy)</i>
0.2	0.1	200	100	–	1	8.79 (346)
0.2	0.1	200	100	–	3	0.17 (6.69)
0.2	0.1	200	100	1200	1	3.54 (139.4)
0.2	0.1	–	300	–	1	8.79 (346)
0.2	0.1	–	300	1200	1	0.39 (15.4)
2.0	1.0	200	2800	–	1	2.87 (113)
2.0	1.0	200	2800	–	3	0.01 (0.39)
2.0	1.0	200	2800	800	1	0.13 (5.1)
2.0	1.0	–	300	–	1	3.71 (146)
2.0	1.0	–	300	1200	1	0.01 (0.39)
6.6	3.3	200	9800	–	1	1.92 (75.6)
6.6	3.3	200	9800	–	3	0.01 (0.39)
6.6	3.3	200	9800	800	1	0 (0)
6.6	3.3	–	300	–	1	1.02 (40)
6.6	3.3	–	300	1200	1	0.02 (0.78)

**Table 9** Effect of zirconium sponge or phosphorous pentoxide on the corrosion of Zr702 in fluoride-containing solutions

<i>Medium</i>	<i>Inhibitor</i>	<i>Temp. (°C)</i>	<i>Corrosion rate, mm year<sup>-1</sup> (mpy)</i>
7.2% AlF <sub>3</sub> + 0.5% HF	None	90	>25.4 (>1000)
7.2% AlF <sub>3</sub> + 0.5% HF	16% Zr Sponge	90	<0.025 (<1.0)
0.2%CaCl <sub>2</sub> + 0.1% MgCl <sub>2</sub> + 620 ppm CaF <sub>2</sub> ; pH = 1	None	80	8.89 (350)
0.2%CaCl <sub>2</sub> + 0.1% MgCl <sub>2</sub> + 620 ppm CaF <sub>2</sub> ; pH = 1	1200 ppm P <sub>2</sub> O <sub>5</sub>	80	0.38 (15)
2%CaCl <sub>2</sub> + 1% MgCl <sub>2</sub> + 620 ppm CaF <sub>2</sub> ; pH = 1	None	80	3.8 (150)
2%CaCl <sub>2</sub> + 1% MgCl <sub>2</sub> + 620 ppm CaF <sub>2</sub> ; pH = 1	1200 ppm P <sub>2</sub> O <sub>5</sub>	80	<0.025 (<1.0)
6.6%CaCl <sub>2</sub> + 3.3% MgCl <sub>2</sub> + 620 ppm CaF <sub>2</sub> ; pH = 1	None	80	1.0 (40)
6.6%CaCl <sub>2</sub> + 3.3% MgCl <sub>2</sub> + 620 ppm CaF <sub>2</sub> ; pH = 1	1200 ppm P <sub>2</sub> O <sub>5</sub>	80	<0.025 (<1.0)
90% HNO <sub>3</sub> + 200 ppm HF	None	25	>25.4 (>1000)
90% HNO <sub>3</sub> + 200 ppm HF	800 ppm Zr sponge	25	0.254 (1.0)

acid. Zirconium would outperform stainless alloys in hydrochloric acid. Moreover, zirconium is not as susceptible to hydrogen embrittlement in hydrochloric acid as tantalum.

Although hydrochloric acid is strongly reducing, the anodic polarization curves of zirconium still do not have an active region as exhibited in [Figure 20](#). However, [Figure 20](#) shows that zirconium may suffer pitting and/or SCC when it is anodically polarized to a potential at or exceeding the pitting potentials. The same types of corrosion problems can be developed in hydrochloric acid when strong oxidizing agents are present. [Figure 21](#) illustrates the detrimental effect of ferric ions in 20% HCl at 100 °C. The presence of ferric ions polarizes the zirconium surface to a potential exceeding the pitting potential. Thus, local breakdown of the passive surface at preferred sites occurs, and a condition develops that favors pitting and/or SCC. Maintaining zirconium at a potential in

its passive region, which is arbitrarily set at 50–100 mV below the corrosion potential, can counteract the detrimental effects resulting from the presence of ferric ions.

### 3.14.3.3.3 Nitric acid

Because of its passivating power, nitric acid is considered to be compatible with passive alloys. However, nitric acid becomes highly corrosive when its temperature is high or when impurities, such as heavy-metal ions, are present. The passivating power favors the formation of oxide films but may also cause the passive films to break down.

Zirconium is considerably more suitable than most passive alloys for handling nitric acid, particularly when the acid is hot, impure, and/or variable in concentration. The excellent corrosion resistance of zirconium in nitric acid has been recognized for more than 30 years.<sup>50–52</sup> Below the boiling point and at 98% nitric acid, and up to 250 °C and at 70% nitric



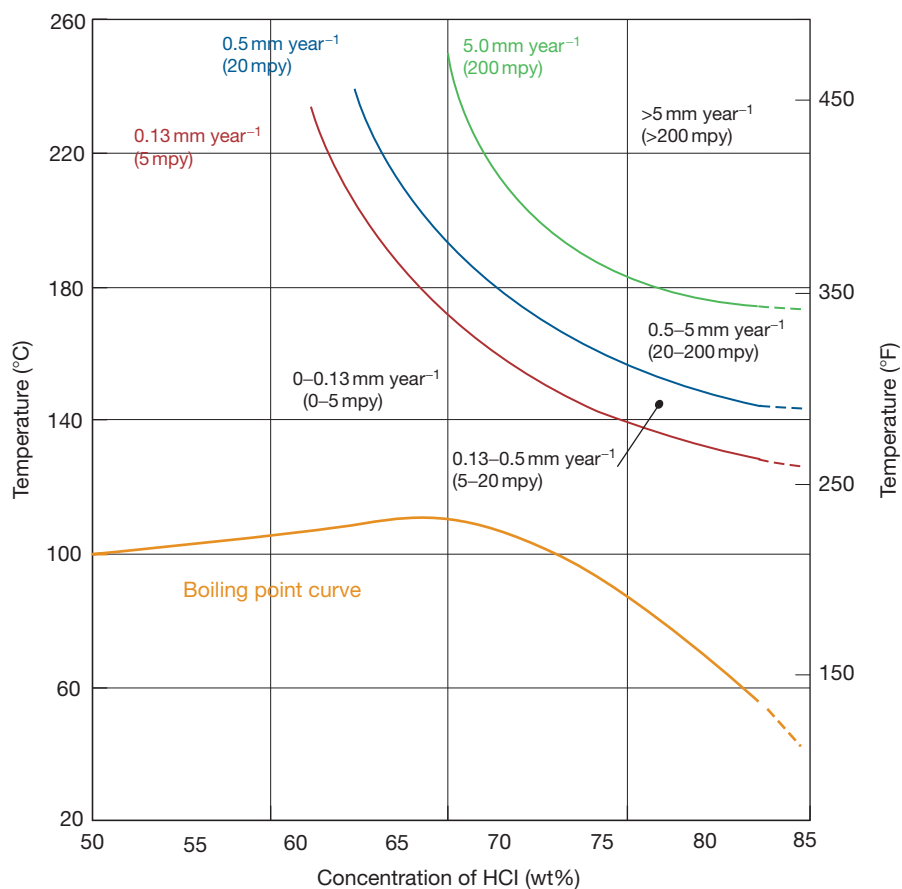


**Figure 19** The isocorrosion diagram of Zr702 in hydrochloric acid.

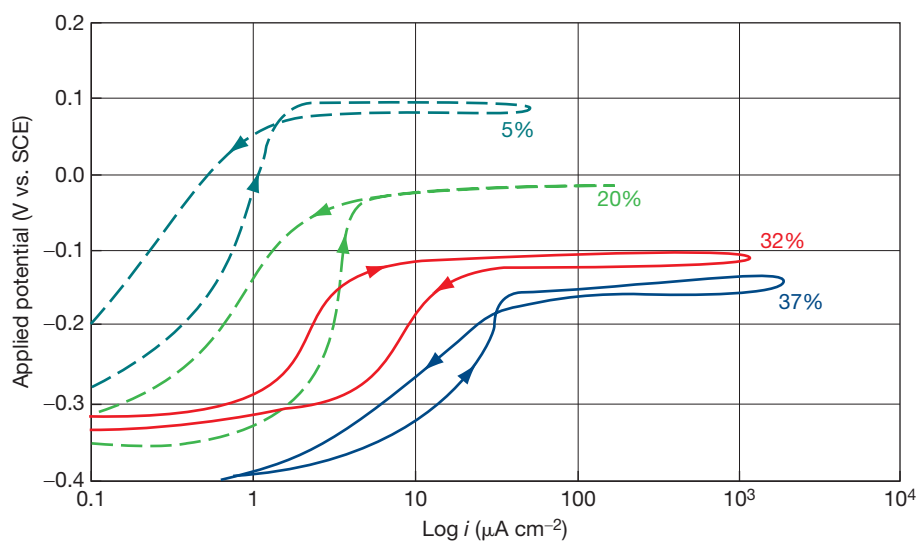


**Figure 20** Anodic polarization curves for Zr702 in hydrochloric acid at near boiling temperature.

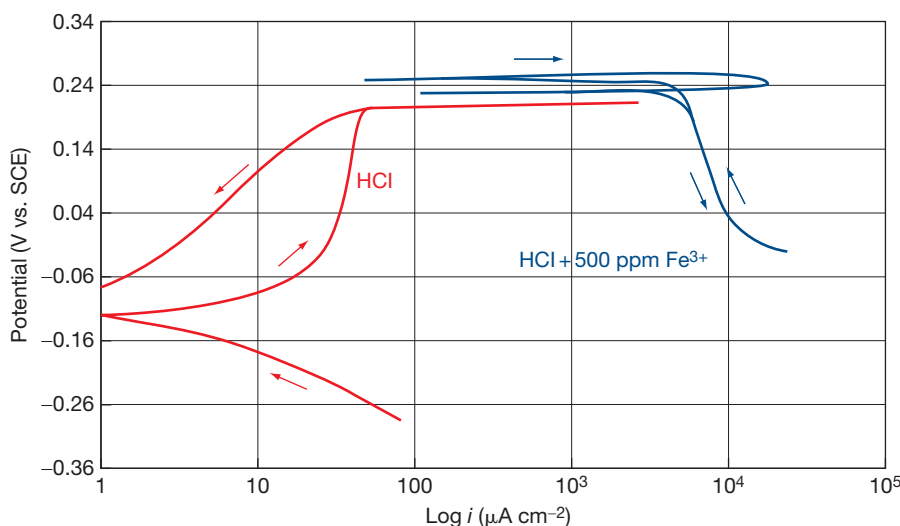


**Figure 21** Effect of 500-ppm ferric ions on the anodic polarization of Zr702 in 20% hydrochloric acid at 100 °C.

acid, the corrosion rate of zirconium is less than  $0.13 \text{ mm year}^{-1}$  as shown in [Figure 22](#).

Zirconium is normally susceptible to pitting in acidic oxidizing chloride solutions. However, nitrate ion is also an inhibitor for the pitting of zirconium because of its passivating power. The minimum  $[\text{NO}_3^-]/[\text{Cl}^-]$  molar ratio required to inhibit pitting of zirconium is between 1<sup>30,51,52</sup> and 5.<sup>53</sup> Results of tests indicate that zirconium's resistance is not degraded in up to 70% nitric acid with dissolved 1% ferric chloride, 1% sodium chloride, 1% seawater, 1% ferric ion, or 1% stainless steel at 204 °C.<sup>54</sup> Still, the presence of an appreciable amount of HCl should be avoided since zirconium is not resistant to aqua regia.

The polarization curves of zirconium in nitric acid are shown in [Figure 23](#). Again, zirconium has the passive-to-transpassive transition similar to that which occurs in sulfuric acid. However, corrosion potentials are noble because of the oxidizing nature of nitric acid. As indicated in the above test results, common oxidizing agents, such as ferric ions, do not affect the corrosion resistance of zirconium in nitric acid. The polarization curves do suggest that, zirconium may be susceptible to SCC in concentrated nitric acid. This is shown by the low passive-to-transpassive potential. This is consistent with the observation of SCC in U-bend specimens in greater than 70% nitric acid.<sup>55</sup> The slow strain-rate technique reveals zirconium's susceptibility to SCC in less than 70% nitric acid.<sup>56</sup> Results of C-ring tests indicate that zirconium specimens will have a long

life when they are stressed below the yield point.<sup>55</sup> Avoiding high-sustained tensile stresses is effective in controlling the SCC of zirconium.<sup>57</sup>

Additional concerns include the accumulation of chlorine gas in the vapor phase and the presence of fluorides. Chlorine gas may be generated by the oxidation of chlorides by nitric acid. Areas that can trap chlorine gas should be avoided for zirconium equipment when chlorides are present in nitric acid. Fluorinated materials should be carefully applied and may be overlooked sources for fluorides.

#### 3.14.3.3.4 Phosphoric acid

Phosphoric acid is less corrosive than other mineral acids. Many materials demonstrate useful resistance in phosphoric acid at least at low temperatures. Corrosion rates often increase with temperature and impurities in the acid. [Figure 24](#) shows that zirconium resists attack in phosphoric acid at concentrations up to 55% and temperatures exceeding the boiling point. Above 55% phosphoric acid, the corrosion rate of zirconium increases with temperature. The most interesting area for zirconium would be dilute acid at elevated temperatures. [Figure 25](#) gives the anodic polarization curves of zirconium in phosphoric acid at near-boiling temperatures. As concentration increases, the passive range diminishes gradually, and the passive current increases progressively. It appears that zirconium passivates more slowly in phosphoric acid than in other mineral acids.

If phosphoric acid contains more than a trace of fluoride ions, attack on zirconium may occur. Because

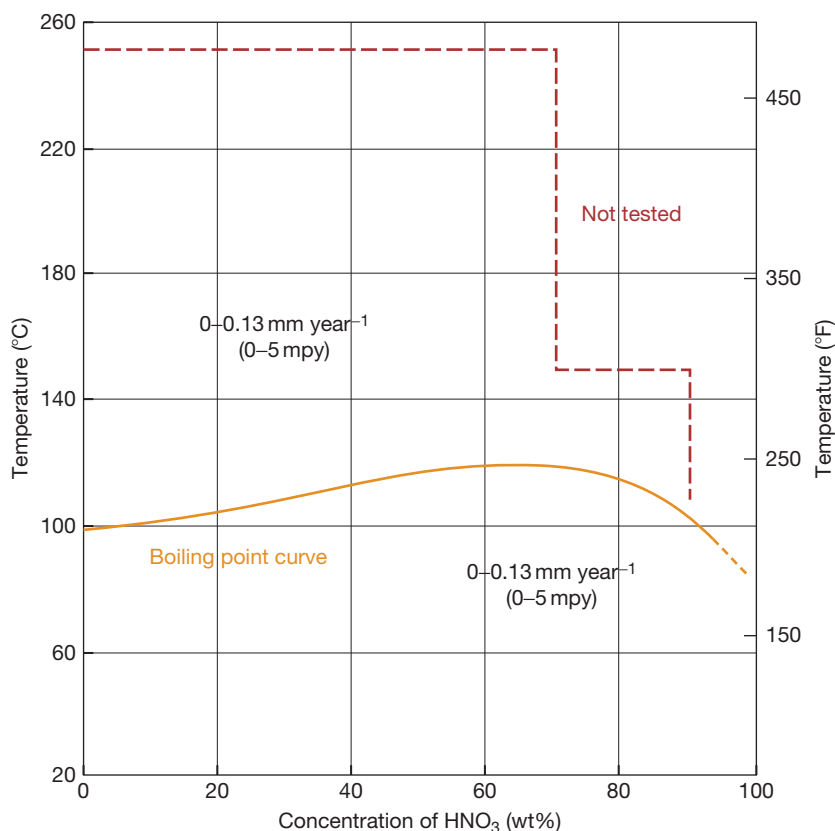


**Figure 22** The isocorrosion diagram of Zr702 in nitric acid.

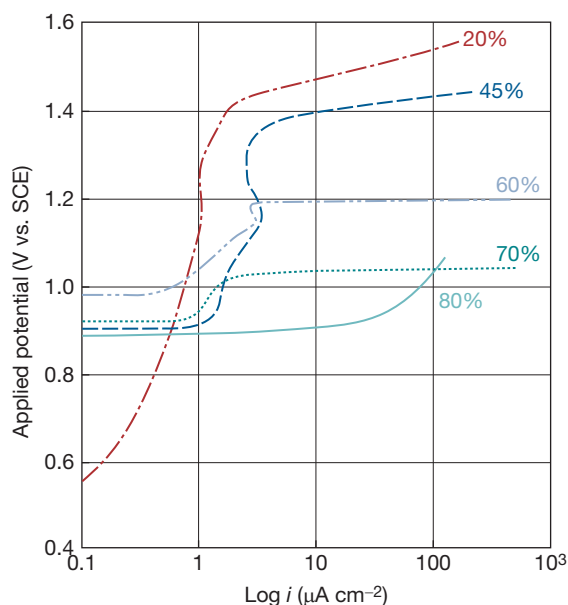


**Figure 23** Anodic polarization curves for Zr702 in nitric acid at near boiling temperature.

fluoride compounds are often present in phosphoric acid, the acid specification is important when zirconium equipment is involved. For example, food grades contain little fluoride ion, while technical grades may contain tens to thousands ppm fluoride ions.

#### 3.14.3.3.5 Other inorganic acids

Zirconium resists chromic acid up to 30% at temperatures to 100 °C<sup>58</sup> but it is not suitable for handling certain chrome-plating solutions that contain fluoride catalysts. Zirconium is also resistant to certain mixed acids that include sulfuric–nitric, sulfuric–hydrochloric, and phosphoric–nitric mixtures. The sulfuric acid concentration must be below 70%.<sup>51,52,59,60</sup> Zirconium is aggressively attacked in 1:3 volume mixtures of nitric and hydrochloric acids (aqua regia). In the volume mixture, zirconium is attacked more slowly than in the aqua regia.<sup>51,52</sup> In mixtures greater than the 3:1 ratio, zirconium becomes resistant. Data for some mixed acid systems are given in [Table 10](#).

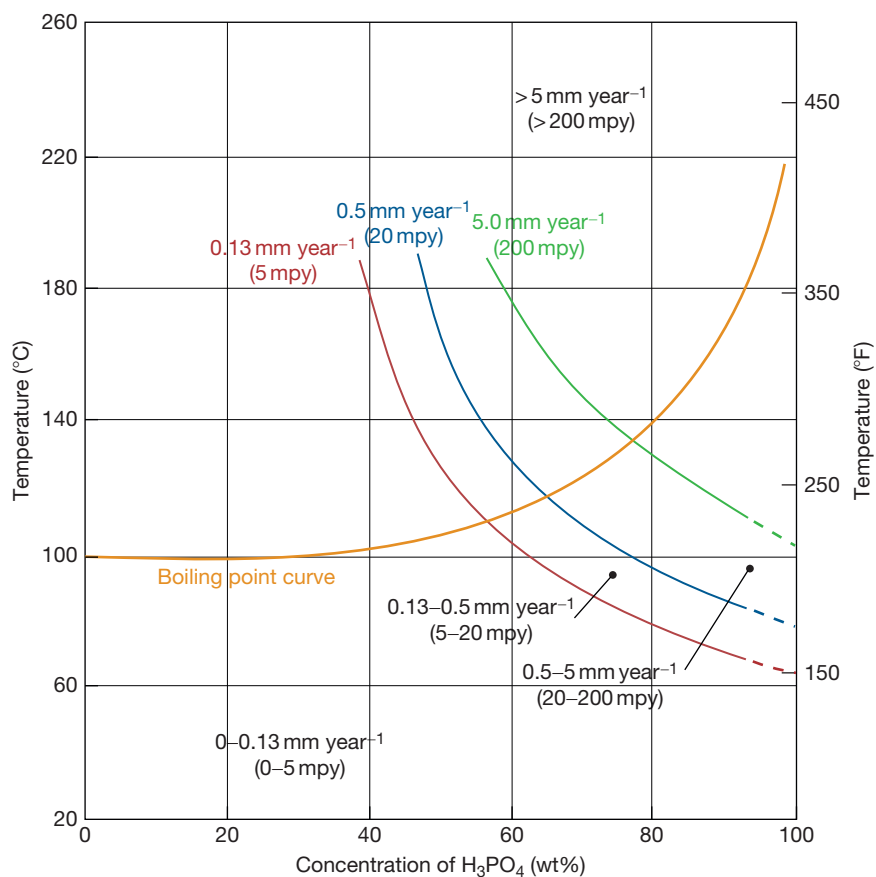


**Figure 24** The isocorrosion diagram of Zr702 in phosphoric acid.

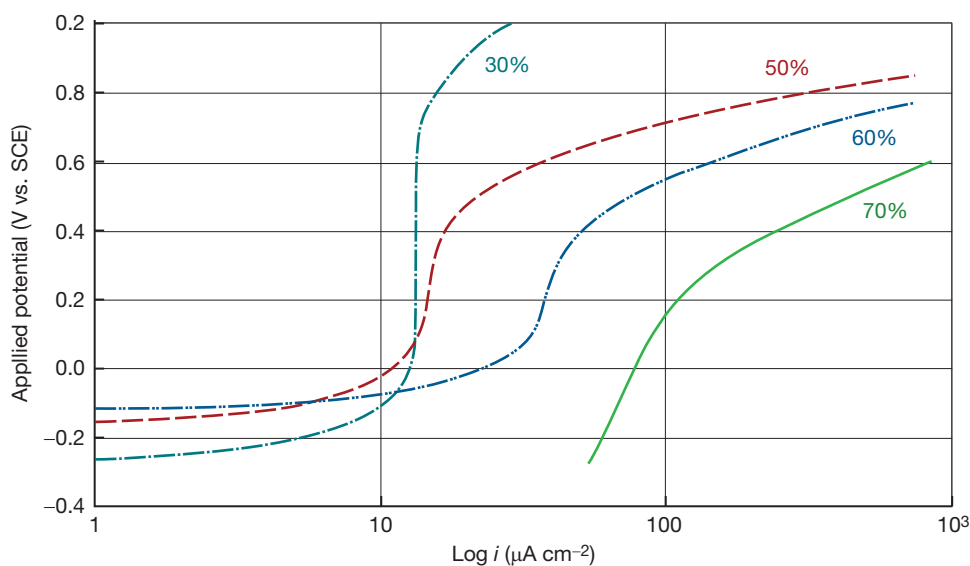


**Figure 25** Anodic polarization curves for Zr702 in phosphoric acid at near boiling temperature.

**Table 10** Corrosion of zirconium in certain mixed acids

Test Solution (wt%)		Temperature (°C)	Corrosion rate, mm year <sup>-1</sup> (mpy)
1% H <sub>2</sub> SO <sub>4</sub>	99% HNO <sub>3</sub>	RT, 100	0.001 (0.06)
10% H <sub>2</sub> SO <sub>4</sub>	90% HNO <sub>3</sub>	RT, 100	WG
14% H <sub>2</sub> SO <sub>4</sub>	14% HNO <sub>3</sub>	Boiling	0.002 (0.1)
25% H <sub>2</sub> SO <sub>4</sub>	75% HNO <sub>3</sub>	100	3.9 (150)
50% H <sub>2</sub> SO <sub>4</sub>	50% HNO <sub>3</sub>	RT	0.016 (0.63)
68% H <sub>2</sub> SO <sub>4</sub>	5% HNO <sub>3</sub>	Boiling	50.8 (2000)
68% H <sub>2</sub> SO <sub>4</sub>	1% HNO <sub>3</sub>	Boiling	0.28 (11)
75% H <sub>2</sub> SO <sub>4</sub>	25% HNO <sub>3</sub>	RT	6.6 (260)
88% H <sub>3</sub> PO <sub>4</sub>	0.5% HNO <sub>3</sub>	RT	0.0 (0.0)
88% H <sub>3</sub> PO <sub>4</sub>	5% HNO <sub>3</sub>	RT	WG
Aqua Regia	–	RT	Dissolved
20% HCl	20% HNO <sub>3</sub>	RT	Dissolved
10% HCl	10% HNO <sub>3</sub>	RT	Dissolved
7.5% H <sub>2</sub> SO <sub>4</sub>	19% HCl	Boiling	0.012 (0.5)
34% H <sub>2</sub> SO <sub>4</sub>	17% HCl	Boiling	0.008 (0.3)
40% H <sub>2</sub> SO <sub>4</sub>	14% HCl	Boiling	0.005 (0.2)
56% H <sub>2</sub> SO <sub>4</sub>	10% HCl	Boiling	0.05 (2.0)
60% H <sub>2</sub> SO <sub>4</sub>	1.5% HCl	Boiling	0.025 (1.0)
69% H <sub>2</sub> SO <sub>4</sub>	1.5% HCl	Boiling	0.12 (5.0)
69% H <sub>2</sub> SO <sub>4</sub>	4% HCl	Boiling	0.38 (15.0)
72% H <sub>2</sub> SO <sub>4</sub>	1.5% HCl	Boiling	0.51 (20.0)

WG, weight gain.

### 3.14.3.4 Other Aqueous Environments

#### 3.14.3.4.1 Hydrogen peroxide

Hydrogen peroxide is a unique and most important covalent peroxide. Many of its physical properties resemble those of water. However, chemically, it is very much different from water. It is not as stable as water. It decomposes into water and oxygen upon heating or in the presence of numerous catalysts, particularly salts of such metals as iron, copper, manganese, nickel, or chromium. Explosion may occur resulting from catalytic decomposition. Often small amounts of stabilizers, for example, tin salts and phosphates, are needed to suppress peroxide decomposition.

Hydrogen peroxide can be corrosive even to highly corrosion resistant metals and alloys such as titanium. In fact, titanium is one of the worst materials for handling hydrogen peroxide solutions. One reason is that hydrogen peroxide has the capability of forming peroxide complex compounds by attacking metals and alloys. These compounds may be soluble and are not as protective as oxide films.

Zirconium is regarded as one of the best materials for hydrogen peroxide service.<sup>61,62</sup> Its corrosion resistance in this medium is excellent. It does not produce active ions to catalytically decompose hydrogen peroxide. It has few problems for use in the production of hydrogen peroxide since it is essential to keep impurities out of process streams.

Nevertheless, zirconium is susceptible to pitting in oxidizing chloride solutions, and hydrogen peroxide is an oxidizer. Zirconium may pit in hydrogen peroxide solutions even when drops of hydrochloric acid are added for acidification.<sup>63</sup> It should be noted that zirconium is fully compatible with other acidic peroxide solutions when acids such as sulfuric acid are added.

#### 3.14.3.4.2 Alkaline solutions

Zirconium resists attack in most alkalis, which include sodium hydroxide, potassium hydroxide, calcium hydroxide, and ammonium hydroxide.<sup>58,64,65</sup> This makes zirconium distinctly different from some other high performance materials, such as titanium, tantalum, glass, graphite, and PTFE, which are attacked by strong alkaline solutions.

U-bends of Zr702 were tested in boiling 50% sodium hydroxide. During the test period, the concentration changed from 50% to about 85%, and temperature increased from 150 to 300 °C. The PTFE washers and tubes used to make the U-bends dissolved. However, the zirconium U-bends remained ductile and did not show any cracks after 20 days.

Coupons of Zr702 were tested in white liquor, paper-pulping solution, which contains sodium hydroxide and sodium sulfide, at 125, 175, and 225 °C. All coupons had corrosion rates of less than

0.025 mm year<sup>-1</sup>. In the same solution, graphite and glass both corroded at 100 °C. Zr702 also exhibited resistance to SCC in simulated white liquor.<sup>66</sup>

#### 3.14.3.4.3 Urea

Zirconium has been recognized as the most corrosion-resistant metal for urea-synthesis service.<sup>68,69</sup> Stainless alloys corrode in urea-synthesis conditions at rates exceeding 2 mm year<sup>-1</sup>.<sup>68</sup> Even silver has a high corrosion rate at 0.76 mm year<sup>-1</sup>. Although titanium does not corrode much, it exhibits several problems, such as erosion<sup>69</sup> and hydrogen embrittlement.<sup>70</sup>

One of the earliest applications of zirconium was in the production of urea. Certain zirconium vessels and heat exchangers have been in service for more than 30 years and show no signs of corrosion. However, the high corrosion rates of stainless steels are greatly reduced when oxygen is added to the process stream. Oxygen or air injection has become popular as the corrosion control measure in urea plants. The advantage of zirconium has been overlooked for many years.

In recent years, zirconium is making a comeback. The driving force for the renewed interest in zirconium is the concern about the presence of heavy metals in fertilizers. Stainless steel equipment still corrodes somewhat even with the oxygen injection measure. To protect the environment, permissible levels for the presence of heavy metal salts in fertilizers are being tightened. The corrosion resistance and nontoxicity of zirconium cannot be ignored in achieving new environmental standards.

#### 3.14.3.5 Organic Acids

##### 3.14.3.5.1 Acetic acid

The importance of acetic acid in the organic chemistry industry is comparable to that of sulfuric acid in the inorganic chemistry industry. Acetic acid can effectively acidify aqueous solutions, increasing their corrosivity. It is not highly corrosive at low temperatures. Many materials, including wood, rubber, aluminum, copper, stainless steels, and titanium, have been used in acetic acid service with different degrees of success. Corrosion problems arise due to variations in acid concentration, temperature, solution impurities or catalysts, and heat transfer.<sup>71</sup>

For over 40 years, zirconium has been recognized as one of the most versatile materials for acetic acid service.<sup>71-74</sup> Zirconium shows nil corrosion rates (<0.025 mm year<sup>-1</sup>) in most acetic acid media at temperatures up to at least 260 °C. In fact, acetate ions have a mildly inhibitive effect on the localized

corrosion of zirconium in halide solutions. Conditions that lead to corrosion are few. They include very dry acid (<650 ppm water) and the presence of copper ions in the acid.<sup>75</sup>

Zirconium has become an important material for the production of acetic acid through the reaction of methanol and carbon monoxide. This technology has been studied for more than 40 years. It could be commercialized in the 1970s only when the corrosion problems of structural materials were managed. In this technology, the reaction must proceed at a high temperature (at or greater than 150 °C) and a high pressure (3.3–6.6 MPa) in the presence of a halide as the catalyst. Process equipment must be made of highly corrosion-resistant materials. Zr702 and Zr705 are often used to construct process equipment, such as reactors, columns, heat exchangers, pumps, valves, piping systems, trays, and packings.

When various alloys were evaluated in acetic acid environments, zirconium was identified as the most corrosion resistant.<sup>72,73</sup> Nevertheless, in certain tests, zirconium exhibited pitting and high corrosion rates in mixtures of acetic acid and acetic anhydride when copper ions were present. Copper ions seem to play a catalytic role in the corrosion process. It is undesirable, therefore, for zirconium equipment to be exposed to acetic acid contaminated with copper ions. Copper ions may come from corrosion of upstream equipment made of copper-containing alloys and may also be added as catalysts in certain processes.

##### 3.14.3.5.2 Formic acid

Formic acid is more easily ionized than acetic acid. Therefore, formic acid is expected to be more corrosive than acetic acid. Indeed, formic acid attacks many common metals and alloys. Steel corrodes rapidly in this acid at all concentrations, even at ambient temperatures. Stainless alloys have some serious limitations. Type 304 stainless steel resists only 1–2% formic acid at boiling. Type 316 stainless steel is attacked by hot formic acid in the intermediate concentrations. Nickel-based alloys may corrode at high rates in the acid with the presence of certain impurities like halides and under heat-transfer conditions. Titanium and its alloys are not consistent due to factors such as aeration and water content. Compared to the mentioned alloys, zirconium is versatile and corrosion resistant in most formic acid solutions.<sup>76</sup>

Zirconium has played a key role in the commercialization of the Leonard–Kemira process.<sup>77,78</sup> In this process, CO gas contacts methanol in the presence of a catalyst to form methyl formate in a reactor.



The methyl formate is hydrolyzed in the presence of a catalyst to yield formic acid and methanol, which are separated by distillation. The methanol is recycled in the first stage of the process. Factors such as elevated temperatures and pressures and the presence of water and catalyst make common materials, including glass lining, resin and plastic coatings, and stainless alloys inadequate as structural materials for this process. Zirconium proves to be the most economical structural material for use in the main equipment for this process.

### 3.14.3.6 Other Organic Environments

Zirconium has excellent corrosion resistance in most organic environments. Exceptions are certain halide-containing organic solutions (e.g., impure methanol) and organic halides (e.g., dichloroacetic and trichloroacetic acids). Zirconium has been extensively tested in organic-cooled reactors where the coolant consists of mixtures of high-boiling aromatic hydrocarbons, for example, terphenyls.<sup>79</sup> These coolants are non-corrosive to zirconium. However, early experiments in the organic coolants indicated that hydriding was a major concern. It was found that chlorine as an impurity in the coolants was the reason for hydriding. Elimination of the chlorine and maintenance of a good surface oxide film by ensuring the presence of some water (>50 ppm) alleviates the hydriding problem. Indeed, the combination of a lack of water and the presence of halogens or halides is the common reason for zirconium to corrode in organic environments. For example, addition of some water suppresses zirconium's susceptibility to SCC in alcohol solutions with halides.<sup>80-82</sup>

On the one hand, zirconium shows excellent corrosion resistance in many chlorinated carbon compounds, such as carbon tetrachloride and dichlorobenzene at temperatures up to 200°C. On the other hand, zirconium is poor in certain chlorinated organic chemicals, such as acetyl halides, even at ambient temperatures. It is well known that certain organic halides are very corrosive to metals in the absence of water and oxygen. Metals can directly incorporate into these compounds to form intermetallic compounds. The reactions were investigated extensively by Grignard during the early 1900s. Today, organometallic halides are termed 'Grignard' reagents. Unsaturated organic compounds and alkyl, aryl, and vinyl halides are commonly used to react with metals in the preparation of organometallic compounds. They are potentially corrosive to metals, including zirconium. From the corrosion

point of view, organic halides can be classified into three groups, that is, water soluble, water insoluble, and water incompatible.

Water-soluble halides, such as aniline hydrochloride, chloroacetic acid, and tetrachloroethane, are not corrosive to zirconium. More active halides, such as dichloroacetic and trichloroacetic acids, are corrosive to zirconium. Corrosion rates of zirconium in these two acids at boiling are greater than 500 and 1250  $\mu\text{m year}^{-1}$  respectively. Water addition and stress relieving could be effective in controlling the corrosion of zirconium in water-soluble halides. Water-insoluble halides, such as trichloroethylene and dichlorobenzene, are not corrosive to zirconium, which is to be expected because of their stability. They do not dissolve in water, and they can be physically mixed together with water. Water-incompatible halides, such as acetyl chloride, may be highly corrosive to zirconium. They are not just unstable, but also react violently with water. There is no chance for water to be present in this type of halides, which are the most undesirable organic compounds for zirconium to handle.

## 3.14.4 High Temperature Degradation

### 3.14.4.1 Oxidation and Hot Corrosion

Zirconium forms a visible oxide film in air at about 200°C. The oxidation rate becomes high enough to produce a loose, white scale on zirconium at temperatures above 540°C. At temperatures above 700°C, zirconium can absorb oxygen and become embrittled after prolonged exposure.

Zirconium reacts more slowly with nitrogen than with oxygen since it has a higher affinity for oxygen than for nitrogen. Also, a layer of oxide film normally protects zirconium from reacting with nitrogen. However, once nitrogen penetrates through the oxide layer, it diffuses into the metal faster than oxygen. Clean zirconium starts the nitriding reaction in ultrapure nitrogen at about 900°C. Temperatures of 1300°C are needed to fully nitride zirconium. The nitriding rate can be enhanced by the presence of oxygen in the nitrogen or on the metal surface.

The oxide film on zirconium provides an effective barrier to hydrogen absorption up to 760°C, provided that small amounts of oxygen are also present in hydrogen for healing damaged spots in the oxide film. In an all-hydrogen atmosphere, hydrogen absorption will begin at a much lower temperature,

that is, 310 °C. Zirconium will ultimately become embrittled by forming zirconium hydrides. Hydrogen can be removed from zirconium by prolonged vacuum annealing at temperatures above 760 °C.

The corrosion and oxidation of zirconium and its alloys in steam are of special interest to nuclear power applications. The alloys can be exposed for prolonged period without pronounced attack at temperatures up to 425 °C. In the 360 °C steam, up to 350 ppm chloride and iodide ions, 100 ppm fluoride ions, and 10 000 ppm sulfate ions are acceptable for zirconium in general applications but not in nuclear power applications.

Zirconium is stable in ammonia up to about 1000 °C, in most gases (carbon monoxide, carbon dioxide, and sulfur dioxide) up to about 300–400 °C, and in dry halogens up to about 200 °C. At elevated temperatures, zirconium forms volatile halides. The corrosion resistance of zirconium in wet chlorine depends on surface condition. Zirconium is susceptible to pitting in wet chlorine unless it has been properly cleaned.

#### 3.14.4.2 Molten Salts and Metals

Zirconium resists attack in some molten salts. It is very resistant to corrosion by molten sodium hydroxide to temperatures above 1000 °C and is also fairly resistant to potassium hydroxide. The oxidation properties of zirconium in nitrate salts are similar to those in air. Zirconium also resists some types of molten metals, but the corrosion resistance is affected by trace impurities such as oxygen, hydrogen, or nitrogen.<sup>83</sup> It has a corrosion rate less than 25  $\mu\text{m year}^{-1}$  in liquid lead to 600 °C, lithium to 800 °C, mercury to 100 °C, and sodium to 600 °C. The molten metals known to attack zirconium include aluminum, zinc, bismuth, and magnesium.

### 3.14.5 Corrosion Protection

#### 3.14.5.1 Protective Film Formation

Zirconium oxide, which forms on zirconium's surface, is among the most insoluble compounds in a broad range of corrosives. This film, although very thin, provides excellent protection for zirconium from corrosion in most media. When the film is mechanically damaged, it will regenerate itself. For corrosion resistance, there is no need to thicken the film before zirconium equipment is placed in a corrosive medium. However, it is desirable to preoxidize

zirconium for meeting heavy mechanical duties. Properly oxidized zirconium has a much-improved performance against sliding forces, although it can be damaged by striking action. Oxidized zirconium pump shafts are an example of common applications. Bolts and nuts are often oxidized for the purpose of preventing galling. Several methods for forming thick layers of oxide films are available. They include anodizing, autoclaving in hot water or steam, oxidation in air or oxygen, and formation in molten salts.

Anodizing forms a very thin film ( $<0.5 \mu\text{m}$ ). The surface of zirconium with anodized films appears in different colors that vary through the entire spectrum. The thickness of the film is in the range of the wavelengths of visible light. Consequently, because of interference of this light, only certain wavelengths are selectively reflected through the film from the zirconium metal underneath. Nevertheless, the film is formed at ambient temperatures and does not adhere to the underlying metal as well as thermally produced films. Anodized films may look beautiful but have very limited capability to protect the metal from mechanical damage.

Autoclaving in hot water or steam is a common practice for determining 'corrosion resistance' in the nuclear industry. In this method, the uniform film of high integrity is formed in pressurized (19 MPa) deionized water at 360 °C for 14 days or in high purity steam (10 MPa) at 400 °C for 1–3 days. In addition to improving corrosion resistance, the rate of hydrogen absorption is greatly reduced.

Oxidation in air or oxygen under well-controlled conditions can produce high quality films on zirconium. The formed films serve as an excellent bearing surface against a variety of materials. For example, a layer of black film forms on a cleaned zirconium component in air at 550 °C for 4–6 h<sup>84</sup> or in a fluidized bed using oxygen during the oxide formation period but using an inert gas during the heating and cooling periods.<sup>85</sup> The resultant oxide layer is approximately 5 and 20  $\mu\text{m}$ , respectively. It is equivalent to sapphire in hardness and is diffusion bonded to the base metal. The oxide layer can be damaged by a striking force, but it serves as an excellent surface for sliding contact.

Film formation in molten salts is useful for small components. In this process, a zirconium subject is treated in fused sodium cyanide containing 1–3% sodium carbonate, or in a eutectic mixture of sodium and potassium chlorides with 5% sodium carbonate.<sup>86</sup> Treatment is carried out at a temperature ranging from 600 to 800 °C for up to 50 h. The thickness of

oxide film formed by this method is 20–30  $\mu\text{m}$ . This film greatly improves resistance to abrasion and galling over thick oxide films grown by many other methods.

### 3.14.5.2 Surface Conditioning

**Figure 11** shows the effect of surface condition on the rest potential of zirconium in 10% HCl + 500 ppm  $\text{Fe}^{3+}$  at 30 °C. Air annealing yields rest potentials nobler than the pitting potential,  $E_{\text{crit}}$ , due to the formed thick oxide during annealing. This does not mean that pitting will occur if the film quality is good. This does put thick oxide coated materials in a position vulnerable to pitting, particularly when there is an anodically applied potential. Surfaces abraded with either 600 grit SiC or  $\text{Al}_2\text{O}_3$  cloth reach the pitting potential quickly and have short pit initiation times. This can be attributed to the presence of embedded particles resulting from rough polishing. Pickled and finely polished surfaces have rest potentials below the pitting potential. They are very resistant to pitting even in oxidizing chloride solutions. This can be attributed to surface homogeneity that favors general corrosion but not localized corrosion. Results of immersion tests indicate that pickled zirconium performs well in boiling 10%  $\text{FeCl}_3$  and in  $\text{ClO}_2$ .<sup>20,87</sup> It is well known that zirconium with a normal surface finish is unsuitable for handling these solutions.

### 3.14.5.3 Electrochemical Protection

Zirconium exhibits a passive-to-transpassive transition with increasing potential in all mineral acids except hydrofluoric acid.<sup>88</sup> The commonly observed active node, as shown in **Figure 8** for many metal–acid systems, is not observed for zirconium. Consequently, zirconium performs well in most reducing media. This can be attributed to zirconium's ability to take oxygen from water to form a stable passive film.

Most passive alloys would need some oxidizing agent, such as the presence of oxygen, for them to form passive films. In fact, zirconium is one of the best metals for handling reducing media. On the other hand, zirconium may experience corrosion problems, such as pitting and SCC, under oxidizing conditions. These problems can be controlled by converting the oxidizing condition to a more reducing condition by various means.

Potentiostatically, by impressing a potential that is arbitrarily 50–100 mV below its corrosion potential, zirconium becomes corrosion resistant in oxidizing chloride solutions.<sup>89</sup> **Tables 11 and 12** demonstrate the benefits of electrochemical protection in controlling pitting and SCC. **Table 11** shows that the general corrosion rates of unprotected zirconium in oxidizing chloride solutions may be low. However, the penetration rates are much higher than the general corrosion rate. Electrochemical protection eliminates this local attack. As indicated in **Table 12**, unprotected U bends of welded zirconium cracked in all but one case shortly after exposure. Protected U bends resisted cracking for the 32-day test interval in all but one acid concentration. Thus, electrochemical protection offers an improvement to the corrosion properties of zirconium in oxidizing chloride solutions.

This technique is also applicable to control the SCC of zirconium in concentrated nitric acid.<sup>57</sup> Because of the strong oxidizing power of the acid, zirconium exhibits a noble corrosion potential. Also, there is a large difference between the corrosion potential and the critical potential to cause SCC. It is desirable to control the potential of zirconium a few hundred millivolts below the corrosion potential or at 740 mV NHE.

### 3.14.5.4 Other Measures

Ferric and cupric ions are the common oxidizing agents experienced in the CPI. Cupric ion is more

**Table 11** Corrosion rate of zirconium in 500 ppm  $\text{Fe}^{3+}$  solution after 32 days

Environment	Acidity	Temp. (°C)	Penetration rate, $\text{mm year}^{-1}$ (mpy)	
			Unprotected	Protected
10% HCl	3 N	60	0.18 (7.1)	<0.003 (<0.12)
		120	1.30 (51.2)	<0.003 (<0.12)
Spent acid (15% Cl)	5 N	65	0.91 (35.8)	<0.003 (<0.12)
		80	0.91 (35.8)	<0.003 (<0.12)
20% HCl	6 N	60	0.09 (3.5)	<0.003 (<0.12)
		107	1.50 (59)	<0.003 (<0.12)

**Table 12** Time to failure of welded zirconium U bends in 500 ppm Fe<sup>3+</sup> solution after 32 days

Environment	Acidity	Temp. (°C)	Time to failure (days)	
			Unprotected	Protected
10% HCl	3 N	60	<0.1	NF <sup>a</sup>
		120	<0.1	NF
Spent acid (15% Cl)	5 N	65	<0.3	NF
20% HCl	6 N	60	NF	NF
		107	<0.1	NF
28% HCl	9 N	60	2	NF
		94	<0.1	NF
32% HCl	10 N	53	1	32
		77	<0.1	20
37% HCl	12 N	30	<0.3	NF
		53	1	NF

<sup>a</sup>NF: no failure.**Table 13** Test results of zirconium (as-received condition) in boiling 500 ppm Cu<sup>2+</sup> containing NaCl solutions after seven 1-day runs

Average corrosion rate, mm year <sup>-1</sup> (mpy)				
No.	% NaCl	pH	Nonwelded coupons	Welded Coupons
1.	3.5	1	0.05 (1.97) <sup>a</sup>	0.60 (23.6) <sup>a</sup>
2.	25	1	0.04 (1.57)	0.55 (21.7) <sup>a</sup>
3.	3.5	4.8	0.01 (0.39) <sup>a</sup>	0.60 (23.6) <sup>a</sup>
4.	25	4.0	0.03 (1.18)	0.56 (22) <sup>a</sup>
5.	3.5	5.0	0.02 (0.78)	0.64 (25) <sup>a</sup>
6.	25	5.0	Nil	Nil
7.	3.5	6.0	Nil	Nil
8.	25	6.0	Nil	Nil
9.	3.5	7.5	Nil	Nil
10.	25	7.5	Nil	Nil

<sup>a</sup>Pitting.

detrimental than ferric ion in promoting the general corrosion and pitting of zirconium in acidic chloride solutions. **Tables 13 and 14** demonstrate the effect of pH, welding, and heat treatment on the corrosion of zirconium in cupric ion-containing solutions. The corrosion problems of zirconium in these solutions can be controlled by adjusting the pH to 6 or higher (**Table 13**) or by high temperature heat treatment (**Table 14**). In ferric ion-containing solutions, it is sufficient to adjust the pH to 3 or higher.

Various inhibitors, such as nitrate, sulfate, and stannous ions, can be used to control the pitting of zirconium in chloride solutions.<sup>20</sup> Furthermore, the solution potential of an oxidizing solution can be lowered when a small amount of hydrofluoric acid is added.<sup>20,57</sup> Therefore, hydrofluoric acid can be used to control pitting and SCC of zirconium in

**Table 14** Effects of heat treatment on the corrosion of zirconium (sand-blasted and pickled) in boiling NaCl + CuCl<sub>2</sub> solutions after seven 1-day runs

Average corrosion rate, mm year <sup>-1</sup> (mpy)				
No.	Metal	Condition	35% NaCl + 500 ppm Cu <sup>2+</sup>	25% NaCl + 500 ppm Cu <sup>2+</sup>
1.	Nonwelded	As conditioned	0.01 (0.39) <sup>a</sup>	0.025 (0.98) <sup>a</sup>
2.	Welded	As conditioned	0.01 (0.39) <sup>a</sup>	0.033 (1.3) <sup>a</sup>
3.	Welded	760°C/AC	<0.003 (0.12) <sup>a</sup>	0.006 (0.24) <sup>a</sup>
4.	Welded	760°C/WQ	<0.003 (0.12) <sup>a</sup>	0.004 (0.16) <sup>a</sup>
5.	Welded	871°C/AC	0.003 (0.12)	0.006 (0.24) <sup>a</sup>
6.	Welded	871°C/WQ	0.003 (0.12)	0.004 (0.16) <sup>a</sup>
7.	Welded	982°C/AC	0.005 (0.20)	0.007 (0.27)
8.	Welded	982°C/WQ	0.005 (0.20)	0.007 (0.27)

<sup>a</sup>Pitting AC, air-cooled; WQ, water-quenched.

oxidizing solutions, such as concentrated nitric acid and ferric chloride solutions. Since hydrofluoric acid is very corrosive to zirconium, the corrosivity of this acid can be neutralized by adding a complexing agent, such as zirconium sponge or zirconium compounds.

Tensile stresses provide a driving force for not just SCC but also for other types of corrosion to occur. Lowering residual stresses by a stress-relieving treatment is useful in controlling pitting as well.

### 3.14.6 Industrial Applications

For more than 40 years, many corrosive applications have been developed for zirconium and its alloys. Zirconium and its alloys are being used as structural materials in fabricating columns, reactors, heat exchangers, vaporizers, pumps, piping systems, valves, and agitators for the chemical process industry. The chemical process industry recognized the advantages of zirconium for solving corrosion problems from zirconium's inception.

#### 3.14.6.1 Processes Using Sulfuric Acid

Zirconium is used for the manufacture of  $\text{H}_2\text{O}_2$  by the electrolysis of acid sulfates. This production process is extremely corrosive and, at one time, graphite equipment was standard for this process. FMC's plant in Vancouver, WA, found that zirconium was superior to graphite and used zirconium equipment to produce up to 90%  $\text{H}_2\text{O}_2$ . The average maintenance-free life of the heat exchanger was 10 years; graphite exchangers failed after 12–18 months of service. The graphite equipment failure was attributed to the leaching of the binder from the graphite by the 35%  $\text{H}_2\text{SO}_4$  feed, which created a porous condition and ultimately caused failure.

The experience of zirconium in peroxide production led to the replacement of the graphite heat exchangers with zirconium shell and tube exchangers in the manufacturing of acrylic films and fibers. In this application, the  $\text{H}_2\text{SO}_4$  concentration was as high as 60% at 150 °C. Another major application in  $\text{H}_2\text{SO}_4$  concerns the manufacture of methyl methacrylate. The system at Rohm and Haas' plant in Deer Park, Texas, includes pressure vessels, columns, heat exchangers, piping systems, pumps, and valves all made from zirconium. A zirconium unit, which was built more than 20 years ago, is still in service.

Zirconium is also widely used for column internals and reboilers in the manufacture of butyl alcohol. The operating conditions are 60–65%  $\text{H}_2\text{SO}_4$  at

temperatures to boiling and slightly above. Zirconium may corrode under upset conditions of elevated concentrations and when such impurities as  $\text{Fe}^{3+}$  are present. Zirconium has been used in  $\text{H}_2\text{SO}_4$  recovery and in recycle systems in which fluorides are not present, and the acid concentration does not exceed 65%. A major application for zirconium is in iron and steel pickling, using hot 5–40%  $\text{H}_2\text{SO}_4$ .

Rayon is a manmade textile fiber, and most of today's rayon is made by the viscose process. Equipment made of graphite was popular for use in the  $\text{H}_2\text{SO}_4$ -affected areas of this process, yet is vulnerable to breakdowns. Avtex Fiber, Inc. began experimenting with zirconium equipment in 1970. Zirconium's excellent performance prompted Avtex to convert more pieces of equipment to zirconium, which included 10 acid evaporators, 14 shell- and tube heat exchangers, and 12 bayonet heat exchangers. In addition to dramatically reducing maintenance costs and downtime, the zirconium equipment improved operating efficiency and lowered overall energy costs.

Hydroxyacetic acid (HAA), also known as glycolic acid, can be produced in a synthetic process other than being extracted from natural sources. Under high pressure (30–90 MPa) and temperature (160–200 °C), formaldehyde reacts with carbon monoxide and water in the presence of an acidic catalyst, such as sulfuric acid, to form HAA. Dupont could not rely on a silver lining for reliable service in this process as silver showed poor erosion resistance in the piping system. There were cases of blowouts in the piping due to failure of the lining. By the mid-1980s, zirconium lining was evaluated when other materials, such as glass, ceramic, stainless alloys, and titanium were found unsuitable. Zirconium is well known for its corrosion resistance in weak sulfuric acid at temperatures up to and above 260 °C. An 8-month field test at Dupont indicated that a zirconium tube would not corrode in the most severe service section of the process. Zirconium's excellent resistance to erosion is also apparent and consequently, Dupont replaced silver lining with zirconium lining in piping sections more than 5 years ago. It was estimated that zirconium lining would last at least three times as long as silver lining.

#### 3.14.6.2 Processes Using Halogen Acids

Zirconium has many applications in HCl, such as the production of concentrated HCl and polymers. Zirconium heat exchangers, pumps, and agitators have been used for more than 15 years in an azo dye

coupling reaction. In addition to being very corrosion resistant in this medium, zirconium does not plate out undesirable salts that would change the color and stability of the dyes.

Lactic acid is commercially produced either by fermentation or by synthesis. The synthetic process is based on lactonitrile, which is prepared by reacting acetaldehyde with hydrogen cyanide at up to 200 °C. Lactonitrile is then hydrolyzed in the presence of HCl to yield lactic acid. In the HCl-affected areas, suitable materials are limited. Glass-lined materials are prone to breakdowns. Stainless alloys corrode and introduce toxic materials to the process stream. Titanium and its alloys are susceptible to crevice corrosion in hot chloride solutions. Zirconium is ideal for this process. Since lactic acid is produced as a fine chemical, contamination has to be prevented in all areas. Oxidizing HCl conditions resulting from the presence of ferric or cupric ions are avoided. Moreover, zirconium is highly resistant to crevice corrosion in chloride solutions. Since the 1970s, zirconium equipment has provided excellent service in lactic acid production.

Other applications in HCl include the breaking down of cellulose in the food industry and the polymerization of ethylene chloride, which is carried out in HCl and chlorinated solvents.

Zirconium and its alloys have been identified to offer the best prospects from a cost standpoint as materials for an HI decomposer in hydrogen production. They resist attack by HI media (gas or liquid) from room temperature to 300 °C. Most stainless alloys have adequate corrosion resistance to HI only at low temperatures.

### 3.14.6.3 Processes Using Nitric Acid

There is an increasing interest in the use of zirconium for HNO<sub>3</sub> service. For example, because of the high degree of concern over safety, zirconium is chosen as the major structural material for the critical equipment used to reprocess spent nuclear fuels.

In most HNO<sub>3</sub> service, stainless steel has been the workhorse for decades. The excellent compatibility between zirconium and HNO<sub>3</sub> was not thought to be needed. This situation changed when nitric acid producers started to modernize their technology in the late 1970s. Conventionally, HNO<sub>3</sub> is manufactured by oxidation of ammonia with air over platinum catalysts. The resulting nitric oxide is further oxidized into nitrogen dioxide and then absorbed in water to form HNO<sub>3</sub>. Acid of up to 65% concentration is

produced by this process. Higher concentration acid is produced by distilling the dilute acid with a dehydrating agent. Before the 1970s, dual-pressure processes were the dominant means of HNO<sub>3</sub> production. A typical dual-pressure process operates the converter at about 500 kPa and the absorber at about 1100 kPa. In the late 1970s, Weatherly, Inc. introduced a high mono-pressure process which operates at 1300–1500 kPa. The advantages of this new process include:

- greater productivity due to higher operating pressure;
- smaller equipment resulting in a lower capital cost;
- higher energy recovery capabilities.

The new process was first tried in 1979 when Mississippi Chemical in Yazoo City, MS, retrofit their existing plant with a new compressor system to increase pressure for greater productivity and energy efficiency. It was at this point that severe corrosion problems were discovered. Prior to the upgrade, the cooler condenser was constructed of type 304L stainless steel tubesheets and type 329 stainless steel tubes. Under the previous operating conditions, the cooler condenser had experienced some corrosion, which was managed by plugging tubes and replacing the unit every 3 to 4 years. Shortly after the upgrade, with an operating temperature and pressure of 200 °C and 1035 kPa, 10% of the type 329 stainless steel tubes were found to be leaking. This condenser was replaced with a unit using type 310L stainless steel, which had to be replaced after 13 months of operation. The original condenser with new tubes of improved grade 329 stainless steel was replaced by the 310L unit. Mississippi Chemical began looking for alternatives.

In an attempt to find a solution to this problem, autoclave tests were conducted on many newer types of stainless steels and zirconium in solutions up to 204 °C and at concentrations up to 65%. Clearly, zirconium was the only suitable material for the mono-pressure process. Corrosion rates of zirconium coupons were consistently below 25 μm year<sup>-1</sup>. The next step was to test zirconium tubes in service. Several tubes were installed into a rebuilt stainless steel condenser. They were destructively examined after 13 months and showed no signs of corrosion. Zirconium tubes were then placed in another condenser for 1 year. Once again, there were no signs of corrosion.

Consequently, Mississippi Chemical replaced its stainless steel cooler condenser with one constructed



from zirconium tubes and zirconium/304L stainless steel explosion-bonded tubesheets. This unit contains more than 18 km of zirconium tubing. In service since 1984, the zirconium unit has already outperformed the stainless steel predecessors. Thereafter, several zirconium cooler condensers have been built for other  $\text{HNO}_3$  producers.

Mono-pressure plants are not the only ones to use zirconium as a solution to corrosion problems. Certain plants use a distillation process to increase the acid concentration. The acid is passed through a reboiler and enters a distillation column to drive off water for concentrating the acid. In 1982, Union Chemicals replaced the bottom portion of each of two distillation columns and the tube bundles of each of two reboilers. The lower parts of the columns had been constructed originally with type 304L stainless steel that experienced corrosion problems. Titanium was tried, but also failed. While glass-lined steel did not have the corrosion problems experienced by type 304L stainless steel and titanium, the maintenance costs were found to be unacceptable. Zirconium provides significantly improved corrosion resistance without adding maintenance costs. Zirconium also solved corrosion problems in the reboilers. Prior to the installation of zirconium tube bundles, both 304L and titanium tube bundles had failed in less than 18 months of operation.

With proper design and fabrication, zirconium's susceptibility to SCC can be suppressed in highly concentrated  $\text{HNO}_3$ . For example, an Israeli chemical plant uses zirconium tubes in a U-tube cooler that processes bleached  $\text{HNO}_3$  at concentrations between 98.5 and 99%. The unit cools the acid from 70–75°C to 35–40°C. Previously, U-tube coolers were made from aluminum, which failed in 2–12 weeks. The zirconium unit has been in service for more than 2 years, operating 24 h a day, 6 days a week.

### 3.14.7 Safety

Zirconium is low in toxicity and is not known to be a carcinogen. The permissible exposure limit for zirconium set by various health agencies is  $5 \text{ mg m}^{-3}$ . For comparison, the limit for iron is  $1 \text{ mg m}^{-3}$ . One major concern is zirconium's reactivity. Under most conditions, the reactivity works toward zirconium's advantage. This reactivity allows zirconium to react spontaneously with oxygen to form a protective film, which suppresses its reactivity. Consequently, zirconium can be safely used under most conditions.

Nevertheless, unsafe situations may develop when this reactive nature is overlooked.

Heat of formation for zirconium dioxide at 25 °C is  $1101.3 \text{ kJ mol}^{-1}$ . It is potently exothermic. The generated heat can be easily absorbed by a large piece of zirconium. After the oxide film is formed, the oxidation rate will decrease quickly and pose no problems. However, when the heat is generated at a very small area, ignition may occur. Care should be exercised in handling fine materials including powder, sponge, machine chips, and thin foils. Ignition of fine materials will result in a very rapid, high temperature fire, which can be extinguished by using dry salt or sand. Attempts to extinguish a large zirconium fire with water will only result in scavenging of the oxygen atoms in the water molecules by the burning zirconium, leaving the hydrogen molecules to act as additional fuel or explosion source. These very large fires should be allowed to burn out by themselves.

It is normally safe to handle a large piece of zirconium. Still, ignition may occur when this piece experiences an enhanced oxidation reaction in a confined space. Under this condition, generated heat cannot easily dissipate, leading to escalated oxidation reaction and ignition becomes possible.

Furthermore, when zirconium's corrosion resistance is grossly exceeded in certain environments, pyrophoric films may form on its surface.<sup>48</sup> These environments include concentrated sulfuric acid and ferric chloride-containing solutions that may induce massive localized corrosion. Consequently, the solid surface is broken down into tiny pieces that contain corrosion products and unreacted zirconium particles. When unreacted particles are fine enough, ignition may occur. This pyrophoricity can be neutralized by treating it with steam.<sup>48</sup> Unreacted particles will oxidize in steam to become stable oxide or cover with a thick layer of oxide film. Treating time is about 20 min when the steam temperature is 250 °C. A longer time is needed when a lower temperature steam is used.

### 3.14.8 Future Possibilities

Trends in the CPI may offer some clues for zirconium's applications in coming years. They include improving product quality, developing new technologies, and assuring safety and environmental protection.

In compatible environments, zirconium yields few zirconium ions, which are colorless and

biocompatible. Zirconium becomes attractive for producers who do not just want to make a product, but want to make a product of high quality without undesirable impurities. The presence of undesirable impurities may affect the product's performance or may be harmful to the environment. The use of zirconium in the urea production is an example. Another example is the use of zirconium in the production of phenolic resins.<sup>75</sup> Purely from the viewpoint of mechanical integrity, iron-based alloys are suitable structural materials. However, in order to make phenolic resins for high-end uses, the products need to be colorless and very low in impurities. Then, zirconium becomes the necessary choice. If this trend continues, zirconium should find more applications in the food, the electronic, and the pharmaceutical industries.

There is the increasing demand for energy and the effort in reducing greenhouse gases. Many technologies are being developed to produce renewable energy. As indicated in the section of halide-containing processes, zirconium looks promising for the production of hydrogen from the decomposition of HI. In certain ethanol processes, the hydrolysis of starch into glucose is accomplished rapidly by treatment with dilute sulfuric acid at elevated temperature. High performance alloys like zirconium are needed for this type of processes.

Moreover, safer, advanced nuclear reactors have been developed. There is a renewed interest in nuclear energy. Many new nuclear power plants are being built and planned. Demand for zirconium in this arena will certainly rise and with it demand for optimized alloys that permit longer service and, consequently, higher utilization of the available uranium fuel.

Finally, developments in nanotechnology create new materials and corrosion challenges. Certain nanodevices process small amounts of corrosives through relatively large areas of corroding surfaces. Alloys of low corrosion rates may be unsuitable as structural materials. Zirconium could be a good match for certain nanodevices.

## References

- McIntyre, D. R. *Chem. Eng.* **1980**, April 7, 107.
- Proceedings of Seminars on Accelerated Crack Propagation of titanium in Methanol, Halogenated Hydrocarbons and Other Solutions, March 6, Battelle's Defense Metals Information Center, 1967.
- Mori, K.; Takamura, A.; Shimose, T. *Corrosion* **1966**, 2, 29.
- Yau, T. L. *Werkst. Korros.* **1992**, 43, 358.
- Rickover, H. G.; Geiger, L. D.; Lustman, B. History of the development of zirconium alloys for use in nuclear reactors, U.S. Energy Research and Development Administration, Division of Naval Reactors; TID-26740, U.S. GPO: Washington, DC, 1975.
- Yau, T. L. *Corrosion Engineering Handbook*; Marcel Dekker: NY, 1996; p 195.
- Yau, T. L.; Sutherland, R. C. *Corrosion: Materials*; ASM Handbook; ASM International: Materials Park, OH, 2005; Vol. 13B, p 300.
- Whitton, J. L. *J. Electrochem. Soc.* **1968**, 115, 58.
- Pourbaix, M. *Atlas of Electrochemical Equilibria in Aqueous Solutions*; Pergamon Press, 1966; p 223.
- Burgers, W. G.; Claassen, A.; Zernike, J. Z. *Phys.* **1932**, 74, 593.
- Charlesby, A. *Acta Metall.* **1953**, 1, 340–347.
- Cox, B. J. *Electrochem. Soc.* **1970**, 117, 654–663.
- Bradhurst, H.; Heuer, P. M. *J. Nucl. Mater.* **1970**, 37, 35–47.
- Roy, C.; David, G. J. *Nucl. Mater.* **1970**, 37, 71–81.
- Godlewski, J.; Gros, J. P.; Lambertin, M.; Wadier, J. F.; Weidinger, H. In *ASTM STP*; ASTM: West Conshohocken, PA, 1991; Vol. 1132, p 416.
- Godlewski, J. In *ASTM STP*; ASTM: West Conshohocken, PA, 1994; Vol. 1245, p 663.
- Khatamian, D.; Lalonde, S. D. *J. Nucl. Mater.* **1997**, 245(1), 10–16.
- Brown, M. L.; Walton, G. N. *J. Nucl. Mater.* **1975**, 58, 321–335.
- Yau, T. L. *Corrosion* **1982**, 38(12), 615.
- Yau, T. L.; Maguire, M. A. *Advances in Localized Corrosion*; NACE: Houston, TX, 1990; p 311.
- Yau, T. L. *Outlook* **1988**, 9(4), 4.
- Yau, T. L.; Holmes, D. R. Fluorides from overlooked sources, Paper presented at Wah Chang's Corrosion Applications Conference, 7–12 September 2003, Coeur d'Alene: ID.
- Kolotyrkin, Y. M. First International Congress on Metallic Corrosion, London; Butterworths: London, 1962; p 10.
- Maguire, M. In *ASTM STP*; ASTM: West Conshohocken, PA, 1984; Vol. 830, p 175.
- Cragolino, G.; Galvele, J. R. *Passivity of Metals*; The Electrochemical Society, 1974; pp 1053–1057.
- Shibato, T.; Ameer, M. A. M. *Corros. Sci.* **1992**, 33, 1633–1643.
- Yau, T. L. *Corrosion* 84; NACE: Houston, TX, 1984; Paper no. 140.
- Yau, T. L. *Corrosion* 83; NACE: Houston, TX, 1983; Paper no. 26.
- Jangg, G.; Webster, R. T.; Simon, M. *Werkst. Korros.* **1978**, 29, 16.
- Maraghini, M.; Adams, G. G.; Russelberghe, P. V. J. *J. Electrochem. Soc.* **1954**, 101, 400.
- Yau, T. L.; Webster, R. T. *Corrosion* **1983**, 39, 218.
- Yau, T. L. In *Stress-Corrosion Cracking: Materials Performance and Evaluation*; Jones, R. H., Ed.; ASM, 1992; p 299.
- Fitzgerald, B. J.; Yau, T. L. In 12th International Corrosion Congress, Houston, TX, 19–24 September 1993; Paper no. 092.
- Yau, T. L.; Webster, R. T. *Corrosion*/95; NACE: Houston, TX, 1995; Paper no. 250.
- Yau, T. L.; Webster, R. T. In *ASTM STP*; ASTM: West Conshohocken, PA, 1985; Vol. 866, pp 36–47.
- Nelson, J. G. In Private communication, 28 April 2000.
- Haffpaur, R.; Hsieh, J.; Coles, M.; Wong, C. 1997 Zirconium – Organics Conference Proceedings; Wah Chang 1998; p 29.

38. Takeda, K.; Anada, H. In *ASTM STP*; ASTM: West Conshohocken, PA, 2000; Vol. 1354, p 592.
39. Yau, T. L. Corrosion Solutions Conference Proceedings; Wah Chang 2001; p 255.
40. Holmes, D. R. Tin in zirconium 702 – Effect in sulfuric acid applications, Paper presented at Wah Chang's Corrosion Applications Conference, 7–12 September 2003, Coeur d'Alene, ID.
41. Kass, S. *Corrosion of Zirconium Alloys*, ASTM; ASTM: West Conshohocken, PA, 1964; Vol. 368, p 3.
42. Thomas, D. E. In *Metallurgy of Zirconium*; Lustman, B., Kerze, F., Jr., Eds.; McGraw-Hill: New York, 1955.
43. Dalgaard, S. B. Proceedings of the Conference on Corrosion Reactor Materials; International Atomic Energy Association 1962; Vol. 2, p 159.
44. Latimer, W. M. *The Oxidation States of the Elements and Their Potentials in Aqueous Solutions*; Prentice-Hall: Englewood Cliffs, NJ, 1952; p 270.
45. Blumenthal, W. B. *Zirconium Compounds*; National Lead Co., TAM Division, 1969.
46. Knittel, D. R.; Webster, R. T. *ASTM STP*; ASTM: West Conshohocken, PA, 1981; Vol. 728, p 191.
47. Yau, T. L. *ASTM STP*; ASTM: West Conshohocken, PA, 1984; Vol. 830, p 203.
48. Yau, T. L. *ASTM STP*; ASTM: West Conshohocken, PA, 1984; Vol. 830, p 124.
49. Yau, T. L. *Corrosion in Desulfurization Systems*; NACE: Houston, TX, 1984.
50. Bishop, C. R. *Corrosion* **1963**, 19, 308t.
51. Andreeva, V. V.; Glukhova, A. I. *J. Appl. Chem.* **1961**, 11, 390.
52. Andreeva, V. V.; Glukhova, A. I. *J. Appl. Chem.* **1962**, 12, 457.
53. Maraghini, M.; Adams, G. G.; Russelberghe, P. V. J. *J. Electrochem. Soc.* **1954**, 101, 400.
54. Yau, T. L. *ASTM STP*; ASTM: West Conshohocken, PA, 1986; Vol. 917, p 57.
55. Yau, T. L. *Corrosion* **1983**, 39, 167.
56. Beavers, J. A.; Griess, J. C.; Boyd, W. K. *Corrosion* **1981**, 36, 292.
57. Yau, T. L. *Corrosion* **1988**, 44, 745.
58. Shetton, S. M. U.S. Bureau of Mines Bull. **1956**, 561.
59. Golden, L. B.; Lane, I. R., Jr.; Acherman, W. L. *Ind. Eng. Chem.* **1952**, 44, 1930.
60. Golden, L. B.; Lane, I. R., Jr.; Acherman, W. L. *Ind. Eng. Chem.* **1953**, 45, 782.
61. Bloom, R., Jr.; Weeks, L. E.; Raleigh, C. W. *Corrosion* **1960**, 16, 164t.
62. Yau, T. L. *Outlook, Wah Chang* **1991**, 12(1), 3.
63. Yau, T. L. *TAPPI J.* **1991**, 74(3), 155.
64. Gegner, P. L.; Wilson, W. L. *Corrosion* **1959**, 15, 341t.
65. Graighead, C. M.; Smith, L. A.; Jaffee, R. I. *Screen tests on metals and alloys in contact with sodium hydroxide at 1000 and 1500 °F*, U.S. Energy Commission Report BMI-707, Battelle Memorial Institute, November 1951.
66. Yau, T. L. *Mater. Perform.* **1993**, 32(6), 65.
67. Golden, L. B. *Zirconium and Zirconium Alloys*; ASM, 1953.
68. McDowell, D. W. *Chem. Eng.* **1974**, 26, 96.
69. Miola, C.; Richter, H. *Werkst. Korros.* **1992**, 43, 396.
70. Krystow, P. E. *Chem. Eng. Prog.* **1971**, 67(4), 59.
71. Corrosion Resistance of Nickel-Containing Alloys in Organic Acids and Related Compound, Publication Number 1285, NiDI, Toronto, Canada 1979.
72. Togano, H.; Osato, K. *Boshoku Gijutsu* **1961**, 10(13), 529.
73. Shimose, T.; Takamura, A.; Segawa, S. *Boshoku Gijutsu* **1966**, 15(2), 49.
74. Yau, T. L. *Outlook, Wah Chang* **1987**, 8(3), 2.
75. Yau, T. L. *J. Test. Eval.* **1996**, 24(2), 110.
76. Yau, T. L. *Outlook, Wah Chang* **1988**, 9(3), 6.
77. Leonard, J. D. Eur. patent 5,998, 12 December 1979.
78. Kemira specifies zircadyne 702 for use in a formic acid application, *Outlook* **1990**, 11(1), 1.
79. Cox, B. In *Advances in Corrosion Science and Technology*; Plenum Press: New York, NY, 1976; Vol. 5, p 173.
80. Mori, K.; Takamura, A.; Shimose, T. *Corrosion* **1966**, 22, 29.
81. De, P. K.; Elayaperumal, K.; Balschandra, J. *Corros. Sci.* **1971**, 11, 579.
82. Cox, B. Reports AECL-3551, 3612, and 3799, Atomic Energy of Canada Ltd. 1970/1971 or 3551 (1970); 3612 (1970) and 3799 (1971).
83. Koenig, R. F. Corrosion of zirconium and its alloys in liquid metals, U.S. Atomic Energy Commission Report No. KAPL-982, 1 October 1953.
84. Watson, R. D. Oxidized zirconium as a bearing material in water lubricated mechanism, Report CRE-996, Atomic Energy of Canada, 1960.
85. Kemp, W. E. *Outlook, Wah Chang* **1990**, 11(2), 4.
86. Haygarth, J.; Fenwick, L. *Thin Solid Films* **1984**, 118, 351.
87. Fahey, J.; Holmes, D. R.; Yau, T. L. *Corrosion* **1997**, 53(1), 54.
88. Magurie, M. A.; Yau, T. L. *Corrosion* **86**; NACE: Houston, TX, 1986; Paper no. 265.
89. Yau, T. L.; Magurie, M. A. *Corrosion* **1984**, 40, 289; **1985**, 41, 397.

## 3.18 Corrosion of Beryllium and its Alloys

**R. S. Lillard**

Los Alamos National Laboratory, Los Alamos, NM, USA

© 2010 Elsevier B.V. All rights reserved.

3.18.1	Metallurgy	2168
3.18.2	Extraction and Fabrication	2168
3.18.3	Aqueous Corrosion Behavior	2169
3.18.3.1	Commercial Grades of Be	2169
3.18.3.2	High-Purity Be	2171
3.18.3.3	Galvanic Effects – The Influence of Be Inclusions	2173
3.18.3.4	Environmental Fracture	2173
3.18.3.5	Corrosion Control	2174
3.18.4	High Temperature Oxidation of Be and the Beryllides	2174
3.18.4.1	Beryllium	2174
3.18.4.2	Beryllides	2177
References		2179

### 3.18.1 Metallurgy

Beryllium is a light metal ( $1.85 \text{ g cm}^{-3}$ ) with a hexagonal close-packed structure (axial ratio 1.568). [Table 1](#) displays the composition of S200D Be versus S200F two common grades of Be (Brush Wellman), both of which are fabricated from powder materials. The main difference between these grades of Be is the concentrations of BeO, iron, and aluminum (Al). Both grades are manufactured by comminuting vacuum cast ingots, followed by grinding or milling to produce powder.<sup>1</sup> In this process, a thin oxide layer forms around the Be powder particles, resulting in a high BeO content and resultant BeO inclusions that form after hot isostatic pressing. The grain sizes of these two grades of Be are on the order of 10–40  $\mu\text{m}$ , which is characteristic of powder products as the BeO particles pin grain boundaries and retard grain growth.

The most notable of its mechanical properties is its low ductility at room temperature. Deformation at room temperature is restricted to slip on the basal plane, which takes place only to a very limited extent. Consequently, at room temperature, beryllium is, by normal standards, a brittle metal, exhibiting only ~2–4% tensile elongation. Mechanical deformation increases this by the development of preferred orientation, but only in the direction of working and at the expense of ductility in other directions. Ductility also increases very markedly at temperatures

above ~300 °C with alternative slip on the (1010) prismatic planes. In consequence, all mechanical working of beryllium is carried out at elevated temperatures. It has not yet been resolved whether the brittleness of beryllium is intrinsic or results from its impurities. Solid solubility of other metals in Be is very low and, to date, it has not been possible to overcome the brittleness problem by alloying.

### 3.18.2 Extraction and Fabrication

Beryllium is extracted from the main source mineral, the aluminosilicate beryl, by conversion to the hydroxide and then through either the fluoride or the chloride to the final metal. If the fluoride is used, it is reduced to beryllium in magnesium by a Kroll-type reaction. The raw metal takes the form of ‘pebble’ and contains much residual halides and magnesium. With the chloride, on the other hand, the pure metal is extracted by electrolysis of a mixture of fused beryllium chloride and sodium chloride. The raw beryllium that results is dendritic in character and contains residual chloride.

Before further processing, the raw metal must be purified. Various methods of leaching have been tried on a laboratory scale, but in practice, the method usually adopted is vacuum induction melting. The ingot so produced is then converted to powder by reducing it to chips/turnings, followed by grinding.

**Table 1** Typical Be S200D and Be S200F chemistries

Constituents	S200F	S200D
Beryllium	≈98.5	≈98.0
Beryllium oxide (BeO)	≤1.5	≤2.0
Aluminum	0.10	0.16
Carbon	0.15	0.15
Iron	0.13	0.18
Magnesium	0.08	0.08
Silicon	0.06	0.08
Other metallic impurities	0.04	0.04

All values are given in weight percent.

On a laboratory scale, the grinding is generally done by ball milling; while in production, milling is carried out between beryllium-faced plates.

The particle size of powder most often used for consolidation is 200 mesh (74 μm sieve aperture), and the most widely practiced method of consolidation is hot pressing *in vacuo*.

Setting aside the necessity for hot working and the toxicity issue, the fabrication of consolidated beryllium generally follows normal lines; rolling, extrusion, drawing, forging, etc. have all been successfully carried out. It is interesting to note that because of the high chemical activity of beryllium, allied to the method of consolidation from powder, the usual grade of metal contains ~1–2% of beryllium oxide as described earlier. It could therefore, be considered almost a mild cermet rather than a conventional pure metal. Specifications for typical chemical composition are detailed in [Table 1](#).

### 3.18.3 Aqueous Corrosion Behavior

#### 3.18.3.1 Commercial Grades of Be

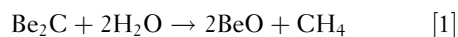
The initial studies of the breakdown of passivity in beryllium focused on those environments expected to be generated in the early ‘development reactors’ where beryllium was used as a neutron reflector, and are not available in the general literature.<sup>2</sup> In these studies, beryllium was exposed to various concentrations of hydrogen peroxide (a water radiolysis product) as a function of solution pH and temperature. At the end of exposure periods, coupons were evaluated for pit density and penetration depth. The effect of coupling beryllium to aluminum and stainless steels on corrosion rate was also investigated. Although beryllium corrosion rates were high in some of the simulated environments, service lifetimes of beryllium reflectors exposed to high-purity,

low-temperature, irradiated water were reported to be good.<sup>3</sup>

At this point, it is worth noting that the Be ion exists only in the Be(II) oxidation state; however, early literature, sometimes incorrectly, reported a Be(I) oxidation state.<sup>4</sup> These reports were later discredited. Sheth used weight loss to study the anodic dissolution of Be in numerous solution, including halides (F<sup>−</sup>, Cl<sup>−</sup>, . . .), sulfates, and phosphates.<sup>5</sup> Thus, reports of the existence of a Be(I) oxidation state can be explained by Sheth’s observation of metal disintegration, unoxidized loss of metal that skewed correlations between charge passed and weight loss data.

In general, early literature on other forms of beryllium corrosion is limited. Although some polarization studies of beryllium in chloride and sulfate environments have been conducted,<sup>6</sup> other investigations focused on weight loss<sup>7</sup> and visual observation<sup>3,8</sup> to evaluate susceptibility to corrosion. Levy found that beryllium is susceptible to pitting attack in chloride at its open circuit potential (OCP) and uniform attack (i.e., ‘. . . a thick, dark anodic film. . .’) in NaNO<sub>3</sub> solution.<sup>6</sup> Similar observations were made by Prochko.<sup>8</sup> Additional studies by Stonehouse and Beaver used humidity cabinet experiments to evaluate the susceptibility of beryllium to corrosion from surface residue deposited during machining.<sup>3</sup>

Other investigations have focused on the corrosion associated with beryllium carbides. One of the primary impurities in historic grades of beryllium is carbon, 0.2 wt% or more, which results in the formation of second-phase particles (Be<sub>2</sub>C). In the presence of water, these carbides react quickly to form BeO ( $\Delta G = -581 \text{ kJ mol}^{-1}$ )



as discussed by Mueller.<sup>9</sup> It may be noted, however, that the relative surface concentration of carbides is low and once the carbide has been consumed by this reaction with water, no further role of carbides is expected.

Gulbrandsen *et al.* studied the passivity of Be in phosphoric acid, oxalic acid, phosphate, borate, carbonate buffer solutions, and sodium hydroxide to characterize the passive current density over a pH of 1–15.<sup>10</sup> It was shown that a minimum in passive current density for beryllium occurs near pH 11 and increases logarithmically in more acidic and alkaline solutions. Moreover, it was also observed for any one solution pH that the passive current density is a function of ionic strength. However, Gulbrandsen did not address the formation of soluble oxalic and phosphoric beryllium complexes that form in some of

the solutions used. This may account for their observation of steady-state passive currents below the thermodynamic limit of pH 2.

More recently, Hill *et al.* studied the passivity and break down of 98.5% pure Be.<sup>11</sup> The solutions used were sulfuric acid adjusted to a solution pH of 1 and 2, 0.25 M boric acid (pH=4.6), 0.05 M sodium borate/0.5 M boric acid (pH=7.2), 0.025 M sodium borate/0.05 M sodium hydroxide (pH=10.7), and sodium hydroxide adjusted to a solution pH of 12.5. A summary of the corrosion current densities and passive current densities as a function of pH is presented in Figure 1. Below pH 2, Be exhibited active dissolution at all applied anodic potentials. In solution pH 2–12.5, it was shown that Be exhibits passive anodic behavior at potentials between the OCP and 0.6 V versus saturated calomel electrode (SCE). Anodic polarization above 0.6 V SCE in the pH range of 2–12.5 led to an abrupt increase in the passive current density, followed by oxygen evolution. This abrupt increase was attributed to a change in the specific resistivity of the passive film, as determined by electrochemical impedance spectroscopy (EIS). EIS experiments were also used to show that the oxide growth rate on Be is  $6.4 \text{ \AA V}^{-1}$  over the potential range of 0–4 V. At higher anodization potentials, the growth rate appeared to be somewhat lower likely due to an increase in oxide conductivity.

Breakdown of passivity was studied in chloride and fluoride solutions. In chloride, the attack was found to be localized. Typical potentiodynamic polarization curves for S200D beryllium in deaerated

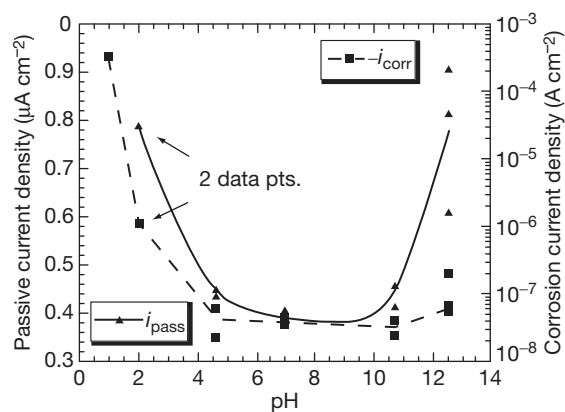


**Figure 1** Passive current density,  $i_{\text{pass}}$ , and corrosion current density,  $i_{\text{corr}}$ , as a function of solution pH. A minimum in  $i_{\text{pass}}$  and  $i_{\text{corr}}$  exists between a pH of 4.5 and 10.7. Reproduced from Hill, M. A.; Butt, D. P.; Lillard, R. S. *J. Electrochem. Soc.* **1998**, 145, 2799, with permission from The Electrochemical Society.

NaCl solutions ranging in concentration from  $10^{-4}$  to 1 M  $\text{Cl}^-$  are presented in Figure 2. For  $\text{Cl}^-$  concentrations below 1 M, the anodic polarization of the sample was characterized by a region of passivity followed by a logarithmic increase in the current density, which corresponded to the onset of pitting corrosion. In deaerated 1 M  $\text{Cl}^-$ , pitting at the OCP was observed. The voltage that corresponded to the onset of pitting corrosion,  $E_{\text{pit}}$ , was found to decrease logarithmically with increasing chloride concentration according to the relationship

$$E_{\text{pit}} = -0.067 \log[\text{Cl}^-] - 1.01 \quad [2]$$

where  $E_{\text{pit}}$  is in volts versus SCE and  $[\text{Cl}^-]$  is the concentration of chloride in molarity (Figure 3). As seen in this relationship, a  $-0.067 \text{ V}$  change in the pitting potential per decade of chloride concentration was observed. A similar relationship between  $E_{\text{pit}}$  and chloride concentration has been noted for pure aluminum (Al); however, the relationship between the pitting potential of Al in  $\text{Cl}^-$  concentration is  $-0.091 \text{ V}$  per decade  $[\text{Cl}^-]$ . For 18Cr–8Ni stainless steel, the pitting potential has been found to vary by  $-0.088 \text{ V}$  per decade  $[\text{Cl}^-]$ . Thus, the pitting potentials of Al and stainless steel are more sensitive to changes in chloride concentration than are those of Be. In addition, as defined by the  $y$ -intercept in eqn. [1], for any one chloride concentration,  $E_{\text{pit}}$  for Be is more negative than those of Al and stainless steel.

Hill *et al.* also investigated the breakdown of passivity in sodium fluoride (NaF) solutions ranging in concentration from  $10^{-1}$  to  $10^{-4} \text{ M F}^-$ . At a

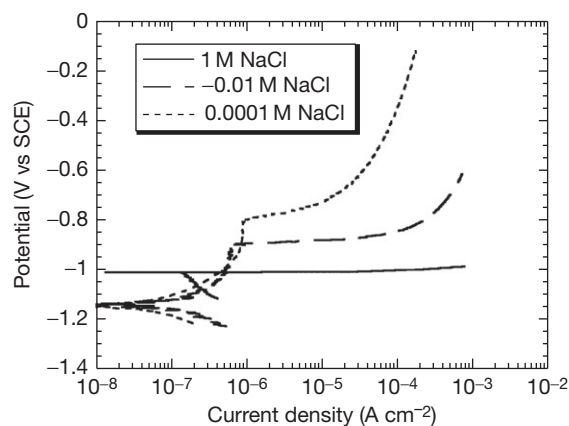


**Figure 2** Beryllium polarization curves as a function of chloride concentration showing a decrease in pitting potential with an increase in chloride concentration. Reproduced from Hill, M. A.; Butt, D. P.; Lillard, R. S. *J. Electrochem. Soc.* **1998**, 145, 2799, with permission from The Electrochemical Society.



$F^-$  concentration of  $10^{-4}$  M, the anodic polarization of the sample was characterized by a region of passivity followed by a logarithmic increase in the current density which corresponded to the onset of pitting corrosion. The pitting potential was found to be  $-0.742$  V SCE. In comparison, for  $10^{-4}$  M  $Cl^-$ , the pitting potential was  $-0.773$  V SCE. Pitting type corrosion was also observed for  $10^{-3}$  M  $F^-$ ; however, no region of passivity was observed upon anodic polarization. While at the lower fluoride concentrations the breakdown of passivity was localized, at the higher fluoride concentrations ( $10^{-1}$  to  $10^{-2}$  M) beryllium was susceptible to uniform attack.

### 3.18.3.2 High-Purity Be

Lillard investigated the factors influencing the transition from metastable to stable pitting high-purity single crystal beryllium.<sup>12</sup> The goal of that work was to determine the relationship between physical bulk

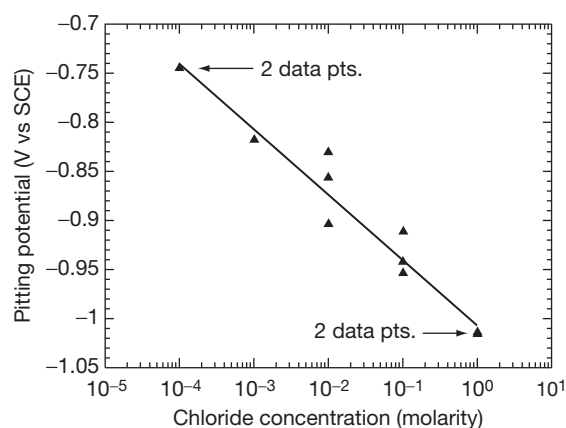


**Figure 3** Pitting potential as a function of chloride concentration displaying a logarithmic relationship between  $E_{pit}$  and  $[Cl^-]$ . Reproduced from Hill, M. A.; Butt, D. P.; Lillard, R. S. J. *Electrochem. Soc.* **1998**, 145, 2799, with permission from The Electrochemical Society.

metal properties, such as crystallographic orientation of the surface, and the critical pitting environments in terms of ohmic and mass transport models on the breakdown of passivity. To accomplish this, electrodes were fabricated from one zone-refined Be single crystal (99.99% Be via ion coupled plasma (ICP) analysis) that was sectioned using electrical discharge machining (EDM). Experiments were conducted on the following surfaces: (0001) the basal plane, (10–10) a Type-I prism plane, and (11–20) a Type-II prism plane. The solutions used in this study were sulfuric acid adjusted to a pH of 2 and near-neutral 0.01 M sodium chloride.

A summary of the critical parameters from the potentiodynamic polarization data for the three orientations investigated is presented in [Table 2](#).  $E_{pit}$  was found to decrease with electrode orientation in the order (0001) > (10–10) > (11–20). The scatter in  $E_{pit}$  for each orientation was moderate, and in only one case did the potential regions overlap; the maximum  $E_{pit}$  for the (11–20) surface was 0.01 V greater than the minimum  $E_{pit}$  for the (10–10) surface. Post-exposure observation found that the corrosion pits were not hemispherical, rather, they were highly crystallographic in nature ([Figure 4](#)). Corrosion pits on the surfaces of prism planes (10–10) and (11–20) were characterized by interiors that had crystallographically oriented, parallel plates of unattacked material. In comparison, the morphology of the corrosion pits in polycrystalline Be are also characterized by parallel plates of unattacked Be, separated by trenches of similar size and shape ([Figure 5](#)). Similar morphologies were also observed by Straumanis in polycrystalline Be.<sup>13</sup> The orientation dependence of pit propagation in single crystal and polycrystalline Be was explained within the context of the metal–metal bond strength as a function of surface orientation.<sup>14</sup> Using the calculations of the electron density distribution, it was proposed that crystallographic pits propagate preferentially at ledges/steps that

**Table 2** Critical parameters from potentiodynamic polarization curves for Be single crystals in 0.01 M NaCl as a function of surface orientation

Surface orientation	$E_{corr}$ (V vs SCE)	$i_{pass}$ ( $A\ cm^{-2}$ )	$E_{pit}$ (V vs SCE)
S200D polycrystalline	$-1.15, \sigma = 0.03$	$6.1 \times 10^{-7}, \sigma = 0.4 \times 10^{-7}$	$-0.862, \sigma = 0.030$
(0001)	$-1.28, \sigma = 0.20$	$1.1 \times 10^{-7}, \sigma = 0.16 \times 10^{-7}$	$-0.644, \sigma = 0.035$
(10–10)	$-1.39, \sigma = 0.12$	$1.8 \times 10^{-7}, \sigma = 0.23 \times 10^{-7}$	$-0.732, \sigma = 0.027$
(11–20)	$-1.28, \sigma = 0.08$	$1.3 \times 10^{-7}, \sigma = 0.34 \times 10^{-7}$	$-0.800, \sigma = 0.047$

The data from polycrystalline S200D grade Be (98.5% Be) from Stonehouse is also presented.

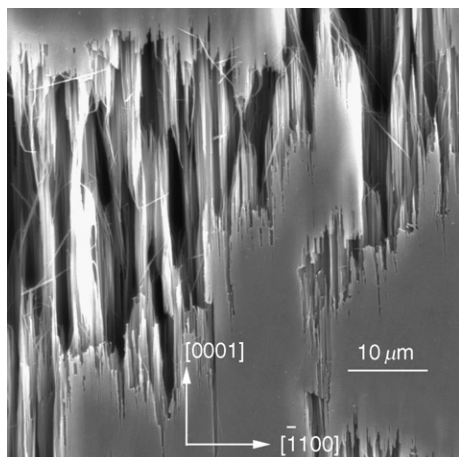


**Figure 4** SEM micrograph of typical corrosion pits in the (11-20) surface of Be after potentiodynamic polarization above the pitting potential in 0.01 M NaCl. Orientation of the lamella (and pit walls) was parallel to the [0001] direction and normal to the (11-20) surface. Reproduced from Lillard, R. S. *J. Electrochem. Soc.* **2001**, 148, B1, with permission from The Electrochemical Society.

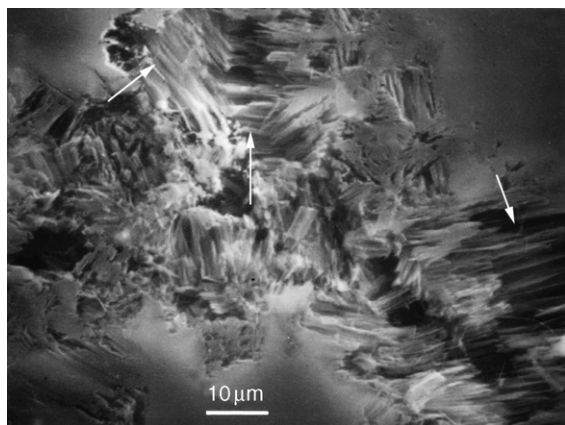
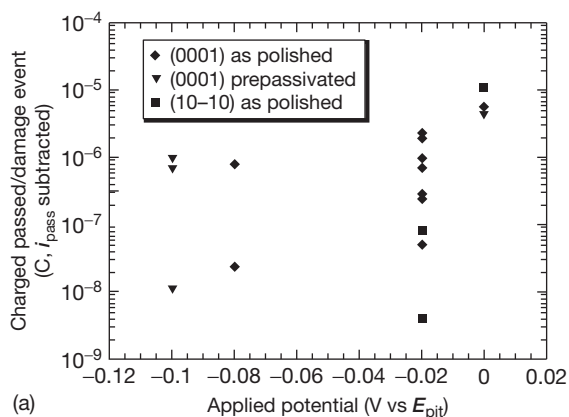


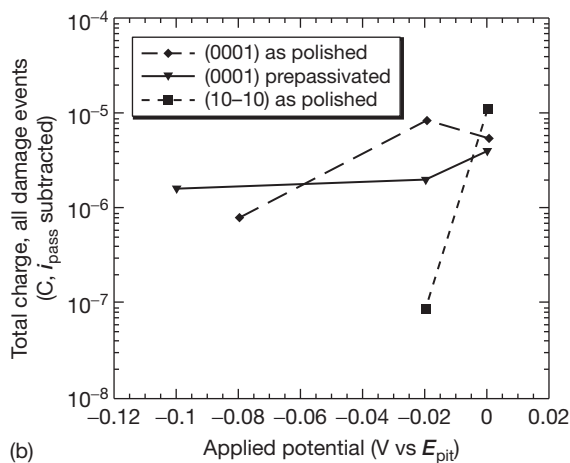
**Figure 5** SEM micrograph of corrosion pits in S200D grade (powder pressed) Be showing orientation of pit walls and parallel plates of unattacked Be lamella (normal to arrows) left behind after pit propagation. The size of any one set of parallel plates is consistent with the grain size of this material ( $\sim 10$ – $40 \mu\text{m}$ ). Reproduced from Lillard, R. S. *J. Electrochem. Soc.* **2001**, 148, B1, with permission from The Electrochemical Society.

expose susceptible lattice positions by removing atoms of lowest bond strength.

At potentials more positive than the repassivation potential,  $E_{\text{rp}}$ , a unique type of current transient was observed in the current/time data collected during potentiostatic experiments. This type of transient



(a)



(b)

**Figure 6** (a) A summary of the damage events; charge passed per event versus applied anodic potential (vs  $E_{\text{pit}}$ ) for the (0001) and the (10-10) surfaces in 0.01 M NaCl solution. (b) A summary of the damage events; total charge passed during all damage events versus applied anodic potential (vs  $E_{\text{pit}}$ ) for the same surfaces in shown in (a). Only damage events that repassivated were considered in these plots. Reproduced from Lillard, R. S. *J. Electrochem. Soc.* **2001**, 148, B1, with permission from The Electrochemical Society.

was always associated with a large amount of charge passed and visible damage on the electrode surface. The average charge passed, peak charge passed, and total number for damage transients increased with increasing anodic potential for each surface orientation are shown in [Figure 6](#). From these results, it was concluded that the transition from metastable to stable pitting is governed by surface damage, and more likely, a bulk property of the metal such as surface energy/metal bond strength.

### 3.18.3.3 Galvanic Effects – The Influence of Be Inclusions

As discussed in Sections 3.18.1 and 3.18.2, commercially available beryllium is generally a powder-processed material. In addition to the relatively high BeO content, most impurity concentrations in commercial beryllium exceed the solubility limit and produce precipitates. The precipitates that form generally are present as both binary and ternary intermetallic phases with Be. Of the possible intermetallics that may form in the commercial grades of Be,  $\text{FeBe}_5$ ,  $\text{TiBe}_{11}$ , and  $\text{FeAlBe}_4$  have been observed on fracture surfaces,<sup>15</sup> although the galvanic relationships between these precipitates and the Be matrix were not defined. These galvanic relationships impact on environmental fracture models from the standpoint of crack tip chemistry and potential, as well as localized corrosion models, from either a cathodic reduction or anodic site chemistry standpoint. In addition, they play an important role in the localized corrosion of Be.<sup>11,16</sup>

To enhance the understanding of the mechanisms of localized corrosion and stress corrosion cracking in commercial grades of beryllium, Hill *et al.* initiated a study of the galvanic relationships between Be and the single phase particles.<sup>17</sup> The beryllides studied were  $\text{TiBe}_{12}$ ,  $\text{FeAlBe}_4$ , and  $\delta$ -phase iron beryllide  $\text{FeBe}_5$  (nominal composition  $\text{FeBe}_{12}$ , crystallographically  $\text{FeBe}_5$ ). They were prepared by arc-melting and casting high-purity elemental material. The solutions studied were of sulfuric acid adjusted to a pH of 2, 0.05 M sodium borate/0.5 M boric acid (pH=7.2), 0.025 M sodium borate, and sodium hydroxide adjusted to a pH of 10.5 and sodium hydroxide adjusted to a solution pH of 12.5.

In a pH range of 7.2–12.5, all of the beryllides exhibited passive behavior. Most notably, a transpassive region was noted in the Fe-containing beryllides at a solution pH of 7.2. With respect to the pH 2 solution, active dissolution of all beryllides was observed at this pH. This was confirmed by post-exposure examinations of the samples, which revealed a large quantity of damage.

A summary plot of OCP values for each beryllide along with that of commercially pure Be is shown in Figure 7 as a function of pH. These data were collected after 48 h of immersion and represent steady-state OCP values. This plot is useful in that it allows one to determine the galvanic relationships between second phase particles in a Be matrix. For example, with respect to  $\text{FeAlBe}_4$ , the OCP is

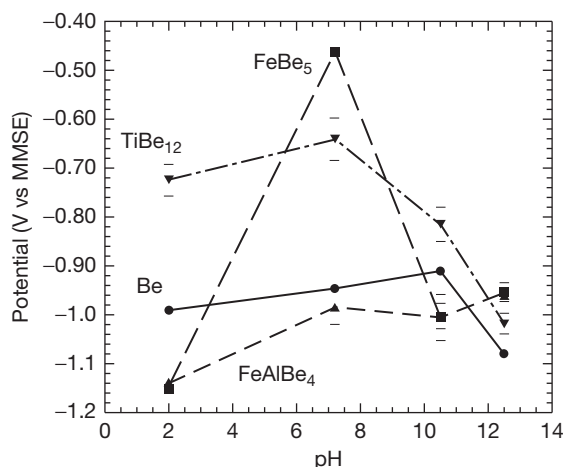


**Figure 7** A summary plot of OCP for  $\text{FeBe}_5$ ,  $\text{FeAlBe}_4$ , and  $\text{TiBe}_{12}$  as a function of solution pH. Data were collected after 48 h of immersion and represent steady-state OCP values. Reproduced from Hill, M. A.; Hanrahan, R. J.; Haertling, C. L.; Schulze, R. K.; Lillard, R. S. *Corrosion* **2003**, 59, 424, with permission from NACE International.

more negative than that of beryllium in the pH range of 2.0–10.5. Thus, from a mixed potential standpoint, when coupled in commercial Be under these conditions, the  $\text{FeAlBe}_4$  may act as a site for active dissolution. This finding was confirmed experimentally in galvanic couple tests.

### 3.18.3.4 Environmental Fracture

Reports on environmental fracture of Be are limited. The first reported work on the stress-corrosion cracking of beryllium related to its use in water containing 0.005 M hydrogen peroxide at pH 6–6.5 and at  $\sim 90^\circ\text{C}$ .<sup>18</sup> Although some pitting occurred in these exposure, there was no evidence of stress corrosion, even though the tests employed extruded metal stressed at up to 90% of the yield stress. Later work included stress corrosion studies of Be tensile bars' exposure to synthetic seawater.<sup>19</sup> In that environment, time to failure decreased from  $\sim 2350$  h at an applied stress of 1220 psi to 40 h at an applied stress of 40000 psi. Further, crack initiation appeared to be related to localized corrosion of the sample. Electron microscopy of the fracture surfaces found the crack habit to be transgranular in character. Subsequent work by the same group studied the influence of applied current, anodic and cathodic, on time to failure.<sup>20</sup> As might be anticipated, applied anodic currents promoted pitting attack and decreased time to failure. However, applied cathodic currents reduced pitting attack and eliminated environmental fracture altogether.

### 3.18.3.5 Corrosion Control

From what has already been indicated, it will be apparent that the use of beryllium in most commercial environments involving moisture will require some form of surface protection to mitigate pitting corrosion. Corrosion control measures range from painting<sup>21</sup> to Zn galvanizing.<sup>22</sup> In addition to those studies, Paine and Stonehouse<sup>23</sup> used a high temperature silicone-based paint on beryllium heat-sinks for aircraft brakes. They also studied cathodic protection in fresh- and saltwater solutions via manganese plating on the steel parts that were mated to Be. Other work on cathodic protection includes the stress corrosion study in aerated synthetic seawater described in [Section 3.18.3.4](#). There, an impressed cathodic potential was used to protect Be from localized attack by chlorides.<sup>20</sup>

Booker examined the application of chromate conversion coatings (CCCs) to mitigate Be corrosion in chloride environments.<sup>24</sup> As the coating bath composition was not specified in that paper, one can only presume that these coatings were based on Alodine® (a nitric acid-based solution containing NaF/KBF<sub>4</sub>/K<sub>2</sub>ZrF<sub>6</sub>/K<sub>3</sub>Fe(CN)<sub>6</sub>). Chromium deposition (and ultimately corrosion protection) was greatly dependent on the manner in which the sample was cleaned and etched. To obtain the best performance, it was necessary to etch the samples in a nitric acid–hydrofluoric acid solution just prior to coating. The need for this F<sup>−</sup> base etch has been confirmed in our laboratory. Samples prepared in this manner were described by Booker as having satisfactory performance in high humidity and salt spray exposures. A similar investigation of CCCs was reported by Levy.<sup>6</sup>

The use of anodization to control Be corrosion has been somewhat problematic. Kerr reported on the anodization of Be in an aqueous solution of 10% nitric acid containing 200 g l<sup>−1</sup> CrO<sub>3</sub> (chromic acid).<sup>25</sup> In that work, samples were anodized at a constant current density of 0.03 A cm<sup>−2</sup>. Although films as thick as 0.35 mm were grown in this solution, when the limiting voltage was reached, the current remained constant with time. Thus, it was concluded that for Be, there is no voltage-dependent limiting oxide thickness as is the case for other valve metals such as aluminum, zirconium, and tantalum. In an attempt to overcome this difficulty, Kerr explored the use of an ammoniacal glycol solution (25 g l<sup>−1</sup> NH<sub>3</sub> in ethylene glycol), which has been used successfully

to grow compact insulating films on aluminum. For current densities of 1.9 mA cm<sup>−2</sup>, limiting thicknesses were formed on Be. However, as was the case in chromic acid, the current remained roughly constant with time and it was concluded that the films formed in this solution were not insulating. Subsequently, Hill has shown that the specific resistivity of the oxide on Be decreases with increasing applied potential and undergoes a transition at ~2 V versus NHE.<sup>11</sup> This was attributed to a change from a compact to a more porous film though this behavior may owe to other factors such as the incorporation of unoxidized metal into the film. Levine has also reported on anodic films grown in ammoniacal glycol solution and nitric acid solutions containing chromic acid.<sup>26</sup> Similarly, films grown in nitric acid were always crystalline, while those grown in ethylene glycol were amorphous. Levine reported current potential relationships similar to Kerr, indicating that these films were not insulating. Shetata has reportedly been able to overcome this problem by growing films on Be in near-neutral ethylene glycol saturate with sodium phosphate dibasic and sodium sulfate.<sup>27</sup> For constant current densities in the order of 2–3 mA cm<sup>−2</sup>, samples anodized in this solution quickly reached limiting voltages of 50 V (<30 s) and, correspondingly, decreasing current density with time. Films grown on Be in this manner were insulating and are of the order of 5 μm thick. Unfortunately, we have not been able to reproduce these results in our own laboratory.

## 3.18.4 High Temperature Oxidation of Be and the Beryllides

### 3.18.4.1 Beryllium

Early high temperature oxidation studies of Be focused on dry and moist oxygen environments. Gulbransen examined the reaction of Be (Brush) with dry oxygen (0.76–7.6 cm O<sub>2</sub>) over the temperature range of 350–950 °C.<sup>28</sup> At lower temperatures (below 825 °C) and high O<sub>2</sub> pressures (7.6 cm O<sub>2</sub>), the oxidation rate appeared to fit a logarithmic or inverse logarithmic law, while at higher temperatures, the rates appeared to be parabolic ([Figure 8](#)). Weight gain data ( $W$ ) as a function of time ( $t$ ) were fit to a parabolic rate law,  $W^2 = Kt + C$ , where  $K$  is the parabolic rate constant. Below 650 °C,  $K$  increased from  $0.93 \times 10^{-16}$  cm<sup>2</sup> s<sup>−1</sup> at 350 °C to  $5.4 \times 10^{-15}$  cm<sup>2</sup> s<sup>−1</sup>; at 950 °C,  $K$  was equal to  $1.0 \times 10^{-12}$  cm<sup>2</sup> s<sup>−1</sup>.

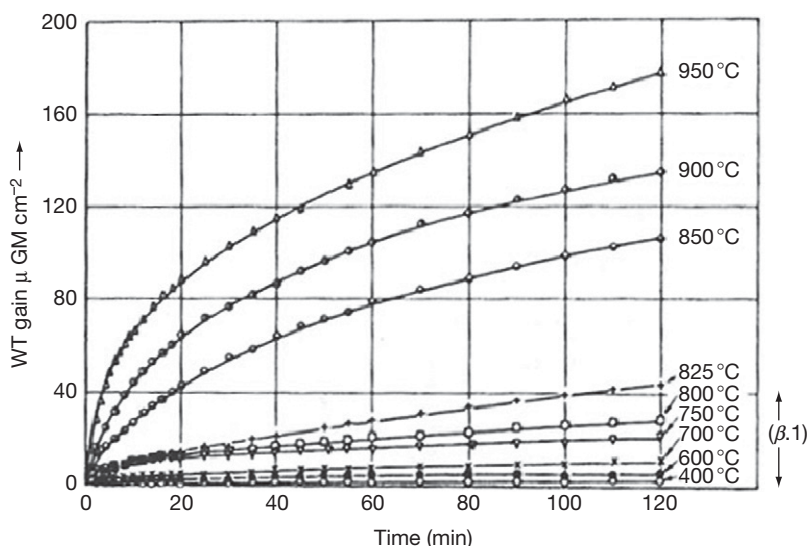


**Figure 8** The influence of temperature on the oxidation rate of Be in dry O<sub>2</sub> at a pressure of 7.6 cm. Reproduced from Gulbransen, E. A.; Andrew, K. F. J. *Electrochem. Soc.* **1950**, 97, 383, with permission from The Electrochemical Society.<sup>28</sup>

Arrhenius plots of  $\log K$  versus  $1/T$  identified two activation energies for oxidation; below 750 °C, the activation energy was equal to 8.5 kcal mol<sup>-1</sup>, while above 750 °C, the activation energy was 50.5 kcal mol<sup>-1</sup> (Figure 9). Similar activation energies in the high temperature range were observed in the later work by Cubicciotti.<sup>29</sup> For Pechiney flake Be (referred to as 'French-flake' being produced in France), Be in 10-cm dry O<sub>2</sub> and temperatures below 650 °C, Alymore found higher oxidation rates and at temperatures greater than 650 °C with break-away oxidation observed.<sup>30</sup> Similar trends were found by Ervin, who concluded that the first stage of Be (Brush/NMC) oxidation is a protective diffusion controlled process (Be vacancies).<sup>31</sup> He further concluded that the formation of pits at accumulation sites of vacancies at the metal–oxide interface in this stage lead to a second, catastrophic stage of oxidation. To date, there is no clear explanation of discrepancy between the Gulbransen–Cubicciotti observations of passive behavior and low oxidation rates in the range of 350–950 °C and the works of Alymore–Ervin that found breakaway oxidation above 650 °C. For example, one investigator did not use powder product as compared with results from pressed disc or flake nor were there clear distinction between vendors (Brush versus Pechiney flake).

With respect to the addition of H<sub>2</sub>O, Alymore investigated oxidation rates for Be in moist O<sub>2</sub>

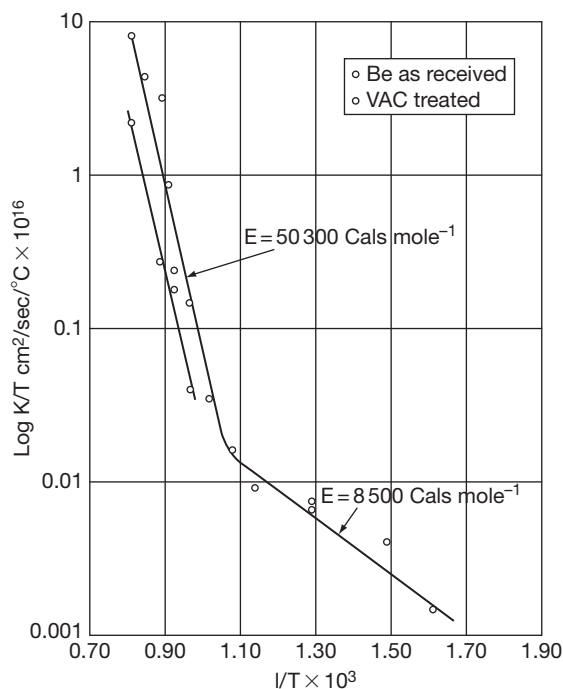


**Figure 9** Arrhenius plot from data in Figure 8 showing the parabolic rate constant as a function of inverse temperature ( $K$ ). Two unique behaviors, and thus activation energies, are observed above and below ~750 °C (1020 K,  $1/T = 0.00098$ ). Reproduced from Gulbransen, E. A.; Andrew, K. F. J. *Electrochem. Soc.* **1950**, 97, 383, with permission from The Electrochemical Society.



(10 cm O<sub>2</sub>, 1.2 cm H<sub>2</sub>O) and water vapor.<sup>32</sup> In 1.2-cm H<sub>2</sub>O and temperatures below 650 °C, oxidation rates were logarithmic/parabolic. After 300 h of exposure, the weight gains were of the order of 20 µg cm<sup>-2</sup>. Above 650 °C, breakaway oxidation was observed. In water vapor below 650 °C, rates were again logarithmic/parabolic and relatively low, less than 50 µg cm<sup>-2</sup>. Above 650 °C, breakaway oxidation was again observed.

The possible use of beryllium in nuclear engineering and in the aircraft industry encouraged considerable investigation into its oxidation characteristics in carbon dioxide and carbon monoxide (dry and moist) at temperatures of up to 1000 °C. For Pechiney-flake Be, Gregg found that the oxidation of Be in dry CO<sub>2</sub> (pressure of 10 cm) was logarithmic at temperatures equal to and below 550 °C and inverse logarithmic between 600 and 750 °C for exposure times up to 300 h (Figure 10).<sup>33</sup> They proposed that film thickening occurs via the outward diffusion of Be<sup>2+</sup> to react with chemisorbed carbon dioxide at the gas-oxide interface where the following reactions take place to form oxide and carbide species.



In moist CO<sub>2</sub> (total CO<sub>2</sub> pressure of 10 cm, with 1.2-cm partial pressure H<sub>2</sub>O) at temperature equal

to and below 650 °C, results were similar to those in dry CO<sub>2</sub>. However, at temperatures greater than 650 °C, breakaway oxidation was observed (Figure 11).<sup>34</sup> Radiotracer experiments in moist CO<sub>2</sub> found the build up of gas in the exposure vessel, which led the authors to conclude that water was reacting with the BeC to form methane:



Unfortunately, no conclusions concerning the mechanism of the breakaway oxidation were reported. Similar rate constants and threshold temperatures were found by Menzies for flake as well as Brush sheet and powder products in 300 psig CO<sub>2</sub>/300 ppm H<sub>2</sub>O for longer exposure periods (up to 8000 h).<sup>35</sup> Higgins investigated Be-CO<sub>2</sub>-H<sub>2</sub>O systems at higher temperatures and higher water content and found similar thresholds.<sup>36</sup> Raine and Robinson found that small additions of calcium greatly improved the resistance of Be to breakaway oxidation.<sup>37</sup> Further, it was found that the addition of Ca modified the pressure dependence of the corrosion reaction in CO<sub>2</sub>.

In dry carbon monoxide, Gregg found that the oxidation rates were greater by at least a factor of 10 than those observed in dry CO<sub>2</sub>; however, the transition temperatures from logarithmic to inverse logarithmic behavior that were reported in that study were similar to those reported by Gulbransen (Figure 8).<sup>38</sup> In this environment, the possible reactions are

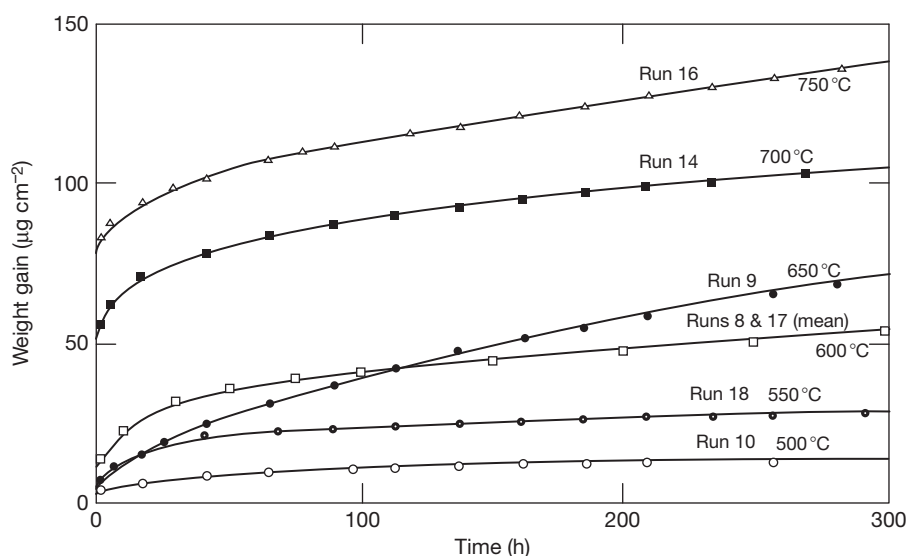


**Figure 10** Oxidation of Be as a function of temperature in dry CO<sub>2</sub> at pressure of 10 cm. Reproduced from Gregg, S. J.; Hussey, R. J.; Jepson, W. B. *J. Nucl. Mater.* **1961**, 3, 175, with permission from Elsevier.<sup>33</sup>



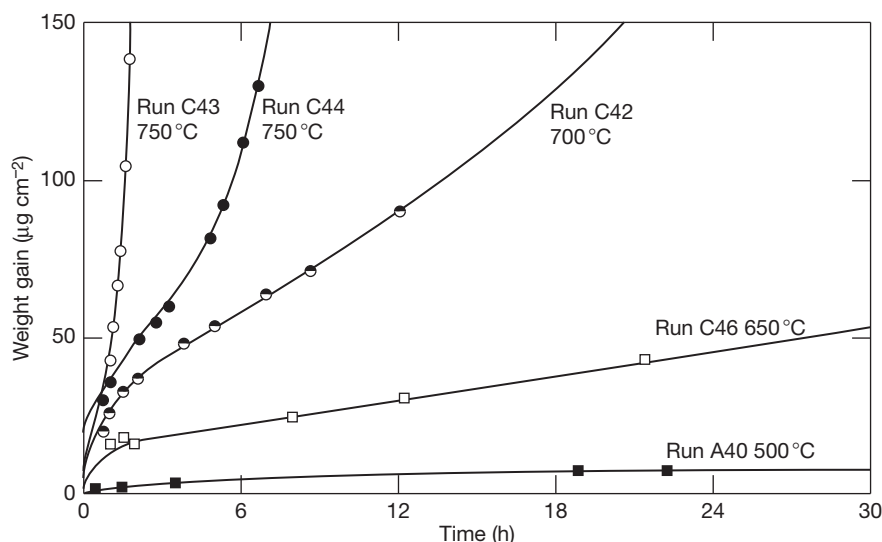
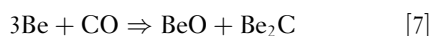
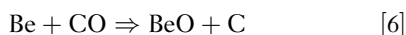


**Figure 11** Oxidation of Be as a function of temperature in moist CO<sub>2</sub> at a total pressure of 10 cm with 1.2-cm partial pressure H<sub>2</sub>O. Reproduced from Gregg, S. J.; Hussey, R. J.; Jepson, W. B. *J. Nucl. Mater.* **1961**, 4, 46, with permission from Elsevier.



The higher oxidation rates observed in CO were attributed to a nonprotective reaction product that spalls from the sample. It was proposed that the lower ratio of BeO to C production in CO oxidation (eqn. [6]), as compared with CO<sub>2</sub> oxidation (eqn. [3]), results in excessive C (or Be<sub>2</sub>C) incorporation, and thus, a less protective film. Subsequent selected-area transmission electron microscope diffraction patterns by Scott confirmed that BeC<sub>2</sub> was in fact incorporated into the oxide during oxidation in CO.<sup>39</sup> Subsequent work on these alloys by Scott found that calcium acted to reduce oxidation rates by decreasing the extent of intergranular oxidation of the metal.<sup>40</sup>

### 3.18.4.2 Beryllides

Beryllium intermetallics are currently being considered as replacement materials for beryllium in demonstration fusion reactors. Although beryllium is commonly used as a neutron multiplier in the fusion blanket, its melting point is low (1285 °C) and the ITER demonstration reactor requires temperature in the 600–900 °C range. Possible replacements include beryllium–copper such as CuNiBe and TiBe<sub>2</sub>. These two intermetallics are representatives of the Laves

phases group C14 and C15. Phases in these groups include CrBe<sub>2</sub>, NbBe<sub>2</sub>, TaBe<sub>2</sub>, and VBe<sub>2</sub> and have been the subject of limited oxidation studies. Paine *et al.* tested the above phases in dry air for 100 h at temperatures up to 1426 °C.<sup>41</sup> Each was shown to have good oxidation resistance under these test conditions. However, the study was heavily biased toward the highest melting point compounds, of which TiBe<sub>2</sub> is one, and therefore, many phases were not examined because they did not appear promising for service above 1371 °C. In a separate study, Alves *et al.* investigated Ti beryllides, Be–5% Ti (Be<sub>12</sub>Ti), and Be–7% Ti, which was a two-phase system consisting of Be<sub>12</sub>Ti surrounded by Be.<sup>42</sup> From surface analytical experiment (X-ray emission and RBS) of samples oxidized at 800 °C for 1–4 h, it was found that the oxidation in the two-phase system was faster than in Be<sub>12</sub>Ti.

By far, the largest amount of information on any beryllide relates to ZrBe<sub>13</sub> and other zirconium-based beryllides. In experiments on powders, Ervin and Nakata found a protective BeO on ZrBe<sub>13</sub> and NbBe<sub>12</sub> between 900 and 1500 °C.<sup>43</sup> The oxidation rate for ZrBe<sub>13</sub> in 0.1-atm oxygen was parabolic and is presented in Figure 12. In comparison, the rates reported by Paine were much higher for air. Paine reported that the oxidation rate for ZrBe<sub>13</sub> in dry air (at 1537 °C) was 10 mg cm<sup>−2</sup> after 100 h and 6 mg cm<sup>−2</sup> for moist air after the same period.<sup>41</sup> The temperature dependence of the rate constants

from the Ervin data is shown in Figure 13 as an Arrhenius plot. As seen in this figure, two activation energies for oxidation ( $Q$ ) were observed. In the range of 1100–1400 °C,  $Q$  was determined to be  $5.6 \times 10^4$  J, while in the range between 1400–1500 °C,  $Q$  was

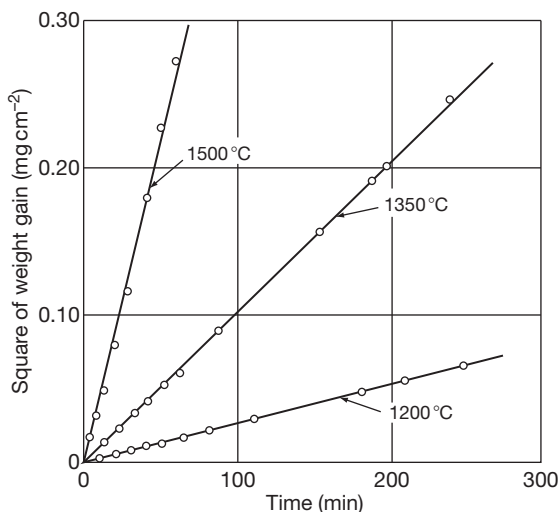


**Figure 12** Oxidation of  $\text{ZrBe}_{13}$  as a function of temperature in 0.1 atm  $\text{O}_2$ . Reproduced from Ervin G., Jr.; Nakata, M. M. *J. Electrochem. Soc.* **1963**, 110, 1103, with permission from The Electrochemical Society.

determined to be  $21.5 \times 10^4$  J. Similar results were found for  $\text{NbBe}_{12}$ ; however, for  $\text{NbBe}_{12}$ ,  $Q$  was constant over the entire temperature range examined and determined to be equal to  $13.0 \times 10^4$  J. Ervin and Nakata reported accelerating oxidation of  $\text{ZrBe}_{13}$  at lower temperatures in 0.1 atm oxygen (Figure 14), while  $\text{NbBe}_{13}$  was immune to this phenomenon. This observation was attributed to “fracture and disintegration of the metal phase causing a continual increase in the exposed metal surface area.” This phenomenon is known as pest and has been reported by several other authors.<sup>44–48</sup> Chou *et al.* reported that the susceptibility of  $\text{ZrBe}_{13}$  to pest is increased in the presence of moist air, although this finding is not uniform amongst other authors investigating Zr-based beryllides. In addition, Chou concluded that the formation of BeO-rich whiskers is important in the pest mechanism of beryllides, but did not report how they might form or why they cause disintegration.

The influence of Be additions on the high temperature oxidation of NiAl and TiAl-based intermetallics has been investigated by Hanrahan.<sup>49</sup> In TGA studies conducted from 800 to 1200 °C for 16 h in air, Be-modified NiAl containing 1, 2, or 5 at.% Be exhibited lower weight gain and comparable or slower oxidation rates than the pure binary material. In addition, the reaction kinetics in these

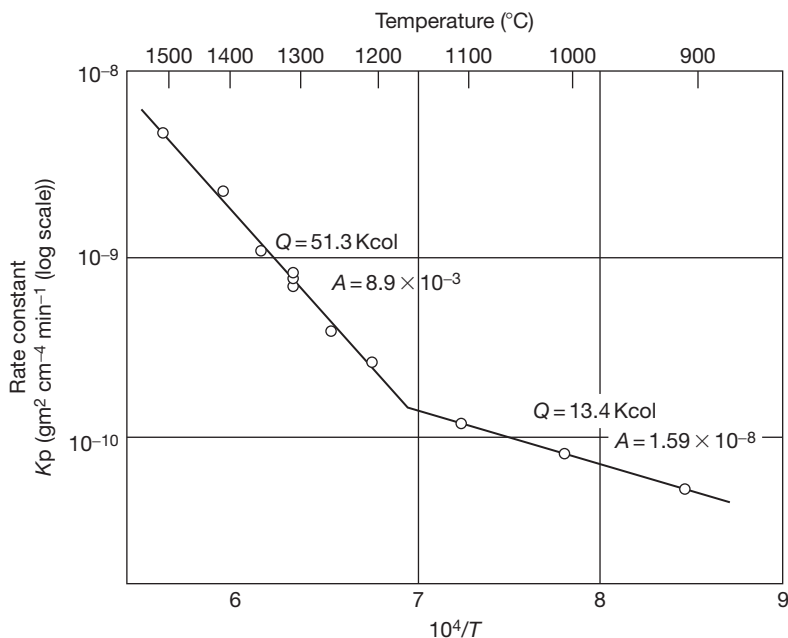


**Figure 13** Arrhenius plot from data in 5.4.2.1 showing the parabolic rate constant as a function of inverse temperature ( $K$ ) for  $\text{ZrBe}_{13}$  in 0.1 atm  $\text{O}_2$ . Reproduced from Ervin G., Jr.; Nakata, M. M. *J. Electrochem. Soc.* **1963**, 110, 1103, with permission from The Electrochemical Society.

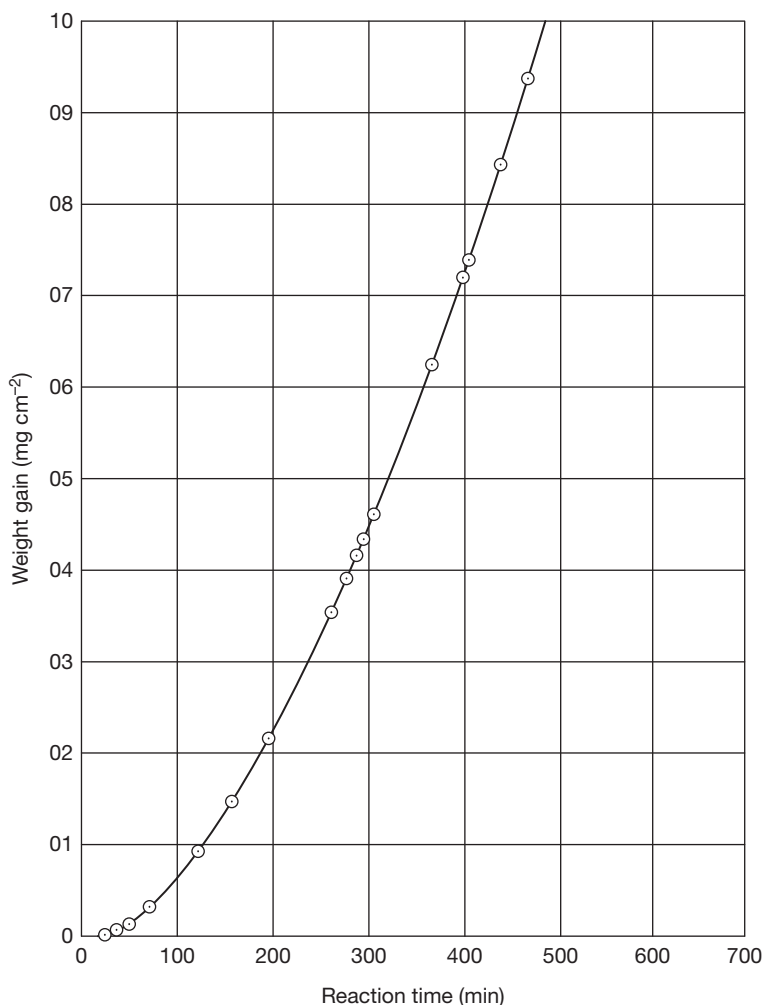


**Figure 14** Low-temperature (600–700 °C) oxidation of  $\text{ZrBe}_{13}$  in 0.1-atm  $\text{O}_2$ . Reproduced from Ervin G., Jr.; Nakata, M. M. *J. Electrochem. Soc.* **1963**, *110*, 1103, with permission from The Electrochemical Society.

experiments were equal to or slower than in NiAl. The surfaces of the Be-modified specimens showed minimal topography, with no evidence of the usual transient alumina phases grown on binary NiAl in this temperature range. From X-ray diffraction and surface analysis, it was found that oxidation did not result in formation of BeO at any of the temperatures. Rather, the presence of layers of  $\text{Al}_2\text{O}_3$  and ternary oxide phases, primarily  $\text{BeO} \cdot \text{Al}_2\text{O}_3$  (chrysoberyl), were observed. It was proposed that the formation of this phase prevents the growth of the transient alumina phases. Thus, lower weight gains and slower reaction kinetics were observed due to the rapid formation of the chrysoberyl phase followed by nucleation of  $\alpha$ -alumina at the scale-metal interface, rather than the formation of transient alumina phases

often observed to form on NiAl. In other studies, Be additions to Ti–Al–Cr-based alloys at 800 °C and 1000 °C in dry air resulted in the formation of a protective  $\text{BeAl}_2\text{O}_4$  spinel phase.<sup>50</sup> In moist air, only Ti–Al–Cr–Be alloys with a high Cr content (10–15 at.%) formed the protective  $\text{Be} \cdot \text{Al}_2\text{O}_4$  scale.

## References

1. Stonehouse, A. J. *J. Vac. Sci. Technol. A* **1986**, *4*, 1163.
2. English, J. L. Interim Report on the Corrosion of Beryllium in Simulated Cooling Water for the Proposed Development Reactor, ORNL-298, Oak Ridge National Laboratory, March, 1949.
3. Stonehouse, A. J.; Beaver, W. W. Corrosion and Protection of Beryllium Metal, BBC-TR 335: The Brush Beryllium Co., 1963.

4. Aida, H.; Elboin, I.; Garreau, M. *J. Electrochem. Soc.* **1971**, *118*, 243.
5. Sheth, K. G.; Johnson, J. W.; James, W. I. *Corros. Sci.* **1969**, *9*, 135.
6. Levy, D. J. The Electrolytic Polarization of Beryllium, LMSC-6-90-61-75.; Lockheed Missiles and Space Division, Sunnyvale, CA, 1961.
7. Miller, P. D.; Boyd, W. K. Corrosion of Beryllium, DMIC Report 242, Defense Metals Information Center, Battelle Memorial Institute, Columbus, 1961.
8. Prochko, R. J.; Myers, J. R.; Saxer, R. K. *Mater. Prot.* **1966**, *5*, 39.
9. Mueller, J. J.; Adolphson, D. R. In *Beryllium Science and Technology*; Floyd, D. R., Lowe, J. N., Eds.; Plenum Press: New York, 1979; Vol. 2, 417.
10. Gulbrandsen, E.; Johansen, A. M. *J. Corros. Sci.* **1994**, *36*, 1523.
11. Hill, M. A.; Butt, D. P.; Lillard, R. S. *J. Electrochem. Soc.* **1998**, *145*, 2799.
12. Lillard, R. S. *J. Electrochem. Soc.* **2001**, *148*, B1.
13. Straumanis, M. E.; Mathis, D. L. *J. Electrochem. Soc.* **1962**, *109*, 434.
14. Lillard, R. S. *Electrochem. Solid-State Lett.* **2003**, *6*, B29.
15. Cotton, J. D.; Field, R. D. *Metall. Trans. A* **1997**, *28*, 673.
16. Venugopal, A.; MacDonald, D. D.; Varma, R. *J. Electrochem. Soc.* **2000**, *147*, 3673.
17. Hill, M. A.; Hanrahan, R. J.; Haertling, C. L.; Schulze, R. K.; Lillard, R. S. *Corrosion* **2003**, *59*, 424.
18. Logan, H. L.; Hessing, H. Summarising Report on Stress Corrosion of Beryllium, NBS-6, Nat. Bur. Stand., Washington, 1955.
19. Miller, R. A.; Myers, J. R.; Saxer, R. K. *Corrosion* **1967**, *23*, 11.
20. King, T. T.; Myers, J. R. *Corrosion* **1969**, *25*, 349.
21. Terlo, G.; Ya, A. D. 628185, Department of Navy, 1966.
22. Beach, J. G.; Faust, C. L. *J. Electrochem. Soc.* **1953**, *100*, 276.
23. Paine, R. M.; Stonehouse, A. J. *Corrosion*/77, 1977, Paper No 26.
24. Booker, J.; Stonehouse, A. J. *Mater. Prot.* **1969**, *8*, 43.
25. Kerr, I. S.; Wilman, H. *J. Inst. Met.* **1955**, *84*, 379.
26. Levin, M. L. *Trans. Faraday Soc.* **1958**, *54*, 935.
27. Shetata, M. T.; Kelly, R. J. *J. Electrochem. Soc.* **1975**, *122*, 1359.
28. Gulbrandsen, E. A.; Andrew, K. F. *J. Electrochem. Soc.* **1950**, *97*, 383.
29. Cubicciotti, D. *J. Amer. Chem. Soc.* **1950**, *72*, 2084.
30. Aymore, D. W.; Gregg, S. J.; Jepson, W. B. *J. Nucl. Mater.* **1960**, *2*, 169.
31. Ervin, G.; Mackay, T. L. *J. Nucl. Mater.* **1964**, *12*, 30.
32. Aymore, D. W.; Gregg, S. J.; Jepson, W. B. *J. Nucl. Mater.* **1961**, *3*, 190.
33. Gregg, S. J.; Hussey, R. J.; Jepson, W. B. *J. Nucl. Mater.* **1961**, *3*, 175.
34. Gregg, S. J.; Hussey, R. J.; Jepson, W. B. *J. Nucl. Mater.* **1961**, *4*, 46.
35. Menzies, I. A. *Corros. Sci.* **1962**, *3*, 35.
36. Higgins, J. K.; Antill, J. E. *J. Nucl. Mater.* **1962**, *5*, 67.
37. Raine, T.; Robinson, J. A. *J. Nucl. Mater.* **1962**, *5*, 341.
38. Gregg, S. J.; Hussey, R. J.; Jepson, W. B. *J. Nucl. Mater.* **1960**, *2*, 225.
39. Scott, V. D. *Nature* **1960**, *186*, 466.
40. Scott, V. D.; Ranzetta, G. V. T. *J. Nucl. Mater.* **1963**, *9*, 277.
41. Paine, R. M.; Stonehouse, A. J.; Beaver, W. W. *Corrosion* **1964**, *20*, 307t.
42. Alves, E.; Alves, L. C.; Franco, N.; da Silva, M. R.; Paul, A. *Mater. Nucl. Sys.* **2007**, *159*, 233.
43. Ervin, G.; Nakata, M. M. *J. Electrochem. Soc.* **1963**, *110*, 1103.
44. Chou, T. C.; Nieh, T. G.; Wadsworth, J. *Scripta Metallurgica* **1992**, *27*, 897.
45. Aitken, E. A.; Smith, J. P. *J. Nucl. Mater.* **1962**, *6*, 119.
46. Lewis, J. R. *J. Met.* **1961**, *13*, 829.
47. Paine, R. M.; Stonehouse, A. J.; Beaver, W. W. In *Nuclear Metallurgy*, International Symposium on Compounds of Interest in Nuclear Reactor Technology; Waber, J. T., Chiotti, P., Miner, W. N., Eds.; AIME: Ann Arbor, 1964; Vol. 10, 495.
48. West Brook, J. H.; Wood, D. L. *J. Nucl. Mater.* **1964**, *12*, 208.
49. Hanrahan Jr, R. J.; Butt, D. P.; Chen, K. C.; Taylor, T. N.; Maggiore, C. J.; Thoma, D. J. Proceedings of the TMS Annual Meeting, 28 Feb.-4 March 1999, San Diego, CA, USA; pp 305-315.
50. Hanrahan, R. J., Jr.; Chen, K. C.; Brady, M. P. Proceedings of the Electrochemical Society 193rd Meeting of the Electrochemical Society; May 3-8, 1998; San Diego, CA; 458.

## 3.19 Corrosion of Uranium and its Alloys

**S. B. Lyon**

Corrosion and Protection Centre, School of Materials, University of Manchester, Oxford Road, Manchester M13 9PL, UK

This article is a revision of the Third Edition article 5.6 by J. E. Antill and R. A. Jarman, volume 1, pp 5:78–5:86,

© 2010 Elsevier B.V.

<b>3.19.1</b>	<b>Introduction</b>	2181
3.19.1.1	Background	2181
3.19.1.2	Applications	2182
3.19.1.3	Metallurgy and Alloying	2182
<b>3.19.2</b>	<b>Aqueous Corrosion</b>	2183
3.19.2.1	Thermodynamics	2183
3.19.2.2	Water	2183
3.19.2.3	Atmospheric Corrosion	2185
3.19.2.4	Effects of Water Radiolysis	2185
3.19.2.5	Galvanic Corrosion	2186
3.19.2.6	Stress Corrosion Cracking	2186
<b>3.19.3</b>	<b>Gases at High Temperatures</b>	2187
3.19.3.1	Carbon Dioxide and Carbon Monoxide	2187
3.19.3.2	Air	2187
3.19.3.3	Steam	2188
<b>3.19.4</b>	<b>Corrosion Processes</b>	2188
3.19.4.1	Protective Coatings	2188
3.19.4.2	Irradiation Effects	2189
3.19.4.3	Corrosion and Dissolution of $\text{UO}_2$	2189
3.19.4.4	Uranium in the Environment	2190
<b>References</b>		2190

### Abbreviations

**DU** Depleted uranium

**PVD** Physical vapor deposition

**RH** Relative humidity

**SCE** Standard calomel electrode

**UTS** Ultimate tensile strength

**YS** Yield stress

### Symbols

$E_{\text{corr}}$  Corrosion potential

## 3.19.1 Introduction

### 3.19.1.1 Background

Uranium is a naturally occurring, and naturally radioactive, element whose predominant commercial interest lies in the ability of the  $^{235}\text{U}$  isotope to undergo nuclear fission with consequent release of large amounts of energy. Uranium metal was first

prepared in 1841 by Peligot using reduction of anhydrous  $\text{UCl}_4$  with potassium. Uranium is an f-block element and a member of the actinide family that has similar, but not identical, chemistry with other elements in its series. Its radioactive nature was not appreciated until 1891 when Becquerel first detected it; however, natural uranium is only mildly radioactive, emitting relatively low-energy  $\alpha$  and  $\beta$  radiation, while material that has been depleted in  $^{235}\text{U}$  can be 30–40% less radioactive than natural uranium.

The main health and safety concern with uranium is its chemical toxicity as a heavy metal, rather than its natural radioactivity, which is relatively easily contained. Prior to the discovery of its fissionable nature in 1938 by Hahn and Strassman, it was used in a number of small-scale applications, predominantly because it imparts an attractive orange color to pottery glazes and a characteristic yellow-green color to glass. Uranium is not a particularly rare element and occurs in greater abundance than, for example, mercury, silver, cadmium, and tungsten and has a similar abundance to molybdenum.<sup>1</sup>

### 3.19.1.2 Applications

The fissionable isotope  $^{235}\text{U}$  comprises about 0.7% of natural isotopic abundance with the majority of the balance consisting of  $^{238}\text{U}$ ;  $^{234}\text{U}$  is also naturally present, but in tiny amounts. By far, the major use of uranium is currently as a nuclear fuel in which the  $^{235}\text{U}$  percentage generally requires enrichment over the natural level, commercial light-water reactors typically being designed to operate with 3–5% of  $^{235}\text{U}$ . The energy released during nuclear fission is approximately 200 MeV per atom or about  $80 \text{ GJ g}^{-1}$  ( $^{235}\text{U}$ ); this is approximately equivalent to 2.7 tons of coal or 13.7 barrels of oil. At 33% thermal efficiency, a 1000 MW electrical generating station consumes about 1 ton of  $^{235}\text{U}$  per year (compared with about 3 000 000 tons of coal per year). Interestingly, coal contains trace quantities of uranium (and thorium, another radioactive element) at levels from 1 to 10 ppm. Thus, a 1000 MW coal-fired power station typically releases between 3 and 30 tons of uranium + thorium into the environment every year of operation: comparable in mass (although very considerably less so in radioactivity) to spent nuclear fuel.

Other applications include those where uranium's exceptional density ( $19.05 \text{ Mg m}^{-3}$ ) is advantageous; these include ballast and counterweights in aircraft and yachts, radiation shielding in medicine and industrial radiography, as well as military uses in defensive armor plating and high-kinetic energy armor-piercing ammunition. Commonly, depleted uranium (DU; typically  $<0.25\%$   $^{235}\text{U}$ , with a radiation level about 40% less than natural uranium) is used as it is a relatively cheap and abundant material with no other significant applications (the world inventory of DU is said to be over 1 million tons).

### 3.19.1.3 Metallurgy and Alloying

Uranium, unusually for a metallic element, has a room-temperature structure that is orthorhombic ( $\alpha\text{-U}$ ) below about  $670^\circ\text{C}$ , tetragonal ( $\beta\text{-U}$ ) from  $670$  to  $770^\circ\text{C}$ , and body-centered cubic ( $\gamma\text{-U}$ ) above about  $770^\circ\text{C}$ . The orthorhombic structure implies significant anisotropy in physical properties, and few alloying elements have significant, if any, room-temperature solubility. The mechanical properties of uranium are more akin to those of tungsten than of gold. Thus, cast commercial-purity uranium has yield and ultimate tensile strengths of, respectively, 200–250 and 600–700 MPa, comparable to austenitic stainless steels, with a ductility of about 25%. It has a ductile to brittle transition at about  $0^\circ\text{C}$ , where its impact strength and fracture toughness fall significantly.

The most common alloys of uranium are titanium ( $\sim 0.75\%$  Ti), niobium ( $\sim 2\text{--}7\%$  Nb), and molybdenum (up to 10% Mo). The alloys are hardenable by solid-solution heat treatment in the  $\gamma$ -phase region, then by quenching and aging to form second-phase particles. Room-temperature aged titanium-containing alloy has a yield stress (YS) of up to 600 MPa and ultimate tensile strength (UTS) of 1200 MPa, which can be increased to over 1200 and 1800 MPa respectively, with negligible ductility by aging at  $500^\circ\text{C}$ . The niobium-containing alloy has lower strength but improved ductility after aging. [Table 1](#) gives property data for some of the more common uranium alloys. In view of these relatively attractive mechanical properties, it has been mooted that uranium might constitute a valuable structural material for specific applications although the dual attributes of its mild radioactivity and relatively poor corrosion resistance are large barriers to any significant adoption.<sup>1</sup>

**Table 1** Properties of some uranium alloys; vacuum-annealed to ensure low hydrogen content

Alloy	Processing	YS (MPa)	UTS (MPa)	Elongation (%)	Corrosion resistance
Unalloyed U	Cast and $\beta$ -quenched	295	700	22	Poor
Unalloyed U	$\alpha$ -Rolled	270	720	31	Poor
U–0.75Ti	$\gamma$ -Quenched	650	1310	31	Fair
U–0.75Ti	$\gamma$ -Quenched, aged $450^\circ\text{C}$ , 6 h	1210	1660	$<2$	Fair
U–2.0Mo	$\gamma$ -Quenched, aged $550^\circ\text{C}$ , 5 h	675	1110	23	Poor
U–2.3Nb	$\gamma$ -Quenched, aged $600^\circ\text{C}$ , 5 h	545	1060	28	Fair
U–4.5Nb	$\gamma$ -Quenched, aged $260^\circ\text{C}$ , 16 h	900	1190	10	Acceptable
U–6.0Nb	$\gamma$ -Quenched	160	825	21	Good
U–10Mo	$\gamma$ -Quenched	900	930	9	Good
U–7.5Nb–2.5Zr	$\gamma$ -Quenched	540	850	23	Good



### 3.19.2 Aqueous Corrosion

#### 3.19.2.1 Thermodynamics

Uranium is an extremely active element and has a complex chemistry, showing all oxidation states from +2 to +6. In the absence of hydride formation, the Pourbaix diagram, [Figure 1](#), shows a significant domain of passivity due to the formation of  $\text{UO}_2$  as well as other, more complex, oxides. Importantly, thermodynamics predict that the passive oxide  $\text{UO}_2$  is susceptible to further oxidation (transpassive dissolution) at both low and high pH, forming soluble uranium species of valency 6; it also transforms to hydrated  $\text{UO}_3$  at intermediate pH. These reactions occur at a slow rate in humid air and, consequently,  $\text{UO}_2$  is not generally protective and the corrosion resistance of unalloyed uranium is poor. Where hydride formation is included in the thermodynamic diagram ([Figure 2](#)),  $\text{UH}_3$  formation is seen also to be stable, although in the presence of humid air the hydride forms only transiently further reacting to  $\text{UO}_2$  and water. Thus, in order to handle uranium without significant degradation, a dry-nitrogen glove-box atmosphere is required. Hydride formation can give rise to severe embrittlement and stress corrosion cracking phenomena, and finely divided uranium can spontaneously ignite and burn pyrophorically.

#### 3.19.2.2 Water

As predicted from the thermodynamic diagram, uranium reacts with water to form uranium dioxide, hydrogen, and uranium hydride. However, the hydride usually has only an ephemeral existence and reacts itself with water to form uranium dioxide and hydrogen. Reaction rates decrease with pH below 2, and it has been suggested that the solid products form by the inward diffusion of hydroxyl ions through the oxide.<sup>3</sup> The oxide is produced mainly as a nonadherent powder, and a linear rate law is obeyed.

Autoclave tests have demonstrated that the rate constant increases markedly with temperature up to at least 300 °C ([Figure 3](#)).<sup>4</sup> The corrosion rate is also influenced by dissolved gases in the water. In particular, the presence of dissolved oxygen decreases substantially the reaction rate<sup>4</sup> but makes the metal susceptible to crevice corrosion and pitting attack. The inhibition is most marked at lower temperatures, at which the oxygen solubility is highest and the hydrogen product is not sufficient to reduce the oxygen content locally. The oxygen could exert its influence by being adsorbed preferentially on the oxide<sup>5</sup> or by removing the disruptive influence of the formation of uranium hydride. An alternative view of such 'hydrogen effects' relates them to changes in the

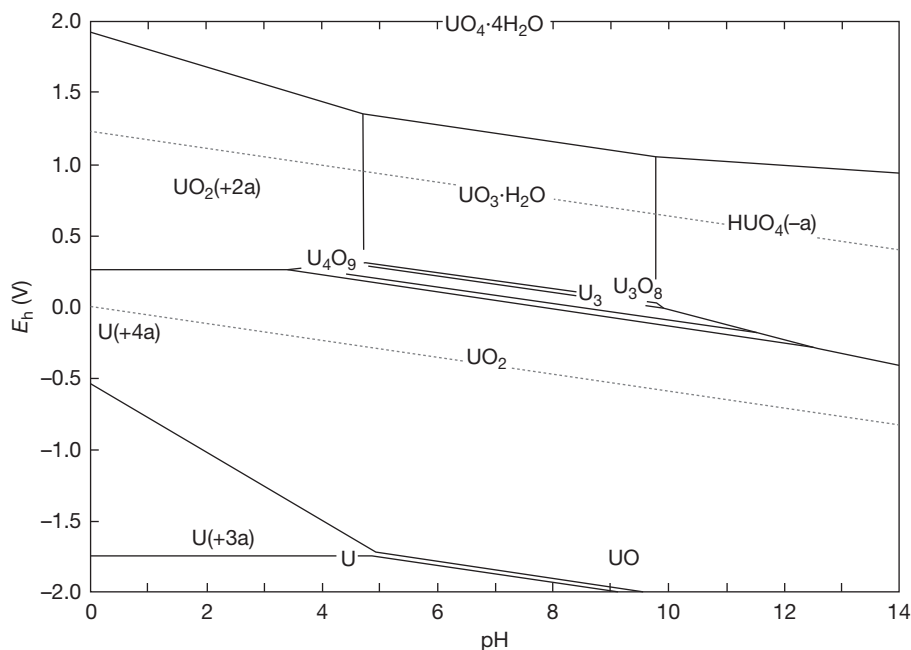


**Figure 1** Pourbaix diagram for uranium (with hydride absent) at a metal ion concentration of  $10^{-5}$  M. Calculated with HSC: Chemistry, version 6.12; Outotec Research Oy: Finland, 2007.

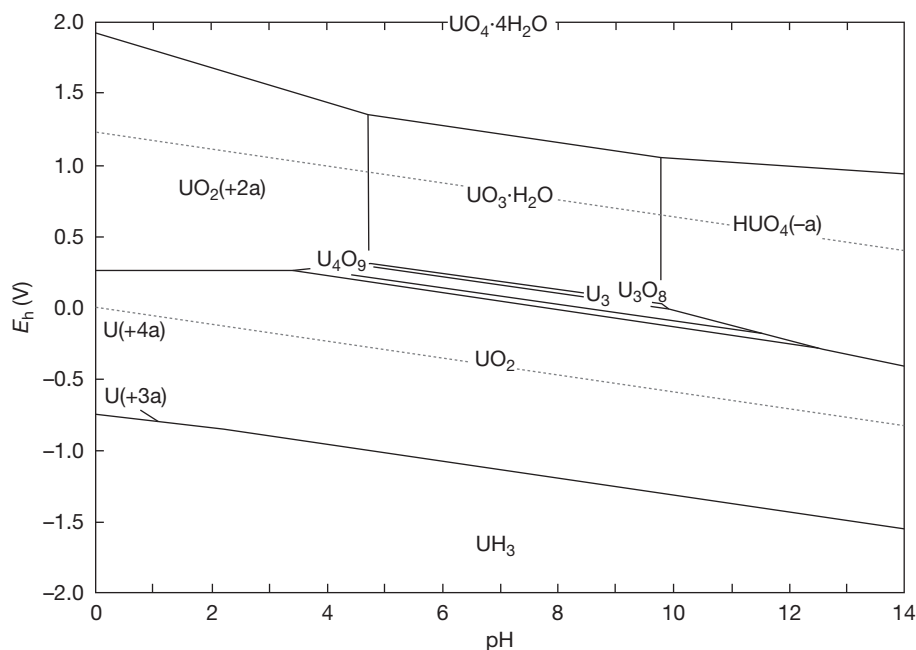


**Figure 2** Pourbaix diagram for uranium (hydride present) at a metal ion concentration of  $10^{-5}$  M. Calculated with HSC: Chemistry, version 6.12; Outotec Research Oy: Finland, 2007.

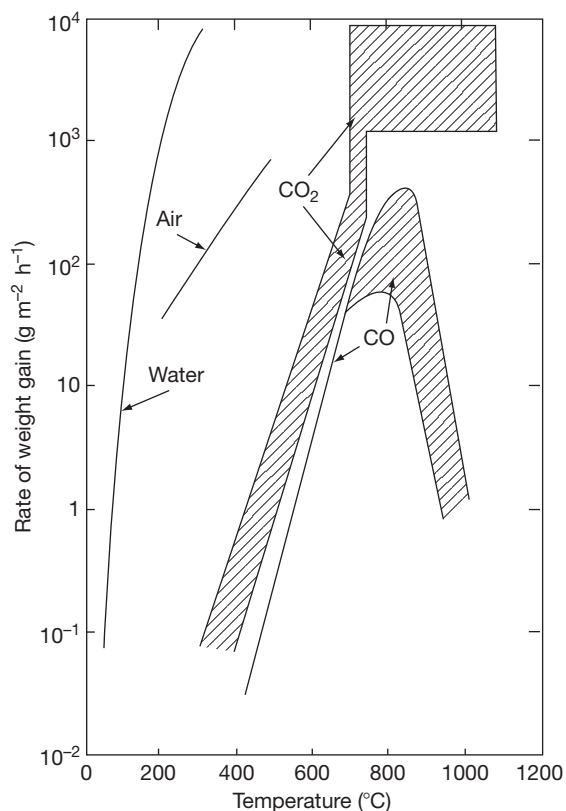


**Figure 3** Oxidation rates of uranium in distilled water, air,  $\text{CO}_2$ , and CO as a function of temperature.

electrical properties of the oxide detected by impedance measurements during corrosion.<sup>6</sup>

Peretrukhin *et al.* studied the corrosion of uranium and its dilute alloys (<0.5% of Zr, Nb, and Ru) in water and bicarbonate aqueous solutions together with the effect of radiolytically generated hydrogen peroxide. No significant difference in corrosion rates for the alloys was found. Regarding the corrosion mechanism, U(III) was found to be rather unstable in neutral solutions and significant precipitation of  $\text{U}(\text{OH})_3$  occurred; no significant quantities of hydride or soluble U(III) species were found.<sup>7</sup>

The atmospheric oxidation kinetics for U(IV) to U(VI) were also studied,<sup>7</sup> where it was shown that U(IV) oxidation by atmospheric oxygen in the pH range 1.5–4.0 resulted in first-order kinetics with respect to uranium. Notably, an induction period for uranium (IV) accumulation was evident, after which the reaction accelerated. The reaction mechanisms differed in the two media: in weakly acid solutions, after the initial appearance of U(VI), evidence for disproportionation of the U(V) intermediate was found. Of mechanistic importance is the formation of a copolymer of U(IV) and U(VI), which at  $\text{pH} \geq 4$  prevents formation of U(V) and limits the oxidation rate. In the presence of hydrogen peroxide, the metallic uranium surface became transpassive and the corrosion rate increased by at least an order of magnitude.

Mechanical failure, which may be associated with stress corrosion as well as hydrogen pickup, has been observed for specimens of uranium<sup>8</sup> and various quenched alloys. For at least the alloys, it is enhanced by chloride ions<sup>9</sup> and is inhibited by cathodic polarization.<sup>10</sup> At higher temperatures, the only resistant metallic materials based upon uranium are alloys containing appreciable amounts of the  $\gamma$ -phase stabilizing elements, molybdenum, niobium, and zirconium,<sup>4</sup> the silicide  $\text{U}_3\text{Si}$ ,<sup>11</sup> and the aluminides. However, the alloys, as distinct from the intermetallic compounds, tend to fail suddenly by disintegration after long periods of exposure, possibly because of internal hydride formation.

The corrosion of DU metal in deaerated ground-water (similar to that at the proposed Yucca mountain nuclear waste repository in the United States) was studied at 90 °C with a view to investigate the rate and products of corrosion: that is,  $\text{UO}_2$ ,  $\text{UO}_{2+x}$ ,  $\text{UH}_3$ , and  $\text{H}_2$ .<sup>12</sup> After exposure over an 81-day period, X-ray powder diffraction revealed the presence of  $\text{UO}_2$  and higher oxides: that is,  $\text{UO}_{2+x}$ ; however, no hydride was detected. The corrosion rate of the uranium metal in the water at 90 °C was determined by measuring the evolution of hydrogen gas, and this revealed a corrosion rate of  $1.42 \text{ mg cm}^{-2} \text{ h}^{-1}$ . This value agreed extremely well with a published Arrhenius-type expression for the corrosion rate of uranium metal in water that had been obtained from a compilation of experimental data<sup>13</sup>:

$$\ln k = 22.34 - \frac{7989}{T}$$

where  $T$  is the absolute temperature (K) and  $k$  is the corrosion rate ( $\text{mg cm}^{-2} \text{ h}^{-1}$ ).

### 3.19.2.3 Atmospheric Corrosion

Uranium tarnishes readily in the atmosphere at room temperature. Electropolishing inhibits the process, while etching in nitric acid activates the surface. Uranium dioxide and hydrated  $\text{UO}_3$  are the principal solid products, although uranium hydride may have a transitory existence. The corrosion is enhanced by water vapor and hence is governed by the humidity conditions.<sup>14</sup> However, the presence of oxygen markedly inhibits attack by water vapor.<sup>5</sup> Danon *et al.* undertook a desorption study of the surface chemistry of chemisorbed species on atmospherically oxidized uranium.<sup>15</sup> The main identified species included water (in different binding forms) and hydrogen. The latter originates from the water–uranium oxidation reaction, which produces uranium dioxide and two types of hydrogen: a near-surface hydride and a surface-chemisorbed form

that desorbs at a lower temperature than the hydride. Water was found to be bound in four forms: (a) a reversibly chemisorbed molecule, (b) tightly bound water molecules, (c) strongly bounded hydroxyl groups and, the most stable (d) a complex water–carboxylate. Hydrogen desorption was also studied, with two main peaks found, one being ascribed to the desorption of lattice hydrogen and the higher temperature peak being related to the decomposition of hydrides.

The corrosion of uranium in water vapor was studied between 50 and 90 °C and from 32% to 86% RH using thermogravimetry.<sup>16</sup> The results show three stages in the uranium–water oxidation reaction. Thus, a rapid initial reaction is followed by a reducing rate and, in the third stage, the corrosion reaction proceeds linearly with an activation energy of about  $43 \text{ kJ mol}^{-1}$  at 74.7% RH.

### 3.19.2.4 Effects of Water Radiolysis

The effect of  $\alpha$ -radiolysis of water on the corrosion potential of  $\text{UO}_2$  has been measured where the cell construction allowed the source to be brought within 30 mm of the  $\text{UO}_2$  electrode.<sup>17</sup> Oxidizing conditions were provided at the  $\text{UO}_2$  surface, and over a period of 30 h, the main process occurring appeared to be the catalytic decomposition of  $\text{H}_2\text{O}_2$  to  $\text{H}_2\text{O}$  and  $\frac{1}{2}\text{O}_2$  with some oxidation of the  $\text{UO}_2$ . The oxidation of uranium by water was studied by Fuller *et al.*<sup>18</sup> using infrared and sorption analysis. Oxidation occurred in cycles forming laminar layers of oxide that tend to spall off because of the strain at the oxide–metal interface. The reaction rate is directly proportional to the amount of adsorbed water on the oxide product, and transport was rapid through the open hydrous product. Dehydration of the hydrous oxide irreversibly forms a more inert oxide which cannot be rehydrated to the degree that prevails in the original hydrous product by uranium oxidation with water. An anomalous temperature dependence was observed for the oxidation of oxycarbide layers on the surface of uranium metal.<sup>19</sup> Normally, oxidation or corrosion reactions are expected to proceed more rapidly as water temperature increases, but the removal of the outermost atomic layers of carbon from uranium oxycarbide by oxygen reproducibly proceeds at a much faster rate at 25 °C than at 280 °C.

The kinetics of  $\text{UO}_2$  fuel oxidation by the products of  $\gamma$  radiolysis of water have been studied by Sunder *et al.* as a function of absorbed dose rate.<sup>20</sup> The radical species formed during water radiolysis are much more effective in promoting  $\text{UO}_2$  oxidation

than molecular oxidants, howsoever formed. Thus,  $\text{UO}_2$  oxidation during  $\gamma$  radiolysis of water occurs in two stages: (a) the formation of a thin layer of  $\text{UO}_{2+x}$  (of composition close to  $\text{UO}_{2.33}$ ); and (b) the subsequent oxidative dissolution of this surface layer to produce soluble U(VI) species and secondary phases, probably hydrated schoepite ( $\text{UO}_3 \cdot x\text{H}_2\text{O}$ ), on the  $\text{UO}_2$  substrate. The first stage occurs in the potential range  $-500 \text{ mV} < E_{\text{corr}} < -100 \text{ mV}$  (versus SCE). The second stage starts around  $E_{\text{corr}} \sim -100 \text{ mV}$  and eventually achieves steady state at a value of  $E_{\text{corr}}$  determined by the  $\gamma$  dose.

### 3.19.2.5 Galvanic Corrosion

Galvanic corrosion reports have emerged from two sources. In the first,<sup>21</sup> the chemical compatibility of uranium carbides and Cr–Fe–Ni alloys was discussed. Evaluation was by thermodynamic modeling and experimental phase studies. Two reaction temperatures (700 and 1000 °C) were used to simulate normal and overtemperature operation of advanced liquid metal fast-breeder reactor fuel-cladding couples. In the second, McIntyre *et al.*<sup>22</sup> coupled depleted U–0.75% Ti to aluminum, magnesium, or mild steel in synthetic seawater. The galvanic current was monitored with time. Gravimetric measurements, polarization resistance measurements, and galvanic currents were monitored over extended periods of time in order to detect changes in galvanic corrosion behavior. Good agreement was obtained for corrosion rates determined electrochemically and those obtained from gravimetric methods.

Galvanic corrosion is also important in metallic coatings applied as protective barriers in uranium. For example, electroplated nickel is an excellent corrosion-resistant barrier; however, when it is subject to localized attack (i.e., pitting), corrosion of uranium occurs at the coating–substrate interface.<sup>23</sup> Rapid failure of the coating tends to ensue because of the volume increase caused by development of uranium corrosion products that causes undermining and cracking of the coating.

### 3.19.2.6 Stress Corrosion Cracking

Uranium alloys are susceptible to stress corrosion cracking (SCC) and knowledge of the surface stresses involved are essential. In an uncoated U–Ti alloy, these have been found to be relatively large and compressive at 365 MPa, but the presence of nickel or zinc coatings led to much smaller compressive stress.<sup>24</sup> The stress corrosion behavior of U–7.5Nb–2.5Zr

in oxygen and hydrogen gases over a temperature range of  $-20$  to  $100^\circ\text{C}$  under pressures varying from  $0.3 \times 10^{-6}$  to  $0.15 \text{ MPa}$  has been analyzed using a fracture mechanics approach.<sup>25</sup> SCC mapping and cracking kinetics were determined as functions of stress intensity factor, temperature, and pressure. It was found that the mechanism responsible for SCC varied with the experimental conditions used.

Powell and his coworkers have explored the hydrogen embrittlement problem associated with uranium alloys.<sup>26,27</sup> Looking at the internal hydrogen embrittlement of  $\gamma$ -stabilized uranium alloys (i.e., containing Mo, Nb), they found that the tensile ductility decreased only slightly with increasing hydrogen content up to a critical hydrogen concentration, above which the tensile ductility dropped to nearly zero.<sup>26</sup> The critical hydrogen content for the ductility loss increased with increasing hydrogen solubility in the alloy. The fracture surfaces were not characteristic of those found under conditions of SCC. Hydrogen embrittlement of U–5.7Nb alloy showed enhanced microvoid coalescence fracture with loss of tensile ductility for hydrogen concentrations less than 23 mg hydrogen per gram of metal, the alloy having been solution-annealed at  $800^\circ\text{C}$  and water-quenched.<sup>27</sup> However, specimens with 36 mg hydrogen per gram of metal had much lower ductilities and exhibited a new, possibly hydride, phase which was associated with brittle transgranular fracture when this phase has a lenticular morphology extending well across the parent metal grains.

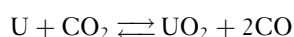
The interactions between aqueous corrosion and mechanical deformation in uranium and alloys involve complex processes of mechanical damage. Various mechanisms are possible for the observed reduction in ductility/fracture toughness during corrosion, including SCC (e.g., via brittle film fracture or film-induced cleavage), hydrogen embrittlement (e.g., via classical mechanisms or by hydride formation), as well as others. Bussiba *et al.*<sup>28</sup> undertook a series of mechanical tests in order to determine the influence of specific mechanisms on the performance of lean uranium alloys (U–0.1Cr and U–0.75Ti) in water and at controlled levels (30, 40, and 80%) of RH. Crack growth rates of between  $10^{-5}$  and  $10^{-9} \text{ m s}^{-1}$  were determined at a stress intensity corresponding to  $16 \text{ MPa m}^{1/2}$ . Cracking appeared to operate discontinuously with trigger events corresponding to acoustic noise generation. In all conditions (i.e., humid air or immersion), surface hydride formation was observed; however, their role in the fracture process could not be confirmed. However,

the rather rapid crack growth velocities seem to imply a triggering mechanism that involves hydrogen embrittlement.

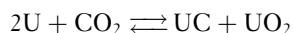
### 3.19.3 Gases at High Temperatures

#### 3.19.3.1 Carbon Dioxide and Carbon Monoxide

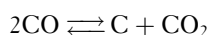
The solid corrosion products resulting from reaction with carbon dioxide and carbon monoxide are uranium dioxide, uranium carbides, and carbon.<sup>29</sup> The major reaction with carbon dioxide results in the formation of carbon monoxide and  $\text{UO}_2$ :



Uranium can also form the carbide with an overall reaction:



The formation of uranium carbide must involve carbon transfer from the gas phase and probably occurs via reactions of carbon monoxide with the metal through pores of the oxide scale. This transfer could occur by direct reaction or via the thermal decomposition of the gas to produce carbon dioxide, which may then react subsequently with uranium, thus forming the carbide:



Diffusion studies on  $\text{UO}_2$  demonstrate that oxygen ions are the major diffusing species in the oxide and, therefore, that the oxide grows by the inward passage of oxygen.<sup>30</sup> Volume changes associated with the oxidation lead to large stresses in the oxide and subsequently to the formation of solid products in the form of powders and/or cracked porous scales.

At the temperatures of interest, a linear rate law is quickly established, and the rate-determining step is believed, in general, to be diffusion of oxygen ions through a thin layer of adherent oxide of constant average thickness at a given temperature. For carbon dioxide, the rate constant (Figure 3) increases steadily with temperature until there is a sudden increase in rate, together with some selfheating from the high heat of reaction, at or near the  $\beta$ - $\gamma$  phase transition in the metal (780 °C); at higher temperatures there is little or no dependence of reaction rate on temperature up to 1000 °C. The majority of the oxide forms as either a nonadherent powder (the particle size of which increases with temperature) or, at the highest temperatures, as a cracked adherent scale. The formation of scale accounts for the lack of temperature dependence

for the rate constant at the highest temperatures and could result either from sintering of the oxide or, more probably, from the growth stresses being relieved by plastic deformation of the oxide and/or the underlying metal, rather than rupture of the oxide. At the highest temperatures, the rate-determining step might be gaseous diffusion through the porous scale.<sup>31</sup> The presence of small amounts of water vapor (greater than 100 ppm) and oxygen (greater than 10 ppm) enhances the attack significantly at the lower temperatures of 400–500 °C,<sup>29</sup> and under these conditions preferential attack is frequently observed at carbide inclusions in the metal.<sup>32</sup> Major alloy additions of silicon (greater than 3.8%) impair oxidation resistance at all temperatures, whereas additions of copper (1%), titanium (5–10%), and molybdenum (10–15%) decrease the rates, but only at the higher temperatures.<sup>33</sup> The beneficial influence of copper is associated with the enrichment of the element at the metal–oxide interface as the  $\text{UCu}_5$  phase.<sup>34</sup> The mechanisms responsible for the effects of the other alloying elements have not been firmly established, but can be attributed to changes in the physical defects and thicknesses of the adherent oxide and, hence, in its protective properties.

The oxidation rates in carbon monoxide (Figure 3) are less than those for carbon dioxide. They increase steadily with temperature up to 800 °C but then decrease markedly by a factor of 100 up to 1000 °C. The decrease in rate can be attributed to the dissociation of carbon dioxide at higher temperatures and to its consequently low partial pressures.

#### 3.19.3.2 Air

Thermal oxidation of uranium dioxide proceeds in air and results ultimately in the formation of  $\text{U}_3\text{O}_8$  at temperatures above 200–300 °C. The lower oxides may also be formed as intermediaries and at lower temperatures. The volume change associated with formation of  $\text{U}_3\text{O}_8$  is greater than for uranium dioxide and, as with carbon dioxide, leads to a linear rate law being established. This gives significantly more rapid oxidation kinetics<sup>35</sup> by comparison with the behavior in carbon dioxide (Figure 3). The rapid reaction rate, coupled with the large enthalpy of reaction, leads to an appreciable selfheating of specimens and an associated increase in reaction rate. In this situation, the supply of oxygen from the air can be rate-determining. The susceptibility of the metal to selfheating increases with the surface area-to-volume ratio of components, and powders may spontaneously ignite at room temperature.<sup>36</sup> However, large blocks



of metal are not normally liable to selfheating until 400–600 °C and then need an external heat source to maintain the situation. Alloy additions of molybdenum (5–15%) markedly reduce reaction rates.<sup>10,37</sup> Minor additions of other elements may either enhance or reduce the susceptibility to ignition<sup>38</sup> (e.g., aluminum or copper, respectively).

### 3.19.3.3 Steam

The mechanisms of corrosion by steam are similar to those for water up to 450 °C, but at higher temperatures are more closely related to the behavior in carbon dioxide. Studies at 100 °C have demonstrated that uranium hydride is produced during direct reaction of the water vapor with the metal and not by a secondary reaction with the hydrogen product. Also, at 100 °C it has been shown that the hydride is more resistant than the metal.<sup>3</sup> Inhibition with oxygen reduces the evolution of hydrogen and does not involve reaction of the oxygen with the uranium.<sup>6</sup> Above 450 °C, the hydride is not stable and hydrogen is released directly to the gas phase. Also, the cohesion and protection provided by the uranium dioxide increase with the formation of a dense scale, at least for short times at the highest temperatures. As a consequence, the extent of reaction after a period greater than 100 min is at a maximum at 300–400 °C with a rate of weight gain of  $10^3 \text{ g m}^{-2} \text{ h}^{-1}$ . The reaction rate increases only slowly with temperature from 500 to 1200 °C, although one piece of work reported a marked increase in attack near the  $\beta$ – $\gamma$  transition in the metal,<sup>39</sup> analogous to that obtained in carbon dioxide. A parabolic rate law has been found to apply at temperatures of 500–1200 °C for periods of 30 min to 6 h,<sup>40</sup> although another work indicates that this law is established for only 1–2 h above 880 °C and that a linear law generally applies.<sup>39</sup> It follows that for a period of 1–2 h, the extent of corrosion in steam straddles that for carbon dioxide, being greater at temperatures less than 700 °C and comparable or less at higher temperatures.

The oxidation rates of uranium in steam were measured between 200 and 550 °C. Arrhenius-type behavior was observed below 300–350 °C, with activation energies of 47 kJ mol<sup>−1</sup> for U foil below 350 °C and 58 kJ mol<sup>−1</sup> for U bar below 300 °C.<sup>41</sup> However, a significant rate reduction was observed at higher temperatures. In all cases, the oxidation products were uraninite-structured  $\text{UO}_{2-x}$  compounds. Non-adherent oxide layers were formed on bar samples below ~300 °C, but became increasingly adherent at higher temperatures. Similarly, the oxide layers on foil

samples below ~350 °C had highly porous cellular structures, whereas the layers formed at higher temperatures were significantly denser. For both materials, the fall in oxidation rate above 300–350 °C was attributed to reduced steam ingress to the underlying metal caused by the increasingly protective surface oxide.

Oxidation of  $\text{UO}_2$  by pure steam at pressures of 7 and 70 atm and 500 and 600 °C was measured using thermogravimetry.<sup>42</sup> Linear kinetics were observed, which varied as the square root of the steam pressure, and is consistent with initial rates extrapolated from higher temperature experiments in 1-atm steam. At temperatures characteristic of normal operation of defective fuel rods, the rate of hydrogen production by thermal oxidation of the fuel in steam is small compared to that due to cladding corrosion. The presence of  $\text{H}_2$  in the steam was found to have much greater influence on reducing the rate of oxidation  $\text{UO}_2$  than on oxidation of cladding.

An experimental study of  $\text{UO}_2$  oxidation in pure steam and in  $\text{H}_2\text{O}/\text{Ar}/\text{H}_2$  mixtures was conducted using a thermal balance at 1 atm in the temperature range 1000–1350 °C.<sup>43</sup> Two surface reaction models were assumed. A phenomenological model assumes that the reaction rate is proportional to the difference between the  $[\text{O}]$  in the solid and the equilibrium  $p\text{O}_2$  in the ambient gas. The results show that this model is a poor fit for oxidation in steam, but is good for  $\text{H}_2\text{O}/\text{Ar}/\text{H}_2$  mixtures. A mechanistic model, based on the assumption that the rate-controlling step was water dissociation at the solid surface, provides a very good fit to all the data. Thus, as long as the pressure is 1 atm, either model can be used to predict nuclear fuel oxidation in severe loss of coolant accidents because the ambient gas invariably contains hydrogen produced by Zircaloy corrosion. However, the kinetics of oxidation in high-pressure steam–hydrogen mixtures are still uncertain. Evidence of uranium volatilization and preferential etching at the grain boundaries at high temperatures were observed.

## 3.19.4 Corrosion Processes

### 3.19.4.1 Protective Coatings

Uranium may be anodized in ethylene glycol containing ammonia and this produces oxide films that are predominantly uranium dioxide in composition<sup>44</sup> and which show considerable resistance to atmospheric corrosion. During film formation at constant current, the voltage rises steeply to a plateau giving predominantly crystalline films. After reaching a



second voltage plateau, the films are largely amorphous. The rate of oxidation during the initial voltage rise, assuming maximum current efficiency, is between 1.6 and 2.0 nm V<sup>-1</sup>.

Metallic and organic-based coatings have been developed to protect uranium from oxidation at low and high temperatures. The work on metallic coatings has covered intermetallic compounds and solid solutions of uranium with aluminum, zirconium, copper, niobium, nickel, and chromium.<sup>45</sup> Aluminum- and zirconium-based coatings<sup>46,47</sup> can be particularly effective in reducing attack over an extended range of temperature. Also, nickel plating can provide protection against atmospheric corrosion.<sup>48</sup> Work on organic coatings has demonstrated that they can enhance resistance to atmospheric corrosion.<sup>49,50</sup> This behavior is attributed to the loss of the inhibiting action of oxygen due to water vapor permeating the coatings more readily than oxygen.

Aluminum, zinc, magnesium, Al-Zn, Al-Mg, nickel, titanium, TiN, and Al/TiN coatings have all been applied by the arc plasma physical vapor deposition (PVD) technique to a DU alloy for corrosion protection assessment.<sup>51</sup> The as-deposited specimens were examined by scanning electron microscopy for surface morphology and tested for adhesion. Electrochemical polarization tests and immersion tests were conducted in aerated 3.5 wt% NaCl solution. Results of electrochemical polarization in 3.5% NaCl solution and observations after long-term exposure tests indicated that both Al-Zn and Al-Mg alloys appear to be the best sacrificial coating materials for improving the corrosion resistance of DU-0.75 Ti.

The effect of various oxyanions (MoO<sub>4</sub><sup>2-</sup>, PO<sub>4</sub><sup>3-</sup>, VO<sub>4</sub><sup>3-</sup>, MnO<sub>4</sub><sup>-</sup>, SiO<sub>4</sub><sup>4-</sup>, and WO<sub>4</sub><sup>2-</sup>) on the corrosion inhibition of U-0.75Ti alloy in nitric acid has been studied.<sup>52</sup> Results indicate that chemical or electrochemical activation of the uranium in 0.1 M HNO<sub>3</sub> + 0.025 M molybdate can lead to the formation of a rudimentary conversion coating. Building on this finding, molybdenum oxide-based coatings were formed on U-0.75Ti alloy<sup>53</sup> using nitric acid in order to activate the metal surface. Successful coatings were produced of the order of 650 nm in thickness. After aging, the coated samples showed an ennobled potential of around 400 mV and a reduced corrosion current density of around 10 times.

### 3.19.4.2 Irradiation Effects

The behavior of irradiated uranium has been studied mainly with respect to the release of fission products

during oxidation at high temperatures.<sup>54</sup> The fission products most readily released to the gas phase are krypton, xenon, iodine, tellurium, and ruthenium. The release can approach 80–100%. For ruthenium, it is dependent upon the environment and only significant in the presence of oxygen to form volatile oxides of ruthenium.

Studies of the influence of irradiation on the kinetics of oxidation have been confined to postirradiation work. In general, prior irradiation increases reactivity, although there are considerable inconsistencies in the enhancements obtained.<sup>17,54,55</sup> The effects can be derived from an increased surface area associated with the swelling voids produced in the metal by the irradiation, and can also probably arise to a lesser extent from chemical effects of the fission products.

The postirradiation examination of two uranium aluminide fuel plates exposed to aqueous corrosion showed failure due to pinhole corrosion during irradiation to about 76% of the maximum burn-up limit.<sup>56</sup> It was thought that the cladding failed by pitting corrosion initiated at preexisting pits at a hot spot. Fuel plate material was washed out through these pinholes due to aqueous corrosion and erosion. Egert<sup>57</sup> also looked at corrosion of coated uranium and found corrosion occurring at defects present in the coating. An equation was derived to predict the extent of substrate corrosion, given the number of defects per unit area and knowledge of the corrosion kinetics of the substrate.

### 3.19.4.3 Corrosion and Dissolution of UO<sub>2</sub>

As noted earlier, uranium dioxide is susceptible to transpassive dissolution to soluble uranium species at low and high pH and at sufficiently high potentials caused by the presence of oxygen in air, or of strongly oxidizing peroxide or radical species formed as a result of water radiolysis. At intermediate potentials, UO<sub>2</sub> may be oxidized to UO<sub>2+x</sub> or hydrated UO<sub>3</sub>. In order to suppress this oxidation, the effects of dissolved hydrogen on the aqueous corrosion of uranium dioxide (UO<sub>2</sub>) under nuclear waste disposal conditions were studied.<sup>58</sup> Measurements of the corrosion potential ( $E_{\text{corr}}$ ) indicate that the oxidation of dissolved hydrogen on noble-metal particles polarizes the UO<sub>2</sub> nuclear fuel surface to reducing potentials (–300 to –400 mV vs. SCE); that is, to  $E_{\text{corr}}$  values more negative than those observed under anoxic (argon-purged) conditions (–200 mV vs. SCE). Thus, noble-metal particles incorporated within UO<sub>2</sub> act catalytically to oxidize H<sub>2</sub>. It is the galvanic coupling of these

particles to the  $\text{UO}_2$  matrix that lowers the corrosion potential, thereby preventing oxidation of the fuel surface.

### 3.19.4.4 Uranium in the Environment

Corrosion of anthropogenic uranium in natural environments is not well understood, but is important for determining potential health risks and mobility in the environment. Buck *et al.* conducted studies of a site in the southwestern United States containing DU that has been weathering for approximately 22 years.<sup>59</sup> The main products of corrosion were found to be schoepite ( $(\text{UO}_2)_4\text{O}(\text{OH})_6 \cdot 6(\text{H}_2\text{O})$ ) and meta-schoepite ( $\text{UO}_3 \cdot 2(\text{H}_2\text{O})$ ), and occur on their own, mixed with clay/silt aggregates, or as coatings upon soil grains. It appeared from this study that local soil geomorphology and chemistry at this site limit uranium mobility and decreases potential health risks. However, changes in land use and/or climate could increase uranium mobility.

There is considerable concern over the use of dense kinetic energy projectiles containing DU in the battlefield and the consequent spread of uranium into the environment. The degradation of a DU penetrator shot in battle in Western Kosovo in 1999 and collected from there in June 2001 was studied.<sup>60</sup> Corrosion products on the surface were confirmed as  $\text{UO}_2$ , with the possible presence of other more oxidized uranium forms, such as  $\text{U}_3\text{O}_8$  and  $\text{UO}_3 \cdot 2(\text{H}_2\text{O})$ . Raman spectra from the surface shows evidence for mobile  $\text{UO}_2^{2+}$  uranyl ions. It can be concluded, therefore, that such projectiles will, in the environment, progressively release mobile uranium species.

In the United Kingdom, the testing of armor-piercing DU 'penetrators' has resulted in the deposition of DU in the sediments of the Solway Firth. Handley-Sidhu *et al.* undertook an investigation of this material by simulating Solway Firth sediments under variable conditions of salinity to study the impact of the corroding DU on the environment, including the microbial population.<sup>61</sup> Under suboxic conditions, the average corrosion rates were  $0.056 \text{ g cm}^{-2} \text{ year}^{-1}$ , implying that complete corrosion of a 120-mm penetrator would take approximately 540 years. Under sulfate-reducing conditions, corrosion ceased because of passivation of the surface. Corroding DU resulted in more reducing conditions and decreased microbial diversity as indicated by DNA sequencing and phylogenetic analysis. Since few uranium species were measured in the sediments adjacent to the DU projectiles, it must be assumed that U was transported

into the surrounding environment through dissolution of  $\text{U(VI)}$ , with subsequent interactions resulting in the formation of secondary uranium species in the sediment.

## References

1. The Encyclopedia of the Earth: Uranium (published at [www.eoearth.org/article/uranium](http://www.eoearth.org/article/uranium)).
2. Argonne National Laboratory, USA: Depleted Uranium and Uranium Alloy Properties, published at: [web.ead.anl.gov/uranium/guide/ucompound/propertiesu/brochure.cfm](http://web.ead.anl.gov/uranium/guide/ucompound/propertiesu/brochure.cfm).
3. McD Baker, M.; Less, L. N.; Orman, S. *Trans. Faraday Soc.* **1966**, 62(2), 513.
4. Wanklyn, J. N.; Jones, P. J. *J. Nucl. Mater.* **1962**, 6, 291.
5. McD Baker, M.; Less, L. N.; Orman, S. *Trans. Faraday Soc.* **1966**, 62(2), 525.
6. Leach, J. S. L. *J. Inst. Met.* **1959**, 88, 24.
7. Peretrukhin, V. F.; Maslennikov, A. G.; Tsvadze, A. Yu.; Delegard, C. H.; Yusov, A. B.; Shilov, V. P.; Bessonov, A. A.; Bulatov, G. S. *Protect. Met.* **2008**, 44(3), 211–232.
8. Hughes, A. N.; Orman, S.; Pictor, G. *Corros. Sci.* **1970**, 10, 239.
9. Magnani, N. J. *J. Nucl. Mater.* **1972**, 42, 271.
10. McLaughlin, B. D. *J. Nucl. Mater.* **1972**, 43, 343.
11. Bourns, W. T. Corrosion Testing of Uranium Silicide Fuel Specimens, AECL-2, 1968; p 718.
12. Fonnesebeck, J. E. *Corros. Eng. Sci. Technol.* **2003**, 38(1), 51–56.
13. Hilton, B. "Review of oxidation rates of DOE spent nuclear fuel: Part 1: metallic fuel," Report ANL-00/24, Argonne National Laboratory, Idaho Falls, ID, USA, 2000.
14. Waber, J. T. "A Review of the Corrosion Behaviour of Uranium," Report LA-2035, Los Alamos Scientific Laboratory, Los Alamos, NM, December 1958.
15. Danon, A.; Koresh, J. E.; Mintz, M. H. *Langmuir* **1999**, 15(18), 5913–5920.
16. Xiong, B.-T.; Meng, D.-Q.; Yang, W.-C.; Luo, W.-H.; Zhang, G.-F.; Lu, Y.-J. *Yuanzineng Kexue Jishu/Atomic Energy Sci. Technol.* **2005**, 39(3), 226–231.
17. Bailey, M. G.; Johnson, L. H.; Shoesmith, D. W. *Corros. Sci.* **1985**, 25, 233.
18. Fuller, E. C.; Fuller, E. L., Jr.; Smyrl, N. R.; Condon, J. B.; Eage, M. H. *J. Nucl. Mater.* **1984**, 120, 174.
19. Ellis, W. P. *Surf. Sci.* **1981**, 109, L567.
20. Sunder, S.; Shoesmith, D. W.; Christensen, H.; Miller, N. H. *J. Nucl. Mater.* **1992**, 190C, 78–86.
21. Beahm, E. C.; Culpepper, C. A. *Nucl. Technol.* **1981**, 54, 215.
22. McIntyre, J. F.; Lefeave, E. P.; Musselman, K. A. *Corrosion* **1988**, 44, 502.
23. Wang, Q.-F.; Ye, H.; Zhang, P.-C.; Lang, D.-M.; Wang, X.-H.; Wang, J.-Y. *Yuanzineng Kexue Jishu/Atomic Energy Sci. Technol.* **2005**, 39(1), 44–48.
24. Sha, W.; Wang, Y.-H. *J. Less Common Met.* **1989**, 146, 179.
25. Lepoutre, D.; Nomine, A. M.; Miannay, D. *J. Less Common Met.* **1986**, 121, 521.
26. Powell, G. L.; Kroger, J. W.; Bennet, R. K. *Corrosion* **1976**, 32, 9.
27. Powell, G. L.; Northcutt, W. G. *J. Nucl. Mater.* **1985**, 132, 47.
28. Bussiba, A.; Alush, H.; Katz, Y. *Mater. Sci. Res. Int.* **1997**, 3(4), 244–251.

29. Pearce, R. J.; Whittle, I.; Hilton, D. A. *J. Nucl. Mater.* **1969**, 33, 1.
30. Belle, J. J. *Nucl. Mater.* **1969**, 30, 3.
31. Pearce, R. J. *J. Nucl. Mater.* **1970**, 34, 332.
32. Hayfield, P. C. S.; Graham, R. L.; Ramshaw, G. In *Institute of Metals Symposium on Uranium and Graphite*, 1962; Paper no. 5.
33. Antill, J. E.; Peakall, K. A. *Less Common Metals* **1961**, 3, 239.
34. Antill, J. E.; Peakall, K. A. *J. Electrochem. Soc.* **1963**, 110, 1146.
35. Baker, L.; Bingle, J. D. *J. Nucl. Mater.* **1966**, 20, 11.
36. Baker, L.; Schnizlein, J. G.; Bingle, J. D. *J. Nucl. Mater.* **1966**, 20, 22.
37. Isaacs, J. W.; Wanklyn, J. N. *AERE R-3* **1960**, 559.
38. Schnizlein, J. G.; Baker, L.; Bingle, J. D. *J. Nucl. Mater.* **1966**, 20, 39.
39. Hopkinson, B. E. *J. Electrochem. Soc.* **1959**, 106, 102.
40. Wilson, R. E.; Martin, P. *ANL* **1962**, 6, 569.
41. Hayward, P. J.; Evans, D. G.; Taylor, P.; George, I. M.; Duclos, A. M. *J. Nucl. Mater.* **1994**, 217(1–2), 82–92.
42. Olander, D. R.; Soo Kim, Y.; Wang, W.-E.; Yagnik, S. K. *J. Nucl. Mater.* **1999**, 270(1), 11–20.
43. Abrefah, J.; Braid, A. D.; Wang, W.; Khalil, Y.; Olander, D. R. *J. Nucl. Mater.* **1994**, 208(1–2), 98–110.
44. Flint, O.; Polling, J. J.; Charlesby, A. *Acta Metall.* **1954**, 2(5), 696–712.
45. Buddery, J. H.; Clark, M. E.; Pearce, R. J.; Stobbs, J. J. *J. Nucl. Mater.* **1946**, 13, 169.
46. Baque, P.; Koch, P.; Dominget, R.; Darras, R. *CEA-R-3* 638.
47. Pearce, R. J.; Giles, R. D.; Tavender, L. E. *J. Nucl. Mater.* **1967**, 24, 129.
48. Orman, S.; Owen, L. W.; Picton, G. *Corros. Sci.* **1972**, 12, 35.
49. Orman, S. *Atom* **1969**, 150, 93.
50. Orman, S.; Walker, P. J. *Oil Colour Chem. Assoc.* **1965**, 48, 233.
51. Chang, F.; Levy, M.; Jackman, B.; Nowak, W. B. *Surf. Coating. Tech.* **1989**, 39–40(1–3 Pt 2), 721–731.
52. Roeper, D. F.; Chidambaram, D.; Clayton, C. R.; Halada, G. P. *Electrochim. Acta* **2005**, 50(18), 3622–3633.
53. Roeper, D. F.; Chidambaram, D.; Clayton, C. R.; Halada, G. P. *Electrochim. Acta* **2005**, 51(3), 545–552.
54. Parker, G. W.; Creek, G. E.; Barton, C. J.; Martin, W. J.; Lorenz, R. A. Oak Ridge National Laboratory Report ORNL-3981, 1967.
55. Fischer, D. F.; Schnizlein, J. G. *J. Nucl. Mater.* **1968**, 28, 124.
56. Vinjami, K.; Hobbins, R. R. *Nucl. Tech.* **1983**, 62, 145.
57. Egert, C. M. *Corrosion* **1988**, 44, 36.
58. Broczkowski, M. E.; Zhu, R.; Ding, Z.; Noel, J. J.; Shoesmith, D. W. *Mater. Res. Soc. Symp. Proc.* **2006**, 932, 449–456.
59. Buck, B. J.; Brock, A. L.; Johnson, W. H.; Ulery, A. L.; *Soil Sediment Contam.* **2004**, 13(6), 545–561.
60. Mellini, M.; Riccobono, F. *Chemosphere* **2005**, 60(9), 1246–1252.
61. Handley-Sidhu, S.; Worsfold, P. J.; Boothman, C.; Lloyd, J. R.; Alvarez, R.; Livens, F. R.; Vaughan, D. J.; Keith-Roach, M. J. *Environ. Sci. Technol.* **2009**, 43(2), 350–355.

## Relevant Websites

[www.world-nuclear.org](http://www.world-nuclear.org) – World Nuclear Organization, London UK.

## 3.20 Corrosion of Amorphous and Nanograined Alloys

**H. Habazaki**

Graduate School of Engineering, Hokkaido University, N13-W8, Kita-ku, Sapporo 060-8628, Japan

© 2010 Elsevier B.V. All rights reserved.

3.20.1	Corrosion of Amorphous Alloys	2192
3.20.1.1	Examples of Corrosion-resistant Amorphous Alloys	2193
3.20.1.2	Mechanism of Extremely High Corrosion Resistance	2194
3.20.1.3	Role of Alloying Elements in Improving Corrosion Resistance	2196
3.20.1.3.1	Phosphorus	2196
3.20.1.3.2	Synergy of corrosion-resistant elements	2198
3.20.1.4	Corrosion Behavior of Bulk Metallic Glasses	2199
3.20.1.4.1	Zr-based bulk metallic glasses	2199
3.20.1.4.2	Corrosion-resistant bulk metallic glasses	2200
3.20.1.5	Corrosion Behavior of Nanocrystalline Alloys	2201
3.20.1.5.1	Nanocrystalline-precipitated amorphous alloys	2201
3.20.1.5.2	Nanocrystallization of conventional crystalline corrosion-resistant materials	2202
References		2202

### Glossary

**Sputter deposition** Sputter deposition is a physical vapor deposition (PVD) method of depositing thin films by sputtering, that is, ejecting material from a target or source, which then deposits onto a substrate – for example, a silicon wafer.

**Amorphous alloy** An amorphous alloy is a metallic material with a disordered atomic-scale structure. In contrast to most metals, which are crystalline and therefore have a highly ordered arrangement of atoms, amorphous alloys are noncrystalline.

**X-ray photoelectron spectroscopy (XPS)** XPS is a quantitative spectroscopic technique that measures the elemental composition, empirical formula, chemical state, and electronic state of the elements that exist within a material. XPS spectra are obtained by irradiating a material with a beam of aluminum or magnesium X-rays while simultaneously measuring the kinetic energy (KE) and number of electrons that escape from the top 1–10 nm of material being analyzed.

**Rutherford backscattering spectroscopy (RBS)** RBS is an analytical technique used in materials science. Sometimes referred to as high-energy ion scattering (HEIS) spectroscopy, RBS is used to determine the

structure and composition of materials by measuring the backscattering of a beam of high energy ions impinging on a sample.

### Abbreviations

**RBS** Rutherford backscattering spectroscopy

**XPS** X-ray photoelectron spectroscopy

### 3.20.1 Corrosion of Amorphous Alloys

Amorphous alloys have been attracting much attention as a new class of metallic materials with excellent physical, mechanical, and chemical properties since their introduction in the late 1960s. The corrosion resistance of amorphous alloys is remarkable and some amorphous alloys are immune even to concentrated hydrochloric acids. Much interest has also been seen in amorphous alloy electrode materials due to their superior electrocatalytic properties as well as high durability, originating from high corrosion resistance. The synergistic effect of various alloying elements homogeneously mixed at the atomic level, in addition to the structurally metastable nature, contributes to the superior chemical properties.

It was believed until the late 1980s that rapid quenching with a quenching rate of more than  $\sim 10^5$  K s<sup>-1</sup> is

required to develop amorphous alloys. During this period, amorphous alloys were produced mostly by melt-spinning and physical vapor deposition (PVD) methods, including sputter deposition. Laser treatment of the alloy surface, as well as ion implantation, was used to develop amorphous alloy surfaces on bulk metallic substrates. In the late 1980s, amorphous alloys with extremely high glass-forming ability were discovered, and bulk amorphous alloys, usually referred to as bulk metallic glasses, are now available in many alloy systems by a conventional casting process. Extremely high glass-forming ability is attained in multicomponent alloy systems with large atomic size ratios of more than 12% and with negative heats of mixing. The discovery of bulk metallic glasses has eliminated the size limitation of amorphous alloys, and their practical importance has been significantly enhanced. Here, corrosion behavior of a range of amorphous alloys, including bulk metallic glasses, is outlined, together with nanocrystalline metallic materials. Interest has also been shown in nanocrystalline alloys due to their enhanced mechanical strength. The influence of nanocrystalline precipitates in an amorphous matrix on corrosion behavior of amorphous alloys will also be discussed here.

### 3.20.1.1 Examples of Corrosion-resistant Amorphous Alloys

Great interest in the corrosion resistance of amorphous alloys was initiated by the early work of Hashimoto and coworkers, which revealed the very high corrosion resistance of iron-metalloid alloys containing chromium even in aggressive hydrochloric acid solutions.<sup>1,2</sup> Results of corrosion tests for the amorphous Fe-10 at.% Cr-13 at.% P-7 at.% C alloy (alloy composition hereafter denoted as Fe-10Cr-13P-7C) and crystalline type-304 stainless steel are shown in Figure 1.<sup>1</sup> The melt-spun amorphous Fe-10Cr-13P-7C alloy reveals no measurable corrosion even in 1 mol dm<sup>-3</sup> HCl solution, while the corrosion rate of type-304 stainless steel increases with the increase in the concentration of HCl, greater than 10 mm s<sup>-1</sup> in 1 mol dm<sup>-3</sup> HCl solution. The amorphous Fe-10Cr-13P-7C alloy is spontaneously passive in HCl solution, and anodic polarization of this alloy does not induce pitting corrosion. The corrosion resistance of Fe-Cr-metalloid alloys was further improved by the addition of molybdenum.<sup>3-6</sup> Amorphous alloys containing sufficient amounts of both chromium and molybdenum were spontaneously passive even in concentrated HCl solution at elevated temperatures.<sup>6</sup>

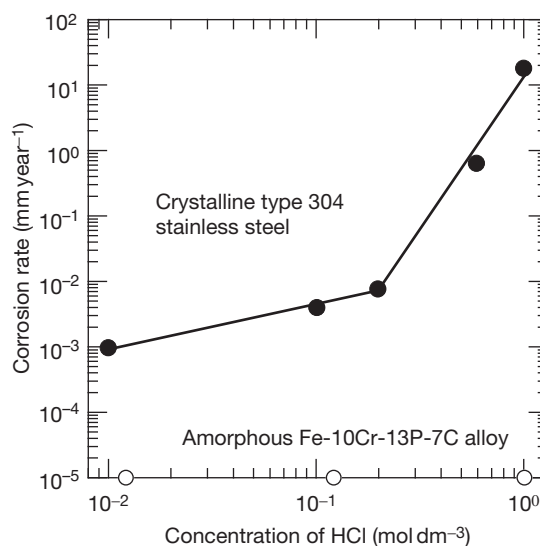


**Figure 1** Example of the greatly enhanced corrosion resistance in 1 mol dm<sup>-3</sup> hydrochloric acid at room temperature of a Fe-based metallic glass (Fe-10Cr-13P-7C) compared to a crystalline, type-304 stainless steel alloy (Fe-18Cr-8Ni).<sup>1</sup>

In addition to Fe-based amorphous alloys, corrosion-resistant nickel-based amorphous alloys were discovered in the late 1980s. Amorphous Ni-based alloys containing 20 at.% or more tantalum were immune to corrosion in boiling 9 mol dm<sup>-3</sup> HNO<sub>3</sub> solution and maintained metallic luster.<sup>7</sup> Ni-Nb alloys containing 40–60 at.% niobium were also highly corrosion-resistant; their corrosion rates were as low as ~1 μm year<sup>-1</sup> in boiling 9 mol dm<sup>-3</sup> HNO<sub>3</sub> solution. Amorphous Ni-Nb and Ni-Nb-Cr alloys were spontaneously passive in 0.1 mol dm<sup>-3</sup> H<sub>2</sub>SO<sub>4</sub> solution, but transpassive dissolution occurred at high anodic potentials.<sup>8</sup> The amorphous Nb-valve metal alloys were also highly corrosion-resistant in hot concentrated phosphoric acid solution as well as in boiling sodium hydroxide solution.<sup>9,10</sup> The addition of small amounts of phosphorus enhances its glass-forming ability as well as its corrosion resistance.<sup>11-16</sup> The role of phosphorus in improving the corrosion resistance of amorphous alloys will be described later.

Most of these corrosion studies were performed using melt-spun amorphous alloy ribbons. In the late 1980s PVD methods, including sputter deposition, were introduced to produce corrosion-resistant amorphous alloys. One of the successful applications of this technique is an aluminum alloy system. The solid solubility of many alloying elements in aluminum at equilibrium is very limited, usually less than a



few atomic percent. None of the existing commercial aluminum alloys have good resistance against localized corrosion. Amorphous Al alloys containing supersaturated alloying elements, including molybdenum, tungsten, chromium, copper, and tantalum, show markedly improved pitting corrosion resistance.<sup>17–27</sup> Some amorphous Al alloys display good corrosion resistance even in hydrochloric acid solutions.<sup>28–30</sup> An example of improved pitting potential by the addition of molybdenum and tungsten is shown in **Figure 2**. The pitting potential of crystalline high-purity aluminum is  $\sim -0.7$  V versus SCE in a borate buffer solution containing  $0.1 \text{ mol dm}^{-3}$  NaCl. The addition of molybdenum ennobles pitting potential by more than one volt, with the addition of tungsten shifting the potential in a more positive direction.<sup>22</sup>

Amorphous alloys with ideally high corrosion resistance, consisting only of corrosion-resistant elements, were developed in the 1990s. Sputter-deposited Cr–X, Mo–X and W–X alloys, in which X denotes Ti, Zr, Nb, or Ta, were shown to be spontaneously passive in concentrated hydrochloric acid.<sup>31–44</sup> The extremely high stability of homogeneous double oxyhydroxides of  $\text{Cr}^{3+}$  and valve metal cations is responsible for the extraordinary corrosion resistance of Cr-valve metal alloys.<sup>45–48</sup>

Intensive studies have recently been conducted on the corrosion behavior of bulk metallic glasses due to

their wide range of potential applications. Bulk metallic glasses with extremely high corrosion resistance even in hydrochloric acid solutions have also been developed in Fe-based and Ni-based alloy systems. Bulk metallic glasses of Fe–Cr–Mo–C–B with and without phosphorus were synthesized over a wide composition range by copper mold casting, and showed high corrosion resistance in concentrated hydrochloric acid with corrosion rates in the range of  $10^3$  to  $10^2 \text{ mm year}^{-1}$ .<sup>49</sup> Bulk Ni-based glasses, containing Nb, Ta, Cr, and Mo in addition to phosphorus, are resistant in concentrated hydrochloric acid.<sup>50,51</sup>

### 3.20.1.2 Mechanism of Extremely High Corrosion Resistance

It was believed that extremely high corrosion resistance of some amorphous alloys is a consequence of the rapid formation of uniform passive films without weak points and with a high concentration of corrosion-resistant alloying element species in the thin passive films. As mentioned above, some amorphous alloys are immune even in concentrated hydrochloric acid. Such excellent corrosion resistance is not achieved by practical crystalline metals and alloys. Single-phase amorphous alloys are structurally and compositionally homogeneous, free from metallurgical heterogeneities such as grain boundaries, second phases, precipitates, inclusions, and segregations. In crystalline alloys, corrosion is often initiated preferentially at such heterogeneous sites. The compositionally uniform nature of amorphous alloys is a key to the coverage of the entire surface of a metallic substrate by a highly protective thin passive film to protect the alloy from severe corrosive attack.

The rapid formation of a highly protective passive film on amorphous alloys was demonstrated in an iron–chromium alloy system.<sup>52</sup> The high corrosion resistance of chromium-containing crystalline and amorphous alloys is attributed to the formation of passive films highly enriched in trivalent chromium species. For instance, immersion of amorphous Fe–10Cr–13P–7C alloy in  $1 \text{ mol dm}^{-3}$  HCl solution for 1 week gives rise to the formation of a passive film consisting exclusively of hydrated chromium oxyhydroxide,  $\text{CrO}_x(\text{OH})_{3-2x}$ .<sup>53</sup> Although chromium-enriched passive films are formed on both crystalline and amorphous chromium-containing alloys, enrichment is more significant for amorphous alloys, contributing to the better corrosion resistance of amorphous alloys. **Table 1** shows the concentrations of  $\text{Cr}^{3+}$  ions in the passive films formed on chromium-containing

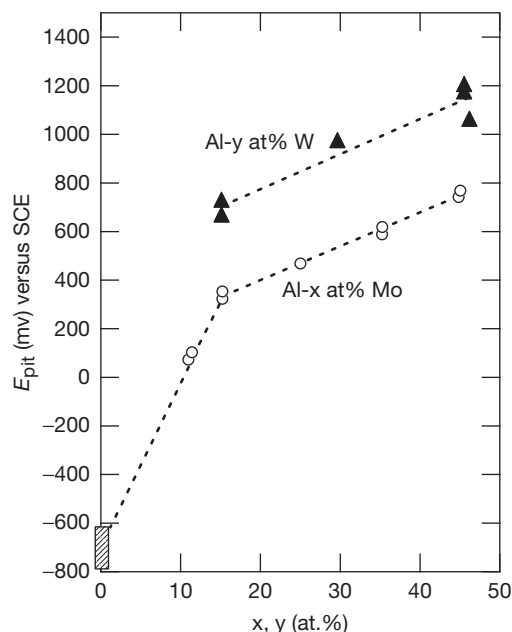


**Figure 2** Pitting potentials of sputter-deposited Al–Mo and Al–W alloys, as well as high purity aluminum, in a borate buffer solution containing  $0.1 \text{ mol dm}^{-3}$  NaCl.<sup>24</sup>

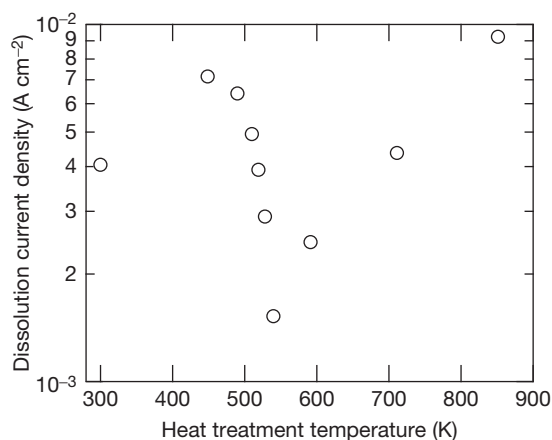


**Table 1** Cationic fractions of  $\text{Cr}^{3+}$  ions in passive films formed on amorphous chromium-containing alloys and stainless steels in  $1 \text{ mol dm}^{-3}$  HCl solution<sup>52</sup>

Alloys	Cationic fraction of $\text{Cr}^{3+}$ ions in passive films	Passivation process
<i>Amorphous alloys</i>		
Fe-10Cr-13P-7C	0.97	Spontaneous passivation
Fe-3Cr-2Mo-13P-7C	0.57	Anodic polarization
Co-10Cr-20P	0.95	Spontaneous passivation
Ni-10Cr-20P	0.87	Spontaneous passivation
<i>Ferritic stainless steels</i>		
Fe-30Cr-(2Mo)	0.75	Anodic polarization
Fe-19Cr-(2Mo)	0.58	Anodic polarization

amorphous and crystalline alloys in  $1 \text{ mol dm}^{-3}$  HCl solution.<sup>52</sup> Crystalline ferritic stainless steels are passivated by anodic polarization, and the cationic concentrations of chromium species in the passive films are 75 and 58 at.% for Fe-30 at.% Cr and Fe-19 at.% Cr, respectively. For amorphous alloys, enrichment of chromium in passive films is more significant, although the contents of chromium in the alloys are lower than those in the crystalline alloys. For the amorphous Fe-10Cr-13P-7C alloy, which shows spontaneous passivation in  $1 \text{ mol dm}^{-3}$  HCl solution, the cationic percentage of chromium is 97 at.% in the passive film and only 3 at.% of cations are  $\text{Fe}^{2+}$  and  $\text{Fe}^{3+}$  ions. The concentration of chromium in the passive film formed on amorphous Fe-3Cr-2Mo-13P-C alloy is comparable to that in the passive film formed on crystalline Cr-19Cr steel. Thus, remarkable enrichment of chromium in the passive film is possible for amorphous alloys even if the chromium content in the alloy is as low as a few atomic percent. Amorphous alloys are metastable and hence surface reactivity is high. High reactivity of alloy surface leads to rapid dissolution of unnecessary alloying constituents, assisting the fast and significant enrichment of chromium species to form a stable and highly protective passive film.

Amorphous alloys are not always corrosion-resistant. The presence of a corrosion-resistant element is essential for improved corrosion resistance. In the absence of a corrosion-resistant element, amorphization increases the reactivity of the metal surface,

**Figure 3** Anodic dissolution rate of amorphous Co-25B alloy at  $-0.3 \text{ V}$  versus SCE in a solution of pH 1.8 containing  $0.5 \text{ mol dm}^{-3}$   $\text{Na}_2\text{SO}_4$ . After heat treatment at several temperatures.<sup>54</sup>

resulting in the occurrence of more aggressive corrosion. For instance, active dissolution rates of amorphous Fe-Cr-P-C alloys are larger than those of crystalline alloys with similar composition.<sup>54</sup> During annealing of amorphous Co-25 at.% B alloy, the alloy crystallizes to a  $\text{Co}_3\text{B}$  phase. The  $\text{Co}_3\text{B}$  phase decomposes to  $\text{Co}_2\text{B}$  and Co by further annealing at higher temperatures. Figure 3 shows the anodic dissolution current density of the Co-25 at.% B alloy at  $-0.3 \text{ V}$  versus SCE in  $0.5 \text{ mol dm}^{-3}$   $\text{Na}_2\text{SO}_4$  (pH 1.8) after annealing at various temperatures.<sup>55</sup> The dissolution rate of the amorphous Co-25 at.% B alloy decreases due to crystallization to  $\text{Co}_3\text{B}$ , indicating higher reactivity of the amorphous surface than that of the crystalline counterpart. Increased dissolution rate again above 623 K is associated with the chemical heterogeneity produced by decomposition of  $\text{Co}_3\text{B}$  to  $\text{Co}_2\text{B}$  and Co.

Another important point for the improved corrosion resistance of amorphous alloys is linked to the fact that amorphous alloys are able to form supersaturated solid solutions containing one or more alloying elements. In amorphous alloys, corrosion-resistant elements can be added uniformly, exceeding the solubility limit at equilibrium. The solid solubility of an alloying element in aluminum is usually less than a few percent. Practical Al alloys consist of an fcc Al phase and an intermetallic compound phase, with concentration of alloying element in the fcc matrix phase remaining low. Thus, the pitting corrosion resistance is not highly enhanced by alloying. However, if the sputter deposition technique is applied for the preparation of aluminum alloys,

a single-phase aluminum alloy supersaturated with an alloying element can be produced in an almost entire composition range and amorphous structure is obtained in a wide composition range.<sup>28</sup> The pitting corrosion resistance of sputter-deposited Al–Mo and Al–W metastable solid solution alloys in a chloride-containing neutral solution increases significantly with an increase in alloying element content, as shown in Figure 2.<sup>22</sup> Corrosion rates of a range of sputter-deposited Al–early transition metal alloys in 1 mol dm<sup>−3</sup> HCl solution also greatly decreases with an increase in content of the alloying element.<sup>28</sup> The improved corrosion resistance of aluminum alloys supersaturated with an alloying element is attributed primarily to the formation of passive films containing corrosion-resistant elements.<sup>28,56–58</sup> Compositions of passive films formed by anodic polarization were examined by X-ray photoelectron spectroscopy (XPS). Based on the results of analysis, it has been proposed that MoO<sub>4</sub><sup>2−</sup>, CrOOH, Ta<sub>2</sub>O<sub>5</sub>, or ZrO<sub>2</sub> present in passive films inhibits the adsorption of chloride ions and increase resistance to pit initiation in chloride-containing neutral solutions.

However, there are also some reports that passive films on solid solution aluminum alloys, including Al–W alloys, are practically free from alloying element species,<sup>59–61</sup> although pitting potential greatly ennobles with increase in content of the alloying element. The improved corrosion resistance of aluminum alloys has also been discussed in terms of local dissolution kinetics; alloying improves pitting resistance through a reduction in the ability of pits to maintain the critical local environment necessary for growth.<sup>62</sup>

A systematic study has been undertaken using transmission electron microscopy and Rutherford backscattering spectroscopy (RBS) to elucidate the growth process of anodic films on single-phase aluminum alloys. During anodizing of most dilute aluminum alloys, only aluminum is oxidized initially at the alloy–film interface, forming an alumina film free from alloying element species.<sup>63</sup> The alloying element is accumulated in a thin alloy layer, ~1–2 nm thick, immediately beneath the anodic film. Once the average composition of the enriched alloy layer reaches a critical level, the alloying element is oxidized and incorporated into the oxide film, with the average composition of the enriched layer maintaining the critical level.<sup>64</sup> It has been proposed that in the enriched alloy layer, clusters of the alloying element or the alloying element-rich clusters are developed (Figure 4). The critical level of enrichment is dependent upon the alloying element. There is a good

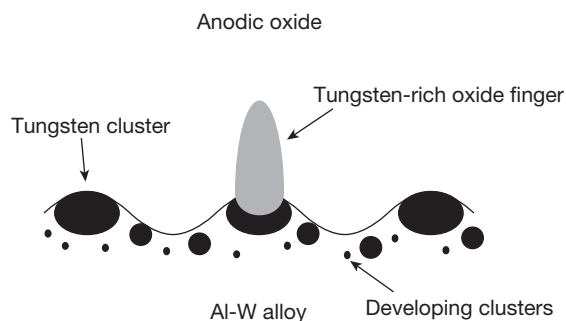


**Figure 4** Schematic illustration showing development of tungsten clusters in the enriched alloy layer, ~2 nm thick, immediately beneath the anodic film, and subsequent oxidation of the cluster with a critical size on a dilute Al–W alloy.

correlation between the critical amount of alloying element in the enriched alloy layer and the Gibbs free energy per equivalent of the formation of alloying element oxide (Figure 5).<sup>63</sup> An element with larger Gibbs free energy per equivalent for formation of oxide, that is, a nobler element, has more significant enrichment. No enrichment of an alloying element occurs when the alloying element has a Gibbs free energy per equivalent for formation of oxide similar to or less than that of Al<sub>2</sub>O<sub>3</sub>. In addition to the growth of anodic films at high current efficiency, preferential oxidation of aluminum and accumulation of an alloying element at the alloy surface also occur during chemical etching of aluminum alloys in alkaline solutions, chemical polishing, and electropolishing.<sup>65,66</sup> In neutral chloride-containing solutions, the dissolution rate of the passive film on aluminum alloys is considerably low unless localized attack occurs. Thus passive films free from alloying element species have been detected by surface analysis. Dissolution of alloy results in accumulation of the alloying element at the alloy surface once local breakdown of passive film occurs. Thus, finally, the passive film containing corrosion-resistant alloying element species may be developed, probably inhibiting the growth of pits.

### 3.20.1.3 Role of Alloying Elements in Improving Corrosion Resistance

#### 3.20.1.3.1 Phosphorus

Amorphous alloys are classified as metal–metal and metal–metalloid alloy systems. Metalloid elements, such as boron, carbon, silicon, and phosphorus, are added primarily for enhancing glass-forming ability.

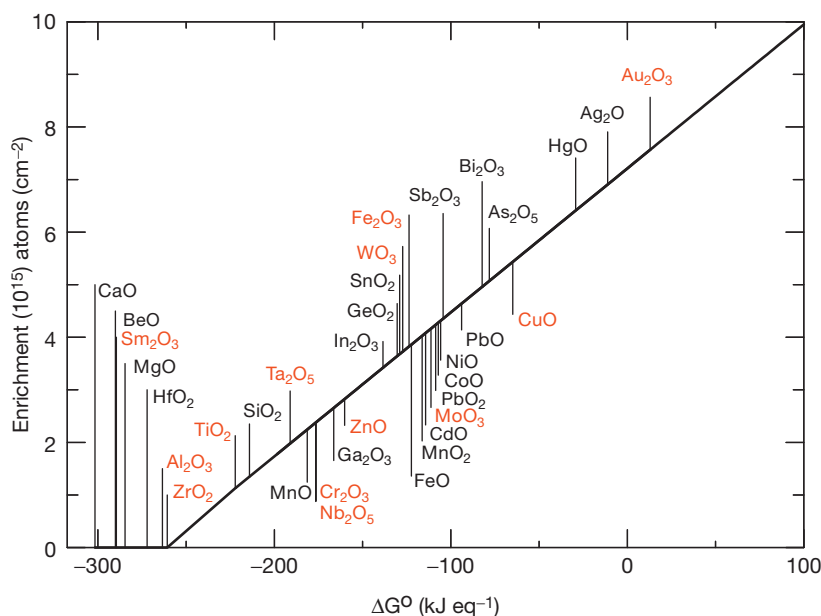


**Figure 5** The steady-state enrichment of the alloy predicted for anodizing of binary aluminum alloys, containing ~1–5 at.% alloying element. Predictions are obtained using the relationship between enrichment and Gibbs free energy per equivalent for formation of the alloying element oxide derived from experimental results for a limited range of alloys anodized at  $50 \text{ A m}^{-2}$  at 298 K.

Among such metalloid elements, phosphorus is particularly beneficial in enhancing corrosion resistance, although it is known that phosphorus segregates at the grain boundaries of stainless steels and induces intergranular corrosion and stress-corrosion cracking of stainless steels. Amorphous Fe–Cr–13Si–7B and Fe–Cr–20B alloys in  $9 \text{ mol dm}^{-3}$   $\text{H}_2\text{SO}_4$  solution dissolve actively and their corrosion rates increase with increasing chromium content. In contrast, the corrosion rates of amorphous Fe–Cr–13P–7C and Fe–Cr–13P–7B alloys in the same solution decrease markedly with the addition of more than 7 at.% chromium.<sup>67</sup> For Ni-based amorphous alloys, the addition of phosphorus reduces the corrosion rate in hydrochloric acid even if a passivating element is absent. The amorphous Ni–20P alloy shows a low corrosion rate of less than  $0.1 \text{ mm year}^{-1}$  even in concentrated HCl solution, in which nickel metal dissolves aggressively.<sup>68</sup> Marked decrease in the corrosion rate has been found with the addition of only small amounts of phosphorus to amorphous Ni–Ta alloys; the addition of 2 at.% phosphorus decreases the corrosion rate by more than four orders of magnitude in boiling  $6 \text{ mol dm}^{-3}$  HCl solution.<sup>7</sup>

The high corrosion resistance of amorphous Ni–P alloys in acid solutions is not associated with oxide-based passivity. The alloys do not reveal a clear

active–passive transition, and the anodic current density increases gradually with anodic potential.<sup>69–71</sup> The corrosion rate of the amorphous Ni–19P alloy is not dependent upon the concentration of HCl—unusual behavior for oxide-based passivity.<sup>72</sup> Chemical passivity by adsorption of hypophosphite ions was proposed on the basis of results of XPS analysis of Ni–P alloy specimens polarized anodically in deaerated HCl and  $\text{H}_2\text{SO}_4$  solutions.<sup>69</sup> In addition to hypophosphite ions, enrichment of elemental phosphorus as a consequence of preferential dissolution of nickel was found by XPS analysis. Kinetic analysis of anodic dissolution of the amorphous Ni–P alloy in HCl solution revealed that the dissolution current density follows Fick’s second law (Figure 6), thus being diffusion-controlled.<sup>73</sup> An explanation of these results is that the elemental phosphorus layer formed by selective dissolution of nickel acts as a diffusion barrier for dissolution of nickel, reducing the dissolution rate of the alloy. The elemental phosphorus layer has high cathodic activity for proton and oxygen reduction. Thus, the formation of an elemental phosphorus layer shifts the corrosion potential in the noble direction as a consequence of the enhancement of cathodic activity and suppression of anodic dissolution. When a passivating element, such as chromium, is present, ennoblement of the corrosion potential promotes

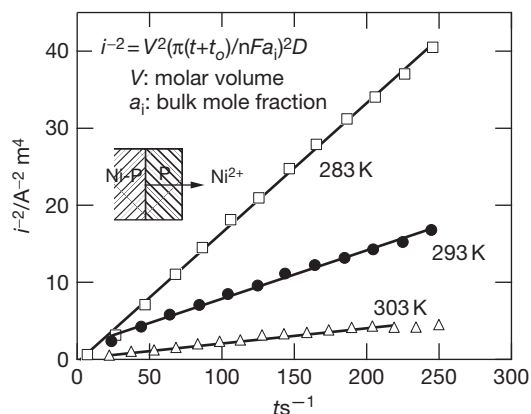


**Figure 6** Reciprocal of square of current density  $i$  for dissolution of nickel from a melt-spun amorphous Ni-19P alloy specimen at 100 mV versus SCE in 1 mol dm<sup>-3</sup> HCl at three different temperature as a function of time  $t$ .<sup>73</sup>

passivation. This may be the reason why many amorphous alloys containing a passivating element and phosphorus, including amorphous Ni-Cr-P and Fe-Cr-P-C alloys, are spontaneously passive even in concentrated acid solutions.

In these studies, the chemical state of phosphorus species has been analyzed by XPS. Special attention must be paid to the characterization of passive films by XPS. Exposure of the specimen surface to air during transfer of the specimen from the electrochemical cell to the spectrometer often changes the chemical state of species in passive films. For instance, surface elemental phosphorus changes to phosphate species.<sup>74</sup> The chemical state of molybdenum in passive films on molybdenum-containing corrosion-resistant alloys also changes from Mo<sup>4+</sup> to Mo<sup>6+</sup> species during exposure to air. For precise identification of the chemical species in passive films by XPS, exposure of specimens to air before introduction into the spectrometer must be avoided.

### 3.20.1.3.2 Synergy of corrosion-resistant elements

It is well known that the addition of molybdenum to stainless steels improves localized corrosion in chloride-containing solutions. Molybdenum also reduces active dissolution rates of stainless steels in acid solutions. Even for amorphous alloys, the addition of molybdenum markedly improves the corrosion resistance of chromium-containing amorphous alloys.<sup>5,75,76</sup> In the active dissolution potential region of chromium, molybdenum is passive, forming stable tetravalent molybdenum species. Such stable molybdenum species

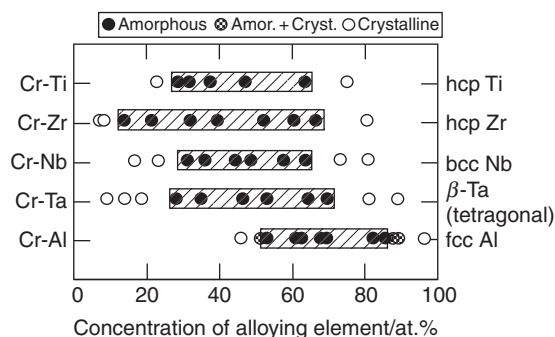


**Figure 7** Structures of sputter-deposited Cr-valve metals alloys identified by X-ray diffraction.

reduce the active dissolution rates of stainless steels and chromium-containing amorphous alloys. In addition to active dissolution rates, the stability of the passivity of stainless steels and amorphous alloys is enhanced by the addition of molybdenum. Because molybdenum dissolves transpassively as molybdate ions in the passive potential region of the alloys, the composition of passive films on molybdenum-containing alloys is often not greatly different from that on molybdenum-free counterparts. There are several reports on the role of molybdenum in enhancing the stability of a passive state.<sup>4,77,78</sup> The precise role of molybdenum in enhancing passivity is still a subject of controversy.

Ideal corrosion-resistant materials should be alloys consisting only of corrosion-resistant elements. Such alloys have been prepared by a magnetron sputtering method, and, interestingly, it has been revealed that the alloys show superior corrosion resistance to that of each alloy-constituting metal. **Figure 7** shows structures of sputter-deposited chromium-valve metal alloys identified by X-ray diffraction.<sup>31-33</sup> The alloys show an amorphous single-phase structure in a wide composition range. Even crystalline alloys are single phase. Their corrosion rates in 6 mol dm<sup>-3</sup> HCl and 12 mol dm<sup>-3</sup> HCl solution are shown in **Figure 8**. In 6 mol dm<sup>-3</sup> HCl solution, chromium and titanium metals dissolve actively, but binary Cr-Ti alloys are spontaneously passive and show extremely low corrosion rates, several orders of magnitude lower than those of the alloy-constituting elements.<sup>33</sup> The binary amorphous Cr-Zr alloys also reveal low corrosion rates in the 6 mol dm<sup>-3</sup> HCl solution, the rates decreasing with increasing chromium content.<sup>32</sup> The binary amorphous Cr-Ta alloys are immune even in 12 mol dm<sup>-3</sup> HCl solution at 303 K in a wide composition range. Corrosion resistance of binary Cr-Nb alloys is also better than that of

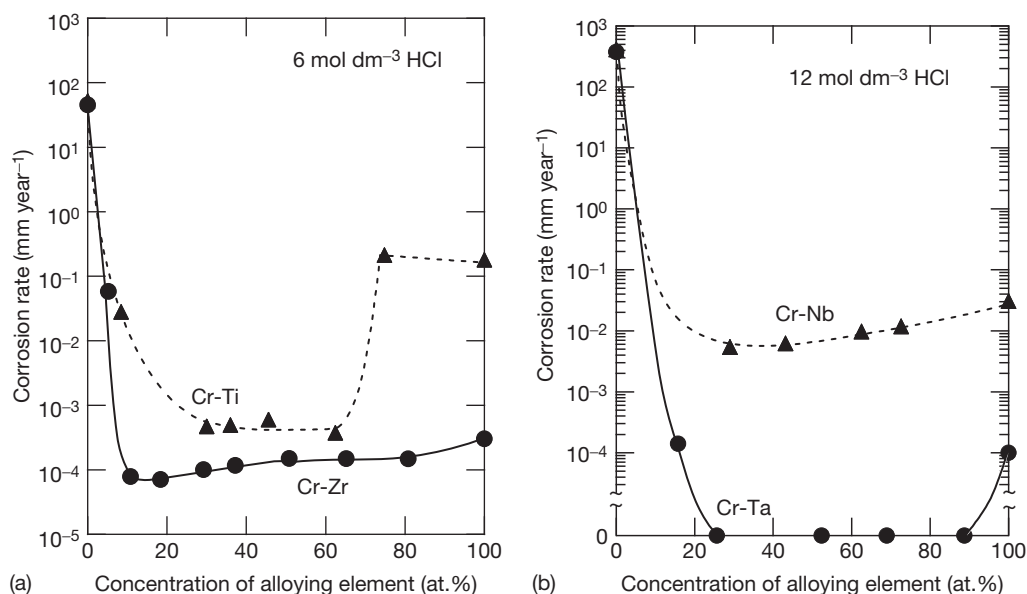


**Figure 8** Corrosion rates of sputter-deposited (a) Cr-Ti and Cr-Zr alloys in 6 mol dm<sup>-3</sup> HCl solutions and (b) Cr-Nb and Cr-Ta alloys in 12 mol dm<sup>-3</sup> HCl solution at 303 K.<sup>31-33</sup>

chromium and niobium metals.<sup>31</sup> Again, corrosion rates decrease with increasing chromium content.

Such excellent corrosion resistance of amorphous Cr-valve metal alloys was interpreted from XPS analyses of passive films; passive films consisting of double oxyhydroxides containing chromium and valve metal cations are remarkably protective in concentrated hydrochloric acids.<sup>45-48</sup> The formation of uniform double oxyhydroxides was identified from the shift of peak binding energies of photoelectrons of each cation. Similarly, Mo-valve metal alloys and W-valve metal alloys prepared by magnetron sputtering reveal high corrosion resistance in concentrated HCl solution. Their corrosion resistance is better than that of the corresponding alloy-constituting metals.<sup>36-40,42,79</sup>

#### 3.20.1.4 Corrosion Behavior of Bulk Metallic Glasses

The discovery in the late 1980s of amorphous alloys with extremely high glass-forming ability has eliminated the shape limitation of amorphous alloys, and a wide variety of applications are now being considered. As described in the review paper by Inoue,<sup>80</sup> a range of bulk metallic glasses, including Zr-based, Ti-based, Fe-based, Ni-based, Mg-based, and Ln-based alloys, have so far been developed by conventional casting and water cooling processes. The high glass-forming ability of these bulk metallic glasses is

associated with the stabilization of supercooled liquids. In metallic alloys, diffusion rates of alloy-constituting elements in their liquid phase are generally very fast at high temperatures just below the melting point. Due to high diffusivity, phase transformation occurs from supercooled liquid to a crystalline phase within a very short time of less than 10<sup>-5</sup> s. In multicomponent alloy systems forming bulk metallic glasses, diffusivity is suppressed, stabilizing the supercooled liquid state. Bulk metallic glasses are therefore obtained even with a slow cooling rate of 1 K s<sup>-1</sup> from liquids. Such metallic glasses with high glass-forming ability reveal in reality a wide temperature range of supercooled liquid region below the crystallization temperature.

Since bulk metallic glasses possess superior mechanical and physical properties, they have potential engineering importance. Thus, the corrosion behavior of bulk metallic glasses in potential service environments needs to be elucidated. Tailoring of extremely corrosion-resistant bulk metallic glasses may allow us to use metallic materials in aggressive environments, in which crystalline metallic materials cannot be used because of corrosion.

##### 3.20.1.4.1 Zr-based bulk metallic glasses

Zr-based bulk metallic glasses have been the most extensively studied glassy alloys. Because of their excellent mechanical properties of high tensile

strength, low Young's modulus, and large elastic elongation limit, Zr–Al–Cu–Ni bulk metallic glasses have been commercialized as golf clubs and pressure sensors. Good corrosion resistance of Zr–Al–Cu–Ni alloys was reported in chloride-free solutions in a wide pH range.<sup>81,82</sup> Their corrosion behavior is similar to that of zirconium metal. Zirconium is one of the valve metals, showing spontaneous passivation and high corrosion resistance in chloride-free acid, neutral, and alkaline solutions.<sup>83</sup> The passive film formed on Zr–Al–Cu–Ni alloys consists mainly of zirconium oxide with a small fraction of aluminum cation. For the Zr–Ti–Nb–Cu–Ni–Al alloy, it was revealed that in 0.5 mol dm<sup>-3</sup> H<sub>2</sub>SO<sub>4</sub> and 1 mol dm<sup>-3</sup> HNO<sub>3</sub> solutions, the fully amorphous alloy showed better passivation stability than nanocrystalline, quasi-crystalline, and crystalline ones with the same composition.<sup>84</sup>

In contrast to their high corrosion resistance in chloride-free solutions, Zr-based metallic glasses suffer pitting corrosion in chloride-containing solutions. The pitting occurs because of the existence of micrometer-sized crystalline inclusions.<sup>82</sup> Inclusions develop during casting at a slow cooling rate, being induced by oxygen in the casting atmosphere; bulk Zr–Al–Cu–Ni alloys containing higher oxygen content develop large fractions of crystalline inclusions.<sup>81</sup> The shape and size of the crystalline inclusions as well as their concentration are largely dependent upon the alloy composition, oxygen content, and cooling rate. The pitting is initiated preferentially at the interface between the amorphous matrix and a crystalline inclusion.

In addition to the reduced fraction of crystalline inclusions, modification of alloy composition is effective in improving pitting corrosion resistance. The addition of 5 at.% of titanium or niobium to Zr–30Cu–10Al–5Ni bulk metallic glass greatly reduces the pitting susceptibility in 0.05 mol dm<sup>-3</sup> NaCl solution.<sup>85</sup> The pitting corrosion resistance of melt-spun Zr–20Cu–10Al–10Ni alloy is enhanced by substituting zirconium with niobium up to 20 at.%.<sup>86</sup> The corrosion rate of the Zr-based alloy in 1 mol dm<sup>-3</sup> HCl solution decreases significantly with increasing niobium content. In 3% NaCl solution, the addition of niobium greatly shifts the pitting potential of the alloy in the positive direction.

Zr-based bulk metallic glasses have also attracted attention as biomaterials because of suitable mechanical properties as well as biocompatibility.<sup>87</sup> The bulk metallic glass of Zr–17.9Cu–14.6Ni–10Al–5Ti, commonly known as Vitreloy 105, possesses a low modulus

that is close to that of bone, as well as high elastic limit and superior strength. An unusual collection of mechanical properties of the bulk metallic glass would be advantageous in various biomedical applications.

As a part of investigations of the biocompatibility of Zr-based bulk metallic glasses, their corrosion behavior has been examined in artificial body fluids.<sup>87–90</sup> It has been found that pitting corrosion occurs on Zr-based metallic glasses in phosphate-buffered saline environments by anodic polarization. However, the susceptibility of pitting is not so high, particularly at low chloride concentrations. The corrosion behavior of the Vitreloy 105 bulk metallic glass has been compared with that of common biomaterials of 316L stainless steel, Ti–6Al–4V, and CoCrMo alloys in a phosphate-buffered saline solution.<sup>87</sup> The corrosion rate of the Zr-based bulk metallic glass was lower than that of 316L stainless steel, being comparable with the corrosion rates of Ti–6Al–4V and CoCrMo alloys. Furthermore, bulk metallic glass showed better localized corrosion resistance than 316L stainless steel. The combined mechanical and electrochemical properties of Zr-based bulk metallic glasses indicate their potential as a new generation of biomaterials.

#### 3.20.1.4.2 Corrosion-resistant bulk metallic glasses

It has been demonstrated that bulk forms of iron-based and nickel-based metallic glasses containing sufficient amounts of corrosion-resistant elements show excellent corrosion resistance in aggressive acid solutions. Corrosion-resistant rod-shaped Ni-based alloys, including Ni–5Cr–5Ta–3Mo–16P–4B, Ni–15Cr–10Mo–16P–4B, Ni–(10–15)Cr–5Ta–16P–4B and Ni–(40–*x*)Nb–*x*Ta–(3–5)P alloys, of 1–2 mm in diameter were successfully prepared by copper mold casting.<sup>51,91,92</sup> These alloys are spontaneously passive in 6 mol dm<sup>-3</sup> HCl solution, showing very low corrosion rates. The corrosion resistance of bulk metallic glasses is comparable to that of metal-spun thin ribbons of the same composition. Thus, the cooling rate does not influence the corrosion behavior of metallic glasses. To obtain sufficient glass-forming ability to form bulk metallic glasses, large amounts of corrosion-resistant elements cannot be added to alloys. However, the combined addition of two or three corrosion-resistant elements to nickel-based and iron-based alloys provides excellent corrosion resistance. The combination of chromium, tantalum, and molybdenum is effective for enhancing corrosion resistance.<sup>50,92</sup>



A bulk form of corrosion-resistant metallic glasses was also successfully prepared by sheath-rolling consolidation of encased amorphous alloy powders. The Ni–10Cr–5Nb–16P–4B metallic glass shows a wide temperature range of supercooled liquid region (more than 50 K) below crystallization. Alloy powders prepared by a gas atomization technique were encased in a stainless steel tube and then heated to temperature of the supercooled liquid region. Sheath-rolling at this temperature produced a bulk metallic glass plate. The potential application of the sheath-rolled and copper-mold cast Ni–10Cr–5Nb–16P–4B bulk metallic glass in an exhaust gas chimney of a waste incinerator has been pointed out.<sup>93</sup> In the environment at 423 K and 463 K, severe corrosion attack occurred on type-316L stainless steel and Alloy B due to dew-point corrosion, whereas bulk metallic glass retained its metallic luster and showed no detectable corrosion weight change for 20 days. Superior corrosion resistance of iron-based bulk metallic glasses containing chromium and molybdenum has also been reported. The availability of corrosion-resistant bulk metallic glasses opens up their applications to very aggressive environments, in which conventional crystalline metallic materials cannot be used due to severe corrosion.

### 3.20.1.5 Corrosion Behavior of Nanocrystalline Alloys

#### 3.20.1.5.1 Nanocrystalline-precipitated amorphous alloys

It is likely that precipitation of crystalline phases in an amorphous alloy matrix containing corrosion-resistant elements is detrimental to its corrosion resistance because of the increased chemical heterogeneity. It is known that amorphous alloys containing corrosion-resistant elements show higher corrosion resistance than fully crystallized alloys with the same composition. This is, however, not always true when nanocrystalline phases are precipitated in an amorphous matrix phase. In certain amorphous Al alloys and Zr alloys,<sup>94–99</sup> it has been demonstrated that good resistance of fully amorphous alloys to localized pitting corrosion is not deteriorated or improved by nanocrystalline precipitation. Nanocrystalline precipitates can be introduced in an amorphous phase by heat treatment of fully amorphous alloys or by utilizing a slow cooling rate during the fabrication of amorphous alloys from the liquid state. The latter condition is required to develop bulk metallic glasses such that they often contain

nanocrystalline precipitates in an amorphous matrix. Thus an understanding of the influence of nanocrystalline precipitates on corrosion behavior is a crucial issue for the practical application of bulk metallic glasses. Furthermore, nanocrystalline-amorphous alloys have attracted attention since they show improved mechanical strength.<sup>100</sup> The crystallization behavior of amorphous alloys is dependent upon alloy composition. For aluminum-rich amorphous alloys, including Al–5Fe–5Gd, Al–8.7Ni–4.3Y, and Al–3Co–7Ce alloys, solute-lean fcc-Al phase nanocrystals are primarily precipitated in an amorphous matrix during heat treatment. Such amorphous–nanocrystalline alloys maintain high pitting potential in chloride-containing solutions comparable to that of fully amorphous alloys, though fully crystallized alloys show considerably low pitting potential.<sup>95–99</sup> For the Al–5Fe–5Gd alloy, even ennobled pitting potential in 0.6 mol dm<sup>−3</sup> NaCl solution by precipitation of 10–15 nm sized nanocrystals has been reported (Figure 9).<sup>98</sup> Ennoblement of pitting potential is also observed for amorphous Zr–Cr alloys; precipitation of hcp Zr nanocrystals of less than 20 nm shifts the pitting potential in the positive direction in 6 mol dm<sup>−3</sup> HCl solution.<sup>94</sup> Ennoblement of the pitting potential is explained by the enrichment of the solute in the amorphous matrix. Precipitation of nanocrystalline Zr induces enrichment of chromium in the amorphous phase, making the matrix phase more pitting-resistant. The presence of a critical size of nanocrystals, that is, 20 nm, in improving localized corrosion resistance has also been pointed out. Below the critical size, a chromium-enriched highly

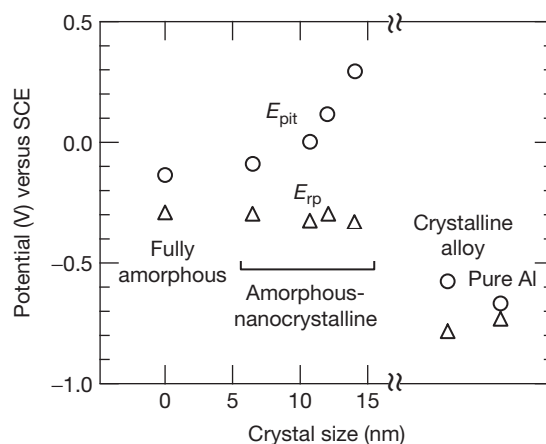


**Figure 9** Pitting and repassivation potentials for Al–5Fe–5Gd in deaerated 0.6 mol dm<sup>−3</sup> NaCl. Pitting and repassivation potentials of pure Al are shown for comparison. Scan rate 0.1 mV s<sup>−1</sup>.<sup>98</sup>

protective passive film can cover the entire alloy surface, but preferential dissolution of a less corrosion-resistant phase occurs when the size of the precipitates exceeds the critical size.

There are also examples of precipitation of nanocrystals less than 10 nm size in amorphous matrix being detrimental in terms of corrosion. The copper-mold cast Ni-10Cr-5Ta-16P-4B bulk metallic glass contains an fcc nickel phase of 2–3 nm in size in the amorphous matrix, showing higher anodic dissolution current than that of fully amorphous alloy ribbon in potentiodynamic polarization curves.<sup>91</sup> Smaller sizes of the fcc Ni precipitates have lower detrimental effect. Sputter-deposited Cr-Nb alloys are spontaneously passive in 6 and 12 mol dm<sup>-3</sup> HCl solutions. The as-deposited alloys crystallize to a two-phase mixture of bcc Cr and Cr<sub>2</sub>Nb, Cr<sub>2</sub>Nb and niobium-rich amorphous phase, Cr<sub>2</sub>Nb and bcc Nb, or chromium-rich amorphous phase and bcc Nb, depending upon alloy composition and heat treatment conditions. The Cr<sub>2</sub>Nb phase has high corrosion resistance, similar to that of the amorphous single phase alloy. The formation of nanocrystalline bcc Cr and bcc Nb phases increases initial passive current density. However, the steady state passive current density is as low as that of the as-deposited alloy, as the amorphous or Cr<sub>2</sub>Nb matrix phase maintains high corrosion resistance. Thus, the formation of soluble nanocrystals in corrosion-resistant matrix phases increases the initial dissolution rate but not always the steady-state anodic dissolution rate.

### 3.20.1.5.2 Nanocrystallization of conventional crystalline corrosion-resistant materials

Finally, it may be worth mentioning that nanocrystallization of conventional corrosion-resistant materials such as stainless steel, markedly improves the susceptibility for localized corrosion without changing the alloy composition. Using a conventional type-304 stainless steel target, nanocrystalline stainless steel films have been prepared by sputter deposition.<sup>101,102</sup> The pitting potential of nanocrystalline films with grain size of 25 nm is ~850 mV more positive than that of conventional bulk material of the same composition, even though enrichment of chromium in the air-formed oxide is lower for nanocrystalline films.<sup>101</sup> Sputter-deposited films have a bcc structure. Improved pitting corrosion resistance may not be related to structural transformation from the fcc phase of bulk material to the bcc phase of nanocrystalline films, because the pitting potential of ferritic bulk stainless

steel containing 18% Cr is even lower than that of austenitic stainless steel with the same Cr content.

It is well accepted that pitting corrosion of stainless steel in chloride-containing environments is usually initiated at manganese sulfide particles in the steel. A recent study also suggests the possibility that pitting is triggered by an attack on chromium-depleted zones around the manganese sulfide particles.<sup>103</sup> In stainless steel films prepared by sputter deposition that produces single-phase materials dissolving most alloying and impurity elements, the chemical heterogeneity of the steel surface should be neglected. By using a process that forms nanograined metastable materials with reduced chemical heterogeneity, corrosion resistance can be improved remarkably without changing chemical compositions, even if there is a high concentration of impurity elements that are generally detrimental to corrosion.<sup>102</sup>

## References

1. Naka, M.; Hashimoto, K.; Masumoto, T. *Jpn. Inst. Met.* **1974**, *38*, 835–841.
2. Naka, M.; Hashimoto, K.; Masumoto, T. *Corrosion* **1976**, *32*, 146–152.
3. Hashimoto, K.; Asami, K.; Naka, M.; Masumoto, T. *Sci. Rep. Res. Inst., Tohoku Univ., Ser. A* **1979**, *27*, 237–245.
4. Hashimoto, K.; Asami, K.; Teramoto, K. *Corros. Sci.* **1979**, *19*, 3–14.
5. Asami, K.; Naka, M.; Hashimoto, K.; Masumoto, T. *J. Electrochem. Soc.* **1980**, *127*, 2130–2138.
6. Hashimoto, K.; Kobayashi, K.; Asami, K.; Masumoto, T. *Metallic Corrosion*, Proceedings of the Eighth International Congress on Metal Corrosion, Mainz, Germany, 6–11 Sept; DEHEMA, Frankfurt am Main, Germany, 1981; pp 70–75.
7. Shimamura, K.; Kawashima, A.; Asami, K.; Hashimoto, K. *Sci. Rep. Res. Inst. Tohoku Univ. Ser. A* **1986**, *33*, 196–210.
8. Singh, I. B.; Misra, R. D. K.; Chaudhary, R. S.; Akhtar, D. *Mater. Sci. Eng.* **1987**, *92*, 173–178.
9. Mitsuhashi, A.; Kawashima, A.; Asami, K.; Hashimoto, K. In *Corrosion, Electrochemistry and Catalysis of Metallic Glasses*, Proceedings of the Symposium of the Electrochemical Society, Honolulu, USA, 1987; Diegle, R. B., Hashimoto, K., Eds.; The Electrochemical Society: Pennington, NJ, USA, 1988; pp 191–200.
10. Shimamura, K.; Miura, K.; Kawashima, A.; Asami, K.; Hashimoto, K. *Sci. Rep. Res. Inst., Tohoku Univ., Ser. A* **1988**, *34*, 107–117.
11. Mitsuhashi, A.; Kawashima, A.; Asami, K.; Hashimoto, K. *Boshoku Gijutsu* **1988**, *37*, 3–8.
12. Lee, H. J.; Akiyama, E.; Habazaki, H.; Kawashima, A.; Asami, K.; Hashimoto, K. *Corros. Sci.* **1995**, *37*, 1313–1324.
13. Lee, H. J.; Akiyama, E.; Habazaki, H.; Kawashima, A.; Asami, K.; Hashimoto, K. *Corros. Sci.* **1995**, *37*, 321–330.
14. Lee, H. J.; Akiyama, E.; Habazaki, H.; Kawashima, A.; Asami, K.; Hashimoto, K. *Mater. Trans., JIM* **1996**, *37*, 383–388.

15. Lee, H. J.; Akiyama, E.; Habazaki, H.; Kawashima, A.; Asami, K.; Hashimoto, K. *Corros. Sci.* **1996**, *38*, 469–485.
16. Lee, H. J.; Akiyama, E.; Habazaki, H.; Kawashima, A.; Asami, K.; Hashimoto, K. *Corros. Sci.* **1996**, *38*, 1269–1279.
17. Kim, Y.; Buchheit, R. G. *Electrochim. Acta* **2007**, *52*, 2437–2446.
18. Janik-Czachor, M.; Jaskiewicz, A.; Kedzierski, P.; Werner, Z. *Mater. Sci. Eng. A* **2003**, *358*, 171–177.
19. Principe, E. L.; Shaw, B. A.; Davis, G. D. *Corrosion* **2003**, *59*, 295–313.
20. Metikos-Hukovic, M.; Radic, N.; Grubac, Z.; Tonejcv, A. *Electrochim. Acta* **2002**, *47*, 2387–2397.
21. Bockris, J. O.; Kang, Y. K. *J. Solid State Electrochem.* **1997**, *1*, 17–35.
22. Wolowik, A.; Janik-Czachor, M.; Werner, Z. *Mater. Chem. Phys.* **1997**, *49*, 164–168.
23. Davis, G. D.; Shaw, B. A.; Rees, B. J.; Pecile, C. A. *Surf. Interf. Anal.* **1995**, *23*, 609–617.
24. Moffat, T. P.; Stafford, G. R.; Hall, D. E. *J. Electrochem. Soc.* **1993**, *140*, 2779–2786.
25. Bockris, J. O.; Minevski, L. V. *J. Electroanal. Chem.* **1993**, *349*, 375–414.
26. Davis, G. D.; Shaw, B. A.; Rees, B. J.; Ferry, M. *J. Electrochem. Soc.* **1993**, *140*, 951–959.
27. Davis, G. D.; Moshier, W. C.; Long, G. G.; Black, D. R. *J. Electrochem. Soc.* **1991**, *138*, 3194–3199.
28. Yoshioka, H.; Yan, O.; Habazaki, H.; Kawashima, A.; Asami, K.; Hashimoto, K. *Corros. Sci.* **1990**, *31*, 349–354.
29. Yoshioka, H.; Habazaki, H.; Kawashima, A.; Asami, K.; Hashimoto, K. *Electrochim. Acta* **1991**, *36*, 1227–1233.
30. Yoshioka, H.; Habazaki, H.; Kawashima, A.; Asami, K.; Hashimoto, K. *Corros. Sci.* **1991**, *32*, 313–325.
31. Kim, J. H.; Akiyama, E.; Habazaki, H.; Kawashima, A.; Asami, K.; Hashimoto, K. *Corros. Sci.* **1993**, *34*, 1947–1955.
32. Kim, J. H.; Akiyama, E.; Habazaki, H.; Kawashima, A.; Asami, K.; Hashimoto, K. *Corros. Sci.* **1993**, *34*, 1817–1827.
33. Kim, J. H.; Akiyama, E.; Yoshioka, H.; Habazaki, H.; Kawashima, A.; Asami, K.; Hashimoto, K. *Corros. Sci.* **1993**, *34*, 975–987.
34. Kim, J. H.; Akiyama, E.; Habazaki, H.; Kawashima, A.; Asami, K.; Hashimoto, K. *Corros. Sci.* **1994**, *36*, 511–523.
35. Bhattarai, J.; Akiyama, E.; Kawashima, A.; Asami, K.; Hashimoto, K. *Corros. Sci.* **1995**, *37*, 2071–2086.
36. Park, P. Y.; Akiyama, E.; Habazaki, H.; Kawashima, A.; Asami, K.; Hashimoto, K. *Corros. Sci.* **1996**, *38*, 1649–1667.
37. Park, P. Y.; Akiyama, E.; Habazaki, H.; Kawashima, A.; Asami, K.; Hashimoto, K. *Corros. Sci.* **1996**, *38*, 1731–1750.
38. Park, P. Y.; Akiyama, E.; Kawashima, A.; Asami, K.; Hashimoto, K. *Corros. Sci.* **1996**, *38*, 397–411.
39. Bhattarai, J.; Akiyama, E.; Habazaki, H.; Kawashima, A.; Asami, K.; Hashimoto, K. *Corros. Sci.* **1997**, *40*, 19–42.
40. Bhattarai, J.; Akiyama, E.; Habazaki, H.; Kawashima, A.; Asami, K.; Hashimoto, K. *Corros. Sci.* **1997**, *39*, 355–375.
41. Bhattarai, J.; Akiyama, E.; Habazaki, H.; Kawashima, A.; Asami, K.; Hashimoto, K. *Corros. Sci.* **1998**, *40*, 1897–1914.
42. Bhattarai, J.; Akiyama, E.; Habazaki, H.; Kawashima, A.; Asami, K.; Hashimoto, K. *Corros. Sci.* **1998**, *40*, 757–779.
43. Bhattarai, J.; Akiyama, E.; Habazaki, H.; Kawashima, A.; Asami, K.; Hashimoto, K. *Corros. Sci.* **1998**, *40*, 155–175.
44. Bhattarai, J.; Akiyama, E.; Habazaki, H.; Kawashima, A.; Asami, K.; Hashimoto, K. *Corros. Sci.* **1998**, *40*, 19–42.
45. Li, X. Y.; Akiyama, E.; Habazaki, H.; Kawashima, A.; Asami, K.; Hashimoto, K. *Corros. Sci.* **1997**, *39*, 1365–1380.
46. Li, X. Y.; Akiyama, E.; Habazaki, H.; Kawashima, A.; Asami, K.; Hashimoto, K. *Corros. Sci.* **1997**, *39*, 935–948.
47. Li, X. Y.; Akiyama, E.; Habazaki, H.; Kawashima, A.; Asami, K.; Hashimoto, K. *Corros. Sci.* **1998**, *40*, 1587–1604.
48. Li, X. Y.; Akiyama, E.; Habazaki, H.; Kawashima, A.; Asami, K.; Hashimoto, K. *Corros. Sci.* **1998**, *40*, 821–838.
49. Pang, S. J.; Zhang, T.; Asami, K.; Inoue, A. *Acta Mater.* **2002**, *50*, 489–497.
50. Katagiri, H.; Meguro, S.; Yamasaki, M.; Habazaki, H.; Sato, T.; Kawashima, A.; Asami, K.; Hashimoto, K. *Corros. Sci.* **2001**, *43*, 183–191.
51. Kawashima, A.; Habazaki, H.; Hashimoto, K. *Mater. Sci. Eng. A* **2001**, *304*, 753–757.
52. Hashimoto, K. In *Passivity of Metals and Semiconductors*; Froment, M., Ed.; Elsevier: Amsterdam, 1983; 235. Proceedings of the Fifth International Symposium, Bombannes, France, May 30–June 3.
53. Asami, K.; Hashimoto, K.; Masumoto, T.; Shimodaira, S. *Corros. Sci.* **1976**, *16*, 909–914.
54. Hashimoto, K.; Osada, K.; Masumoto, T.; Shimodaira, S. *Corros. Sci.* **1976**, *16*, 71–76.
55. Huerta, D.; Heusler, K. E. *J. Non-Cryst. Solids* **1983**, *56*, 261–266.
56. Davis, G. D.; Moshier, W. C.; Fritz, T. L.; Cote, G. O. *J. Electrochem. Soc.* **1990**, *137*, 422–427.
57. Moshier, W. C.; Davis, G. D.; Cote, G. O. *J. Electrochem. Soc.* **1989**, *136*, 356–362.
58. Moshier, W. C.; Davis, G. D.; Ahearn, J. S.; Hough, H. F. *J. Electrochem. Soc.* **1986**, *133*, 1063–1064.
59. Shaw, B. A.; Davis, G. D.; Fritz, T. L.; Rees, B. J.; Moshier, W. C. *J. Electrochem. Soc.* **1991**, *138*, 3288–3295.
60. Janik-Czachor, M.; Wolowik, A.; Szummer, A.; Lublinska, K.; Hofmann, S.; Kraus, K. *Electrochim. Acta* **1998**, *43*, 875–882.
61. Wolowik, A.; Janik-Czachor, M. *Mater. Sci. Eng. A* **1999**, *267*, 301–306.
62. Frankel, G. S.; Newman, R. C.; Jahnes, C. V.; Russak, M. A. *J. Electrochem. Soc.* **1993**, *140*, 2192–2197.
63. Habazaki, H.; Shimizu, K.; Skeldon, P.; Thompson, G. E.; Wood, G. C.; Zhou, X. *Trans. Inst. Met. Finish.* **1997**, *75*, 18–23.
64. Habazaki, H.; Shimizu, K.; Skeldon, P.; Thompson, G. E.; Wood, G. C. *Philos. Mag. B* **1996**, *73*, 445–460.
65. Liu, Y.; Colin, F.; Skeldon, P.; Thompson, G. E.; Zhou, X.; Habazaki, H.; Shimizu, K. *Corros. Sci.* **2003**, *45*, 1539–1544.
66. Zhou, X.; Thompson, G. E.; Habazaki, H.; Shimizu, K.; Skeldon, P.; Wood, G. C. *Thin Solid Films* **1997**, *293*, 327–332.
67. Im, B. M.; Akiyama, E.; Habazaki, H.; Kawashima, A.; Asami, K.; Hashimoto, K. *Corros. Sci.* **1993**, *34*, 1829–1839.
68. Zhang, B. P.; Kawashima, A.; Asami, K.; Hashimoto, K. *Boshoku Gijutsu* **1989**, *38*, 384–389.
69. Diegle, R. B.; Sorensen, N. R.; Clayton, C. R.; Helfand, M. A.; Yu, Y. C. *J. Electrochem. Soc.* **1988**, *135*, 1085–1092.
70. Diegle, R. B.; Sorensen, N. R.; Clayton, C. R.; Helfand, M. A. In *Corrosion, Electrochemistry and Catalysis of Metallic Glasses*; Diegle, R. B., Hashimoto, K., Eds.; The Electrochemical Society, Pennington, NJ, USA, 1988; pp 80–103. Proceedings of the Symposium of the Electrochemical Society, Honolulu, USA, 1987.
71. Krolkowski, A.; Karbownicka, B.; Jaklewicz, O. *Electrochim. Acta* **2006**, *51*, 6120–6127.

72. Zhang, B. P.; Habazaki, H.; Kawashima, A.; Asami, K.; Hashimoto, K. *Corros. Sci.* **1992**, *33*, 667–679.
73. Habazaki, H.; Ding, S. Q.; Kawashima, A.; Asami, K.; Hashimoto, K.; Inoue, A.; Masumoto, T. *Corros. Sci.* **1989**, *29*, 1319–1328.
74. Zhang, B. P.; Habazaki, H.; Kawashima, A.; Asami, K.; Hashimoto, K. *Corros. Sci.* **1992**, *33*, 103–112.
75. Habazaki, H.; Kawashima, A.; Asami, K.; Hashimoto, K. *Mater. Sci. Eng. A* **1991**, *134*, 1033–1036.
76. Habazaki, H.; Kawashima, A.; Asami, K.; Hashimoto, K. *Corros. Sci.* **1992**, *33*, 225–236.
77. Sugimoto, K.; Sawada, Y. *Corros. Sci.* **1977**, *17*, 425–437.
78. Clayton, C. R.; Lu, Y. C. *Corros. Sci.* **1989**, *29*, 881–898.
79. Bhattarai, J.; Akiyama, E.; Habazaki, H.; Kawashima, A.; Asami, K.; Hashimoto, K. *Corros. Sci.* **1998**, *40*, 155–175.
80. Inoue, A. *Proc. Jpn. Acad. Ser. B* **2005**, *81*, 156–171.
81. Gebert, A.; Buchholz, K.; Leonhard, A.; Mummert, K.; Eckert, J.; Schultz, L. *Mater. Sci. Eng. A* **1999**, *267*, 294–300.
82. Gebert, A.; Mummert, K.; Eckert, J.; Schultz, L.; Inoue, A. *Mater. Corros.* **1997**, *48*, 293–297.
83. Pringle, J. P. S. *Electrochem. Acta* **1980**, *25*, 1420–1437.
84. Mudali, U. K.; Scudino, S.; Kühn, U.; Eckert, J.; Gebert, A. *Scr. Mater.* **1994**, *50*, 1379.
85. Raju, V. R.; Kuhn, U.; Wolff, U.; Schneider, F.; Eckert, J.; Reiche, R.; Gebert, A. *Mater. Lett.* **2002**, *57*, 173–177.
86. Pang, S. J.; Zhang, T.; Kimura, H.; Asami, K.; Inoue, A. *Mater. Trans. JIM* **2000**, *41*, 1490–1494.
87. Morrison, M. L.; Buchanan, R. A.; Leon, R. V.; Liu, C. T.; Green, B. A.; Liaw, P. K.; Horton, J. A. *J. Biomed. Mater. Res. A* **2005**, *74A*, 430–438.
88. Hiromoto, S.; Tsai, A. P.; Sumita, M.; Hanawa, T. *Mater. Trans.* **2002**, *43*, 3112–3117.
89. Hiromoto, S.; Asami, K.; Tsai, A. P.; Hanawa, T. *Mater. Trans.* **2002**, *43*, 261–266.
90. Hiromoto, S.; Tsai, A. P.; Sumita, M.; Hanawa, T. *Corros. Sci.* **2000**, *42*, 1651–1660.
91. Habazaki, H.; Sato, T.; Kawashima, A.; Asami, K.; Hashimoto, K. *Mater. Sci. Eng. A* **2001**, *304*, 696–700.
92. Katagiri, H.; Meguro, S.; Yamasaki, M.; Habazaki, H.; Sato, T.; Kawashima, A.; Asami, K.; Hashimoto, K. *Corros. Sci.* **2001**, *43*, 171–182.
93. Hashimoto, K.; Katagiri, H.; Habazaki, H.; Yamasaki, M.; Kawashima, A.; Izumiya, K.; Ukai, H.; Asami, K.; Meguro, S. *Mater. Sci. Forum* **2001**, *377*, 1–8.
94. Mehmood, M.; Zhang, B. P.; Akiyama, E.; Habazaki, H.; Kawashima, A.; Asami, K.; Hashimoto, K. *Corros. Sci.* **1998**, *40*, 1–17.
95. Sweitzer, J. E.; Scully, J. R.; Bley, R. A.; Hsu, J. W. P. *Electrochem. Solid State Lett.* **1999**, *2*, 267–270.
96. Sweitzer, J. E.; Shiflet, G. J.; Scully, J. R. *Electrochim. Acta* **2003**, *48*, 1223–1234.
97. Lucente, A. M.; Scully, J. R. *Electrochem. Solid State Lett.* **2007**, *10*, C39–C43.
98. Lucente, A. M.; Scully, J. R. *Corros. Sci.* **2007**, *49*, 2351–2361.
99. Goldman, M. E.; Unlu, N.; Shiflet, G. J.; Scully, J. R. *Electrochem. Solid State Lett.* **2005**, *8*, B1–B5.
100. Choi, G. S.; Kim, Y. H.; Cho, H. K.; Inoue, A.; Masumoto, T. *Scr. Met. Mater.* **1995**, *33*, 1301–1306.
101. Inturi, R. B.; Szklarskasmialowska, Z. *Corrosion* **1992**, *48*, 398–403.
102. Fujimoto, S.; Hayashida, H.; Shibata, T. *Mater. Sci. Eng. A* **1999**, *267*, 314–318.
103. Ryan, M. P.; Williams, D. E.; Chater, R. J.; Hutton, B. M.; McPhail, D. S. *Nature* **2002**, *415*, 770–774.

## 3.21 Corrosion of Noble Metals

**S. B. Lyon**

Corrosion and Protection Centre, School of Materials, The University of Manchester, Oxford Road, Manchester M13 9PL, UK

This article is a revision of the Third Edition article 6.1 by G. W. Walkiden and R. A. Jarman, volume 1, pp 6:3–6:27,  
© 2010 Elsevier B.V.

<b>3.21.1</b>	<b>Introduction</b>	2206
<b>3.21.2</b>	<b>Properties</b>	2206
3.21.2.1	Silver and Gold	2206
3.21.2.2	Platinum Group Metals	2208
3.21.2.2.1	Platinum–rhodium	2209
3.21.2.2.2	Alloys of platinum with other PGMs	2209
3.21.2.2.3	Dispersion strengthened alloys	2209
<b>3.21.3</b>	<b>Thermodynamic Behavior</b>	2209
3.21.3.1	Silver	2209
3.21.3.2	Gold	2210
3.21.3.3	Platinum Group Metals	2210
<b>3.21.4</b>	<b>Corrosion and Electrochemistry</b>	2212
3.21.4.1	Silver	2212
3.21.4.1.1	Anodic processes	2212
3.21.4.1.2	Atmospheric corrosion and tarnishing	2213
3.21.4.2	Gold	2214
3.21.4.2.1	Anodic processes	2214
3.21.4.2.2	Gold extraction	2214
3.21.4.2.3	Dealloying and nanoporous materials	2215
3.21.4.3	Platinum Group Metals	2215
3.21.4.3.1	Anodic processes	2215
3.21.4.3.2	Platinum extraction and secondary recovery	2216
3.21.4.3.3	Cathodic processes: Hydrogen evolution	2216
<b>3.21.5</b>	<b>High temperature Properties</b>	2217
3.21.5.1	Silver and Gold	2217
3.21.5.2	Platinum Group Metals	2217
<b>3.21.6</b>	<b>Selected Applications</b>	2218
3.21.6.1	Chemical Process Equipment	2218
3.21.6.1.1	Linings	2218
3.21.6.1.2	Bursting discs	2218
3.21.6.1.3	Spinnerets	2218
3.21.6.2	High temperature Materials	2219
3.21.6.2.1	Molten glasses and salts	2219
3.21.6.2.2	Metal joining	2219
3.21.6.2.3	Furnace windings	2219
3.21.6.2.4	Temperature measurement	2220
3.21.6.2.5	Gas turbine applications	2220
3.21.6.3	Dental and Medical Applications	2220
3.21.6.3.1	Dental restorations	2220
3.21.6.3.2	Medical sensing and electrodes	2221
3.21.6.4	Electrical Contact Materials	2221
3.21.6.5	Anodes	2221
3.21.6.5.1	Dimensionally stable anodes	2221
3.21.6.5.2	Cathodic protection	2222
<b>References</b>		2222

## Glossary

**Noble metal** A metal generally characterized by having relatively positive potentials and low corrosion rates when immersed in an aqueous environment by virtue of its relative thermodynamic stability with respect to its simple hydrated ions in solution (and not solely by its passivity).

**PGMs** The platinum group of metals that comprises: platinum, palladium, rhodium, ruthenium, osmium and iridium; or (PGM) a single element of that group.

**Sterling silver** An alloy containing at least 92.5% silver plus other (unspecified) alloying additions, commonly copper. In the United Kingdom, this level of purity is the minimum standard guaranteed by hallmark.

**Troy ounce** A historic unit of measurement common in medieval Europe and said to derive from the city of Troyes, France; approximately equal to 31.1 g. Currently used in the weighing, trading, and description of precious metals and jewels.

### 3.21.1 Introduction

The group of noble metals comprises adjacent elements from the second and third row of the transition metals and from groups 8b (platinum group metals – PGMs) and 1b (silver and gold) of the periodic table. They are characterized by their exceptional resistance to corrosive attack by a wide range of liquid and gaseous substances and their relative stability at high temperatures, conditions under which base metals would be rapidly oxidized. This resistance to chemical and oxidative attack arises principally from the inherent, high thermodynamic stability of the noble metals. Apart from gold (which does not form an oxide in aqueous media), in other noble metals a thin film of adsorbed oxygen or oxide may form under oxidizing or anodic conditions, which can enhance their corrosion resistance via passivity. In some materials, for example silver in halide solutions, salt films can accomplish a similar passivation effect.

Their high initial cost, combined with a mechanical strength which is generally inferior to that of the base metals, results in only a limited number of corrosion-related applications for the noble metals, and they are as used only as sheaths, linings, or coatings, for example,

electrodeposits. However, noble metals have some critical applications, for example, equipment for fine chemical and pharmaceutical production, for fiber drawing, in the glass industry, and for crystal growth.

Silver is produced in a number of countries, generally as a by-product from mining other materials, particularly lead, zinc, copper, nickel, and gold, although some significant primary mines operate in Australia, Mexico, and Russia. (Basic information regarding physical and mechanical properties, application, and production of the noble metals were obtained from the references listed.) The largest producers are in Latin America (e.g., Peru, Mexico, Chile), while China, Australia, and Eastern Europe also produce significant quantities. Gold is mined as a primary product in a number of countries (e.g., South Africa, Australia, Ghana), but is also produced as a secondary product from other mining operations (e.g., Peru, Indonesia). By far, the majority (>80%) of the PGMs are produced from primary resources in South Africa and Russia, with lesser amounts from secondary resources. [Table 1](#) shows estimated supply and demand figures for all the noble metals. Note the relatively small volumes of material recovered. In years of excess of supply over demand, stocks are built-up, which are then released when demand exceeds supply. This is demonstrated for ruthenium demand in 2006. Noble metals are subject to large fluctuations in price according to market demands.

### 3.21.2 Properties

Although in the majority of their applications the choice of noble metals is determined by their chemical property rather than by their physical and mechanical properties, some consideration of the latter is necessary. Therefore, important physical and mechanical properties are reported in [Tables 2 and 3](#).

#### 3.21.2.1 Silver and Gold

Silver in the fully annealed state is a soft, ductile metal, which is easily fabricated into the very wide range of forms employed in industry by the normal metal-working techniques such as drawing, spinning, rolling, etc. Silver work-hardens appreciably during fabrication. The mechanical strength of silver is markedly affected by an increase in temperature and falls to about 25% of the initial value of cold, hard-worked silver when the metal is heated to just over 200 °C. Silver has the highest electrical and thermal conductivities of all



**Table 1** Estimated supply/demand and average prices for noble metals in 2006

<i>Metal</i>	<i>Supply (tons)</i>	<i>Demand (tons)</i>	<i>Volume (m<sup>3</sup>)</i>	<i>Average Price (\$/oz: \$/kg)</i>	<i>\$/kg</i>
Silver	26 900	–	2569	11.5	370
Gold	3 400	–	176	635	20 450
Platinum	218	218	9.18	1140	36 650
Palladium	259	213	21.6	320	10 290
Rhodium	27.1	27.6	1.98	4550	146 300
Ruthenium	26 (est.)	41.5	3.11	195	6 200
Iridium	–	3.94	0.174	350	11 250
Osmium	–	<0.1	<0.004 5	–	–

Basic information regarding physical and mechanical properties, application, and production of the noble metals were obtained from the references listed.

Source: Matthey, J. *Platinum Metals Market Review*; 2007.

**Table 2** Physical properties of the noble metals

<i>Property</i>	<i>Ag</i>	<i>Au</i>	<i>Ru</i>	<i>Rh</i>	<i>Pd</i>	<i>Os</i>	<i>Ir</i>	<i>Pt</i>
Atomic number	47	79	44	45	46	76	77	78
Relative atomic mass	107.9	196.9	101.1	102.9	106.4	190.2	192.2	195.1
Room temperature structure	fcc	fcc	hcp	fcc	fcc	hcp	fcc	fcc
Density (mg m <sup>-3</sup> )	10.49	19.32	12.45	12.41	12.02	22.61	22.65	21.45
Melting point (K)	1234	1337.6	2523	2236	1825	3300	2716	2045
Boiling point (K)	2438	3130	4423	3970	3237	5285	4701	4100
Resistivity ( $\times 10^{-6} \Omega \text{ cm}$ )	1.59	2.06	6.80	4.33	9.93	8.12	4.71	9.85
Thermal conductivity (W m <sup>-1</sup> K <sup>-1</sup> )	419	311	105	150	76	87	148	73

Source: The PGM database. Available at: [www.platinummetalsreview.com/jmpgpm/](http://www.platinummetalsreview.com/jmpgpm/)

HSC 6.1: *Thermochemical Database*; Outotec, 2007.

**Table 3** Room temperature mechanical properties of the noble metals and some alloys

<i>Metal (annealed)</i>	<i>Melting point (K)</i>	<i>Proof stress at 0.2% (MPa)</i>	<i>Ultimate tensile strength (MPa)</i>	<i>Elongation (%)</i>	<i>Young's modulus (GPa)</i>
Silver	1234	40	180	60	82
Gold	1337.6	30	120	70	72
Ruthenium	2523	370	430	3	420
Rhodium	2236	80	700	15	315
Palladium	1825	50	190	40	115
Osmium	3300	Brittle	Brittle	Brittle	555
Iridium	2716	235	1100	10	515
Platinum	2045	45	150	40	170
+5% Rhodium	2098	55	210	35	170
+10% Rhodium	2123	65	310	35	180
+20% Rhodium	2173	80	480	30	215
+30% Rhodium	2193	95	510	30	–
+40% Rhodium	2213	100	580	30	–
Pt–10Rh + dispersed ZrO <sub>2</sub>	2123	240	355	30	190

Source: The PGM database. Available at: [www.platinummetalsreview.com/jmpgpm/](http://www.platinummetalsreview.com/jmpgpm/)

the metals, and these properties are sometimes utilized for specialist applications. Silver is available in several grades, including fine silver, the normal commercial product containing a minimum of 99.95% silver, and

chemically pure silver containing a minimum of 99.99% silver, used for catalytic and special purposes where the presence of certain trace impurities may adversely affect its resistance to corrosion.

Silver is available in many standard forms – sheet, strip, foil of thicknesses down to 0.013 mm, rod, wire down to 0.013 mm diameter, gauze, tubes, bimetal as silver-clad copper or phosphor-bronze, and many others. It is easily fabricated by the normal techniques of rolling, spinning, drawing, etc., and readily binds to itself by fusion-welding using argon-arc welding. Flame welding may be used, but the resulting welds are often not as satisfactory, owing to the possibility of oxygen absorption while the metal is molten, followed by embrittlement by hydrogen. Fine silver filler rods may be used, and hammering the weld fillet down to the contour of the surrounding metal produces a very strong joint.

Gold is an extremely soft and ductile metal and exhibits little work hardening during deformation. Applications of gold are almost entirely restricted to thin linings or electrodeposits on base-metal equipment. It is available for industrial purposes in a grade containing a minimum of 99.9% gold in a wide range of forms – sheet, foil, tube, wire, etc. It is easily fabricated, and when it is being joined to itself, it may be fusion-welded with an oxy-hydrogen flame or hammer-welded at temperatures well below the melting point.

### 3.21.2.2 Platinum Group Metals

Pure platinum is soft, ductile, and easily fabricated, although its mechanical properties are affected by the degree of cold working and the presence of impurities or alloying constituents. In its applications, it is frequently alloyed with other PGMs; the melting points of its alloys with Rh, Ir, Os, and Ru being higher than the parent metal, those with Pd being lower. In most cases, the strength, rigidity, hardness, and resistance to corrosion are improved by alloying. Contamination with certain base metals (e.g., iron), however, can lead to embrittlement and failure of platinum and its alloys and, for example, if steel tongs are used to handle platinum at high temperatures, then they should be platinum-tipped to avoid iron pick-up.

The PGMs have a range of often unique properties that find critical use in a number of key applications, for example, in automotive catalysts, chemical catalysts, electronics, and jewelry; however, such applications are outside the scope of this chapter. Apart from palladium, the other PGMs are seldom used in isolation for corrosion-resistant applications, mainly because of their cost and availability. Palladium has very similar properties to platinum but is less corrosion resistant. Its remarkable ability to absorb large quantities of hydrogen is used in hydrogen permeation

membranes and in similar applications such as solid-state hydrogen reference electrodes. Iridium and osmium are characterized by their extreme densities, their high melting points, and their low ductility and high hardness, which are sometimes utilized in specialist corrosion and wear-resistant applications for hard alloys: for example, the traditional use of iridium–osmium tipped fountain pens and precision pivots and bearings. Rhodium, ruthenium, and iridium are used as alloying additions to platinum in order to improve the mechanical and physical properties. Iridium is used in specialist equipment for fine crystal growth (e.g., in electronics), especially from 1600 to 1900 °C. Both iridium and osmium form oxides that are volatile at modest temperatures, which, in the case of osmium, forms and volatilizes at room temperature.

Platinum is available as sheet, foil down to 0.0064 mm thick, tube, rod, wire down to 0.0064 mm diameter, wire down to 0.001 mm diameter, and clad on thin sections of base metals, for example, copper, nickel, Inconel, etc. Platinum, palladium, and the normal alloys of platinum used in industry are easily workable by the normal techniques of spinning, drawing, rolling, etc. To present a chemically clean surface of platinum and its alloys after fabrication, they may be pickled in hot concentrated hydrochloric acid to remove traces of iron and other contaminants; this is important for certain catalytic and high temperature applications. In rolling or drawing thin sections of platinum, care must be taken to ensure that no dirt or other particles are worked into the metal, as these may later be chemically or electrolytically removed, leaving defects in the platinum.

When platinum or its alloys are joined, properties of the weld or solder must be such that it is no less corrosion- or oxidation-resistant for the application in question than the parent metal. Platinum and its alloys are readily joined to themselves and to certain base metals, for example, iron, nickel, and copper. The principal methods for joining platinum are as follows

1. Fusion welding, using a platinum or alloy filler rod of the same composition as the parent metal and a shielded electric arc or an oxy-hydrogen flame (an oxy-acetylene flame may cause carbon pick-up by the molten metal). The weld fillets are then cold hammered to the contours of the surrounding metal to provide a strong joint.
2. Platinum and rhodium–platinum alloys when cleaned are readily hammer-welded to themselves and to each other at temperatures in the range 800–1000 °C. The welds so produced are completely homogeneous.

3. Fine gold, copper, silver–palladium, or platinum–palladium–gold–copper alloys may be used to solder platinum to itself and to its alloys, or to steels, nickel, etc. No fluxes are used, and soft solders should not be employed.

#### 3.21.2.2.1 Platinum–rhodium

Rhodium alloys readily with platinum in all proportions, although the workability of the resulting alloy decreases rapidly with increasing rhodium content. Alloys containing up to about 40% rhodium, however, are workable and find numerous applications. Alloys that contain more than 40% rhodium, while very difficult to fabricate, are almost immune from attack by oxidizing acids. The Pt–10Rh alloy is particularly resistant to attack by free wet chlorine such as that produced by the combustion of halogenated organic vapors.

The resistance of rhodium–platinum alloys to corrosion is about the same as, or slightly better than, that of pure platinum, but they are much more stable at high temperatures. They have excellent resistance to creep above 1000 °C, a factor which largely determines their extensive use in the glass industry, where continuous temperatures sometimes exceeding 1500 °C are encountered. Rhodium additions to platinum reduce appreciably the volatilization of pure platinum at high temperatures.

#### 3.21.2.2.2 Alloys of platinum with other PGMs

Iridium alloys with platinum in all proportions and alloys containing up to about 40% iridium are workable, although considerably harder than pure platinum. The creep resistance of iridium–platinum alloys is better than that of rhodium–platinum alloys at temperatures below 500 °C. Their stability at high temperatures, however, is lower, owing to the higher rate of formation of a volatile iridium oxide. Additions of ruthenium increase the hardness of platinum substantially, but the limit of workability is reached at about 15% ruthenium. Apart from a somewhat greater tendency to oxide formation at temperatures above 800 °C, the resistance to corrosion of ruthenium–platinum alloys is comparable with that of iridium–platinum alloys of similar composition.

#### 3.21.2.2.3 Dispersion strengthened alloys

Platinum–rhodium alloys are used extensively in high temperature applications for crucibles and related equipment, especially in the glass industry. The increasing cost of rhodium and platinum provides a strong driver to reduce overall costs, and this

has led to the development of a range of oxide dispersion strengthened alloys and composite alloys using, for example, platinum coatings on palladium cores.<sup>1</sup> The most common formulation is of zirconia-dispersed Pt–10Rh alloy<sup>2</sup> with somewhat higher room temperature strength than Pt–10Rh and 2–3 times the creep rupture properties of Pt–40Rh at 1400 °C (Table 3).

### 3.21.3 Thermodynamic Behavior

The behavior of the noble metals (indeed all metals) in different environments is determined by three principal factors:

1. their relative thermodynamic stability (nobility);
2. the formation of passive protective films;
3. their tendency to form complex ions in solution.

In the absence of species that form soluble complex ions, the noble metals are extremely resistant to corrosion by aqueous solutions of alkalis, salts, and acids. However, the resistance of silver to oxidizing acids is generally lower than that of the other noble metals, while in halogen acids, it forms a protective film of insoluble halide. Silver also differs from the other noble metals in forming a sulfide tarnish film in the presence of reduced sulfur compounds. Where complexing species are present and they stabilize the metal ions in solution (e.g., cyanide) the noble metals will corrode.

#### 3.21.3.1 Silver

Silver, with a standard electrode potential  $E_{\text{Ag}^+/\text{Ag}} = 0.79 \text{ V}$ , is exceeded in nobility only by gold and the PGMs. The Pourbaix diagram for silver (Figure 1) shows that at potentials below about 0.4 V and in the absence of complexing ions, silver is immune to attack over almost the whole pH range.

The situation is different in the presence of complexing agents, such as cyanide, or with species with which silver forms an insoluble salt, such as chloride. Thus, the presence of halides (with the exception of fluoride) substantially increases the zone of passivity, because of the formation of halide salt films as passivation layers;<sup>1</sup> at 25 °C, the solubility product of AgCl is  $1.7 \times 10^{-10}$ , of AgBr is  $5.0 \times 10^{-13}$ , and AgI is  $8.5 \times 10^{-17}$ ; AgF is soluble. Silver will also passivate in solutions containing sulfate. However, in the presence of sulfide, silver can form Ag<sub>2</sub>S tarnish films, even in the absence of air.

Silver, therefore, is thermodynamically stable in reducing acids, for example, hydrochloric acid, acetic

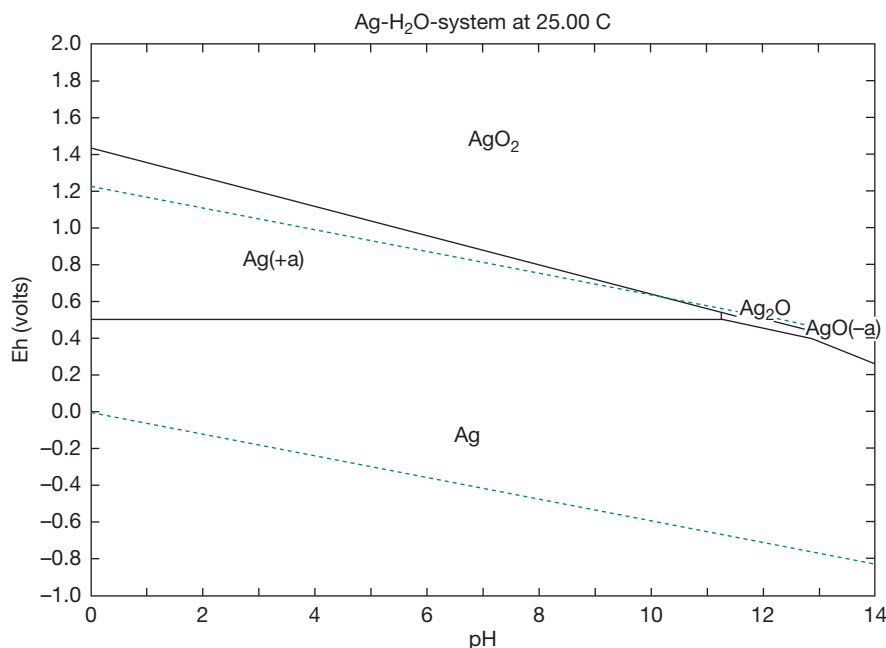


**Figure 1** Pourbaix ( $E$ -pH) diagram for silver at a metal ion concentration of  $10^{-5}$  M. Reproduced from *HSC 6.1: Thermochemical Database*; Outotec, 2007.

acid, phosphoric acid, provided oxidizing substances are absent. Oxidizing acids, for example, nitric acid, hot sulfuric acid at concentrations exceeding 80%, and reducing acids containing oxidizing agents will be corrosive to silver, and the diagram shows that an extensive zone of corrosion occurs at elevated potentials in the acid region. When silver is passivated by a halide film, as is formed for example in hydrochloric acid, the film is tenacious, self-healing, and highly insoluble. However, such films are easily reduced, for example, by galvanic coupling to a less noble metal such as zinc, aluminum, and passive stainless steels and nickel-based alloys. In such instances, silver will continuously corrode. In highly alkaline solution, silver corrodes only within a narrow region of potential, provided complexants and oxidants are absent. It is thus suitable to handle aqueous solutions of sodium or potassium hydroxides at all concentrations; it is also unaffected by fused alkalis.

### 3.21.3.2 Gold

The high resistance of gold to attack by a very wide range of corrosive media results from its exceptional thermodynamic stability in aqueous conditions. The Pourbaix diagram for gold (Figure 2) shows immunity from attack over the whole range of pH values and, uniquely, gold's zone of thermodynamic stability

includes the entire region of water stability; thus, it is immune from corrosion in aerated water. Gold, however, is easily complexed, and its solubility in hydrochloric acid containing an oxidizing agent (e.g., nitric acid) results from a combination of high redox potential and the formation of chloroaurate complex ions ( $\text{AuCl}_4^-$ ). The unstable  $\text{Au}^+$  ion and the easily reducible  $\text{Au}^{3+}$  ion also readily form stable complexes. Gold is unaffected in alkaline solutions, but in the presence of cyanides the soluble  $\text{Au}(\text{CN})_2^-$  ion is readily formed by air oxidation. This reaction forms the basis for the extraction of gold from its ores on an industrial scale.

### 3.21.3.3 Platinum Group Metals

All the six PGMs are highly resistant to corrosion by most acids, alkalis, and other chemicals. As may be seen from the potential-pH diagram (Figure 3), platinum is immune to attack at almost all pH levels, although it will corrode slowly in aqua regia (concentrated hydrochloric acid + nitric acid). It should also be noted that platinum is significantly less noble than gold and is covered by an oxide film in air (unlike gold, which is oxide free).

Platinum is unaffected by most organic compounds, although some compounds may catalytically decompose or become oxidized on a platinum surface at

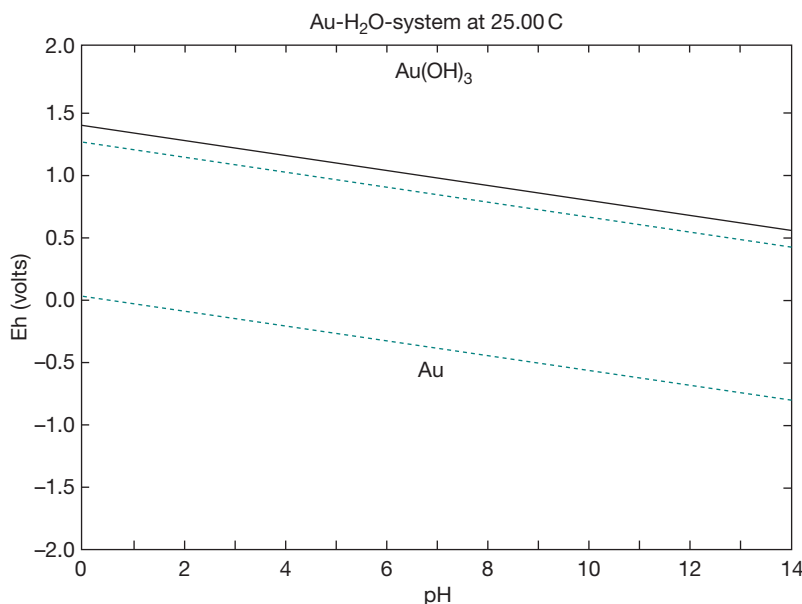


**Figure 2** Pourbaix diagram for gold at a metal ion concentration of  $10^{-5}$  M. Reproduced from *HSC 6.1: Thermochemical Database*; Outotec, 2007.

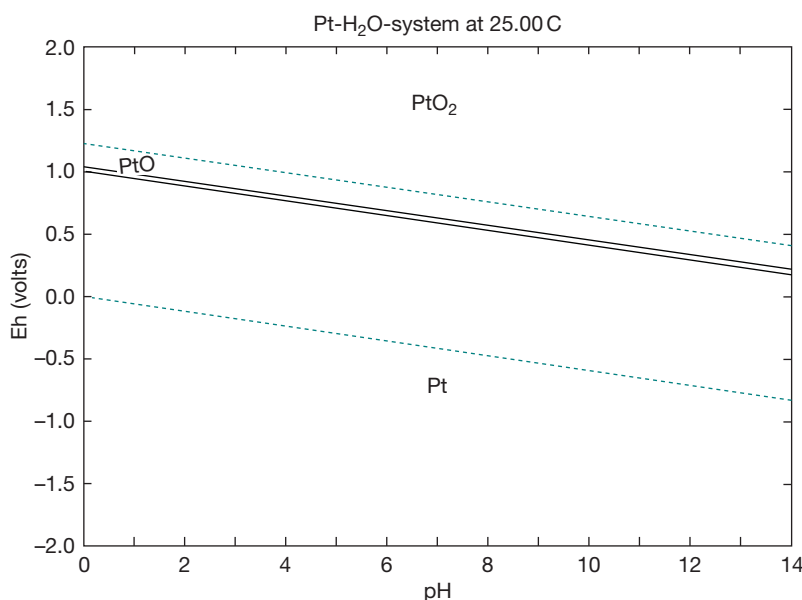


**Figure 3** Pourbaix diagram for platinum at a metal ion concentration of  $10^{-5}$  M. Reproduced from *HSC 6.1: Thermochemical Database*; Outotec, 2007.

elevated temperatures, resulting in an etched appearance of the metal.

Compared with platinum, palladium is significantly less noble, as can be seen from its Pourbaix diagram (Figure 4), where an extended passive oxide region is notable (PdO) and simple  $\text{Pd}^{2+}$  aquo-ions are stable at low pH and high potential (compare with platinum). However, palladium is relatively stable in the presence

of aqueous solutions of all pH values with the exception of strong oxidizing agents and complexing substances. Nonoxidizing acids, for example, acetic, oxalic, hydrofluoric, and sulfuric acids, have no effect on the metal at ordinary temperatures. Strongly oxidizing acids, however, for example, hydrochloric acid containing nitric acid, rapidly attack palladium. Dilute nitric acid attacks palladium only slowly, but the metal

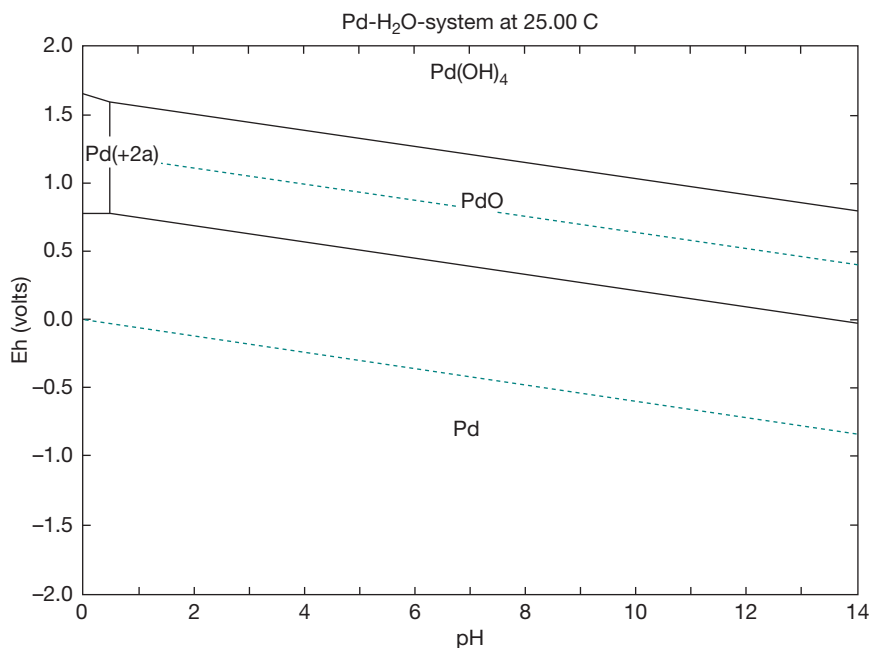


**Figure 4** Pourbaix diagram for palladium at a metal ion concentration of  $10^{-5}$  M. Reproduced from *HSC 6.1: Thermochemical Database*; Outotec, 2007.

is rapidly corroded by the concentrated acid. Alloys of palladium with platinum, however, retain most of the corrosion resistance of platinum. In ordinary atmospheres, palladium is resistant to tarnish, but some discoloration due to sulfide-film formation may take place in industrial atmospheres containing sulfur dioxide. Alkaline solutions, even in the presence of oxidizing agents, are without significant effect.

The resistance of rhodium and iridium to chemical attack is very similar to that of platinum, although with a wider domain of stability, particularly, at low pH in oxidizing solution. Additions of rhodium or iridium to platinum generally raise the overall corrosion resistance of the alloy to a very wide range of reagents. Like the other noble metals, in the absence of complexing agents both rhodium and iridium are stable in aqueous solutions at all pH values. Both metals are unattacked by alkalis, acids or oxidizing agents in aqueous solution, although oxidizing molten salts (e.g., potassium nitrate) are more corrosive. Iridium, in particular, has excellent resistance to fused lead oxide, silicates, and molten copper and iron at temperatures up to 1500 °C.

Ruthenium and osmium are decidedly less noble than the other four elements in the platinum group. Both exist in numerous valency states and very readily form complexes. Ruthenium is not attacked by water or noncomplexing acids, but is easily corroded by oxidizing alkaline solutions, such as peroxides and

alkaline hypochlorites. Osmium forms a volatile (and toxic) oxide at room temperature in air, and hence, should be handled with care.

### 3.21.4 Corrosion and Electrochemistry

There is great interest in the electrochemistry of the noble metals; many of them having scientifically interesting and sometimes unique properties that can result in commercially useful attributes, for example, in electrocatalysis. However, it is impossible to provide a fully comprehensive review in this section and it is not even attempted. Thus, the general electrochemistry of the materials is only superficially considered here. From the perspective of corrosion, one of the most interesting and potentially valuable effects is the substantial reduction in the corrosion rate of passive alloys (i.e., stainless steels) as a consequence of the addition of small amounts of noble metal. For further detailed information the reader is referred to the separate chapter on cathodic modification of stainless steels and titanium.

#### 3.21.4.1 Silver

##### 3.21.4.1.1 Anodic processes

Silver generally corrodes anodically below the reversible oxygen potential, unless an insoluble



oxide or salt is formed. When silver is used as an anode in sulfuric acid solutions, its behavior shows an analogy with that of lead. Silver sulfate,  $\text{Ag}_2\text{SO}_4$ , is first formed, and this acts as a passive film.<sup>3</sup> When the potential is raised the sulfate is oxidized to  $\text{AgO}$ , which may be cathodically reduced back to  $\text{Ag}_2\text{SO}_4$  at a potential lower than that required for its initial formation. When made anodic in nitrate solutions, silver generally dissolves quantitatively as  $\text{Ag}^+$ , and this forms the basis of the electrorefining techniques widely used in the industry. Similar considerations apply to the anodic behavior of silver in cyanide solutions, where silver forms a cyanide complex. In chloride solutions, silver anodes become covered with a layer of silver chloride.<sup>4</sup> The anodic oxidation and reduction of silver in alkaline solutions is of interest in battery applications, and a few percent of alloying additions of palladium or gold improve the capacity of silver oxide electrodes.<sup>5</sup>

Silver is not generally resistant to sulfidizing environments, as is commonly demonstrated by the atmospheric tarnishing of silver (see below), generally the formation of a sulfide film of varying thickness. The aqueous corrosion of silver in sulfide solution was studied using electrochemical and analytical methods in order to elucidate the mechanisms.<sup>6</sup> Under anodic polarization, silver initially forms  $\text{Ag}_2\text{S}$ , which is then further oxidized to  $\text{Ag}_2\text{O}$  at higher potentials. The limiting anodic current density was found to be proportional to the sulfide concentration in solution, and this was thought to be due to diffusion of  $\text{SH}^-$  ion to the silver surface. The reaction rate increased as the pH increased, which is consistent with the change in speciation of  $\text{SH}^-$  ion in solution; little effect on corrosion rate was found with dissolved oxygen content. X-ray diffraction and Raman spectroscopy indicated the formation of  $\text{Ag}_2\text{S}$  as the main reaction product.

#### 3.21.4.1.2 Atmospheric corrosion and tarnishing

Silver is traditionally used decoratively and functionally in fine cutlery and tableware and is valued for its high luster and long life. It has also been widely used in electrical contact applications because of its high conductivity. Although silver is stable to oxidation, it forms a tarnish film in atmospheres containing inorganic or organic sulfur species and chlorides. This dulls the surface and detracts from appearance; the film also increases contact resistances. Atmospheric levels below 0.1 ppm of  $\text{H}_2\text{S}$ ,  $\text{SO}_2$ , and  $\text{HCl}$  are sufficient to tarnish silver at measurable growth rates. Dry nitrogen atmospheres stops tarnish film growth, which

suggests that the process is electrochemical and occurs in a thin adsorbed water layer on the metal surface and requires air as oxidant.<sup>7</sup> Long chain organic molecules containing sulfur were also found to strongly interact with silver surfaces, giving tarnish films of similar composition to those found in  $\text{H}_2\text{S}$ .<sup>8</sup>

The sulfidation of silver was studied in a tubular reactor, with well-controlled mass transfer characteristics. In dry air,  $\text{H}_2\text{S}$  slowly reacted with silver at a constant rate, independent of the flow. The mechanism is surface controlled, and was found to involve atmospheric oxygen; the rate being increased significantly in the presence of an alternative oxidant ( $\text{NO}_x$ ). In humid air, corrosion was over 1000 times faster, with the kinetics now controlled by mass transfer of  $\text{H}_2\text{S}$  in the gas phase.<sup>9</sup> In a series of comprehensive studies, the effect of carbon oxysulfides ( $\text{COS}$ ) was also investigated and it was concluded that the sulfidation of silver by  $\text{COS}$  was at least as significant as by  $\text{H}_2\text{S}$ ; the detailed mechanisms of film growth were also determined.<sup>10</sup>

Significant research effort has been expended on preventing (or at least reducing) the kinetics of the tarnishing process. These apply one of three strategies: coating the silver, alloying the silver, or use of a tarnish (corrosion) inhibitor. In the electronics sector, electroplating with gold is commonly used in order to limit corrosion of contacts and consequent increase in contact resistance, and is generally a successful solution. However, if the excellent appearance of decorative silver is required, gold plating (i.e., a gilt finish) is not acceptable.

A number of treatments have been considered for tarnish protection, including palladium or rhodium plating (importantly the latter causes very little color change on silver), tarnish inhibitors incorporated into commercial polishes (commonly using organic thiols),<sup>11</sup> treatments with lacquers or plasma-polymerized coatings, and formation of self-assembled monolayers.<sup>12</sup> In a comparative evaluation of their performance, the commercial tarnish inhibitors were found not to provide significant protection, while the most effective treatment was an organic lacquer, followed by rhodium plating and the self-assembled monolayer treatment.<sup>13</sup>

The search for a tarnish-resistant silver alloy has been ongoing for at least 70 years with, until recently, comparatively little success. Although alloys of silver that substitute some of the copper content for palladium, nickel, zinc, or tin do tarnish more slowly than standard sterling silver,<sup>14</sup> they have no compelling advantage. Novel formulations for decorative silver alloys are constrained by the need to stay

within the purity level for hallmarked sterling silver (i.e., more than 92.5% silver content). Until recently, no novel alloy had significant proven advantages in this application. However, an alloy containing germanium has been shown to be relatively resistant to sulfide tarnishing, and is now marketed as 'Argentium'.<sup>15</sup> The improved surface properties are due to preferential oxidation of germanium, resulting in a continuous protective oxide layer, and the high diffusivity of germanium, which permits the layer to be reestablished rapidly if damaged.

### 3.21.4.2 Gold

#### 3.21.4.2.1 Anodic processes

Gold is thermodynamically stable to corrosion in ordinary aerated noncomplexing environments, and, of course, it neither tarnishes in the atmosphere nor in biological fluids. It is, therefore, ideal for applications in the decorative, medical and dental (*in vivo*), and electrical (contacts and connectors) areas. It is also used extensively (as is platinum) as a nonreactive electrode substrate for laboratory electrochemical studies of redox reactions of species in solution, however, such applications are not within the scope of this discussion.

The anodic oxidation of gold itself is of interest (indeed it is among the most studied of oxidation processes), as it can elucidate generic mechanisms for film formation and metal dissolution under anodic dissolution. In general terms, on anodic polarization in noncomplexing electrolytes, for example, sulfate, perchlorate, hydroxide, etc., gold will reversibly passivate by forming an oxide/hydroxide film above about +1.4 V (SHE) at pH 0. Thus, in sulfuric acid gold dissolves transiently to the Au(I) species but rapidly passives forming a film of hydroxide,<sup>16</sup> containing Au(III) species consisting generally of Au(OH)<sub>3</sub>. Evidence for lower oxides is no longer convincing. Conway's extensive and thorough review describes in detail the adsorption and oxidation on noble metal surfaces.<sup>17</sup> Unlike conventional corrosion, anodic oxidation on gold proceeds predominantly by surface chemical processes, involving submonolayer adsorption of hydroxide and oxide species (hydroxide electrolytes) that eventually grow by coalescence and thickening, eventually forming a macroscopic multilayer hydrous oxide film, probably by field assisted ion migration. In the presence of other anions, a competitive chemisorption with, for example, HSO<sub>4</sub><sup>-</sup>, ClO<sub>4</sub><sup>-</sup>, Cl<sup>-</sup>, occurs, which inhibits the onset of surface oxidation. Studies using scanning tunneling microscopy (STM) and atomic

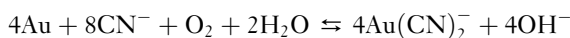
force microscopy (AFM) on single-crystal gold surfaces has shown the development of single-atom dimensioned pits, and have demonstrated that atomic rearrangement (or dissolution) is more difficult from atom terraces than from edges.<sup>18</sup>

In solutions where gold forms a soluble complex ion, gold may dissolve or may passivate (depending on the concentration of the complexing ion and the potential). On anodic polarization in acidic chloride solutions, gold initially dissolves, due to formation of the AuCl<sub>4</sub><sup>-</sup> ion, at potentials greater than about +1.3 V (SHE, pH = 0), depending on the chloride ion concentration; no evidence is seen for dissolution in the Au(I) state. At higher potentials greater than about +1.6 V, gold passivates forming an oxide film.<sup>19</sup> In alkaline cyanide solutions (pH = 13), which are of obvious interest for gold extraction and in electroplating, dissolution proceeds above about -0.66 V (SHE) by competitive adsorption of the cyanide ion on gold, followed stepwise by single-electron transfer and then adsorption of another cyanide ion, leading to the formation of the Au(CN)<sub>2</sub><sup>-</sup> ion. No convincing evidence for formation of the Au(III) state, Au(CN)<sub>4</sub><sup>-</sup>, is found at higher potentials, instead passivation terminates dissolution at potentials above about +0.38 V (SHE, pH = 13) due to formation of an Au(OH)<sub>3</sub> film.<sup>20</sup>

In addition to cyanide and chloride, gold forms complexes with a number of other common species in acid or alkaline conditions, including thiosulfate, thiocyanate, thiourea, sulfite, bromide, and iodide. The anodic dissolution of gold in these environments was reviewed by Nicol in 1980.<sup>21</sup> In view of the toxicity of cyanide, there is obvious interest in using alternative leaching agents for gold recovery, and thiourea, thiocyanate, and bromide processes have been considered. Of more academic interest is the surface chemistry and electrochemistry of gold in the presence of sulfur-containing species, where many detailed studies have been carried out; however, these are beyond the scope of this section.

#### 3.21.4.2.2 Gold extraction

Since the late nineteenth century, most recovery of gold from crushed ore has been via the MacArthur-Forrest cyanidation process. This utilizes the stability of the gold cyanide complex ion (Au(CN)<sub>2</sub><sup>-</sup>:  $K = 10^{-38}$ ) to dissolve gold, which may then be recovered by electrodeposition or via zinc dust (Merrill-Crowe process).<sup>22,23</sup> The principle dissolution reaction is given by Elsener's equation:



For the sake of efficient extraction and to minimize loss of cyanide as volatile HCN, the leaching is done ideally at pH close to 10.5. The cyanidation process requires an oxidant to be present (usually dissolved oxygen), and the efficiency of extraction is reduced if insufficient oxidant is present. Other factors that reduce leaching efficiency (present in so-called 'refractory' ores) include the presence of sulfides, copper, iron, and zinc. Pretreatment of crushed ores is often required as is the use of additional oxidants (chemical or biological – i.e., sulfur oxidizing bacteria).

Once leached, the gold has to be recovered from the relatively dilute cyanide solution. One of the largest gains in efficiency of gold recovery from more dilute cyanide liquors is the absorption of the gold complex on activated carbon, and a variety of processes are in use, for example, the carbon-in-pulp process.<sup>22</sup> For cyanide processes, there is also the considerable problem of cyanide disposal. To counter this, various other processes have been considered, with some in active development. These include the use of bromine, chlorine, thiourea, and thiosulfate. Although these have advantages, much research needs to be done to optimize them. Currently, therefore, the cyanide process is generally still the most economical.

#### 3.21.4.2.3 Dealloying and nanoporous materials

Dealloying as a corrosion phenomenon has been known for over 100 years, the classical case being dezincification (i.e., selective dissolution of zinc from brass leaving a copper-rich, mechanically weak, layer). Dealloying typically occurs in an alloy where at least two of the components have relatively well-separated equilibrium potentials in the environment. In such cases, where the alloy is polarized between these values, the less noble component of the alloy is selectively dissolved, leaving the remaining more noble component. This mechanism invariably produces layers that have profoundly altered mechanical properties usually of very low fracture toughness (i.e., they are brittle). These have been found to have profound influence on many stress-corrosion cracking processes in alloys.<sup>24,25</sup> Although it was not called such, and the mechanism was not then known, dealloying was first developed as a process to produce porous nickel (by selective dissolution of aluminum from a nickel–aluminum alloy – Raney nickel), which is used a catalyst in various chemical processes.<sup>26</sup>

Selective dissolution in, for example, Cu–Au and Ag–Au alloys has been well studied in order to determine generic aspects of the dealloying mechanism in

these and other more commercially important alloys. Increasingly, controlled dealloying is being used in its own right to produce tailored nanoporous gold substrates for chemical sensing and catalytic applications. The ordered intermetallic alloy Cu<sub>3</sub>Au is an excellent template to study dealloying phenomena. At low overpotentials for copper dissolution, scanning tunneling microscopy has demonstrated 2-dimensional clustering of gold, while at higher overpotentials the surface is mostly covered by gold and effectively passivates in two dimensions, although small regions of material continue to dissolve generating 3-dimensional roughness and porosity.<sup>27</sup> Above a threshold potential, global surface roughening occurs, which is strongly influenced by adsorption of species such as sulfate, chloride, and alkyl-thiols on the surface of the gold atoms. This process has been modeled using a continuum model such that porosity during dealloying develops on a length scale that is characteristic of the surface aggregation (diffusion) of the noble metal atoms.<sup>28</sup>

The formation of nanoporosity in Ag<sub>0.7</sub>Au<sub>0.3</sub> and Ag<sub>0.65</sub>Au<sub>0.35</sub> alloys during dealloying in perchloric acid has been studied. Without halide addition, the pores were of the order of 8 nm, while with chloride, bromide, and iodide, the pore size changed, respectively, to 17, 16, and 67 nm. This coarsening can be interpreted as an increase in surface mobility of the gold atoms in the presence of halides.<sup>29</sup> Gold substrates with tailored nanostructures can thus be prepared by controlled electrochemical dealloying. Although development is still required, in particular, to resist coarsening of the porosity during application, nanoporous gold substrates have many potential applications, for example, in electrocatalysis,<sup>30</sup> fuel cells,<sup>31</sup> and chemical and biochemical sensing.<sup>32</sup>

#### 3.21.4.3 Platinum Group Metals

##### 3.21.4.3.1 Anodic processes

The PGMs are characterized by their intrinsic thermodynamic stability and in this they are similar to gold. The key difference between them is that gold remains oxide-free in aerated noncomplexing aqueous environments; however, the PGMs are predicted to retain an oxide film that contributes to their passivity. The PGMs have many important properties and applications in catalysis, which are beyond the scope of this section.

For many years, it was assumed that platinum and other PGMs were oxide-free in air and in aerated

solutions; however, the advent of rapid cyclic sweep voltammetry techniques has allowed the elucidation of the redox processes between platinum and oxygen, and this research was reviewed extensively by Conway in 1995.<sup>17</sup> After initial adsorption of oxygen-containing species, a place exchange mechanism takes place between Pt and O to effectively develop a 2-dimensional and then a 3-dimensional oxide film. Oxygen adsorption, reduction, and place exchange occur via a variety of steps, with the rate-determining processes for each part of the mechanism determined; however, a full discussion is well beyond the scope of this chapter. Like gold oxide, formation on, and dissolution of, platinum occurs as a function of crystallography. On low-index surfaces, oxide formation passivates the surfaces more easily, resulting in lower dissolution rates at higher potentials, while nanofaceted surfaces dissolve more rapidly, which is the evidence that atomic edges and corners are the main locations of dissolution.<sup>33</sup> Perhaps the most interesting finding is that although like gold, anion adsorption plays a role, it appears to be much less important, which reflects the increased stability of PGMs to complexing species such as halides, cyanides, etc.

PGMs are, therefore, extremely resistant to dissolution in almost all aqueous environments under almost all conditions. For example, and in contrast to gold and silver, high pressures and temperatures are required for the dissolution of platinum in cyanide to occur at significant rates. Table 4 shows the corrosion resistance of the PGMs in various environments; importantly, PGMs are one of the few non-polymeric materials that can successfully handle fluorides and HF without significant problems.

**Table 4** Corrosion resistance of PGMs in various environments

Environment	Ru	Rh	Pd	Os	Ir	Pt
HF (40%, 20 °C)	A	A	A	A	A	A
HCl (36%, 100 °C)	A	A	B	A	A	B
H <sub>2</sub> SO <sub>4</sub> (96%, 100 °C)	A	B	C	A	A	A
HNO <sub>3</sub> (62%, 100 °C)	A	A	D	D	A	A
HCl + HNO <sub>3</sub> (aqua regia, 100 °C)	A	A	D	D	A	D
H <sub>3</sub> PO <sub>4</sub> (100 °C)	A	A	B	D	A	A
HClO <sub>4</sub> (100 °C)			C			A
KCN (100 °C)			D			C
NaOCl (100 °C)	D	B	C	D		A

A – No attack; B – Minor attack but can be used; C – Major attack and cannot be used; D – Rapid attack.

Source: Darling, A. S. In *Electronic Design Materials*; Waller, W. F., Ed.; Macmillan, 1971; Chapter 3.

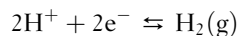
### 3.21.4.3.2 Platinum extraction and secondary recovery

As noted earlier, ambient temperature and pressure cyanide leaching is not effective for the recovery of PGMs from crushed ore bodies. Thus, after mining and concentration by gravity and/or froth flotation, the materials are smelted on a copper–nickel matte (sulfide-rich intermediate), which is further separated into copper and nickel anode materials and are purified electrolytically. The PGMs remain within the (insoluble) anode slime and were traditionally recovered using wet chemical methods, including sequential precipitation. Current technology uses a liquid–liquid solvent extraction technique that is more efficient, offering enhanced recovery and lower cost.<sup>34</sup>

Efficient secondary recovery of PGMs from, for example, vehicle exhaust catalysts, and recovery and separation from other metals from, for example, electronic circuit boards, is critical for their sustainable use. In such cases, higher temperatures and pressures, as well as more corrosive solutions, can be used. Several leaching processes have been proposed, the majority using strong hydrochloric acid containing an oxidant (i.e., aqua regia)<sup>35,36</sup> at high temperature and pressure leaching with cyanide.<sup>37,38</sup> The pressure cyanide processes are better developed and can, under ideal conditions, extract over 95% of the platinum and palladium and about 85–90% of rhodium.

### 3.21.4.3.3 Cathodic processes: Hydrogen evolution

The PGMs are well-known for their outstanding electrocatalytic activity, especially for the evolution of hydrogen. The exchange current density for the overall hydrogen evolution reaction



varies by about 10 orders of magnitude from mercury and lead to platinum (Table 5).

The large exchange current density of PGMs implies a correspondingly low overpotential for hydrogen evolution. This property finds extensive applications in electrocatalysis in general, and in hydrogen storage and release, hydride batteries, and fuel cells, where nanosized PGM particles are used, to increase surface area and to reduce the quantity of expensive material used. An important application is noble metal alloying of passive metals (stainless steels and titanium), where small amounts (0.2%) of noble metals (typically Pt, Pd, or Ru) causes spontaneous passivation in acids by increasing the cathodic rate of hydrogen evolution.

**Table 5** Exchange current densities for the evolution of hydrogen on various metals in various environments

Environment	Metal	Exchange current density, $i_o$ ( $A\text{ cm}^{-2}$ )
1 M $\text{H}_2\text{SO}_4$ at 20 °C	Palladium	$10^{3.0}$
	Platinum	$10^{3.1}$
	Rhodium	$10^{3.6}$
	Iridium	$10^{3.7}$
	Nickel	$10^{5.2}$
	Gold	$10^{5.4}$
	Titanium	$10^{8.2}$
	Aluminium	$10^{-10.0}$
0.1 M HCl at 20 °C	Lead	$10^{12.0}$
	Mercury	$10^{12.3}$
	Platinum	$10^{-2.6}$
	Palladium	$10^{-3.2}$
	Silver	$10^{-5.6}$
	Gold	$10^{-5.6}$
	Iron	$10^{-6.0}$
	Nickel	$10^{-6.0}$
	Copper	$10^{-6.8}$
	Lead	$10^{-13.2}$

Source: Parsons, R. *Handbook of Electrochemical Constants*; Butterworths, 1959.

Bockris, J. O. M.; Reddy, A. K. N. *Modern Electrochemistry*, 2nd ed.; Springer, 1998.

The PGMs are somewhat susceptible to a reduction in their catalytic activity as a consequence of 'poisoning' with other surface active species, including metallic impurities with lower exchange current density, which will tend to plate out onto cathodically polarized surfaces.<sup>39</sup> On the other hand, noble metal oxides, in particular, ruthenium and iridium oxide, are almost as effective cathodic electrocatalysts as platinum and palladium; they are almost immune to poisoning by metal ions in solution.<sup>40,41</sup>

### 3.21.5 High temperature Properties

#### 3.21.5.1 Silver and Gold

Owing to their relatively low melting points and mechanical strengths, silver and gold find very few applications at elevated temperatures. Silver below its melting point has considerable resistance to oxide-film formation, but molten silver dissolves appreciable quantities of oxygen, which precipitates as silver oxide or bubbles dispersed throughout the metal when the metal solidifies. Gold is not subject to oxide-film formation at any temperature up to its melting point, but may be covered by a thin adsorbed layer of oxygen. The absence of an oxide film enables gold to be pressure-welded at room temperatures.

#### 3.21.5.2 Platinum Group Metals

The excellent resistance of platinum, rhodium, and iridium to oxidation at high temperatures finds numerous applications in technology, in particular, in the form of platinum-based alloys. Osmium and ruthenium form volatile oxides and are therefore not suitable for high temperature use on their own.

Platinum, while it does not form a measurable oxide film, is covered by thin adsorbed layer of oxygen,<sup>42</sup> which volatilizes at an increasing rate as its temperature rises above 1000 °C, via a volatile metastable oxide.<sup>43</sup> In the presence of flowing oxygen or air, the rate of volatilization is considerably increased. Rhodium, iridium, and palladium exhibit oxide-film formation, at a temperature as low as 600 °C.<sup>44</sup> However, palladium oxide dissociates above 870 °C, the metal then appearing bright up to its melting point. Absorption of oxygen without film formation occurs, however, and palladium increases in weight. Platinum loses more mass via this volatilization mechanism compared with rhodium and iridium, from 900 to 1200 °C, but their volatilities are about the same at temperatures around 1300 °C. However, below 1100 °C, alloys of platinum with rhodium and palladium lose less mass than do pure platinum, but palladium-platinum alloys absorb oxygen detrimentally. Rhodium-platinum alloys at high temperatures show no preferential loss of either metal, and are widely used. Iridium-platinum alloys show greater loss of weight on heating in air, because of the greater rate of oxidation of iridium and the higher volatility of the oxide of this metal. Iridium is thus lost preferentially from iridium-platinum alloys. Selected properties of the PGM oxides are shown in Table 6.

Volatilization of platinum and its alloys at high operating temperatures may be substantially reduced by avoiding contact with air or oxygen, especially if the environment is flowing, for example, due to convection currents. This may be achieved by completely embedding the metal in high-purity alumina refractory; flame-sprayed coatings, for example, are effective in preventing free circulation of air over the metal. Only alumina that is largely free from silica and other oxides that are more easily reduced can be used, otherwise contamination and embrittlement of the platinum may result from partial reduction of such oxides.

Grain growth of platinum and its alloys when operating continuously at high temperatures is often responsible for failure of the metal, resulting from weaknesses developed by large intercrystal boundaries. This defect may be largely eliminated by the use of



**Table 6** Selected properties of PGM oxides

Oxide	Molar Mass	Density	Pilling–Bedworth ratio	Properties at high temperature
RuO <sub>2</sub>	133.1	6.97	2.31	Dissociates at 930–950 °C
RuO <sub>4</sub>	165.1		–	Sublimes at 40 °C
RhO	118.9			Dissociates above 1000 °C
Rh <sub>2</sub> O <sub>3</sub>	253.8	8.2	1.87	Dissociates above 1100 °C
PdO	122.7	8.31	1.66	Dissociates above 870 °C
OsO <sub>2</sub>	222.2	11.29	2.33	Dissociates at 650 °C
OsO <sub>4</sub>	254.2	4.95	6.09	Boils without decomposition at 131 °C
IrO <sub>2</sub>	224.2	11.69	2.24	Decomposes at 400 °C
PtO	211.1	14.9	1.56	Dissociates above 1100 °C
Pt <sub>3</sub> O <sub>4</sub>	649.3	8.89	2.68	Decomposes when heated
PtO <sub>2</sub>	227.3	10	2.63	Thermally unstable

Source: Savitskii, E. M. *Physical Metallurgy of Platinum Group Metals*; Elsevier, 1979.

sintered metal produced by powder-metallurgical techniques, or by the incorporation of a small amount of a refractory oxide, carbide, or nitride in powder form in the body of the metal, such as zirconia-dispersed platinum–rhodium alloys.<sup>44</sup>

### 3.21.6 Selected Applications

#### 3.21.6.1 Chemical Process Equipment

##### 3.21.6.1.1 Linings

Traditionally, noble metal linings were used in chemical and pharmaceutical production as linings for steel and copper equipment and occasionally as vessels, condensers, and other equipment. However, such uses have generally been superseded either by more cost-effective coating materials (e.g., tantalum, glass lining), or alternative construction materials (e.g., stainless steel, graphite).

Linings may be of two types: either loose or bonded. Loose linings provide good contact between vessel and lining – adequate for good heat transfer – but are not suitable to be used in reduced pressure as the gap between vessel and lining will expand causing the lining to fail. Traditionally, silver linings for chemical plant were used particularly for highly alkaline environments in which silver has excellent performance; where used, silver linings are generally 0.5–1 mm thick. Solid silver construction, 1–2.5 mm thick, may be employed for condenser coils, distillation heads, etc. Traditional bonded silver linings for mild steel or copper vessels are generally soldered *in situ* onto the walls of the vessel using a tin–silver solder. Such soft-soldered linings should not exceed 200 °C for their maximum continuous operating temperature. However, bonded linings are suitable

for operation under vacuum conditions, and provide excellent heat-transfer characteristics.

Platinum, rhodium–platinum, and iridium–platinum alloys are employed in line and sheath autoclaves,<sup>45</sup> reaction vessels and tubes, calorimeters,<sup>46</sup> and a range of other laboratory and commercial equipment.<sup>47</sup> Linings are generally 0.13–0.38 mm thick, and for certain applications coextruded platinum-lined nickel-based alloys (Inconel 625), or other metal reactor or cooling tubes are fabricated. In such cases, the platinum is bonded to the base metal, but in all other instances platinum linings are of the ‘loose’ type.

##### 3.21.6.1.2 Bursting discs

Bursting discs are a simple and effective (fail-safe) protection against overpressurization in a closed system. The protection of pressure vessels containing corrosive materials presents a special problem for the selection of bursting discs as bursting discs should not corrode (and hence weaken) until they are required to fracture under an overpressure. For this reason, corrosion resistant, high reliability bursting discs have been traditionally fabricated from noble metals,<sup>48</sup> although other cost-effective alternatives now exist (e.g., tantalum or niobium). The recommended maximum temperatures for continuous use are 80 °C for gold, 150 °C for silver, 300 °C for palladium, and 450 °C for platinum.

##### 3.21.6.1.3 Spinnerets

The spinning of viscose rayon for the production of yarn, tire cord, and staple fiber involves the extrusion of an alkaline solution of cellulose into an acid bath. The orifices through which individual fibers are extruded are often extremely small – down to



30  $\mu\text{m}$  or less in diameter – and their dimensional accuracy must be maintained to a very high degree for long periods, while operating in two highly corrosive media simultaneously. Platinum–gold alloys are the traditional material of construction for rayon spinnerets, in particular, Au–30Pt + 0.5Rh as a grain-refining additive. This alloy has greater hardness, which permits a high polish to be produced in a scratch-resistant exit face, while the small grain size ensures that the holes produced have a high grade of uniform circularity. Other noble metal alloys for spinneret construction include rhodium–platinum, iridium–platinum, iridium–rhodium–platinum, ruthenium–platinum, ruthenium–palladium, and platinum–palladium. The use of these alloys in this application is being superseded by the introduction of tantalum, which has comparable corrosion resistance at lower cost.<sup>49</sup>

### 3.21.6.2 High temperature Materials

#### 3.21.6.2.1 Molten glasses and salts

A principal application of PGM metals is in the production of fine, optical glasses and glass fibers; platinum–alloy crucibles and spinnerets are generally resistant to molten glasses at temperatures from 1200 to 1500 °C, with continuous operation at 1400 °C. Traditionally, Pt–Rh alloys were used for this purpose with typically 10% Rh added to improve high temperature creep-rupture performance and to reduce evaporation loss. Useful gains in creep-rupture properties can be made using zirconia-dispersed materials, either of pure platinum or of Pt–10Rh alloy.<sup>2</sup> Materials may be used as sheet for fabricated metal crucibles, as thin foil liners for covering ceramic (i.e., alumina) crucibles, and as flame-sprayed coatings<sup>50</sup> on a ceramic substrate. Also, flame-sprayed or plasma-evaporated alumina coatings can be used to protect PGM materials from evaporation losses at high operation temperatures.<sup>51</sup>

Platinum is generally highly resistant to air-saturated oxide glasses because of the formation of a thin stable layer of oxide that passivates the metal.<sup>52</sup> Stressing during immersion in molten glass (and hence cracking the passive oxide) greatly increases the dissolution rate of the metal in the glass.<sup>53</sup> Under reducing conditions, for example, nonoxide glasses and/or with an inert gas atmosphere, platinum is much less resistant to molten glass, with increased dissolution and additional reaction to form embrittling intermetallic compounds.<sup>54</sup> Where platinum cannot be used, or where

even higher temperatures are required (1500–2000 °C), iridium crucibles can be used.<sup>55</sup>

Platinum crucible materials are also generally suitable for containing molten salts over similar temperature ranges as for molten glass. However, salts that can easily form complex ions with platinum will cause its corrosion; also, coupling to other metals can result in enhanced dissolution if it encourages the formation of the complex ionic species in the melt.<sup>56</sup> Platinum and iridium crucibles and equipment are extensively used in single crystal growth production from molten precursors.

#### 3.21.6.2.2 Metal joining

Solders and brazes (although the distinction is not clear, solders are useful for ‘lower’ temperatures, while brazes are suitable for ‘higher’ temperatures) are widely used materials for metal joining. Their key characteristics are that

1. their melting point is lower than the parent material to be joined;
2. a metallurgical bond, usually by intermetallic development or interdiffusion, is formed between the solder and the parent material.

One common formulation of a tin-based lead-free solder contains several percent silver and is more corrosion resistant than the material it replaces. For use in higher temperature, silver-based brazing alloys are widely used. In both cases, galvanic corrosion of the parent (joined) material should be considered as the joining alloy is commonly significantly more noble. Thus, where silver brazing alloys are used to join stainless steel, a narrow zone of corrosion on the stainless steel often occurs on subsequent exposure in tap water.<sup>57</sup>

PGM brazing alloys, commonly containing palladium with alloying additions, including gold, silver, nickel, copper, are also utilized. They have significant advantages, including high temperature strength and stability as well as corrosion resistance, and have been used to join stainless steels,<sup>58</sup> nickel-based superalloys,<sup>59</sup> and other refractory materials, with minimal corrosion problems. Their low vapor pressure gives them advantages in high vacuum systems, and their low toxicity (if nickel-free) gives them advantages as a dental brazing alloy.<sup>60</sup>

#### 3.21.6.2.3 Furnace windings

Rhodium–platinum alloys containing up to 40% Rh have been traditionally used in the form of wire or

ribbon in electrical resistance windings for furnaces to operate continuously at temperatures up to 1750 °C. Such windings are usually completely embedded in a layer of high-grade alumina cement or flame-sprayed alumina to prevent volatilization losses from the metal due to the free circulation of air over its surface. However, these types of furnace windings have been largely superseded by molybdenum disilicide materials, which are resistant in air at a similar temperature. For reducing (hydrogen) atmospheres, Pt–Rh alloy windings are still useful, although molybdenum metal windings may also be used at considerably lower cost.

#### 3.21.6.2.4 Temperature measurement

Until 1968, platinum–rhodium thermocouples (type S) were used as the standard interpolating thermometer in IPTS-68 (International Practical Temperature Scale of 1968) because of their good thermal stability. However, the present temperature scale ITS-90 (International Temperature Scale of 1990) now uses a Standard Platinum Resistance Thermometer.<sup>61</sup> The particular advantages of PGM materials in temperature measurement are, of course, their excellent stability to oxidation and corrosion. Thus, platinum resistance thermometers offer a more reliable temperature measurement than the traditional thermocouples up to around 600–650 °C and are unaffected by the environment. At higher temperatures, Pt/Pt–10Rh (type S) or Pt/Pt–13Rh (type R) thermocouples may be used for accurate temperature measurement in essentially all atmospheres up to 1450 °C. Both types of thermocouple have a short-term stability, typically better than 0.5 °C, with a long-term reproducibility of better than 2.0 °C. For higher temperatures up to 1800 °C, Pt–6Rh/Pt–30Rh (type B) thermocouples can be used.

#### 3.21.6.2.5 Gas turbine applications

Improvements to gas turbine operating efficiency require an increase in the gas temperature of the turbine and combustion chamber. Since most gas turbine materials are now optimized more for their high temperature strength and creep resistance, their hot corrosion and oxidation resistance has become relatively poorer. Platinum aluminide coatings have been developed, which, in combination with other coating types, offer improved performance for nickel-based superalloys.<sup>62</sup> Platinum, by substituting for nickel in the aluminide, eliminates chromium-rich precipitates from the outer coating layer and

limits the diffusion of refractory transition elements such as molybdenum, vanadium, and tungsten into the outer coating layer.<sup>63</sup>

### 3.21.6.3 Dental and Medical Applications

#### 3.21.6.3.1 Dental restorations

Generally, the noble metals, particularly gold, have excellent biocompatibility, and the use of gold and gold–palladium alloys in dental restorations is very common. However, they are too soft to be used on their own and require alloying (typically with copper, silver, and palladium, plus other minor components), and this increases corrosion susceptibility. There are a number of classification schemes for these alloys: First, based on their strength, and second, on their metal content. There are numerous alloys, many proprietary and many designed for specific aspects of the dental restoration task; the main classes are listed in Table 7.

The oral environment is corrosive and materials for use must be correspondingly corrosion resistant; thus, the general corrosion of dental alloys is of interest partly with a view to increase the service life of implants and partly for biocompatibility. The main issues are

1. tarnishing and discoloration, usually caused by foods and drinks that contain sulfur;<sup>64</sup>
2. galvanic corrosion between adjoining oral alloys of differing composition;<sup>65</sup>
3. galvanic corrosion caused by microsegregation of alloy components at grain boundaries or in the interdendritic regions in cast materials.

Failure modes exhibited include generation of expansive corrosion products causing disbonding of the implant, general thinning of the material, and cracking.

**Table 7** Classification for dental alloys

	<i>Yield stress (MPa)</i>	<i>Elongation (%)</i>
Type I	<140	18
Type II	140–200	18
Type III	200–340	12
Type IV	>340	10
Typical composition		
High noble	Au > 40% + total noble metals > 60%	
Noble	Total noble metals > 25%	
Base	Total noble metals < 25%	

Source: Wataha, J. C. *J. Prost. Dent.* **2002**, 87, 351–363.

Conventional mercury amalgam restorations are typically anodic to noble and more noble alloys and will corrode preferentially<sup>66</sup> and can lead to cracking. Therefore, care has to be taken in mixing restorative alloy materials. For example, cracking of gold crowns has been observed as a consequence of intergranular–interdendritic corrosion in association with corrosion of an underlying mercury-based amalgam alloy.<sup>67</sup> Electrochemical and corrosion tests in ammonium and sodium sulfide solutions, as a simulation of the oral environment, has demonstrated that the tarnishing is particularly related to the silver and copper contents of the alloys.<sup>68</sup> Generally, as might be expected, the higher the noble metal content of the alloy used, the more the corrosion resistant,<sup>69</sup> hence, selection of the correct restorative alloy is a balance between mechanical and other required properties and corrosion resistance.<sup>70</sup>

### 3.21.6.3.2 Medical sensing and electrodes

Unalloyed noble metal (or high noble metal content) body implants are used for a number of purposes, with generally few or no corrosion issues arising. Reference above has been made to the production of nanoporous gold electrodes of exceptionally high surface area. These have a number of potential applications in medical sensing; for example, insulin determination.

Noble metals, particularly platinum and platinum alloys, find use as electrode materials for *in vivo* nerve stimulation (e.g., heart, neural, auditory electrode implants, etc.). The applied potentials used are generally transient in nature (i.e., a pulse waveform), and significant corrosion of electrode materials can be observed. For example, Pt, Au, Rh, Ir, Pt–10Ir, and Pt–10Rh electrodes were severely corroded under a bipolar current pulse of  $1 \text{ A cm}^{-2}$ , while Rh was moderately attacked. At  $0.1 \text{ A cm}^{-2}$ , Au, Rh, and Ir were resistant to corrosion.<sup>71</sup> However, although examination of heart pacemaker electrodes has shown evidence of corrosion in all cases, in no case had this resulted in the failure of the implant.<sup>72</sup>

### 3.21.6.4 Electrical Contact Materials

High reliability electrical contacts are frequently plated with noble metals (Ag, Au, Pd, etc.) in order to limit any corrosion and consequent increase in contact resistance with time. This is because uncoated copper contact materials are particularly susceptible to corrosion and contact failure mechanisms involving vibration (e.g., in motor vehicles), giving rise to wear–fretting effects in addition to corrosion.

Silver coatings are liable to grow intrusive whiskers in sulfidizing, and to a lesser extent in chloridizing environments, although much less than copper or tin. The main environmental driver is the presence of hydrogen sulfide at or above 200 ppb, which can be reached, for example, in pulp and paper processing,<sup>73</sup> where significant failures have occurred.

Gold alloys and gold coatings are also extensively used for electrical contacts, especially in the electronics industry. Corrosion failure mechanisms are associated with the growth of gold shorts from cathodic conductors, especially where chloride ions are present. On anodically biased conductors, a voluminous reaction product of  $\text{Au}(\text{OH})_3$  is produced by anodizing.<sup>74,75</sup>

### 3.21.6.5 Anodes

#### 3.21.6.5.1 Dimensionally stable anodes

Nonconsumable anode materials are used extensively in electroplating, electrowinning, chlorine production, and water electrolysis (oxygen evolution) and have traditionally variously utilized silver, lead, magnetite, graphite, and noble metals. Of these, chlorine production by electrolysis of brine is among the most energy intensive and industrially important.

For chlorine evolution, platinum generally shows very low rates of attack, and platinum anodes can be used for both cathodic protection in seawater and for chlorine production at low overvoltage.<sup>76</sup> This attribute takes advantage of using platinum-coated titanium or niobium substrate materials; the substrates are stable to the conditions of electrolysis, while the electrode reaction (e.g., chlorine evolution) occurs on the platinum surface. At low current densities, the platinum can be corroded, especially at low pH; however, at high current densities, passivation of the platinum occurs and corrosion reduces considerably. However, the corrosion rate of platinum can be much higher if an alternating current component is present, as this tends to thicken the passive film. Rhodium and iridium are as resistant to anodic corrosion as platinum, but are more resistant to the influence of alternating currents.

The single most important advance in anodes for chlorine evolution is in the replacement of noble metal coatings on stable substrates with oxide coatings using ruthenium modified by iridium ('mixed metal oxides').<sup>77</sup> These provide efficient production of chlorine at low overvoltage, with no corrosion, provided the overpotential is kept below a critical value.<sup>78</sup> Such anodes are called 'dimensionally stable'

because, in principle, they do not need replacement throughout the life of the plant, provided they are operated within the correct parameters.<sup>79</sup> They are also responsible for a reduction of about 20% in the energy usage per unit of chlorine production.

Given the success of noble metal oxide-doped anodes in chlorine evolution, they are being trialed in a number of other applications that would benefit from improved electrocatalysis.

### 3.21.6.5.2 Cathodic protection

Although there are a wide range of possible anode systems for impressed current cathodic protection, noble metal-coated titanium mesh anodes have been used for many years in a wide variety of applications, including protection of reinforcement steel in concrete and cathodic protection systems in seawater (e.g., for vessels, etc.). In severe environments, or where the system requires a high driving voltage, platinum-coated niobium anodes are used because of the increased stability of niobium (compared with titanium) to chlorides. More recently, the use of noble metal oxide-coated electrodes has also become increasingly important, with their advantages of higher current density and increased lifetime under polarization.<sup>80</sup>

## References

- Rowe, M. S.; Heywood, A. E. *Mater. Des.* **1984**, *5*, 30–33.
- McGrath, R. B.; Badcock, G. C. *Platinum Met. Rev.* **1987**, *31*, 8–11.
- Jones, P.; Thirsk, H. R. *Trans. Faraday Soc.* **1954**, *50*, 732–739.
- Altukhov, V. K.; Shatalov, V. G. *Sov. Electrochem.* **1998**, *23*, 912–915.
- Grozdić, T. D.; Stojić, D. L. *J. Power Sources* **1999**, *79*, 1–8.
- Lee, J. I.; Howard, S. M.; Keller, J. J.; Cross, W.; Han, K. N. *Metall. Mater. Trans. B* **2001**, *32*, 895–901.
- Rice, D. W.; Peterson, P.; Rigby, E. B.; Phipps, P. B. P.; Cappell, R. J.; Tremoureux, R. *J. Electrochem. Soc.* **1981**, *128*, 275–284.
- Sinclair, J. D. *J. Electrochem. Soc.* **1982**, *129*, 33–40.
- Volpe, L.; Peterson, P. J. *Corros. Sci.* **1998**, *29*, 1179–1187, 1189–1196.
- Graedel, T. E. *J. Electrochem. Soc.* **1992**, *139*, 1963–1970.
- Karlucke, D.; Scholz, R. R.; Funk, M. J.; Baumgartner, M. E. *Galvanotechnik* **1992**, *83*, 1918–1926.
- Burleigh, T. D.; Gu, Y.; Donahey, G.; Vida, M.; Waldeck, D. H. *Corrosion* **2001**, *57*, 1066–1074.
- McEwan, J. J.; Scott, M.; Goodwin, F. E. In Proceedings of the South African Institute of Mining and Metallurgy, 8th International Corrosion Conference, Johannesburg 2006.
- Ray, K. W.; Baker, W. N. *Indust. Eng. Chem.* **1932**, *24*, 778–781.
- Johns, P. G.; Davis, S. In Proceedings of the 31st International Precious Metals Institute Conference 2007.
- Jirsa, F.; Buryanek, O. Z. *Z. Elektrochem. Angew. Physik. Chem.* **1923**, *29*, 126–135.
- Conway, B. E. *Prog. Surf. Sci.* **1995**, *49*, 331–452.
- Schneeweiss, M. A.; Kolb, D. M.; Liu, D.; Mandler, D. *Can. J. Chem.* **1997**, *75*, 1703–1709.
- Ye, S.; Ishibashi, C.; Shimazu, K.; Uosaki, K. *J. Electrochem. Soc.* **1998**, *145*, 1614–1623.
- Kirk, D. W.; Foulkes, F. R.; Graydon, W. F. *J. Electrochem. Soc.* **1978**, *125*, 1436–1443; *J. Electrochem. Soc.* **1979**, *126*, 2287–2288.
- Nicol, M. J. *Gold Bull.* **1980**, *13*, 46–55, 105–111.
- Marsden, J. O.; House, C. I. *The Chemistry of Gold Extraction*; Society of Mining Engineers, 2006.
- Prasad, M. S.; Mensah-Biney, R.; Pizarro, R. S. *Miner. Eng.* **1991**, *4*, 1257–1277.
- Sieradzki, K.; Kim, J. S.; Cole, A. T.; Newman, R. C. *J. Electrochem. Soc.* **1987**, *134*, 1635–1639.
- Newman, R. C.; Corderman, R. R.; Sieradzki, K. *Br. Corros. J.* **1989**, *24*, 143–148.
- Raney, M. US Patent 1,628,190, 1927.
- Moffat, T. P.; Fan, F.-R. F.; Bard, A. J. *J. Electrochem. Soc.* **1991**, *138*, 3224–3235.
- Erlebacher, J.; Aziz, M. J.; Karma, A.; Dimitrov, N.; Sieradzki, K. *Nature* **2001**, *410*, 450–453.
- Dursun, A.; Pugh, D. V.; Corcoran, S. G. *J. Electrochem. Soc.* **2003**, *150*, B355–B360.
- Jia, F.; Yu, C.; Ai, Z.; Zhang, L. *Chem. Mater.* **2007**, *19*, 3648–3653.
- Zhang, J.; Liu, P.; Ma, H.; Ding, Y. *J. Phys. Chem. C* **2007**, *111*, 10382–10388.
- Hu, K.; Lan, D.; Li, X.; Zhang, S. *Anal. Chem.* **2008**, *80*, 9124–9130.
- Komanicky, V.; Chang, K. C.; Menzel, A.; Markovic, N. M.; You, H.; Wang, X.; Myers, D. J. *J. Electrochem. Soc.* **2006**, *153*, B446–B451.
- Charlesworth, P. *Platinum Met. Rev.* **1981**, *25*, 106–112.
- Tyson, D. R.; Bautista, R. G. *Separ. Sci. Technol.* **1985**, *22*, 1149–1167.
- Gaita, R.; Al-Bazi, S. J. *Talanta* **1995**, *42*, 249–255.
- Kuczynski, R. J.; Atkinson, G. B.; Dolinar, W. J. In Proceedings of the TMS Fall Meeting, 1995; pp 527–541.
- Chen, J.; Huang, K. *Hydrometallurgy* **2006**, *82*, 164–171.
- Savadogo, O.; Amuzgar, K.; Piron, D. L. *Int. J. Hydrogen Energy* **1990**, *15*, 783–788.
- Blouin, M.; Guay, D. J. *J. Electrochem. Soc.* **1997**, *144*, 573–581.
- Kötz, E. R.; Stucki, S. J. *Appl. Electrochem.* **1987**, *17*, 1190–1197.
- Andreeva, V. V.; Shishakov, N. A. *J. Appl. Chem.* **1961**, *11*, 388–389.
- Alcock, C. B.; Hooper, G. W. *Proc. R. Soc. A* **1960**, *254*, 551–561.
- Raub, E.; Plate, W. Z. *Metall.* **1957**, *48*, 529–539.
- Ziemniak, S. E.; Guilmette, P. A.; Turcotte, R. A.; Tunison, H. M. *Corros. Sci.* **2008**, *50*, 449–462.
- Bailey, J. J.; Gehring, D. G. *Anal. Chem.* **1961**, *33*, 1760–1762.
- Rowe, M. S.; Heywood, A. E. *Platinum Met. Rev.* **1984**, *28*, 7–12.
- Barrell, J. D. *Platinum Met. Rev.* **1982**, *26*, 13–15.
- Butyagin, P. A.; Bakshiev, I. P.; Zakharova, R. I. *Fibre Chem.* **1997**, *29*, 251–252.
- Coupland, D. R. *Platinum Met. Rev.* **1993**, *37*, 62–70.
- Panfilov, P.; Bochegov, A.; Yermakov, A. *Platinum Met. Rev.* **2004**, *48*, 47–55.
- Le Haret, P. *Glass* **2003**, *80*, 345.

53. Rytvin, E. I.; Medovoi, L. A. *Mater. Sci.* **1976**, *11*, 488–490.
54. Rapin, C.; Vilasi, M.; Podor, R.; Carton, A.; Gaillard-Allemand, B.; Berthod, P.; Steinmetz, P. *Mater. Sci. Forum* **2004**, 461–464, 1125–1132.
55. Couderc, C.; Williams, P.; Coupland, D.; Matthey, J. *Glass* **2007**, *84*, 24–27.
56. Hara, M.; Shinata, Y.; Hashimoto, S. *Corros. Sci.* **1997**, *39*, 627–638.
57. Steffens, H.-D.; Wielage, B.; Brandl, W. *Welding J.* **1989**, *68*, 151–157.
58. Leinenbach, C.; Gelder, N.; Bissig, V.; Gattiker, F.; Klotz, U. E. *Sci. Technol. Welding Joining* **2007**, *12*, 708–717.
59. Bose, D.; Datta, A.; Rabinkin, A.; De Cristofaro, N. J. *Welding J.* **1989**, *65*, 23–29.
60. Bessing, C.; Bergman, M.; Sjögren, M. *Swed. Dent. J.* **1991**, *15*, 7–14.
61. Preston-Thomas, H. *Metrologia* **1990**, *27*, 3, 107.
62. Wing, R. G.; McGill, I. R. *Platinum Met. Rev.* **1981**, *25*, 94–105.
63. Tawancy, H. M.; Abbas, N. M.; Rhys-Jones, T. N. *Surf. Coat. Technol.* **1991**, *49*, 1–7.
64. Laub, L. W.; Stanford, J. V. *Gold Bull.* **1981**, *14*, 13–18.
65. Holland, R. I. *Eur. J. Oral Sci.* **1980**, *88*, 269–272.
66. Karov, J.; Hinberg, I. *J. Oral Rehabil.* **2001**, *28*, 212–219.
67. Odén, A.; Tullberg, M. *Acta Odontol. Scand.* **1985**, *43*, 15–17.
68. Angelini, E.; Zucchi, F. *Surf. Technol.* **1984**, *21*, 179–191.
69. Meyer, J.-M.; Reclaru, L. *J. Mater. Sci. Mater. Med.* **1995**, *6*, 534–540.
70. Upadhyay, D.; Panchal, M. A.; Dubey, R. S.; Srivastava, V. K. *Mater. Sci. Eng. A* **2006**, *432*, 1–11.
71. Johnson, P. F.; Hench, L. L. *Brain Behav. Evol.* **1977**, *14*, 23–45.
72. Parsonnet, V. P.; Villanueva, A.; Driller, J.; Bernstein, A. D. *Pacing Clin. Electrophysiol.* **1991**, *4*, 289–296.
73. Chudnovsky, B. H. In Proceedings of the Annual Holm Conference on Electrical Contacts, 2001, pp 140–150.
74. Frankenthal, R. P.; Becker, W. H. *J. Electrochem. Soc.* **1979**, *126*, 1718.
75. Frankenthal, J. P.; Kruger, J. *Gold Bull.* **1985**, *18*, 46.
76. Conway, B. E.; Novak, D. M. *J. Electroanal. Chem.* **1979**, *99*, 133–156.
77. Burke, L. D.; O'Neill, J. F. *J. Electroanal. Chem.* **1979**, *101*, 341–349.
78. Consonni, V.; Trasatti, S.; Pollak, F.; O'Grady, W. E. *J. Electroanal. Chem.* **1987**, *228*, 393–406.
79. Trasatti, S. *Electrochim. Acta* **2000**, *45*, 2377–2385.
80. Kroon, D. H.; Ernes, L. M. *Mater. Perform.* **2007**, *46*, 26–29.

## Further Reading

Cotton, S. A. *Chemistry of Precious Metals*; Springer, 1997.

The Silver Institute, Information resource about silver. [www.silverinstitute.org](http://www.silverinstitute.org)

The Gold Institute, Information resource about gold. [www.gold.org](http://www.gold.org)

Gold Bulletin, Current and back issues of this journal are freely available online at [www.goldbulletin.org](http://www.goldbulletin.org)

Platinum Metals Review, Current and back issues of this journal are freely available online at [www.platinummetalsreview.com](http://www.platinummetalsreview.com)

The PGM Database, Comprehensive physical, metallurgical and chemical data on the platinum group metals and their alloys available as a searchable online database and linked off the Platinum Metal Review homepage and also from: [www.noble.matthey.com](http://www.noble.matthey.com)

*Corrosion Handbook*; ASM International, 2008; Vol. 13B.

## 3.22 Corrosion of Passive Alloys: The Effect of Noble Metal Additions

**J. H. Potgieter**

School of Chemical and Metallurgical Engineering, University of the Witwatersrand, Johannesburg, South Africa

© 2010 Elsevier B.V. All rights reserved.

---

<b>3.22.1</b>	<b>Introduction</b>	2225
<b>3.22.2</b>	<b>Cathodic Modification and Passivation</b>	2225
<b>3.22.3</b>	<b>Origin of Cathodic Modification</b>	2226
<b>3.22.4</b>	<b>Requirements for Cathodic Modification</b>	2227
<b>3.22.5</b>	<b>Principle of Cathodic Modification</b>	2227
3.22.5.1	Active State	2227
3.22.5.2	Active–Passive State	2227
3.22.5.3	Passive State	2227
3.22.5.4	Transpassive State	2228
<b>3.22.6</b>	<b>Mechanism of Cathodic Modification</b>	2229
<b>3.22.7</b>	<b>Cathodic Modification of Cr and Cr-Based Alloys</b>	2230
3.22.7.1	Effect of the Addition of Noble Metals	2230
3.22.7.1.1	Cathodic modification	2230
3.22.7.1.2	Kinetic effect	2230
<b>3.22.8</b>	<b>Cathodic Modification of Stainless Steels</b>	2231
3.22.8.1	Addition of Noble Metals to Fe–Cr Stainless Steels	2231
3.22.8.2	Addition of Noble Metals to Fe–Cr–Mo Stainless Steels	2233
<b>3.22.9</b>	<b>Cathodic Modification of Fe–Cr–Ni Stainless Steels</b>	2235
3.22.9.1	Addition of Noble Metals to Fe–Cr–Ni Stainless Steels	2235
3.22.9.2	Addition of Noble Metals to Fe–Cr–Ni–Mo and Fe–Cr–Mn–Ni Stainless Steels	2236
3.22.9.3	Galvanic Coupling in Fe–Cr–Ni Stainless Steels	2237
<b>3.22.10</b>	<b>Cathodic Modification of Duplex Stainless Steels</b>	2237
<b>3.22.11</b>	<b>Surface Alloying with PGMs</b>	2239
3.22.11.1	Cathodically Modified Cr Coatings	2239
3.22.11.2	Surface Alloying in Fe–Cr Alloys	2240
3.22.11.3	Surface Alloying Fe–Cr–Ni Stainless Steel	2240
<b>3.22.12</b>	<b>Summary of the Effect of PGMs and other Noble Metals on the Corrosion Resistance of Cr-Based Alloys</b>	2241
<b>3.22.13</b>	<b>The Nature of the Passive Film on Cathodically Modified Alloys</b>	2242
<b>3.22.14</b>	<b>Russian Studies</b>	2242
<b>3.22.15</b>	<b>The Fe–40% Cr–PGM System</b>	2243
<b>3.22.16</b>	<b>Other Quaternary and Ternary Fe–Cr Alloys with PGMs</b>	2244
<b>3.22.17</b>	<b>Summary of the Current Observations about the State of Passive Film Compositions on Cathodically Modified Alloys</b>	2245
<b>3.22.18</b>	<b>Noble Metal Corrosion Resistance in Reducing Acids</b>	2246
3.22.18.1	Hydrochloric Acid	2246
3.22.18.2	Sulfuric Acid	2246
<b>3.22.19</b>	<b>Final Conclusions</b>	2247
<b>References</b>		2247

---



## Abbreviations

**SCE** Saturated calomel electrode  
**SHE** Standard hydrogen electrode

## Symbols

$i_p$  passive current density  
 $i_{cr}$  critical current density  
 $i_{co}$  corrosion current density  
 $i_{cath}$  current density of cathodic process  
 $i_{tr}$  transpassive current density  
 $E_{co}$  corrosion potential  
 $E_p$  passivation potential  
 $E_O^A$  anodic potential of base metal or alloy  
 $E_O^C$  potential of cathodic component  
 $E_{tr}$  transpassive potential

### 3.22.1 Introduction

Pt-group metals (PGMs), together with silver and gold, constitute the group known as noble metals. These metals find wide application in a number of different fields, such as catalysts, fuel cells and metal winning electrodes, dental alloys, and even semiconductors. The focus of this chapter will be limited to the addition of PGMs, and in some cases silver and gold, to Cr-based stainless steel alloys used in process industries where prevailing reducing acid conditions create major challenges for the corrosion resistance of equipment construction materials, and failures as a result of corrosion can create serious safety hazards and cause substantial maintenance and production losses. It will also not consider PGM-based alloys in which the majority of alloying elements consist of the PGM, although these alloys are becoming increasingly important for high temperature corrosion resistant applications. Two excellent reviews appeared recently<sup>1,2</sup> describing the manufacturing of such alloys, as well as their physical, mechanical, and corrosion properties.

Owing to the very specialized nature of the topic under discussion, it is not surprising that research on the addition of noble metals to alloys for the improvement of corrosion resistance, or cathodic alloying of materials, has not been widely investigated or described in literature. Another reason might be that the major producers of the PGMs used in the enhancement of corrosion resistance, namely Pd (Pd) and Ru (Ru), have traditionally been South Africa and Russia (old

USSR), and they are the obvious beneficiaries of an increased demand for their produce should this approach of adding PGMs to stainless steels markedly increase the demand for the elements in question. It seems that research work on this was mainly done by the Tomashov's group (in Russia), Higginson and others at Mintek (Council for Mineral Technology, South Africa), the University of the Witwatersrand in collaboration with Mintek, and Tjong and coworkers in Hong Kong. As a result, there has been little discussion of the topic in the literature, and no comprehensive review paper on the subject appeared to date. The present review, therefore, covers previous work carried out by various groups from different laboratories and, in addition, discusses some more recent results from the past two decades. Furthermore, this review will be restricted to aqueous corrosion in reducing acid media, and will not specifically consider high temperature corrosion resistance of cathodically modified stainless steels. Conclusions are drawn from earlier results, and possible areas for future research are outlined.

### 3.22.2 Cathodic Modification and Passivation

During the course of the past 50 years, a number of papers concerning the application of cathodic modification and the corrosion behavior of cathodically modified alloys have been published, especially by the Tomashov group in Russia. However, none of these provides a comprehensive description of the electrochemistry of the cathodic modification phenomenon and of the mechanisms involved. One of the purposes of this review, therefore, is to present in detail all aspects concerning the electrochemistry of cathodic modification. The practical applications of cathodic modification in different alloy systems, and the corrosion behavior of cathodically modified alloys in different acidic media, will be dealt with later in the review.

An examination of the mechanisms of corrosion processes by Tomashov<sup>3</sup> indicates that there are four possible ways in which corrosion-resistant alloys can be produced and the resistance of alloys against electrochemical attack increased, namely:

- an increase in the degree of thermodynamic stability;
- retardation of the kinetics of the cathodic processes;
- retardation of the kinetics of the anodic processes; and
- the production of stable passivating oxide layers.

The thermodynamic stability of commercial steels can be increased in only a limited number of cases, for example, Cr-containing steel can be alloyed with a nickel or molybdenum.<sup>3,4</sup> Cathodic reactions can be retarded in two ways: by the elimination of active cathodic impurities, such as iron or copper in zinc, from alloys and by the increase of overvoltage of the cathodic process, for example, by the alloying of manganese or zinc to magnesium alloys, and of arsenic or antimony to steel. Stable passivating oxide layers can be obtained by adding Cr, which is thermodynamically less stable than iron, to iron to produce stainless steel which owes its corrosion resistance to the formation of passivating oxide layers on the surface of the steel. Retarded cathodic reactions can change the polarization curves as shown in **Figure 1**.

The anodic reaction can be retarded as a result of an increase in the ability of the alloy to be passivated. This can be done in various ways, including the alloying of iron, nickel and ferronickel steels with Cr, or the introduction of active cathodes into the alloy, for example, the alloying of stainless steels and titanium with PGMs. The latter technique is known as cathodic modification.

### 3.22.3 Origin of Cathodic Modification

Cathodic modification is not widely known and practiced outside USSR, but it is by no means a new

discovery or concept. As early as 1911, Monnartz<sup>5</sup> reported that the rapid corrosion of Fe–Cr alloys in certain acids can be prevented either by the winding of a Pt wire around the sample used in the corrosion test, or by the alloying of the steel with Pt. Nobody seems to have shown much interest in this discovery until Tomashov *et al.*<sup>6</sup> first confirmed it in 1948, and then further developed the concept of ‘cathodic alloying’ in their work on stainless steels and titanium and its alloys. Other contributions have been made mainly by Stern and coworkers<sup>7–11</sup> and Cotton.<sup>12–15</sup>

In principle, passivity can be induced in a base metal or an alloy by the addition of a noble metal (one of the PGMs, gold, or silver) having a high cathodic exchange current density, provided that the passive region of the base alloy extends to potentials that are more negative than the redox potential of the environment. This is schematically represented in **Figure 2**, in which line A represents the cathodic polarization curve for the metal and B, the cathodically modified alloy. Hence, for metals and alloys that exhibit stable passivity at potentials sufficiently more negative than the existing hydrogen potential in the system, spontaneous passivation will be possible in the absence of any substance or compound more oxidizing than hydrogen ions. The effect of cathodic modification should therefore be most pronounced in nonoxidizing acid environments, for example, deaerated hydrochloric and sulfuric acids.

This conclusion has been confirmed by Greene *et al.*<sup>11</sup> who found that, while addition of PGMs to Cr

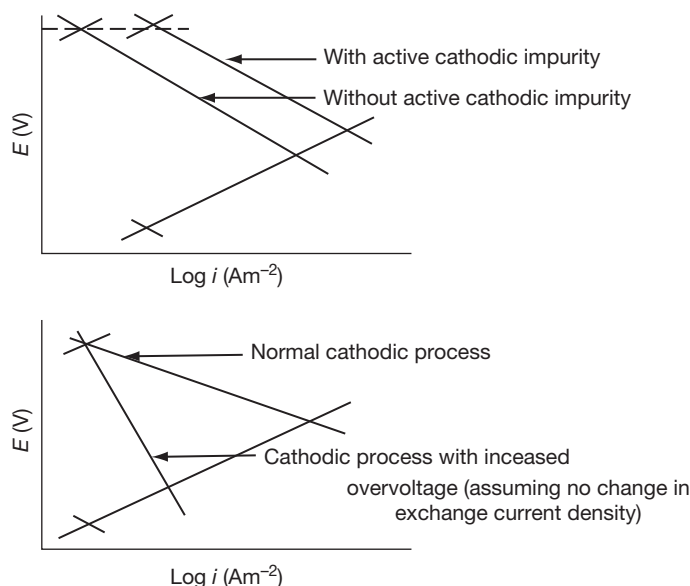


**Figure 1** Schematic representation of ways in which cathodic reactions can be retarded.

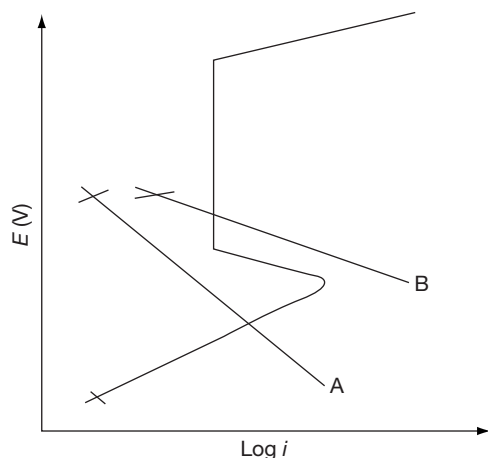


**Figure 2** Schematic illustration of the effect of cathodic modification. A is the cathodic polarization curve for the parent metal, while B is the cathodic polarization curve for the cathodically modified alloy.

in nonoxidizing acids (hydrochloric and sulfuric acids) improved its corrosion resistance, they had a detrimental effect in oxidizing acid (nitric acid) because the oxidizing acid increased the potential to a value in the transpassive range.

### 3.22.4 Requirements for Cathodic Modification

The basic conditions required for successful cathodic alloying can be summarized as follows<sup>3</sup>:

- The base alloy must have a small critical current density ( $i_{cr}$ ) that will be easily exceeded by the current of the hydrogen cathodic reaction on the added noble metal at the given passivation potential ( $E_p$ ).
- The passivation potential ( $E_p$ ) of the base metal must be sufficiently negative to allow the cathodic component that has been introduced to change the corrosion potential ( $E_{co}$ ) of the alloy to a value in the passive range that is more positive than ( $E_p$ ) but less positive than the potential associated with the onset of transpassive processes ( $E_{tr}$ ).
- The transpassive potential ( $E_{tr}$ ) of the base alloy should be sufficiently electropositive to allow a wide passive range.

Furthermore, the cathodic alloying component should itself satisfy certain basic conditions<sup>3</sup>: it should have a higher exchange current density  $i_0$  (and lower overvoltage) for the cathodic process of hydrogen evolution than the base metal or the alloy, and it should be corrosion resistant under the given

conditions. In nonoxidizing acids (such as sulfuric and hydrochloric acids), the conditions requiring a sufficiently negative passivation potential are satisfied by stainless steels, Cr-based alloys and titanium-based alloys, while the PGMs have the necessary high exchange current density,  $i_0$  (and low overvoltage), for hydrogen evolution.

### 3.22.5 Principle of Cathodic Modification

**Figure 3** presents schematic diagrams of the four distinct states that can be displayed by a system with an active–passive transition. The different states depend upon the relative efficiency of the cathodic process (or processes) in each case.

#### 3.22.5.1 Active State

When the rate of the cathodic process is relatively low (as shown by the solid line in **Figure 3(a)**), the system will be in the active state. The metal or alloy undergoes stable active dissolution at a potential of  $E_{co}$  with a current density of  $i_{co}$ , and the following conditions prevail:

$$E_O^A < E_{co} < E_p \text{ and } i_{cath}(E_p) < i_{cr}$$

The active state is established spontaneously. Hence, if an external perturbation causes the system to move momentarily into the passive potential range, the active state will be spontaneously reestablished.

#### 3.22.5.2 Active–Passive State

For a higher, intermediate rate of the cathodic process (as shown by the solid line in **Figure 3(b)**), there are three possible conditions for the system. These conditions are given at the three points A, B, and C at which the cathodic line and anodic curve intersect.

At potential C ( $E_p$ ), anodic dissolution of the metal or alloy occurs at a relatively high corrosion rate. At potential B ( $\sim E_p$ ), the system is in an unstable state rarely observed in practice. At potential A ( $> E_p$ ), the system is in the passive state, and the corrosion rate is very low. If the system is perturbed, the different conditions of the active–passive state will not be spontaneously reestablished.

#### 3.22.5.3 Passive State

For a high rate of the cathodic process (as shown by the solid line in **Figure 3(c)**), the anodic and cathodic

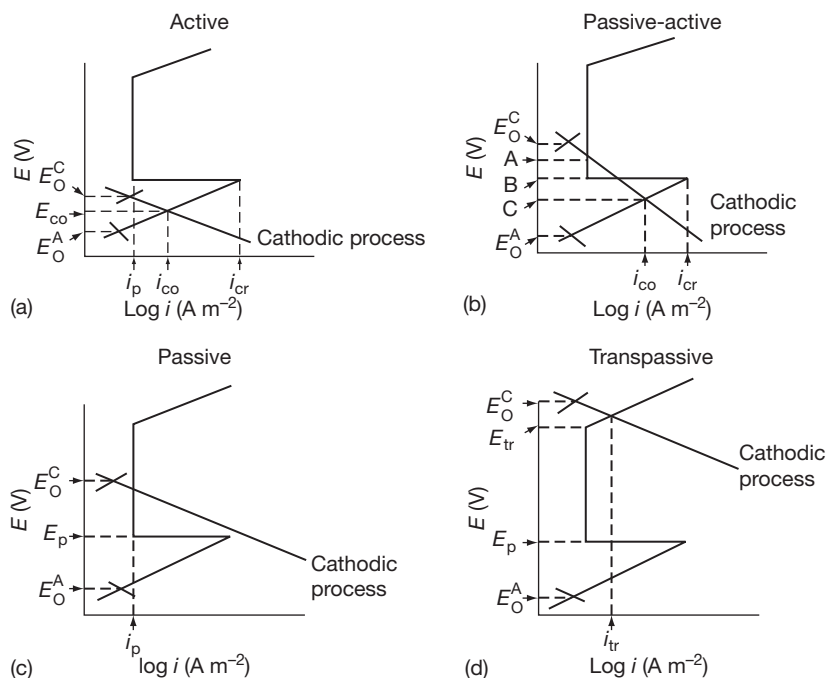


**Figure 3** Different active-passive status in an alloy system.

curves intersect at only one point. The system is in a stable, passive state. The following conditions prevail:

$$E_O^C > E_p \text{ and } i_{cath}(E_p) < i_{cr}$$

The rate of metal or alloy dissolution is very low and is equal to the passive current density  $i_p$ . The passive state is also spontaneously stable, which means if the passivity is momentarily disturbed, the passive state will be spontaneously reestablished.

This kind of system is typical of cathodically modified Cr, stainless steel, and titanium alloys in nonoxidizing acid environments. The Cr, stainless steel, and titanium alloys all have passivation potentials more negative than the evolution potential of hydrogen in acidic media. When a PGM is added to any of these alloys, a large increase in the rate of hydrogen evolution will occur, which is large enough to move the corrosion potential of the cathodically modified alloy in the region of stable passivity. Spontaneous passivation of the alloy will therefore be the result.

#### 3.22.5.4 Transpassive State

For a very high rate of the cathodic process (as shown by the solid line in **Figure 3(d)**), or in highly oxidizing environments, it is possible that  $E_O^C > E_{tr}$ . At this high potential, the metal or alloy will have a higher rate of dissolution than it will at potentials in the passive range, and considerable corrosion can take place.

A comprehensive study by Stern and Wissenberg<sup>8</sup> on the effect of various PGMs and other noble metals in causing the spontaneous passivation of titanium in boiling dilute sulfuric and hydrochloric acids showed that the increase in corrosion resistance of the titanium depends on the concentration of the PGMs added and also that alloying additions of as little as 0.1% (by mass) resulted in a pronounced improvement in corrosion resistance. They found that the effect of the various alloying elements in improving the corrosion resistance of an alloy generally decreased in the order:

$$Ir > Rh > Ru > Pt > Pd > Os > Au > Re$$

According to the available comparable data, there seems to be a reasonable parallel between the hydrogen exchange current densities and the extent to which additions of the various PGMs improve corrosion resistance, although a close examination shows that exceptions do occur, and that this agreement is not conclusive.<sup>16</sup>

The relatively high exchange current density of Pd indicates that it should be an effective alloying element in conferring stable passivity. Although equivalent data under these conditions are not available for Ru, it is widely considered to be a more effective cathode for hydrogen evolution than is Pd. It should therefore be a fairly effective cathodic modifying agent. Streicher<sup>17</sup> tested Pd, Pt, iridium, osmium, rhodium, and Ru as cathodic additives to ferritic

stainless steels, and showed that Ru additions (0.2%) indeed produced better corrosion resistance than did Pd additions (0.2%). Higginson<sup>18</sup> also confirmed that Ru confers better corrosion resistance on ferritic stainless steels than does Pd. The commercial titanium alloy Ti–0.2% Pd containing 0.2% Pd which was developed by the Tomashov group proves that cathodically modified alloys can be economically viable corrosion resistant materials for severe reducing conditions.

### 3.22.6 Mechanism of Cathodic Modification

Upon formation of the alloy, it is conceivable that the atoms of each alloying component maintain their electrochemical individuality. Consequently, although it is a solid solution, the surface of the alloy is electrochemically heterogeneous at an atomic level, and the atoms of the solid solution do not possess identical corrosion resistance. It seems that the PGMs can inhibit corrosion in two ways, namely;

- by acting as a catalyst for hydrogen evolution (and thus increasing the efficiency of the cathodic process); and
- by inhibiting the anodic dissolutions of the metal or alloy to which they are added.

As a result of the initial interaction of the different atoms of the alloy with the corrosive media, there is a rearrangement of atoms at the alloy surface resulting in a redistribution of the PGM on the surface of the alloy, before passivity is established.<sup>19,20</sup> Three separate mechanisms have been proposed<sup>18</sup> to account for the distribution process, namely:

- dissolution of the PGMs followed by diffusion through the electrolyte and, secondarily, electrochemical deposition of the noble metal on the alloy surface;
- volume diffusion (from the bulk alloy) of the PGM atoms; and
- surface diffusion of the PGM atoms.

The dissolution–deposition model was proposed in some early research into the cathodic modifications of titanium alloys.<sup>15</sup> Diffusion of the PGM ions (or complexes) through the electrolyte to the surface of the alloy could easily occur at a sufficient rate to account for the observed redistribution. However, it is impossible for the PGMs to be oxidized in the potential range associated with the dissolution of the

cathodically modified alloy, and this fact is a major obstacle, providing a fundamental objection to this mechanism.

The volume-diffusion and surface-diffusion mechanisms do not involve dissolution of the PGM, although the latter model does not preclude the possibility of partial solvation of PGM atoms. However, the difficulty initially associated with these mechanisms was that the diffusion rates associated with similar processes were not high enough to account for the redistribution of PGM atoms at relatively low temperatures. This objection remains valid for the volume-diffusion mechanism.

The important feature of the surface-diffusion mechanism concerns the nature of the surface undergoing anodic dissolution. In recent years, an increasing amount of evidence has emerged which favors the surface-diffusion mechanism in alloying systems that undergo selective dissolution. Forty and Durkin<sup>21</sup> showed that, for silver alloys containing 10 at.% gold, the surface diffusion of the more noble component of the alloy (gold) is responsible for substantial reordering of the surface during anodic dissolution in nitric acid. Pickering<sup>22</sup> classified the polarization curves of alloys in terms of their tendency towards selective dissolution and the surface enrichment of the more noble metal. He also pointed out that the morphology of cathodically modified alloys should be that of a solid planar surface enriched in the noble metal. Work by Tomashov *et al.*<sup>23,24</sup> on cathodically modified alloys has also provided evidence in favor of a surface-diffusion mechanism.

A surface undergoing anodic dissolution is an extremely disturbed surface because selective dissolution causes a high concentration of defects in the surface. This, in turn, can cause rapid diffusion of the atoms of the noble-metal component to the surface of the alloy. Normally, diffusion coefficients associated with surface diffusion are considerably higher than those for volume diffusion, particularly at ambient temperature. A diffusion coefficient of  $10^{-2} \text{ cm}^2 \text{ s}^{-1(25)}$  which is estimated for Cr atoms from a surface analysis of a ferro-Cr alloy undergoing dissolution in a 0.1 M solution of hydrochloric acid, is several orders of magnitude higher than the diffusion coefficients required for volume–bulk diffusion, and proves that the observed redistribution rates in cathodically modified alloys can be accounted for by a surface-diffusion mechanism.

It therefore seems that the most important results of noble metal additions to Cr, stainless steel, and other alloys are:



- a. Cathodic modification can increase the corrosion resistance of materials in nonoxidizing acids by increasing the potential to a value that is in the passive potential range.
- b. During anodic dissolution, noble-metal atoms are redistributed on the surface of the alloy, probably by a surface-diffusion mechanism.

### 3.22.7 Cathodic Modification of Cr and Cr-Based Alloys

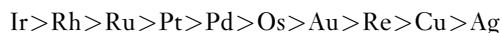
Since 1948, both Tomashov *et al.*<sup>6</sup> and Stern *et al.*<sup>8</sup> have proved that the tendency to passivation and the corrosion resistance of Cr in a nonoxidizing acid environment can be increased by the addition of small amounts of PGMs to these alloys.<sup>6,8,11,26–30</sup> Alloying with these cathodic additives causes dramatic improvements in corrosion resistance, and does not reduce the low-temperature plasticity of the Cr. It therefore opens up extensive possibilities for the use of these alloys in new industrial applications.

#### 3.22.7.1 Effect of the Addition of Noble Metals

##### 3.22.7.1.1 Cathodic modification

Greene *et al.*<sup>11</sup> conducted a comprehensive investigation into the influence of small additions of various PGMs, as well as some other noble metals, on the corrosion resistance of Cr in both nonoxidizing acids (hydrochloric, sulfuric) and an oxidizing acid (nitric). The tests carried out for the determination of the loss in mass in boiling sulfuric acid (5–98%), in hydrochloric acid (5–15%), and in nitric acid (65%) showed that an addition of as little as 0.1% PGMs to Cr (Cr–0.1% Pt) could cause a decrease in the corrosion rate of the Cr by a factor  $10^5$  or more. Each of the alloying additions improved the corrosion resistance in nonoxidizing environments, whereas several of the PGMs, particularly Pt and Ru, actually accelerated corrosion in nitric acid, which is a highly oxidizing environment. This phenomenon can be explained by the fact that the corrosion potential of Cr in a boiling solution of 65% nitric acid is very noble, and is very close to the beginning of its transpassive region. Alloying with an inert element having a large exchange-current density for the reduction of nitric acid can shift the existing high positive potential of the alloy into the transpassive region, resulting in an increased dissolution of the metal.

In electrochemical tests carried out at room temperature, a decrease in the critical anodic current density for passivation was found in all the Cr alloys containing noble elements, except those containing rhenium, silver and gold. The decreasing order of effectiveness of the various alloying additions in causing corrosion resistance in sulfuric and hydrochloric acids is as follows:



This can be correlated with the hydrogen-overvoltage behavior of these elements.

The corrosion of ductile Cr alloyed with Ru, osmium, iridium, Pt, Pd, and rhenium in solutions of 5–60% sulfuric acid at various temperatures has been described by Tomashov *et al.* in various papers.<sup>27–30</sup> Tomashov<sup>3</sup> found that Cr that has no cathodic additives (PGMs) corrodes at a high rate, while cathodically modified alloys self-passivate easily, and their corrosion resistance is several orders of magnitude higher than that of pure Cr. An increase in the concentration of the alloying component also increases the stability of the passive state.

A detailed study of Cr–Pd (0.1–0.4%) and Cr–Pt (0.1–0.4%) alloys in a 50% solution of sulfuric acid at 98°C<sup>30</sup> revealed that the addition of small amounts of nitrate ions (0.02%  $\text{NO}_3^-$  or 0.2 g dm<sup>−3</sup>  $\text{NO}_3^-$ ), which serve as an oxidizing agent, considerably increased the stability of the passive state in this aggressive condition. On the other hand, concentrations of up to 10 mg dm<sup>−3</sup> of chloride ions in solutions of 40% sulfuric acid at 65°C delayed the onset of self-passivation, and also narrowed the range of the passivation region for ductile Cr–0.3% Ru, and Cr–0.4% Ru alloys.<sup>6</sup> Work by Kato and Sakaki<sup>31</sup> on Cr with Pd and Ru additions, confirmed the beneficial effect of both on the increased corrosion resistance of the Cr in sulfuric acid, as well as the fact that Ru is more effective than Pd in this regard.

##### 3.22.7.1.2 Kinetic effect

Tomashov *et al.*<sup>27,29,32,33</sup> investigated the effect of PGMs on the active dissolution of ductile Cr in sulfuric acid. Results of the dissolution kinetics of ductile Cr alloyed with Ru, iridium, Pd, and Pt (0.1–0.4%) in a solution of 40% sulfuric acid at 65°C and at a fixed potential of −175 mV (SHE) show that the PGM alloying elements decrease the anodic dissolution rate of Cr, and also that the corrosion resistance of the alloy depends on the concentration and nature of the alloying addition.



Investigations of the Cr-PGM alloys by electron microscopy after active corrosion had taken place showed that the accumulating PGMs formed separate islets rather than a homogeneous layer on the surface of the alloy. It is presumed that the dissolution of Cr from the Cr-PGM alloy occurs by means of successive transfer into the solution of the atoms that are at the corners and edges of the crystal lattice and those that have an enhanced activity. If these sectors of the crystal lattice are blocked by more corrosion-resistant PGM atoms, anodic dissolution of the Cr atoms that lie on the flat steps of the alloy lattice and that bind more firmly to it will take place less readily. The PGM atoms gradually lose their bonding with the neighboring Cr atoms, and remain on the surface in the form of adsorbed atoms or adatoms.<sup>32-34</sup> The further surface diffusion of such adatoms results in the formation of microcrystals of pure PGMs, which are metals that preserve the electric contact with the substrate alloy.<sup>32,33</sup> Thus, with an increase in the PGM content of the alloy, more active surface centers are blocked by the added PGM atoms, and the rate of Cr solution from the alloy in the active state decreases. While Tomashov *et al.*<sup>32-34</sup> do not preclude the possibility of the partial solvation of the PGM atoms, they conclude that the changing distribution of the PGM metal occurs mainly as a result of a surface diffusion mechanism.

The retardation of the anodic dissolution of Cr by all the PGM additives seems to occur as a result of the operation of two mechanisms. The dominant mechanism is a blocking mechanism, in which the PGMs (as adatoms) block the active sites in the crystal lattice of Cr, thus preventing corrosion as described earlier. A lesser effect was also observed to occur as a result of a 'screening' mechanism, in which a layer of the PGM adatoms and trapped hydrogen in the pores between the cathodic component particles partly screen the surface of the alloy, causing a decrease in the active anodic surface and in corrosion.

### 3.22.8 Cathodic Modification of Stainless Steels

#### 3.22.8.1 Addition of Noble Metals to Fe-Cr Stainless Steels

The Tomashov group has made the main contribution to the knowledge of corrosion resistance of Fe-Cr alloys cathodically modified with noble metals in various acid media at different concentrations and temperatures.

In the 1960s, Tomashov<sup>35</sup> demonstrated the beneficial effect of the addition of Pt, Pd, rhenium, and copper to Fe-27% Cr alloys in 20–30% sulfuric acid at between 10 and 25 °C. Even small additions (less than 0.5%) of Pt, Pd, and rhenium reduced the corrosion in the Fe-27% Cr alloy by as much as 99.85%.<sup>17</sup> With its higher hydrogen overvoltage, copper is less effective as a cathodic additive. The addition of 0.2% Pd to Fe-18% Cr in 20% sulfuric acid of 20 °C resulted in a large increase in the corrosion resistance of the Fe-Cr alloy. Under these conditions, the corrosion resistance of Fe-18% Cr-0.2% Pd is comparable with that of an Fe-18% Cr-3% Mo alloy. When 0.2% Pd was added to Fe-25% Cr in 30% sulfuric acid at 20 °C, the alloy became even more corrosion resistant than Fe-25% Cr steels with additions of either 3% molybdenum or 6% nickel. The higher corrosion resistance of an Fe-18% Cr-3% Mo-0.2% Pd steel when compared to that of Fe-18% Cr-0.2% Pd and Fe-18% Cr-3% Mo steels illustrated, for the first time, the synergistic beneficial effect of the simultaneous additions of molybdenum and Pd to an alloy. This effect was later confirmed by Bieffer<sup>36</sup> and Higginson.<sup>18</sup>

After demonstrating the cathodic modification effect in Fe-Cr stainless steels, the Tomashov group discovered that the effect of cathodic additions was enhanced with an increasing Cr content (above 25%) in an alloy.<sup>37</sup> Investigations carried out on Fe-Cr alloys with varying Cr contents (25–100%) to which 0.2% Pd was added indicated that Fe-40% Cr-0.2% Pd had the optimum passivation characteristics in 10–50% sulfuric acid and 1% hydrochloric acid at 100 °C. Under these conditions, the Fe-40% Cr-0.2% Pd alloy required the minimum time for self-passivation and displayed the minimum corrosion in the passive range, as well as a small critical current density and a highly negative passivation potential. The addition of 0.2% Pd to the Fe-40% Cr steel caused a dramatic decrease of a factor of  $2 \times 10^5$  in the corrosion rate in a boiling solution of 40% sulfuric acid. The remarkable corrosion resistance of the Fe-40% Cr-0.2% Pd alloy when compared to that of other alloys can be clearly seen from Table 1.

Although the effect of the addition of Pd in improving the corrosion resistance is much less in hydrochloric acid, the corrosion rate in the passive state is still reduced by a factor of  $\sim 100$ . The alloy was found to have high corrosion rates in a solution of hydrochloric acid at concentrations of more than 1%.

This extraordinary corrosion resistance in sulfuric acid was confirmed by Higginson,<sup>18</sup> who found that

**Table 1** Corrosion rate (CR) of some acid-resistant alloys in 40% sulfuric acid at 100 °C

Alloy	CR (mm year <sup>-1</sup> )
Fe-40% Cr	~10 000 <sup>37</sup> ; ~5 000 <sup>38</sup> (10% acid)
Fe-23% Cr-28% Ni-3% Mo	3 <sup>37</sup>
Hastelloy A, B	0.2 <sup>37</sup>
C	0.3 <sup>37</sup>
Ti-30% Mo	0.18 <sup>37</sup>
Fe-40% Cr-0.2% Pd	0.05 <sup>37</sup>
Fe-40% Cr-0.2% Ru	0.03 <sup>38</sup>
Fe-29% Cr-4% Mo-2% Ni	~ 8000 <sup>39</sup>
Fe-29% Cr-4% Mo-2% Ni-0.2% Ru	12.93 <sup>39</sup>

an improvement was obtained in the corrosion rate of a factor of  $(1-5) \times 10^4$  for Fe-40% Cr-0.2% Pd and Fe-40% Cr-0.2% Ru alloys compared to that of Fe-40% Cr in a boiling solution of 10% sulfuric acid. The alloy containing Ru was more resistant than the alloy containing Pd. The greater effect of the Ru was explained on the basis that it is a more effective cathode for the evolution of hydrogen than is Pd. A similar investigation conducted by Howarth<sup>40</sup> indicated that no improvement in corrosion resistance is gained by the use of Pt rather than Ru for purposes of cathodic modification. Higginson<sup>18</sup> also observed that the critical time and charge density for spontaneous passivation of Fe-40% Cr-Ru alloys depends on the concentration of Ru in the alloy, and the kind of acid (hydrochloric or sulfuric) in which the corrosion takes place.

Work by Potgieter and van Bennekom<sup>41</sup> indicated that although the optimum Cr concentration for maximum corrosion resistance in Fe-Cr-0.2% Pd alloys was 40% Cr, there was no difference in the corrosion resistance of an Fe-40% Cr-0.2% Ru and an Fe-30% Cr-0.2% Ru alloy. This implies that in Ru containing alloys, the maximum Cr content can be restricted to 30% by mass, which means that it can be produced commercially in the same way as the patented Fe-28Cr-4% Mo superferritic stainless steel. It also means huge gains in the physical and mechanical properties of the alloy, as Fe-40% Cr alloys are very brittle and difficult to form. A later work by Wolff *et al.*<sup>42</sup> indicated that further additions of 5% Al to Fe-35/40% Cr-0.2% Ru not only improved the high temperature hot corrosion resistance at elevated temperatures, but also aqueous corrosion resistance against sulfuric acid solutions of 10% at room temperature. The Fe-40% Cr and

Fe-35% Cr-5% Al alloys corroded actively in 10% sulfuric acid, while the alloys containing 0.2% Ru additions passivate spontaneously, with the one containing the Al having the lowest corrosion rate. However, this latter alloy of Fe-35% Cr-5% Al had inferior pitting corrosion resistance compared to the Fe-40% Cr one in a 3.5% NaCl solution. Once again it was observed that the addition of 0.2% Ru to both the alloys increased their pitting resistance in the salt solution.

Detailed investigations were carried out by Tomashov<sup>43</sup> on Fe-25% Cr steels alloyed with 0.3% and 2.0% Pd and Ru in 5–50% sulfuric acid and 1 and 5% hydrochloric acid at 50–100 °C. It was found that the general and pitting corrosion resistance was higher in the alloys containing Ru than in the alloys containing Pd.

These results were attributed to several factors:

- Ru reduces the overvoltage of cathodic hydrogen generation more effectively than does Pd, thereby increasing the efficiency of the cathodic process.
- Ru, unlike Pd, reduces the rate of anodic dissolution by reducing the critical current density required for passivation, especially in media containing chloride ions. This observation was confirmed by both Bieffer<sup>36</sup> and Higginson.<sup>18</sup>
- Ru is susceptible to the adsorption of oxygen and the formation of phase oxides, and thus enters the composition of the hydroxide and oxide layers formed on the surface of the steel, while Pd remains as a separate metallic phase in the surface layer.
- Because the passivating oxide layers on the steel contain Ru as well as Cr, the resistance of the steel to the activating effect of chloride ions increases. Thus, Ru does not impair the resistance to pitting corrosion, but Pd does impair this resistance.

An electron microscopy investigation<sup>23</sup> into the accumulation of Pd on the surface of Fe-25% Cr-(0.1–0.5%) Pd in 10% sulfuric acid at 25–100 °C revealed that the size and amount of accumulated particles on the surface of the alloy depend not only on the initial concentration of the Pd in the alloy, but also on the temperature at which active dissolution takes place. The size and distribution of the accumulated Pd particles are explained on the basis of the theory of Erdey-Gruz and Volmer, which states that nuclei of crystallization arise at a definite supersaturation of adsorbed atoms on the surface of the alloy. An increase in the concentration of the Pd should therefore result in both an increase in the number of nuclei

and decrease in the particle size. Higginson<sup>18</sup> confirmed this in a study of the accumulation of Ru on Fe–40% Cr–(0.1–0.2%) Ru alloys corroding in 0.5 M sulfuric acid (4.9%) and 0.5 M hydrochloric acid (1.8%). He also found that a greater amount of accumulation occurred in a solution of hydrochloric acid than in sulfuric acid, apparently as a result of the adsorption of chloride ions, which increases the surface diffusion rate of Ru atoms during anodic dissolution.

Tjong<sup>44</sup> investigated the corrosion behavior of an Fe–24% Cr alloy with sputter-deposited Pd thin films on the surface in 0.5 M HCl solutions at room temperature, and found that prolonged corrosion protection against active dissolution in the hydrochloric acid medium is due to the formation of a sufficiently thick Pd-enriched surface layer containing Fe–Cr. Auger analysis of the passive surface revealed that a thick Cr oxide layer forms with and on the Pd-enriched surface, thus confirming the earlier work by Tomashov described above.<sup>3,23</sup> Recent work by Tjong and Chu<sup>45</sup> investigated the same parent alloy, but this time with Ru ion implanted on the surface, and in sulfuric acid. They found that the basic alloy with Ru does not passivate in the 0.5-M sulfuric acid solution, whereas the one containing ion-implanted Ru atoms does. Furthermore, XPS analysis of the passivated surface showed that Ru is incorporated as Ru<sup>4+</sup> species in the hydrated Cr oxyhydroxide passive film formed on the Ru-implanted Fe–24% Cr alloy, which is once again in agreement with the results from Tomashov<sup>3</sup> discussed above.

Bieffer<sup>36</sup> assessed the influence of several transition metals, as well as additions of Pd and rhenium in different concentrations to type 430 ferritic stainless steel (17% Cr) in 0.5-M sulfuric acid at ambient temperature (24 °C). The results indicate that the addition of 0.46% Pd to 430 stainless steel resulted in spontaneous passivation, but insufficient levels of Pd (0.06–0.26%) increased the active corrosion rate by a factor of as high as 10.

It was found that in 1-M hydrochloric acid (3.6%), the additions of Pd to steel 430 were strongly deleterious, and increased the corrosion rate from a factor of 10 to a factor of 30. Further, it was observed that Pd was deleterious to the pitting corrosion of ferritic stainless steels. However, at levels of 0.99% Pd, 430 stainless steel appears to have a superior corrosion resistance even to that of highly alloyed austenitic stainless steels in concentrated sulfuric acid at high temperatures.

Although Tomashov<sup>35</sup> concluded that the addition of 0.2% Pd to Fe–18% Cr steel was sufficient to result in spontaneous passivation in 20% sulfuric acid at 20 °C, Bieffer<sup>36</sup> found that type 430 stainless steel with an addition of 0.26% Pd did not passivate spontaneously in 0.5 M sulfuric acid at 24 °C. A probable reason for this discrepancy is the presence of relatively high amounts of carbon and impurities in the 430 stainless steel. Lizlovs and Bond<sup>46</sup> showed, in measurements of anodic polarization, that the performance of a standard type-430 steel was surpassed by that of a 17% Cr steel of high purity.

### 3.22.8.2 Addition of Noble Metals to Fe–Cr–Mo Stainless Steels

Tomashov *et al.*<sup>47–49</sup> investigated the corrosion characteristics of several Fe–Cr stainless steels containing molybdenum (2–3%) and Pd (0.1–0.5%) in sulfuric acid (1–80%) at temperatures varying from 10 °C to boiling point (about 100 °C). The results indicated that, when molybdenum is added to an Fe–25% Cr steel containing 0.3% Pd, the concentration and temperature ranges in which the steels self-passivate in sulfuric acid are narrowed.

According to them, the simultaneous alloying of Fe–24% Cr with molybdenum and Pd leads to a marked increase in the stability of the passive film in sulfuric acid, because molybdenum is incorporated in the passivating film on the steel, resulting in a more protective surface layer.<sup>48</sup> The shrinkage of the region of passive behavior was also confirmed by Agarwala and Bieffer<sup>50</sup> in their investigation of type-430 stainless steel, especially at high concentrations of sulfuric acid. They found that type-430 steels with additions of 3% Mo–0.5% Pd and 2% Mo–1% Pd had comparatively large regions of spontaneous passivity in sulfuric acid up to concentrations of 25% at temperatures near boiling point. They even passivated in the presence of 2–3% sodium chloride in sulfuric acid solutions at 24 °C, thus showing much more resistance to chlorides than steels that contain only Pd.

The Tomashov group<sup>49</sup> showed further that Fe–18% Cr–2% Mo alloyed with 0.3% Pd self-passivates, is corrosion resistant in 1–40% sulfuric acid at between 10 and 100 °C and has a lower corrosion rate than commercial Fe–18% Cr–10% Ni stainless steel under the same conditions.

Streicher<sup>17,51</sup> also investigated the effect of additions of PGMs to an Fe–Cr–Mo alloy. Without these additions, the rate of attack on an Fe–28.5%Cr–4% Mo alloy in a 10% solution of boiling sulfuric acid

was found to be  $\sim 52\,000\text{ mm year}^{-1}$ . Each of the six added PGMs, when present in excess of a certain minimum amount that varied from 0.005 to 0.2%, passivated the Fe–28.5% Cr–4% Mo alloy in 10% boiling sulfuric acid. The minimum concentration of PGMs required to passivate the base alloy decreased with an increase in the Cr content. Additions of a PGM at a concentration lower than the required to produce passivity actually increased the corrosion rate as compared to that of Fe–28.5% Cr–4% Mo. This was also observed by Bieffer<sup>36</sup> for Fe–17% Cr (type 430 steel). Scheers *et al.*<sup>52</sup> and McEwan *et al.*<sup>53</sup> found that Fe–29% Cr–4% Mo–2% Ni with small amounts of Ru also performed excellently in phosphoric acid solutions, and that Ru greatly enhances the corrosion resistance of the base alloy. Further work by Potgieter *et al.*<sup>39</sup> on these Fe–29% Cr–4% Mo–2% Ni alloys with various levels of Ru and silver additions, as well as a partial copper substitution for Ni, confirmed that excellent corrosion resistance can be achieved against sulfuric acid solutions as concentrated as 30–40% at boiling point with decreases in corrosion rates by a factor of  $10^2$  to  $10^3$ . A level of at least 0.2% Ru is required for a worthwhile and significant corrosion resistance improvement, and silver additions, even in much larger concentrations than Ru, are not as effective as Ru to improve corrosion resistance of the base alloy. Substitution of half of the Ni with a similar amount of Cu does not seem to have a major beneficial or detrimental effect, except in severely aggressive conditions (40%  $\text{H}_2\text{SO}_4$  at boiling point), where the effect is decidedly detrimental. This is shown in **Table 2**, which also includes a value of a duplex stainless steel discussed further on in this report.

The observation made by both Tomashov *et al.*<sup>48</sup> and Agarwala and Bieffer<sup>50</sup> that the simultaneous

presence of Pd and molybdenum in Fe–Cr steels promotes more stable passivity than the presence of each individual element alone was confirmed by both Streicher<sup>17,51</sup> and Higginson.<sup>18</sup> Higginson found that Fe–40% Cr that had been alloyed with both 1.8% molybdenum and 0.1% Ru passivated far more quickly in sulfuric acid (0.5 M) than did an Fe–40% Cr–0.1% Ru alloy. According to Tomashov *et al.*<sup>48</sup> this is true not only for solutions of sulfuric acid, but also for solutions of dilute hydrochloric acid (1–3%). However, Higginson<sup>18</sup> showed that the addition of 0.1% Ru to an Fe–40% Cr–1.8% Mo steel could not cause the spontaneous passivation of the alloy to occur in a solution of 0.5 M hydrochloric acid. The fact that Tomashov *et al.*<sup>48</sup> could achieve spontaneous passivation while Higginson could not, can be attributed to different conditions in their respective investigations.

The addition of molybdenum has different effects on the corrosion resistance of Cr steels in the active state in solutions of sulfuric and hydrochloric acid. In solutions of sulfuric acid, the presence of molybdenum reduces the corrosion rate, but in solutions of hydrochloric acid, it increases the rate. The corrosion potential in both acids of steel containing molybdenum is more positive than that of steel without molybdenum. This fact can be explained if it is assumed that molybdenum not only retards anodic dissolution, but also increases the effectiveness of the cathode process owing to the reduced overvoltage of hydrogen on molybdenum. The predominant action of molybdenum on the anodic process appears in solutions of sulfuric acid but, in hydrochloric acid, where passivation is hindered by the presence of chloride ions, it is mainly the cathodic influence of molybdenum that prevails. This leads to a marked increase in the rate of dissolution of steel, because the

**Table 2** Corrosion roles of a superferritic SS with various Ru and Ag additives in boiling sulfuric acid solutions

Alloy	$[\text{H}_2\text{SO}_4]$ %			
	10	20	30	40
Fe–29% Cr–4% Mo–2% Ni–0% Ru	0.0083	1.733	1.884	–
Fe–29% Cr–4% Mo–2% Ni–0.05% Ru	0.0012	0.0205	1.0044	4687
Fe–29% Cr–4% Mo–2% Ni–0.10% Ru	0.0008	0.0031	0.4219	4099
Fe–29% Cr–4% Mo–2% Ni–0.20% Ru	0.0006	0.0027	0.0645	12.93
Fe–29% Cr–4% Mo–1% Ni–1% Cu–0.20% Ru	0.0152	0.0518	0.0892	3550
Fe–29% Cr–4% Mo–0.20% Ru	0.2300			
Fe–29% Cr–3% Mo–14% Ni–0.20% Ru	0.000			
Fe–29% Cr–4% Mo–2% Ni–0.1% Ag	0.0227	3.719		
Fe–29% Cr–4% Mo–2% Ni–0.5% Ag	0.0333	1.560		
Fe–29% Cr–4% Mo–2% Ni–1.0% Ag	0.1183	0.4726		

effectiveness of the cathodic process on molybdenum in hydrochloric acid is insufficient to bring the steel into the passivated state. The simultaneous presence of Pd and molybdenum in steel produces a more effective cathodic process<sup>48</sup> and could possibly lead to passivation. Thus, in sulfuric acid molybdenum affects not only the cathodic process (together with PGMs), but also retards the anodic process. The combined influence of molybdenum and PGMs on the anodic and cathodic processes of Fe–Cr stainless steel in sulfuric acid is summarized schematically in **Figure 4**.

Streicher<sup>51</sup> also carried out investigations into the pitting corrosion of Fe–28% Cr–4% Mo alloys to which PGMs in several halide media had been added.

The results show clearly that Pd destroys the pitting resistance in all of the three pitting solutions tests, while rhodium impairs the resistance in ferric chloride and the bromine–bromide solution. None of the other four PGMs had any influence on the pitting resistance in these media, except for Pt, which caused failure in the bromine–bromide solution. No mechanism was suggested as an explanation for these observations. Streicher concluded that, of the six PGMs only iridium, osmium, and Ru can be used to produce the passivity of stainless steels in sulfuric acid without impairing their resistance to pitting corrosion in oxidizing chloride and bromide environments. Recent

investigations by Sherif El-Sayed *et al.*<sup>54</sup> on the behavior of Fe–Cr–Ni–Mo–(0–0.3% Ru) in chloride media confirmed the beneficial effect of Ru on the pitting corrosion resistance of stainless steels.

As far as organic media are concerned, it was found<sup>35</sup> that the addition of 0.1% Pd to Fe–25% Cr in a solution of 50% formic acid at 100 °C decreased the corrosion rate of steel by a factor of approximately 60. An Fe–25% Cr–3% Mo steel is stable under these conditions, both with and without Pd.

### 3.22.9 Cathodic Modification of Fe–Cr–Ni Stainless Steels

Although the effect of cathodic alloying additives on Fe–Cr–Ni stainless steels is not as dramatic as for Fe–Cr steels, it can nevertheless bring about marked improvement in the corrosion resistance of Fe–Cr–Ni alloys, especially in fairly aggressive conditions.<sup>55</sup>

#### 3.22.9.1 Addition of Noble Metals to Fe–Cr–Ni Stainless Steels

The addition of 0.1–0.5% Pt, 0.1–0.9% Pd and 1.2% Cu to Fe–18% Cr–9% Ni (an austenitic stainless steel) in 20–40% sulfuric acid at 20 °C reduced the corrosion of the Fe–Cr–Ni alloy by as much as 99.85%.<sup>17,56</sup> The results also indicated that the effectiveness of the alloying additions increased in the order Cu < Pd < Pt.

An electrochemical investigation into the alloying of Fe–25% Cr–6% Ni steel with Pd<sup>57</sup> (0.1%, 0.2%, and 0.5%) showed that the corrosion rate is reduced by more than an order of magnitude in 20% sulfuric acid at 100 °C over that for steel without Pd. However, steels containing Pd (0.1–0.5%) do not reach the stable passive region, and continue to dissolve at a considerable rate. The corrosion rate of Fe–25% Cr–6% Ni–0.5% Pd in a solution of 10% sulfuric acid at 100 °C is lower by a factor of 4 compared with the steel without any Pd.

Tomashov<sup>35</sup> also demonstrated that the addition of 0.2% Pd to an Fe–18% Cr–10% Ni alloy greatly reduced the corrosion of this austenitic stainless steel. The substitution of part of the nickel by manganese (Fe–18% Cr–2% Ni–8% Mn) produced an austenitic stainless steel with a corrosion performance that was not nearly as good as that of a steel with 10% nickel. The alloying of this manganese substituted steel with 0.2% Pd rectified this impaired corrosion resistance, and resulted in a steel with similar

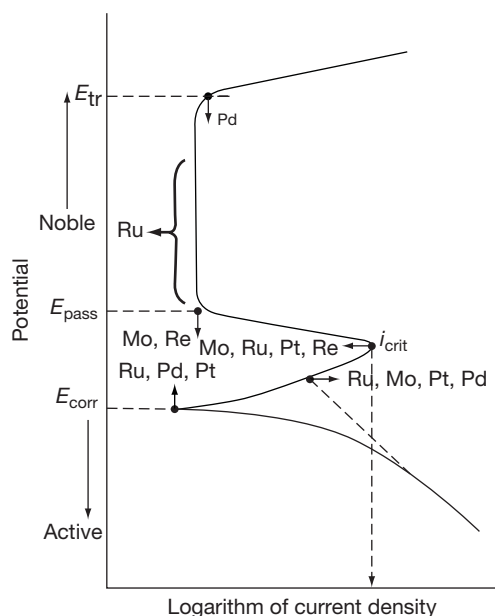


**Figure 4** Summary of the effects of alloying additions on the polarization characteristics of Fe–Cr stainless steel in sulfuric acid.



corrosion characteristics to that of an Fe–18% Cr–10% Ni–0.2% Pd alloy.

A recent study by Peled and Itzhak<sup>58</sup> into the effect of silver, Pd, and gold on the corrosion behavior of hot-pressed and sintered type 316 stainless steel in 0.5-M sulfuric acid at 25 °C indicated that the corrosion resistance of the base alloy could be dramatically improved by additions of noble metals. Silver concentrations of less than or equal to 1% improved the corrosion resistance of the sintered stainless steel only for limited periods of exposure. Pt additions of about 2% were found to be sufficient to preserve the sintered stainless steel in the passive state. However, high Pt contents (about 5%) resulted in a tendency for the passive layer to break down. Samples containing additions of gold at various concentrations (1–5%) exhibited clear anodic active-passive transitions with a wide range of passivation. The addition of 5% gold to the sintered stainless steel caused the alloy to remain passive.

An interesting beneficial synergistic effect between nickel and Ru was noticed by Streicher.<sup>51</sup> Lower concentrations of Ru (0.1%) and nickel (0.1%) were needed to passivate Fe–28% Cr–4% Mo in a 10% solution of boiling sulfuric acid than the concentrations of either Ru (0.2%) or nickel (0.25%) that were needed when they were used alone. Although it seemed that Higginson<sup>18</sup> was unaware of that since he neither confirmed nor disproved it; he nonetheless found that the addition of 1% nickel to a Fe–40% Cr–0.1% Ru alloy resulted in an increase in the time needed for the occurrence of spontaneous passivation in 0.5 M sulfuric acid. He also concluded that the inhibition of the anodic dissolution reaction in sulfuric acid was much greater for the alloy containing both nickel and Ru than for that containing only 0.1% Ru. The alloying of Fe–40% Cr–0.1% Ru with 1% nickel also caused spontaneous passivation to occur approximately seven times faster in 0.5 M hydrochloric acid than for the Fe–40% Cr–0.1% Ru alloy. Thus, while an addition of 1% nickel to Fe–40% Cr–0.1% Ru was advantageous and lowered the passivation time in hydrochloric acid, the same did not apply when sulfuric acid was used since the passivation time increased. This synergistic effect between Ni and Ru was also confirmed by Potgieter and Kincer<sup>38</sup> in sulfuric acid, in their work on Fe–40% Cr–Ni–Ru alloys in 0.5 M hydrochloric and sulfuric acids. Their results indicated that less expensive Ni can be substituted for Ru to improve corrosion resistance effectively in sulfuric acid, but not in hydrochloric acid.

As far as organic acid media are concerned, work by the Tomashov group<sup>35,55</sup> indicated that an Fe–25% Cr–6% Ni–0.1% Pd alloy in a solution of 50% formic acid at 100 °C had a significantly reduced rate of corrosion when compared with the alloy without Pd. An alloy of 26% Cr–0.5% Ni to which noble metals had been added (0.5% Pt and 0.5–1.0% Pd) could withstand solutions of 50% formic acid and 10% oxalic acid at 100 °C for better than a similar alloy without the additions of any noble metals.

### 3.22.9.2 Addition of Noble Metals to Fe–Cr–Ni–Mo and Fe–Cr–Mn–Ni Stainless Steels

Investigations by Tomashov *et al.*<sup>35,55,59,60</sup> into the corrosion resistance of nitrided stainless steels revealed that an addition of 3% molybdenum to Fe–25% Cr–6% Ni steel in a solution of 30% sulfuric acid at 20 °C produced a sufficiently stable alloy in which the further addition of Pd (0.1%) did not result in any significant improvement in the corrosion resistance.<sup>55</sup> This occurs as a result of the fact that molybdenum not only retards the anodic dissolution of steel, but also promotes the cathodic evolution of hydrogen. Passivation is thus caused by the increased effectiveness of the cathodic process as well as the inhibition of the anodic process.

The work of the Tomashov group also showed that highly nitrided (0.7–0.9%) Fe–25% Cr–3% Ni–2% Mo–Mn stainless steels to which 0.1–0.5% Pd had been added had a very high corrosion resistance in mildly aggressive conditions, such as in solutions of 20–40% sulfuric acid at 20–100 °C, as well as in solutions of 1–3% hydrochloric acid at 20–50 °C.<sup>59</sup> However, at least 0.2% Pd is needed for self-passivation and high corrosion resistance to occur under more aggressive conditions (2% or higher hydrochloric acid at 50 °C or higher and 30% or more sulfuric acid at 50 °C or higher).<sup>55</sup> In mildly aggressive media, the corrosion resistance of the steel depends on the ability of the molybdenum to cause self-passivation as a result of the increased effectiveness of the cathodic process and inhibition of the anodic process. The simultaneous addition of Pd and molybdenum in a stainless steel broadens the region of self-passivation of the steel. The favorable influence of Pd on the corrosion resistance of stainless steel is due primarily to the cathodic modification of the steel and, in the presence of molybdenum, to its beneficial effect on the stability of the passive state.



Results also indicated that Fe–25% Cr–6% Ni–3% Mo–0.2% Pd that does not contain nitrogen could not be passivated in a solution of hydrochloric acid. Only a high nitrogen content (0.5% or more) leads to an increase in the corrosion resistance and self-passivation of these alloys in solutions of dilute hydrochloric acid (2–5% hydrochloric acid at 50 °C).<sup>60</sup> The positive influence of nitrogen occurs as a result of its influence on the structure of steel. A high nitrogen content creates a more homogeneous austenitic structure, and thus prevents the partitioning of Cr, molybdenum, and nickel in a two-phase austenitic–ferritic structure. Steel containing Pd but no nitrogen cannot be passivated in solutions of hydrochloric acid, apparently owing to the heterogeneity of the structure, which contains ~40% ferrite. The presence of appreciable amounts of both austenite and ferrite phases in the alloy, which cause a galvanic interaction between the two electrochemically different phases, is possibly responsible for this observed corrosion behavior.

Work carried out by Tjong<sup>61</sup> on Fe–24Cr–6V–Ru (0–0.2%) and Potgieter<sup>62</sup> on Fe–22% Cr–5% Ni–3% Mo–(0–0.3%)Ru and having a very low nitrogen content, showed that in these ferritic steels Ru has a major beneficial effect in increasing the corrosion resistance of the base alloy towards attack by 1 M H<sub>2</sub>SO<sub>4</sub> solutions. The effect increases by increasing the Ru contents, and the Ru in all cases caused a shift in the open-circuit corrosion potential towards more noble values. Under conditions of active–passive transition behavior, Ru additions also lowered the critical current density required for passivation and lowered the cathodic Tafel slope.

Tomashov *et al.*<sup>59</sup> proved that Fe–Cr–Ni–Mn and Fe–Cr–Mn alloys containing 0.5% Pd self-passivated, and had a high corrosion resistance in solutions of 20% sulfuric acid at 100 °C. However the steels containing only 0.2% Pd did not self-passivate in solutions of 2 and 3% hydrochloric acid at 25 °C, and had a low resistance to corrosion. Manganese shifts the complete passivation potential of Fe–Cr steel to values that are more positive, but to a lesser degree than nickel. The beneficial effect obtained when Cr steels are alloyed with nickel and manganese can be ascribed to the fact that they cause a smaller shift in potential to the positive direction upon complete passivation than occurs when they are alloyed with nickel alone. The further addition of nickel to Cr–Mn steels also lowers the critical current density at the onset of passivation. This permits better self-passivation, and a higher corrosion resistance upon cathodic alloying.

### 3.22.9.3 Galvanic Coupling in Fe–Cr–Ni Stainless Steels

Bianchi *et al.*<sup>63</sup> investigated the galvanic coupling of different stainless steels with sheet Pt in various non-oxidizing acid solutions at various concentrations and temperatures. For example, it was found that, in an aerated solution of 38% sulfuric acid at 25 °C, types 316, 304, and 430 (a ferritic alloy) stainless steel resisted corrosion when the ratio of the area of Pt to that of the stainless steel was 1, 10, and 100, respectively. This acquired corrosion resistance was attributed to the anodic protection of the stainless steels by Pt, which is a more efficient cathode for the reduction of oxygen. This greater efficiency of Pt for the reduction of oxygen shifted the potential of the stainless steel to a value in the passive range, thereby enhancing the resistance to corrosion. The same effect is observed when Pt is alloyed with steel, and is known as a cathodic modification of the stainless steel by the PGM. The galvanic coupling of two austenitic stainless steels, AISI 304 (18% Cr–8% Ni) and AISI 316 (18% Cr–8% Ni–2% Mo) with Pt, was studied electrochemically by Kabi *et al.*<sup>64</sup> in solutions of 2 and 5 M sulfuric acid at 28 °C. They confirmed that galvanic coupling with Pt enhanced the corrosion resistance of both steels, since the critical current density was lowered at the onset of passivation, as was the passivating current density. The corrosion potential of both alloys also shifted to a more positive value.

### 3.22.10 Cathodic Modification of Duplex Stainless Steels

The development of the duplex stainless steels (steels containing a ferrite–austenite mixture) was first reported by Bain and Griffiths<sup>65</sup> as early as 1927. Duplex stainless steels combine the advantages of ferritic and austenitic stainless steels and, although a large amount of data has been collected and published about duplex stainless steels, very little work has been reported in the literature about the addition of noble metals to these steels.

It appears that Tomashov's is the only group that has carried out any work on the influence of the addition of noble metals on duplex stainless steels. Furthermore, it appears that their work on the addition of Pd to duplex stainless steels was purely incidental, their main thrust having been focused on the investigation of the effect of Pd on the corrosion characteristics of

highly nitrated austenitic stainless steel (some containing molybdenum as well) in non-oxidizing acid solutions. The occurrence of two phases (ferrite and austenite) in some highly nitrated austenitic stainless steels also led to investigations of duplex stainless steels that were alloyed with Pd.<sup>59</sup>

In one of the investigations by the Tomashov group<sup>60</sup> into the corrosion resistance of Fe–Cr–Ni stainless steels in hydrochloric acid, two duplex stainless steels were produced with low levels of nitrogen (0.03% or more). The Fe–25% Cr–6% Ni–3% Mo alloy contained 30% ferritic phase, while the Fe–25% Cr–6% Ni–3% Mo–0.2% Pd alloy contained 40% ferrite phase. Both steels were found to corrode actively in a solution of 3% hydrochloric acid at 50 °C.

A higher corrosion rate was found in the duplex steel containing Pd because, in conditions in which the steel does not self-passivate and in which it corrodes with the evolution of hydrogen, the presence of an effective cathodic additive with a low hydrogen over-voltage enhances the cathodic reaction and increases the corrosion rate.

This investigation showed that duplex stainless steels containing Pd cannot be passivated in a solution of up to 3% hydrochloric acid at 50 °C because of the heterogeneity of its structure. Both Cr and molybdenum are powerful ferrite stabilizers, while nickel is primarily an austenite stabilizer. Therefore, the distribution of the different components in the two phases differs by several percentage points as a result of partitioning. The austenitic phase, being depleted of Cr and molybdenum and enriched with nickel, experienced difficulty in achieving passivation.

In another paper on the corrosion resistance of highly nitrated austenitic stainless steels alloyed with Pd, Tomashov *et al.*<sup>59</sup> produced some duplex stainless steels that typically consisted of 18–25% Cr, 7–11% Mn, ~2% Mo, and nearly 1% N, with a varying ferrite content of 36–50%. These steels were additionally alloyed with 0.1–0.5% Pd. No nickel was present in any of these alloys.

Corrosion tests conducted in solutions of 20–50% sulfuric acid at 20–100 °C indicated that all the duplex alloys containing Pd initially corroded intensively after immersion and activation before they became self-passivated. The time required for self-passivation decreased with an increase in both the Pd content of the steel and an increase in temperature, but increased with an increase in the concentration of acid (20–40% sulfuric acid). In a solution of 20% sulfuric acid at 100 °C, only the steels containing

0.4% and 0.5% Pd self-passivated. This investigation also showed that duplex stainless steels containing Pd had a greater corrosion resistance in 2–3% hydrochloric acid at 20–50 °C than did similar cathodically modified austenitic stainless steels.

Potgieter<sup>66</sup> carried out an extensive investigation into the corrosion behavior of different stainless steel groups cathodically modified with Ru in sulfuric acid solutions at various temperatures. Three groups of low nitrogen duplex stainless steels were investigated, namely Fe–22% Cr–3% Mo, Fe–29% Cr–3% Mo, and Fe–35% Cr–3% Mo, with sufficient amounts of Ni added to each group (9.14% and 18% respectively) to ensure a fully duplex structure containing approximately equal amounts of austenite and ferrite in each case after suitable heat treatment. Varying amounts of Ru, namely 0.1–0.3%, were added to each of the base alloys in each group, yielding a total of twelve alloys. One of the reasons for the selection of the three groups was to determine whether the effect of the Ru in inhibiting corrosion would become more enhanced with an increasing Cr content in the alloy, as was the case with the ferritic and superferritic stainless steel. The choice of Ru was motivated by two factors, that is, the fact that it was more effective than Pd, and the huge excess being produced in South Africa for which there is currently no alternative applications. The compositions of the various alloys are given in **Table 3**.

The results obtained from mass loss tests indicated that significant decreases in the corrosion rates of duplex alloys could be obtained by the addition of small amounts of Ru to the base alloys. The increase in the corrosion resistance was the most

**Table 3** Chemical composition (%m/m) of the duplex stainless steels investigated

Alloy	Cr	Ni	Mo	Ru
377	22.0	9.07	2.81	–
378	22.1	9.20	2.89	0.14
379	22.4	9.14	2.82	0.22
380	22.4	9.24	2.92	0.28
413	28.5	14.4	2.70	–
414	28.4	14.0	2.70	0.06
398	29.6	14.3	2.73	0.17
399	30.1	14.8	2.88	0.28
400	34.7	18.6	2.72	–
416	33.9	17.4	2.60	0.15
448	35.0	18.8	2.50	0.23
446	34.5	18.5	2.80	0.28

For each alloy the balance of the composition is made up of Fe.

pronounced in the alloy group with the lowest Cr and nickel content. Electrochemical measurements indicated that the corrosion potentials of all the alloys containing Ru were raised to more noble values in sulfuric acid solutions. Under conditions where the alloys passivated spontaneously, a decrease in cathodic Tafel slopes occurred. When the alloys were actively corroding, Ru additions decreased the critical as well as the passive current densities of all three groups of alloys. Increasing acid concentrations and temperatures were found to increase the corrosion rates, critical current densities and passive current densities of all the alloys investigated. At the same time a lowering in the corrosion potential occurred for each individual alloy with increasing severity of the corrosive environment. In contrast to commercial duplex stainless steel, where the potential of the specimen with respect to the environment determines the phase that would preferentially corrode, only the ferrite phase corroded preferentially in these low nitrogen duplex alloys through a range of active to passive potentials investigated.

The effect of the various acid concentrations and temperatures used in the investigation on the different duplex stainless steel group can best be described by the compiled isocorrosion curves presented in Figure 5. Areas to the left and below each curve indicate the conditions where stable (spontaneous) passivation occurs, while areas to the right and above each curve indicate active corroding conditions. The beneficial effects of increased Cr and nickel additions in improving the corrosion resistance between each of the groups of duplex stainless steels are clearly visible, while the beneficial effect of increasing Ru additions in each group can also be easily distinguished.

### 3.22.11 Surface Alloying with PGMs

Unlike bulk alloying, which requires the introduction of a considerable amount of a noble-metal component to obtain a protective effect, surface alloying seems to be a more economical way to achieve the same purpose. It is therefore not surprising that a fair amount of research has been conducted to establish the corrosion resistance of various alloys with PGM surface coatings.

#### 3.22.11.1 Cathodically Modified Cr Coatings

Tomashov *et al.*<sup>67</sup> showed that the corrosion resistance of electrolytic Cr plating could be substantially

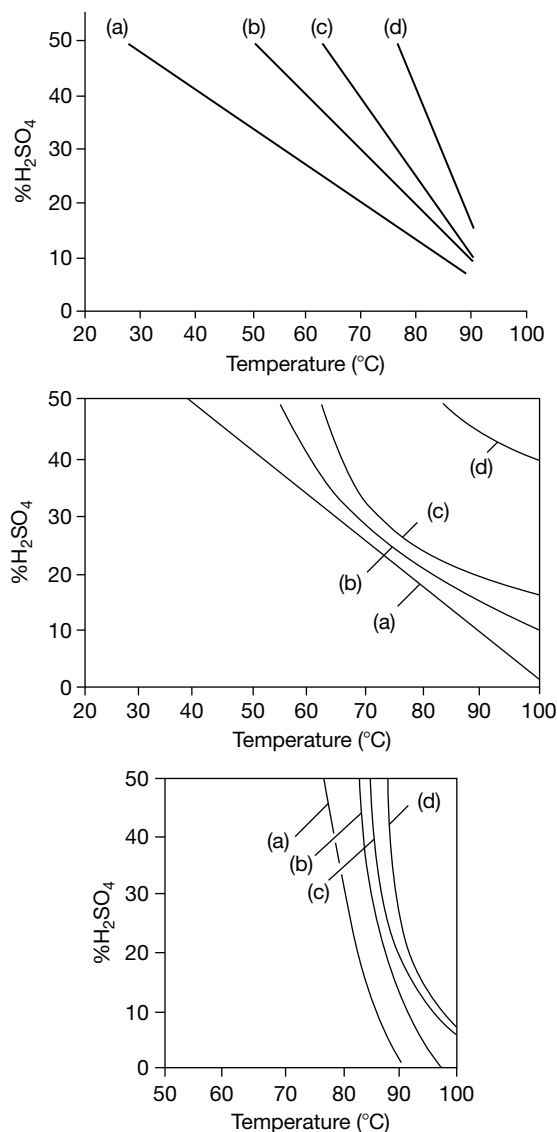


**Figure 5** Isocorrosion curves of different duplex stainless steel group with varying Ru concentrations (i) 22% Cr–9% Ni–3% Mo (a = 0% Ru; b = 0.1% Ru; c = 0.2% Ru; d = 0.3% Ru); (ii) 29% Cr–13% Ni–3% Mo (a = 0% Ru; b = 0.1% Ru; c = 0.2% Ru; d = 0.3% Ru); and (iii) 35% Cr–17% Ni–3% Mo (a = 0% Ru; b = 0.1% Ru; c = 0.2% Ru; d = 0.3% Ru).

increased in solutions of nonoxidizing acids when Cr and Pd were deposited layer by layer. Small additions of Pd (1–3%) significantly increased the corrosion resistance of Cr coatings in solutions of 20% sulfuric acid and 5–10% hydrochloric acid. The sequence of alternating Cr and Pd layers, as well as subsequent heat treatment (annealing) after plating, also influenced the corrosion characteristics.

### 3.22.11.2 Surface Alloying in Fe–Cr Alloys

When Fe–27% Cr is surface alloyed with Pd (0.1–0.5  $\mu\text{m}$ ) by an electroplated coating followed by annealing, it acquires a high resistance to corrosion in solutions of 20% sulfuric acid at 100 °C.<sup>68–70</sup> While steel that does not contain Pd was nonresistant, the corrosion rate in the coated steel decreased by several orders of magnitude. The annealing of the samples did not hinder the corrosion resistance, despite the diffusion of a considerable amount of Pd into the base metal. In milder conditions, the introduction of less Pd into the surface layer is even sufficient to prevent corrosion. It was calculated<sup>69</sup> that the minimum amount of Pd that is necessary per unit surface area to impart corrosion resistance is about 0.1 g m<sup>−2</sup>, which corresponds to mean Pd layer thickness of  $\sim 10$  nm.

The electrospark method of coating<sup>68–70</sup> yields similar results for corrosion resistance in Fe–27% Cr, and may offer a convenient method for increasing the corrosion resistance of large structures that cannot be electroplated with Pd in baths.

Agarwala and Bieffer<sup>50</sup> agree with the Tomashov group that the surface deposition of Pd appears to be a relatively inexpensive way of obtaining good corrosion resistance in stainless steels. They found that the deposition of Pd from a Pd chloride solution onto type 430 stainless steel and type 430 stainless steel plus 2% molybdenum cause the specimens to passivate spontaneously when exposed to 0.5-M sulfuric acid. The molybdenum-bearing steel was more readily passivated than the molybdenum-free steel. They concluded that this behavior supports statements that Pd enriched the surface of an alloy during the initial period of corrosion.

### 3.22.11.3 Surface Alloying Fe–Cr–Ni Stainless Steel

Work on the cathodic alloying of Fe–Cr–Ni stainless steel surfaces was first carried out by Bianchi *et al.*<sup>71</sup> who electroplated a Fe–19% Cr–11% Ni alloy with Pt. They concluded that, even with a Pt coverage of as low as 20 mg m<sup>−2</sup>, the Pt provides efficient protection of the stainless steel in solutions of concentration up to 75% H<sub>2</sub>SO<sub>4</sub> at 25 °C. They attributed this greater corrosion resistance of the stainless steel to two factors. First, Pt is a more efficient cathode for the reduction of oxygen than is stainless steel and, second, the selective deposition of Pt in the form of small round particles ( $\sim 0.01$   $\mu\text{m}$  in diameter) blocked the most active sites of the stainless steel surface. Electron microscopy was carried out on thin-film samples, and provided evidence for the selective

electrodeposition of Pt at emerging dislocations and grain boundaries.

Tomashov *et al.*<sup>68,72</sup> investigated this possibility using two different methods of applying Pd to the surface of an Fe–18% Cr–10% Ni alloy, namely electrolytic plating, and electrospark alloying. The Fe–18% Cr–10% Ni alloy with electrolytically deposited coatings of Pd (0.1–5  $\mu\text{m}$ ) acquire high corrosion resistance in a solution of 20% sulfuric acid at 100 °C. Under less aggressive conditions, even less Pd is required in the surface layer to protect the steel from corrosion. When the Fe–18% Cr–10% Ni stainless steel was modified by electrospark alloying, stable passivity was once again obtained. When an Fe–40% Cr–0.2% Pd alloy was used for the coating, the concentration of Pd on the surface of the Fe–18% Cr–10% Ni steel was  $\sim 1\%$ , which increased to between 12 and 18% as self-passivation was established. It was found that spark alloying with this combined Cr and Pd alloying addition produced better resistance against corrosion than that obtained when alloying was carried out with Pd alone. However, electrolytic deposition produced a smoother more continuous coating than was produced by spark alloying.

In acid solutions (20% H<sub>2</sub>SO<sub>4</sub> at 100 °C), the simultaneous presence of a specimen of carbon steel, which dissolves with the evolution of hydrogen, causes the potential of the specimen coated with Pd (1  $\mu\text{m}$ ) to shift towards a more negative value, and causes the stainless steel to dissolve actively. This situation arises irrespective of whether or not there is contact between the carbon steel and the stainless steel coated with Pd.

Potgieter and van Bennekom<sup>73</sup> investigated the corrosion behavior of 316 austenitic stainless steel electrolytically plated with silver and heat treated to diffuse the silver into the material in various sulfuric acid solutions at temperatures of 25, 45, and 75 °C. Table 4 gives an indication of the performance of the base and plated alloys in the various H<sub>2</sub>SO<sub>4</sub> solutions. As can be expected, the best corrosion resistance was observed in the solutions at 25 °C, while the most severe corrosion occurred in the solutions at 75 °C. The silver plated alloy by far outperformed the unplated base alloy under all test conditions, and caused a marked improvement in corrosion resistance. Furthermore, silver has the advantage that it is substantially cheaper than Ru, almost by a factor of 10.

Potgieter *et al.*<sup>74</sup> investigated the effect of Ru evaporated by an electron beam onto an Fe–22% Cr–9% Ni–3% Mo duplex stainless steel on the corrosion

**Table 4** Electrochemical parameters of surface alloyed and nonsurface alloyed 316 SS at 25 °C

$H_2SO_4$ (%)	Nonalloyed with Ag		Surface alloyed with Ag			
	$i_{crit}$ ( $A\ cm^{-2}$ )	$i_{corr}$ ( $A\ cm^{-2}$ )	$E_{corr}$ (mV)	$i_{crit}$ ( $A\ cm^{-2}$ )	$i_{corr}$ ( $A\ cm^{-2}$ )	$E_{corr}$ (mV)
1	37.1	12.84		21.1	6.18	
10		28.48	102		11.15	264
20	87.4	37.41	−310	42.6	13.43	285
30	99.6	90.91	−120	63.3	24.30	280

**Table 5** Main features of the influence of noble metal additions on the corrosion resistance of various alloy systems

Alloy system	$H_2SO_4$	HCl
Ductile chromium	5–98% at boiling point 0.1% PGM additions cause a decrease in the corrosion rate by a factor of $10^5$ or more Decreasing order of effectiveness of PGMs: Ir > Rh > Ru > Pt > Pd > Os.	5–15% at boiling point
Ferritic stainless steels	20–30% at 25 °C. Additions of <0.5% PGMs decrease the corrosion rate by as much as 99.85% Synergistic beneficial effect on corrosion rate if both a PGM and Mo are present in an alloy. Effect of PGM on corrosion rate increase with increasing chromium content (above 25% in an alloy). Fe–40% Cr–0.2% Pd even more resistant than Hastelloy alloys in 10–50% at boiling point	1% at boiling point
Austenitic stainless steels	Ru a better cathodic additive than Pd. Insufficient cathodic additive accelerates corrosion Behaviour of PGM alloyed ferritic SSs different in $H_2SO_4$ and HCl media. Effect of PGM additions not as dramatic as for ferritic stainless steels, but increase corrosion resistance nonetheless, especially in fairly aggressive conditions. Synergistic beneficial effect on corrosion rate if both a PGM and nickel are present in an alloy.	
Duplex stainless steel	Also possible to enhance corrosion resistance by galvanic coupling with Pt. 20–50% at 20–100 °C PGM additions (0.5%) cause self-passivation	3% at 50 °C. Alloys with low nitrogen content corrode actively even with PGM additions. 2–3% at 20–50 °C Highly nitrided manganese substituted duplex SSs with PGM additives more resistant than similar cathodically modified austenitic SS

resistance of the alloy in 10%  $H_2SO_4$ , and compared it with that of a bulk alloyed sample containing 0.2% Ru. It was found that the two alloys performed similarly and that both had improved corrosion resistance compared to the base alloy without any Ru addition to it.

The main features of the influence of noble-metal additions on the corrosion resistance of the various alloy systems are summarized in Table 5.

### 3.22.12 Summary of the Effect of PGMs and other Noble Metals on the Corrosion Resistance of Cr-Based Alloys

From the above discussion, it can be concluded that cathodic alloying additives (PGMs) greatly increase the corrosion resistance of Cr in nonoxidizing acid environments. The processes of active dissolution

and passivation of cathodically modified Cr can be satisfactorily interpreted from a comparison of the different electrochemical processes; the anodic process on Cr, and the process on the cathodic component. It is also evident that the corrosion resistance of Fe–Cr stainless steels can be significantly increased in nonoxidizing media over a large range of concentrations and temperatures by small additions (0.5% or less) of PGMs. The amount of PGMs needed to produce passivity in Fe–Cr alloys can be decreased by an increase in the Cr content. When molybdenum is also present in the base alloy, a further beneficial synergistic effect between molybdenum and the PGMs can decrease the concentration of the PGMs needed for stable passivity even further. The pitting corrosion resistance of Fe–Cr–Mo steels can be impaired by some of the PGMs. The use of various methods for surface alloying has also proved



successful in reducing high corrosion rates, and similar results to those achieved by use of bulk alloying can be achieved in increasing the resistance to corrosion. However, long-term assessment has to be carried out on surface alloying before any conclusive judgment can be reached.

Similarly, the alloying of multicomponent stainless steels with Pd can also lead to a significant increase in the corrosion resistance of such steels especially in more aggressive environments. However, the corrosion resistance of these steels also depends, to a large extent, on the presence and combination of other components, for example, molybdenum, manganese, and nitrogen.

The work carried out by Tomashov *et al.*<sup>59,60</sup> provides some insight into the corrosion behavior of cathodically modified duplex stainless steels. The effect of the addition of Ru on the corrosion mechanism and the corrosion of each phase in duplex stainless steels were further investigated by Potgieter,<sup>66</sup> who found that the increase in corrosion resistance was the most pronounced in the alloy group with the lowest Cr and Ni content. Furthermore, it was shown that the Ru additions lowered the cathodic Tafel slopes, the critical current densities required for passivation and only the ferritic phases underwent preferential dissolution under conditions of active corrosion.

Evidence indicates that, for all cathodically modified alloys of titanium, stainless steel, and Cr, there is an enrichment of the PGMs on the surface of the alloy at the onset of passivation. It seems that, in all cases, the enrichment of the surface of the alloy during the corrosion process can be explained as being due to a diffusion mechanism.

### 3.22.13 The Nature of the Passive Film on Cathodically Modified Alloys

There are various ways in which the corrosion resistance of an alloy can be improved. The formation of stable oxide layers constitutes one such method. Stainless steels owe their corrosion resistance largely to the formation of passivating oxide layers on the surface of the alloys. However, the effect of PGMs and/or their incorporation in stainless steels on the composition of the passive surface layer has not yet received much attention.

Initially, there is an atmospheric oxide film present on the surface of the cathodically modified alloy.<sup>75</sup> Auger analyses have indicated that the composition and structure of the passive film on some cathodically

modified alloys are similar to those on other stainless steels.<sup>76</sup> It is accepted that the less noble components of stainless steel, for example Cr and iron, oxidize the fastest during the initial stage of active dissolution, thus leaving the noble metal atoms originally present in solid solution as adatoms on the surface of the alloy. Since the noble metal atoms do not oxidize at the low potentials normally encountered during active dissolution, they accumulate on the surface of the alloy. Once a sufficient quantity has accumulated, it can cause spontaneous passivation of the alloy to occur. Although there is ample evidence from various sources<sup>11,23,32,55,75–77</sup> that there is an accumulation of the cathodic component, present in solid solution in the alloy, on the surface of the alloy during the first few minutes of active dissolution, before the passive state is established, very little is known about the nature of the passive film itself, and only a few investigations have been carried out.

### 3.22.14 Russian Studies

Tomashov *et al.*<sup>60</sup> concluded that, in the absence of preliminary etching, Pd which is originally present in solid solution in the alloy, is incorporated into the passive film formed on a Fe–25% Cr–6% Ni–3% Mo–N–0.2% Pd alloy after exposure in HCl, but that in the case of preliminary etching in the active region, Pd accumulates on the surface of the alloy in the form of an independent phase. Furthermore, it seems that Pd increases the stability of the passive film. It was also found that the simultaneous presence of Pd and molybdenum in an Fe–25% Cr–2% Mo–0.3% Pd alloy in nonoxidizing acids promotes more stable passivity than do either Pd or molybdenum alone.<sup>48</sup> This is attributed to the direct influence of molybdenum on the anodic process, as well as the assumption that molybdenum was incorporated in the passivating film on the steel.

Tomashov *et al.*<sup>77</sup> also determined that an Fe–25% Cr alloy to which Ru is added, passivated easier in 5–50% H<sub>2</sub>SO<sub>4</sub> and 1–5% HCl at 50–100 °C than did a similar alloy with an equal Pd content.

Electron microscopy indicated that the surface layer on the Fe–25% Cr–2% Pd alloy consisted mainly of a chromic oxide (Cr<sub>2</sub>O<sub>3</sub>) film with metallic Pd precipitates, while no metallic Ru particles were detected in the chromic oxide film on the surface of the Fe–25% Cr–2% Ru alloy. On this basis it was concluded that one of the reasons for the better resistance of the Ru-containing alloy as



compared to the Pd-containing one, was due to the fact that a large fraction of the accumulated Ru was not present in the form of an independent phase, but was included in the composition of hydroxide and oxide layers that had formed on the surface of the alloy, thereby increasing the resistance of these layers.

A detailed electron microscopy study, by Tomashov *et al.*<sup>23</sup> of the accumulation of Pd on the surface of an Fe–25% Cr steel during active corrosion in H<sub>2</sub>SO<sub>4</sub> revealed that the particle size of the accumulated Pd depends on the temperature at which dissolution took place, as well as on the Pd concentration in the steel. This was confirmed by Higginson *et al.*,<sup>76</sup> who also found that the concentrations of Ru were higher on the passive surfaces of Fe–40% Cr–0.1% Ru alloys than on the passive surfaces of Fe–40% Cr–0.2% Ru. He furthermore established that the accumulation of Ru on the surfaces of Fe–40% Cr–(0.1–0.2%) Ru also depended on the kind of acid in which corrosion took place.

The composition and morphology of the passive surfaces of the cathodically modified alloys studied by Higginson *et al.*<sup>76</sup> are those predicted by Pickering<sup>22</sup> in his review of selective dissolution for alloys containing low concentrations of the noble metal. These results in addition confirm that the chloride ion tends to produce a coarser distribution, thus supporting the suggestion that the chloride ion increases the rate of surface diffusion of Ru during selective dissolution.

### 3.22.15 The Fe–40% Cr–PGM System

Although Higginson *et al.*<sup>76</sup> detected Ru with Auger analysis in the Fe–40% Cr–(0.1–0.2%) Ru alloy after spontaneous passivation in 0.5 M HCl and in the Fe–40% Cr–0.1% Ru alloy after spontaneous passivation in 0.5 M H<sub>2</sub>SO<sub>4</sub>, they only concluded that the enrichment in Ru occurred at the metal oxide film interface, without elaborating on the possible inclusion of the Ru in the passive film. Finer detail about the precise nature of the passive film on Fe–40% Cr–Ru alloys was obtained in a study by Tjong.<sup>61</sup> Tjong confirmed observations by Higginson *et al.*<sup>76</sup> that more Ru is present on the surface of the Fe–40% Cr–0.1% Ru alloy after spontaneous passivation in 0.5 M HCl than in the case of the alloy containing 0.2% Ru and ascribes this to the fact that active dissolution preceding passivation of the 0.1% Ru alloy in 0.5 M HCl is

faster than that of the Fe–40% Cr–0.2% Ru alloy. As a result, larger amounts of Ru adatoms are accumulated on the surface of the alloy containing 0.1% Ru than on that of the alloy containing 0.2% Ru. In both alloys passivating spontaneously in 0.5 M HCl, considerable enrichment of Cr as well as Ru occurs in the passive films. Tjong<sup>61</sup> estimated that the thickness of the passive film on the Fe–40% Cr–0.2% Ru alloy, after spontaneous passivation in 0.5 M HCl, was ~3.2 nm.

Tjong<sup>61</sup> also agrees with Higginson *et al.*<sup>76</sup> that Ru is only incorporated in the passive film of the Fe–40% Cr–0.1% Ru alloy after spontaneous passivation in 0.5 M H<sub>2</sub>SO<sub>4</sub> and could not be detected for the Fe–40% Cr–0.2% Ru under similar conditions. However, when X-ray photoelectron spectroscopy (XPS) was used, the presence of Ru in the passive film on Fe–40% Cr–0.2% Ru after passivation in 0.5 M H<sub>2</sub>SO<sub>4</sub> was detected in the form of Ru<sup>4+</sup>. Tjong<sup>61</sup> concluded that it is likely that both Ru hydroxide as well as RuO<sub>2</sub> may be present in the passive film. It was pointed out earlier by Tomashov *et al.*<sup>77</sup> that in Cr steel containing Ru, that the Ru tends to be incorporated into the hydroxide or oxide layers formed on the Cr steel. The presence of Ru<sup>4+</sup> was also detected in the passive films formed on Fe–40% Cr–0.1% Ru after exposure to 0.5 M H<sub>2</sub>SO<sub>4</sub> and both Fe–40% Cr–0.1% Ru and 0.2Ru after spontaneous passivation in 0.5 M HCl. Tjong<sup>61</sup> thus proved that Cr and Ru are both incorporated in the passive films formed spontaneously on the Fe–40% Cr–0.1% Ru and Fe–40% Cr–0.2% Ru alloys in both hydrochloric and sulfuric acid solutions as Ru<sup>4+</sup> and Cr<sup>3+</sup> species. Further evidence for the incorporation of Ru into the passive film as Ru<sup>2+</sup> species, comes from the work of Kato and Sakaki<sup>31</sup> who investigated the passivation of Cr–Ru materials in sulfuric acid with AES and XPS.

In another study of the Fe–40% Cr alloy system, Tjong<sup>78</sup> found a remarkable difference in the nature of the passive films formed on an Fe–40% Cr–0.2% Pd alloy that passivated spontaneously and under potentiostatic control in 0.5 M HCl at 25 °C. A comparison of the AES composition depth profiles as well as in the [Cr]/[Cr] + [Fe] concentration ratios with sputtering time reveals that there is a marked difference in the composition of the passive films formed under different conditions. The passive film on the Fe–40% Cr–0.2% Pd alloy that underwent spontaneous passivation in 0.5 M HCl was estimated to be 2.4 nm thick and was enriched in Pd relative to Cr. The enrichment of Pd was responsible for the occurrence of spontaneous passivation. In the passive film formed on this same

alloy under potentiostatic control at 220 mV for 40 min, strong enrichment in Cr was found. No Pd was incorporated into this passive film. XPS measurements on both passive surfaces indicated that the Pd is present in the spontaneously passivated film as  $\text{Pd}^{2+}$ , whereas Cr is present as  $\text{Cr}^{3+}$ . This is a significant finding which indicates that there is a difference in the type of oxide formed by different PGMs when spontaneous passivation of Fe-40% Cr-0.2% PGM alloys occur in 0.5 M HCl.

In another investigation<sup>79</sup> of the passivation of Fe-40% Cr-(0.1–0.2)% Pt alloy in 0.5 M HCl at 25 °C, Tjong<sup>79</sup> found that the passive film that formed on these alloys is extremely thin, that is,  $\sim 1.6$  nm. Although Auger spectra did not detect the presence of Pt in the passive surfaces of the Fe-40Cr-Pt system, XPS measurements revealed the existence of the Pt-passivating species and the fact that the surface film contains two Pt species, that is,  $\text{Pt}^{2+}$  and  $\text{Pt}^0$  (metallic Pt).

### 3.22.16 Other Quaternary and Ternary Fe-Cr Alloys with PGMs

Tjong<sup>80</sup> also investigated the passivation characteristics of an FeCrNiMoRu ferritic stainless steel containing 22% Cr, 5% Ni, 3% Mo, and 0–0.3% Ru in 0.5 M HCl at 25 °C. XPS analysis of the passive film on the FeCrNiMo alloy containing 0.3% Ru after spontaneous passivation in 0.5 M HCl showed the presence of three molybdenum species, namely  $\text{Mo}^0$ ,  $\text{Mo}^{4+}$ , and  $\text{Mo}^{6+}$ , in the passive film. The presence of molybdenum in the spontaneously formed passive film indicated that the film is thin enough to allow escape of photoelectrons ejected from the substrate alloy through the film. It was also found that nickel and Ru were absent and did not accumulate in the passive film.

Auger and XPS analyses on passivated films on Fe-24% Cr containing sputter-deposited Pd and exposed to 0.5-M HCl, revealed that a thick Cr oxide layer formed on the Pd enriched surface of the alloy.<sup>44</sup> XPS analysis of a similar base alloy containing ion implanted Ru after exposure to 0.5 M  $\text{H}_2\text{SO}_4$  showed that Ru is incorporated as  $\text{Ru}^{4+}$  in the passive film formed on the alloy.

Studies by Potgieter *et al.*<sup>81</sup> and Baradlai *et al.*<sup>82</sup> on Fe-22% Cr-9% Ni-3% Mo-(0–0.3%) Ru alloys spontaneously passivated in 1–20% sulfuric and 1–2% hydrochloric acid with *in situ* radiotracer methods, AES and XPS analyses, indicate a strong bisulphate/sulphate

accumulation on the alloys' surfaces that is related to the redistribution of the main alloying elements (Cr, Ni, Mo), as well as Ru, in the surface oxide films formed on the steels. The steel containing 0.3% Ru which passivated spontaneously in the HCl showed a significant enrichment of Mo. Cr seems to be mostly present as  $\text{Cr}_2\text{O}_3$  (deeper region) or  $\text{Cr}(\text{OH})_3$  (outermost range). Various types of iron oxides ( $\text{Fe}_3\text{O}_4$ ,  $\text{Fe}_2\text{O}_3$  and  $\text{FeO}(\text{OH})$ ) were also observed. The  $\text{Fe}_3\text{O}_4$  and  $\text{Cr}_2\text{O}_3$  contents were higher in the samples containing Ru than in those without it. Another investigation by the same group<sup>83</sup> using ordinary type-316 stainless steel and a 316 alloy containing 0.5% Ru, shows that after exposing it to HCl and  $\text{H}_2\text{SO}_4$ , selective dissolution of the less noble components occur first, while the majority of the surface defect sites are occupied by Cr, Ni, Mo, and Ru species. The enhanced protection and stability of the passive layers on the 316 + 0.5% Ru are most likely related to the changes in the chemical state and redistribution of these alloying elements on the surface. Myburg *et al.*<sup>84</sup> compared the surface composition of passive layers of an Fe-22% Cr-9% Ni-3% Mo with and without 0.3% Ru after passivation in 0.1 M HCl and 1 M  $\text{H}_2\text{SO}_4$  with each other after AES and XPS analyses, and concluded that the passive film of the alloy having a Ru addition contained more  $\text{Cr}_2\text{O}_3$  and  $\text{Fe}^{2+}$  than  $\text{Cr}(\text{OH})_3$  and  $\text{Fe}^{3+}$ , than was found for the alloy without Ru. Their observations correlated with the fact that Ru and Ni act as blocking agents and therefore increase the probability to form a stable passive layer.

Olefjord and Elstrom<sup>85</sup> have reported that the beneficial effect of nickel is not connected with the occurrence of this metal in the passive film. Instead the accumulation of nickel in the underlying alloy surface decreases the dissolution rate in the active condition and thereby enhances the formation of the anodic passive film.<sup>86</sup> It has been pointed out previously by Tomashov *et al.*<sup>87</sup> that Ru blocks lattice point defects during active dissolution and thereby decreases the dissolution rate of Cr from the active sites. It is believed that molybdenum exhibits similar blocking characteristics. It is therefore clear that Mo, Ni, and Ru are competing species in promoting self-passivation. The absence of Ru from the XPS spectra can be explained by taking into account the fact that the molybdenum concentration is  $\sim 10$  times higher than that of the Ru. Therefore, the molybdenum adatoms presumably blocked the majority of the active surface sites prior to passivation, while only a small number of defect sites are blocked by Ru adatoms. After spontaneous passivation the molybdenum adatoms were incorporated into the film as  $\text{Mo}^{4+}$  and

Mo<sup>6+</sup> species. The XPS measurements also showed that the outermost zone of the passive film that formed on the spontaneously passivated FeCrNiMo alloy with 0.3% Ru consists of Cr and molybdenum hydroxides.

In another investigation on the corrosion behavior of a Fe–24% Cr–6% V alloy containing various amounts of Ru (0.12–0.35%), Tjong<sup>88</sup> concluded from the Auger spectrum that Ru was absent in the passive film on the alloy that passivated spontaneously in 5% HCl solution at 25 °C. This was in contrast to what was found for a spontaneously passivated Fe–40% Cr–0.2% Ru alloy in 0.5 M HCl, where Ru was detected in the passive film. However, the Auger spectrum does show the presence of both Cr and vanadium in the spontaneously formed passive film. It therefore seems that the presence of Ru in the passive film not only depends on experimental conditions, but also on the alloy composition and the presence of other alloying elements.

According to Tjong,<sup>88</sup> the absence of Ru in the spontaneously formed passive film on the Fe–25% Cr–6% V–0.35% Ru alloy can be explained in terms of the competition between vanadium and Ru in blocking the surface-defect sites of the lattice. Because the concentration of vanadium is about 20 times greater than that of Ru, most of the surface defect sites are blocked by vanadium rather than Ru. It was also found that both Cr and vanadium were enriched in the passive film formed on this alloy. The thickness of the passive film was estimated to be approximately 1.8 nm.

Peled and Itzhak<sup>89</sup> investigated the nature of the passive films on hot pressed and sintered 316 stainless steel containing Cu, Au, Pd, and Pt additions of various concentrations after spontaneous passivation occurred in 0.5 M H<sub>2</sub>SO<sub>4</sub>. Auger spectroscopy indicated a maximum in the molybdenum concentrations at a depth of about 0.6 nm in all the passive steel samples, regardless of the composition. These observations mean that molybdenum is accumulated in the passive film. Furthermore, it was found that the oxide-film thickness of passive samples containing Au, Pd, and Pt was about 12–15 nm as compared to about 2–3 nm for passive sintered 316 stainless steel. This was ascribed to the low cathodic overpotential of Au, Pd, and Pt which enhance hydrogen evolution in the cathodic areas and promote the creation of a passive oxide layer in the anodic areas, thus resulting in a thicker oxide film. However, marked enrichment of copper was found on the surface of the passive, Cu-containing, sintered stainless steel samples after exposure to H<sub>2</sub>SO<sub>4</sub>, while only a slight

surface enrichment of the noble alloying elements was observed in the passive samples containing Au, Pd, and Pt.

### 3.22.17 Summary of the Current Observations about the State of Passive Film Compositions on Cathodically Modified Alloys

The following statements can be made to summarize the current state of knowledge regarding passive films formed in reducing acid media:

- i. Accumulation of PGMS originally present in solid solution in the alloy occurs on the surface of the alloy during the initial dissolution period.
- ii. Alloying elements such as Mo, V, and Ni can compete with the PGMs in blocking active surface sites during the initial stage of the corrosion process. This might result in the PGMs not being detected in the formed passive film, especially if the concentration of the other alloying elements is significantly higher (>10 ×) than that of the PGMs.
- iii. The amount, particle size, and morphology of the accumulated PGM on the surface alloy depend on the temperature at which the dissolution occurs as well as the medium in which it is taking place. Greater amounts of PGMs are found on surfaces of alloys that corroded in HCl than on those that were placed in H<sub>2</sub>SO<sub>4</sub>. This is attributed to increased surface-diffusion rates of the PGM adatoms in the presence of Cl<sup>−</sup> ions. Another factor that influences the accumulation of PGMs on the alloy surface is its initial concentration in the alloy. In alloys with lower PGM concentrations, active dissolution occurs faster and results in more adatoms accumulated on the final passive surface.
- iv. There is a difference in the passive films formed spontaneously and those formed under potentiostatic control. In the former case the PGM is incorporated in the passive film as an oxide, while in the latter case it is not, and is only present in an accumulated metallic form.
- v. Different PGMs form different types of oxides on passivated surfaces. Ru occurs as Ru<sup>4+</sup> in the passive film after spontaneous passivation in H<sub>2</sub>SO<sub>4</sub> and HCl, while Pd is incorporated into the passive film as Pd<sup>2+</sup> after spontaneous passivation of the same base alloy in HCl, or occurs in

the  $\text{Pd}^0$  form on the surface. Pt can occur in both the  $\text{Pt}^{2+}$  and  $\text{Pt}^0$  states in the passive film.

- vi. Determinations of the thicknesses of the passive films formed on cathodically modified stainless steels were carried out on a limited number of ferritic stainless steels that passivated spontaneously in HCl. Vast opportunities exist to extend this kind of investigations to other stainless steels in the same or different media (e.g., in  $\text{H}_2\text{SO}_4$ ) under a variety of conditions. Such an endeavor would shed more light on the role of PGMs and other alloying elements in enhancing the corrosion resistance of cathodically modified alloys.

### 3.22.18 Noble Metal Corrosion Resistance in Reducing Acids

Before closing this chapter, it is necessary to briefly take cognizance of the corrosion resistance of pure PGMs and other noble metals under reducing conditions (typically in hydrochloric and sulfuric acid solutions) to complete the description and understanding of their effects in various alloying systems exposed to such reducing acid conditions. The interest in recent times and the latest information is a result of renewed interest in the use of PGMs and their respective alloy or oxides combinations in various anode configurations for the chlorine–alkali industry for the electrolytic manufacture of chlorine, as well as the use of PGMs in fuel cell applications.

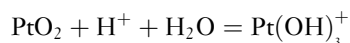
#### 3.22.18.1 Hydrochloric Acid

Kuhn and Wright<sup>90</sup> quoted evidence that the electrochemical behavior of platinum (Pt) in strong hydrochloric acid solutions can be ascribed to a  $\text{PtCl}_6$  corrosion product that changes to  $\text{PtCl}_4$  after passivation. Other sources quoted by Kodera *et al.*<sup>91</sup> confirmed that in the presence of  $\text{Cl}^-$  ions, Pt dissolves as the  $\text{PtCl}_4^{2-}$  or  $\text{PtCl}_6^{2-}$  complex. Apparently the specific adsorption of chloride ions on the electrode surface begins immediately after hydrogen desorption. In the same report it is mentioned that iridium (Ir) resist corrosion more than Pt and that it dissolved as  $\text{IrCl}_6^{3-}$  and  $\text{IrCl}_2^{2-}$  if the HCl concentration in solution is stronger than 3 M. Ru corrodes more readily than Pt and Ir, and Llopis and coworkers<sup>92,93</sup> have found that  $\text{RuO}_4$  was formed on ruthenium (Ru) electrodes which partially dissolved, presumably as  $\text{H}_2\text{RuO}_5$ , during anodic CV sweeps in hydrochloric acid solutions.

Sandenbergh and van der Lingen<sup>94</sup> calculated Pourbaix diagrams for Pd–Cl– $\text{H}_2\text{O}$  and Ru–Cl– $\text{H}_2\text{O}$  systems with 250 g l<sup>-1</sup> HCl using Stabcal software with the NBS and Uncritical databases and found that Ru should only oxidize (corrode) at potentials more positive than 0.347 V (vs. SHE) or 0.106 V (vs. SCE), while for Pd the values should be more positive than 0.180 V (vs. SHE) or -0.061 V (vs. SCE). Their experimental results were in excellent agreement with these theoretical predictions, thus lending credibility to their reported values of  $3.6 \times 10^{-6}$  and  $2.8 \times 10^{-3}$  A cm<sup>-2</sup> for the exchange current densities of Ru and Pd in 25% (m/m) HCl, respectively. These authors cautioned though that the values that were obtained are dependent on prior exposure time and surface enrichment of the alloying elements and should not be interpreted as steady state data.

#### 3.22.18.2 Sulfuric Acid

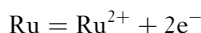
Pourbaix's diagram predicts that Pt metal will dissolve as  $\text{Pt}^{2+}$  during anodic polarization in strong acid solutions. In sulfuric or nitric acid solution the electrolyte enhances the passivation of Pt, especially in 0.5–5 M solutions, and the extent of corrosion seems to be dependent on the formed platinum oxide,<sup>91</sup> which is presumably  $\text{PtO}$ .<sup>90</sup> In more concentrated sulfuric acid solutions of 14–18 M, sulfur deposition seems to occur on the Pt electrode surface by cathodic polarization, which induces Pt corrosion under anodic polarization. The corrosion mechanism is thus different in dilute and concentrated sulfuric acid solutions, something which has also been observed in terms of nickel's behavior as an alloying element in stainless steels.<sup>95</sup> In an effort to understand and improve the dissolution behavior of Pt in polymer electrolyte fuel cells (PEFCs), Mitsushima *et al.*<sup>96</sup> reported a solubility of Pt of  $3 \times 10^{-6}$  M at 25 °C in 1 M  $\text{H}_2\text{SO}_4$  which increases with higher temperatures and increasing acid concentration. They postulated that platinum solubility in an oxygen-containing atmosphere would occur according to the dissolution reaction:



Ota *et al.*<sup>97</sup> reported a dissolution rate of  $5 \mu\text{g A}^{-1} \text{h}^{-1}$  for Pt in 1 M  $\text{H}_2\text{SO}_4$  at 40 °C and the formation of a monolayer of platinum oxide, probably  $\text{PtO}$ , when Pt is anodized under mild conditions. It was found that the corrosion of Pt is always lower in

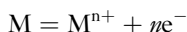
sulfuric acid solutions than in hydrochloric acid solutions of similar concentration, because the sulphate anions do not coordinate with the dissolved Pt ions in the way the chloride ions form chlorocomplexes referred to earlier.

In sulfuric acid solution Ru can passivate due to the formation of  $\text{RuO}_4$ .<sup>92</sup> Lezna *et al.*<sup>98</sup> reported electrochemical evidence which indicated that the O-layer formation and reduction of Ru in sulfuric acid depend on the range over which the potential is cycled. The anodic reaction initiated when the potential exceeds the equilibrium potential of 0.455 V for the reaction:



yields the equivalent of a monolayer of probably a mixture of oxygen-containing species such as  $\text{Ru}_2\text{O}$ ,  $\text{Ru}(\text{OH})$ , or  $\text{RuO} \cdot \text{H}_2\text{O}$  during the first stage of the electrooxidation process. This can change to  $\text{Ru}_2\text{O}_3$  and  $\text{RuO}_2$  as the potential is increased to 1.4–1.5 V (vs. SCE). Although no specific formula is given for it, a formal oxide of Ir begins to form at about the potential of oxygen evolution in 0.5 M  $\text{H}_2\text{SO}_4$ , and this oxide is only reduced in the hydrogen adsorption and evolution region.<sup>92,93</sup>

According to Pourbaix<sup>99</sup> the standard potentials for several noble metals dissolving are 0.80 V for  $\text{Rh}/\text{Rh}^{3+}$ , 0.99 V for  $\text{Pd}/\text{Pd}^{2+}$ , 1.19 V for  $\text{Pt}/\text{Pt}^{2+}$  and 1.50 V for  $\text{Au}/\text{Au}^{3+}$  versus RHE. Rand and Woods<sup>100</sup> reported similar values in their investigating on the dissolution of Pt, Pd, Rh, and Au electrodes in 1-M sulfuric acid solutions at 25 °C and emphasized that the amount of metal dissolved during a potential sweep (e.g., as in CV) will depend both on the nature and pretreatment of the electrode, on the experimental conditions, any stirring of the solution and the surface's structure. Their work supported a direct anodic dissolution mechanism of the noble metals according to the general reaction:



and the amounts of dissolved metals analyzed in solution correlated well with their electrochemical measurements and other reported values in the literature. It should be kept in mind that all the postulated oxide species formed on the surfaces of PGMs and noble metals during oxidation/corrosion were based on electrochemical data and little evidence could be found of surface analytical measurements to support the electrochemical data.

### 3.22.19 Final Conclusions

Despite the work during the last 50–60 years in this field, there are still a number of unanswered questions, and matters to be resolved. It is clear that the effects of cathodic modification in enhancing corrosion resistance are definitely more dramatic in ferritic stainless steels than in austenitic or duplex stainless steels. If Pd is replaced by Ru, then the maximum Cr content at which the largest decrease in the corrosion rate in superferritic (Fe–40% Cr) alloys is observed, can be lowered by at least 10%, which can have enormous cost and workability advantages. Because surface alloying seem to be equally efficient to bulk alloying in increasing the corrosion resistance of various stainless steels, it is definitely a more cost effective option to exploit in terms of practical applications of cathodically modified stainless steels for process equipment manufacture. However, it is not clear if cathodically modified stainless steels will always remain too expensive for uses other than those where safety hazards are the overriding concern and everything else is therefore of secondary importance.

### References

1. Cornish, L. A.; Süß, R.; Watson, A.; Preussner, J.; Prins, S. N.; Wenderoth, M.; Völkl, R.; Glatzel, U. *J. SAImm* **2007**, *107*, 713–724.
2. Cornish, L. A.; Süß, R.; Völkl, R.; Wenderoth, M.; Vorberg, S.; Fischer, B.; Glatzel, U.; Douglas, A.; Chown, L. H.; Murakumo, T.; Preussner, J.; Lupton, D.; Glaner, L.; Maledi, N. B.; Potgieter, J. H.; Sephton, M.; Williams, G. *J. SAImm* **2007**, *107*, 697–711.
3. Tomashov, N. D. *Prot. Met.* **1986**, *22*, 679.
4. Tomashov, N. D. *Corrosion* **1958**, *14*, 229.
5. Monnart, P. *Metallurgie* **1911**, *8*, 161.
6. Tomashov, N. D.; Sinelschtschikova, G. P.; Vedineeva, M. A. *Ber. Akad. D. Wissenschaft (Dokl. Akad. Nauk SSSR) (Moscow 1962) Bd.* **1948**, *1*, 105–108.
7. Stern, M. *J. Electrochem. Soc.* **1958**, *105*, 638.
8. Stern, M.; Wissenberg, H. *J. Electrochem. Soc.* **1959**, *106*, 751–764.
9. Stern, M.; Bishop, C. R. *Prepr. Am. Soc. Metals* **1959**, *51*, 165; *ASM* **1960**, *52*, 239.
10. Stern, M.; Bishop, C. R. *Trans. ASM* **1961**, *54*.
11. Greene, N. D.; Bishop, C. R.; Stern, M. *J. Electrochem. Soc.* **1961**, *108*, 836–841.
12. Cotton, J. B. *Chem. Ind.* **1958**, 68–9, 492; *Werkstoffe und Korrosion* **1960**, *1*, 152.
13. Cotton, J. B. *Chem. Eng.* **1960**, *67*, 166.
14. Cotton, J. B. *Chem. Eng.* **1959**, *66*, 200.
15. Cotton, J. B. *Ber. 111. Int. Congr. Metallic Corr. Moscow*, **1966**, 54.
16. Bockris, J. O. M.; Bonciocat, N.; Guthmann, F. *An Introduction to Electrochemical Science*; Sykeham Publishers: London, 1974; 72.
17. Streicher, M. A. *Platin. Met. Rev.* **1977**, *21*, 51–55.



18. Higginson, A. Ph.D Thesis, University of Manchester (UMIST), Manchester, U.K, 1987.
19. Tomashov, N. D. *Prot. Met.* **1967**, 3, 3; **1986**, 22, 679.
20. Tomashov, N. D. *Prot. Met.* **1981**, 17, 11.
21. Forty, A. B.; Durkin, J. A. *Philos. Mag.* **1980**, 42, 295.
22. Pickering, H. W. *Corros. Sci.* **1983**, 23, 1107–1120.
23. Tomashov, N. D.; Chernova, G. P.; Volkov, L. N.; Yakharov, A. P.; Sheshenina, Y. E. *Prot. Met.* **1973**, 9, 289–292.
24. Tomashov, N. D.; Chernova, G. P.; Ustinskii, E. N.; Chalykh, A. E.; Ilin, M. I.; Matveev, V. V.; Rubitsov, A. E. *Prot. Met.* **1984**, 20, 158.
25. Brox, B.; Olejford, I. In Proceedings of the Stainless Steel 84 Conference, Institute of Metals: London, 1985; 134.
26. Tomashov, N. D.; Chernova, G. P. *Passivity and Protection of Metals Against Corrosion*; Nauka: Moscow, 1965; pp 89–97. Translated from Russian by B.H. Tytell, Plenum Press, New York, 1967.
27. Tomashov, N. D.; Chernova, G. P.; Ustinskii, E. N. *Platin. Met. Rev.* **1979**, 23, 143–149.
28. Tomashov, N. D.; Chernova, G. P.; Trevilov, V. I.; Ratinski, A. N.; Poryadchenko, N. E.; Savranski, E. F.; Ustinskii, E. N. *Prot. Met.* **1980**, 16, 208–213.
29. Tomashov, N. D.; Chernova, G. P.; Ustinskii, E. N. *Prot. Met.* **1980**, 16, 452–455.
30. Tomashov, N. D.; Chernova, G. P.; Trevilov, V. I.; Ratinski, A. N.; Poryadchenko, N. E.; Savranski, E. F.; Ustinskii, E. N. *Prot. Met.* **1983**, 19, 89–93.
31. Kato, M.; Sakaki, T. *J. Jpn. Inst. Met.* **1993**, 57(4), 410–416.
32. Tomashov, N. D.; Chernova, G. P.; Ustinskii, E. N. *Prot. Met.* **1981**, 17, 325–330.
33. Tomashov, N. D.; Chernova, G. P.; Ustinskii, E. N. *Corrosion* **1984**, 40, 134–138.
34. Tomashov, N. D.; Chernova, G. P.; Ustinskii, E. N.; Chalykh, A. E.; Ilin, M. I.; Matveev, V. V.; Rubstov, A. E. *Prot. Met.* **1984**, 20, 158–162.
35. Tomashov, N. D. *Werkstoffe Korrosion* **1967**, 8, 694–707.
36. Bieffer, G. J. *Can. Metall. Q.* **1970**, 9, 537–550.
37. Tomashov, N. D.; Chernova, G. P. *Prot. Met.* **1975**, 11, 379–384.
38. Potgieter, J. H.; Kincer, M. U. *S. Afr. J. Chem.* **1991**, 44, 47–50.
39. Potgieter, J. H.; Machio, C. N.; Olubambi, P. A.; Sherif, E. M. In Proceedings Eurocorr 2007, Freiburg in Breisgau, Germany 9–13 Sept 2007.
40. Howarth, D. Unpublished results, Randburg, Council for Mineral Technology, 1987.
41. Potgieter, J. H.; Van Bennekom, A. *Can. Metall. Q.* **1995**, 34, 143–146.
42. Wolff, I. M.; Iorio, L. E.; Rumpf, T.; Scheers, P. V. T.; Potgieter, J. H. *Mater. Sci. Eng. A* **1998**, 241(1–2), 264–276.
43. Tomashov, N. D.; Chernova, G. P.; Chigirinskaya, L. A.; Nasedkina, E. A. *Prot. Met.* **1986**, 22, 704–710.
44. Tjong, S. C. *Appl. Surf. Sci.* **1991**, 51, 157–164.
45. Tjong, S. C.; Chu, P. K. *Surf. Coat. Technol.* **2007**, 201, 6781–6784.
46. Lizlovs, E. A.; Bond, A. P. *J. Electrochem. Soc.* **1969**, 116, 574.
47. Tomashov, N. D.; Chernova, G. P.; Markova, O. N. *Prot. Met.* **1973**, 9, 616–618.
48. Tomashov, N. D.; Chernova, G. P.; Golovanenko, S. A.; Ul'yanin, E. A.; Goronkova, A. D. *Prot. Met.* **1980**, 16, 83–89.
49. Tomashov, N. D.; Chernova, G. P.; Ryabchenkov, A. V.; Gerasimov, V. I.; Aksenova, L. I.; Agakishiev, O. D.; Chigirinskaya, L. A. *Prot. Met.* **1985**, 21, 155–159.
50. Agarwala, V. S.; Bieffer, G. J. *Corrosion* **1972**, 28, 64–74.
51. Streicher, M. A. *Corrosion* **1974**, 30, 77–91.
52. Scheers, P. V. T.; McEwan, J. J.; Knight, D. *Corros. Coat.* **1994**, 1–4.
53. McEwan, J. J.; Knight, D.; Scheers, P. V. T. *Proceedings of the XVth CMMI Congress; SAIMM* **1994**; Vol. 2, pp 151–155.
54. Sherif El-Sayed, M.; Potgieter, J. H.; Comins, J. D.; Cornish, L. A.; Olubambi, P. A.; Machio, C. N. In Proceedings Eurocorr 2007, 9–13 Sept, Freiburg in Breisgau, Germany 2007.
55. Tomashov, N. D.; Chernova, G. P. Chigirinskaya, L. A. *Corrosion* **1978**, 34, 445–446.
56. Hoar, T. P. *Platin. Met. Rev.* **1958**, 2, 117–119.
57. Tomashov, N. D.; Chernova, G. P.; Volkov, L. N. *Prot. Met.* **1970**, 6, 388–390.
58. Peled, P.; Itzhak, D. *Corros. Sci.* **1988**, 28, 1019–1028.
59. Tomashov, N. D.; Chernova, G. P.; Lakomskii, V. I.; Torkhov, G. F.; Chigirinskaya, L. A.; Slyshankova, V. A. *Prot. Met.* **1977**, 13, 6–11.
60. Chernova, G. P.; Chigirinskaya, L. A.; Tomashov, N. D. *Prot. Met.* **1980**, 16, 1–5.
61. Tjong, S. C. *Appl. Surf. Sci.* **1990**, 44, 7–15.
62. Potgieter, J. H. *J. Mater. Sci. Lett.* **1996**, 15, 1408–1411.
63. Bianchi, G.; Barosi, A.; Trasatti, S. *Electrochim. Acta* **1965**, 10, 83–95.
64. Kabi, C.; Mukherjee, K. P.; Rastogi, M. C. *J. Electrochem. Soc. India* **1985**, 34, 256–260.
65. Bain, E. C.; Griffith, W. E. *Trans. Metall. Soc. AIME* **1927**, 75, 166–213.
66. Potgieter, J. H. *S. Afr. J. Chem.* **1993**, 46(3/4), 58–64.
67. Tomashov, N. D.; Chernova, G. P.; Fedoseeva, T. A. *Prot. Met.* **1976**, 12, 1–3.
68. Tomashov, N. D.; Chernova, G. P.; Fedoseeva, T. A.; Kornienko, L. P. *Prot. Met.* **1981**, 17, 406–411.
69. Tomashov, N. D.; Chernova, G. P.; Reshetnikov, S. M.; Fedoseeva, T. A.; Vdovin, S. F.; Kornienko, L. P. *Prot. Met.* **1979**, 15, 525–528.
70. Tomashov, N. D.; Chernova, G. P.; Fedoseeva *Corrosion* **1980**, 36, 201–27.
71. Bianchi, G.; Camona, G. A.; Fiori, G.; Mazza, F. *Corros. Sci.* **1968**, 8, 751–757.
72. Tomashov, N. D.; Chernova, G. P.; Fedoseeva, T. A.; Kornienko, L. P. *Surf. Technol.* **1981**, 13, 241–256.
73. Van Bennekom, A.; Potgieter, J. H. *Surf. Eng.* **2001**, 17(1), 71–74.
74. Potgieter, J. H.; Wentzel, E.; Myburg, G. *Surf. Eng.* **1992**, 8(4), 289–292.
75. Tomashov, N. D.; Chernova, G. P.; Ustinski, E. N. *Platin. Met. Rev.* **1979**, 23, 147.
76. Higginson, A.; Newman, R. C.; Proctor, R. P. *Corros. Sci.* **1989**, 29, 1293–1318.
77. Tomashov, N. D.; Chernova, G. P.; Chigirinskaya, L. A.; Nasedkina, E. A. *Prot. Met.* **1986**, 22, 704–720.
78. Tjong, S. C. *Surf. Coat. Technol.* **1982**, 38, 46–52.
79. Tjong, S. C. *Appl. Surf. Sci.* **1990**, 45, 301–318.
80. Tjong, S. C. *Werkstoffe Korrosion* **1989**, 40, 729–734.
81. Potgieter, J. H.; Barnard, G.; Myburg, G.; Varga, K.; Baradlai, P.; Tomcsanyi, L. *J. Appl. Electrochem.* **1996**, 26, 1103–1110.
82. Baradlai, P.; Potgieter, J. H.; Barnard, W. O.; Tomcsanyi, L.; Varga, K. *Mater. Sci. Forum* **1995**, 185–188, 759–768.
83. Varga, K.; Baradlai, P.; Barnard, W. O.; Myburg, G.; Halmos, P.; Potgieter, J. H. *Electrochim. Acta* **1997**, 42(1), 25–35.
84. Myburg, G.; Varga, K.; Barnard, W. O.; Baradlai, P.; Tomcsanyi, L.; Potgieter, J. H.; Louw, C. W.; van Staden, M. J. *Appl. Surf. Sci.* **1998**, 136, 29–35.



85. Olefjord, I.; Elfstrom, B. O. *Corrosion* **1982**, *38*, 46–52.
86. Olefjord, I.; Brox, B.; Jelvestam, U. *J. Electrochem. Soc.* **1985**, *132*, 2854–61.
87. Tomashov, N. D.; Chernova, G. P.; Ustinski, E. N. *Corrosion* **1984**, *40*, 134–8.
88. Tjong, S. C. *ISIJ* **1990**, *30*, 397–402.
89. Peled, P.; Itzhak, D. *Corros. Sci.* **1991**, *32*, 83–90.
90. Kuhn, A. T.; Wright, P. M. *Electroanal. Chem. Interf. Electrochem.* **1973**, *41*, 329–349.
91. Kodera, F.; Kuwahara, Y.; Nakazawa, A.; Umeda, M. *J. Power Sources* **2007**, *172*, 698–703.
92. Llopis, L.; Tordesillas, I. M.; Alfayate, J. M. *Electrochim. Acta* **1966**, *11*, 623–632.
93. Llopis, L.; Vazquez, M. *Electrochim. Acta* **1966**, *11*, 633–640.
94. Sandenbergh, R. F.; Van der Lingen, E. *Corros. Sci.* **2005**, *47*, 3300–3311.
95. Potgieter, J. H.; Olubambi, P. A.; Machio, C. N.; Cornish, L.; Sherif, E. S. M. *Corros. Sci.* **2008**, *50*, 2572–2579.
96. Mitsushima, M.; Koizumi, Y.; Uzuka, S.; Ota, K. I. *Electrochim. Acta* **2008**, *54*, 455–460.
97. Ota, K. I.; Nishigori, S.; Kamiya, N. *J. Electroanal. Chem.* **1988**, *257*, 205–215.
98. Lezna, R. O.; De Tacconi, N. R.; Arvia, A. J. *J. Electroanal. Chem.* **1983**, *151*, 193–207.
99. Pourbaix, M. *Atlas of Electrochemical Equilibria in Aqueous Solution*; Pergamon Press: Oxford, 1966.
100. Rand, D. A. J.; Woods, R. *Electroanal. Chem. Interf. Electrochem.* **1972**, *35*, 209–218.

## 3.24 Degradation of Carbon and Graphite

**S. B. Lyon**

Corrosion and Protection Centre, School of Materials, The University of Manchester, Oxford Road, Manchester M13 9PL, UK

© 2010 Elsevier B.V. All rights reserved.

3.24.1	Technical Carbon and Graphite	2271
3.24.1.1	Introduction	2271
3.24.1.2	Baked Carbon	2272
3.24.1.3	Industrial Graphite	2272
3.24.1.4	Glassy Carbon	2273
3.24.1.5	Pyrolytic Graphite	2273
3.24.1.6	Carbon Fiber and Carbon Composites	2273
3.24.1.7	Other Forms of Carbon: Fullerenes and Carbon Nanostructures	2274
3.24.1.8	Final Manufacture and Surface Finishing	2274
3.24.2	General Characteristics	2274
3.24.3	Applications	2275
3.24.4	Degradation of Carbon and Graphite	2276
3.24.4.1	Aqueous Corrosion	2276
3.24.4.2	Aqueous Environments	2276
3.24.4.3	Galvanic Corrosion	2278
3.24.4.4	High Temperature Oxidation	2278
3.24.4.5	High Temperature Environments	2279
3.24.4.6	Protection against Degradation	2279
3.24.5	Nuclear Graphite	2280
3.24.5.1	Radiation Damage	2280
3.24.5.2	Enhanced Radiolytic Oxidation	2281
References		2281

### Glossary

**Exfoliation** The process of separation or shedding of layers of a structure, caused by mechanical abrasion, or particularly intercalation within a structure, resulting in the disruption of the bonding forces between 2-dimensional sheets of a material, such as graphite.

**Fullerene** A generic molecular structure for carbon, comprising linked polygonal sheets that build into a 3-dimensional structure such as a tube or ball and which resembles the geodesic dome structures originally designed by the architect Buckminster Fuller, after whom such structures are named.

**Intercalation** An ionic or molecular process that comprises the entry, or exchange, of species into a 2- or 3-dimensional lattice structure, for example, between the 2-D-layered

sheets that constitute graphite. Such entry often results in significant changes in physical or chemical properties of the structure.

### 3.24.1 Technical Carbon and Graphite

#### 3.24.1.1 Introduction

Natural flake graphite was known in ancient times as a mineral with well described properties, albeit in small volumes. However, the material became of technical interest only when an electric resistance furnace, capable of graphitization of carbonaceous materials and production of materials in large dimensions, was developed by Acheson in 1895.<sup>1</sup> Currently, only a few mines supply natural graphite, the main producing countries being China, Ukraine, Brazil, Russia, and Canada, although many mines produce

the less-valuable amorphous material in small volumes and not the more-valuable flake graphite. In the United Kingdom, a small graphite mine near Kendal was the basis of the Lakeland pencil manufacturing industry.

Baked carbon and industrial graphite can be manufactured from almost any form of carbonaceous precursor that leaves a carbon-rich material when heated in the absence of air. The main difference between the two substances is that graphitization requires furnace baking for much longer periods at higher temperatures and is therefore considerably more costly. However, its properties, for example, electrical conductivity, high temperature strength, etc., are greatly superior to baked carbon. In view of the limited natural resources, the main carbon precursors for carbon and graphite manufacture are generally cokes derived either from petroleum or coal, the former giving the highest purity and lowest ash content.

Carbon atoms can coordinate in several different ways with adjacent atoms. Thus, in the  $sp^3$  form, carbon is tetragonally coordinated in 3 dimensions, while in the  $sp^2$  form, carbon is trigonal planar.<sup>2</sup> Although carbon is obviously most abundant in nature in the form of various coals (largely, amorphous carbon containing various amounts of volatile materials and ash), this key difference in bonding is well exhibited in carbon's naturally occurring allotropes: graphite ( $sp^2$  bonding in 2-D macromolecular sheets), and most appealingly, diamond ( $sp^3$  bonding in 3-D macromolecules). In recent years, however, it has also been recognized that carbon can form a multitude of polymeric-like structures and macromolecules based particularly on  $sp^2$  bonding, for example, fullerenes.

### 3.24.1.2 Baked Carbon

At atmospheric pressure, carbon does not melt, but sublimates at very high temperatures (above 4000 °C). It can, therefore, only be manufactured using conventional ceramic processing routes. Thus, the precursor material (e.g., coal-derived coke) is initially ground to a desired particle size range, and then a clay-like green compact is formed with petroleum pitch or coal tar as binder. This is then formed into a final or near-net shape compact typically by extrusion, die-molding, or isostatic pressing. Significant anisotropy may be developed during such compact formation, especially with extruded materials. Also, the considerable shrinkage that will take place during heating has to be taken into account in the initial

dimensions of the green compact. After formation, the green compact is then baked in a pyrolysis furnace (i.e., with the exclusion of air) in order to eliminate oxidation and to ensure the carbonization of the pitch binder and the removal of volatile species by diffusion. During this process, it is important to limit the initial heating rate and temperature in order to ensure dimensional stability of the material. Depending on the application and the precursor, the initial pyrolysis temperatures are typically from 200 to 500 °C, with a final baking temperature of 650–900 °C. To avoid excessive cracking and porosity, large dimensioned samples require slow heating and cooling with furnace cycles of tens of days possible.

Carbon products from a single baking cycle are usually relatively porous (15–25 % porosity). Thus, although there are some uses for porous carbons (e.g., for the infiltration of copper for carbon brushes in electric motors, etc.), such products are, more generally, subjected to repeated cycles of pitch infiltration and baking in order to reduce porosity to desired levels (Figure 1).

### 3.24.1.3 Industrial Graphite

Baked carbon precursors may be graphitized by further heat treatment, using direct resistance heating with water-cooled electrodes. This further improves the mechanical and electrical properties of the material and also reduces the ash and volatile content. However, additional shrinkage takes place during the graphitization process. Initially, the temperature is raised to between 900 and 1200 °C where any residual pitch filler is fully carbonized. Thereafter, the temperature is raised in stages: from 1500 to 2000 °C, residual impurities such as hydrogen and sulfur are volatilized; above 2200 °C, a significant graphite crystallization commences; above 2600 °C, the graphite crystallite growth predominates; finally, at ~3000 °C, the electrical and mechanical properties become optimal. At this point, the residual impurity content (mostly as nonvolatile metal-containing ashes) should be below 1000 ppm, which is sufficient for the majority of purposes. Prolonged treatment at higher temperatures can further reduce this value to 200–300 ppm. The total cycle time of heating and cooling may take several tens of days.

Normally, the levels of residual impurity after high temperature graphitization are adequate for most purposes. However, very high-purity grades such as nuclear graphite require further lower-temperature thermal treatment using halogens, or

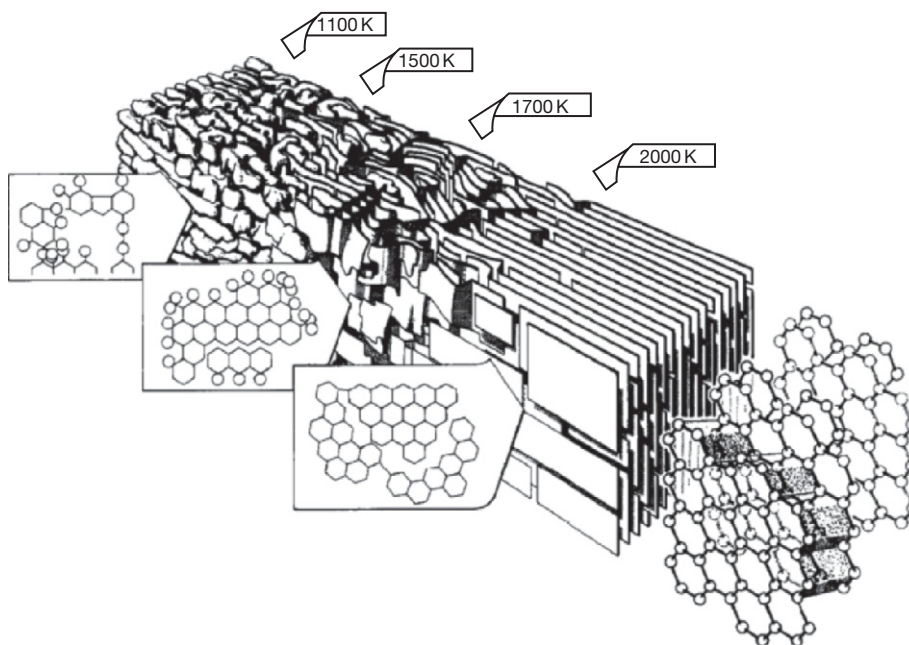


**Figure 1** Schematic diagram showing the progressive graphitization of carbon. Reproduced from Marsh, H. *Carbon* 1991, 29, 703–704, with permission from Elsevier Publications.<sup>3</sup>

more commonly, halogen-containing compounds (e.g., carbon tetrachloride) in order to convert residual metal species to volatile halides. In this way, the residual impurity level can be reduced to below 1 ppm.

#### 3.24.1.4 Glassy Carbon

Vitreous or glassy carbon is important because of its low reactivity (high corrosion resistance). These are generally produced by the pyrolytic decomposition of thermoset polymer resins (e.g., phenolic resins), with or without fiber reinforcement (e.g., by cellulose or rayon).<sup>4</sup> Carbonization occurs in the solid phase, and there is no significant crystallite growth or porosity development even at graphitizing temperatures. The production of this type of carbon requires moderate and carefully controlled baking rates, because large volumetric contractions occur (~50%) and considerable volumes of volatiles are emitted.

#### 3.24.1.5 Pyrolytic Graphite

Carbon may be directly deposited on a heated substrate by the decomposition of hydrocarbons such as methane, benzene, or acetylene. The reaction conditions determine how the deposition occurs (i.e., surface or gas phase polymerization), but it is essential

to avoid soot formation in the gas. The structure of pyrolytic graphite can be varied from randomly oriented (i.e., essentially isotropic and nanocrystalline) to highly oriented material of near theoretical density. The high anisotropy of this latter material leads to markedly different properties in directions parallel and perpendicular to the graphite planes. This feature is an advantage particularly in heat transfer applications where high conductivity in one or two directions is desired to be combined with poor conductivity in a third direction.

#### 3.24.1.6 Carbon Fiber and Carbon Composites

Carbon fibers essentially comprise long bundles of linked graphite plates in a highly oriented crystal structure layered parallel to the fiber axis. This results in extreme anisotropy, with elastic moduli of up to 200–400 GPa on-axis versus only 35 GPa off-axis. Carbon fibers can be manufactured from several different precursor fibers, such as polyacrylonitrile, rayon, etc., and by high temperature pyrolysis with or without pretensioning, usually in a two-stage process with initial carbonization at ~1500 °C followed by graphitization at ~3000 °C. In such ways, the properties of the resulting fibers can be varied somewhat to emphasize

either high strength (2000–5000 MPa) or high stiffness (200–400 GPa). Given the range of densities for carbon fibers ( $1.7\text{--}1.85\text{ g cm}^{-3}$ ), they have outstanding specific strength and stiffness characteristics.

Carbon fibers may be used with a variety of matrix phases, including polymer composites (e.g., epoxy–carbon) and carbon–carbon composites (fiber-reinforced graphite). The latter can be made via vapor deposition routes; however, these are generally slow and costly. Alternatively, methods involving fibers can be impregnated into a thermoset resin (e.g., phenolic) or petroleum pitch, followed by further pyrolysis steps.

### 3.24.1.7 Other Forms of Carbon: Fullerenes and Carbon Nanostructures

Until 1985, carbon was thought to exist only in two allotropes: diamond and graphite. This changed when, using mass spectroscopy, an entirely new form of carbon was found in which the atoms are arranged in closed structures. The original discovery, for which the Nobel Prize for Chemistry was awarded in 1996, was for the isolation and the identification of the  $C_{60}$  molecule, which is shaped like a soccer ball (i.e., consisting of alternating pentagons and hexagons). Such closed-shaped molecules are named fullerenes because of their resemblance to the geodesic domes first constructed by the architect R. Buckminster Fuller. Since 1985, many additional fullerene molecules have been identified, and furthermore, several additional molecular shapes, often based on rolled up sheets of graphite, have been identified, for example, carbon nanotubes. Many of these materials have interesting electrical and other characteristics, and there is hope that they will eventually outgrow the laboratory and become industrially useful.

### 3.24.1.8 Final Manufacture and Surface Finishing

Baked carbon and industrial graphite are both fully machinable with the use of conventional tools, although carbide or diamond-tipped tools are preferable especially when cutting lower-porosity glassy carbon because of its higher hardness. Additional treatments that seal the surface and/or internal porosity are also often used. These include, for example, sealing/impregnation with organic materials such as phenolic resins or Polytetrafluoroethene

(PTFE) (although this will limit the application temperature to below  $\sim 200^\circ\text{C}$ ) and a final impregnation with pitch followed by a low-temperature pyrolysis process. High temperature degradation (usually by oxidation) may be reduced by impregnation with inorganic salts, such as borates and phosphates, which melt at operating temperatures, sealing the pores. All forms of carbon may be coated with, for example, silicon carbide, silicon nitride, or high-density pyrolytic graphite by chemical vapor deposition. Such treatments can provide greatly improved oxidation and chemical (wet corrosion) resistance.

## 3.24.2 General Characteristics

Carbon and graphite have a number of useful and even unique properties that may be summarized as follows:

- retention of modulus, strength, and erosion resistance to very high temperatures (up to  $3200^\circ\text{C}$  in nonoxidizing atmospheres);
- low coefficient of thermal expansion and high thermal conductivity (25% of copper), giving rise to excellent thermal shock resistance;
- high corrosion resistance and a wide resistance to chemical attack except to strongly oxidizing species;
- significant electrical conductivity especially in fully graphitized materials;
- low friction and self-lubrication in graphitized grades;
- controllable porosity, giving a spectrum of structures from dense, hard materials to nanoporous materials with very high surface area;
- efficient moderation of fast neutrons and scattering of thermal (i.e., slow) neutrons, coupled with a low-absorption cross section for both thermal and fast neutrons in high-purity grades

The physical properties of a number of grades of carbon are summarized in [Table 1](#). It should be noted, however, that the material properties will vary over a wide range depending upon the original source of carbon (e.g., natural graphite, petroleum coke, or coked coal), the original powder size prior to sintering, the binder used (e.g., petroleum pitch, coal tar, etc.), and the temperature and time of heat treatment, including the number of cycles of pitch infiltration and recarbonization. Also, depending on the initial morphology of the input carbon source

**Table 1** Typical properties of carbon and graphite materials<sup>5</sup>

Property	Baked carbon	Industrial graphite	Glassy carbon	Pyrolytic graphite
Bulk density ( $\text{mg m}^{-3}$ )	1.65–1.8	1.7–1.9	1.3–1.5	2.1–2.2
Nominal porosity (%)	15–20%	9–18%	25–30%	<1%
Compressive strength (MPa)				–
Modulus of elasticity (GPa)	8–14	10–15	12–20	28–31
Tensile strength (MPa)	0.007–0.016			8–12 //c 110 //ab
Coefficient of thermal expansion ( $\text{K}^{-1}$ )	$3.5\text{--}5.5 \times 10^{-6}$			15–25 //c –1–1 //ab
Thermal conductivity ( $\text{W m}^{-1} \text{K}^{-1}$ )	30–100	100–200	4–10	1–3 //c 190–390 //ab
Electrical conductivity ( $\Omega^{-1} \text{m}^{-1}$ )	200–1000			300–1000 //c 20 000–25 000 //ab
Ash content	<0.2%	<0.1%	1–2%	<1 ppm

(e.g., natural flake graphite), materials produced by extrusion and related processes may retain significant anisotropy in the final manufactured product. Thus, one purpose in using the increasing grinding of the input carbon source is to produce small particle sizes that reduce or eliminate this anisotropy.

Carbon and graphite are unusual in that (in the absence of oxidative degradation) their strength and Young's modulus generally increase with temperature. Thus, the tensile strength of industrial graphite is about twice the room temperature value at 2500 °C, while its modulus is ~40% higher. Fully dense (pyrolytic) graphite generally has outstanding high temperature properties, especially if isotropic (i.e., essentially containing randomly oriented nanocrystallites). More normally, however, its properties are highly directional and vary within the graphite basal plane (*ab*-direction) and across the planes (*c*-direction). This variation is due to the large difference in interatomic distance between in-plane atoms and out-of-plane atoms. This directionality of properties can be utilized for advantage in certain applications, for example, where good heat transfer in one direction is required to be coupled with poor heat transfer in another direction (Figure 2).

The oxidation of carbon and graphite materials leads to the formation of gaseous products (i.e., CO and/or CO<sub>2</sub>) and results in a rapid decrease in properties, especially strength. These reactions begin to become significant above ~350 °C, but can be controlled by reducing or eliminating the porosity of the materials, in which case slow reaction will occur only on the surface of the material, leading to a steady loss of thickness. In the absence of oxidation, the dimensional stability of carbon and graphite materials is

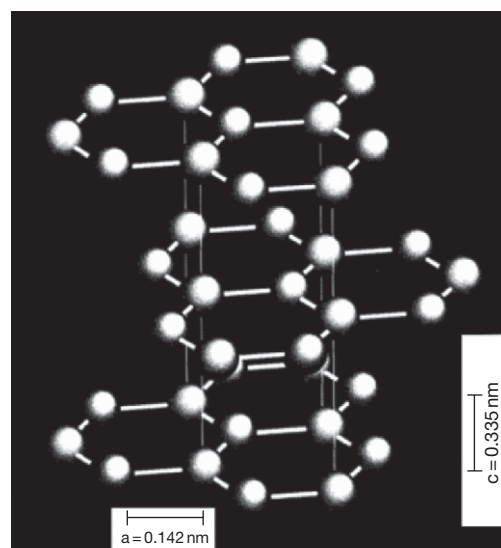


**Figure 2** Schematic diagram showing the atomic structure of graphite. Reproduced from European Carbon and Graphite Association, Avenue de Broqueville 12, B-1150 Bruxelles, with permission from Elsevier Publications.

excellent, provided their final heat treatment temperature is not exceeded. If this occurs, then additional graphitization may take place, leading to shrinkage.

### 3.24.3 Applications

Carbon is relatively inert chemically and thus may be used in all its forms under a variety of corrosive conditions. Many applications depend upon the acceptable electrical and excellent heat conductivity



of carbon and graphite and upon the unique retention of significant strength at very high temperatures. Thus, current major uses include

- carbon anodes in the Hall–Heroult aluminum cell and in electric arc furnaces such as for steel production and remelting; this is by far the greatest tonnage usage;
- heat exchangers, gaskets, seals, etc. for use in the chemical industry;
- furnace linings (e.g., in the iron blast furnace) as well as other high temperature furnace components, including crucibles;
- resistive and inductive susceptor elements in furnace and related specialist activities (e.g., graphite tube furnaces for atomic absorption spectroscopy);
- dies for optical glass fiber drawing and related operations;
- reaction vessels, crucibles, and supports in the electronics industry for Si wafer and especially for III–V semiconductor manufacture;
- heat transfer in brake blocks and other friction components, as well as low friction bearing materials, seals, etc. in the automotive and aerospace industries;
- conductive brushes for slip rings and commutator components in electric motors, etc;
- neutron moderator and reflector materials in the nuclear industry;
- heat-resisting components in aerospace and rocketry;
- biomedical applications (carbon is fully biocompatible);
- Electrodes for conventional batteries and ultrahigh surface area electrodes for lithium ion cells and supercapacitors.
- electrodes in electrolysis cells (e.g., chloralkali production) and cathodic protection anodes, etc.

### 3.24.4 Degradation of Carbon and Graphite

#### 3.24.4.1 Aqueous Corrosion

In aqueous conditions and at room temperature, carbon is thermodynamically unstable to direct oxidation to carbon dioxide, the bicarbonate ion, or the carbonate ion, depending upon the pH, and to direct reduction to methane at all pH. In practice, these reactions are severely kinetically hindered, and apart from oxidation at pH below  $\sim 1$ , occur at negligible rates at all pH up to 100 °C. The only significant

aqueous oxidation processes occur in strongly oxidizing environments such as concentrated nitric acid, perchloric acid, chromic acid, and chromates, or at highly oxidizing (positive) potentials. Thus, at pH 0 and under appropriate conditions, carbon will slowly form carbon dioxide at potentials more positive than  $\sim 0.45$  V on the hydrogen electrode scale (SHE). This implies that carbon/graphite is a relatively noble element – indeed, it is slightly more noble than copper. Therefore, while coupling graphite components to other metals, this important factor should be taken into account.

Most degradation of industrial graphite under aqueous conditions occurs not as a result of oxidation, but as a consequence of the reaction within pores of the material, for example, with residual impurities or binder phases, causing initially localized mechanical damage, but ultimately macroscopic mechanical failure of the component. Alternatively, where chemical species (e.g., chloride ion) can intercalate between the graphite layers, thus causing exfoliation, degradation is greatly increased.

#### 3.24.4.2 Aqueous Environments

The performance of glassy carbon electrodes in sulfuric acid under anodic polarization has been examined at room temperature as a function of acid concentration and anodic current density.<sup>6</sup> It was found that the dominant process of mass removal was via a mechanical mechanism with initial selective oxidative attack in regions of apparent lower density. This appeared to result in a mechanical stress, thus giving rise to local spallation. The formation of  $\text{CO}_2$  as the oxidative product was also confirmed. Degradation did not occur below the potential for oxygen evolution, but above this value was approximately linear with applied anodic current density and with acid concentration up to 4 M  $\text{H}_2\text{SO}_4$ . A degraded surface film,  $\sim 2\text{--}4$   $\mu\text{m}$  in thickness, formed after passage of  $\sim 80\,000$   $\text{C m}^{-2}$ .

The corrosion of industrial graphite was examined in 30% (5.5 M) phosphoric acid at 25 and 80 °C.<sup>7</sup> Under free corrosion conditions in air, the electrochemical potential fell in the range 0.59–0.62 V (SHE), which is somewhat greater than the theoretical value of 0.45 V. Potentiodynamic polarization implied the presence of a surface film, most likely of adsorbed oxygen and hydroxide species. Secondary ion mass spectrometry confirmed this hypothesis and also demonstrated significant penetration of phosphorus within the graphite, either as an

intercalated species, or more likely, adsorbed onto internal porosity (Figure 3).

The mass-loss rates for carbon electrolysis anodes used in brines for chlorine production were examined as a function of temperature, current density, and NaCl concentration.<sup>8</sup> The mass-loss rate was found to decrease with increase in chloride concentration and increase with temperature. The maximum degradation rate was at approximately neutral pH, the rate falling off by a factor of 2–3 under acid (pH 1) and alkaline (pH 11) conditions; at neutral pH, the degradation rate was found to be a function of current density. The degradation mechanism occurred via the reaction of an adsorbed chloride–graphite intermediate. Significant reductions in degradation rate were achieved as the overall porosity of the anodes decreased, and particularly, when the average pore size decreased below  $\sim 5\ \mu\text{m}$ .

The oxidation of high-purity (nuclear) graphite was studied in nitric acid at temperatures between 275 and 300 °C and at 100–120 bar pressure.<sup>9</sup> Under these extreme conditions, graphite is smoothly oxidized to carbon dioxide, while the nitric acid is reduced to nitrogen. Average reaction rates from 0.4 to 1 mol h<sup>-1</sup> were obtained under these conditions.

The corrosion of small graphite tube furnaces, used in atomic adsorption spectroscopy, was studied primarily in order to ascertain the effect of their degradation on the accuracy of analysis.<sup>10</sup> However,

it was found that the order of acid reactivity followed the trend:  $\text{HNO}_3 < \text{HF} < \text{HCl} < \text{HClO}_4$ . This was explained by two tendencies: first, the ability of the aggressive species to intercalate between the graphite sheets, and second, the ability of the species to oxidize the graphite. Thus, hydrochloric acid, which is nonoxidizing but which can intercalate easily because of the small size of the chloride ion, is more aggressive than nitric acid, resulting in mechanical damage (exfoliation) to the graphite.

The electrochemical degradation of glass-like carbon (GC), diamond-like carbon (DLC), and highly ordered pyrolytic graphite (HOPG) were studied in nitric–hydrofluoric acid mixtures at 50 °C.<sup>11</sup> Under repeated potential cycling within the range for water stability, small pits became apparent on the GC electrode and the HOPG electrode became severely roughened. However, a few, if any, morphological changes were evident on the DLC electrode. The heavy degradation of the HOPG electrode was ascribed to the oxidation of intercalated species and the consequent exfoliation of the graphite sheets.

The stability of graphite-reinforced epoxy-composite materials was studied under both galvanic coupling (i.e., where the graphite was a net cathode) and anodic polarization in order to understand electrochemically induced degradation processes. When the composite was connected to sacrificial anode materials in seawater, it suffered a significant (30%) reduction in strength over 140 days' exposure.<sup>12</sup> This was found to be due to the degradation of the graphite–epoxy bond probably via a similar mechanism to cathodic disbondment of organic coatings. Under anodic polarization, significant damage was apparent even at comparatively low current densities of 1  $\mu\text{A cm}^{-2}$ . This was ascribed to direct oxidation of the graphite fibers at local potentials above the oxygen evolution reaction.<sup>13</sup> Consequently, care has to be taken when using carbon fiber reinforcement composite materials where they may become electrochemically polarized.

In summary, all forms of technically important carbon may be degraded in aqueous conditions by two main mechanisms: electrochemical oxidation under anodic polarization (or chemical oxidation using a strong oxidizing agent) and the intercalation of small species between the graphite sheets with consequent swelling leading to the exfoliation of the sheets. Both of these processes may be greatly reduced in extent by use of dense materials of low overall porosity and/or with pore sizes in the micron range.

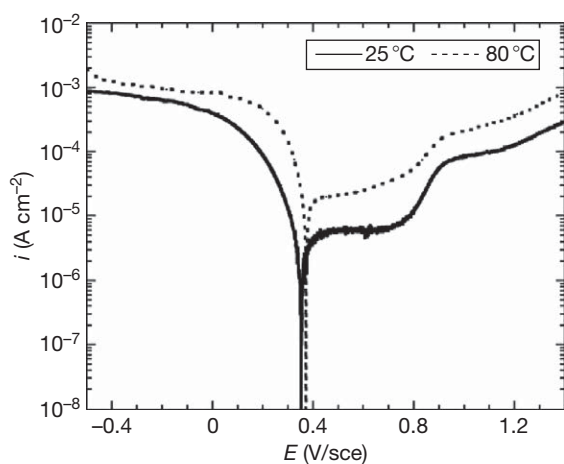


**Figure 3** Potentiodynamic polarization of graphite in phosphoric acid. Reproduced from Guenbour, A.; Kebkab, N.; Bellaouchou, A.; Iken, H.; Boulif, R.; BenBachir, A. *Appl. Surf. Sci.* **2006**, 252, 8710–8715, with permission from the European Carbon and Graphite Association (page 4 on presentation: “The element C”).

### 3.24.4.3 Galvanic Corrosion

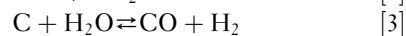
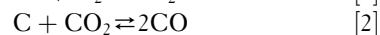
Since carbon/graphite is relatively noble, care has to be taken to ensure its galvanic compatibility with metals in which it is in contact. Thus, graphite is cathodic to most common metals such as steels, and particularly, the light metals aluminum and magnesium. Indeed, early aluminum airframes, which were commonly marked out for cutting using graphite pencils, suffered from corrosion along the residual pencil marks.<sup>14</sup> Also, a cathodic residue of carbon, deposited from lubrication oils during tube drawing, is responsible for the pitting of copper tubing in some natural drinking supply waters. Thus, the general assumption should be that electrical contact between carbon/graphite and other metals under aqueous corrosion conditions should generally be avoided.

As an example, the galvanic corrosion behavior of graphite fiber-reinforced epoxy composites coupled to a series of materials (aluminum alloys AA2024, 7075, and 5052, stainless steels AISI301, 302, 321, 15-5PH, and 17-7PH, carbon steel AISI4340, nickel–aluminum–bronze, and titanium Ti–6Al–4V) was studied.<sup>15</sup> The graphite composite was found to be cathodic in 3.5% NaCl to all of the alloys studied. Relatively high galvanic currents were evident when coupled to all aluminum alloys and to the carbon steel: the corrosion in these cases was effectively limited by cathodic oxygen reduction at the graphite cathode. Dealloying was evident for the nickel–aluminum–bronze material, and hence, coupling this material to graphite is also not recommended. Of the passive alloys, minor pitting was observed for the lower grades of stainless steel, while only titanium was deemed to be wholly safe.

Although graphitic materials are not generally recommended where oxygen reduction is the dominant cathodic process, they are relatively widely used as gasket materials in a crevice situation: where oxygen depletion would be expected. Under these conditions, the electrochemical potential of the graphite will become significantly depressed tending to that of the hydrogen evolution reaction. The likelihood of crevice attack with graphite gaskets was explored by experiment and modeling<sup>16</sup> where it was predicted that, in nonchlorinated seawater, graphite is likely to become anodic to duplex stainless steels, and hence protective, in a tight crevice because of oxygen depletion. However, for lower grades such as AISI316, where initiation is due to micropitting, such protection would not be effective.

### 3.24.4.4 High Temperature Oxidation

Carbon is largely nonreactive in air or oxygen at temperatures below  $\sim 350^\circ\text{C}$ . However, above  $400^\circ\text{C}$  the rate of reaction increases significantly. The principle oxidants are air (i.e.,  $\text{O}_2$ ), steam ( $\text{H}_2\text{O}$ ), and carbon dioxide ( $\text{CO}_2$ ), the main reaction equilibria being:



The  $\text{CO}_2$  shift reaction [2] and the water gas reaction [3] are both thermodynamically unfavorable below  $\sim 700^\circ\text{C}$ , but start to become kinetically significant above  $\sim 750^\circ\text{C}$ . The kinetic reactivity<sup>17</sup> differs greatly as a function of the material's porosity, its residual ash content (i.e., on the presence of oxidative catalysts, such as metallic impurities), and interestingly, also on the form of carbon. Studies of the thermal stability of diamond, graphite, carbon black,  $\text{C}_{60}$  and  $\text{C}_{70}$  fullerenes, and carbon nanotubes were carried out by thermal gravimetric analysis in nitrogen and air.<sup>18</sup> In nitrogen, the low molecular weight materials (i.e., the fullerenes and the carbon black) started to sublime above  $\sim 300\text{--}400^\circ\text{C}$ ; however, graphite and diamond showed mass losses of less than 3% up to  $900^\circ\text{C}$ . In flowing air, the onset temperatures for the reaction of  $\text{C}_{70}$  and  $\text{C}_{60}$  fullerenes were  $\sim 430^\circ\text{C}$  and  $530^\circ\text{C}$ , respectively. Carbon black commenced reaction at  $\sim 505^\circ\text{C}$ , graphite showing significant mass losses above  $\sim 610^\circ\text{C}$ . The carbon nanotube structures were most resistant, with an onset temperature of  $820^\circ\text{C}$ , while diamond had an onset temperature of  $800^\circ\text{C}$ . However, once reaction commenced, oxidation was found to progress rapidly (Figure 4).

Thus, the kinetics of oxidation of different forms of carbon are clearly very different at lower temperatures. However, as the oxidation temperature increases, the surface reactivity becomes less rate-limiting, and above  $800^\circ\text{C}$ , the oxidation rate is determined by mass transfer in the gas phase.<sup>19</sup> For example, the reaction of nuclear graphite with air was found to follow three regimes as a function of temperature.<sup>20</sup> In the lowest temperature range from  $400$  to  $600^\circ\text{C}$ , the reaction exhibited the highest activation energy ( $\sim 160\text{ kJ mol}^{-1}$ ) and was chemical reaction rate controlled. In the intermediate range from  $600$  to  $800^\circ\text{C}$ , the activation energy fell to  $72\text{ kJ mol}^{-1}$ , with the reaction kinetics controlled by

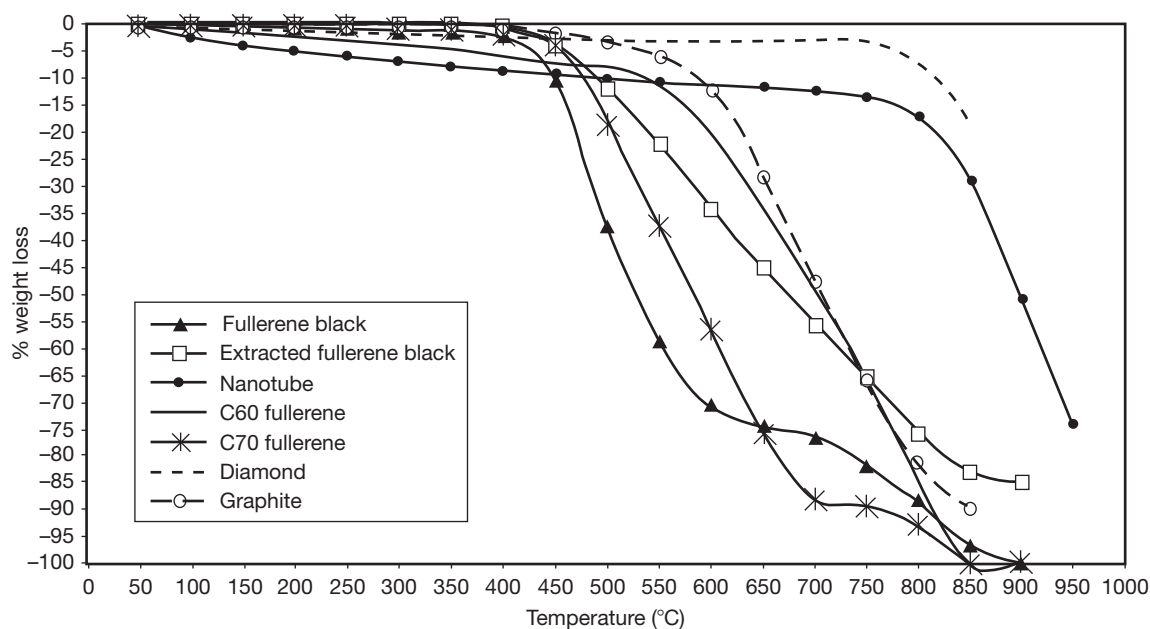


**Figure 4** Thermal gravimetric analysis on carbon materials in flowing air at  $20^{\circ}\text{C min}^{-1}$ . Reproduced from Cataldo, F. *Fullerenes, Nanotubes and Carbon Nanostruct.* **2002**, *10*, 293–311, with permission from Taylor and Francis.

the diffusion of reactant and products within the pores in the material. Above  $800^{\circ}\text{C}$ , the activation energy was low-to-negligible, the rate-controlling step in the oxidation process being boundary diffusion in the bulk gas phase.

#### 3.24.4.5 High Temperature Environments

Carbon will react directly at high temperatures with many nonmetallic elements such as sulfur and halogens and with metallic elements that can dissolve significant quantities of carbon (e.g., iron). The layered structure of graphite is also susceptible to intercalation with a range of species both ionic and molecular (e.g., from molten salts), leading to the disruption and the exfoliation of the graphite layers.<sup>21</sup> This phenomenon is critical in the use of graphite intercalation electrodes in Li-ion rechargeable cells in room temperature molten salts.<sup>22</sup>

Many molten metals will dissolve significant quantities of carbon, iron being the most obvious example of this. Notwithstanding this factor, carbon refractory materials are a critical component of many smelting and purification processes particularly for their outstanding resistance to thermal shock. For example, the hot-air zone of the iron blast furnace (i.e., close to the tuyeres or hot air nozzles) is an extreme environment requiring high temperature stability with resistance to hot gas erosion and large

temperature fluctuations. In view of this, carbon refractories, often impregnated with oxide materials such as zirconia to improve abrasion and erosion resistance, are the materials of choice.<sup>23</sup>

#### 3.24.4.6 Protection against Degradation

For high temperature use, it is normal to protect carbon from oxidation, as relatively small mass losses (e.g., 5–10%) have been found to result in losses of mechanical properties of up to 50%.<sup>19</sup> Alternative gas atmospheres such as  $\text{H}_2$  or  $\text{N}_2$  are most easily used; however, at temperatures above  $\sim 1500$ – $1600^{\circ}\text{C}$ , hydrogen will react to form methane, while nitrogen will react at temperatures above  $\sim 1700^{\circ}\text{C}$  to form cyanogen. Thus, at very high temperatures, inert gas atmospheres, such as argon or helium, are essential. Careful matching of the grade of carbon or graphite to the application, for example by the selection of low porosity (high density) grades, will also help to limit degradation rates both at high temperature and in aqueous conditions.

There has long been a search for coating methods to protect carbon from high temperature degradation, which is predominantly an oxidation problem. Such coatings should match the thermal expansion properties of carbon (to avoid spallation on thermal cycling), should adhere well, should have a low permeability to oxygen, and clearly, should not

themselves degrade/oxidize under the conditions of operation. Coatings that are molten at the operating temperature (i.e., glazes) are obviously resistant to cracking and are self-healing.<sup>24</sup> The most successful of such glazes are based on boron oxide ( $B_2O_3$ ), which melts at  $\sim 500^\circ C$  and starts to volatilize significantly above  $1200^\circ C$ , although their upper limit of operation is  $\sim 900^\circ C$  when their permeability to oxygen starts to become significant.<sup>25</sup> Phosphorus-type glazes may also be used successfully in a similar manner.<sup>26</sup>

Above  $\sim 900^\circ C$ , single layer coatings become increasingly ineffective and multilayer coatings are required. Many types of oxide, carbide, and nitride coatings have been applied with a view to limiting oxidation. The most successful are those based on silicon carbide either in conjunction with boron oxide (i.e., as self-healing agent)<sup>24</sup> or in functional coatings with graded thermal expansion coefficients matched to the substrate.<sup>27</sup> Coatings can be formed using a variety of methods, including sol-gel, pack cementation, and chemical or physical vapor deposition. Silicon carbide is successful, partly because it oxidizes to silicon oxide; however, the upper temperature limit for  $SiO_2$  is  $\sim 1700\text{--}1800^\circ C$  when its vapor pressure starts to become significant; thus, in practice, the practical temperature limit is  $\sim 1650^\circ C$ . Above  $1800\text{--}2000^\circ C$ , nonoxide ceramics become increasingly susceptible to oxidation and many oxide ceramics are not stable to carbothermic reduction. However, for specialist uses, such as rocketry components, which require only a few minutes' or hours' operation at maximum temperature, coatings such as hafnium and zirconium carbides and borides have been implemented successfully.

### 3.24.5 Nuclear Graphite

#### 3.24.5.1 Radiation Damage

The main purpose of graphite in a fission reactor is to slow ('thermalize') fast neutrons, which are emitted during fission, so that they can be recaptured by heavy nuclei in order to maintain the fission chain reaction. Graphite can also act to reflect slow neutrons back into the reactor core, thus improving neutron usage and may find use in a similar role in future fusion reactor systems. To accomplish this goal satisfactorily, nuclear graphite has exceptionally low impurity levels, that is, below a few parts per million. This is because elemental impurities will unacceptably increase the neutron capture cross-section of the graphite. Apart from this difference in

purity, the microstructures of nuclear grades of graphite are essentially similar to other graphite grades except that they generally have lower porosity resulting in improved mechanical properties.

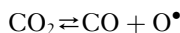
Fast neutrons typically emerge from a fission event with a mean energy of  $\sim 2\text{ MeV}$  (a velocity of  $15\,000\text{ km s}^{-1}$ ). This needs to be reduced to  $\sim 1\text{ km s}^{-1}$  ( $\sim 50\text{--}100\text{ eV}$ ), which is approximately in equilibrium with the surrounding temperature, and hence, these neutrons are known as 'thermal'.<sup>28</sup> Radiation damage in graphite thus occurs as a result of inelastic scattering between the neutrons and carbon atoms that result in the displacement of the carbon from their preferred lattice positions. An incoming neutron will typically require between 500 and 1000 of such scattering events, and travel  $\sim 500\text{ nm}$  (i.e., significant in terms of the lattice spacing), before it is in thermal equilibrium; this results in a significant displacement of the carbon atoms, and consequently, a significant storage of energy (Wigner energy) in the form of an unstable lattice. For room temperature irradiation of graphite, this energy can reach over  $20\text{ MJ kg}^{-1}$ . This is easily more than sufficient, when released in an uncontrolled manner, to raise the temperature of the material spontaneously by several hundred degrees. Graphite-moderated power reactors, however, generally operate at temperatures that are sufficiently high to result in a continuous thermal annealing of the graphite such that the storage of Wigner energy is insignificant.

Neutron irradiation of graphite also results in significant dimensional changes as a consequence of the difference between inelastic scattering within (*ab*-direction) and between (*c*-direction) the graphite layers.<sup>28</sup> Thus, in single crystal graphite, there is a significant expansion in the between-plane direction and a slight contraction in the in-plane direction. In macroscopic graphite, this results in an initial shrinkage of components, but an ultimate expansion of component sizes giving rise to a significant stress generation.<sup>29</sup> Both these factors have to be taken into account in reactor designs. The physical properties of graphite also change as a result of irradiation.<sup>30</sup> In particular, irradiation induces creep within the graphite and also reduces the elastic modulus of the material in the *c*-direction by  $\sim 6\%$ . Also produced are many radiation-induced dislocation structures with the graphite, which disrupts normal lattice vibrations, and hence, the thermal conductivity of irradiated graphite is reduced substantially (by up to two orders of magnitude).



### 3.24.5.2 Enhanced Radiolytic Oxidation

In graphite-moderated, carbon dioxide-cooled nuclear power reactors,  $\gamma$ -irradiation modifies the chemistry of the reaction between graphite and  $\text{CO}_2$ . This takes the form of a radiolytic decomposition<sup>31</sup> of carbon dioxide to carbon monoxide and an oxygen radical as follows:



Although this decomposition is only transient because of the back reaction, the generation of gas-phase oxygen radicals (and related oxidizing species) is significant enough to comprise the major in-reactor oxidative degradation process for nuclear graphite. As the oxidation of small amounts of graphite can lead to relatively large reductions in mechanical properties, it is important to limit this process as much as possible. In practice, this is achieved in a number of ways. First, the addition of 1–1.5% of carbon monoxide into the coolant tends to scavenge the oxygen radicals produced in the gas-phase, although this process becomes less efficient above 1.5% CO. Thus, in order to maintain long-term integrity of the graphite moderator core, smaller amounts of methane and hydrogen are also added. The former decomposes within the graphite structure to form a sacrificial carbon layer, while the addition of hydrogen limits significant carbon deposition on the fuel rods (which would reduce the reactor efficiency).

## References

1. Acheson, E.G. U.S. Patent 542982, 1985; U.S. Patent 568 323, 1896.
2. Morgan, P. *Carbon Fibres and Their Composites*; CRC Press, 2005; Chapter 2.
3. Marsh, H. *Carbon* **1991**, 29, 703–704.
4. Chekanova, V. D.; Fialkov, A. S. *Russ. Chem. Rev.* **1971**, 40, 413–428.
5. European Carbon and Graphite Association, Avenue de Broqueville 12, B-1150 Bruxelles.
6. Neffe, S. *Carbon* **1988**, 26, 687–692.
7. Guenbour, A.; Kebkab, N.; Bellaouchou, A.; Iken, H.; Boulif, R.; BenBachir, A. *Appl. Surf. Sci.* **2006**, 252, 8710–8715.
8. Rabah, M. A.; Nassif, N.; Abdul Azim, A. *Carbon* **1991**, 29, 165–171.
9. Farrell, J. P.; Haas, P. A. *Ind. Eng. Chem.* **1967**, 6, 277–280.
10. Rohr, U.; Ortner, H. M.; Schlemmer, G.; Weinbruch, S.; Welz, B. *Spectrochim. Acta B* **1999**, 54, 699–718.
11. Swain, G. M. *J. Electrochem. Soc.* **1994**, 141, 3382–3393.
12. Sloan, F. E.; Talbot, J. B. *Corrosion* **1992**, 48, 830–838.
13. Sloan, F. E.; Talbot, J. B. *Corrosion* **1992**, 48, 1020–1026.
14. Dr. Brian Johnson, UMIST, Personal communication.
15. Bellucci, F. *Corrosion* **1992**, 48, 281–291.
16. Turnbull, A. *Corrosion* **1999**, 55, 206–212.
17. McKee, D. W. In *Chemistry and Physics of Carbon*; Walker, P. L., Thrower, P. A., Eds.; Marcel Dekker: New York, 1980; Vol. 16.
18. Cataldo, F. *Fullerenes, Nanotubes and Carbon Nanostruct.* **2002**, 10, 293–311.
19. Pickup, I. M.; McEnaney, B.; Cooke, R. G. *Carbon* **1985**, 24, 535–543.
20. Xiaowei, L.; Jean-Charles, R.; Suyuan, Y. *Nucl. Eng. Des.* **2004**, 227, 273–280.
21. Wang, Z. D.; Inagaki, M. *J. Mater. Chem.* **1992**, 2, 629–632.
22. Doughty, D. H. *Soc. Adv. Mater. Process Eng. J.* **1996**, 32, 75–81.
23. Vernilli, F. Jr.; Justus, S. M.; Silva, S. N.; Mazine, A.; Baldo, J. B.; Longo, E.; Varela, J. A. *Mater. Corros* **2005**, 56, 475–480.
24. de Castro, D.; McEnaney, B. *Corros. Sci.* **1992**, 33, 527–542.
25. McKee, D. W.; Spiro, C. L.; Lamby, E. J. *Carbon* **1984**, 22, 507–511.
26. McKee, D. W.; Spiro, C. L.; Lamby, E. J. *Carbon* **1984**, 22, 285–290.
27. Kwon, O. S.; Hong, S. H.; Kim, H. J. *Eur. Ceram. Soc.* **2002**, 23, 3119–3124.
28. Telling, R. H.; Heggie, M. I. *Philos. Mag.* **2007**, 87, 4717–4846.
29. Li, H.; Fok, A. S. L.; Marsden, B. J. *J. Nucl. Mater.* **2008**, 372, 164–170.
30. Tanabe, T.; Maruyama, T.; Iseki, M.; Niwase, K.; Atsumi, H. *Fusion Eng. Des.* **1995**, 29, 428–434.
31. Best, J. V.; Stephen, W. J.; Wickham, A. J. *Prog. Nucl. Energy* **1985**, 16, 127–178.

## Further Reading

European Carbon and Graphite Association, Avenue de Broqueville 12, B-1150 Bruxelles, <http://www.carbonandgraphite.org>  
 Ishikawa, T.; Nagaoki, T. *Recent Carbon Technology*; JEC Press, 1983.  
 Pierson, H. O. Ed. *Handbook of Carbon, Graphite, Diamonds and Fullerenes: Processing, Properties and Applications*; Applied Science: New York, 1994.



## 3.23 Corrosion of Metal Matrix Composites

**L. H. Hihara**

Department of Mechanical Engineering, Holmes Hall 302, College of Engineering, University of Hawaii at Manoa, 2540 Dole St., Honolulu, HI, USA

© 2010 Elsevier B.V. All rights reserved.

<b>3.23.1</b>	<b>Introduction</b>	2251
<b>3.23.2</b>	<b>Types of MMCs</b>	2251
3.23.2.1	Continuous-Reinforced MMCs	2251
3.23.2.2	Discontinuous-Reinforced MMCs	2252
<b>3.23.3</b>	<b>MMC Applications</b>	2252
3.23.3.1	Examples of Applications for CF MMCs	2252
3.23.3.2	Examples of Applications for DR MMCs	2252
<b>3.23.4</b>	<b>Corrosion Characteristics</b>	2253
3.23.4.1	Electrochemical Effects Related to the Primary MMC Constituents	2253
3.23.4.1.1	Environment	2254
3.23.4.1.2	Matrix metal	2254
3.23.4.1.3	Reinforcement electrochemistry	2255
3.23.4.1.4	Reinforcement photoelectrochemistry	2256
3.23.4.1.5	Reinforcement resistivity	2257
3.23.4.1.6	Reinforcement area fraction	2258
3.23.4.1.7	Microstructure	2259
3.23.4.2	Electrochemical Effects of the Interphases	2262
3.23.4.3	Chemical Degradation in MMCs	2262
3.23.4.3.1	Aluminum carbide hydrolysis	2263
3.23.4.3.2	Mica degradation	2263
3.23.4.4	Secondary Effects	2263
3.23.4.4.1	Intermetallics	2263
3.23.4.4.2	Dislocation density	2264
3.23.4.4.3	MMC processing	2264
3.23.4.5	Corrosion in Environments	2264
3.23.4.5.1	Immersion exposure	2265
3.23.4.5.2	Humidity chamber exposure	2266
3.23.4.5.3	Outdoor exposure	2266
<b>3.23.5</b>	<b>Corrosion Protection of MMCs</b>	2267
<b>3.23.6</b>	<b>Conclusions</b>	2267
<b>References</b>		2268

### Abbreviations

**B MF** Boron monofilament

**B<sub>MF</sub><sup>E</sup>** B<sub>MF</sub> electrode with MF ends exposed

**B<sub>MF</sub><sup>S</sup>** B<sub>MF</sub> electrode with MF circumferential surface exposed

**CD** Current density

**HP** Hot-pressed

**MMC** Metal–matrix composite

**SC** Semiconductor

**SiC MF** Silicon carbide monofilament

**SiC<sub>MF</sub><sup>E</sup>** SiC<sub>MF</sub> electrode with MF ends exposed

**SiC<sub>MF</sub><sup>S</sup>** SiC<sub>MF</sub> electrode with MF circumferential surface exposed

### Symbols

<sup>E</sup> Electrode with fiber or MF ends exposed  
(e.g., SiC<sub>MF</sub><sup>E</sup>)

**E<sub>APPLIED</sub>** Applied potential

**E<sub>pit</sub>** Pitting potential

$E_{\text{GALV}}$	Galvanic couple potential
g	Gaseous state
Gr	Graphite
Gr <sup>E</sup>	Gr electrode with fiber ends exposed
$i$	Current density
$i_a$	Anodic current density
$i_c$	Cathodic current density
$i_{\text{CORR}}$	Corrosion current density
$i_{\text{GALV}}$	Galvanic current density
l	Liquid state
s	Solid state
S	Electrode with fiber or MF circumferential surface exposed (e.g., SiC <sub>MF</sub> <sup>S</sup> )
$t$	Thickness
$V_{\text{SCE}}$	Volts versus a calomel electrode
$x_c$ or $X_c$	Cathodic area fraction
$\rho$	resistivity

### 3.23.1 Introduction

Metal–matrix composites (MMCs) are metals that are reinforced with either continuous or discontinuous constituents usually in the form of fibers (F), monofilaments (MF), particles (P), whiskers (W), or short fibers (SF). The reinforcements can be metals (e.g., tungsten), nonmetals (e.g., carbon, silicon), or ceramics (e.g., silicon carbide, boron carbide, or alumina). The selection of the matrix metal and reinforcement constituent is usually based on how well the combination interacts to achieve the desired properties. MMCs are usually stiff, strong, and lightweight, but they are also engineered for other properties. Reinforcements have been used in MMCs to increase stiffness,<sup>1</sup> strength,<sup>1</sup> thermal conductivity,<sup>2</sup> neutron shielding, and vibration damping capacity; and to reduce weight,<sup>1</sup> thermal expansion,<sup>3</sup> friction,<sup>4</sup> and wear.<sup>5</sup> Some, but not all, MMC properties are governed by the rule of mixtures.<sup>6</sup> Although MMCs

have properties more useful than those of their individual constituents, resistance to corrosion is usually sacrificed. The corrosion behavior of MMCs is often significantly different from that of their monolithic matrix alloys because of the presence of the reinforcements that alter the microstructure, electrochemical properties, and corrosion morphology.

The different types, typical applications, corrosion characteristics, and corrosion protection of MMCs will be summarized below.

### 3.23.2 Types of MMCs

A variety of MMCs have been developed with matrices such as aluminum, magnesium, lead, depleted uranium, stainless steel, titanium, copper, and zinc. Only MMCs with aluminum matrices, however, are extensively available.<sup>3</sup> Reinforcement constituents for MMCs include boron (B), graphite (Gr), silicon (Si), silicon carbide (SiC), boron carbide (B<sub>4</sub>C), titanium diboride (TiB<sub>2</sub>), alumina (Al<sub>2</sub>O<sub>3</sub>), mica, quartz, tungsten, yttria, and zircon. The reinforcement constituents usually range from 10 to 60 vol.%.

In this chapter, the MMC types will be denoted as matrix type/reinforcement composition/vol.% reinforcement type. Hence, aluminum/Al<sub>2</sub>O<sub>3</sub>/50 P MMC denotes an aluminum matrix MMC reinforced with 50 vol.% of Al<sub>2</sub>O<sub>3</sub> particles.

#### 3.23.2.1 Continuous-Reinforced MMCs

Continuous-reinforced (CR) MMCs are reinforced with continuous fibers or MF generally resulting in anisotropic properties, with substantial enhancements in the longitudinal direction of the reinforcement. The reinforcement diameter generally varies from 10  $\mu\text{m}$  for fibers (Figure 1(a)) to 150  $\mu\text{m}$  for MF (Figure 1(b)). Continuous reinforcements are usually much more

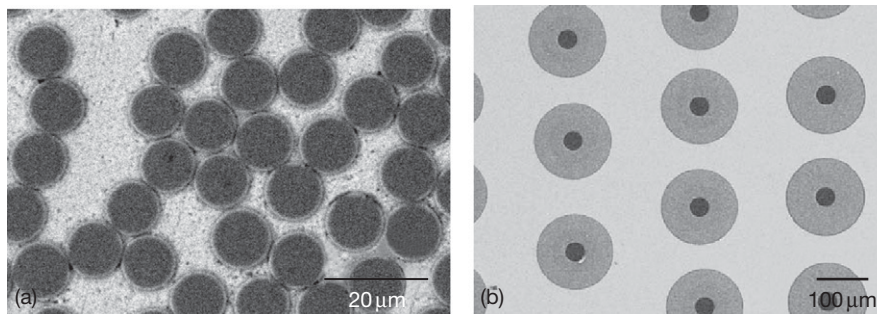


**Figure 1** Micrographs of (a) pure Al/Al<sub>2</sub>O<sub>3</sub>/50 F MMC (courtesy of J. Zhu) and (b) Ti-6Al-4V/SiC/MF MMC (courtesy of R. Srinivasan).

expensive than their discontinuous counterparts. Fabrication costs of CR MMCs are also higher than that of discontinuous-reinforced (DR) MMCs.

### 3.23.2.2 Discontinuous-Reinforced MMCs

DR MMCs are reinforced with particles, whiskers, or SF, and generally have isotropic properties and lower material and fabrication costs as compared to CR MMCs. Enhancements in properties of DR MMCs, however, are usually modest in comparison to CR MMCs. Reinforcement volume percents range from ~15 to 25% for structural MMCs (Figure 2(a)), and greater than 30% for MMCs used in electronic packaging (Figure 2(b)). Uniform particle and particle-size distribution are preferred in structural MMCs for optimal mechanical properties. In electronic-grade MMCs, the particle and particle-size distribution may not be uniform in order to maximize the reinforcement volume fraction. The high reinforcement loading in electronic-grade MMCs is necessary to reduce the coefficient of thermal expansion (CTE) to levels closer to that of electronic materials such as silicon and gallium arsenide.

### 3.23.3 MMC Applications

MMCs are being used in the aerospace, automotive, electronics, utilities, sports, and defence industries.

#### 3.23.3.1 Examples of Applications for CF MMCs

Aluminum/B/MF MMCs have been used for structural tubes in the space shuttle, resulting in 44% reduction in weight over aluminum alloys in the

original design.<sup>7</sup> Aluminum/Gr/F MMCs, which have unique properties such as negative to near-zero CTE, have been used as antenna booms in the Hubble Space Telescope.<sup>3</sup> In the automotive industry, Al/Al<sub>2</sub>O<sub>3</sub>/F MMCs have been used to replace cast iron components. Al/Al<sub>2</sub>O<sub>3</sub>/F MMCs with low weight, high temperature tensile and fatigue strengths, low thermal conductivity and expansion, and superior wear resistance are used in engine blocks, pistons, and cylinder heads.<sup>8</sup> Other types of Al/Al<sub>2</sub>O<sub>3</sub>/F MMCs with low weight, high strength, and high damping capacity are used for automotive push rods, resulting in increased horsepower generation.<sup>9</sup> These Al/Al<sub>2</sub>O<sub>3</sub>/F MMCs are also used as load-carrying core wires in high-current capacity and low-sag aluminum conductor cables (Figure 3). The Al/Al<sub>2</sub>O<sub>3</sub>/F MMCs core wires impart desirable properties to the cable such as high strength at ambient and elevated temperatures, low CTE, and lightweight.

#### 3.23.3.2 Examples of Applications for DR MMCs

Aluminum/SiC/20 P MMCs were used to replace aluminum tubes in the catamaran 'Stars and Stripes '88,' resulting in 20 wt% savings in comparison with monolithic aluminum.<sup>3</sup> Aluminum/Si/43 P MMCs, which are machinable, lightweight, and possess a low CTE, are used for electronic packaging (Figure 4(a)). For thermal management applications, copper-matrix MMCs are reinforced with milled graphite fibers that have negative CTEs and thermal conductivities exceeding that of copper. Accordingly, the resulting Cu/Gr MMCs have lower CTEs and higher thermal conductivity than copper.<sup>10</sup> In the automotive sector, DR MMCs are used for engine

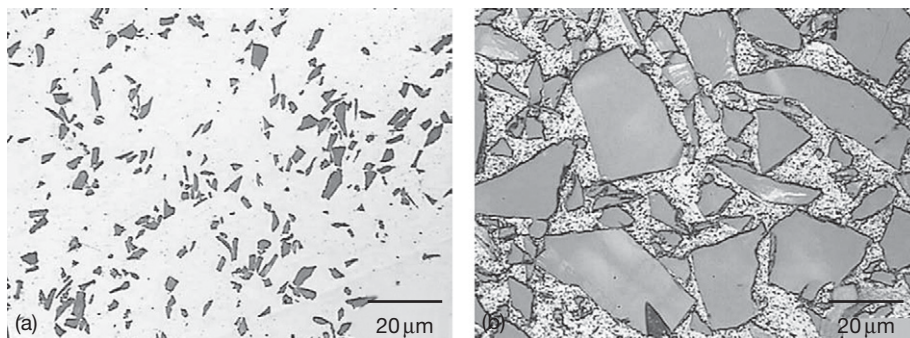


**Figure 2** Micrographs of (a) Al 6092/SiC/10 P-T6 MMC and (b) Al 6092/SiC/50 P-T6 MMC. Courtesy of G. Hawthorn.

pistons, piston connection rods, rear wheel driveshafts, break calipers, cylinder liners, push rods, rocker arms, and valve guides.<sup>11</sup> DR MMCs are also used in the sports industry for high-performance bicycle frames and components, golf clubs, and baseball bats.<sup>11</sup> In the aircraft industry, examples of DR MMCs' used are fan exit guide vanes in turbine engines, ventral fins, helicopter blade sleeves (**Figure 4(b)**), and fuel access covers.<sup>12</sup> Other potential emerging applications for DR MMCs are shoes for tracked vehicles and light-weight armor.

### 3.23.4 Corrosion Characteristics

The presence of the reinforcements and the processing associated with MMC fabrication can lead to accelerated corrosion of the metal matrix. Special concerns regarding corrosion become important in MMCs as compared to the corrosion of the monolithic matrix alloys. Accelerated corrosion in MMCs

may originate from electrochemical, chemical, and physical interaction between MMC constituents because of their intrinsic properties or those induced by processing. Galvanic interaction between the reinforcement, matrix, and interphases can accelerate corrosion. Interphases and reinforcements may undergo chemical degradation, which is not electrochemical in nature. The microstructure of MMCs can influence corrosion by inducing segregation, intermetallic formation, and dislocation generation. Processing deficiencies may result in unexpected forms of corrosion.

The parameters affecting MMC corrosion that will be discussed are (1) electrochemical effects related to the primary MMC constituents; (2) electrochemical effects of the interphases; (3) chemical degradation in MMCs; and (4) secondary effects caused by the microstructure and processing. Corrosion in selected environments and corrosion protection will also be covered.

#### 3.23.4.1 Electrochemical Effects Related to the Primary MMC Constituents

Galvanic corrosion between the matrix and reinforcements is one of the primary concerns regarding the corrosion behavior of MMCs. Depending on the electrochemical properties of the MMC constituents, the galvanic corrosion rate can be controlled by either the anodic or cathodic reaction, or by both. Anodic control prevails when the cathodic reaction is depolarized (**Figure 5(a)**); cathodic control prevails when the anodic reaction is depolarized (**Figure 5(b)**); and there is mixed control when both the anodic and cathodic reactions polarize (**Figure 5(c)**).<sup>13</sup> For a galvanic couple with equal matrix and reinforcement

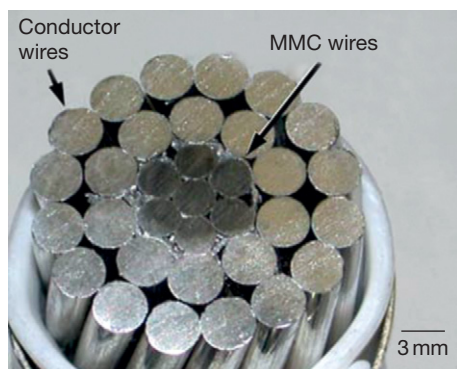


**Figure 3** Aluminum conductor composite reinforced cable specimen. Notice the seven inner Al/Al<sub>2</sub>O<sub>3</sub>/F MMC core wires.

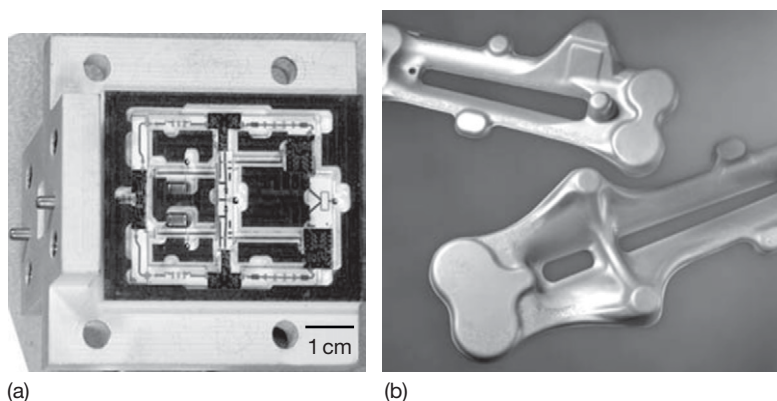


**Figure 4** (a) Pure Al/Si/43 P MMC electronic package, and (b) 2009 Al/SiC/15 P-T4 helicopter blade sleeves (courtesy of DWA Aluminum Composites).



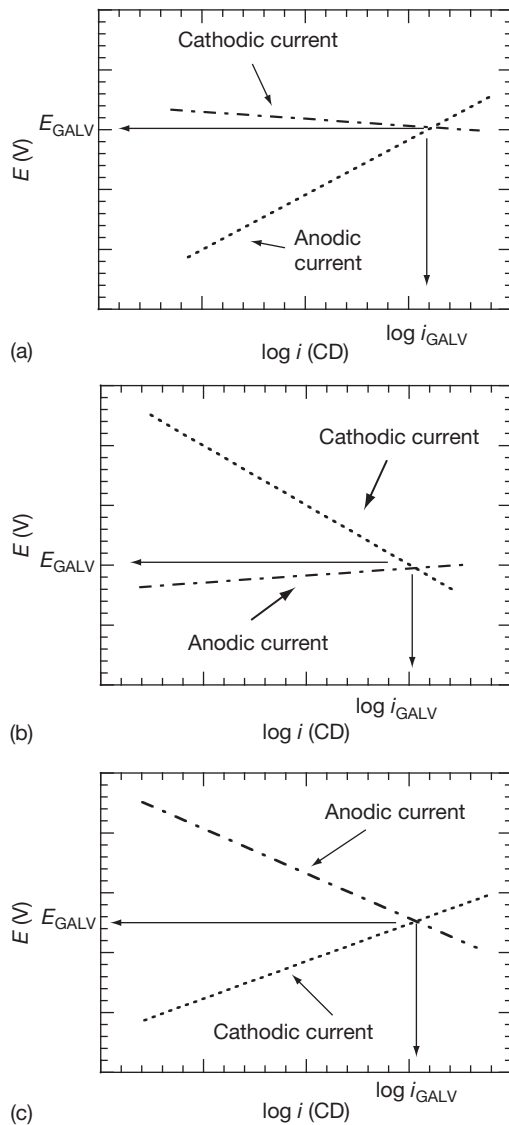


**Figure 5** Polarization diagrams showing (a) anodic control, (b) cathodic control, and (c) mixed control in galvanic corrosion.

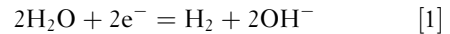
area fractions, the intersection of the anodic polarization curve of the matrix metal and the cathodic polarization curve of the reinforcement indicates the magnitude of the galvanic corrosion current density ( $i_{\text{GALV}}$ ) (Figure 6). Hence, the degree of galvanic corrosion depends on the environment, matrix alloy, reinforcement electrochemistry, resistivity, and area fraction.

#### 3.23.4.1.1 Environment

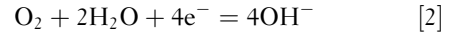
The environment has a significant effect on galvanic corrosion rates. The two most primary factors are

usually dissolved-oxygen content and electrolyte composition (e.g., presence of aggressive ions).

In deaerated environments, the governing cathodic reaction for corrosion is hydrogen evolution:



In aerated solutions, oxygen reduction can also operate, and generally results in higher corrosion rates:



For example, if pure magnesium is coupled to an equal area of SiC MF with the ends exposed ( $\text{SiC}_{\text{MF}}^{\text{E}}$ ), the galvanic corrosion rate between Mg and  $\text{SiC}_{\text{MF}}^{\text{E}}$  would increase by  $\sim 4$  times if the solution is oxygenated (Figure 6). Interestingly, the normal corrosion rate of uncoupled pure magnesium does not significantly change in the presence of dissolved oxygen<sup>14</sup> since hydrogen evolution is the governing cathodic reaction for magnesium, as exemplified in Figure 6. Hence, it is important to recognize that the corrosion behavior and trends of the MMC could be significantly different than that of the monolithic matrix alloy.

The presence of aggressive ions can greatly increase the corrosion rate, especially for alloys to lose passivity. For example, the galvanic corrosion rate between a passive metal matrix and conductive reinforcements would be limited to the passive current density (CD), as demonstrated with the polarization diagram Al 6061-T6 plotted with those of various reinforcements in aerated chloride-free 0.5 M  $\text{Na}_2\text{SO}_4$  (Figure 7). In the presence of aggressive ions that breakdown passivity, the galvanic corrosion rates can dramatically increase (Figure 7). Using Al 6061-T6 coupled to an equal area of P100 graphite fibers with the ends exposed ( $\text{P100 Gr}^{\text{E}}$ ) as an example, the galvanic corrosion rate increases  $\sim 300$  times in aerated 3.15 wt% NaCl as compared to that in aerated 0.5 M  $\text{Na}_2\text{SO}_4$  (Figure 7).

#### 3.23.4.1.2 Matrix metal

Galvanic corrosion in MMCs reinforced with conductive, noble reinforcements is a concern in environments in which the matrix metal corrodes actively. For example, for MMCs reinforced with an equal area fraction of graphite fibers,  $i_{\text{GALV}}$  in aerated 3.15 wt% NaCl (Figure 8) would be only  $5 \times 10^{-7} \text{ A cm}^{-2}$  for Ti-15V-3Cr-3Sn-3Al (Ti-15-3), 1.5 orders of magnitude larger for pure copper ( $10^{-5} \text{ A cm}^{-2}$ ), and 3 orders of magnitude larger for Al 6061-T6 ( $3 \times 10^{-4} \text{ A cm}^{-2}$ ). The passivity of Ti-15-3 prevents  $i_{\text{GALV}}$  from exceeding the passive-CD (Figure 8).

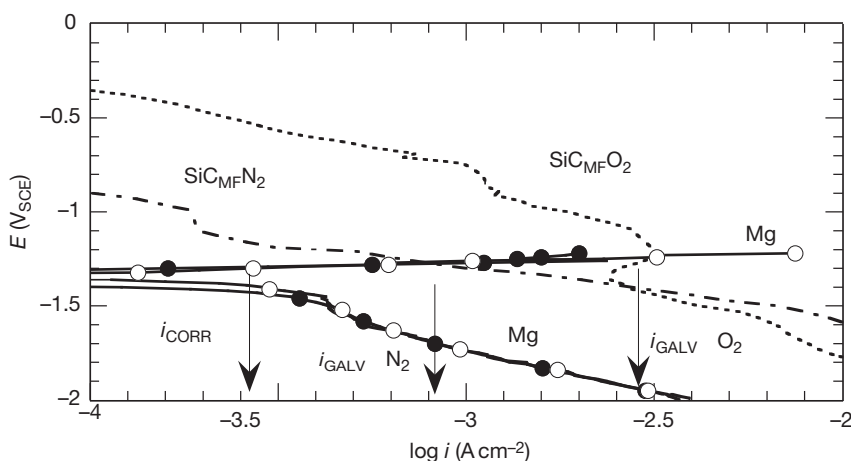


**Figure 6** A collection of anodic and cathodic polarization curves of Mg (99.95%) exposed to aerated (open circles) or deaerated (solid circles) 0.5 NaNO<sub>3</sub> at 30 °C, and cathodic polarization curves of SiC<sub>MF</sub><sup>E15</sup> exposed to deaerated or aerated 0.5 NaNO<sub>3</sub> at 30 °C. Scan rate = 0.1 mV s<sup>-1</sup>. Superscript E denotes MF ends were exposed.

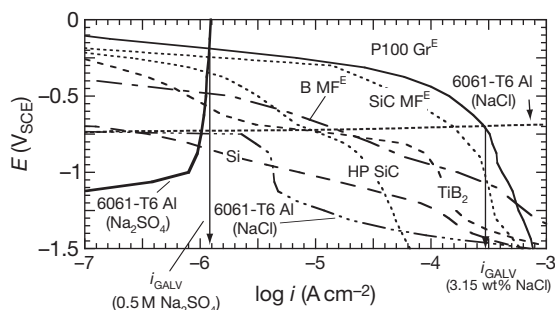


**Figure 7** A collection of anodic polarization diagrams of Al 6061-T6<sup>16</sup> exposed to aerated 0.5 M Na<sub>2</sub>SO<sub>4</sub> or 3.15 wt% NaCl at 30 °C, and cathodic polarization diagrams of P100 Gr<sup>E</sup>,<sup>16</sup> hot-pressed (HP) SiC,<sup>16</sup> SiC<sub>MF</sub><sup>E15</sup> and Si,<sup>17</sup> TiB<sub>2</sub>, and B<sub>MF</sub><sup>E</sup> exposed to aerated 3.15 wt% NaCl at 30 °C. Scan rate = 0.1 mV s<sup>-1</sup>.

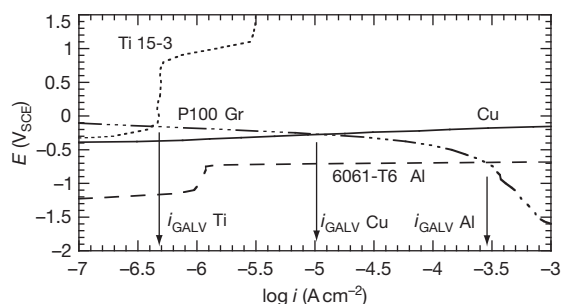


**Figure 8** Anodic polarization diagrams of Ti 15-3,<sup>18,19</sup> pure Cu (99.999%), and Al 6061-T6<sup>16</sup> in deaerated 3.15 wt% NaCl at 30 °C. Cathodic polarization diagram of P100 Gr fibers<sup>16</sup> in aerated 3.15 wt% NaCl at 30 °C. Scan rate = 0.1 mV s<sup>-1</sup>.

In the case of pure copper,  $i_{\text{GALV}}$  is about 1 order of magnitude less than the normal copper corrosion CD ( $10^{-4}$  A cm<sup>-2</sup>) in the aerated 3.15 wt% NaCl; hence, galvanic action would increase corrosion of copper, but not significantly.

### 3.23.4.1.3 Reinforcement electrochemistry

In cases where galvanic corrosion is under cathodic control, the type of reinforcement may have a significant effect on the rate of galvanic corrosion. For example, in aluminum MMCs, the galvanic corrosion rates between Al 6061-T6 and various reinforcements ranked from the highest to lowest in aerated 3.15 wt% NaCl is as follows (Figure 9): P100 Gr > carbon-cored SiC<sub>MF</sub><sup>E</sup> with ends exposed > tungsten-cored B<sub>MF</sub><sup>E</sup> with ends exposed > hot-pressed (HP) SiC > Si. It should also be noted that ceramic reinforcements may vary in purity and structure, and some reinforcements are in themselves composites. This leads to interesting electrochemical behavior. For example, SiC MFs have carbon-rich outer layers and carbon cores, and their polarization diagrams have a stronger resemblance to P100 Gr<sup>E</sup> than to HP SiC. The orientation of reinforcements may also affect electrochemical behavior. SiC MFs have carbon cores and B MFs have tungsten cores. The polarization behavior of the circumferential surface of the MFs are different compared with the behavior of the ends of the MFs that expose the carbon and tungsten cores (Figure 9 compares cathodic curves for SiC MF<sup>S</sup> versus SiC MF<sup>E</sup>, and B MF<sup>S</sup> versus B MF<sup>E</sup>).

Therefore, the composition of the reinforcement is important to the extent that it affects the kinetics of hydrogen evolution and oxygen reduction.



For reinforcements of very high resistivity, galvanic corrosion can also be limited by a large ohmic drop through reinforcement.

### 3.23.4.1.4 Reinforcement photoelectrochemistry

If the MMC reinforcements or constituents are semiconductors (SCs), galvanic currents between the matrix metal and SC could be suppressed or accelerated depending on whether the SC is n-type or p-type, respectively.<sup>22</sup>

#### n-Type SCs

An n-type semiconductor is photoanodic, and under illumination promotes photooxidation reactions. One such reaction is the oxidation of water. In the presence of moisture and illumination on MMCs that contain n-type SCs, photogenerated electrons could polarize the MMC to more negative potentials inducing cathodic protection (Figure 10).<sup>22</sup> While the MMC

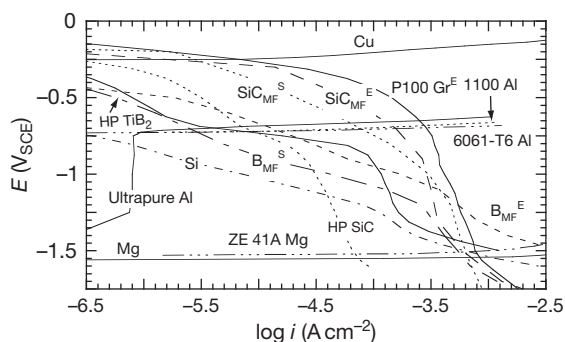


**Figure 9** A collection of anodic polarization diagrams of ultrapure Al (99.999%),<sup>16</sup> Al 1100,<sup>17</sup> and Al 6061-T6<sup>16</sup> and cathodic polarization diagrams of P100 Gr<sup>E</sup>,<sup>16</sup> HP SiC,<sup>16</sup> SiC<sub>MF</sub><sup>E</sup>,<sup>20</sup> SiC<sub>MF</sub><sup>S</sup>,<sup>20</sup> Si,<sup>17</sup> B<sub>MF</sub><sup>E</sup>,<sup>21</sup> and B<sub>MF</sub><sup>S</sup>,<sup>21</sup> exposed to aerated 3.15 wt% NaCl at 30 °C. Scan rate = 0.1 mV s<sup>-1</sup>.

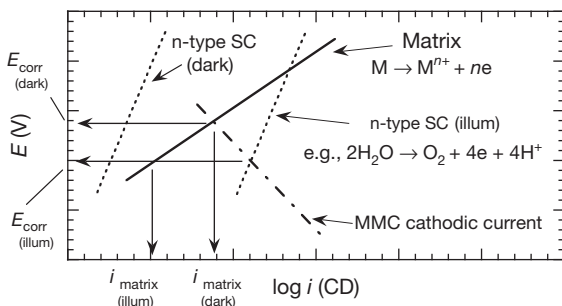


**Figure 10** Polarization diagrams showing the effect of an illuminated n-type semiconductor (SC) on the corrosion current density (CD) of the MMC matrix.

is under illumination,  $E_{\text{corr}}$  shifts from  $E_{\text{corr}}$  (dark) to  $E_{\text{corr}}$  (illum), and the dissolution from the matrix decreases from  $i_{\text{matrix}}$  (dark) to  $i_{\text{matrix}}$  (illum). Accordingly, during anodic polarization of Al 6092/Al<sub>2</sub>O<sub>3</sub>/20 P-T6 MMCs that were immersed in air-exposed 0.5 M Na<sub>2</sub>SO<sub>4</sub> solutions, anodic current densities increased sharply during illumination which were attributed to photoanodic currents generated by water oxidation on TiO<sub>2</sub> particles that were likely introduced with the Al<sub>2</sub>O<sub>3</sub> reinforcements.<sup>23</sup> The open-circuit potentials also decreased upon illumination. In these MMCs exposed to outdoors, corrosion films were also thinner on the topside of specimens exposed to sunlight as compared with the backside of the specimens not exposed to sunlight.<sup>24</sup> Interestingly, MMCs containing p-type SCs had thicker corrosion films on the sunlit surfaces as opposed to the shaded surfaces.<sup>24</sup>

#### p-Type SCs

A p-type SC is photocathodic and under illumination promotes photoreduction reactions. Depending on the electrolyte conditions, proton or oxygen reduction may be enhanced at the p-type semiconductor. In the presence of moisture and illumination on MMCs that contain p-type SCs, photoreduction causes cathodic current to increase, raising the corrosion potential and corrosion rates (Figure 11).<sup>22</sup> While the MMC is under illumination,  $E_{\text{corr}}$  shifts positive from  $E_{\text{corr}}$  (dark) to  $E_{\text{corr}}$  (illum), and the dissolution from the matrix increases from  $i_{\text{matrix}}$  (dark) to  $i_{\text{matrix}}$  (illum). Accordingly, during cathodic polarization of pure Al/Si/43 P MMCs<sup>25</sup> and various Al 6092/SiC/P-T6 MMCs<sup>22</sup> that were immersed in air-exposed 0.5 M Na<sub>2</sub>SO<sub>4</sub> solutions, cathodic current densities increased sharply during illumination, which were attributed to photocathodic currents on

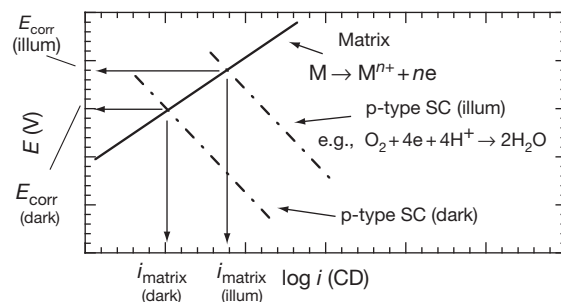


**Figure 11** Polarization diagrams showing the effect of an illuminated p-type SC on the corrosion CD of the MMC matrix.

the Si or SiC particles. The open-circuit potentials also increased upon illumination.<sup>22</sup> In these MMCs exposed to outdoors, corrosion films were also thicker on the sunlit surfaces as opposed to the shaded surfaces.<sup>24</sup>

### 3.23.4.1.5 Reinforcement resistivity

Reinforcement materials generally fall into the categories: insulators, SCs, or conductors (Table 1). For reinforcements that are insulators, galvanic corrosion is not possible. For SCs, the degree of galvanic corrosion will be restricted by the magnitude of ohmic losses through the reinforcements. This is demonstrated<sup>21</sup> by plotting (Figure 12) the cathodic curve derived from the hydrogen evolution on P100 Gr<sup>26</sup> exposed to aerated 3.15 wt% NaCl at 30 °C and incorporating a term for hypothetical ohmic losses through the electrode (eqn [3]).

$$E_{\text{APPLIED}}(V_{\text{SCE}}) = -0.67 - 0.081 \times \log i + ipt \quad [3]$$

The ohmic loss term  $ipt$  corresponds to a planar electrode having a thickness  $t$  and resistivity  $\rho$ , and one-dimensional current flow through the thickness. Equation [3] was plotted for various resistivity values and an electrode thickness of 5  $\mu\text{m}$  with that of anodic polarization diagrams of copper, Al 6061-T6, ZE 41A Mg, and pure magnesium in 3.15 wt% NaCl. Notice the effect of ohmic losses on the cathodic polarization diagrams and decreasing galvanic current densities as the reinforcement resistivities increase (Figure 12). For example,  $i_{\text{GALV}}$  of Al 6061-T6 is  $\sim 10^{-4} \text{ A cm}^{-2}$  for an ohmic loss  $IR_1$  resulting from a reinforcement resistivity of  $10^7 \Omega \text{ cm}$ . The value of  $i_{\text{GALV}}$  reduces

to  $\sim 10^{-7} \text{ A cm}^{-2}$  when the ohmic loss is increased to  $IR_2$  by a reinforcement resistivity of  $10^{10} \Omega \text{ cm}$ . The effect of reinforcement resistivity on the galvanic corrosion rate is also dependent on the type of matrix metal. The limiting effect on galvanic corrosion rates on copper only manifests at very high reinforcement resistivities (e.g.,  $>10^7 \Omega \text{ cm}$  in Figure 12); whereas, effects are seen on Al 6061-T6, ZE 41A Mg, and magnesium at lower resistivities. Note that the  $i_{\text{GALV}}$  values correspond to galvanic couples having equal anode and cathode areas.

Figure 12 is based on a fixed electrode thickness, but note that the critical resistivity to limit the galvanic corrosion rate below a particular level is also dependent on the thickness of the reinforcement since the ohmic loss is equal to  $ipt$ . Hence, if ohmic losses are to limit galvanic corrosion, reinforcements having higher resistivity are needed as the thickness or particle size of the reinforcement decreases. For example, to maintain an ohmic drop of 0.5 V at a galvanic CD of  $10^{-4} \text{ A cm}^{-2}$ , a 50- $\mu\text{m}$  particle would need a resistivity of  $10^6 \Omega \text{ cm}$ ; whereas, a 5- $\mu\text{m}$  particle would need a resistivity of  $10^7 \Omega \text{ cm}$  to achieve the same ohmic loss. If the reinforcements that are used in MMCs are not of high purity, resistivities may drop significantly allowing galvanic corrosion to ensue. For example, Al/SiC MMCs are fabricated from both high-purity green SiC and lower-purity black SiC, depending on the application. The resistivity of SiC may vary by  $\sim 18$  orders of magnitude depending on its purity.<sup>27</sup> Boron MFs are more conductive than pure boron due to tungsten and tungsten borides in the core.<sup>28</sup> In fact, many

**Table 1** Resistivities of reinforcement materials

Material	Resistivity ( $\Omega \text{ cm}$ )	Temperature ( $^{\circ}\text{C}$ )	Notes	Ref.
$\text{Al}_2\text{O}_3$	$>10^{14}$	30	99.7% $\text{Al}_2\text{O}_3$	29
Mica	$10^{13} - 10^{17}$	–	Muscovite $\text{KAl}_3\text{Si}_3\text{O}_{10}(\text{OH})_2$	30
SiC	$10^{-5} - 10^{13}$	–	Function of purity	27
B	$6.7 \times 10^5$	25	Pure	31
$\text{B}_4\text{C}$	$10^0$	–	–	32
Si	$10^{-2} - 10^5$	–	Function of purity	29
P100 Gr fiber	$2.5 \times 10^{-4}$	–	Thornel	33
P55S Gr fiber	$7.5 \times 10^{-4}$	–	Thornel	33
$\text{SiC}_{\text{MF}}^{\text{E}}$	$4 \times 10^{-2}$	25	The superscript 'E' indicates that electrical contact was made with the end of the MF exposing the core; the 'S' indicates that electrical contact was made with only the MF circumferential surface (excluding the core). SiC MFs have carbon cores and B MFs have tungsten cores.	21
$\text{SiC}_{\text{MF}}^{\text{S}}$	$2 \times 10^{-2}$	25		
$\text{B}_{\text{MF}}^{\text{E}}$	$2 \times 10^{-1}$	25		
$\text{B}_{\text{MF}}^{\text{S}}$	$5 \times 10^{-1}$	25		

reinforcement materials have resistivities that are not high enough to stifle galvanic corrosion. The resistivities of some reinforcement materials are shown in [Table 1](#). The treatment above for the ohmic losses through reinforcement particles should only be considered as an approximation since one-dimensional current flow was assumed. In the actual case, the ohmic drop through the edges of the particle could be much less than through the thickness. The galvanic corrosion rate can also significantly increase as the area fraction of the reinforcements increases.

### 3.23.4.1.6 Reinforcement area fraction

The galvanic corrosion rate generally increases with the area fraction of the reinforcement. This is demonstrated ([Figure 13](#)) using the anodic polarization diagrams of copper, Al 1100, Al 6061-T6, pure

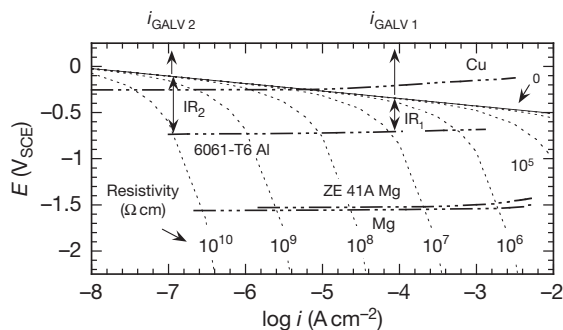


**Figure 12** Plots of the Tafel equation for oxygen reduction on P100 Gr<sup>E</sup> incorporating the effect of hypothetical ohmic losses based on various resistivities [eqn \[3\]](#) in aerated 3.15 wt% NaCl at 30 °C.<sup>21</sup> The anodic polarization diagrams of Cu, Al 6061-T6,<sup>16</sup> pure Mg, and ZE 41A Mg are also shown. The pure Mg and ZE41A Mg diagrams correspond to oxygenated solutions. Scan rate = 0.1 mV s<sup>-1</sup>.

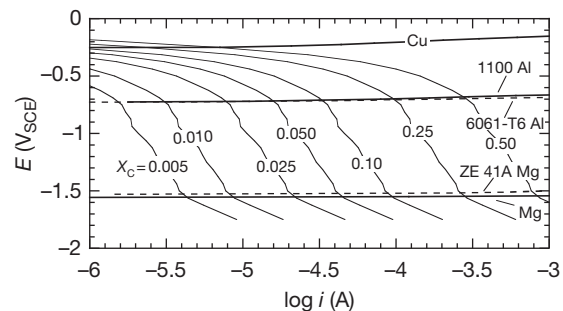


**Figure 13** Anodic polarization diagrams of Cu, Al 1100, Al 6061-T6, Mg, and ZE 41A Mg, and cathodic polarization diagrams of P100 Gr<sup>E</sup> showing the effect of the P100 Gr<sup>E</sup> area fraction  $X_C$  on the galvanic current in aerated 3.15 wt% NaCl at 30 °C. Scan rate = 0.1 mV s<sup>-1</sup>.<sup>21</sup> The electrode area of the anodic diagrams corresponds to 1 cm<sup>2</sup>.

magnesium (99.95% metallic purity), and ZE 41A Mg, and the cathodic polarization diagram of P100 Gr.<sup>16</sup> The cathodic curve for P100 Gr<sup>E</sup> shifts to higher currents as its area fraction is increased, causing the galvanic current with the various metals and alloys to increase. Since the galvanic couples are predominately under cathodic control, the catchment area principle<sup>34</sup> can be used to determine  $i_{\text{GALV}}$  as a function of the area fraction of the cathodic reinforcement.<sup>16</sup>

$$i_{\text{GALV}} = i_C(X_C/1 - X_C) \quad [4]$$

The parameter  $i_{\text{GALV}}$  is the dissolution CD of the matrix (i.e.,  $i_{\text{GALV}}$ /anode area);  $i_C$  is the CD of the cathode;  $X_C$  is the area fraction of the cathode; and  $(1 - X_C)$  is the area fraction of the anode. The value of  $i_C$  can be set equal to the CD of the cathodic constituents at the galvanic couple potential. For example, the galvanic couple potentials of ultrapure aluminum, Al 1100, and Al 6061-T6 couple to various reinforcements are coincident with the pitting potentials of the aluminum alloys (i.e.,  $\sim -0.75$  V<sub>SCE</sub>). Hence, the values of  $i_C$  for a variety of reinforcements were read at  $\sim -0.75$  V<sub>SCE</sub> from [Figure 7](#). By plotting [eqn \[4\]](#), a graph ([Figure 14](#)) was generated from which  $i_{\text{GALV}}$  of ultrapure aluminum, Al 1100, or Al 6061-T6 can be obtained as a function of the area fraction of P100 Gr<sup>E</sup>, SiC MF<sup>E</sup>, B MF<sup>E</sup>, HP SiC, and Si with exposure to aerated 3.15 wt% NaCl at 30 °C.<sup>21</sup> [Figure 14](#) shows that to sustain a galvanic corrosion rate equal to the normal corrosion rate of Al 6061-T6, it would take less than 0.05 area fraction of P100 Gr<sup>E</sup> or SiC MF<sup>E</sup>, between 0.2 and 0.3 area fraction of B MF<sup>E</sup> and HP SiC, and more

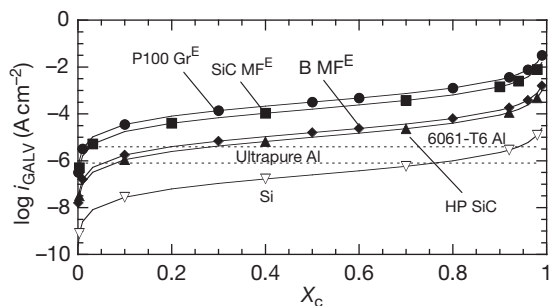


**Figure 14** Graphs showing the galvanic corrosion current density  $i_{\text{GALV}}$  of ultrapure Al (99.999%), Al 1100, or Al 6061-T6 as a function of the area fraction  $X_C$  of P100 Gr<sup>E</sup>, SiC MF<sup>E</sup>, B MF<sup>E</sup>, HP SiC, and Si for exposure to aerated 3.15 wt% NaCl at 30 °C. The horizontal dashed lines represent the normal corrosion rates of ultrapure Al and Al 6061-T6. Reproduced from Hihara, L. H. *Corros. Rev.* **1997**, 15(3-4), 361.

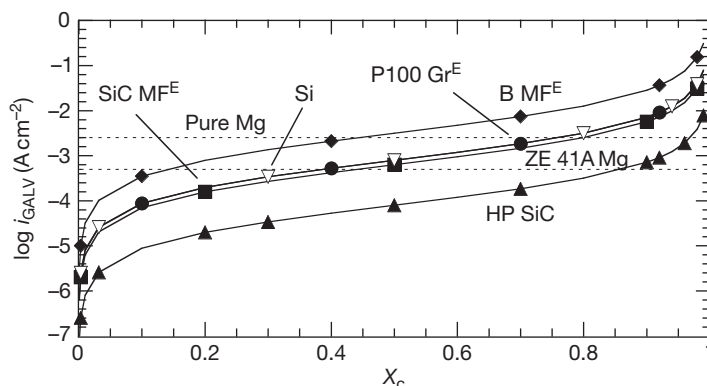


**Figure 15** Graphs showing the galvanic corrosion current density  $i_{\text{GALV}}$  of pure Mg and ZE 41A Mg as a function of the area fraction  $X_C$  of P100 Gr<sup>E</sup>, SiC MFE, B MFE, HP SiC, and Si for exposure to aerated 3.15 wt% NaCl at 30 °C. The horizontal dashed lines represent the normal corrosion rates of pure Mg and ZE 41A Mg.

than 0.9 area fraction of Si. It should be noted that for those reinforcements for which  $i_C$  was read in the diffusion-limited regime for oxygen reduction, galvanic corrosion rates could increase with additional convection. A similar figure was developed for pure magnesium and ZE 41A Mg (Figure 15).

The above discussion did not take into consideration the distribution of the anodic and cathodic current densities over the MMC microstructure. In some cases, for very low levels of conductive particles, localized corrosion can be induced by solution alkalization, as will be discussed below.

### 3.23.4.1.7 Microstructure

The physical presence of the reinforcements also greatly affects MMC corrosion. The reinforcements, which are usually inert in comparison to the matrix, are often left in relief as the matrix corrodes leaving behind a network of fissures that trap corrosion products and exacerbate corrosion (Figure 16). The initiation and propagation of corrosion sites are generally influenced by the electrical resistivity and volume fraction of the MMC constituents, including the reinforcements, interphases, and intermetallics. The corrosion behavior of MMCs in the open-circuit condition can be quite different from what might be expected based on anodic polarization diagrams of the MMCs. For example, in near-neutral 0.5 M Na<sub>2</sub>SO<sub>4</sub> solutions, various aluminum MMCs passivate (Figure 17)<sup>35,36</sup> during anodic polarization, but in the open-circuit condition, the same MMCs are susceptible to localized corrosion. The localized corrosion in the open-circuit condition is caused by the development of localized anodic and cathodic

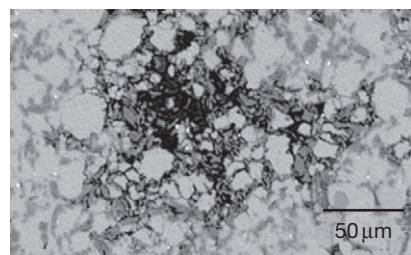


**Figure 16** SEM micrograph of region of localized corrosion on Al 6092/SiC/20 P-T6 MMC exposed for 24h in aerated 0.5 M Na<sub>2</sub>SO<sub>4</sub> at 30 °C in the open-circuit condition. Micrograph courtesy of H. Ding.

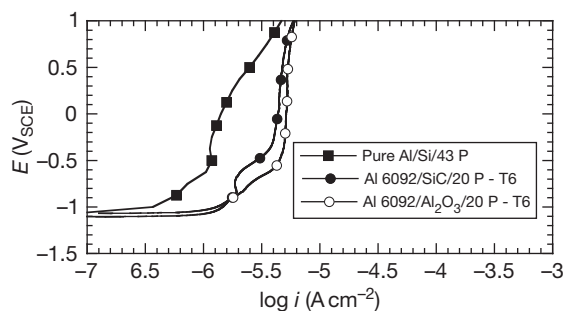


**Figure 17** Anodic polarization curves of various Al MMCs exposed to 0.5 M Na<sub>2</sub>SO<sub>4</sub> at 30 °C. Scan rates are 1 mV s<sup>-1</sup> (Al 6092-T6 MMCs) and 0.1 mV s<sup>-1</sup> (pure Al/Si/43 P MMC).

sites. The alkalinity in cathodic regions and acidity in anodic regions are accentuated by the formation of microcrevices in the network of reinforcement particles in relief. In the case of Al MMCs, aluminum loses its passivity in both the acidic and alkaline environments because of the amphoteric nature of aluminum oxide.

When an MMC is exposed to an electrolyte in the open-circuit condition, the sum of anodic current  $I_a$  is equal to the sum of cathodic current  $I_c$ :

$$I_a = I_c \quad [5]$$

Hence, the anodic and cathodic current densities are related by eqn [6],<sup>35</sup>

$$i_c = i_a \frac{(1 - x_c)}{x_c} \quad [6]$$

where  $i_c$  and  $i_a$  are the cathodic and anodic current densities, respectively, and  $x_c$  is the area fraction of cathodic constituents, here assumed to be conductive reinforcement, interphase, or intermetallic particles.

From eqn [6], the cathodic CD over cathodic constituents in the MMC microstructure can be approximated if the anodic CD of the matrix  $i_a$ , and the area fraction of cathodic constituents  $x_c$  are known. Experimental results on Al MMCs have indicated that the corrosion initiation sites depended on the amount of electrically conductive cathodic constituents that are present in the MMC microstructure. If the area fraction of cathodic constituents were low, corrosion initiated around the cathodic constituents because of solution alkalization; if the area fraction of cathodic constituents were high, corrosion initiation appeared more random around the reinforcement constituents.

Equation [6] was used to calculate the cathodic CD (Table 2) emanating from cathodic sites based on the area fraction  $x_c$ , and the assumption that the passive CD of the aluminum matrix was  $\sim 4 \times 10^{-6} \text{ A cm}^{-2}$ , based on the passive CD of various Al 6092-T6 MMCs (Figure 17). This passive CD should also be approximately equal to the initial anodic CD  $i_a$  of the Al matrix in the MMC at the open-circuit potential, prior to the development of significant pH gradients.

#### Low content of cathodic constituents

When the amount of cathodic sites is relatively low, cathodic current densities become concentrated over

the few cathodic sites resulting in hydroxide ion buildup. If the matrix material is not stable at high pH levels, localized corrosion can result. Table 2 shows the values of  $i_c$  as a function of  $x_c$ , assuming a value for  $i_a$  to be equal to  $4 \times 10^{-6} \text{ A cm}^{-2}$ , which is an estimate of the passive CD of an Al 6092-T6 matrix.

When values of  $x_c$  become less than  $\sim 0.04$  (Table 2), the cathodic current densities begin to exceed  $10^{-4} \text{ A cm}^{-2}$ , which can lead to solution alkalization by oxygen reduction and hydrogen evolution. Cathodic current densities of the order of  $10^{-4} \text{ A cm}^{-2}$  causes phenolphthalein dye in 0.5 M  $\text{Na}_2\text{SO}_4$  solutions to transform from clear to red for electrodes in quiescent solutions. The color change of phenolphthalein occurs in a pH range from 8.3 to 9.8. Aluminum corrosion rates increase exponentially when the pH exceeds  $\sim 8$ .<sup>37</sup> Hence, corrosion can be expected around cathodic constituents if their area fractions are low.

Accordingly, corrosion was observed on an Al 6092/ $\text{Al}_2\text{O}_3$ /20 P-T6 MMCs around intermetallic particles (Figure 18) in 0.5 M  $\text{Na}_2\text{SO}_4$ , in which Al passivates during anodic polarization.

In these MMCs, the  $\text{Al}_2\text{O}_3$  particles are insulators and cannot serve as cathodes; however, several types of particles, including titanium suboxides with compositions close to that of  $\text{Ti}_6\text{O}$ ,  $\text{Ti}_3\text{O}$ ,  $\text{Ti}_2\text{O}$ , and  $\text{TiO}$ ;  $\text{TiO}_2$  (likely doped); Ti–Zr–Al containing oxides; and Fe–Si–Al intermetallics<sup>23</sup> were found. Of these particles, the titanium suboxides,  $\text{TiO}_2$ , and the Fe–Si–Al intermetallics supported significant cathodic activity.<sup>23</sup> The area fraction of the non- $\text{Al}_2\text{O}_3$  particles in the MMCs was estimated to be of the order of 0.01 using image analysis.<sup>35</sup> Hence, if the area fraction of the cathodic constituents was less than 0.01, cathodic current densities in excess of  $10^{-4} \text{ A cm}^{-2}$  could result in significant solution alkalization and corrosion.

The scanning vibrating electrode technique (SVET) and scanning ion-selective electrode technique (SIET) revealed that localized corrosion over Al 6092/ $\text{Al}_2\text{O}_3$ /20 P-T6 MMCs immersed in 0.5 M  $\text{Na}_2\text{SO}_4$  was coinciding with that in alkaline, cathodic regions.<sup>38</sup>

The type of corrosion discussed above was suppressed in pH 7 buffered solutions. Only staining was observed around the intermetallics (Figure 19).

#### High content of cathodic constituents

MMCs that contain relatively high levels of cathodic sites should generally be more immune to corrosion

**Table 2** Values<sup>a</sup> of  $i_c$  as a function of  $x_c$

$i_c \text{ (A cm}^{-2}\text{)}$	$x_c$
$4 \times 10^{-3}$	0.001
$4 \times 10^{-4}$	0.01
$1 \times 10^{-4}$	0.04
$4 \times 10^{-5}$	0.1
$2 \times 10^{-5}$	0.2
$9 \times 10^{-6}$	0.3
$4 \times 10^{-6}$	0.5

<sup>a</sup> $i_c$  values correspond to  $i_a = 4 \times 10^{-6} \text{ A cm}^{-2}$ .



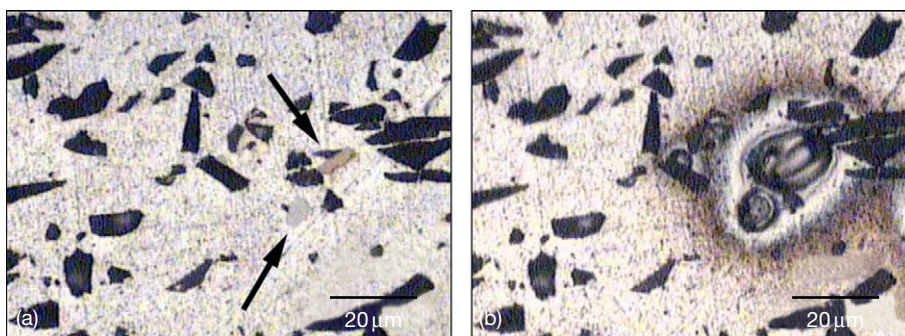


**Figure 18** Virgin Al 6092/Al<sub>2</sub>O<sub>3</sub>/20 P-T6 MMC (a) and after 2 days of immersion (b) in air-exposed 0.5 M Na<sub>2</sub>SO<sub>4</sub> at 30 °C. Intermetallic particles appear as light gray, and Al<sub>2</sub>O<sub>3</sub> appears as near black.

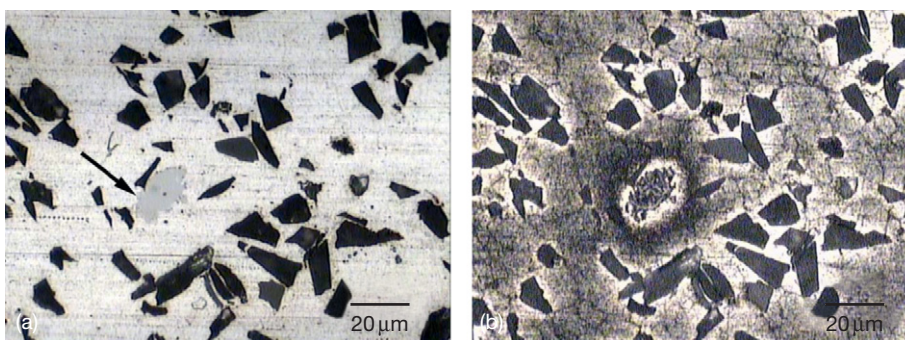


**Figure 19** Al 6092/Al<sub>2</sub>O<sub>3</sub>/20 P-T6 MMC in the virgin state (a) and after immersion for 17 days in air-exposed pH 7 buffered solution at 30 °C (b). Notice staining of the matrix around the intermetallic particle, but lack of localized corrosion.

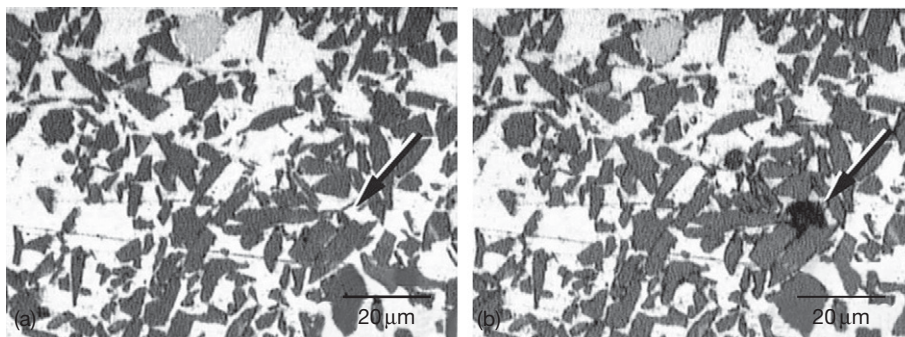


**Figure 20** Al 6092/SiC/40 P-T6 MMC in the virgin state (a) and after immersion for 2 days (b) in air-exposed 0.5 M Na<sub>2</sub>SO<sub>4</sub> at 30 °C.

initiation caused by extensive hydroxide ion buildup around the cathodic constituents, since the cathodic current is dispersed over more sites.

For example, in Al MMCs that are exposed to Na<sub>2</sub>SO<sub>4</sub> solutions in which the Al matrix passivates, the cathodic current densities are estimated to be relatively low (i.e.,  $\leq 4 \times 10^{-5} \text{ A cm}^{-2}$ ) (Table 2) for  $x_c$  greater than  $\sim 0.1$ . Accordingly, corrosion initiation

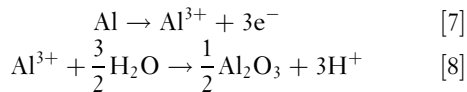
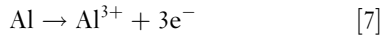
sites on Al 6092-T6 MMCs reinforced with semiconductive SiC (Figure 20) and B<sub>4</sub>C (greater than 10 vol. %) were different in appearance from the alkali-induced corrosion around intermetallics (Figure 18) in the Al 6092/Al<sub>2</sub>O<sub>3</sub>/20 P-T6 MMC.<sup>35</sup>

One possible source of the corrosion initiation sites on the Al 6092-T6 MMCs reinforced with SiC or B<sub>4</sub>C could be the formation of crevices at SiC–Al



or  $B_4C$ –Al interfaces by the hydrolysis of  $Al_4C_3$ , which is a reaction product of SiC and Al<sup>39</sup>, and  $B_4C$  and Al.<sup>40</sup>  $Al_4C_3$  readily hydrolyses upon contact with moisture and could leave fissures in the SiC–aluminum and  $B_4C$ –aluminum interface (see Section 3.23.4.3).

Once a crevice is formed at the particle–matrix interface, crevice corrosion can ensue. If the reinforcement particles are electrically conductive, they can serve as cathodic sites for hydrogen and/or oxygen reduction. As a result, for Al MMCs, the environment in the crevice will become acidic:



The acidified solution in the crevice can breakdown passivity because of the amphoteric nature of  $Al_2O_3$  and exacerbate corrosion. Eventually, corrosion spreads and encompasses adjacent particles forming a network of microcrevices caused by reinforcement particles in relief (Figures 21). The solution above the network of microcrevices has been measured to be acidic in the initial stages of growth.<sup>38</sup> The region around the centralized anodic region becomes alkaline because of the reduction of oxygen in surrounding regions.<sup>38</sup>

### 3.23.4.2 Electrochemical Effects of the Interphases

During the fabrication processing of MMCs, reactions between the reinforcement and matrix may lead to the formation of an interphase at the reinforcement–matrix interface. The presence of the interphase may lead to corrosion behavior different from what might

be expected based on virgin MMC constituents. For example, Pohlman<sup>41</sup> could not measure galvanic currents between virgin B MFs and Al 2024 or Al 6061 in 3.5% NaCl solutions, indicating that galvanic corrosion between aluminum matrices and B MFs should be negligible. In actual Al/B/MF MMCs, however, galvanic corrosion takes place between the aluminum matrix and the aluminum boride interphase on the surface layers of the B MFs.<sup>41</sup> Pohlman measured galvanic currents between the aluminum alloys and B MFs that were extracted from the matrix. A 4- $\mu m$ -thick layer of aluminum boride enveloped the extracted B MFs. Galvanic currents measured between the aluminum alloys and aluminum boride were similar to those between the alloys and the extracted B MFs. When the layer of aluminum boride was removed from the extracted B MFs, the galvanic current ceased, which indicated that the aluminum boride interphase was necessary for galvanic corrosion.

### 3.23.4.3 Chemical Degradation in MMCs

MMCs may also degrade by chemical reactions that cannot be directly assessed by electrochemical measurements. Interphases and reinforcement phases may undergo chemical degradation which cannot be detected, for example, with the aid of anodic polarization. In aluminum MMCs, the hydrolysis of the  $Al_4C_3$  interphase is one such example. Aluminum carbide degradation can affect Al/Gr, Al/SiC, and Al/ $B_4C$  MMCs. Reinforcement phases may also experience degradation. For example, mica particles have been reported to undergo exfoliation in Al/mica MMCs.

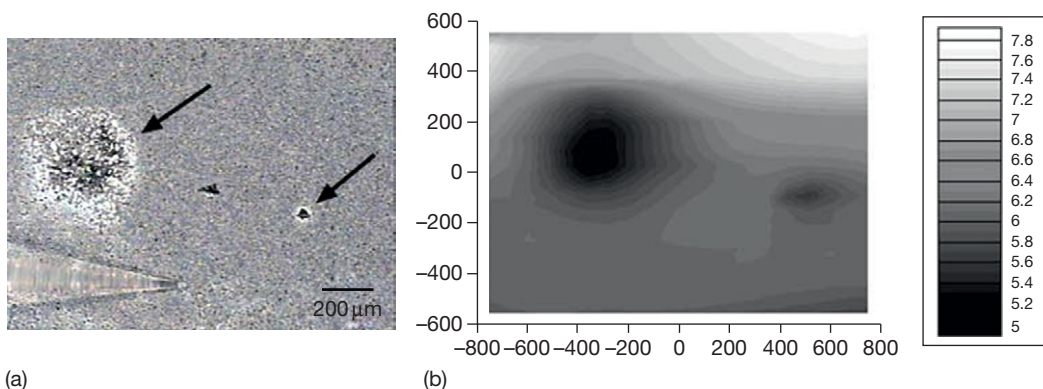


**Figure 21** Al 6092/SiC/20 P-T6 MMC in air-exposed 0.5 M  $Na_2SO_4$  (a), and pH profile over the specimen (b). Notice acidification of localized corrosion sites, and the alkalinization of surrounding cathodic sites.

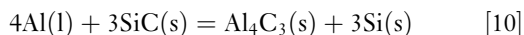
### 3.23.4.3.1 Aluminum carbide hydrolysis

Aluminum carbide forms by the reaction of aluminum and carbon,<sup>42</sup>



and its formation is substantial in Al/Gr MMCs during processing if temperatures are significantly higher than the liquidus temperature. At lower temperatures,  $\text{Al}_4\text{C}_3$  formation can be controlled.<sup>43</sup>

Aluminum carbide also forms by the reaction of aluminum and SiC,



and has been found at SiC–Al interfaces if the Si activity in liquid aluminum is low.<sup>39</sup>

The formation of  $\text{Al}_4\text{C}_3$  by the reaction of Al and  $\text{B}_4\text{C}$  is reported to occur rapidly at 900 °C. In addition, many other Al–B–C compounds are known to form.<sup>40</sup>

In the presence of moisture,  $\text{Al}_4\text{C}_3$  hydrolyzes to liberate methane gas by the reaction



Methane evolution has been detected from Al/Gr MMCs containing  $\text{Al}_4\text{C}_3$ .<sup>44,45</sup> The rate of  $\text{Al}_4\text{C}_3$  hydrolysis was measured to be ~1% per hour for HP  $\text{Al}_4\text{C}_3$  (78% of theoretical density and porous) exposed to pure water at 30 °C.<sup>26</sup> Buonanno<sup>45</sup> reported that  $\text{Al}_4\text{C}_3$  hydrolysis in Al/Gr MMCs leaves fissures at fiber–matrix interfaces. The hydrolysis of  $\text{Al}_4\text{C}_3$ , therefore, could result in rapid penetration into the MMC microstructures through fiber–matrix interfaces, and lead to the formation of microcrevices at reinforcement–matrix interfaces.

### 3.23.4.3.2 Mica degradation

Muscovite mica  $\text{KAl}_3\text{Si}_3\text{O}_{10}(\text{OH})_2$  particles of ~70  $\mu\text{m}$  in size<sup>46</sup> have been used in Al MMCs developed for potential use in applications where good antifriction, seizure resistance, and high-damping capacity are required.<sup>47</sup> During exposure to nonde-aerated 3.5 wt% NaCl solutions, the mica particles appeared to have absorbed moisture, swelled, and then exfoliated.<sup>48</sup>

### 3.23.4.4 Secondary Effects

The presence of the reinforcement phases in the MMCs may alter the microstructural features in the matrix material in ways that are nonexistent in the monolithic matrix alloys. Two examples that are discussed here are

the formation of intermetallic phases around reinforcements by solute rejection during solidification,<sup>49</sup> and the mismatch in the CTE between reinforcements and matrices that can lead to dislocation generation,<sup>50</sup> which potentially could lead to higher corrosion in some metals.<sup>51</sup>

### 3.23.4.4.1 Intermetallics

Intermetallics may have potentials and corrosion resistance different from that of the matrix. Table 3 shows corrosion potentials, pitting potentials, and normal corrosion current densities of various metals and intermetallics.<sup>52</sup> Noble and inert intermetallics may induce galvanic corrosion of the matrix; whereas, active intermetallics may go into dissolution and leave fissures or crevices.

In Al/ $\text{Al}_2\text{O}_3$  MMCs,  $\text{Al}_8\text{Mg}_5$  and  $\text{Mg}_2\text{Si}$ , intermetallics provided corrosion paths along fiber–matrix interfaces.<sup>53</sup> Pits in Al/ $\text{Al}_2\text{O}_3$  MMCs exposed to NaCl solutions containing  $\text{H}_2\text{O}_2$  were attributed to the dissolution of  $\text{MgAl}_3$ , which is rapidly attacked at low potentials.<sup>54</sup> In Al/mica MMCs, a dendritic

**Table 3** Corrosion data<sup>a</sup> of intermetallics

Constituent	$E_{\text{corr}}$ (mV <sub>SCE</sub> )	$E_{\text{pit}}$ (mV <sub>SCE</sub> )	$i_{\text{corr}}$ (A cm <sup>-2</sup> )
Cu (99.9)	−232	−30	$1.8 \times 10^{-6}$
Si (99.9995)	−441	—	—
Cr (99.0)	−506	297	—
$\text{Al}_3\text{Fe}$	−539	106	$2.1 \times 10^{-6}$
$\text{Al}_7\text{Cu}_2\text{Fe}$	−551	−448	$6.3 \times 10^{-6}$
$\text{Al}_{20}\text{Cu}_2\text{Mn}_3$	−565	−428	$3.4 \times 10^{-7}$
Al–4%Cu	−602	−406	$2.3 \times 10^{-6}$
$\text{Al}_3\text{Ti}$	−603	−225	$5.6 \times 10^{-7}$
$\text{Al}_2\text{Cu}$	−665	−544	$7.3 \times 10^{-6}$
Al–2% Cu	−672	−471	$1.3 \times 10^{-6}$
$\text{Al}_3\text{Zr}$	−776	−275	$2.5 \times 10^{-6}$
$\text{Al}_6\text{Mn}$	−779	−755	$6.3 \times 10^{-6}$
$\text{Al}_{12}\text{Mn}_3\text{Si}$	−810	−621	$1.7 \times 10^{-6}$
Al (99.9999)	−823	−610	$3.9 \times 10^{-6}$
$\text{Al}_2\text{CuMg}$	−883	80	$2.0 \times 10^{-6}$
Mg (AlCu)	−943	−2	$2.3 \times 10^{-5}$
7075-T651 Al	−965	−739	$1.1 \times 10^{-6}$
Zn (99.99)	−1000	—	$1.2 \times 10^{-6}$
$\text{Al}_{32}\text{Zn}_{49}$	−1004	—	$1.4 \times 10^{-5}$
$\text{Mg}_2\text{Al}_3$	−1013	−846	$4.8 \times 10^{-6}$
$\text{MgZn}_2$	−1029	—	$8.4 \times 10^{-5}$
Mn (99.9)	−1323	—	—
$\text{Mg}_2\text{Si}$	−1538	—	$7.7 \times 10^{-6}$
Mg (99.9)	−1586	−1391	$5.5 \times 10^{-6}$

<sup>a</sup>Aerated, pH 6, 0.1 M NaCl.

Source: Data from Birbilis, N.; Buchheit, R. G. *J. Electrochem. Soc.* 2005, 152(4), B140–B151.

phase, which was probably  $\text{Mg}_2\text{Al}_3$  or  $\text{Al}_8\text{Mg}_5$ , and spheroidized  $\text{CuMgAl}_2$  were preferentially attacked in nondeaerated 3.5 wt%  $\text{NaCl}$ .<sup>55</sup>

#### 3.23.4.4.2 Dislocation density

The high strengths of particulate MMCs in comparison to their monolithic alloys are generated by high dislocation densities caused by a mismatch in the CTE between reinforcement and matrix, and heating and cooling histories.<sup>50</sup> Since cold working, which is the result of generating high dislocation densities, is known to change the corrosion behavior of metals such as steel<sup>51</sup> and aluminum,<sup>56</sup> the corrosion behavior of MMCs may also be affected by high dislocation densities.<sup>21</sup> It has been suggested that corrosion near the  $\text{SiC}$ - $\text{Al}$  interface in  $\text{Al/SiC}$  MMCs could be caused by high dislocation density because of a mismatch of the CTE between  $\text{SiC}$  and  $\text{Al}$ .<sup>57,58</sup>

#### 3.23.4.4.3 MMC processing

Processing-induced corrosion is not inherently caused by the primary components of the MMC system, but results from processing deficiencies. The corrosion of diffusion bonds in  $\text{Al/B}$  MMCs and corrosion due to microstructural chlorides in some  $\text{Al/Gr}$  MMCs are two examples.

#### Low-integrity diffusion bonds

The open-circuit potentials of  $\text{Al}$  MMCs reinforced with  $\text{B}$  MFs were active as that of their monolithic matrix alloys in aerated  $\text{NaCl}$  solutions,<sup>59,60</sup> which were not expected since  $\text{B}$  MFs had open-circuit potentials that were noble to that of the monolithic matrix alloy. On the basis of the mixed-potential theory, it was expected that the MMCs would equilibrate at potentials between that of the noble  $\text{B}$  MF and the monolithic matrix alloy. To investigate the origin of this discrepancy, Bakulin *et al.*,<sup>60</sup> measured the open-circuit potentials of HP stacks of aluminum foil processed in the same way as the MMC (but without the  $\text{B}$  MFs), and found that the HP aluminum stacks were active as that of the monolithic alloy as well as the MMCs. The only difference between the HP stacks of aluminum foil and the monolithic aluminum was crevices in the diffusion bonds between adjacent foils which served as additional anodic sites.

#### Microstructural chlorides

Some types of  $\text{Al 6061/Gr/50 F-T6}$  MMCs were found to have been contaminated with microstructural chlorides during processing<sup>61</sup> by the  $\text{Ti-B}$  vapor

deposit method<sup>62</sup> that utilizes  $\text{TiCl}_4$  and  $\text{BCl}_3$  gases. The presence of microstructural chlorides in the  $\text{Al/Gr}$  MMCs was confirmed during microstructural analyses, and the effect of the chlorides was evident in anodic polarization diagrams.<sup>63</sup> These MMCs are pitted at  $\sim -0.6 \text{ V}_{\text{SCE}}$  in 0.5 M  $\text{Na}_2\text{SO}_4$ <sup>63</sup>; whereas, both the matrix alloy and other types of  $\text{Al/Gr}$  MMCs are processed by pressure infiltration without the use of chlorides passivate in 0.5 M  $\text{Na}_2\text{SO}_4$ .<sup>45</sup> The residual microstructural chlorides also make these MMCs inherently unstable, and as a result, some specimens have suffered from corrosion initiating subcutaneously beneath monolithic  $\text{Al}$  skins after long storage in laboratory air (Figure 22). This type of subcutaneous corrosion has also been observed in a similar type of  $\text{Mg/Gr}$  MMC (Figure 23).

#### 3.23.4.5 Corrosion in Environments

A comprehensive study of  $\text{Al 6092-T6}$  MMCs reinforced with black  $\text{SiC}$  (5, 10, 20, 40, and 50 vol%), green (high purity)  $\text{SiC}$  (50 vol%),  $\text{B}_4\text{C}$  (20 vol%), and  $\text{Al}_2\text{O}_3$  (20 vol%) has been examined in a battery of immersion, humidity-chamber exposure, and outdoor exposure tests.<sup>64</sup> The wide range of reinforcement types and testing conditions allows trends in corrosion behavior to be made and will be

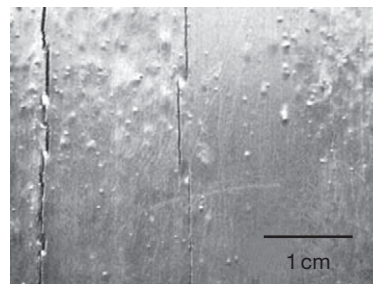


**Figure 22** Subcutaneous corrosion in  $\text{Al/Gr}$  MMC with over 10 years exposure in laboratory air.

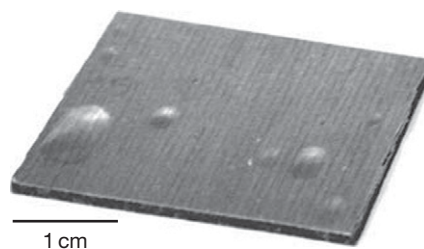


**Figure 23**  $\text{Mg/Gr}$  MMC showing subcutaneous corrosion after more than 15 years in storage.

highlighted here. Since galvanic corrosion between the Al 6092-T6 matrix and reinforcement particles depends on the ability of the particle to conduct electricity, the electronic resistivities of the particle should have an effect on the corrosion behavior. The resistivity of  $B_4C$  is  $\sim 10^0 \Omega \text{ cm}$ ,<sup>32</sup> that of SiC ranges from  $\sim 10^{-5}$  to  $10^{13} \Omega \text{ cm}$  depending on its purity,<sup>27</sup> and that of  $Al_2O_3$  is  $10^{14} \Omega \text{ cm}$ .<sup>29</sup> The green SiC possessing high electrical resistivity should be less likely to promote galvanic corrosion of the aluminum matrix as compared to black SiC, which is of lower purity and resistivity.

### 3.23.4.5.1 Immersion exposure

Immersion studies were conducted for 90 days in 3.15 wt% NaCl, ASTM seawater, real seawater, 0.5 M  $Na_2SO_4$ , and ultrapure 18  $\Omega \text{ cm}$  water exposed to air at 30 °C. The dimensions of the specimens were  $\sim 2.54 \text{ cm} \times 2.54 \text{ cm} \times 0.25 \text{ cm}$ . Specimens in triplicate were examined, but data correspond to results from two specimens for each testing condition (Figure 24). The third specimen was reserved for further surface analyses.

Corrosion rates were generally highest for the MMCs immersed in 3.15 wt% NaCl. The rates were much lower in ASTM seawater because of the formation of a film on the MMC surfaces, which was likely composed of Al–Mg hydrotalcite-like compounds.<sup>65</sup> The film may have impeded the diffusion of dissolved oxygen to cathodic regions limiting the corrosion rate. For most of the specimens, the

corrosion rates in  $Na_2SO_4$  were similar to those in NaCl. Although Al MMCs generally passivate in  $Na_2SO_4$  solutions during anodic polarization, they corrode in the open-circuit condition because of the formation of localized acidic and alkaline regions (see Section 3.23.4.1.7).

Most of the trends observed in the corrosion rate versus the reinforcement composition and type indicated that the level of galvanic corrosion between the matrix and reinforcements increases as the reinforcement electrical resistivity decreases, and as the reinforcement content increases. For the MMCs with 20 vol% of particulates, the corrosion rates were generally highest for that reinforced with  $B_4C$ , followed by that with black SiC, and least for that with  $Al_2O_3$ . Of the three types of reinforcements, the  $B_4C$  has the lowest electrical resistivity, and  $Al_2O_3$  has the highest. For the MMCs reinforced with 5, 10, 20, 40, and 50 vol% black SiC, the corrosion rates also generally increased as the volume fraction increased. For the MMCs reinforced with 50% black or green SiC, corrosion rates were higher for those that were reinforced with the lower purity, more conductive, black SiC in ASTM seawater and 0.5 M  $Na_2SO_4$ . It was expected that this trend would also be observed for the 3.15 wt% NaCl solution, but the results in this solution were skewed because of crevice and localized corrosion on one of the MMCs reinforced with the higher-purity, less-conductive, green SiC. A crevice formed on the specimen because of contact with the specimen holder, and a highly localized corrosion

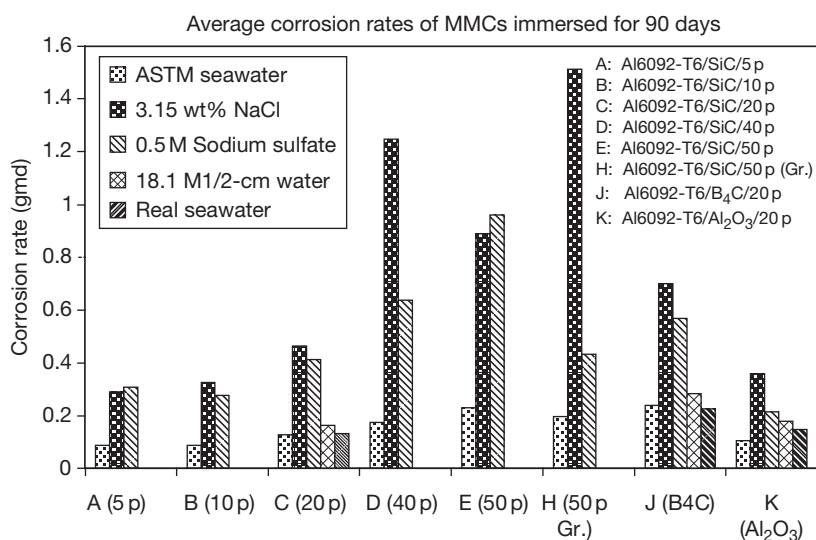


**Figure 24** Corrosion rates of Al 6092-T6 MMCs under immersion conditions in air-exposed solutions for 90 days at 30 °C. Reproduced from Hawthorn G. A. MS Thesis, University of Hawaii at Manoa, Honolulu, 2004.

site formed in a region of high plastic deformation where the specimen was stamped for identification.

### 3.23.4.5.2 Humidity chamber exposure

Humidity chamber studies were conducted for 90 days at 85% RH (relative humidity) and 30 °C. The dimensions of specimens were  $\sim 2.54 \text{ cm} \times 2.54 \text{ cm} \times 0.25 \text{ cm}$ . The specimens were treated in 3.15 wt% NaCl, ASTM seawater, actual seawater, and 0.5 M  $\text{Na}_2\text{SO}_4$  by immersion in the electrolyte for 1 min, air-dried, and then placed in the humidity chamber. Specimens in triplicate were examined, but data correspond to results from two specimens for each testing condition (Figure 25). The third specimen was reserved for further surface analyses.

The corrosion rates of specimens treated with ASTM seawater were generally comparable to or exceed those treated with NaCl, as the hydrotalcite-like films cannot form in the absence of an electrolyte. The specimens treated with  $\text{Na}_2\text{SO}_4$  generally had the lowest corrosion rates. Corrosion rates also generally increased for the MMCs reinforced with black SiC as the SiC content increased. For the MMCs reinforced with 50 vol% SiC, corrosion rates were lower for those having the high-purity, higher resistivity, and green SiC.

### 3.23.4.5.3 Outdoor exposure

The MMC specimens were exposed to six outdoor sites. The specimens were  $\sim 9 \text{ cm}$  in diameter and

2.5 mm in thickness. Specimens in triplicate were examined, but data correspond to results from two specimens for each testing condition (Figure 26). The third specimen was reserved for further surface analyses.

The test sites were industrial (Campbell Industrial Park), agricultural (Ewa Nui), arid (Waipahu), marine (Kahuku and Coconut Island sites), and rain forest (Lyon Arboretum). Weather and environmental data are provided for the 180-day exposure period (Table 4).

Some trends are clearly visible in the corrosion data (Figure 26). The corrosion rates of the MMCs reinforced with black SiC generally increased with an increase in volume fraction of the reinforcement. This would be expected due to galvanic action between the black SiC and aluminum matrix. For the MMC reinforced with 50 vol% SiC, those having the black SiC corroded at higher rates than those reinforced with the high-purity, higher-resistivity, and green SiC. For the three types of MMCs with 20 vol% particulates, those reinforced with  $\text{B}_4\text{C}$  generally corroded at a higher rate than those reinforced with less-conductive SiC or  $\text{Al}_2\text{O}_3$ .

The highest corrosion rates were generally observed at the Manoa (very wet), Coconut Island (marine), and Kahuku (marine) test sites. The high corrosion rate at Manoa is likely due to persistent rain since chloride levels are negligible at that site.

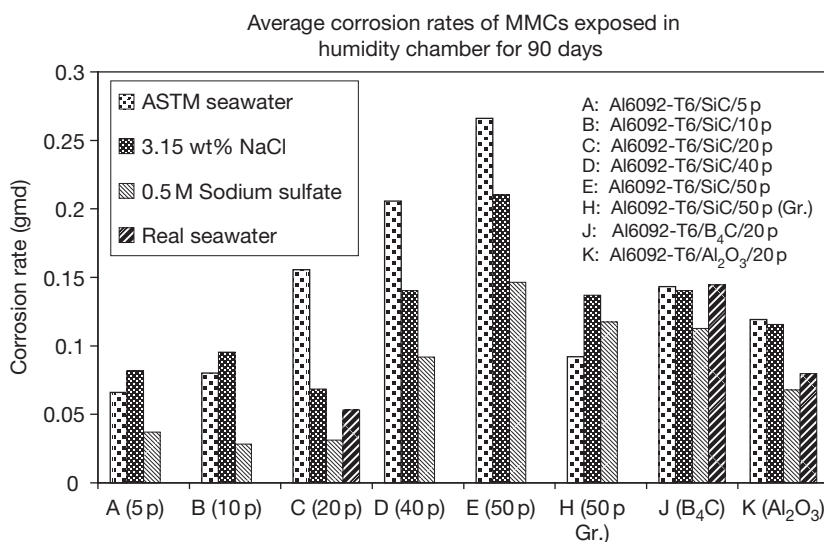


**Figure 25** Corrosion rates of Al 6092-T6 MMCs treated with various salts and exposed to 85% RH for 90 days at 30 °C. Reproduced from Hawthorn G. A. MS Thesis, University of Hawaii at Manoa, Honolulu, 2004.



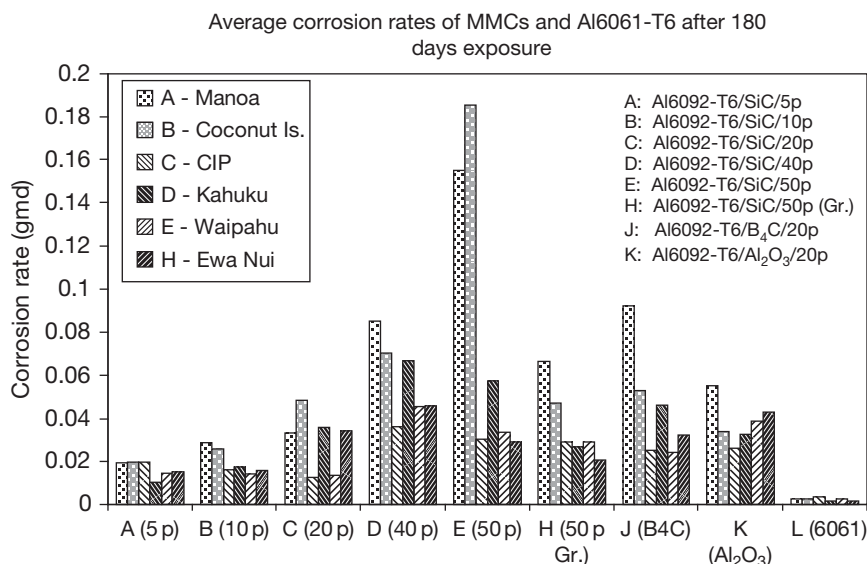


**Figure 26** Corrosion rates of Al 6092-T6 MMCs exposed to outdoor test sites for 180 days. Reproduced from Hawthorn G. A. MS Thesis, University of Hawaii at Manoa, Honolulu, 2004.

**Table 4** Weather and atmospheric data for 180-day exposure at test sites

Test site	Avg. temp (°C)	Rain (cm)	% of exposure time when TOW = 0 <sup>a</sup>	% of exposure time when TOW = 15 <sup>a</sup>	Avg. Cl <sup>-</sup> deposition rate (mg m <sup>-2</sup> day <sup>-1</sup> )	Avg. humidity (%RH)
Manoa	22.9	357.9	60.6	26.4	— <sup>b</sup>	83.1
Coconut Is.	25.8	65.0	54.8	9.2	58.3	74.9
Campbell	27.2	45.5	66.5	4.6	24.4	63.2
Kahuku	25.6	132.1	59.6	15.1	89.9	73.4
Waipahu	26.3	79.0	80.3	7.1	10.7	66.9
Ewa Nui	25.9	82.6	77.6	6.5	9.4	67.4

<sup>a</sup>A TOW sensor value of zero indicates that the specimens are dry and a value of 15 indicates that the specimens are wet.

<sup>b</sup>Below detectable level of 7.0.

Source: Hawthorn, G. A. MS Thesis, University of Hawaii at Manoa, Honolulu, 2004.

### 3.23.5 Corrosion Protection of MMCs

Corrosion of metals can be prevented with the use of protective coatings and inhibitors. The type of coating (e.g., impervious, inhibitive, or cathodically protective) will depend on the application; for example, immersion or atmospheric exposure. For MMCs, however, a proven coating system for the matrix alloy may not be suitable. Poor adhesion and wettability between the coating and reinforcement or differences in the electrochemical properties of the alloy and the MMC may render a good coating system for the ineffectiveness of alloy for the MMC. Other coating techniques such as anodization could also be ineffective or even deleterious to the MMC. Various studies on the corrosion protection of MMCs utilizing

organic coatings, inorganic coatings, anodization, chemical conversion coatings, and inhibitors have been summarized elsewhere.<sup>66</sup>

### 3.23.6 Conclusions

The corrosion of MMCs is significantly more complicated and less predictable than that of their monolithic alloys. MMC systems that consist of active metal matrices and noble reinforcements have inherent galvanic corrosion problems. Some systems, such as those containing aluminum and carbon, may also be susceptible to interphase formation of the deleterious Al<sub>4</sub>C<sub>3</sub>, which hydrolyses in the presence of moisture. Other complications arise when reinforcements are



SCs, which have electrical resistivities that can span orders of magnitude and are sensitive to impurity levels. In addition, impurities in semiconducting reinforcements may cause them to become n-type or p-type which can lead to photo-induced corrosion or even beneficial photoinduced cathodic protection. The presence of the reinforcements may also influence the formation of intermetallics and the generation of dislocations, which also affect corrosion behavior. These additional concerns make designing and utilizing MMCs a significant, but worthy, engineering challenge. Many of the extraordinary mechanical and physical properties of MMCs cannot be achieved with conventional metal alloys. Standardization of MMC constituents (e.g., purity levels in reinforcements) and the stringent control of processing temperatures and histories could help develop MMCs with more predictable corrosion behavior.

## References

- Weeton, J. W.; Peters, D. M.; Thomas, K. L. *Guide to Composite Materials*; American Society for Metals: Metals Park, OH, 1987; pp 2–2.
- Park, G. B.; Foster, D. A. International Technical Conference Proceedings, SUR/FIN'90, Boston, MA, July, 1990; American Electroplaters and Surface Finishers Society: Boston, MA, 1990; pp 1349–1369.
- Harrigan, W. C. J. *Metal Matrix Composites: Processing and Interfaces*; Academic Press, 1991; pp 1–16.
- Liu, Y.; Rohatgi, P. K.; Ray, S.; Barr, T. L. In Conference Proceedings, ICCM/8, 1991; Tsai, S. W., Springer, G. S., Eds.; Society for the Advancement of Material and Process Engineering (SAMPE), 1991; p 20H.
- Lim, T.; Lee, C. S.; Kim, Y. H.; Han, K. S. In Conference Proceedings, ICCM/8, 1991; Tsai, S. W., Springer, G. S., Eds.; Society for the Advancement of Material and Process Engineering (SAMPE), 1991; pp 20E.
- Ashby, M. F.; Jones, D. R. H. *Engineering Materials*, 2nd ed; Butterworth Heinemann, 1998; Vol. 2.
- Buck, M. E.; Suplinskas, R. J. In *Engineered Materials Handbook on Composites*; ASM International: Metals Park, Ohio, 1987; Vol. 1, pp 851–857.
- Saffil Saffil. [www.saffil.com](http://www.saffil.com) (May).
- 3M Metal Matrix Composites, [www.3m.com/market/industrial/mmc/](http://www.3m.com/market/industrial/mmc/www.3m.com/market/industrial/mmc/) (May).
- FiberNide, <http://fibernide.com/copper.html> October 2007.
- DWA Technologies Inc., <http://dwatechnologies.com/> October 2007.
- ALMMC Aluminum Metal–Matrix Composites Consortium, [www.almmc.com](http://www.almmc.com)
- Wesley, W. A.; Brown, R. H. *The Corrosion Handbook*, 1st ed; Uhlig, H. H., Ed.; Wiley: New York, 1948; pp 481–495.
- Uhlig, H. H.; Revie, R. W. *Corrosion and Corrosion Control*, 3rd ed; Wiley: New York, 1985; p 354.
- Hihara, L. H.; Kondepudi, P. K. *Corros. Sci.* **1994**, *36*, 1585–1595.
- Hihara, L. H.; Latanision, R. M. *Corrosion* **1992**, *48*(7), 546–552.
- Lin, Z. J. M.S. Thesis, University of Hawaii at Manoa, Honolulu, 1995.
- Tamirisa, C. M.S. Thesis, University of Hawaii at Manoa, Honolulu, HI, 1993.
- Hihara, L. H.; Tamirisa, C. *Mater. Sci. Eng. A* **1995**, *198*, 119–125.
- Hihara, L. H.; Latanision, R. M. *Int. Mater. Rev.* **1994**, *39*, 245.
- Hihara, L. H. *Corros. Rev.* **1997**, *15*(3–4), 361.
- Ding, H.; Hihara, L. H. In 212th ECS Meeting, Washington, DC, October 7–12, 2007, Washington, DC, 2007.
- Ding, H.; Hihara, L. H. In 212th ECS Meeting, Washington, DC, October 7–12, 2007, Washington, DC, 2007.
- Adler, R. P. I.; Snoha, D. J.; Hawthorn, G.; Hihara, L. H. In *Characterization of Environmentally Exposed Aluminum Metal Matrix Composite Corrosion Products as a Function of Volume Fraction and Reinforcement Specie*, paper 06T029; Tri Service Corrosion Conference, Orlando, Florida, 2005; Beatty, J., Adler, R. P. I., Eds., Orlando, Florida, 2005.
- Ding, H.; Hihara, L. H. *J. Electrochem. Soc.* **2008**, *155*(5).
- Hihara, L. H. Ph.D. Thesis, Massachusetts Institute of Technology, Cambridge, MA, 1989.
- Ichinose, N. *Introduction to Fine Ceramics*; John Wiley and Sons, 1987; p 50–52.
- Tsirlin, A. M. In *Strong Fibres (Handbook of Composites)*; Watt, W., Perov, B. V., Eds.; Elsevier Science Publishers, 1985; Vol. 1, pp 155–199.
- Bolz, R. E.; Tuve, G. L. *CRC Handbook of Tables for Applied Engineering Science*, 2nd ed.; CRC Press: Boca Raton, FL, 1973; pp 262–264.
- Clauser, H. R. *The Encyclopedia of Engineering Materials and Processes*; Reinhold Publishing Corporation, 1963; p 429.
- Greenwood, N. N.; Earnshaw, A. *Chemistry of the Elements*; Pergamon Press, 1984.
- Yamada, S.; Hirao, K.; Yamauchi, Y.; Kanzaki, S. *Ceram. Int.* **2003**, *29*, 299.
- Weeton, J. W.; Peters, D. M.; Thomas, K. L. *Guide to Composite Materials*; American Society for Metals: Metals Park, OH, 1987; pp 5–10.
- Evans, U. R. *Metallic Corrosion, Passivity and Protection*; Edward Arnold and Co.: London, 1937; pp 513–516.
- Hihara, L. H.; Devarajan, T. S.; Ding, H.; Hawthorn, G. A. In *Corrosion Initiation and Propagation in Particulate Aluminum–Matrix Composites*, Tri-Service Corrosion Conference, Orlando, Florida, November 14–18, 2005; Orlando, Florida.
- Hihara, L. H.; Lin, Z. J. In Seventh Japan International SAMPE Symposium and Exhibition: Tokyo, Japan, 1999.
- Deltombe, E.; Vanleugenhaghe, C.; Pourbaix, M. In *Atlas of Electrochemical Equilibria in Aqueous Solutions*; Pourbaix, M., Ed.; National Association of Corrosion Engineers: Houston, TX, 1974; pp 168–176.
- Ding, H.; Hihara, L. H. *J. Electrochem. Soc.* **2005**, *152*, 4.
- Iseki, T.; Kameda, T.; Maruyama, T. *J. Mater. Sci.* **1984**, *19*, 1692–1698.
- Grytsiv, A.; Rogl, P. In *Light Metal Systems. Part 1: Selected Systems from Ag–Al–Cu to Al–Cu–Er*; Springer: Berlin Heidelberg, 2004; p 11A1.
- Pohlman, S. L. *Corrosion* **1978**, *34*, 156–159.
- Becher, H. J. In *Handbook of Preparative Inorganic Chemistry*, 2nd ed.; Brauer, G., Ed.; Academic Press, 1963; Vol. 1, p 832.
- Kendall, E. G. In *Metal Matrix Composites*; Kreider, K. G., Ed.; Academic Press: New York, 1974; Vol. 4, pp 319–397.
- Portnoi, K. I.; Timofeeva, N. I.; Zambolotskii, A. A.; Sakovich, V. N.; Trefilov, B. F.; Levinskaya, M. K.; Polyak, N. N. *Poroshkovaya Metallurgiya* **1981**, *218*(2), 45–49.

45. Buonanno, M. A. Ph.D. Thesis, Massachusetts Institute of Technology, Cambridge, MA, 1992.
46. Deonath, S. K.; Bhat, R. T.; Rohatgi, P. K. *J. Mater. Sci.* **1980**, *15*, 1241–1251.
47. Rohatgi, P. K.; Asthana, R.; Das, S. *Int. Mater. Rev.* **1986**, *31*, 115.
48. Deonath, S. K.; Namboodhiri, T. K. *Composites* **1988**, *19*, 237–243.
49. Mortensen, A.; Cornie, J. A.; Flemings, J. J. *Met.* **1988**, *40*, 12.
50. Arsenault, R. J. In *Metal Matrix Composites: Mechanisms and Properties*; Everett, R. K., Arsenault, R. J., Eds.; Academic Press: New York, 1991; pp 79.
51. Uhlig, H. H.; Revie, R. W. *Corrosion and Corrosion Control*, 3rd ed.; Wiley: New York, 1985; p 123.
52. Birbilis, N.; Buchheit, R. G. *J. Electrochem. Soc.* **2005**, *152* (4), B140–B151.
53. Bruun, N. K.; Nielsen, K. In *Metal Matrix Composites-Processing, Microstructure and Properties*, 12th Riso International Symposium on Materials and Science, 1991; Hansen, Ed., 1991; pp 257–264.
54. Yang, J. Y.; Metzger, M. In *Extended Abstracts*; The Electrochemical Society: Denver, CO, 1981; Vol. 81-2, Abstract no. 115.
55. Deonath, S. K.; Namboodhiri, T. K. *Corros. Sci.* **1989**, *29*, 1215–1229.
56. Butler, G.; Ison, H. C. K. In *Corrosion and Its Prevention in Waters*; Robert, E., Ed.; Krieger Publishing: New York, 1978; p 149.
57. Ahmad, Z.; Paulette, P. T.; Aleem, B. J. A. *J. Mater. Sci.* **2000**, *35*, 2573–2579.
58. Yao, H.-Y.; Zhu, R.-Z. *Corrosion* **1998**, *54*(7), 499–503.
59. Sedriks, A. J.; Green, J. A.; Novak, D. L. *Metall. Trans.* **1971**, *2*, 871–875.
60. Bakulin, A. V.; Ivanov, V. V.; Kuchkin, V. V. *Zaschita Metallov* **1978**, *14*(1), 102–104.
61. Hihara, L. H.; Latanision, R. M. *Mater. Sci. Eng.* **1990**, *A126*, 231–234.
62. Harrigan, W. C. J.; Flowers, R. H. In *Failure Modes in Composites*; Cornie, J. A., Crossman, F. W., Eds.; The Metallurgical Society of AIME: Warrendale, PA, 1979; Vol. IV, pp 319–335.
63. Hihara, L. H.; Latanision, R. M. *Corrosion* **1991**, *47*, 335–341.
64. Hawthorn, G. A. MS Thesis, University of Hawaii at Manoa, Honolulu, 2004.
65. Ding, H.; Hawthorn, G. A.; Hihara, L. H. *ECS Trans.* **2008**, *26*(24), 29.
66. Hihara, L. H. In *ASM Handbook, Corrosion: Materials*; Cramer, S. D., Covino, J., Eds.; ASM International: Materials Park, OH, 2005; Vol. 13B, pp 538–539.

## Further Reading

Aylor, D. M. In *Metals Handbook, 9th ed.; Corrosion*; ASM International: Metals Park, Ohio, 1987; pp 859–863.

Jones, R. H. In *Environmental Effects on Engineered Materials*; Jones, R. H., Ed.; Marcel Dekker, 2001; pp 379–390.

Lucas, K. A.; Clarke, H. *Corrosion of Aluminum-Based Metal Matrix Composites*; Research Studies Press: England, Wiley: New York, 1993.

Trzaskoma, P. P. In *Metal Matrix Composites: Mechanisms and Properties*; Everett, R. K., Arsenault, R. J., Eds.; Academic Press, 1991; pp 383–404.

## 3.25 Degradation of Engineering Ceramics

**R. Morrell**

National Physical Laboratory, Teddington, Middlesex TW11 0LW, UK; Institut für Strucktur-und Funktionskeramik, Montanuniversität Leoben, A8700 Leoben, Austria

© 2010 Elsevier B.V. All rights reserved.

<b>3.25.1</b>	<b>Ceramic Materials as Engineering Products</b>	2283
3.25.1.1	Ceramic Materials and Applications	2283
3.25.1.2	Mechanical and Thermal Limitations	2284
<b>3.25.2</b>	<b>Microstructure and Corrosion Processes</b>	2284
3.25.2.1	Role of Microstructure	2284
3.25.2.2	Corrosion Processes	2285
3.25.2.3	Subcritical Crack Growth	2285
3.25.2.4	Corrosion/Erosion	2286
<b>3.25.3</b>	<b>Testing Procedures and Standards</b>	2286
3.25.3.1	Standards	2286
3.25.3.2	Procedures	2287
3.25.3.2.1	Equipment	2287
3.25.3.2.2	Assessment techniques	2287
3.25.3.3	Testing Standards	2288
<b>3.25.4</b>	<b>Performance of Specific Material Types</b>	2289
3.25.4.1	Oxide-Based Materials	2289
3.25.4.1.1	Porcelains and aluminosilicates	2289
3.25.4.1.2	Alumina	2289
3.25.4.1.3	Zirconia	2294
3.25.4.1.4	Other oxide ceramics	2296
3.25.4.1.5	Glasses and glass-ceramics	2296
3.25.4.2	Nonoxide-Based Materials	2297
3.25.4.2.1	Silicon carbides	2297
3.25.4.2.2	Silicon nitrides	2299
3.25.4.2.3	Boron nitrides	2301
3.25.4.2.4	Specialist materials	2301
3.25.4.3	Comparative Attack Rates	2302
<b>3.25.5</b>	<b>Some Specific Applications Requiring Corrosion Resistance</b>	2302
3.25.5.1	Chemical Process Vessels	2302
3.25.5.2	Rotating Seals	2303
3.25.5.3	Flow-meter Bodies	2303
3.25.5.4	Food Processing	2303
3.25.5.5	Valves	2303
3.25.5.6	Medical	2303
<b>3.25.6</b>	<b>Selecting the Right Material</b>	2303
<b>References</b>		2304

### Glossary

#### **Advanced (advanced technical, fine) ceramic**

A highly engineered, high-performance, predominantly nonmetallic, inorganic, ceramic material having specific functional attributes (*Note:* US – advanced ceramic;

Europe – advanced technical ceramic; Japan (English term) – fine ceramic; Germany – Hochleistungskeramik).

**Ceramic** An inorganic, nonmetallic material consolidated by the action of heat.

**Chemical porcelain** A ceramic material manufactured principally from clays, feldspars and quartz, and/or alumina, and generally of low iron content.

**Chemical stoneware** A ceramic material manufactured principally from clays, feldspars and quartz, and/or alumina, designed to retain dimensions during firing, and manufactured in large pieces.

**Chemical vapor deposition (CVD)** Method of producing a coating on a body (and more rarely a solid object on a mandrel) by reaction between gases at high temperature, for example,  $\text{SiCl}_4 + \text{CH}_4$ , producing  $\text{SiC}$ .

**Corrodant** Substance causing corrosion.

**Delayed failure** The sudden failure of a ceramic component without detectable creep as a result of subcritical crack growth under stress.

**Flexural strength** The fracture stress of a defined beam test-piece loaded in flexure and computed as the nominal tensile surface stress; usually applied to ceramic and other brittle materials.

**Glass-ceramic** A material fabricated as a glass which is then subjected to a controlled crystallization (devitrification) process to give a fine-grained microstructure with desired properties.

**Hardmetal** A metal/ceramic composite material comprising typically a hard ceramic phase with a metallic binder phase. Examples: WC/Co, WC/Ni, TiC/Fe.

**High-alumina ceramic** An advanced ceramic material comprising principally a compound of aluminium and oxygen with or without other minor components to aid densification or control properties.

**Hydration** The formation of a hydroxide material, especially at the corrosion interface of a material, especially a ceramic.

**Mullite** A ceramic phase comprising a compound of alumina and silica.

**Nonoxide ceramic** An advanced ceramic material comprising principally borides, carbides, nitrides, or silicides, for example, silicon nitride, molybdenum disilicide.

**Reaction bonding** A process for ceramic manufacture in which a ceramic bond between grains is produced *in situ* by chemical reaction between relevant species,

for example, between silicon and nitrogen to produce silicon nitride.

**Subcritical crack growth** The process of crack extension over time without complete failure.

**TZP (tetragonal zirconia polycrystals)** A zirconia ceramic, typically, but not exclusively, partially stabilized with yttria (hence Y-TZP) and with submicrometer grain size to retain principally the tetragonal phase of zirconia, resulting in high strength.

**Zirconia ceramic** An advanced technical ceramic material comprising principally a compound of zirconium and oxygen with or without other minor components to provide phase stabilization, to aid densification or to control properties.

## Abbreviations

**CBN** Cubic boron nitride

**CVD** Chemical vapor deposition

**HBN** Hexagonal boron nitride

**PTFE** Polytetrafluoroethylene

**TZP** Tetragonal zirconia polycrystal

## 3.25.1 Ceramic Materials as Engineering Products

### 3.25.1.1 Ceramic Materials and Applications

For many years, ceramic materials have formed a vital part of the palette of materials available for engineers, but with the principal disadvantage that they are brittle and may not be available in particularly large sizes. In former times, the choice was limited to porcelain-like products, which could be made for items such as pestles, mortars, mills, and chemical plant tower packings. Such materials generally have good resistance to being attacked by aqueous solutions up to 100 °C. Their principal advantage is that they produce no corrosion scale layers and no obvious metallic contamination of the process for which they are used. However, such materials are not particularly strong and/or wear resistant. Over the last half-century, the development of a wider range of harder and stronger materials for general engineering applications has greatly widened the field of applications from a corrosion

perspective. Such newer products have improved the performance of a wide range of existing devices compared with the use of metallic components, and have enabled new applications and processes to be developed, upon which the entire world now relies.

### **3.25.1.2 Mechanical and Thermal Limitations**

The main disadvantage of ceramic materials is that they are, in engineers' terms, brittle. They generally show linear elastic behavior to fracture, which occurs at strains of less than 0.5%, usually less than 0.1%. They therefore have to be treated with care from the design and application point of view. There must be an avoidance of stress concentrations that initiate fracture, which means that the designer should change his/her mindset, throw away his/her metallic designs with all their in-built assumptions, and start from scratch with chunky designs, which minimize stresses and thus maximize reliability. Failures in trials often result from poor or inappropriate design and a failure to understand stress concentrations and thermal gradients, as much as from attempting to use an inappropriate material.

A further consequence of brittleness is a limitation to thermal stress and thermal shock resistance. Steep temperature gradients or sudden changes of surface temperature, particularly downshock, can result in internal stresses, which are not relaxed by plastic deformation processes, but which can cause rapid failure. The larger the item, the more it is prone to thermal stress failure. Care is needed in the choice of material to withstand thermal shock. In general, for dense, fine-grained materials, thermal stress is reduced and thermal shock resistance is improved with reductions in thermal expansion coefficient and elastic modulus, and with increases in thermal conductivity and strength. Materials that have larger grain sizes, perhaps some open porosity, and lower elastic modulus, such as many refractory products, may show better thermal shock resistance than do finer-grained, denser, stronger materials, because the elastic energy developed is less, and damage takes the form of microcracking rather than macrocracking. Changing the material to maximize thermal shock resistance may have limitations in terms of resistance to corrosive attack. Therefore, care in material selection has to be taken. Unless parts are of thin sections, where concerns about thermal stress are less, it may be better to design the whole function to restrict thermal

stressing occurring while retaining the corrosion resistance of the material of choice.

## **3.25.2 Microstructure and Corrosion Processes**

### **3.25.2.1 Role of Microstructure**

Ceramic materials are typically made by a powder route, with a high temperature consolidation process to form the final microstructure. This process may be *via* solid state diffusion or sintering, or *via* a liquid phase mechanism, or *via* a combination of the two. In many cases, it leaves a continuous second phase, often of a glassy or partially crystallized nature, running between the grains. This is a key aspect of ceramic microstructures that needs to be considered from the point of view of corrosion. It means that not only the base crystalline phase or phases, but also the secondary, often unspecified, continuous phase, has to be resistant to corrosion in the medium under consideration.

An example of this is the series of materials known as high-alumina ceramics. By itself, high-purity alumina powder requires a high sintering temperature, and particularly expensive raw materials. Usually, a small amount of MgO is added to control grain growth during sintering, and this tends to segregate to grain boundaries along with any residual impurities such as sodium. For control of electrical properties such as dielectric loss, small additions of silica are made to create a glassy phase. Reductions in firing temperature can be achieved by adding additional components such as CaO. Although the alumina grains themselves are corrosion resistant, the resulting continuous grain boundary phase may not be, especially in acid media where the material can be penetrated through this phase without necessarily any change in dimensions or appearance. Such penetration can be disastrous for strength, wear, and erosion resistance, as well as for any process containment. Thus, although there may be claims that might seem to indicate that high-alumina ceramics have generically good corrosion resistance, which would be borne out for high-purity materials, it is not generally the case. Materials have to be chosen for their individual fitness for purpose, balanced against the ability to make the size and shape required. Often, it is necessary to undertake a test under the specific conditions of anticipated use to prove that they have the required corrosion resistance.

The majority of ceramic materials contain some residual porosity as a result of the process route

used in their fabrication. For engineering purposes, selected materials should be specified as being 'impervious,' in which case the pores are individual, and mostly not connected to each other. Liquids cannot penetrate the material except by dissolving a continuous phase. In some cases, this porosity is 'open,' that is, it is accessible from the exterior of the body, and there is a large accessible internal surface area that is subject to corrosive attack. With some materials, notably with chemical porcelains and stonewares, the integrity of the item may rely on an intact, impervious skin, which, if broken, permits corrodants to access the more-porous bulk.

Further details concerning individual material types are found in later sections.

### 3.25.2.2 Corrosion Processes

While corrosion of metallic alloys involves the dissolution or oxidation/hydroxylation of metal atoms at the surface, usually with electrolytic drivers, oxide ceramics are already oxides, and are usually quite stable against further hydration except under hydrothermal conditions (temperatures of 300–500 °C and pressures of 10s or 100s of atmospheres). They may possess a surface monolayer of hydroxide, but typically, this is stable. Removal of material from such a surface by aqueous environments requires chemical dissolution of the ceramic structure itself. In materials such as high-purity, single-phase alumina or silicon carbide, this is difficult; hence the corrosion resistance.

Some single-phase products have only moderate corrosion resistance in acidic or alkaline environments, notably those that are based primarily on alkaline or acidic oxides. Thus, magnesium and calcium silicates and some aluminosilicates tend not to be acid resistant, while silica and highly siliceous glasses tend to be relatively resistant to acids, but are attacked by strongly alkaline environments.

In structures with corrosion-resistant primary grains and secondary phases such as glasses, attack may be much more rapid, especially if the glassy network is highly disrupted by locally high levels of alkaline and alkaline earth ions. Acidic environments can much more readily attack this glassy phase. It is quickly leached of its alkaline ions, leaving a porous siliceous gel acting as a diffusion medium for the corroding species. Another example is of the free silicon phase in some versions of silicon carbide ceramics. The result is that the material can be penetrated down the grain boundaries without the

generation of any surface layers and without loss of dimensions.

In nonoxide ceramics, which are free from oxide phases, the first step to dissolution is oxidation or hydration. In silicon carbide and silicon nitride, the surface comprises a protective layer of silica. To progressively remove material, not only does this layer have to be removed, requiring a strongly alkaline condition, but also the underlying material then has to be oxidized. Only certain corrodant conditions will achieve this, hence the corrosion resistance of such materials. In some cases, the material oxidizes or hydrates readily. An example is the soft, crystallographically hexagonal form (HBN) of boron nitride. The oxide product is boric oxide, which readily reacts with water. Once hydration occurs at a significant rate, dissolution is continuous, and there is no protective skin.

The majority of commonly available ceramics for structural purposes are not electrically conducting to any significant extent at temperatures up to 500 °C. Consequently, they do not suffer from electrolytic effects, and hence from corrosion processes that involve this type of process. Only in materials that are electronically or ionically conducting, one might see such effects. With a few exceptions (e.g., siliconized silicon carbide), such materials are generally not employed for corrosion-resisting functions. However, an interesting example of a study of electrolytic corrosion of titanium-based ceramics and ceramic composites (TiN, Ti(C,N), TiB<sub>2</sub>) in seawater has been made by Lavrenko *et al.*<sup>1</sup> They showed that the rate of corrosion was three or four orders of magnitude less than in the majority of metallic materials, and that the process was dominated by the formation of a TiO<sub>2</sub>-based layer, which was analyzed in detail.

### 3.25.2.3 Subcritical Crack Growth

It is well established that the strength of many types of ceramic materials is determined by small defects or 'flaws,' which can be located in the bulk or at the surface. The combination of the largest flaw and the most highly stressed location determines the short-term strength. If such flaws are accessible to the external environment, the strength may be controlled by that environment through its effect on the process of breaking atomic bonds at the tips of stressed flaws. The net effect of this 'subcritical crack growth' is that both the short-term strength and the lifetime under steady applied stress are reduced.



The key element in this process is the presence of water, or more exactly,  $\text{OH}^-$  ions at the crack tip. The effect is accelerated by high temperature, and is influenced by pH. Glasses are the most susceptible of materials, followed by oxide-based ceramics and nonoxide-based materials with oxidic continuous secondary phases. Nonoxides that are inert to water, such as some silicon carbides, show very little effect.

The susceptibility of materials to this effect can be determined either by conducting strength tests at a wide range of stressing rates (four or more orders of magnitude), or by undertaking crack growth experiments on long-crack fracture toughness test-pieces. The information derived may be of importance for applications in which the actual bulk corrosion rates are very low or negligible, but the material is highly stressed.

#### 3.25.2.4 Corrosion/Erosion

There is a strong synergistic effect of corrosion and wear or erosion. There are two principal processes:

- The enhanced reaction between the medium and the ceramic surface, brought about by raised local temperature and the simultaneous removal of the reaction product;
- The undercutting of surface grains by the corrodant penetrating grain boundaries, followed by the mechanical removal of grains.

The first mechanism occurs in dense materials in which the grain boundaries are not preferentially penetrated. An example is in silicon carbide or silicon nitride subjected to sliding wear against a similar counterface. In these cases, the wear process enhances hydration of the surface to silica, which is progressively removed through the sliding process. The rate may be low, but is the principal damage mechanism in sliding seal wear. The second mechanism is when the rate-determining factors are chemical penetration and grain loosening.

### 3.25.3 Testing Procedures and Standards

#### 3.25.3.1 Standards

Testing standards for aqueous-based corrosion performance are generally flexible in corrodant conditions and duration to allow for a very wide range of potential applications in which particular conditions

may arise. For example, ASTM C 650 for ceramic tile permits any corroding substance of application relevance, advises against the use of HF because of its obvious rapid attack on any silicate-based material, and suggests that a general indication of respectively acid or alkali resistance can be obtained by the use of 10% HCl or 10% KOH at room temperature for 24 h. This standard uses visual color and texture change as the main indicator of attack, preferred to the measurement of change of gloss or mass change. A similar test is available as EN ISO 10545-13 (superseeding EN 106 and EN 122) for both unglazed and glazed tiles, using visual assessment of changes in surface appearance, and for glazed tiles, a 'pencil' test for the roughening of a glazed surface. The test duration is rather more extended than in ASTM C 650.

A test with a specific purpose in mind is described in BS4789 for alumina and beryllia ceramics for vacuum envelopes. It involves boiling in concentrated nitric acid (sp. gr. 1.42), followed by washing in water, then dilute ammonia, and again in water. The test-pieces are then conditioned by heating to 1200 °C for 30 min before weighing and calculation of mass loss. There is also a requirement to inspect for local cracking and spalling. The original intention behind this test was to determine whether the ceramic materials could withstand the removal of metallizing by acid digestion, followed by reprocessing at high temperature, and still maintain integrity and vacuum-tightness. This test originated from work reported by Binns.<sup>2</sup> Experience has shown that it is indeed very effective in identifying those materials that can be rapidly penetrated by acids.

A more general procedure is listed in CEN EN 12923-1. This provides guidance on the use of various criteria in deciding the extent of corrosive attack under any aqueous-based conditions. It provides options for characterization microstructurally, by mass change, dimension change, hardness change, flexural strength change, and by analysis of species dissolved into the reactant.

ISO 17092 provides methods for acid and alkali attack based on standardized HCl and NaOH solutions that are similar in principle to ASTM C 650, but intended for engineering type materials.

ISO 6474 (alumina) and ISO 13356 (zirconia) specifying ceramics for human body implantation such as in orthopedics require evidence that there is no change in strength after immersion in a simulated body fluid (saline, bovine serum, or the like) as one of the criteria for acceptability.

ASTM C 1368 and EN 843-3 provide methods for studying subcritical crack growth in an optional medium, which can include corrosive liquids. It is based on flexural strength testing at a series of rates over at least four orders of magnitude in loading or straining rate. The variation of mean strength with stressing or straining rate is used to compute the subcritical crack growth exponent  $n$ . This method is typically limited to tests of a few hours' duration, and therefore, if longer durations of exposure (and slower rates of attack) are relevant, the alternative method is dead-load 'delayed failure' testing, but this method has only been standardized so far in ASTM C 1576.

### 3.25.3.2 Procedures

#### 3.25.3.2.1 Equipment

In conducting corrosion tests in highly corroding media, it is necessary to consider carefully the containment vessels, and whether they themselves will be corroded to an extent that may affect the outcome of the test. Borosilicate glass vessels are usually perfectly adequate for acid tests at ambient pressure, but may have limited life under alkali tests. Test-pieces can be suspended in baskets or from wires, but should be separate from each other and should not rest on the bottom of the vessel to avoid erosion or damage, notably during boiling tests.

In the modern era, the safest way of undertaking aggressive corrosion tests is to use polytetrafluoroethylene (PTFE)-lined digestion bombs placed in an oven at the relevant temperature. Tests at temperatures of up to 200 °C can usually be undertaken without damaging the PTFE, giving pressures of up to 10 atm dictated by the certified maximum for the vessel. The advantage is the small volume of corrodant being handled, especially if it is subsequently being analyzed for dissolved species. The disadvantage is the limited volume of corrodant that can be employed, which might lead to exhaustion, and the fact that it is static within the vessel, which can lead to some areas of corrosion shielding.

It is sometimes necessary to understand the performance of materials in the presence of combined corrosion and erosion or abrasion. Such tests are certainly relevant to plant operation where fluids and possibly abrasive debris are being circulated, but are more difficult to set up in a meaningful way and to control in the laboratory. Cox and Morrell<sup>3</sup> describe a method of acidic and alkaline slurry erosion based on a spinning disc, applied to alumina

ceramics for chemical plant pipeline use. Wear of baffles intended to induce turbulence to avoid laminar flow films, coupled with changes in dimensions of the test discs led to some nonlinearity of conditions. Nevertheless, differences between different materials and corrodants were adequately demonstrated.

Standardized abrasive wear testing of hard materials is typically undertaken in rotating wheel experiments using loose abrasive, which becomes trapped between the wheel and the test-piece. Examples are ASTM B 611 (hard metals, steel wheel, brown alumina grit in water), ASTM G 65 (general applications, rubber edged wheel, sand, dry), and the light wear ball-cratering test (CEN EN 1071-6 intended for ceramic coatings). With suitable precautions, these tests can also be used with acidic or alkaline environments, which can be fed along with the abrasive. This approach can be used to study the synergistic effect of simultaneous corrosion and abrasion.

#### 3.25.3.2.2 Assessment techniques

##### *Mass change*

Measurements of mass change following corrosion can be misleading with ceramics. This type of test works well for materials that are uniformly dissolved, but if there is grain boundary penetration, corrosion products can be variably trapped in the developed porosity. Washing and drying, even refiring to high temperature, does not necessarily remove them all. It is even possible to obtain a mass gain despite clear penetration, which is clearly misleading if candidate materials are ranked solely using mass change. It is recommended that mass change tests are always used in conjunction with a test that is not influenced by residual corrosion products.

##### *Change of cross-section*

This test has the same limitations and problems as with testing metallic materials. It may not provide a particularly relevant result on ceramics under aqueous corrosion conditions, because generally size changes are very small if the primary phases are not attacked, and of course, penetration is not characterized. In some cases, the method may have value, where there is clear loss in section, for example, when corrosion is combined with erosion or wear.

The most reliable method is usually the preparation of a cross-section and its dimensioning using a measuring microscope.

**Dye penetration**

This is an extremely useful test. Test-pieces are simply immersed for an hour or two in a suitable dye solution after corrosion and washing. After washing in solvent, the greater retention of dye compared with uncorroded material is an initial indicator of some penetration, which can be confirmed by sectioning or fracturing the test item. If the corrosion tests have been conducted on flexural strength test bars (see the following section), the depth of penetration is easily seen after fracture.

**Flexural strength**

For smaller-sized parts, which may suffer a risk of fracture in the intended application, knowledge of any reduction in strength as a result of corrosion can be important. Such tests are normally performed on standardized flexural strength test-pieces, typically  $>45 \text{ mm} \times 4 \text{ mm} \times 3 \text{ mm}$  tested in four-point flexure (ASTM C 1161, CEN EN 843-1, ISO 14704) for advanced technical ceramics. It is recommended that at least 10 test-pieces are used for any one corrosive condition, as well as for the uncorroded reference state, in order to allow for the typical spread of strengths typically obtained with brittle materials.

**Change of surface texture**

The roughening or pitting of a ceramic surface can occur in corrosion, and this can be characterized using conventional roughness measurement techniques. Caution is needed with the texture characterization of ceramic surfaces in general, and the guidance given in EN 623-4 is intended to encourage good and relevant practice.

**Hardness**

Surfaces that suffer penetration lose apparent hardness. They may even become soft enough to be scratched or chipped using a knife, while micro- or macrohardness tests can be used to quantify such an effect (see EN 843-4, ISO 14706). The method is appropriate for small penetration depths, up to say  $20\text{--}50 \mu\text{m}$ , which might not reveal themselves as changes in strength, but not for larger depths where the test may become meaningless.

**Chemical changes to the corrodant**

Chemical analysis of the corrodant after the test can offer an insight into which species in a multicomponent material are being preferentially removed. Very sensitive techniques are available.

**General comments**

Care should be taken to ensure that any loose or precipitated material is fully accounted for. Material can be dissolved and reprecipitated elsewhere, including the vessel walls and sample suspension system. An example of what can be achieved and some of the pitfalls are given by Öhman *et al.*,<sup>4</sup> who studied the leaching of high-purity alumina by sodium bicarbonate buffered water. They determined that in this case, gravimetric methods of determining material loss give significantly greater values than determined by using a fluoroscopic method of analyzing the corrodant solution. An analysis of solution equilibrium calculations showed that precipitation was unlikely, but far more likely was the development of a surface skin by a hydration/precipitation mechanism, which when dried out for test-piece weighing gave a friable surface, which was readily lost.

**3.25.3.3 Testing Standards**

Following are the standards providing testing methods relevant to various varieties of ceramics:

EN 12923-1:2006 Advanced technical ceramics – Monolithic ceramics – Part 1: General practice for undertaking corrosion tests (Generic standard for technical and engineering materials providing procedures for determining attack, appropriate for any reagent.)

ISO 17092:2005 Fine ceramics (advanced ceramics, advanced technical ceramics) – Determination of corrosion resistance of monolithic ceramics in acid and alkaline solution. (Testing in 6 N  $\text{H}_2\text{SO}_4$  and NaOH boiling solutions for 24 h with attack criteria being mass loss, dimension changes, and loss of mechanical strength.)

EN ISO 10545-13:1997 Ceramic tiles – Part 13: Determination of chemical resistance. (A variety of test solutions permitted, including ammonium chloride (representing household cleaning products), sodium hypochlorite (swimming pools), HCl, citric acid, KOH, and lactic acid (foodstuffs), used for 24 h on glazed surfaces. Criteria based on visual inspection, reflectivity, and ‘pencil’ test.)

EN 993-16:1995 Methods of test for dense shaped refractory products. Determination of resistance to sulfuric acid

ISO 28706-4 Vitreous and porcelain enamels. Determination of resistance to chemical corrosion. Part 1: Determination of resistance to chemical corrosion by acids at room temperature.

Part 2: Determination of resistance to chemical corrosion by boiling acids, neutral liquids, and/or their vapors.

Part 3: Determination of resistance to chemical corrosion by alkaline liquids, using a hexagonal vessel

Part 4: Determination of resistance to chemical corrosion by alkaline liquids, using a cylindrical vessel

### 3.25.4 Performance of Specific Material Types

#### 3.25.4.1 Oxide-Based Materials

##### 3.25.4.1.1 Porcelains and aluminosilicates

The longevity of many silica-based materials, including earthenware, porcelains, and even some glasses, in wet environments is eminently demonstrated by archaeological evidence. Most clay-based materials comprise crystalline phases such as quartz, cristobalite, and mullite embedded in a glassy matrix produced by melting mineral phases containing alkalis and alkaline earth species. The solubility of such glasses in water is limited, and while the attack does slowly occur by a leaching/hydration process, it does not restrict their use in many applications. In fact, they will also withstand some aggressive, aqueous environments, such as strong acid and alkaline solutions.

For applications in the kitchen and the laboratory, so-called ‘chemical porcelains’ with very low or zero open porosity without glazes have been in use for many years, particularly in the pharmaceutical industry, and are not radically different in structure from materials used for electrical insulators. They have been employed in a range of applications, the most commonly known one being pestles and mortars, up to some moderate-sized items for use as one-piece corrosion and abrasion-resistant linings. However, one of the limitations of such materials is their manufacture in large pieces. The shrinkage obtained on firing makes shape and dimension control difficult. One long-standing route around this problem is to restrict the shrinkage by adding prefired refractory particulates to the clay mix. However, this allows porosity to be developed, and often a product will only remain impervious if the surface skin, which effectively seals the bulk microstructure, remains intact. Such materials, often called ‘chemical stoneware,’ can be made in the large pieces required for chemical tower packing, and still remain the preferred

option for large-sale use. Similar materials are used for corrosion-resistant hygienic tiling of surfaces.

In addition, similar materials are available in brick form for building structural chemical plant linings. Varieties are available with microstructures appropriate for acid or alkali resistance. These would be grouted with appropriate acid- or alkaline-resistant cements, which although not as corrosion resistant as the bricks, survive sufficiently for the vessel to survive and prevent corrosion of external steelwork. The scientific literature on such materials is very limited, but Charlebois<sup>5</sup> has described a number of such applications, including sulfite digesters in the paper industry, sodium chlorate tanks, and tanks for HCl leaching of TiO<sub>2</sub> ore.

Bennett<sup>6</sup> reports on sulfuric acid testing of four aluminosilicate brick materials made from different sources of red shale or fireclay, but all show rather higher rates of attack than SiC, silica, carbon, or alumina, minimum rates being obtained with carbon and alumina.

Marcus and Ahrens<sup>7</sup> show that highly siliceous materials (fused silica glass, sintered mullite, and sintered clay/zircon) have rather lower corrosion rates in concentrated phosphoric acid at 204 °C than many nonsiliceous oxides (alumina, beryllia, spinel), cordierite (2MgO·2Al<sub>2</sub>O<sub>3</sub>·5SiO<sub>2</sub>) showing intermediate behavior.

##### 3.25.4.1.2 Alumina

The ceramic family most commonly employed for engineering components is that based on aluminum oxide (alumina, Al<sub>2</sub>O<sub>3</sub>), being generally stronger, harder, and more abrasion resistant than porcelains. There is a huge spectrum of types of alumina ceramic depending on their intended engineering function. Containing more than 80% by mass of Al<sub>2</sub>O<sub>3</sub>, but more typically in excess of 95%, they usually have additional components added to control the sintering process, to reduce the sintering temperature, or to modify the final properties. It is probably true to say that no two alumina ceramics from different sources are the same in all respects, but some generalizations may be helpful (more details can be found in Morrell<sup>8</sup>):

1. High-purity alumina without additions does not sinter well and tends to suffer from exaggerated grain growth. Such materials tend to be used only for crucibles.
2. High-purity alumina with small controlled amounts of MgO or Y<sub>2</sub>O<sub>3</sub> when in ultrafine powder form can be sintered to full density with control of grain

size. Such products include biomedical implants (fine-grained) or translucent lamp envelopes (medium-coarse grained).

3. Aluminas of lesser purity (sometimes called 'debased' alumina) used for lower value-added products, for example, in electronics, usually have deliberate additions of MgO, SiO<sub>2</sub>, and CaO. This produces a distinct secondary glassy phase, which can act as a sink for impurities such as alkalis, and thereby control dielectric properties, especially loss tangent.
4. Alumina ceramics for general engineering may be similar to those for electrical purposes in terms of compositions; indeed often, a given product is treated as multifunctional. Others, such as those sintered using MnO and TiO<sub>2</sub>, which produce a low-temperature eutectic liquid during firing, tend to have applications restricted to mechanical ones. More generally, if strength and wear/erosion resistance is an important feature, products tend to be of finer grain size than used for many electrical applications.
5. While the majority of aluminas are highly resistant to corrosion in high pH or neutral solutions, only a few products are designed for resistance to aqueous corrosion at low pH. This requires control of the nature of the secondary phase composition.

There is an extensive literature on corrosion resistance. Thermodynamically, Al<sub>2</sub>O<sub>3</sub> is not stable in water, but is attacked only very slowly. Öhman *et al.*<sup>4</sup> evaluated the rate of attack of simulated groundwater on a high-purity alumina hot-pressed material substantially free from secondary phases. The buffered sodium bicarbonate solution used gave pH 8.5. In tests of up to 90 days' duration and at temperatures in the range 40 °C–100 °C, depths of corrosion determined by mass loss and fluoroscopic analysis for aluminum in the corrodant solution were of the order of only a few nanometers. As mentioned earlier, the factor of 5 discrepancy between the two analysis methods was ascribed to the development of a hydrated surface skin, which was readily lost when dried. A similar very thin deposited layer was found by Real *et al.*<sup>9</sup> in tests on a similar sintered material boiled for 2 weeks in 5% salt solution. This treatment did not significantly affect the strength or the apparent hardness of the material.

One of the first systematic studies of corrosion resistance was made on a fairly high-purity crucible material, conducted by Jaeger and Kraseman.<sup>10</sup> Attack by various acidic and alkaline solutions at 95 °C for 3 days was very significant for HF and

**Table 1** Corrosion resistance of alumina ceramics<sup>11</sup>

Body no.	Composition (wt%)				Mass loss, 50% HNO <sub>3</sub> , RT, 18 h (mg cm <sup>-2</sup> )
	Al <sub>2</sub> O <sub>3</sub>	CaO	MgO	SiO <sub>2</sub>	
1	94.1	1.8	0.7	3.4	7.0
2	94.7	1.7	1.2	2.4	5.0
3	95.2	1.0	0.7	3.1	3.5
4	95.8	0.6	0.7	3.0	0.6
5	94.7	0.6	0.7	3.4	0.2
6	94.7	0.6	1.1	3.7	0.1
7	96.6	–	1.3	2.2	0.04

HF/H<sub>2</sub>SO<sub>4</sub> and for strong (1:2) NaOH solution. For many other acids, attack was slow.

Richards<sup>11</sup> reported the corrosion resistance of experimental 'debased' alumina ceramics in HNO<sub>3</sub> as a function of secondary phase composition. From the data provided (Table 1), it can be seen that the mass loss rate can vary by more than a factor of 100, depending on the ratio of MgO:CaO:SiO<sub>2</sub>. It can be concluded that the best resistance is achieved when the ratio of alkaline earths to silica in the secondary phase is small, and when the amount of CaO is minimized. Commercial products are available that are free from CaO for maximized resistance to acidic corrosion, but have a disadvantage that they tend to have lower toughness because of an increased thermal expansion mismatch between the alumina grains and the secondary phase.

These findings are supported by the work undertaken at NPL during the 1970s.<sup>12, 13</sup> A variety of alumina ceramics of between 95% and 99.8% were tested in H<sub>2</sub>SO<sub>4</sub> (10%, v/v, boiling, 72 h), HCl (20%, w/v, boiling, 72 h), HNO<sub>3</sub> (35%, w/v, boiling, 72 h), HF (40% solution, 20 °C, 72 h), and KOH (10%, w/v, boiling, 72 h). The criteria used were weight loss and spalling tendency on reheating to 1000 °C (Figure 1), dye penetration (Figure 2), strength loss, and hardness loss. The principal results are shown in Table 2.

A summary of some of the conclusions is as follows:

1. A translucent high-purity alumina was found to be resistant to all acids with no detectable weight loss, dye penetration, or tendency to spall.
2. A number of refractory or electrical aluminas (up to 99.7% Al<sub>2</sub>O<sub>3</sub>) were badly attacked in all acids, and some pitted badly or disintegrated when reheated indicating the presence of trapped corrosion products. There were significant losses in strength and hardness, indicating the development



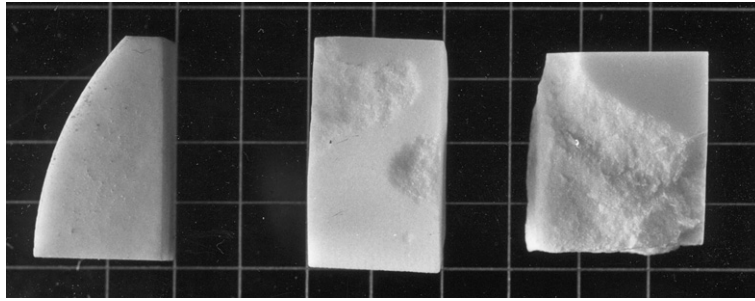


**Figure 1** The entrapment of corrosion products within the surface of corroded alumina ceramics produces spalling on reheating to 1000 °C. Exposure to HF for 72 h at room temperature; left to right: Materials C, G, and K (see Table 2, Ref. 14). Reproduced with permission of HMSO through National Physical Laboratory.

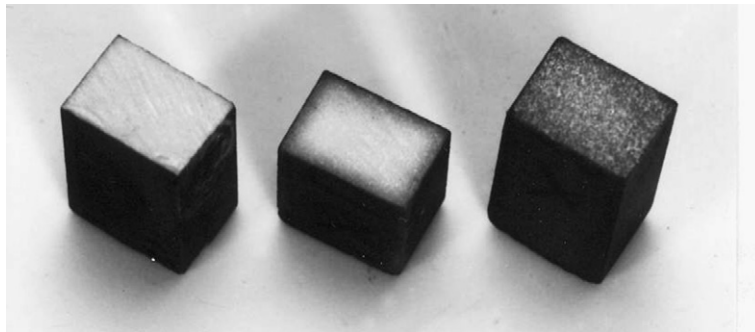


**Figure 2** Fracture surfaces of test-bars after 72 h immersion in boiling H<sub>2</sub>SO<sub>4</sub> followed by dye impregnation, showing a range of degrees of attack.<sup>13,14</sup> Reproduced with permission of HMSO through National Physical Laboratory.

**Table 2** Corrosion tests on high-alumina ceramics<sup>12–14</sup>

Material	Al <sub>2</sub> O <sub>3</sub> (%) <sup>a</sup>	Mass loss (mg cm <sup>-2</sup> )					Flexural strength after exposure (% of original)				
		HCl	HNO <sub>3</sub>	H <sub>2</sub> SO <sub>4</sub>	HF	KOH	HCl	HNO <sub>3</sub>	H <sub>2</sub> SO <sub>4</sub>	HF	KOH
A <sup>c</sup>	99.8	0	0	–	0	0					
B <sup>c</sup>	(96)	6.4	2.5	3.6	–	<0.1					
C <sup>b</sup>	99.8	1.5	1.0	1.0	0.05	–1.0	34			48	
D <sup>b</sup>	99.4	D	PP	D	D	<0.1					
E <sup>b</sup>	99.2	D	D	0.65	0.76	0					
F <sup>b</sup>	99.6	D	0.3	D	P	0					
G <sup>b</sup>	99.6	P	S	S	SS	0					
H <sup>d</sup>	94.6	0.07	0.06	0.08	15	0.77	91	95	92	45	58
I <sup>c</sup>	97.5	SS	PP	2.5	D	<0.1	44	51	58	25	97
J <sup>c</sup>	99.1	0.25	P	0.35	0.66	<0.1	65	73	76	21	86
K <sup>c</sup>	99.5	P	D	S	D	<0.1	26	27	27	34	84

<sup>a</sup>By XRF analysis except (–);

<sup>b</sup>Refractory grades;

<sup>c</sup>Engineering grades;

<sup>d</sup>'Acid-resisting' grade.

Appearances after heating to 1000 °C: P = surface pits, PP = bad pitting, S = surface spalling, SS = severe spalling, D = disintegrated.

of a porous layer, but without any significant loss in dimensions.

3. A 95% material claimed to be acid resistant was found to be so compared with most others, except in HF, which attacks the siliceous phase. In this

material, most of the CaO is replaced by MgO, and the SiO<sub>2</sub> content raised to provide a relatively corrosion-resistant intergranular glassy phase.

4. Alumina itself is slowly dissolved by strong alkalis, but there is much less preferential penetration



through any intergranular phase, resulting in a progressive removal of the surface rather than the penetration seen with acids. Strength as measured in a flexural test on small test-pieces, which preferentially stresses the corroded surface, tends to be better maintained than in acids.

Later work at NPL<sup>3</sup> evaluated the effects of combined corrosion and erosion in acids and alkalis on a small range of alumina ceramics. Three alumina ceramics were employed, two fine-grained, of nominal 99.5%, and one coarse-grained, of nominal 97.5% alumina. Tests were made on discs spinning in a heated corrosive liquid, with and without SiC as a hard particle erodant, as well as on test-bars suspended in the liquid. All the three materials were significantly penetrated by acidic solutions, HCl being the most aggressive. The 97.5% alumina was attacked much faster than were the 99.5% materials, but these showed significant differences in behavior. **Figure 3** shows the change in flexural strength measured at room temperature for different corrodant types. Immersion in KOH solution produced the least effect. There were very minor changes in both mass and strength as a result of immersion in water.

The addition of 5% (v/v) SiC grit to acidic corrodants in these tests resulted in an acceleration in the rate of mass loss by a factor of between 2 and 4

compared with tests in liquid only. This is explained by the fact that the removal of the secondary phase renders the remaining material rather weaker and more readily eroded. By comparison, the erosion rate in KOH solution was only slightly faster than that in water at the same temperature, indicating that the microstructure is not weakened in the same way.

Engell and Jakobsen<sup>15</sup> have reviewed corrosion mechanisms in alumina ceramics used for liquid pump parts, including brown-colored versions incorporating MnO and TiO<sub>2</sub> as low-temperature liquid phase formers. Tests were run for up to 5000 h at 90 °C at pH 5.5, 9, and 12 buffered by NaOH. **Figure 4** summarizes some of their results. The rates of attack increase with increasing pH over this range, but there are significant variations between the materials.

Genthe and Hausner<sup>16</sup> studied single-crystal sapphire and ruby, and high-purity hot-pressed aluminas with and without MgO and Cr<sub>2</sub>O<sub>3</sub> dopants. The dissolution rates in HCl and H<sub>2</sub>SO<sub>4</sub> (180 °C, 168 h) were minimal for single-crystal materials, but greater for polycrystalline ones, which was attributed to the preferential removal of the grain boundary phase. In H<sub>2</sub>SO<sub>4</sub>/H<sub>3</sub>PO<sub>4</sub> mixtures, attack rates were significantly higher owing to the dissolution of alumina itself, although increasing amounts of Cr<sub>2</sub>O<sub>3</sub> tended to suppress this process.

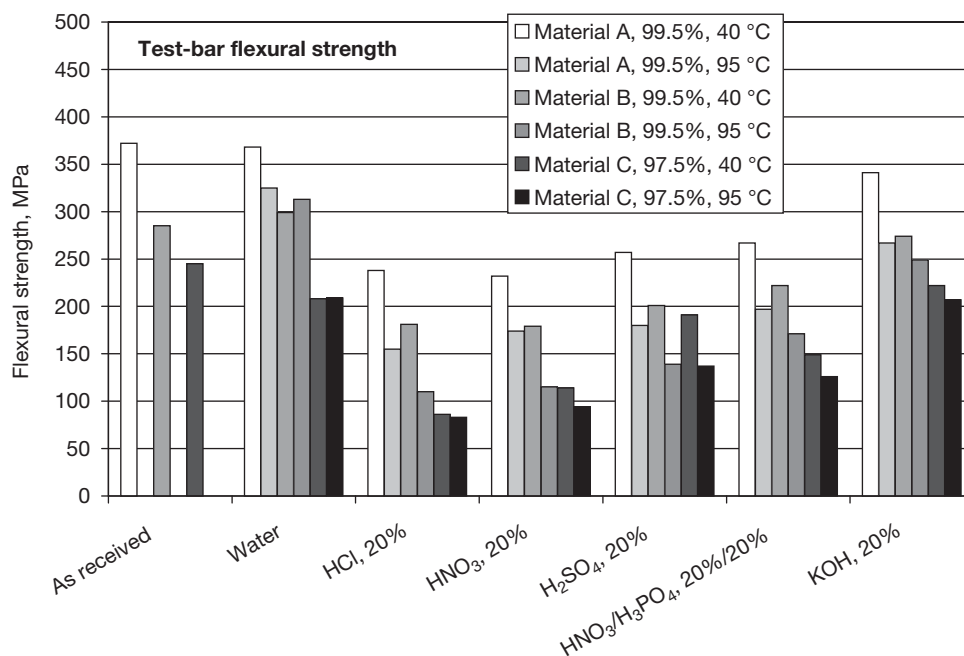


**Figure 3** Loss in strength of test-bars immersed in flowing liquid for 23 h in various corrodants (data from Ref. 3).

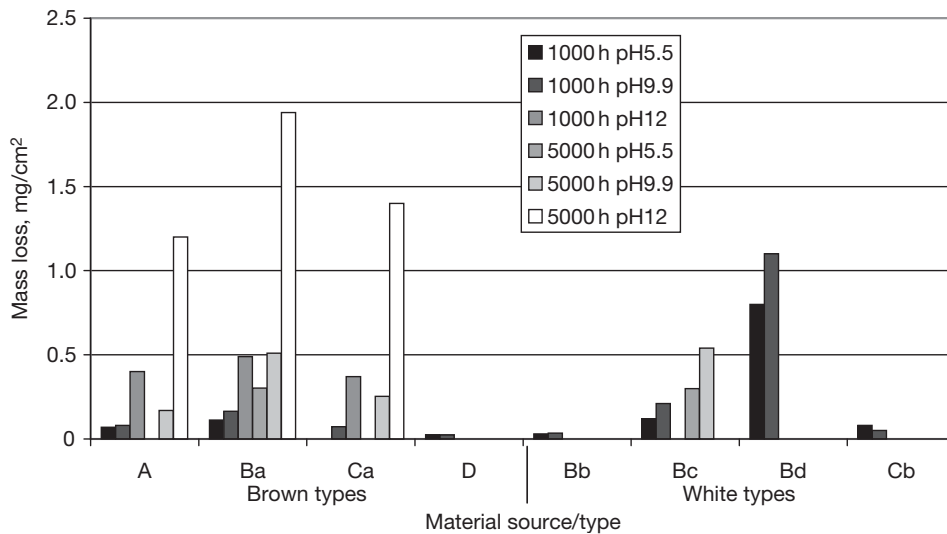


**Figure 4** Corrosion test results from Ref. 15 at 90 °C on brown and white alumina ceramics from different manufacturers. (Note: not all combinations were tested.)

Mikeska *et al.*<sup>17</sup> report that all alumina ceramics, including those of nominally very high purity, other than single-crystal sapphire are very significantly attacked by HF at 90 °C as a result of grain boundary phases, the effect being worst with high levels of silica in the secondary phase. Fang *et al.*<sup>18</sup> show that an 85% alumina is rapidly penetrated by a 1% HF + 5% HCl solution at room temperature, to leave a porous layer that was readily eroded in a subsequent wet sand erosion test.

Tests on 94% and 99% aluminas in concentrated (96%) phosphoric acid have been reported by Marcus and Ahrens.<sup>7</sup> At room temperature, the dissolution rate was minimal over a period of a month, but at 204 °C, the higher-purity material was attacked faster with a dissolution rate equivalent to 450 mm year<sup>-1</sup>, compared with 35 mm year<sup>-1</sup> for the 94% material. This is likely to be a result of a slower reaction with the continuous glassy phase than with alumina itself.

Sato *et al.*<sup>19</sup> tested two aluminas at 150–200 °C in 0.1 M to 25 M NaOH. A 93% alumina material was attacked several times faster than was a 99.5% alumina, primarily by dissolution of the secondary phase. Small test-pieces (3 × 4 × 20 mm) were essentially consumed by the 25 M solution within a day at 200 °C and within 5 days at 160 °C.

This wide range of performance implies that although alumina ceramics generally show good resistance to weak and neutral solutions, great care must be taken to select the most appropriate product if aggressively acidic service conditions are intended.

Materials not designed for acid resistance may be penetrated much faster than might be expected.

Dailly *et al.*<sup>20</sup> evaluated the stress-corrosion behavior of several types of electrical substrate alumina ceramic in air and in Ringer's solution (saline, appropriate for biomedical environments), using the double torsion plate method. In this method, the test-piece is rapidly loaded, and then the machine cross-head is stopped and the stress relaxation monitored as the crack progresses along the length of the plate. The crack velocity was determined from the relaxation rate. In all the cases, the crack velocity exponent ( $n$  in the relationship  $v = AK_I^n$  where  $v$  is the crack velocity,  $K_I$  is the stress intensity factor, and  $A$  is a constant) was in the range 17–30, indicating the clear existence of subcritical crack growth. This value was lower in saline than in moist air, that is, the material becomes more susceptible to crack growth. The results given do not provide a clear indication of what features of the composition, especially the relative proportions of the secondary components, control the behavior, but the authors suggest that the presence of MgO is disadvantageous. Byrne *et al.*<sup>21</sup> used the same technique on a variety of materials and found significant differences in crack growth in strong acids and alkalis. Barinov *et al.*<sup>22</sup> report similar large changes in  $n$  with different pH values for one alumina, but not another, using the method of flexural strength testing over a very wide range of testing rates.

Circumstantial evidence from *in vitro* and *in vivo* failures of highly loaded alumina femoral

components suggests that high-purity materials are not immune to the phenomenon, although Ferber and Brown<sup>23</sup> have found that the values of  $n$  are higher.

### 3.25.4.1.3 Zirconia

#### Material types

Zirconia in its pure form undergoes two solid-state phase transformations on cooling from the melt (cubic–tetragonal–monoclinic), making the production of useful ceramic materials impossible. Structural stabilization is required. To stabilize the cubic form, MgO, CaO, or Y<sub>2</sub>O<sub>3</sub> can be used in sufficient quantity; such products are known as *stabilized zirconia*. Such materials find uses as crucibles and oxygen sensors, but are not particularly strong or tough.

Developments in the 1970s were made with partially stabilized materials that enabled much stronger tougher products to be made. With MgO additions, a ceramic shape sintered in the cubic phase field is subjected to a programmed cooling schedule in which a fine-scale tetragonal phase precipitate is developed inside the large cubic grains (~30 µm). The destructive martensitic-like conversion of the tetragonal phase to the monoclinic phase with significantly lower density is avoided by constraint of the cubic phase and by retaining a small precipitate size. Such products are known as *transformation toughened partially stabilized zirconia*, but often just ‘partially stabilized zirconia.’ Mixed stabilizers are sometimes used instead of just MgO.

An alternative approach is with yttria additions, most commonly with 3 mol%. In this case, a very fine powder (<100 nm) is prepared at which size scale tetragonal zirconia is stable to below room temperature. This is sintered to a dense ceramic at a relatively low temperature (~1450 °C) in order to avoid excessive grain growth. Such materials typically have a grain size of ~0.5 µm, which is mostly the tetragonal phase, although the surface layer may contain some monoclinic phase. Such products are known as *tetragonal zirconia polycrystals* or more commonly as ‘TZP.’ When the stabilizer is yttria (‘Y-TZP’), this product has a high strength, and a wide range of applications, including biomedical devices such as hip joints, but has a limited performance at raised temperature because of an increased risk of progressive transformation from the surface. To circumvent this problem, alternative or mixed stabilizers have been proposed.<sup>24</sup> Research has been conducted on the use of other lanthanides, such as scandia, but such materials are

primarily intended for oxygen ion conduction and are not generally commercially available.

The principle of transformation suppression in tetragonal ZrO<sub>2</sub> is also used to improve the strength of other ceramic materials, notably alumina.

#### Stabilized zirconia

Compared with TZP materials (see the later sections), cubic stabilized zirconia (CSZ) has been considered to be more stable to hydrothermal degradation. However, as shown by Guo and He,<sup>25</sup> an 8Y–ZrO<sub>2</sub> material typical of that used for oxygen ion sensors showed precipitation of the monoclinic phase after exposure to 0.026 atm. water vapor pressure at 250 °C, and some tendency to cracking, but with an increase in electrical conductivity.

Lay<sup>14</sup> reports significant rates of attack by boiling acid solutions on a CaO-stabilized material, especially H<sub>2</sub>SO<sub>4</sub>, but no attack by 80 °C solution of KOH. 6Y-CSZ and 8Y-CSZ are reported to be highly corrosion resistant, especially in neutral or alkaline solutions.<sup>26</sup>

#### Transformation toughened partially stabilized materials

Sato *et al.*<sup>27</sup> report that an MgO partially stabilized material does not undergo tetragonal-to-monoclinic transformation in 1 M HCl and 1 M sodium acetate–acetic acid pH 3 solution at up to 140 °C for up to 40 days, but some transformation and a loss of strength occurred when exposed to water at above 200 °C, Mg<sup>2+</sup> ions being detected in solution.

Fang *et al.*<sup>18</sup> report on corrosion testing of a UK origin material, partially stabilized with MgO and Y<sub>2</sub>O<sub>3</sub> and containing some SiO<sub>2</sub>, in an HF/HCl solution, simulating an oil pipeline cleaning solution. They noted that HF tended to attack the grain-boundary silica, while HCl attack tended to leach the yttrium and to destabilize and dissolve the zirconia grains. The process was thought to be such that the surface of the material was progressively removed with no significant influence on strength or erosion rate in a subsequent sand jet wet erosion test.

Mikeska *et al.*<sup>17</sup> report a corrosion penetration rate >100 mm year<sup>−1</sup> in HF at 90 °C.

#### Y-TZP, Ce-TZP, and Ce-Y-TZP

There is extensive literature on the problem of destabilization of Y-TZP in water or steam in the temperature range 150–400 °C, but there is no conclusive explanation. The most likely process is the diffusion of water into the ceramic, annihilating oxygen vacancies, releasing yttrium ions, and leaving the zirconia

grains with insufficient stabilization.<sup>28–31</sup> It has been suggested that the impurity content of the material affects this process, changing the level of stability,<sup>32–37</sup> but the exact mechanisms have not been conclusively determined. The net result is the expansile growth of groups of monoclinic zirconia grains on the surface, giving small raised regions that can be plucked out leaving a pit.<sup>31</sup> In the short term, such pits do not necessarily affect the strength of the material, but eventually macrocracking can occur.

Researchers usually characterize the process using X-ray diffraction and report the percentage of monoclinic phase at the surface. Using this approach, it has been shown that there is a nucleation delay for the process, of length determined by temperature, which has allowed prediction of rates at temperatures as low as 37 °C (orthopedic applications at human body temperature<sup>32</sup>). The process has also been found to be surface preparation dependent. Grinding the surface of this material caused some transformation to occur, often considered to be beneficial by creating high surface residual compressive stresses. Subsequent rates of transformation of such surfaces are different from those of as-fired surfaces, as illustrated in Figure 5. Other recent literature on this problem includes Refs. 29, 31, 39, and 40.

Bastide *et al.*<sup>24</sup> determined that the material containing 1 mol%  $Y_2O_3$  and 7 mol%  $CeO_2$  was stable at well below room temperature, was not quite as strong as 3 mol% Y-TZP, but possessed a good strength retention after exposure to steam at up to 300 °C up to 2000 h. Similar results have been reported.<sup>41,42</sup>

However, this product is not yet commercially available. Another route to improving the stability has been shown to be carbonitriding the surface in a  $ZrN + C$  bed at high temperature.<sup>43</sup> In contrast,  $Sc_2O_3$  stabilization has been found not to be effective in restricting hydrothermal transformation.<sup>44</sup>

In more severe chemical environments, Shojai and Mantyla<sup>45</sup> report that 3Y-TZP zirconia ceramic membranes lost weight in both acid and alkaline solutions at room temperature, but suggest that the material did not transform at a significantly enhanced rate compared with exposure to water.

For 3Y-TZP, Mikeska *et al.*<sup>17</sup> report a corrosion penetration rate  $>100$  mm year<sup>-1</sup> in HF at 90 °C.

Kritzer *et al.*<sup>46</sup> report on corrosion tests on a Ce-TZP, using HF and HBr at 24 MPa pressure at 500 °C. Some intergranular attack was noted, HF being less corrosive than HBr, but no weight loss or phase transformation was found.

Kalin *et al.*<sup>47</sup> describe Y-TZP ball on alumina disc wear test experiments, in which the rate of wear of the balls in the severe wear condition is pH-controlled. A low pH of 0.9 resulted in much lower friction and milder wear than did high pH values where the formation of distinct tribolayers led to grain fracture, rough surfaces, and high friction coefficients.

#### Composites with $ZrO_2$

Hisamori and Mimura<sup>48</sup> studied the role of Y- $ZrO_2$  additions to alumina, and found that with optimized amounts of the addition, there were some small improvements in average strength after exposure to deionized water at 200 °C and 1.59 MPa pressure,

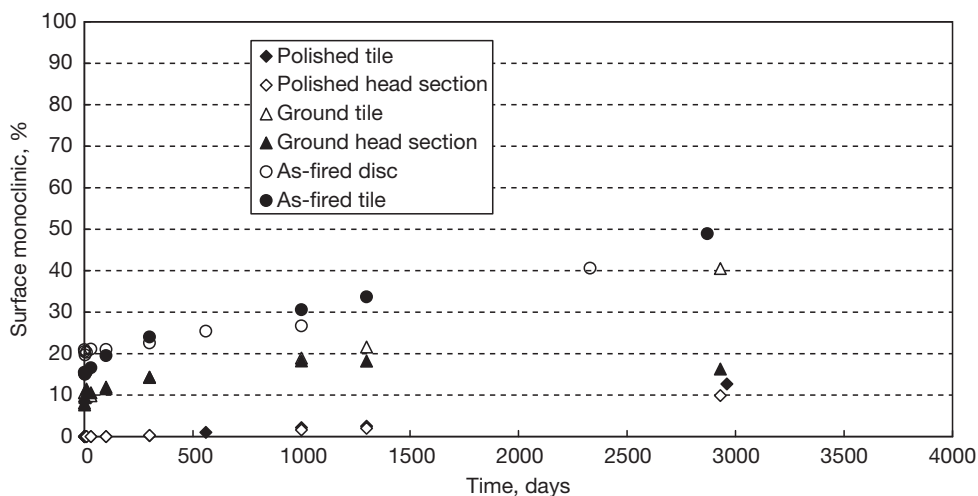


**Figure 5** The transformation of Zyranox® Y-TZP material formed as flat tiles and as ceramic femoral heads as a function of time of exposure to simulated body fluid at 37 °C.<sup>38</sup>

although it was unclear why this should be the case. Microstructural analysis of the surface of the test-pieces showed that the presence of zirconia induced pitting with associated microcracks that might be associated with the transformation of surface-connected or near-surface zirconia grains. Herrmann *et al.*<sup>49</sup> demonstrate similar microstructural effects, and show that the corrosion rate under such conditions is higher than in pure alumina. Material made by Hirano and Inada<sup>50</sup> and by Nakanishi *et al.*<sup>51</sup> showed no change in monoclinic content after high temperature aging in water.

Thompson and Rawlings<sup>52</sup> identified structural changes in such a material when subjected to HCl attack. In medium- to long-term tests at room temperature, microcracking was associated with the leaching of yttria from the zirconia phase, and this eventually led to macrocracking. There was increased transformation of near-surface zirconia from the tetragonal to the monoclinic form. There was also a progressive loss in strength, compared with an initial drop and then a plateauing of the strength of the same alumina without reinforcement.

#### **3.25.4.1.4 Other oxide ceramics**

Mullite – Yoshio *et al.*<sup>53</sup> studied water attack at 300 °C and 8.6 MPa pressure on various synthetic mullite materials, and found that the mechanism of attack was dissolution of silica and the formation of a hydrated layer of boehmite (AlOOH). The composition of the mullite and the processing route adopted affect the results.

#### **3.25.4.1.5 Glasses and glass-ceramics**

##### **Glasses**

The majority of technical glasses are based on a network-forming oxide (such as silica, boric oxide, phosphoric oxide, etc.) modified with a range of other oxides. Of these, the silicate glasses are the more corrosion resistant, while the others tend to be readily attacked by water. In general, the greater the proportion of the network-modifying components in glasses, the less resistant they are to corrosion, because the remaining silicate network is more readily broken up, and the modifiers are more easily removed. Thus, many specialized glasses that are designed with specific control on expansion coefficients and glass transformation temperatures, for example, for sealing applications, tend to have a lesser ability to resist corrosion than does even window or bottle glass.

The ability of corrosive solutions to attack glasses thus depends primarily on glass composition and corrodant pH. Under near-neutral conditions, silicate glasses are very slowly hydrated at the surface, the surface being depleted of network modifying ions, such as Ca and Na by ion exchange. Silica itself is almost insoluble in water, except at elevated temperature and pressure. Good corrosion resistance is reported for high-silica, some borosilicate (e.g., Pyrex<sup>®</sup>), aluminosilicate, and high-lead compositions. Soda-lime, alkali-lead, lead borosilicate, and low-melting borosilicate sealing glasses have less good properties, while high-alkali, calcium aluminate, phosphate, and borate glasses have poor properties.

Under strongly acid conditions, network-modifying species are removed more readily, but the adequate stability of glass at room temperature is well demonstrated by the use of ordinary soda-lime glass containers for the long-term storage of mineral acids. Similarly, sodium borosilicate glasses are widely used for chemical processing in the laboratory and in chemical plant, but have the advantage of improved thermal shock resistance because of their lower expansion coefficients. High-silica glasses have the best acid resistance, while softer sealing glasses can be very rapidly attacked in mineral acids. An exception to this behavior is with HF, which attacks the silicate network, producing SiF<sub>4</sub>, so that many glass etchants and cleaning solutions contain HF as a primary component.<sup>54</sup> Glasses with a high CaO content are the most resistant to HF because of the formation of insoluble CaF<sub>2</sub>, which impedes the corrosion process.

Attack by strongly alkaline solutions is often more rapid than attack by mineral acids, because these actually dissolve the silicate network. Many dishwasher detergents are mildly alkaline, and over time can destroy the surface of glassware or glazed china-ware. The rate of corrosion is less composition dependent than with acid corrosion, aluminosilicate and special alkali-resistant compositions faring the best.

At higher temperatures, glasses become much less stable toward water-based corrodants. The surface layer can become like a sponge as the network modifiers are leached out. This has been exploited in the Vycor<sup>®</sup> process<sup>55</sup> for making high-silica glass; a sodium borosilicate glass is heat treated to cause two-phase separation to give interpenetrating silica-rich and silica-poor phases, the latter being readily removed by acids. A second heat treatment is used to densify the porous body.

### Glass-ceramics

Glass-ceramics are produced by the homogeneous nucleation and crystallization (sometimes known as 'devitrification') of special glass compositions.<sup>56</sup> This process allows the exploitation of glass-making to form ceramic and ceramic-glass shapes that have special characteristics not readily achievable by conventional ceramic sintering routes. There is a huge variety of compositional types for different purposes. Some examples include

Lithium aluminosilicates:	Low and near-zero expansion coefficients, for thermally shock-resistant cookware and cooker hobs (e.g., Pyroceram®), and for optical components such as telescope mirrors (e.g., Zerodur®). Photosensitive glasses, which after heat treatment can be selectively etched
Magnesium aluminosilicates:	Medium-to-low expansion coefficients, for electronic substrates, heat exchangers, high temperature uses
Lithium zinc silicates:	Medium-to-high expansion coefficients, for glass-metal sealing, lead throughs, etc.
Fluorine-silicates:	These devitrify to fluorine-based micas to give machinability, for example, Macor®, for prototype work, including dental ceramics.

The first two types listed have also been used for the fabrication of fiber-reinforced ceramic composites, using silicon carbide fibers and a hot-pressing route to manufacture.

In general, glass-ceramics are seldom optimized for aqueous-based corrosion resistance, and tend to be attacked faster than the parent glass. The baseline glass composition is devised to permit processing as a glass, while permitting control over the devitrification. Therefore, the microstructure generally comprises intended crystalline silicate phase assemblage plus a residual glassy phase. Like glasses, all will be rapidly attacked by HF, but in other common chemical species behavior will be very much composition dependent. Some examples of recent studies of corrosion behavior are given in Refs. 57–59.

Data on the corrosion resistance of Macor® machinable glass-ceramic are shown in Figure 6, taken from the manufacturer's brochure.<sup>60</sup> Compared with other oxide ceramics and glasses, the material appears to be significantly attacked by water. It is possible that the leaching of fluorine ions from the fluorine-based mica phase creates HF in solution. This

results in accelerating attack on the silicate phases if the HF is not removed by solvent replacement.

Some examples of stress-corrosion effects in water are given in Refs. 61–65.

### 3.25.4.2 Nonoxide-Based Materials

#### 3.25.4.2.1 Silicon carbides

##### Material types

Silicon carbides are among the most acid resistant of ceramics at up to 100 °C, but the behavior differs among the different types available for use in engineering and chemical applications:

1. Reaction-bonded silicon carbide is made by infiltration of silicon into a SiC/C mass, a process which forms bonding SiC and leaves a generally interpenetrating, continuous silicon phase filling the pore space. The principal advantage of this process route is the minimal size change that occurs.
2. Sintered silicon carbide is made by a high temperature sintering process, producing either a dense or a porous, nominally single-phase material. The material can be either  $\alpha$ -SiC (hexagonal structure) or  $\beta$ -SiC (cubic structure). There is usually some residual porosity.
3. Liquid-phase sintered silicon carbide is made by employing additions of typically yttria and alumina to form a liquid phase at the sintering temperature. This phase solidifies to a continuous second phase.

In addition, for special purposes, other microstructural modifications can be employed, including the addition of graphite flakes for the reduction of friction in sliding seals, and the deliberate generation of closed porosity to act as a liquid reservoir, also for seals.

##### Reaction-bonded silicon carbides

Tests at NPL have shown no significant mass loss or penetration of several types of reaction-bonded SiC for a range of acids. The most aggressive was boiling orthophosphoric acid, in which a mass loss of 0.3 mg cm<sup>-2</sup> was obtained in 30 min.<sup>12</sup> Similar results are cited by Marcus and Ahrens.<sup>7</sup> The only acid combination to produce much more rapid attack is HF/HNO<sub>3</sub>, which attacks the residual silicon phase by the dual process of oxidizing the surface to silica and the latter's immediate removal by HF. This combination can be used to remove completely any residual silicon, but it leaves a weakened, open-porous



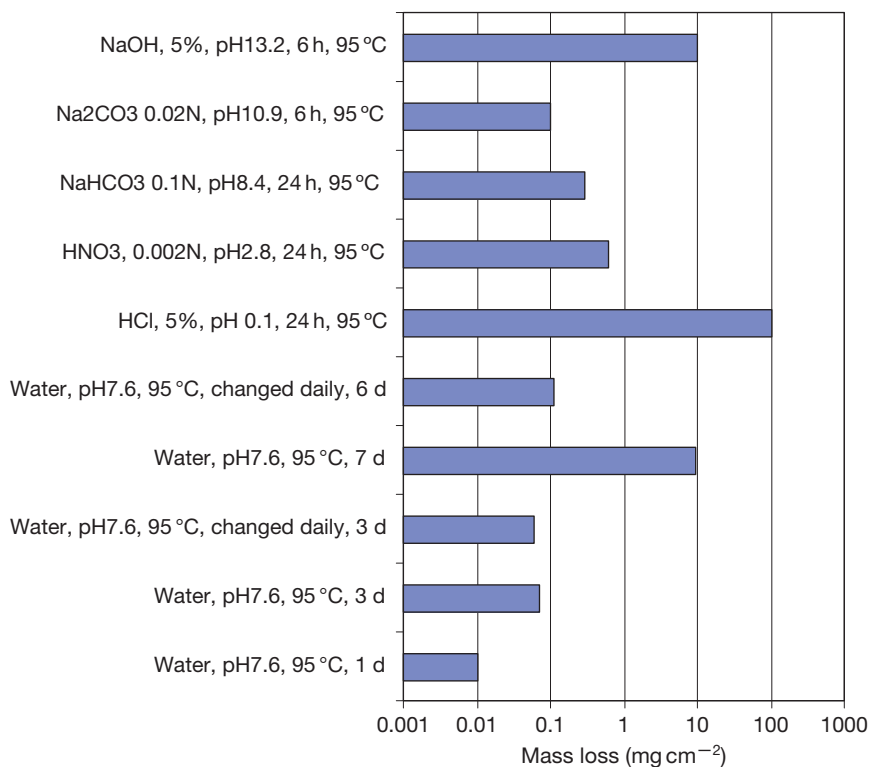


**Figure 6** Corrosion test results on Macor® machinable glass-ceramic.<sup>60</sup>

material. In contrast, Fang *et al.*<sup>18</sup> show that an HF/HCl mixture at room temperature produces only a very slow attack rate. Strong alkalis, as exemplified by tests using 10% KOH at 80 °C for 168 h, also attack the material by direct rapid dissolution of the silicon phase, 30 mg cm<sup>-2</sup> mass loss being obtained.

At higher temperatures, hydrothermal conditions result in oxidation and the removal of the oxide. Thus in steam at 220 °C (20 bar) for 24 h, a mass loss of 1.9 mg cm<sup>-2</sup> was obtained. More recently, more extreme conditions have been evaluated on three materials with different free Si contents in water at 360 °C for 7 days.<sup>66</sup> The rate of mass loss increased with increasing Si content, the Si phase being leached away by water oxidation and by dissolution as silicic acid. The rate increased further when an initially alkaline solution (pH 9) was used, rather than pH 6 of deionized water.

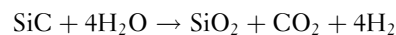
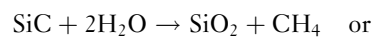
Mikeska *et al.*<sup>17</sup> used 20 M HF at 90 °C and found a significant rate of penetration by the removal of the silicon phase through the formation of H<sub>2</sub>SiF<sub>6</sub>.

#### Sintered silicon carbides

In this form, silicon carbide is one of the most resistant of all ceramics to both acidic and basic aqueous-based

corrosion, and finds a wide range of applications, including components in paper-making plant, cement plants, and heat exchangers.

In water, sintered silicon carbide is quite stable up to ~400 °C, but at higher temperatures, hydrothermal decomposition can take place at the surface by the following reactions (Yoshimura *et al.*<sup>67</sup> working with powders):



The authors suggest that water diffuses faster than oxygen through the thin protective surface layer of amorphous silica that is always present, accelerating the reaction compared with the oxidation rate in dry air. The silica is progressively dissolved allowing further oxidation to occur. At lower temperatures, the removal of the silica by abrasive or sliding wear processes exposes fresh surface, which oxidizes, and this defines the rate of surface removal.

Acid attack on a sintered material (B and C sintering acids) has been shown by Genthe *et al.*<sup>68</sup> to be minimal at 240 °C, 168 h for HCl, HNO<sub>3</sub>, and HF, but significant in an HNO<sub>3</sub>/HF mixture

( $\sim 270 \text{ mg cm}^{-2}$ ) as a result of a combined oxidation and dissolution effect.

Marcus and Ahrens<sup>17</sup> have evaluated two forms of porous sintered SiC in 96%  $\text{H}_3\text{PO}_4$  at 204 °C, and found minimal rates of attack.

The alkaline corrosion resistance of two forms of sintered silicon carbide has been examined by Sato *et al.*<sup>69</sup> They found that there was sensibly no attack by up to 25 M NaOH held at up to  $\sim 200$  °C for 3 days. Above this temperature and up to 300 °C, there was still no attack, provided that there was no free oxygen, but in the presence of oxygen, attack became significant, the surface layer of the material becoming penetrated and minor grain boundary phases being removed, leading to a significant loss in strength. This process greatly increases the exposed surface area of silicon carbide, which is then attacked *via* a hydrolysis type reaction given earlier, the silica being dissolved by the alkaline solution. The authors fitted a shrinking core model to the depth of penetration observed.

#### Liquid phase sintered silicon carbides

Liquid phase sintering is a recent development for SiC compared with the other process methods, and has been exploited in an attempt to improve strength and toughness of a SiC-based material. Like the situation with silicon nitride (explained later), it involves the use of additives such as alumina and yttria to promote densification at high temperature, and leaves these components as a grain boundary phase on completion of the process. The corrosion resistance of this type of product has not been widely studied, but it is likely to be poorer than the solid-state sintered version with some penetration likely in strong acids and strong alkalis.

#### Chemical vapor deposited (CVD) SiC

Generally, one would expect CVD SiC to behave similar to the sintered versions. Kim *et al.*<sup>70</sup> have studied the behavior of CVD SiC in water at 360 °C in comparison with sintered material, and found that the former performed better. Under these conditions, slow grain-boundary attack occurred, leading to an initially parabolic weight loss with time, but after some days resulting in the loosening of surface grains with a step increase in mass loss.

Mikeska *et al.*<sup>17</sup> showed that this material has excellent resistance to HF at 90 °C, and recommended its use as a coating to protect other forms of SiC that corrode down grain boundaries.

#### Other SiC composites

The corrosion properties of particulate composite materials based on SiC/TiC mixtures with alumina as a sintering aid have been studied<sup>68</sup> using a range of acids. It was established that the attack rates were very low in concentrated HCl ( $\leq 4 \text{ mg cm}^{-2}$  after 168 h at 210 or 240 °C), most of the attack being surface removal of TiC. An HF and  $\text{HNO}_3$  mixture proved to attack an order of magnitude faster, probably because the SiC phase was also removed, while an HF/ $\text{HNO}_3$  mixture attacked yet another order of magnitude faster at only 100 °C in 24 h because of the synergistic effects oxidizing the SiC and removing the  $\text{SiO}_2$  formed.

#### 3.25.4.2.2 Silicon nitrides

##### Material types

Like SiC, there are several routes by which silicon nitride materials can be produced. The first materials were produced by *hot-pressing* with, typically, MgO, and although this method has been extensively used and data on test materials have been widely reported in the literature, this method is nowadays rarely used for technical products because of the cost and a lack of shaping flexibility. The other widely researched early method was *reaction bonding* in which a preform of powdered silicon was converted to silicon nitride by heating in nitrogen. This material has open porosity, and therefore, is seldom employed for its corrosion resistance except as a crucible material for high temperature melts. In recent decades, the focus has switched to *sintering* the material using additions such as alumina and yttria, although a whole range of more exotic sintering aids has been explored with the aim of maximizing high temperature performance, particularly oxidation and creep resistance. The sintering process is relatively complex, and usually requires an overpressure of nitrogen in order to suppress high temperature dissociation, known as *gas-pressure sintering*. An alternative process is to first use the reaction bonding process at  $\sim 1350$ – $1400$  °C on a silicon-based shape containing sintering aids, and then to raise the temperature to  $\geq 1750$  °C to induce the sintering process. Such products are usually termed *sintered reaction-bonded* silicon nitride. The lowest closed porosity levels in any sintered products, and hence the highest densities, often require *hot isostatic pressing*. Sometimes this is done as part of the primary fabrication route, and sometimes as a second operation. Some versions of sintered silicon nitride have optimized fracture

toughness through the development of elongated silicon nitride grains; products of this type are typically used for corrosion-resistant rolling bearings.

The term 'sialon' is used for materials in which the composition is adjusted such that a solid solution between alumina and silicon nitride is produced as the primary phase. The secondary phases contain sintering aids, and thus such products can be considered as rather similar to sintered silicon nitrides in most respects, including corrosion resistance. There is no defined boundary between the two types.

Silicon nitride in its purest state can be prepared by chemical vapor deposition, but is not widely available. Because of the absence of secondary phases, this material has better corrosion resistance than do materials containing secondary phases to aid sintering.

Composites between silicon nitride and other nonoxides have been developed, with additions of BN, TiB<sub>2</sub>, TiN, MoSi<sub>2</sub>, but these are outside the scope of this chapter.

### **Sintered silicon nitrides**

Perhaps the most detailed published ambient pressure study is that of Okada and Yoshimura,<sup>71</sup> who evaluated a dense gas-pressure sintered silicon nitride in boiling sulfuric acid. This material contained secondary components alumina and yttria, which form a grain-boundary phase that is, for the most part, continuous. Flexural strength and mass loss were determined as a function of time at a range of boiling acid concentrations. It was found that in a 1 h test, pH 3 solution boiling at 103 °C created the biggest loss in strength and mass, with higher concentrations have a lesser effect. In prolonged exposure, there was a progressive loss of mass and of nominal flexural strength, the latter attributable to the development of a weakened porous surface skin. After 72 h exposure to 6 N sulfuric acid at 105 °C, the strength had dropped from an initial level of  $888 \pm 57$  MPa to  $445 \pm 45$  MPa. Some of this drop may be attributable to the removal of residual stresses due to machining the original test-pieces. The surface layer thickness, as a measure of penetration rate, increased from 100  $\mu\text{m}$  after 24 h to more than 250  $\mu\text{m}$  after 72 h, approximating to a rate of  $\sim 3 \mu\text{m h}^{-1}$  after an initial transient, but without loss of physical cross-section. The mechanism of corrosion is not discussed, but is likely to be a simple dissolution process of the yttria part of the secondary phase, while the silicon nitride itself is not significantly attacked. This type of attack has also been reported by Lin *et al.*<sup>72</sup> and is likely to be found in most commercial

products with alumina and yttria as the sintering aids. Similar attack processes have been found for a material with yttria and lanthana as the sintering aids.<sup>73</sup> Products with alternative rare-earth additions rather than yttria are likely to be more corrosion resistant. Fang *et al.*<sup>18</sup> show that a sintered sialon material with a glassy second phase is reasonably resistant to corrosion by a 1% HF + 5% HCl solution.

Sato *et al.*<sup>74</sup> tested a series of hot isostatically pressed silicon nitrides containing Y<sub>2</sub>O<sub>3</sub> and Al<sub>2</sub>O<sub>3</sub> sintering aids in 1 M HCl at 70 °C for 50–240 h. Analysis of the test solution showed that Al and Y dissolved preferentially from the grain boundary phase, and that retained strength progressively reduced with ageing time. It was further found that when the solution concentration was less than 1 M, the corrosion rate was controlled by the reaction at the surface, and when greater than 5 M, the rate was determined by diffusion through the corrosion product layer. In a material containing no additives, no attack occurred.

Sato *et al.*<sup>75</sup> have compared the rates of attack of a 25 M NaOH solution at 150–200 °C for 3 days on hot-pressed and sintered silicon nitrides of similar composition, both containing Al<sub>2</sub>O<sub>3</sub> and Y<sub>2</sub>O<sub>3</sub> as densification aids. It was found that the rate of attack in terms of mass loss was low at 150 °C, but at higher temperatures, the sintered material with 5.2 wt% additions was attacked more rapidly than was the hot-pressed material with 4.7 wt% additions. This was ascribed to the preferential dissolution of silica. However, the hot-pressed material lost strength in a more catastrophic way with a total weight loss greater than in the sintered material, although the reasons for this are not entirely clear.

Sato *et al.*<sup>76</sup> have reported experiments on three materials with differing grain boundary phase compositions, conducted under neutral hydrothermal conditions (200–300 °C) for 3 days. A white deposit developed on the surface of the material, which was found to contain hydrated silica and grain boundary phases of alumina and yttria. The material in which this phase remained glassy appeared to perform better than those in which it is partially crystallized. Strength was found to drop from an initial 630 MPa toward 400 MPa.

### **Reaction-bonded silicon nitride**

Being open-porous, this material is not widely used for liquid environments at low temperature, and therefore, few data are reported, but if substantially

free from impurities, it will, like hot-pressed and some sintered versions, show good corrosion resistance to acids. Marcus and Ahrens<sup>7</sup> report minimal rates of attack in  $\text{H}_3\text{PO}_4$  at 204 °C.

### 3.25.4.2.3 Boron nitrides

#### Material types

Boron nitride exists in two forms: the crystallographically cubic form (CBN) is akin to diamond in properties, while the hexagonal form (HBN) is akin to graphite. CBN is difficult to densify, but is made in monolithic form as a cutting tool and die material. In contrast, HBN is available as a hot-pressed, machinable form for general applications, and via a vapor phase route, when it is usually termed 'pyrolytic.'

#### CBN

CBN is widely claimed to be corrosion resistant, but no specific information is available at this time. The binder phase employed to aid the compaction process is likely to control performance.

#### HBN

Corrosion performance is limited by a hydration process that converts BN to boric acid with the release of nitrogen. Oda and Yoshio<sup>77,78</sup> have shown that the rate of attack on a solid material under hydrothermal conditions (150–300 °C, 1–10 days) is related to crystal orientation, because the oriented grains in pyrolytic material are attacked more slowly than the more randomly orientated hot-pressed material, as shown by micrographic evidence. Figure 7 shows their results for the linear portions of the trends of mass loss as function of time, ignoring an initial

transient. The activation energy for the hydrolysis process was computed as 60 kJ mol<sup>-1</sup>, based on equivalent tests on powdered material.

Moderate rates of attack by both acids and alkalis were found in NPL tests at 140 °C/23 h. Marcus and Ahrens<sup>7</sup> report moderate rates of attack at 204 °C in  $\text{H}_3\text{PO}_4$ .

### 3.25.4.2.4 Specialist materials

AlN – Young and Duh<sup>79</sup> report that corrosion rates at room temperature in alkaline solutions are much faster than in neutral or acid solutions as a result of a catalyzed hydration process with the formation of aluminates as intermediaries. Marcus and Ahrens<sup>7</sup> report rapid dissolution in  $\text{H}_3\text{PO}_4$  at 204 °C.

TiC – Genthe *et al.*<sup>68</sup> have tested hot-pressed material, and shown some slow acid attack in HCl and HF, but rapid attack in  $\text{HNO}_3$  and HF– $\text{HNO}_3$  mixture.

TiB<sub>2</sub> – Monticelli *et al.*<sup>80</sup> demonstrate that hot-pressed material with 1.5% Ni behaves like a passive metal in 3.5% salt solution at 25–65 °C, with the formation of a corrosion-resistant TiO<sub>2</sub> layer on the surface. However, tests at NPL have shown that hot-pressed material is rapidly attacked by acids at 140 °C/23 h, especially HCl, but is very resistant to KOH solutions. Marcus and Ahrens<sup>7</sup> showed that a hot-pressed material was attacked faster than a sintered material in  $\text{H}_3\text{PO}_4$  at 204 °C.

MoSi<sub>2</sub> – Marcus and Ahrens<sup>7</sup> report slow attack by  $\text{H}_3\text{PO}_4$  at 204 °C.

B<sub>4</sub>C – NPL tests have shown negligible attack by acids and alkalis at 140 °C/23 h on a hot-pressed material, except an  $\text{HNO}_3$  +  $\text{H}_3\text{PO}_4$  mixture, which gave slight attack. Mikeska *et al.*<sup>17</sup> report minimal

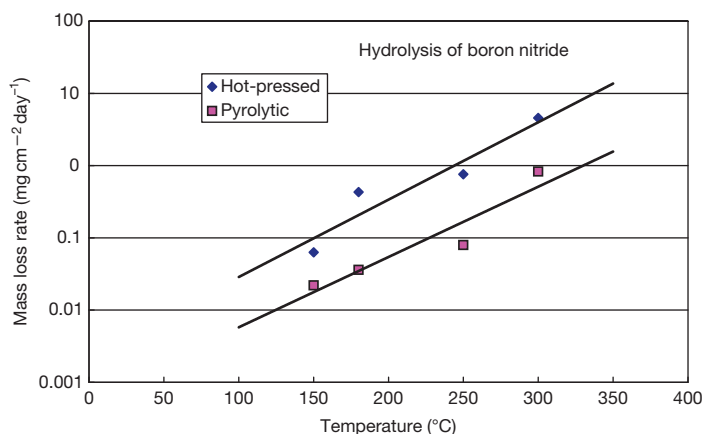


Figure 7 Hydrolysis of dense boron nitride as a function of temperature.<sup>77,78</sup>

attack by HF at 90 °C. Marcus and Ahrens<sup>7</sup> report negligible attack rates by H<sub>3</sub>PO<sub>4</sub> at 204 °C.

Pure WC, CaF<sub>2</sub>, MgF<sub>2</sub> show excellent resistance to HF at 90 °C.<sup>17</sup>

### 3.25.4.3 Comparative Attack Rates

From the foregoing, it will be appreciated that the performance of any one material is highly dependent not only on its composition and microstructure, but also on the conditions to which it is subjected and how the effects of corrosion are measured. It is therefore particularly difficult to give a clear appreciation of the comparative performance of the huge range of materials now available. There are relatively few sources of directly comparative numerical data over a wide range of products. Some appreciation can be obtained from unpublished NPL work<sup>13</sup> given in Figure 8.

## 3.25.5 Some Specific Applications Requiring Corrosion Resistance

### 3.25.5.1 Chemical Process Vessels

There has been a long history of the use of technical ceramics for chemical process vessels, both as the lining and as furniture inside them. If the vessels are limited in dimensions to typically 500 mm or less,

they can be made from monolithic shells of dense, chemically resistant porcelain, which provide a long life except perhaps with the most aggressive of reagents. Examples include digesters and ball mills. If the vessels are larger, a lining of chemically resistant brickwork is required, usually bedded into a chemically resistant mortar. The mortar may be the life-limiting factor, but despite this, successful applications have been achieved for many years. A review of such applications may be found in Charlebois.<sup>5</sup>

Furniture, such as so-called 'tower packing,' is often made from a chemically resistant stoneware, a product much coarser in texture than porcelain, but with similar properties, provided that the as-fired surface skin remains intact. This skin acts as a glaze, which seals access to internal porosity. In some aggressive environments, their successful application may be reliant on preservation of the skin. More expensive options rely on alumina ceramics, but these tend to be available only in rather smaller pieces. Other applications reliant on alumina include filter plates, filters, nozzles, pipe linings, etc.

In the laboratory, chemical porcelains continue to be used for pestles, mortars, and other corrosion-resistant parts for chemical handling. Low thermal expansion glass-ceramics are used for hot-plate and stirrer plate units, minimizing the risks of corrosion from common chemicals. Similar materials are used in the kitchen for cookware and for cooker hobs.

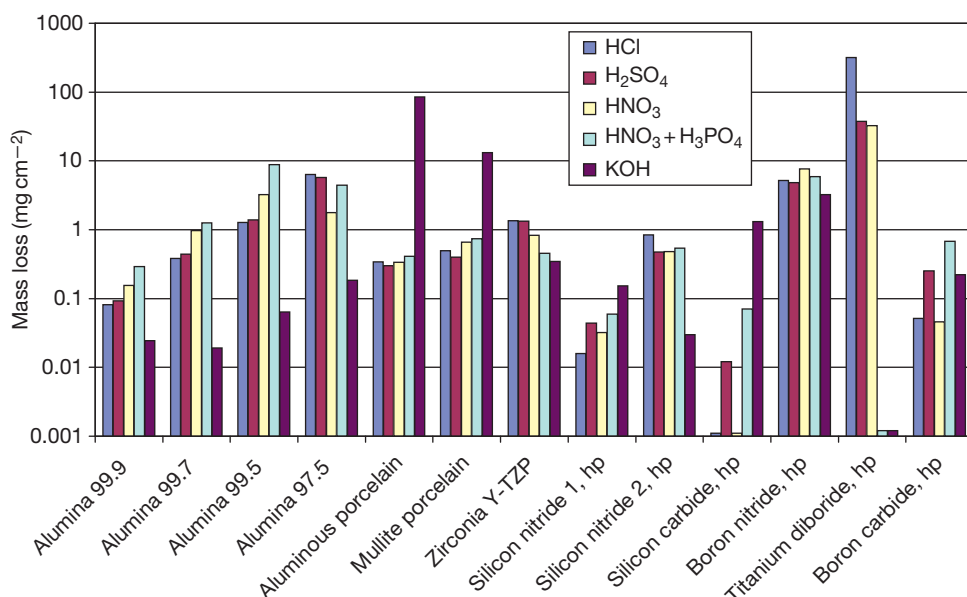


**Figure 8** Comparative rates of mass loss after exposure in PTFE-lined digestion bombs to various 20% by volume solutions at 140 °C for 23 h.

### 3.25.5.2 Rotating Seals

Rotating seal faces for pumps are usually made from a hard material such as a ceramic and an abradable material, often carbon or graphite based. Alumina ceramics are the most commonly employed hard faces for water and organic liquid-based media, and have demonstrably long lives in the absence of excessive abrasion or very high or very low pH. Examples include central heating pumps, light-duty chemical process pumps, and food processing pumps. Where there is additional loading, such as abrasive particles, a harder material is usually employed, such as silicon carbide. For vehicular water cooling pumps, silicon nitride has been widely used because of its better strength and thermal shock resistance compared with alumina.

For highly acidic conditions, secondary phases in alumina limit corrosion/abrasion performance and silicon carbide-based materials are often employed.

Silicon carbide is also often the material of choice in gas bearings and gas pump seals.

### 3.25.5.3 Flow-meter Bodies

Flow-meters for highly corrosive chemical plant circuits based on electroconduction are typically made from alumina ceramics. Insulated electrodes can be sealed through the wall to provide the sensing circuit, and provided that the right choice of material is made, the life can be much longer than that of the attached pipework.

### 3.25.5.4 Food Processing

The linings of food processing equipment can often, with advantage, be made from alumina ceramics, which resist corrosion from food acids as well as abrasion. Food is not contaminated in the same way as it might be with metallic linings such as stainless steel. The key requirement is that the materials withstand typical chlorinated steam cleaning processes, which can be more aggressive than the food itself. Materials with good resistance to hydrochloric acid at elevated temperatures are required.

### 3.25.5.5 Valves

Seal faces for valves, including shower mixers, quarter-turn faucets, gas valves, etc., are typically made from pairs of alumina ceramics plates with flat lapped faces. These resist corrosion from normal

water supplies to elevated temperature, and have a long, corrosion-free life that is usually limited only by risks of mechanical damage from the metallic components used to operate them, or from the deposition of lime-scale, which can jam them, or lead to excessive wear.

Corrosion-resistant ball valves used for chemical plant are also made typically up to 150 mm diameter. The choice of material for this application is critical, as in the case of flow-meters.

### 3.25.5.6 Medical

The human body places unusually corrosive conditions on materials used for implants, but because of their corrosion resistance, ceramics are successfully being employed for both dentistry and orthopedics. In the mouth, glassy porcelains are used for individual tooth crowns, and the literature contains increasing number of reports of the use of machinable glass-ceramics for forming tooth shapes, and of zirconia (Y-TZP type) for prosthetic bridges. For orthopedics, the combination of strength and corrosion resistance of, particularly, alumina is exploited for balls and cups for hip replacement. Zirconia (Y-TZP type) has also been used, and offers higher mechanical strength, but as described earlier, there are some potential limitations of phase stability at body temperature. Increasingly, alumina-zirconia composite materials are being employed to overcome the instability problem, and silicon nitride is on the horizon, already widely employed for rolling bearing balls.

Other corrosion-resistant ceramics used in the body include glassy carbons for heart valves, and hydroxyapatite as a fully biocompatible ceramic, which can be used as a coating on metallic components to enhance osseointegration, or as a free-standing material to assist in bone reconstruction. Bioglasses and bioglass-ceramics also have specialized applications in which reaction with the body is deliberately exploited in their function.

## 3.25.6 Selecting the Right Material

It is hard to predict performance, and, therefore, it is important when selecting ceramic materials for corrosion-resisting applications to undertake some relevant testing to check potential performance, unless there is direct previous experience with a particular type of product. Often, ceramic materials are not specifically optimized for applications



requiring corrosion resistance, and may contain species that are readily removed. Simple ranking tests will provide a guide, as in [Figure 8](#).

In addition, there are other factors which may dictate material choice, including price, availability in the shape and dimensions required, aspects of mechanical performance, and aspects of joining to other components. For those not experienced with the use for ceramic components, specialist advice should be sought.

## References

- Lavrenko, V. A.; Panasyuk, A. D.; Desmaison-Brut, M.; Schvets, V. A.; Desmaison, J. J. *Eur. Ceram. Soc.* **2005**, *25*, 1813–1818.
- Binns, D. B. *The Use of Ceramics in Valves*; British Ceramic Research Association Special Publication no. 48, **1965**, p 157.
- Cox, J. M.; Morrell, R. *Brit. Ceram. Proc.* **1989**, *43*, 29–40.
- Öhman, L. O.; Ingri, N.; Tegman, R. *Bull. Amer. Ceram. Soc.* **1982**, *61*(5), 567–571 and 581.
- Charlebois, G. W. *Mater. Perform.* **1991**, *3*, 71–75.
- Bennett, J. P. Corrosion resistance of selected ceramic materials to sulfuric acid, Report of Investigations 9011; US Bureau of Mines, 1986.
- Marcus, L.; Ahrens, R. L. *Bull. Amer. Ceram. Soc.* **1981**, *60*(4), 490–493.
- Morrell, R. *Handbook of Properties of Technical and Engineering Ceramics. Part 2, Data Reviews, Section 1, High-Alumina Ceramics*; HMSO: London, 1987.
- Real, M.; Cooper, D. R.; Morrell, R.; Rawlings, R.; Weightman, B.; Davidge, R. W. *J. Phys. Coll.* **1986**, *C1*(2), C1-763–C1-766.
- Jaeger, G.; Kraseman, R. *Werkstoffe Korrosion* **1952**, *3*(11), 401–415.
- Richards, G. *Trans. Br. Ceram. Soc.* **1981**, *80*(4), 120–124.
- Lay, L. A. *The Resistance of Ceramics to Chemical Attack*; NPL Report CHEM 96; National Physical Laboratory: Teddington, Middlesex, UK, 1979.
- Lay, L. A. Unpublished NPL results, 1980.
- Lay, L. A. *Corrosion Resistance of Technical Ceramics*, 2nd ed.; HMSO: London, 1991.
- Engell, J.; Jakobsen, P. *Danish Materials Society Yearbook* 1990, pp 89–112.
- Genthe, W.; Hausner, H. *Euroceramics* **1989**, *3*, 3.463–3.467.
- Mikeska, K. R.; Bennison, S. J.; Grise, S. L. *J. Am. Ceram. Soc.* **2000**, *83*(5), 1160–1164.
- Fang, Q.; Sidky, P. S.; Hocking, M. G. *Corros. Sci.* **1997**, *39*(3), 511–527.
- Sato, T.; Sato, S.; Okuwaki, A.; Tanaka, S. *J. Am. Ceram. Soc.* **1991**, *74*(12), 3081–3084.
- Dailly, D. F.; Hastings, G. W.; Lach, S. *Proc. Br. Ceram. Soc.* **1981**, *31*, 191–200.
- Byrne, W. P.; Hanney, M. J.; Morrell, R. *Proc. Br. Ceram. Soc.* **1982**, *32*, 303–314.
- Barinov, S. M.; Fateeva, L. V.; Ivanov, N. V.; Orlov, S. V.; Shevchenko, V. Ja. *Scripta Mater.* **1998**, *38*(6), 975–980.
- Ferber, M. K.; Brown, S. D. *J. Am. Ceram. Soc.* **1980**, *63*, 424–429.
- Bastide, B.; Canale, P.; Odier, P. *J. Eur. Ceram. Soc.* **1989**, *5*, 289–293.
- Guo, X.; He, J. *Acta Mater.* **2003**, *51*(17), 5123–5130.
- Kawakubo, T.; Hirayama, H.; Kaneko, T. *J. Soc. Mater. Sci. Jpn.* **1990**, *39*(438), 312–317.
- Sato, T.; Endo, T.; Shimada, M.; Mitsudome, T.; Otabe, N. *J. Mater. Sci.* **1991**, *26*(5), 1346–1350.
- Ohmichi, N.; Kamioka, K.; Ueda, K.; Matsui, K.; Ohgai, M. *J. Jpn. Ceram. Soc.* **1999**, *107*(2), 128–133.
- Yasuda, K.; Arai, S.; Itoh, M.; Wada, K. *J. Mater. Sci.* **1999**, *34*(15), 3597–3604.
- Pecharromán, C.; Bartolomé, J. F.; Requena J., Moya, J. S.; Deville, S.; Chevalier, J.; Fantozzi, G.; Torrecillas, R. *Adv. Mater.* **2003**, *15*(6), 507–511.
- Ikeda, J.; Pezzotti, G.; Iwamoto, M.; Ueno, M. *Key Eng. Mater.* **2007**, *330–332*(2), 1203–1206.
- Chevalier, J. *Biomaterials* **2006**, *27*(4), 535–543.
- Chevalier, J.; Gremillard, L.; Deville, S. *Ann. Rev. Mater. Res.* **2007**, *37*, 1–32.
- Chevalier, J. J.; Deville, S.; Münch, E.; Jullian, R.; Lair, F. *Biomaterials* **2004**, *25*(24), 5539–5545.
- Butt, D. P.; Payyapilly, J. J. *J. Nucl. Mater.* **2007**, *360*(2), 92–98.
- Gremillard, L.; Chevalier, J.; Epicier, T.; Fantozzi, G. *J. Am. Ceram. Soc.* **2002**, *85*(2), 401–407.
- Tagigawa, Y.; Naka, Y.; Higashi, K. In *Proceedings of Conference Materials in Clinical Applications VII Trans Tech: Zürich, Switzerland, 2006*; pp 106–111.
- Murray, M.; Stuart, J.; Morrell, R. In *Performance Evaluation of Zirconia Femoral Heads*; Proceedings of the Conference on Engineers Meet the Surgeons; Inst. Mechanical Engineers: London, 2002.
- Lance, M. J.; Vogel, E. M.; Reith, L. A.; Cannon, W. R. *J. Am. Ceram. Soc.* **2001**, *84*(11), 2731–2733.
- Kosmac, T.; Dakskobler, A.; Oblack, C.; Jevnikar, P. *Int. J. Appl. Ceram. Technol.* **2007**, *4*(2), 164–174.
- Lin, J. D.; Duh, J. G.; Lo, C. L. *Mater. Chem. Phys.* **2003**, *77*(3), 808–818.
- Hernandez, M. T.; Jurado, J. R.; Duran, P.; Fierro, J. L. G. *J. Am. Ceram. Soc.* **1991**, *74*(6), 1254–1258.
- Zhao, Z.; Liu, C.; Northwood, D. O. *Ceram. Eng. Sci. Proc.* **2001**, *22*(4), 59–66.
- Basu, D.; Das Gupta, A.; Basu, M. K.; Sarkar, B. K. *J. Eur. Ceram. Soc.* **1996**, *16*(6), 613–617.
- Shojai, F.; Mantyla, T. A. *J. Am. Ceram. Soc.* **2001**, *21*(1), 37–44.
- Kritzer, P.; Schacht, M.; Dinjus, E. *Mater. Corros.* **1999**, *50*(9), 505–516.
- Kalin, M.; Dražič, G.; Novak, S.; Vižintin, J. *J. Eur. Ceram. Soc.* **2006**, *26*, 223–232.
- Hisamori, N.; Kimura, Y. *J. Soc. Mater. Sci. Jpn.* **1999**, *48*(3), 275–281.
- Herrmann, M.; Seipel, B.; Schilm, J.; Nickel, K. G.; Michael, G.; Krell, A. *J. Eur. Ceram. Soc.* **2005**, *25*(10), 1805–1812.
- Hirano, M.; Inada, H. *J. Mater. Sci.* **1991**, *26*(18), 5047–5052.
- Nakanishi, T.; Sasaki, M.; Ikeda, J.; Mijaji, F.; Kondo, M. *Key Eng. Mater.* **2007**, *330–332*, Part 2, 1267–1270.
- Thompson, I.; Rawlings, R. D. *J. Mater. Sci.* **1992**, *27*, 2823–2830.
- Yoshio, T.; Oda, K.; Suemasu, T.; Kohno, A. *J. Jpn. Ceram. Soc.* **1992**, *100*(5), 668–674.
- Holland, L. *The Properties of Glass Surfaces*; Chapman and Hall: London, 1964.
- Hood, H. P.; Nordberg, M. E. British Patent 2,221,709, 1934.
- McMillan, P. W. *Glass-Ceramics*, 2nd ed.; Academic Press: London, 1979.
- Salama, S. N.; Salman, S. M. *J. Eur. Ceram. Soc.* **1994**, *13*(6), 521–528.

58. Demirkesen, E.; Göller, G. *Ceram. Int.* **2003**, 29(4), 463–469.
59. Livingston, F. E.; Adams, P. M.; Helvajian, H. *Appl. Phys. A: Mater. Sci. Eng.* **2007**, 89(1), 97–107.
60. Corning Inc., Company brochure on Macor.
61. Li, C. G.; Si, W. J.; Zhang, W. F. *Key Eng. Mater.* **2007**, 336–338(part 3), 2429–2431.
62. Hiratsuka, A.; Yoshikawa, A.; Ogwara, K.; Adachi, K. *Mater. Sci. Forum*, **2003**, 426–429, 4471–4476.
63. Studart, A. R.; Filser, F.; Kocher, P.; Gaukler, L. J. *Biomaterials* **2007**, 28(17), 2695–2705.
64. Teixeira, E. C.; Piascik, J. R.; Stoner, B. R.; Thompson, J. Y. *J. Mater. Sci. – Mater. Med.* **2007**, 18(6), 1219–1224.
65. Qiao, G. J.; Wang, Y. L.; Jin, Z. H.; Zhou, H. J. *Int. J. Fatigue* **1996**, 18(8), 523–527.
66. Kim, W. J.; Hwang, H. S.; Park, J. Y. *J. Mater. Sci. Lett.* **2002**, 21, 733–735.
67. Yoshimura, M.; Kase, J.; Somiya, S. *J. Mater. Res.* **1986**, 1(1), 100–103.
68. Genthe, W.; Robayie, J. K.; Hausner, H. *cfi/Ber. Deut. Ker. Ges.* **1991**, 68(6), 262–265.
69. Sato, T.; Taura, K.; Okuwaki, A. *Brit. Ceram. Trans. J.* **1992**, 91, 181–185.
70. Kim, W. J.; Hwang, H. S.; Park, J. Y.; Ryu, W. S. *J. Mater. Sci. Lett.* **2003**, 22, 581–584.
71. Okada, A.; Yoshimura, M. *Key. Eng. Mater.* **1996**, 113, 227–236.
72. Lin, C. H.; Komeya, K.; Meguro, T.; Tatami, J.; Abe, Y.; Komatsu, M. *J. Jpn. Ceram. Soc.* **2003**, 111(7), 452–456.
73. Monteverde, F.; Mingazzi, C.; Giogi, M.; Bellosi, A. *Corros. Sci.* **2001**, 43(10), 1851–1863.
74. Sato, T.; Tokunaga, Y.; Endo, T.; Shimada, M.; Komeya, K.; Komatsu, M.; Kameda, T. *J. Am. Ceram. Soc.* **1988**, 71(12), 1074–1079.
75. Sato, T.; Sato, S.; Tamura, K.; Okuwaki, A. *Br. Ceram. Trans. J.* **1992**, 91, 117–120.
76. Sato, T.; Murakami, T.; Endo, T.; Shimada, M.; Komeya, K.; Kameda, T.; Komatsu, M. *J. Mater. Sci.* **1991**, 26, 1749–1754.
77. Oda, K.; Yoshio, T. *Nippon Seramikkusu Kyokai Gakujutsu Ronbunshi* **1989**, 97(9), 903–910.
78. Oda, K.; Yoshio, T. *J. Jpn. Ceram. Soc.* **1993**, 101(8), 855–859.
79. Young, C. D.; Duh, J. G. *J. Mater. Sci.* **1995**, 30(1), 185–195.
80. Monticelli, C.; Frignani, A.; Bellosi, A.; Brunoro, G.; Trabanelli, G. *Corros. Sci.* **2001**, 43(5), 979–992.

## 3.26 Degradation of Glass and Glass Ceramics

**S. Oliver and B. A. Proctor**

Pilkington Ltd., St. Helens WA10 3TT, UK

**C. A. May**

School of Engineering, University of Greenwich, London SE10 9LS, UK

This article is a revision of the Third Edition article 18.2 by D. S. Oliver and B. A. Proctor, volume 2, pp 18:9–18:26,

© 2010 Elsevier B.V.

<b>3.26.1</b>	<b>Introduction</b>	2307
<b>3.26.2</b>	<b>Commercial Glasses</b>	2307
<b>3.26.3</b>	<b>Physical Properties</b>	2308
3.26.3.1	Structure	2308
3.26.3.2	The Nature of the Glass Surface	2309
3.26.3.3	Thermal Expansion	2309
<b>3.26.4</b>	<b>Mechanical Properties</b>	2310
3.26.4.1	Strength	2310
3.26.4.2	Elastic Modulus	2310
3.26.4.3	Thermal Shock Resistance	2310
<b>3.26.5</b>	<b>Chemical Properties</b>	2310
3.26.5.1	Degradation	2310
3.26.5.2	Glass Durability Tests	2311
3.26.5.2.1	Grain tests	2311
3.26.5.2.2	Whole-article tests	2311
<b>3.26.6</b>	<b>Mechanisms of Glass Corrosion</b>	2311
3.26.6.1	General Properties	2311
3.26.6.2	Corrosion Mechanisms	2313
3.26.6.3	The Action of Water and Acids	2313
3.26.6.4	Attack by Alkali Solution, Hydrofluoric Acid, and Phosphoric Acid	2313
3.26.6.5	Chemical Attack by Other Agents	2313
3.26.6.6	Cleaning of Glass	2313
3.26.6.7	Applications	2314
<b>3.26.7</b>	<b>Vitreous Silica</b>	2314
3.26.7.1	Manufacturing	2314
3.26.7.2	Structure and Physical Properties	2314
3.26.7.2.1	Polymorphism of silica	2314
3.26.7.2.2	Thermal expansion	2314
3.26.7.2.3	Heat resistance	2315
3.26.7.2.4	Thermal conductivity	2315
3.26.7.2.5	Electrical characteristics	2315
3.26.7.3	Resistance to Chemical Attack	2315
3.26.7.3.1	Boiling water and steam	2315
3.26.7.3.2	Fluorine, hydrofluoric acid, and alkaline solutions	2315
3.26.7.3.3	Basic oxides	2316
3.26.7.3.4	Metals	2316
3.26.7.4	Applications of Vitreous Silica	2316
<b>3.26.8</b>	<b>Glass Ceramics</b>	2317
3.26.8.1	Definition and Properties	2317
3.26.8.2	Chemical Durability of Glass-Ceramics	2317
<b>References</b>		2318

## Glossary

**Glass** A solid material that is characterized by lack of crystallinity; that is, with short-range but not long-range order.

**Glass-ceramic** An initially glassy material that, when heat-treated, forms a crystalline phase such that the material, on cooling, comprises a composite containing the crystalline phase surrounded by the remaining glassy material; such materials generally have enhanced mechanical properties compared to either a typical glass or a typical ceramic of similar composition.

**Network former** A compound such as silica ( $\text{SiO}_2$ ) that, when cooled at a sufficient rate, will on its own form a glass.

**Network modifier** A compound such as soda ( $\text{NaO}$ ) or calcia ( $\text{CaO}$ ) that will not form a glass on cooling and, when combined with a network former, will disrupt network bonds.

**Static fatigue** The process of delayed fracture below the normal fracture stress of a glass that results from cracks growing from flaws on the glass surface, usually exacerbated by the presence of moisture or humidity.

**Vitreous** The glass-like state of a material that might otherwise crystallize (e.g., vitreous silica is the glassy state of the compound  $\text{SiO}_2$ , while quartz is one of the crystalline phases of the same compound).

### 3.26.1 Introduction

One of the most important properties of commercial glasses is their great resistance to corrosion; any chemical laboratory apparatus, window, or wind-screen provides an excellent illustration. Windows remain virtually unchanged for centuries, resisting the influences of atmosphere and radiation. A vast range of products may be safely stored in glass for decades at ordinary temperatures, and the fact that glass can be used with alkaline, neutral, and acid environments allows the same equipment to be used for a variety of processes.

The principal difficulty associated with the use of glass equipment is the fact that glass fractures rather than deforms on severe impact. Thus, although it may be toughened by thermal treatment or ion exchange,

glass remains a material that has intrinsically a relatively low value of fracture toughness and small critical flaw size. Glass is also more prone than metals to damage by thermal shock, although this difficulty can be largely avoided by the use of low-expansion glass formulations. Finally, the size of glassware that can readily be fabricated is sometimes below the needs of a particular process.

### 3.26.2 Commercial Glasses

The term glass defines a family of materials that exhibit as wide a range of differences among themselves as exists among metals and alloys. The great variety of physical and chemical properties available arises from the possibility of including almost all the stable oxides, sulfides, halides, etc. throughout the periodic table in different glass formulations. Many branches of the family, for example, those borates, silicates, and phosphates which are water-soluble, are of little interest in the present context. It is, however, worth bearing in mind that glasses can be designed to combine particular physical properties with good chemical resistance.

For most of the commercial oxide glass families, silica ( $\text{SiO}_2$ ) is the main ingredient. However, lower melting points and greater flexibility of properties are achieved with the addition of other oxides and modifiers. Depending upon the choice of these additional constituents, glasses are classified into groups, including fused silica, soda-lime glasses, leaded glasses, aluminosilicate glasses, borosilicate glasses, etc. A cross section of some commercial glass compositions is given in [Table 1](#).<sup>1</sup>

*Fused silica* is a general classification within which is a range of varieties and types of material with differences in purity, transmission, and grade. This type of glass may be used up to 900 °C in continuous service; it resists attack by a great many chemical reagents, rapid attack occurring only in hydrofluoric acid and concentrated alkali solutions.

*Container glass* is suitable for the storage of beverages, medicines, cosmetics, household products, and a wide range of laboratory reagents.

*Tubing glass* is suitable for general laboratory use and chemical apparatus construction, though neutral or hard borosilicate are preferred for more severe conditions, these representing the most resistant glasses available in bulk form.

*Neutral glasses* are generally less resistant than the hard borosilicate type, but are more easily melted

**Table 1** Typical glass compositions

	1	2	3	4	5	6	7	8	9	10	11
SiO <sub>2</sub>	100%	72.7%	72.8%	71.4%	71.5%	80.3%	57.2%	67.5%	54.2%	63.6%	57.1%
Al <sub>2</sub> O <sub>3</sub>	—	1.1%	1.7%	2.2%	5.5%	2.8%	1.0%	4.8%	14.3%	2.9%	4.6%
B <sub>2</sub> O <sub>3</sub>	—	—	—	—	10.0%	12.3%	—	—	8.3%	5.0%	11.8%
MgO	—	3.8%	—	3.9%	—	—	—	—	4.5%	3.2%	—
CaO	—	8.4%	10.5%	4.6%	0.2%	—	—	0.1%	17.7%	7.3%	0.4%
BaO	—	—	—	0.8%	3.0%	—	—	12.0%	—	2.6%	—
Na <sub>2</sub> O	—	13.1%	14.5%	15.0%	8.0%	4.0%	4.0%	7.2%	0.6%	14.5%	14.2%
K <sub>2</sub> O	—	0.5%	—	1.7%	1.2%	0.4%	8.5%	6.9%	0.1%	0.6%	0.8%
ZrO <sub>2</sub>	—	—	—	—	—	—	—	—	—	—	3.8%
TiO <sub>2</sub>	—	—	—	—	—	—	—	—	—	—	7.5%
PbO	—	—	—	—	—	—	29.0%	—	—	—	—
Li <sub>2</sub> O	—	—	—	—	—	—	—	0.5%	—	—	—
Others	—	0.4%	0.5%	0.4%	0.6%	0.2%	0.3%	0.3%	0.3%	0.3%	0.4%

1, fused silica; 2, window glass; 3, container glass; 4, fluorescent tubing; 5, neutral glass; 6, hard borosilicate; 7, lead glass; 8, TV tube and screen; 9, textile glass fiber; 10, glass wool insulation; 11, superfine glass wool.

and shaped. They are formulated so that the pH of aqueous solutions is unaffected by contact with the glass, making it particularly suitable in pharmaceutical use for the storage of pH-sensitive drugs.

*Borosilicate glasses* are, in terms of different types available, the most versatile types of glass produced. In general, borosilicate glasses are grouped into five types: low-expansion glass, low electrical-loss glass, materials for seals to metals, glasses for laboratory apparatus, and optical-grade glasses, including those with enhanced transmission beyond the visible spectrum. The example given, that is, hard borosilicate glass, is typically used for ovenware, laboratory apparatus, etc., and combines low expansion and high chemical resistivity with chemical stability. These types of glasses generally require high fabrication temperatures compared with soft soda glasses.

*Electronic grade glasses* are used in cathode ray tube screens and similar applications, and contain higher quantities of heavy elements (e.g., lead, barium, etc.) in order to absorb radiation. These glasses do not operate under severe corrosion conditions, but surfaces must not leach excessive alkali under damp conditions or electrical breakdown can occur.

*Glass fibers* present particular problems in corrosive environments because of their very high surface/volume ratios. Glasses for electrical insulation are generally formulated from alkali-free aluminoborosilicate glasses (generally known as E-glass) and are frequently specified as containing less than 1% alkali (Na<sub>2</sub>O and K<sub>2</sub>O). This type of glass is also used extensively for the reinforcement of plastics where its high resistance to moisture attack ensures a durable product.

*Glass wools* are used for less demanding applications and generally contain some alkali to aid in processing. Superfine wool contains zirconia and titania to enhance the chemical resistance while retaining the properties necessary for economic fine fiber formation.

### 3.26.3 Physical Properties

#### 3.26.3.1 Structure

Glass has been defined as 'an inorganic product of fusion which has cooled to a rigid condition without crystallizing.' The atomic structure of glasses is more closely related to liquids than to crystals. The properties of glasses are manifestations of this structure, being governed in particular by the random liquid-like disposition of the network-forming ions (commonly Si<sup>4+</sup> and B<sup>3+</sup>); the presence of mobile, interstitial alkali ions; and the 'single-molecule' nature of the lattice. The bonding within the atomic network is partly covalent and partly ionic. Thus, the network bonds are highly directional with a range of interbond angles, bond lengths, and bond energies; the bonding electrons are restricted to particular energy levels within the bonds. The network-modifying ions (commonly alkali and alkaline-earth ions) are ionically bound to the network although the field strength and diameter of the alkali ions allow them some mobility as a function of temperature.

The random nature of the glass structure imparts a range of bond energies in the network, and hence a characteristic feature of glasses is a continuous

softening over a range of temperature, a continuous viscosity/temperature curve, and the absence of a true melting point. For convenience in comparing the viscosity behavior of different glasses, arbitrary temperatures at which the glass has specific viscosities are often quoted.<sup>2</sup> The Littleton softening point<sup>3</sup> is most commonly used. At this temperature, the glass has a viscosity of  $10^{6.6}$  Pa s.

The glass transition temperature  $T_g$  corresponds to a viscosity between  $10^{12}$  and  $10^{13}$  Pa s depending on the definition and on the method of measurement. Glass behaves as a Newtonian liquid at temperatures well above the glass transition. It is this behavior that prevents the necking generally observed during plastic deformation of metals and which allows glass to be easily formed into such a large number of useful configurations.

In practice, an important range of viscosities are those from  $10^{11}$  to  $10^{13.5}$  Pa s, known as the annealing range. The annealing point and the strain point are generally taken as the temperatures at which the glass has a viscosity of  $10^{12.4}$  and  $10^{13.6}$  Pa s, respectively. Within this range, the glass is effectively a solid, but internal stresses can be relieved within a practical time scale. Rapid cooling of glass articles through the annealing range eventually results in permanent and sometimes catastrophic thermal stresses. However, it is possible to cool the glass relatively quickly from the lower end of the annealing range.

The structural features are reflected in the characteristic properties of inorganic glasses and bring about a broad overall similarity in behavior as summarized below. Values for the physical properties of the glasses listed in Table 1 are given in Table 2.

### 3.26.3.2 The Nature of the Glass Surface

It is widely accepted that the composition of the surface of a glass is different from that of its interior.

Alkali loss during forming, grinding, polishing, and surface treatments affects the structure of the surface, but a more basic difference is brought about by the effect of the unbalanced force fields at the surface on the ions within the glass.

Glass is composed of glass-forming cations (e.g.,  $B^{3+}$ ,  $Si^{4+}$ ,  $P^{5+}$ ) surrounded by polyhedra of oxygen ions in the form of triangles or tetrahedra. Two types of oxygen ions exist: bridging and nonbridging. The former, bonded to two network-forming ions, link polyhedra, and the latter, bonded to one network-forming ion only, carry an excess negative charge. To compensate for this, charged cations of low positive charge and large size (e.g.,  $Na^+$ ,  $K^+$ ,  $Ca^{2+}$ ) are located within the structure. Silicon may be substituted by other cations of large positive charge and small size; these are collectively known as network formers.

The difference in size and field strength between ions is reflected in the polarizabilities of each ion and their final position relative to the glass surface. Since the force field is unbalanced, ions of low polarizability will remain near the surface and ions of higher polarizability will move towards the interior of the glass. A strong feature of chemical reactions associated with the surface is the need to screen adequately (and not merely to neutralize) those cations that have strong electric fields. If the unbalanced field is removed by the presence of materials, liquid, adsorbed vapor, or solid in contact with the glass, there is sufficient mobility within the glass surface zone for it to revert to a more normal structure by the diffusion of ions towards the surface.

### 3.26.3.3 Thermal Expansion

Glasses having coefficients of linear thermal expansion of from  $5 \times 10^{-7}$  to over  $10^{-5} K^{-1}$  are available. However, high-expansion glass compositions do not

**Table 2** Physical property data for the glasses of compositions listed in Table 1<sup>1</sup>

	1	2	3	4	5	6	7	8	9	10	11
Density ( $mg\ m^{-3}$ )	2.2	2.49	2.46	2.49	2.42	2.24	3.03	2.62	2.58	2.57	2.54
Strain point ( $^{\circ}C$ )	987	520	490	495	518	515	—	448	616	—	—
Annealing point ( $^{\circ}C$ )	1082	545	540	524	565	565	—	470	657	—	—
Littleton softening point ( $^{\circ}C$ )	1594	735	720	705	780	820	631	670	843	688	710
Resistivity ( $\Omega\ m$ at $20\ ^{\circ}C$ )	$10^{15}$	$10^{13}$	—	$10^{15}$	$10^{15}$	—	—	—	—	—	—
Dielectric constant (at 1 kHz)	3.8	7.4	—	7.8	—	5.1	7	—	—	—	—
$\tan \delta$ (at 1 MHz)	small	—	—	0.008	—	0.02	0.001	—	—	—	—
Refractive index	1.48	1.52	—	1.51	1.49	1.47	1.56	1.51	1.55	—	—
Thermal conductivity ( $W\ m^{-2}\ K^{-1}$ )	1.38	1.05	1.02	1.04	1.04	1.13	0.84	1.01	0.97	—	—
Thermal expansion ( $\times 10^7\ K^{-1}$ )	5.4	79.3	87	85.5	50	33	84	85.5	49	83	—
Specific heat ( $J\ kg^{-1}$ )	775	987	821	833	819	794	—	733	796	—	—
Young's modulus (GPa)	7.3	7.4	—	—	—	6.3	5.75	7.4	7.2	—	—



generally have long-term chemical durability. Glass-ceramic materials, on the other hand, are remarkable for the very wide range of thermal expansion coefficients that can be obtained. At one extreme, materials having negative coefficients are available, while for other compositions very high positive coefficients can be obtained. Between these two extremes, there exist glass-ceramics having thermal expansion coefficients practically equal to zero and others whose expansion coefficients are similar to those of ordinary glasses or ceramics or to those of certain metals and alloys and, hence, allow thermal compatibility. This range of expansion coefficients is allied with good chemical durability.

### **3.26.4 Mechanical Properties**

Characteristically, glasses are susceptible to brittle fracture under tension but tend to have significantly higher compressive strengths. The ionic and directional nature of the bonds and the localization of bonding electrons to pairs of atoms preclude bond exchange. This, coupled with the random nature of the atomic lattice, that is, the absence of close-packed planes, makes gross slip or plastic flow extremely difficult.

#### **3.26.4.1 Strength**

If flaws and stress concentrators, which emphasize the brittle nature of glass, can be avoided, then a glass article behaves as though its strength is governed by the high interatomic bond strength. Glasses are therefore inherently very strong materials, theoretically capable of exhibiting a tensile strength of about 7 GPa. In practice however, surface flaws act as stress concentrators under tensile loading, and commercial glasses in bulk show a mean strength in tension of only about 40 MPa. The statistical variation of strength about this figure makes it desirable to allow a substantial safety margin and to design using a figure of about 7 MPa.<sup>4</sup>

The strength of glass can be increased to about 200 MPa by commercial (generally thermal) toughening processes. The use of such glasses is not possible, however, at elevated temperatures since resoftening will occur. Undamaged commercial glass fibers display strengths of about 2 GPa, which is dependent upon surface protection, given usually by organic coatings. Removal of the coating results in a marked decrease in strength due to the introduction of small surface flaws.

#### **3.26.4.2 Elastic Modulus**

Up to the fracture stress, glass behaves, for most practical purposes, as an elastic solid at ordinary temperatures. Most silicate-based commercial glasses display an elastic modulus of about 70 GPa, that is, about one-third the value for steel. If stress is applied at temperatures near the annealing range, then delayed elastic effects will be observed and viscous flow may lead to permanent deformation.

The brittle nature of glasses at normal temperatures makes them inappropriate for use in locations where severe impacts are likely to be encountered. In the design of pipelines or other equipment, it is possible to use normal engineering assembly techniques provided that suitable gaskets or cushioning are provided at joints and supports and that care is taken in tightening bolts to avoid unequal or localized stresses.

#### **3.26.4.3 Thermal Shock Resistance**

The ability of a glass article to withstand sudden changes of temperature depends primarily on its thermal expansion coefficient, its thickness, and its design. For articles of identical shape, a low-expansion glass (such as a commercial borosilicate) will withstand appreciably greater temperature shocks than will glass of a higher expansion coefficient. Thermal shock-resistance testing is usually carried out by transferring the articles from a hot environment to a cold vessel containing water at a predetermined temperature.<sup>5</sup> In general, transitions from a hot to a cold environment are more likely to produce failure than those in the opposite direction since they tend to induce tensile stresses at the surface.

### **3.26.5 Chemical Properties**

#### **3.26.5.1 Degradation**

Technical glasses are now used so extensively and in such widely varying circumstances that it is necessary to be as accurate as possible in describing their chemical properties. The deterioration of individual glasses is dependent on composition, manufacture, and use and, unless the degradation processes are accelerated, may be observable only after very long periods of time. A typical figure for the corrosion rate of an ordinary soda-lime-silica glass would be less than  $10 \mu\text{m year}^{-1}$ . The effect is accelerated when the exposure takes place at higher temperatures, for example, in boiling

**Table 3** The corrosion resistance for commercial glasses listed in Table 1

	Glass				
	1	2	3	6	7
Water	A	B	B	A-B	B-C
Acid	A	B	B	A-B	B-C
Weathering	A	C	C	A-B	B-C

A, essentially resistant; B, possibility of degradation; C, certain degradation.<sup>1</sup>

water or in an autoclave. Table 3 compares the corrosion resistance of some commercial glasses.

One of the most commonly used measures of durability, that is, loss of sodium from the glass, is important to the pharmaceutical and chemical industries, but other changes such as loss of surface quality, are of equal importance for optical and window glasses. The properties of a wide range of technical glasses are well catalogued,<sup>5-7</sup> but the data are often inadequate when considering a particular application and where possible nonstandard 'whole article' tests are advisable.

### 3.26.5.2 Glass Durability Tests

In selecting a glass for chemical durability, regard must be paid to the temperature and concentration of the corrosive agent, length of exposure, ratio of reagent volume to surface exposed, and mechanical operating conditions. Guidelines on the durability of many commercial glasses in some attacking media are available from standard durability tests. There are two types of durability tests for glassware: 'grain' or 'powder' tests and 'whole article' tests.

#### 3.26.5.2.1 Grain tests

In these tests, samples of glass crushed and graded to a specified sieve size are exposed under standard conditions of time and temperature to the attacking medium. The temperatures commonly used are 98 °C (water bath) and 121 °C (autoclave) and the attacking media are water, acid, and alkali. The amounts of a particular glass constituent (usually soda or total alkali) removed from a standard weight in a given time are determined. Various standard test methods have been established.<sup>8-11</sup> However, variability is found between different laboratories, and using a particular grain test has shown considerable divergence, and it appears that

to obtain consistent results very close adherence to the details of the standard procedures is necessary.<sup>12</sup>

#### 3.26.5.2.2 Whole-article tests

Grain tests are open to the criticism that they do not necessarily reflect the behavior of the finished product in service, and hence various tests on complete glass articles have been developed. These are normally carried out under accelerated conditions, and on completion various relevant factors are determined, such as loss in weight, alkali or other constituents extracted, the weight of soluble and insoluble materials in the extract, and an assessment of surface condition. Analytical microscopy and other surface analytical tools can be of great assistance in determining mechanisms.

Whole-article tests are particularly useful in the evaluation of window and optical glasses. Various tests have been proposed for window glass, but no standards exist. The usual procedure is to subject the glass to an accelerated humidity/temperature weathering cycle and to assess the surface conditions after a given period of treatment. The degree of haze formation has been suggested as a method of measuring surface damage, but generally visual comparison with a standard is used. Figure 1 illustrates the application of such a test to various optical glasses.

Many optical glasses are much less resistant to attack than are container and window glasses, and less severe tests are necessary. A commonly used method is to immerse specimens in either dilute nitric acid or standard acetate solution (pH 4.6) for specified periods at room temperature, and then to examine the surfaces.

Glass fibers present a particular problem in that the resistance of the base glass is unlikely to be representative of the performance of the final product. Generally, empirical methods are used to test the glass fibers *in situ* in a composite material: for example, the fibers are made up into rods or rings with the appropriate partly polymerized plastic; the composites are then cured under specified conditions; and the breaking strength is determined after various exposures to water or steam.

## 3.26.6 Mechanisms of Glass Corrosion

### 3.26.6.1 General Properties

Glass surfaces may react with corrosive agents in one or a combination of the following ways:

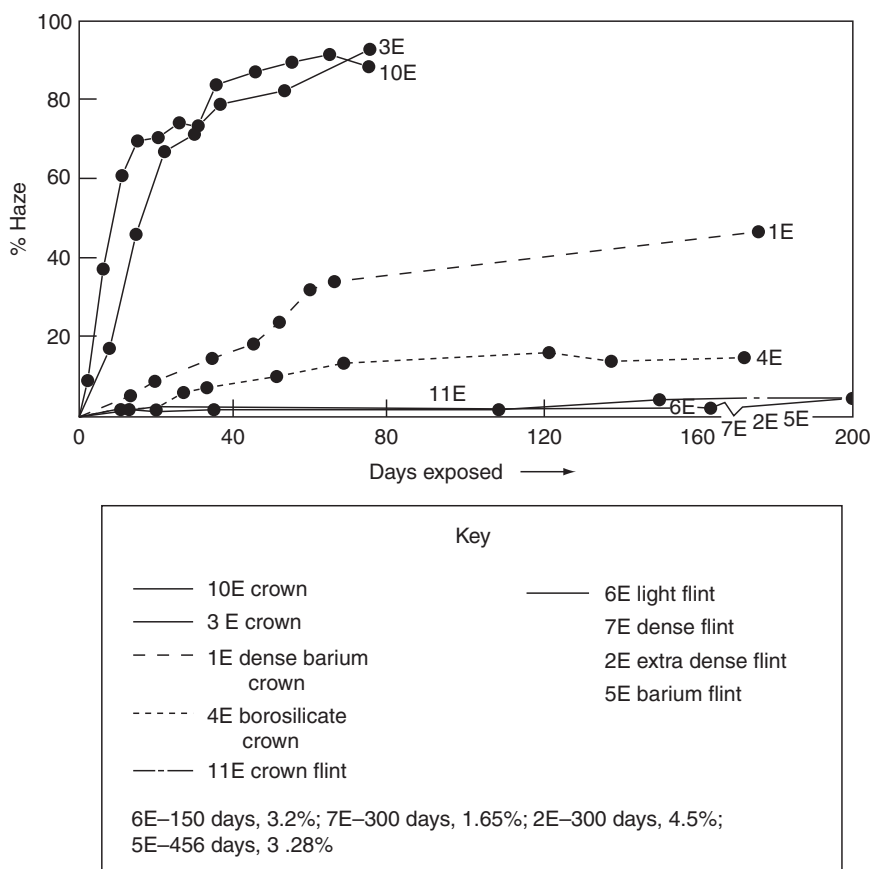


**Figure 1** Comparison of optical glasses after exposure to an alkaline solution. Simpson, H. E. *J. Soc. Glass Technol.* **1953**, 37, 249; *J. Am. Ceram. Soc.* **1953**, 36, 143-146.<sup>13</sup>

- by forming new compounds on the surface;
- by selectively losing material from a leached porous layer;
- by continuous dissolution leaving a freshly exposed surface.

Important effects on glass durability in aqueous conditions, due to the interrelation between glass composition and environmental pH, have been reviewed by Doremus<sup>14</sup> and Adams.<sup>15</sup> To some extent, durability can be predicted on thermodynamic grounds.<sup>16,17</sup> In general, additions of CaO (calcia) and Al<sub>2</sub>O<sub>3</sub> (alumina) to a basic alkali silicate glass confer water resistance; additions of zirconium, lanthanum, tin, and chromium oxides improve alkali resistance; and reducing the levels of boron, aluminum, or lead oxides, in glasses where they are present, improves acid resistance. Predictions of the effects of added oxides on glass durability should, however, be treated with caution. Structural factors, such as

occurrence of phase separation, coordination state, mixed alkali effect, and/or kinetic effects resulting from the presence or absence of insoluble reaction product layers on the glass surface, can influence durability to a significant extent.

More generally, Valez *et al.*<sup>18</sup> have reviewed the corrosion behavior of silicate and borate glasses in contact with alkali metals and molten salts, as well as in aqueous conditions.

Another important aspect of glass corrosion behavior that should be emphasized is the effect of applied stresses. Glass is subject to stress-enhanced corrosion, which is often described as static fatigue. Under a continuously applied stress, and in the presence of normal environmental moisture (or other more aggressive corrosion conditions), cracks may grow from flaws on the glass surface and this can lead to delayed failure at stresses below the strength level that is measured in a short-term loading test.<sup>17,19</sup> As a consequence, common silicate glasses are usually expected to have a

load-bearing capacity at one-quarter to one-third the short-term strength when continuously loaded over some 50 years in the normal atmosphere.

### 3.26.6.2 Corrosion Mechanisms

There is no serious challenge to the view that the alkali or alkaline-earth ions are removed from glass in water by an ion exchange process in which  $H^+$  ions diffuse into the glass to preserve the electrical neutrality of the system. However, only under certain circumstances can the rate-controlling process be directly related to the diffusion of sodium in the glass. Most glass/corrosive agent systems are treated as unique cases, since in addition to the concentration of the attacking agent, temperature, rate of flow, and reaction time contribute to what is observed. General chemical principles of electrophilic and nucleophilic types of general attack can be applied to glasses.<sup>20</sup> The first is considered as an attack on nonbridging oxygen atoms by reagents with an electron deficiency and the second as an attack on bridging oxygens by reagents with an electron excess.

For the most common series of corrosive agents – water, steam, acids, alkalis, and salts – the hydrolytic processes peculiar to each determine the mechanism of attack. Thus, under the right circumstances, hydrolytic attack on bridging oxygen atoms can occur, which is an irreversible reaction resulting in permanent damage to the glass network. The corrosion process is modified by the physical state of the surface. Grinding and polishing processes, in particular, leave the structure with a degree of roughness and residual stress; all can contribute to accelerated corrosion.

### 3.26.6.3 The Action of Water and Acids

During attack, the alkali and alkaline-earth network-modifying ions are exchanged by  $H^+$  or  $H_3O^+$  from an acid solution. In some glasses the exchange process can go to completion causing only a small degree of network damage. In water, the exchange process proceeds at a very much slower rate relative to the acid conditions, and some attack of the network is possible as a result of the presence of alkali ions from the glass moving into solution. This is most pronounced when glass is attacked by steam at high temperature and where there is no mechanism for the removal of alkali from the hydrolyzed zone. Acid solutions mitigate this form of attack by neutralizing the alkali as it is formed.

The attack of most glasses in water and acid is diffusion controlled, and the thickness of the porous

layer formed on the glass surface consequently depends on the square root of the time. There is ample evidence that the diffusion of alkali ions and basic oxides is thermally activated, suggesting that diffusion occurs either through small pores or through a compact body. The reacted zone is porous and can be further modified by attack and dissolution, if alkali is still present, or by further polymerization. Consolidation of the structure generally requires thermal treatment.

### 3.26.6.4 Attack by Alkali Solution, Hydrofluoric Acid, and Phosphoric Acid

A common feature of these corrosive agents is their ability to disrupt the network. This process is not encumbered by the formation of porous layers, and the amount of leached matter is linearly dependent on time. Consequently, the extent of attack by strong alkali is usually far greater than either acid or water attack. Both  $HF$  and  $H_3PO_4$  form compounds of silicon as a result of attack on the network: silicon fluoride from hydrofluoric acid and silicic phosphate from phosphoric acid.

### 3.26.6.5 Chemical Attack by Other Agents

If the hydrogen ion concentration is sufficiently high, the glass loses a substantial amount of weight by leaching, but these reactions are dependent on the nature of the ions in solution. Certain salts, especially those of  $Zn$ ,  $Al$ , and  $Be$ , if present as trace amounts, can have a beneficial effect by poisoning the process and limiting the occurrence of leaching.

### 3.26.6.6 Cleaning of Glass

There is no universally ideal technique for either cleaning glass or avoiding contamination of the surface. In the most severe circumstances of corrosion, the only methods capable of restoring an acceptable surface finish consist of grinding and polishing or removing the contamination and corroded layers by strong etching agents such as hydrofluoric acid. Less severe conditions may respond to treatment by various detergent solutions or organic solvents, these being considerably aided by ultrasonic vibration. Manual washing or ultrasonic cleaning can be used to remove massive dirt accumulations. Vapor solvent degreasing processes, for example using isopropyl alcohol, has minimal corrosive action on the glass.

To restore old stocks of corroded glass, treatment in hot 1% sodium hydroxide solution followed by

rinsing in 5% hydrochloric acid and a final rinse in pure water at room temperature is recommended.<sup>21</sup>

### 3.26.6.7 Applications

Over recent years, a number of new applications of glasses have grown out of increased understanding and control of glass corrosion behavior. Conventional silicate and borosilicate glasses are subject to severe corrosive attack in highly alkaline solutions (pH 12–13.5), such as those found in Portland cement, and there is rapid and drastic loss of strength in fibers formed from soda or borosilicate compositions. To counter this, alkali-resistant glass fibers have been developed from silicate glass compositions and containing about 16 wt% of zirconia<sup>22,23</sup> and these have formed the basis for development of a range of glass-fiber reinforced cement (GRC) materials, analogous to glass-fiber reinforced plastics (GRP). In the GRP field, it has been shown that E-glass borosilicate fibers are prone to strength loss and stress corrosion in acidic environments<sup>24,25</sup> – this in turn led to the development of an acid-resistant version of E-glass for use in such conditions.

## 3.26.7 Vitreous Silica

Vitreous silica, also referred to as quartz glass, fused quartz, or fused silica, is a material of considerable importance, possessing a unique combination of high softening temperature, excellent resistance to chemical attack, and high transparency. Its general, physical, and mechanical characteristics are common to all glasses, the difference being that the high purity (>98.7% SiO<sub>2</sub>) maximizes the durability, fusion temperature, and volume stability. The general superiority of the properties of fused silica over conventional glasses is well illustrated in [Table 1](#). It has excellent high temperature properties in excess of 1000 °C, high resistivity, high chemical stability, and excellent thermal shock resistance due to its low coefficient of expansion. However, the high softening point makes it much more difficult to fabricate than conventional glasses.

### 3.26.7.1 Manufacturing

The raw materials for the production of vitreous silica are either high-purity rock crystal from which the transparent form is produced, or vein quartz (high-grade glass sand) from which impurities have

been removed by acid leaching. The persistence of liquid and gaseous inclusions is partly responsible for the translucency of cheaper forms of vitreous silica. Ground quartz is melted at around 2000 °C by induction heating in a graphite crucible. Even at this temperature, the melt viscosity is so high (10<sup>5</sup>–10<sup>6</sup> Pa s) that trapped gas bubbles do not float to the melt surface and can only be removed by vacuum treatment. At high temperature, the SiO<sub>2</sub> partly dissociates to the monoxide SiO, which is volatile.

Vitreous silica produced by this route contains small amounts of impurities such as Fe, Cr, Al, and Ca. These may be removed by reaction to form volatile metal chlorides, whereupon the remaining SiCl<sub>4</sub> can be hydrolyzed in a flame to produce fine molten droplets of SiO<sub>2</sub> which then deposit on a cold base; impurity levels below 10<sup>−7</sup>% can be reached in this process and are essential in applications such as optical fibers.

### 3.26.7.2 Structure and Physical Properties

#### 3.26.7.2.1 Polymorphism of silica

Although vitreous silica is nominally a homogeneous isotropic amorphous material, and should normally remain so during its service life, it is in fact in a metastable condition. The tendency to revert to crystalline forms with attendant deterioration in mechanical durability places severe limitations on the range of applications. [Figure 2](#) illustrates the polymorphic forms of silica, and the dimensional changes accompanying each transition.

Changes from one polymorphic form of crystalline SiO<sub>2</sub> to another, as from tridymite to quartz at temperatures below 870 °C and to cristoballite above 1470 °C, involve the breaking of Si–O bonds. High energies are required for these ‘reconstructive’ changes, and changes from one form to another require very long periods for completion. On the other hand, inversions from high- to low-temperature forms of quartz or cristoballite involve only changes in the angles between adjoining SiO<sub>4</sub> tetrahedra, and these ‘displacive’ transformations are accomplished almost instantaneously. The accompanying volume changes lead to disruption of ware containing significant amounts of quartz or cristoballite.

#### 3.26.7.2.2 Thermal expansion

The coefficient of thermal expansion of vitreous silica is very small (5.4×10<sup>−7</sup> over the range 0–1000 °C), about one-sixth that of porcelain. It is thus highly resistant to thermal shock.

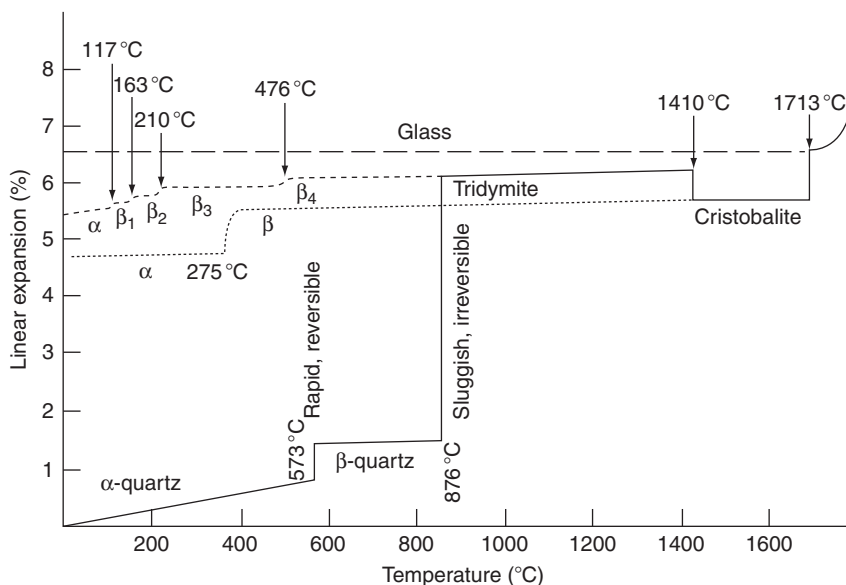


**Figure 2** Polymorphism and dimensional changes in silica as a function of temperature.

### 3.26.7.2.3 Heat resistance

Being a glass, vitreous silica softens progressively as it approaches its melting point of 1713 °C. The maximum recommended working temperature is 1050 °C in an oxidizing atmosphere, though it may be taken to 1350 °C for short periods. Surface devitrification to cristoballite occurs above this temperature. This causes some loss of transparency, but chemical and mechanical durability are unaffected provided the temperature does not fall below the  $\beta$ - $\alpha$  inversion temperature (275 °C), which would lead to the initiation of cracks. It should be noted that devitrification is accelerated by traces of alkali-metal compounds, particularly potassium and lithium salts, sodium tungstate, and ammonium fluoride. Devitrification is also enhanced by water vapor and oxygen, but inhibited by neutral or reducing atmospheres.

### 3.26.7.2.4 Thermal conductivity

The thermal conductivity of fused silica is low ( $1.38 \text{ W m}^{-2} \text{ K}^{-1}$ ). The transparent form passes infrared radiation with little loss up to wavelengths of 3.5  $\mu\text{m}$ .

### 3.26.7.2.5 Electrical characteristics

The insulating properties of glass are excellent. At ordinary temperatures, the resistivity of the translucent form is  $10^{15} \Omega \text{ m}$ , and it is capable of withstanding high-frequency discharges at high voltages. See also [Table 1](#) for data on other physical properties and for comparison with other glasses.

### 3.26.7.3 Resistance to Chemical Attack

Most glasses suffer chemical attack and deterioration due to ion exchange of sodium ions to form a highly alkaline solution, which subsequently attacks the network. As network-modifying oxides are absent from fused silica, this mode of attack does not occur. Hence fused silica is highly resistant to most aqueous solutions, even aqua regia at elevated temperatures having no effect. Reagents that attack the network silica directly, such as strong alkalis and fluorides, cause serious damage and are therefore to be avoided.

#### 3.26.7.3.1 Boiling water and steam

There is limited reaction with water and steam at moderate temperatures and pressures. However, silica is slightly soluble up to around 6 ppm. However, at temperatures in the range 400–500 °C and pressures of the order of 3.5 MPa the solubility rises to 0.14% for the translucent form and 0.035% for the transparent.

#### 3.26.7.3.2 Fluorine, hydrofluoric acid, and alkaline solutions

Silica is susceptible to attack by all three reagents, the rate of corrosion increasing with temperature and concentration. Although 5% caustic soda solution can be contained in fused silica at room temperature, attack becomes significant at pH values greater than 9, as shown in [Figure 3](#).



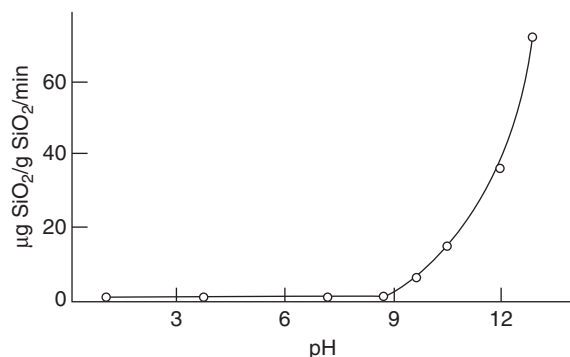


**Figure 3** Effect of pH on the rate of silica extraction from vitreous silica powder at 80 °C. Reproduced from El-Shamy, T. M. M.; Douglas, R. W. *J. Am. Ceram. Soc.* **1967**, 50, 1–7.

The essential step in the dissolution reaction of silica is the breaking of a siloxane bond Si–O–Si. This bond, although strong, is polar, and may be represented as (Si<sup>δ+</sup>–O<sup>δ–</sup>). The excess positive charge associated with the silicon atom makes it susceptible to attack by nucleophilic reagents such as the hydroxide ion, which attaches itself to the silicon, rupturing the network at that point. The attack by HF on silica is thought to proceed by a similar mechanism in which there is simultaneous nucleophilic and electrophilic attack on the network silicon and oxygen atoms, respectively. It should be pointed out the H<sup>+</sup> ion cannot effect disruption of the siloxane bond without the simultaneous action of the F<sup>–</sup> ion. Consequently, sulfuric and nitric acids do not initiate attack even at temperatures up to 1000 °C.

Sodium fluoride also attacks silica, as do sodium metaphosphate and sodium polyphosphate, and to a lesser extent sodium carbonate and sodium cyanide. Attack is particularly vigorous for fused alkalis, alkali halides, and phosphates.

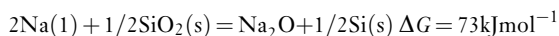
### 3.26.7.3.3 Basic oxides

As an acidic oxide, SiO<sub>2</sub> is resistant to attack by other acidic oxides, but has a tendency towards fluxing by basic oxides. An indication of the likelihood of reaction can be obtained by reference to the appropriate binary phase equilibrium diagram. The lowest temperature for liquid formation in silica oxide binary systems is shown below:

Oxide	Al <sub>2</sub> O <sub>3</sub>	BeO	CaO	MgO	ThO <sub>2</sub>	TiO <sub>2</sub>	ZrO <sub>2</sub>
Eutectic (°C)	1546	1670	1436	1543	1700	1540	1675

### 3.26.7.3.4 Metals

Silica is decomposed only by those metals that have a high thermodynamic affinity for oxygen. On this basis, molten sodium should be compatible with silica:



Although the equilibrium levels of the reaction products are very small, both can dissolve in liquid sodium; also sodium oxide can form compounds with silica. As a consequence, the reaction moves to the right, leading to further reduction of silica. Nevertheless, vitreous silica crucibles have been used successfully for containing molten antimony (850 °C), copper (1210 °C), gallium (1100 °C), germanium (1100 °C), lead (500 °C), and tin (900 °C).

In accordance with the free energy predictions, silica is readily attacked by molten aluminum, lithium, magnesium, and calcium.

### 3.26.7.4 Applications of Vitreous Silica

The high thermal and electrical resistance of vitreous silica, and its imperviousness to chemical attack, make it suitable for a wide range of applications. These include chemical and physical laboratory apparatus, tubes and muffles for gas and electric furnaces (including vacuum furnaces), pyrometers, insulators for high-frequency and high-tension electrical work, mercury-vapor and hydrogen-discharge lamps, high-vacuum apparatus, plants (complete or partial) for chemical and related industries, equipment for the manufacture of pure chemicals, tubes, chimneys and radiants for the gas- and electric-heating industries, component material in refractory and ceramic mixtures, etc.

It is used for pipes to carry hot gases and acids and in acid distillation units, condensing coils, S-bend coolers, hydrochloric acid cooling and absorption systems, nitrating pots, and cascade basin concentrators for sulfuric acid. The resistance of vitreous silica to most acids is also utilized in the manufacture of electric immersion heaters and plate heaters for acidic liquors in chemical processes and electroplating baths. Vitreous silica wool is used for filtration of acidic liquids and filtering hot gases. The resistance of vitreous silica to water and steam at normal temperatures and pressures makes it applicable in the production of pure water for the manufacture of highly purified chemicals. Because of its thermal properties, it is used for the construction of muffles of oval cross section used for the bright-annealing of metal strip and wires. Special products include transparent vitreosil components, which are ideal

**Table 4** Property data for some glass-ceramics

	A	B	C	D	E
Compositional type	Lithium aluminosilicate	Lithium aluminosilicate	Potassium magnesiasilicate	Lithium aluminosilicate	Lithium aluminosilicate
Density ( $\text{mg m}^{-3}$ )	2.55	2.5	2.53	2.5	2.5
Thermal expansion coefficient ( $\times 10^{-7} \text{ K}^{-1}$ )	6	12.7	97	4.2	-3
Transition point ( $^{\circ}\text{C}$ )	820	—	—	—	—
Softening point ( $^{\circ}\text{C}$ )	950	—	—	1250	—
Service limit ( $^{\circ}\text{C}$ )	800	1000	1500	—	810
Bend strength (MPa)	120	180	88	110	130

A: 'Heatron-T', B: 'Neoceram-15', C: 'Corning 9650' (machinable), D: 'Pyroceram 9608', E: 'Hercuvit'.

for continuous measurement in corrosive atmospheres, and quick-immersion thermocouple protection sheaths for rapid temperature measurement.

### 3.26.8 Glass Ceramics

#### 3.26.8.1 Definition and Properties

Glass-ceramics are a family of materials that are polycrystalline in nature and are formed from the liquid or glassy state. A glass-ceramic article is made by the heat treatment of a vitreous body in two stages:

1. *Nucleation*: The glass is held at a temperature below its softening point for a period of minutes or hours to allow nuclei to develop.
2. *Crystallization*: The temperature of the nucleated glass is raised to just below the softening point when crystals form and grow around the nuclei.

Ideally the product is a fine-grained ceramic containing interlocking crystal grains of sizes ranging from less than 10 nm in transparent glass-ceramics to several micrometers, with a residual, usually small, glass content. The behavior of the material is largely determined by the choice of the crystalline phase; by suitable choice, a range of useful properties has been obtained.

As a class of materials, glass-ceramics have the following general characteristics:

1. Impervious, with moderate densities similar to those of glasses.
2. Improved fracture toughness compared with glass or ceramic materials.
3. Relatively high tensile strengths (a consequence of item 2).
4. Stiff, elastic (Hookean) limited-to-zero plasticity.
5. Considerable hardness and resistance to abrasion.

6. Chemical stability and resistance to corrosion.
7. Resistance to medium-high temperatures (higher temperatures than most glasses but lower than the refractory oxides) and low thermal conductivity.
8. Resistance to the passage of electrical current.

Special characteristics can be developed in individual materials depending on the cations present and their arrangement relative to each other and to the oxygen anions. The most important of these characteristics is low, medium, or high reversible thermal expansion. The properties of some commercially available glass-ceramics are summarized in [Table 4](#).

#### 3.26.8.2 Chemical Durability of Glass-Ceramics

While the chemical behavior of a glass-ceramic is strongly influenced by the chemical composition of the parent glass, several different crystalline compounds together with a residual glass phase are likely to be present. The relative resistances of these phases to attack by water or other reagents will determine the chemical stability. In general, a glass that exhibits poor chemical stability is unlikely to give rise to a glass-ceramic of high stability. To this extent, the factors that govern the stability of glass-ceramics can be equated to those that determine the chemical stability of glasses.

In most cases, glass-ceramics possess good chemical stability and certainly compare favorably in this respect with other ceramic materials. [Table 5](#) summarizes manufacturers' data for chemical attack on the materials listed in [Table 4](#).

Certain types of glass-ceramic have good resistance to attack by corrosive chemical reagents. Low-expansion glass-ceramics derived from lithium aluminosilicate glasses are only slightly inferior to

**Table 5** Chemical resistance data for the glass-ceramics listed in Table 4

	A	B	C	D	E
<i>Powder method</i>					
Water solubility (mg Na <sub>2</sub> O/mg sample)	0.29	0.8	128	0.1–0.3	0.12
Acid solubility (mass loss in %)	0.06	3.5	5	0.02–0.1	0.2
Alkali solubility (mass loss in %)	0.13				4
<i>Surface method</i>					
H <sub>2</sub> O (90 °C, 24 h) (mass loss in mg cm <sup>-2</sup> )	0	0.13			
5% HCl (90 °C, 24 h) (mass loss in mg cm <sup>-2</sup> )	0.04				
5% NaOH (90 °C, 24 h) (mass loss in mg cm <sup>-2</sup> )					

borosilicate chemically resistant glass with regard to attack by strong acids and are somewhat more resistant to attack by alkaline solutions. Materials derived from magnesium aluminosilicate glass compositions are slightly less resistant to attack by strong acids and alkalis than are chemically resistant borosilicate glasses. Even at high temperatures, these types of glass-ceramic retain resistance to attack by corrosive gases. For certain applications, it is important that the glass-ceramic should be unaffected by contact with reducing gases at high temperatures. In such cases, the composition must not include any oxides such as lead, which are easily reduced to the metal.

## References

1. Oliver, S.; Proctor, B. A.; May, C. A. In *Shreir's Corrosion*, 3rd ed.; Butterworth-Heinemann, 1994; Chapter 18.3.
2. Cole, H. *Viscosity-Temperature Relations in Glass: 1. Viscosity in Glass*; International Commission on Glass, 1970.
3. ASTM Method C338-93: Standard Method of Test for Softening Point of Glass; American Society for Testing and Materials, 2008.
4. BS 2598-4:1980, ISO 4704:1977 – Glass plant, pipeline and fittings: Specification for glass plant components.

5. BS 3517:1991, ISO 718:1990 – Methods for thermal shock tests on laboratory glassware.
6. Volf, M. B. *Technical Glasses*; Pitman: London, 1961.
7. Wessel, H. *Silikattechnik* **1967**, 18, 205–211; **1968**, 19, 6–10.
8. ASTM Method C 225-68: Standard Methods of Test for Resistance of Glass Containers to Chemical Attack.
9. DIN 12116:2001: Testing of glass – Resistance to attack by a boiling aqueous solution of hydrochloric acid – Method of test and classification; DIN EN 12122:2005: Chemicals used for treatment of water intended for human consumption – Ammonia solution.
10. BS 3473 Parts 1–5: Chemical resistance of glass used in the production of laboratory glassware, 1991.
11. ISO 695:1991: Glass – Resistance to attack by a boiling aqueous solution of mixed alkali – Method of test and classification; ISO 719:1985: Glass – hydrolytic resistance of glass grains at 98 °C – Method of test and classification.
12. Wiegel, E. *Glastechnische Berichte* **1956**, 29, 137–144.
13. Simpson, H. E. *J. Soc. Glass Technol.* **1953**, 37, 249; *J. Am. Ceram. Soc.* **1953**, 36, 143–146.
14. Doremus, R. H. *Treatise Mater. Sci. Technol.* **1979**, 17, 41–67.
15. Adams, P. B. *J. Non-Cryst. Solids* **1984**, 67, 193–205.
16. Paul, A. *J. Mater. Sci.* **1977**, 12, 2246–2268.
17. Newton, R. G.; Paul, A. *Glass Technol.* **1980**, 21(6), 307–309.
18. Velez, M. H.; Uhlmann, D. R.; Tuller, H. L. *Rev. Latinoamericana Metall. Mater.* **1982**, 11(1).
19. Kurkjian, C. R. Ed. *Strength of Inorganic Glass*; NATO Conference Series VI, *Materials Science*, Vol. 11; Plenum Press: New York, 1985.
20. Budd, S. M. *Phys. Chem. Glasses* **1961**, 2, 111–114; Budd, S. M.; Frackiewicz, J. *Phys. Chem. Glasses* **1961**, 2, 115–118.
21. Tichane, R. M. *Am. Ceram. Soc. Bull.* **1963**, 42, 441.
22. Majumdar, A. J.; Ryder, J. F. *Glass Technol.* **1968**, 9(3), 78–84.
23. Proctor, B. A.; Yale, B. *Philos. Trans. Roy. Soc. London A* **1980**, 294, 427–436.
24. Metcalfe, A. G.; Gulden Mary, E.; Schmitz, G. K. *Glass Technol* **1971**, 12, 15–23.
25. Torp, S.; Arvesen, R. In 34th Annual Technical Conference, Reinforced Plastics/Composites Institute, SPI, 1979; Session 13-D.

## Further Reading

- Clark, D. E.; Zaitos, B. K. *Corrosion of Glass, Ceramics and Ceramic Superconductors*; William Andrew Publishing/Noyes, 1992.
- Doremus, R. H. *Glass Science*, 2nd ed., Wiley, 1994.
- Lewis, M. H. *Glasses and Glass-Ceramics*; Chapman and Hall, 1989.
- Shelby, J. H. *Introduction to Glass Science and Technology*, 2nd ed.; Royal Society of Chemistry, 2005.
- Varshneya, A. K. *Fundamentals of Inorganic Glasses*; Academic Press, 1993.

## Relevant Websites

- [www.sgt.org](http://www.sgt.org) – Society of Glass Technology
- [www.ceramics.org](http://www.ceramics.org) – Glass and Optical Materials Division of The American Ceramic Society

## 3.27 Degradation of Glass Linings and Coatings

**G. Schäfer**

Pfaudler Werke GmbH, Pfaudlerstrasse, D-68723 Schwetzingen, Germany

© 2010 Elsevier B.V. All rights reserved.

3.27.1	Introduction	2320
3.27.2	Manufacturing of Glass-Lined Steel Equipment	2320
3.27.2.1	Glass Formulations	2320
3.27.2.2	Glass Preparation	2321
3.27.2.3	Metal Preparation	2322
3.27.2.4	Certifications	2322
3.27.2.5	Lining Process	2323
3.27.3	Properties of Glass on Steel	2323
3.27.3.1	Mechanical Properties	2323
3.27.3.2	Thermal Properties	2323
3.27.3.3	Chemical Properties	2324
3.27.3.4	Testing Methods	2324
3.27.3.5	Surface Properties	2325
3.27.3.6	Enamel Behavior in Service	2325
3.27.3.7	General Aspects of Glass Enamel Corrosion	2325
3.27.3.8	Attack by Water	2325
3.27.3.9	Attack by Alkaline Solutions	2326
3.27.3.10	Attack by Acid	2326
3.27.3.10.1	Mineral acids	2326
3.27.3.10.2	Organic acids	2326
3.27.3.11	Further Possibilities of Corrosive Attack on Glass	2326
3.27.3.11.1	Attack by complex formation	2326
3.27.3.11.2	Attack by fluorides	2326
3.27.3.12	Inhibition of Corrosion Attack	2327
3.27.3.13	Effect of Leaching – Temperature Dependence	2327
3.27.4	Damage Monitoring and Analysis	2327
3.27.4.1	<i>In Situ</i> Sensing Technology	2327
3.27.4.2	Repairs to Enamel Damage	2328
3.27.4.3	Recent Developments	2328
References		2328

### Glossary

**Adhesion (enamel-basis metal)** Amount of the force required to separate a coating from its basis metal and the area of the corresponding surface.

**Blister** Defect that appears as a localized bubble under the surface of the fired vitreous enamel.

**CIP** Cleaning in place – standard procedure in chemical plants to avoid or remove surface contaminations or settlements. Normally carried out after several production batches. pH and temperature are often just the

opposite of the regular production conditions.

**Cover coat** Vitreous enamel with specific chemical and/or esthetic properties as the final coat.

**Crazing** Defect resembling a network of fine hairline cracks in a coating.

**Fishscaling** Small half-moon shaped defects occurring in the vitreous enamelled surface. Can occur immediately on cooling or after some time has elapsed following firing. This defect originates from supersaturation of the substrate with hydrogen (acquired during firing), which explosively fractures the

enamel coating because of the pressure that has accumulated with time at the enamel–steel interface.

**Ground coat** Vitreous enamel, containing adherence-promoting agents and applied directly to the substrate to function as an intermediate bonding layer between the substrate and the cover coat.

**Scale** Oxide formed on the surface of a metal during heating at elevated temperatures.

**Spark test** High-voltage electrical test in which a spark is used to detect discontinuity in coating. Applied voltages can be as high as 20 kV.

**Technical enamel/vitreous enamel** Product formed by the heating of an inorganic mixture, to a temperature just high enough for fritting, or uniform fusion to occur. It is designed for application to metallic surfaces for protective, functional, and/or aesthetic purposes, and specifically will exhibit cubic thermal expansion of between 150 and  $450 \times 10^{-7} \text{ K}^{-1}$ , in the temperature range 20–100° C, the actual value varying specifically with the type of substrate and the field of application.

## Abbreviations

**ORP** Oxidation/reduction potential

**APAVE** Association des propriétaires d'appareils à vapeur et électriquest

**ASME** American Society of Mechanical Engineers

**ISO** International Organization for Standardization

**WWG** World Wide Glass: Pfudler trademark for a high chemically inert vitreous enamel

**PPG** Pfudler Pharma Glass: Trademark for a specially designed glass with both very high acidic and alkaline resisitivity

**PTFE** Polytetrafluorethylene

### 3.27.1 Introduction

While glass can provide many of the desirable features of an almost ideal inert material, manufacturing difficulties and safety considerations prevent its use in large-scale dimensions for chemical process equipment, and mechanical considerations would, in any

case, make it necessary to treat any such equipment with great care.

The high chemical resistance, and the nontoxic, nonflammable, nonflavorable, and thermal resistant properties of glass, can, however, be combined with the mechanical strength of metals by covering metal surfaces exposed to corrosive media with a layer of suitable glass. It thus becomes feasible to produce large-scale storage or transport tanks or to run large-scale reactors under high overpressures and extended temperature profiles. Reaction vessels, storage tanks, all-glass-lined pump smoke stacks, distillation columns, etc. can all be made of glass-lined equipment.

The principal advantage of glass linings is the increased size as well as the mechanical and thermal strength that are possible compared with all-glass equipment and the flexibility of operation with different chemicals compared with all-metal equipment. The increased heat transmission, in comparison with glass equipment, can also be an advantage.

The principal disadvantages are the loss of transparency and the potential vulnerability of the lining to mechanical damage unless sensible precautions are taken in handling, installation, and service. A variety of metals can be protected in this way, including copper, gold, stainless steel, titanium, and aluminum, but by far the most extensive use is for carbon steel based equipment.

The actual size of glass-lined equipment varies from 4 l autoclaves up to storage tanks that exceed a size of 120 000 l. The pressure regime under service can range from vacuum up to 25 bars in standard operation processes. Because of the often severe application properties run in glass-lined equipment, the sensor probes used to monitor production processes have to be made of glass or of glass-lined parts. These include acidity (pH) and potential (ORP-redox) probes, temperature sensors, conductivity measurements, and also glass-lined radar probes as well as oscillating sensing forks for fluid level measurement.

## 3.27.2 Manufacturing of Glass-Lined Steel Equipment

### 3.27.2.1 Glass Formulations

Glass frits used in vitreous enamels may contain as many as 20 components, though these may be classified in three functional categories: glass formers ( $\text{SiO}_2$  and  $\text{B}_2\text{O}_3$ , which constitute the random network of the glass), the dioxides ( $\text{ZrO}_2$ ,  $\text{CeO}_2$ , and  $\text{TiO}_2$ , which all enhance alkali resistance and are



also opacifiers), and the alkali and alkaline earths (which lower fusion temperature and increase the expansion coefficient). While high alkali (e.g., sodium, potassium) content lowers resistance to acid attack, adequate amounts are required to dissolve the oxides on the surface of the steel. Alkaline earth elements (e.g., calcium, barium), on the contrary, increases the chemical resistivity up to a certain extent. A kind of 'mixed alkali effect' additionally enhances the properties of the enamel by creating nanosized local stress inside the glass matrix thereby reducing the amount of easily dissolvable species. A relatively infusible ground-coat frit becomes supersaturated in iron oxide, which eventually crystallizes in the enamel, a defect known as 'copper heading.' Compromise is necessary, as too fluid a ground-coat results in over-rapid reaction and 'burning off,' precipitating the chipping of the enamel coating later on. Ground-coat frits contain much more boron oxide than the enamels used for the cover coat. Additions of alumina can be used to control viscosity, surface smoothness, and mechanical hardness of the glass.

Depending on the field of application, specific chemical, surface, and manufacturing properties of the enamel are required, resulting in compositions most appropriate for the area of the specific subject. This results in two different composition schemes 'A' and 'B' for technical enamels and enamels for domestic appliances respectively, which are schematically shown in the composition triangle in **Figure 1**. **Table 1** lists the oxides most often used for glass making. A high silica-to-boric oxide ratio composition is used for industrial enamels in reaction vessels and in hot water tanks where the higher firing temperature is required for improved chemical and thermal resistance.

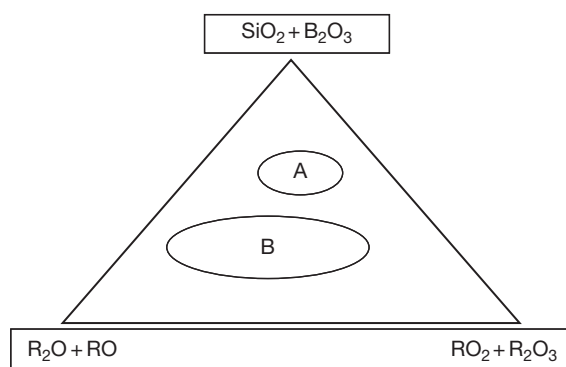


**Figure 1** Area 'A' represents the chemical composition of technical enamels, 'B' shows the much wider area of enamels used for domestic appliances, such as cookware, burner cups, fridges, ovens, bath tubs, architectural panels, etc.

### 3.27.2.2 Glass Preparation

Most of the manufacturers of glass-lined equipment have their own glass formulations, although frit manufacturers also sell appropriate frits. In most cases, the chemical constitution has not been disclosed, but the more successful types are borosilicates containing high amounts of silicate (>55 wt%), aluminum, and alkaline earth oxides than do the typical heat-resistant borosilicates.

In formulations for ground coating the steel, the glass composition contains more cobalt and manganese oxide than do ordinary glasses to enable a better adhesion to the plain steel surface and to form a chemical bond between the metal and the glass. The thermal expansion coefficients of the glasses are of the order of  $(8-9) \times 10^{-6} \text{ K}^{-1}$  for this application, but vary for other metallic substrates. The disparity between these figures and the higher expansion coefficient of the steel, which is in the order of  $14 \times 10^{-6} \text{ K}^{-1}$ , is quite deliberate and results in the development of compressive stresses in the glass layer after processing (i.e., after cooling from the sintering temperature). The stress developed gives more resistance to thermal shock or external stresses than if the expansion coefficient of the glass and steel were accurately matched.

The raw materials required to produce the particular glass composition are thoroughly mixed and melted at temperatures above  $1300^\circ\text{C}$ . The melt is normally quenched directly into cold water, but often quenching is carried out using cooled copper-based rolling blades. While the directly quenched melts produce irregularly shaped, cracked particles, the rollers form disc-like shapes.

Both types of frits are ground in the same way, either dry to form powders or wet-milled with clay and quartz added to form a viscous slip. It can be applied to steel by spraying or dipping, depending on the shape, size, and design of the structure.

**Table 1** Oxides used in glass manufacture

Glass former	Glass modifier $R_2O$	Glass modifier $RO$	Glass former $RO_2, R_2O_3$	Adhesion promoter
$SiO_2$	$Li_2O$	$MgO$	$TiO_2$	$CaF_2$
$B_2O_3$	$Na_2O$	$CaO$	$ZrO_2$	$MnO_2$
	$K_2O$	$SrO$	$SnO_2$	$CoO$
		$BaO$	$Fe_2O_3$	$NiO$
		$ZnO$	$Al_2O_3$	



### 3.27.2.3 Metal Preparation

A low-carbon ( $<0.2\%$  C) steel is usually used in the manufacturing of chemical process reactors or storage tanks, distillation columns, and the like; the steel quality is defined in several standards,<sup>1–3</sup> which include also the minimum and maximum content of other constituents than that of iron, and stipulate surface standards prior to the lining process. For other parts of the reactor, such as nozzle parts, pipes, etc., specific requirements are defined in various EN standards.<sup>4,5</sup>

These requirements contain the maximum content and diffusivity of hydrogen, amount of slacks, and define test methods for estimating the propensity for defects such as fishscaling, blistering, crazing, scaling, and poor adhesion. Cast iron is frequently used in equipment such as valve bodies and pipe unions. It should be of good quality, close-grained gray iron, free from blow-holes, cavities, and porosity. Repair of such defects by filling is not permissible in the reactor field.

Conventional welding techniques are used in production and assembly of the steel body, but special precautions must be taken to ensure that the weld metal is of a similar composition to the base metal. Moisture-free electrodes must be used.<sup>6–8</sup> According to the assigned production place, the equipment has to fulfill different local requirements, which are all specified in technical rules.<sup>2</sup>

### 3.27.2.4 Certifications

This knowledge about industrial enamel and the glass lining process is the basis of the European glass lining industry. It is used to manufacture highly sophisticated products according to ISO 9001, APAVE, ASME, Druckgeräterichtlinie, China Code, etc., which are certified regularly by external audits of the manufacturers.

The design and dimensioning of a specific vessel results from customer requests and should be in accordance to the local laws and standards. **Table 2** lists some of them.

All these regulations define how a vessel has to be designed and also how the required quality has to be controlled. They assess criteria for welding and lay down instructions that define accompanying material tests to ascertain the overall quality of a vessel. All these instructions increase the amount of testing enormously, and make the production more costly,

**Table 2** List of technical rules to define good manufacturing procedures used for manufactured products related to chemical industry

<i>AD 2000 Merkblatt HP-0</i>	<i>ATEX 94/9/EG</i>	<i>DIN EN 729-2</i>
DGRL97/23/EG	ASME R	TRD 201
SVTI	ASME NB	CODAP
UIC	ASME U	DIN 6700-2
AQSIQ	DIN ISO 9001:2000	

but ensure a safe running of a chemical plant where they are applied to. In the end, they lead to the international reputation of equipment manufactured in Europe (**Table 3**).

Typically, a completed steel assembly is examined in detail by ultrasonic and X-ray detection to check for defects likely to impair serviceability. It is then often normalized above  $860^{\circ}\text{C}$  to relieve stresses arising from fabrication and to reduce hydrogen content. The heat treatment also has the advantage of burning off organic contamination and carbon residues localized near the steel surface. After cooling, the vessel is sand-blasted either with silica grit or steel shot to remove the scale formed during the normalization procedure and promote mechanical keying of the glass ground-layer to be applied (by roughening the surface). Degreasing and chemical descaling is no longer used for large-scale equipment because of the risk of hydrogen uptake and consequent fishscaling and also for environmental restrictions.

Important points in vessel design are

1. The metal thickness should be as uniform as possible throughout, avoiding heavy bosses, lucks, or brackets.
2. Sharp edges must be avoided under all circumstances, the minimum radius recommended for all curved surfaces is  $\sim 8\text{ mm}$ , at complex-shaped parts, and with smaller dimensions, radii can be as small as  $3\text{ mm}$ . The risk of sudden shaling increases as the radius decreased. Therefore, for such parts, thickness limitations are defined.
3. The risk of distortion on firing is greater if the design includes numerous apertures in the vessel or its cover.
4. The minimum metal thickness must take into consideration that the mechanical strength of steel decreases sharply during heating. Several standards<sup>9</sup> define maximum tolerances for deviations from the original design.

**Table 3** List of technical standards which define technical requirements and material flow and documentation procedures for manufactured products related to chemical industry

EN 14483-1 to 5	Defines physical and chemical properties of glass coatings. Describes testing devices and procedures
EN 14430	Defines spark testing devices and technical spec for glass linings
EN 15159-1 to 2	Technical delivery conditions, min spec of glass linings and vessels defined
CODAP	French standards, include welding procedures, heat treatment and material flow until delivery of glass-lined devices
Swiss standard	Swiss standards, include welding procedures, heat treatment and material flow until delivery of glass-lined devices

### 3.27.2.5 Lining Process

The first coat consists of a ground-coat, which is sprayed as the first layer in the form of a wet slip. After drying, it is normally fired at temperatures above 900 °C. The alternative, directly dusting hot parts with dry powder, has diminished completely. After inspection, either a second ground-coat or several cover coats are applied directly. Each coating allows a buildup of ~0.3–0.5 mm of glass, which means that an average of 4–6 coats are required to build up a desired glass thickness of 1.5–2 mm.

Each coat is dried thoroughly and is fired according to a firing program, especially designed for each part. Cover coats are fired between 780 and 850 °C, depending on the size of the part, glass type, and coat number. To avoid thermal-induced stresses within the glass lining, slow cooling is most appropriate for a high standard of quality. Inadequate cooling rates lead to a number of severe defects,<sup>10</sup> which are not accepted by customers.

To avoid any kind of defect, for example, blisters, bubbles, scale, etc., visual inspection and spark testing at 20 kV after each coat reveals the integrity of the coating. To ensure pore-free quality, small defects are ground and refilled with cover coat slip, blisters are ground down to the steel, and, by using special patch grounds in combination with cover coats slips locally, a homogeneous and sound layer of glass can be built up again.

## 3.27.3 Properties of Glass on Steel

### 3.27.3.1 Mechanical Properties

With a properly formulated glass and correct firing, the lining withstands stresses up to the elastic limit of steel without breaking. Impacts sufficiently severe to dent steel will probably cause fractures in the lining. The hardness and abrasion-resistance of the lining exceeds the properties of all-glass equipment, and a smooth and easily cleaned surface is

produced during firing. The combined effect of mechanical keying of the glass to the metal and the chemical bonding developed between glass and steel results in very high adhesive strength.<sup>11</sup> Thus, at room temperature, the typical bond strength of glass to steel can be greater than 100 MPa, the fracture toughness is  $\sim 70 \text{ MPa m}^{-1/2}$  and compressive strength reaches 800 MPa.

### 3.27.3.2 Thermal Properties

The thermal shock resistance of glass-lined equipment, that is, the safe limit of the temperature difference between the glass surface of the vessel and any charge introduced varies to some extent according to general operation conditions. Minimum values are defined in the EN standard 15159-2. To fulfill the requirements of chemically inert industrial enamel, a value of at least 190 °C is required. Modern industrial vitreous enamels are much better and can withstand even sudden temperature changes of 220 °C, on defined standardized test plates.

For reactors, a maximum temperature difference of 140 °C, according to EN 15159-3, is allowed. This value is very close to the thermal shock borderline of steel, where a sudden temperature difference leads to plastic deformation of the steel substrate, causing severe cracking in the glass.

Plant operation temperatures vary nowadays from –150 up to 280 °C, with the maximum operating temperature limited by the corrosivity of the liquid in contact with the enamel. The heat transfer coefficient for heating in glass-lined equipment is of the order of  $400 \text{ W m}^{-2} \text{ K}^{-1}$  but can be increased by agitation. For cooling, corresponding figures would be<sup>12</sup>  $280 \text{ W m}^{-2} \text{ K}^{-1}$ . The numerical values depend on the thickness of the glass coating, increasing with decreasing glass thickness, and the figures quoted represent the behavior of an average coating of 1.4 mm in thickness.

### 3.27.3.3 Chemical Properties

The general pattern of chemical durability of glass linings is higher than for all-glass equipment. Water absorption is negligible, chemical resistance is very high to all acids except hydrofluoric acid and at high temperatures and concentrations of phosphoric acid. Attack by water is measurable only with great difficulty, leading to deviations caused largely by quality of the used water. Almost all organic solvents produce no measurable effect, and strong alkaline solutions (e.g., 20 wt% NaOH) are satisfactorily handled up to at least 60 °C; above that temperature, there might be appreciable reaction. For most types of chemicals, corrosion of the enamel can be assessed by measuring the loss in thickness either in weight per unit area and time or by directly calculating thickness loss when exposed to the liquid.<sup>13</sup>

Conditions in service vary widely. Many cold liquids (milk, ketchup, and beverages) have little corrosive action, and the chosen glass lining need not be very acid-resistant. By contrast, very often base chemicals are produced, which need high temperatures and strong inorganic acids often under high pressure for processing; glasses, therefore, have to be extremely chemically resistant. Further needs are high durability against leaching effects. Thus, the modern semiconductor industry asks for impurity concentrations of their products (pigments, LCD crystals) at the ppb level. Only a few of the modern industrial enamels fulfill these exacting requirements. In the life-science industry, normally acid-based reactions are carried

out, but cleaning in place (CIP) often requires the use of strong alkaline solutions at high temperatures, so the resistance to caustic attack needs to be much higher than in the past.

### 3.27.3.4 Testing Methods

Investigations recently carried out on the leaching effects during corrosion tests showed that the time used for running the tests has a significant influence on the achieved results. Excessive time periods lead to an increase in dissolved glass constituents, which then again further hinder corrosion of the glass. This inhibition effect, described by the mass balance equation, is an ongoing process of glass corrosion. New EN standards with drastically increased concentrations of corrosive media and reduced reaction times especially for alkaline testing have overcome these effects and now lead to better and reproducible data.<sup>14</sup> The values hold for both immersion and vapor-phased conditions, depending on the media used (Table 4).

The effect of temperature on alkaline corrosion is illustrated by data from Pfadler.<sup>11</sup> There are various glass compositions in service, and it is important to ensure that the lining is appropriate for the particular process to be carried out. An example of the behavior of two different technical enamels compared with borosilicate and lime glass is shown in Table 5. This table gives some resistance data with regard to typical acids and alkalis, all data measured according to EN 14483-1-5.<sup>13,14</sup>

**Table 4** The durability of several materials against chemical attack

Material	Acidic solutions			Alkaline solutions		
	HCl (20%)	H <sub>2</sub> SO <sub>4</sub> (60%)	HNO <sub>3</sub> (25%)	NaOH (5%)	Na <sub>2</sub> CO <sub>3</sub> (10%)	NH <sub>3</sub> (1%)
WWG	0.039 (108 °C)	0.1 (160 °C)	0.1 (135 °C)	0.51 (80 °C)	0.10 (56 °C)	0.1 (82 °C)
PPG	0.046 (108 °C)	0.1 (160 °C)	0.1 (135 °C)	0.32 (80 °C)	0.10 (63 °C)	0.1 (92 °C)
Borosilicate glass	0.056 (108 °C)	No data available	No data available	1.2–4.1 (80 °C)	No data available	0.29 (80 °C)
Soda lime glass	0.245 (108 °C)	No data available	No data available	1.57 (80 °C)	No data available	No data available
Hastelloy C4 2.4610	0.51 (62 °C)	0.1 (50 °C)	0.125 (60 °C)	No data available	0.05 (135 °C)	No data available
Stainless steel 1.4571	Dissolves fast	≥10 (100 °C)	0.1 (124 °C)	Stress corrosion cracking	No data available	No data available
Carbon steel 1.0488	Dissolves fast	Dissolves fast	1 (20 °C)	Stress corrosion cracking	2.2 (20 °C)	No data available

The numbers indicate thickness loss in (mm year<sup>-1</sup>).

Data for WWG, PPG, borosilicate, and soda lime glass are from Schäfer,<sup>15</sup> hastelloy from Dechema-Werkstoff Tabelle,<sup>16</sup> stainless and carbon steel from "Key to Steel" Handbook.<sup>17</sup>

**Table 5** Comparative corrosion tests between borosilicate glass, soda lime glass, and technical enamels

Material (glass or enamel)	Chemical corrosion tests – comparison of technical enamel and glass			
	Acid resistivity EN 14483-1 (mm year <sup>-1</sup> )	Acid resistivity EN 51174 (mm year <sup>-1</sup> )	Alkaline resistivity DIN 2743 (mm year <sup>-1</sup> )	Alkaline resistivity EN 14483-5 (mm year <sup>-1</sup> )
	20% HCl, 108 °C, 168 h	20% HCl, 140 °C, 24 h	0.1 M NaOH (0.4%), 80 °C, 24 h	1N NaOH (4%), 80 °C, 48 h
WWG <sup>a</sup>	0.038–0.043	0.20–0.24	0.27–0.3	0.48
PPG <sup>a</sup>	0.046–0.05	0.22	0.13–0.2	0.32–0.35
Duran 8330	From 0.245 (1 d) to 0.06 (5d)	0.385	0.848–1.615	1.23–4.13
AR glass <sup>b</sup>	0.056	0.313	1.18	1.57

<sup>a</sup>WWG and PPG are trademarks of technical enamels produced by Robbins and Myers Inc.

<sup>b</sup>AR Glass: Sodium–calcium silicate glass (soda lime glass).

Source: Lorentz, R. *Werkst. Korros.* **1982**, 33, 247.

### 3.27.3.5 Surface Properties

For several applications, the smoothness of the glass surface is the most important factor, making glass more attractive than stainless steel vessels, for example. Polymer producers ask for very smooth surfaces with nonstick behavior, thereby improving the cleanability of the enameled reactor walls compared with stainless steel ones. Even if the thermal properties of a glass-lined reactor are worse than those of stainless steel, because of higher sticking rates of polymer particles on stainless steel, glass-lined reactors achieve at least similar performance rates during service.

### 3.27.3.6 Enamel Behavior in Service

Enamels, although resistant to many alkalis, are not necessarily completely resistant. Thus, weight loss from enameled iron test pieces has been related to resistance to detergent attacks, but field assessment of the effect of alkaline materials upon enamel does not always agree with accelerated laboratory tests. In such a case, the fitting of a glass-lined test piece into the vessel is required. The production test can last for several weeks, allowing a realistic calculation of the durability of the glass. Often, large differences between enamels occur depending on their chemical composition. Often, also minor changes in the production process have a drastic influence and increase on the performance of a glass lining. As an example, addition of caustic soda above 80 °C is often used to neutralize a product.

If the addition is done solely through a nozzle at the upper bottom, no fast mixing between the two liquids occurs, which would corrode the glass within a distinct zone near the edge of the liquid level. By using a dip pipe for the addition of the caustic soda,

complete mixing and dilution occurs immediately, drastically reducing the chemical attack and also improving the performance of the process.

### 3.27.3.7 General Aspects of Glass Enamel Corrosion

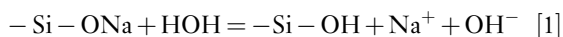
Evidence (about the interaction of liquids with glass surfaces) has come from the results of research work in developing corrosion-resistant glass compositions and there is now better understanding of the mode of chemical attack on glass. Reaction on the surface occurs through ion exchange, dissolution, and absorption. Signs of these reactions are a dimming of gloss, thin film interference colors, and surface-roughening on general degradation. In the beginning, the corrosion becomes apparent as a loss of gloss, but there is no direct correlation between gloss and chemical degradation by ongoing attack. Continued penetration of the glass structure by some ions could lead to its decomposition. The thickness of the ion-exchanged surface layer is related to the durability of the glass and initial reactions are rapid.<sup>18,19</sup> An intermediate phase is formed whose structure, thickness, and durability depends on the glass composition as well as the temperature and pH of the attacking/reacting liquid.<sup>20</sup>

The borosilicate glasses on coated steel contain silica and alkali metal oxides and the reactions can be considered as involving silicate networks. Attacks begin as an interaction between silicate lattice ions and protons from the liquid with the consequent leaching of monovalent and divalent ions.

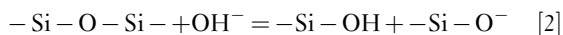
### 3.27.3.8 Attack by Water

No enamel or glass is thermodynamically stable against attack by water. The durability is caused by

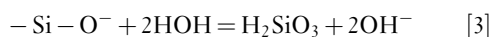
the diffusivity of alkali ions inside the silica network. This can generally be described by a diffusion kinetics and thus follows a  $\sqrt{t}$ -relationship. Initially, there is the replacement of an alkali ion in the glass by a proton (H) from the water,



The released hydroxyl ion shifts the pH of the solution and interacts with the siloxane bond in the vitreous network



This open oxygen interacts with a water molecule to form dissolved silicic acid

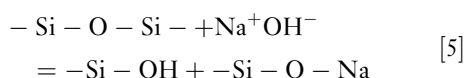


The resulting hydroxyl ion is available for further reaction in reaction [2]. As the hydrogen ions replace alkali (R) ions, a surface film forms, which has properties different from the solid glass. This film swells, acting as a barrier to further diffusion of ions into and out of the bulk material, thus inhibiting further attack. If this layer dries out, the thin films produce characteristic, iridescent interference colors. Depending on the chemical durability of the glass, the mechanism of attack varies. Highly chemical-resistant enamels withstand the  $\text{OH}^-$  attack, and corrosion is mainly caused by ion exchange and proton interaction. This leads to the general equation



### 3.27.3.9 Attack by Alkaline Solutions

With the migration of alkali ions ( $\text{R}^+$ ) into the leachant, attack is no longer solely by water. If  $\text{R}^+$  is sodium, the attack on the glass is



Alkaline ions in solution increase the pH with two consequences. The rate of silica extraction increases with rise in pH value above 8–9 and the rate of alkali exchange is reduced. However, as the higher alkalinity favors dissolution of silica, further alkali is released by the lattice. The quantity of alkali extracted can be used as a measure of the resistance of the glass to attack.

### 3.27.3.10 Attack by Acid

#### 3.27.3.10.1 Mineral acids

The mode of attack with mineral acids is similar to that by water, namely at the site of siloxane bond  $-\text{Si}-\text{O}-\text{Si}-$ . Hydrochloric, sulfuric, and nitric acids all attack through similar mechanisms. Phosphoric acid, when almost water-free, is no more corrosive than the other mineral acids. However, diluted phosphoric acid forms polyanionic networks that are good complexing agents and increase the leaching of monovalent and divalent cations from the vitreous network (via the formation of alkaline and alkaline earth silicyl phosphates).

#### 3.27.3.10.2 Organic acids

Some glasses are more prone to attack by organic acids than by other acids with a lower pH value. These acids form complex ions in solution, which increase the glass solubility. Many vitreous enamels contain larger divalent cations in their network, specifically Ca, Sr, and Ba ions reduce ion diffusivity in the lining.

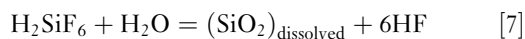
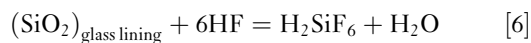
### 3.27.3.11 Further Possibilities of Corrosive Attack on Glass

#### 3.27.3.11.1 Attack by complex formation

Chelating agents sequester polyvalent cations and, if present in a corrosive liquid, can increase the rate of attack on the glass. The cations  $\text{Mg}^{2+}$ ,  $\text{Ca}^{2+}$ ,  $\text{Al}^{3+}$ ,  $\text{Zr}^{4+}$ , and  $\text{Ti}^{4+}$  are known to stabilize the siliceous surface film and so aid corrosion resistance, but in the presence of say, ethylenediaminetetraacetic acid (EDTA), with which these ions interact, this protective action is increasingly nullified as the ions are removed from the silicate surface. Complexes are formed between  $\text{Si}^{4+}$  and some organic acids, notably gallic acid and tannic acid.

#### 3.27.3.11.2 Attack by fluorides

All silicates are severely attacked by hydrofluoric acid and its constituents with  $\text{F}^-$  ion acting as a catalyst. Only the form of the silica network influences to some extent the reaction rate.

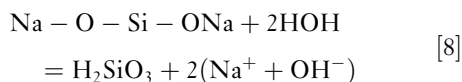


Although neutralization reduces the rate of fluoride attack, no inhibition of this process is so far known.



### 3.27.3.12 Inhibition of Corrosion Attack

The reaction routes of chemical attack aforementioned also open the possibility for inhibiting the attack on glass by altering the chemical equilibrium to favor the reactant (glass) side of the equations. Thus, appropriate chemical additions can reduce the glass dissolution rate considerably. This holds especially for attack of protons on glass where the addition of dissolved  $\text{SiO}_2$  into the process fluid shifts the equilibrium constant towards a higher stability of the vitreous glass matrix. Formally, reaction [8] is used to calculate the amount of dissolved  $\text{SiO}_2$  necessary to stabilize the lining.



Equilibrium is achieved when the dissolution concentration of the main constituent  $\text{SiO}_2$  reaches saturation level.  $[\text{H}_2\text{SiO}_3]_{\text{diss}}$  describes the amount of dissolved  $\text{SiO}_2$ ,  $[\text{Na}_2\text{SiO}_3]_{\text{glass}}$  stands for the glass matrix containing alkaline ions.

$$K = \frac{[\text{H}_2\text{SiO}_3]_{\text{diss}} [\text{NaOH}]^2}{[\text{Na}_2\text{SiO}_3]_{\text{glass}} [\text{H}_2\text{O}^2]} \quad [9]$$

The addition of a small amount (normally 100–300 ppm) of  $\text{SiO}_2$ , according to eqn [9], shifts the equilibrium towards the reactant side and therefore hinders glass corrosion.

### 3.27.3.13 Effect of Leaching – Temperature Dependence

The quantity of alkali extracted from a glass matrix in a fixed time increases with increasing temperature. Depending on the composition of the glass coating and the alkali present (ions of different size behave differently) the amount leached approximately doubles for each  $10^\circ\text{C}$  rise in temperature. This temperature dependence can be expressed by the equation (Arrhenius):

$$A = B \exp(-\Delta E/RT) \quad [10]$$

where  $A$  is the specific reaction rate changing with temperature,  $B$  is a constant,  $R$  is the gas constant,  $T$  is

the absolute temperature, and  $\Delta E$  the activation energy for the process of alkali removal from the glass. Alkali extraction is always associated with changes in pH and such changes depend on the quantities of alkali and silica released. For details, see the mechanism of water attack. Where glass linings are exposed to water or steam at temperatures above  $160^\circ\text{C}$  and/or at extreme pH values, the plant manufacturers should be consulted.

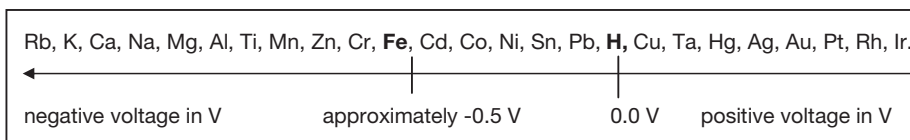
## 3.27.4 Damage Monitoring and Analysis

### 3.27.4.1 In Situ Sensing Technology

Glass damage or corrosion may be monitored by applying a low voltage to the coated metallic substrate and recording the resulting current, which must necessarily flow from any damaged parts of the coating that significantly expose the metallic substrate. Provided that a history of the plant process and the type of insulating material used on the equipment installed is known, this can provide a record of the percentage of damaged (or unharmed) coating. Three methods are used to monitor glass defects, which have no need of additional installed test samples: Low DC voltage method that measures the overall ohmic resistance of a vessel<sup>21</sup>; electrochemical noise analysis that records and analyses the frequency-dependant noise spectrum of a vessel<sup>22</sup>; potentiometric decomposition analysis that measures the electrochemical potential of steel in a conductive solution.<sup>23,24</sup>

All three methods require at least some electrical conductivity of the solution, and all use the vessel (i.e., metallic substrate) as one of the working electrodes.

1. Simple voltage–current measurements are restricted by the specific conductivity of the liquid (must be high enough – works normally in all water-based liquids) and all installed parts demonstrate insulating behavior. A defect is recorded if the current exceeds a previously defined level. The method can lead to a large number of false alarms and, as such, is often not so useful (with the monitoring equipment being shut down).





2. Electrochemical noise analysis records the frequency spectrum (from mHz up to a few kHz) on the sample and looks for deviations from historic records that can indicate ongoing corrosion. However, the noise spectrum can often change drastically depending on the process conditions where this does not imply defect formation. Interpretation is thus quite difficult and automatic computation does not work well. Often the onset of corrosion is unseen or misinterpreted.
3. The potentiometric decomposition analysis overcomes these limitations. Recent developments allow the monitoring of glass defects also if metal parts such as nickel-based inlet tubes or graphite-filled polytetrafluorethylene (PTFE) linings or metal-based distillation columns are used. The method is based on the EMF build-up by an electrochemical cell. It makes use of the specific electrochemical potential of each element which is unique among all types of solutions and compositions, pH values, or temperatures.

The potentiometric method is based on the definition of electrochemical potentials, where the zero point is defined as the standard hydrogen electrode of potential equal to 0 V at 25 °C at 1 bar pressure of hydrogen and a solution that is 1 molar in proton concentration. Noble metals produce positive potentials, base metals negative ones.

Advantages of the method include ease of adjustment to a computer-based monitoring system, short time cycles (within minutes), and relative lack of dependence on changes in pH, temperature, or composition of the solutions.

### 3.27.4.2 Repairs to Enamel Damage

Repair cements are quite satisfactory and economical for mild chemical service over lengthy periods. For severe chemical service, enameled areas up to 120 mm in diameter can be repaired by specialists with tantalum plugs, discs, and PTFE gaskets. These materials have a similar chemical resistance to that of glass. Larger areas of damage or corrosion need special glass-lined plates (covers) fixed with several studs and cement.

Complete reenameling of equipment is feasible, but is often accompanied by a microstructural changes in the metal, and for this reason, it is limited to 4–5 times. With each reenameling distortion becomes larger and the process may consequently be uneconomical. For this reason, a complete inspection of a vessel is required to allow a decision as to whether reenameling or a new vessel is the more economical alternative.

### 3.27.4.3 Recent Developments

The traditional method of producing glass-lined vessels involves stages of annealing, degreasing, shot blasting, acid pickling, followed by application of up to two ground coats and five cover coats, each with a separate firing. Tighter legislation and higher energy costs have led to the development of processes in which one or more of these stages may be omitted. These advances are achieved through greater understanding and control of glass composition, and by adopting more sophisticated powder-handling techniques. This includes statistical methods of running a vessel mixture of various shapes, dimensions, and different coats-to-finish in one furnace run.

The more demanding the requirements of customers using enameled vessels for their production, the finer the resolution of analytical instruments being developed and the lower the permitted amounts of dissolved glass constituents in the products. These implications are requested especially by life-science companies and the semiconductor industry, as they call for decreases in the allowed level of leached impurities to almost 1 ppb. Mainly, impurity levels of transition metal oxides reduce the yield of product drastically, making it impossible to produce them in the qualities demanded. Typical examples are enantioselective oxidation reactions of proteins, manufacturing of LCD crystals, and photoresistant chemicals for the chip industry. This has led to the development of new enamels that consists only of biologically nontoxic metal oxides and that therefore remove CoO, NiO, MnO, Fe<sub>2</sub>O<sub>3</sub>, SnO<sub>2</sub>, ZnO, Cr<sub>2</sub>O<sub>3</sub>, SrO, and BaO from the glass compositions.

## References

1. DGRL 97/23/EG.
2. ASME R, ASME Boiler and Pressure Vessel Code, R – Stamp.
3. EN 10028-1: Flat products made of steel for pressure purposes – general requirements.
4. EN 15711: Vitreous and porcelain enamels – glass lined flanged steel pipes and flanged steel fittings – quality requirements.
5. EN10209: Cold rolled low carbon steel flat products for vitreous enamelling – technical delivery conditions.
6. EN 12536: Welding consumables – rods for gas welding of nonalloy and creep resisting steels.
7. EN ISO 15607\_2004-03: Specification and approval of welding procedures for metallic materials Part 1: General rules for fusion welding.
8. EN287-1: Qualification test of welders – fusion welding.
9. EN 15159-1: Vitreous and porcelain enamels – glass lined apparatus for process plants – quality requirements.

10. EN 51176-1: Vitreous and porcelain enamels – presentation and characterization of defects Part 1: Enamels for chemical service and vessels.
11. Pfaudler glass linings **614-1e**, Pfaudler Werke GmbH, D-68723 Schwetzingen, Germany, 2007.
12. Reinemuth, J.; Heinzmann, M. *CIT* **2007**, 79, 53–67.
13. EN 14483-1: Vitreous and porcelain enamels – determination of resistance to chemical corrosion Part 1.
14. EN 14483-5: Vitreous and porcelain enamels – determination of resistance to chemical corrosion Part 5.
15. Schäfer, G. *Mitt. DEV* **2004**, 6, 90–95.
16. Dechema-Werkstoff Tabelle DECHEMA e.V. Theodor-Heuss-Allee 25, D-60486 Frankfurt am Main.
17. “Key to Steel” Handbook, Verlag Stahlschlüssel Wegst GmbH Theodor-Heuss-Str 36, 71672 Marbach a.N., 2001.
18. Lorentz, R. *Werkst. Korros.* **1982**, 33, 247.
19. Petzold, Pöschmann: Email und Emailiertechnik, Deutscher Verlag für Grundstoffindustrie, 2. Auflage 1992.
20. Gesche, G. *Mitt. VDEfa* **1958**, 6, 101.
21. Bard, A. J.; Faulkner, L. R. *Electrochemical Methods*; John Wiley, 1980.
22. Göllner, J.; Burkert, A. *Mater. Corros.* **1998**, 49, 614.
23. Harrison, J. A.; Thirsk, H. R. *Electroanalyt. Chem.* **1971**, 5, 67–148.
24. Trampert, R. *CAV* **2007**, 3, 34.

## 3.28 Degradation of Vitreous Enamel Coatings

**T. Curtis**

Research and Development Director, Escol Products Ltd, UK

This article is a revision of the Third Edition article 16.1 by N. S. C. Millar and C. Wilson, volume 2, pp 16:3–16:12, © 2010, Elsevier B.V.

3.28.1	Nature of Vitreous Enamels	2330
3.28.2	Metal and Metal Preparation	2331
3.28.2.1	Cast Iron	2331
3.28.2.2	Steel	2331
3.28.2.3	Enamel Bonding	2332
3.28.2.4	Enamel Application and Fusion	2332
3.28.3	Properties of Enamel Coatings Affecting Corrosion	2332
3.28.3.1	Mechanical Properties	2332
3.28.3.2	Thermal Properties	2333
3.28.3.3	Chemical Resistance	2333
3.28.3.3.1	Acid resistance	2334
3.28.3.3.2	Alkali and detergent resistance	2335
3.28.3.3.3	Resistance to water and atmosphere	2335
References		2336

### Glossary

**Frit** A complex of oxides of boron and silicon with alkali and transition metals forming a glass that is suitable for fusing onto a metal, thus forming a vitreous enamel coating.

### 3.28.1 Nature of Vitreous Enamels

A vitreous enamel coating is, as the name implies, a coating of a glassy substance which has been fused onto the basis metal to give a tightly adherent hard finish, resistant to many abrasive and corrosive materials. The purpose of modern vitreous enamels is twofold, that is, to confer corrosion protection to the metal substrate and at the same time provide permanent color, gloss, and other aesthetic values.

Most of the corrosion resistance, and indeed other properties of the finish, are determined by the composition of the vitreous enameller's raw material *frit*, although other factors can influence them to a minor degree. Frit, for application to sheet and cast iron, is essentially a complex alkali-metal alumino borosilicate and is prepared by smelting together an intimate

mixture of refractory materials such as silica, titania, feldspar, china clay, etc. at temperatures between 1100 and 1450°C with fluxes exemplified by borax, sodium silicofluoride and nitrates and carbonates of lithium, sodium and potassium. Smelting continues until all the solid matter has inter-reacted to form a molten mass; but unlike true glass, this liquid does contain a degree of bubbles. At this stage the melt is quenched rapidly by either pouring it into water or between water-cooled steel rollers to form 'frit' or 'flake.'

Frit may be milled dry or wet. The long established dry process is used for cast iron baths and for chemical plants. Where possible the preferred process for vitreous enamel application today is dry electrostatic. The frit is milled with low level additions of refractory and/or inorganic pigments together with typically 0.3–0.4% of a silicone. The silicone imparts the required electrical characteristics to the ground frit to enable efficient application of the powder to the metal substrate. This is achieved in cylinders using balls of porcelain, steatite or denser alumina, or with pebbles of flint, to produce a fine powder of predetermined size.

In the more common wet process, frit is milled with water, colloidal clay, opacifier, coloring oxide, refractory and various electrolytes in a ball mill to a closely controlled fineness or coarseness.

The standard method of cleaning cast iron for enameling is by grit or shot blasting, which may be preceded by an annealing operation.

### 3.28.2.2 Steel

Two general types of sheet steel are in current use, *viz.* cold-rolled mild steel and decarburized steel. A typical analysis for cold-rolled steel is 0.1% C, 0.5% Mn, and 0.04% S. It can be obtained in regular, deep drawing or extra-deep drawing grades. This type of steel is normally used with a ground coat including cobalt and nickel, as shown in [Table 1](#).

Decarburized steel is mild steel that has undergone heat treatment in a controlled atmosphere to reduce carbon content to about 0.005%. White or coloured enamel can then be applied directly to this type of steel without the need for a ground coat layer.

Sheet steel is normally prepared for application of enamel by a sequence of operations including thorough degreasing, acid pickling, and neutralization. A nickel

[illegible]

Frit	100	
Water	35–40	
Titania	1	
Clay	2.5	Grind to fineness of 1 g residue on 200 mesh sieve (50ml sample)
Bentonite	0.3	
Sodium nitrite	0.05	
Potassium carbonate	0.1	

dip stage is often included to deposit a thin, porous layer of nickel applied at about  $1\text{gm}^{-2}$ , especially when the conventional ground coat is not used.

### 3.28.2.3 Enamel Bonding

For effective performance, the enamel must be firmly bonded to the underlying metal and this bond must persist during use. The bond is formed by the molten enamel flowing into 'pits' in the metal, that is, mechanical adhesion, and by solution of the metal in the glass, that is, chemical adhesion. The coefficient of thermal expansion of the enamel in relation to the cast iron or sheet steel and enamel setting temperature determines the stress set up in the coating. As enamel, like glass, is strongest under compression, its thermal expansion should be slightly less than the metal.

### 3.28.2.4 Enamel Application and Fusion

Vitreous enamel is normally applied to the prepared metal or over a ground coat by spraying or dipping. Alternative wet techniques are used, of which the most common has been electrostatic wet spraying. Electrophoretic deposition from slurry has been found to be highly suitable for some components.

On sheet iron, a ground coat including cobalt and nickel, is generally used, but for mass production (e.g., cookers) use of decarbonized steel and direct application of colors is more common. This involves more complex steel pretreatment.

After drying the applied slurry, the enamel is fused onto sheet steel at about  $800\text{--}850^\circ\text{C}$  for about 4–5 min. For cast iron, a longer time and lower temperature are normal.

The old dry process enameling of cast iron (baths etc.) is no longer widely used. The method consisted of sieving finely powdered frit onto preheated casting and inserting it back into a furnace at about  $900^\circ\text{C}$  to produce the smooth finish.

In recent years increasing use has been made of the electrostatic application of a dry powder spray by many manufacturers, who require a limited range of colors. Dry electrostatic finishes are fused at temperatures in the same range as conventional ones.

## 3.28.3 Properties of Enamel Coatings Affecting Corrosion

### 3.28.3.1 Mechanical Properties

This group includes surface hardness, that is, scratch and abrasion resistance, adhesion and resistance to chipping, crazing, and impact. All these and other

properties depend upon adhesion between the vitreous enamel layer and the metal being good and remaining so.

There is no single test that will give a quantitative assessment of adhesion; all those which have been proposed cause destruction of the test plan. It has already been stated that this property is dependent upon mechanical and chemical bonds between enamel and metal. One must, however, also consider stresses set up at the interface and within the glass itself during cooling after fusion or after a delay.

The coefficient of thermal expansion is primarily determined by frit composition, although mill additions can have a minor influence. As a general rule, superior acid and thermal shock resistance are obtained with low expansion enamel, and the skill of the frit manufacturer is in obtaining good resistance and maintaining a sufficiently high expansion to prevent distortion of the component (pressing or casting). Several workers have produced a set of factors for expansion in relation to the enamel oxides that constitute the frit, which provides a guide to the frit producer. However, as these factors are derived from a study of relatively simple glasses smelted to homogeneity, it must be emphasized that they are only a guide. The effect of substituting certain oxides for others in standard titanium superopaque enamel is given in [Table 2](#). The use of a nickel dip improves adhesion by minimizing iron oxide formation, but it should be noted that some iron oxide formation is necessary to produce enamel/metal adhesion. In the most common methods of testing for adherence to sheet iron, the coated metal is distorted by bending, twisting, or impacting under a falling weight. In the worst cases the enamel is removed leaving the metal bright and shiny, but in all others a dark-colored coating remains with slivers of fractured enamel adhering to a greater or lesser degree. With cast

**Table 2** Effect of frit ingredients on enamel expansion

<i>Constituent varied</i>	<i>Expansion change</i>
Increase alkali metal	Increase
Replace $\text{Na}_2\text{O}$ by $\text{Li}_2\text{O}$	Increase
Replace $\text{Na}_2\text{O}$ by $\text{K}_2\text{O}$	Decrease
Increase fluorine	Decrease
Increase $\text{B}_2\text{O}_3$	Decrease
Replace $\text{SiO}_2$ by $\text{TiO}_2$	Increase
Increase $\text{TiO}_2$	Slight increase
Replace $\text{SiO}_2$ by $\text{Al}_2\text{O}_3$	Slight increase
Introduce $\text{P}_2\text{O}_5$	Slight increase
Introduce $\text{BaO}$	Increase
Increase $\text{SiO}_2$	Decrease

iron enameling it is not possible to distort the metal and in this case an assessment of adhesion is obtained by dropping a weight on to the enamel surface and examining for fractures. Erroneous results can be obtained in that often thicker enamel coatings appear to be better bonded and resistant to impact, whereas in fact the converse is true. Provided the bond is adequate, this test really gives an indication of the strength of the enamel itself.

According to Andrews<sup>1</sup> a typical sheet iron ground coat has a tensile strength of about 10 kg mm<sup>-2</sup>. In small cross-sections, however, the tensile strength of glass is improved and fine threads, for example, as in glass fiber, are quite strong. Enamels under compression are 15–20 times stronger than an equal thickness under tension.

The hardness of an enamel surface is an important property for such items as enameled sink units, domestic appliances, and washing machine tubs which have to withstand abrasive action of buttons, etc. On Moh's scale, most enamels have a hardness of up to 6 (orthoclase). There are two types of hardness of importance to users of enamel, *viz.* surface and subsurface. The former is more important for domestic uses when one considers the scratching action of cutlery, pans, etc. whereas subsurface hardness is the prime factor in prolonging the life of enameled scoops, buckets, etc. in such applications as elevators or conveyors of coal and other minerals.

Of the several methods of measuring this property, those specified by the Porcelain Enamel Institute and the Institute of Vitreous Enamellers are the best known and most reliable. Both consist of abrading a weighed enamel panel with standard silica or other abrasive suspended in water and kept moving on an oscillating table with stainless steel balls. The loss in weight is measured periodically and a graph of time versus weight loss indicates both the surface and subsurface abrasion resistance. Pedder<sup>2</sup> has quoted relative weight loss figures for different types of enamel. They are shown in Table 3.

Fine bubbles uniformly distributed throughout the coat improve elasticity and thus mill additions and under and over firing influence this property. The greatest effect on elasticity is enamel thickness and most developments are aimed at obtaining a satisfactory finish with minimum thickness.

### 3.28.3.2 Thermal Properties

These properties are made use of in many applications ranging from domestic cookers to linings which

**Table 3** Comparison of abrasion resistance of different enamels<sup>a</sup>

<i>Types of enamel</i>	<i>Average loss in weight (g)<sup>b</sup></i>
Acid resisting titania based	$56 \times 10^{-4}$
Acid resisting non-titania	$342 \times 10^{-4}$
Antimony white cover coat	$582 \times 10^{-4}$
High refractory enamel	$129 \times 10^{-4}$
Plate glass	$70 \times 10^{-4}$

<sup>a</sup>Data from Pedder.<sup>2</sup>

<sup>b</sup>Overall figure for tests under standardized conditions for each grade of enamel.

must withstand heat from jet engines. There is simple heat resistance, that is, the ability of the enamel to protect the underlying metal from prolonged heat and also thermal shock resistance, which is the ability to resist sudden changes in temperature without failure occurring in the coating. These thermal properties depend upon the relative coefficient of thermal expansion of enamel and metal, enamel setting point, adhesion, enamel thickness, and geometry of the shape to which the finish is applied.

It is obvious that adhesion must be good in order to prevent rupture at the enamel/metal interface during heating and cooling. Thick coatings are liable to spall when subjected to thermal change due to the differential strain set up within the enamel layer itself, caused by poor heat conductivity of the glass. Thus again thin coatings are desirable.

Compressive forces on enamel applied to a convex surface are less than when a concave surface is coated, and it is therefore apparent that the sharper the radius of the metal, the weaker the enamel applied to it will be. This fact is also relevant to mechanical damage.

Thermal shock resistance is important for gas cookers, pan supports and hotplates where spillage is liable to occur; but in oven interiors heat resistance is more relevant.

The softening point of conventional cast and sheet iron enamels is about 500°C, but special compositions are obtainable, which operate successfully at 600°C. Other more specialized enamels withstand service conditions ranging from being in excess of dull red heat, for example, as obtained in fire backs, to those capable of enduring short exposure to temperatures of around 1000°C, for example, in jet tubes, after burners, etc.

### 3.28.3.3 Chemical Resistance

That examples of glass and glazes manufactured many centuries ago still exist is an indication of the



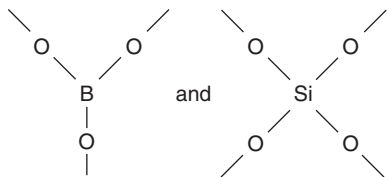
good resistance of such ceramics to abrasion, acids, alkalis, atmosphere, etc.

In this section, chemical resistance will be divided into three parts, *viz.* acid, alkali (including detergents), and water (including atmosphere). Normally enamel is formulated to withstand one of the corrosive agents more specifically than another, although vitreous enamel as a general finish has good 'all round' resistance, with few exceptions such as hydrofluoric acid and fused or hot concentrated solutions of caustic soda or potash.

### 3.28.3.3.1 Acid resistance

This property is best appreciated when the glass structure is understood. Most enamel frits are complex alkali metal borosilicates and can be visualized as a network of  $\text{SiO}_4$  tetrahedra and  $\text{BO}_3$  triangular configurations containing alkali metals such as lithium, sodium and potassium or alkaline earth metals, especially calcium and barium, in the network interstices.

Fused silica may be regarded as the ultimate from the acid resistance aspect but because of its high softening point and low thermal expansion, it cannot be applied to a metal in the usual manner. Rupturing or distorting this almost regular  $\text{SiO}_4$  lattice makes the structure more fluid. Thus to reduce its softening point  $\text{B}_2\text{O}_3$  is introduced whereby some of the Si–O bonds are broken and an irregular network is formed. Further distortion of the network is obtained by introducing alkali and alkaline earth metals into the lattice. If fluorine is included in the frit, more bonds are broken; in this case an oxygen atom (–O–) linking two silicon or boron atoms is replaced by a fluorine atom (F–) – which, being monovalent, cannot join two Si or B atoms and hence causes bond rupture. A study of relevant phase diagrams and eutectics proves useful in formulating low firing enamels.



Thus all frit ingredients act as either network formers or modifiers and with the principal exception of silica, titania, and zirconia, all cause diminution in acid resistance. The reacting acid causes an exchange between metal ions in the network modifier of the glass and hydrogen ions from the acid. This naturally occurs at the enamel surface, but as the etching or

leaching reaction proceeds, a resulting thin layer of silica-rich material inhibits further reaction. Thus acid attack is dependent upon enamel composition and pH, with time and temperature playing a part. Sodium oxide and boric acid are both leached out by acid attack, and it has been found that the  $\text{Na}_2\text{O}/\text{B}_2\text{O}_3$  ratio is constant for any enamel and is dependent upon enamel composition.

An increase in titania content of the frit acts in a similar way to increasing silica in enhancing acid resistance with the added advantage that the coefficient of expansion is also raised slightly and the glass viscosity is not increased as much as by the equivalent  $\text{SiO}_2$  increment. This only applies to the titania remaining in solution in the glass and does not necessarily hold when the frit is supersaturated with  $\text{TiO}_2$ , which occurs with the modern opaque sheet iron covercoats when some of the pigment recrystallizes and causes opacification on cooling from the firing process.

In formulating holloware enamels, the degree of acid resistance required is less than for chemical plant, for example, reaction vessels. Consequently the  $\text{RO}_2$  ( $\text{SiO}_2$  and  $\text{TiO}_2$ ) is lower, thus permitting increased quantities of fluxes to be fired at lower temperatures and having superior chip resistance. Conversely, chemical plant enamels are higher in silica and dissolved titania and require harder firing. An example of such an enamel is shown in [Table 1](#).

The acid resistance required for domestic appliances varies with the particular component, for example, the oven interior of a gas cooker necessitates higher resistance than the outer sides – the former being at least Class A using 2% sulfuric acid while the latter can have a lower grading based on less aggressive citric acid tests. These tests are detailed in EN 14483-1:2004.

The enamel mill addition, degree of firing, and furnace atmosphere all affect acid resistance. An increase in clay and alkaline electrolyte detracts from this property and underfiring also has an adverse effect. The use of organic suspending agents is thus preferable to clays, from this aspect, but other factors must also be considered. Similarly replacement of 1% milling clay by 0.25% of the more colloidal bentonite is beneficial. Large additions of quartz at the mill improve heat resistance, and, provided the firing temperature is increased to dissolve a sufficient quantity of this silica in the glass, acid resistance is also enhanced.

In the glass-bottle industry bottles can be cooled in a dilute  $\text{SO}_2/\text{SO}_3$  atmosphere to increase chemical resistance. A similar effect has been noted with

vitreous enamel. It has been postulated that a thin layer of  $-OH$  groups or  $-OH-H_2O$  (hydronium) ions is adsorbed on the surface of fired enamel. These ions are transformed into  $-OSO_2$  or  $-OSO_3$  in the presence of oxides of sulfur which are more resistant to further acid attack. It is known that the acid resistance of a recently fired enamel improves with ageing, probably due to enamel reaction with  $SO_2/SO_3$  in the atmosphere and it is quite common for the grading to improve from Class A to Class AA (EN 14483-1:2004).

In enamels for chemical plant such as autoclaves, it is not only the degree of acid resistance which is important but also the freedom of the finish from minute flaws detectable by high frequency spark testing or chemical methods. Chemical methods depend upon a color change when the reagent such as ammonium thiocyanate reacts with the iron exposed at the bottom of the pinhole or flaw in the finish. Alternatively, an electric cell can be formed via the exposed iron in the flaw and detected chemically.

In general, strong mineral acids are more severe in their attack on enamel than weak organic acids. Vargin<sup>3</sup> has stated that the severity of action of organic acids on enamel increases with the increase in the dissociation constant of the acid. Temperature plays a major part in acid resistance – the nearer the boiling point the greater the rate of attack. It is more significant than acid concentration.

It is recognized that vitreous enamel possesses good acid resistance, but an exception is hydrofluoric acid. This is due to the relative ease of reaction between this acid and the silica (which is the largest constituent in the frit) to form silicon tetrafluoride. This reaction is made use of in some 'de-enameling' plants.

### 3.28.3.3.2 Alkali and detergent resistance

The usual method of de-enameling sheet iron is by immersion in fused or hot strong aqueous solutions of caustic soda where the silica network is broken down to form sodium silicate. However, in spite of this fact, enamels are capable of withstanding detergents and mild alkalis and this finish is often used very successfully in washing machines, baths, sink units, etc. where alkaline conditions prevail. Such enamels are usually higher in alumina than acid-resisting enamel and often contains zirconia in the frit. Other elements which aid alkali resistance are barium, calcium, lead, and zinc, and their function in this context is to increase the bond with the essentially silica network and form insoluble silicates which act as a protective coating slowing down the formation of soluble

sodium silicate. The necessity for alkali resistance is relatively limited when compared with detergent resistance and it has been shown that while these two properties are similar, a finish resistant to one is not necessarily a resistant to the other.

The Institute of Vitreous Enamellers produced a report on detergent resistance in 1959<sup>5</sup> and the following facts are brought out:

1. Semi-opaque acid-resistant titania enamel and alkali-resistant frit generally have good detergent resistance whereas non-acid-resistant sign enamel and  $Al_2O_3/B_2O_3/P_2O_5$ -based finishes have poor resistance.
2. Initially, detergent attack is accompanied by a deposit on the enamel surface which can be abraded off resulting in an apparently unaffected glossy appearance. This contrasts with acid attack when a progressive weight loss occurs and original gloss cannot be restored once it has been lost or diminished. After more prolonged detergent attack it is not possible to restore the original high gloss.
3. The rate of attack is very dependent upon temperature. At boiling temperature it is several times greater than that at room temperature.
4. An increase in milling clay has a marked effect on improving this property.
5. Increased detergent concentration, coarser grinding of the frit, and nonstandard firing all cause minor deterioration in resistance.

In the design of an enamel for a washing machine tub, detergent resistance alone is not sufficient and the enamel must also be capable of withstanding the possible abrasive action of buttons, zip fasteners, etc.

### 3.28.3.3.3 Resistance to water and atmosphere

These properties are of particular importance in enameled signs, architectural panels, cooking utensils, and hospital ware subjected to repeated sterilization. That such enameled signs as 'Stephen's Inks', etc. are still in existence and in good condition after many years of outside exposure coupled with the fact that the use of vitreous enamel as a finish for architectural panels is growing, are ready pointers to the good water and atmospheric resistance of enamel. Enameled hospital utensils such as kidney bowls score over organic finishes because of ease of sterilization and also because they are less accommodating to germs, bacteria, etc. on account of their lower electrostatic type attraction for such microbes.

Action of water on enamel is in many ways similar to that of acids in that the network modifier is the weak link and through hydrolysis can be removed from the glass system resulting in loss of gloss and porous surface. As with acids and alkalis, attack on the glass by water can be continued in extreme cases, by an attack on the inorganic coloring matter initially liberated or made more active. In an enclosed system the soluble salts first leached out from the enamel by water become in turn the corrosive element and further attack is dependent upon the pH of such a salt, or, for example, on the  $\text{Na}_2\text{O}/\text{B}_2\text{O}_3$  ratio.

Introduction of divalent calcium and barium oxides into frits in preference to monovalent sodium and potassium generally increases water resistance. Further, oxides of tetravalent and pentavalent metals have a favorable effect on the resistance of glasses and enamel to water. The influence of  $\text{B}_2\text{O}_3$  and fluorine in the frit on chemical resistance is variable and is dependent upon the content and balance of the frit constituents, but they usually cause diminution in resistance. In general, mill-added clay, silica, and opacifier increase water resistance provided the firing or fusing of the enamel is at the optimum.

As is expected, atmospheric resistance is related to water and the acid formed from  $\text{CO}_2$ ,  $\text{SO}_2$ ,  $\text{SO}_3$ , etc. The action of ultraviolet light has no apparent effect on vitreous enamel unlike the case with organic finishes.

There is good correlation between atmospheric and acid resistance, and this fact is helpful to manufacturers of architectural panels as they can easily and quickly determine the latter property and do not have to carry

out lengthy exposures to relatively unpolluted air. An exception, however, occurs with reds and yellows where strict correlation is not always true, and in these cases a test based upon exposure to a saturated copper sulfate solution under illumination by a white fluorescent light has been advocated.

In the main the comments recorded in this section apply to enamel fused onto sheet and cast iron. Enamel is, however, applied to aluminum, stainless steel, copper, and noble metals on account of its aesthetic value and also to confer durability to the base metal. With low melting point metals such as aluminum it is obvious that superb resistance to chemicals is not as feasible as in the case of iron as the base. Nevertheless, such metals are vitreous enameled in growing quantities and sold, indicating that the range of color and durability obtained is superior to that possible with alternative finishes.

It can justly be claimed that vitreous enamel coating applied to sheet or cast iron (or indeed any other metal) will confer to the basic shape color, gloss, texture, and high degree of resistance to corrosive influences.

## References

1. Andrews, A. I. *Porcelain Enamels*; Gerrard Press, Champaign, IL.
2. Pedder, J. W. G. *Inst. Vit. Enam.* **1959**, 9(9).
3. Vargin, V. V. Ed. *Technology of Enamels*; Maclaren & Sons Ltd., 1967; pp 31, 78.
4. Krauter, J. C.; Kraaijveld, Th. B. *Inst. Vit. Enam.* **1970**, 21(2).
5. I.V.E. Technical Sub-committee Report, *Bull. Inst. Vit. Enam.* **1960**, 10, 285.

## 3.29 Degradation of Ceramic Masonry Linings

**D. I. Hughes**

Hanson Building Products, Accrington Nori Factory, Accrington, Lancashire BB5 6NR, UK

© 2010 Elsevier B.V. All rights reserved.

<b>3.29.1</b>	<b>Introduction</b>	2338
<b>3.29.2</b>	<b>Ceramic Masonry Linings</b>	2338
<b>3.29.2.1</b>	<b>Chemically Resistant Bricks</b>	2338
3.29.2.1.1	Acid-resistant brick	2338
3.29.2.1.2	High-density fireclay	2339
3.29.2.1.3	Carbon/graphite	2339
3.29.2.1.4	Silicon carbide	2339
3.29.2.1.5	Foamed glass	2339
3.29.2.1.6	Alumina	2340
3.29.2.1.7	Porcelain	2340
3.29.2.1.8	Silica	2340
3.29.2.1.9	Cast basalt	2340
3.29.2.1.10	Granite	2340
3.29.2.1.11	Refractory bricks	2340
<b>3.29.2.2</b>	<b>Mortars</b>	2341
3.29.2.2.1	Silicate-based mortars	2341
3.29.2.2.2	Synthetic and natural resins	2341
<b>3.29.3</b>	<b>Chemically Resistant Membranes</b>	2342
3.29.3.1	Asphalt/epoxy Mastic	2342
3.29.3.2	Ceramic Paper/Potassium Silicate	2343
3.29.3.3	Fluorocarbons	2343
3.29.3.4	Lead	2343
3.29.3.5	Thermoplastic	2343
3.29.3.6	Glass Fiber Reinforced Resins	2343
3.29.3.7	Rubber	2343
<b>3.29.4</b>	<b>Design and Construction of Ceramic Masonry Linings</b>	2343
<b>3.29.4.1</b>	<b>Vessel Linings</b>	2344
3.29.4.1.1	Fabrication of suitable steel vessels	2344
3.29.4.1.2	Storage of materials	2345
3.29.4.1.3	Surface preparation	2345
3.29.4.1.4	Application of a membrane	2345
3.29.4.1.5	Mortar	2345
3.29.4.1.6	Brick laying	2345
3.29.4.1.7	Inspection and quality control	2346
3.29.4.2	Linings to Flooring, Pits, and Trenches	2346
3.29.4.3	Linings to Chimneys	2347

### Abbreviations

**ASTM** American Society for Testing and Materials

**BS** British Standard

**PTFE** Polytetrafluoroethylene

**PVDF** Polyvinylidene fluoride

**PVC** Polyvinyl chloride

**SSPC** Steel Structures Painting Council

### 3.29.1 Introduction

Ceramic materials have been used for many years as linings to process equipments, chimneys, and chemical resistant flooring. The materials utilized have been both man-made and naturally occurring. By using ceramics, the engineer is employing a material which offers excellent corrosion resistance, abrasion and impact resistance, as well as (generally) an excellent thermal barrier.

Chemical resistant masonry is generally emplaced to act as a barrier to prevent corrosion of a substrate, which is most commonly steel but may also be any suitable structural material such as concrete or glass reinforced plastic. The protection system, therefore, acts effectively as a lining that generally comprises multiple layers supported by a shell (i.e., the substrate) that provides strength and rigidity. The lining system that prevents corrosive chemicals from reaching the shell generally consists of a membrane and one or more layers of chemical resistant bricks, bonded with a chemical resistant mortar. The three products used in chemical resistant construction are therefore:

1. chemically inert ceramic products such as brick, stone or blocks,
2. chemically resistant mortars,
3. chemically resistant membranes

Traditional ceramic materials are usually derived from clays and are thus based on silicate/silica chemistry. They can be classified into structural ceramics, such as pottery, porcelain, refractories, glasses, etc.; and inorganic binders such as cements, gypsum, etc. Most of these materials consist of crystallographic grains of one or more phases that are bound together by another phase that is commonly glassy and melts at the sintering temperature for the material.

That corrosion/degradation of ceramics and glasses does occur is incontrovertible. However, it is important to remember that, unlike in metals, it is a chemical dissolution process and not an electrochemical process. Thus, the dominant controlling mechanisms for the degradation of ceramic materials are the

rate of the surface chemical reactions and the rate of diffusion of reacting species to and from the surface.

### 3.29.2 Ceramic Masonry Linings

#### 3.29.2.1 Chemically Resistant Bricks

##### 3.29.2.1.1 Acid-resistant brick

The man-made chemical resistant ceramic products generally offered are of two types, categorized by the raw materials from which they were manufactured:

- red shale acid-resistant products
- fireclay acid-resistant products

These products, often referred to as 'acid brick,' are visually identified by their respective colors of red and off-white. Historically the red shale products have been favored by British and North American manufacturers. The fire clay products are manufactured often as a refractory by-product. Their properties are dependant upon the structure of the raw material and the manufacturing methods. Both products are manufactured from clays containing low levels of acid soluble components. By firing at relatively high temperatures and by prolonging the firing time these products become partially vitrified throughout the entire body of the brick. This produces a strong brick with low water absorption, which is practically chemically inert ([Table 1](#)).

The performance of these ceramic products is very similar although differences exist due to their relative density and porosity. The red shale product being a highly vitrified dense bodied ceramic is excellent in applications covering a wide range of acid concentrations and temperatures. Red shale bricks have a surface porosity of practically zero percent, preventing penetration of chemicals into the body of the ceramic avoiding chemical spalling. The fireclay materials that have lower levels of flux within the clay generally fire to lower degrees of vitrification and hence exhibit higher porosity. As a result fireclay bricks unfortunately are susceptible to chemical spalling, as their relatively high porosity extends throughout the body of the brick. Chemical spalling is the

**Table 1** Typical physical properties of red shale and fireclay bricks

Property	Test method	Red shale	Fireclay
Density ( $\text{Mg cm}^{-3}$ )	ASTM C 20	2.45	2.15
Water absorption (%)	ASTM C 20	2	5
Apparent porosity (%)	ASTM C 20	5	11
Cold crushing strength (MPa)	ASTM C 133	>150	>80
Acid solubility (%)	ASTM C 279	7	6
Thermal spalling (no. of cycles at 450 °C)	DIN 51068	5	10

result of crystallization of salts that have penetrated the brick. The crystal growth weakens the structure of the brick causing it to fracture. The thermal spalling resistance of red shale is lower than that of the fireclay product. The fireclay products being more open bodied give improved thermal spalling resistance. They are often used in 'refractory' applications. Thermal spalling is not a problem normally encountered in liquid phases, where temperatures are generally below 150 °C. Due to its low porosity the red shale product usually conforms to the standard Type III in ASTM C 279. The fireclay product is described as meeting Type II in ASTM C 279.

Both products are manufactured in a variety of different shapes. The shapes can be specifically manufactured to suit the complex arrangements often found in chemical reaction vessels. The two products are used in similar applications; the choice between them generally made purely on economic considerations.

### 3.29.2.1.2 High-density fireclay

This material is similar to the low density fireclay, however, the density is increased to 2.3 Mg m<sup>-3</sup> and the porosity lowered to 5%. As a result the cold crushing strength is improved as is the acid solubility. The somewhat improved performance over the two previously mentioned products is offset by a considerable increase in cost.

### 3.29.2.1.3 Carbon/graphite

Carbon brick is used in conditions where shock resistance is of prime importance. Due to their much higher porosity and lower coefficients of expansion these materials are capable of withstanding thermal and pressure shock to a much higher degree than those products previously mentioned. Carbon brick can be used to absorb surface stresses in brick linings which would otherwise cause compressive failure of red shale or fireclay bricks. Carbon brick also exhibits resistance to attack by both strong alkali and hydrofluoric acid.

Carbon brick is generally derived either from coking coal or from petroleum coke. The petroleum cokes offer a higher purity containing very low levels of ash. Often clays are used as binding agents during brick manufacture. The nature of the ash and binding agent must be considered when specifying carbon brick types as they will alter the chemical resistance of the brick. In particular the resistance to strong alkali and hydrofluoric acid can be adversely affected by the composition of the ash or binding agent. Carbon brick is generally stable to very high temperatures in the absence of an oxidizing atmosphere. However, in air the temperature limit for carbon brick is 350 °C, above which the carbon brick will be destroyed by oxidation to carbon dioxide (Table 2).

### 3.29.2.1.4 Silicon carbide

Silicon carbide brick is made from SiC (80–90%) normally nitride bonded with Si<sub>3</sub>N<sub>4</sub>. This relatively high porosity material gives good thermal spalling resistance along with a general high chemical resistance. The bricks and special shapes made from this product can be used at high temperatures where high abrasion resistance is required (although alumina brick can offer a slightly higher abrasion resistance) (Table 3).

### 3.29.2.1.5 Foamed glass

Foamed borosilicate glass or aluminosilicate glass is formed into blocks which have zero percent water absorption. This is a highly efficient impermeable insulating material with good chemical resistance to all acids, except hydrofluoric acid. This product cannot be used in the presence of alkali solutions. Foamed glass offers a very good thermal barrier having a particularly low thermal conductivity. Foamed glass blocks are available in a variety of different shapes and grades. The grading of the product is related to its density. Foamed glass blocks can be easily cut with a 'wood' saw. The application of this material is limited by its extremely low crushing strength and abrasion resistance (Table 4).

**Table 2** Typical physical properties of carbon bricks

Property	Petroleum-derived coke	Coal-derived coke
Bulk density (Mg m <sup>-3</sup> )	1.50	1.60
Apparent porosity (%)	25	19
Cold crushing strength (MPa)	40	80
Modulus of elasticity (GPa)	12	10
Tensile strength (MPa)	6	7
Coefficient of linear thermal expansion (K <sup>-1</sup> )	$3.5 \times 10^{-6}$	$5.4 \times 10^{-6}$
Thermal conductivity (25 °C–400 °C) (W m <sup>-1</sup> K <sup>-1</sup> )	4–6	4–4.5
Upper temperature limit (in air) (°C)	350	350
Ash content (%)	<1.0	6.6



**Table 3** Typical physical properties of nitride-bonded silicon carbide bricks

Property	Value
Bulk density ( $\text{Mg m}^{-3}$ )	2.63
Apparent porosity (%)	16
Modulus of rupture (MPa)	38
Cold crushing strength (MPa)	165
Abrasion resistance – BS1902 ( $\text{cm}^3$ )	30
Thermal conductivity at 200 °C ( $\text{W m}^{-1} \text{K}^{-1}$ )	20

**Table 4** Typical physical properties of foamed glass

Property	Test method	Value
Specific weight ( $\pm 10\%$ tolerance)	C165	$0.12 \text{ Mg m}^{-3}$
Thermal conductivity ( $\pm 10\%$ )	C203	$0.038 \text{ W m}^{-1} \text{K}^{-1}$
At 0 °C		$0.040 \text{ W m}^{-1} \text{K}^{-1}$
At 10 °C		
Compressive strength (average at break point)	C 240-85	700 kPa
Flexural strength	C 303	400 kPa
Flexural modulus of elasticity	C 518	800 MPa
Coefficient of thermal expansion	E 96	$9 \times 10^{-6} \text{ K}^{-1}$
Specific heat	E 136	$0.84 \text{ kJ kg}^{-1} \text{K}^{-1}$
Thermal diffusivity	ISO8302	$4.2 \times 10^{-7} \text{ cm}^2 \text{s}^{-1}$

### 3.29.2.1.6 Alumina

Fine grain, high grade alumina shapes are manufactured from an exceptionally pure, uniformly controlled alpha aluminum oxide and are engineered to be one of the best wear resistant materials available to counteract fine particle abrasion. Preengineering and advanced processing techniques enable the manufacture of alumina products in a variety of geometries from simple to complex shapes. Grid support beams and packing internals for sulfuric acid towers are normally manufactured from high alumina clays ([Table 5](#)).

### 3.29.2.1.7 Porcelain

Similar to high alumina brick, porcelain is an extremely dense material manufactured from high alumina content materials (85%). Its zero water absorption and excellent chemical resistance can be put to use where it is important to maintain product purity. The density of this product generally exceeds  $2.45 \text{ Mg m}^{-3}$ .

### 3.29.2.1.8 Silica

High silica content bricks (>98%) can be used for a wide range of very high concentration acids. Their

**Table 5** Typical physical properties of sintered alumina

Property	Value
Bulk density ( $\text{Mg m}^{-3}$ )	2.52
Alumina content (wt%)	>90
Water absorption (%)	0
Gas permeability (%)	0
Compressive strength (GPa)	1.77
Young's modulus (GPa)	270
Thermal conductivity ( $\text{W m}^{-1} \text{K}^{-1}$ )	18
Thermal expansion ( $\text{K}^{-1}$ )	$8.30 \times 10^{-6}$
Vickers hardness (GPa)	9.00

**Table 6** Typical physical properties of silica bricks

Product	Low density	High density
Bulk density ( $\text{Mg m}^{-3}$ )	0.80	1.90
Crushing strength (MPa)	4	51
Modulus of rupture (MPa)	1	15
Thermal conductivity ( $\text{W m}^{-1} \text{K}^{-1}$ )		
At 100 °C	0.175	0.645
At 250 °C	0.195	0.700
At 400 °C	0.215	0.725

use must be avoided in the presence of hydrofluoric acid and strong alkali. They are available as both a high density product and also as a low density silica product. The low density product combines excellent chemical resistance with good thermal insulating properties ([Table 6](#)).

### 3.29.2.1.9 Cast basalt

Basalt rock is quarried, crushed, and then melted and poured into moulds. Extremely complex shapes can be manufactured. This product offers excellent chemical resistance and abrasion resistance. It is used for lining bunkers, hoppers, and chutes carrying abrasive chemicals ([Table 7](#)).

### 3.29.2.1.10 Granite

Granite has been used for centuries as a chemical resistant block. Simply cut to shape from deposits of granite rock this product can be used in a variety of different chemical and abrasion resistant applications. The properties of granite can vary immensely from one source to another. Large shaped granite blocks have found use throughout the steel industry as 'skid blocks' in steel pickling tanks ([Table 8](#)).

### 3.29.2.1.11 Refractory bricks

A large range of refractory bricks are manufactured throughout the world. They are occasionally used in chemical resistant linings acting normally as an

**Table 7** Typical physical properties of cast basalt rock

Property	Value
Density ( $\text{Mg m}^{-3}$ )	2.9
Mohs hardness	>8
Compressive strength (MPa)	>450
Water absorption (%)	0

**Table 8** Typical physical properties of granite block

Property	Value
Nominal composition (%)	
$\text{SiO}_2$	>70.0
$\text{Al}_2\text{O}_3$	<18.0
$\text{K}_2\text{O}, \text{Na}_2\text{O}$	<10.0
$\text{TiO}_2$	<1.0
$\text{Fe}_2\text{O}_3$	<2.0
$\text{CaO}, \text{MgO}$	<2.5
Bulk density BS1902 ( $\text{Mg m}^{-3}$ )	>2.40
Water absorption BS3921 (%)	<1
Cold crushing strength ISO 179.3:N12 (MPa)	>200
Modulus of rupture (MPa)	>25

insulating brick behind the ‘true’ chemical resistant brick. The manufacturers do not list chemical resistance amongst the properties of these products. Their physical properties vary greatly from one product to the other. When designing chemical resistant linings using these products their selection should consider the following points: (1) the type of chemicals likely to contact the product should not damage the product. Higher temperatures can increase the chemical solubility of the product. (2) The compressive stress that the brick will experience must be below the compressive strength of the brick. (3) The thermal conductivity and brick thickness should be as much as needed to give the required temperature drop. The products used most commonly in chemical resistant construction include the following:

*Insulating firebricks* are manufactured from low iron silica/alumina clays. They have properties of low density and high porosity. Having high porosity makes them unsuitable in applications where total immersion in liquid chemicals is a probable condition. Their temperature range can extend to 1000 °C.

*Mullite bricks* are manufactured from clays having a preponderance of alumina over silica. Hence, the fired bricks contain little free alumina. The partial vitrification produces a brick offering good chemical resistance and high compressive strength. These bricks can be used in low duty chemical resistant applications when ‘acid brick’ is not available.

### 3.29.2.2 Mortars

#### 3.29.2.2.1 Silicate-based mortars

In chemical resistant masonry construction the choice of mortar is determined by the chemical and thermal conditions of the process. Care must be taken when using these mortars, as deviation from the manufacturers mixing instructions and recommendations regarding their use can result in a mortar with poor strength and chemical resistance.

These mortars consist of sodium or potassium silicate liquid mixed with a silica filler. The hardening process is accelerated by the use of a catalyst, for example, polyphosphate, silicofluoride, amines, and lead oxide. The advantage of polyphosphate hardened mortars is a low fluid absorption (2% for sodium polyphosphate). Potassium silicate mortars, utilizing silicofluorides must be washed with weak acid as part of the curing process. This also assists in lowering the fluid absorption.

These mortars have excellent chemical resistance to low and high concentration acids. Their temperature limit is 800 °C. A disadvantage of these mortars is their high porosity >12%. They are not suitable for contact with hydrofluoric acid and alkali solutions. Potassium silicate mortar is the most widely used. The use of sodium silicate mortar has declined due to its relatively high water solubility. With the addition of suitably graded fillers the potassium silicate mortar can be modified to produce a potassium silicate concrete that can be cast in a similar manner to Portland cement (Table 9).

#### 3.29.2.2.2 Synthetic and natural resins

##### Furane resin

Furane resin mortars have found wide popularity in the United Kingdom and North America due to their excellent chemical resistance and ease of use. This is the standard mortar for low sulfuric acid concentration (<70%) applications in vessel linings and flooring. They consist of furane resin liquid mixed with filler. The fillers available are silica, graphite or carbon. The normal filler is silica. For hydrofluoric acid and hot concentrated alkaline conditions carbon filled grades of furane mortar should be used. The carbon filled variety of this mortar is the mortar of choice when bonding carbon brick. The cheaper silica filled furane resin mortar should always be used when bonding acid brick. Furane mortars offer good erosion resistance and a service temperature of up to 200 °C. Some specialist furane mortars can withstand temperatures up to 300 °C (Table 10).

**Table 9** Typical physical properties of potassium silicate mortar

Property	Value
Density ( $\text{Mg m}^{-3}$ )	>1.85
Tensile strength (MPa)	3.5
Compressive strength (MPa)	>21
Modulus of rupture (MPa)	10
Coefficient of expansion ( $\text{K}^{-1}$ )	$15 \times 10^{-6}$
Water absorption (%)	15
Temperature limit ( $^{\circ}\text{C}$ )	800
Conformance	ASTM C 466

**Table 10** Typical physical properties of silica filled furane mortar

Property	Value
Tensile strength (MPa)	4
Compressive strength (MPa)	38
Flexural strength (MPa)	17.5
Bond strength (MPa)	1.5
Density ( $\text{Mg m}^{-3}$ )	1.985
Water absorption (%)	0.2
Temperature limit ( $^{\circ}\text{C}$ )	200
Conformance	ASTM C 395

**Modified phenolic resin**

Phenolic mortars offer chemical resistance over a wide range of both acid and alkali conditions. A choice of either carbon or silica based fillers are available. Being phenol based, care must be taken when using these mortars. In recent years the safety precautions required when using this mortar have resulted in a reduction in its use. Graphite filler and a double hardener system permit this mortar to be utilized in prestressing brickwork which places the brick lining in permanent compression. The porosity of these mortars is extremely low. They exhibit a good degree of erosion resistance and have a maximum service temperature of  $190^{\circ}\text{C}$  (Table 11).

**Epoxy resin**

Epoxy resin mortars are supplied as a two- or multi-component system. The chemical resistance of these mortars is good. They can be used to withstand medium strength acid and alkali. They exhibit extremely high bond strength between brick and steel. Epoxy mortars are limited by a maximum temperature of  $90^{\circ}\text{C}$ . Epoxy resins have found extensive use as monolithic screed coatings for concrete in flooring applications (Table 12).

**Table 11** Typical physical properties of phenolic resin mortar

Property	Value
Tensile strength (MPa)	3
Compressive strength (MPa)	44
Bond strength (MPa)	1.2
Density ( $\text{Mg m}^{-3}$ )	2
Water absorption (%)	0.3
Temperature limit ( $^{\circ}\text{C}$ )	190
Conformance	ASTM C 395

**Table 12** Typical physical properties of epoxy resin mortar

Property	Value
Tensile strength (MPa)	7
Compressive strength (MPa)	52
Bond strength (MPa)	2.0
Density ( $\text{Mg cm}^{-3}$ )	2
Water absorption (%)	0.3
Temperature limit ( $^{\circ}\text{C}$ )	90
Conformance	ASTM C 395

**Polyester resin**

This family of mortars includes bisphenols, chlorinated polyester and vinylester based products. These mortars offer good resistance to acid, especially oxidizing acids. They have poor resistance to organic solvents with the exception of acetic acid. Epoxy mortars have better resistance to organic solvents. The bond strength is equivalent to epoxy. The compressive strength of polyester mortar is the highest of all resin based mortars (65 MPa).

**3.29.3 Chemically Resistant Membranes**

The membrane is the final line in defense for the shell and the first material in the system to be applied during installation. The membrane should, where possible, be impervious. Its selection, however, is often determined by temperature and chemical resistance considerations.

**3.29.3.1 Asphalt/epoxy Mastic**

A nonrigid material is applied directly to the vessel shell. The degree of flexibility is generally governed by the amount of epoxy and hardener that is used in the mix. Asphalt and bitumen are often used on their own as a membrane for chemical resistant floors.

**Table 13** Typical physical properties of PTFE sheet

Property	Value
Density ASTM D 792 ( $\text{Mg m}^{-3}$ )	2.1–2.2
Water absorption ASTM D 570 (%)	<0.01
Tensile strength ASTM D 638–D 1708 (MPa)	25–30
Elongation ASTM D 638–D 1708 (%)	250–400
Tensile modulus ASTM D 638–D 1708 (MPa)	750
Flexural modulus ASTM D 638–D 1708 (MPa)	44–52
Coefficient of linear expansion ASTM D 696 ( $\text{K}^{-1}$ )	$10\text{--}15 \times 10^{-5}$
Thermal conductivity ASTM C177 ( $\text{W m}^{-1} \text{K}^{-1}$ )	0.2–0.45

### 3.29.3.2 Ceramic Paper/Potassium Silicate

The ceramic paper (high purity chemical resistant paper made from aluminosilicate refractory fibres) is soaked in sodium silicate and pasted onto the substrate in sheets (similar to applying wallpaper), forming an impervious membrane. This membrane is often used in high strength acid applications. Temperature resistance is excellent.

### 3.29.3.3 Fluorocarbons

Fluorocarbons, such as PTFE and PVDF, offer excellent chemical resistance and thermal resistance up to  $250^\circ\text{C}$  and are applied usually in sheet form. Given their intrinsic 'nonstick' surfaces, their use is limited by the performance of the bonding agent either epoxy or asphaltic mastic. Often the surface of the sheet is 'etched,' to improve bonding. The sheet thickness is often very thin: 0.125 or 0.25 mm (Table 13).

### 3.29.3.4 Lead

For best performance, this excellent membrane should be homogeneously applied. In service, temperatures must be kept below  $70^\circ\text{C}$  to avoid creep. A lack of personnel with the necessary installation skills has led to a reduction in the use of lead as a membrane.

### 3.29.3.5 Thermoplastic

Sheets of a thermoplastic material such as Hypalon (chlorosulfonated polyethylene) may be applied to the shell with adhesive. Being a thermoplastic material the joints may be welded and the sheets are often reinforced with a polyester scrim. This membrane is nonrigid and has an upper limit of sulfuric acid

**Table 14** Typical physical properties of Hypalon sheet

Property	Value
Breaking strength ASTM D751 (N)	500
Tongue tear ASTM D751 (N)	250
Temperature resistance (high) ASTM D2136 ( $^\circ\text{C}$ )	160
Water absorption (%)	3.0
Density (for black unreinforced) BS903 ( $\text{Mg m}^{-3}$ )	1.6
Thermal expansion coefficient ASTM C864 ( $\text{K}^{-1}$ )	$20 \times 10^{-5}$
Thermal conductivity ( $\text{W m}^{-1} \text{K}^{-1}$ )	0.11
DC electrical resistivity at $125^\circ\text{C}$ ( $\Omega \text{cm}$ )	$2.3 \times 10^{11}$

concentration of 70%. It may be used as a membrane for both vessel and flooring applications (Table 14).

### 3.29.3.6 Glass Fiber Reinforced Resins

These are rigid membranes. The glass fiber reinforces furane, phenolic, or epoxy based compounds to reduce the susceptibility to hairline cracks.

### 3.29.3.7 Rubber

Either hard or soft rubbers, both natural and synthetic can be used as membranes behind acid bricks. They are not suitable for high acid concentrations and have temperature limitations of  $90^\circ\text{C}$ . Petroleum products can damage butyl rubber. PVC can be used in the presence of oxidizing chemicals. There are numerous types of rubber available; the most popular being bromobutyl, chlorobutyl, and neoprene. These products are often combined to produce calendered sheets which are frequently used to protect steel substrates. A bromobutyl/neoprene rubber sheet membrane (neoprene as the backing sheet to give improved bond strength) has found great success in lining vessels for the metallurgical industry (Table 15).

## 3.29.4 Design and Construction of Ceramic Masonry Linings

Ceramic masonry lining systems are utilized extensively to prevent corrosion of vessel shell materials, chimney shell materials and concrete floors. This is an extremely complex subject which cannot be effectively dealt with in this publication. The following guidelines will be of use to the engineer involved in the design of ceramic masonry corrosion resistant linings. The engineer is recommended to approach

**Table 15** Typical physical properties of BIIR/CR rubber sheet

<i>Property</i>	<i>Value</i>
Tensile strength (MPa)	$\geq 7$
Elongation at break (%)	$\geq 350$
Hardness (Shore A)	$50 \pm 5$
Rebound resilience (%)	$\geq 10$
Abrasion ( $\text{mm}^3$ )	$< 225$
Density ( $\text{Mg cm}^{-3}$ )	$1.26 \pm 0.02$
Bonding strength on steel ( $\text{N mm}^{-1}$ )	$> 4$
Electrical resistance ( $\Omega$ )	$> 108$
Test voltage	$> 10$
Max. continuous operating temperature ( $^{\circ}\text{C}$ )	$< 90$
Thermal conductivity ( $\text{W m}^{-1} \text{K}^{-1}$ )	0.28

the ceramic product manufacturer, the membrane manufacturer, the mortar manufacturer and the specialist installer for advice regarding ceramic lining design.

### 3.29.4.1 Vessel Linings

A multitude of different structures may require lining after specification. The most important fact to be remembered when designing ceramic lined structures is that the most likely form of failure is tension or shear. Ceramic lined units must, therefore, be designed to make the most of the excellent properties of compressive *strength* shown in ceramics and avoid possible tensile failure of the lining.

General process parameters will determine the type of mortar, membrane and ceramic material to be utilized. Once these have been specified the thickness and number of layers of brick must be determined. Temperature gradients must be calculated in order to check the membrane and substrate temperatures thus avoiding excursions beyond material performance limits. Stress-strain calculations can be performed to determine the structural integrity of the lining system.

Vessels are generally cylindrical, offering curved surfaces to be brick lined. This is an ideal situation, provided the thermal expansion of the shell is kept under control when the brickwork will be placed into compression during operation. Circular bricks should be used against curved surfaces. The use of thin tiles as backing courses and square bricks on tapered joints is not recommended due to the difficulty of transferring the stress evenly. This 'cheap' design which has been adopted recently by some manufacturers/installers is prone to movement resulting in shear which causes cracking of the mortar joints and tiles.

The bases of vessels are often flat. A superior base design is a dished base lined with at least two layers of brick, generally radial end arch bricks installed in concentric circles or radial stretchers installed in a cruciform arrangement. If a flat base is a necessity then multiple layers of bricks must be utilized if lifting of the lining is to be avoided.

Great care must be taken in designing the ceramic brick elements used in forming nozzles and manholes. The use of special shaped ceramic units for this application is highly recommended. Forming nozzles by cutting standard bricks during installation can only be successful provided an extremely skilled craftsman performs the work.

A number of specialist vessels may require supports for packed beds. Due to their excellent corrosion resistance ceramic products are utilized to form support structures for tower packing in sulfuric acid plant drying and absorption towers. Two designs are currently available:

- (i) support wall and beams
- (ii) self supporting dome

The first method has an extremely successful track record. The use of the self supporting dome, however, has led to gas channeling at a number of installations, especially on larger diameter towers. The ceramic product is a most effective product for this structure. The design choice is left with the engineer.

To optimize the corrosion resistance of the lining it is essential that the ceramic masonry lining is installed by experts following strict guidelines issued by the manufacturers of the lining components. The guides will cover a number of important areas, including vessel shell construction and preparation, material storage, mixing of products, installation technique for the membrane, mortar and brick, the curing process and inspection. The following general guide is the basis for all ceramic masonry lining systems.

#### 3.29.4.1.1 Fabrication of suitable steel vessels

All welded joints shall be continuous and ground smooth to a minimum of 3 mm radius for convex corners and to a minimum of 6 mm radius for concave corners. All surfaces shall be free of weld splatter of foreign material. Voids, gaps, holes, pockets, or undercut welds are not permitted. Vessels should be fabricated to an appropriate constructional code, for example: PD5500 (UK), GOST (Russia), ASME VIII (USA), AD2000 (Germany), ODAP2000 (France).

### 3.29.4.1.2 Storage of materials

Where possible, all materials to be used in the brick lining shall be stored in such areas and under such cover as to prevent water from entering any of the packages or from soaking the brick. In addition, for 16–24 h before use, all materials shall be maintained at temperatures not below 16 °C (in cold weather) or above 32 °C (in hot weather). If the materials have become damp (e.g., during transportation) then they must be thoroughly dried with blown dry air before use.

### 3.29.4.1.3 Surface preparation

Prior to applying the membrane, the contractor shall prepare the surface to be lined in accordance with SSPC-SP10 or SA 2½; blast cleaning should be carried out using silica grit to ensure that the surface is free of all rust and foreign matter. Following cleaning, all dust and silica shall be removed. The surfaces to be lined shall be fully dry and, if necessary, dried to achieve this.

### 3.29.4.1.4 Application of a membrane

The membrane must be applied before the steel surface develops a visible rust film. Any rusted surface must be cleaned again. Spot cleaning may be done by wire brushing followed by solvent cleaning. The membrane is installed in accordance with the manufacturer's recommendations. For sheet rubber membranes, this operation may require specialist rubber lining labor.

### 3.29.4.1.5 Mortar

The mortar shall be mechanically mixed in the ratio quoted on the manufacturer's specification sheet. No water or other foreign matter or unauthorized fillers, extenders or fluids shall be added to the mix. Mixing equipment shall be clean at the start of mixing and all surplus or unused mortar shall be removed between batches to prevent excessive inter-batch contamination and retempering of spent mortar.

In general, the mortar shall be completely free of lumps, dried mortar particles and foreign material. The mortar shall be capable of being spread uniformly over a brick surface without dragging. When the set of the mortar has advanced to the point that it will no longer wet the brick properly, no more of that batch shall be used and the balance shall be discarded.

### 3.29.4.1.6 Brick laying

All cutting of brick shall be done with a brick saw outside the vessels to prevent chips and small

particles from falling on the membrane backing. After cutting, all brick shall be fully air dried, wiped with an absorbent cloth and mortared into position when dry.

All joints shall be full and tight, the brick double buttered (i.e., all brick surfaces in mortar joints or against vessel membrane shall be buttered on both surfaces) and pressed firmly in place. All bricks shall be laid with a sliding motion to eliminate the possibility of air pockets and shall be firmly pressed into place and tapped until all surplus mortar is forced out of joints. Any excess mortar must be cut off cleanly with a trowel before initial set takes place. This mortar may be used to butter brick surfaces. Excessive waste of mortar must be avoided.

Large joints are unacceptable. The mason should aim for 3–4 mm joints. The width of mortar will be checked by an inspector. The top surface of brick shall not be coated with mortar until the next course of brick is placed. At the start of brickwork each day, all surplus mortar projecting from end joints of brickwork laid on the previous day shall be struck off the area on which the new brickwork is to be applied. Joints between courses and layers shall be staggered for maximum strength and to eliminate the possibility of straight line penetration from the interior directly to the vessel wall.

The brick lining subcontractor shall maintain proper material and internal air temperatures, and provide for full cure time as required by the mortar manufacturer. No bricks shall be laid when the temperature is less than 3 °C above the dewpoint and during winter time, all work areas shall be kept at a minimum temperature of 21 °C day and night until the mortar has set. No excessive moisture is acceptable (such as condensation on the steel plate in the vessel) where bricks are being installed. Condensation may be prevented by portable heaters (preferably electric) inside the vessels. Any brickwork less than 5 days old which has been wetted shall be replaced. Care should be taken to prevent condensation on or behind the brickwork from blowers or other devices used for heating.

The following is a guide to hardening time for potassium silicate mortar:

Temperature (°C)	Time (days)
10	10
16	8
21	6
27	4



In order to develop the optimum mortar strength, the curing shall be a minimum of 6 days or the above guide time, whichever is longer. After the completion of curing, the joints (when using potassium silicate mortar) shall be washed with 10% sulfuric acid to protect the surface against moisture or high humidity damage, unless the equipment is being placed immediately into acid service. Please note that acid washing of potassium silicate mortar is a vital part of the curing process and must not be omitted. Furane based mortars do not require acid washing.

All waste materials, spoiled and unused brick and mortar, water and cleaning materials shall be kept away from all acid proof masonry until it is cured.

#### **3.29.4.1.7 Inspection and quality control**

Work areas (mixing, brick cutting and installation areas) shall be maintained sufficiently clean so that foreign matter is not introduced into the lining system. Adequate lighting shall be maintained in the vessel during installation work to enable a sound lining to be obtained in accordance with this standard. The work will be inspected by the client's inspector at the following stages:

1. before the application of membrane, to ensure that all metal surfaces are clean and dry;
2. after the application of membrane, to ensure that complete coverage has been achieved;
3. during the laying of brick, to ensure that the specified conditions are followed.

Lining installations which are not in accordance with the specification or in which injurious defects, improper application, or excessive repairs are indicated shall be subject to rejection. A full inspection report shall be submitted to the manufacturer prior to the equipment being placed in service.

#### **3.29.4.2 Linings to Flooring, Pits, and Trenches**

Ceramic masonry lining systems have been successfully utilized to protect floors, pits, and trenches from the action of corrosive chemicals for many decades. Just as with vessel lining systems the total package consists of the three main components – membrane, brick, and mortar. The specification of the three component is entirely dependant upon the process conditions; taking careful consideration of the chemical types, temperatures and exposure times. Correct product specification, design and installation technique will produce a corrosion resistant lining which will

maintain many years of trouble free service. The lining offers not only corrosion resistance but also thermal resistance, abrasion resistance and impact resistance. The use of an acid brick system will permit heavy loading such as those experienced in chemical tanker loading bays.

For the majority of applications an asphalt/epoxy membrane, acid brick and furane mortar are used for the lining system. The membrane and mortar can be altered to suit specific process conditions. For high concentration acids Hypalon sheet membrane is often specified. In the presence of hot alkali or hydrofluoric acid carbon bricks may substitute acid bricks.

Both acid brick and acid tile are used for masonry lining systems. A tile is recognized internationally as a masonry unit with a thickness of 30 mm or less. Tiles are available in most of the materials mentioned previously for brick products. Their corrosion resistance is material and manufacturing method dependant. The choice between brick or tile is primarily one of determining the appropriate thickness of the masonry unit for the application. The thickness of the masonry unit must be sufficient to offer structural stability, mechanical protection and thermal protection.

It is worth stating, again, that ceramic masonry lining systems offer excellent performance provided they are placed in *compression*. Tensile and shear stresses are unacceptable. It is therefore essential that the substrate to which the ceramic masonry lining is to be applied has sufficient strength and rigidity to support the lining under all anticipated loads. In order to achieve sufficient rigidity it is recommended that the floor, pit or trench be constructed from reinforced concrete. The use of sheet steel, wood or concrete blocks as a substrate is unadvisable.

Concrete floors generally contain expansion and construction joints to permit movement. These joints must be mated to similar joints in the ceramic masonry lining. The joints are a potential source of leakage and therefore serious corrosion to the underlying substrate. The positioning of the joints, the material used for the joints and the design of joints is important if the integrity of the floor is to be maintained. The manufacturers should be consulted over the design of chemical resistant expansion joints.

There a number of corrosion resistant expansion joint materials available. The type of compression/expansion must be considered when specifying the joint material. Many joint materials deform under compression and then protrude from the joint. This would be totally unacceptable in enclosed joints, which may be employed in multi layer brickwork

systems. In a single layer brickwork system the protruding joint may be cut off. A brief list of the corrosion resistant expansion joint material, currently available, is as follows:

Plasticized PVC	Polyurethane foam	Natural rubber
Ceramic blanket	Silicone sealants	Teflon felt
Polyester foam	Flexible epoxy	Carbon sponge

Flexible epoxy has the best overall chemical resistance combined with a temperature resistance of 75 °C. For precise details of expansion joint corrosion and temperature resistance the manufacturer should be consulted.

### 3.29.4.3 Linings to Chimneys

Combustion processes invariably produce acid gases. In order to reduce energy wastage in power stations the flue gas temperatures have been steadily reduced over the last four decades. Flue gas desulfurization has also led to a reduction in flue gas temperatures. It is now commonplace to have flue gas temperatures below 90 °C, which is below the sulfuric acid and water dewpoints. As a result, acid condenses on the inside of the chimney causing corrosion of the flue liner and, hence, precautions against this occurrence have to be taken.

Ceramic masonry chimney linings serve as a chemical and abrasion resistant barrier against gases, liquids, and solids thereby protecting the chimney shell (windshield). There are generally three distinct lining systems for concrete or steel windshields:

- full height, free standing flues;
- multilevel flues (as single or multiflue systems);
- full height linings as an integral component of the windshield.

Lining materials are carefully chosen to suit the flue gas conditions. Nonmetallic lining materials include acid brick, foamed glass block, synthetic rubber and glass fiber reinforced resins.

Flues constructed entirely of acid brick and chemical resistant mortars (normally potassium silicate) have an excellent proven track record. They are the only nonmetallic material capable of withstanding high temperature gases and a wide variety of corrosive

chemicals. As free standing brickwork elements, unconstrained by an outer shell, the brick flues have a tendency to exhibit tensile failure, when operated at elevated temperatures. Large cracks in the brick flues are evidence of this type of failure. The use of interlocking bricks and high bond strength mortars has reduced the incidence of stress cracks in brick flues. With the advent of chimneys operating with low temperature flue gases, tensile failure is no longer a problem and the brick flues can give an extremely long trouble free service.

The key benefits of acid brick flues are:

- durability,
- suitability for use in FGD and non-FGD systems,
- cost effective,
- long service life,
- excellent track record.

A large number of chimneys, throughout the world, have been built either entirely of steel or a concrete windshield with steel flues. The production of acid condensates in the flue gases, due to lower flue gas temperatures causing serious corrosion problems in these chimneys. Most of these chimneys now require the installation of a corrosion protective lining. Due to loading limitations on the foundations, the large weight of acid brick and mortar precludes this product as a viable solution. Foamed glass blocks bedded and jointed in chemical resistant mortars offer a suitable answer to the problem of corrosion prevention. The foamed glass block combines light weight with excellent acid resistance and thermal insulation properties. The choice of chemical resistant mortar is dependant upon the flue gas conditions. The mortar can also be used as the membrane applied to the steel shell, behind the foamed glass blocks.

### Further Readings

McCauley, R. A. Ed. *Corrosion of Ceramic and Composite Materials*, 2nd ed.; CRC Press, 2004.  
 Sheppard, W. L. Ed. *Corrosion and Chemical Resistant Masonry Materials Handbook*; William Andrew, 1986.  
 Bennet, J. P. In *Corrosion of Glass, Ceramics and Ceramic Superconductors*; Clark, D. E., Zaitos, B. K., Eds.; Noyes Publications, 1992; Chapter 15.

## 3.30 Degradation of Cement and Concrete

**P. Lambert, R. Brueckner, and C. Atkins**

Materials & Corrosion Engineering, Spring Bank House, 33 Stamford Street, Altrincham WA14 1ES, UK

© 2010 Elsevier B.V. All rights reserved.

---

<b>3.30.1</b>	<b>The Chemistry of Cement</b>	2349
3.30.1.1	Cement Types	2349
3.30.1.2	Compounds Present in Portland Cement	2349
<b>3.30.2</b>	<b>The Hydration of OPC</b>	2350
3.30.2.1	The Silicates	2350
3.30.2.2	Tricalcium Aluminate	2351
3.30.2.3	Tetracalcium Aluminoferrite	2351
<b>3.30.3</b>	<b>Stages in Cement Hydration</b>	2351
3.30.3.1	The First Stage	2351
3.30.3.2	The Second Stage	2352
3.30.3.3	The Third Stage	2352
3.30.3.4	Admixed Chlorides and the Rate of Hydration	2352
3.30.3.5	Summary of the Hydration of Cement	2353
<b>3.30.4</b>	<b>High Alumina Cement</b>	2353
<b>3.30.5</b>	<b>Pozzolanic Materials</b>	2354
3.30.5.1	Ground Granulated Blast Furnace Slag	2354
3.30.5.2	Pulverized Fuel Ash	2354
3.30.5.3	Silica Fume	2354
3.30.5.4	Inert Fillers	2355
<b>3.30.6</b>	<b>Concrete</b>	2355
3.30.6.1	Aggregate	2355
3.30.6.2	Water	2356
3.30.6.3	Admixtures	2356
3.30.6.4	Concreting	2356
3.30.6.5	Strength of Concrete	2357
<b>3.30.7</b>	<b>Degradation</b>	2358
3.30.7.1	Cracking	2358
3.30.7.1.1	Plastic settlement cracking	2358
3.30.7.1.2	Plastic shrinkage cracking	2358
3.30.7.1.3	Early age thermal cracking	2358
3.30.7.1.4	Long-term drying shrinkage	2358
<b>3.30.7.2</b>	<b>Corrosion of Steel in Concrete</b>	2358
3.30.7.2.1	Chloride attack	2359
3.30.7.2.2	Sources of chloride ions	2359
3.30.7.2.3	Carbonation	2359
3.30.7.2.4	Chloride ion diffusion	2359
3.30.7.2.5	The diffusion cell	2360
3.30.7.2.6	Immersion testing	2360
3.30.7.2.7	Resistivity measurements	2360
3.30.7.2.8	Errors in diffusion experiments	2361
3.30.7.2.9	Corrosion ladder	2361
3.30.7.2.10	Tests on retrieved samples	2361
3.30.7.2.11	Chloride ion selective electrodes	2362
<b>3.30.7.3</b>	<b>Alkali-Silica Reaction</b>	2362
<b>3.30.7.4</b>	<b>Sulfate Attack</b>	2363
3.30.7.4.1	Conventional sulfate attack	2363

---

3.30.7.4.2	Thaumasite form of sulfate attack	2364
3.30.7.4.3	Delayed ettringite formation	2365
3.30.7.5	<b>Mechanical Damage</b>	2366
3.30.7.5.1	Abrasion/erosion	2366
3.30.7.5.2	Cavitation	2366
3.30.7.5.3	Frost	2366
3.30.7.5.4	Exfoliation	2366
3.30.7.5.5	Fire	2367
References		2367

## Symbols

<b>A</b>	Aluminum oxide
<b>C</b>	Calcium oxide
<b>C<sub>(x)</sub></b>	Concentration
<b>C<sub>o</sub></b>	Surface concentration
<b>c</b>	Number of ions per unit volume
<b>D<sub>c</sub></b>	Diffusion coefficient (m <sup>2</sup> s <sup>-1</sup> )
<b>e</b>	Electron charge
<b>F</b>	Iron oxide
<b>F(x)</b>	Flux
<b>f<sub>ck,cyl</sub></b>	Minimum characteristic cylinder strength (N mm <sup>-2</sup> )
<b>f<sub>ck,cu</sub></b>	Minimum characteristic cube strength (N mm <sup>-2</sup> )
<b>k</b>	Boltzmann constant
<b>N̄</b>	NaO <sub>2</sub> -equivalent
<b>S</b>	Silicon oxide
<b>T</b>	Absolute temperature (K)
<b>t</b>	Time (s)
<b>w/c</b>	Water–cement ratio
<b>x</b>	Distance from the exposed face (m)
<b>X<sub>d</sub></b>	Depth of chloride penetration (m)
<b>Z</b>	Valency
<b>σ</b>	Conductivity (Ω <sup>-1</sup> m <sup>-1</sup> )

## Abbreviations

<b>AFm</b>	Tricalcium-aluminate-ferrite-monosulfate
<b>Aft</b>	Tricalcium-aluminate-ferrite-trisulfate
<b>ASR</b>	Alkali silica reaction
<b>BRE</b>	Building Research Establishment
<b>C–A–H</b>	Calcium aluminate hydrate
<b>C–S–H</b>	Calcium silicate hydrate
<b>DEF</b>	Delayed ettringite formation
<b>GGBS</b>	Ground granulated blast furnace slag
<b>HAC</b>	High alumina cement
<b>IStructE</b>	Institute of Structural Engineers
<b>OPC</b>	Ordinary Portland cement
<b>PFA</b>	Pulverized fuel ash

<b>pH</b>	Potential hydrogenii
<b>SRPC</b>	Sulfate resisting Portland cement
<b>TEG</b>	Thaumasite Expert Group
<b>TF</b>	Thaumasite formation
<b>TSA</b>	Thaumasite form of sulfate attack

## 3.30.1 The Chemistry of Cement

### 3.30.1.1 Cement Types

EN 197-1:2000 defines cement as “a hydraulic binder, i.e., a finely ground inorganic material which, when mixed with water, forms a paste which sets and hardens by means of hydration reactions and processes and which, after hardening, retains its strength and stability even under water.” The hardening of cement is mainly a result of the hydration of calcium silicates and, to a lesser extent, of aluminates.

Portland cement consists of cement clinker and various other constituents, which determine its classification. These additional constituents can be granulated blast furnace slag, natural and industrial pozzolanic materials, burnt shale, limestone, silica fume, and calcium sulfate, which are added during the manufacture to control setting. EN 197-1:2000 covers 27 common cement products, which are grouped into five main cement types as follows:

- CEM I – Portland cement
- CEM II – Portland–composite cement
- CEM III – Blast furnace cement
- CEM IV – Pozzolanic cement
- CEM V – Composite cement

### 3.30.1.2 Compounds Present in Portland Cement

Ordinary Portland cement (OPC) is made up of the compounds listed in Table 1. The abbreviations are in the standard cement chemist’s notation: C = calcium

**Table 1** Compounds present in anhydrous cement

<i>Cement component</i>	<i>Abbreviation</i>	<i>% in OPC</i>	<i>Hardening rate</i>
Tricalcium silicate	C <sub>3</sub> S	>50	Rapid
Dicalcium silicate	C <sub>2</sub> S	<20	Slow
Tricalcium aluminate	C <sub>3</sub> A	<10	Rapid
Tetracalcium aluminoferrite	C <sub>4</sub> AF	<10	Extremely slow

oxide, S = silicon oxide, A = aluminum oxide, and F = iron oxide.

It is, however, more customary to express the composition of cements in terms of oxide analysis, that is, CaO, SiO<sub>2</sub>, Al<sub>2</sub>O<sub>3</sub>, Fe<sub>2</sub>O<sub>3</sub>, NaO<sub>2</sub>, and so on. From this it is possible to calculate the so-called 'Bogue compositions' shown in **Table 1**. The following equations are based on solving certain simultaneous equations and were first derived by Bogue.

For the system C<sub>3</sub>S–C<sub>2</sub>S–C<sub>3</sub>A–C<sub>4</sub>AF:

$$C_3S = 4.01710CaO - 7.6024SiO_2 - 1.4297Fe_2O_3 \\ - 6.7187Al_2O_3 (-2.852SO_3)$$

$$C_2S = 8.6024SiO_2 + 1.0785Fe_2O_3 \\ + 5.0683Al_2O_3 - 3.0710CaO$$

$$C_3A = 2.6504Al_2O_3 - 1.6920Fe_2O_3$$

$$C_4AF = 3.0432Fe_2O_3$$

The equations were produced by assuming that all the Fe<sub>2</sub>O<sub>3</sub> reacts with Al<sub>2</sub>O<sub>3</sub> and CaO to form the C<sub>4</sub>AF, the remaining Al<sub>2</sub>O<sub>3</sub> reacts with CaO to form the C<sub>3</sub>A. The CaO then reacts with the SiO<sub>2</sub> to form C<sub>2</sub>S and any CaO left reacts with the C<sub>2</sub>S to form C<sub>3</sub>S.

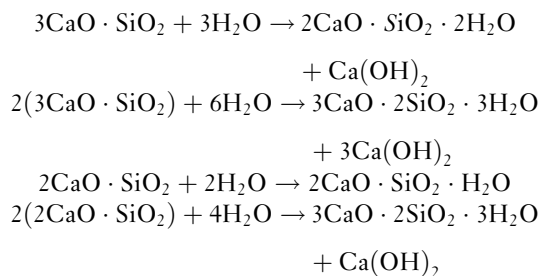
It should be recognized that in commercial manufacture, equilibrium conditions are unlikely to be achieved. Coarse particles may not be completely converted because some of the reactions occurring in manufacture are between liquid and solid phases and also resolution during cooling of previously crystallized phases may not be complete. Component parts may be embedded in each other where the liquid may not be able to act upon them or the liquid may crystallize independently without the formation of equilibrium products. The minor components of cements such as sodium, potassium, and magnesium oxides will also have an effect. Despite the aforementioned problems, the ability to produce a simplified equation for the composition of the

cement from its constituent parts has obvious benefits for the cement industry and also for scientific research.

### 3.30.2 The Hydration of OPC

#### 3.30.2.1 The Silicates

There is an empirical character to the information available with respect to the hydrolysis of the calcium silicates because of a wide variation in water contents and lime–silica ratios between component parts of the system. Also, products of the same composition can be represented by several phases, and it is difficult to prepare large crystals representative of those produced during cement hydration because the hydrates are in the form of gels.<sup>1</sup> In general, the reactions are considered to be as follows:



It is worth noting that Joisel<sup>2</sup> reports that there is no stoichiometrically defined hydrate of calcium silicate, and as a consequence, during hydration, intermediate compositions may exist locally between C<sub>2</sub>SH<sub>2</sub> and CH. Taylor<sup>3</sup> states that the composition of calcium, silica, and water varies between CS(aq.) and C<sub>3</sub>S<sub>2</sub>(aq.) without significant change in the X-ray diffraction pattern. It is the C–S–H that imparts the cementing action in concrete, derived from surface forces interacting over the large surface area of the C–S–H.

The rate of early hydration of silicates is controlled by the rate of dissolution of calcium and hydroxide ions into a liquid phase from the C–S–H layer produced around the cement grains.<sup>4</sup>

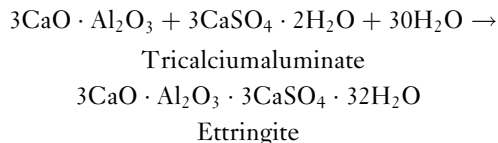
There is some debate whether or not the calcium silicate hydrate binds chlorides. Ramachandran<sup>5</sup> investigated the hydration of tricalcium silicate supplied by the Portland Cement Association in the presence of calcium chloride, using various techniques and concluded that there is evidence for the presence of various states of chloride. Ramachandran attributed this to two mechanisms: one due to the positively charged surface of the C–S–H adsorbing

negatively charged chloride ions and the second being the formation of some interlayer chloride, which was irremovable by leaching with ethyl alcohol but could be removed by leaching with water. Water molecules are more readily able to access the finer pores than does ethyl alcohol because of their smaller size. He added that the chloride ions incorporated into the C–S–H are not mobile enough in water to cause corrosion in reinforced systems.

Lambert *et al.*<sup>6</sup> used tricalcium silicate produced by firing a mixture of calcium oxalate, alumina, and magnesia to produce Jeffrey's Alite<sup>7</sup> ( $C_5S_16AM$ ), which is reported to be a reasonable approximation of  $C_3S$ . They reported, using pore water extraction to monitor the pore solution, that when the chlorides are added as sodium chloride no binding takes place. This is supported by the fact that the pH remained at  $\sim 12.5$ , which is the pH of saturated calcium hydroxide, which agreed with work done on microsilica binding using sodium chloride.<sup>8</sup>

### 3.30.2.2 Tricalcium Aluminate

Tricalcium aluminate is reported to preferentially react with calcium sulfate as follows:<sup>9</sup>



The term 'ettringite' has come into use in a generic sense to represent the calcium aluminate or ferrite trisubstituted hydrates (AFt) formed as a result of the reaction of tricalcium aluminate hydrating with gypsum and water.

If chlorides are present, the tricalcium aluminate mainly reacts with the sulfates present first to form the chloroaluminate,  $3CaO \cdot Al_2O_3 \cdot CaCl_2 \cdot 10H_2O$ , more commonly known as Friedel's salt.<sup>10</sup> It is worth noting that the formation of Friedel's salt will only take place if anhydrous tricalcium aluminate is present, and therefore, it would be expected that diffused chlorides will only be bound to a small extent. When tricalcium aluminate is hydrated in the presence of both gypsum and calcium chloride, a small amount of chloroaluminate is formed immediately, but the main consumption of chlorides begins only after the supply of sulfate ions is exhausted.

### 3.30.2.3 Tetracalcium Aluminoferrite

Tetracalcium aluminoferrite hydration is not well understood,<sup>11</sup> but is generally regarded as similar to the hydration of tricalcium aluminate under comparable conditions.  $Fe(OH)_3$  gel, AFt,  $C_2(A,F)H_8$ ,  $C_4(A,F)H_{13}$ , and  $Al(OH)_3$  gel have also been observed.  $C_4AF$  has a general formula of  $2CaO \cdot (Al_2O_3)_x (Fe_2O_3)_{(1-x)}$  where  $x$  is between 0 and 0.7. In most Portland cements  $x$  is usually 0.5.<sup>12</sup>

Ettringite is also produced and will undergo the same series of subsequent reactions as that formed during the tricalcium aluminate hydration. A chloro-ferroaluminate phase produced by the hydration of tetracalcium aluminoferrite in the presence of calcium chloride and analogous to Friedel's salt has also been identified.<sup>13</sup>

### 3.30.3 Stages in Cement Hydration

There are three main stages in the hydration of OPC.

#### 3.30.3.1 The First Stage

When OPC is mixed with water, a rapid reaction takes place, which forms a supersaturated solution. After this rapid period of initial hydration lasting less than 15 min, a period of very slow hydration lasting for several hours called the dormant or induction period occurs. There are four main theories for the cause of this period.

The first is that a layer of hydration products precipitate over the surface of the cement grains. After a period of time this splits, either by pressure caused by the formation of hydration products under this protective layer<sup>14</sup> or by osmotic pressure building up under the surface of the grain<sup>15</sup> and hydration commences again. The second theory states that hydration only starts when an initial hydrate of low permeability converts into one of a higher permeability<sup>16</sup> and therefore is similar to the first. The third proposes that the induction period ends because of calcium hydroxide crystallizing into solution, and thus forming nuclei that act as seed crystals for further calcium hydroxide, thereby allowing hydration of the silicates to proceed.<sup>17</sup>

The final theory reports that the induction period exists due to a potential barrier corresponding to a critical size of calcium silicate hydrate (C–S–H) nuclei.<sup>18</sup> According to this theory, C–S–H is initially only formed on imperfect preferential sites on the



surface of calcium silicates. Only after the hydrate nuclei reach a critical size does hydration extend to other parts of the surface and hence hydration accelerates.

The first theory is the simplest and has some evidence for its validity. Jennings and Pratt<sup>19</sup> concluded that, as hydration at the end of the dormant period is characterized by hollow spines growing out of the grains, this suggests that a membrane has ruptured and the interior of the grains flows out through these spines and hydrates on contact with the exterior solution. However, they also state that the environment of the experiment was artificial because it was at a water solids ratio of 20, and therefore, the procedure may be flawed although fibers such as those that were created in the experiment have been found in cement in practical situations. They suggest that when cement comes into contact with water, the calcium quickly passes into solution and a silica-rich layer forms a gelatinous coating containing alumina. This coating allows the passage of ions such as sulfates, potassium, and calcium along with water but not aluminum and silicon ions.

Odler and Dörr<sup>20</sup> studied the hydration of tricalcium silicate and concluded that the fourth theory was more accurate in this application. Addition of 'seed crystals' of calcium hydroxide did not affect the induction period, but the addition of prehydrated tricalcium silicate had a marked effect, thus discounting the third theory. They also stated that the preinduction period was controlled by the concentration of calcium hydroxide in the solution, and hence discounted the precipitation theory.

The time of inception and the duration of the dormant period depend mainly on the water–cement ratio, fineness of the cement, and its composition. The cement paste at this stage appears to be a suspension of fine powder in water. Odler and Dörr<sup>21</sup> state that the amount of tricalcium silicate that hydrates in the preinduction period can be altered by experimental procedure and the presence of defects in the crystalline lattice. The tricalcium silicate anneals with time, resulting in a lower number of lattice defects, resulting in an extension of the dormant period, thus further discounting the precipitation theory and supporting the final one.

During the dormant period a certain amount of sedimentation takes place, known as bleeding. This is undesirable because the water rises to the surface carrying fine cement particles with it, resulting in the formation of a high water–cement ratio slurry on the surface, called laitance, which has a low

strength. This causes problems when trying to continue construction up a column or wall and should be removed before casting continues. Also, flow channels of low cement content, and therefore low strength, can occur in the body of concrete structures. In reinforced concrete structures, this bleeding can cause voids beneath the reinforcement, which are reported to be sites for potential corrosion attack.<sup>22</sup>

### **3.30.3.2 The Second Stage**

The growth of plastic strength begins after the end of the dormant phase and can be divided into two stages. At the end of the dormant phase a period of hydration takes place, known as 'setting,' which lasts to about 30% of the total hydration. During this stage, the cement loses its plasticity and the cement paste becomes hard. Coagulation of the structure takes place and is characterized by the presence of a three-dimensional network formed by disordered coupling of the finest particles in the disperse phase through thin layers of the dispersion medium, resulting in a network low in strength. In this stage, crystallization only occurs in the form of individual crystallites, mainly in the form of calcium hydroxide and sulfoaluminate.

The onset of this phase is known as the initial set, and the end of the set, marked by the total loss of plasticity, is known as the final set.

### **3.30.3.3 The Third Stage**

After the final set, the hydration process slows down and the 'hardening period' begins, during which the cement gains most of its mechanical strength. In this stage, more intense crystal formation is accompanied by crystal bonding, forming a strong crystalline network. Subsequent strength development comes from the growth of hydrated calcium silicate crystalline structure as crystals are formed from the supersaturated solution. The rate of this stage is controlled by diffusion through the cement matrix. If mechanical deformation is applied at the onset of this stage, it is usually detrimental to its ultimate strength.

### **3.30.3.4 Admixed Chlorides and the Rate of Hydration**

Calcium chloride falls into the category of accelerating admixtures and, being a low-priced industrial by-product, was extensively used. In 1977, however, due to the increased risk of corrosion of reinforcement

steel, the use of chloride-based accelerators was prohibited in all reinforced or prestressed concrete in the United Kingdom.

Accelerators increase the initial rate of chemical reaction between the cement and the water so that the concrete stiffens, hardens, and develops strength more rapidly. This is a benefit because it allows the earlier striking (i.e., removal) of formwork. They have a negligible effect on workability and 28-day strengths are rarely affected. The addition of small amounts ( $<1$  mass%) of calcium chloride sometimes retards the set; however, this effect is very variable. Larger amounts produce an acceleration, and amounts over 3% have been known to cause a flash set. Sodium chloride produces a less pronounced change in the rate of hydration and the effect is more erratic, sometimes accelerating, sometimes retarding.

### 3.30.3.5 Summary of the Hydration of Cement

The hydration products of the silicates are basically a calcium silicate hydrate gel of varying morphology and composition between  $1 < C/S < 2$  and calcium hydroxide. Contained within this gel are areas where iron, sulfate, and aluminum ions have been adsorbed into the lattice. It is probable that some chlorides can also be absorbed in this way. Chlorides may also form complexes with hydrating calcium silicates. Specific information about the calcium silicate hydrates is hard to obtain because they are poorly crystalline, which leads to difficulty in analysis. Also, variations occur throughout the cement matrix, which are time dependant because of the nature of the solid solutions formed.

Aluminate hydrates also form solid solutions, leading to time-dependant variations as compounds migrate through the matrix. Chlorides are predominantly bound to the aluminate compounds by the formation of Friedel's salt. The hydration products of the aluminoferrites are similar to those of the aluminates with iron substituting for aluminum in varying quantities.

The hydration of cement takes place in three stages. A period of rapid hydration occurs as water is added to the anhydrous cement. After about 15 min this stops and a period of little activity takes place, known as the dormant period. This lasts for about 3–4 h, after which hydration recommences. The end of the dormant period is thought to be caused by the break down of some protective membrane of hydration products covering the surface of the cement

grains or by the transformation of a hydrate to a more porous form or by the volume of hydrates on the surface of the grain reaching a critical mass. The post dormant phase of hydration is known as the setting period, when crystallites of calcium hydroxide and sulfoaluminate are known to form. Eventually, the hydration products build up and this causes the process to become diffusion controlled. It is during this hardening period that the cement gains its mechanical strength.

### 3.30.4 High Alumina Cement

High alumina cement (HAC), as the name suggests, contains a large proportion of alumina; typically about 40% each of alumina and lime with around 15% of ferrous and ferric oxides, plus 5% silica.

HAC was developed as an alternative to OPC because of its increased resistance to sulfate attack, and in this respect, it performs well. This resistance to sulfate attack is due to the absence of  $\text{Ca}(\text{OH})_2$  in hydrated HAC and also due to the protective influence of the relatively inert alumina gel formed during hydration. HAC is not attacked by  $\text{CO}_2$  dissolved in pure water, and while it is not acid resisting, it can tolerate very dilute solutions of acids ( $\text{pH} > \sim 4$ ) found in industrial effluents but not hydrochloric, hydrofluoric, or nitric acids.

Another positive feature of HAC is its very high rate of strength development. About 80% of its ultimate strength is reached in 24 h, and even at 6–8 h the concrete is strong enough for the side formwork to be struck and for the preparation for further concreting to take place. It is for this attribute that it became popular for the production of precast beams used in floor and roofing systems in the late 1960s and early 1970s.

Because a number of high profile catastrophic failures occurred in the early 1970s, the suitability of HAC concrete for use in structural components has been of concern. The Building Research Establishment (BRE) subsequently carried out a major investigation<sup>23</sup> and identified that HAC is subject to a process known as conversion.

Conversion occurs due to the primary hydrates present in the material being chemically unstable. The conversion process involves a change in the mineralogy of the cement, which becomes increasingly porous and friable with age and also loses alkalinity. Under conditions where the overall dimensions of the body are constant, as is the case in set

cement paste, conversion results in an increase of porosity of the paste.

The strength of hydrated cement paste or of concrete is very strongly affected by its porosity; a porosity of just 5% can reduce the strength by more than 30%. As a result, conversion markedly reduces the strength of HAC. Also, the increased porosity means the concrete is more susceptible to other forms of attack such as alkali, sulfate attack, or carbonation.

As the concrete becomes more porous, it allows easier movement of oxygen and water as well as aggressive species like chloride ions. This, combined with the loss of alkalinity, can result in the increased possibility of reinforcement corrosion, which can also cause deterioration of the concrete. This deterioration is accelerated by the presence of excess water, for example, from leakages, condensation, or groundwater.

The effects of conversion on the strength of beams depend on the original strength and quality of concrete used. In some cases, the increase in porosity has been reported to allow moisture to react with unhydrated cement particles and produce an increase in strength. In other cases, significant strength reduction can take place.

### **3.30.5 Pozzolan Materials**

A number of materials are available that can be used to partly replace the cement content of a concrete mix, saving cement and usually providing additional benefits in terms of performance and durability; these include blast furnace slag, fly ash, metakaolin, and natural volcanic ashes. Such materials, whether natural or human-made, have been thermally modified to produce potentially reactive compounds of silica and alumina.

The first hydraulic cements based on pozzolanic materials date back to Roman times. These were materials that reacted with lime water to produce a hardened mass and employed the volcanic ash obtained from the slopes of Mount Vesuvius, in the vicinity of the Italian town of Pozzuoli from which the term Pozzolan originates. The term is now commonly used to represent any material that reacts with alkaline water to harden. There are a number of industrial by-products that are used in this way to replace a proportion of the cement used in concrete.

There are typically two main benefits. The first is a reduction in cost, as the by-products are typically cheaper than the cement they replace. The second

is a perceived enhancement in the properties of the concrete produced. This can take the form of increased resistance to aggressive materials, enhanced strength, or slower curing (which for large concrete pours is a benefit as the heat generated is reduced and consequently the risk of thermal-induced cracking when the concrete cools). There is a further potential benefit with regards to sustainability, as there is less cement used and it consumes what would otherwise be an industrial by-product.

#### **3.30.5.1 Ground Granulated Blast Furnace Slag**

Typically up to 70% of the cement used in a mix can be replaced with ground granulated blast furnace slag (GGBS). This means that a relatively standard concrete mix containing 300 kg of cement per cubic meter of concrete would contain 90 kg of OPC and 210 kg of GGBS. The benefits of GGBS are typically a reduced heat of hydration for large pours, and an increase in the overall durability of the concrete. This is both due to an increased resistance to the effects of aggressive chemicals on the concrete and due to a reduced rate of passage for aggressive species such as chlorides into the concrete.

The reduced heat of hydration produces a slower strength gain and a longer setting time. This means that the concrete may require more careful placement and curing techniques to minimize the risk of plastic cracking problems. The slower hydration may also produce substandard strength gain, resulting in a difficulty in achieving a target strength (the common method used to assess the quality control of concrete on a construction site). Some cases have been found where a portion the GGBS did not hydrate, but this is rare.

#### **3.30.5.2 Pulverized Fuel Ash**

Pulverized fuel ash or fly ash (PFA) is a by-product of coal-fired power stations and can achieve similar effects to GGBS, that is, an increase in durability and a reduction in heat of hydration, with a risk of plastic cracking problems because of difficult curing. The replacement quantities are lower than GGBS (typically up to 35%).

#### **3.30.5.3 Silica Fume**

Silica fume, also known as microsilica and nanosilica, is a highly reactive pozzolanic filler, which is used to achieve high strength and dense concrete. Silica

fume is a by-product of the manufacture of silicon and ferrosilicon alloys from high-purity quartz and coal in a submerged-arc electric furnace. The  $\text{SiO}_2$  content is generally in the range between 80 and 98 mass%. The process produces a very fine material, which has a high pozzolanic reactivity. The silica particles react with the calcium hydroxide of the cement paste and form calcium silicate hydrates. The hydrates fill the space between the cement hydration products, and in particular, the weaker calcium hydroxide interface around aggregate particles increases the strength and density of the concrete. Contrary to the other cement replacements, the use of silica fume leads to a more rapid hydration and typically higher strengths.

#### 3.30.5.4 Inert Fillers

Fillers are very finely ground materials, which have a similar particle size to Portland cement. Fillers, such as limestone or quartz powder, are inert or quasiinert materials, which mainly improve the density and stability of the cement paste. The workability, permeability, bleeding, or cracking tendency are also improved. Inert fillers do not contribute to the hydration; however, limestone powder can be beneficial for the hydration. It is able to form monoaluminate carbonate hydrates and supports the formation of ettringite.<sup>24</sup>

Modern UK and European Portland cements (CEM I), BS EN 197-1:2004, are permitted to contain up to 5% limestone filler as a minor addition. This can lead to a higher susceptibility to thaumasite formation because of a considerable internal source of carbonate ions.<sup>25</sup>

### 3.30.6 Concrete

Concrete has been an important construction material for more than the last 100 years. Concrete is a three-phase system consisting of cement, aggregate, and water. Nowadays, concrete is usually a five-phase system because of the addition of additives and admixtures for property improvements and cost reduction. The binder compounds cement and additives are discussed in [Sections 3.30.1.1](#) and [3.30.5](#), respectively.

#### 3.30.6.1 Aggregate

Aggregates occupy more than 75% of the volume of concrete and hence form one main indicator of

the strength. The properties of aggregate characterize the performance of concrete. According to the density of aggregate, concrete is divided into three groups of lightweight ( $400 < 2000 \text{ kg m}^{-3}$ ), normal ( $2000\text{--}2800 \text{ kg m}^{-3}$ ), and heavyweight concrete ( $\geq 2800 \text{ kg m}^{-3}$ ).

Aggregate is a cheap compound in relation to cement. Hence, it is desired to use as much aggregate as possible, but with the restriction to achieve a durable concrete. Aggregate influences physical, chemical, and thermal characteristics and may affect the durability. Beside the economic factors, aggregate is used to increase the concrete's stability, that is, reduction of shrinkage, to decrease the susceptibility to chemical attack due to the reduction of susceptible cement paste, and to decrease thermal effects. Cement paste is susceptible to shrinkage-induced cracking, carbonation, sulfate attack, and mechanical attack such as erosion and fire. However, aggregate can cause concrete deterioration such as alkali-silica reaction, frost attack, and in the case of salt contamination, corrosion may be initiated. Organic impurities may affect the hydration, and coating of fine particles such as clay may reduce the bond.

To obtain good quality concrete, the compactness of the aggregate bulk has to be high, that is, to follow certain particle size distributions. This is mainly achieved using at least two size groups: fine (0–5 mm) and coarse (>5 mm) particles. The fine particles are also referred to as sand.

Another point of division of aggregate is based on their source. There are natural and industrial manufactured aggregates. Industrial products are mainly light- and heavyweight aggregates. Examples of natural aggregates are basalt, granite, limestone, quartz, and gabbro.

The strength of natural occurring aggregates is mostly higher than the cement paste; therefore, the weakest part within the concrete system is the cement paste, and in particular, the interface between cement paste and aggregate. The strength of cement correlates well with the concrete strength of a three-phase system. On the other hand, lightweight aggregates have a lower strength than do the cement paste. There are three different crack patterns that relate to the strength relation between aggregate and cement paste in concrete. Concrete under stress may crack either within the cement paste or along the aggregate-paste interface or through the cement paste and aggregate particle or within the aggregate materials.

### 3.30.6.2 Water

Water is the third main phase within the concrete system, beside cement and aggregates. Water is essential for the formation of the strength giving hydrates within the cement paste such as the C–S–H phases. Hydration of cement is discussed in [Section 3.30.3](#). The effects of the quantity of water, the water–cement ratio, on the strength are discussed in [Section 3.30.6.5](#).

Natural occurring water and recycled water from concrete production can be used. The suitability depends on secondary substances in the water. Impurities may affect the hydration and consequently the strength of concrete. Organic substances should not be present. Seawater should not be used in reinforced concrete. The use of recycled water is specified in EN 1008. The usable amount of recycled water depends on the actual density showing the percentage of fine particles. Recycled water should not be used in concrete with air entrainment.

### 3.30.6.3 Admixtures

Admixtures are an additional ingredient of concrete. They are used to improve fresh concrete properties, such as workability and bleeding behavior, combined with an increase in strength and durability.

BS EN 934-2:2001 defines admixtures as “materials which are added during the mixing process of concrete in a quantity not more than 5% by mass of the cement content of the concrete, to modify the properties of the mix in the fresh and/or hardened state.” They are mainly based on chemicals. Admixtures can be classified according to their function in

- water reducing/plasticizing,
- high range water reducing/superplasticizing,
- water retaining,
- air entraining,
- set accelerating,
- hardening accelerating,
- set retarding,
- water resisting,
- set retarding/water reducing/plasticizing,
- set retarding/high range water reducing/superplasticizing, and
- set accelerating/water reducing/plasticizing admixture.

The application of admixtures should always be in accordance to the manufacturers' guidance. The dosages should be within the recommended range

because of the high sensitivity of concrete to the admixture.

Plasticizers are used to reduce the water–cement ratio in order to gain early and high-strength concrete with increased durability. Air entraining admixtures are used to increase the freeze–thaw resistance. Accelerating admixtures are commonly used in the precast sector and for cold weather concreting, whereas retarding admixtures are used to counteract the effects of hot weather on hydration.

Admixtures are a relative expensive component of concrete, however, the positive effects, such as increased workability and durability, can reduce total costs.

### 3.30.6.4 Concreting

Concrete should be mixed so that a homogenous mix is ready for transport and placement. The time between first contact of cement and water and final placing is limited to 90 min. The temperature of the concrete when placed is also limited so that the concrete temperature should be in the range of 5–30 °C. Concreting should be suspended when the air temperature is 3 °C and falling. The temperature of concrete placed in hot weather conditions can be reduced using cooled aggregates, ice as water replacement, or special curing methods to prevent excessive core and surface temperatures.

The placed concrete should be properly vibrated so that the reinforcement is enclosed and air voids (<1 mm) are reduced to less than 2%. However, over-vibration may cause loss of homogeneity because of segregation. The following curing process mainly determines the durability of the concrete. This is of special importance during cold and hot weather concreting. Concrete placed in cold weather should be cured longer to allow for the retardation of the hydration. The temperature gradient between core and surface should be minimized and the concrete should be prevented from freezing during its early stages of hydration. All surfaces should be protected against any weather effects. The rate of hydration increases with increasing temperatures so that special curing measures have to be taken into account in hot weather conditions. These may be cooling systems within the core of the concrete to prevent temperature above 60 °C, protection of the surface against sun, wind, and evaporation, and continuous humidification to achieve high grades of hydration within the surface layer.

Improper curing in cold weather may cause excessive bleeding, increased pore volume due to freezing, plastic cracking and thermal cracking caused by high temperature gradients. Wind and sun may cause extensive surface evaporation, causing a highly porous, less durable surface. Excessive core temperature can cause cracking and thermodynamical changes within the hydration products, causing delayed ettringite formation (DEF).

### 3.30.6.5 Strength of Concrete

The compressive strength of concrete is the most expressive property to describe the quality, and therefore, the long-term performance of concrete. This characteristic mainly determines the durability and permeability and can primarily be described with the water–cement ratio ( $w/c$  ratio). Secondary parameters affecting the concrete strength are aggregate–cement ratio, the properties of the aggregate, including the maximum aggregate size and the degree of compaction. In addition to the strength of concrete, the curing regime is of significant importance to achieve a durable and long-performing concrete structure.

The water–cement ratio is inversely proportional to the strength under the condition that the concrete is well compacted, allowing an air void content of less than 2%. The inverse proportionality is not valid below a  $w/c$  ratio of 0.38. The amount of water required for the total theoretical hydration of cement is in the range of 0.26–0.28; however, water is also physically bound within the cement matrix, that is, water is absorbed. A  $w/c$  ratio of 0.38 is required for the total hydration, including chemical and physical bond. Below this value, the degree of hydration and compaction decrease causing loss of strength. The increase of the  $w/c$  ratio above 0.38 causes the formation of capillarity pores, and hence, a reduction in strength. Water–cement ratios commonly used in the field are in the range of 0.45–0.60 or admixtures are added to achieve workability by low  $w/c$  ratios.

The effective water–cement ratio available for the hydration varies to the amount of water added to the mix. Additional water may be supplied by surface moisture of aggregate or water may be withdrawn from the mix because of absorption from the not saturated aggregates.

Various types of pores are present in the hydrated cement matrix, which may affect strength and durability. Gel and shrinkage pores formed during the hydration of cement are a usual compound within

the matrix. Capillary pores form above  $w/c = 0.38$  by total hydration; however, these pores may form below this value by reduced degree of hydration. The capillary pores are responsible for all transport processes within the concrete. Continuity between the capillary pores should be prevented until a  $w/c$  ratio of  $\sim 0.45$ , providing a durable concrete. Air voids formed during the mixing process can have a diameter up to 1 mm. To improve the freeze–thaw resistance artificial air pores can be introduced by using an air entrainment admixture. These pores are round and not connected and have a maximum diameter of 300  $\mu\text{m}$  to allow the freezing water to expand. The last type of porosity is due to compaction voids, which mainly arise from variable workmanship.

The amount of cement within the mix can affect the strength. Very low cement contents and cement contents exceeding about 530  $\text{kg m}^{-3}$  decrease the performance. High cement contents may cause extensive hydration shrinkage leading to large cracks in the paste. The properties of the aggregates are another secondary parameter, as partly discussed in [Section 3.30.6.1](#). Beside the type of aggregate, the moisture, surface texture, grading, and strength influence the strength of concrete.

Concretes are classified in EN 206-1:2000 according to their compressive strength after 28 days, see [Table 2](#). The classification for lightweight concrete is similar and can be found in EN 206-1:2000.

**Table 2** Standard concrete strengths according to EN 206-1:2000

Concrete compressive strength class	Minimum characteristic cylinder strength $f_{ck,cyl} (\text{N mm}^{-2})$	Minimum characteristic cube strength $f_{ck,cube} (\text{N mm}^{-2})$
C8/10	8	10
C12/15	12	15
C16/20	16	20
C20/25	20	25
C25/30	25	30
C30/37	30	37
C35/45	35	45
C40/50	40	50
C45/55	45	55
C50/60	50	60
C55/67	55	67
C60/75	60	75
C70/85	70	85
C80/95	80	95
C90/105	90	105
C100/115	100	115



### 3.30.7 Degradation

#### 3.30.7.1 Cracking

There are many different types of crack that can occur in concrete. The consequences of these can range from purely aesthetic to structurally significant, and care should be taken when assessing them. It should always be borne in mind that concrete will always typically crack, but that cracks may or may not be structurally significant. Cracks may be as a result of the manner in which it performs structurally, as concrete has a low tensile strength. These are discussed in the order they occur, in the following sections.

##### 3.30.7.1.1 Plastic settlement cracking

During concrete hydration, there is a period where it is a solid suspended in a liquid phase. This is known as the plastic stage. If this stage lasts too long, or the mix contains a significant amount of water, the solid particles can settle, see [Figure 1](#). Mixes that hydrate slowly, such as those placed in cold weather, or with a high proportion of cement replacements are typically more vulnerable to this type of cracking. This typically manifests itself in the form of cracks immediately over the reinforcement steel, which provides a shorter path for the ingress of potentially aggressive species. If plastic settlement cracks are visible on a new structure, there is a significant possibility that extensive cracking has occurred and the surface should be grit blasted to identify the true extent of the problem before remedial measures are considered.

##### 3.30.7.1.2 Plastic shrinkage cracking

If during hydration water is lost to the atmosphere quicker than it can be replenished from the hydrating

concrete, the surface undergoes plastic shrinkage cracking. This typically takes the form of many small cracks over the surface of the structure and can be minimized with careful curing. As with plastic settlement cracking, if this is visible on the surface of concrete, the true extent needs to be identified before embarking on remedial measures. This can be achieved by a light grit blast.

##### 3.30.7.1.3 Early age thermal cracking

As concrete hydrates, it generates heat. If this heat is not adequately controlled, then the concrete will cool after hydration, and as a result, will shrink. This may result in visible cracks forming. For water retaining structures, the basic approach is to limit the width of cracks by having a higher number of smaller cracks.

##### 3.30.7.1.4 Long-term drying shrinkage

Over a significant period of time, concrete tends to shrink as shown in [Figure 2](#). This will produce cracks and can be the basis or the allowable movement at structural joints. If the movement does not occur at the joints, there is additional restraint or the joints are incapable of movement, shrinkage cracks may occur. These are typically uniformly spaced across a structure as the concrete tends to shrink in a uniform manner.

#### 3.30.7.2 Corrosion of Steel in Concrete

The single commonest cause of degradation of reinforced concrete is corrosion of the reinforcement. The pore water in concrete is highly alkaline and in a strongly alkaline environment steel is passivated, and does not corrode, by the formation of a stable and adherent oxide coating, thought to be  $\text{Fe}_2\text{O}_3$ . However,



**Figure 1** Plastic settlement cracking.



**Figure 2** Shrinkage.

this passive film can become unstable due to two mechanisms: those of chloride ion attack and carbonation. This is instigated by either carbon dioxide penetration reducing the pH, or by the presence of chlorides. Once corrosion has initiated, the rust produced is typically insoluble and has a greater volume than the original steel. As a result, tensile stresses develop in the concrete and the cover delaminates. This typically occurs with section losses below that, which are structurally sensitive; however, the falling concrete can pose a significant hazard. In addition, the corrosion may be taking place in an unobservable area, and hence the damage may go unnoticed until significant corrosion has taken place. In addition, the original design may have a limited factor of safety by current standards, and hence any corrosion may be intolerable.

#### 3.30.7.2.1 Chloride attack

Chloride ions are considered to be the major cause of corrosion of reinforcement, see [Figure 3](#). The level at which chlorides are generally considered to represent a risk of corrosion is typically greater than 0.4 mass% of cement.

#### 3.30.7.2.2 Sources of chloride ions

The main source of chloride ions is typically from external sources such as deicing salts on roads or from the marine environments, the sea. However, there are situations whereby chlorides can end up in the concrete mix prior to casting of the concrete. Chlorides from this source are known as internal chlorides, and during the hydration of cement, a quantity of these are bound to the cement hydrates. For any particular cement, the relationship is thought to be primarily governed by the ratio of chloride to cement by mass. Internal sources can be from aggregate contamination by using marine-dredged

aggregates that have not been washed properly, or by using contaminated water in the mix. Note that in some parts of the world, it is difficult to obtain chloride-free aggregates and chloride-free water. Chlorides have been deliberately added to the mix to control the hydration rate, although this practice has been discouraged.

#### 3.30.7.2.3 Carbonation

Carbonation occurs where carbon dioxide in the atmosphere dissolves in water to form carbonic acid. This reacts with the alkaline concrete and reduces the pH to a value below 10, see [Figure 4](#). It has been reported<sup>26</sup> that carbonation also increases the concentration of free chloride in the pore solution by releasing bound chlorides.

As the above processes require some diffusion through the concrete to the steel any factor that influences the rate of these processes also affects the corrosion rate, thus dense well compacted concrete with adequate cover can provide excellent protection to embedded steel and there are oil platforms in the North Sea that have survived 17 years<sup>27</sup> with no observable corrosion of the reinforcement bars taking place. Cement replacements are often used to provide an enhanced durability and resistance to passage of aggressive ions but do require more care in placement or these benefits may not be realized.

#### 3.30.7.2.4 Chloride ion diffusion

As stated above, chloride ion ingress is the major cause of deterioration of reinforced concrete structures. Therefore, knowledge of the nature of diffusion of chloride ions through concrete would be necessary for any structure to have a designed lifetime. Ideally,



**Figure 3** Chloride-induced corrosion.



**Figure 4** Carbonated concrete sample treated with phenolphthalein indicator (magenta color represents uncarbonated concrete).

it would be possible to calculate a figure for the time taken for chlorides to reach the steel in sufficient quantities to cause depassivation from the mix design and cover. This has led to certain experimental procedures being developed that attempt to model chloride diffusion on a laboratory scale and these methods are outlined below.

Generally, current investigations into this topic can be divided into three types: those using the diffusion cell method, those using immersion into solution, and those using electrical properties of concrete to monitor diffusion, usually resistivity. The first two methods apply laws developed by Adolf Fick in 1858, which govern diffusion on a quantitative basis, to obtain diffusion coefficients for the materials under test; the third infers a diffusion coefficient from the change in the total quantity of ions in the pore solution with time, which manifests itself by an increase in ionic conductivity.

### 3.30.7.2.5 The diffusion cell

In this type of experiment, slices of cement mortar are taken and inserted into a diffusion cell.<sup>28</sup> Both sides of the cell are filled with either deionized water, saturated calcium hydroxide, or dilute sodium hydroxide, with one side containing chloride ions added in the form of sodium chloride. This method applies Fick's first law after the rate of change of chloride ion concentration in compartment one becomes constant:

$$-\mathcal{J}(x) = \frac{dC}{dt} = D_c \frac{dC(x)}{dx}$$

where  $\mathcal{J}(x)$  is the flux of  $x$ ,  $D_c$  is the diffusion coefficient ( $\text{m}^2 \text{s}^{-1}$ ), and  $C$  is the concentration.

Tests such as this can take a significant length of time to achieve steady state. To avoid this, a direct current voltage can be applied to accelerate the test and calculate the flux of ions from the total current flowing. The problems with this method are that current is used in transporting all ions, not just the chlorides, and also a certain amount of heat is developed.

A modified version of this test was used by Luping and Nilsson,<sup>29</sup> who applied the test to both cement paste and mortar samples of varying water–cement ratios and applied a voltage of 30 V across a 70-mm-long cured samples with solutions of saturated calcium hydroxide and 3% sodium chloride. They compared the results obtained in this manner with conventional diffusion cell data and recorded current and temperature (a rise of only a few degrees after 8 h

of testing) and obtained chloride profiles by sectioning the samples after 2 months of testing. The following equation was produced as a method of calculating the diffusion coefficient from the depth of chloride penetration, derived from a combination of electrochemical and ionic diffusion equations.

$$D_c = 1.189 \times 10^{-11} \frac{X_d - 1.061 X_d^{0.589}}{t}$$

where  $D_c$  is the diffusion coefficient ( $\text{m}^2 \text{s}^{-1}$ ),  $X_d$  is the depth of chloride penetration (m), and  $t$  is the time (s).

This suggests a clearly defined depth of chloride penetration, which is not necessarily the case. As an alternative, Fick's second law can be applied to calculate the diffusion coefficient under non-steady-state conditions.

$$\frac{\delta C}{\delta t} = D_c \frac{\delta^2 C}{\delta x^2}$$

where  $D_c$  is the effective diffusion coefficient ( $\text{m}^2 \text{s}^{-1}$ ).

### 3.30.7.2.6 Immersion testing

As the name suggests, in this type of diffusion, testing blocks of concrete are taken, all but one of their surfaces are sealed, and the blocks are immersed in a solution. After a time, the blocks are removed and chloride ion profiles are obtained. Sections of the block are taken using either dry drilling or cutting with a diamond saw. The solutions in which the samples are immersed vary considerably from sodium chloride to seawater. For unidirectional diffusion into a semiinfinite medium, an accepted solution to Fick's second law is:

$$C_{(x,t)} = C_o \left( 1 - \operatorname{erf} \frac{x}{2\sqrt{D_c t}} \right)$$

Where  $\operatorname{erf}(z) = \frac{2}{\sqrt{\pi}} \int_0^z e^{-y^2} dy$ ,  $x$  is the distance from the exposed face (m),  $C_o$  is the surface concentration, and  $t$  is the time (s).

### 3.30.7.2.7 Resistivity measurements

Although not a direct method of measuring diffusivity of ions into concrete, this technique has been applied to infer variations in ionic concentrations in the pore solution. The use of conductivity in concrete as a measure of diffusivity was first suggested by Brace<sup>30</sup> for use in analyzing the properties of rocks. If a material is made up of a solid, insulating phase, with a

liquid phase distributed through it, then diffusion and conductivity are controlled by the same process and are related using the Einstein relationship.

$$\sigma = \frac{e^2}{kT} \sum_j c_j Z_j D_j$$

where  $\sigma$  is the conductivity ( $\Omega^{-1} \text{ m}^{-1}$ ),  $e$  is the electron charge,  $k$  is the Boltzmann constant,  $T$  is the absolute temperature (K),  $c_j$  is the number of ions per unit volume of  $j$ ,  $Z_j$  is the valency of  $j$ , and  $D_j$  is the diffusion coefficient of  $j$ .

Buenfeld and Newman<sup>31</sup> continued this work, on the basis that the conductivity of concrete when wet is  $5 \times 10^8$  times more than that of the dry material, and therefore electrical conductance takes place through the pore water. They point out, however, that the conductance depends entirely on the composition of the pore water solution, and therefore, variations in conductivity could be due to any increase in any ions in the pore solution, or the variations could be due to surface changes in the concrete itself.

### 3.30.7.2.8 Errors in diffusion experiments

The fundamental purpose of the above experiments is to obtain a value characteristic of the rate of ionic movement of chlorides through concrete. Ideally, it would be then possible to take this figure and apply it in the design stages of a structure to provide an accurate life expectancy.

This approach is flawed for concrete structures as design lives are very long, 120 years for bridges, and over this period of time, the environment can change considerably; for example, consider how much the world has developed over the past 120 years. With design lives of this scale the problem becomes one of adequate maintenance and repair rather than an initial design and build problem, although, of course, the ability to maintain the structure must be designed for.

Accelerated testing for diffusion involves either using thin sections or applying a voltage across the samples to accelerate the ionic flux. The first method must be questioned, because if used as an accelerated test, it may miss important effects that occur later in the life of the sample, as the morphology of the pore structure changes on contact with the solution. The second is additionally unsafe, because in concrete, charge balance is maintained as chloride ions diffuse in by the migration of hydroxide ions (see later). This would not be the case if using an applied voltage, and

therefore, too much emphasis may be placed on the diffusion of cations in the process.

Chatterji<sup>32</sup> states that the assumption of constant diffusivity is seldom satisfied, with results suggesting that an increasing or decreasing depth of penetration could be observed depending on history. He adds that the use of a measured diffusion coefficient by any method to calculate the long-term chloride penetration depth is uncalled for and may be misleading.

Theoretically, Fick's second law cannot be used to analyze the chloride ion migration data through cementitious materials, as no account is made for any chemical reactions that take place during the process. Saetta *et al.*<sup>33</sup> reported that temperature, relative humidity, and degree of hydration all have an effect on the effective diffusion coefficients.

### 3.30.7.2.9 Corrosion ladder

This is a proprietary corrosion sensor developed by Raupach *et al.*<sup>34</sup> to allow monitoring of the indication of potential corrosion problems in new structures. Steel bars are cast parallel to the reinforcement at varying depths from the concrete surface up to and beyond the depth of rebar at strategic places in the structure. The potentials of these are recorded and when they change from a passive state to an active one, it is an indication that the steel has depassivated either due to the presence of chlorides or by carbonation. The occurrence of corrosion can be checked by connecting the mild steel electrodes to the stainless steel. If the mild steel has depassivated, then a current will flow, which can be measured using a zero resistance ammeter.

One possible problem with this method of monitoring is that when the chlorides reach the steel, it starts to corrode, producing voluminous corrosion products, and hence causes the concrete to spall. It is possible that only a small area of the steel has enough chlorides to cause activation and this test may therefore be unrepresentative of the overall state of the structure. In addition to this, very accurate positioning of the steel would be required in a small distance of concrete not greater than 150 mm. The size of the probe may also cause difficulties in areas of high stress, where the presence of the probe may reduce the load-bearing capacity of the section.

### 3.30.7.2.10 Tests on retrieved samples

The following testing methods all involve taking a sample of concrete. This is done by collecting the dust from a drilled hole and treating this with nitric acid to extract the free and bound chlorides into



solution. This solution is then usually neutralized and a known quantity is taken for testing by an external laboratory. The locations for testing are invariably limited by available time and access, and therefore, care must be taken in assessing the results.

### 3.30.7.2.11 Chloride ion selective electrodes

As the potential of the silver–silver chloride electrode depends on the chloride ion activity, the temperature, and the standard electrode potential of both the ion selective electrode and the reference electrode (it is compared with), in laboratory tests, the chloride-sensitive electrode is first calibrated in a set of solutions of known concentration. When a plot of potential against the log of chloride concentration is made, a straight line is obtained, and therefore, when the ion-selective electrode is submerged into an unknown solution, the chloride concentration of the solution can easily be calculated from the calibration plot. The potential obtained can be affected by the presence of bromide ions from a marine environment as there is some bromide in seawater. This approach has been used to produce a commercially available probe that has been installed in a number of structures.

### 3.30.7.3 Alkali-Silica Reaction

Alkali silica reaction (ASR) is a type of the more known ‘Alkali-aggregate reaction’ and was first reported in the United States by T.A. Stanton in 1940.<sup>35</sup> The reaction between alkali and aggregate as the cause of concrete degradation has been investigated since the early 1920s due to the occurrence of ASR in a dam in California, where opal was used as aggregate. Europe and the United Kingdom generally assumed that ASR was a degradation process which only occurred in North America until first cases were discovered in the early 1970s. Nowadays, ASR is present and recognized throughout the world. The causes of ASR and the protective measures to minimize the risk are well documented.

ASR is a chemical reaction between various forms of silica from the aggregate and alkali hydroxides (NaOH, KOH) from the pore solution in presence of moisture. The alkalis mainly derive from the cement. The reaction product, the alkali–silica gel, is more voluminous than the concrete and, after exceeding the tensile strength of the concrete, forms a distinctive crack pattern, see **Figure 5**. The cracks formed have the appearance of a spider web; however, affected prestressed elements tend to show cracks parallel to the stress direction.

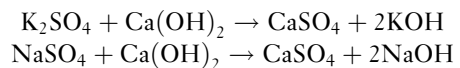


**Figure 5** Typical crack pattern of ASR.

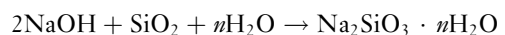
The reaction affects the appearance and serviceability of a structure, although generally its structural integrity, particularly the compressive strength, is not affected. However, the formation of cracks can enhance the penetration of various aggressive compounds, leading to acceleration of other types of degradation. ASR is often observed in combination with corrosion and sulfate attack and can be their predecessor.

The reaction can be described in accordance to Wieker *et al.*<sup>36</sup> as follows.

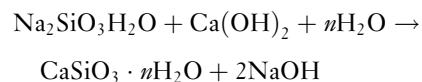
Formation of alkali hydroxides (NaOH, KOH) during cement hydration



Water intake and expansion



The reaction can proceed when further water ingress takes place. The gel, an alkali–silica hydrate, is able to react with water and calcium hydroxide to form calcium silicate hydrates and alkali hydroxides, which can form more gel and degrade concrete over a long term.



This reaction is a definite process because the majority of the alkalis remain in the gel.

The formation of the alkali–silica gel causes swelling<sup>37</sup> and the expansion pressure developed during this process can reach up to  $20 \text{ N mm}^{-2}$ , exceeding the tensile strength of concrete, which is in the range  $2\text{--}5 \text{ N mm}^{-2}$ .

The reactivity of aggregate depends on the mineralogical structure of the  $\text{SiO}_2$  and its proportion of amorphous and other reactive forms of silica. The reaction between  $\text{SiO}_2$  and alkalis always occurs; however, this reaction is destructive in the presence of reactive  $\text{SiO}_2$ . All amorphous and cryptocrystalline  $\text{SiO}_2$  minerals can be considered as reactive.<sup>24</sup> These include opal, chalcedony, greywacke, granite, and porphyry. ASR can be prevented when one of the three risk factors, alkalis, reactive  $\text{SiO}_2$ , and moisture, is minimized or eliminated. Moisture cannot be entirely controlled. The use of reactive aggregates is difficult to exclude because of the regional availability of aggregate. The transportation of nonreactive aggregates is commercially inefficient.

The amount of available alkalis can be controlled during the manufacture of cement so that the  $\text{Na}_2\text{O}$ -equivalent ( $\bar{N}$ ) is less than 0.6,<sup>38</sup> which conforms to a hydroxide ion concentration of around  $500 \text{ mmol l}^{-1}$ . The use of GGBS, PFA, microsilica, or other pozzolanic material increases this threshold. Alkalis react with the high reactive fine pozzolanic particles during the early stages of the cement hydration before setting.  $\text{Ca}^{2+}$  ions are bound in reaction products of the pozzolanic material. These two reactions bind the alkalis in insoluble compounds with the cement matrix. Pozzolanas increase the density of the concrete, and hence, reduce the permeability of external and mobility of internal alkalis.

In the case of confirmed ASR degradation in structural elements, there are series of measures to monitor and control ASR. The IStructE<sup>39</sup> described these measures as follows:

- Regular monitoring of the structure to check that deterioration does not reach dangerous proportions. This requires experienced engineering judgment.
- Detailed check on the structural details to establish criticality, in particular, a critical examination of the robustness of the reinforcement detailing.
- Measures to reduce the amount of water available to the structure.
- Limited strengthening of the structure.
- Partial or full demolition followed by rebuilding.

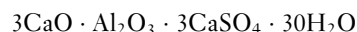
The appropriate measure should be assessed through a series of investigations comprising the documentation of the degradation, a desk study to gain information about the materials used, the type of construction, and the rate of degradation. Destructive investigations should include the retrieval of cores in degraded and sound areas and their assessment in the

laboratory. This may include strength tests, petrographic examination, and visual inspection.

### 3.30.7.4 Sulfate Attack

#### 3.30.7.4.1 Conventional sulfate attack

The damaging influence of sulfates on concrete has been known since 1877, and first investigations were performed by Candlot<sup>40</sup> and Michaelis<sup>41</sup> at the end of the nineteenth century. They identified a complex water-enriched compound in the damaged matrix and described it as



Michaelis called the salt formed ‘cement bacillus,’ and nowadays it is known as ‘ettringite,’ and this is the main reaction product in various forms of sulfate attack. Several forms of sulfate attack have been identified that affect various phases of the cement hydration products.<sup>42</sup>

Sulfate attack can result in one of two forms of deterioration, the first is due to leaching of the calcium containing phases, particularly portlandite [ $\text{Ca}(\text{OH})_2$ ] as shown in Figure 6. The second is the more familiar expansive form caused by formation of more voluminous reaction products such as gypsum, monosulfate, and ettringite. The expansive form can



Figure 6 External sulfate attack.



be categorized by the location of the supplied sulfate whether there is an external or internal source.

The main reaction products of sulfate attack are gypsum and/or ettringite, and the reaction mechanism is generally accepted as portlandite transforms into gypsum and calcium aluminate hydrate into ettringite, the latter being the more expansive reaction. These findings allowed the development of sulfate-resisting Portland cement (SRPC-BS 4027-1996), which is mainly characterized by a limited tricalcium aluminate content ( $C_3A < 3.5\%$ ). The low presence of the main ingredient for the deteriorative reaction hinders the formation of the more voluminous reaction products, which is mainly ettringite. Guidelines, such as BS EN 206, BS EN 1992, and BS 8500, have also been produced resulting in the solution to the majority of problems caused by sulfate attack.

#### **3.30.7.4.2 Thaumassite form of sulfate attack**

The thaumasite form of sulfate attack differs to the forms described earlier, including the conventional sulfate attack in that the calcium silicate hydrates (C-S-H phases), the main binding agent in all Portland cement binders, is targeted rather than the calcium aluminate hydrates (C-A-H phases) and the highly soluble calcium hydroxide ( $Ca(OH)_2$ ).

Although TSA has been recognized for many years, it did not receive any serious attention from either industry or the research community until the discovery of 10 cases of the thaumasite form of sulfate attack in the foundations of overbridges along the M5 motorway in Gloucestershire in 1998.<sup>43</sup> The seriously attacked columns had been all buried in backfilled Lower Lias Clay and were discovered during strengthening works. In response to this discovery, the UK Government convened the Thaumassite Expert Group (TEG) with “the remit to produce interim advice and guidance on the implications for existing buildings and structures and for the design and specification of new constructions in the UK.”

The TEG emphasized that deterioration as a result of the formation of thaumasite has become a separate form of sulfate attack, which has the potential to affect a wide variety of components and a range of building materials. The TEG gave thaumasite two classifications. The first being the ‘thaumasite form of sulphate attack’ (TSA) where significant damage of the concrete–mortar matrix has occurred as a consequence of replacement of cement hydrates

by thaumasite. In this case, the TSA-affected concrete transforms into a soft, mushy mass with a distinctive white coloration. The second classification the ‘thaumasite formation’ (TF) refers to the occurrence of thaumasite as precipitations in pre-existing voids and cracks without causing deterioration of the host concrete or mortar. However, thaumasite formation can be a precursor of the thaumasite form of sulfate attack and constitute an early stage in the deterioration process, as suggested by Sims and Huntley,<sup>44</sup> who suggested changing the term TF to ‘incipient TSA’.

In their report, the TEG recognized two sets of conditions for the formation of TSA in buried concretes, these are four primary and four secondary risk factors. The TEG emphasizes “that all of the four primary risk factors need to be present before significant TSA will occur within a buried Portland cement-based concrete.” The primary risk factors are defined as

- a source of sulfates and/or sulfides in the ground;
- a source of carbonate;
- presence of mobile groundwater; and
- low temperatures ( $<15^\circ\text{C}$ ).

The source of silicate, which is also a necessary component, was not included into the risk factors as it is an actual element in all Portland cement-based materials and is mainly present as calcium silicate hydrate phases (C-S-H phases).

The four secondary risk factors are identified by the TEG as

- type and quantity of cement used in concrete;
- quality of concrete mix, compaction;
- changes to ground chemistry and water regime resulting from construction; and
- type, depth and geometry of buried concrete.

On the basis of the findings of the TEG and other researchers, conventional sulfate attack and thaumasite form of sulfate attack have to be considered as two separate forms, which occur in different environments. TSA takes mainly place in low temperatures ( $<15^\circ\text{C}$ ), whereas conventional sulfate attack is predominantly at ambient temperatures of  $>15^\circ\text{C}$ . However,  $15^\circ\text{C}$  cannot be considered as a threshold between both types of attack.

Low temperatures favor the formation of thaumasite where generally less than  $15^\circ\text{C}$  is necessary with an optimum value of  $\sim 5^\circ\text{C}$ . The formation ability increases with the decrease of the temperature, that

is, the lower the temperature the faster the formation of thaumasite.

One reason for the increase in deterioration rate with reduced temperature is solubility. The solubility of carbon dioxide increases with decreasing temperature, leading to about twice the amount of dissolved carbonate in solution at 0 °C than at 25 °C; portlandite is also more soluble at low temperatures, whereas thaumasite is in the order of a hundred times less soluble. From this follows an increased rate of deterioration at low temperatures.<sup>45</sup> On the other hand, lower temperatures lead to a better stability of the six-coordinated  $[\text{Si}(\text{OH})_6]^{2-}$  groups that are present in the structure of thaumasite. The cut-off point where the mineral formed changes from thaumasite to ettringite should be between 15 and 20 °C. The typical temperature conditions in the ground at foundation depth in the United Kingdom range from about 9 to 12 °C and are therefore in the optimum range of below 15 °C.<sup>46</sup>

The more frequent detection of TSA during the past decade is most probably due to the development of more selective analytical and diagnostic techniques, which are able to differentiate unambiguously between ettringite and thaumasite as well as mixed crystals of both. Crammond<sup>47</sup> suggests that TSA is not a recent phenomenon and has occurred likely in the past, but has not been recognized as such because of several reasons:

- failure to detect thaumasite in standard sulfate resistance tests;
- improved analytical techniques;
- buried concretes rarely inspected;
- postconstruction enhancement of sulfate levels in the ground; and
- changes in the composition of modern cements.

Many other cases of TSA may remain unidentified or have been reported spuriously as 'sulfate attack' caused by ettringite formation because of misidentification due to the structural similarities. Furthermore, the traditional diagnosis 25 years ago was performed using chemical analysis alone, and this method is not able to distinguish between ettringite and thaumasite. Nowadays, the mechanisms of the different types of sulfate attack are well known and the facilities for an unambiguous identification are available.

#### 3.30.7.4.3 Delayed ettringite formation

Ettringite is a hydration product with two faces. The formation of ettringite during the first stage of

cement hydration controls the setting time of the paste. Ettringite formation is responsible for the workability of fresh concrete. Ettringite can be destructive when it forms in the hardened cement paste. This degradation process has been mainly observed in heat-treated elements with high strengths and high density exposed to external conditions; however, the formation can also occur in non-heat-treated elements.

The destructive ettringite formation was first observed in a structural element at the beginning of the twentieth century. Ettringite is common hydrate in concrete and the presence does not need to conclude that a deterioration process had occurred.

The effect of increased heat on young concrete can be the formation of delayed ettringite. Causes are heat treatment of concrete elements and extensive heat development in mass concrete or under hot external conditions. Heat treatment of concrete accelerates the hydration and strength gain, respectively, and enables the manufacturer shorter stripping off times for the elements. Hot weather conditions can cause DEF during mixing and hydration as well as in already hardened concrete.

Temperature influences the stability of monosulfate and ettringite. The increase in temperature decreases the stability of both monosulfate and ettringite; however, the rate of the decrease of ettringite is higher, that is, monosulfate is thermodynamically more stable above 90 °C. Alkalis in pore solution reduce this threshold to 50–60 °C.<sup>48</sup> These changes of the stability of ettringite lead to the formation of monosulfate, free available sulfates ( $\text{Na}_2\text{SO}_4$ ) in pore solution, and sulfates bound in the C–S–H phases above the critical temperature. Calcium silicate hydrates are able to bind sulfate ions during the hydration. Monosulfate becomes metastable when the temperature drops below the critical threshold.

If the concrete element is exposed to changeable weather conditions, that is, wet–dry cycles, then the sulfate ions in the pore solution and within the C–S–H phases react with the metastable monosulfate and  $\text{C}_3\text{AH}_6$  to form the more voluminous ettringite. This reaction can cause expansion and cracking within the cement paste. The volume of ettringite is eight times greater than  $\text{C}_3\text{A}$  and 2.3 times greater than monosulfate. Ettringite can also form in pores and is not destructive.

Pozzolanas, latent hydraulic material, and microsilica reduce the susceptibility of concrete to DEF. Heat-treated elements should undergo special procedures, such as initial storage before treatment,

controlled warming, constant heat control, controlled cooling, and an after treatment.

### 3.30.7.5 Mechanical Damage

#### 3.30.7.5.1 Abrasion/erosion

Abrasion or erosion can be defined as the wearing away of surfaces. It is commonly considered that it requires the action of a hard material on a softer one, but this is not the case. Over a significant period of time, a soft material can slowly wear away a harder one.

Concrete is no exception to this and will be subject to abrasion with time. Typically, it is a very slow process, unless it is subject to other mechanisms discussed later. For conventional reinforced concrete, the abrasion is likely to be of most of the concern if it results in an uneven surface for traffic, or if it significantly reduces cover to the reinforcement. Uneven surfaces often allow puddles of water to form, which can markedly accelerate the abrasion process, see [Figure 7](#). When water is trapped while being subject to wheel loading, a significant pressure is exerted in the horizontal plane. This can rapidly lead to undermining of the surrounding surfaces, or opening up of existing defects, leading to increasingly more widespread surface degradation.

#### 3.30.7.5.2 Cavitation

Cavitation occurs when liquids undergo a change in pressure to a point where the pressure in the liquid is below its vapor pressure. This produces bubbles in the liquid, which subsequently collapse and produce shockwaves. This can result in a very aggressive environment and extremely high rates of abrasion. This process is accepted as a mechanism that results in

coastal erosion whereby air pockets within water are forced into fissures. The continuing inflow of water results in the collapsing of pockets and a range of shock waves being produced that result in degradation.

#### 3.30.7.5.3 Frost

Frost damage is caused by a simple mechanism. Moisture within the concrete expands as it freezes, and as a result, tensile stresses form near to the surface. This can result in the surface crazing then scaling off, see [Figure 8](#). In areas vulnerable to frost, a common approach to controlling the risk of frost action is to include an air entraining admixture. There are a range of products available to achieve this. The use of an air entraining admixture produces a series of evenly dispersed discontinuous pores within the concrete that are relatively uniform in diameter, the majority of which are less than 0.3 mm. This provides two benefits. The first is that the surface absorbency is reduced, because the pores are discontinuous. The second is that they are able to absorb the stresses induced by frost, because the pores remain air filled, and hence, unsaturated.

#### 3.30.7.5.4 Exfoliation

Exfoliation is caused by a similar principle to frost, in that the pore structure becomes filled with a material that subsequently expands, see [Figure 8](#). In this case, it is a solution containing soluble salts. As the moisture dries out, the solution becomes more and more concentrated until ultimately the soluble salts recrystallize. The recrystallized salts may be greater in volume than the original solution, and therefore, tensile stresses are imparted into the concrete.



**Figure 7** Erosion of concrete by flowing water.



**Figure 8** Exfoliation of a seawater outfall.

It should be noted that the surface of concrete that is exposed to the solution may not be the one that suffers from exfoliation. If one face of a concrete surface is adjacent to a highly concentrated solution, and the other is exposed to a drying environment, the salt solution can be drawn a significant distance to the drying face, where the recrystallization takes place. This can be a problem in immersed tunnels. Typically, the solution on the exterior of the tunnel is chloride contaminated and the capillary absorption that takes place will cause corrosion as well as exfoliation.

The first thing to note is that concrete already contains a supersaturated solution of calcium hydroxide. However, calcium salts typically have a relatively low solubility, and therefore, as the moisture dries out, the salts that are precipitated do not have a large volume expansion associated with them. For exfoliation to occur, a more soluble salt is usually present. In many cases in natural environments, this is sodium chloride based, but any highly soluble salt can produce a similar effect.

Coatings or waterproofing for concrete are commonly vapor permeable to prevent osmotic blistering. As a result, this can cause a drying out of the coated concrete. If the concrete is contaminated with a soluble salt, the concentrations in the pores under the coating will increase, until the salts precipitate. This can cause the surface to exfoliate, which can result in coating failure. It should also be noted that solubilities typically increase with temperature. As a result, exfoliation may also occur due to a temperatures change.

To control the risk of exfoliation or frost attack, the basic approach is to either prevent significant salt ingress or prevent drying of the surface. Typically, a coating system would provide protection against salt ingress, but note that a vapor permeable coating can increase drying out of the concrete and may therefore cause exfoliation if the substrate is heavily contaminated.

### 3.30.7.5.5 Fire

Following the great fire of Chicago in 1871, all iron- and steel-framed structures were coated with a basic form of concrete fire protection. When cement hydrates, it chemically combines with a significant amount of water. In the case of fire, as the temperature increases, the hydrated compounds break down and release the water, thus dissipating heat and energy. This means that while the surface of the

concrete may have been subject to high temperatures, the depth of damage may be limited.

After a fire, the appearance of any structure can give the impression of a scene of total destruction. Because of the smoke, everything will be blackened. There will be areas where concrete has cracked and may have spalled. The levels of damage may appear significant but due to concrete's ability to dissipate heat, the actual damage may well be recoverable.

If the temperature of the concrete has not exceeded 300 °C on cooling, the residual strength is commonly considered to not be significantly affected.<sup>49</sup> The reduction in strength is often offset by factors that resulted in the concrete having higher strengths than required by the original structural capacity. A word of caution should be raised as it is often assumed that the concrete strength increases with time beyond that required by the design. For older cements, this was the case, as in order to achieve the required strength at 28 days, the ultimate strength needed to be higher. Cements are more finely ground and cement producing companies have improved quality control systems that mean the factors of safety included to ensure the concrete meets the required 28 days strength are now lower. The ultimate strength achieved may not be significantly greater than that obtained at 28 days.

The temperature at which significant structural deterioration occurs coincides with a color change in many concretes, where the material develops a pink hue. This discoloration is due to the presence of ferrous salts in the aggregates, and may not occur if these are not present. It is important to note that this does not apply in every case, and the levels of heat damage and degradation of the cement should be confirmed using petrographic analysis on samples. Where temperatures exceed 500 °C, the strength is usually severely compromised.

## References

1. Bernal, J. D. In *Proceedings of Symposium on the Chemistry of Cement*, London, 1952.
2. Joisel, A. In *Proceedings of the 5th International Symposium on the Chemistry of Cement*, Tokyo, 1968; Vol. 2, p. 268.
3. Taylor, H. F. W. *J. Chem. Soc.* **1950**, 3682.
4. Kondo, R.; Daimon, M. *J. Am. Ceram. Soc.* **1969**, 58, 87.
5. Ramachandran, V. S. *Mater. Construct* **1971**, 4(19), 1.
6. Lambert, P.; Page, C. L.; Short, N. R. *Cement Concr. Res.* **1985**, 15, 675.
7. Jeffrey, J. W. In *Proceedings of the 3rd International Symposium on the Chemistry of Cement*, 1952; Cement and Concrete Association: London, 1954; p. 30.

8. Page, C. L.; Vennesland, O. *Mater. Construct.* **1983**, 6(91), 19.
9. Collepardi, M.; Baldini, G.; Pauri, M.; Corradi, M. *Cement Concr. Res.* **1978**, 8, 571.
10. Friedel, M. G. *Bull. Soc. France Mineral* **1897**, 20, 122.
11. Liang, T.; Nanru, Y. *Cement Concr. Res.* **1994**, 24, 150.
12. Tamas, F. D.; Vertes, A. *Cement Concr. Res.* **1973**, 3, 575.
13. DeKeyser, W. L.; Tenoutasse, N. In Proceedings of the 5th International Symposium on the Chemistry of Cement, 1968; Vol. II, p. 379.
14. Hansen, W. L. In The 3rd Pacific Area National Meeting of the ASTM, San Francisco, 1959.
15. Powers, T. C. *J. Res. Dev. Lab. Portland Cement Association* **1961**, 3(1), 47.
16. de Jong, J. G. M.; Stein, H. N.; Stevels, J. M. *J. Appl. Chem.* 1972, 17, 246.
17. Tadros, M. E.; Skalny, J.; Kalyoncu, R. S. *J. Am. Ceram. Soc.* 1976, 59, 344.
18. Fujii, K.; Kondo, W. *J. Am. Ceram. Soc.* **1974**, 57, 492.
19. Jennings, H. M.; Pratt, P. L. *Cement Concr. Res.* **1979**, 9, 501.
20. Odler, I.; Dörr, H. *Cement Concr. Res.* **1979**, 9, 277.
21. Odler, I.; Dörr, H. *Cement Concr. Res.* **1981**, 11, 765.
22. Tremper, B.; Beaton, J. L.; Stratful, R. F. Federal Highway Research Road Bulletin No 182, Washington, DC, 1959; p. 18.
23. BRE Digest 392, Assessment of existing high alumina cement concrete construction in the UK, BRE, UK, March, 1994.
24. Stark, J.; Wicht, B. *Dauerhaftigkeit von Beton – Der Baustoff als Werkstoff (Durability of Concrete)*; Birkhäuser: Basel, 2001 (in German).
25. Department of the Environment, Transport and the Regions. The thaumasite form of sulphate attack: Risks, diagnosis, remedial works and guidance on new construction. Report of the Thaumasite Expert Group, DETR, London January 1999.
26. Kayyali, O. A.; Haque, M. N. *Cement Concr. Res.* **1988**, 18, 636.
27. Cathodic Protection of Offshore Structure Marine Technology Directorate Publications G0/102.
28. Page, C. L.; Short, N. R.; El-Tarras, A. *Cement Concr. Res.* **1981**, 11, 395.
29. Luping, T.; Nilsson, L. *Am. Concr. Mater. J.* **1992**, 89(1), 49.
30. Brace, W. F. *J. Geophys. Res.* **1977**, 82, 3343.
31. Buenfeld, N. R.; Newman, J. B. *Mag. Concr. Res.* **1984**, 36, 67.
32. Chatterji, S. *Cement Concr. Res.* **1995**, 25, 299.
33. Saetta, A. V.; Scotta, R. V.; Vitaliani, R. V. *ACI Mater. J.* **1993**, 90(5), 441.
34. Raupach, M.; Schiessl, P. In Proceedings of the 6th International Conference on Structural Faults and Repair; Forde, M.C., Ed.; Engineering Technical Press, 1995; p. 221.
35. Stanton, T. A. In Proceedings of American Society of Civil Engineers 1940, pp. 1781–1811.
36. Wieker, W.; Herr, R.; Huebert, C. *Betonwerk Fertigteil-Technik* 1994, 60(11), 86–90.
37. Taylor, H. F. W. *Cement Chemistry*, 2nd ed.; Thomas Telford: London, 1997.
38. Locher, F. W.; Sprung, S. Ursache und Wirkungsweise der Alkalireaktion *Betontechnische Berichte* 1973, Duesseldorf: Betonverlag, 1974; pp. 101–123.
39. IStructE Report 62, Structural effects of alkali-silica reaction: technical guidance on appraisal of existing structures, 1992; pp. 48.
40. Candlot, E. *Bull. Soc. Encour. Ind. Nat.* **1890**, 89, 682–689.
41. Michaelis, W. *Tonindustrie-Zeitung* **1892**, 6, pp. 105–106.
42. Brown, P. W. *Cement Concr. Compos.* **2002**, 24, 301–303.
43. Halcrow Group Ltd.: Halcrow Thaumasite Investigation – Final Interpretative Report, 2000.
44. Sims, I.; Huntley, S. A. *Cement Concr. Compos.* **2004**, 26, 837–844.
45. Collett, G.; Crammond, N. J.; Swamy, R. N.; Sharp, J. H. *Cement Concr. Res.* **2004**, 34, 1599–1612.
46. Crammond, N. J.; Collett, G. W.; Longworth, T. I. *Cement Concr. Compos.* **2003**, 25, 1035–1043.
47. Crammond, N. J. *Cement Concr. Compos.* **2003**, 25, 809–818.
48. Wieker, W.; Huebert, C.; Schubert, H. Untersuchungen zum Einfluss der Alkalien auf die Stabilität der Sulfoaluminathydrate in Zementstein und –moerteln bei Warmbehandlung. Schriftenreihe des Institutes fuer Massivbau und Baustofftechnologie, Universitaet Karlsruhe, 1996, pp. 175–186.
49. Concrete Society Technical Report 33, Assessment and repair of fire-damaged concrete structures, Concrete Society, UK, 1990.



## 3.31 Degradation of Plastics and Polymers

**D. J. Hourston**

Department of Materials, Loughborough University, UK

This article is a revision of the Third Edition article 18.6 by J. A. Brysdon, volume 2, pp 18:53–18:77, © 2010 Elsevier B.V.

<b>3.31.1</b>	<b>Introduction</b>	2370
<b>3.31.2</b>	<b>Definition of ‘Plastics’</b>	2371
<b>3.31.3</b>	<b>The Chemical Nature of Plastics</b>	2371
3.31.3.1	Free-Radical Addition Polymerization of Monomers with Double Bonds	2371
3.31.3.2	Step-Growth Polymerization	2372
3.31.3.3	Rearrangement Polymerization	2372
3.31.3.4	Ionic Polymerization	2372
<b>3.31.4</b>	<b>The Physical Nature of Plastics</b>	2372
3.31.4.1	Thermoplastics	2373
3.31.4.1.1	Amorphous thermoplastics	2373
3.31.4.1.2	Rubber-modified amorphous polymers	2374
3.31.4.1.3	Plasticized amorphous thermoplastics	2374
3.31.4.1.4	Crystalline thermoplastics	2374
3.31.4.2	Thermosetting Plastics	2375
3.31.4.3	Reinforced Plastics	2375
<b>3.31.5</b>	<b>Polymer Orientation</b>	2376
<b>3.31.6</b>	<b>The Chemical Properties of Polymers</b>	2376
3.31.6.1	Resistance to Chemical Attack	2377
3.31.6.2	Polymer Solubility	2378
3.31.6.2.1	Amorphous nonpolar polymers and amorphous nonpolar solvents	2379
3.31.6.2.2	Crystalline nonpolar polymers and amorphous solvents	2379
3.31.6.2.3	Amorphous nonpolar polymers and crystalline solvents	2380
3.31.6.2.4	Amorphous polar polymers and solvents	2380
3.31.6.2.5	Crystalline polar polymers and solvents	2381
3.31.6.2.6	Rubbers and thermosetting plastics	2381
3.31.6.3	Resistance to Cracking in Aggressive Environments	2381
3.31.6.4	Diffusion	2382
<b>3.31.7</b>	<b>Review of Commercial Plastics</b>	2382
3.31.7.1	Amorphous Thermoplastics	2382
3.31.7.1.1	Polyvinyl chloride	2382
3.31.7.1.2	Polystyrene	2382
3.31.7.1.3	Acrylonitrile–styrene–butadiene polymers (ABS)	2382
3.31.7.1.4	Poly(methyl methacrylate)	2382
3.31.7.1.5	Polyvinyl acetate and derivatives	2382
3.31.7.1.6	Cellulose-based plastics	2383
3.31.7.2	Crystalline Plastics	2383
3.31.7.2.1	Polyethylene	2383
3.31.7.2.2	Polypropylene	2383
3.31.7.2.3	Other polyolefins	2383
3.31.7.2.4	Polytetrafluorethylene	2383
3.31.7.2.5	Other fluorine-containing plastics	2383
3.31.7.2.6	Polyamides (nylons)	2383
3.31.7.2.7	Polyformaldehydes (polyoxymethylenes, polyacetals)	2383
3.31.7.2.8	Other polyethers	2383
3.31.7.2.9	Linear polyesters	2383
3.31.7.2.10	Polycarbonates and polysulfones	2384



3.31.7.3	Thermosetting Resins	2384
3.31.7.3.1	Phenol–formaldehyde (phenolic) plastics	2384
3.31.7.3.2	Aminoplastics	2384
3.31.7.3.3	Unsaturated polyesters	2384
3.31.7.3.4	Epoxy and furan resins	2384
3.31.7.3.5	Silicones	2384
3.31.7.3.6	Polyurethanes	2384
3.31.8	Polymers with Enhanced Heat Resistance	2384
3.31.9	Thermoplastic Rubbers	2385
References		2386

## Glossary

**Glass transition temperature** The temperature at which polymer molecules cease being effectively locked into position and have sufficient rotational energy to be able to coil and uncoil.

**Polymer resin** A polymerized synthetic or chemically modified natural material, including thermoplastic materials such as polyvinyl chloride and thermosetting materials such as epoxy resins, which are used with other components such as fillers to form plastics.

**Thermoplastic** A polymeric material (e.g., nylon) which is capable of being repeatedly softened by increases in temperature and hardened by decreases in temperature.

**Thermoset/thermosetting** A polymeric material (e.g., an epoxy resin) which, upon curing, results in a three-dimensional structure and that decomposes rather than melts upon heating.

**PTFE** Polytetrafluoroethylene

**PVC** Polyvinyl chloride

**PVdC** Polyvinylidene chloride

**PVdF** Polyvinylidene fluoride

**SBR** Styrene butadiene rubber

**SBS** Styrene butadiene styrene triblock copolymer

## Symbols

$\Delta G$  Change in Gibbs's free energy

$\Delta H$  Change in enthalpy

**L** Latent heat of vaporisation

**P** Partial polarity

$\Delta S$  Change in entropy

$T_g$  Glass transition temperature

$T_m$  Melting temperature

## Abbreviations

**ABS** Acrylonitrile butadiene styrene polymers

**DSC** Differential scanning calorimetry

**FEP** Fluorinated ethylene propylene resins

**HIPS** High impact polystyrene

**MBS** Methacrylate butadiene styrene polymers

**PBT** Polybutylene terephthalate

**PEEK** Polyetheretherketone

**PES** Polyether sulfone

**PMMA** Polymethylmethacrylate

**PP** Polypropylene

**PPO** Polyphenylene oxide

**PPS** Polyphenylene sulfide

**PS** Polystyrene

## 3.31.1 Introduction

From ancient times, organic materials, such as beeswax, have been used for surface protection of metallic and other artifacts. The nineteenth and especially the twentieth centuries saw huge advances<sup>1,2</sup> in surface coatings for the protection of metals against corrosion. This development continues apace right up to the present day. Some of the drivers of these developments are not only the ever-present desire to improve protection, but also to find materials and systems which are less polluting and which conform with increasingly stringent environment protection legislation. The latter driver has, for example, led to much work on waterborne coatings<sup>3</sup> to replace systems containing organic solvents, which were traditionally simply lost to the atmosphere. It is also the driving force behind the spectacular rise of polymeric materials which has led to the replacement of metals as the structural material in a vast range of manufactured

items. A glance around any room will reveal many plastic items which formerly would have been metallic.

In the past, corrosion control has involved, in the main, the use of metal alloys, protective coatings, inhibitors, etc. Corrosion problems may now often be circumvented by the use of organic polymers in the form of plastics or rubbers.<sup>1</sup> It must, however, be stressed that such polymeric materials are not totally inert to chemicals in their immediate environment, including, possibly, to metallic substrates or contacts.

### 3.31.2 Definition of 'Plastics'

In this section, both the terms 'polymer' and 'plastic' are encountered. The former is much easier to define than the latter. A polymer, or macromolecule, may be defined as a species with a molar mass much greater than that encountered in common organic substances such as alcohol, petrol, chloroform, etc., and which is comprised of smaller, repetitive molecular units. Although there is no specific definition that can universally define the polymeric (macromolecular) state, a molecular mass of at least several thousand is generally taken as indicating its start. Such polymer molecules may be linear, branched, have a network structure, etc. These different molecular geometries influence the properties of the given polymer very significantly.<sup>4,5</sup>

It is difficult to provide a satisfactory definition of the term 'plastics'. Attempts at reasonably concise definitions tend to include certain materials such as rubbers, adhesives, fibers, glasses and surface coatings which are not usually considered as plastics, and to exclude a number of materials such as bituminous plastics, shellac and polytetrafluorethylene which usually are considered as plastics. In reality, the term becomes defined by common usage rather than by a physical/chemical description. However, in general, it may be said that plastics are usually high-molecular-weight polymers that at some stage in their existence are capable of flow, but may also be brought into a non-fluid form in which they have sufficient toughness and strength to be useful in self-supporting applications. Although they may be self-supporting, this does not exclude the possibility of reinforcing the plastics with fibers, or other fillers, or laminating them with other materials. Sometimes metals are coated with plastics, but usually at a greater thickness than is common with surface coatings such as paint films (which are, of course, also polymers).

The rapid rise of the plastics industry may be attributed to a number of factors. Foremost has been the fact that while many materials of construction

have been subjected to continual increase in their price, the development of the petrochemicals industry and economies of scale have, for most of the time, led to reductions in the prices of plastics materials. Thus, with the passage of time, more and more products constructed from traditional materials have become cheaper to produce from plastics. The trend of increased plastics usage seems bound to continue in the foreseeable future, now driven by our ever-increasing ability to make polymer molecules (plastics) with better controlled molecular architectures<sup>6</sup> and by better processing technologies.<sup>7</sup>

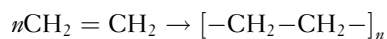
Such a growth also requires, of course, that plastics possess properties suitable for the end uses envisaged. It is now possible, by control of synthesis, by chemical modification, by careful control of the relevant processing technology (injection molding, extrusion, etc.) or by the selective use of additives such as fibers, nanofillers, etc., to make products varying widely in their properties. The following is a list of some of the salient properties expected of plastics materials.

1. Tenacity. While some plastics are rigid and others flexible, all commercial materials show a degree of strength and toughness when stressed rapidly, superior to simple crystals and common glass.
2. Low thermal conductivity.
3. Low electrical conductivity.
4. Low heat resistance compared with common metals. The vast majority of plastics will not withstand 100 °C for extended periods and only a very few highly specialized products will withstand temperatures of 400 °C and above.

### 3.31.3 The Chemical Nature of Plastics

#### 3.31.3.1 Free-Radical Addition Polymerization of Monomers with Double Bonds

In this case, the reactive double bond in a small molecule, such as ethylene or propylene, allows it to join another similar molecule.<sup>5</sup> These small molecules are known as monomer molecules. The chemical equation below shows this process for ethylene. The value of  $n$  in the equation can typically exceed 10 000 and can rise above 1 000 000.

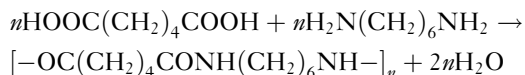


Such a molecule is referred to as a polymer, in this case polyethylene. Styrene, propylene, vinyl

chloride, vinyl acetate, and methyl methacrylate are other examples of monomers that can polymerize in this way. Sometimes, two monomers may be reacted together so that residues of both are to be found in the same chain. Such materials are known as copolymers and are exemplified by ethylene–vinyl acetate copolymers and styrene–acrylonitrile copolymers. If there are three such repeat units in a given polymer, it is termed a terpolymer.

### 3.31.3.2 Step-Growth Polymerization

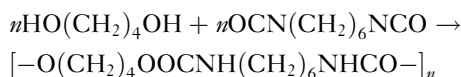
In this case, reaction between two functional groups occurs, which leads to the production of a polymer and also a small molecule. This is a condensation reaction. A good example of this type of chemistry is the reaction between adipic acid and hexamethylene diamine, which yields nylon-6,6 and water as the small molecule:



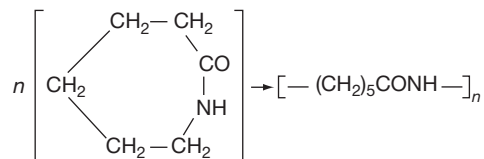
Most nylons, polyesters, phenolics and a number of other plastics are produced by this route.<sup>8</sup>

### 3.31.3.3 Rearrangement Polymerization

Here the mechanism resembles step-growth polymerization, but no small molecule is split at each individual reaction step. In the first example, 1,4-butane diol reacts with hexamethylene di-isocyanate to give polyurethane:



In the second,  $\epsilon$ -caprolactam, a ring compound opens up to give nylon-6:



The polymerization of  $\epsilon$ -caprolactam is commonly known as a ring-opening polymerization, a technique also used with other cyclic compounds such as ethylene oxide, propylene oxide and tetrahydrofuran.

### 3.31.3.4 Ionic Polymerization

In the case of ionic polymerization, the growing polymer molecules (commonly referred to as

polymer chains) are temporarily terminated by ionic groups, which may be anionic (anionic polymerization) or cationic (cationic polymerization). The major advantage of this type of polymerization is that it offers good control over the resulting molecular architecture.<sup>8</sup>

Polymers may also be obtained from biological sources.<sup>9,10</sup> Cellulose, the principal constituent of cotton and a major constituent of wood, is such a polymer. So also are lignin, chitin from crustacean shells, natural rubber, gutta percha, and proteins. Sand (silica) may be considered as an inorganic polymer. While many of these are unmodified, some, like cellulose, cannot be considered as plastics in their natural state, but if chemically modified, useful plastics materials such as cellulose acetate, celluloid, and ethyl cellulose may be obtained. Natural rubber is clearly the basis of a huge worldwide industry.

## 3.31.4 The Physical Nature of Plastics

Many polymers, such as polystyrene, consist of long chain-like molecules of high molecular weight. A typical average molecular weight for a polystyrene sample is about 200 000 and since the molecular weight of the monomer is 104 this implies that there are around 2000 repeat units joined together in a typical molecule taken from that sample. It is the case in nearly all plastics that a given sample contains molecules covering a distribution of molecular weights. This distribution, in some cases, may be very wide.<sup>5</sup> Since the backbone carbon–carbon bonds can rotate relatively freely, such molecules are most unlikely to be stretched out, but are more likely to be coiled up into what is referred to as a random-coil conformation.<sup>11</sup>

In the case, for example, of polystyrene, the molecules at room temperature do not have enough rotational energy to twist around the backbone chemical bonds and so, in the mass, the polymer is rigid. On heating above a certain temperature, sufficient energy for such subchain movement is obtained and on application of a shearing stress in processing such as extrusion, the polymer molecules partly uncoil. Chain segments slip past each other and, in the mass, flow occurs. On cessation of stress, slippage ceases, the chains again coil up and, on cooling, the mass again hardens. If desired, the whole process of heating, shearing and cooling may be repeated. Materials that behave in this way are known as

thermoplastics.<sup>7,11</sup> Two points should, however, be noted. Firstly, if cooling is faster than the chain recoiling process, then a frozen-in molecular orientation will result. This can grossly affect the polymer properties, in some cases adversely. Secondly, repeated heating and shearing may be accompanied by changes such as oxidation and polymer degradation, which will limit, in practice, the number of times heating and cooling can be applied on a particular polymer sample. In terms of tonnage, the bulk of plastics produced are thermoplastics, a group that includes the polyethylenes, polypropylene, polystyrene, polyvinyl chloride (PVC), the nylons, polycarbonates and cellulose acetate. There is, however, a second class of materials, the thermosetting plastics.<sup>7,11</sup> They comprise long-chain molecules, similar to a typical thermoplastic molecule, however, as rather smaller molecules. They are formed, often in a mold, into the desired final shape and then subjected to chemical reaction, often by heating, in such a way such that the molecules link with one another to form a cross-linked network as shown in **Figure 1**. As the molecules are now interconnected, they can no longer slide extensively past one another and the material is said to have set, cured or cross-linked. Plastic materials behaving in this way are designated as thermosetting plastics, a term which is also used to include those materials that can be cross-linked with suitable catalysts at room temperature. Important thermosetting plastics include the phenolic resins, melamine-formaldehyde resins, the epoxy resins and unsaturated polyester resins used in glass-reinforced plastics.

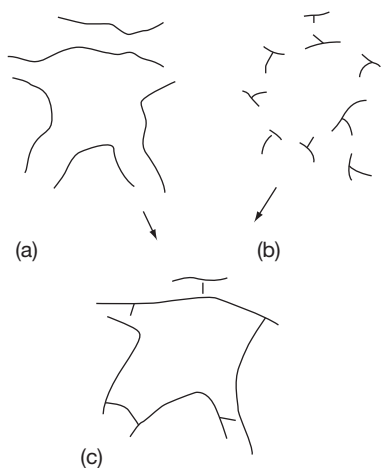


**Figure 1** Joining up of (a) long-chain molecules or (b) branched molecules to produce (c) a cross-linked polymer.

### 3.31.4.1 Thermoplastics

Thermoplastics may be considered in four subclasses: (a) amorphous thermoplastics; (b) rubber-modified amorphous thermoplastics; (c) plasticized amorphous thermoplastics, and (d) crystalline thermoplastics.

#### 3.31.4.1.1 Amorphous thermoplastics

These are made from polymers that have a sufficiently irregular molecular structure to prevent them from crystallizing. Examples of such materials include polystyrene and polymethyl methacrylate. The structural irregularity in these examples arises from the free-radical addition polymerization process used in their synthesis. This results in the repeat unit side groups being present in essentially random configurations,<sup>5</sup> which is sufficient to prevent crystallization.

At very low temperatures, these materials are glass-like and rigid. On heating, a temperature is eventually reached where the material softens. If the polymer is of sufficiently high molecular weight, it becomes rubbery above this temperature. The temperature at which this occurs is known as the glass transition temperature ( $T_g$ ),<sup>5,11</sup> and is in effect the temperature at which the polymer molecules have sufficient rotational energy to be able to coil and uncoil. As the individual polymer molecules, in their random-coil conformations, interpenetrate each other, the resulting chain entanglements prevent flow. At higher temperatures there are two possibilities. Polymers of moderate molecular weight may achieve such energy that they can flow, while high molecular weight materials may decompose before the flow point is reached. This is shown schematically in **Figure 2**,

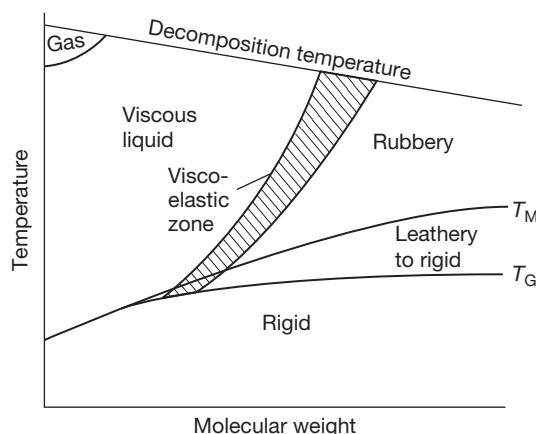


**Figure 2** Temperature-molecular weight phase diagram for amorphous polymers.

which indicates the phases in which this type of polymer can occur. It should be stressed that the boundary lines will change position with change of polymer type.

It can be seen that up to a certain molecular weight a polymer may be processed either as a liquid (by injection molding, extrusion, etc.) or as a rubber (by vacuum forming, sheet blowing, hot pressing). In the case of a polymer of much higher molecular weight, it can be seen that it can only be shaped in the rubbery state, and if it is intended to be processed by, say, injection molding, then the molecular weight may first have to be reduced. An important illustration of this is with well-known acrylic materials such as Perspex (polymethyl methacrylate), which can have too high a molecular weight to be injection-molded.

It is possible to make some generalizations about the properties of amorphous thermoplastics.

1. The  $T_g$  will determine the maximum temperature of use of the material as a rigid thermoplastic. For amorphous rubbers, the  $T_g$  value will determine the minimum temperature of use.
2. Below  $T_g$ , most amorphous polymers show a more or less linear stress-strain curve with no yield point. The tensile strengths are typically around 50 MPa, elongation at failure usually less than 10%, and the elastic modulus typically around 2.5 GPa. Since the area under the curve provides a measure of the energy required to rupture the specimen, and since this area is small, such polymers will have a low impact strength (which is closely related to the energy to break) and will break with a brittle fracture.
3. They are generally more permeable to gases than crystalline polymers. This is more so above  $T_g$  than below.
4. They usually have a much wider range of solvents than crystalline polymers.

#### **3.31.4.1.2 Rubber-modified amorphous polymers**

The brittleness of amorphous polymers has been a hindrance in their commercial development. However, for reasons now substantially understood, the addition of rubbery polymers as dispersed droplets into the glassy polymer can often lead to substantial increases in impact strength,<sup>12</sup> albeit usually at some cost to tensile strength and, in many cases, to transparency.

The most important polymers of this important class are as follows.

1. High-impact polystyrene (a polystyrene modified with a styrene-butadiene rubber (SBR) or a polybutadiene rubber).
2. ABS, which is based on a copolymer of acrylonitrile, butadiene and styrene.
3. Methacrylate-butadiene-styrene polymers (MBS) and related materials, which are chemically similar to ABS but are often available in transparent form.
4. Rubber toughened epoxy resins.
5. High-impact PVC; in this case the impact modifiers are not always rubbers, but the mechanism of their action is probably similar.

#### **3.31.4.1.3 Plasticized amorphous thermoplastics**

Certain plastics may be mixed with high boiling temperature, low-volatility liquids to give products of lower  $T_g$ . The most important example of this class occurs with PVC, which is often mixed with liquids such as di-*iso*-octyl phthalate, tritolyl phosphate, or other diesters to bring the  $T_g$  below room temperature. These liquids work by increasing the free volume in the materials, thereby facilitating the segmental motions that constitute the glass transition process. If their volatility is a problem in a given case, it may be possible to use either a polymeric plasticizer<sup>13</sup> or a chemically bound plasticizer.<sup>14</sup> The resultant plasticized PVC is flexible and to some degree quite rubbery. Other commonly plasticized materials are cellulose acetate and cellulose nitrate.

It is essential to appreciate that such plasticizers may also considerably modify the chemical properties of the plastic material since the plasticizer may be readily extracted by certain chemicals and chemically attacked by others while the base polymer may be unaffected.

#### **3.31.4.1.4 Crystalline thermoplastics**

While polymers such as polyethylene and nylon-6,6 do not show any regular external form, which is characteristic of crystals, closer examination reveals that they have many properties common to crystalline materials. They exhibit distinct X-ray diffraction patterns<sup>5</sup> and exhibit specific melting in differential scanning calorimetry (DSC).<sup>5</sup> Although the exact nature of this crystallinity is not fully resolved in some cases, it would appear that polymer segments pass through zones in which molecular arrangement is highly ordered, that is, crystalline. In some ways these zones act like knots, or cross-links, holding the individual molecules of such materials together.



The effect of heating crystalline polymers from low temperatures is more complex than with amorphous polymers. Initially, the material is rigid and hard. As the temperature goes through the  $T_g$ , light crystalline materials soften slightly and become leather-like, but highly crystalline materials show relatively little change in properties. Further heating results in the crystals melting, often over quite a wide temperature range, and the polymer becomes rubbery. Whether or not it melts or decomposes first on further increase in temperature will depend on both the particular polymer and its molecular weight.

A typical phase diagram for such polymers is given in **Figure 3**. With such crystalline polymers, the melting point,  $T_m$ , replaces the  $T_g$  as the factor usually determining the maximum service temperature of thermoplastics and minimum service temperature of rubbers. However, it is more difficult to make generalizations about properties. The following remarks may, however, be pertinent for crystalline polymers.

1. Below  $T_g$ , tensile strengths are usually at least as high for crystalline polymers as for amorphous ones. Between  $T_m$  and  $T_g$ , the strength and rigidity will be very dependent on the degree of crystallinity and to some extent on the molecular weight. Tensile strengths commonly range from below 10 to around 90 MPa.
2. In most cases, crystal densities differ from those of amorphous polymers. This leads to differences in refractive index, which in turn cause scattering of light at boundaries between amorphous and crystalline zones. Such materials are opaque, except in certain instances where the crystal structure can be carefully oriented to prevent such scattering of light.

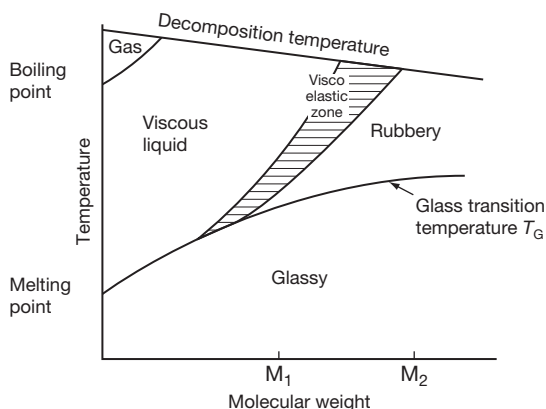


**Figure 3** Temperature-molecular weight phase diagram for crystalline polymers.

3. The close molecular packing makes diffusion more difficult than with amorphous polymers compared under similar circumstances, that is, either below  $T_g$ , or above  $T_g$  but below  $T_m$ , of the crystalline polymer.
4. Thermodynamic considerations lead to considerable restriction in the range of solvents available for such polymers.<sup>5,11</sup>

### 3.31.4.2 Thermosetting Plastics

If glycerol, a trihydric alcohol, reacts with phthalic anhydride, three ester links can be made from each glycerol unit. Continued reaction will eventually cause the molecules to link up in a three-dimensional network in which, theoretically at least, the whole polymer mass becomes one giant molecule.

For reasons of production feasibility, such cross-linked plastics are normally prepared in two stages. In the first stage, either a low-molecular-weight branched polymer or a higher-molecular-weight linear (unbranched) polymer is produced. Such materials are thermoplastic and in most cases soluble in some solvents. At a convenient (later) time, this intermediate is subjected to heat, electromagnetic radiation (such as ultraviolet), or chemical reactants, such that the branched molecules join together, or the linear polymers cross-link, thereby producing an infusible, insoluble material. Since, in the early days of the plastics industry, the cross-linking processes required heat, these materials became known as 'thermosetting plastics.' Today this term is commonly extended to materials which can cross-link at room temperature: for example, many organic coating systems (or paints).

Because thermosetting plastics have an irregular form, they are amorphous, and because of their network structure, they are invariably rigid. They do not dissolve without decomposition, but may swell in appropriate solvents, the amount of swelling decreasing with increasing cross-link density. Well-known thermosetting plastics include the phenolics, urea-formaldehyde and melamine-formaldehyde resins, unsaturated polyesters and epoxy resins.

### 3.31.4.3 Reinforced Plastics

The mechanical properties of plastic materials may often be considerably enhanced by embedding fibrous materials in the polymer matrix.<sup>15</sup> While such techniques have been applied to thermoplastics, the greatest developments have taken place with the thermosetting plastics. The most common reinforcing materials are



glass and cotton fibres,<sup>16</sup> but many other materials including paper, carbon fiber, inorganic whiskers, particulates including nanoscale particulates,<sup>15</sup> are used. Reinforcing fibers normally have a modulus of elasticity that is substantially greater than the resin, so that under tensile stress much of the load is borne by the fibers. The modulus of the composite is, therefore, intermediate to that of the fiber and of the resin.

In addition to the nature of resin and fiber, the laminate properties also depend on the degree of bonding between the two main components and on the presence of other additives, including entrained air bubbles. Because of this, some parts, fabricated by simple hand build-up techniques, may exhibit strengths no better, or even worse, than unreinforced materials. This problem is often worst with glass fibers, which are, therefore, normally treated with special finishes to improve the resin–glass bond.

The highest mechanical strengths are usually obtained when the fiber is used in fine fabric form, but for many purposes the fibers may be used in mat form, particularly glass fiber. The chemical properties of such laminates are largely determined by the nature of the polymer, but capillary attraction along the fiber–resin interface can occur when some of these interfaces are exposed at a laminate surface. In such circumstances, the resistance of both the reinforcement and the matrix must be considered when assessing the suitability of a laminate for use in chemically demanding situations. For more information, the reader is referred to the article on polymer–matrix composites.

### 3.31.5 Polymer Orientation

It is not difficult to appreciate that if polymer molecules are aligned, as in **Figure 4(a)**, then a much higher tensile strength will be obtained if a test is carried out in the X–X direction as opposed to the Y–Y direction. It is also not difficult to understand

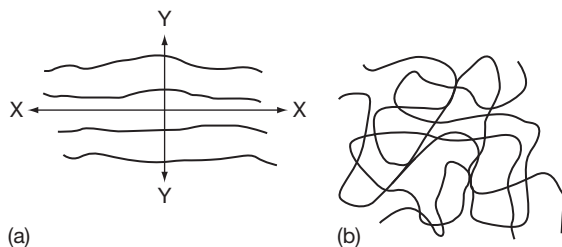


**Figure 4** Polymer segment alignment: (a) parallel and (b) random.

why such a material has lower impact strength than a randomly coiled mass of molecules, **Figure 4(b)**, because of the ease of cleavage of the material parallel to the X–X direction.<sup>15</sup>

Similar remarks may also be made where crystal structures, or fiber reinforcements, are aligned rather than the individual molecules. For fibers and filaments such orientation is desirable, but for solid objects where impact strength is often more important than tensile strength such orientation is usually unwelcome. It can also have further unwanted effects. This arises from the fact that oriented molecules are thermodynamically unstable and will at the first opportunity try to achieve random-coil conformations. Thus, on heating samples up to temperatures near  $T_g$ , severe distortion can occur, leading to warped moldings.

Another serious effect, solvent stress cracking,<sup>17</sup> occurs with liquids which are not in themselves solvents but which may wet the polymer surfaces. These facilitate relief of frozen-in stresses by surface cracking, which can be a severe problem in using many injections and blow moldings with specific chemicals. Examples of this are white spirit with polystyrene, carbon tetrachloride with polycarbonates and soaps and silicone oils with low-molecular-weight polyethylenes.

In addition to orientation in one direction (monoaxial orientation), biaxial orientation is possible. This is achieved when the sheet is stretched in two directions, resulting in layering of the molecules. This can increase the impact strength, tensile strength and solvent cracking resistance of polymers, and with crystalline plastics the polymer clarity may also be improved.

### 3.31.6 The Chemical Properties of Polymers

It is common practice to talk about the chemical resistance of polymers, unaware of the fact that this can mean different things. To avoid this it is probably wiser to differentiate between the following.

1. Resistance of a polymer to chemical attack resulting in breakdown of some covalent bonds and the formation of new ones. This could involve molecular breakdown initiated by heat or radiation, including ultraviolet light.
2. Resistance to dissolution by liquids.
3. Resistance to cracking in aggressive environments.
4. Permeability to gases and liquids.

It is also important to bear in mind that, for specific end uses, polymers are commonly mixed with a number of additives such as plasticizers, stabilizers, antioxidants, fillers, fire retardants, pigments, dyes and other polymers, and that this may well have an important influence on their chemical properties. The following discussion will, however, be confined to pure polymers.

### 3.31.6.1 Resistance to Chemical Attack

Expressed simply, the resistance of a polymer to chemical attack may be said to be determined by the following factors:

- the nature of the chemical bonds present,
- interactions between chemical groups that occur repeatedly along the molecular chain, and
- the presence of occasional 'weak-links.'

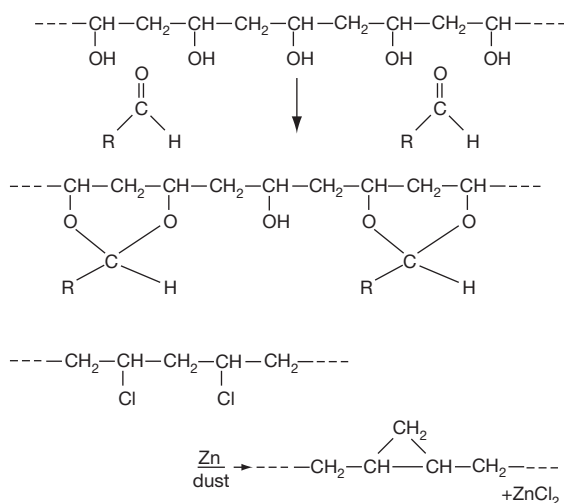
In commercial polymers, there are a rather limited number of chemical bond types to be found and it is possible to make a number of general observations about the chemical reactivity in the following list of examples.<sup>5,8,18</sup>

1. Polyolefins such as polyethylene and polypropylene contain only C–C and C–H bonds and may be considered simply as high-molecular-weight paraffins. Like the simpler paraffins, they are somewhat inert, and their major chemical reaction is a substitution reaction, for example, halogenation. In addition, the branched polyethylenes and all the higher polyolefins contain tertiary carbon atoms which are reactive sites for oxidation. Because of this, it is necessary to add antioxidants to stabilize the polymers against such oxidation. Some polyolefins may be cross-linked by peroxides.
2. Polytetrafluoroethylene (Teflon) contains only C–C and C–F bonds. These are both very stable and the polymer is exceptionally inert.<sup>19</sup> A number of other fluorine-containing polymers are available, which may contain in addition C–H and C–Cl bonds. These are somewhat more reactive, and those containing C–H bonds may be cross-linked by peroxides and certain diamines and diisocyanates.
3. Many polymers, such as the diene rubbers, contain double bonds. These will react with many agents such as oxygen, ozone, hydrogen halides and halogens. Ozone, and in some instances oxygen, will lead to scission of the main chain at the site of the repeat-unit double bond and this will have a

catastrophic effect on the molecular weight. The rupture of one such bond per chain will halve the average molecular weight.

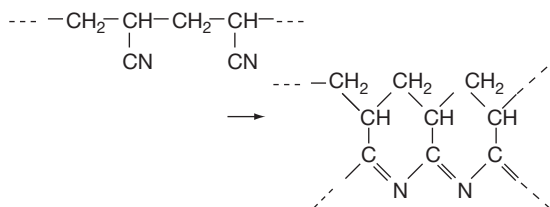
4. Ester, amide, and carbonate groups are susceptible to hydrolysis. When such groups are found in the main chain, their hydrolysis will also result in a reduction of molecular weight. Where hydrolysis occurs in a side chain, the effect on molecular weight is usually insignificant. The presence of benzene rings adjacent to these groups may offer some protection against hydrolysis, except where organophilic hydrolyzing agents are employed.
5. Hydroxyl groups are extremely reactive. These occur attached to the backbones, for example, of cellulose and polyvinyl alcohol.
6. Benzene rings in both the backbone structure and on the side groups can be subjected to substitution reactions. Such reactions do not normally cause great changes in the fundamental nature of the polymer. They seldom lead to chain scission or cross-linking. However, the phenolic resins provide an important exception to this.

There are numerous examples of chemical reactions consequent upon chemical groups that occur repeatedly along a chain. In some cases, the reaction occurs randomly between adjacent pairs of groups such as in the reaction between aldehydes and polyvinyl alcohol and of zinc dust with polyvinyl chloride:



In other instances the reactions appear to occur in sequence down individual chains, for example, in the depolymerization reactions of polyformaldehyde (polyacetal) and polymethyl methacrylate, which are referred to sometimes as unzipping reactions.

In other cases, cyclization reactions can occur such as on heating polyacrylonitrile.



It is commonly found that polymers are less stable, particularly to molecular breakdown at elevated temperatures, than low-molecular-weight compounds containing similar groupings. In part, this may be due to the regular repetition of groups along a chain as discussed above, but more frequently it is due to the presence of weak links along the chain. These may be at the end of the chain (terminal) arising from specific mechanisms of chain initiation and/or termination, or nonterminal, and due to such factors as impurities that become built into the chain, an aberration in the *modus operandi* of the polymerization process or, perhaps, to branch points.<sup>20</sup>

The combination of weak links and unzipping can be catastrophic and has been a particular problem in the commercial development of some polymers, in particular polyacetals.<sup>21</sup>

### 3.31.6.2 Polymer Solubility

The solution properties of polymers have been subjected to intensive study, in particular to complex mathematical treatment.<sup>5,22,23</sup> This section will, however, confine the discussion to a qualitative and practical level.<sup>5</sup>

One chemical will be a solvent for another if the molecules are able to co-exist on a molecular scale, that is, the molecules show no tendency to separate. In these circumstances, the two species are said to be compatible. The definition concerns equilibrium properties and gives no indication of the rate of solution, which will depend on other factors such as temperature, the molecular size of the solvent and the size of voids in the solute.

Molecules of two different species will be able to coexist if the force of attraction between different molecules is not less than the forces of attraction between two like molecules of either species. This is shown more clearly by reference to Figure 5, which shows two types of molecules A and B. The average forces between the like molecules are  $F_{AA}$  and  $F_{BB}$ ,

and the average forces between dissimilar molecules are  $F_{AB}$ . If  $F_{AA}$  was the largest of these three forces, then the A molecules would tend to congregate or cohere, rejecting the B molecules. A similar phase separation would occur if  $F_{BB}$  was the greatest.

It is, therefore, seen that only when  $F_{AB} \geq F_{AA}$  and  $F_{AB} \geq F_{BB}$  will coexistence or compatibility be possible. Obviously, if it is possible to obtain some measure of these forces, it should be possible to make predictions about polymer solubility. What then is a suitable measure of the forces holding like molecules together? One would expect the latent heat of vaporization,  $L$ , to exceed that cohesion energy by an amount corresponding to the work done by evaporation, an amount approximating to  $RT$ , where  $R$  is the gas constant and  $T$  the absolute temperature. Such a diagram of  $(L - RT)$  might be a sufficient measure if all of the molecules were of about the same size.

However, it is reasonable to suppose that compatibility should not be greatly affected by molecular size and that the shorter polymer molecules in Figure 6(a) should be just as compatible as the longer ones in Figure 6(b), although their theoretical latent heats of vaporization will be greatly different. In such circumstances, a reduced diagram of  $(L - RT)/M$  will give a measure of intermolecular energy per unit weight. Similarly, a measure of the intermolecular

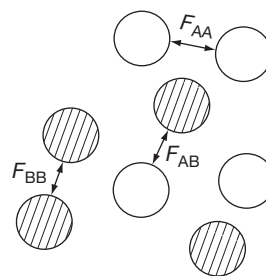


**Figure 5** Two different molecular species will be compatible if  $F_{AB} \geq F_{AA}$  and  $F_{AB} \geq F_{BB}$ . In other circumstances the molecules will tend to separate if they have sufficient energy for molecular movement.

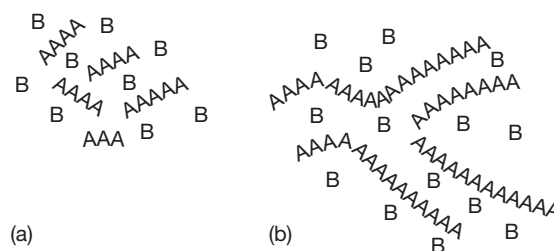


**Figure 6** Polymer molecules: (a) short and (b) long.

or cohesion energy per unit volume will be given by the following expression, where  $D$  is the density.

$$\frac{L - RT}{M/D}$$

This expression is known as the cohesive energy density<sup>5,24</sup> with units of megapascal. The square root of this expression is more commonly encountered in quantitative studies and is known as the solubility parameter and given the symbol  $\delta$ .

$$\delta = \sqrt{\frac{L - RT}{M/D}} \text{MPa}^{1/2}$$

The solubility parameter is, thus, an experimentally determinable property, at least for low-molecular-weight materials. In the case of polymers that cannot be vaporized without decomposition, a method of calculating from a knowledge of structural formula has been devised by Small and others.<sup>24,25</sup> It is now possible to provide an estimate of  $F_{AA}$  and  $F_{BB}$ , but the magnitude of  $F_{AB}$  has to be considered separately for each different system.

### 3.31.6.2.1 Amorphous nonpolar polymers and amorphous nonpolar solvents

It is generally assumed in these circumstances, by analogy with gravitational and electrostatic attractions, that  $F_{AB}$  will be equal to the geometric mean of  $F_{AA}$  and  $F_{BB}$ . Thus, if by definition  $F_{AA} > F_{BB}$ , then,  $F_{AA} > F_{AB} > F_{BB}$ . Considering these conditions, it can be seen that compatibility will occur between amorphous nonpolar polymers and solvents only when  $F_{AA} = F_{AB} = F_{BB}$ ; that is, when polymer and solvent

have similar solubility parameters (in practice to within about  $2 \text{MPa}^{1/2}$ ). Reference to the values of  $\delta$  in **Tables 1 and 2** provides examples of this. For example, natural rubber (unvulcanized) ( $\delta = 16.5$ ) is soluble in toluene ( $\delta = 18.2$ ) and carbon tetrachloride ( $\delta = 17.5$ ) but not in ethanol ( $\delta = 25.9$ ). Cellulose diacetate ( $\delta = 23.2$ ) is soluble in acetone ( $\delta = 20.4$ ), but not in methanol ( $\delta = 29.6$ ) or toluene ( $\delta = 18.2$ ). It should be noted that apart from the problem of achieving a molecular level of dispersion, it is not necessary for the solvent to be liquid; it may be an amorphous solid. Such tables are of greatest use with nonpolar materials with values of  $\delta$  not exceeding  $19.4 \text{MPa}^{1/2}$  and when the polymers are amorphous.

### 3.31.6.2.2 Crystalline nonpolar polymers and amorphous solvents

Most polymers of regular structure will crystallize if cooled below the melting point,  $T_m$ . This is in accordance with the thermodynamic law that a process will occur only if there is a decrease in Gibbs free energy ( $-\Delta G$ ) in going from one state to another. Such a decrease occurs on crystallization as the molecules pack in a regular fashion. Since a process occurs only when it is accompanied by a decrease in free energy, there is no reason why a crystalline nonpolar polymer should dissolve in a solvent at temperatures well below the melting point. However, as the melting point is approached, the  $T \Delta S$  term in the equation below increases.

$$\Delta G = \Delta H - T \Delta S$$

**Table 1** Solubility parameters ( $\delta$ ) of polymers

Polymer	$\delta \text{ (MPa}^{1/2}\text{)}$	Polymer	$\delta \text{ (MPa}^{1/2}\text{)}$
Polytetrafluorethylene	12.6	Polyethyl acrylate	18.8
Polychlorotrifluoroethylene	14.7	Polysulfide rubber	18.4–19.2
Polydimethyl siloxane	14.9	Polystyrene	18.8
Ethylene-propylene rubber	16.1	Polychloroprene rubber	18.8–19.2
Polyisobutylene	16.1	Polymethyl methacrylate	18.8
Polyethylene	16.3	Polyvinyl acetate	19.2
Polypropylene	16.3	Polyvinyl chloride	19.4
Polyisoprene (natural rubber)	16.5	Bisphenol A polycarbonate	19.4
Polybutadiene	17.1	Polyvinylidene chloride	20.0–24.9
Styrene-butadiene rubber	17.1	Ethylcellulose	17.3–21.0
Poly- <i>t</i> -butyl methacrylate	16.9	Cellulose dinitrate	21.5
Poly- <i>n</i> -butyl methacrylate	17.7	Polyethylene terephthalate	21.8
Poly- <i>n</i> -hexyl methacrylate	17.5	Acetal resins	22.6
Polybutyl acrylate	18.0	Cellulose diacetate	23.1
Polyethyl methacrylate	18.4	Nylon 66	27.7
Polymethylphenyl siloxane	18.4	Polymethyl $\alpha$ -cyanoacrylate	28.8
		Polyacrylonitrile	28.8

**Table 2** Solubility parameters ( $\delta$ ) and partial polarities ( $P$ ) of some common solvents

<i>Solvent</i>	$\delta$ (MPa <sup>1/2</sup> )	<i>P</i>	<i>Solvent</i>	$\delta$ (MPa <sup>1/2</sup> )	<i>P</i>
Dimethylpropane	12.9	0	Chloromethane	19.8	–
2-Methylpropene	13.7	0	Dichloromethane	19.8	–
Hexane	14.9	0	1,2-Dichloroethane	20.0	0
Ethoxyethane	15.1	0.03	Cyclohexane	20.2	–
Octane	15.5	0	Carbon disulfide	20.4	0
Methylcyclohexane	15.9	0	Acetone	20.4	0.69
2-Methylpropanoate	16.1	–	Octanol	21.0	0.04
2,4-Dimethylpentan-3-one	16.3	0.3	Butanenitrile	21.4	0.72
2-Methyl butyl acetate	16.3	–	Hexanol	21.8	0.06
Cyclohexane	16.7	0	2-Butanol	22.0	0.11
2,2-Dichloropropane	16.7	–	Pyridine	22.2	0.17
3-Methyl-1-butyl acetate	16.9	–	Nitroethane	22.6	0.71
Pentylacetate	17.3	0.07	Butanol	23.3	0.10
Tetrachloromethane	17.5	0	Cyclohexanol	23.3	0.08
Hexan-2-one	17.7	0.4	2-propanol	23.4	–
Piperidine	17.7	–	Propanol	24.3	0.15
Xylene	18.0	0	Dimethyl formamide	24.7	0.77
Methoxymethane	18.0	–	Hydrogen cyanide	24.7	–
Toluene	18.2	0	Acetic acid	25.7	0.30
1,2-Dichloropropane	18.4	–	Ethanol	25.9	0.27
Ethyl acetate	18.6	0.17	Formic acid	27.5	–
Benzene	18.8	0	Methanol	29.6	0.39
4,4-Hydroxymethylpentan-2-one	18.8	–	Phenol	29.6	0.06
Trichloromethane	19.0	0.02	Glycerol	33.7	0.47
1,1,2-Trichloroethene	19.0	0	Water	47.7	0.82
Tetrachlorethane	19.2	0.01			
2-Hydroxyethoxyethan-2-ol	19.6	–			

Here,  $T$  is the absolute temperature,  $\Delta S$  the entropy change, and  $\Delta H$  the enthalpy change. So, with increasing temperature,  $\Delta G$  can become negative and dissolution can therefore occur.

Hence, at room temperature, there are no solvents for polyethylene, polypropylene, poly-4-methylpentene-1, polyacetal or polytetrafluoroethylene, but at temperatures of about 30°C below their melting points solvents of similar solubility parameter are effective. It should also be noted that at room temperature swelling may occur in the amorphous zones of the polymer in the presence of solvents of similar solubility parameter.

### 3.31.6.2.3 Amorphous nonpolar polymers and crystalline solvents

This situation is identical to the previous one, and occurs, for example, when paraffin wax is mixed into rubber above its melting point. On cooling, the paraffin wax tends to crystallize, some of it on the surface of the rubber. Such a bloom is one way of protecting a diene rubber from ozone attack.

### 3.31.6.2.4 Amorphous polar polymers and solvents

Molecules are held together by one, or more, of four types of forces: dispersion, dipole, induction and hydrogen bonding. In the case of aliphatic hydrocarbons, the so-called dispersion forces predominate. However, many covalent bonds contain dipoles, with one end being partially positively charged and the other partially negatively charged. Such dipoles may interact with dipoles on other molecules and lead to enhancement of the total intermolecular attraction. Molecules that possess dipoles and interact in this way are said to be polar. Many well-known solvents (e.g., water) and polymers (e.g., PVC) are polar, and it is generally considered that for interaction both the solubility parameter and their degrees of polarity should match. This is usually expressed in terms of partial polarity,<sup>24</sup> which expresses the fraction of total forces due to dipole bonds. Some figures for partial polarities ( $P$ ) for solvents are given in Table 2, but there is a lack of quantitative data on the partial polarities of polymers. A comparison of



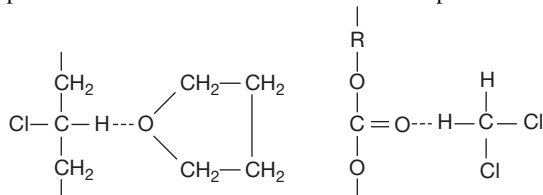
polarities has to be made by common sense rather than a quantitative approach. For example, hydrocarbon polymers would be expected to have a negligible polarity and would then be more likely to dissolve in toluene rather than diethyl ketone, although both have similar solubility parameters.

### 3.31.6.2.5 Crystalline polar polymers and solvents

It has already been pointed out that at temperatures well below their melting point crystalline nonpolar polymers will not interact with solvents, and similar considerations can apply to a large number of polar crystalline polymers. It has, however, been possible to find solvents for some polar, crystalline polymers such as the nylons, polyvinyl chloride and the polycarbonates. This is because of specific interactions between polymer and solvent that may often occur by, for example, hydrogen bonding.

For example, nylon-6,6 will dissolve in formic acid, glacial acetic acid and phenol, solvents that not only have similar solubility parameters but also are capable of acting as proton donors while the carbonyl groups on the nylon act as proton acceptors.

More interesting examples are given with PVC and the polycarbonate of bis-phenol A – both are slightly crystalline polymers. It is noticed here that while dichloromethane is a good solvent and tetrahydrofuran a poor solvent for the polycarbonate, the reverse is true for PVC, yet all four materials have similar solubility parameters. It would seem that the explanation is that a form of hydrogen bonding occurs between the polycarbonate and methylene chloride and between PVC and tetrahydrofuran. In other words, there is a specific interaction between each solvent pair:



Many studies have been made to assess the propensity to hydrogen bonding of chemical structures.<sup>24</sup> As a result, the following broad generalizations may be made.

1. Proton donors include highly halogenated compounds such as chloroform and pentachlorethane; less halogenated materials are weaker donors.
2. Polar acceptors include, in roughly descending order of strength, amines, ethers, ketones,

aldehydes, and esters, with aromatic materials usually being more powerful than aliphatic ones.

3. Some materials such as water, alcohols, carboxylic acids, and primary and secondary amines may be able to act simultaneously as proton donors and acceptors. Cellulose and polyvinyl alcohol are two polymers that also function in this way.
4. A number of solvents such as the hydrocarbons, carbon disulfide and carbon tetrachloride are quite incapable of forming hydrogen bonds.

### 3.31.6.2.6 Rubbers and thermosetting plastics

Covalently cross-linked rubbers and plastics cannot dissolve without chemical change. They will, however, swell in solvents of similar solubility parameter, the degree of swelling decreasing with increasing cross-link density. The solution properties of the thermoplastic elastomers, which are two-phase materials, are much more complex and dependent on whether or not the rubber phase and the thermoplastic domains are dissolved by the solvent.

### 3.31.6.3 Resistance to Cracking in Aggressive Environments

It has been found with many rigid plastics materials that, under stresses well below the normal yield stress, cracking occurs in environments where the polymer will be unaffected when free of stress. The mechanism for this stress-cracking phenomenon is not fully understood and, indeed, there may well be different mechanisms in different circumstances. There do, however, appear to be four main types.

- Solvent cracking of amorphous polymers.
- Solvent cracking of crystalline polymers.
- Environmental stress cracking.
- Thermal cracking.

Examples of solvent cracking of amorphous polymers<sup>26</sup> are polystyrene with white spirit, polycarbonate with methanol and polysulfone with ethyl acetate. The propensity to solvent stress cracking is, however, far from predictable, and intending users of a polymer should check on this before use.

In the case of crystalline polymers, it may be that solvents can cause cracking by activity in the amorphous regions of these more complex morphologies. Examples of this are benzene and toluene with polyethylene. In polyethylene, however, a greater problem is that of environmental stress cracking,<sup>17</sup> which



occurs with materials such as soap, alcohols, surfactants and silicone oils. Many of these are highly polar materials that cause no swelling, but are simply absorbed either into, or on to, the polymer. This appears to weaken the surface and allows cracks to propagate from minute flaws. Cracking caused by heat (thermal cracking) appears to act in a similar manner, but in this case oxygen is the aggressive environment, becoming active at 70–80 °C with some polyethylenes.

### 3.31.6.4 Diffusion

The efficacy of polymers when used to protect metals from corrosive environments is, of course, strongly influenced by their efficiency as barrier materials. When applied to metals by some techniques, such as fluidized-bed coating, there is always the danger of ‘macrodiffusion’ through pinholes, which are gross imperfections in the surface region and which do not have to be visible to be very much greater than the dimensions of penetrating molecules.

Assuming, however, that the film is continuous, the concern then is with the permeability of the corrosive fluids in the polymer film. This involves both the dissolution of the fluid into the polymer, which will be determined by the conditions discussed previously, and the rate of diffusion of the fluid through the polymer. This has been discussed elsewhere<sup>18,27</sup> in detail, but may be summarized as follows.

1. The lowest diffusion rates occur with crystalline polymers below the  $T_g$ , since there is very little space through which diffusing molecules may pass.
2. Amorphous polymers below the  $T_g$  have a somewhat higher permeability, but diffusion is still difficult.
3. For amorphous polymers above the  $T_g$ , that is, in the flexible and rubbery states, there is more space (free volume) available through which diffusing molecules may pass, and so these materials show comparatively high diffusion rates with low-molecular-weight diffusing fluids.
4. For crystalline polymers between  $T_g$  and  $T_m$ , the diffusion rate is very dependent on the degree of crystallization.

## 3.31.7 Review of Commercial Plastics

### 3.31.7.1 Amorphous Thermoplastics

#### 3.31.7.1.1 Polyvinyl chloride

PVC<sup>28</sup> is one of the two most important plastics in terms of tonnage and shows many properties typical

of rigid amorphous thermoplastics. However, PVC is not a truly amorphous polymer in that it has short stereoregular repeat unit sequences which can lead to crystallinity values up to about 10 vol.%. PVC softens at about 70 °C, burns only with difficulty, but is thermally unstable. To reduce this instability, stabilizers are invariably compounded into the polymer.

Being slightly crystalline, there are a few good solvents, the best known of which are nitrobenzene, cyclohexanone, and tetrahydrofuran. When mixed with certain nonvolatile solvents such as some phthalates, adipates, and phosphates, flexible materials are obtained, which are referred to as plasticized PVC.

In order to improve toughness, many rubbers and other soft polymers may be used as additives to modify the compound. Some copolymers based on vinyl chloride are available of which the most important are the vinyl chloride–vinyl acetate materials used in flooring compositions and surface coatings.

#### 3.31.7.1.2 Polystyrene

The volume of expanded polystyrene (PS) produced probably exceeds the total volume production of all other plastics (excluding the polyurethanes). About half the tonnage of polystyrene produced is in the form of high-impact polystyrene (HIPS): a complex blend containing styrene–butadiene rubber or polybutadiene.<sup>7,19</sup> Styrene–acrylonitrile (SAN) has improved heat resistance, oil resistance and slightly better impact strength.

#### 3.31.7.1.3 Acrylonitrile–styrene–butadiene polymers (ABS)

These are complex blends and copolymers of excellent toughness.<sup>7,19</sup>

#### 3.31.7.1.4 Poly(methyl methacrylate)

Poly(methyl methacrylate) (PMMA)<sup>7,19</sup> is used mainly where high light transmission and excellent weathering properties are of greatest importance. This polymer is the most well known of a very wide range of acrylic polymers that find use as rubbers, fibers, plastics, adhesives and surface coatings. The sheet forms (Perspex, Plexiglas, Oroglass) are often of high molecular weight and dissolve only with some difficulty.

#### 3.31.7.1.5 Polyvinyl acetate and derivatives

Polyvinyl acetate is used largely for coating applications,<sup>7,19</sup> but the derivative polyvinyl alcohol will, provided there are some residual acetate groups, dissolve in water. Reaction products of polyvinyl

alcohol with aldehydes such as polyvinyl formal and polyvinyl butyral are also commercially available materials.

#### **3.31.7.1.6 Cellulose-based plastics**

These long-established materials<sup>9,10</sup> have limited chemical resistance. Ethyl cellulose is, however, often used in conjunction with mineral oil for hot-melt strippable coatings for protecting metal parts against corrosion and marring during transport and storage.

### **3.31.7.2 Crystalline Plastics**

#### **3.31.7.2.1 Polyethylene**

The polyethylenes (high density, low density, linear low density, etc.) are among the largest tonnage polymeric materials produced worldwide.<sup>7,19</sup> They are attacked by only a few chemicals, are not swollen by water or common organic solvents, but are susceptible to environmental stress cracking in the presence of certain detergents, esters, alcohols and silicones. Commercial materials vary in the regularity of their molecular structure, the more regular grades having a higher density and rigidity and lower gas permeability.

#### **3.31.7.2.2 Polypropylene**

Polypropylene has similar chemical properties to polyethylene, but is less susceptible to environmental stress cracking. It may also be used at somewhat higher temperatures.<sup>7,19</sup>

#### **3.31.7.2.3 Other polyolefins**

A variety of other crystalline polyolefins such as polybutene-1 (improved creep resistance over polyethylene), poly-4-methyl pentene-1 (excellent temperature deformation resistance) and ethylene-vinyl acetate polymers (greater flexibility) are available.<sup>7</sup>

#### **3.31.7.2.4 Polytetrafluorethylene**

Polytetrafluorethylene (PTFE) does not absorb water, has no solvents and is almost completely inert to chemical attack, except by molten alkali metals and sodium in liquid ammonia. Furthermore, it does not soften below 320°C, is electrically inert and has a very low coefficient of friction. It is more expensive than general-purpose plastics, requires special fabrication techniques, is degraded by high-energy radiation and has a low creep resistance.<sup>7,19</sup>

#### **3.31.7.2.5 Other fluorine-containing plastics**

These materials<sup>7,19</sup> in general, attempt to compromise between the exceptional end-use properties of PTFE and the greater ease of processing of other thermoplastics. Examples include polychlorotrifluoroethylene, tetrafluoroethylene-hexafluoropropylene copolymers (FEP resins), and polyvinylidene fluoride. Polyvinyl fluoride is available in film form with excellent weathering resistance.

#### **3.31.7.2.6 Polyamides (nylons)**

The main types of nylon<sup>7,19</sup> are oil and petrol resistant, but on the other hand susceptible to high water absorption and hydrolysis. There are a few solvents which include phenol and formic acid. Special grades include a water-soluble nylon, amorphous copolymers and low-molecular-weight grades used in conjunction with epoxy resins. Transparent amorphous polyamides are also now available.<sup>7</sup>

#### **3.31.7.2.7 Polyformaldehydes (polyoxymethylenes, polyacetals)**

These are physically similar to general-purpose nylons, but with greater stiffness and lower water absorption. There are no common solvents, but swelling occurs in liquids of similar solubility parameter. Poor resistance to ultraviolet light and limited thermal stability are two disadvantages of these materials.<sup>7,19</sup>

#### **3.31.7.2.8 Other polyethers**

The chlorine-containing polyether 'Penton' has excellent resistance to mineral acids, strong alkalis and most common solvents.<sup>29</sup> However, it is not recommended for use with oxidizing acids such as fuming nitric acid. Poly-2,6-dimethyl phenylene oxide (PPO) and certain related materials are similar to the nylons, but have superior heat resistance. These polymers are somewhat liable to stress-cracking problems.<sup>7,19</sup> Several polyethers are used as intermediates in the preparation of polyurethane foams, while others such as polyethylene glycol are water soluble.<sup>7</sup>

#### **3.31.7.2.9 Linear polyesters**

Polyesters<sup>7,19</sup> may be obtained in a wide variety of forms including rubbers, fibers, films, laminating resins, surface coatings and thermoplastic molding powders. The last named are somewhat similar to the nylons, but are more rigid. Chemical applications are limited because of their sensitivity to alkaline solutions and hot water.

**3.31.7.2.10 Polycarbonates and polysulfones**

These are tough materials with heat resistance better than most thermoplastics. They are resistant to attack by acids and alcohols, but the polycarbonates are sensitive to alkalis.<sup>7,19</sup>

**3.31.7.3 Thermosetting Resins**

These materials<sup>7,19</sup> often have better heat resistance than thermoplastics. Thermosetting resins are used in a variety of guises including surface coatings, but as plastics they are most frequently used in molding compositions and laminates. The tensile strength of unfilled rigid thermosetting resins is of the same order as for amorphous thermoplastics, that is, about 55 MPa, but this value may be greatly affected by the choice of fillers. For example, polyester–glass chopped-mat laminates often have tensile strengths in excess of 100 MPa, while values several-fold higher may be achieved by using carbon or boron fibers with epoxy resins. Further increases are becoming possible through the use of nanofillers.

**3.31.7.3.1 Phenol–formaldehyde (phenolic) plastics**

The chemical resistance is affected by the type of phenol used, cresols giving the best acid resistance, while xylenols are often used to obtain the best alkali resistance. For chemical-resistant applications, the fillers used in the molding powder and in the reinforcing material in laminates should be inorganic, for example, glass. These resins<sup>7,19</sup> are usually dark in color.

**3.31.7.3.2 Aminoplastics**

In this group, melamine–formaldehyde resins<sup>7,19</sup> with their good heat resistance, scratch resistance, and stain resistance, are usually preferred to urea–formaldehyde resins, where chemical resistance is important. Unlike the phenolics, these materials are not restricted to dark colors.

**3.31.7.3.3 Unsaturated polyesters**

It is possible to prepare unsaturated polyester-based laminates without application of external heat and pressure, thereby facilitating the manufacture of large objects such as boats using simple equipment. The laminates have somewhat limited chemical resistance, being attacked by many acids, alkalis and organic solvents.<sup>7,19</sup> Glass fiber is the common reinforcing agent, and in some products there is a tendency

for capillary action to occur along the fiber bundles. Distilled water, in general, is more active in this respect than aqueous salt solutions, including seawater.

**3.31.7.3.4 Epoxy and furan resins**

These important materials,<sup>7,19</sup> somewhat more expensive than the polyesters, may also be fabricated without the use of pressure, and at ambient temperatures, if so desired. They are markedly superior to polyesters in chemical resistance, particularly towards alkalis.

**3.31.7.3.5 Silicones**

This term is given to a wide range of polymers<sup>7,19</sup> including fluids, rubbers and thermosetting resins. Although rather expensive compared to most other plastics, they are particularly noted for their thermal stability and their water repellency.

**3.31.7.3.6 Polyurethanes**

These are another large class of polymers<sup>7,19,30</sup> that are available in a wide range of forms, including rigid and flexible rubbers, foams, surface coatings and adhesives. The solid polymers, including the rubbers, have particularly good abrasion resistance. The polyurethanes, as a class, are somewhat lacking in resistance to acids and alkalis, and to the prolonged action of water and steam.

**3.31.8 Polymers with Enhanced Heat Resistance**

Very often, a desirable feature of a plastic material is its low softening point which enables it to be melt-processed at temperatures much lower than those normally used for metals and inorganic glasses. The ever-more sophisticated uses to which plastics materials have been put have, however, led to the demand for newer polymers with improved heat resistance to supplement those materials already available such as PTFE and the polycarbonates. For example, the polyimides (e.g., bismaleimides) are a developing class of polymer with good high temperature properties.<sup>7,19</sup>

Factors that need to be taken into account at high temperatures are the flammability of the polymer, or a compound from it, and the smoke evolution characteristics of the polymer and its degradation compounds. In general, the maximum service temperature for which a polymer may be used in a given application (i.e., prior to serious oxidative degradation, including burning) depends generally on two independent factors.

1. The thermal stability of the polymer, particularly in air.
2. The softening behavior of the polymer.

Polymer thermal stability is largely concerned with chemical reactivity, which may involve oxygen, ultra-violet radiation or depolymerization reactions. The presence of weak links and the possibility of chain reactions involving polymer chains may lead to polymers having lower thermal stability than predicted from studies of low-molecular-weight analogues.

The softening behavior of a thermoplastic material depends to a large extent on the flexibility of the chains and their ability to crystallize. Significant cross-linking of a reasonably stiff-chained polymer will lead to material that is unlikely to soften below its decomposition temperature. Intermediate to the linear and cross-linked polymers are various 'ladder polymers' in which the polymer molecule consists of a pair of more or less parallel chains bridged in a manner analogous to the rungs of a ladder.<sup>31,32</sup>

Resistance to burning depends on many factors. It is, however, to be noted that those polymers that burn only in air enriched with oxygen tend to have high carbon-to-hydrogen ratios and/or may also emit materials during degradation, such as hydrogen chloride, which are inherent flame retardants. Low smoke emission is also often associated with a high carbon-to-hydrogen ratio. Table 3 gives some collected data for the limiting oxygen index, the minimum percentage of oxygen in an oxygen/nitrogen mixture that will sustain combustion under a specified set of test conditions.

Polyimides, obtained by reacting pyromellitic dianhydride (1,2,4,5-benzenetetracarboxylic anhydride) with aromatic amines, can have ladder-like structures and commercial materials that may be used up to temperatures in excess of 300 °C are available. They are, however, somewhat difficult to process. Thus, the polyamide-imides, which are easier to process but have lower heat resistance, have been developed. One disadvantage of polyimides is their limited resistance to hydrolysis; therefore, they may crack in aqueous environments above 100 °C.<sup>7,19</sup>

The polyether imides show much better hydrolytic stability with little change in tensile strength after exposure to water at 100 °C for 1 year. These materials also show exceptional resistance to mineral acids and are unharmed by most hydrocarbons including gasoline (petrol) and oils.

Although all commercial polysulfones are, in fact, polyethersulfones, the latter term is given to specific polysulfones that have improved heat resistance.

**Table 3** Limiting oxygen index data for a variety of polymers (unfilled)

<i>Polymer</i>	<i>Limiting oxygen index (%)</i>
Polyacetal	15
Polymethyl methacrylate (Perspex)	17
Polypropylene (PP)	17
Polyethylene (PE)	17
Polybutylene terephthalate (PBT)	18
Polystyrene (PS)	18
Polyethylene terephthalate (PET)	21
Nylon 6	21–34
Nylon 66	21–30
Nylon 11	25–32
Polyphenylene oxide (PPO)	29–35
Acrylonitrile butadiene styrene (ABS)	29–35
Polycarbonate of bisphenol A	26
Polysulfone	30
Polyimide	32
Polyarylate	34
Polyether sulfone (PES)	34–38
Polyether ether ketone (PEEK)	35
Phenol-formaldehyde resin	35
Polyvinyl chloride (PVC)	23–43
Polyvinylidene fluoride (PVdF)	44
Polyamide-imide	42–50
Polyphenylene sulfide (PPS)	44–53
Polyvinylidene chloride (PVdC)	60
Polytetrafluoroethylene (PTFE)	90

Commercial polymers now have values of  $T_g$  ranging from 190 to well above 300 °C, but the cost generally increases sharply with  $T_g$ .<sup>7,19</sup> Polyether ether ketones (PEEKs)<sup>7,19</sup> are similar to polyethersulfones; however, unlike the polysulfones, these materials are crystalline and have higher maximum service temperatures. They also have better resistance to hydrolysis at elevated temperatures than the polyimides. Polyarylates are highly aromatic linear polyesters with relatively high values of  $T_g$  (up to 194 °C) and are self-extinguishing.<sup>7,19</sup>

Polyphenylene sulfides,<sup>7,19</sup> when glass-fiber filled, have high temperature ratings, second only to PEEKs among commercial thermoplastics. These materials often have better resistance to environmental stress cracking than the polysulfones and have found use in automotive applications because of their resistance to corrosive engine exhaust gases, ethylene glycol and gasoline.

### 3.31.9 Thermoplastic Rubbers

These materials<sup>7,19</sup> have characteristics of both rubbers and thermoplastics. At room temperature they

behave like cross-linked rubbers, but at elevated temperatures the cross-links, in the form of separated phases in block copolymers such as SBS (styrene-butadiene-styrene triblock copolymer), or ionic clusters or crystallites, break down and the materials may be processed like a thermoplastic. Unlike truly cross-linked (vulcanized) rubbers, these materials may be capable of dissolution in solvents, although not necessarily at room temperature.

SBS thermoplastic elastomer is a block copolymer consisting of a block of butadiene units end-capped by polystyrene blocks. Below the  $T_g$ , the polystyrene blocks from different chains congregate into polystyrene domains, which act as both cross-links and reinforcing fillers. The polymers will dissolve in certain hydrocarbon solvents. Hydrogenated SBS materials have better resistance to ageing.

Thermoplastic polyester rubbers<sup>7,19</sup> are also block copolymers consisting of polyether and polyester sequences. The polyester groups are capable of crystallization and the crystal structures, in this case, act as the physical cross-links. These materials have good hydrocarbon resistance. Similar thermoplastic polyamide rubbers are also available. Thermoplastic polyolefin rubbers are usually blends based on polypropylene and ethylene-propylene rubbers. They are not resistant to hydrocarbons.

## References

- Orr, E. W. *Performance Enhancement in Coatings*; Hanser: Munich, 1998.
- Marrion, A. R. *The Chemistry and Physics of Coatings*, 2nd ed.; Royal Society of Chemistry: Cambridge, 1994.
- Glass, J. E. *Technology of Waterborne Coatings*; American Chemical Society: Washington, DC, 1997.
- Sperling, L. H. *Introduction to Physical Polymer Science*; Wiley: New York, 1986.
- Cowie, J. M. G.; Arrighi, V. *Polymers: Chemistry & Physics of Modern Materials*, 3rd ed.; CRC Press, 2007.
- Moad, G.; Solomon, D. H. *The Chemistry of Radical Polymerisation*, 2nd ed.; Elsevier: New York, 2005.
- Brydson, J. A. *Plastics Materials*, 7th ed.; Elsevier: New York, 1999.
- Odian, G. *Principles of Polymerisation*; McGraw-Hill: New York, 1970.
- Kennedy, J. F.; Phillips, G. O.; Wedlock, D. J.; Williams, P. A. *Cellulose and its Derivatives*; Ellis Horwood: Chichester, 1985.
- Young, R. A.; Rowell, R. M. *Cellulose Structure, Modification and Hydrolysis*; Wiley-Interscience: New York, 1986.
- Sperling, L. H. *Introduction to Physical Polymer Science*, 2nd ed.; Wiley: New York, 1992.
- Collyer, A. A. *Rubber Toughened Engineering Plastics*; Chapman & Hall: London, 1994.
- [http://www.dsm.com/en\\_US/html/drs/polymericplasticizers.htm](http://www.dsm.com/en_US/html/drs/polymericplasticizers.htm)
- Wilson, A. S. *Plasticisers Principles and Practice*; The University Press: Cambridge, 1995.
- Ward, I. M.; Hadley, D. W. *An Introduction to the Mechanical Properties of Solid Polymers*; Wiley: Chichester, 1993.
- Dyson, R. W. *Engineering Polymers*; Blackie: New York, 1990.
- Brostow, W.; Corneliussen, R. D. *Failure of Plastics*; Hanser: Munich, 1986.
- Brydson, J. A. *Plastics Materials*, 5th ed.; Butterworth-Heinemann: London, 1989.
- Alfredo Campo, E. *Industrial Polymers*; Hanser: Munich, 2008.
- Singh, B.; Sharma, N. *Polym. Degrad. Stabil.* **2008**, 93, 561–584.
- Flynn, J. H. *Handbook of Thermal Analysis and Calorimetry*; Elsevier: Amsterdam, 2002; Vol. 3.
- Yamakawa, H. *Modern Theory of Polymer Solutions*; Harper & Row: New York, 1971.
- Richards, E. G. *An Introduction to Physical Properties of Large Molecules in Solution*; Cambridge University Press: Cambridge, 1980.
- Van Krevelen, D. W. *Properties of Polymers: Their Correlation with Chemical Structure; Their Numerical Estimation and Prediction from Additive Group Contributions*, 3rd ed.; Elsevier: Amsterdam, 1990.
- Small, P. A. J. *J. Appl. Chem.* **1953**, 3, 71–78.
- Andrews, E. H.; Bevan, I. *Mechanics and Mechanism of Environmental Cracking in a Polymeric Glass*; Elsevier: New York, 1972.
- Crank, J.; Park, J. S. *Diffusion in Polymers*; Academic Press: London/New York, 1968.
- Grossman, R. F. *Handbook of Vinyl Formulating*, 2nd ed.; Wiley-Interscience: New Jersey, 2008.
- <http://www.gaylordchemical.com/bulletins/bulletin105b/Bulletin105B-15.html>
- Ulrich, H. *Chemistry and Technology of Isocyanates*; Wiley: Chichester, 1996.
- <http://chem.chem.rochester.edu/~chem424/ladder.htm>
- Schluter, A. D.; Offler, M.; Enkelmann, V. *Nature* **1994**, 368, 831–834.



## 3.32 Degradation of Polymer Matrix Composites

**R. H. Martin**

Materials Engineering Research Laboratory Ltd, Wilbury Way, Hitchin SG4 0TW, UK

© 2010 Elsevier B.V. All rights reserved.

3.32.1	Introduction	2388
3.32.2	Ageing Mechanisms	2390
3.32.2.1	Physical Ageing and Time-Dependent Effects	2391
3.32.2.2	Hygrothermal Effects	2391
3.32.2.3	Thermooxidative Degradation	2392
3.32.2.4	Chemical Ageing	2393
3.32.2.5	UV and Weathering Degradation	2393
3.32.2.6	Mechanical Degradation	2394
3.32.2.7	Fire Testing	2394
3.32.2.8	Synergistic Effects	2394
3.32.3	Accelerated Ageing	2395
3.32.4	Ageing Associated with Supersonic Flight	2396
3.32.5	Ageing in the Oil and Gas Industry	2398
3.32.6	Ageing in the Chemical Processing Industry	2401
3.32.6.1	ASTM Standard for Long-Term Chemical Resistance	2403
3.32.6.2	The Arrhenius Relationship	2403
3.32.6.3	Using a Semiempirical Corrosion Approach	2404
3.32.7	Ageing in the Marine Industry	2404
3.32.8	Concluding Remarks	2405
	References	2405

### Glossary

**Extrusion** A manufacturing process in which a softened blank of plastic material is forced through a shaped die to produce a continuous ribbon of the formed product.

**Gelcoat** A polymer material that is used to provide a high-quality finish to the visible surface of a fiber reinforced composite material.

**Polymer resin** A polymerized synthetic or chemically modified natural material including thermoplastic materials such as polyvinyl, and thermosetting materials such as epoxies, that are used with other components such as fillers to form plastics.

**Pultrusion** A manufacturing process that consists of pulling a fiber reinforcing material through a resin impregnation bath and a shaping die prior to final curing.

**Thermoplastic** A polymeric material (for example nylon) which, upon curing, forms one- or two-dimensional molecular structures and is capable of being repeatedly softened by

increases in temperature and hardened by decreases in temperature.

**Thermoset/thermosetting** A polymeric material (e.g., epoxy) which, upon curing, results in a three-dimensional structure and decomposes rather than melting upon heating.

### Abbreviations

**CPI** Chemical processing industry

**CRA** Corrosion resistant alloy

**DCB** Double cantilever beam

**DMA** Dynamic mechanical analysis

**DSC** Differential scanning calorimeter

**ECR** Corrosion resistant e-glass

**ESC** Environmental stress cracking/corrosion

**FRP** Fiber reinforced plastic

**FTIR** Fourier transform infrared

**GC** Gas chromatography

**GRP** Glass reinforced plastic

**MS** Mass spectroscopy



**TGA** Thermogravimetric analysis  
**TMA** Thermomechanical analysis  
**UV** Ultraviolet  
**Vf** Fiber volume fraction

## Symbols

**c** Chlorine dioxide concentration ( $\text{g l}^{-1}$ )  
**t** Time (s)  
 **$T_g$**  Glass transition temperature  
 **$t_{95}$**  Time to reach 95% of original property (s)  
**B** Factor in the presence of deposits  
**D** Diffusion coefficient ( $\text{m}^2 \text{s}^{-1}$ )  
 **$E_a$**  Activation energy ( $\text{J mol}^{-1}$ )  
 **$E_{11}$**  Young's modulus in the fiber direction (GPa)  
 **$E_{22}$**  Young's modulus transverse to the fiber direction (GPa)  
 **$G_{12}$**  Shear modulus (GPa)  
 **$M_t$**  Total mass absorbed at time t (kg)  
 **$M_\infty$**  Total mass at equilibrium (kg)  
**R** Universal gas constant ( $\text{J K}^{-1} \text{mol}^{-1}$ )  
**T** Temperature (K)  
**W** Rate of weight loss ( $\text{kg s}^{-1}$ )  
 **$\alpha$**  Corrosion depth factor  
 **$\Phi$**  Depth of corrosion (m)

### 3.32.1 Introduction

In the past, the primary reason for the use of fiber reinforced plastics (FRPs) is because of weight saving

for their relative stiffness and strength. As an example, a carbon fiber composite can be five times stronger than 1020 grade steel while having only one-fifth the weight. Aluminum (6061 grade) is much nearer in weight to carbon fiber composite, but the composite can have twice the modulus and up to seven times the strength. A comparison of some properties of metals and composites is shown in **Figure 1**.

A composite, which is generically a material that is made up of two or more distinct (i.e., macroscopic, not microscopic) materials, comes in different configurations but is essentially a plastic material within which there are embedded fibers or particles. The plastic, or more correctly a polymer, is more often termed the matrix or sometimes the resin. The fibers or particles dispersed within the polymer are known as the reinforcement. The reinforcement is generally orders of magnitude stiffer than the matrix, thus resulting in a stiffened plastic. This stiffer reinforcement can either be randomly distributed short fibers or continuous fibers (sometimes in mat form) that are laid in a particular direction within the matrix. The resulting material thus may have different properties in different directions (anisotropic or orthotropic, depending on the lay-up). This characteristic is usually exploited to optimize the design and results in the composite material being tailorable in that its mechanical properties can be formed to meet specific directional loading.

Most engineering materials are essentially isotropic. That is, they have the same properties such as strength and modulus in any direction. There may be 'grain' in some metals because of the manufacturing

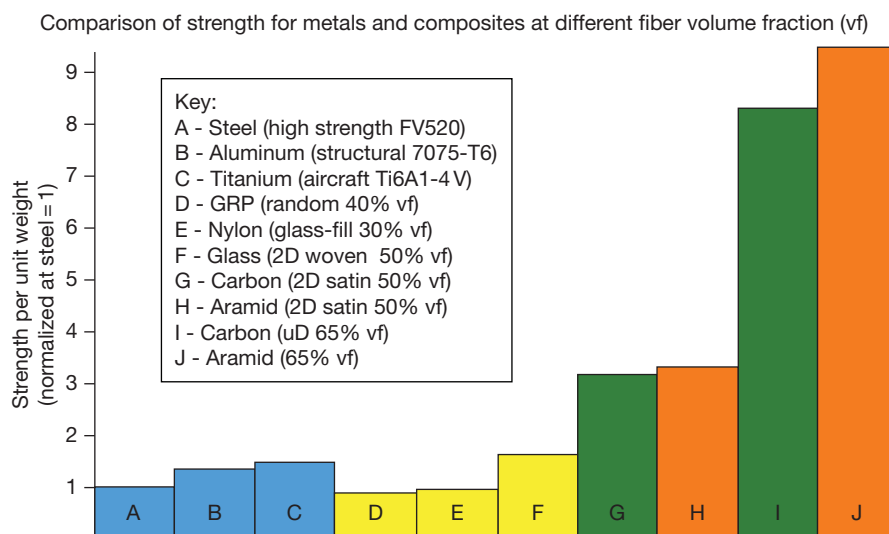


**Figure 1** Comparison of specific strength of different metals and FRPs ([www.merl-ltd.co.uk](http://www.merl-ltd.co.uk)).

process, but it is only in critical applications that this matters. Most machining or casting processes do not have to take directional differences into account. Because of the different fiber orientation, mentioned above, most composites will have very different properties in different directions. For example, a carbon FRP may be up to 100 times stronger under tension than it is in shear, and the stiffness may differ in the two directions by similar ratios.

Several different terms have been used by different industries to describe a composite material, and these acronyms have become jargons. More technical descriptions include:

GRP	Glass reinforced plastic (in which the fiber is glass and the resin is any of the polymer resins)
GRE	Glass reinforced epoxy (in which the fiber is glass and the resin is an epoxy)
FRP	Fiber reinforced plastic (in which the fiber may be any of those listed above and the resin is any of the polymer resins)
CFRP	Carbon FRP (in which the fiber is carbon and the resin is any of the polymer resins)
PMC	Polymer matrix composite

None of these terms are incorrect, although some cover a wider range of material classes. FRP is a generic term and will be used throughout this chapter when referring to composite materials generically.

Both thermosetting and thermoplastic polymers can be used for the matrix material, and the most common thermosetting matrix materials include polyester, vinyl ester and epoxy, and bismaleimide for higher-temperature applications. Thermoplastic matrix materials tend to have higher performance ability and include polymers such as polyimide, phenolic, polypropylene, polyetheretherketone (PEEK), and polyphenylene sulfide (PPS).

Another primary benefit of FRPs is their durability in hostile environments, often termed corrosive environments, although in reality, composite materials do not 'corrode.' While the matrix is primarily the binder that transfers the load to the reinforcement, it is also very resilient to environmental attack. The type of resin needs to be carefully selected so that it can withstand the service temperature (high or low) conditions, and it should not be significantly affected within its lifetime by fluids (gases or liquids) with which the FRP will come into contact. Hence,

FRPs are used in very corrosive applications such as for acid storage in the chemical processing industry and longevity in marine environments such as in vessels and offshore oil and gas applications. These applications are discussed in more detail in this chapter.

The effect of exposure to various environments such as heat, moisture, solvents, acids, ozone, hydrocarbons, loads, etc., and more importantly a combination of these parameters, may degrade the material's key properties. For load bearing applications, these properties may include stiffness and strength. Cracks may appear and accumulate ultimately leading to failure. For fluid containment applications, cracks may coalesce leading to a leak path for this fluid even though the structure is globally still intact. Despite these safety critical uses, the degradation of an FRP is still not a well understood phenomenon compared to the corrosion of metals.

The reason that the long-term degradation of FRPs is not well understood is because it is a very complex process with many interrelated factors and has led to much ongoing research into the topic. Degradation is often given the generic term 'ageing' that can include the more benign physical ageing effects such as swelling from moisture absorption, that is largely reversible, to the more serious chemical ageing where material properties are permanently (irreversibly) degraded. Additionally, synergistic effects to ageing from mechanical loading, such as creep, need to be considered in isolation (or in addition) to that associated with the environment and often change the rate of degradation. Environmental ageing of FRPs occurs from the surface or edge inwards and requires time to penetrate into the material's center, and the rate of ageing can be directional (like the mechanical properties); further, it is generally dependent on the temperature and stresses. The complexity described above makes predicting ageing around detailed geometries such as stress concentrations nontrivial.

Added to the issue of ageing of FRP materials is the variety of different manufacturing methods available to manufacture components. The reader is pointed toward the works of Jones,<sup>1</sup> Matthews *et al.*,<sup>2</sup> and in ASM Handbook<sup>3</sup> for detailed information on manufacturing. The methods available depend very much on the nature and quality of the component to be manufactured. For the low-end marine industry, uncured resin is poured over chopped glass fibers laid in a mould to form what is often termed 'fiberglass.' A step-up on this approach is known as filament

winding where the fibers are wrapped around a net-shape mandrel, and the resin poured on or the fibers are dipped in the resin before winding. Both methods are low-cost manufacturing techniques and the resin is generally cured at room temperature. Alternative lower-cost manufacturing methods include injecting the resin into a mould or extruding or pultruding the composite profile through a die to form the part desired. Additionally, resin-rich layers, known as gel coats can be put on the outside of the parts for better resistance or appearance. To improve the quality and performance of the resin, vacuum, pressure and temperature are used in a variety of combinations. A vacuum is employed by placing the component in a bag and the vacuum is used to help to pull the resin through the fibers and, more importantly, to remove air and other gases from the final composite part reducing porosity. Pressure is used on the outside of the vacuum bag to help form and consolidate the part again, helping to reduce porosity. Temperature is used for stronger resins to assist in curing and consolidation. The combination of these three manufacturing parameters requires an autoclave and produces a high-quality, high-strength part and is still the manufacturing method of choice for the aerospace industry.

A further difficulty is introduced with the need to predict long-term ageing using short-term testing and analysis. For long-term life prediction based on short-term data, representing the true service history (load, temperature, time, fluid, etc.) for long-term structural life prediction is a vital step to validate any short-term-based predictive methodology. The coupon tests must reflect the effect of ageing on the polymer (i.e., matrix-dominated properties) because the fibers may mask any property loss in the resin. However, fibers can sometimes degrade in some environments quicker than the polymer and additionally the fiber–matrix interface can be attacked and this too must be represented in any accelerated ageing methodology. Further, the chemical bond between the fiber and resin itself (often known as the interface region) can be degraded. All of these degradation methods are important to understand. Loss of fiber properties greatly reduces the strength and stiffness of the FRP laminate because that is their main purpose. Similarly, a break down of the bond between the fiber and the resin leads to the fibers not providing stiffness and strength through transfer of shear between the two. Reduction of properties of the resin is also important because it provides the load transfer between fibers.

It is this shortage of long-term data or of an accelerated ageing methodology to determine the

residual properties of a FRP component at any time in its life that still hinders the uptake of FRPs in some applications. However, over the decades when composites have been used, much has been learned, and this chapter addresses some of this work detailing the nature of ageing of composites and the use of composites in certain industry sectors where corrosion or degradation is an issue. This chapter will describe how it is the degradation or ageing of a composite that needs to be understood when these materials are used in hostile environments. This chapter is not intended to be a general introduction to FRPs; there are many publications available for this purpose<sup>1–3</sup> or informative internet-based sites such as The Virtual Composite Material Consultant.<sup>4</sup>

### 3.32.2 Ageing Mechanisms

The ageing of an FRP comprises an ongoing development of damage that is dependent on the type of polymer matrix, the fiber type and architecture, the fiber volume fraction and the operating conditions of temperature, relative humidity, oxidative attack, solvent infusion, internal moisture concentration, air pressure, mechanical loads, and the time of exposure. These degradation factors are often related and varying. For example, a FRP pipe used to transport hydrocarbons may experience hot oil field fluids internally, ultraviolet (UV) radiation from sunlight, and moisture externally, external loads from supports and other loading. The external temperature may vary between  $-40$  and  $+40^{\circ}\text{C}$  depending on the location while the internal temperature may be that of the oil at temperatures up to  $+100^{\circ}\text{C}$ . However, a fuselage or wing FRP structure may experience temperature cycles of  $-55$  to  $+40^{\circ}\text{C}$  between flight and ground with ice, cleaning solutions, moisture, jet fuel, ozone, UV and other environmental conditions, making the determination of residual life a complex procedure. Therefore, ideally these conditions must be represented in any simulation of ageing for predictive purposes to accurately reproduce the degradation mechanisms. In reality, only the key conditions considered to be the more potentially damaging may be investigated. In any test program, it is important to use relevant material or structural properties as an indicator of the state of ageing of the material. This may be the mass change, the glass transition temperature  $T_g$ , the crack density, the modulus, strength or a combination of these properties. Therefore, a complete understanding of all the degradation processes should be known or an

assumption made on what is the primary degradation mechanism. The section below describes some of the key degradation mechanisms that individually or combined form the ageing of a composite material.

### 3.32.2.1 Physical Ageing and Time-Dependent Effects

Polymers, both in their rubbery (above  $T_g$ ) and in their glassy state (below  $T_g$ ), are characterized by viscoelasticity, a time-dependent mechanical behavior. The characteristic times of this constitutive behavior are much longer in the glassy state and decrease at temperatures near and above  $T_g$ . Typical evidences of viscoelasticity are creep and stress relaxation. Creep is a time-dependent deformation that usually has three stages when under a constant load, rapid primary creep, a steady-state secondary creep rate and a rapid acceleration in the creep rate leading to rupture. Stress relaxation is a related phenomenon where stresses are relieved when under a constant deformation. In composite materials, the stress transfer between the viscoelastic matrix and the elastic reinforcement, or between layers with different fiber directions (laminae) needs to be considered for long-term ageing characterization. For long-term property estimation, especially when considering FRP properties that are more dominated by the resin than the fiber, long-term viscoelastic behavior can be accelerated by adopting the time-temperature superposition principle.<sup>5,6</sup> This principle is based on the premise that the behavior for long time periods at low temperatures corresponds to that for short time periods at higher temperatures. This is because in a polymer, the polymer chains are more mobile and easier to arrange at higher temperature resulting in a higher compliance or lower modulus. The time-temperature superposition principle is evident from the compliance curves in creep experiments (or modulus curves for stress-relaxation experiments) at different temperatures that are related to one another by a simple temperature-dependent shift on the log time scale.

The fundamentals on physical ageing and the dependency of mechanical properties on time and temperature become more pronounced when testing close to the  $T_g$ . The  $T_g$  itself may well be affected by moisture; lowering  $T_g$  and service temperatures may be close to wet  $T_g$  requiring aspects of physical ageing to be a vital part of a durability analysis.

With physical ageing, polymers below their  $T_g$  exhibit a time-dependent rearrangement of their

structure. The mutual interaction between viscoelasticity and physical ageing imposes the introduction of time-ageing and time-temperature shift factors. Other time-shifting effects may also exist based on the applied stress, moisture condition and other environmental factors. These time-dependent properties and physical ageing has an affect on the material's overall strength and stiffness. Thus, ideally an accelerated ageing analysis needs to include an aspect of physical ageing such that the strength/failure criteria includes time-dependent coefficients and a nonlinear viscoelastic-viscoplastic damage analysis.

For accelerated physical ageing tests, the relationships are obtained from short-term tests using the time-dependent experimental data described above. It is important that no chemical ageing (discussed further below) is included. The typical properties measured depend on the application, but most testing presented in the literature has been on off-axis plies because they give a good representation of matrix-dominated properties.<sup>6</sup> However, the literature often falls short in producing such time-dependent relationships for more useful design properties such as static properties of FRP laminates with or without holes.

### 3.32.2.2 Hygrothermal Effects

Hygrothermal effects are related to the uptake of water molecules from a humid environment or water in direct contact with the FRP when the component is submerged in water (or other solution). The water is absorbed by the polymer matrix and results in plasticization of the matrix leading to hydrolytic degradation or hydrolysis which lowers the molecular weight and hence mechanical properties of the FRP. The rate of hydrolysis may be accelerated by the application of load or more significantly with elevated temperature and high- or low-pH conditions. In contact with the polymer, low molecular weight liquids are absorbed by and diffuse into the polymer until saturation (equilibrium) is reached. The rate of diffusion and equilibrium are dependent on the chemical structure and morphology, such as the degree of crystallinity of the polymer. For an FRP, these properties are also related to the type of fibers, the volume fraction and the nature of the fiber-matrix interface.

The relationship between time and moisture mass uptake can classically be characterized using simple approaches such as Fick's law, but generally for FRPs, diffusion is more complex with competing factors affecting the rate of diffusion.<sup>7</sup> With time, moisture diffuses into the FRP through the surfaces and there

is a moisture-content concentration gradient through the thickness. Indeed, for some FRPs there may be a different concentration through the edges than through the surfaces. If the moisture content or temperature is cycled, this will lead to local dryness at the surface plies compared to the centre of the laminate. This moisture distribution can lead to significant residual stresses within the laminate that can in turn cause outer ply delamination of blisters.

Short-term hygrothermal effects on FRPs may extend beyond plasticization of the matrix and lead to mechanical damage such as the creation of microvoids, matrix cracking and blistering. These microcracks, in turn, provide fast diffusion paths (for both liquid water and water vapor) and then alter the moisture-absorption characteristics of the laminate.

Long-term exposures may not cause mechanical damage, described above, but the plasticization may well change matrix-dominated mechanical properties such as interlaminar and intralaminar shear modulus and the transverse tensile strength and modulus. Properties like compression modulus and strength are greatly affected by the shear properties of the matrix; hence, under hot and wet conditions compression properties may be severely degraded. The high temperature and humidity exposure of FRPs effectively plasticizes the matrix, more so closer to the  $T_g$  of the material which reduces when the material is saturated.

Post-cure reactions, hydrolysis and leaching of products within the FRP coupled with the decrease of  $T_g$  when moisture is absorbed, make modeling the effects of moisture complex and warrant further investigation. Such modeling can supply important information to establish the effects of moisture on time-temperature shift factors, by scaling the temperature axis on the basis of  $T_g$  change. As a result, Fick's law needs to be extended to model three-dimensional diffusion in anisotropic materials. For FRPs, the value of the diffusion coefficient,  $D$ , for the neat polymer needs to be modified to account for the tortuous path created by the presence of the fibers (their size, distribution, aspect ratio, orientation, etc.). Hence,  $D$  becomes an anisotropic property that is dependent on fiber direction. In FRP laminates with several layers of different orientation, the different diffusivity in each layer must be considered for the overall laminate. In ideal Fickian behavior, moisture absorption increases linearly with the square root of time for values of  $M_t/M_\infty \leq 0.5$  (where  $M_t$  is the total amount of moisture absorbed at time  $t$  and  $M_\infty$  is the total amount absorbed at equilibrium). Time-thickness scaling allows the long-term prediction

of absorption in thick laminates from thin-sample measurement, when Fick's law applies. Diffusion can be accelerated by increasing the temperature and follows the Arrhenius relationship eqns [1]

$$D = D_0 \left[ \exp \left( \frac{-E_a}{RT} \right) \right] \quad [1]$$

Where  $E_a$  is the activation energy of the diffusion rate,  $R$  is the universal gas constant, and  $T$  is the absolute temperature of the exposure in Kelvin.

As discussed above, Fickian law may not always be demonstrated in composites where, following reaching equilibrium, there can be a slow long-term increase in mass uptake or a decrease in mass or both. The decrease may arise from products leaching from the FRP over time and the increase from a two-stage absorption process where the first is Fickian and the second a relaxation-based phenomenon.<sup>8</sup>

### 3.32.2.3 Thermooxidative Degradation

While the application of temperature and moisture can have negative effects on the composite, exposure to temperature in an air environment can cause thermooxidative ageing. This ageing mechanism arises from the thermal instability of the polymer and leads to oxidative attack that comprises chain scission, cross-linking, and thermooxidative reactions. Thermal degradation of FRPs, in an inert atmosphere, is exclusively a thermolysis phenomenon, while in air it is dominated by oxidation. Thermolysis is the result of breaking of covalent bonds in the polymer network and, in general, thermal stability of high-performance polymers in an inert atmosphere is very good.<sup>6,8-11</sup> Oxidation is usually characterized in terms of weight loss generally from the surfaces of the laminate. This weight loss is predominantly from the matrix and will penetrate into the laminate at higher temperatures and long exposures. Eventually, microcracks will form leading to a larger reduction in the mechanical properties of the FRP. These weight losses are generally permanent (irreversible) and even a small weight change can be an indication of the onset of damage at the surface. For oxidation to occur at the center of the laminate, the diffusion process must be understood, including the diffusion of oxygen and reactions products throughout the polymer matrix in a similar manner to liquid diffusion discussed above. The pattern of oxidation reactions and subsequent chemical changes depends on the exposure temperature, the resin system, and the oxygen content. Simply



increasing the temperature to accelerate the characterization of oxidation is nontrivial. The changes in mechanical properties postexposure are a function of sample thickness and surface protection as well as the ageing temperature and the material's  $T_g$ . Therefore, the examination of the thermooxidative stability of an FRP must include not only the degradation of mechanical properties, but also the failure mechanisms to ensure that they are consistent when comparing two laminates aged at different temperatures in an attempt to accelerate thermooxidative ageing.

#### 3.32.2.4 Chemical Ageing

Chemical ageing follows principles very similar to oxidative ageing but occurs when the environmental fluid is an acid, alkali solvent, or many other fluids to which an FRP may be exposed. These chemicals actually attack the resin, the fiber, or the fiber–matrix interface (or any combination of these three). When the FRP is subjected to exposure to, for example, an acid solution, depending on the concentration of the solution, competing ageing mechanisms may occur. The liquid will first be absorbed in a hygrothermal fashion as described above. In time (dependent on the strength and nature of the chemical involved and the compatibility of the polymer), the material will chemically react with the FRP. This results in an increase in cross-linking density that can severely affect the mechanical properties by densification and increasing the  $T_g$ . Also, products may be leached out of the FRP in an irreversible manner. This will result in weight loss and a potential decrease in properties. With further time, actual physical material loss can occur, resulting in a more dramatic change in properties.

In order to perform studies of long-term and accelerated chemical ageing, usually a large test program is required with long periods of time and a selection of parameters (temperature, chemicals, loads). A variety of specimen types is also required to assess the degradation of mechanical properties parameters such as specimen type, lay-up, thickness, material, etc. As with other ageing types, chemical ageing is a diffusion-related phenomenon. Therefore, the use of thick specimens will delay observable changes in mechanical properties although significant surface damage may have occurred. Different lay-ups will affect the interlaminar stresses, which will affect diffusion rates.<sup>12</sup> Additionally, edge effects can play a role and this is often where mechanical failure can initiate. As a result, chemical ageing exposures are often conducted on panels of FRP and mechanical specimens cut from

these panels once the ageing is complete. Another approach is to coat the free edges of the test specimens with a resilient coating to prevent unrepresentative edge damage.

An additional approach to characterizing chemical ageing to better understand the change in the polymer is to conduct thermal analysis on the FRP or the matrix. Of all the properties,  $T_g$  is the most common one measured using thermal analysis because it is a good indication of physical changes. Methods and approaches to measure  $T_g$  vary and all are reasonably well established as standards. These include dynamic mechanical analysis (DMA) that may be performed in torsion or flexure depending on the test apparatus; differential scanning calorimetry (DSC); or thermomechanical analysis (TMA). These methods all raise the temperature of the FRP and look for inflection points of peaks in the property being measured. The DMA tends to be more sensitive than the DSC for materials such as phenolics. Thermogravimetric analysis (TGA) is used to measure the rate of change of weight versus time and temperature in a controlled gas environment. TGA is highly dependent on the available surface of the specimens placed into the test chamber and hence the size of the pieces of materials that are used can effect measurements. It is sometimes useful to identify how the polymer has changed during ageing and other equipments such as Fourier transform infrared (FTIR) spectroscopy and gas chromatography (GC) as well as mass spectroscopy (MS) are used to evaluate the degradation products. These techniques can also be used for thermooxidative ageing.

#### 3.32.2.5 UV and Weathering Degradation

Similar to oxidative ageing, weathering affects the surface of the FRP laminate. Generally, UV ageing affects the appearance of the laminate (particularly color loss) and this degradation in appearance can be considered failure (aesthetically). Often, the change in color has a minor effect on structural performance. Weathering is a combination of ultraviolet radiation, temperature from the sun, oxygen and any ambient moisture such as humidity or precipitation.<sup>13,14</sup> With the use of coatings and additives, the structural performance of FRPs can be maintained and the weathering effects tend to be surface related and appear as:

- fading and darkening;
- yellowing;
- blooming; and
- loss of gloss and chalking.



Yellowing, fading, and darkening are generally due to chemical degradation in the polymer. Blooming can be caused by an additive coming to the surface, whereas loss of gloss is generally caused by erosion of the surface layer. While the loss of surface quality may be considered benign, it can lead to leaks and weakening.

The severity of the ageing due to weathering is strictly dependent on the nature of the climate or the geographical region, for example, tropical, desert, arctic, etc. Predicting the weathering performance of FRPs is carried out both in laboratories using artificial weathering and in long-term experimental field ageing. The latter takes several years and becomes very specific to the material and location selected for the study. The specimens are directly exposed to outdoor conditions at a fixed angle relative to the horizontal and in a fixed direction. To accelerate weathering, the UV radiation is concentrated onto the test specimen using special mirrors. Also, locations with high levels of sunshine, for example, Florida and Arizona are used to compare with longer-duration exposures in regions with less sunshine hours.

There are a larger number of laboratory-based ageing tests along with actual case studies where specimens are exposed to UV radiation from a variety of UV light sources. There are currently three key laboratory methods used for artificial weathering.<sup>14</sup> The carbon arc lamp uses two strong emission bands that peak at 358 and 386 nm which are much more intense than natural sunlight. These have a lower effect than solar radiation on materials that absorb only short-wavelength UV radiation. The xenon arc lamp gives a broad spectrum of light that matches the solar spectrum quite closely. Filters are used to reduce the short-wavelength UV light from these lamps that are not present in sunlight. Fluorescent lamps have special phosphors selected to emit UV light at a particular waveband. Exposure is carried out under controlled conditions of temperature and moisture. With the varied nature of weather, conducting accelerated tests to simulate specific weather exposure for predictive purposes is difficult. As a result, accelerated methods tend to focus on the worst-case weather scenarios and any correlations must be qualitative.

### **3.32.2.6 Mechanical Degradation**

This chapter focuses more on the ageing of FRPs under environmental loads, and, strictly speaking, mechanical degradation is not part of ageing. Nevertheless, it is often a consequence of ageing. Mechanical damage processes such as matrix cracking, delamination, plastic strain,

interfacial failure are generally irreversible. In an FRP, some of these damage modes may be seen to be benign or subcritical; however, the damage may accumulate or lead to damage elsewhere by transferring load ultimately leading to failure. The most common mechanical degradation, especially when operating at high temperature, is the formation of cracks in the matrix either within the ply or transverse to the ply. Fatigue, environmental loading, and residual stresses can all promote the onset and accumulation of these cracks. The laminate strength, stiffness, and thermal properties as well as failure modes can be affected by transverse matrix cracking which can also promote higher uptake of moisture deeper in the laminate. The prediction of these failure modes are often parts of a long-term durability assessment, especially under fatigue loads. The reader is directed towards Jones,<sup>1</sup> Mathews and Rawlings,<sup>2</sup> and ASM Handbook,<sup>3</sup> for a description of predicting mechanical failure in FRP laminates.

### **3.32.2.7 Fire Testing**

While the above sections discuss various environmental forms of ageing, FRPs are often, perhaps surprisingly, used in high-risk fire applications. These include the aerospace industry in the event of on-board fires and crashes, marine vessels with very high requirements for resistance to fire, railways, where the fire resistance for underground trains is perhaps the most stringent, and offshore oil and gas requirements. Many of these fire-resistance requirements arise from unfortunate incidents. Glass and carbon fibers do not burn but the resin may well set alight or give off noxious fumes or both. Different resins have different fire resistance to jet fires (where a flame is concentrated on one spot) and pool fires. The combination of low thermal conductivity, resin endotherm effects, structural integrity and coatings mean FRPs can have excellent fire-resistance performance but this does need to be strictly controlled using established small-scale tests to evaluate the combustibility and ignitability. Models based on the energy flux involved in decomposition have been used to predict fire performance of materials.<sup>15</sup> However, no further discussion on fire testing is given in this chapter because it goes beyond the scope of less severe forms of ageing and degradation.

### **3.32.2.8 Synergistic Effects**

Each of the sections above described individual possible ageing mechanisms that may occur to an FRP

laminate. However, an FRP component is a combination of fibers, the fiber–matrix interface, and the polymer matrix that may be subject to long-term ageing of a combination of the above ageing scenarios. Hence, the mechanical properties and fitness for purpose may change through a combination of thermal oxidation, physical ageing, hygrothermal effects, UV exposure, and chemical attack. Therefore, macroscopic changes need to account for the synergies between these ageing mechanisms and any accelerated ageing methodology should really account for these combined factors – a nontrivial task!

### 3.32.3 Accelerated Ageing

As discussed above, one of the biggest advantages of composite materials is their long life in harsh environments. Ironically, it is this long life and the difficulties in being able to reliably predict the long life that has hindered the uptake of composites. The development of a robust accelerated ageing methodology is a key technology development for FRPs. An accelerated-ageing methodology should accelerate the action of degradation factors without altering the underlying molecular mechanisms of ageing. The analogy that a chicken does not hatch quicker from the egg by boiling the egg applies here. As discussed, the ageing process may cause both reversible and irreversible changes and the accelerated ageing methodology must simulate these processes. The design of an accelerated methodology relies on the knowledge of material properties and their relationship with environmental conditions (temperature, pressure, loads, relative humidity, UV, etc.) and upon the fundamental ageing or damage mechanisms as described in the previous section.

The purpose of accelerated ageing methodology is simply to speed up the accumulation of damage or deformation, potentially leading to failure. This is achieved by establishing relationships between time and various parameters, such as temperature, fluid concentration, load, etc. that can be related back to the in-service conditions. Accelerated testing also aims to determine the material microstructure and damage at the end-of-life or ideally at any time during the life of the component. For most structural applications, the durability and mechanical fatigue are the main degradation processes in which frequency and load are the main acceleration factors used. For FRPs in corrosion applications, exposure temperature is the primary means of accelerating

ageing, but other parameters include increasing the concentration of a degradative chemical, applying pressure, or a load. Most accelerated ageing experiments consider a single accelerating factor because it is difficult to test multiple accelerated conditions and understand the synergistic effects as discussed above. The preferred approach is to incrementally subject samples to accelerated conditions. For the approach to be valid, a fundamental understanding of material response and the reversible and irreversible degradation processes is required and needs to be incorporated into the modeling.

An accelerated test methodology must follow the following steps<sup>16</sup>:

- (a) identification of the material, including the polymeric matrix and the fiber (including type, volume fraction, orientation, sizing, etc.);
- (b) identification of the primary ageing mechanism for the environment, for example, thermooxidation, hydrolysis, UV ageing, etching, . . .;
- (c) identification of the physical properties, most important to the application, to be measured in the accelerated ageing test (e.g., mass loss, stress, strength, toughness, leak resistance, color, . . .);
- (d) selection of the environmental acceleration of degradation factors such as temperature, time, concentration, etc.;
- (e) carry out the accelerated tests under conditions given in (c) and (d);
- (f) use theoretical modeling (e.g., Arrhenius relationship, time–temperature superposition, curve-fitting) of the degradation factors; and
- (g) validating some of the modeling by performing long-term tests that are representative of in-service conditions.

For accelerated ageing, the synergistic effects of time, pressure, and conditions on FRP degradation should be established. Free space exists between molecular chains to a greater or lesser degree leading to a balance between stiffness and flexibility. However, this same free space can mean that polymers can absorb fluids to which they are exposed, especially those with similar solubility parameters. Such absorption can physically weaken the polymer to provide an effect of ageing. In addition, the fluid might chemically attack the polymer to provide an additional effect. The kinetics of these two ageing effects is governed by; (i) diffusion, and (ii) chemical kinetics, both of which are governed by Arrhenius relationships with regard to the influence of temperature. This characterization is commonly based on

weight loss and, where possible, mechanical property reduction measurements as a function of time and temperature. The rate of weight loss ( $W$ ) versus time can be modeled by using an Arrhenius relationship, eqns [2].<sup>8</sup>

$$W = A \left[ \exp \left( \frac{-E_a}{RT} \right) \right] \quad [2]$$

where  $W$  represents the ratio between the weight loss and the starting weight of the sample and  $A$  is an empirical factor. However, because the thermooxidative degradation in an FRP laminate occurs at the surface, the above equation does not necessarily relate to the same reduction in mechanical properties that are dominated by the bulk properties, and not just the surface properties. A good example of this is an interlaminar fracture test such as the double cantilever beam (DCB)<sup>17</sup> where the fracture data are measured from a delamination in the centre of the specimen. During an ageing test, much of this delamination is not exposed to the environment.

There are few published works on experimental work using a change in a specific mechanical property of relevance, say modulus or strength in eqns [3], to allow modeling of the global effect on a component from local ageing degradation at the surface. Chemical kinetics, classically involving concentrations of reactants and products, can employ the fact that for cross-linked polymers, concentration of cross-links is approximately proportional to the modulus or stiffness. Hence, measurements of changes in modulus from ageing can be plotted logarithmically against linear time (for first-order reactions) at each temperature. From a series of such ageing plots at different temperatures, times to attain the same degree of modulus change can be used to develop the Arrhenius plot, eqns [3].

$$\ln \frac{1}{t_{95}} = A \frac{-E_a}{RT} \quad [3]$$

where  $t_{95}$  is the time for a property to reach 95% of its original value (although other values can be used),  $T$  is the absolute temperature,  $R$  is the universal gas constant ( $8.314 \text{ J deg}^{-1} \text{ mol}^{-1}$ ),  $A$  is a constant, and  $E_a$  the activation energy. This expression holds well where there is only one degradation mechanism taking place and this is seldom the situation in the chemical processing environments.

The mechanics and chemistry of degradation can be different at higher-temperature exposures to that at lower-temperature exposures. Mass-loss curves can change significantly with temperature because

of different mechanism occurring, including removal of volatiles, additional cross-linking, and structural rearrangements of the matrix. Testing at temperatures too close to the  $T_g$  gives degradation rates that are nonlinear, making estimates of useful remaining life invalid.

One acceleration method for thermooxidative stability is to increase the temperature and the pressure of the oxygen,<sup>18</sup> thus accelerating the rate of degradation due to oxidation. However, other attempts to accelerate ageing in acids by increasing the acid concentration were less successful, with only small increases in the ageing rate being achieved.<sup>19</sup>

While the above sections have described the current technology and gaps in predictive methodologies, there are FRP components in-service with long duration lives. The approaches used to give some estimation on long-term life include single-point data (properties after a specific set of ageing conditions) and short-term ageing extrapolation. The following section describes some applications where ageing has been considered.

### 3.32.4 Ageing Associated with Supersonic Flight

Many of the earliest applications of carbon FRPs were in military aircraft where the main ageing mechanisms were hygrothermal. As discussed above, this reduced the modulus of the matrix lowering some mechanical properties. As a result, most aircraft with FRP components use hot wet properties as part of the design allowables. Several aerospace programmes have been concerned with commercial supersonic aircraft to replace the Concorde. Long-term thermooxidative ageing became a key technology development for these aircraft. The first major study on ageing of FRPs for supersonic aircraft was performed by Kerr and Haskins.<sup>20</sup> The materials investigated included carbon- and boron-epoxy and carbon polyimide that were exposed to elevated temperatures for up to 50 000 h. The effect of altitude was also included representing the reduced oxygen levels at high altitudes. The laminates used were typically  $[0^\circ/\pm 45^\circ]_s$  and temperatures ranging from 122 to 177 °C representing temperatures up to Mach 2.4 flight. The tests performed included tensile, compression, and shear and also tests to study the effects of moisture and creep after the exposures in an attempt to identify the thermooxidative ageing mechanisms. These tests were chosen as those

typically used in an aircraft design process as opposed to those required to identify the effects of ageing.

For some materials, edge cracking and severe property degradation was identified at temperatures of 177 °C after 5000 h of ageing with a 0.1 MPa pressure. This degradation was not noted after 25 000 h at the same temperature but at 0.014 MPa. Degradation was observed for epoxy specimens at times under 5000 h when aged at 177 °C, which was close to the  $T_g$  of materials. Degradation was a severe crumbling of the matrix at the specimen surface. Ageing damage was far less at 122 °C after many more hours exposure. This demonstrates that raising the temperature to accelerate ageing may not be a valid approach when the exposure temperature reaches  $T_g$ . The polyimide-based specimens had much better thermooxidative stability. At 232 °C, after 50 000 h the tensile properties decreased, although no macroscopic damage to the resin could be observed, although clearly some degradation had occurred from the weight-loss results. In this instance, the selection of a matrix-based mechanical test during the ageing program would perhaps identify matrix degradation after shorter exposure times.

During NASA's High-Speed Research (HSR) programme in the 1990s, studies were conducted that focused mainly on high temperature polymers for a new generation of High-Speed Civil Transport (HSCT) aircraft with a speed target between Mach 2.0 and 2.4 with a design requirement of 60 000–120 000 h. The work in this program focused on new materials' development for high temperature use and included carbon bismaleimides and polyimides.

One of the primary difficulties in characterizing the effects of ageing on changes in structural properties is the correlation of 'ageing'-related data, such as weight loss, to changes in material mechanical properties such as strength, stiffness, and toughness. An investigation in the change of lamina properties ( $E_{11}$ ,  $E_{22}$ , and  $G_{12}$ ),  $T_g$  and weight loss for this programme can be found elsewhere.<sup>20</sup> An IM7/8320 carbon thermoplastic and an IM7/5260 carbon bismaleimide were aged in air-circulating ovens at 125 and 175 °C for 5000 h (representing 10% of the life of proposed life for HSCT). In this time frame, the materials showed little signs of ageing at 125 °C. The IM7/5260 had a 2% weight loss after 5000 h at 175 °C. This corresponded to a 10% decrease in  $E_{22}$  and a 2% decrease in  $G_{12}$ , but no significant change in  $T_g$  or  $E_{11}$ .

A test program to evaluate the synergistic effects of stress, temperature, moisture, time, radiation, and oxygen level on the properties of bismaleimide

composites was conducted as part of the HSR programme.<sup>10,11,18,21–23</sup> Isothermal ageing as well as thermal cycling, and creep tests were conducted at temperatures up to 250 °C. As for the Kerr and Haskins work, exposure temperatures close to the materials  $T_g$  led to very rapid ageing and anomalous effects that made it difficult to develop an accelerated ageing approach.

Martin<sup>17</sup> has investigated the delamination onset under thermal mechanical fatigue with modeling used to predict delamination onset. To verify the methodology, isothermal statics tests were conducted at temperatures of 125 and 175 °C (representing Mach 2 and Mach 2.4 flight, respectively) on quasi-isotropic laminates fabricated from carbon bismaleimide (IM7/5260). Raising the temperature had the effect of decreasing the value of strain energy release rate ( $G$ ) at the edge by reducing residual thermal stresses. However, the materials fracture toughness was also lower at higher temperatures. The isothermal ageing results of these materials discussed by Kerr *et al.*<sup>20</sup> would need to be incorporated as additional effects of ageing. These would need to be included in addition to the change in properties related to temperature and fatigue.

For aerospace applications, open-hole tension and compression of laminates are important properties for damage tolerance designs. As discussed above, thermooxidative ageing attacks the surface and an investigation was conducted by Morgan *et al.*<sup>22</sup> to determine the influence on isothermal ageing of laminates with a hole drilled before and after ageing and edge cut before and after ageing. Quasi-isotropic laminates fabricated from IM7/5260, IM7/8320, and IM7/K3B a carbon polyimide added to the HSR program were aged at temperatures of 125 and 175 °C (additional exposures at 200 °C were carried out on the IM7/K3B) for periods up to 5000 h. For IM7/5260 and IM7/8320, significant damage was seen on the surfaces and this degraded the stress to cause delamination at the edges but did not affect ultimate strength of the laminate, because of the presence of 0° fibers in the loading direction. Removal of these damaged edge by cutting them off brought the edge delamination stress back to the undamaged value demonstrating that thermooxidative ageing begins at the surface. For the K3B laminate, no edge delamination was observed before lamination failure reflecting the higher toughness of this material and hence the better resistance to thermooxidative ageing. Little difference was identified whether the holes were drilled before or after ageing. While there would be some damage to

the matrix within the holes after ageing, the failure is still dominated by the local stress concentration on the 0° fibers at the hole.

### 3.32.5 Ageing in the Oil and Gas Industry

FRPs are key candidate materials for replacing carbon steel in the Oil and Gas Industry because of their good corrosion resistance and light weight. However, this industry is very risk averse and the uptake of these materials has been slow and is directly related to the operational risks for that component. The shortage of long-term performance data of FRPs in oil and gas applications does not aid their uptake. However, the potential improvements in component and system performance using FRPs will ultimately reduce capital and maintenance requirements, and this fact has enabled some usage of composites in the industry.<sup>24,25</sup>

The environments in the oil and gas industry can be very harsh. The fluids with which FRPs might come into contact include those illustrated in **Figure 2**, along with some of the potential ageing effects. The composition of crude oil varies around

the world from well to well. It mainly comprises aliphatic alkanes (hydrocarbons) such as hexane, octane, decane, etc. Aromatic hydrocarbons may also be present and these are known to swell epoxy matrices. The presence of corrosive media such as hydrogen sulfide or even carbon dioxide in water (carbonic acid) can chemically attack the entire composite, especially if a GRP is under load promoting environmental stress cracking/corrosion (ESC). In addition, most oil and gas operations are conducted at high temperatures (up to 200 °C) and at high pressures, helping to accelerate ageing of the material.

The notable uses of FRPs in this industry are in pipeworks, gratings, and blast and fire protection. Apart from hundreds of kilometers of GRP pipe used for transporting hydrocarbon and water lines in the Middle East, FRPs are also being increasingly used to line steel pipes where the FRP provides corrosion protection for the pipe bore by acting as a barrier to the passage of transported fluids. The composite-lined pipe solution is in direct competition with conventional corrosion-resistant alloy (CRA) systems for downhole and flowline/pipeline applications. Statoil Hydro pioneered the use of downhole tubing with composite materials in the North Sea. A Duoline 20 liner was examined after five years of

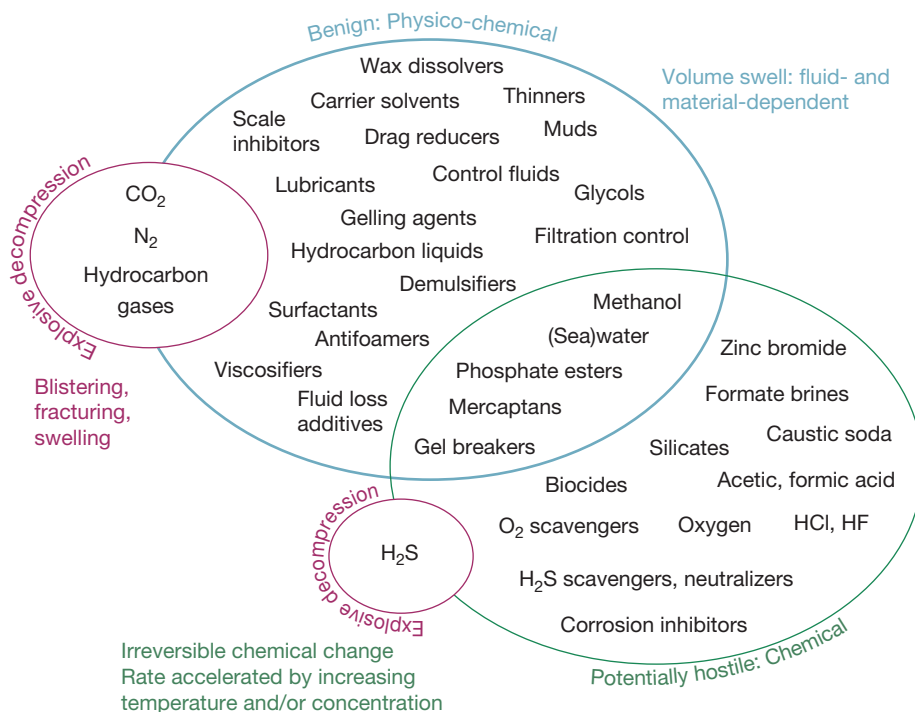


**Figure 2** Possible fluids used in the oil and gas industry and their effects on polymers.



service at up to 110°C and was found to be in excellent condition.<sup>26</sup> The technology has generally been confined to water injection service. A consortium project has been run by Oil States Industries UK to help understand the chemical compatibility of various types of FRP exposed to different oil field fluids, with the aim of obtaining 20-year life.<sup>27</sup> These liners see a variety of hostile media including hydrocarbons at temperatures up to 160°C, and short exposures to methanol, HCl/HF, and other fluids for cleaning operations. As part of the materials screening tests conducted at MERL, Hitchin, UK, single-point data was generated for specific conditions such as several days at 160°C in hydrocarbon and brine mix, 8 h of HCL exposure, etc. Several postexposure tests were conducted to ascertain surface degradation, weight change and mechanical property change of the liners. A picture of a glass-epoxy liner exposed to HCl for 8 h shows complete degradation (Figure 3).

GRP piping onshore is primarily filament-wound glass-epoxy and it has been successfully installed in 100 km runs in the Middle East for transport of hydrocarbons and other fluids. One of the shortcomings for these pipes is that the corrosion science of metals is much more developed and understood than the ageing and degradation of these materials. International standards exist for the design and installation of such pipework where short-term tests are used to account for such degradation and sufficient safety factors employed. DNV-OS-C501 standard discusses the various effects on mechanical properties under the influence of temperature, moisture and chemicals, and suggests that "... the degradation rates shall be obtained for the actual materials in question..." but gives no method for quantifying these effects in the long term. The ISO 14692 Part 2 Annex

D provides information on defining partial factors A1/A2 to account for temperature and chemical resistance, respectively. These factors are used to give knockdowns on properties that were measured at standard temperatures. While values for determining A1 are well established, A2 can be generated for water but is less well identified for other chemicals. The standard makes recommendations of other standards (such as ASTM C 581) that can be used for deriving these factors for other chemicals, although these standards were not specifically written for determining A2 (see Section 3.32.6). While these approaches have allowed GRP piping to be specified, it is generally accepted that an improved approach of quantifying such degradation is needed.

Ageing from contact of the transport fluid in these GRP pipes occurs from the surface inwards and requires time to penetrate into the material's centre, as discussed above. The ageing or degradation of an FRP pipe has many stages and it is up to the user to determine at which phase failure is said to have occurred, Figure 4. Almost immediately at Stage 1, the fluid will diffuse into the polymer causing immediate physical changes. This is a complex phenomenon for an FRP material in contact with mixed fluids and is discussed further below. In Stage 2, the fluids would have diffused further into the FRP and the inner surface might have begun to chemically age. In Stage 3, the ageing is such that it has caused mechanical damage on the inner surface. Fluid diffusion and chemical ageing continue in Stage 3, but with the presence of cracks the fluid can now penetrate quicker. In Stage 4 diffusion, chemical ageing and mechanical damage has continued, but now the mechanical damage on the inner surface is sufficient for material to be removed. Stage 4 also shows cracks

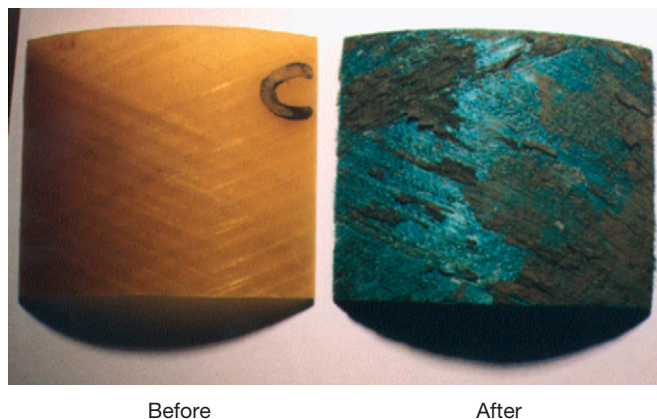


**Figure 3** Section of glass-epoxy liner submitted to an HCl exposure. Courtesy of MERL.



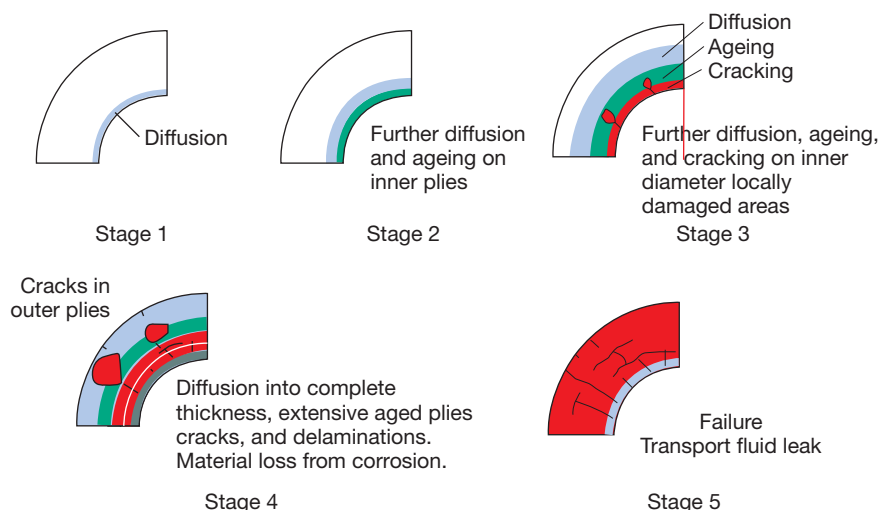


**Figure 4** A schematic of GRP degradation when transporting a hostile fluid.

on the outside of the pipe from other damages such as erosion or UV degradation. Stage 5 shows complete damage through the pipe wall and subsequent leaking.

In most pipe designs, 'failure' should be considered as somewhere between Stages 1 and 3 and the influence on strength of the system evaluated to allow for sufficient safety factors (e.g., A2) to be applied.

In order to predict the life of an FRP laminate the following information needs to be known:

- The aged condition of the material and the profile through the thickness. This can be determined by knowing the rate of ageing (physical and chemical) for a given set of conditions (fluid type, temperature profile, time, etc.).
- The key material properties at a given amount of ageing. This depends on what is classed as the residual life of the pipe (see next bullet). The mechanical properties that are used to determine this residual life are those that have to be measured.
- The residual life of the structure with given damage and degradation profile; this is dependent on what is considered as failure for example, leak, global change in stiffness, % loss of material, inner cracking.

The technology for generating the information above does not exist at the time of publication.

The advantages of FRP gratings used offshore are obvious in the improved resistance to corrosion in a sea water environment and their durability and light weight, compare to metallic options, [Figure 5](#). The products are generally pultruded glass reinforced,



**Figure 5** A glass-phenolic grating on the Mars Platform in the Gulf of Mexico, Courtesy of Strongwell.

offering a cost-effective manufacturing method. The use of phenolic resins allows the parts to meet fire-resistance requirements offshore. An important driver for GRP gratings has been the ease of installation compared to steel. The ageing of these materials follows the same aspects as marine composites discussed in [Section 3.32.7](#) and includes hydrolysis and UV ageing. The fire resistance of these phenolic gratings is also a key reason behind their selection, but fire properties goes beyond the scope of this chapter.

Composites are also being increasingly used to protect subsea structures such as wellheads, and flowlines, protecting them from impact events such as dropped objects and commercial fishing operations. This is an accepted area of use where the perceived risks of adoption are outweighed by the benefits in performance and corrosion resistance. Another example of the use of composites in hostile



**Figure 6** Composite fire-blast protection enclosure. Reproduced with permission from Solvent Composite Systems Ltd.

environments is a ProTek(tm) Jet Fire and Blast protection enclosure manufactured from composite panels by Solent Composite Systems Ltd., **Figure 6**. This enclosure was installed at the LNG plant in the Arctic town of Hammerfest in northern Norway to protect emergency shutdown equipment. The composite structure resists an explosion pressure equivalent to 7 tonnes per square meter and protects against 90 min exposure to the erosive and heating effects of a hydrocarbon jet fire with a flame temperature of 1150°C resulting from a high pressure gas leak. During this period the equipment temperature does not exceed 65°C. The ageing aspects of long-term water exposure, biofouling, and hydrolysis are covered in **Section 3.32.7**.

### 3.32.6 Ageing in the Chemical Processing Industry

In the chemical processing industry (CPI), the environments for equipment such as reactor vessels, storage tanks, scrubbing towers, stacks, piping, valves, etc. may be extremely harsh (**Figure 7**). In many instances, corrosion-resistant alloys including highly alloyed stainless steel, titanium, and nickel-based alloys have

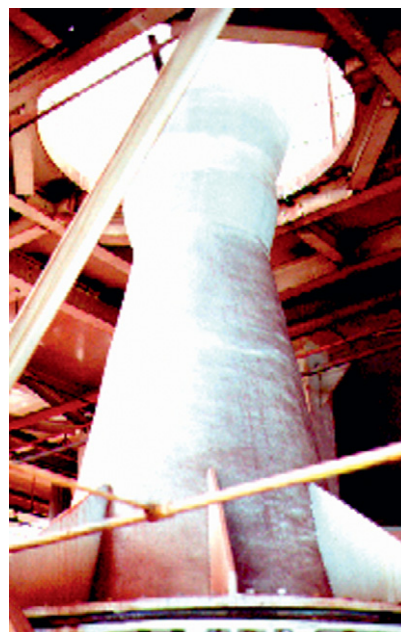


**Figure 7** FRP scrubbing tower. Courtesy of Dow Chemicals.

to be used and even these can corrode in these environments. One solution adopted in this industry is the use of FRPs in manufacturing this equipment.

FRP materials are used to a large extent in plants which manufacture chlorine, chlorate and concentrated acids (e.g., sulfuric, hydrochloric, hydrofluoric, nitric) as well as metal chloride solutions (e.g., NaCl, FeCl<sub>3</sub>, AlCl<sub>3</sub>, MgCl<sub>2</sub>, NiCl<sub>2</sub>).<sup>28</sup> FRPs are now also used in desulfurization plants (flue-gas ducting, scrubbers, etc.) which also have applications in oil and gas production. In many instances, a thermoplastic liner is used in the metallic and FRP pipes to act as a corrosion or permeation barrier, or both. The thermoplastic lining may be PA11, PVC, or PP; or for more aggressive service, PVDF. Because of the environmentally hostile nature of some of the chemicals being transported or stored, failure is unacceptable. However, failures do occur (**Figure 8**).<sup>29</sup> These failures may not only be very costly, but also present a health and safety risk to the workers at the plant, local residents and environment. The consequences and liability of equipment failure, even minor leaks, are becoming increasingly severe and have resulted in a very strict regulatory climate. Although FRP is often used to solve problems of corrosion on various metallic materials, these materials can still be affected by these fluids.<sup>30</sup>

The types of resins and fibers depend very much on the application being considered. Thermosetting

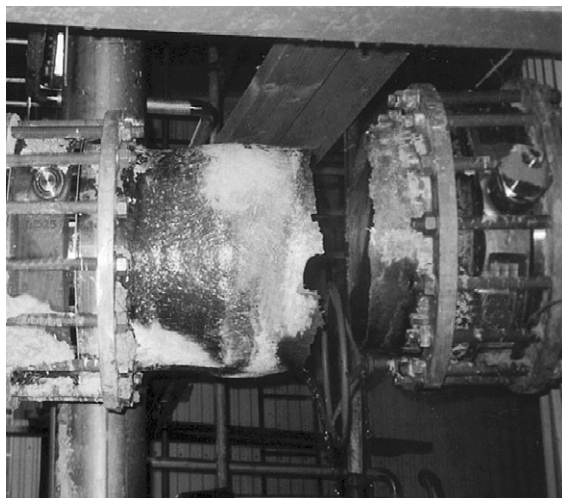


**Figure 8** Failure in alkaline aqueous solution at 70 °C. Courtesy of G. Bergman.

resins are suitable for large moldings and for filament wound pipes. The most important resin systems used for corrosion protection in the CPI include polyesters, epoxies, bismaleimides, phenolics, and vinyl esters.<sup>28,31</sup> Epoxies have certain advantages, in that they have lower cure shrinkage, adhere better to steel substrates, and offer better chemical resistance than polyesters towards hot alkalis. Vinyl esters are favored because they offer a compromise between epoxies and polyesters, offering good corrosion resistance with moderate relative cost. E-glass fiber is used as the reinforcement for the main structural part with a more chemical resistant fiber such as ECR-glass used in the layer in contact with the corrosive fluid. A protective resin-rich layer is often used on the surface adjacent to the acid.

Prediction methods for FRPs in the CPI must account for chemical ageing and include diffusion, hydrolysis and ultimately cracking, blisters and other damage. Eventually, this degradation may continue and lead to actual material loss from the inside of the vessels (Figure 9).<sup>32</sup>

Degradation in FRP composites may be defined as one of any of the following in the exposed surface:

• cracks	• loss of fiber	• etching
• pitting	• softening	• delamination
• thickness change	• blistering	• discoloration
• charring	• leaching	• fiber blossomin
• resin loss		

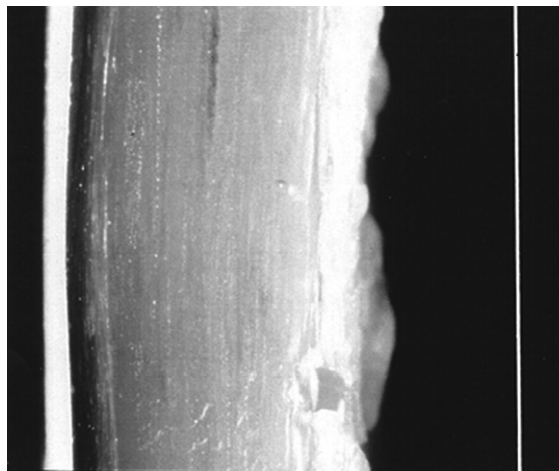


**Figure 9** Uniform corrosion in an FRP pipe after 14 years of service. The white line shows the original thickness. Courtesy of G. Bergman.

The published work related to chemical resistance of FRP materials in different environments has focused on immersion testing, rather than the more realistic single-sided exposure. Much of the published data quote only single-point data, for example, “The mass of material X increases by 10% in methanol after 10 days at 60 °C.” This information may be misleading because the overall trend may involve a mixture of competing mechanisms as discussed in previous sections. For hybrid materials (e.g., the use of a corrosion-resistant veil), the prediction method must account for the time for the ageing to reach each layer.

Further, FRPs may be subject to step changes in property changes leading to failure such as resin embrittlement. This failure is often termed environmental stress cracking (ESC) and also applies to the glass fibers when undergoing strains in excess of 2% and exposed to even dilute acids.<sup>33</sup> In any long-term evaluation, it is necessary to use diagnostic equipment to ensure that the cause for the change in properties of the FRP is understood.

Estimates of remaining life of FRP equipment in the CPI often rely on periodic visual inspection, intuition, and experience of the inspector. The inspector searches out defects such as blistering, delamination, or signs of leaking. Often a bright light is shone on the opposite side of the laminate to help reveal flaws. The inspector often also checks the condition of the laminate surface with a Barcol indentation tester. Drastic reduction in Barcol readings since the previous inspection indicates degradation. On the basis of these findings, the inspector will judge whether the equipment is still safe to operate and when the next inspection should occur.<sup>30</sup>



### 3.32.6.1 ASTM Standard for Long-Term Chemical Resistance

Materials are generally approved for long-term usage in the CPI using ASTM C 581 *Standard Practice for Determining Chemical Resistance of Thermosetting Resins Used in Glass-Fiber-Reinforced Structures Intended for Liquid Service*. This standard requires immersion of a material in a fluid at a single temperature. Various properties (Barcol hardness, flexural modulus and strength, and  $T_g$ ) are determined at intervals normally within one year. If the properties do not decrease by a certain amount, the material may be approved for long-term usage. However, this method does not offer an approach to allow an extrapolation to longer-term usage at varied of temperatures and is therefore little more than a screening test.

To demonstrate the use of ASTM C 581, an FRP laminate that may be used for the linings of tanks and vessels used to store acids was tested.<sup>30</sup> Plaques of materials were immersed in concentrated HCl or  $H_2SO_4$  for 12 months. Periodically, Barcol hardness, mass change, and flexural properties were measured on specimens cut from these plaques. The mass change is shown in Figure 10, illustrating that the material shows weight loss early in the exposures and the rate of weight loss begins to reduce as the test progresses. The change in Barcol hardness, shown in Figure 11, shows that there is an initial increase in both exposures, indicating that some form of local hardening has occurred. After 6 months' exposure, the hardness begins to decrease, leading to 10–15% from the starting values after 12 months. This indicates that there is more than one ageing mechanism

occurring and the resulting change in properties cannot be taken from only the end data point.

### 3.32.6.2 The Arrhenius Relationship

Using the different test parameters used in ASTM C 581 in the previous section, the feasibility of using an Arrhenius relationship was presented elsewhere.<sup>30</sup> Key to this approach being successful is that the elevated temperature exposures do not cause a change in the ageing mechanisms observed at lower temperatures.

A Derakane 411 vinyl ester resin was tested with two plies of 45g E-Glass chopped-strand mat, with a 0.25-mm C-glass veil. The materials were exposed to 37% HCl at temperatures of 40, 60, and 80 °C. Before and after the exposures, thickness and weight in air and water were measured to determine any changes. Following the ageing and the weighing, suitable specimens were cut from the plaques. Three point-bend tests were conducted and showed that the modulus initially increased before decreasing, whereas at the higher temperatures, the modulus and strength continually decreased, showing a change in mechanism at the different temperatures. The work demonstrated that there is an overall trend from test to test of a property change with exposure time, the rate of which increases with time. It is this general concept that lays foundation for developing accelerated ageing approaches using the Arrhenius equation if a single mechanism is present. The 5 and 10% change of flexural strength were plotted against the reciprocal of the absolute exposure temperature and a straight line fitted. The shorter-term,

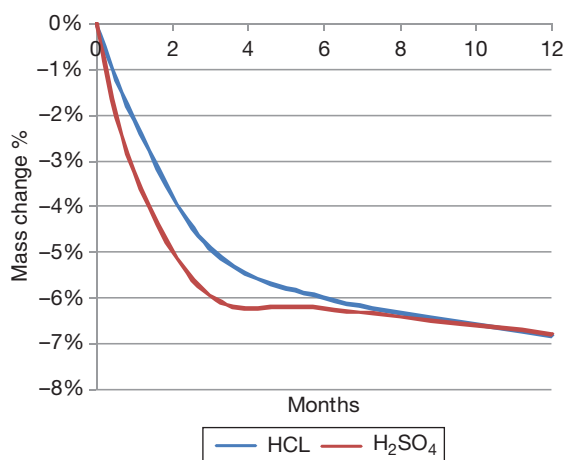


Figure 10 Mass change of an FRP in concentrated acid.

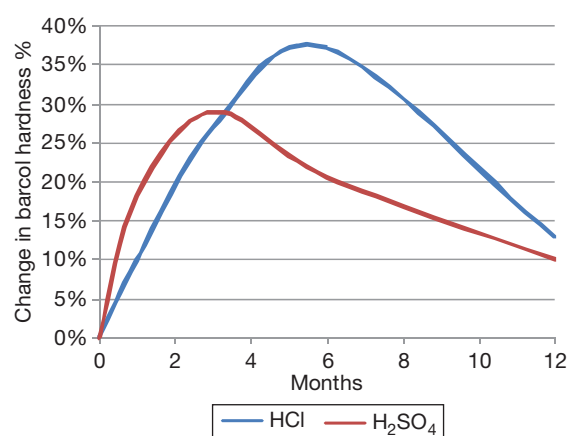


Figure 11 % Change in Barcol hardness of an FRP in concentrated acid.

higher-temperature exposure tests were able to predict the properties at lower-temperature exposures. The energy of activation for this change is in the region of  $80 \text{ kJ mol}^{-1}$ , which is indicative of chemical ageing. However, an Arrhenius curve cannot be drawn for the modulus because of the initial increase in modulus in the early exposure times, this invalidating this method unless the different mechanisms are separated.

### 3.32.6.3 Using a Semiempirical Corrosion Approach

Another approach to the long-term ageing of FRPs is to relate the effects of ageing to those of corrosion in metals, because on the macrolevel the results are very similar. Many types of corrosion found in metals can also be found in FRP, such as uniform corrosion (material loss), localized corrosion (pitting), selective corrosion, stress corrosion, corrosion fatigue, erosion corrosion, and layer corrosion (delamination). CFRPs are conductive and galvanic corrosion effects may arise when being coupled to a metal component.

On the basis of the results of corrosion analyses of samples taken from FRP equipment used for different chlorine dioxide environments in various pulp mill applications over a period of 20 years, a semiempirical relationship for uniform corrosion behavior of FRP in chlorine dioxide environments has been established,<sup>32</sup>

$$\Phi = Bt^\alpha cA \exp\left(\frac{-E_a}{RT}\right) \quad [4]$$

where  $\Phi$  is the depth of corrosion (mm),  $B$  is a special factor in case of protective deposits on the surface (usually  $B = 0$  or  $1$ ),  $t$  is the time in service (years),  $\alpha$  is a factor which depends on the thickness and degree of degradation of the corroded surface layer (usually  $\alpha$  is between  $0.5$  and  $1$ ),  $c$  is the concentration of chlorine dioxide ( $\text{g l}^{-1}$ ),  $A$  is a material constant which depends on the type of resin, the degree of curing, and the laminate structure,  $E_a$  is the activation energy of the rate-controlling step of the corrosion process ( $\text{kJ mol}^{-1}$ ),  $R$  is the general gas constant ( $8.3 \text{ J mol}^{-1} \text{ K}$ ),  $T$  is the temperature (K).

This expression is not proven for other applications and environments, although the premise should hold.

### 3.32.7 Ageing in the Marine Industry

One of the more established uses of FRPs with long and chopped fiber resins in marine vessels from small

dinghies to racing yachts. A review of marine composites is given elsewhere.<sup>34,35</sup> The FRP materials are mainly E-glass reinforced polyester and epoxy, but with the high-performance vessels carbon fiber composites and a range of sandwich materials are now used. Almost always, a protective outer coating or gelcoat is used to help prevent diffusion and to give a better appearance. There is much experience on the ageing of these materials in this environment. However, similar to the studies in other industries, research studies on ageing for this industry have focused on short-term ageing tests under severe conditions that may have little relationship with in-service use.

Leisure craft or pleasure boats, defined as vessels built for recreational purposes, were one of the first applications of FRPs. The average lifetime of a FRP pleasure boat is 30 years, demonstrating the anticipated long use life of these materials. For commercial vessels including fast ferries, lifeboats, fishing boats, and some military vessels have been made from a conventional GRP material since the 1960s. Some vessels such as mine countermeasure vessels are in excess of 40 m length and the nonmagnetic and conducting properties of the GRP add another advantage to the use of these materials. The low weight of FRP materials make them attractive for submarine use in internal and external structures such as sonar domes.

Woven or chopped glass strand mats in a polyester resin is the typical FRP use in marine applications and much work on ageing of these materials in a sea water environment has been conducted.<sup>36</sup> Higher-end materials, including stitched multiaxial cloth, carbon epoxy are used for the higher end applications where ageing may be less of a concern such as in racing yachts. The document also provides a database of material properties to be used if test data are not available. Typical hull laminate thicknesses vary from 5 mm for pleasure craft up to 150 mm for hulls that must survive underwater explosions. The difference in thickness has an affect on the time to reach equilibrium and hence begin hydrolytic ageing. Manufacturing techniques have been developed over the past 10 years to utilize resin infusion to draw the resin through the dry fibers. This has resulted in the ability to have a higher fiber to resin volume fraction giving thinner laminates with the same strength as the previously used wet lay-up manufacturing methods with lower volume fractions. Sandwich panels comprising a core (foam or balsa-wood) surrounded by thin layers or skins of FRP are a preferred manufacturing method for large hulls. However, the thin skins, their bonding to the core

and degradation of the core material present further concerns for ageing. As mentioned above, a gelcoat is almost always used and this serves to protect the laminate.

There are a number of different damage modes for marine composites and the gelcoats, including osmosis, blisters, pinholes, wrinkling, debonding/delamination, crazing, etc., can all be considered a form of ageing. Blisters are a particular ageing damage mode in marine environments, where the osmotic pressure is developed between the gelcoat and the FRP. This is built up from products such as glycols leached from the base FRP and can cause local delamination or blisters and is particularly apparent with a gelcoat that is more permeable than the base laminate. The temperature and the composition of the seawater, which varies around the world, are important aspects in considering ageing of marine FRPs as well as the loading from wave load, slamming load, hydrostatic pressure, etc. Antifoul treatments are used on many boats to prevent biofouling or marine growth. These are applied to the gelcoat and may in themselves age the coating.

Conventional marine ageing of a marine FRP follows the same degradation mechanisms as discussed in [Section 3.32.2.2](#). This is physical ageing causing plasticization and swelling (potentially leading to interfacial debonding and delaminations) and chemical ageing such as hydrolysis of the matrix and, in saltwater environments, the fiber and the fiber–matrix interface. Many of the ageing studies are conducted at higher temperatures to reduce the ageing times. A number of case studies are presented in Searle and Summerscales,<sup>36</sup> where an attempt to better understand the changes due to ageing of properties that can be used for design were studied. In one study, weight change was measured along with shear strength and modulus for three GRPs (polyester, vinyl ester, and epoxy, all with the same glass reinforcement). The work demonstrated that the resin and fiber interface within an FRP absorbs water, not just the resin. In the same work, FRP materials were exposed to an accelerated exposure (elevated temperature), and the same panels were exposed to the sea for up to a year. The results suggest that without due attention to the various ageing conditions, the accelerated test will overpredict changes in properties.

For realistic accelerated ageing of marine FRPs, several aspects need to be considered. Virtually, all laminates, as stated above, will have a gelcoat. While not an impermeable layer, it is a resin-rich layer and needs to be considered in ageing analysis. The work in Searle and Summerscales<sup>36</sup> demonstrated that the

composition of the water can greatly affect the ageing of the FRP. Seawater will diffuse into polymers slower than distilled water, and ageing exposure using distilled water may be overly conservative. In addition, during ageing, products may leach out of the FRP into the water. These products will themselves change the composition of the water more significantly if small vessels and hence small volumes of water are used. As for other applications, the use of temperature as an ageing accelerator must be used with caution. The increase in temperature can serve to promote further cross-linking in partially cured polyesters and use of ageing temperatures near or above the  $T_g$  can cause degradation mechanisms that will never occur at lower temperatures. For true comparisons for sea environments, it is the inclusion of biofilms that will develop, followed by biofouling, resulting in a complete covering. This needs to be considered when conducting weight-gain/loss measurements and the influence of the living matter on the properties of the composites needs to be better understood.

### 3.32.8 Concluding Remarks

This chapter has described some of the more common forms of ageing of FRPs. Ageing is a summation word for degradation and can include physical changes of the matrix such as swelling or irreversible chemical changes such as hydrolysis or oxidation. The extent of the degradation is very much dependent on the exposure the FRP material will experience including the fluid in contact, time, pressure, temperature, load applied, if any, etc. Some attempts have been to develop predictive modeling capability for the long-term durability assessment of FRP components, but this still remains an area for further research. As the use of FRP materials increases and the demands for extended performance grow, so does the need and importance to develop predictive capability for assigning the fitness for the purpose of an FRP structure at any time during its service.

### References

1. Jones, R. M. *Mechanics of Composite Materials*; Scripta Book Company: Washington DC, 1975.
2. Matthews, F. L.; Rawlings, R. D. *Composite Materials: Engineering and Science*; Woodhead Publishing: Cambridge, England, 2002.
3. *ASM Handbook, Volume 21 Composite*; ASM International: Ohio, 2001.



4. [www.vircon-composites.com](http://www.vircon-composites.com)
5. Struik, L. C. *Physical Ageing in Amorphous Polymers and Other Materials*; Elsevier Scientific: New York, 1978.
6. Gates, T. In *Ageing of Composites*; Martin, R., Ed.; Woodhead Publishing: Cambridge, England, 2008; Chapter 1.
7. Jones, F. R. In *Reinforced Plastics Durability*; Pritchard, G., Ed.; Woodhead Publishing: Cambridge, England, 1999; Chapter 3.
8. Mensitieri, G.; Iannone, M. In *Ageing of Composites*; Martin, R., Ed.; Woodhead Publishing: Cambridge, England, 2008; Chapter 9.
9. Harris, C. E.; Gates, T. S. Eds. *High Temperature and Environmental Effects on Polymeric Composites*; ASTM STP 1174; American Society for Testing and Materials: Pennsylvania, 1993.
10. Martin, R. H.; Siochi, E. J.; Gates, T. S. In *Proceedings of the American Society for Composites Seventh Technical Conference*, University Park Pennsylvania, 13–15 October 1992; pp 207–217.
11. Tsotsis, T. In *Ageing of Composites*; Martin, R., Ed.; Woodhead Publishing: Cambridge, England, 2008; Chapter 5.
12. Weitsman, Y. *Mech. Phys. Solids* **1987**, 35(1), 73–93.
13. Layton, J. In *Reinforced Plastics Durability*; Pritchard, G., Ed.; Woodhead Publishing: Cambridge, England, 1999; Chapter 6.
14. Halliwell, S. *Ageing of Composites*; Martin, R., Ed.; Woodhead Publishing: Cambridge, England, 2008; Chapter 15.
15. Dodds, N.; Gibson, G. In *Composite Materials for Offshore Applications*; American Bureau of Shipping, 1999; pp 77–92.
16. Gates, T. S. On the use of accelerated test methods for characterisation of advanced composite materials, NASA TP-2003-212407, May 2003.
17. Martin, R. H. In *High Temperature and Environmental Effects on Polymeric Composites*; ASTM STP, 1174; Harris, C. E., Gates, T. S., Eds.; American Society for Testing and Materials: Pennsylvania, 1993.
18. Tsotsis, T. K.; Lee, S. M. *Compos. Sci. Technol.* **1998**, 58, 355–368.
19. Hogg, P. J.; Hull, D. In ; Harris, B., Ed.; In *Developments in GRP Technology*, Harris, B., Ed.; Applied Science: London, UK, 1983; Vol. 1, pp 37–90.
20. Kerr, J. R.; Haskins, J. F. Time temperature stress capabilities of composite materials for advanced supersonic technology applications, NASA CR-178272, May 1987.
21. Martin, R. H.; Siochi, E. J.; Gates, T. S. In *7th Technical Conference on Composite Materials*, The Pennsylvania University, American Society for Composites, October 1992.
22. Morgan, R. J.; Shin, E.; Dunn, C.; Fouch, E.; Jurek, B.; Jurek, A. In *Proceedings of the 39th International SAMPE Symposium*, April 1994, pp 1564–1575.
23. Martin, R. H. In *AIAA/ASME/ASCE/AHS/ACE 35th Structures, Structural Dynamics and Materials Conference*, Hilton Head, SC, April 1994; pp 18–20.
24. Martin, R. H. A Technology Gap Review of Composites in the UK Oil and Gas Industry, March 2007 [www.merl-ltd.co.uk](http://www.merl-ltd.co.uk).
25. Frost, S. In *Ageing of Composites*; Martin, R., Ed.; Woodhead Publishing: Cambridge, England, 2008; Chapter 14.
26. Melve, B.; Nice, P. In *Statoil, MERL Oilfield Engineering with Polymers Conference*; London, 2003.
27. [http://medlicott.uk.com/bus/osiuk\\_jip.htm](http://medlicott.uk.com/bus/osiuk_jip.htm)
28. Kelly, P. *Reinforced Plastics Durability*; Pritchard, G., Ed.; Woodhead Publishing: Cambridge England, 1999; Chapter 9.
29. Bergman, G. *Corrosion*; 2004; NACE Paper 04611.
30. Martin, R. H. *Ageing of Composites*; Martin, R., Ed.; Woodhead Publishing: Cambridge England, 2008; Chapter 17.
31. Pritchard, G. In *Advanced Composites*; Elsevier Applied Science, 1989; pp 163–196.
32. Bergman, G. *J. Hazard. Mater.* **2007**, 142(3), 695–704.
33. French, M. A.; Pritchard, G. *Compos. Sci. Technol.* **1993**, 47, 257–263.
34. Davies, P.; Choqueuse, D. In *Ageing of Composites*; Martin, R., Ed.; Woodhead Publishing: Cambridge England, 2008; Chapter 12.
35. Choqueuse, D.; Davies, P. In *Ageing of Composites*; Martin, R., Ed.; Woodhead Publishing: Cambridge England, 2008; Chapter 18.
36. Searle, T. J.; Summerscales, J. In *Reinforced Plastics Durability*; Pritchard, G., Ed.; Woodhead Publishing: Cambridge England, 1999; Chapter 7.

## 3.33 Degradation of Natural Rubber and Synthetic Elastomers

**A. bin Samsuri**

Department of Polymer Technology, MARA University of Technology (UiTM), 40450 Shah Alam, Selangor, Malaysia

© 2010 Elsevier B.V. All rights reserved.

<b>3.33.1</b>	<b>Introduction</b>	2409
<b>3.33.2</b>	<b>Classifications of Rubber and Elastomers</b>	2410
3.33.2.1	Classification in Terms of Origins	2410
3.33.2.2	Classification in Terms of Purposes	2411
3.33.2.3	Classification in Accordance with International Organization for Standardization	2411
<b>3.33.3</b>	<b>General Properties of Elastomers</b>	2413
3.33.3.1	Structure–Property Relationship	2413
3.33.3.1.1	Mechanical strength	2413
3.33.3.1.2	Oxidation and ozone resistance	2415
3.33.3.1.3	Swelling resistance	2415
3.33.3.1.4	Glass-transition temperature $T_g$	2416
<b>3.33.4</b>	<b>Rubber Technology and Compounding</b>	2416
3.33.4.1	Mastication and Mixing	2416
3.33.4.2	Rubber Compounding	2416
3.33.4.3	Vulcanization	2417
<b>3.33.5</b>	<b>Rubber-to-Metal Bonding – Engineering and Automotive Applications</b>	2418
3.33.5.1	Bonding of Rubber to Metal	2420
3.33.5.1.1	Preparation of metal plates	2420
3.33.5.1.2	Types of bonding agent and methods of applications of bonding agent to metal plates	2420
3.33.5.1.3	Molding of rubber-to-metal bonded parts	2420
3.33.5.2	Vulcanization	2421
3.33.5.2.1	Low or high pressure steam	2421
3.33.5.2.2	Water curing technique	2421
3.33.5.2.3	Hot air or ambient temperature vulcanization	2421
3.33.5.3	Types of Bond Failure and Possible Remedies	2421
<b>3.33.6</b>	<b>Oxidation of Rubber</b>	2422
<b>3.33.7</b>	<b>Ozone Cracking of Rubber</b>	2424
<b>3.33.8</b>	<b>Heat Aging Resistance</b>	2426
<b>3.33.9</b>	<b>Flex Cracking</b>	2426
<b>3.33.10</b>	<b>Oil Absorption</b>	2427
3.33.10.1	Effect of Crosslink Concentration and Polarity on Swelling Resistance	2428
<b>3.33.11</b>	<b>Water Absorption</b>	2429
<b>3.33.12</b>	<b>Protective Measures</b>	2431
3.33.12.1	Selection of Elastomer	2431
3.33.12.2	Blends of Elastomers	2431
3.33.12.3	Antidegradants	2432
3.33.12.3.1	Mechanism of antiozonant action	2433
3.33.12.3.2	Theories of layer formation	2433
3.33.12.4	Blooming of Wax	2435
3.33.12.5	Choice of Vulcanization System	2435
3.33.12.5.1	Sulfur vulcanization system and types of crosslinks on aging resistance	2436
3.33.12.5.2	Peroxide vulcanization system	2436

3.33.12.5.3	Vulcanization with urethane	2437
3.33.12.5.4	Metallic oxide vulcanization	2437
3.33.12.5.5	Resin vulcanization	2437
3.33.12.5.6	Quinonedioximes vulcanization	2437
<b>3.33.13</b>	<b>Future Developments in Materials or Applications</b>	<b>2437</b>
<b>References</b>		<b>2438</b>

## Glossary

### Damping Basic property of an

elastomer to dampen, absorb or reduce vibrations. High damping elastomers are those having high glass-transition temperature ( $T_g$ ), which are widely used to isolate vibrations.

**Glass-transition temperature ( $T_g$ )** It denotes the temperature below which the elastomer becomes glassy and brittle, above which it is soft and rubbery.  $T_g$  reflects molecular mobility and hence the internal viscosity of the elastomer. High  $T_g$  indicates low molecular mobility or high internal viscosity and vice versa.

**Heat build-up** The amount of heat accumulated in the elastomer when subject to cyclic deformation. It is closely related to hysteresis.

**Hysteresis** It is a term to denote energy dissipated as heat when the elastomer is subject to cyclic stresses or in a single stress-strain cycle. The area bounded by the extension and retraction curve gives a quantitative measure of hysteresis.

**Raw rubber** Fresh rubber or an elastomer as received from the supplier.

**Scorch** It is a rubber technology term to denote the occurrence of a premature crosslink, which is an undesirable feature during the shaping process.

**Vulcanize or vulcanized elastomer** Indicates rubber or elastomer that has been vulcanized or cured, and thus, contains network structure or chemical crosslinks.

**CM** Cement metal failure

**CP** Cement primer failure

**CR** Polychloroprene rubber

**CSM** Chlorosulfonated polyethylene rubber

**DCP** Dicumyl peroxide

**DOPPD** Dioctyl-*p*-phenylenediamines

**ECO** Copolymer of epichlorohydrin rubber

**ENR50** Epoxidized natural rubber (50 mol% epoxidation)

**EPM** Ethylene propylene rubber

**EV** Efficient vulcanization

**GRG** General rubber goods

**IHRD** International Rubber Hardness Degrees

**IIR** Isobutylene isoprene (butyl) rubber

**IR** Synthetic polyisoprene rubber

**IRG** Industrial rubber goods

**ISO** International Organization for Standardization

**MRB** Malaysian Rubber Board

**MRPRA** Malaysian Rubber Producers Research Association

**MS** Malaysian standard

**NBR** Nitrile rubber

**NR** Natural rubber

**PP** Polypropylene

**PTR** Polysulphide rubber

**SBR** Styrene butadiene rubber

**TAC** Triallyl cyanurate

**TAIC** Triallylisosyanurate

**TARRC** Tun Abdul Razak Research Centre

**UiTM** Mara University of Technology

**UV** Ultraviolet light

**XNBR** Carboxylated nitrile rubber

## Abbreviations

**ACM** Polyacrylic rubber

**ASTM** American Society for Testing Materials

**CED** Cohesive energy density

**CIIR** Chlorinated butyl rubber

## Symbols

**A** Cross-sectional area ( $\text{m}^2$ )

**$A_0$**  Unstrained (original) cross-sectional area ( $\text{m}^2$ )

**B** Crack growth constant

**c** Crack length (mm, m)

**$c_0$**  Natural flaw size (mm, m)

**$C_0$**  Concentration of antiozonant ( $\text{mg cm}^{-2}$ )

<b>C<sub>s</sub></b>	Concentration of antiozonant at the rubber surface (mg cm <sup>-2</sup> )
<b>D</b>	Diffusion coefficient (m <sup>2</sup> s <sup>-1</sup> )
<b>dc/dt</b>	Crack growth rate (m s <sup>-1</sup> )
<b>f</b>	Force (N)
<b>f<sub>f</sub></b>	Frequency (Hz)
<b>h</b>	Height (m)
<b>k<sub>c</sub></b>	Compression stiffness (N m <sup>-1</sup> )
<b>k<sub>s</sub></b>	Shear stiffness (N m <sup>-1</sup> )
<b>l</b>	Half thickness of film sheet (mm, m)
<b>L</b>	Length (m)
<b>M</b>	Molecular weight (g mol <sup>-1</sup> )
<b>M<sub>∞</sub></b>	Total mass of liquid absorbed after an infinite time (g, kg)
<b>M<sub>L</sub></b>	Mass of layer per unit area of surface (g mm <sup>-2</sup> , kg m <sup>-2</sup> )
<b>M<sub>t</sub></b>	Total amount of liquid absorbed per unit area after immersion time, <i>t</i> (g mm <sup>-2</sup> s <sup>1/2</sup> )
<b>N</b>	Number of molecules per unit volume of rubber (mol cm <sup>-3</sup> )
<b>N<sub>f</sub></b>	Fatigue life (number of cycles of failure) (cycles, kilocycles)
<b>R</b>	Molar gas constant (8314 J mol <sup>-1</sup> K <sup>-1</sup> )
<b>S</b>	Shape factor
<b>T</b>	Absolute temperature (K)
<b>t</b>	Time (s)
<b>T<sub>g</sub></b>	Glass-transition temperature (°C, K)
<b>V<sub>1</sub></b>	Molar volume of solvent (m <sup>3</sup> )
<b>v<sub>f</sub></b>	Volume fraction of seeding particles present in the rubber
<b>v<sub>r</sub></b>	Volume fraction of rubber in the swollen gel
<b>W</b>	Width (m)
<b>W<sub>s</sub></b>	Strain energy density (J m <sup>-3</sup> )
<b>[X]<sub>phy</sub></b>	Physically manifested crosslink concentration (mol kg <sup>-1</sup> )
<b>δ</b>	Solubility parameter (MPa) <sup>1/2</sup>
<b>ΔH</b>	Latent heat of vaporization (J)
<b>λ</b>	Extension ratio
<b>ρ</b>	Density (kg m <sup>-3</sup> )
<b>χ</b>	Rubber-solvent interaction parameter

### 3.33.1 Introduction

Natural rubber and elastomers belong to the same group of materials known as high molecular weight polymers. According to the International Organization for Standardization (ISO) rubber vocabulary,<sup>1</sup> an elastomer is a macromolecular material which returns rapidly to approximately its initial dimensions and shape after substantial deformation by a weak stress

and release of the stress. However, an elastomer has always been recognized as a synthetic elastic polymer.<sup>1</sup> A polymer is a high molecular weight material having many units of small molecules chemically joined or linked by normal covalent bonds to form long chain molecules. These flexible and soft materials find wide uses in many engineering applications, such as natural rubber (NR) bridge bearings, and earthquake and seismic bearings. Indeed NR has had a sound track record in many engineering applications for over 150 years.<sup>2</sup> Elastomers have some unique properties that metals do not have. These include

- high bulk modulus (2000–3000 MPa) relative to their Young's modulus (0.5–3.0 MPa),
- some inherent damping, and
- large strain deformation.

Rubbers having high bulk modulus hardly change their volume when deformed. In simple words, rubber is incompressible. Like incompressible liquids, it has a Poisson's ratio close to 0.5. If rubber is constrained, to prevent changes in shape, it becomes much stiffer, a feature that is used to full advantage in the design of compression springs. Elastomeric bridge bearings and seismic bearings are examples of products that rely on these properties.

The damping inherent in the elastomer is a very important property as it helps to prevent the amplitude of the vibration of the spring from becoming excessive if resonant frequencies are encountered. Elastomeric products such as vibration isolators and engine mounts rely on the inherent damping properties of the elastomer.

The elastomer undergoes large strain deformation (a few hundred percent) without failure by an applied stress below its breaking stress. This means that it can store much more energy per unit volume than steel. Elastomeric dock fender systems make use of its large stored energy capacity to absorb shocks, blows and the impact exerted by ships.

Some of the merits of elastomeric springs over metal springs are as follows<sup>2</sup>:

- no maintenance is required,
- the energy storage capacity is high,
- with correct design, the rubber spring can provide different stiffness in different directions, or nonlinear load–deflection characteristics,
- a certain amount of misalignment is tolerable as the rubber spring can accommodate this tolerance,
- easier to install,
- hysteresis inherited by the elastomer is able to dampen dangerous resonant vibrations.



Another important property of an elastomer is its strong resistance to inorganic acids, salts, and alkalis. In contrast, acids attack metals. For these reasons, the linings of chemical tanks and pipes, especially those containing caustic solutions, are made from elastomers. The function of the elastomer here is to protect the metal against attack by corrosive chemicals.

Every product has its own life span. The designed lifetime of a product depends on the environmental conditions and the nature of the application. It is very important to choose the materials correctly to meet the intended service conditions and the surrounding environment. The aging process is the determining factor that limits the life span of the product. The term aging is always associated with the degradation or corrosion process as applied to metals, which may take many forms. In metals, corrosion takes place in the form of rusting, which involves oxygen and moisture. In elastomers, the term degradation is preferred to corrosion and covers a wider scope than that of metals. Degradation takes place in the form of oxidation, ozone cracking, flex cracking, liquid absorption and heat aging. Degradation in elastomers is very complex as it involves oxygen, ozone, mechanical strain, heat, trace metals, etc. There are other agencies such as solvents, oils, fuels, hot air (steam) and water, which may degrade elastomers and affect the service life of elastomeric products. A specific section on the degradation of elastomers discusses all these issues again later.

### 3.33.2 Classifications of Rubber and Elastomers

#### 3.33.2.1 Classification in Terms of Origins

Natural rubber comes from trees known as *Hevea brasiliensis*, and shrubs called guayule. The pictures in Figure 1 show typical rubber trees grown in the hot tropical climate of Malaysia, and the fresh latex that exudes from the bark of the rubber tree, after tapping with a sharp tapping knife. The fresh latex that exudes from the tree known as field latex contains about 70% water. After removing this large amount of unwanted water, the latex is known as concentrated latex and has about 60% of rubber content. Centrifuging is the preferred method of concentrating field latex because of its efficiency and rapidness compared to creaming and evaporation methods. Apart from latex, natural rubbers are available commercially in standard bale form, weighing about 33.33 kg. These bales of NR are produced specifically to meet certain



**Figure 1** Pictures of (a) natural rubber trees (top), (b) NR latex exudes from natural rubber tree (middle), and (c) closer view of NR latex collected in a cup (bottom).

technical requirements such as minimum dirt content, viscosity consistency, ash content, etc.

All synthetic elastomers are produced by the polymerization process. The early production of synthetic elastomers such as styrene butadiene rubber (SBR), polychloroprene rubber (CR), and nitrile rubber (NBR) relied on emulsion polymerization. One of the main drawbacks of emulsion polymerization is the lack of uniformity of polymer molecules with respect to stereo regularity. This is due to the

different ways in which diene monomer molecules can react, and it applies to all free radical polymerization processes of diene monomers. However, there was a real breakthrough with the discovery of the Ziegler–Natta catalyst in 1954, which enabled the control of the microstructure of polyisoprene.<sup>3</sup> Synthetic polyisoprene is produced by the solution polymerization process using catalysts of the alkyl lithium types such as trialkyl aluminum/titanium tetrachloride mixtures.<sup>3</sup> The Al/Ti mole ratio is critical for achieving high cis content. Currently, there are about 27 types of rubbers or more commercially available in the market. The choice depends on the nature of application, service conditions and environment.

### 3.33.2.2 Classification in Terms of Purposes

Elastomers can be classified further either as general-purpose rubbers or as specialty rubbers. General-purpose rubbers are those elastomers that are widely used in the manufacture of tires, industrial rubber goods (IRG), and general rubber goods (GRG). Most of the general-purpose elastomers cannot meet high service temperature and high oil resistance specifications or the combinations of these two requirements. The most common general-purpose rubbers include NR, SBR, CR, NBR, ethylene–propylene–diene rubber (EPDM), and BR. In contrast, specialty rubbers are those elastomers that are tailor made to meet certain specific requirements, such as low temperature flexibility, high swelling resistance towards oil (hydrocarbon, fuel, gasoline, etc.) and very high service temperature or combinations of these requirements. Specialty rubbers include silicone rubber, fluoroleastomers, epichlorohydrin, chlorosulfonated rubber, etc. [Table 1](#) shows some of the rubbers which belong to these grades and their typical applications.

### 3.33.2.3 Classification in Accordance with International Organization for Standardization

Elastomers can also be classified according to the ISO 4632/1-1982(E)<sup>4</sup> which provides information about rubber as a material with specifications. They are classified and designated in terms of their performance to heat aging, swelling resistance towards oil and low temperature flexibility. This method of classification is very helpful as it facilitates the purchasers and suppliers to make the correct selection of suitable materials, and avoid wasting time and energy.

These designations are determined by a type based on resistance to heat aging, by a class based on resistance to swelling in oil, and by a group based on low temperature resistance.<sup>4</sup> These classification criteria are used to establish a characteristic material designation consisting of three capital letters, where

- the first letter signifies Type (heat resistance)
- the second letter signifies Class (oil resistance)
- the third letter signifies Group (low temperature resistance).

[Tables 2–4](#) show the heat aging temperature, limits of volume swell and brittleness temperature for establishing Type, Class and Group respectively.<sup>4</sup> Type is determined by the maximum temperature at which heat (air oven) aging for 70 h, in accordance with ISO 188, causes a change in tensile strength of not more than  $\pm 30\%$ , a change in elongation at break of not more than  $-50\%$ , and a change in hardness of not more than  $\pm 15$  International Rubber Hardness Degrees (IHRD). Class is based on the resistance of the material to swelling in American Society for Testing Materials (ASTM) Oil No. 3, when tested in accordance with ISO 1817. In the test, the immersion time shall be 70 h at a temperature determined in [Table 2](#). Group is based on the brittleness temperature of the material when measured in accordance with ISO/R 812.

Thus if an elastomer is designated as BCD, it means that it is classified as Type B, Class C and Group D. This implies that the elastomer resists temperatures up to  $100^{\circ}\text{C}$ , with volume swelling not exceeding 120% in oil No. 3 and is not brittle at  $-40^{\circ}\text{C}$ .

Most of the general purpose elastomers shown in [Table 1](#) have poor heat resistance except for ethylene propylene rubber (EPM) as shown in [Figure 2](#). EPM can withstand service temperature of about  $150^{\circ}\text{C}$  as it is categorized as Type D. General purpose elastomers also have poor swelling resistance towards hydrocarbon oil except nitrile rubber (NBR) which is classified as Class H with maximum volume swell of 30%. A majority of the specialty elastomers shown in [Table 1](#) have both excellent heat resistance and swelling resistance. From the chart shown in [Figure 2](#), silicone rubber having both methyl and vinyl substituent groups on the polymer chain (VMQ) has equivalent heat resistant (Type G) with silicone rubber having methyl, vinyl, and fluorine substituent groups on the polymer chain (FVMQ). However, they have different Class with respect to swelling resistance. VMQ belongs to Class E while FVMQ belongs to Class J. Clearly



**Table 1** General purpose rubbers and specialty rubbers

<i>General purpose rubbers</i>	<i>Typical applications</i>	<i>Specialty rubbers</i>	<i>Typical applications</i>
Natural rubber (NR)	Mainly for tires, industrial and general rubber goods, bridge and earthquake bearings, bridge expansion joints, etc.	Carboxylated nitrile rubber (XNBR)	Oil resistant hoses, boots, seals and gaskets and other automotive components with very good oxidation resistance
Synthetic polyisoprene (IR)	Tires, sports goods, earthquake rubber bearings, IRG.	Polysulphide rubber (PTR)	Used mainly where good resistance to solvents is required
Styrene butadiene rubber (SBR)	Passenger car tires, IRG, GRG	Polyurethane rubber (AU, EU)	Gaskets, seals, solid tires, and foams
Butyl rubber (IIR)	Tire tubes, tube liners, enclosures, air bags, and curing bladders	Silicone rubber (Si)	Able to withstand a very wide range of service temperatures from $-45$ to $200^{\circ}\text{C}$ . Various grades are available covering a very wide range of applications such as baby teats, catheters, medical applications, wire and cables, electronic components, etc.
Butadiene rubber (BR)	Tires, sports goods	Chlorosulfonated polyethylene rubber (CSM)	Electrical insulator in cable and wire industry, tank lining, colored-stable weather-resistance products, oil resistant hoses and gaskets
Ethylene-propylene-diene rubber (EPDM)	Gaskets, seals, automotive components, IRG, and GRG	Polyacrylic rubber (ACM)	Seals and gaskets for high temperature applications, $180-200^{\circ}\text{C}$
Polychloroprene rubber (CR)	Hoses, rubber bearings, expansion joints, belts, and conveyors	Fluorocarbon rubber (FPM)	Products which are resistant to chemicals, oils and solvents. Able to withstand high service temperatures exceeding $250^{\circ}\text{C}$ . Outstanding oxidation and ozone resistance. Flame resistant. Hoses, gaskets and seals for aircraft, jets, and rockets
Nitrile rubber (NBR)	Oil-resistant hoses, seals, O-rings, gaskets	Epichlorohydrin rubber (ECO)	Automotive industry – gasket, seals, hoses to withstand service temperatures above $130^{\circ}\text{C}$

**Table 2** Heat aging temperature for establishing Type<sup>4</sup>

	<i>Type</i>									
	A	B	C	D	E	F	G	H	J	K
Test temperature ( $^{\circ}\text{C}$ )	70	100	125	150	175	200	225	250	275	300

**Table 3** Limits of volume swelling for establishing Class<sup>4</sup>

	<i>Class</i>										
	A	B	C	D	E	F	G	H	J	K	L
Vol. swell max. (%)	No rqmt.	140	120	100	80	60	40	30	20	10	5

**Table 4** Limiting brittleness temperatures for establishing Group<sup>4</sup>

	Group						
	A	B	C	D	E	F	G
Limiting brittleness temperature (°C)	0	−10	−25	−40	−55	−75	−85

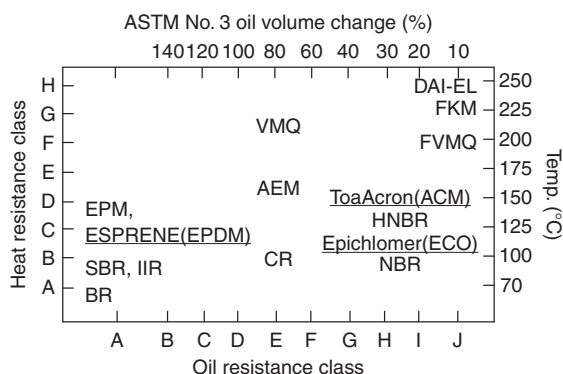


**Figure 2** A chart showing type and class of elastomers. Adapted from Hashimoto, K.; Maeda, A.; Hosoya, K.; Todani, Y. *Rubb. Chem. Technol.* **1998**, 70(3), 449–519, with permission from American Chemical Society.

FVMQ is more resistant to swelling towards the solvent than VMQ grade, as the fluorine atom is highly polar. **Figure 3** shows the general chemical structure of silicone rubber with different substituent groups.

The main backbone chain is made of repeating  $-\text{Si}-\text{O}-$  groups while the methyl groups are attached at the side. Both  $\text{Si}-\text{O}$  and  $\text{Si}-\text{CH}_3$  bonds are thermally stable. This explains why VMQ and FVMQ grades have the same Type of heat resistance, as the main chain backbone is the same for both. The  $\text{Si}-\text{O}$  bond is partially ionic and it is relatively easy to be broken by concentrated acids and alkalis even at room temperature. Another important feature of the chemical structure of silicone rubber is the relatively large bond angle of  $\text{Si}-\text{O}$  (about  $140^\circ$ – $160^\circ$ ).<sup>7</sup> The intermolecular forces between silicone chains are very low probably because of the large distance between the adjacent chains, as silicone atoms are relatively large. Thus this facilitates ease of chain rotation which accounts for the lowest glass-transition temperature  $T_g$  ( $\sim -120^\circ\text{C}$ ) among the commercially available elastomers. The dimethyl rubbers swell more in aliphatic and aromatic hydrocarbons than in acetone and diesters. However, the swelling resistance towards hydrocarbon oil can be enhanced by the replacement of one methyl group on each silicon atom by a more polar group such as trifluoropropyl group ( $-\text{CH}_2\text{CH}_2\text{CF}_3$ ), that is, the FVMQ grade.

### 3.33.3 General Properties of Elastomers

All elastomers have some common properties such as being flexible, tough, relatively impermeable to both water and air, and elastic when vulcanized. One of the unique features of a vulcanized elastomer is its ability to exhibit high elasticity: the elastomer can be stretched to a few hundred percent and recover its original shape and dimensions almost instantaneously when the deforming force is released. For a material to exhibit high elasticity, it must fulfill the following conditions:

- flexible long chain molecules with relatively low molecular interaction forces,
- the long chain molecules must be cross linked (at least 2% cross linked network),
- rubbery above  $T_g$

The elasticity of an ordinary solid such as metal is associated with its internal energy. In contrast, the elasticity of rubber is entropy driven.

Elastomers are also well known for their good resistance to acids, alkali and chemical solutions. Elastomers have a proven record of accomplishment as the material used for tank lining or related chemical vessels. Beyond these common characteristics, each rubber has its own unique properties depending on the chemical structure as discussed briefly below.

#### 3.33.3.1 Structure–Property Relationship

The effects of chemical structure on some important physical and technological properties are summarized in **Table 5**.

##### 3.33.3.1.1 Mechanical strength

Tensile strength, tear strength, crack-growth resistance and fatigue life of the vulcanized elastomer depend on the chemical structure and its geometrical configurations. Elastomers having regular microstructure are able to crystallize, and those that have irregular microstructure are amorphous. **Figure 4** shows the chemical structure of general-purpose elastomers such

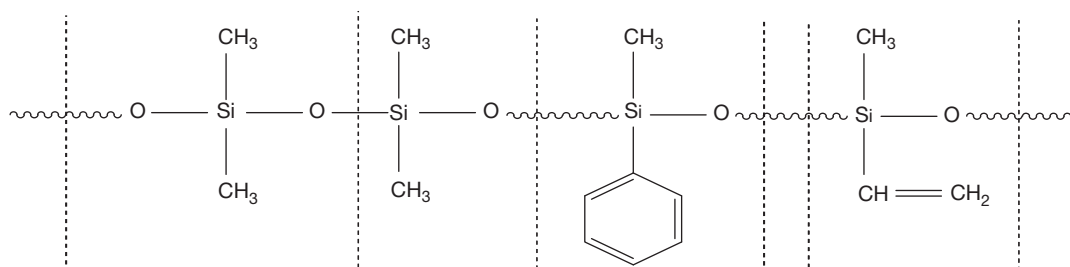


**Figure 3** Chemical structure of silicone rubber: MQ grade consists of methyl, PMQ grade consists of benzene rings and VMQ grade consists of vinyl.

**Table 5** Influence of chemical structure on physical and technological properties of elastomers

Basic structure	Technological significance
1. Nature of carbon-carbon backbone chain (i) Double bonds (ii) Single bonds	Unsaturated elastomers (having double bonds) are capable of being vulcanized with sulfur. Saturated elastomers (having single bonds) cannot be vulcanized with sulfur, but with peroxide. Unsaturated elastomers have poorer ozone cracking resistance and poorer oxidative resistance than saturated elastomers
2. Geometrical configurations	Regular microstructure would favor crystallization. Irregular microstructure leads to amorphous elastomers. The degree of crystallization affects mechanical strength
3. Polarity	Affects the degree of swelling resistance, rubber to metal bond strength, $T_g$ and electrical resistivity
4. Chain flexibility and glass transition temperature, $T_g$	Affects hysteresis and damping, and other related properties such as resilience, heat build-up, mechanical strengths, etc.
5. Molecular weight distribution	Broad molecular weight distribution provides easier processing than narrow molecular weight distribution

as natural rubber (NR), styrene butadiene rubber (SBR) and polychloroprene rubber (CR).

Natural rubber is 100% *cis*-1,4-polyisoprene indicating that it has regular microstructure, thus enabling it to crystallize. NR will crystallize at low temperatures. Crystallization has its own kinetic; in the case of NR the maximum rate of crystallization occurs at  $-26^\circ\text{C}$ .<sup>2,6</sup> When the rubber crystallizes, it hardens progressively and eventually loses its flexibility and rubber-like elasticity. The maximum amount of crystalline region is about 33% in the case of NR. However, if a tensile strain (more than 200%) is applied to NR it crystallizes almost instantaneously even at high temperatures. This phenomenon is known as strain-induced crystallization. Since crystallization is a reversible process, the crystals are completely melted once the applied strain is removed.

Low temperature crystallization brings few disadvantages to NR, particularly when it involves mixing. When NR crystallizes, it becomes very stiff and may cause damage to the mills. To overcome this problem, the common practice is to place the crystallized NR in a hot room (oven) to melt the crystals so that the rubber regains its flexibility. Any unmelted crystals

present during the mixing process would interfere with the incorporation and dispersion of the compounding ingredients. In contrast, strain-induced crystallization offers a big advantage in that it helps to enhance the mechanical strength of the rubber. For example, an unfilled or gum NR vulcanizate gives higher tensile strength (23–27 MPa) than unfilled SBR gum vulcanizate (2–3 MPa). Unfilled (gum) vulcanizate refers to a vulcanized rubber containing no filler apart from the compounding ingredients necessary for vulcanization. The crystals that are formed during straining act like a reinforcing filler to enhance the tensile strength. Thus for a noncrystallizing elastomer, it is necessary to incorporate a reinforcing filler into the rubber to enhance its strength.

In addition to the reinforcing filler, the types of chemical crosslink such as polysulfidic (C–S<sub>x</sub>–C), monosulfidic (C–S–C), or carbon-carbon (C–C) also affect the strength of the vulcanized elastomer.<sup>8</sup> Polysulfidic crosslinks are weak and labile with lower bond energy than monosulfidic and carbon-carbon links. Polysulfidic crosslinks enhance mechanical strengths such as tensile and tear strengths because these weak and labile crosslinks relieve stresses by ‘yielding.’<sup>8</sup>

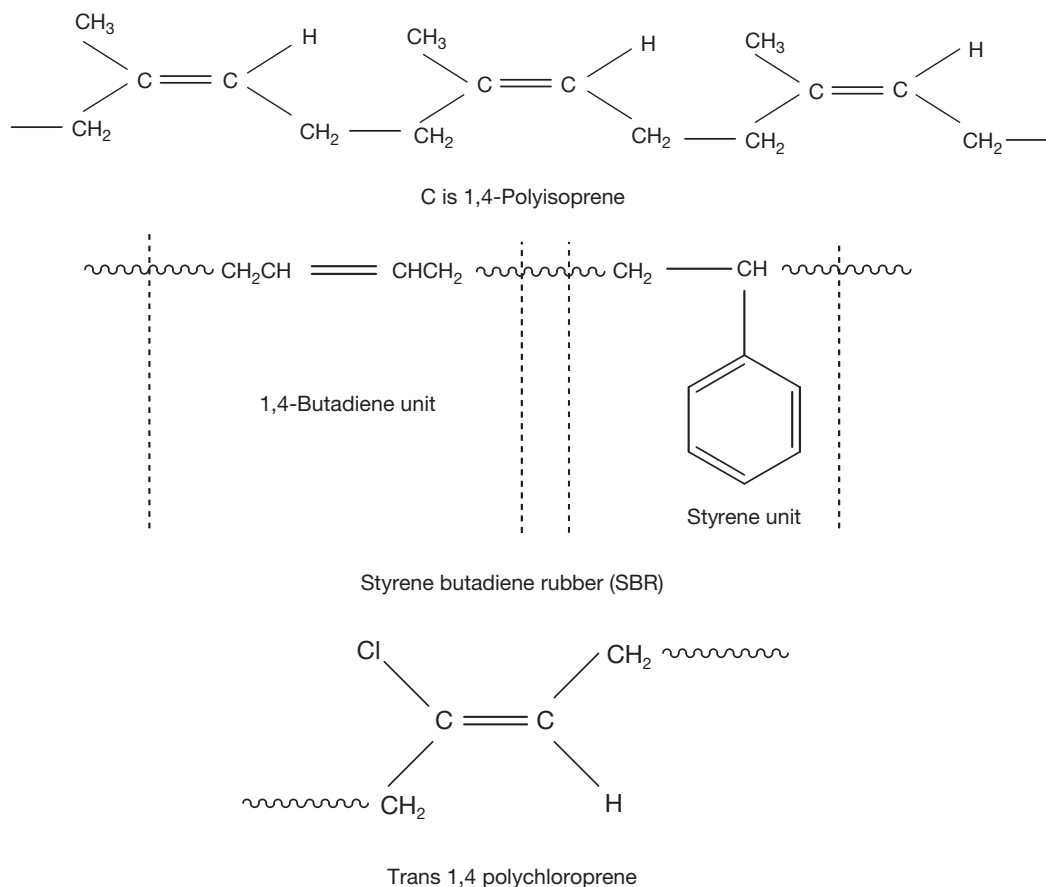


**Figure 4** Chemical structure of general-purpose elastomers.

Besides NR, polychloroprene rubber (CR) can also crystallize. Indeed CR crystallizes more readily than NR does because trans 1,4 configuration allows better molecular packing than cis 1,4 configuration.

### 3.33.3.1.2 Oxidation and ozone resistance

All unsaturated elastomers are susceptible to attack by oxygen and ozone which ultimately leads to chain scission followed by progressive loss in the physical properties. This aspect of oxidation will be discussed further in a later section. Almost all specialty elastomers have saturated bonds on the main backbone as well as high bond dissociation energy. Thus, specialty elastomers are highly resistance to heat, oxidation and ozone cracking.

### 3.33.3.1.3 Swelling resistance

The swelling resistance of rubber towards hydrocarbon oil depends on the extent of the polarity of the elastomer. The more the polar groups attached to the rubber molecules the higher is the polarity, and

the better is the swelling resistance towards hydrocarbon oil. The solubility parameter of elastomers and liquids determines the extent of compatibility and swelling resistance. The closer the solubility parameters between the elastomer and the liquid, the better is their compatibility. Indeed, the greater the thermodynamic compatibility between liquid and elastomer, the greater the absorption of liquid occurring when both have similar solubility parameters. The solubility parameter  $\delta$  is related to a parameter to measure the specific interaction between molecules known as cohesive energy density (CED) by the following mathematical relationship.

$$\delta = (\text{CED})^{1/2} \quad [1]$$

$$\text{CED} = (\Delta H - RT)/(M/\rho) \quad [2]$$

where  $\Delta H$  is the latent heat of vaporization,  $T$  is the absolute temperature,  $M$  is the molecular weight of the polymer,  $\rho$  is the density of the polymer, and  $R$  is the molar gas constant. For example, natural rubber has a solubility parameter value of 16.7 and NBR has

a solubility parameter between 21.0 and 22.0 MPa<sup>1/2</sup>. Most of the petroleum oils have a solubility parameter of 16.3 MPa<sup>1/2</sup>. Thus NR will swell markedly in petroleum oil because their solubility parameters are similar. In contrast, NBR has a solubility parameter very much higher than that of petroleum oil, so the two are not compatible. For this reason, polar NBR shows higher swelling resistance than nonpolar NR towards petroleum oil. Elastomers with higher polarity such as polyurethane rubber (AU) show even higher swelling resistance to nonpolar solvents than nonpolar elastomers. Based on the solubility parameter, polar rubbers swell more in polar solvents. Nonpolar rubbers are resistant to swelling in polar solvents.

#### 3.33.3.1.4 Glass-transition temperature $T_g$

The glass-transition temperature ( $T_g$ ) is the temperature at which molecular mobility begins to take place, below which molecular mobility is frozen and the elastomer becomes rigid and glassy. The  $T_g$  of the elastomer depends on the chemical structure of the elastomer. The presence of a polar atom, side groups, length of side chains, and crosslink reduces molecular mobility which would increase  $T_g$  of the elastomer. The glass-transition temperature affects a number of important technological properties such as strength, damping, low temperature flexibility, rolling resistance, wet grip, etc. High  $T_g$  elastomers are preferred to low  $T_g$  elastomers for applications where high mechanical strength, high damping, and excellent wet traction are required. For applications where excellent low temperature flexibility, low heat

generation, high resilience and low rolling resistance are required, low  $T_g$  elastomers are preferred to high  $T_g$  elastomers.

**Table 6** summarizes the respective  $T_g$ , ozone cracking resistance, chemical resistance and heat aging resistance of some of the important commercial elastomers.

### 3.33.4 Rubber Technology and Compounding

#### 3.33.4.1 Mastication and Mixing

Rubbers find very limited applications in their raw form. In their raw form, rubbers may be suitably used as binders and adhesives because of their inherent tack. To become useful products, they have to undergo various processes from mastication, mixing, shaping or fabrication prior to molding, as shown by the schematic flow chart in **Figure 5**.

#### 3.33.4.2 Rubber Compounding

Rubber compounding is the term used to denote the art and science of selecting and combining elastomers and additives to obtain an intimate mixture that will develop the necessary physical and chemical properties for a finished product. In compounding, one must cope with literally hundreds of variables in materials and equipment. There are three main areas of concern in rubber compounding, namely, (i) to secure certain properties in the finished product to

**Table 6** Some important technological properties of some important commercial elastomers

Elastomer	$T_g$ (°C)	O <sub>3</sub> resistance	Swelling resistance (%) <sup>a</sup>	Heat resistant up to (°C) <sup>b</sup>
NR	-72	L	200 (120 °C)	100
SBR	-63	L	130 (120 °C)	100
BR	-112	L	>140 (70 °C)	100
EPDM	-55	H	>140 (70 °C)	150
IIR	-66	M	120 (120 °C)	150
CIIR	-66	M	>140 (150 °C)	150
ACM	-22 to -40	H	25 (150 °C)	175
CO	-26	H	5 (150 °C)	150
CR	-45	M	65 (120 °C)	125
NBR (med ACN)	-34	L	10 (100 °C)	125
MVQ	-120	VH	50 (150 °C)	225
CSM	-25	H	50 (150 °C)	150
H-NBR	-30	H	15 (150 °C)	150
FKM	-18 to -50	VH	2 (150 °C)	250
EU	-55	H	40 (100 °C)	100

<sup>a</sup>Swelling after 70 h in ASTM oil 3.<sup>5,9</sup>

<sup>b</sup>Classification after ISO/TR 8461, aerobic condition, Method ISO 4632/1 3 days, (Retention properties).<sup>9</sup>

L = low resistance M = medium resistance H = high resistance.<sup>5,9</sup>

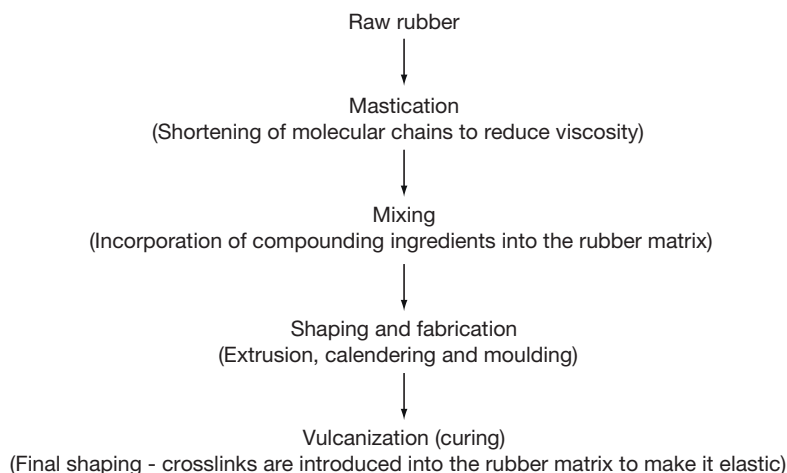


**Figure 5** Schematic flow process chart.

satisfy service performance; (ii) to be able to meet processing characteristics for efficient utilization of available equipment, and (iii) to meet conditions (i) and (ii) at the lowest possible cost. In other words, the most important criteria in compounding are to secure an acceptable balance among demands arising from the three concerned areas.

Theoretically, a rubber compound may consist of an elastomer and a cross linking agent. However, in practice, a rubber compound may contain 5 ingredients or even more than 10 ingredients, depending on the intended products, types of application and their service conditions. Each ingredient has a specific role and function(s). Each has an impact on properties, processability, and price. The real challenge is to develop a high quality rubber product at the lowest cost possible. The materials utilized by the rubber compounder can be classified into nine major categories, which are defined as follows:

- **Elastomers:** The basic component of all rubber compounds may be in the form of rubber alone, or master batches of rubber–oil, rubber–carbon black, or rubber–oil–carbon black.
- **Vulcanization agents:** These materials are necessary for vulcanization processes where chemical crosslinks are introduced into the rubber matrix to form a three-dimensional network. Crosslinks inhibit permanent flow under deformation or heat and prevent dissolution in solvents. Strength, stiffness and resilience increase upon cross linking, and set, stress-relaxation and creep decrease.
- **Accelerators:** In combination with vulcanizing agents, these materials reduce the vulcanization time (cure time) by increasing the rate of vulcanization. In most

cases, the physical properties of the products are also improved.

- **Activators:** These ingredients form chemical complexes with accelerators, and thus aid in obtaining the maximum benefit from an acceleration system by increasing vulcanization rates and improving the final properties of the products.
- **Age-resistors:** Antioxidants, antiozonants, and other materials are used to slow down ageing processes in the vulcanizates.
- **Fillers:** These materials are used to reinforce or modify physical properties, impart certain processing properties, and reduce cost.
- **Processing additives:** Formerly known as processing aids, the new term currently used is processing additives. These are materials used to modify rubber during the mixing or processing steps, or to aid in a specific manner during extrusion, calendering, or molding operations.
- **Softeners:** They are materials that can be added to rubber either to aid mixing, produce tack, or extend a portion of the rubber hydrocarbon (e.g., oil extended).
- **Miscellaneous ingredients:** These materials can be used for specific purposes but are not normally required in the majority of rubber compounds. They include retarders, colors, blowing agents, abrasives, dusting agents, odorants, etc.

### 3.33.4.3 Vulcanization

Vulcanization is a process of cross-linking rubber molecules chemically with organic/inorganic substance through the action of heat and pressure. The



rubber which is cross linked chemically is known as vulcanizate. The introduction of crosslinks into the rubber matrix may be comparatively few in number but are sufficient to prevent unrestricted flow of the whole molecules past neighboring ones. The low concentration of crosslinks implies that the vast majority of the segments making up the long chain molecules are free to move by virtue of kinetic energy. An unvulcanized rubber dissolves completely in its solvent. In contrast, a vulcanized rubber only swells. The chemical crosslinks prevent complete dissolution. A vulcanized rubber in this sense is a solid and will retain its shape and dimensions.

Vulcanization is a very important process in the rubber industry and conducted at relatively high temperatures (140–200 °C). For latex dipped goods, vulcanization is conducted at relatively low temperatures (60–120 °C) and requires no pressure as the latex is in fluid form and flows to take the final shape of the former and mold.

One of the most important chemicals in vulcanization is the cross linking agent. Elemental sulfur is the most widely used cross linking agent in the rubber industry because it is very cheap, abundant and easily available. Besides, sulfur is very easy to mix and readily soluble in the rubber. By varying the amount of sulfur to the accelerator ratio one can get different types of crosslink in the rubber matrix. Table 7 summarizes the types of sulfur vulcanization system,<sup>10</sup> nature of crosslinks produced and their influence on technological properties. Thus sulfur vulcanization provides flexibility as one can control the type of crosslink intended for specific use or applications. The most basic requirement for sulfur vulcanization is the availability of double bonds on the rubber hydrocarbon. The nonsulfur cross-linking agents include organic peroxides, quinines and their oximes and imines, metallic oxides and high energy radiation. The detailed mechanisms of vulcanization with these vulcanizing agents are discussed by Elliot and Tidd.<sup>10</sup>

There is another type of sulfur vulcanization system known as soluble efficient vulcanization (EV)<sup>10</sup> intended for engineering products that require consistent stiffness, low creep, low stress-relaxation and low set. This vulcanization system employs certain soluble accelerators, activators, and sulfur that completely dissolve in rubber giving a truly homogeneous compound.<sup>10</sup> In practice, this is achieved by selecting accelerators and activators that have a fairly high solubility in rubber at room temperature. Suitable accelerators for soluble EV include diphenyl guanidine, tetrabutylthiuram disulphide and *N*-oxydiethylenebenzothiazole-2-sulphenamide. Zinc oxide is insoluble in rubber, but it has to be included in the system as it plays a major role in sulfur vulcanization. However, 2-ethyl hexanoic replaces the common coactivator stearic acid as the latter reacts with zinc to form an insoluble zinc stearate which induces creep and the former forms a rubber-soluble zinc salt. The sulfur dosage employed in soluble EV must not exceed 0.8 pphr (parts per hundred of rubber) to ensure that it remains dissolved in the rubber and with no tendency to bloom to the rubber surface.

Nonsulfur vulcanization such as the peroxide vulcanization system produces carbon-carbon type of crosslink that gives excellent heat aging resistance and very low compression set. However, the mechanical strengths are lower than polysulfidic and monosulfidic crosslinks. The choice of vulcanization system depends on the service environment as well as the mode of deformation for the intended rubber product.

### 3.33.5 Rubber-to-Metal Bonding – Engineering and Automotive Applications

Most of the rubber springs involve bonding of rubber to metal. In many cases the metal parts are required for fixing purposes, particularly those of automotive components such as rubber bushes, engine mounts

**Table 7** Sulfur vulcanization systems, types of crosslink produced and their effect on technological properties

<i>Vulcanization system</i>	<i>Sulfur</i>	<i>Accelerator</i>	<i>Type of crosslink</i>	<i>Technological properties</i>
Conventional	2.0–3.5	1.0–0.4	Polysulfidic	Increase tensile and tear strengths, high compression set, and poor heat aging
Efficient (EV)	0.3–0.8	6.0–2.5	Monosulfidic	Excellent heat aging, low compression set, low tensile, and tear strengths
Semi-EV	1.0–1.7	2.5–1.0	Mixtures of poly, di- and mono	Compromise or balance in terms of strength and heat aging

and couplings. **Figure 6** shows some typical rubber-to-metal bonded products. In tank lining, the main function of rubber is to protect the metal against attack by corrosive chemicals as well as to protect the metal parts from oxidation by air and moisture, which leads to rusting.

The laminated rubber bearing consists of alternate layers of metal plates. The metal plates serve to restrain the lateral expansion of the rubber on compression. Because of restriction at the rubber metal interface, due to friction or when the rubber is bonded to metal, the rubber bulges at the end plates to maintain a constant volume. As a result, the effective compression modulus is dependent on the shape factor,  $S$ , defined as the ratio of loaded area to force free area.<sup>2</sup>

$$S = \text{Loaded area/Force free area} \quad [3]$$

For a rectangular rubber block of length  $L$ , width  $W$  and thickness  $h$ , shape factor  $S$  is given by eqn [4]:

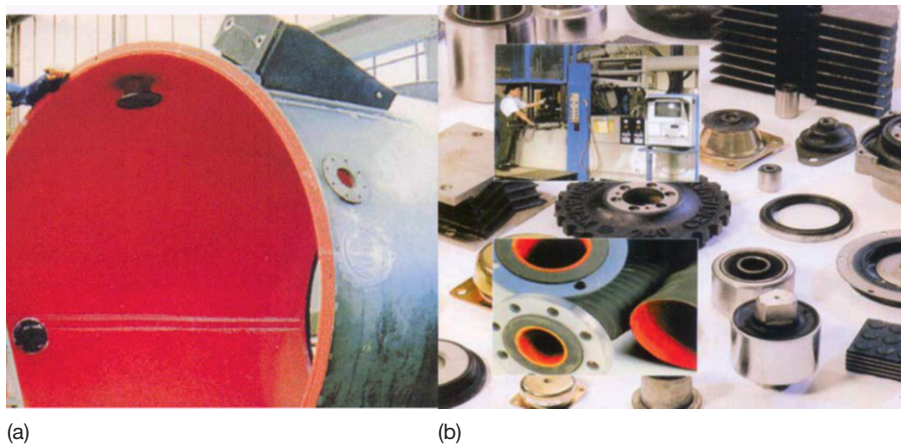
$$S = LW/[2b(L + W)] \quad [4]$$

The dependence of the compression modulus on the shape factor has a significant advantage where the vertical stiffness increases substantially, by inserting horizontal metal spacer plates into the rubber. For a rectangular rubber block having length  $L$ , width  $W$  and height  $h$ , the shear stiffness and compression stiffness are given by eqns [5] and [6] respectively.

$$k_s = GA/b \quad [5]$$

$$k_c = 3G(1 + 2S^2)A/b \quad [6]$$

Here,  $G$  is the shear modulus of the vulcanizate and  $A$  is the cross-sectional area of the rubber surface subjected to shear or compression. Equation [6] shows



Rubber bearing



**Figure 6** Rubber-to-metal bonding products – (a) tank lining (LHS), (b) various automotive rubber products (RHS) and (c) below rubber bridge bearing.

that the compression stiffness can be increased substantially by increasing the shape factor. The shape factor does not affect shear stiffness. For these reasons, laminated steel rubber bearings are used in bridges, where high compression stiffness is necessary to support all dead and live loads of the deck, and very low shear stiffness to accommodate movements associated with thermal expansion and contraction due to temperature changes.

To achieve efficient bonding at the rubber–metal interface, it is necessary that the rubber is chemically bonded to the metal surface. This is achieved in practice by following proper procedures laid down in the following section.

### **3.33.5.1 Bonding of Rubber to Metal**

#### **3.33.5.1.1 Preparation of metal plates**

The metal plates must be clean and free from any contamination such as oil, grease, protective coating, and rust. Exposing the contaminated metal surface to the vapor of a suitable organic solvent (e.g., chlorinated solvent) removes oil and grease. The next step is to remove metal oxides and rust on the metal surface, usually by the sandblasting technique or wire brushing. Apart from cleaning, sandblasting increases the surface area, which is very beneficial for strengthening the bonded area. Acid etching provides an alternative means of removing metal oxides from the metal surface.

It is very vital that the metal surface is completely free from oil, grease and rust to ensure efficient wetting of the bonding agent on the metal surface so that during vulcanization the bond formed between rubber and metal via the bonding agent is very strong. However, a few precautions need to be observed when sandblasting on the metal surface. The grit size, gun pressure and shooting distance must be correct to get the right surface topology, thus avoiding excessive wear or too little wear.

#### **3.33.5.1.2 Types of bonding agent and methods of applications of bonding agent to metal plates**

The common bonding agents for bonding rubbers to metals include ebonite solution or sheet, brass and proprietary adhesives. In the past, the bonding agent as well as the lining material for making tank lining was ebonite solution and calendered ebonite sheet. The ebonite compound contains a high amount of sulfur, about 25–35 pphr. This high sulfur content makes ebonite a hard and brittle material. Indeed ebonite is a thermoset as it is highly cross linked.

The high sulfur content of ebonite introduces high polarity that makes it a very suitable bonding agent. Despite the superior chemical resistance of ebonite, there are a few limitations such as its brittleness after cure, long cure time and potential of fire hazard due to exothermic reaction during curing, especially when a thicker lining is involved. For this reason, soft rubber linings are preferred to ebonite linings.

Brass is a very good bonding agent, and is widely used in the tire industry. Brass is coated on steel wire cords by the electroplating process. Brass-coated steel wire cords are used as breakers or belts placed underneath the tread and on top of the carcass of the green tire. During vulcanization, the sulfur forms covalent bonds with both the rubber and the component metals of the brass, leading to a very strong bond.<sup>11</sup>

In most rubber-to-metal bonded products, a proprietary bonding agent is preferred to the other two bonding agents. A proprietary bonding agent usually requires two coatings, *viz.* a primer and an adhesive cement. There are reasons why a two-coat system offers more insurance for the rubber to metal bond. The first coating known as a primer helps to eliminate corrosion in corrosion-prone metals when they are in contact with the rubber.<sup>12</sup> By using a primer, secondary cement (second coating–adhesive) that has a greater degree of bondability to the stock being used can be selected, rather than a one-coat system.<sup>12</sup> It is claimed that the two-coat system allows more metal adhesion into the primer, and more stock adhesion into the cement coat.<sup>12</sup> This results in a higher intrinsic bond with the two-coat system than a single coat system.

Bonding agents are applied by painting, spraying or dipping on treated metal parts in the form of a solution or aqueous suspension.

#### **3.33.5.1.3 Molding of rubber-to-metal bonded parts**

Finally, the dried, coated metal parts are loaded into the mold and the rubber is vulcanized in contact with these substrates by the conventional rubber molding techniques such as compression, transfer and injection molding. It is during this vulcanization process that the rubber is chemically bonded to the metal surface when the cross linking agents react with the adhesive.

However, in the case of tank lining, the method is different from the conventional rubber-to-metal bonded products. The method of applying calendered rubber sheeting onto the prepared metal surfaces is

analogous to that of applying rolls of wallpaper to the walls of a room. However, care must be taken to avoid entrapment of air between rubber and metal. The rubber sheet is laid down at the correct angle, and is rolled down into close contact with the adhesive. Applying the rubber sheet at the corner or edges of the tank is quite tricky. In practice, this is achieved by making joints at corners by inserting and rolling down an extruded rubber fillet of triangular cross-section and forming the sheet joints on top of the fillet. This technique gives to the lining a well finished appearance and reduces the danger of weak joints occurring in corners.

Upon completion of laying the rubber sheet onto the metal surface, the covered lining tank is usually allowed to rest for at least 24 h before being vulcanized. This resting period allows any air trapped between rubber and metal to diffuse, apart from enabling the adhered rubber sheet to recover and settle down before it is heated.

### 3.33.5.2 Vulcanization

It is usually done in an open steam autoclave for tanks or vessels that are small enough to go into the autoclave. When the lined vessel is too large to be accommodated in an autoclave it may be vulcanized in one of the following methods:

#### 3.33.5.2.1 Low or high pressure steam

This method is applicable to a vessel that has sufficient strength to withstand internally applied pressure. This procedure can be adopted if the vessel such as road or rail tank cars can be lined and then sealed and bolted to give a strong and steam proof pressure container. The steam pressure is passed through the lined vessel to the desired vulcanization temperature until the rubber is fully vulcanized. There are some elements of danger when dealing with high pressure steam. So it is very important that all the safety regulations are met in terms of design and material of the vessel. The work should be done under skilled engineering supervision.

#### 3.33.5.2.2 Water curing technique

This method is suitable for tanks or vessels that are too weak structurally to be put under steam pressure. Here, the lined tank is filled with water or brine. The water is heated by passing live steam into the water until it approaches boiling point. This temperature is maintained for a few hours until the rubber is fully vulcanized. Care must be taken to ensure that live steam does not impinge on the rubber lining to

avoid the occurrence of a large blister between the rubber and metal at the point of impingement. It is necessary to conserve heat by shielding the unit against draughts and cold to minimize temperature variations which would affect the uniformity of the cure.

#### 3.33.5.2.3 Hot air or ambient temperature vulcanization

This method is suitable for tanks or vessels which do not work with the methods discussed above. The choice of accelerator is very important. Ultrafast or very fast accelerator is usually used in the rubber compound. Care has to be taken to ensure that the rubber does not vulcanize prematurely (scorched) before it is applied onto the treated metal surface. One of the means to overcome the problem is to avoid mixing the accelerator and sulfur together, but to prepare sulfur masterbatch and accelerator masterbatch separately. The two masterbatches are blended together just prior to calendering, and the calendered sheet applied as soon as possible to the metal to avoid the risk of being scorched.

### 3.33.5.3 Types of Bond Failure and Possible Remedies

A rubber shear mount may be expected to deform up to 300% shear strain, and the mean shear stress acting on the rubber-to-metal bond can be as high as 10 MPa or 2/3 tons per square inch.<sup>11</sup> Steel laminated rubber bearings for bridges must have a minimum bond strength of about 9 N mm<sup>-1</sup> (MS 671, 1991).

It is important to observe the failure mode that occurs in rubber-to-metal bonded products because it throws some light and clues to the root cause of the problem. It is usual to conduct peel test to determine the interfacial bond strength between the rubber and metal. There are two basic types of bond failure either adhesive or cohesive. Adhesive failure may occur at the interfacial between the rubber and substrate, or between cement and substrate. Cohesive failure occurs within the rubber itself. There are three modes of adhesive failure.<sup>13</sup> First is called CM failure that takes place between primer and metal interface. Second is CP failure that occurs at the primer to cover cement interfacial. Third is RC failure where the bond fails at the rubber–cover cement interface. RC failures are the most common and the most difficult to solve.<sup>13</sup> There are a number of causes, which bring about these bond failures. They include the following: metal surface not cleaned efficiently due to poor cleaning procedure,



contamination of metal surface during handling, incomplete wetting of adhesive on the metal surface, variations of temperature of metal surface, precured adhesive, sweeping of adhesive during molding etc.<sup>13</sup> There are remedies to overcome these problems. First, ensure that the metal surface is free from all forms of contamination. Second, avoid contamination of metal surface during handling. Third, apply the primer and adhesive cement onto the metal surface evenly by taking care of the correct viscosity of the adhesive, and correct spraying distance and thickness of the adhesive film. Fourth, use the correct type of adhesive and follow strictly the instruction and procedure recommended by the chemical supplier.

If during the peel test, cohesive failure occurs within the bulk of the rubber, then this indicates that the interfacial bond strength between the rubber and metal plate via the bonding agent is stronger than the cohesive strength of the rubber itself.

### 3.33.6 Oxidation of Rubber

Metals oxidize in the presence of air and water and consequently they corrode, become rusty and weak. **Figure 7** shows the old version of using steel rollers to accommodate movements of the bridge deck brought about by expansion and contraction due to temperature changes.<sup>14</sup> The steel rollers corroded and suffered high wear and tear. In contrast, laminated steel rubber bearing did not show any sign of wear out after nearly twenty years of installation.<sup>14</sup> However, this does not mean that elastomeric bearing will last forever. Like metals, rubbers are also prone to corrosion. Corrosion of rubbers is associated with the aging process known as degradation. All unsaturated rubbers are subject to degradation due to the attack of heat, ultraviolet (UV) light, oxygen,

ozone etc. The more is the amount of unsaturation the more it is susceptible to degradation. The term aging as applied to rubber, covers a variety of phenomenon arising out of the factors described above. Aging properties of raw rubber differ from vulcanized rubber because of the latter's specific network structure and extra network material. When natural rubber is heat-aged in the presence of oxygen or air, it invariably loses strength, in particular its tensile strength decreases. The pattern of modulus change during aging is not so straight forward because there are two opposing reactions which can occur simultaneously. One is degradation of the molecular chains and crosslinks which causes softening; the other is additional cross linking which causes stiffening. Under any given set of aging conditions (time and temperature) either softening or stiffening reactions may predominate depending on the type of vulcanization system, type of filler and antidegradants employed in the rubber compound.

Oxygen reacts with rubber only after the rubber has been acted upon by energy. This is usually from UV light, heat or mechanical energy (flexing). This energy dislodges a hydrogen atom from the rubber molecule, resulting in the formation of a radical. The oxidation of polymer with elemental oxygen is called autoxidation because it is an autocatalytic. The rate of autoxidation is affected by temperature, the presence of catalyst and also the presence of antioxidant. When the oxygen attacks the rubber it produces hydroperoxide. The hydroperoxides break to form free radicals. This is an autocatalytic, self generated free radical process. The autoxidation process involves three main stages, namely, initiation, propagation and termination. In view of the complexity of autoxidation reaction with rubber, Bolland and Gee<sup>15,16</sup> used model olefins to study the kinetics of autoxidation. **Figure 8** shows the mechanism of autoxidation as proposed by Bolland.<sup>15,16</sup>

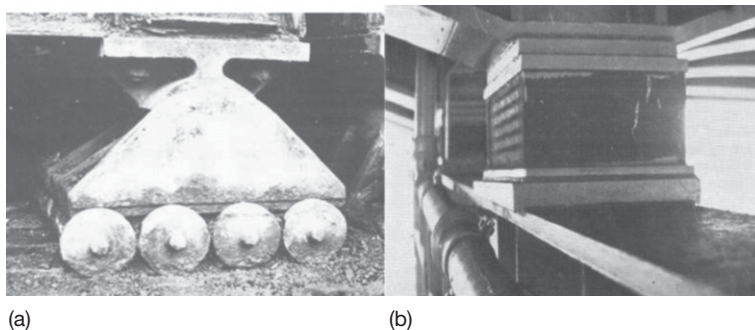


**Figure 7** (a) Steel roller bridge bearing and (b) steel laminated rubber bearing installed in 1955. Adapted from Mullins, L. *Proc. Rubb. in Eng. Conf.* Kuala Lumpur, 1974, pp. 1–20, with permission from the Malaysian Rubber Board.

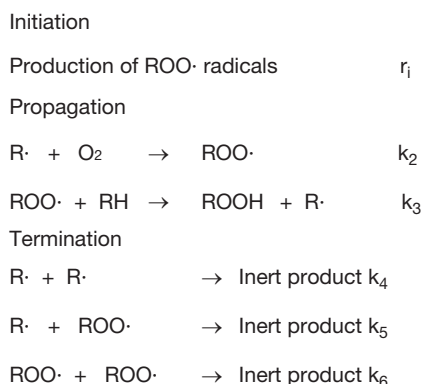


**Figure 8** Mechanism of autoxidation of natural rubber as outlined by Bolland. Adapted from Barnard, D.; Lewis, P. M. In *Natural Rubber Science and Technology*; Robert, A. D., Ed. Oxford University Press, 1988; Chapter 13, pp 621–673, with permission from . . .

The autoxidation is initiated with the generation of free radicals due to the relatively facile homolysis of traces of peroxide present in the elastomer.<sup>17</sup> The rate of oxidation is related to the concentration of the hydroperoxide [ROOH] as shown by eqn [I] below<sup>16</sup>.

$$r_i = k_i[\text{ROOH}]^2 \quad [\text{I}]$$

The resultant free radicals react with oxygen to form the deleterious peroxides and propagate the autoxidation reaction. The rate of propagation is controlled by the hydroperoxide yields and those of decomposing. The hydroperoxide yields for a large number of olefins range from almost 100% downwards to values controlled by side reactions of the peroxy radicals, such as addition to olefinic double bonds, when hydrogen abstraction becomes relatively difficult.<sup>16</sup> Such side reactions would continue the propagation chain. However, when the value of the rate constant  $k_2$  becomes large, the reaction of alkenyl radicals with oxygen become independent of oxygen pressure. Under these conditions, rate-determining step is no longer controlled by the rate constant  $k_3$ , of the hydrogen abstraction step. Termination would occur primarily by the interaction of alkenyl radicals. Then the propagation rate is given by eqn [II] below<sup>16</sup>.

$$r = r_i^{1/2} k_2 k_4^{-1/2} [\text{O}_2] \quad [\text{II}]$$

Termination occurs solely by the mutual destruction of peroxy radicals and represented by the following rate equation<sup>16</sup>:

$$r = r_i^{1/2} k_3 k_6^{-1/2} [\text{RH}] \quad [\text{III}]$$

The outcome of this autoxidation is either chain-scission or cross-linking. If chain-scission occurs, the degraded rubber will be soft and tacky. On the other hand, if cross linking occurs the degraded rubber will be hard and brittle. In both cases, the mechanical strength of the rubber decreases markedly. Model olefins were used to study the mechanism of oxidation of NR due to complexity of the oxidation reaction in particular when the rubber is vulcanized.<sup>16</sup> The oxidation of rubber vulcanizate is technologically important since the absorption of only a small amount of oxygen (1%) by rubber vulcanizate results in a considerable change in the physical properties.

It is believed that the oxidation of natural rubber follows the same route and analogous to that of the model olefins where the polyisoprene chain undergoes scission.<sup>16</sup> An essential concept of this process is the number of molecules of oxygen absorbed per scission event. According to Bolland,<sup>15</sup> the oxidation reaction would finally lead to an alkoxy radical disproportionate to butan-2-one-4-al rather levulinaldehyde, and the vinylic radical would have to be oxidized further to the methyl ketone end group. Minute amount of certain heavy metals such as copper, iron and manganese catalyze autoxidation reactions. However, this catalytic action can be prevented by applying protective or chelating agent such as metal deactivator like *p*-phenylenediamines.

In the case of vulcanized rubber, the oxidation reaction is more complex than that of raw rubber since the various different types of crosslink (e.g., polysulfidic, disulfidic, monosulfidic, cyclic sulfides, conjugated dienes and treines, etc.) present in the network structure may affect oxidation in some way or another.<sup>16</sup> Most types of sulfur vulcanizates initially hardens on aging before degradation occurs. This hardening is due to cross linking associated with oxidative reactions of sulfur species in the network that takes place before chain scissions take place.<sup>16</sup>

Barnard and Lewis<sup>16</sup> listed out some useful and important points concerning chain scission mechanism for unprotected NR at modest temperature as follows:

- Scission occurs once approximately for every 20 molecules of oxygen absorbed.
- The scission is of the rubber chain even in peroxide or sulfur vulcanizates although concomitant crosslink can occur in the latter.
- Kinetically, scission appears to take place in the propagation step.



- Each scission event results in a stable terminal ketone group being formed on one of the new chains and a transient terminal aldehyde group on the other.

Since autoxidation results in chain scission, means and ways were introduced to determine accurately chain scissions caused by a known quantity of oxygen absorbed. A parameter known as scission efficiency  $\varepsilon$  defined as the number of molecules of oxygen absorbed which bring about one scission event<sup>16</sup> was introduced to monitor chain scission quantitatively. There are two methods either physical or chemical to monitor chain scission. The common physical methods involved measuring molecular weight reduction, stress-relaxation, sol-gel analysis, and stress-strain characteristics.<sup>16</sup> For example, in stress-relaxation method, a rubber sample of a uniform cross-section is held at a constant extension and maintained at a constant temperature. When a network is oxidized due to the cleavage of stress-supporting chains, then the stress would decay and this event would lead to occurrence of stress-relaxation. The change in moles of stress-supporting chains per gram can be calculated from eqn [7]<sup>16</sup>:

$$f_t/f_0 = N_t/N_0 \quad [7]$$

where the subscripts  $t$  and  $0$  refer to the samples after time  $t$  and time zero respectively, and  $f$  derived from the statistical theory of rubber elasticity<sup>18</sup> is given by eqn [8]:

$$f = \rho NRTA_0(\lambda - \lambda^{-2}) \quad [8]$$

where  $\rho$  is the density of rubber,  $N$  is the number of moles of stress-supporting chains per gram,  $R$  is the gas constant,  $T$  is the absolute temperature,  $A_0$  is the unstrained cross-sectional area, and  $\lambda$  is the extension ratio. Stress-relaxation method has the advantage of being able to monitor scission event continuously, and if the amount of oxygen absorbed is also known then the scission efficiency  $\varepsilon$  can be calculated.<sup>16</sup> However, on a short time scale, the decay in stress level as function of time at constant deformation and temperature is associated with the rearrangement of molecular chains and it is predominantly attributed to viscoelastic behavior of the rubber.

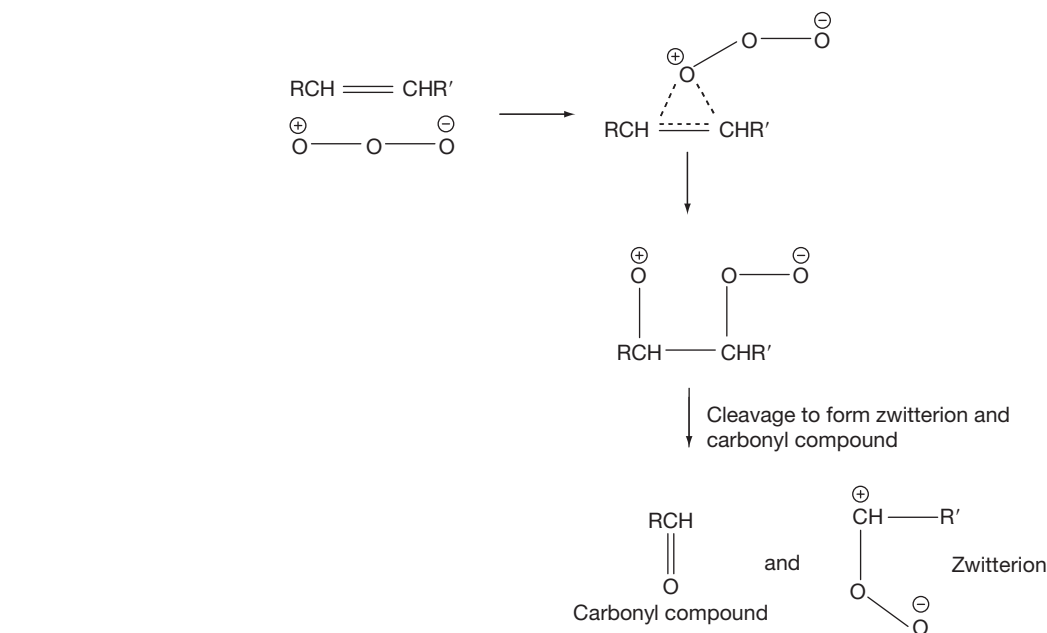
Almost all technical specifications of elastomeric products require passing an aging test. The use of aging tests is extremely important in assessing the service life of elastomeric products because properties of vulcanizate could change during service.

The basic principle of the test is to expose rubber test-pieces to air at an elevated temperature (70 or 100 °C) for a specified period (7 or 14 days or longer). This so-called accelerated aging test causes deterioration of rubber in air due to combined effects of oxidative and thermal aging. The tensile properties, set and hardness are measured on these samples before and after ageing. If minor changes in these properties result, long service life may be expected; if appreciable changes occur, service life may be short. However, it must be stressed here that accelerated ageing test is a useful quality control and specification tests. There are significant difficulties in predicting service life from accelerated aging test. Use of test temperatures much above the anticipated service temperature is not advisable because the correlation between the results of such tests and service performance becomes increasingly tenuous.

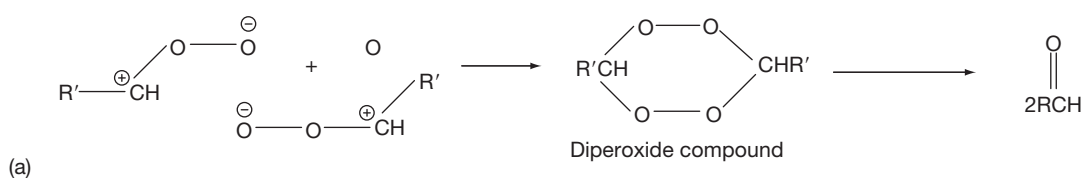
### 3.33.7 Ozone Cracking of Rubber

Apart from oxygen, all unsaturated elastomers are also susceptible to ozone attack although ozone concentration in the outdoor atmosphere at ground level is about 1 pphm (part per hundred million of air by volume).<sup>19,20,21</sup> However, this can be significant because the reaction of ozone with the double bond is extremely fast and causes cracking on strained rubber. The cracks appear slowly at right angle to the direction of the strain applied, that grow slowly and consequently lead to a break of the vulcanizate. Ozone being very reactive attacks the double bonds of the rubber and produces ozonide that cleaves to produce zwitterions.<sup>17</sup> The zwitterions are unstable and will breakdown to form other zwitterions. These zwitterions may react with other zwitterions to produce diperoxide compound, or react with carbonyl compound to produce ozonide. In both cases, the ultimate result is chain scission. The mechanism of ozone attack on olefin is as shown in Figure 9.<sup>17</sup>

However, there is a subtle difference between ozone cracking and auto-oxidation where the former requires a certain critical strain level ( $\sim 5\%$  for unprotected NR) for its occurrence.<sup>19,20,21</sup> The severity of ozone cracking increases rapidly with strain level. Braden and Gent,<sup>19</sup> and subsequently Lake *et al.*<sup>20,21</sup> investigated various factors affecting ozone cracking. For example, Lake and Thomas<sup>20</sup> came out with a boundary layer theory for ozone attack on rubber surface to explain the rate of ozone crack growth. According to their theory, the variation in



The zwitterion may react with other zwitterion to give diperoxide compound



Or with carbonyl compound to give ozonide

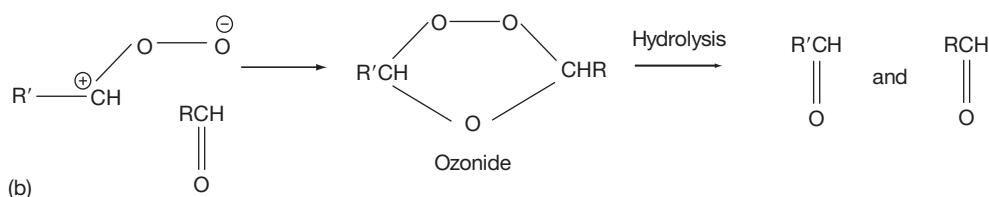


**Figure 9** Mechanism of ozone attack on olefins.

the rate of ozone attack on stretched rubber surfaces produced by changes in the air velocity and magnitude of the strain is controlled by the diffusion of ozone across the relatively stationary boundary layer adjacent to rubber surface. The boundary layer effect is important because of the readiness with which ozone is destroyed by stretched rubber.<sup>20</sup> As mentioned earlier, ozone cracking occurs only in elastomers subject to tensile stresses. Elastomeric components used in compression will crack only in the regions of the surface where tensile stresses are induced. These cracks are unable to penetrate very

far because they soon encounter compressive rather than tensile stresses. Thus ozone cracking is not a serious problem for large elastomeric components such as rubber bearings which are used in compression. Nevertheless, ozone cracks are unsightly and may initiate fatigue crack growth, which ultimately leads to mechanical failure. In view of this deleterious effect, it is necessary to carry out test on ozone resistance. The test involves exposing the stretched test-pieces (20% strain) in an ozone-rich atmosphere at a fixed temperature (23 or 40 °C) and inspecting the surfaces for cracks with the aid of a magnifying

glass at intervals of time. If cracks are not observed after completion of test, the vulcanizate is said to have good resistance to ozone cracking.

### 3.33.8 Heat Aging Resistance

Elastomers can survive over long periods in service at ambient temperatures without any measurable deterioration if the products are sufficiently thick. For a thick section of rubber, the availability of oxygen will be limited by diffusion, and components with bulky rubber layers can be considerably more resistant to elevated temperatures than thin rubber sections. For example, bearing pads of NR installed in 1890 had been examined, and although the outer 1–2 mm of rubber had degraded after 96 years of exposure to the atmosphere, the inner core of the rubber was still in good condition as shown by the photograph in [Figure 10](#).<sup>2</sup> Rubber samples taken from the interior portion were found to retain good physical properties as that of freshly prepared compounds.<sup>2</sup> At sufficiently elevated temperatures, all types of elastomer will undergo degradation. However, conventional NR vulcanizates can be used safely at 60 °C, the maximum ambient temperature likely to be encountered practice.<sup>2</sup> At temperatures of 300 °C and above, NR vulcanizates first softens as molecular breakdown

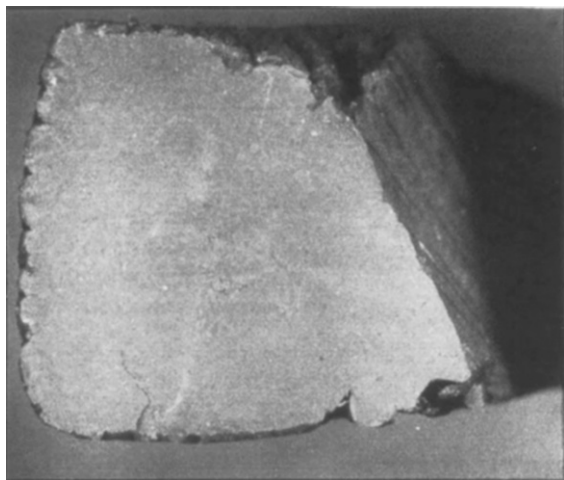


**Figure 10** Cross-sectioned view of a 100-year old bridge bearing pad showing the very small depth of penetration of atmospheric degradation. Adapted from Fuller, K. N. G.; Muhr, A. H. *Engineering design with natural rubber*, NR Technical Bulletin, 5th ed.; The Malaysian Rubber Producers' Research Association, London, 1992; pp 1–33, with permission from Tun Abdul Razak Research Centre, Brickendonbury Hertford, England.

occurs, then resinify, becoming hard and brittle.<sup>2</sup> Flammable vapor are emitted and ignition occurs. However, the rate of burning is extremely slowly for the case of large block rubber.<sup>2</sup>

In recent years, new performance demands for automotive elastomers have been proposed<sup>22</sup> to perform at high operating temperatures. This move was made to accommodate increasing concern for improved fuel economy, which resulted in a significant downsizing and redesign of the automobile. Concomitantly the engine compartment became smaller and more difficult to cool thus raising the temperature of the under hood. Current automotive elastomers are expected to perform well under a 120 °C in-service temperature at least until the life of the car.<sup>22</sup>

There is a growing expectation those future automotive elastomers to perform well in a 150 °C environment for over 100 000 miles.<sup>22</sup> This is a clear signal that specialty elastomers would find very strong markets over general-purpose elastomers for high temperature performance.

### 3.33.9 Flex Cracking

Flexing and cyclic stresses can lead to premature failure during service. There are two basic mechanisms of crack growth, (i) ozone crack growth, due to primarily chain scission, and (ii) mechanico-oxidative crack growth, due to mechanical rupture at the tip of a flaw, which is considerably facilitated by the presence of oxygen.<sup>23</sup> Both types of growth can occur under static or dynamic conditions or together. The amount of crack growth in a given time is directly proportional to the ozone concentration. The crack growth rate  $dc/dt$  of a single ozone crack under static conditions is given by [eqn \[9\]](#):

$$dc/dt = \alpha q \quad [9]$$

where  $q$  is the ozone concentration and  $\alpha$  a constant (the rate at unit ozone concentration) which is a property of the rubber.<sup>23</sup> The cyclic crack growth rate is given by [eqn \[10\]](#):

$$r = (dc/dn)_{\text{ozone}} = (F/f_f)\alpha q \quad [10]$$

where  $F$  is the time fraction of cycle for which the test-piece is strained, and  $f_f$  is the frequency.<sup>23</sup> Based on fracture mechanics approach, and assuming that the growth of naturally occurring flaws of a fatigue test has the same characteristics as that of a crack growth test, Lake and Lindley<sup>23</sup> worked out

the fatigue life of vulcanized elastomer as given by eqn [11]:

$$N_f = 1/(16BW_s^2c_0) \quad [11]$$

where  $N_f$  is the number of cycles to failure from a naturally occurring flaw of size  $c_0$ .  $B$  is the crack growth constant, and  $W_s$  is the strain energy density. Thus the fatigue life  $N$  can be predicted from known parameters of eqn [11].

### 3.33.10 Oil Absorption

An unvulcanized elastomer becomes solution when immersed in its solvent; in contrast, a vulcanized elastomer will only swell. The extent of swell depends on the amount of solvent absorbed, which in turn depends on the crosslink concentration and types of solvent. Swelling is undesirable because apart from dimensional instability, the modulus and mechanical strengths are all decreased making the

swollen vulcanizate unsuitable for most engineering applications.<sup>2</sup> In the case of rubber-to-metal bonded, bond failure occurs if the liquid is able to reach the metal plate. **Figures 11 and 12** show some of the typical automotive elastomeric components such as fuel and oil hoses, gaskets, O-rings and seals which are in contact with automotive fuels. These rubber components are thin and susceptible to damages when swollen excessively by the oil. Additives such as ethanol, methanol, and methyl *t*-butyl ether are being placed in gasoline with a view to improve its octane number.<sup>22</sup> Increasing the alcohol content of the gasoline increases the amount of swell, which is very undesirable not only because of dimensional instability, but also reduces tensile strength and elongation at break of the swollen elastomer.

It is well established that swelling is diffusion-controlled and the volume of liquid absorbed is initially proportional to the square root of the time of immersion.<sup>2</sup> For most organic liquids, the rate of penetration depends on their viscosity rather than

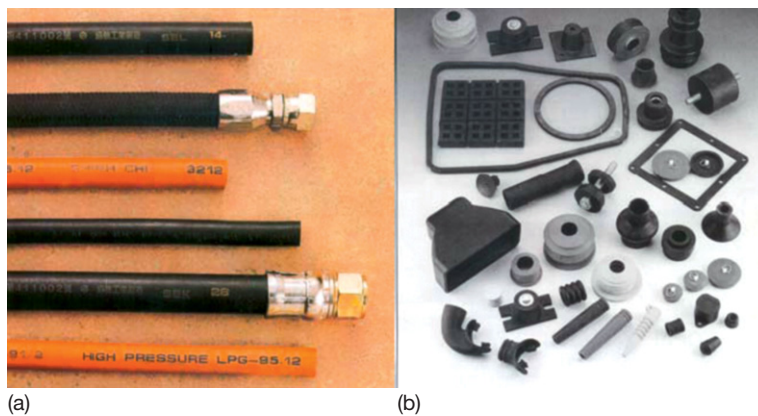


**Figure 11** Automotive rubber products in contact with oil and heat: (a) hoses – hydraulic, fuel, gasoline pump, and steam hose and (b) gaskets, O-rings, seals, and exhaust hanger, etc.

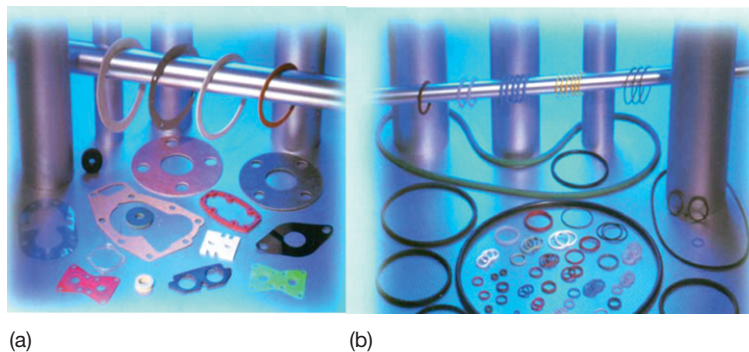


**Figure 12** Automotive rubber components: (a) gaskets and (b) O-rings and seals.

their chemical nature<sup>2</sup>. Figure 13 shows the time–viscosity relationship for the liquid to penetrate 5 mm into the rubber interior.<sup>2</sup>

For NR, it takes about 4 days for a volatile liquid such as toluene to penetrate 5 mm depth, 1–2 years for engine lubricating oil, and about 30 years for a petroleum jelly, even with continuous immersion.<sup>2</sup> It is possible to estimate the distance of liquid in a given time provide that the penetration rate is known.<sup>2</sup> Alternatively, the viscosity of the liquid may be used if penetration rate is not known since the penetration rate is related to viscosity as shown earlier in Figure 13.

Southern<sup>24</sup> has introduced a nomogram as illustrated in Figure 14 to facilitate the calculation in estimating the penetration depth of liquid into the elastomer. Although the data were obtained for NR, but would be expected to work with other elastomers of similar  $T_g$ .<sup>24</sup> As an illustration to use the nomogram, Southern<sup>24</sup> has calculated, a liquid with penetration rate of  $7 \times 10^{-5} \text{ cm s}^{-1/2}$  would take 4 weeks to penetrate 1 mm, but 100 years to penetrate 40 mm of the rubber block. The penetration rate–viscosity relationship does not hold for water because of the presence of hydrophilic impurities which complicate transport of water in elastomers.<sup>24</sup>

### 3.33.10.1 Effect of Crosslink Concentration and Polarity on Swelling Resistance

Natural rubber (NR) latex has found very wide applications in the glove industry since the 1920s. This is attributed to the excellent tear and puncture

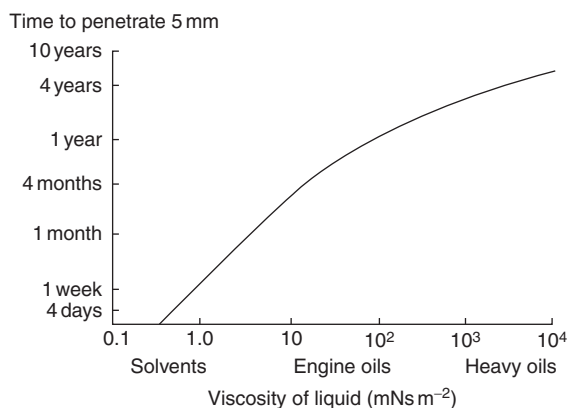


**Figure 13** Effect of viscosity of liquid on penetration time. Adapted from Fuller, K. N. G.; Muhr, A. H. *Engineering design with natural rubber*, NR Technical Bulletin, 5th ed.; The Malaysian Rubber Producers' Research Association, London, 1992; pp 1–33, with permission from Tun Abdul Razak Research Centre, Brickendonbury Hertford, England.

resistance of NR latex films. Besides, NR latex film exhibits very high extensibility (600–1000%) before its breaking point. These properties make NR latex film an excellent barrier protection against infectious liquids and gases. Most of the examination and surgical NR latex gloves are used in hospitals and clinics. However, recently NR latex gloves have entered the fast food industry where good swelling resistance is an essential requirement. Being a nonpolar rubber, NR latex gloves have a poor swelling resistance which limits its application in the fast-food industry. The fast-food industry is growing very fast all over the world. There is a growing concern over the cleanliness and hygiene of the food. It is essential that the workers wear rubber gloves to avoid contact with the food they serve. Rahim and Samsuri<sup>25</sup> investigated the effect of crosslink concentration and effect of blending carboxylated nitrile rubber (XNBR) with NR latex on the swelling resistance of NR latex film towards cooking oil. The amount of sulfur was varied to produce different crosslink concentrations. The crosslink concentration was determined by immersing the latex film sample in a solvent until equilibrium swelling was attained. The crosslink concentration was calculated by using the Flory–Rehner equilibrium swelling equation as proposed by Mullins<sup>18</sup> given by eqn [12]:

$$-\ln(1 - v_r) - v_r - \chi v_r^2 = 2\rho V_1 [X]_{\text{phy}} v_r^{1/3} \quad [12]$$

where  $v_r$  is the volume fraction of rubber in the swollen gel,  $\rho$  is the density of rubber,  $V_0$  is the molar volume of solvent,  $\chi$  the rubber–solvent interaction parameter, and  $[X]_{\text{phys}}$  is the physically manifested crosslink concentration. The diffusion coefficient  $D$  was calculated from eqn [13]<sup>24</sup>:

$$M_t/M_\infty = (2/l)(Dt/\pi)^{1/2} \quad [13]$$

where  $M_t$  is the total amount of liquid absorbed per unit area of the sheet after immersion for time  $t$ ,  $M_\infty$  is the amount of liquid absorbed after infinite time (in this case time to reach equilibrium swelling), and  $l$  is the half thickness of the film sheet. It is necessary to plot  $M_t$  against square root time as shown in Figure 15 to calculate  $D$  in eqn [13].

The effect of crosslink concentration on the diffusion coefficient of cooking oil in the latex film is shown in Table 8.<sup>25</sup> The results show that increasing the crosslink concentration decreases the diffusion coefficient significantly. Increasing the sulfur content from 0.6 to 3 pphr increases the crosslink concentration by about 90%, which merely decreases the



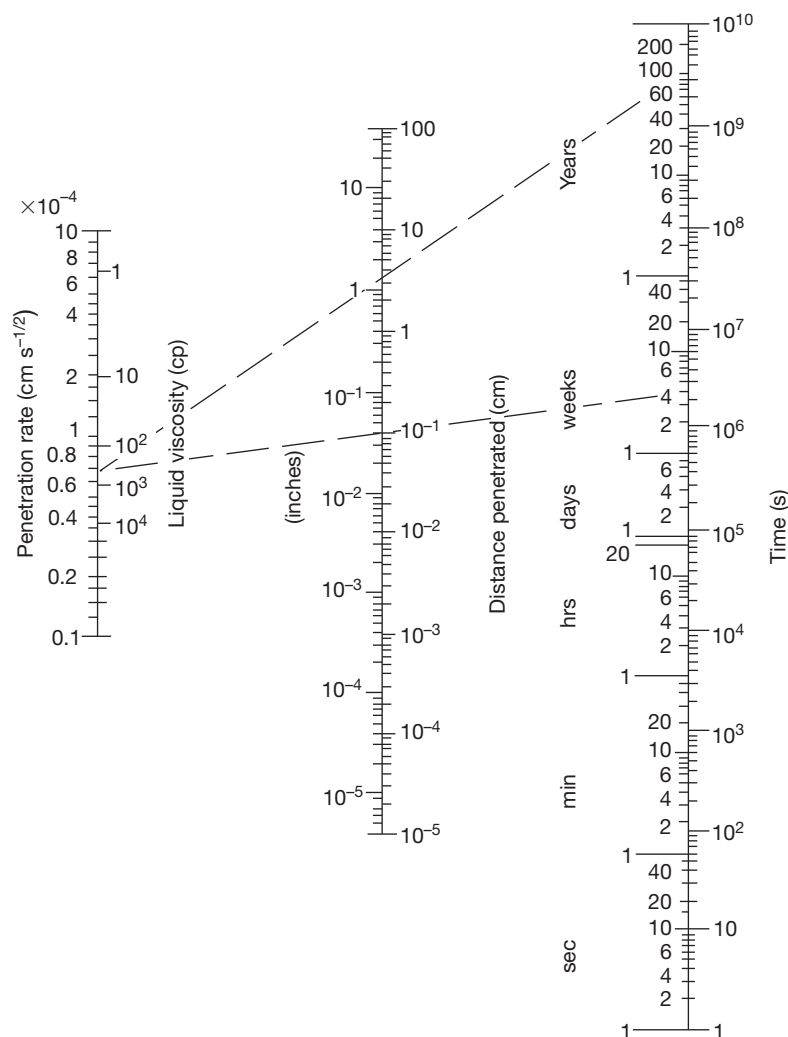


**Figure 14** Nomogram to facilitate rapid calculation of distance penetrated by liquid into rubber. Adapted from Muniandy, K.; Southern, E.; Thomas, A. G. In *Natural Rubber Science and Technology*; Robert, A. D., Ed.; Oxford University Press, Oxford, UK, 1988; Chapter 13, pp 820–851, with permission from Oxford University Press.

diffusion coefficient by about 23%. However, the most efficient method to increase swelling resistance is through physical blending of NR latex with XNBR latex, where the diffusion coefficient  $D$  of the oil into the film decreases by a factor of 2.7 compared with NR latex having the highest crosslink concentration. Thus, this work shows strong evidence that blending of nonpolar elastomer with polar elastomer enhances the swelling resistance of the former.

### 3.33.11 Water Absorption

Elastomers find wide uses in marine and offshore engineering applications. The application of elastomers

in water management is attributed to its high impermeability to water. A rubber sheet is used to line the water reservoir and pond, while inflatable rubber is used as a dam. Rubber dock fenders rely on the energy absorption capacity of the rubber. Inevitably, the rubber will absorb some quantity of water as these rubber products spend a considerable time under water. It is of great concern whether the absorption of water would impair the strength of the rubber.

The true solubility of water in rubber is very low.<sup>24</sup> Nonetheless, relatively large amounts of water can be absorbed during prolonged immersion as shown in [Figure 16](#).<sup>2</sup> The diffusion of water in elastomers is not straightforward, but complicated by the presence of hydrophilic materials. In the case of NR it is mainly

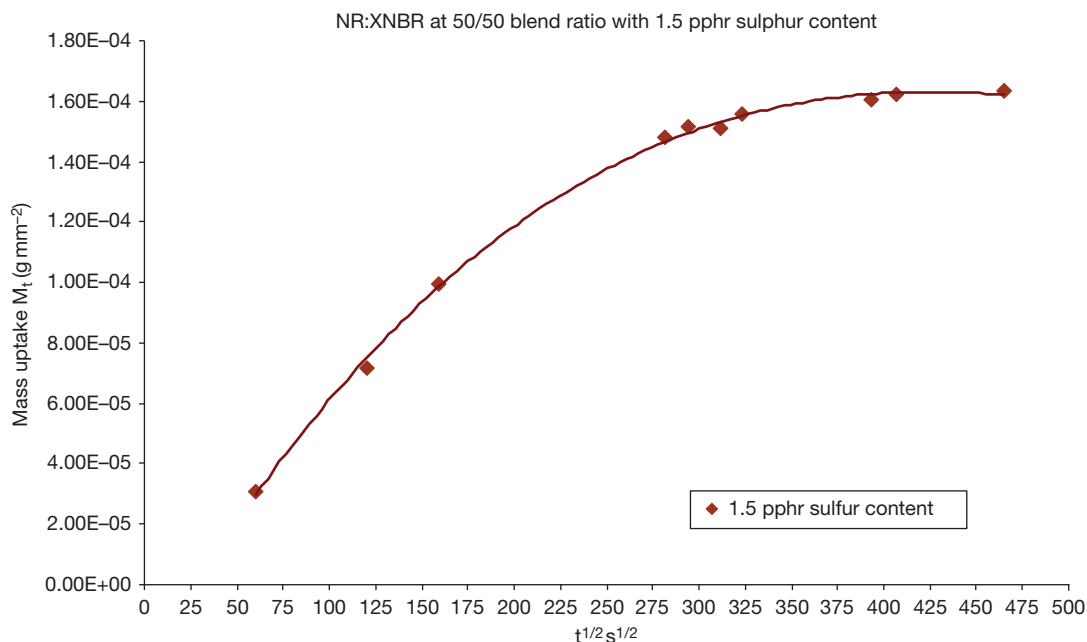


**Figure 15** Typical mass uptake curve for NR/XNBR blend latex film.<sup>25</sup>

**Table 8** Effect of crosslink concentration on diffusion coefficient  $D$  of cooking oil into NR latex film

Sulfur level (pphr)	$[X]_{phy}$ (mol per kg RH)	$D$ ( $m^2 s^{-1} \times 10^{-13}$ )
0.6	$4.46 \times 10^{-2}$	4.70
1.0	$4.60 \times 10^{-2}$	4.00
2.0	$4.89 \times 10^{-2}$	3.70
3.0	$5.82 \times 10^{-2}$	3.57
NR:XNBR (50:50) 1.5	—	1.30

proteinaceous.<sup>24</sup> When water diffuses into the rubber, the water-soluble hydrophilic materials dissolve forming droplets of solution within the rubber. Osmotic pressure gradient would exist between watery domains in the rubber and that of the external solution immersing the rubber.<sup>24</sup> This results in more water diffusing into the internal solution droplet. Water absorption reaches its equilibrium when the elastic stresses acting on the droplets balance the osmotic pressure difference. Muniandy and Thomas<sup>24</sup> proposed a mathematical model for water absorption to derive equations for the equilibrium water uptake and to evaluate the kinetics of water absorption and desorption. From the model, they calculated the equilibrium water uptake and the apparent diffusion coefficient. They found very good agreement between theory and experimental results.

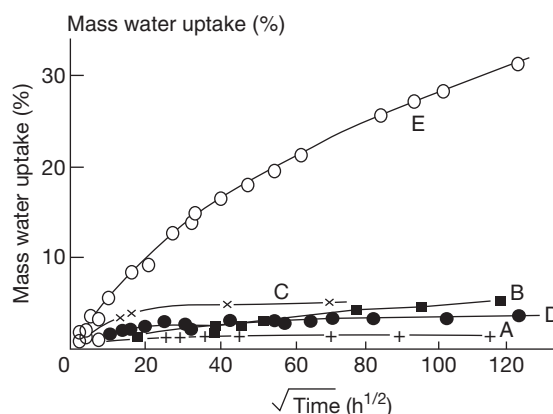


**Figure 16** Corrected mass uptake measurements for engineering rubbers in seawater at 23 °C: (a) deproteinized NR, (b) lead oxide cured polychloroprene, (c) nitrile rubber, (d) conventional NR, and (e) conventional polychloroprene. Adapted from Fuller, K. N. G.; Muhr, A. H. *Engineering design with natural rubber, NR Technical Bulletin*, 5th ed.; The Malaysian Rubber Producers' Research Association, London, 1992; pp 1–33, with permission from Tun Abdul Razak Research Centre, Brickendonbury Hertford, England.

Later, Lake<sup>26</sup> investigated the kinetics of water (tap water) absorption in elastomers and their effects on properties. He reported that when the absorption was large (50% or more), the rubber test-piece degraded. Severe degradation leads to porosity of the surface layer, and when pressed, water exudes.<sup>26</sup> However, at a low level of absorption, Lake observed

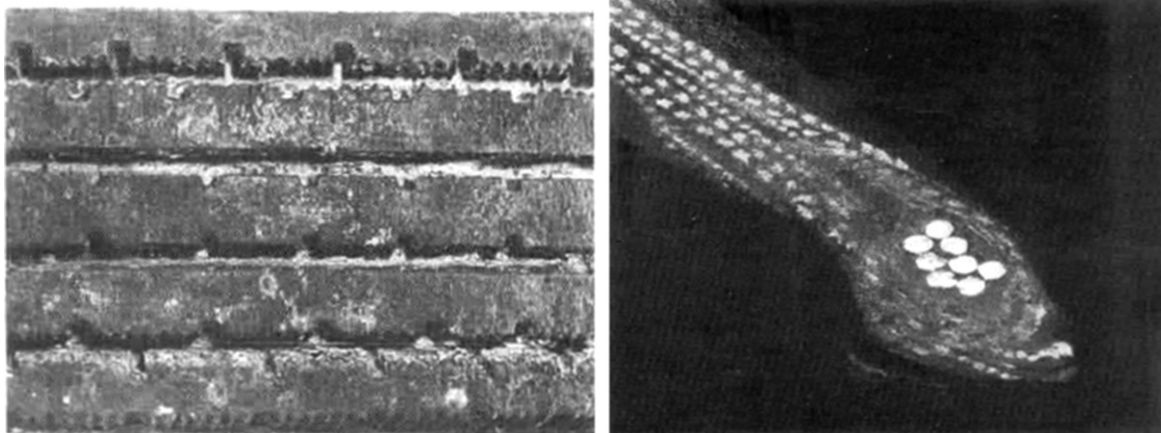


**Figure 17** A natural rubber tire after 40 years' exposure to seawater. Adapted from Mullins, L. *Proc. Int. Rubb. Conf.* Kuala Lumpur, 1985, with permission from Malaysian Rubber Board.

the formation of droplets similar to the blisters that occur in plastics or under protective coatings, consistent with an osmotic diffusion mechanism.<sup>24</sup> In salt-water, water absorption reached steady state at much lower levels than in freshwater, again consistent with an osmotic pressure mechanism. Thus seawater is less damaging than freshwater and may not have any serious consequences for many elastomers. This latter point is consistent with findings of Ab. Malek and Stevenson<sup>27</sup> who evaluated the physical properties of a rubber tire as shown in [Figure 17](#), recovered from seawater at a depth of 80 ft. They found that the rubber tire had absorbed about 5% of seawater after 42 years of immersion. They found no evidence of microbiological attack. What is more interesting, the physical properties of the rubber tire were within normal specifications for new rubber of the same type. They even suggested storing elastomers in deep seawater in view of its inert nature. Indeed, elastomer is a very suitable material to coat metal surfaces against corrosion in deep seawater. The photograph in [Figure 17](#) shows clear evidence that the steel cords making up the bead of the tire are corrosion-free after a 42-year immersion in seawater.<sup>27</sup>

### 3.33.12 Protective Measures

#### 3.33.12.1 Selection of Elastomer

All elastomers experience aging. Some age faster than others. The rate of aging depends on a number of factors such as the chemical structure of the polymer, service environment, which includes length of exposure to heat and light, oxygen and ozone concentration, size and shape of elastomers, and mechanical

stresses. One cannot stop the aging process, but one can slow it down. The most effective means of combating aging is to select the correct elastomers to meet the maximum service temperature and environment. Fully saturated elastomers having high bond dissociation energy making up their backbone chains are the best choice to meet high service temperature applications. Fully saturated rubbers such as ethylene propylene copolymer and very low unsaturation butyl rubber are excellent resistance to heat aging, oxidation and ozone cracking. Not only the maximum service temperature, but also other environmental factor such as oil or solvent determines the aging resistance. In cases like these, the elastomers having high bond dissociation energy and solvent resistance are desired. These include specialty elastomers such as acrylic (ACM), chloro-sulfonyl-polyethylene (CSM), ethylene propylene copolymer (EPM), fluoroelastomers (FKM), silicones (MQ, VMQ), polyester urethanes (AU), etc. Alternatively, for unsaturated elastomers are to use antioxidants and antiozonants, with correct vulcanization system can slow down the aging process quite efficiently.

#### 3.33.12.2 Blends of Elastomers

It is a common practice to blend two elastomers of different properties with a view to combining the best features in terms of technical and economic values. Natural rubber is blended with EPM for applications requiring very high resistance to attack by ozone as the latter is fully saturated. A blend of NR and EPDM is used for applications that require a combination of good resistance to attack by ozone and high

strength properties. Nitrile rubber (NBR) is blended with EPM to meet the requirements for very good oil resistance as well as conferring high resistance to oxidation and ozone cracking. The former is polar rubber and provides very good oil resistance, while the latter provides excellent weather resistance. However, blending two or more elastomers is not as easy as one would imagine. The work on blending various elastomers conducted by Tinker<sup>28</sup> and coworkers has thrown some light on the importance of compatibility, distribution of crosslinks in each rubber phase, distribution of filler and plasticizer and interfacial tension of each phase which have very strong influence on the service performance of the blend. When the elastomers are not compatible with each other, the associated problems that may arise include maldistribution of crosslinks, partition of chemicals (sulfur, accelerators, etc.) due to mechanism associated with preferential solubility and others. Lewan<sup>29</sup> worked on crosslink density distribution in NR/NBR blend and reported the effects of large difference in polarity and solubility parameters between these two rubbers. The large difference in polarity has the following effects:

- (i) causes high interfacial tension that is detrimental to mixing since it interferes with efficient mixing at the interface, hence minimizing the opportunity for crosslinking between the rubbers;
- (ii) causes poor phase morphology, which is characterized by large phase sizes;
- (iii) causes uneven distribution of crosslinks arises through preferential solubility of the curatives and vulcanization intermediates. Sulfur will be preferentially soluble (partition in favor of) the more polar NBR. One phase is over-crosslinked and the other is lowly crosslinked.

However, Lewan<sup>29</sup> overcame these problems by selecting the correct type of curing system such as semi-EV based on sulfur – TBBS, to obtain an even distribution of crosslinks in each phase and maximizing crosslinking between rubbers at the interface. The use of compatibilizer is highly recommended to enhance the compatibility between rubber phases. Polychloroprene rubber serves as a very good compatibilizer for the NR/NBR blend with just a small quantity (5 pphr) added to the blend. The addition of this compatibilizer reduced phase sizes, gave an even distribution of crosslinks and increased tensile strength.<sup>30</sup> Blends of elastomers provide alternative means of improving both aging resistance and oil resistance.

### 3.33.12.3 Antidegradants

Chemical antioxidants and antiozonants combat aging by scavenging harmful radicals, absorbing UV light, deactivating catalytic metals like copper, manganese, iron, etc., and decomposing initiating peroxides.<sup>16,17</sup> Two main types of chemical antioxidants and antiozonants are widely used in rubber compounds; they are amines and phenolics. Amine types are more effective and powerful antioxidants than phenolic types. However, the former is staining and the latter is not. Thus, this limits applications of amine types to black and dark colored elastomeric products. Phenolic types are exclusively used for white and bright colored products, especially in electrical wire insulation where colors are useful for identification purposes. Both amines and phenolics provide protection against aging by scavenging the harmful free radicals during the oxidative chain reaction.<sup>16,17</sup> The proposed mechanism<sup>17</sup> by which these two types of antioxidants work is shown in **Figure 18**. During the initiation stage, the free radicals produced by the peroxides abstract a labile hydrogen atom from the antioxidant and produce an antioxidant radical. This antioxidant radical is more stable than the peroxy radical, which terminates by reaction with other radicals in the system.<sup>16,17</sup>

The transfer step (c) and termination step (f) remove the free radical functionality from the elastomer, which consequently halts the oxidative degradation reaction.<sup>17</sup> Metal deactivators such as 2-mercaptobenzimidazole and its salt when added into the rubber compound containing amine or phenolic antioxidant give a synergistic effect to enhance the protection against aging.<sup>31</sup> These chemicals form

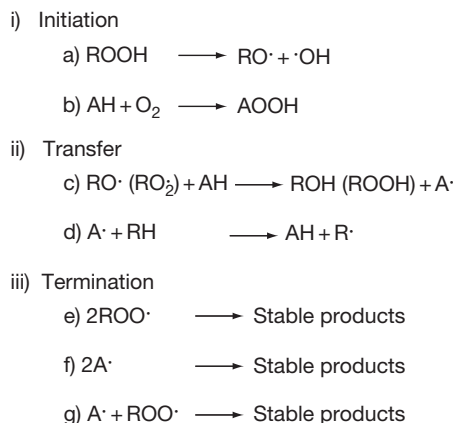


**Figure 18** Mechanism of amine and phenolic antioxidant activity, where AH is the antioxidant.<sup>17</sup>

coordination complexes with catalytic metals and inhibit metal-activated oxidation. Carbon black is a natural UV light absorber, and for nonblack compounds, it is useful to incorporate a UV light absorber such as benzotriazole derivative.

### 3.33.12.3.1 Mechanism of antiozonant action

The mechanism by which an antiozonant protects unsaturated rubber against ozone cracking has received attention from many rubber chemists and physicists. A number of suggestions have been proposed as to how antiozonants confer protection, ranging from competitive reaction with ozone (scavenging) to various types of protective layer formation.<sup>17,19–21</sup> There are three theories to describe the mechanism of antiozonant action<sup>17</sup>:

- (i) The antiozonant blooms to the surface of the rubber compound and reacts preferentially with the incident ozone.
- (ii) The antiozonant blooms to the surface of the rubber and forms a protective layer of film on the surface.
- (iii) The antiozonant reacts with intermediates formed in the ozonation of rubber, preventing chain scission or recombining severed rubber chains.

Lake<sup>32</sup> has conducted some work to elucidate the mechanism of antiozonant action to protect natural rubber against ozone cracking. He used dioctyl-*p*-phenylenediamines (DOPPD) antiozonant for his rubber compound. Exposing the rubber test-piece to ozone-rich atmosphere has reportedly resulted in a layer of film  $10^{-3}$  cm thick and visible to the naked eye forming on the rubber surface.<sup>32</sup> The protective layer can be removed by physical means either by scraping or using adhesive tape, or by swabbing with cotton wool dipped in acetone. The mass of the film can be determined by weighing the test-piece before and after its removal. In this way, the kinetics of layer formation can be determined by monitoring changes in weight after various periods of exposure to ozone.

Lake<sup>32</sup> has derived a mathematical expression to relate the mass of layer per unit area of surface  $M_L$  formed after time  $t$  to the concentration  $C_0$  of antiozonant in the rubber and diffusion coefficient  $D_L$  as shown by eqn [14]:

$$M_L = [2\rho_L D_L S_L C_0 t]^{1/2} \quad [14]$$

where  $\rho_L$  is the density of the layer material and  $S_L$  is the solubility, relative to that in the rubber, of the antiozonant in the layer. In deriving this equation,

Lake<sup>32</sup> assumed that the layer to be formed entirely of reacted antiozonant and the concentration of unreacted material within it to be small. The product  $D_L S_L$  was determined experimentally by measuring the rate of transfer of antiozonant through the layer formed on a test-piece to a controlled rubber test-piece containing no antiozonant initially. This was done experimentally by pressing two cylindrical discs (test-piece A contains antiozonant, test-piece B has no antiozonant) together so their surfaces are in intimate contact with each other. The antiozonant from test-piece A would migrate into test-piece B as a function of time. The mass of the layer formed per unit area of surface was plotted against the square root of time to produce a straight line whose slope gave the value of  $M_L/t^{1/2}$ , that is mass of film deposited per square root time. Lake<sup>32</sup> obtained very good agreement between theory and experimental data.

Lake<sup>32</sup> proposed the mechanism of antiozonant action as follows: The protective layer formed on the rubber surface is composed predominantly of the antiozonant which has reacted with ozone. The film formed remained essentially in the unstrained state, independent of the type of deformation applied. For this to happen, it is necessary that the antiozonant is soluble in the rubber, and that its reaction product should be insoluble. However, once the protective layer becomes coherent and compact, it will reduce substantially the flux of ozone reaching the rubber surface. Thus it appears that the ability of the antiozonant to prevent cracking is likely to be determined by what occurs during the initial stages of exposure when the layer is starting to form, rather than by the long-term behavior. Indeed, Lake<sup>32</sup> suggested that a coherent monomolecular layer of film that formed on the rubber surface is sufficient to confer protection against ozone cracking. However, the time for this monolayer to form must be faster than the time for the crack to grow to the same depth, so that the monolayer is able to bridge any cracks that have begun to grow.

### 3.33.12.3.2 Theories of layer formation

The thin layer of protective film covering the rubber surface is a direct consequence of the chemical reaction between chemical antiozonant and ozone. Lake and Mente<sup>21</sup> proposed two diffusion models to work out a theory for layer formation. The two models are shown in Figure 19. The first model describes the rate of layer formation that is controlled by the diffusion of the antiozonant across the already-formed layer to react with ozone at its outer surface. Under



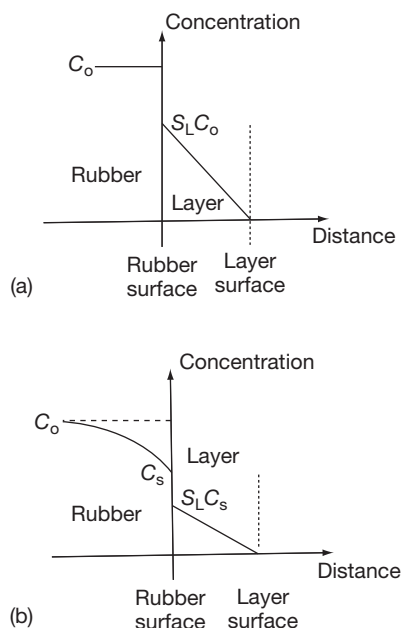


**Figure 19** Diffusion models for antiozonant layer formation: (a) rate governed by diffusion of antiozonant within the layer only, and (b) rate governed by both diffusion in the layer and in the rubber. Adapted from Lake, G. J.; Mente, P. G. *J. Nat. Rubb. Res.* **1992**, 7(1), 1–13, with permission from Malaysian Rubber Board.

these circumstances, the mass per unit area  $M_L$ , of layer formed after time  $t$  is given by eqn [14].<sup>21,32</sup> The concentration gradient in the layer will be essentially linear as shown in Figure 19(a). The second diffusion model takes into account diffusion within the rubber in addition to diffusion across the layer. In this case, an equation similar to eqn [14] applies, when  $C_0$  is replaced by  $C_s$ , the concentration at the rubber surface is lower than  $C_0$  as shown schematically in Figure 19(b).  $C_s$  is a function of  $C_0$  and the relative permeabilities of the rubber and the layer to the antiozonant, and with the assumptions made, are given by eqn [15]:

$$C_s/C_0 = 1 + \xi - [(1 + \xi)^2 - 1]^{1/2} \quad [15]$$

where

$$\xi = (\pi/4)(\rho_L D_L S_L / D C_0) \quad [16]$$

and  $D$  is the diffusion coefficient of the antiozonant in the rubber. The mass of layer per unit area of surface plotted against square root of time as shown in Figure 20 enabled Lake and Mente<sup>21</sup> to determine the rates of layer formation of the antiozonants formed on NR, ENR 50, and NBR 34, respectively. These three rubbers differ greatly in terms of

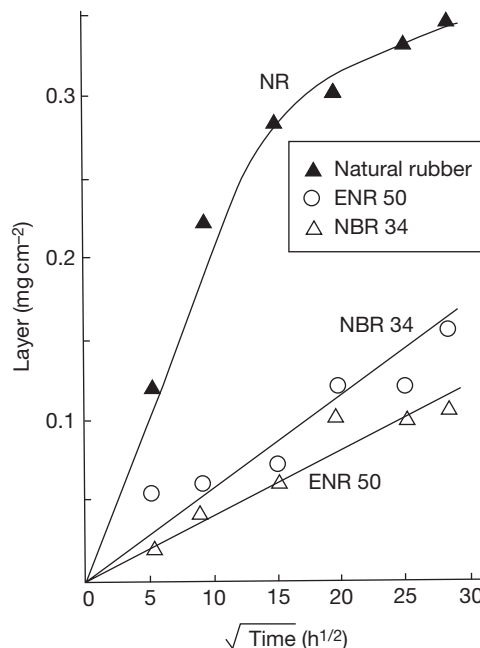


**Figure 20** Dependence of the mass of antiozonant layer formed on the square root of the time of exposure to an ozone concentration of 200 pphm at 40 °C for vulcanizates of NR, ENR 50, and NBR 34. Adapted from Lake, G. J.; Mente, P. G. *J. Nat. Rubb. Res.* **1992**, 7(1), 1–13, with permission from Malaysian Rubber Board.

polarity and glass-transition temperature, which may affect the rate of film formation on the rubber surface. Their experimental results as shown in Figure 20 indicate that the rate of layer formation for NR is about four times faster than that of NBR 34 and ENR 50, which is in accordance with the dependence of the diffusion coefficient on the glass-transition temperature of the rubber. The diffusion coefficient decreased in the increasing order of the  $T_g$  of the rubber.<sup>21</sup> Thus the diffusion coefficient of NR is fastest and that of ENR 50 is the slowest as  $T_g$  of NR is about  $-69$  °C and that of ENR 50 is about  $-24$  °C.<sup>21</sup> NBR34 has a slightly faster diffusion coefficient than ENR 50 as its  $T_g$  ( $-28$  °C)<sup>19</sup> is slightly lower than that of ENR 50. Lake and Mente<sup>21</sup> also conducted experiments to investigate the effect of temperature on layer formation on the NR surface at  $-17$  and  $23$  °C respectively as shown in Figure 21. They found that the rates of layer formation at these two temperatures were the same for NR. However, the diffusion coefficient of this particular antiozonant (DOPPD) in NR at  $-17$  °C was very similar to that in ENR 50 and NBR 34 at  $23$  °C. They attributed this finding to the partitioning of the antiozonant

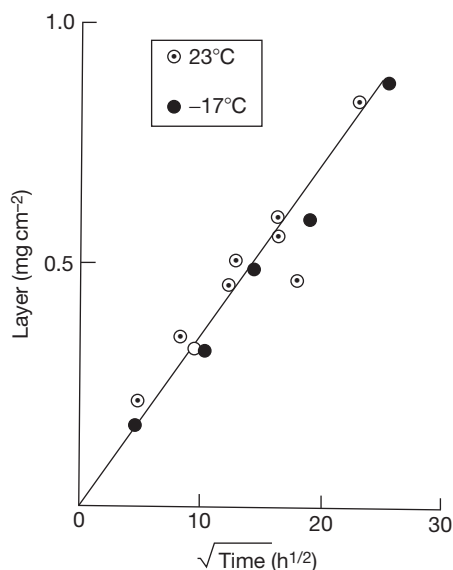


**Figure 21** Mass of antiozonant layer formed versus square root of the time of exposure to  $10^5$  pphm ozone for an NR vulcanizate containing 10 phr DOPPD at 23 and  $-17^\circ\text{C}$ . Adapted from Lake, G. J.; Mente, P. G. *J. Nat. Rubb. Res.* **1992**, 7(1), 1–13, with permission from Malaysian Rubber Board.

between the elastomer and the layer material, as the polarity of the elastomer affects the solubility of the antiozonant in the rubber. The solubility of the antiozonant varies in the ascending order of polarity of elastomer, that is  $\text{NR} < \text{NBR } 34 < \text{ENR } 50$ .<sup>21</sup> Lake and Mente concluded that for elastomers with high  $T_g$ , the antiozonant offers better protection at temperatures above room temperature than at low temperature, as the protective agents are more mobile at high temperatures rather than at low temperatures.

### 3.33.12.4 Blooming of Wax

Besides chemical antiozonants, paraffin wax is also a useful ingredient to confer protection against ozone cracking. Wax provides a protective layer surrounding the surface of the elastomer through the diffusion process commonly known as blooming, which prevents direct contact between ozone and the elastomer. Blooming occurs when the supersaturated solution of the ingredient in the rubber crystallizes more readily on the surface than in the rubber itself.<sup>24,33</sup> This basic mechanism of blooming is not only applicable to wax but other ingredients as well. When other ingredients such as sulfur, accelerators and stearic acid bloom to the rubber surface, they reduce the tackiness of the rubber, which can bring detrimental effects to

products relying on adhesion and bond strength involving different components plied together. These include rubber-to-metal bonded components, tires, belts, and hoses. However, blooming of waxes and antioxidants brings advantages.

Nah and Thomas<sup>33</sup> investigated the mechanism and kinetics of diffusion of wax to the rubber surface. They envisaged that the driving force for the blooming process arises from the elastic forces acting around the wax precipitates in the rubber when the wax concentration is in excess of its equilibrium solubility. They then proposed a model and theory for wax blooming base on thermodynamic concept of diffusion, where the driving force of the diffusion process is predominantly associated with free energy gradient rather than the concentration gradient of the wax that is dissolved in the rubber. The initial rate of wax bloom per unit area ( $M_t/t^{1/2}$ ) is given by eqn [17]<sup>33</sup>:

$$(M_t/t^{1/2})_{x=0} = [(24v_f D_t s_x \rho_x V_x G)/RT]^{1/2} (d\lambda/dy)_0 \quad [17]$$

where  $D_t$  is diffusion coefficient,  $v_f$  is volume fraction of seeding particles or flaws present in the rubber.  $s_x$  is solubility of wax in the rubber,  $\rho_x$  is density of wax, and  $V_x$  is molar volume of solid wax.  $G$  is shear modulus of the rubber,  $R$  is molar gas constant,  $T$  is absolute temperature.  $(d\lambda/dy)_0$  is equivalent to the concentration gradient of the wax at the surface of the rubber, and is determined by numerical methods for the appropriate boundary conditions and a suitable value of  $v_f$ . The symbol  $\lambda$  stands for the extension ratio of the rubber around the precipitated wax particle, assumed spherical. Nah and Thomas<sup>33</sup> verified eqn [17] experimentally, and obtained satisfactory agreement between their experimental and theoretical values for the migration of paraffin waxes in peroxide cured natural rubber. The theory was applicable to predict the blooming of wax mixtures with success, indicating that the mechanism of wax blooming has been identified correctly. Although Nah and Thomas developed the theory for blooming of wax, with minor adjustments, it is also applicable to predict migration and blooming of sulfur, fatty acids and antidegradants in vulcanized elastomers.

### 3.33.12.5 Choice of Vulcanization System

Anaerobic aging usually decreases the stiffness, resilience, and tensile, tear and fatigue properties; the extent is mainly determined by the type of vulcanization system, which affects aging of elastomers. There are three types of sulfur vulcanization systems known as conventional, efficient (EV) and

semi-efficient (semi-EV) respectively<sup>8,10</sup> as discussed briefly in [Section 3.33.4.3](#). The conventional system has a higher sulfur dosage than the accelerator that produces predominantly polysulfidic crosslinks, where the rubber molecular chains are linked by three or more sulfur atoms. Polysulfidic crosslinks have poor resistance to heat aging because the  $-S-S-$  bond has low thermal stability. In contrast, EV makes use of the low sulfur level and high accelerator dosage. This EV system produces predominantly monosulfidic crosslinks which are thermally very stable. The rubber network consists of other structural features as described briefly in subsequent sections.

### **3.33.12.5.1 Sulfur vulcanization system and types of crosslinks on aging resistance**

#### **Polysulfidic crosslink**

A chain of three or more sulfur atoms (maximum of six atoms) in this crosslink bridges two polymer chains. The bond energy of this crosslink is less than  $268 \text{ kJ mol}^{-1}$ , which is relatively low.<sup>10</sup> A polysulfidic crosslink can be produced by using the conventional vulcanization system where the quantity of sulfur is more than the quantity of the accelerator in the ratio 5:1 (sulfur: accelerator). Therefore the conventional sulfur cure system is not suitable for high temperature applications.

#### **Disulfidic crosslink**

In a disulfidic crosslink, there are two sulfur atoms bridging the two polymer chains. Its bond energy is about  $268 \text{ kJ mol}^{-1}$ . Little is known of the properties of this crosslink, mainly because it is very difficult to prepare a network in which disulfides are predominant. In both conventional and efficient sulfur vulcanizes the proportion of disulfidic crosslink is seldom more than 20–30% of the total.

#### **Monosulfidic crosslink**

In the case of a monosulfidic crosslink, the two polymer chains are bridged by one sulfur atom. Its bond energy<sup>10</sup> is relatively high, about  $285 \text{ kJ mol}^{-1}$ . A monosulfidic crosslink can be produced from an EV system where the amount of the accelerator is higher than the amount of sulfur, about 5:1 (accelerator:sulfur). Thus the EV system is suitable for medium high temperature applications.

#### **Cyclic sulfides**

These are intra-crosslinks which are useless as the crosslinks are formed on the same polymer chain.

This phenomenon is also known as main chain modification. The main source of these main chain modifications is the thermal decomposition of polysulfide crosslinks. The conventional vulcanization system creates more cyclic sulfides than the EV system as the former produces more polysulfide crosslinks than the latter.

#### **Conjugated diene and triene groups**

These main chain modifications are also formed by the thermal decomposition of polysulfide crosslinks. The concentration of these conjugated groups increases on overcure. The presence of these groups tends to catalyze oxidative aging as they are much more susceptible to oxidation than the polyisoprene main chain.<sup>8,10,16</sup>

#### **Pendent accelerator group**

It is generally accepted that in accelerated sulfur vulcanization, crosslinks are formed from initial rubber-bound pendent groups in which disulfide or polysulfide chains are terminated by accelerator fragments. Like the crosslink, some of these intermediates undergo progressive desulfuration and are converted into stable monosulfidic links between the polymer chain and accelerator fragments. The extent of main chain modification will depend on the amount of accelerator available and on the ease with which the initial pendent group can be desulfurated.

#### **Extra-network material**

The extra-network material formed by a sulfur vulcanizing system can be put into two categories. The first consists of unreacted zinc oxide and fatty acid activators, their zinc soap reaction products and zinc sulfide. The second consists of accelerator reaction products.

### **3.33.12.5.2 Peroxide vulcanization system**

Unlike sulfur vulcanization, peroxide vulcanization does not require the presence of double bonds. In fact, peroxide vulcanization is possible for rubbers having either saturated or/and unsaturated carbon-carbon backbone chains. However, peroxide vulcanization is quite impossible with the following elastomers because of their tendency to decompose:

- IIR – butyl rubber
- CIIR – chlorinated butyl rubber
- CO – polyepichlorohydrin rubber
- ECO – copolymer of epichlorohydrin and ethylene oxide
- PP – polypropylene
- ACM – polyacrylic rubber

The most common peroxide is dicumyl peroxide (DCP or dicup). Others include ditert butyl peroxide, dibenzoyl peroxide and bis(2,4-dichlorobenzoyl) peroxide. Peroxide vulcanization<sup>10</sup> produces a vulcanizate which will impart good aging resistance and excellent resistance to compression at high temperatures (70–100 °C). To obtain the best compression set performance, freedom from certain other compounding ingredients, especially zinc oxide and stearic acid, is essential. Peroxide vulcanization is essentially nonreverting. However, there are certain deficiencies such as poor hot tear strength and incompatibility with chemical antiozonants. Other technical limitations include slow cure rate with no delayed action, and degradation of the rubber giving a sticky surface if it comes into contact with air during the cure. Thus peroxides are not suitable for hot-air or steam-pan curing. The reaction of peroxide must be carried through to completion to obtain the best heat resistance; therefore long cure times are inevitable. In addition, nearly all antidegradants and aromatic oils affect the efficiency of the peroxide cure.

Co agents, which are highly reactive materials, are usually added in peroxide vulcanization to increase the efficiency of the organic peroxide, but do not affect the rate of cure.<sup>10,31</sup> They are used either to enhance the modulus and hardness or to reduce the level of peroxide required. They can be absolutely essential for the efficient cure of chlorinated polyethylene. Typical solid coagents are zinc diacrylate, zinc dimethacrylate, and *m*-phenylene dimaleimide. Liquid coagents are materials such as triallyl cyanurate (TAC), triallylisocyanurate (TAIC), etc. High vinyl polybutadiene is a polymer which can act as a coagent.

### 3.33.12.5.3 Vulcanization with urethane

This (urethane) crosslinking system for natural rubber was developed in the early 1980s by the scientists at the Malaysian Rubber Producers Research Association (MRPRA).<sup>10,31</sup> It was marketed under the trademark Novor. The basic reagent is a reaction product of a nitroso compound and a diisocyanate which dissociates at vulcanizing temperatures into its component species. The free nitroso compound then reacts by addition to rubber molecules giving attached pendent groups which subsequently react with the diisocyanate to form urea type crosslinks. The main features of the vulcanizates are excellent reversion resistance and, when protected with a TMQ/ZMBI antioxidant combination, excellent heat aging resistance.

### 3.33.12.5.4 Metallic oxide vulcanization

Elastomers containing halogens can be cured with metallic oxides such as oxides of zinc, magnesium, and lead. The oxides form an ether type of crosslink (R–O–R') which gives good heat aging resistance. Elastomers which can be vulcanized with metallic oxides are polychloroprene, halogenated butyls, and polychlorosulphonated rubber.

### 3.33.12.5.5 Resin vulcanization

Resin vulcanization has established itself to some degree in butyl (IIR) crosslinking, giving excellent heat and steam stability.<sup>10</sup> Example of a typical resin cross linker is polymethylolphenolic resin. The amount used is at the level of 5–12 pphr.

### 3.33.12.5.6 Quinonedioximes vulcanization

*p*-Benzoquinonedioxime (CDO) as well as its dibenzoyl derivative are cross linkers for many rubbers because of their free radical reactions.<sup>10</sup> Best known and of greatest interest is their use in IIR because of the excellent heat and steam stability that can be obtained. They are used mainly for rubbers having low unsaturation where sulfur vulcanization is slow. They have been unimportant for the classic diene rubbers.

## 3.33.13 Future Developments in Materials or Applications

Natural rubber and synthetic elastomers are likely to maintain their roles and contributions in domestic and industrial applications, buildings and structures, automobiles, and marine and engineering products. With the emergence of nanomaterials for rubber compounding, it is envisaged that future elastomeric products will provide better service and longer life performance than they are capable of providing now. High heat resistant elastomers and highly oil resistant elastomers are the main players of the future to meet the high demands of the automotive industry and aeronautical engineering. More developmental work in these areas is expected.

## Acknowledgements

I am very grateful to Dr. Stuart Lyon, Reader in Corrosion Control Engineering, School of Materials (Corrosion and Protection Centre), University of Manchester, England, who gave me the opportunity to write as part of the prestigious Shier's Corrosion

book. I feel much honored to be among the experts who contributed to this fourth edition of Shier's Corrosion.

It gives me great pleasure to thank the Publication Divisions of the Malaysian Rubber Board (MRB) (formerly Rubber Research Institute of Malaysia), and its sister concern the Tun Abdul Razak Research Centre (TARRC) (formerly Malaysian Rubber Producers Research Association) at Brickendonbury Hertford, England. In particular, Dato' Dr. Kamarul Baharin Basir, Director General, MRB and Mdm Rabeatun Awaliah Awalludin, MRB, and Dr. A.J. Tinker (Director Research) TARRC and Ms. K. Lawson TARRC who helped me to obtain the permission to reproduce data and figures from their respective Publication Divisions.

I would like to express my sincere appreciation and thanks to Oxford University Press and the American Chemical Society (Rubber Division) for giving permission to reproduce figures and data from their respective publications.

Last but not least, Associate Prof. Dr. Mohamad Kamal Harun, Dean of Faculty of Applied Sciences, MARA University of Technology, Malaysia (UiTM) for his encouragement.

## References

1. International Standard, Rubber – Vocabulary, ISO1382, 3rd Ed, 1996-08-01.
2. Fuller, K. N. G.; Muhr, A. H. *Engineering design with natural rubber, NR Technical Bulletin*, 5th ed.; The Malaysian Rubber Producers' Research Association: London, 1992; pp 1–33.
3. Chadwick, J. C. *Shell Polym.* **1981**, 5, 44–50.
4. ISO 4632/1-1982 (E), ISO Classification system.
5. Hashimoto, K.; Maeda, A.; Hosoya, K.; Todani, Y. *Rubb. Chem. Technol.* **1998**, 70(3), 449–519.
6. Fogg, G.; Swift, P. M. *NRPRA Tech. Bull.* **1962**, 4, 1–26.
7. Brydson, J. A. *Plastics Materials*, 4th ed.; Butterworths: Newton, MA, 1989; Chapter 29, pp 730.
8. Brown, P. S.; Porter, M.; Thomas, A. G. In *Proceedings of the International Rubber Conference*; Kuala Lumpur, October 21–25, 1985, RRIM, 1986; pp 20–46.
9. Hofmann, W. *Rubber Technology Handbook*; Hanser, 1989; Chapter 3, Synthetic Rubber, pp 1–171.
10. Elliott, D. J.; Tidd, B. K. *Prog. Rubb. Technol.* **1974**, 34, 83–126.
11. Gregory, M. J. In *Rubber to metal bonding, Adhesives, Sealants, and Encapsulants Conference*, London, November 5–7, 1985.
12. Gage, F. J. *IRI* **1968**, 47–49.
13. Gibbs, E. H., Jr.; Seber, J. N. ACS Rubber Division Mtg., Indianapolis, IN, May 1984, pp 1–9.
14. Mullins, L. In *Proc. Rubb. in Eng. Conf.* Kuala Lumpur, 1974, pp 1–20.
15. Bolland, J. L.; Hughes, H. J. *Chem. Soc.* **1949**, 492.
16. Barnard, D.; Lewis, P. M. In *Natural Rubber Science and Technology*; Robert, A. D., Ed.; Oxford University Press: Oxford, UK, 1988; Chapter 13, pp 621–673.
17. Keller, R. W. *Rubb. Chem. Technol.* **1985**, 58, 637–651.
18. Mullins, L. J. *Polym. Sci.* **1956**, 19, 225–236.
19. Braden, M.; Gent, A. N. *J. Appl. Polym. Sci.* **1960**, 3, 90–106.
20. Lake, G. J.; Thomas, A. G. In *Proceedings of the Int. Rubb. Conf.* 1967, Maclarens: London.
21. Lake, G. J.; Mente, P. G. *J. Nat. Rubb. Res.* **1992**, 7(1), 1–13.
22. Kinro, H.; Akio, M.; Kiyoshi, H.; Yoshihiro, T. Speciality Elastomers for Automotive Applications, *Rubber Chemistry Technology*; **1998**, 71(3).
23. Lake, G. J.; Lindley, P. B. *Rubber J.* **1964**, 10, 24–30, 79, 11, 30–36, 39.
24. Muniandy, K.; Southern, E.; Thomas, A. G. In *Natural Rubber Science and Technology*; Robert, A. D., Ed.; Oxford University Press: Oxford, UK, 1988; Chapter 13, pp 820–851.
25. Rahim, R.; Samsuri, A., Effect of crosslink concentration and XNBR:NR ratio on swelling resistance of NR latex film towards cooking oil, in press.
26. Lake, G.J. In *Conf. Polymers in a Marine Environment*, London, 31 Oct.–2 Nov., 1984, pp 157–160.
27. Ab-Malek, K.; Stevenson, A. J. *Mater. Sci.* **1986**, 21, 147–154.
28. Tinker, A. J. In *Blends of Natural Rubber*; Tinker, A. J., Jones, K. P., Eds.; Chapman & Hall: London, 1998; Chapter 1, pp 1–7.
29. Lewan, M. V. In *Blends of Natural Rubber*; Tinker, A. J., Jones, K. P., Eds.; Chapman & Hall: London, 1998; Chapter 5, pp 53–67.
30. Kongsin, K.; Lewan, M. V. In *Blends of Natural Rubber*; Tinker, A. J., Jones, K. P., Eds.; Chapman & Hall: London, 1998; Chapter 7, pp 80–93.
31. The Natural Rubber Formulary and Property Index, Malaysian Rubber Producers' Research Association, 1984, pp 1–24.
32. Lake, J. G. *Rubb. Chem. Chem.* **1970**, 43, 1230–1238.
33. Nah, S. H.; Thomas, A. G. *J. Polym. Sci., Polym. Phys. Ed.* **1980**, 18, 511–521.



## 3.33 Degradation of Natural Rubber and Synthetic Elastomers

**A. bin Samsuri**

Department of Polymer Technology, MARA University of Technology (UiTM), 40450 Shah Alam, Selangor, Malaysia

© 2010 Elsevier B.V. All rights reserved.

<b>3.33.1</b>	<b>Introduction</b>	2409
<b>3.33.2</b>	<b>Classifications of Rubber and Elastomers</b>	2410
3.33.2.1	Classification in Terms of Origins	2410
3.33.2.2	Classification in Terms of Purposes	2411
3.33.2.3	Classification in Accordance with International Organization for Standardization	2411
<b>3.33.3</b>	<b>General Properties of Elastomers</b>	2413
3.33.3.1	Structure–Property Relationship	2413
3.33.3.1.1	Mechanical strength	2413
3.33.3.1.2	Oxidation and ozone resistance	2415
3.33.3.1.3	Swelling resistance	2415
3.33.3.1.4	Glass-transition temperature $T_g$	2416
<b>3.33.4</b>	<b>Rubber Technology and Compounding</b>	2416
3.33.4.1	Mastication and Mixing	2416
3.33.4.2	Rubber Compounding	2416
3.33.4.3	Vulcanization	2417
<b>3.33.5</b>	<b>Rubber-to-Metal Bonding – Engineering and Automotive Applications</b>	2418
3.33.5.1	Bonding of Rubber to Metal	2420
3.33.5.1.1	Preparation of metal plates	2420
3.33.5.1.2	Types of bonding agent and methods of applications of bonding agent to metal plates	2420
3.33.5.1.3	Molding of rubber-to-metal bonded parts	2420
3.33.5.2	Vulcanization	2421
3.33.5.2.1	Low or high pressure steam	2421
3.33.5.2.2	Water curing technique	2421
3.33.5.2.3	Hot air or ambient temperature vulcanization	2421
3.33.5.3	Types of Bond Failure and Possible Remedies	2421
<b>3.33.6</b>	<b>Oxidation of Rubber</b>	2422
<b>3.33.7</b>	<b>Ozone Cracking of Rubber</b>	2424
<b>3.33.8</b>	<b>Heat Aging Resistance</b>	2426
<b>3.33.9</b>	<b>Flex Cracking</b>	2426
<b>3.33.10</b>	<b>Oil Absorption</b>	2427
3.33.10.1	Effect of Crosslink Concentration and Polarity on Swelling Resistance	2428
<b>3.33.11</b>	<b>Water Absorption</b>	2429
<b>3.33.12</b>	<b>Protective Measures</b>	2431
3.33.12.1	Selection of Elastomer	2431
3.33.12.2	Blends of Elastomers	2431
3.33.12.3	Antidegradants	2432
3.33.12.3.1	Mechanism of antiozonant action	2433
3.33.12.3.2	Theories of layer formation	2433
3.33.12.4	Blooming of Wax	2435
3.33.12.5	Choice of Vulcanization System	2435
3.33.12.5.1	Sulfur vulcanization system and types of crosslinks on aging resistance	2436
3.33.12.5.2	Peroxide vulcanization system	2436

3.33.12.5.3	Vulcanization with urethane	2437
3.33.12.5.4	Metallic oxide vulcanization	2437
3.33.12.5.5	Resin vulcanization	2437
3.33.12.5.6	Quinonedioximes vulcanization	2437
<b>3.33.13</b>	<b>Future Developments in Materials or Applications</b>	<b>2437</b>
<b>References</b>		<b>2438</b>

## Glossary

### Damping Basic property of an

elastomer to dampen, absorb or reduce vibrations. High damping elastomers are those having high glass-transition temperature ( $T_g$ ), which are widely used to isolate vibrations.

**Glass-transition temperature ( $T_g$ )** It denotes the temperature below which the elastomer becomes glassy and brittle, above which it is soft and rubbery.  $T_g$  reflects molecular mobility and hence the internal viscosity of the elastomer. High  $T_g$  indicates low molecular mobility or high internal viscosity and vice versa.

**Heat build-up** The amount of heat accumulated in the elastomer when subject to cyclic deformation. It is closely related to hysteresis.

**Hysteresis** It is a term to denote energy dissipated as heat when the elastomer is subject to cyclic stresses or in a single stress-strain cycle. The area bounded by the extension and retraction curve gives a quantitative measure of hysteresis.

**Raw rubber** Fresh rubber or an elastomer as received from the supplier.

**Scorch** It is a rubber technology term to denote the occurrence of a premature crosslink, which is an undesirable feature during the shaping process.

**Vulcanize or vulcanized elastomer** Indicates rubber or elastomer that has been vulcanized or cured, and thus, contains network structure or chemical crosslinks.

**CM** Cement metal failure

**CP** Cement primer failure

**CR** Polychloroprene rubber

**CSM** Chlorosulfonated polyethylene rubber

**DCP** Dicumyl peroxide

**DOPPD** Dioctyl-*p*-phenylenediamines

**ECO** Copolymer of epichlorohydrin rubber

**ENR50** Epoxidized natural rubber (50 mol% epoxidation)

**EPM** Ethylene propylene rubber

**EV** Efficient vulcanization

**GRG** General rubber goods

**IHRD** International Rubber Hardness Degrees

**IIR** Isobutylene isoprene (butyl) rubber

**IR** Synthetic polyisoprene rubber

**IRG** Industrial rubber goods

**ISO** International Organization for Standardization

**MRB** Malaysian Rubber Board

**MRPRA** Malaysian Rubber Producers Research Association

**MS** Malaysian standard

**NBR** Nitrile rubber

**NR** Natural rubber

**PP** Polypropylene

**PTR** Polysulphide rubber

**SBR** Styrene butadiene rubber

**TAC** Triallyl cyanurate

**TAIC** Triallylisosyanurate

**TARRC** Tun Abdul Razak Research Centre

**UiTM** Mara University of Technology

**UV** Ultraviolet light

**XNBR** Carboxylated nitrile rubber

## Abbreviations

**ACM** Polyacrylic rubber

**ASTM** American Society for Testing Materials

**CED** Cohesive energy density

**CIIR** Chlorinated butyl rubber

## Symbols

**A** Cross-sectional area ( $\text{m}^2$ )

**$A_0$**  Unstrained (original) cross-sectional area ( $\text{m}^2$ )

**B** Crack growth constant

**c** Crack length (mm, m)

**$c_0$**  Natural flaw size (mm, m)

**$C_0$**  Concentration of antiozonant ( $\text{mg cm}^{-2}$ )

<b>C<sub>s</sub></b>	Concentration of antiozonant at the rubber surface (mg cm <sup>-2</sup> )
<b>D</b>	Diffusion coefficient (m <sup>2</sup> s <sup>-1</sup> )
<b>dc/dt</b>	Crack growth rate (m s <sup>-1</sup> )
<b>f</b>	Force (N)
<b>f<sub>f</sub></b>	Frequency (Hz)
<b>h</b>	Height (m)
<b>k<sub>c</sub></b>	Compression stiffness (N m <sup>-1</sup> )
<b>k<sub>s</sub></b>	Shear stiffness (N m <sup>-1</sup> )
<b>l</b>	Half thickness of film sheet (mm, m)
<b>L</b>	Length (m)
<b>M</b>	Molecular weight (g mol <sup>-1</sup> )
<b>M<sub>∞</sub></b>	Total mass of liquid absorbed after an infinite time (g, kg)
<b>M<sub>L</sub></b>	Mass of layer per unit area of surface (g mm <sup>-2</sup> , kg m <sup>-2</sup> )
<b>M<sub>t</sub></b>	Total amount of liquid absorbed per unit area after immersion time, <i>t</i> (g mm <sup>-2</sup> s <sup>1/2</sup> )
<b>N</b>	Number of molecules per unit volume of rubber (mol cm <sup>-3</sup> )
<b>N<sub>f</sub></b>	Fatigue life (number of cycles of failure) (cycles, kilocycles)
<b>R</b>	Molar gas constant (8314 J mol <sup>-1</sup> K <sup>-1</sup> )
<b>S</b>	Shape factor
<b>T</b>	Absolute temperature (K)
<b>t</b>	Time (s)
<b>T<sub>g</sub></b>	Glass-transition temperature (°C, K)
<b>V<sub>1</sub></b>	Molar volume of solvent (m <sup>3</sup> )
<b>v<sub>f</sub></b>	Volume fraction of seeding particles present in the rubber
<b>v<sub>r</sub></b>	Volume fraction of rubber in the swollen gel
<b>W</b>	Width (m)
<b>W<sub>s</sub></b>	Strain energy density (J m <sup>-3</sup> )
<b>[X]<sub>phy</sub></b>	Physically manifested crosslink concentration (mol kg <sup>-1</sup> )
<b>δ</b>	Solubility parameter (MPa) <sup>1/2</sup>
<b>ΔH</b>	Latent heat of vaporization (J)
<b>λ</b>	Extension ratio
<b>ρ</b>	Density (kg m <sup>-3</sup> )
<b>χ</b>	Rubber-solvent interaction parameter

### 3.33.1 Introduction

Natural rubber and elastomers belong to the same group of materials known as high molecular weight polymers. According to the International Organization for Standardization (ISO) rubber vocabulary,<sup>1</sup> an elastomer is a macromolecular material which returns rapidly to approximately its initial dimensions and shape after substantial deformation by a weak stress

and release of the stress. However, an elastomer has always been recognized as a synthetic elastic polymer.<sup>1</sup> A polymer is a high molecular weight material having many units of small molecules chemically joined or linked by normal covalent bonds to form long chain molecules. These flexible and soft materials find wide uses in many engineering applications, such as natural rubber (NR) bridge bearings, and earthquake and seismic bearings. Indeed NR has had a sound track record in many engineering applications for over 150 years.<sup>2</sup> Elastomers have some unique properties that metals do not have. These include

- high bulk modulus (2000–3000 MPa) relative to their Young's modulus (0.5–3.0 MPa),
- some inherent damping, and
- large strain deformation.

Rubbers having high bulk modulus hardly change their volume when deformed. In simple words, rubber is incompressible. Like incompressible liquids, it has a Poisson's ratio close to 0.5. If rubber is constrained, to prevent changes in shape, it becomes much stiffer, a feature that is used to full advantage in the design of compression springs. Elastomeric bridge bearings and seismic bearings are examples of products that rely on these properties.

The damping inherent in the elastomer is a very important property as it helps to prevent the amplitude of the vibration of the spring from becoming excessive if resonant frequencies are encountered. Elastomeric products such as vibration isolators and engine mounts rely on the inherent damping properties of the elastomer.

The elastomer undergoes large strain deformation (a few hundred percent) without failure by an applied stress below its breaking stress. This means that it can store much more energy per unit volume than steel. Elastomeric dock fender systems make use of its large stored energy capacity to absorb shocks, blows and the impact exerted by ships.

Some of the merits of elastomeric springs over metal springs are as follows<sup>2</sup>:

- no maintenance is required,
- the energy storage capacity is high,
- with correct design, the rubber spring can provide different stiffness in different directions, or nonlinear load–deflection characteristics,
- a certain amount of misalignment is tolerable as the rubber spring can accommodate this tolerance,
- easier to install,
- hysteresis inherited by the elastomer is able to dampen dangerous resonant vibrations.

Another important property of an elastomer is its strong resistance to inorganic acids, salts, and alkalis. In contrast, acids attack metals. For these reasons, the linings of chemical tanks and pipes, especially those containing caustic solutions, are made from elastomers. The function of the elastomer here is to protect the metal against attack by corrosive chemicals.

Every product has its own life span. The designed lifetime of a product depends on the environmental conditions and the nature of the application. It is very important to choose the materials correctly to meet the intended service conditions and the surrounding environment. The aging process is the determining factor that limits the life span of the product. The term aging is always associated with the degradation or corrosion process as applied to metals, which may take many forms. In metals, corrosion takes place in the form of rusting, which involves oxygen and moisture. In elastomers, the term degradation is preferred to corrosion and covers a wider scope than that of metals. Degradation takes place in the form of oxidation, ozone cracking, flex cracking, liquid absorption and heat aging. Degradation in elastomers is very complex as it involves oxygen, ozone, mechanical strain, heat, trace metals, etc. There are other agencies such as solvents, oils, fuels, hot air (steam) and water, which may degrade elastomers and affect the service life of elastomeric products. A specific section on the degradation of elastomers discusses all these issues again later.

### 3.33.2 Classifications of Rubber and Elastomers

#### 3.33.2.1 Classification in Terms of Origins

Natural rubber comes from trees known as *Hevea brasiliensis*, and shrubs called guayule. The pictures in Figure 1 show typical rubber trees grown in the hot tropical climate of Malaysia, and the fresh latex that exudes from the bark of the rubber tree, after tapping with a sharp tapping knife. The fresh latex that exudes from the tree known as field latex contains about 70% water. After removing this large amount of unwanted water, the latex is known as concentrated latex and has about 60% of rubber content. Centrifuging is the preferred method of concentrating field latex because of its efficiency and rapidness compared to creaming and evaporation methods. Apart from latex, natural rubbers are available commercially in standard bale form, weighing about 33.33 kg. These bales of NR are produced specifically to meet certain



**Figure 1** Pictures of (a) natural rubber trees (top), (b) NR latex exudes from natural rubber tree (middle), and (c) closer view of NR latex collected in a cup (bottom).

technical requirements such as minimum dirt content, viscosity consistency, ash content, etc.

All synthetic elastomers are produced by the polymerization process. The early production of synthetic elastomers such as styrene butadiene rubber (SBR), polychloroprene rubber (CR), and nitrile rubber (NBR) relied on emulsion polymerization. One of the main drawbacks of emulsion polymerization is the lack of uniformity of polymer molecules with respect to stereo regularity. This is due to the



different ways in which diene monomer molecules can react, and it applies to all free radical polymerization processes of diene monomers. However, there was a real breakthrough with the discovery of the Ziegler–Natta catalyst in 1954, which enabled the control of the microstructure of polyisoprene.<sup>3</sup> Synthetic polyisoprene is produced by the solution polymerization process using catalysts of the alkyl lithium types such as trialkyl aluminum/titanium tetrachloride mixtures.<sup>3</sup> The Al/Ti mole ratio is critical for achieving high cis content. Currently, there are about 27 types of rubbers or more commercially available in the market. The choice depends on the nature of application, service conditions and environment.

### 3.33.2.2 Classification in Terms of Purposes

Elastomers can be classified further either as general-purpose rubbers or as specialty rubbers. General-purpose rubbers are those elastomers that are widely used in the manufacture of tires, industrial rubber goods (IRG), and general rubber goods (GRG). Most of the general-purpose elastomers cannot meet high service temperature and high oil resistance specifications or the combinations of these two requirements. The most common general-purpose rubbers include NR, SBR, CR, NBR, ethylene–propylene–diene rubber (EPDM), and BR. In contrast, specialty rubbers are those elastomers that are tailor made to meet certain specific requirements, such as low temperature flexibility, high swelling resistance towards oil (hydrocarbon, fuel, gasoline, etc.) and very high service temperature or combinations of these requirements. Specialty rubbers include silicone rubber, fluoroleastomers, epichlorohydrin, chlorosulfonated rubber, etc. [Table 1](#) shows some of the rubbers which belong to these grades and their typical applications.

### 3.33.2.3 Classification in Accordance with International Organization for Standardization

Elastomers can also be classified according to the ISO 4632/1-1982(E)<sup>4</sup> which provides information about rubber as a material with specifications. They are classified and designated in terms of their performance to heat aging, swelling resistance towards oil and low temperature flexibility. This method of classification is very helpful as it facilitates the purchasers and suppliers to make the correct selection of suitable materials, and avoid wasting time and energy.

These designations are determined by a type based on resistance to heat aging, by a class based on resistance to swelling in oil, and by a group based on low temperature resistance.<sup>4</sup> These classification criteria are used to establish a characteristic material designation consisting of three capital letters, where

- the first letter signifies Type (heat resistance)
- the second letter signifies Class (oil resistance)
- the third letter signifies Group (low temperature resistance).

[Tables 2–4](#) show the heat aging temperature, limits of volume swell and brittleness temperature for establishing Type, Class and Group respectively.<sup>4</sup> Type is determined by the maximum temperature at which heat (air oven) aging for 70 h, in accordance with ISO 188, causes a change in tensile strength of not more than  $\pm 30\%$ , a change in elongation at break of not more than  $-50\%$ , and a change in hardness of not more than  $\pm 15$  International Rubber Hardness Degrees (IHRD). Class is based on the resistance of the material to swelling in American Society for Testing Materials (ASTM) Oil No. 3, when tested in accordance with ISO 1817. In the test, the immersion time shall be 70 h at a temperature determined in [Table 2](#). Group is based on the brittleness temperature of the material when measured in accordance with ISO/R 812.

Thus if an elastomer is designated as BCD, it means that it is classified as Type B, Class C and Group D. This implies that the elastomer resists temperatures up to  $100^{\circ}\text{C}$ , with volume swelling not exceeding  $120\%$  in oil No. 3 and is not brittle at  $-40^{\circ}\text{C}$ .

Most of the general purpose elastomers shown in [Table 1](#) have poor heat resistance except for ethylene propylene rubber (EPM) as shown in [Figure 2](#). EPM can withstand service temperature of about  $150^{\circ}\text{C}$  as it is categorized as Type D. General purpose elastomers also have poor swelling resistance towards hydrocarbon oil except nitrile rubber (NBR) which is classified as Class H with maximum volume swell of  $30\%$ . A majority of the specialty elastomers shown in [Table 1](#) have both excellent heat resistance and swelling resistance. From the chart shown in [Figure 2](#), silicone rubber having both methyl and vinyl substituent groups on the polymer chain (VMQ) has equivalent heat resistant (Type G) with silicone rubber having methyl, vinyl, and fluorine substituent groups on the polymer chain (FVMQ). However, they have different Class with respect to swelling resistance. VMQ belongs to Class E while FVMQ belongs to Class J. Clearly



**Table 1** General purpose rubbers and specialty rubbers

<i>General purpose rubbers</i>	<i>Typical applications</i>	<i>Specialty rubbers</i>	<i>Typical applications</i>
Natural rubber (NR)	Mainly for tires, industrial and general rubber goods, bridge and earthquake bearings, bridge expansion joints, etc.	Carboxylated nitrile rubber (XNBR)	Oil resistant hoses, boots, seals and gaskets and other automotive components with very good oxidation resistance
Synthetic polyisoprene (IR)	Tires, sports goods, earthquake rubber bearings, IRG.	Polysulphide rubber (PTR)	Used mainly where good resistance to solvents is required
Styrene butadiene rubber (SBR)	Passenger car tires, IRG, GRG	Polyurethane rubber (AU, EU)	Gaskets, seals, solid tires, and foams
Butyl rubber (IIR)	Tire tubes, tube liners, enclosures, air bags, and curing bladders	Silicone rubber (Si)	Able to withstand a very wide range of service temperatures from $-45$ to $200^{\circ}\text{C}$ . Various grades are available covering a very wide range of applications such as baby teats, catheters, medical applications, wire and cables, electronic components, etc.
Butadiene rubber (BR)	Tires, sports goods	Chlorosulfonated polyethylene rubber (CSM)	Electrical insulator in cable and wire industry, tank lining, colored-stable weather-resistance products, oil resistant hoses and gaskets
Ethylene-propylene-diene rubber (EPDM)	Gaskets, seals, automotive components, IRG, and GRG	Polyacrylic rubber (ACM)	Seals and gaskets for high temperature applications, $180$ – $200^{\circ}\text{C}$
Polychloroprene rubber (CR)	Hoses, rubber bearings, expansion joints, belts, and conveyors	Fluorocarbon rubber (FPM)	Products which are resistant to chemicals, oils and solvents. Able to withstand high service temperatures exceeding $250^{\circ}\text{C}$ . Outstanding oxidation and ozone resistance. Flame resistant. Hoses, gaskets and seals for aircraft, jets, and rockets
Nitrile rubber (NBR)	Oil-resistant hoses, seals, O-rings, gaskets	Epichlorohydrin rubber (ECO)	Automotive industry – gasket, seals, hoses to withstand service temperatures above $130^{\circ}\text{C}$

**Table 2** Heat aging temperature for establishing Type<sup>4</sup>

	<i>Type</i>									
	A	B	C	D	E	F	G	H	J	K
Test temperature ( $^{\circ}\text{C}$ )	70	100	125	150	175	200	225	250	275	300

**Table 3** Limits of volume swelling for establishing Class<sup>4</sup>

	<i>Class</i>										
	A	B	C	D	E	F	G	H	J	K	L
Vol. swell max. (%)	No rqmt.	140	120	100	80	60	40	30	20	10	5

**Table 4** Limiting brittleness temperatures for establishing Group<sup>4</sup>

	Group						
	A	B	C	D	E	F	G
Limiting brittleness temperature (°C)	0	−10	−25	−40	−55	−75	−85

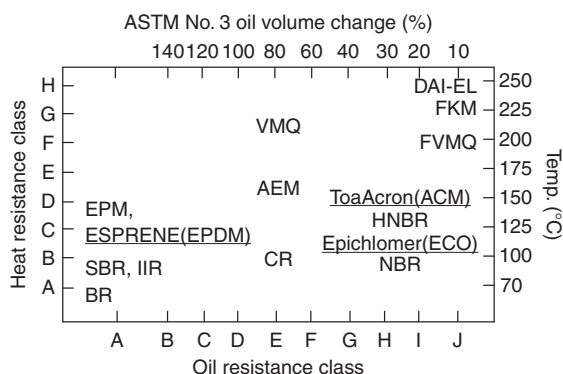


**Figure 2** A chart showing type and class of elastomers. Adapted from Hashimoto, K.; Maeda, A.; Hosoya, K.; Todani, Y. *Rubb. Chem. Technol.* **1998**, 70(3), 449–519, with permission from American Chemical Society.

FVMQ is more resistant to swelling towards the solvent than VMQ grade, as the fluorine atom is highly polar. **Figure 3** shows the general chemical structure of silicone rubber with different substituent groups.

The main backbone chain is made of repeating  $-\text{Si}-\text{O}-$  groups while the methyl groups are attached at the side. Both  $\text{Si}-\text{O}$  and  $\text{Si}-\text{CH}_3$  bonds are thermally stable. This explains why VMQ and FVMQ grades have the same Type of heat resistance, as the main chain backbone is the same for both. The  $\text{Si}-\text{O}$  bond is partially ionic and it is relatively easy to be broken by concentrated acids and alkalis even at room temperature. Another important feature of the chemical structure of silicone rubber is the relatively large bond angle of  $\text{Si}-\text{O}$  (about  $140^\circ$ – $160^\circ$ ).<sup>7</sup> The intermolecular forces between silicone chains are very low probably because of the large distance between the adjacent chains, as silicone atoms are relatively large. Thus this facilitates ease of chain rotation which accounts for the lowest glass-transition temperature  $T_g$  ( $\sim -120^\circ\text{C}$ ) among the commercially available elastomers. The dimethyl rubbers swell more in aliphatic and aromatic hydrocarbons than in acetone and diesters. However, the swelling resistance towards hydrocarbon oil can be enhanced by the replacement of one methyl group on each silicon atom by a more polar group such as trifluoropropyl group ( $-\text{CH}_2\text{CH}_2\text{CF}_3$ ), that is, the FVMQ grade.

### 3.33.3 General Properties of Elastomers

All elastomers have some common properties such as being flexible, tough, relatively impermeable to both water and air, and elastic when vulcanized. One of the unique features of a vulcanized elastomer is its ability to exhibit high elasticity: the elastomer can be stretched to a few hundred percent and recover its original shape and dimensions almost instantaneously when the deforming force is released. For a material to exhibit high elasticity, it must fulfill the following conditions:

- flexible long chain molecules with relatively low molecular interaction forces,
- the long chain molecules must be cross linked (at least 2% cross linked network),
- rubbery above  $T_g$

The elasticity of an ordinary solid such as metal is associated with its internal energy. In contrast, the elasticity of rubber is entropy driven.

Elastomers are also well known for their good resistance to acids, alkali and chemical solutions. Elastomers have a proven record of accomplishment as the material used for tank lining or related chemical vessels. Beyond these common characteristics, each rubber has its own unique properties depending on the chemical structure as discussed briefly below.

#### 3.33.3.1 Structure–Property Relationship

The effects of chemical structure on some important physical and technological properties are summarized in **Table 5**.

##### 3.33.3.1.1 Mechanical strength

Tensile strength, tear strength, crack-growth resistance and fatigue life of the vulcanized elastomer depend on the chemical structure and its geometrical configurations. Elastomers having regular microstructure are able to crystallize, and those that have irregular microstructure are amorphous. **Figure 4** shows the chemical structure of general-purpose elastomers such

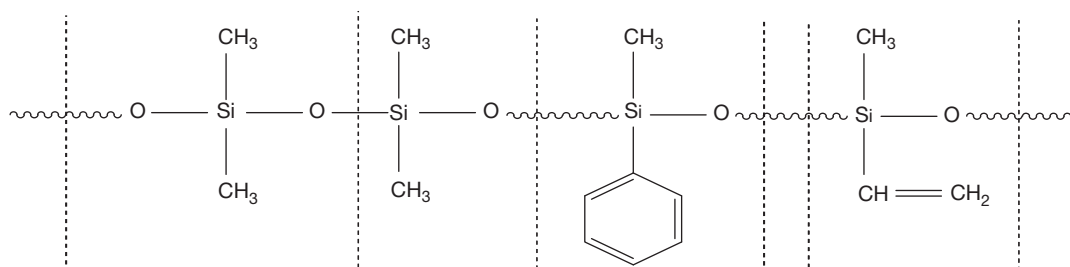


**Figure 3** Chemical structure of silicone rubber: MQ grade consists of methyl, PMQ grade consists of benzene rings and VMQ grade consists of vinyl.

**Table 5** Influence of chemical structure on physical and technological properties of elastomers

Basic structure	Technological significance
1. Nature of carbon-carbon backbone chain (i) Double bonds (ii) Single bonds	Unsaturated elastomers (having double bonds) are capable of being vulcanized with sulfur. Saturated elastomers (having single bonds) cannot be vulcanized with sulfur, but with peroxide. Unsaturated elastomers have poorer ozone cracking resistance and poorer oxidative resistance than saturated elastomers
2. Geometrical configurations	Regular microstructure would favor crystallization. Irregular microstructure leads to amorphous elastomers. The degree of crystallization affects mechanical strength
3. Polarity	Affects the degree of swelling resistance, rubber to metal bond strength, $T_g$ and electrical resistivity
4. Chain flexibility and glass transition temperature, $T_g$	Affects hysteresis and damping, and other related properties such as resilience, heat build-up, mechanical strengths, etc.
5. Molecular weight distribution	Broad molecular weight distribution provides easier processing than narrow molecular weight distribution

as natural rubber (NR), styrene butadiene rubber (SBR) and polychloroprene rubber (CR).

Natural rubber is 100% *cis*-1,4-polyisoprene indicating that it has regular microstructure, thus enabling it to crystallize. NR will crystallize at low temperatures. Crystallization has its own kinetic; in the case of NR the maximum rate of crystallization occurs at  $-26^\circ\text{C}$ .<sup>2,6</sup> When the rubber crystallizes, it hardens progressively and eventually loses its flexibility and rubber-like elasticity. The maximum amount of crystalline region is about 33% in the case of NR. However, if a tensile strain (more than 200%) is applied to NR it crystallizes almost instantaneously even at high temperatures. This phenomenon is known as strain-induced crystallization. Since crystallization is a reversible process, the crystals are completely melted once the applied strain is removed.

Low temperature crystallization brings few disadvantages to NR, particularly when it involves mixing. When NR crystallizes, it becomes very stiff and may cause damage to the mills. To overcome this problem, the common practice is to place the crystallized NR in a hot room (oven) to melt the crystals so that the rubber regains its flexibility. Any unmelted crystals

present during the mixing process would interfere with the incorporation and dispersion of the compounding ingredients. In contrast, strain-induced crystallization offers a big advantage in that it helps to enhance the mechanical strength of the rubber. For example, an unfilled or gum NR vulcanizate gives higher tensile strength (23–27 MPa) than unfilled SBR gum vulcanizate (2–3 MPa). Unfilled (gum) vulcanizate refers to a vulcanized rubber containing no filler apart from the compounding ingredients necessary for vulcanization. The crystals that are formed during straining act like a reinforcing filler to enhance the tensile strength. Thus for a noncrystallizing elastomer, it is necessary to incorporate a reinforcing filler into the rubber to enhance its strength.

In addition to the reinforcing filler, the types of chemical crosslink such as polysulfidic (C–S<sub>x</sub>–C), monosulfidic (C–S–C), or carbon-carbon (C–C) also affect the strength of the vulcanized elastomer.<sup>8</sup> Polysulfidic crosslinks are weak and labile with lower bond energy than monosulfidic and carbon-carbon links. Polysulfidic crosslinks enhance mechanical strengths such as tensile and tear strengths because these weak and labile crosslinks relieve stresses by ‘yielding.’<sup>8</sup>

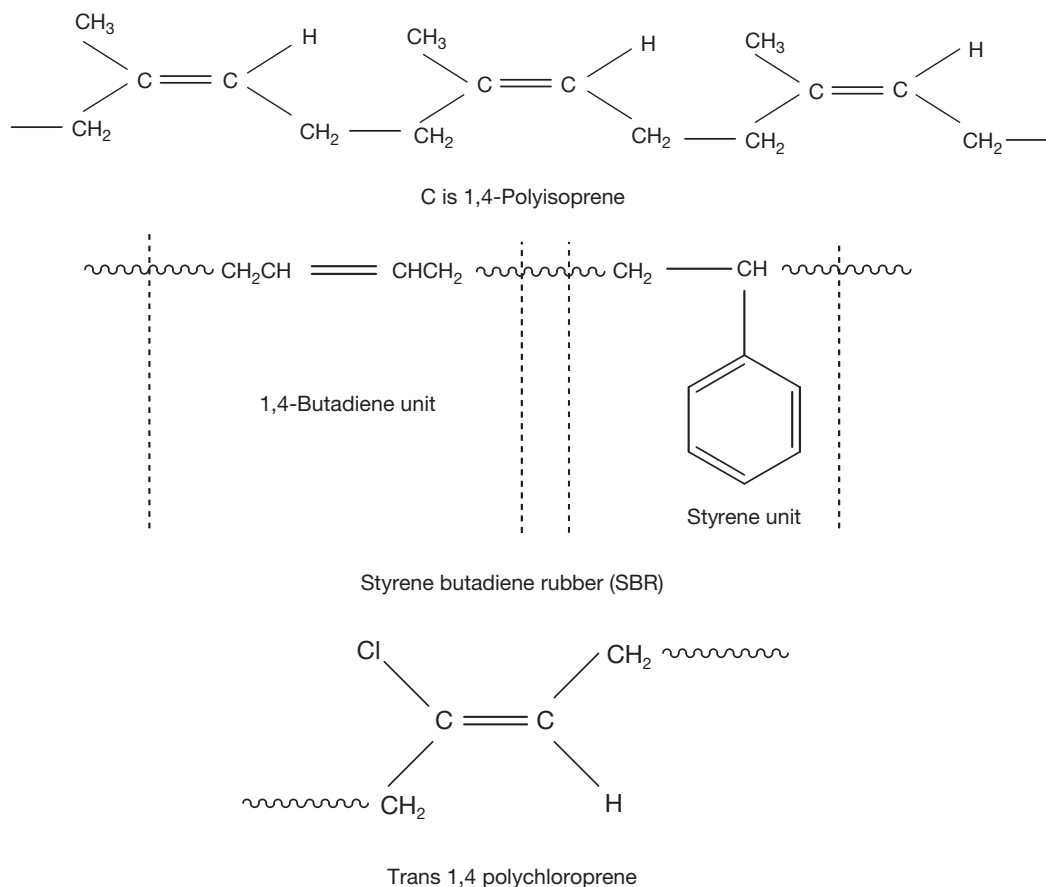


**Figure 4** Chemical structure of general-purpose elastomers.

Besides NR, polychloroprene rubber (CR) can also crystallize. Indeed CR crystallizes more readily than NR does because trans 1,4 configuration allows better molecular packing than cis 1,4 configuration.

### 3.33.3.1.2 Oxidation and ozone resistance

All unsaturated elastomers are susceptible to attack by oxygen and ozone which ultimately leads to chain scission followed by progressive loss in the physical properties. This aspect of oxidation will be discussed further in a later section. Almost all specialty elastomers have saturated bonds on the main backbone as well as high bond dissociation energy. Thus, specialty elastomers are highly resistance to heat, oxidation and ozone cracking.

### 3.33.3.1.3 Swelling resistance

The swelling resistance of rubber towards hydrocarbon oil depends on the extent of the polarity of the elastomer. The more the polar groups attached to the rubber molecules the higher is the polarity, and

the better is the swelling resistance towards hydrocarbon oil. The solubility parameter of elastomers and liquids determines the extent of compatibility and swelling resistance. The closer the solubility parameters between the elastomer and the liquid, the better is their compatibility. Indeed, the greater the thermodynamic compatibility between liquid and elastomer, the greater the absorption of liquid occurring when both have similar solubility parameters. The solubility parameter  $\delta$  is related to a parameter to measure the specific interaction between molecules known as cohesive energy density (CED) by the following mathematical relationship.

$$\delta = (\text{CED})^{1/2} \quad [1]$$

$$\text{CED} = (\Delta H - RT)/(M/\rho) \quad [2]$$

where  $\Delta H$  is the latent heat of vaporization,  $T$  is the absolute temperature,  $M$  is the molecular weight of the polymer,  $\rho$  is the density of the polymer, and  $R$  is the molar gas constant. For example, natural rubber has a solubility parameter value of 16.7 and NBR has

a solubility parameter between 21.0 and 22.0 MPa<sup>1/2</sup>. Most of the petroleum oils have a solubility parameter of 16.3 MPa<sup>1/2</sup>. Thus NR will swell markedly in petroleum oil because their solubility parameters are similar. In contrast, NBR has a solubility parameter very much higher than that of petroleum oil, so the two are not compatible. For this reason, polar NBR shows higher swelling resistance than nonpolar NR towards petroleum oil. Elastomers with higher polarity such as polyurethane rubber (AU) show even higher swelling resistance to nonpolar solvents than nonpolar elastomers. Based on the solubility parameter, polar rubbers swell more in polar solvents. Nonpolar rubbers are resistant to swelling in polar solvents.

#### 3.33.3.1.4 Glass-transition temperature $T_g$

The glass-transition temperature ( $T_g$ ) is the temperature at which molecular mobility begins to take place, below which molecular mobility is frozen and the elastomer becomes rigid and glassy. The  $T_g$  of the elastomer depends on the chemical structure of the elastomer. The presence of a polar atom, side groups, length of side chains, and crosslink reduces molecular mobility which would increase  $T_g$  of the elastomer. The glass-transition temperature affects a number of important technological properties such as strength, damping, low temperature flexibility, rolling resistance, wet grip, etc. High  $T_g$  elastomers are preferred to low  $T_g$  elastomers for applications where high mechanical strength, high damping, and excellent wet traction are required. For applications where excellent low temperature flexibility, low heat

generation, high resilience and low rolling resistance are required, low  $T_g$  elastomers are preferred to high  $T_g$  elastomers.

**Table 6** summarizes the respective  $T_g$ , ozone cracking resistance, chemical resistance and heat aging resistance of some of the important commercial elastomers.

### 3.33.4 Rubber Technology and Compounding

#### 3.33.4.1 Mastication and Mixing

Rubbers find very limited applications in their raw form. In their raw form, rubbers may be suitably used as binders and adhesives because of their inherent tack. To become useful products, they have to undergo various processes from mastication, mixing, shaping or fabrication prior to molding, as shown by the schematic flow chart in **Figure 5**.

#### 3.33.4.2 Rubber Compounding

Rubber compounding is the term used to denote the art and science of selecting and combining elastomers and additives to obtain an intimate mixture that will develop the necessary physical and chemical properties for a finished product. In compounding, one must cope with literally hundreds of variables in materials and equipment. There are three main areas of concern in rubber compounding, namely, (i) to secure certain properties in the finished product to

**Table 6** Some important technological properties of some important commercial elastomers

Elastomer	$T_g$ (°C)	O <sub>3</sub> resistance	Swelling resistance (%) <sup>a</sup>	Heat resistant up to (°C) <sup>b</sup>
NR	-72	L	200 (120 °C)	100
SBR	-63	L	130 (120 °C)	100
BR	-112	L	>140 (70 °C)	100
EPDM	-55	H	>140 (70 °C)	150
IIR	-66	M	120 (120 °C)	150
CIIR	-66	M	>140 (150 °C)	150
ACM	-22 to -40	H	25 (150 °C)	175
CO	-26	H	5 (150 °C)	150
CR	-45	M	65 (120 °C)	125
NBR (med ACN)	-34	L	10 (100 °C)	125
MVQ	-120	VH	50 (150 °C)	225
CSM	-25	H	50 (150 °C)	150
H-NBR	-30	H	15 (150 °C)	150
FKM	-18 to -50	VH	2 (150 °C)	250
EU	-55	H	40 (100 °C)	100

<sup>a</sup>Swelling after 70 h in ASTM oil 3.<sup>5,9</sup>

<sup>b</sup>Classification after ISO/TR 8461, aerobic condition, Method ISO 4632/1 3 days, (Retention properties).<sup>9</sup>

L = low resistance M = medium resistance H = high resistance.<sup>5,9</sup>



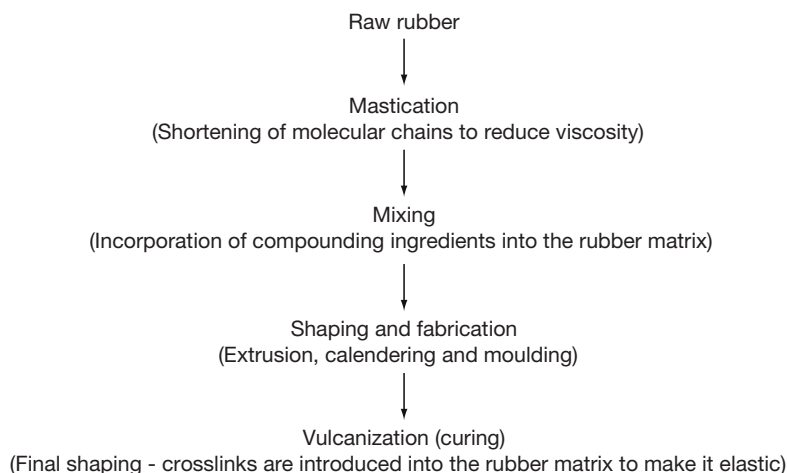


**Figure 5** Schematic flow process chart.

satisfy service performance; (ii) to be able to meet processing characteristics for efficient utilization of available equipment, and (iii) to meet conditions (i) and (ii) at the lowest possible cost. In other words, the most important criteria in compounding are to secure an acceptable balance among demands arising from the three concerned areas.

Theoretically, a rubber compound may consist of an elastomer and a cross linking agent. However, in practice, a rubber compound may contain 5 ingredients or even more than 10 ingredients, depending on the intended products, types of application and their service conditions. Each ingredient has a specific role and function(s). Each has an impact on properties, processability, and price. The real challenge is to develop a high quality rubber product at the lowest cost possible. The materials utilized by the rubber compounder can be classified into nine major categories, which are defined as follows:

- **Elastomers:** The basic component of all rubber compounds may be in the form of rubber alone, or master batches of rubber–oil, rubber–carbon black, or rubber–oil–carbon black.
- **Vulcanization agents:** These materials are necessary for vulcanization processes where chemical crosslinks are introduced into the rubber matrix to form a three-dimensional network. Crosslinks inhibit permanent flow under deformation or heat and prevent dissolution in solvents. Strength, stiffness and resilience increase upon cross linking, and set, stress-relaxation and creep decrease.
- **Accelerators:** In combination with vulcanizing agents, these materials reduce the vulcanization time (cure time) by increasing the rate of vulcanization. In most

cases, the physical properties of the products are also improved.

- **Activators:** These ingredients form chemical complexes with accelerators, and thus aid in obtaining the maximum benefit from an acceleration system by increasing vulcanization rates and improving the final properties of the products.
- **Age-resistors:** Antioxidants, antiozonants, and other materials are used to slow down ageing processes in the vulcanizates.
- **Fillers:** These materials are used to reinforce or modify physical properties, impart certain processing properties, and reduce cost.
- **Processing additives:** Formerly known as processing aids, the new term currently used is processing additives. These are materials used to modify rubber during the mixing or processing steps, or to aid in a specific manner during extrusion, calendering, or molding operations.
- **Softeners:** They are materials that can be added to rubber either to aid mixing, produce tack, or extend a portion of the rubber hydrocarbon (e.g., oil extended).
- **Miscellaneous ingredients:** These materials can be used for specific purposes but are not normally required in the majority of rubber compounds. They include retarders, colors, blowing agents, abrasives, dusting agents, odorants, etc.

### 3.33.4.3 Vulcanization

Vulcanization is a process of cross-linking rubber molecules chemically with organic/inorganic substance through the action of heat and pressure. The

rubber which is cross linked chemically is known as vulcanizate. The introduction of crosslinks into the rubber matrix may be comparatively few in number but are sufficient to prevent unrestricted flow of the whole molecules past neighboring ones. The low concentration of crosslinks implies that the vast majority of the segments making up the long chain molecules are free to move by virtue of kinetic energy. An unvulcanized rubber dissolves completely in its solvent. In contrast, a vulcanized rubber only swells. The chemical crosslinks prevent complete dissolution. A vulcanized rubber in this sense is a solid and will retain its shape and dimensions.

Vulcanization is a very important process in the rubber industry and conducted at relatively high temperatures (140–200 °C). For latex dipped goods, vulcanization is conducted at relatively low temperatures (60–120 °C) and requires no pressure as the latex is in fluid form and flows to take the final shape of the former and mold.

One of the most important chemicals in vulcanization is the cross linking agent. Elemental sulfur is the most widely used cross linking agent in the rubber industry because it is very cheap, abundant and easily available. Besides, sulfur is very easy to mix and readily soluble in the rubber. By varying the amount of sulfur to the accelerator ratio one can get different types of crosslink in the rubber matrix. Table 7 summarizes the types of sulfur vulcanization system,<sup>10</sup> nature of crosslinks produced and their influence on technological properties. Thus sulfur vulcanization provides flexibility as one can control the type of crosslink intended for specific use or applications. The most basic requirement for sulfur vulcanization is the availability of double bonds on the rubber hydrocarbon. The nonsulfur cross-linking agents include organic peroxides, quinines and their oximes and imines, metallic oxides and high energy radiation. The detailed mechanisms of vulcanization with these vulcanizing agents are discussed by Elliot and Tidd.<sup>10</sup>

There is another type of sulfur vulcanization system known as soluble efficient vulcanization (EV)<sup>10</sup> intended for engineering products that require consistent stiffness, low creep, low stress-relaxation and low set. This vulcanization system employs certain soluble accelerators, activators, and sulfur that completely dissolve in rubber giving a truly homogeneous compound.<sup>10</sup> In practice, this is achieved by selecting accelerators and activators that have a fairly high solubility in rubber at room temperature. Suitable accelerators for soluble EV include diphenyl guanidine, tetrabutylthiuram disulphide and *N*-oxydiethylenebenzothiazole-2-sulphenamide. Zinc oxide is insoluble in rubber, but it has to be included in the system as it plays a major role in sulfur vulcanization. However, 2-ethyl hexanoic replaces the common coactivator stearic acid as the latter reacts with zinc to form an insoluble zinc stearate which induces creep and the former forms a rubber-soluble zinc salt. The sulfur dosage employed in soluble EV must not exceed 0.8 pphr (parts per hundred of rubber) to ensure that it remains dissolved in the rubber and with no tendency to bloom to the rubber surface.

Nonsulfur vulcanization such as the peroxide vulcanization system produces carbon-carbon type of crosslink that gives excellent heat aging resistance and very low compression set. However, the mechanical strengths are lower than polysulfidic and monosulfidic crosslinks. The choice of vulcanization system depends on the service environment as well as the mode of deformation for the intended rubber product.

### 3.33.5 Rubber-to-Metal Bonding – Engineering and Automotive Applications

Most of the rubber springs involve bonding of rubber to metal. In many cases the metal parts are required for fixing purposes, particularly those of automotive components such as rubber bushes, engine mounts

**Table 7** Sulfur vulcanization systems, types of crosslink produced and their effect on technological properties

<i>Vulcanization system</i>	<i>Sulfur</i>	<i>Accelerator</i>	<i>Type of crosslink</i>	<i>Technological properties</i>
Conventional	2.0–3.5	1.0–0.4	Polysulfidic	Increase tensile and tear strengths, high compression set, and poor heat aging
Efficient (EV)	0.3–0.8	6.0–2.5	Monosulfidic	Excellent heat aging, low compression set, low tensile, and tear strengths
Semi-EV	1.0–1.7	2.5–1.0	Mixtures of poly, di- and mono	Compromise or balance in terms of strength and heat aging

and couplings. **Figure 6** shows some typical rubber-to-metal bonded products. In tank lining, the main function of rubber is to protect the metal against attack by corrosive chemicals as well as to protect the metal parts from oxidation by air and moisture, which leads to rusting.

The laminated rubber bearing consists of alternate layers of metal plates. The metal plates serve to restrain the lateral expansion of the rubber on compression. Because of restriction at the rubber metal interface, due to friction or when the rubber is bonded to metal, the rubber bulges at the end plates to maintain a constant volume. As a result, the effective compression modulus is dependent on the shape factor,  $S$ , defined as the ratio of loaded area to force free area.<sup>2</sup>

$$S = \text{Loaded area/Force free area} \quad [3]$$

For a rectangular rubber block of length  $L$ , width  $W$  and thickness  $h$ , shape factor  $S$  is given by eqn [4]:

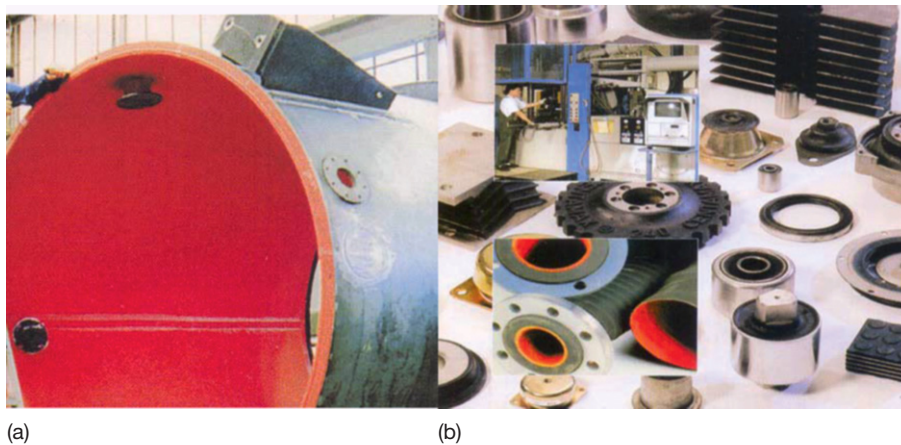
$$S = LW/[2b(L + W)] \quad [4]$$

The dependence of the compression modulus on the shape factor has a significant advantage where the vertical stiffness increases substantially, by inserting horizontal metal spacer plates into the rubber. For a rectangular rubber block having length  $L$ , width  $W$  and height  $h$ , the shear stiffness and compression stiffness are given by eqns [5] and [6] respectively.

$$k_s = GA/b \quad [5]$$

$$k_c = 3G(1 + 2S^2)A/b \quad [6]$$

Here,  $G$  is the shear modulus of the vulcanizate and  $A$  is the cross-sectional area of the rubber surface subjected to shear or compression. Equation [6] shows



Rubber bearing



**Figure 6** Rubber-to-metal bonding products – (a) tank lining (LHS), (b) various automotive rubber products (RHS) and (c) below rubber bridge bearing.

that the compression stiffness can be increased substantially by increasing the shape factor. The shape factor does not affect shear stiffness. For these reasons, laminated steel rubber bearings are used in bridges, where high compression stiffness is necessary to support all dead and live loads of the deck, and very low shear stiffness to accommodate movements associated with thermal expansion and contraction due to temperature changes.

To achieve efficient bonding at the rubber–metal interface, it is necessary that the rubber is chemically bonded to the metal surface. This is achieved in practice by following proper procedures laid down in the following section.

### **3.33.5.1 Bonding of Rubber to Metal**

#### **3.33.5.1.1 Preparation of metal plates**

The metal plates must be clean and free from any contamination such as oil, grease, protective coating, and rust. Exposing the contaminated metal surface to the vapor of a suitable organic solvent (e.g., chlorinated solvent) removes oil and grease. The next step is to remove metal oxides and rust on the metal surface, usually by the sandblasting technique or wire brushing. Apart from cleaning, sandblasting increases the surface area, which is very beneficial for strengthening the bonded area. Acid etching provides an alternative means of removing metal oxides from the metal surface.

It is very vital that the metal surface is completely free from oil, grease and rust to ensure efficient wetting of the bonding agent on the metal surface so that during vulcanization the bond formed between rubber and metal via the bonding agent is very strong. However, a few precautions need to be observed when sandblasting on the metal surface. The grit size, gun pressure and shooting distance must be correct to get the right surface topology, thus avoiding excessive wear or too little wear.

#### **3.33.5.1.2 Types of bonding agent and methods of applications of bonding agent to metal plates**

The common bonding agents for bonding rubbers to metals include ebonite solution or sheet, brass and proprietary adhesives. In the past, the bonding agent as well as the lining material for making tank lining was ebonite solution and calendered ebonite sheet. The ebonite compound contains a high amount of sulfur, about 25–35 pphr. This high sulfur content makes ebonite a hard and brittle material. Indeed ebonite is a thermoset as it is highly cross linked.

The high sulfur content of ebonite introduces high polarity that makes it a very suitable bonding agent. Despite the superior chemical resistance of ebonite, there are a few limitations such as its brittleness after cure, long cure time and potential of fire hazard due to exothermic reaction during curing, especially when a thicker lining is involved. For this reason, soft rubber linings are preferred to ebonite linings.

Brass is a very good bonding agent, and is widely used in the tire industry. Brass is coated on steel wire cords by the electroplating process. Brass-coated steel wire cords are used as breakers or belts placed underneath the tread and on top of the carcass of the green tire. During vulcanization, the sulfur forms covalent bonds with both the rubber and the component metals of the brass, leading to a very strong bond.<sup>11</sup>

In most rubber-to-metal bonded products, a proprietary bonding agent is preferred to the other two bonding agents. A proprietary bonding agent usually requires two coatings, *viz.* a primer and an adhesive cement. There are reasons why a two-coat system offers more insurance for the rubber to metal bond. The first coating known as a primer helps to eliminate corrosion in corrosion-prone metals when they are in contact with the rubber.<sup>12</sup> By using a primer, secondary cement (second coating–adhesive) that has a greater degree of bondability to the stock being used can be selected, rather than a one-coat system.<sup>12</sup> It is claimed that the two-coat system allows more metal adhesion into the primer, and more stock adhesion into the cement coat.<sup>12</sup> This results in a higher intrinsic bond with the two-coat system than a single coat system.

Bonding agents are applied by painting, spraying or dipping on treated metal parts in the form of a solution or aqueous suspension.

#### **3.33.5.1.3 Molding of rubber-to-metal bonded parts**

Finally, the dried, coated metal parts are loaded into the mold and the rubber is vulcanized in contact with these substrates by the conventional rubber molding techniques such as compression, transfer and injection molding. It is during this vulcanization process that the rubber is chemically bonded to the metal surface when the cross linking agents react with the adhesive.

However, in the case of tank lining, the method is different from the conventional rubber-to-metal bonded products. The method of applying calendered rubber sheeting onto the prepared metal surfaces is

analogous to that of applying rolls of wallpaper to the walls of a room. However, care must be taken to avoid entrapment of air between rubber and metal. The rubber sheet is laid down at the correct angle, and is rolled down into close contact with the adhesive. Applying the rubber sheet at the corner or edges of the tank is quite tricky. In practice, this is achieved by making joints at corners by inserting and rolling down an extruded rubber fillet of triangular cross-section and forming the sheet joints on top of the fillet. This technique gives to the lining a well finished appearance and reduces the danger of weak joints occurring in corners.

Upon completion of laying the rubber sheet onto the metal surface, the covered lining tank is usually allowed to rest for at least 24 h before being vulcanized. This resting period allows any air trapped between rubber and metal to diffuse, apart from enabling the adhered rubber sheet to recover and settle down before it is heated.

### 3.33.5.2 Vulcanization

It is usually done in an open steam autoclave for tanks or vessels that are small enough to go into the autoclave. When the lined vessel is too large to be accommodated in an autoclave it may be vulcanized in one of the following methods:

#### 3.33.5.2.1 Low or high pressure steam

This method is applicable to a vessel that has sufficient strength to withstand internally applied pressure. This procedure can be adopted if the vessel such as road or rail tank cars can be lined and then sealed and bolted to give a strong and steam proof pressure container. The steam pressure is passed through the lined vessel to the desired vulcanization temperature until the rubber is fully vulcanized. There are some elements of danger when dealing with high pressure steam. So it is very important that all the safety regulations are met in terms of design and material of the vessel. The work should be done under skilled engineering supervision.

#### 3.33.5.2.2 Water curing technique

This method is suitable for tanks or vessels that are too weak structurally to be put under steam pressure. Here, the lined tank is filled with water or brine. The water is heated by passing live steam into the water until it approaches boiling point. This temperature is maintained for a few hours until the rubber is fully vulcanized. Care must be taken to ensure that live steam does not impinge on the rubber lining to

avoid the occurrence of a large blister between the rubber and metal at the point of impingement. It is necessary to conserve heat by shielding the unit against draughts and cold to minimize temperature variations which would affect the uniformity of the cure.

#### 3.33.5.2.3 Hot air or ambient temperature vulcanization

This method is suitable for tanks or vessels which do not work with the methods discussed above. The choice of accelerator is very important. Ultrafast or very fast accelerator is usually used in the rubber compound. Care has to be taken to ensure that the rubber does not vulcanize prematurely (scorched) before it is applied onto the treated metal surface. One of the means to overcome the problem is to avoid mixing the accelerator and sulfur together, but to prepare sulfur masterbatch and accelerator masterbatch separately. The two masterbatches are blended together just prior to calendering, and the calendered sheet applied as soon as possible to the metal to avoid the risk of being scorched.

### 3.33.5.3 Types of Bond Failure and Possible Remedies

A rubber shear mount may be expected to deform up to 300% shear strain, and the mean shear stress acting on the rubber-to-metal bond can be as high as 10 MPa or 2/3 tons per square inch.<sup>11</sup> Steel laminated rubber bearings for bridges must have a minimum bond strength of about 9 N mm<sup>-1</sup> (MS 671, 1991).

It is important to observe the failure mode that occurs in rubber-to-metal bonded products because it throws some light and clues to the root cause of the problem. It is usual to conduct peel test to determine the interfacial bond strength between the rubber and metal. There are two basic types of bond failure either adhesive or cohesive. Adhesive failure may occur at the interfacial between the rubber and substrate, or between cement and substrate. Cohesive failure occurs within the rubber itself. There are three modes of adhesive failure.<sup>13</sup> First is called CM failure that takes place between primer and metal interface. Second is CP failure that occurs at the primer to cover cement interfacial. Third is RC failure where the bond fails at the rubber-cover cement interface. RC failures are the most common and the most difficult to solve.<sup>13</sup> There are a number of causes, which bring about these bond failures. They include the following: metal surface not cleaned efficiently due to poor cleaning procedure,



contamination of metal surface during handling, incomplete wetting of adhesive on the metal surface, variations of temperature of metal surface, precured adhesive, sweeping of adhesive during molding etc.<sup>13</sup> There are remedies to overcome these problems. First, ensure that the metal surface is free from all forms of contamination. Second, avoid contamination of metal surface during handling. Third, apply the primer and adhesive cement onto the metal surface evenly by taking care of the correct viscosity of the adhesive, and correct spraying distance and thickness of the adhesive film. Fourth, use the correct type of adhesive and follow strictly the instruction and procedure recommended by the chemical supplier.

If during the peel test, cohesive failure occurs within the bulk of the rubber, then this indicates that the interfacial bond strength between the rubber and metal plate via the bonding agent is stronger than the cohesive strength of the rubber itself.

### 3.33.6 Oxidation of Rubber

Metals oxidize in the presence of air and water and consequently they corrode, become rusty and weak. **Figure 7** shows the old version of using steel rollers to accommodate movements of the bridge deck brought about by expansion and contraction due to temperature changes.<sup>14</sup> The steel rollers corroded and suffered high wear and tear. In contrast, laminated steel rubber bearing did not show any sign of wear out after nearly twenty years of installation.<sup>14</sup> However, this does not mean that elastomeric bearing will last forever. Like metals, rubbers are also prone to corrosion. Corrosion of rubbers is associated with the aging process known as degradation. All unsaturated rubbers are subject to degradation due to the attack of heat, ultraviolet (UV) light, oxygen,

ozone etc. The more is the amount of unsaturation the more it is susceptible to degradation. The term aging as applied to rubber, covers a variety of phenomenon arising out of the factors described above. Aging properties of raw rubber differ from vulcanized rubber because of the latter's specific network structure and extra network material. When natural rubber is heat-aged in the presence of oxygen or air, it invariably loses strength, in particular its tensile strength decreases. The pattern of modulus change during aging is not so straight forward because there are two opposing reactions which can occur simultaneously. One is degradation of the molecular chains and crosslinks which causes softening; the other is additional cross linking which causes stiffening. Under any given set of aging conditions (time and temperature) either softening or stiffening reactions may predominate depending on the type of vulcanization system, type of filler and antidegradants employed in the rubber compound.

Oxygen reacts with rubber only after the rubber has been acted upon by energy. This is usually from UV light, heat or mechanical energy (flexing). This energy dislodges a hydrogen atom from the rubber molecule, resulting in the formation of a radical. The oxidation of polymer with elemental oxygen is called autoxidation because it is an autocatalytic. The rate of autoxidation is affected by temperature, the presence of catalyst and also the presence of antioxidant. When the oxygen attacks the rubber it produces hydroperoxide. The hydroperoxides break to form free radicals. This is an autocatalytic, self generated free radical process. The autoxidation process involves three main stages, namely, initiation, propagation and termination. In view of the complexity of autoxidation reaction with rubber, Bolland and Gee<sup>15,16</sup> used model olefins to study the kinetics of autoxidation. **Figure 8** shows the mechanism of autoxidation as proposed by Bolland.<sup>15,16</sup>

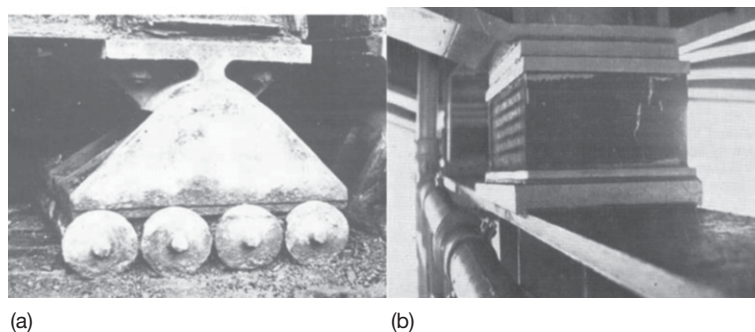


**Figure 7** (a) Steel roller bridge bearing and (b) steel laminated rubber bearing installed in 1955. Adapted from Mullins, L. *Proc. Rubb. in Eng. Conf.* Kuala Lumpur, 1974, pp. 1–20, with permission from the Malaysian Rubber Board.

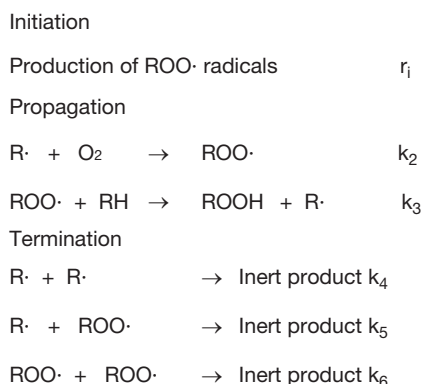


**Figure 8** Mechanism of autoxidation of natural rubber as outlined by Bolland. Adapted from Barnard, D.; Lewis, P. M. In *Natural Rubber Science and Technology*; Robert, A. D., Ed. Oxford University Press, 1988; Chapter 13, pp 621–673, with permission from . . .

The autoxidation is initiated with the generation of free radicals due to the relatively facile homolysis of traces of peroxide present in the elastomer.<sup>17</sup> The rate of oxidation is related to the concentration of the hydroperoxide [ROOH] as shown by eqn [I] below<sup>16</sup>.

$$r_i = k_i[\text{ROOH}]^2 \quad [\text{I}]$$

The resultant free radicals react with oxygen to form the deleterious peroxides and propagate the autoxidation reaction. The rate of propagation is controlled by the hydroperoxide yields and those of decomposing. The hydroperoxide yields for a large number of olefins range from almost 100% downwards to values controlled by side reactions of the peroxy radicals, such as addition to olefinic double bonds, when hydrogen abstraction becomes relatively difficult.<sup>16</sup> Such side reactions would continue the propagation chain. However, when the value of the rate constant  $k_2$  becomes large, the reaction of alkenyl radicals with oxygen become independent of oxygen pressure. Under these conditions, rate-determining step is no longer controlled by the rate constant  $k_3$ , of the hydrogen abstraction step. Termination would occur primarily by the interaction of alkenyl radicals. Then the propagation rate is given by eqn [II] below<sup>16</sup>.

$$r = r_i^{1/2} k_2 k_4^{-1/2} [\text{O}_2] \quad [\text{II}]$$

Termination occurs solely by the mutual destruction of peroxy radicals and represented by the following rate equation<sup>16</sup>:

$$r = r_i^{1/2} k_3 k_6^{-1/2} [\text{RH}] \quad [\text{III}]$$

The outcome of this autoxidation is either chain-scission or cross-linking. If chain-scission occurs, the degraded rubber will be soft and tacky. On the other hand, if cross linking occurs the degraded rubber will be hard and brittle. In both cases, the mechanical strength of the rubber decreases markedly. Model olefins were used to study the mechanism of oxidation of NR due to complexity of the oxidation reaction in particular when the rubber is vulcanized.<sup>16</sup> The oxidation of rubber vulcanizate is technologically important since the absorption of only a small amount of oxygen (1%) by rubber vulcanizate results in a considerable change in the physical properties.

It is believed that the oxidation of natural rubber follows the same route and analogous to that of the model olefins where the polyisoprene chain undergoes scission.<sup>16</sup> An essential concept of this process is the number of molecules of oxygen absorbed per scission event. According to Bolland,<sup>15</sup> the oxidation reaction would finally lead to an alkoxy radical disproportionate to butan-2-one-4-al rather levulinaldehyde, and the vinylic radical would have to be oxidized further to the methyl ketone end group. Minute amount of certain heavy metals such as copper, iron and manganese catalyze autoxidation reactions. However, this catalytic action can be prevented by applying protective or chelating agent such as metal deactivator like *p*-phenylenediamines.

In the case of vulcanized rubber, the oxidation reaction is more complex than that of raw rubber since the various different types of crosslink (e.g., polysulfidic, disulfidic, monosulfidic, cyclic sulfides, conjugated dienes and treines, etc.) present in the network structure may affect oxidation in some way or another.<sup>16</sup> Most types of sulfur vulcanizates initially hardens on aging before degradation occurs. This hardening is due to cross linking associated with oxidative reactions of sulfur species in the network that takes place before chain scissions take place.<sup>16</sup>

Barnard and Lewis<sup>16</sup> listed out some useful and important points concerning chain scission mechanism for unprotected NR at modest temperature as follows:

- Scission occurs once approximately for every 20 molecules of oxygen absorbed.
- The scission is of the rubber chain even in peroxide or sulfur vulcanizates although concomitant crosslink can occur in the latter.
- Kinetically, scission appears to take place in the propagation step.

- Each scission event results in a stable terminal ketone group being formed on one of the new chains and a transient terminal aldehyde group on the other.

Since autoxidation results in chain scission, means and ways were introduced to determine accurately chain scissions caused by a known quantity of oxygen absorbed. A parameter known as scission efficiency  $\varepsilon$  defined as the number of molecules of oxygen absorbed which bring about one scission event<sup>16</sup> was introduced to monitor chain scission quantitatively. There are two methods either physical or chemical to monitor chain scission. The common physical methods involved measuring molecular weight reduction, stress-relaxation, sol-gel analysis, and stress-strain characteristics.<sup>16</sup> For example, in stress-relaxation method, a rubber sample of a uniform cross-section is held at a constant extension and maintained at a constant temperature. When a network is oxidized due to the cleavage of stress-supporting chains, then the stress would decay and this event would lead to occurrence of stress-relaxation. The change in moles of stress-supporting chains per gram can be calculated from eqn [7]<sup>16</sup>:

$$f_t/f_0 = N_t/N_0 \quad [7]$$

where the subscripts  $t$  and  $0$  refer to the samples after time  $t$  and time zero respectively, and  $f$  derived from the statistical theory of rubber elasticity<sup>18</sup> is given by eqn [8]:

$$f = \rho NRTA_0(\lambda - \lambda^{-2}) \quad [8]$$

where  $\rho$  is the density of rubber,  $N$  is the number of moles of stress-supporting chains per gram,  $R$  is the gas constant,  $T$  is the absolute temperature,  $A_0$  is the unstrained cross-sectional area, and  $\lambda$  is the extension ratio. Stress-relaxation method has the advantage of being able to monitor scission event continuously, and if the amount of oxygen absorbed is also known then the scission efficiency  $\varepsilon$  can be calculated.<sup>16</sup> However, on a short time scale, the decay in stress level as function of time at constant deformation and temperature is associated with the rearrangement of molecular chains and it is predominantly attributed to viscoelastic behavior of the rubber.

Almost all technical specifications of elastomeric products require passing an aging test. The use of aging tests is extremely important in assessing the service life of elastomeric products because properties of vulcanizate could change during service.

The basic principle of the test is to expose rubber test-pieces to air at an elevated temperature (70 or 100 °C) for a specified period (7 or 14 days or longer). This so-called accelerated aging test causes deterioration of rubber in air due to combined effects of oxidative and thermal aging. The tensile properties, set and hardness are measured on these samples before and after ageing. If minor changes in these properties result, long service life may be expected; if appreciable changes occur, service life may be short. However, it must be stressed here that accelerated ageing test is a useful quality control and specification tests. There are significant difficulties in predicting service life from accelerated aging test. Use of test temperatures much above the anticipated service temperature is not advisable because the correlation between the results of such tests and service performance becomes increasingly tenuous.

### 3.33.7 Ozone Cracking of Rubber

Apart from oxygen, all unsaturated elastomers are also susceptible to ozone attack although ozone concentration in the outdoor atmosphere at ground level is about 1 pphm (part per hundred million of air by volume).<sup>19,20,21</sup> However, this can be significant because the reaction of ozone with the double bond is extremely fast and causes cracking on strained rubber. The cracks appear slowly at right angle to the direction of the strain applied, that grow slowly and consequently lead to a break of the vulcanizate. Ozone being very reactive attacks the double bonds of the rubber and produces ozonide that cleaves to produce zwitterions.<sup>17</sup> The zwitterions are unstable and will breakdown to form other zwitterions. These zwitterions may react with other zwitterions to produce diperoxide compound, or react with carbonyl compound to produce ozonide. In both cases, the ultimate result is chain scission. The mechanism of ozone attack on olefin is as shown in Figure 9.<sup>17</sup>

However, there is a subtle difference between ozone cracking and auto-oxidation where the former requires a certain critical strain level ( $\sim 5\%$  for unprotected NR) for its occurrence.<sup>19,20,21</sup> The severity of ozone cracking increases rapidly with strain level. Braden and Gent,<sup>19</sup> and subsequently Lake *et al.*<sup>20,21</sup> investigated various factors affecting ozone cracking. For example, Lake and Thomas<sup>20</sup> came out with a boundary layer theory for ozone attack on rubber surface to explain the rate of ozone crack growth. According to their theory, the variation in

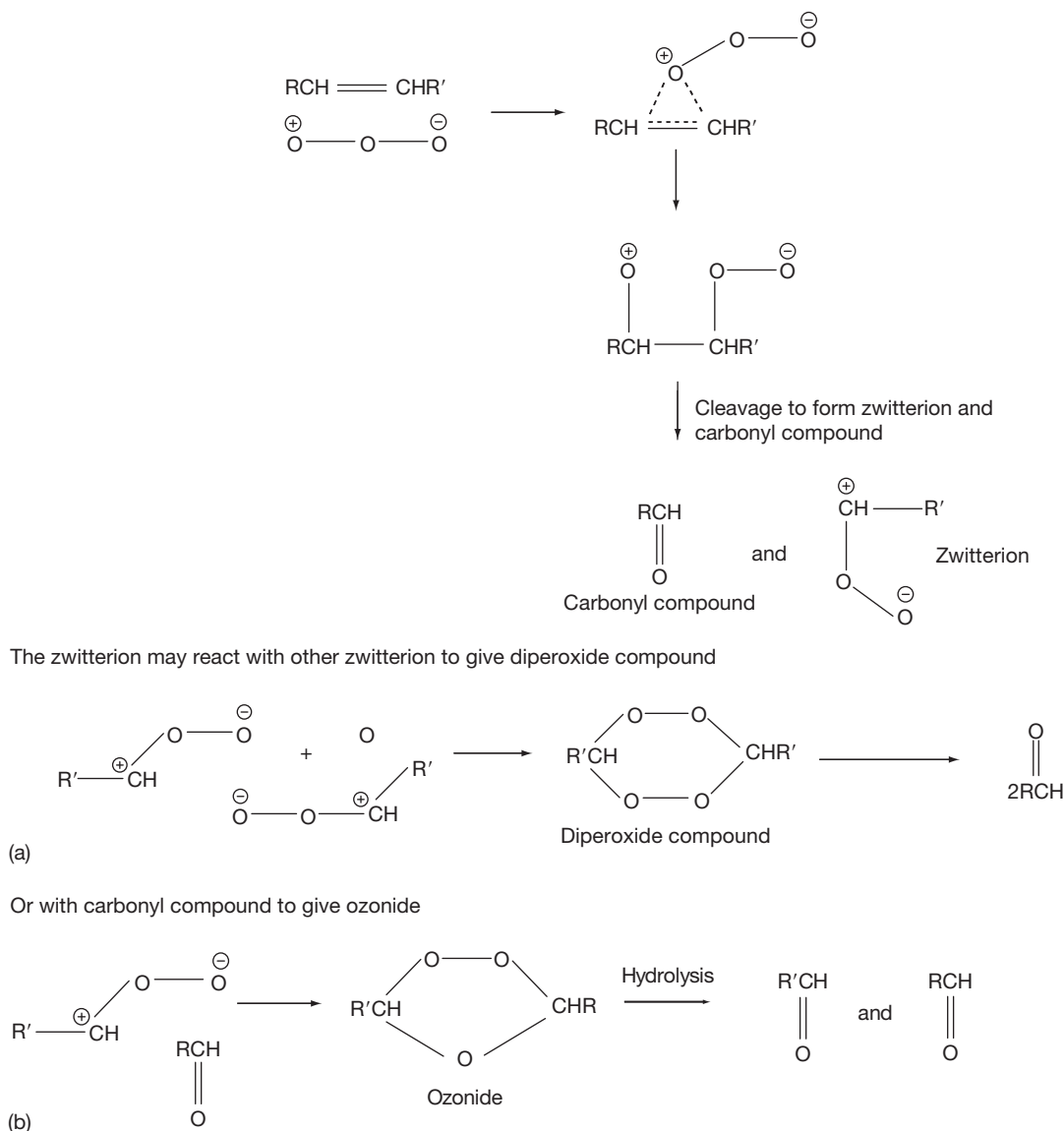


**Figure 9** Mechanism of ozone attack on olefins.

the rate of ozone attack on stretched rubber surfaces produced by changes in the air velocity and magnitude of the strain is controlled by the diffusion of ozone across the relatively stationary boundary layer adjacent to rubber surface. The boundary layer effect is important because of the readiness with which ozone is destroyed by stretched rubber.<sup>20</sup> As mentioned earlier, ozone cracking occurs only in elastomers subject to tensile stresses. Elastomeric components used in compression will crack only in the regions of the surface where tensile stresses are induced. These cracks are unable to penetrate very

far because they soon encounter compressive rather than tensile stresses. Thus ozone cracking is not a serious problem for large elastomeric components such as rubber bearings which are used in compression. Nevertheless, ozone cracks are unsightly and may initiate fatigue crack growth, which ultimately leads to mechanical failure. In view of this deleterious effect, it is necessary to carry out test on ozone resistance. The test involves exposing the stretched test-pieces (20% strain) in an ozone-rich atmosphere at a fixed temperature (23 or 40 °C) and inspecting the surfaces for cracks with the aid of a magnifying

glass at intervals of time. If cracks are not observed after completion of test, the vulcanizate is said to have good resistance to ozone cracking.

### 3.33.8 Heat Aging Resistance

Elastomers can survive over long periods in service at ambient temperatures without any measurable deterioration if the products are sufficiently thick. For a thick section of rubber, the availability of oxygen will be limited by diffusion, and components with bulky rubber layers can be considerably more resistant to elevated temperatures than thin rubber sections. For example, bearing pads of NR installed in 1890 had been examined, and although the outer 1–2 mm of rubber had degraded after 96 years of exposure to the atmosphere, the inner core of the rubber was still in good condition as shown by the photograph in [Figure 10](#).<sup>2</sup> Rubber samples taken from the interior portion were found to retain good physical properties as that of freshly prepared compounds.<sup>2</sup> At sufficiently elevated temperatures, all types of elastomer will undergo degradation. However, conventional NR vulcanizates can be used safely at 60 °C, the maximum ambient temperature likely to be encountered practice.<sup>2</sup> At temperatures of 300 °C and above, NR vulcanizates first softens as molecular breakdown

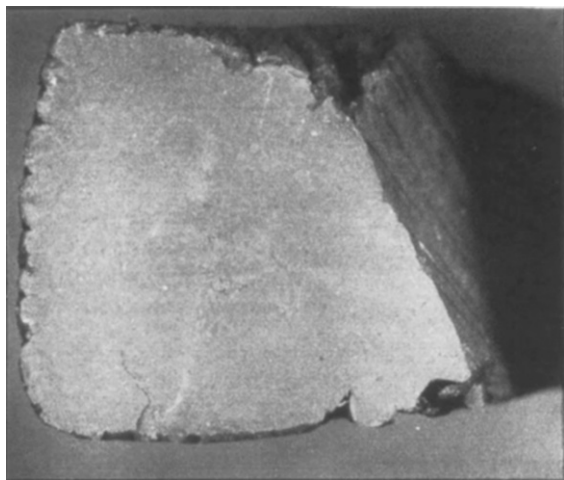


**Figure 10** Cross-sectioned view of a 100-year old bridge bearing pad showing the very small depth of penetration of atmospheric degradation. Adapted from Fuller, K. N. G.; Muhr, A. H. *Engineering design with natural rubber*, NR Technical Bulletin, 5th ed.; The Malaysian Rubber Producers' Research Association, London, 1992; pp 1–33, with permission from Tun Abdul Razak Research Centre, Brickendonbury Hertford, England.

occurs, then resinify, becoming hard and brittle.<sup>2</sup> Flammable vapor are emitted and ignition occurs. However, the rate of burning is extremely slowly for the case of large block rubber.<sup>2</sup>

In recent years, new performance demands for automotive elastomers have been proposed<sup>22</sup> to perform at high operating temperatures. This move was made to accommodate increasing concern for improved fuel economy, which resulted in a significant downsizing and redesign of the automobile. Concomitantly the engine compartment became smaller and more difficult to cool thus raising the temperature of the under hood. Current automotive elastomers are expected to perform well under a 120 °C in-service temperature at least until the life of the car.<sup>22</sup>

There is a growing expectation those future automotive elastomers to perform well in a 150 °C environment for over 100 000 miles.<sup>22</sup> This is a clear signal that specialty elastomers would find very strong markets over general-purpose elastomers for high temperature performance.

### 3.33.9 Flex Cracking

Flexing and cyclic stresses can lead to premature failure during service. There are two basic mechanisms of crack growth, (i) ozone crack growth, due to primarily chain scission, and (ii) mechanico-oxidative crack growth, due to mechanical rupture at the tip of a flaw, which is considerably facilitated by the presence of oxygen.<sup>23</sup> Both types of growth can occur under static or dynamic conditions or together. The amount of crack growth in a given time is directly proportional to the ozone concentration. The crack growth rate  $dc/dt$  of a single ozone crack under static conditions is given by [eqn \[9\]](#):

$$dc/dt = \alpha q \quad [9]$$

where  $q$  is the ozone concentration and  $\alpha$  a constant (the rate at unit ozone concentration) which is a property of the rubber.<sup>23</sup> The cyclic crack growth rate is given by [eqn \[10\]](#):

$$r = (dc/dn)_{\text{ozone}} = (F/f_f)\alpha q \quad [10]$$

where  $F$  is the time fraction of cycle for which the test-piece is strained, and  $f_f$  is the frequency.<sup>23</sup> Based on fracture mechanics approach, and assuming that the growth of naturally occurring flaws of a fatigue test has the same characteristics as that of a crack growth test, Lake and Lindley<sup>23</sup> worked out



the fatigue life of vulcanized elastomer as given by eqn [11]:

$$N_f = 1/(16BW_s^2c_0) \quad [11]$$

where  $N_f$  is the number of cycles to failure from a naturally occurring flaw of size  $c_0$ .  $B$  is the crack growth constant, and  $W_s$  is the strain energy density. Thus the fatigue life  $N$  can be predicted from known parameters of eqn [11].

### 3.33.10 Oil Absorption

An unvulcanized elastomer becomes solution when immersed in its solvent; in contrast, a vulcanized elastomer will only swell. The extent of swell depends on the amount of solvent absorbed, which in turn depends on the crosslink concentration and types of solvent. Swelling is undesirable because apart from dimensional instability, the modulus and mechanical strengths are all decreased making the

swollen vulcanizate unsuitable for most engineering applications.<sup>2</sup> In the case of rubber-to-metal bonded, bond failure occurs if the liquid is able to reach the metal plate. **Figures 11 and 12** show some of the typical automotive elastomeric components such as fuel and oil hoses, gaskets, O-rings and seals which are in contact with automotive fuels. These rubber components are thin and susceptible to damages when swollen excessively by the oil. Additives such as ethanol, methanol, and methyl *t*-butyl ether are being placed in gasoline with a view to improve its octane number.<sup>22</sup> Increasing the alcohol content of the gasoline increases the amount of swell, which is very undesirable not only because of dimensional instability, but also reduces tensile strength and elongation at break of the swollen elastomer.

It is well established that swelling is diffusion-controlled and the volume of liquid absorbed is initially proportional to the square root of the time of immersion.<sup>2</sup> For most organic liquids, the rate of penetration depends on their viscosity rather than

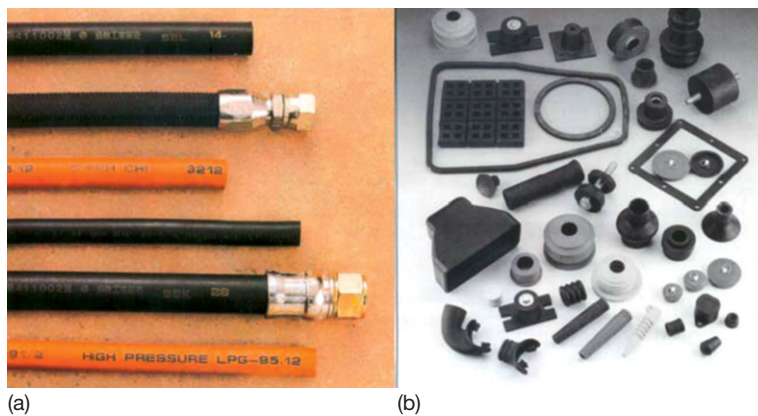


**Figure 11** Automotive rubber products in contact with oil and heat: (a) hoses – hydraulic, fuel, gasoline pump, and steam hose and (b) gaskets, O-rings, seals, and exhaust hanger, etc.

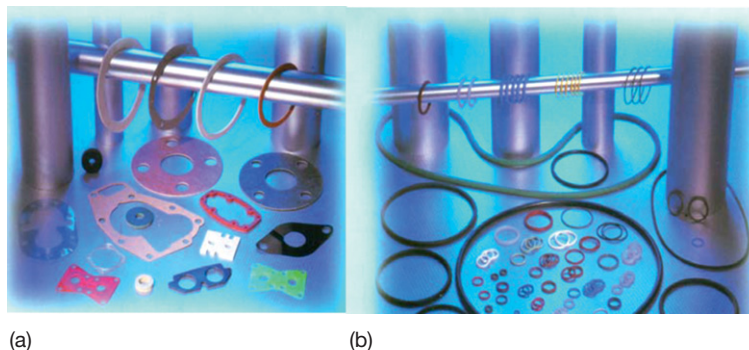


**Figure 12** Automotive rubber components: (a) gaskets and (b) O-rings and seals.

their chemical nature<sup>2</sup>. Figure 13 shows the time–viscosity relationship for the liquid to penetrate 5 mm into the rubber interior.<sup>2</sup>

For NR, it takes about 4 days for a volatile liquid such as toluene to penetrate 5 mm depth, 1–2 years for engine lubricating oil, and about 30 years for a petroleum jelly, even with continuous immersion.<sup>2</sup> It is possible to estimate the distance of liquid in a given time provide that the penetration rate is known.<sup>2</sup> Alternatively, the viscosity of the liquid may be used if penetration rate is not known since the penetration rate is related to viscosity as shown earlier in Figure 13.

Southern<sup>24</sup> has introduced a nomogram as illustrated in Figure 14 to facilitate the calculation in estimating the penetration depth of liquid into the elastomer. Although the data were obtained for NR, but would be expected to work with other elastomers of similar  $T_g$ .<sup>24</sup> As an illustration to use the nomogram, Southern<sup>24</sup> has calculated, a liquid with penetration rate of  $7 \times 10^{-5} \text{ cm s}^{-1/2}$  would take 4 weeks to penetrate 1 mm, but 100 years to penetrate 40 mm of the rubber block. The penetration rate–viscosity relationship does not hold for water because of the presence of hydrophilic impurities which complicate transport of water in elastomers.<sup>24</sup>

### 3.33.10.1 Effect of Crosslink Concentration and Polarity on Swelling Resistance

Natural rubber (NR) latex has found very wide applications in the glove industry since the 1920s. This is attributed to the excellent tear and puncture

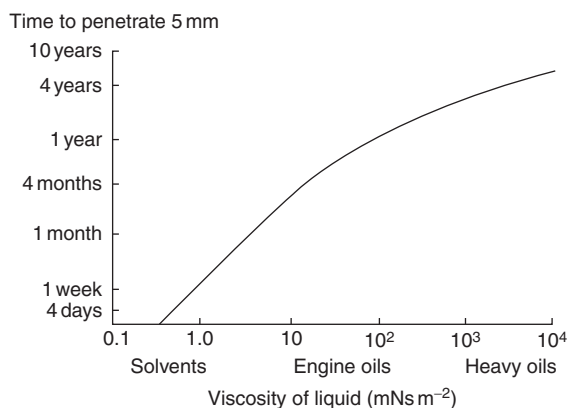


**Figure 13** Effect of viscosity of liquid on penetration time. Adapted from Fuller, K. N. G.; Muhr, A. H. *Engineering design with natural rubber*, NR Technical Bulletin, 5th ed.; The Malaysian Rubber Producers' Research Association, London, 1992; pp 1–33, with permission from Tun Abdul Razak Research Centre, Brickendonbury Hertford, England.

resistance of NR latex films. Besides, NR latex film exhibits very high extensibility (600–1000%) before its breaking point. These properties make NR latex film an excellent barrier protection against infectious liquids and gases. Most of the examination and surgical NR latex gloves are used in hospitals and clinics. However, recently NR latex gloves have entered the fast food industry where good swelling resistance is an essential requirement. Being a nonpolar rubber, NR latex gloves have a poor swelling resistance which limits its application in the fast-food industry. The fast-food industry is growing very fast all over the world. There is a growing concern over the cleanliness and hygiene of the food. It is essential that the workers wear rubber gloves to avoid contact with the food they serve. Rahim and Samsuri<sup>25</sup> investigated the effect of crosslink concentration and effect of blending carboxylated nitrile rubber (XNBR) with NR latex on the swelling resistance of NR latex film towards cooking oil. The amount of sulfur was varied to produce different crosslink concentrations. The crosslink concentration was determined by immersing the latex film sample in a solvent until equilibrium swelling was attained. The crosslink concentration was calculated by using the Flory–Rehner equilibrium swelling equation as proposed by Mullins<sup>18</sup> given by eqn [12]:

$$-\ln(1 - v_r) - v_r - \chi v_r^2 = 2\rho V_1 [X]_{\text{phy}} v_r^{1/3} \quad [12]$$

where  $v_r$  is the volume fraction of rubber in the swollen gel,  $\rho$  is the density of rubber,  $V_0$  is the molar volume of solvent,  $\chi$  the rubber–solvent interaction parameter, and  $[X]_{\text{phys}}$  is the physically manifested crosslink concentration. The diffusion coefficient  $D$  was calculated from eqn [13]<sup>24</sup>:

$$M_t/M_\infty = (2/l)(Dt/\pi)^{1/2} \quad [13]$$

where  $M_t$  is the total amount of liquid absorbed per unit area of the sheet after immersion for time  $t$ ,  $M_\infty$  is the amount of liquid absorbed after infinite time (in this case time to reach equilibrium swelling), and  $l$  is the half thickness of the film sheet. It is necessary to plot  $M_t$  against square root time as shown in Figure 15 to calculate  $D$  in eqn [13].

The effect of crosslink concentration on the diffusion coefficient of cooking oil in the latex film is shown in Table 8.<sup>25</sup> The results show that increasing the crosslink concentration decreases the diffusion coefficient significantly. Increasing the sulfur content from 0.6 to 3 pphr increases the crosslink concentration by about 90%, which merely decreases the

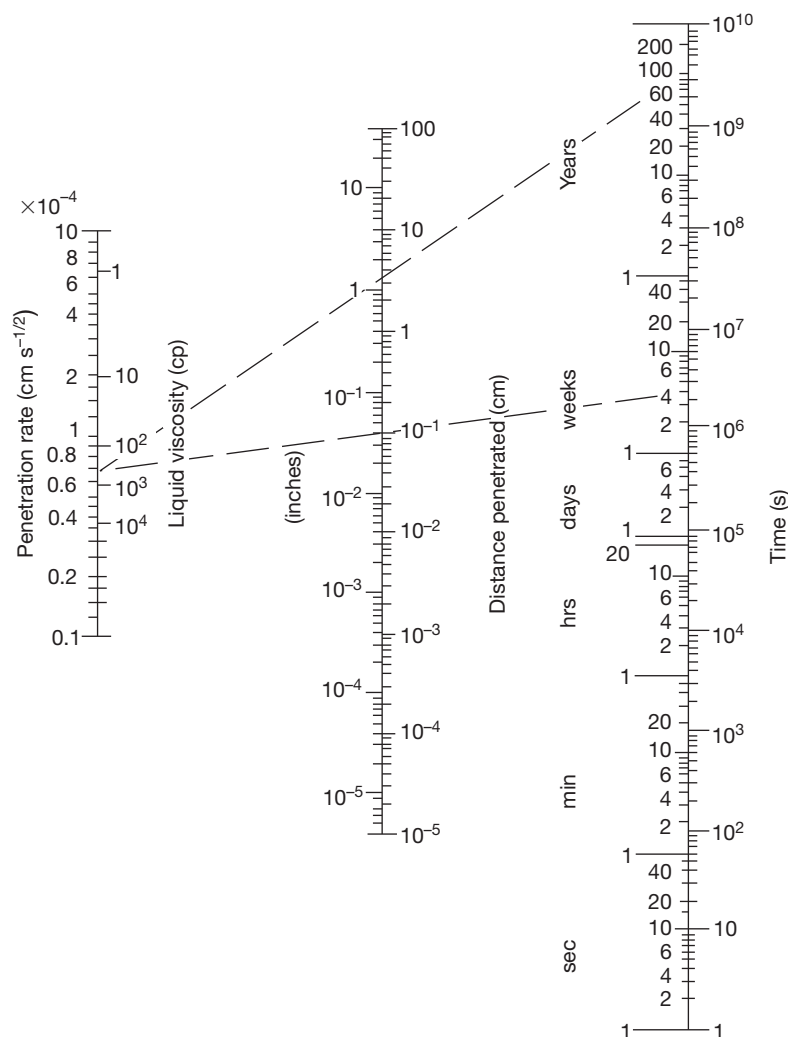


**Figure 14** Nomogram to facilitate rapid calculation of distance penetrated by liquid into rubber. Adapted from Muniandy, K.; Southern, E.; Thomas, A. G. In *Natural Rubber Science and Technology*; Robert, A. D., Ed.; Oxford University Press, Oxford, UK, 1988; Chapter 13, pp 820–851, with permission from Oxford University Press.

diffusion coefficient by about 23%. However, the most efficient method to increase swelling resistance is through physical blending of NR latex with XNBR latex, where the diffusion coefficient  $D$  of the oil into the film decreases by a factor of 2.7 compared with NR latex having the highest crosslink concentration. Thus, this work shows strong evidence that blending of nonpolar elastomer with polar elastomer enhances the swelling resistance of the former.

### 3.33.11 Water Absorption

Elastomers find wide uses in marine and offshore engineering applications. The application of elastomers

in water management is attributed to its high impermeability to water. A rubber sheet is used to line the water reservoir and pond, while inflatable rubber is used as a dam. Rubber dock fenders rely on the energy absorption capacity of the rubber. Inevitably, the rubber will absorb some quantity of water as these rubber products spend a considerable time under water. It is of great concern whether the absorption of water would impair the strength of the rubber.

The true solubility of water in rubber is very low.<sup>24</sup> Nonetheless, relatively large amounts of water can be absorbed during prolonged immersion as shown in [Figure 16](#).<sup>2</sup> The diffusion of water in elastomers is not straightforward, but complicated by the presence of hydrophilic materials. In the case of NR it is mainly

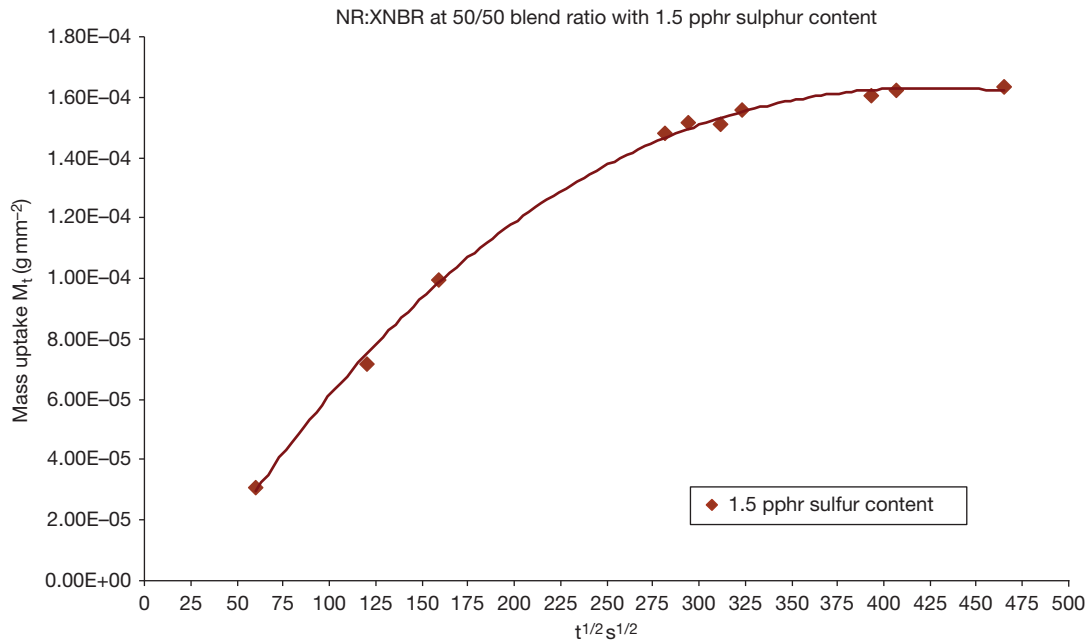


**Figure 15** Typical mass uptake curve for NR/XNBR blend latex film.<sup>25</sup>

**Table 8** Effect of crosslink concentration on diffusion coefficient  $D$  of cooking oil into NR latex film

Sulfur level (pphr)	$[X]_{phy}$ (mol per kg RH)	$D$ ( $m^2 s^{-1} \times 10^{-13}$ )
0.6	$4.46 \times 10^{-2}$	4.70
1.0	$4.60 \times 10^{-2}$	4.00
2.0	$4.89 \times 10^{-2}$	3.70
3.0	$5.82 \times 10^{-2}$	3.57
NR:XNBR (50:50) 1.5	—	1.30

proteinaceous.<sup>24</sup> When water diffuses into the rubber, the water-soluble hydrophilic materials dissolve forming droplets of solution within the rubber. Osmotic pressure gradient would exist between watery domains in the rubber and that of the external solution immersing the rubber.<sup>24</sup> This results in more water diffusing into the internal solution droplet. Water absorption reaches its equilibrium when the elastic stresses acting on the droplets balance the osmotic pressure difference. Muniandy and Thomas<sup>24</sup> proposed a mathematical model for water absorption to derive equations for the equilibrium water uptake and to evaluate the kinetics of water absorption and desorption. From the model, they calculated the equilibrium water uptake and the apparent diffusion coefficient. They found very good agreement between theory and experimental results.

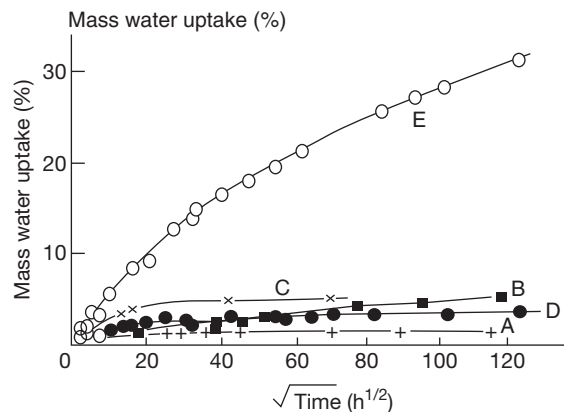


**Figure 16** Corrected mass uptake measurements for engineering rubbers in seawater at 23 °C: (a) deproteinized NR, (b) lead oxide cured polychloroprene, (c) nitrile rubber, (d) conventional NR, and (e) conventional polychloroprene. Adapted from Fuller, K. N. G.; Muhr, A. H. *Engineering design with natural rubber*, NR Technical Bulletin, 5th ed.; The Malaysian Rubber Producers' Research Association, London, 1992; pp 1–33, with permission from Tun Abdul Razak Research Centre, Brickendonbury Hertford, England.

Later, Lake<sup>26</sup> investigated the kinetics of water (tap water) absorption in elastomers and their effects on properties. He reported that when the absorption was large (50% or more), the rubber test-piece degraded. Severe degradation leads to porosity of the surface layer, and when pressed, water exudes.<sup>26</sup> However, at a low level of absorption, Lake observed

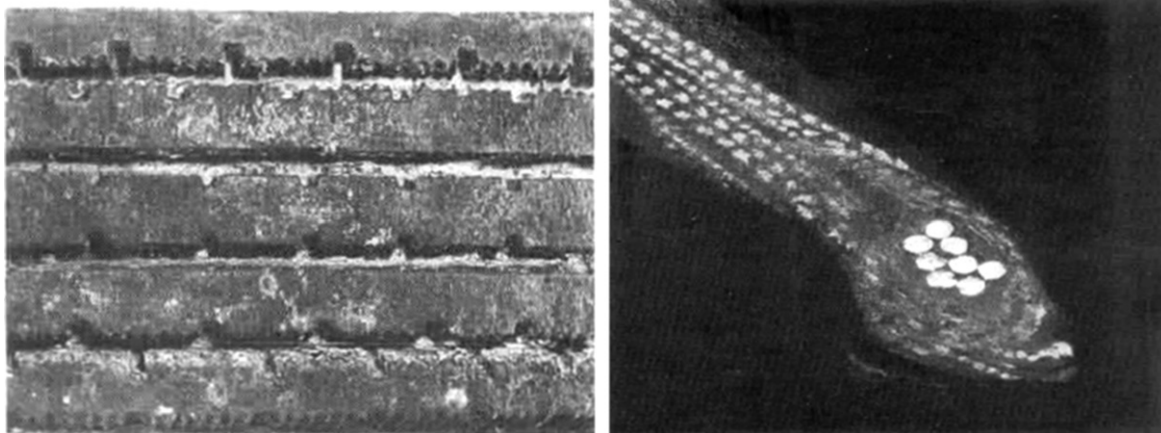


**Figure 17** A natural rubber tire after 40 years' exposure to seawater. Adapted from Mullins, L. *Proc. Int. Rubb. Conf.* Kuala Lumpur, 1985, with permission from Malaysian Rubber Board.

the formation of droplets similar to the blisters that occur in plastics or under protective coatings, consistent with an osmotic diffusion mechanism.<sup>24</sup> In salt-water, water absorption reached steady state at much lower levels than in freshwater, again consistent with an osmotic pressure mechanism. Thus seawater is less damaging than freshwater and may not have any serious consequences for many elastomers. This latter point is consistent with findings of Ab. Malek and Stevenson<sup>27</sup> who evaluated the physical properties of a rubber tire as shown in [Figure 17](#), recovered from seawater at a depth of 80 ft. They found that the rubber tire had absorbed about 5% of seawater after 42 years of immersion. They found no evidence of microbiological attack. What is more interesting, the physical properties of the rubber tire were within normal specifications for new rubber of the same type. They even suggested storing elastomers in deep seawater in view of its inert nature. Indeed, elastomer is a very suitable material to coat metal surfaces against corrosion in deep seawater. The photograph in [Figure 17](#) shows clear evidence that the steel cords making up the bead of the tire are corrosion-free after a 42-year immersion in seawater.<sup>27</sup>

### 3.33.12 Protective Measures

#### 3.33.12.1 Selection of Elastomer

All elastomers experience aging. Some age faster than others. The rate of aging depends on a number of factors such as the chemical structure of the polymer, service environment, which includes length of exposure to heat and light, oxygen and ozone concentration, size and shape of elastomers, and mechanical

stresses. One cannot stop the aging process, but one can slow it down. The most effective means of combating aging is to select the correct elastomers to meet the maximum service temperature and environment. Fully saturated elastomers having high bond dissociation energy making up their backbone chains are the best choice to meet high service temperature applications. Fully saturated rubbers such as ethylene propylene copolymer and very low unsaturation butyl rubber are excellent resistance to heat aging, oxidation and ozone cracking. Not only the maximum service temperature, but also other environmental factor such as oil or solvent determines the aging resistance. In cases like these, the elastomers having high bond dissociation energy and solvent resistance are desired. These include specialty elastomers such as acrylic (ACM), chloro-sulfonyl-polyethylene (CSM), ethylene propylene copolymer (EPM), fluoroelastomers (FKM), silicones (MQ, VMQ), polyester urethanes (AU), etc. Alternatively, for unsaturated elastomers are to use antioxidants and antiozonants, with correct vulcanization system can slow down the aging process quite efficiently.

#### 3.33.12.2 Blends of Elastomers

It is a common practice to blend two elastomers of different properties with a view to combining the best features in terms of technical and economic values. Natural rubber is blended with EPM for applications requiring very high resistance to attack by ozone as the latter is fully saturated. A blend of NR and EPDM is used for applications that require a combination of good resistance to attack by ozone and high



strength properties. Nitrile rubber (NBR) is blended with EPM to meet the requirements for very good oil resistance as well as conferring high resistance to oxidation and ozone cracking. The former is polar rubber and provides very good oil resistance, while the latter provides excellent weather resistance. However, blending two or more elastomers is not as easy as one would imagine. The work on blending various elastomers conducted by Tinker<sup>28</sup> and coworkers has thrown some light on the importance of compatibility, distribution of crosslinks in each rubber phase, distribution of filler and plasticizer and interfacial tension of each phase which have very strong influence on the service performance of the blend. When the elastomers are not compatible with each other, the associated problems that may arise include maldistribution of crosslinks, partition of chemicals (sulfur, accelerators, etc.) due to mechanism associated with preferential solubility and others. Lewan<sup>29</sup> worked on crosslink density distribution in NR/NBR blend and reported the effects of large difference in polarity and solubility parameters between these two rubbers. The large difference in polarity has the following effects:

- (i) causes high interfacial tension that is detrimental to mixing since it interferes with efficient mixing at the interface, hence minimizing the opportunity for crosslinking between the rubbers;
- (ii) causes poor phase morphology, which is characterized by large phase sizes;
- (iii) causes uneven distribution of crosslinks arises through preferential solubility of the curatives and vulcanization intermediates. Sulfur will be preferentially soluble (partition in favor of) the more polar NBR. One phase is over-crosslinked and the other is lowly crosslinked.

However, Lewan<sup>29</sup> overcame these problems by selecting the correct type of curing system such as semi-EV based on sulfur – TBBS, to obtain an even distribution of crosslinks in each phase and maximizing crosslinking between rubbers at the interface. The use of compatibilizer is highly recommended to enhance the compatibility between rubber phases. Polychloroprene rubber serves as a very good compatibilizer for the NR/NBR blend with just a small quantity (5 pphr) added to the blend. The addition of this compatibilizer reduced phase sizes, gave an even distribution of crosslinks and increased tensile strength.<sup>30</sup> Blends of elastomers provide alternative means of improving both aging resistance and oil resistance.

### 3.33.12.3 Antidegradants

Chemical antioxidants and antiozonants combat aging by scavenging harmful radicals, absorbing UV light, deactivating catalytic metals like copper, manganese, iron, etc., and decomposing initiating peroxides.<sup>16,17</sup> Two main types of chemical antioxidants and antiozonants are widely used in rubber compounds; they are amines and phenolics. Amine types are more effective and powerful antioxidants than phenolic types. However, the former is staining and the latter is not. Thus, this limits applications of amine types to black and dark colored elastomeric products. Phenolic types are exclusively used for white and bright colored products, especially in electrical wire insulation where colors are useful for identification purposes. Both amines and phenolics provide protection against aging by scavenging the harmful free radicals during the oxidative chain reaction.<sup>16,17</sup> The proposed mechanism<sup>17</sup> by which these two types of antioxidants work is shown in **Figure 18**. During the initiation stage, the free radicals produced by the peroxides abstract a labile hydrogen atom from the antioxidant and produce an antioxidant radical. This antioxidant radical is more stable than the peroxy radical, which terminates by reaction with other radicals in the system.<sup>16,17</sup>

The transfer step (c) and termination step (f) remove the free radical functionality from the elastomer, which consequently halts the oxidative degradation reaction.<sup>17</sup> Metal deactivators such as 2-mercaptobenzimidazole and its salt when added into the rubber compound containing amine or phenolic antioxidant give a synergistic effect to enhance the protection against aging.<sup>31</sup> These chemicals form

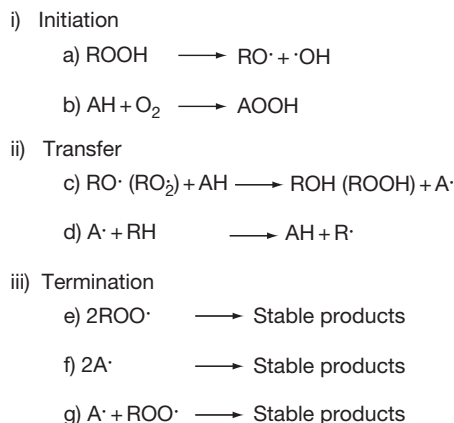


**Figure 18** Mechanism of amine and phenolic antioxidant activity, where AH is the antioxidant.<sup>17</sup>

coordination complexes with catalytic metals and inhibit metal-activated oxidation. Carbon black is a natural UV light absorber, and for nonblack compounds, it is useful to incorporate a UV light absorber such as benzotriazole derivative.

### 3.33.12.3.1 Mechanism of antiozonant action

The mechanism by which an antiozonant protects unsaturated rubber against ozone cracking has received attention from many rubber chemists and physicists. A number of suggestions have been proposed as to how antiozonants confer protection, ranging from competitive reaction with ozone (scavenging) to various types of protective layer formation.<sup>17,19–21</sup> There are three theories to describe the mechanism of antiozonant action<sup>17</sup>:

- (i) The antiozonant blooms to the surface of the rubber compound and reacts preferentially with the incident ozone.
- (ii) The antiozonant blooms to the surface of the rubber and forms a protective layer of film on the surface.
- (iii) The antiozonant reacts with intermediates formed in the ozonation of rubber, preventing chain scission or recombining severed rubber chains.

Lake<sup>32</sup> has conducted some work to elucidate the mechanism of antiozonant action to protect natural rubber against ozone cracking. He used dioctyl-*p*-phenylenediamines (DOPPD) antiozonant for his rubber compound. Exposing the rubber test-piece to ozone-rich atmosphere has reportedly resulted in a layer of film  $10^{-3}$  cm thick and visible to the naked eye forming on the rubber surface.<sup>32</sup> The protective layer can be removed by physical means either by scraping or using adhesive tape, or by swabbing with cotton wool dipped in acetone. The mass of the film can be determined by weighing the test-piece before and after its removal. In this way, the kinetics of layer formation can be determined by monitoring changes in weight after various periods of exposure to ozone.

Lake<sup>32</sup> has derived a mathematical expression to relate the mass of layer per unit area of surface  $M_L$  formed after time  $t$  to the concentration  $C_0$  of antiozonant in the rubber and diffusion coefficient  $D_L$  as shown by eqn [14]:

$$M_L = [2\rho_L D_L S_L C_0 t]^{1/2} \quad [14]$$

where  $\rho_L$  is the density of the layer material and  $S_L$  is the solubility, relative to that in the rubber, of the antiozonant in the layer. In deriving this equation,

Lake<sup>32</sup> assumed that the layer to be formed entirely of reacted antiozonant and the concentration of unreacted material within it to be small. The product  $D_L S_L$  was determined experimentally by measuring the rate of transfer of antiozonant through the layer formed on a test-piece to a controlled rubber test-piece containing no antiozonant initially. This was done experimentally by pressing two cylindrical discs (test-piece A contains antiozonant, test-piece B has no antiozonant) together so their surfaces are in intimate contact with each other. The antiozonant from test-piece A would migrate into test-piece B as a function of time. The mass of the layer formed per unit area of surface was plotted against the square root of time to produce a straight line whose slope gave the value of  $M_L/t^{1/2}$ , that is mass of film deposited per square root time. Lake<sup>32</sup> obtained very good agreement between theory and experimental data.

Lake<sup>32</sup> proposed the mechanism of antiozonant action as follows: The protective layer formed on the rubber surface is composed predominantly of the antiozonant which has reacted with ozone. The film formed remained essentially in the unstrained state, independent of the type of deformation applied. For this to happen, it is necessary that the antiozonant is soluble in the rubber, and that its reaction product should be insoluble. However, once the protective layer becomes coherent and compact, it will reduce substantially the flux of ozone reaching the rubber surface. Thus it appears that the ability of the antiozonant to prevent cracking is likely to be determined by what occurs during the initial stages of exposure when the layer is starting to form, rather than by the long-term behavior. Indeed, Lake<sup>32</sup> suggested that a coherent monomolecular layer of film that formed on the rubber surface is sufficient to confer protection against ozone cracking. However, the time for this monolayer to form must be faster than the time for the crack to grow to the same depth, so that the monolayer is able to bridge any cracks that have begun to grow.

### 3.33.12.3.2 Theories of layer formation

The thin layer of protective film covering the rubber surface is a direct consequence of the chemical reaction between chemical antiozonant and ozone. Lake and Mente<sup>21</sup> proposed two diffusion models to work out a theory for layer formation. The two models are shown in Figure 19. The first model describes the rate of layer formation that is controlled by the diffusion of the antiozonant across the already-formed layer to react with ozone at its outer surface. Under

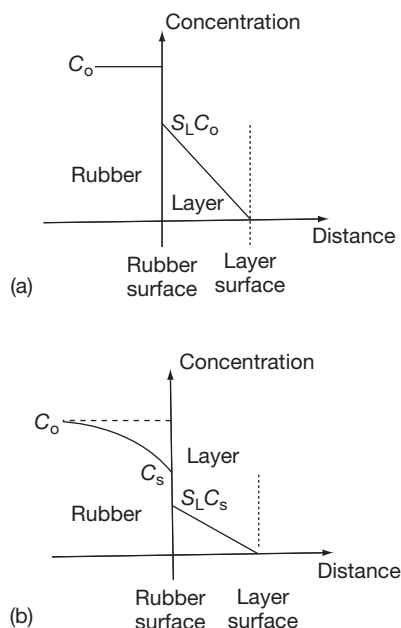


**Figure 19** Diffusion models for antiozonant layer formation: (a) rate governed by diffusion of antiozonant within the layer only, and (b) rate governed by both diffusion in the layer and in the rubber. Adapted from Lake, G. J.; Mente, P. G. *J. Nat. Rubb. Res.* **1992**, 7(1), 1–13, with permission from Malaysian Rubber Board.

these circumstances, the mass per unit area  $M_L$ , of layer formed after time  $t$  is given by eqn [14].<sup>21,32</sup> The concentration gradient in the layer will be essentially linear as shown in Figure 19(a). The second diffusion model takes into account diffusion within the rubber in addition to diffusion across the layer. In this case, an equation similar to eqn [14] applies, when  $C_0$  is replaced by  $C_s$ , the concentration at the rubber surface is lower than  $C_0$  as shown schematically in Figure 19(b).  $C_s$  is a function of  $C_0$  and the relative permeabilities of the rubber and the layer to the antiozonant, and with the assumptions made, are given by eqn [15]:

$$C_s/C_0 = 1 + \xi - [(1 + \xi)^2 - 1]^{1/2} \quad [15]$$

where

$$\xi = (\pi/4)(\rho_L D_L S_L / D C_0) \quad [16]$$

and  $D$  is the diffusion coefficient of the antiozonant in the rubber. The mass of layer per unit area of surface plotted against square root of time as shown in Figure 20 enabled Lake and Mente<sup>21</sup> to determine the rates of layer formation of the antiozonants formed on NR, ENR 50, and NBR 34, respectively. These three rubbers differ greatly in terms of

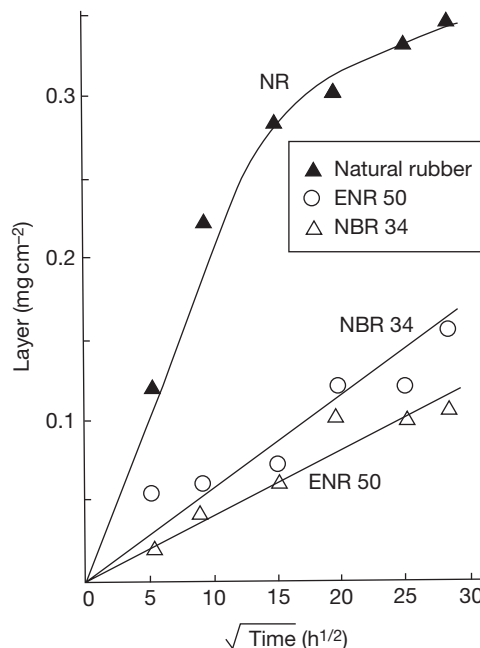


**Figure 20** Dependence of the mass of antiozonant layer formed on the square root of the time of exposure to an ozone concentration of 200 pphm at 40 °C for vulcanizates of NR, ENR 50, and NBR 34. Adapted from Lake, G. J.; Mente, P. G. *J. Nat. Rubb. Res.* **1992**, 7(1), 1–13, with permission from Malaysian Rubber Board.

polarity and glass-transition temperature, which may affect the rate of film formation on the rubber surface. Their experimental results as shown in Figure 20 indicate that the rate of layer formation for NR is about four times faster than that of NBR 34 and ENR 50, which is in accordance with the dependence of the diffusion coefficient on the glass-transition temperature of the rubber. The diffusion coefficient decreased in the increasing order of the  $T_g$  of the rubber.<sup>21</sup> Thus the diffusion coefficient of NR is fastest and that of ENR 50 is the slowest as  $T_g$  of NR is about  $-69$  °C and that of ENR 50 is about  $-24$  °C.<sup>21</sup> NBR34 has a slightly faster diffusion coefficient than ENR 50 as its  $T_g$  ( $-28$  °C)<sup>19</sup> is slightly lower than that of ENR 50. Lake and Mente<sup>21</sup> also conducted experiments to investigate the effect of temperature on layer formation on the NR surface at  $-17$  and  $23$  °C respectively as shown in Figure 21. They found that the rates of layer formation at these two temperatures were the same for NR. However, the diffusion coefficient of this particular antiozonant (DOPPD) in NR at  $-17$  °C was very similar to that in ENR 50 and NBR 34 at  $23$  °C. They attributed this finding to the partitioning of the antiozonant

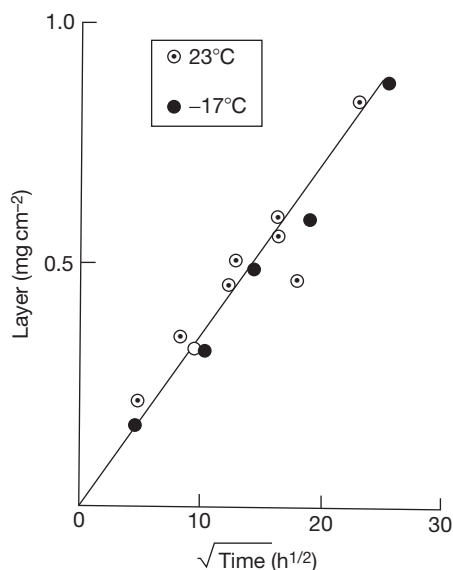


**Figure 21** Mass of antiozonant layer formed versus square root of the time of exposure to  $10^5$  pphm ozone for an NR vulcanizate containing 10 phr DOPPD at 23 and  $-17^\circ\text{C}$ . Adapted from Lake, G. J.; Mente, P. G. *J. Nat. Rubb. Res.* **1992**, 7(1), 1–13, with permission from Malaysian Rubber Board.

between the elastomer and the layer material, as the polarity of the elastomer affects the solubility of the antiozonant in the rubber. The solubility of the antiozonant varies in the ascending order of polarity of elastomer, that is  $\text{NR} < \text{NBR } 34 < \text{ENR } 50$ .<sup>21</sup> Lake and Mente concluded that for elastomers with high  $T_g$ , the antiozonant offers better protection at temperatures above room temperature than at low temperature, as the protective agents are more mobile at high temperatures rather than at low temperatures.

### 3.33.12.4 Blooming of Wax

Besides chemical antiozonants, paraffin wax is also a useful ingredient to confer protection against ozone cracking. Wax provides a protective layer surrounding the surface of the elastomer through the diffusion process commonly known as blooming, which prevents direct contact between ozone and the elastomer. Blooming occurs when the supersaturated solution of the ingredient in the rubber crystallizes more readily on the surface than in the rubber itself.<sup>24,33</sup> This basic mechanism of blooming is not only applicable to wax but other ingredients as well. When other ingredients such as sulfur, accelerators and stearic acid bloom to the rubber surface, they reduce the tackiness of the rubber, which can bring detrimental effects to

products relying on adhesion and bond strength involving different components plied together. These include rubber-to-metal bonded components, tires, belts, and hoses. However, blooming of waxes and antioxidants brings advantages.

Nah and Thomas<sup>33</sup> investigated the mechanism and kinetics of diffusion of wax to the rubber surface. They envisaged that the driving force for the blooming process arises from the elastic forces acting around the wax precipitates in the rubber when the wax concentration is in excess of its equilibrium solubility. They then proposed a model and theory for wax blooming base on thermodynamic concept of diffusion, where the driving force of the diffusion process is predominantly associated with free energy gradient rather than the concentration gradient of the wax that is dissolved in the rubber. The initial rate of wax bloom per unit area ( $M_t/t^{1/2}$ ) is given by eqn [17]<sup>33</sup>:

$$(M_t/t^{1/2})_{x=0} = [(24v_f D_t s_x \rho_x V_x G)/RT]^{1/2} (d\lambda/dy)_0 \quad [17]$$

where  $D_t$  is diffusion coefficient,  $v_f$  is volume fraction of seeding particles or flaws present in the rubber.  $s_x$  is solubility of wax in the rubber,  $\rho_x$  is density of wax, and  $V_x$  is molar volume of solid wax.  $G$  is shear modulus of the rubber,  $R$  is molar gas constant,  $T$  is absolute temperature.  $(d\lambda/dy)_0$  is equivalent to the concentration gradient of the wax at the surface of the rubber, and is determined by numerical methods for the appropriate boundary conditions and a suitable value of  $v_f$ . The symbol  $\lambda$  stands for the extension ratio of the rubber around the precipitated wax particle, assumed spherical. Nah and Thomas<sup>33</sup> verified eqn [17] experimentally, and obtained satisfactory agreement between their experimental and theoretical values for the migration of paraffin waxes in peroxide cured natural rubber. The theory was applicable to predict the blooming of wax mixtures with success, indicating that the mechanism of wax blooming has been identified correctly. Although Nah and Thomas developed the theory for blooming of wax, with minor adjustments, it is also applicable to predict migration and blooming of sulfur, fatty acids and antidegradants in vulcanized elastomers.

### 3.33.12.5 Choice of Vulcanization System

Anaerobic aging usually decreases the stiffness, resilience, and tensile, tear and fatigue properties; the extent is mainly determined by the type of vulcanization system, which affects aging of elastomers. There are three types of sulfur vulcanization systems known as conventional, efficient (EV) and

semi-efficient (semi-EV) respectively<sup>8,10</sup> as discussed briefly in [Section 3.33.4.3](#). The conventional system has a higher sulfur dosage than the accelerator that produces predominantly polysulfidic crosslinks, where the rubber molecular chains are linked by three or more sulfur atoms. Polysulfidic crosslinks have poor resistance to heat aging because the  $-S-S-$  bond has low thermal stability. In contrast, EV makes use of the low sulfur level and high accelerator dosage. This EV system produces predominantly monosulfidic crosslinks which are thermally very stable. The rubber network consists of other structural features as described briefly in subsequent sections.

### **3.33.12.5.1 Sulfur vulcanization system and types of crosslinks on aging resistance**

#### **Polysulfidic crosslink**

A chain of three or more sulfur atoms (maximum of six atoms) in this crosslink bridges two polymer chains. The bond energy of this crosslink is less than  $268 \text{ kJ mol}^{-1}$ , which is relatively low.<sup>10</sup> A polysulfidic crosslink can be produced by using the conventional vulcanization system where the quantity of sulfur is more than the quantity of the accelerator in the ratio 5:1 (sulfur: accelerator). Therefore the conventional sulfur cure system is not suitable for high temperature applications.

#### **Disulfidic crosslink**

In a disulfidic crosslink, there are two sulfur atoms bridging the two polymer chains. Its bond energy is about  $268 \text{ kJ mol}^{-1}$ . Little is known of the properties of this crosslink, mainly because it is very difficult to prepare a network in which disulfides are predominant. In both conventional and efficient sulfur vulcanizes the proportion of disulfidic crosslink is seldom more than 20–30% of the total.

#### **Monosulfidic crosslink**

In the case of a monosulfidic crosslink, the two polymer chains are bridged by one sulfur atom. Its bond energy<sup>10</sup> is relatively high, about  $285 \text{ kJ mol}^{-1}$ . A monosulfidic crosslink can be produced from an EV system where the amount of the accelerator is higher than the amount of sulfur, about 5:1 (accelerator:sulfur). Thus the EV system is suitable for medium high temperature applications.

#### **Cyclic sulfides**

These are intra-crosslinks which are useless as the crosslinks are formed on the same polymer chain.

This phenomenon is also known as main chain modification. The main source of these main chain modifications is the thermal decomposition of polysulfide crosslinks. The conventional vulcanization system creates more cyclic sulfides than the EV system as the former produces more polysulfide crosslinks than the latter.

#### **Conjugated diene and triene groups**

These main chain modifications are also formed by the thermal decomposition of polysulfide crosslinks. The concentration of these conjugated groups increases on overcure. The presence of these groups tends to catalyze oxidative aging as they are much more susceptible to oxidation than the polyisoprene main chain.<sup>8,10,16</sup>

#### **Pendent accelerator group**

It is generally accepted that in accelerated sulfur vulcanization, crosslinks are formed from initial rubber-bound pendent groups in which disulfide or polysulfide chains are terminated by accelerator fragments. Like the crosslink, some of these intermediates undergo progressive desulfuration and are converted into stable monosulfidic links between the polymer chain and accelerator fragments. The extent of main chain modification will depend on the amount of accelerator available and on the ease with which the initial pendent group can be desulfurated.

#### **Extra-network material**

The extra-network material formed by a sulfur vulcanizing system can be put into two categories. The first consists of unreacted zinc oxide and fatty acid activators, their zinc soap reaction products and zinc sulfide. The second consists of accelerator reaction products.

### **3.33.12.5.2 Peroxide vulcanization system**

Unlike sulfur vulcanization, peroxide vulcanization does not require the presence of double bonds. In fact, peroxide vulcanization is possible for rubbers having either saturated or/and unsaturated carbon-carbon backbone chains. However, peroxide vulcanization is quite impossible with the following elastomers because of their tendency to decompose:

- IIR – butyl rubber
- CIIR – chlorinated butyl rubber
- CO – polyepichlorohydrin rubber
- ECO – copolymer of epichlorohydrin and ethylene oxide
- PP – polypropylene
- ACM – polyacrylic rubber



The most common peroxide is dicumyl peroxide (DCP or dicup). Others include ditert butyl peroxide, dibenzoyl peroxide and bis(2,4-dichlorobenzoyl) peroxide. Peroxide vulcanization<sup>10</sup> produces a vulcanizate which will impart good aging resistance and excellent resistance to compression at high temperatures (70–100 °C). To obtain the best compression set performance, freedom from certain other compounding ingredients, especially zinc oxide and stearic acid, is essential. Peroxide vulcanization is essentially nonreverting. However, there are certain deficiencies such as poor hot tear strength and incompatibility with chemical antiozonants. Other technical limitations include slow cure rate with no delayed action, and degradation of the rubber giving a sticky surface if it comes into contact with air during the cure. Thus peroxides are not suitable for hot-air or steam-pan curing. The reaction of peroxide must be carried through to completion to obtain the best heat resistance; therefore long cure times are inevitable. In addition, nearly all antidegradants and aromatic oils affect the efficiency of the peroxide cure.

Co agents, which are highly reactive materials, are usually added in peroxide vulcanization to increase the efficiency of the organic peroxide, but do not affect the rate of cure.<sup>10,31</sup> They are used either to enhance the modulus and hardness or to reduce the level of peroxide required. They can be absolutely essential for the efficient cure of chlorinated polyethylene. Typical solid coagents are zinc diacrylate, zinc dimethacrylate, and *m*-phenylene dimaleimide. Liquid coagents are materials such as triallyl cyanurate (TAC), triallylisocyanurate (TAIC), etc. High vinyl polybutadiene is a polymer which can act as a coagent.

### 3.33.12.5.3 Vulcanization with urethane

This (urethane) crosslinking system for natural rubber was developed in the early 1980s by the scientists at the Malaysian Rubber Producers Research Association (MRPRA).<sup>10,31</sup> It was marketed under the trademark Novor. The basic reagent is a reaction product of a nitroso compound and a diisocyanate which dissociates at vulcanizing temperatures into its component species. The free nitroso compound then reacts by addition to rubber molecules giving attached pendent groups which subsequently react with the diisocyanate to form urea type crosslinks. The main features of the vulcanizates are excellent reversion resistance and, when protected with a TMQ/ZMBI antioxidant combination, excellent heat aging resistance.

### 3.33.12.5.4 Metallic oxide vulcanization

Elastomers containing halogens can be cured with metallic oxides such as oxides of zinc, magnesium, and lead. The oxides form an ether type of crosslink (R–O–R') which gives good heat aging resistance. Elastomers which can be vulcanized with metallic oxides are polychloroprene, halogenated butyls, and polychlorosulphonated rubber.

### 3.33.12.5.5 Resin vulcanization

Resin vulcanization has established itself to some degree in butyl (IIR) crosslinking, giving excellent heat and steam stability.<sup>10</sup> Example of a typical resin cross linker is polymethylolphenolic resin. The amount used is at the level of 5–12 pphr.

### 3.33.12.5.6 Quinonedioximes vulcanization

*p*-Benzoquinonedioxime (CDO) as well as its dibenzoyl derivative are cross linkers for many rubbers because of their free radical reactions.<sup>10</sup> Best known and of greatest interest is their use in IIR because of the excellent heat and steam stability that can be obtained. They are used mainly for rubbers having low unsaturation where sulfur vulcanization is slow. They have been unimportant for the classic diene rubbers.

## 3.33.13 Future Developments in Materials or Applications

Natural rubber and synthetic elastomers are likely to maintain their roles and contributions in domestic and industrial applications, buildings and structures, automobiles, and marine and engineering products. With the emergence of nanomaterials for rubber compounding, it is envisaged that future elastomeric products will provide better service and longer life performance than they are capable of providing now. High heat resistant elastomers and highly oil resistant elastomers are the main players of the future to meet the high demands of the automotive industry and aeronautical engineering. More developmental work in these areas is expected.

## Acknowledgements

I am very grateful to Dr. Stuart Lyon, Reader in Corrosion Control Engineering, School of Materials (Corrosion and Protection Centre), University of Manchester, England, who gave me the opportunity to write as part the prestigious Shier's Corrosion

book. I feel much honored to be among the experts who contributed to this fourth edition of Shier's Corrosion.

It gives me great pleasure to thank the Publication Divisions of the Malaysian Rubber Board (MRB) (formerly Rubber Research Institute of Malaysia), and its sister concern the Tun Abdul Razak Research Centre (TARRC) (formerly Malaysian Rubber Producers Research Association) at Brickendonbury Hertford, England. In particular, Dato' Dr. Kamarul Baharin Basir, Director General, MRB and Mdm Rabeatun Awaliah Awalludin, MRB, and Dr. A.J. Tinker (Director Research) TARRC and Ms. K. Lawson TARRC who helped me to obtain the permission to reproduce data and figures from their respective Publication Divisions.

I would like to express my sincere appreciation and thanks to Oxford University Press and the American Chemical Society (Rubber Division) for giving permission to reproduce figures and data from their respective publications.

Last but not least, Associate Prof. Dr. Mohamad Kamal Harun, Dean of Faculty of Applied Sciences, MARA University of Technology, Malaysia (UiTM) for his encouragement.

## References

1. International Standard, Rubber – Vocabulary, ISO1382, 3rd Ed, 1996-08-01.
2. Fuller, K. N. G.; Muhr, A. H. *Engineering design with natural rubber, NR Technical Bulletin*, 5th ed.; The Malaysian Rubber Producers' Research Association: London, 1992; pp 1–33.
3. Chadwick, J. C. *Shell Polym.* **1981**, 5, 44–50.
4. ISO 4632/1-1982 (E), ISO Classification system.
5. Hashimoto, K.; Maeda, A.; Hosoya, K.; Todani, Y. *Rubb. Chem. Technol.* **1998**, 70(3), 449–519.
6. Fogg, G.; Swift, P. M. *NRPRA Tech. Bull.* **1962**, 4, 1–26.
7. Brydson, J. A. *Plastics Materials*, 4th ed.; Butterworths: Newton, MA, 1989; Chapter 29, pp 730.
8. Brown, P. S.; Porter, M.; Thomas, A. G. In *Proceedings of the International Rubber Conference*; Kuala Lumpur, October 21–25, 1985, RRIM, 1986; pp 20–46.
9. Hofmann, W. *Rubber Technology Handbook*; Hanser, 1989; Chapter 3, Synthetic Rubber, pp 1–171.
10. Elliott, D. J.; Tidd, B. K. *Prog. Rubb. Technol.* **1974**, 34, 83–126.
11. Gregory, M. J. In *Rubber to metal bonding, Adhesives, Sealants, and Encapsulants Conference*, London, November 5–7, 1985.
12. Gage, F. J. *IRI* **1968**, 47–49.
13. Gibbs, E. H., Jr.; Seber, J. N. ACS Rubber Division Mtg., Indianapolis, IN, May 1984, pp 1–9.
14. Mullins, L. In *Proc. Rubb. in Eng. Conf.* Kuala Lumpur, 1974, pp 1–20.
15. Bolland, J. L.; Hughes, H. J. *Chem. Soc.* **1949**, 492.
16. Barnard, D.; Lewis, P. M. In *Natural Rubber Science and Technology*; Robert, A. D., Ed.; Oxford University Press: Oxford, UK, 1988; Chapter 13, pp 621–673.
17. Keller, R. W. *Rubb. Chem. Technol.* **1985**, 58, 637–651.
18. Mullins, L. J. *Polym. Sci.* **1956**, 19, 225–236.
19. Braden, M.; Gent, A. N. *J. Appl. Polym. Sci.* **1960**, 3, 90–106.
20. Lake, G. J.; Thomas, A. G. In *Proceedings of the Int. Rubb. Conf.* 1967, Maclarens: London.
21. Lake, G. J.; Mente, P. G. *J. Nat. Rubb. Res.* **1992**, 7(1), 1–13.
22. Kinro, H.; Akio, M.; Kiyoshi, H.; Yoshihiro, T. Speciality Elastomers for Automotive Applications, *Rubber Chemistry Technology*; **1998**, 71(3).
23. Lake, G. J.; Lindley, P. B. *Rubber J.* **1964**, 10, 24–30, 79, 11, 30–36, 39.
24. Muniandy, K.; Southern, E.; Thomas, A. G. In *Natural Rubber Science and Technology*; Robert, A. D., Ed.; Oxford University Press: Oxford, UK, 1988; Chapter 13, pp 820–851.
25. Rahim, R.; Samsuri, A., Effect of crosslink concentration and XNBR:NR ratio on swelling resistance of NR latex film towards cooking oil, in press.
26. Lake, G.J. In *Conf. Polymers in a Marine Environment*, London, 31 Oct.–2 Nov., 1984, pp 157–160.
27. Ab-Malek, K.; Stevenson, A. J. *Mater. Sci.* **1986**, 21, 147–154.
28. Tinker, A. J. In *Blends of Natural Rubber*; Tinker, A. J., Jones, K. P., Eds.; Chapman & Hall: London, 1998; Chapter 1, pp 1–7.
29. Lewan, M. V. In *Blends of Natural Rubber*; Tinker, A. J., Jones, K. P., Eds.; Chapman & Hall: London, 1998; Chapter 5, pp 53–67.
30. Kongsin, K.; Lewan, M. V. In *Blends of Natural Rubber*; Tinker, A. J., Jones, K. P., Eds.; Chapman & Hall: London, 1998; Chapter 7, pp 80–93.
31. The Natural Rubber Formulary and Property Index, Malaysian Rubber Producers' Research Association, 1984, pp 1–24.
32. Lake, J. G. *Rubb. Chem. Chem.* **1970**, 43, 1230–1238.
33. Nah, S. H.; Thomas, A. G. *J. Polym. Sci., Polym. Phys. Ed.* **1980**, 18, 511–521.

## 3.35 Corrosion of Metal Joints

**G. Pimenta**

Materials Laboratory, Instituto de Soldadura e Qualidade, Av. Prof. Cavaco Silva 33 – Talaide, 2780-994 Porto Salvo, Portugal

**R. A. Jarman**

Formerly School of Engineering, University of Greenwich, Old Royal Naval College, Park Row, Greenwich, London SE10 9LS, UK

© 2010 Elsevier B.V. All rights reserved.

3.35.1	Introduction	2448
3.35.2	Mechanical Fasteners	2449
3.35.3	Soldering and Brazing	2450
3.35.3.1	Soldered Joints	2450
3.35.3.2	Brazed Joints	2451
3.35.4	Welded Joints	2452
3.35.4.1	Welding Processes	2452
3.35.4.2	Weld Defects	2453
3.35.4.3	Factors Affecting Weldment Corrosion	2453
3.35.4.3.1	Weldment design	2453
3.35.4.3.2	Weldment backing	2454
3.35.4.3.3	Welding procedure or technique	2455
3.35.4.3.4	Residual stresses and stress concentration	2455
3.35.4.3.5	Postweld heat treatment	2456
3.35.4.3.6	Filler metal composition	2456
3.35.5	Welding of Specific Materials	2456
3.35.5.1	Introduction	2456
3.35.5.2	Carbon and Low-Alloy Steels	2456
3.35.5.3	Stainless Steels	2458
3.35.5.3.1	Ferritic and martensitic stainless steels	2458
3.35.5.3.2	Austenitic stainless steels	2458
3.35.5.3.3	Duplex stainless steels	2459
3.35.5.3.4	Sensitization	2460
3.35.5.3.5	Localized corrosion at weldments	2460
3.35.5.4	Nickel Alloys	2461
3.35.5.5	Aluminum Alloys	2461
3.35.6	Protection of Welded Joints	2461
References		2462

### Glossary

**Bead** A single run of weld metal on a surface.

**Brazing** A metal joining process that is identical to soldering except that the joining takes place at temperatures generally above 500 °C. The molten non-ferrous filler metal is distributed between properly fitted surfaces of the joint by capillary attraction.

**Butt joint** A connection between the ends or edges of two parts making an angle to one another of 135°–180° inclusive in the region of the joint.

**Edge preparation** The preparation of an edge, by squaring, grooving, chamfering, or bevelling, prior to welding.

**Electroslag welding** A fusion welding process that utilizes the combined effects of current and electrical resistance in a consumable electrode and conducting bath of molten slag, through which the electrode passes into a molten pool, both the pool and the slag being retained in the joint by cooled shoes which move progressively upwards.

**Electron-beam welding** A welding process in which the joint is made by fusing the parent metal by the impact of a focused beam of electrons.

**Filler metal** The metal that is added during welding, braze welding, brazing, or surfacing.

**Flux** A material that is used during welding, brazing, or braze welding to clean the surfaces of the joint, prevent atmospheric oxidation, and to reduce impurities.

**Friction welding** A welding process by which the joint metals are fused together by the conjoint action of frictional heating and pressure.

**Fusion penetration** The depth to which the parent metal has been fused.

**Fusion zone** That part of the parent metal which is melted into the weld metal.

**Heat affected zone** That part of the parent metal that is metallurgically affected by the heat of the joining process, but not melted.

**Laser welding** A welding process employing a laser as the source of heat.

**Metal arc welding** An arc welding process that uses a consumable metal electrode.

**MIG welding** Metal-inert gas arc welding using a consumable electrode.

**Gas welding** A welding process in which the heat source is a flammable gas (commonly acetylene) that is burnt in an oxygen atmosphere.

**Parent metal** The metal that is to be joined.

**Pressure welding** A welding process in which a weld is made by a sufficient pressure to cause plastic flow of the surfaces, which may or may not be heated.

**Resistance welding** A welding process in which force is applied to surfaces in contact and in which the heat for welding is produced by the passage of electric current through the electrical resistance at, and adjacent to, these surfaces.

**Run** The metal melted or deposited during one passage of an electrode, torch, or blow-pipe.

**Soldering** A metal joining process that is identical to brazing except that the joining takes place at temperatures generally below 500 °C. The molten nonferrous filler metal is distributed between closely fitted surfaces of the joint by capillary attraction.

**Submerged arc welding** Metal-arc welding in which a bare wire electrode is used; the arc is enveloped in flux, some of which fuses to form a removable covering of slag on the weld.

**TIG welding** Tungsten inert-gas arc welding using a nonconsumable electrode of pure or activated tungsten.

**Thermal cutting** The parting or shaping of materials by the application of heat with or without a stream of cutting oxygen.

**Weld** A union between pieces of metal at faces rendered plastic or liquid by heat or by pressure, or by both. A filler metal whose melting temperature is of the same order as that of the parent material may or may not be used.

**Welding** The making of a weld.

**Weld metal** All metal melted during the making of a weld and that is retained in the weld.

**Weld zone** The zone containing the weld metal and the heat-affected zone.

## Abbreviations

**CP** Cathodic protection

**HAZ** Heat affected zone

**IGA** Intergranular attack

**MIG** Metal inert gas

**MMA** Manual metal arc

**PWHT** Postweld heat treatment

**SCC** Stress corrosion cracking

**SSCC** Sulfide stress corrosion cracking

**TIG** Tungsten inert gas

## Symbols

$\Delta K$  Stress intensity range (MPa m<sup>1/2</sup>)

### 3.35.1 Introduction

A jointed fabrication is the one in which two or more components are held in position by one of:

1. A mechanical fastener (screw, rivet, bolt, etc.).
2. A fusion joining process (e.g., welding, brazing, soldering, etc.).
3. An adhesive bond.

The components of the joint may be metals of similar or dissimilar composition and structure, metals and nonmetals, or they may be wholly nonmetallic. Since the majority of fabrications are joined at some stage of their manufacture, the corrosion behavior of joints is of utmost importance, and the nature of the materials involved in the joint, and in the geometry of the joint, may lead to a situation in which one of the materials is subjected to accelerated and/or localized attack. Although galvanic corrosion is dealt with elsewhere in this book, it is necessary to emphasize the following in relation to corrosion at joints in which the metals involved may be either identical or similar:

1. A difference in electrochemical potential may result from differences in structure or stress brought about during or subsequent to the joining process.
2. Large differences in area may exist in certain jointed structures, for example, between weld metal and parent metal.
3. Many joining processes lead to a crevice, with the consequent possibility of crevice corrosion.

The corrosion of adhesive joints is described in a separate chapter in this book.

### 3.35.2 Mechanical Fasteners

These require little further description and take the form of bolts, screws, rivets, etc. Mechanical failure may occur as a result of the applied stress in shear or tension exceeding the ultimate strength of the fastener, and can normally be ascribed to poor design. However, other failure modes are possible, including the failure of steel fittings below their ductile-to-brittle transition temperature, or by hydrogen embrittlement. Also, failure mechanisms that combine mechanical and corrosion aspects are of particular risk, that is, corrosion fatigue, stress corrosion cracking (SCC), etc. Thus, the corrosion problems associated with mechanical fixtures are often one of three types, that is, crevice corrosion, galvanic corrosion, or stress related.<sup>1-3</sup> Individually, these topics are dealt with in some detail in the relevant chapters elsewhere in this book.

As an example, the mechanical joining of aluminum alloys to steel using rivets and bolts, a combination which is difficult to avoid in the shipbuilding industry, represents a typical example of a situation where subsequent galvanic corrosion could occur. Similarly, other examples of an ill-conceived choice of materials, which should normally be avoided, can

be found in, for example, brass screws used to attach aluminum plates or steel pins used in the hinges of aluminum windows.

The relative areas of the metals being joined is of primary importance in galvanic corrosion. For example, stainless steel rivets can be used to join aluminum sheet (small cathode, large anode), whereas the reverse situation would lead to rapid deterioration of aluminum rivets (large cathode, small anode). However, in the former case a more dangerous situation could arise if a crevice was present, for example, a loose rivet, since under these circumstances the effective anodic area of the aluminum sheet would be reduced, with consequent localized attack. In general, under severe environmental conditions, it is always necessary to insulate the components from each other by use of insulating washers, sleeves, gaskets, etc. as shown in [Figure 1](#). The greater the danger of galvanic corrosion, the greater the necessity to ensure complete insulation; washers may suffice under mild conditions but a sleeve must be used additionally when the conditions are severe.<sup>4</sup>

The fasteners themselves may be protected from corrosion and made compatible with the metal to be fastened by the use of a suitable protective coating, for example, a metallic or organic coating, etc. The choice of fastener and protective coating, or the materials from which it is manufactured, must be made in relation to the components of the joint and environmental conditions prevailing. A point that cannot be overemphasized is that, in the long term, stainless steel fasteners should always be used for securing joints of stainless steel parent metal.

In the case of protection with organic coatings, it is dangerous to confine the paint to the more anodic component of the joint because if the paint is scratched, intense localized attack is likely to occur on the exposed metal. In general, organic coatings should be applied to both the anodic and cathodic metal, but if this is not possible, the more cathodic metal rather than the more anodic metal should be painted. The use of high-strength steels for bolts for fastening mild steel does not normally present problems, but a serious situation could arise if the structure is to be cathodically protected, particularly if an impressed current system is to be used, since failure could then occur by hydrogen embrittlement; in general, the higher the strength of the steel and the higher the stress, the greater the susceptibility to cracking.

In summary, mechanical joints are important joining methods. However, attention must be given to materials compatibility in order to avoid dissimilar metal



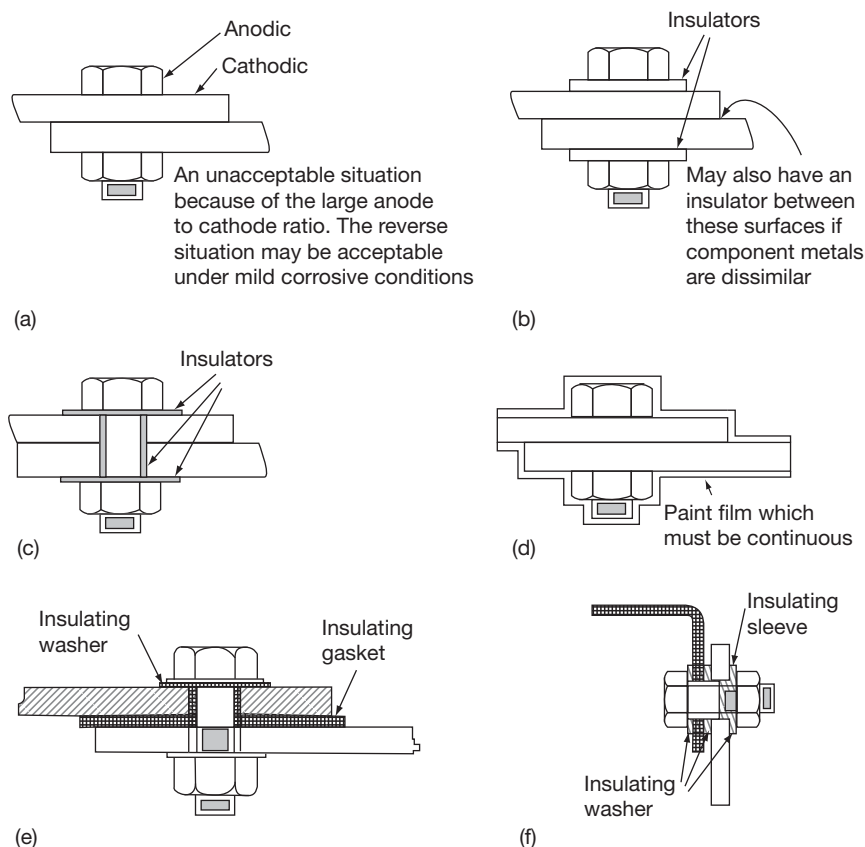


**Figure 1** Design of insulated joints. Reproduced from Layton, D. N.; White, P. E. *Br. Corros. J.* **1966**, 1(6), 213.

corrosion problems, crevice corrosion, for example, for aluminum,<sup>5,6</sup> stress corrosion, and corrosion fatigue.

### 3.35.3 Soldering and Brazing

These metal joining processes are essentially identical apart from the temperature of joining, which is lower for soldering (generally below  $\sim 500^\circ\text{C}$ ) than for brazing (generally above  $\sim 500^\circ\text{C}$ ). A characteristic of both processes is the formation of an interdiffusion layer between the parent and filler metal that, if properly formed, constitutes the main metallurgical bond, which results in the strength of the joint. Since a filler material is used for joining which is necessarily different from the parent metal, galvanic corrosion is one of the characteristic failure mechanisms.

#### 3.35.3.1 Soldered Joints

Soldering and brazing are methods of joining components together with a lower-melting-point alloy such that the parent metal (the metal or metals to be joined)

is not melted. Traditional alloys for this purpose are summarized in [Table 1](#), although it should be noted that many of the lead-containing alloys are no longer in use. In the case of soft soldering, the maximum temperature employed is usually of the order of  $250^\circ\text{C}$ , and the filler alloys used for joining are generally based on a tin alloy composition. The components must present a clean surface to the solder to allow efficient wetting and flow of the molten filler and to provide a joint of adequate mechanical strength. To obtain the necessary cleanliness, degreasing and mechanical abrasion may be required followed by the use of a flux to remove any remaining oxide film and to ensure that no tarnish film develops on subsequent heating.

Soldered joints present their own characteristic corrosion problems usually in the form of dissimilar metal attack often aided by inadequate flux removal after soldering. Such joints have always been a source of concern to the electrical industry.<sup>7,8</sup> However, in view of the toxicity of lead and its alloys, the use of lead solders, particularly in contact with potable waters and foodstuffs, is effectively no longer permitted.

**Table 1** Traditional soldering and brazing alloys

<i>Process</i>	<i>Temperature range(°C)</i>	<i>Typical fillers</i>	<i>Fluxes</i>
Soldering Hot iron, oven, induction, ultrasonic, dip, resistance, wave and cascade	60–300	70Pb–30Sn 40Pb–60Sn 70Pb–27Sn–3Sb 40Pb–58Sn–2Sb Sn–Zn–Pb	Chloride based Fluoride based Resin based
Brazing Torch, dip, salt bath, furnace, induction, resistance	500–1200	90Al–10Si 50Ag–15Cu–17Zn–18Cd Ag–Cu–Ni–In 60Ag–30Cu–10Zn 50Cu–50Zn 97Cu–3P 70Ni–17Cr–3B–10Fe 82Ni–7Cr–5Si–3Fe 60Pd–40Ni	Borax based Fluoride based Hydrogen gas Town's gas Vacuum

In the case of carbon and stainless steels, and many of the nonferrous alloys, the fluxes are based on acidic inorganic salts, for example, chlorides, which are highly corrosive to the metal unless they are removed subsequently by washing in hot water. For soldering tinplate, copper, and brass, it is possible to formulate resin-based fluxes having noncorrosive residues, and these are essential for all electrical and electronic work. Activators are added to the resin to increase the reaction rate, but these must be such that they are thermally decomposed at the soldering temperature if subsequent corrosion is to be avoided.<sup>9</sup> Corrosion is always a particular risk with soldered joints in passive materials such as aluminum owing to the relatively large difference in electrochemical potential between the filler alloy and the parent metal and the highly corrosive nature of the flux that is generally used for soldering. With aluminum soldering, it is imperative that the joints be well cleaned both prior and subsequent to the soldering operation, and the design should avoid subsequent trapping of moisture.

### 3.35.3.2 Brazed Joints

When stronger joints or higher temperature service are required, brazing may be used.<sup>10</sup> The filler alloys employed generally melt at much higher temperatures (600–1200 °C), but the effectiveness of the joining process still depends upon surface cleanliness of the components to ensure adequate wetting and spreading. Metallurgical and mechanical hazards may be encountered in that the filler may show poor spreading or joint filling capacity in a certain situation or may suffer from

hot tearing, whilst during furnace brazing in hydrogen-containing atmospheres there is always the possibility that the parent metal may be susceptible to hydrogen embrittlement or steam cracking. Furthermore, brittle diffusion products may be produced at the filler base-metal interface as a result of the reaction of a component of the filler alloy with a base-metal component, for example, phosphorus-bearing fillers used for steel in which the phosphorus diffuses into the steel.

Damage during the brazing procedure can be caused by excessive diffusion into the parent metal of the molten brazing alloy, especially where the parent contains residual or applied stresses, which can lead to liquid metal embrittlement. Nickel and nickel-rich alloys are particularly prone to liquid-braze-filler attack especially when using silver-based braze fillers at temperatures well-below the annealing temperature of the base metal, since under these conditions there is no adequate stress relief of the parent metal at the brazing temperature. The problem may be avoided by annealing prior to brazing and ensuring the maintenance of stress-free conditions throughout the brazing cycle. A range of silver-, nickel-, and palladium-based braze fillers of high oxidation and corrosion resistance have been developed for joining the nickel-rich alloys; however, the presence of sulfur, lead, or phosphorus in the base-metal surface or in the filler can be harmful, since quite small amounts can lead to interface embrittlement. In the case of nickel–copper alloys, the corrosion resistance of the joint is generally less than that of the parent metal and the design must be such that as little as possible of the joint is exposed to the corrosive media.

With carbon and low-alloy steels, the braze fillers are invariably noble to the steel so that there is less likelihood of corrosion (small cathode/large anode system). However, for stainless steels a high-silver braze filler alloy is often used to retain the corrosion resistance of the joint. However, embrittlement of the filler is always a possibility if any zinc, cadmium, or tin are present. An interesting example of the judicious choice of braze filler is to be found in the selection of silver alloys for the brazing of stainless steels to be subsequently used in a tap-water environment.<sup>11</sup> Although the brazed joint may appear to be quite satisfactory, after a relatively short exposure period, failure of the joint occurs by a mechanism which appears to be due to the breakdown of the bond between the filler and the base metal. Dezincification is a prominent feature of the phenomenon<sup>12,13</sup> and zinc-free braze alloys based on the Ag–Cu system with the addition of nickel and tin have been found to inhibit this form of attack. A similar result is obtained by electroplating of nickel over the joint area prior to brazing with a more conventional Ag–Cu–Zn–Cd alloy. Interface corrosion of brazed stainless steel joints has been reviewed by Kuhn and Trimmer,<sup>14</sup> whilst Lewis<sup>15</sup> has used X-ray photo-electron spectroscopy to confirm the dezincification theory. On the other hand, the corrosion resistance of a high temperature brazed joint in a Mo-containing low-C stainless steel exposed to drinking water gave no problems.<sup>16</sup>

When, in an engineering structure, an aluminum–bronze alloy is selected for corrosion resistance, the choice of braze filler becomes important. Thus, although copper–zinc brazing alloys are widely used, the corrosion resistance of the resultant joint (effectively of brass) will be significantly worse than that of the bronze. Crevice corrosion has also been found when joining copper tubes using Cu–Ag–P fillers, the presence of scale adjacent to the joint being deemed responsible.<sup>17</sup> Brazing with copper alloys is unsuitable for equipment exposed to ammonia and various ammoniacal solutions because of the likelihood of increased corrosion, especially SCC with copper- and nickel-base alloys; however, an alloy based on Fe–3.25B–4.40Si–50.25Ni has been shown to be suitable for such applications.<sup>18</sup>

### 3.35.4 Welded Joints

#### 3.35.4.1 Welding Processes

A weld differs from all other forms of joint in that the intention is to ideally obtain a homogeneous material

(i.e., continuous and of similar microstructure and composition) throughout the volume of the welded joint. There are a large variety of processes by which this may be achieved, most of which depend upon the application of thermal energy to bring about a plastic or molten state of the metal surfaces to be joined. The more common processes used are classified in **Table 2**.

Examination of a welded joint shows several distinct zones, namely the fusion zone with its immediate surroundings, the heat affected zone (HAZ) adjacent, and the parent metal that remains unaffected, **Figure 2**. It is apparent that welding necessarily produce differences in microstructure between the (effectively) cast deposit, the HAZ which has undergone a variety of thermal cycles, and the parent plate. Furthermore, differences in chemical composition are often present between parent and weld metal. Other characteristics of welding include:

1. The production of a residual stress system which remains after welding is completed, and which, in the vicinity of the weld, is tensile and can exceed yield.
2. In the case of fusion welding, the surface of the deposited metal has a generally rough surface profile that is both a stress raiser and a site for the condensation of moisture.
3. The joint area is covered with an oxide scale and possibly a slag deposit which may be chemically reactive, particularly if hygroscopic.
4. Protective coatings on the metals to be joined are inevitably removed during welding so that the weld and the parent metal in its vicinity become unprotected compared with the bulk of the plate.

**Table 2**     Typical joining processes

<i>Joining process</i>	<i>Types</i>
Mechanical fasteners	Nuts, bolts, rivets, screws
Soldering and brazing	Hot iron, torch, furnace, vacuum
Fusion welding	Oxyacetylene, manual metal arc, tungsten inert gas, metal inert gas, carbon dioxide, pulsed arc, fused arc, submerged arc, electro slag, and electron beam
Resistance welding	Spot, seam, stitch, projection, butt, and flash butt
Solid-phase welding	Pressure, friction, ultrasonic and explosive

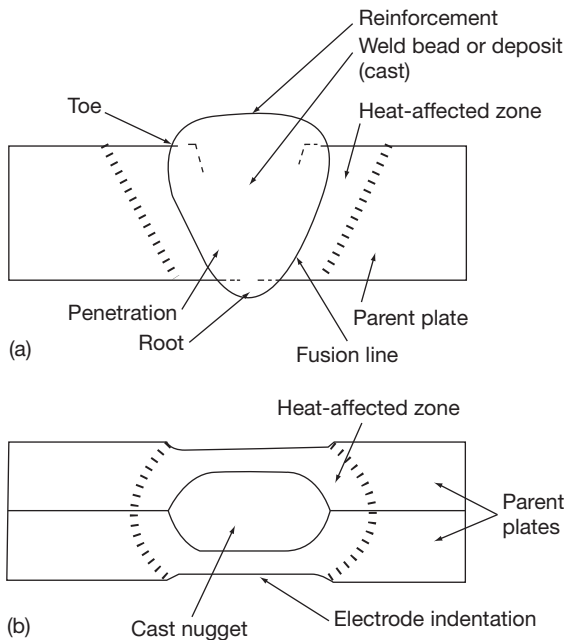


**Figure 2** Weld definitions. (a) fusion weld and (b) resistance spot weld.

Therefore, the use of welding as a method of fabrication may modify the corrosion behavior of an engineering structure, and this may be further aggravated by removal of protective systems applied before welding, whilst at the same time the use of such anticorrosion coatings may lead to difficulties in obtaining satisfactorily welded joints.<sup>19–21</sup>

### 3.35.4.2 Weld Defects

There is no guarantee that defect-free joints will automatically be obtained when fabricating 'weldable' metals. This is a result of the fact that weldability is not a specific material property but a combination of the properties of the parent metals, filler metal (if used), and various other factors that are summarized in Table 3.<sup>22</sup> The consequence of the average structural material is to produce a situation where defects may arise in the weld deposit or HAZ, as summarized in Table 3 and Figure 3.

It is obvious that these physical defects are dangerous in their own right but it is also possible for them to lead to subsequent corrosion problems, for example, pitting corrosion at superficial nonmetallic inclusions and crevice corrosion at pores or cracks. Other weld irregularities which may give rise to crevices include the joint angle, the presence of backing strips and spatter, as summarized in Figure 4 and Table 4.

**Table 3** Factors affecting weldability after Lundin

Parent metal	Filler metal	Other factors
Composition	Composition	Degree of fusion (Joint formation)
Thickness	Impact strength	Degree of restraint
State of heat treatment	Toughness	Form factor (Transitions)
Toughness	Hydrogen content	Deposition technique
Temperature	Purity	Skill and reliability of the welder
Purity	Homogeneity	
Homogeneity	Electrode diameter (heat input during welding)	

Source: Lundin, S. *ESAB, Göteborg 1963*, 2.

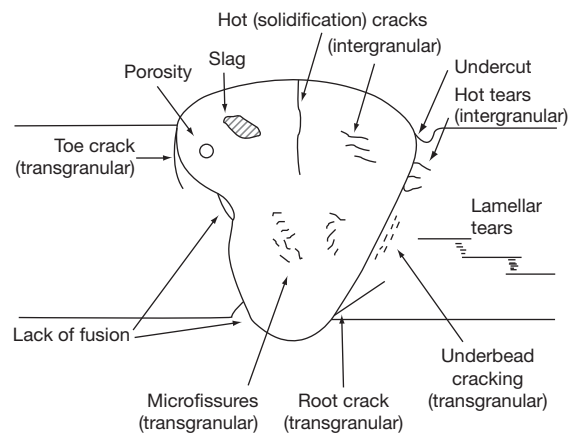


**Figure 3** Possible weld defects.

### 3.35.4.3 Factors Affecting Weldment Corrosion

Corrosion of welds may result from one or more of a number of factors, including:

1. Deficient weld design
2. Residual stresses
3. Inadequate consumables
4. Deficient welding procedure or welding technique
5. Incomplete penetration
6. Weld features such as the geometry of the weld bead
7. Surface finish, due, for example, to oxide film or scales on the weld surface, weld slag or spatter.

#### 3.35.4.3.1 Weldment design

Weld joint design is a relevant factor to be considered in the overall corrosion performance assessment of equipment, and the design stage provides the best

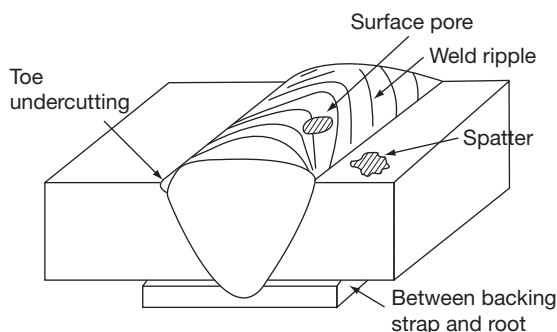


**Figure 4** Possible crevice sites.

opportunity to avoid future corrosion problems relating to both the weld material and the weld geometry. The specification of the ideal geometry in regard to corrosion resistance has sometimes to be sacrificed in favor of the necessity to attend to other relevant construction aspects, for example, component flexibility. When possible, the weld should be located in an easily accessible area that allows for easy inspection, for example by nondestructive testing or even by visual inspection, and avoids stress concentration.

Some of the more significant features of weldment geometry are those that might cause crevice corrosion problems. These can be eliminated at the equipment design stage by a proper weld design, for example, by the use of butt rather than overlap welds. Weld joint geometry may affect the corrosion performance of a welded structure by creating conditions leading to dead volumes that may lead to accumulation of debris or corrosion products. These causes exacerbate corrosion by:

1. Allowing the area to remain wet longer than the rest of the equipment.
2. Contributing to the accumulation of aggressive species beneath them.
3. Allowing differentiated access of oxygen to the surface.
4. Preventing adequate drainage of equipment during downtime periods, rendering the fluid stagnant, and increasing the localized corrosion rate.

Some weld joint geometries may also cause crevice corrosion. For example, an overlap or T weld is an inevitable crevice former. Also, the use of skip welding instead of continuous welding introduces crevices, as illustrated in [Figure 5](#). In principle, these problems can be avoided by the application of a sealing weld. However, sometimes the solution is

**Table 4** Weld defects

<i>Defect</i>	<i>Causes</i>	<i>Remedies</i>
Hot cracks	Large solidification range Segregation Stress	More crack-proof filler Less fusion
Under bead cracks	Hardenable parent plate Hydrogen Stress	Low hydrogen process Planned bead sequence Preheating
Microfissures	Hardenable deposit Hydrogen	Low hydrogen process Pre- and post-heating
Toe cracks	Stress High stress Notches Hardenable parent plate	Planned bead sequence Pre-heating Avoidance of notches
Hot tears	Segregation Stress	Less fusion Cleaner parent plate
Porosity	Gas absorption	Remove surface scale Remove surface moisture Cleaner gas shield

not so straightforward because this might introduce unacceptable constraints into the equipment that can cause cracking or even promote other corrosion phenomena, such as SCC.

#### **3.35.4.3.2 Weldment backing**

A common deficiency of weld joint geometry is faulty weld penetration through the complete thickness of the section to be joined. Incomplete or excess penetrations are the two most serious defects in root passes, both of which have an impact on corrosion performance. In some geometries and welding positions, the root pass liquid weld metal pool tends to fall toward the interior of the structure resulting in excessive penetration. This can cause flow disturbance, particularly in small diameter pipes. Furthermore, splatter can also form on the internal surface. Both defects can compromise the corrosion performance of the equipment, and welders often tend to produce incompletely penetrated welds, which produce crevices in which corrosion can occur by the accumulation of aggressive species. To avoid this, backing rings can be used. These accessories help control the weld pool on the root pass, which is essential to produce a



satisfactory weld, allowing an easier inner surface alignment and an acceptable internal root profile. Furthermore, backing rings can have a chilling effect on the weld metal and the HAZ, reducing the total heat input which often has a positive impact on the HAZ width and weldment microstructures resulting from the welding operation. A common backing material is copper, which has a high thermal conductivity. However, other backing materials are also used such as anodized aluminum, stainless steel, mild steel, or even nonmetallic materials like ceramics.

Although the use of backing materials is positive from the welding standpoint, a permanent backing material may reduce the corrosion resistance of the weld joint. It creates an internal obstruction that will disturb flows and may induce erosion–corrosion, a crevice that may lead to crevice corrosion and possible galvanic incompatibility that may promote galvanic corrosion if the material is not chosen correctly. To overcome the disadvantages associated with permanent backings, inserts have been developed, that are consumed in the root pass, assuring complete penetration and a smooth root pass.

#### 3.35.4.3.3 Welding procedure or technique

Apart from incomplete or excessive penetration, other incorrect or inadequate aspects of welding operations can have an impact on the weldment corrosion performance. A weld is always a metallurgically inhomogeneous area compared to the parent material. Often, depending on welding parameters or cooling rates, this may lead to the formation of second phases, precipitates, grain boundary segregation, or even grain growth, which has consequences for the mechanical and corrosion properties of the weldment. Thus, an inappropriate thermal cycle can lead to a severe reduction in fracture toughness due to martensite formation in the case of carbon or low alloy steels, sensitization in the case of stainless steels, an inappropriate proportion of phases as in the case of

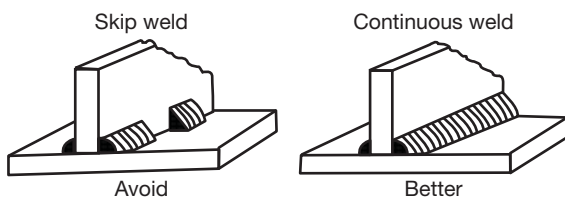


**Figure 5** Skip welding and crevice corrosion versus continuous welding. Reproduced from Landrum, R. J. *Fundamentals of Designing for Corrosion Control*; NACE, 1989.

duplex stainless steels, or secondary phase formation/distribution in the case of aluminum alloys.

Weld metal surface roughness or finish, or even the geometrical transition of the weld cap to the parent material, can provide stress raisers and therefore crack initiators in conditions with the potential for SCC or corrosion fatigue. Also, weld slag or spatter can create the conditions for crevice corrosion. Insufficient shielding gas protection can produce excessive oxidation of the welded area resulting in the formation of films or even scales that reduce the localized corrosion resistance, particularly in the case of stainless steels. Note that welding is much more readily controlled in the fabrication shop than in the field, and field repair welding presents particular challenges in relation to the control of procedures and techniques.

#### 3.35.4.3.4 Residual stresses and stress concentration

A weld is a geometric discontinuity that may concentrate residual, service, or applied stresses. Thermal contraction in the cooling stage and phase transition resulting from the welding process may introduce residual stresses in or at the vicinity of the weld joint, as shown schematically in [Figure 6](#). Furthermore, surface irregularities associated with the roughness of the weld bead or other defects may act as stress raisers. The resulting applied stress, that is, the sum of all stresses in a component, may introduce a vulnerability to phenomena such as corrosion fatigue, SCC, hydrogen induced cracking, or hydrogen embrittlement. The crack orientations will vary with the relevant stress fields:

1. Longitudinal cracks oriented parallel to the weld cord arise as consequence of transverse contraction.
2. Longitudinal cracks located on the middle of the weld cord arise as a consequence of an abnormal

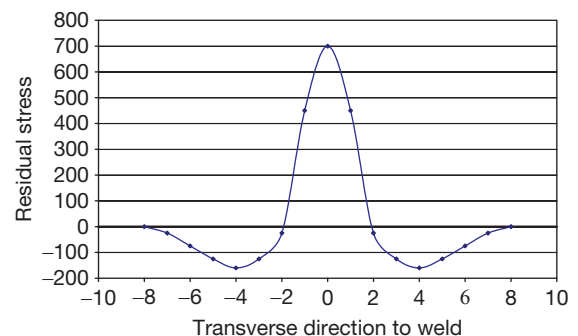


**Figure 6** Schematic diagram of typical stress distribution across a butt weld.

stress level on the weld cord resulting from an improper welding technique.

3. Cracks on the weld edges result from the contraction stresses amplified by an edge effect.
4. Cracks on the HAZ parallel to the weld arise as a consequence of transverse contraction.

#### **3.35.4.3.5 Postweld heat treatment**

Sometimes, welding procedures require a postweld heat treatment (PWHT). This may be required by the construction code and may have an impact on the corrosion behavior of the weld area. PWHT is undertaken for a number of reasons depending on the requirements of the joint:

1. Annealing to produce recrystallization and eventually grain growth.
2. Softening to reducing the weld hardness in the HAZ.
3. Precipitation hardening to increase the strength
4. Stress relieving to reduce residual fabrication stresses.

These heat treatments may have an impact on the corrosion performance of the weld area to the extent that they might change the microstructure of the weld metal and HAZs, as well as the material surface condition, namely in regard to oxide formation. If a heat treatment is required and it is not adequately performed, it can induce detrimental changes, such as the sensitization of stainless steels or secondary phase precipitation that will strongly affect the corrosion performance of the weld. One of the most common examples of softening relates to materials intended for sour service in the oil and gas industry where materials are submitted to environments in which sulfide stress corrosion cracking (SSCC) may occur.

#### **3.35.4.3.6 Filler metal composition**

The weld metal composition is important from the corrosion standpoint. If the weld metal has a lower potential than the materials to be joined, it will corrode preferentially. Furthermore, due to its lower surface area, the corrosion current density for the corrosion process will be very high. In the case of autogenous welds, in which there is no separate filler material, the composition of the weld, *albeit* not necessarily the microstructure, is determined by the adjacent parent material. However, if a filler material is used, it should ideally be more noble than the material, or materials to be joined. Furthermore, when possible, the weld root should face the most aggressive fluid, because it will expose a smaller area.

### **3.35.5 Welding of Specific Materials**

#### **3.35.5.1 Introduction**

A review of the extensive work that has been undertaken since the previous edition on the corrosion performances of weldments in specific materials is beyond the scope of this chapter and the reader is referred to other sources such as *The Corrosion of Weldments*, edited by J. R. Davis, published by ASM International and the publications of relevant alloy suppliers. The pointers to weldment performance that are provided in the following sections are based mostly upon the material published in the previous edition with only minor updating.

#### **3.35.5.2 Carbon and Low-Alloy Steels**

Carbon steels undergo metallurgical transformations across the weld and HAZ, and a wide range of microstructures can be developed depending on cooling rates that in turn depend on factors, such as energy input, preheat, metal thickness, weld bead size, etc. Some typical microstructures for a carbon steel weld are shown in [Figure 7](#). Clearly, weld metal microstructures will be very different from those of the HAZ and parent material. Preferential corrosion of the HAZ is a common feature in a wide range of aqueous environments. Hardness levels will tend to be lower for high heat input processes such as submerged-arc welding than lower energy processes such as shielded metal arc.

The subject of weldment corrosion in offshore engineering was reviewed by Turnbull.<sup>23</sup> Galvanic effects are possible if the steel weld metal is anodic to the surrounding parent plate and is enhanced by the high anode to cathode surface area ratio that exists. Lundin<sup>24</sup> showed, for carbon steel, that weld metal deposited using a basic flux was less noble; acid fluxes resulted in a more noble weld metal, while rutile-based fluxes were intermediate. The nature of the surface and its prior treatment (e.g., peening) seemed to have no effect. It was also noted that the HAZ was no less corrosion resistant than the unaffected plate. Millscale and other heat oxides should always be removed by grit blasting as its presence can cause serious corrosion problems around welded joints. On the other hand, Saarinen and Onnela<sup>25</sup> considered that weld metal corrosion can be eliminated by using a suitably balanced electrode type, the remaining problem then being in the HAZ whose tendency to corrode (i.e., become more active) increased with increasing Mn content. Thus, the heat input during welding must be

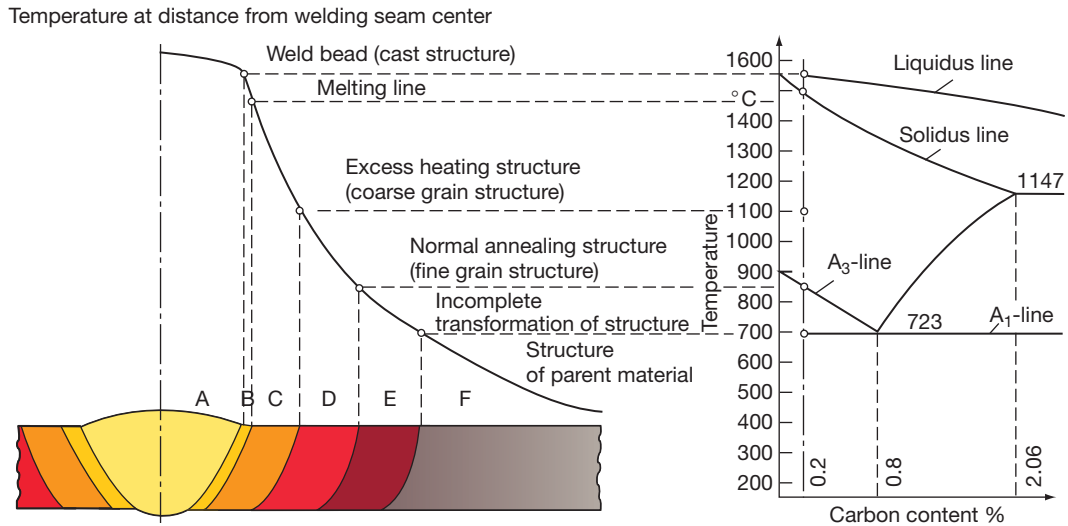


**Figure 7** Variation of weld structure with distance from the welding seam center. Reproduced from ISQ training material.

important since a significant factor will be the cooling rate of the HAZ after welding. These findings have been substantiated by Ousyannikov *et al.*<sup>26</sup> using a scanning reference electrode probe. Increasing the heat input changed the weld metal from anodic to cathodic relative to the parent plate, although the presence of Ni reduced the magnitude of the effect.

The problem of grooving corrosion in line-pipe steel welded by high frequency induction or electric resistance welding has been studied. In sea water, it seems to be related to high sulfur content in the weld zone, the type of environment, its temperature, and velocity.<sup>27</sup> The importance of sulfur is significant since Drodten and Herbsleb have reported that localized corrosion at welded joints is more a function of S, Si, microstructure, and nonmetallic inclusion type and shape than of the local oxygen concentration.<sup>28</sup>

One of the major concerns in offshore construction is that of the corrosion fatigue. Turnbull<sup>24</sup> discusses this at length. Cracks usually originate at weld toes, the point of initiation being associated with crack-like defects (slag, nonmetallics, cold laps, undercuts, hot tears). These can constitute sharp notches situated at a point of maximum stress concentration due to the weld geometry. It is to be noted that although cracks initiate in the HAZ at the weld toe, the majority of crack propagation occurs in what is essentially unaffected parent plate. In air, it is possible to have cracks that grow at a decelerating rate until no further growth occurs, this is the 'short crack' problem widely discussed by Miller,<sup>29</sup> and the cracks are referred to as

nonpropagating cracks. On the other hand, similar cracks may continue to grow at an accelerating rate in a corrosive environment even though the stress may be below the fatigue limit. Burns and Vosikovsky<sup>30</sup> have given considerable attention to corrosion fatigue of tubular joints in structural and line-pipe steels. Crack initiation at the toe occurs after a small fraction of life, and long surface cracks can exist for over 50% of the life. On the other hand, laboratory tests on plate-to-plate welded specimens of the cruciform type show cracks which are much smaller for a larger percentage of the life, but their growth rate accelerates as the depth increases.

In sea water, the effects of cyclic frequency, stress ratio, electrochemical potential, oxygen content, and intermittent immersion at 5–12 °C have all been evaluated.<sup>31</sup> There is some evidence that at lower temperatures, seawater is less detrimental to fatigue life, but at all temperatures studied, the crack growth rate was always faster than in air. At intermediate ranges of stress intensity range ( $\Delta K$ ), there was a significant reduction in crack growth rate as the seawater temperature was reduced from 25 °C to 0 °C. Whilst the cracks are small and  $\Delta K$  low, calcareous blocking is very effective, and under these conditions and correctly applied cathodic protection (CP) consequently reduces the crack growth rate. As the crack length increases, blocking becomes less effective and the increased hydrogen embrittlement can accelerate the growth rate to values greater than experienced for the unprotected joints. Similarly,

Nibbering *et al.*<sup>31</sup> obtained data showing that CP raises the initial fatigue crack resistance but has little effect at a later stage of crack propagation. Even so, they considered that CP is still the most effective method for prolonging structural life under corrosion fatigue conditions. This is not unreasonable since crack initiation and early growth can represent a large proportion of the total life.

Marine fouling leading to the local production of H<sub>2</sub>S increases crack growth rate, but what the effect is when combined with CP is uncertain. Some of the factors mentioned earlier in connection with other steel corrosion problems are important to sulfide stress-corrosion cracking (SSCC). For example, the use of high strength low alloy steels in which carbon is reduced to below 0.05% combined with reduced sulfide segregation are beneficial to preventing SSCC of weldments.<sup>32,33</sup> SSCC of weld repairs in well-head alloys was investigated by Watkins and Rosenberg<sup>34</sup> who found that the repairs were susceptible to this problem because of the hard HAZs developed by welding. Postweld heat treatment was an essential but not complete cure compared with unrepaired castings. In the case of hydrogen-assisted cracking of welded structural steels, composition is more important than mechanical properties and the carbon equivalent should be <0.5%.<sup>35,36</sup> McMinn has presented much useful data concerning the fatigue crack growth rate in simulated HAZs of A533-B steels,<sup>37</sup> whilst Ray *et al.* have demonstrated the role of pitting corrosion of mild steel on crack initiation.<sup>38</sup>

### 3.35.5.3 Stainless Steels

There are four groups of stainless steels, each possessing their own characteristic welding problems:

1. Ferritic: Welding tends to result in a large grain size throughout the weld zone causing significant reduction in ductility. Also, the ferritic microstructure is susceptible to hydrogen embrittlement.
2. Martensitic: HAZ cracking is likely and may be remedied by employing the normal measures required for the control of hydrogen-induced cracking.
3. Austenitic: These steels may be readily welded but are susceptible to hot cracking, which may be controlled by permitting a small amount of residual delta ferrite in the weld.
4. Duplex: Welding of duplex alloys requires correct choice of weld material and procedures, in particular weld heat input, in order to ensure the retention of a satisfactory weld microstructure.

The corrosion of stainless steel welds was reviewed in the 1970s by Pinnow and Moskowitz<sup>39</sup> and, although this article is clearly dated in detail, the main general issues are still of relevance. Thus, main problems that might be encountered are weld decay, knife-line attack, and SCC, as illustrated in **Figure 8**.

#### 3.35.5.3.1 Ferritic and martensitic stainless steels

The more traditional compositions with a relatively high (C + N): Cr ratio carry a risk of martensite formation in the HAZ during cooling.

Furthermore, there is a risk for carbide precipitation and therefore, for intergranular corrosion. More modern grades of ferritic stainless steel have a low (C + N): Cr ratio and possess stabilizing elements added to the material to reduce the likelihood of intergranular corrosion. Ferritic stainless steels are also liable to grain growth in the HAZ, as illustrated in **Figure 9**. Therefore, heat input should be kept to a minimum, **Figure 9**. Also, insufficient gas protection during welding may lead to chromium nitride formation due to N<sub>2</sub> uptake from the atmosphere, and consequently, to embrittlement and decreased corrosion resistance. Finally, the gas used for shielding as well as the metal surface should be free of H<sub>2</sub> sources (e.g., moisture, oil, and grease) in order to avoid hydrogen embrittlement.

#### 3.35.5.3.2 Austenitic stainless steels

Although readily welded, these are susceptible to hot cracking which may be overcome by balancing the weld metal composition to allow the formation of a small amount of  $\delta$ -Fe (ferrite) in the deposit, optimum crack resistance being achieved with a  $\delta$ -ferrite content of 5–10%, as illustrated in **Figure 10**. More than this

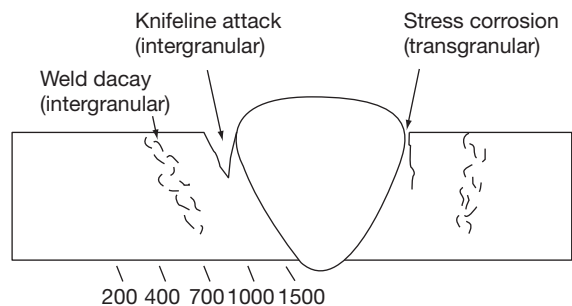


**Figure 8** Common sites of corrosion in stainless steel welds; typical peak temperatures attained during welding (°C) are given at the foot of the diagram. Note that knife-line attack has the appearance of a sharply defined line adjacent to the fusion zone.

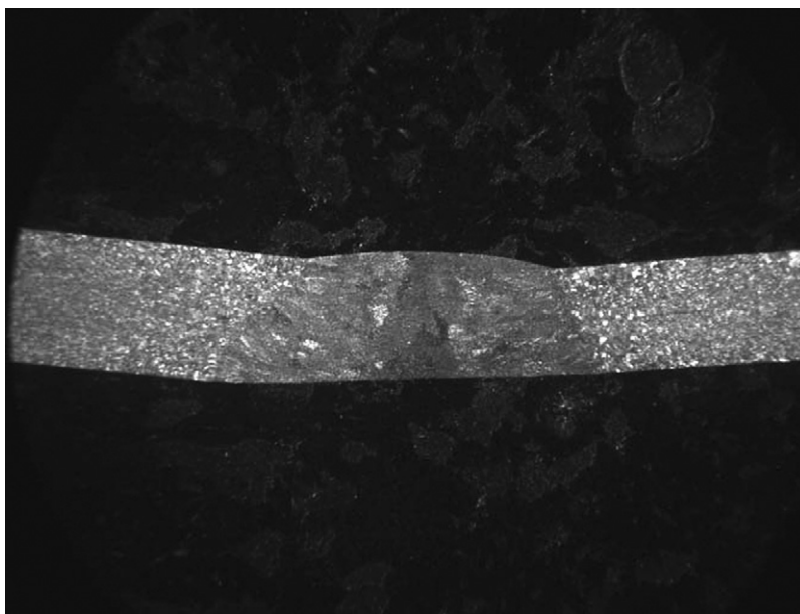


**Figure 9** Ferritic stainless steel weld showing large grain size in the weld and heat affected zone.

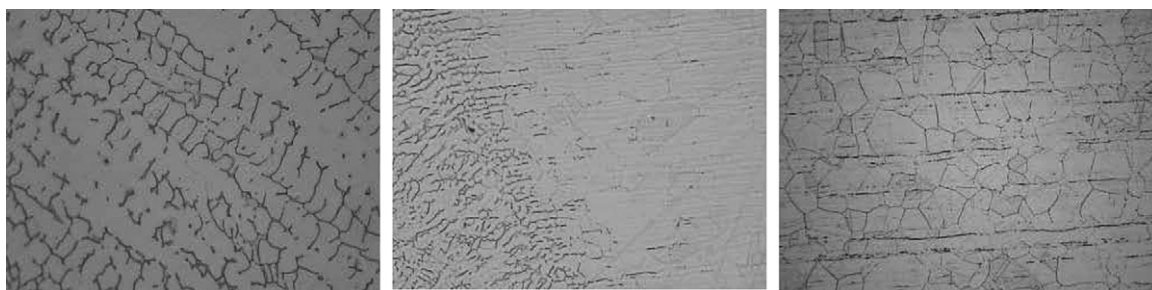


**Figure 10** Dendritic ferrite in an austenite weld (left); heat affected zone (center); equiaxed austenitic grains in the parent metal (right).

concentration increases the possibility of  $\sigma$ -phase formation if the weldment is used at elevated temperature consequently reducing both mechanical and corrosion properties. Any adverse effects of the  $\delta$ -ferrite on corrosion resistance are usually overcome by slight enrichment of the filler metal composition relative to the parent material. However, in certain critical applications such as the manufacture of urea,  $\delta$ -ferrite can reduce corrosion resistance to an unacceptable extent in which case fully austenitic welds are required.

Prasad Rao and Prasanna Kumar<sup>40</sup> undertook electrochemical studies of austenitic stainless steel claddings to find that heat input and delta ferrite content significantly affected the anodic polarization behavior under active corrosion conditions, whilst Herbsleb and Stoffelo found that two-phased weld claddings of the

24Cr–13Ni type were susceptible to intergranular attack (IGA) as a result of sensitization after heat treatment at 600 °C.<sup>41</sup>

### 3.35.5.3.3 Duplex stainless steels

These steels have a better weldability than ferritic steels. They are purely ferritic at high temperatures, and if quenched rapidly they may remain predominantly ferritic and the ferrite phase is sensitive to chromium nitride and brittle phase formation. Modern duplex stainless steels have a high content of nitrogen, which is an austenite stabilizer. This facilitates austenite formation at high temperatures and consumes the nitrogen, preventing the formation of nitrides in the ferritic phase. Duplex filler metal is also formulated with more nickel than the parent



material to promote austenite formation. As a result, the as-welded structure has a balance of ferrite and austenite that is close to the equilibrium structure of the parent material. Nitrogen additions to the weld shielding gases also assist in maintaining the correct composition of the weld and heat affected zones. Duplex stainless steels are also susceptible to intermetallic phase formation approximately in proportion to their chromium and molybdenum contents. This decreases the corrosion resistance and mechanical properties such as toughness. Precipitation of intermetallic phases is favored by high heat inputs that need to be controlled, particularly in thick sections, to avoid adverse effects.

#### 3.35.5.3.4 Sensitization

Carbide precipitation and growth causes the formation of a chromium depleted area around the grain boundaries and chromium carbide formation at the grain boundaries. When sensitized material is subjected to an aggressive medium, preferential attack occurs.

Sensitization results from exposure of the material to high temperatures, either during production, or as a result of welding operations. Sensitization temperatures are in the range 425–815 °C. Although sensitization is primarily caused by chromium and carbon, other elements present in the stainless steel may play a secondary role in sensitization. Thus, Ni increases carbon activity in the solid matrix; favoring carbide precipitation and Mo has behavior similar to chromium, although it is usually present in lower amounts.

Nowadays, most commercial grades of stainless steel are of an 'L' grade and low in carbon. Hence, sensitization rarely occurs; as can be seen in [Figure 11](#), reduction in carbon concentration greatly increases the time required for sensitization to occur. However, surface sensitization, most commonly from surface hydrocarbon contamination (i.e., from oil and grease) remains an issue. Sensitization can only be reversed by heat-treatment to affect a re-solution of the chromium carbide (preferably at ~1050 °C), which is generally impractical in most structures.

Under certain conditions, it is possible for a weldment to suffer corrosive attack which has the form of a fusion line crack emanating from the toe of the weld; this is termed knife-line attack. It is occasionally experienced in welded stainless steels that have been stabilized against sensitization by addition of titanium, niobium, or tantalum. The niobium-stabilized steels are more resistant than the titanium-stabilized types by virtue of the higher solution temperature of NbC, but the risk may be minimized by limiting the carbon

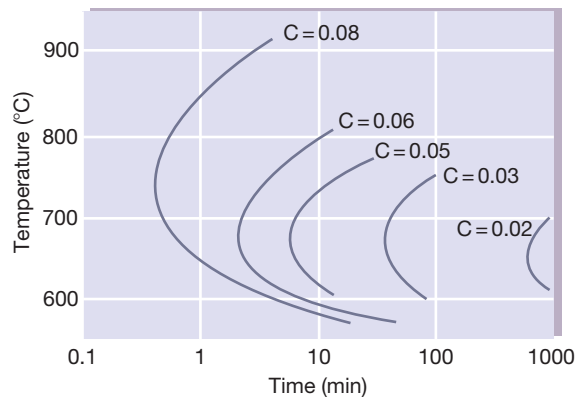


**Figure 11** Time-temperature diagram for IGA of 18Cr 9Ni stainless steels with different carbon contents in sulfuric acid-copper sulfate tests showing that lower carbon contents increase the time required for sensitization. Reproduced from *Corrosion Handbook, Stainless Steels*; AB Sandvik Steel, 1994.

content of the steel. Knife-line attack is described in detail in [Chapter 2.24, Corrosion in Nitric Acid](#).

#### 3.35.5.3.5 Localized corrosion at weldments

The various forms of SCC are described in separate chapters in this book. SCC is particularly dangerous because of the insidious nature of the phenomenon. The residual stresses arising from welding are often sufficiently high to provide the necessary stress condition, whilst a chloride-containing environment in contact with the austenitic stainless steels induces the typically transgranular and branched cracking. Increased nickel content marginally improves the resistance of the steel to this type of attack. Also, the ferritic steels and duplex steels with at least 50% ferrite have high resistance to chloride-induced transgranular SCC.

IGA, pitting, and crevice corrosion are problems commonly associated with the stainless steels and their welds. For example in the duplex stainless steels, the corrosion resistance, particularly in terms of pitting and crevice corrosion, depends on microstructure, that is, the relative proportions of ferrite and austenite, the lattice concentration of dissolved nitrogen, and the segregation of alloying elements between the ferrite and austenite phases.<sup>42–44</sup> These may be affected by heat input and welding procedures.<sup>45</sup> Grekula *et al.*,<sup>46</sup> studying pitting corrosion of gas tungsten arc welds in austenitic steels, found that the final interdendritic regions to solidify in primary austenite welds and the austenite interfaces in primary  $\delta$ -ferrite welds are the most susceptible sites for pit initiation. Sulfur also affects pitting

potential and increases the pit density but has no effect on the pit growth rate.<sup>47</sup> Also, pitting in or adjacent to tungsten inert gas (TIG) weld beads in tap-water may be caused by the surface oxides formed during welding and is generally due to inadequate root gas shielding.<sup>48</sup> It is essential, for optimum resistance to localized corrosion initiation, to remove any weld tint using appropriate pickling fluids/pastes such as nitric acid or light blasting with, for example, rounded glass beads.

Controlled additions of nitrogen have been made to 439 steel weld metal to prevent IGA,<sup>49</sup> whilst additions of Y or Ce to an 18Cr–12Ni steel have also been found to be beneficial.<sup>50</sup> In the case of TIG-welded Mo-containing stainless steels,  $\sigma$ -phase formation can be responsible for IGA in hot oxidizing (e.g., nitric) acids.<sup>51</sup>

#### 3.35.5.4 Nickel Alloys

In the main, welding does not seriously affect the corrosion resistance of the high nickel alloys, and the resistance to stress corrosion is particularly high. Earlier versions of the N–Cr–Mo and Ni–Mo families of alloys had limited thermal stability and were vulnerable to the precipitation of deleterious intermetallic phases during welding. Thus, in the case of the Ni–Cr–Mo–Fe–W type alloys, Samans<sup>52</sup> suggested that the material should be given a two-stage heat treatment prior to single-pass welding in order to produce a dependable microstructure with a thermally stabilized precipitate. In the case of the Ni–28Mo alloy, it was suggested that a special case of selective corrosion analogous to the weld-decay type of attack could be removed by solution treatment or using an alloy containing 2% V.<sup>53</sup> The more recent grades of these alloys have been alloyed to provide much greater thermal stability and are much less vulnerable to loss of corrosion resistance during welding. The chromium-containing alloys can be susceptible to weld decay and should be thermally stabilized with titanium or niobium, and where conditions demand exposure to corrosive media at high temperatures a further post-weld heat treatment may be desirable.

Of the weldability problems, nickel and nickel-based alloys are particularly prone to solidification porosity, especially if nitrogen is present in the arc atmosphere, but this may be controlled by ensuring the presence of titanium as a denitrider in the filler and maintaining a short arc length. The other problem that may be encountered is hot cracking, particularly in alloys containing Cr, Si, Ti, Al, B, Zr, S, Pb, and P. For optimum corrosion resistance, it is recommended that

similar composition fillers be used wherever possible, although overmatching with, for example, molybdenum can compensate for any elemental segregation inherent in the weld metal. Obviously any flux residues that may be present must be removed.

#### 3.35.5.5 Aluminum Alloys

These alloys are susceptible to hot solidification cracking and in order to overcome this problem some aluminum alloys have to be welded with a compensating filler of different composition from that of the parent alloy; this difference in composition may lead to galvanic corrosion. A further problem in the welding of these materials is the high solubility of the molten weld metal for gaseous hydrogen which causes extensive porosity in the seam on solidification; the only effective remedy is to minimize hydrogen pick-up by using a hydrogen-free gas shield with dry, clean consumables (e.g., welding rods, wire), and parent plate.

In general, however, the corrosion resistance of many aluminum alloys is not significantly reduced by welding. Any adverse effects that may be encountered with the higher strength alloys can be largely corrected by postweld heat treatment; this is particularly true of the copper-bearing alloys. Pure aluminum fillers impart the best corrosion resistance, although the stronger Al–Mg and Al–Mg–Si fillers are normally suitable; the copper-bearing fillers are not particularly suitable for use in a corrosive environment.

The HAZ may become susceptible to SCC, particularly in the high-strength precipitation hardened alloys. In this context for Al–Zn–Mg type alloys, it has been shown that maximum sensitivity appears to occur when there is a well-developed precipitation at the HAZ grain boundaries adjacent to the fusion line, a fine precipitate within the grain and a precipitate-free zone immediately adjacent to the grain boundaries.<sup>54</sup>

#### 3.35.6 Protection of Welded Joints

Structural steels are frequently protected from corrosion by means of a paint primer, but these materials can have an adverse effect on the subsequent welding behavior, and this is mainly observed as porosity.<sup>20</sup> Hot-dip galvanizing for long-term protection can also lead to porosity and intergranular cracking after welding, in which case it may be necessary to remove the zinc coating from the edges of the parent material prior to welding. The presence of zinc can also lead to operator problems due to the toxicity of the fume

evolved unless adequate fume extraction is employed. After welding and prior to painting, all welding residues must be removed and the surface prepared by grinding, grit blasting, wire brushing, or chemical treatment. This preparation is of fundamental importance, the method of applying the paint and the smoothness of the bead apparently having little effect on the final result.<sup>55</sup>

In the electric-resistance welding of hot-dipped galvanized steel, welding had little effect on the seawater corrosion of the coated steel when compared with the uncoated steel, the latter showing considerable corrosion after 12 months exposure.<sup>56</sup> The subject of galvanizing and the welding of structural steels has been given special attention by Porter,<sup>57</sup> but by far the most common method of protection is by painting which McKelvie<sup>58</sup> discusses in terms of fundamentals of paint as a corrosion barrier and the cleaning and coating procedures necessary to achieve protection of welded structures. In these articles, he covers the type of contaminants arising from welding as well as cleaning methods, blast primers, galvanizing, coating removal for repair welding, wire brushing, and chemical treatments. Lloyds Register of Shipping lists the proprietary products that have no significant deleterious effects on subsequent welding work.<sup>59</sup>

## References

- Booth, F. F. *Br. Corros. J.* **1967**, 2(2), 55.
- Everett, L. H.; Tarleton, R. D. *J. Br. Corros. J.* **1967**, 2(2), 61.
- Layton, D. N.; White, P. E. *Br. Corros. J.* **1967**, 2(2), 65.
- Layton, D. N.; White, P. E. *Br. Corros. J.* **1966**, 1(6), 213.
- Hahn, F. P. *Ind. Corros.* **1984**, 2(6), 16.
- Bauer, I. C. O. *Aluminium* **1982**, 58(5), E146.
- Costos, L. P. *Weld. J.* **1982**, 61(10), 320s.
- Yamaguchi, S. *Werkstoffe Korros.* **1982**, 33(11), 617.
- Allen, B. M. *Soldering Handbook*; Iliffe: London, 1969.
- Collard Churchill, S. *Brazing*; The Machinery: London, 1963.
- Sloboda, M. H. *Czech. Conf. Brazing* **1969**, 18.
- Jarman, R. A.; Myles, J. W.; Booker, C. J. L. *Br. Corros. J.* **1973**, 8(1), 33.
- Linekar, G. A. B.; Jarman, R. A.; Booker, C. J. L. *Br. Corros. J.* **1975**, 10.
- Kuhn, A. T.; Trimmer, R. M. *Br. Corros. J.* **1982**, 17(1), 4.
- Lewis, G. *Corros. Sci.* **1980**, 20(12), 1259.
- Lugscheider, E.; Minarski, P. *Schweissen Schneiden* **1989**, 41(11), 590.
- Stevernazel, G. *Werkstoffe Technik.* **1981**, 12(12), 439.
- Stenerson, R. N. *Welding J.* **1969**, 48(6), 480.
- Gooch, T. G.; Gregory, E. N. *Br. Corros. J.* **1968**, 348.
- Baker, R. G.; Whitman, J. G. *Br. Corros. J.* **1967**, 2(2), 34.
- Hoar, T. P. *Br. Corros. J.* **1967**, 2(2), 46.
- Lundin, S. *ESAB, Göteborg* **1963**, 2.
- Turnbull, A. *Rev. Coat. Corros.* **1982**, 5(1-4), 43.
- Lundin, S. *Svetsaren (ESAB)* **1967**, 2(2).
- Saarinén, A.; Onnela, K. *Corros. Sci.* **1970**, 10(11), 809.
- Ousyannikov, V. Yu.; Chernov, B. B.; Semenchenko, V. S.; Tyul'kin Yu, K. *Svar. Proizvod.* **1986**, 4, 38.
- Düren, C.; Treiss, E.; Herbsleb, G. *Mater. Perform.* **1986**, 25(9), 41.
- Drodtten, P.; Herbsleb, G.; Schwenk, W. *Steel Res.* **1989**, 60(10), 471.
- Miller, K. J. *Fatigue Eng. Mater. Struct.* **1982**, 5(3), 223.
- Burns, D. J.; Vosikowsky, O. *Time-Dependent Fracture*; Krauz, A. S., Ed.; Martinus Nijhoff: Dordrecht, 1985; pp 53.
- Nibbering, J. J. W.; Buisman, B. C.; Wildschut, H.; Rietbergen, E. *Laser Tech.* **1986**, 9, 187.
- Choi, J. K.; Kim, H. P.; Pyun, S. I. *Korean Inst. Met.* **1986**, 24(1), 14.
- Terasaki, F.; Ohtani, H.; Ikeda, A.; Nakanishi, M. *Proc. Inst. Mech. Eng. A. Power Process Eng.* **1986**, 200(A3), 141.
- Watkins, M.; Rosenberg, E. L. *Mater. Perform.* **1985**, 22(12), 30.
- Pircher, H.; Sussek, G. *Stahl und Eisen* **1982**, 102(10), 503.
- Drodtten, P. *Stahl und Eisen* **1982**, 102(7), 359.
- McMinn, A. *FCGR in HAZ-Simulated A533-B steel*; H.M.S.O.: London, 1982.
- Ray, G. P.; Jarman, R. A.; Thomas, J. G. N. *Corros. Sci.* **1985**, 25(3), 171.
- Pinnow, K. E.; Moskowitz, A. *Weld. J.* **1970**, 49(6), 278.
- Prasad Rao, K.; Prasanna Kumar, S. *Corrosion* **1985**, 41(4), 234.
- Herbsleb, G.; Stoffelo, H. *Werkstoffe Korros.* **1978**, 29(9), 576.
- Tamaki, K.; Yasuda, K.; Kimura, H. *Corrosion* **1989**, 45(9), 764.
- Fujiwara, K.; Tomasi, H. *Corros. Eng.* **1988**, 37(11), 657.
- Angelini, E.; Zucchi, F. *Br. Corros. J.* **1986**, 21(4), 257.
- Grekula, A. I.; Kujaanpaa, V. P.; Karjalainen, V. P. *Corrosion* **1984**, 40(11), 569.
- Chen, J. S.; Levine, T. M. *Corrosion* **1989**, 45(1), 62.
- Edling, G. *Svetsen* **1979**, 38(3), 61.
- Engelhard, G.; Mattern, U.; Pellkofer, D.; Seibold, A. *Weld. Cutting (Düsseldorf)* **1988**, 40, 19.
- Deverell, H. E. *Mater. Perform.* **1985**, 24(2), 47.
- Watanabe, T.; El, K.; Nakamura, H. *J. High Temp. Soc. Japan* **1988**, 14(4), 185.
- Zingales, A.; Quartarone, G.; Moretti, G. *Corrosion* **1985**, 41(3)m, 136.
- Samans, C. H.; Meyer, A. R.; Tisinai, G. F. *Corrosion* **1966**, 22(12), 336.
- Lancaster, J. F. *Metallurgy of Joining*; Chapman and Hall: London, 1986.
- Kent, K. G. *Met. Revs.* **1970**, 15(147), 135.
- Keane, J. D.; Bigos, J. *Corrosion* **1960**, 16(12), 601.
- Roswell, S. C. *Met. Constr.* **1978**, 104(4), 163.
- Porter, F. C. *Met. Constr.* **1983**, 15(10), 606.
- McKelvie, A. N. *Met. Constr.* **1981**, 13(11/12), 693-744.
- Approved Prefabrication Primers and Corrosion Control Coatings*; Lloyds Register of Shipping: London, 1983.

## Further Reading

Davis, J. R. Ed. *Corrosion of Weldments*; ASM International: Materials Part, OH, 2006.

## 3.36 Role of Corrosion in the Failure of Adhesive Joints

**J. F. Watts**

Surrey Materials Institute and Faculty of Engineering & Physical Sciences, University of Surrey, Guildford, Surrey, GU2 7XH, UK

© 2010 Elsevier B.V. All rights reserved.

---

<b>3.36.1</b>	<b>Introduction</b>	2463
<b>3.36.2</b>	<b>Mechanisms of Failure</b>	2464
3.36.2.1	Hydrodynamic Displacement	2464
3.36.2.2	Adhesive Plasticization	2465
3.36.2.3	Corrosion Induced Failure	2466
3.36.2.3.1	Cathodic failure	2466
3.36.2.3.2	Anodic failure	2468
<b>3.36.3</b>	<b>Identification of Locus of Failure and Failure Classification</b>	2469
<b>3.36.4</b>	<b>Adhesively Bonded Substrate Materials</b>	2473
3.36.4.1	Low Carbon Steel Substrates	2473
3.36.4.2	Aluminum Substrates	2475
3.36.4.3	Zinc Substrates	2479
<b>3.36.5</b>	<b>The Improvement of Bond Durability</b>	2480
<b>3.36.6</b>	<b>Conclusions</b>	2480
<b>References</b>		2481

---

### 3.36.1 Introduction

It may seem rather at odds with the general scope of Shreir's Corrosion to include a section on adhesives as these materials are not normally employed as a mechanism of combating corrosion, or recognized as being susceptible to it, although they will, and do undergo environmental degradation. The justification is, however, very straightforward; adhesives are now widely used to bond metal components; metal components corrode, and such corrosion processes may compromise the performance of an adhesive joint, either at the bonded interface or adjacent to it. This chapter seeks to bring together the current state of knowledge regarding failure mechanisms in adhesive joints (much of it obtained from studies of the behavior of organic coatings applied to effect corrosion protection of a metallic substrate) and provide guidelines as to how various failure types may be identified.

Adhesive bonding has reached a level in manufacturing industry where the process can truly be said to be ubiquitous. Applications range from the rapid robotic assembly of small components to the structural adhesive bonding of massive parts in the aerospace and civil engineering industries. Against this background, there is a need to understand failure mechanisms that

may occur in adhesively bonded structures during their lifetime and design out such weaknesses. In terms of the initial load-bearing capacity, and subsequent lifetime under well defined conditions, of an adhesive joint, this can be readily determined from standard monotonic or fatigue tests. Arguably, however, the most important attribute of an adhesive joint is the durability that it possesses, that is the level of the original joint strength that will be retained over the lifetime of the structure. The life expectation of an adhesive joint can vary from a few days or weeks for foodstuffs packaging to more than 25 years for an aircraft! Thus, the focus of much adhesive bonding research over the last three decades has sought to catalogue and understand the issues associated with the durability of adhesive joints. The term durability in its strictest sense refers to the exposure of an adhesive joint or adhesively bonded structure to any aggressive liquid (or vapor) phase and as such includes reagents as diverse as fuel, deicing liquid and brake fluid! The generally accepted definition, however, of joint durability refers to the environmental exposure to water. The reason for this is that although durability is the performance of an adhesive bond in any chosen environment, the most aggressive environment as far as the metallic substrate–adhesive interface is concerned is water, and the term durability,

when applied to adhesives, has become synonymous with bond performance when exposed to water in its vapor or liquid form.

In seeking to understand the role of water on the degradation of joint durability, one must be aware that there are several distinct processes that can take place, leading to failure, resulting from different diffusion paths for water molecules in the adhesive and the presence, or otherwise, of electrochemical activity at the coated metallic surface. This gives rise to three distinct failure processes; interfacial failure as a result of hydrodynamic displacement of the adhesive from the substrate, the degradation of the adhesive itself in the environs of the substrate–adhesive (known in the adhesives community as plasticization), and the interfacial failure as a result of cathodic or anodic activity at the substrate, referred to as either cathodic delamination or anodic undermining. The mechanistic aspects of these three processes are well understood and can be related to exposure parameters.

The kinetics of failure is a function of both the environment and design parameters. In some situations, there may be more than one mechanism in operation, and the one that proceeds fastest will invariably become the rate-controlling step, but although it may prove possible to stifle such a mechanism, failure may still occur, albeit at a slower pace, as a result of the kinetics associated with the minor process. A number of authors have attempted to relate experimental observables to a unified mechanism that may serve as a design guide. Test geometries employed have varied from very simple tension or peel geometries to more sophisticated fatigue test pieces. Similarly, some authors have set out to investigate a particular failure process, such as cathodic delamination, while others have set out to study joint performance and have related durability to corrosion processes in an effort to gain a complete understanding of how failure has occurred. This chapter reviews mechanisms of failure, considers the various rate models that have been derived on the basis of empirical results, and finally, suggest ways in which adhesive joint design and specification can be used to reduce the detrimental effects of corrosion on joint durability.

### 3.36.2 Mechanisms of Failure

#### 3.36.2.1 Hydrodynamic Displacement

The interfacial thermodynamics associated with an adhesive joint are readily addressed using the concepts of interfacial free energy of the substrate,

adhesive, and water. Following is the well known Young–Dupré, which defines the thermodynamic work of adhesion ( $W_A$ ) as

$$W_A = \gamma_S + \gamma_A - \gamma_{AS} \quad [1]$$

where  $\gamma_S$  is the surface free energy of the (oxidized) metal substrate,  $\gamma_A$  is the surface free energy of the adhesive (normally a figure for a generic type of adhesive, such as epoxies, will be used), and  $\gamma_{AS}$  is the interface free energy associated with the substrate–adhesive junction. In a dry environment, the  $W_A$  parameter will assume a positive value indicating that the joint is thermodynamically stable. Something that is self evident by visual inspection and mechanical testing will invariably yield a failure within the adhesive layer, often at about the midpoint of the glue line thickness. The important feature here is that from both a thermodynamic standpoint and by experiment, when tested in a dry environment, the interface between substrate and adhesive is strong and stable. The exception to this observation is if a contaminant layer is present on the substrate, such an occurrence will compromise joint strength and lead to an interfacial failure. For this reason, such contamination, known as a weak boundary layer, is to be avoided at all costs in adhesive bond fabrication.

Although stable in a dry atmosphere, the exposure of such a joint to a humid or wet environment can lead to the diffusion of water along the interface, from the exposed joint edge, as indicated in [Figure 1](#). Following the approach of Gledhill and Kinloch,<sup>1</sup> [eqn \[2\]](#) can be written to predict the work of adhesion  $W_A^*$  in the presence of a third liquid phase, considering the three interfaces that are now involved:

$$W_A^* = \gamma_{SL} + \gamma_{AL} - \gamma_{AS} \quad [2]$$

where the addition of subscript L indicates the interface free energy of substrate or adhesive in contact with the liquid, as indicated in [Figure 1](#). Gledhill and Kinloch were able to show that when the values of

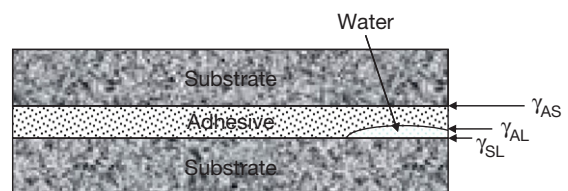


**Figure 1** The spontaneous displacement of an adhesive layer on an oxidized metal substrate (e.g., aluminum); the quantity  $W_A^*$  will be negative as predicted by [eqn \[2\]](#).



$W_A^*$  were negative (indicating that the process is thermodynamically favorable), there was a good correlation with empirical results in which a variety of joints were exposed to various liquids. Calculated values of  $W_A^*$  from these systems were either positive or negative, and those with a negative value showed spontaneous (but not instantaneous) separation when exposed to the liquid. (The term spontaneous is used in the thermodynamic sense, meaning energetically favorable, and has no implications regarding the kinetics of the process. This usage should not be confused with the same word taken in a sense to mean instantaneous, as in the term spontaneous combustion much favored by the popular press!)

Although outside the scope of this article, it must be appreciated that such an approach is only valid when the forces of adhesion are a result of van der Waals forces, more usually subdivided into dispersion and polar forces. These forces are generally rather weak and readily compromised by the presence of water. Specific interaction at interfaces, such as covalent bonds or donor–acceptor interactions (also known as acid–base bonds, of which hydrogen bonds are an important subcategory), are not so susceptible to degradation by water, and for this reason, the energetics approach described above is not applicable, and the presence of such bonds at the substrate–adhesive interface has, in itself, the propensity to improve bond durability.

Thermodynamic considerations indicate a true interfacial failure, as described above, and this can be established by the use of surface analysis methods such as X-ray photoelectron spectroscopy (XPS) and time-of-flight secondary ion mass spectrometry (ToF-SIMS). As some failure mechanisms may leave vanishingly thin adhesive residues on the substrate (<5 nm), the use of optical or scanning microscopy, analysis by EDX or FT-IRS is really not good enough, and methods that can explicitly provide a chemical analysis of such very thin layers are required.

Although the study of organic coatings provides valuable mechanistic information regarding failure modes that can be transferred directly to studies of the failure of adhesive joints, there is one major difference that must be considered when making this analogy. In the case of coatings, downward diffusion of water molecules, perhaps mitigated by the concomitant diffusion of solvated ions, is always likely to occur, whereas in the case of adhesively bonded substrates, this is only an important consideration if one or other substrate is permeable to water. This is clearly not the case in the adhesive bonding of

metallic substrates, although it may become so if one or other of the substrates is a polymeric material, or if so-called ‘open-face’ model joints are being considered. Thus, the usual pathway for the diffusion of water and other aggressive or deleterious species is laterally from the joint edge, either along the interface, as considered in Figure 1, or within the adhesive layer itself. This route gives rise to a characteristic failure that moves inwards from the edge of the joint, giving rise to the characteristic picture-frame morphology as illustrated in Figure 2. This failure appearance may be a result of thermodynamic displacement or any of the other failure mechanisms discussed in the following section.

In summary, the presence of water at the interface of an adhesive joint generally leads to instability at the interface, resulting in interfacial failure, readily identified by XPS and ToF-SIMS. Simple thermodynamic calculations enable joint stability to be predicted from the knowledge of surface and interface free energies. It must be noted, however, that it provides no indication of the kinetics of failure, which must be established by empirical studies.

### 3.36.2.2 Adhesive Plasticization

All polymeric adhesives are permeable to water, and although water molecules can only enter through the edge of the joint, there is then the possibility that they can diffuse throughout the glue-line thickness. This can give rise to a degradation of the mechanical properties of the adhesive that is usually known by the catch-all term of plasticization. Water molecules can aggregate close to the interface with the substrate, which leads to swelling of the polymer and the subsequent reduction in durability. This process is analogous to the wet adhesion phenomenon observed in paints and shows the same behavior, in that, it is reversible to a large extent. Heating, or simply leaving joints that have been exposed to

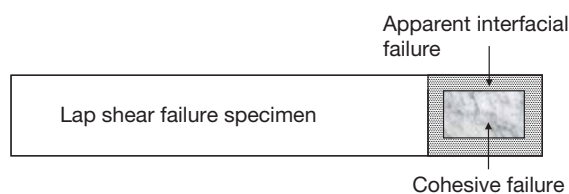


**Figure 2** Picture frame failure, the typical appearance of a joint, which has been exposed to water, leading to an apparent interfacial failure from the edge inwards (the picture frame) and a central cohesive region (the picture), which has not been affected by water and provides the joint with residual strength.

water in relatively dry air is able to remove the water, and values approaching the original dry strength can easily be achieved.<sup>2,3</sup> The diagnostic of this type of failure is once again made by a careful examination of the substrate failure surface. Unless there is ready route to the interface from the bulk of the adhesive for the water molecules, they will not aggregate at the interface but only very close to it. Once again, surface analysis has an important role to play in the forensic analysis of failures in order to define the locus of failure at the molecular level. **Figure 3** indicates, schematically, the concepts of interfacial and cohesive failure, and the thinner the layer of adhesive remaining on the substrate in the cohesive example, the more challenging the analysis. The role of surface analysis in adhesion studies has recently been reviewed,<sup>4</sup> and examples of different failure types, as deduced from the application of such methods, will be presented at the end of this section.

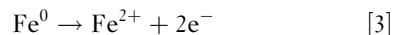
### 3.36.2.3 Corrosion Induced Failure

#### 3.36.2.3.1 Cathodic failure

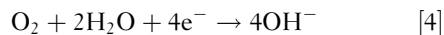
The occurrence of corrosion at the exposed substrate of an adhesive joint leads to a localized corrosion phenomenon, in that the anodic and cathodic sites are separated with the exposed metal undergoing anodic oxidation, and the electrons produced are

consumed at a cathodic site at the adhesive–substrate interface, where hydroxide ions are produced by the reduction of water and oxygen molecules. The reactions involved are the standard ones and are given below for an iron substrate.

At the exposed metal, the anodic reaction occurs



While at the cathode, two reactions are possible depending on the electrode potential, the more usual one being



Although at potentials more noble than 1020 mV (versus the saturated calomel electrode), water reduction, leading to the evolution of hydrogen, is dominant:



Reaction [5] occurs at a potential below that, which develops at the free corrosion potential of iron, and is generally considered to be important only when metal substrates are deliberately polarized cathodically, such as in impressed current cathodic protection schemes or laboratory based simulations of the same. Both cathodic reactions lead to the generation of hydroxide ions, which creates an alkaline environment in and around the adhesive–substrate interface.

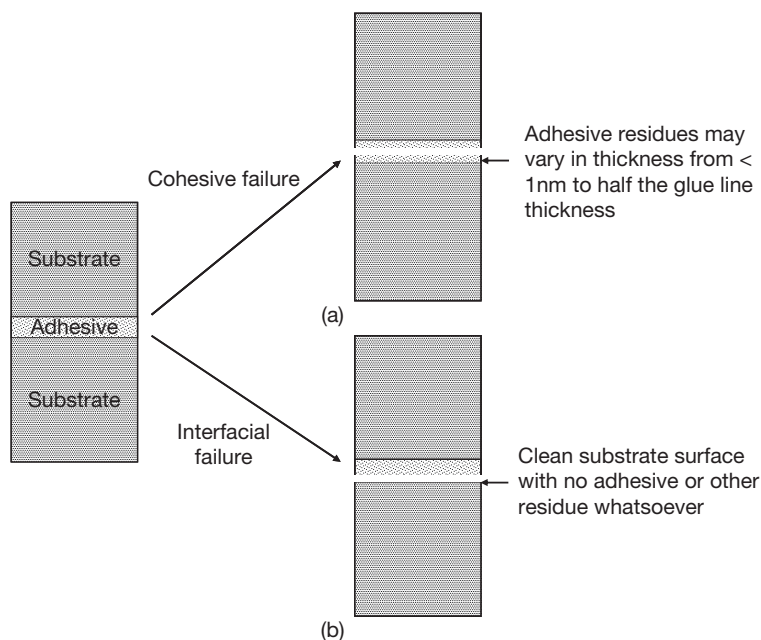


**Figure 3** Schematic representation of (a) cohesive and (b) interfacial loci of failure.

The deleterious effect of such an alkaline environment on polymer to metal adhesion was first reported by Evans in 1929<sup>5</sup> in a paper entitled ‘The Electrochemical Corrosion of Painted Steel with Special Reference to the *Alkaline Peeling* of the Coat.’ This phenomenon received scant attention until the 1970s when the term cathodic disbondment (or variously disbonding or delamination) was coined to describe the separation of a polymer from the cathodic region of a coated metal. At the time, the examples of cathodic delamination that were cited included the adhesion loss of a paint film adjacent to a stone chip on an automobile or the failure of powder coatings on cathodically protected gas and oil transmission line pipe. Interestingly, both these examples had important technological consequences and led to an upsurge in research activity in the process of the mechanisms of cathodic delamination, most notably by groups led by Leidhesier, using electrochemical methods<sup>6,7</sup> and Dickie (at Ford USA)<sup>8,9</sup> and Castle (at the University of Surrey UK),<sup>10,11</sup> using XPS. The various mechanisms implicated in the cathodic delamination process were reviewed in the following decade by Leidhesier<sup>12</sup> and Watts.<sup>13</sup> Castle attempted to shed fresh light on the process in 1996, with a critical assessment of the role of water within the polymer in the failure process.<sup>14</sup>

The basic premise of cathodic delamination is very straightforward in that oxygen and water arrives at the cathodically polarized metal surface and, following eqn [4], hydroxide ions are produced, leading to an increase in the pH in the environs of the polymer–metal interface. This underfilm alkalinity attacks the interfacial bonding directly, in the manner proposed by Evans,<sup>5</sup> leading to adhesion loss. In practice, such a failure is observed visually on low carbon steel as the rather unusual and counter intuitive observation in that the organic coating readily peels from the steel, but the steel has a very clean, unruined, appearance. The classic situation of a localized defect in an organic coating on steel is indicated in Figure 4. In this situation, the exposed metal undergoes anodic dissolution, the electrons produced are consumed in the annular cathodic zone surrounding the initial defect, water may arrive at the tip of the disbondment crevice by lateral diffusion from the defect or by downwards diffusion through the thickness of the coating, and the process which supplies the water molecules most quickly will be the one that is rate controlling. As the process continues, the anodic area will grow, consuming the delaminated cathodic area that will also extend, leading to increased coatings failure. This type of failure is

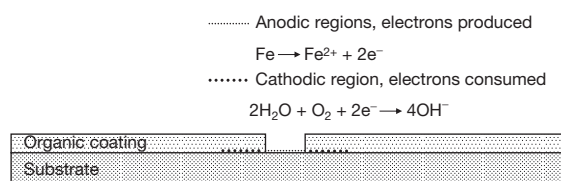


**Figure 4** The electrochemical reactions that occur at a defect in an organic coating exposed to an aqueous solution. The anodic reaction occurs at the defect and cathodic reduction of water is localized within an extending crevice beneath the coating.

readily observed on painted steel structures where macroscopic or microscopic defects in the coating have developed. The cathodic and anodic areas are visually quite easy to separate, but in some cases, there is a need to be absolutely certain about the mechanism of failure, and in such cases, a useful analytical solution is to make use of the observation that electrode surfaces will retain their electrochemical signature once removed from the electrolyte and analyzed by a surface analysis method such as XPS.<sup>15</sup> In essence, the surface alkalinity needs metal cations (often  $\text{Na}^+$ ) to balance the cathodically generated hydroxide ions, and as most electrolytes will have sufficient ionic species, the cathodic region can be identified by retained cations of this type. In a similar vein, anodic regions will retain marker anions such as  $\text{Cl}^-$ . Although the concentration of such ions is at monolayer coverage or less, it is a routine matter to determine their presence and concentration by XPS. Thus, in XPS, there is a useful methodology in which mechanism of failure can be confirmed, as will be shown in the next section.

The scenario of Figure 4 is clearly the situation that exists when a polymer–metal system, be it adhesive or coating, is at the rest potential (free corrosion potential) of the metallic substrate. Although this situation occurs quite often, there is another regime that can render the cathodic delamination process even more destructive, that is, when the metal substrate bearing the adhesive or coating is polarized cathodically. This can occur as a result of a deliberately applied potential (as is the situation with impressed current cathodic protection), but more often, it occurs when the metal is coupled to a more active metal. Much of the early work relating to cathodic delamination was carried out in this manner using either an ASTM Specification<sup>16</sup> in which coated steel was coupled to a zinc anode or a UK approach<sup>17</sup> in which the coated panel was polarized

cathodically to a potential of 1.5 V versus the saturated calomel electrode, as shown in **Figure 5**. This latter test was much favored by the coatings end-users who found that it was able to discriminate coating performance very rapidly at a fairly rudimentary level. Many in the business found that it was a very severe test, with oxide reduction occurring as a precursor to coatings failure, something which the Pourbaix diagram for iron predicts will only happen at the extremes of cathodic potential and pH! Notwithstanding these possible shortcomings, this test is widely used, and performance of high performance fusion bonded coatings is frequently quoted against such a test by coatings manufacturers.

The mechanisms for destruction of the polymer-metal interface and failure of coating or adhesive appear to be fairly similar, irrespective of the source and magnitude of the cathodic potential; however, the kinetics of failure vary quite considerably, and this in turn is a direct consequence of the flux of hydroxide ion produced during the cathodic reduction process. It is informative to consider the quantities involved using data published many years ago.<sup>11</sup> In the examination of the delamination of a powder sprayed epoxy coating from a cathodically polarized ( $-1.5$  V versus SCE) mild steel substrate, a delamination rate of  $0.4 \text{ mm day}^{-1}$  was established for a range of surface profiles once a correction for interfacial path length had been made. By converting the delamination rate to a more convenient unit, one arrives at a crack growth rate of  $5 \text{ nm s}^{-1}$ . From the knowledge of the rate at which a typical interface separates, the rate at which such an interface is exposed can be calculated, and then, by the application of Fick's law of diffusion, the flux of hydroxide ions required to

sustain these kinetics can be inferred. The results of such a modeling approach lead to a flux of  $10^{-15}$  mole of hydroxide ions per second, and the application of Fick's Law indicates a concentration gradient within a disbondment crevice of  $10^{-3} \text{ mole dm}^{-3} \text{ cm}^{-1}$ , that is, a pH of at least 11. Using a similar approach, the current density required to sustain a rate of  $5 \text{ nm s}^{-1}$  is estimated at  $6 \times 10^{-11} \text{ A cm}^{-2}$ . This is extremely low, and it is unlikely that this is the rate-controlling step in the disbondment process, and this leads one to the inescapable conclusion that diffusion of hydroxide ions along the metal-polymer interface is, indeed, the rate-controlling step, and when the required concentration gradient is maintained, the process will continue unabated.

### 3.36.2.3.2 Anodic failure

The two failures described above, hydrodynamic displacement of the organic phase, and the cathodic delamination of the coating or adhesive as a result of a local increase in pH, are routinely observed, whereas the failure of the polymer-metal interface as a result of localized anodic activity is unusual. In the coatings field, there are well documented examples of the anodic undermining of a lacquer on tin plate for foodstuffs<sup>18</sup> and the failure of an acrylic repair coat on an aluminum brass substrate,<sup>19</sup> but otherwise, examples are rare. In the examination of the failure mode of adhesively bonded hot dipped galvanized steel, Fitzpatrick and Watts<sup>20</sup> showed that failure was a result of localized microelectrodes occurring at the metal-adhesive interface, but it was in the regions of cathodic activity that interfacial failure occurred; the other failure regions, presumably in the region of the microanodes, were essentially cohesive in nature,

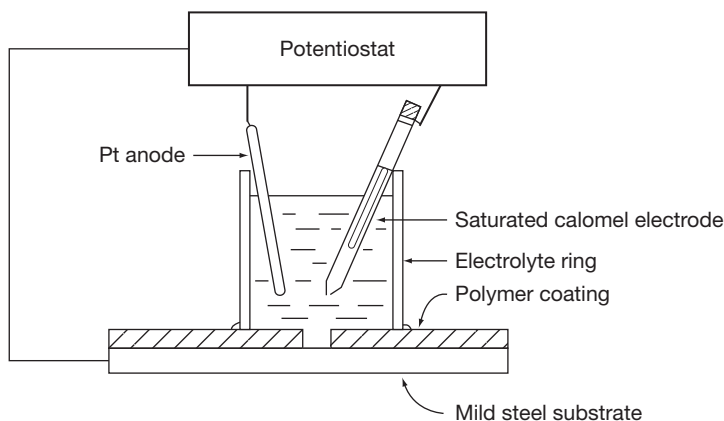


**Figure 5** Schematic representation of the cathodic disbondment test.

indicating that the electrochemical activity in the environs of the anodic sites was not as deleterious as the increase in pH experienced at the microcathodes.

### 3.36.3 Identification of Locus of Failure and Failure Classification

As described above, there are four possible failure mechanisms that may be encountered as a result of the exposure of an adhesive joint to water. If we also consider the cohesive failure that may occur in a dry joint or a joint exposed to water for a relatively short time, there are five potential modes of failure. Of these five, four may look remarkably similar, and upon cursory examination, all will be described as an interfacial failure. This can be a gross oversimplification, and it is now informative to consider the characteristics of the failure modes that will be generated by each process in turn. The types of failure can be divided into cohesive failure within the adhesive (**Figure 3(a)**) or interfacial failure, when separation occurs exactly at the junction between substrate and adhesive (**Figure 3(b)**). Although conceptually easy, this definition is extremely difficult to confirm in practice as the layer of adhesive remaining on the substrate can range from many hundreds of micrometers (which can be established with the naked eye) to vanishingly thin layers of a few nanometers or less, which require surface analysis methods to detect and identify them. Thus, one of the greatest problems faced by those attempting to classify a failure mode can be the experimental techniques at their disposal; at some point, if only microscopy is used, a cohesive failure will appear, and be classified, as an interfacial failure!

If a joint is tested in a dry condition or if only exposed to water for a short time, the expectation is that the locus of failure will run through the glue-line thickness, a phenomenon that is readily observed by optical or electron microscopy and even, in some instances, by the naked eye. The diagnosis of such a failure is simple, but the edges of the joint should be examined for evidence of an interfacial failure generated by water diffusion along the interface. Even in instances of dry failure, it is possible that under some loading geometries, the locus of failure will pass so close to the metal–adhesive interface that the failure will appear interfacial to all forms of microscopy. This is the nub of any investigation into an adhesive joint failure – the identification of the failure path (or locus of failure to use the adhesion scientists term) at the molecular level. Thus, unless a failure

is demonstrably within the glue-line thickness, the emphasis is on the investigator to use techniques that are appropriate to characterize the exact locus of failure and also the thermodynamic or electrochemical cause of the failure under consideration. The most useful method for failure analysis in this type of investigation has been shown to be XPS, which is a surface chemical analysis technique with a characteristic sampling depth of  $\sim 5$  nm. In addition, XPS is able to provide chemical specificity, a quantitative analysis, overlayer thickness values and the identification of any characteristic ions from solution that are associated with the failure, and for this reason, it has been widely used in adhesion investigations over the last three decades.<sup>21–23</sup> The XPS characteristics of a cohesive failure close to the metal polymer interface are shown in **Figure 6**. This sample is a tin free steel substrate coated with an epoxy lacquer that has been hot molded to nylon, and then tested on a lap shear configuration. A macroscopic image (**Figure 6(a)**), shows that the failure appears to occur between metal substrate and epoxy or epoxy and nylon, depending on the position on the failure surface. Small spot XPS analyses (at  $400\mu\text{m}$ ) were taken from the region that appeared to be a metal interfacial failure surface and a mirror image position on the adhesive side. These spectra (**Figures 6(b) and 6(c)**) are extremely similar, and the characteristic of the epoxy coating itself is showing that the locus of failure is within this phase and not at the epoxy–steel interface, as one would assume from a visual inspection of the failure surfaces. Moving on to the situation wherein water is responsible for the (hydrodynamic) displacement of the adhesive from the metal substrate, an example can be seen in the work of Kinloch *et al.*<sup>24</sup> on the structural adhesive bonding of aluminum. After fatigue tests of a tapered double cantilever beam test piece, the joint is cracked open, and XPS analysis of the metal failure surface (**Figure 7(b)**), when compared with the unbonded surface (**Figure 7(a)**), indicates that an interfacial failure has occurred. However, the absence, in the spectrum, of any specific marker ion indicating electrochemical activity leads to the conclusion that this failure has been the result of the thermodynamic displacement, by water, of the adhesive from the metal substrate. This conclusion is entirely logical as the aluminum substrate will be covered with a passive oxide film and will only be susceptible to localized corrosion at points of metallurgical heterogeneity such as intermetallic precipitates (which will be cathodic to the surrounding matrix).

The observation that the electrochemical history of an electrode could be deduced from the spectrum



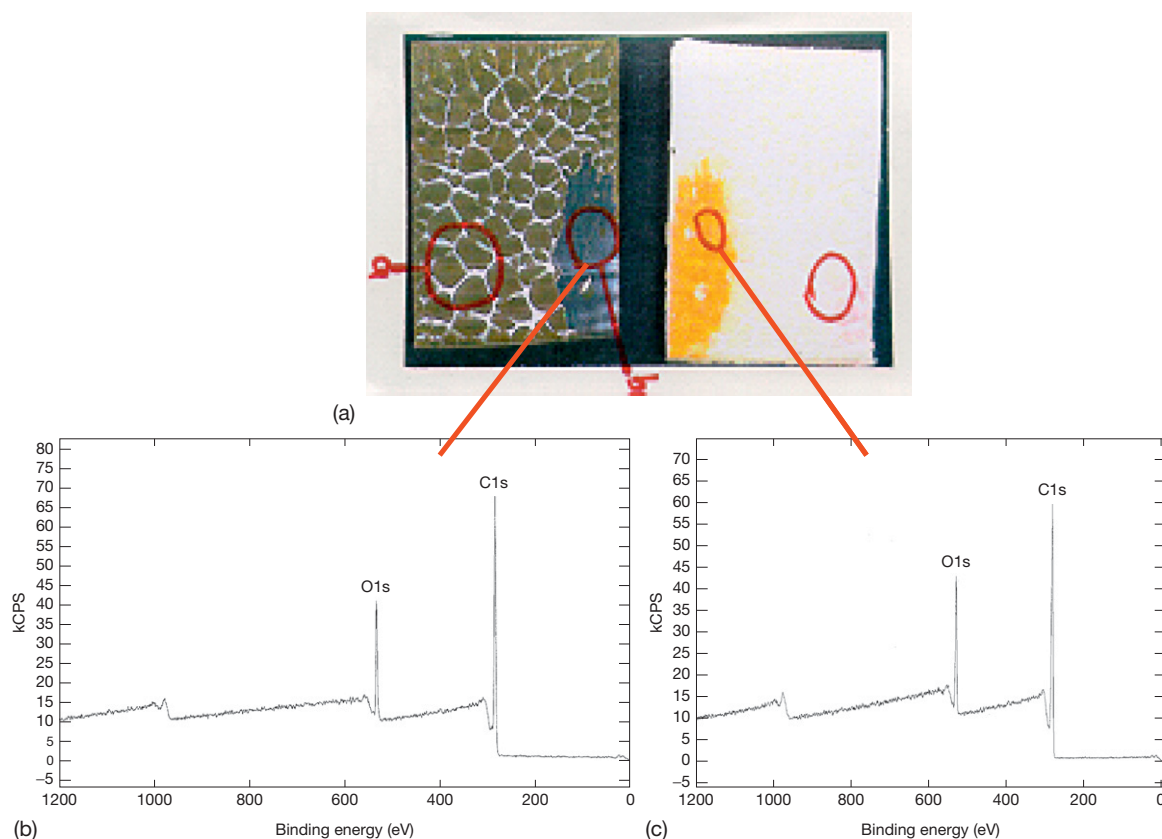


**Figure 6** Optical microscopy image of a failure between epoxy coated tin-free steel and a nylon coating (a). XPS survey spectra taken from the apparent interfacial failure between the steel substrate (b) and epoxy coating (c). The similarity of the spectra establish unambiguously that the failure is a cohesive failure within the epoxy lacquer.

of ions adsorbed on the surface was first made by Castle and Epler,<sup>15</sup> using XPS, and more recently, work from the authors laboratory has extended this approach to analysis using ToF-SIMS. The important observation, initially made more than 30 years ago, was that if a metal electrode is exposed to a cathodic potential in an aqueous electrolyte, it will, not unreasonably, adsorb cations from the electrolyte. On removal from the electrolyte and subsequent washing, these adsorbed ions are retained (often at submonolayer concentrations) on the electrode surface and can be detected and quantified by a surface chemical analysis technique such as XPS. Initial work envisaged that such an approach would be useful in identifying whether a corrosion feature, such a pit, was active or benign, but the widest application of this approach is probably in guiding the definition of failure mode of organic coating and adhesives. This can be illustrated from very early work on the delamination of an organic coating from cathodically

polarized ( $-1.5\text{ V}$  versus saturated calomel electrode in  $0.5\text{ M NaCl}$ ) steel.<sup>10</sup> The test was set up as shown in Figure 5 with a central defect in the coating so that the cathodic reduction reaction could readily occur at the exposed metal surface and lateral diffusion of hydroxide ions could occur unimpeded. In addition, water could diffuse through the thickness of the coating in regions well removed from the coating defect. The metal interfacial failure surfaces that are generated in these two regions are very different, as shown in Figures 8(a) and 8(b). The failure close to the defect is once again characterized by an interfacial failure, but the very intense sodium concentration ( $\sim 7\text{ at.}\%$ ) shows that there has been cathodic activity, the  $\text{Na}^+$  acting as a counter ion for the cathodically generated  $\text{OH}^-$ . Farther from this defect, the carbon peak in the spectrum is very intense and the Fe 2p peak (at a binding energy of  $\sim 710\text{ eV}$ ) is barely visible, being identified by an abrupt change in the background region of the spectrum. This change in background is

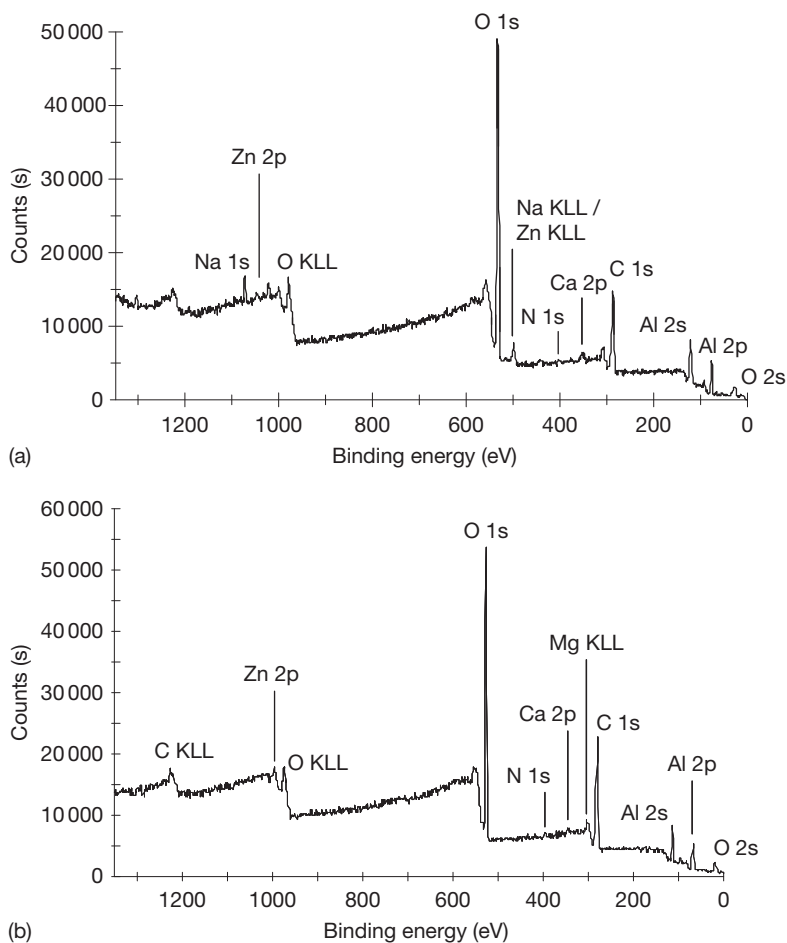


**Figure 7** XPS survey spectra from grit blasted/degreased aluminum surfaces (a) prior to bonding and (b) following failure after exposure to liquid water. Reproduced from Kinloch, A. J.; Korenberg, C. F.; Tan, K. T.; Watts, J. F. *J. Mater. Sci.* **2007**, *42*, 6353–6370.

itself very informative, in that it indicates to the electron spectroscopist that most of the iron signal is being attenuated by a thin overlayer of, in this case, carbon (polymeric coating). Thus, this spectrum indicates that the failure is cohesive within the polymer but with a very thin (<10 nm) overlayer, indicating the locus of failure is ~10 nm from the metal oxide–polymer interface.

Although failure of adhesion as a result of cathodically generated alkali is one of the most usual failure mechanisms when corrosion is involved, there are very few documented examples of the advancing disbondment front acting as an anodic crevice. The most cited system and example of great importance to the food packaging industry is the anodic undercutting of the tin coating on tinplate<sup>18</sup> in times gone by but less so nowadays. An example of the manner in which the polymer–metal interface may develop as

anodic crevice is afforded by the work of Castle *et al.*<sup>19</sup> who investigated the failure of an acrylic coating on aluminum brass on exposure to hot saline solution. The XPS survey spectra of Figure 9 are from the interfacial failure metal surfaces of the acrylic–aluminum brass systems when subjected to a mechanical test before exposure (Figure 9(a)) and the failure following saline exposure (Figure 9(b)). Both failures are cohesive, as indicated by the intense C 1s peak at a binding energy of ~285 eV, and the intense Cl 2p peak for the exposure surface (Figure 9(b)) is in marked contrast to the failure surfaces of Figure 8(a) and indicates that the system is behaving as an anodic crevice. The localization of anodic activity within the crevice was reported to be enhanced by the application of increased thickness of organic coating, which represents a situation similar to that in adhesive bonds.

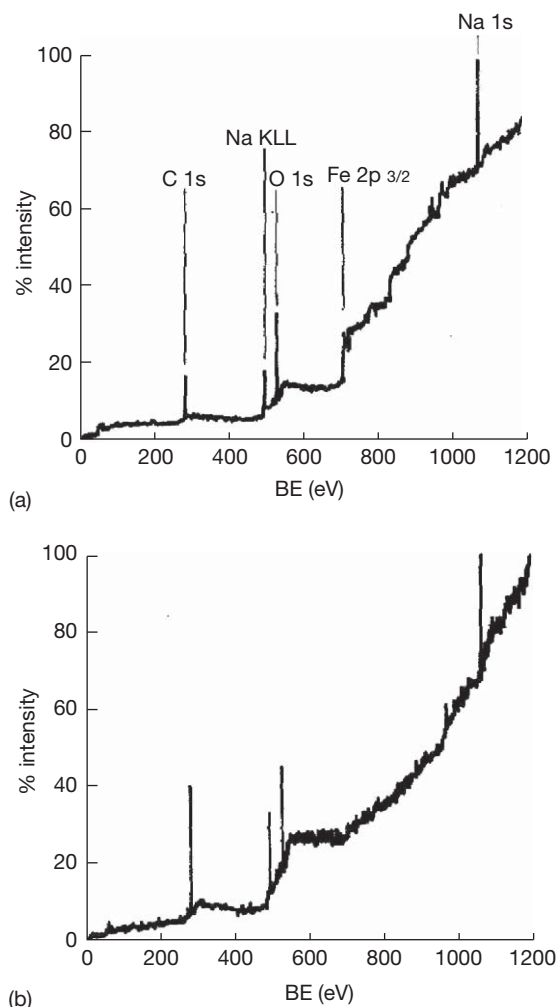


**Figure 8** Failure of a polybutadiene coating on steel exposed to the cathodic disbondment test of [Figure 5](#). XPS survey spectra from (a) immediately adjacent to the defect, resulting from the cathodic generation and lateral diffusion of hydroxide ions and (b) the wet adhesion failure region well removed from the defect arising from the downward diffusion of water molecules through the thickness of the coating. Reproduced from Watts, J. F.; Castle, J. E. *J. Mater. Sci.* **1983**, *18*, 2987–3003.

In this section, the various mechanisms that may be observed in adhesive joints exposed to aqueous environments have been reviewed. When inspecting a failure surface, the first step in establishing the process responsible for failure is the assessment of the exact locus of failure. If failure is clearly within the glue-line thickness, as established by visual inspection or optical or electron microscopy, then it is reasonable to assume that failure is a result of exceeding the load-bearing capacity of the adhesive, and corrosion does not play a significant role in the

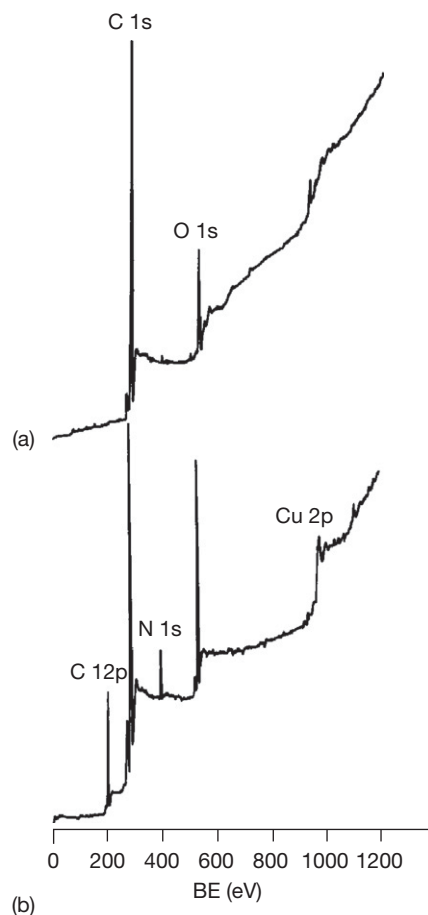


**Figure 9** The failure of an acrylic coating on brass. XPS survey spectra of the interfacial metal surface following (a) dry test and (b) test in hot saline solution. Reproduced from Castle, J. E.; Luklinska, Z. B.; Parvizi, M. S. *J. Mater. Sci.* **1984**, *19*, 3217–3223.

failure process. If the failure path is very close to the substrate–adhesive interface, it is very likely that degradation based on exposure to water or corrosion reactions is responsible for failure, and without resorting to surface analysis techniques, such as XPS, it is probable that the locus of failure will be described as interfacial, even if examined at high resolution in an SEM. The reason for this is that failure is often extremely close (within 10 nm) to the interface, and thus, to fully understand failure, a surface chemical analysis is needed. A true interfacial failure can be easily recognized (although there will be a small amount of adventitious carbon – 20–35 at.% in a quantitative surface analysis), and this may be a result of hydrodynamic separation on exposure to water or cathodic delamination, which is recognized by the adsorption of cations, such as sodium, from the

test solution. If there is a small residual layer of adhesive on the substrate, it may be a result of water- or alkali-induced degradation of the polymer phase; once again, the presence of cations will indicate a significant involvement of the cathodic reduction process. The presence of anions, such as chloride, to excess, is unusual and is indicative of failure being the result of a developing anodic crevice, and seems to be associated with a cohesive failure.

Having reviewed the corrosion processes that may be responsible for failure of an adhesive joint and the manner in which the forensic analysis of failed surfaces can help identify the failure mechanism, and the role of corrosion in the failure process, it is helpful to consider the failure characteristics of various adhesively bonded substrate materials.

### 3.36.4 Adhesively Bonded Substrate Materials

In this section, the role of corrosion in adhesive bond failure will be considered with a series of case histories involving common metallic substrates for adhesive bonding. It is interesting to note that some authors set out to establish performance data, which can be used for adhesive bond design purposes, and the unraveling of the failure mechanism, takes on a secondary role, while others set out with the main purpose of establishing failure mechanism and use durability data on a merely comparative basis. It is important to note that there are two clear philosophies that are in use regarding the durability testing of adhesive joints; the first, easiest, and probably least realistic is to expose the joint to the aggressive environment with no load applied: at the point of test, the joint is removed from the test solution, dried, and

tested, to obtain performance data. The alternative approach is to load (either monotonically or in cyclic mode) within the test environment, and once failure has occurred, remove specimens for microscopy and/or analysis. Both methods have their own particular merits; the first practice avoids the possibility of post-failure contamination (or back deposition) from the test solution, while the second is clearly much more realistic and generates data that can be included in the appropriate design codes. Examples of both types of testing will be considered in this section.

#### 3.36.4.1 Low Carbon Steel Substrates

As one might imagine, the rapid corrosion that is experienced by adhesively bonded low carbon steel, if the joint is not protected by additional measures, leads to the domination of cathodic delamination as a failure process, and significant problems in the post failure analysis of failed joints as all surfaces that have been exposed during failure will inevitably become anodic sites. There are two potential measures for alleviating these difficulties; the cathodic polarization of the entire joint and the exposure of a joint in water with a low concentration of dissolved oxygen. Both approaches have been successfully employed, and examples are described below.

The bonding of neoprene to mild steel is of particular importance in the maritime industry, and there is a fairly extensive body of literature dealing with the failure modes of this system when the steel substrate is protected by either impressed current or sacrificial anode cathodic protection. The mechanistic aspects of the failure of this system was investigated by Boerio *et al.*<sup>25,26</sup> who employed a strip blister specimen, illustrated in Figure 10, polarized at a

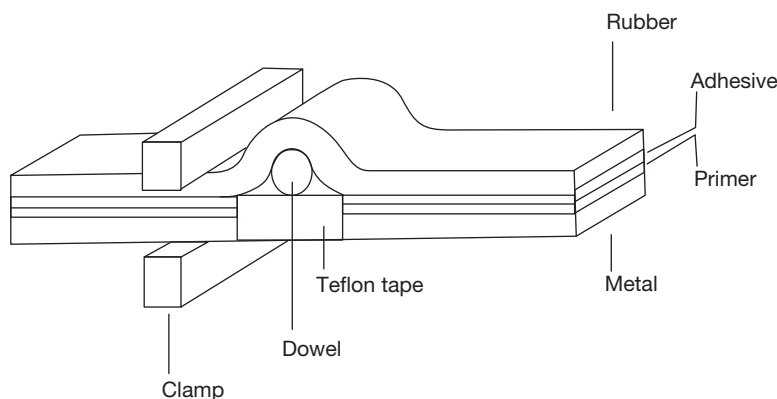


**Figure 10** Schematic diagram of the strip specimen used for the study of the cathodic delamination of neoprene rubber from steel. Reproduced from Boerio, F. J.; Hudak, S. J.; Miller, M. A.; Hong, S. G. *J. Adhes.* **1987**, 99–114.

potential of  $-1.5\text{ V}$  versus the saturated calomel electrode. They were able to show, by XPS and FT-IRS analysis of the failure surfaces, that degradation occurred as a result of the degradation of the phenolic primer and dehydrohalogenation of the rubber in both the primer and the adhesive.<sup>25</sup> Such dehydrochlorination resulted in the formation of inorganic solutes soluble in the alkaline solution used as a test medium. These authors also showed a critical dependence on surface roughness, indicating the importance of mechanical effects in the performance of adhesive joints, presumably as a result of the increased extent of interfacial contact achieved with the rougher substrate. In subsequent work, Boerio and Hong<sup>26</sup> used FTIR to refine the chemistry of the failure mechanism, and showed that methylene groups linking phenyl species in the primer were rapidly oxidized in alkaline solution to form benzophenone linkages, which could oxidize further to carboxylic acids and quinines.  $\text{ZnCl}_2$  was observed to form a soluble reaction product at the bondline, as a result of the reaction between chlorine from the chlorinated rubber and  $\text{ZnO}$  filler in the primer. It is concluded, on the basis of these studies, that both the oxidation of phenolic resins in the primer and osmotic effects related to  $\text{ZnCl}_2$  have important roles to play in the failure mechanism of rubber to steel adhesive joints. Complemented by the studies of Hamade and Dillard, in a series of papers spanning almost 20 years, have concentrated on relating the experimental observables (strength and extent of disbondment) to experimental parameters, such as time, temperature, and cathodic potential. The study of these authors is informative as it shows how a simple, diffusion-based model can be developed to provide a semiempirical model that is able to accurately predict the disbondment rates upon exposure to cathodic environments. These authors also differentiate between a separated zone (the picture-frame failure appearance) and a weakened zone ahead of the true delamination zone. Although mechanistic aspects of this are not fully explored, one assumes that the separated zone is the region of cathodic delamination resulting from alkaline attack of the interfacial bonding, while the weakened zone results from aqueous plasticization of the adhesive. The latter zone may show recovery of strength on removal from the aqueous environment as described by Watts *et al.* in their work on epoxy and other systems.<sup>27</sup> Hamade *et al.* in their extensive studies have produced data on the rate of disbondment in both the failed and weakened zone, and also strain energy release

rate,  $G$ , as a function of time. This led to the development of a semiempirical model for the cathodic weakening of adhesive joints,<sup>28,29</sup> in which failure kinetics were related to the harshness of the environment (as exemplified by extent of cathodic activity and temperature of test) and the strain energy release rate. This can be represented very conveniently in the diagram of **Figure 11**, which illustrates the generic behavior of delamination rate ( $\log dZ_2/dt$ ) versus strain energy release rate for weakening (region I), delamination (region II) as well as region III, where environmental and corrosion process play no discernible role in the failure process. These authors also provide guidance on the extent of delamination that will occur for a given set of exposure conditions in the form of nomographic scales or nomograms. In this manner, the extent, for a particular bond, in a particular aqueous environment, can be estimated as a function of cathodic potential and temperature. Two such nomograms are reproduced in **Figure 12** for a mild steel adhesively bonded system of a chlorinated rubber adhesive and a phenolic resin/chlorinated rubber primer. **Figure 12(a)** represents the calculated delamination values ( $Z_2$ ) for the above system in artificial seawater, while **Figure 12(b)** represents complementary data in a 1M NaOH environment. The arrows on the nomograms indicate example applications for the time for 12 mm of delamination to occur in the strip blister test of **Figure 10** at a potential of  $-1100\text{ mV}$  and at a temperature of 298 K. In the case of artificial seawater, a time of 180 days is predicted, while in 1M NaOH, a much reduced time of  $\sim 30$  days is indicated. Although very specifically related to a certain system, such nomographs are clearly of much practical use, allowing changes in environment and pretreatment to be predicted.

An alternative way in which gross corrosion of a mild steel substrate can be alleviated in order to examine the interfacial chemistry associated with failure is to expose the joints in water containing a low concentration of dissolved water. In studies of this type, Davis and Watts<sup>30</sup> assembled adhesively bonded mild steel coupons in a lap shear configuration and then immersed them in pure water in sealed glass jars, removing specimens periodically for mechanical testing and surface analysis of the interfacial failure surfaces. After 1200 h of testing, a characteristic picture-frame failure surface was observed, while after 7500 h, the picture was greatly reduced in size, and visual and spectroscopic differences were observed at the surrounding metal surface. In the early stages of exposure, adhesive-substrate separation is driven by cathodic delamination, but on longer exposure times,



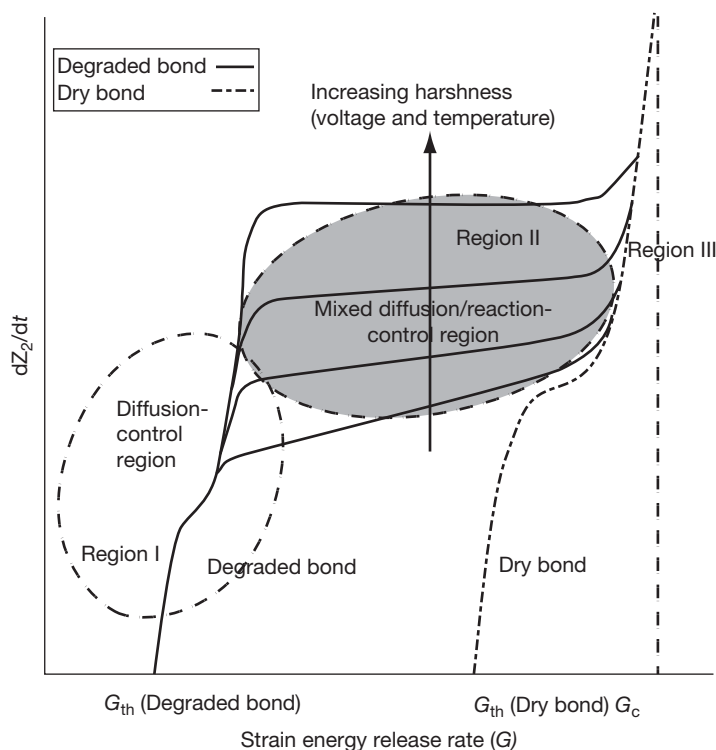


**Figure 11** A plot illustrating the generic behavior of log delamination rate ( $\log dZ_2/dt$ ) versus  $\log G$ . The diagram shows the regimes of diffusion control, leading to weakening (region I), the mixed diffusion/reaction control region (region II) and the environment independent region (region III). Reproduced from Hamade, R. F.; Seif, C. Y.; Merhij, F.; Dillard, D. A. *J. Adhes. Sci. Technol* **2008**, 22, 775.

the crevice opens at the mouth as a result of oxide thickening, which appears as a dull rather than bright outer region. XPS analysis confirmed oxide dissolution at the crack tip with oxide growth subsequently occurring, as indicated in [Figure 13](#). As the experiments were undertaken in pure water, the deposition of marker cations was at a very low concentration (below the detection limit of XPS); however, ToF-SIMS, with its better detection limit, allowed such marker ions to be profiled across the failure crevice. This example illustrates the concept of a so-called zero volume debond (sometimes referred to as a kissing bond in the aerospace industry) in which the adhesive and failure surfaces are in contact but have no load carry ability as a result of the adhesion between the two, having been compromised.

### 3.36.4.2 Aluminum Substrates

As a result of its importance in the aerospace industry, the adhesive bonding of aluminum has been studied very widely over the last three decades, and there is a large body of literature relating to the

mechanical performance and durability of these systems. Generalized corrosion of aluminum is unusual, and it has very rarely been identified as a primary cause of failure in adhesively bonded systems, although localized corrosion in the form of pitting may sometimes be seen on test pieces immersed in water. The more usual forms of failure are associated with adhesive degradation at short exposure times, and interfacial separation of adhesive and oxidized aluminum substrate is as a result of thermodynamic displacement of adhesive by water. Using simple T-peel joints, exposed to water prior to testing, Watts *et al.*<sup>27</sup> were able to show failure associated with adhesive degradation at the edge of the joint. [Figure 14](#) shows the physical appearance of the failure surface of adhesively bonded chromic acid anodized aluminum following 10 weeks exposure at 50°C in deionized water. The characteristic picture-frame type of failure morphology is seen running along the length of the joint, and visual assessment would identify the edge effect as being an interfacial failure. Small area XPS analyses were recorded from the interfacial failure surfaces at the edge of the joint and the centre of the

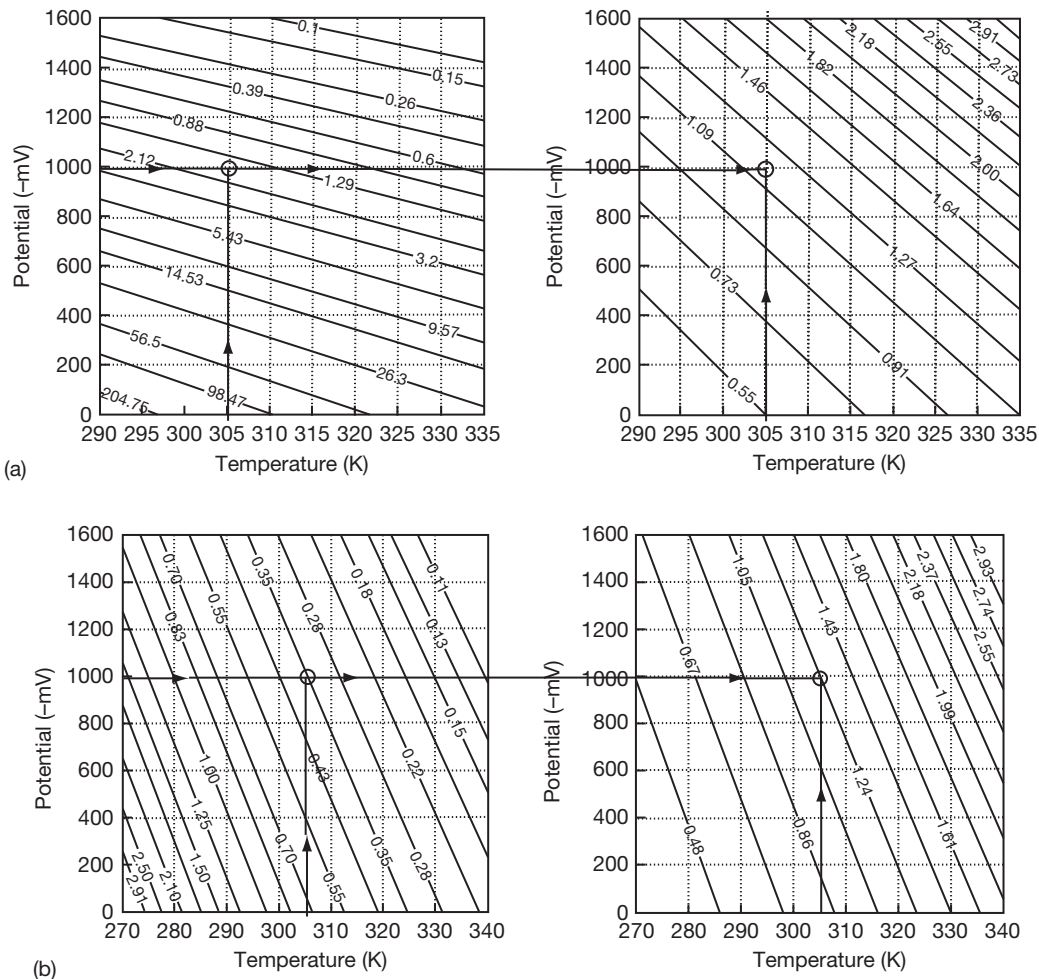


**Figure 12** Nomographs for estimating bond weakening distances in (a) artificial seawater and (b) 1M NaOH. The left plot of each pair represents the contours of the square root of delay time,  $t_d$ , while the right plots represent contours of the bond weakening rate  $WR_b$ . Examples of the use of such nomographic scale are provided in the original reference. Reproduced from Hamade, R. F.; Dillard, D. A. J. *Adhes. Sci. Tech.* **2003**, 1235–1264.

joint width. As expected, the general cohesive failure zone yields a spectrum characteristic of the bulk adhesive with no unexpected elements present, but the spectrum from the edge region, **Figure 15(a)**, is of an oxidized aluminum substrate attenuated with  $\sim 5$  nm of adhesive. This clearly indicates that failure is associated not with environmental attack of the adhesive–substrate interface but with the aqueous degradation of the adhesive itself. Work in this paper also shows that such degradation is physical rather than chemical in nature and that a drying schedule at elevated temperature is able to reverse the damage, the locus of failure moving into the bulk of the adhesive, as observed in the central part of the joint of **Figure 15(b)**.

As part of a wide-ranging fracture mechanics study, Kinloch *et al.*<sup>24</sup> have studied the durability of

adhesively bonded aluminum joints, steel joints, and aluminum–steel couples bonded in a similar manner. In the case of the aluminum and steel joints, the failure mechanisms were as expected; in the case of bonded 7075 aluminum, there is little corrosion observed, and failure is attributed to the thermodynamic displacement of the adhesive from the substrate as predicted by eqn [2]; when the substrates are both medium carbon (0.6%), steel failure follows the predicted path of cathodic delamination, both failure mechanisms being confirmed by an extensive XPS and ToF-SIMS study. In the case of dissimilar substrates (aluminum and steel beams), the situation is rather complex, and it is worthwhile considering this situation in some detail as an exemplar of how corrosion processes may have an unexpected role to

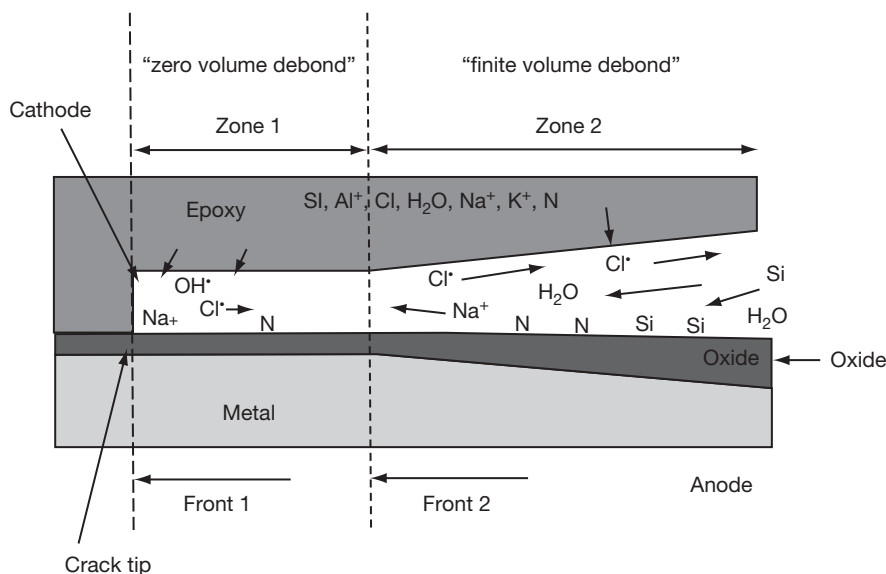


**Figure 13** Schematic illustration of the failure processes that occur within the extending crevice at the edge of an adhesive joint exposed to an aqueous solution with a low partial pressure of oxygen. The crevice mouth acts as the anode and subsequently opens as a result of oxide growth and other processes, while the crevice tip forms the cathodes and leads to a zero-volume debond within which mass transport of the reactive and other species is restricted. Reproduced from Davis, S. J.; Watts, J. F. *J. Mater. Chem.* **1996**, 6, 479–494.

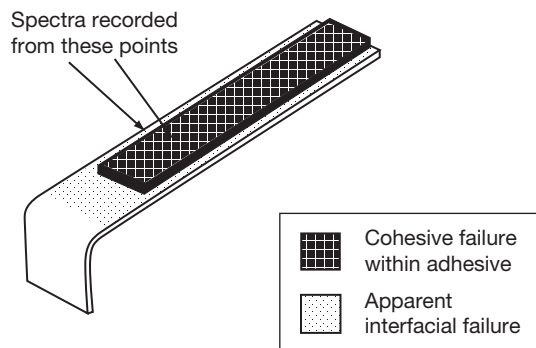


**Figure 14** The schematic appearance of the failure surface of a T-peel assembly of adhesively bonded aluminum exposed for water at 50°C prior to testing. Reproduced from Watts, J. F.; Blunden, R. A.; Hall, T. J. *Surf. Interf. Anal.* **1990**, 16, 227–235.

play in the failure of an adhesively bonded structure, and the manner in which it is necessary to consider the environment surrounding the joint as well as the specific environs of the bondline itself. In the case described by Kinloch *et al.*, the joints were assembled in a tapered cantilever beam geometry (to ensure constant compliance as crack propagation occurs) and tested under fatigue loading in pure water. Failure always occurred adjacent to the adhesive–steel interface, and not at the aluminum–adhesive interface. At first sight, the occurrence of the failure at the

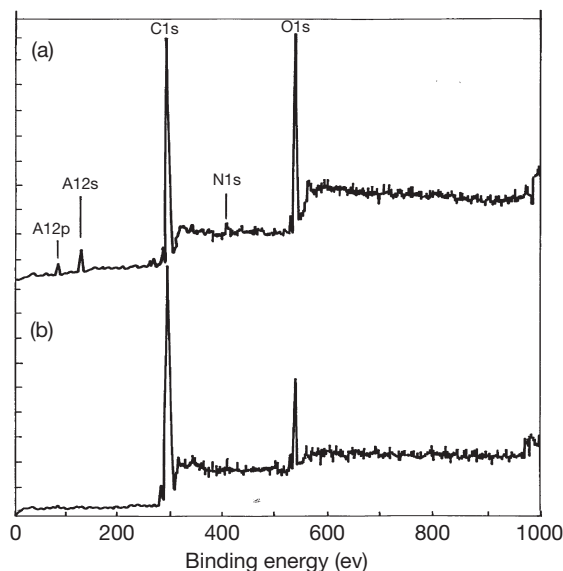


**Figure 15** Small area XPS (250 μm) taken from the edge (a) and the central (b) regions of the failure illustrated in Figure 14.

steel–adhesive interface would seem to be the simple case of galvanic corrosion, as an aluminum alloy will be at the more active end of the galvanic series than steel. For such galvanic coupling to occur, there needs to be electrical contact between the aluminum–alloy

and steel substrates. This was not the case, and experiments were performed to ensure that there was no electrical coupling of the two substrates. There was also extensive corrosion on the steel beam, which would not be present had the beam been the cathodic part, in its entirety, of a galvanic cell. Now, the reason for the inferior durability of the dissimilar joints lies in the diffusion of oxygen molecules into a developing crevice and the concomitant outward diffusion of the cathodic reaction product ( $\text{OH}^-$ ). It is helpful at this point to consider the situation in terms of the oxygen supply that exists for the steel–steel joint. Along the sides of both beams, the anodic reaction will take place, and soluble  $\text{Fe(II)}$  ions will pass into the solution, leading to a local increase in density. Thus, this solution of water and  $\text{Fe(II)}$  ions will sink to the bottom of the testing tank, and the solution in the environs of the adhesive layer will be refreshed with aerated water. This situation ensures that there is a ready supply of reactants for the cathodic reaction, which develops a crevice normal to the direction of crack propagation (i.e., the length of the test piece). As the diffusion of hydroxyl ions is known to be rapid in aqueous solution, it is more likely that the aggregation of these species at the crack tip is modest; in other words, the diffusion coefficient of water molecules into the crevice is much the same as that of hydroxide ions diffusing outwards. Thus, the rate-controlling step may be taken to be the rate of arrival of the water molecules, which must feed the two developing cathodic crevices. This situation is illustrated schematically in **Figure 16**. In the case of an aluminum–alloy–steel

joint, the two metal interfaces will not behave in the same manner; the steel adhesive interface will develop a cathodic crevice as described above, but as the aluminum–alloy has a passivated film present, the extent of cathodic reactions at this surface will be confined to regions surrounding localized corrosion, such as pitting on the failure surface of the beam. Thus, any corrosion on the aluminum–alloy beam will be a post-failure event. This means that the majority of the oxygen molecules dissolved in the aqueous bath adjacent to the adhesive layer are available for consumption by the cathodic half reaction at the steel–adhesive interface. Assuming the outward diffusion of hydroxide ions remain the same, the situation that now exists is that the inward diffusion of oxygen molecules exceeds the outward diffusion of hydroxide ions. This will lead to an aggregation of hydroxide ions at the crevice tip and an increase in pH in this region. This will have an increased damaging effect on the level of adhesion between adhesive and steel substrate and the associated reduction in performance. To summarize, the increased concentration of oxygen molecules available in solution to feed the crevice developing normal to the beam side at the steel–adhesive interface weakens the joint and leads to more rapid advancement of the crack tip. As the crevice develops, the crevice mouth becomes anodic and the corrosion product is back deposited, reducing the inward diffusion of water and oxygen molecules, but by this time, the damage is already done and the mechanical perturbation of the reduced area at the advancing crack tip has brought about failure. The development of the cathodic crevice

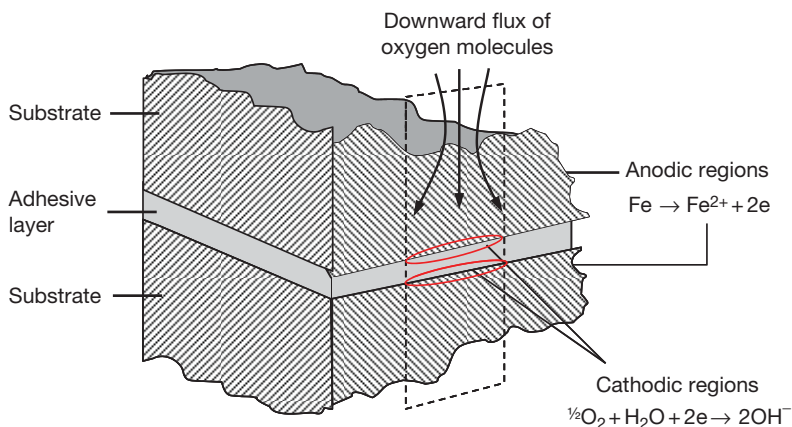


**Figure 16** Schematic illustration of the supply of oxygen to the crevices developing at the adhesive–substrate interface of an adhesive joint. As freshly aerated water arrives, it must supply oxygen to both crevices in the case of a steel–steel joint, but only the steel–adhesive interface in the case of an aluminum–steel joint. Reproduced from Kinloch, A. J.; Korenberg, C. F.; Tan, K. T.; Watts, J. F. *J. Mater. Sci.* **2007**, *42*, 6353–6370.

happens along the beam simultaneously; thus the effect is most serious in the mid-regions where the crevice has developed significantly but not been blocked by corrosion product. The situation is summarized schematically in **Figure 17**.

### 3.36.4.3 Zinc Substrates

The need to bond zinc structures is, of course, very specialized and outside the scope of the review; however, the bonding of zinc coated steel (whether hot dipped or electrogalvanized (HDGS or EGS)) is becoming increasingly important as a production process, particularly in the automobile industry. In essence, the failure is brought about by the gross corrosion of the substrate, a situation that is improved by the chemical pretreatment of the substrate, for example, by the application of a zinc phosphate process. Dickie *et al.* showed quite convincingly that the failure

of adhesively bonded EGS in an aqueous environment is a result of an electrochemically driven process,<sup>31</sup> with the XPS survey spectra of both the metal and adhesive interfacial failure surfaces being dominated by zinc oxide. These observations indicate that failure is associated with gross corrosion of the zinc when the surface is not stabilized by the application of an appropriate treatment, such as a conversion coating. Work by Fitzpatrick *et al.*<sup>20,32</sup> points the way to a better understanding of the manner in which such a conversion coating improves bond durability. Studies by small area XPS indicate that failure initiation is associated, at least in part, by the dissolution of the phosphate crystal by cathodically-generated alkali in regions of some 50–100  $\mu\text{m}$  in size within 1 mm of the edge of the adhesive bond. ToF-SIMS successfully identifies electrochemical activity, although not gross phosphate dissolution, within the central region of the joint, and it is clear that this precedes the

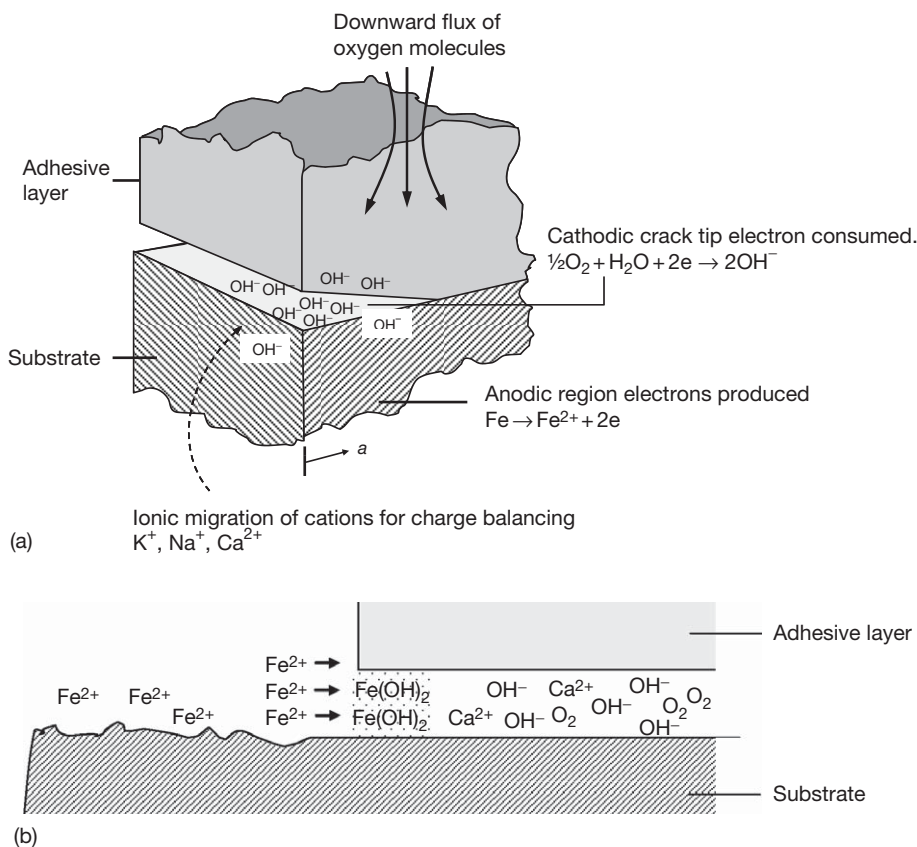


**Figure 17** Schematic representation of the factors influencing supply of oxygen in the developing crevices. (a) In the early stages of failure, oxygen is supplied at the advancing crevice tip as the crack proceeds along the length of the beam and also normal to the direction of crack growth to establish a small but significant developing crevice at the edge of the specimen. (b) The edge crevice may become blocked with corrosion products in this manner in the later stages of joint failure and thus have a disproportionate effect on the failure kinetics. Reproduced from Kinloch, A. J.; Korenberg, C. F.; Tan, K. T.; Watts, J. F. *J. Mater. Sci.* **2007**, *42*, 6353–6370.



phosphate degradation process identified at the bond edge. This points the way to a more purposeful design and selection of conversion coatings for the pretreatment of zinc-coated steel for adhesive bonding, the use of those that have a better resistance to alkaline dissolution than the traditional zinc phosphate product.

### **3.36.5 The Improvement of Bond Durability**

The solution to the need to improve the resistance of adhesive joints to the ravages of corrosion-related phenomena, leading to premature failure, is well-catalogued and can be readily appreciated by consideration of the examples above. There are two potential routes by which durability can be improved; one is the exclusion or immobilization of water by the adhesive so that the kinetics of diffusion toward the reaction zone are reduced to a manageable or acceptable level. The other is to modify the interface in some manner so that the forces responsible for adhesion become less susceptible to cathodically generated alkali or the interfacial path length between substrate and adhesive, which is increased to such an extent that the delamination process at the interface translates to a lateral or planar value that will no longer compromise the joint performance.

Exclusion of water is most commonly achieved by the simple expedient of the application of a bead of silicone, polysulfide or similar sealant along the external surface of the adhesive. Similar in use to a typical domestic product for bathroom use, such a sealant not only seals the joint against the ingress of water, but being hydrophobic, it also physically repels water from the vicinity of the joint. A similar approach is to use a hydrophobic binder for the adhesive, which will repel water from the adhesive, although not necessarily from the interface region. An alternative possibility, not widely explored, is to add extenders to the pigment that will either absorb and immobilize water or increase the path length for water to reach the interface.

The modification of the interface to improve performance would seem to be a much more elegant approach to take, and clear improvements in performance can be achieved by the use of organo-functional silanes as either primers<sup>24,28</sup> or components of the adhesives formulation, and most commercial structural adhesives have these additives included by the manufacturer. The benefit derives from the formation of a bond more resistant to both hydrodynamic displacement

and cathodic delamination; that is a covalent bond as opposed to van der Waals bonding.<sup>33</sup> The increase of the interfacial path length is achieved by simple expedients, such as grit blasting, but in the case of aluminum, this is never adequate, and the complex microtopography achieved by acid anodizing processes is always required.<sup>34</sup> The porous deposit produced by these processes is filled by the adhesive on joint manufacture forming an interlocking region sometimes referred to as a microcomposite interphase zone.

The empirical test approach for a particular set of variables (substrates, adhesive type, loading conditions and environment) is an important way of extending our understanding of failure mechanisms and at the same time providing an indication of the manner in which improved performance can be obtained. This does not necessarily help the design engineer and certainly provides no predictive capability outside the narrow spectrum of conditions that have been examined. The solution to this, as outlined by many authors in recent years, is to develop predictive models that take into account the important variables that are experienced by adhesive joints. There are two basic approaches here that can be described, by analogy with nanotechnology production methods, as top-down or bottom-up. Models based on empirical results, of the required level of sophistication, can be extended to accommodate different adhesive bonding situations, and elegant examples of this approach is provided by the work of Kinloch<sup>24</sup> and Hamade.<sup>35</sup> The alternative approach is to consider a particular joint geometry, load and environment, and the development of closed form adhesive joint stress analyses as described by Crocombe.<sup>36</sup> The particular challenge with this method has been the incorporation of environmental degradation into such closed form solutions, and recent work shows that this can be achieved in a relatively straightforward manner.<sup>37</sup>

### **3.36.6 Conclusions**

There is a very large body of literature that documents the deleterious effect of water on adhesively bonded metal structures, and the prime causes of joint failure are well understood. Corrosion of the substrate, leading to cathodic delamination of the adhesive from the metal is particularly important in the failure of steel joints, while for aluminum, with its passive native oxide layer, thermodynamic displacement of the adhesive from the substrate by the water is the most

commonly encountered failure mode. If the interface is modified chemically (e.g., using an organosilane) or physically to increase surface topography and then the interfacial path length, environmental degradation of the adhesive itself may occur. In order to improve a joint performance, it is necessary to first define the failure mode, and the surface analysis methods of XPS and ToF-SIMS have important roles to play here, not only in the exact definition of the locus of failure, measurement of the thickness of vanishingly thin residual adhesive layers, and relating their composition to the adhesive formulation, but also in the identification of tracer anions and cations, which can indicate whether the region of the substrate that the adhesive has separated from has experienced anodic or cathodic condition as an electrochemical cell has been set up.

There is still much active research to establish new pretreatments that will improve the durability of joints and provide improved corrosion resistance of the substrate. The driving force over the last decade has been to remove hexavalent chromium from pretreatment processes, and the stage is almost upon us where this reagent can be removed totally from the pretreatment stage of the bonding process, even in the aerospace industry, with no adverse effect on performance.

## References

1. Gledhill, R. A.; Kinloch, A. J. *J. Adhes.* **1974**, *6*, 315–330.
2. Watts, J. F.; Castle, J. E.; Hall, T. J. *J. Mat. Sci. Lett.* **1988**, *7*, 176–178.
3. Leidheiser, H., Jr; Funke, W. J. *Oil Colour Chem. Assoc.* **1987**, *70*, 121–132.
4. Watts, J. F. In *Handbook of Surface and Interface Analysis: Methods for Problem Solving*; Riviere, J. C., Myhra, S., Eds.; Marcel Dekker, 1998; pp 781–833. Second Edition in press, publication 2009.
5. Evans, U. R. *Trans. Electrochem. Soc.* **1929**, *5*, 243–248.
6. Leidheiser, Jr. H.; Kendig, M. W. *Corrosion* **1976**, *32*, 69–76.
7. Standish, J.; Leidheiser, H., Jr. In *Corrosion Control by Organic Coatings*; Leidheiser, H., Jr., Ed.; NACE: Houston, TX, 1981; pp 38–44.
8. Hammond, J. S.; Holubka, J. W.; de Vries, J. E.; Dickie, R. A. *Corr. Sci.* **1981**, *21*, 239–253.
9. Dickie, R. A.; Hammond, J. S.; Holubka, J. W. *Ind. Eng. Chem. Prod. Res. Dev.* **1981**, *20*, 339–343.
10. Watts, J. F.; Castle, J. E. *J. Mater. Sci.* **1983**, *18*, 2987–3003.
11. Watts, J. F.; Castle, J. E. *J. Mater. Sci.* **1984**, *19*, 2259–2272.
12. Leidheiser, H., Jr. *J. Adhes. Sci. Technol.* **1986**, *1*, 79–98.
13. Watts, J. F. *J. Adhes.* **1989**, *31*, 73–85.
14. Castle, J. E. In *Organic Coatings*; AIP Conference Proceedings 354; Lacaze, P.-C., Ed.; AIP Press: Woodbury, NY, 1996; pp 432–449.
15. Castle, J. E.; Epler, D. C. *Surf. Sci.* **1975**, *53*, 286–296.
16. ASTM G8–72.
17. British Gas Specification PS/CW6.
18. Koehler, E. L. *J. Electrochem. Soc.* **1985**, *132*, 1005–1009.
19. Castle, J. E.; Luklinska, Z. B.; Parvizi, M. S. *J. Mater. Sci.* **1984**, *19*, 3217–3223.
20. Fitzpatrick, M. F.; Watts, J. F. *Surf. Interf. Anal.* **1999**, *27*, 705–715.
21. Watts, J. F.; Castle, J. E.; Ludlam, S. J. *J. Mater. Sci.* **1986**, *21*, 2965–2971.
22. Watts, J. F.; Dempster, B. R. *Surf. Interf. Anal.* **1992**, *19*, 115–120.
23. Sautrot, M.; Abel, M.-L.; Watts, J. F.; Powell, J. J. *Adhes.* **2005**, *81*, 163–187.
24. Kinloch, A. J.; Korenberg, C. F.; Tan, K. T.; Watts, J. F. *J. Mater. Sci.* **2007**, *42*, 6353–6370.
25. Boerio, F. J.; Hudak, S. J.; Miller, M. A.; Hong, S. G. *J. Adhes.* **1987**, *99*–114.
26. Boerio, F. J.; Hong, S. G. *J. Adhes.* **1989**, *30*, 119–134.
27. Watts, J. F.; Blunden, R. A.; Hall, T. J. *Surf. Interf. Anal.* **1990**, *16*, 227–235.
28. Hamade, R. F.; Dillard, D. A. *J. Adhes. Sci. Technol.* **2003**, *1235*–1264.
29. Hamade, R. F.; Dillard, D. A. *Int. J. Adhes. Sci. Technol.* **2005**, *147*–163.
30. Davis, S. J.; Watts, J. F. *J. Mater. Chem.* **1996**, *6*, 479–494.
31. Dickie, R. A.; Haack, L. P.; Jethwa, J. K.; Kinloch, A. J.; Watts, J. F. *J. Adhes.* **1998**, *1*–37.
32. Fitzpatrick, M. F.; Ling, J. S. G.; Watts, J. F. *Surf. Interf. Anal.* **2000**, *29*, 131–138.
33. Abel, M.-L.; Fletcher, I. W.; Digby, R. P.; Watts, J. F. *Surf. Interf. Anal.* **2000**, *29*, 115–125.
34. Clearfield, H. M.; McNamara, D. K.; Davis, G. D. In *Adhesive Bonding*; Lee, L.-H., Ed.; Plenum Press: New York, NY, 1991; pp 203–238.
35. Hamade, R. F.; Seif, C. Y.; Merhij, F.; Dillard, D. A. *J. Adhes. Sci. Technol.* **2008**, *775*–793.
36. Crocombe, A. D. In *Adhesive Bonding: Science, Technology and Applications*; Adams, R. D., Ed.; Woodhead Publishing Ltd.: Cambridge, UK, 2005; pp 91–122.
37. Crocombe, A. D. *J. Adhes.* **2008**, *84*, 212–230.

# COMPREHENSIVE CORROSION



## 4.01 Surface Pretreatment

### G. L. Higgins

Chemetall Ltd, Aylesbury, UK

### R. S. Hullcoop

Ray Hullcoop and Associates, High Wycombe, UK

### S. Turgoose

CAPCIS-INTETECH, Manchester, UK

### W. Bullough

Corus Research Centre, Rotherham, UK

This article is a revision of the Third Edition articles 11.1 and 11.2 by G. L. Higgins and R. S. Hullcoop & S. Turgoose and W. Bullough, volume 2, pp 11:3–11:23, © 2010 Elsevier B.V.

4.01.1	Introduction	2484
4.01.2	Chemical Cleaning	2484
4.01.2.1	Solvent Cleaning	2484
4.01.2.1.1	Vapor degreasing	2484
4.01.2.1.2	Emulsifiable cleaners (water rinsable cold solvent cleaning)	2485
4.01.2.1.3	Emulsion cleaners	2485
4.01.2.2	Neutral Cleaners	2485
4.01.2.3	Acidic Cleaners	2485
4.01.2.4	Alkaline Cleaners	2486
4.01.2.5	Acid Pickling of Ferrous Materials	2487
4.01.2.5.1	Formation of millscale	2487
4.01.2.5.2	Mechanism of scale removal	2488
4.01.2.5.3	Hydrogen embrittlement	2489
4.01.2.5.4	Pickling of alloy steels	2489
4.01.2.5.5	Pickling inhibitors	2489
4.01.2.6	Acid Pickling of Nonferrous Metals	2491
4.01.2.6.1	Electrochemical cleaning	2491
4.01.2.7	Ultrasonic Cleaning	2491
4.01.3	Mechanical Cleaning	2491
4.01.3.1	Flame Cleaning	2491
4.01.3.2	Manual Cleaning	2491
4.01.3.3	Abrasive Blast Cleaning	2492
4.01.3.3.1	Surface finish	2492
4.01.3.3.2	Surface profile	2492
4.01.3.4	Ultrahigh Pressure Water Jetting	2492
4.01.3.5	Health, Safety, and the Environment	2492
4.01.4	Standards	2493
References		2493

### Glossary

**Millscale** An oxide that forms on steel during high temperature processing (e.g., hot rolling) and must be effectively removed prior to the application of any subsequent surface protection.

**Surfactant** A substance that lowers the surface tension of a liquid, allowing easier spreading across the surface of a material.

**Workpiece** The item, component, or material that is undergoing surface pretreatment.

### Abbreviations

**BS** British Standard

**EDTA** Ethylene diamine tetra-acetic acid

**EN** European Norm  
**ISO** International Standards Organisation  
**TLV** Threshold limit values  
**VOC** Volatile organic compounds

#### **4.01.1 Introduction**

The attainment of a clean surface prior to the application of any subsequent treatment or coating is essential, whether this subsequent operation is electroplating, anodizing, chemical treatment, or organic coating. The standard of cleanliness which must be achieved has been stated to be “that which will allow the subsequent process to be carried out satisfactorily”; however, this is an almost meaningless statement. Often it is industry experience that provides a guide to the standard of surface preparation required. As an example, the degree of cleanliness required to satisfactorily zinc plate from an acid solution is somewhat higher than that required prior to zinc plate from a high-cyanide alkali zinc solution. However, this should never be taken as a license to skimp on surface preparation and in another example the arguments over the degree of pretreatment required for ‘surface-tolerant’ paint coatings abound and will probably continue. It should be remembered that it is to a large extent true that problems of early failure in metal finishing are traceable to incorrect or insufficient surface preparation.

#### **4.01.2 Chemical Cleaning**

Chemical contamination consists of oils, greases, preservatives, or old paint coatings which must be removed prior to further finishing. Paint coatings can be removed by chemical paint strippers (e.g., solvent or alkali based); however, these methods will not be discussed further here. Sources of most organic contamination are, for example, cutting and machining fluids, preservatives, oils, and greases from, for example, rolling operations, press lubricants, and mechanical or manual handling operations. Various means of removal have been proposed: mechanical action; solvency; detergency; and chemical reaction. In all cleaning operations one or more of these mechanisms will contribute more or less to the overall cleaning procedure, dependent upon the cleaning method and solution employed.

With chemical cleaning, performance will be enhanced by the use of mechanical action, such as brushing, air agitation, spraying, electrolysis or ultrasonic agitation. Solvency is where the materials to be

removed dissolve in the cleaning medium, for example mineral oil in chlorinated solvents. Detergency is the ‘lifting’ action attributed to some alkalis and to special surface-active agents commonly referred to as surfactants. Chemical reaction is characterized by, for example, the saponification of some oils in strong alkali, or the reaction of rust with acid solutions. The main types of cleaners used for the removal of organic contaminants are solvent cleaners, neutral cleaners, acid cleaners, and alkali cleaners.

##### **4.01.2.1 Solvent Cleaning**

The traditional use of flammable hydrocarbon solvents (e.g., white spirit or paraffin) used either by immersion or by manual application is not to be recommended as an effective or particularly safe method of degreasing. When used by immersion, the holding tank can become heavily contaminated and the contaminants will remain on the work after the solvent has evaporated. The use of solvent-soaked rags, although a time-honored procedure, is now being frowned upon on the grounds of operator safety; aqueous based prewipes are available.

###### **4.01.2.1.1 Vapor degreasing**

The use of hot/boiling solvents, with either immersion of the articles to be cleaned in the bulk solvent or in the overlying vapor using specially designed installations, is an effective use of solvents for cleaning purposes. The solvent, which traditionally was of a halogenated hydrocarbon type, is held in a sump at the base, which is heated by any suitable means and under thermostatic control. Above this may be a wire mesh on which the workpieces are rested. The solvent is condensed near the top of the chamber by cooling coils; thus, between the mesh and the coils is created a region where the solvent is in vapor form. When cold items are introduced, the vapor condenses upon them and liquid solvent flows off, thereby removing contamination. To a large extent, only clean solvent is vaporized, thus ensuring that only fresh solvent is used to clean the workpiece until the sump becomes overcontaminated, when the solvent must be cleaned or replaced. Care should be exercised with some metals, notably aluminum, that solvent with free chloride is not used, as this could lead to pitting of the metal surface.

Currently, the use of chlorinated solvents is increasingly deprecated in view of the extent of release of volatile organic compounds (VOC). Therefore, the advice of the manufacturers of the installation and the suppliers of the solvent should always be heeded in the operation of these installations to ensure



their trouble-free running. Effective fume control must be available above the installation and the work must be removed slowly enough to ensure that all the solvent has evaporated from the work before it leaves the extracted area. Also, as per governing legislative rules, exposure limits for solvents are increasingly being reduced and current advice must be sought.

#### **4.01.2.1.2 Emulsifiable cleaners (water rinsable cold solvent cleaning)**

Emulsifiable cleaners (sometimes incorrectly referred to as emulsion cleaners) are blends of organic solvent (often hydrocarbons) with surface active agents and dispersed in an aqueous medium. The work is immersed in the unheated solution for a sufficient time for the cleaner to penetrate the surface thoroughly. The articles are then removed and water rinsed. Additives in the cleaner allow the solvent to emulsify in the water thus removing the contamination. Spray rinsing or agitation in an immersion rinse will aid removal of the residues. This form of cleaning creates disposal problems as the rinse water cannot be merely disposed of into sewerage systems. Thus, the effluent will require storage and the emulsion is broken up before discharge of the water layer and approved disposal of the organic material. As with all solvent-based materials, the need to observe threshold limit values (TLV) for personal exposure and the need for the work to be carried out only under effective fume extraction must be taken into account when considering this type of cleaning product.

The cleanliness of the surface produced by emulsifiable cleaners is not of the highest standard, and additional cleaning may well be necessary before further finishing operations. However, in the use of this method prior to some chemical conversion coating processes (e.g., immersion in phosphate baths), the crystal growth can be quite refined because of the absence of the passivation effect often encountered with some heavy-duty alkali cleaners. Needless to say, manufacturers' recommendations should be followed at all times and the suitability of any particular cleaning/pretreatment combination should be confirmed. Another benefit gained from the use of emulsifiable cleaners is that the surface produced is usually hydrophobic and therefore, to an extent, resistant to tarnishing and corrosion in storage.

#### **4.01.2.1.3 Emulsion cleaners**

These are materials, containing blends of organic solvents and surfactants, which are added to water to form an emulsion. Typical concentrations are in the range 0.5–5%. Such emulsions are normally used

by spray, as either a preclean in a multistage pretreatment line, or as the cleaner in an industrial washing machine. Such washing machines are often used to clean parts which are contaminated with cutting oils and which require inspection before storage. Like the emulsifiable cleaners, the emulsion cleaners, after rinsing, often leave a hydrophobic surface which is resistant to short-term corrosion. Emulsion cleaners can be used hot or cold. Heat generally improves the cleaning action but, in most cases, leads to an objectionable increase in the smell associated with solvent products.

#### **4.01.2.2 Neutral Cleaners**

These are rapidly replacing emulsion and alkali products for use in industrial washing machines and are generally used at pH 7.5–9, which is considerably lower than that of the corresponding alkali products. Neutral cleaners are on the basis of chemical soaps, with additions of surfactant (to improve cleaning, wetting, penetration, and defoaming), corrosion inhibitors (which may be nitrite or organic), and a bactericide.

Neutral cleaners provide the benefits of generally lower operating temperatures, reduced odor, easier effluent treatment, and improved health and safety considerations over the alkali or emulsion products. Because of the inhibited nature of the surface produced, such products are used for inter stage cleaning and prior to assembly. The surface is generally not suitable for immediate painting.

#### **4.01.2.3 Acidic Cleaners**

The vast majority of acid-based cleaning products are designed for the removal of scale, rust, and other oxide films. These products may also contain solvents and surfactants to degrease and derust simultaneously. There are, however, certain acid-based materials which can primarily be construed as cleaners. One such type of material is used in the cleaning of aluminum cans prior to treating and lacquering. Such cleaners are normally on the basis of sulfuric or phosphoric acid, with, generally, additions of hydrofluoric acid and surfactants. These materials are sprayed on to preformed cans to remove the lubricant used during the can-forming operation. The fluoride is present to enhance the removal of fine metal swarf as well as to remove the oxide film.

Fluoride-free acid cleaners are used for general pretreatment cleaning of aluminum as an alternative to strong alkali materials. Although more expensive in terms of initial make-up and plant requirements the rate of material loss through cleaning and etching is reduced. Furthermore, the need for an acid de-smut (required after alkali cleaning) can be eliminated.

As the surface smoothing and leveling effects are somewhat limited, the use of acid cleaners prior to anodizing or electropainting, where surface defects can be enhanced, is not common. Care must be taken here not to confuse acid cleaners with high-strength, phosphoric acid-based chemical polishes and chemical brighteners, which are used to obtain specific types of attractive surface finish. Also in the category of acid cleaners could be considered the lightweight alkali-metal phosphating cleaner-coater solutions; a fuller discussion of such materials is best left to specialist publications on metal pretreatment chemicals.

#### 4.01.2.4 Alkaline Cleaners

Alkali cleaners can be used before almost every conceivable metal finishing operation at one stage or another; they can be used by spray, by immersion, by manual application or by all three, or maybe by two out of the three methods. They can come as powders or as made-up liquids. They may be single or multipack, to be used as supplied or at a range of dilutions. They may require high temperatures or work successfully at ambient temperature. They may be suitable for cleaning one metal only or have multimetal capability. The user thus has an immense range from which to choose.

Consideration will first be given to the inorganic species used to produce the base material. The pH values of several commonly used materials are shown in [Table 1](#). Hydroxides are the simplest, strongest alkalis and most commonly used. A major effect of hydroxides in cleaning is saponification: the conversion of certain oils and greases to water-soluble soap-type materials.

Beside the benefits of hydroxides must be placed certain disadvantages:

1. The possible passivation of iron and steel surfaces; this can be a problem prior to chemical conversion coatings.

2. The soaps produced by saponification may give excessive foam during spray cleaning or react with hard-water salts to form scum and scale.
3. Amphoteric metals, such as zinc and aluminum, can be attacked (i.e., corroded) more than is desirable.
4. Powder products formulated with too much hydroxide can be hygroscopic and thus tend to form solid blocks in storage rather than remaining as free-flowing powders.
5. Spray cleaners based on hydroxide can pick up carbon dioxide from the atmosphere and such carbonated solutions become less effective.

Carbonates and bicarbonates are used as lower alkalinity adjuncts or substitutes for hydroxide and are more resistant to carbonation during spraying than hydroxide-only solutions. Powder products blended with light sodium carbonate are much less hygroscopic and the carbonate can be a useful 'carrier' for liquid additives, such as surfactants and solvents.

Silicates can offer an almost complete cleaning system on their own. Sodium silicate, the most commonly used of these materials, has a high enough pH value to cause saponification on its own and the anion formed gives a certain degree of detergency and inhibition. Thus, silicates are often found in multimetal cleaners. Light metals, such as zinc and aluminum will generally not be attacked if the silicate level is sufficiently high and the free hydroxide level sufficiently low. However, cleaners containing silicate can cause problems. They should not be used prior to an alkaline process on aluminum, owing to the formation on the surface of alkali-insoluble aluminum silicate. Cleaners containing silicates can also cause problems if used prior to some surface-sensitive treatments, such as use of zinc phosphating solutions.

Other common ingredients of alkaline cleaners include phosphates, which have both detergent and dispersive properties; also, the polyphosphates have water softening capabilities. In addition, borates are often the base for light-duty cleaners, because of their inhibiting action and less alkaline pH. They can also be used, to a certain extent, as a substitute for phosphates when a phosphate-free product is required. The organic acid salts, such as EDTA and heptonate, are included for water softening properties and to assist in the removal of solid particles. Gluconate and heptonate, in particular, are effective in the highly alkaline solutions used for etching aluminum and prevent the precipitation of aluminum hydroxide scale and sludge.

Surfactants are probably the materials which most affect the performance of alkali cleaners. Surfactants

**Table 1** pH values of selected alkalis as 1 wt% solution at 50°C

<i>Alkali</i>	<i>pH</i>
NaOH	12.7
Na <sub>2</sub> CO <sub>3</sub>	11.3
Na <sub>2</sub> SiO <sub>3</sub>	12.2
Na <sub>3</sub> PO <sub>4</sub>	11.8
Na <sub>2</sub> P <sub>2</sub> O <sub>7</sub>	10.6
Na <sub>5</sub> P <sub>3</sub> O <sub>10</sub>	9.8
Na <sub>2</sub> B <sub>4</sub> O <sub>7</sub>	9.3
NaC <sub>7</sub> H <sub>13</sub> O <sub>8</sub>	7.8

are chemicals that modify the solubility of various materials in, and their surface affinity for, oil and water. The diverse composite which makes up the surface of a metal object must be fully wetted out if the cleaner is to perform properly. Surfactants lower the surface tension to allow wetting out to occur. Oils and greases must either be dissolved off the surface or lifted from it; surfactants assist in both areas.

There are four broad categories of surfactant on the basis of the charge associated with the active part

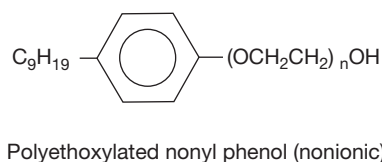
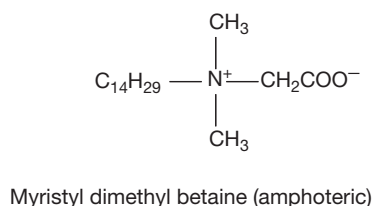
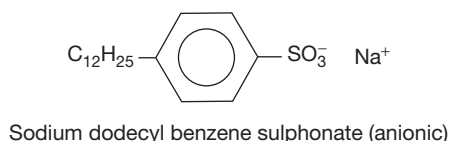
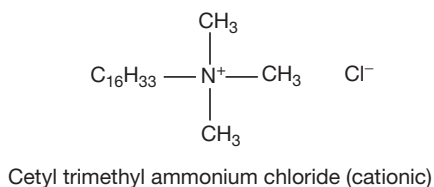


**Figure 1** Common surfactants of each main category.

of the molecule (typical examples of each are given in [Figure 1](#)):

1. cationic, where the residual charge is positive;
2. anionic, where the residual charge is negative;
3. amphoteric, where there exists both positive and negative charge centers;
4. nonionic, where there is no residual charge.

Care must be taken with some surfactant-containing cleaners not to exceed certain temperature and concentration limits. Thus, it is not always true that the hotter and more concentrated the solution, the better the cleaning. Many commonly used surfactants have limited solubility in alkali and become less soluble as the alkalinity, ionic strength, and temperature rise. A point can, therefore, be reached when the surfactants come out of solution and, in immersion cleaning especially, performance will suffer drastically. Similarly, some spray cleaners are designed to work above a certain minimum temperature and strength. In this case, a surfactant is designed to come out of solution to act as a defoamer for the system. Examples of typical simple formulations for various types of alkali cleaners are given in [Table 2](#).

#### 4.01.2.5 Acid Pickling of Ferrous Materials

The hot rolling of steel produces a surface layer of complex oxides known as 'millscale.' It is unstable and must be removed prior to painting if reliable performance is to be obtained. Removal of millscale may be accomplished by a variety of methods but it is traditionally removed by pickling in strong acid containing one or more corrosion inhibitors.

##### 4.01.2.5.1 Formation of millscale

When mild steel is heated in air an oxide or scale will form on the steel surface. This scale consists of three well defined layers, whose thickness and composition depend on the duration and temperature of heating. In general, the layers, from the steel base outwards,

**Table 2** Typical formulations for alkali cleaners

Constituent			Composition (%)		
NaOH	20	60	20	0	0
Na <sub>2</sub> SiO <sub>3</sub>	50	20	40	60	0
Na <sub>2</sub> CO <sub>3</sub> /NaHCO <sub>3</sub>	20	10	20	10	20
Na <sub>3</sub> PO <sub>4</sub>	—	—	12	20	20
EDTANa <sub>4</sub>	5	5	5	5	8
Na <sub>2</sub> B <sub>4</sub> O <sub>7</sub>	—	—	—	—	50
Surfactant	5	5	3	5	2
Substrate application	Steel immersion	Steel electrocleaning	Zinc electrocleaning	Multimetal immersion	Aluminium spray

comprise a relatively thick layer of wüstite, the composition of which approximates to the formula  $\text{FeO}$ , a layer of magnetite ( $\text{Fe}_3\text{O}_4$ ), and a thin layer of hematite ( $\text{Fe}_2\text{O}_3$ ).

When the steel is rapidly cooled, the thickness and composition of these layers remain more or less unchanged, but when it is slowly cooled through  $575^\circ\text{C}$  the scale becomes enriched in oxygen and the remaining wüstite layer breaks down to some extent into an intimate mixture of finely divided iron and magnetite.<sup>1</sup> Holding the temperature between  $400$  and  $575^\circ\text{C}$  causes the iron particles to agglomerate and the scale becomes further enriched in oxygen. As wüstite is unstable below  $575^\circ\text{C}$ , scales produced at temperatures lower than this contain magnetite and hematite only. In addition, the scales are often cracked and porous. This is due to the difference in contraction between scale and metal on cooling and to the change in volume when the metal is oxidized.

#### 4.01.2.5.2 Mechanism of scale removal

When steel that has been slowly cooled through  $575^\circ\text{C}$  is immersed in mineral acid, the acid penetrates through the cracks and pores in the upper layers of scale and rapidly attacks the oxide layers (Figure 2). The iron, being anodic, dissolves to form ferrous ions and the magnetite, being cathodic, is reduced, forming more ferrous ions. As the three constituents of these cells are good electrical conductors, their resistance is sufficiently small so that the rate of dissolution is largely governed by the rate at which acid diffuses in through the cracks and the rate at which spent acid diffuses out through them. A similar but slower action occurs between the

exposed metal and the magnetite and hematite layers which have not been detached.

The mechanisms of oxide dissolution and scale removal have been widely studied and have been thoroughly reviewed by Frenier and Growcock,<sup>2</sup> who concluded, in agreement with others,<sup>3</sup> that oxide removal from the surface of steel occurs predominantly by a process of reductive dissolution, rather than by chemical dissolution, which is slow in mineral acids. In this process the reduction of the ferric components of the scale is coupled to oxidation of the base metal, both reactions yielding ferrous species readily soluble in the acid. For magnetite the processes are:

1.  $\text{Fe}_3\text{O}_4 + 8\text{H}^+ + 2\text{e}^- = 3\text{Fe}^{2+} + 4\text{H}_2\text{O}$
2.  $\text{Fe} = \text{Fe}^{2+} + 2\text{e}^-$

Scale removal is also assisted by the dissolution of the underlying metal by normal acid corrosion processes, which undermines the scale, and by the physical effect of hydrogen gas evolved in this latter reaction.

In general there does not appear to be any direct correlation between the rate of the chemical dissolution of oxides and the rate of scale removal, although most work on oxide dissolution has concentrated on magnetite. For example, Gorichev and coworkers have studied the kinetics and mechanisms of dissolution of magnetite in acids<sup>4,5</sup> and found that it is faster in phosphoric acid than in hydrochloric, while scale removal is slower in the former. Also, ferrous ions accelerate the dissolution of magnetite in sulfuric, phosphoric and hydrochloric acids, whereas the scale removal rate is reduced by the addition of ferrous ions. These observations appear to emphasize the importance of reductive dissolution and undermining in scale removal, as opposed to direct chemical dissolution.

As further confirmation of this Rozenfeld<sup>3</sup> has reviewed Russian work on this subject and reports that in pickling with sulfuric acid the amount of acid used in scale dissolution is only about one-tenth that consumed by the dissolution (corrosion) of the underlying metal. However, in hydrochloric acid the direct scale dissolution occurs to a much greater degree, and is responsible for about 40% of the acid consumption.

A mechanism such as that given above provides explanations for the known effects of many process variables. The reductive dissolution and undermining processes require access of the acid to the metal surface, hence the benefits obtained by the deliberate introduction of cracks in the oxide by cold-working prior to pickling. Also the increase in pickling rate with agitation or strip velocity can be explained in

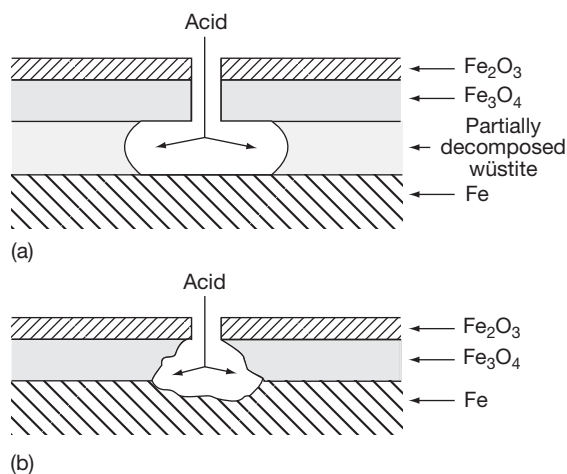


**Figure 2** Mechanism of scale removal with acid: (a) high temperature scale and (b) low-temperature scale.

terms of the avoidance of acid depletion at the oxide–solution interface.

#### 4.01.2.5.3 *Hydrogen embrittlement*

Although the majority of the hydrogen produced on the cathodic areas is evolved as gas and assists the removal of scale, some of it diffuses into the steel in the atomic form and can render it brittle. Hardened and higher carbon ferritic steels are particularly susceptible to this hydrogen embrittlement and cracks may appear during pickling. Austenitic steels, however, are much more resistant to embrittlement because of the lower diffusivity of hydrogen in the face-centered cubic lattice. Certain impurities (e.g., arsenic, sulfur, antimony, etc.) promote the dissolution of hydrogen into the metal (or inhibit the hydrogen recombination reaction generating hydrogen gas, which amounts to the same thing). Consequently, this increases the quantity of hydrogen that diffuses into the steel and the consequent risk of embrittlement. Several theories of the mechanism of embrittlement have been put forward<sup>6,7</sup> and these are discussed in more detail elsewhere in this volume.

As well as causing brittleness, absorbed gas may combine to form molecular hydrogen on the surface of inclusions and voids within the steel. Thus a gas pressure is set up in the voids and this may be sufficient to cause blisters to appear either during pickling or during subsequent processing such as hot-dip galvanizing. The embrittlement effect can be largely removed by heat treatment of the steel at 150–200 °C, but even then the original ductility may not be entirely restored. In estimating the degree of embrittlement, the temperature and rate of testing have an important effect. Thus the embrittlement tends to disappear at very low and very high temperatures and is reduced at high strain rates.

#### 4.01.2.5.4 *Pickling of alloy steels*

The furnace scales which form on alloy steels are thin, adherent, complex in composition, and more difficult to remove than from nonalloy steels. Several mixed acid pickles have been recommended for stainless steel, the type of pickle depending on the composition and thickness of the scale.<sup>8</sup> For lightly-scaled stainless steel, a nitric–hydrofluoric acid mixture is suitable, the ratio of the acids being varied to suit the type of scale. Strict chemical control of this mixture is necessary, as it tends to pit the steel when the acid is nearing exhaustion. For heavy scale, two separate pickles are often used. The first conditions the scale and the second removes it. For example, a sulfuric–hydrochloric acid mixture is recommended

as a scale conditioner on heavily scaled chromium steels and a nitric–hydrochloric acid mixture for scale removal. A ferric sulfate–hydrofluoric acid mixture has advantages over a nitric–hydrofluoric acid mixture in that the loss of metal is reduced and the pickling time is shorter, but strict chemical control of the bath is necessary.

Electrolytic pickling of stainless steel in 5–10% (w/v) sulfuric acid at 50 °C can be used for removing the majority of the scale. The strip is first made anodic, when a little metal dissolves, and then cathodic, when the evolved hydrogen removes the loosened scale. To complete the pickling, a nitric plus hydrofluoric acid dip is given for austenitic steels and a nitric acid dip for ferritic steels.

The chromium-containing oxides on stainless steels are more resistant to reductive dissolution and harder to remove than oxides on mild steel. Typically mixed acids and multistage treatments are used and many formulations have been reported.<sup>9</sup> Scale conditioning can be carried out in acids, in molten salts (e.g., sodium hydroxide plus sodium nitrate) or in alkaline solutions (e.g., alkaline permanganate). Scale removal can be obtained with a variety of acids, the commonest being a nitric/hydrofluoric mixture. Rozenfeld<sup>3</sup> also reports effective pickling with ferric sulfate plus sulfuric acid mixtures and considers that the effect of the ferric ions is to speed up the dissolution of the underlying metal. Organic acids, such as citric acid, also have a role in the cleaning of lightly corroded alloy steels.<sup>10</sup>

#### 4.01.2.5.5 *Pickling inhibitors*

##### *Organic inhibitors*

During the pickling of scaled steel, the thinner and more soluble scale is removed before the thicker and less soluble scale. Consequently, some exposed base metal is attacked before the pickling operation is complete. In order to reduce this acid attack to a minimum, corrosion inhibitors are used. Although an effective inhibitor reduces acid attack, it does not prevent the attack of oxidizing agents on the exposed base metal. Thus, the ferric ions resulting from the gradual dissolution of the detached magnetite and hematite may, even in the presence of an inhibitor, attack the exposed steel causing pitting.

Clearly, the selected inhibitor should not decompose during the life of the pickle nor decrease the rate of scale removal appreciably. Some highly efficient inhibitors, however, do reduce pickling speed a little. It would be expected that as the hydrogen evolution is reduced the amount of hydrogen absorption and



embrittlement would also be reduced. This is not always the case; thiocyanate inhibitors, for example, actually increase the absorption of hydrogen.

Many organic substances soluble in acid or colloidal-dispersible have been shown to have inhibiting properties. The most effective types contain a non-polar group such as a hydrocarbon chain and a polar group such as an amine. They contain oxygen, nitrogen, sulfur, or other elements of the fifth and sixth groups of the Periodic Table. They include alcohols, aldehydes, ketones, amines, proteins, amino acids, heterocyclic nitrogen compounds, mercaptans, sulfoxides, sulfides, substituted ureas, thioureas, and thiazoles.

The efficiency of an inhibitor ( $I$ ) under a given set of conditions can be expressed by the ratio of the decreased corrosion rate as a function of the original uninhibited corrosion rate (as a percentage):

$$I = \frac{(\text{Uninhibited corrosion rate} - \text{Inhibited corrosion rate})}{\text{Inhibited corrosion rate}} \times 100\%$$

In general the efficiency increases with an increase in inhibitor concentration; typically an effective inhibitor gives >95% inhibition at a concentration of 0.01 wt% and ~90% at ~0.005 wt%. Provided the inhibitor is stable, increase in temperature usually increases the efficiency although the actual acid attack may be greater. A change in acid concentration, or in type of steel, may also alter the efficiency. Thus, the conditions of a laboratory determination of efficiency should closely simulate the conditions expected in commercial practice.

Figure 3 shows the relationship between efficiency and concentration of some thiourea derivatives and gelatin in the pickling of cold-reduced and annealed strip in 6 wt% sulfuric acid at 85 °C. The thiourea derivatives, diluted with sodium chloride, gelatin and a wetting agent, are used commercially. Mono- and di-*O*-tolyl thioureas are stable in this pickle for at least 50 h, but diphenyl thiourea and gelatin decompose after 4 or 5 h.

The principles behind the selection of effective inhibitors for steel in the various acids have been reviewed by Schmitt<sup>11</sup> and Gardner.<sup>12</sup> The selection of an inhibitor is dependent on both the metal and the acid. For steel, in general, nitrogen-based inhibitors (e.g., amines and heterocyclic compounds) are used in hydrochloric acid, whereas sulfur-containing ones (e.g., thiourea and its derivatives) find more favor in sulfuric acid.

Given the reductive dissolution process involved and the contributions from undermining and

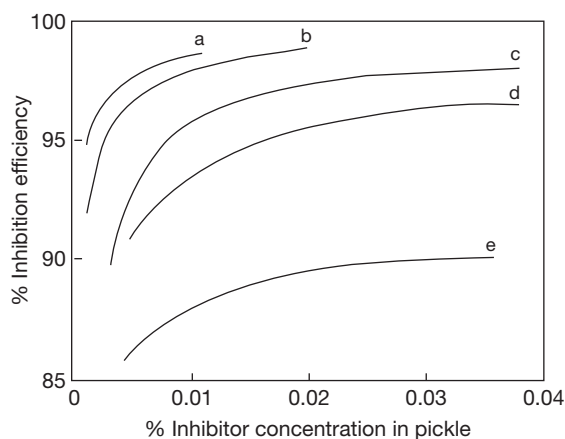


**Figure 3** Relationship between % inhibitor efficiency and inhibitor concentration in 6 wt%  $\text{H}_2\text{SO}_4$ : (a) di-*o*-tolyl thiourea; (b) mono-*o*-tolyl thiourea; (c) commercial inhibitor containing 20% di-*o*-tolyl thiourea; (d) commercial inhibitor containing 20% diphenyl thiourea; and (e) gelatin.

hydrogen evolution in scale removal, inhibitors might be expected to affect the rate of this removal. Also, if the inhibitor adsorbs on the oxide surface then the rate of chemical dissolution of the oxide may be affected. Experimental evidence suggests that these effects may occur, depending on the acid and the inhibitor. Cumper<sup>13</sup> has shown that pyrrole and indole can increase the rate of dissolution of magnetite in hydrochloric acid. It has been reported<sup>14</sup> that commercial amine-based inhibitors can either increase or decrease the rate of scale removal in the same acid. Other reports suggest that the presence of inhibitor has little effect on scale removal rate in hydrochloric acid but markedly decreases it in sulfuric acid. One area that has not been widely studied is the effectiveness of inhibitors on scaled surfaces, but there is experimental evidence that the presence of magnetite scales can significantly affect the performance of nitrogen-based inhibitors in alkaline solutions used for chemical cleaning.

#### Inorganic inhibitors

Inorganic inhibitors are salts of metals having a high hydrogen overvoltage, for example, antimony and arsenic salts. The inhibiting action is associated with the formation of a coating of the metal, which, being cathodic to the steel and having a high hydrogen overvoltage, prevents the discharge of hydrogen ions and so stops the dissolution of the steel. These inhibitors are seldom used in commercial practice, but antimony chloride dissolved in concentrated hydrochloric acid is used in the laboratory for stripping

deposits of zinc, cadmium, tin, and chromium from steel, and with the addition of stannous chloride for removing scale and rust.<sup>15</sup>

#### 4.01.2.6 Acid Pickling of Nonferrous Metals

Although less common, acids are also used for the removal of oxide and scale from nonferrous metals and alloys. Table 3 summarizes a number of pickling solutions for selected materials.

##### 4.01.2.6.1 Electrochemical cleaning

A significant increase in immersion cleaning performance can be achieved by local agitation caused by vigorous gas evolution on the surface of the workpiece. Thus, the use of an applied cathodic voltage evolves hydrogen, which provides a 'scrubbing' action, greatly enhancing the cleaning process. However, during cathodic cleaning any dissolved metal ions in solution will tend to plate-out on the metal surface, so the work will normally be given a short anodic cycle at the end of the cleaning time to dissolve this contamination. Also, periodic reverse cathodic-anodic cycling is another way of achieving the same effect. Anodic cleaning can also be performed as a small fraction of the metal is dissolved, thereby simultaneously removing any contamination; however, this should be done with care, as otherwise the workpiece may be destroyed.

For electrocleaning, care must be taken that a solution of sufficiently high conductivity is used to prevent solution voltage drops and 'burning' of workpieces in high current density areas. Clearly, excessively high anode current densities should be avoided as these will cause excess corrosion/dissolution of the

workpiece. Care must also be taken during cathodic cleaning of steel alloys as hydrogen embrittlement, which must always be considered a risk during cathodic cleaning, must be either avoided or allowed for.

#### 4.01.2.7 Ultrasonic Cleaning

Another method for introducing mechanical action into immersion cleaning is by the use of ultrasonic agitation. Here, a high frequency vibration is imparted to the solution. At the surface to be cleaned, minute bubbles are formed by local cavitation of the fluid. When they collapse, they impart a high degree of local agitation, thereby efficiently removing any surface contamination.

#### 4.01.3 Mechanical Cleaning

##### 4.01.3.1 Flame Cleaning

Now little used as a preparatory method, flame cleaning is a process whereby an intensely hot flame is played on the surface of the steel. In theory, differential expansion causes millscale to detach. In practice, there is evidence that the treatment may not remove thin, tightly adhering millscale. Also, steel less than 5 mm thick can buckle. Finally, the process can 'burn in' chemicals deposited on the surface, causing premature paint failure.

##### 4.01.3.2 Manual Cleaning

The term encompasses all manual and mechanical methods of cleaning other than blast-cleaning, for example abrasive discs, wire brushes, scrapers, vibratory needle guns and chipping hammers are all

**Table 3** Pickling solutions for nonferrous metals

<i>Metal</i>	<i>Acid</i>	<i>Temperature</i>	<i>Time</i>
Copper and brass (60–90% Cu, 10–40% Zn)	7–25% (w/w) H <sub>2</sub> SO <sub>4</sub> or 15–25% (w/w) HCl	15–60 °C	1–10 min
Aluminium bronze (82–95% Cu, 5–10% Al, 0–5% Fe, 0–5% Ni)	Scale conditioned with 10% (w/w) NaOH followed by H <sub>2</sub> SO <sub>4</sub> or HCl as above	15 °C	1–3 min
Copper–silicon alloys (96–97% Cu, 1–3% Si)	7–25% (w/w) H <sub>2</sub> SO <sub>4</sub> + 1–3% (w/w) HF	75 °C	2–5 min
Nickel–copper alloys (55–90% Cu, 10–30% Ni, 0–27% Zn)	10% (w/w) HCl + 1.5% (w/w) CuCl <sub>2</sub>	15 °C	1–5 min
Nickel–chromium alloys (35–80% Ni, 16–20% Cr, 0–45% Fe, 0–2% Si)	10% (w/w) HCl + 1.5% (w/w) CuCl <sub>2</sub>	80 °C	30 min
Aluminium alloys (0–10% Cu, 0–30% Mg, 0–6% Zn, 0–12% Si)	Scale conditioned with 20% NaOH + 5% (w/w) KMnO <sub>4</sub> followed by 20% (w/w) HNO <sub>3</sub> + 4% (w/w) HF	100 °C	1–2 h
Magnesium alloys (0–10% Al, 0–3% Zn, 0–0.2% Mn)	25% (w/w) H <sub>2</sub> SO <sub>4</sub> + 5% (w/w) CrO <sub>3</sub>	50 °C	5–30 min
	40% (w/w) HNO <sub>3</sub> + 1–5% (w/w) HF	65 °C	20 min
	10–20% (w/w) CrO <sub>3</sub> + 3% (w/w) H <sub>2</sub> SO <sub>4</sub>	15 °C	1–5 min
		100 °C	1–30 min
		25 °C	15 s

available. Manual cleaning removes neither tightly adhering millscale nor deep-seated rust from pits. None the less, it is often used for maintenance work or for the preparation of new steelwork to be exposed in nonaggressive conditions. Manual cleaning is rarely used in conjunction with, as it is inappropriate for, high-performance long-life systems, for example, two-pack chemically curing coatings which require a high standard of blast cleaning.

#### **4.01.3.3 Abrasive Blast Cleaning**

Abrasive blast cleaning uses the action of abrasive particles suspended in a fluid (e.g., air or water) in order to remove surface contamination by mechanical action. Thus, abrasive particles are directed at high velocity against the blasted surface by means of compressed air, high-pressure water, or centrifugal force from an impeller wheel. As the surface removal rate can be controlled by choice of equipment, abrasive grit and blast parameters, all kinds of surfaces may be prepared including heavily rusted steel and concrete, as well as lightly contaminated surfaces.

##### **4.01.3.3.1 Surface finish**

Surface 'finish' commonly means surface cleanliness. It is important to remember that cleanliness refers not only to the degree of residual rust present, but also to the level of surface chemical contamination from soluble salts and from condensed moisture layers, all of which will detrimentally affect coating adhesion and ultimate performance.

##### **4.01.3.3.2 Surface profile**

Blast-cleaning produces a roughened surface, the size and nature of which is largely determined by the type and size of the abrasive used. The nature of the profile is important, especially for application of organic coatings (paints) and for thermally sprayed metal coatings. This is because the profile acts to aid the mechanical 'keying' of the coating to the surface and, hence, greatly increases coating adhesion. Likewise, the peak-to-trough profile roughness should not be excessive as this causes rogue peaks from the substrate to penetrate beyond the coating surface. Finally, profiles should be relatively open as excessively compressed surfaces will contain pores and defects underneath the coating that can act as reservoirs for chemical contamination and certainly will prevent coating penetration to the complete surface.

#### **4.01.3.4 Ultrahigh Pressure Water Jetting**

Water jetting is a convenient method for light cleaning and washing of surfaces. However, if the pressure of the water is increased significantly, the fluid becomes capable of removing, with high efficiency, relatively loosely adherent materials on a surface, including organic coatings. Water jetting also leaves surfaces relatively free of soluble salt contamination, which is a considerable advantage. Because of the kinetic energy of the water droplets on hitting the blasted surface, ultrahigh pressure water jetting leaves a dry, slightly warm surface that is free of dust and which dries relatively quickly; therefore, repainting can be carried out without significant delay.

The recent trend is to increase pressures as less volume of water is used. Thus, ultrahigh pressure (>170 MPa) water jetting equipment is becoming preferred as disposal costs for contaminated water are reduced. Water jetting cannot change an existing surface profile; hence if this is inadequate, abrasive blasting is to be preferred. However, for surfaces that have an adequate abrasive blast profile, it is sufficient to merely remove the defective coating and water jetting can be a highly economical option to achieve this end.

#### **4.01.3.5 Health, Safety, and the Environment**

In all surface preparation methods, including chemical and mechanical cleaning options, health, safety and environmental concerns are essential. Organic solvents are toxic and clearly have high VOC levels while aqueous alternatives may still possess significant organic content; in both cases operator protection and chemical disposal need to be addressed adequately. Organic-free chemical cleaners are frequently highly corrosive (acidic or alkaline), and also require correct neutralization and disposal procedures. Mechanical cleaning operations contain their own danger, not the least of which is the safety of the operator; to this end correct operator training, especially for abrasive and water jetting operations, is essential. Finally, waste abrasive grit and paint are frequently contaminated by toxic heavy metals previously used as corrosion inhibitive pigments (i.e., lead, chromium, etc). Removal and disposal of such materials often require a special license and certainly require great care and attention to detail.

#### 4.01.4 Standards

Generally standards for surface preparation, especially for surfaces subsequently to be painted, use visual comparisons. In all such standards, some caution should be exercised because the color reproduction may vary from one copy to another.

Standards for degrees of surface rusting are described in ISO 8501-1 as follows:

- (a) Steel surface largely covered with adhering mill scale, but little if any rust.
- (b) Steel surface which has begun to rust and from which mill scale has begun to flake.
- (c) Steel surface on which the mill scale has rusted away or from which it can be scraped, but with slight pitting visible under normal vision.
- (d) Steel surface on which the mill scale has rusted away and on which general pitting is visible under normal vision.

Surface rust and millscale must be removed before surface protection is applied. Where this is done by abrasive blasting, standards of surface cleanliness are also described in ISO 8501-1 and are on the basis of the original Swedish SIS 05 5900:

- Sa 1: Light blast cleaning.
- Sa 2: Thorough blast cleaning.
- Sa 2½: Very thorough blast cleaning.
- Sa 3: Blast cleaning to visually clean steel.

The minimum standard that is normally accepted for organic coating of steel structures is the Sa 2½ grade, which is generally achievable in the field using hand-held equipment. Sa 3, which is effectively blasting to white metal, can be achieved using modern automated shot-blast plant under factory conditions.

#### References

1. Pfeil, L. B. *J. Iron Steel Inst.* **1931**, 123, 237.
2. Freiner, W. W.; Growcock, F. B. *Corrosion* **1984**, 40, 663.
3. Rozenfeld, I. L. *Corrosion Inhibitors*; McGraw-Hill, 1981.
4. Gorichev, I. G.; Klyuchnikov, N. G.; Bibikova, Z. P.; Boltovskaya, I. G. *Russ. J. Phys. Chem.* **1976**, 50.
5. Gorichev, I. G.; Gorsheneva, V. F.; Boltovskaya, I. G. *Russ. J. Phys. Chem.* **1979**, 53, 1293.
6. Petch, N. J.; Stables, P. *Nature (London)* **1952**, 169, 842.
7. Morlet, J. G.; Johnson, H. H.; Troiano, A. R. *J. Iron Steel Inst.* **1958**, 189, 37.
8. Spencer, L. F. *Metal Finish.* **1954**, 52(2), 54.
9. Roberts, W. J. In *Cleaning Stainless Steel*; ASTM Special publ. 538, 1972; p 77.
10. Blume, W. J. In *Cleaning Stainless Steel*; ASTM Special publ. 538, 1972; p 43.
11. Schmitt, G. *Br. Corros. J.* **1984**, 19, 165.
12. Gardner, G. In *Corrosion Inhibitors*; Nathan, C. C., Ed.; NACE, 1973; p 156.
13. Cumper, C. W. N.; Grzeskowiak, R.; Newton, P. *Corros. Sci.* **1982**, 22, 551.
14. Riggs, O. L.; Hurd, R. M. *Corrosion* **1968**, 24, 45.
15. Clarke, S. G. *Trans. Electrochem. Soc.* **1936**, 69, 131.

#### Further Reading

Hudson, R. *Guide to Good Practice in Corrosion Control: Surface Preparation for Coatings*; National Corrosion Service, National Physical Laboratory: UK, 2000.  
 Freeman, D. B. *Phosphating and Metal Pre-treatment*; Woodhead, 1986.  
 Plaster, H. S. *Blast Cleaning and Allied Processes*; Industrial Newspapers, 1972/1973; Vol. I/II.

#### Relevant Websites

[www.waterjetting.org.uk](http://www.waterjetting.org.uk) – Water Jetting Association.  
[www.sspc.org](http://www.sspc.org) – Steel Structures Painting Council/Society for Protective Coatings (SSPC).

#### Standards

Swedish Standard SIS 05 5900: "Pictorial surface preparation standards for painting steel surfaces"  
 BS 7079:2009: "General introduction to standards for preparation of steel substrates before application of paints and related products"  
 BS EN ISO 8501: "Preparation of steel substrates before application of paints and related products: Visual assessment of surface cleanliness"  
 BS EN ISO 8502: "Preparation of steel substrates before application of paints and related products: Tests for the assessment of surface cleanliness"  
 BS EN ISO 8503: "Preparation of steel substrates before application of paints and related products: Surface roughness characteristics of blast-cleaned steel substrates"  
 BS EN ISO 8504: "Preparation of steel substrates before application of paints and related products: Surface preparation methods"  
 BS EN ISO 11124: "Preparation of steel substrates before application of paints and related products: Specifications for metallic blast-cleaning abrasives"  
 BS EN ISO 11125: "Preparation of steel substrates before application of paints and related products: Test methods for metallic blast-cleaning abrasives"  
 BS EN ISO 11126: "Preparation of steel substrates before application of paints and related products: Specification for nonmetallic blast-cleaning abrasives"  
 BS EN ISO 11127: "Preparation of steel substrates before application of paints and related products: Test methods for nonmetallic blast-cleaning abrasives"  
 BS ISO 27831: "Metallic and other inorganic coatings: Cleaning and preparation of metal surfaces"

## 4.02 Phosphate Coatings

**M. O. W. Richardson**

University of Loughborough, Loughborough, Leicestershire, UK

**R. E. Shaw**

ICI Paints, UK

This article is a revision of the Third Edition article 15.2 by M. O. W. Richardson and R. E. Shaw, volume 2, pp 15:22–15:37, © 2010 Elsevier B.V.

4.02.1	Introduction	2494
4.02.2	Phosphate Coating Formation	2495
4.02.2.1	Deposition Mechanism	2495
4.02.2.2	Accelerators	2496
4.02.3	Nature of Coatings	2496
4.02.3.1	Types of Coating	2496
4.02.3.2	Effect of Metal Surface	2497
4.02.3.3	Effect of Phosphate Solution	2497
4.02.3.4	Composition and Structure	2498
4.02.3.5	Post-phosphating Treatment: Rinses	2499
4.02.4	Performance	2499
4.02.4.1	Corrosion Protection	2499
4.02.4.2	Testing	2500
4.02.4.3	Phosphophyllite–Hopeite Ratio	2501
References		2501

### Glossary

**Diacetone alcohol** 4-Hydroxy-4-methyl-2-pentanone:  $(\text{CH}_3)_2\text{C}(\text{OH})\text{CH}_2\text{COCH}_3$

**Hopeite** Hydrated zinc phosphate of composition:  $\text{Zn}_3(\text{PO}_4)_2 \cdot 4\text{H}_2\text{O}$

**Hureaulite** Hydrated manganese iron phosphate of composition:  $(\text{Mn,Fe})_5(\text{PO}_4)_4 \cdot 4\text{H}_2\text{O}$

**Phosphophyllite** Hydrated iron–zinc phosphate of composition:  $\text{FeZn}_2(\text{PO}_4)_2 \cdot 4\text{H}_2\text{O}$

**Scholzite** Hydrated zinc calcium phosphate of composition:  $\text{CaZn}_2(\text{PO}_4)_2 \cdot 2\text{H}_2\text{O}$

**Vivianite** Hydrated iron phosphate of composition:  $\text{Fe}_3(\text{PO}_4)_2 \cdot 8\text{H}_2\text{O}$

### Abbreviations

**BS** British Standard

**BSTSA** British Surface Treatment Suppliers Association

**EN** European Norm

**ISO** International Standards Organisation

**Me** In a chemical equation, represents the metal ion (e.g., Fe, Zn, Mn, etc.).

### 4.02.1 Introduction

Phosphate treatments are readily adaptable to production requirements for articles of all sizes, and for large or small numbers. Mild steel sheet is the material most frequently subjected to phosphate treatment, but a great variety of other ferrous surfaces is also processed. Examples include cast-iron plates and piston rings, alloy steel gears, high-carbon steel cutting tools, case-hardened components, steel springs and wire, powdered iron bushes and gears, etc. Phosphate treatments designed for steel can also be used for the simultaneous treatment of zinc die-castings, hot-dipped zinc, and zinc-plated articles. However, if there is a large quantity of these nonferrous articles, it is often more economical to phosphate them without the steel. Aluminum articles may also be phosphated; however, these require somewhat different bath chemistries.

The usual method of applying phosphate coatings is by immersion, using a sequence of tanks that includes degreasing and phosphating stages, with their respective rinses. The treatment time ranges from 3 to 5 min for thin zinc phosphate coatings and up to 30–60 min for thick zinc, iron, or manganese phosphate coatings. The accelerated zinc phosphate processes lend themselves to application by power



spray, and the processing time may then be reduced to 1 min or less. Power spray application is particularly advantageous for mass-production articles such as motorcars and refrigerators, as the conveyor can run straight through the spray tunnel, which incorporates degreasing, rinsing, phosphating, rinsing, and drying stages. Flow-coating and hand spray-gun application are sometimes employed when a relatively small number of large articles have to be phosphated.

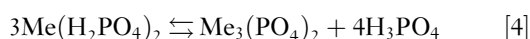
## 4.02.2 Phosphate Coating Formation

### 4.02.2.1 Deposition Mechanism

All conventional phosphate coating processes are based on dilute phosphoric acid solutions of iron, manganese, and zinc dihydrogen phosphates either separately or in combination. The free phosphoric acid in these solutions reacts with the iron surface undergoing treatment in the following manner<sup>1</sup>:



Thus, ferrous dihydrogen phosphate is produced and hydrogen is liberated. Local depletion of phosphoric acid occurs at the metal-solution interface. As the dihydrogen phosphates of iron, manganese, and zinc dissociate readily (i.e., are soluble) in aqueous solution, the following reactions take place:



The neutralization of free phosphoric acid by reaction [1] alters the position of equilibrium of equations [2]–[4] towards the right and thereby leads to the deposition of the sparingly soluble hydrogen phosphates and insoluble phosphates on the metal surface.

As reaction [1] takes place even when the phosphating solution contains zinc or manganese phosphate with little or no dissolved iron, it will be seen that the simple (or nonaccelerated) phosphate treatment gives coatings that always contain iron phosphate derived from the ferrous parts being processed. After prolonged use, a manganese phosphate bath often contains more iron in solution than manganese and produces coatings with an iron content 2–3 times that of manganese.

The relation between free phosphoric acid content and total phosphate content in a processing bath, whether based on iron, manganese, or zinc, is very

important; this relation is generally referred to as the acid ratio. An excess of free acid will retard the dissociation of the dihydrogen and hydrogen phosphates and hinder the deposition of the insoluble phosphate coating; sometimes excessive loss of metal takes place and the coating is loose and powdery. When the free acid content is too low, dissociation of phosphates takes place in the solution as well as at the metal/solution interface and leads to precipitation of insoluble phosphates as sludge. Nonaccelerated processes operated near boiling generally work best with a free-acid titration between 12.5% and 15% of the total acid titration.

A zinc phosphate solution tends to produce coatings more quickly than iron or manganese phosphate solutions, and dissociation of zinc dihydrogen phosphate proceeds rapidly through reaction [2] to [3] or directly to zinc phosphate via reaction [4]. Even so, a processing time of 30 min is usual with the solution near boiling. Another factor in the initiation of the phosphate coating reaction is the presence in the processing solution of phosphate, either as a colloidal suspension or as fine particles.<sup>2</sup> This effect is most apparent in zinc phosphate solutions, which produce good coatings only when turbid. The zinc phosphate particles can be present to a greater extent in cold processing solutions and may act as nuclei for the growth of many small crystals on the metal surface, thereby promoting the formation of smoother coatings.

Similarly, the ferric phosphate sludge formed during the processing of steel in a zinc phosphate solution can play a useful part in coating formation.<sup>3</sup> The solubility of ferric phosphate is greater at room temperature than at elevated temperatures, and is increased by the presence of nitrate accelerators. To allow for saturation at all temperatures, it is desirable always to retain some sludge in the processing bath. Coatings with optimum corrosion resistance are produced when the temperature of the bath is rising and causing supersaturation of ferric phosphate.

With zinc/iron/phosphate/nitrate baths, the iron content of the coating comes predominantly from the processing solution and very little from the surface being treated.<sup>4</sup> This greatly diminished attack on the metal surface by accelerated baths has a slight disadvantage in practice in that rust is not removed, whereas the vigorous reaction of the nonaccelerated processes does remove light rust deposits. The solution of iron represented in eqn [1] takes place at local anodes of the steel being processed, while discharge of hydrogen ions with simultaneous dissociation and deposition of the metal phosphate takes place at the

local cathodes.<sup>1</sup> Thus, factors that favor the cathode process will accelerate coating formation and, conversely, factors favoring the dissolution of iron will hinder the process.

Application of a cathodic potential to the treated surface exerts an accelerating action, as the reaction at all cathodic areas is assisted and the formation of a phosphate layer is speeded accordingly. Conversely, an anodic potential results in the dissolution of iron at local anodes and hinders phosphate coating formation. An oxidizing agent acts as an accelerator by depolarization of the cathodes, raising the density of local currents so that rapid anodic passivation of active iron in the pores takes place. This inactivation of local anodes favors the progression of the cathodic process. The accelerating effect of alternating current is explained by the practical observation that the cathodic impulse acting protectively greatly exceeds in its effect the anodic impulse which dissolves iron. In a similar manner, the electrolytic pickling of iron with alternating current can dissolve iron at a slower rate than when no current is used.

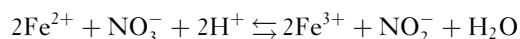
Reducing agents have the same ultimate effect as cathodic depolarization in that they convert anodic regions into cathodic regions and increase the ratio of cathodic to anodic areas. Nitrogenous organic components such as toluidine, quinoline, aniline, etc. all act as inhibitors to the anodic reaction between metal and acid and thereby favor the cathodic reaction and accelerate the process.

#### 4.02.2.2 Accelerators

The majority of phosphate processes in use are 'accelerated' to obtain shorter treatment times and lower processing temperatures. The most common mode of acceleration is by the addition of oxidizing

agents such as nitrate, nitrite, chlorate, and hydrogen peroxide. By this means, a processing time of 1–5 min can be obtained at temperatures of 45–70 °C. The resultant coatings are much smoother and thinner than those from nonaccelerated processes, and, while the corrosion resistance is lower, they cause less reduction of paint gloss and are more suited to mass-production requirements.

The presence of nitrate as accelerator has a pronounced effect on the amount and composition of gas evolved from the work being treated<sup>1</sup> (Table 1). It will be observed that hydrogen evolution drops to a very low figure with the zinc/nitrate baths. The formation of nitrite arises from the oxidation of ferrous ion by nitrate leading to ferric ions, which will then deposit out as ferric phosphate:



In acid solution, the nitrite ion acts as an oxidizing agent. A slight degree of acceleration can be obtained by introducing traces of metals which are more noble than iron, for example nickel, copper, cobalt, and silver. These metals are deposited electrochemically over the iron surface undergoing treatment, thereby providing more active cathodic centers and promoting phosphate deposition. This method of acceleration has the disadvantage of leaving minute particles of the noble metal in the coating, and, in the case of copper, this can seriously inhibit the drying of some types of paint coatings.

#### 4.02.3 Nature of Coatings

##### 4.02.3.1 Types of Coating

Although there is a limited number of phosphate coating types, there are many specific bath compositions

**Table 1** Amount and composition of the gases evolved on phosphating of 1 m<sup>2</sup> of sheet metal for deep drawing

Phosphate solution	Pointage <sup>a</sup>	Time (min)	Amount of gas (cm <sup>3</sup> m <sup>2</sup> )	H <sub>2</sub> (%)	N <sub>2</sub> (%)	O <sub>2</sub> (%)	N <sub>2</sub> O + NO (%)
Manganese phosphate	30	60	7000	87.5	11.4 <sup>b</sup>	1.1	–
Zinc phosphate	40	30	2540	92.7	6.4 <sup>b</sup>	0.9	–
Manganese phosphate (accelerated with nitrate)	30	15	3500	84.6	9.1	1.3	3.0
Zinc phosphate (accelerated with nitrate)	70	5	78	16.7	75.3	8.0	–
Zinc phosphate containing 1.5–2 g l <sup>-1</sup> iron (accelerated with nitrate)	70	5	85	32.1	57.0	1.6	9.3

<sup>a</sup>A measure of the total of a phosphating solution, as indicated by the number of ml of 0.1 N sodium hydroxide (4.0 g l<sup>-1</sup>) needed to neutralise 10 ml of the phosphating solution to phenolphthalein.

<sup>b</sup>Presumably from anrides present in the steel.

that have been formulated for optimization of particular applications and processes.<sup>5</sup> Lightweight amorphous iron phosphates provide excellent paint adhesion and are of low cost; however, the corrosion resistance is relatively poor. Lightweight (microcrystalline) zinc phosphate coatings offer higher corrosion resistance while still retaining very good adhesion for organic coatings. Heavy macrocrystalline zinc phosphates are used in applications such as fastener coatings or wire and tube drawing aids. Where used in this fashion, the coating provides excellent adhesion and a slightly porous surface that can act as a reservoir for drawing lubricants such as soaps and/or oils. Likewise, heavy-weight manganese-iron phosphates and calcium-zinc phosphates may be used to reduce galling on mating surfaces such as valve train components or hypoid gears. These coatings have good oil absorbing properties and provide good corrosion resistance when used with a rust-preventing oil. Military ordnance components are often finished by this method. **Table 2** provides a summary of some types and applications of phosphate coatings.

#### 4.02.3.2 Effect of Metal Surface

The state of the metal surface has a pronounced effect on the texture and nature of phosphate coating produced by orthodox processes. Heavily worked surfaces tend to be less reactive and lead to patchy coatings. Surface abrasive blasting greatly simplifies treatment and gives uniform phosphate coatings. Accidental contamination of sheet steel with lead has been shown to have an adverse effect on the corrosion resistance and durability of phosphate coatings and paint.<sup>6</sup>

Cleaning operations that make use of strong acids or strong alkalis tend to lead to the formation of

excessively large phosphate crystals which do not completely cover the metal surface and therefore show inferior corrosion resistance; this is particularly serious if rinsing is inadequate between the preparatory treatment and the phosphating. Adherent dust particles can also lead to the formation of relatively large phosphate crystals, whereas surfaces that have been wiped beforehand show much smoother and more uniform phosphate coatings.

On the other hand, the provision of vast numbers of minute nuclei assists the phosphate coating reaction to start at a multitude of centers, resulting in a finely crystalline coating. This effect can be obtained chemically by a predip in a solution of sodium phosphate containing minutely dispersed traces of titanium or zirconium salts<sup>7</sup> or in weak solution of oxalic acid. This type of predip entirely eliminates any coarsening effect due to previous treatment in strong alkalis or acids.

#### 4.02.3.3 Effect of Phosphate Solution

Improved nucleation within the phosphate solution itself can produce smoother coatings without the necessity of recourse to preliminary chemical treatment. This may be accomplished by introducing into the phosphating bath the sparingly soluble phosphates of the alkaline-earth metals or condensed phosphates such as sodium hexametaphosphate or sodium tripolyphosphate. Such modified phosphating baths produce smoother coatings than orthodox baths and are very much less sensitive to cleaning procedures.

Very thin coatings of iron phosphate can be produced by treatment with solutions of alkali-metal phosphate. These serve a useful purpose for the treatment of office furniture, toys, etc. where a high

**Table 2** Types of phosphate coating

Type	Mineral name	Formula	Coating weight ( $\text{g m}^{-2}$ )	Appearance
Lightweight iron phosphate	Vivianite	$\text{Fe}_3(\text{PO}_4)_2 \cdot 8\text{H}_2\text{O}$	0.3–0.9	Iridescent pink/yellow/blue to light gray
Microcrystalline zinc phosphate	Hopeite or phosphophyllite	$\text{Zn}_3(\text{PO}_4)_2 \cdot 4\text{H}_2\text{O}$ ; $\text{FeZn}_2(\text{PO}_4)_2 \cdot 4\text{H}_2\text{O}$	1.4–2.7	Light gray
Macrocrystalline zinc phosphate	Hopeite or phosphophyllite	$\text{Zn}_3(\text{PO}_4)_2 \cdot 4\text{H}_2\text{O}$ ; $\text{FeZn}_2(\text{PO}_4)_2 \cdot 4\text{H}_2\text{O}$	7.5–30	Light gray
Manganese iron phosphate	Hureaulite	$(\text{Mn,Fe})_5(\text{PO}_4)_4 \cdot 4\text{H}_2\text{O}$	7.5–30	Dark gray to black
Calcium zinc phosphate	Scholzite	$\text{CaZn}_2(\text{PO}_4)_2 \cdot 2\text{H}_2\text{O}$	1.6–6.5	Light gray

Source: British Surface Treatment Suppliers Association, Technical Brochure: "Metal pre-treatment." Available for download from <http://www.bstsa.org.uk>.

degree of protection is not required, and also as a base for phenolic varnishes or resin varnishes requiring high temperature curing, for example, at over 200 °C. The coating is of heterogeneous nature and contains less than 35% iron phosphate ( $\text{FePO}_4 \cdot 8\text{H}_2\text{O}$ ) with the remainder probably  $\gamma\text{-Fe}_2\text{O}_3$ .<sup>8</sup>

Thin phosphate coatings can be formed by application of phosphoric acid solution alone, that is, not containing metallic phosphates, to a steel surface, sufficient time being allowed after application to enable complete reaction to take place. In this way, a thin film of iron phosphate can be formed. In practice, it is difficult to obtain complete conversion, and the remaining traces of phosphoric acid can cause blistering of paint coatings. This effect may be insignificant on rough, absorbent steel surfaces, for example, ship's plating, where heavy coats of absorbent paint are applied, and under these circumstances the treatment can enhance the corrosion resistance of the finishing system.

#### 4.02.3.4 Composition and Structure

The simplest phosphate coating that is formed from a solution containing only ferrous phosphate and phosphoric acid consists of dark gray to black crystals of ferrous phosphate,  $\text{Fe}_3(\text{PO}_4)_2$  and ferrous hydrogen phosphate,  $\text{FeHPO}_4$ , with a small proportion of ferric phosphate,  $\text{FePO}_4$ . Coatings formed from manganese phosphate solutions consist of  $\text{Mn}_3(\text{PO}_4)_2$ , and those from zinc phosphating solutions consist of  $\text{Zn}_3(\text{PO}_4)_2$ . With both the manganese and zinc type of coating, insoluble iron phosphates, derived from iron present in the bath, may also be present in solid solution. Iron from the surface being treated can also be present in the coating, particularly at the metal-phosphate interface. The  $\text{PO}_4^{3-}$  content of coatings may vary from 33% to 50%, whereas the theoretical  $\text{PO}_4^{3-}$  content is lowest, at 41%, in  $\text{Zn}_3(\text{PO}_4)_2 \cdot 4\text{H}_2\text{O}$  and highest, at 63%, in  $\text{FePO}_4$ .

X-ray diffraction studies have given very good correlation between the mineral hopeite,  $\text{Zn}_3(\text{PO}_4)_2 \cdot 4\text{H}_2\text{O}$ , and the zinc phosphate coatings that form on steel.<sup>9</sup>  $\text{Zn}_3(\text{PO}_4)_2 \cdot 4\text{H}_2\text{O}$  appears in three crystal forms:  $\alpha$ -hopeite (rhombic plates),  $\beta$ -hopeite (rhombic crystals), and  $\delta$ -hopeite (triclinic crystals). Their transition points are at 105, 140, and 163 °C, respectively. It has been observed<sup>10</sup> that zinc phosphate coatings heated in the absence of air lose their corrosion resistance at between 150 and 163 °C probably due to disruption in coating integrity due to the volume changes arising from the phase change. Likewise, manganese phosphate coatings lose their corrosion

resistance at between 200 and 218 °C, where they lose between 75 and 80% of their water of hydration. It is assumed that this results in a volume decrease of the coating which causes voids and thereby lowers the corrosion resistance. Figure 1 shows the loss of water of hydration from zinc, iron, and iron-manganese phosphate coatings.

The heating of phosphate coatings in the absence of air provides conditions similar to those prevailing during the stoving of paint on phosphated articles, but in general the paint stoving temperatures and times are well below those at which damage to zinc phosphate coatings takes place. The loss of water from conventional zinc and manganese phosphate coatings heated in air is from 10 to 20% higher than the loss on heating in the absence of air. It is thought that this greater loss may be due to oxidation of the iron phosphate present in the coatings.

The most important uses for phosphate coatings entail sealing with oil or paint and it is therefore of interest to study absorption values. Table 3 compares the absorption of diacetone alcohol into coatings of widely differing thicknesses and composition; despite these differences, values of 10.5–13  $\text{g m}^{-2}$  are obtained throughout. It is therefore evident that absorption is predominantly a surface effect and not appreciably influenced by coating thickness.

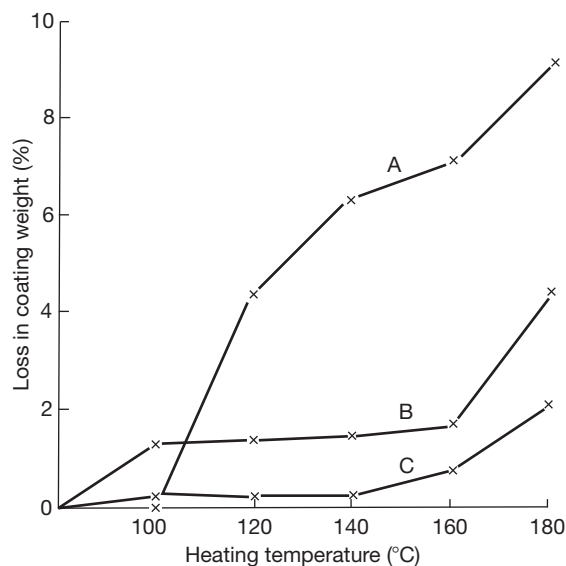


**Figure 1** Effect of heating on phosphate coatings for 16 h at various temperatures, showing loss of water of hydration: (a) zinc phosphate; (b) iron phosphate, and (c) iron manganese phosphate. Reproduced from B.S.I. Phosphate Coatings (Drafting) Panel, *J. Iron Steel Inst.* 1952, 170, 13.

**Table 3** Analytical tests on industrial phosphate coatings

Process <sup>a</sup>	P	S	T	Q	V	R
Main cation in phosphate bath	Fe	Mn	Zn	Zn	Zn	Zn
Method of application	Immersion	Immersion	Spraying	Immersion	Immersion	Immersion
Duration of treatment (min)	15	30	1.5	4	5	12
Change in weight on phosphating ( $\text{g m}^{-2}$ )	-26.1	-26.4	2.61	3.37	1.63	5.87
Coating weight ( $\text{g m}^{-2}$ )	14.2	21.2	4.46	5.43	3.48	12.28
$\text{PO}_4^{3-}$ ( $\text{g m}^{-2}$ )	7.0	8.9	1.96	2.07	1.20	4.46
Moisture ( $\text{mg m}^{-2}$ )	81.5	76.1	152.2	396.6	173.9	771.7
$\text{PO}_4^{3-}$ content of coating (%)	49.0	42.0	44.0	38.0	34.0	36.0
Moisture content of coating (%)	0.6	0.4	3.4	6.9	5.0	6.4
Hygroscopicity of coating (%)	0.3	0.2	1.2	1.3	1.0	1.5
Absorption value (diacetone alcohol ( $\text{g m}^{-2}$ ))	11.4	10.9	10.9	13.04	10.87	11.96

<sup>a</sup>The letters used for designation indicate proprietary process.

Data reproduced courtesy of the *Journal of the Iron and Steel Institute*, 1952, 170, 11.

#### 4.02.3.5 Post-phosphating Treatment: Rinses

After phosphating, thorough rinsing with water is necessary in order to remove soluble salts which would otherwise tend to promote blistering under a paint film. Care should also be taken to ensure that the water supply itself is sufficiently free from harmful salts. Experience has shown that a water supply is potentially injurious if it exceeds any one of the three following limits:

1. 70 ppm total chlorides and sulfates (calculated as  $\text{Cl}^- + \text{SO}_4^{2-}$ );
2. 200 ppm total alkalinity (calculated as  $\text{CaCO}_3$ ); and
3. a maximum of 225 ppm of (1) and (2) together.

Improved corrosion resistance and reduced tendency to blistering was traditionally obtained by treating the final rinse with chromic acid, or preferably with phosphoric and chromic acids combined. Normally, a total acid content of 0.05% was used, with higher concentrations of chromate increasing corrosion resistance. However, legislation restricting the use of chromates has now eliminated this practice. The use of demineralized water for rinsing purposes is recommended, especially before electrophoretic painting, as this practice reduces residual surface contamination. The demineralized water is generally applied by misting jets at the end of all other pretreatment stages and allowed to flow back into the last rinse tank. In certain cases, rinsing may be dispensed with after nonaccelerated phosphate treatment, but blistering of

paint due to local concentration of solution in seams and crevices may occur. Thus, it is good practice to employ rinsing, regardless of the type of phosphate process.<sup>11</sup>

#### 4.02.4 Performance

##### 4.02.4.1 Corrosion Protection

The corrosion protection provided by phosphate coatings without a sealing treatment is of a low order; their value when sealed is considerably greater. Unsealed corrosion tests are therefore of little value except perhaps for studying porosity or efficiency of coatings destined to be sealed only with oil. It is usually necessary to control the acid ratio of phosphating baths, particularly those of iron, manganese, and zinc operating near boiling point that produce heavy coatings. The best performing coatings are obtained when the free acidity is maintained between 12.5% and 15%; above this figure, coatings with progressively lower corrosion resistance are obtained. Note that heavy, that is, thicker phosphate coatings do not necessarily have better corrosion resistance than lighter coatings. Even with a single process, for example, zinc/iron/phosphate/nitrate, no consistent relationship has been found between corrosion resistance and either coating weight or weight of metal dissolved. Jaudon<sup>12</sup> tested phosphate coatings and found the salt-spray resistance, as judged by the first appearance of rust, while only a few minutes for base steel, was around a few hours for phosphated steel.



**Table 4** Typical phosphate coating processes

<i>Phosphate coating solution</i>	<i>Accelerator</i>	<i>Immersion time (min)</i>	<i>Type of coating</i>	<i>Coating weight (g m<sup>-2</sup>)</i>
Iron	None	30	Heavy	10.87–32.61
Iron/manganese	None	30	Heavy	10.87–32.61
Manganese	Nitrate	15	Heavy	8.70–32.61
Zinc	Nitrate	15	Medium	3.26–32.61
Zinc	Nitrate/nitrite or chlorate	3	Light	1.09–6.52
Sodium/ammonium	None	1–2 (spray)	Very light	0.22–0.65

Phosphating prior to painting doubled the observed time to first rusting.

Phosphate processes containing little or no oxidizing agent and based on manganese or zinc tend to accumulate iron in solution from the work being processed. With a manganese content from 0.2% to 0.5%, it is best to control the iron between 0.2% and 0.4%; a higher iron content reduces the corrosion resistance and may lead to the formation of thin powdery coatings, while a lower iron content gives soft coatings. Similarly, a zinc process operates best with 0.15–0.5% zinc and 0.4–0.5% iron. Again, with a higher iron content corrosion resistance falls off and powdery coatings may be formed, and soft coatings result from lower iron content.

Within broad limits, phosphate processes can be classified according to the main metallic radical of the processing solution and the type of accelerator used; typical processes are given in [Table 4](#). The selection of process and of coating weight is mainly dependent on the end-use of the article being processed; the general requirements for corrosion resistance and wear prevention are given in [Table 5](#).

#### 4.02.4.2 Testing

Heavy phosphate coatings are generally used as protection against corrosion in conjunction with a sealing film of oil or grease. The porosity or free pore area of these coatings should be kept to a minimum. Machu<sup>13</sup> devised a method of examination based on the quantity of electricity necessary to effect passivation of the bare steel and used this to determine the free pore area which, in the phosphate coatings tested, varied from 0.27% to 63%; however, this method is insufficiently sensitive to evaluate thin zinc phosphate coatings. A method for making rapid measurements of the electrical resistance of phosphate coatings has been described by Scott and Shreir.<sup>14</sup>

The most widely used accelerated tests are based on salt spray, whose main value is in the evaluation of

**Table 5** Typical uses of phosphate coatings on steel

<i>Coating weight (g m<sup>-2</sup>)</i>	<i>For corrosion resistance</i>	<i>For wear prevention and metal forming</i>
21.74–32.61	–	Critical cold extrusion
10.87–21.74	Military equipment, etc. requiring oil or grease finish	Normal cold extrusion 'Running in' treatment for piston rings, gears and tappets
5.43–10.87	Nuts, bolts, clips, brackets	Wire and tube drawing Sheet steel pressing
2.17–2.72	Cars, refrigerators, washing machines	Light metal pressing
1.63–2.17	Steel drums, bicycles, office machinery	
0.22–0.65	Toys, office furniture Strip steel, for painting and forming	

the effectiveness of phosphate coatings in restricting the spread of rust from scratches or other points of damage in a paint film.<sup>15</sup> This feature is of particular interest to the automotive industry, as vehicles are often exposed to marine atmospheres and to moisture and salt when the latter is used to disperse ice and frost from road surfaces. Great care is needed in the interpretation of a salt-spray test, as it has been found to favor thin iron phosphate coatings more than is justified by experience with natural weathering. Humidity tests are generally of more practical use than salt-spray tests, particularly where painting is employed, as the thoroughness of rinsing may be checked by this means. The use of contaminated water can leave water-soluble salts in the phosphate

**Table 6** Weights of phosphate coatings

Class of phosphate process	Coating weight (g m <sup>-2</sup> )	
	Min.	Max.
A 1. Heavyweight (Mn or Fe)	7.61	–
A 2. Heavyweight (Zn)	7.61	–
B Medium weight (Zn, etc.)	4.34	–
C Lightweight (Zn, etc.)	1.09	4.34
D Extra lightweight (Fe)	0.33	1.09

Source: BS EN 12476: Phosphate conversion coatings of metals. Method of specifying requirements.

coating and lead to blistering of the paint film under humid conditions, as paint films are permeable to water vapor. Immersion in water, or subjection to high humidity in a closed cabinet, will generally show any defects of this kind within a few days.

Phosphate coating weight determinations are generally performed by dissolving the coating from weighed panels using inhibited acid (e.g., by immersion in a solution of 20 g dm<sup>-3</sup> of antimony trioxide in concentrated hydrochloric acid at a temperature of 13–21 °C. Thin iron or zinc phosphate coatings can be removed for weight determination by immersion in 5% chromic acid solution at 70 °C, but this solution should also be used only once, as the presence of more than a trace of phosphate leads to pitting of the steel and false results. Zinc phosphate coatings can be removed by immersion in 10% sodium hydroxide at boiling temperature, aided by rubbing during rinsing.

BS EN 12476 contains information on the operation of phosphate processes to obtain optimum results and on the testing of phosphate coatings.<sup>16</sup> The classification of coatings according to composition and weight is shown in Table 6. The inspection and testing includes determination of coating weight, freedom from corrosive residues as shown by a humidity test, and resistance to corrosion by salt spray. BS EN ISO 12944-1 is also a valuable source of information.<sup>17</sup>

#### 4.02.4.3 Phosphophyllite–Hopeite Ratio

There is evidence that the ratio of phosphophyllite to hopeite (the so-called P/(P + H) ratio) can be used as a predictive measure of the performance of phosphated steel when coated with cathodic electroprimer and paint.<sup>18,19,20,21</sup> In this context, P is defined as the intensity of X-rays diffracted from the (100) plane of phosphophyllite, FeZn<sub>2</sub>(PO<sub>4</sub>)<sub>2</sub>·4H<sub>2</sub>O, and H is defined as the intensity of X-rays diffracted from the (020) plane of hopeite, Zn<sub>3</sub>(PO<sub>4</sub>)<sub>2</sub>·4H<sub>2</sub>O,

and it has been suggested that higher values of this ratio (i.e., a low volume fraction of hopeite) are synonymous with good corrosion performance.<sup>18</sup> However, other factors to be considered include the need for homogeneous phosphate layers of controlled thickness, the direct attachment of the primer to a coherent layer, and the level of interlayer cohesion within the coating. Some papers<sup>21</sup> indicate that adhesion failure results from internal fracture of the phosphate coating and that it is concentrated at the junction between a primary microcrystalline or even amorphous layer close to the metal substrate and a secondary layer exhibiting relatively coarse crystallinity. The primary layer is comprised essentially of a zinc phosphate material, and the Zn/P ratio in the retained primary layer after fracture is lower than that in the detached material, though close enough to be considered essentially similar.

Finally, it is worth noting that the quality of the steel substrate can have an effect on the corrosion resistance promoted by any subsequent treatment by phosphating and painting. Indeed, it has been reported<sup>22</sup> that interesting results are obtained when cold-rolled steel panels, with different amounts of surface contamination, are zinc phosphated, then coated with anionic or cationic electrocoat primers, and followed by a conventional filler-topcoat system. In salt-spray, scab, and filiform corrosion tests, it is apparently possible to distinguish between different surface contamination levels and primer coatings. Carbonaceous residues on the steel can have a detrimental effect, and this can be confirmed in the case of anionic primer during salt-spray tests. In the scab corrosion and filiform corrosion tests, however, anionic primer performance actually increases with surface contamination. It can be concluded that the steel condition and the type of coating affect the corrosion resistance of the entire system by inducing changes in the phosphate layer. With the current low level of surface contamination of commercial steels and the highly resistant modern coating formulations, it is suggested<sup>22</sup> that the phosphate layer is the weakest link in the entire system.

## References

1. Machu, W. *Die Phosphatierung — Wissenschaftliche Grundlagen und Technik*; Verlag Chemie: Weinheim, 1950.
2. Wusterfeld, H. *Arch. Metallk* **1949**, 3, 233.
3. Determination of the solubility of ferric phosphate in phosphating solutions using radioiron, US Department of Commerce, Office of Technical Services, Rep. no. PB 111, 1953; p 399.

4. Radiometric study of phosphating problems, US Department of Commerce, Office of Technical Services, Rep. no. PB 111, 1951; p 396.
5. British Surface Treatment Suppliers Association, Technical Brochure: "Metal pre-treatment." Available for download from <http://www.bstsa.org.uk>.
6. Wirshing, R. J.; McMaster, W. D. *Can. Paint Varn. Mag.* **1956**, 30(5), 42, 55.
7. Jernstedt, G. *Chem. Eng. News* **1943**, 21, 710; *Trans. Electrochem. Soc.* **1943**, 83, 361.
8. A radiometric study of the iron phosphating process, US Department of Commerce, Office of Technical Services, Rep. no. PB 111, 1953; p 400.
9. X-ray diffraction study of zinc phosphate coatings on steel, US Department of Commerce, Office of Technical Services, Rep. no. PB 111, 1954, p 486.
10. Doss, J. *Org. Finish.* **1956**, 17(8), 6.
11. B.S.I. Phosphate Coatings (Drafting) Panel. *J. Iron Steel Inst.* **1952**, 170, 13.
12. Jaudon, E. *Peint.-Pigm.-Vernis.* **1949**, 25, 224.
13. Machu, W. *Korros, Metallsch.* **1944**, 20, 1.
14. Scott, J. W.; Shreir, L. L. *Chem. Ind. (Rev.)* **1957**, 807.
15. BS EN ISO 9227: Corrosion tests in artificial atmospheres: Salt spray tests.
16. BS EN 12476: Phosphate conversion coatings of metals. Method of specifying requirements.
17. BS EN ISO 12944-1: Paints and varnishes. Corrosion protection of steel structures by protective paint systems.
18. Miyawaki, T.; Okita, H.; Umehara, S.; Okabe, M. *Proc. Interfinish.* **1980**, 80, 303.
19. Richardson, M. O. W.; Freeman, D. B.; Brown, K.; Djaroud, N. *Trans. I.M.F.* **1983**, 61, 155.
20. Freeman, D. B.; Brown, K.; Richardson, M. O. W.; Tiong, H. *Finishing* **1984**, 27–28.
21. Cooke, B. A. Proceedings of the IX International Conference on Organic Science and Technology, Athens; 1983; pp 29–46.
22. Soepenbergh, E. N.; Vrijburg, H. G.; van Ooij, W. J.; Vries, O. T. The Influence of Steel Quality, Pretreatment and Coating Systems on the Corrosion of Automotive Steel, 1984; pp 381–393.

## Relevant Websites

<http://www.bstsa.org.uk> – British Surface Treatment Suppliers Association, Birmingham, UK.

## 4.03 Coatings Produced by Anodic Oxidation

**X. Zhou**

University of Manchester, Manchester, M13 9PL, UK

**P. G. Sheasby**

Alcan International, Banbury, UK

**B. A. Scott**

British Aluminium Company, UK

This article is a revision of the Third Edition article 15.1 by P. G. Sheasby and B. A. Scott, volume 2, pp 15:3–15:21,

© 2010 Elsevier B.V.

4.03.1	Practice of Anodizing	2504
4.03.2	Mechanism of Formation of Porous Oxide Coatings	2505
4.03.3	Properties of Coatings	2507
4.03.3.1	Composition	2507
4.03.3.2	Density	2508
4.03.3.3	Mechanical Properties	2508
4.03.3.3.1	Hardness	2508
4.03.3.3.2	Flexibility	2509
4.03.3.4	Electrical Properties	2509
4.03.3.5	Physical Properties	2509
4.03.3.6	Thermal Properties	2510
4.03.3.7	Optical Properties	2510
4.03.3.8	Effect of Anodizing on Mechanical Properties	2511
4.03.3.9	Measurement of Film Thickness	2511
4.03.4	Corrosion Resistance	2511
4.03.4.1	Atmospheric Exposure	2513
4.03.4.2	Maintenance	2513
4.03.5	Recent Developments	2514
4.03.5.1	Practice of Anodizing	2514
4.03.5.2	Mechanism of Anodizing	2515
4.03.5.3	Properties of Coatings	2516
4.03.5.4	Test Methods	2516
References		2516

### Glossary

**Barrier anodic film** An oxide coating deliberately formed on a valve metal (commonly aluminum) that is generally relatively featureless and provides an electrical and physical barrier to the bare metal surface.

**Porous anodic film** An oxide coating deliberately formed on a valve metal (commonly aluminum) that generally contains self-organized directional porosity; all porous anodic films are terminated by a form of barrier anodic film adjacent to the base metal surface.

**Plasma electrolytic oxidation** A process for anodizing that uses relatively high voltages that deliberately induce dielectric breakdown,

with associated sparking, on the treated component; also called micro-arc oxidation.

**Valve metal** An element from the group: aluminum, titanium, zirconium, hafnium, tungsten, niobium and tantalum. Such elements will develop protective oxide films when polarized anodically in a suitable electrolyte.

### Symbols

**MAO** Micro-arc oxidation

**PEO** Plasma electrolytic oxidation

**SHE** Standard Hydrogen Electrode

### 4.03.1 Practice of Anodizing

Anodic oxidation or anodizing, as applied to metallic surfaces, is the production of a coating, generally of oxide, on the surface by electrolytic treatment in a suitable solution, the metal being the anode. Although a number of metals,<sup>1</sup> including aluminum, magnesium, tantalum, titanium, vanadium and zirconium, can form such anodic films, only aluminum and its alloys, and to a lesser extent magnesium, are anodized on a significant commercial scale for corrosion protection.

The anodic oxidation of magnesium does not normally produce a film that has sufficient corrosion resistance to withstand exposure without further protection by painting, and the solutions used are complex mixtures containing phosphates, fluorides and chromates. In the case of aluminum, a relatively simple treatment produces a hard, compact, strongly adherent film of oxide, which affords considerably increased protection against corrosive attack.<sup>2,3</sup>

A further advantage of this process lies in the decorative possibilities of the oxide film, which may be almost completely transparent on very high purity aluminum (99.99% Al) and certain alloys based on this purity, and thus protects the surface without obscuring its polish or texture. On metal of lower purity, and other alloys, the oxide layer may become slightly milky, or colored grey or yellowish, although the deterioration is hardly apparent with purities down to 99.7–99.8% Al. The appearance and character of the film may also be influenced by the type of anodizing treatment, and the oxide film may be dyed to produce a wide range of colored finishes. Anodizing characteristics of a number of aluminum alloys are listed by Wernick and Pinner.<sup>3</sup> The anodizing procedures in general use are shown in Table 1, sulfuric acid being the most commonly used electrolyte. Treatment time is 15 min to 1 h.

The articles to be anodized should be free from crevices where the acid electrolyte can be trapped. They may be given a variety of mechanical and chemical pretreatments, including polishing, satin-finishing, etching, etc. but before anodizing, the surface must be clean and free from grease and polishing compound.

After the anodic treatment, the work is removed from the tank and carefully swilled with cold water to remove all traces of acid. At this stage, the anodic film is absorptive, and care should be taken to avoid contamination with oil or grease, particularly if the work is to be dyed. Dyeing may be carried out by immersion for about 20 min in an aqueous solution of the dyestuff at a temperature of 50–60 °C. Inorganic pigments may also be incorporated in the oxide layer by a process involving double decomposition. Finally, both dyed and undyed work are sealed by treatment in boiling water (distilled or deionized) or steam, which enhances the corrosion resistance and prevents further staining or leaching of dye. Solutions of metal salts, for example nickel or cobalt acetates, are often used to seal work after dyeing. Traditionally sealing in 5–10% dichromate solution, which gives the coating a yellow color, was used to impart the highest degree of corrosion resistance. However, the use of chromates is being increasingly phased out due to environmental concerns.<sup>4</sup>

In the architectural field, use is being made of integral color anodizing which is capable of producing self-colored films in a number of fade-resistant tints ranging from gray, through bronze and brown, to a warm black. The electrolytes are developments of the oxalic acid solution and consist of various dibasic organic acids, such as oxalic, malonic or maleic, or sulfonated organic acids such as sulfosalicylic acid, together with a small proportion of sulfuric acid. For constant and reproducible results, a close analytical control of the electrolyte must be maintained, particularly with respect to aluminum which dissolves as

**Table 1** Traditional anodizing processes for aluminum (the chromic acid treatment is historic and is being increasingly phased out)

<i>Electrolyte</i>	<i>Temperature (°C)</i>	<i>Applied voltage (V)</i>	<i>Current density (A m<sup>-2</sup>)</i>	<i>Film thickness (μm)</i>	<i>Appearance</i>
5–10% sulfuric acid	17–22	12–24	110–160	3–25	Transparent: colorless to milky
3–10% chromic acid	30–45	30–45	30–35	2–8	Opaque: light to dark gray
2–5% oxalic acid	20–35	30–60	110–215	10–60	Transparent: light yellow to brown



treatment proceeds, and ion-exchange resins are frequently used to regenerate the relatively expensive electrolyte and keep the aluminum in solution between controlled limits. Some typical color anodizing treatments are summarized in **Table 2**.

Alloys are generally of the Al–Mg–Si type with additions of copper and chromium or manganese. Color varies with the particular alloy and the film thickness. For optimum control of color, the alloy must be carefully produced with strict attention to composition, homogenization and heat-treatment, where appropriate, and the anodizing conditions must be maintained within narrow limits. It is usual to arrange matters, preferably with automatic control, such that current density is held constant with rising voltage up to a selected maximum, after which voltage is held steady; the whole cycle being for a fixed time. Refrigeration of the electrolyte may be necessary to maintain the temperature at the working level, owing to the relatively high wattage dissipation.

Hard anodic films, 50–100  $\mu\text{m}$  thick, for resistance to abrasion and wear under conditions of slow-speed sliding, can be produced in sulfuric acid electrolytes at high current density and low temperature.<sup>5–7</sup> Current densities range from 250 to 1000  $\text{A m}^{-2}$ , with or without superposed alternating current in 20–100  $\text{g l}^{-1}$  sulfuric acid at  $-4$  to  $10^\circ\text{C}$ . Under these conditions, special attention must be paid to the contact points to the article under treatment, in order to avoid local overheating.

The films are generally dark in color and often show a fine network of cracks due to differential expansion of oxide and metal on warming to ambient temperature. They are generally left unsealed, since sealing markedly reduces abrasion resistance, but may be impregnated with silicone oils<sup>8</sup> to improve the frictional properties. Applications include movable instrument parts, pump bodies and plungers, etc. Decorative self-colored films<sup>9</sup> can also be produced in sulfuric acid under conditions intermediate between normal and hard anodizing.

Continuously anodized sheet, foil and wire, which may be given a dyed finish, are produced through a series of cleaning, etching and anodizing tanks, with a film thickness up to about 6  $\mu\text{m}$ . Uses include electrical windings for transformers and motors, where the light weight of aluminum and the insulating and heat-resistant properties of the film are of value, and production of small or light-section articles by stamping or roll-forming.

#### 4.03.2 Mechanism of Formation of Porous Oxide Coatings

It has been established that in the case of electrolytes, such as boric acid or ammonium phosphate solutions, in which aluminum oxide is insoluble, this anodic passivity is due to the formation of a thin compact layer of aluminum oxide whose thickness is proportional to the applied voltage. In neutral phosphate solutions, for example, film growth practically ceases when the thickness corresponds to about  $1.4 \text{ nm V}^{-1}$ , and a similar value has been found for many other electrolytes of this type. These thin films have a high electrical resistance, and can withstand several hundred volts under favorable conditions.

In electrolytes in which the film has a moderate solubility, film growth is possible at lower voltages, for example, in the range 12–60 V, since the rate of formation of the oxide exceeds its rate of solution and current flow continues owing to the different structure of the oxide layer. Electron microscopy has revealed the characteristic porous structure of these films.<sup>10</sup> The pore diameter appears to be a function of the nature and concentration of the electrolyte and of its temperature, being greatest in a solution of high solvent activity, while the number of pores per unit area varies inversely with the formation voltage. In any given electrolyte, the lower the temperature and concentration, and the higher the voltage, the denser will be the coating, as the number of pores per unit

**Table 2** Traditional integral color anodizing processes

<i>Electrolyte</i>	<i>Temperature (<math>^\circ\text{C}</math>)</i>	<i>Current density (<math>\text{A m}^{-2}</math>)</i>	<i>Voltage (V)</i>	<i>Time (min)</i>
Sulfosalicylic acid ( $100 \text{ g l}^{-1}$ ) + sulfuric acid ( $50 \text{ g l}^{-1}$ )	22–25	215–320	25–70	20–45
4- or 5-Sulfophthalic acid ( $75\text{--}100 \text{ g l}^{-1}$ ) + sulfuric acid ( $8\text{--}10 \text{ g l}^{-1}$ )	15–30	130–370	>70	30
Oxalic acid ( $80 \text{ g l}^{-1}$ to saturation)	15–25	130–160	35–70	50–90

area are reduced under these conditions; Table 3 illustrates these points.

In order to account for the relatively high potential required to maintain the current it was suggested by Setoh and Miyata<sup>11</sup> that a thin barrier-layer, similar to that formed in nonsolvent electrolytes, is present below the porous layer. This view has been supported by later work involving capacity and voltage-current measurements, which have allowed the thickness of the barrier-layer to be computed.<sup>12</sup> As in the case of electrolytes which produce barrier films, the thickness has been found to be proportional to the anodizing voltage, but is lower than the limiting growth rate of  $1 \text{ nm V}^{-1}$  and varies with the anodizing conditions (Table 4). The morphology of the anodic film is shown in Figure 1 and diagrammatically in Figure 2.

The more or less regular pattern of pores imposes a cellular structure on the film, with the cells approximating in plan to hexagons, each with a central pore.<sup>13-15</sup> A barrier layer separates the pores from the aluminum, the alumina cells can self-organize to a close-packed arrangement,<sup>13,16</sup> with groups of cells having a potential for organization into regular patterns.<sup>13,16-18</sup> The pore diameter and barrier layer thickness are related to the anodizing voltage, with

ratios of about  $1.0 \text{ nm V}^{-1}$ , with an increased ratio of about  $2.8 \text{ nm V}^{-1}$  for the cell width.<sup>19</sup> The metal surface underlying the film, therefore, consists of a close-packed regular array of nearly hemispherical depressions which increase in size with the anodizing voltage. The thickness of the individual cell walls is approximately equal to that of the barrier-layer.<sup>20</sup>

In view of its position in the electrochemical series ( $E^0 \text{ Al}^{3+}/\text{Al} = -1.66 \text{ V (SHE)}$ ), aluminum would be expected to be rapidly attacked even by dilute solutions of relatively weak acids. In fact, the rate of chemical attack is slow, owing to the presence on the aluminum of a thin compact film of air-formed oxide. When a voltage is applied to an aluminum anode there is a sudden initial surge of current, followed by a rapid fall to a lower, fairly steady value. It appears that this is due to the formation of a barrier-layer. Before the limiting thickness is reached; however, the solvent action of the electrolyte initiates a system of pores at weak points or discontinuities in the oxide barrier-layer.

Pore initiation may be associated with irregularities in original air-formed film on the metal. The development of locally thicker film regions with subsequent pore initiation in the thinner film region is related to the substrate texture. Initial uniform film thickening is apparent, followed by development of locally thicker film material above the distinct metal ridges upon the aluminum surface after pretreatment, and eventual pore development in preferred regions of thinner film between the protuberances, as shown in Figure 3.<sup>21-23</sup>

Growth of oxide continues on a series of hemispherical fronts centered on the pore bases, provided that the effective barrier-layer thickness between the metal surface and the electrolyte within the pores, represented by the hemisphere radius, is approximately  $1 \text{ nm V}^{-1}$ . As anodic oxidation proceeds at a uniform rate, a close-packed hexagonal cell-pattern is produced, the inward extension of the pore due to solution of oxide keeping pace with the inward movement of the oxide-metal interface, as shown by the arrows in Figure 2.

Radiochemical and electron microscopy studies<sup>21-25</sup> indicate that the pore base is the actual site of formation of aluminum oxide. The high electric field that exists across the barrier layer drives the transport of  $\text{Al}^{3+}$  and  $\text{O}^{2-}$  ions through the barrier layer, which is necessary for film growth.<sup>23,26</sup> The formation of porosity has mainly been attributed to field-accelerated dissolution of anodic alumina at the base of each pore,<sup>22,23</sup> which is also enhanced by the heating

**Table 3** Number of pores in anodic oxide coatings

Electrolyte	Temperature (°C)	Applied voltage (V)	Pores ( $\text{cm}^{-2}$ )
15% sulfuric acid	10	15	$77 \times 10^9$
	10	20	$51 \times 10^9$
	10	30	$28 \times 10^9$
3% chromic acid	49	20	$22 \times 10^9$
	49	40	$8 \times 10^9$
	49	60	$4 \times 10^9$
2% oxalic acid	24	20	$36 \times 10^9$
	24	40	$12 \times 10^9$
	24	60	$6 \times 10^9$

Data reproduced from Keller, F.; Hunter, M. S.; Robinson, D. L. *J. Electrochem. Soc.* **1953**, *100*, 411.

**Table 4** Barrier-layer thickness in various electrolytes

Electrolyte	Temperature (°C)	Barrier layer growth ratio
15% sulfuric acid	10	1.00
3% chromic acid	38	1.25
2% oxalic acid	24	1.18

Data reproduced from Hunter, M. S.; Fowle, P. J. *Electrochem. Soc.* **1954**, *101*, 481.

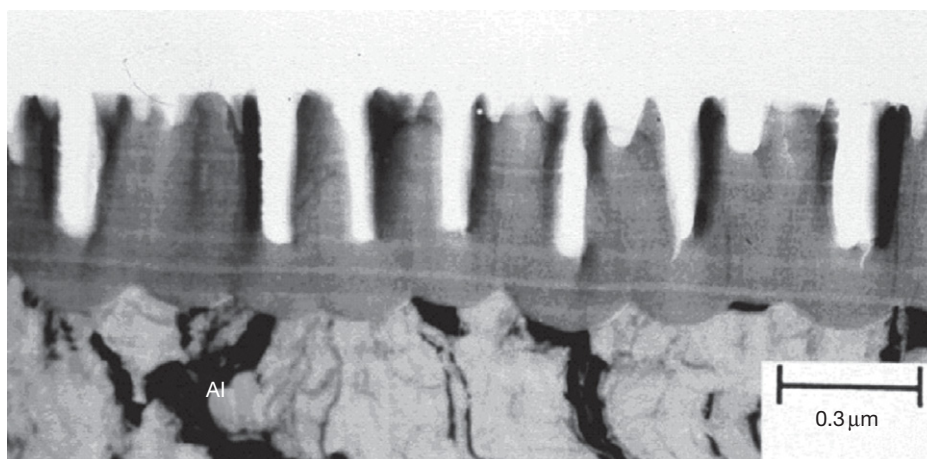


**Figure 1** Transmission electron micrographs of ultramicrotomed cross section of porous anodic film, revealing pores at the centers of cells that pass perpendicular to metal surface and the barrier layer present at the base of pore.

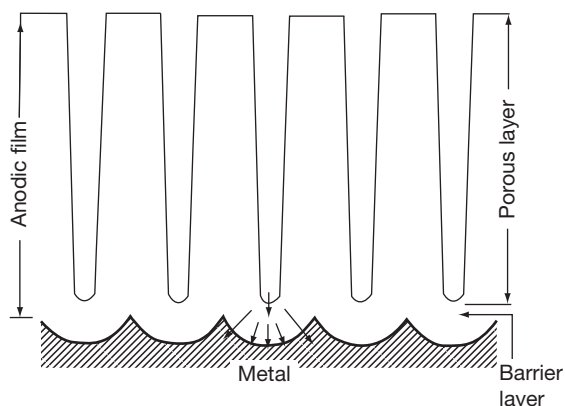


**Figure 2** Diagrammatic cross-section of porous anodic oxide film.

effect of the current, but will also be limited by diffusion. In a process that is separate to field-assisted dissolution, the  $\text{Al}^{3+}$  ions that migrate to the pore base are ejected directly to the electrolyte,<sup>23</sup> that is, without formation of anodic alumina, such that new film is formed due to the inward migration of  $\text{O}^{2-}$  ions. It has been shown that the freshly formed oxide,  $\alpha\text{-Al}_2\text{O}_3$ , is amorphous.<sup>27</sup> The very early stages of pore growth have been extensively studied, and the importance of surface topography and flaw sites in the preexisting oxide established by O'Sullivan, Wood<sup>24</sup> and Thompson and Wood<sup>28</sup> using electron microscopy. Prolonged action of the acid electrolyte on thick films may cause the pores to become conical in section, widening towards the upper surface of the film. This will impose an upper limit on film thickness in solvent electrolytes, as found in practice.

For color anodizing, although it might seem at first sight that dyestuffs are merely held mechanically within the pores, and this view is probably correct in the case of inorganic pigments, there is some support for the opinion that only those dyestuffs which form aluminum–metal complexes produce really light-fast colorations. The effect of hot water sealing is to convert anhydrous  $\gamma\text{-Al}_2\text{O}_3$  into the crystalline monohydrate,  $\text{Al}_2\text{O}_3 \cdot \text{H}_2\text{O}$ , which occupies a greater volume and blocks up the pores, thus preventing further absorption of dyes or contaminants. The monohydrate is also less reactive.

### 4.03.3 Properties of Coatings

#### 4.03.3.1 Composition

The main constituent of the film is aluminum oxide, in a form which varies in constitution between amorphous  $\text{Al}_2\text{O}_3$  and  $\gamma\text{-Al}_2\text{O}_3$ , together with some monohydrate,  $\text{Al}_2\text{O}_3 \cdot \text{H}_2\text{O}$ . In the presence of moisture, both the anhydrous forms are gradually transformed into the monohydrate, and the water content of as-formed films is, therefore, somewhat variable.

After sealing in boiling water, the composition of the completely hydrated film obtained when using sulfuric acid approximates to: 70%  $\text{Al}_2\text{O}_3$ , 17%  $\text{H}_2\text{O}$ , 13%  $\text{SO}_3$ . It is probable that the  $\text{SO}_3$  is combined with the aluminum as a basic sulfate. Sealed films show the electron diffraction pattern of the monohydrate, beohmite.

Anion incorporation in the film is a further important factor affecting film characteristics. It has been

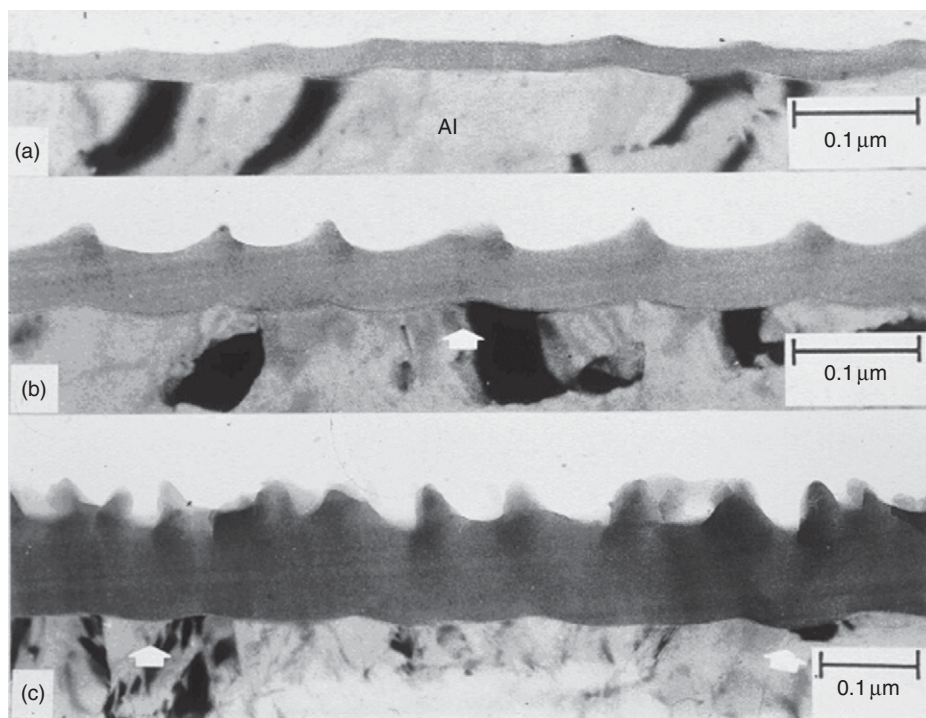


**Figure 3** Transmission electron micrographs of ultramicrotomed cross-section of porous anodic film in the early stages of development. The arrow in (b) highlights a local crack/repair event.

found that anion species are incorporated into the films produced in the main acids, including oxalic acid, sulfuric acid, phosphoric acid and boric acid-formamide electrolytes.<sup>29</sup> The levels of acid anion incorporation are generally in the order: sulfuric acid > phosphoric acid > oxalic acid > chromic acid. Using a radiotracer technique and electron probe microanalysis, sulfur incorporation in films formed in sulfuric acid were determined. A typical level of 4–18 wt% sulfur was found, distributed uniformly throughout film thickness, by different researchers.<sup>30–33</sup> Anodizing in chromic acid produces contrasting results from films formed in sulfuric, oxalic, phosphoric acids; the films contain relatively low levels of chromate incorporation.

The distribution of the anion present after anodizing in oxalic acid has been studied by Rutherford back scattering (RBS) and Auger electron spectroscopy (AES).<sup>34</sup> Carbon is present in the oxide layer in measurable concentrations. The carbon concentration shows a maximum at the surface, a slow decrease through the oxide, and with no signal within a thin oxide region adjacent to the metal. An oxalate content of about 2.4 wt% in films formed in oxalic acid was reported.<sup>35</sup>

#### 4.03.3.2 Density

Owing to the variable degree of porosity of the anodic film, it is only possible to determine the apparent density, which varies with the anodizing conditions and also with the film thickness. **Figure 4** shows the variation in density with thickness for steam-sealed anodic films produced in sulfuric acid on aluminum of 99.99% and 99.5% purity. A mean figure of  $2.7 \text{ g cm}^{-3}$  for sealed, and  $2.5 \text{ g cm}^{-3}$  for unsealed films is accepted by the British Standard for anodized aluminum.<sup>36</sup>

#### 4.03.3.3 Mechanical Properties

##### 4.03.3.3.1 Hardness

It is not possible to obtain a reliable figure for the hardness of anodic coatings with either the indentation or scratch methods, because of the influence of the relatively soft metal beneath the anodic film, and the presence of a soft outer layer on thick films. On Moh's scale, the hardness of normal anodic films lies between 7 and 8, that is, between quartz and topaz.

Methods are available for the determination of relative abrasion resistance using either a mixed jet

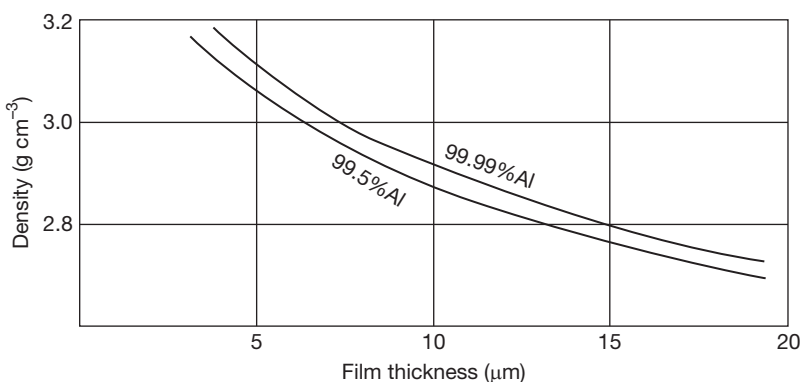


**Figure 4** Apparent density of anodic film as a function of film thickness. Reproduced from *Aluminium, Berl.* **1938**, 32, 126.

of air and abrasive, as recommended in the appropriate British Standard<sup>37</sup> or an abrasive wheel or disc. Owing to variations in the quality of the abrasive, and the performance of individual jets, a standard comparison sample is included in each batch.

The hardness of the film is markedly affected by the conditions of anodizing. By means of special methods involving dilute electrolytes at low temperatures and relatively high voltages, with or without superimposed alternating current, it is possible to produce compact abrasion-resistant films with thicknesses of 50–75 μm and hardness of 200–500 Vickers, for special applications.

#### 4.03.3.3.2 Flexibility

The normal anodic film begins to crack if subjected to an extension exceeding about 0.5%. Thinner films up to 5 μm in thickness appear to withstand a greater degree of deformation without obvious failure, and are often used for dyed coatings on continuously anodized strip from which small items may be punched or stamped. Continuously anodized wire can be bent round a radius of 10–15 times its diameter without visible crazing. A greater degree of flexibility is also shown by the more porous coatings produced in 20–25% sulfuric acid at 35–40 °C, while hard films are much less flexible. Unsealed films are only slightly more flexible than films sealed in water or dichromate solution.

#### 4.03.3.4 Electrical Properties

The specific resistance of the dry anodic film is  $4 \times 10^{15} \Omega \text{ cm}$  at 20 °C,<sup>38</sup> while the dielectric constant of anodic oxide films has been found to be 5.0–5.9 for sulfuric films, and 7–8 for oxalic films. A mean value of 7.45 has been quoted for barrier-layer films,<sup>1</sup> but more recent work favors a value closer to 8.7.<sup>39</sup>

The breakdown voltage of an anodic film varies with the method of measurement and conditions of anodizing, and shows fluctuations over the surface. In the case of unsealed films, breakdown voltage also depends on the relative humidity at the time of measurement. It is normally measured by applying a slowly increasing alternating voltage between a loaded hemispherical probe on the upper surface of the film, and the underlying metal, contact to which may be established by removing a portion of the film. The breakdown voltage–thickness relationship for sealed films up to about 20 μm is approximately linear, and the slope of the curve for sulfuric acid films varies from 30 to 40 V μm<sup>-1</sup>. These results were obtained with a relatively high loading on the probe; with reduced load (approx. 60 g and below on a hemispherical probe of 1.6 mm radius) values of 60–100 V μm<sup>-1</sup> can be reached. The higher figures probably represent limiting values which will apply to the conditions between adjacent laps or turns on coils wound from anodized strip or wire.

#### 4.03.3.5 Physical Properties

The thermal expansion of the film is only about one-fifth that of aluminum,<sup>1</sup> and cracking or crazing is observed when anodized aluminum is heated above 80 °C. The fine hair-cracks produced do not seem to impair the protective properties of the coating if anodizing conditions have been correct.

The thermal conductivity of anodized films is approximately one-tenth that of aluminum.<sup>2</sup> Also, apart from hair-cracks, little change is observable in the anodic film on heating up to 300–350 °C, although some dyed finishes may change color at 200–250 °C, but at higher temperatures up to the melting point of



the metal, films may become opaque or change color, owing to loss of combined water, without losing their adhesion.

#### 4.03.3.6 Thermal Properties

**Table 5** shows the total heat emissivity of various aluminum surfaces, as a percentage of that of a black body. The emissivity of anodized aluminum rises rapidly with film thickness up to 3  $\mu\text{m}$  after which the rate of increase diminishes.

The heat reflectivity of as-rolled aluminum is about 95%, but this high value may not be maintained for long in a corrosive atmosphere, although it is less affected by surface finish than is optical reflectivity. Anodizing reduces the heat reflectivity, owing to absorption by the oxide layer; this effect increases with film thickness. There is a deep absorption trough in the region corresponding to a wavelength of 3  $\mu\text{m}$ ; this is probably due to the  $-\text{OH}$  grouping in the hydrate, the effects of which may be minimized

**Table 5** Relative heat emissivity of various aluminum surfaces

Surface	Heat emissivity (%)
Highly polished	4.3–6.4
Etched	6.4–8.5
Bright roll finish	5.3–7.4
Malt roll finish	8.5–16
Aluminum paint	17–32
Diecast	16–26
Sandcast	26–36
Anodized, according to film thickness	38–92
Black body	100

Data recalculated from Hase, R. *Aluminium*, Berl. **1942**, 24, 140.

by sealing the heated film in oil instead of water.<sup>40</sup> This treatment is particularly valuable for heat reflectors in apparatus using sources running at 900–1000 °C, which show a peak emission in the 2–3  $\mu\text{m}$  region. **Figure 5** shows the heat reflectivity of anodized superpurity aluminum for a source of this type plotted against film thickness. The benefits of the modified sealing treatment are obvious.

#### 4.03.3.7 Optical Properties

The refractive index of the clear anodic film produced on aluminum of the highest purity in sulfuric acid is 1.59 in the as-formed condition, rising to 1.62 after sealing.<sup>41</sup> The total and specular reflectivities of an anodized aluminum surface are controlled by both the condition of the metal surface, polished or matt, and the absorption or light-scattering properties of the oxide layer. Total reflectivity may be defined as the percentage of the incident light reflected at all angles, while specular reflectivity is that percentage reflected within a relatively narrow cone with its axis along the angle of reflection. For many years, the standard instrument for measuring specular reflectivity has been that designed by Guild,<sup>42</sup> but more recently a modified gloss head giving rather greater discrimination has been described by Scott.<sup>43</sup> Other instruments, while placing a number of surfaces of varying specularly in the same relative order, may give different values for the specular reflectivity.

The general brightness of a surface is chiefly dependent upon the total reflectivity  $T$ , while specular reflectivity  $S$  controls the character of the reflected image. In assessing the subjective brightness of a surface the eye tends to be influenced more by

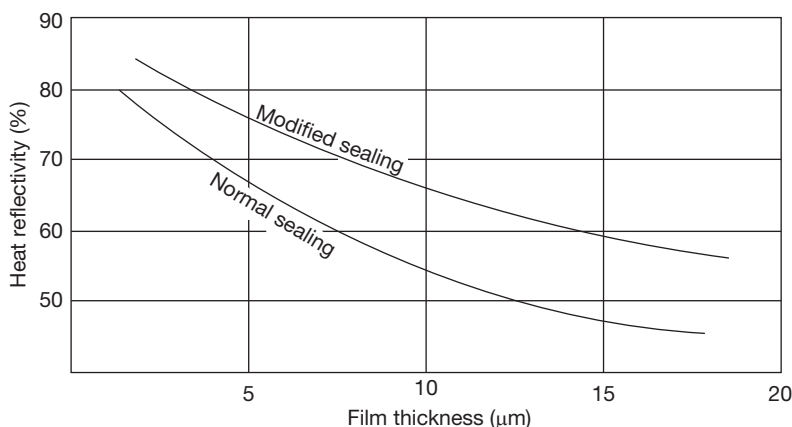


**Figure 5** Heat reflectivity of anodized aluminum. Reproduced from Pearson, T. G.; Phillips, H. W. L. *Metallurg. Rev.* **1957**, 2(8), 348.



the  $S/T$  ratio or image clarity than by the total reflectivity.

For a high degree of specularity, the metal surface must be given a high polish by mechanical means; this may be followed (or replaced) by electrochemical or chemical brightening. When such a brightened surface is protected by anodizing, however, insoluble impurities (mainly iron and silicon) present in the aluminum will be incorporated in the anodic film and will increase its tendency to absorb or scatter light. Only metal of the highest purity, 99.99% Al, produces a fully transparent oxide film, while lower purities show decreased total reflectivities and the fraction of specular reflectivity ( $S$ ) as a function of total reflectivity ( $T$ ), the  $S/T$  ratio, after anodizing because of the increased opacity of the anodic film. **Table 6** demonstrates these effects. The figures were obtained using the Guild meter on electrobrightened and anodized metal.

#### 4.03.3.8 Effect of Anodizing on Mechanical Properties

The tensile strength of thin sections of aluminum may be somewhat reduced by anodizing, owing to the brittleness of the coating and the reduction in metallic cross-section, but this effect is normally very slight. Thin sheet, less than about 0.6 mm with a relatively thick anodic coating, also has a tendency to break more easily on bending. The incompressibility of the anodic film on the inside of the bend

probably enhances this effect, which is also seen on anodized wire.

Anodizing should be used with caution on components likely to encounter high stresses, owing to the deterioration in fatigue properties liable to result under these conditions, but under light loading and with the thinner coatings, the reduction is negligible. In some cases,<sup>44</sup> an actual improvement has been reported. The coefficient of friction of the sealed anodic film is 0.76, falling to 0.19 after impregnation with silicone oil.<sup>45</sup> These results were obtained with anodized wire.

#### 4.03.3.9 Measurement of Film Thickness

The thickness of an anodic film may be determined by a variety of nondestructive methods. Some of these are capable of a high degree of precision, while simpler methods are available for rough sorting. A number of instruments employing the eddy-current principle, with which, after prior calibration, a rapid estimate of film thickness may be made, are now available. With the best instruments, an accuracy of  $\pm 1 \mu\text{m}$  can be obtained. For approximate determinations of thickness, the breakdown voltage of the film may be measured. Breakdown voltage shows wide variations with anodizing conditions and metal or alloy composition. A separate calibration curve is, therefore, needed for each treatment. Accuracy is comparatively low, rarely being greater than  $\pm 2\%$  of the total film thickness.

Alternatively, the loss in weight<sup>46</sup> of an anodized sample of known area may be found after the film has been stripped in a boiling solution made up with phosphoric acid (specific gravity 1.75) 3.5 vol.% and chromic acid 2.0 wt%. Immersion for 10 min is usually sufficient to remove the film without the metal being attacked. Further, film thickness can be precisely determined by cross-sectional examination in a scanning electron microscope or a transmission electron microscope.

#### 4.03.4 Corrosion Resistance

Since the natural passivity of aluminum is due to the thin film of oxide formed by the action of the atmosphere, it is not unexpected that the thicker films formed by anodic oxidation afford considerable protection against corrosive influences, provided the oxide layer is continuous, and free from macropores. The protective action of the film is considerably enhanced by effective sealing, which plugs the mouths of the micropores formed in the normal course of anodizing with hydrated oxide, and still

**Table 6** Effect of metal purity and anodic film thickness on reflectivity

Metal purity (%)	Film thickness ( $\mu\text{m}$ )					
	2		5		10	
	$T$	$S/T$	$T$	$S/T$	$T$	$S/T$
99.5	80	0.84	79	0.83	77	0.78
99.8	82	0.95	83	0.95	—	—
99.99 (super purity)	84	0.99	84	0.99	84	0.99
Super purity + 0.5 Mg	84	0.98	84	0.98	83	0.97
Super purity + 1.25 Mg	83	0.99	83	0.99	82	0.99
Super purity + 0.7 Mg, 0.3 Si, 0.25 Cu	82	0.99	79	0.98	—	—

$S$ , Specular reflectivity;  $T$ , Total reflectivity.

Data reproduced from Pearson, T. G.; Phillips, H. W. L. *Metallurg. Rev.* **1957**, 2(8), 348.

further improvement may be afforded by the incorporation of corrosion inhibitors, such as dichromates, in the sealing solution. Chromic acid films, in spite of their thinness, show good corrosion resistance.

The protective action of sulfuric films is mainly controlled by the anodizing conditions, compact films formed at temperatures below 20 °C in 7% (v/v) sulfuric acid being more resistant than the films formed at higher temperatures in more concentrated acid. The wider pores of the latter result in less protection but these films are more readily dyed. Greater protection is also given by thicker films, and a thickness of about 25 µm is generally considered adequate for architectural work in a normal urban environment. In a heavily polluted industrial area, even thicker films may be desirable, while in rural areas some reduction would be permissible. Bright anodized motorcar trim is generally given a film thickness of about 7 µm.

Alumina monohydrate in the mass is very unreactive, being rapidly attacked only by hot sulfuric acid or caustic soda solutions, and the anodic coating shows similar characteristics to some degree. The presence in the film of macropores due to localized impurities, intermetallic particles or contaminations in the metal and overlying oxide can bring about rapid penetration, owing to the concentration of attack at the few vulnerable points. Metal of good quality specially produced for anodizing should therefore be used in order to ensure that such weak points are absent. For vessels and tanks for holding liquids, it may be preferable to use unanodized aluminum, and to accept generalized corrosive attack rather than run the risk of perforation, which may occur with anodized metal.

For ordinary atmospheric exposure, it is usually possible to arrange that thin spots of the film, such as the contact points of the anodizing jigs, are located in relatively unimportant positions on the article and are hidden from view.

Since the corrosion resistance of anodic films on aluminum is markedly dependent on the efficacy of sealing (provided the film thickness is adequate for the service conditions), tests for sealing quality are frequently employed as an index of potential resistance to corrosion. While it is admitted that an unequivocal evaluation of corrosion behavior can only be obtained by protracted field tests in service, accelerated corrosion tests under closely controlled conditions can also provide useful information in a shorter time within the limitations of the particular test environment employed.

Tests for sealing include dye staining tests such as that specified in BS EN 12373-4:1999, involving preliminary attack with acid, followed by treatment with dye solution. Nitric acid<sup>47,48</sup> or a sulfuric acid/fluoride mixture may be used for the initial attack, and a rapid spot test<sup>49</sup> has been developed using the acid/fluoride mixture, followed by a solution of 10 g l<sup>-1</sup> Aluminum Fast Red B3LW. Poor sealing is revealed by a deep pink to red spot, while good sealing gives nearly colorless to pale pink colorations. The test can be applied to architectural or other material on site.

Physical tests of film impedance<sup>50</sup> using an a.c. bridge have also been recommended, although the correlation with corrosion resistance is necessarily empirical. Film impedance increases at an approximately linear rate with sealing time and film thickness.

Exposure of the samples to a controlled moist atmosphere containing sulfur dioxide, as recommended in ISO 12473:2006, is an example of a test bridging the gap between sealing tests and accelerated corrosion tests. After exposure for 24 h at 25 ± 2 °C, poorly sealed films show a persistent heavy white bloom, while good sealing produces at the most a slight superficial bloom.

A rapid immersion test in a hot aqueous solution containing sulfur dioxide has also been developed by Kape<sup>44</sup> and is specified in ISO 12473:2006. Results are similar to those obtained in the preceding test, Method H. The method can also be made quantitative by measuring the weight loss.

The accelerated corrosion test in most general use is the copper accelerated acetic acid (CASS) test<sup>51</sup> in which the articles are sprayed intermittently with a solution made up with 5% NaCl, 0.026% CuCl<sub>2</sub>·H<sub>2</sub>O acidified to pH 2.8–3.0 with acetic acid. The specimens are clamped at an angle of 15° to the vertical in a baffled enclosure maintained at 50 °C, and the exposure time is 24–96 h. Corrosive attack of inadequately sealed or thin films is shown by pitting.

A derivative of the CASS test is known as the Ford Anodized Aluminium Corrosion Test (FACT).<sup>52</sup> This makes use of a controlled electrolytic attack using the CASS solution. The electrolyte is contained in a glass test cell and clamped against the anodized surface with a Neoprene sealing gasket. A d.c. voltage of 200 V in series with a high resistance is maintained between an anode of platinum wire and the aluminum test piece as cathode. The integrated fall in potential across the cell over a fixed period of 3 min as corrosion proceeds and an increasing current flows, is taken as a measure of the corrosion resistance. Remarkably good correlation has been obtained between

the readings of this instrument and the amount of pitting after exposure at a number of outdoor sites.<sup>53,54</sup> Comprehensive reviews of sealing techniques including test methods and corrosion behavior have been published by Thomas<sup>55</sup> and Wood.<sup>56</sup>

The behavior of samples under the actual conditions of service is the final criterion, but unfortunately such observations take a long time to collect and assess, and the cautious extrapolation of data from accelerated tests must be relied on for forecasting the behavior of anodized aluminum in any new environment.

#### 4.03.4.1 Atmospheric Exposure

Table 7 shows the effects of thin anodic oxide films on the resistance to industrial and synthetic marine atmospheres (intermittent salt spray) of three grades of pure aluminum. The results show how relatively thin films produce a marked improvement in both environments.

In an industrial atmosphere, an anodic film only 6.5  $\mu\text{m}$  thick provides a twofold increase in life over unprotected metal, and the effect under salt-spray conditions is even greater. It is interesting to note that both the industrial atmosphere and salt-spray results show parallel trends. A similar improvement in expectation of life for thin anodic coatings has been reported by Phillips<sup>57</sup> for 99.5% Al, and for alloys of the following compositions: Al–1.25Mn; Al–2Mg–1Mn; Al–1Mg–1Si. The results for a high-copper alloy were less good.

An interesting paper by Lattey and Neunzig<sup>58</sup> shows that the better the surface finish of the aluminum

the thinner the coating required for protection. Neunzig<sup>59</sup> has also studied the effect of the hair-cracks produced by heating or bending on corrosion resistance. Although pitting was initiated by such cracks in thin films (5  $\mu\text{m}$ ), serious pitting in thicker films (15  $\mu\text{m}$ ) was observed only if anodizing had been carried out at 25 °C; films produced at 16–17 °C were more resistant to corrosive attack. This reemphasizes the importance of maintaining correct anodizing conditions for maximum corrosion resistance.

Results of exposure tests for 10 years in a severe industrial environment at Stratford, London, have been reported by the Fulmer Research Institute.<sup>60</sup> A range of pure and alloy specimens, anodized to a maximum film thickness of about 25  $\mu\text{m}$ , was exposed at an angle of 45°. Corrosion was assessed visually, by determination of weight loss after cleaning, and by reflectivity measurements. All specimens showed signs of pitting, and there was a considerable loss of reflectivity, the under surface being more affected than the upper. A striking feature of the results was the accelerating rate of deterioration in the final five years of exposure. Although none of the samples was completely protected, results were better for the purer specimens and the thicker films.

#### 4.03.4.2 Maintenance

In architectural work, particular care must be taken to avoid destructive attack of the anodic film by alkaline mortar or cement during erection, and temporary coatings of spirit-soluble waxes, or acetate–butyrate lacquers are frequently applied to window frames and the like to protect against mortar splashes,

**Table 7** Corrosion tests on unprotected and anodized pure aluminum

Corrosive effect		Grade 1B (99.5%)			Grade 1A (99.8%)		Super purity (99.99%)	
		Film thickness ( $\mu\text{m}$ )			Film thickness ( $\mu\text{m}$ )		Film thickness ( $\mu\text{m}$ )	
		0	6.5	0	4	6.5	0	4
Industrial atmosphere (7 years exposure)	Appearance <sup>a</sup> (life in years)	2.5	5	2.5	.5	5	3.5	6
	Mechanical properties (life in years)	2.75	5.5	3	4.5	6	3	5
	Pitting <sup>b</sup> (depth in mm)	0.18	0.20	0.18	0.25	0.25	0.20	0.13
Marine atmosphere (11 years exposure)	Appearance <sup>a</sup> (life in years)	<1	4	1	4	5	3	4
	Mechanical properties <sup>c</sup> (life in years)	5	>11	8	7	>11	>11	>11
	Pitting <sup>b</sup> (depth in mm)	0.30	0.18	0.15	0.33	0.15	0.15	0.08

<sup>a</sup>No of years to deterioration surface appearance to a fixed arbitrary level.

<sup>b</sup>Mean depth of Pitting obtained statistically.

<sup>c</sup>No of years to deterioration mechanical properties to a fixed arbitrary level.

Data reproduced from Champion, F. A.; Spillet, E. E. *Sheet Metal Ind.* **1956**, 33, 25.

which in any event should be removed at the earliest possible moment.

The resistance of properly anodized aluminum exposed to the weather can be considerably enhanced by correct and regular cleaning. Deposits of soot and dirt should be removed by washing with warm water containing a nonaggressive detergent; abrasives should not be used. For window frames this washing may conveniently be carried out when the glass is cleaned in the normal way. In such circumstances the life of the coating may be prolonged almost indefinitely, as exemplified by the good condition of the chromic-anodized window frames of Cambridge University Library which were installed in 1933, and of the sulfuric-anodized window frames of the New Bodleian Library, Oxford University, installed in 1938.

### 4.03.5 Recent Developments

#### 4.03.5.1 Practice of Anodizing

Although there have been few changes in the basic anodizing practices, and sulfuric acid is the electrolyte used in most plants, there have been many developments in the pretreatment, coloring and sealing processes associated with anodizing.

The increasingly stricter regulations on the toxicological and environmental issues associated with hexavalent chromium have pushed research efforts focused on the replacement of chromic acid anodizing.<sup>61–65</sup> Different weak organic acid additions, such as boric acid<sup>66</sup> or tartaric acid<sup>67</sup> to sulfuric acid anodizing baths have been proposed. Tartaric/sulfuric acid anodizing (TSA) has proven to produce porous anodic film comparable to those formed in chromic acid baths.

Over recent years, new anodizing processes have been developed. These processes do not utilize hexavalent chromium species and hydrofluoric acid and as such have environmental advantages over some earlier processes. For instance, research on plasma electrolytic oxidation (PEO),<sup>68–78</sup> also known as microarc oxidation (MAO), has been revived since the late 1980s. PEO is an electrochemical surface treatment process for generating oxide coatings on metals. It is an anodizing processes with the use of relatively high voltages that lead to dielectric breakdown, with sparking, on the treated component. During the process, discharges occur and the resulting plasma modifies (and enhances) the structure of the oxide layer. This process can be used to grow thick (tens or hundreds of micrometers), largely crystalline, oxide coatings on metals such as aluminum,

magnesium and titanium. The resultant coatings can offer protection against wear, corrosion or heat as well as electrical insulation due to their high hardness and a continuous barrier layer.

The trend in architectural applications has been towards more matt finishes, and the sodium hydroxide-based etchants used frequently contain additives such as sodium nitrate or nitrite or sodium fluoride. Chelating agents such as gluconates, heptonates or sorbitol are added to complex the aluminum produced, and other additives such as sulfides may be present in the etchant to complex zinc dissolved from the alloy, and allow it to be used continuously without dumping.<sup>79</sup>

In terms of anodizing itself, the introduction of a standard for architectural applications of anodized aluminum,<sup>80</sup> and the European development of the Qualanod quality labeling scheme for architectural anodizing,<sup>81,82</sup> have been significant factors in the general improvement in the standard of anodizing. Both of these standards require the use of thick coatings (20 or 25  $\mu\text{m}$ ), which are sealed to a high quality level. The production of such coatings requires good control of operating parameters, particularly the anodizing electrolyte temperature, which should be below 21 °C.<sup>83</sup>

The field of color anodizing has changed considerably since the late 1960s. At that time the integral color anodizing processes were dominant in architectural applications, and electrolytic coloring was relatively new. Now, mainly because of the high energy costs associated with integral color processes, electrolytic coloring is by far the most widely used technique.

In order to produce color by this method, the anodized work is rinsed and transferred to a suitable metal salt solution. The process is electrolytic, and a.c. is passed between the work and a metal or graphite counter-electrode, causing the metal present in the solution to be deposited at the base of the pores of the anodic coating.<sup>84</sup> The height of the metal deposited in the pores controls the depth of color, and a range of shades is produced by varying the applied voltage and time. Ranges of bronze and black finishes are produced in nickel-, cobalt-, or tin-based electrolytes, and pink, maroon, or black finishes in electrolytes based on copper. The electrolytes usually contain the appropriate metal sulfate, with many other additives present to adjust or control pH, to improve throwing power, or to make dark colors easier to produce. Nickel and cobalt electrolytes are used at pH values of 4–6, and tin and copper electrolytes at pH values of 1–2; an applied voltage of the order of 10–20 V and a current density of about 30–50  $\text{A m}^{-2}$  are normally required.

The finishes produced have very good light fastness and corrosion resistance, and, unlike integral color finishes, the shade is largely independent of the aluminum alloy and the anodic film thickness used. The whole range of shades can be produced on films as thin as 5  $\mu\text{m}$ , so the finishes are also being used in trim applications.<sup>85</sup> Many patents and publications in the electrolytic coloring field now exist and they have been reviewed by many authors.<sup>86,87</sup>

In order to obtain a wider range of colored finishes, electrolytic coloring processes have been combined with conventional dyeing.<sup>88</sup> The work is anodized normally to the required film thickness, electrolytically colored in a cobalt- or tin-based electrolyte to a light bronze shade, and then over-dyed in an appropriate dyestuff to give muted shades of red, blue, yellow, or brown. Again the main application is architectural, and the finishes have good light fastness and durability. An alternative approach to widening the color range with electrolytic coloring has been the development of finishes based on optical interference effects,<sup>89</sup> whereby quite different colors can be produced in the same electrolyte. An intermediate treatment in a phosphoric acid anodizing electrolyte is normally required, between anodizing and electrolytic coloring, to produce these effects.

With the increasing use of color anodized finishes, sealing quality has become very important, and seal quality tests and standards have all improved. Sealing smut is more visible on colored than on clear anodized surfaces, and it has become common practice to try to eliminate this chemically, rather than removing it by hand wiping. Approaches to this include dipping in mineral acids after sealing,<sup>90</sup> and adding surface active agents which prevent smut forming.<sup>91,92</sup>

Sealing is normally carried out in boiling water and the high energy costs involved have led to the development of alternative, lower-energy methods. Approaches have included the use of boehmite accelerators such as triethanolamines to shorten the sealing time,<sup>93</sup> and the use of so-called 'cold' sealing systems. These latter approaches have mainly been developed in Italy,<sup>94</sup> and are based on the use of nickel salts in the presence of fluorides. They are used at a temperature of about 30 °C for a time of 15 min, and are claimed to give good corrosion resistance.

#### 4.03.5.2 Mechanism of Anodizing

The development of sophisticated electron-optical techniques now allows the direct observation of the barrier layer and the pore structure of all types of

anodic coating. Much of the most relevant work has been carried out at the University of Manchester.

For example using a tungsten tracer layer that is incorporated into the anodic film from the aluminum substrate has indicated a major role for oxide growth stresses in the origin of porosity.<sup>95–98</sup> The stresses result in flow of the relatively plastic film material in the barrier layer region of the porous film, which proceeds from beneath the pores toward the cell walls. The redistribution of film material contributes to an enhanced thickness of the film relative to that of the metal consumed. Such stress-driven pore generation is probably an important factor in the potential for self-ordering of porosity in anodic alumina.<sup>99, 100</sup> The behavior is contrary to expectations of a dissolution model of pore formation.

The morphology of porous anodic films are significantly affected by alloying elements in aluminum alloys. Thus, morphologies of porous anodic alumina films on aluminum alloys containing copper often differ greatly from that on high purity aluminum, as shown in [Figure 6](#). The well-developed cellular morphology of the classic porous film<sup>11,101,102</sup> is largely absent. In contrast, the porosity in the anodic film is irregular and can incorporate a component with a lateral alignment in cross-sections of the film.

From studies of barrier films, it was revealed that alloying elements with Gibbs free energies of oxide formation per equivalent greater than that of alumina enrich at the alloy–film interface; when a critical enrichment is reached, oxidation of the alloying elements occurs; for alloying elements with oxides of lower Gibbs free energies than that of alumina, immediate oxidation, along with aluminum, is evident from the commencement of anodizing.<sup>103–108</sup> For copper-containing alloys, copper can be significantly enriched in the alloy immediately beneath the anodic film, up to 40 at.% Cu, by the initial formation of a copper-free alumina film.<sup>109–111</sup> The enriched alloy layer is typically about 2 nm in thickness. Following enrichment, copper can be oxidized, and incorporated into the anodic film as  $\text{Cu}^{2+}$  species.<sup>112</sup> About the same time that the oxidation of copper commences, oxygen is generated within the anodic film, with associated formation of bubbles of high pressure gas.<sup>113,114</sup>

The pore morphology of the porous anodic films formed on copper-containing alloys is associated with the generation of oxygen gas bubbles and their subsequent disruption. The film disruption leads to an altered direction of pore propagation, before the pore reestablishes a normal orientation with respect



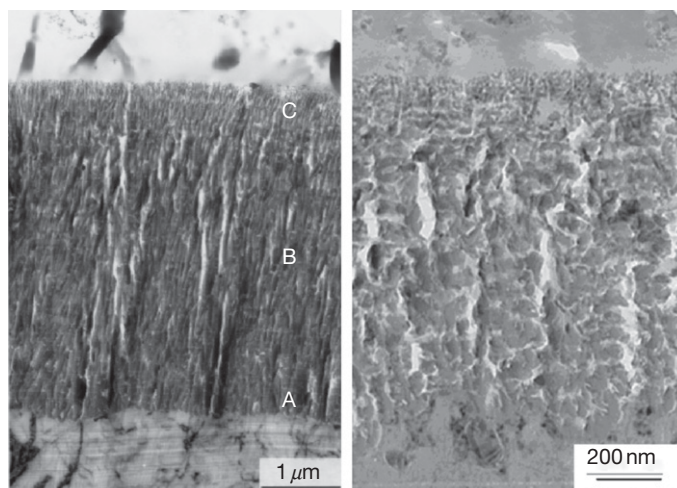


**Figure 6** Transmission electron micrographs of ultramicrotomed sections of aluminum alloys following anodizing in chromic acid (DEF STAN 03-24/2): (a) AA1050 and (b) AA2024. Reproduced from Zhou, X.; Thompson, G. E.; Skeldon, P. In Proceedings of the 17th International Corrosion Congress, Las Vegas, USA, 2008; Paper 3972.

to the local alloy–film interface. The changing directions of pores contribute to a lateral aspect of the pore morphology.<sup>101,115</sup>

The mechanism of coloring with integral color finishes has been shown to depend on the presence of free metallic aluminum in the film, as well as on the inclusion of intermetallic constituents.<sup>116</sup> With electrolytic coloring processes, color is produced by light scattering effects, with the tiny metallic deposits within individual pores acting as light scattering centers.<sup>126</sup> Distribution of metal in the pores varies from one electrolyte to another, and this can affect the corrosion resistance of the final product.<sup>127</sup>

The mechanism of sealing has been shown to involve an initial dissolution and reprecipitation of hydrated aluminum oxide on the pore walls, pseudo-boehmite gel formation within the pores, and conversion of this to crystalline boehmite at the film surface.<sup>117</sup> The presence of an intermediate layer close to the film surface, in which the identity of the original pores has been lost, has also been recognized.<sup>118</sup>

#### 4.03.5.3 Properties of Coatings

The hardness and abrasion resistance of anodic coatings have never been easy properties to measure, but the development of a British Standard on hard anodizing<sup>119</sup> has made this essential. Film hardness is best measured by making microhardness indents on a cross-section of a film,<sup>120,121</sup> but a minimum film thickness of 25 μm is required. For abrasion resistance measurements, a test based on a loaded abrasive

wheel,<sup>122</sup> which moves backwards and forwards over the film surface, has improved the sensitivity of such measurements.

#### 4.03.5.4 Test Methods

Tests for quality of sealing of anodic coatings have become internationally standardized. They include dye spot tests with prior acid treatment of the surface (ISO 2143:1981 and BS EN 12373-4:1999), measurement of admittance or impedance (ISO 2931:1983 and BS EN 12373-5:1999), or measurement of weight loss after acid immersion (ISO 3210:1983 and 12373-6:1999, BS EN 12373-7:2002). Of these the chromic-phosphoric acid immersion test (ISO 3210) has become the generally accepted reference test.

The revision of the main anodizing standard (BS 1615:1987) has changed it from a ‘specification’ to a ‘method for specifying,’ but it provides all the information necessary to write an appropriate specification for any anodized product.

## References

1. Young, L. *Anodic Oxide Films*; Academic Press: New York, 1961.
2. Schenk, M. *Werkstoff Aluminium und seine Anodische Oxydation*; Francke: Berne, 1948.
3. Wernick, S.; Pinner, R. *The Surface Treatment and Finishing of Aluminium and its Alloys*, 3rd ed.; Robert Draper: Teddington, 1964.
4. Processes for the Anodic Oxidation of Aluminium and Aluminium Alloy Parts, DTD 910C, H.M.S.O.: London, 1951.

5. Campbell, W. J. Conference on Anodising Aluminium, A.D.A., Nottingham, Paper 11, Sept. 1961.
6. Csokan, P. *Metalloberfläche* **1965**, 19(8), 252.
7. Csokan, P. *Trans. Inst. Met. Fin.* **1964**, 41, 51.
8. Tsuji, Y. *Trans. Inst. Met. Fin.* **1963**, 40, 225.
9. Scott, B. A. *Trans. Inst. Met. Fin.* **1965**, 43, 1.
10. Edwards, J. D.; Keller, F. *Trans. Amer. Inst. Min. (Metall.) Engrs.* **1944**, 156, 288.
11. Setoh, S.; Miyata, A. *Sci. Pap. Inst. Phys. Chem. Res. Tokyo* **1932**, 17, 189.
12. Hunter, M. S.; Fowle, P. J. *Electrochem. Soc.* **1954**, 101, 481.
13. Masuda, H.; Yamada, H.; Satoh, M.; Asoh, H.; Nakao, M.; Tamamura, T. *Appl. Phys. Lett.* **1997**, 71, 2770.
14. Shingubara, S.; Morimoto, K.; Sakaue, H.; Takahagi, T. *Electrochem. Solid-State Lett.* **2004**, 7, 2004.
15. Ono, S.; Saito, M.; Asoh, H. *Electrochem. Solid-State Lett.* **2004**, 7, B21.
16. Masuda, H.; Fukada, K. *Science* **1995**, 268, 1466.
17. Li, F.; Zhang, L.; Metzger, R. M. *Chem. Mater.* **1998**, 10, 2470.
18. Nielsch, K.; Choi, J.; Schwirn, K.; Wehrspohn, R. B.; Gösele, U. *Nano Lett.* **2002**, 2, 677.
19. Wood, G. C.; O'Sullivan, J. P. *Electrochim. Acta* **1970**, 15, 1865.
20. Keller, F.; Hunter, M. S.; Robinson, D. L. *J. Electrochem. Soc.* **1953**, 100, 411.
21. Lewis, J. E.; Plumb, R. C. *J. Electrochem. Soc.* **1958**, 105, 496.
22. Hoar, T. P.; Mott, N. F. *J. Phys. Chem. Solids* **1959**, 9, 97.
23. Siejka, J.; Ortega, C. J. *Electrochem. Soc.* **1977**, 124, 883.
24. O'Sullivan, J. P.; Wood, G. C. *Proc. Royal Soc.* **1970**, A317, 511.
25. Thompson, G. E.; Xu, Y.; Skeldon, P.; Shimazu, K.; Han, S. H.; Wood, G. C. *Philos. Mag. B* **1987**, 55(6), 651-667.
26. Cherki, C.; Siejka, J. *J. Electrochem. Soc.* **1973**, 120, 784.
27. Verwey, E. J. W. *Z. Kristallogr.* **1935**, 91, 65.
28. Thompson, G. E.; Wood, G. C. In *Corrosion: Aqueous Processes and Passive Films*; Scully, J. C., Ed.; Academic Press: New York, 1983.
29. Tajima, S.; Baba, N.; Mori, T.; Shimura, M. *Electrochim. Acta* **1967**, 45, 174.
30. Brace, A. W.; Baker, H. *Trans. IMF* **1963**, 40, 31.
31. Pullen, N. D. *Metal Ind.* **1939**, 56, 327.
32. Liechti, F.; Rreadwell, W. T. *Helv. Chim. Acta* **1947**, 30, 1024.
33. Spooner, R. C. *Proc. Am. Electropl. Soc.* **1951**, 44, 1321.
34. Sarganov, V.; Jansson, C.; Nielsen, J. G.; Morgen, P.; Gorokh, G.; Larsen, A. N. *Electrochim. Acta* **1988**, 33, 517.
35. Alvay, C. E. Ph.D. Thesis, UMIST, 1974.
36. Aluminium and aluminium alloys anodizing: Method for specifying decorative and protective anodic oxidation coatings on aluminium, BS EN 12373-1: 2001.
37. Aluminium and aluminium alloys anodizing: Measurement of mean specific abrasion resistance of anodic oxidation coatings using an abrasive wheel/jet test apparatus, BS EN 12373-9: 1999; 12373-10: 1999.
38. Franckenstein, G. *Ann. Phys.* **1936**, 26, 17.
39. van Geel, W. Ch.; Schelen, B. J. J. *Philips Res. Rep.* **1957**, 12, 240.
40. Gwyer, A. G. C.; Pullen, N. D. *Metallurgia Manchr.* **1939**, 21, 57.
41. Edwards, J. D. *Mon. Rev. Amer. Electropl. Soc.* **1939**, 26, 513.
42. Guild, J. J. *Sci. Inst.* **1940**, 17, 178.
43. Scott, B. A. *J. Sci. Inst.* **1960**, 37, 435.
44. Kape, J. M. *Metal Industry* **1959**, 95(6), 115.
45. Vevers, H. H. In Conference on Anodising Aluminium, A.D.A., Nottingham, Discussion on Section 4, Sept. 1961.
46. Aluminium and aluminium alloys anodizing: Assessment of quality of sealed anodic oxidation coatings by measurement of the loss of mass after immersion in phosphoric acid/chromic acid solution with/without prior acid treatment BS EN 12373-7: 2002; 12373-6: 1999.
47. Neunzig, H.; Rohrig, V. *Aluminium* **1962**, 38(3), 150.
48. Sacchi, F.; Paolini, G. *Aluminio* **1961**, 6, 9.
49. Scott, B. A. *Electroplating and Metal Finishing*, Feb. 1965.
50. Wood, G. C. *Trans. Inst. Met. Fin.* **1964**, 41, 99.
51. ASTM B368-97 (2003) e1, Standard Method for Copper-Accelerated Acetic Acid-Salt Spray (Fog) Testing (CASS Test).
52. Quality Laboratory and Chem. Eng. Physical Methods, MA-P, BQ7-1, Ford (USA), Feb. 1970.
53. Carter, V. E.; Edwards, J. *Trans. Inst. Met. Fin.* **1965**, 43, 97.
54. Carter, V. E. *Trans. Inst. Met. Fin.* **1967**, 45, 64.
55. Thomas, R. W. In Symposium on Protecting Aluminium, Aluminium Federation: London, 1970.
56. Wood, G. C. *Trans. Inst. Met. Fin.* **1959**, 36, 220.
57. Phillips, H. W. L. *Institute of Metals Monograph* 1952, Vol. 13.
58. Lattey, R.; Neunzig, H. *Aluminium, Berl.* **1956**, 32, 252.
59. Neunzig, H. *Aluminium, Berl.* **1958**, 34, 390.
60. Liddiard, E. A. G.; Sandersen, G.; Penn, J. E. In Annual Technical Conference, Institute of Metal Finishing, Brighton, 28 May 1971.
61. Thompson, G. E.; Zang, L.; Smitz, C. J. E.; Skeldon, P. *Corrosion* **1999**, 55, 1052.
62. Eichinger, E. *Met. Finish* **1997**, 95, 36.
63. Smith, C. J. E.; Baldwin, K. R.; Garrett, S. A.; Gibson, M. C.; Hewins, M. A. H.; Lane, P. L. *ATB Metall.* **1997**, 37, 266.
64. Wilcox, G. D.; Gabe, D. R.; Warnick, M. E. *Corr. Rev.* **1986**, 6, 327.
65. Moutarlier, V.; Gigandet, M. P.; Ricq, L.; Pagetti, J. *Appl. Surf. Sci.* **2001**, 183, 1.
66. Moutarlier, V.; Gigandet, M. P.; Pagetti, J. *Appl. Surf. Sci.* **2003**, 206, 237.
67. Boeing Co. EP 0, 405, 624, 1991.
68. Patel, J. L.; Saka, N. *J. Interferom.* **2001**, 50, 398.
69. Shatrov, A. S.; Samsonov, V. I. U.S. Patent 6,896,785, 2005.
70. Kurze, P.; Banerjee, D.; Kletke, H.-J. U.S. Patent 5,385, 662, 1995.
71. Saakian, L. S.; Yefremov, A. P.; Ropyak, L. Y.; Apelfeld, A. V. *Corrosion Control and Environment Protection*. Informative survey, VNIIOENG, Moscow, 6, 1986.
72. Fyedorov, V. A.; Kan, A. G.; Maksutov, R. P. *Surface Strengthening of Oil and Gas Trade Facilities by Micro Arc Oxidation*, VNIIOENG, Moscow, 6, 1989, in Russian.
73. Markov, G. A.; Gizatullin, B. S.; Rychazhkova, I. B. USSR Patent 926,083, Bul. Inv. 17, 1982.
74. Snezhko, L. A.; Tchernenko, V. I. USSR Patent 973,583, Bul. Inv. 23, 1982.
75. Gradkovsky, R. J.; Bayles, S. N. U.S. Patent 3,956,080, May 11, 1974.
76. Brown, S. D.; Kuna, K. J.; Van, T. B. *J. Am. Ceram. Soc.* **1971**, 54(8), 384.
77. Monfort, F.; Berkani, A.; Matykina, E.; Skeldon, P.; Thompson, G. E.; Habazaki, H.; Shimizu, K. *Corros. Sci.* **2007**, 49(2), 672.
78. Yerokhin, A. L.; Nie, X.; Leyland, A.; Matthews, A.; Dowey, S. J. *Surf. Coat. Technol.* **1999**, 122(2-3), 73-93.

79. Kape, J. M. *Trans. Inst. Met. Fin.* **1971**, 49, 22.
80. Specification for anodic oxidation coatings on wrought aluminium for external architectural applications, BS EN 3987: 1991.
81. Qualanod, Specifications for the Quality Sign for Anodic Oxidation Coatings on Wrought Aluminium for Architectural Purposes, Zürich, 1983.
82. Carter, V. E. *Trans. Inst. Met. Fin.* **1977**, 55, 9.
83. Architectural Anodising: Sulphuric Acid Anodic Film Quality, British Anodising Association, 1981.
84. Sheasby, P. G.; Cooke, W. E. *Trans. Inst. Met. Fin.* **1974**, 52, 103.
85. Short, E. P.; Fern, D.; Kellermann, W. M. In SAE Conference, Detroit, 1983, Paper 830389.
86. Brace, A. W.; Sheasby, P. G. *The Technology of Anodising*; Aluminium Technology Ltd.: UK, 1979.
87. John, S.; Balasubramaniam, V.; Shenoi, B. A. *Fin. Ind.* **1978**, 2, 32.
88. Grossman, H.; Speier, C. Th. *Aluminium* **1979**, 55, 141.
89. Sheasby, P. G.; Patrie, J.; Badia, M.; Cheetham, G. *Trans. Inst. Met. Fin.* **1980**, 58, 41.
90. Aluminium Co. of America, U.S. Patent 3,822,156, 1974.
91. Göhausen, H. J. *Galvanotechnik* **1978**, 69, 893.
92. Speiser, C. Th. *Aluminium* **1983**, 59, E350.
93. Olin Mathieson Chemical Corp., U.S. Patent 3,365,377, 1968.
94. Strazzi, E. *Alluminio* **1981**, 50, 496.
95. Garcia-Vergara, S. J.; Iglesias-Rubianes, L.; Blanco-Pinzon, C. E.; Skeldon, P.; Thompson, G. E.; Campestri, P. *Proc. R. Soc. A* **2006**, 462, 2345.
96. Skeldon, P.; Thompson, G. E.; Garcia-Vergara, S. J.; Iglesias-Rubianes, L.; Blanco-Pinzon, C. E. *Electrochem. Solid State Lett.* **2006**, 9, B47.
97. Garcia-Vergara, S. J.; Skeldon, P.; Thompson, G. E.; Habazaki, H. *Electrochim. Acta* **2006**, 52, 681.
98. Garcia-Vergara, S. J.; Skeldon, P.; Thompson, G. E.; Habazaki, H. *Corros. Sci.* **2007**, 49, 3772–3782.
99. Ono, S.; Saito, M.; Asoh, H. *Electrochim. Acta* **2005**, 51, 827.
100. Jessensky, O.; Müller, F.; Gösele, U. *Appl. Phys. Lett.* **1998**, 22, 1173.
101. Zhou, X.; Thompson, G. E.; Skeldon, P. In Proceedings of the 17th International Corrosion Congress, Las Vegas, USA, 2008, Paper 3972.
102. Garcia-Vergara, S. J.; El Khazmi, K.; Skeldon, P.; Thompson, G. E. *Corros. Sci.* **2006**, 48, 2937.
103. Habazaki, H.; Shimizu, K.; Skeldon, P.; Thompson, G. E.; Wood, G. C.; Zhou, X. *Corros. Sci.* **1997**, 39, 731–737.
104. Paez, M. A.; Foong, T. M.; Ni, C. T.; Thompson, G. E.; Shimizu, K.; Habazaki, H.; Skeldon, P.; Wood, G. C. *Corros. Sci.* **1996**, 38, 59.
105. Habazaki, H.; Paez, M. A.; Shimizu, K.; Skeldon, P.; Thompson, G. E.; Wood, G. C.; Zhou, X. *Corros. Sci.* **1996**, 38, 1033.
106. Habazaki, H.; Shimizu, K.; Paez, M. A.; Skeldon, P.; Thompson, G. E.; Wood, G. C.; Zhou, X. *Surf. Interf. Anal.* **1995**, 23, 892.
107. Zhou, X.; Habazaki, H.; Shimizu, K.; Skeldon, P.; Thompson, G. E.; Wood, G. C. *Thin Solid Films* **1997**, 293, 327.
108. Habazaki, H.; Zhou, X.; Shimizu, K.; Skeldon, P.; Thompson, G. E.; Wood, G. C. *Electrochim. Acta* **1997**, 42, 2627.
109. Paez, M. A.; Bustos, O.; Thompson, G. E.; Skeldon, P.; Shimizu, K.; Wood, G. C. *J. Electrochem. Soc.* **2000**, 147, 1015.
110. Habazaki, H.; Paez, M. A.; Shimizu, K.; Skeldon, P.; Thompson, G. E.; Wood, G. C.; Zhou, X. *Corros. Sci.* **1996**, 38, 1033.
111. Habazaki, H.; Shimizu, K.; Skeldon, P.; Thompson, G. E.; Wood, G. C.; Zhou, X. *Trans. Inst. Met. Finishing* **1997**, 75, 18.
112. Zhou, X.; Thompson, G. E.; Robinson, J.; Skeldon, P. *J. Electrochem. Soc.* **2005**, 152, B393.
113. Skeldon, P.; Thompson, G. E.; Wood, G. C.; Zhou, X.; Habazaki, H.; Shimizu, K. *Philos. Mag. A* **1997**, 76, 729.
114. Zhou, X.; Thompson, G. E.; Paez, M. A.; Skeldon, P.; Habazaki, H.; Shimizu, K.; Wood, G. C. *J. Electrochem. Soc.* **2000**, 147, 1747.
115. Iglesias-Rubianes, L.; Garcia-Vergara, S. J.; Skeldon, P.; Thompson, G. E.; Ferguson, J.; Beneke, M. *Electrochim. Acta* **2006**, 52, 7148.
116. Wefers, K.; Evans, W. T. *Plating Surf. Fin.* **1975**, 62, 951.
117. Wefers, K. *Aluminium* **1973**, 49, 553.
118. Thompson, G. E.; Furneaux, R. C.; Wood, G. C. *Trans. Inst. Met. Fin.* **1975**, 53, 97.
119. Specification for hard anodic oxidation coatings on aluminium and its alloys for engineering purposes BS EN 5599:1993.
120. Metallic and other inorganic coatings: Vickers and Knoop microhardness tests, BS EN ISO 4516: 2002.
121. Thomas, R. W. *Trans. Inst. Met. Fin.* **1981**, 59, 97.
122. Göhausen, H. J. *Trans. Inst. Met. Fin.* **1978**, 56, 57.
123. Thompson, G. E.; Furneaux, R. C.; Goode, J. S.; Wood, G. C. *Trans. IMF* **1978**, 56, 159.
124. Thompson, G. E.; Furneaux, R. C.; Wood, G. C. *Trans. IMF* **1979**, 57, 123.
125. Stickley, G. W.; Howell, F. M. *Proc. Am. Soc. Test. Mater.* **1950**, 50, 735.
126. Goad, D. G. W.; Moskovits, M. J. *Appl. Phys.* **1978**, 49, 2929.
127. Sheasby, P. G. Paper presented at Aluminum Finishing Seminar, St. Louis, 1982.

## 4.04 General Principles of Protection by Coatings

**D. R. Gabe and G. D. Wilcox**

Department of Materials, Loughborough University, Leicestershire LE11 3TU, UK

**V. E. Carter**<sup>†</sup>

Formerly at British Non-Ferrous Research Association, London

This article is a revision of the Third Edition article 13.1 by D. R. Gabe and V. E. Carter, volume 2, pp 13:3–13:18,

© 2010 Elsevier B.V.

4.04.1	Introduction	2519
4.04.2	Anodic and Cathodic Coatings	2520
4.04.3	Factors Affecting Choice of Coating	2521
4.04.3.1	Resistance to the Corrosive Environment	2521
4.04.3.2	Practicability of Application	2521
4.04.3.3	Compatibility of Galvanic Coupling	2522
4.04.3.4	Effect of Coating Process on Substrate Properties	2523
4.04.3.5	Coating Properties	2523
4.04.3.6	Economics	2524
4.04.4	Coatings in Practical Use – Overview	2524
4.04.4.1	Zinc	2524
4.04.4.2	Cadmium	2524
4.04.4.3	Tin	2525
4.04.4.4	Aluminum	2525
4.04.4.5	Nickel	2525
4.04.4.6	Lead	2525
4.04.4.7	Copper	2525
4.04.4.8	Chromium	2526
4.04.4.9	Precious Metals	2526
4.04.5	Recent Developments	2526
4.04.5.1	Galvanic Coupling	2527
4.04.5.2	Porosity	2528
4.04.5.3	Environment Classification	2528
4.04.6	Alternative Coating Systems	2528
4.04.7	Multilayer Coatings	2528
4.04.8	Metal Whiskers	2529
References		2530

### Abbreviations

**ASTM** American Society for Testing of Materials

**BS** British Standard

**CVD** Chemical vapor deposition

**FCC** Face centered cubic

**GMR** Giant magnetoresistive

**HE, DTD** Aluminum alloy designation codes

**NASA** National Aeronautics and Space  
Administration

### 4.04.1 Introduction

The application of metallic coatings for the protection of metals may be required for one or more of the following reasons:

- to prevent or reduce corrosion of the substrate metal;
- to modify the physical or mechanical properties of the substrate metal;

<sup>†</sup>Deceased.

- (c) to achieve and maintain some desired decorative effect.

Many coatings also have a role in wear resistance and may have other important properties to be considered, for example, silver electrodeposits for electrical contacts.

Although the initial choice of coating material applied for reasons (b) or (c) may be dictated by the particular properties required, the corrosion behavior of the composite metal coating–metal substrate system must also be taken into consideration insofar as it may affect the maintenance of the desired properties. Consequently, in all cases where protective metal coatings are used, the corrosion performance of both coating and substrate requires careful consideration.

The choice of substrate metal is usually governed by cost and weight as well as general physical, mechanical or, fabrication properties, and these factors will normally dictate a very limited number of possible materials none of which may be ideal in resisting the corrosive environment that will be encountered in service. Ideally, a protective metal coating should exclude completely the corrosive environment from the substrate metal and, if this can be achieved, only the resistance of the coating metal itself to that corrosive environment needs to be considered. However, in practice, discontinuities in the coating may occur during application or be produced subsequently by mechanical damage or by the corrosion of the coating itself. In these cases, the corrosion performance of the bimetallic system so produced is of major importance.

#### **4.04.2 Anodic and Cathodic Coatings**

A detailed discussion of galvanic corrosion between dissimilar metals in contact in a corrosive environment is given in the chapter on galvanic corrosion in this book. In the case of coating discontinuities, the effect of the anode–cathode area relationship and the nature of any corrosion products formed at small discontinuities may modify any choice made on strict considerations of general galvanic corrosion theory based on the potentials of the coating and substrate in the environment under consideration.

Thus, coatings which are anodic or cathodic to the substrate are both used in practice, but the former will provide sacrificial protection at a coating discontinuity, and the latter may stimulate attack on any exposed substrate. The sacrificial consumption of an

anodic coating at a pore or discontinuity results in a gradual increase in the area of substrate exposed and a corresponding decrease in the corrosion current density, which, in time, may become insufficient to maintain protection in the centre of the exposed area. The rate of sacrificial consumption of an anodic coating is reduced by several factors such as the resistance of the electrolyte solution within the discontinuity, blocking of the discontinuity by corrosion products, or the formation of protective films on the exposed substrate which may be encouraged by an increase of electrolyte pH by the cathodic reaction at the discontinuity. Under these circumstances, the life of the anodic coating will be prolonged.

Zinc and cadmium are both anodic to steel and provide sacrificial protection to the substrate when used as coating metals. On exposure to industrial atmospheres, zinc will protect steel for a longer period than cadmium, whereas in many marine or rural environments, cadmium provides a longer period of protection. Layton<sup>1</sup> attributes this difference in behavior to the nature of the corrosion products formed in the different environments. In industrial atmospheres, soluble sulfates of both zinc and cadmium are produced and are removed by rain so that corrosion can continue freely. Under these conditions, zinc, which has a more negative potential than cadmium in most environments, is a more efficient anode than cadmium and gives a longer period of protection to the substrate. In rural and marine exposure, however, the cadmium carbonates and basic chlorides that are formed are insoluble and corrosion is stifled to a greater extent than in the case of the more soluble zinc carbonates and basic chlorides, so tending towards a longer life with cadmium coatings.

When cathodic coatings are used, the sacrificial action is reversed, the substrate being attacked and the coating protected. This attack on the substrate can be highly localized and can lead to rapid penetration through the thickness of the metal. The effect is appreciably reduced by electrolyte resistance and by the stifling action of corrosion products, as mentioned above for anodic coatings, and the production of substrate corrosion products within the discontinuity can significantly decrease the corrosion rate and delay penetration.

Decorative coatings of nickel plus chromium are cathodic to steel or zinc alloy substrates, and with these protective systems, deliberate use may be made of discontinuities in the chromium topcoat where corrosion of the underlying nickel will occur. If the number of these discontinuities in the chromium



layer is greatly increased, the current density at each individual corrosion site is reduced; the penetration of corrosion through the thickness of the nickel layer is thus slowed down, and the period of protection of the substrate metal is prolonged.

In general, the choice between cathodic or anodic coatings will be governed by the service application. Where cathodic coatings are used, any attack on the substrate will be highly localized, leading to rapid perforation of thin sections with a consequent loss of functional integrity. Anodic coatings, on the other hand, will protect exposed areas of substrate metal by sacrificial action until the area exposed exceeds that, over which cathodic polarization of the corrosion reaction can be maintained, after which time the substrate itself will corrode freely.

With both anodic and cathodic coating systems, account must be taken of the extent to which the presence and nature of corrosion products on the surface may impair either the decorative aspects or the functional use of the article. For example, the presence of small amounts of corrosion products on the surface of gold-plated electrical contacts can markedly increase the electrical contact resistance and cause malfunctioning; the problem may be overcome by increasing the thickness of the gold deposit – thus reducing its porosity – or by interposing an undercoat of a more resistant metal to act as a barrier layer between the gold and the substrate.

Because of the many variables which can influence the corrosion reaction, the use of the e.m.f. series of metals to predict the behavior of galvanic couples in a given service environment can be hazardous and misleading. Numerous examples of coatings expected to act cathodically but have, in fact, been anodic have been reported in the literature,<sup>2-5</sup> and specialized lists of galvanic couples in different environments have been compiled.<sup>6-8</sup>

#### **4.04.3 Factors Affecting Choice of Coating**

Many factors are involved in the choice of coating material to be used for any particular application, and these will now be described.

##### **4.04.3.1 Resistance to the Corrosive Environment**

The principal difficulty in assessing the resistance of a coating material to a corrosive environment

lies in an adequate and accurate definition of that environment. Metals exposed to natural atmospheres will corrode at markedly different rates depending upon the degree of pollution present and a number of interrelated meteorological factors. Atmospheric corrosion rates for most of the metals in common use have been published by many authors and by official organizations such as the American Society for Testing and Materials (ASTM).<sup>9</sup> These tables may be consulted for general guidance but must always be used with caution by choosing data for environments that most nearly approach the service conditions concerned. However, purely local conditions can markedly affect the rate of attack. An example of this, in the authors' knowledge, involved the corrosion of galvanized-steel air-intake louvres on the roof of a building in a severe industrial environment; most of the louvres gave satisfactory service, but premature rusting occurred on those that faced in a westerly direction where the prevailing winds exposed them to additional chloride contamination picked up from a nearby river estuary. A detailed knowledge of both the macro- and microenvironmental conditions to be encountered is thus seen to be essential if the best choice of coating is to be made, and it is often desirable to make site inspections before recommending a coating system for a particular application.

When the corrosive environment consists of water or other liquids, the effect of the presence of minor constituents in the liquid as well as the degree of aeration and rate of flow must be taken into account.

##### **4.04.3.2 Practicability of Application**

It is essential to choose a material and a method of application that will provide a coating of adequate thickness with good coverage and distribution over the surface of the article.

Hot-dipped tin coatings are difficult to apply outside the thickness range of 8–38 mm,<sup>10</sup> and hot-dipped zinc coatings do not normally greatly exceed 50 mm in thickness. Hollow sections and excessively large articles may be impractical to handle by the hot-dipping process, and very thin sections may be subject to much distortion.

Electrodeposited coatings may range in thickness from about 0.1 mm to about 25 mm for decorative and protective purposes, though considerably greater thicknesses may be applied in the case of coatings for wear resistance purposes. The shape of the article to be plated greatly influences the thickness and coverage of the electrodeposit. Copper and nickel deposits

cover well and throw well into recesses, and leveling can be obtained during electrodeposition. Zinc gives good coverage but poor leveling, and chromium has a very poor throwing power leading to bare areas in deep recesses of the plated article. Precious metals, because of cost, tend to be electrodeposited in thicknesses of less than 1 mm, and at these thicknesses, porosity of the electrodeposit is a significant factor; acid gold electrodeposits tend to be less porous than the deposits from alkaline baths.

Sprayed metal coatings may be applied without limitations of size of the article to be processed such as may apply for hot-dipping processes, and the thickness and coverage of the coating can be readily controlled during application. Problems can arise, however, with applications involving complex shapes or hollow sections. Coating thicknesses are normally in the range 50–250 mm but considerably greater thicknesses may be built up for applications involving wear resistance, and diffusion heat-treatments may be subsequently applied in order to improve the resistance further. Sprayed metal coatings are of a porous nature and contain a high proportion of oxides produced by the method of application. In service, corrosion products may build up in the pores of the coating which can contribute materially to a stifling of the corrosion reaction, but even so, sacrificial protection of the substrate exposed at any coating discontinuities may still be maintained.

Cladding by pressing, rolling or extrusion can produce a coating in which the thickness and distribution can be readily controlled over wide ranges, and the coatings so produced will be completely free from porosity. Although there is very little practical limit to the thickness of coatings that can be produced in this way, the application of the process is limited to comparatively simple-shaped articles that do not require much subsequent mechanical deformation. Among the principal uses are lead and aluminum sheathing for cables, lead-sheathed sheets for architectural applications and composite extruded tubes for heat exchangers.

#### 4.04.3.3 Compatibility of Galvanic Coupling

Most of the published data on galvanic corrosion concern solid metal couples rather than bimetallic coating systems, and it is important to bear in mind that the same galvanic relationships do not necessarily apply in both cases; nevertheless, useful guidance can be obtained from the data for the solid-couple

systems exposed to suitable environments. Data have been reported<sup>11</sup> for combinations of metals commonly used in the electrical industry; couples involving plated brass, copper, and aluminum were exposed to a 1% salt spray and the corrosion currents (mA) were measured over a 1-week test period. The relative ratings in this test are shown in **Table 1**, and items of particular interest in this table are coatings of aluminum on either brass or copper that are unsatisfactory because of the active galvanic corrosion that occurs at discontinuities. If tin plating is used as an undercoat to the aluminum, corrosion of the substrate is prevented, but if tin is applied as a topcoat over the aluminum (particularly by means of the conventional zincate process) it is sufficiently porous to allow the aluminum to continue to function as an active anode and corrosion can continue.

**Table 1** Performance of various crimped metallic couples in 1% salt spray

---

<i>A. Completely Satisfactory Combinations</i>	
Copper/nickel-plated copper	
Copper/gold-plated copper	
Tin-plated copper/aluminum	
Tin-plated copper/nickel-plated copper	
Tin-plated copper/solder-dipped copper	
Tin-plated brass/aluminum	
Solder-dipped copper/nickel-plated copper	
Nickel-plated copper/gold-plated copper	
Nickel-plated copper/silver-plated copper	
Gold-plated copper/silver-plated copper	
Aluminum/tin-plated aluminum (no copper undercoat)	
<i>B. Satisfactory Combinations, Slight Galvanic Corrosion</i>	
Copper/silver-plated copper	
Solder-dipped copper/tin-plated aluminum	
Copper/tin-plated copper	
Copper/solder-dipped copper	
Copper/reflowed tinned copper	
Silver-plated copper/tin-plated copper	
Silver-plated copper/solder-dipped copper	
Gold-plated copper/tin-plated copper	
Aluminum/tin-plated aluminum (zincate process)	
<i>C. Borderline, Moderate Galvanic Corrosion</i>	
Gold-plated copper/solder-dipped copper	
Tin-plated aluminum/nickel-plated copper	
Aluminum/solder-dipped aluminum	
<i>D. Unsatisfactory, Severe Galvanic Corrosion</i>	
Aluminum/brass	
Aluminum/copper	
Tin-plated aluminum/copper	
Aluminum/nickel-plated copper	
Aluminum/nickel-plated brass	
Aluminum/silver-plated copper	
Tin-plated aluminum/silver-plated copper	
Aluminum/gold-plated copper	
Tin-plated aluminum/gold-plated copper	

---

The relationships given in [Table 1](#) apply to the specific environment quoted, and it must always be remembered that if the conditions are varied, even to only a small extent, different galvanic effects may be produced.

#### 4.04.3.4 Effect of Coating Process on Substrate Properties

The application of any coating process may affect the physical or mechanical properties of the substrate material and any such effects should be considered when choosing the type of coating to be used and its method of application.

With hot-dipping processes, apart from the risk of distortion previously mentioned, the high temperatures involved can produce annealing, for example, softening of brass and copper during hot-tinning. Furthermore, hard and brittle intermetallic-alloy zones are produced during hot-dipping as a result of diffusion of the liquid coating metal into the solid basis metal, for example,  $\text{FeSn}_2$  in the tinning of steel,  $\text{Cu}_6\text{Sn}_5$ , and  $\text{Cu}_2\text{Sn}$  in the tinning of copper – the extent and depth of the alloy formation depending on temperature and time of dipping. Thus, too long a dipping time in hot-dip galvanizing can lead to flaking during subsequent mechanical deformation.<sup>12,13</sup>

Evolution of hydrogen during some electrodeposition processes can cause embrittlement if it diffuses into the substrate; the effect has been reported for chromium and cadmium plating of high-strength steels,<sup>14</sup> and provision is made in relevant standards<sup>15,16</sup> for diffusion heat-treatments after plating to reduce the hazard. Alternatively, zinc or cadmium coatings may be applied by vacuum deposition, thus avoiding any embrittlement of the steel – a process of this nature having been developed by the Royal Aircraft Establishment, Farnborough. Cases have also occurred where cracks in a highly stressed electrodeposit have acted as stress-raisers, which initiate stress-corrosion of susceptible substrate metals.

Although the annealing effects of overheating are avoided when coatings are applied by metal spraying processes – provided that those processes are properly applied – it has been reported<sup>17</sup> that compressive stresses imparted to the substrate by the grit-blasting pretreatment can alter the fatigue properties of the material. Cladding involves extensive cold-working, which may necessitate annealing of the composite material before use.

#### 4.04.3.5 Coating Properties

A number of physical and mechanical properties of coating metals need to be considered when making a choice of metal to be used in a particular application.

Appearance, color, and brightness are important in decorative applications. Copper, zinc, cadmium, nickel, silver, and gold can be readily plated in a bright condition, while tin normally plates as a dull deposit but may be brightened by flash-melting after electroplating (flow brightening process). Aluminum and lead deposits are always dull, but reflective aluminum coatings can be produced by roll-cladding using highly polished rolls. Colors may range from the blue-white of chromium through yellows for gold or brass to the reds of bronzes. Reflectivity after polishing also varies with the coating metal, being very high for silver and rhodium and progressively decreasing in the order aluminum and palladium, tin, zinc, gold, iron, and lead.

Hardness, strength, and wear resistance are prime properties, not necessarily interrelated. For example, rubbing contact between two hard surfaces may produce more wear than with two soft surfaces, though, in general, rubbing contact between one hard and one soft surface causes wear in the softer material. However, mechanical design factors can alter this wear relationship so that the harder material wears to a greater extent, for example, the case of the rapid wear imposed on a steel record needle rubbing against a vinyl record surface. In general, the hardest deposits are those of chromium, nickel and rhodium; with iron, copper, zinc, cadmium, and silver in an intermediate hardness group; with tin, lead, gold, and indium being relatively soft.

Temperature resistance, that is, a combination of melting point and oxidation resistance, may be of prime importance. A general correlation exists between melting point and hardness since both reflect the bond strength of the atoms in the crystal lattice, and the preferred order of coating metals for use in high temperature applications as temperature is increased is silver, aluminum, nickel, rhenium, chromium, palladium, platinum, and rhodium.

The electrical conductivity of coatings is often of secondary importance since they are of thin section and are in parallel with a metallic substrate of larger cross section, which is generally a good electrical conductor. A more important property for coatings used as electrical contacts is surface hardness and the ability to remain free from oxide and tarnish films.

Thus, although aluminum has almost four times the conductivity of tin, it is often tin-plated to improve its electrical contact properties. Other coating metals commonly used for low-voltage applications are gold, tin/lead, silver, palladium, copper, rhodium, and nickel.

#### **4.04.3.6 Economics**

Economic factors are obviously of prime importance when choosing both the coating material and its method of application. Individual items in the economic balance sheet will vary not only with the material and the process but also with availability, local labor costs and factors unique to the design and use of the articles concerned. A further factor that frequently does not receive adequate importance in costing is the ease or otherwise of maintaining the finish to ensure an adequate and efficient service life for the component. In general, though with many exceptions, processing costs may range in ascending order from hot-dipping to plating, spraying, and cladding. The lowest cost group of metals includes zinc, copper, iron, and lead; the intermediate group contains nickel, tin, tin/lead, cadmium, and aluminum; and the highest cost group comprises silver, palladium, gold, and rhodium, though cost relationships may vary from time to time as a result of price fluctuations in response to supply and demand.

Experience in the application of metal-coating processes can materially affect economics. Thus, although it is possible to apply aluminum by electrodeposition, the process is difficult to operate and few metal finishers apply the process; the application of aluminum coatings by hot-dipping or by metal spraying is much more readily accomplished, and more of these types of installations are becoming available on the metal-finishing market.

### **4.04.4 Coatings in Practical Use – Overview**

In modern coating technology, the range of materials used is ever increasing and specific coatings may be chosen and applied, often by specially designed techniques, for particular applications. Details of the behavior of various specific metal coatings are given elsewhere in this book, but some general information on a number of the more commonly applied coating metals is as follows.

#### **4.04.4.1 Zinc**

This is an anodic coating material that may be applied by hot-dipping, metal spraying or electrodeposition, with a good corrosion resistance to most neutral environments, particularly when used in combination with chromate or phosphate passivation treatments. In most cases of atmospheric exposure, zinc will provide good protection to steel, particularly where any sulfur pollution is present, but in rural and pure marine environments the conditions of humidity and chloride pollution level can reduce the effectiveness of zinc coatings and make the use of cadmium more suitable, though the same degree of protection may often be achieved at lower cost by increasing the thickness of the zinc coating. Zinc is the preferred coating for steel used under immersed conditions in scale-forming waters or sea-water and, since it is less toxic than cadmium, it should be used in applications involving welding.

The life of zinc coatings is generally proportional to thickness and independent of the method of application, though it has been reported<sup>18,19</sup> that zinc electrodeposited from the sulfate bath gives a better performance than when deposited from the cyanide bath. Hudson<sup>20</sup> has reported lives for 42-mm-thick zinc coatings on steel ranging from 3½ years in a severe industrial environment (Sheffield) to more than 10 years in a rural environment (Llanwrtyd Wells), and Gilbert<sup>21</sup> quotes lives of 4–5 years in London, 9 years in Cambridge, and 18 years in Brixham.

#### **4.04.4.2 Cadmium**

Cadmium also provides a sacrificial coating to steel and gives better protection than zinc in applications where strong acids and alkalis may be encountered and those involving immersion in stagnant or soft neutral waters. It should be used in applications involving bimetallic contact with aluminum and in electrical applications where ease of solderability is important. Cadmium has a low torque resistance and should be used as a coating material in cases where bolted assemblies have to be frequently dismantled. It also provides better protection than zinc in enclosed spaces where condensation can occur, particularly when there is contamination by organic vapors.

Cadmium is more expensive than zinc. It is usually applied by electrodeposition in thicknesses up to about 25 mm and has a superior tarnish and stain resistance to that of zinc. As with zinc, the life

of cadmium coatings is proportional to thickness; Hudson<sup>20</sup> quotes a life of only 9 months at Sheffield for a 25-mm-thick coating and ~8 years for a 42-mm-thick coating exposed to a marine environment at Calshot.

#### 4.04.4.3 Tin

Tin is applied by hot-dipping or electrodeposition and has a similar corrosion behavior as that of zinc. Coating thicknesses are usually in the range 12–50 mm, and in the lower portion of this range coating porosity can be a factor to be taken into account (see discussions by Kochergin,<sup>22</sup> and Gonser and Strader<sup>23</sup>).

Tin coatings are widely used in the electrical industry because of their good contact properties and in the food industry because of low toxicity. In addition to pure tin coatings, a number of alloy coatings have been developed for special applications, for example, tin–lead (terne plate), tin–zinc, tin–cadmium, tin–bronze, and tin–nickel. Reference should be made to the relevant chapter in this book and to the publication by Britton<sup>24</sup> for data on the corrosion of tin and its alloys.

#### 4.04.4.4 Aluminum

Aluminum may be applied as coatings by metal spraying, cladding, hot-dipping and electrodeposition, though the last-named process is difficult to apply, and by far, the largest proportion of aluminum-coated metals are produced by the first two methods.

In atmospheric exposure to industrial environments, its corrosion rate is only about one-third that of zinc and the corrosion reaction is stifled by the tenacious oxide which is produced; nevertheless, it can frequently function as an anodic coating both for steel and for the less corrosion-resistant aluminum alloys.

Hudson<sup>20</sup> reported lives of about 4½ years for 38-mm-thick metal-sprayed aluminum coatings on steel exposed at Sheffield, and more than 11½ years for coatings 75 mm thick. Sprayed aluminum coatings (~125 mm thick) have also provided complete protection against exfoliation and stress corrosion to aluminum–copper–magnesium (HE15) and aluminum–zinc–magnesium (DTD 683) alloys in tests lasting up to 10 years in industrial and marine environments.<sup>25,26</sup>

#### 4.04.4.5 Nickel

Nickel has an inherently high corrosion resistance, particularly in chloride-free atmospheres, and is

widely used as a coating material in the chemical industry. When exposed to the atmosphere, rapid tarnishing and slow superficial corrosion occur; for this reason, nickel coatings are seldom used alone, but they are widely used as undercoats beneath bright chromium to give decorative and protective schemes for steel, zinc-alloy and copper-alloy consumer goods notably in the automobile and domestic hardware industries. Used in this way, corrosion of the nickel undercoat is confined to localized pitting that develops at discontinuities in the chromium layer and which will eventually penetrate into the substrate. Many special processing variations have been developed to improve the corrosion resistance of these composite coatings, and recommended systems are detailed in standards documents such as BS 1224 (1970).<sup>16</sup>

#### 4.04.4.6 Lead

Lead coatings are mainly applied by cladding and find principal use in the chemical industry for resistance to sulfuric acid, for cable sheathing resistant to attack by soils and in architectural applications where resistance to industrial atmospheres is particularly good. They rely for their protective action on the formation of insoluble corrosion products that stifle the corrosion reaction and lead to very long service lives, but the corrosion resistance is impaired when chlorides are present.

#### 4.04.4.7 Copper

Except in the case of certain decorative and electrical applications, copper is seldom used as a coating material in its own right owing to the rapidity with which it tarnishes, particularly in sulfur-polluted environments. Nevertheless, its atmospheric corrosion resistance is good owing to the development of the well-known green patina of basic copper salts, which give protection against further corrosion of the metal. When copper coatings are used for their decorative effect, the high luster and distinctive color are retained by applying a protective coating of transparent lacquer which may contain an inhibitor, for example, benzotriazole.

By far, the largest use of copper as a coating metal is in the form of undercoats to other protective schemes, such as the nickel plus chromium systems, where they offer great benefit by leveling the surface to improve the brightness of the finished article. Their role in the corrosion protection of the substrates is complex; they are themselves often preferentially attacked when overlay coatings are penetrated by



corrosion, and can stimulate enhanced corrosion of the substrate when penetration through their thickness occurs. On the other hand, however, in the case of coatings of bright nickel plus microdiscontinuous chromium, the use of a copper undercoat is known to improve corrosion resistance and to extend the period of protection of the substrate.<sup>27</sup>

#### 4.04.4.8 Chromium

Chromium is highly resistant to atmospheric corrosion, being almost inert in most atmospheres, and is therefore used as a thin, bright overlay to other coatings to retain decorative appeal for long periods. The thickness of these coatings, applied by electrodeposition, is normally in the range 0.3–1.3 mm. In the lower thickness range, the coating contains minute discontinuities which cannot be eliminated by increasing the thickness, since spontaneous cracking of the deposit occurs as the thickness builds up. The tendency to cracking of chromium electrodeposits is encouraged and put to good use by inducing cracking on a microscale by processing modifications. When this is done, the microcracked deposits so produced provide greater protection to nickel-plated steel and zinc-alloy substrates exposed to the atmosphere by increasing the area of nickel exposed at the microdiscontinuities, and thereby reducing the corrosion current density at individual corrosion sites with a consequent reduction in the rate of penetration through the nickel layer.

Chromium is also a very hard metal with excellent wear resistance, and so is widely used as a coating material for engineering applications. For these purposes, coatings are applied by electrodeposition which may be several millimeters thick. These hard engineering chromium coatings invariably contain fine cracks and fissures which can allow corrodents to attack the substrate, but this is not often a hazard in service and in many cases they are advantageous in providing a means of retaining lubricant on the working surface during use.

#### 4.04.4.9 Precious Metals

Gold and platinum, being highly noble metals, can provide highly corrosion-resistant coatings, but are rarely used for this application alone because of cost. Silver, though cheaper than gold or platinum, has a somewhat lower corrosion resistance since it is very prone to attack by sulfides, which cause dark tarnishing.

The principal use of gold is as a very thin coating about 0.05 mm thick for electrical and electronic applications. Because of the thinness of gold electrodeposits, porosity must be very carefully controlled since seepage of corrosion products from substrate or undercoat exposed at these pores can have serious adverse effects on both appearance and electrical properties of the composite. The porosity can vary with the thickness of the deposit (**Figure 1**), and with the type of plating bath and with its method of operation (**Figure 2**), and the phenomenon has been extensively studied by Clarke and many others.

#### 4.04.5 Recent Developments

The general principles of protection of metal substrates by metallic coatings are, of course, clear. Nevertheless, detailed considerations and particular aspects have received continued attention and some

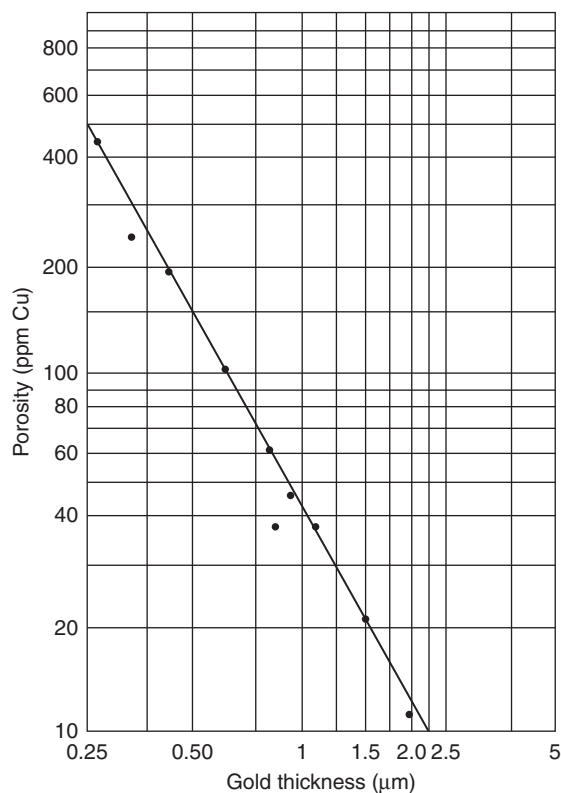


**Figure 1** Log-log plot of gold-plate porosity against thickness for the conventional hot-cyanide gold-plating bath on copper substrate. The porosity was determined by the amount of copper (ppm) dissolved under standard conditions by an ammonia–ammonium persulfate test solution.



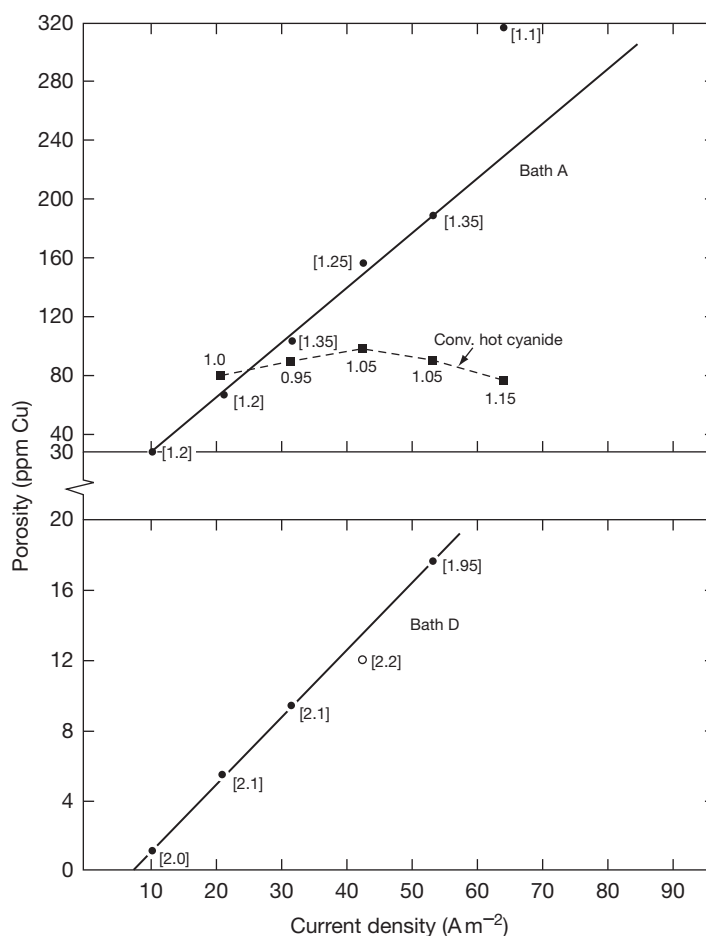


**Figure 2** Linear plots of the effect of current density on the porosity, expressed as ppm Cu, for three different gold-plating baths. The numbers next to each point show the actual average thickness (in mm) for each test. Bath A was a proprietary alkaline cyanide bath using silver as a brightener. Bath D was an acid gold bath containing cobalt and an ethylenediaminetetraacetic acid (EDTA) gold complex.

of these developments can be highlighted. Among general treatments, several books may be noted dealing with the coating spectrum and the theory of protection,<sup>28–30</sup> and a book on the testing of such coatings for product performance assessment in relation to quality assurance is also available.<sup>31</sup>

#### 4.04.5.1 Galvanic Coupling

This particular topic remains vital but often controversial especially when attempts are made to codify practice and opinion. The British Standards Institution have published a ‘Commentary on corrosion at bimetallic contacts and its alleviation,’<sup>32</sup> which represents an important first attempt to produce such a code. It lists 23 metals and alloys coupled to each other in three atmospheric and two immersed environments using a four-point subjective scale to describe behavior.

The shortcomings of such a code are mainly attributable to the limited number of environments considered because specific behavior is generally related to specific metal–electrolyte behavior which can result in substantial potential changes or even polarity reversals. A polarity reversal implies a large potential at one or both metal electrodes and may be attributed to two main factors:

1. onset of passivity on the more base (negative) metal, thereby raising its surface potential to more noble values;
2. solution complexants reacting with free metal ions of the corroding metal thereby lowering that metal’s corrosion potential.

The features of instances of such potential reversals have been described<sup>33</sup> and include tin coatings on steel in various foodstuffs, particularly acid fruits,<sup>34,35</sup>

cadmium coatings on steel in hard waters,<sup>36</sup> and zinc and aluminum for cathodic protection of steel in natural groundwaters.<sup>37,38</sup>

#### 4.04.5.2 Porosity

The study of coating porosity and its effect on corrosion rates continues to be an important subject and is generally directed at establishing the minimum thickness that can be allowed in a specification, related of course to a test/service corrosion environment. Porosity usually decreases exponentially with coating thickness (Figure 1 represents a relationship for part of the range only) and the minimum acceptable thickness can be defined according to 0, 0.5, 1.0%, etc. porosity level or to a threshold corrosion rate. The ability to measure porosity rapidly and precisely is therefore of importance and the whole subject has been critically reviewed by Clarke.<sup>39</sup> In many cases, the purpose of such testing is to separate effects on porosity of the coating process itself and the substrate preparation and roughness; the latter is often the aspect most susceptible to improvement.

The comparative tests for porosity are not very accurate or susceptible to statistical analysis. A number of electrochemical tests have been devised that are more sensitive and give better numerical data; such tests depend upon selection of a suitable solution for each coating–substrate combination but have shown considerable promise and commercial instruments have been marketed.<sup>40–42</sup>

#### 4.04.5.3 Environment Classification

All testing has to be related to environmental conditions whose characteristics must be defined. The relation of accelerated corrosion test condition to real service conditions is one aspect, while another is defining classes of environment and relating them to characteristic corrosion performance in order to produce useful specification guidelines. BS5493:1977 is an attempt to do this using four categories appropriate primarily to the United Kingdom (Table 2). Such a classification is clearly an oversimplification, but represents an important step in this particular direction.

#### 4.04.6 Alternative Coating Systems

The drive of financial economy has been manifest in terms of the need to establish alternative coating

**Table 2** Atmospheric corrosion environments<sup>a</sup>

Type 1	Nonpolluted inland	Rural areas, town suburbs
Type 2	Polluted inland	Industrial towns and cities
Type 3	Nonpolluted coastal	Type 1 but with marine spray
Type 4	Polluted coastal	Type 2 but with marine spray

<sup>a</sup>BS 5493:1977.

systems for particular applications based not on technical performance alone but also on cost saving and sometimes environmental or ecological considerations. Thus expensive metals may be challenged by cheaper metals and alloys, and cheap metals by non-metals. Every coating is under such economic pressure; some have withstood by reducing thickness, improving quality, and maintaining performance, but some have succumbed to the competition. Gold in particular has faced competition from brass electrodeposits in the cheap market, titanium carbonitride (CVD produced) for wear-resistant applications and Pd-Ni alloy electrodeposit for electrical connectors and contacts, each representing cost saving and improvement in selected properties.<sup>40–42</sup>

The desire to replace cadmium is generally attributed to its toxicity, both in terms of process pollution and product corrosion, and several alternatives are feasible: thicker zinc, tin–zinc alloy or tin–nickel alloy depending upon the precise application.<sup>43</sup> The demise of decorative nickel–chrome systems in the automotive industries of the world is partly due to cost and partly to market image, and not to technical performance where major improvements took place in the period 1960–1975 through the establishment of duplex nickel underlayers and microdiscontinuous chromium top layers. In the 1980s, the trend has been towards black finishes produced generally by powder-applied epoxy polymers.

A recent publication by Dini<sup>47</sup> provides a relatively novel text covering the material science of coatings and substrates.

#### 4.04.7 Multilayer Coatings

The use of layered electrodeposits has been practiced since the 1800s and has continued to the present day. The usual reason is for the use of a thick functional underlayer with a thin decorative or

cosmetic top layer; cost of a top layer such as gold is clearly an important factor. In the case of chromium, which is stressed and liable to cracking in service, the underlayers of nickel provide both protection against corrosion and resistance against crack continuation to the substrate. Nickel has been a common underlayer but recently concerns of nickel allergy with consumer-jewellery products have led to nickel-free underlayers, for example, Cu–Sn–Zn, being used. Such underlayers are usually of 1–20  $\mu\text{m}$  thickness, the top layer being 0.1–2  $\mu\text{m}$  thick. The history and wider development of such layered systems have been reviewed elsewhere.<sup>48–50</sup>

Underlayers for electrodeposits are deliberately added and are now an integral part of the coating specification. The origin has clearly been the need to increase corrosion resistance with a vulnerable top layer. The logic has been that if one layer can have a dramatic effect, perhaps many layers will continue the trend. The technique has been to use pulse techniques with specially formulated solutions and often potential, not current, control. In this way, an alloy plating solution of A and B can be pulsed to yield alternate layers of A-rich and B-rich layers. The length of the current pulses determines the layer thickness by a Faraday–Coulomb calculation. A number of layered electrodeposits have been studied, for example, Zn–Ni, Zn–Co, Zn–Fe, and enhanced corrosion resisting performance has been reported using layer thicknesses of  $\sim 1 \mu\text{m}$ . It has been noted that for steel, it is generally better to use an initial layer rich in zinc, and total thicknesses up to 50  $\mu\text{m}$  have been produced. (It should be noted that the alternative production technique of using two solutions with the substrate being moved from solution to solution is possible but is much less elegant because of the need to rinse between plating stations and the risk of passivation during the transfer.) Similarly, pumping alternate solutions and rinses through a fixed cell is possible but again rather inconvenient.

The ideal alloy system has often been stated to be Cu–Ni, as the alloy is one continuous FCC phase. This has also been well studied but for enhanced magnetic characteristics (giant magnetoresistive (GMR) applications). The solution requires a mild complexant, typically citrate or tartrate, in a simple acid formulation to be most effective.

The same principles have been adapted to attain enhanced coating hardness or strength for which thicknesses in the nanometer range are needed, and some promising results have been achieved. The nanometer thickness appears to exploit the grain

interfaces as dislocation ‘wave’ guides, thereby restricting ductility in depth direction.

These layering techniques have long been recognized as coating design opportunities and should always be part of any specification. Substantial development can be expected leading to more widespread incorporation into standard specifications.<sup>48–50</sup>

#### 4.04.8 Metal Whiskers

Metal whiskers are primarily, but not exclusively, found on electrodeposited coatings during product storage generally over relatively long periods of time. The phenomenon of such spontaneous metallic whisker growth can be identified, commonly, for metals such as tin, zinc, and cadmium. The first real documented evidence is from such growths emanating from cadmium-electroplated surfaces in capacitors in aircraft radios during the Second World War.<sup>51</sup> It soon became evident that such growths were more problematic on tin and perhaps, to a lesser extent, zinc surfaces. Whisker growths can vary in their morphology, with filamentous and nodular outcrops being the most common. Long filaments often pose the biggest potential problems because of their size and propensity and becoming detached from the metal surface from which they are growing. With tin finishes widely utilized in electronics, the chances of such growths causing reliability issues are obvious.

A single mechanism for whisker growth still eludes researchers. Many attempts have been made to provide such a theory: well known mechanisms include dislocation theories involving Frank–Read sources,<sup>52</sup> recrystallization,<sup>53</sup> two-stage dislocation involving climbing and gliding of dislocation loops,<sup>54</sup> and a cracked oxide theory.<sup>55</sup> With electronic devices reducing in size and intercomponent spacing becoming commensurately less, the threat from failures, particularly ‘shorting,’ is ever present. Until recently, one way of reducing the negative effects of tin whiskers was through alloying the metal with lead. However, with the advent of environmental concerns over the use of lead in electronics (and elsewhere) and the implementation of the so-called Pb-free solders, the occurrence of tin whisker growth may become more problematic. The continued use of tin finishes (particularly bright tin) is also problematic from a whisker growth viewpoint.

Recent investigations<sup>56</sup> have suggested that electrodeposited Sn–Mn alloys are capable of producing

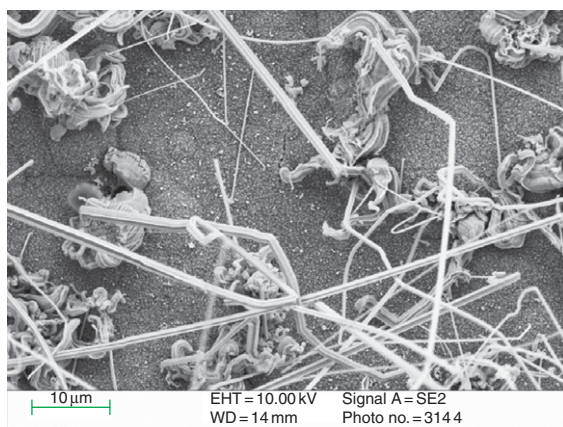


**Figure 3** Scanning electron micrograph of tin whisker growth on an electrodeposited tin–manganese alloy coating.<sup>57</sup>

whisker growth after only a few hours at room temperature following coating formation (see [Figure 3](#)). Subsequent whisker growth was rapid and profuse.

Although the occurrence of cadmium whiskers may not be a major cause for concern due to its reduced usage (due to a poor environmental status), zinc whisker growth has come into prominence in recent years due to the metal's use as a protective coating in raised flooring in computer rooms. One particular incident in the United States involving computers in the Colorado Department of State's data center failing has been highlighted as a serious concern.<sup>58</sup> The occurrence of zinc-electroplated finishes in the vicinity of electronic components (e.g., on steel casings) must also be a cause for concern. The recent discovery of zinc whiskers on hot dip-galvanized surfaces<sup>59</sup> is a further indication of the potential size of the problem.

The perceived future problems associated with metal whisker growth, particularly on tin and zinc coated surfaces, are a cause for concern. The reasons for the occurrence of these types of growth need to be understood. At present, mitigation strategies are mainly based around the use of polymeric conformal coatings on areas of concern. The coatings do not preclude whisker growth underneath and, depending on the coating type and thickness, actual breaches of the coating layers have been reported.

For those wanting more information on whisker growth, a NASA website exists that is generally regarded as an excellent and comprehensive source of information.<sup>60</sup>

## References

1. Layton, D. N. *Trans. I.M.F.* **1965**, 43(14), 153.
2. Hoar, T. P. *Trans. Faraday Soc.* **1934**, 30, 472.
3. Koehler, E. L. *J. Electrochem. Soc.* **1956**, 103, 486.
4. La Que, F. L. *Corrosion, News Section* 8(1), April **1952**.
5. Compton, K. G.; Mendizza, A.; Bradley, W. W. *Corrosion* **1955**, 11, 35.
6. La Que, F. L.; Cox, G. L. *Proc. Am. Soc. Test. Mat.* **1940**, 40, 670.
7. Evans, U. R.; Rance, V. E. *Corrosion and its Prevention at Bimetallic Contacts*; HMSO: London, 1958.
8. McKay, R. J.; Worthington, R. *Corrosion Resistance of Metals and Alloys*; ACS Monograph Series, 1936.
9. *Metal Corrosion in the Atmosphere*; A.S.T.M. Special Technical Publication No. 435, 1968.
10. Hoare, W. E. *Hot Tinning*; Tin Research Institute: Perivale, Middlesex, 1947; p 7.
11. Frant, M. S. *Electron. Des.* **1961**, 20, 112.
12. Mathewson, C. H. *Zinc*; Reinhold: New York, 1959; pp 462–465.
13. Spencer, L. F. *Metal Prod. Manuf.* **1960**, 17, 27.
14. Cotton, W. L. *Plating* **1960**, 47, 169.
15. BS EN12329-30:2000 – Electroplated Coatings of Cadmium and Zinc on Iron and Steel (formerly BS 1706).
16. BS EN12540:2000 – Electroplated Coatings of Nickel and Chromium (formerly BS 1224).
17. Whittaker, J. A.; King, H.; Liddiard, E. A. G. In *Proceedings of the 2nd International Congress on Metallic Corrosion*, 1966, pp 229–235.
18. Hippensteel, C. L.; Borgmann, C. W. *Trans. Am. Electrochem. Soc.* **1930**, 58, 23.
19. Biestek, T. *Met. Finish.* **1970**, 68(4), 48.
20. Hudson, J. C.; Stanners, J. E. *J. Iron and Steel Inst.* **1953**, 175, 381.
21. Gilbert, P. T. *J. Appl. Chem.* **1953**, 3, 174.
22. Kochergin, V. P. K.; Prostkov, M. F.; Nimvitskaya, T. A. *Konserv. Ovoshchesushil. Prom.* **1959**, 14, 22.
23. Gonser, B. W.; Strader, J. E. In *The Corrosion Handbook*; Uhlig, H. H., Ed.; Wiley: New York, 1948.
24. Britton, S. C. *The Corrosion Resistance of Tin and Tin Alloys*; Tin Research Institute: Perivale, Middlesex, 1951.
25. Carter, V. E.; Campbell, H. S. *J. Inst. Met.* **1960**, 89, 472.
26. Carter, V. E.; Campbell, H. S. *Br. Corros. J.* **1969**, 4(1), 15.
27. Clauss, R. J.; Klein, R. W. In *Proceedings of the 7th International Metal Finishing Conference, Hanover (Interfinish 68)*, **1968**, p 124.
28. Carter, V. E. *Metallic Coatings for Corrosion Control*; Newnes-Butterworths, 1977.
29. Gabe, D. R., *Principles of Metal Surface Treatment and Protection*, 2nd ed.; Pergamon, 1978.
30. Gabe, D. R. Ed. *Coatings for Protection*; Inst. Prod. Eng.: London, 1983.
31. Carter, V. E. *Corrosion Testing for Metal Finishing*; Butterworths, 1982.
32. PD6484: 1979, British Standards Institution, London.
33. Gabe, D. R. *Bull. Inst. Corros. Sci. Technol.* **1981**, 19(3), 2–4.
34. Willey, A. R. *Brit. Corros. J.* **1972**, 7, 29–35.
35. Sherlock, J. C.; Britton, S. C. *Brit. Corros. J.* **1972**, 7, 180–183.
36. Zanker, L.; Yahalom, J. *Corros. Sci.* **1969**, 9, 157–167.
37. Ashworth, V.; Fairhurst, D. *Corros. Sci.* **1975**, 15, 669–686.
38. Gabe, D. R.; Shirkhanzadeh, M. *Brit. Corros. J.* **1980**, 15, 216–221.
39. Clarke, M. In *Properties of Electrodeposits: Their Measurement and Significance*; Sard, R., Leidheiser, H., Ogburn, F., Eds.; Electrochemical Society: USA, 1975.

40. Notter, I. M.; Gabe, D. R. *Corros. Rev.* **1992**, *10*, 217.
41. Notter, I. M.; Gabe, D. R. *Trans. I.M.F.* **1990**, *68*, 59.
42. Notter, I. M.; Gabe, D. R. *Corros. Sci.* **1993**, *10*, 217.
43. Stevenson, J. S. *Trans. I.M.F.* **1981**, *59*, 113–117.
44. Whitlaw, K. J. *Trans. I.M.F.* **1982**, *60*, 141–146.
45. Graham, A. H.; Pike-Bieganski, M. J.; Updegraff, S. W. *Plating Surf. Finish.* **1983**, *70*(11), 52–57.
46. Carter, V. E. *Met. Finish. J.* **1972**, *18*, 304–309.
47. Dini, J. W. *Electrodeposition: The Material Science of Coatings and Substrates*; Noyes Publications: Park Ridge, NJ, 1993.
48. Gabe, D. R. *Electrochim. Acta* **1994**, *39*, 115.
49. Gabe, D. R. *J. Korean Inst. Surf. Eng.* **1999**, *32*, 195.
50. Gabe, D. R.; Wilcox, G. D. *Met. Finish. (USA)* **2002**, *100*(4), 18.
51. Reported in Cobb, H. L. *Monthly Rev. Am. Electroplaters Soc.* **1946**, *33*(28), 28.
52. Eshelby, J. A. *Phys. Rev.* **1953**, *91*, 755.
53. Ellis, W. C.; Gibbons, D. F.; Treuting, T. C. In *Growth and Perfection of Crystals*; Doremus, R. H., Roberts, B. W., Turnbull, D., Eds.; Wiley: New York, 1958; p 102.
54. Lindborg, U. *Acta Metall.* **1976**, *24*, 181.
55. Tu, K. N. *Phys. Rev. B* **1994**, *49*, 2030.
56. Chen, K.; Wilcox, G. D. *Phys. Rev. Lett.* **2005**, *94*, 066104.
57. Lu, D.; Chen, K.; Wilcox, G. D. Unpublished work.
58. Svaldi, A. *The Denver Post*, Denver, CO, USA, 2004; p C01 1 July.
59. Lahtinen, R.; Gustafsson, T. E. *J. Appl. Surf. Finish* **2007**, *2*(1), 15.
60. NASA Goddard Space Flight Centre. <http://nepp.nasa.gov/whisker>

## 4.05 Diffusion Coatings

**J. R. Nicholls, K. A. Long, and N. J. Simms**

Cranfield University, Cranfield, Bedfordshire MK43 0AL, UK

© 2010 Elsevier B.V. All rights reserved.

4.05.1	Introduction	2532
4.05.2	The Pack Cementation Process	2534
4.05.2.1	The Pack Aluminide Process	2534
4.05.2.2	Inward Growth Diffusion Coatings	2537
4.05.2.3	Outward Grown Diffusion Coatings	2538
4.05.3	Other Process Methods to Form Diffusion Coatings	2538
4.05.3.1	Slurry Cementation	2538
4.05.3.2	Fluidized Bed Techniques	2540
4.05.3.3	Metallizing	2541
4.05.3.4	Molten Salt Baths	2541
4.05.3.5	Gas and Vapor Phase Chemical Vapor Deposition Processes	2542
4.05.4	Modified Aluminide Coatings	2543
4.05.4.1	Platinum Aluminide Coatings and Bondcoats	2544
4.05.4.2	The Role of Impurities Introduced in Coating Manufacture	2546
4.05.4.3	Chromium- and Silicon-Modified Aluminides	2548
4.05.4.4	Reactive Element-Modified Aluminide Coatings	2549
4.05.5	Mitigating Substrate Alloy Interdiffusion Effects	2550
4.05.5.1	Smart Coating Concepts	2551
4.05.6	Summary and Conclusions	2552
References		2553

### Abbreviations

<b>APS</b>	Air plasma spray
<b>CVD</b>	Chemical vapour deposition
<b>DBTT</b>	Ductile to brittle transition temperature
<b>EB-PVD</b>	Electron beam physical vapour deposition
<b>FBR-CVD</b>	Fluidized bed reactor-chemical vapour deposition
<b>HTLA</b>	High temperature, low activity – referring to Al activity in the CVD process
<b>HVOF</b>	High velocity oxy-fuel
<b>LTHA</b>	Low temperature, high activity – referring to Al activity in the CVD process
<b>MCFC</b>	Molten carbonate fuel cell
<b>PVD</b>	Physical vapour deposition
<b>TCP</b>	Topological close packed
<b>TMF</b>	Thermo-mechanical fatigue
<b>VPS</b>	Vacuum plasma spray

### 4.05.1 Introduction

Diffusion coating processes have been applied for more than half a century as a cost-effective method of improving the environmental resistance of a base alloy by enriching the surface in Al, Cr, Si, B, Ti, Zn, etc. The choice of surfacing material to be used depends on the base alloy and the final application of the component once surface-treated. For example, bolt stock are widely available zinc-coated using the sheradizing process to resist atmospheric and aqueous corrosion, while for high temperature applications, similar bolt materials could be chromized, that is, surface-enriched in chromium to produce a stainless steel surface layer. Probably the most exotic of these is the current practice to plate turbine blades with 5–10  $\mu\text{m}$  of platinum, diffuse and then vapor-aluminize to produce a platinum aluminide, a high temperature oxidation-resistant coating that may be also used as a



bondcoat for thermal barrier coatings for first-stage turbine blades in aero and industrial gas turbines.

Advanced applications include the surface engineering of materials and components for aerogas turbines, industrial gas turbines, medium speed diesels, automotive petrol engines, steam turbines, various power plant components, heat exchanges as well as catalytic reactors in chemical and petrochemical process plant. These illustrate the breadth of diffusion-coating applications.

From a surface engineering perspective, the final selection of the most suitable surface treatments/coatings must consider the following:

- (i) the operating temperature, both of the component in service and the part/component during coating manufacture and heat treatment;
- (ii) the service environment, duty cycle, and load-bearing capability of the treated components;
- (iii) the desired design life and the influence of the service temperature and duty cycle on long-term metallurgical stability, with respect to oxidation, corrosion and interdiffusion with the substrate;
- (iv) ease of manufacture, reproducibility, and the unit cost of the coating, compared to other manufacturing routes that may involve more costly corrosion-resistant alloys.

Obviously, loss of surface protection (passivation) can result in very high rates of attack to the substrate. In many cases, failure of a surface coating could make substrate attack worse, and may, on occasions, lead to catastrophic component failure. Even when not catastrophic, it is bound to be costly as a result of unplanned outage, downtime, and loss of production. Hence, the principal reason for applying a surface treatment of coating is to ensure that the coating is capable of operating efficiently throughout its design life. Diffusion coatings often are proven to be a cost-effective solution in this respect. Many diffusion-coating processes are so well established that international standards exist for their manufacture: for example, ASTM B 874-96 (2008) 'Standard specification for chromium diffusion coating applied by pack cementation'<sup>1</sup>; ASTM B 875-96 (2008) 'Standard specification for aluminum diffusion coating applied by pack cementation'<sup>2</sup>; and British Standard BS 4921 'zinc deposition using the "sherardising" process.'<sup>3</sup>

Pack-chromizing was in widespread use in the early 1950s<sup>4</sup> to increase the oxidation/corrosion resistance of low alloy steels. In the late 1960s, aluminizing was first used for the protection of superalloy gas turbine

aerofoils.<sup>5-7</sup> Aluminide diffusion coatings are now routinely applied to nickel-base superalloy blades and vanes used in the hot sections of gas turbines to enhance their resistance to high temperature oxidation and hot corrosion. Plain aluminides have provided cheap and cost-effective solutions to protect superalloy components within the high-pressure turbine of both aero and industrial gas turbines. As such, they are probably the most widely used coatings in service within the gas-turbine industry. There was renewed interest in siliconizing and silicon-modified aluminide diffusion coatings for high temperature service in the early 1970s<sup>8-11</sup> when novel solutions to the low-temperature hot corrosion problems associated with contaminants in marine turbine plants burning impure fuels were required. This interest continues with development of multifuel-capable plants that may be fired on gasified coal, biomass, or waste-derived fuels<sup>12</sup> and as coating methods to coat the internal cooling passages of turbine blades.<sup>13,14</sup>

These aluminizing, chromizing, and siliconizing processes result in enhanced corrosion resistance through the formation of protective thermally grown oxides of  $\text{Al}_2\text{O}_3$ ,  $\text{Cr}_2\text{O}_3$ , and  $\text{SiO}_2$  as discussed elsewhere in this book. It is also possible to produce diffusion coatings containing a combination of aluminum and chromium (chromaluminizing)<sup>15-26</sup> or aluminum and silicon<sup>8-13</sup> plus modified aluminides containing precious metals (Pt, Pd)<sup>6,27-34</sup> or reactive elements (Y, Hf and Zr).<sup>35-45</sup> The performance of these modified aluminide coatings will be discussed later in this chapter.

Diffusion coatings can be applied to hot gas components using a variety of techniques including pack cementation, slurry cementation, and metallizing. Comprehensive reviews of the methods of deposition of diffusion coatings are given in Goward *et al.*,<sup>5</sup> Goward and Boone,<sup>6</sup> Grisaffe,<sup>7</sup> Streiff and Boone,<sup>30</sup> Meier and Pettit,<sup>31</sup> Pichoir,<sup>46</sup> Goward,<sup>47</sup> Goward and Cannon,<sup>48</sup> Mevrel,<sup>49</sup> Nicholls,<sup>50,51</sup> and Pomeroy.<sup>52</sup> All diffusion coatings, whether depositing zinc vapor onto steels (sheradizing) for aqueous/atmospheric corrosion protection, or forming high temperature oxidation-resistant nickel or platinum aluminides, are formed as a result of two distinctly similar process steps, no matter what the manufacturing method used.

1. *The solute elements must be brought into contact with surface to be coated* In the sheradizing process (zinc deposition), the vapor pressure of zinc within the pack (it is a pack cementation-based process) is sufficiently high that no vapor-phase activator is

required; thus, zinc vapor generated in the pack directly deposits onto the component surface, ready for step 2, which is the 'diffusion' process. However, for most metallic systems, this is not the case; instead, an intermediate step is required, which is the production of a vapor species with a high solute metal content. This is most commonly achieved through the use of a halide salt, or salt mix, which may involve fluoride, chloride, or iodide species. Bromide species are almost never used for health reasons, although thermodynamically there is no reason why they should not be used. These halide additions are known as 'halide activators' in the industry.

2. *The solute diffuses into the component surface* Step 2 is a key stage in the manufacture of a diffusion coating. This diffusion step forms the surface alloy or intermetallic compound. The process temperature influences the rate of diffusion, which species may diffuse and the metallurgy of the surface compound that may form and is, therefore, a critical parameter in the processing and manufacture of diffusion coatings. This aspect will be explained in more detail using the 'pack-aluminizing' process as a case study (see [Section 4.05.2.1](#)). As well, time at temperature defines the thickness of the coating formed during this diffusion step.

Thus, the main differences between diffusion-coating process routes reflect the method by which solute and substrate are brought into contact. The time at temperature controls the degree of interdiffusion, establishes the concentration gradients that will develop from the surface to the interior of the coating and defines the various layers that may form as dictated by thermodynamic and kinetic considerations.

**Table 1** summarizes the currently available diffusion-coating process routes, together with a selection of elements that may be enriched into the substrate surface using these methods. Each of these process routes will be briefly reviewed.

#### **4.05.2 The Pack Cementation Process**

Pack cementation is still the traditional route used to apply diffusion coatings, with standard procedures established for chromium,<sup>1</sup> aluminum,<sup>2</sup> and zinc deposition.<sup>3</sup> For example, within the gas turbine industry, pack cementation was introduced into aero-engine service in 1957<sup>48</sup> and has been widely used to

coat turbine components since the mid-1960s.<sup>6,46–48</sup> The coatings produced were based on the formation of nickel or cobalt aluminides and this class of coating is still extensively used, probably satisfying some 75–80% of the current world market, for protecting turbine blades under aero, marine, and industrial turbine service.

In this process, the components to be coated are buried in a 'pack,' contained in a sealed retort. **Figure 1** shows a schematic diagram of a typical retort used to produce diffusion coatings, and **Figure 2** shows a photograph of the quarter-size commercial production facility at Cranfield University.

The retort is heated to the desired processing temperature under either an inert gas or hydrogen atmosphere to prevent oxidation. The exact process cycle, time, and temperature are dependent on the required coating, coating thickness and the subsequent substrate heat treatment. The pack contains a donor alloy that releases solute material at a known rate and hence determines the pack activity, a halide activator that dissociates during the process cycle and acts to transport the solute material from the pack to the component to be coated and an inert oxide diluent to prevent pack sintering.

Typical pack compositions used to produce a range of metallic coatings are given in **Table 2**. Of these, the three diffusion-coating processes that are most widely used are: 'sheradizing' to zinc-alloy coat many small steel parts in a wide range of manufacturing sectors from the building industries, through domestic white goods to many automotive parts to impart corrosion resistance<sup>3</sup>; 'chromizing' which may be used to coat a wide range of steel, stainless steel and nickel or cobalt-based superalloys to impart improved corrosion resistance for temperatures up to and sometimes in excess of 800 °C<sup>1</sup>; and 'aluminizing' which is widely used in the aero and industrial gas turbine sector to develop intermetallic surface layers that impart enhanced corrosion resistance, thermal stability and, for some applications, wear-resistant properties. The pack aluminizing process will be used as an example. The formation of aluminide coatings by pack cementation has been extensively studied, and details of the process and characteristics of the coating are well documented in the literature.<sup>3,5,6,15–18,20–31,35–42,46–52</sup>

##### **4.05.2.1 The Pack Aluminide Process**

During the aluminizing process, material from the pack is transferred to the component surface through the formation of intermediate volatile aluminum

**Table 1** Diffusion coating process routes

Process route	Process characteristics	Diffusion coatings that may be produced on ferrous materials and superalloys												
		Al	B	C	Cr	Cu	Mo	N	Nb	Si	Ta	Ti	V	Zn
Pack cementation	<ul style="list-style-type: none"> <li>Gas phase transport</li> <li># source material as a powder</li> <li># halide activator</li> <li># 700–1200 °C</li> <li>Solid state diffusion</li> <li># source material as a fine powder</li> <li># temperature below the alloy melting point</li> <li># no activator</li> </ul>	■	■	■	■	■	■		■	■	■	■	■	■
Slurry cementation	<ul style="list-style-type: none"> <li>Spray or dip coat application</li> <li># coating material, halide activator and organic binder prepared as a paint or slurry</li> <li># heat treated after coating</li> <li>700–1200 °C</li> </ul>	■			■					■				
Fluidized bed methods	<ul style="list-style-type: none"> <li>Activated gas fluidization</li> <li># the halide activator is incorporated in the fluidizing gas</li> <li># the coating material is in the fluidizing bed</li> <li># 500–1100 °C</li> </ul>	■		■	■					■		■		
Molten salt bath processes	<ul style="list-style-type: none"> <li>Direct thermochemical processing</li> <li># 500–900 °C</li> </ul>		■	■	■			■						
	<ul style="list-style-type: none"> <li>Metallizing</li> <li># an electrolytic process in alkali fluoride solvents</li> <li># 500–1200 °C</li> </ul>	■				■		■						
Gas or vapor phase processes	<ul style="list-style-type: none"> <li>Over pack process</li> <li># similar to pack process, but components processed in the gas above the pack</li> <li># 900–1200 °C</li> </ul>	■			■									
	<ul style="list-style-type: none"> <li>Vapor phase sources</li> <li># Halide vapor phase sources generated in a separate vapor generator</li> <li># 900–1200 °C</li> </ul>	■		■	■			■						

monohalide gas, and as such the coating process is probably more accurately described as a chemical vapor deposition (CVD) process. Interdiffusion between the depositing aluminum and the substrate

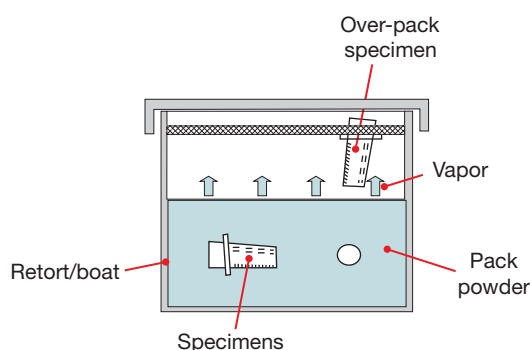


**Figure 1** Schematic of a pack cementation facility.

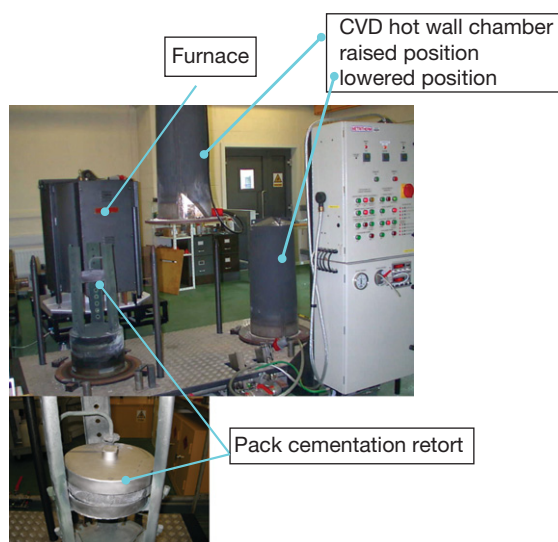


**Figure 2** Pack cementation facility at Cranfield University: this is quarter size of an industrial production facility.

alloy results in the formation of the intermetallic coating, primarily NiAl, CoAl, FeAl, or TiAl depending on the alloy base, but containing, to a degree, most of the elements present in the base alloy, either in solution or as dispersed phases.

The CVD aluminizing process is best illustrated and described by the schematic in **Figure 3**, which describes the various chemistries involved during aluminum deposition and the formation of a nickel aluminide coating from an aluminizing pack. The processes involved in diffusion coating are complicated even when only nickel and aluminum are considered, as illustrated schematically in **Figure 3**. This behavior reflects the thermodynamic stability of the various phases in the nickel–aluminum binary system; the range of compositions for which each nickel aluminide phase is stable (which varies with process temperature); and the dominant diffusion processes in the newly (near surface) formed alloy due to the interdiffusion processes (which also depends on alloy composition).

The deposition rate and morphology of the coating depend on pack activity, process time and temperature. **Table 3** presents two pack compositions used in research at Cranfield to produce nickel aluminide coatings described in this section and illustrated in **Figures 4 and 5**. Coatings are classified as either ‘high activity,’ when inward diffusion of aluminum occurs or ‘low activity,’ when outward diffusion of nickel occurs. Thus the first pack composition in **Table 3**, with a higher aluminum content, is used at lower temperatures, 700–950 °C. This forms ‘low-temperature high-activity (LTHA)’ nickel aluminide coatings. (See **Figure 4** for a sample micrograph of this coating produced on the nickel-based superalloy CMSX4.) For this case, a surface layer of Ni<sub>2</sub>Al<sub>3</sub> forms and a further heat treatment is required to convert this brittle surface layer to NiAl. This step is usually combined with the heat treatment required

**Table 2** Typical compositions and deposition temperatures for halide activated pack cementation

Coating	Pack composition (wt%)	Deposition temperature (°C)
Al	1.2–2.7% Al, 0.8–1.2% NaF, bal. Al <sub>2</sub> O <sub>3</sub>	900
B	80% B, 16% Na <sub>2</sub> B <sub>4</sub> O <sub>7</sub> , 4KBF <sub>4</sub>	900
Cr	48%Cr, 48% Al <sub>2</sub> O <sub>3</sub> , 4NH <sub>4</sub> Cl	850–1050
Cu	50% CuO, 50% NH <sub>4</sub> Cl	–
Mo	75% Mo, 6% Mg, 18% TiO <sub>2</sub> , 1% NH <sub>4</sub> Cl	–
Nb	NbFe, Al <sub>2</sub> O <sub>3</sub> , NH <sub>4</sub> Cl	1000–1100
Ti	77% Ti, 20% TiO <sub>2</sub> , 3% NH <sub>4</sub> Cl	–
V	40–50% FeV, 2% NH <sub>4</sub> Cl bal. Al <sub>2</sub> O <sub>3</sub>	900–1200
Zn	37.5% Zn, 43.5% ZnCl <sub>2</sub> , 19% KCl	300–350

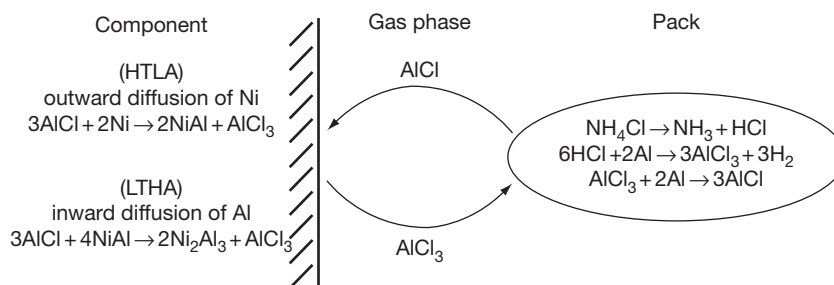


**Figure 3** Schematic illustration of the chemistry involved in the 'pack aluminizing' process.

**Table 3** Example aluminide pack compositions

Pack Constituent	Low-temperature high-activity (LTHA) pack	High temperature low-activity (HTLA) pack
Process temperature	700–950 °C	950–1100 °C
Aluminum flake: (to BS 388) <sup>40</sup>	1.7–2.7 wt%	1.2–1.5 wt%
Activator		
NaF	0.8–1.2 wt%	0.8–1.2 wt%
KHF	0.05–0.15 wt%	0.05–0.15 wt%
NH <sub>4</sub> Cl	0.1–0.2 wt%	0.1–0.2 wt%
AlF <sub>3</sub>	Trace	Trace
Alumina	Balance	Balance
Uncombined water	<0.3 wt%	<0.3 wt%

to recover substrate properties. This coating was deposited using an aluminizing pack containing 2% Al at 900 °C, and was heat-treated for 2 h at 1120 °C and then for 24 h at 845 °C. **Figure 5** illustrates, similarly, a nickel aluminide coating produced using a high temperature low-activity (HTLA) process. The HTLA process results in the outward diffusion of nickel from the superalloy to react with the depositing aluminum to form a monophase  $\beta$ -NiAl intermetallic surface layer. The pack composition (**Table 3**) used to deposit this coating has a lower aluminum content but is processed at high temperatures, 950–1100 °C.

From this simple illustration, it is clear that the properties and performance of an aluminide coating (or for that matter any diffusion coating) will depend upon the process methodology used, the substrate temperature and the subsequent heat treatment. For aluminide coating (also modified aluminizing coatings such as platinum aluminides, see **Section 4.05.4.1**), the critical difference in the processes reflects whether the coating is formed by inward aluminum diffusion, that is, inward grown diffusion coatings, or outward nickel diffusion, that is, outward grown diffusion coatings.

#### 4.05.2.2 Inward Growth Diffusion Coatings

When the aluminizing process parameters are chosen such that the aluminum activity at the component surface is high, then reaction between the nickel-based superalloy ( $\gamma$ -Ni +  $\gamma'$ -Ni<sub>3</sub>Al matrix) and the depositing aluminum forms a surface layer of  $\delta$ -Ni<sub>2</sub>Al<sub>3</sub>, over a subsurface layer of  $\beta$ -NiAl. This reaction is evident in the simple Ni–Al binary phase diagram, for process temperatures between 854 and 1133 °C (**Figure 6**), but may be further complicated by the addition of tertiary and quaternary elements which may modify the equilibrium phase structures.

In  $\delta$ -Ni<sub>2</sub>Al<sub>3</sub>, the diffusivity of nickel is near zero when compared to aluminum, which diffuses rapidly (Janseen and Rieck measured this diffusion rate as  $1.8 \times 10^{-8} \text{ cm}^2 \text{ s}^{-1}$  at 600 °C)<sup>53</sup>; thus, the formation of a surface layer of  $\delta$ -Ni<sub>2</sub>Al<sub>3</sub> ensures that the coating growth results from the inward diffusion of aluminum. Phase equilibria require that beneath this layer  $\beta$ -NiAl is formed to accommodate the aluminum flux. This  $\beta$ -NiAl phase can react further with the inward diffusing aluminum to form more  $\delta$ -Ni<sub>2</sub>Al<sub>3</sub>.



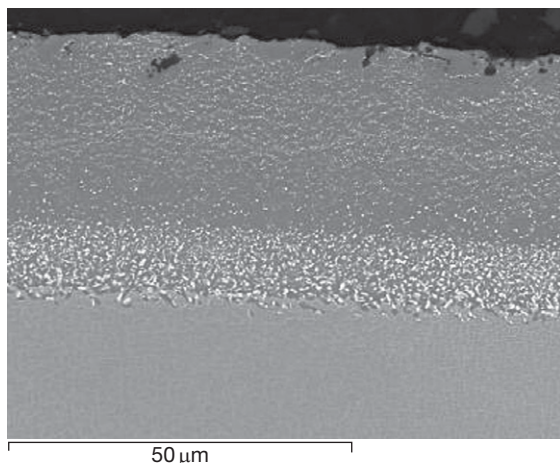


**Figure 4** A nickel aluminide diffusion coating produced using a low-temperature high-activity (LTHA) pack cementation process.

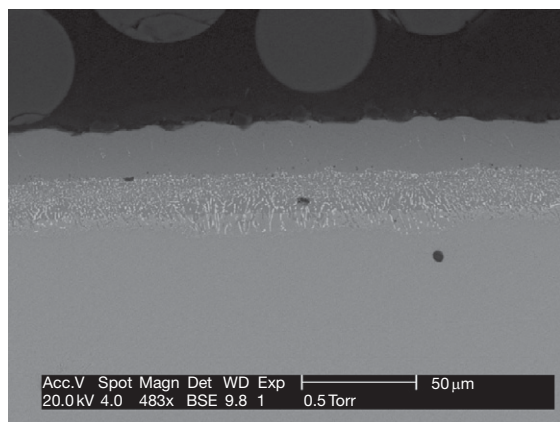


**Figure 5** A nickel aluminide diffusion coating produced using a high temperature low-activity (HTLA) pack cementation process.



As a consequence of this inward growth process, slowly diffusing alloying elements within the substrate can be entrapped in the inwardly growing aluminide coating. Thus, a high-activity aluminide coating contains precipitates that are rich in W, Mo, Ta, Re, and Cr within the  $\beta$ -NiAl phase.

After aluminizing, the coated material is given a high temperature heat treatment (usually linked to the heat treatment necessary to recover the base alloys' mechanical properties). During this heat treatment, nickel is able to diffuse outward from the substrate, which results in the transformation of the brittle  $\delta$ -Ni<sub>2</sub>Al<sub>3</sub> phase into an aluminum-rich  $\beta$ -NiAl

( $\beta$ -NiAl has a wide solubility range for nickel and aluminum, from 46 to 74 at% Ni, 36 to 54 at% Al measured at 1100 °C).

#### 4.05.2.3 Outward Grown Diffusion Coatings

When the aluminizing process parameters are selected such that the aluminum activity at the component surface is low (low aluminum content in the pack, high process temperatures), then aluminum is deposited on the surface, but at a reduced rate, and nickel simultaneously diffuses outward to the surface. A  $\beta$ -NiAl surface layer now forms. For stoichiometric and substoichiometric NiAl (Al contents less than 51 at%),<sup>55</sup> the diffusivity of nickel in  $\beta$ -NiAl is much higher than that of aluminum. **Figure 7** presents the variation in nickel to aluminum diffusivity at 1100 °C as a function of the aluminum content of the  $\beta$ -NiAl phase.<sup>55</sup> Thus, this rapid nickel diffusion to the surface, coupled with the low aluminum activity at the surface, effectively holds the surface aluminum content at 51 at%. Hence, HTLA coatings are near-stoichiometric at the surface and nickel-rich within the subsurface  $\beta$ -NiAl phase that has formed. This structure ensures outward nickel transport and the outward growth of the coating microstructure. Another important outcome of this outward diffusion process is that slowly diffusing elements from the substrate are unable to diffuse to form significant concentration levels in the outwardly growing  $\beta$ -NiAl. The outer zone of this coating therefore appears much 'cleaner' and is free from such precipitates as observed in the inwardly grown, aluminum-rich coating formed at lower temperatures and higher aluminum activities.

### 4.05.3 Other Process Methods to Form Diffusion Coatings

#### 4.05.3.1 Slurry Cementation

Slurry-based diffusion coatings are commercially available, offering similar chemistries to those found in conventional pack cementation aluminide coatings. In slurry cementation, the coating materials and halide activator are blended as a slurry or particle-loaded paint system, using either an organic binder or a water-based emulsion. The slurry/paint system can be applied to the part to be coated through dipping or spraying at or near room temperature. The slurry spray is then cured onto the part through a low-temperature thermal treatment, typically around 200 °C. The cured pre-diffusion coating



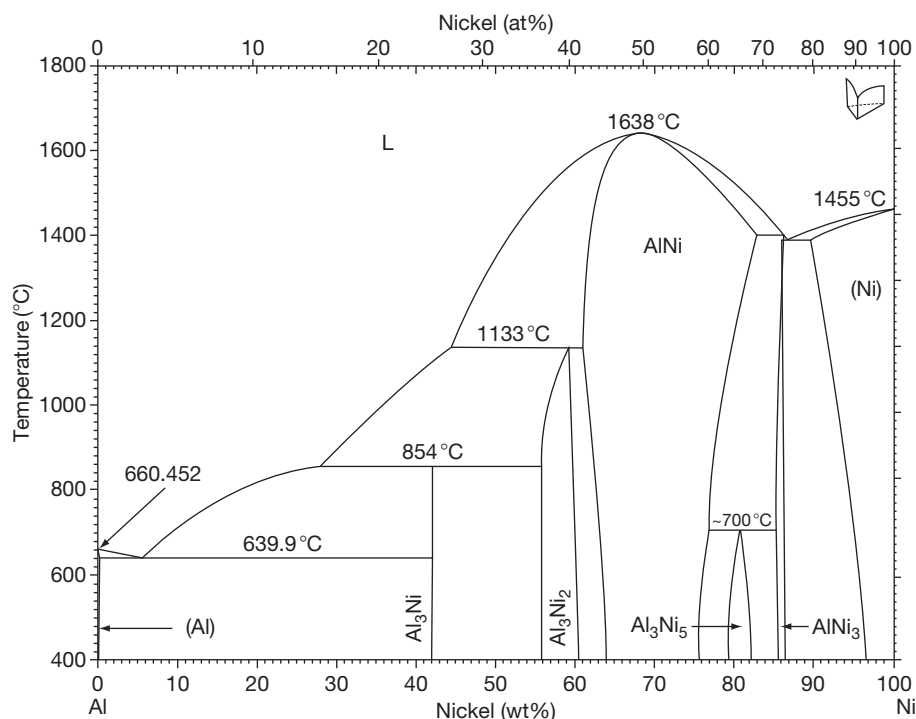


**Figure 6** The Ni-Al binary phase diagram. Reproduced from Singleton, M. F.; Murray, J. L.; Nash, P. In *Binary Alloy Phase Diagrams*; Massalski, T. B., Ed.; ASM Materials Park: OH, 1990; Vol. 1, p 142.<sup>54</sup>

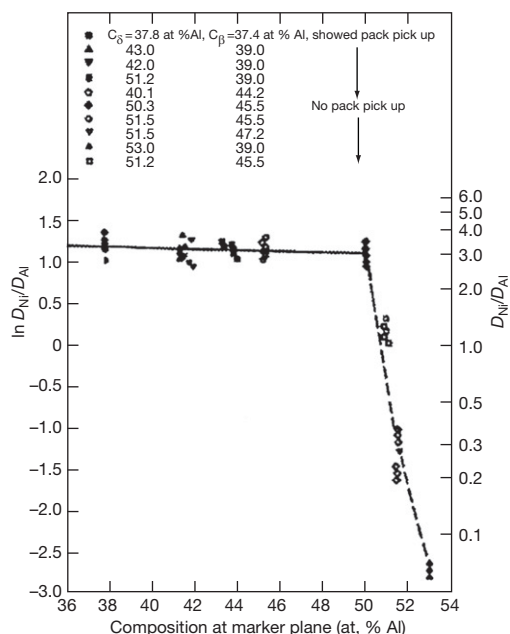


**Figure 7** Variation of  $D_{Ni}/D_{Al}$  with composition in  $\beta$ -NiAl at 1100°C. Reproduced from Shanker, S.; Siegle, L. L. *Met. Trans.* **1978**, 9A, 1467.

may contain only aluminum, aluminum + chromium, aluminum + silicon, or aluminum + chromium + silicon, depending on the final service conditions envisaged. After this overlay of binder, activator and reactive metals has been built up, the aluminum, silicon and other additions are diffused into the substrate by heating the precoated parts in a furnace at temperatures between 650 and 1100°C depending on the substrate to be coated and its final application. The temperature is chosen such that the coating material contained in the slurry reacts and interdiffuses with the substrate to form the final intermetallic coating. Reaction temperatures and the reaction chemistries are similar to those for pack cementation for halide-activated slurry systems. For systems not involving halide activation, diffusion occurs through direct contact between the molten aluminum or aluminum-silicon particles in the precured cement and the substrate to be coated.

Sermatech was an early protagonist of this form of coating, with Sermaloy J (**Figure 8**) – one of the first widely adopted slurry aluminide coatings – providing outstanding resistance to type II hot corrosion.<sup>56–58</sup>

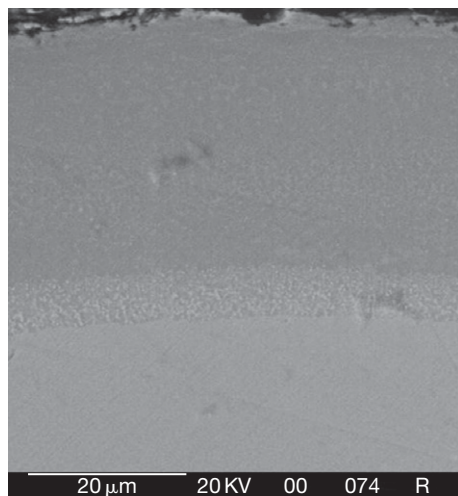


**Figure 8** Micrograph of SermaLoy J.

This slurry aluminide coating forms a silicon-enriched outer layer containing  $\text{Cr}_2\text{Si}$  phases in  $\beta\text{-NiAl}$ , and provides oxidation and corrosion protection up to  $1000^\circ\text{C}$ .<sup>56–58</sup> Later, as engine technologies advanced and directional solidified or single-crystal alloys were more widely adopted, less chromium was available within the alloy to form  $\text{CrSi}_2$  (a critical phase within SermaLoy J)<sup>56</sup>; thus, joint research between Sermatech and Rolls Royce led to the development of SermaLoy 1515,<sup>59</sup> a multilayered structure slurry aluminide coating containing bands of  $\text{CrSi}_2$ . This variant is capable of providing hot corrosion protection to low-chromium-containing single-crystal alloys.<sup>58,59</sup> Other variants of the slurry aluminide process are now available commercially, including IP1041 developed by Indestructible Paints in the UK, and Ceral 10 by BWD Turbines Ltd. The latter uses a water-based slurry process to deposit the prediffused overlay coating prior to heat treatment and reaction to form the Si-containing aluminide coating. Most recently, slurry aluminide coating methods have been researched as a potential method for providing oxidation protection of Fe–Cr ferritic steels for steam power plants,<sup>60–62</sup> where the ability to form an iron aluminum oxidation-resistant coating at temperatures as low as  $650^\circ\text{C}$ , coupled with the capability to coat large steam turbine components at reasonable costs, makes the process commercially competitive.

#### 4.05.3.2 Fluidized Bed Techniques

Fluidized bed reactor-chemical vapor deposition (FBR-CVD) offers a cross between pack cementation and CVD processes. In addition, because of the

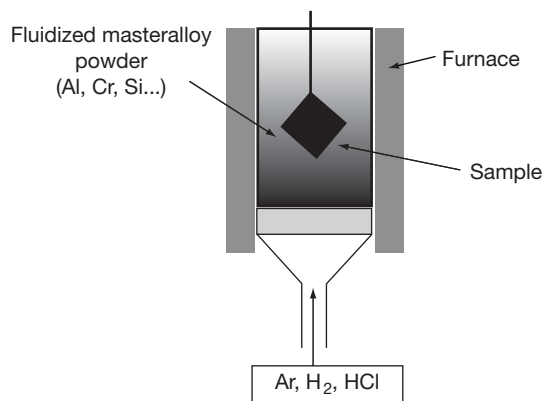


**Figure 9** Schematic of a fluidized bed chemical vapor deposition system.

excellent mixing and dispersion within the bed, efficient heat and mass exchange is ensured, giving uniform coatings on complex-shaped parts.<sup>63–65</sup> This allows uniform aluminide coatings to be produced on ferritic steels in relatively short times at temperatures below  $700^\circ\text{C}$ .<sup>66,67</sup> For FBR-CVD, the fluidized bed (Figure 9) consists of a mixture of the material to be deposited and an inert diluent, which forms the bulk of the fluidized bed and is most often alumina or silica. The halide activator is carried in vapor form by the fluidizing gas and is introduced into the fluidizing gas usually from a separate vapor generator or directly as HCl gas. This latter process is widely used in laboratory-scale systems by fluidizing the bed in a once-through cycle with HCl in the fluidizing gas.<sup>66,68</sup> In more commercial-size plants, the fluidizing gas is recirculated and the level of HCl to  $\text{H}_2$  in the feed gas adjusted to control the generation of the precursor vapor species. Also, when a vapor generator is used, it is possible to control the chemical activity of the active vapor supply to the fluidized bed reactor.

Components to be coated can be hung in the fluidized bed or supported on custom-designed fixtures, depending on their size. The chemistries in FBR-CVD has been extensively studied<sup>60–68</sup> and is similar to the LTHA aluminizing process of the pack cementation method, when aluminum powder is part of the fluidized bed medium. The primary differences are that the halide vapors are flowing, rather than diffusing, and that the carrier particle density is much lower in the fluidized bed than in the pack. Specifically, the gas flow rate must be greater than the minimum fluidization velocity; for a small laboratory experimental system, this would require argon

gas flow rates between 0.35 and 1.1 l min<sup>-1</sup>, with the fluidizing gas containing 5–30 vol% H<sub>2</sub> and 0.5–3 vol% HCl.<sup>66,68</sup> Given a reactor tube diameter of 3.5 cm in this laboratory scale system,<sup>66</sup> this equates to a linear fluidization velocity between 0.6 and 2.0 cm s<sup>-1</sup> when the fluidized bed has a height of 3 cm. Scaling to large fluidizing vessel sizes, therefore, requires high gas flows; for example, for a once-through cycle, a 35-cm-diameter bed would require gas flows in excess of 100 l min<sup>-1</sup>. Thus, large quantities of activator (HCl) and reactive gas (AlCl<sub>3</sub> in the case of aluminizing) would be lost to the scrubbing system. For these reasons, commercial fluidized bed systems use recirculating fluidizing gases, but this requires that the pumps, pipework and flow control equipment are designed for HCl service.

However, the benefits are that the use of a fluidized bed reactor for CVD deposition offers rapid and uniform heating of parts to be coated and good long-term stability (typically  $\pm 0.5\%$  variation in bed temperature, even when the bed is 15 m in diameter). These properties reflect the high heat and mass transport rates reported for fluidized bed systems,<sup>63,64</sup> improved process flexibility, lower capital and operating costs, precise process control, better environmental control, and the ability to automate the coating process.<sup>67</sup> Thus, in addition to aluminizing, fluidized bed systems have been proposed for chromizing, boronizing, nitriding, and carburizing.<sup>68–72</sup>

#### 4.05.3.3 Metallizing

Metallizing uses molten alkali and alkaline-earth fluorides as solvents for the electrolytic deposition of diffusion coatings. This process is well documented for the formation of alloy and intermetallic coatings following high temperature electrolysis in these molten salts.<sup>73–78</sup> The process is usually carried out at temperatures in the range 500–1200 °C in metallic vessels under inert gas, principally argon. The metallizing process is a specific method to deposit highly reactive metals that cannot be normally plated from aqueous solutions. Thus, aluminum, various refractory metals, the actinides, and many rare-earth metals can be deposited using the metallizing process. This capability to deposit refractory metals means that the metallizing process provides a coating route for niche-market applications. It has been used to manufacture protective refractory metal carbide coatings to protect components in contact with nuclear fuel<sup>73</sup> and to manufacture protective coatings for nickel cathodes (Ni<sub>3</sub>Nb) for use in molten carbonate fuel cells (MCFCs).<sup>76</sup>

The metallizing process was patented by N.C. Cook in the 1960s,<sup>79,80</sup> then at General Electric, to manufacture alloy and intermetallic coatings. Although process temperatures between 500 and 1200 °C are quoted, it is now acknowledged that many of the surface layers that are formed are thin unless processed above 800 °C.<sup>73</sup> The process consists of a galvanic cell where the anode is the reactive metal to be deposited and the cathode is the component to be coated.<sup>79–81</sup> Three modes of coating manufacture are now cited<sup>81</sup>:

1. Electrodeposition of a pure reactive metal onto the cathode, followed by interdiffusion of the metallic layers to form the alloy or intermetallic coating.
2. Metallizing, using a galvanic cell, as originally proposed by Cook.<sup>79,80</sup> In this metallizing process, interdiffusion occurs alongside the electrodeposition to form the alloy or intermetallic coating.
3. Thus, mode 1 can be used to deposit a surface coating from a molten salt in the temperature range 500–800 °C, which is subsequently diffused at higher temperatures or for longer times at the deposition temperature, whereas mode 2, the original patented metallizing process, requires higher process temperatures, in excess of 800 °C.
4. The third mode is similar to mode 1 but involves deposition of the coating at the ‘under potential’ for the alloy formation, following some interdiffusion process.<sup>81</sup>

In general, the purity of the fluoride solvents must be very high if a good and reproducible diffusion coating is to be formed. Any impurity cations in the melt will be codeposited.

Since metallizing reagents are electrochemically more reactive than the components to be coated, each coating material can only be deposited onto a specific group of metals to produce diffusion coatings. The more active the metal, the larger the scope of metallic substrates that can be coated. The most useful metallizing reactions include boriding, aluminizing, siliciding, titanizing, chromizing, zirconizing, and most recently the deposition of niobium and tantalum intermetallic coatings ‘niobiding’ and ‘tantalizing’ for the niche metal carbonate fuel cell markets.<sup>73,76</sup>

#### 4.05.3.4 Molten Salt Baths

Molten salt baths have been widely used for the direct thermochemical formation of diffusion coatings.

The formation of chromized coatings for corrosion protection and chromized, carburized, carbo-nitrided, nitrided, and borided diffusion coatings for wear protection are classic commercial examples of this form of diffusion coating manufacture.

In this process, components are treated in a bath containing a molten salt of the species to be deposited, which is then diffused into the component surface. For example, a mixture of chromous and chromic chlorides is used to form a 'chromized' diffusion coating.

Sodium and potassium cyanides are used in the salt baths for carburizing, carbonitriding, and nitriding. At a given temperature, the percentage of sodium or potassium cyanate generated in the bath determines whether a carburized or nitrided surface is produced. For low cyanate and high cyanide concentrations, carburization of the component surface occurs. At cyanate concentration around 10% and for temperatures between 750 and 900 °C, mixed carbonitride surface coatings are produced. Increasing the cyanate concentration to around 25% at temperatures between 500 and 750 °C results in the formation of a nitride-rich surface layer (all salt bath nitriding processes produce iron carbides as well as iron nitrides).

Thermochemical liquid-phase boriding processes are based on molten borax to which reducing agents such as ferroboration or boron carbide are added.

#### 4.05.3.5 Gas and Vapor Phase Chemical Vapor Deposition Processes

Gas and vapor phase processes offer the most diverse range of diffusion/chemical conversion coatings. The largest volume production of coatings based on gas and vapor phase CVD is used to combat wear. Pyrolysis of hydrocarbon gases, such as methane and propane, is used to carburize metal components. This method is generally cheaper to operate and more widely used for high-volume production than any other method aimed at producing a carburized surface treatment. The addition of ammonia to the hydrocarbon gas results in the formation of carbon nitride coatings; while pyrolysis of ammonia at temperatures between 500 and 525 °C produces a nitrided surface.

Chromized, boronized, siliconized, and aluminized diffusion coatings can also be produced by vapor decompositions but not generally at the commercial scale used for carburized and nitrided surface treatments.

In the corrosion field, especially high temperature oxidation and corrosion, chromizing and aluminizing are the most widely applied CVD coatings. Although, pack cementation (Section 4.05.2) is probably the most versatile and easiest-to-install small-batch process, the better process control of CVD – particularly the ability to codeposit metals and add small reactive element additions (see Section 4.05.4.4) – has seen an increased use of CVD and vapor phase coating routes to deposit high temperature corrosion-resistant coatings. A further advantage of these purely gas phase processes is the ability to coat internal cooling passages of the gas turbine blades, by directly feeding the vapor species into the existing cooling passages cast into the turbine blades.<sup>13,14,43,44</sup> Pressure 'pulse aluminizing'<sup>82</sup> can also be used to aid vapor transport into these narrow internal cooling passages.

(a) *The out-of-pack or over-pack process* operates in a manner very similar to pack cementation, except that the parts to be coated are suspended either above the pack or downstream from the pack (vapor generating) retort. The coating vapors ( $\text{AlCl}$  and  $\text{AlCl}_3$ , if aluminizing, depending on temperature and aluminum activity) are transported to the parts to be coated by an inert carrier gas. This approach results in a much cleaner coating, with no entrapped bed particles, but because of the longer path lengths for vapor transport, out-of-pack processes favor a low activity-type process, with outward coating growth and reduced coating deposition rates and thus longer processing times at any given temperature.

Figure 10, illustrates the modified retort used at Cranfield University to provide vapor phase coating deposition using an over-source deposition process. The process is entirely vapor phase using a process very similar to the Snecma vapor phase aluminizing process.<sup>83</sup> No longer is a powder pack required as a vapor source; instead, the source material is a crushed Cr–Al intermetallic alloy, which plays two roles: it lowers the aluminum activity creating a low-activity, outwardly grown aluminide coating, but does not melt at the desired processing temperatures. This means that it is no longer necessary to blend pack composition, and activation of the process only requires addition of the halide activator salt. Figure 11 illustrates a micrograph of the nickel aluminide coating produced using this vapor phase route, using NaF as the activator and a deposition temperature of 1050 °C.

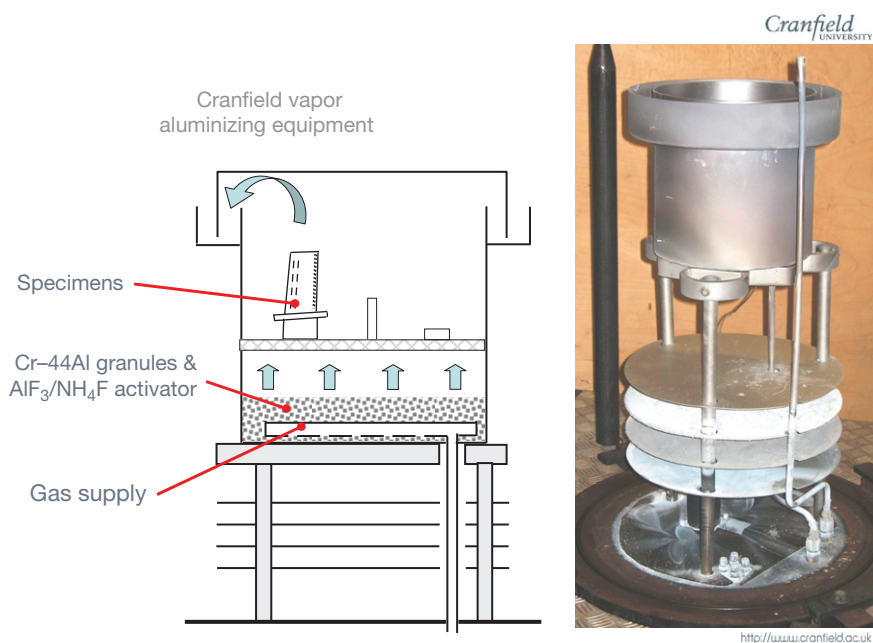


**Figure 10** Modified retort to permit vapor phase aluminizing using an 'over-source' process.

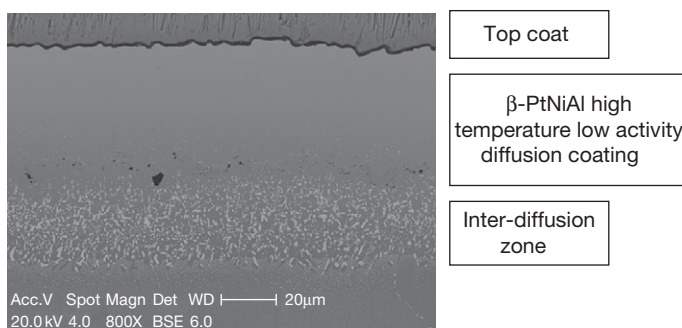


**Figure 11** Micrograph of a nickel aluminide coating produced by the Cranfield vapor aluminizing process at a deposition temperature of 1050 °C.

- (b) Gas phase chemical vapor deposition process reaction gases are metered into the reaction vessel from external sources, see [Figure 12](#). Thus, the aluminum halide source gas is generated in an external vaporizer prior to being introduced into the reaction chamber. This enables better control over the reaction, since temperature, pressure, chemical activity and the flow path of the active gas can all be controlled independently. Further, separate vapor sources can be used for the external and internal aerofoil vapor circuits, permitting the outer gas-washed surface and the internal cooling passages to be coated with different compositions/thicknesses. With recent interest in adding active elements (see [Section 4.05.4.4](#))

and modifying coating compositions through codeposition, the ability to use a number of separated, controllable vapor sources permits more repeatable and reliable manufacture of the more complex coating formulations. Recent patents by Howmet have identified this approach as a method to ensure cleaner 'diffusion coatings.'<sup>84,85</sup>

#### 4.05.4 Modified Aluminide Coatings

From the foregoing, it is clear that the properties of an aluminum coating (or for that matter any diffusion coating) depend on the process methodologies used to deposit the coating, the substrate composition,



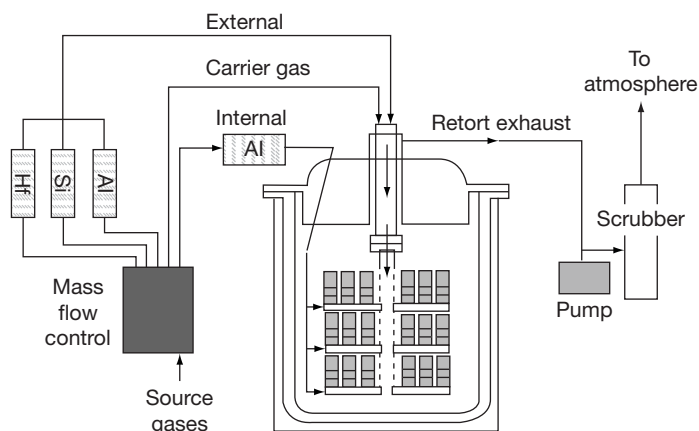


**Figure 12** Schematic diagram of Howmet's vapor aluminizing process using gas phase CVD. Reproduced from Warnes, B. M.; Punola, D. C. *Surf. Coat. Technol.* **1997**, 94–95, 1–6.

and the subsequent heat treatment. Thus, coatings produced by 'pack cementation,' 'out-of-pack' processes or 'chemical vapor deposition' will all differ in performance as discussed later in [Section 4.05.4.2](#). Similarly, a 'pack aluminide' coating whether a simple aluminide or modified aluminide on IN100,<sup>83,86,87</sup> IN738,<sup>84,88–91</sup> IN792,<sup>34</sup> CMSX4,<sup>31–34,52</sup> AM1,<sup>83</sup> Rene 80,<sup>31</sup> or PWA 1480<sup>31</sup> would all be expected to behave differently. Typically, a 'high activity' pack aluminide coating (e.g., PWA73) would be 50  $\mu\text{m}$  thick (65  $\mu\text{m}$  including the interdiffusion zone), with an aluminum content in excess of 30 wt% in the near-surface region of the diffusion coating.<sup>33,34</sup> Such pack aluminide coatings offer satisfactory performance for many aviation, industrial and marine applications and provide satisfactory performance at relatively low cost. It is a mature technology first patented in 1961 and in wide service for protecting turbine blades and vanes since 1970 (as cited by Goward<sup>48</sup> while reviewing the historical perspective of high temperature coatings). However, at temperatures above 1050  $^{\circ}\text{C}$ , especially under cyclic conditions, or under severe hot corrosion, these simple aluminide coatings offer limited protection. Thus, from the 1970s onwards, developments in diffusion coating technologies included modification of the aluminide coatings.

Modified aluminides have been fabricated using one of the following techniques:

1. codeposition of elements from the same pack;
2. codeposition from two separate vapor sources (generated using the over-pack process or by CVD);
3. pretreatment of the superalloy before pack-aluminizing (or vapor phase aluminizing), for example, chromizing a part prior to aluminum;

4. deposition of a metallic layer, using electroplating or PVD (physical vapor deposition) techniques, prior to aluminizing, for example, a platinum-aluminide coating produced by depositing platinum onto the superalloy prior to the aluminizing treatment.

Alloy additions may include chromium,<sup>15–26,92–97</sup> silicon,<sup>8–13,56–58</sup> platinum,<sup>6,27–34,50,93,100–113</sup> and, most recently, various reactive element additions, including Hf, Zr, Ce, and Y.<sup>35–45</sup> Probably the most significant advance in this area was the development of the platinum-modified aluminum class of coating. The first commercial coating in this class was designated LDC-2 and was produced by electrodepositing a thin layer of Pt, followed by a pack-aluminizing treatment at 1100  $^{\circ}\text{C}$ .<sup>84</sup> Since 1970, this process has been licensed to many manufacturers who produce their own variants of this basic coating design, see [Figures 14–16](#) for examples. Platinum aluminide coatings have much improved high temperature performance over diffusion aluminides. Although typically 2–3 times costlier than a conventional pack aluminide coating, they may last up to 3 times longer, depending on the service environment and duty cycle. Much of this most recent work results from the recognition in the 1990s that platinum-modified aluminide coatings develop stable alumina scales and hence perform as a useful bondcoat for EB-PVD thermal barrier coatings (see [Section 4.05.4.1](#)).

#### 4.05.4.1 Platinum Aluminide Coatings and Bondcoats

Most commercial platinum aluminide coatings are manufactured by first electroplating typically 5–7  $\mu\text{m}$



of platinum onto the component surface, and then heat-treating the platinum-plated component to diffuse the platinum into the nickel-based superalloy surface, prior to aluminizing. The quantity of platinum varies from one manufacturer to another, with between 2 and 10  $\mu\text{m}$  in common usage. There is a commercial drive to reduce the platinum thickness to produce platinum-lean platinum aluminides with the performance enhanced by adding various reactive elements<sup>114</sup> (see Section 4.05.4.4). Equally, platinum need not be electroplated, and in a drive to develop 'clean' coating methods, alternative routes involving the PVD (physical vapor deposition) of platinum have been investigated, although electroplating methods are still the most widely used in industry.

Both high-activity and low-activity aluminizing may be used following platinum plating and its partial diffusion into the component surface. Thus, platinum aluminide coatings have been produced commercially using pack cementation, out-of-pack or over-pack processes and gas phase CVD (Warnes and Punola<sup>84</sup> provides a comparison of pack cementation and gas phases CVD for the production of

platinum aluminum coatings, and will be discussed in more detail in Section 4.05.4.2 on the role the coating process has on introducing impurities into the coating). Depending on the initial Pt thickness, its diffusion heat treatment and the mode of aluminizing, together with aluminizing parameters, a range of microstructures can be produced. The four most widely found structures are illustrated schematically in Figure 13. Thus the platinum aluminide coating can be single-phase ( $\beta$ -PtNiAl) platinum aluminide, for example, MDC150, MDC150L, or CN91 (see Figure 14 for example), or a two-phase platinum aluminide, classified into one of three microstructures: an outer zone consisting of a two-phase  $\beta$ -PtNiAl + PtAl<sub>2</sub> over an inner  $\beta$ -phase NiPtAl layer (an RT22 type), an outer zone of PtAl<sub>2</sub> over an NiPtAl  $\beta$  phase and a structure that is a mix of both these morphologies, consisting on an outer PtAl<sub>2</sub> layer, a middle zone of PtAl<sub>2</sub> +  $\beta$  PtNiAl, and an inner layer of  $\beta$ -NiPtAl.

Figure 15 illustrates the single phase  $\beta$ -PtNiAl microstructure manufactured using the coating facilities at Cranfield to produce a microstructure similar to CN91. The coating was produced by PVD

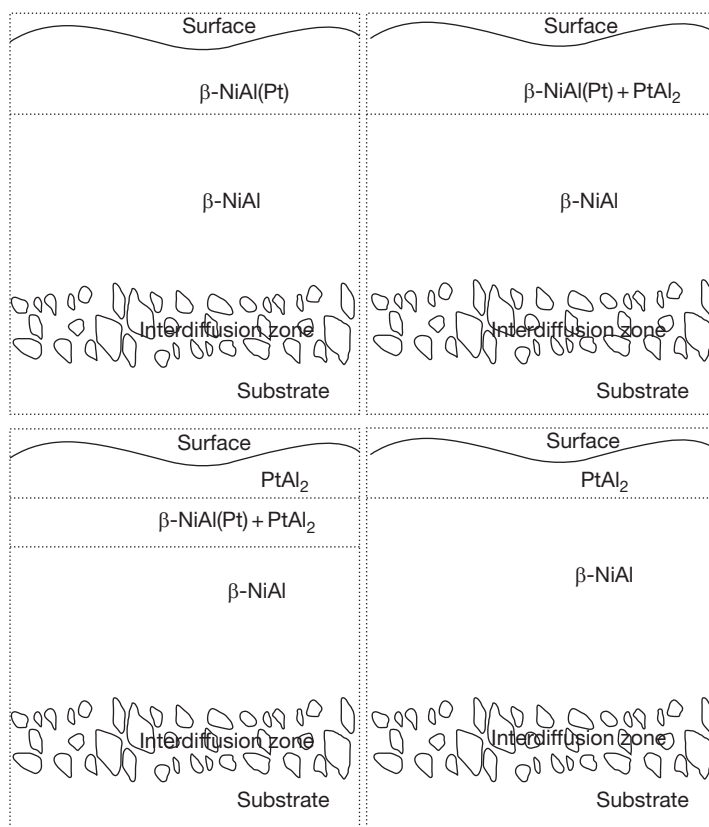


**Figure 13** Schematic microstructures of platinum-modified diffusion coatings.

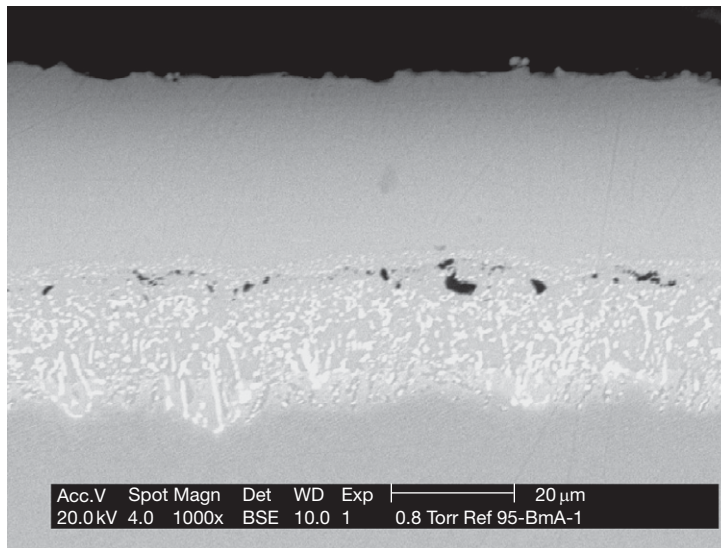


**Figure 14** Micrograph of MDC150L platinum aluminide coating, produced by a gas-phase CVD process.

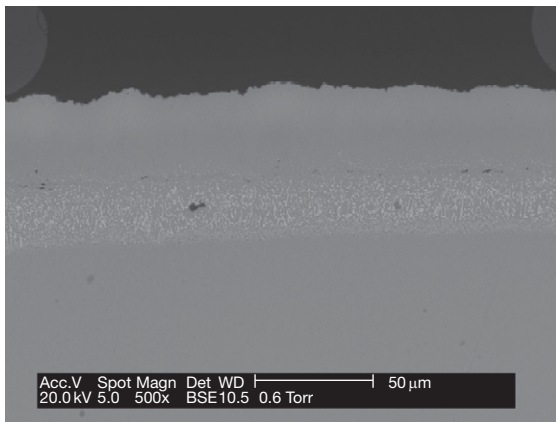


**Figure 15** Single-phase platinum aluminide coating (CN91 type).

deposition of platinum to a thickness of 7 μm, heat-treated, then over-pack aluminized at 1080 °C using a HTLA process.

**Figure 16** illustrates a two-phase  $\text{PtAl}_2 + \beta\text{-PtNiAl}$  microstructure manufactured at Cranfield. The platinum layer was again 7 μm by PVD and heat-treated, but the aluminizing treatment was a high-activity pack aluminizing process at 970 °C.

During service at elevated temperatures (above 850 °C), the microstructure of the coating continuously evolves with time and temperature. The effect of ageing up to 4000 h at 1000 °C and 1050 °C on the microstructure of RT22 is illustrated in **Figure 17**, which demonstrates the effect of platinum diffusion into the substrate: aluminum

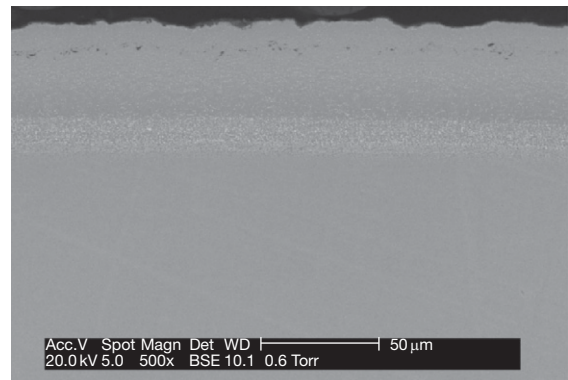


**Figure 16** Two-phase platinum aluminide coating (RT22 type).

consumption by interdiffusion, oxidation, and the formation of various TCP precipitate phases containing refractory metals that have diffused into the platinum aluminide coating from the substrate.

#### 4.05.4.2 The Role of Impurities Introduced in Coating Manufacture

As discussed above, the way the coating is made as well as its final microstructure and composition can have a major influence on its performance and lifetime. With the aim of increasing oxidation life, Howmet<sup>84</sup> undertook a research program on the role of tramp impurities, introduced through the manufacturing process, on the cyclic oxidation lifetime of platinum aluminide coatings.

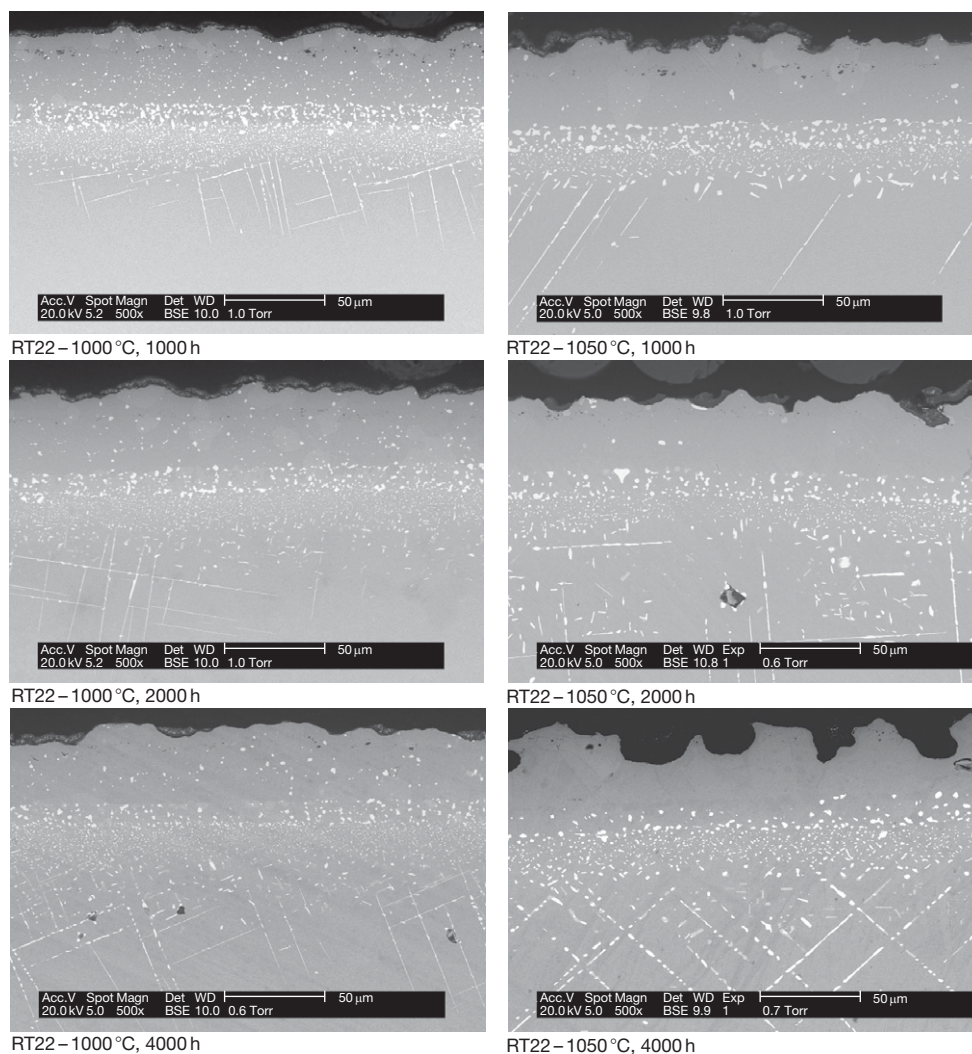


**Figure 17** Influence of long-term exposure on the microstructured degradation of the platinum aluminide coating RT22 at 1000 °C and 1050 °C.

This research investigated three alternative routes to manufacture a platinum aluminide coating deposited onto an IN738 nickel-based superalloy substrate. A common platinum plating method was used for all three platinum aluminides with difference only in the method of undertaking the aluminizing process. The processes were:

- LDC2E: a high aluminum activity pack cementation process, resulting in inward aluminum diffusion.
- MDC-150: a high aluminum activity, gas phase CVD process. An inwardly grown aluminide coating activated by  $\text{AlCl}_3$  generated external to the CVD retort.
- MDC-150L: a low-activity aluminide coating formed by outward nickel diffusion using the

gas phase, and external  $\text{AlCl}_3$  vapor source used to manufacture the MDC-150 coating.

Four tramp impurity levels were studied: B, P, S, and W. Three of these perceived harmful impurities come from the IN738 substrate alloy, namely B, S, and W, while the fourth (P) comes from the electroplating of platinum. [Table 4](#) illustrates the chemical analysis results.<sup>84</sup>

The four elements were selected because they could be introduced into the coating from three potential sources:

- the superalloy substrate: W, S, P, and B;
- the platinum plating process: P;
- the aluminizing process: S and B.

**Table 4** Bulk chemical analysis of coated IN738 foils

<i>Element</i>	<i>As platinum plated</i>	<i>LDC2E coated</i>	<i>MDC 150 coated</i>	<i>MDC 150L coated</i>
B	120	140	150	50
P	450	440	390	140
S	6	7	8	5
W	23 900	23 000	5700	1300

All concentrations are in parts per million by weight (ppm).

Source: Warnes, B. M.; Punola, D. C. *Surf. Coat. Technol.* **1997**, 94–95, 1–6.

Bulk chemical analysis of the coated foils reveals some interesting results. First, the ‘low activity’ CVD aluminizing process is able to ‘clean up’ the coating with respect to these tramp additions, reducing significantly the level of each tramp element addition. Second, the high-activity aluminide processes increase the level of B and S in the coating over that of the ‘as-plated’ condition. For the pack aluminide process (LDC 2E) this was thought to be due to transfer of S and B from the source alloy (analysis of the aluminum–chromium source gave 22 ppmw S and 310 ppmw B); however, the high-activity vapor aluminizing process used 99.999 wt% Al as a source in the  $\text{AlCl}_3$  vapor generator.

Further microprobe studies showed that in the MDC150L coating, where the low activity aluminide appeared to clean the process, concentrations of impurities peaked in the interdiffusion zone and dropped in the diffusion coating surface, with levels at the surface significantly below that found in the IN738 substrate. Such behavior is consistent with the aluminizing process removing contaminants from the surface as a result of a gas–solid surface reaction.<sup>84</sup> In the ‘as-coated’ condition, both ‘high activity’ processes (LDC-2E and MDC-150) had a two-phase ( $\text{NiPtAl} + \text{PtAl}_2$ ) microstructure, while the MDC-150L had a single-phase  $\text{NiPtAl}$  microstructure. After solution heat-treatment of the IN738, all of the coatings were single phase, but varied in thickness and surface aluminum and platinum contents: LDC-2E 74  $\mu\text{m}$  thick, 20.0 wt% Al, 30.6 wt% Pt; MDC150 88  $\mu\text{m}$  thick, 23.2 wt% Al, 22.6 wt% Pt; MDC-150L 77.5  $\mu\text{m}$  thick, 19.5 wt% Al, 19.0 wt% Pt (the quoted thickness included the coating and interdiffusion zone).

Cyclic oxidation tests at 1100 °C (50 min at temperature, 10 min cooling) on these three coating variants (Figure 18) showed that the MDC150L (low-activity aluminide, formed by outward nickel diffusion) had a significantly longer life. The lifetime was defined as the time to ‘zero crossover’ (see Figure 21 to illustrate this definition).

A very important conclusion from this study is that minor tramp element contaminants can influence the oxidation cyclic life, with higher contaminant levels lowering the life. Even more important is the fact that the choice of processing route can influence the level of tramp contaminants in the coating and that through a correct choice of processing it is possible to ‘clean up’ the coating, thereby, giving between 20% and 40% improvement in lifetime, using rounded numbers.

#### 4.05.4.3 Chromium- and Silicon-Modified Aluminides

To combat hot corrosion, additions of chromium<sup>56,57,92–97</sup> and silicon<sup>98–100,103</sup> were extensively researched in the 1970s and 1980s. Research into the influence of these additions still continues as additions to both standard aluminides and platinum-modified aluminides, especially when considering coating on the latest third- and fourth-generation low-chromium-containing single-crystal alloys.

This early research plus service experience has shown that chromium additions to aluminide coatings offer little advantage over standard aluminide coatings under high temperature oxidation conditions. However, chromium additions are found to be beneficial and offer improved performance in industrial and marine turbine applications burning high-sulfur fuels.<sup>15,19,20,46,49,94,97</sup>

Additions of silicon are also known to improve hot corrosion resistance, but may also benefit the high temperature oxidation performance of aluminide coatings. Since the early work in the late 1970s and early 1980s, a number of researchers have investigated the role of Si, both for high temperature oxidation resistance and hot corrosion resistance, in diffusion aluminide coatings.<sup>10,56–114</sup> The possibility of using silicon aluminides for protecting internal cooling passages has also been investigated.<sup>14,115</sup>

The most commonly used silicon aluminide is the commercial coating SermaLoy J, a  $\text{CrSi}_2$ -dispersed



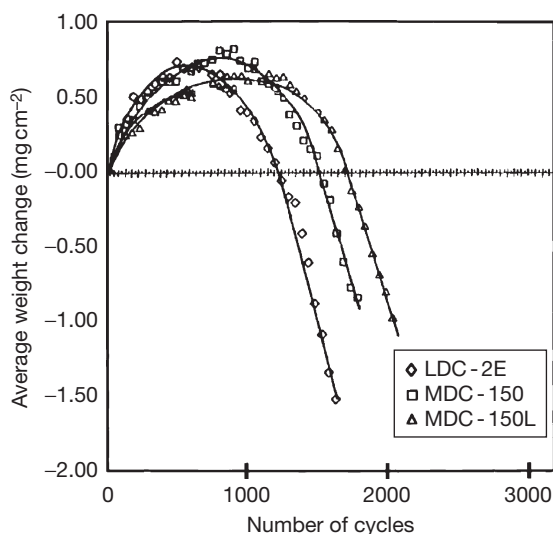


**Figure 18** Cyclic oxidation lifetimes for various platinum aluminide coatings on IN738 at 1100 °C: The cycle is 50 min at temperature, 10 min cool, cycled hourly, with failure defined as the time to zero mass gain cross over (the cyclic lives were calculated from data present in Warnes and Punola).<sup>84</sup>

$\beta$ -NiAl diffusion coating.<sup>11,56–58,100</sup> The microstructure of this coating is illustrated in **Figure 8**. Sermaloy J is manufactured using a slurry aluminizing process route. At about 10 wt% silicon in a diffusion aluminide coating, the silicon aluminide coating provides unsurpassed resistance to type I and II hot corrosion.<sup>11,58,100</sup> It is, however, somewhat brittle and this limits its use for internal cooling passage applications at this level of silicon content. Later, as engine technologies advanced and single-crystal alloys were widely adopted, with lower chromium contents, there was less chromium available within the alloy to form the  $\text{CrSi}_2$  precipitates – a critical component of Sermaloy J<sup>56–58</sup> – thus a research program between Sermatech and Rolls Royce led to the development of Sermaloy 1515. Sermaloy 1515 is a layer-structured slurry aluminide diffusion coating containing bands of  $\text{CrSi}_2$  precipitates as illustrated in **Figure 19**. Sermaloy 1515 is, thus, specifically designed to provide hot corrosion resistance on low-chromium-containing single-crystal alloys.<sup>56,58,59</sup>

For cooling passage applications,<sup>115,116</sup> this silicon content of the aluminide has to be reduced such that it does not impact on the alloy mechanical performance but must be sufficiently high to confer good oxidation and hot corrosion protection. Reducing the silicon level to between 1 and 2 wt% meets this criteria. Testing coatings with silicon levels in this range under Cyclic oxidation at 1100 °C and 1 h hot dwell

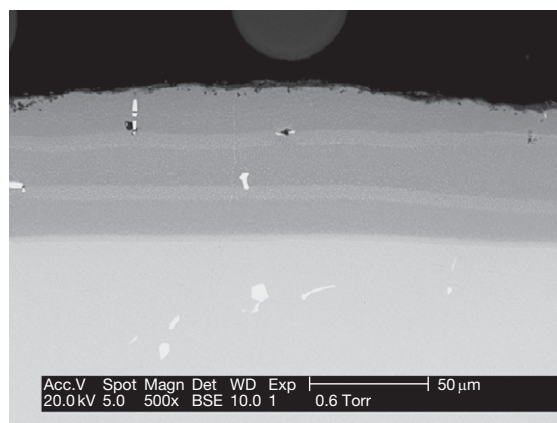


**Figure 19** Sermaloy 1515 silicon aluminide coating on IN738 produced by a repeat slurry aluminizing process route.

cycles gives a lifetime of 280–320 cycles.<sup>116</sup> A result superior to that of a standard aluminide (HTLA aluminide) was obtained, for which the cyclic lifetime varied between 25 and 120 cycles, but was inferior to a platinum aluminide. The worst of the platinum aluminides in **Figure 18** gave a lifetime of 1174 cycles under similar test conditions.

Under hot corrosion conditions, both type I and type II, this coating with 1–2% silicon addition was superior to a conventional aluminide, lasting approximately twice as long to through coating penetration, but was inferior to the performance of Sermaloy J containing a higher silicon content.

#### 4.05.4.4 Reactive Element-Modified Aluminide Coatings

There has been continued interest in the ability to incorporate active elements in  $\beta$ -NiAl to improve cyclic oxidation resistance through enhanced scale adherence. The benefits of oxygen-active elements are well documented in the literature; for example, yttrium levels below 0.5 wt% are widely added to commercial overlay coatings to reduce oxidation rates and improve scale adhesion. Even in the development of the earliest MCrAlY coatings this was recognized.<sup>48</sup> The most recent MCrAlY overlays are far more complex and may contain multiple active elements, including Y, Si, Hf, Zr, Ta, etc.<sup>11,28,99,117–120</sup> and even minor addition of precious metals.<sup>31,104–106,117</sup>

For systems based on  $\beta$ -NiAl, the systems are far less advanced, with few reactive-element-modified diffusion coatings commercially available.<sup>43,44</sup> Most of the research has been on model alloys<sup>36,121–125</sup> and



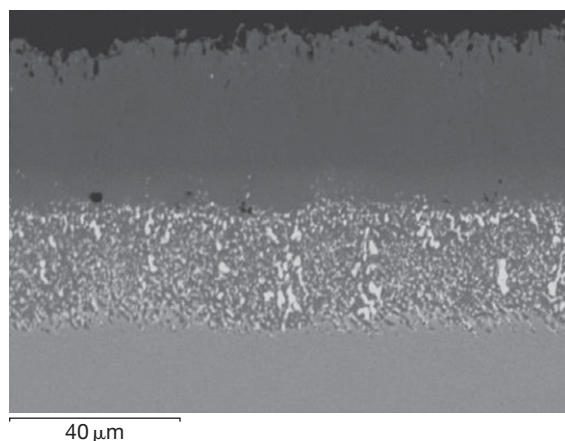


**Figure 20** Yttrium-modified aluminide 'over pack' CVD coating.

in particular on the roles of hafnium, zirconium, and yttrium. Some research papers have considered the incorporation of reactive elements as part of the CVD process.<sup>35–44</sup> Early published work by Bianco and Rapp<sup>35–37</sup> introduced reactive elements into the CVD process such that codeposition of the reactive element with the aluminide occurred. This approach has also been adopted in the one published commercial application in which Howmet used multiple vapor sources to blend the vapor phase environment from which the codeposited active-element-modified aluminide is formed.<sup>84,114</sup> In the work of Kim *et al.*,<sup>42</sup> a yttrium-modified aluminide was formed by first pack-aluminizing the substrate alloy (in this case IN738) and then depositing a thin layer of yttrium by electron beam evaporation, prior to heat treatment to interdiffuse the coating. It is only recently that yttrium-modified aluminide has been able to be produced using a simple pack cementation or the 'over-pack' CVD process.<sup>126</sup> **Figure 20** illustrates a micrograph of a yttrium-modified aluminide using the 'over-pack' CVD process developed at Cranfield. **Figure 21** compares the cyclic oxidation performance (1100 °C, 1 h hot dwell) of various aluminide and modified aluminide coatings produced using facilities at Cranfield University on an IN738 substrate alloy. The improvement in performance of the modified aluminides can be seen relative to that for an uncoated IN738 alloy and IN738 aluminized using a high-activity aluminide process. The uncoated alloy failed (zero net mass gain crossover point) at  $30 \times 1$  h cycles and the high-activity aluminide failed at  $620 \times 1$  h cycles, while the monophasic (high temperature, low activity) platinum aluminide and the

yttrium-modified aluminide did not fail (zero net mass gain crossover) at the end of the test ( $900 \times 1$  h cycles at 1100 °C). Extrapolation of the oxide spalling regime leads to an estimated life of  $1000 \times 1$  h cycles for both the platinum aluminide coating and the yttrium aluminide coating, based on the zero net mass gain crossover point. However, whereas the platinum aluminide coating started to spall at  $170 \times 1$  h hot cycles, the yttrium aluminide did not start to spall until  $800 \times 1$  h hot cycles at 1100 °C.

#### 4.05.5 Mitigating Substrate Alloy Interdiffusion Effects

As is evident from the earlier sections reviewing diffusion coating manufacture, all diffusion coatings must involve an underlying material, usually the substrate alloy, as part of the coating manufacturing process. It is for this reason that similar diffusion coating processes but on different substrate alloys produce different coating systems, and hence the lifetimes of such coatings, be it oxidation, cyclic oxidation or high temperature corrosion, will be influenced by alloying additions diffusing out from the substrate into the coating. Some elements can be beneficial, for example Cr, Si, Hf, Y, etc., while others are clearly detrimental, such as W, Mo, V, possibly Ru, either to the cyclic oxidation or hot corrosion performance of the coating.

One of the benefits of the high temperature low-activity aluminizing processes is the reduction of refractory metals, such as W and Mo, that move outward from the substrate into the coating owing to the fact that the coating is formed as a result of outward nickel transport, and the refractory metals diffuse outward much more slowly than nickel. This observation highlights one way of mitigating the detrimental effects of alloy additions and tramp elements moving from the substrate into the coating during manufacture: that is, to precoat the alloy with some form of temporary or partial barrier (nickel plating the substrate, for example, in its simplest form) prior to aluminizing. A second is to deposit an MCrAlY overlay coating as a partial diffusion barrier and then aluminize the MCrAlY overlay coating.

Commercially, variants on this approach have been used. General Electric has a patented process for over-aluminizing an MCrAlY coating, previously sprayed or EB-PVD-deposited onto the alloys surface. GT29+ and GT33+ are examples of the 'over-aluminized' version of GT29 (Co28Cr6Al0.5Y) and

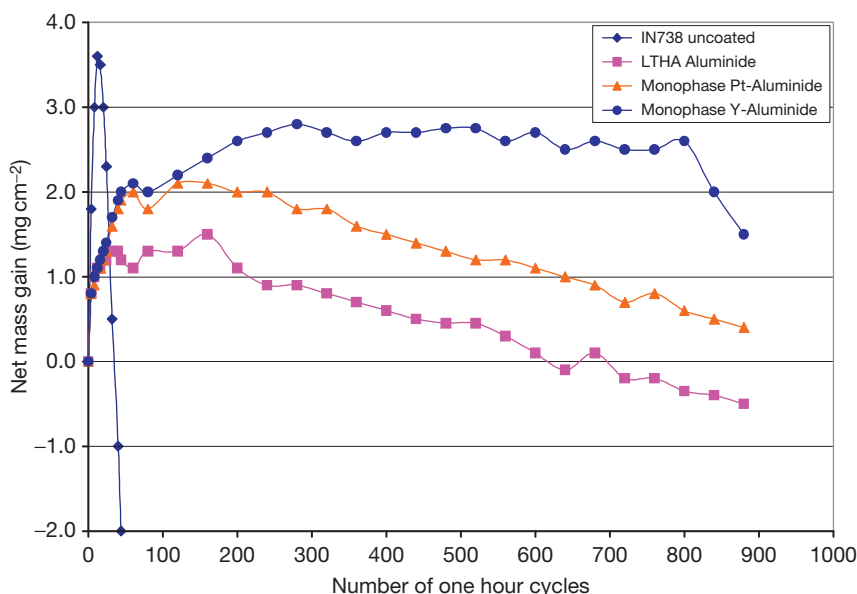


**Figure 21** Cyclic oxidation performance of modified aluminide coatings, produced at Cranfield University: 1100 °C, 1 h hot dwell cycles (data from Long and Nicholls and Nicholls and Wing).<sup>116,126</sup> (Note: ↑ equals point of zero crossover for a LTHA aluminide.)

GT33 (Ni22Cr9Al0.5Y). These coatings are used on blades and vanes of GE industrial engines, models 7/9EA and 7/9FA/FA+,<sup>127</sup> making the performance of the coating less dependent on the substrate alloy chemistry from an oxidation and/or corrosion perspective. These dual-layered over-aluminized MCrAlY alloys provide surface layers with up to 25 wt% Al for good oxidation resistance, while the MCrAlY base confers better hot corrosion resistance because of the higher levels of Co and Cr.<sup>127</sup> Additionally, the incorporation of Y from the MCrAlY into the surface aluminide layer confers improved scale adhesion to the alumina scale, improving the cyclic oxidation resistance of this dual layer coating. The surface aluminide layer is brittle, however, and the higher ductile to brittle transition temperature (DBTT) makes the surface layer prone to thermo-mechanical fatigue (TMF) cracking during start/stop cycling. The more ductile MCrAlY underlayer can blunt these cracks, thereby, limiting their propagation into the substrate. The presence of an outer aluminide layer on a CoNiCrAlY basecoat (GT33+ compared to GT33) can lower the TMF life by a factor of 2.5 at high strain ranges, while at low strain ranges (0.45%ε), the TMF lives are comparable.<sup>127</sup>

Howmet now also offers these duplex MCrAlY + aluminide coatings.<sup>128</sup> However, they claim that by using low-activity aluminizing in addition to

the MCrAlY alloy, they can further improve the oxidation performance when compared to a similar coating made by pack cementation.

#### 4.05.5.1 Smart Coating Concepts

Smart overlay coatings<sup>129–131</sup> are functionally gradient coating systems designed to provide high temperature oxidation and corrosion protection over a wide range of operating conditions. The SMARTCOAT concept is a natural extension of the ideas embodied in GT29+ and GT33+, the over-aluminized MCrAlYs, which involves surface-treating a base overlay coating using diffusion coating processes to obtain improved performance and durability, but now extended to produce a chemically graded structure that can provide both high temperature oxidation protection as well as more optimized protection to type I and II corrosion. Thus, the SMARTCOAT design consists of an MCrAlY base coating, which can be deposited by any spray deposition method (air plasma spray (APS), Vacuum plasma spray (VPS), and high velocity oxy-fuel (HVOF)), by occluded electroplating or by EB-PVD, which is overcoated with successive layers to produce the chemical gradient structure. A second layer, enriched in chromium and/or silicon, is then deposited prior to surface aluminizing, which then generates the required gradient chemical structure.

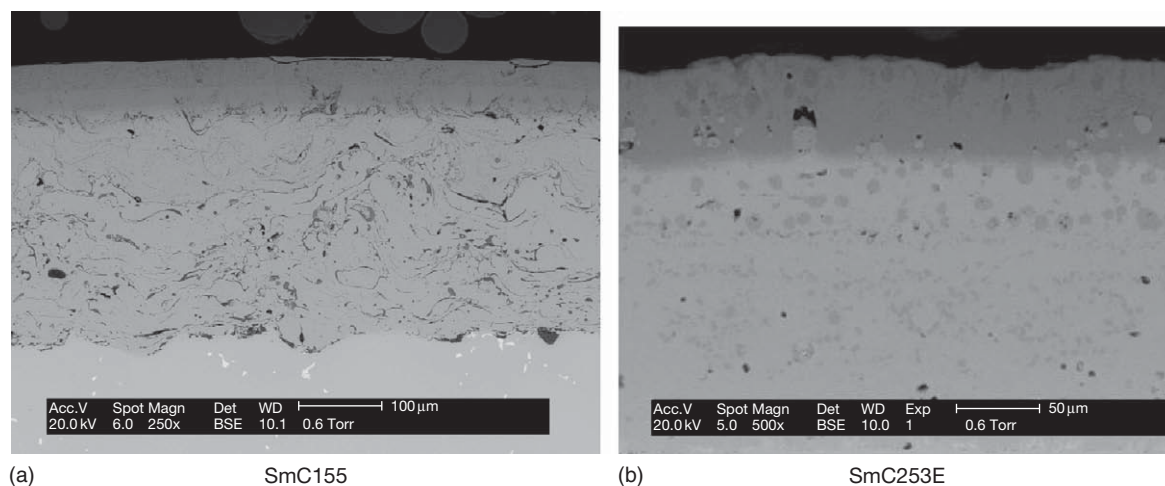


**Figure 22** Micrographs of two SMARTCOAT structures: (a) SmC155, showing the three-layered structure characteristic of SMARTCOAT, but produced using air plasma spraying; (b) SmC253E, produced by occluded electroplating of the basecoat and chromium-rich interlayer.

**Figures 22(a) and 22(b)** illustrates two variants of this SMARTCOAT design. SmC155 (**Figure 22(a)**) is produced by surface-treating an Amdry 995 basecoat that has been deposited by air plasma spraying. The chromium-rich interlayer is also deposited by air plasma spraying before the bi-layer structure is aluminized to give the final SMARTCOAT design. The composition of the three-layered microstructure critically affects performance. The outer aluminide layer varies in composition between those of Ni–15Cr–32Al and Ni–10Cr–21Al, with small additions of Y as a result of the aluminizing of an MCrAlY base alloy, and is designed to produce a protective alumina scale for oxidation- and cyclic-oxidation-protection at temperatures above 900 °C. However, at lower temperatures, this alumina scale does not reform fast enough to confer a protection under type II hot corrosion conditions. SMARTCOAT is, therefore, designed with an intermediate chromium-rich layer, which permits the rapid formation of chromia, which are healing areas of type II corrosion damage. Research into optimum corrosion-resistant alloy compositions<sup>132,133</sup> defined the useful composition range of this interlayer, in the final chemical gradient structure, between Ni–60Cr–20Al and Ni–35Cr–40Al, adding tantalum may be beneficial. The basecoat may be any MCrAlY alloy, Amdry 995 (Co–32Ni–21Cr–8Al–0.5Y) for the SmC155 variant of SMARTCOAT.

**Figure 22(b)**, a second variant of SMARTCOAT, is produced using occluded electroplating<sup>134</sup> to deposit the basecoat and interlayer. Ghost images of the original particles in the occluded electroplate can still be seen. The base alloy is Amdry 963: a NiCrAlY

alloy; otherwise the coating procedure matches that of the aluminized, plasma-sprayed MCrAlY, but with the difference that the basecoat and interlayer were deposited by electroplating.

**Figure 23** illustrates the comparative performance of three variants of SMARTCOAT, when compared to two platinum aluminide coatings RT22 and CN91, and an over-aluminized CoNiCrAlY – a similar process and structure to that of GT29+, a General Electric proprietary coating. For each coating system, the substrate was IN738. The hot corrosion tests were of 500 h duration and conducted at 700 and 800 °C, using a salt recoat test procedure with daily replenishment of an 80% Na<sub>2</sub>SO<sub>4</sub>/20% K<sub>2</sub>SO<sub>4</sub> salt mix at an equivalent salt deposition flux of 0.015 mg cm<sup>–2</sup> h<sup>–1</sup>. The test was conducted in an air + 300 vpm SO<sub>2</sub>/SO<sub>3</sub> gaseous environment.

Under hot corrosion conditions, only the outer aluminide region of the smart coatings was attacked. The corrosion front effectively stopped at the chromium-rich interlayer, whereas the platinum aluminide coating was consumed down to the interdiffusion zone at 700 °C and completely penetrated at 800 °C. For the over-aluminized CoNiCrAlY, the worst attack was observed at 700 °C, as a result of severe type II pitting of the Co,Ni aluminide, and the underlying CoNiCrAlY basecoat layer.

#### 4.05.6 Summary and Conclusions

This chapter reviewed the methods and applications of diffusion coatings. Diffusion coatings can offer a

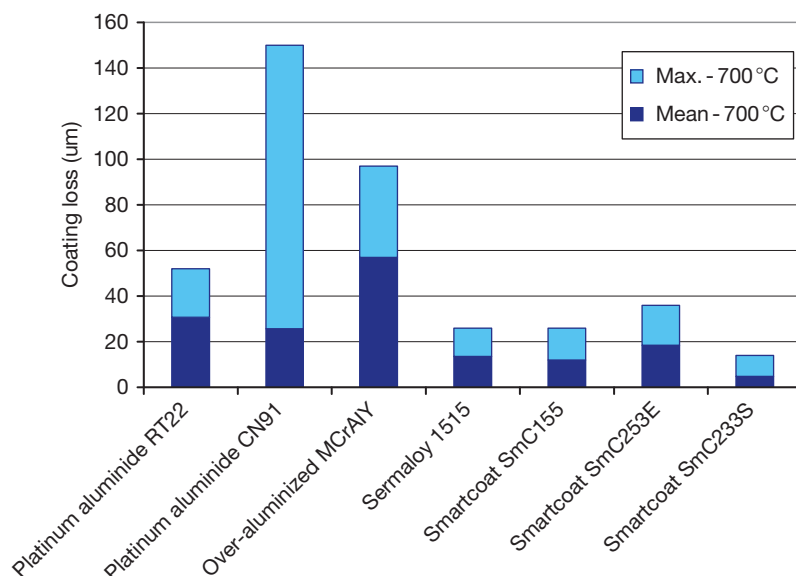


**Figure 23** Hot corrosion performance of SMARTCOAT SmC155 and SmC253E, relative to an over-aluminized CoNiCrAlY and platinum aluminide coatings (RT22 and CN91) at 700 °C.

low-cost solution for providing environmental protection, or can be a part manufacture of more sophisticated custom-designed coatings.

Applications may vary from aqueous corrosion protection through to high temperature oxidation and hot corrosion environments, and can encompass industries as diverse as aerospace, motor sports, petrochemical processes, chemical industries, steam turbines and advanced combined-cycle power generation plants.

Coating solutions vary from the low-cost aluminide diffusion coatings, first introduced into gas turbine service in 1957, through to platinum aluminide bondcoats for thermal barrier coatings.

To the future, one can foresee the development of 'custom surface engineering' solutions, where the component and coating are designed as a material system. SMARTCOAT is one such design for high temperature aggressive service condition, and there are many others. CVD and diffusion coating processes will form an important part of such functional surface engineering solutions.

## References

1. ASTM 874-96. Standard specification for chromium diffusion coating applied by pack cementation, 2008.
2. ASTM B 875-96. Standard specification for aluminium diffusion coating applied by pack cementation, 2008.
3. BS4921: The sherardizing process, 1973.
4. Samuel, R. L.; Lockington, N. A. *Met. Treat. Drop Forging* **1951**, 18, 354–359, 407–415, 440–444, 495–502, 506.
5. Goward, G. W.; Boone, D. H.; Giggins, C. S. *Trans. ASM* **1967**, 60, 228–241.
6. Goward, G. W.; Boone, D. H. *Oxid. Met.* **1971**, 3, 475–495.
7. Grisaffe, S. J. In *The Superalloys*; Sims, C. T., Hagel, W. C., Eds.; Wiley: New York, 1972; p 341.
8. Felix, P.; Erdos, E. *Werkst. Korros.* **1972**, 23, 626–636.
9. Fitzer, F.; Schlichting, J. In *High Temperature Corrosion*; Rapp, R. A., Ed.; NACE: Houston, TX, 1983; pp 604–614.
10. Grünling, H. W.; Bauer, W. *Thin Solid Films* **1982**, 95, 3.
11. Van Roode, M.; Hsu, L. *Surf. Coat. Technol.* **1989**, 37, 461–481.
12. Agüero, A.; Muelas, R.; Scarlin, B. In *Materials for Advanced Power Engineering*; Lecomte-Beckers, J., et al., Eds.; Forschungszentrum Julich 21 (II), 1143–1157 (2002).
13. Long, K. Ph.D. Thesis, Cranfield University, 2004.
14. Kohlsheer, J.; Stock, H. R. *Surf. Coat. Technol.* **2008**, 203, 476–479.
15. Pichoir, R. In *High Temperature Alloys for Gas Turbines*; Coutouradis, D., et al. Eds.; Applied Science: London, 1978; pp 191–208.
16. Gupta, B. K.; Seigle, L. L. *Thin Solid Films* **1980**, 73, 365–371.
17. Malik, M.; Morbioli, R.; Huber, P. In *Proceedings of the High Temperature Alloys for Gas Turbines*; Brunetaud, R., et al. Eds.; D. Reidel: Dordrecht, 1982; pp 87–98.
18. Duret, C.; Davin, A.; Marrijnissen, G.; Pichoir, R. In *Proceedings of the High Temperature Alloys for Gas Turbines*; Brunetaud, R., et al. Eds.; D. Reidel: Dordrecht, 1982; pp 83–87.
19. Restall, J. E.; Malik, M.; Singheiser, L. In *Proceedings of the Conference on High Temperature Alloys for Gas Turbines and Other Applications 1986*; Betz, W., et al. Eds.; D. Reidel: Dordrecht, 1986; pp 357–404.

20. Mevrel, R.; Duret, C.; Pichoir, R. *Mater. Sci. Technol.* **1986**, 2(3), 201–206.
21. Luthra, K. L.; LeBlanc, O. H. *Mater. Sci. Eng.* **1987**, 88, 329.
22. Choquet, P. A.; Naylor, E. R.; Rapp, R. A. *Mater. Sci. Eng. A* **1989**, 121, 413–418.
23. Geib, F. D.; Rapp, R. A. *Oxid. Met.* **1993**, 40, 213–228.
24. Da Costa, W.; Gleeson, B.; Young, D. J. *Electrochem. Soc.* **1994**, 141, 1464–1471.
25. Da Costa, W.; Gleeson, B.; Young, D. J. *Electrochem. Soc.* **1994**, 141, 2690–2697.
26. Da Costa, W.; Gleeson, B.; Young, D. *Surf. Coat. Technol.* **1996**, 88, 165–171.
27. Lehnert, G.; Meinhardt, H. W. *Electrodepos. Surf. Treat.* **1972**, 1, 189.
28. Levin, S. R.; Caves, R. M. *J. Electrochem. Soc.* **1973**, 120, C232.
29. Pint, B. A. *Mater. Sci. Forum* **1997**, 251–254, 397.
30. Streiff, R.; Boone, D. J. *Mater. Eng.* **1988**, 10, 15.
31. Meier, G. H.; Pettit, F. S. *Surf. Coat. Technol.* **1989**, 39–40, 1.
32. Angenete, J.; Stiller, K. *Mater. High Temp.* **2000**, 17, 179.
33. Angenete, J.; Stiller, K. *Surf. Coat. Technol.* **2002**, 150, 107.
34. Vialas, N.; Monceau, D. *Surf. Coat. Technol.* **2006**, 201, 3846–3851.
35. Bianco, R.; Rapp, R. A. *Oxid. Met.* **1992**, 38, 33–43.
36. Bianco, R.; Rapp, R. A. *J. Electrochem. Soc.* **1993**, 140, 1181–1190.
37. Bianco, R.; Rapp, R. A.; Smialek, J. L. *J. Electrochem. Soc.* **1993**, 140, 1191–1203.
38. Xiang, Z. D.; Datta, P. K. *Mater. Sci. Eng. A* **2003**, 363, 185–192.
39. Quraishi, M. A.; Sharma, H. S. *Anti-corros. Meth. Mater.* **2004**, 51, 41.
40. Haynes, J. A.; Pint, B. A.; Moore, K. L.; Zhang, Y.; Wright, I. G. *Oxid. Met.* **2002**, 58, 513–544.
41. Nicholls, J. R.; Wing, R. In *Materials for Advanced Power Engineering 2002*; Lecomte-Beckers, J., et al. Eds.; Forschungszentrum Julich: Germany, 2002; Part 1, pp 57–71.
42. Kim, K. Y.; Jun, J. H.; Lee, J. K. *J. Phys. IV* **1993**, 3, 521–529.
43. Warnes, B. M.; Punola, D. C.; Smith, J. S.; Daniel, N. L. *U.S. Patent 6* **2004**, 689, 422.
44. Warnes, B. M. *Surf. Coat. Technol.* **2001**, 146–147, 7–12.
45. Nicholls, J. R.; Bordenet, B. In *Materials for Advanced Power Engineering 2006*; Lecomte-Beckers, J., et al. Eds.; Forschungszentrum Julich: Germany, 2006; Part 111, p 1696.
46. Pichoir, R. In *Materials and Coatings to Resist High Temperature Corrosion*; Holmes, D. R.; Rahmel, A., Eds.; Applied Science: London, 1978; pp 271–291.
47. Goward, G. W. *Surf. Coat. Technol.* **1998**, 108–109, 73.
48. Goward, G. W.; Cannon, L. W. ASME Paper 87-GT-50 American Society of Mechanical Engineers: New York, 1988.
49. Mevrel, R. *Mater. Sci. Eng. A* **1989**, 120, 13–24.
50. Nicholls, J. R. *J. Met.* **2000**, 52, 28.
51. Nicholls, J. R. *MRS Bull.* **2003**, 28(9), 659–670.
52. Pomeroy, M. J. *Mater. Des.* **2005**, 26, 223–231.
53. Janssen, M. M. P.; Rieck, G. D. *Trans. Met. Soc. AIME* **1967**, 239, 1372.
54. Singleton, M. F.; Murray, J. L.; Nash, P. In *Binary Alloy Phase Diagrams*; Massalski, T. B., Ed.; ASM Materials Park: OH, 1990; Vol. 1, p 142.
55. Shanker, S.; Siegle, L. L. *Met. Trans.* **1978**, 9A, 1467.
56. McMordie, B. G.; Weatherill, A. In *Proceedings of the Turbine Forum*; Nice: France, 2002.
57. Meelu, M. C.; McMordie, B. G.; Loretto, M. H.; Jones, A. In *The Processing, Properties and Application of Metallic and Ceramic Materials*; Loretto, M. H., Beevers, C. J., Eds.; EMAS Publishing: Washington, 1992; Vol. II, p 1250.
58. Berry, D.; Meelu, M. C.; McMordie, B. G.; Kircher, J. A. ASME Pub. 95-GT-359, 1995.
59. SermaLoy 1515, U.S. Patent 5,547,700.
60. Scheefer, M.; Knodler, R.; Scarlin, B.; Bruna, A. A.; Tsipas, D. N. *Mater. Corros.* **2005**, 56, 907–915.
61. Aguero, A.; Muelas, R.; Gutierrez, M.; Van Vulpen, R.; Osgerby, S.; Banks, J. P. *Surf. Coat. Technol.* **2007**, 201, 6253–6260.
62. Aguero, A. *Mater. High Temp.* **2008**, 25, 257–265.
63. Sanjuro, A.; Lau, K.; Wood, B. *Surf. Coat. Technol.* **1992**, 54–55, 219–223.
64. Tsipas, D. N.; Anthymidis, K. G.; Flitris, Y. J. *Mater. Process Technol.* **2003**, 134, 145–152.
65. Kinkel, S.; Angelopoulos, G. N.; Dahl, W. *Surf. Coat. Technol.* **1994**, 64, 234–240.
66. Perez, F. J.; Hierro, M. P.; Trilleros, J. A.; Carpintero, M. C.; Sanchez, L.; Brossard, J. M.; Bolivar, F. J. *Intermetallic* **2006**, 14, 811–817.
67. Lau, K. H.; Sanjuro, A.; Wood, B. J. *Surf. Coat. Technol.* **1992**, 54–55, 234–240.
68. Perez, F. J.; Hierro, M. P.; Pedraza, F.; Gomez, C.; Carpintero, M. C.; Trilleros, J. A. *Surf. Coat. Technol.* **1999**, 122, 281–289.
69. Anthymidis, K. G.; Stergioudis, G.; Tsipas, D. N. *Mater. Lett.* **2001**, 51, 156–160.
70. Anthymidis, K. G.; Stergioudis, G.; Tsipas, D. N. *Sci. Tech. Adv. Mater.* **2002**, 3, 303–311.
71. Anthymidis, K. G.; Maragoudakis, N.; Stergioudis, G.; Haidar, O.; Tsipas, D. N. *Mater. Lett.* **2003**, 57, 2399–2403.
72. Reynoldson, R. W. *Heat Treatment in Fluidised Bed Furnaces*; ASM International: Ohio, USA, 1993; p 111.
73. Taxil, P.; Chamelot, P.; Massot, L.; Hamel, C. *J. Mining Metallurgy* **2003**, 39, 177–200.
74. Trusov, G. N.; Goliasheva, E. P.; Gorachenko, B. A.; Mikheev, V. S. Cited in Ref. 73.
75. Taxil, P. *Appl. J. Electrochem.* **1985**, 17, 261.
76. Fang, B.; Zhou, C.; Liu, X.; Duan, S. *Appl. J. Electrochem.* **2001**, 31, 201.
77. Comminellis, Ch.; Vercesi, G. P. *Appl. J. Electrochem.* **1991**, 21, 335.
78. Cardarelli, F.; Taxil, P.; Savall, A. *Appl. J. Electrochem.* **1998**, 28, 245.
79. Cook, N. C. U.S. Patents 2,970,091, 1961; 3,024,176, 1962; 3024b117, 1966; 30,232,853, 1966.
80. Cook, N. C. *Sci. Am.* **1969**, 221, 38.
81. Taxil, P.; Qiao, Z. Y. *Molten Salts Chemistry-Principle and Applications*; The Metallurgical Industry Press: Beijing, 1987.
82. Restall, J. E.; Hayman, C. In *Proceedings of the Workshop on Coatings for Heat Engines*; Clarke, R. L., et al. Eds.; US Department of Energy: Washington DC, 1984; pp 347–357.
83. Benoist, J.; Badawa, K. F.; Malie, A.; Ramade, C. *Surf. Coat. Technol.* **2004**, 182, 14–23.
84. Warnes, B. M.; Punola, D. C. *Surf. Coat. Technol.* **1997**, 94–95, 1–6.
85. Warnes, B. M. *Surf. Coat. Technol.* **2003**, 163–164, 106–111.
86. Lindblad, N. R. *Oxid. Met.* **1969**, 1, 143.
87. Sivakumar, R. *Oxid. Met.* **1982**, 17, 27.
88. Jackson, M. R.; Rairden, J. R. *Met. Trans. A* **1977**, 8, 1697.
89. Niu, Y.; Wu, W. T.; Boone, D. H.; Smith, J. S.; Zhang, J. Q.; Zhen, C. L. *J. Phys. IV* **1993**, 3, 511.



90. Calliari, I.; Dabala, M.; Zambon, A. *J. Mater. Eng. Perform.* **2001**, *10*, 258.
91. Elsawy, A.; Soda, H.; McLean, A. *Mater. Corros.* **2005**, *56*, 669.
92. Nicholls, J. R.; Hancock, P. *Ind. Corros.* **1987**, *5*(4), 8–18.
93. Goward, G. W. In *Proceedings of the Conference on High Temperature Corrosion, NACE-6*; Rapp, R. A., Ed.; NACE: Houston, TX, 1983; pp 553–560.
94. Nicholls, J. R.; Saunders, S. R. J. In *High Temperature Materials for Power Engineering*; Bachelet, E., et al. Eds.; Kluwer Academic Publishers: Dordrecht, 1990; pp 865–875.
95. Mom, A. J. A. NLR Report MP 81003U, Amsterdam, 1981.
96. Novak, R. C. Cited in *Coatings for High Temperature Structural Materials*, National Materials Advisory Board Report; National Academy Press: Washington, DC, 1996.
97. Luthra, K. L.; LeBlanc, O. H. *Mater. Sci. Eng.* **1987**, *88*, 329.
98. Fitzer, F.; Schlichting, J. In *High Temperature Corrosion, NACE-6*, 1984; pp 604–614.
99. Davis, F. N.; Grinnell, C. E. ASME Pub. 82-GT-244 1982.
100. Stringer, J.; Viswanathan, R. In *Advanced Materials and Coatings for Combustion Turbines*; Swaminathan, V. P., Cheruvu, N. S., Eds.; ASM, 1994; p 6.
101. Stringer, J.; Viswanathan, R. In *Proceedings of ASM 1993 Materials Congress Materials Week'93*, Pittsburgh, Pennsylvania, October 17–21; ASM International: Materials Park, OH, 1993; pp 1–21.
102. Czech, N.; Schmitz, F.; Stamm, W. *Surf. Coat. Technol.* **1994**, *68–69*, 17–21.
103. Pint, B. A. *Oxid. Met.* **1997**, *48*, 303–333.
104. Pint, B. A.; Wright, I. G.; Lee, W. Y.; Zhang, Y.; Prüssner, K.; Alexander, K. B. *Mater. Sci. Eng. A* **1998**, *245*, 201–211.
105. Tawancy, H. M.; Abbas, N. M.; Rhys Jones, T. N. *Surf. Coat. Technol.* **1992**, *54–55*, 1.
106. Tawancy, H. M.; Sridhar, N.; Abbas, N. M.; Rickerby, D. S. *Scr. Metall. Mater.* **1995**, *33*, 1431.
107. Felten, E. J. *Oxid. Met.* **1976**, *10*, 23–28.
108. Felten, E. J.; Pettit, F. S. *Oxid. Met.* **1976**, *10*, 189–223.
109. Fountain, J. G.; Golightly, F. A.; Stott, F. S.; Wood, G. C. *Oxid. Met.* **1976**, *10*, 341–345.
110. Allam, I. M.; Akuezlte, H. C.; Whittle, D. P. *Oxid. Met.* **1980**, *14*, 517–530.
111. Vogel, D.; Newman, L.; Deb, P.; Boone, D. H. *Mater. Sci. Eng.* **1987**, *88*, 227.
112. Malik, M.; Morbioli, R.; Huber, P. In *Proceedings of the Conference on High Temperature Alloys for Gas Turbines*; Brunetaud, R., et al. Eds.; D. Reidel: Dordrecht, 1982; pp 87–98.
113. Nicholls, J. R.; Stephenson, D. J.; Hancock, P.; Wood, M. I.; Restall, J. E. *Proceedings of the Workshop on Gas Turbine Materials in a Marine Environment* 1984; Paper 7.
114. Warnes, B. M. *Surf. Coat. Technol.* **2001**, *146–147*, 7–12.
115. Michels, H. T.; Friend, W. Z. *Corrosion of Nickel and Nickel*; Electrochemical Society, 1980; p 49.
116. Long, K.; Nicholls, J. R. in press.
117. Zhang, Y.; Haynes, J.; Lee, W. Y.; Wright, I. G.; Pint, B. A.; Cooley, K. M.; Laiw, P. K. *Metall. Mater. Trans. A* **2001**, *32*, 1727.
118. de Wit, J. H. W.; Van Manen, P. A. *Mater. Sci. Forum* **1994**, *154*, 109.
119. Dickey, E. C.; Pint, B. A.; Alexander, K. B.; Wright, I. G. In *High Temperature Surface Engineering*; Nicholls, J. R., Rickerby, D. S., Eds.; IoM Communications: London, 2000; pp 115–128.
120. Fisher, G.; Datta, P. K.; Burnell-Gray, J. S.; Chan, W. Y.; Wing, R. In *High Temperature Surface Engineering*; Nicholls, J. R., Rickerby, D. S., Eds.; IoM Communications: London, 2000; pp 1–11.
121. Pint, B. A.; More, K. L.; Wright, I. G. *Mater. High Temp.* **2003**, *20*, 375–386.
122. Bennett, I. J.; Sloof, W. G. *Mater. High Temp.* **2002**, *20*, 395–403.
123. Schumann, E.; Yang, J. C.; Graham, M. J.; Ruhle, M. *Mater. Corros.* **1996**, *47*, 631–632.
124. Pint, B. A.; Garrett-Reed, A. J.; Hobbs, L. W. *Microsc. Oxid.* **1993**, *2*, 463–475.
125. Pint, B. A.; Wright, I. G.; Lee, W. Y.; Zhang, Y.; Prüssner, K.; Alexander, K. B. *Mater. Sci. Eng. A* **1998**, *245*, 201.
126. Nicholls, J. R.; Wing, R. In *Materials for Advanced Power Engineering 2002*; Lecomte-Beckers, J., et al. Eds.; Forschungszentrum Julich: Germany, 2002; Part 1, pp 57–71.
127. Cheruvu, N. S.; Chan, K. S.; Viswanathan, R. *Energy Mater.* **2006**, *1*, 33–47.
128. Warnes, B. M. *Surf. Coat. Technol.* **2003**, *163–164*, 106–111.
129. Nicholls, J. R.; Simms, N. J.; Chan, W. Y.; Evans, H. E. *Surf. Coat. Technol.* **1992**, *149*, 236.
130. Nicholls, J. R.; Simms, N. J.; Neseiyif, S.; Evans, H. E.; Ponton, C.; Taylor, M. J. *Electrochem Soc.* **2002**, *99*(38), 305–316.
131. Nicholls, J. R.; Simms, N. J.; Taylor, M.; Evans, H. E. *Proceedings of the Turbine Forum*; Nice, France, 2002.
132. Nicholls, J. R.; Hancock, P.; Al Yasiri, L. H. *Mater. Sci. Technol.* **1989**, *5*, 799–805.
133. Nicholls, J. R.; Lawson, K. J.; Al Yasiri, L. H.; Hancock, P. *Corros. Sci.* **1993**, *35*(5–8), 1209–1223.
134. Honey, F. J.; Kedward, E. C.; Wride, V. J. *Vac. Sci. Technol A* **1986**, *4*, 2593–2597.

## 4.06 Hot Dipped Coatings

**W. J. Smith**

UK Galvanizers Association, Sutton Coldfield, West Midlands B72 1SY, UK

**F. E. Goodwin**

International Lead Zinc Research Organization Inc., International Zinc Association Suite 120, Durham NC 27713, USA

© 2010 Elsevier B.V. All rights reserved.

---

<b>4.06.1</b>	<b>Introduction</b>	2556
<b>4.06.2</b>	<b>Corrosion Characteristics of Zinc</b>	2557
4.06.2.1	General Considerations	2557
4.06.2.2	Atmospheric Corrosion	2558
4.06.2.3	Water Corrosion	2562
4.06.2.4	Soil Corrosion	2562
4.06.2.5	Other Corrosion Media	2562
<b>4.06.3</b>	<b>Corrosion Characteristics of Aluminum</b>	2564
<b>4.06.4</b>	<b>Corrosion Characteristics of Tin</b>	2564
<b>4.06.5</b>	<b>Applying Coatings by Hot Dipping</b>	2565
4.06.5.1	Introduction	2565
4.06.5.2	Principles of the Hot Dipping Operation	2565
4.06.5.2.1	Cleaning	2565
4.06.5.2.2	Dipping	2566
4.06.5.2.3	After treatments	2566
<b>4.06.6</b>	<b>Hot Dip Galvanizing</b>	2566
4.06.6.1	Introduction	2566
4.06.6.2	Design for Hot Dip Galvanizing	2566
4.06.6.3	Degreasing and Pickling	2567
4.06.6.4	Fluxing	2567
4.06.6.5	Galvanizing	2568
4.06.6.5.1	Coating development and reactivity of steel	2568
4.06.6.5.2	Alloying additions the zinc melt	2569
4.06.6.6	Post-Galvanizing Treatments	2570
<b>4.06.7</b>	<b>Continuous Zinc and Zinc Alloy Coating</b>	2570
<b>4.06.8</b>	<b>Hot Tinning</b>	2571
<b>4.06.9</b>	<b>Hot Dip Aluminizing</b>	2572
<b>4.06.10</b>	<b>Hot Dip Coatings with Applied Organics: Duplex Systems</b>	2572
<b>4.06.11</b>	<b>Applications for Hot Dip Coated Products</b>	2572
<b>4.06.12</b>	<b>Standards</b>	2573
<b>4.06.13</b>	<b>Recent and Future Developments</b>	2573
<b>References</b>		2574

---

### 4.06.1 Introduction

Hot-dipped coatings are prepared by cleaning a metal substrate, usually steel, and also other metals such as copper, and immersing it in a bath of molten (lower melting point) metal. During dipping, a reaction takes place to form a metallurgically bonded coating. The most widely used hot dip coating is zinc or alloys of zinc with other metals, followed by aluminum and tin

coatings. Typical thicknesses of hot dip zinc coatings on steel depend upon the application process. Pre-fabricated steel articles, such as structurals, dipped in zinc have coatings between 85 and 250- $\mu\text{m}$  thick, continuous galvanized sheet have between 10 and 20 $\mu\text{m}$  thick, and fasteners that are hot dip galvanized and then centrifuged have coatings around 50 $\mu\text{m}$  thick. Zinc–aluminum coatings are normally between 5 and 33 $\mu\text{m}$  thick. Aluminum–silicon coatings on

steel sheet are most often supplied between 6 and 33  $\mu\text{m}$  of thickness. The hot dip zinc coating not only serves as a protective barrier coating for iron and steel, with a generally much lower rate of corrosion than steel in the application environment, but is also electronegative to iron and protects it sacrificially.<sup>1</sup> Aluminum coatings also serve as barrier coatings, and provide sacrificial protection of steel in chloride-bearing environments. Tin coatings serve as barrier coatings, but are generally cathodic to steel in many environments and thus derive their utility from their corrosion resistance in selected application environments, such as food canning, together with other processability attributes.<sup>2</sup> The metallurgical reaction during hot dipping results in coatings that have two components: a reaction layer of intermetallic compound that is formed on the base of the steel, and an overlay of the molten coating bath that solidifies on top of this reaction layer and can be controlled to desired thicknesses during the hot dipping operation. The reaction layer thickness and character varies widely with the type of hot dip coating, for example, in the Zn–5% Al continuous galvanized coating, it is on the scale of nanometers, while after fabrication, galvanizing of reactive steels can give reaction layer thicknesses in excess of 60  $\mu\text{m}$ .<sup>3,4</sup> Both the overlay and reaction layers are important components in the ability of the hot dip coating to protect the substrate to which it is applied. Pure zinc is mostly used for general galvanizing, while zinc alloyed with about 0.2% aluminum is generally used for continuous galvanized sheet. In recent years, new alloy coatings have entered both sectors to improve either processability or corrosion resistance.<sup>5</sup>

In many cases, the hot dip coating is also given a surface treatment, either a chemical conversion layer such as chromate or an organic layer such as paint. A wide range of paints, meeting different demands for formability, weathering resistance, and appearance are available for galvanized steel. Aluminized steels are generally chromated but occasionally painted, while tin coatings can be lacquered if required.

## 4.06.2 Corrosion Characteristics of Zinc

### 4.06.2.1 General Considerations

Zinc coatings generally corrode as a result of the slow general dissolution of zinc from the surface. Zinc has the ability to form protective layers comprising basic carbonates, oxides, or hydrated sulfates, depending upon the nature of the environment. When protective

layers have formed and completely covered the surface of the coating, corrosion proceeds at a greatly reduced rate. Localized pitting occurs only under special conditions, for example, in waters where a calcareous scale may crack locally, exposing a small area of zinc. Provided that specifications are adhered to, intergranular corrosion of zinc is not a problem; however, certain impurities, especially in zinc aluminum alloy coatings, can cause intergranular corrosion. By its very nature, the protection of galvanized steel by zinc can result in bimetallic corrosion when steel surfaces are exposed, such as at cut edges, drilled holes, or when uncoated fasteners are inserted into structural items. Good design will minimize the amount of steel that is exposed to the environment and therefore minimize metallic corrosion.

The ability of zinc to maintain a protective layer is mainly determined by the pH of the environment, especially acidic pollutants. Because zinc forms an amphoteric oxide, strong alkalinity can also adversely effect zinc's corrosion behavior by interfering with the formation of protective layers. **Figure 1** shows that the corrosion rate of zinc varies with pH and shows that attack is most severe at pH values below 6 and above 12.5, while within this range, corrosion is

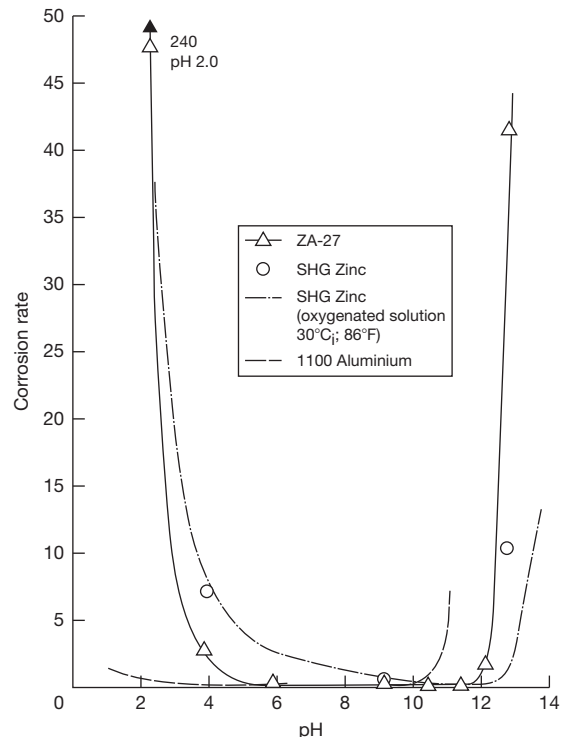


**Figure 1** Variation of corrosion rate with pH. Based on Noranda, *Designing zinc castings for corrosion resistance*; 1993; 24, and earlier data.

very slow. The actual rates of corrosion shown in this figure are not of direct relevance in any particular application, but mainly serve as a guide to the relative severity of corrosion.

Aluminum is particularly beneficial in zinc coatings and has resulted in development of trade name products such as Microzinc D4 (Zn->3%Al), Zinkopal (Zn-5% Al), Supergalva (Zn-5%Al), Galfan (Zn-5% Al), and Galvalume (Zn-55%Al). In these coatings with 5 and 55% aluminum, respectively, the surface is made up of mixed compounds of zinc and aluminum, which increase corrosion performance in many applications. **Figure 2** shows the effect of aluminum content on the corrosion resistance of Al-Zn coatings.

Zinc-iron alloys are present in a reactive layer formed on coatings prepared by dipping prefabricated steel in nearly pure zinc baths and also in the continuous galvanized sheet product termed 'galvanneal.' When coatings on prefabricated items are exposed for a sufficient time, the pure zinc overlay coating will be removed and expose the underlying zinc-iron reaction layer, causing a red staining. This is often confused with attack of the underlying steel; however, in many cases, this intermetallic layer, which contains in excess of 85% zinc, is capable of protecting the

underlying steel for many additional years. The galvanneal coating produced on continuous galvanized sheet is a fully alloyed coating with no zinc overlay. Its rough surface makes it particularly useful as a substrate for application of paints, while the ~85% zinc content of this intermetallic layer provides good protection to the steel substrate. Painted galvanneal has found widespread applications in automobile bodies and structures.

#### 4.06.2.2 Atmospheric Corrosion

Zinc and zinc alloy coatings have good resistance to atmospheric corrosion. Atmospheres are usually classified subjectively as industrial, urban, rural, or marine. In the first three classifications, the severity of corrosion is usually related to the amount of sulfur dioxide in the atmosphere, whereas in the latter the presence of chloride is an important determinant of corrosion rate. Guidelines for life expectancies of zinc coatings exposed to different atmospheres are shown in **Table 1**. The corrosion rate of zinc coatings is approximately linear with time in most aggressive atmospheres. Milder atmospheres allow the protective films formed on zinc to enable a decrease

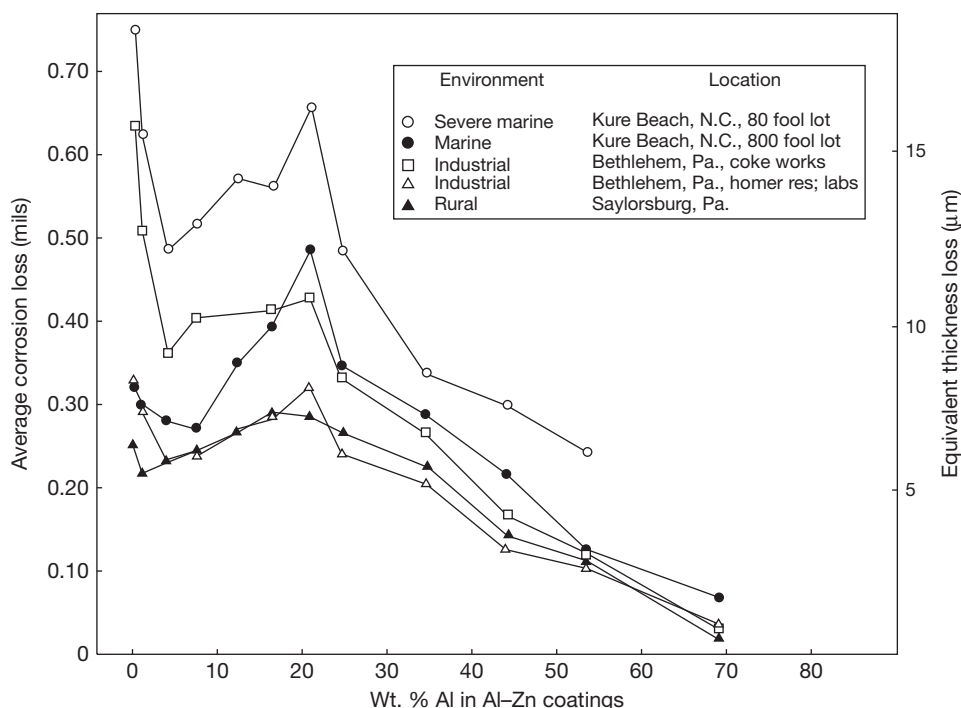


**Figure 2** Five-year corrosion tests on early zinc-aluminum alloys; effect of aluminum content on corrosion performance of aluminum-zinc alloy coatings after exposure in various atmospheres: 1 mm = 25.4  $\mu\text{m}$ , 1 ft = ~0.035 m. Zoccola, J. C.; Townsend, H. E.; Borzillo, A. R. and Horton, J. B. In *Atmospheric Factors Affecting the Corrosion of Engineering Metals*, STP 646, Coburn, S. K. Ed.; American Society for Testing and Materials: Philadelphia, PA, 1978; pp 165-184.

**Table 1** Description of typical atmospheric environments related to the estimation of corrosivity categories and average corrosion rates for zinc

<i>Corrosivity category (C), Corrosion rate (based upon one year exposures), <math>r_{\text{corr}}</math> (m per annum), and corrosion level</i>	<i>Typical environments (examples)</i>	
	<i>Indoor</i>	<i>Outdoor</i>
C1 $r_{\text{corr}} \leq 0.1$ Very low	Heated spaces with low relative humidity and insignificant pollution, e.g., offices, schools, museums	Dry or cold zone, atmospheric environment with very low pollution and time of wetness, e.g., certain deserts, central Arctic/Antarctica
C2 $0.1 < r_{\text{corr}} \leq 0.7$ Low	Unheated spaces with varying temperature and relative humidity. Low frequency of condensation and low pollution, e.g., storage, sport halls	Temperate zone, atmospheric environment with low pollution ( $\text{SO}_2 < 5 \mu\text{g m}^{-3}$ ), e.g., rural areas, small towns. Dry or cold zone, atmospheric environment with short time of wetness, e.g., deserts, subarctic areas
C3 $0.7 < r_{\text{corr}} \leq 2$ Medium	Spaces with moderate frequency of condensation and moderate pollution from production process, e.g., food-processing plants, laundries, breweries, dairies	Temperate zone, atmospheric environment with medium pollution ( $\text{SO}_2$ : $5\text{--}30 \mu\text{g m}^{-3}$ ) or some effect of chlorides, e.g., urban areas, coastal areas with low deposition of chlorides, e.g., Subtropical and tropical zone, atmosphere with low pollution
C4 $2 < r_{\text{corr}} \leq 4$ High	Spaces with high frequency of condensation and high pollution from production process, e.g., industrial processing plants, swimming pools	Temperate zone, atmospheric environment with high pollution ( $\text{SO}_2$ : $30\text{--}90 \mu\text{g m}^{-3}$ ) or substantial effect of chlorides, e.g., polluted urban areas, industrial areas, coastal areas, without spray of salt water, exposure to strong effect of deicing salts, e.g., subtropical and tropical zone, atmosphere with medium pollution
C5 $4 < r_{\text{corr}} \leq 8$ Very high	Spaces with very high frequency of condensation and/or with high pollution from production process, e.g., mines, caverns for industrial purposes, unventilated sheds in subtropical and tropical zones	Temperate and subtropical zone, atmospheric environment with very high pollution ( $\text{SO}_2$ : $90\text{--}250 \mu\text{g m}^{-3}$ ) and/or important effect of chlorides, e.g., industrial areas, coastal areas, shelter positions at coastline
CX $8 < r_{\text{corr}} \leq 25$ Extreme	Spaces with almost permanent condensation or extensive periods of exposure to extreme humidity effects and/or with high pollution from production process, e.g., unventilated sheds in humid tropical zones with penetration of outdoor pollution including airborne chlorides and corrosion stimulating particulate matter	Subtropical and tropical zone (very high time of wetness), atmospheric environment with very high pollution $\text{SO}_2 (>250 \mu\text{g m}^{-3})$ including production and industrial zones and/or strong effect of chlorides, e.g. extreme industrial areas, coastal and off shore areas, occasionally contact with salt spray

Proposal for update to EN ISO 14713: 1999 incorporating corrosion rates for zinc set out in ISO 9223, UK Galvanizers Association, 2006.

in corrosion rate with time. Therefore, a straight line relationship will have a substantial safety margin in milder atmospheres. Corrosion rates increase as the amount of sulfur deposition in the atmosphere increases. Chlorides and nitrogen oxides usually are not as significant in determining corrosion resistance

as sulfur compounds, but, in combination with sulfur, can significantly increase corrosion rates. Corrosion resistance also increases with time of wetness. Therefore, the relative humidity and the amount of rainfall both influence the observed corrosion rate. [Table 2](#) gives the results from the ISOCORRAG



**Table 2** Zinc 1-year corrosion rates and ratio of steel corrosion and site atmospheric characteristics to zinc corrosion<sup>a</sup>

Test site	Code	Zinc corrosion 1-year results ( $\mu\text{m}$ )		Steel/zinc ratio (mean) 1-year results		Environmental characteristics <sup>b</sup>		
		Flat	Helix of wire	Flat	Helix	$\text{Cl}^-$ mean ( $\text{mg m}^{-2}$ )	$\text{SO}_2$ mean ( $\mu\text{g m}^{-3}$ )	Time of wetness (TOW), mean (h per annum)
Iguazu	ARG1	1.6		4		Semiarid, wet, rural		5680
Camet	ARG2	1.3		28		Subtropical, marine, wet		6088
Buenos Aires	ARG3	1.0		16		Subtropical, marine, wet		4645
San Juan	ARG4	0.2		23		Subtropical, dry, rural		855
Yubany Base	ARG5	1.9		19		Antarctic, desert		2693
Boucherville	CND1	1.4	2.0	17	14	59	16	1396
Kasp Hory	CS1	1.9	2.2	14	22	Rural	17	3206
Praha-Bechov	CS2	2.8	3.3	17	21	Urban	67	2991
Kopisty	CS3	3.5	4.8	20	23	Industrial	90	2444
Helsinki	SF1	1.3	2.6	26	16	4	19	3578
Otaniemi	SF2	0.9	1.8	28	21	3	15	3256
Athari	SF3	0.7	1.2	18	13	Rural	4	3105
St. Denis, Paris	F1	1.5	3.6	25	14	28	50	4268
Ponteau Mart	F2	2.6	13.4	28	9	241	87	3846
Picherande	F3	0.9	2.2	18	10	7	9	4171
St. Remy	F4	1.5	4.2	29	23	378	30	6310
Salin de Gir	F5	4.6	5.7	16	23	184	20	3311
Ostende (Belgium)	F6	5.1	10.6	19	12	173	24	6083
Paris	F7	3.0	2.8	14	18	Urban	53	3189
Auby	F8	5.6	8.5	19	17	16	188	4571
Biarritz	F9	4.3	8.2	20	8	193		
Bergisch Glad	D1	1.6	1.8	23	29	Urban	18	4267
Choshi	J1	1.4	2.8	31	33	56	8	5704
Tokyo	J2	1.5	1.5	26	26	4	15	2173

Okinawa	J3	3.4	8.8	22	12	97	11	3852
Judgeford, Wellington	NZ1	0.7	1.2	29	30	Rural-marine		
Oslo	N1	1.3	1.8	19	19	2	14	2641
Borregaard	N2	3.8	5.7	16	16	9	44	3339
Birkenes	N3	2.3	2.0	9	14	Acid rain	1	4138
Tananger	N4	3.0	3.3	20	22	308	4	4583
Bergen	N5	2.1	2.2	13	15	7	9	4439
Svanvik	N6	0.8	1.4	25	21	1	17	2605
Murmansk	SU1	1.1	2.1	28	25	19	5	3227
Batum	SU2	1.6	2.0	18	14	1	26	3216
Vladivostok	SU3	2.3	3.1	11	22	18	29	3920
Oymyakon	SU4	0.4	0.6	2	3	Cold	5	381
Madrid	E1	0.6	1.6	46	18	Urban	44	2060
El Prado	E2	0.5	1.2	31	18	Urban	5	3223
Lagoas-Vigo	E3	1.0	2.5	27	14	29	49	2840
Baracaldo-Vizcaya	E4	1.2	2.6	37	22	25	32	4375
Stockholm Vana	S1	0.6	1.5	41	28	Urban	10	
Kattesand	S2	1.5	2.8	23	22	76	5	
Kvarnvik	S3	1.8	3.5	34	19	650	5	
Stratford	UK1	1.7	1.5	23	34	Industry	20	5783
Crowthorne	UK2	1.1	1.2	34	48	Rural		
Rye	UK3	2.5	2.0	23	46	Marine	21	
Fleet Hall	UK4	1.3	2.3	29	25	Urban		
Kure Beach	US1	2.0	3.9	19	21	102	10	4289
Newark	US2	2.0	2.2	13	12	Industrial		
Panama CZ	US3	17.5	7.6	21	39	619 <sup>c</sup>	52	7598
Research Triangle	US4	0.8		28		Urban		
Point Reyes	US5	1.7	3.5	23	42	Marine		
Los Angeles	US6	1.1	1.8	20	11	Urban, marine	20	4003

<sup>a</sup>The zinc corrosion results are normally the mean of 18 determinations (3 replicates for 6 1-year exposures) starting in spring and autumn for 3 years.

<sup>b</sup>Where no atmospheric data are available, a qualitative description of the site is given.

<sup>c</sup>Marine, splash zone.

Source: Knotkova, D. Atmospheric Corrosivity Classification. Results of the International Testing Programme ISOCORRAG, In International Corrosion Conference, Houston, TX, USA, 1993; 16 pp.

tests for a 3-year period in many locations around the world.<sup>6</sup> The ISOCORRAG severity classification is given. The steel/zinc ratio is shown for both flat and helical-shaped samples together with environmental characteristics that govern atmospheric corrosion.

#### 4.06.2.3 Water Corrosion

Zinc coatings provide good protection for steel in hard waters, where the scale forming ability of the hardness salts allow for development of passive layers. Less favorable corrosion resistance is seen in distilled and soft waters. Zinc, being an amphoteric metal, exhibits good corrosion resistance in water having a pH near neutral. The corrosion rates of both galvanized and aluminized steels in four potable waters in the Soviet Union are shown in Table 3. The normal application of galvanized steel with potable water is in the form of supply pipes.

Seawater corrosion of galvanized steel is moderate in temperate climates, but more severe in the tropics. In temperate seawater, magnesium salts are sufficient to act as inhibitors. Typical corrosion rates are 25  $\mu\text{m year}^{-1}$  in the tropics and half that in the temperate seas such as the North Atlantic. In tidal areas, in which twice daily immersion occurs, or in areas splashed by waves, the corrosion rate is typically twice as great as that for completely immersed areas.

#### 4.06.2.4 Soil Corrosion

There is a wide variation and composition of natural soils, and therefore, a wide range of corrosion rates that can be expected from galvanized steel, but sandy,

well aerated soils with neutral or slightly alkaline pH are likely to cause only limited corrosion of zinc-coated steel. Zinc coatings prevent pitting of steel in soil, and even when the zinc coating is destroyed, the coated steel corrodes much less than do the bare specimens. The controlled use of backfilled materials can allow for satisfactory use of zinc-coated steel in soil contact applications. Typical corrosion rates of galvanized steel pipe in contact with a variety of soils in the United States are shown in Table 4. Here, it is indicated that inorganic oxidizing soils should allow an 85  $\mu\text{m}$  coating to provide at least 10 years of protection. In most inorganic reducing soils, a 130- $\mu\text{m}$  coating should give 10 years of life; however, this thickness would not be sufficient to protect steel in soils containing highly reducing organic or inorganic matter, or in cinders.<sup>7</sup>

#### 4.06.2.5 Other Corrosion Media

Alkaline solutions of ordinary laundry soaps develop a protective coating when in contact with zinc coatings. Satisfactory corrosion rates are observed with both warm and cold applications. Detergent solutions are more corrosive; however, the better grades include inhibitors that reduce corrosion and allow the use of zinc-coated containers. Strong alkalis will result in excessive corrosion.

Many inorganic chemicals may be used in contact with zinc; however, in the presence of moisture, or with water in solution, many inorganic chemicals react with zinc. Mixtures of chemicals can sometimes be more corrosive than the sum of their separate effects, but in many cases, there are often inhibitors present that

**Table 3** Corrosion rates for galvanized and aluminized steel in four waters of the Soviet Union

*Rate of Corrosion*  
( $\mu\text{m per annum}$ )

Water	Duration of testing (h)		Galvanized Specimens			
	Total	Actual (in the given regime)	Of Steel Specimens (uncoated)	Specimens galvanized with additions of 0.11–0.15% Al	Galvanized specimens subsequently heat-treated at 500 °C for 10 min	Aluminized specimens (coated in a bath of molten Al)
Dnieprovsk	8 000	3000	0.460	0.042	0.011	0.003
Moskovorents	24 300	3000	0.207	0.017	0.009	0.016
Volzhs	24 300	3000	0.280	0.028	0.020	0.180
Nevsk	24 300	3000	1.01	Pitting corrosion of the coating		0.100 <sup>a</sup>

<sup>a</sup>Total duration of testing 10 800 h; actual duration, 2000 h.

Source: Proskurkin, E. V.; Bakalyuk, Ya. K. L.; Zholudev, M. D.; *et al. Water. Supply Sanit. Technol.* 1981, 10, 16–18.

**Table 4** Corrosion of galvanized steel pipe in contact with a variety of soils in the United States

<i>Weight loss (<math>\text{g m}^{-2}</math>)<sup>a</sup> and maximum pit depth (mm) after burial for years stated</i>								
<i>Soil type</i>	<i>Loss after 2.1 years</i>	<i>Max. pit depth</i>	<i>Loss after 4.0 years</i>	<i>Max. pit depth</i>	<i>Loss after 9.0 years</i>	<i>Max. pit depth</i>	<i>Loss after 12.7 years</i>	<i>Max. pit depth</i>
<i>Inorganic oxidizing acid soils</i>								
Cecil clay loam	90	0.23	430	0.15	180	<0.15	180	<0.15
Hagerstown loam	90	<0.15	300	0.20	210	0.15	180	<0.15
Susquehanna clay	300	0.23	700	0.23	270	<0.15	240	<0.15
<i>Inorganic oxidizing alkaline soils</i>								
Chino silt loam	330	<0.15	700	0.15	490	<0.15	330	<0.15
Mojave fine gravelly loam	480	0.15	1000	0.20	330	<0.15	330	<0.15
<i>Inorganic reducing acid soils</i>								
Sharkey clay	180	0.15	460	0.30	210	<0.15	330	0.15
Acadia clay	1000	0.15			1460	0.20		
<i>Inorganic reducing alkaline soils</i>								
Docas clay	980	0.20	490	0.23	490	0.25	490	<0.15
Merced silt loam	640	0.20	130	0.30	30	0.15	400	0.20
Lake Charles clay	1130	0.13	1190	0.18	1680	0.33	4210	1.68
<i>Organic reducing acid soils</i>								
Carlisle muck	360	0.20	1040	0.28	915	0.20	1040	<0.15
Tidal marsh	360	<0.15	640	0.25	610	0.20	1460	1.32
Muck	1310	0.33	1650	0.53	2750	1.63	3260	1.93
Rifle peat	1310	0.25	2200	0.30	5980	2.11	5950	2.23
<i>Cinders</i>								
Cinders	2040	1.57	1650	1.14	1710	0.53	3630	1.22

<sup>a</sup>To obtain weight loss in micrometers, divide  $\text{g m}^{-2}$  result by 7.2.

Normal mass coating,  $915 \text{ g m}^{-2}$  of exposed area, is the mass of coating on one side of the pipe;  $915 \text{ g m}^{-2}$  is equivalent to approximately 0.13 mm thickness of coating.

Source: Romanoff, M. *Underground Corrosion*; National Association of Corrosion Engineers (NACE): Houston, TX, 1989. (Originally Issued by the National Bureau of Standards, Circular 579, 1957).

give a net beneficial effect. A short immersion trial is desired for water-based solutions, from which results can be linearly extrapolated to give the worse possibility, because attack often reduces with time.

Many organic chemicals can be used with zinc-coated steel, and many of these organic liquids are inert in contact with zinc. Air entrapped during encapsulation and vapor from polymeric materials such as epoxy resin can cause corrosion. When 85–90% humidity is present, zinc can deteriorate in contact with several synthetic organic chemicals.

Zinc-coated steel is not highly corroded when it is placed in contact with pure fuels, but sulfur or water in ordinary fuels may form compounds with zinc that can both cause high corrosion rates and also form compounds that can clog small orifices. Surface treatments that provide resistance to sulfur or moisture impurities are recommended in this application.

Many lubricants, when in contact with galvanized steel, produce a smooth lightly etched surface, and therefore, form a natural protective coating. Lubricants should be stable and free from acidity. Lubricants

of mineral origin are completely satisfactory, while those containing animal or vegetable oils or fats should be avoided.

Chromated zinc coatings are widely used in contact with concrete in reinforced concrete applications. Galvanized reinforcing bar in concrete has a much higher tolerance for chloride contamination of the concrete resulting from marine exposure or contact with deicing salts. Zinc corrosion products are much less expansive than are iron corrosion products, greatly reducing the risk of cracking, rust staining, and spalling of concrete. Static strength and bond strength of the reinforcement in concrete is not affected by the presence of the coating.

One form of general corrosion that is not protective is 'white rust,' more properly called wet storage stain. This corrosion occurs when there is access for water but limited supply of oxygen and carbon dioxide. The presence of chlorides and sulfates accelerates wet storage stain formation. White rust is particularly found in newly galvanized, bright surfaces, and especially in crevices between closely

packed galvanized articles. In such cases, the surfaces come into contact with moisture, and it cannot dry quickly. Zinc surfaces that already have a normal protective layer of corrosion products are seldom attacked. The presence of white rust does not affect the functional corrosion resistance of the zinc coating. Short-term protection against white rust is attained by chromating or phosphating. Freshly galvanized work should always be stored, so that all surfaces are well ventilated and water allowed to easily run off the surfaces.

### 4.06.3 Corrosion Characteristics of Aluminum

Low corrosion rates are seen with aluminum-coated steel between pH levels of 5 and 8.5. Like zinc, aluminum is amphoteric and its corrosion dependence on pH of several media is shown in **Figure 3**. Aluminum corrodes under both acidic and alkaline conditions; however, when the corrosive environment is highly oxidizing, the aluminum oxide film will be more protective. Also, in several specific cases, the oxide film is not soluble in acidic or alkaline solutions. Two notable examples are acetic acid and sodium disilicate, which are shown in **Figure 3**. Ammonium hydroxide with >30% concentration by weight, nitric acid at >80% weight concentration, and sulfuric acid of 98–100% concentration are also exceptions. There is no general relationship between pH level and the rate of attack, because specific ions largely regulate corrosive behavior. Aluminum coatings are inert to strong nitric or acetic acid solutions, but are easily attacked in dilute nitric, sulfuric, or

hydrochloric acid solutions. Similarly, solutions with a pH as high as 11.7 may not attack aluminum alloys, provided silicate inhibitors are present, but in the absence of silicates, appreciable attack may occur at pH levels as low as 9.0. Generally, less corrosion occurs in the near-neutral pH range of chloride-containing solutions, 5.5–8.5, than in more distinctly acid or alkaline solutions.

Aluminum coatings are not appreciably corroded by distilled water even at temperatures up to 180°C. For this reason, aluminum-coated steel can be used in many distilled water storage and handling applications, provided the coating is continuous, so that the underlying steel is not exposed. Freshwaters vary widely in their composition, and in many cases, the use of aluminum-coated steel in contact with many freshwaters will be satisfactory. However, certain waters may cause severe localized attack or pitting. Pitting is of special importance when coatings are thin. However, aluminized culvert is widely used for freshwater drainage applications. In this case, the greater hardness of aluminized coatings provides better abrasion resistance compared with zinc, even though the aluminized coating provides only barrier, and not sacrificial protection of the steel.

Corrosion of aluminum coatings in seawater is mainly characterized by pitting. Rates of pitting usually range from 3 to 6  $\mu\text{m year}^{-1}$  during the first year and from 0.8 to 1.5  $\mu\text{m year}^{-1}$  after that.

### 4.06.4 Corrosion Characteristics of Tin

As with other metal coatings, the corrosion rate of tin in the atmosphere is highly influenced by moisture. In dry conditions, slow growth of tin oxide is expected; however, in wet conditions, tin coatings behave in a manner similar to that of steel. In wet conditions, tin behaves as a cathode for steel, being more noble than steel in the electromotive series. The only barrier offered by tin to steel under such conditions is as a physical barrier.<sup>2</sup>

Liquid phase corrosion of tin has been extensively studied because of the use of tin steel in food-containment applications. However, the necessary control of process temperatures and times of cooling to ensure product safety, usually results in the avoidance of tin corrosion problems. However, poor drying of cans may initiate corrosion that is only observed later. Also, poor practice regarding external

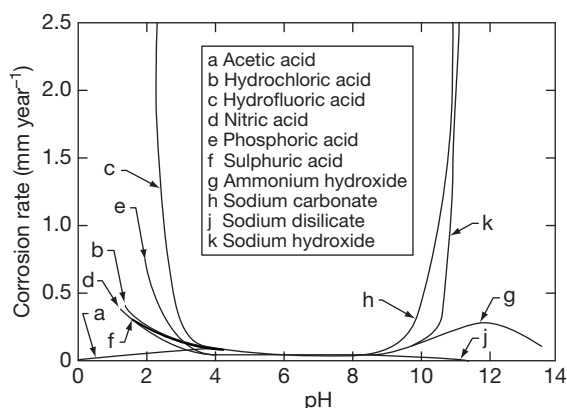


**Figure 3** Relation to pH of the corrosivities towards 1100-H14 alloy sheet of various chemical solutions. Revie, W. R. *Uhlig's Corrosion Handbook*, 2nd ed.; Wiley, 2000; Chapter 40, pp 677–714.



packaging, such as shrink wrapping of wet cans may trap water and cause noticeable tin corrosion. Uptake of chloride from cardboard in contact with food cans may also cause local attack.

Within tin cans, the corrosion of tin is largely affected by the character of the contained food or other substances such as beverages, domestic cleaners, paints, and decorative materials, together with a wide variety of other materials that are stored or transported in tin cans. Organic complexes such as citrate or tartrates can result in conditions that influence the nature of tin corrosion. Pesticide residues or the residues from nitrate fertilizers may also be present. Some foods and beverages are themselves likely to attack steel. Thus, cola-type drinks having phosphate as well as citrate ions and low pH tend to be iron dissolvers. As these products are normally packed in lacquered cans, the potential effects of a large tin cathode are minimized and hence perforation is uncommon. Tinned meats, fish, and vegetables (such as peas) can contain sulfur-bonded protein species. During processing, these may breakdown to yield hydrogen sulfide, which can react readily with both tin and steel. Although they offer no food contamination problems because of the low solubility, they are unsightly. This can be controlled by using internal lacquers pigmented with zinc carbonate or oxide. The sulfide reacts with these pigments, but the resulting zinc compound is off-white and causes no concern to the customer.

#### **4.06.5 Applying Coatings by Hot Dipping**

##### **4.06.5.1 Introduction**

Dipping of metals into molten lower melting point metals is the oldest, simplest, and generally, the cheapest method of forming a surface coating. The base metal must withstand the dipping temperature without undesirable changes in properties. To obtain a coating, the coating metal must be wetted and alloyed with the substrate. The coating metal, in addition to having a lower melting point, must be inexpensive and must confer the desired properties: corrosion resistance is the most important, but often the coated product is required to be formed and must have reasonable abrasion resistance. Commercial coating of zinc, aluminum, tin, and their alloys are most important. Steel is by far the most important metal that is coated by hot dipping. Cast irons are also coated by hot dipping and some copper is coated with tin or tin alloys. Stainless steel is hot dip

coated with aluminum, mainly for use in automotive exhaust systems. Other hot dip coatings are only applied for special purposes.

The dipping processes are of three basic types: (1) continuous lengths of strip, wire, or tube pass through the molten coating metal; (2) semimanufactured products (such as cut tube lengths or sheets) are dipped into the molten metal in batches in specially designed and automatically operated plants; and (3) fabricated products are dipped into the molten metal.

The coatings produced are designed to differ because with most semifabricated materials, such as sheet, the final coating needs to be formed as easily as the base metal, whereas on fabricated products this does not apply and thicker coatings with better corrosion resistance are provided. The vast majority of coatings are zinc based: more than 20 times as much zinc is used for hot dip coatings as the total of all other hot dip metallic coatings. All three types of processes apply for hot dip zinc (galvanizing) and zinc–5% aluminum coatings. Hot dip aluminum coatings (aluminizing), while used in the past on fabricated products, are now expanding for continuously coated strip and also for wire. The 55% aluminum–43.5% zinc–1.5% silicon coating (Galvalume type) and Zn–Al–Mg coatings are used similarly for continuous coating of strips where the coating operation can be in a controlled atmosphere. Hot tinning is used to protect food containers and also to facilitate the soldering of steel, copper, brass, and other metals, for example, copper wire is often tinned. With continuously coated steel sheet and wire, in addition to thin coatings, the ‘terne’ coating, an alloy of lead usually with 2–25% tin, continues in industrial use as a coating for steel sheet and wire, although because of environmental concerns, it has largely been replaced by lead-free materials.

##### **4.06.5.2 Principles of the Hot Dipping Operation**

Most of the principles of hot dipping are common to galvanizing, tinning, terne coating, and aluminizing.

###### **4.06.5.2.1 Cleaning**

The surface must be cleaned of oil, grease, and other surface contaminants and also scale and oxide, using degreasing and/or pickling treatments as required. The original Sendzimir pretreatment of steel strip by oxidation followed by reduction at high temperature or other high temperature gaseous treatments, developed more recently, eliminates the necessity for

these operations and also for fluxing, although electrolytic cleaning can be used before the gaseous treatment processes, to obtain the highest quality hot dip coatings on strip.

Keeping the material in a controlled atmosphere is often sufficient to retain a clean surface until coating takes place, but where exposure to air occurs (as with most coating of fabricated articles), a flux coating is usually applied to keep the surface clean and free from oxide. Fluxing may be by immersion in an aqueous prefluxing bath, followed by drying, or by passing through the molten flux floating on the bath of molten metal, or both of these. Molten flux attacks the surface, cleaning it and promoting the wetting of the base metal by the molten metal in which it is dipped.

#### 4.06.5.2.2 Dipping

Strip or wire is coated continuously, up to  $4 \text{ m s}^{-1}$  in speed. Continuous coating plants in which the sheet is continuously uncoiled, passed through the coating equipment, and then recoiled have largely replaced cut sheet plants, except in developing countries. Fabricated articles are either dipped in batches, mounted on suitable jigs if small, or singly if large, and the operation may be mechanized. Small articles and threaded work are dipped in perforated baskets suitable for subsequent centrifuging before the coating solidifies. Assuming that the articles to be coated have been properly cleaned and fluxed, the base metal and the molten coating metal interact on dipping, producing an alloy layer. If the article is colder on entry than the melting point of the coating metal, there may be a short intermediate stage where a solid skin forms around the article. Frequently, the base metal (or article) is preheated to avoid this.

For any given pair of metals, the total amount of alloy increases with the duration of immersion and is also affected by the temperature of the bath.

The amount and nature of the alloy layer may also be profoundly affected by additions to the molten bath, such as silicon to an aluminum bath or aluminum to a galvanizing bath. The change in the composition of the base metal may also have a marked effect, for example, mild steel containing a little silicon continues to react with zinc at a steady state throughout immersion, whereas with steel without silicon, the reaction rate decreases with time. Although the alloy layer is always referred to as if it were a single layer, it is usually made up of two or more layers, corresponding to known metallurgical phases. Reaction can occur after the work has left the molten metal bath while the coating is solidifying and cooling.

#### 4.06.5.2.3 After treatments

These include processes intended to produce one or more of the following results:

- Reduction of coating thickness by reducing the amount of molten metal adhering to a substrate as it leaves the bath. Air or gaseous jets are used for control of the coating thickness of continuous sheet and wire and tubes. For fabricated articles, this is done by centrifuging while the coating is still molten.
- Improvement of the properties or appearance of the coating for substrates. Such improvements include quenching (to avoid unwanted alloy growth), chromating and phosphating, and special treatments in both chemical and mechanical types for sheet such as temper rolling and stretch leveling.
- Change in the character of the coating – as distinct from the more superficial treatments listed under (b). Hot-dipped zinc coatings are sometimes annealed to convert the whole of the coating into alloy as are aluminum coatings intended for heat resistance.

### 4.06.6 Hot Dip Galvanizing

#### 4.06.6.1 Introduction

Large tonnages of fabricated steelwork are hot dip galvanized each year. Over 6 million tons of steel were hot dip galvanized within the European Union in 2006.<sup>8</sup> The principles of hot dip galvanizing have remained unchanged for 150 years; however, a vast amount of research has enabled the industry to become technically advanced over this period. Many changes to plant configuration have also been brought about in response to modern national and European environmental and health and safety legislation. The hot dip galvanizing process essentially consists of cleaning the articles (degreasing and pickling), fluxing the work, and then immersing the work in a bath of molten zinc. Coated work can then be either quenched or allowed to air cool.

#### 4.06.6.2 Design for Hot Dip Galvanizing

Steelwork intended for processing should ideally be designed with the coating process in mind.<sup>9</sup> When an article is received for hot dip galvanizing it is assessed for suitability for further processing. It should be free from contamination, which would not be removed in

the normal pretreatment process prior to galvanizing. It is important that the design allows adequate handling through the process and for the access and egress of all pretreatment solutions and molten zinc. Articles containing sealed volumes should not be hot dip galvanized, because any residual water or other solutions contained within the void will evaporate and are likely to generate sufficient pressure to cause an explosion – ejecting molten zinc from the galvanizing bath and compromising operator safety. Distortion can occur in some fabrications because of relief of unbalanced steel production stresses and or fabrication stresses in combination with the thermal stresses brought about during dipping. Articles destined for galvanizing, having been fabricated from elements with very dissimilar geometries (thickness), utilizing high-strength steels, and particularly those adopting designs that incorporate highly restrained joints, can in specific circumstances become more susceptible to steel cracking during galvanizing by one or more mechanisms (strain-age embrittlement, hydrogen embrittlement, or liquid metal assisted cracking), and guidance exists to manage these risks.<sup>10,11</sup>

#### 4.06.6.3 Degreasing and Pickling

Steelwork is commonly degreased in acid or alkaline solutions prior to rinsing in cold water. The work is then pickled in either a sulfuric acid solution or a hydrochloric acid solution. Sulfuric acid is usually operated at a strength of around 14% and at a temperature of 60–80°C, whereas hydrochloric acid would normally be operated across a range of ~5–14% and at ambient temperatures.<sup>12</sup> Inhibitors are added to the acid to reduce potential for overpickling on clean areas of steelwork. Rather than operate a separate process tank, acidic degreasers can also be added to a pickle tank obviating the need for a separate degreasing stage. Pickling will be followed by another water rinse stage.

Grit blasting is often used to remove tenacious contamination on castings, to remove welding slag from fabricated steelwork, or in specific instances where a rougher steel surface profile is required in order to attract development of a thicker galvanized coating. Where grit blasting is carried out, the work is normally ‘flash pickled’ to remove any residual loose contamination prior to further processing. Hydrofluoric and mixed acids can also be used to pickle castings, but these are extremely dangerous chemicals and great care is needed when working with these agents.

#### 4.06.6.4 Fluxing

After degreasing and pickling, work is fluxed to prevent further oxidation of the surface and to aid wetting of the surface when it comes into contact with the molten zinc. Fluxing has historically taken place in a variety of ways – ‘old dry,’ ‘dry,’ and ‘wet’ methods **Figure 4**. The ‘dry’ method dominates for general galvanizing, while the ‘wet’ method is still used when processing smaller articles in spin-galvanizing operations for instance.

The ‘old dry’ method consists of drying the work after pickling and allowing the dried on salts to provide the fluxing action prior to dipping in the molten zinc. The ‘dry’ method involves dipping the pickled and rinsed work into a flux solution and afterwards drying the work in a pit or oven prior to dipping the work into the molten zinc. The ‘wet’ method involves passing the pickled and rinsed work through a blanket of flux floating on the top of the zinc melt.

Where the ‘dry’ process of prefluxing is used, the solutions adopted are usually based upon zinc ammonium chloride (a common form being the double salt  $\text{ZnCl}_2 \cdot 3\text{NH}_4\text{Cl}$ ). Operating strength is usually up to 30% and operating temperatures of up to 80°C can

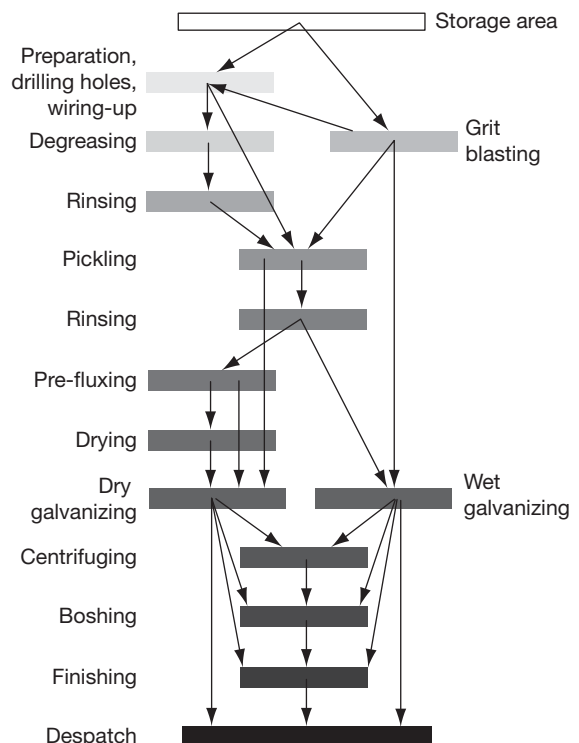


**Figure 4** Flow diagram showing handling operations in the galvanizing process. *General Galvanizing Practice*; Galvanizers Association: UK; 1999; p 3.12.

be used. Other fluxes, which include a proportion of sodium chloride or potassium chloride, can also be used. These fluxes, while requiring more care for optimum operation, have been reported to produce fewer fumes during dipping of the work than do the traditional zinc ammonium chloride solutions.<sup>13,14</sup>

When drying the work prior to dipping in the molten zinc, care is needed to ensure that the flux on the work is not degraded by overheating. Normally, article surface temperatures are limited to 150°C maximum. The time between fluxing and dipping in the molten zinc should be minimized to maintain the effectiveness of the flux.

#### 4.06.6.5 Galvanizing

Upon immersion of the prepared article into the molten zinc a series of iron–zinc intermetallic compounds are formed on the surface of the article (gamma ( $\Gamma$ ), delta ( $\delta$ ), zeta ( $\zeta$ )). Upon withdrawal of the article from the galvanizing bath, a proportion of molten zinc is also withdrawn on the work (forming the eta ( $\eta$ ) layer). This solidifies as the work cools (see **Figure 5**).

‘Spin-galvanizing’ or ‘centrifuge galvanizing’ is a variation of the general galvanizing process where articles are contained within a perforated basket during pretreatment and dipping in the zinc melt. After withdrawal, the basket is placed in a container, which spins the work to remove a proportion of the free (semimolten) zinc from the coating. This type of process is often used for small articles such as fasteners and washers. The spinning process produces a thinner coating than that of the general galvanizing process, a factor that is reflected in the standards and specifications associated with products processed in this way.<sup>15</sup>

##### 4.06.6.5.1 Coating development and reactivity of steel

Conventional operating temperatures for galvanizing are between 445 and 465°C. High temperature galvanizing is carried out between 530 and 560°C. Galvanizing processes are not operated at temperatures between these two ranges.<sup>16</sup> Operators of the higher temperature process use ceramic galvanizing baths to overcome problem of the increased reaction rate between steel and zinc at these high temperatures. For silicon-free steel, the reaction rate between iron and zinc is parabolic with time in the temperature range 420–490°C (the lower parabolic range). At temperatures between 490 and 510°C, the reaction rate is approximately linear with time (known as the linear region). The reaction rate reverts to a parabolic relationship at temperatures above 530°C (the upper parabolic region).

The thickness of the alloy layers within the coating formed on a steel article will depend principally on (a) the chemistry of the surface of the steel, (b) the surface roughness of the steel, (c) the temperature of the galvanizing bath, (d) the time of immersion, and (e) the rate of cooling.<sup>17</sup>

The role of silicon and phosphorus in development of alloy layers in a galvanized coating has been subject to intense research over many years.<sup>18,19</sup>

Silicon-killed steels, containing Si over 0.3%, produce a thick gray galvanized coating on processing. These thick gray coatings consist predominantly of all zinc–iron alloy (see **Figure 6**). While offering extended periods of corrosion protection, they are often less resistant to mechanical damage. Steels containing between 0.15% and 0.25% Si often produce

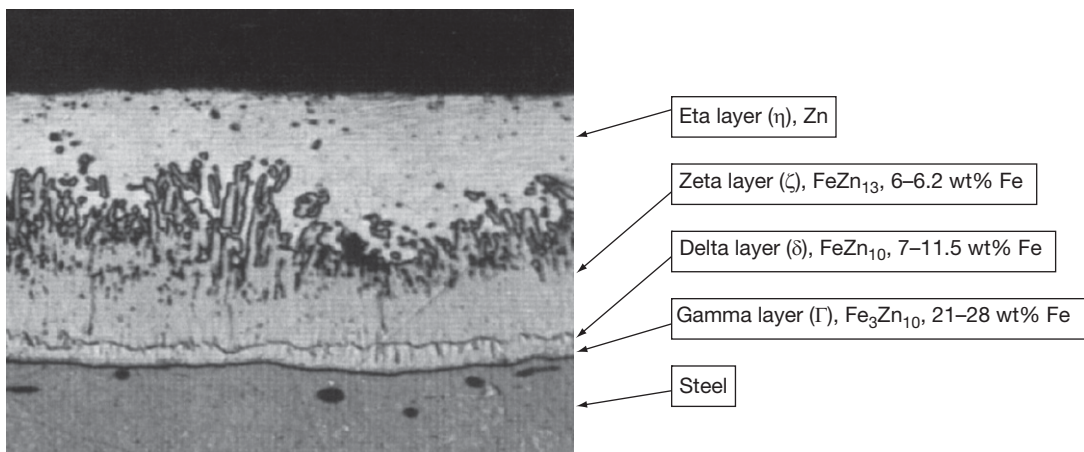


**Figure 5** Structure of a galvanized coating on a normal (un killed) steel. *The Engineers and Architects' Guide: Hot Dip Galvanizing*; UK Galvanizers Association Publication, 1999.

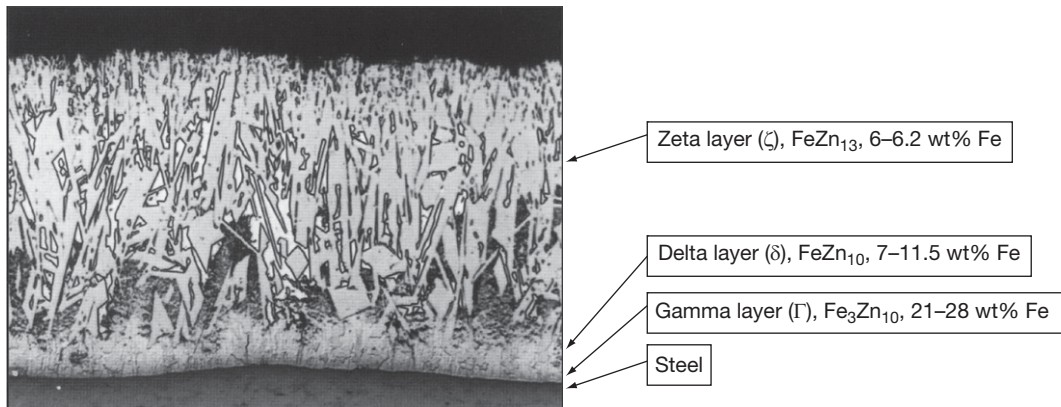


**Figure 6** Structure of a galvanized coating on a reactive (silicon-killed) steel. *The Engineers and Architects' Guide: Hot Dip Galvanizing*; UK Galvanizers Association Publication, 1999).

coatings that retain a proportion of zinc on top of the zinc–iron alloy layers.

Where semikilled steels are processed, the results are less predictable. Steels containing between 0.04% and 0.14% Si often produce coatings that are very thick and exhibit poor cohesion. This reactivity range (see [Figure 7](#)) is often known as the ‘Sandelin peak,’ named after the researcher who described the effect some years ago.<sup>20</sup> Phosphorous is more influential in determining coating characteristics at these lower silicon concentrations. The International Lead Zinc Research Organization (ILZRO) has set out a classification system for reactivity of steels, which is broadly in line with the Sandelin data.<sup>21</sup> Hot dip galvanizing of reactive steels is often associated with increased zinc usage.

The effect of silicon can be suppressed by galvanizing at higher temperatures (530–560°C). High temperature galvanizing is often (but not exclusively) used to process small work also, adopting the ‘centrifuge’ or ‘spinning’ process.<sup>15</sup>

Alloy layers tend toward increased thickness on rougher steel surfaces, and because of the increased surface area, they are able to take part in the reaction between the zinc and the iron.<sup>22</sup> In practice, a maximum uplift in coating of ~50% can be achieved for steel that has been grit blasted prior to galvanizing compared with the coating developed on a steel of similar thickness and surface chemistry that has not been subject to blasting.

The alloy layers grow more rapidly as temperature increases – but there are practical limits to the extent to which this factor can be used to control alloy layer growth.<sup>23</sup>

Coating development normally tends to follow a parabolic reaction rate when articles are first immersed in the zinc melt. Very reactive steels

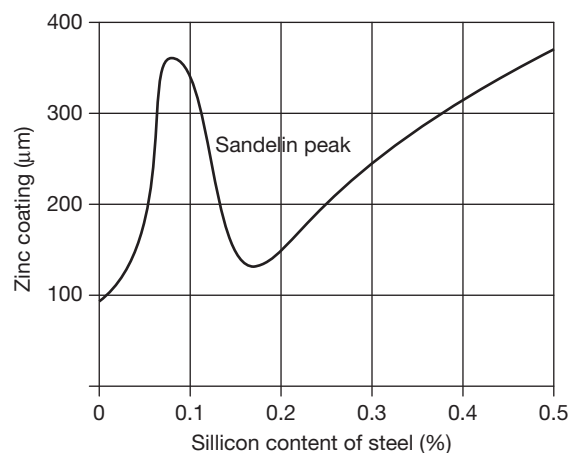


**Figure 7** Illustration of the ‘Sandelin’ curve – Hot dip galvanized coating development with increasing steel surface silicon concentration. *General Galvanizing Practice*; Galvanizers Association: UK; 1999; 1.8.

(particularly those with high (>0.25%) or critical levels (0.04–0.14%) of silicon and phosphorus) exhibit a reaction rate for coating growth that is more linear with time (see [Figure 8](#)).

The alloy layer may continue to grow slowly during the cooling of the work after galvanizing. This is rarely an important consideration except when very heavy sections are being processed. In extreme cases, the alloy layer diffuses to the surface to form grey patches. This is often referred to as a ‘gray coating’ or ‘gray bar.’<sup>24</sup>

#### 4.06.6.5.2 Alloying additions the zinc melt

Alloying additions to the galvanizing zinc melt can be made to control the rate of coating development for reactive steels. Depending upon the specific alloying element(s) being introduced to the galvanizing zinc



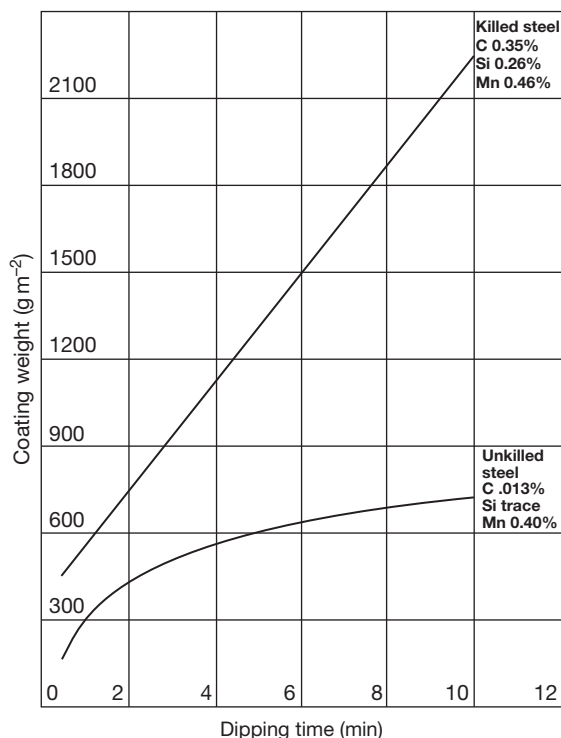


**Figure 8** Illustration of galvanized coating development with time for normal (unkilled) and reactive (silicon-killed) steel. *General Galvanizing Practice*; Galvanizers Association: UK, 1999; 1.8.

melt, these additions can be made directly or in the form of a master-alloy.

Most galvanizing melts will contain ~98.5% zinc. Lead will be found in zinc melts produced by melting zinc stock originating from a thermal production route (e.g., imperial smelting process). Although the solubility of lead in zinc is ~1.4% at 450°C, common concentrations of lead in zinc melts will run up to ~1%. Lead assists wetting of the steel surface and reduces the surface tension of zinc, thereby encouraging greater fluidity and better drainage from the article.<sup>25,26</sup>

Nickel additions to the zinc melt of ~0.05–0.06% have been found to be most effective for controlling coating development on steels that exhibit silicon concentrations up to 0.2%, effectively eliminating the development of reactive coatings in this range.<sup>27,28</sup> The effects of bismuth on the zinc–nickel-based melt have also been studied.<sup>29</sup>

Historically, aluminum additions of up to 0.005% have been used to aid brightening of the work and reduce the rate of oxidation of the zinc.<sup>30,31</sup> Galvanizing melts commonly operate using aluminum levels of ~0.001–0.002%.

Tin additions to the zinc melt at concentrations up to around 2% had been found to be effective in controlling steel reactivity across the range of common silicon concentrations in steels and providing coatings with bright finishes.<sup>32,33</sup> Although the role of tin during galvanizing for concentrations up to 5.0% have also been investigated,<sup>34</sup> tin levels of ~0.3%, particularly when used in combination with bismuth (around 0.1% maximum to improve melt fluidity), have found wider currency in Europe for controlling steel reactivity. Zinc alloy melts using total for tin, bismuth, and aluminum (total Sn/Bi/Al < 1%) have also been developed, which provide a smooth, bright, spangled finish to the galvanized coating.<sup>35</sup> The additions of tin to the melt allow for operation of higher aluminum levels without detriment to coating continuity (development of bare spots).

Use of other alloying additions (alone or in combinations), such as vanadium,<sup>36,37</sup> manganese, and titanium,<sup>38</sup> have also been investigated to either control steel reactivity or develop a more consistent coating thickness, texture, or appearance while maximizing profitability and minimizing production of waste streams.

Almost from 2002, zinc–5% aluminum coatings have also been developed for application through the general galvanizing process, albeit on a more limited scale than coatings developed through conventional zinc melts (zinc concentration 98.5% minimum).<sup>39</sup> Coatings of Zn–23% Al have also been investigated.<sup>40</sup>

#### 4.06.6.6 Post-Galvanizing Treatments

Work which has been galvanized is often either left to air-cool or quenched in water. The quench water may contain a passivation treatment (chromate or phosphate), which retards the early onset of wet storage staining during transport or storage.<sup>41</sup> Quenching the work has the advantage of removing potential flux residues that might stain the work and allowing more rapid cooling of the work, thereby reducing the potential for development of all alloy layered coatings on components fabricated from reactive steels. The work will also be cooler to handle, allowing earlier movement of work away from the processing area.

#### 4.06.7 Continuous Zinc and Zinc Alloy Coating

Large tonnages of wire and sheet are galvanized on automated lines by continuously uncoiling the steel,

passing it through the coating line, and recoiling it. In the past 20 years, development of techniques for coating steel sheet with zinc and zinc alloys, and pretreating advanced high-strength steels now demanded by automakers, have been the major advances.<sup>42</sup>

Surface pretreatment is now principally by gaseous treatments in most strip lines and some wire lines; pickling remains for other products. In the gaseous pretreatment processes, steel is fed into the galvanizing bath through a snout, which dips below the surface of the molten zinc and protects the surface against reoxidation. This eliminates the need for fluxing. The strip enters the molten zinc at a temperature of 470–480°C; most of the heat required for the galvanizing bath is supplied by the sheet itself.

Chemical cleaning and fluxing (wheeling process) without gaseous treatment also has limited use, mainly for building panels and other sheets in which economical development of high tensile strengths is desired. External coating of small diameter tubes in which zinc is pumped over the steel instead of the steel being dipped uses either an inert atmosphere or a flux pretreatment.

Painting of galvanized sheet best involves no-spangle or minimum spangle galvanized surfaces that provide good specular reflectivity without the substrate surface structure being visible. The traditional spangled galvanized surface is now only rarely seen on sheet intended for painting. Spangle reduction is achieved by sweeping the coating with narrow jets of steam or air or by depositing a large number of crystallization nuclei on the surface just before solidification. A skin pass, with a reduction of <1%, after solidification is an alternative method. Paintability (and weldability) is also improved by converting the surface to a zinc-iron alloy (galvannealing) in line.

Steel wire is also galvanized on a continuous basis and the principles of the Sendzimir sheet galvanizing process and later developments have been applied as an alternative to wet cleaning and pickling. Certain grades of wire that require tensile strength may require redrawing of the wire after coating.

For annealed wire, the strands of wire are first taken through a bath of molten lead, where the desired softening and a partial cleaning effect, termed patenting, is achieved. Strands are then pickled, fluxed, and galvanized. Wiping of the wire after galvanizing controls coating thickness. Wires with heavier coatings are drawn through a bed of charcoal, while for thinner coatings, wiper pads are held against the wire by various means. At higher line speeds, gas wiping is practised.

#### 4.06.8 Hot Tinning

Like zinc coatings, hot dip tin coatings possess an intermetallic coating covered with the solidified metallic coating. Cleaning and pickling treatments for prefabricated article are similar to hot dip galvanizing. The aqueous flux solution is also similar to galvanizing solution, consisting typically of 240 g l<sup>-1</sup> of zinc chloride, 60 g l<sup>-1</sup> of sodium chloride, 30 g l<sup>-1</sup> of ammonium chloride, and 6–12 ml l<sup>-1</sup> of hydrochloric acid (sp. gr. 1.14). Articles, wet with flux solution, are lowered into a bath of molten tin at about 280°C, having a layer of fused flux floating on it, covering about two-thirds of its surface. The flux cover is composed of a mixture of dry chlorides in the same proportions by weight, as the flux solution being carried over with the work. After the article reaches the temperature of the tinning bath, flux is removed from the immediate surface of the bath and the article is immediately withdrawn through the flux free area of the tin surface. Coating quality may be improved by redipping in a second tinning pot where the tin is covered with a layer of molten grease such as tallow at a temperature of 240–270°C. Small articles may be tinned in batches using jigs or baskets and then spun in a heated centrifuge to remove excess tin. The brightness of the tin coating may be preserved by quenching the articles in a layer of paraffin or kerosene, 50–100-mm thick, floating on water. Small parts can be separated from one another before the tin coating solidifies by allowing them to fall on a paddle wheel rotating at 500–1000 rpm. For strip, pretreatment uses electrolytic alkaline degreasing followed by electrolytic pickling. Work then passes downward through a layer of molten zinc chloride flux into the molten tin at 300–320°C on emerging sheet passed through pressure rolls and palm oil at 240°C to remove tin. A hot dip tin coating on a steel layer has a layer of FeSn<sub>2</sub> at the interface between the tin and the steel. This alloy grows very slowly in comparison with the more complex alloy layers formed in galvanizing and then aluminizing. It usually comprises 10–20% of the total coating thickness. Tin-lead coatings containing two or more percent of tin may be applied by hot dip processes to steel, copper, and copper alloys. Steel sheets are commonly coated with alloys containing 7%, 10%, or 25% tin. These are called terne plate with the name tin-terne, sometimes applied to the higher tin coating. Coating quality can be improved by electroplating the steel substrate with nickel before hot dipping in the terne bath.

### 4.06.9 Hot Dip Aluminizing

Fabricated articles are less commonly hot dip aluminized now, than in the past. Coatings are applied after cleaning the work, including degreasing, pickling in hydrochloric acid, and then preheating. The work is then immersed in a molten salt bath, a flux or reducing atmosphere, prior to immersion in the bath of molten aluminum. Alloying occurs between iron and aluminum at the interface.

Type I aluminized steel strip (used in high temperature conditions) is coated with aluminum–silicon alloy containing typically 5–11% silicon, whereas the Type II grade (for corrosion prevention) is coated with a heavier layer of ‘pure’ aluminum, although heavier aluminum–silicon coatings are also referred to as ‘Type II’. A disadvantage of silicon-containing aluminum coatings is that they darken when subjected to atmospheric corrosion; Type I grade of aluminized steel possesses total coating thicknesses, including the alloy layer, between 14 and 25  $\mu\text{m}$  (80–150  $\text{g m}^{-2}$  including both sides) whereas Type II grade has in excess of 40  $\mu\text{m}$  (230  $\text{g m}^{-2}$  including both sides). In both cases, about 2–4% of iron is present in the coating alloy. This is iron dissolved from the strip and the coating bath hardware. An alloy layer containing intermetallic compounds can be seen between the coating layer and the steel substrate in both grades. This layer is thicker in the Type II grade. As intermetallic compounds are generally very brittle, it is desirable to keep the alloy layer fairly thin. Silicon additions help control the thickness of the alloy layer. In both grades, it thickens with time and temperature, at a rate that is generally parabolic, but there is a slower rate of thickening of the alloy layer in the Type I grade, likely because of a combination of a higher dissolution rate and a slower solid state growth rate.

Post annealing, an overageing heat treatment carried out for an hour at 400–500°C, can slightly increase ductility. A coating which has a total thickness of 25  $\mu\text{m}$  in which the alloy layer occupies about 25% of the total has satisfactory bending properties. Excessive deformation causes cracking of the alloy layer or delamination of the coating. The thicker alloy layer in the Type II grade tends to crack more readily than that on Type I.

Aluminized steel has far better heat resistance than do galvanized steel, maintaining a bright metallic surface on exposure to temperatures up to ~500°C. Higher temperatures will lead to the conversion of any free aluminum at the surface to iron aluminum

compounds. Exposure to temperatures up to 700°C are possible without promoting breakdown of the steel substrate. Aluminized steel does not suffer from the intergranular embrittlement problems arising from intergranular diffusion of zinc reported for galvanized steel at high temperatures. Galvalume, a strip product coated with an alloy containing 55% Al–43.5% Zn–1.5% Si, has also been reported to suffer from intergranular embrittlement at temperatures close to 500°C, although this can be prevented by increasing the phosphorus content of the substrate steel above 0.04%.

### 4.06.10 Hot Dip Coatings with Applied Organics: Duplex Systems

Hot dip galvanized coatings by themselves provide a long lasting and cost-effective means of corrosion protection for iron and steel articles in most applications. When organic systems are applied on top of the galvanized article, this becomes known as a duplex coating. Duplex coatings are often used to add color for aesthetic reasons (camouflage or contrast), to increase the economic life of the structure by providing additional corrosion protection, or to provide greater protection in aggressive corrosive environments.

Organic systems used in conjunction with galvanized coatings often provide a life for a structure, which are longer than the sum of the lives of the coatings used independently.<sup>43</sup> EN ISO 12944 provides information on preparation of galvanized coating prior to application of wet paint systems, together with life to first maintenance periods for duplex-coated articles in a variety of exposures (the predicted life to first maintenance relates only to the need for repair of the organic coating and so is likely to be much shorter than the life expected from use of the galvanized coating alone).<sup>44</sup> EN 13438 provides performance requirements for duplex systems involving powder organic coatings applied to galvanized articles.<sup>45</sup>

### 4.06.11 Applications for Hot Dip Coated Products

All industrial sectors use hot dip coated products of one form or another. [Table 5](#) illustrates a range of application sectors for hot dip coated products. The growing need for cost-effective, long-life, sustainable corrosion protection systems has led to increasing usage of hot dip coated products worldwide. The construction industry and street and outdoor furniture sectors

dominate the take up of hot dip galvanized products, followed by agricultural sector and many other, smaller, market segments. Development of coatings with greater formability for application to higher strength steel has increased the usage of these types of coatings in the vehicle manufacturing sector.

#### 4.06.12 Standards

The development of standards for hot dip coatings within the European region, through Comité

**Table 5** Applications for use of hot dip coated products

<i>Application</i>	<i>Examples</i>
Agricultural	Animal pens, buildings, cattle grids, farm machinery, gates, grain hoppers, glass houses, livestock trucks, and sprinklers
Building components	Balconies, downpipes, fire escapes, gutters, lintels, louvres, reinforcing bar, and window frames
Construction	Bridges, building frames, car parks, telecom masts, ski lifts, tunnels, siding/cladding, corrugated roofing
Industrial	Access bridges, cat ladders, checker plate, conduit, handrail, pipe bridges, stairways and walkways, and platforms
Marine	Boat hulls, buoys, chains, docking pontoons, fish farm equipment, handrailing, offshore platforms
Miscellaneous	Brackets, castings, fasteners, nails
Power generation/distribution	Cable tray, cooling towers, flues, power station equipment, pylons, transformer boxes, wind turbines
Storage and handling	Conveyor systems, cranes, drums, pallets, racking, and stillages
Street furniture	Benches, bollards, bus stops, crash barrier, lighting columns, manhole covers, palisade fencing, playground equipment, and safety barriers
Transport	Fencing, footbridges, rail gantries, motorway signal gantries, railway station platforms, trailers, and vehicle chassis
Automotive	Components, subframe, body-panels, fuel tanks, baffles, brackets, filler caps
Food	Packaging (cans)
Domestic	Mufflers, furnaces, ovens, ranges, heaters, water heaters, fireplaces, baking pans, air conditioner housings and drying ovens, lighting fixtures

Source: UK Galvanizers Association, 2007.

Européen de Normalisation (CEN), and on a global scale, through the International Standards Organisation (ISO), has burgeoned over the last decade. **Table 6** shows a selection of relevant international and European standards for hot dip coatings on articles. **Table 7** shows a selection of relevant American standards (developed by the American Society for Testing and Materials (ASTM) International). Where standards are specified, the latest dated document should be used.

#### 4.06.13 Recent and Future Developments

Since the previous edition was written, several new directions for development have emerged, and are likely to continue into the future:

**Table 6** Selected international and European reference standards relevant for specification and use of hot dip coated sheet/articles

<i>EN/ISO</i>	<i>Title</i>
ISO 752	Zinc ingots
ISO 9223	Corrosion of metals and alloys – Corrosivity of atmospheres – Classification
EN 1179	Zinc and zinc alloys – Primary zinc
EN 10240	Internal and/or external protective coatings for steel tubes. Specification for hot dip galvanized coatings applied in automatic plants
EN 13283	Zinc and zinc alloys – Secondary zinc
EN 13438	Paints and varnishes. Powder organic coatings for galvanized or sherardized steel products for construction purposes
EN ISO 1460	Metallic coatings. Hot dip galvanized coatings on ferrous materials. Gravimetric determination of the mass per unit area
EN ISO 1461	Hot dip galvanized coatings on fabricated iron and steel articles – Specifications and test methods
EN ISO 1462	Metallic coatings – Coatings other than those anodic to the base metal – Accelerated corrosion tests – Method for the evaluation of results
EN ISO 10684	Fasteners – Hot dip galvanized coatings
EN ISO 12944 Parts 1-8	Paints and varnishes. Corrosion protection of steel structures by protective paint systems.
EN ISO 14713	Protection against corrosion of iron and steel in structures – Zinc and aluminium coatings – Guidelines

Source: UK Galvanizers Association, 2007.

**Table 7** Selected ASTM standards relevant to hot dip coating of steel sheet/articles

ASTM	Title
A90/A90M	Standard Test Method for Weight (Mass) of Coating on Iron and Steel Articles with Zinc or Zinc-Alloy Coatings
A123/A123M	Standard Specification for Zinc (Hot-Dip Galvanized) Coatings on Iron and Steel Products
A143/A143M	Standard Practice for Safeguarding Against Embrittlement of Hot-Dip Galvanized Structural Steel Products and Procedure for Detecting Embrittlement
A153/A153M	Standard Specification for Zinc Coating (Hot-Dip) on Iron and Steel Hardware
A308/A308M	Standard Specification for Steel Sheet, Terne (Lead-Tin Alloy) Coated by the Hot-Dip Process
A384/A384M	Standard Practice for Safeguarding Against Warpage and Distortion During Hot-Dip Galvanizing of Steel Assemblies
A463/A463M	Standard Specification for Steel Sheet, Aluminum-Coated, by the Hot-Dip Process
A653/A653M	Standard Specification for Steel Sheet, Zinc-Coated (Galvanized) or Zinc-Iron Alloy-Coated (Galvannealed) by the Hot-Dip Process
A792/A792M	Standard Specification for Steel Sheet, 55% Aluminum-Zinc Alloy-Coated by the Hot-Dip Process
A875/A875M	Standard Specification for Steel Sheet, Zinc-5% Aluminum Alloy-Coated by the Hot-Dip Process
A924/A924 M	Standard Specification for General Requirements for Steel Sheet, Metallic-Coated by the Hot-Dip Process
A1046/A1046M	Standard Specification for Steel Sheet, Zinc-Aluminum-Magnesium Alloy-Coated by the Hot-Dip Process

Source: UK Galvanizers Association, 2007.

- Zinc alloy coatings to control reactivity in galvanizing and fabricated articles.<sup>46</sup>
- Development of zinc–aluminum–magnesium and composite coatings for continuous sheet galvanizing.<sup>47</sup>
- Development of lead-free coatings<sup>46</sup> and duplex coatings.<sup>48</sup>

Very recently, an explanation of the beneficial effects of magnesium alloying in zinc hot dip coatings has

emerged. As magnesium is added to zinc coatings, up to around 8 wt% magnesium, a magnesium-based oxide layer gradually replaces the zinc-based oxide layer. It is known that magnesium oxide has a higher band gap than do zinc oxide (5.2 eV compared with 3.5 eV, respectively), and therefore a lower ability to transfer electrons. This results in a reduced efficiency of oxygen reduction. As magnesium in the coating is further increased, the corrosion resistance does not improve and indeed decreases as hydrogen depolarization becomes easier in the higher magnesium content phases that then exist in the coating, for example, ZnMg. At this point, the optimal composition appears to be one that allows for bulk zinc metal to be present in the coating giving an anode, together with magnesium oxide in the surface layer, with its low ability to reduce oxygen.<sup>49</sup> Further improvements are being seen with zinc–aluminum–magnesium hot dip coatings whose mechanisms for improvement appear to be similar to that of zinc–magnesium coatings, but are not yet fully understood.<sup>50</sup>

## References

1. Zhang, G. Z. *Corrosion and Electrochemistry of Zinc*; Plenum, New York, 1986; Chapter 7, pp 213–217.
2. Revie, W. R. *Uhlig's Corrosion Handbook*, 2nd ed.; Wiley, 2000; Chapter 40, pp 677–714; Chapter 46, pp 853–862; Chapter 48, pp 887, 903.
3. Lamberigts, M.; Goodwin, F. E. In *Process—structure Relationships in Commercial Galvan-Coated Steel Steels*, *The Physical Metallurgy of Zinc Coated Steel*; Marder, A. R., Ed.; The Minerals, Metals and Materials Society (TMS), 1993; pp 79–87.
4. Mackowiak, J.; Short, N. R. *Int. Metals Rev.* **1979**, 24(1), 1–19 (reprinted by UK Galvanizers Association).
5. Marder, A. R. *Prog. Mater. Sci.* **2000**, 45(3), 191.
6. Knotkova, D. *International Corrosion Conference*, Houston, TX, USA, 1993; 16.
7. Porter, F. C. *Corrosion Resistance of Zinc and Zinc Alloys*; Marcel Dekker: New York, 1994; Chapter 4, 341.
8. Garcia, C. Assembly 2007 The George Hotel, Edinburgh, UK, June 2007, Proceedings of the European General Galvanizers Association, 2008.
9. EN ISO 14713. Protection against Corrosion of Iron and Steel in Structures – Zinc and Aluminium Coatings – Guidelines British Standards Institution: Chiswick, UK, 1999.
10. *The Engineers and Architects' Guide: Hot Dip Galvanizing*; UK Galvanizers Association Publication, 2007.
11. The British Constructional Steelwork Association Limited. Publication 40/05, Galvanizing Structural Steelwork – An Approach to the Management of Liquid Metal Assisted Cracking, 2005.
12. Viljoen, C. L.; Kirkbride, A. N.; van Wyk, D. In A Comparative Study of the use of HCl and H<sub>2</sub>SO<sub>4</sub> in Acid Pickling in the South African Hot Dip Galvanizing Industry, Proceedings of the 16th International Galvanizing Conference, Barcelona, Spain, European General Galvanizers Association, 1991.



13. Allen, C.; Kolisnyk, P. S.; Anderson, N. In Fumeless Flux Developments, Proceedings of the 2nd Asian Pacific General Galvanizing Conference, Kobe, Japan, 1994.
14. Vazquez, A. J.; Garcia, J. In Galvanizing Fluxes without Fumes, Proceedings of the 20th International Galvanizing Conference (Intergalva 2003) Amsterdam 2003, European General Galvanizers Association, UK, 2003.
15. Porter, F. C. *Zinc Handbook: Properties, Processing, and Use in Design*; Marcel Dekker: New York, 1991; Chapter 10, pp 224–225.
16. Porter, F. C. *Zinc Handbook: Properties, Processing, and Use in Design*; Marcel Dekker: New York, 1991; Chapter 10, pp 211–213.
17. *General Galvanizing Practice*; Galvanizers Association: UK, 1999; 1.9.
18. Richards, R. W. In Relationship between Steel Surface Chemistry and the Galvanizing Behaviour of Reactive Steels, Proceedings of the 16th International Galvanizing Conference (Intergalva 1991) Barcelona, Spain, 1991, European General Galvanizers Association, UK, 1991; pp GF4/1–GF4/20.
19. Horstmann, D. Proceedings of the 14th International Galvanizing Conference (Intergalva 1985), Munich, Germany FR, Zinc Development Association, 1985; pp 6/1–6/5.
20. Kirkbride, A. N.; Wells, A. In Studies Relating to the Galvanizing Behaviour of Sandelin Alloys, Proceedings of the Fifteenth International Galvanizing Conference, Rome, Italy, 1988, pp GC1/1–GC1/16.
21. International Lead Zinc Research Organization Inc. Galvanizing Reactive Steels – A Guide for Galvanizers and Specifiers Englewood, 1996.
22. *General Galvanizing Practice*; Galvanizers Association, UK, 1999; 1.11.
23. Porter, F. C. *Zinc Handbook: Properties, Processing, and Use in Design*; Marcel Dekker: New York, 1991; Chapter 10, 222.
24. Horstmann, D. *Faults in Hot Dip Galvanizing*, 2nd ed.; Verlag Stahleisen mbH, Dusseldorf, 1983; pp 64, 65.
25. Reumont, G.; Perrot, P. In Fundamental Study of Lead Additions in Industrial Zinc Baths, Proceedings of the 18th International Galvanizing Conference (Intergalva 1997) Birmingham, UK 1997, European General Galvanizers Association, UK, 1997.
26. Krepski, R. P. In The Influence of Lead in After-fabrication Hot Dip Galvanizing, Proceedings of the 14th International Galvanizing Conference (Intergalva 1985), Munich, Germany FR, Zinc Development Association, 1985; pp 6/6–6/12.
27. Taylor, M.; Murphy, S. In A decade of Technigalva, Proceedings of the 18th International Galvanizing Conference (Intergalva 1997) Birmingham, UK 1997, European General Galvanizers Association, UK, 1997.
28. Lewis, G. P.; Pederson, N. In Optimizing the Nickel–Zinc Process for Hot Dip Galvanizing, Proceedings of the 3rd Asian Pacific General Galvanizing Conference, Queensland, Australia, 1996.
29. Pederson, J. In The Effects of Bismuth on Nickel–Zinc Galvanizing, Proceedings of the 4th Asian Pacific General Galvanizing Conference Kuala Lumpur, 1999.
30. Krepski, R. P. *The Influence of Bath Alloying Additions in Hot Dip Galvanizing*; St. Joe Minerals Corporation, Monaca, PA, 1980.
31. Davies, J. R. *Surface Engineering for Corrosion and Wear Resistance*; ASM International, 2001; Chapter 6, pp 139–142.
32. Pankert, R. In Five years' experience with the Galveco Alloy, Proceedings of the 10th Hot Dip Galvanizing Conference, 4–6 October 2004, Hotel Plejsy, Krompachy, Slovak Republic; Czech Galvanizers Association & Slovak Galvanizers Association, 2004; pp 18–26.
33. Gilles, M.; Sokolowski, R. In The Zinc–Tin Galvanizing Alloy: A Unique Zinc Alloy for Galvanizing any Reactive Steel, Proceedings of the 18th International Galvanizing Conference (Intergalva 1997) Birmingham, UK 1997, European General Galvanizers Association, UK, 1997.
34. Avettand-Frénöel, M. N.; Reumont, G.; Perrot, P. In The Effect of Tin on the Reactivity of Silicon-Containing Steels, Proceedings of the 21st International Galvanizing Conference (Intergalva 2006) Naples 2006, European General Galvanizers Association, UK, 2006.
35. Zervoudis, J.; Anderson, G. A Review of Bath Alloy Additives and their Impact on the Quality of the Galvanized Coating, 6th Asian Pacific General Galvanizing Conference Cairns: Australia, May 29–June 2, 2005.
36. Zervoudis, J. In Reactive Steel Galvanizing with Zn–Sn–V (Ni) alloys, Proceedings of the 19th International Galvanizing Conference (Intergalva 2000) Berlin 2000, European General Galvanizers Association, UK, 2000.
37. Alonso, C.; Fullea, J.; Recio, F. J.; Sanchez, M.; Soldado, R.; Bernal, M.; Tierra, P. In The Adhesion of Hot Dip Galvanized Coatings and Zn–Ni–V (Ecozinc) Alloy to Steel Reinforcement, Proceedings of the 21st International Galvanizing Conference (Intergalva 2006) Naples 2006, European General Galvanizers Association, UK, 2006.
38. Reumont, G.; Foct, J.; Perrot, P. In New Possibilities for the Galvanizing Process: The Addition of Manganese and Titanium to the Zinc Bath, Proceedings of the 19th International Galvanizing Conference (Intergalva 2000) Berlin 2000, European General Galvanizers Association, UK, 2000.
39. Memmi, M.; Cecchini, M.; Colibri, C.; Goodwin, F. In New Batch Zinc–5% Aluminium Hot Dip Galvanizing Process for Fabricated Steel Parts (Part II: Process Simplification), Proceedings of the 21st International Galvanizing Conference (Intergalva 2006) Naples 2006, European General Galvanizers Association, UK, 2006.
40. van Ooij, W.; Ranjan, M.; Joshi, A.; Verstappen, J.; Zervoudis, J.; Poag, G. In Update on the Status of the Development of a High-Al Alloy for General Galvanizing, Proceedings of the 21st International Galvanizing Conference (Intergalva 2006) Naples 2006, European General Galvanizers Association, UK, 2006.
41. *General Galvanizing Practice*; Part 4; Galvanizers Association: UK, 1999; pp 4.1–4.4.
42. Fujine, M. In Expectation for Steel Sheet in View for Future Automobile Application, Proc. Galvatech 2007, Osaka, 18–22, ISIJ, Tokyo, Nov 2007; pp 374–379.
43. van Eijnsbergen, J. F. H. *Duplex Systems – Hot-dip Galvanizing plus Painting*; Elsevier: New York, 1994; Chapter 2, pp 7–9.
44. EN ISO 12944: Paints and Varnishes – Corrosion Protection of Steel Structures by Protective Paint Systems, British Standards Institution, Chiswick, UK.
45. EN 13438. Paints and Varnishes – Powder Organic Coatings for Galvanized or Sherardised Steel Products for Construction Purposes British Standards Institution: Chiswick, UK, 2005.
46. Proceedings of the 21st International Galvanizing Conference (Intergalva 2006) Naples 2006; European General Galvanizers Association, UK, 2006.
47. Schuhmacher, B.; Klare, B.; Steinhorst, M.; Schulzki, R. In Novel Surface Coated Products for ThyssenKrupp Steel – Innovation Road Map of DOC Dortmund Oberflächencentrum GmbH, Proc. Galvanizing Steel Sheet Forum, 30–31 May 2006, Dusseldorf, Germany, International Lead Zinc Research Org., Inc, 2006.

48. Bjordal, M.; Knudsen, O. O.; Haarberg, S.; Osen, K. S. In Pinholes in Powder Coatings on Hot Dip Galvanized Steel – Sources and Prevention, Assembly 2005, Radisson SAS Alacron Hotel, Prague, Czech Republic, June 2005, Proceedings of the European General Galvanizers Association, 2005.
49. Prosek, T.; Nazarov, A.; Bexell, U.; Thierry, D.; Serak, J. In Corrosion Properties of Model Zinc-Magnesium Alloys, Proc. Galvatech, Osaka, 18–22 Nov 07, ISIJ, Tokyo, 2007; pp 592–597.
50. Vlot, M.; Bleeker, R.; Maalman, T.; van Perlstein, E. In MagiZinc – a new generation of hot-dip galvanised products, Proc. Galvanizing Steel Sheet Forum, 30–31 May 2006, Dusseldorf, Germany, International Lead Zinc Research Org., Inc, 2006.
- Porter, F. C. Corrosion Resistance of Zinc and Zinc Alloys Marcel Dekker: New York, 1994.
- Porter, F. C. Zinc Handbook: Properties, Processing, and Use in Design Marcel Dekker: New York, 1991.
- van Eijnsbergen, J. F. H. Duplex Systems – Hot-dip Galvanizing plus Painting Elsevier: New York, 1994.
- European General Galvanizers Association, UK. General Assembly and Intergalva Proceedings 1994–2007. *General Galvanizing Practice*; Galvanizers Association: UK, 1999.
- High Temperature Galvanizing*; International Lead Zinc Research Organization, 1980.

## Further Reading

Zhang, G. Z. Corrosion and Electrochemistry of Zinc Plenum: New York, 1986.

## Relevant Websites

[www.galvalume.com](http://www.galvalume.com).  
[www.galfan.com](http://www.galfan.com).  
[www.galvanizing.co.uk](http://www.galvanizing.co.uk).  
[www.galvanizeit.org](http://www.galvanizeit.org).

## 4.07 Plated Coatings

**D. R. Gabe**

Department of Materials, Loughborough University, Leicestershire, UK

**M. Clarke**

City of London Polytechnic, London, UK

This article is a revision of the Third Edition article 12.1 by D.R. Gabe and M. Clarke, volume 2, pp 12:3–12:50,

© 2010 Elsevier B.V.

---

4.07.1	Approach	2578
4.07.2	Origin	2578
4.07.3	Substrates	2578
4.07.4	Pretreatments	2579
4.07.4.1	Metallic Substrates <sup>17–21</sup>	2579
4.07.4.1.1	Degreasing	2579
4.07.4.1.2	Removal of oxides and corrosion products	2579
4.07.5	Nonconductors	2580
4.07.5.1	Mechanical Pretreatments	2580
4.07.6	Plating Processes	2581
4.07.6.1	Electroplating	2581
4.07.6.2	Aqueous Electrolytes	2582
4.07.6.3	Simple and Complex Ions	2584
4.07.6.4	Conducting Salts, Addition Agents, and Other Ingredients of Plating Baths	2585
4.07.6.5	Electroplating Anodes	2586
4.07.6.6	Corrosion of the Cathode	2588
4.07.6.6.1	Zinc diecastings: complex baths and undercoats	2589
4.07.6.6.2	Silver plating: 'strike' baths	2589
4.07.6.6.3	Electroplating passive alloys	2590
4.07.6.6.4	Service corrosion effects	2591
4.07.6.6.5	Corrosion potentials in plating baths	2591
4.07.6.6.6	Agitation and high-speed electrodeposition	2591
4.07.6.6.7	Pulse plating	2592
4.07.6.7	Factors Influencing Structure	2593
4.07.6.7.1	Substrate effects: epitaxy and pseudomorphism	2593
4.07.6.7.2	Electrolyte effects	2595
4.07.6.7.3	Form of current passed through cell	2596
4.07.6.8	Industrial Electroplating Techniques	2597
4.07.6.9	Rinsing	2597
4.07.6.10	Postplating Treatments	2598
4.07.7	Properties of Electrodeposits	2598
4.07.7.1	Thickness	2598
4.07.7.2	Throwing Power	2599
4.07.7.3	Current Path Geometry	2600
4.07.7.4	Structure-Dependent Properties	2601
4.07.7.4.1	Composition of the electrodeposit	2601
4.07.7.5	Internal Stress	2601
4.07.7.6	Ductility, Hardness, Wear, Strength	2602
4.07.7.7	Interdiffusion with the Substrate	2603
4.07.7.8	Porosity	2603
4.07.8	Plating from Ionic Liquids	2605
4.07.9	Recent Developments	2606
References		2608

---

**Abbreviations****ABS** Acrylonitrile–butadiene–styrene**AC** Alternating current**DC** Direct current**IMF** Institute of Metal Finishing (Birmingham, UK)**PNS** Post-nickel strike**TFS** Tin-free steel**4.07.1 Approach**

There are books and reviews dealing with electroplating which approach it as a commercial technology, a useful art, or an interesting process for scientific enquiry. In this case, the emphasis is on the production of coatings for the control of corrosion and the consequences of action taken at various stages of electroplating for the control of corrosion events. Corrosion control is not the sole function of electroplated coatings; indeed most authors play down corrosion control in favor of ‘more positive’ virtues such as decoration (sales appeal), reflectivity, wear resistance, solderability, or low contact resistance. However, to preserve these properties, it is essential to prevent corrosion; in essence, electroplated metal coatings are required to confer corrosion resistance together with one or more of the other properties, the nature of which provides the criteria on which selection of a coating is made. Corrosion protection is a common factor.<sup>1–7</sup>

**4.07.2 Origin**

The production of electricity by metallic corrosion in Volta’s pile (1786) was followed by the reduction of metal ions to metal by electrons at a metal–solution interface.<sup>8</sup> Electroplating is an application of electrodeposition to produce thin, coherent, adherent coatings of solid metal, and is one of the important methods for producing coatings. Brugnattelli,<sup>9</sup> a Professor of Chemistry at the University of Pavia, published an account of silver plating in 1800, and is said to have gold plated silver coins using Volta’s pile as early as 1805. Wollaston deposited copper (presumably a very small quantity) on silver wire using current from an electrostatic generator. Electrodeposition was developed energetically in the succeeding three decades, and by 1840, commercial electroplating had advanced to the stage where patent protection was being sought for various processes. The breakthrough was made in

1839–1840 through the discovery of cyanide as a versatile complexant for first silver and gold and later other metals. The main source of electricity for the first six or seven decades was the primary galvanic cell, and progress was aided by the invention of cells such as those of Daniell, Meidinger, Grove, and Bunsen, which were capable of delivering large currents for long periods without polarisation. Faraday discovered electromagnetic induction in 1831, and Pixii used the commutator in 1832 to produce a direct current generator, but it was not until about 1870 that several independent inventors used electromagnetic field coils to generate the heavy currents needed for electrolysis. Large scale electroplating enterprises were established by the latter part of the nineteenth century. In 1883, the Postal Telegraph Company of New York used 200 copper plating cells to deposit 250 kg day<sup>−1</sup> onto steel wire. Aqueous solutions have always been by far the most important electrolytes. There have been many investigations of nonaqueous solutions or ionic melts, and Davy deposited the alkali metals from the latter in 1807. Aqueous solutions and their associated pre- and postplating treatments are so well established that they are likely to remain preeminent for the immediate future.<sup>8–16</sup>

**4.07.3 Substrates**

Metallic substrates which are good electron conductors and nonmetallic ones which are not can both be electroplated with adherent coatings, but the preliminary procedures or ‘pretreatment’ differ markedly. The commonly plated metal substrates are mild and low-alloy steels, zinc alloys for diecasting, and copper or high-copper alloys like brasses, bronzes, and beryllium coppers. A large number of other alloys can be electroplated, but their use is restricted to particular industries, and they often require special pretreatments. Aluminum alloys, stainless steels, titanium alloys, and refractory metals are examples. The three major substrates are plated with corrosion control as one of the important objectives, but with less common substrates this may not be the case. There has been a rapid growth in electroplated parts made from plastic material. The main objective is to make the part look metallic for reasons of appearance rather than function. A complicated acrylonitrile–butadiene–styrene copolymer dispersion (ABS) was the first plastic material to be plated on a large scale. It was followed by polypropylene, and the development of plating grades of other plastics (e.g., polysulphone, polycarbonate, epoxide resins, glass-reinforced polyester) is

at hand. Metallic corrosion problems arise as soon as plastics have been plated, creating a new field for the corrosion enthusiast to investigate.

By exercising ingenuity, most nonconducting objects may be electroplated, and this is a long-established small-scale operation. The usual aim is artistic or a search for novelty, a good example being the preparation of a heavily gold-plated haggis for the 1973 conference of the Institute of Metal Finishing, which took place in Edinburgh.

## 4.07.4 Pretreatments

### 4.07.4.1 Metallic Substrates<sup>17-21</sup>

This is considered in detail in **Chapter 1.08, Stress Effects in High Temperature Oxidation**, but a brief review is relevant here in relation to electroplating.

Metallic articles arrive at the electroplating stage with a surface film of soil derived from earlier production processes. These are divided into three classes:

- Organic films, oils, greases, and perhaps polymeric films.
- Fine particles suspended in (a), often of siliceous material, that is, dirt.
- Films of the substrate oxide or other corrosion products.

With few exceptions, it is more efficient and economical to use at least two different pretreatments, that is, degreasing processes which deal with (a) and (b), and pickling processes which remove oxide and corrosion films. Degreasing comes first, as pickling processes fail on hydrophobic surfaces.<sup>17-21</sup>

#### 4.07.4.1.1 Degreasing

Hydrocarbon or mineral oils are removed by solvents; vapor degreasing with chlorinated solvents or emulsification, is a common alternative. Greases of animal or vegetable origin, which are fatty acids, alcohols, or esters, are removed with hot aqueous solutions of high-pH (alkaline degreasing). They react with alkali to form water-soluble soaps. Electrolytic alkaline degreasing is considerably faster than soak cleaning. The work, immersed in hot alkali, is usually the cathode. A mass of hydrogen bubbles formed at the solution-metal interface undermines and removes the grease very effectively; saponification takes place more slowly later. Ferrous metals may be degreased anodically, the metal surface becoming passive, but nonferrous metal anodes corrode in hot alkaline solutions. Anodic cleaning produces only half the volume of gas

(oxygen) and is less effective on that count. However, there is an advantage. During use, small amounts of metal enter the cleaning solution; other metals enter as impurities in the salts and make-up water. A thin metal film may be electrodeposited during cathodic cleaning, which if it remains can decrease the corrosion resistance of the main deposit. Anodic cleaning avoids this danger, even when the cleaning bath is contaminated. For steel and occasionally for copper alloys, a cleaning cycle is employed, with the work being cathodic for degreasing; but the current is reversed for the final few seconds, during which any thin film of metal impurity is removed by anodic dissolution.

Alkaline cleaning solutions are compounded from sodium hydroxide, trisodium phosphate (TSP), sodium silicate, sodium carbonate, soaps and detergents, and other materials. The higher the pH, the more effective is the saponification, but with nonferrous metals, the greater is the danger of corrosion. Zinc diecastings and aluminum need much less aggressive alkalis than those which are safe with steel. For aluminum and its alloys, a high concentration (10%) of sodium silicate acts as a corrosion inhibitor and as a cleaner.

To check the efficacy of grease removal, the alkali solution is rinsed away or neutralized by dipping in dilute acid. If, after removal from the acid, the draining metal surface remains wetted evenly all over for 30–60 s (or until it dries by evaporation), hydrophobic soils have been removed. Traces of grease cause the surface to dewet, and surface tension draws the water into separate droplets. This is the water-break test. Traces of grease which remain when the work is plated do not prevent electrodeposition, but are detrimental to adhesion and corrosion resistance by increasing the incidence of coating porosity.

Particulate dirt is usually removed together with the grease which binds it, although there are a few exceptions. Sheet steel may carry a 'smut' of finely divided carbon (or perhaps iron carbide) left from pickling processes in steelmaking. This is not removed with grease, and if evenly distributed, it is not apparent until the work is rubbed locally. Left in place, it leads to porous and poorly adherent coatings. While it can be removed by mechanical means, for example, vigorous brushing, this is impracticable when automatic plating machines are used. Steel which shows this defect may be unsuitable for plating.

#### 4.07.4.1.2 Removal of oxides and corrosion products

Oxide and corrosion-product films are removed by dissolution in aqueous solutions. Hydrochloric and



sulfuric acid are the most common. Concentrations and temperatures are varied according to the substrate. For mild steel, for example, cold 15 wt% HCl is suitable, but for zinc diecastings the concentration must be reduced to 0.25 wt%, and the pickling time must be kept very short to avoid excessive attack. Rust is more quickly removed by acid pickling when, in the prior degreasing stage, the work is made the cathode rather than the anode. Cathodic cleaning partially reduces rust to magnetite and iron, which undergo rapid reductive dissolution in the acid. Mixed acids containing wetting agents are supplied as proprietary mixtures; hydrochloric, sulfuric, and phosphoric acids are common. Inhibitors – generally amino compounds – may be added, but strongly adsorbed films of inhibitors or their breakdown products may cause trouble later. Electrolytic pickling is used for special purposes, but hydrochloric acid is unsuitable for this purpose because of its volatility and the possibility of chlorine evolution. Cathodic pickling of steel in 10–20 wt% sulfuric acid enables thick rust or scale to be dissolved without losing metal, which is cathodically protected. Anodic pickling in 42 vol.% (about 55 wt%) sulfuric acid is used to remove a thin surface layer from steel. A high current density is used and dissolution, which is under diffusion control, is uniform. After 10–20 s, the metal becomes passive and dissolution ceases. Disordered and fragmented metal produced by abrasion or machining is removed to leave a surface which favors good adhesion of an electrodeposit. Oxide and corrosion products on copper and its alloys may be removed in hydrochloric or sulfuric acids, less concentrated than that used for steel. Sulfuric acid allows the dissolved copper to be recovered and the acid to be regenerated by electrolysis. However, when copper alloys are cathodically degreased, cuprous oxide is reduced to loose copper particles which do not dissolve in acid. An electroplated coating over loose metal is likely to be defective. A much more aggressive mixture of sulfuric and nitric acids known as a bright dip or sometimes (wrongly) aqua fortis is used. This is a rudimentary chemical-polishing system and produces a bright surface from which the loose particles have been removed.

#### 4.07.5 Nonconductors

Plating plastic articles has become a widespread commercial process fairly recently. The main plastics in use at the time of writing are ABS and

polypropylene. Both replace diecast and pressed metal in various fields. Molded parts have smooth surfaces unsuited to producing adherent plate, and the first step is to ‘etch’ the plastic surface by using strongly oxidizing acids, usually chromic plus sulfuric acid mixtures. The plastic must have dispersed in its surface small areas more susceptible to oxidation than the surrounding matrix, and these are introduced in a variety of ways during manufacture. Etching produces a pattern of small pits. The second step is to produce within the pits and over the surface a fine metallic precipitate. One method is to dip in solutions of stannous and palladium salts in succession, which produces fine palladium particles, but there is a variety of proprietary processes available. The metal particles become nuclei for the deposition of a metal coating from an electroless plating bath. This is an aqueous solution of a metal salt containing a reducing agent that is able to reduce the metal ions to metal. The solution is unstable, but is compounded and used so that homogeneous electron transfer does not occur, and there is neither homogeneous precipitation of metal, nor heterogeneous precipitation on nonconducting surfaces, but only on the metallic nuclei on the plastic surface. Several electroless plating processes have been devised, but only those for copper or nickel are widely used for plastics. Once a continuous coating of metal has been produced, the substrate can be transferred to an electroplating bath for the application of any desired coating. Most plastic articles are finished with nickel and chromium.<sup>22–32</sup>

##### 4.07.5.1 Mechanical Pretreatments

Mechanical processes which cold-work a substrate have important effects on electrodeposits. Examples are grinding and abrasive polishing, grit and shot blasting, cold rolling, and severe cold deformation. They alter the metallurgical structure of the substrate, reducing the surface grain size and in some cases produce small crevices filled with nonmetallic debris. Abrasive processes which act parallel to the surface (e.g., grinding, polishing) may leave splinters and leaves of metal attached at one end but otherwise separated from the surface on which they lie. In addition, nonmetallic abrasive material is embedded in the surface. Surfaces which are neither annealed nor otherwise treated to remove mechanically disturbed surface layers, affect the structure and properties of metal electroplated over them, as mentioned below. In many cases, one result of the modification of the electrodeposit is to reduce the corrosion protection it affords. Where the same

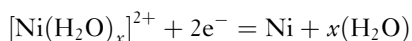
topographical alteration of a substrate can be achieved by nonmechanical means, for example, electrochemical polishing, electrochemical machining, chemical milling, the surface left is not cold-worked and does not disturb an electrodeposit to the same extent.<sup>33–40</sup>

## 4.07.6 Plating Processes

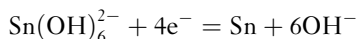
### 4.07.6.1 Electroplating

The metallic substrate, clean and rinsed, is immersed wet in the plating cell. The base metals which are usually plated present an essentially metallic surface to the electrolyte, and the slight corrosive action of the rinse water in preventing the formation of any substantial oxide film is important. A critical balance of corrosion processes in the initial stages is vital for successful electroplating, and for this reason, there is a severe restriction on the composition of the electroplating bath which may be used for a particular substrate. This will be discussed later. The substrate is made of the cathode of the cell; it may be immersed without applied potential ('dead' entry) or may be already part of a circuit which is completed as soon as the substrate touches the electrolyte ('live' entry). Live entry reduces the tendency for the plating electrolyte to corrode the substrate in the period before the surface is covered by the coating. The main cathodic process is usually the reduction of dissolved ions to metal in the form of an adherent, coherent coating.

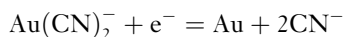
The ions reduced may be aquo cations, for example,



or oxyanions, for example,

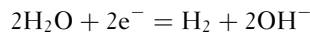


or complex ions, usually cyanides, for example,

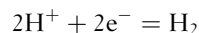


Cations are assisted by the electric field to migrate to the cathode. On the other hand, the field impedes the migration of anions, and diffusion has to overcome this. It is rare for metal reduction to be the sole cathode process, as water and other dissolved substances are reduced simultaneously. Many compounds are added intentionally to take part in the cathode process, with the object of modifying the nature of the coating. Such materials are called addition agents and are subdivided into classes on the basis of their

main effect (e.g., brighteners, levelers, grain refiners, stress reducing agents). In all aqueous solutions, water may be reduced: either



or



This reaction becomes thermodynamically possible whenever the cathode potential falls below

$$E = \frac{RT}{2F} \ln \frac{(a^2\text{H}^+)}{p\text{H}_2} \quad [1]$$

where  $R$  is the gas constant,  $T$  the temperature (K),  $F$  the Faraday constant, and  $p\text{H}_2$  is the relative partial pressure (strictly, the fugacity) of hydrogen in solution, which for continued evolution, becomes the total external pressure against which hydrogen bubbles must prevail to escape (usually 1 atm). The activity of water  $a\text{H}_2\text{O}$  is not usually taken into account in elementary treatments, as it is assumed that  $a\text{H}_2\text{O} = 1$ , and for dilute solutions this causes little error. Note that in some concentrated plating baths  $a\text{H}_2\text{O} \neq 1.0$  and neither is it in baths which use mixtures of water and miscible organic liquids (e.g., dimethyl formamide). However, by far the most important term is the hydrogen ion activity; this may be separated so that eqn [1] becomes

$$E = -\frac{RT}{2F} \ln p\text{H}_2 - \frac{2.303RT}{F} pH \quad [2]$$

As  $p\text{H}_2 \approx 1 (\approx a\text{H}_2\text{O})$

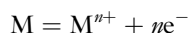
$$E \approx -0.059 pH \quad [3]$$

These considerations have been entirely on the basis of thermodynamics and take no account of the overpotential, which is dependent on the rate of the process and the nature of the surface at which the reaction occurs. For this reason, the rate of reduction of  $\text{H}^+$  or  $\text{H}_2\text{O}$  is usually low, and remains so to potentials from 0.5 to 1.0 V, below that given in eqn [1]. Even so, the instability of water is an insuperable obstacle to electrodepositing metals whose ions are so stable in aqueous solutions (e.g.,  $\text{Al}^{3+}$  aq.) that water reduction becomes the sole cathode process.

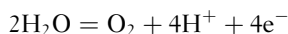
Much time has been devoted in recent years to study the mechanism of electrodeposition. Most investigators have assumed that electrodeposition should follow a mechanism akin to that for the deposition of a crystalline coating by condensation of a vapor. The

solvated metal ion approaches and adsorbs on the cathode, losing some of its solvation sheath as the cathode gains the requisite electrons. The adion, which is mobile, diffuses over the cathode surface until it reaches an atomic step. It adsorbs on the step, losing more water of solvation, and having its freedom reduced to diffusion along the step. Further desolvation and coordination follows when it reaches a kink in the step, at which stage it is immobilized. When other adions following this path eventually join and submerge the first, coordination with water in the electrolyte is exchanged fully for coordination with metal ions in the metallic lattice. This view of the mechanism of electrodeposition is plausible and compatible with both current views on metallic crystals and their defects, and certain properties of electrodeposits. It is, however, a preconceived notion, and considerable experimental difficulties in the way of producing evidence are responsible for both the numerous different investigations in the field, and the fact that the evidence produced is impressive more for its volume than its conclusive force.

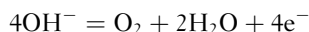
Current enters through the metal–electrolyte interface of the anode, which is usually made from the same metal as is plated on the cathode. The anode dissolves replacing the metal lost at the cathode:



The overall process is metal transfer from anode to cathode via the solution. The form of anode corrosion is important, and materials may be added both to the anode metal and to the electrolyte, to influence it. There are important instances where an insoluble anode is used, and the anode reaction becomes the oxidation of water or hydroxyl ions: either



or



and also the oxidation of any other susceptible materials. Oxidation of water may occur at an anode, which was intended to be soluble, if the metal becomes passive. The minimum potential, above which the anode must rise before oxidation of water occurs, is:

$$E = E^0 + \frac{RT}{4F} \ln(pO_2 \times a_{H^{+}}^4) \quad [4]$$

In this equation,  $E^0$  is the standard electrode potential of the water/oxygen reaction, that is,  $-\Delta G_{H_2O}^0/nF$ . Simplifying, eqn [4] at 298 K becomes

$$E = 1.23 - 0.059 pH \quad [5]$$

There is often an overpotential of about 0.5 V before the rate of oxidation of water becomes rapid.<sup>41–43</sup>

#### 4.07.6.2 Aqueous Electrolytes

Aqueous solutions have a complex structure. Liquid water is anomalous; properties estimated by interpolation from those of neighboring hydrides in the periodic table fall wide of the observed properties. For example, estimated melting and boiling points are  $-43$  and  $-11$  °C, respectively. Molecular interaction (hydrogen bonding) imposes short range order in the liquid, which the anomalous properties reflect. Some of the crystal structure of ice is retained in the liquid, though the structure is less open, and water shares this peculiarity with diamond, silicon, and germanium, as in each case the liquid is denser than the solid at the melting point. A simple view of water is as a fluid with two species, small local regions with an ice structure and others with a strongly associated but irregular structure  $(H_2O)_n$ . The ‘icebergs’ and random groups are in dynamic equilibrium, exchanging individual molecules throughout the lifetime of the larger groups, which are not themselves permanent.

Water has a permanent dipole moment (strictly it is a quadrupole moment) caused by the asymmetry of the molecule and the greater electron affinity of oxygen. When soluble strong electrolytes, for example, nickel sulphate, dissolve, they dissociate completely, and the interactions between the charged ions and the dipole water molecules considerably modify the water structure. The small nickel ions with their high charge density will cause more disruption than the larger sulphate ion, but both become strongly associated with a sheath of water molecules (Figure 1). The bonding between the ion and solvation sheath confers a high degree of stability on the

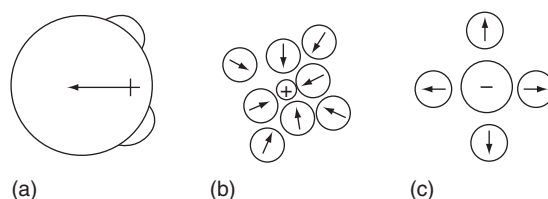
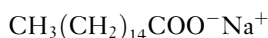


**Figure 1** (a) Water molecule, dipole structure, (b) solvation of a small cation, for example,  $Ni^{2+}$  and (c) solvation of a larger anion, for example,  $SO_4^{2-}$ .

ions in aqueous solutions. The dipolar nature of the solvent, able to stabilize ions of either charge sign equally well, makes water an excellent ionic solvent. Ionic solvation destroys the ice-like component of the liquid with a result similar to that observed on melting, that is, a decrease in volume as the 'space-wasting' ice structure is removed, and many strong electrolytes have a negative volume of mixing.

Aqueous solutions of nonelectrolytes, especially of nonpolar solutes, may show the reverse effect and increase the proportions of ice-like components. The nonpolar part of organic electrolytes such as soaps and wetting agents may predominate in increasing the ice component. Thus solutes can be divided into two classes: structure making and structure breaking, and in some metal-finishing process solutions of both types of solute may be added. In certain cases, it is impossible to satisfy both, and there is a decrease in solubility of the least successful component. For example, a soap such as sodium palmitate, which in water is mainly



is very soluble, and the proportion of ice-like water increases to minimize interaction with the hydrophobic hydrocarbon chain. If sodium chloride is added to a concentrated soap solution, the ice-like structure is broken, and the increased concentration of 'free water' causes the palmitate to separate. Polar nonelectrolytes such as the lower alcohols have an even greater effect on the water structure than soaps. Being themselves capable of forming hydrogen bonds, they enter the 'iceberg' structure, increasing its stability. Methyl or ethyl alcohol added to solutions saturated with structure-breaking electrolytes, for example,  $\text{NiSO}_4$ , in a plating bath, can withdraw water from the ionic solvation sheaths to form ice-like water, and now it is the electrolyte whose solubility falls. Soap, on the other hand, is more soluble in alcohol-water mixtures.

The ability of water to be oxidized or reduced at the plating-bath electrodes is in practice an important advantage, though it has a few drawbacks. The drawbacks are overemphasized in textbooks and the advantages ignored. An ion which is much more stable towards reduction than water is unaffected in the region of the cathode during electrolysis. With the margin of polarization of 0.5–1.0 V, the manganous aquocation is the most stable that can be reduced in aqueous solutions, but because of the shortcomings of the metallic coating, manganese is not used, and the zinc aquocation is the most stable ion that can be

reduced in large scale electroplating. A drawback is that the aquocations of aluminum, titanium, zirconium, niobium, and tantalum are too stable. Their known corrosion resistance would make them important coatings, but they cannot be electrodeposited. On the other hand, there are numerous electrolytes whose presence is desirable in a plating bath but whose cations must not be reduced during electrolysis. The complete stability of cations like  $\text{Na}^+$ ,  $\text{K}^+$ ,  $\text{NH}_4^+$ ,  $\text{Li}^+$ ,  $\text{Mg}^{2+}$ ,  $\text{Ca}^{2+}$ , and  $\text{Al}^{3+}$  is then an advantage. Should the cathode be depressed (accidentally) below the normal working value, they are safe from reduction as hydrogen evolution acts as a 'safety valve' for excessive currents. The products of water reduction, hydrogen gas and  $\text{OH}^-$  ions, are less likely to contaminate a large volume of valuable solution than are the reduction products of other materials.

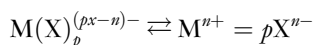
Similar considerations apply to oxidation. An anion, which is considerably more stable than water, will be unaffected in the neighborhood of the anode. With a soluble anode, in principle, an anion only needs be more stable than the dissolution potential of the anode metal, but with an insoluble anode, it must be stable at the potential for water oxidation (eqn [4] or [5]), plus any margin for polarization. The metal salts, other than those of the metal being deposited, used for electroplating are chosen to combine solubility, cheapness, and stability to anode oxidation and cathode reduction. The anions most widely used are  $\text{SO}_4^{2-}$ ,  $\text{Cl}^-$ ,  $\text{F}^-$  and complex fluorides  $\text{BF}_4^-$ ,  $\text{SiF}_6^{2-}$ ,  $\text{Br}^-$ ,  $\text{CN}^-$  and complex cyanides. The nitrite ion is usually avoided because it is too easily reduced at the cathode. Sulfite, which is used for gold plating, is nevertheless too readily oxidized at the anode, and provides an example of an ion used in one instance despite its drawbacks. The oxidation of water at the anode is also a reaction which does not contaminate the solution.

Much laboratory work has been performed to develop nonaqueous plating baths, using either organic solvents or ionic melts. Insofar as the reduction of water is concerned, there are two rather different aims in view. Firstly, there is a search for solvents or melts sufficiently stable to allow electrodeposition of coatings of aluminum, titanium, etc., which is impossible with water as the solvent. Secondly, there is a need for a nonaqueous solvent for metals such as cadmium, whose electrodeposition from water, while practicable and satisfactory, is always accompanied by hydrogen which can embrittle cathodes of certain high strength steels and other alloys. Here, the aim is to avoid hydrogen discharge.

A practical drawback to the use of nonaqueous solvents is the accumulation of the by-products of solvent-electrode reactions leading eventually to the bath being poisoned.<sup>44</sup>

#### 4.07.6.3 Simple and Complex Ions

Amongst the common metals of the electroplating industry, only nickel is invariably reduced from its aquocation. Copper, silver, gold, cadmium, and zinc are normally deposited from solutions of complex cyanides; tin and chromium from oxyanions, and tin, in other cases, from a complex fluoride. Platinum-metal plating baths contain ions, all of which are complex; it is doubtful if any platinum-metal aquocation can exist in aqueous solution, as such is the high tendency of these metals to form complexes. If a ligand, such as cyanide, can displace water from an aquocation to form a complex ion, the complex must be more stable, and the deposition potential is always more negative for a complex ion than for the equivalent simple ion. Let the equilibrium between aquocation  $M^{n+}$ , ligand  $X^{x-}$  and complex ion  $\{M(X)_p\}^{(px-n)-}$  be:



and

$$K = \frac{aM^{n+} \times a^p X^{x-}}{aM(X)_p^{(px-n)-}}$$

where  $K$  is the instability constant for the complex ion,  $p$  is the coordination number. The potential below which deposition becomes possible is

$$E = E^0 + \frac{RT}{nF} \ln \frac{K \times aM(X)_p^{(px-n)-}}{a^p X^{x-}}$$

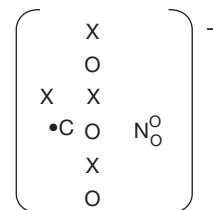
or

$$E = E^0 + \frac{RT}{nF} \ln K + \frac{RT}{nF} \ln \left( \frac{aM(X)_p^{(px-n)-}}{a^p X^{x-}} \right) \quad [6]$$

where  $E^0$  is the standard electrode potential for the simple ion-metal equilibrium. The two bracketed terms on the right of eqn [6] constitute a sort of ' $E^0$ ' for the complex ion, and as  $K$  is usually very small, the second term is negative.

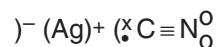
Complex ions used for electroplating are anions. The cathode tends to repel them, and their transport is entirely by diffusion. Conversely, the field near the cathode assists cation transport. Complex cyanides deserve some elaboration in view of their commercial

importance. It is improbable that those used are covalent coordination compounds, and the covalent bond breaks too slowly to accommodate the speed of electrode reactions. The electronic structure of the cyanide ion is shown below.

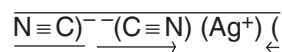


Here, electrons are contributed by the carbon atom (x), the nitrogen atom (o), and the cation (•), for example,  $Na^+$  in the case of a sodium cyanide solution.

A soluble cyanide added to silver nitrate solution precipitates silver cyanide as an ionic compound:



The precipitate redissolves in excess soluble cyanide, and the complex ion is probably an ion-dipole coordination compound, that is,



The solubility of  $Ag(CN)_2^-$  in water stems from the overall negative charge encouraging solvation with water dipoles, which uncharged  $AgCN$  does not. It is likely that the other cyanide complex ions of low coordination number have a similar structure.

When ions with this structure diffuse to the vicinity of a negative cathode, the ion is distorted by the field to become polarized, with the positive silver core nearest the cathode (see Figure 2). Once within a critical distance the field can assist transport of the distorted complex, discharge the silver core and eventually repel the released cyanide anions. There are several practical advantages in plating from complex cyanides. The reduction in deposition potential is most important in the application of relatively noble metals to base substrates, when avoiding severe cathode corrosion. The important case of the copper cyanide bath is discussed later. The impeded diffusion of the complex anion, the energy needed to polarize and reduce the anion, and the diffusion 'barrier' produced by the high concentration of cyanide near the cathode, all contribute to a high overpotential for electrodeposition, which aids the production of even coatings on cathodes of uneven shape. The cyanide ions released after discharge of the metal from the



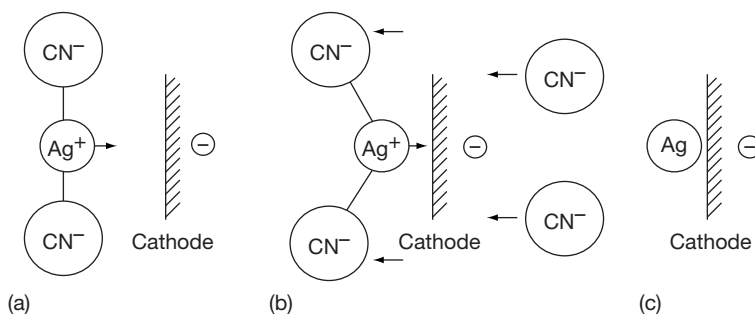


**Figure 2** Ion distortion by the field in the vicinity of a negative cathode. (a) Diffusion of anion to cathode, (b) diffusion and migration of distorted complex and (c) release of  $\text{CN}^-$  ions and incorporation of  $\text{Ag}$  into the lattice.

complex modify the structure of the coating in a manner similar to that of addition agents, and it is probable that some cyanide is adsorbed. The result is that cyanide bath coatings are fine grained, hard, and may contain small amounts of carbon.

Some disadvantages stem from the same phenomena: impeded diffusion reduces the maximum practical rate of plating to well below that possible with aquocation baths. The cyanide ion is not entirely stable; both oxidation and reduction products accumulate, including carbonate. Carbonate is also formed in the alkaline cyanide baths (all cyanide baths are alkaline except some based on aurocyanides) by absorption of  $\text{CO}_2$  from the air, and it is necessary either to replace or purify baths periodically. Much has been made of the toxicity of cyanides, but the other process solutions used in plating are generally extremely toxic and corrosive or caustic, and it is necessary to treat them all with respect.

Oxyanions are important in chromium and tin plating. Although chromium plating baths have a simple formulation (chromium trioxide, sulfuric acid, and water), hydrolysis and side reactions form a variety of polychromate ions. The cathode reactions are numerous and imperfectly elucidated; only about 5% of the charge passed produces chromium. As in cyanide baths, the by-products behave as addition agents. The grain size of chromium electroplated under the normal conditions is the smallest encountered amongst metals. Tin coatings plated from stannate solutions are reduced from the  $\text{Sn}(\text{OH})_6^{2-}$  ions, and are fine-grained.

The platinum-group metals are necessarily plated from complex solutions, as all platinum-metal salts form complex ions in water. The development of aqueous baths has hinged upon finding complex ions sufficiently unstable to be reduced; all the platinum group cyanides are far too stable. Because all the platinum metals are good catalysts for hydrogen

evolution (high exchange current density) there is no useful margin of hydrogen overpotential over that predicted by eqn [2]. Nevertheless, aqueous plating baths have been devised for the entire platinum group, although only palladium, rhodium, and platinum find commercial use at present.

The complex cyanides of transition metals, especially the iron group, are very stable in aqueous solution. Their high coordination numbers mean the metal core of the complex is effectively shielded, and the metal–cyanide bonds, which share electrons with unfilled inner orbitals of the metal, may have a much more covalent character. Single electron transfer to the ferricyanide ion as a whole is easy (reducing it to ferrocyanide, with no alteration of coordination), but further reduction does not occur.<sup>45</sup>

#### 4.07.6.4 Conducting Salts, Addition Agents, and Other Ingredients of Plating Baths

Plating baths contain a number of salts and compounds in addition to those of the ion to be reduced to metal. Much commercial electroplating is from ‘proprietary’ solutions whose use is covered by patents, and which are supplied completely or partly compounded. The precise composition is generally a trade secret, and the patents may sometimes be very widely drawn to include a larger range of compositions and ingredients than is successful. A broad classification of additional ingredients includes the following:

- Those which maintain certain conditions but do not take part in electrode reactions; examples are electrolytes added to improve conductivity, pH buffer systems, and ions which maintain complex ion equilibria.
- Those which take part in the anode reaction, added to promote efficient dissolution of a soluble anode.

- (c) Those which take part in the cathode reaction by adsorption, codeposition, or both, or by modifying the reaction; these ingredients alter the structure and properties of the coating and have an important bearing on its corrosion properties. The term addition agents is generally used for this class.

A particular ingredient often acts in more than one category.

Conducting salts are usually sodium, potassium, or ammonium salts, or the acid of a stable ion already present from other ingredients. Apart from energy conservation, the higher the conductivity of a bath the better the distribution of thickness on complex shapes.

Addition agents are subdivided according to the main effect they have on the coating, that is, grain refiners, brighteners (primary), brighteners (secondary), levelers, stress reducers, and antipitting agents. Apart from the last, all these addition agents modify the growth process profoundly. They may be the ions of foreign metals which can codeposit, or polar or ionic organic materials. They introduce irregular atoms or molecular fragments into the metal lattice or grain structure of the main metal of the coating, and alter the crystal structure. The macroscopic results are suggested by the terms: smaller grain size, mirror-like surface, or a relatively smooth (level) surface on an initially rough substrate. These characteristics are not achieved without corresponding disadvantages. Foreign material from the addition agent is incorporated, up to 5% by weight for metallic codeposition, less for organic agents. First- and second-order tensile stresses usually increase, hardness rises, and ductility falls. First-order tensile stress can exceed the tensile strength of the coating, but for some metals, particularly nickel, addition agents (stress reducers) are known which decrease first-order stress, though second-order stress is not reduced. The mechanical results are detrimental to corrosion protection, but the topographical results, fine grain, and level and bright coatings, are favorable. The chemical results, on the evidence available, vary. The most extensively investigated case is nickel. Here, it is almost universal practice to employ several addition agents together in a bright plating bath, one of which causes the incorporation of a small amount (about 0.02%) of sulfur, and reduces the corrosion resistance of bright nickel. There are other systems (benzotriazole brighteners in copper, aldehyde-amine brighteners in tin) which enhance corrosion resistance.<sup>46-49</sup>

#### 4.07.6.5 Electroplating Anodes

The anode is usually soluble, and is made from a high purity form of the metal being deposited, or occasionally from an alloy. A soluble anode is often the cheapest and most convenient means of replacing the metal reduced at the cathode. Effective anode corrosion is important, and different examples present a variety of types of dissolution.

Copper anodes in the acid sulphate bath are an example of active anodic dissolution. They etch uniformly with low polarization at 100% efficiency, forming little anode debris or sludge. Idle anode corrosion is very slow with dissolved oxygen reduction as the cathodic reaction. Copper anodes in the cyanide bath corrode easily provided that there is sufficient excess or 'free' cyanide present. Polarization is higher than in the acid bath, with a much lower maximum current density. At high current densities, the rate of dissolution of copper exceeds the rate of supply of cyanide ions needed to form the cuprocyanide complex, and blue cupric aquocations form. Eventually, the anode becomes passive and evolves oxygen. For special purposes where anode area is limited (e.g., in a Hull cell), an insoluble mild-steel anode avoids these troubles. A proportion of insoluble anodes or alternate use of soluble and insoluble ones is necessary, because anode efficiency exceeds cathode efficiency, and the metal content of the solution would rise continually if soluble anodes alone were used.

Nickel is normally plated from mixed solutions of nickel sulphate and chloride using soluble anodes. The standing potential of pure nickel anodes indicates they are passive in the idle bath, while in operation dissolution is by pitting corrosion brought about by chloride (Figure 3). In all sulphate solutions, nickel anodes are passive and insoluble. Dissolution is aided by adding small amounts of sulfur or carbon to the nickel anode, which aid the breakdown of passivity ('depolarized anodes'). Nickel anodes produce a fine particulate 'anode sludge'; anode bags of finely woven cloth are used to retain much of this, and continuous filtration is needed to remove the rest, otherwise the corrosion resistance of the coating is severely degraded. Nickel can be used in the form of small 'chips' in baskets of titanium mesh. The titanium is passive and the surface is effectively insulated from electrolytic current exchange, but electrons released by the dissolving chips of nickel are able to pass via the metal-semiconductor contact with the basket to the outside circuit. Anode efficiency slightly exceeds cathode efficiency, but not sufficiently to increase the metal



**Figure 3** Part of an anode from a nickel plating bath, showing dissolution by pitting corrosion.

concentration, unless rigorous precautions are taken to return all the solution lost on surfaces removed from the bath.

Tin anodes dissolve by etching corrosion in acid baths based on stannous salts, but in the alkaline stannate bath, they undergo transpassive dissolution via an oxide film. In the latter, the  $\text{OH}^-$  ion is responsible for both film dissolution and for complexing the tin. Anodes must not be left idle because the film dissolves and thereafter corrosion produces the detrimental divalent stannite oxyanion. Anodes are introduced 'live' at the start of deposition, and transpassive corrosion is established by observing the color of the film (pale yellow for correct operation) and the anode polarization, and by adjusting the immersed area. The anodes retain a smooth, quasipolished surface, and no anode bags are needed. An alternative, where anode filming is inconvenient, is to use insoluble (passive) mild-steel anodes, and replaces tin by adding a colloidal dispersion of stannic oxide.

Chromium plating from hexavalent baths is carried out with insoluble lead-lead peroxide anodes, as chromium anodes would be insoluble (passive). There are three main anode reactions: oxidation of water, reoxidation of  $\text{Cr}^{3+}$  ions (or more probably complex polychromate compounds) produced at the cathode, and gradual thickening of the  $\text{PbO}_2$  film. The anode current density must balance the reduction and reoxidation of trivalent chromium so that the concentration reaches a steady state. From time to time, the  $\text{PbO}_2$  film is removed as it increases electrical resistance.

Gold plating is another process where insoluble anodes are the rule. Soluble gold anodes would be technically satisfactory in some baths, but too tempting to thieves. A factor in their decline is the disappearance of gold coins, whose temporary sojourn in the anode circuit is alleged to have provided a form of corrosion beneficial to gold platters of earlier times. Insoluble stainless-steel anodes are now widely used, with graphite, platinized titanium, and platinum mesh as alternatives. All suffer gradual deterioration. Stainless-steel anodes are pitted, especially in areas of high current density, and the corrosion products may eventually give trouble. Platinized titanium sheds its platinum coating, becoming steadily more polarized. Platinum anodes used with cyanide solutions slowly corrode.

The potentials and corrosion data for some anodes in typical plating baths are listed in [Table 1](#).<sup>50,51</sup>

With the exception of  $\text{Pb/PbO}_2$  for chromium plating, the main or even sole anode reaction is oxygen evolution from water. Selection of insoluble anode materials traditionally only took account of mechanical stability and corrosion resistance, and not of the evolution overvoltage which usually lies in the range 1–3 V. This represents a significant (and unproductive) proportion of the total cell or tank voltage drop of 5–9 V. Consequently, searches for anodes with lower overvoltages have led to adoption of the so-called catalytic anodes, which in the context of chlorine and seawater cathodic production technologies have been termed dimensionally stable anodes (DSAs). These were originally based on titanium substrates coated with platinum; product development has led to niobium or tantalum substrates with palladium, iridium, ruthenium, and mixed oxide coatings depending upon the application. In particular, the use of mixed oxides on titanium has established a reputation as the most catalytic anode available. Such anodes are specialist products and offer good service lives when carefully chosen.

However, the criteria for that reputation have been very misleading. They have been based on chlorine electrochemistry initially and later the oxygen reaction itself without regard to side reactions which might occur. One class of side reaction has proved to be problematical, that is, the possible oxidation of organic additives in solution for the purposes of brightening, leveling, wetting, etc. This has always been recognized as a loss, because of the slow oxidation by air used for agitation in industrial operations, but the loss has increased substantially and unacceptably since the introduction of catalytic anodes. The remedy may therefore be threefold:

**Table 1** Behavior of anodes in plating baths

Plating bath	Anodes	Corrosion process		Current density ( $\text{Am}^{-2}$ )	Potential (V) (vs.SHE)
		Idle	Working		
1. Watts' nickel $\text{NiSO}_4 \cdot 7\text{H}_2\text{O}$ , 330 $\text{gl}^{-1}$ $\text{NiCl}_2 \cdot 6\text{H}_2\text{O}$ , 45 $\text{gl}^{-1}$ $\text{H}_3\text{BO}_3$ , 30 $\text{gl}^{-1}$ pH 2.5 55 °C	Nickel slab	Passive	Pitting	0 65 130 195	+0.08 +0.23 +0.27 +0.30
2. Bright nickel as (1) plus saccharin and 2–3 butyne 1–4 diol pH 2.2 50 °C	Nickel slab	Passive	Pitting	0 390	+0.03 +0.36
3. Acid copper $\text{CuSO}_4 \cdot 5\text{H}_2\text{O}$ , 150 $\text{gl}^{-1}$ $\text{H}_2\text{SO}_4$ , 50 $\text{gl}^{-1}$ pH < 0 18 °C	Pure copper	Slow etching	Uniform etching	0 130 260 390	+0.28 +0.32 +0.35 +0.38
4. Rochelle copper $\text{CuCN}$ , 27 $\text{gl}^{-1}$ $\text{NaCN}$ , 38 $\text{gl}^{-1}$ $\text{Na}_2\text{CO}_3$ , 35 $\text{gl}^{-1}$ $\text{KNaC}_4\text{H}_4\text{O}_6 \cdot 4\text{H}_2\text{O}$ , 45 $\text{gl}^{-1}$ pH 12.0 55 °C	Pure copper	Slow etching	Uniform etching	0	–0.38
5. Silver $\text{AgCN}$ , 50 $\text{gl}^{-1}$ $\text{KCN}$ , 30 $\text{gl}^{-1}$ $\text{K}_2\text{CO}_3$ , 50 $\text{gl}^{-1}$ pH 11.5 25 °C	Fine silver	Slow etching	Uniform etching ↓ passive. evolving $\text{O}_2$	0 32 ↓ 65	–0.24 –0.01 +6.0
6. Acid zinc $\text{ZnSO}_4 \cdot 7\text{H}_2\text{O}$ , 250 $\text{gl}^{-1}$ $\text{NH}_4\text{Cl}$ , 15 $\text{gl}^{-1}$ $\text{Al}_2(\text{SO}_4)_3 \cdot 18\text{H}_2\text{O}$ , 30 $\text{gl}^{-1}$ Dextrose, 75 $\text{gl}^{-1}$ pH 4.0 18 °C	Zinc	Etching, rather rapid, $\text{H}_2$ evolved	Uniform etching	0 163 325	–0.63 +0.30 +1.86
7. Chromium $\text{CrO}_3$ , 400 $\text{gl}^{-1}$ $\text{H}_2\text{SO}_4$ , 4 $\text{gl}^{-1}$ pH < 0 37 °C	Pb/ $\text{PbO}_2$	Passive	Passive, evolving $\text{O}_2$ , reoxidising $\text{Cr}^{3+}$ , etc.	0 1075	+1.5 +2.65

- be more careful in the selection of anode by distinguishing between reductions of the oxygen overvoltage;
- introduce an organic reductant to be 'sacrificially' oxidised by the anode, for example, ascorbic acid;
- introduce an inorganic redox metal ion, for example, iron, to divert the oxidizing tendency.

The first choice is clearly the best, because it avoids further additions, which may cause build-up of products and be more expensive. Furthermore, the other choices are patented. The incentive is obvious – the

saving of 1–2 V or 10–15% of power supplied to the process. Other uses can also be identified; for example, the oxidation of  $\text{Cr}^{3+}$  to  $\text{CrO}_4^{2-}$  in a solution drag-out recovery operation for which diamond-like coatings may be the best. Similarly, the use of a selected anode can achieve oxidation of  $\text{CN}^-$  in a cyanide destruction stage of effluent treatment.<sup>52–55</sup>

#### 4.07.6.6 Corrosion of the Cathode

At the start, the cathode is invariably a metal different from that to be deposited. Frequently, the aim is to

coat a base metal with a more noble one, but it may not be possible to do this in one step. When a metal is immersed in a plating bath, it will corrode unless its potential is sufficiently low to suppress its ionization. Fortunately, a low rate of corrosion is tolerable for a brief initial period. There are cases, where even when a cathode is being plated at a high cathodic (net) current density, the substrate continues to corrode rapidly, because the potential (determined by the metal deposited) is too high. No satisfactory coating forms, if the substrate dissolves at a high rate concurrently with electrodeposition. This problem can be overcome by one or more of the following procedures:

- The use of a complex anion bath.
- The use of a 'strike' bath.
- The use of intermediate electrodeposits (undercoats or underplates).

The principles are illustrated by the following important commercial examples.<sup>52–57</sup>

#### 4.07.6.6.1 Zinc diecastings: complex baths and undercoats

Diecastings are made from zinc with up to 8% aluminum, but from the viewpoint of corrosion they behave like zinc. Diecast parts are often plated with nickel and chromium for protection and decoration, but when zinc is immersed in a typical nickel plating solution, it corrodes rapidly. There are two cathodic reactions: hydrogen is evolved and spongy nickel precipitates. If a diecasting is immersed 'live,' corrosion and electrodeposition occur together as the potential for nickel deposition still leaves the cathode too positive to suppress zinc corrosion (Figure 4). Standard practice is first to plate the zinc with an undercoat of copper, which is too noble to evolve hydrogen or reduce nickel ions. In the bath to which the data of Figure 4 are applied, the potential of copper was +0.042 V. Prolonged immersion led only to slow copper corrosion, with the reduction of dissolved oxygen as the cathodic reaction. This does not interfere with satisfactory nickel plating, and is entirely suppressed by live entry. The problem of applying a copper undercoat is solved by using the cuprocyanide complex bath. The acid cupric bath would present a worse problem than the nickel bath, with its lower pH and the greater oxidizing power of the cupric ion. The stabilities of zinc and copper are reversed in alkaline cyanide, and zinc will not displace copper from cuprocyanide. Zinc immersed in the cuprocyanide bath can corrode to form either zincate

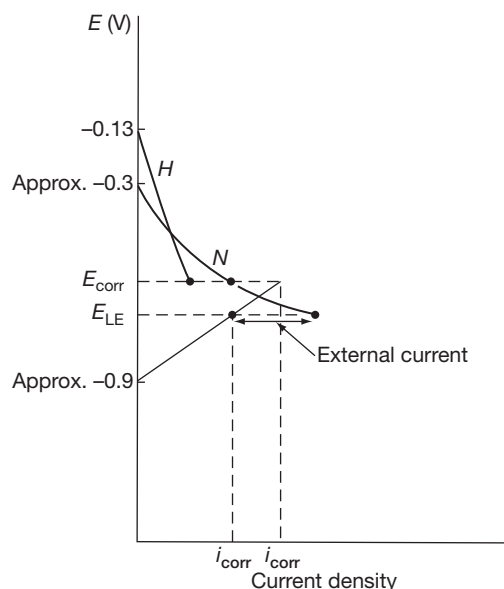


**Figure 4** Corrosion diagram for a zinc diecasting in a nickel plating bath, pH 2.2. There are two possible cathodic reactions, hydrogen evolution (H) and nickel ion reduction (N). The corrosion current  $i_{\text{corr}}$  is the sum of the partial cathode currents. Even with 'live entry' the potential ELE is still too high to suppress corrosion, though the rate is reduced to  $i_{\text{corr}}$ .

or a complex zinc cyanide ion  $\text{Zn}(\text{CN})_4^{2-}$ , with two possible cathodic corrosion reactions, that is, dissolved oxygen reduction or hydrogen evolution. However, high polarization prevents either supporting rapid corrosion, and the situation is like that for copper in the nickel bath; a sound coating is possible and live entry suppresses corrosion. Once a coherent copper coating envelopes the zinc, the part is rinsed and transferred to the nickel bath.

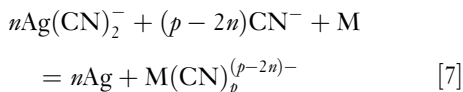
The cuprocyanide plating bath is invaluable in numerous similar cases, where a base substrate cannot be plated directly with the chosen coating. Steels, brass, bronze, beryllium copper, and other substrates are copper underplated. Aluminum articles are ennobled, usually in two stages, that is, first coated with zinc, which is in turn copper plated as described. Such is the utility of the cuprocyanide bath in circumventing cathode corrosion that although copper finds no significant use as a coating in its own right, cuprocyanide baths are found in almost every electroplating establishment.

#### 4.07.6.6.2 Silver plating: 'strike' baths

A 'strike' is usually a solution of special composition in which electroplating is initiated. After a short period of 10–150 s, the cathode is transferred to a



normal bath. The term strike is also used when plating is initiated in the normal bath, but for 10–150 s under very different conditions (often much higher current density), continuing normally afterwards. Silver is electroplated from argentocyanide anions, that is,  $\text{Ag}(\text{CN})_2^-$ . The bath is alkaline and contains ‘free’  $\text{CN}^-$ . The argentocyanide ion is the least stable of the soluble complex cyanides, and therefore,  $\text{Ag}(\text{CN})_2^-$  is a strong oxidizing agent towards other metals which form soluble cyanide complexes. Generally, the reaction



proceeds as written where M is a more base metal of valency  $n$ . Copper, gold, zinc, iron, etc. are all base metals by comparison, so a copper undercoat does not solve the problem. An immersion deposit of silver leads to blistering and loss of adhesion, if electrodeposition is continued over it. The ‘nobility gap’ between copper and silver can be bridged by combining a shift in the equilibrium of eqn [7] with live entry. As a first step, the cathode may be given a copper undercoat. The deposition potential for silver (special case of eqn [7]) is

$$E = E^0 + \frac{RT}{F} \ln K_{\text{instab.}} + \frac{RT}{F} \ln \frac{a\text{Ag}(\text{CN})_2^-}{a^2\text{CN}^-} \quad [8]$$

where

$$K_{\text{instab.}} = \frac{a\text{Ag} + a^2\text{CN}^-}{a\text{Ag}(\text{CN})_2^-} = 1.8 \times 10^{-19}$$

At 298 K, eqn [8] is

$$E = -0.310 + 0.059 \log \frac{a\text{Ag}(\text{CN})_2^-}{a^2\text{CN}^-} \quad [9]$$

and may be depressed by reducing the ratio in the last term. Therefore, a silver strike bath has a small concentration of metal and a large concentration of free cyanide. Equation [7] shows that a high concentration of free cyanide further decreases the nobility of the substrate, so some of the advantage is lost. One way of redressing the balance would be to have the substrate complex  $\text{M}(\text{CN})_p^{(p-n)-}$  present in solution. Silver strike baths are formulated with cuprocyanide in solution, but curiously these are usually recommended for striking steel, while those recommended for copper alloys omit the cuprocyanide. The author uses the cuprocyanide silver strike for ferrous and copper alloys alike. The combination of low silver and high cyanide concentrations means the cathode

potential at a relatively high current density is very low, and both charge transfer and diffusion polarization are high. With live entry, the low potential suppresses substrate ionization, and a detrimental immersion deposit of silver is avoided. A thin underplate – called a flash – is deposited from the strike, after which the normal bath is used. Dilute strike baths working at high current density cannot deposit thick coatings; continued electrolysis produces incoherent, powdery material. They have a low cathode efficiency and evolve considerable hydrogen.

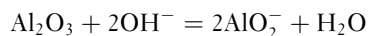
#### 4.07.6.6.3 Electroplating passive alloys

Another application of strike baths reverses the case illustrated in the previous example. The strike is used to promote a small amount of cathode corrosion. When the passivation potential of a substrate lies below the cathode potential of a plating bath, deposition occurs onto the passive oxide film and the coating is nonadherent. Stainless steel plated with nickel in normal baths retains its passive film and the coating is easily peeled off. A special strike bath is used with a low concentration of nickel and a high current density, so that diffusion polarization (transport overpotential) depresses the potential in the active region. The bath has a much lower pH than normal. The low pH raises the substrate passivation potential  $E_{\text{pass}}$ , which theoretically follows a relation

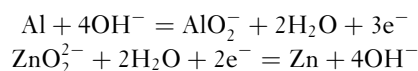
$$E_{\text{pass.}} = E_{\text{pass.}}^0 - 2.303 \frac{RT}{F} \text{pH} \quad [10]$$

When stainless steel is ‘struck,’ the passive film is reduced and an adherent flash of nickel forms on the active metal surface. Deposition is continued in a normal bath.

Electroplating aluminum and its alloys require a similar technique. In aqueous solutions, it is impossible to lower the potential sufficiently to reduce an alumina film, so the substrate is immersed in a strongly alkaline solution capable of dissolving it:



The solution also contains a high concentration of zinc (as zincate), which is noble relative to aluminum. As metallic aluminum is exposed, it corrodes, reducing zincate ions and forming a coating of zinc:



The immersion deposit is necessarily somewhat defective, for the reasons already mentioned, though immersion deposits from complex ions are finer grained and more satisfactory than those reduced from aquocations. The zinc coating is, under the best conditions, an acceptable basis for a copper undercoat from the cuprocyanide bath, on which other coatings can be plated, but there is usually a fair proportion of rejects in commercial operation. Other processes similar in principle use tin or bronze immersion coatings.<sup>56–61</sup>

#### 4.07.6.6.4 Service corrosion effects

Undercoats, 'flash' deposits produced by strike baths, and immersion deposits are potential sources of weakness. If their structure is faulty, it affects the subsequent layers built on the faulty foundation. The greater the number of stages, the higher is the probability of faults. Additional metal layers can create bimetallic corrosion cells, if discontinuities appear in service. The layer of copper beneath cadmium plate on aluminum (using a zincate plus cuprocyanide deposition technique) can cause corrosion problems. When aluminum is plated with nickel and chromium, rapid service corrosion in the zinc layer causes exfoliation.

#### 4.07.6.6.5 Corrosion potentials in plating baths

The standing potentials of steel and copper (before application of current) are shown in Table 2,

together with the standing potential of the plated metal and the potential below which hydrogen should, in theory, be evolved. The potential of the cathode during deposition at a typical current density is also given.

#### 4.07.6.6.6 Agitation and high-speed electrodeposition

There are a number of applications for electrodeposition where high speed is the essence. These include coated strip (e.g., tinplate and galvanized steel), electroforming, and jet plated connectors/contacts. Such high speeds can be achieved either by exploiting solution characteristics or by applying agitation techniques. In simple terms, this can be understood by consideration of the Nernst diffusion equation, where the limiting current density is defined as,

$$i_L = nFCD/\delta(1 - t)$$

Thus  $i_L$  is maximized by increasing  $C$ , the metal concentration in solution, through using near-saturated solutions, selection of highly soluble salts or complexes, or increasing  $D$ , the diffusion coefficient, by using high temperatures. Alternatively it can be maximized by minimizing  $\delta$ , the cathode diffusion layer thickness, by agitation or reducing  $t$ , the transport number, or by using highly conducting solutions through use of support salts (e.g., acids) in solution. In practice, all these can be exploited within the

**Table 2** Corrosion potentials of substrates of copper and steel, plated and unplated in same plating solutions

Plating bath	Copper	Steel	During plating	Plated copper	Plated steel	Hydrogen evolved below
Watts nickel, pH 2.5, 55 °C (not agitated)	+0.112	−0.238	−0.65 (130)	+0.132	−0.173	−0.148
Bright nickel, pH 2.2, 50 °C (air agitated)	+0.042	−0.293	−1.22 (388)	−0.003	−0.138	−0.130
Cupric sulphate, pH < 0, 20 °C	+0.275	approx. −0.35	−0.15 (388)	+0.265	−	>0
Cuprocyanide, pH 12, 55 °C	−0.378	−0.353	−1.21 (130)	−0.378	−0.388	−0.71
Argentocyanide, pH 11.5, 20 °C	−	−	−0.58 (65)	−0.24	−	−0.68
	immersion deposit impedes measurement)					
Zinc sulphate, pH 4.0, 20 °C	+0.122	−0.578	−1.213 (162)	−0.64	−0.65	−0.24
18% (w/v) HCl pickle for ferrous metal, pH < 0	−	−0.17				>0
3% (w/v) HCl pickle for copper alloys, pH 0	+0.17					0

Deposition potential is accompanied by current density ( $A\ m^{-2}$ ) in parentheses; the plated substrate's coating thickness was 2.5 mm. The final column gives the potential below which hydrogen evolution is possible; only in the cuprocyanide is it observed.

constraints of practicality, such as solution boiling and evaporation, heat loss costs, effluent treatment, etc. Thus, high speed solutions have been formulated for tin, zinc, nickel, gold, and silver using these principles.

Agitation has been more problematical. In the past, poor distinction has been made between solution mixing and diffusion layer thickness reduction. Traditional methods of cathode reciprocating movement and air bubbling or sparging are simple and cheap, but not very effective in the context of high-speed electrodeposition. Consequently, other techniques have been developed. Moving the cathode at high velocity is very effective provided it has symmetry of shape and can be done equally for all points on the deposition surface, for example, coating of continuous strip or wire substrates, or rotation of the cathode is possible as for cylinders, flywheels, tubes, bearings, etc. Alternatively, pumping the solution along or at the electrode interface is feasible by using focused jets or capillary-type gaps at the interface. The use of submerged eductor jets has become ecologically important, because there is little or no atmospheric spray produced and the venturi-induced flow can be substantially greater than the direct pumped flow.

Specialist forms of agitation have been developed for certain types of process. For example, deposition of composite coatings requires the particles to be suspended in solution and captured by the growing deposit. This is difficult with pumped flow agitation, where the particles are in fast continuous movement. In these situations vibratory agitation may be best or the solution could be made more viscous and agitation disregarded.

Comparison of the efficacy of agitation techniques has always been problematical because speed *per se* is inadequate – deposit quality must be assured. Theoreticians may prefer to define diffusion layer thicknesses or mass-transport numbers, but in practical terms the current density to attain a given deposit quality is easier to measure. From this, an agitation enhancement factor (EF) can be used for comparison, the EF value for a static solution being taken to be unity. Typical values are then as follows:

Cathode reciprocation	EF = 2
Air bubbling	2–5
Cathode movement	5–20
Cathode rotation	5–50
Jetting/eductor flow	10–25

Distinction should be made between agitative fluid flow and ultrasonic agitation. Ultrasonics are effective at displacing solids from interfaces in a cleaning mode and for modifying physical properties of the growing deposit but are not specifically effective at moving or thinning the liquid-phase diffusion layers.<sup>62–64</sup>

#### 4.07.6.6.7 Pulse plating

The use of pulsed current as a means of improving deposition rates and yielding improved deposits is a development of periodic reverse techniques, long used in the metal extraction and refining industries to produce smoother/leveled deposits. The reasoning was that high currents may give high deposition rates but generally yield rougher surfaces. However, reversing the current for a short time can ideally cause preferential anodic dissolution of the protruberances, thereby, leading to smoother surfaces. Thus a degree of inefficiency of overall production can be withstood in the attainment of better deposit surfaces. The times for forward and reverse currents are usually of the order of minutes.

While it may be easy to use sine wave alternating current waveforms, this is limited to 50 or 60 Hz and square waves are usually generated by an electronic waveform generator. The waves themselves may be on/off, but more usually, pulse/reverse, superimposed pulses, duplex pulse, etc. The choice depends upon intention with regard to electrode kinetics or mass transfer, electrocrystallization modification, deposit properties, etc. Furthermore, the technique has been explored for virtually every metal and alloy, which can or has been researched. Some metals, alloys, and solutions are more susceptible than others although in some cases the systematic research may not have been adequate. Successes have commonly been to modify deposit grain size and stress, to improve surface smoothness, distribution and brightness, to increase net deposit rates, and to enable layered deposits to be produced. The literature is now so large that it must be referred to by search engines and not general reviews.

When the time intervals are of seconds or less, the term pulse plating has become usual, for which a number of terms must be defined:

- The waveform is the shape of the current/time graph; it is usually square but could be sine wave. The pulses may be forward only or pulse/reverse (forward and negative). Other patterns are possible.

- The pulse frequency is the number of pulse cycles per second.
- The duty cycle (%) is the on time related to the total time.
- The mean current is the duty cycle  $\times$  the peak current

Many plating processes have been studied but relatively few have been used industrially or commercially. A number of reasons can be noted, especially the cost of pulsing large currents because of the dissipation of energy; but a particular reason is that each metal and solution has its own characteristics, which normally have to be individually studied or optimized, with transposition from another system only rarely successful. Consequently, apparent failure is often because of lack of perseverance! Puipe and Leaman in 1986<sup>65</sup> have demonstrated the huge stock of research data; what is lacking is this perseverance.

#### 4.07.6.7 Factors Influencing Structure

##### 4.07.6.7.1 Substrate effects: epitaxy and pseudomorphism

Both the words epitaxy and pseudomorphism are derived from classical Greek, the former meaning literally, close to or close upon an arrangement, row or series (technically an arrangement imposed upon a skin or layer, for example, an electrodeposit, which is close upon a substrate) and the latter, false form (technically a mineral or crystal displaying a form more characteristic of another material than its usual one). For many years, the two terms were held to be synonyms for one phenomenon in electrodeposits. Since 1936, it has become clear that there are two related phenomena, on each of which one of the names is bestowed. Not all authors recognize this, nor is the usage employed here adopted uniformly. Both phenomena are of great practical importance.

Pseudomorphism received methodical study from about 1905. A microsection taken across the interface between a substrate and an electrodeposit shows the grain boundaries of the former continue across the interface into the deposit (Figure 5). As grain boundaries are internal faces of metal crystals, when they continue into the deposit, the latter displays in the form of the substrate. Hotherhall's 1935 paper contains numerous excellent illustrations with substrates and deposits chosen from six different metals, crystallizing in different lattice systems and with different equilibrium spacing. Grain boundary continuation

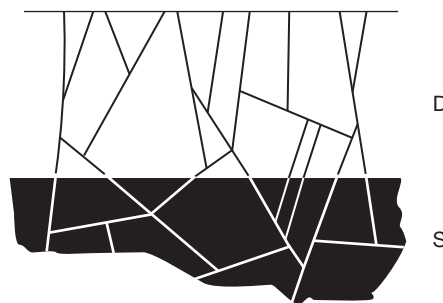


**Figure 5** Pseudomorphism; grain boundaries in the substrate (S) are continued in the electrodeposit (D).

and hence pseudomorphism is evident despite the differences.

Epitaxy is a relation on the atomic scale between substrate and electrodeposit. Imagine that the interface of the microsection is magnified about 107 times so that the rows of atoms in the metal lattice become visible. If the deposit shows epitaxy, there will be an ordered and regular relation between substrate and deposit atom positions (Figure 6(a)). A nonepitaxial deposit shows no such relation (Figure 6(b)). Direct experimental demonstration of epitaxy was first made in 1936 by Finch and Sun. Earlier, metallographers argued that pseudomorphism (which they could see) meant there must be epitaxy (which they could not), as grain boundaries are surfaces where the direction of lattice rows of atoms changes; if epitaxy were assumed to exist, pseudomorphism should result. Reversing the argument, pseudomorphism was taken as evidence for epitaxy (Figure 6(c)).

Electron diffraction investigations showed that epitaxy did indeed exist when one metal was electrodeposited on another, but that it persisted for only tens or hundreds of atomic layers beyond the interface. Thereafter, the atomic structure (or lattice) of the deposit gets altered to one characteristic of the plating conditions. Epitaxy ceases before an electrodeposit is thick enough to be seen with an optical microscope, and at thicknesses well below those at which pseudomorphism is observed.

Epitaxy reflects the formation of metallic bonds between the dissimilar atoms at the interface. When the two metals crystallize in different systems, their relative orientation is that which promotes the maximum coordination and the maximum metallic bonding. The stability achieved by epitaxy overrides any lost because of the lattice strains imposed. These strains may be considerable; 'stresses' calculated from the bulk elastic moduli are correspondingly high, and sometimes puzzle the uninitiated if they

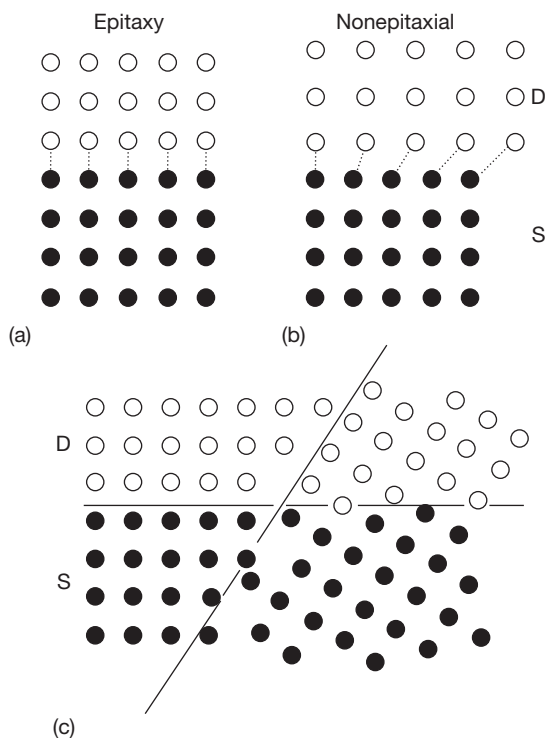


**Figure 6** (a) Coordination across a substrate S-electrodeposit D interface on the atomic scale produces epitaxy, (b) a nonepitaxial deposit has no coordination and (c) epitaxy would be expected to produce grain boundary continuation at the interface, though in fact grain boundaries often continue to thicknesses far greater than those at which epitaxy disappears.

exceed the bulk tensile strength. It is an oversimplification to regard the interface as being highly stressed; were the 'stress' which seems to be parallel to the interface reduced by some means to zero, the energy that would have to be put into the bonds normal to the interface would be much greater than that released. The simple concept of stress in a homogeneous alloy is not applicable to the peculiar case of a substrate-electrodeposit interface. The latter is unique in having metallic bonds carried across a very sharp boundary.

The practical result of epitaxy is a very high degree of adhesion between coating and substrate. The force needed to separate the interface is similar to that needed to break the metals on either side. Where a true metallic bond forms at an epitaxial interface, it is only possible to measure adhesion if the bond is the weakest of the three near the interface. An adhesion test based on breaking the joint indicates only which of the three is weakest. For practical purposes, any epitaxial joint will have strength more than adequate for service conditions.

Nonepitaxial electrodeposition occurs when the substrate is a semiconductor. The metallic deposit cannot form strong bonds with the substrate lattice, and the stability conferred by coordination across the interface would be much less than that lost by straining the lattices. The case is the converse of the metal-metal interface; the stable arrangement is that in which each lattice maintains its equilibrium spacing, and there is consequently no epitaxy. The bonding between the metallic lattice of the electrodeposit and the ionic or covalent lattice of the substrate arises only from secondary or van der Waals' forces. The force of adhesion is not more than a tenth of that to a metal substrate, and may be much less.

Epitaxial growth is prevented if semiconducting films of grease, oxide, sulfide, etc. cover the cathode surface. These occur when pretreatment is inadequate, when plating baths are contaminated, or when, as with stainless steel, aluminum, titanium, etc. an oxide film reforms immediately after rinsing. Low adhesion resulting from nonepitaxial electrodeposition is used in electroforming to promote easy separation of deposit and substrate. When semiconductors or nonconductors are to be electroplated, a form of dovetail mechanical joint (achieved as outlined above) is essential. Means similar to those for stainless steel and aluminum have been devised to deal with other alloys, which are passivated readily. Sometimes, even with special methods, some oxide remains so that the electroplated coating is anchored only by small epitaxial areas. There is risk of failure. Thermal stress or relatively mild abrasion may part the interface and cause the unanchored areas to blister. Adhesion is improved by postplating annealing. The oxide at the interface is dissolved in one or other metal, or diffuses to grain boundaries and alloying at the interface produces the desired metallic bond.

Pseudomorphism has less desirable consequences, and usually means are sought to suppress it. If the substrate has been scratched, ground, or abrasively polished, or if it has been cold rolled or cold formed, the surface is left in a peculiar state. Cold working reduces the surface grain size, and produces deformed, shattered, and partly reoriented metal. It may produce microcrevices between the deformed grains, and, with some processes, nonmetallic impurities and oxides are embedded in the surface. The disturbed state of the substrate is copied by a pseudomorphic electrodeposit with several consequences (Figure 7). One is aesthetic, as it has often been noted that almost invisible abrasion of the substrate develops, as more prominent markings in the



deposit. A chalk mark on steel produces local abrasion, hardly noticeable when the chalk is wiped away. If a strongly pseudomorphic electrodeposit is applied, the chalk mark reappears indelibly on its surface. A bright deposit may have its luster greatly reduced by pseudomorphic growth on a deformed surface (Figure 8). The corrosion protection is reduced if pseudomorphism with a deformed substrate leads to discontinuities at ill-fitting deposit grains (Figure 9). A pseudomorphic coating usually presents a dull or rough crystalline appearance. When the crystal form of the substrate is copied in the deposit, growth generates faces of simple index. An artificial face of high index soon grows out when plated. Tradition demands a featureless mirror surface on metal coatings, and a way of producing this, which has attracted much commercial effort, is by using brightening addition agents. Microsections of electrodeposits from the more effective bright plating

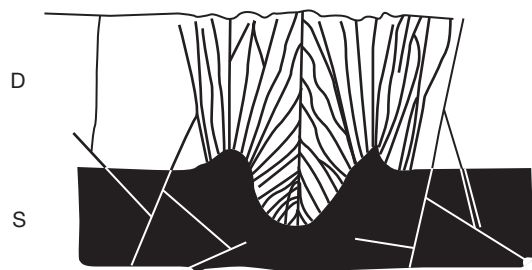


**Figure 7** The disturbed structure of a scratch, with fragmented and distorted grains, is perpetuated by a strongly pseudomorphic electrodeposit.

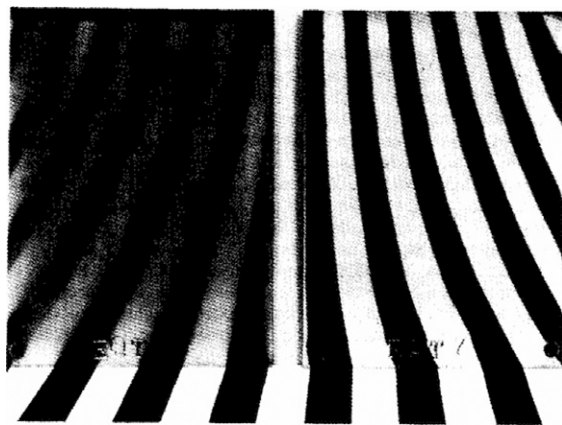


**Figure 8** A fairly strongly pseudomorphic bright tin deposit (left) has its brightness impaired by the shattered surface layer produced on steel by cold rolling. When this layer is removed, the deposit is mirror bright (right). Coating 5 mm thick.

baths do not exhibit pseudomorphism. The deposit usually shows no grain structure, but instead a series of light and dark grain bands parallel to the substrate (Figure 10). Pseudomorphism is suppressed by the addition agent adsorbing on, and blocking areas taking part in, pseudomorphic growth. In the initial stages of bright plating, the addition agents adsorb at similar points on the substrate. Growth commences from fewer substrate nuclei when annealed nickel is plated in a bright nickel bath than in a dull (Watts') bath without additions. In the earliest stages of deposition, replicas of the surface show evidence of pseudomorphism even in bright baths (the substrate grain boundaries are carried into the deposit) but this is suppressed rapidly as the thickness increases. The aim with bright plating baths is to inhibit growth sufficiently to suppress pseudomorphism, but not so much as to suppress epitaxy and adhesion. An excessive concentration of addition agent will also suppress epitaxy, so that deposition occurs on to an adsorbed layer of brightener. Brightener adsorption is often potential dependent and trouble may occur first at high current density (low potential) areas.<sup>58-64</sup>

#### 4.07.6.7.2 Electrolyte effects

As a deposit becomes thicker, the influence of the substrate diminishes, and eventually the structure is characteristic only of the electrolyte composition, the temperature, current density, and mode of agitation. A great variety of structures are observed; some are analogous to those seen in cast metals, but others are obtained only by electrodeposition. Crystalline deposits

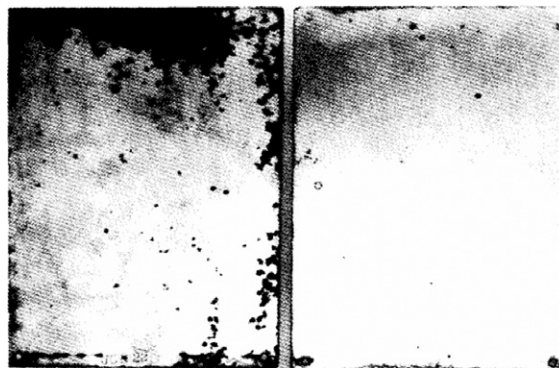


**Figure 9** Corrosion resistance of tin–nickel electrodeposit impaired by pseudomorphic porosity originating on cold-rolled steel surface (left). Panel on right has had the shattered grain surface removed by chemical polishing (0.125 mm removed). Coating thickness 15 mm; panels exposed 6 months to marine atmospheric corrosion (Hayling Island).

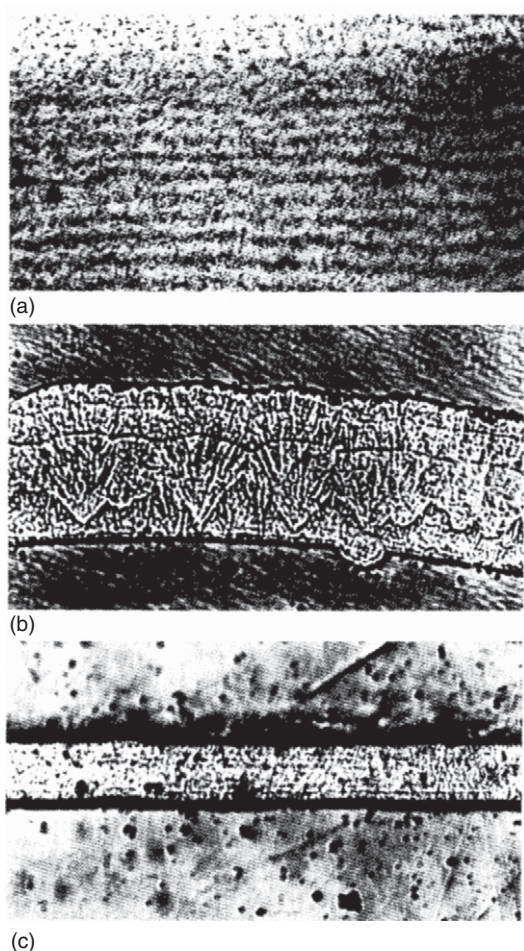


**Figure 10** Banding often observed in microsections of bright electrodeposits. (a) Bright tin (courtesy of the Tin Research Institute), and (b) and (c) bright gold.

from baths containing little or no addition agent often develop a preferred orientation texture. Some bright deposits show a texture, but in general as growth processes are progressively inhibited by increasing addition agent concentration or by using more active materials, the deposit becomes progressively finer grained and loses preferred orientation textures.

The compositions of baths, chosen for practical use, result in initial rates of lateral growth much greater than the rate of outward growth. This is a desirable feature; it causes the coating to become continuous at low thicknesses. The opposite condition of a faster rate of outward growth is undesirable, and results in a noncoherent deposit. Predominantly, outward growth occurs when the transport of metal ions becomes slow compared to their rate of discharge, that is, it is favored by high current density, low temperature, and lack of agitation. Lateral

growth processes are then starved of material to support them, but outward growth moves the deposit towards the supply, and the prominences formed benefit from greater diffusive flux. There are strong pressures in industrial production to increase electroplating rates, which carries a danger of using high current density and causing a shift to outward growth. In baths where the coating is electroplated from aquocations at high cathode efficiency, the onset of lateral growth is fairly sharp. Cathodes have a range of local current density, and the coating on the high current density areas becomes friable, dark colored, and rough as the transition is reached. Such coatings are termed 'burnt' and the corrosion protection is degraded. With baths working in the acid pH range, there is the complication that once an appreciable part of the current is used to reduce water, the pH at the cathode rises and insoluble hydroxides are precipitated and incorporated in the coating. With complex cyanide baths, the onset of 'burning' is less sharp. There is normally considerable simultaneous hydrogen discharge, and as the current density rises, there is no sharp limiting current density for metal discharge. Addition agents raise the lateral-outward transition to higher current densities by inhibiting outward growth. Nevertheless, all electroplated coatings show signs of deteriorating properties if the baths in which they are produced are worked at sufficiently high current density.<sup>66-70</sup>

#### **4.07.6.7.3 Form of current passed through cell**

Commercial electroplating began with pure DC from galvanic cells. Later, for many years, DC generators were used. Their current output is unidirectional but with a superimposed ripple. Part of the ripple stems from the angular motion of the armature coils during the period they supply current to a commutator segment and part from variations of contact resistance at the commutator. Generators have been superseded by transformers and rectifiers. Copper-oxide, mercury-arc, selenium, germanium, and silicon rectifiers have been used and examples of each are to be found in service. These devices supply varying unidirectional current whose form depends on the number of phases in the input and the circuit used. A half-wave single-phase rectifier provides a pulsating current; a full-wave three-phase set has a much smoother output.

Alternating currents with asymmetric forms have been used, mainly for electroforming and thick engineering deposits. Where the cycles are slow,

for example, several seconds, the term periodic reverse current (p-r-c) is used. The benefit claimed for p-r-c plating is that smoother, thick deposits result from selective dissolution of peaks in the reverse part of the cycle. This assumes the electrode process reverses during the anodic period, which is not always the case. In chromium plating, the coating becomes passive in anodic periods, while in acid gold baths based on aurocyanide, the process is also irreversible. More recently, asymmetric AC with a much higher frequency of 500 Hz was found to alter beneficially the properties of nickel from chloride baths.

Pulses of unidirectional current have been used to modify coating properties. When plating starts, it is possible, for a time, to use a current much higher than the steady-state limit, drawing on the stock of ions near the cathode. Provided sufficient time is allowed between pulses, a coating can be built of layers plated at much higher current density than normal. Improved gold coatings were produced by relatively rapid pulses. The technique of barrel plating results in pulse plating of an irregular sort, with pulse durations of the order of seconds and inactive periods rather longer.

Chromium plating from chromic acid baths is more sensitive to the source of current than most other processes, sufficiently so for commercial operators to use at least three-phase rectifiers as a rule, and to take precautions against any temporary break of current during voltage regulation. A recent investigation showed that the ripple introduced by thyristor control of rectifiers was detrimental to chromium electrodeposits.<sup>71-80</sup>

#### 4.07.6.8 Industrial Electroplating Techniques

Electroplating is usually a finishing technique applied after an article has been completely fabricated. Fairly large articles, from cutlery to motorcar bumpers, are dealt with by vat plating. They are suspended by a conducting connection in a rectangular tank or vat of electrolyte. The anodes are arranged about the periphery of the tank. For small runs the cathodes may be suspended by copper wire wrapped round a suitable part, but for longer runs a plating jig is used. This is a copper frame with phosphor bronze spring contacts to hold the work and insulated, usually with a PVC coating, on all but the contact points. The point of contact between wire or jig and the article becomes a weak part in the coating, and some thought should be given to providing or selecting contact points in insignificant areas.

Vat plating is used sometimes with articles too large for complete immersion. Printing, calendering, drying, and similar rolls are part-immersed and revolved continuously during plating. However, it is much more difficult to plate half an object, reverse it, and complete the other half later; the 'join' between the two deposits is rarely satisfactory.

Small objects, nuts, bolts, screws, and small electrical parts are plated in a revolving barrel. Electrical connection is made by a conductor immersed in the tumbling mass, and electrodeposition, which is confined to the outer layer of the mass at any instant, takes place in intermittent stages for any individual object. The coating is abraded during the process. The peculiarities of chromium deposition set it apart, and the normal barrel-plating processes are not used. In the so-called chromium barrels, the small parts travel and tumble along a helix inside a rotating cylinder during deposition, and are electroplated for a much greater proportion of the time than are parts in normal barrels.

Brush plating is a special technique which dispenses with a container and uses a swab soaked in electrolyte applied to the work. In jet plating, a stream of electrolyte is applied to the cathode. Both are methods of selective plating, applying an electrodeposit to only a part of an article. Little has been published about the techniques or the properties of coatings they produce.

Continuous plating of wire and strip is, unlike the preceding techniques, a prefabrication process. The production of tinplate is the largest scale continuous operation, but any electrodeposit may be applied this way. Subsequent fabrication processes are likely to damage the coating, so that precoating is best reserved for ductile coatings which are anodic to the substrate in service, as is the case for tin.<sup>81-83</sup>

#### 4.07.6.9 Rinsing

Between all stages of immersion (cleaning, pickling, plating, postplating treatment) work has to be rinsed. Once the hydrophobic solid has been removed, metal surfaces withdrawn from solutions carry a film of liquid. The solution lost this way is known as drag-out. A film 10 mm thick is the minimum retained by smooth, well drained, vertical surfaces. On rough or horizontal surfaces, and in recesses it is much thicker, as it is also with viscous solutions. During rinsing, the film is diluted, and the ratio of the final concentration to that present initially is the dilution ratio. The dilute material is carried forward to the next process,



and clearly the highest concentration of impurity permissible before the subsequent process is affected adversely determines the maximum dilution ratio that can be allowed. Sometimes there is a minimum dilution ratio; between nickel plating and chromium plating it is essential that the rinsed metal surface does not become passive, and prolonged rinsing carries a danger of eliminating the slight but important amount of rinse water corrosion which keeps the surface active between stages.

Usually rinsing troubles are caused by a dilution ratio that is too high. If incoming work passes through a process stage, and the drag-out from that stage is in turn discarded in a subsequent rinse, the maximum concentration of material carried into the bath is equal to that in the film carried over. However, there is an increasing tendency to conserve materials and steps are taken to return drag-out losses. In so doing, the impurities are also returned, so conservation measures require a reduction in the dilution ratio of the preceding rinse. Inadequate intermediate rinses are detrimental to the corrosion resistance of the coating because carried-over impurities impair the functioning of plating baths. Inadequate final rinsing leads to increased corrosion of the coating, and to staining. Staining, which is a serious aesthetic problem with decorative coatings, may itself arise from corrosion. Some stains are caused by the precipitation of dissolved solids when rinse water evaporates, but in other cases, they are caused by corrosion supported by the presence of an electrolyte in the rinse water.<sup>84-93</sup>

#### 4.07.6.10 Postplating Treatments

Where the corrosion resistance of a coating depends upon its passivity, it is common to follow plating with a conversion coating process to strengthen the passive film. Zinc, cadmium, and tin in particular are treated with chromate solutions which thicken their protective oxides and also incorporate in it complex chromates. There are many proprietary processes, especially for zinc and cadmium. Simple immersion processes are used for all three coatings, while electrolytic passivation is used on tinplate lines. Chromate immersion processes are known to benefit copper, brass, and silver electrodeposits, and electrolytic chromate treatments improve the performance of nickel and chromium coatings, but they are not used to the extent common for the three first named.

The tin coatings as deposited in tinplate manufacture are not bright. Until comparatively recently,

bright tin electrodeposition was not practiced commercially, there being no reliable addition agents. To produce bright tin on tinplate and other products, the process of flow melting or flow brightening is used; tinplate is heated by induction or resistance, and plated articles are heated by immersion in hot oil to melt the tin, which flows under surface tension to develop a bright surface. While the tin is molten it reacts to form an alloy layer with the substrate. The alloy layer alters the corrosion behavior.

Other electroplated articles are heated after plating to expel hydrogen which has entered the substrate during cleaning, pickling, and plating, and which embrittles some metals, mainly high-strength steels. Generally speaking, alteration of the deposit structure and properties is not desired. Another use of postplating heat treatment is to improve adhesion, as already mentioned (Section 4.07.6.7.1).

Mechanical polishing, formerly the principal means of producing bright coatings, has become less important with the extension of the use of brightening addition agents. Mechanical polishing reduces the thickness of a coating, and may cut through to the substrate. As corrosion resistance is related to thickness, mechanical polishing can be detrimental. It may also increase porosity.<sup>94-97</sup>

### 4.07.7 Properties of Electrodeposits

#### 4.07.7.1 Thickness

Coating thickness is one of the most important quantities connected with corrosion resistance, and its measurement and control are features common to all electroplating operations and in all quality specifications. In some cases, coating thickness has functional importance, for example, where there are fitting tolerances, as with screw threads. However, in most cases, it is the connection with corrosion resistance that makes thickness important. Where the coating is anodic to an area of substrate exposed at a discontinuity, the coating is slowly consumed by corrosion, but the criterion of failure is the appearance of substrate corrosion product. This does not form until almost all the coating is consumed. Coatings which are cathodic to the substrate must have no discontinuities if substrate corrosion is to be suppressed.

The criterion of failure is usually the same. Freedom from discontinuity is also related to thickness. Discontinuities have three origins: spontaneous cracking to relieve internal stress, pores formed during the growth of the coating, and abrasion and wear.

The last two causes, that is, porosity and wear, both exhibit diminishing incidences as thickness rises. Apart from the peculiar case of electrodeposited chromium, internal stress cracking is a sign of incorrect plating conditions. Broadly speaking, thickness and corrosion resistance increase together. The thickness of an electroplated coating is never uniform. On the significant area (i.e., that on which corrosion resistance and other special properties are important) of a plated surface, there are two important thicknesses, that is, (a) average thickness, which determines the production rate and plating costs; and (b) minimum local thickness, which, as the weakest link in the chain, determines the corrosion resistance. The ideal is to make these equal; the larger the difference the greater the waste of metal. The difference can be reduced by special procedures, but at a cost.

When the cathode is being plated, the electrical field is not uniform. Both electrodes are equipotential surfaces, so that prominent parts of the cathode, for example, corners, edges, protuberances, etc. which are relatively nearer to the anode are plated at a higher average current density, resulting in a thicker coating. Recesses and more distant parts are more thinly plated. Distribution of thickness tends to be the reverse of that found with paints, hot-dipped articles, and other coatings that are applied as liquids. Liquid-applied coatings are thin on sharp edges, and thick in recesses because of the effects of surface tension and radii of curvature.

The numerous factors which contribute to the thickness distribution can be divided into two groups, that is, (a) those connected with the nature of the plating bath (see below), and (b) those to do with the geometry of current paths in the bath, including the shapes of the electrodes. (Reference should be made to publications on electrodeposit specifications of the British Standards Institution, American Standards Institution and other standardizing bodies.)

#### 4.07.7.2 Throwing Power

In a given plating cell, thickness distribution is found to vary with bath composition, current density, temperature, and agitation. It is common to speak of the throwing power of a plating bath. The throwing power of chromic acid baths is poor, that is, there is a relatively large difference between maximum and minimum local thickness; conversely, the throwing power of alkaline stannate baths is good, that is, there is much less difference in the local thicknesses.

Strictly speaking, the bath composition should be qualified by the conditions of use, as they affect throwing power. Otherwise, the usual conditions are implied. A numerical throwing index can be calculated from the performance of a plating bath in a cell of standard geometry. Two widely used cells are, (a) the Haring–Blum cell, and (b) the Hull cell (Figure 11). The Haring–Blum cell was devised for throwing index measurement; the Hull cell is used mainly to study the effects of varying bath composition.

The Haring–Blum cathode is divided into two equal plane areas, distant  $l_1$  and  $l_2$  from a common anode, and a quantity called the primary current density ratio  $P$  is defined as

$$P = l_2/l_1$$

This is the ratio in which the current would divide, if electrolytic resistance were to control its flow entirely. The metal distribution ratio  $M$  is the ratio of the thicknesses of the coating actually deposited during a measurement. There are several numerical scales of throwing index  $T$ , but Field's is widely adopted:

$$T = 100 \frac{P - M}{P + M - 2} \% \quad [11]$$

On this scale, zero represents the case when  $M = P$ , and electrolyte resistance is the main factor. Throwing power can be worse, down to a limit  $T = -100\%$  when  $M = \infty$ , that is, no deposit at all on the far cathode. Conversely, when  $M < P$ ,  $T$  is positive, where  $M$  to reach 1.0 despite the difference in position,  $T = +100\%$ . At one time,  $+100\%$  was regarded as an unrealizable limit, but conditions have been found for which  $T = +150\%$  in a Haring–Blum cell equation.

The Hull cell cathode has a continuous variation of current density along its length, and there are

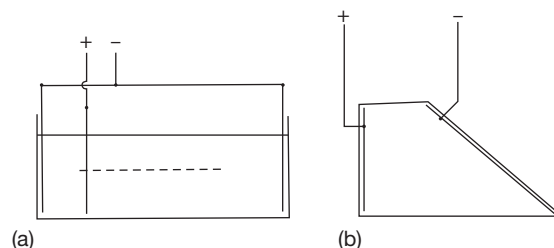


**Figure 11** (a) Haring–Blum cell for throwing index measurement, in elevation and (b) Hull cell (plan view) which can also be used for measuring throwing indices.



equations which give the primary current density at any point not too near the end. If the local thickness is measured at two points for which  $P$  is known,  $T$  can be calculated. The real current distribution is a function of cathode and anode polarization as well as of the resistance of the electrolyte. The metal distribution ratio will be

$$M = \frac{(V - \Delta E_1)}{(V - \Delta E_2)} \times \frac{l_2}{l_1} \times \frac{\varepsilon_1}{\varepsilon_2} \quad [12]$$

where  $V$  is the cell potential difference between anode and cathode,  $\Delta E$  is the total potential difference caused by polarization (anode and cathode) on the cathode area indicated by the subscript, and  $\varepsilon$  is the cathode efficiency as indicated by the subscript.

As  $\Delta E$  will be a function of current density,  $T$  will be a function of electrode area, and comparisons should, therefore, be made with cells of standard size. Equation [12] shows that high throwing indices will result when polarization rises steeply with current ( $\Delta E_1/\Delta E_2$ ) and cathode efficiency falls steeply ( $\varepsilon_2/\varepsilon_1$ ). The primary current ratio,  $P = l_2/l_1$ , affects the result because by altering the currents the polarization terms are altered. For example, with an acid copper bath in a Haring–Blum cell,  $194 \text{ A m}^{-2}$  average CD:

$P$	2	5	11	23
$T$ (%)	+7	+11	+22	+41

An increase in conductivity usually increases  $T$  because it increases the proportion of polarization in the total cell potential difference and lowers the ratio  $(V - \Delta E_1)/(V - \Delta E_2)$ . Changing the conductivity, an acid copper bath with sulfuric acid produced the following result ( $291 \text{ A m}^{-2}$  average CD,  $P = 5$ ):

Conductivity ( $\text{S cm}^{-1}$ )	0.08	0.15	0.26	0.30
$T$ (%)	+5	+11	+13	+27

where S is the SI unit of conductance (Siemens).

Many baths in which metal is reduced from complex anions (e.g., cyanide baths, stannate baths) give high throwing indices because both polarization and cathode efficiency variation favor a low value of  $M$ . The cathode efficiency for a typical copper cyanide bath ( $40^\circ\text{C}$ ) was

Cathode current density ( $\text{A m}^{-2}$ )	199	253	384	763	1785	5130	30800
Cathode efficiency (%)	0	5.9	11.9	13.9	18.8	22.7	24.4

The throwing index for the cyanide bath is usually about +40% and rises as the cell current is increased to as high as +85%. Aquocation baths give values near  $T = 0$ , though conditions may be selected which give much higher figures if there is a steeply rising section of the polarization curve. Chromium plating baths invariably have large negative throwing indices, despite deposition from a complex ion. The cause is the anomalous rising trend of cathode efficiency with current density and the existence of a minimum current density below which the efficiency is zero. A typical bath ( $400 \text{ g l}^{-1} \text{ CrO}_3$ ,  $4 \text{ g l}^{-1} \text{ H}_2\text{SO}_4$ ,  $38^\circ\text{C}$ ) gave the following data:

Current density ( $\text{A m}^{-2}$ )	32	65	129	258	388
Cathode efficiency	76	68	56	34	21

If the current density on the far cathode in a Haring–Blum cell was  $199 \text{ A m}^{-2}$  or less,  $T = -100\%$ .

Throwing indices measured in a Hull cell differ from those in a Haring–Blum cell because of the differences in geometry. In a Hull cell, several pairs of points can be found, which have the same primary current ratio, but for which  $M$  and hence  $T$  are found to vary because of polarization changes.<sup>98–105</sup>

#### 4.07.7.3 Current Path Geometry

The polarization and cathode efficiency terms in eqn [12] cannot be altered in practice to improve thickness distribution, as they tend to be decided by overriding considerations. It is usual to accept the distribution obtained without special precautions as being the best commercial solution, although the average thickness needed to achieve the necessary minimum local thickness may be high. Where this approach does not serve, there are a number of methods of altering the term  $l_2/l_1$  in eqn [12]:

- By using shaped (conforming) anodes, additional (auxiliary) anodes or ‘bipolar’ anodes to bring anode areas nearer to cathode recesses. Insoluble anodes are better where they are applicable, as they do not alter the original shape during use.

- (b) By using nonconducting shields of plastic or glass to equalize the current path lengths.
- (c) By placing auxiliary cathodes ('robbers' or 'thieves') near high-current-density points to divert deposition. This does not save metal, but has the merit that auxiliary cathodes can be incorporated into jigs for long runs in automatic plating machines. Auxiliary cathodes are used in heavy chromium deposition, where metal waste is secondary to the cost of removing excess chromium when grinding to precise dimensions. Where a number of small parts are plated together on a jig, it is usually possible to dispose them so that they serve as 'robbers' for each other.
- (d) By paying attention to certain 'rules' when designing articles which will be finished by electroplating. Many external contours are chosen for reasons of style. It helps to avoid features like sharp recesses, which are bound to cause trouble. A simple rule is the '1 in ball test' or perhaps the '25 mm ball test': if there is any part of a surface which a ball of this diameter cannot touch when rolled over it, there will be difficulties. There are other design aspects, covered in specialist publications, attention to which improves the corrosion resistance, which can be imparted by plating.<sup>106-110</sup>

#### 4.07.7.4 Structure-Dependent Properties

##### 4.07.7.4.1 Composition of the electrodeposit

Attention has been drawn to the dependence of structure on both substrate and plating conditions, and to the transition in properties which occurs across the section of a deposit. Most commercial electrodeposits have a high purity, yet in a sense impurities are vital to their successful application. Alloy electrodeposition possesses the literature whose bulk attests the subject's fascination for research (which the authors share), but is out of proportion to the extremely limited commercial applications. Alloys in general metallurgical practice provide a variety of mechanical properties; in electroplating the range of properties desired is narrower, and it can generally be achieved by altering the structure of a single metal deposit through changes in the plating bath composition or plating conditions. The microstructure of an electrodeposit can be altered much more than that of a cast and worked metal. This is because the deposit forms well below its melting point, where crystallization processes are hindered by the virtual absence of

solid-state diffusion. Consequently, very small amounts of 'impurity' absorbed at important growth sites on the surface cause large changes in the structure of what is, chemically, almost pure metal. The structure is metastable, but permanent as long as the electrodeposit is not heated. A variety of mechanical and physical properties are a reflection of the structure: hardness, ductility, tensile strength, internal stress, electrical and thermal conductivity, etc. As the structure of an electrodeposited metal is altered by changing the plating conditions, the mechanical and physical properties also alter. A plot of structure-dependent properties against the plating variable usually shows the various properties moving in parallel or inverse motion, and over ranges not accessible in cast and worked metal of the same composition. However, if electrodeposits are heated to temperatures where moderate mobility of the atoms is possible, their properties rapidly revert to 'normal.' The corrosion resistance of electrodeposits depends much more on chemical composition than on structure, so that the corrosion resistance of a particular metal is retained for a wide range of mechanical and physical properties.

The 'impurities' responsible for modifying the structure may originate from water (dispersed oxides); adsorbing ions, especially cyanides; organic addition agents parts of which are incorporated; or ions of a second metal which are codeposited. Some regard deposits in which the impurity is a small amount of a second metal as an alloy, but generally, they have the same sort of metastable structures as are obtained with nonmetallic impurities, rather than the structures of stable alloys of the same composition. The 'alloying' metal serves to cause and perpetuate a nonequilibrium structure whose real basis is the low temperature of the electrocrystallization process. Generally, the corrosion properties of the various different structures of a given metal are much the same, with the notable exception of nickel containing sulfur from addition agents, which has already been mentioned.<sup>111-116</sup>

##### 4.07.7.5 Internal Stress

Electrodeposits are usually in a state of internal stress. Two types of stress are recognized. First order, or macrostress, is manifest when the deposit as a whole would, when released from the substrate, either contract (tensile stress) or expand (compressive stress) (**Figure 12**). Second order, or microstress, occurs when individual grains or localities in the

metal are stressed, but the signs and directions of the microstresses cancel on the larger scale. The effects of first-order stress are easily observed by a variety of techniques.

Second-order stress is difficult to observe and much less extensively studied. The causes of internal stress are still a matter for investigation. There are broad generalizations, for example, 'frozen-in excess surface energy,' 'a combination of edge dislocations of similar orientation,' and more detailed mechanisms advanced to explain specific examples.

Tensile first-order stress is a corrosion hazard in coatings cathodic to the substrate. Compressive stress is not usually troublesome, nor is the stress of either sign in anodic coatings. Less can be said about high

second-order stress, though it may well cause brittleness. If tensile stress is large enough, the coating cracks and a cathodic coating will fail to protect, as illustrated in **Figure 13**. Tensile stress below the level needed for spontaneous cracking lowers the fatigue limit of a substrate. Tensile stress can in several cases be reduced to safe values by fairly minor changes in microstructure and plating conditions, insufficient to upset other desirable properties. Saccharin is an addition agent for reducing stress in nickel; additions of ammonium chloride reduce stress in tin–nickel alloy; and small changes in bath temperature and  $\text{CrO}_3\text{:H}_2\text{SO}_4$  ratio reduce stress in chromium.

The effects of tensile stress in the various layers of nickel plus chromium coatings are complex, and internal stress in both chromium and nickel (post-nickel strike or PNS) layers can be harnessed to produce beneficial cracking ('microcracking')<sup>117–120</sup>.

#### 4.07.7.6 Ductility, Hardness, Wear, Strength

The mechanical properties reflect very closely the structures of electrodeposits. The softest, most ductile, weakest form of a particular metal is that with a large crystal size, deposited with minimum polarization from baths, which have no addition agents. This is the type of deposit in which pseudomorphism is strongest. In terms of the accepted deposition mechanism, there is the least inhibition of adion mobility as the deposit grows, and least inhibition of those sites at which equilibrium growth would occur. This electrodeposit has properties the nearest to those for the annealed metal, but even so tends to be somewhat harder. Because of pseudomorphism the properties near the substrate interface may be greatly modified if the latter has a metastable structure, especially one

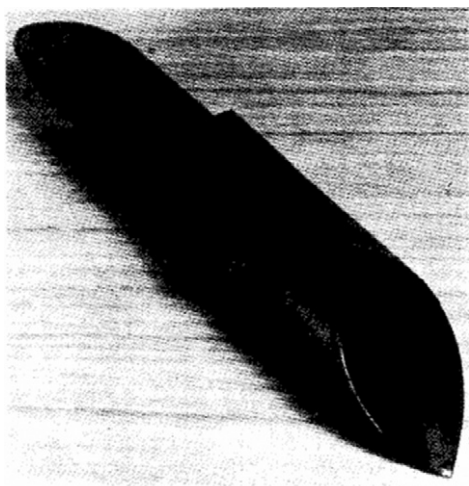


**Figure 12** An electrodeposit showing unusually high compressive stress. A 150 × 150 mm copper sheet was insulated with lacquer on one side and electroplated with Sn-35 Ni alloy. The high compressive stress has caused the sheet, originally flat, to coil in the manner shown, with the electrodeposit outside.

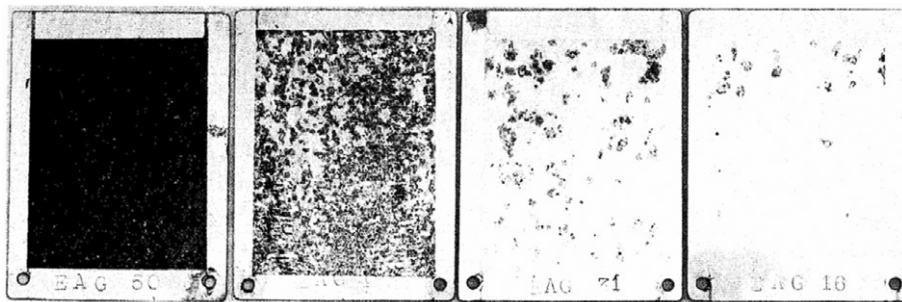


**Figure 13** Cracking in a cathodic coating due to a tensile stress that exceeds the cracking strength, leading to loss of protection. All 5  $\mu\text{m}$  coatings of Sn–Ni alloy on steel. From left to right, values of stress in  $\text{N mm}^{-2}$ : 134 tensile, 86 tensile, 57 tensile, and 127 compressive.

with very small grains produced by mechanical working. The deposit in turn becomes 'work hardened' by pseudomorphous growth.

When electrodeposition is inhibited, the metal becomes harder and less ductile, and tensile strength is increased. Metals deposited from acidic solutions of aquocations become harder when the pH is raised to near the value at which the hydroxide precipitates. Codeposited oxide acts as an addition agent, giving small-grained, hard deposits. Hard nickel is produced for engineering surfacing from high-pH baths. Many metals can be electrodeposited in extremely hard forms from inhibited baths, but they tend to become brittle, with high internal stress, so that the true tensile strength is hard to establish. Ductility necessarily falls as hardness rises, and coatings become more susceptible to damage by impact, reducing their protective value if they are cathodic to the substrate. Some applications of electroplating depend on the production of unusually hard and wear-resistant forms of corrosion-resistant metals. Thick coatings of chromium and nickel are applied to numerous steel parts to combine wear resistance with corrosion resistance. Thick or engineering chromium electrodeposits crack repeatedly during deposition, but the cracks are subsequently sealed and none should traverse the entire coating. Thick chromium coatings have practically no ductility, and because of their defective structure they have a low effective strength. They serve best on stiff substrates.

Gold coatings on separable electric contacts and slip rings make use of the high hardness possible with electrodeposition to resist wear. Rhodium is another metal which can be exceptionally hard. Thick coatings have a cracked-sealed structure similar to that of chromium.<sup>121-124</sup>

#### 4.07.7.7 Interdiffusion with the Substrate

A thin metal coating on a metal substrate is not a stable entity; greater stability would be attained if the coating were to diffuse evenly throughout the substrate. Fortunately, at ambient temperatures most of the usual combinations interdiffuse sufficiently slowly to present no practical problem. At high temperatures, however, many coatings diffuse quickly. Diffusion in a few systems at moderate temperatures causes corrosion problems. Difficulties can occur with tin, which, with its low melting point of 231 °C, is relatively 'hot' at room temperature. On copper and copper-alloy substrates, diffusion transforms the tin into the intermetallic phases  $\text{Cu}_6\text{Sn}_5$

and  $\text{Cu}_3\text{Sn}$ . At 100 °C, the transformation is accelerated, and 5 mm of tin may become wholly alloyed within a year. The alloy coating may pass as tin having a silvery color, but it is much harder and has a very stable passivity. One use of tin on copper is to facilitate easy joining by soldering, but the alloy has a high melting point and is not easily wet by solder. Thin 'tin' coatings on copper which have become wholly alloyed in storage are difficult to solder. Sometimes extremely thin coatings (0.25 mm) used purely for solderability become wholly alloyed in a few weeks. Parts should not be stored too long and very thin coatings are a false economy.

Tin will protect copper from corrosion by neutral water. Pure tin is anodic to copper, and protects discontinuities by sacrificial corrosion. Both intermetallic phases are strongly cathodic to copper and corrosion is stimulated at gaps in wholly alloyed coatings. An adequate thickness of tin is needed for long service, for example, 25–50 mm. Another diffusion problem occurs with tin-plated brass. Zinc passes very quickly to the tin surface, where under conditions of damp storage zinc corrosion products produce a film which greatly impairs solderability. An underplate of copper, or better still nickel, usually cures this trouble.

A similar problem, that is, diffusion of the substrate through the coating to corrode at the surface, arises with gold-plated copper. Many gold coatings are used to ensure a low electric contact in electrical connectors. Gold is preeminent because of the absence of stable-corrosion-product films under most service conditions, but it is expensive, so coatings are kept as thin as possible. Electronic devices may operate at fairly high temperatures (100–150 °C), and significant amounts of copper may diffuse through the coating to produce a film of oxide on the surface, nullifying the contact value of the gold. Nickel underplate mitigates this trouble (though increasing plating difficulties). To reduce costs, attempts have been made to dilute gold with cheaper metals, while retaining gold-like corrosion properties. Cadmium has been used as a diluent, but while quite high cadmium-golds are gold-like at 25 °C, at higher temperatures, cadmium gets oxidized at the surface. Pure gold is preferred for high temperature contacts.<sup>125,126</sup>

#### 4.07.7.8 Porosity

In the very earliest stages of electroplating, the substrate carries discontinuous areas of deposit growing around nuclei. Lateral growth causes the great



majority of growing edges to coalesce with sufficient perfection to be impervious to corrosive gases and liquids. On normal metallic substrates, a few edges do not grow together, and a gap remains in the coating. As the coating thickens, the gap is propagated as a channel through the coating, to form a pore. Under the conditions chosen for practical electroplating, pores diminish in cross section as deposition continues, and pore density (pores per unit area) falls as thickness increases. The corrosion which occurs when pores allow liquid and gaseous corrosive agents to reach the substrate varies in importance according to the relation between the corrosion potentials of deposit and substrate, the corrosive environment, and the function of the coating.

If the environment favors wet corrosion processes, relative polarity is the main consideration. If the coating is anodic, porosity is seldom of any serious consequence. The cathode is the very small area of substrate exposed at the base of the pore, and the restricted channel limits the diffusion of reactants and products. The large anode area provided by the coating reduces the bimetallic corrosion current density thereon. Two important examples of this type are zinc coatings on steel in cold waters or the atmosphere and tin coatings on steel on the inside (but not the outside) of a sealed, air-free can of wet food. In the first case, oxygen is the cathodic reactant; in the second it is hydrogen ions (or water). Where the coating is cathodic, porosity enables the exposed substrate to corrode. In most cases, this is detrimental; the exception is found in some multi-layer nickel plus chromium coatings where certain forms of porosity in the chromium layer are harnessed to divert the direction of corrosion to the overall benefit of coating life. In other cases, corrosion at pores causes trouble. In wet atmospheric corrosion, substrate corrosion product, if colored and insoluble, spoils decorative appearance. In immersed conditions or humid atmospheres, if the corrosion product is soluble, intense pore corrosion will perforate sheet metals. Here, a porous coating may accelerate corrosion when compared to the uncoated substrate.

Porosity causes little trouble when corrosion is restricted to dry processes (oxidation). Corrosion products block the pores and stifle the reaction.

There was much research into the causes of porosity in nickel deposits when it was thought to be the main cause of failure in nickel and chromium plates. Much was discounted as it became clear that nickel pitting at discontinuities in the chromium was the factor determining service life. Porosity remains

relevant to the corrosion resistance of simpler cathodic coatings, and especially for gold. The use of gold for contact surfacing since around 1950 has revived the importance of studies of porosity. Pores in gold coatings allow films of substrate corrosion product to contaminate the surface and to destroy the low contact resistance of the gold. Sulfides, which are one of the products of corrosion by service atmospheres, have a particularly high rate of spreading over gold in the solid state (**Figure 14**).

Pores originate on substrate areas known as precursors, which are of at least three types. Firstly, an obvious cause is an inclusion of foreign material which is a semiconductor or insulator – particles of oxide, sulfide, slag, polishing abrasive, etc. When electrodeposition starts, inclusions will not be nucleation sites, and they will impede the lateral growth and coalescence of crystals from neighboring nuclei. Secondly, substrates whose surface grain structure has been severely disturbed by cold working (abrasion, cold rolling, drawing, etc.) have precursors whose physical state (rather than chemical difference as in the first type) precludes coalescence of the electrodeposit. This is probably an effect of pseudomorphic growth. Relatively low-temperature annealing (as low as 210 °C for steel) greatly reduces the effect, and further cold work increases it again (**Figure 15**). The third type of precursor is a crevice in the substrate. If the depth is great relative to the width, the electric field is excluded and deposition does not occur within the crevice. Lateral growth is impeded once the edges from neighboring nuclei reach it in much the same way as with a nonconducting inclusion. A pore caused by any type of precursor in one

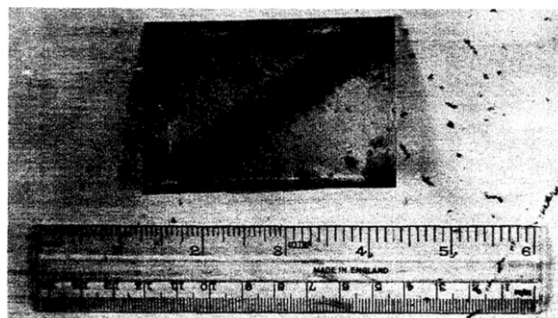


**Figure 14** Spread of silver sulphide from discontinuities in gold electrodeposits on silver substrates. The gold was deliberately scratched and the specimen exposed for 24 h to an atmosphere containing 10% SO<sub>2</sub>. Immediately after this the sulphide stain extended 0.2 mm. Five years later, the stain extends to about 13 mm, after storage in a normal indoor atmosphere.



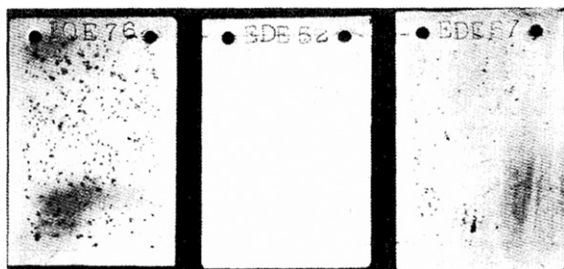


**Figure 15** Porosity caused by a cold-worked substrate. Left (EQE 76) cold-rolled steel as received; centre (EDE 52) steel bright-annealed in vacuum before plating, 2.5 h at 700 °C; right, annealed steel, further cold-rolled (0.914 mm to 0.864 mm) produces porosity again. No steel was removed from the surface; 5 mm tin-nickel electrodeposit.

electrodeposit becomes in turn a precursor for a second deposit plated over it. There may be other forms of precursor.

In a particular area of substrate, there will be a number of precursors, distributed over a range of sizes, and reflecting the nature, composition, and history of the metal. In principle, anything affecting the substrate surface will affect porosity in an electroplated coating.

As deposition continues, growth gradually diminishes the surface opening of a pore and, if continued to a sufficient thickness, closes it, leaving a sealed cavity filled with solution. Small precursors will generate pores which seal relatively early, large ones will require greater thicknesses. The total pore density, revealed by a test which renders pore sites visible, falls as thickness increases. The minimum thickness required to seal a precursor of fixed size will depend on the rate of narrowing of the surface opening, and as a growth process, this will reflect the plating conditions. Because of this, the density of pores still open at a fixed thickness is a function of all the plating conditions, that is, the composition of the plating bath, temperature, current density, agitation, and anything affecting deposit growth.

Postplating treatments affect pore density, either by closing pores which are still open or opening sealed ones. It has been asserted that mechanical polishing in general and flow-melting for tin are both processes which could seal pores and reduce porosity. It is also conceivable that polishing might cut-open sealed pores, and likewise under flow-melting conditions, the vaporization of solution trapped in sealed pores could disrupt the coating and recreate discontinuities. The author has come across no convincing demonstration of porosity reduction by either treatment, but has found experimental evidence for porosity increases (**Figure 16**).<sup>127–139</sup>



**Figure 16** Increase in porosity of an electrodeposit caused by mechanical polishing. Left, 7.5 mm unpolished coating; right, polished with lime finishing compound. The average thickness removed by abrasion was 0.1 mm.

#### 4.07.8 Plating from Ionic Liquids

At first, this concept seems to be obvious and indeed the name is not well chosen. It relates to essentially nonaqueous solutions which are conducting and ionic, a field that was formerly referred to as organic or nonaqueous plating. None of these titles are entirely satisfactory.

The need arises from several difficulties with conventional processes:

- The reactive base metals (e.g., Al, Mg, Ti) cannot be deposited from aqueous solutions.
- If the base metals can be deposited, inevitably the current efficiency is poor (e.g., Cr).
- If the substrate is steel, the inefficient production of hydrogen may be disastrous for its mechanical properties.

In the 1960s, the driving force lays with aluminum on the basis that aluminum-coated steel was an ideal combination for many corrosion needs; hot-dipped coatings were limited to thicknesses over  $\sim 20\ \mu\text{m}$ . A number of solvents based on alcohols, ethers, and ketones were used which gave poor results with major fire hazards; processes by Philips and Siemens had much publicity but no commercial success. Since 1990, alternative organic solvents based on low melting point ( $<100\ ^\circ\text{C}$ ) eutectic mixtures have been explored; the eutectic is formed from a metal complex salt such as borofluoride, phosphofluoride, or thicyanate and a methyl or ethyl imidazolinium, pyridinium, or quaternary ammonium (choline) salt. The requirement is that the mixture should be highly

conductive, have low viscosity, high metal solubility, and no propensity to absorb water.<sup>140,141</sup>

Research progress has been fairly rapid and all the common metals have been studied with especial concentration on Al, Cr, and Zn and its alloys. The possibility of electroless deposition has also been considered. No commercial operation has been reported yet, probably because while the cathode efficiencies are high, the practical current densities are still rather low: a report on an EU project *IONMET* has stated the challenges succinctly. However, the field must be considered promising for future development.<sup>140–143</sup>

#### 4.07.9 Recent Developments

Although the basic principles of electroplating remain unchanged, the extent of development and variety of application have widened substantially.<sup>144</sup> In this section, some notable developments will be cited.

The development of new solutions and processes continues unabated, driven, as ever, by commercial and proprietorial needs as well as pressure from pollution and effluent control demands and simply for the need to supersede some less-than-satisfactory solutions. Noncyanide solutions are continually being sought for metals such as gold, copper, cadmium, and zinc, but cyanide remains preeminent as the most effective and best understood complexant available and few competitors have been discovered. The other ecological *bête-noire* is hexavalent chromium, and several commercial bodies offer nontoxic trivalent chromium plating solutions, both aqueous- and organic-based, although only the former is believed to be industrially viable. The solutions are on the basis of chromic sulphate or chloride salts, a complexant such as hypophosphite, glycollate, thiocyanate, etc. and a depolarizing anode reactant which could include ammonium ions or a separated anode compartment. The cathode efficiency is still below 50% and only thin coatings can be reproducibly produced (10  $\mu\text{m}$  max.), but pollution difficulties are largely eliminated. This has proved to be a difficult area, but the number of successes is expected to increase.<sup>145–148</sup>

A separate problem is the establishment of a good process for electroplating aluminum which must necessarily be on the basis of a nonaqueous electrolyte. This field is a history of many discoveries, but few developed processes have been claimed, although recent work suggests that at least two good

possibilities exist which may make inroads in the electronics field rather than in the other important area of wide steel strip aluminizing.<sup>149,150</sup>

In his classic treatise, Brenner<sup>2</sup> reported that over 500 alloy electrodeposition systems had then been studied in depth – that number has now been substantially increased – yet barely 10–20 have any real degree of industrial exploitation. The list continues to grow and the present type of work on alloys can be divided into three classes:

1. The development of new alloys in new fields; for example the development of alloys of molybdenum and tungsten with iron, cobalt, or nickel for coating of dies and nozzles, or the development of palladium–nickel alloy as an alternative to gold for connectors.
2. The development of new alloys as a means of modifying existing electrodeposits; for example the production of hard gold alloy by codeposition of copper, cadmium, etc., to yield 23 or 18 carat alloys, or the use of zinc alloys for improved electrogalvanized coatings.
3. The development of new solutions for established alloys; for example, the replacement of fluoborate for lead–zinc brasses.

With industry proving to be so conservative about binary alloys, it is hardly surprising that ternary alloys receive little attention. Nevertheless, two ternary alloys at least have become commercially available: iron–chromium–nickel (so-called stainless steel) for both functional and domestic markets and an electronic connector and solderable alloy based on copper–zinc–tin.

The field of composite materials has been the major growth area of materials engineering in the last twenty years, based mainly on ceramic and polymer materials. While electroplated (and electroless) composites show more modest growth, this is attributable to the necessary limitation of metal matrices. Thus, the principle is to take a well established metal deposition process (gold, cobalt, copper, nickel, tin) and to induce codeposition of second-phase particles, thereby, enhancing coating properties such as hardness, wear, and oxidation resistance. The key to successful codeposition is having particles of appropriate size and density, typically 0.1–10  $\mu\text{m}$  size, suitably suspended in solution by a nonswirling agitation technique, that is, codeposition occurring by physical entrapment or electrophoretic attraction. Such particles include oxides (e.g.,  $\text{Al}_2\text{O}_3$ ,  $\text{TiO}_2$ ,  $\text{ZrO}_2$ , etc.) or refractory hard compounds (e.g.,  $\text{Cr}_7\text{C}_3$ , WC,  $\text{Mo}_2\text{C}$ , etc.), abrasives such as diamond, lubricants such as  $\text{MoS}_2$  or graphite, and low-friction material

such as PTFE. A substantial literature exists, relating to both process and product characteristics and reference should be made to two notable reviews.<sup>151,152</sup> Several obvious applications have, to a large extent, been achieved; for example, second-phase hardening by  $\text{Al}_2\text{O}_3$  of gold without serious loss of electrical conductivity, high temperature erosion or wear resistance of nickel, nickel–cobalt gas turbine, or jet engine alloys improved by using carbide incorporation, and improved surface lubrication of nickel by incorporation of PTFE particles.

The use of current or voltage pulsing during electroplating has long been known to have a beneficial effect on the deposition process rate and on the deposit itself in terms of grain-size variation, internal stress, leveling, etc. Periodic reverse techniques (cycle time of 10–102 s) are widely employed in electrowinning and electrefining operations while pulse plating (cycle time of  $10^{-3}$  to 1 s), which requires more sophisticated electronics, is now of considerable interest for metal finishing. The basic theory has been discussed by Ibl<sup>153</sup> who has defined the parameters involved. Claims for improved brightening, leveling and throwing power are of especial interest in electronics but are not yet fully substantiated in many instances.<sup>154</sup> The cooperation of industrial and engineering designers with the metal finishers, who are frequently required to perform the near-impossible as a consequence of poor communication, is notoriously bad, largely as a consequence of the nature of subcontract industrial relationships. To meet this need, an important new standard – BS 4479 – has been issued; although it is ostensibly a revision of the old standard, it is in reality a new standard written essentially as a code of practice. Invaluable advice is given to finishers and designers alike: the challenge now is to have it widely read and appreciated!

Increasing awareness of the cost-effectiveness of electroplating processes has led to critical appraisals being made of cell design, not only to improve the product through improved efficiency and economics of the process itself, but also typically through the costs of electricity. Thus the use of more conductive solutions, combined with minimization of the anode–cathode spacing can yield a 40% saving in electrical power. However, not all of this saving is necessarily desirable if chemical costs, thereby, increase and the peripheral cost of solution heating has also to be increased. Similarly, improved agitation and filtration may also be considered for optimization studies. This ‘chemical engineering’ approach has found increasing value,<sup>155–159</sup> not least in the development of new types

of plating cell specifically for metal recovery from trade effluent, dragouts, and rinses.<sup>160–162</sup> In fact, the number of new designs far outnumbers the number of optimizing and independent assessment studies so that it is not possible to name a ‘best-buy,’ and time is needed for commercial realities to eventually declare a winner, albeit not on entirely objective terms.

The largest-scale electroplating activities have always been carried out by the steel industry in an atmosphere largely divorced from traditional metal finishing. Upwards of 20% of all steel produced may be coated, the products of relevance to this chapter being tinplate, its alternative for packaging ‘tin-free steel,’ and zinc electrogalvanized steel in the form of sheet, strip, and wire. During the last twenty years, little advance has been made in the electroplating stage of tinplate production, the electrolytes and additives have changed little, and the plant design remains essentially the same – marked changes have occurred in other aspects of tinplate production, however. The alternative ‘tin-free steel’ or TFS, has settled into a well established sector of the market, largely for lacquered beer and beverage cans and noncritical container applications such as oil, polish, some paints, etc. Its invention is attributed to Japan in the period 1958–1965, and it has been widely exploited. The technology is on the basis of that of tinplate, as a fast cathodic process (1–20 s) in a chromic acid-based solution yielding a coating (<0.1 mm) consisting of chromium metal and chromium oxide,  $\text{Cr}_2\text{O}_3$ .<sup>163,164</sup> Its virtue is cost-effectiveness for every specific application, and as such, it has replaced tinplate for 10–40% of the market, depending upon the country concerned.

By contrast, the zinc coating product area is seeing rapid developments after a relatively static period when hot-dipped and electrogalvanized products occupied well defined niches for thick (20–150  $\mu\text{m}$ ) and thin (5–20  $\mu\text{m}$ ) coatings, respectively. The driving force can be found in the automotive industry which is looking towards car bodies having 5–10-year warranties for which paint and phosphating treatments on steel sheet are inadequate. Two separate types of coated product are emerging. First, electrogalvanizing combined with a modified TFS process giving a highly passivated zinc coating: this is probably the cheapest and easiest option.<sup>165</sup> Second, alloyed zinc electrogalvanizing to give improved sacrificial corrosion performance whilst remaining relatively thin (<15  $\mu\text{m}$ ), a requirement imposed by the body-forming processes. To this end, the zinc alloys favored are those with nickel, iron, manganese, or tin at 0.5–10% levels.<sup>166</sup> It is too early to predict which alloy will dominate the field.

**References**

- Blum, W.; Hogaboom, G. B. *Principles of Electroplating and Electroforming*; McGraw-Hill: New York, 1949.
- Brenner, A. *The Electrodeposition of Alloys*; Academic Press: New York, 1963.
- Dennis, J. K.; Such, T. E. *Nickel and Chromium Plating*; Newnes-Butterworths: London, 1972.
- Graham, A. K.; Pinkerton, H. L. Eds. *Electroplating Engineering Handbook*; Reinhold: New York, 1956.
- Lowenheim, F. A. Ed. *Modern Electroplating*; Wiley: New York, 1974.
- Raub, E.; Müller, K. *Fundamentals of Metal Deposition*; Elsevier: Amsterdam, 1967.
- Vagramyan, A. T.; Soloveva, Z. A. *Technology of Electrodeposition*; Robert Draper: Teddington, 1961.
- Barclay, W. R. J. *Electrodepositors' Tech. Soc.* **1937**, 12, 169.
- Brugnatelli, L. *Ann. Chim. (Pavia)*. **1800**, 18, 152. (Silver).
- Dubpernell, G. *Plating* **1960**, 47, 35. (History of chromium plating).
- Dubpernell, G. *Plating* **1959**, 46, 599. (History of nickel plating).
- Durose, A. H. *Plating* **1970**, 57, 793. (USA developments).
- Elkington, G. R.; Elkington, H. U.K. Patent 8 447, March 1840.
- Passal, F. *Plating* **1959**, 46, 629. (Copper).
- Smee, A. *Elements of Electrometallurgy*, 2nd ed.; Longmans Green: London, 1843.
- Wormwell, R. *Electricity in the Service of Man*; Cassell: London, 1897.
- Edwards, J.; Swanson, C. J. J. *Electrodepositors' Tech. Soc.* **1953**, 29, 290.
- Graham, A. K. *Trans. Inst. Met. Fin.* **1954**, 31, 259.
- Meyer, W. R. *Trans. Inst. Met. Fin.* **1954**, 31, 290.
- Moreley, E. *Trans. Inst. Met. Fin.* **1956**, 33, 102.
- Westman, A. E. R.; Mohrnhelm, F. A. *Plating* **1955**, 42, 154, 281, 417.
- Beacom, S. E. *Plating* **1969**, 56, 129.
- Hepfer, I. C.; Hampel, K. R.; Vollmer, T. L.; Boehm, D. R. *Plating* **1971**, 58, 333.
- Jostan, J. L.; Bogenschütz, A. F. *Plating* **1969**, 56, 399.
- Logi, G. R.; Rantell, A. *Trans. Inst. Met. Fin.* **1968**, 46, 91.
- Murphy, N. F.; Swansey, E. F. *Plating* **1971**, 58, 583.
- Perrins, L. E. *Trans. Inst. Met. Fin.* **1972**, 50, 38.
- Prince, D. E. *Plating* **1971**, 58, 588.
- Rantell, A. *Trans. Inst. Met. Fin.* **1969**, 47, 197.
- Saubestre, E. B. *Trans. Inst., Met. Fin.* **1969**, 47, 228.
- Saubestre, E. B.; Khara, R. P. *Plating* **1971**, 58, 464.
- Woldt, G. *Trans. Inst. Met. Fin.* **1969**, 47, 236.
- Moore, A. J. W. J. *Electrodepositors' Tech. Soc.* **1952**, 28, 117.
- Pinner, W. L. *Proc. Amer. Electroplaters' Soc.* **1953**, 40, 83.
- Raub, E.; Mietka, M.; Beeskow, H. *Metallüberfläche* **1959**, 13, B153.
- Samuels, L. E. *Electroplat. Met. Fin.* **1959**, 11, 130.
- Samuels, L. E. *J. Inst. Met.* **1956**, 85, 177.
- Samuels, L. E. *Plating* **1961**, 48, 46.
- Research Report No. 38, American Electroplaters' Society, 1958.
- Research Report No. 39, American Electroplaters' Society, 1959.
- Fleischmann, M.; Thirsk, H. R. In *Advances in Electrochemistry and Electrochemical Engineering*; Delahay, P., Tobias, C. W., Eds.; Interscience: New York, 1963; Vol. 3, ch. 3.
- Vetter, K. J. *Electrochemical Kinetics*, English edn.; Academic Press: New York, 1967.
- Bockris, J. O. M.; Razumney, G. A. *Fundamental Aspects of Electrocrystallisation*; Plenum Press, 1967.
- Eisenberg, D.; Kauzmann, W. *The Structure and Properties of Water*; Oxford University Press, 1969.
- Lyons, E. H. In *The Chemistry of Co-ordination Compounds*; Bailar, J. C., Ed.; Reinhold: New York, 1956.
- Edwards, J. *Trans. Inst. Met. Fin.* **1964**, 41, 169.
- Kendrick, R. J. *Plating* **1961**, 48, 1099.
- Saubestre, E. B. *Plating* **1958**, 45, 927.
- Saubestre, E. B. *Plating* **1958**, 45, 1219.
- Hardisty, D. W. *Plating* **1969**, 56, 705.
- Knapp, B. B. *Plating* **1971**, 58, 1187.
- Gabe, D. R. *Met. Fin. J.* **1971**, 7(11), 276–282.
- Gabe, D. R. In *Oxides and Oxide Films*; Vijn, A. K., Ed.; Dekker: New York, 1981; Vol. 6, pp 147–250.
- Gabe, D. R.; Cobley, A. *Trans. IMF.* **2002**, 80, B13–B16.
- Gabe, D. R.; Cobley, A. J. *Circuit World* **2006**, 32(3), 3–10.
- Bailey, G. L. J. *J. Electrodepositors' Tech. Soc.* **1951**, 27, 233.
- Beyer, S. J. *Plating* **1969**, 56, 257.
- Longkind, J. C. *Trans. Inst. Met. Fin.* **1967**, 45, 155.
- Vandenberg, R. V. *Trans. Inst. Met. Fin.* **1967**, 45, 161.
- West, E. G. J. *Electrodepositors' Tech. Soc.* **1946**, 21, 211.
- Wyszynski, A. E. *Trans. Inst. Met. Fin.* **1967**, 45, 147.
- Cobley, A. J.; Gabe, D. R. *Circuit World* **2001**, 27(3), 19–25.
- Gabe, D. R. *Trans. IMF* **2003**, 81, 7–12.
- Gabe, D. R. *Trans. IMF* **2006**, 84, 67–78.
- Puippe, J. Cl.; Leaman, F. *Theory and Practice of Pulse Plating*; Amer. Electropl. Surf. Fin.: Orlando, FL, 1986.
- Brenner, A.; Zentner, V.; Jennings, C. W. *Plating* **1952**, 39, 865.
- Clarke, M.; Chakrabarty, A. M. *Trans. Inst. Met. Fin.* **1970**, 48, 124.
- Fischer, H. *Elektrolytische Abscheidung und Elektrokristallisation von Metallen*; Springer-Verlag: Berlin, 1954.
- Weil, R. *Met. Fin.* **1955**, 53(11), 60. 53(12), 60.
- Wilman, H. *Trans. Inst. Met. Fin.* **1955**, 32, 281.
- Avila, A. J.; Brown, M. J. *Plating* **1970**, 57, 1105.
- Baeyens, P. A. *Trans. Inst. Met. Fin.* **1954**, 31, 429.
- Beckmann, M. E.; Maass-Craefe, F. *Metallüberfläche*. **1951**, 5, A161.
- Crossley, J. A.; Kendrick, R. J.; Mitchell, W. I. *Trans. Inst. Met. Fin.* **1967**, 45, 59.
- Davies, G. R. *Trans. Inst. Met. Fin.* **1973**, 51, 47.
- Hicklin, A.; Rothbaum, H. P. *Trans. Inst. Met. Fin.* **1957**, 34, 53. 199.
- Jernstedt, G. W. U.S. Patents 2,451,340 and 2,451,341 1948.
- Kendrick, R. J. *Trans. Inst. Met. Fin.* **1966**, 44, 78.
- Vagramyan, A. T.; Soloveva, Z. A. *Technology of Electrodeposition*; Robert Draper: Teddington, 1961. ch. 3.
- Wernlund, C. J. U.S. Patent 2,701,234 1955.
- Geissmann, W.; Carlson, R. *Proc. Am. Electroplaters' Soc.* **1952**, 39, 153.
- Nanis, L. *Plating* **1971**, 58, 805.
- Rasmerova, N. J. J. *Electrodepositors' Tech. Soc.*; **1937**, 13, paper 11.
- Clarke, M. *Chem. Indust.* **1970**, 329.
- Clarke, M. *Trans. Inst. Met. Fin.* **1968**, 46, 201.
- Clarke, M.; Ashburn, R. J. *Trans. Inst. Met. Fin.* **1969**, 47, 18.

87. Clarke, M.; Kieszkowski, M. *Trans. Inst. Met. Fin.* **1974**, 52, 79.
88. Clarke, M.; Zaya, P. *Trans. Inst. Met. Fin.* **1972**, 50, 54.
89. Soderberg, K. G. *Proc. Amer. Electroplaters' Soc.* **1936**, 24, 233.
90. Tallmadge, J. A.; Buffam, B. A. *J. Water Pollution Control Fed.* **1961**, 33, 817.
91. Tallmadge, J. A.; Mattson, R. A. *J. Water Pollution Control Fed.* **1962**, 34, 723.
92. Tallmadge, J. A.; Barbolini, R. R. *J. Water Pollution Control Fed.* **1966**, 38, 1461.
93. Walker, C. A.; Tallmadge, J. A. *Chem. Eng. Prog.* **1959**, 55(3), 73.
94. Hoare, W. E. *Tinplate Handbook*; Tin Research Institute: Greenford, various editions, 1950, 1956, 1965.
95. Jenkins, H. A. H.; Freeman, D. B. *Trans. Inst. Met. Fin.* **1964**, 42, 163.
96. Raub, E.; Müller, K. *Fundamentals of Metal Deposition*; Elsevier: Amsterdam, 1967. Section 5.6.
97. Thwaites, C. J. *The Flow Melting of Electrodeposited Tin Coatings*; Tin Research Institute: Greenford, 1956.
98. Agar, J. N.; Hoar, T. P. *Disc. Faraday Soc.* **1947**, 1, 162.
99. Clarke, M.; Bernie, J. A. *Electrochem. Acta.* **1967**, 12, 205.
100. Field, S. *Metal. Ind. (London)* **1934**, 33, 564.
101. Garmon, L. B.; Leidheiser, H. *Plating* **1961**, 48, 1003.
102. Leffler, E. B.; Leidheiser, H. *Plating* **1957**, 44, 388.
103. Wagner, C. J. *Electrochem. Soc.* **1951**, 98, 116.
104. Wagner, C. *Plating* **1961**, 48, 997.
105. Watson, S. A. *Trans. Inst. Met. Fin.* **1960**, 37, 28.
106. de Bruijn, W. J. *Electrodepositors' Tech. Soc.* **1951**, 27, 1.
107. Layton, D. N. *Design for Electroplating*; International Nickel Co.: London, BS4479, 1991.
108. Leadbeater, C. J. *J. Electrodepositors' Tech. Soc.* **1944**, 19, 35.
109. Tope, N. A. *J. Electrodepositors' Tech. Soc.* **1947**, 22, 29.
110. *Design for Metal Finishing*; Institute of Metal Finishing: London, 1960.
111. MacNaughtan, D. J.; Hothersall, A. W. *Trans. Faraday Soc.* **1935**, 31, 1168.
112. MacNaughtan, D. J.; Gardam, G. E.; Hammond, R. A. F. *Trans. Faraday Soc.* **1935**, 31, 729.
113. Mohrheim, A. F. *J. Electrochem. Soc.* **1970**, 117, 833.
114. O'Sullivan, J. B. *Trans. Faraday Soc.* **1930**, 26, 89.
115. Schlotter, M. *Trans. Faraday Soc.* **1935**, 31, 1177.
116. Dennis, J. K.; Such, T. E. *Nickel and Chromium Plating*; Butterworths: London, 1972.
117. Kendrick, R. J. *Trans. Inst. Met. Fin.* **1963**, 40, 19.
118. Walker, R. *Internal Stress in Electrodeposited Metal Coatings*; Industrial Newspapers: London, 1968.
119. Watson, S. A. *Trans. Inst. Met. Fin.* **1963**, 40, 41.
120. Weil, R. *Plating* **1970**, 57, 1231; **1971**, 58, 50; **1971**, 58, 137. Review and Bibliography.
121. Angus, H. C. *Trans. Inst. Met. Fin.* **1962**, 39, 20; **1965**, 43, 135; **1966**, 44, 41.
122. Antler, M. In *Proceedings of the 6th International Conference on Electr. Contact Phenomenon*, Chicago 1972.
123. Fairweather, A. *Proc. Inst. Elec. Eng.* **1953**, 100A, 174.
124. *Nickel Plating*; International Nickel Co.: London, 1963.
125. Britton, S. C.; Clarke, M. *Trans. Inst. Met. Fin.* **1959**, 36, 230.
126. Clarke, M.; Britton, S. C. *Trans. Inst. Met. Fin.* **1963**, 40, 205.
127. Berdick, M.; Lux, G. A. *Proc. Am. Electroplaters' Soc.* **1942**, 30, 19.
128. Britton, S. C.; Clarke, M. In *Proceedings of the 3rd European Corrosion Congress*, 1963.
129. Clarke, M. *Trans. Inst. Met. Fin.* **1973**, 51, 150.
130. Clarke, M.; Britton, S. C. *Trans. Inst. Met. Fin.* **1959**, 36, 58; **1960**, 37, 110, 230.
131. Clarke, M.; Chakrabarty, A. M. *Trans. Inst. Met. Fin.* **1970**, 48, 99; **1972**, 50, 11.
132. Clarke, M.; Leeds, J. *Trans. Inst. Met. Fin.* **1965**, 43, 50; **1968**, 46, 1, 81; **1969**, 47, 163.
133. Clarke, M.; Sansum, A. J. *Trans. Inst. Met. Fin.* **1972**, 50, 211.
134. Evans, U. R.; Shome, S. C. *J. Electrodepositors' Tech. Soc.* **1950**, 26, 137.
135. Frant, M. S. *J. Electrochem. Soc.* **1960**, 107, 1009.
136. Hothersall, A. W.; Hammond, R. A. F. *Trans. Electrochem. Soc.* **1938**, 73, 449.
137. Jones, M. H.; et al. *Proc. Am. Electroplaters' Soc.* **1957**, 44, 53; **1958**, 45, 45; **1959**, 46, 113.
138. Shome, S. C.; Evans, U. R. *J. Electrodepositors' Tech. Soc.* **1951**, 27, 129.
139. Clarke, M.; Subramanian, R. *Trans. Inst. Met. Fin.* **1974**, 52, 48.
140. Wasserscheid, P.; Walton, T. *Ionic Liquids in Synthesis*, 2nd ed.; Wiley-VCH: Weinheim, 2008.
141. Ohno, H. Ed. *Electrochemical Aspects of Ionic Liquids*; Wiley: New York, 2005.
142. Abbott, A. P.; Ryder, K. S.; König, U. *Trans. Inst. Met. Fin.* **2008**, 86, 106.
143. König, U.; Sessler, B. *Trans. Inst. Met. Fin.* **2008**, 86, 183.
144. Romankiw, L. T.; Turner, D. R. Eds. *Proceedings of the Electrochemical Society, USA*, **1987**; pp 87–17.
145. Crowther, J. C.; Renton, S. *Electropl. Met. Fin.* **1975**, 28(5), 6.
146. Lyde, D. M. *Prod. Fin. (London)* **1978**, 31(9), 14.
147. Hoare, J. P. *J. Electrochem. Soc.* **1979**, 126, 190.
148. Smart, D.; Such, T. E.; Wake, S. J. *Trans. Inst. Met. Fin.* **1983**, 63, 104.
149. Daene, T.; van der Berg, J.; Dijk, G. V. *Trans. Inst. Met. Fin.* **1985**, 63, 104.
150. Birkle, S.; Gehring, I.; Stoger, K.; Vries, H. *Metallurgy* **1982**, 36, 673.
151. Celis, J. P.; Roos, J. R. *Rev. Coat. Corros.* **1982**, 5, 1.
152. Simon, H.; Thoma, M. *Angewandte Oberflächentechnik für metallische Werkstoffe*; Carl Hanser: Munich, 1985.
153. Ibl, N. *Surf. Technol.* **1980**, 10, 81.
154. Puippe, J. C.; Leamon, F. *Theory and Practice of Pulse Plating*; Amer. Electropl. Soc.: Orlando, FL, 1986.
155. Newman, J. S. *Electrochemical Reactor Design*; Prentice-Hall: New Jersey, 1973.
156. Pickett, D. J. *Electrochemical Reactor Design*, 2nd ed.; Elsevier: Amsterdam, 1979.
157. Coeuret, F.; Storck, A. *Elements de genie electrochimique*; Lavoisier: Paris, 1984.
158. Snyder, D. D.; Landau, U.; Sard, R. In *Proceedings of the Electrochemical Society, Pennington, USA*, **1983**; pp 83–112.
159. White, R. E. Ed. *Electrochemical Cell Design*; Plenum Press: New York, 1984.
160. Gabe, D. R. *I. Chem. E. Symp. Ser.* **1983**, 77, 291.
161. Gabe, D. R.; Mäkanjuola, P. A. *I. Chem. E. Symp. Ser.* **1986**, 96, 221.
162. Marshall, R. J.; Walsh, F. C. *Surf. Technol.* **1985**, 24, 45.
163. Fukuda, N., et al. *J. Electrochem. Soc.* **1986**, 116, 398.
164. Yonezaki, S. *Sheet Metal Ind.* **1971**, 48(1), 25.
165. Memmi, M.; Bruno, R.; Palladino, M. *Mat. Perform.* **1983**, 22(2), 9.
166. Sard, R. *Plating Surf. Fin.* **1987**, 74(2), 30.



## 4.08 Sprayed Coatings

**K. T. Voisey**

Department of Mechanical, Materials and Manufacturing Engineering, Faculty of Engineering, University of Nottingham,  
University Park, Nottingham NG7 2RD, UK

© 2010 Elsevier B.V. All rights reserved.

<b>4.08.1</b>	<b>Coating Deposition Techniques</b>	2610
4.08.1.1	Nonthermal Spray Deposition Techniques	2610
4.08.1.1.1	Air spraying	2610
4.08.1.1.2	Electrostatic spray deposition	2611
<b>4.08.2</b>	<b>Thermal Spraying: An Overview</b>	2611
<b>4.08.3</b>	<b>Thermal Spraying: Variants</b>	2612
4.08.3.1	Flame Spraying	2612
4.08.3.1.1	Variants of flame spraying	2613
4.08.3.2	Wire Arc Spraying	2613
4.08.3.2.1	Variants of wire arc spraying	2613
4.08.3.3	Plasma Spraying	2614
4.08.3.3.1	Variants of plasma spraying	2614
4.08.3.4	High Velocity Oxy-Fuel Spraying	2615
4.08.3.5	Detonation Gun Spraying	2616
4.08.3.6	Cold Gas Dynamic Spraying	2616
4.08.3.7	Other Thermal Spray Techniques and Variants	2617
4.08.3.8	Liquid Feedstock	2617
4.08.3.8.1	Nanostructured coatings	2617
4.08.3.8.2	Laser-hybrid techniques	2617
4.08.3.9	Thermal Spraying: Periphery Processes	2618
4.08.3.9.1	Preprocessing processes	2618
4.08.3.9.2	Postprocessing techniques	2618
<b>4.08.4</b>	<b>Corrosion Applications of Metallic Sprayed Coatings</b>	2618
<b>4.08.5</b>	<b>Corrosion Applications of Inorganic Sprayed Coatings</b>	2620
<b>References</b>		2620

### Abbreviations

**APS** Atmospheric plasma spraying  
**CAPS** Controlled atmosphere plasma spraying  
**CGDS** Cold gas dynamic spraying  
**D-Gun** Detonation gun  
**ESD** Electrostatic spray deposition  
**HPPS** High-pressure plasma spraying  
**HVAF** High-velocity air fuel  
**HVLP** High-volume low pressure  
**HVOF** High-velocity oxy-fuel  
**HVOLF** High-velocity oxy-liquid-fuel  
**HVSFS** High-velocity suspension flame spraying  
**IPS** Inert plasma spraying  
**LPPS** Low-pressure plasma spraying  
**PTA** Plasma-transferred arc  
**RF** Radio frequency  
**RFS** Reactive flame spraying

**SPS** Shrouded plasma spraying  
**TBC** Thermal barrier coating  
**VPS** Vacuum plasma spraying  
**YSZ** Yttria stabilized zirconia

### 4.08.1 Coating Deposition Techniques

#### 4.08.1.1 Nonthermal Spray Deposition Techniques

##### 4.08.1.1.1 Air spraying

Paints, including inorganic paints, may be deposited by a variety of spray guns. Air spraying has also been used to deposit conversion coatings.<sup>1</sup> Air spray guns are simple devices that operate in atmospheric conditions, though they may be housed in a spray booth to

contain fumes and paint spray. Air spray guns are based on venturis. A stream of high-velocity gas is passed through a tube connected to the paint reservoir. The high velocity of the gas lowers the pressure in the venturi and this draws paint from the reservoir and atomizes it. The paint droplets are then propelled toward the substrate by the gas flow. Paint spray guns can be gravity fed or pumped. The high-velocity gas stream is usually compressed air.

High-volume low-pressure (HVLP) spraying is an air spraying variant, which uses a lower-pressure gas supply. The advantage of HVLP is that the deposition efficiency is increased to ~65% compared with something in the region of 30% for standard air spraying. The deposition efficiency can be further improved by using low-volume low-pressure air spraying; however, the coverage rate is decreased.

#### **4.08.1.1.1 Variants of air spraying**

Airless spraying is achieved by using a high-pressure pump to force paint through a spray gun. The advantages of this technique are that uniform thick coats of paint are produced, reducing the number of times an area must be coated. The high pressure also increases the penetration of the paint into surface features such as crevices. Spin spraying is a hybrid process combining spray coating with spin coating.<sup>2</sup> Spray pyrolysis is another hybrid process; a liquid precursor is deposited by air spraying and the coated substrate is then heated to induce pyrolysis.<sup>3</sup>

#### **4.08.1.1.2 Electrostatic spray deposition**

In electrostatic spray deposition (ESD), the deposition efficiency is improved by the use of an applied potential difference between the spray nozzle and the substrate. A liquid feedstock is atomized and charged by being pumped through the nozzle. The electrostatic field between the nozzle and the substrate accelerates the charged droplets toward the substrate.<sup>4</sup> Functional ceramic thin films are one type of coating that has been produced using ESD.<sup>5</sup>

### **4.08.2 Thermal Spraying: An Overview**

The overall technology of thermal spraying is now a century old. A whole list of thermal spraying variants is now currently used in industry, with further developments constantly being made. Dedicated professional and academic societies such as the International Thermal Spray Association, the ASM Thermal Spray

Society, and Japan Thermal Spray Society actively disseminate research results and good practice. There is a high degree of research activity in the area: a brief search of the scientific literature shows that 967 thermal spray papers and patents were published in 2007, as against 624 in 2000, 442 in 1990, and 78 in 1980.

Despite the proliferation of thermal spray variants, the coatings produced in each case share many common features and would all be recognized as thermal spray coatings by Max Ulrich Schoop, the Swiss inventor of thermal spraying, who first established the technology around the beginning of the twentieth century.

In all thermal spray technologies, particles of the coating material are propelled toward the substrate. On impact, the particles deform and adhere to the substrate primarily by mechanical interlocking.

The differences between the various thermal spraying techniques are primarily in the details of how the particles are propelled toward the substrate. Different methods of propulsion result in the particles experiencing different temperatures and velocities while in flight between the spray gun and the substrate. Depending on the process used, particles arrive at the substrate in solid, molten, or partially molten form. Additional variations on the thermal spray theme are created by the form of the feedstock coating material: powder, wire, or molten metal; the use of additional processes to produce hybrid processes such as laser-assisted thermal spraying; the atmosphere in which the spraying is carried out: vacuum or atmospheric.

Thermal spray coatings have a distinctive lamellar microstructure due to the formation of the coating from individual deformed particles, frequently referred to as splats. Porosity is an important issue in thermal spray coatings. Insufficient particle deformation on impact can create intersplat pores. For particles which arrive partially or completely molten, solidification shrinkage can add to porosity. Oxides may also be present in thermally sprayed coatings, which is a particular issue for metallic corrosion-resistant coatings, as in-flight oxidation of particles can result in discontinuous and hence nonprotective oxides in the coating. Another characteristic of as-sprayed thermally sprayed coatings is the distinct substrate-coating interface. In metallic coatings on metallic substrates, this interface is frequently strengthened and simultaneously made more diffusive by a diffusion heat treatment.

Thermal spraying techniques which induce extensive melting, including plasma spraying, flame spraying, and arc spraying suffer from high residual

stresses. These limit the thickness of the coating that will remain adhered to the substrate.

### 4.08.3 Thermal Spraying: Variants

The following table gives an overview of the typical key features of the main thermal spraying variants. Further details of each process are given in the following text ([Table 1](#)).

#### 4.08.3.1 Flame Spraying

Flame spraying is the original thermal spraying process used by the first thermal sprayer, Max Ulrich Schoop. Approximately 100 years later, the technique is still in widespread use. Metals, alloys, ceramic,<sup>8</sup> and polymer coatings may all be formed by flame spraying.<sup>7</sup>

A flame spraying torch is relatively simple, consisting of a flame combined with a system that introduces the feedstock coaxially with the flame. A fuel gas–oxygen mixture is combusted to produce the flame: oxyacetylene is typically used. The feedstock material, which may be in the form of powder, wire, or rod, is continuously fed into the flame and melted. For wire and rod feedstock, the melted material is broken into discrete particles by jets of compressed air. This is not required when a powder feedstock is used. The molten particles are accelerated toward the substrate by the expanding gas flow from the

flame, additional acceleration coming from the compressed air jets if present.<sup>7</sup> Spray distances are typically 120–250 mm.<sup>6</sup>

The type of feedstock used can affect the properties of the final coating. The atomization of molten rod or wire tends to generate finer particles than are found in powder feedstock. The resultant coatings are generally found to be smoother and denser than those formed using powder. The increased smoothness simply results from the finer droplet, and hence splat, size. The effect on density is largely due to the greater degree of melting, which is achieved for rods and wires, as their positioning in the flame can be controlled more precisely than for powder feedstocks.<sup>7</sup>

In addition to atomizing the molten feedstock and providing some acceleration of the sprayed particles, compressed air jets can be used to modify the shape, and hence temperature and flow characteristics of the flame.<sup>7</sup>

The flame may also be controlled by modifying the fuel–oxygen ratio. The highest flame temperatures are achieved when a stoichiometric fuel–oxygen mixture is used. Excess fuel or oxygen will cool the flame simply due to the introduction of a noncombusting material. Fuel-rich mixture is used when spraying metallic coatings, which results in a reducing environment in the flame and hence minimizes in-flight oxidation.

Flame spraying is a low-cost thermal spraying technique. Interfacial bond strengths achievable by flame spraying are generally lower than those of

**Table 1** Characteristics of the different thermal spray techniques

<i>Spraying process</i>	<i>Materials that can be sprayed</i>	<i>Powder size (<math>\mu\text{m}</math>)</i>	<i>Particle velocities (<math>\text{m s}^{-1}</math>)</i>	<i>Deposition rates (<math>\text{m}^2 \text{h}^{-1}</math>)</i>	<i>Interfacial bond strength (MPa)</i>	<i>Coating porosity (%)</i>
Flame	Metals, alloys, ceramics, polymers (with specialist torches) <sup>6</sup>	5–100 <sup>6</sup>	50–100 <sup>7</sup>	1–23 <sup>6</sup>	30 (metals and alloys) <sup>6</sup>	10–20 <sup>6</sup>
Wire arc	Metals, alloys, cermets <sup>6</sup>	Wire size 1.6–5 mm <sup>6</sup>	50–150 <sup>6,7</sup>	50–1000 g min <sup>−16</sup>	10–70 <sup>6,7</sup>	10–20 <sup>6</sup>
Plasma	Metal, alloys, ceramics <sup>6</sup>	20–90 <sup>6</sup>	200–800 <sup>7</sup>		70 (metals and alloys) <sup>6</sup>	1–10 <sup>6,7</sup>
Vacuum/low pressure plasma	Metals, alloys	5–20 <sup>6</sup>	200–600 <sup>7</sup>		>80 <sup>6</sup>	1–10 <sup>6,7</sup>
Detonation gun	Carbide reinforced composites <sup>6</sup>	5–60 <sup>6</sup>	800 <sup>7</sup>		70–83 <sup>6</sup>	0.5–2 <sup>6</sup>
HVOF	Metals, alloys, cermets, ceramics	5–45 <sup>6</sup>	200–1000 <sup>7</sup>		68–90 <sup>6,7</sup>	1–5 <sup>6,7</sup>
Cold spray	Metals, alloys, cermets <sup>6</sup>	5–20 <sup>6</sup>	600 <sup>6</sup>		26–62 <sup>6</sup>	3–5 <sup>6</sup>

other thermal spraying variants.<sup>9</sup> Reproducibility issues are a concern for all thermal spraying methods, but have been reported as being a particular issue for flame-sprayed coatings.<sup>10</sup>

#### 4.08.3.1.1 Variants of flame spraying

High-velocity suspension flame spraying (HVSFS) is a recent development of flame spraying. The key advantage is that very fine powders can be sprayed. Fine powders are normally very difficult to thermally spray, since they do not flow easily. Forming a liquid suspension enables fine powders to be handled in a controlled manner. Once the suspension feedstock is injected into the flame, the liquid is evaporated or burnt off leaving the fine powder in the flame to be heated and accelerated as in any other thermal spray process. The technique is still at a very early stage and the process needs to be optimized; however, demonstration such as the deposition of  $\sim 50\text{-}\mu\text{m}$  thick  $\text{CaO-ZrO}_2\text{-SiO}_2$  indicates that this technique has great potential for corrosion applications.<sup>11</sup>

Reactive flame spraying (RFS) is another process that has been developed from flame spraying. RFS combines flame spraying with self-propagating high temperature synthesis to give a single process in which the feedstock material is both produced and deposited.<sup>12</sup> Clearly, this technique is suitable only for materials that can be formed by self-propagating high temperature synthesis:  $\text{TiC-Fe}$  cermet coatings<sup>12</sup> have been successfully formed by this method. The advantage is that the reaction products are fine scaled; the overall process is low in cost and the energy released by the exothermic reaction acts as an additional heat source.<sup>12</sup>

Flame spraying can be combined with an induction heating postprocessing step to improve corrosion performance by fusing the coating, thereby decreasing porosity and increasing the effectiveness of the coating as a barrier.<sup>13</sup> This has been demonstrated on nickel-based self-fluxing alloys used to protect furnace wall tubes in Taiwanese waste incineration plants.<sup>13</sup>

There are numerous corrosion protection applications for flame-sprayed zinc and aluminum.<sup>9</sup> Flame-sprayed zinc is generally used to protect structural steelwork, and aluminum is used in more demanding applications.<sup>9</sup> Flame-sprayed  $\text{Zn/15Al}$  can provide cathodic protection to steel substrates.<sup>14</sup>  $\text{SiO}_2\text{-Al}_2\text{O}_3\text{-Y}_2\text{O}_3$  glasses have been deposited by flame spraying as candidate corrosion-resistant coatings for engine applications.<sup>15</sup>

#### 4.08.3.2 Wire Arc Spraying

Wire arc spraying is also known as electric arc spraying or arc spraying. In this spraying process, the coating feedstock is a pair of metallic wires, between which an electric arc is struck. The arc melts the ends of the wires; the molten material is then atomized and accelerated toward the substrate by a jet of compressed air.<sup>9</sup> Materials that can be arc sprayed must be electrically conductive, and hence the technique is generally used for metals. Arc spraying is often used to deposit aluminum coatings for anticorrosion applications in the marine and petrochemical industries.<sup>9</sup>

The thermal efficiency of wire arc spraying is greater than that of other thermal spray processes, since the feedstock material is directly heated by the arc.<sup>7</sup> Heating occurs only at the ends of the wires where the arc forms. As soon as the atomized droplets of molten material start to be propelled toward the substrate, they start to cool.<sup>7</sup> Unlike other thermal spray processes, there is no in-flight heating in wire arc spraying, since the droplets are propelled by an air jet as opposed to any kind of flame. Relatively short spray distances of 50–170 mm are used to minimize the in-flight oxidation.<sup>6,7</sup>

Another consequence of the highly localized heating is that the heat input to the substrate is low, primarily because there is no hot gas or plasma jet directed at the substrate.<sup>7</sup> Hence, wire arc spraying can be used to form coatings on materials such as polymers that would not withstand the heat input from other thermal spray processes.<sup>7</sup>

The electric arc must be stable for the spraying process itself to be stable and proceed in a uniform manner.<sup>7</sup> This means that the positioning of the ends of the wires is very important; both the absolute position and feed rate must be accurately controlled in order to maintain a stable arc.<sup>7</sup> The straightness of the wires is therefore significantly more important in wire arc spraying than it is in other wire feedstock thermal spray methods. Wire arc spraying is well suited to high-rate deposition, and hence is used for coating large steel structures including bridges and storage tanks.<sup>7</sup>

##### 4.08.3.2.1 Variants of wire arc spraying

Shrouded arc spraying is a variant of wire arc spraying where an inert gas is used to isolate the sprayed droplets from the surrounding environment, thereby minimizing in-flight oxidation.

### 4.08.3.3 Plasma Spraying

Plasma spraying produces denser and more adherent coatings than does flame spraying.<sup>15</sup> The increased complexity of the spray gun, the power consumption, the requirements of water cooling, and regular electrode replacement as well as the cost of process gases all combine to make plasma spraying costlier than flame spraying.

In plasma spraying, a plasma torch is used to heat and accelerate the feedstock material. The plasma temperature is very high, in the region of 10000K. The flame is capable of melting any material, and consequently, plasma spraying is frequently used to deposit coatings of otherwise difficult-to-melt materials such as zirconia, which are hard to deposit using other thermal spray methods.

The plasma spray gun consists of a central cathode, around which the process gases flow to exit through the anode, which forms the nozzle at the end of the gun. The central cathode is made from thoriated tungsten, as it not only has a high melting point but is also a good thermionic emitter, meaning that it easily releases the electrons required to maintain the arc.<sup>7</sup> The addition of thoria enhances the arc initiation process. The anode is copper, chosen for its high thermal and electrical conductivity, and must be water cooled.

The plasma is generated by a high-voltage discharge between the cathode and the anode. This discharge ionizes the gas between the cathode and the anode, forming a conductive path, which allows an arc to form. The arc heats the gas to temperatures that may exceed 10000K. Due to the very high temperatures created, the gas ionizes to form a plasma. The plasma then expands through the nozzle of the gun, creating a plasma jet, which heats and accelerates any feedstock material injected into it.

A variety of gases may be used to form the plasma. Argon and helium have low enthalpies of ionization; hence it is relatively easy to form a plasma from these gases.<sup>7</sup> An additional benefit of argon is its high atomic mass, which helps to stabilize the arc.<sup>7,16</sup> Nitrogen and hydrogen may also be used, despite their larger enthalpies of ionization, since they improve heat transfer from the plasma to the coating particles.<sup>6</sup> Gas viscosity also needs to be considered: higher gas viscosity reduces the mixing of the plasma with the surrounding air.<sup>10,16</sup> This is advantageous as the hot core of the plasma jet is maintained over a longer distance, improving heat and momentum transfer. In the temperature range of interest, that is, 10000K and above,

argon and helium have high viscosities.<sup>16</sup> Taking these factors into consideration, the gases and gas mixtures used are typically argon, argon–helium, argon–hydrogen, argon–nitrogen, and nitrogen–hydrogen.<sup>6,7</sup> Three gas mixtures of argon–helium–hydrogen and argon–helium–nitrogen have also been used,<sup>7,10,17</sup> an argon–helium–hydrogen mixture being commercially available.<sup>6</sup>

Electrode erosion is an important issue in plasma spraying. A combination of high temperatures and the intense arc means that the electrodes are operating in extreme conditions and consequently need to be periodically replaced. The erosion of the anode is more severe than the erosion of the cathode, resulting in anodes being replaced two to five times more often than cathodes.<sup>7</sup> Electrode lifetimes depend on the operating conditions, but are typically in the range of tens to hundreds of hours.<sup>7</sup> The heat flux in the regions where the arc terminates at each electrode can be in the region of  $10^8 \text{ W m}^{-2}$ .<sup>7</sup> The resulting electrode deterioration can result in the failure of the spray gun and can lead to coating contamination by fragments of the electrodes.<sup>7</sup>

Electrode erosion is most severe when a single arc is struck consistently in the same place. Two approaches have been used to minimize electrode erosion: vortex stabilization and multielectrode guns. Vortex stabilization ensures that the anodic arc root is constantly moving over the anode surface. This is achieved by simply ensuring that the plasma-forming gases have a vortex flow.<sup>7</sup> An alternative is the use of multielectrode guns. Instead of having a single arc, these guns have multiple arcs, each carrying a fraction of the current, and thus decreasing the damaging heat flux at the arc root.<sup>10,18</sup>

#### 4.08.3.3.1 Variants of plasma spraying

The mixing of the plasma jet with surrounding air during air plasma spraying can result in in-flight oxidation of metallic particles.<sup>7</sup> This is generally undesirable, and therefore, several plasma spraying variants have been developed to ensure lower levels of oxidation.

Shrouded plasma spraying (SPS) uses an inert gas to surround the plasma jet in an effort to separate it from the surrounding atmosphere.<sup>7</sup> This can be achieved by simply flooding the area between the nozzle and the substrate with a blanket of inert gas, usually argon or nitrogen.<sup>7,19</sup> The disadvantage of this approach to shrouding is that large volumes of inert gas are used.<sup>7</sup> An alternative that results in a lower usage rate of inert gas is to surround the plasma jet by



a layer of inert gas.<sup>7</sup> These approaches are each achieved by attaching a gas flow device to the front of a plasma spray gun.<sup>7</sup> Both the processes have been shown to produce metallic coatings with significantly lower oxide levels than would be possible with non-SPS. CoNiCrAlY SPS coatings have been reported with 0.3% oxide content,<sup>20</sup> approximately a third to a half of the extent of oxidation expected from atmospheric plasma spraying (APS).<sup>7</sup>

SPS is the cheapest way of plasma spraying in an inert environment, but not the most effective. In order to provide greater separation of the plasma jet from atmospheric air, it is necessary to spray in an enclosed chamber. Such a chamber may be filled with an inert gas as is the case in inert plasma spraying (IPS), or evacuated as it is done in vacuum plasma spraying (VPS) or low-pressure plasma spraying (LPPS).<sup>6</sup> Using such processes essentially eliminates oxidation, oxygen levels of 1500 ppm and 700 ppm being reported for LPPS<sup>21</sup> and VPS<sup>22</sup> respectively.

Another controlled atmosphere variant is high-pressure plasma spraying (HPPS), which is carried out in a pressurized gas-filled chamber, with typical pressures of 100–350 kPa.<sup>23</sup> The higher gas pressures used in HPPS increase heat transfer to the sprayed particles.<sup>23,24</sup> Hence, HPPS is well suited to the spraying of higher melting point materials and is generally used for ceramics. Compared with APS, HPPS coatings have lower porosity levels, improved properties, and uniformity.<sup>23,25</sup> Lower levels of oxidation and contamination are additional advantages.<sup>25</sup>

For IPS, VPS, LPPS, and HPPS, there is a significant increase in equipment cost compared with air plasma spraying due to the requirement of an air-tight or pressure chamber.<sup>10</sup> However, once a plasma spray gun has been installed in an air-tight chamber, it is of course possible to use it in different ways. Controlled atmosphere plasma spraying (CAPS) is an umbrella term covering IPS, VPS, LPPS, and HPPS. CAPS systems are commercially available, which can operate in IPS, VPS, LPPS, and HPPS modes as well as APS.<sup>23,25</sup>

Another plasma spraying variant is radio frequency (RF) induction plasma spraying.<sup>26</sup> An induction coil surrounds the gun, through which the plasma gas and powder feedstock are injected axially.<sup>27</sup> RF torches have a large internal nozzle diameter, which results in relatively low plasma jet velocities, and hence, low particle velocities.<sup>7,27</sup> These are typically 20–50 m s<sup>-1</sup>, that is, an order of magnitude lower than is generally seen for other plasma spray processes.<sup>7,27</sup> This results in particles being in the hot plasma jet for a longer

time, typically ~20 ms compared with ~1 ms for other plasma spray processes,<sup>28</sup> resulting in an increased overall heat transfer.<sup>27</sup> The extensive melting produced by RF plasma spraying results in good spreading of the particles on impact and the production of nearly fully dense coatings.<sup>28</sup> The improved heat transfer also means that larger powder sizes can be used while retaining a high level of particle melting.<sup>27</sup> The key advantage of this is that larger, and hence generally cheaper, feedstock powder can be used.<sup>10,27</sup> Another important advantage of RF induction plasma spraying, particularly for metallic coatings, is the lower levels of oxidation resulting directly from the lower surface-to-volume ratio of larger feedstock powder.<sup>10</sup>

A further development is supersonic RF plasma spraying. In order to generate the higher particle velocities desirable for improved coating properties, supersonic nozzles have been fitted to RF plasma spray guns.<sup>27</sup> In these systems, melting occurs while the particles are at low velocity; they are then accelerated by gas expansion resulting in particle velocities of up to 600 m s<sup>-1</sup> comparable to other plasma spray techniques.<sup>7,27</sup> Another advantage of RF spraying is the absence of electrodes.<sup>28</sup> There is no danger of coating contamination by electrode erosion.<sup>7</sup> It is also possible to use reactive gases in RF, which is ruled out in other plasma spray methods, since contact with the hot electrodes would severely reduce electrode life.<sup>7,28,29</sup>

In plasma-transferred arc (PTA) spraying, an arc is initially generated between a central tungsten cathode and a water-cooled copper anode. The interaction of this arc with the gases flowing through the gun generates a plasma. So far, this is exactly the same as in normal plasma spraying. The difference in PTA is that the ionized gas that forms the plasma provides a conductive path and the arc transfers from the anode and instead strikes the substrate surface.<sup>30</sup> The resulting high heat flux at the substrate surface induces substrate melting. Therefore, on solidification, a metallurgical bond is formed between the coating and the substrate,<sup>30</sup> which is much stronger than the mechanical interlocking that is found in other sprayed coatings. Some dilution of the coating with the substrate is unavoidable, the dilution generally being 5–10%.<sup>31</sup> Since the workpiece becomes part of the electrical circuit, this technique is restricted to electrically conductive coatings and substrates.

#### 4.08.3.4 High Velocity Oxy-Fuel Spraying

The high-velocity oxy-fuel (HVOF) process and the closely related high-velocity air fuel (HVOF) process

both produce relatively dense and oxide-free coatings by accelerating feedstock powder to relatively high velocities in a relatively cool flame. This cool, fast approach ensures sufficient plastic deformation to produce an adherent coating. Due to the lower temperatures used, melting, and hence oxidation, is minimized. HVOF coatings typically have less than 1% porosity. WC-Co coatings are frequently deposited by HVOF; an additional advantage of the lower temperatures is that carbide decomposition is minimized.<sup>10</sup>

In HVOF spraying, powder feedstock is heated and accelerated by expanding combustion gases. Fuel gases are usually hydrogen or hydrocarbon gases like ethylene, propylene, propane, or acetylene,<sup>6,7</sup> though liquid fuels such as kerosene may also be used.<sup>7</sup> As for detonation gun (D-Gun) spraying, the HVOF gun is relatively simple, consisting of a combustion chamber linked to a barrel by a nozzle. Powder injection may be axial or radial.<sup>7</sup> HVOF spray guns require water cooling.<sup>6</sup> Spray distances used in HVOF tend to be a bit higher than those used in plasma spraying due to the enthalpy release in the flame, which may lead to excessive convective heating of the substrate.<sup>6</sup>

A key feature of HVOF spraying is the limited extent of melting. This makes it one of the few thermal spraying processes suitable for spraying nanostructured feedstock, since the feedstock microstructure is retained. The specific corrosion-related interest in forming nanostructured coatings is that the refined grain size may increase the density of fast diffusion paths, hence increasing the speed and effectiveness of passivation.<sup>32</sup> Ji *et al.*<sup>32</sup> have successfully created nanostructured HVOF FeAl-based coatings; however, the corrosion resistance was less than that of the bulk material. Current densities of  $10^{-2}$  A cm<sup>-2</sup> and  $10^{-4.4}$  A cm<sup>-2</sup> were measured in the passive region of potentiodynamic tests in 0.5 M H<sub>2</sub>SO<sub>4</sub> for the sprayed coating and bulk material respectively.<sup>32</sup>

The relatively low temperatures encountered in HVOF and HVOF spraying limit the materials that can be deposited by these methods, since some materials do not exhibit sufficient plasticity at the combustion temperatures, ~3300 and 2300 K, encountered in HVOF and HVOF flames respectively. This means that HVOF and HVOF spraying of high melting point brittle materials such as ceramics becomes difficult.<sup>33</sup> This has led to interest in more highly thermal-efficient guns, such as those with two chambers, which enable easier HVOF spraying of these otherwise problematic materials.<sup>33</sup>

HVOF is a variant of HVOF, which uses a liquid fuel, that is, kerosene. Using a liquid fuel produces

higher gas velocities, and hence higher particle velocities and a lower temperature.<sup>34</sup> This can result in lower oxide content for HVOF coatings compared with those made using HVOF.<sup>34</sup> A disadvantage of using a liquid fuel is the lower deposition efficiency, typically only two-thirds that of a gas-fuelled HVOF gun.<sup>7</sup>

Hasan *et al.*<sup>35</sup> have designed and demonstrated a multipowder feed variant of HVOF, which can create functionally graded materials by simply adjusting the flow rate of powder from each of two separate powder feeders to continuously control the composition of the coating deposited. The idea is that the resultant coating has a gradual change in composition with thickness, which decreases the overall residual stresses.<sup>35</sup>

#### 4.08.3.5 Detonation Gun Spraying

D-Gun spraying is a Union Carbide/Praxair technology that was initially available only as a service with research work appearing only from the mid 1990s onwards,<sup>10</sup> D-Gun WC-Co coatings being a popular research area.

D-Gun spraying can be considered a variant of HVOF spraying, sharing HVOF's advantages of high particle velocity and low temperatures. In D-Gun, spraying powder is injected into the gun along with a mixture of oxygen and fuel. A spark ignites the oxygen-fuel mixture, which explosively combusts. The powder in the combustion chamber is heated and accelerated by the expanding combustion gases, and is directed toward the substrate by the geometry of the gun barrel. This process is repeated at a frequency of 1–55 Hz with a nitrogen purge between each shot.<sup>6</sup>

#### 4.08.3.6 Cold Gas Dynamic Spraying

In thermal spraying, the feedstock is generally heated, commonly to a molten state, to ensure sufficient deformation, and hence bonding on impact. Cold-gas dynamic spraying (CGDS) takes a different approach; here, the emphasis is on increasing particle velocity while maintaining a low particle temperature. Deformation on impact is then solely due to the large momentum of the particles. There is a material-dependent critical velocity, dependent on both particle size and material yield strength, which must be exceeded for deposition to occur. The lack of any significant heating means that CGDS can be used to spray substrates, such as polymers, that would be thermally damaged by other higher heat input thermal spray processes.

Despite the name, there is some heating in CGDS. A carrier gas, typically nitrogen, or helium, or a mixture of one or both of these with air, is compressed and then heated.<sup>6</sup> Helium is more effective than nitrogen at transferring momentum to the injected powder; however, it is also more expensive. Powder is injected into the gas, which then passes through a converging–diverging de Laval nozzle that accelerates the gas to supersonic velocities.<sup>6</sup> The gas is heated, and hence there is some heating of the feedstock powder; however, this is insignificant compared with other thermal spray processes. The temperature of the powder remains well below the melting point<sup>6</sup> and particle temperatures of 500 K have been calculated for CGDS Cu.<sup>6,36</sup>

Although details of particle adhesion in the CGDS process are still under investigation, it can be said that particle melting is avoided and adhesion of particles requires plastic deformation on impact. Therefore, CGDS is suited only to materials that can undergo plastic deformation in the solid state. This rules out ceramics and makes CGDS best suited to ductile metals. CGDS has been successfully used to deposit aluminum,<sup>37</sup> copper,<sup>38</sup> titanium,<sup>39</sup> nickel,<sup>40</sup> nickel alloys<sup>40</sup> as well as some composite coatings such as aluminum with SiC and Al<sub>2</sub>O<sub>3</sub> inclusions,<sup>41</sup> and NiCr with Cr<sub>3</sub>C<sub>2</sub>.<sup>42</sup>

The key advantage of CGDS is the low thermal input, which results in low oxide levels and enables the spraying of substrates that would be thermally damaged by other thermal spray processes.

#### 4.08.3.7 Other Thermal Spray Techniques and Variants

Metallic glasses have good corrosion resistance; however, they are expensive to produce. There is, therefore, interest in producing metallic glass coatings. Iron-based metallic glass has been successfully deposited by gas tunnel plasma spraying.<sup>43</sup> This is a variant of plasma spraying where a vortex flow is used to produce a higher-temperature and higher-energy density plasma than is typical of other plasma spray processes.<sup>44</sup>

#### 4.08.3.8 Liquid Feedstock

Thermal spraying using a liquid feedstock is the current area of interest.<sup>11</sup> Liquid feedstock variants of plasma spraying and HVOF<sup>11,45</sup> have been reported. These including high velocity suspension flame spraying, see [Section 4.08.3.1.1](#). An important advantage of

using a liquid feedstock is that finer particles can be sprayed by spraying a liquid suspension,<sup>11</sup> for example, plasma spraying of submicron WC–Co powder.<sup>46</sup> This results in finer splats, and consequently, a denser microstructure<sup>11</sup>; fully dense Inconel 625 coatings have been reported formed by HVOF spraying of a suspension of fine particles of Inconel 625.<sup>47</sup> For metallic coatings a simple suspension of fine particles is used. There is a second form of liquid feedstock that may be used for ceramic coatings: a liquid containing precursors, referred to as solution precursor plasma spraying.<sup>45</sup>

##### 4.08.3.8.1 Nanostructured coatings

Reports of increased fracture toughness of nanostructured ceramic coatings have led to interest in this area.<sup>48</sup> For processes such as HVOF, where the feedstock powder is not fully melted, it is possible to obtain a nanostructured coating by using a nanostructured feedstock powder.<sup>48</sup> Other thermal spray variants suited for the generation of nanostructured coatings are suspension plasma spraying and solution precursor plasma spraying.<sup>49</sup>

##### 4.08.3.8.2 Laser-hybrid techniques

The various laser-thermal spray hybrid techniques use the additional heat input from a laser beam to enhance the extent of melting to produce a denser coating, thereby improving corrosion resistance, as ingress of corrosive species is inhibited.<sup>50–52</sup> Antou *et al.* showed that an *in situ* laser remelting technique could reduce the interconnectivity of the porosity present in APS YSZ coatings, thus improving the effectiveness of the coating as a barrier to ingress of foreign species.<sup>51</sup> Techniques that melt the entire coating also enhance coating adhesion, as the usual mechanically bonded interface is replaced by metallic bonding.<sup>52,53</sup> An additional advantage is the reduction of residual stresses. The laser treatment and thermal spraying may happen simultaneously<sup>52</sup>; they may alternate or the thermally sprayed coating may simply be laser melted some time after spraying.<sup>53</sup> Provided that suitable laser processing parameters are used to ensure crack-free coatings, laser remelting can significantly improve corrosion resistance.<sup>52</sup> One of the many examples is the use of a hybrid laser-flame spraying method to generate Metco 12C coatings with a superior corrosion resistance to similar HVOF coatings.<sup>52</sup>

An extreme of the hybrid spray techniques is surface alloying of a preplaced thermally sprayed coating, a method, which can be used to enhance corrosion

resistance.<sup>54</sup> Electron beam melting of a flame-sprayed Al coating has been used to enhance the corrosion resistance of the underlying Mg alloy substrate.<sup>54</sup>

#### **4.08.3.9 Thermal Spraying: Periphery Processes**

##### **4.08.3.9.1 Preprocessing processes**

Abrasive blasting is widely used to achieve suitable surface roughness and to activate the surface by removing any preexisting oxides.<sup>55</sup> Substrate preheating is less widely used and its effectiveness varies with the deposition method. It has been shown to enhance substrate wettability for flame spraying. A similar, though lesser, effect was seen for plasma spraying of Al on mild steel. In HVOF spraying, minimal melting occurs, and hence there is no wettability-linked effect of preheating; however, some increase in adhesion was noted, highlighting the different bonding mechanism in HVOF coating.<sup>55</sup>

##### **4.08.3.9.2 Postprocessing techniques**

Various posttreatments are frequently used with thermally sprayed coatings. These enable higher quality coatings to be produced than can be formed from simply optimizing spraying parameters.<sup>50</sup> The prime reason for this is a desire to eliminate the detrimental effect of porosity, particularly interconnected porosity. Organic sealants can be applied to seal the sprayed coating<sup>56,57</sup>; however, such sealants may have a relatively low maximum operating temperature.<sup>58</sup> Alternatively, corrosion resistance can be ensured by adding a corrosion-resistant layer between the substrate and coating. This technique is used when the outer coating has an additional function. Aluminum bond coats have been successfully used in this role in HVOF wear-resistant WC–Co coatings on Mg alloy substrates that otherwise corrode rapidly in salt spray tests.<sup>56</sup> MCrAlY bond coats are widely used in the same role in thermal barrier coatings. A further variant has been demonstrated by Ishikawa *et al.*,<sup>58</sup> who used a duplex wire flame-sprayed system consisting of an 80Ni–20Cr underlayer covered with a layer of aluminum. The outer aluminum layer then improved corrosion resistance by acting both as a sacrificial anode and essentially as a sealant.<sup>58</sup>

Laser remelting has successfully improved the salt spray resistance of plasma-sprayed Ni-coated WC coatings by densification on resolidification, reducing the porosity from an initial 6.67% to 0.76%.<sup>59</sup> The alternative process of vacuum annealing was also used on the same coatings, which also decreased the

porosity but was less effective, resulting in 2.24% porosity.<sup>59</sup> Induction heating is another remelting process that has successfully been used to seal porosity, and hence improve the effectiveness of thermally sprayed coatings as barriers to corrosive species.<sup>13</sup>

#### **4.08.4 Corrosion Applications of Metallic Sprayed Coatings**

Large scale steel structures such as bridges, girders, and ski lifts are commonly provided with corrosion protection by thermally sprayed coatings.<sup>6,7</sup> For such applications, zinc and aluminum, as well as their alloys, are widely used.<sup>7</sup> Coating thicknesses of 50–500  $\mu\text{m}$  are typical.<sup>7</sup> Thermally sprayed aluminum coatings are also used to protect a large number of steel marine structures, including components on off-shore oil rigs.<sup>7</sup> These coatings are generally deposited by arc spraying<sup>6</sup> or flame spraying.<sup>7</sup> Zinc is also used for some immersion applications such as components on dams.<sup>7</sup> Other uses of thermally sprayed aluminum include preventing corrosive chemicals from attacking storage containers.<sup>7</sup> For most of these applications, any porosity present, as is typical of thermal spray coatings, will not be a great problem, because both zinc and aluminum provide cathodic protection. Hence, the corrosion protection provided by these coatings is not lost by simple breaches in the coating.<sup>7</sup> However, if the coatings are to be used in immersed conditions or if there is any danger of aluminum–thermite sparking, a sealant is used.<sup>7</sup>

In the automotive industry, wire arc- or flame-sprayed aluminum coatings are used to protect various exhaust components from hot corrosion.<sup>7</sup> Wire arc-sprayed zinc has been used to provide corrosion protection for steel steering stop brackets.<sup>7</sup> There is a clear driving force for the increased use of light alloys, specifically aluminum and magnesium alloys in the automotive industry. In many potential automotive applications, coatings are required to improve both the wear and corrosion resistance of the underlying alloy. Magnesium alloys particularly need to be protected against corrosive environments. There is great scope for the use of thermally sprayed coatings, particularly APS and HVOF, in such applications.<sup>60</sup>

The relatively low melting point of aluminum, 660°C, restricts the use of these coatings to maximum service temperatures of  $\sim 550^\circ\text{C}$ .<sup>7</sup> MCrAlY coatings tend to be used for high temperature corrosion protection; such coatings would generally be deposited by plasma spraying or HVOF.<sup>61</sup>

The harsh operating environments encountered in gas turbines are withstood only with the aid of various coatings. MCrAlY alloys are widely used to provide high temperature corrosion resistance. These alloys are used both as overlay coatings on components such as stators and as the bond coat in thermal barrier coatings.<sup>7</sup> VPS and LPPS are the techniques most commonly used to deposit these coatings.<sup>6</sup> This minimizes the formation of noncontinuous, nonprotective oxides during coating deposition, which would decrease the corrosion protection offered by the coating.

Boilers require high temperature corrosion resistance in aggressive environments; these are frequently thermal sprayed to protect against temperature, abrasion, and corrosive elements from fuel.<sup>6,7</sup> Plasma spraying, wire arc spraying, and HVOF coatings of stainless steel,<sup>6</sup> nickel alloys, high-chromium alloys, and chromium–nickel alloys<sup>7</sup> have been used to extend the life of boiler components such as superheater tubes and waterwalls.

Very demanding corrosive conditions are encountered in the glass-making industry.<sup>7</sup> The only materials that can withstand extended contact with molten glass are the precious metals and their alloys.<sup>7</sup> Precious metal glass-making components are often coated with thermally sprayed ceramics in order to extend corrosion life.<sup>7</sup> Plasma-sprayed molybdenum or molybdenum alloys are used to protect a variety of glass-making components, including moulds and stirrers.<sup>7</sup>

Unsurprisingly, corrosion-resistant coatings are required in the chemical processing industry where aggressive chemicals are stored and piped.<sup>7</sup> APS nickel-based alloys, including Hastelloy C, Hastelloy B, and Inconel 600, have been successfully used to extend the service life of pressure vessels.<sup>7</sup> Plasma-sprayed niobium doped with palladium has been used to protect welds in aluminum alloy tanks used to contain nitric acid.<sup>7</sup> Various glass-lined chemical reactors have been repaired using APS tantalum.<sup>7</sup> HVOF spraying of a molybdenum coating on stainless steel components used in a high temperature sulfur and ammonia environment has proved to be a cost-effective alternative to component replacement.<sup>6,62</sup>

Applications of thermally sprayed corrosion resistance coating in the petrochemical industry include HVOF-sprayed tungsten carbide coatings used to increase wear as well as corrosion resistance of valves.<sup>7</sup> Such coatings are also used to protect the blades of cutting machines in the paper industry.<sup>7</sup> HVOF stainless steel coatings with high molybdenum contents are

used to provide corrosion resistance to dryer rolls used in tissue making.<sup>7</sup> APS NiCrSiB/CuSn/MoS<sub>2</sub> coatings have successfully increased the lifetime of steel hydraulic mine props by providing protection against corrosive attack by mine water.<sup>6,63</sup>

The formation of sacrificial anodes for cathodic protection systems is another corrosion-related application of thermal spraying.<sup>7</sup> Plasma spraying and arc spraying have been used to deposit zinc and titanium sacrificial anodes; flame spraying has also been used for zinc.<sup>7</sup> Whether or not a given coating will act as a sacrificial anode depends on the substrate material and the surrounding electrolyte as well as any impressed current.<sup>7</sup> Semiconducting ceramics can be used as sacrificial anodes in impressed current systems. These can also be made by thermal spraying.<sup>7</sup> Plasma-sprayed ferrite coatings have cathodically protected metals such as titanium, niobium, and tantalum when they have been used in oil or specific chemical environments.<sup>7</sup>

The general increasing acidity of printing inks as well as the tight tolerances required result in several applications of thermally sprayed coatings in the printing industry.<sup>7</sup> Engraver rolls are coated with APS ceramic, either TiO<sub>2</sub>–Al<sub>2</sub>O<sub>3</sub> or Cr<sub>2</sub>O<sub>3</sub>, which, as for TBCs, is deposited on top of a metallic bond.<sup>7</sup> The bond coats used for engraver rolls are made using APS.<sup>7</sup> In this application, it is interesting to note that the large size of the components is instrumental in the choice of thermal spray method, the rolls being far too large for any CAPS chamber.<sup>7</sup>

APS may also be used for the large rolls used in continuous annealing lines.<sup>6</sup> These rolls require coatings that provide both wear and corrosion resistance<sup>6</sup>: cermets such as Cr<sub>2</sub>C<sub>3</sub>/NiCr and MCrAlY/oxide deposited by APS, D-Gun, or HVOF spraying.<sup>6,64</sup>

The provision of alternative coatings to hard chrome is an important area in which thermal spraying can be applied.<sup>7,65</sup> HVOF WC–Co is widely used as a hard chrome replacement. Both the US air force and navy use HVOF WC–Co, which resulted from the work of the Hard Chrome Alternatives Team (HCAT) set up by the United States military, on landing gear components.<sup>7</sup> However, the dimensions of HVOF guns rule out HVOF spraying of some components, particularly inner diameters of landing gear and hydraulic components.<sup>66</sup> For such applications, plasma spraying may be used. The Sulzer Metco F300 gun has been demonstrated to be able to coat components with inner diameters of 1.6 in.<sup>66</sup> A standard spray gun is fitted with an extension to permit insertion into internal diameters. These tend to



be 12 or 24 in. long, and it is the length of the extension that limits the depth to which spraying can occur.<sup>66</sup> Both Praxair and Sulzer Metco produce guns specifically for inner-diameter spraying applications.<sup>66</sup> The rotation of the component around the gun ensures uniform coating deposition.<sup>66</sup>

In other applications, such as the coating of engine cylinders, a rotating gun is used. These are commercially available and include the SulzerMetco RotaPlasma<sup>®</sup>. From approximately 2000 onwards, Volkswagen has routinely used a 200- $\mu\text{m}$  thick air plasma-sprayed Fe–Mo coating on the cylinder walls of diesel and petrol engines. These coatings enhance both the tribological performance of the underlying aluminum alloy and corrosion resistance.<sup>67</sup>

#### 4.08.5 Corrosion Applications of Inorganic Sprayed Coatings

Thermal barrier coatings (TBCs) are perhaps the most widely known example of thermally sprayed inorganic corrosion-resistant coatings. TBCs consist of two layers. The inner layer is a metallic bond coat, which is frequently a VPS- or LPPS-deposited MCrAlY ( $M = \text{Co}, \text{Ni}, \text{or NiCo}$ ) coating.<sup>61</sup> A relatively recent innovation is the use of HVOF to deposit denser bond coats.<sup>61</sup> An important role of the bond coat is to enhance adhesion of the outer layer. For nonrotating components, APS zirconia is frequently used for the outer layer, with electron beam physical vapor deposition used to deposit the ceramic outer layer on rotating components. The main role of this outer ceramic layer, the top coat, is to form a thermal barrier, protecting the underlying component from the high temperatures of the hot gas path, and thus improving corrosion resistance. A  $\sim 250\text{ }\mu\text{m}$  top coat can reduce the surface temperature of the underlying component by 200K.<sup>68</sup> The thermally grown oxide that forms on the underlying MCrAlY bond coat in service is the main corrosion protection mechanism in TBCs.<sup>68</sup> TBCs are used on various components along the hot gas path, including combustors and nozzle guide vanes.

Among other corrosion uses of thermally sprayed ceramic coatings, APS  $\text{Al}_2\text{O}_3\text{--TiO}_2$  coatings have been used to protect blast furnace stove cooling pipes from carburization.<sup>6,69</sup>

Conversion coatings are widely used to enhance corrosion resistance. The chemical treatment of the material to be protected produces a surface layer of insoluble compounds, usually oxides, chromates, or phosphates.<sup>70</sup> This layer acts as a barrier between the

substrate and the corrosive environment.<sup>70</sup> Air spray is one method that has been used for the deposition of cerium oxide conversion coatings, which are chromate-free alternatives to chromate conversion coatings.<sup>1,71</sup>

There is a wide variety of commercially available zinc-pigmented paints and zinc-rich coatings. These typically consist of zinc in an organic binder; however, inorganic versions are available. The inorganic zinc-based coatings use a silicate binder in place of the epoxy binders used in the more established organic zinc-based coatings. Zinc silicate coatings can outperform zinc epoxy coatings.<sup>72</sup> As with the organic versions of such coatings, the inorganic zinc coatings can also be used in multilayer coating systems.<sup>72</sup>

#### References

1. Jones, P. S.; Yu, P.; Pinc, W. R.; O'Keefe, M. J.; Fahrenholtz, W. G.; O'Keefe, T. J. *Int. J. Appl. Ceram. Technol.* **2008**, *5*, 63–73.
2. Hai, T. H.; Van, H. T. B.; Phong, T. C.; Abe, M. *Physica B: Condens. Mater.* **2003**, *327*, 194–197.
3. Ibáñez, R. L.; Barrado, J. R. R.; Martín, F.; Brucker, F.; Leinen, D. *Surf. Coat. Technol.* **2004**, *188–189*, 675–683.
4. Huang, H.; Yao, X.; Wu, X.; Wang, M.; Zhang, L. *Microelectron. Eng.* **2003**, *66*, 688–694.
5. Chen, C. H.; Emond, M. H. J.; Kelder, E. M.; Meester, B.; Schoonman, J. J. *Aerosol. Sci.* **1998**, *30*, 959–967.
6. Pawlowski, L. *The Science and Engineering of Thermal Spray Coatings*; Wiley, 2008.
7. Davis, J. R. *Handbook of Thermal Spray Technology*; ASM International, 2004.
8. Lima, R. S.; Krugera, S. E.; Marplea, B. R. *Surf. Coat. Technol.* **2008**, *202*, 3643–3652.
9. Thermal Spray Coatings Protect Petro-Chemical Components from Corrosion. *International Thermal Spray & Surface Engineering*, 2008. 16–18.
10. Fauchais, P.; Vardelle, A.; Dussoubs, B. *The International Thermal Spray Conference*; ASM International: Singapore, 2001.
11. Bolelli, G.; Rauch, J.; Cannillo, V.; Killinger, A.; Lusvardi, L.; Gadow, R. *Mater. Lett.* **2008**, *62*, 2772–2775.
12. Liu, H. Y.; Huang, J. H.; Yin, C. F.; Zhang, J. G.; Lin, G. B. *Ceram. Int.* **2007**, *33*, 827–835.
13. Matsubara, Y.; Sochi, Y.; Tanabe, M.; Takeya, A. *J. Therm. Spray Technol.* **2007**, *16*, 195–201.
14. Panossian, Z.; Mariaca, L.; Morcillo, M.; Flores, S.; Rocha, J.; Peña, J. J.; Herrera, F.; Corvo, F.; Sanchez, M.; Rincon, O. T., et al. *Surf. Coat. Technol.* **2005**, *190*, 244–248.
15. Sainz, M. A.; Osendi, M. I.; Miranzo, P. *Surf. Coat. Technol.* **2008**, *202*, 1712–1717.
16. Aubreton, J.; Elchinger, M. F.; Fauchais, P.; Rat, V.; André, P. J. *Phys. D: Appl. Phys.* **2004**, *37*, 2232–2246.
17. Janisson, S.; Vardelle, A.; Coudert, J. F.; Meillot, E.; Pateyron, B.; Fauchais, P. J. *J. Therm. Spray Technol.* **1999**, *8*, 545–552.
18. Schein, J.; Zierhut, J.; Dzulko, M.; Forster, G.; Landes, K. D. *Contrib. Plasma Phys.* **2007**, *47*, 498–504.

19. Planche, M. P.; Liao, H.; Coddet, C. *Surf. Coat. Technol.* **2007**, *202*, 69–76.
20. Sakakibara, N.; Manabe, Y.; Hiromoto, Y.; Kobayashi, Y. *Sci. Technol. Weld. Joining* **2008**, *13*, 344–348.
21. Steffens, H. D.; Hohle, H. M.; Erturk, E. *Thin Solid Films* **1980**, *73*, 19–29.
22. Vasen, R.; Doring, J. E.; Dietrich, M.; Lehmann, H.; Stover, D. *International Gas Turbine Conference*, Tokyo, 2003.
23. Beauvais, S.; Guipont, V.; Borit, F.; Jeandin, M.; Español, M.; Khor, K. A.; Robisson, A.; Saenger, R. *International Thermal Spray Conference*; ASM International: Singapore, 2001.
24. Guipont, V.; Español, M.; Borit, F.; Llorca-Isern, N.; Jeandin, M.; Khor, K. A.; Cheang, P. *Mater. Sci. Eng. A* **2002**, *325*, 9–18.
25. Sarafoglou, C. I.; Pantelis, D. I.; Beavais, S.; Jeandin, M. *Surf. Coat. Technol.* **2007**, *202*, 155–161.
26. Boulos, M. I. *J. Therm. Spray Technol.* **1991**, *1*, 33–48.
27. Fauchais, P. *J. Phys. D: Appl. Phys.* **2004**, *37*, R86–R108.
28. Boulos, M. I. *J. Therm. Spray Technol.* **1992**, *1*, 33–48.
29. Fauchais, P.; Vardelle, A.; Denoirjean, A. *Surf. Coat. Technol.* **1997**, *97*, 66–78.
30. Deuis, R. L.; Yellup, J. M.; Subramanian, C. *Compos. Sci. Technol.* **1998**, *58*, 299–309.
31. d'Oliveira, A. S. C. M.; Vilar, R.; Feder, C. G. *Appl. Surf. Sci.* **2002**, *201*, 154–160.
32. Ji, G.; Elkedim, O.; Grosdidier, T. *Surf. Coat. Technol.* **2005**, *190*, 406–416.
33. Evdokimenko, Y. I.; Kisel, V. M.; Kadyrov, V. K.; Korol, A. A.; Podchernyaeva, I. A.; Panasyuk, A. D. *Powder Metall. Met. Ceram.* **2003**, *42*, 578–586.
34. Zhang, D.; Harris, S. J.; McCartney, D. G. *Mater. Sci. Eng. A* **2003**, *344*, 45–56.
35. Hasan, M.; Stokes, J.; Looney, L.; Hashmi, M. S. J. *Surf. Coat. Technol.* **2008**, *202*, 3215–3220.
36. Stoltzenhoff, T.; Voyer, J.; Kreye, H. *International Thermal Spraying Conference*; Essen, 2002.
37. Lee, H.; Shin, H.; Lee, S.; Ko, K. *Mater. Lett.* **2008**, *62*, 1579–1581.
38. Calla, E.; McCartney, D. G.; Shipway, P. H. In *International Thermal Spray Conference*, Osa: Japan, 2004.
39. Price, T. S.; Shipway, P. H.; McCartney, D. G. *J. Therm. Spray Technol.* **2006**, *15*, 507–512.
40. Raletz, F.; Vardelle, M.; Ducos, M. *International Thermal Spray Conference*, Osa: Japan, 2004.
41. Lee, H. Y.; Yu, Y. H.; Lee, Y. C.; Hong, Y. P.; Ko, K. H. *J. Therm. Spray Technol.* **2004**, 184–189.
42. Lima, R. S.; Karthikeyan, J.; Kayb, C. M.; Lindemann, J.; Berndt, C. C. *Thin Solid Films* **2002**, *416*, 129–135.
43. Kobayashi, A.; Yano, S.; Kimura, H.; Inoue, A. *Surf. Coat. Technol.* **2007**, *202*, 2513–2518.
44. Arata, Y.; Kobayashi, A. *J. Appl. Phys.* **1986**, *59*, 3038–3044.
45. Berghaus, J. O.; Legoux, J. G.; Moreau, C.; Tarasi, F.; Chraska, T. *J. Therm. Spray Technol.* **2008**, *17*, 91–104.
46. Berghaus, J. O.; Marple, B.; Moreau, C. *J. Therm. Spray Technol.* **2006**, *15*, 676–681.
47. Ma, X. Q.; Roth, J.; Gandy, D. W.; Frederick, G. J. *J. Therm. Spray Technol.* **2006**, *15*, 670–675.
48. Varis, T.; Knuuttli, J.; Turunen, E.; Lelvo, J.; Silvonen, J.; Oskala, M. *J. Therm. Spray Technol.* **2007**, *16*, 524–532.
49. Fauchais, P.; Rat, V.; Coudert, J. F.; Etchart-Salas, R.; Montavon, G. *Surf. Coat. Technol.* **2008**, *202*, 4309–4317.
50. Coddet, C. *Surf. Coat. Technol.* **2006**, *201*, 1969–1974.
51. Antou, G.; Montavon, G.; Hlawka, F.; Cornet, A.; Coddet, C.; Machi, F. *Surf. Coat. Technol.* **2004**, 180–181.
52. Suutala, J.; Tuominen, J.; Vuoristo, P. *Surf. Coat. Technol.* **2006**, *201*, 1981–1987.
53. Voisey, K. T.; Liu, Z.; Stott, F. H. *Surf. Coat. Technol.* **2006**, *201*, 637–648.
54. Ye, H.; Yan, Z. L. *5th International Conference on Surface Engineering*; Dalian Univ Technol: alian, China, 2007.
55. Paredes, R. S. C.; Amico, S. C.; d'Oliveira, A. S. C. M. *Surf. Coat. Technol.* **2006**, *200*, 3049–3055.
56. Parco, M.; Zhao, L.; Zwick, J.; Bobzin, K.; Lugscheider, E. *Surf. Coat. Technol.* **2006**, *201*, 3269–3274.
57. Mazraeh, M.; Hocking, M. G.; Sidky, P. S. *International Conference on Corrosion in Refinery Petrochemical and Power Generation Plants*; Venice, Italy.
58. Ishikawa, K.; Suzuki, T.; Tobe, S.; Kitamura, Y. *J. Therm. Spray Technol.* **2001**, *10*, 520–525.
59. Xie, G.; Lin, X.; Wang, K.; Mo, X.; Zhang, D.; Lin, P. *Corros. Sci.* **2007**, *49*, 662–671.
60. Friedrich, C.; Gadow, R.; Scherer, D. *Functional Ceramic and Metallurgical Coatings on Magnesium Components* The International Thermal Spray Conference; ASM International: Singapore, 2001.
61. Lima, C. R. C.; Guilemany, J. M. *Surf. Coat. Technol.* **2007**, *201*, 4694–4701.
62. Moskowitz, L. N. *The 1st Gorham's International Thermal Spray Coatings Conference*, Cambridge, MA, USA, 1992.
63. Matejka, D.; Berezovsky, M.; Palka, V.; Kolanciak, V.; Ivan, L. *1st Plasma Technik Symposium*, 1988.
64. Fukubayashi, H. H. *International Thermal Spray Conference*; Osaka, Japan, 2004.
65. Wasserman, C.; Boecking, R.; Gustafsson, S. *Replacement for Hard Chrome Plating in Printing Machinery*; International Thermal Spray Conference; ASM International: Singapore, 2001.
66. Legg, K. *Replacement of Internal Diameter Hard Chrome with Plasma Spray Coatings at NADEP Jacksonville – Implementation Assessment*; Rowan Technology Group: Libertyville, IL, 2004.
67. Lampe, T.; Eisenberg, S.; Cabeo, E. R. *Surf. Coat. Technol.* **2003**, 174–5; 1–7.
68. Padture, N. P.; Gell, M.; Jordan, E. H. *Science* **2002**, *296*, 280–284.
69. Hoffman, J. W. *International Thermal Spray Conference*; The Hague, The Netherlands, 1980.
70. Gray, J. E.; Luan, B. *J. Alloys Compd.* **2002**, *336*, 88–113.
71. Johnson, B. Y.; Edington, J.; Williams, A.; O'Keefe, M. J. *Mater. Charact.* **2005**, *54*, 41–48.
72. Keijman, J. M. *PCE '99 Conference*, Brighton, UK, 1999.

## 4.09 Laser Applied Coatings

**Z. Liu**

Corrosion and Protection Centre, School of Materials, The University of Manchester, Oxford Road, Manchester M13 9PL, UK

© 2010 Elsevier B.V. All rights reserved.

4.09.1	<b>Lasers and Laser Beam Interactions with Materials</b>	2623
4.09.2	<b>Solidification Microstructures</b>	2623
4.09.3	<b>Laser Applied Coatings</b>	2624
4.09.3.1	Laser Cladding	2624
4.09.3.2	Laser Surface Melting	2626
4.09.3.3	Laser-Assisted Thermal Spray	2627
4.09.3.4	Laser Melt/Particle Injection	2628
4.09.3.5	Pulsed Laser Deposition	2628
4.09.3.6	Laser Chemical Vapor Deposition	2629
4.09.3.7	Laser Surface Alloying	2630
4.09.4	<b>Advantages and Limitations of Laser Applied Coatings</b>	2633
References		2634

### Glossary

**Laser-assisted thermal spray** Laser-assisted thermal spraying is a one-step coating method, in which a high-power laser is combined with thermal spraying to create denser and more adherent coatings, with a metallurgical bond between the coating and the base material, than achieved by normal thermal spraying processes.

**Laser chemical vapor deposition (LCVD)** Laser chemical vapor deposition is a technique to deposit thin to moderate films by a chemical reaction activated by a laser beam inside a gas chamber via either a pyrolytic or a photolytic effect.

**Laser cladding (LC)** Laser cladding is a process for fusing a powdered/wire/sheet material by using a laser on a substrate with minimum dilution.

**Laser melt/particle injection (LMI)** Laser melt/particle injection is a process for generating a metal matrix composite on a substrate by the injection of ceramic/higher melting point particles into a laser-induced melt pool.

**Laser surface alloying (LSA)** Laser surface alloying is a process that utilizes a laser to melt a metal coating and a portion of the underlying substrate to form a surface layer that is different from the coating and the substrate.

**Laser surface melting (LSM)** Laser surface melting is a process in which a thin layer of substrate surface is melted by a high-power laser beam and followed by rapid solidification to alter surface microstructures.

**Pulsed laser deposition (PLD)** Pulsed laser deposition is a thin-film deposition technique in which the target material is ablated by a high-power pulsed laser beam inside a vacuum or an inert-gas chamber and then deposited as a thin film on a substrate.

### Abbreviations

**CVD** Chemical vapor deposition  
**HPDL** High-power diode laser  
**HVOF** High-velocity oxy-fuel  
**LC** Laser cladding  
**LCVD** Laser chemical vapor deposition  
**LGN** Laser gas nitriding  
**LMI** Laser melt/particle injection  
**LSA** Laser surface melting  
**MMC** Metal matrix composite  
**Nd:YAG** Neodymium-doped yttrium aluminium garnet  
**PLD** Pulsed laser deposition  
**PVD** Physical vapor deposition  
**TBC** Thermal barrier coating  
**YSZ** Ytria stabilised zirconia

**Symbols****G** Thermal gradient ( $\text{K m}^{-1}$ )**R** Solidification rate ( $\text{m s}^{-1}$ )**4.09.1 Lasers and Laser Beam Interactions with Materials**

LASER is an acronym for light amplification by stimulated emission of radiation. Material processing with lasers takes advantage of virtually all the characteristics of the laser beam, including monochromaticity, coherency, high radiance, low beam divergence, and the ability to focus on a small spot.

When a laser beam strikes an opaque surface, a part of the radiation is reflected and the remaining part is absorbed in the substrate of the material. The absorption process depends on beam wavelength, temperature, and nature of the surface. Shorter wavelengths, elevated temperatures, and rougher surfaces usually lead to a higher absorptivity for metallic materials. The absorption of laser energy results in the excitation of free electrons (in metals), vibrations (in insulators), or both (in semiconductors). This excitation energy is rapidly converted into heat, and followed by various heat transfer processes such as conduction into the material and radiation from the surface. The generation of heat at the surface and its conduction into the material establish the temperature distribution in the material. Depending on the thermophysical properties of the material and laser parameters, a thin layer of the material surface could be heated, melted, or even vaporized, and then followed by rapid solidification to generate refinement/homogenization of microstructures.

Many types of lasers have been operated in material processing, but only four types of lasers are of sufficient energy and robustness to be used effectively for surface treatments: the  $\text{CO}_2$  laser (with wavelength of  $10.6 \mu\text{m}$ ), the Nd:YAG laser ( $1.06 \mu\text{m}$ ), the high-power diode laser (HPDL:  $800\text{--}950 \text{ nm}$ ), and the excimer laser ( $248 \text{ nm}$  for KrF). Due to their long wavelengths, surface modification by continuous-wave (CW) multikilowatt  $\text{CO}_2$ , Nd:YAG, and HPDLs occurs through heating effects, with a typical melt depth in the range of  $50 \mu\text{m}\text{--}2 \text{ mm}$ . In contrast, the excimer laser is pulsed and ranges in energy up to  $1 \text{ J}$  per pulse. Due to the short wavelength, surface modification by an excimer laser occurs through a combination of photochemical and heating effects. The typical melt depth caused by

an excimer laser is a few micrometers, with a much faster cooling rate compared with the other three lasers. Recently, many special features of HPDL interaction with materials have been identified.<sup>1</sup> These features include better surface finish, better beam absorption, better morphological characteristics, more consistent and repeatable results, fewer cracks, and less porosity generation. These benefits are due to the multiple beam integration and shorter wavelength of the HPDLs, compared with Nd:YAG and  $\text{CO}_2$  lasers. In addition, HPDLs have the advantages of being potentially low in cost, high in energy efficiency, and more reliable, as well as having longer service life, and portability. Therefore, HPDLs are ideal for industrial applications of surface treatments.

**4.09.2 Solidification Microstructures**

Solidification induced by a laser beam leads to high solidification rates due to the rapidly moving temperature fields and the associated high cooling rates and large supercooling. At very high solidification rates (greater than the local diffusion rate), equilibrium at the interface cannot be established and the solute atoms are frozen into solid at the same composition as they arrive at the interface (solute trapping).<sup>2</sup> This provides a unique opportunity for the development of a wide variety of novel alloys with extended solid solution. These alloys with nonequilibrium phases offer the possibility of new materials with properties that cannot be achieved by conventional processing techniques. In addition, the rapid cooling rate results in the homogenization/refinement of microstructure and dissolution/redistribution of precipitates or inclusions. In the case of CW lasers with a multikilowatt power level, a cooling rate of  $10^3\text{--}10^6 \text{ K s}^{-1}$  is quite common. The cooling rate can rise up to  $10^{11} \text{ K s}^{-1}$  for the low energy input surface skin processes.<sup>3</sup> The solidification microstructure is determined by the constitutional supercooling theory. For a specific alloy, the solidification microstructure depends on the local solidification conditions, that is, solidification rate,  $R$ , and temperature gradient,  $G$ , at the solid-liquid interface. In general, the morphology of solidification microstructures can be described as planar, cellular, cellular/dendritic, or dendritic, depending on  $GR$ . The values of  $G$ ,  $R$ , and  $G/R$  vary within the melt pool. Therefore, different solidification morphologies can be found, for example, with a planar front zone at the melt pool-substrate interface and then cellular and dendritic

structure toward the surface of the melt pool. On the other hand, the size of microstructure, which is often characterized by the secondary dendritic arm spacing, is determined by  $G/R$ , which is the cooling rate. The higher the cooling rate, the finer the resulting microstructure.

### 4.09.3 Laser Applied Coatings

A wide range of laser applied coating techniques is available today. Laser cladding (LC) and laser melt/particle injection are usually used to provide thick coatings with minimum dilution of substrate material. Laser surface remelting is applied to coatings produced by conventional techniques, such as thermal spraying, in order to modify microstructures and eliminate defects for the improvement in properties. Laser-assisted thermal spraying, also called laser hybrid spraying, is a one-step coating method, in which a high-power laser is combined with thermal spraying, to create denser and adherent coatings with much increased processing efficiency than normal thermal spray process. Pulsed laser deposition (PLD) and laser-assisted chemical vapor deposition (LCVD) produce thin films. Laser surface alloying (LSA), on the other hand, is applied to alter surface chemistry and composition by melting and mixing the substrate, with a coating material or a component of a gas, and can be used for either thick coatings or thin films.

#### 4.09.3.1 Laser Cladding

LC is used to produce a relatively thick, typically from 50  $\mu\text{m}$  to 2 mm, and homogeneous overlay of coating material on the substrate with a fusion bond. LC can be achieved by a high-power laser beam to slightly melt the surface of the substrate with simultaneous delivery of powdered materials into the molten pool, as described in [Figure 1](#). LC can be also performed by completely melting materials predeposited on the substrate or through wire feeding with minimum dilution.

LC has many advantages over conventional cladding techniques such as thermal spray and arc welding. These advantages include a fusion bond and a reduction (or elimination) of porosity and cracks in comparison with thermal spray; a reduction in dilution (typically <5%), extremely narrow heat-affected zones with a low thermal distortion, and a reduction in postcladding machining costs in comparison with

arc welding. For most LC applications in the field of surface protection, CW  $\text{CO}_2$  and Nd:YAG lasers are typically used. However, in recent years, HPDLs have been increasingly used, especially in industrial environments, with the advantages of a reduction of operating and investment cost, high plug efficiency, and compact size. LC enables the generation of very fine, homogenous microstructures and nonequilibrium alloys due to the inherent rapid cooling rate associated with the process, which promotes the formation of either an amorphous phase or nonequilibrium crystalline phases with extended solid solution.

LC has found relatively widespread use for the protection of materials against corrosion and oxidation in a variety of applications, including Al alloys, Mg alloys, carbon steels, stainless steels, and various metal matrix composites. LC on Mg alloys with Al, Al alloys, and other alloying elements significantly enhances the corrosion resistance, along with wear resistance. For example, the corrosion rate of laser-clad  $\text{Mg}_{27}\text{Al}_{73}$  is one order of magnitude lower than that of commercially produced AZ91B and two orders of magnitude lower than that of Mg in 3.5% NaCl solution.<sup>2</sup> This is due to the passive film on the clad material, which is much more stable than that of the AZ91B and Mg substrates, due to the refinement of microstructure and extended solid solution of Al. Additionally, LC of amorphous alloy  $\text{Zr}_{65}\text{Al}_{7.5}\text{Ni}_{10}\text{Cu}_{17.5}$ , with a thickness of 1.5 mm, on a commercially pure Mg substrate resulted in corrosion resistance and wear resistance superior to those of the uncoated substrate, with the corrosion current density being lowered by three orders of magnitude in 3.5% NaCl solution.<sup>5</sup> In addition, the corrosion current density of laser-clad  $\text{Al}_2\text{O}_3$  is three orders of magnitude lower than that of AZ91HP Mg alloy in 3.5% NaCl solution.<sup>6</sup>

LC can also be applied for extending the solid solubility limits of rare-earth additions (e.g., yttrium, rhenium hafnium, and cerium) in nickel-based superalloys to improve their resistance to oxidation at elevated temperatures. Under equilibrium conditions, the maximum solid solubility of rare-earth metals is  $\sim 0.2 \text{ wt}\%$  at room temperature. However, alloys produced by LC of Ni-(Fe,Cr)-Al-Hf-Re resulted in a uniform distribution of alloying elements in the clad matrix with an extended solid solubility of alloying additions, a greatly refined microstructure, and the formation of metastable rhenium- and hafnium-rich phases.<sup>7,8</sup> Under thermal cycling oxidation conditions, the clad material exhibits negligible change in weight, while the substrate



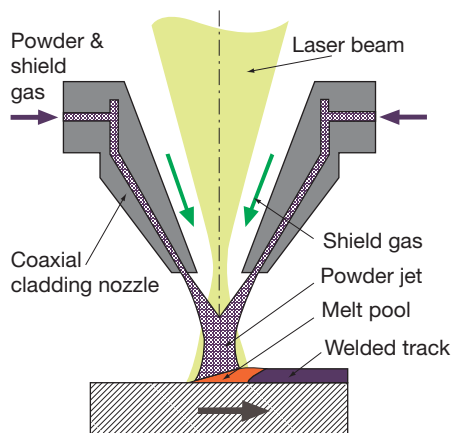
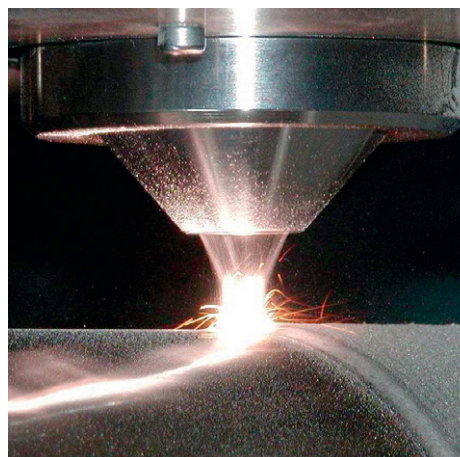


**Figure 1** Laser cladding with coaxial powder feeding.<sup>4</sup>



(Rene80) suffers from extensive spalling of the scale.<sup>9</sup> In addition, LC of NiCrAlY alloy on a Hastelloy X substrate produces a columnar dendritic structure, free of porosity and microcracks, consisting of  $\gamma$ -Ni solid solution and a small amount of  $\text{Al}_5\text{Y}_3\text{O}_{12}$  close to the surface, which exhibits excellent isothermal oxidation behavior.<sup>10</sup>

A new type of thermal barrier coating (TBC) has been developed for gas turbine blades by LC of yttria-stabilized zirconia (YSZ) on superalloy substrates.<sup>11</sup> The LC produces an oriented epitaxial growth, closely packed columnar structure during rapid solidification processing. This promotes the formation of an alumina layer between the NiCoCrAlY layer and the columnar ceramic layer that provides the adherence of the columnar layer to the NiCoCrAlY layer. A good metallurgical bond between the  $\text{ZrO}_2$  layer and the NiCoCrAlY alloying layer, and between the alloying layer and the substrate. The chemical modification of  $\text{ZrO}_2$  can be adopted to eliminate microcrackings of the coatings. The oxidation resistance of such laser-clad thermal barrier coatings in air at  $1200^\circ\text{C}$  is significantly higher than that of plasma-sprayed coatings. In addition, LC with 60% Ni, 19% Cr, 11% Al, and 6.4% Fe showed an excellent corrosion resistance than the Incoloy 800H,<sup>12</sup> so that these coatings can be used as an oxidation barrier in high temperature applications at temperature levels over the maximum limit where the Incoloy 800H can be used.

Titanium-based alloys are high-strength, light materials used extensively in the aerospace industries for airframe structures and component parts of aircraft engines (e.g., airfoils). However, titanium alloys have poor oxidation resistance at temperatures above

$600^\circ\text{C}$ . The most critical section of the airfoil is its tip, which is generally exposed to high temperatures  $>500^\circ\text{C}$  during engine operating conditions. LC of 50Nb–50Ti alloy on the tip of airfoils (Ti–6Al–4V alloy) has resulted in an excellent oxidation resistance at  $1000^\circ\text{C}$  in air. In contrast, the unclad Ti–6Al–4V alloy formed a 500- $\mu\text{m}$  thick, porous oxide layer, which tends to spall from the substrate, forming a 100- $\mu\text{m}$  oxide in 48 h with a good adherence.<sup>13</sup> Important features of such LC processes for industrial applications include that the laser beam is capable of following the contour of the airfoils; good bonding between the laser-clad niobium and airfoils, and readily controlled thickness and composition of the clad.

In municipal waste incinerators (MWI), critical components such as superheater or boiler tubes are often degraded by corrosion. Especially in modern waste-to-energy (WTE) plants, the need for increased efficiency requires operation at higher temperatures, which in turn enhances the corrosion rates. LC has been successfully used for the production of anticorrosion and antierosion coatings on superheater and boiler tubes. Compared with protective coatings produced by flame spraying, LC is virtually porosity free and ensures metallurgical bonding to the substrate, so that the clad tubes can be bent without any damage from cracking or spalling. This is an important development for the construction of the bends of the superheater coils and the production of integral laser clad superheater assemblies. One automatic diode laser workstation available for industrial production of MWI superheater and boiler clad tubes has been demonstrated and installed in European MWI plants.<sup>14</sup>

#### 4.09.3.2 Laser Surface Melting

In the laser surface melting (LSM) process, a thin surface layer is rapidly melted by a high-power laser beam, followed by a rapid solidification to produce a microstructure different from that of the bulk material. High cooling rates of the molten surface layer can promote the formation of an amorphous material, metastable phases, or a fine-grained microstructure resulting in improved surface properties, such as wear, corrosion, and fatigue resistance. The principal advantage of LSM is that it alters the microstructure without changing the composition, compared with other laser surface modification techniques introduced later. More importantly, LSM has been utilized as a posttreatment for other surface coating techniques. The most commonly encountered example is laser melting of thermally sprayed coatings. In this case, it is also referred to as laser remelting.

Thermal spraying processes are widely used to apply a variety of coatings, including metallic coatings, metal matrix composite coatings (MMC), and ceramic coatings, on different substrates. However, despite the efforts made to improve spraying techniques, such as high-velocity oxy-fuel (HVOF) and plasma spraying, the coatings may still exhibit certain defects such as unmelted particles, oxide layers at splat boundaries, porosity, and microcracks, which are detrimental to corrosion performance. Furthermore, the bonding to the substrate is usually not metallurgical or fusion based. Interconnected porosity and lamellar grain, splat-structures, with oxide inclusions at interlayer boundaries, result in potential failure of the coatings due to penetration of corrosive agents into the interlayer and eventual debonding of the coatings. The use of LSM to modify the structures of thermal sprayed coatings is referred to as laser sealing or laser glazing. In this technique, melting is induced in the near-surface coating by a relatively high intensity and short duration of laser irradiation.

For thermally-sprayed metallic coatings, laser melting is an effective technique for a significant improvement in the corrosion resistance by elimination of defects in the original thermal-sprayed layers. Normally, high-power CW lasers, such as CO<sub>2</sub> laser, Nd:YAG laser, and HPDLs, are chosen with appropriate selection of laser operating conditions enabling fully controllable melt pool dimensions. Therefore, thermal-sprayed coatings can be either partially melted (i.e., top-layer only), or fully melted (i.e., whole layer together with a small portion of substrate material). In both the cases, the defects in the original

thermal-sprayed coatings can be completely eliminated, while fully melting offers an advantage of the formation of a metallurgical bond compared with the mechanical interlocking in the original coatings. For example, plasma-sprayed Ni31Cr11Al0.6Y coating on Alloy 800H, as a physical barrier to carbon ingress, improves the metal dusting resistance, with limitation due to the presence of interconnected porosity. Laser remelting of such coatings further improves the metal dusting resistance of the thermal-sprayed coated alloys due to improving the effectiveness of the coating by elimination of interconnected porosity.<sup>15</sup> In addition, laser remelting of HVOF-sprayed Inconel 625 coatings resulted in the homogenization of the sprayed structure, and the removal of oxide inclusions between splats and interconnected porosity, leading to a significant improvement in resistance to wet corrosion and high temperature corrosion. The corrosion resistance of the sprayed coatings after laser treatment is equivalent to that of the wrought alloy.<sup>16</sup>

For MMC, which are normally applied using HVOF, apart from the role of common defects of thermal-sprayed coatings described earlier, the corrosion processes are dominated by complex microgalvanic and interfacial mechanisms. First, the interface between the hard phase and the matrix represents a physical microcrevice, providing an inherent driving force for localized attack due to classic mechanisms of differential aeration; second, the difference in electrochemical potentials between the coating constituents provides additional driving force for localized corrosion due to microgalvanic corrosion. Third, the existence of interconnected porosity and lamellar grains, splat-structures with oxide inclusions at interlayer boundaries results in another major concern to the failure of the coatings due to corrosion penetration into the interface and eventually debonding of the coatings. Laser remelting of such HVOF MMC coatings is an obvious option owing to its unique features over conventional heat-treatments, for example, precise control of treatment depth with or without melting. The resultant microstructural homogenization, such as the removal of the splat-structure and porosity, the reduction of sharp compositional gradient between the hard phase and the matrix, and the improvement in adhesion bonding between coating and substrate, can be readily achieved. Compared with metallic coatings, special attention should be paid to an appropriate selection of laser operating conditions to avoid formation of

cracks and porosity within laser-melted layers. Laser remelting of Inconel 625-based tungsten carbide (WC) HVOF-sprayed MMC coatings significantly improves the corrosion resistance as a result of the elimination of a discrete splat-structure, microcracks, and porosity, and also reduces the microgalvanic driving force between the WC and the metal matrix. In addition, an improved wear resistance of the laser-treated coatings results due to the formation of a faceted dendritic structure of the WC phase.<sup>17</sup> Therefore, laser remelting shows potential benefits for the improvement in HVOF coatings in tribocorrosive environments.

A typical example of ceramic coatings is thermal barrier coatings consisting of  $\text{ZrO}_2 + 8 \text{ wt\% Y}_2\text{O}_3$  as the outer coating and NiCrAlY layer as a bond-coat on Ni-base substrate. Such TBC coatings, normally applied by plasma spray on hot-section components of gas turbines, offer significant advantages of increased operating temperatures and protecting the coatings from hot corrosion. The coatings retain a substantial amount of interconnected pores and microcracks, with high porosity providing a better thermal protection. However, the life of the coatings is limited by the oxidation of the metallic bond coat due to the penetration of corrosive fuel through the porosity, which causes the failure of the coatings by the spalling of ceramic coating layer. Laser surface remelting shows great potential for the improvement in plasma-sprayed thermal barrier coating properties by reducing surface roughness, eliminating open porosity on the surface, and modifying microstructures from lamellar to columnar. In laser-melted ceramic materials, cracks frequently occur in the densified layer perpendicular to the surface, generated by shrinkage and thermally induced stresses. However, it is possible to generate a controlled segmented crack network by properly selecting laser operating conditions, so that improvement in thermal shock resistance can be achieved. For example, laser glazing increases thermal cyclic lifetimes of plasma-sprayed thermal barrier coatings about fourfold by improving the strain accommodation through segmented cracks.<sup>18</sup> Laser glazing has also resulted in enhancement, approximately fourfold, in the lifetimes of plasma-sprayed thermal barrier coatings by in high temperature corrosion tests involving  $\text{V}_2\text{O}_5$  salts.<sup>19</sup> However, the existence of macroscopic vertical cracks may provide a path for oxygen and molten salts to attack the TBC system. Therefore, special care must be taken in the consideration of a compromise between the desirable and undesirable properties.

#### 4.09.3.3 Laser-Assisted Thermal Spray

As described earlier, the improvement in integrity and performance of thermal-sprayed coatings can be achieved by laser remelting. However, such a process requires additional steps. Although LC has a potential to be developed as an effective technique for coatings in practice, it is inefficient for large-area coverage in industrial applications; more than 10 times slower than thermal spraying in terms of materials deposition rate. In addition, LC of ceramic materials also produces numerous macrocracks.

An effective combination of laser processing and conventional thermal spray systems, namely laser-assisted thermal spray, has been developed and provided the opportunity for depositing dense coatings on large surface areas with improved structural integrity and performance, and acceptable process efficiencies for industrial applications. The laser in such a combined system can be used to reduce microstructural defects, improve cohesion within the coatings, and achieve fusion bonding between the coating and the substrate. The thermal spray jet can provide an effective heat source for increasing the processing rate (relative to LC) and controlling the temperature gradients and thermal stresses during processing. This could be of considerable benefit to process and manufacturing engineers.

Lasers can be combined with various types of thermal spray techniques. For example, laser-assisted flame hybrid spraying process has been developed to deposit alumina coatings on alumina-based refractory ceramics.<sup>20</sup> Flame spraying is a cost-effective and highly flexible surface coating technique; however, the resulting coatings are porous and have a low mechanical bonding to the substrates. LSM can produce very dense surfaces and fused bonded layers; however, cracks in the treated layers readily occur and the process velocity is often too slow for industrial applications. The combination of flame spraying and laser beam decreases, and may even overcome the drawbacks of the individual processes, thus forming an efficient method for depositing coatings with improved structural integrity. Coatings with dense microstructures and fusion-bonded to the substrate are especially desirable for refractory materials used for lining furnaces and incinerators. In addition, laser-assisted plasma spray systems have been used to produce dense NiCrBSi coatings on small mild steel components,<sup>21</sup> and to deposit a Ni/Ti coating onto a Ti-6Al-4V substrate.<sup>22</sup> The shear strength of the Ni/Ti coating was increased sixfold compared

with a conventional plasma coating, as a result of the improved bond between the coating and the substrate.<sup>22</sup> A similar laser-plasma hybrid spraying system has been applied to deposit  $Y_2O_3$  stabilized  $ZrO_2$  thermal barrier coatings, with modified crack system and pore connectivity leading to a significantly decreased permeability in the produced coatings compared with laser posttreated coatings. Therefore, combined laser and thermal spray processes are promising for depositing denser coatings, with much increased processing efficiency, to achieve improved structure integrity and performance.<sup>23</sup>

#### 4.09.3.4 Laser Melt/Particle Injection

Laser melt/particle injection (LMI) can be considered as a special form of LC, which is aimed at producing a metal-matrix composite layer on top of a substrate. The laser beam melts the substrate locally while particles of additional material with a high melting temperature, usually ceramics, are simultaneously injected. Another version of LMI uses a laser beam to melt coaxially fed metallic powder and simultaneously inject ceramic particles into the melt pool. These particles are trapped when the melt pool rapidly solidifies after the laser beam has passed. Unlike LC, in LMI, the interaction between ceramic particles and laser beam is limited so that the ceramic particles remain mainly in the solid state, but with partial dissolution of the ceramic particulate into the melt pool, forming new phases at/around the interface between the particles and metal matrix.

MMC coatings are normally used for the improvement in wear performance. However, MMC coatings often have poor resistance to corrosion, and applications of such coatings in corrosive environment can be limited. Therefore, there is a need to achieve excellent wear performance with acceptable corrosion resistance. As described earlier, the corrosion properties of MMC coatings produced by thermal spraying are dominated by complex microgalvanic and interfacial mechanisms, as well as by oxide inclusions and porosity. However, it is possible to control the corrosion performance of LMI-produced MMC coatings by suitably adjusting the laser operating parameters to partially dissolve ceramic particles, to promote the formation of interfacial phases, and to eliminate other coating defects. For example, LMI-produced TiC-Ti-6Al-4V exhibits an excellent corrosion resistance in seawater after 1 month exposure.<sup>24</sup> In addition, MMC coatings of  $Al_2O_3$  particle injected Ni-Cr-Al-Hf produced by

LMI are possible candidates to meet the technical challenges of particular turbine components, such as the tips of turbine airfoils, requiring thermal stability, high temperature oxidation resistance, and wear resistance.<sup>25</sup> Compared with MMC coatings produced by thermal spray techniques, such as HVOF, LMI results in an improved corrosion resistance by (1) reducing the sharp composition gradient between the matrix and the hard phase through promoting some interdiffusion; (2) forming a uniform distribution of the phase and composition with a much lower number of defects such as porosity and microcracks in MMC coatings.

#### 4.09.3.5 Pulsed Laser Deposition

PLD is a thin-film deposition technique using high-energy laser pulses to vaporize the surface of a solid target inside a vacuum chamber and condensing the vapor on a substrate to form a thin film up to a few micrometers in thickness. Figure 2 shows a schematic diagram of a typical PLD process.

The main advantage of PLD derives from the laser material removal mechanism. PLD relies on a photon interaction to create an ejected plume of material from any target based on rapid explosion of the target surface region due to superheating. Unlike thermal evaporation, which produces a vapor composition dependent on the vapor pressures of the elements in the target material, the laser-induced expulsion produces a plume of material with stoichiometry similar to that of the target. Therefore, it is generally easier to obtain the desired film stoichiometry for multielement materials using PLD than with other deposition technologies.<sup>27</sup> On the other hand, the kinetic

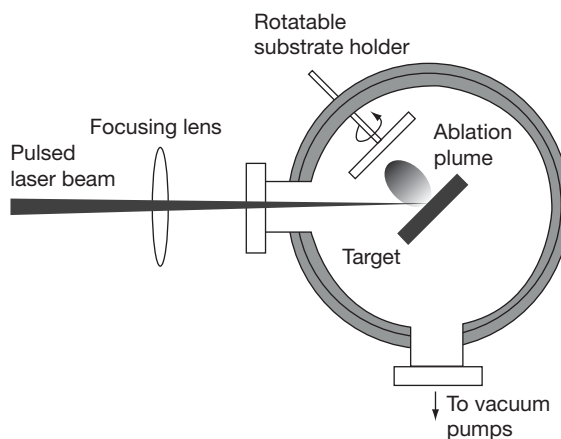


**Figure 2** Schematic diagram of PLD process.<sup>26</sup>

energies of ablated particles are typically high enough to promote surface diffusion, but not so high as to induce bulk damage. Thus, PLD can create thin films of a wide range of materials, including metals, semiconductors, and insulators with excellent adhesion. Since PLD results in a high cooling rate during film formation, it is likely to form nanocrystalline or even amorphous alloy films. Some of the films have been applied as protective barriers in corrosive environments.<sup>28–30</sup> For example, amorphous Ta–Ni films produced by PLD offer extremely high corrosion resistance in both acid and alkaline solutions.<sup>28</sup> A 160-nm thick film of  $Y_2O_3$  deposited on Zn–22Al–2Cu alloy produces an improvement of up to 75% in corrosion resistance in aerated water of pH 4.5, compared with the alloy without the  $Y_2O_3$  film.<sup>29</sup> In addition, the PLD technique can be used to form alumina-stabilized zirconia films on fused silica substrate making for both corrosion resistance and thermal barrier purposes.<sup>30</sup>

Since it is possible to control microstructures in a wide range, from amorphous dense to microcrystalline porous, by properly selecting laser operating conditions, PLD offers significant advantages and manufacturing flexibilities for the formation of graded coatings for thermal and corrosion barriers, compared with other methods such as electron beam–physical vapor deposition (EB-PVD) and atmospheric plasma spraying (APS). A German National Science Foundation program has reported a successful

deposition of functionally graded thermal barrier coatings on Cu substrates by PLD to sustain extremely high thermal loadings in a hot gas environment.<sup>31</sup> A columnar–lamellar microstructure, with designed column size, graded profile of lamellae thickness and interface modification can be produced, to a large extent, by means of PLD using a combination of nano- and microsecond laser beam pulses.

#### 4.09.3.6 Laser Chemical Vapor Deposition

Laser chemical vapor deposition (LCVD) is employed to generate solid deposits on a substrate by laser beam-induced chemical reactions in a chemical vapor reactant. LCVD processes can be divided into two main categories: photolytic and pyrolytic, depending on the mechanism that activates the chemical reactions.

Photolytic LCVD, as shown in **Figure 3(a)**, utilizes photons of a laser beam to break chemical bonds within the reactive gases. The molecules either recombine or decompose to form a solid deposit on the surface of the substrate. Pulsed lasers in the ultraviolet wavelength, typically excimer lasers with photon energies of several electron volts, are used for photolytic reactions. The main advantage of photolytic reactions is the absence of high temperatures that may adversely affect the substrate or build up thermal stresses within the deposited layers. In pyrolytic LCVD, the energy of a laser beam is used to heat

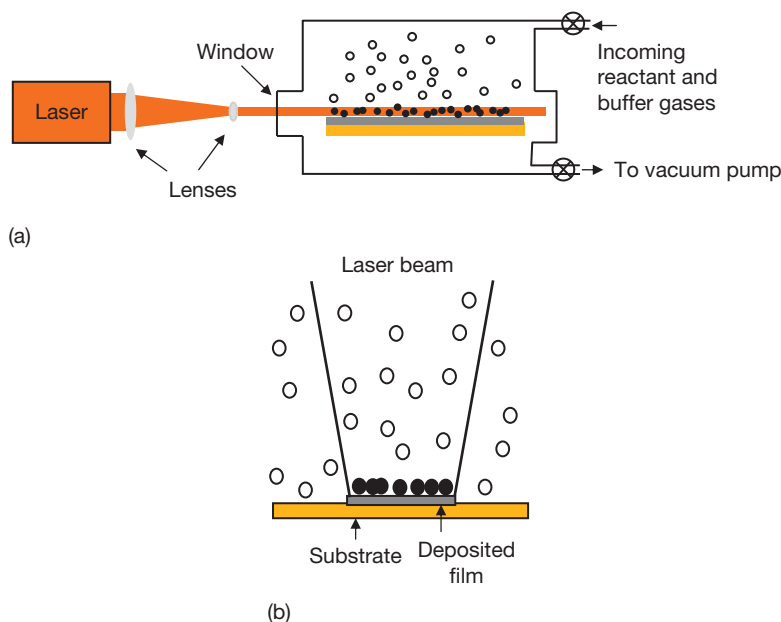


**Figure 3** Schematic diagrams of LCVD (a) photolytic and (b) pyrolytic process.



the surface of a substrate to the temperature required for thermally driven chemical deposition, as shown in **Figure 3(b)**. Typically lasers with infrared wavelengths such as  $\text{CO}_2$ , Nd:YAG, and HPDLs, are used for such processes. Compared with the traditional thermal CVD, LCVD offers the significant advantage of avoiding the heating of the entire substrate to the reaction temperature.

Silica coatings on metallic substrates have been produced using an ArF excimer laser to photolytically induce the reaction between  $\text{SiH}_4$  and  $\text{N}_2\text{O}$ .<sup>32</sup> This technique is capable of producing complex silica coatings with graded density, thus efficiently solving the potential problem caused by thermal expansion coefficient mismatch between the metallic substrate and the coating. Protective coatings withstood thermal cycling and long-term corrosion tests at a temperature of  $450^\circ\text{C}$  without spallation. This excellent performance is associated with the reduced elastic modulus of the less dense coating in contact with the metallic substrate and the improved diffusion barrier provided by the fully dense silica deposited on top.<sup>32</sup> In addition,  $\text{Ta}_2\text{O}_5$  films with columnar, dense structures, prepared by KrF excimer laser CVD from tantalum-pentamethoxide ( $\text{Ta}(\text{OCH}_3)_5$ ), have been shown to reduce the corrosion current density of iron by six orders of magnitude, indicating that the dense LCVD- $\text{Ta}_2\text{O}_5$  coating was effective in increasing the corrosion resistance of an iron substrate.<sup>33</sup>

Although CVD has often been considered to be a slow process for the production of thick coatings, a laser CVD process has achieved high deposition rates for YSZ coatings with either a columnar structure (**Figure 4(a)**,  $230\ \mu\text{m h}^{-1}$ ) or a cone structure (**Figure 4(b)**,  $660\ \mu\text{m h}^{-1}$ ). At high deposition rates, a large number of nanopores are formed within grains

(**Figure 4(c)**), resulting in a thermal conductivity of  $0.7\ \text{W mK}^{-1}$ , which is almost the same as that of EB-PVD YSZ coatings. However, the nanopores in the laser CVD YSZ are relatively stable such that the thermal conductivity does not increase significantly after heat-treatment for more than 20 h at high temperatures of  $\sim 1000\text{--}1100^\circ\text{C}$ .<sup>34</sup> Laser CVD is also capable of forming other oxides, such as  $\text{Al}_2\text{O}_3$  and  $\text{TiO}_2$  coatings, at deposition rates  $\sim 1\text{--}2\ \text{mm h}^{-1}$ . The thick coatings, of more than several  $100\ \mu\text{m}$ , provides at high speeds by laser CVD may find many industrial applications in industries requiring corrosion and abrasion resistance.<sup>34</sup>

#### 4.09.3.7 Laser Surface Alloying

LSA is a process that is used to incorporate additional alloying elements into the surface of a component, by utilizing a laser beam with high power density to melt metal coatings and a portion of the underlying substrate. The typical thickness of the alloyed surface layer ranges from  $1\ \mu\text{m}$  to  $2\ \text{mm}$ . The thickness and the composition of the treated surface can be adjusted by controlling the laser power intensity and the interaction time. Due to the high cooling rate associated with LSA, nonequilibrium phases and supersaturated solid solutions can be readily achieved. LSA processes may be divided into two classes, namely, thin-film alloying and thick-layer alloying.<sup>35</sup>

The thin-film alloying process involves the use of short energy pulses (width range from some nanoseconds up to a few microseconds). The typical alloyed thickness is a few micrometers. The mixing process is based on a diffusion mechanism of mass transfer, with cooling rates of up to  $10^{11}\ \text{K s}^{-1}$ , leading to a strong decrease of the alloying elements' concentration with

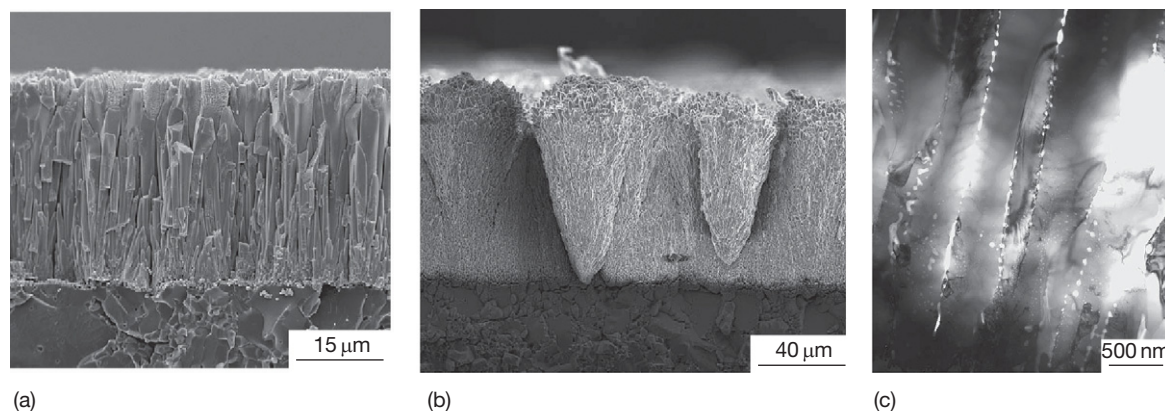


**Figure 4** Cross-section of YSZ coatings prepared by laser CVD at a deposition rate of  $230\ \mu\text{m h}^{-1}$  (a),  $660\ \mu\text{m h}^{-1}$  (b), and nanostructure of the YSZ coatings (c).<sup>34</sup>

the increase of the depth in the modified layer. The thick-layer alloying process involves the use of either energy pulses of duration from 1 up to 20 ms or CW radiation, resulting in cooling rates of  $10^4$  to  $10^6 \text{ K s}^{-1}$ . The typical alloyed thickness is in the range of 0.1 mm to a few millimeters. The mixing process within the melt pool is mainly controlled by a convective mechanism of mass transfer. Therefore, the chemical compositional homogeneity of the melted layer can vary from relatively uniform to highly nonuniform, depending on the turbulent stirring effect within the melt pool driven by surface tension gradients that result from thermal gradients, that is, Marangoni effect. For metals, the convection speed is several orders of magnitude higher than the laser scanning speed, leading to a rapid homogenization. When the melting temperature of the alloying elements is considerably higher than the melting temperature of the substrate material, or when the alloying elements react with the melt pool material to form insoluble high melting temperature phases, alloying may be difficult.

A main characteristic of LSA is the possibility of producing an almost unlimited range of alloy composition for the surface layer, with fine and homogenized microstructures, tailor-made for the requirement. However, it is difficult sometimes for certain elements to be alloyed into certain material substrates. In selecting elemental combinations for LSA, attention needs to be paid to the relative melting temperature, vaporization temperature, and vapor pressure of alloying elements and substrate materials. Processing will be difficult if the added element vaporizes at a temperature that is lower than the melting temperature of the substrate material; for example, in LSA of Zn into a Cu substrate, since at 1 atm Zn boils at  $\sim 900^\circ\text{C}$ , while Cu does not melt until  $\sim 1100^\circ\text{C}$ .

The rapid cooling rate associated with LSA provides a unique opportunity for the generation of nonequilibrium alloys. The thickness and composition of the treated surface can be adjusted by properly choosing the type of laser and appropriately controlling the laser power intensity and interaction time. In LSA, the extent of solid solubility can be increased as a result of solute trapping arising from rapid rates of cooling. Therefore, more alloying elements can be retained in solid solution, with beneficial effects on corrosion properties or wear properties. There are other methods of producing nonequilibrium metallic alloys, using rapid solidification technology (RST), such as atomization, twin roll quenching, and melt spinning. However, in order to make an engineering component, the

materials must be consolidated, involving temperature and pressure cycles that can induce phase transition in a metastable material.<sup>2</sup> Therefore, laser processing has potential benefits for the generation of nonequilibrium materials for industrial applications.

Surface alloying of transition-metal elements, such as Cr, Ni, and Mo, has been applied on low-carbon steel substrates for corrosion protection. For example, LSA of Cr into mild steel produces a uniform Cr distribution in the alloy layer, and consequently, a decrease in the critical current density required for passivation and a decrease in the passive current density in the passive range.<sup>36</sup> In addition, LSA of Mo into 304 stainless steel increases in the critical pitting potential on potentiodynamic polarization in 0.1 M NaCl solution. The critical pitting potential for surface alloys containing 3% Mo is comparable with that of bulk 316 alloy, while surface alloys containing 9% Mo indicate no breakdown up to the oxygen evolution potential.<sup>36</sup> In addition, surface alloys rich in Ni–Mo produced by LSA of 304 stainless steel substrate result in a pitting resistance above that of AISI 316 stainless steel.<sup>37</sup> Fe–Cr–Ni–Mo–C surface alloys with different compositions can be produced on carbon steel.<sup>38</sup> The pitting potential of the Fe–18.7Cr–6.3Ni–3.8Mo–0.14C laser surface alloy is  $\sim 200 \text{ mV}$  higher than that of AISI 316 stainless steel and Fe–23.2Cr–7.3Ni–4.7Mo–0.13C laser surface alloy does not suffer pitting corrosion in anodic polarization tests in 3% NaCl.

LSA of nonferrous substrates has been applied for the improvement in corrosion properties. LSA of Al + Mn into a Mg alloy (MEZ) produces an alloyed surface consisting of dendrites of Al + Mn and Al + Mg, which significantly reduces the corrosion rate in 3.56 wt.% NaCl solution to 250 mpy, compared with 1520 mpy of the MEZ substrate. This improved corrosion resistance was due to the presence of  $\text{Al}_2\text{O}_3$  and  $\text{Mn}_3\text{O}_4$  layer on the alloyed surface, while the microhardness of the alloyed zone was enhanced up to 1250–350 VHN, compared with 35 VHN for the substrate.<sup>39</sup> LSA of Zircaloy-4 with niobium (Nb) significantly improves the resistance to localized corrosion in a chloride solution at  $80^\circ\text{C}$  due to the combined effects of a rapidly cooled, fine microstructure and the Nb alloying. However, it should be noted that the corrosion resistance of such an alloyed surface is reduced in steam at  $400^\circ\text{C}$ .<sup>40</sup>

LSA is a potential option for the improvement in the high temperature oxidation resistance of high temperature alloys. The high temperature oxidation resistance of laser-surface-alloyed Incoloy-800H with

Al is significantly improved at 1000 °C in air, due to the formation of an Al-rich layer close to the surface, which acts as a barrier against oxygen diffusion into the bulk.<sup>41</sup> In a similar way, LSA of Incoloy-800H with Al and Si improves the resistance to metal dusting.<sup>42</sup>

When LSA is used for thin-film alloying by use of excimer lasers, it provides a unique opportunity to produce concentrated alloying elements extending to depths of submicrometers to a few micrometers, without bulk heating or the requirement of a vacuum. A typical example is LSA of 50- $\mu\text{m}$  thick Ti foil with Pd layer of 310-nm thick, using a KrF excimer laser.<sup>43</sup> Using this technique, it was possible to form homogeneous surface-alloy regions by rapid diffusion and intermixing, and demonstrate a major improvement in the corrosion resistance in 0.1 M  $\text{H}_2\text{SO}_4$  solution at 80 °C, as shown in **Figure 5**, due to the shifting of the potential to the region of passivity of titanium. Such Pd-alloyed Ti foils have been of interest for increasing the life of titanium foils that are used as electron-transparent windows in the removal of  $\text{SO}_2$ ,  $\text{NO}_x$ , and volatile organic compounds from flue gas by EBs.

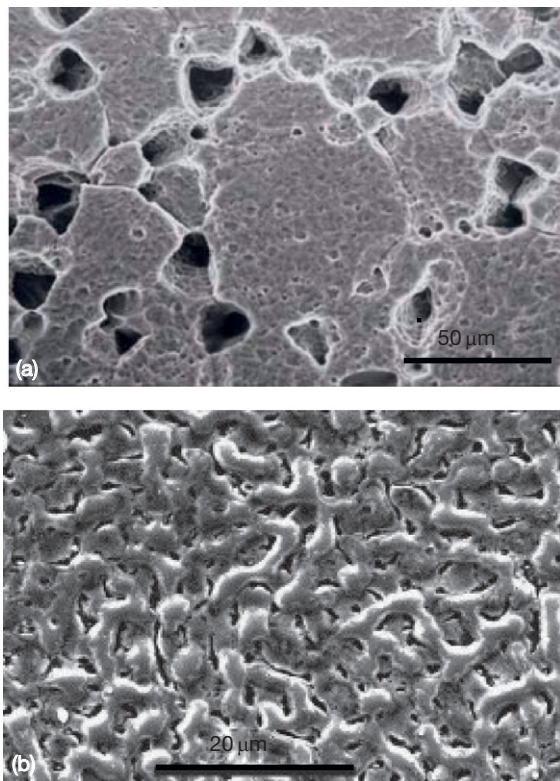


**Figure 5** Corrosion morphology of untreated titanium foil (a) and laser-alloyed with Pd after immersion in  $\text{H}_2\text{SO}_4$  solution (b) at 80 °C.<sup>43</sup>

Laser gas nitriding (LGN) is a special form of LSA by laser melting of a metal surface in a nitrogen gas environment to form a nitride layer on the irradiated surfaces by chemical reactions. Many metals, including iron, carbon steels, stainless steels, and aluminum alloys, can be nitrided by lasers. These layers are metallurgically bonded with the substrate and have better interfacial properties than those produced by other nitriding techniques such as PVD, CVD, and ion implantation. Depending on the type of laser, the typical depth of nitrided surface layers can be in the range of a few microns or up to a few hundred microns. In the LGN process, a major problem to be addressed is cracking. There are two types of cracks on laser nitrided Ti-6Al-4V surfaces: (1) macrocracks induced by the accumulation of tensile stresses during the laser melting process; and (2) microcracks related to the inherent brittleness of TiN.<sup>44</sup> However, such cracks can be eliminated by proper selection of laser operating conditions, such as energy level, pulse width, traverse velocity, and gas environment (e.g., diluted nitrogen gas). **Figure 6** shows a typical example of LGN of Ti-6Al-4V alloy, using a Nd:YAG laser with a pulse width of 200  $\mu\text{s}$ .<sup>45</sup> In cross sections, the microstructures mainly consist of an outer thin continuous layer of TiN, followed by a region of nearly perpendicular TiN dendrites, and an intermixture region of small dendrites and large needles of nitrogen-enriched  $\alpha$ -Ti phase. The density of TiN dendrites decreases gradually toward the interface between the nitrided layer and the substrate. An improvement in pitting corrosion behavior in 3.5% NaCl solution, associated with the presence of the TiN coating, can be achieved.

When an excimer laser is used for nitriding, the mechanism of formation of the nitrided thin-films

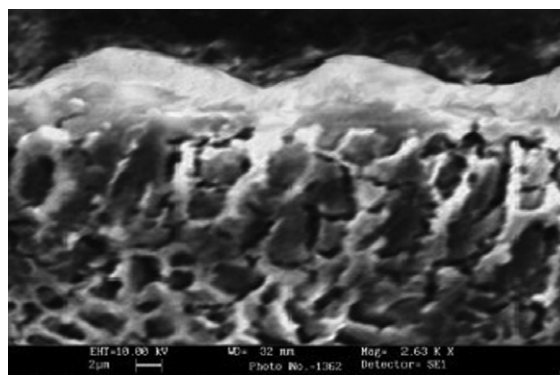


**Figure 6** Typical cross-sectional microstructure of laser nitrided Ti-6Al-4V surface.<sup>45</sup>

differs from that with other types of lasers. In the excimer laser nitriding process, the laser beam is focused on an alloy surface in a chamber containing nitrogen gas. At each pulse, the laser-surface interaction leads to metal heating and vaporization. Vapor plasma expands from the surface and a shock wave dissociates and ionizes nitrogen. It is assumed that nitrogen from the plasma in contact with the surface penetrates to some depth, to form a nitride layer several micrometers thick.<sup>46</sup> For example, excimer laser nitriding of  $\text{AlSi}_7\text{Mg}_{0.3}$  alloy produces an AlN (columnar microstructure) top layer (200–500 nm thick) standing on an AlN (grains) in the alloy diffusion layer.<sup>46</sup> Excimer LSM of aluminum alloy 6013 under nitrogen atmospheres forms AlN– $\text{Al}_2\text{O}_3$  films, which are barriers against corrosion in 3.5% NaCl solution as demonstrated by a reduction in corrosion current density of three orders of magnitude compared with the untreated alloy.<sup>47</sup> Excimer LSM of an Al-2009/ $\text{SiC}_w$  composite in nitrogen gas presents an improved corrosion resistance in 3.5% NaCl solution, due to the formation of AlN in the laser-modified layer. In addition, the reduction of both the

number of SiC whiskers, caused by excimer laser ablation, and the amount of Cu-bearing compounds in the laser-modified layer were also attributed to the improvement in corrosion performance.<sup>48</sup>

#### 4.09.4 Advantages and Limitations of Laser Applied Coatings

**Table 1** summarizes the laser applied coating techniques introduced in this chapter.

Since a laser generates extremely concentrated beam energy, laser-applied coatings offer significant advantages over more conventional surface engineering techniques. The laser techniques can be used to selectively modify surface composition and microstructure without affecting surrounding material properties and causing thermal distortion. Hence, these processes are applicable to processing of critical regions of a component. In addition, a unique advantage of laser coating techniques is the rapid cooling rate, which enables the formation of amorphous or microcrystalline surfaces, modification of

**Table 1** Summary of various laser applied coating techniques introduced in this chapter

Coating techniques		Coating thickness	Coating materials	Type of lasers
Laser cladding		Thick-layer (50 μm to 2 mm)	Metallic alloys; ceramics	CW CO <sub>2</sub> , CW Nd:YAG, HPDL
Laser melt/particle injection		Thick-layer (a few hundred micrometers to 2 mm)	Metal matrix composites	CW CO <sub>2</sub> , CW Nd:YAG, HPDL
Laser surface remelting (laser sealing; laser glazing) of thermal sprayed coatings		Fully or partially melting (melt depth greater than/equal to or less than thermal sprayed coating thickness)	Metallic alloys; metal matrix composites; ceramics	CW CO <sub>2</sub> , CW Nd:YAG, HPDL
Laser-assisted thermal spray		Thick-layer (50 μm to 2 mm)	Metallic alloys; metal matrix composites; ceramics	CW CO <sub>2</sub> , CW Nd:YAG, HPDL
Pulsed laser deposition		Thin-film (up to a few μm)	Metallic alloys; ceramics.	High energy pulsed lasers with ns pulse width, e.g., Excimer laser.
Laser chemical vapor deposition	Pyrolytic	Thin to moderate films (a few micrometers to a few hundred micrometers)	Metallic alloys, ceramics.	CW CO <sub>2</sub> ; CW Nd:YAG, HPDL
	Photolytic	Thin-film (up to a few micrometers)	Metallic alloys	Excimer laser
		Thick-layer (up to 2 mm)		CW CO <sub>2</sub> ; CW Nd:YAG; HPDL
Laser surface alloying		Thin-film (up to a few micrometers)		Pulsed Nd:YAG laser with ns pulse width; Excimer laser
Laser nitriding		Thick-layer	Metal nitrides	CW CO <sub>2</sub> , CW Nd:YAG; HPDL
		Thin-film		Pulsed Nd:YAG laser with ns pulse width; Excimer laser.



grain size and orientation, and control of inclusion morphology and distribution for improved surface microstructure at both the micro and macro levels. For thick coatings, laser techniques produce relatively pore-free surfaces compared with thermal spray coatings, which are integral to the substrate, and thereby eliminate the problem of debonding. For thin-film deposition, laser processing penetrates to greater substrate depths compared with ion beam treatments, which may result in a longer lifetime of the coatings.

On the other hand, a laser beam with sufficient energy density for coating processes has a limited size. Therefore, a laser-applied coating technique is less efficient than other conventional methods like thermal spraying, in terms of coverage rate; in addition, coverage of large area components by laser-applied coatings requires overlapping of individual tracks. This overlapping process could result in an inherently nonuniform microstructure in the treated surface due to the reheating of a small portion of the previous track. Such microstructural changes may or may not have significant influence on corrosion properties, depending on coating materials.

Generally, laser coating techniques, except PLD, require no vacuum conditions, thereby providing substantial manufacturing flexibility. They provide chemically clean, noncontact, possibly remotely operated procedures that can be automated and integrated into other conventional production processes. Therefore, laser-applied coatings have become the preferred choice in many applications. Applications of laser-applied coating techniques can be limited to small areas, complex shapes, and high value/high cost items. However, the interest in laser-applied coatings, especially LC, of large components is increasing. With reductions in the cost of laser power, increased reliability and output power, and capacity of fiber delivery systems, coatings over large areas have become cost effective. These improvements have enabled lower-value items to benefit from laser-based coating techniques. For example, the power generation industry has begun to use LC of boiler tubes and water walls in steam generators, which can be justified in terms of the environmental improvement resulting from the reduced use of chromium. In addition, the development of an effective combination of laser processing and conventional thermal spray systems has provided a new opportunity for depositing dense coatings with improved structural integrity and performance on large surface areas at acceptable process efficiencies for industrial applications.

As with all laser-based processes, a lack of familiarity with the process may be an obstacle to industrial application. However, as more sophisticated operating systems become available, in which computer-generated models are integrated with automated beam and alloy delivery, the scope of applications of laser-applied coating is increasing considerably.

## References

1. Li, L. *Opt. Lasers Eng.* **2000**, 34, 231–253.
2. Mazumder, J. In *Non-equilibrium Synthesis by Laser for Tailored Surface*, Proceeding of the NATO Advanced Study Institute on Laser Processing: Surface Treatment and Film Deposition, Sesimbra, Portugal, July 3–16 1994.
3. Wu, J. D.; Wu, C. Z.; Song, Z. M.; Li, F. M. *Thin Solid Films* **1997**, 311, 62–66.
4. [http://www.ccl.fraunhofer.org/download/innovations\\_in\\_diode\\_laser\\_cladding.pdf](http://www.ccl.fraunhofer.org/download/innovations_in_diode_laser_cladding.pdf).
5. Yue, T. M.; Su, Y. P.; Yang, H. O. *Mater. Lett.* **2007**, 61, 209–212.
6. Gao, Y. L.; Wang, C. S.; Yao, M.; Liu, H. B. *Appl. Surf. Sci.* **2007**, 253, 5306–5311.
7. Singh, J.; Mazumder, J. *Acta Mater.* **1987**, 35, 1987.
8. Singh, J.; Naganathan, K.; Mazumder, J. *High Temp. Technol.* **1987**, 5, 131–137.
9. Ribaud, C.; Mazumder, J. *Mater. Sci. Eng. A* **1989**, 121, 531.
10. Paetes, K.; Giolli, C.; Borgioli, F.; Bardi, U.; Seefeld, T.; Vollertson, F. *Surf. Coat. Technol.* **2008**, 202, 2208–2213.
11. <http://www.shvoong.com/exact-sciences/1607816-structure-oxidation-properties-thermal-barrier/>.
12. Dedamborenea, J.; Lopez, V.; Vazquez, A. J. *Surf. Coat. Technol.* **1994**, 70, 107–113.
13. Singh, J. *J. Mater. Sci.* **1994**, 29, 5232–5258.
14. Fantini, V. In *Laser Cladding: A New Technology for Corrosion and Erosion Protection of Boiler Tubes*, Proceedings of the International Thermal Spray Conference and Exposition, May 14–17, 2007. Beijing, China.
15. Voisey, K. T.; Liu, Z.; Stott, F. H. *Surf. Coat. Technol.* **2006**, 201, 637–648.
16. Tuominen, J.; Vuoristo, P.; Mantyla, T.; Kylmalahti, M.; Vihinen, J.; Andersson, P. H. *J. Therm. Spray Technol.* **2000**, 9, 513.
17. Liu, Z.; Cabrero, J.; Niang, S.; Al-Taha, Z. Y. *Surf. Coat. Technol.* **2007**, 201, 7149–7158.
18. Tsai, P. C.; Hsu, C. S. *Surf. Coat. Technol.* **2004**, 183, 29.
19. Tsai, P. C.; Lee, J. H.; Hsu, C. S. *Surf. Coat. Technol.* **2007**, 201, 5143–5147.
20. Li, J. F.; Li, L.; Stott, F. H. *Thin Solid Films* **2004**, 453–454, 67–71.
21. Nowotny, S.; Scharek, S.; Zieris, R.; Naumann, T.; Beyer, E. In *Innovations in Laser Cladding*, Proceedings of the 19th International Congress on Applications of Lasers & Electro-Optics (ICALEO), 89, A11–15 Michigan, October, 02–05, 2000.
22. Hiraga, H.; Inoue, T.; Kamado, S.; Kojima, Y.; Matsunawa, A.; Shimura, H. *Surf. Coat. Technol.* **2001**, 139, 93–100.
23. Antou, G.; Montavon, G.; Hlawka, F.; Cornet, A.; Coddet, C.; Machi, F. *J. Eur. Ceram. Soc.* **2006**, 26, 3583–3597.
24. Cooper, K. P.; Sleboznick, P. L.; Lucas, K. E.; Hogan, E. A. *J. Mater. Sci.* **1998**, 33, 3805–3816.



25. Wolfe, D.; Singh, J. J. *Mater. Sci.* **1998**, 33, 3677–3692.
26. Michael, N. R.; Ashfold, F. C.; Gareth, M. F.; Henley, S. J. *Chem. Soc. Rev.* **2004**, 33, 23–31.
27. <http://pulsedlaser.net/index.html>.
28. Yano, T.; Ooie, T.; Yoneda, M.; Katsumura, M. In *Proceedings of the Laser Materials Processing Conference*, 1996; Vol. 81, pp A67–A74.
29. Guerrero, R.; Farias, M. H.; Cota-Araiza, L. *Surf. Coat. Technol.* **2002**, 154, 218–222.
30. Qadri, S. B.; Horwitz, J. S.; Chrisey, D. B.; Donovan, E. P.; Skelton, E. F. *Surf. Coat. Technol.* **1996**, 86–87, 149–152.
31. Schulz, U.; Peters, M.; Bach, F.-W.; Tegeder, G. *Mater. Sci. Eng. A*, **2003**, 362, 61–80.
32. Pou, J.; González, P.; García, E.; Fernández, D.; Serra, J.; León, B.; Saunders, S. R. J.; Pérez-Amor, M. *Appl. Surf. Sci.* **1994**, 79/80, 338–343.
33. Mukaida, M.; Osato, K.; Watanabe, A.; Imai, Y.; Kameyama, T.; Fukuda, K. *Thin Solid Films* **1993**, 232, 180–184.
34. Goto, T. *Surf. Coat. Technol.* **2005**, 198, 367–371.
35. Smurov, I.; Ignatiev, M. In *Innovative Intermetallic Compounds by Laser Alloying*, Proceedings of Laser Processing: Surface Treatment and Film Deposition, Sesimbra, Portugal, July 3–16, 1994.
36. McCafferty, E.; Moore, P. G. *J. Electrochem. Soc.* **1986**, 133, 1090–1096.
37. Grover, A. K.; Kumar, D.; Goswami, G. L.; Pappachan, A. L.; Totlani, M. K. *Lasers Eng.* **1998**, 7, 119–131.
38. Anjos, M. A.; Vilar, R.; Li, R. *Surf. Coat. Technol.* **1995**, 70, 235–242.
39. Majumdar, J. D.; Maiwald, T.; Galun, R.; Mordike, B. L.; Manna, I. *Lasers Eng.* **2002**, 12, 147–169.
40. Lee, S.; Park, C.; Lim, Y.; Kwon, H. *J. Nucl. Mater.* **2003**, 321, 177–183.
41. Gutierrez, A.; de Damborenea, J. *Oxid. Met.* **1997**, 47, 259–275.
42. Ejaz, M.; Prescott, R.; Liu, Z. In *Resistance to Metal Dusting by Aluminium Laser-Alloyed Alloy 800H*, EURCORR 2007.
43. Blanco-Pinzon, C.; Liu, Z.; Voisey, K.; Bonilla, F. A.; Skeldon, P.; Thompson, G. E.; Piekoszewski, J.; Chmielewski, A. G. *Corros. Sci.* **2005**, 47, 1251–1269.
44. Xue, L.; Islam, M.; Koul, A. K.; Bibby, M.; Wallace, W. *Adv. Perform. Mater.* **1997**, 4, 25–47.
45. Razavi, R. S.; Salehi, M.; Monirvagheft, M.; Mozafarinia, R. *ISIJ Int.* **2007**, 47, 709–714.
46. Sicard, E.; Boulmer-Leborgne, C.; Andrezza-Vignolle, C.; Frainais, M. *Appl. Phys. A* **2001**, 73, 55–60.
47. Yue, T. M.; Mei, S. M.; Chan, K. C.; Man, H. C. *Mater. Lett.* **1999**, 39, 274–279.
48. Xu, W. L.; Yue, T. M.; Man, H. C. *Surf. Eng.* **2007**, 23, 284–290.

## 4.10 Paint Application

**N. R. Whitehouse**

PRA Coatings Technology Centre, 14 Castle Mews, High Street, Hampton TW12 2NP, UK

© 2010 Elsevier B.V. All rights reserved.

4.10.1	Introduction	2637
4.10.2	Methods of Applying Paints and Coatings	2637
4.10.2.1	Brush Application	2638
4.10.2.2	Roller Application	2638
4.10.2.3	Air Atomized Spray Application	2638
4.10.2.4	High Volume Low Pressure (HVLP) Spray Application	2639
4.10.2.5	Airless Spray Application	2639
4.10.2.6	Air-Assisted Airless Spray Application	2640
4.10.2.7	Heated Spray Application	2640
4.10.2.8	Electrostatic Spray Application	2640
4.10.2.9	Dip Coating	2641
4.10.2.10	Fluidized Bed Coating	2641
4.10.2.11	Flow Coating	2641
4.10.3	Application Conditions	2641
4.10.4	The Applicator	2641
References		2641

### Glossary

**Thinners** A low-viscosity liquid, commonly a solvent, which is added to paint prior to coating application in order to reduce its viscosity and permit easier and more rapid paint application, especially by spraying.

**Transfer efficiency** The ratio, as a percentage, of liquid paint to the quantity of organic coating that is applied to the surface. This can approach 100% for manual brush and roller application but is usually in the 40–70% range for spray application.

### Abbreviations

**HVLP** High velocity low pressure

**ICATS** Industrial coatings applicator training scheme

**ICorr** UK Institute of Corrosion

**VOC** Volatile organic compounds

### 4.10.1 Introduction

Paints and organic coatings may be applied by many methods,<sup>1,2</sup> and it is not possible to consider all of them in detail in a chapter of this size. The main emphasis has been placed, therefore, on the methods of paint application used most commonly to protect constructional steelwork from corrosion<sup>3,4</sup> at either the fabrication stage or when the maintenance painting is required.

### 4.10.2 Methods of Applying Paints and Coatings

There are four main methods of applying paints and coatings for corrosion protection:

- by spreading, for example, by brush or roller;
- by spraying, for example, by air-assisted spray, airless spray and electrostatic spray;
- by dip coating and flow coating;
- by electrodeposition (this method is considered elsewhere in this volume).

For most steel fabrications and structures, protective coating systems are applied by spray. Application by brush is used to a much lesser extent, mainly for minor coating repairs during maintenance painting programs. At factory work, pipes and small fabrications may be dip coated and, during maintenance, some small, relatively inaccessible tanks, for example, may be flow coated.

#### **4.10.2.1 Brush Application**

The application of paints by brush is labor-intensive and time-consuming. Success depends to a very large extent on the quality and suitability of the brush, the rheological properties of the coating, and the diligence of the painter. Industrially, therefore, more rapid and efficient methods of paint application are now preferred.

Brushing is still seen, however, as a very suitable method of application for maintenance painting of small areas, for stripe coating of sharp edges and for coating awkward or restricted areas where spray application would be either difficult, or may not be permitted for reasons of health and safety.

When paints are applied by brush, there is minimal wastage and, usually, very little contamination of adjacent areas. A transfer efficiency approaching 100% is possible. Brushes can also be cleaned easily after use and, thereby, maintained in good condition.

The shape, length, and mechanical properties of the bristles of a paint brush determine its potential performance. The bristles must be capable of holding sufficient paint to allow coverage of a reasonable area from each loading. Bristles made from Chinese hog are excellent in this respect and continue to be favored by many painters, over brushes made with synthetic bristles of nylon or polyester fiber.

The size and shape of a paint brush determine its suitability for a particular coating task. Wide, flat brushes, for example, are most appropriate for coating large flat surfaces. Small round or oval brushes are most appropriate for specialist tasks, such as the coating of more complex surfaces with bolt heads and possible crevices. The action of brushing paint into relatively inaccessible spaces forces the coating into contact with the surface and promotes the wetting needed for full coverage and subsequent good adhesion.

Brushing is not a suitable method of application for paints, which dry rapidly by solvent evaporation, such as vinyl coatings, for example, as the viscosity of the applied film can increase rapidly and may quickly become difficult to apply satisfactorily to give an even film, free from brush marks.

#### **4.10.2.2 Roller Application**

The application of paints manually by roller to large, flat areas can be up to four times faster than coating the same area with a brush. Brushes may still be needed, however, to coat corners and edges satisfactorily. As cleaning of the roller after use can be time-consuming, industrial painters will often discard some types of roller cover (the cheaper ones), without cleaning: these thus become effectively 'single-use' items. The roller cover types used most commonly are mohair, lambswool, nylon and polyester. The cover material selected and the length of the nap will be determined usually by the type of coating to be applied and the surface finish required. The roller itself must be resistant chemically to solvents in the coating and also to any thinners used.

While most hand rollers are loaded simply by dipping them into a tray of paint, it is possible also to mechanize the procedure and feed paint to the roller with an electric pump. The inlet to the pump, typically a flexible tube with a filter on the end, is immersed in the can of paint. Flow to the roller is then controlled by a finger valve on the applicator handle. It is possible to achieve very high transfer efficiency, often better than 95%, when paints are applied by roller.

#### **4.10.2.3 Air Atomized Spray Application**

Air atomized spray guns were the first type of spray guns to be used commercially. They allow paint to be applied up to eight times more quickly than by brush, with better control and uniformity of film thickness. Losses of paint are, however, considerably higher than those incurred by either brush or roller application and considerable skill is needed to produce quality finishes at an economic cost.

In air atomized spray application, also known as conventional spray application, compressed air is used not only to atomize the paint, but also to propel it towards the surface to be coated. As the paint passes through the orifice of the fluid nozzle, it is mixed with compressed air and atomized at pressures, typically between 0.2 and 0.4 MPa.

Paint may be fed to the spray gun by gravity, by suction or by compressed air from a pressurized container. In the gravity feed system, the paint is placed in a cup on top of the spray gun and is fed to the nozzle by gravity. Gravity fed guns are ideal for small spray painting tasks, as they can be cleaned relatively easily after use. In the suction feed system,

the paint is contained in a cup fixed to the underside of the gun and is drawn upwards into the gun as a result of the partial vacuum created at the nozzle by the flow of compressed air. The most common conventional spray gun, when used to paint large areas, relies on the paint being fed to the nozzle by compressed air, via a hose from a pressurized container.

Over-spray and bounce back are the two main disadvantages of conventional air atomized systems. Transfer efficiency is relatively poor and is, typically, between 30 and 45%. Overspray occurs when the paint misses the object being coated. The extent of overspray will depend on the size and shape of the object. It is influenced also by the spraying pressure, spraying distance, skill of the sprayer, and characteristics of the paint itself. Overspray may often contaminate other nearby surfaces on which it settles.

Bounce-back is a consequence of the high pressure of compressed air needed to atomize the paint. The air 'bounces' off the component, or the surface being sprayed, and, in doing so, creates an air barrier to the paint sprayed subsequently. The result is a fog or mist of the atomized paint, a characteristic feature of this method of application.

#### 4.10.2.4 High Volume Low Pressure (HVLP) Spray Application

HVLP spray application is not a new process, but a novel spraying technique that has been developed further commercially to improve transfer efficiency and reduce the emission of volatile organic compounds (VOCs) to the environment, when solvent-borne coatings are applied by an air atomizing spray method. HVLP spray guns have now replaced conventional air atomized spray guns for many paint finishing operations. The HVLP spray gun still relies on air atomization but uses higher volumes of air at low pressures. Paint is delivered to the nozzle of the gun under pressure and is then atomized by this low-pressure air. In order to accommodate the larger volumes of air required, the air passages in the spray cap of the HVLP gun are much larger than those in a conventional spray gun.

HVLP spray application systems were developed originally in France in the 1950s. The earliest systems used a turbine to generate the high volumes of low-pressure air required. They were self-contained, requiring only an electrical supply to power them. Today, most HVLP spray guns use standard compressed-air systems for motive power. In the compressed-air HVLP spray application system,

the air entering the gun is at a pressure of around 0.5 MPa. It is converted to low pressure, typically 0.05 MPa, inside the gun through either a series of valves and chambers designed to promote rapid expansion of the compressed air, or by means of a specially designed baffle located near the tip of the gun. At the low pressures which result, the forward velocity of the spray pattern is reduced considerably, in comparison with the forward velocity of atomized paint from a conventional compressed-air spray gun. As a consequence, there is significantly less overspray and substantially less bounce-back because of the lower velocity of the paint. The combined benefit is a much improved transfer efficiency of at least 65%. Speed of application is comparable with that of conventional air atomized spraying.

#### 4.10.2.5 Airless Spray Application

This method of spray application is very different from the conventional techniques described previously. In airless spray equipment, the paint is not atomized by air. A fluid pump is used to force paint at high pressure through a fluid hose to the gun. Atomization is achieved by the release of highly pressurized liquid paint through a small orifice in the spray tip. Fluid nozzle sizes range, typically, in diameter from 0.03 to 0.15 mm. On exit from the small orifice in the spray tip, the paint atomizes into a cloud of ultrafine particles which then move forward slowly towards the surface to be coated. The slowing down is caused by the resistance of the atmospheric air and the cloud of ultrafine particles impacts on to the surface at a relatively slow speed, in comparison with conventional spray application. As there is no overspray and no bounce back, a transfer efficiency of well over 50% can usually be achieved. Penetration of the paint into crevices and recesses is good and, in the absence of entrained atomizing air, little or no solvent evaporation occurs during the spraying process. As a result, the subsequent flow out of liquid paint on the surface of the work piece is good.

Typically, the fluid pumps used with airless spray equipment have multiplication ratios of 48:1 or 60:1. This is the ratio of fluid output pressure to air input pressure. As the fluid output pressure at the spray tip can be of the order of 27 MPa, airless spray guns can deliver paint very rapidly and enable large areas of steel structures, for example, to be coated quickly. A surface area of 300 m<sup>2</sup>, for example, can be coated in 1 h. The skill and experience of the sprayer will always determine the evenness of coverage and the

final quality of the finish. Careful choice of tip size and spray width (the 'fan') is critical to success and the guidance given by the paint manufacturer on the technical data sheet for the coating product to be sprayed needs always to be observed.

It is important to note that airless spray guns can be dangerous in unsafe hands because, close to the nozzle, the paint being delivered is at a very high pressure. To prevent operators from carelessly, in effect, 'injecting' them with paint, all airless spray guns are fitted with tip safety guards.

#### **4.10.2.6 Air-Assisted Airless Spray Application**

As its name implies, air-assisted airless spray is a hybrid of airless spray application and conventional air atomized spray application. The purpose of introducing a compressed air supply is to aid atomization and improve fan pattern shaping, without creating excessive bounce back. Air-assisted spray application requires a lower fluid pressure than airless spray application; typically between 3 and 10 MPa. Spray tips with larger nozzle orifices can, therefore, be used. Transfer efficiency is typically between 65 and 70%.

The major difference in construction between an air-assisted airless spray gun and an air atomized spray gun is the atomizing tip. The air-atomizing tip has a fluid nozzle and an air cap which delivers a ring of atomizing air around the fluid nozzle. In addition, two fine jets of air are emitted from ports in small 'shoulders' on each side of the tip. The purpose of these two air jets is to break up any large droplets of paint, formed as a consequence of lowering the fluid pressure, and complete the atomization.

#### **4.10.2.7 Heated Spray Application**

Both conventional air atomized spray and airless spray equipment can be used to apply paint coatings which have first been heated to 60–80 °C. Raising the temperature of the paint to this level lowers its viscosity (by as much as two-thirds of its viscosity at ambient temperature), aids flow and reduces drying time. If the heated paint is applied by the conventional air atomized spray, for example, the air pressure needed can often be halved and transfer efficiency improved. If the heated paint is applied by airless spray, a lower fluid pressure is needed and the efficiency of the equipment as a whole is improved.

More sophisticated heated spray application equipment has been developed in previous years to apply some solvent-free two-pack coatings, notably epoxies. In this type of spray equipment, base and curing agent are heated separately, pumped to the gun and then mixed either with a small agitator in the gun itself or, with arguably less efficiency, in the turbulence of the emerging spray. Accurate metering of the two components is essential whichever mixing method is used and this is achieved with the aid of carefully calibrated pumps. Twin-feed heated airless spray equipment is expensive and needs always to be maintained well. Specially trained operators are usually required.

#### **4.10.2.8 Electrostatic Spray Application**

This application method takes advantage of electrostatic attraction to improve transfer efficiency. When paint droplets are passed through a powerful electrostatic field, they become charged. If the work piece is earthed, the charged droplets are attracted and will coat not only the front face of the work piece but also some of the back face. The extent of coating 'wrap round' achieved, will depend on the size of the work piece and its depth.

In most manual electrostatic spray guns, the power pack delivers, typically, a voltage of 60–85 kV at a current of 150  $\mu$ A to a point electrode close, but external to the spray head. The air in the immediate vicinity of the spray head becomes highly charged and the charge is transferred partially to the atomized paint droplets, as they pass through. It is also possible for paint to be charged directly by an electrode fitted inside the gun itself. For electrostatic spray guns with internal charging, an operating voltage of 30 kV is typical.

All of the spray application methods, which have been described above, can benefit from the addition of electrostatic charging. Transfer efficiency is improved throughout, often by as much as 20%. For steelwork, the main advantage of applying paints by electrostatic spray is gained when long runs of perimeter-fencing or similar 'open' structures need to be coated.

Electrostatics add significantly to the cost of the spray equipment and, as a consequence of the charge imparted to the spray droplets, only relatively thin coatings can be applied easily. Electrostatic spraying methods are used most commonly for industrial finishing operations, in particular the automated application of coating powders.<sup>5</sup>



#### 4.10.2.9 Dip Coating

Small fabrications, which may be both difficult and time-consuming to paint satisfactorily by brush and difficult to paint by spray, can often be painted more effectively by dipping. Steel pipes are also often coated in this way. Specially formulated liquid paints are needed for dipping tanks and, in use regular checks on the viscosity of the paint are required. Additions of solvent have to be made from time to time to adjust the viscosity of the paint to its specified level. Dip coating is a rapid process in which all accessible areas are coated at one time. However, controlled withdrawal of the work piece from the bath is critical to success to minimize the presence of 'runs' and sags in the finish. Sharp edges, if present in the work piece, will not be coated to the same thickness as the main surfaces.

#### 4.10.2.10 Fluidized Bed Coating

Thermoplastic coating powders can be applied, at works, to heavy metal pipes by a somewhat different dipping method called *fluidized bed coating*.<sup>5</sup> The coating powder to be applied is loaded on a porous membrane near the bottom of the dip tank and air, at low pressure and in high volume, is passed upwards through the membrane to 'fluidize' the powder. Low-pressure air blowers are used for this purpose. The work piece is first heated to a little above the melting point of the coating powder. It is then lowered into the fluidized bed and subsequently withdrawn. The dwell time, which may range from a few seconds to several minutes, as required, will determine the thickness of coating achieved. If the coating powder being applied is a thermosetting type, the coated work piece will need then to be postcured in an oven. Very thick powder coatings can be built up on heavy gauge steel pipes very satisfactorily by this relatively simple application method.

#### 4.10.2.11 Flow Coating

In a variation on the dipping process of paint application, small fixed items of intricate shape are often best recoated on site by flow coating. Electrical transformer radiator tanks, for example, can be recoated most effectively in this way.<sup>3</sup> Paint is poured into a temporary tank built around the item and allowed to flow into any corners and crevices. The excess paint is then drained; if still clean, can be used again.

Specially formulated paints are again required. For the process to be successful, very thorough precleaning, usually with solvent, is essential.

### 4.10.3 Application Conditions

The main environmental conditions which can have a bearing on the success of any paint application method are temperature, relative humidity and ventilation. The paint itself needs also to be in good condition and within shelf-life. Temperature will influence the viscosity of the paint, rate of evaporation of solvent (which may be water), drying time, and curing time of the coating. Application of paints at low ambient temperatures to cold surfaces will extend drying time, curing time and increase the overcoating interval. Conversely, application of paints at high ambient temperatures will increase solvent evaporation, drying time, curing time and may shorten the overcoating interval.

The level of moisture present in the air when paint is being applied is equally important. If the relative humidity is too high, unwanted condensation may occur on the surface of the workpiece. Any moisture on the surface may interfere with paint adhesion and may also interfere with the curing of some two-pack chemically cured coatings. Conversely, if the coating being applied relies on the presence of moisture in the air to cure it, then low relative humidity can also become a problem. Good ventilation is always desirable, as it will aid initial drying of the coating and help to maintain air safety in the working environment.

### 4.10.4 The Applicator

The final outcome of any paint application process will be determined, to a great extent, by the skill and diligence of the applicator. In 2005, the UK Institute of Corrosion (ICorr) launched an Industrial Coating Applicator Training Scheme<sup>6</sup> (ICATS). The scheme, which is operated through the ICorr trading subsidiary Correx Ltd., is a comprehensive structured program for the training, certification and registration of industrial surface preparation and coating operatives.

## References

1. Roobol, N. R. *Industrial Painting: Principles and Practices*; Hanser, 1997.
2. Tank, G. F. *Industrial Paint Finishing Techniques and Processes*; Ellis Horwood, 1991.

3. Chandler, K. A.; Bayliss, D. A. *Corrosion Protection of Steel Structures*; Elsevier, 1985.
4. Bayliss, D. A.; Deacon, D. H. *Steelwork Corrosion Control*; Taylor & Francis, 2002.
5. Cowley, M.; Griffiths, M. *Coating Powders and their Application: A Practical Guide*; Paint Research Association, 2004.
6. Goldie, B. P. F. *Corros. Mgmt* **2005**, 64, 10–11.

## 4.11 Paint Formulation

### G. P. Bierwagen

Coatings and Polymeric Materials, North Dakota State University, Room No. 216B, 1735 Research Park Drive, Fargo, ND 58102, USA

### A. M. Huovinen

Coatings and Polymeric Materials, North Dakota State University, 1735 Research Park Drive, Fargo, ND 58102, USA

© 2010 Elsevier B.V. All rights reserved.

---

<b>4.11.1</b>	<b>Introduction</b>	2644
4.11.1.1	Materials Used in Coatings	2645
4.11.1.2	Protection of Surfaces by Paints and Organic Coatings	2645
4.11.1.3	Unique Properties of Paints and Coatings for Corrosion Control	2646
4.11.1.4	Formulation as a Scientific Design Activity	2646
4.11.1.5	Testing of Corrosion Protection by Paints and Organic Coatings and Feedback to Coatings Design	2646
<b>4.11.2</b>	<b>Overview of Corrosion Control by Paints and Organic Coatings</b>	2647
4.11.2.1	Barrier Protection by Coatings	2647
4.11.2.2	Active Metal Pigmentation and Cathodic Protection	2648
4.11.2.3	Inhibitor Release Coatings	2649
4.11.2.4	Comments on 'Smart Coatings' and their Relative 'Intelligence'	2650
<b>4.11.3</b>	<b>Components of Organic Coatings for Corrosion Control</b>	2650
4.11.3.1	Polymer(s) for Corrosion Control Coatings	2651
4.11.3.1.1	Epoxies	2651
4.11.3.1.2	Isocyanate-based polymers: polyurethanes and polyureas	2652
4.11.3.1.3	Acrylics	2652
4.11.3.1.4	Alkyds	2652
4.11.3.1.5	Vinyl polymers	2652
4.11.3.1.6	Mixtures including silicones	2652
4.11.3.1.7	Sol-gel and hybrids	2652
4.11.3.2	Pigments	2652
4.11.3.2.1	Inhibitive pigments	2652
4.11.3.2.2	Reactive metal pigments: spherical, lamellar, and platelet/flake	2653
4.11.3.2.3	Inert/extenders pigments	2653
4.11.3.2.4	Colored pigments	2653
4.11.3.3	Additives: Surfactants, Rheological Control Agents, Flow Agents, Defoamers, Wetting Agents, Dispersants, etc.	2653
4.11.3.4	Solvents/Carrier Fluids	2654
4.11.3.5	Catalysts for Reactive Polymer (Usually Two Component) Curing	2654
<b>4.11.4</b>	<b>Coatings Application Methods and Corrosion Protection</b>	2654
<b>4.11.5</b>	<b>Coating Wetting and Adhesion in Coatings</b>	2655
<b>4.11.6</b>	<b>Coatings Formulation/Design</b>	2655
4.11.6.1	Principle Objectives of Formulation – Coatings Design	2655
4.11.6.2	Volume Effects in Coatings	2657
4.11.6.3	Setting Formulation Goals	2659
4.11.6.3.1	Use of combinatorial methods in coating design and choice	2661
<b>4.11.7</b>	<b>Coatings Design and Testing: Choosing the Final Formula</b>	2663
<b>4.11.8</b>	<b>Summary and Conclusions</b>	2664
<b>References</b>		2664

---

**Abbreviations**

<b>AA 2024T3</b>	An aluminum alloy commonly used in aircraft; see common alloy numbering system
<b>ASTM</b>	American Society for Testing and Materials
<b>B117</b>	Salt spray accelerated aging testing protocol, as per ASTM B117
<b>CPVC</b>	Critical pigment volume concentration
<b>EDX</b>	Energy dispersive X-ray (spectroscopy)
<b>EIS</b>	Electrochemical impedance spectroscopy
<b>ENM</b>	Electrochemical noise methods
<b>FBE</b>	Fusion bonded epoxy
<b>NACE</b>	National Association of Corrosion Engineers
<b>NDSU</b>	North Dakota State University
<b>OCP</b>	Open circuit potential or free corrosion potential
<b>OEM</b>	Original equipment manufacturer
<b>PUR</b>	Polyurethane system
<b>PVC</b>	Pigment volume concentration
<b>RM</b>	Raw material
<b>SEM</b>	Scanning electron microscopy
<b>SSPC</b>	Society for Protective Coatings
<b>UV</b>	Ultraviolet light, light in the frequency range of 10–400 nm
<b>XPS</b>	X-ray photoelectron spectroscopy
<b>XRD</b>	X-ray diffraction

**Symbols**

$E_{\text{corr}}$	Open-circuit potential (OCP) or free corrosion potential
$F$	Formula
$h$	Thickness of a coating
$R_{\text{ft}}(t)$	Electrochemical noise resistance as a function of time
$R_{\text{n}}$	Electrochemical noise resistance
$T_{\text{g}}$	Glass transition temperature
$ Z(t)_0 $	Low-frequency electrochemical impedance modulus as a function of time
$ Z_0 $	Low-frequency impedance modulus
$Z(\omega)$	Electrochemical impedance as a function of frequency $\omega$
$\Delta$	Reduced PVC, pigment volume concentration/critical pigment volume concentration. A quick and useful number for indicating whether a given PVC is above or below the system's CPVC
$\phi$	Volume concentration or fraction of a species

**4.11.1 Introduction**

How does one formulate/design a corrosion protective coating? This is the key question that this chapter seeks to answer. Before 1900, the process of formulating/designing organic coatings was an art form, similar to that of developing food recipes. Around the dawn of the twentieth century, awareness of natural oil film formation and crosslinking began to be developed, as well as the optical and physical effects of pigmentation. (It is noteworthy, in the context of the timing of coating science development, that research and development on paints and coatings began formally at North Dakota State University in 1905, and the authors' academic department is a direct descendant of this coatings research program.) The first science impacting directly on coatings was chemistry, and later chemistry's great twentieth century offshoot, polymer chemistry and science. Since then, optical physics, composite science, and materials science<sup>1</sup> have all contributed to the science and design/formulating of organic coatings. One of the most important functions of organic coatings is to protect substrates of all types. When the substrate is a metal, the primary function of the coating is to protect the metal substrate from corrosion. Most OEM coatings, whether for automobiles, aircraft, or metal furniture, have the primary function to protect against corrosion. The entire class of coatings known as 'industrial maintenance' coatings have corrosion protection as their primary purpose. The least expensive method, in reality, of protecting an object against corrosion is to coat the object with a film of the proper organic coating system. Consider making a car entirely from stainless steel versus producing it as a painted steel frame, galvanized steel sheet outer system, and plastic composite bumper system that is the modern car. From this, one easily sees the efficiencies in cost and appearance in using organic coatings for protecting against materials degradation.

The objectives of this chapter are as follows:

- describe briefly the material components of coatings;
- describe how the performance requirements of a corrosion protective coating are specified;
- describe how one designs a corrosion protective coating;
- describe briefly how a corrosion protective coating is tested to determine whether it meets its performance requirements.

While pursuing these objectives, we have to include general discussions concerning the component materials of a coating, specifying coating performance requirements, the process of the coating design, and the testing of coatings. As much as possible, the focus of these discussions will be on corrosion protective coatings, and the emphasis will be on considerations of the rapid and efficient design of such coatings.

All the components of a corrosion-protective coating system must function properly for it to provide all the elements of physical protection and optical performance that it was designed to provide. To ensure proper coating system functions over its desired lifetime, one must have the capacity to define, measure, and evaluate the properties that determine these functions in use. For corrosion-protective organic coatings, the desired properties can be summarized as mechanical/chemical protection of the metal substrate, with acceptable appearance parameters. This is easily enough said, but difficult to achieve in practice. There are many properties one can measure in a corrosion-protective coating system. Indeed, the present cohort of designers and users of these systems are uncertain about which set of measurements to choose. They seek the set that will give the maximum amount of pertinent information with least effort and expense. The *sine qua non* of such properties is yet to be determined, but the current 'best practice' thinking among the coating-science community focuses on adhesion, solvent resistance, corrosion protection, and appropriate optical performance over its lifetime. It also takes into account the effects of UV exposure, hot and cold organic fluids, seawater, humidity and temperature cycles, mechanical stress, and abrasion. All these must be considered while choosing the tests/results protocol that the coatings/pretreatment must undergo to be 'fit for use.' We discuss the current thinking on the measurements/exposures for corrosion protective coatings as well as the accuracy/validity they provide in practice. We also discuss spectral, optical, and electrochemical testing of coatings system properties and their changes in simulated and field exposure. The differences between test performance and real use performance are considered, especially with respect to film application uniformity and film damage<sup>2</sup> (taken with some changes from the introduction/abstract of Bierwagen and Tallman).<sup>2</sup>

One of the overriding themes of this chapter is that organic coatings, especially those for corrosion protection, are random two-phase composite materials and must be specified, designed and tested as such.<sup>3</sup> As clearly stated in Chapter 1 of *Random*

*Heterogeneous Materials*,<sup>4</sup> the proper way to interpret the behavior of pigmented organic coatings is as a random heterogeneous composite where the volume fraction of the pigment phase is a crucial measure of concentration of materials. This measure, known now in the coatings industry as the pigment volume concentration (PVC),<sup>3,5,6</sup> is the crucial measure of pigment concentration for the characterization and design of pigmented coatings. Another crucial measure of pigmentation for coatings formulation is the critical pigment volume concentration (CPVC). We discuss this in [Section 4.11.6.1](#).

#### 4.11.1.1 Materials Used in Coatings

In general, when considering liquid coatings, one chooses the materials comprising a corrosion-protective coating from the three classes of materials shown in [Figure 1](#). Many of the negative environmental impacts of coatings come from the solvents emitted during coating application and curing/drying. If one uses powder coatings, for example, the use of solvents is abandoned. One should note here, that in many dispersions, because of environmental considerations, water is a carrier liquid for a fine particle dispersion of polymer and pigment rather than a true molecular solvent for the coating. The resins are the organic polymer matrices of coatings; pigments are the solid, insoluble particles that assist the coating in supplying color and other functions, including protection of a substrate.

#### 4.11.1.2 Protection of Surfaces by Paints and Organic Coatings

[Figure 2](#) gives a general description of the methods by which one stops corrosion. A proper choice of substrates may accomplish some of these, but often, a coating is also used as a supplemental protection.

Corrosion-protective coatings work in three modes<sup>7</sup>: (i) barrier protection; (ii) cathodic/sacrificial protection (i.e., zinc rich coatings)<sup>8–10</sup>; and (iii) inhibitive/passivation protection (i.e., coatings formulated with partially soluble inhibitive pigments and/or additives). The latter two modes are what may be designated as 'active' protection, that is, a protection that is provided to the metal substrate in damaged areas of a coating by such processes as dissolution,

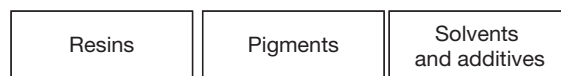


**Figure 1** Primary components of organic coatings.



mass transport, chemical reaction, and adsorption. Barrier protection is the passive mode, by which intact coatings provide protection to metal substrates, and is the protection provided by the reduction of the transport of materials, ions, or charge.<sup>11–13</sup> Barrier properties that are important for coatings are the resistance to the transport (small diffusion coefficients) of the chemical species of the corrosion reactions, which are in most cases  $\text{H}_2\text{O}$ ,  $\text{O}_2$ , and electrolyte ions.

#### 4.11.1.3 Unique Properties of Paints and Coatings for Corrosion Control

Coatings decorate and protect the substrate to which they are applied. One can summarize the unique features required in corrosion-protective organic coatings for the protection of metal substrates. Such a coating must have a combination of barrier, sacrificial and inhibition/passivation protection of the coating–metal substrate interface. For this protection to occur, the prime features of the painted metal system are as follows:

Dry film properties:

- A. Wet/dry adhesion-keeping coating in contact with the substrate under exposure conditions;
- B. Low ion, water, and oxygen permeability of the coating film – barrier effects;
- C. Low coating/film conductivity – minimize flow of current in local corrosion cells and stop ion and electron motion in film;
- D. Coating/film stability to its environment, stability to hydrolysis and UV radiation, thermal stability, etc.;

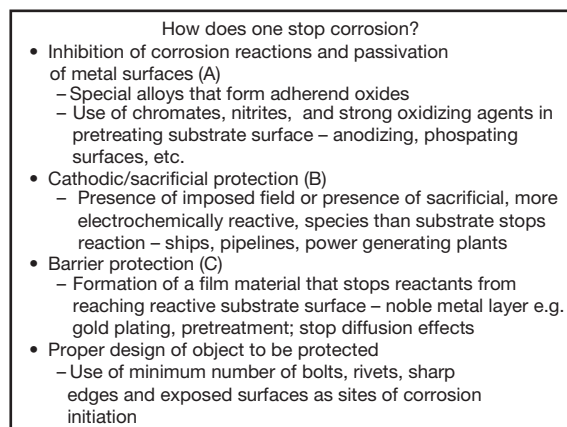


**Figure 2** Summary of modes of corrosion protection of metal substrates.

- E. Strong adsorption of coating to substrate interface – good wetting of the substrate by the coating system;
- F. Coating pigmentation for passivation/inhibition (chromates), sacrificial (Zn-rich coatings,  $A = 1$ ), or barrier ( $A = \text{PVC/CPVC} \cong 0.85$ ) coatings.

System properties:

- A. Good quality metal substrate and pretreatment;
- B. Coating film be applied uniformly in a defect-free manner to metal substrates of all shapes and sizes.

In this list, adhesion to metal substrates, strong absorption to metal substrates, and wetting of metal substrates are all unique features of organic systems, as they interact with metal–metal oxide surfaces. The ability to be applied uniformly with no defects is crucial to the performance of corrosion-protective coatings. This means that for corrosion protective coatings, the method of application is almost as important as the properties of the coating being applied. Each of these topics will be discussed in more detail below.

#### 4.11.1.4 Formulation as a Scientific Design Activity

The basics of coating formulation have been discussed often,<sup>14</sup> but the primary issues of designing a coating still remain the same. The complexity of the design process is quite extensive. This has been noted as a general issue of the design process, as well as specifically for coating designs (Figure 3).<sup>15,16</sup>

#### 4.11.1.5 Testing of Corrosion Protection by Paints and Organic Coatings and Feedback to Coatings Design

The final stage of coating design is the testing of the coating to determine whether it meets the design

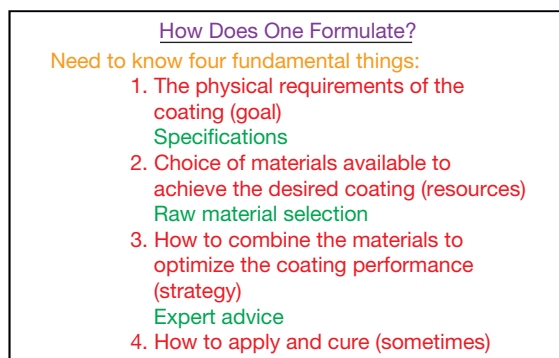


**Figure 3** Schematic of multilayer coating system.

specifications. This is often done using standardized test methods (often from ASTM or SSPC) for measuring the obvious parameters such as color, density, and hardness.<sup>17</sup> The testing of corrosion performance is often much less of a standardized issue, and many of the ASTM Test Methods for Corrosion Protection by Coatings, including B117, have met with serious disagreement from many researchers in their application. Much of the work on the testing of coatings for corrosion protection has involved the use of electrochemical methods to supplement or even replace the more traditional subjective test methods still in use for this purpose.<sup>18</sup> This is discussed in more detail in subsequent sections.

As the coating is tested, many small incremental modifications of the original design are made to achieve the best combination of the properties that still satisfy the original specifications. The final design is thus a nonideal choice of materials, which optimizes the total performance, but is often less than optimal among the many physical and chemical properties of the coating.

#### 4.11.2 Overview of Corrosion Control by Paints and Organic Coatings

As stated earlier, there are several general routes by which paints and coatings protect metal substrates from oxidation/corrosion. More specifically, they provide barrier protection for the substrate, cathodic/sacrificial protection by metal pigments more reactive than the metal substrate, and inhibition/passivation of the metal substrate by dissolution/ion exchange/controlled release from pigments or additives in the coating. Coatings are applied to substrates largely to protect them from the corrosive environments in which they function. Therefore, one can say that the passive barrier function of coatings is the primary mode by which they protect substrates. The active corrosion protective functions of coatings, the release or dissolution of inhibitors, or passivating chemicals, and sacrificial protection, occur in most cases when the coating is damaged and then breached, or by defects in the coating application process, which give incomplete coverage to the substrate.

Most often in the use of organic coatings for corrosion protection, the total coating system is multilayered.<sup>2</sup> The first organic coating layer applied to the metal substrate, or as is often the case, over a thin inorganic pretreatment layer on the metal substrate, is often called the primer layer. This layer is that

portion of a coating system that most frequently contains the active components, metal pigments, or soluble pigments that give active functionality to the total coating system. The subsequent coatings on top of the primer often provide most of the barrier properties of the total system. For example, the multilayered coating system usually contains (at a minimum) a primer/pretreatment layer, primer, base coat, and top coat. The optical functions of the total coating system, such as hiding, color, and camouflage, are provided most often by the coatings applied over the primer.

##### 4.11.2.1 Barrier Protection by Coatings

It is known that the primary function of a corrosion-protective coating system is to be a barrier between the coating system and the environment. However, no coating system now in use stops completely the transport of oxygen, water, and ions to the coatings-metal interface. Barrier protection is the reduction of the transport of materials, ions, or charge to the surface of the metal substrate.<sup>11-13</sup> Barrier properties that are important for coatings are resistance to the transport (small diffusion coefficients) of the chemical species of the corrosion reactions, in most cases,  $\text{H}_2\text{O}$ ,  $\text{O}_2$ , and electrolyte ions usually  $\text{Cl}^-$ ,  $\text{SO}_4^{2-}$ , and a mixture of cations such as  $\text{Na}^+$ ,  $\text{K}^+$ ,  $\text{NH}_4^+$ , and  $\text{Ca}^{2+}$ . Along with these barrier properties, high resistance to the flow of charge, electronic and ionic, is also important, as has been observed by Mayne<sup>12</sup> and Funke.<sup>11</sup> The barrier properties of polymer and paint films are known to be increased by their exposure to various gases and liquids.<sup>13</sup> The exposure of polymer and paint films to solvents that plasticize them greatly increases the transport properties of these films if they reduce the effective  $T_g$  of the films below the temperature of film use. Also, the exposure of these films to aqueous electrolyte solutions causes many coating films to swell and develop conductive pathways not present in the film before exposure.<sup>19</sup> These also severely reduce the barrier properties of the coating.

Let us examine an idealized multilayered coating system of three layers as shown in Figure 4.

In most coating systems, the outermost layer, in this case Coating III, is the layer whose primary function is barrier protection. This means that the polymer of this layer has to reduce the transport of water, and of oxygen to a lesser extent, into the coating film, as well as prevent the movement of dissolved ionic species through the film. The coating

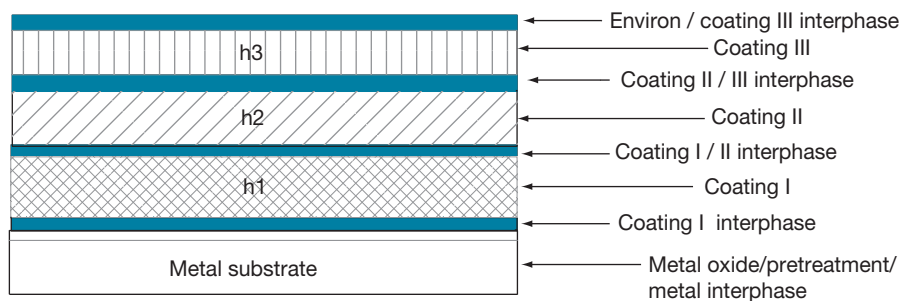


**Figure 4** Schematic of multilayer coating system.

polymers that achieve this best are those that are hydrophobic and resist photooxidation in exposure. Examples of these are exterior quality urethanes, fluorourethanes, and fluorocarbon-based polymers such as kynar. One should note that the interphase region between each layer in the coating is separately identified, because this region often performs in a manner superior to the bulk of the coating *vis à vis* resistance to transport. In a recent paper from this laboratory, the interfacial region was identified separately in an equivalent circuit description of a coating, and this enabled one to identify this region and its contribution to the barrier properties of the system.<sup>20</sup> The issue of the interfacial layer and its importance in coating design performance are described in detail in several references.<sup>3,21</sup>

The barrier properties of coatings can be estimated by the use of electrochemical impedance spectroscopy (EIS) and electrochemical noise methods (ENM).<sup>22–24</sup> The monitoring of the low-frequency impedance modulus and/or the electrochemical noise resistance with exposure time (either natural exposure or accelerated exposure),  $|Z(t)_{\text{lowf}}|$  or  $R_n(t)$ , have shown themselves to be very useful techniques for following the changes in coating performance in the field or accelerated testing. Measuring the diffusion of water into a coating by single frequency EIS measurements is also a powerful tool for monitoring aqueous diffusion in coatings.<sup>25</sup> This group of electrochemical techniques provides a strong set of measurement tools for examining the barrier properties of organic coatings over metal substrate. Permeability measurements for water and oxygen performed by the use of a film and a sensing device of a gravimetric measurement for the permeant have also been performed, for example, for water, weight change in a desiccant on the other side of a film. There is a considerable literature in this area.<sup>26</sup> Gravimetric measurement of water pickup by coatings can supplement the methods just described.

#### 4.11.2.2 Active Metal Pigmentation and Cathodic Protection

The other modes in which coatings provide corrosion protection are active modes. In the case of metal-rich coatings, the protection comes from the chemical activity, or oxidation of an active metal pigment to provide sacrificial, cathodic protection to a less active metal substrate. Metal-rich coatings provide protection for metal substrates in a unique manner. They provide cathodic protection to the underlying substrate through high volume concentration of a more reactive metal than the substrate.<sup>27,28</sup> At the later stages of their performance, the basic metal oxides created from the particulate metal in the coating help to generate a barrier and passivation protection. A general description of these coatings is that they are designed with high volume fraction of metal pigment particles (near CPVC) dispersed in a non-conductive polymer or inorganic matrix. They were originally designed in the late 1930s with particulate Zn in matrix over steel. As particle volume fraction is high enough to give almost complete particle-to-particle contact, when a coating is applied to a metal substrate, it provides sacrificial/cathodic protection to the substrate. In effect, Zn-rich coatings act as a galvanizing layer that can be applied *in situ* to metal objects that cannot receive a galvanizing Zn or Zn/Al alloy layer. Metal-rich coatings are most often used as a primer, with a decorative or functional top-coat, which mainly provides barrier protection. Metal-rich coatings need basic material research to enhance their design and function. North Dakota State University has been active in this area recently applying metal-rich methods to the protection of Al alloys and other metals more reactive than steel.<sup>29–31</sup> This work indicates that Mg-rich coatings can provide similar protection to aerospace Al alloys such as AA 2024 T-3. This is the first completely Cr-free (no Cr-based pigments or pretreatments) protection system that gives long-term protection to such alloys.

The protection of automobile steel sheet outer bodies by galvanizing was first introduced by Porsche in circa 1970, and has been extended to all types of automobiles throughout the world. In conjunction with cationic electrodeposition coatings at about the same time, galvanized sheet steel increased the corrosion protected lifetime of the automotive coating systems considerably. Pure Zn as well as Zn–Al alloys are the common metallic layers used to protect sheet steel.<sup>32</sup> The warranties in cars for perforation corrosion protection are now commonly about 10 years<sup>33</sup> and the automotive companies have current goals of 15 years of perforation protection with 10 years of cosmetic appearance protection. The use of Zn-rich coatings has always aimed at providing protection similar to the galvanizing metal layers used on sheet steel. A review of the production and properties of galvanized steels has been published fairly recently.<sup>34</sup> Further, the problems in edge protection by galvanized layers have been studied recently and remain some of the major problems in the use of galvanized sheet.<sup>35</sup>

In the original paper on Mg-rich coatings,<sup>29</sup> a summary of the performance of a Zn-rich coating was given and was utilized to design and predict the performance of metal-rich coatings in general. This summary is paraphrased as follows:

1. This class of coatings uses either organic or inorganic matrices, and is used mainly as a primer.
2. They are pigmented with particulate Zn, in either spherical, random shape, or flake form.
3. The PVC of the Zn pigment in the coating should equal or exceed the CPVC for the coating to properly provide sacrificial/cathodic protection to the underlying steel substrate. At or above the CPVC, the Zn particles are all in mutual contact as well as in electrical contact with the steel substrate. The CPVC values in Zn-rich coatings range from 40 to 60%. There is some evidence that the electrical connectivity of the Zn particles carries over from the  $PVC = CPVC$  ( $\sim 60$ – $70\%$  by volume) to  $PVC = \text{volume percolation threshold}$ <sup>36</sup> for Zn ( $\sim 30\%$  by volume for spherical particles). Therefore, some sacrificial protection occurs over this range even while the Zn is being consumed by sacrificial oxidation. The percolation threshold for flake pigments may be different depending on particle alignment.<sup>37</sup>
4. The mode of protection is sacrificial as long as the Zn is electrically connected to the steel, as the Zn is more anodic (reactive) than Fe (major constituent of steel) in the electrochemical series. Then the

mixed Zn oxides formed in the sacrificial oxidation fill the damaged areas and also sometimes passivate the steel surface by their basic nature.

5. The organic or inorganic matrix of the coating must be stable under the basic conditions created by the zinc oxide, hydroxide, etc., formed from the oxidation of Zn in the presence of the electrolyte. It must also adhere well to the steel alloys and be stable in a corroding environment.
6. These primer coatings are usually top-coated to function optimally and have a long field lifetime. When used properly, these primers provide almost as much protection to steel as galvanizing. The coating system of a Zn-rich primer and an exterior durable topcoat provide both barrier and damage (sacrificial/cathodic) protection to steel substrates.

Much of what has been said concerning Zn-rich coatings holds true for Mg-rich coatings as well.<sup>29–31</sup>

Other metals and alloys have also been used as active metals in metal-rich coatings. Mn in particulate form has been used in coatings as an active metal pigment in the protection of steel<sup>38</sup>; various blends of Al pigments and Zn pigments have been proved to give corrosion protection to various steel alloys.<sup>39</sup> In summary, if one can get a stable metal  $M_1$  pigment – organic (or inorganic) matrix dispersion formed, and cast a film that will adhere to a less active metal  $M_2$  substrate such that there is electrical connectivity between the  $M_1$  particles and the  $M_2$  substrate, this substrate is now cathodically protected. For practical protection, the mixed potential developed at the  $M_2$  substrate surface,  $E_{M_1/M_2}$ , should be 100 mV below the  $M_1$  open circuit potential (OCP).

#### 4.11.2.3 Inhibitor Release Coatings

Like the cathodic protective coatings described, inhibitor release coatings that provide corrosion protection are active coatings, not just a passive barrier. In this class of coatings, the physical activity of dissolution and the physicochemical activity of substrate inhibition give protection to the substrate. Inhibitors are always discussed in books<sup>40,41</sup> and articles on corrosion control, but they are very far from being understood. Inhibitor release coatings are almost always designed and pigmented in an empirical manner with inhibitor release rates and time of release sustenance most often chosen by trial-and-error experimentation rather than by rational design. A paper by del Amo *et al.* is an example of this type of formulation methodology.<sup>42</sup> Sinko<sup>43</sup> gives an

interesting description of how important the solubility properties and other nonelectrochemical properties of inhibitive chromate pigments are to their successful use in coatings, and the challenges faced by those seeking to replace them for environmental reasons. Kendig and Buchheit also review chromates as inhibitors for Al alloy protection in coatings and give some very useful observations on the requirements for inhibitor pigments and the problems in controlling the 'controlled release' of inhibitors from coatings.<sup>44</sup> There are a considerable number of recent publications discussing new corrosion inhibitors and inhibitive pigments, but very little is said about their release rates in a lifetime of effective corrosion inhibition.

Water or aqueous electrolyte solutions, are the primary solvents that cause release of inhibitors from coatings. Therefore, the barrier properties of the coating toward water are important in inhibitor release. Very few studies have been published on the modeling of inhibitor release and the effects of solubility, water, geometry of coating, damage to coating, etc.<sup>45,46</sup> In general, organic inhibitors are more soluble and tend to leach out of the coatings much more rapidly than inorganic inhibitors. Many of the inorganic inhibitors used are so slightly soluble that they are classified as pigments. As is the case in most issues of coating design, the coating matrix polymer also helps to determine the release rate of inhibitors. The inhibitor release from a primer is minimized by the barrier properties of the topcoat in areas of no physical damage or defects. It appears that in undamaged coating systems, the small amounts of inhibitor dissolved near the primer coating–substrate interface may play a role in keeping any corrosion that occurs under the coating general and uniform at a low rate. Most inhibitors are controlled release materials in that they are only dissolved and become mobile in the presence of water, but many materials dissolve and disappear at a rate much faster than is necessary for corrosion inhibition, and hence have short lifetimes in coatings. An example of this is molybdate pigments, compared to chromate pigments. Even though the former may give inhibition, their solubility is great enough to leach out so rapidly that they cannot be considered true substitutes for chromates.

#### **4.11.2.4 Comments on 'Smart Coatings' and their Relative 'Intelligence'**

Much has been written lately about 'smart coatings,' and 'smart corrosion inhibitors'.<sup>47,48</sup> It is clear that most

of the authors seek to describe any coating or pigment from which the process of release is not 'dumb.' (Dumb apparently means that it dissolves in an uncontrolled manner whenever water is present.) They are trying to describe a coating system in which the release or chemical reaction within the coating that provides protection to the metal substrate occurs only in response to some external stimuli. Dramatic claims for release in the presence of threat from 'physical damage' or chloride ion concentration provide arguments for new designs of pigments or encapsulated inhibitors. This author insists on great care in accepting many of these arguments in differentiating one material from another. None of the writings in this field shows any numerical modeling or analysis of inhibitor release and substrate passivation and lifetime prediction, but only describes release testing into bulk solutions or trial-and-error formulated coating testing. This area of research has only been active for about 5 years (see, for example, Provder and Baghdachi,<sup>49</sup> and the coatings market place is very slow to accept new ideas or materials, so it is unlikely that many of these 'smart' coatings will appear in common use soon.

### **4.11.3 Components of Organic Coatings for Corrosion Control**

As described in [Section 4.11.1.1](#), the four basic component classes of a coating are polymeric binders, pigments, solvents, and additives. The polymeric binder matrix of a coating is the continuous phase of a well formed coating, which often provides a major part of the barrier protection provided by the coating. A brief survey of the most commonly used polymer classes for corrosion protective coatings follows. For further details on the properties of such polymers and their use, one needs to examine the general textbooks on coatings.<sup>16,50,51</sup> The focus in the following discussion is on the properties and uses of coating polymers unique to corrosion protection. The *Journal of Protective Coatings and Linings*, *Materials Performance* and the *Journal of Coatings Technology* often present articles on polymer suppliers and users and details of specific polymer use in corrosion protective coatings. In a general net or preapplication coating system, the solvent composition by volume ranges from 10 to 50% (zero in powder coatings), the polymer volume fraction ranges from 20 to 50%, the pigment volume concentrations range from 0 to 35%, and additives usually are at 15% or less.



### 4.11.3.1 Polymer(s) for Corrosion Control Coatings

In [Section 4.11.1.3](#), the desired attributes of a corrosion protective coating are given, and from these, the specific properties required of polymers for use in a corrosion-protective coating can be listed as follows:

1. Wet/dry adhesion – keeping the coating in contact with the substrate.
2. Low ion, water, and oxygen permeability – physical barrier effects.
3. Low conductivity – inhibit flow of current in local corrosion cells and stop ion and electron motion in film – electrical barrier effects.
4. Stability to its environment, stability to OH-driven basic hydrolysis and UV radiation, thermal stability, etc.
5. Strong adsorption of coating polymer to substrate interface – provides good wetting of substrate by coating system and reinforces the wet adhesion of the polymer mentioned in property 1.

These attributes are somewhat vague in qualitative definition and hard to define in numerical terms. All the properties described in the list can be altered by a detailed polymer composition as well as additives such as wetting agents. This must be taken into account when considering the information given on specific polymer classes as given in the following sections ([Table 1](#)).

#### 4.11.3.1.1 Epoxies

Perhaps the class of polymer type most commonly used in corrosion protective organic coatings is the epoxy class of polymers because of their good wetting of metal-metal oxide surfaces, excellent adhesion to most substrates, good to excellent chemical resistance, good dry electrical properties, relatively easily controlled crosslinking, wide range of commonly available molecular weights, relative ease of forming

pigment dispersions, wide range of crosslinking reactions available, and relatively good water resistance; epoxy type polymers can be modified to become a polymer engineer's dream. Epoxy polymers are very stable in the locally high pH ranges encountered due to oxygen reduction at metal substrates when corrosion occurs. Because of the good wetting and adhesion properties, epoxy-based coatings are more tolerant of poor substrate preparation than are many other polymer types. These polymers wet pigments and fibers well, and form stable composite films and structures with many pigments and fillers. A wide range of curing temperatures can be achieved, and by a suitable choice of the crosslinker, a wide range of polymer physical properties is available. Epoxies have a relatively strong tendency to pick up water due to humidity effects as well as in immersion, and they are plasticized by water.<sup>23,25</sup> Further, as a general class of polymers, epoxies tend to have poor UV resistance, because many epoxy precursors have phenyl groups in their structure. For this reason, many two-layer corrosion-protective coating systems use epoxy-based primers, while using a more UV-resistant polymer in the topcoat.

Epoxy materials can be designed to require heat curing as well as ambient curing. They have been applied in all types of commonly used equipment and can be used as solvent-borne systems, powder coatings, and waterborne, high-solid, and 100% solid variations. One specific class of epoxies that deserves special notice is the so-called fusion bonded epoxy (FBE) pipeline coatings class. Epoxy-polyamide polymers are often used in Zn-rich coatings because of their chemical resistance and adhesion to steel substrates. These coatings are high temperature cured epoxy powder coatings used for pipeline corrosion protection.<sup>52</sup> Further, qualitative comments specific to epoxy polymer use in corrosion protective coatings are given in several introductory texts discussing this class of polymeric materials.<sup>40,41</sup>

**Table 1**

Polymer	Property 1 wet adhesion	Property 2 chemical barrier	Property 3 electrical resistance	Property 4 exterior durability	Property 5 substrate wetting	Relative cost
Epoxies	+	+	+	+	+	Medium
Polyurethanes/polyureas	+	+	+	+	—	Medium to high
Acrylics	—	—	—	—	—	Medium
Alkyds	—	—	—	—	—	Low
Silicones	—	—O <sub>2</sub> /+H <sub>2</sub> O	—	+	—	Medium
Inorganic/sol-gels, etc.	—/+	—	—	+	+	Medium to high
Vinyls	—	+	+	—	—	Low

#### **4.11.3.1.2 Isocyanate-based polymers: polyurethanes and polyureas**

The second most commonly used class of polymers used for corrosion protection is isocyanate-based polymers, which includes polyurethanes of all types and the so-called polyurea coatings. Polyurethanes provide an excellent matrix for corrosion-protective coatings, but they are less tolerant as a class, being ill prepared substrates compared to epoxy coatings, with less wetting and adhesion properties. Aliphatic polyurethane (PUR) coatings are often used as topcoats in corrosion-protective systems because of their excellent UV resistance and barrier properties. Chemical resistance, abrasion resistance, and design flexibility are among the other strengths of coatings in this class of polymers. Aircraft coating systems,<sup>2</sup> chemical agent resistant coatings for military vehicles, and many other coating systems, including bridge coatings, have aliphatic PUR topcoats. Polyurethanes are based on reactions of monomeric or oligomeric isocyanates with polyhydroxyl oligomers<sup>53</sup> and vary in use from room temperature reactive curing to high temperature blocked isocyanate chemistry.<sup>54</sup> Most types of pigments, including active metal pigments such as Zn, have been used in PUR coatings. PUR-type coatings are sometimes difficult to use in primers as they are difficult to wet and adhere to as a substrate.

#### **4.11.3.1.3 Acrylics**

Acrylic polymers have been used in the coating industry for some time<sup>55</sup> and have great usefulness because of their UV stability and wide range of use. There are very many acrylic monomers so that copolymers of many types can be prepared using basic acrylic free radical polymerization. Similarly, very many side-groups of acrylic monomers are available, which allow crosslinking chemistries with many other polymer types.

#### **4.11.3.1.4 Alkyds**

Alkyds are among the longest used polymer classes in the modern coating era. They still have extensive use because of their relatively low costs and wide range of use. This class of polymers is, however, sensitive to basic hydrolysis, so use of unmodified alkyd polymers in purely corrosion-protective systems is definitely on the decline.

#### **4.11.3.1.5 Vinyl polymers**

Vinyl polymers is a name often used to identify polymers based on the vinyl group,  $\text{NCH}=\text{CH}_2$ ,

but really has been used to identify polymers and copolymers of vinyl chloride.<sup>3,16,40,41</sup> These polymers have been used extensively in the past for corrosion protective systems, but they often need large amounts of strong solvents to be applied properly, and thus their use has been heavily curtailed by VOC regulations for coatings. They also as a class have poor outdoor durability in UV exposure. They do, however, have excellent barrier properties, especially water resistance, and they are still used in some situations. They are often used as thick films applied in multiple layers. Chlorinated rubbers are often considered in this class of polymers.

#### **4.11.3.1.6 Mixtures including silicones**

Many of the polymer matrix systems for corrosion-protective coating systems are mixtures of more than one type of polymer. A full discussion of all the types of polymer chemistries available, is beyond the scope of this chapter, but is available in reviews and textbooks.<sup>41,50</sup>

#### **4.11.3.1.7 Sol-gel and hybrids**

Some coating matrix systems use ceramic-like chemistries for film formation, and have found use in corrosion-protective coatings, especially in Zn-rich primers (see Chapter 10 of Smith<sup>41</sup>). There is a current review on how these systems can handle a broad range of coating problems.<sup>56</sup>

### **4.11.3.2 Pigments**

Pigments are the second group of materials from which coatings are designed/formulated. As the heterogeneous phase in what might best be called a random two-phase particulate composite, pigments perform appearance functions and help provide protective functions. As discussed earlier, pigments help coatings provide corrosion protection by cathodic protection, barrier protection, and inhibitor release protection. In addition, colored pigments are used in corrosion-protective coatings for appearance purposes or to provide visual feedback to applicators about proper film thickness/opacity coverage.

#### **4.11.3.2.1 Inhibitive pigments**

Inhibitive pigments are perhaps the largest class of pigments used in corrosion-protective organic coatings. They include partially soluble inorganic compounds such as chromates, which are used in aircraft primers<sup>43,57</sup> and phosphates<sup>58</sup> as well as other related materials such as molybdates.<sup>59</sup> Other materials of this type are organic inhibitive pigments, controlled

release pigments<sup>60</sup> (the inhibitor is given off by the pigment in a controlled release manner), and ion exchange pigments.<sup>61</sup> These materials dissolve or release materials at a slow rate in the presence of water, and are thus present in high concentrations near a damaged site in a coating in exterior exposure. The release of materials from such pigments has been studied by several authors and found to be related to the efficiency of the pigment/coating polymer system.<sup>43,62</sup> The commercial literature of this area of materials is full of a lot of claims, and the formulator of coatings using such pigments is cautioned to carefully study coatings based on inhibitive pigments in tests that reflect the proper use conditions. In the case of chromate-replacement pigments, especially, matching release rates and inhibitive performance with no-chromate materials is very difficult indeed, and claims of replacement pigment manufacturers should be examined very carefully.

#### **4.11.3.2.2 Reactive metal pigments: spherical, lamellar, and platelet/flake**

The next class of pigments important in the formulation of corrosion-protective coatings are the reactive metal pigments used in formulating metal-rich, cathodic protective coatings. As discussed in [Section 4.11.2.2](#), metal-rich coatings are formulated with active metal pigments that are more reactive than the metal substrate the coating protects. Zn-rich coatings used for steel were the first such coatings of this type, and much of the literature on pigments for metal-rich coatings perforce concerns Zn pigments. However, this class of materials is expanding, and now includes Al,<sup>39</sup> Mg,<sup>29,30</sup> and Mn<sup>38</sup> pigments. A recent publication has even described the use of nano-Ti particles in corrosion-protective coatings, but gives no claims of cathodic protection.<sup>63</sup>

The important properties of metal pigments for use in coatings are as follows:

1. Particle size;
2. Particle size distribution;
3. Particle shape;
4. Surface oxide layer thickness or pretreatment.

The reactivity of metal particles is determined by their size (surface-to-volume ratio, specifically), increasing ( $3/\text{radius}$ ) for spherical particles. The shape of the particles, flakelike, needlelike, or spherical, affects their connectivity and thus their connectivity and percolation threshold.<sup>36,37</sup> Because of the importance of connectivity, metal-rich primer coatings are formulated near the CPVC, and thus particle

size, size distribution, and particle packing efficiency in such coatings are very important formulating issues that must be considered in the design of such coatings.<sup>1,3,27</sup> Their shape is also important for connectivity and percolation threshold determination, and the advantages of flakelike Zn pigments compared to an equivalent volume of spherical Zn pigments have been claimed.<sup>37</sup>

#### **4.11.3.2.3 Inert/extenders pigments**

The other class of coatings important for their use in corrosion-protective coatings is the inert/extender pigments. These pigments are used to control the PVC-related properties of coatings such as the dielectric, transport, and mechanical properties. They also tend to be lower in cost than other pigments, which helps explain their extensive use. Their function in coatings has been extensively discussed elsewhere,<sup>1,3,5,51</sup> and will not be discussed here. However, a subclass of extender pigments that is extensively used in corrosion-protective coatings is inertflake pigments such as Al, mica, exfoliated clays, and related materials. Because such pigments often align parallel to the substrate during coating film formation, they decrease transport in such films more effectively on a volume basis than spherically shaped pigments. Thus, if one wishes to increase the barrier properties by a given volume of extender pigments, those in a flakelike form are the most efficient if they align parallel to the substrate.<sup>62</sup>

#### **4.11.3.2.4 Colored pigments**

Colored pigments are used in corrosion-protective films to help provide a more pleasing appearance to such coatings and the substrates they protect. The use of colored pigments also helps provide a visual guide to hand-applied coatings. The major issues requiring consideration in colored pigments in corrosion-protective coatings is whether the coatings will be used on the exterior or the interior. For the former, pigments should be UV stable and not cause photo-oxidation, as do untreated TiO<sub>2</sub> pigments. Most often, inexpensive colorants such as iron oxide red, carbon black, or yellow iron oxide are used in corrosion protection systems because of their stability.

#### **4.11.3.3 Additives: Surfactants, Rheological Control Agents, Flow Agents, Defoamers, Wetting Agents, Dispersants, etc.**

The term additives is a general term used for describing those materials that are added in small amounts,

usually less than 1% by weight, to coatings to control the properties of the liquid coating before and during application. Included in this class of materials for coating formulation and design are surface active materials, such as wetting agents, pigment dispersants and defoamers, biocides, and materials for rheological control of the liquid coatings. Coalescents and plasticizers, which affect the short-term behavior of polymers during film formation, are also included in this class of materials. Some additives are used to control and improve the properties of the solid film, and these include UV absorbers, light stabilizers, mildew retardants, and fire retardants.<sup>36,37</sup>

#### 4.11.3.4 Solvents/Carrier Fluids

Solvents and dispersion carrier fluids (i.e., water in latex-based paints) play a key role in coatings, as they are liquids that enable the coating to be in liquid form for proper coating application. For cost, environmental, and legal reasons, the minimum amount of solvent is used in formulating a coating, and the type of solvents one can use in coatings is subject to severe restrictions. The legislation in this area is continually changing, and the formulator is advised to check on the specific regulations on solvent use that apply to the location of his coatings.

For corrosion-protective coatings, a primary consideration is, whether the solvent remains in the coating long enough for the coating to complete film formation, and then leaves the coating and does not interfere with the full development of coating properties. For example, if the formulator uses a solvent that does not completely leave the film during film formation, the residual solvent can act as a plasticizer and lower the effective  $T_g$  of the coatings, which will reduce the coating barrier properties. If the solvent leaves the film before polymer crosslinking is complete, the film formation process will remain incomplete, and the full development of coating properties will not occur. Again, the formulator is referred to monographs on coatings for further guidance on solvent choice and usage.<sup>51</sup>

#### 4.11.3.5 Catalysts for Reactive Polymer (Usually Two Component) Curing

Catalysts to accelerate the curing of coating polymers are also an important type of additive.<sup>50,58</sup> Many of the polymers used in corrosion protective coatings are two-component systems that use reactive cure as the mode of film formation. These curing systems

often require catalysts to crosslink and undergo film formation properly.<sup>16,17,52–54</sup> Epoxy-based coatings require catalysis in their use, and detailed information on individual coating polymers is most often available from the polymer manufacturer. Similarly, catalysts are commonly used in polyurethane/polyurea coatings, but recommendations from the manufacturer of the polymer under consideration are probably the best starting point for formulation practice in PUR systems.

#### 4.11.4 Coatings Application Methods and Corrosion Protection

Since corrosion in coated metal substrates is a problem that begins locally and then may grow into a global concern, the elimination of all coating defects during the coating application process is of great concern. For this reason, the method by which a corrosion-protective coating is applied to the metal substrate is extremely important for the successful use of such a coating. Also very important to the proper performance of a corrosion-protective coating is the proper preparation of the metal surface to receive the coating. For example, an improperly applied spray coating will make a coating-metal substrate system liable to corrosion. For this reason, corrosion-protective coatings that are field applied are inspected after application to ensure that no defects are present before a coating system is allowed to go into field use. The Society for Protective Coatings (SSPC, see [www.sspc.org](http://www.sspc.org)) has several manuals for coating inspection and the National Association of Corrosion Engineers, Intl (NACE, see [www.nace.org](http://www.nace.org)) has an extensive set of training programs for training personnel as coating inspectors.

A corrosion-protective coating correctly applied to a well prepared metal substrate is crucial for achieving the proper performance from the coating substrate system. This is especially crucial for systems in situations where field repair of coating imperfections is not achievable, such as buried pipelines or off-shore oil platforms. Because of this, proper coating application is paramount for corrosion-protective coatings. Much of the high-quality corrosion protection inherent in recent automobiles is due to the use of cathodic electrodeposition primers used over Zn/Zn-alloy galvanized steel.

A more detailed discussion of the application methods and procedures of corrosion-protective organic coatings is given in this volume, and this

subject receives no further discussion here. For further reading in this area, see the references listed under Further Reading.

#### 4.11.5 Coating Wetting and Adhesion in Coatings

General wisdom has it that adhesion, especially ‘wet adhesion,’ is a key attribute for corrosion-protective coatings.<sup>7</sup> To function properly, a coating must wet and adhere to the metal substrate it is being used to protect.<sup>1,11</sup> Many adhesion problems in actual use are solved by properly preparing the surface of the substrate for the coating application process. Additives for improved wetting are often used in corrosion-protective coatings. Because of their high surface energies, the ideal surfaces for wetting have been considered to be clean metals or metal oxides. Such surfaces, along with coatings that strongly wet them, such as epoxy-polyamide-based coatings over pretreated steel, have given excellent adhesion of the coatings and thus good corrosion protection. However, recent developments in science have been giving the hope of achieving improved adhesion by true covalent bonding across the coating-substrate interface. There are many claims for such pretreatments/coatings, which achieve covalent bonding directly across the coating-substrate interface. Many of these claims are based on the use of functional silanes and their metallic analogs. The surface density of such covalent bonds is still highly variable, and no good tests are available to measure the extent of covalent bonding across an interface in the coating-metal substrate situation. Most of the difficulties in this area lies with issues of measurement of ‘adhesion’ several recent articles<sup>65,66</sup> indicate that there measurements in ‘adhesion’ have improved and that further improvements in this area may be expected soon.<sup>67,68</sup>

#### 4.11.6 Coatings Formulation/Design

##### 4.11.6.1 Principle Objectives of Formulation – Coatings Design

For many systems, the coating design process can be summarized as shown in Figure 5. One first determines the desired properties (specifications) of the coating, translates these to the physical properties required of the coatings, and then attempts to convert these requirements to material choices for the composite, that is, the coating. Converting materials

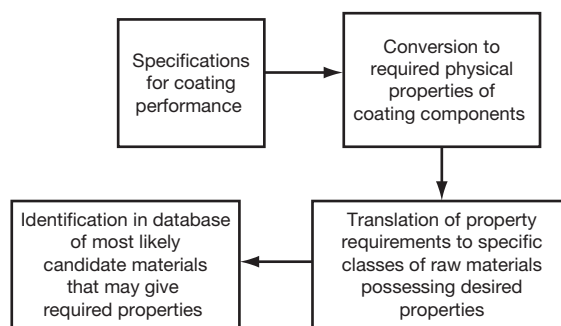


**Figure 5** Idealized case of raw material selection.

specifications to materials choice is one of the most difficult steps in the design process.<sup>15</sup> Additionally, it should also be noted that the ‘best’ coating for any situation is likely going to be a balance between minimizing cost while achieving – within tolerances – the performance requirements.

While working on coating design, work at North Dakota State University (NDSU) has been performed to accomplish the following:

- Put coating design on the same strong technical basis as any other type of engineering design;
- Identify the logic of paint formulation;
- Emulate as much as possible the practice of paint formulation development;
- Determine steps in setting coating specifications – performance property requirements – and converting them into a set of raw material identities, concentrations, and rules for coating manufacture (order of addition, etc.) and application to a substrate;
- Develop basis for coating design system to assist coating formulators;
- Software development for formulator support.

One can think of each of the processes shown in Figure 5 as an operation on a set of databases of material information, specification information, and coating application information. From this alternative viewpoint, the process of formulation would schematically appear as shown in Figure 6. (At the bottom of Figure 6, the  $F$  is used to represent formula.) One might think of each step in choosing materials and processes and applying specifications, as applying a mathematical filter to a database of choices yielding reduced databases, from which the formulator/designer makes his final choices. This type of analysis of the formulation process seeks to reduce the often intuitive reasoning that is common in many paint laboratories to a more scientific process analogous to the design process used in many scientific disciplines.<sup>69,70</sup>



Another description of the coating 'formulation' or design process is given in **Figure 7**, in which the consideration of legal/environmental restrictions, curing restrictions due to the site or substrate, and the requirements of individual coating classes are also considered. Other constraints faced by the formulator/designer are production equipment capacity for producing paints of various classes, application equipment available to the user, and substrate size, solvent and temperature sensitivity, corrosion sensitivity, and surface preparation.

There are various ways to organize a database for formulation, and in the following section, several

schemes that fit in with the logic of **Figures 6 and 7** are presented.<sup>14</sup> **Figure 8** shows a raw material (RM) database structure compatible with these operational methods of formulation. **Figure 9** gives an alternative RM data base focusing on polymer/binder classes for coatings as well as coatings classes.

If the RM databases are cast in the proper format, one can use the formulation/design logic discussed earlier, shown in a more detailed form in **Figure 10**.

If one wishes to consider previous formulations/designs to reduce the amount of decision making that needs to be performed in these processes, one can use the flow process shown in **Figure 11**. Once an original candidate coating design/formulation is available, the development and testing protocol found in **Figure 12** can be used.

These processes can be quite slow when run in the sequential, serial form as shown in **Figure 12**. There are also several problems in trying to reduce the formulation process to a computer-driven procedure. Among these are difficulties in the correlation of coating specifications with design rules developed for translating RM properties to RM choice, the need to narrow the range of raw material availability, or conversely, database limitations due to RM availability. Raw material variability from single or multiple sources is another problem that must be

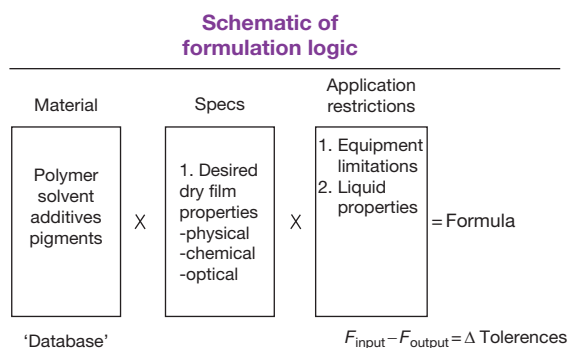


**Figure 6** Schematic of formulation logic – alternative view.

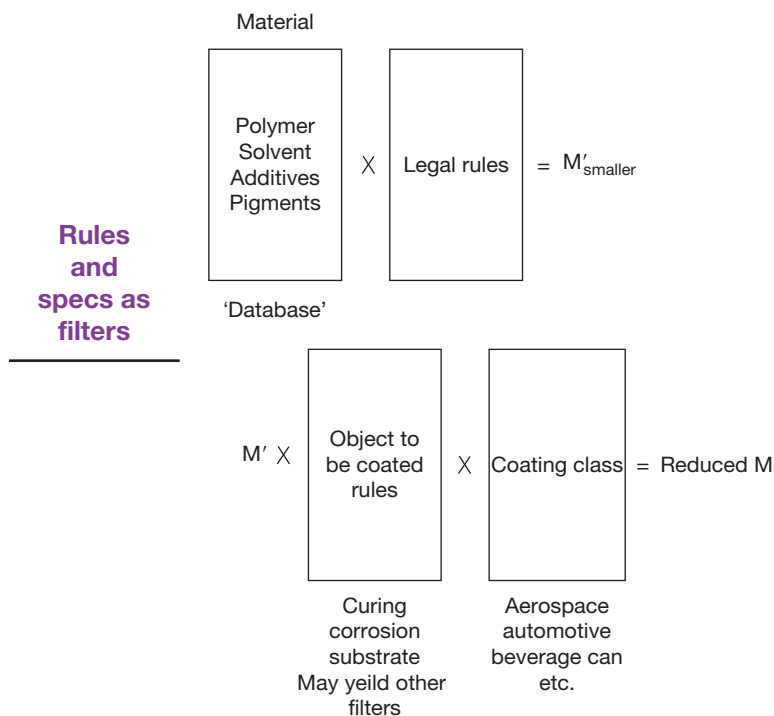


**Figure 7** Alternate schematic of materials choice in coating design/formulation.

### Pigment and additive raw material classes

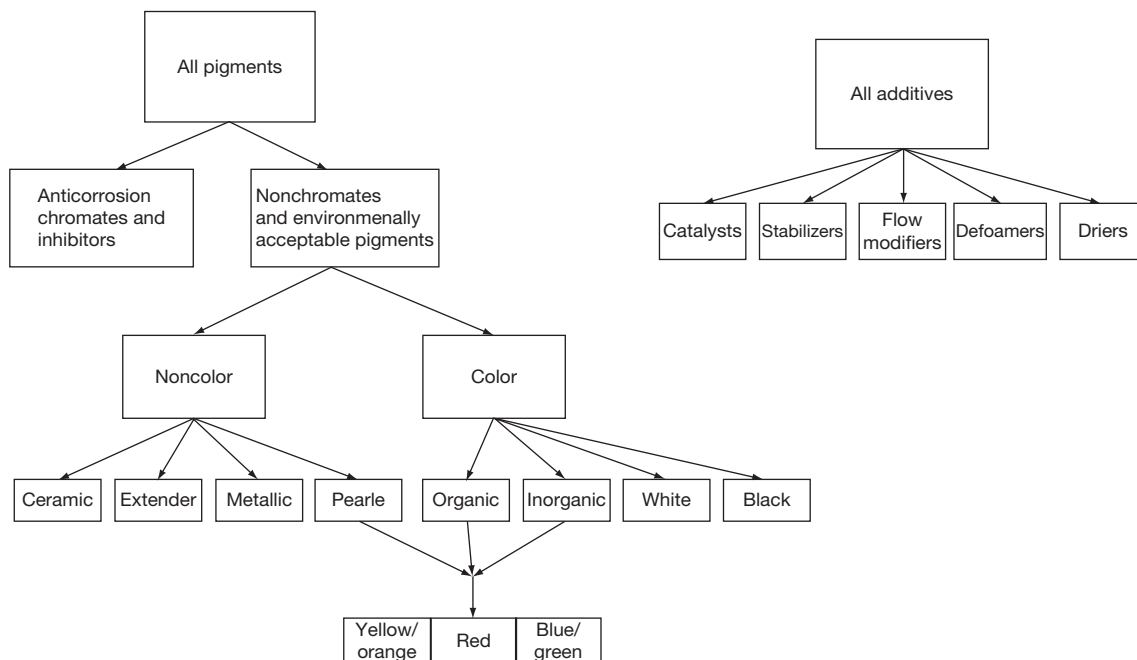


**Figure 8** Schematic of possible coatings raw material database organization.

considered, and procedures included in the formulation process to examine the final properties and quality of the coating for sensitivity to RM variability.

#### 4.11.6.2 Volume Effects in Coatings

As mentioned earlier, and reiterated in a recent publication,<sup>1</sup> volume effects are extremely important in pigmented organic coatings, as the volume concentration of materials is the relevant concentration parameter for many of the physical properties of coatings. This is especially true for pigments and the term PVC is commonly used in coating studies. Because of system requirements, it is often considered fruitful to formulate at fairly high PVC levels. Although the specifics differ for every coating system, in general the most expensive component of the system is the pigment or colorant. This is followed by the binder system. The least expensive materials are the solvent (which is not present in the dry film) and the filler or extender pigment. This has made knowledge of the CPVC an important formulating variable, and crucial to coating design and the understanding of corrosion-protective coatings.<sup>71</sup> The CPVC measures the highest volume fraction of solid pigment that can

be packed into a coating without introducing air voids. The parameter  $A$  ( $\equiv$  PVC/CPVC, the reduced pigment volume concentration) is often used in interpreting and predicting coating behavior. Coating properties that are directly affected by  $A$  are given in [Table 2](#). The use of  $A$  in coatings design is discussed extensively in Bierwagen,<sup>1,6,7</sup> Bierwagen *et al.*,<sup>3</sup> Hare,<sup>27</sup> and Nanna and Bierwagen.<sup>29</sup> Theoretical studies of nonuniformities in particle packing and their impact on CPVCs in ‘real’ coating systems have given further insight into PVC issues in coatings.<sup>72,73</sup> The knowledge of coating performance as a function of  $A$  is often utilized in coating design once the pigments to be used in the coating are identified. As discussed in [Section 4.11.3.2.2](#), this is especially critical in metal-rich coatings.

Numerical guidelines for  $A$  levels for formulation of corrosion-protective coatings have focused on the effects of the CPVC on coating performance characteristics. Some figures describing the qualitative variation of coating properties with PVC or  $A$ , pertinent to corrosion protection are given in the following section. [Figure 13](#) (taken and modified from Bierwagen *et al.*)<sup>3</sup> shows the relation between pigment and polymer components, including the adsorbed layer on the pigment and void fraction above the CPVC, that occur

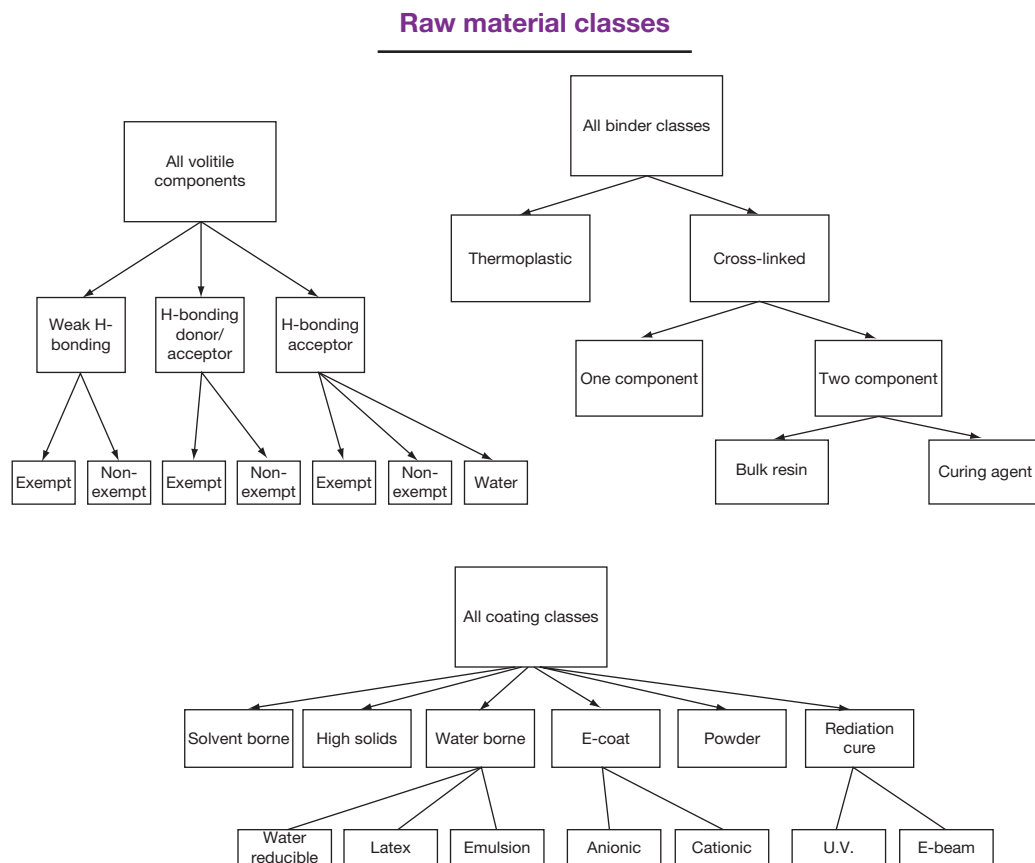


**Figure 9** Alternate coating raw material database organization.

in the coating as a random two-phase (below the CPVC) and three phase (above the CPVC) composite. **Figure 14** shows schematically the increase in permeability that occurs in a coating above the CPVC, while **Figure 15** shows the sudden drop in film resistance measured by the low-frequency impedance modulus  $|Z_0|$  or noise resistance,  $R_n$ , that occurs at the CPVC. Similarly, the film capacitance measured in an aqueous electrolyte will increase drastically above the CPVC because of water intrusion into voids and corrosion resistance, measured in accelerated testing salt spray, will increase drastically above the CPVC.<sup>71</sup> Thus, a coating formulated above the CPVC provides hardly any barrier protection and often gives poor adhesion in certain types of polymers. Primers can be formulated above the CPVC, if they are coated with a topcoat formulated below the CPVC. This gives a total coating system that does not have a porous structure open to water/electrolyte intrusion. This is often done with Zn-rich primers that are formulated near the CPVC.

The barrier properties of coating are ideally maximized at the CPVC, but in practice, it is known that voids sometimes appear in real coating systems

below the CPVC.<sup>1</sup> These voids form in local areas of the coating where the local PVC exceeds the CPVC because of the nonuniform distribution of pigment and polymer throughout the coating film. This can be described by a parameter named coarseness (from Torquato),<sup>4</sup> used to analyze these results properly. It helps to interpret correctly what happens in films as the PVC approaches the CPVC.<sup>74,75</sup> A schematic of these effects, taken from calculations described in earlier work from this lab, is shown in **Figure 16**.

The interpretation of these data were based on an analysis of coatings as a random composite in which the local PVCs could vary from the calculated (global average) PVC as measured by the coarseness of the system. These variations could occur in coatings due to poor manufacture, film formation or application problems, or other processes in the coating that tend to separate the pigments from the polymer, such as flocculation in storage. Incorporating the coarseness parameter in the analysis, enables one to numerically predict the effect of poor, nonuniform distribution of particulate materials in a coating. The analysis also showed how such coarseness could affect many of the

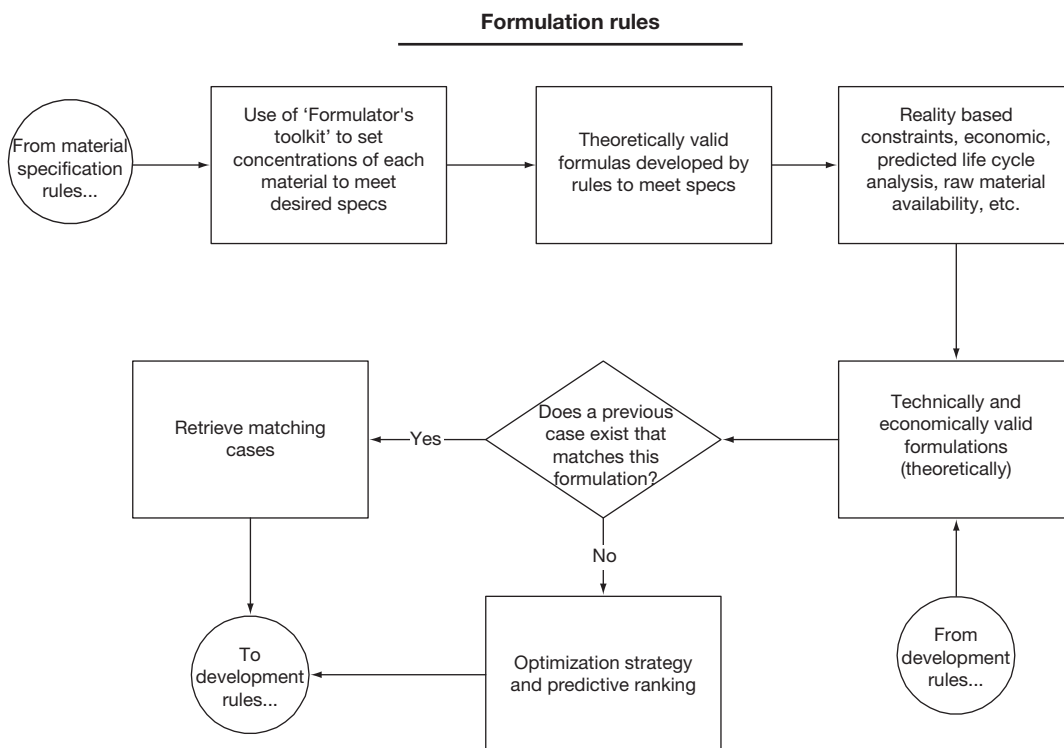


**Figure 10** Raw materials choice flow process for coating design.

properties of coating films, especially those related to corrosion protection. These results helped to interpret the empirical observation that most corrosion-protective primer formulae, dependent on barrier effects as part of their protective properties, had  $\lambda$  values of  $\sim 0.85$ . One would actually expect that these coatings would be formulated at  $\lambda \approx 1$  for maximum barrier protection, because one would assume that it would be the best value for corrosion protection. However, if one analyzes the onset of voids as a function of coarseness, one rapidly determines that there is a very small but finite probability for voids occurring above  $\lambda = 0.85$ , but below this PVC value, the probability is very small. The margin of tolerance formulating at  $\lambda$  values of  $\sim 0.85$  given to the designer of primer barrier coatings is crucial for avoiding completely the onset of voids in the coating film.

There are no efficient experimental methods other than the manual interpretation of SEM cross-sections to estimate coarseness. A proper microview of the coating system is necessary to properly analyze the manifestations of coarseness throughout a film. We have been trying to use SEM photomicrographs for estimating coarseness, but a detailed three-dimensional characterization of pigment particle distribution in a paint film is necessary for an accurate estimate of coarseness.

#### 4.11.6.3 Setting Formulation Goals

A coating is chosen for purchase, or designed/formulated, based on the requirements of the customer or as translated by sales/marketing and given to technical/research personnel. For example, corrosion-protective coatings often have a lifetime of performance measured by a specific accelerated test method in a specific set of conditions. An idealized list of specified properties for an organic coating is given in [Table 3](#). These specifications could be considered in a design process, as shown in [Figure 7](#).

The specifications for a coating are usually determined by the following:

1. Exposure environment(s) of use;
2. Properties of substrate – asset to be protected
  - a. general chemical and mechanical properties of bulk substrate and its surface
  - b. pretreatment of the substrate and resultant surface properties;
3. Desired lifetime of use.

The specifications can often be converted into the required properties of coating under the following classifications:

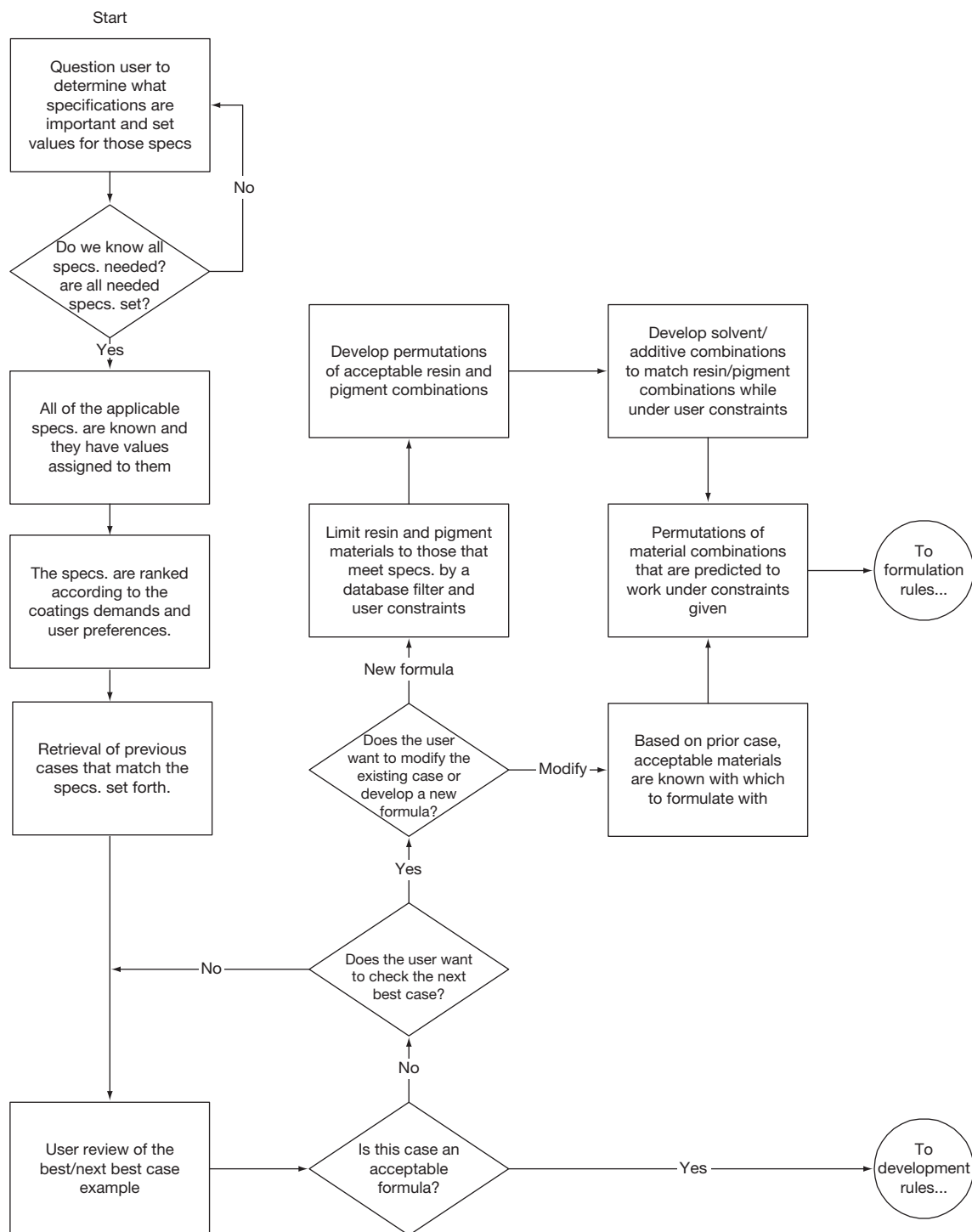


**Figure 11** Flow process for coatings formulation with former formula for use as precedent and guide.

1. Diffusion and transport;
2. Thermal and mechanical;
3. Electrical;
4. Optical and color;
5. Chemical resistance;
6. Acid/base resistance;
7. UV resistance;
8. Degree of crosslinking;
9. Solvent and water resistance.



### Development rules

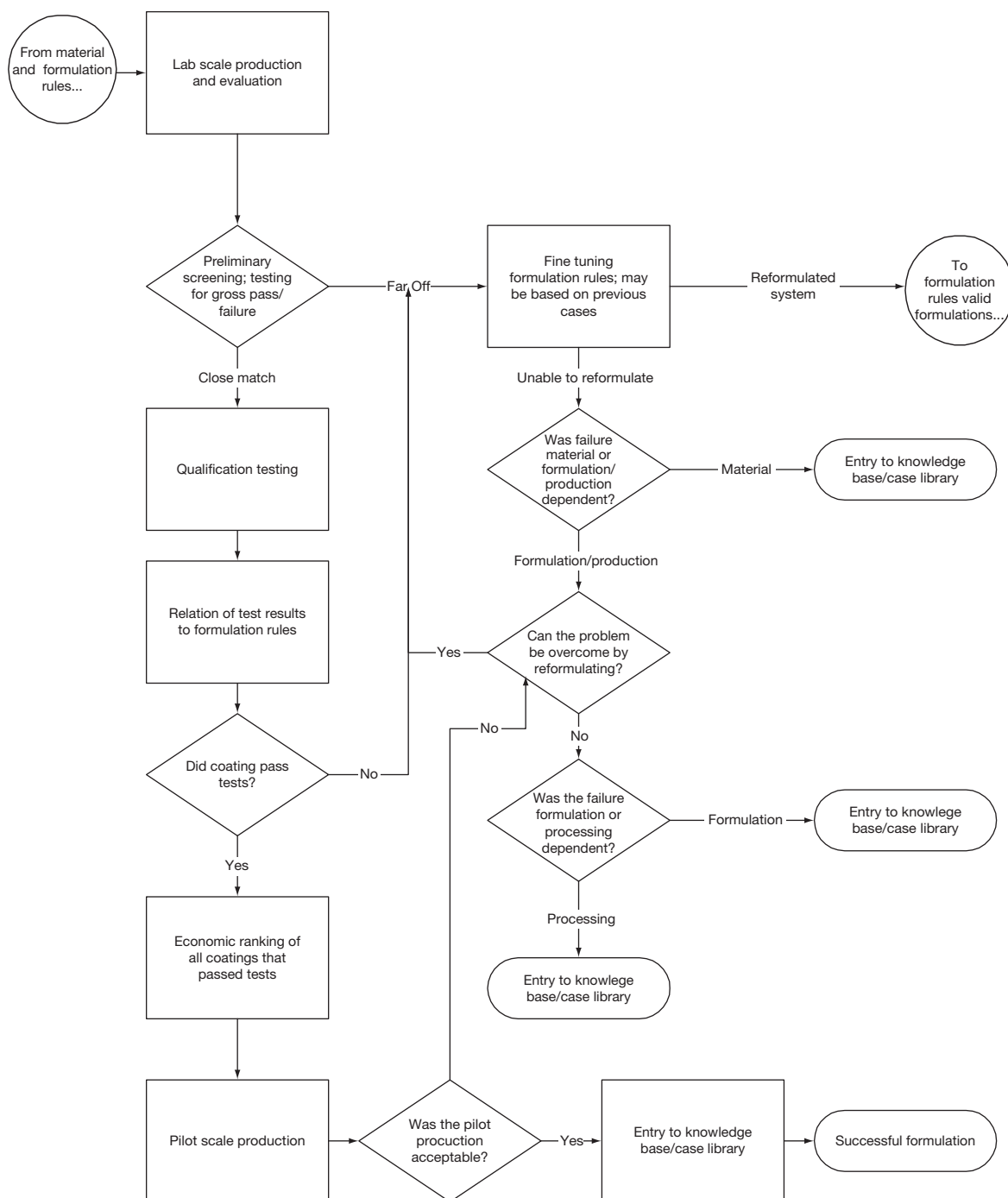


**Figure 12** Development, testing, and pilot scale production flow process once an initial formula is proposed.

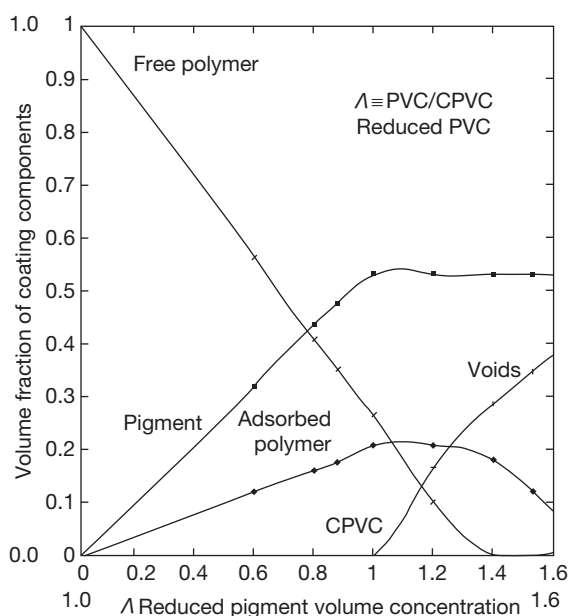
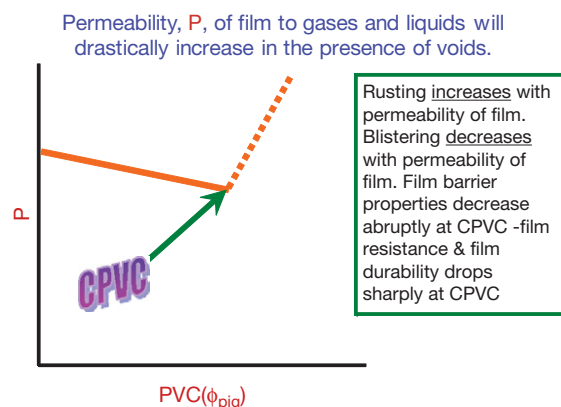
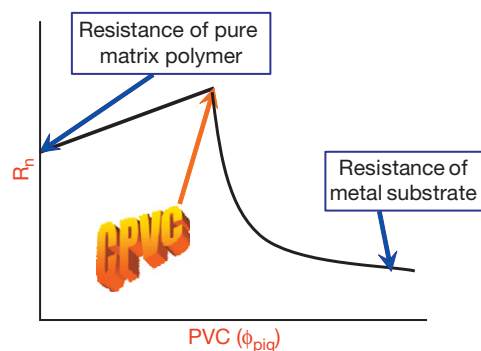
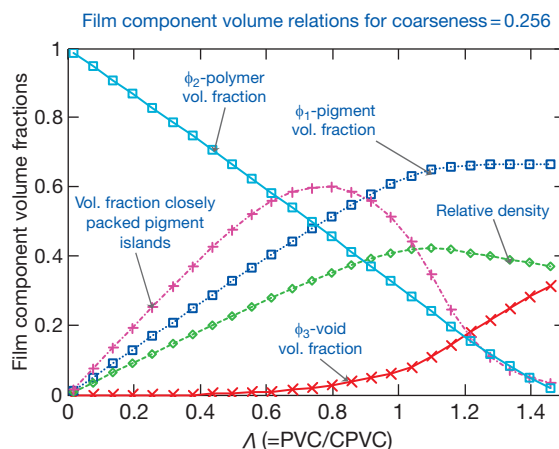
As described earlier, these requirements are converted into material properties, and material selections are made based on availability, material cost, and cost restrictions of the customer, subject to legal, toxicity, and ecological restrictions.

#### 4.11.6.3.1 Use of combinatorial methods in coating design and choice

The new combinatorial methodologies developed for the pharmaceutical and electronics industries are now being applied to improving coatings.<sup>76,77</sup> These

**Table 2** Paint properties affected by  $\Lambda$ , the reduced pigment volume concentration (PVC/CPVC)

Gloss	Blistering
Flexibility (elongation)	Enamel holdout
Tensile strength	Penetration control over porous
Color development (tint acceptance)	Density (specific volume)
Hiding – contrast ratio	Durability
Block resistance	Electrical resistance
Permeability	Cold crack resistance
Wet abrasion (scrubbability)	Dielectric constant
Stain removal	Adhesion
Corrosion resistance (salt spray resistance)	Dispersion

**Figure 13** Coating film component variations with PVC.**Figure 14** Organic coating film permeability.**Figure 15** Film resistance as  $R_n$  or  $|Z_0|$  or vs. PVC.**Figure 16** Film component volume relations with coarseness effects for CPVC = 0.66.

methods speed up considerably the time-consuming conversion of material requirements to material choice in the design of coatings and related materials. Combinatorial methods convert one-at-a-time serial methods of sample preparation and testing into parallel methods that, in the case of coating testing, convert single sample testing to 24-samples-at-a-time high-speed testing. For example, these methods have been used in a crude form to modify an automotive coating to one suitable for the corrosion protection of bronze statuary.<sup>78</sup> More recent developments have focused on the development of high throughput screening methods for testing<sup>79,80</sup> and designing corrosion-protective coatings.<sup>81</sup> Coupled with the database-driven material choice methods described earlier, the numerical methods available for polymer and pigment choice, combinatorial coating design, and testing will greatly accelerate the design and testing cycle for corrosion-protective organic coatings.

**Table 3** Simplified coating specification list for coatings design

---

Issues determining coatings design/formulation coatings systems specifications/performance requirements
Cost
Number of layers (more than one layer $\equiv$ system)
Topcoat properties – usually contain color and optical properties plus the barrier and chemical and UV resistance properties
Primer properties (usually contains corrosion resistance properties)
System physical properties including color and mechanical properties
System chemical resistance properties
System exposure resistance properties
Application method and flow properties

---

#### 4.11.7 Coatings Design and Testing: Choosing the Final Formula

The final stages of coating design involve the examination of experimental formulations according to tests that have been chosen to determine whether the coating films resulting from a proper application of the prototype formulations meet the specifications for the new coating system. The type of tests performed often is discussed in the literature,<sup>2,17,82</sup> but no one set of specifications is agreed upon by all users. There have been many arguments about the validity of test methods to evaluate protective coating systems, including disagreements on whether cyclic or continuous exposure tests are more accurate and predictive. Many of these issues have been discussed in previous reports of this laboratory.<sup>83</sup>

The testing of corrosion protection is discussed in detail in earlier volumes of this series and will not be discussed in detail here. The steps in coating development are

1. Developing the prototype formula;
2. Converting formulation specifications to qualification tests;
3. Short-term lab testing;
4. High-throughput combinatorial testing;
5. Modifying the prototype formula;
6. Accelerated testing/lifetime prediction.

One can see how these steps fit in the schematic of **Figure 12** on coating development and testing. As shown in **Figure 12**, no information from testing should ever be discarded or unrecorded.

As mentioned earlier, this laboratory has been working on metal-rich primer coatings for corrosion protection. A brief discussion of the testing involved in the Zn-rich subclass of such coatings will illustrate the type of corrosion-related testing done. There has been some recent work on lifetime of protection of Zn-rich primers,<sup>84,85</sup> but little has been done on characterizing quantitatively their performance or their lifetime of corrosion protection. Unfortunately, the science and technology of Zn-rich primers is assumed to be a ‘mature’ technology, to which little technical improvement can be made. This is definitely not true, as clearly indicated by the recent work of Marchebois *et al.*,<sup>86</sup> and Böhm and co-workers.<sup>36</sup> There is a need to re-examine Zn-rich coatings over steel substrates by the experimental and theoretical methods that we have developed for the examination of Mg-rich coatings over Al alloys.

The characterization tools previously used on metal-rich coatings for the active protection of metal substrates are as follows:

Open Circuit Potential (OCP)( $E_{\text{corr}}$ ) measurements versus exposure time to verify electrochemical cathodic protection;  
 Electrochemical Impedance Spectroscopy;  
 Electrochemical Noise Studies;  
 Weight Gain/loss;  
 Optical Microscopy and local XRD;  
 SEM, EDX, some local XPS for Zn reaction product ID.<sup>32,33,37,84–86</sup>

Little that is new in characterization methodology has been introduced for this class of coatings in recent years, and subsequently, little that is new in coating technology or product protection performance for this class of coatings has entered the marketplace recently. Specifically, very little data acquisition and analysis, focused on improving costing system performance or lifetime, has been described in the recent literature. Further, little has been done to acquire proper time series data for lifetime/durability prediction. There has been no true detailed modeling of Zn-rich coatings as a material system to assist material design based on advanced characterization. Surprisingly, in the face of their successful use in many areas of electrochemical science, there has been no inclusion of new local measurement techniques, especially scanning probe methods for the characterization and modeling of Zn-rich coating performance. No analyses of cyclic transport and no electrochemical data from drying cycles have been made as aqueous electrolyte required for data acquisition.

### 4.11.8 Summary and Conclusions

The design/formulation of a corrosion-protective organic coating is a very challenging design procedure, often involving 20–40 individual materials that must be properly chosen, mixed, packaged, and applied as a final coating to a metal substrate. The design procedure is quite complex, as also the formulation of the proper choice of matrix polymer and pigments of the corrosion-protective coating system. The basic information on such choices has been given, and the process of choosing raw materials has been described. A general bibliography on monographs and textbooks pertinent to corrosion-protective coating design is given.

## References

- Bierwagen, G. J. *Coatings Technol. Res.* March 2008; Online, 2007 Matiello Lecture.
- Bierwagen, G. P.; Tallman, D. E. *Prog. Org. Coat.* **2001**, *41*, 201–217.
- Bierwagen, G. P.; Fishman, R. S.; Storsved, T.; Johnson, J. *Prog. Org. Coat.* **1999**, *35*, 1–10.
- Torquato, S. *Random Heterogeneous Materials*; Springer: New York, 2001; Chapter 1.
- Bierwagen, G. P.; Hay, T. K. *Prog. Org. Coat.* **1975**, *3*, 28.
- Bierwagen, G. P. *J. Coat. Technol.* **1992**, *64*(806), 71–75.
- Bierwagen, G. P. *Prog. Org. Coat.* **1996**, *28*, 43–48.
- Feliu, S. Jr.; Morcillo, M.; Bastidas, J. M.; Feliu, S. *J. Coat. Technol.* **1993**, *65*(26), 43–48.
- Feliu, S. Jr.; Morcillo, M.; Bastidas, J. M.; Feliu, S. *J. Coat. Technol.* **1991**, *63*(793), 31–34.
- Szauer, T.; Miszczyk, A. In *Polymeric Materials for Corrosion Control*; Dicke, R. A., Floyd, F. L., Eds.; ACS Symposium Series 322; American Chemical Society: Washington, DC, 1986; Chapter 21.
- Funke, W. In *Polymeric Materials for Corrosion Control*; Dicke, R. A., Floyd, F. L., Eds.; ACS Symposium Series 322; American Chemical Society: Washington, DC, 1986; Chapter 20.
- Mayne, J. E. O. *Met. Finish. J.* **1966**, *12*(143), 437–441.
- Thomas, N. L. *Prog. Org. Coat.* **1991**, *19*, 101–121.
- Johnson, J. Ph.D. thesis; Department of Polymers & Coatings, North Dakota State University: Fargo, ND, May 2000.
- Ashby, M. F.; Johnson, K. *Materials and Design*; Butterworth Heinemann-Elsevier Science: Oxford, UK, 2002.
- Wicks, Z. W.; Jones, F. N.; Pappas, S. P.; Wicks, D. A. *Organic Coatings: Science & Technology*, 3rd ed.; John Wiley: New York, 2007; Chapter 34.
- Koesleske, J. V. Ed. *Paint and Coating Test Manual: 14th Edition of the Gardner-Sward Handbook*; ASTM Manual Series MNL 17; ASTM: Philadelphia, PA, 1995.
- Bierwagen, G.; Tallman, D.; Li, J.; He, L.; Jeffcoate, C. *Prog. Org. Coat.* **2003**, *46*, 148–157.
- Kinsella, E. M.; Mayne, J. E. O.; Scantlebury, J. D. *Br. Polym. J.* **1971**, *3*, 41–43.
- Allahar, K. N.; Su, Q.; Bierwagen, G. P. *Corrosion* **2008**, *64*, 860–870.
- Dill, K.; Bromberg, S.; Stitger, D. *Molecular Driving Forces*; Taylor & Francis: New York, 2003; Chapter 33.
- Bierwagen, G. P.; Jeffcoate, C.; Mills, D. J.; Li, J.; Balbyshev, S.; Tallman, D. E. *Prog. Org. Coat.* **1996**, *29*, 21–30.
- Li, J.; Jeffcoate, C. S.; Bierwagen, G. P.; Mills, D. J.; Tallman, D. E. *Corrosion* **1998**, *54*, 763–771.
- Bierwagen, G.; Tallman, D.; Li, J.; He, L.; Jeffcoate, C. *Prog. Org. Coat.* **2003**, *46*, 148–157.
- Allahar, K. N.; Hinderliter, B. R.; Bierwagen, G. P.; Tallman, D. E.; Croll, S. G. *Prog. Org. Coat.* **2008**, *62*, 87–95.
- Thomas, N. L. *Prog. Org. Coat.* **1991**, *19*, 101–121.
- Hare, C. In *Uhlig's Corrosion Handbook*; 2nd ed.; Review, R. W., Ed.; John Wiley: New York, 2000; Chapter 55, pp 1023–1038.
- Felix, S.; Barajas, R.; Bastidas, J. M.; Morcillo, M.; Feliu, S. In *Electrochemical Impedance Spectroscopy, ASTM STP 1188*; Scully, J. R., Silverman, D. C., Kendig, M., Eds.; American Society for Testing and Materials (ASTM): Philadelphia, PA, 1993; pp 438–449.
- Nanna, M. E.; Bierwagen, G. P. *J. Coat. Technol. Res.* **2004**, *1*, 69.
- Battocchi, D.; Simões, A. M.; Tallman, D. E.; Bierwagen, G. P. *Corros. Sci.* **2006**, *48*, 1292–1306.
- Battocchi, D.; Simões, A. M.; Tallman, D. E.; Bierwagen, G. P. *Corros. Sci.* **2006**, *48*, 2226–2240.
- Panossian, Z.; Mariaca, L.; Morcillo, M.; Flores, S.; Rocha, J.; Peñ, J. J.; Herrera, F.; Corvo, F.; Sanchez, M.; Rincon, O. T.; Pridyballo, G.; Simancas, J. *Surf. Coat. Technol.* **2005**, *190*, 244–248.
- Amirudin, A.; Thierry, D. *Prog. Org. Coat.* **1996**, *28*, 59–76.
- Marder, A. R. *Prog. Mater. Sci.* **2000**, *45*, 191.
- Brown, S. G. R.; Barnard, N. C. *Corros. Sci.* **2006**, *48*, 2291–2303.
- Böhm, S.; Holness, R. J.; McMurray, H. N.; Worsley, D. A. In *Eurocorr*; 2000, Queen Mary and Westfield College, London, pp 10–14, September 2000.
- Kalendová, A.; Kuckačová, A. *Macromol. Symp.* **2002**, *187*, 377–386.
- Selvaraj, M.; Guruviah, S. *Prog. Org. Coat.* **1996**, *28*, 271–277.
- Chen, W.-B. et al. *Appl. Surf. Sci.* **2002**, *187*, 1254–1264.
- Schweitzer, P. A. *Paint and Coatings: Applications and Corrosion Resistance*; CRC-Taylor & Francis: New York, 2006.
- Smith, L. M. Ed. *Generic Coatings Types: An Introduction to Industrial Maintenance Coating Materials*; SSPC 95-08; Technology Publishing: Pittsburgh, PA, 1996.
- del Amo, B.; Romagnoli, R.; Vetere, V. F.; Hernandez, L. S. *Prog. Org. Coat.* **1998**, *33*, 28–35.
- Sinko, J. *Prog. Org. Coat.* **2001**, *42*, 267–282.
- Kendig, M. W.; Buchheit, R. G. *Corrosion* **2003**, *59*, 359–400.
- Wang, H.; Presuel, F.; Kelley, R. G. *Electrochim. Acta* **2004**, *49*, 239–255.
- Pommersheim, J. M.; Nguyen, T.; Zhang, Z.; Hubbard, J. B. *Prog. Org. Coat.* **1994**, *25*, 23–41.
- Deya, C. G.; Romagnoli, D.; del Amo, B. *J. Coat. Technol. Res.* **2007**, *4*, 167–175.
- Kendig, M. W. In *Proceedings of the 4th International Symposium on Aluminum Surface Science & Technology*, Beaune, France, May 2006.
- Provier, T.; Baghdachi, J. *Smart Coatings*, ACS Symposium Series, 957; American Chemical Society Press: Washington, 2007.
- Lambourne, R.; Strivens, T. A. Eds. *Paint and Surface Coatings: Theory and Practice*, 2nd ed.; Woodhead: Cambridge, UK, 1999.

51. Goldschmidt, A.; Streitberger, H.-J. *The BASF Handbook on Basics of Coatings Technology*; Vincentz Network: Hannover, Germany, 2003.
52. Kehr, J. A. *Fusion Bonded Epoxy (FBE): A Foundation for Pipeline Corrosion Protection*; NACE: Houston, TX, 2003.
53. Chattopadhyay, D. K.; Raju, K. V. S. N. *Prog. Polym. Sci.* **2007**, *32*, 352–418.
54. Wicks, D. A.; Wicks, Z. W. *Prog. Org. Coat.* **2001**, *41*, 1–83.
55. Weiss, K. D. *Prog. Polym. Sci.* **1991**, *22*, 203–245.
56. Wang, D.; Bierwagen, G. P. *Prog. Org. Coat.* **2009**, *64*, 327–338.
57. Twite, R. L.; Bierwagen, G. P. *Prog. Org. Coat.* **1998**, *33*, 91–100.
58. Hare, C. H. *Paint Coat. Indust.* **1997**, *13*, 50–56.
59. Austin, M. J. *Raw Materials and Their Usage*; Surface Coatings, 3rd ed.; Vol. 1, Chapman & Hall, 1993; Chapter 25.
60. Kil, S.; Johansen, K. D.; Weinell, C. E.; Pedersen, M. S. *Prog. Org. Coat.* **2002**, *45*, 423–434.
61. Chico, B.; Simancas, J.; Vega, J. M.; Granizo, N.; Díaz, I.; de la Fuente, D.; Morcillo, M. *Prog. Org. Coat.* **2008**, *61*, 283–290.
62. Amiuidin, A.; Barrear, C.; Hellouin, R.; Thierry, D. *Prog. Org. Coat.* **1995**, *25*, 339–355.
63. Zhang, X.; Wang, F.; Du, Y. *Surf. Coat. Technol.* **2007**, *201*, 7241–7245.
64. Moggridge, G. D.; Lape, N. K.; Yang, C.; Cussler, E. L. *Prog. Org. Coat.* **2003**, *46*, 231–240.
65. Perrin, X.; Merlatti, C.; Aragon, E.; Margaillan, A. *Prog. Org. Coat.* **2009**, *64*, 466–473.
66. Soera, W. J.; Minga, W.; Koringb, C. E.; van Benthem, R. A. T. M.; Mold, J. M. C.; Terryn, H. *Prog. Org. Coat.* **2009**, *65*, 94–103.
67. Ashby, M.; Johnson, K. *Materials and Design: The Art and Science of Material Selection in Product Design*; Elsevier Science: Oxford, 2002.
68. Bohl, A. H. Ed. *Computer Aided Formulation*; VCH Publishers: New York, 1990.
69. Wang, D.; Bierwagen, G. P. *Prog. Org. Coat.* **2009**, *64*, 327–338.
70. Pathak, S. S.; Sharma, A.; Khanna, A. S. *Prog. Org. Coat.* **2009**, *65*, 206–216.
71. Skerry, B. S.; Chen, C. T.; Ray, C. J. *J. Coat. Technol.* **1992**, *64*(806), 77–86.
72. Fishman, R. S.; Kurtze, D. A.; Bierwagen, G. P. *Prog. Org. Coat.* **1993**, *21*, 387.
73. Fishman, R. S.; Hill, E. S.; Storsved, T. K.; Bierwagen, G. P. *J. Appl. Phys.* **1996**, *79*, 729.
74. Fishman, R. S.; Kurtze, D. A.; Bierwagen, G. P. *J. Appl. Phys.* **1992**, *72*, 3116–3124.
75. Fishman, R. S.; Kurtze, D. A.; Bierwagen, G. P. *Prog. Org. Coat.* **1993**, *21*, 387–403.
76. Chisholm, B. J.; Webster, D. C. *J. Coat. Technol. Res.* **2007**, *4*, 1–12.
77. Chisholm, B.; Potyrailo, R.; Cawse, J.; Shaffer, R.; Brennan, M.; Molaison, C.; Whisenhunt, D.; Flanagan, B.; Olson, D.; Akhave, J.; Saunders, D.; Mehrabi, A.; Licon, M. *Prog. Org. Coat.* **2002**, *45*, 313–321.
78. Shedlosky, T. J.; Huovinen, A.; Webster, D.; Bierwagen, G. In *Metal 04: Proceedings of the International Conference on Metals Conservation*, Canberra, Australia, 4–8 October 2004, p. 400.
79. Bonitz, V. S.; Hinderliter, B. R.; Bierwagen, G. P. *Electrochim. Acta* **2006**, *51*, 3558–3565.
80. Hie, J.; Bahr, J.; Chisholm, B.; Li, J.; Chen, Z.; Balbyshev, S.; Bonitz, V.; Bierwagen, G. *J. Comb. Chem.* **2008**, *10*, 704–713.
81. Chisholm, B. J.; Berry, M.; Bahr, J.; He, J.; Li, J.; Balbyshev, S.; Bierwagen, G. P. *J. Coat. Technol. Res.* **2009**.
82. Grundmeier, G.; Simões, A. Corrosion and Oxide Films; Bard, A., Stratman, M., Eds.; *Encyclopedia of Electrochemistry*, Vol. 4 Wiley-VCH: New York, 2003; Chapter 5.4.
83. Bierwagen, G.; Li, J.; He, L.; Tallman, D. In *Proceedings of the 2nd International Symposium on Service Life Prediction Methodology and Metrologies*, Monterey, CA, 14–17 November 1999; Martin, J., Bauer, D., Eds.; ACS Symposium Series 805; ACS: Washington, DC, 2001; Chapter 14; pp 316–350.
84. Knudsen, O. Ø.; Steinsmo, U.; Bjordal, M. *Prog. Org. Coat.* **2005**, *54*, 224–229.
85. Abreu, C. M.; Izquierdo, M.; Merino, P.; Nóvoa, X. R.; Pérez, C. *Corrosion* **1999**, *55*, 1173.
86. Marchebois, H.; Savall, C.; Bernard, J.; Touzain, S. *Electrochim. Acta* **2004**, *49*, 2945–2954.

## Further Readings

- Ashby, M.; Johnson, K. *Materials and Design: The Art and Science of Material Selection in Product Design*; Elsevier Science: Oxford, UK, 2002.
- Bierwagen, G. Ed. *Organic Coatings for Corrosion Control*; ACS Symposium Series 689; American Chemical Society: Washington, DC, 1998.
- Bohl, A. H. Ed. *Computer Aided Formulation*; VCH: New York, 1990.
- Fedrizzi, L. Terryn, H.; Simoes, A. Eds. *Innovative Pretreatment Techniques to Prevent Corrosion of Metallic Surfaces*; European Federation of Corrosion – Publication No. 54 Woodhead/CRC Press: Boca Raton, FL, 2007.
- Martin, J. W.; Bauer, D. R. Eds. *Service Life Prediction: Methodology and Metrologies*; ACS Symposium Series 805; American Chemical Society: Washington, DC, 2001.
- Scantlebury, D.; Kendig, M. *Advances in Corrosion Protection by Organic Coatings II*; Proceedings of the Electrochemical Society, Vol. 95–13; The Electrochemical Society: Pennington, NJ, 1995.
- Sekine, I.; Kendig, M.; Scantlebury, D.; Mills, D. *Advances in Corrosion Protection by Organic Coatings III*; Proceedings of the Electrochemical Society, Vol. 94–41; The Electrochemical Society: Pennington, NJ, 1997.
- Taylor, S. R. Isaacs, H. S.; Brooman, E. W. Eds. *Environmentally Acceptable Inhibitors and Coatings*; Proceedings of the Electrochemical Society; Vol. 95–16; The Electrochemical Society: Pennington, NJ, 1997.
- Wicks, Z. W.; Jones, F. N.; Pappas, S. P.; Wicks, D. A. *Organic Coatings: Science & Technology*, 3rd ed.; John Wiley: New York, 2007.
- Zarras, P.; Wood, T.; Richey, B.; Benicewicz, B. C. *New Developments in Coatings Technology*; ACS Symposium Series 962; The American Chemical Society: Washington, DC, 2006.



## 4.12 Mechanisms of Protection by Paints

**J. E. O. Mayne**

Department of Materials Science and Metallurgy, University of Cambridge, Cambridge, CB2 3QZ, UK

© 2010 Elsevier B.V. All rights reserved.

4.12.1	Introduction	2666
4.12.2	The Corrosion of Iron and Steel	2667
4.12.2.1	The Cathodic Reaction	2667
4.12.2.1.1	Diffusion of water	2668
4.12.2.1.2	Diffusion of oxygen	2668
4.12.2.2	The Anodic Reaction	2669
4.12.3	Mechanisms of Paint Protection	2669
4.12.3.1	Cathodic Protection	2669
4.12.3.2	Anodic Passivation	2670
4.12.3.2.1	Basic pigments	2670
4.12.3.2.2	Soluble pigments	2670
4.12.3.3	Resistance Inhibition	2671
4.12.3.3.1	Electrolytes underneath the film	2671
4.12.3.3.2	Ionogenic groups in the film substance	2671
4.12.3.3.3	Water and electrolytes outside the film	2672
4.12.3.4	Physical Factors Affecting Resistance	2675
4.12.3.4.1	Temperature	2675
4.12.3.4.2	Concentration of electrolyte	2675
4.12.3.4.3	Film thickness	2675
4.12.3.4.4	Solvents	2676
4.12.4	Prediction of Paint Performance	2676
References		2676

### Glossary

**D conduction** The behavior of a paint film (or an area of a paint film) whose trends in conductivity follow directly the solution in which it is immersed.

**Donnan effect** Where species of a particular size or charge are unable to pass through a semipermeable membrane, an additional osmotic pressure is created across the membrane.

**I conduction** The behavior of a paint film (or an area of a paint film) whose conductivity follows inversely to the solution in which it is immersed.

**Ionogenic** Capable of forming ions; used especially of a molecule that can dissociate into fixed ions and mobile counterions

**Isoelectric (point)** The pH at which a particular molecule or surface carries no net electrical charge.

**Zwitterion** A chemical compound that is electrically neutral but carries formal positive and negative charges on different atoms.

### Abbreviations

**AC** Alternating current

**DC** Direct current

**PVC** Pigment volume concentration

**RH** Relative humidity

### 4.12.1 Introduction

From time to time, astronomical estimates are made of the annual destruction of metals, particularly iron and steel, by corrosion. Paint is one of the oldest methods used for delaying this process. However,

it is somewhat surprising that its protective action has only recently been systematically examined.

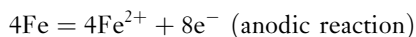
Since iron is the commonest structural material, the following discussion will be limited to the behavior of this metal. The general principles can readily be extended to nonferrous metals.

#### 4.12.2 The Corrosion of Iron and Steel

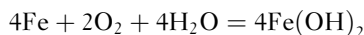
Corrosion is essentially the conversion of iron into a hydrated form of iron oxide, that is, rust. The driving force of the reaction is the tendency of iron to combine with oxygen. It has long been known that iron is not visibly corroded in the absence of either water or oxygen. The overall reaction in their presence may be written as:



When the supply of oxygen is restricted, the corrosion product may contain ferrous ions. The overall reaction can be broken down into two reactions, one producing electrons and the other consuming them:

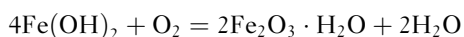
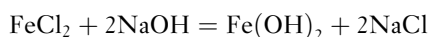


Or, combining these:



In the presence of oxygen, the ferrous hydroxide will be further converted into one of the forms of rust, for example,  $\text{Fe}_2\text{O}_3 \cdot \text{H}_2\text{O}$ .

Ferrous hydroxide is soluble (9%) in pure water, but slight oxidation renders it appreciably less soluble. Thus, in the presence of water and oxygen alone, the corrosion product may be formed in close contact with the metal and attack will consequently be stifled. In the presence of an electrolyte such as sodium chloride, however, the anodic and cathodic reactions are modified, ferrous chloride being formed at the anode and sodium hydroxide at the cathode. These two compounds are highly soluble and not easily oxidized, so they diffuse away from the sites of formation and react at a distance from the metal surface to form ferrous hydroxide, or a basic salt, which then combines with oxygen to form rust with the regeneration of sodium chloride:



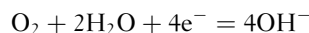
Consequently, rust is formed at a distance from the metal, and so stifling cannot occur.

It follows that when iron rusts, the conversion is accompanied by a flow of electrons in the metal from the anodic to the cathodic regions and by the movement of ions in solution. This conclusion has been firmly established by Evans<sup>1</sup> and his coworkers, who have shown that in the case of a number of metals under laboratory conditions, the spatial separation of the anodic and cathodic zones on the surface of the metal was so complete that the current flowing was equivalent to the corrosion rate. In order to inhibit corrosion, it is necessary to stop the flow of current. This can be achieved by suppressing either the cathodic or the anodic reaction, or by inserting a high resistance in the electrolytic path of the corrosion current. These three methods of suppression are called cathodic, anodic, and resistance inhibition, respectively.

The effect of paint films on the cathodic and anodic reactions will now be considered and the factors which influence the electrolytic resistance of paint films will be discussed.

#### 4.12.2.1 The Cathodic Reaction

The cathodic reaction in neutral solutions usually involves oxygen, water, and electrons:



If a paint film is to prevent this reaction, it must be impervious to electrons; otherwise, the cathodic reaction is merely transferred from the surface of the metal to the surface of the film. Organic polymer films do not contain free electrons, except in the special case of pigmentation with metallic pigments; consequently, it will be assumed that the conductivity of paint films is entirely ionic. In addition, the films must be impervious to either water or oxygen, so that they prevent either of them from reaching the surface of the metal.

The rate of corrosion of unpainted mild steel immersed in seawater, found by Hudson and Banfield,<sup>2</sup> was found to be  $0.089 \text{ mm year}^{-1}$ . Hudson<sup>3</sup> obtained a similar average value for steel exposed to the open air under industrial conditions ( $0.051 \text{ mm year}^{-1}$  at Motherwell and  $0.109 \text{ mm year}^{-1}$  at Sheffield). This rate of corrosion corresponds to the destruction of  $0.07 \text{ g cm}^{-2}$  of iron per year. Assuming that the corrosion product was  $\text{Fe}_2\text{O}_3 \cdot \text{H}_2\text{O}$ , this rate of attack represents the consumption of  $0.011 \text{ g cm}^{-2}$  of water per year and  $0.03 \text{ g cm}^{-2}$  of oxygen per year.

**4.12.2.1.1 Diffusion of water**

The diffusion of water through paint films has been measured by various workers. The weight of water, which could diffuse through three clear vehicles and eight paint films, each 0.1-mm thick, at a relative humidity (RH) of 85–100%, has been calculated on the assumption that the water would be consumed as soon as it reached the metal surface, that is, the rate-controlling step was the rate of diffusion of water through the film, as shown in [Table 1](#).<sup>4,5</sup>

By means of an ingenious instrument, which measured the ‘wetness’ of a painted surface, Gay<sup>6</sup> found that although the relative humidity of the atmosphere varies appreciably, this is not reflected in the behavior of paint films. He found that under normal conditions, paint films are saturated with water for about half of their life, and for the remainder, the water content corresponded with an atmosphere of high humidity; furthermore, the relative humidity of sea water is about 98%. It follows from [Table 1](#) that the rate at which water passes through paint and

varnish films is many times greater than the water consumed by an unpainted specimen exposed under industrial conditions or immersed in the seawater.

**4.12.2.1.2 Diffusion of oxygen**

The diffusion of oxygen through polymer films has been examined by a number of workers. Guruviah<sup>5</sup> measured the permeability to oxygen of films cast from five paints ([Table 2](#)) and compared the results with the corrosion rates of painted steel panels, when exposed to salt spray and humidity for 1000 h. He concluded that “the low corrosion rate could be explained by the low permeability to oxygen of the films”; however, when his values for the permeability are plotted against the corrosion, it is clear that this conclusion is without foundation.

The mass of oxygen, which could diffuse through unit area of a 0.1-mm thick film under a pressure gradient of 2 kPa of oxygen, has been calculated, and is shown in [Table 2](#).<sup>5,7,8</sup> Baumann<sup>9</sup> has claimed that these figures are about 100 times too high, but

**Table 1** Diffusion of water through paint films of thickness 0.1 mm

<i>Vehicle</i>	<i>Pigment</i>	<i>Rate of water consumed (g cm<sup>-2</sup> year<sup>-1</sup>)</i>	<i>Reference</i>
Glycerol phthalate varnish	None	0.825	4
Phenolformaldehyde varnish	None	0.718	4
Epoxy coal tar	None	0.391	5
Glycerol phthalate varnish	Flake aluminum	0.200	4
Phenolformaldehyde varnish	Flake aluminum	0.191	4
Linseed oil	Lithopone	1.125	4
Ester gum varnish	White lead/zinc oxide	0.122	4
Linseed penta-alkyd	Iron oxide, 15% PVC	0.840	5
Linseed penta-alkyd	Iron oxide, 35% PVC	0.752	5
Epoxy polyamide	Iron oxide, 35% PVC	1.810	5
Chlorinated rubber	Iron oxide, 35% PVC	1.272	5

Unpainted steel consumes water at a rate of 0.008–0.023 g cm<sup>-2</sup> year<sup>-1</sup>.

**Table 2** Diffusion of oxygen through paint films of thickness 0.1 mm

<i>Vehicle</i>	<i>Pigment</i>	<i>Rate of water consumed (g cm<sup>-2</sup> year<sup>-1</sup>)</i>	<i>Reference</i>
Asphalt	None	0.053	7
Epoxy coal tar	None	0.002	5
Polystyrene	None	0.013	8
Polyvinyl butyral	None	0.027	8
Asphalt	Talc	0.039	7
Linseed penta-alkyd	Iron oxide, 15% PVC	0.003	5
Linseed penta-alkyd	Iron oxide, 35% PVC	0.003	5
Epoxy polyamide	Iron oxide, 35% PVC	0.002	5
Chlorinated rubber	Iron oxide, 35% PVC	0.006	5

Unpainted steel consumes oxygen at a rate of 0.020–0.030 g cm<sup>-2</sup> year<sup>-1</sup>.

this is because he compared the amount which could pass through in a day with that passing in a year. Haagen and Funke<sup>10</sup> concluded that the permeation of water was too great and that of ions too small to be the controlling factor and suggested that the rate controlling step was the rate of the diffusion of oxygen. However, if this were the case then painted steel upon exposure should corrode at a rate varying from that of unpainted steel to about a tenth of that value. Since painted steel upon exposure does not corrode immediately at this rate, it is concluded that the rate of the diffusion of oxygen is not the controlling factor.

The general conclusion drawn from these considerations is that paint films are so permeable to water and oxygen that they cannot inhibit corrosion by preventing water and oxygen from reaching the surface of the metal, that is to say they cannot inhibit the cathodic reaction.

#### 4.12.2.2 The Anodic Reaction

The anodic reaction consists of the passage of iron ions from the metallic lattice into solution, with the liberation of electrons, which are consumed at the cathode by reaction with water and oxygen. There are two ways in which the anodic reaction can be suppressed:

- (a) If the electrode potential of iron is made sufficiently negative, positively charged iron ions will not be able to leave the metallic lattice, that is, cathodic protection.
- (b) If the surface of the iron becomes covered with a film impervious to iron ions, then the passage of iron ions into solution will be prevented, that is, anodic passivation.

### 4.12.3 Mechanisms of Paint Protection

#### 4.12.3.1 Cathodic Protection

In order to make the potential of iron more negative, the iron must receive a continuous supply of electrons. As has already been pointed out, polymer films do not contain free electrons; there remains the possibility of obtaining these from a pigment. The only pigments which contain free electrons are metallic ones, and such pigments will protect iron cathodically if the following conditions are fulfilled:

- (a) The metallic pigment must be of a metal less noble than iron, otherwise the iron will supply

electrons to the pigment, which will be protected at the expense of iron.

- (b) The pigment particles must be in metallic, that is, electronic, contact with each other and with the coated iron; if they are not, the movement of electrons cannot occur.

It has been shown<sup>11</sup> that zinc dust is the only commercially available pigment which fulfils both conditions. Paints capable of protecting steel cathodically can be prepared with zinc dust, provided that the pigment content of the dried film is of the order of 95 wt%; both organic and inorganic binders have been used, the latter being very useful when resistance to oil or organic solvents is required.

These paints are quite porous and function satisfactorily only in the presence of an electrolyte – for example, water containing a trace of salt, or acid – which completes the circuit formed by the two metals. It might be thought that the useful life of these paints is limited to the life of the electronic contact between the zinc particles, but this is not correct. Under normal conditions of exposure, the electrons supplied by the zinc to the steel are consumed at the surface of the steel by reaction with water and oxygen (cathodic reaction), with the formation of hydroxyl ions. Consequently, the surface becomes coated with a deposit of the hydroxides, or carbonates of zinc, calcium, or magnesium, which blocks the pores in the film and renders it very compact, adherent, and impervious. Thus, although metallic contact between the steel and the zinc dust particles is essential in the early stages of exposure, the paints provide good protection after that contact has been lost. Paints containing less zinc dust have been known for a long time, but as the zinc dust concentration is decreased, protection at scratch lines or at gaps in the coating decreases; however, such paints frequently afford good general protection owing to the formation of deposits (consisting of oxides and carbonates) on the metal at the base of the coating.

Recently, it has been pointed out that manganese satisfies both conditions since the oxide film around the particles contains ions in two states of oxidation, and it has been claimed that cathodically protective paints can be prepared with this pigment.<sup>12</sup> Exposure trials in this country have indicated that at an inland site their behavior is comparable with the zinc dust controls, but that they were inferior to zinc-rich paints under severe marine conditions. It has been suggested that they might be of interest where zinc was unsuitable owing to toxicity.<sup>13</sup>

#### 4.12.3.2 Anodic Passivation

When a piece of iron is exposed to the air, it becomes covered with an oxide film. Upon immersion in water or solutions of certain electrolytes, the air-formed film breaks down and corrosion ensues. In order to prevent corrosion, the air-formed film must be reinforced with similar material, or a ferric compound, and there are two ways in which this may be achieved:

- (a) The pigment may be sufficiently basic to form soaps when ground in linseed oil; in the presence of water and oxygen these soaps may autoxidize to form soluble inhibitive degradation products.
- (b) The pigment itself may be an inhibitor of limited solubility.

##### 4.12.3.2.1 Basic pigments

Typical pigments in this class include basic lead carbonate, basic lead sulfate, red lead, and zinc oxide.

It has been established that water becomes non-corrosive after contact with paints prepared by grinding basic pigments in linseed oil,<sup>14</sup> it was also shown that lead and zinc linoleates, prepared by heating the oxide with linseed oil fatty acids in xylene, behave in a similar way. Later, this observation was extended to the linoleates of calcium, barium, and strontium.<sup>15</sup>

Determinations have been made of the solubility of lead linoleate prepared in the absence of oxygen and extracted with air-free water.<sup>16</sup> Under these conditions, lead linoleate had a solubility of 0.002% at 25 °C, and the extract was corrosive when exposed to the air. However, when the extraction was carried out in the presence of air, the resulting extract contained 0.07% solid material and was noncorrosive. It was concluded that in the presence of water and oxygen lead linoleate yielded soluble inhibitive degradation products.

In order to obtain information regarding the composition of these degradation products, aqueous extracts of the lead soaps of the linseed oil fatty acids were analyzed, mainly by chromatography. The extracts contained formic acid 46%, azelaic acid 9%, and pelargonic acid and its derivatives 27%, the remaining 18% consisting of a mixture of acetic, propionic, butyric, suberic, pimelic, and adipic acids. It was shown that whereas the salts of formic acid were corrosive, those of azelaic and pelargonic acid were very efficient inhibitors.

Mayne and Ramshaw<sup>17</sup> have obtained information regarding the origin of these various acids by examining the degradation products of the lead soaps of the individual acids present in linseed oil. They found that it was only the unsaturated acids which degraded

to give inhibitive materials, and that the lead soaps of linoleic and linolenic acid yielded in addition short-chain acids which were corrosive. He also examined the relative inhibiting powers of the lead, calcium and sodium salts of a range of mono- and dibasic acids in the pH range 4–6 at concentrations of  $10^{-3}$  to  $10^{-5}$  M.<sup>18</sup> Under these conditions the lead salts were always more efficient than the sodium and calcium salts, and the optimum efficiency occurred when both the mono- and dibasic acids had a chain length of 8–9 carbon atoms.

The mechanism of inhibition by the salts of the long-chain fatty acids has been examined.<sup>19</sup> It was concluded that in the case of the lead salts, metallic lead was first deposited at certain points and that at these points oxygen reduction proceeded more easily. Consequently, the current density was kept sufficiently high to maintain ferric film formation; in addition, any hydrogen peroxide present may assist in keeping the iron ions in the oxide film in the ferric condition, consequently the air-formed film is thickened until it becomes impervious to iron ions. The zinc, calcium, and sodium salts are not as efficient inhibitors as the lead salts and recent work has indicated that inhibition is due to the formation of ferric azelate, which repairs weak spots in the air-formed film. This conclusion has been confirmed by the use of  $^{14}\text{C}$ -labelled azelaic acid, which was found to be distributed over the surface of the mild steel in a very heterogeneous manner.<sup>20</sup>

Zinc phosphate was introduced as an inhibitive pigment by Barraclough and Harrison,<sup>21</sup> and in the early tests, vehicles based on drying oils were used. Later, it was claimed<sup>22</sup> that it was an effective inhibitive pigment when used with all paint media in current use.

Variable results have been reported with this pigment and an examination of its inhibitive action<sup>23</sup> has led to the conclusion that under rural and marine conditions, where the pH of the rainwater is above 5, it behaves as an inert pigment owing to its limited solubility. However, in industrial and urban areas, where the pH of the rainwater may be in the region of 4 or lower, it is converted into the more soluble monohydrogen phosphate. This reacts, in the presence of oxygen, with the steel surface to form a mixture of tribasic zinc and ferric phosphates, which being insoluble protects the steel from further attack.

##### 4.12.3.2.2 Soluble pigments

The most important pigments in this class are the metallic chromates, which range in solubilities from



17.0 to  $0.00005 \text{ g l}^{-1}$  as  $\text{CrO}_3$ .<sup>24</sup> An examination has recently been carried out of the mechanism of inhibition by chromate ions and it has been shown by chemical analysis of the stripped film, Mössbauer spectroscopy and electron microprobe analysis that the air-formed film is reinforced with a more protective material in the form of a chromium-containing spinel.<sup>25</sup> The situation is, however, complicated by the possibility that some chromates, particularly the basic ones, may inhibit through the formation of soaps. There is evidence that lead chromate can function in this way.

It has been found that red lead, litharge, and certain grades of metallic lead powder render water alkaline and inhibitive<sup>14</sup>; this observation has been confirmed by Pryor.<sup>26</sup> The effect is probably due to a lead compound, for example, lead hydroxide, in solution. Since, however, atmospheric carbon dioxide converts these lead compounds into insoluble basic lead carbonate, thereby removing the inhibitive materials from solution, these pigments may have only limited inhibitive properties in the absence of soap formation.

Work by Beckmann<sup>27</sup> indicated that lead hydroxide was only very slightly better as an inhibitor than sodium hydroxide, and the mechanism of inhibition is probably similar to that suggested for alkaline solutions.<sup>28</sup>

Owing to the low dielectric constant of organic vehicles, these pigments can ionize only after water has permeated the film; consequently, their efficiency is associated with the nature of the vehicle in which they are dispersed, a point which is sometimes overlooked when comparing the relative merits of chromate pigments.

#### 4.12.3.3 Resistance Inhibition

It has been shown that paint films are so permeable to water and oxygen that they cannot affect the cathodic reaction, and that the anodic reaction may be modified by certain pigments. There are, however, many types of protective paints which do not contain inhibitive pigments. It is concluded that this class of paints prevents corrosion by virtue of its high ionic resistance, which impedes the movement of ions and thereby reduces the corrosion current to a very small value.

It is assumed that conduction in polymer films is ionic; it is difficult to see how it could be otherwise. The factors which break down the ionic resistance, or render it ineffective, will now be considered.

The effective resistance of paint films may be influenced by ions derived from three sources:

- (a) electrolytes underneath the film;
- (b) ionogenic groups in the film substance;
- (c) water and electrolytes outside the film, that is, arising from the conditions of exposure.

##### 4.12.3.3.1 Electrolytes underneath the film

Atmospheric exposure trials, carried out in Cambridge, established the fact that when rusty specimens were painted in the summer, their condition, after some years' exposure, was very much better than that of similar specimens painted in the winter.<sup>29</sup> It was found that steel weathered in Cambridge carried spots of ferrous sulfate, deeply imbedded in the rust, and that the quantity of ferrous sulfate/unit area was very much greater in the winter than in the summer<sup>30</sup>; this seasonal variation was attributed to the increased sulfur dioxide pollution of the atmosphere in the winter, caused by the combustion of coal in open grates. It was concluded that there was a causal relationship between the quantity of ferrous sulfate and the effective life of the paint. It was suggested that these soluble deposits of ferrous sulfate short-circuit the resistance of the paint film, and since paint films are very permeable to water and oxygen, the ferrous sulfate will become oxidized and hydrolyzed with the production of voluminous rust, which will rupture the film at numerous points, thus giving rise to the characteristic type of failure seen on painted rusty surfaces.

It can be claimed that the problem of painting rusty surfaces is now understood. A method for estimating the ferrous sulfate content of any rusty surface has been put forward,<sup>30</sup> but the amount of ferrous sulfate which can be tolerated by various paints has not yet been established. Thus, it is a bad practice to apply paints to surfaces carrying electrolytes.

##### 4.12.3.3.2 Ionogenic groups in the film substance

Ionogenic (ion-producing) materials may be present, in the form of electrolytes, in both the pigments and the vehicle. Their presence in the pigments may be eliminated by the selection of suitable raw materials by the paint manufacturer; though it does not concern us here, it is important to consider the possibility of the existence of ionogenic groups, such as carboxyl groups, in the polymer itself.

When paint films are immersed in water or solutions of electrolytes, they acquire a charge.

The existence of this charge is based on the following evidence. In a junction between two solutions of potassium chloride, 0.1 and 0.01 M, there will be no diffusion potential, because the transport numbers of both the  $K^+$  and the  $Cl^-$  ions are almost 0.5. If the solutions are separated by a membrane equally permeable to both ions, there will still be no diffusion potential, but if the membrane is more permeable to one ion than to the other a diffusion potential will arise; it can be calculated from the Nernst equation that when the membrane is permeable to only one ion, the potential will have the value of 58 mV at 20 °C.

It is easy to measure the potential of this system and it has been found<sup>31</sup> that membranes of polystyrene, linseed oil, and a tung oil varnish yielded diffusion potentials of 43–53 mV, the dilute solution being always positive to the concentrated. Similar results have been obtained with films of nitrocellulose,<sup>32</sup> cellulose acetate,<sup>33</sup> alkyd resin, and polyvinyl chloride.<sup>34</sup>

This selective permeability is ascribed to the presence on the membrane of a negative charge, which is attributed to carboxyl groups attached to the polymer chains. Paint films can, therefore, be regarded as very large anions.

It has been shown that the charge influences the distribution of the primary corrosion products, and work<sup>35</sup> has indicated that the existence of carboxyl groups in the polymer film has an important influence on its behavior when immersed in potassium chloride solutions.

#### **4.12.3.3.3 Water and electrolytes outside the film**

Here, we are concerned with the effect of ions in the environment on the resistance of polymer films.

Kittelberger and Elm<sup>36</sup> measured the rate of diffusion of sodium chloride through a number of paint films. Calculations based on their results<sup>31</sup> showed clearly that the rate of diffusion of ions was much smaller than the rate of diffusion of either water or oxygen. Furthermore, they found that there was a linear relationship between the rate of diffusion and the reciprocal of the resistance of the film. This relationship suggests that sodium chloride is diffused through the membrane as ions and not as ion pairs, since the diffusion through the film of unionized material would not affect the resistance, because if a current is to flow, either ions of similar charge must move in one direction, or ions of opposite charge must move in opposite directions.

An examination has, therefore, been made of the effect of solutions of potassium chloride on the electrolytic resistance of films cast from a pentaerythritol alkyd, a phenolformaldehyde tung oil, and an epoxy-polyamide varnish.<sup>37,38</sup> Potassium chloride was chosen because its conductivity is well known and unpigmented films were first examined in order to eliminate the complexities of polymer-pigment interaction.

The experimental procedure consisted of casting the varnish on glass plates by means of a spreader bar having a gap of 0.102 mm; this produced a wet film of thickness 0.051 mm that yielded a dried film of 0.025 mm. This standard thickness was used throughout and resistances are quoted in  $\Omega\text{cm}^2$ . The cast films were dried for 48 h in a glove box followed by a further 48 h in an oven at 65 °C.

The films were then soaked in water and removed from the plates. Portions were mounted in glass cells which were filled with potassium chloride solution; two Ag/AgCl electrodes were inserted into the limbs of the cells and the unit was placed in a thermostat. The resistance of the films was determined, from time to time, by connecting the cells in series with a known resistance and applying a potential of 1 V to the combination; the potential drop across the standard resistance was measured by means of a valve potentiometer.

When samples of about 1 cm<sup>2</sup> were taken from a single cast film of 100 × 200 mm<sup>2</sup> of a number of paint and varnish films, their resistances varied with the concentration of potassium chloride solution in one of two ways (Figure 1). Either the resistance increased with increasing concentration of the electrolyte (inverse or I conduction) or the resistance of the film followed that of the solution in which it was immersed (direct or D conduction). The percentage of I and D samples taken from different castings varied, but average values for a number of castings were 50% D for the pentaerythritol alkyd and the tung oil phenol formaldehyde varnishes, 57% for urethane alkyd, 76% for epoxypolyamide, and 78% for polyurethane varnishes.<sup>39</sup>

The effect of iron oxide, zinc oxide, and red lead on the percentage of D areas has been determined. Three vehicles were used, a pentaerythritol alkyd, a tung oil phenolic, and an epoxypolyamide.<sup>40</sup> In the case of iron oxide, the D areas increased with all the three vehicles; in contrast, zinc oxide had very little effect on the percentage of D areas. However, red lead when dispersed in the alkyd and tung oil vehicles behaved in a similar way to iron oxide, whereas red

lead when dispersed in the epoxypolyamide vehicle had very little effect.

A careful examination has been made of the properties of I films when immersed in solutions of

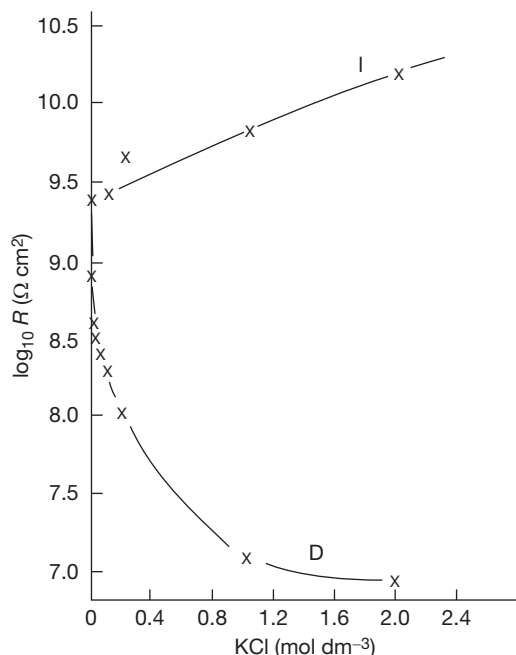


**Figure 1** Relationship between the logarithm of the resistance of D and I films of a pentaerythritol alkyd paint, containing 6.1% iron oxide by volume, and the concentration of the potassium chloride solutions in which they were immersed. Reproduced from *Brit. Polym. J.* **1971**, 3, 41.

electrolytes. It was found that when a film of a pentaerythritol alkyd varnish was transferred from 0.001 to 3.5 N KCl its resistance rose, fell upon returning it to the 0.001 N KCl, rose again to the same high value when immersed in a sucrose solution isotonic with 3.5 N KCl and fell to the original value when returned to the dilute KCl solution (Figure 2). It was concluded that the changes in resistance were dependent only upon the available water in the solution and were associated, therefore, with the entry of only water into the varnish film.<sup>37</sup>

In contrast, D films followed the resistance of the solution in which they were immersed, and this behavior was originally explained by assuming that D films contained holes, or pores, filled with solution that controlled the resistance of the film. Thus, a typical value for the resistance of a D film in 3.5 M potassium chloride is  $108 \Omega \text{ cm}^2$  and if this resistance was due to a pore, then it would have a radius of about 50 nm. In order to test this explanation, the distribution of I and D areas in a given piece of film has been determined by means of a series of gaskets fitted into a dismountable cell.<sup>41</sup> It was found that I films were free from D areas, but in the case of the three vehicles examined, samples of D films always contained a mixture of I and D areas in an interlocking mosaic structure. It was concluded that those portions of the film having D properties were distributed over an appreciable area of the sample and not confined to a single area, as would have been the case had the sample contained a single pore.

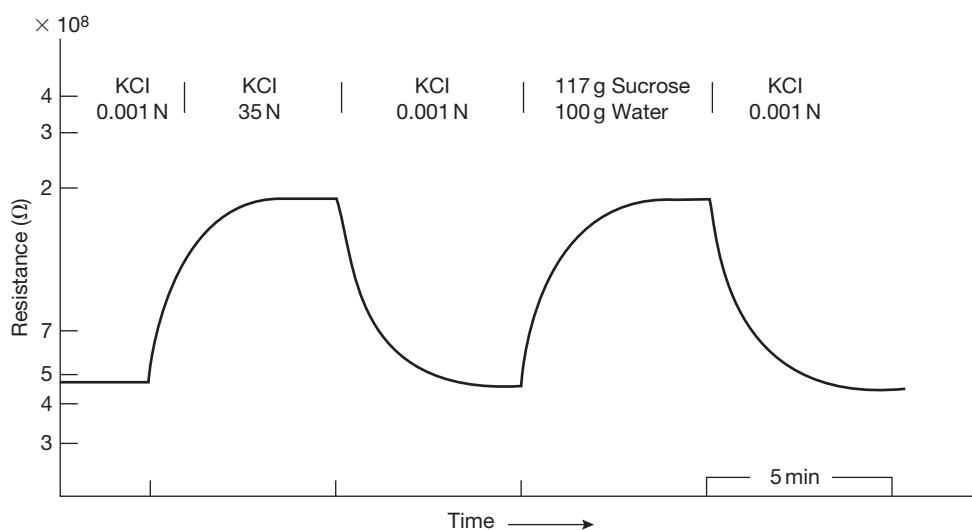


**Figure 2** Relationship between the resistance of an I film (log scale) and the concentration of the solute. Reproduced from *Official Digest* **1970**, 34(452), 972–990.

It was concluded that D conduction cannot be attributed to the presence of pores, unless they were of molecular dimensions.

In general, the water uptake of D films tended to be higher than that of I films, but a more significant difference was shown by microhardness measurements. The results obtained with all the three vehicles showed that the D areas were significantly softer than the I areas and that the distribution of the hardness values corresponded to that of the resistances. It was concluded that these films have a very heterogeneous structure and that I and D areas are brought about by differences in cross-linking density within the film.

An investigation has been made of the factors that control I and D conduction and it has been found that the difference is only one of degree and not of kind.<sup>42</sup> Thus, if the varnish films are exposed to solutions of decreasing water activity, then the resistance falls with increasing concentration of electrolyte, but a point is eventually reached when the type of conduction changes and the films exhibit I-type behavior. It appears that D films can be converted into I films, the controlling factor being the uptake of water.

The discussion so far has been limited to the behavior of polymer films after immersion in potassium chloride solutions for only a short time. When varnish films were immersed in potassium chloride solutions for a month or more, a steady fall in resistance took place. Further experiments indicated that the effect was reversible and dependent on both the pH of the solution and the concentration of potassium chloride. It was concluded that an ion-exchange process was operative.<sup>37</sup>

In view of this, the properties of I films were examined after they had been subjected to increasing amounts of ion exchange.<sup>38</sup> In order to do this, detached films were exposed at 65 °C for 7 h to a universal buffer adjusted to a suitable pH and the resistance of the film measured at 25 °C in 3 M and 0.001 M potassium chloride. The results obtained with a pentaerythritol alkyd are shown in Figure 3 from which it can be seen that as the pH of the conditioning solution increased, the resistance of the film fell, until at a pH of about 7.5 when it suddenly dropped. The resistance of the film then followed that of the solution in which it was immersed, that is, it became a D-type film. Similar results were obtained with films of a tung oil phenolic varnish, although in this case the change-over point occurred at a higher pH, that is, about 9.

In the case of the epoxypolyamide varnish, however, as the pH increased the resistance of the film at

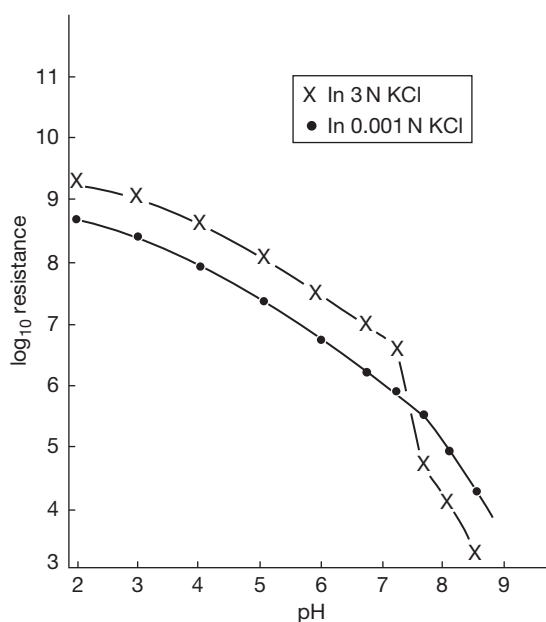


**Figure 3** Variation of the resistance of I films (log scale) with the pH of the conditioning solutions.

first rose, then at about pH 8.8 it started to fall until at pH 11 the change-over in the type of conduction occurred. This suggests that the resin was acting as a zwitterion with an isoelectric point at about pH 8.8. Thus, before the isoelectric point, the membrane would be positively charged and an increasing concentration of hydroxyl ions would depress the ionization of the ionogenic groups; above the isoelectric point, the membrane would be negatively charged and ion exchange with potassium ions would take place. This conclusion was confirmed by diffusion potential measurements.

In the case of all the three varnishes, after the ion exchange had taken place, a point was reached when the type of conduction changed from I to D. The change-over in the type of conduction was found to occur at the same pH as a fall in the temperature coefficient of resistance, and the lower value corresponded to that of the aqueous solution.

The phenomenon of ion exchange has been confirmed by chemical analysis.<sup>43</sup> Films were exposed to potassium chloride solutions of increasing pH, ashed and their potassium content determined by flame photometry. It was found that the potassium content of the films increased as the pH of the solutions rose until saturation was reached at a value which corresponded to that of the change-over in the mechanism of conduction. It was concluded that the change-over in the mechanism of conduction corresponded to the

point at which the exchange capacity of the film had reached its limit.

Rothwell<sup>44</sup> found by resistance measurements that ion exchange occurred in films of eight unpigmented varnishes, and he confirmed this for pentaerythritol alkyd films by the determination of the uptake of radioactive potassium in the form of  $^{42}\text{KCl}$ ; however, his films, with one exception, were all D type.

Fialkiewicz and Szandorowski<sup>45</sup> examined the penetration of  $^{90}\text{Sr}$  and  $^{36}\text{Cl}$  ions through air-dried films of a styrenated alkyd pigmented with iron oxide over the range 10–60% PVC (pigment volume concentration) and found intense penetration of the strontium cations, but negligible penetration of the chloride ions.

Ulfvarson *et al.*<sup>46</sup> examined the ion exchange properties of free films of a soya alkyd, and later Khullar and Ulfvarson<sup>47</sup> extended the examination to clear films of 20 vehicles. They concluded that those binders with low ion-exchange capacities provided the best protection. In a later study,<sup>48</sup> they examined the relationship between ion-exchange capacity and corrosion protection of 22 paints based on three alkyd binders and concluded that ion exchange was not the dominating factor, but a secondary one. This conclusion was confirmed by van der Heyden,<sup>49</sup> who suggested that a process of ion exchange combined with diffusion of cations into the film was operative.

#### 4.12.3.4 Physical Factors Affecting Resistance

##### 4.12.3.4.1 Temperature

An examination has been made of the effect of temperature on the structural changes in polymer films produced from the three vehicles described earlier.<sup>50</sup> Three methods were used: dilatometry, water absorption, and ionic resistance. It was concluded that dilatometry was the most reliable method and water absorption is difficult to determine. Both methods use appreciable quantities of film, which contain both D and I areas. Resistance measurements, however, can be carried out on small areas of film and the relative properties of D and I areas studied.

It was established that significant changes in resistance took place at the transition temperature and consequently sharp changes in protective properties. The resistance always fell with an increase in temperature and this may provide an explanation for the fact that accelerated tests using the same corrosion cycle may not produce the same results if carried out at different temperatures.

##### 4.12.3.4.2 Concentration of electrolyte

Myer and Sievers<sup>51</sup> applied the Donnan equilibrium to charged membranes and developed a quantitative theory of membrane selectivity. They expressed this selectivity in terms of a selectivity constant, which they defined as the concentration of fixed ions attached to the polymer network. They determined the selectivity constant of a number of membranes by the measurement of diffusion potentials. Nasini *et al.*<sup>52</sup> and Kumins<sup>53</sup> extended the measurements to paint and varnish films.

When the Donnan equilibrium is operative, the entry of ions into the membrane is restricted. Consequently, as the concentration of ions in the solution increases the resistance of the membrane remains constant until the concentration of ions in the solution reaches that of the fixed ions attached to the polymer network. At this point, their effect will be swamped and the movement of ions will be controlled by the concentration gradient.

Films of a pentaerythritol alkyd, a tung oil phenolic and an epoxy–polyamide pigmented with iron oxide in the range 5–7% PVC were exposed to solutions of potassium chloride in the range 0.0001–2.0 M.<sup>54</sup> It was found that in all cases, the resistance of the films steadily decreased as the concentration of the electrolyte increased. Since the resistances of the films were at no time independent of the concentration of the electrolyte, it was concluded that the Donnan equilibrium was not operative and that the resistance of the films were controlled by the penetration of electrolyte moving under a concentration gradient.

##### 4.12.3.4.3 Film thickness

Varnishes prepared from the three standard polymers were cast on two thicknesses and the percentage of D areas compared with that obtained from the films produced by casting one thin coat, allowing it to dry and then casting a second coat on top.<sup>59</sup> Similar results were obtained from all the three varnishes and the results obtained with the epoxy–polyamide varnish are given in Table 3.

**Table 3** Percentage of D areas on cast films epoxy–polyamide varnish

	Thickness ( $\mu\text{m}$ )	% D-type
Single coat	35–40	80
Single coat	75–80	50
Double coat	70–75	0–5



Earlier, it was shown that D type areas are relatively small; consequently, the chance of D areas overlapping each other is low. It follows that two coats of all the three varnishes, which are based on cross-linking polymers, are more effective in improving the resistance of the films than single coats of equal thickness.

#### 4.12.3.4.4 Solvents

All the films discussed so far have been cast from paints or varnishes containing solvents. In order to examine the effect of solvents, films of a solvent-free epoxy-polyamine were cast, mounted in cells, and their resistances measured in dilute and concentrated potassium chloride solution.<sup>55</sup> All the films had I properties with resistances in the range  $10^{10}$ – $10^{12} \Omega \text{ cm}^2$ .

It appears that during the drying of paint or varnish films, the presence of solvent molecules interferes with the process of cross-linking; consequently, the films have a heterogeneous structure and films of improved protective quality arise when solvents are eliminated.

It is suggested that future work should be directed toward the pigmentation of solvent-free systems, either with inert pigments, when they would form coatings of high electrolytic resistance which would protect by the exclusion of ions, or as sealing coats applied over primers containing inhibitive pigments.

### 4.12.4 Prediction of Paint Performance

If protection by paints or varnish films is due to their ability to restrict the penetration of corrosive ions, then it follows that resistance measurements should form the basis of the prediction of their behavior. In 1948, Bacon *et al.*<sup>56</sup> measured the resistance of over 300 paint systems immersed in seawater using a direct current (DC) technique, and concluded that for good performance, coatings should have a resistance in excess of  $10^8 \Omega \text{ cm}^2$ . Coatings having resistances in the range  $10^6$ – $10^8 \Omega \text{ cm}^2$  were found to be unreliable, and those of lower resistance behaved poorly.

It has frequently been suggested that during direct current measurements the specimens become polarized, consequently alternating current (AC) should be used. A comparison of DC and AC methods has been made and it was found that at a frequency of 1592 Hz and over the range 0.2–20 kHz, the values of the resistances were always lower when AC was used.<sup>57</sup>

The situation has now been clarified,<sup>58</sup> and it has been shown that, with AC, the values obtained are

controlled by the capacitance until the frequency has fallen to about 1 Hz. It was shown that under these circumstances, in the absence of corrosion, the resistances of paint films measured by DC or AC were the same; furthermore, no polarization resistance was detected.

The conclusions are that when coatings have resistances greater than  $10^8 \Omega \text{ cm}^2$  (i.e., when corrosion is absent) then their resistances may be measured by either DC or AC. However, DC measurements can be made more quickly; they are easier to make and the apparatus is less costly. It has also been suggested that such measurements provide a basis for the prediction of performance. On the other hand, when corrosion starts, the AC should be used, since the values obtained can be resolved into two components, which provide a means of detecting and following the corrosion beneath the coating.

### References

1. Evans, U. R. *The Corrosion and Oxidation of Metals*; Arnold: London, 1960; Chapter 21.
2. Hudson, J. C.; Banfield, T. A. *J. Iron Steel Inst.* **1946**, 154, 229.
3. Hudson, J. C. *The Corrosion of Iron and Steel*; Chapman and Hall: London, 1940; p 66.
4. Edwards, J. D.; Wray, R. I. *Ind. Eng. Chem.* **1936**, 28, 549.
5. Guruviah, S. J. *Oil Col. Chem. Assoc.* **1970**, 53, 669.
6. Gay, P. J. *J. Oil Col. Chem. Assoc.* **1948**, 31, 481.
7. Anderson, A. P.; Wright, K. A. *Ind. Eng. Chem.* **1941**, 33, 991.
8. Davis, D. W. *Mod. Packag.* **1946**, 19, 145–149.
9. Bauman, K. *Plaste Kautschuk* **1972**, 19, 694.
10. Haagen, H.; Funke, W. *J. Oil. Col. Chem. Assoc.* **1975**, 58, 359.
11. Mayne, J. E. O. *J. Soc. Chem. Ind.* **1947**, 66, 93.
12. Kelkar, V. M.; Putambekar, S. V. *Chem. Ind.* **1964**, 1, 315.
13. Wild, G. L. E. *Paint Technol.* **1966**, 30, 9.
14. Mayne, J. E. O. *J. Soc. Chem. Ind.* **1946**, 65, 196; **1949**, 68, 272.
15. Mayne, J. E. O. *Oil Col. Chem. Assoc.* **1951**, 34, 473.
16. Mayne, J. E. O.; van Rooyen, D. *J. Appl. Chem.* **1954**, 4, 384.
17. Mayne, J. E. O.; Ramshaw, E. H. *J. Appl. Chem.* **1963**, 13, 553.
18. Mayne, J. E. O.; Ramshaw, E. H. *J. Appl. Chem.* **1960**, 10, 419.
19. Appleby, A. J.; Mayne, J. E. O. *J. Oil Col. Chem. Assoc.* **1967**, 50, 897.
20. Mayne, J. E. O.; Page, C. L. *Br. Corros. J.* **1970**, 5, 94; **1972**, 7, 111, 115.
21. Barraclough, J.; Harrison, J. B. *J. Oil. Col. Chem. Assoc.* **1965**, 48, 341.
22. Harrison, J. *Br. Corros. J.* **1969**, 4, 55.
23. Burkill, J. A.; Mayne, J. E. O. *J. Oil. Col. Chem. Assoc.* **1988**, 71, 273.
24. Sherman, L. R. *Official Digest* **1956**, 28, 645.
25. Bancroft, G. M.; Mayne, J. E. O.; Ridgway, P. *Br. Corros. J.* **1971**, 6, 119.
26. Pryor, M. J. *J. Electrochem. Soc.* **1954**, 101, 141.

27. Beckman, P.; Mayne, J. E. O. *J. Appl. Chem.* **1971**, *10*, 417.
28. Gilroy, D.; Mayne, J. E. O. *Br. Corros. J.* **1966**, *1*, 161.
29. Mayne, J. E. O. *J. Iron St. Inst.* **1954**, *176*, 143.
30. Mayne, J. E. O. *J. Appl. Chem.* **1959**, *9*, 673.
31. Mayne, J. E. O. *Research, Lond.* **1952**, *6*, 278.
32. Sollner, K. J. *Phys. Chem.* **1945**, *49*, 47, 147, 265.
33. Meyer, K. H.; Sievers, J. F. *Helv. Chim. Acta.* **1936**, *19*, 665.
34. Nasini, A. G.; Poli, G.; Rava, V. In *Premier Congrès Technique International de Industrie des Peintures*, Paris, 1947; p 299.
35. Mayne, J. E. O. *J. Oil Col. Chem. Assoc.* **1957**, *40*, 183.
36. Kittleberger, W. W.; Elm, A. C. *Ind. Eng. Chem.* **1952**, *44*, 326.
37. Maitland, C. C.; Mayne, J. E. O. *Official Digest* **1962**, *34*, 972.
38. Cherry, B. W.; Mayne, J. E. O. In *First International Congress on Metallic Corrosion*, Butterworths, London, 1962; p 539.
39. Mills, D. J.; Mayne, J. E. O. *Corrosion Control by Organic Coatings*; NACE, 1981; p 12.
40. Mills, D. J.; Mayne, J. E. O. *J. Oil. Col. Chem. Assoc.* **1983**, *66*, 88.
41. Mayne, J. E. O.; Scantlebury, J. D. *Br. Polym. J.* **1970**, *2*, 240.
42. Kinsella, E. M.; Mayne, J. E. O. *Br. Polym. J.* **1969**, *1*, 173.
43. Cherry, B. W.; Mayne, J. E. O. In *Second International Congress on Metallic Corrosion*; National Association of Corrosion Engineers: Houston, TX, 1966; p 680.
44. Rothwell, G. W. *J. Oil Col. Chem. Assoc.* **1969**, *52*, 219.
45. Fialkiewicz, A.; Szandorowski, M. *J. Oil. Col. Chem. Assoc.* **1974**, *57*, 258.
46. Ulfvarson, U.; Khullar, M. L.; Wåhlin, E. *J. Oil. Col. Chem. Assoc.* **1967**, *50*, 254.
47. Khullar, M. L.; Ulfvarson, U. In *IX Congres Fatipeec*, Fédération d'Associations de Techniciens des Industries des Peintures (FATIPEC): Brussels, 1968; Section 3, p 165.
48. Ulfvarson, U.; Khullar, M. L. *J. Oil. Col. Chem. Assoc.* **1971**, *54*, 604.
49. van der Heyden, L. A. In *XI Congres Fatipeec*, Fédération d'Associations de Techniciens des Industries des Peintures (FATIPEC): Brussels, 1972; p 475.
50. Mayne, J. E. O.; Mills, D. J. *J. Oil. Col. Chem. Assoc.* **1982**, *65*, 138.
51. Meyer, K. H.; Sievers, J. F. *Helv. Chem. Acta* **1936**, *19*, 649.
52. Nasini, A. G.; Poli, G.; Rava, V. In *Premier Congrès Technique International de l'Industrie des Peintures et des Industries Associées*, **1947**; p 299.
53. Kumins, C. A. *Official Digest* **1962**, *34*, 843.
54. Maitland, C. C.; Mayne, J. E. O.; Scantlebury, J. D. In *Proceedings 8th International Congress on Metallic Corrosion*, Dechema, Frankfurt, **1981**; p 1032.
55. Mayne, J. E. O. *Advances in Corrosion Protection by Organic Coatings*; Electrochemical Society PV, 1989; 89-13.
56. Bacon, R. C.; Smith, J. J.; Rugg, F. M. *Ind. Eng. Chem.* **1948**, *40*, 162.
57. Buller, M.; Mayne, J. E. O.; Mills, D. J. *J. Oil. Col. Chem. Assoc.* **1976**, *59*, 351.
58. Burstein, G. T.; Gao, G.; Mayne, J. E. O. *J. Oil. Col. Chem. Assoc.* **1989**, *72*, 407.

## 4.13 Temporary Protectives

**T. N. Tate and E. W. Beale**

Defence Research Agency, Materials Quality Assurance Directorate, Woolwich, London, UK

This article is a revision of the Third Edition article 16.3 by T. N. Tate, D. R. A. Swynnerton and E. W. Beale, volume 2, pp 16:24–16:33, © 2010 Elsevier B.V.

4.13.1	Introduction	2678
4.13.2	Types of Temporary Protectives	2678
4.13.2.1	Soft-Film Materials	2678
4.13.2.2	Hard-Film Materials	2679
4.13.2.3	Oil-Type Materials	2680
4.13.2.4	Strippable Coatings	2680
4.13.2.5	Special Materials	2680
4.13.2.5.1	Water displacing agents	2680
4.13.2.5.2	Volatile corrosion inhibitors	2680
4.13.3	Scope for Temporary Protectives	2680
4.13.4	Causes of Failure	2681
4.13.5	Application of Protectives	2681
4.13.6	Choice of Protective	2681

### Abbreviations

**VCI** Volatile corrosion inhibitor

#### 4.13.1 Introduction

There are many temporary protectives in the market and it would be impracticable to describe them individually. However, they may be classified according to the type of film formed, that is, soft film, hard film, and oil film; the soft film may be further sub-divided into solvent-deposited thin film, hot-dip thick film, smearing, and slushing types. All these types are removable with common petroleum solvents. There are also strippable types based on plastics (deposited by hot dipping or from solvents) or rubber latex (deposited from emulsions); these do not adhere to the metal surfaces and are removed by peeling. In addition, there are volatile corrosion inhibitors (VCI) consisting of substances, the vapor from which inhibits corrosion of ferrous metals. The types of temporary protectives in common use are given in [Table 1](#).

#### 4.13.2 Types of Temporary Protectives

##### 4.13.2.1 Soft-Film Materials

Protectives that are deposited in the cold from a solvent usually consist of waxy substances such as

lanolin or petrolatum mixtures dissolved in solvents such as white spirit. Films formed in this way are thinner than other soft films deposited by different methods. On the other hand, protectives applied by dipping the article in the hot molten material are usually based on petrolatum.

Corrosion prevention depends largely on the barrier provided by the film, but for improved protection, corrosion inhibitors such as sodium nitrite or benzoate may be added. The film may be relatively hard and waxy or quite soft like pharmaceutical petroleum jelly. Corrosion-inhibited petroleum-based waxes deposited from solvent find application for the supplementary protection of hollow sections of finished products. These waxes are applied by airless or air-assisted pressure-feed spraying techniques to clean and dry, but often painted, surfaces to provide increased protection against corrosion due to humid and corrosive atmospheres during both transit and use.

The smearing types of protective material usually consist of lubricating grease compositions, that is, blends of soaps and lubricating oil, but may be mixtures containing petrolatum, oil, lanolin or fatty material. They are softer than the hot-dip materials to permit cold application by smearing. Slushing compounds are a variant of the smearing types and possess some flow properties at room temperature. Thus, they can be brush applied and marks produced after application are reduced. Some materials contain solvent, so that they are free-flowing as applied, but stiffen when the solvent evaporates.

**Table 1** Types of temporary protective in general use

<i>Types of protective</i>	<i>Typical ingredients</i>	<i>Method of application</i>	<i>Properties of film</i>
Solvent-deposited hard film		Dipping spraying, brushing	Solid, thin, tough, nonsticky, removable by wiping with solvent
(a) ordinary grade	(a) Plasticised bitumens, plasticised resins, white spirit, coal tar naphtha, chlorinated solvents		
(b) water-displacing grade	(b) As (a) above together with water displacing agents		
Solvent-deposited soft films		Dipping, spraying, brushing	Solid, thin, greasy, removable by wiping with solvent
(a) ordinary grade	(a) Lanolin, petrolatum, with and without specific corrosion inhibitors and antioxidants, white spirit, coal tar naphtha, chlorinated solvents		
(b) water-displacing grade	(b) As (a) above together with water displacing agents		
Hot-dipping soft film	Petrolatum, lanolin, with and without specific corrosion inhibitors	Dipping in molten material	Solid, thick, waxy or greasy, removable by wiping with solvent or immersing in hot oil
Smearing	Metallic soap and mineral oil, soft petrolatum, lanolin (castor oil/lead stearate for rubber-containing components)	Smearing, brushing	Solid, thick, greasy, removable by wiping with solvent
Slushing	Metallic soap and mineral oil, oil-softened petrolatum, lanolin, small amounts of solvent	Smearing, brushing	As for smearing protective
Oil	Mineral oil, specific corrosion inhibitors and antioxidants	Dipping, rinsing, spraying	Liquid, thin, oily
Strippable			
(a) hot-dipping grade	(a) Ethyl cellulose, cellulose acetate butyrate, mineral oil, plasticiser, resins, stabilisers	(a) Dipping in molten material	(a) Solid, tough, nonadherent. Often leaves oily film with lubricating properties; film removed by stripping.
(b) cold-applied grade	(b) Vinyl copolymer resins, plasticisers, stabilisers, flammable or nonflammable solvents	(b) Spraying, dipping	(b) Solid, tough, nonadherent film, removed by stripping
Volatile corrosion inhibitor (V.C.I.)	Organic amino salts (e.g. dicyclohexylamine nitrite, cyclohexylamine carbonate)	From solution by spraying, as a powder by sprinkling, by wrapping with V.C.I. impregnated paper	Adsorbed, nonvisible film

#### 4.13.2.2 Hard-Film Materials

These were developed to facilitate handling after treatment and to avoid contamination of adjacent components. The films are deposited in the cold and should be tough and neither sticky nor brittle. The deposited films may be plasticized polymer resins, bitumens, etc. which are varied according to the subsidiary properties required, such as transparency and

color. The solvents used vary according to the solubility of the ingredients, drying-time requirements, flammability, and permissible toxicity in given circumstances. As with the soft-film solvent-deposited materials, the surface coverage is large, and for this reason, and because they can be applied at room temperature, hard and soft-film solvent-deposited protectives are widely used.

### 4.13.2.3 Oil-Type Materials

These are usually mineral oils of medium or low viscosity, which contain specific corrosion inhibitors and antioxidants. In spite of the relatively low protective properties of the fluid films, which are not nearly as great as those of the previously described solid films, these materials have an established field of use on the internal surfaces of tanks and assembled mechanisms, and where solid material or solvent cannot be tolerated.

### 4.13.2.4 Strippable Coatings

The most important of these to date are those applied by hot dipping. Many are based on polymer resins with comparatively high dipping temperatures ( $\sim 190^{\circ}\text{C}$ ). They rely mainly on the thickness ( $< 2\text{ mm}$ ) and toughness of the coatings for their extremely good protective properties. They have the added advantage of giving protection against mechanical damage so that little added packaging is required for transport. Reuse of the material is frequently possible. The disadvantages are the necessity for special dipping tanks and cost; the latter may, however, be offset by saving in packaging materials. Strippable films deposited from solvents in the cold are much thinner ( $0.05\text{--}0.25\text{ mm}$ ) than those from the hot-dip materials and their protective properties are generally not nearly so effective.

Strippable coatings based on such polymer resins as vinyl, acrylic, and polyethylene are finding increasing favor for applying to finished products to protect them during transit. These coatings offer excellent temporary protection against moisture, chemicals, and weathering and some stand up well to such fabricating techniques as bending and deep forming. The coatings are easy to apply and some are removed simply by piercing the film and peeling it off, others by washing away by applying an alkaline solution or solvent.

### 4.13.2.5 Special Materials

#### 4.13.2.5.1 Water displacing agents

These have been developed for special uses. For example, as petroleum-based materials harm natural rubber, greases based on castor oil are available for use on the steel parts of rubber bushes, engine mountings, hydraulic equipment components, etc. (but are not for use on copper alloys). Some soft-film solvent-deposited materials have water-displacing properties and are designed for use on surfaces which cannot be

dried properly, for example, internal combustion engine cooling systems, boilers, etc.

An application of this type of fluid is assistance in the removal of ingested salt spray from jet aircraft compressors and the neutralization of corrosive effects. Other types of water-displacing fluids are claimed to have fingerprint neutralizing properties or to be suitable for use on electrical equipment. Some oil-type materials serve temporarily as engine lubricants and contain suitable inhibitors to combat the corrosive products of combustion encountered in gasoline engines.

#### 4.13.2.5.2 Volatile corrosion inhibitors

Volatile corrosion inhibitors are a special type of protective, which when present as a vapor inhibit the corrosion of metals. They are generally used as an impregnant or coating on paper or synthetic film; as a powder, either loose or in a porous container; or in the form of a 5% (w/v) solution in nonaqueous solution (e.g., alcohol) with application by either swab or spray. Their effectiveness in preventing corrosion depends not only upon the inherent activity of the material but also upon their volatility and rate of release from the supporting medium. Being volatile, some form of enclosure is necessary for continued effectiveness, whether it is by the closing of orifices with bungs or overwraps when protecting internal surfaces, or by sealing the outer container for other packed stores. Volatile corrosion inhibitors should be used with caution in the presence of nonferrous metals which may be attacked, particularly in the presence of free water. Care should also be taken with painted surfaces and with some plastics and other organic materials which may become discolored or damaged.

### 4.13.3 Scope for Temporary Protectives

Temporary protectives against corrosion should be used only where removal is subsequently necessary for the fitting or the working of surfaces to which they are applied. For example, coatings are designed to protect packaged engineering materials against corrosion due to a humid atmosphere, in both rural and general industrial conditions, during transit and storage. Where conditions are severe, extra packaging may be required or, in the case of thick soft-film materials, extra thicknesses may be applied. The coatings are also often used to protect unpackaged spares during shelf storage.



In normal thicknesses, temporary protectives are unsuitable for outdoor exposure and they should be protected against gross liquid water by coverings or wrappings. The wax and grease-based thick-film materials will, however, give adequate protection outdoors if they are applied extra thickly. Protection cannot be expected if the surfaces remain in contact with waterlogged packing material.

Corrosion preventives should be applied to surfaces which are clean and dry or corrosion may well continue beneath the coating. Materials with special properties such as water displacement or the ability to neutralize fingerprints should not be used in place of drying and clean handling, but only where the application demands it.

#### 4.13.4 Causes of Failure

In practice it is usually difficult to establish the reasons for failure as a number of factors may be simultaneously responsible, such as (1) application of the protective to dirty surfaces, (2) carelessness in application, (3) inherent inadequacy of the material, (4) exposure to unreasonably severe conditions, and (5) inevitable difficulties in application. Point (3) includes inadequacy not only in protective properties but, in the case of the hard-film materials, in certain physical properties, for example, the film may become brittle and flake when handled, may remain too sticky and become contaminated with dirt or adhere to the wrapping paper more strongly than to the surface to be protected, may age to form an insoluble material and become difficult to remove, or may not remain flexible and adherent at low temperatures. Point (4) includes, for example, the use of soft-film materials in hot conditions at temperatures too near to their melting point. As regards (5), it may be difficult to avoid thin places in the film arising from contact with other surfaces during the process of application, drying-off of the solvent, or cooling; when such thinning occurs, good surface-active properties are advantageous. In this connection, it may be pointed out that scraping in transit and stacking and local thinning due to grit, dirt, etc. are common; it follows therefore that shelf storage of unpacked items should be avoided if possible.

#### 4.13.5 Application of Protectives

Application by dipping gives the most complete film, is the most economical in material, and is usually the

quickest for large quantities of articles. This method should be chosen whenever possible. Spraying is the next best. Brushing and hand-smearing should be adopted only when dipping or spraying is not feasible.

During the dipping process, articles with recesses should be rotated in the bath so that air can escape. Dipping baths should be kept covered when not in use to prevent contamination and, in the case of solvent-containing materials, to prevent concentration by evaporation of the solvent, as this would lead to excessive film thicknesses and long drying times. The composition of a bath of solvent-containing material should be checked periodically. Unaided evaporation of the solvent from solvent-deposited films is usual, but the process can be speeded up by blowing air over the articles or by gentle warming; the heating, however, should not be excessive.

During hot-dipping, film thickness can generally be varied by altering the temperature of dipping and the duration of immersion. The molten material will first chill on to a cold article put in the bath, the solid coating bridging small crevices. This may give sufficient protection, but it may be desirable for the article to attain the temperature of the bath so that the material will fully penetrate into all the crevices, for example, between the ball and race of a rolling bearing. The article may then be withdrawn, allowed to cool and given a further dip to build up the film thickness.

#### 4.13.6 Choice of Protective

Hard-film protectives can be applied to most types of single articles and are especially suitable in mass-production systems. They should not be applied to assemblies because the hard film is liable to cement mating surfaces together and considerable difficulty may arise in the removal of the protective film. This type of protective should be removed before the article is put into use.

The soft-film solvent-deposited type can be used broadly for the same purposes as the hard-film type. A grease-resistant wrapping is required as an inner wrapping (as for all soft-film types) in packaging. Grades of this material, consisting essentially of lanolin in a solvent, have been found to give better protection to packaged articles than some of the best available hard-film materials and are to be preferred for articles with very high precision surfaces. The film is usually dispersible in lubricating oil and it

is therefore not so important to remove it from surfaces when an article comes into use except when it has become contaminated with grit and dirt.

The thick soft films produced by hot dipping are suitable for highly finished as well as normal machined surfaces. Grades with drop-points substantially higher than 50 °C are preferable for tropical storage as, otherwise, marked softening and possible thinning of the protective film are likely to occur. These films can be applied to many types of assemblies, the chief exceptions being assemblies with inaccessible interiors that cannot readily be blanked-off and fine mechanisms where any residue might interfere with the free movement of parts or their subsequent lubrication with low viscosity oil. These films can also be used on parts which might be affected by the solvent from the thin or soft film protectives, but they should not be applied to items having plastics or leather components.

Greases are usually applied by brush or smearing; the brush must be sufficiently stiff to give intimate contact with the surface yet not so stiff as to leave deep brush marks. Greases should not be melted and therefore cannot be applied by dipping or spraying; also, no attempt should be made to dissolve them in a solvent for application. They are particularly useful where only part of the surface of the item requires protection, because of the ease of application by cold smearing. They can be used in this way also in conjunction with solvent-deposited protectives for assemblies of a low degree of complexity, by coating screw threads and filling clearance spaces before dipping the article in the solvent-containing protective. Grease films can be made thick enough to give the desired level of protection. Wrapping is desirable to protect the very soft film. Removal before use is chiefly for the purpose of removing grit and dirt.

The slushing material finds its most useful application on big machinery requiring protection of large areas during storage or during intervals of idleness in

machine shops. The effect of dust and dirt contamination should therefore be considered an important factor in assessing the quality of these materials.

The lower protective quality of oil-type materials largely restricts their use on internal surfaces of, for example, internal combustion engine cylinders, and gearbox and back-axle assemblies of motor vehicles. Such materials are widely used to fulfill the simultaneous functions of a protective and lubricating oil; for example, in machinery the protective can also serve as a lubricant during its initial period of use. The functions of corrosion inhibitor and hydraulic oil are also often combined. Oil-type materials are also used on small nuts, screws, and washers which cannot easily be protected by solid-film materials; in this case, protection must be reinforced by good packaging.

The hot-dip strippable coating is applicable when a high standard of protection from corrosion and mechanical damage is required, as on gauges and tools which so often have their working surfaces facing outwards. Assemblies must have orifices plugged so that molten material cannot penetrate during the dipping.

Volatile corrosion inhibitors are particularly useful when oil, grease or other adherent films are unsuitable. They should be used in conjunction with a primary wrap which should form as close an approach to a hermetically sealed pack as possible. They are widely used to provide protection to precision tools, moulds, and dies and also on a larger scale to car body components.

## **Further Reading**

Protection of Metals from Corrosion in Storage and Transit, by Donovan, P. D.; Ellis-Horwood, (1986).  
Guide to Temporary Corrosion Protectives, National Corrosion Service, National Physical Laboratory (2003).

## 4.14 Marine Paints

**P. Jackson**

International Paint Ltd, Stoneygate Lane, Felling, Gateshead, Tyne & Wear NE10 0JY, UK

© 2010 Elsevier B.V. All rights reserved.

4.14.1	Introduction and Overview of the Marine Industry	2683
4.14.2	Corrosion Breakdown of Marine Coatings and the Factors Influencing Coating Performance	2685
4.14.3	Coating Processes in the Marine Market	2689
4.14.3.1	Newbuilding	2689
4.14.3.2	Maintenance and Repair	2690
4.14.4	Coating Selection for Different Vessel Areas	2691
4.14.4.1	Underwater Hull	2691
4.14.4.2	Ballast Tanks	2692
4.14.4.3	Cargo Tanks	2694
4.14.4.4	Chemical and Product Tankers	2695
4.14.4.5	Cargo Holds	2696
4.14.4.6	Other Vessel Areas	2698
4.14.4.6.1	External decks	2698
4.14.4.6.2	Topsides and superstructure	2699
4.14.4.6.3	Vessel interiors	2699
4.14.5	Future Trends	2699
References		2700

### Glossary

**Block** Modern ships are constructed in sections (called blocks). A typical block will contain 2000–3000 m<sup>2</sup> of steel which requires coating.

**Block join-up** After construction and coating, the block is transferred to the building dock where it is welded to other blocks to produce the ship.

**Boot top** Area on the outer hull, which is immersed when the vessel is loaded and is out of the water when the vessel is not carrying a load.

**Fender damage** Fenders are applied on the side of docks to prevent the ship impacting with the dock wall.

**Grit blasting** A high velocity jet of an abrasive material is directed at the steel substrate to remove rust and coating and to introduce a surface profile onto the steel substrate. The process can be automated (at Newbuilding) or manual.

**Hydroblasting** Surfaces are treated with a high-pressure jet of water which is capable of removing coatings.

**Slurry blasting** A variant on hydroblasting in which abrasive is added to the high-pressure water jet.

**Ullage space** Space above the cargo (crude oil) and the top of the tank.

### Abbreviations

**FDA** Food and Drugs Administration

**VLCC** Very large crude carrier

### Symbols

**T<sub>g</sub>** Glass transition temperature

### 4.14.1 Introduction and Overview of the Marine Industry

Providing effective corrosion protection on ships and other marine structures presents a major challenge. The structure, which is normally constructed from

mild steel, may be subject to continuous immersion, cyclic wet–dry exposure, and extremely aggressive environments, including many of the cargoes ships transport. Corrosion protection is primarily obtained through applying high-performance coatings that are specifically designed for use on the different vessel types and vessel areas.

The current world fleet comprises 94 936 vessels, of which 50 214 are cargo carrying.<sup>1</sup> The market is currently growing at 6.6% per annum. Market growth is primarily driven by the current high freight rates, major economic growth in Asia, increased demand for liquid natural gas (LNG) carriers, and regulations requiring the phasing out of single-hulled oil tankers by 2010. **Table 1** shows the percentage of the world fleet by class of ship, in terms of both the number of ships and gross tonnage.<sup>1</sup>

This chapter primarily focuses on coatings for the high gross tonnage vessel types, because these represent the largest area of steel requiring protection, and therefore the largest coating volumes. The coating of smaller vessels, such as yachts and other marine structures, offshore platforms, etc., will not be considered in this chapter.

There are a number of distinct areas on ships as indicated in **Figure 1**: ballast tanks, underwater hull,

**Table 1**     World fleet by class of ship

<i>Ship type</i>	<i>Market % (by number of vessels)</i>	<i>Market % (by gross tonnage)</i>
Fishing vessels	25	2
Cargo carriers (including ro-ro/ reefer/container ships)	25	28
Supply ships/tugs/dredgers	22	3
Tankers, product, and chemical	9	9
Bulk (dry cargo) carriers	8	28
Passenger vessels/Ferries	7	4
Tankers, crude oil	3	22
Liquid gas carriers	1	4

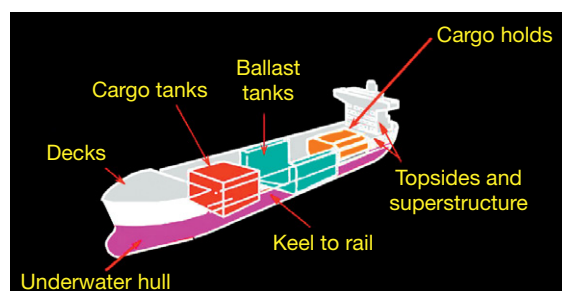


**Figure 1**     Different areas on a ship.

cargo tanks (dry cargo, oil, chemicals), decks, topsides and superstructure, and the vessel interior. Each area presents different challenges to the coating system.

**Table 2** shows the area of steel that requires coating for the different areas on the largest type of double-hull oil tanker, a VLCC vessel.

Over the last 20 years, there have been major changes in shipbuilding processes, ship operational procedures, and the marine coatings market, for example,

- Increase in Newbuilding shipyard productivity and reduction in vessel build times through the introduction of high-speed welding and cutting techniques, automation of certain fabrication processes and the adoption of block stage construction, and coating processes. To be compatible with the new shipyard procedures, coatings require fast cure/drying characteristics and flexible overcoating intervals.
- Changes in ship design and in-service operation. Examples include: (1) the move from single-hull to double-hull oil tankers, driven by major pollution incidents associated with damage to single-hull tankers (e.g., Exxon Valdez, MIT Erika); double-hull tankers have a significantly increased (at least 2 times) ballast tank area<sup>2</sup> as indicated in **Figure 2**, (2) the increased use of high-tensile steel in ship construction, and (3) increased cargo loading and unloading rates on bulk carriers.
- Environmental and health and safety issues together with changes in legislation have lead to

**Table 2**     M<sup>2</sup> of steel in the different areas on a VLCC tanker

<i>Vessel area</i>	<i>m<sup>2</sup> of steel</i>
Ballast tanks	235 000
Underwater hull	37 000
Boot top area	1600
Topsides	4300
Decks	21 800

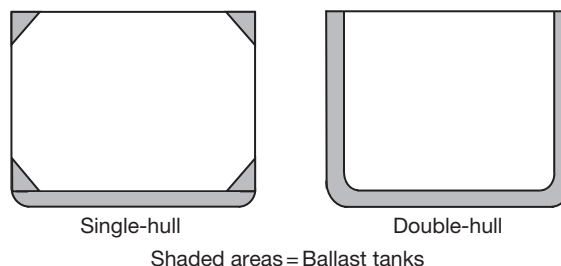


**Figure 2**     Ballast tanks on single-hull and double-hull oil tankers.

(1) a reduction in solvent emissions through the use of higher solids or waterborne coatings and (2) the gradual phasing out of a number of marine coating types, including coal tar epoxy anticorrosives and antifouling paints based on tin copolymers. The reduction in solvent emissions has increasingly resulted in a change from one pack thermoplastic to two-pack thermoset coatings.

- A trend toward higher performance coatings with a longer service life and a reduced frequency of coating maintenance, for example, the new International Maritime Organization (IMO) regulations relating to the coating of ballast tanks<sup>3,4</sup>; these regulations are intended to improve the corrosion protection obtained in this critical vessel area.

As a result, the types of coatings used in the marine market have changed significantly from the coating systems described in earlier reviews.<sup>5,6</sup>

Prevention of corrosion on ships is essential; corrosion is recognized as one of the key factors that contribute to the loss of vessels at sea. In 2006, 25 vessels accounting for 409 000 gross tones were lost at sea.<sup>7</sup> Corrosion reduces the steel thickness and structural integrity of the vessel. Studies have shown that the corrosion rates are highest in the ballast tanks<sup>8</sup> where steel losses in excess of 1 mm year<sup>-1</sup> can be observed in uncoated tanks. Given the clear link between corrosion and vessel safety, ship operations are regulated by the classification societies who establish and apply technical requirements for the design, construction, and in-service survey of vessels. Ships and the coatings applied to ships are subject to regular surveys, and where the required remedial action, that is, the replacement of steel or the coating system, becomes mandatory in order for the vessel to be maintained in class. Class renewal/surveys are carried out every 1–5 years; this requires dry-docking of the vessel, which provides an opportunity to carry out major refurbishment of the coating system.

In addition to the benefits with regard to reduced corrosion, the application of coating systems, which provide effective long-term protection, is also important financially. The steel areas coated and the volume of paint applied to ships are significant. A VLCC tanker at Newbuilding will typically need >200 000 l of paint with a paint cost in excess of \$1 million. Surface preparation and the application process further add to the costs. Although coatings are designed to have a long service life, breakdown does occur, and given that the average lifetimes of oil tankers and bulk carriers are 28 and 30 years, respectively,

coating systems will need to be reapplied during the vessel's lifetime. At major refurbishment, the surface preparation costs, for noncomplex areas such as the underwater hull, are of the order of \$8 m<sup>-2</sup> (for an Sa2 blast), while application costs are typically \$1 m<sup>-2</sup>, highlighting the high costs associated with the application of marine coatings and the importance of specifying the correct coating systems.

#### 4.14.2 Corrosion Breakdown of Marine Coatings and the Factors Influencing Coating Performance

Marine coatings are designed to provide different performance characteristics depending on the vessel type and vessel area:

- corrosion protection (all vessel areas);
- fouling control (underwater hull);
- damage resistance (cargo holds);
- chemical resistance (chemical tanks);
- decorative effect (topsides, superstructure).

Although the primary attribute of many coatings is not corrosion protection, it is important to recognize that degradation and failure of the coating, for example, a cargo hold or chemical tank coating, will lead to conditions that result in corrosion of the steel substrate. The types of coatings used on different vessel areas and the specific modes of in-service failure associated with the coatings will be discussed in [Section 4.14.4](#).

Considering the corrosion breakdown of coatings on ships, it is clear that there are a number of different failure mechanisms, including:

- *Through film breakdown.* Corrosion occurs through the film in the absence of any macroscopic defect. Breakdown is attributed to the presence of pores in the coating which act as pathways for the transport of ions to the coating–steel interface.<sup>9,10</sup> Academic studies<sup>10,11</sup> have clearly demonstrated that coatings do not act as effective barriers to oxygen and water transport and that ion transport normally determines the rate of corrosion.

All coatings will contain microscopic pores and defects that are produced during the application, film formation, and coating ageing processes. However, the presence of pores does not mean that through film corrosion breakdown is inevitable as evident by the fact that marine epoxy–amine anticorrosive coatings can remain free from visual



corrosion over a period of many years. The pore size and pore distribution are important factors as is the potential for the pores to become blocked with corrosion product, which retards the corrosion process. The onset of through-film corrosion after many years in-service is indicative of chemical or physical changes occurring in the coating, which reduce the coating's barrier properties and promote ion transport and corrosion breakdown.

- Blistering:** Osmotic blistering of coatings, subject to full or periodic immersion, is due to the presence of water-soluble ionic contamination on the steel surface prior to coating application or soluble material present in the coating, which migrates to the coating-steel interface. Osmotic blisters are usually relatively small; larger blisters are produced by electroendosmosis, which can occur when the growing blister contains a pore. Anodic and cathodic blisters, associated with active corrosion cells, can also be observed.
- Cathodic disbonding at areas of coating damage:** At sites of impact and abrasion damage where the coating is removed exposing the steel substrate, rapid corrosion takes place. The high pH environment associated with the cathodes in the corrosion cell has the potential to attack the coating-steel interface, leading to the loss of adhesion and disbonding of the coating. When cathodic protection systems are used, the rate of cathodic disbonding may increase as the entire defect will act as a cathode. The extent of disbonding can extend over significant distances, and where there are multiple sites of damage, this can result in complete disbonding of the coating. A number of factors have been shown to influence the rate of cathodic disbonding,<sup>12</sup> including the coating thickness, substrate type and pretreatment, type and concentration of electrolyte, oxygen concentration, potential at the cathode, and the temperature.
- Rust jacking:** This type of failure is observed toward the end of the coating life. Where corrosion products are produced below the coating, the increase in volume of the rust, typically by a factor of 10, acts to lever the coating from the steel substrate as shown in **Figure 3**.
 

Disbonding of the coating will further accelerate the corrosion process. A similar failure mode can be observed for the calcareous deposits produced at the steel-coating interface for coatings under cathodic protection.
- Cracking of coatings:** This is now recognized as one of the potential early failure modes of anticorrosive

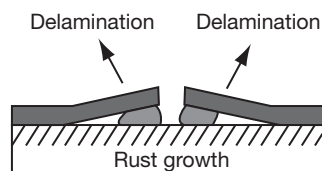


**Figure 3** Rust jacking.



**Figure 4** Cracking of coating in a ballast tank.

coatings applied in ballast tanks.<sup>13,14</sup> Cracking, an example of which is shown in **Figure 4**, is primarily observed on welds, corners, stiffeners, and other structural areas where stress concentration occurs.

Once cracking has occurred exposing the steel substrate, rapid corrosion breakdown follows. A number of factors influence the cracking susceptibility of coatings, including the stresses and strains imposed on the ship structure during operation, the intrinsic mechanical properties (flexibility, etc.) of the coating, internal and thermal stresses developed in the coating, and the coating film thickness. Cracking can also be observed on the block join-up areas, which have been power tool prepared, suggesting that the surface profile on the steel and the coating-substrate adhesion are also important factors. However, a recent study of cracking on erection joint weld seams prepared to different

standards found that the coating properties had the greatest influence on the cracking susceptibility.<sup>15</sup>

Cracking of ballast tank coatings appears to have increased on moving from single-hull to double-hull tankers. This potentially reflects the increased use of lower thickness high-tensile steel plates in double-hull tankers and the associated increase in the flexibility of the ship structure.<sup>16</sup>

In developing coatings and coating systems to provide long-term corrosion protection on ships, it is important to recognize that the coatings' composition and intrinsic performance characteristics are only two of the factors which will determine the in-service performance of the coating. The corrosion protection obtained will be influenced by:

1. The quality of the surface preparation prior to coating application. It is essential that contaminants, which may adversely affect the coating adhesion or lead to osmotic blistering, are removed. Potential contaminants include oils and grease, moisture, weld spatter, welding and cutting fume, corrosion products, and water-soluble salts. A range of surface cleaning procedures are available: solvent cleaning, abrasive blasting, water washing, hydroblasting, and power tool preparation. The appropriate technique or techniques are selected based on the nature of the contamination, the vessel area, and the conditions under which the surface preparation is carried out (there are major differences in the surface preparation procedures adopted at Newbuilding and Maintenance and Repair). Paint manufacturers normally recommend that the level of water-soluble salts on the steel surface is below 50 or 100  $\mu\text{g cm}^{-2}$ , this is supported by a number of studies<sup>17</sup> noting that the salt type, coating type, and ship vessel area have an

influence on the blistering characteristics, and several authors have proposed that the salt level should be significantly lower. The profile introduced onto the steel, by abrasive blasting or power tool cleaning, improves both the coating-substrate adhesion and the anticorrosive performance of the coated steel, particularly with regard to resistance to cathodic disbonding. The blast profile is determined by the type of blasting media selected and the standard of blast cleaning carried out; the latter is specified in a number of international standards as indicated in [Table 3](#).

Typical blast profiles, measured as the average peak to valley distance are 80–120  $\mu\text{m}$  for steel grit and 50–70  $\mu\text{m}$  for steel shot.<sup>18</sup>

2. Selection of the correct coating type. From a corrosion protection perspective, important characteristics are: good barrier properties, good adhesion to steel, mechanical properties and stress behavior required to minimize in-service cracking of the coatings, and environmental stability (resistance to degradation on long-term exposure). Given the highly alkali environments associated with corrosion cells and cathodic protection systems, the coating should be resistant to saponification. Epoxy-amine anticorrosives are currently the corrosion protection coatings of choice, particularly for vessel areas (underwater hull, ballast tanks) subject to permanent or periodic immersion.
3. Control of the application and cure conditions. In the marine market, it is not possible to control the environmental conditions, and coatings must be designed to be tolerant to application under a range of temperatures and humidities. Application at relatively high temperatures ( $>40\text{ }^{\circ}\text{C}$ ) can cause problems with excessive solvent loss during

**Table 3** International standards for abrasive blasting

	<i>NACE (National Association of Corrosion Engineers)</i>	<i>Swedish Standard/ ISO SIS055900 (1967)</i>	<i>Japanese Shipbuilding Research Association – Standard 1984</i>
White metal (all millscale rust, foreign matter removed)	NACE #1	Sa3	JaSh3 or JaSd3
Near white metal (only traces of millscale, rust, foreign matter remain)	NACE #2	Sa2½	JaSh2 or JaSd2
Commercial blast (almost all millscale, rust, foreign matter removed)	NACE #3	Sa2	JaSh1 or JaSd1
Brush off blast (loose millscale, rust, foreign matter removed)	NACE #4	Sa1	–

Similar standards exist for hydroblasting, power tool, and hand tool preparation of the substrate.

spray application, which will adversely affect the flow characteristics of the applied paint and can result in poor coalescence of the paint droplets. Poor coalescence will potentially reduce the barrier properties of the coating and lead to early corrosion breakdown. For thermoset coatings, such as epoxy-amine systems, the rate of cure is significantly reduced as the temperature is lowered. If the coating enters service before an adequate degree of cure has been achieved, this can lead to early corrosion breakdown. So-called 'winter workable' epoxy-amine coatings have been developed, which are designed to cure rapidly at temperatures down to  $-5^{\circ}\text{C}$ . Although coatings are generally tolerant to variations in the relative humidity, it is important that the coatings are not applied onto steel surfaces where condensation has occurred. Paint application should not take place when the steel temperature is less than  $3^{\circ}\text{C}$  above the dew point. Air flow and ventilation, which is particularly important when coating enclosed areas such as tanks, can have a significant impact on the rate of solvent loss from the coating. If the coating has a high level of retained solvent on service entry, this can have an adverse effect on the in-service performance.

4. Control of coating thickness. If the coating is under-applied, this will reduce the barrier properties and potentially lead to early corrosion breakdown. Over-application of the coating, which frequently occurs when coating complex structures in confined areas, such as ballast tanks, can also have an adverse effect on performance. With increasing film thickness, the internal and environmental stresses developed in the coating will be higher, which increases the potential for cracking and loss of adhesion at the coating-steel interface. Overapplication will also increase the amount of retained solvent in the coating.

The coating of edges presents a further problem. Due to the difficulty of spraying coatings onto the edges and the surface tension driven flow of the coating away from the edge, achieving the specified coating thickness is difficult and in-service corrosion breakdown of coatings is often observed at edges. This is shown in [Figure 5](#).

Several approaches to improve the edge protection can be adopted:

- Changing the edge profile by grinding the edge.
- Brush or roller application of stripe coats of the paint to the cut edge. Normal practice for coating cut edges in a ballast tank would be

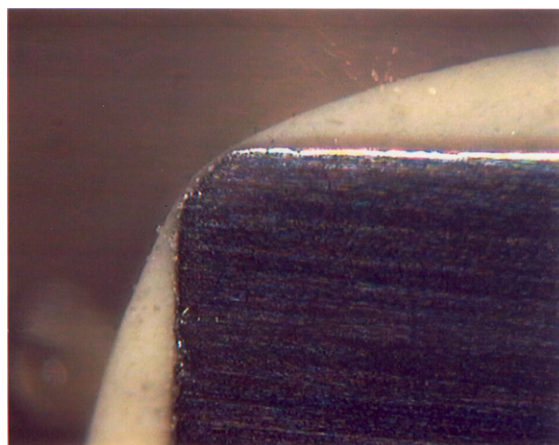


**Figure 5** Flow of paint away from an edge.

spray coat-stripe coat-spray coat-stripe coat. Stripe coating is also used to improve the coating thickness control on fillet welds.

- Formulation of the coating to improve edge retention. This involves modifying the rheological characteristics of the paint to reduce the surface tension driven flow.
5. Use of a cathodic protection system on vessel areas that are continuously or periodically immersed. Such systems are used on the underwater hull, ballast tanks, and in cargo holds, which are also ballasted. The cathodic protection system will significantly reduce corrosion of any exposed steel. At the exposed steel, the cathodic reaction produces hydroxide ions, which react with metal ions and  $\text{CO}_2$  in the seawater to produce an insoluble calcareous deposit, which provides a degree of protection to the steel. It should be noted that cathodic protection systems in ballast tanks do not protect when the tank is empty, which typically accounts for 50–60% of the vessels operation. The cathodic protection system needs to be correctly designed and operated, as overprotection can in itself lead to coating breakdown through blistering and calcareous deposit jacking.
  6. Effective maintenance of the coating. In vessel areas that are readily accessible to the ship's crew, coating breakdown due to corrosion can be routinely repaired. The ship operator will monitor the coating condition in other vessel areas and put in place a strategy to either repair or replace coatings that are showing a significant degree of breakdown. Major refurbishment of the coating may only be possible when the ship is in dry-dock.

### 4.14.3 Coating Processes in the Marine Market

#### 4.14.3.1 Newbuilding

The fabrication and coating processes at Newbuilding have been designed to increase productivity, lower costs, and reduce the build time for new vessels.

Ships are primarily constructed from hot-rolled steel. During the steel manufacturing process, a relatively thick (20–50  $\mu\text{m}$ ) oxide layer, referred to as mill scale, is produced on the steel surface. As the mill scale is cathodic to the steel, rapid pitting corrosion is observed where there are breaks in the scale layer. It is therefore essential that the mill scale is fully removed prior to coating application. The steel is normally blasted with shot to an Sa2½ standard, using an automated rotary or wheel blasting unit.<sup>19</sup> The blast profile introduced on the steel should be less than 100  $\mu\text{m}$  peak-to-valley, as a larger profile may lead to peak coverage issues when the low film thickness shop primer coating is applied. After blast cleaning, it is important to apply a protective coating, a shop primer, as soon as possible to avoid corrosion of the cleaned surface. In practice, the blasting and primer coating processes are carried out on the same automated pretreatment line and the coating application takes place immediately after blasting.

The shop primer coating, which is typically applied at 15–20  $\mu\text{m}$  thickness, must have the following performance characteristics in order to meet the requirements of the shipyard:

- Dry rapidly to allow handling of the coated steel within 2–3 min.
- Provide effective corrosion protection of the steel during the ship fabrication process. As the build cycle varies in different shipyards, the corrosion protection period required is typically between 3 and 9 months. The low film thickness coating of shop primer is formulated to effectively follow the contours of the 50–100  $\mu\text{m}$  profile on the steel introduced during the shot blasting process.
- Be compatible with high-speed cutting and welding processes and have no detrimental effect on the weld quality.
- Resistant to mechanical damage during fabrication.
- Overcoatable with the full range of marine coatings.

Historically, a number of different types of shop primers have been used: phenolic–polyvinylbutyral (PVB) primers, epoxy coatings pigmented with iron

oxide, inhibitor pigments, or zinc and zinc silicate coatings. The current market is, however, dominated by solvent-borne zinc silicate shop primers; this reflects (1) the improved cutting and welding characteristics obtained through the use of an inorganic binder system and (2) the enhanced corrosion protection. The zinc pigment galvanically protects the steel substrate and the zinc corrosion products produced, while providing protection, act to block pores in the coating, leading to an increase in the coating barrier properties.<sup>20</sup> Solvent-borne zinc silicate shop primers are two-pack coatings based on a prehydrolyzed tetraethyl orthosilicate binder system, the cure of which is acid catalyzed.<sup>19,21</sup> Unlike the high-build zinc silicate anticorrosive coatings used in the protective coatings market, the amount of zinc in the coating is kept as low as possible, while maintaining effective corrosion protection; this is because zinc can have an adverse effect on the welding process. Coatings are normally formulated above the critical pigment volume concentration (CPVC) and the applied coatings are therefore porous. The shop primer coating is applied using automated airless or high-volume low-pressure (HVLP) spray processes.

Solvent emission legislation, particularly in Europe and the United States, is impacting on the use of the high solvent content (typically 650 g l<sup>-1</sup>) zinc silicate shop primers. As it is difficult to formulate this type of product with higher solids, the Newbuilding shipyard has two options to reduce emissions: (1) to install solvent abatement equipment on the pretreatment line and continue to use the current solvent-borne products or (2) to move to an alternative low or zero solvent content shop primer. Although waterborne zinc silicate coatings are commercially available, the conventional formulations based on alkali silicate binders are unsuitable for use in the marine market because of their high water-soluble salt content and susceptibility to osmotic blistering when overcoated and immersed. New waterborne coatings, which overcome this limitation have recently been commercialized<sup>22</sup> or are under development. A further issue with the use of zinc silicate shop primers is the potential for the formation of zinc corrosion products (so-called white rust) on the coating surface. If overcoated, the corrosion products may produce a mechanically weak interface and adversely affect the in-service performance of the coating scheme. Normal shipyard practice is to carry out secondary surface preparation (sweep blasting with grit) to remove any white rust immediately



prior to applying subsequent coatings. Certain solvent-borne zinc silicate shop primers have been formulated to produce low levels of white rust, which allows direct overcoating without the need for secondary surface preparation.

The shop-primed steel plates and bars are cut and welded to produce subassemblies, and eventually, blocks. In high-productivity shipyards, the application of the main epoxy anticorrosive system and many of the other coatings takes place at the block stage. In certain shipyards, 80–90% of the coatings can be applied at the block stage. A typical block from a VLCC tanker is shown in [Figure 6](#).

Coating of the blocks is carried out indoors, allowing better control over the environmental conditions. Normal practice is to apply the full anticorrosive scheme, for example,  $2 \times 150 \mu\text{m}$  coats of epoxy plus stripe coating of welds and cut edges, followed by the cosmetic finish or antifouling paint. Coatings are airless spray applied. Although it is possible to apply different epoxy coatings onto different areas of the block, reflecting where the block will be positioned in the final ship construction, a current industry trend is the move to ‘universal primer’ coatings, which are designed for use on all areas of the ship, except certain specialist areas such as potable water and chemical tanks. The use of a universal primer simplifies the coating process, providing both time and cost savings. The coated blocks are subsequently transferred to the building

dock where they are welded together. Prior to applying coatings to the block join-up areas, the steel surface has to be prepared. Grit blasting cannot be carried out due to concerns over damaging the coatings already applied to the block, so the join-up areas are manually prepared using power tools and associated techniques. Following construction of the ship, any remaining coatings are applied; chemical tank coatings are always applied postconstruction and many shipyards choose to apply the antifouling paint and finishes at this stage.

#### 4.14.3.2 Maintenance and Repair

Although the cost of repairing coatings is relatively high, when the surface preparation, labor, and paint costs are considered, this cost is low in comparison with the cost of steel replacement, which would be required if extensive corrosion takes place.

Two different scenarios need to be considered: (1) major refurbishment of the vessel where the existing coating is either fully replaced or subject to significant repair and (2) on-board maintenance (OBM) where the ship's crew carries out routine repair of the coating on those vessel areas (decks, superstructure, certain areas in ballast tanks) that are readily accessible.

At major refurbishment, the coatings used are essentially the same as those applied at Newbuilding. The surface preparation procedures are, however, significantly different

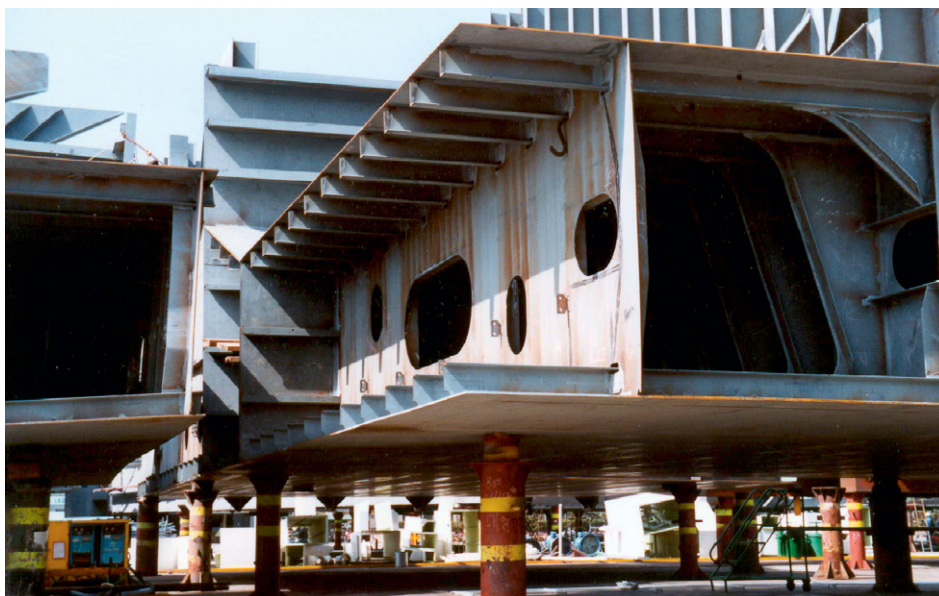


**Figure 6** Block section from a VLCC.



- Due to the potential for high levels of salt contamination on the coating surface, thorough high-pressure water washing is essential prior to preparation of the surface.
- Although grit blasting continues to be widely used, concerns over the amount of dust (grit and removed coatings) released to the atmosphere have seen an increase in the use of hydroblasting and slurry blasting techniques.<sup>19</sup> Although hydroblasting is very effective at removing old coatings and cleaning corrosion pits, it is important to recognize that it does not introduce a new blast profile (the profile applied at Newbuilding is however retained) and the technique can also lead to flash rusting of the steel substrate.

Following the replacement of any heavily corroded steel, the removal of existing coatings, and surface preparation, the new coating scheme will be applied by airless spray. As at Newbuilding, stripe coating of cut edges and welds is essential.

The objectives of OBM are (1) to maintain the ship's appearance by periodically applying new finishes to the deck and superstructure and (2) to repair areas of coating breakdown and corrosion. Manual surface preparation, using power tools and discs, is carried out at sites of corrosion breakdown, but is generally confined to the areas of visible corrosion, leaving potential active corrosion cells under the intact coating. Finishes are normally applied directly over the existing coating scheme, which will be prepared by solvent degreasing (where required) and high-pressure water washing. One-pack alkyd finishes are widely used in this market and the application is by brush and roller. Alkyd and epoxy primers are used; these can be significantly different from the products used at Newbuilding and major refurbishment, and are designed to have improved surface tolerance (to damp and contaminated surfaces, residual rust, aged coatings) and for application under the variable environmental conditions encountered at sea. One important difference in the OBM market is that the coating systems used are not subject to any regulations on solvent emissions. Lower solids coatings can therefore be used in the OBM market.

#### 4.14.4 Coating Selection for Different Vessel Areas

##### 4.14.4.1 Underwater Hull

The coating system has two primary functions: (1) to provide effective corrosion protection on a vessel

area that is subject to permanent sea water immersion and (2) to prevent the attachment of marine organisms to the hull; fouling increases the hull's roughness and significantly reduces the vessel's fuel efficiency. Corrosion protection is provided by a combination of a high-build epoxy anticorrosive (refer to [Section 4.14.4.2](#)) and cathodic protection, using either an impressed current system or sacrificial zinc or aluminum anodes. As previously discussed, the cathodic protection system must be correctly designed and installed to avoid overprotection issues, which can lead to premature breakdown of the coating.

Antifouling coatings are classified as either biocidal or nonbiocidal foul release systems.

The biocidal coatings contain pigments, such as copper oxide, copper thiocyanate, and copper metal, which in the presence of seawater, produce biocidal copper ions. Organic booster biocides are also introduced to further improve the antifouling performance, particularly against slimes and weeds. The use of biocides is increasingly subject to regulatory review in Europe<sup>23</sup> and it is likely that the range of biocides approved for use in marine antifoulings will reduce in the future. Biocidal antifoulings are further classified in terms of the binder type<sup>24</sup>:

- *Self-polishing copolymers (SPC)*: At the coating–water interface, the binder undergoes controlled hydrolysis and is converted from a water-insoluble to a water-soluble polymer. The coating slowly dissolves and the dissolution process effectively maintains a constant rate of release of the biocide throughout the coating lifetime. The coating dissolution also reduces the coating roughness introduced during application and further improves the vessel's fuel efficiency. SPC antifoulings were originally based on acrylic copolymers of tributyltin-methacrylate; however, these coatings have now been phased out because of environmental concerns over the released tributyltin oxide (TBTO). Alternative binder systems based on metal (copper or zinc) acrylate and silyl ester polymers have recently been developed.
- *Controlled depletion polymers (CDP)*: An intrinsically water-soluble material, normally gum rosin, is blended with a water-insoluble vinyl or acrylic polymer. The advantage of this coating type is the lower solvent content. However, CDP antifoulings do not show the smoothing effect observed for SPC coatings and the in-service lifetime of CDP coatings is normally limited to 3 years rather than the 5 years achievable from SPC coatings.

- *Hybrid coatings:* Rosin and a self-polishing copolymer are combined.

Typical coating schemes applied on the underwater hull are summarized in [Table 4](#).

Biocidal antifouling coatings are one-pack solvent-borne coatings with solid volumes in the range 45–55% and typically contain up to 60 wt% biocidal pigments in the dry film.

The selection of the antifouling type and applied coating thickness is, in part, determined by the time period between dry-docking of the vessel, normally 2.5 or 5 years, depending on the classification society rules and the vessel activity. It is essential that the antifouling maintains effective performance throughout this period in-service.

At major refurbishment of the vessel, the underwater hull will either (1) be high-pressure washed, fully blasted, and recoated with both the anticorrosive and antifouling, or (2) be high-pressure washed, have areas of damage spot repaired, and a new coating of antifouling applied to the underwater hull.

Nonbiocidal foul release coatings were originally based on silicone elastomers.<sup>25</sup> The coatings are highly hydrophobic, low surface energy, low  $T_g$  materials, which present surfaces that are difficult to adhere to. If the coating remains static, fouling will occur; however, movement of the vessel causes release of the fouling. To be effective, the vessel should be operating at speeds in excess of 10 or 15 knots for >80% of its service life. As shown in [Table 4](#), the silicone antifouling comprises a silicone tie coat and a silicone topcoat, the topcoat being modified with a silicone fluid to optimize the foul release characteristics. Due to the low surface energy of the silicone coating, the coating cannot be applied directly to the epoxy anticorrosive, so hybrid epoxy–silicone tie coats containing adhesion promoters are used to obtain effective adhesion.

**Table 4** Typical coating schemes for the underwater hull

<i>Antifouling coating type</i>	<i>Coating scheme (dft)</i>	
Tin free SPC (60-month scheme)	Epoxy anticorrosive SPC antifouling	2×150 μm 3×125 μm
CDP (36-month scheme)	Epoxy anticorrosive CDP antifouling	2×150 μm 2×125 μm
Foul release coating	Epoxy anticorrosive Silicone tie coat Silicone or fluoropolymer finish coat	2×150 μm 1×100 μm 1×150 μm

Recently introduced fluoropolymer topcoats offer a further enhancement in the antifouling performance.

Foul release coatings are more expensive, on a \$ m<sup>-2</sup> basis, than the biocidal antifouling. However, significant through life cost benefits can be obtained. Major refurbishment costs are reduced; the normal procedure is to carry out only touchup repair and apply a further thin coat of the topcoat every 5 years.

The amount of corrosion breakdown observed on the underwater hull is normally relatively low; this reflects the fact that (1) the submerged areas are not subject to mechanical damage, (2) the antifouling paint prevents marine organisms adhering to and potentially damaging/removing the coating, and (3) the hull is cathodically protected. Corrosion breakdown primarily takes place at the waterline, the so-called Boot-top area on the vessel, because of a combination of the repeated wet–dry cycling of the coating, UV exposure, and fender damage.

The use of copper or copper oxide (which contains low levels of copper metal) pigmented antifouling paints can lead to severe pitting corrosion on aluminum hull vessels.<sup>26</sup> As copper has a more positive electrochemical potential than does aluminum, if there are defects in the epoxy primer system, a galvanic cell will be set up with the aluminum hull acting as a sacrificial anode.

#### 4.14.4.2 Ballast Tanks

The corrosion rates in ballast tanks, if left uncoated, are usually the highest of any vessel area.<sup>8</sup> This reflects the severity of the conditions experienced in ballast tanks, as the tank alternates between full immersion in seawater when in ballast and a high humidity environment when deballasted. The latter condition is more aggressive from a corrosion perspective, in part, because any cathodic protection system used in the ballast tanks will not be active. Ballast tanks are also subject to large variations in temperature, which can both accelerate corrosion and contribute to a premature breakdown of coatings through cracking and other processes. The increased ballast tank area in double-skin tankers and the structured complexity of the tanks, with many welds and edges, makes the effective protection of the tanks with coatings both essential and a major challenge. [Figure 7](#) shows a typical area in a ballast tank.

It is important that coatings applied at Newbuilding provide long-term protection as the cost of replacing the coating is potentially financially prohibitive;

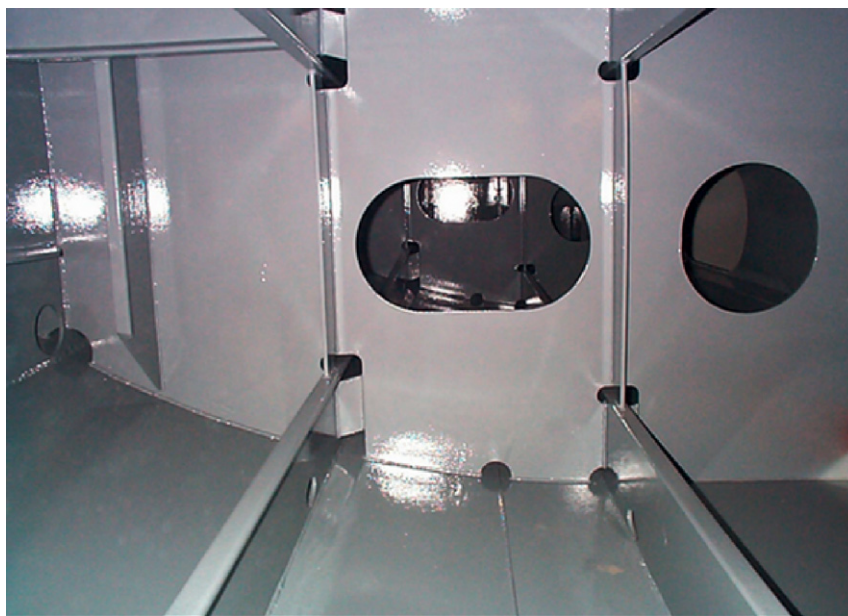


**Figure 7** Interior of a typical ballast tank.

Mills<sup>2</sup> suggests that it would take 250 days and cost about \$20million to fully recoat a VLCC tanker with 250 000 m<sup>2</sup> of ballast tanks. This issue is currently being addressed, at least in part, by the new IMO ballast tank coating standard for Newbuilding,<sup>3,4</sup> which defines procedures for the design of the coating systems, surface preparation, acceptable application conditions, and the inspection of the applied coating. A coating service life of 15 years is targeted, which means that major refurbishment of the ballast tank coating will normally still be required during the vessel's lifetime.

The coating systems used in ballast tanks are almost exclusively based on epoxy-amine resins. The coatings are relatively high solids ( $\geq 70\%$  volume solids), solvent-borne systems. This coating type has a number of characteristics: excellent barrier properties, good adhesion to steel and shop primer, resistance to hydrolytic and high pH degradation, and potential for rapid cure under ambient conditions, which make it particularly suitable for use in ballast tanks and as a universal primer applied at Newbuilding. Epoxy ballast tank coatings contain a relatively high loading of barrier pigments such as mica and talc. Corrosion inhibitor pigments are not used due to concerns over the potential for osmotic blistering. The coating is normally light colored to make in-service inspection and the detection of the onset of corrosion easier. A number of different types

of epoxy-amine ballast tank coatings are available; all are based on aromatic, bisphenol A, or to a lesser extent, bisphenol F, epoxy resins:

- *Coal tar epoxy:* The epoxy-amine resin system is combined with a naturally occurring coal tar. A two-phase, heterogeneous, binder is produced, which is very hydrophobic. Although coal tar coatings have a long track record of providing excellent corrosion protection in ballast tanks, this type of product is currently being phased out due to (1) health and safety concerns over materials present in the coal tar, and (2) the dark color of the coatings.
- *Pure epoxy and modified epoxy coatings:* The distinction between the two coatings is that the modified epoxy coatings contain either (1) nonepoxy resins, for example, acrylate functional materials, which can react into the epoxy-amine binder, or more commonly, (2) nonreactive liquid or solid resins, typically hydrocarbons, which modify the properties of both the liquid and cured coating. A concern with the use of modified epoxy coatings is the potential for extraction of the nonreactive resin on long-term immersion. There has been considerable debate concerning the relative merits of pure and modified epoxy coatings,<sup>27,28</sup> the pure epoxy being claimed to have the better barrier properties and the modified epoxy improved tolerance to

application onto surfaces with reduced preparation. If correctly formulated, both coating types can provide good long-term anticorrosive performance.

- *Aluminum pigmented coatings:* The amount of aluminum flake pigment added to coatings has to be maintained at a relatively low level in the cured coating, typically less than 10 wt%, to avoid potential safety issues associated with the generation of sparks when the coating is subject to impact or abrasion. Aluminum pigmented epoxy coatings can provide excellent corrosion protection, and in particular, very good resistance to cathodic disbonding at defects. Although the lamellar aluminum flake pigmentation may improve the coating barrier properties, recent studies<sup>29</sup> have demonstrated that the aluminum pigment also reacts with the hydroxide ions produced at the cathodic sites in the corrosion cell.
- *Solvent-free epoxy coatings:* A recent development to address the increasing legislative restrictions on solvent emissions. To maintain an acceptable viscosity for application, the paints are normally formulated with a reduced level of pigmentation, may contain high levels of reactive or nonreactive diluents, and may require the use of heated application equipment.

A more detailed consideration of the coating chemistry and formulation guidelines can be found in other reference works.<sup>30,31</sup> In addition to epoxy-amine coatings, these references also discuss both the polyurethane and alkyd coating systems that are used on other vessel areas.

The epoxy-amine coatings are two-pack products, which are mixed immediately prior to application. Coatings are normally applied by airless spray. Typical coating schemes are indicated in **Table 5**.

Stripe coating of welds and cut edges, by brush or roller, is important if effective corrosion protection is to be achieved, and this is now a mandatory requirement in the new IMO coating regulations.<sup>3,4</sup>

Because of the wide range of temperatures experienced during application and cure of the coatings,

for example, in Korean Newbuilding shipyards, paints are applied at temperatures as low as  $-5^{\circ}\text{C}$ , epoxy coatings are often formulated in 'summer' and 'winter' versions. The type of amine curing agent and level of catalyst are varied in order to obtain the rapid cure characteristics required by the shipyard.

Cathodic protection systems based on sacrificial zinc or aluminum anodes are used in ballast tanks. The system is either installed at Newbuilding or can be introduced several years into the coating life; this largely depends on the vessel operator's preference.

Other approaches to improve the corrosion protection in ballast tanks are also being considered, including the use of deoxygenation of the ballast water<sup>32</sup> and the use of gas inertion systems.<sup>33</sup> Neither of these approaches is considered as a replacement for the coating system, but they may enhance the coating performance.

Given that the average life expectancy of ships is in excess of 25 years, repair and/or replacement of the ballast tank coatings applied at Newbuilding will be required. The coating systems and schemes outlined in **Table 6** are also applied at Maintenance and Repair. Other more surface and damp-tolerant epoxy and one-pack vinyl coatings have also been developed for the OBM market. An IMO standard for the maintenance of ballast tank coatings is currently under discussion.

Future IMO regulations, due to be implemented from 2009, will require the treatment of ballast tank water to prevent the transport of marine organisms between different geographic locations in the ballast water. A number of different treatment technologies, including electrolysis, UV radiation, addition of chemicals, and deoxygenating, are currently being proposed. There are concerns that the water treatments could increase the corrosion rates in ballast tanks,<sup>34</sup> and testing of the new technologies in conjunction with ballast tank coatings is required.

#### 4.14.4.3 Cargo Tanks

As indicated in **Table 1**, cargo tankers, which transport crude oil, account for 22% of the world fleet (considered as gross tonnage). Until recently, normal practice was to leave the cargo tanks uncoated, as the oil was considered to be a relatively inert material and the oil film remaining on the tank walls, on emptying the tank, provided a degree of corrosion protection.<sup>5</sup> However, corrosion was frequently observed in cargo tanks primarily at the top (the deck head) and on the floor (the tank top) of the tank, and the corrosion rates

**Table 5** Coating schemes for ballast tanks

Coating type	Coating scheme (dft)
Coal tar epoxy	$1 \times 250 \mu\text{m} + \text{stripe coat or } 2 \times 125 \mu\text{m} + 2 \text{ stripe coats}$
Modified and pure epoxy	$2 \times 125 \text{ or } 2 \times 150 \mu\text{m} + 2 \text{ stripe coats}$
Aluminum pigmented epoxy	$2 \times 125 \text{ or } 2 \times 150 \mu\text{m} + 2 \text{ stripe coats}$
Solvent-free epoxy	$1 \times 300 \mu\text{m} + 2 \text{ stripe coats}$



**Table 6** Coating systems for chemical and product tanks

Coating type	Typical scheme (dft)	End use/potential limitations
Epoxy-amine	2×125 µm or 3×80 µm or 3×100 µm	Primarily used for product carriage
Zinc silicate	1×100 µm	Cannot carry strongly acidic or basic cargoes Unsuitable for carriage of vegetable oils
High-performance epoxy (epoxy-isocyanate)	3×90 µm	Chemical carriage Relatively low solids products
Epoxy phenolic	3×100 µm	Chemical carriage To obtain optimum performance the coating needs to be postcured

were typically 2–3 times higher than those expected for uncoated steel.<sup>35</sup> Corrosion breakdown was primarily attributed to<sup>35</sup>

1. the low level of water in the crude oil, which on storage, settles to produce a thin layer below the oil. The water can have a strongly acidic pH due to water-soluble materials, such as sulfates, present in the oil;
2. microbial-induced corrosion, particularly associated with acid-producing bacteria (APB) and sulfate-reducing bacteria (SRB); and
3. corrosive materials present in the ullage space above the crude oil. Gases such as hydrogen sulfide can be released from the oil. The inert gas system, which is used to prevent the buildup of oil vapor in the ullage space, contains sulfur dioxide and nitrous oxides as well as other impurities.<sup>13</sup>

Factors (1) and (2) lead to the corrosion of the floor of the tank and can result in severe pitting of the steel.

More general corrosion breakdown is observed on the deck head.

Changes in ship design have also contributed to the increased rates of corrosion. Double-skin tankers retain the heat of crude oil (certain heavy crude oils are loaded into the tank at 80–100 °C) more effectively than do the older single-skin tankers and the higher temperature will accelerate any corrosion processes. The increased use of high-tensile steels has resulted in more flexible ships and the increased flexing of the structure acts to loosen scale and rust on the deck head, exposing a new layer of steel to the corrosive environment.<sup>36</sup> Vessels constructed from thermomechanically controlled process (TCMP) steel can also show increased susceptibility to pitting corrosion.<sup>35</sup>

Given the corrosion issues observed in cargo tanks, coatings are now normally applied to the top

and bottom 2–3 m of the tank. The rest of the tank is not coated with anything other than the low film thickness zinc silicate shop primer applied at Newbuilding. Coal tar epoxy coatings were very effective in cargo tanks due to their excellent acid resistance; however, this product type is being phased out due to health and safety concerns. Modified or pure epoxy-amine coatings, essentially the same coatings as applied in ballast tanks, are currently used in cargo tanks. The coating will be applied as a 2×125 or 2×150 µm film thickness scheme. The coatings provide long-term protection and will not normally be replaced during the vessel's 20–30 year lifetime. Proposed IMO regulations are expected to make the coating of the deck head and the top of cargo tanks mandatory at Newbuilding.<sup>37</sup> A potential amendment to the new regulations currently under discussion is the option of constructing the tank, or parts of the tank, from corrosion-resistant steels, which have improved resistance to the environments present in cargo tanks. The corrosion-resistant steel would not require coating.

#### 4.14.4.4 Chemical and Product Tankers

Although crude oil carriage represents by far the largest sector of the cargo tanker market, there has been an increasing trend toward shipping refined oil products (aliphatic hydrocarbons, gasoline, diesel, aviation fuel) and chemicals (organic and inorganic chemicals, vegetable oils/animal fats). Coating of the tanks on chemical and product tankers is essential; certain cargoes can chemically attack the steel, and after carriage of a cargo, the tank will be subjected to a rigorous cleaning regime, using water and often acidic or basic cleaning chemicals. If corrosion occurred in the tank, the corrosion products could contaminate the cargo.

High-performance coatings are used in the chemical and product tanker market. The coatings must be



resistant to the wide range of cargoes carried and impose minimum restrictions on the carriage of the subsequent cargoes. The coating should also exhibit low cargo absorption and/or any absorbed cargo should be rapidly desorbed during the venting and cleaning of the tanks between cargoes – this is important to avoid the absorbed cargo being desorbed into the next cargo, resulting in contamination. Obtaining good coating–substrate adhesion and accurate film thickness control are also essential; to achieve this, high-quality surface preparation and coating application are required. At Newbuilding, the chemical tank coatings are applied post vessel erection rather than at block stage, the entire tank is reblasted to an Sa2½ standard and the coating is applied under a defined range of environmental conditions (temperature, relative humidity).

As an alternative to coated tanks, the ship owner has the option of constructing the tanks from stainless steel. However, stainless steel is expensive, more difficult to fabricate and weld, and can still be attacked by certain chemicals (e.g., chlorides). As a result, most vessels use coated mild-steel tanks or a combination of mild and stainless steel tanks.

A number of different coating types can be used as shown in [Table 6](#).

The selection of the coating is largely dependent on the chemicals that will be carried. The epoxy–amine coatings, which are of the pure epoxy resin type discussed in the ballast tank section, provide very effective protection against refined oil products and certain chemicals. Cargo absorption is, however, an issue. Zinc silicate coatings, which can be either solvent-borne or waterborne, offer excellent chemical resistance together with low cargo absorption and cross contamination. However, this type of coating cannot be used for strongly acidic or basic cargoes because of the potential for rapid dissolution of the zinc pigmentation. The high-performance epoxy and epoxy phenolic coatings are designed to have polymer networks with very high crosslink densities to reduce cargo absorption. The epoxy–isocyanate coatings are relatively low solids due to the requirement to use hydroxide functional epoxy resins for reaction with the isocyanate, and certain owners also have health and safety concerns over the use of isocyanates. As a result, the market has increasingly moved to using epoxy–phenolic coatings for the most demanding applications. The epoxy–phenolic coatings, which are relatively high cost in comparison with the epoxy–amine and zinc silicate systems, produce a high crosslink density through a ‘dual cure’

mechanism. The epoxy phenolic resin is partially cured with an amine and the residual epoxy functionality is homopolymerized using a suitable catalyst. The homopolymerization reaction primarily takes place at elevated temperature (60–100 °C), and prior to the carriage of certain cargoes, the epoxy phenolic coating needs to be postcured. Postcure can be via heating with hot-air blowers or applying hot water onto the coating through the tank cleaning system; alternatively, the carriage of heated cargoes can produce an effective postcure.

In addition to meeting the demanding performance requirements of the chemical and product tanker markets, the coatings should also be compliant with the appropriate regulations relating to the carriage of foodstuffs in contact with coatings. If the coating is not appropriately certified, it cannot carry certain cargoes.

Chemical tank coatings typically have to be replaced every 5–7 years. At Major Refurbishment, the tank is fully blasted to an Sa2½ standard and the coating system reapplied.

#### 4.14.4.5 Cargo Holds

Bulk carrier vessels transport dry cargoes, primarily coal, iron ore, grains, and bauxite/alumina. In 2007, ~1800 million tones of cargo was transported worldwide and the market is growing at typically 4–5% per annum fuelled by the rapid industrial growth in China and other Far East countries. The coatings applied in cargo holds have to resist the mechanical damage caused by the hard angular cargoes and the conditions experienced during cargo loading and unloading and while the vessel is at sea. The holds are normally loaded by dropping the cargo, using a conveyor or mechanical grab, from above the deck height (typically 30 m from the deck to the bottom of the cargo hold), while unloading is by mechanical grab. These processes have the potential to produce significant impact damage of the coating, particularly on the coated shedder plates and hopper sides at the bottom of the hold. Further damage of the coating can be caused by the slow settlement of the cargo during transportation; this produces a gouging action on the coating applied to the vertical walls of the hold,<sup>38</sup> and to minimize the damage the coating should have excellent abrasion resistance. An example of settlement damage of coatings is shown in [Figure 8](#).

Where coating damage occurs and the mild steel substrate is exposed, rapid corrosion will occur, particularly as (1) certain cargoes, such as coal, contain

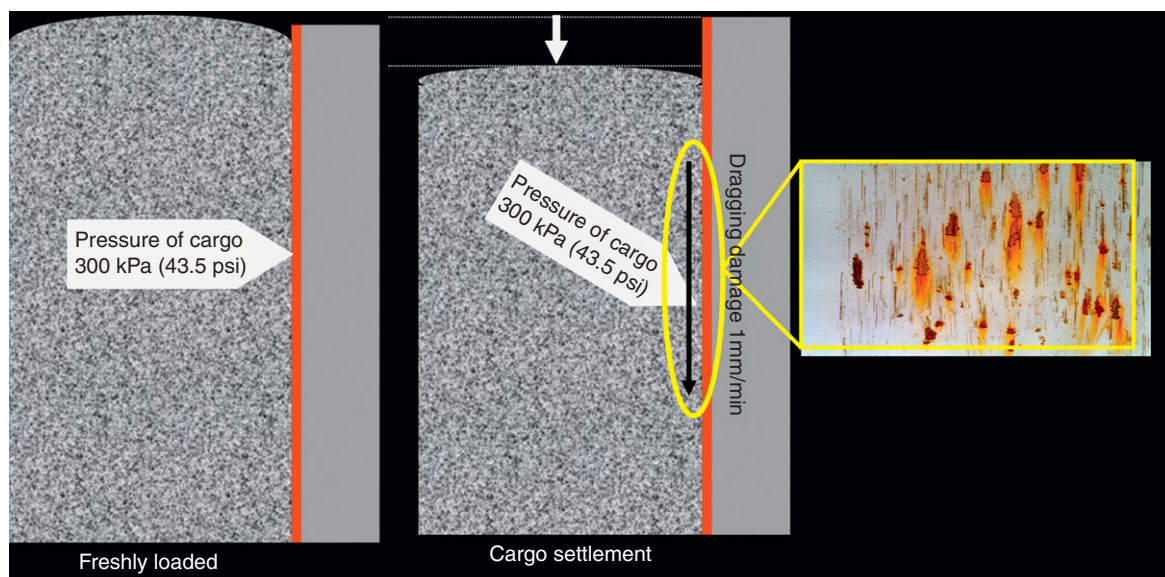


**Figure 8** Settlement damage in a cargo hold.

**Table 7** Coating systems for cargo holds

Coating type	Typical specification (dft)		
Abrasion resistant epoxy	2×150 μm	↑ Increasing performance	↑ Increasing cost
Pure epoxy	2×150 μm		
Modified epoxy	2×125 μm		
Alkyd	2×75 μm		

impurities that accelerate the corrosion process and (2) several of the cargo holds will be fully or partially ballasted during the normal operation of the vessel.

For the carriage of grain, the impact and abrasion issues are greatly reduced; however, any coating, which is in contact with grain, should comply with the appropriate food contact regulations, for example, should be FDA certified.

The different types of coatings used in the cargo hold market are summarized in [Table 7](#). At New-building or Major Refurbishment, the coatings are applied by airless spray.

Although high volumes of one-pack alkyd products are used, it is recognized that the coatings offer only limited damage resistance, and extensive, frequent, repair of the coating will be required if coal or iron ore are carried in the hold. The alkyd coatings are, however, FDA certified and therefore represent a cost-effective coating system for vessels that specialize in grain carriage. Two-pack pure and modified epoxy-amine coatings provide improved damage resistance

and also have good intrinsic anticorrosive performance; the coatings are the same as those specified for use in ballast tanks and on the underwater hull. Hydrocarbon modification of the epoxy coating can have a detrimental effect on the damage resistance, while the aluminum pigmented pure epoxy-amine coatings are particularly resistant to gouging damage. The abrasion resistant epoxy-amine coatings contain a high loading of 'hard' pigments, such as bauxite and amorphous silica, and the polymer network is designed to provide excellent mechanical properties.

The coatings should develop good damage resistance shortly after application, including under the poor ventilation and low-temperature conditions frequently experienced in the bottom of the hold. Otherwise, high levels of coating damage may occur on loading and carriage of the first cargo. Avoiding over application of the coating and minimizing solvent retention are also important requirements.<sup>39</sup>

Epoxy-amine coatings provide effective damage resistance by transferring the impact energy through

to the steel substrate. An alternative approach is to use a highly elastomeric coating, which absorbs the impact energy. High-build, solvent-free, polyurethane elastomer coatings are used, albeit to a limited extent in comparison with epoxy-amine coatings, to protect the shedder plates and hopper sides, which are subject to the high levels of impact damage. Polymer sheet linings, based on high-density polyethylene, can also be used to protect specific areas in the cargo hold; these lining materials have found applications on certain specialist self-unloaded vessels.

The in-service lifetime of the cargo hold coating will depend on the coating type, the cargos carried, and the amount of OBM of the coating carried out by the crew. Typical lifetimes are modified epoxy 3–5 years, pure epoxy 5–7 years, abrasion resistant epoxy 10–12 years.<sup>38</sup> At Major Refurbishment, the entire cargo hold will be reblasted to an Sa2 standard and the coating system reapplied. As previously discussed, a large amount of OBM can be carried out in cargo holds, for both the alkyd and epoxy-amine coatings types. The same coatings applied at Newbuilding and Major Refurbishment can be used for OBM; however, a range of more surface-tolerant epoxy coatings are also used.

A current trend in the bulk carrier market is an increase in the vessel cargo loading speeds used in certain countries. Loading rates of between 3000 and 17 000 tones per hour are being achieved. The new high-speed conveyor and loading systems can, depending upon the procedure adopted, fire the cargo at high speed against the coated walls of the hold, leading to increased damage of the coating on the forward and aft bulkheads. It is currently unclear whether the current high-performance hold coatings will provide effective long-term protection for vessels using the new high-speed loading procedures.

#### 4.14.4.6 Other Vessel Areas

The preceding sections have focused on coatings for the vessel load carrying areas (cargo holds, cargo tanks, and chemical tanks) and the underwater hull and ballast tanks, which are critical areas with regard to fouling control and corrosion protection. There are a number of other areas on the vessel that also require coating: decks, topsides and superstructure, and internals. In general, the corrosion protection challenge in these areas is lower, reflecting the fact that the coated structure is not subject to permanent or periodic seawater immersion, or in extended contact with potentially damaging liquid or dry cargos. However,

exposure to a marine atmosphere is one of the most aggressive nonimmersion corrosive environments and the coating system can also be subject to UV degradation, which may lead to both a loss of aesthetic appearance and cracking of the coating. If cracking occurs, it may reduce the corrosion protection provided.

A wide range of coatings, both anticorrosive primers and cosmetic finishes, are applied on these vessel areas and the coating scheme selected is often determined by a combination of (1) the conditions that the coating will experience, (2) the required in-service lifetime of the coating, and (3) the ship owner's coating preferences, including potential cost restrictions.

##### 4.14.4.6.1 External decks

Coating systems for decks are required to provide damage and chemical resistance, cosmetic appearance, as well as effective corrosion protection. Representative coating schemes are indicated in [Table 8](#).

Increasingly stringent solvent emission legislation has resulted in a phasing out or a significant reduction in sales volumes of the low solids chlororubber-based coatings and thermoplastic acrylic finishes, which were previously widely used in the marine market. High volumes of the relatively low-cost alkyd coatings are used on decks, including zinc phosphate pigmented primers; however, there is an increasing trend toward specifying higher-performance epoxy primer systems. The epoxy primers are of the pure and modified epoxy type discussed in [Section 4.14.4.2](#). In general, the epoxy primers do not contain corrosion inhibitor pigmentation.

Significant differences are observed in the UV stability and durability of the different cosmetic finishes. Epoxy finishes undergo rapid UV degradation and chalking of the coating will be observed, while the more expensive polyurethane finishes

**Table 8** Typical coating schemes for external decks

Coating system	Scheme (dft)
Alkyd primer + alkyd finish	2×75 µm primer + 40 µm finish
Epoxy primer + epoxy finish	2×125 µm primer + 50 µm finish
Zinc silicate + epoxy primer + epoxy finish	75 µm zinc silicate + 75 or 150 µm epoxy primer + 50 µm finish
Epoxy primer + polyurethane finish	2×125 µm primer + 50 µm finish
Epoxy primer finish	2×150 µm
Epoxy primer + one-pack thermoplastic acrylic finish	2×125 µm primer + 40 µm finish

have excellent long-term stability. Alkyd finishes also exhibit good durability, but can be prone to yellowing on long-term exposure.

If required, nonskid characteristics can be introduced into the deck coating by the addition of aggregate pigmentation, either present in the liquid coating or applied onto the wet coating, immediately following spray application.

At Newbuilding and Major Refurbishment, coatings will be applied by airless spray, while for OBM, which will regularly be carried out by the crew, roller and brush application is widely used.

#### 4.14.4.6.2 Topsides and superstructure

The key performance requirements for the coating scheme are effective corrosion protection and good aesthetic appearance. As shown in Table 9, the typical coating schemes are similar to the schemes applied on decks.

Polysiloxane finishes, which provide excellent long-term durability, are being increasingly specified on vessels such as cruise liners where the aesthetic appearance is particularly important. The cost of the polysiloxane coating is higher than the other finishes used in the marine market.

#### 4.14.4.6.3 Vessel interiors

The main coating requirement is cosmetic appearance. Low-cost, fast drying, alkyd primers often containing zinc phosphate anticorrosive pigmentation are normally applied typically at  $1 \times 75 \mu\text{m}$  dft. The primer will either be topcoated with  $40 \mu\text{m}$  of an alkyd finish or wood veneers are attached over the primer. Waterborne one-pack acrylic primers and finishes have recently been introduced for use on vessel interiors. Although generally costlier than the alkyd system, the waterborne system provides significantly reduced solvent emissions.

**Table 9** Typical coating schemes for topsides and superstructures

Coating system	Scheme
Epoxy primer + polysiloxane finish	$2 \times 100 \mu\text{m}$ primer + $100 \mu\text{m}$ finish
Epoxy primer + polyurethane finish	$2 \times 125$ or $2 \times 150 \mu\text{m}$ primer + $1 \times 50$ or $2 \times 50 \mu\text{m}$ finish
Epoxy primer + epoxy finish	$1 \times 150 \mu\text{m}$ primer + $2 \times 50 \mu\text{m}$ finish
Alkyd primer + alkyd finish	$2 \times 75 \mu\text{m}$ primer + $40 \mu\text{m}$ finish

For interior areas, such as the floor in the engine room, which may be exposed to more aggressive conditions, epoxy-based coatings will be specified.

A number of specialist coating systems have also been developed for use on decks, topsides, and the vessel superstructure:

- Low solar absorption (LSA) coatings, which are designed to reduce the amount of near-infrared radiation absorbed by the coating, thereby reducing the coating temperature. LSA coatings are widely used on military vessels where it is important to control the temperature of the electronic defense systems in the vessel interior. Use of LSA coatings can also reduce the air conditioning requirements on other vessel types. LSA is primarily achieved through the careful selection of the pigments used in the coating.<sup>40</sup>
- Finish coatings that reduce the level of rust staining on the topsides and superstructure, a major issue on cruise liners and other vessels. The coatings contain a chelating agent, which coordinates with the ferrous ions to produce a colorless product.
- Deck coatings for military ships, which are designed to resist the short duration high temperatures associated with vertical take-off aircraft.

### 4.14.5 Future Trends

Obtaining effective long-term corrosion protection in the marine industry represents a major challenge. High-performance coating systems have been developed, which provide both long-term protection, thereby reducing coating maintenance costs and meet the other requirements of the shipyards and ship owners – coatings compatible with shipbuilding processes, minimize the application time and costs, compliance with environmental regulations, etc.

The last 20 years have seen major changes in the marine industry, which have resulted in significant changes to the type of coating systems used to protect ships. Continued change in the ship construction processes, ship operational procedures, and environmental and industry regulations are envisaged and will require further development of the coating systems used in the marine market. Future trends may include:

- Further reduction in permissible solvent emissions driven by environmental legislation. Increased use of high-solids, solvent-free, and waterborne coating systems can be anticipated. It is important to



recognize that, at present, waterborne coatings are not widely used in the marine market. This reflects (1) the temperature and humidity restrictions on the use of this type of product, (2) the higher cost, depending upon coating type, and (3) concerns over the anticorrosive performance and osmotic blistering susceptibility of waterborne epoxy anticorrosive coatings if used on areas subject to permanent or periodic immersion.

- Increasing health and safety concerns over certain materials used in marine coatings, for example, low molecular weight epoxy resins, amine curing agents, biocides, and isocyanates.
- A requirement for increased coating lifetimes in key vessel areas such as ballast tanks and cargo holds.
- Changes in the design of ships. The use of composite materials as a replacement for steel<sup>41</sup> and the use of steel-laminate-steel structural laminates<sup>42</sup> have recently been proposed. Aluminum is being increasingly used in the fast ferry market.
- Changes to the ship construction and Newbuilding coating processes. The use of higher-speed and alternative welding and cutting techniques, for example, laser welding.<sup>43</sup> The potential use of robotic coating application as a route to reduce application costs and improve the coating thickness control. Development of ultra fast drying anticorrosive coatings, which significantly reduce the time required to paint the blocks, which can be a major bottleneck in the ship construction process. For this last opportunity both modified epoxy and polyurea/polyurethane coatings are currently being investigated.<sup>44,45</sup>

## References

1. Lloyds Register World Fleet Statistics 2006.
2. Mills, G.; Eliasson, J. Future Cargo and Ballast Tank Coatings – Forward Looking Technology SSPC October, 2003.
3. Performance standard for protective coatings for dedicated seawater ballast tanks of all types of ships and double side skin spaces of bulk carriers. 2006: SOLAS regulations II – 1/3-2 and regulation XII/6.3.
4. Howarth, D. *Asia Pacific Coatings J.* **2007**, 12–14.
5. Banfield, T. A. In *Corrosion, Corrosion Control*, 3rd ed.; Shrier, L. L., Ed.; 1994; Vol. 2; Section 14.7.
6. Lambourne, R. In *Paint and Surface Coatings, Theory and Practice*, 2nd ed.; Lambourne, R., Strivens, T. A., Eds.; 1999; Chapter 13 (The Painting of Ships).
7. World Shipyard Monitor Vol. 14 No 5; 2007 Clarkson Research Services.
8. Wang, G.; Spencer, J. S.; Olson, D. L.; Mishra, B.; Saidarasamoot, S.; Thuanboon, S. *Handbook of Environmental Degradation of Materials*; Myer, K., Ed.; 2005; Chapter 25 (Tanker Corrosion).
9. Nguyen, T.; Hubbard, J. B.; Pommersheim, J. M. *J. Coat. Technol.* **1996**, 855, 45–56.
10. Greenfield, D.; Scantlebury, D. *J. Corros. Sci. Eng.* **2000**, 3, Paper 5.
11. Mayne, J. E. O. *J. Oil and Colour Chem. Assoc. (JOCCA)*. **1949**, 352, 481–487.
12. Leidheiser, H.; Wang, W. *J. Coat. Technol.* **1981**, 672, 77–84.
13. Eliasson, J.; Rauta, D.; Gunner, T. Ballast Water Tank Coatings of the Future, NACE Corrosion Conference 2005.
14. Song, E. H.; Lee, H. I.; Chung, M. K.; Park, C. S.; Lee, C. H.; Shin, C. S.; Lee, S. K.; Baek, K. K. NACE 61st Annual Conference and Exposition 2006, Paper 6015.
15. Park, C. S.; Son, S. M.; Shin, C. S.; Chung, M. K.; Baek, K. K. NACE 62nd Annual Conference and Exposition 2007, Paper 7004.
16. Koch, G. H.; Brongers, M. P. H.; Thompson, N. G.; Virmani, Y. P.; Payer, J. H. Corrosion Cost and Preventative Strategies in the United States, Office of Infrastructural Research and Development Federal Highway Administration, report no FHWA-RD-01-156 2001.
17. ISO/TR 15235:2001(E) Preparation of steel substrates before application of paint and related products – collected information on the effect of water soluble salt contamination.
18. Ward, D. NACE 62nd Annual Conference and Exposition Paper 7001, 2007.
19. Munger, C. G. Corrosion Prevention by Protective Coatings National Association of Corrosion Engineers, 1999.
20. Feliu, S.; Barajas, R.; Bastidas, J. M.; Marcillo, M. *J. Coat. Technol.* **1989**, (775), 63–70, 71–76.
21. Hare, C. H. Paint Film Degradation SSPC: The Society for Protective Coatings, 2001, Chapter 64.
22. International Coatings WO 00/55260 2000.
23. Biocide Products Directive in the European Union 98/8/EC.
24. Yebra, D. H.; Kill, S.; Dam-Johansen, K. *Biofouling* **2004**, 75–104.
25. Chambers, L. D.; Stokes, K. R.; Walsh, F. C.; Wood, R. J. *K. Surf. Coat. Technol.* **2006**, 3642–3652.
26. Woods Hole Oceanographic Institution Upper Ocean Process Group Technical Note 9508, 1995.
27. Callow, L. *Protective Coat. Eur.* **2001**, 20–24.
28. Alveberg, B. E.; Busklein, J. I.; Alveberg, J. J. *Protective Coat. Eur.* **2002**, 10–13.
29. Knudsen, O. O. PhD Thesis, Norwegian University of Science and Technology, 1998.
30. Muller, B.; Poth, U. *Coatings Formulation*; Vincentz Network GmbH & Co. KG: Hannover, 2006.
31. Hare, C. H. Protective Coatings Fundamentals of Chemistry and Composition, SSPC: The Society for Protective Coatings, 1998.
32. Lee, J. S.; Ray, R. I.; Little, B. J.; Lemieux, E. J. *Corrosion* **2005**, 12, 1173–1187.
33. Makoto, K.; Kobuchi, S. *Zairyo* **2000**, 11, 118–1192.
34. Dragsund, E.; Johannessen, B. O.; Anderson, A. B. *Protective Coat. Eur.* **2005**, 4–9.
35. Huang, R. T. International Workshop on Corrosion Control for Marine Structures and Pipelines, 9–11 February 1999, Galveston: Texas, USA.
36. Towers, R. J. *Protective Coat. Linings* March **2000**, 30–42.
37. MSC 82/23/4 proposal for a new SOLAS regulation II – 1/3–9, coating of cargo oil tanks of oil tankers.
38. Propeller Magazine (International Paint Publication) 2005 November, 13–15.
39. Parry, T. J. *Protective Coat. Linings* **2000**, 40–43.
40. Brady, R. F.; Wake, L. V. *Prog. Org. Coat.* **1992**, 1–25.
41. Dodkins, A. R. *Inst. Mech. Eng. IMechE C536/024* **1998**, 189.



42. Lloyds Register Special Report September 2000. A new concept for a new age – the sandwich plate system (SPS) for shipbuilding.
43. Zeyffarth, P.; Hoffman, J. *Laser Technol.* **2000**, 9–15.
44. Son, S. H.; Chang, M. K.; Kim, K. H.; Shin, C. S.; Baek, J. J.; Baek, K. K. Feasibility Evaluation of Rapid Cure Coatings for Ships Water Ballast Tanks PACE 2007, Dallas Convention Centre Feb 11–14 2007.
45. Kaznoff, A. I.; Evans, M.; Verbogt, J. The Future of Marine Coatings Technology in the US Navy, Marine Coatings Conference, 27–28 September 2006, SMM Fairgrounds Hamburg.

## 4.15 Coatings for Structures in Contact With the Ground

**D. Fairhurst**

Corrosion Engineering Consultant, 12 Handside Close, Welwyn Garden City, Hertfordshire AL8 6SR, UK

© 2010 Elsevier B.V. All rights reserved.

4.15.1	Introduction	2703
4.15.2	Properties Required of Coatings for Steel in Contact with Soil	2704
4.15.3	Preparation of Metal Surfaces	2705
4.15.4	Specific Coating Material Types and Their Applicability	2705
4.15.4.1	Liquid-Applied Coatings (Paint)	2705
4.15.4.2	Cold-Applied Tapes	2707
4.15.4.2.1	Petrolatum tapes	2707
4.15.4.2.2	Pressure-sensitive tapes	2707
4.15.4.2.3	Laminated tapes	2707
4.15.4.3	Line Pipe Coatings	2707
4.15.4.3.1	General	2707
4.15.4.3.2	Coal tar and asphalt/bitumen enamels	2709
4.15.4.3.3	FBE powder coatings	2709
4.15.4.3.4	Polyolefin coatings	2710
4.15.4.4	Field Joint Coatings	2711
4.15.4.4.1	General	2711
4.15.4.4.2	Liquid-applied field joint coatings	2711
4.15.4.4.3	Radiation cross-linked heat shrink sleeves	2712
4.15.4.4.4	FBE powder coatings	2712
4.15.4.4.5	FBE-polypropylene	2713
4.15.5	Pipeline Coatings for Thermal Insulation	2715
4.15.6	Pipeline Coating Rehabilitation	2716
4.15.7	Quality Control During Coating Application	2717
References		2718

### Glossary

**Bell hole** Area of ground excavation around a pipeline that allows inspection and/or repair work to be carried out on the pipeline in a selective location.

**Cup shot** A sample of a liquid coating taken during the coating application usually in a plastic cup or similar receptacle. Once the liquid coating has fully cured, tests can be carried out to verify that the coating components have been mixed in the correct proportions.

**Cut back** When line pipe is coated, a small area at each end of the pipe is left free of protective coating so that adjacent sections of pipe can be welded together without the heat from the welding damaging the coating. The area of the joint (the field joint) is prepared and coated after welding.

**Fusion-bonded epoxy (FBE) powder** A protective coating supplied in powder form, containing both a base resin and a curing agent. The powder is stable at room temperature. When the powder is heated to within a certain temperature range, the powder melts and a chemical reaction takes place between the two components, which results in a complex stable polymer film.

**Intelligent pig** An electromechanical device which travels inside a pipeline measuring the pipe wall thickness.

**LPG** Liquid petroleum gas, that is, either liquefied butane or liquefied propane.

**Off ratio** Two-component coatings like epoxies and polyurethanes require the two components to be mixed in the

correct ratio to achieve optimum performance from the finished coating. The correct mixing ratio is prescribed by the coating manufacturer with an appropriate tolerance. If the actual mixing ratio is outside of the prescribed tolerance, that is, off ratio, then the optimum coating performance will not be achieved.

**Pot life** Protective coatings such as epoxies and polyurethanes are supplied to the applicator in two parts: a base and a curing agent. The two parts must be thoroughly mixed together before application in order for their corrosion protection qualities to be fully realized. Once the coating has been thoroughly mixed, the applicator has a finite time in which to apply it. This is known as the pot life. For many solvent-containing epoxies and polyurethanes, the pot life will be of the order of 1–2 h. For solvent free formulations, the pot life may be as short as 1–2 min, depending on the application temperature. If the coating is applied outside of the pot life, its protective qualities may be severely compromised.

**Tenting** Where discontinuities occur in the surface of a structure, for example at weldments, certain semirigid coating types, in particular cold-applied tapes, experience difficulty in conforming to the discontinuity. Instead, the discontinuity is bridged and a tent is formed at the location providing a weakness in the corrosion protection.

## Abbreviations

**HDPE** High density polyethylene

### 4.15.1 Introduction

The most important types of steel structures affected by corrosion because of contact with the ground are: buried transmission pipelines and buried process piping networks, structural support piles, well casings, and above- and belowground storage tanks. A detailed discussion of the protective coatings applied to these structures is considered to be the best means of

describing coatings for corrosion protection where steel is in contact with the ground.

The corrosivity of soil is determined by many factors, the principal ones being

- the soil type (sand, clay, chalk, carbonaceous, etc.)
- the degree of compaction,
- the water content and salinity,
- the oxygen content, and
- the extent and the prevalence of sulfate-reducing bacteria.

For buried steel structures, maintenance may be difficult or even impossible, and it is usually necessary to provide some form of corrosion protection in order for the structure to meet its design life. The corrosion protection will normally involve a protective coating often supplemented by cathodic protection. Protective coatings used on buried structures act as physical barriers, which isolate the structure from the surrounding environment. They must be sufficiently robust to withstand construction activities, including transportation to site, handling, and burial, and can vary in thickness from 500  $\mu\text{m}$  to several millimeters. In service, the cathodic protection prevents corrosion from occurring at holidays in the coating, which result mainly from mechanical damage.

Improvements are continually being made to the quality of protective coating materials and to their methods of application. Nevertheless, it is virtually impossible to produce a protective coating that will protect 100% of the surface of a buried structure for the full design life at an economic cost. This is largely due to the skills required to apply these coatings successfully and the many opportunities, which exist for the coating to become damaged. The coating may suffer handling damage, during transportation to site and during construction. It may be penetrated by rocks during backfilling and by ground settlement following construction. Air–soil interfaces on partially buried items can be particularly vulnerable to mechanical damage. Some pipe coatings have been known to split because of the stressing of the coating in-service as a result of the repeated cycle of wetting and drying of the surrounding soil. All of these events inevitably result in isolated areas of bare metal being exposed to the possibility of soil corrosion. In the majority of cases, the combination of a protective coating with cathodic protection offers the best economic solution to soil corrosion. Therefore, protective coatings used on buried structures need to be compatible with cathodic protection.

Protective coatings used on buried structures may be divided into several generic types, namely

- liquid coatings (paint) applied manually by brush, by airless or conventional spraying, by roller, or by dipping;
- tape wrappings applied by hand or by wrapping machine;
- radiation cross-linked heat-shrinkable materials;
- reinforced coal tar or asphalt enamel coatings, applied in the factory or at site;
- fused (mostly epoxy) powder coatings applied by flock spray or fluidized bed, mainly under factory conditions; and
- multilayer coatings comprising a polyolefin outer layer applied on top of an adhesive with or without a fusion bonded epoxy (FBE) powder coating applied as a first coat. These are factory-applied coatings and their use is confined to pipelines.

The selection of the type of coating will be strongly influenced by the size and geometry of the item, the method of construction, and the operating conditions. For multiple items of the same geometry, such as sections of straight line pipe, factory application of the coating to individual pipe lengths on a continuous production line represents the most economical method of applying a protective coating. Numerous coatings have been developed, which lend themselves to this type of application, and will be dealt with in more detail later.

For single, large, or complex geometry items, such as storage tanks, buried piping networks at process sites, valves, etc., liquid coatings applied by spray, brush, or dipping (where size allows) represent the most practical solution.

For some applications, such as pipelines through marshland, or coastal inlets, the protective coating may be supplemented with an outer concrete compression coating to provide additional mechanical protection and negative buoyancy.<sup>1</sup>

For all coating types and methods of application, quality control at every stage is crucial to the long-term performance of the selected coating. The quality of surface preparation is arguably the single most important factor, which determines the lifespan of the coating (see [Section 4.15.3](#)). More will also be said about quality control in [Section 4.15.7](#).

#### **4.15.2 Properties Required of Coatings for Steel in Contact with Soil**

The purpose of applying a coating to a buried structure is to prevent direct contact with the surrounding

soil over the lifetime of the structure. With this requirement in mind, the characteristics required of a protective coating for buried steel are as follows:

1. *Ease of application:* It must be possible to apply the coating in the factory, the coating yard, or in the field at an economical rate, using the standard tools and equipment that are available.
2. *Resistance to handling damage:* It must be possible for the structural item to be handled reasonably quickly after the coating has been applied without damaging the coating. For liquid-applied materials, this means a short drying time.
3. *Good adhesion to the metal surface:* The coating must have an excellent bond to steel. To this end, some coating systems include specific primers to promote superior adhesion of the complete system to the substrate.
4. *Resistance to impact:* The coating must be able to withstand reasonable levels of impact without cracking, chipping, or disbondment.
5. *Resistance to abrasion:* Where relative movement between the coated item and the ground, or other structures is inevitable during construction, then the coating must have good abrasion resistance. This is particularly important in the case of driven piles and water or hydrocarbon well casings.
6. *Flexibility:* The coating must be flexible enough to withstand such deformation as may occur during construction, for example, during field bending or laying of pipe and during the lifting and placement of buried storage tanks, etc. The coating must also accommodate any expansion or contraction that may occur because of significant changes in environmental or operating temperatures.
7. *Resistance to soil stress:* Coatings on buried structures are often subject to very high shear stresses, due, for instance, to the contraction of clay soils during periods of very dry weather. The coating must be able to resist such stresses without suffering damage.
8. *Water resistance:* The coating should display a low rate of water absorption and be resistant to water or water-vapor transmission through it.
9. *High electrical resistance:* The coating must be an electrical insulator free of any significant amounts of electrically conductive material.
10. *Chemical and physical stability:* The physical properties of the coating must remain stable, showing negligible change under the prevailing operating conditions.

11. *Resistance to bacteria:* The coating must be resistant to the action of destructive effect of any bacteria in the soil.
12. *Resistance to marine organisms:* For structures buried in coastal areas, the coating should be resistant to penetration by marine organisms.
13. *Resistance to cathodic disbondment:* Where the coating is to be used in conjunction with cathodic protection, it must be resistant to the high levels of pH, which are generated at coating breaks, as the protective current flows to the exposed steel surface.

### 4.15.3 Preparation of Metal Surfaces

The single most important factor determining the lifespan of a protective coating is the quality of the surface preparation. Before applying a protective coating, it is essential to ensure that the surface is free from rust, mill scale, moisture, loose dust, grease, or any other form of surface contamination. The best time for achieving the optimum standard of surface preparation is when the item is new. Once significant corrosion has taken place, it is far more difficult to achieve the high standard of surface preparation required for coating longevity.

The first stage in the preparation process should be the complete removal of all dirt and grease using either a proprietary detergent–water solution followed by freshwater, or an organic solvent.<sup>2</sup> Once all grease and dirt have been removed, a number of surface preparation methods may be used to remove rust, mill scale, and old coatings as follows:

1. *Mechanical cleaning:* This includes the use of wire brushes or abrasive paper either handheld or mounted on rotary power tools, and scrapers, and needle guns. Although scrapers, wire brushes, and abrasive paper are able to remove loose rust and scale, they do not remove more adherent layers and tend to polish the steel surface. Protective coatings adhere best to surfaces that are contaminant-free and not smooth. They need to have a surface profile or anchor pattern in addition to being clean. Needle guns are more effective at removing tightly adherent rust and scale, but progress is slow and this form of surface preparation is impracticable for anything other than small areas.
2. *Dry abrasive blast cleaning:* The projection of small particles of hard nonmetallic particles, or steel shot or steel grit at metal surfaces, using compressed air or centrifugal wheels is an extremely efficient form of removing all rust, mill scale, and old coatings. Abrasive blasting is capable of leaving a very clean steel surface and a surface profile, which optimizes coating adhesion. The cost of attaining a very high standard of cleanliness is considerable, and careful consideration should always be given to specifying the correct level of abrasive blasting for the particular application.<sup>3</sup>
3. *Pickling:* Dipping in inhibited hydrochloric or sulfuric acid is a commonly used factory method of removing mill scale from steel, particularly in conjunction with hot phosphoric acid dipping (the Footner process). It is mainly used in the steel manufacturing industry and for the pretreatment of steel prior to the application of specialized coatings such as hot dip galvanizing and electrodeposits. It is rarely used as a method of surface preparation before the application of the types of protective coatings used on buried structures. Published specifications are available covering the pickling process.<sup>4</sup>

Before the application of any coating, the quality of the prepared surface should meet specific inspection requirements with regard to the visual appearance,<sup>2</sup> the degree of dust contamination,<sup>5</sup> and the surface profile.<sup>6</sup>

Both before and during surface preparation and coating application, it is necessary to ensure that condensation is not likely to occur to the detriment of the final protective coating quality.<sup>7</sup> Regardless of which method of cleaning is adopted, it is important to apply the first coating layer as soon as possible after the cleaning operation and before any deterioration in the prepared surface.

### 4.15.4 Specific Coating Material Types and Their Applicability

#### 4.15.4.1 Liquid-Applied Coatings (Paint)

The earliest coating types used on buried steel were based upon coal tar or bitumen often blended with a volatile solvent. In the absence of the solvent, the coating material had to be heated until molten and then poured onto the steel surface or the item had to be coated by being dipped into a hot bath of the liquid coating. When blended with a volatile solvent, the coating could be applied at room temperature and dried by evaporation of the solvent, to leave a



protective film on the steel surface. The solvent-blended coatings could be applied very simply by brush, or for smaller compact items, by dipping. Regardless of the coating type and the application method, the coatings were brittle and prone to mechanical damage. Significant improvements in mechanical properties were made by the addition of fillers, and in the case of coal tar coatings for pipelines, the inclusion of fabric reinforcement. More will be said about reinforced enamel pipeline coatings later.

Today, the most commonly used liquid-applied coatings for buried steel are based on two-component epoxy or polyurethane formulations.<sup>8,9</sup> Both types require thorough mixing of their two components before application. A chemical reaction takes place resulting in cross-linking of the molecules of the base resin by molecules of the curing agent. The fully cured coatings adhere rigidly to well prepared steel and are very resistant to mechanical damage. Until recently, epoxy and polyurethane formulations containing coal tar were very popular for protecting buried steel, such types having built up a strong reputation of long-term performance over many years because of the improved chemical resistance that coal tar imparts at reduced cost. However, health and safety concerns over the carcinogenic nature of the polycyclic aromatic compounds contained within coal tar and released during heating have led to a significant decrease in the availability of epoxy and polyurethane formulations containing this material in recent times.

Additional health and safety concerns over solvent emissions and the demand from customers for rapid curing have led to significant developments in epoxy and polyurethane coating technology. Solvent-free formulations now exist that satisfy health and safety legislation but require an enhanced degree of sophistication during application, due mainly to the short pot life of the mixed constituents. The principle method of application is by airless spray without any premixing of the two components. Instead, the two components are pumped separately to a mixing chamber just ahead of the spray gun to ensure that the short pot life of the fully mixed coating is accommodated. The curing rate can be further enhanced by thermostatically controlled heating of each separate component prior to mixing, with the final application temperatures being as high as 80°C for some formulations. As a result, the coatings fully cure in a matter of hours, which is a major advantage for the applicator, as coated items can be handled a few hours after coating compared with several days for the solvent-based alternatives. The principal use of epoxy and polyurethane coatings is in the protection from soil corrosion of buried tanks and associated piping, and pipeline components such as thrust bore sections, field joints, preformed pipe bends, and valves. **Figure 1** shows several LPG storage tanks coated with a solvent-free coal tar polyurethane prior to encapsulation in a burial mound.

Liquid-applied epoxies and polyurethanes have also found use on above-ground storage tanks, specifically



**Figure 1** Large LPG storage tanks externally coated with a solvent-free coal tar urethane awaiting burial.

on the undersides of the floor plates where the steel is in intimate contact with the tank mound. This is to help reduce the risk of under-floor corrosion, which can lead to perforation of the floor plates and the loss of product containment. Complete coverage of the undersides of the floor is not possible because of the method of construction. The plates can be coated prior to laying down the floor, but the edges have to be left bare to accommodate welding. Once welded in place, the undersides of the weldments are not accessible and have to be left bare. Nevertheless, the practice of painting the undersides of the plates before laying down the floor significantly reduces the area of bare metal in contact with the foundation mound and enhances the spread of protection from the cathodic protection system.

#### **4.15.4.2 Cold-Applied Tapes**

##### **4.15.4.2.1 Petrolatum tapes**

Petrolatum has, like lanolin, long been recognized as possessing corrosion preventative properties. Petrolatum tapes consist of a synthetic fabric carrier impregnated with petrolatum. Modern petrolatum formulations incorporate biocides to inhibit bacterial growth. The tapes are applied by hand over a soft petrolatum-based paste primer and are sufficiently conformable to accommodate irregular surfaces, such as flanges, large bolts, etc. They do tend to remain sticky to the touch long after application.

##### **4.15.4.2.2 Pressure-sensitive tapes**

Unlike petrolatum tapes, which possess corrosion-inhibitive properties, pressure-sensitive tapes rely entirely upon the prevention of the ingress of moisture to the metal surface to prevent corrosion. The tapes usually comprise a polyethylene or polyvinylchloride film of 0.25–0.5 mm thickness, with the inner surface coated with a thin layer of adhesive, often rubber-based. The adhesive is usually between 25 and 100- $\mu$ m thick. They have minimal conformability and therefore cannot be used to wrap complex shapes. In addition, their resistance to mechanical damage and adhesion to steel are also limited. These tapes resemble those commonly used by electricians to bind electrical wiring and have limited use in corrosion protection applications other than as a temporary solution to a minor problem.

##### **4.15.4.2.3 Laminated tapes**

In a more general use as protective coatings for buried pipework are tape wrappings comprising a

polyvinyl chloride or polyethylene carrier with a minimum thickness of 0.75 mm and an inner layer of a self-adhesive bituminous rubber compound with a minimum thickness of 0.8 mm.<sup>10</sup> These tape coating systems include a quick-drying primer with good adhesion to both the bituminous rubber compound and the prepared steel substrate. As with pressure sensitive tapes, laminated tapes have limited conformability and their use is mostly restricted to uniform cylindrical shapes such as buried pipe work. Laminated tapes are usually applied by hand or wrapping machine as a 55% minimum overlapping spiral, starting and ending with a double wrap and a neat square end. The application is easier and the performance is likely to be superior on smaller diameter pipe (<250 mm, say). During the application, care has to be taken to avoid tenting at weld seams, and where the weld cap is prominent, this may require the use of weld seam cover tape or proprietary mastic filler. Tenting may result in water channeling beneath the coating and localized corrosion of the substrate.

Laminated tape components are thermoplastic and the tapes have limited environmental and operating temperature resistance. Allowing tape-wrapped items to sit out in the hot sun prior to burial can result in distortion, disbondment, and blistering of the tape. Service at elevated temperatures may result in the movement of the tape wrapping relative to the coated item, exposing the substrate to soil corrosion.

#### **4.15.4.3 Line Pipe Coatings**

##### **4.15.4.3.1 General**

In the oil and gas industry, transmission pipelines are almost always of an all-welded construction. At the pipe mill, the pipe is manufactured in fixed lengths, usually 12 m, and is supplied to the pipeline construction site already factory coated to within several inches of the pipe ends. The coating cut-back is provided at each end in order to minimize damage to the coating from the heat generated during field welding operations. Once the field weld has been completed and inspected, the bare steel at the weld area and at the adjacent cut-back is cleaned and prepared (see [Section 4.15.3](#)), and a field joint coating is applied. The first 50–75 mm of the factory-applied coating is also prepared and the field joint coating overlapped onto it. Clearly, the factory coating and the line pipe coating have to be compatible and of a similar durability.

At the pipeline design stage, it is customary for the selection of an economic pipe wall thickness to be dominated by pressure containment considerations and any corrosion allowance is normally limited to a few millimeters at most. Thus, the integrity of the protective coating is paramount in ensuring the long-term integrity of the pipeline.

**Figure 2** shows a schematic of the typical layout of a line pipe coating factory. The manufactured pipe enters the coating factory via the incoming pipe racks, and all dirt and grease are removed as the pipe passes through the washing unit. The pipe is then heated to typically 40–80 °C to drive off any residual moisture and ensure that the pipe temperature is maintained above the dew point throughout the ensuing surface preparation stage. The warm pipe enters an enclosed wheelabrator cabinet, where a mixture of steel shot and grit from a vertical hopper is propelled at high velocity on to the pipe surface via bladed wheels rotating at very high speeds. The steel shot, impacting on the surface with great force, breaks up the surface mill scale. The steel grit produces an angular surface profile on the pipe surface, which is necessary for optimum coating adhesion. After emerging from the cabinet, any surface debris, such as dust, spent grit, etc., is removed by vacuuming or brushing with stiff bristle brushes or a combination of the two.

Debris is normally removed from the inside of each pipe by air blowing (not shown). Inspection racks are normally provided to permit inspection of the surface preparation quality before coating application.

Following the inspection and acceptance of the prepared surface, the pipe is transferred from the inspection racks onto a second conveyor system where a surface chemical pretreatment may be applied before further preheating and coating application. If chemical pretreatment is used, it usually involves the application of either a phosphate or chromate solution, sometimes, both in succession. The chemicals used are proprietary, being individually formulated for use with specific coating systems in line pipe coating plants.<sup>11</sup>

The specific example shown in **Figure 2** involves the application of a three layer FBE–polyethylene coating, but the basic layout is typical of most modern line pipe coating factories. In the example shown in the figure, the prepared pipe is induction heated to the required temperature before the FBE powder is applied by electrostatic air spray. A polyethylene adhesive is then side extruded on to the FBE coating, followed by the side extrusion of the polyethylene outer coating.

The completed coating is cold water quenched to enable the coated pipe to be handled safely and

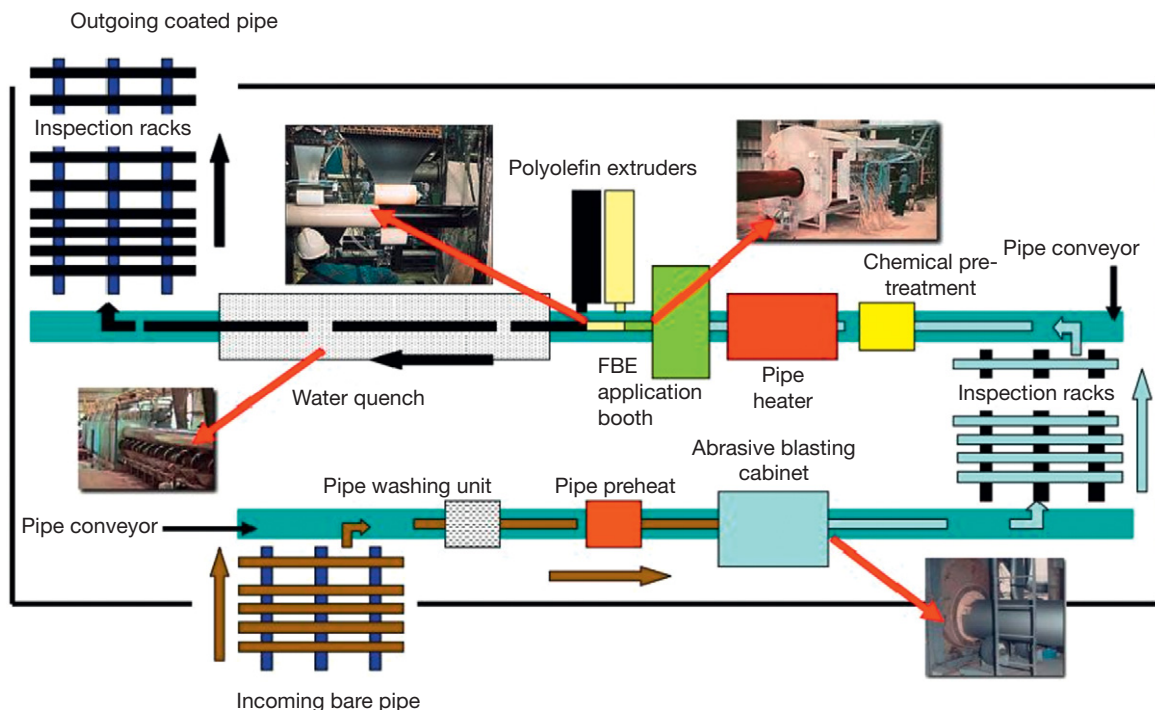


**Figure 2** Schematic of a modern line pipe coating plant.

moved without damaging the coating. More will be said about this line pipe coating system later.

#### **4.15.4.3.2 Coal tar and asphalt/bitumen enamels**

Coal tar and bitumen were first used to protect pipelines from external corrosion in the 1870s. However, until the end of nineteenth century, these materials were not satisfactory as pipeline coatings, being, for the most part, brittle at low temperatures and soft and sticky at higher temperatures. Progressive developments included the incorporation of pulverized coal in coal tars and mineral fillers in both coal tar and asphalt coatings. These increased-viscosity formulations gave thicker films, but poorer wetting of the steel surface and necessitated the introduction of low-viscosity priming coats. The incorporation of reinforced glass inner wraps and asbestos felts, then to be replaced by the more modern glass fiber outer wraps, resulted in a much increased coating strength, and correspondingly, an enhanced protection against impact and soil stressing. Throughout all of the early developments, the importance of surface preparation on coating performance appears to have received little attention, the removal of oil and grease from the steel surface being the only major concern. Despite this apparent absence of rigorous substrate preparation, there are reports of coal tar enamel coatings on pipelines still being in good condition after more than 70 years in service. The early coatings were invariably applied on site using 'over the ditch methods' comprising various forms of line traveling equipment.

Only with the introduction of the more modern coatings, such as fusion bonded epoxies, in the early 1960s (see later), did the importance of good surface preparation and application under factory conditions to the consistency of asphalt or coal tar enamel coating performance become fully appreciated.

Hot-applied asphalt and coal tar coatings with their priming systems are now well classified, described, and specified in BS 4164:1967 (coal tar)<sup>12</sup> and BS 4147:1967 (bitumen),<sup>13</sup> but no guidance is given in these standards on the application procedure. The procedure commences with the application of a thin-film primer to the prepared pipe surface usually by spraying. Once the primer is dry, the hot molten enamel (200–240°C) is poured over the rotating pipe. The hot enamel layer is immediately over wrapped with a continuous spiral of fibre glass inner reinforcement tape applied under just-sufficient tension to imbed the outer half of the still molten

enamel layer. A second wrap or outer wrap of glass fiber preimpregnated with enamel is subsequently applied to produce a coating of 5 mm minimum thickness.<sup>14,15</sup>

Asphalt enamel coatings are generally regarded as inferior to coal tar enamel coatings because of their higher rate of water uptake and poorer mechanical strength, and this has resulted in the decline of the popularity of asphalt enamels in favor of coal tar over the past 30 years. Coal tar contains polycyclic aromatics, which are known carcinogens, and this has led to at least one major protective coating manufacturer's removing coal tar completely from their protective coating formulations. For these reasons, the use of asphalt and coal tar enamel coatings on buried pipelines has largely been superseded by more modern alternatives described in the following sections.

#### **4.15.4.3.3 FBE powder coatings**

Fusion-bonded epoxy (FBE) powder, thermosetting resin, thin-film coatings were first used as stand-alone coatings on pipelines in the early 1960s. FBEs cure by chemical reaction of a curing agent with a base resin analogous to liquid epoxies, except that elevated temperatures (180–240°C) are required for the chemical reaction to take place. Early formulations had poor flexibility and coated pipes could not be field bent. Over the next 20 years, developments in resin and curing agent formulations resulted in FBE coatings with improved flexibility without significant compromises in hot water and cathodic disbondment resistance.<sup>16</sup> Today, it is claimed that, there are in excess of 100 000 km of FBE-coated pipe installed throughout the world, mostly belowground. Originally developed as a single-coat system, typically 350–600-μm thick, more recent developments have included thicker dual-coating layer combinations. The main advantage of the dual-layer systems has been that they either increase the resistance to mechanical damage during transport and construction or improve the performance at high pipeline operating temperatures (>90°C). As mentioned previously (see introduction to this section and [Figure 2](#)), FBE coatings have also become established as the primer layer in three-layer polyolefin coatings. A first layer of FBE enables polyolefin coating adhesion strengths of steel to be achieved, which are an order of magnitude higher than those possible without FBE. More will be said about polyolefin line pipe coating systems later.

One of the major advantages of FBE coatings is that they can be applied to line pipe, bends, fittings,



and field joints, enabling just one coating system to be specified for the entire pipeline. This eliminates problems associated with the selection of the coating at field joints where, otherwise, two generically different coatings may have been applied to the parent line pipe on either side of the field joint, presenting significant coating compatibility problems.

FBE coatings are less forgiving of substandard surface preparation than are the reinforced enamel coatings, and a satisfactory long-term FBE coating performance is reliant upon a rigid adherence to established surface preparation and coating application procedures regardless of whether the coating is applied in the factory or the field.

The FBE application process is as follows: once the pipe surface preparation is complete, including chemical treatment (where specified), and the standard is acceptable, the pipe is induction heated to a temperature usually in the range 210–240°C. The coating, which is in dry powder form, is electrostatically sprayed onto the rotating pipe using a number of low-pressure spray guns. The powder melts as it hits the hot pipe surface, thoroughly wetting the steel substrate. The axial and rotational speed of the pipe is carefully controlled to ensure that the correct coating thickness is applied using a set number of spray guns. Most FBE coating plants incorporate a reclaim system for collecting, cleaning, and recycling any surplus powder that has failed to make contact with the hot pipe. At such high substrate temperatures, the coating on the pipe cures within 1–2 min, and the coated pipe is immediately quenched, as it travels through a water cascade system. This allows the pipe to be handled and inspected very soon after the coating has been applied.

#### **4.15.4.3.4 Polyolefin coatings**

The early 1960s also saw the emergence of polyethylene as a commercial external pipeline coating system. Its inherent toughness was seen as the answer to the mechanical damage suffered by asphalt and coal tar enamel pipeline coatings, either during pipeline construction or in service. Poor or nonexistent grading of the pipeline trench backfill through rocky terrain can be particularly damaging for reinforced enamel coatings. The first polyethylene coatings were applied either as a powder by sintering or by hot extrusion as a film over a soft mastic adhesive. Neither of these application methods resulted in satisfactory adhesion of the coating to the steel substrate. In the case of the latter, the adhesive was brittle at temperatures close to 0°C, and its viscosity was drastically reduced above 50°C enabling the outer

polyethylene sleeve to move relative to the pipe. Furthermore, the early grades of polyethylene were difficult to extrude and the coatings would suffer shrink back from the pipe ends, following application. The differential expansion rates between polyethylene and steel could also result in the crimping of the field joint coating at the joints, and the early polyethylene films also suffered environmental stress, cracking in service. Improvements in the grade of polyethylene used plus the development of a hard ethylene copolymer adhesive gave better adhesion quality and a more robust coating. A two-layer polyethylene/rubberized asphalt adhesive external pipeline coating system (yellow jacket<sup>®</sup>) is still used in the United States and Australia.<sup>17</sup>

A major break through in the adhesive bonding of polyethylene to steel came in 1982 with the advent of the three-layer FBE–polyethylene pipeline coating system. The development of a polyethylene copolymer that could cross link with FBE during the gel stage of the epoxy application process enabled peel adhesion strengths between polyethylene and steel to be obtained of a magnitude, perhaps never envisaged before.<sup>18</sup> As the FBE powder hits the hot pipe, it melts and becomes gel-like for a finite time, which is governed by the applied FBE powder coating thickness and the pipe temperature. For a typical FBE powder, the gel time can vary from 5 to 60 s depending upon these variables. Hence, the speed of the pipe plus the proximity of the extruders to the FBE application chamber must be carefully adjusted to ensure contact between the FBE in gel form and the polyolefin copolymer, and cross-linking between the two. The application process for three-layer polyethylene is shown in [Figure 2](#). The application procedure for the FBE first layer is identical to that described earlier for standalone FBE coatings. The extrusion temperatures for the polyethylene adhesive and the polyethylene outer coating are normally in the ranges 190–210°C and 200–240°C, respectively. The FBE coating thickness is controlled by the number of electrostatic spray guns and the lateral and rotational speed of the pipe. For the polyethylene adhesive and top coat, the thickness is also governed by the speed of the pipe and also the width settings on the extruders. Typical specified individual layer thicknesses are FBE 75–350 µm, adhesive 400–600 µm, and top coat 1.5–2.5 mm.

The full coating system is cold water quenched to allow early handling and inspection.

An extension of this technology to polypropylene followed in 1989, and with it, the development, for



the first time, of a coating with the ability to perform satisfactorily at operating temperatures up to 125°C.<sup>19</sup> By comparison, the upper operating temperature limits for FBE–polyethylene coatings are normally in the range 70–80°C. The factory coating application process for three-layer polypropylene is almost identical to that for three-layer FBE–polyethylene shown in [Figure 2](#).

Three-layer coating systems combine the good adhesion of FBE to steel, with the enhanced mechanical and environmental degradation resistance of the modern thermoplastic polyolefins.

#### 4.15.4.4 Field Joint Coatings

##### 4.15.4.4.1 General

Before the advent of factory coating application to line pipe, asphalt and coal tar enamel coatings were applied on site over or adjacent to the pipeline trench. This meant that the field joints were not, in themselves, a specific concern, as the coating could be applied in a more or less continuous manner to long sections of welded pipe along the pipeline way before burial. It was only when these coating materials began to be applied to individual lengths of pipe under factory conditions that field joints became a subject of attention. At first, the field joints on coal tar and asphalt enamel factory-coated line pipe were coated in a manner analogous to the coating of the line pipe, that is, using hot enamel and fabric reinforcement applied as a full circumferential wrap. This archaic procedure has been largely superseded over the last 30 years by the application of cold-applied synthetic rubber adhesive backed PVC or polyethylene tapes (see [Section 4.15.4.2.3](#)), radiation cross-linked

heat shrink sleeves (see [Section 4.15.4.4.3](#)), or liquid-applied coal tar modified two-pack epoxies and polyurethanes (see [Section 4.15.4.4.2](#)).

Liquid epoxies and polyurethanes, cold-applied tapes, and radiation cross-linked shrink sleeves have all been used to coat the field joints on FBE and two- and three-layer polyethylene-coated line pipe in recent times.

Three-layer FBE–polypropylene coatings are usually selected for the line pipe coating where a high resistance to mechanical damage is required and the operating temperature exceeds that, which can be handled satisfactorily by any of the alternative line pipe coating systems available and previously described. Correspondingly, it is usual to specify an analogous FBE–polypropylene coating system for the field joints in order to ensure that the performance of the field joint coating approaches that of the line pipe coating.

Driven by a need to achieve consistent field joint coating quality at economic production rates, the pipeline coating industry has made significant technological developments in field joint coating procedures in the last 20 years. Modern application methods necessitate the use of induction coils and invertors, fluidized beds, thermostatically controlled heaters, automated spray, or wrapping equipment plus diesel generators to provide the necessary power. All of the equipment needed is containerized and the containers are mounted on lorries or caterpillar-tracked vehicles, see [Figure 3](#).

##### 4.15.4.4.2 Liquid-applied field joint coatings

The major developments in solvent-free two-pack liquid epoxy and polyurethane coating technology



**Figure 3** Typical field joint coating spread, including weatherproof shelters.

have already been mentioned in [Section 4.15.4.1](#). These materials are widely used as field joint coating materials and are regularly applied using automated spray equipment of the type shown in [Figure 4](#). The temperature of the separate components is thermostatically controlled inside furnished containers. The separate components travel to the spray head mounted on the carriage via a thermally insulated umbilical. A mixing chamber located just before the spray head ensures thorough mixing before application. A third process line in the umbilical allows the mixing chamber and spray head to be flushed with solvent to prevent them from becoming blocked between successive spray applications. During spraying, the spray head rotates around the pipe first in one direction and then in the other a sufficient number of times, depending upon the required coating thickness.

#### **4.15.4.4.3 Radiation cross-linked heat shrink sleeves**

The standard radiation cross-linked heat shrink sleeve comprises an expanded polyethylene backing with a heat-sensitive adhesive and is applied either over a steel surface primer or directly on to the field joint area. Heat is applied both before and after the application of the sleeve and care must be taken to ensure that the heating process does not damage the parent coating on either side of the field joint. Careful fitup and controlled uniform heating are essential to ensure uniform shrinkage and to avoid bubbling and blistering of the sleeve during the shrinking process. Although an open flame torch is the preferred method of both pre- and postheating

by most applicators, induction heating provides a superior method of ensuring a uniform heat distribution at the preheat stage.

As with cold-applied tape wrappings, the components of polyethylene heat shrink sleeves remain thermoplastic after application, and their service temperatures are therefore limited.

In addition to their use on asphalt and coal tar enamel factory-coated pipe, heat shrink sleeves have also been used at field joints on FBE and two- and three-layer polyethylene-coated line pipe.

Recent developments have included an expanded polypropylene version for use with three-layer FBE–polypropylene factory-coated line pipe at high service temperatures ( $>60^{\circ}\text{C}$ ). The application of this latter product requires a much higher heat input to the field joint area both before and following sleeve fitup but provides significantly improved levels of adhesion to both the pipe and the polypropylene factory coating at elevated service temperatures.

#### **4.15.4.4.4 FBE powder coatings**

Reference has already been made to the use of FBE as a field joint coating material for FBE-coated line pipe. The field application of FBE is similar, in most respects, to the factory application in that an induction coil is used to heat the field joint area to the required temperature ( $210\text{--}240^{\circ}\text{C}$ ) before the powder coating is applied by low pressure air spray. The process requires a substantial amount of portable equipment, including a hinged induction coil (see [Figure 5](#)) and inverter and a fluidized bed, from which the airborne powder is conveyed to the



**Figure 4** Application of a two-pack solvent-free liquid coating to field joints on large diameter pipe.



**Figure 5** An induction coil being lowered into place over a prepared field joint on a large diameter pipe.

application jig. The application equipment comprises a hinged cylindrical frame, which fits around the field joint area and contacts the pipe via a number of wheels (see [Figure 6](#)). The frame is motorized so that it can be rotated around the pipe, first in one direction and then the other. The FBE powder is sprayed onto the hot pipe from a low-pressure air spray head mounted on the frame as the frame rotates around the pipe.

#### 4.15.4.4.5 FBE–polypropylene

The introduction of the three-layer FBE–polyolefin coatings initially created a dilemma for field joint coating system specifiers as a few, if any, of the traditional field joint coating systems mentioned earlier adhere to polyolefin surfaces to a totally satisfactory degree, particularly at operating temperatures above  $\sim 40^{\circ}\text{C}$ . Correspondingly, the last 5–10 years have seen considerable development activity on behalf of the field joint coating specifiers and application contractors, to produce a field joint coating with the ability to match the performance of and be compatible with three-layer FBE–polypropylene line pipe coating.<sup>20</sup> As a result, six different field joint coating systems have been used. They may be summarized as follows:

1. Sintered polypropylene copolymer.
2. Coextruded polypropylene sheet.
3. Injection molded polypropylene.
4. Flame sprayed polypropylene copolymer.
5. Coextruded polypropylene tape.
6. Polypropylene heat shrink sleeve.

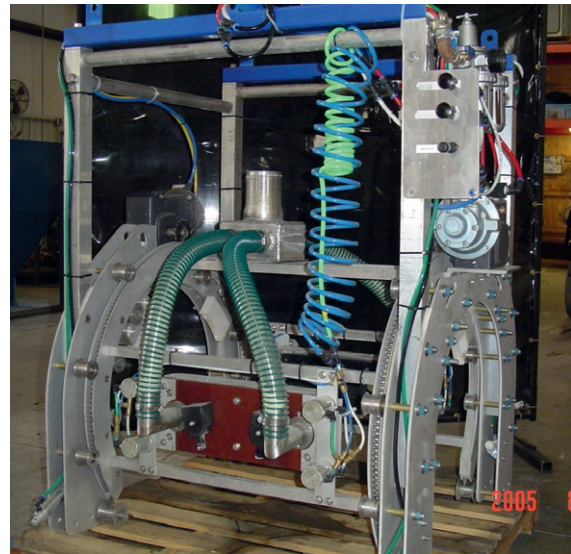


**Figure 6** A typical coating application frame used for the application of FBE powder coatings at field joints. Courtesy by Offshore Joint Services, Houston, TX.

With the exception of the polypropylene heat shrink sleeve, which is described earlier, all of these systems incorporate the application of FBE as the first coating layer in the manner described earlier. This is followed immediately by a sprayed layer of polypropylene copolymer adhesive powder usually from a second coating head mounted on the FBE coating frame (see [Figure 6](#)). As with the factory application of three-layer FBE–polyolefins, the polypropylene copolymer must be applied within the gel time of the FBE powder in order to ensure adequate chemical cross-linking and a good chemical bond between the two. It is the subsequent and final step in the field joint coating procedure that differentiates between each of the first five polypropylene field joint coating types listed.

1. The sintered polypropylene copolymer field joint coating application method involves the buildup of the copolymer coating, by flock spraying as a dry powder, making use of the residual heat in the field joint to melt, and coalesce the copolymer particles. As polyolefins have a low thermal conductivity, the total coating thickness that can be achieved is limited usually to less than 1 mm without the application of additional external heat in between successive copolymer powder applications. In addition, the final copolymer layer may be porous because of a lack of fusion between adjacent particles of powdered polyolefin, which have failed to reach their melt temperature.



2. In the coextruded polypropylene sheet method, the field joint area is wrapped with a sheet of polypropylene–polypropylene adhesive coextruded sheet. Preheating of the sheet is required as is further heating of the field joint area to ensure good fusion between the sheet and the flock-sprayed layer of adhesive applied previously. Sealing of the longitudinal and circumferential edges of the sheet by plastic extrusion welding is also required, using a polypropylene consumable, see **Figures 7 and 8**. Although this method is capable of giving a sound field joint coating with properties equivalent to those of the line pipe coating, it is time consuming to apply it correctly. It has been superseded by a second generation extruded polypropylene copolymer sheet, which is capable of bonding directly to the field joint area, the line pipe coating, and itself. This can be applied as a complete wrap, overlapping the factory coating circumferentially and itself axially, and avoiding the need for extrusion welding.
3. The injection molding of polypropylene at field joints has been considered for buried pipelines, but to date, has been used exclusively on offshore pipelines. It requires bulky and sophisticated equipment to both melt the polypropylene and pump it into the mold, which fits around the field joint area, see **Figure 9**. It consumes a lot of energy and is expensive compared with the alternative systems available. Nevertheless, it gives an extremely robust field joint with properties almost identical to the factory coating on the line pipe.
4. Of all of the polypropylene field joint coatings that have been developed, flame spraying is perhaps the most versatile as, in addition to field joints, it can also be used to coat fittings and preformed bends at a wide range of coating thicknesses. During flame spraying, the polypropylene copolymer powder is blown through the center of a circular gas flame under inert-gas pressure. The pressure of the inert gas propels the heat-softened polypropylene particles toward the substrate. The softened particles impact on the pipe surface coalescing with themselves and the existing layer of copolymer adhesive, see **Figures 10 and 11**. The application is a highly skilled process, as the heat input to the substrate and the sprayed powder need to be carefully controlled in order to buildup the coating thickness without compromising the quality of the coating. Too much heat can result in a reduction in the long-term environmental stability of the finished coating.
5. The coextruded polypropylene tape is the most recent development and is an extension of the



**Figure 7** Coextruded polypropylene sheet in place over the field joint.



**Figure 8** Final appearance after plastic welding at the horizontal and circumferential seams.



**Figure 9** Injection molded polypropylene field joint coating application to pipe test pieces.



**Figure 10** Flame spray application of polypropylene to pipeline field joints inside a weatherproof shelter.



**Figure 11** Close up of flame spray polypropylene application trial. Note the completed trial field joint coating in the foreground.

coextruded sheet method. Being more flexible than the sheet, it is applied to the field joint as a spiral wrap in the same way as a cold-applied tape. Good adhesion between successive spirals of the tape, between the tape and the pipe, and between the tape and the line pipe coating requires preheating of the pipe and the tape, and postheating of the applied wrapping. An example of the automated polypropylene tape application equipment is shown in [Figure 12](#).

#### 4.15.5 Pipeline Coatings for Thermal Insulation

In certain circumstances, it may prove necessary for a buried pipeline to be thermally insulated. The justification for thermal insulation will be



**Figure 12** Spiral wrapping of polypropylene coextruded tape.

determined by the nature of the product being transported and/or the condition the product needs to be in, at the point of delivery. For multiphase hydrocarbon flow lines, flow assurance may well be the major concern. Maintaining the product temperature above a certain level will ensure that neither wax deposition nor hydrate formation will jeopardize the product flow rate over the projected lifespan of the project. For gas pipelines, the gas delivery specification may include a minimum temperature to be maintained to avoid liquid drop out and attendant problems with fluid handling at the reception facilities.

It is a common misconception that applying a thermal insulation system will also prevent external corrosion of the pipe. In practice, thermal insulation systems are invariably breached by moisture, resulting in localized corrosion rates well in excess of those to be anticipated if no thermal insulation system were in place. In addition, with thermal insulation, any applied cathodic protection is unlikely to be effective because of the high electrical resistivity of the thermal insulation. It is a good engineering practice, therefore, to ensure that steel pipelines are protected using one of the coating systems previously described, before thermal insulation is applied.

The most commonly used thermal insulation systems for buried piping usually employ polyurethane foam as the insulant with an outer protective layer. This outer layer needs to be mechanically robust as polyurethane foam has a low compressive strength and is easily damaged. A well established factory application system used for district heating purposes comprises a high-density polyethylene (HDPE) outer pipe arranged concentrically over the transmission pipe using spacers.<sup>21</sup> The annular space between the



two pipes is filled with blown polyurethane foam. Temporary end caps ensure that the foam is not lost from the open ends of the HDPE pipe. At the field joints, the continuity of the thermal insulation must also be ensured. Various field joint insulation systems have been employed using some preformed polyurethane foam half shells with either heat shrink sleeves or cold-applied tapes to provide the outer protection for the foam. Because of the problems resulting from poor half shell fitup and correspondingly difficult field application procedures, track records with such systems have been indifferent, leading to severe corrosion in some cases. The use of such systems is difficult to justify on pipelines carrying hazardous products such as hydrocarbons.

A novel line pipe insulation system developed for a gas transmission pipeline in the early 1990s comprised of an FBE powder protective coating, 50–150 mm of polyurethane foam and an 8-mm poured polyurethane outer coating.<sup>22</sup> Using advanced polyurethane foam and liquid polyurethane application technology, each 12-m length of line pipe was first coated with FBE, then thermally insulated and the insulation was sealed. The insulation application process resulted in a tapered insulation profile at each end with an outer layer of solid polyurethane providing mechanical protection and a complete seal at the foam-coated pipe interface, see [Figure 13](#). During pipeline construction, the field joints were coated with FBE in the traditional manner (see earlier) and then thermally insulated using preformed foamed polyurethane half shells fitted around the joint area, and then fully encapsulated in liquid polyurethane pumped into suitably sized molds; see [Figure 14](#).

#### **4.15.6 Pipeline Coating Rehabilitation**

The decision to refurbish an external coating on an ageing, but still required, buried pipeline will normally be determined by an analysis of the results from a combination of the following: the leak history investigation, aboveground nonintrusive surveys (e.g., cathodic protection status), wall thickness measurements using intelligent pigs, and direct visual inspection of the condition of both the coating and pipe surface at a representative sample of bell holes. In many instances, the cost of excavation, pipe repairs and external coating refurbishment, and reburial will be prohibitive when compared against partial or total pipeline replacement. From a production standpoint,



**Figure 13** Thermally insulated line pipe awaiting pipeline construction.



**Figure 14** Moulded thermally insulated field joints.

the consequences of taking the pipeline out of service for extended periods of time also need to be addressed.

Once the decision to refurbish the pipeline has been reached, the selection of the equipment needed for the removal of the old coating, for repairs to the pipe and for surface preparation and new coating application, has to be made at an early stage. This is so that questions regarding the extent of pipe excavation can be addressed and sufficient clearance can be provided around the pipe for all of the required equipment to function fully as intended.

Proprietary line travel equipment exists for refurbishing external coatings on long continuous pipeline sections. This equipment incorporates separate devices for the removal of old coatings, abrasive blasting of the steel surface, and application of the new coating. Preference should be given to the use of

equipment that captures removed coating materials and spent abrasives for disposal, in accordance with local government legislation. Such equipment will often require a greater clearance around the pipe than usually required with manual methods of coating removal, surface preparation, and coating application.

The removal of old coatings will require one or more equipment types – scrapers, high-pressure water jetting ( $\leq 20\,000$  psi), abrasive blasting, etc., depending on the coating type and its condition. For optimum performance from the new coating, the final stage in the surface preparation process should be abrasive blasting. The ideal surface condition is one that complies with grade Sa2.5 in accordance with the visual standard in ISO 8501–1. An angular surface profile with minimum amplitude of  $50\mu\text{m}$  is an additional advantage. Although some coating material suppliers would claim this requirement to be unnecessary,<sup>23</sup> careful consideration of the pipeline operating conditions, diameter, and projected further life is required before this advice is to be considered viable.

Protective coatings used for the refurbishment of old pipelines include all of those considered in the previous sections of this chapter with the exception of FBE powder and two- and three-layer polyolefins. The application of these coatings employs too high a level of sophistication to be practical on a scale larger than applicable to field joints only.

Today, liquid-applied epoxy and polyurethanes, mainly solvents-free (see [Section 4.15.4.1](#)) tend to be the coatings most regularly chosen for pipeline coating rehabilitation, as these provide superior mechanical damage resistance particularly at elevated temperatures ( $\geq 50^\circ\text{C}$ ), and the potential for longer-term external corrosion protection when compared with the alternatives available.<sup>24,25</sup> However, where partial refurbishment of existing coatings is to be carried out, over short sections such as at bell holes, for example, considerations of compatibility with the existing coating, or materials availability, for example, may justify the use of one of the different generic alternatives available.<sup>26</sup>

#### 4.15.7 Quality Control During Coating Application

As with all protective coatings, the lifespan of those used to protect buried steel will be greatly enhanced by close attention to quality control during surface preparation and coating application. The cost of excavation and reburial on top of surface preparation and

coating application emphasize the need to ensure that the risk of premature coating failure is avoided.

The cornerstone of good quality is the coating specification. The specification should define the following:

1. What exactly is to be coated in terms of the boundary limits and interfaces with other work.
2. The responsibilities of the different parties involved in the work, not just those actually carrying out the surface preparation and the coating application. This includes those responsible for ensuring that the specification is followed and all quality control activities are completed, which is usually the coating contractor, the supplier(s)/manufacturer(s) of the coating materials and those responsible for rectifying any damage caused during handling and transportation.
3. The reference standards to which the work is to be carried out, including all quality control measurements and test procedures.
4. The specific materials to be used, both for surface preparation and coating application and the number and thickness of each coat.
5. All quality control measurements and tests, their frequency, and the results to be achieved.

The location where the work is to be carried out may well have a significant bearing upon the specification. Surface preparation and coating application in the factory have the major advantages over site work of (1) being independent of the weather and (2) not being confined to daylight hours, as power and light are normally readily available. Equipment can be more easily maintained and testing and inspection can be more sophisticated and rigorous compared with work on site. The specification should recognize the conditions under which the work is to be carried out and the constraints imposed accordingly.

Quality control tests during surface preparation should include visual assessments of the surface condition both before and after preparation. Visual standards are available against which to compare the surface of the prepared item before application of the first coat.<sup>3</sup> Inspection of the surface should also include the assessment of dust<sup>5</sup> and where items to be coated have been stored in coastal areas, the level of salt contamination.<sup>27</sup> For abrasive blasted surfaces, quality control tests should include the measurement of the surface profile.<sup>6</sup>

Quality control tests on applied coatings should always include as a minimum coating thickness,<sup>28</sup> holiday detection,<sup>29</sup> and adhesion. There are several standard test methods available for determining

the adhesion quality of thin-film coatings of limited flexibility.<sup>30–32</sup> For thicker, more flexible coatings, such as polyolefins, the quality of the adhesion is best determined using the peel adhesion test.<sup>17</sup> All of these standard adhesion test methods are destructive, requiring coating repairs at the test site. Thus it is often more convenient for coated test samples to be prepared in an identical manner so that the quality of the adhesion can be determined without incurring coating repairs on the work item. Such test samples can also be used to determine the resistance of the coating to cathodic disbondment.<sup>17,18</sup>

With multicomponent solvent free liquid-applied coatings such as polyurethanes and epoxies, it is also good practice to take cup shots of the mixed material at various stages during the coating application process. This is to verify that a consistent mixing ratio is being achieved within the coating manufacturer's recommended tolerances throughout the coating application process. The physical properties of the fully cured samples can be subjected to gravimetric analysis, hardness, tensile strength measurements, etc., to verify that the optimum mixing ratio is being achieved. This type of testing is particularly useful where the coating is being applied, using automated equipment such as that shown in **Figure 4** where there is a risk of the material going off ratio due to a component malfunction.

FBE powder coatings require a minimum substrate temperature for the coating to fully cure and provide optimum corrosion protection. It is therefore a standard practice to remove small samples of the applied coating from the substrate in order to confirm that full cure has been achieved. The removed coating samples are examined using a differential scanning calorimeter (DSC).<sup>33</sup> This equipment is able to determine the thermal characteristics of the coating, in particular, the glass transition temperature, from which the degree of cure can be ascertained.

It is very common for structures manufactured from steel and buried underground to have a design life in excess of 30 years. A sound coating selection process, good surface preparation, and coating application practice supported by a rigorous quality control system are necessary at construction if such aspirations are not to prove unrealistic.

## References

1. National Association of Pipe Coating Applicators. Bulletin 18–99. Application Procedures For Concrete Weight Coating Applied by the Compression Method to Steel Pipe <http://www.napca.com/>
2. Steel Structures Painting Council. Specification SP1 Solvent Cleaning. <http://www.sspc.org/>
3. International Standards Organisation. ISO 8501–1: Preparation of Steel Substrates Before Application of Paints and Related Products.
4. Steel Structures Painting Council Specification SP8 Pickling. <http://www.sspc.org/>
5. International Standards Organisation. ISO 8502–3: Preparation of steel substrates before application of paints and related products – Tests for the assessment of surface cleanliness – Part 3: Assessment of dust on steel surfaces prepared for painting. (Pressure sensitive tape method.)
6. International Standards Organisation. ISO 8503–1: Preparation of Steel Substrates Before Application of Paints and Related Products – Surface Roughness Characteristics of Blast-Cleaned Steel Substrates Part 1: Specifications and Definitions for ISO Surface Profile Comparators for the Assessment of Abrasive Blast-Cleaned Surfaces.
7. International Standards Organisation. ISO 8502–4: Preparation of steel substrates before application of paints and related products – Tests for the assessment of surface cleanliness – Part 4: Guidance on the estimation of the probability of condensation prior to paint application.
8. BS EN 10289: Steel tubes and fittings for onshore and offshore pipelines – External liquid applied epoxy and epoxy-modified coatings.
9. BS EN 10290: Steel tubes and fittings for onshore and offshore pipelines – External liquid applied polyurethane and polyurethane-modified coatings.
10. ANSI/AWWA C209: Cold Applied Tape Coatings for Special Sections, Connections and Fittings for Steel Water Pipelines.
11. Bates, C. R. 15th International Conference on Pipeline Protection Proceedings, Aachen, Germany, 29–31 October. BHR Group Limited, The Fluid Engineering Centre, Cranfield, Bedfordshire, UK, 2003; p 33.
12. BS 4164: 1967: Specification for coal tar-based hot-applied coating materials for protecting iron and steel, including a suitable primer.
13. BS 4147: 1967: Specification for bitumen-based hot-applied coating materials for protecting iron and steel, including suitable primers where required.
14. National Association of Pipe Coating Applicators. Specification and Plant Coating Guide 1-65-94 thru 17–98. <http://www.napca.com/>
15. ANSI/AWWA C203: Standard for coal tar protective coatings and linings for steel water pipelines – Enamel and tape – Hot applied <http://www.awwa.org/>
16. Neal, D. *Fusion Bonded Epoxy Coatings. Application and Performance*; Harding & Neale: Texas, 1997.
17. CAN/CSA Z245.21-02: External Polyethylene Coating For Pipe (System A) <http://www.csa.ca/contact/>
18. CAN/CSA Z245.21-02: External Polyethylene Coating For Pipe (System B) <http://www.csa.ca/contact/>
19. Waterton, K. C.; Woolf, L.; Fowler, C. M.; Palmer, A. C. NACE Canadian Region Western Conference Proceedings; Calgary: Alberta, February, 1990; pp 20–22.
20. Fairhurst, D.; Willis, D. J. *Prot. Coat. Linings* 1997.
21. Socotherm/Socologstor. Adria, Italy <http://www.socotherm.com/>
22. Gower, S.; Fairhurst, D. *Oil Gas J* **1992**, 219(8), 49–63.
23. Weber, T. J. 15th International Conference on Pipeline Protection Proceedings; Aachen, Germany, Oct 29–31; BHR Group Limited, The fluid Engineering Centre. Cranfield: Bedfordshire, UK, 2003; pp 337.

- 
24. Norman, D.; Swinburne, R. 13th International Conference on Pipeline Protection Proceedings, Edinburgh, UK, Sep 29–Oct 1; BHR Group Limited, The fluid Engineering Centre. Cranfield: Bedfordshire, UK, 1999; pp 199.
  25. John, R. 15th International Conference on Pipeline Protection Proceedings, Aachen, Germany; Oct 29–31 Papers presented at 15th International Conference on Pipeline Protection. BHR Group Limited: Cranfield, 2003; pp 331.
  26. NACE Technical Committee Report Item No 24202: Coatings for repair and rehabilitation of the external coatings on buried steel pipelines July 1999.
  27. ISO 8502-6: Preparation of steel surfaces before application of paints and related products – Tests for surface cleanliness – Part 6: Sampling of soluble impurities on surfaces to be painted – Bresle Method.
  28. ASTM B499: Test method for measurement of coating thickness by the magnetic method: Nonmagnetic coatings on magnetic basis metals.
  29. ASTM G62-87: Standard test methods for holiday detection in pipeline coatings.
  30. ASTM D 6677: Standard test method for adhesion by knife.
  31. ASTM D3359: Standard test method for measuring adhesion by tape test.
  32. ISO 4624: Paints and varnishes – Pull-off test for adhesion.
  33. CAN/CSA Z245.20-06: External Fusion Bonded Epoxy Coating For Steel Pipe (System A) <http://www.csa.ca/contact/>

## 4.16 Inspection of Paints and Painting Operations

**N. R. Whitehouse**

PRA Coatings Technology Centre, 14 Castle Mews, High Street, Hampton TW12 2NP, UK

© 2010 Elsevier B.V. All rights reserved.

4.16.1	Introduction	2720
4.16.2	Duties of the Painting Inspector/Types of Inspection	2720
4.16.2.1	Introduction	2720
4.16.2.2	Inspection Records and Reports	2721
4.16.2.3	Additional Inspection Services	2721
4.16.2.4	The Importance of Precontract Discussions	2722
4.16.3	The Training and Certification of Painting Inspectors	2722
4.16.4	Specific Aspects of Inspection	2722
4.16.4.1	Initial Inspection of Liquid Paints and Blast Cleaning Abrasives	2722
4.16.4.2	Inspection of Surface Preparation	2723
4.16.4.3	Inspection of Surface Profile	2724
4.16.4.4	Inspection of Steel Surfaces for Chemical Cleanliness	2725
4.16.4.5	Monitoring of Ambient Conditions	2726
4.16.4.6	Inspection during Paint Application	2726
4.16.4.7	Inspection after Paint Application	2726
4.16.5	Concluding Remarks	2727
References		2727

### Abbreviations

**BSI** British Standards Institute

**ICorr** UK Institute of Corrosion

**ISO** International Standards Organisation

**NACE** National Association of Corrosion Engineers

### 4.16.1 Introduction

It is not always easy to apply the concepts of quality control, which have become routine on coating production lines, to new steel structures. In many steelwork fabrication shops, much of the day-to-day throughput does not require a high-performance paint system to be applied. For most major new constructions, however, a protective coating system is needed to ensure the best possible corrosion protection. It is for these types of project that painting inspection is an essential requirement. The full performance of any protective coating system will only be realized if it is applied to a well prepared surface, under suitable environmental conditions. The paint system must have good adhesion to the substrate and must be free from defects. Each individual coat must also be applied at the correct film thickness.

For most protective coating projects, therefore, the skill and diligence of the blasters and sprayers involved will determine whether a particular paint system will provide the long-term corrosion protection required or fail prematurely. Inspection of both surface preparation and each stage of paint application by a suitably trained, and preferably independent, painting inspector is the best way to ensure that the protective coating of new constructional steelwork or the maintenance painting of an existing asset is successful. The primary purpose of painting inspection, therefore, is to ensure that the coating specification is met fully by the contractor, on time and, wherever possible, on budget. Inspection is never a substitute for adequate supervision, nor is it a satisfactory way of overcoming the shortfalls of a badly written specification.

### 4.16.2 Duties of the Painting Inspector/Types of Inspection

#### 4.16.2.1 Introduction

The duties of a painting inspector will be determined by the scope of his engagement. As a minimum, the inspector will check and report that all elements of the coating schedule have been completed satisfactorily.



The painting inspector's duties will usually extend beyond this, however, to ensuring that the specification, as written, is met fully and that, if any deficiencies in workmanship are discovered, they are brought to the attention of the client at the earliest possible moment. It is important to note that a painting inspector has no power to order work to stop, unless the power has been delegated to him, which is unlikely.

For the high-performance protective coating systems specified today, some projects will require the maximum level of surface preparation and will benefit from continuous inspection at every stage. For many minor painting programs, however, less intensive inspection may be adequate. It is the responsibility of the client to determine the appropriate level of inspection needed and to make provision accordingly. One of the following three possible levels of inspection is usually selected:

- *Full inspection:* The inspector is on site throughout the project to witness that preparation and painting work complies with the requirements of the specification, at all times. Work is inspected at each stage of the program and only when formal approval has been given is the next coat of the paint system applied, for example. For the largest projects, more than one inspector may be needed.
- *Intermittent inspection:* The inspector is not on site at all times and observes work in progress at agreed intervals. Intermittent inspection is, by its nature, less costly than full inspection, but is also less complete.
- *Occasional inspection:* The inspector observes the initial work by the applicator and agrees the standard to be achieved for subsequent work. He then returns to site infrequently to inspect the work done and to check that the agreed standard of application has been maintained. Although the cost savings that can result on inspection are considerable, the overall benefit to the client technically is very much reduced.

The level of inspection chosen will be determined, most often, by the nature of the project and the complexity of the protective coating work involved. A strong case for full inspection on a minor maintenance painting program, therefore, or a relatively undemanding new construction project can rarely be made.

#### 4.16.2.2 Inspection Records and Reports

The compiling of adequate inspection reports is an important aspect of a painting inspector's duties. Inspection reports not only provide a record of progress on a contract, but also become a source of useful information when maintenance painting is due. In the event of an

unexpected coating failure, an investigation into the cause can often be moved forward more quickly, when access to inspection records can be provided.

The painting inspector will usually complete a daily inspection record and provide a weekly summary report. The inspector's daily and weekly records will be issued to the client and may also be circulated to other interested parties, as required. The permanent record of progress provided by the inspector will be retained on file by the client and, subsequently, will become an integral part of the archived project documentation. A daily paint inspection report will usually include, as a minimum, information on

1. The general weather conditions and the local ambient temperature, relative humidity, dew point, and steel temperature.
2. The location of the work area that day and the number of blasters and painters involved.
3. Whether surface preparation work is being undertaken and, if so, the condition of steel surface before and after preparation, together with details of the method of surface preparation used.
4. Whether paints are being applied and, if so, the product reference and the batch number of each paint coating, together with a note on their method of application.
5. While inspecting, a description of the inspection methods and instruments used, together with the results obtained.
6. Whether the requirements of the specification have been met fully in the areas inspected and, if not, the nature and extent of any noncompliance.

#### 4.16.2.3 Additional Inspection Services

Most specialist providers of painting inspectors will usually offer a number of additional services, when required, including

1. Constructive comments on the coating specification, wherever appropriate, to alert the client to any ambiguities, inaccuracies, or omissions.
2. A preliminary discussion on the painting contractor's proposed method of working and any foreseen health and safety hazards.
3. Liaison with the paint manufacturer directly on the coating products selected and any critical requirements for their successful application.
4. The drafting and presentation of an inspection schedule, setting out precisely how and at what stages of the coating program, inspection will be carried out and reported.

5. Where there is a requirement for precontract inspection of the blast cleaning and painting contractor's facilities and equipment, specialist providers of painting inspection will usually offer this preliminary service as well.

The purpose of a precontract inspection at works is to confirm that the facilities are adequate and that the equipment that will be used has been well maintained and is currently in good working order. The cleanliness of the paint shop and the tidiness of the paint store can often give a telling indication of the seriousness with which the workforce takes the surface preparation and protective coating of steelwork.

The purpose of a precontract inspection on site is to ensure that any scaffolding and access platforms needed will provide safe access to the work, that compressors are in good working order, that any temporary sheeting needed will be effective and that extraction equipment is available to remove solvent vapors and dust particles.

#### **4.16.2.4 The Importance of Precontract Discussions**

Precontract discussions involving the client, the main contractor, the steel fabricator, the painting contractor and, in particular, the painting inspection company can be invaluable, as they provide a forum in which potential problems with the program, as a whole, can be 'ironed out' before any work on the project commences. Precontract discussions enable agreement to be reached on, for example

1. Any features of the design that, if not modified, may be difficult to coat successfully.
2. Arrangements and facilities for the testing of materials, including coatings.
3. The measures to be adopted to reduce coating damage during handling, transport, and subsequent erection on site.
4. The chain of authority to be followed in cases of difficulty or disagreement.

When the minutes of such discussions are recorded accurately, they can serve as a useful adjunct to the contract.

#### **4.16.3 The Training and Certification of Painting Inspectors**

The protective coating of constructional steelwork has advanced technically in recent years, and as a

consequence, industry pressure for the development and provision of programs of formal training and certification of painting inspectors has increased. Initiatives over the last two decades, in both the United Kingdom and the United States, first to certificate painting inspectors and then to provide enabling training programs have culminated in the Institute of Corrosion's (ICorr) Painting Inspector Scheme in the United Kingdom and the National Association of Corrosion Engineers' (NACE) Coating Inspector Training and Certification Scheme. For both of these now well established certification schemes, candidates attain initially a Level 1 Certificate. With further study and verifiable work experience, inspectors can then progress to Level 2 and, ultimately, to Level 3 certification. For many high-profile, new construction projects and for programs of critical coating maintenance on important assets, the use of NACE- or ICorr-certificated painting inspectors has become very much the preferred option.

#### **4.16.4 Specific Aspects of Inspection**

##### **4.16.4.1 Initial Inspection of Liquid Paints and Blast Cleaning Abrasives**

Supplies of the liquid paints specified for a project and the blast cleaning abrasives to be used for surface preparation should be checked by the painting inspector initially to ensure that they are of the correct type, that they are being stored correctly, and that they have been supplied in sufficient quantities to allow surface preparation and paint application to proceed smoothly. For some projects, it may be a requirement of the inspection contract for tests on the paints to be performed, in a laboratory, to a predetermined schedule. In this event, the inspector may be required only to take the liquid samples needed for the testing program and forward them to the test house. Typically, the routine checks made by a painting inspector on liquid paints delivered to a steel fabricator's works, or to site, for a project will include the following:

1. Checking that the paints delivered correspond to the coating products specified, for example, manufacturer, product type, product name, and color.
2. Checking that the paints delivered are of the correct type for the method of application to be used, for example, spraying grade or brushing grade.
3. Checking that the paint store does not suffer from extreme temperatures and is both safe and secure.

Typically, the temperature inside the paint store should be above  $+3^{\circ}\text{C}$  and below  $+30^{\circ}\text{C}$ .

4. Checking that the paints have been delivered in sufficient quantities for the amount of steelwork to be coated (and, if not, that further supplies can be obtained quickly when needed).

The painting inspector should record the batch numbers and expiry dates of all paints held in the store. The subsequent withdrawal of paint, when coating work commences, should then be controlled and monitored by the inspector to ensure that the stocks are always rotated properly and that the paint used is always well within its shelf life.

When cans of paint are opened for use, the inspector will observe that they are first mixed thoroughly and that any settlement, if found, can be reincorporated into the bulk of the paint easily and satisfactorily. For two-pack paints, the inspector will observe that the base and hardener are always mixed together in the correct proportions and that any induction period before application is observed. The inspector will also ensure that any two-pack paints that cannot be applied within their pot life are discarded.

In cold weather conditions, it may be necessary to add small amounts of solvents to paints in order to lower their viscosity for spraying. Whenever any addition of thinners are made to the paints, the inspector will normally note the additions being made and ensure that they do not exceed, in percentage terms, the recommendations given by the manufacturer. Guidance on the preparation of samples of paints and coatings for testing and their subsequent examination may be found in BS EN ISO 1513.<sup>1</sup>

When abrasive blast cleaning is the method of surface preparation used, the inspector may be required to carry out checks on the abrasive itself. The extent of inspection of an abrasive will be determined by the requirements of the specification. As a minimum, however, it would be usual to check that the abrasive is of the correct type, for example, steel grit, steel shot, or copper slag, that it is of the correct particle size, and that it is dry. In the unlikely event that either the purity or the cleanliness of the abrasive is in doubt, then tests may be needed to determine, for example, the presence of foreign matter and the presence of water-soluble contaminants.

Guidance on test methods for metallic blast-cleaning abrasives may be found in BS EN ISO 11125<sup>2</sup> and guidance on test methods for nonmetallic blast-cleaning abrasives may be found in BS EN ISO 11127.<sup>3</sup>

#### 4.16.4.2 Inspection of Surface Preparation

The primary objective of surface preparation is to produce a clean surface to which the first coat of a paint system will adhere well. For protective coating systems on steelwork, an inspector may be asked to examine the initial condition of the steel surface and then to examine the condition of the steel surface after preparation for painting. He will usually inspect prepared surfaces for physical cleanliness, chemical cleanliness, and surface roughness (profile) by visual assessment and appropriate test methods. Constructional steelwork is prepared for painting, most often, by abrasive blast cleaning, hand- and power-tool cleaning, or high-pressure water jetting. Fabrication of the steelwork is likely to have involved both cutting and welding operations.

Inspection of the surface preparation of steelwork prior to painting has been assisted greatly by the development of relevant national standards over the past 40 years; most notably in Sweden, the United Kingdom, and the United States. These national standards have led, in more recent years, to the publication of four series of International (ISO) Standards. In the United Kingdom, these multipart ISO Standards have been issued by BSI as BS EN ISO 8501–8504. The second edition of a general introduction to these BS EN ISO Standards, BS 7079,<sup>4</sup> provides a concise overview of their scope and content. The inspector's working standards for the surface preparation of steelwork are laid out in Parts 1 to 4 of BS EN ISO 8501.

BS EN ISO 8501-1 specifies a series of rust grades and preparation grades (subsequent degrees of visual cleanliness) for uncoated steel surfaces. The various rust and preparation grades are defined by written descriptions and by photographs that are representative examples. There are twenty eight photographs in total. Four rust grades of uncoated steel, designated A, B, C, and D and three series of preparation grades, designated Sa, St, and Fl, according to the method of surface preparation used, are described and illustrated.

For abrasive blast cleaning (Sa series), four preparation grades are designated as follows:

- Sa 1 Light blast-cleaning;
- Sa 2 Thorough blast-cleaning;
- Sa 2 1/2 Very thorough blast-cleaning;
- Sa 3 Blast-cleaning to visually clean steel.

For hand- and power-tool cleaning (St series), two preparation grades are designated as follows:

- St 2 Thorough hand- and power-tool cleaning;
- St 3 Very thorough hand- and power-tool cleaning.

For flame cleaning (Fl), there is only one preparation grade, namely

- Fl Flame cleaning.

BS EN ISO 8501-1 is an important inspection tool. It enables the inspector to compare the appearance of uncoated steel, and the same steel after it has been prepared for painting by one of these methods, with internationally agreed written descriptions and representative photographic examples.

A number of different abrasives may be used to blast clean steelwork. If the abrasive used is nonmetallic, dark in color, and becomes embedded in the surface profile, it can alter the visual appearance of the surface finish. In contrast, some hard, metallic abrasives can create an apparently darker surface finish as a result of shadows in deep-sided pits. To assist the inspection of such surfaces, a further six photographic examples of such effects have been included in BS EN ISO 8501-1, as an informative annex.

BS EN ISO 8501-2:2001 complements BS EN ISO 8501-1, and in a similar way, provides written descriptions and representative photographic examples of steel surfaces after the localized removal of previous paint coatings. BS EN ISO 8501-2 provides detailed guidance on the visual inspection of surface preparation in, for example, a maintenance painting program where the complete removal of all previously applied coatings may not be required.

Welds, cut edges, and minor imperfections in steelwork are often starting points for corrosion. Inspection of the surface preparation of these areas, prior to paint application, is assisted by BS EN ISO 8501-3. The standard defines three preparation grades for making steel surfaces with imperfections suitable for application of paints and related products. For each grade, requirements for the preparation of commonly found imperfections are tabulated and are also illustrated with line drawings.

While dry abrasive blast cleaning, and to a lesser degree, low-pressure water/abrasive blast cleaning are still used widely for the surface preparation of steelwork, the use of high-pressure water jetting has increased in recent years, as it offers an effective method of removing rust, previous coatings, foreign matter, and water-soluble contaminants, all at the same time.

BS EN ISO 8501-4 is a new standard that has been developed to stand alongside BS EN ISO 8501-1 and provide a comparable tool for the visual assessment and inspection of initial surface conditions, preparation

grades and flash rust grades on steelwork prepared for the application of paints and related products by high-pressure water jetting. The preparation grades are again defined by written descriptions and photographs that are representative examples within the tolerances of each grade, as described in words. There are 23 photographs in total.

Specifically, five initial surface conditions are defined, three of which are applicable to degraded paint coatings and two of which are applicable to damaged prefabrication primers. Three preparation grades for each initial surface condition, after partial or full removal of previous paint coatings by high-pressure water jetting, indicate the degree of cleaning required. Three grades of flash rusting of the steel surface that develop when high-pressure water jetting is the method of preparation used are also specified.

#### **4.16.4.3 Inspection of Surface Profile**

Preparation of steelwork by abrasive blast cleaning not only removes surface contaminants, such as rust and mill scale, but also introduces a surface profile. The magnitude of the surface roughness (peak-to-trough height) that results when this is the method of surface preparation selected will be determined by the particle size of the abrasive used and the air pressure at the nozzle. Measurement of surface profile and checks each day on the air pressure at the nozzle of the blast cleaning equipment being used will form part of the inspector's duties on many contracts. Ensuring that the specified surface profile is achieved is important. If the profile is too low, the adhesion of the coating may be compromised. If the profile is too high, there is a danger that the tallest peaks will not be covered adequately by the coating and so will corrode in service.

Surface comparators are used most commonly today by inspectors for assessing the grade of surface profile on steel surfaces. In parts 1-4 of BS EN ISO 8503, the requirements for these comparators are specified and two laboratory procedures for their calibration are defined. BS EN ISO 8503 is in five parts, and in part 5, an alternative method of measuring surface profile on site with the aid of replica tape and a micrometric gauge is defined.

Two surface profile comparators have been specified in BS EN ISO 8503: Reference Comparator 'G' is for grit-blasted surfaces and Reference Comparator 'S' is for shot-blasted surfaces. Each comparator has four segments (numbered 1-4) each of a

peak-to-trough height defined by nominal values and associated tolerances. For Comparator 'G', for example, the nominal values and tolerances are as follows:

Segment	Nominal reading ( $\mu\text{m}$ )	Tolerance ( $\mu\text{m}$ )
1	25	3
2	60	10
3	100	15
4	50	20

'Fine', 'medium' and 'coarse' profiles are then defined, as follows:

- Fine: Profiles equal to segment 1 and up to but excluding segment 2;
- Medium: Profiles equal to segment 2 and up to but excluding segment 3;
- Coarse: Profiles equal to segment 3 and up to but excluding segment 4.

In use, the inspector compares the blast-cleaned surface to be graded visually with the segments on the appropriate comparator and determines whether the work surface is 'fine,' 'medium,' or 'coarse.' This relatively simple approach to grading surface profile is generally adequate.

Many specifications continue to rely on the final inspection of the blast-cleaned surface as the procedure for acceptance. This approach is reasonable as long as the blast-cleaning equipment used has been well maintained and is functioning satisfactorily. When problems do arise with the equipment, however, the inspector may be required also to check the air pressure at the blasting nozzle and the quality of the compressed air emitted. The checks required are simple and can be performed quickly.

In order to check the air pressure at the nozzle of the blast-cleaning equipment, the hypodermic needle of a special pressure gauge is inserted into the blasting hose, close to the nozzle, and the pressure is measured. The small hole made in the hose by the hypodermic needle seals quickly when the needle is withdrawn and the subsequent operation of the hose is not compromised. Typically, the air pressure required at the nozzle is 80–100 psi (550–690 kPa).

The compressed air itself must be clean and dry, in order not to contaminate the blast-cleaned steel surface. The quality of the compressed air can only be checked by the inspector, with the abrasive supply switched off. A clean white cloth (or filter paper) placed in front of the nozzle allows the inspector to see unwanted water

and oil contaminants. If any contamination is found, the inspector will then require the contractor to check his equipment and rectify the problem.

#### 4.16.4.4 Inspection of Steel Surfaces for Chemical Cleanliness

For steelwork that will be coated and then exposed, in service, to aggressive industrial and marine environments, the chemical cleanliness of the steel is of equal importance to the physical cleanliness of the surface and the surface roughness. The BS EN ISO 8502 Series of Standards addresses this requirement and defines field and associated laboratory test methods to determine both the physical and chemical surface cleanliness of steel substrates before application of paints and related products. There are currently nine parts to the 8502 Standard.

The test methods in 8502 describe suitable field procedures for the extraction of soluble ferrous salts and the analysis, on site, of the extract for the presence of ferrous ions, chloride ions, and sulfate ions. In the case of chloride ions, a procedure intended only for use in the laboratory is also provided. The field test methods include the use of ion-detection tubes for chlorides, measurement of conductivity for water-soluble salts, and measurement of turbidity for water-soluble sulfates. There is also a field test method for the refractometric determination of moisture; guidance on estimating the probability of condensation on a steel surface and a simple procedure, involving the use of pressure-sensitive tape, to determine whether a steel surface prepared for painting is free from dust and debris.

While it may be a requirement for an inspector to test steel surfaces for the presence of soluble ferrous salts after preparation for painting, it may not be necessary for him/her to determine whether soluble ferrous salts, when found, are chlorides or sulfates, for example. In such situations, the potassium ferricyanide test, first described in British Standard Code of Practice 5493,<sup>5</sup> is still often relied upon. For this test, an area of the blast-cleaned steel surface is moistened with distilled water, and when the surface is almost dry, a test paper that has been impregnated previously with a dilute aqueous solution of potassium ferricyanide is placed on the steel surface. Deep blue spots (a Prussian blue complex is formed) develop quickly on the yellow test paper wherever ferrous salts are detected. The test method is qualitative and very sensitive. It provides an easily conducted pass/fail procedure for routine site inspection work.



#### **4.16.4.5 Monitoring of Ambient Conditions**

An important aspect of the inspection of both surface preparation and paint application is the monitoring of ambient conditions. Specifications may require abrasive blast cleaning to be carried out under ambient conditions that will ensure that the freshly blast-cleaned surface will not deteriorate quickly and will be preserved until paint can be applied a few hours later. Specifications may also require paint to be applied only under defined ambient conditions.

The painting inspector will normally monitor the air temperature, the steel temperature, and the relative humidity, two or three times during the working day. On some projects, continuous measurement of air temperature and relative humidity may be provided by the client and the data logged electronically. For most projects, however, the monitoring of ambient conditions remains the duty of the inspector. Typically, a painting inspector will use a whirling hygrometer to determine the relative humidity and also to measure the air temperature. A contact thermometer will be used to measure the surface temperature of the steel. From the relative humidity, the dew point will then be calculated and recorded.

Specifications will usually require that steel temperatures should be at least 3 °C above the dew point, in order to avoid the possibility of moisture condensing on the work surface during preparation and painting operations. Relative humidity not greater than 85% and ambient air temperature not less than 4 °C are also usually prescribed. Ambient conditions outside these limits or deteriorating weather conditions that, it can be anticipated, will lead quickly to rainfall or relative humidity and air temperature outside the prescribed limits will be reasons for the inspector to advise the painting contractor to cease blast cleaning and painting.

#### **4.16.4.6 Inspection during Paint Application**

Monitoring paint application is an important aspect of a painting inspector's duties. The inspector will record climatic conditions; ensure that the paint is applied in accordance with that specified; and note that the correct method of application is being used. Application methods will depend on the type of coating product, the nature of the substrate, and the surface area to be painted. For most constructional steelwork, the method of paint application will be airless spray.

Paints almost always need to be mixed before being applied, to ensure that there has not been any settlement of pigment in the can. In the case of two-pack paints, thorough mixing of base and hardener, in the correct proportions, is essential. Thinning of some paints may also be needed prior to spray application, especially in colder winter months. The inspector will ensure that all of these procedures are carried out correctly and at the appropriate times.

A primer needs to cover the entire surface profile of the steel substrate and each coat of the paint system applied subsequently needs then to cover all areas completely and needs to be as uniform as possible in thickness. During paint application, therefore, the inspector may wish to measure the wet-film thickness of paint being applied. He should need only to make such checks infrequently, when the work is progressing smoothly, as the painters themselves should be checking wet-film thicknesses regularly as they proceed. Simple measurements with a wet-film thickness comb gauge are all that is required.

As the paint application progresses from primer to intermediate coats and finish, the inspector will ensure that each over-coating interval stated on the paint manufacturer's technical data sheet is observed and that any particulate contamination on intermediate painted surfaces, should it occur, is removed and is not painted over. The diligence of the painting inspector during the paint application phase of a project will influence, to a significant extent, the potential of the paint system ultimately to achieve its expected level of performance in service. A good rapport with the painting supervisor is always beneficial during this phase of the work program.

#### **4.16.4.7 Inspection after Paint Application**

When the paint system has been built up satisfactorily and has cured, the painting inspector can progress to the final phase of his inspection duties. Key requirements such as total dry film thickness, adhesion between individual coats, and curing of the paint system, as a whole, will all now need to be checked and reported. In addition, the inspector may be required to check the coating system for freedom from pinholes and to conduct other specific tests, if required by the client.

Methods for the measurement of paint film thickness are described in BS EN ISO 2808.<sup>6</sup> The procedure for checking nominal dry-film thickness is usually agreed between the inspector and his client.

Unless agreed otherwise, individual dry-film thicknesses of less than 80% of the nominal dry film thickness will not be acceptable. Values between 80% and 100% of the nominal dry-film thickness are acceptable, provided that the overall average value is equal to or greater than the nominal dry-film thickness. It is usually recommended that the dry-film thickness of a coating should not exceed three times the nominal film thickness.

These guidelines give the inspector a framework in which to analyze his/her results and to define any areas where coatings have been found to be either too thin or too thick. It is generally not the case that 'thicker is better.' Excessively thick films of paint and coatings will usually sag and may take an excessively long time to achieve full cure.

Good adhesion of the primer to the substrate and good adhesion of subsequent coats one to another is a prime requirement of a protective coating system and will usually be checked by the painting inspector. Guidance on cross-hatch adhesion tests is provided in BS EN ISO 2409<sup>7</sup> and guidance on pull-off adhesion tests is provided in BS EN ISO 4624.<sup>8</sup> As all adhesion testing is destructive, the inspector will not carry out more adhesion tests than required. On many painted surfaces, a simple St Andrews Cross cut with a sharp knife will give a good indication of poor paint adhesion and prompt the inspector to investigate further.

The full properties of a protective coating system will not be achieved if the paints have not cured properly. An inspector will usually use a solvent-rub test to determine whether, or not, a coating has achieved a full cure. Methyl ethyl ketone is the solvent used most often. Any softening or loss of coating during the test indicates an incomplete cure.

In addition to specific coating tests, an inspector will also examine painted surfaces visually for good coverage, uniformity of color, and for obvious defects such as sagging, wrinkling, and pinholes. The absence of pinholes is particularly important where protective coating systems are required to provide chemical resistance and barrier properties. Checks for the

presence of pinholes can be made by the inspector with a low-voltage or a high-voltage pinhole detector, as appropriate. High-voltage pinhole detectors need to be used with caution and understanding. If the voltage is set too high, there is a risk that the instrument will introduce small holes in the coating rather than detecting them.

#### 4.16.5 Concluding Remarks

The demand for well trained, certificated painting inspectors has increased in recent years, as the importance of thorough surface preparation has been recognized fully and advances in paint technology have led to the introduction of new generations of protective coating systems. Painting inspection can not only provide quality control throughout a painting contract but also ensure that the specification is met and that the client's expectations for robust corrosion protection are delivered.

#### References

1. BS EN ISO 1513: *Paints and Varnishes: Examination and Preparation of Samples for Testing*; British Standards Institution: London, 1995.
2. BS EN ISO 11125: *Preparation of Steel Substrates before Application of Paints and Related Products: Test Methods for Metallic Blast-Cleaning Abrasives*; British Standards Institution: London, 1997.
3. BS EN ISO 11127: *Preparation of Steel Substrates before Application of Paints and Related Products: Test Methods for Non-Metallic Blast-Cleaning Abrasives*; British Standards Institution: London, 1998.
4. BS 7079: *General Introduction to Standards for Preparation of Steel Substrates before Application of Paints and Related Products*; British Standards Institution: London, 2008.
5. BS 5493:1977: *Code of Practice for Protective Coating of Iron and Steel Structures against Corrosion*, Appendix G. British Standards Institution: London, 1977. [Obsolescent, Superseded largely by BS EN ISO 12944].
6. BS EN ISO 2808: *Paints and Varnishes: Determination of Film Thickness*; British Standards Institution: London, 2007.
7. BS EN ISO 2409: *Paints and Varnishes: Cross-Cut Test*; British Standards Institution: London, 2007.
8. BS EN ISO 4624: *Paints and Varnishes: Pull-Off Test for Adhesion*; British Standards Institution: London, 2003.

## 4.17 Paint and Coating Failures and Defects

### B. Fitzsimons

Pyeroy Ltd, St, Omers Road, Dunston, Gateshead, Tyne & Wear NE11 9EZ, UK

### T. Parry

Scientific & Technical Services Ltd, Summerhill, Blaydon, Tyne & Wear NE21 4JR, UK

© 2010 Elsevier B.V. All rights reserved.

---

<b>4.17.1</b>	<b>Coating Failures and Defects</b>	<b>2729</b>
4.17.1.1	Adhesion Failure (Delamination/Flaking)	2730
4.17.1.2	Alligatoring (also Known as Crocodiling)	2730
4.17.1.3	Aluminum Corrosion	2731
4.17.1.4	Bittiness	2731
4.17.1.5	Bleaching (also see Fading)	2731
4.17.1.6	Bleeding (also Called 'Bleed Through')	2731
4.17.1.7	Blistering	2732
4.17.1.8	Bloom (Blush)	2732
4.17.1.9	Bridging	2732
4.17.1.10	Brush Marks (also Laddering, Ladders, or Ropiness)	2733
4.17.1.11	Bubbles or Bubbling	2733
4.17.1.12	Chalking	2733
4.17.1.13	Checking (also see Cracking)	2733
4.17.1.14	Cheesiness (Soft Coating)	2734
4.17.1.15	Cissing (also Referred to as Crawling)	2734
4.17.1.16	Cobwebbing	2734
4.17.1.17	Cracking (also see Alligatoring and Checking)	2734
4.17.1.18	Cratering	2735
4.17.1.19	Crowsfooting (also see Wrinkling)	2735
4.17.1.20	Delamination (also see Adhesion Failure and Flaking)	2735
4.17.1.21	Dryspray (also see Overspray)	2736
4.17.1.22	Efflorescence	2736
4.17.1.23	Erosion	2736
4.17.1.24	Fading (also see Bleaching)	2736
4.17.1.25	Filiform (Corrosion)	2737
4.17.1.26	Flaking (also see Delamination and Adhesion Failure)	2737
4.17.1.27	Flocculation	2737
4.17.1.28	Flooding (also see Flotation)	2737
4.17.1.29	Flotation (also see Flooding)	2738
4.17.1.30	Grinning (also see Grinning Through)	2738
4.17.1.31	Grit Inclusions	2738
4.17.1.32	Growth (on the Surface of Paint Film)	2738
4.17.1.33	Incorrect Coating System	2739
4.17.1.34	Impact Damage (Star Cracking)	2739
4.17.1.35	Lamination or Shelling (of Cast Iron)	2739
4.17.1.36	Misses/Skips/Holidays	2739
4.17.1.37	Mud Cracking	2739
4.17.1.38	Orange Peel (also Known as Pock-Marking)	2740
4.17.1.39	Overspray (also see Dry spray)	2740
4.17.1.40	Peeling (also see Flaking)	2740
4.17.1.41	Pinholes	2741
4.17.1.42	Rain Damage – Water Spotting	2741

---

4.17.1.43	Rippled Coating	2741
4.17.1.44	Runs or Sags (also Described as Curtains or Wrinkles)	2741
4.17.1.45	Rust Rashing (to Thermal Spray Coating)	2742
4.17.1.46	Rust Spotting (also Referred to as Rash Rusting)	2742
4.17.1.47	Rust Staining	2742
4.17.1.48	Saponification	2743
4.17.1.49	Settlement	2743
4.17.1.50	Solvent Lifting (also see Wrinkling)	2743
4.17.1.51	Solvent Popping	2743
4.17.1.52	Tackiness	2743
4.17.1.53	Undercutting	2744
4.17.1.54	Water Spotting (also see Rain Spotting)	2744
4.17.1.55	Wrinkling/Rivelling (also see Crowsfooting)	2744
4.17.1.56	Zinc Carbonates	2745
Reference		2745

### 4.17.1 Coating Failures and Defects

Coatings can be very complex materials and their principal constituents are resin, tinting pigments (colorants), and solvent. Other ingredients can be extender pigments (fillers), nonreactive diluents, thixotropes, curing agents, catalysts, film forming agents, etc. Not all coatings will contain all of the different types of ingredients, but most are complex mixtures that have to be carefully formulated to satisfy the design and performance criteria. The percentage by weight of a particular ingredient will vary between the type of coating and the supplier of the coating.

The coatings, single pack, two pack, or three pack, are mixed in the correct proportions for the two and three pack materials prior to application as a thin film by various methods. The application can take place at different levels of surface preparation under a wide range of environmental conditions that can vary from one part of a structure to another.

The applied coating after curing would be expected to retain its cosmetic qualities and perform and protect the substrate from the general elements such as variable levels of heat, cold, and humidity as well as wind, rain, sunlight, and oxygen. Coatings may also be subject to special conditions such as immersion in seawater or chemicals such as a specialist tank lining.

Considering all the variables, it is inevitable that some coatings fail earlier than anticipated. Coating defects may also be expected; however, this may not necessarily lead to a coating failure. For example, alligatoring may be considered as a coating defect,

but the system will still perform, and therefore, this defect does not necessarily constitute a coating failure.

In general terms, a coating failure can be related to formulation deficiencies, application problems, inadequate surface preparation, or external factors such as exposure to an environment to which it is not resistant. Coating failure is not always attributed to a single source, and often a number of contributing factors have to be considered in evaluating the breakdown mechanism. Coating defects normally fall into three categories: those arising during application such as sagging and cissing, those arising after application but prior to service entry such as blushing and wrinkling, and those appearing after entry into service such as chalking.

Probably the most common reasons for coating failure are inadequate surface preparation in terms of applying the coating to a lower standard of preparation than it was designed for, inadequate correction of steel defects, and inadequate removal of soluble salts. The coating failure could therefore be attributed to poor workmanship and/or incorrect specification requirements.

Application-related failures are common, particularly in the industrial and marine coatings industry where basic application faults, such as inadequate film thickness, misses, lack of stripe coating, incorrect over coating times, and inadequate curing times and temperatures prior to entry into service, frequently lead to early coating failure.

Coating selection is important; many coating failures being related to improper coating selection for

the specific environment to which it would be exposed, that is, the use of a product for a purpose for which it was not designed. Environments can also change with time, a prime example being tank linings on chemical carriers where variables of different cargoes, different temperatures, and tank cleaning on a cyclic basis place great stress on the coating system.

No matter how carefully a coating is formulated, laboratory testing is relied upon, to a great extent, to simulate in-service conditions and the results, together with those from field trials, are used to evaluate the coating prior to launch. Laboratory testing, however, cannot cover all of the in-service variables, and in addition, has to be of an accelerated nature; hence, only long-term use of the product is likely to highlight any formulation problems.

The following examples of coating failures and defects have been chosen to illustrate how coatings can fail prematurely or exhibit application defects. The photographs are examples only, as the type of failure or defect could manifest itself in a different way. It is not intended to make the reader an instant 'paint expert,' as the establishment of a failure mechanism is often difficult because of the number of potential contributory factors.

#### **4.17.1.1 Adhesion Failure (Delamination/Flaking)**

**Description:** Flaking, generally accepted as the detachment of the paint system from the substrate, and delamination, used to describe intercoat detachment in a multicoat system, are both forms of adhesion failure where a coating has failed to adhere to the substrate or the underlying paint coating.



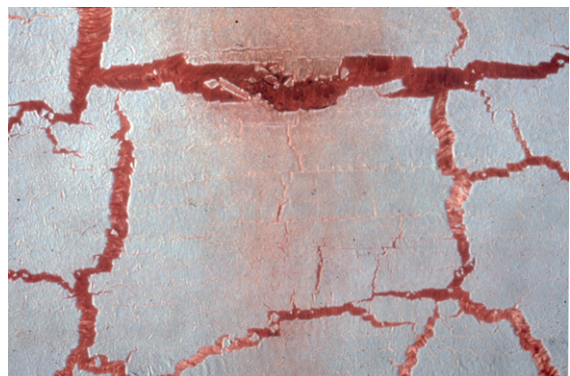
**Probable causes:**

Adhesion failures can be as a result of either internal stress alone or internal stress plus the exacerbating effect of one or more other factors. The contributory factors could be related to formulation, inadequate surface profile, surface contamination, exceeding over-coating times, application to a glossy paint surface, amine bloom, incorrect surface preparation, and differential expansion/contraction of the paint coating and the substrate, particularly in the painting of timber.



#### **4.17.1.2 Alligatoring (also Known as Crocodiling)**

**Description:** Very large (macro) checking or cracking that resembles the skin of an alligator or crocodile. Cracks may penetrate to the undercoat, but generally not down to the substrate.

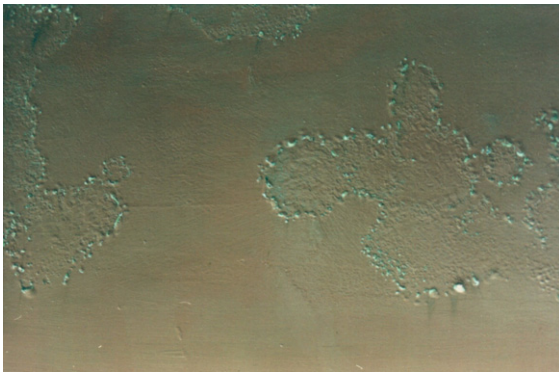




Probable causes: Internal stresses in the coating where the surface shrinks faster than the body of the paint film. Can be caused by excessive film thickness and limited paint flexibility and on paint systems having a flexible undercoat with a hard topcoat.

#### 4.17.1.3 Aluminum Corrosion

Description: Blistering and/or lifting of the paint coating because of the formation of aluminum corrosion products under the paint.



Probable causes: Pinholes in the coating, porosity of flame-sprayed aluminum, or insufficient coating thickness.

#### 4.17.1.4 Bittiness

Description: Film contaminated by particles of paint skin, gel, flocculated material, or foreign matter, which project above the paint surface to give a rough appearance. The term *Pep-pery* is used when the bits are small and uniformly distributed.



Probable causes: The main cause is contamination within or on the surface of the paint film by paint skin, gelled particles, airborne sand and grit, or contamination from brushes or rollers.

#### 4.17.1.5 Bleaching (also see [Fading](#))

Description: Total loss of the color of a coating.



Probable causes: Bleaching due to weathering or chemical attack.

#### 4.17.1.6 Bleeding (also Called 'Bleed Through')

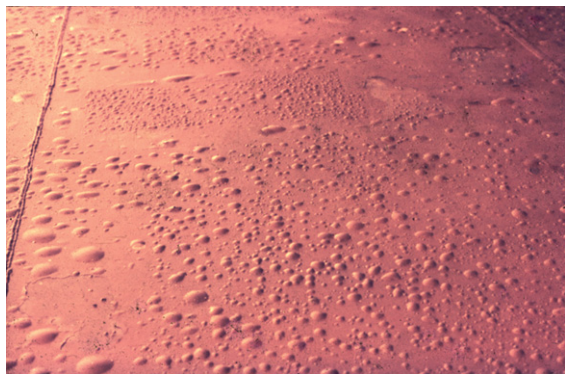
Description: Staining of a paint film by diffusion of a soluble, colored substance from the underlying paint to give undesirable discoloration or staining. Very often, this is seen where bitumen or tar-based products are overcoated with alkyd-based or other conventional topcoats. It can also occur with emulsion paints.



Probable causes: 'Bleed through' is generally a full or partial redissolving of the previous coat and can happen when strong solvents are used in the topcoats.

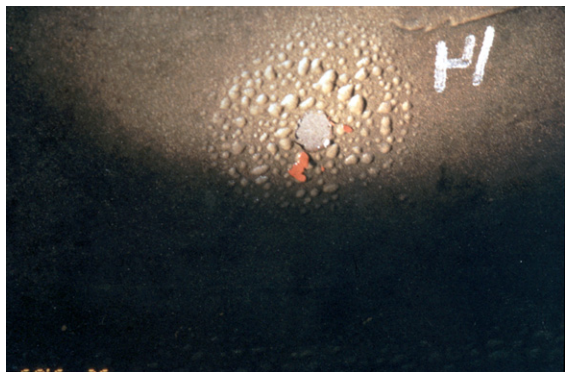
**4.17.1.7 Blistering**

**Description:** Dome-shaped projections in the dry paint film through local loss of adhesion from the underlying surface. The blisters may contain liquid or gas, or may be dry.

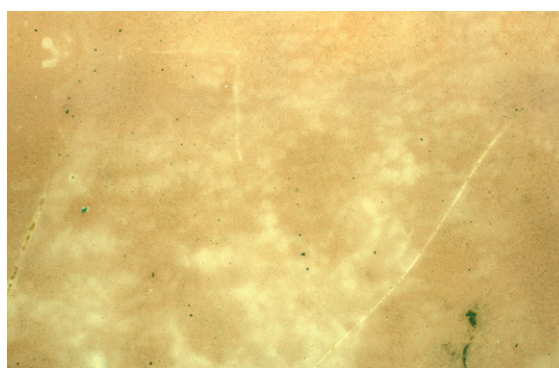


**Probable causes:**

Osmotic blistering is commonly associated with the presence of soluble salts, soluble pigments, retained solvents, or the absorption and retention of low molecular weight water-miscible solvents, typically from the carriage of chemical cargoes. Nonosmotic blistering, commonly described as cathodic blistering, is often seen as a circular pattern of blisters around a coating defect where the substrate is exposed. Non-osmotic blistering can also occur due to a cold-wall effect producing condensation. Where coatings are used with cathodic protection, hydrogen production is possible and the resultant hydrogen vapor pressure could produce blisters.

**4.17.1.8 Bloom (Blush)**

**Description:** A hazy deposit on the surface of the paint film, resembling the bloom on grape resulting in a loss of gloss and a dulling of the color.



**Probable causes:**

Paint film exposed to condensation or moisture during curing (common phenomenon with amine-cured epoxies). Incorrect solvent blends can also contribute to blooming.

**4.17.1.9 Bridging**

**Description:** The covering over of unfilled gaps such as cracks or corners with a film of the coating material. This causes a weakness in the paint film, which may crack, blister, or flake off.



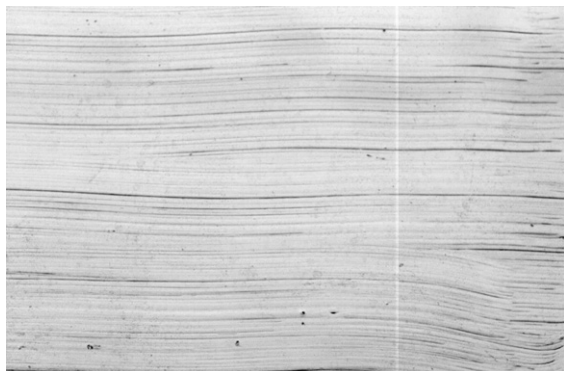
**Probable causes:**

Poor application, high-viscosity paint, or failure to brush paint into corners and over welds.



#### 4.17.1.10 Brush Marks (also Laddering, Ladders, or Ropiness)

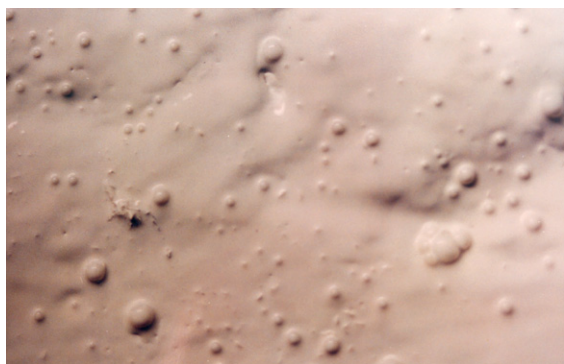
**Description:** Undesirable ridges and furrows that remain in a dry paint film after brush application where the paint film has not flowed out. May be found as a cross-hatch pattern (laddering) where alternate coats have been applied in opposite directions. Pronounced brush marks are known as ropiness.



**Probable causes:** Viscosity of material may be too high for brush application, incorrect thinners used in the paint, inadequate mixing, or poor application technique. Two-pack paints may have exceeded their application pot-life.

#### 4.17.1.11 Bubbles or Bubbling

**Description:** Bubbles within a paint film appear as small raised blisters and may be intact or broken to leave a crater. They are found in excessively thick paint films, especially if spray applied, and also with roller application. This defect should not be confused with blistering.



**Probable causes:**

Trapped air/solvent within the coating, which is not released before the surface dries. They are also associated with factory-applied coatings where application is by dipping, electrodeposition, or roller coating.

#### 4.17.1.12 Chalking

**Description:** A friable, powdery layer on the surface of a paint film, often associated with a change of color or fading. Chalking rates vary with pigment concentration and choice of binder, and are a known characteristic of certain paints for example, amine- or amide-cured epoxy paints.



**Probable causes:**

The deterioration of the paint binder on exposure to weathering and/or UV light, leaving a powdery layer of underbound pigment at the surface.

#### 4.17.1.13 Checking (also see [Cracking](#))

**Description:** Fine cracks that do not penetrate to the substrate. Some checking can be so minute that it is impossible to see without magnification.



Probable causes: Typically, a formulation and/or a specification problem where the paint has limited flexibility. Surface stresses are developed, which cause the surface of the paint film to become brittle and crack.

#### **4.17.1.14 Cheesiness (Soft Coating)**

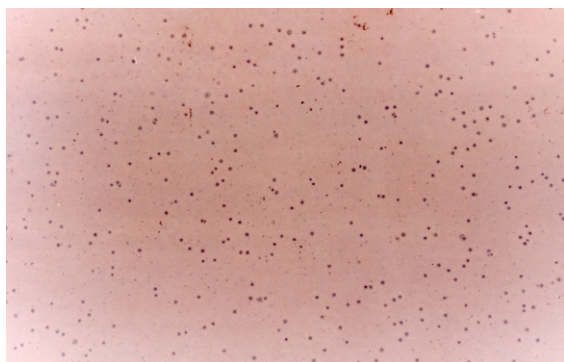
Description: The coating remains soft, even after a prolonged drying time.



Probable causes: Wrong mixing ratio for two-pack paints, too low a drying/curing temperature, or excessive solvent retained within the coating.

#### **4.17.1.15 Cissing (also Referred to as Crawling)**

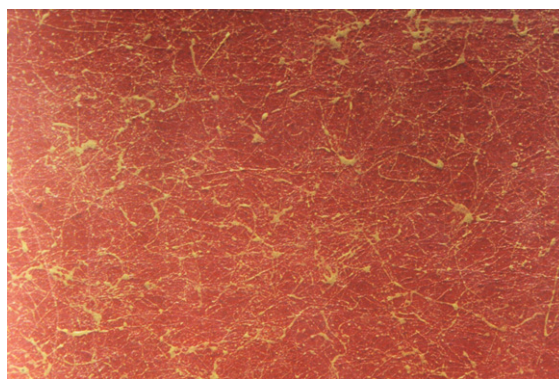
Description: Surface breaks in a wet paint film, where the paint has receded to expose the underlying substrate, because the paint is unable to wet-out the substrate. The individual areas involved can be very large.



Probable causes: Surface contamination by either moisture or foreign matter such as oil, grease, silicone, etc. and is also known to happen when incorrect solvent blends have been used.

#### **4.17.1.16 Cobwebbing**

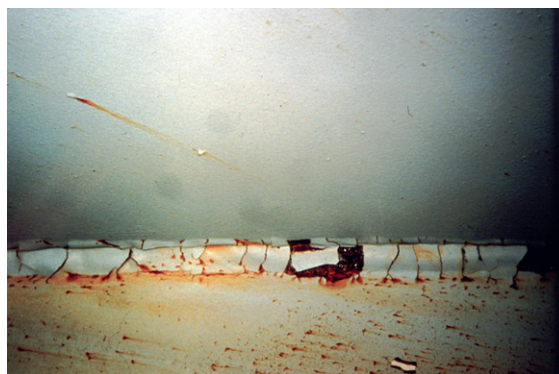
Description: The production of fine filaments instead of normal, atomized particles when some solutions of high-molecular weight polymers are sprayed.



Probable causes: Too high a viscosity with some types of polymer solutions.

#### **4.17.1.17 Cracking (also see [Alligatoring](#) and [Checking](#))**

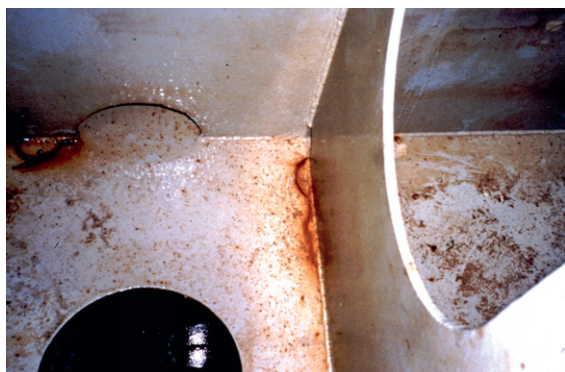
Description: Paint coatings with visible cracks, which generally penetrate to the substrate. Cracking comes in several forms and ranges from minor cracking to severe cracking.





Probable causes:

Cracking is generally related to internal stress within the body of the coating. Factors involved in cracking are formulation, high film thickness, thermal cycling, substrate geometry, substrate movement, ageing, absorption/desorption of water or chemicals, and inadequate surface profile. One or more contributory factors exacerbates the internal stress in the coating.



#### 4.17.1.19 Crowsfooting (also see [Wrinkling](#))

Description: The development of small wrinkles in the paint film, which occur in a pattern resembling that of a crow's foot.

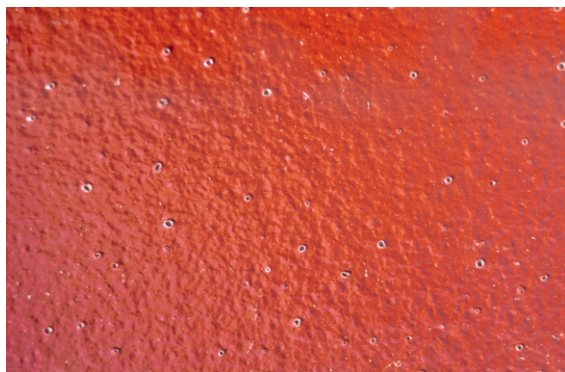


Probable causes:

Usually due to the surface drying rapidly to form a skin, which then wrinkles as the solvent slowly evaporates from the soft, underlying paint layer.

#### 4.17.1.18 Cratering

Description: The formation of small bowl-shaped depressions in the paint film, which are not to be confused with cissing.



Probable causes:

Trapped air bubbles that have burst to leave small craters as the coating dries and the coating has had insufficient time to flow out as a uniform film.

#### 4.17.1.20 Delamination (also see [Adhesion Failure](#) and [Flaking](#))

Description: Loss of adhesion between coats of paint.



Probable causes:

Provided compatible paint materials have been used, delamination defects are generally related to contamination between coats, including amine bloom, exceeding overcoat times, or application to a glossy surface.



**4.17.1.21 Dryspray (also see [Overspray](#))**

**Description:** Rough and uneven finish to the surface of the paint film where the particles are insufficiently fluid to flow together and are often poorly adhered.



**Probable causes:** Incorrect spray application, for example, gun distance. Also associated with fast drying products and too high an application temperature.

**4.17.1.22 Efflorescence**

**Description:** The formation of a white (powdery) substance on the substrate of concrete, brick, masonry, and plaster, or on the surface of the paint. The efflorescence, which comes from the migration of salts, can lift the paint from the substrate where impermeable films are involved.



**Probable causes:** Soluble salts within the substrate. Moisture brings the salts to the surface of the substrate, resulting

in coating adhesion failure, or they deposit on the coated surface where more porous films are involved.

**4.17.1.23 Erosion**

**Description:** Selective removal of paint films from areas of high spots.



**Probable causes:** The wearing away of the paint film by various elements such as rain, snow, wind, sand, etc. and found to be more prominent on brush applied coatings because of the uneven finish.

**4.17.1.24 Fading (also see [Bleaching](#))**

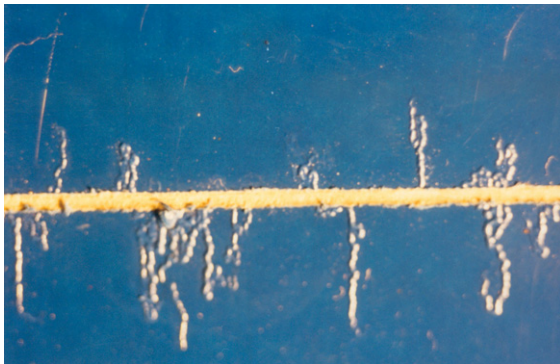
**Description:** Gradual decrease in the color of the paint when exposed to sunlight/weather, which tends to occur more rapidly in the presence of moisture and may be accompanied by a loss of gloss. In some situations, it may resemble chalking but without the powdery surface.



Probable causes: Incorrect pigmentation, the use of organic pigments, atmospheric contamination, or a porous substrate.

#### 4.17.1.25 Filiform (Corrosion)

Description: Random threads of corrosion that develop beneath thin lacquers and other coating films from a growing head or point. Often seen on old 'tin' food cans with thin electroplating, but also seen on painted aluminum and other surfaces.



Probable causes: Contamination on the metallic substrate or damage to the coating, which allows a corrosion cell to develop at the tip and advance under the coating.

#### 4.17.1.26 Flaking (also see [Delamination](#) and [Adhesion Failure](#))

Description: A form of adhesion failure where the paint flakes from the substrate, which is a familiar sight on wood substrates and on galvanizing.

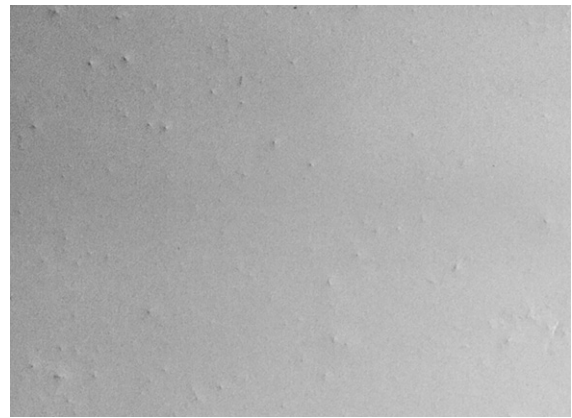


Probable causes: Incorrect paint system used. Either none or incorrect pretreatment

used for certain substrates such as nonferrous or galvanized. May also be attributed to differential expansion and contraction of paint and substrate, for example, wood, and can be the result of the ageing of the paint system.

#### 4.17.1.27 Flocculation

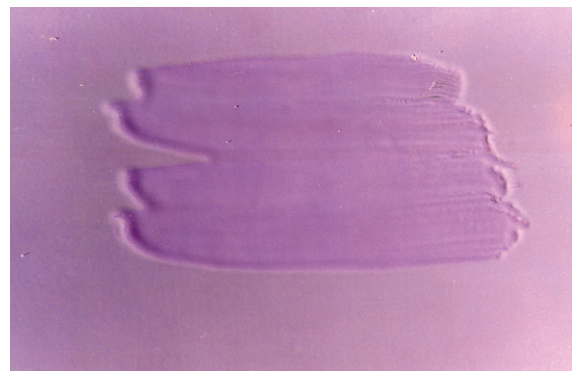
Description: The development of loosely coherent pigment agglomerates in a coating material.



Probable causes: Nonuniform pigment dispersion, which results in the pigments forming agglomerations, arising from the use of unsuitable thinners, inadequate mixing, or inappropriate surfactants.

#### 4.17.1.28 Flooding (also see [Flotation](#))

Description: A defect that appears soon after application due to pigment separation, the visual appearance being a change of color where the affected area dries to a different shade than that of the remainder of the surface.





Probable causes: Pigment separation and settlement.

#### 4.17.1.29 Flotation (also see [Flooding](#))

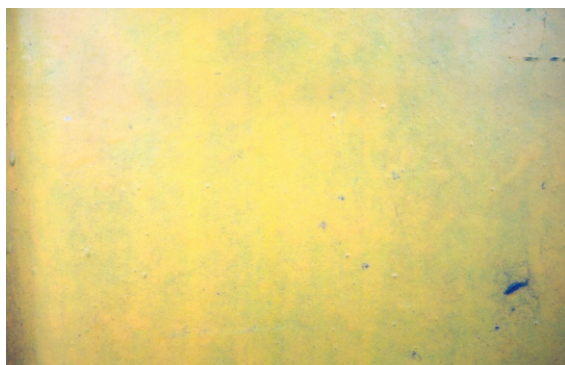
Description: Occurs in colored materials containing mixtures of different pigments and closely resembles flooding, although a mottled or streaky effect is produced when the different pigments separate.



Probable causes: The mottled effect, which is visible to the eye, is caused by the separation of the different colored pigments and may also result from the addition of excessive thinners.

#### 4.17.1.30 Grinning (also see [Grinning Through](#))

Description: The underlying surface is visible through the paint film due to inadequate hiding power of the coating material. It is sometimes called grinning-through and is often seen where dark colors are overcoated with lighter colors.



Probable causes: Low film thickness of topcoat, poor opacity and covering power of topcoat, or strong color of the penultimate coat.

#### 4.17.1.31 Grit Inclusions

Description: Particles of grit and dust embedded within or adhering to the surface of the coating system.



Probable causes: Failure to remove used blast cleaning abrasive from the surface prior to the application of the paint. Contamination of the wet primer or undercoat with abrasive from other blast-cleaning operations, wind blown grit particles adhering to the topcoat, or poor housekeeping.

#### 4.17.1.32 Growth (on the Surface of Paint Film)

Description: Growth and attachments of natural organisms to the surface of finished products, which vary in form, size, and lifespan, for example, algae, mosses, etc.



Probable causes: Generally, natural organisms within moist, wet, or immersed conditions. Growth may continue after attachment.

#### 4.17.1.33 Incorrect Coating System

Description: An unsuitable or incompatible coating system has been used that results in rapid failure.



Probable causes: The use of incompatible or unsuitable coating materials.

#### 4.17.1.34 Impact Damage (Star Cracking)

Description: Cracks that radiate from a point of impact.



Probable causes: Impact damage to a relatively brittle coating, which is often seen on glass fiber reinforced plastics.

#### 4.17.1.35 Lamination or Shelling (of Cast Iron)

Description: The photograph shows flaking or shelling of sections of cast iron

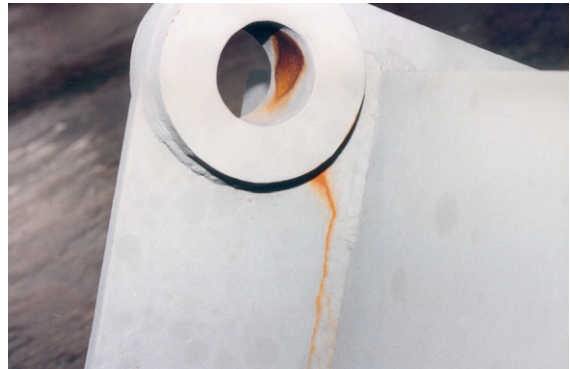
from the surface that has been overpainted, which has led to subsequent rust staining.



Probable causes: Failure to remove or treat delaminated sections prior to the application of the coating system.

#### 4.17.1.36 Misses/Skips/Holidays

Description: Exposed areas of substrate or previous coat when the intention was to coat the entire area. Could be confined to a single coat in a multi-coat paint system.

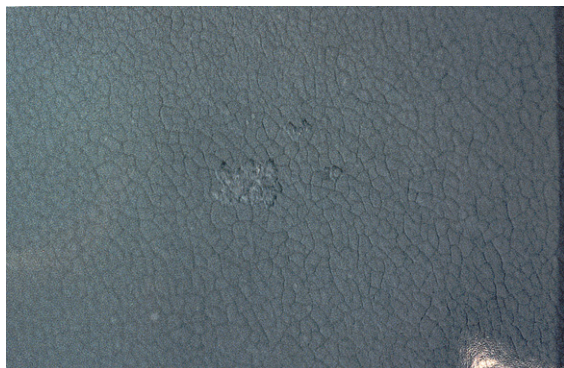


Probable causes: Poor application techniques or a lack of quality control, or both.

#### 4.17.1.37 Mud Cracking

Description: The dried paint film has the appearance of a dried-out mud bath where the cracks can vary in size and amount, but form a network of cracks.





**Probable causes:** Generally, overapplication of heavily pigmented primers such as inorganic zinc silicates or water-based coatings, although it can occur with other systems that are thickly applied.

#### **4.17.1.38 Orange Peel (also Known as Pock-Marking)**

**Description:** The uniform pockmarked appearance, in particular, of a sprayed paint film, in which the surface of the paint film resembles the skin of an orange.



**Probable causes:** Failure of the paint film to flow out. Usually caused by poor application techniques or by incorrect solvent blend.

#### **4.17.1.39 Overspray (also see [Dry spray](#))**

**Description:** Small particles of paint adhering to the surface of the previous dry

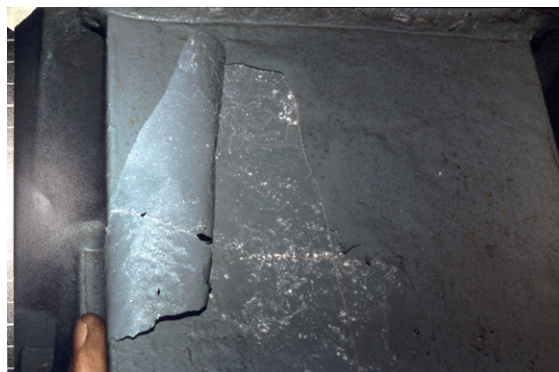
coat, generally adjacent to the area being sprayed, and often appears as a pebbly surface, similar to dry spray.



**Probable causes:** Particles of wet paint falling outside of the spray pattern, too rapid a solvent evaporation, or spray application under windy conditions.

#### **4.17.1.40 Peeling (also see [Flaking](#))**

**Description:** Similar to flaking, although peeling tends to involve soft and pliable coatings that can be pulled away from, or spontaneously flake away from the substrate or from between coats because of loss of adhesion.



**Probable causes:** Peeling is due to a reduction in bond strength of the paint film because of inadequate surface preparation, contamination, or incompatibility of coats.



#### 4.17.1.41 Pinholes

**Description:** The formation of minute holes in the wet paint film during application and drying due to air or gas bubbles that burst giving rise to small craters or holes, which fail to coalesce before the film dries.



**Probable causes:** Solvent or air entrapment within a paint film, which is a common problem when coating porous substrates such as zinc-filled primers, zinc silicates, and metal-sprayed coatings. Pinholes can also be caused by incorrect spray application or incorrect solvent blend.

#### 4.17.1.42 Rain Damage – Water Spotting

**Description:** Craters and water marks on the surface of the paint film, caused by rain or heavy condensation.



**Probable causes:** Rain falling on a freshly painted surface causes craters and/or water marks to form on the surface before it has hardened sufficiently.

#### 4.17.1.43 Rippled Coating

**Description:** A rippled effect on the surface of the paint.



**Probable causes:** Strong wind blowing across the surface of wet paint causes it to ripple and this occurs on the underside; the ripples can hang down in the form of small stalactites. Can also be caused by poor application techniques.

#### 4.17.1.44 Runs or Sags (also Described as Curtains or Wrinkles)

**Description:** The downward movement of paint that appears soon after application to vertical surfaces because of excessive paint application and appears as tears, or in severe situations, it may be described as curtains.



**Probable causes:** Overapplication of paint, addition of excessive thinners, lack of or wrong curing agent, and in extreme circumstances, could be a formulation problem.

**4.17.1.45 Rust Rashing (to Thermal Spray Coating)**

**Description:** Spots of rust develop within the pores of sprayed metal coating, similar to rust spotting of a paint film.



**Probable causes:** A phenomenon that can develop on aluminum thermal-sprayed coatings soon after application when moisture is absorbed into the metal coating and reacts with the ferrous substrate. Early sealing with an appropriate coating prevents such events.

**4.17.1.46 Rust Spotting (also Referred to as Rash Rusting)**

**Description:** Fine spots of rust that appear on a paint film, usually a thin primer coat, which frequently starts as localized spotting, but rapidly spreads over the surface.



**Probable causes:** Where the rust spotting emanates from the substrate, low film

thickness, pinholes, and defects in the steel such as untreated laminations, or too high a surface profile causing penetration of peaks through a paint film are probable causes. Where the rust spotting does not penetrate to the substrate, it is probably from the metallic contamination of a coated surface by ferrous grinding debris.

**4.17.1.47 Rust Staining**

**Description:** A red/brown staining on the surface of the paint.

**Probable causes:** Water run-off from a rusty surface adjacent to a soundly coated surface. Rust staining occurs when the rust is wetted-out and contaminated water runs over and discolors other items or locations. It is usually more of an eyesore than a defect where the coating itself may not be defective, only stained.





#### 4.17.1.48 Saponification

**Description:** The coating appears to be soft and sticky, and can occur as sporadic isolated spots or as an overall effect.



**Probable causes:** Chemical breakdown of the binder, for example in alkyd and oleo resinous paints by reaction with alkali. Commonly seen when these types of paint are used on concrete or cement render.

#### 4.17.1.49 Settlement

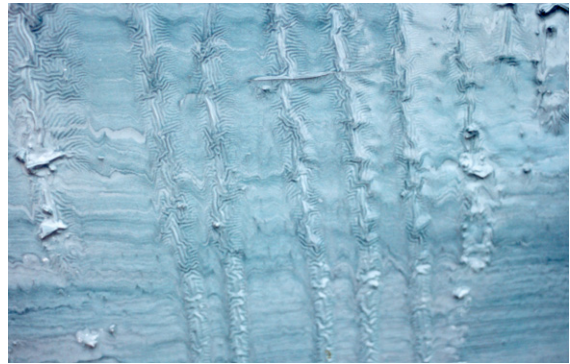
**Description:** A term used to describe the settlement of pigment/solid in a liquid prior to application, occurring during paint storage. Settlement, which occurs after mixing and during application, can result in a variation in color in different areas.



**Probable causes:** Old stock, heavily pigmented paint, wrong formulation, or contamination of product. Can be a problem with zinc-rich primers.

#### 4.17.1.50 Solvent Lifting (also see [Wrinkling](#))

**Description:** Eruption of the surface of the paint film by wrinkling and blistering, which leads to a weak surface and ultimate coating breakdown.



**Probable causes:** Incompatible paint system used, topcoats with a strong solvent blend can attack underlying coatings with a weaker solvent blend, or overcoating before the previous coat has adequately hardened.

#### 4.17.1.51 Solvent Popping

**Description:** Solvent bubbles on the surface of the paint film soon after application.



**Probable causes:** Incorrect solvent blends, porous surfaces, or wrong environmental conditions.

#### 4.17.1.52 Tackiness

**Description:** Soft surface film of the applied coatings. Although, beyond the

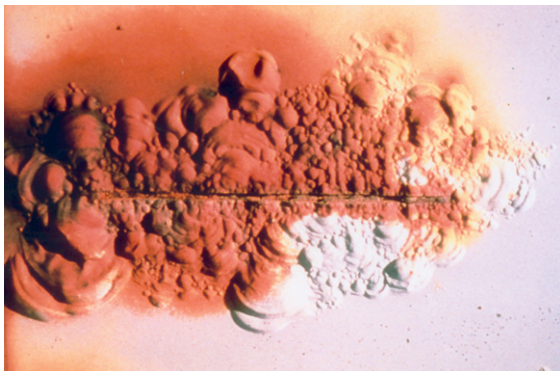
wet and liquid stage, the paint film remains as a tacky and soft surface, sometimes only apparent on touching.

Probable causes:

There are various reasons why paint will remain tacky, including overthickness, addition of excessive thinners, incorrect, insufficient, or lack of curing agent, low drying/curing temperature, or the use of coating beyond its shelf life.

#### 4.17.1.53 Undercutting

**Description:** Corrosion beneath a paint film. Corrosion travels beneath the paint film and lifts the paint from the substrate, and in severe cases, can show as flaking, cracks, and exposed rust.

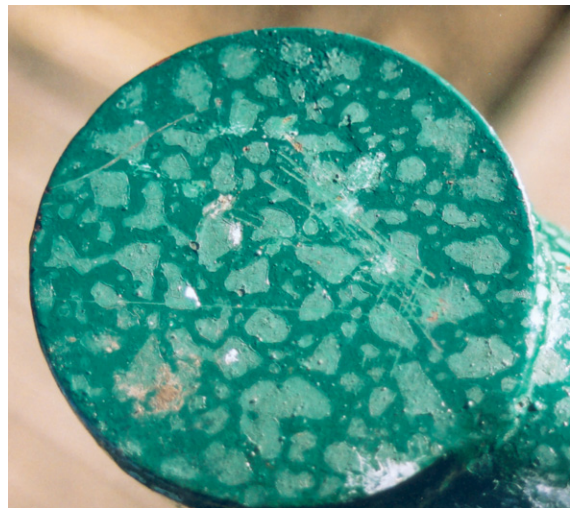


Probable causes:

The application of paint to a corroded substrate and/or rust creep from areas of mechanical damage and/or missing primer coats. Can be found in areas of poor design or access where inadequate preparation and coating thickness were applied and could also be due to a lack of maintenance.

#### 4.17.1.54 Water Spotting (also see [Rain Spotting](#))

**Description:** The spotty appearance of the paint film caused by drops of water on the surface, which remains after the water has evaporated. The effect may or may not be permanent.

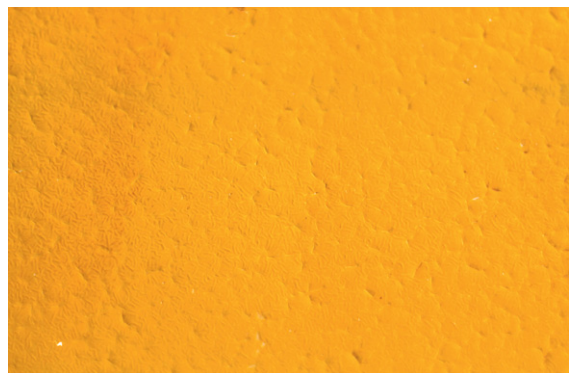


Probable causes:

Rain drops falling on to a wet paint film, leaving permanent marks, or falling on a freshly dried but hard surface where after the water has evaporated, marks may be seen, which can be rubbed off.

#### 4.17.1.55 Wrinkling/Rivelling (also see [Crowsfooting](#))

**Description:** The development of wrinkling in the paint film during drying, appearing as wrinkling, swelling, and blistering of the coating.

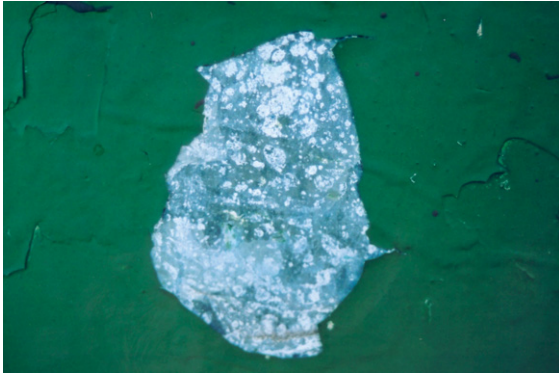


Probable causes:

Usually due to the initial formation of a surface skin with solvent-based paints and related to shrinkage stress as the lower area of the film cures after the top surface. Can arise from overcoating before the previous coat has adequately hardened and swelling of the coating from reaction with solvent.

#### 4.17.1.56 Zinc Carbonates

**Description:** The loss of adhesion to galvanized surfaces and blistering of paint on a galvanized surface.



**Probable causes:**

White rust or carbonates on the surface of galvanizing prior to the application of the paint coating. Corrosion of zinc under the paint surface.

For a full and comprehensive range of definitions, see BS EN ISO 4618: Paints and Varnishes.

Terms and definitions for coating material, general terms, and BS 2015 glossary of paint and related terms.

#### Reference

Fitz's Atlas of Coating Defects. Fitzsimons, Weatherhead, and Morgan ISBN 0 9513940 2 9.



## 4.18 Principles of Cathodic Protection

V. Ashworth

This article is a revision of the Third Edition article 10.1 by V. Ashworth, volume 2, pp 10:3–10:28, © 2010 Elsevier B.V.

4.18.1	Historical Background	2747
4.18.2	Electrochemical Principles	2748
4.18.2.1	Aqueous Corrosion	2748
4.18.2.2	Cathodic Protection	2748
4.18.2.3	Oxygen Reduction	2749
4.18.2.4	Hydrogen Evolution	2750
4.18.3	Methods of Applying Cathodic Protection	2751
4.18.3.1	Impressed Current Method	2751
4.18.3.2	Sacrificial Anodes	2752
4.18.4	Proof of Protection	2753
4.18.4.1	Steel	2753
4.18.4.2	Other Metals	2755
4.18.4.3	Steel in Concrete	2755
4.18.4.4	Potential Measurements	2756
4.18.5	Current Requirements	2757
4.18.6	Coatings and Cathodic Protection	2758
4.18.7	Calcareous Deposit	2759
4.18.8	Potential Attenuation in Impressed-Current Systems	2759
4.18.9	Summary	2761
References		2762

### Abbreviations

**AC** Alternating current  
**BS** British Standard  
**DC** Direct current  
**emf** Electromotive force  
**EN** European Norm  
**NACE** National Association of Corrosion Engineers  
**SRB** Sulfate-reducing bacteria

***IR*** Ohmic drop (equivalent to a voltage)

***R*** Resistance

***η*** Overpotential

### Symbols

***E*** Potential  
***E*<sup>°</sup>** Equilibrium potential  
***E*<sub>a</sub>** Anodic potential  
***E*<sub>c</sub>** Cathodic potential  
***E*<sub>corr</sub>** Corrosion potential  
***I*** Current  
***I*<sub>a</sub>** Anodic current  
***I*<sub>c</sub>** Cathodic current  
***I*<sub>corr</sub>** Corrosion current  
***I*<sub>lim</sub>** Limiting current

### 4.18.1 Historical Background

In recent years, it has been regarded as somewhat passé to refer to Sir Humphry Davy in a text on cathodic protection. However, his role in the application of cathodic protection should not be ignored. In 1824, Davy presented a series of papers to the Royal Society in London,<sup>1</sup> in which he described how zinc and iron anodes could be used to prevent the corrosion of copper sheathing on the wooden hulls of British naval vessels. His paper shows a considerable intuitive awareness of what are now accepted as the principles of cathodic protection. Several practical tests were made on vessels in harbor and on sea-going ships, including the effect of various current densities on the level of protection of the copper. Davy also considered the use of an impressed current

device based on a battery, but did not consider the method to be practicable.

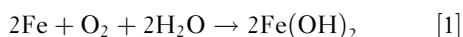
The first ‘full-hull’ installation on a vessel in service was applied to the frigate HMS Samarang in 1824. Four groups of cast iron anodes were fitted, and virtually perfect protection of the copper was achieved. So effective was the system that the prevention of corrosion of the copper resulted in the loss of the copper ions required to act as a toxicide for marine growth, leading to increased marine fouling of the hull. Since this led to some loss of performance from the vessel, interest in cathodic protection waned. The beneficial action of the copper ions in preventing fouling was judged to be more important than preventing deterioration of the sheathing. Cathodic protection was therefore neglected for 100 years, after which it began to be used successfully by oil companies in the United States to protect underground pipelines.<sup>2</sup>

It is interesting that the first large-scale application of cathodic protection by Davy was directed at protecting copper rather than steel. It is also a measure of Davy’s grasp of the topic that he was able to consider the use of two techniques of cathodic protection, namely sacrificial anodes and impressed current, and two types of sacrificial anode, namely zinc and cast iron.

## 4.18.2 Electrochemical Principles

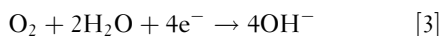
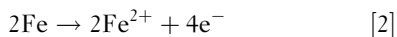
### 4.18.2.1 Aqueous Corrosion

The aqueous corrosion of iron under conditions of air access can be written as



The product, ferrous hydroxide, is commonly further oxidized to magnetite ( $\text{Fe}_3\text{O}_4$ ) or a hydrated ferric oxide ( $\text{FeOOH}$ ), that is, rust.

It is convenient to consider separately the metallic and nonmetallic reactions in eqn [1]:



To balance eqns [2] and [3] in terms of electrical charge, it has been necessary to add four electrons to the right-hand side of eqn [2] and to the left-hand side of eqn [3]. However, simple addition and rationalization of eqns [2] and [3] yield eqn [1].

We conclude that corrosion is a chemical reaction [1] occurring by an electrochemical mechanism (eqns [2] and [3]), that is, by a process involving electrical and chemical species. Figure 1 is a

schematic representation of aqueous corrosion occurring at a metal surface.

Equation [2], which involves consumption of the metal and release of electrons, is termed an anodic reaction. Equation [3], which represents consumption of electrons and dissolved species in the environment, is termed a cathodic reaction. Whenever spontaneous corrosion reactions occur, all the electrons released in the anodic reaction are consumed in the cathodic reaction; no excess or deficiency is found. Moreover, the metal normally takes up a more or less uniform electrode potential, often called the corrosion or mixed potential ( $E_{\text{corr}}$ ).

### 4.18.2.2 Cathodic Protection

It is possible to envisage what might happen if an electrical intervention was made in the corrosion reaction by considering the impact on the anodic and cathodic reactions. For example, if electrons were withdrawn from the metal surface, it might be anticipated that reaction [2] would speed up (to replace the lost electrons) and reaction [3] would slow down, because of the existing shortfall of electrons. It follows that the rate of metal consumption would increase.

By contrast, if additional electrons were introduced at the metal surface, the cathodic reaction would speed up (to consume the electrons) and the anodic reaction would be inhibited; metal dissolution would be slowed down. This is the basis of cathodic protection.

Figure 2 shows the effect on the corrosion reaction shown in Figure 1 of providing a limited supply of electrons to the surface. The rate of dissolution

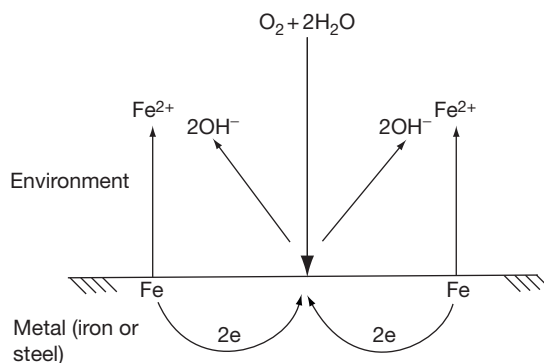


**Figure 1** Schematic illustration of the corrosion of steel in an aerated environment. Note that the electrons released in the anodic reaction are consumed quantitatively in the cathodic reaction, and that the anodic and cathodic products may react to produce  $\text{Fe}(\text{OH})_2$ .

slows down because the external source rather than an iron atom provides two of the electrons. **Figure 3** shows the effect of a greater electron supply; corrosion ceases since the external source provides all the requisite electrons. It should be apparent that there is no reason why further electrons could not be supplied, when even more hydroxyl ( $\text{OH}^-$ ) ion would be produced, but without the possibility of a concomitant reduction in the rate of iron dissolution. Clearly, this would be a wasteful exercise.

The corrosion reaction may also be represented on a polarization diagram (**Figure 4**). The diagram

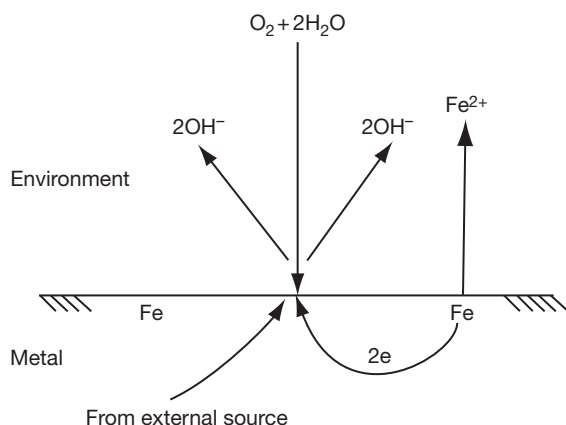


**Figure 2** Schematic illustration of partial cathodic protection of steel in an aerated environment. Note that one of the anodic reactions shown in **Figure 1** has been annihilated by providing two electrons from an external source; an excess of  $\text{OH}^-$  ions over  $\text{Fe}^{2+}$  now exists at the surface.

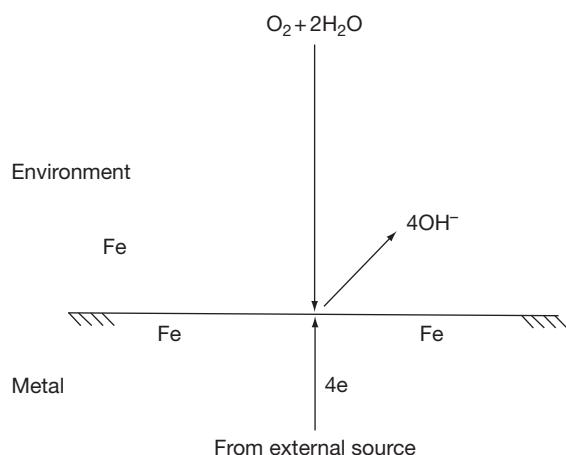


**Figure 3** Schematic illustration of full cathodic protection of steel in an aerated environment. Note that both anodic reactions shown in **Figure 1** have now been annihilated, and there is an accumulation of  $\text{OH}^-$  at the surface.

shows how the rates of the anodic and cathodic reactions (both expressed in terms of current flow  $I$ ) vary with electrode potential  $E$ . Thus, at  $E_a$ , the net rate of the anodic reaction is zero and it increases as the potential becomes more positive. At  $E_c$ , the net rate of the cathodic reaction is zero and it increases as the potential becomes more negative. (To be able to represent the anodic and cathodic reaction rates on the same axis, the modulus of the current has been drawn.) The two reaction rates are electrically equivalent at  $E_{\text{corr}}$ , the corrosion potential, and the corresponding current  $I_{\text{corr}}$  is an electrical representation of the rate of the anodic and cathodic reactions at that potential, that is, the spontaneous corrosion rate of the metal. That is, at  $E_{\text{corr}}$  the polarization diagram represents the situation referred to above; namely, that when spontaneous corrosion occurs, the rate of electron release equals the rate of electron consumption, and there is no net current flow although metal is consumed, and meanwhile the metal exerts a single electrode potential.

To hold the metal at any potential other than  $E_{\text{corr}}$  requires that electrons be supplied to, or be withdrawn from, the metal surface. For example, at  $E'$ , the cathodic reaction rate  $I'_c$  exceeds the anodic reaction rate  $I'_a$ , and the latter does not provide sufficient electrons to satisfy the former. If the metal is to be maintained at  $E'$ , the shortfall of electrons given by  $(|I'_c| - I'_a)$  must be supplied from an external source. This externally supplied current serves to reduce the metal dissolution rate from  $I_{\text{corr}}$  to  $I'_a$ .

At  $E_a$ , the net anodic reaction rate is zero (there is no metal dissolution) and a cathodic current equal to  $I''_c$  must be available from the external source to maintain the metal at this potential. It may also be apparent from **Figure 4** that, if the potential is maintained below  $E_a$ , the metal dissolution rate remains zero ( $I_a = 0$ ), but a cathodic current greater than  $I''_c$  must be supplied; more current is supplied without achieving a benefit in terms of metal loss. There will, however, be a higher interfacial hydroxyl ion concentration.

#### 4.18.2.3 Oxygen Reduction

In illustrating the corrosion reaction in eqn [1], the oxygen reduction reaction [3] has been taken as the cathodic process. Moreover, in **Figures 1–4**, oxygen reduction has been assumed. While there is a range of cathodic reactions that can provoke the corrosion of a metal (since to be a cathodic reactant, any particular species must simply act as an oxidizing

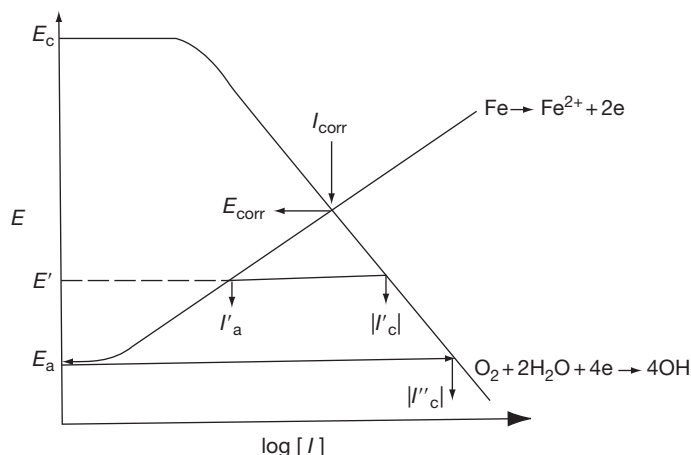


**Figure 4** Polarization diagram representing corrosion and cathodic protection. A corroding metal takes up the potential  $E_{\text{corr}}$  spontaneously and corrodes at a rate given by  $I_{\text{corr}}$ . If the potential is to be lowered to  $E'$ , a current equal to  $(|I'_c| - I'_a)$  must be supplied from an external source; the metal will then dissolve at a rate equal to  $I'_a$ .

agent to the metal), the most common cathodic reactant present in natural environments is oxygen. It is for this reason that the oxygen reduction reaction has been emphasized here.

When corrosion occurs, if the cathodic reactant is in plentiful supply, it can be shown both theoretically and practically that the cathodic kinetics are semilogarithmic, as shown in **Figure 4**. The rate of the cathodic reaction is governed by the rate at which electrical charge can be transferred at the metal surface. Such a process responds to changes in electrode potential, giving rise to the semilogarithmic behavior.

Because oxygen is not very soluble in aqueous solutions ( $\sim 10$  ppm in cool seawater, for example), it is not freely available at the metal surface. As a result, it is often easier to transfer electrical charge at the surface than for oxygen to reach the surface to take part in the charge transfer reaction. The cathodic reaction rate is then controlled by the rate of arrival of oxygen at the surface. This is often referred to as mass transfer control. Since oxygen is an uncharged species, its rate of arrival is unaffected by the prevailing electrical field and responds only to the local oxygen concentration gradient. If the cathodic reaction is driven so fast that the interfacial oxygen concentration is reduced to zero (i.e., the oxygen is consumed as soon as it reaches the surface), the oxygen concentration gradient to the surface reaches a maximum and the reaction rate attains a limiting value. Only an increase in oxygen concentration or an increase in flow velocity will permit an increase in the limiting value. The cathodic kinetics under mass transfer control will be as shown in **Figure 5**.

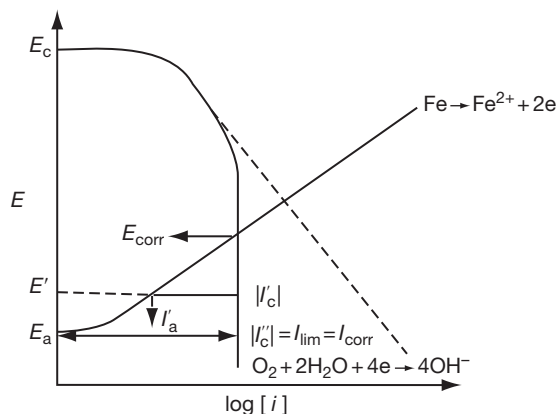
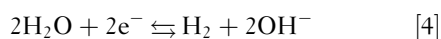


**Figure 5** Polarization diagram representing corrosion and cathodic protection when the cathodic process is under mass transfer control. The values of  $E_{\text{corr}}$  and  $I_{\text{corr}}$  are lower than when there is no mass transfer restriction, that is, when the cathodic kinetics follows the dotted line.

**Figure 5** demonstrates that, even when semilogarithmic cathodic kinetics is not observed, partial or total cathodic protection is possible. Indeed, **Figure 5** shows that the corrosion rate approximates to the limiting current for oxygen reduction ( $I_{\text{lim}}$ ), and the current required for protection is substantially lower than when semilogarithmic cathodic behavior prevails.

#### 4.18.2.4 Hydrogen Evolution

In principle, it is possible for water to act as a cathodic reactant with the formation of molecular hydrogen:



Indeed, in neutral solutions, the corrosion of iron with concomitant hydrogen evolution deriving from the reduction of water is thermodynamically feasible. In practice, this cathodic reaction is barely significant because the reduction of any oxygen present is both thermodynamically favored and kinetically easier. In the absence of oxygen, the hydrogen evolution reaction at the corrosion potential of iron is so sluggish that the corrosion rate of the iron is vanishingly small.

Nevertheless, hydrogen evolution is important in considering the cathodic protection of steel. Although hydrogen evolution takes little part in the corrosion of steel in aerated neutral solutions (see **Figure 6**), as the potential is lowered to achieve cathodic protection, it plays a larger, and eventually dominant, role in determining the total current demand. This too is demonstrated in **Figure 6** where, it must be remembered, the current supplied from the external source at any potential must be sufficient to sustain the total cathodic reaction, that is, both oxygen reduction and hydrogen evolution reactions at that potential. It will be seen that to lower the potential much below  $E_a$  entails a substantial increase in current and significantly more hydrogen evolution.

### 4.18.3 Methods of Applying Cathodic Protection

There are two principal methods of applying cathodic protection, namely the impressed current technique and the use of sacrificial anodes.

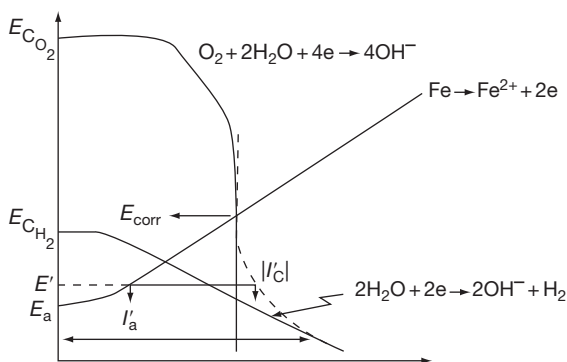


**Figure 6** Polarization diagram showing the limited role hydrogen evolution plays at the corrosion potential of steel in aerated neutral solution, the larger role in determining cathodic protection currents, and the dominant role in contributing to current requirements at very negative potentials. The dotted line shows the total cathodic current due to oxygen reduction and hydrogen evolution.

The former includes the structure as part of a driven electrochemical cell, and the latter includes the structure as part of a spontaneous galvanic cell.

#### 4.18.3.1 Impressed Current Method

**Figure 7** illustrates the use of an external power supply to provide the cathodic polarization of the structure. The circuit comprises the power source, an auxiliary or impressed current electrode, the corrosive solution, and the structure to be protected. The power source drives a positive current from the impressed current electrode through the corrosive solution and onto the structure. The structure is thereby cathodically polarized (its potential is lowered), and the positive current returns through the circuit to the power supply. Thus, to achieve cathodic protection, the impressed current electrode and the structure must be in both electrolytic and electronic contact.

The power supply is usually a transformer/rectifier that converts AC power to DC. Typically, the DC output will be in the range 15–100 V and 5–100 A, although 200 V/200 A units are not unknown. Thus, fairly substantial driving voltages and currents are available. Where mains power is not available, diesel or gas engines, solar panels, or thermoelectric generators have all been used to provide suitable DC.

It will be seen that the impressed current electrode discharges positive current, that is, it acts as an anode in the cell. There are three generic types of anode used in cathodic protection, namely consumable, nonconsumable, and semiconsumable. The consumable electrodes undergo an anodic reaction that involves their consumption. Thus, an anode made of scrap iron produces positive current by the reaction

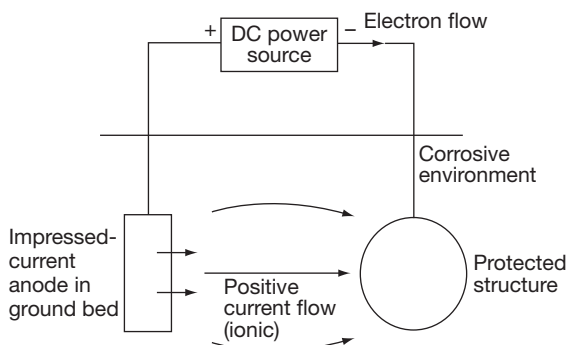
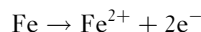
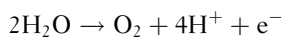


**Figure 7** Schematic diagram of cathodic protection using the impressed-current technique.

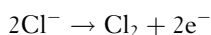


The ferrous ions then enter the environment as a positive current carrier (although in practice the current will be carried in the environment by aqueous ions such as  $\text{Na}^+$  and  $\text{Cl}^-$ ). Since the dissolving anode must obey Faraday's law, it follows that the wasting of the anode will be proportional to the total current delivered. In practice, the loss for an iron anode is approximately  $9 \text{ kg A}^{-1} \text{ year}^{-1}$ . Thus, consumable anodes must be replaced at intervals, or be of sufficient size to remain as a current source for the design life of the protected structure. This poses some problems in design because, as the anode dissolves, the resistance it presents to the circuit increases. More important, it is difficult to ensure continuous electrical connection to the dissolving anode.

Nonconsumable anodes sustain an anodic reaction that decomposes the aqueous environment rather than dissolves the anode metal. In aqueous solutions the reaction may be



or in the presence of chloride ions



Anodes made from platinized titanium or niobium belong to this category.

Because these anodes are not consumed faradaically, they should not, in principle, require replacement during the life of the structure. However, to remain intact, they must be chemically resistant to their anodic products (acid and chlorine) and, where the products are gaseous, conditions must be produced that allow the gas to escape and not interfere with anode operation. This is particularly true of the platinized electrodes because they can operate at high current density ( $>100 \text{ A m}^{-2}$ ) without detriment, but will then produce high levels of acidity ( $\text{pH} < 2$ ) and large volumes of gas. Ground-bed design (the way in which the anode is installed) is therefore crucial.

Although the anodes are described as non-consumable, they do suffer some loss of the thin ( $\sim 2.5\text{--}10 \text{ mg m}^{-3}$ ) platinized coating. This loss, which unfortunately has become known as the wear rate although there is no question of the loss being due to mechanical wear, is usually small, related to the total current passed, and increased if the applied current has an AC component. Typically, values for the loss rate are  $8 \text{ mg A}^{-1} \text{ year}^{-1}$  for platinized titanium, which may be increased 10-fold if an AC component of  $<100 \text{ Hz}$  is present. Negative-going current spikes, such as may be induced by a poorly designed thyristor switching

device, even given otherwise clean DC, can produce a 100-fold increase in the rate of loss.

The semiconsumable electrodes, as the name implies, suffer rather less dissolution than Faraday's law would predict and substantially more than the nonconsumable electrodes. This is because the anodic reaction is shared between oxidizing the anode material (causing consumption) and oxidizing the environment (with no concomitant loss of metal). Electrodes made from silicon-iron, chromium-silicon-iron and graphite fall into this category.

**Table 1** gives a brief summary of the behavior of some impressed current anodes, and protection by impressed current is discussed in more detail elsewhere.

#### 4.18.3.2 Sacrificial Anodes

Using the impressed-current technique, the driving voltage for the protective current comes from a DC power source. The sacrificial anode technique uses the natural potential difference that exists between the structure and a second metal in the same environment to provide the driving voltage. No power source is employed. Moreover, the dissolution of the second metal, that is, the sacrificial anode, provides the source of electrons for cathodic polarization of the structure. Thus, while the impressed-current anode may be more noble or more base than the protected structure because the power source forces it to act as an anode, the sacrificial anode must be spontaneously anodic to the structure, that is, be more negative in the galvanic series for the given environment. Thus, in principle, zinc, aluminum, or magnesium could be used to protect steel, and iron to protect copper. **Figure 8** illustrates the use of a sacrificial anode for cathodic protection.

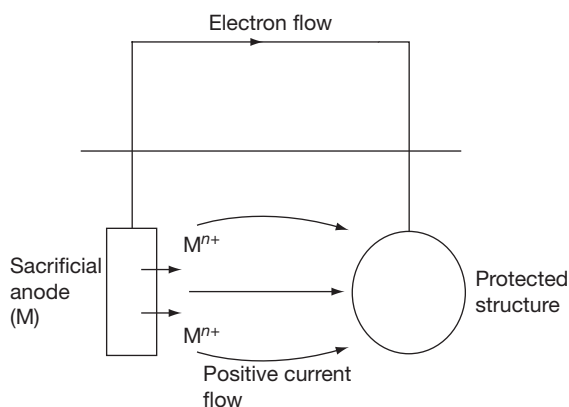
In practice, pure metals are never used as sacrificial anodes. There are a variety of reasons for this, which includes the need for

1. a reliable, reproducible and negative operating potential for the anode;
2. a high and reproducible capacity ( $\text{A h kg}^{-1}$ ) for the anode;
3. uniform dissolution of the anode so that all metal is consumed usefully in providing cathodic protection and not wastefully by mechanical loss;
4. freedom from any loss of activity by the anode due to passivation.

For these reasons, alloying elements appear in all the commercial anodes, and very careful quality control

**Table 1** Impressed-current anode materials

Material	Consumption rate or operating current density	Notes
Consumable:		
Scrap iron	$\sim 9 \text{ kg A}^{-1} \text{ year}^{-1}$	Cheap: suitable for buried or immersed use
Cast iron	$< 9 \text{ kg A}^{-1} \text{ year}^{-1}$	Cheap; buried or immersed use; carbon skeleton reduces consumption
Semiconsumable:		
Silicon cast iron (Fe-14Si-(3 Mo)	$5\text{--}50 \text{ A m}^{-2}$ (in freshwater or soil)	Buried or immersed use; consumption ( $< 1 \text{ kg A}^{-1} \text{ year}^{-1}$ ); Mo reduces consumption in seawater
Graphite	$2.5\text{--}10 \text{ A m}^{-2}$	Consumption rate very much less than steel or cast iron ( $< 1 \text{ kg A}^{-1} \text{ year}^{-1}$ ); chloride ions reduce consumption
Nonconsumable:		
Lead alloys:		
1. Pb-6Sb-1Ag	$< 50\text{--}200 \text{ A m}^{-2}$ (in seawater)	PbO <sub>2</sub> film restrains consumption
2. Pt-activated	$< 50\text{--}500 \text{ A m}^{-2}$ (in seawater)	PbO <sub>2</sub> film protective
Platinized Ti, Ta, or Nb	$< 1000 \text{ A m}^{-2}$ (consumption)	Discontinuities in Pt coat protected by oxide film on substrate; sensitive ( $< 100 \text{ Hz}$ ) AC ripple in DC or negative current spikes causing electrode consumption; maximum operating potential with Ti substrate: 9 V

**Figure 8** Schematic diagram of cathodic protection using sacrificial anodes. In practice, the anode, which will be mounted on a steel core, can be attached directly to the structure.

is required to keep disadvantageous tramp elements (notably iron and copper) below defined threshold levels. Many anode failures can be attributed to poor production quality control. A guide to minimum quality standards has been produced.<sup>3</sup>

**Table 2** gives electrochemical properties for various generic anode types. It will be apparent that the driving voltages that are available from sacrificial anodes are substantially less than those available from power sources. At best, an anode will produce 1 V to steel, whereas an impressed current power source may produce up to 100 V.

A more detailed treatment of cathodic protection by sacrificial anodes is provided elsewhere in this book.

## 4.18.4 Proof of Protection

### 4.18.4.1 Steel

**Figure 4** demonstrates that the rate of dissolution of iron (or any other metal) decreases as the potential is made more negative. **Figure 6** shows that the current required to reach any given potential below the corrosion potential ( $E_{\text{corr}}$ ) will vary according to the composition of the corrosive solution. Thus **Figure 6** shows that, in the absence of oxygen, the current requirement would be low, but would increase to a value approximating to the limiting current in its presence. Moreover, since the limiting current can be increased by increasing the oxygen concentration or the solution flow rate, the current required for protection will change predictably with change in either of these parameters.<sup>4</sup> It follows that the current required to prevent corrosion completely (i.e., in principle to achieve  $E_a$ ) will vary according to the environment and the environmental dynamics. As a consequence, there is no single current that will assure protection in all cases. Current supplied is not, therefore, an unequivocal indication of the effectiveness of protection.

By contrast, it appears from **Figures 4 and 6** that a potential measurement would be more reliable: specifically, that  $E_a$  (the equilibrium potential for the

**Table 2** Typical sacrificial anode compositions and operating parameters

Alloy	Environment	Operating voltage vs. Ag/AgCl/seawater (V)	Driving voltage <sup>a</sup> (V)	Capacity (Ah/kg)
Al-Zn-Hg	Seawater	-1.0 to -1.05	0.20-0.25	2600-2850
Al-Zn-In	Seawater	-1.0 to -1.10	0.20-0.30	2300-2650
Al-Zn-In	Marine sediments	-0.95 to -1.05	0.15-0.25	1300-2300
Al-Zn-Sn	Seawater	-1.0 to -1.05	0.20-0.25	925-2600
Zn <sup>b</sup>	Seawater	-0.95 to -1.03	0.15-0.23	760-780
Zn <sup>b</sup>	Marine sediments	-0.95 to -1.03	0.15-0.23	750-780
Mg-Al-Zn	Seawater	-1.5	0.7	1230
Mg-Mn	Seawater	-1.7	0.9	1230

It is often important to control impurities and especially Fe, Cu, Ni, and Si, although a controlled Si content is essential to some aluminum alloys.

<sup>a</sup>The driving voltage to bare steel, that is, protection potential of steel-anode operating potential.

<sup>b</sup>US Military Specification.

iron/ferrous-ion electrode given a suitably low ferrous ion concentration) would always represent the achievement of full protection for iron.

Almost without exception, all the accepted criteria for full cathodic protection of iron are based on a potential measurement. The various recommended practices published by the U.S. National Association of Corrosion Engineers (NACE) give six criteria for full protection.<sup>5-11</sup> The current British Standard Code of Practice<sup>12</sup> gives one. These are summarized in **Table 3**. Only the first three are useful; the remaining ones are of dubious value or expressions of pious hope.

The most widely accepted criterion for protection of steel at room temperature (the protection potential) in aerobic conditions is -0.85 V with respect to a Cu/CuSO<sub>4</sub> reference electrode. In anaerobic conditions, -0.95 V (versus Cu/CuSO<sub>4</sub>) is the preferred protection potential because of the possible presence of active sulfate-reducing bacteria (SRB).

Various limitations on the most negative potential that may be imposed during cathodic protection are often quoted for high-strength steels (typically -1.0 V versus Cu/CuSO<sub>4</sub> for steels in the 700-800 MPa tensile strength range). The restriction is to limit the evolution of hydrogen at the structure and thereby prevent hydrogen absorption with the possibility of embrittlement of the steel, possibly leading to fracture. The consequence is that the useful window of potential in which the steel can operate is severely restricted, especially under anaerobic conditions.

It must not be assumed that the protection potential is numerically equal to the equilibrium potential for the iron/ferrous-ion electrode ( $E_a$ ). The standard equilibrium potential ( $E^\circ$ ) for the iron/ferrous-ion is -0.440 V (versus the standard hydrogen electrode).

**Table 3** Cathodic protection criteria: after British Standard Code of Practice<sup>12</sup> and NACE Recommended Practices<sup>5-11</sup>

1.  $\leq -0.85$  V w.r.t Cu/CuSO<sub>4</sub> with current applied but minimizing  $IR$  error
2. Negative shift  $\geq 300$  mV when current applied
3. Positive shift  $\geq 100$  mV when current interrupted
4. More negative than beginning of Tafel segment of cathodic polarisation ( $E - \log i$ ) curve
5. A net protective current in the structure at former anodic points
6. Polarize all cathodic areas to open circuit potential of most active anode areas

If the interfacial ferrous ion concentration when corrosion ceases is approximately  $10^{-6}$  M, then according to the Nernst equation, the equilibrium potential ( $E_a$ ) is given by

$$E_a = E^\circ + \frac{2.303}{2F} RT \log(a_{\text{Fe}^{2+}})$$

where  $a_{\text{Fe}^{2+}}$  is the activity or thermodynamic concentration of the ferrous cation,  $R$  is the gas constant,  $F$  is Faraday's constant, and 2 represents the number of units of charge transferred (i.e., the doubly charged ferrous ion). Thus,  $E_a = -0.62$  V versus the standard hydrogen electrode or -0.93 V versus Cu/CuSO<sub>4</sub>. This is a value substantially more negative than the accepted protection potential (-0.85 V).

A simple calculation based on the solubility product of ferrous hydroxide and assuming an interfacial pH of 9 (due to the alkalization of the cathodic surface by reaction [3]) shows that, according to the Nernst equation, at -0.85 V (versus Cu/CuSO<sub>4</sub>), the ferrous ion concentration then present is sufficient to permit deposition of the hydroxide ion. It appears that the ferrous hydroxide formed may be protective,

and that the practical protection potential ( $-0.85$  V), as opposed to the theoretical protection potential ( $E_a = -0.93$  V), is governed by the thermodynamics of precipitation and not those of dissolution.

It is also worth noting that the exact achievement of the so-called protection potential is not essential to excellent corrosion control. **Figures 4–6** show the anodic kinetics as semilogarithmic in character. Behavior approaching this is observed in practice for steel in many environments. Thus, the first increment of negative potential shift will reduce the anodic dissolution rate substantially. A second equal shift will be 10 times less effective and will require the application of very much more current. A third equal shift will be 10 times less effective again. That is, the dissolution rate decreases asymptotically as the full protection potential is approached; a small shortfall in cathodic polarization is not, therefore, disastrous. By contrast, the current required to achieve the protection potential, and more particularly to exceed it, is often very substantial and may increase exponentially. There may often be good economic reasons for permitting a minor shortfall of polarization.

#### 4.18.4.2 Other Metals

In principle, all metals may be protected by cathodic protection. In practice, it is not always relevant, either because the metals are, to all intents and purposes, naturally immune to corrosion (the noble metals) and often not used as engineering materials or, being base metals, they are well protected by the spontaneous formation of a passive film in aqueous solution (aluminum or a stainless steel, for example).

Copper-base alloys will corrode in aerated conditions. It is, therefore, sometimes appropriate to consider cathodic protection. It becomes particularly relevant when the flow rates are high or when the design of an item causes the copper to be an anode in a galvanic cell (e.g., a copper alloy tube plate in a titanium-tubed heat exchanger). Corrosion can be controlled by polarization to approximately  $-0.6$  V (versus Cu/CuSO<sub>4</sub>) and may be achieved using soft-iron sacrificial anodes.

Some metals are amphoteric: that is, they form simple cations (in acid solutions) and soluble oxyanions (in alkaline solution); only in the mid-pH range is a protective film stable. Since cathodic protection produces alkali at the structure's surface, it is important to restrict the polarization, and thereby the amount of hydroxyl ion produced, in these cases. Thus both lead and aluminum will suffer cathodic

corrosion under cathodic protection if the potential is made excessively electronegative.

Many passive metals suffer pitting attack when aggressive ions (usually chloride) enter the system. It is possible to forestall pitting, or to stop it once started, using cathodic protection. It is not necessary to polarize to the protection potential of the metal; a negative shift of 100 mV from the natural corrosion potential in the environment will often be sufficient. This technique has been applied to various stainless steels and to aluminum.<sup>13</sup> The philosophy is not unlike that applied to rebar in concrete.

Where there is a perceived risk of crevice corrosion, cathodic protection can often be used to prevent its initiation. Once more, a 100-mV cathodic polarization will usually prove sufficient. However, it is doubtful whether cathodic protection can arrest crevice corrosion once started and, despite claims to the contrary, whether it could be effective in arresting stress-corrosion cracking. The problem lies in the fundamental difficulty of forcing cathodic current into an occluded area.

Some recommended protection potentials for other metals are given in **Table 4**.

#### 4.18.4.3 Steel in Concrete

Concrete is a very benign environment for steel so long as its natural pH remains high and no aggressive species enters. The low corrosion rate experienced by the steel is due to the formation of a protective passive film. There are a number of circumstances that allow chloride ions to enter reinforced concrete. When these ions reach the reinforcing bar (rebar), they may cause localized corrosion damage to it, with consequent cracking or even spalling of the concrete. The result is both unsightly and potentially dangerous. Impressed-current cathodic protection has been used to overcome the problem, and significant beneficial effects have been claimed.<sup>14–16</sup>

The proof of protection is more difficult to establish in this case for two reasons. First, the object is to

**Table 4** Recommended protection potentials for other metals<sup>12</sup>

<i>Metal</i>	<i>Protection potential (V vs. Cu/CuSO<sub>4</sub>)</i>
Lead	$-0.6$
Copper-base alloys	$-0.5$ to $-0.65$
Aluminum	
Positive limit	$-0.95$
Negative limit	$-1.2$

restore passivity to the rebar and not to render it virtually immune to corrosion. Second, it is difficult to measure the true electrode potential of rebars under these conditions. This is because the cathodic-protection current flowing through the concrete produces a voltage error in the measurements made (see below). For this reason, it has been found convenient to use a potential decay technique to assess protection rather than a direct potential measurement. Thus, a 100-mV decay of polarization in 24 h once current has been interrupted has been adopted as the criterion for adequate protection.<sup>17</sup> It will be seen that this proposal does not differ substantially from the decay criterion included in **Table 3** and recommended by NACE for assessing the full protection of steel in other environments. Of course, in this case, the cathodic polarization is intended to inhibit pit growth and restore passivity, not to establish effective immunity.

#### 4.18.4.4 Potential Measurements

It is clear that to ensure adequate protection of a structure under cathodic protection, it is necessary to measure its electrode potential. This can be achieved only by using a reference electrode placed in the same environment as the structure and measuring the emf of the cell so formed. Since the electrode potentials of different types of reference electrode vary, it is clear that the measured emf will also vary according to the particular reference electrode used. It follows that the potential measured must always be recorded with respect to the reference electrode deployed, which must always be stated.

The protection potential for a given metal is numerically different according to the reference electrode used. Thus the protection potential for iron in aerobic environments is

- −0.85 V versus Cu/CuSO<sub>4</sub>;
- −0.80 V versus Ag/AgCl/seawater;
- −0.77 V versus Ag/AgCl/1 M KCl;
- −0.84 V versus Ag/AgCl/0.1 M KCl;
- −0.55 V versus standard hydrogen electrode.

It is fundamental that a reference electrode should have a stable and reproducible potential. Not all reference electrodes are suitable for all environments or circumstances. For example, a Cu/CuSO<sub>4</sub> electrode is suitable for use in soil, but should never be used in seawater or on concrete. Contamination of the electrode can occur, which will produce serious changes in the reference potential.

The Ag/AgCl/seawater electrode should be used only in seawater since the electrode is merely

a Ag/AgCl element that provides a known stable reference potential when immersed in clean seawater. Immersion in any other chloride-containing fluid will produce a different reference potential depending on the chloride concentration present in the environment. Only if appropriate allowance is made for the particular chloride content present, will the potentials measured be reliable. Commercial Ag/AgCl electrodes are available in which the element is encapsulated within an environment containing a fixed chloride content. The electrodes are very stable and suitable for short-term use in fluids containing any concentration of chloride or no chloride ions at all. They are not suitable for continuous immersion in fluids in which the chloride concentration of the encapsulation will change with time as a result of chloride leaching (e.g., in distilled water) or chloride ion ingress (e.g., in seawater).

Finally, calomel electrodes (and particularly hydrogen electrodes) are not suitable for field measurements because they are not sufficiently robust. The calomel electrodes are, however, essential for calibrating the field reference electrodes. Saturated KCl calomel electrodes are the most suitable because there is then no doubt about the reference potential of the calibrating electrode. Lack of adequate calibration is a common cause of cathodic protection system mismanagement.

Incorrect potential measurement technique leads to another management problem. If the potential of a freely corroding metal is measured, the values recorded will remain constant wherever the reference electrode is placed in the environment. If the same metal is under cathodic protection, the positioning of the reference electrode is crucial. This is because the cathodic protection current flowing through the corrosive environment produces an electric field gradient as the current  $I$  flows through the environment of resistance  $R$ . Thus, when the reference electrode is placed remote from the metal surface, the measured potential comprises the true electrode potential of the metal and the potential difference in the environment between the metal and the reference electrode due to the electric field. As the reference electrode is moved closer to the metal surface, less of the electric field is included in the measurement and the potential of the metal appears more positive (**Figure 9**). That is, with current flowing, a remote reference electrode ensures measurement of a more negative potential for the metal (it appears better protected than it is), while the closer the reference electrode is placed to the



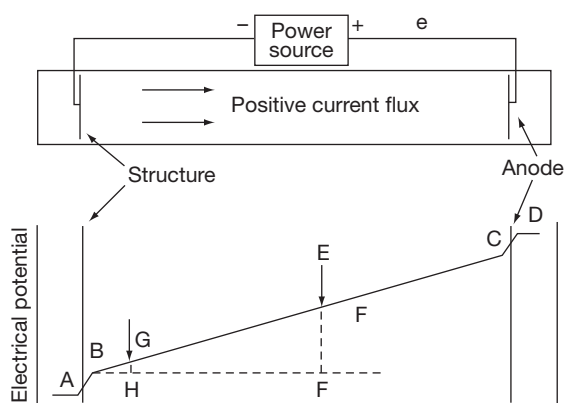


**Figure 9** Diagram illustrating the source of the  $IR$  error in potential measurements on a cathodically protected structure. BA is the absolute electrode potential of the structure; CD is the absolute electrode potential of the anode; and CB is the field gradient in the environment due to cathodic protection current flux. A reference electrode placed at E will produce an  $IR$  error of EF in the potential measurement of the structure potential. If placed at G, the error will be reduced to GH. At B there would be no error, but the point is too close to the structure to permit insertion of a reference electrode. If the current is interrupted, the field immediately becomes as shown by the dotted line, and no  $IR$  is included.

metal, the more positive, and more reliable, the measurement becomes.

The deviation from the correct potential value by inclusion of the field gradient in the measurement is often called the  $IR$  error, and it must be minimized in assessing the state of polarization of a cathodically protected structure. The recommended protection potentials all assume no significant  $IR$  error in the measurement.

It is desirable to measure the potential of a structure without an  $IR$  error. It is not always possible to place the reference electrode close to the structure to minimize the  $IR$  error but it can be achieved using the so-called instant-off technique. The technique relies on the fact that when the current is interrupted, the  $IR$  effect, being ohmic, dissipates immediately but the polarization decays much more slowly. Thus, if the current is switched off and the potential is measured immediately, the  $IR$ -free polarized potential of the structure can be measured. Where the cathodic protection system uses multiple power sources, it is necessary to switch off all the units simultaneously if true  $IR$ -free conditions are to be achieved.

In an impressed-current cathodic protection system, the power source has a substantial capacity to deliver current and it is possible to change the state of polarization of the structure by altering that current.

Thus, effective control of the system depends on credible potential measurements. Since the current output from any given anode is substantial, the possibility of an  $IR$  error, which may reach many hundreds of millivolts in any potential measurements made, is high. Thus the instant-off technique (or some other means of avoiding  $IR$  error) is essential to effective system management.

By contrast, a cathodic protection system based on sacrificial anodes is designed from the outset to achieve the required protection potential. If this is not achieved in practice, there is no control function that can be exercised to improve the situation. Some remodeling of the system will be required. Moreover, the current from each current source (the sacrificial anodes) is modest so that field gradients in the environment are not significant. It is at once clear that potential measurements are less significant in this case and instant-off measurements are neither necessary nor possible.

#### 4.18.5 Current Requirements

It was indicated earlier that the cathodic current is a poor indicator of adequate protection. While, to a first approximation, the protection potential is a function of the metal, the current required for protection is a function of the environment and, more particularly, of the cathodic kinetics it entails. From **Figure 4**, it is apparent that any circumstance that causes the cathodic kinetics to increase will cause both the corrosion rate and the current required for full ( $I''_c$ ) or partial ( $|I'_c| - I'_a$ ) protection to rise. For example, an increase in the limiting current in **Figure 5** produced by an increase in environmental oxygen concentration or in fluid flow rate will increase the corrosion rate and the cathodic protection current. Similarly, if the environment is made more acidic, the hydrogen evolution reaction is more likely to be involved in the corrosion reaction and it also becomes easier and faster; this too produces an increased corrosion rate and cathodic current demand.

In short, the current demand for cathodic protection varies according to the aggressiveness of the corrosive environment. It is for this reason that cathodic protection finds its greatest application where the pH is close to neutral. The more acidic environments entail a current output that rapidly becomes uneconomical. The more alkaline environments prove less aggressive to the structure and therefore often do not justify cathodic protection.

#### 4.18.6 Coatings and Cathodic Protection

Coatings (e.g., paints) applied to metal surfaces can be extremely effective in containing the corrosion of the substrate in many environments. This is particularly true for steel in natural environments. However, no freshly applied coating is entirely free from defects and so there will always be small areas which are exposed directly to the corrosive environment. It is possible to reduce, but not eliminate, these defects by paying attention to workmanship. In practice, it becomes increasingly expensive to achieve fewer and fewer defects because of the need for high-grade inspection as well as the detection and repair of individual defects.

Large structures, even in near-neutral pH environments, require a considerable current for cathodic protection. As a result, structure coatings are an almost mandatory requirement when cathodic protection is contemplated. The coating then provides the major part of the protection, and the cathodic protection provides the protection at the coating defects. This apparently ideally complementary behavior occurs because the coating defects represent a low resistance path, and therefore a preferred route, to the structure, for the cathodic protection current. It is now apparent that the coating does not need to achieve total surface coverage and the cathodic protection system must deliver only a fraction (often less than 1%) of the current that would be required to protect a bare structure. **Figure 10** shows

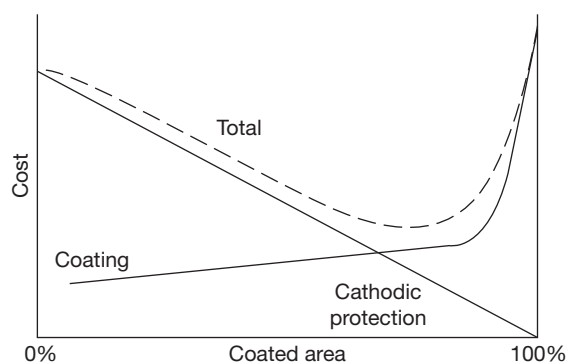


**Figure 10** Schematic diagram illustrating the economic benefit of the conjoint use of coating and cathodic protection. The increasing cost of coating as the coating is made progressively more defect free is shown; the corresponding cost of applying cathodic protection to the holidays decreases. The dotted line shows the total cost, and that there is overall benefit in using a good coating reinforced by cathodic protection.

schematically that there is an optimum combination of coating quality and cathodic protection that minimizes the cost of protecting a structure.

A coating deteriorates chemically and mechanically during its lifetime. This leads to a progressive increase in both the number of defects and the current required to protect the steel as they occur. Fortunately, each new defect represents a new low-resistance path and the cathodic protection current will flow to it to provide protection. Of course, this means that the cathodic protection system as installed must have sufficient reserve to provide this necessary extra current. This is readily accommodated in an impressed-current system where, if correctly designed, the voltage output can be increased to provide the requisite current. It is rather more difficult in the case of a sacrificial anode system because, as the anodes get smaller (by dissolving sacrificially), they are not capable of delivering more current. Thus increasing current demand develops alongside decreasing current availability. Of course, it is possible to provide anodes capable of delivering substantially more current initially in order to be able to provide sufficient current for later demand. This entails anodes operating in their early life at low current densities, which has sometimes been known to result in anode passivation and failure to deliver any significant current when it is needed.

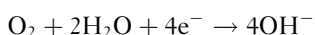
Notwithstanding this latter difficulty, cathodic protection is usually applied to coated structures. Thus, ships, many piers and jetties, and virtually all buried pipelines are coated when cathodic protection is applied. Liquid storage tanks standing on sand or bitumen sand often have the underside of their base plate under cathodic protection. Here coating is often omitted, but this is more often due to ignorance of the designer than a conscious decision not to coat. Only offshore oil production platforms, particularly in the North Sea, are cathodically protected but often deliberately uncoated. There are two reasons for this. First, these structures are almost all protected using sacrificial anodes and it is easier to design for a more or less constant current demand than for an increasing current demand in these systems. Second, the construction of the platforms is made against a tight schedule; any weather conditions that prevented completion of coating would involve launching a platform with an incomplete coating and insufficient anodes to protect the now partially coated structure. It is certainly true that the first platforms in the North Sea were coated and cathodically protected. However, at that time the only reliable marine anodes

were based on zinc alloys which entailed a heavy weight penalty (because they have a low capacity) and there was thus a pressing need to reduce anode weight by coating.

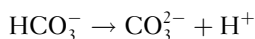
#### 4.18.7 Calcareous Deposit

It has been noted that the total current required to protect large structures can be substantial even in mildly corrosive environments. In seawater, for example, an initial current in the region of  $200 \text{ mA m}^{-2}$  for bare steel might well be required in the North Sea. This is because the relatively high oxygen concentration and the tide and wave action all contribute to a facile cathodic reaction. Fortunately, this current diminishes with time. The reason for this is the protective scale on the steel surface, which forms during cathodic protection by decomposition of the seawater.

During cathodic protection, the dissolved oxygen is reduced to produce hydroxyl ions:

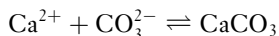


causing an increase in the pH at the interface. Seawater contains carbonate and bicarbonate ions that are in a pH-dependent equilibrium with one another:



The higher the pH of the seawater, the greater will be the proportion of carbonate ions present (since as the pH increases, so the  $\text{H}^+$  concentration decreases, thereby moving the equilibrium to the right). It follows that at a surface under cathodic protection, the hydroxyl ion produced has the effect of increasing the local carbonate ion concentration.

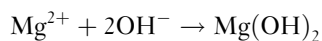
Seawater also contains calcium ions which form an insoluble carbonate with carbonate ions:



An increase in carbonate-ion concentration moves the equilibrium in favor of calcium carbonate deposition. Thus, one secondary effect of cathodic protection in seawater is the production of  $\text{OH}^-$ , which favors the production of  $\text{CO}_3^{2-}$ , which in turn promotes the deposition of  $\text{CaCO}_3$ . Cathodically protected surfaces in seawater will often develop an aragonite ( $\text{CaCO}_3$ ) film. This film is commonly referred to as a calcareous deposit.

Similarly, the seawater contains magnesium ions which can react with the hydroxyl ion directly to

form magnesium hydroxide:



Thus, brucite,  $\text{Mg}(\text{OH})_2$ , is also commonly found on surfaces under cathodic protection in seawater. Because more hydroxyl ions (higher pH) are required to cause magnesium hydroxide to precipitate, the magnesium is virtually always found in the calcareous deposits associated with calcium.<sup>18</sup>

The practical consequences of these events are that, once the calcareous film has formed, a cathodic current density at least an order of magnitude lower than that required to protect bare steel is needed to maintain protection. Although temporary damage to the film (e.g., storm action) may create a temporarily increased current demand, the film soon repairs and the lower current demand is restored. There is, however, a danger in excessive cathodic polarization: hydrogen is evolved at the steel surface, which, as it emerges, can itself disrupt the film mechanically. Since hydrogen continues to be produced so long as there is excessive polarization, there is continuing mechanical damage to the film and a more or less permanent increase in the cathodic current required for protection.

On the basis of laboratory experiments, it is widely believed, but there is little field evidence to prove, that high initial cathodic current densities promote the development of thinner, more compact, and more protective calcareous deposits. If this could be proved, some reduction in the sacrificial anode burden on a structure might be possible. As a result, some attention has been paid to the possibility of designing cathodic protection systems capable of delivering a high initial current with a view to reducing the total lifetime current required to attain and maintain protection. In general, this approach has involved proposals to use a limited number of high-current-output magnesium alloy sacrificial anodes to reinforce the anode burden (usually aluminum alloy) installed to provide long-term protection. It remains to be seen whether this is, or could be, successful.

#### 4.18.8 Potential Attenuation in Impressed-Current Systems

An impressed-current cathodic protection system circuit comprises an anode, the power source, the structure, and the environment in which it is placed. In addition, there are electrical connections between the power source and the anode and between the

power source and the structure (at the so-called negative drain point). The voltage available from the power source is used to polarize the anode and the structure and to overcome the electrical resistance of the environment and the metallic circuit, including that of the structure itself. It follows that the overall circuit resistance to various parts of a very large structure will differ and, where the resistance is higher, the voltage available for polarization of the structure will be lower. Thus, on large structures protected by a limited number of anodes, some lateral variation in the level of polarization is to be expected. This variation of potential is referred to as attenuation. Given that to ensure full protection the structure should everywhere be polarized at least to the protection potential, some part of it must be polarized to a greater extent. We have seen that more polarization requires more cathodic current. In the interest of economy, it is important to minimize attenuation as far as possible. One practical way to achieve this is to use a protective coating and thus limit the total current in the circuit. It may then still prove desirable to use more than one anode grounded to render the attenuation less extreme. To pursue this latter course, it is helpful to have some assessment of the likely level of attenuation that will be experienced on a given structure.

No exact mathematical analysis of potential attenuation for all structures has yet been developed. Some indicative analysis has been achieved for a buried pipeline,<sup>19</sup> which is perhaps the simplest case.

In making the analysis, it is assumed that the anode grounded is remote from the pipeline. That is, the length of the pipeline in question stands in what is virtually a uniform anode field, as shown in **Figure 11**. Since the electrical potential on the soil

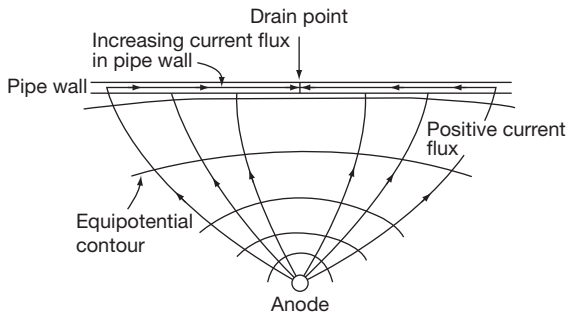


**Figure 11** Schematic diagram showing an impressed-current anode installed in a groundbed remote from a pipeline. The positive current produces a field gradient in the soil, but the gradient tends to zero close to the line, producing a uniform lateral electrical potential on the soil side.

side is constant, any electrical potential change in the pipeline metal due to current flow within it reflects an equal electrode potential change at the pipe-soil interface. The change is also numerically equal to the cathodic overpotential, that is, the shift in electrode potential from the spontaneous corrosion potential.

We assume that the current enters the pipeline from the soil side through defects in the coating and returns to the power source via the line and one of the drain points, as shown in **Figure 12**. If the total current in the pipeline at a point a distance  $x$  from a drain point is  $I_x$ , then the change in current per unit length at  $x$  is the current entering at  $x$ :

$$\frac{dI_x}{dx} = -2\pi r i_x \quad [5]$$

where  $r$  is the radius of the pipeline and  $i_x$  is the current density entering at  $x$ .

The electrical potential change along the pipeline at  $x$  is

$$\frac{d\phi_x}{dx} = -R_L I_x$$

where  $\phi_x$  is the electrical potential at  $x$  and  $R_L$  the resistance of the metallic pipeline/unit length. However, since the rate of electrical potential change is equal to the rate of change of overpotential, given a remote grounded, it follows that

$$\frac{d\eta_x}{dx} = -R_L I_x \quad [6]$$

where  $\eta_x$  is the overpotential and is the difference between the actual potential at  $x$  and the free corrosion potential of the metal.

From eqns [5] and [6]:

$$\frac{d^2\eta_x}{dx^2} = R_L (2\pi r i_x) \quad [7]$$

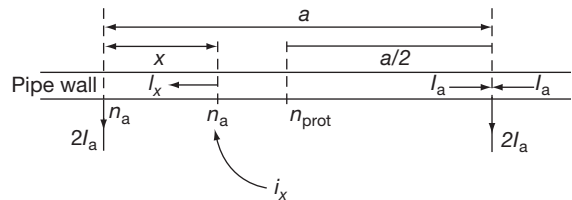


**Figure 12** Schematic representation of a pipewall subject to cathodic protection (see text).  $\eta_x$  = overpotential at  $x$ ;  $\eta_a$  = overpotential at  $x = 0$ ;  $\eta_{prot}$  = overpotential at  $x = a/2$ ;  $I_x$  = current line at  $x$ ;  $i_x$  = current density entering line at  $x$ ;  $I_a$  = current in line at  $x = 0$  from one side of drain point ( $2I_a$  = total current drain);  $a$  = distance between the drain points.

Now, when  $i_x$  is small, the polarization of the pipeline is approximately directly proportional to the true current density ( $i'_x$ ) at the holidays in the coating. Thus

$$\eta_x = k' i'_x \quad [8]$$

Also,

$$i'_x = \frac{i_x}{f}$$

where  $f$  is the fraction of the surface covered by holidays in the coating and is inversely proportional to the resistance of the coating/unit area ( $z$ ).

Thus

$$\eta_x = k' i'_x = \frac{k' i_x}{f} = K i_x z \quad [9]$$

where  $K$  is a constant that depends on the nature of the structure to be protected and the properties of the soil.

From eqns [7] and [9]:

$$\frac{d^2 \eta_x}{dx^2} = R_L \left( \frac{2\pi r}{Kz} \right) \eta_x \quad [10]$$

The solution to eqn [10] for an infinite pipeline, that is, when  $\eta_x = 0$ ,  $x = \infty$  and when  $\eta_x = \eta_a$ ,  $x = 0$ , is

$$\eta_x = \eta_a \exp \left[ - \left[ \frac{2\pi r R_L}{Kz} \right]^{1/2} x \right] \quad [11]$$

However, if the pipeline has multiple drain points separated by distance  $a$ , and the aim is that the pipeline electrode potential should just reach the protection potential at the mid-point ( $x = a/2$ ), then  $\eta_x = a/2$  is equal to  $\eta_{prot}$  (the overpotential required just to achieve the protection potential). At  $x = a/2$ , the current in the line is zero and  $(d\eta_x/dx)_x = a/2$  is also zero. Thus

$$\eta_x = \eta_{prot} \cosh \left[ \left[ \frac{2\pi r R_L}{Kz} \right]^{1/2} \left[ x - \frac{a}{2} \right] \right] \quad [12]$$

and

$$\eta_x = \eta_{prot} \cosh \left[ - \left[ \frac{2\pi r R_L}{Kz} \right]^{1/2} \frac{a}{2} \right] \quad [12a]$$

The current in an infinite pipeline is obtained by differentiating eqn [11] and substituting into eqn [6]:

$$I_x = \left[ \frac{2\pi r R_L}{Kz} \right]^{1/2} \frac{\eta_a}{R_L} \exp \left[ - \left[ \frac{2\pi r R_L}{Kz} \right]^{1/2} x \right] \quad [13]$$

The drainage current (i.e.,  $2I_x = 0$ ) is therefore

$$2 \left[ \frac{2\pi r R_L}{Kz} \right]^{1/2} \frac{\eta_a}{R_L} \quad [13a]$$

This analysis is far from exact since it assumes a remote groundbed, uniform soil resistivity, and uniform defect density in the coating. At best, it demonstrates that attenuation is likely to follow an exponential decay and that it will be less severe for larger diameter pipes than for smaller diameter ones. The problem is more difficult to solve for more complex structures (e.g., congested pipeline networks) and especially so for marine installations where the development of the calcareous deposit introduces the possibility of temporal variations in attenuation.

The question of attenuation is not significant in the case of sacrificial anode protection systems where the individual source outputs are small.

#### 4.18.9 Summary

Cathodic protection is a long-established and proven technique for protecting metals from corrosion. While in principle it may be used to protect any metal in an aqueous environment, in practice it is used mainly to protect carbon steels in natural environments such as water, soil, and sand. Other metals often do not require protection because they do not corrode significantly under these circumstances. More aggressive environments render cathodic protection less attractive because of the substantial cost of providing the requisite current. Nevertheless, cathodic protection is applied to a vast area of metal on structures such as buried pipelines, ships, piers and jetties, oil production platforms, and liquid storage tanks. More recently, the protection of reinforcing bar in concrete has received attention. Cathodic protection is therefore of great technological significance.

There are two methods of applying cathodic protection, namely using an impressed current or a sacrificial anode. The former requires a source of DC power, but is then capable of delivering large voltages (<100 V) and currents (<100 A). A sacrificial anode operates independently of a source of DC power but only delivers a voltage of about 1 V and a current that will rarely exceed 5 A. The relative advantages of the two methods largely derive from these differences.

Cathodic protection benefits from its conjoint use with a coating on the structure; the current required for protection is reduced. However, in seawater,



the application of the technique encourages deposition of protective salts which to some extent achieves the same objective.

Since cathodic protection, if operated correctly, can prevent the corrosion of a metal entirely, it is unique among all the methods of corrosion control.

## References

1. Davy, H. *Philos. Trans. Roy. Soc.* **1824**, 114, 151, 242, 328.
2. Scherer, L. F. *Oil Gas J.* **1939**, 38(27), 179.
3. *Metallurgical and Inspection Requirements for Cast Sacrificial Anodes for Offshore Applications*; SP 0387–2006; NACE: Houston, TX, 2006.
4. Ashworth, V. *Hot Risers: Managing the Corrosion Problem*; Oyez: London, 1979.
5. *Recommended Practice: Control External Corrosion on Underground or Submerged Metallic Piping Systems*, SP 0169–2007; NACE: Houston, TX, 2007.
6. *Recommended Practice: Internal Cathodic Protection Systems in Oil Treating Vessels*, SP 0575–2007; NACE: Houston, TX, 2007.
7. *Cathodic Protection of Pipeline Transportation Systems – Offshore Pipelines*; ISO 15589-2: 2004 (also ANSI/NACE SP 0607–2007), ISO: Geneva, 2004.
8. *Corrosion Control of Submerged Areas of Permanently Installed Steel Offshore Structures Associated with Petroleum Production*, SP 0176–2007 NACE: Houston, TX, 2007.
9. *Recommended Practice: Cathodic Protection of Pulp and Paper Mill Effluent Clarifiers*, RP-0181–2001; NACE: Houston, TX, 2001.
10. *Recommended Practice: Corrosion Control of Underground Storage Tank Systems by Cathodic Protection. Control of External Corrosion on Metallic Buried, Partially Buried or Submerged Liquid Storage Systems*, RP 0285–2002; NACE: Houston, TX, 2002.
11. *Recommended Practice: Application of Cathodic Protection of External Surfaces of Well Casings*, SP 0186 (2007); NACE: Houston, TX, 2007.
12. *Cathodic Protection: Part 1: Code of Practice for Land and Marine Applications* (formerly CP 1021). BS 7361: Part 1: 1991; BSI: London, 1991.
13. Dees, D. D. In *Corrosion/87*; NACE: Houston, TX, 1987; Paper no. 73.
14. Stratfull, K. F. *Corrosion* **1959**, 15(6), 65.
15. Stratfull, R. F. *Transport. Res. Rec. (USA)* **1974**, 500, 1.
16. Anderson, G. H. In *Proceedings of the Conference on Cathodic Protection of Reinforced Concrete Bridge Decks* NACE: Houston, TX, 1985.
17. European Standard, *Cathodic Protection of Steel in Concrete*, BS EN 12696: 2000; BSI: London.
18. Yague-Murillo, O. Ph.D. Thesis, Victoria University of Manchester, England, 1983.
19. Uhlig, H. H. *Corrosion and Corrosion Control*; Wiley: New York, 1971.

## Further Reading

BS EN12473: General principles of cathodic protection in sea water  
 BS EN12495: Cathodic protection for fixed offshore structures  
 BS EN12696: Cathodic protection of steel in concrete  
 BS EN12954: Cathodic protection of buried or immersed metallic structures: General principles and applications for pipelines  
 BS EN13173: Cathodic protection for steel offshore floating structures  
 BS EN13174: Cathodic protection for harbor installations  
 BS EN13509: Cathodic Protection measurement techniques  
 BS EN13636: Cathodic protection of buried metallic tanks and related piping  
 BS EN14505: Cathodic protection of complex structures  
 BS EN15257: Cathodic protection – Competence levels and certification of cathodic protection personnel

## 4.19 Sacrificial Anodes

**R. F. Crundwell**

Chartley Consultants, Foar Oaks, Sutton Coldfield B74 4TH, UK

© 2010 Elsevier B.V. All rights reserved.

---

<b>4.19.1</b>	<b>Principles of Operation</b>	2764
4.19.1.1	Applications of Sacrificial Anodes	2764
<b>4.19.2</b>	<b>Sacrificial Anode Basics</b>	2764
4.19.2.1	Anode Operating Potential, Protection Potential, and Driving Voltage	2764
4.19.2.2	Anode Capacity and Anode Efficiency	2765
4.19.2.3	Anode Requirements	2765
<b>4.19.3</b>	<b>Sacrificial Anode Materials</b>	2766
<b>4.19.4</b>	<b>Factors Affecting Anode Performance</b>	2766
4.19.4.1	Alloy Composition	2766
4.19.4.2	Impurities	2767
4.19.4.3	Alloying Additions	2767
4.19.4.4	Metallurgical Factors	2769
4.19.4.5	Environmental Factors	2770
<b>4.19.5</b>	<b>Selecting the Appropriate Anode Material</b>	2771
4.19.5.1	Zinc	2771
4.19.5.2	Aluminum	2772
4.19.5.3	Magnesium	2773
<b>4.19.6</b>	<b>Anode Testing</b>	2773
<b>4.19.7</b>	<b>Cathodic Protection System Design</b>	2774
4.19.7.1	Design Parameters	2774
<b>4.19.8</b>	<b>Area of Steel Requiring Protection and Coating Considerations</b>	2774
<b>4.19.9</b>	<b>Cathodic Current Densities for Protecting Steel</b>	2774
<b>4.19.10</b>	<b>System Life</b>	2775
4.19.10.1	Calculating the Weight and Number of Individual Anodes	2775
4.19.10.2	Anode Size and Shape	2775
4.19.10.3	Anode Output	2775
4.19.10.4	Anode Resistance	2776
4.19.10.5	Anode Life	2776
4.19.10.6	Number of Anodes	2777
4.19.10.7	Anode (End Current) Distribution	2777
4.19.10.8	The Anode Insert	2778
4.19.10.9	Utilization Factor	2778
4.19.10.10	Backfills for Anodes	2779
<b>4.19.11</b>	<b>Other Considerations</b>	2779
4.19.11.1	Calcareous Scale	2779
4.19.11.2	Combined Alloy Anodes for Rapid Structure Polarization	2779
4.19.11.3	Flame Sprayed Aluminum	2780
4.19.11.4	Protection of High-Alloy Steels	2780
<b>References</b>		2780

---

**Abbreviations****ASTM** American Society for Testing and Materials**DNV** Det Norsk Veritas**FSA** Flame sprayed aluminum**Symbols****E** Anode consumption rate**L** Anode lifetime**M** Mass of single anode**N** Total number of anodes**U** Utilisation factor of anode**W** Total mass of all anodes**4.19.1 Principles of Operation**

When two different metals are immersed in the same electrolyte, they will usually exhibit different electrode potentials. If they are connected by an electronic conductor, there will be a tendency for the potentials of the two metals to move toward one another; they are said to mutually polarize. The polarization will be accompanied by a flow of ionic current through the solution from the more negative metal (the anode) to the more positive metal (the cathode); therefore, electrons will be transferred through the conductor from the anode to the cathode. Thus, the cathode will benefit from the supply of electrons in that it will dissolve at a reduced rate; it is said to be 'cathodically protected.' Conversely, in supplying electrons to the cathode, the anode will be consumed more rapidly and will act as a 'sacrificial anode.'

From the above discussion, it is clear that, for an anode material to offer sacrificial protection, it must have an open-circuit potential that is more negative than that of the structure being protected (the cathode). The extent of protection experienced by the cathode will depend on the potential it attains. This is dependent on the electrochemical properties of the anode which in turn are governed by its composition and the environment to which it is exposed.

**4.19.1.1 Applications of Sacrificial Anodes**

The first recorded work on the application of sacrificial anodes was in the 1820s when Sir Humphrey Davy and his assistant Michael Faraday's work for the Royal Navy was reported in Philosophical Transactions of the Royal Society.<sup>1-3</sup> Their work centered

on the reduction of the corrosion of copper sheets attached to the wooden hulls of naval vessels. Davy identified that the corrosion was associated with differences in potential across the sheets of copper and, especially, where adherent corrosion products were present. By attaching pieces of zinc wire to a coil of copper wire, Davy demonstrated the process of sacrificial anode cathodic protection; he expanded this to larger scale trials and, finally, to full-scale trials on the HMS Sammarang and the Carnbrea Castle using anodes of cast iron.

When iron hulls became more common later in the nineteenth century, zinc sacrificial anodes were used to reduce corrosion; however, impurities, particularly iron, in the then commercially available zinc resulted in the formation of adherent nonconducting corrosion products of zinc on the anodes, which stifled the protection current flow and reduced the driving potential to unacceptable level.

Examples of the application of sacrificial anodes include ship, hulls and ballast tanks, offshore oil and gas drilling rigs, production platforms semisubmersibles and support facilities, underwater pipelines, underground pipelines, buried structures, harbor piling and jetties, floating dolphins, buoys, lock gates, and submerged concrete structures. There are many other uses including a large range of industrial equipment in which the surfaces are in contact with corrosive electrolytes, for example, heat exchangers, pump impellers, and vessel internals.

**4.19.2 Sacrificial Anode Basics****4.19.2.1 Anode Operating Potential, Protection Potential, and Driving Voltage**

The operating potential of an anode material is its potential when coupled with the structure under protection (i.e., the closed-circuit potential). Since commercial anode materials are formulated to suffer only limited polarization, under most conditions of exposure, the operating potential approximates to the open-circuit potential. Indeed, any substantial difference ( $>50$  mV) between these two potentials questions the suitability of the anode in the particular environment. For this reason, the open-circuit potential is usually used in design calculations wherein the operating potential is more precise but generally unknown at the time when the design is undertaken.

The protection potential refers to the potential at which experience shows that corrosion of a metal

**Table 1** Anode potentials of various alloys used in cathodic protection

<i>Alloy</i>	<i>Anode potential (V vs Ag/AgCl/ Seawater)</i>	<i>Max anode capacity (A h kg<sup>-1</sup>)</i>
Al-Zn-Hg	-1.0 to -1.05	2830
Al-Zn-Sn	-1.0 to -1.05	2600 (heat treated)
Al-Zn-In	-1.05 to -1.15	2700
Zn-Al-Cd	-1.05	780
Mg-Mn	-1.70	1230
Mg-Al-Zn	-1.50	1100-1230

will cease. Different materials have different potentials (Table 1). Occasionally, a less negative potential will be specified because some degree of corrosion is permissible. It should be noted that in a mixed metal system, the protection potential for the most base metal is adopted although the designer should take into account any deleterious effect that over protection may have on the nobler component and the need to supply excessive current if it is an efficient cathode. The cathodic protection of mixed metal systems can be a complex subject and is discussed in detail later in the chapter.

The driving voltage is the difference between the anode operating potential and the potential of the polarized structure to which it is connected. For design purposes, the driving voltage is taken as the difference between the anode open circuit potential (unless there are data on how the anode material will actually behave) and the required protection potential of the structure.

#### 4.19.2.2 Anode Capacity and Anode Efficiency

The anode capacity is the total coulombic charge (current  $\times$  time) produced by the unit mass of an anode as a result of electrochemical dissolution. It is normally expressed in ampere hours per kilogram (A h kg<sup>-1</sup>); however, the inverse of anode capacity, that is, the consumption rate (kg A<sup>-1</sup> year<sup>-1</sup>), is also sometimes used.

The theoretical anode capacity can be calculated according to Faraday's law. From this, it can be shown that 1 kg of aluminum should provide 2981 Ah of charge. In practice, the realizable capacity of the anode is less than the theoretical value. The significance of the actual (as opposed to the theoretical) anode capacity is that it is a measure of the amount of cathodic current an anode can give. Since anode capacity varies among anode materials, it is the

parameter against which the anode cost per unit anode weight should be evaluated.

The anode efficiency is the percentage of the theoretical anode capacity that is achieved in practice:

$$\text{Anode efficiency} = \frac{\text{Anode capacity}}{\text{Theoretical capacity}} \times 100\%$$

Anode efficiency is of little practical significance and can be misleading. For example, magnesium alloy anodes often appear to have an efficiency of around 50%, while for zinc alloys, the value exceeds 90%; it does not follow that zinc alloy anodes are superior to those based on magnesium. Efficiency will be encountered in many texts on sacrificial anode cathodic protection.

#### 4.19.2.3 Anode Requirements

The fundamental requirements of a sacrificial anode are to impart sufficient cathodic protection to a structure economically and predictably over a defined period, and to eliminate, or reduce to an acceptable level, corrosion that would otherwise take place.

In view of the above criteria, the following properties are prerequisites for the viability of a sacrificial anode<sup>4,5</sup>

1. The material must have a potential more negative than the potential at which corrosion ceases on the material being protected (i.e., the anode must exhibit a driving potential relative to the protected cathode). Thus, for steel, which is considered protected at potentials more negative than 0.8 V negative to the silver chloride seawater reference electrode, the driving voltage must be capable of overcoming the ohmic resistances of the anode cathode and the electrolyte in order to make the anode deliver the protection current. In practice this means a driving potential of at least 0.2 V more negative than the metal to be protected.
2. The driving potential of the anode must be stable with respect to time and must be predictably affected by the passage of current, that is, the anode material must have known and have acceptable polarization characteristics.
3. The anode material must have adequate capacity; that is, it must deliver an adequate and predictable number of ampere hours for every kilogram consumed.
4. The alloy must be capable of being formed by simple and economical processes into shapes in which it may be used, and it must have adequate

mechanical strength to remain in the desired form throughout its designed life.

5. The alloy must be commercially viable; that is, it must be capable of being produced in significant quantities (the world production of sacrificial anodes runs into many tens of thousands of tons per annum) and sold at a price that is acceptable to the users.

#### 4.19.3 Sacrificial Anode Materials

While cathodic protection can be used to protect most metals from aqueous corrosion, it is most commonly applied to carbon steel in natural environments (waters, soils, and sands). In a cathodic protection system, the sacrificial anode must be more electronegative than the structure. There is, therefore, a limited range of suitable materials available to protect carbon steel. The range is further restricted by the fact that the most electronegative metals (Li, Na, and K) corrode extremely rapidly in aqueous environments. Thus, only alloys based on magnesium, aluminum, and zinc are viable possibilities. These metals form the basis of the three generic types of sacrificial anodes.

In practice, with one minor exception (pure zinc), the commercially pure metals are unsuitable as sacrificial anode materials. This is because they fail to meet one or more of the prerequisites outlined above. For each basis metal, alloying elements are added to ensure more acceptable properties.

**Table 2** gives a list of the more important anode materials by broad categories, and some indication of their operating parameters. It is clear that there are major differences in performance between one generic type and another. Thus, the magnesium alloys have

very negative operating potentials and are therefore able to provide a large driving voltage for cathodic protection; zinc and aluminum alloys are more modest in this respect. Aluminum alloys, by contrast, provide a substantial current capacity which is more than twice that available from the zinc and magnesium alloys. It might appear that this implies that if the driving voltage is the most important feature in a given cathodic protection system (e.g., when there is a need for short-term high currents or a high resistivity to overcome), then magnesium alloys are to be preferred, but if a high capacity is required (e.g., steady delivery of current over a long life), aluminum alloys would be better. In practice, selection is significantly more complicated, and the topic is discussed in more detail in later sections.

Even within a generic type of alloy, there are significant performance differences. Thus, for example, Al–Zn–In alloys provide a higher driving voltage but a lower current capacity than Al–Zn–Hg alloys. Once a decision to use a generic type of alloy has been made, these apparently small differences in performance may become important in the final selection.

Alloying additions are made to improve the performance of an anode material.<sup>5</sup> Of equal importance is the control of the levels of impurity in the final anode, since impurities (notably iron and copper) can seriously adversely affect anode performance. Careful quality control of the raw materials used and the manufacturing process adopted is essential to sound anode production.

An intimate knowledge of the factors influencing the operation of sacrificial anodes and design parameters is essential if a full appreciation of how best to select an anode and achieve optimum performance is to be realized. The following considerations deal with those factors, which ultimately determine anode performance.

#### 4.19.4 Factors Affecting Anode Performance

##### 4.19.4.1 Alloy Composition

The constituent elements of anode materials, other than the basis metal, are present as a result of either being impurities in the raw materials or deliberate alloying additions. Impurity elements can be deleterious to anode performance; therefore, it is necessary to control the quality of the input materials in order to achieve the required anode performance. Since this will usually have an adverse impact on costs, it may

**Table 2** Typical basis material composition requirements for anode alloys

99.90% Magnesium		99.99% Zinc	
Cu	0.02 max	Pb	0.003 max
Mn	0.01 max	Cu	0.001 max
Sn	0.01 max	Cd	0.003 max
Ni	0.001 max	Fe	0.002 max
Pb	0.01 max	Sn	0.001 max
Others	0.05 max	Zn	99.99 min
Mg	99.90 min		
99.85% Aluminum (P0610)		99.90% Aluminum (P0506)	
Fe	0.10 max	Fe	0.06 max
Si	0.06 max	Si	0.05 max
Cu	0.003 max	Cu	0.003 max
Ni	0.003 max	Ni	0.003 max
Cd	0.002 max	Cd	0.002 max



be desirable to tolerate a level of impurities and to overcome their action by making alloying additions. Alloying elements may also be added for other reasons, which are important to anode production and performance.

In general, sacrificial anode alloy formulations are proprietary and may be covered by patents. The patent documents are often very imprecise when they relate to compositions that will produce effective anodes and quite inaccurate in ascribing the function to a given alloying element. While the commercial literature is more specific when it relates to compositions, it rarely details the purpose of an alloying addition. In discussing alloy composition here, the treatment derives from the technical literature and is necessarily a broad-brush account. The reader is referred to the wealth of literature published over the past 50 years, for example, as reviewed by Googan.<sup>6</sup>

#### 4.19.4.2 Impurities

One important feature of an anode alloy is that it should dissolve with a capacity approaching the theoretical value. That is, all the electrons released by the metal dissolving should be transferred to the structure to support the cathodic reaction there, and should not be wasted in local cathodic reactions on its own surface.

In all the generic types of sacrificial anode alloys, the presence of iron is found to be deleterious. This is because an intermetallic compound formed between it and the basis metal proves to be a good cathode. Its presence will result in a substantial lowering of the capacity of an anode. Moreover, the presence of this cathodic material will often raise (make less negative) the anode operating potential and may, in the limit, promote actual passivation. Thus, the driving force available from the anode is reduced or completely destroyed. For example, when the solid solubility of iron in zinc (~14 ppm) is exceeded, the anode operating potential becomes more positive. This has been attributed to the formation of  $\text{Zn}(\text{OH})_2$  around intermetallic precipitates of  $\text{FeZn}_{13}$ .<sup>7</sup> The presence of iron has a similar adverse effect in aluminum<sup>8</sup> and magnesium<sup>5</sup> alloys.

There are two ways of avoiding the iron problem: to control the iron added with the basis metal or to sequester the iron in some way to render it ineffective. In practice, it is not possible to permit more than a limited iron content because sequestering is only economic and practicable within defined limits. The wider availability of electrolytically smelted zinc

with iron levels around 20 ppm means that iron is no longer an issue in the production of zinc anodes. The same is true for aluminum as world demand for higher purity ingot for the electronics industry means that aluminum with a notional purity of 99.85% is readily available with less than 0.08% iron and 99.90% with iron levels selectable at below 0.05%.

Other heavy metal impurities (especially copper and nickel) have similar adverse effects on all generic alloy types. In their case, sequestering has not proved successful, and control of input quality is used to keep their concentration acceptably low.<sup>5</sup> It is important that these impurities are specified at the time of selecting a supplier as what is a deleterious impurity to one application may be a beneficial ingredient to another; for example, levels of nickel in aluminum sourced in the Middle East were not considered relevant for most applications but resulted in significant reduction in capacity when used for anode production. Similarly, naturally occurring levels of gallium present in aluminum feedstock sourced in the United States for the development of Al–Zn–Si–In alloys contributed to the activation process, but when the alloy was licensed for production in the United Kingdom, locally sourced aluminum did not have the gallium impurity, and it had to be deliberately added to achieve the desired properties.

#### 4.19.4.3 Alloying Additions

We have seen that the adverse effect of impurities can, within limits, be controlled by alloying additions. Thus, silicon and aluminum are added to zinc and manganese to magnesium, to counter the effect of iron.

Additions are made for other purposes, all of which aim to improve the performance of the anode. These include lowering the anode operating potential to increase the driving voltage, avoiding passivation, increasing the anode capacity, improving the dissolution morphology, modifying the mechanical properties of the dissolution product to promote detachment, and improving the mechanical properties of the anode.

Table 3 lists some common zinc anode alloys. In three cases, aluminum is added to improve the uniformity of dissolution and thereby reduce the risk of mechanical detachment of undissolved anode material.<sup>5</sup> Cadmium was traditionally added to encourage the formation of a soft corrosion product that readily crumbles and falls away so that it cannot accumulate to hinder dissolution<sup>7</sup>; however, its use is now restricted due to environmental concerns. The Military Specification<sup>9</sup> material was developed to avoid the alloy

**Table 3** Standard zinc anode alloys

<i>Alloy Component (wt%)</i>	<i>ASTM B4 18-88 Type I</i>	<i>ASTM B 418-88 Type II</i>	<i>US Mil Spec A 18001 K</i>	<i>DNV Elevated temp</i>
Al	0.10–0.50	0.005 max	0.10–0.50	0.10–0.20
Cd	0.025–0.07	0.003 max	0.025–0.07	0.03–0.06
Fe	0.005 max	0.0014 max	0.005 max	0.002 max
Cu	0.005 max	0.002 max	0.005 max	0.005 max
Pb	0.006 max	0.003 max	0.006 max	0.006 max
Si	—	—	—	0.125 max
Others(total)	0.1 max		0.10 max	—
Zn	Remainder	Remainder	Remainder	Remainder
o/c potential Ag/AgCl/ seawater	–1.05 V	–1.05 V	–1.05 V	–1.05 V
Capacity (A h kg <sup>–1</sup> )	780	780	780	780

passivating as a result of the presence of iron.<sup>5</sup> It later became apparent that this material suffered intergranular decohesion at elevated temperatures (>50 °C) with the result that the material failed by fragmentation.<sup>10</sup> The material specified by Det Norske Veritas<sup>11</sup> was developed to overcome the problem: the aluminum level was reduced under the mistaken impression that it produced the problem. It has since been shown that decohesion is due to a hydrogen embrittlement mechanism,<sup>12</sup> and that it can be overcome by the addition of small concentrations of titanium.<sup>13</sup> It is not clear whether the titanium acts as a getter for hydrogen or simply serves to refine the grains and increase the grain boundary area thereby diluting the embrittlement effect. It is claimed that recently developed alloys with magnesium additions are also resistant to intergranular attack at elevated temperatures.<sup>5,10</sup>

Although aluminum is a base metal, it spontaneously forms a highly protective oxide film in most aqueous environments; that is, it passivates. Consequently, it has a relatively noble corrosion potential and is then unable to act as an anode to steel. Low level mercury, indium, or tin additions have been shown to be effective in lowering (i.e., making more negative) the potential of aluminum; they act as activators (depassivators). Each element has been shown to be more effective with the simultaneous addition of zinc. Zinc additions of up to 5% lower the anode operating potential, but above this level, no benefit is gained. Below 0.9% zinc, there is little influence on the performance of aluminum anodes.<sup>5</sup> **Table 4** lists a number of the more common commercial alloy groups.

The best capacities in seawater are obtained from alloys containing zinc and mercury, but this is achieved at the expense of a somewhat more noble operating potential. Higher zinc additions at around 5% result in an alloy highly tolerant of burial in seabed muds.

**Table 4** Proprietary aluminum anode alloys

<i>Alloy Component (wt%)</i>	<i>Al–Zn–In</i>	<i>Al–Zn–Sn</i>	<i>Al–Zn–Hg</i>
Fe	0.12 max	0.13 max	0.08 max
Si	0.05–0.20	—	0.11–0.21
Zn	2.0–6.5	4.0–6.0	0.35–0.5
Hg	—	—	0.035–0.050
In	0.01–0.02	—	—
Sn	—	0.1	—
Cu	0.006 max	–.01 max	0.006 max
Ti	0.02 max	0.02 max	0.02 max
Others	0.02 max	0.02 max	0.02 max
o/c potential Ag/AgCl/ seawater	–1.10 V	–1.10 V	–1.05 V
Capacity (A h kg <sup>–1</sup> )	2700	Variable	2830

Mercury has become associated with environmental issues and is now seldom used in offshore applications. Zinc and indium additions give a less noble operating potential but are associated with a lower capacity. In practice this effect on the operating potential can be quite significant. The driving voltage between Al–Zn–Hg (open circuit/operating potential –1.05 V) and steel (protection potential –0.80 V) is 0.25 V. The use of Al–Zn–In provides a 20% increase in the driving voltage and thereby the possibility of a higher current output from equal sized anodes. Thus, both alloys have important advantages and disadvantages.

The Al–Zn–Sn alloys require careful solution heat treatment in their production to achieve optimum properties. Inevitably, this leads to more expense, longer production times, and a need for greater quality control. The advent of the alloys containing mercury or indium rendered these alloys very much

less attractive. Magnesium additions (0.1–2.0%) to Al–Zn–In alloys have been made, but it is not known whether this was a deliberate addition to improve a particular property or because the starting point for alloy development was an existing structural alloy. These materials can harden with age and hence suffer reduced ductility; since this can subsequently lead to longitudinal cracking of the anodes, they should not be cast in thin sections or stored at elevated temperatures (full sun in hot climates). Higher levels of magnesium (up to 8%), while improving strength and casting characteristics, incur the disadvantage of a reduced capacity.

Both titanium and boron can be added as grain refiners to ensure small grain size and hence high surface area grain boundaries.<sup>14</sup> This reduces the risk of preferential attack at grain boundaries and promotes more uniform dissolution. This effect also results in an alloy that is less susceptible to ‘hot shortness.’

Typical proprietary magnesium anode materials are given in **Table 5**. Magnesium anodes comprise two distinct types, the Mg–Mn and Mg–Al–Zn alloy systems. Addition of up to 1.5% manganese to high-purity magnesium yields a material with an operating potential of –1.7 V versus Ag/AgCl/seawater. The Mg–Mn alloys therefore exhibit very high driving potential and thus find application in particularly resistive environments. Mg–Al–Zn anodes have an operating potential (–1.5 V versus Ag/AgCl/seawater) 200 mV above that of the Mg–Mn alloys. This is very favorable in view of problems with overprotection. Thus, they are more popular in typical environments than the Mg–Mn alloys. The alloys also contain manganese, which is added to overcome the deleterious effects of iron.<sup>5</sup> Alloying additions of

aluminum, zinc, and manganese to magnesium serve to improve the anode capacity and reduce the operating potential, compared with that of pure magnesium. There is, however, no difference between the capacity of Mg–Mn and Mg–Al–Zn anodes. Mg–Al–Zn alloys are called ‘high purity’ when produced from virgin magnesium to distinguish them from a series of alloys developed after the Second World War when large amounts of magnesium alloy scrap were available.

#### 4.19.4.4 Metallurgical Factors

In producing anodes, the production method must not compromise the benefits of alloy formulation. A number of undesirable anomalies can occur during production, which may detract from the desired anode properties. Some of these anomalies are discussed below. A detailed account of finished anode requirements can be found elsewhere.<sup>11,15</sup>

Although most anodes are made by gravity casting, some are made by continuous or semicontinuous casting or extrusion. The method of casting affects the physical structure of the anode. That is, the associated cooling process will influence the segregation or distribution of alloying constituents. In some cases, it is undesirable to permit segregation since this may lead to preferential attack at grain boundaries. However, it is believed that segregation of activating elements during cooling benefits the performance of some alloys. This mechanism is a suggested explanation for the mercury- and indium-rich phases round on the surfaces of aluminum anodes.<sup>13</sup> The increased surface concentrations of these elements aid activation and are therefore beneficial.

Significant porosity within the anode is an indicator of the presence of dissolved gasses in the molten alloy and is an indicator of poor foundry practice and should be a cause for rejection and further investigation. The inclusion of extraneous matter, as a consequence of unclean foundry practices, may increase the tendency to fragmentation.

Cracking of anodes during casting is, in some cases, unavoidable due to the stresses imposed by cooling particularly those occurring between the cooling contracting anode and the mould heating and expanding. The problem is more common in Al–Zn–Hg anodes and less common when continuous or semicontinuous casting is used. Longitudinal cracks cannot be accepted, as these will lead eventually to mechanical loss of material. A greater tolerance to transverse cracks can be exercised although foundry practice and the use of grain refinement additions can

**Table 5** Proprietary magnesium anode alloys

<i>Alloy Component (wt%)</i>	<i>Mg–Mn (Galvomag®)</i>	<i>Mg–Al–Zn (high purity)</i>
Cu	0.02 max	0.02 max
Al	0.01 max	5.3–6.7
Si	–	0.10 max
Fe	0.03 max	0.003 max
Mn	0.5–1.3	0.15 min
Ni	0.001 max	0.002 max
Zn	–	2.5–3.5
Sn	0.01 max	–
Pb	0.01 max	–
o/c potential vs. Ag/ AgCl/seawater	–1.7	–1.5
Capacity Ahrs/kg	1230	1230

minimize their occurrence. For example, one quality specification permits an anode completely supported by the insert to have transverse cracks of unlimited length and depth provided that there are no more than ten cracks per anode and their width does not exceed 5 mm.<sup>15</sup> This is somewhat arbitrary but emphasizes the point that cracks that threaten anode integrity are of greatest importance.

The anode material must stay firmly attached to the steel insert, which is necessary to conduct the current from the anode so that the structure remains effective, throughout its design life. Consequently, surface preparation of the insert prior to casting to ensure a sound bond with the anode material is essential. Voids at the insert–anode material interface are undesirable, as these will also affect the bond integrity. Dry blast cleaning to near white metal at the time of casting is the usual preparation for aluminum alloy anodes,<sup>15</sup> and coating by hot dip galvanizing or electrogalvanizing is used for inserts of zinc or magnesium anodes. Zinc coating of inserts for aluminum anodes must not be used as the coating enables the molten alloy to dissolve the insert.

#### 4.19.4.5 Environmental Factors

The conditions of environmental exposure play a key role in determining anode performance. Indeed, specific environments often preclude, or necessitate, the use of particular anode materials.

This section is not intended to deal with those environmental factors that influence cathodic current demand (e.g., oxygen availability or the presence of calcareous deposits) but those that directly affect the performance of the anodes.

Temperature is of particular importance to the performance of anodes, especially when anodes are buried. Anodes may often be used to protect pipelines containing hot products. Thus, temperature effects must be considered. Al–Zn–In anodes experience greatly reduced capacity in open seawater at temperatures above 70 °C<sup>16</sup> (down to 1200 A h kg<sup>-1</sup> at 100 °C) and in seabed muds in excess of 50 °C<sup>16,17</sup> (900 A h kg<sup>-1</sup> at 80 °C). At elevated temperatures, passivation of both aluminum alloys and pure zinc can occur.<sup>18</sup> Considerable improvement in performance (capacity, and to a lesser extent operating potential) has been claimed for a range of modified Al–Zn–In anode materials containing a deliberate alloying addition of silicon.

Zinc anodes have also experienced problems at elevated temperatures in saline mud, suffering intergranular decohesion at approximately 70 °C.<sup>19</sup> Later work by the same authors showed the threshold

for damage to be ~50 °C. The material is not recommended above 40 °C<sup>10</sup> although special zinc based materials for temperatures exceeding 50 °C have been developed.<sup>11</sup> Pure zinc, which does not suffer intergranular decohesion, will passivate under these conditions. It is claimed that newly developed Zn–Al–Mg anodes will perform satisfactorily at elevated temperatures.<sup>10</sup> Nevertheless, Al–Zn–In anodes have been specified for operation above 50 °C.<sup>10</sup> Furthermore, steps are now taken to ensure that the anode design prevents anode material being exposed to elevated temperatures under buried conditions.

It must be observed that most anode testing and development for use at elevated temperatures both in laboratories and in the field has been under isothermal conditions, and it is often erroneously assumed that the anode temperature is that of the product, whereas the anode is probably at a significantly lower temperature but is operating under high heat transfer conditions and that consideration should be given to placing a thermal barrier between the anode and the structure to minimize both temperature and heat transfer effects.

The presence of H<sub>2</sub>S (from bacterial activity in anaerobic saline mud, for example) can result in a significant decrease (16%) in capacity and loss of operating potential for Al–Zn–In anodes.<sup>17</sup>

Environmental resistivity and chloride content will affect anode performance. Aluminum alloy anodes require the presence of chloride ions to prevent passivation. Land-based applications generally provide insufficient chloride levels for this purpose. Consequently, aluminum alloy anodes predominantly find application in marine environments although some water produced from oil or gas wells is both saline and hot, and aluminum anodes find application in corrosion protection in vessels handling these fluids. The capacity and operating potential, of aluminum alloy anodes in particular, illustrated in [Figures 1 and 2](#), are dependent on the degree of salinity. With reducing salinity, the anode capacity will decrease and the operating potential rise. This becomes increasingly significant below 10–20% seawater strength and is important for design in estuarine conditions. Passivation of aluminum zinc indium alloy anodes may occur as a consequence of electrolyte stagnation, particularly, if the anode is immersed in silt or sand; zinc and Al–Zn(5%)–Hg perform reasonably under these conditions.

The capacity of an anode is dependent on the anode operating current density.<sup>16</sup> To some extent, it will be governed by its environment but, in part, is within the control of the design. Certainly, wholly unsuitable current densities can usually be avoided

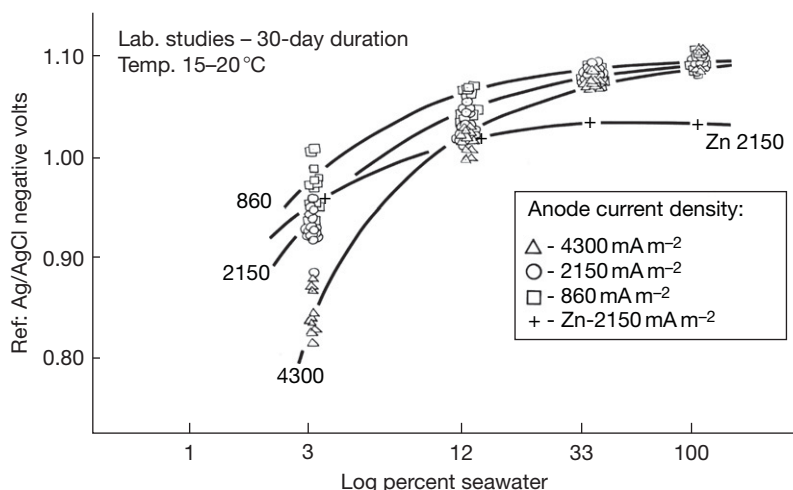


**Figure 1** Electrochemical potential of aluminum and zinc anodes as a function of salinity and current density.

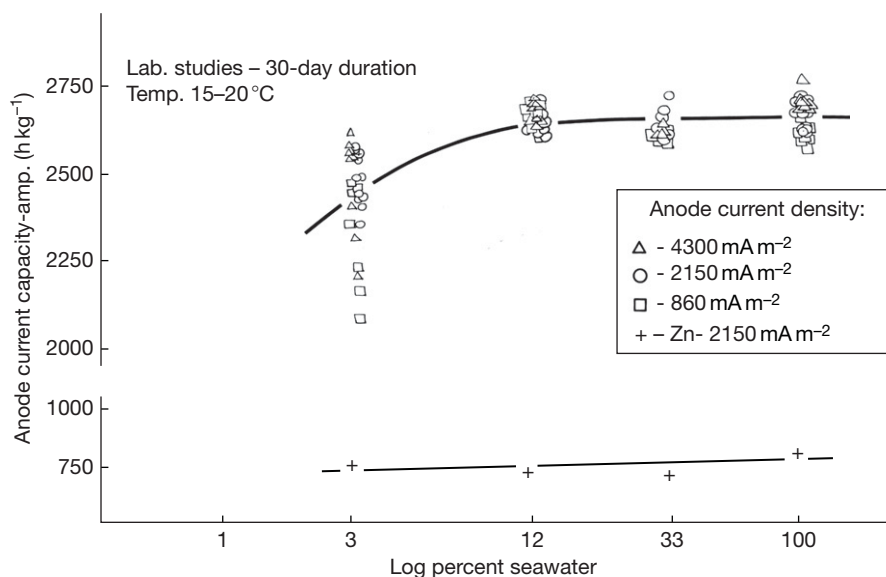


**Figure 2** Capacity of aluminum and zinc anodes as a function of chloride ion concentration and current density.

by correctly sizing the anodes. At lower operating current densities, some anodes exhibit reduced capacity; this is shown in [Figure 3](#). Long periods of low operating current density can lead to passivation. This may result in failure to activate when the current demand increases (as can occur with anodes on coated structures when the coating deteriorates).

#### 4.19.5 Selecting the Appropriate Anode Material

It is desirable to choose an anode material with the lowest cost per ampere hour of current supplied.

However, the choice is often governed by other constraints and frequently becomes a compromise.

##### 4.19.5.1 Zinc

Of all the anode materials, zinc is arguably the most reliable. It has, with few exceptions, reliable electrochemical performance; the exceptions lie within the area of high temperature operation. Zinc provides the lowest driving voltage of the generic alloy types. It is therefore unsuitable in highly resistive soils, except possibly as a ribbon, and in low salinity waters. However, an operating potential of  $-1.05$  V versus



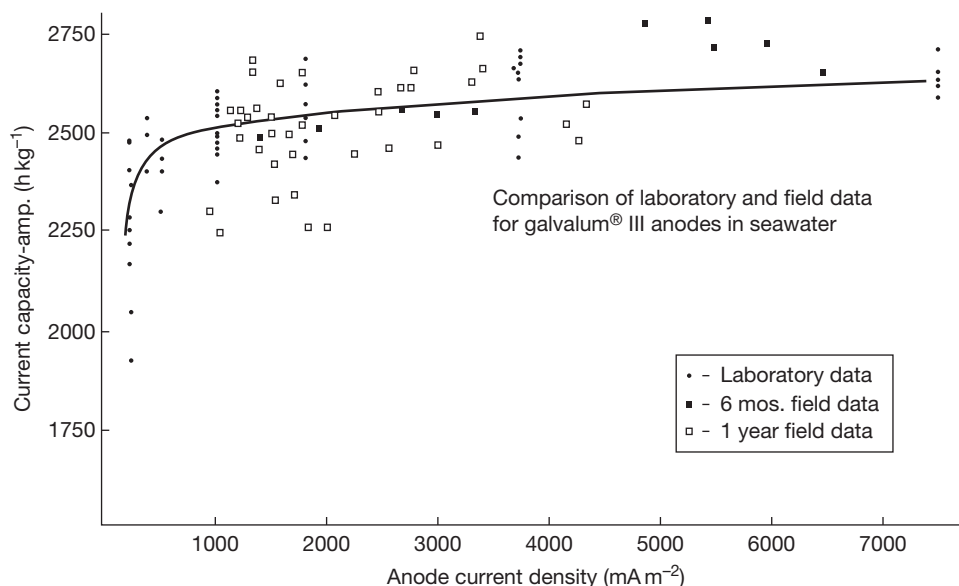


**Figure 3** Capacity of an aluminum anode as a function of current density in seawater.

Ag/AgCl/seawater cannot lead to overprotection, which is an advantage where concerns for coating disbondment and hydrogen damage of high strength steel ( $>700$  MPa) exist.<sup>11</sup>

Zinc anodes have a poor capacity ( $780 \text{ A h kg}^{-1}$ ) compared with aluminum ( $>2500 \text{ A h kg}^{-1}$ ) although with its much higher density equivalent life anodes are frequently of similar dimensions. However, zinc is not susceptible to passivation in low chloride environments or as a consequence of periods of low operating current density. The reliable operational characteristics of zinc often outweigh the apparent economic attraction of aluminum, which can passivate under such conditions. At the time of writing, raw zinc costs about half the price of aluminum, which can significantly contribute to enhancing the appeal of zinc.

Zinc anodes do not find application at temperatures in excess of  $50^\circ\text{C}$ . Zn–Al–Cd alloys suffer intergranular decohesion, and high purity zinc will passivate. Zinc anodes are not predominant in onshore or offshore applications, but they find use under both conditions. The use of zinc anodes on fixed structures in the North Sea is now proscribed under EU regulation (Paris Convention).

#### 4.19.5.2 Aluminum

The great attraction of aluminum anodes is their very high capacity, over three times that of zinc. They are attractive from a cost point of view and also offer

substantial weight savings, which can be of great importance (e.g., offshore structures wherein the float-out weight is of paramount importance and the cost of increased weight of anodes can be many times the cost of the anodes and their installation).

Aluminum anodes comprise essentially three generic types: Al–Zn–In, Al–Zn–Hg, and Al–Zn–Sn. Since Al–Zn–Sn alloys have largely been superseded, they will not be discussed further. Indium and mercury are added to aluminum to act as activators, that is, to overcome the natural passivation of aluminum. Despite this, aluminum anodes are not suitable for low chloride environments, which would lead to passivation. These anodes are therefore not used for land-based applications (although examples of use in environments such as swamps do exist). Similarly, their use in low chloride aqueous environments such as estuaries must be viewed with caution.

Traditionally, the technical choice between Al–Zn–In and Al–Zn–Hg anodes is influenced by their respective operating potentials and capacities; however, more recently the environmental concerns have restricted the use of mercury-containing anodes. Where an additional driving voltage is required (such as in seabed mud), Al–Zn–In anodes may be preferred to ensure adequate structure polarization. Alternatively, a lower driving potential may be acceptable where the additional capacity (and hence weight saving) is the predominant factor; this favors Al–Zn–Hg anodes.

Aluminum anodes are less constant in their electrochemical characteristics than zinc. This presents no major problem provided the designer is aware of their properties. They suffer from reduced capacity and increased operating potential (and hence risk of passivation) with increasing temperatures above approximately 50 °C, decreasing salinity (Figure 2) and decreasing operating current density (Figure 3).

Aluminum alloys are susceptible to thermite sparking when dropped on to rusty surfaces. Consequently, their use may be subject to restrictions. For example, in ships' tanks where explosive gases or mixtures of gases can accumulate, the weight of the anode and the height at which it is suspended are strictly controlled. This is because thermite sparking is dependent on the kinetic energy of the anode released on impact, should it fall.

#### 4.19.5.3 Magnesium

Magnesium anodes are of two generic types, Mg–Mn and Mg–Al–Zn. Both alloy systems have a high driving voltage and therefore find application in high resistivity environments: soils and fresh, or brackish waters, for example. The Mg–Mn alloy is useful in particularly resistive environments (up to 6000  $\Omega$  cm) as a result of an available driving voltage 200 mV greater than Mg–Al–Zn anode. Because magnesium is nontoxic, its use is permissible in potable water systems wherein the conductivity is low.

The high driving voltage may, however, result in overprotection. Combined with relatively poor capacity (1230 A h kg<sup>-1</sup>) and high unit cost, these disadvantages mean that magnesium rarely finds application in subsea environments where alternatives are available. Despite this, Mg–Al–Zn anodes have been used in seabed mud and for rapid polarization of structures (in ribbon form).

The susceptibility of magnesium to thermite sparking when dropped onto rusty surfaces precludes its consideration for applications involving a spark hazard, for example, tankers carrying inflammable petroleum products.

#### 4.19.6 Anode Testing

Tests or sacrificial anode materials are generally conducted for three reasons: for screening (or ranking), performance information, and quality control. The application of sacrificial anodes for the protection of structures requires the development of suitable anode materials for the exposure environment.

1. Screening tests enable the rapid selection of materials that show potential as candidates for the given application. These tests may typically use a single parameter (e.g., operating potential at a defined constant current density) as a pass/fail criterion and are normally of a short duration (usually hours) with test specimen weights of the order of a few tens or hundreds of grams. The tests are not intended to simulate field conditions precisely and often include cutting samples from larger castings and surface preparation to give uniformity/across tests.
2. Performance testing is long term (months to years). Once a potentially attractive formulation has been identified, it is usual to produce detailed data on its performance and behavior as an anode material under the anticipated exposure conditions. For this reason, the test should mirror as closely as possible the expected operating conditions, or where practicable be conducted in the field. Large specimens (tens or hundreds of kilograms) in the as cast condition would be used for these tests.
3. Quality control tests are intended to detect produced materials that deviate from manufacturing specifications, and thus may result in questionable performance. This area of anode testing has probably been the subject of more debate and controversy than any other. The anode alloy is usually subjected to chemical analysis usually by spark emission spectroscopy, which is the primary quality control check. The preparation of samples for this testing, especially if small samples from the melt or samples that are cut from a full anode are to be used, must be validated to ensure that analysis is not corrupted by surface preparation. The risk is reduced if the analytical technique uses dissolution of the sample when surface preparation is irrelevant.
4. Exposure testing has generated a whole industry of quite dubious value to the final product. It was first developed to act as a quality check on the efficacy of solution heat treatment of Al–Zn–Sn alloy anodes when a simple capacity test based on measurement of hydrogen evolved under impressed current was used as a go or no-go acceptance test. Samples, heat treated alongside full sized anodes, were tested overnight. Unfortunately, the results were expressed in the same units as anode capacity, and electrochemical testing has now been mandated to do a job that was never intended, that is, to confirm the actual long-term performance of full sized anodes in service. The use of short-duration (hours or days) tests on small samples, which have had some form of surface treatment not typical of

full-sized anodes, in which the test conditions attempt to reflect the environment of operation, for example, using artificial seawater for a marine application, cannot and never will reflect full-scale operation. In more than 30 years of experience, this author has not heard of a single instance in which a sensible sized anode (>10 kg) made from a correctly formulated alloy has failed to deliver electrochemical performance as expected. Conversely, the examples of small-scale tests on samples giving erratic results are legion, and the subsequent contractual and so called scientific wrangles have contributed nothing to corrosion control.

#### 4.19.7 Cathodic Protection System Design

##### 4.19.7.1 Design Parameters

Before a satisfactory cathodic protection system using sacrificial anodes can be designed, the following information has to be available or decided upon:

1. the area of the steelwork to be protected;
2. the type of coating, if any, that is to be used;
3. the cathodic current density;
4. cathodic protection system life.

While the data given here is general guidance for many situations, detailed guidance will be given in classification society or client rules, and these will take precedence and may change based on the experience gained in actual operation.

#### 4.19.8 Area of Steel Requiring Protection and Coating Considerations

The area of bare steel to be protected is usually calculated from drawings and knowledge of the actual structure and must account for all electrically continuous steelwork exposed to the electrolyte. Steelwork not specified in drawings and subsequently overlooked is a common cause of underdesign. In one classic example, the current drain to the conductors of an offshore production platform was ignored with near disastrous consequences and a requirement for a gigantic retrofit program. In practice, the area is usually taken assuming the steel surfaces to be flat without corrugations, indentations, or surface roughness. An allowance for uncertainties in real area is normally involved.

Many structures, especially pipelines, are coated. Thus, the presented area far exceeds the area of steel

to be protected, which is restricted to uncoated areas and holidays in the coating. It is therefore good practice to assume an arbitrary level of coating breakdown for coated areas to obtain the area of metal requiring cathodic protection. During installation of larger diameter subsea pipelines (>8 in. dia), pipe sections are prepared in 40 ft lengths onshore where coating integrity can be rigorously controlled; however, field joints are often made under severe constraints as the pipe is prepared to go over the stinger. It is therefore often assumed that these field joints will fail, and 2.5% coating loss is used as the basis for design

$$\text{Area to be protected} = \frac{\text{Presented area} \times \% \text{ breakdown}}{100}$$

Breakdown will vary through the life of a structure with the result that the area requiring protection will change. Various estimates of coating breakdown have been made, and Table 6 provides an example based on a single coat epoxy coating system on blast cleaned steel exposed to seawater, for example, a subsea completion structure. Table 6 reasonably assumes a rate of breakdown that varies with time; this will be much greater for fully exposed surfaces compared, for example, to pipeline coatings which may be overlaid with several centimeters of reinforced concrete which are then trenched into the seabed, as are shown alongside. A ship's hull may be expected to lose 10–20% or even more of its coating system in a relatively short period dependant on operating location. The significance of the area of steelwork is that the greater the area, the greater the weight and/or the area of anode material required for protection.

#### 4.19.9 Cathodic Current Densities for Protecting Steel

Examples of current density requirements for the protection of steel (to achieve a steel potential of  $-0.8$  V

**Table 6** Guidance on coating breakdown for offshore structures

<i>Steel structures fully exposed simple epoxy coating</i>			
Lifetime (years)	Coating breakdown %		
	Initial	Mean	Final
10	2	7	10
20	2	15	30
30	2	25	60
40	2	40	90
<i>Pipeline with glass fiber/bitumen and 70-mm reinforced concrete weight coat</i>			
40	1	2.5	5

**Table 7** Guidance on current density for cathodic protection of bare steel

Location	Current density (mA m <sup>-2</sup> )		
	Initial	Mean	Final
Northern North Sea	180	90	120
Southern North Sea	150	90	100
Arabian Gulf	130	70	90
Indian Ocean	130	70	90
Australia	130	70	90
Brazil	130	70	90
West Africa	130	70	90
Gulf of Mexico	110	60	80
Indonesia	110	60	80
Saline mud	25	20	15

versus Ag/AgCl/seawater) are given in [Tables 7](#). It should be realized that the current demand of a structure will be influenced by, *inter alia*, temperature, degree of aeration, flow rate, protective scales, burial status, presence of bacteria, and salinity.

It is important that the correct current density requirement is assigned for design purposes. If too high a value is used the structure may be overprotected and anode capacity wasted. On the other hand, if too small a value is used it will mean that the protection system will not achieve its design life.

#### 4.19.10 System Life

Cathodic protection systems may be designed with a life as short as 1 year or more than 40 years. The greater the time of protection, the greater the mass or anode material that is required.

Intermittent exposure and local conditions need to be considered also. The ballast or storage tanks of ships will experience periods of complete submergence and partial coverage, and may at times be empty. Similarly, the wetted areas of offshore structures may be governed by tidal and seasonal variations. Local requirements must therefore be considered in order to achieve the optimum amount of anodic material to achieve the life of the system.

##### 4.19.10.1 Calculating the Weight and Number of Individual Anodes

Firstly, the total weight of anode required to protect the structure for its projected life is calculated. This is given by:

$$W = \frac{i_{av} A l \times 8760}{C}$$

where  $W$  is the total mass of anode material (kg);  $A$ , the structure area to be protected (m<sup>2</sup>);  $i_{av}$ , the mean structure current density demand (A m<sup>-2</sup>);  $l$ , the design life in years (1 year = 8760 h); and  $C$  is the anode capacity (A h kg<sup>-1</sup>).

Obviously, the total weight of the anode material must be equal to or be greater than the total weight,  $W$ , calculated above. Similarly, each anode must be of sufficient size to supply current for the design life of the cathodic protection system. The anodes must also deliver sufficient current to meet the requirements of the structure at the beginning and end of the system's life. That is, if current demand increases (as a result of coating breakdown, for example), the output from the anodes should meet the current demands of the structure.

##### 4.19.10.2 Anode Size and Shape

In practice, while there is often an extensive range of suitable anode sizes to select from, economics may dictate a bespoke anode for a project depending on its precise requirements. Computer programs are used to optimize (minimize) the number of anodes required to satisfy the often conflicting protection requirements. The cost of the anode insert in a platform anode may be close to that of the anodic material, and the cost of lifting, welding, etc. is substantially more than that of the anode. Furthermore, after a set of moulds has been used to produce several thousand anodes, they will probably only be fit for recycling.

The current output from an anode will depend on its resistance, which will be a direct function of shape and size. Generally, larger anodes will have a higher current output. Anodes of the same weight but differing shape can have different outputs because the surface area to weight ratio will not be equal for all possible dimensions. Thus, for a given weight of anode, the shape will offer a degree of flexibility when considering current output.

##### 4.19.10.3 Anode Output

Anode output is the current available from the anode under the design conditions. It will depend on the shape of the anode, the resistivity of the environment, the protection potential of the structure, and the anode operating potential. It is defined as:

$$I = \frac{[E_2 - E_1]}{R}$$

$I$  is the anode output (A);  $E_1$ , the operating potential of the anode (V);  $E_2$ , the protection potential (V); and  $R$  is the anode resistance ( $\Omega$ ).

The protection potential of steel in aerobic environments is taken as  $-0.80\text{ V}$  (versus  $\text{Ag}/\text{AgCl}/\text{seawater}$ ).

#### 4.19.10.4 Anode Resistance

**Table 8** lists some of those formulae suitable for the calculation of anode resistance,  $R$ , under submerged conditions. Some are based on earth resistance effects and modifications of the formulae used in the design of electrical earthing systems, while others are purely empirical. Similar formulae exist for anodes in buried conditions. These have been extensively researched and reviewed.<sup>20–24</sup>

To calculate the anode resistance, a knowledge of the environmental resistivity is required. For submerged anodes, the water resistivity can be obtained from graphical representations such as in **Figure 4**, provided that the temperature and water density are

known. However, field data are preferable, and, in the case of soils that can have widely varying resistivities, they are essential.

#### 4.19.10.5 Anode Life

Having calculated the resistance, and hence the current output, the anode life,  $L$ , is checked by the calculation:

$$L = \frac{MU}{IE}$$

where  $L$  is the effective life of anode (years);  $M$ , the mass of single anode (kg);  $U$ , the utilization factor, for example, 0.75–0.80 for bracelet anodes and 0.95 for platform anodes;  $E$ , the consumption rate of the anode ( $\text{kg A}^{-1} \text{ year}^{-1}$ ) (inverse of capacity in suitable units); and  $I$  is the anode output (A).

**Table 8** Table of anode resistance formulae DnV RP B401

Anode type	Resistance formula
Long slender stand-off <sup>a,b</sup> $L \geq r$	$R_a = \frac{\rho}{2\pi L} \left( \ln \frac{4L}{r} - 1 \right)$
Short slender stand-off <sup>a,b</sup> $L < 4r$	$R_a = \frac{\rho}{2\pi L} \left[ \ln \left\{ \frac{2L}{r} \left( 1 + \sqrt{1 + \left( \frac{L}{2L} \right)^2} \right) \right\} + \frac{r}{2L} - \sqrt{1 + \left( \frac{r}{2L} \right)^2} \right]$
Long flush-mounted <sup>b</sup> $L \geq 4$ width and $L > 4$ thickness	$R_a = \frac{\rho}{2S}$
Short flush-mounted, bracelet and other types	$R_a = \frac{0.315\rho}{\sqrt{A}}$

<sup>a</sup>The equation is valid for anodes with minimum distance 0.30 m from protection object. For anode-to-object distance minimum 0.15 m the same equation may be applied with a correction factor 1.3.

<sup>b</sup>For noncylindrical anodes:  $r = c/2\pi$  where  $c(\text{m})$  is the anode cross-sectional periphery.

Source: DnV RP B401 (2005) – Recommended practise for cathodic protection design.

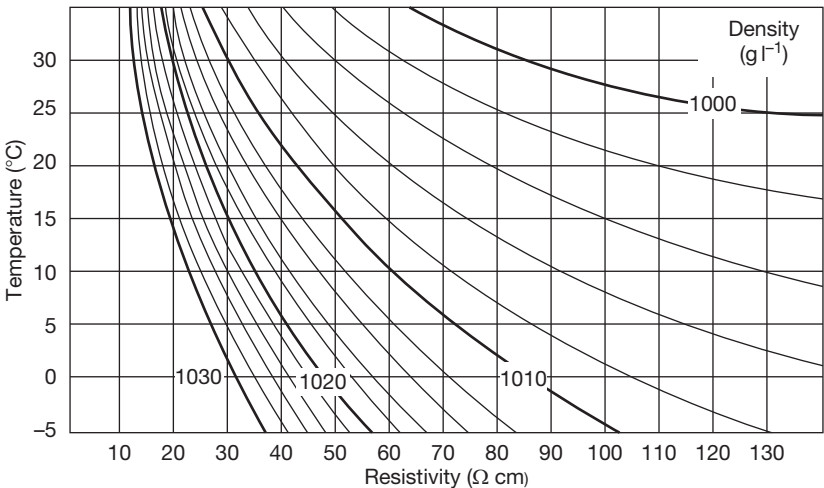


**Figure 4** Resistivity as a function of specific gravity for seawater/fresh water mixtures.



$U$  is purely a function of anode geometry and is the fraction of anode material consumed when the remaining anode material cannot deliver the current required or the anode can no longer be supported by its insert.

Excessive anode life is of no benefit. If the calculated life is unsuitable a different anode size and/or shape should be considered. However, this may not always be possible, especially for short-life, coated structures, when dimensional constraints on the anodes may be imposed.

#### 4.19.10.6 Number of Anodes

The total number of anodes,  $N$ , is calculated from:

$$N = \frac{Ai_{ay}}{I}$$

This calculation should yield a practicable number of anodes; that is, 10 or 10 000 anodes are both clearly unacceptable for the distribution of protection. On an offshore oil production platform,  $N \times M$  must be equal to, or greater than, the total weight or anode material,  $W$ , required.

It is also useful at this point to consider the limitations imposed by the production processes and the actual application of the anode. For a platform anode, hypothetically, the anode could be almost as long as the water depth, but first such an anode would have such a large mass and consequently inertia that it would be unlikely to survive the installation or piling processes and would be torn off. Using a stronger insert and attachment configuration would result in such a large diameter core relative to the body cross section that the anode material could reasonably be expected to split longitudinally during the solidification and subsequent cooling. Some of these could be overcome by semicontinuous casting rather than horizontal gravity casting. However, this process, originally developed for production of extrusion ingots still, has the limitation of the depth of the pit into which the casting is discharged and the lifting equipment servicing it. In order to minimize the likelihood of some or all of these, for all practical purposes, the maximum core diameter of a platform anode is 150 mm, and for this to be cast into an anode, the cross section would have to give at least 100-mm depth of cover of the anodic material over the insert. While some foundries design a small cross-section taper over the length of the anodes, others use very heavy preheated wall moulds and inserts (or both) to minimize anode mould interaction. Unless the mould/insert is heated to the casting temperature of

the anode alloy, the mould and insert will continue to expand as the anode solidifies and contracts, and transverse cracking of the anode becomes more probable. Grain refinement increases the high strength of the alloy, but there are limits to how much can be done. Typically, a maximum anode length of 3 m and a maximum weight of 500 kg have been imposed as practical limitations. Bracelet anodes for submarine pipelines are often sized to match a weight coating thickness where there is no weight coating. The thinner the anode, the lesser the impact as it goes over the stinger during laying. Many of the same limitations that applied to platform anodes also apply to bracelets although thin wall moulds and water cooling have assisted reducing anode thickness where necessary. Bracelet diameters are governed by pipe diameters and thickness by laying or coating considerations, but they are unlikely to be viable at more than 1.5 m long and 400 kg in weight. Needless to say, some readers will be able to quote examples of anodes larger than those implied here, but they will be few and far between and almost certainly associated with some special circumstance; for example, a very large platform anode mounted on a sea bed sled or a bracelet designed to be mounted on a large pipe to be retrofitted to a platform to compensate for a shortfall in the original design.

It can be difficult to achieve both the exact current output and precise weight of anode material simultaneously although, as mentioned previously, the use of iterative calculation by a computer program can optimize this. Where a compromise is necessary, both must at least match design requirements.

A check to ensure that the anodes will deliver sufficient current to protect the structure at the end of the design life should be conducted. This entails calculating the expected anode output at the end of its life and checking that it meets the demands of the structure. Generally, the output is calculated using a modified resistance based on an anode that is 90% consumed.

#### 4.19.10.7 Anode (End Current) Distribution

It is evident that a greater number of anodes distributed over the structure will improve current distribution. However, aside from the unacceptable cost incurred by attaching excessive numbers of anodes, an anode must continue to function throughout the life of the structure and must, therefore, be of sufficient size to meet the design life. A very large number of heavy anodes is clearly impracticable and uneconomic.

It is essential to ensure adequate current distribution such that all of the exposed structure remains

protected; particularly important, for example, for the nodes of an offshore steel structure. Similarly, over-protection should be avoided. Thus, sacrificial anodes need to be distributed to ensure that the protection potential over the whole structure is achieved.

The proximity of the anodes to structures is also important. For example, if the sacrificial anodes are placed on or very close to the steel pipework in soil, then the output from the face of the anodes next to the steelwork can be severely limited. Alternatively, in high conductivity environments, corrosion products may build up and wedge between the anode and the structure. The resulting stresses can lead to a mechanical failure of the anode. On the other hand, when anodes are located at an appreciable distance from the steelwork, part of the potential difference will be consumed in overcoming the environmental resistance between the anode and cathode.

Complex computer models are now available to assist in defining the optimum anode distribution.<sup>25</sup>

#### 4.19.10.8 The Anode Insert

The anode insert must be strong enough to support the weight of the anode and must be capable of being welded, or mechanically fixed to the cathode.

It should be appreciated that the attachment may be required to withstand the launching and pile driving of a steel jacket for offshore applications.

Consideration must be given to the ease and speed of anode fixing, as this is a significant part of the total installation cost. The methods of fixing anodes to flat, vertical or horizontal surfaces are relatively well known and simple. The methods of fixing anodes to curved surfaces of pipelines and immersed structures are more complex, and generally require more steel insert. **Figure 5** shows typical anodes in common use offshore on jackets and pipelines.

While catalogues of proprietary platform anodes often show a wide variety of attachment arrangements involving tube, angle, channel, and other sections, it must be remembered that most anodes are attached to structural tubular members of a stressed structure subject to significant cyclic forces during installation, piling, and service (wave impacts). The welds between anode insert and structure have to be designed to avoid fatigue failure; not only will this involve, in most cases, the doubler plates of a metal compatible with both anode and structure but also full penetration welds that are subject to most stringent inspection (probably radiography) and the avoidance of stress raisers,

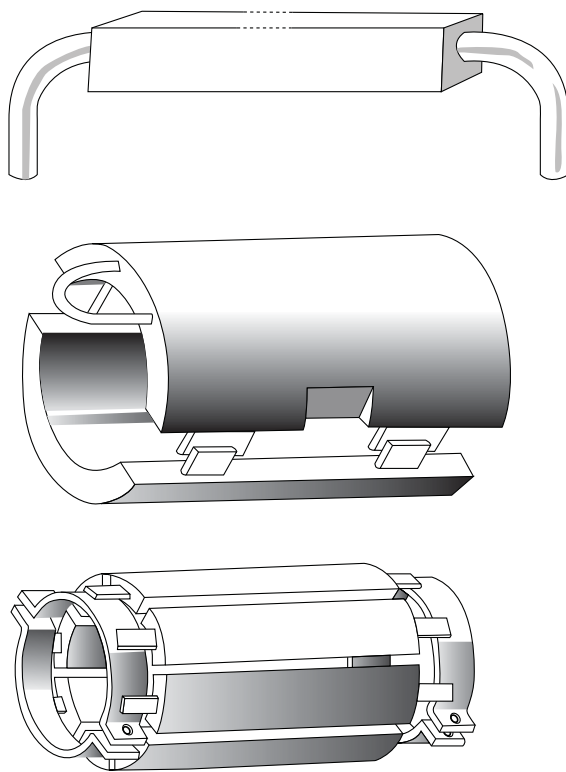


**Figure 5** Typical anodes in common use offshore on jackets and pipelines.

meaning that only all tubular inserts are likely to be acceptable. Bracelet anodes are usually clamped around the pipe with little or no welding between inserts, and pipe steel electrical connection is achieved by a low temperature connection process such as copper thermite welding or pin brazing with a very small contact area, but even then usually to an expendable doubler plate.

#### 4.19.10.9 Utilization Factor

This component of anode design calculation is worthy of serious consideration as too often a figure of 0.9 or 90% is used for platform anodes and 0.75–0.85 or 75–85% for bracelets without understanding where it originates from. Essentially, the utilization factor reflects how much of the net weight of an anodes delivers useful cathodic protection before it becomes structurally unstable and (literally) falls to pieces. Examination of long thin anodes, which are cast on tubular inserts, towards the end of their life reveals that the attack on the original rectangular cross section approaches a final circular appearance.

Moreover, the attack is preferential towards the ends of the anode such the overall appearance approximates to a traditional 'cigar' shape while it remains supported by the insert. Anodes with a stand-off at least 300 mm from the structure being protected in open seawater are unlikely to be seriously affected by proximity and corrode nonuniformly. Anodes installed close to the structure should have an inert nonconducting coating (coal tar epoxy) on the face closest to the structure to minimize preferential attack on the close face and the possibility of anode corrosion products building up behind the anode and forcing it off. This is of particular importance for bracelet or hull anodes and much less so for platform anodes.

For pipeline or hull anodes, the distance through the anode that the insert is placed directly influences the utilization factor since; if, for example, the insert is in the centre of the anode mass, the utilization factor will be 0.5 or 50%; if it were on the front face, the  $U/F$  would theoretically be zero and on the back face, 1.0, although none of these would be practical. Thus, if the insert is 75% of the depth of the anode from the front face, then the utilization factor is likely to approximate to 75%. Ingenious designs of insert involving a backing plate with a mesh embedded in the back face of the anode material in order to approach a  $U/F$  of 1.0 have been patented but are not in common use.

#### 4.19.10.10 Backfills for Anodes

When zinc or magnesium anodes are used for cathodic protection onshore,<sup>25–28</sup> they are usually surrounded by a backfill, which decreases the electrical resistance of the anode. Small anodes are usually surrounded with backfill in bags and large anodes are usually surrounded with a loose backfill during installation. The backfill prevents the anode coming into contact with the soil and suffering local corrosion, thus reducing the capacity. By surrounding the anodes with a backfill, the combination of the anode with soil salts is reduced, and this helps prevent the formation of passive films on the anode surface.

The effect of the backfill is to lower the circuit resistance and thus reduce potential loss due to the environment. The additive resistances of the anode/backfill and backfill/soil are lower than the single anode/soil resistance. Backfills attract soil moisture and reduce the resistivity in the area immediately round the anode. Dry backfill expands on wetting,

and the package expands to fill the hole in the soil and eliminate voids.

For use in high resistivity soils, the most common mixture is 75% gypsum, 20% bentonite, and 5% sodium sulfate. This has a resistivity of approximately 50 ohm cm when saturated with moisture. It is important to realize that carbonaceous backfills are relevant to impressed current anode systems and must not be used with sacrificial anodes. A carbonaceous backfill is an electronic conductor and noble to both sacrificial anodes and steel. A galvanic cell would therefore be created causing enhanced dissolution of the anode, and eventually corrosion of the structure.

### 4.19.11 Other Considerations

#### 4.19.11.1 Calcareous Scale

A consequence of cathodic protection in seawater is the formation of a protective calcareous scale.<sup>29</sup> The increased local pH at the steel surface caused by hydroxyl production (a product of the cathodic reaction) favors the deposition of a mixed scale of  $\text{CaCO}_3$  and  $\text{Mg(OH)}_2$ . This scale is beneficial since it is protective and nonconducting, thus reducing the cathodic current density. Ensuring a high current density in the early period of operation will encourage calcareous scale deposition and thus reduce the current requirements in the long term.

The build-up of calcareous deposits is a complex topic. Very high current densities will not necessarily result in the most protective scale. In the extreme, hydrogen evolution may rupture the scale resulting in reduced protection. An optimum current density will exist, and this should be recognized.

#### 4.19.11.2 Combined Alloy Anodes for Rapid Structure Polarization

Combined (or binary) alloy sacrificial anodes have been developed.<sup>30</sup> An aluminum anode, for example, might have attached to it a short-life supplementary magnesium anode, or anodes, for quick polarization of the structure. The overall reduction in structure current requirements is claimed to result in an anode weight saving of 35–50%. This derives from the increased current output from the anode early in its operating life, giving rise to a relatively protective calcareous scale, which then reduces the current demand for protection later in life.

**4.19.11.3 Flame Sprayed Aluminum**

The use of flame sprayed aluminum (FSA) with a silicon sealer paint has been applied to protect high-strength steel tension legs of a North Sea production facility.<sup>32</sup> The FSA system primarily acts as a very effective barrier coating. In addition, the coating has significant anodic capability and aluminum corrosion products serve to plug coating defects. The sealer, although reducing the anodic current output, serves to increase the service life of the FSA coating. This coating system is subject to strict control of application procedures.

**4.19.11.4 Protection of High-Alloy Steels**

High-alloy pipeline steels (e.g., austenitic–ferritic or duplex) have been used where the product stream demands materials with better corrosion resistance than carbon steel. In practice, the external corrosion resistance of these materials cannot be guaranteed, so cathodic protection is employed to protect areas which may be subject to corrosion.

Concern about hydrogen damage has led to much debate regarding limits for protection potentials of high-alloy steels. However, it is thought that under normal seawater service and cathodic protection conditions, these materials will not be adversely affected provided that the microstructure has at least 40% of austenite present. This latter point is of particular importance to welds and their heat affected zone where careful control of heat input is necessary to maintain a favorable microstructure.

The latter part of this chapter has dealt with the design considerations for a sacrificial anode cathodic protection system. It has outlined the important parameters and how each contributes to the overall design. This is only an introduction and guide to the basic principles of cathodic protection design using sacrificial anodes and should be viewed as such. In practice, the design of these systems can be complex and can require experienced personnel who will have to not only satisfy the needs of the protection system but also the client and the classification body, and not all of these are mutually compatible.

**References**

1. Davy, H. *Philos. Trans. Royal Soc. (London)* **1824**, 114(1), 117.
2. Davy, H. *Philos. Trans. Royal Soc. (London)* **1824**, 114(2), 242.
3. Davy, H. *Philos. Trans. Royal Soc. (London)* **1825**, 115(2), 328.
4. Crundwell, R. F. In *NACE Corrosion 82*, Houston TX, March 1982; Paper no. 166.
5. Crundwell, R. F. In *Cathodic Protection Theory and Practice*, 2nd International Conference, Stratford upon Avon, June 1989.
6. Googan, C. G. Ph.D. Thesis, Institute of Science and Technology, University of Manchester, 1979.
7. Salleh, M. M. B. H. Ph.D. Thesis, University of Manchester, 1978.
8. Klinghoffer, O.; Linder, B. In *NACE Corrosion/87*, San Francisco, CA, March 1987; Paper no. 59.
9. US Military Specification MIL-A-18001 K, 1991.
10. Jensen, F. O.; Torleif, J. In *Corrosion/87*, San Francisco, CA, March 1987; Paper no. 72.
11. Det Norske Veritas Recommended Practice, Cathodic Protection Design, RP B401. 1986, revised 1993, revised 2005.
12. Ahmed, D. S.; Ashworth, V.; Scantlebury, J. D.; Wyatt, B. S. *Br. Corros. J.* **1989**, 24, 149.
13. Ashworth, V. Private communication.
14. Lennox, T. J.; Peterson, M. H.; Groover, R. E. *Mater. Protect.* **1968**, 7(2), 33.
15. NACE Standard Recommended Practice RP0387-87, Metallurgical and Inspection Requirements for Cast Sacrificial Anodes for Offshore Applications; NACE: Houston, TX, 1990.
16. Schreiber, C. F.; Murray, R. W. In *Corrosion/88*; St. Louis, March 1988; Paper no. 32.
17. Schreiber, C. F.; Murray, R. W. *Mater. Perform.* **1981**, 20(3), 19.
18. Houghton, C. J.; Ashworth, V. *Mater. Perform.* **1982**, 21(7), 20.
19. Ashworth, V.; Googan, C. G.; Scantlebury, J. D. *Br. Corros. J.* **1979**, 14(1), 46.
20. Dwight, H. B. *Electrical Engineering*; 1936, Vol. 55, 1319–1328.
21. Sunde, E. D. *Earth Conduction Effects in Transmission Systems*; Van Nostrand: New York, NY, 1949.
22. Cochran, J. In *Corrosion 82*, Houston, TX, March 1982; Paper no. 169.
23. Nisancioglu, K. In *Corrosion 84*; New Orleans LA, April 1984; Paper no. 255.
24. Morgan, J. H. *Cathodic Protection*, 2nd ed.; NACE: Houston, TX, 1987.
25. Nisancioglu, K. In *Cathodic Protection Theory and Practice*, 2nd International Conference, Stratford upon Avon June 1989.
26. Osborn, O.; Robinson, H. A. *Corrosion* **1952**, 8, 114–129.
27. Craven, D. *The Protected Gas Service*; Institution of Gas Engineers: Cardiff, 1969.
28. Peabody, A. W. *Control of Pipeline Corrosion*; NACE: Houston, TX, 1971.
29. Evans, T. E. In *Cathodic Protection Theory and Practice*, 2nd International Conference, Stratford upon Avon June 1989.
30. Schreiber, C. F.; Reding, J. T. In *Corrosion/90*; Las Vegas, NV, April 1990; Paper no. 381.

## 4.20 Impressed-current Anodes

**W. R. Jacob**

The Corrosion Consultancy Limited, Tatton House, 3 Manor Farm, Little Wenlock, Shropshire TF6 5BZ, UK

© 2010 Elsevier B.V. All rights reserved.

4.20.1	Introduction	2782
4.20.2	Ferrous Materials	2782
4.20.2.1	Steel	2782
4.20.2.2	Cast Iron	2782
4.20.2.3	Stainless Steel	2783
4.20.2.4	High-Silicon Irons (HSI)	2783
4.20.2.4.1	Iron-silicon alloys	2783
4.20.2.4.2	Silicon-molybdenum iron	2784
4.20.2.4.3	High-silicon-chromium iron	2784
4.20.2.5	Magnetite Anodes	2784
4.20.2.6	Ferrite Anodes	2785
4.20.3	Lead-Based Materials	2786
4.20.3.1	Lead Alloys	2786
4.20.3.2	Lead/Platinum Bielectrodes	2787
4.20.3.3	Lead/Magnetite Composites	2788
4.20.3.4	Lead Dioxide on other Substrates	2788
4.20.4	Carbonaceous Materials	2788
4.20.4.1	Graphite	2788
4.20.4.2	Carbonaceous Backfills	2789
4.20.4.3	Conductive Polymers	2791
4.20.4.4	Conductive Overlay Systems	2791
4.20.4.5	Conductive Paints	2792
4.20.5	Platinum Anodes	2792
4.20.5.1	Platinum	2792
4.20.5.2	Platinized Titanium	2792
4.20.5.3	Platinized Niobium and Tantalum	2795
4.20.5.4	Mixed Metal Oxide Coated Titanium	2796
4.20.6	Ceramic Anodes	2797
4.20.7	Applications of Impressed-Current Anodes	2798
4.20.7.1	Offshore and Marine	2798
4.20.7.2	Onshore	2798
4.20.7.3	Internal	2798
4.20.7.4	Concrete	2798
References		2799

### Glossary

**Backfill** A material having preferred properties, such as conductivity, noncorrosiveness, etc., and that is emplaced around an anode in order to enhance its performance.

**Groundbed** The location of one or more buried anodes in, for example, soil, mud, etc.

### Abbreviations

**AC** alternating current

**ASTM** American Society for Testing and Materials

**BS** British Standard

**DC** direct current

**DSA** Dimensionally stable anodes

**HSI** High-silicon iron

**MMO** Mixed metal oxides



## 4.20.1 Introduction

The ideal anode for impressed-current cathodic protection (CP) would be capable of passing the required current into the environment, at a low operating overpotential, with insignificant loss of material with time. The first application of impressed-current systems used steel anodes which were Faradaically consumed during operation. Later anodes replaced such metal dissolution with the evolution of oxygen or chlorine, depending on the composition of the environment. The lower anode dissolution rate associated with such evolution then depends on the properties of the surface film produced (usually an oxide) and its resistance to the evolved oxidizing gases. Thus, the oxygen evolved on graphite forms some carbon dioxide consuming some of the carbon in the process. Lead and silicon iron anodes rely on the formation of an insoluble but conductive oxide film allowing current to pass while significantly reducing, but not eliminating, metal loss.

This reduction in anode consumption because of oxide formation is most efficient on platinum, where the loss rate is of the order of  $1.0\text{--}10\ \mu\text{g A}^{-1}\text{h}^{-1}$ . Further reductions in dissolution rate have come with the development of the most recent anode materials, which effectively dispense with the underlying dissolving metal by using a coating consisting solely of oxides (e.g., mixed metal oxides, MMO), supported on an anodically inert substrate (titanium). Even at high currents, these anodes are consumed at a rate which can be as much as an order of magnitude less than that seen on platinum. These latter materials probably represent the ultimate to be achieved in anode performance.

The various types of materials which have been, or are, used as anodes in impressed-current systems may be classified as follows:

- Ferrous materials: steel, cast iron, iron, stainless steel, high-silicon iron, high-silicon molybdenum iron, high-silicon chromium iron, magnetite, ferrite.
- Lead materials: lead–antimony–silver, lead with platinum alloy microelectrodes, lead/magnetite, lead dioxide/titanium, lead dioxide/graphite.
- Carbonaceous materials: graphite, carbon, coke breeze, conductive polymer, conductive paint.
- Precious metals and oxides: platinum, platinized titanium, platinized niobium and tantalum, mixed metal oxide-coated titanium, titanium oxide-based ceramics.

Each group is discussed in detail in the following sections, while the final sections briefly describe those that are presently employed in common CP scenarios.

## 4.20.2 Ferrous Materials

### 4.20.2.1 Steel

One of the earliest materials to be used in impressed current CP was carbon steel. Although it has severe limitations, it has sometimes been found to be cost effective in situations where steel scrap is available in suitable quantities and geometry, and it is only in such situations where its use would now be considered. Steel anodes have found particular use in seawater, with a surprising variety of forms being reported to have been utilized, for example, pipes, piling, machinery, rails, and even obsolete ships which have not been economic to salvage. When used as an anode, the consumption rate of steel is close to the theoretical, Faradaic value of  $9.1\ \text{kg A}^{-1}\text{year}^{-1}$ . Consumption rates in excess of the theoretical value have been reported for steel in some waters.<sup>1</sup>

When buried, ferrous anodes tend to exhibit high resistance polarization because of the formation of a voluminous corrosion product. This can be alleviated by closely surrounding the anode with carbonaceous backfill; this of course increases the cost if the backfill is also not a locally available by-product. It is necessary to ensure compactness and homogeneity of backfill at all areas around the anode, as otherwise rapid loss of metal at poorly compacted areas can occur.

In recent years, deep-well groundbeds for the protection of clusters of oil or gas wells have been provided by using the steel casings of otherwise abandoned wells in the same area. In order to provide conductance to the active length of the casing, the wells have been filled with carbonaceous backfill, such as coke breeze. Commercial examples of such installations are known to be working well after the period of 28 years.<sup>2</sup> It is necessary to take considerable care to ensure the integrity of anode cable connections and to use multiple connections to ensure redundancy in the event of cable failure. Connections must be encapsulated to protect them from the environment.

### 4.20.2.2 Cast Iron

Cast iron may be used under similar circumstances to steel, but has inferior mechanical properties. It has

been used, although not in recent times, for internal CP, of cooling water systems, where it has been demonstrated that the presence of ferrous ions in the cooling water is of benefit in reducing sulfide-induced attack on Cu alloy tube plate and tubes.<sup>3</sup> Ferrous sulfate dosing is now used as a more reliable means of achieving the same end.

#### 4.20.2.3 Stainless Steel

Stainless steel has been tried as an inert anode, mainly under laboratory conditions and with only partial success. Even at low current densities, the majority of alloys pit rapidly in fresh water, although others show the ability to remain passive at a low current density.<sup>4,5</sup> However, at practical current densities, the presence of chloride ions, deposits on the anode, or crevice corrosion at the anode support leads to rapid failure,<sup>6</sup> but it may be possible that stainless steel could give useful service under certain conditions and with particular alloys.<sup>7</sup>

#### 4.20.2.4 High-Silicon Irons (HSI)

##### 4.20.2.4.1 Iron-silicon alloys

High-silicon iron (HSI) anodes are cast-iron alloys that contain 14–18% Si and were first developed in 1912,<sup>8</sup> although it was not until 1954 that they were first evaluated for use as impressed-current anode materials in CP.<sup>1</sup> Their major disadvantages are those of a hard brittle material unable to withstand thermal or mechanical shock. HSI has a long and successful history as a corrosion-resistant material in the chemical industry for such items as acid storage vessels and has been used in this application for more than 60 years. A typical analysis for HSI anodes is 14.5% Si, 0.75% Mn, 0.95% C, and remainder Fe. The anodes conform to either BS 1591:1975 or ASTM A518–80 Grade 2. The latter lists the permissible Si content range as between 14.20 and 14.75. As the material is not readily machined, it is cast into standard sizes to suit the general requirements of the CP industry. Anodes can be cast as solid rods, or centrifugally cast cylinders.

Used as an anode, HSI readily forms a protective film, which is reformed if removed mechanically. The film is gray-white in appearance and has a tendency to flake under the compressive stress produced at thickened areas. The film is 50% porous and contains 72–78% SiO<sub>2</sub>.<sup>8</sup> It is a fairly good electron conductor,

even though SiO<sub>2</sub> in its natural state is a dielectric. The mechanism whereby the SiO<sub>2</sub> becomes a conducting oxide has been reviewed in some detail by Shreir and Hayfield,<sup>9</sup> and is probably associated with doping of the SiO<sub>2</sub> with Fe ions.

HSI anodes are subject to severe pitting in the presence of halide ions, and this precludes their use in seawater or other environments in which these ions may be present. They are suitable for freshwater applications (below 200 ppm Cl<sup>−</sup>), although not suitable for temperatures above 38°C. The addition of Mo or Cr to the alloy can improve performance under these conditions, with an upper limit temperature of 56°C,<sup>10</sup> which may be affected by the composition of the water and the operating conditions.

The consumption rate of HSI depends upon the current density and the environment in which the anode is used. HSI is superior to graphite in waters with resistivity greater than 10 Ω m, but in waters of 0.5 Ω m and below, it is susceptible to pitting. Experience in fresh water in the pH range 3 to 10 indicates a nominal consumption rate of approximately ~0.1 kg A<sup>−1</sup> year<sup>−1</sup> at 20°C. The precise value is dependent upon the solution composition and the temperature.<sup>11</sup> A number of reports on the performance of HSI anodes in different environments have been produced.<sup>11–14</sup>

The consumption rate of HSI anodes buried directly in soils will vary depending upon the soil composition and will be excessive in chloride-containing soils. In quicksand, consumption rates of ~0.35 kg A<sup>−1</sup> year<sup>−1</sup> have been reported,<sup>11</sup> while in other soils, consumption rates in the region of 1 kg A<sup>−1</sup> year<sup>−1</sup> are possible. A consumption rate in the region of 0.1–0.25 kg A<sup>−1</sup> year<sup>−1</sup> would be expected in a correctly installed carbonaceous backfill, when operating in a soil of insignificant chloride content and a surface current density of no more than 20 A m<sup>−2</sup>. Higher consumption rates would result from high local current densities, often caused by inadequate backfill, partial submersion, or silting. A coke-breeze backfill can be installed around the anodes when buried in higher resistivity soil, so as to reduce the overall resistance to the earth and enabling the use of higher current groundbeds. There is a tendency for the surface resistance of a buried anode to increase, but not to an extent that it affects performance. The large resistance changes sometimes reported for carbonaceous beds are usually due to gaseous polarization (gas blocking) caused by poor venting or by inadequate compaction of backfill.

With any impressed current anode, an effective connection is vital. Loss of insulation at the connection point or penetration of water into the anode cable seal will bring about rapid failure. Hydrostatic pressure should be borne in mind when considering the seal required for any depth of water. End connections for solid rod anodes use compression, cast lead, or taper pin connections, sealed by a combination of epoxy filling and heat shrinkable sleeves. Cylindrical anodes have center connections with taper wedges or cast lead. The useful life of HSI anodes is usually considered at an end after a 33% reduction in diameter, but this depends upon the original diameter, the amount of pitting sustained, and the mechanical stresses to be withstood. Therefore, doubling the cross-sectional area may more than double the effective life of the anode.

#### 4.20.2.4.2 *Silicon-molybdenum iron*

The addition of 1–3% Mo to HSI modifies the anodic oxide film resulting in improved performance in solutions containing above 200 ppm chloride or at temperatures of 38 °C or above. In seawater at 10 A m<sup>-2</sup>, the addition of Mo reduced the consumption rate from 0.22 to 0.15 kg A<sup>-1</sup> year<sup>-1</sup> at ambient temperatures and from 0.63 to 0.21 kg A<sup>-1</sup> year<sup>-1</sup> at 51 °C.<sup>15</sup> However, a considerably higher rate of 0.9 kg A<sup>-1</sup> year<sup>-1</sup> at 10.8 A m<sup>-2</sup> has been reported for molybdenum-containing silicon iron in chloride-containing waters.<sup>11</sup> Because the addition of Cr results in even greater improvements in performance, the molybdenum-enhanced alloy has been little used.

#### 4.20.2.4.3 *High-silicon-chromium iron*

High-silicon chromium iron alloy (HSCI) came into commercial use by about 1959.<sup>15</sup> The addition of chromium, together with silicon, results in a film that has a high resistance to pitting in waters containing halide ions and these alloys can, therefore, be used with confidence in seawater- or chloride-containing soils. A typical analysis is 14.5% Si, 0.75% Mn, 1.0% C, 4.5% Cr, and remainder Fe. In the United Kingdom, this anode is manufactured to BS 1591:1975, which permits a variation in silicon content from 14.25% to 15.25% and of chromium from 4.0% to 5.0%, with a maximum carbon content of 1.40%. The equivalent US standard is ASTM A 518-64 Grade 2 with a silicon content of 14.2–14.75% and a chromium content of 3.25–5.00%. Neglecting possible mechanical damage and anode/cable joint failure, it is possible, in view of the very minor pitting sustained in free suspension, for the

anode to continue operating until almost totally consumed. Note that HSCI anodes cannot be used in potable waters because of the possibility of chromium contamination.

Comparative tests of silicon iron and chromium-containing silicon iron in seawater at 93 °C and 10.8 A m<sup>-2</sup> produced consumption rates of 8.4 kg A<sup>-1</sup> year<sup>-1</sup> and 0.43 kg A<sup>-1</sup> year<sup>-1</sup>, respectively.<sup>16</sup> These figures show that in seawater the consumption rate of HSI without the addition of chromium may approach that of steel, but because of the very deep pitting experienced in chlorides, and the fragility of HSI, it is effectively inferior to steel. However, in fresh waters, HSI has a far lower corrosion rate than steel. The consumption rate of chromium-containing variety, freely suspended in seawater, increased from 0.33 kg A<sup>-1</sup> year<sup>-1</sup> at 10.8 A m<sup>-2</sup> to 0.48 kg A<sup>-1</sup> year<sup>-1</sup> at 53.8 A m<sup>-2</sup>. Direct burial in seawater silt or mud also increases the consumption rate, with value of 0.7 kg A<sup>-1</sup> year<sup>-1</sup> at 8.5 A m<sup>-2</sup> increasing to 0.94 kg A<sup>-1</sup> year<sup>-1</sup> at 23.4 A m<sup>-2</sup>.<sup>17</sup> A recent evaluation of HSCI anodes in different soil conditions has been conducted by Jakobs and Hewes.<sup>18</sup> They report a consumption rate for different HSCI alloys between 0.32 and 0.87 kg A<sup>-1</sup> year<sup>-1</sup> in 3% NaCl, at a current density of 21.5 A m<sup>-2</sup>, depending upon the alloy composition; while in soils containing 2% SO<sub>4</sub><sup>2-</sup>, consumption rates varied between 0.29 and 0.53 kg A<sup>-1</sup> year<sup>-1</sup>, again depending upon the alloy composition.

Improvements in anode construction have been carried out to reduce the nonuniform material loss along the length of the HSCI anode, the so-called ‘end effect’ phenomenon. This involves incorporating a taper in the anode casting at the connection end, or the use of hollow, centrifugally cast anodes of uniform wall thickness with a centrally located interior electrical connection.<sup>19</sup> Similar configurations are now used for HSI anodes. Cable connections for solid rod anodes use compression, cast lead, or taper pin connections, sealed by a combination of epoxy filling and heat shrinkable sleeves. Cylindrical anodes have centre connections with taper wedges or cast lead. Care must be taken to ensure that the cable insulation and sheathing are adequate for use in an oxidizing environment, in which chlorine evolution occurs. Kynar and high molecular weight polyethylene are commonly used.

#### 4.20.2.5 *Magnetite Anodes*

A compound, rather than an alloy, of iron, magnetite (Fe<sub>3</sub>O<sub>4</sub>) has been in use since the 1970s as a CP

anode, although its use as an anode material had been known for some time previously.<sup>20</sup> As an oxide, and being very brittle, it cannot be formed into an anode by conventional means. Magnetite has a melting point of 1540 °C and can be cast using special techniques and with the addition of certain alloying elements.<sup>21</sup> The anodes are in the form of a cast alloyed magnetite shell, the centre of which is hollow. The internal surfaces of the magnetite shell are then lined with an electronic conductor so as to ensure a uniform distribution of current density over the external surface. This technique overcomes the longitudinal current attenuation that would occur because of the relatively high resistivity of magnetite (3.3  $\Omega\text{m}$  quoted by Linder<sup>21</sup> and 0.8  $\Omega\text{m}$  by Kofstad).<sup>22</sup> Magnetite anodes can be operated at elevated temperatures up to 90 °C, with the limitation in temperature being failure of the anode cable connection and not the magnetite itself.

In early magnetite anodes, the internal lining consisted of a thin copper layer, but the poor electrical contact between the copper layer and the magnetite, together with the fact that the cable-to-anode connection was made at the anode head, resulted in a nonuniform current density on the external magnetite surface, which contributed, in part, to the poor performance reported for some of the early anodes. Subsequently, the manufacturers perfected a method of electrodepositing a lead alloy lining onto the internal magnetite surface with spring-loaded cable-to-anode connection made at the mid-point of the anode. Special care and some ingenuity in design are required in insulating the connection.

Magnetite anodes exhibit a relatively low consumption rate and can be used in seawater, freshwater, and soils. This low consumption rate enables a light-weight anode construction to be utilized. For example, the anode described by Linder<sup>21</sup> is 800 mm in length, 60 mm in diameter, 10-mm wall thickness, and 6 kg in weight. Tests carried out in seawater over the current density range 30–190  $\text{A m}^{-2}$  showed the consumption rate to be dependent upon current density, increasing from 1.4 to 4  $\text{g A}^{-1}\text{year}^{-1}$  over the current density range studied (with the recommendation that to achieve the required life, the current density should not exceed 115  $\text{A m}^{-2}$ ).<sup>23</sup> Later work by Jakobs and Hewes<sup>18</sup> indicated the consumption rate in seawater to be less than 1  $\text{g A}^{-1}\text{year}^{-1}$  at 21.6  $\text{A m}^{-2}$ , while at 32.4  $\text{A m}^{-2}$  a consumption rate of 12–41  $\text{g A}^{-1}\text{year}^{-1}$  was observed. Higher consumption rates were reported for magnetite anodes in soils containing 2%  $\text{SO}_4^{2-}$ ; namely 75  $\text{g A}^{-1}\text{year}^{-1}$

at current densities of 21.6 and 32.4  $\text{A m}^{-2}$ . Jakobs<sup>24</sup> also conducted a survey of different anode systems in soils and found magnetite anodes after 2 years' exposure and operating at a current density of 43  $\text{A m}^{-2}$  to be in good condition with little evidence of attack.

The main disadvantages of magnetite anodes are that they are brittle and susceptible to high-impact shocks, as is the case with silicon iron anodes, while some of the earlier anodes were subject to failure from thermal cycling.<sup>9,21</sup> Indeed, one evaluation of magnetite anodes reported a high incidence of failure,<sup>24</sup> and a more recent report<sup>25</sup> suggests an increased tendency to failure of magnetite anodes when compared with other, more conventional, anode materials. These failures were mainly associated with poor installation practice and operation at current densities in excess of the manufacturers' maximum recommended values (77  $\text{A m}^{-2}$  for seawater and 30  $\text{A m}^{-2}$  for soil). Improvements in design have now led to a more reliable anode with a decrease in the level of reported failures.<sup>26</sup>

Magnetite may also be used in combination with lead or electrodeposited onto a titanium substrate.<sup>27</sup> The latter anode system has been shown to exhibit good operating characteristics in seawater but at present it is only of academic interest showing no benefit over platinized and mixed metal oxide anodes.

#### 4.20.2.6 Ferrite Anodes

Sintered and sprayed ceramic anodes have been developed for CP applications. The ceramic anodes are composed of a group of materials classified as ferrites with iron oxide as the principal component. The electrochemical properties of divalent metal oxide ferrites in the composition range around 0.1MO–0.9 $\text{Fe}_2\text{O}_3$ , where M represents a divalent metal, for example, Mg, Zn, Mn, Co, or Ni, have been examined by Wakabayashi and Akoi.<sup>28</sup> They found that nickel ferrite exhibited the lowest consumption rate in 3% NaCl (of 1.56  $\text{g A}^{-1}\text{year}^{-1}$  at 500  $\text{A m}^{-2}$ ) and that an increase in the NiO content to 40 mol%, that is, 0.4NiO–0.6 $\text{Fe}_2\text{O}_3$  reduced the dissolution rate to 0.4  $\text{g A}^{-1}\text{year}^{-1}$  at the expense of an increase in resistivity from 0.02 to 0.3  $\Omega\text{cm}$ .

Ceramic anodes may be cast or sintered around a central steel core which acts as the electrical conductor. However, anodes produced in this form are brittle and susceptible to mechanical shock. Ceramic anodes based on a plasma-sprayed ferrite coating on a titanium or niobium substrate have also been developed. These consist of plasma-sprayed

lithium, nickel, or cobalt ferrite on a machined Ti or Nb button-shaped substrate fitted into a plastic electrode holder.<sup>29</sup> This method of anode construction is durable and not as prone to mechanical damage as the sintered ceramic anode, while the ceramic coating is abrasion resistant and has a long operational life. Kumar *et al.*<sup>29</sup> report a dissolution rate for a sprayed lithium ferrite of  $1.7 \text{ g A}^{-1} \text{ year}^{-1}$  at a current density of  $2000 \text{ A m}^{-2}$  in seawater. The anode exhibited good performance with no damage on the ceramic coating observed during a two-month trial. However, the normal restrictions on operating voltages for titanium electrodes (discussed below) were still found to apply, with pitting<sup>30</sup> of the titanium substrate reported at 9.66 V versus SCE.

## 4.20.3 Lead-Based Materials

### 4.20.3.1 Lead Alloys

Investigations into the use of lead and lead alloys for CP were carried out in the early 1950s<sup>31–33</sup> and a practical material had been developed by 1954. The general use of lead alloys in seawater had previously been established.<sup>34,35</sup> The anodic behavior of lead varies depending upon the electrolyte composition and the electrode potential and has been the subject of a number of reviews.<sup>9,35,36</sup> In  $\text{NO}_3^-$ ,  $\text{CH}_3\text{COO}^-$ , and  $\text{BF}_4^{2-}$  solutions, lead will form highly soluble salts, while in  $\text{Cl}^-$  and  $\text{SO}_4^{2-}$  solutions, insoluble salts are formed.

The use of lead as an anode depends on the formation and maintenance of a hard layer of lead oxide,  $\text{PbO}_2$ . The  $\text{PbO}_2$  acts as an inert anode, with the lead acting both as a source of  $\text{PbO}_2$  and an electrical conductor.  $\text{PbO}_2$  is relatively insoluble in seawater and its dissipation is more usually associated with mechanical wear and stress than electrochemical action. In alkaline solutions approaching pH 10,  $\text{PbO}_2$  dissolves and for this reason lead anodes should be mounted clear of cathodic areas, where alkalinity will form. It should be noted that lead dioxide will discharge if electronically connected to a more base material, when in an unenergized state, with the consequent formation of lead chloride and corrosion of the anode.

Lead alloys have found considerable use as anodes in a wide variety of electrochemical applications, with studies dating back to 1924.<sup>36–38</sup> Pure lead has been tried as an anode in seawater and shown to be unsuitable, because of the formation of  $\text{PbCl}_2$  beneath the  $\text{PbO}_2$  which insulates the  $\text{PbO}_2$  from the substrate. The anodic behavior of lead in  $\text{Cl}^-$

solutions depends upon  $\text{Cl}^-$  ion concentration, solution pH, and the presence of passivating anions such as  $\text{CO}_3^{2-}$ ,  $\text{HCO}_3^-$ , and  $\text{SO}_4^{2-}$ . At low current densities and low  $\text{Cl}^-$  concentration, dissolution of Pb will occur and a  $\text{PbCl}_2$  deposit will not be formed at the anode. In high  $\text{Cl}^-$  concentrations and at high current densities, the rate of formation of  $\text{Pb}^{2+}$  will be high enough for the solubility product for  $\text{PbCl}_2$  to be exceeded and  $\text{PbCl}_2$ , not  $\text{PbO}_2$ , will be deposited at the anode. The formation of a  $\text{PbO}_2$  coating on lead, when it is anodically polarized in  $\text{Cl}^-$ , is achieved more readily by alloying lead with silver or other metals or by incorporating inert conducting micro-electrodes on the Pb surface.

Lead alloys have been investigated to determine their suitability as anodes for CP. Tests<sup>39</sup> were carried out on lead–silver alloys and found that Pb–1%Ag was suitable for use in seawater provided that the current density did not exceed  $100\text{--}200 \text{ A m}^{-2}$ , as at higher current densities an insulating film formed. Morgan<sup>39,40</sup> found that Pb–6Sb–1Ag alloy gave a lower consumption rate and exhibited a harder  $\text{PbO}_2$  film than Pb–6Sb or Pb–1Ag. Pb–6Sb–2Ag alloys are slightly better, but ~50% more expensive. Other work<sup>41</sup> has also shown that additions of Mn to Pb–2Ag alloys may have a beneficial effect on anode performance in seawater. The Pb–6Sb–1Ag alloy is commonly used where lead–silver anodes are specified. The results of tests on Pb–6Sb–1Ag given in **Table 1** are of interest in recognizing the scope for the use of lead alloys in waters of differing resistivity.

Additions of antimony, bismuth, and tin to the lead appear to be detrimental for anode applications. Dispersion-hardened lead alloys have been unsatisfactory, showing pronounced spalling in the direction of extrusion. There is an indication that the addition of 0.1% Ag is almost as effective as 1% and additions as low as 0.01% that have been utilized in practice. Pb–0.1Te–0.1Ag has been also used with apparent success.<sup>42</sup>

In electrolytes containing sulfate and chloride ions, the sulfate ion favors the formation of lead sulfate which is rapidly transformed to lead dioxide. The continuing satisfactory operation of the anode depends upon the initial conditions of polarization. In solutions containing higher sulfate concentrations, or when the water is agitated, the lead dioxide is of better quality and more adherent when formed below  $108 \text{ A m}^{-2}$ .<sup>43</sup>

It is important to realize that a minimum current density is necessary to ensure the passivation of lead–silver anodes and that anodes operating below this



current density may experience rapid consumption rates. A minimum value of  $32.3 \text{ A m}^{-2}$  is quoted by Barnard *et al.*<sup>34</sup> The consumption rate of lead-silver is high in the initial stages of operation as can be seen from Table 1. However, the rate in seawater, over an extended period, is generally taken as  $0.06 \text{ kg A}^{-1} \text{ year}^{-1}$ . If a lead alloy is used as a ship's hull anode, consideration should be given both to the make-up of the water in which the anode is initially passivated and that in which it will normally operate. The same consideration will apply for static structures in estuarine waters.

Experience with Pb-6Sb-1Ag (and Pb/Pt) anodes operating in seawater at depths greater than 25 m has revealed a marked increase in consumption rate compared with that found on the surface. Hollandsworth and Littauer<sup>44</sup> have calculated that on a fully formed anode at  $400 \text{ A m}^{-2}$ , only  $6 \times 10^{-5}\%$  of the current is used to maintain the passive film, but at a depth of 180 m, this percentage increases to  $2 \times 10^{-3}\%$  and results in a 30-fold increase in consumption rate. They propose that a combination of the mechanical forces acting on the  $\text{PbO}_2$  at increased depths and the reduction in the evolution of chlorine are responsible for the increased consumption rate. It is, therefore, recommended that lead anodes are not used at depths below 25 m.

**Table 1** Behaviour of Pb-6Sb-1Ag anodes

Resistivity of electrolyte at 35°C ( $\Omega\text{m}$ )	Average wastage rate at $108 \text{ A m}^{-2}$ ( $\text{kg A}^{-1} \text{ year}^{-1}$ )	Length of trial (days)	Note
0.163 (sea)	0.086	236	1
0.163 (NaCl)	1.99	1-75	2
0.5 (sea)	0.0145	234	1
0.5 (NaCl)	0.654	1-75	3
10 (sea)	23.80	5-75	4
10 (NaCl)	23.70	1-75	4
50 (sea)	0.10	236	5
50 (NaCl)	11.64	1-75	5

Notes:

1. Service indicates a practical consumption of between  $0.057$  and  $0.114 \text{ kg A}^{-1} \text{ year}^{-1}$ . Under laboratory conditions,  $\text{PbO}_2$  has been formed at current densities as low as  $21.6 \text{ A m}^{-2}$ . Typical operating current densities are  $54\text{--}270 \text{ A m}^{-2}$  at wastage rates of  $0.045$  to  $0.082 \text{ kg A}^{-1} \text{ year}^{-1}$ .
2. Similar performance between  $0.7$  and  $270 \text{ A m}^{-2}$ : formation of this adherent film of  $\text{PbO}_2$ .
3. Similar performance between  $2.7$  and  $160 \text{ A m}^{-2}$ ; thick nodules of  $\text{PbO}_2$  in some areas; severe deterioration at  $270 \text{ A m}^{-2}$ .
4. Tests have indicated failure to form  $\text{PbO}_2$ ; rapid deterioration, although at  $100 \text{ A m}^{-2}$  it shows down after several weeks. Increasing silver content results in some improvement. Anode passivated in  $0.163 \text{ ohm m}$  water continues to operate whilst  $\text{PbO}_2$  is undamaged.
5. Above  $22 \text{ A m}^{-2}$ , deterioration rate may be low, but  $\text{PbO}_2$  coating is poor and interspersed with  $\text{PbCl}_2$ .

### 4.20.3.2 Lead/Platinum Bielectrodes

The insertion of platinum microelectrodes into the surface of lead and some lead alloys has been found to promote the formation of lead dioxide in chloride solutions.<sup>45,46</sup> Experiments with silver and titanium microelectrodes have shown that these do not result in improvement.<sup>42</sup> Similar results to those when using platinum have been found with graphite and iridium, and although only a very small total surface area of microelectrodes is required to achieve benefit, the larger the ratio of platinum to lead surface, the faster the rate of formation of the oxide layer.<sup>44</sup> Platinized titanium microelectrodes have also been utilized.

Lead dioxide will readily form on lead with a platinum electrode as small as  $0.076 \text{ mm}$  in diameter.<sup>44,45,47</sup> It has been observed that the current density on the platinum is considerably less than that on the lead dioxide once polarization has been achieved, the proportion of current discharged from the platinum decreasing with increase in total current. A typical anode for practical use would be in the order of  $25\text{--}48 \text{ mm}$  in diameter, with hard platinum alloy pins of  $0.50\text{-mm}$  diameter by  $10\text{-mm}$  length, spaced every  $150\text{--}300 \text{ mm}$  and progressively positioned around the circumference.<sup>48</sup> The pins are a press fit into holes in the lead or lead alloy and lie flush with the surface. The lead is peened around the pins to improve mechanical and electrical contact.

The action of platinum microelectrodes has been extensively studied.<sup>9,36</sup> Trials carried out by Peplow<sup>49</sup> have shown that lead/platinum bielectrodes can be used in high velocity seawater at current densities up to  $2000 \text{ A m}^{-2}$  and that blister formation with corrosion under the blisters is decreased by the presence of platinum microelectrodes. The current density range in which the anode is normally operated is  $200\text{--}750 \text{ A m}^{-2}$  with the maximum working current density quoted as  $1000 \text{ A m}^{-2}$ . The consumption rate of these anodes ranged from  $0.0014$  to  $0.002 \text{ kg A}^{-1} \text{ year}^{-1}$  at  $500 \text{ A m}^{-2}$ , but increased to  $0.003 \text{ kg A}^{-1} \text{ year}^{-1}$  at  $2000 \text{ A m}^{-2}$ .<sup>49</sup> The results of work in this field<sup>44,47,50,51</sup> can be summarized as follows:

- Pt acts as a stable electrode for nucleation of  $\text{PbO}_2$  and limits  $\text{PbCl}_2$  formation.
- In the case of a lead anode (without a platinum microelectrode), the  $\text{PbO}_2$  thickens during prolonged polarization with the consequent development of stresses in the film.
- The stresses result in microcracks in the  $\text{PbO}_2$ , thus, exposing the underlying lead, which corrodes with the formation of voluminous  $\text{PbCl}_2$ , resulting

in blisters; the resistance of the anode increases and high voltages are required to maintain the current (if the voltage is maintained constant the current falls to a low value).

- The platinum microelectrode appears to act as a potentiostat and maintains the potential of the lead–solution interface at any crack at a value that favors the reformation of  $\text{PbO}_2$ , rather than the continuous formation of  $\text{PbCl}_2$ , which would otherwise result in excessive corrosion.

It is known that an increase in the resistance of a lead electrode indicates that corrosion is taking place with the formation of an insulating film of a lead compound and this is confirmed in practice by observation of the anodes, which reveal localized areas coated with white corrosion products, although the  $\text{PbO}_2$  remains intact at other areas. However, it is possible that an insulating film forms over the whole surface, thus, isolating the conducting  $\text{PbO}_2$  from the lead. Wheeler<sup>52</sup> suggested that the sole function of the platinum is to provide a conducting bridge between the lead and the  $\text{PbO}_2$ . It has been demonstrated that, although initially the  $\text{PbO}_2$  nucleates at the surface of the platinum, the initially formed  $\text{PbCl}_2$  is rapidly converted into the  $\text{PbO}_2$  that is in direct contact with the lead.<sup>44</sup>

The formation of  $\text{PbO}_2$  is favored in the solutions containing passivating anions such as  $\text{SO}_4^{2-}$  and in the chloride solutions of intermediate concentrations; very high and very low concentrations of chloride inhibit the formation of  $\text{PbO}_2$ . The platinum/lead bielectrode performs best in seawater and is not recommended for use in waters of high resistivity.

#### 4.20.3.3 Lead/Magnetite Composites

It has been demonstrated that the particles of magnetite in a lead matrix can produce results similar to those produced by platinum, acting as stable nucleation sites for  $\text{PbO}_2$  formation.<sup>53</sup> Composite Pb/ $\text{Fe}_3\text{O}_4$  anodes containing 10, 15, and 20%  $\text{Fe}_3\text{O}_4$  were prepared by mixing powders of the constituents (Pb 30–60 mesh,  $\text{Fe}_3\text{O}_4$  72 mesh) and compacting at a pressure of 300 MPa.<sup>9,54</sup> These anodes were found to operate successfully in both artificial seawater (resistivity  $0.25 \Omega \text{ m}$ ) and in the same water diluted with distilled water to give a higher resistivity of  $10 \Omega \text{ m}$ .

In seawater, the anodes were found to operate best in the current density range  $100\text{--}1000 \text{ A m}^{-2}$ , a weight loss of  $50 \text{ g A}^{-1} \text{ year}^{-1}$  being recorded for a 20% composite anode at  $300 \text{ A m}^{-2}$ . No initial rise

in voltage at a constant current density was observed, as is the case with Pb/Pt electrodes, where the potential increases because of the formation of  $\text{PbCl}_2$ . The steady-state potential of the anode was found to be dependent upon the  $\text{Fe}_3\text{O}_4$  content. In freshwater solutions, the composite Pb–10%  $\text{Fe}_3\text{O}_4$  anodes were also able to form a  $\text{PbO}_2$  film, although an induction period was necessary before stabilization was complete. Hill reports that at current densities less than  $150 \text{ A m}^{-2}$ , the anodes were unable to stabilize. Consumption rates similar to those in artificial seawater were reported for the Pb–20%  $\text{Fe}_3\text{O}_4$  composites, which were found to give the optimum performance. However, in tapwater with a high  $\text{SO}_4^{2-}$  and  $\text{CO}_3^{2-}$  concentration and low  $\text{Cl}^-$  concentration (36 ppm), a consumption rate of  $100 \text{ g A}^{-1} \text{ year}^{-1}$  was recorded.

#### 4.20.3.4 Lead Dioxide on other Substrates

Lead dioxide on graphite or titanium substrates has been utilized as an anode in the production of chlorate and hypochlorites<sup>55</sup> and on nickel as an anode in lead–acid primary batteries.<sup>56</sup> Lead dioxide on a titanium substrate has also been tested for use in the CP of heat exchangers<sup>11</sup> and in seawater may be operated at current densities up to  $1000 \text{ A m}^{-2}$ .<sup>57</sup> However, this anode has not gained general acceptance as a CP anode for seawater applications, as platinized Ti anodes are more robust.

### 4.20.4 Carbonaceous Materials

#### 4.20.4.1 Graphite

Graphite is the dense, crystalline, form of carbon. Graphite anodes are prepared by heating calcined petroleum coke particles with a coal tar pitch binder. The mix is then shaped as required and heated to  $\sim 2800^\circ\text{C}$  to convert the amorphous carbon to graphite.<sup>58</sup> Graphite is used in preference to amorphous carbon as it is a less porous and more reliable anode material, particularly in saline conditions. It is current practice to impregnate the graphite, traditionally with linseed oil, although synthetic resins are also successful. The concept behind impregnation is to reduce the porosity and hence inhibit subsurface gas evolution or carbon oxidation which would initiate spalling and early anode failure. Being a natural lubricant, the material can easily be machined. It has a negligible contact resistance and it is relatively simple to make a sound cable joint. It can be DC

welded under high pressure argon. It is brittle but a little more shock resistant than silicon iron, in that it can absorb energy by localized damage, and it is a much lighter material to handle. Cable-to-anode joints need to be designed and made with the same care as those for high-silicon iron anodes.

The performance of graphite in seawater, where chlorine is the principal gas evolved, is considerably better than that in fresh water where oxygen is produced. Graphite is effectively immune to chlorine and has a long history in the chemical industry in this and similar applications.<sup>59</sup> In freshwater applications, considerable amounts of free oxygen are produced at the anode surface, which can attack both the carbon and any organic binders used to reduce porosity, resulting in a high consumption rate. The corrosion product is predominantly carbon dioxide. For this reason, graphite anodes for underground service are used in conjunction with a carbonaceous backfill.

If all the oxygen produced were to combine with the carbon, the maximum theoretical consumption rate would be of the order of  $1 \text{ kg A}^{-1} \text{ year}^{-1}$ .<sup>60</sup> However, in practice, the rate is usually of the order of  $0.2 \text{ kg A}^{-1} \text{ year}^{-1}$  and in coke breeze may be as low as  $0.05 \text{ kg A}^{-1} \text{ year}^{-1}$ . In seawater, where chlorine is the predominant gas produced, any oxygen formed will be quickly removed and the corrosion rate may be very low. Electrode reactions occur to a depth of 0.5 mm below the surface of the anode and the true current density can be shown to be only 1/400th of the value indicated by the superficial geometrical area.<sup>61</sup> Acidity has been found to increase the consumption rate,<sup>62</sup> as has the presence of sulfate ions.<sup>63</sup> Interestingly, when buried in soils containing 2%  $\text{SO}_4^{2-}$  Jakobs and Hewes<sup>18</sup> report the graphite consumption rates of  $1.56 \text{ kg A}^{-1} \text{ year}^{-1}$  at  $21.6 \text{ A m}^{-2}$ , which is considerably higher than the theoretical maximum consumption rate.

The anode is not recommended for use in water at above  $50^\circ\text{C}$ , where the consumption rate increases rapidly and erratically. It is no longer the practice to use this material in cooling water plants where a secondary attack from contact with the relatively noble pieces of anode may occur, should pieces break off the anode.

**Table 2** gives some results obtained with graphite under different conditions. Results obtained with one particular installation using a 100 mm diameter anode of 1 m length operating at  $6.9 \text{ A m}^{-2}$  indicate a predicted life of 20 years.<sup>64</sup>

Graphite anodes, when used in soils, are invariably placed in a carbonaceous backfill. This helps

**Table 2** Performance of graphite anodes

<i>Environment</i>	<i>Wastage rate (<math>\text{kg A}^{-1} \text{ year}^{-1}</math>)</i>	<i>Current density (<math>\text{A m}^{-2}</math>)</i>
Backfill	0.9	10.8
Hot water	0.9	
<b>Seawater</b>	<b>0.045</b>	<b>4.5–115</b>
Seawater	Little	10.8
Fresh water	0.45	3.5
Fresh water	0.45	2.7
Mud	0.91–1.36	71

Data reproduced from corresponding article in 3rd Edition of Shreir's Corrosion.

compensate for the lower electrical resistivity of graphite when compared with silicon iron. In such an environment, no build-up of a film of high resistance between the anode and backfill occurs, unlike silicon-iron anodes where the resistance can increase with time.<sup>65</sup>

Failures of graphite anodes can occur by corrosion of the anode connection, high current densities at either end of the anode resulting in excessive consumption rates often referred to as 'end effect' corrosion, sealant failure, or surface contamination.

#### 4.20.4.2 Carbonaceous Backfills

Carbonaceous backfill, either coke breeze, or, more recently, calcined petroleum coke, is used to surround a buried solid anode, or anodes, to produce an anode groundbed with an increased surface area, thus, significantly lowering the resistance to the surrounding environment. Groundbeds may be horizontal, vertical, or deep-well in form, depending on the soil resistivity in which they are installed. Such backfills have been used in conjunction with a number of different 'primary' anodes, including silicon iron, graphite, platinized titanium, and mixed metal oxide coated titanium. Canister anodes consist of a spirally wound galvanized steel outer casing containing a pre-packed carbonaceous backfill which surrounds the primary anode element which may be graphite, silicon iron, platinized titanium, mixed metal oxide-coated titanium, or platinized niobium. Such anodes allow ease of installation and are often used as shallow vertical linear arrays.

By using carbonaceous backfill, the consumption of the primary anode is reduced, as the majority of the conduction from the anode to the backfill becomes electronic rather than electrolytic. The electrochemical and physical nature of the backfill results in the spread of the anode reaction (formation of  $\text{CO}_2$  and  $\text{O}_2$ , or  $\text{Cl}_2$ )

over a large surface area, thereby reducing attack on the primary anode. The coke is slowly oxidized, primarily to carbon dioxide, which in a suitably vented groundbed will escape into the atmosphere together with any oxygen or chlorine formed. If all the oxygen reacted with the carbon, consumption would be  $1.02 \text{ kg A}^{-1} \text{ year}^{-1}$ , but in practice the rate is of the order of  $0.25 \text{ kg A}^{-1} \text{ year}^{-1}$ ,<sup>65</sup> depending upon the environment.

Some typical properties of coke breeze and similar materials are shown in **Tables 3–5**. The densities given in **Table 3** are for bulk material and are dependent upon grading. Flake graphite is not recommended

**Table 3** Densities of carbonaceous backfill

<i>Backfill in bulk</i>	<i>Density range (<math>\text{kg m}^{-3}</math>)</i>	<i>Typical density (<math>\text{kg m}^{-3}</math>)</i>
Coal coke breeze	650–800	690
Calcined petroleum coke granules	700–1100	720–850
Natural graphite granules	1100–1300	–
Man-made graphite, crushed	1100–1300	–

Data reproduced from corresponding article in 3rd Edition of Shreir's Corrosion.

**Table 4** Typical coal coke specification for CP

To pass 16-mm screen	100%
To pass between 16-mm and 8-mm screen	8.9–9.8%
To pass between 8-mm and 1-mm screen	78–90%
To pass 1-mm screen	1–14%
Fixed carbon	82.7 min to 91% max
Volatile matter	0.1%
Ash	8.6%
Moisture	5% max, typically 4%
Sulfur	1.2% max, typically
Phosphorus	0.42–0.7%
Resistivity (uncompacted)	0.55 $\Omega\text{m}$ max, (typically 0.35 $\Omega\text{m}$ )
Specific gravity	1.4

Data reproduced from corresponding article in 3rd Edition of Shreir's Corrosion.

**Table 5** Resistivities of carbonaceous backfills ( $\Omega\text{m}$ )

<i>Material</i>	<i>Dry</i>	<i>Tamped</i>	<i>Wet</i>
Coal coke	0.55	0.45	0.15
Graphite granules	1.50	1.20	0.20

Data reproduced from corresponding article in 3rd Edition of Shreir's Corrosion.

for use in groundbeds as it tends to conglomerate and prevent gas emission.

The grading of the coke is of some importance in that too large a particle size offers large local contact resistance, leading to uneven consumption, while an excessively fine material leads to over-tight compaction and resultant gas blocking (gaseous polarization). Chemicals are sometimes added, for example, calcium hydroxide (5–10 wt%), to counteract the tendency to lose moisture by electroosmosis, as it is essential that an aqueous electrolyte is present to replace water consumed in the anodic reaction and conduct the current to the protected structure. The alkaline material also serves to neutralize anodically formed acid. Calcium sulfate is sometimes used in very dry conditions. A typical specification for coke suitable for CP groundbed use is given in **Table 4**.

The coke breeze is tamped down at a minimum pressure of 15 Pa. This ensures integrity of the groundbed while in operation and allows for the reduction in volume produced by chemical oxidation. A pressure of this magnitude will also reduce the initial bulk resistivity of the coke. In practice, resistivities between 0.08 and 0.29  $\Omega\text{m}$  have been recorded on coke samples used in typical groundbeds. The effect of pressure on the measured value for resistivity of different coke samples has also been reported elsewhere.<sup>66</sup> The resistivity of bulk metallurgical coke is given as 0.024  $\Omega\text{m}$  with a slightly lower value of 0.020  $\Omega\text{m}$  at a pressure of 0.43 Pa, while for calcined fluid petroleum coke at zero applied pressure the resistivity was 0.02  $\Omega\text{m}$ , which decreased to 0.002  $\Omega\text{m}$  when tested at an applied pressure of 1.31 MPa.

The backfill cross-section, in a typical horizontal groundbed, is normally  $\sim 300 \times 300 \text{ mm}$ . Deep-well groundbeds have a diameter of 150–300 mm. Bed length depends upon the required current output and the surrounding soil resistivity. In freshwater soil conditions, higher than average current density at the ends of the primary anodes can be prevented by not exceeding a primary anode spacing of twice its length. As the electrolyte resistance decreases, with a consequent increase in current density at the ends of the primary anodes, either a reduction in anode spacing or an increase in backfill cross-section should be considered.

Calcined petroleum coke breeze is often used in deep-well applications. The material has a low particle size and, with suitable additives, may be converted into a slurry and pumped into a borehole. The sulfur content of this material is high (1.4%), but moisture

(0.2%), ash (0.4%), and volatiles (0.4%) are low. The typical resistivity of this material is  $0.15 \Omega\text{m}$ . A petroleum coke with spherical grains is available, specifically for borehole CP applications.<sup>67</sup> The round grains ensure high bed porosity and enable gas to escape, allowing the coke to sink to the base of the borehole. The resistivity of this material is quoted as  $0.1 \Omega\text{m}$ .

#### 4.20.4.3 Conductive Polymers

A continuous carbon loaded polymer anode system has been developed specifically for the CP of buried pipelines and tanks. The anode, marketed under the trade name AnodeFlex,<sup>68</sup> consists of a continuous stranded copper conductor (6AWG), which is encased in a thick jacket of carbon-loaded polymer, with overall diameter of 12.5 mm. To prevent unintentional short circuits an insulating braid is sometimes applied to the outer surface of the conductive polymer. The anode may be operated in the temperature range  $-18$ – $65^\circ\text{C}$  and at currents up to 0.05 A per linear meter in soil and 0.01 A per linear meter in water, which corresponds to effective maximum surface current densities of  $0.66 \text{ A m}^{-2}$  in soil and  $0.13 \text{ A m}^{-2}$  in water. No precise details on the anode consumption rate have been provided by the manufacturer, but as the active component is carbon, the consumption rate would be expected to be of a similar order to that exhibited by graphite anodes. The anode may be installed in conventional groundbeds or laid in close proximity to the cathode, for example, parallel to a pipeline route. The anode may be buried either directly in soil or in carbonaceous backfill. The intended applications for this material are external tank base protection, internal vessel protection, mitigation of poor current distribution, and to supplement conventional CP systems by providing increased levels of CP in underprotected areas.

The disadvantage of this anode system for the CP of pipelines is that the anode length provided is by one single connection to the DC. Power source is limited by resistive losses along the copper conductors. Thus, the required current output per unit length and soil resistivity are limiting factors and a number of anode connections may be required to protect long lengths of pipeline. The anode has a poor chemical resistance to oils and should not be used in situations where oil spillage may occur.

A similar conductive polymer electrode has been designed specifically for the CP of steel reinforcing bars in concrete and has been marketed under the

trade name Ferex.<sup>69</sup> The anode consists of a 16AWG stranded copper conductor surrounded by a carbon-loaded polymeric coating similar to that used on the AnodeFlex system<sup>68</sup> to provide a nominal anode diameter of 8 mm.<sup>70</sup> The manufacturer claims that at a maximum recommended current density of  $0.08 \text{ A m}^{-2}$  the anode life in concrete will be 32 years with a proportionately longer life at lower current densities. The anode is fixed to the concrete using nonmetallic fixings and may be supplied as a prefabricated mesh or more often as a continuous anode strand which is laid over the surface of the structure to be protected. The spacing between the anode strands may be adjusted to give the required current distribution and current density per unit area of concrete necessary to provide CP to a particular structure. A number of anode connections are made to the DC power source using proprietary splice kits (approximately one for every  $60$ – $80 \text{ m}^2$  of concrete to be protected). This will provide redundancy for anode failure and reduce resistive losses along the anode cable. Care must also be taken not to expose the copper conductor during installation or anode failure will take place. Once fitted to the concrete surface, a 15-mm thick cementitious overlay (gunite) is applied above the anode mesh, as recommended by the anode manufacturer, although thicknesses of up to 35–40 mm have been applied in some instances.

The major electrochemical reactions at the anode surface are oxygen and chlorine evolution coupled with oxidation of the active carbon to carbon dioxide. Eventually, all the carbon is removed from the anode coating and this allows perforation of the copper conductor leading to ultimate anode failure. Failures due to delamination of the concrete overlay coating have been reported in the United States, but have not been observed to any significant extent in Europe,<sup>71</sup> although some early failures of the anode system have been associated with high local current densities in areas of low concrete cover and high moisture or salt content.<sup>72</sup> The major application of this anode system is, therefore, on structures that are relatively dry with a uniform current requirement.

#### 4.20.4.4 Conductive Overlay Systems

Early systems used for the protection of reinforced concrete bridge decks were on the basis of the use of a continuous layer of coke breeze/asphaltic cement (85%/15%) to ensure uniform current distribution.<sup>73</sup> Electrical connection was made using silicon iron anodes held in position using a nonconductive



epoxy and covered with a conductive cement. Fromm<sup>74</sup> investigated the performance of different coke breeze/asphalt mixes and developed a mix containing only 45% coke breeze which had a resistivity of  $0.03 \Omega \text{ m}$  and a void content of 5%. This was reported to give good results. The conductive mix was applied over the primary anodes, either silicon iron or graphite, to a total thickness of 50 mm and then given a protective top coat.

Schutt<sup>75</sup> reported that the coke breeze specification and conditions in which the mix is prepared are important factors in determining the optimum operation of such overlay systems, while further details on the coke breeze asphalt mix composition are given by Anderson.<sup>76</sup> Conductive concrete mixes with a polymer binder have also been developed as an anode system specifically for reinforced concrete CP systems.<sup>77</sup>

Conductive overlay systems are not practical propositions on vertical surfaces or surfaces where weight restrictions are important. However, they are proven CP systems and can be considered in conjunction with other reinforced concrete CP system anodes.

#### 4.20.4.5 Conductive Paints

Carbon loaded conductive coatings may be used for the CP of steel reinforcing bars in concrete. They are always used in conjunction with a primary anode material, for example, a platinized-niobium or platinized-titanium wire or a conductive polymer rod. Brown and Fessler<sup>78</sup> have conducted a laboratory evaluation of conductive mastics that can be brushed or sprayed onto the concrete surface to achieve the necessary thickness. However, the most extensive study on conductive paints for CP purposes was undertaken by the US Federal Highway Authority.<sup>77</sup> Nine commercially available resins were evaluated in this work. It was shown that neither thermal cycling, freeze thawing nor the application of CP currents resulted in any deterioration of the most successful paint system, now referred to as DAC-85, a solvent-based acrylic mastic containing graphite. Minor failures with this system have been reported but only in localized areas with a high chloride content. The anode system generally consists of platinized titanium or niobium wire laid in strips with the layers of carbon fiber interleaved between the strips. The paint is then mixed and applied on site. The paint consists of blends of resin and fine particles of coke. The performance of some paint systems is poor

because of attempts to operate the anodes at currents in excess of  $0.1 \text{ A m}^{-2}$ .

The advantages of conductive paints are that they are easy to apply and a concrete overlay is not required. They can be applied to complex shapes and are not a problem where weight restrictions are imposed.

### 4.20.5 Platinum Anodes

#### 4.20.5.1 Platinum

The properties of platinum as an inert electrode in a variety of electrolytic processes are well known, and in CP, it is utilized as a thin coating on a suitable substrate. In this way, a small mass of Pt can provide a very large surface area, and thus, anodes of this type can be operated at high current densities in certain electrolyte solutions, such as seawater, and can be economical to use. When platinum is made the anode in an aqueous solution, a protective electron-conducting oxide film is formed. Once this film has formed, current flow then occurs by oxygen evolution. In chloride-containing solutions, evolution of chlorine will also occur and is usually the predominant anodic reaction even at low chloride concentrations, for example, brackish waters. The relative proportions of oxygen and chlorine evolved will be dependent upon the chloride concentration, solution pH, anode potential, degree of agitation and nature of the electrode surface, with only a fraction of the current being used to maintain the passive platinum oxide film.<sup>79</sup> This results in a very low platinum consumption rate.

The dissolution rate of solid rods of high purity platinum over the current density range  $1180\text{--}4600 \text{ A m}^{-2}$  has been investigated. Values of  $17.5\text{--}26.3 \text{ mg A}^{-1} \text{ year}^{-1}$  were reported over the first year, but the rate decreased to a limiting value of  $2.6\text{--}4.4 \text{ mg A}^{-1} \text{ year}^{-1}$  over a 5-year period.<sup>80</sup> The high initial rate was attributed to preferential dissolution at grain boundaries and other high free energy sites. Tests carried out in the United Kingdom<sup>81,82</sup> on electrodeposited platinum on a titanium substrate indicate a consumption rate in seawater of  $8.8 \text{ mg A}^{-1} \text{ year}^{-1}$ , although values of up to  $15 \text{ mg A}^{-1} \text{ year}^{-1}$  have been quoted elsewhere.<sup>83</sup>

#### 4.20.5.2 Platinized Titanium

Titanium, which has been in commercial production since 1950,<sup>84</sup> is thermodynamically a very reactive metal, but has a strong tendency to passivate, that is, to form a highly stable oxide film which, although

only a few atoms thick, is highly protective in most natural environments. When made anodic in a chloride-containing solution, this anodic film thickens with increase in voltage, remaining protective until a potential of  $\sim 8$  V is reached, at which point localized film breakdown occurs with subsequent pitting. Until pitting occurs, the resistive nature of the oxide film prevents significant current, making titanium itself unsuitable for use as an anode material. However, this inertness makes titanium an eminently suitable substrate for platinum, which may be applied to the metal in the form of a thin coating. The presence of platinum allows electronic conduction across the oxide, with the resultant composite behaving in a similar manner to solid platinum. Any titanium exposed at discontinuities in the platinum layer remains protected by the anodically formed oxide film, provided surface potentials are maintained below  $\sim 8$  V. Platinized titanium, therefore, provides an economical method of utilizing the inertness and electronic conductivity of platinum on a relatively inexpensive, yet inert substrate.

Titanium can be forged, bent, cut, stamped, rolled, extruded, and successfully welded under argon, making possible a large variety of electrode shapes, that is, rod, sheet, tube, wire, or mesh. It is a very light yet strong material with a high resistance to abrasion. Cotton<sup>85,86</sup> was the first to publish results on platinized titanium as an anode material and the first commercial installation utilizing platinum plated titanium anodes was completed in 1958 at Thameshaven for the protection of a large shipping jetty.

Platinized titanium anodes are usually produced by the electrodeposition of a thin coating of platinum from aqueous solutions<sup>9</sup> on to chemically etched titanium. Warne<sup>87</sup> states that electrodepositing coatings from aqueous plating solutions have the advantage that control of thickness is easily achieved, irregularly shaped substrates can be plated, and the electrodeposited coatings are hard and abrasion resistant, by virtue of interstitial hydrogen codeposited in the plating process. Titanium is a very difficult metal to electroplate because of the presence of the oxide film. Sophisticated pretreatments with acids are necessary to remove the oxide film and achieve good adhesion. Improvements in the level of adhesion can be obtained by heat treatment after plating.<sup>88</sup>

From aqueous solutions, platinum can only be applied as a relatively thin porous layer. Although the porosity decreases with increase in deposit thickness, so does the internal stress and if the platinum adhesion is poor, the coating may exfoliate. As a

consequence, platinum thicknesses of 2.5–7.5  $\mu\text{m}$  are normally used, although it is possible with care to apply coatings of 12.5  $\mu\text{m}$  in one operation and still achieve good adhesion.<sup>79</sup> However, 7.5  $\mu\text{m}$  is generally considered the maximum thickness from one plating operation. Thicker deposits may be obtained by deposition in a number of stages, with interstage anneals to expel codeposited hydrogen and relieve internal stresses.

Platinum electrodeposits may also be produced from molten salt electrolytes. The high temperature process has the advantage that the deposits are diffusion bonded to the titanium substrate and, thus, have good adhesion; if necessary, thick deposits can be produced. However, they have the disadvantages that, because of the complexity of the process, there is a limitation on the size and shape of the object to be plated, and the resultant deposits are softer and less wear resistant than those deposited from aqueous solutions.<sup>89</sup>

Metallurgically bonded platinized anodes have also been produced. These are achieved by wrapping a thin platinum sheet over a cylindrical billet of titanium, vacuum encapsulating within a copper can, which acts as a lubricant, and extruding it to the required shape.<sup>9</sup> When used in seawater systems, the resultant copper layer has the advantage that it prevents fouling of the anode prior to energizing. Low porosity, ductile platinum coatings can be produced, but only on rod or wire anode forms. A variant has been produced that consists of a titanium rod spirally wound with platinum wire spot welded to the surface of the rod.<sup>90</sup>

As indicated above, platinized titanium anodes have the disadvantage that the protective passive film on the titanium can break down and pit at high applied anodic voltages, leading ultimately to anode failure. The potential at which the breakdown of titanium occurs is dependent upon the solution composition. In seawater, the breakdown potential of titanium is often considered to be  $\sim 9.5$  V versus SHE,<sup>81</sup> while values as low as 6 V in 5.8% NaCl have been reported.<sup>91</sup> The value of the breakdown potential for titanium is dependent upon the  $\text{Cl}^-$  concentration and in high purity waters may be relatively high.<sup>92</sup> The presence of certain anions for example  $\text{SO}_4^{2-}$ , favors passivation. At sulfate, when chloride ratios are above 4:1, the breakdown voltage increases from  $\sim 8$  to 35 V.<sup>93</sup> The presence of bromides and iodides significantly reduce the pitting potential for titanium (down to as low as 2 V), while fluorides and sulfates will increase it to as much as

35 V.<sup>93</sup> Temperature also has a significant effect on the anodic breakdown voltage of titanium, with an increase in temperature decreasing the breakdown potential. A prudent maximum operating potential for platinized titanium in seawater is 8.0 V.

Platinized titanium anodes may be operated at current densities as high as  $5400 \text{ A m}^{-2}$  (<sup>94</sup>); however, at these current densities there is the possibility that the breakdown potential of titanium may be exceeded. The normal operating current density range in seawater is  $250\text{--}750 \text{ A m}^{-2}$  (<sup>79</sup>) while that in brackish waters is given as  $100\text{--}300 \text{ A m}^{-2}$  (<sup>95</sup>) with values within the range  $100\text{--}150 \text{ A m}^{-2}$  being favored.<sup>9</sup> The consumption rate for platinized titanium anodes in seawater over the current density range  $300\text{--}5000 \text{ A m}^{-2}$  has been found to be directly related to the charge passed, with values of  $1\text{--}2 \mu\text{g A}^{-1} \text{ h}^{-1}$  being generally used as the basis for system design. The consumption rate is also dependent upon solution composition, the rate increasing with decreasing chloride concentration and may reach a peak value of  $435 \text{ mg A}^{-1} \text{ year}^{-1}$  at a chloride concentration to be associated with the concurrent evolution of oxygen and chlorine, the rates of which are about equal in a neutral solution containing  $2.5 \text{ g dm}^{-3} \text{ NaCl}$ .<sup>81</sup> In brackish waters, the platinum consumption rate may be as high as  $20 \mu\text{g A}^{-1} \text{ h}^{-1}$ , more than ten times the rate in seawater and increases with increase in current density. Baboian<sup>96</sup> reports consumption rates of  $\sim 13 \text{ mg A}^{-1} \text{ year}^{-1}$  in seawater over the current density range  $11.8\text{--}185 \text{ A m}^{-2}$ , while those in  $350 \Omega \text{ cm}$  water (brackish river water) he reports as  $92.3 \text{ mg A}^{-1} \text{ year}^{-1}$  at  $11.8 \text{ A m}^{-2}$ , increasing to  $117.8 \text{ mg A}^{-1} \text{ year}^{-1}$  at  $185 \text{ A m}^{-2}$ . The effect of temperature on the consumption rate of platinized titanium anodes has not been found to be significant over the ranges normally encountered in CP installations.

Failures of platinized titanium anodes have been found to occur for reasons other than consumption of platinum or attack on the titanium substrate caused by voltages incompatible with a particular electrolyte. The following are examples:

- Attack on the substrate when covered in mud or marine growth, prior to energizing, has been found to be a possible cause of failure, because of a buildup of acidity (reduction in pH) once the current is applied.<sup>97,98</sup> Some commercial guarantees require that the exposure period during which anodes remain unenergized must exceed 8 weeks.<sup>99</sup> If anodes are to be installed in seawater for extended periods prior to energizing, they

should be coated with a copper antifouling paint or electrodeposit.<sup>81</sup> The copper coating will dissolve when the anode is energized and will not affect the anode's subsequent performance or operation.

- Attack on the substrate by contact with calcareous scale can also cause platinum loss to occur. Anodes located close to the cathode or operating at high current densities can lead to a rapid build up of calcareous deposit, the major constituents of which are  $\text{Mg(OH)}_2$  and  $\text{Ca(OH)}_2$ .<sup>100</sup> The alkaline conditions so generated can lead to rapid dissolution of the platinum. The calcareous deposit can be removed by washing with dilute nitric acid.
- The formation of deposits on platinized anodes can cause anode degradation.<sup>88,97</sup> Thus, dissolved impurities present in water, which are liable to oxidation to insoluble oxides, for example Mn, Fe, Pb, and Sn, can have a detrimental effect on anode life. In the case of  $\text{MnO}_2$  films, it has been observed that  $\text{MnO}_2$  may alter the relative proportions of  $\text{Cl}_2$  and  $\text{O}_2$  produced and thereby, increase the Pt dissolution rate.<sup>9</sup> The oxides may be incorporated into the  $\text{TiO}_2$  oxide film and decrease the breakdown potential<sup>97</sup> or form thick deposits. The latter may limit electrolyte access and lead to the development of localized acidity, at concentrations sufficient to attack the underlying substrate.<sup>9</sup>
- The superimposition of AC ripple on the DC output from a transformer rectifier can, under certain circumstances, lead to increased platinum consumption rates and has been the subject of considerable research.<sup>97,101–103</sup> Indeed, when platinized titanium anodes were first used, it was recommended that the AC component was limited to 5% of the DC voltage.<sup>9</sup>
- The frequency of the superimposed AC voltage signal has also been shown to affect the consumption rate of platinum, which increases with decrease in frequency. At  $100\text{--}120 \text{ Hz}$  (the frequency of the AC component signal from a full-wave single-phase transformer rectifier) and above, the AC signal has a negligible effect on consumption rate, provided that the AC component did not allow the electrode to become negative. If negative potential 'spikes' do occur in the output wave form, even at  $100 \text{ Hz}$ , a considerable increase in platinum dissolution can occur.<sup>104</sup> This could be the case with a thyristor-controlled transformer rectifier operating at a relatively low current

output. At low-frequency AC (2 Hz), an increase in platinum dissolution rate of two to three times has been reported, while negative current spikes of a few milliseconds duration at this frequency can cause dissolution rates of  $\sim 190 \text{ mg A}^{-1} \text{ year}^{-1}$ . It is, therefore, recommended that all spurious waveforms on the DC supply to platinized anodes be avoided.

- Organic impurities in the electrolyte have also been quoted as increasing the rate of platinum dissolution when the metal is used as an anode in electroplating.<sup>97</sup> Saccharose was observed to increase the anodic dissolution of platinum by a factor of ten in a 3% brine solution,<sup>105</sup> but did not affect the anodic breakdown voltage for titanium. Other organic compounds that may also have an effect are brightening agents for Ni plating solutions of the naphthalene trisulfonic acid type, detergents, or wetting agents.
- Fatigue failure of cantilever anodes in flowing electrolytes can occur as a result of vortex shedding.<sup>106</sup> However, with proper design and adequate safety factors, these failures can be avoided.<sup>97,107</sup>
- Attention must be paid to end effects, particularly on cantilever anodes, for example, on long anodes that extend away from the cathode surface. Under these circumstances, the anode surface close to the cathode may be operating at a considerably higher current density than the mean value, with the exact values dependent upon the system geometry. The life of the platinized anode in this region would then be reduced in inverse proportion to the current density.

In seawater and brackish waters, platinized–titanium installations have now been in use for 50 years for jetties, offshore installations, ships and submarines,<sup>9,107</sup> and for internal protection, particularly of cooling-water systems.<sup>108</sup> Anode forms include rod, tubular, mesh, and plate. For the protection of heat exchangers, an extruded wire of copper-cored titanium–platinum has shown a reduction in current requirement, together with improved longitudinal current spread, over cantilever anodes.<sup>109,110</sup> This ‘continuous’ or coaxial anode is usually fitted around the water box periphery a few centimeters away from the tube-plate.

Although not suitable for direct burial, platinized–titanium anodes may also be used in soils when surrounded by a carbonaceous backfill. Warne and Berkeley<sup>111</sup> have investigated the performance of platinized–titanium anodes in carbonaceous backfills

and concluded that the anodes may be successfully operated in this way at current densities of up to  $200 \text{ A m}^{-2}$ . This also supplements the findings of Lewis,<sup>112</sup> who states that platinized–titanium anodes may be used in carbonaceous backfill without breakdown of the titanium oxide film. In a properly constructed groundbed, there will be little ionic conduction at the platinum surface, the primary conduction to the carbon being electron transfer.

Under some circumstances, platinized titanium can be used in open-hole groundbeds extending below the water table. However, the water chemistry within a borehole can be complex and may, in certain circumstances, contain contaminants which favor breakdown of the anodic film on titanium. In addition, the pH of the solution in a confined space will tend to decrease, and this will result in an increase in the corrosion rate of the platinum.

#### 4.20.5.3 Platinized Niobium and Tantalum

Platinum electrodeposition onto tantalum had been carried out as early as 1913<sup>113</sup> and the use of platinized tantalum as an anode was suggested in 1922,<sup>114</sup> while platinum electrodeposition on to niobium was first successfully carried out in 1950.<sup>115</sup> These anodes are similar in principle to their titanium equivalent, differing only in the fact that they can tolerate much higher operating potentials and hence, they can operate at much higher current density. They are considerably more expensive than platinized titanium, especially when expressed in terms of price per unit volume.<sup>88</sup> As niobium is cheaper than tantalum, the use of the latter has become rare. The extra cost of Nb anodes may be offset in certain applications by their superior electrical conductivity and higher breakdown voltages. **Table 6** gives the comparative breakdown potentials of Ti, Nb, and Ta in various solutions under laboratory conditions.

**Table 6** Comparison of breakdown potential

<i>Solution</i>	<i>Ti</i>	<i>Nb</i>	<i>Ta</i>
Seawater	9	120	120
Sulfate/Carbonate	60	255	280
Phosphate/Borate	80	250	280
Drinking water	37.5	250	280
Bromides	2–3		

Data reproduced from corresponding article in 3rd Edition of Shreir’s Corrosion.

There have been instances reported in the literature where the breakdown potential for Nb and Ta in seawater has been found to be lower than the generally accepted value of 120 V, with reported values in extreme instances as low as 20–40 V.<sup>116,117</sup> This has been attributed to contamination of the niobium surface from machining operations, grit blasting, or traces of copper lubricant used in anode manufacture. These traces of impurities, by becoming incorporated in the oxide film, decrease its dielectric properties and, thus, account for the lower breakdown voltage. Careful control of surface contamination in the manufacture of platinized niobium is, therefore, essential to minimize the lowering of the breakdown potential of niobium.

Lower breakdown potentials, leading to unexpected premature failure, have also been observed on platinized niobium anodes which have become buried in seabed silt.

Platinized niobium anodes can be prepared by electrodepositing platinum onto grit-blasted niobium, metallurgical coprocessing (cladding) or by welding platinum or platinum/iridium wire to niobium rod.<sup>116</sup> They cannot be prepared by thermal deposition because niobium oxidizes at 350 °C and good adhesion cannot be obtained. Both materials may be welded under argon, utilizing butt or plasma welding techniques.

Platinized niobium and tantalum anodes have found use in applications where their high breakdown voltages and hence higher operational current densities can be utilized. These include ship and cooling system anodes, which may need to operate in estuarine waters and therefore, require higher driving voltages, offshore structures where high reliability in service is required, domestic water tanks,<sup>118</sup> and deep-well open-hole groundbeds.<sup>119</sup> Efrid<sup>104</sup> found the consumption rate of platinized niobium in seawater over the range 5000–10 000 A m<sup>-2</sup> to be similar to that of platinized titanium, that is, 1 µg A<sup>-1</sup> h<sup>-1</sup>. However, at a current density of 30 000 A m<sup>-2</sup>, he observed an increase in the platinum consumption rate to 2 µg A<sup>-1</sup> h<sup>-1</sup> and concluded that this was the limiting current density for operating these anodes. Warne and Berkeley<sup>111</sup> report that the maximum current density for these anodes in seawater is 2000 A m<sup>-2</sup>, with a working current density of 500–1000 A m<sup>-2</sup>. The operating current density selected should, however, be commensurate with the desired anode life, platinum coating thickness, and platinum consumption rate in a given environment.

In open-hole deep-well groundbeds, platinized niobium anodes have been successfully operated at

a current density of 215 A m<sup>-2</sup> (<sup>120</sup>) and in the range 100–267 A m<sup>-2</sup>.<sup>121</sup> Toncre and Hayfield<sup>95</sup> have conducted work on the operating parameters of platinized niobium anodes in brackish waters and simulated groundbed environments. For an open-hole groundbed, they concluded that operational current densities of 400 A m<sup>-2</sup> or higher were the most economical, as they led to a lower consumption rate in sulfate-containing groundwaters. The platinum consumption rate in a deep-well environment may well alter because of variations in the environmental conditions. On extruded platinized niobium anodes a consumption rate of 175 mg A<sup>-1</sup> year<sup>-1</sup> was considered for design purposes, while that for electroplated platinized niobium was taken as 87.6 mg A<sup>-1</sup> year<sup>-1</sup>. In a backfilled deep-well groundbed, dissolution rates comparable with those for an open-hole environment were reported, that is, 87.6 mg A<sup>-1</sup> year<sup>-1</sup> at 200 A m<sup>-2</sup>. At lower current densities, it seems likely that the electrochemical processes would be limited to oxidation reactions involving coke alone and no electrochemical loss would occur on platinized niobium. Indeed, Baboian<sup>122</sup> reports negligible Pt consumption rates in carbonaceous backfill at current densities from 11.8 to 29 A m<sup>-2</sup>, increasing to 11.9 mg A<sup>-1</sup> at 57.9 A m<sup>-2</sup> and 13.5 mg A<sup>-1</sup> year<sup>-1</sup> at 185 A m<sup>-2</sup>. The wear rates at 57.9 and 185 A m<sup>-2</sup> were comparable to those Baboian observed in seawater. The relative merits of platinized titanium and niobium in a deep-well environment, in comparison with those of other anode materials, have been discussed by Stephens.<sup>123</sup>

#### 4.20.5.4 Mixed Metal Oxide Coated Titanium

Mixed metal oxide (MMO) anodes, as their name suggests, consist of a layer of precious metal oxide intermixed with titanium or tantalum oxide, on a titanium substrate. They were originally developed, by Beer,<sup>124,125</sup> for the production of chlorine and chlorates,<sup>126,127</sup> where they were used as a more corrosion resistant replacement for graphite at the very high current densities (10 000 A m<sup>-2</sup>) and extreme environmental conditions experienced in those applications. They are sometimes alternatively referred to as dimensionally stable anodes (DSA).

They have now gained wide acceptance as impressed current anodes for CP and have been in use for this purpose since 1971. The anode consists of a thin film of metal oxides deposited onto a chemically etched titanium substrate by thermal



decomposition of a solution of metal salts, usually chlorides, in an organic solvent. The solution is applied by painting or spraying on to the titanium surface and then allowing the solvent to evaporate. The anode is heated in a controlled atmosphere to a temperature at which the metal salts decompose (between 350 and 600 °C)<sup>128</sup> and form the oxides. Multiple layers are applied and heated until the required deposit thickness, which is typically 2–12.5 µm, is obtained. Thicker deposits become brittle and poorly adherent,<sup>129</sup> although deposits up to 25-µm thick can be produced. Only titanium substrates can be coated in this way because at the temperatures required by the anode manufacturing process niobium oxidizes excessively.

MMO coatings are usually on the basis of the use of ruthenium or iridium oxides, in combination with titanium or tantalum oxides, although palladium has also been used for some applications and additions of tin oxide are also sometimes used. The composition of mixed metal oxide used is dependent on the environment in which the anode will operate and is adjusted to favor either oxygen or chlorine evolution by varying the relative proportions of iridium and ruthenium. For chlorine production, RuO<sub>2</sub>-rich coatings are preferred, while for oxygen evolution IrO<sub>2</sub>-rich coatings are utilised.<sup>130</sup> The former would be used in seawater, and the latter for buried or concrete CP application. The precise composition of the coating is generally considered proprietary information and is not divulged by the anode manufacturers.

MMO coated anodes have a significantly lower consumption rate than those using platinum metal. In seawater, with the anode evolving chlorine, the consumption rate is 0.5–1 mg A<sup>-1</sup> year<sup>-1</sup>, while in freshwaters and soils where oxygen evolution predominates the rate is 6 mg A<sup>-1</sup> year<sup>-1</sup>.<sup>(128)</sup> These are one fifth to one tenth of the platinized anode loss rate. The current densities normally used for design purposes are 600 A m<sup>-2</sup> for seawater, and 100 A m<sup>-2</sup> for fresh water, saline mud, and coke breeze backfill.<sup>131</sup> Higher current densities may be utilized in certain circumstances, but this reduces the anode life for a given coating thickness. MMO coatings are porous and, therefore, the limitations on operating voltage for platinized titanium anodes apply equally to MMO coated titanium electrodes. It has been reported that breakdown of mixed metal oxide anodes may occur at 50–60 V in low-chloride concentration water but at only 10 V in chloride-rich environments.<sup>128</sup>

MMO anodes, like platinized Ti, can be supplied in a number of different forms including rod, tube,

plate, and wire. Their application is similar to that for platinized anodes, except that, with a suitable MMO formulation, they can be directly buried without the use of carbonaceous backfill. LIDA<sup>®</sup> anodes, consisting of tubular anodes distributed on a length of cable which passes through the tubes, which are then swaged to connectors at their center points, have been developed specifically for use in groundbeds, both deep-well and horizontal.

Another specific development has been the use of MMO coated titanium mesh for the CP of reinforcing steel in concrete structures.<sup>132,133,134</sup> The anode mesh is made from commercially pure titanium sheet ~0.5–2-mm thick expanded to provide a very open, diamond-shaped, mesh. The mesh size selected is dictated by the required cathode current. The anode mesh is joined on site using spot welded connections to a titanium strip or by niobium crimps, while electrical connections to the DC power source are made at selected locations using suitably encapsulated or crimped connections. The mesh is fixed to the concrete using nonmetallic fixings. The MMO in this application is usually a combination of iridium and tantalum oxides. The material once installed is then covered with a concrete or mortar coating, the minimum thickness of cover above the anode mesh being 10 mm, while 15 mm is preferred. Alternative methods of application for concrete structures have included installation of anode strips in diamond cut slots and MMO coated titanium rods inserted in grouted holes. As well as being suitable for controlling reinforcement corrosion in existing structures by CP, all these anode variants can be installed in new structures to provide cathodic prevention, the advantage of the latter being that much lower current densities are required for ‘prevention’ rather than ‘protection.’

#### 4.20.6 Ceramic Anodes

An electrically conductive titanium oxide based ceramic material has been developed and is marketed under the trade name ‘Ebonex.’<sup>®135</sup> This material consists principally of Ti<sub>4</sub>O<sub>7</sub> but may also contain some higher oxides. It is black in color, has an electrical resistivity of less than  $2 \times 10^{-4} \Omega \text{m}$  and can be operated at current densities up to 100 A m<sup>-2</sup> in 10% NaCl; however, if coated with a precious metal, it can be operated at considerably higher current densities up to 400 A m<sup>-2</sup>.<sup>(136)</sup> Consumption rates, even in concentrated sulfuric acid, are negligible. It is both porous and brittle, although its mechanical strength

can be improved and porosity reduced by resin impregnation, preferably with inorganic fillers. It has a high over-potential for oxygen evolution, is not affected by current reversal, and has no restriction on operating voltage, and the makers claim that it has an excellent resistance to both acid and alkali. It is, however, difficult and expensive to produce, requiring heating of pure compacted titanium oxide powder in hydrogen at  $\sim 1350^\circ\text{C}$ .

To date, the material has been used as an electrode in electrowinning, electrochlorination, batteries, and electrostatic precipitators. In tubular form, it has been used as a discrete anode on concrete CP and prevention. One feature restricting its more widespread application is the difficulty of making good, consistent electrical connection having sufficient reliability.

#### **4.20.7 Applications of Impressed-Current Anodes**

As will be clear from the discussions above, the types of anodes available for use in impressed-current CP have become more advanced with time, starting with steel, which is fully consumed with use and proceeding with increasing resistance to anodic dissolution, through silicon containing cast iron, graphite (and carbonaceous backfill), lead based alloys (including bielectrodes), platinized titanium to mixed metal oxide coated titanium. The current use of these materials in a number of CP applications is briefly outlined in the following sections. The final choice will be on the basis of a combination of operational factors (design life, environment, consumption rate, and ease of installation) and cost.

##### **4.20.7.1 Offshore and Marine**

The majority of offshore installations are protected from corrosion by the use of sacrificial-anode CP. A number of impressed current systems have been installed, but they have a number of disadvantages, most notably a need for continuing control and maintenance, and a tendency to mechanical failure. Where impressed-current protection has been used, it has been with platinized titanium or platinized niobium. MMO anodes have, on occasion, been used to retrofit protection to structures where life extension has been needed.

Impressed-current systems are more often used with marine structures such as jetties, where the

possibility of automatic current control allows for the varying current demand because of tidal movements. Very early systems used scrap steel anodes. The use of lead–silver was common up to  $\sim 30$  years ago, when platinized titanium became widely available. Most modern systems utilize MMO coated titanium in rod, tube, or plate form.

Systems for the protection of ship's hulls and, recently, floating production units used to use lead–silver anodes, but most installations today take advantage of the very low consumption rate of MMO materials.

##### **4.20.7.2 Onshore**

Most CP for onshore installations is provided using anode groundbeds backfilled with a carbonaceous material. The primary conductor anode is now commonly MMO coated titanium, which offers advantages in weight and ease of installation. However, silicon–iron is still in extensive use, while graphite and magnetite anodes are also available for these applications.

Canistered anodes utilize silicon–iron, platinized titanium or MMO anodes in carbonaceous backfill within a galvanized steel canister. Where ground conditions allow the use of open-hole deep-well groundbeds, silicon–iron or MMO anodes are usually used although again graphite and magnetite are also sometimes employed. Platinized niobium may be used where very high groundbed current output is required.

Under the bases of large diameter above-ground tanks, MMO coated titanium wire can be used to ensure good current distribution to the entire base surface. Conductive polymer coated wire is occasionally used for this application.

##### **4.20.7.3 Internal**

The earliest systems for the protection of the water boxes of seawater cooled condensers used steel or cast-iron anodes. The tendency now is to use platinized or MMO anodes, with occasional use of magnetite.

##### **4.20.7.4 Concrete**

Reinforced concrete structures that are fully immersed or buried in a corrosive environment may generally be protected using conventional cathodic protection groundbed design. However, for the CP of above-ground reinforced concrete structures,

for example, bridge decks, jetties, tunnel parking garages, and concrete buildings, a number of specific anode systems have been developed.

Some of the earliest systems were for bridge decks and used conductive asphalts. Where the additional weight and thickness can be accommodated, modern systems use an MMO coated mesh attached to the surface and covered with a layer of sprayed concrete or mortar. If weight is an issue or the additional thickness of mortar cannot be accepted, conductive coating can be used, or, alternatively strip or rod anodes can be incorporated in the concrete by slot cutting or drilling, respectively. Titanium oxide ceramic has sometimes been used as an alternative to MMO coated rods.

## References

- Kimmel, A. L. *Corrosion* **1956**, 12(1), 63.
- Peabody, A. W. *Mater. Prot.* **1970**, 9(5), 13–18.
- Bengough, G. C.; May, R. J. *Inst. Met.* **1924**, 32(2), 5.
- Cotton, J. B. *Chem. Ind. Rev.* **1958**, 68, 492.
- Brand, J. W. L. F.; Tullock, D. S. 1965, CWE International Report, London.
- Redden, J. C. *Mater. Prot.*, **1966**, 5(2).
- Applegate, L. M. *Cathodic Protection*; McGraw Hill: New York, 1960.
- Bryan, W. T. *Mater. Prot. Perf.* **1970**, 9(9), 25–29.
- Shreir, L. L.; Hayfield, P. C. S. In *Impressed Current Anodes*; Conference on Cathodic Protection Theory and Practice – The Present Status, Coventry, 28–30 April, 1982.
- Peabody, A. W. *Control of Pipeline Corrosion*; NACE: Houston, TX, 1967.
- Tudor, S.; Miller, W. L.; Ticker, A.; Preiser, H. S. *Corrosion* **1958**, 14(2), 93t–99t.
- NACE T-2B Report. *Corrosion* **1960**, 16(2), 65t–69t.
- NACE T-2B Report. *Corrosion* **1957**, 13(2), 103t–107t.
- NACE T-2B Report. *Corrosion* **1955**, 10(12), 62–66.
- Doremus, G. L.; Davis, J. G. *Mater. Prot.* **1967**, 6(1), 30–39.
- Bryan, W. T. *Mater. Prot. Perform.* **1970**, 9(9), 25–29.
- Durion Company, Dayton, OH, USA, Technical Data Bulletin DA/7c, 1984.
- Jakobs, J. A.; Hewes, F. W. In *Proceedings of Corrosion '81*; NACE International: Houston, TX, 1981; Paper no. 222.
- McKinney, J. W. *Mater. Perform.* **1979**, 18(11), 34–39.
- Allmand, A. J.; Ellingham, H. J. T. *Applied Electrochemistry*; Edward Arnold: London, 1931.
- Linder, B. *Mater. Perform.* **1979**, 18(8), 17–22.
- Kofstad, P. *Nonstoichiometry, Diffusion and Electrical Conductivity in Binary Metal Oxides*; Wiley Interscience: New York, 1972.
- Miller, J. Danish Corrosion Centre Report, May 1977.
- Jakobs, J. A. *Mater. Perform.* **1981**, 20(5), 17–23.
- Matlock, G. L. In *Proceedings of Corrosion 84*; NACE International: Houston, TX, 1984; Paper no. 340.
- Technical Data Sheet, Bergsoe Anti Corrosion.
- Kubicki, J.; Trzepieczynska, J. *Ochr. Przed. Koroz.* **1980**, 11–12, 301–303.
- Wakabayashi, S.; Aoki, T. *J. Phys.* **1977**, 4, pCl.
- Kumar, A.; Segan, E. G.; Bukowski, J. *Mater. Perform.* **1984**, 23(6), 24–28.
- Tefsuo, F. *et al. Corros. Eng.* **1980**, 29(4), 180–184.
- Moller, G. E.; Patrick, J. T.; Caldwell, J. W. *Mater. Prot.* **1962**, 1(2), 46–57.
- Littauer, E. L.; Shreir, L. L. In *Proceedings of the 1st International Congress on Metallic Corrosion*, Butterworths, London, 1961; p 374.
- Shreir, L. L. *Corrosion* **1961**, 17, 188t.
- Barnard, K. N.; Christie, G. L.; Gage, D. E. *Corrosion* **1959**, 15(11), 501t–586t.
- Von Fraunhofer, J. A. *Anti Corrosion*, November 9–14 and December 4–7, 1986.
- Kuhn, A. T. *The Electrochemistry of Lead*, Academic Press: London, 1979.
- Fink, C. G.; Pan, L. C. *Trans. Electrochem. Soc.* **1924**, 46(10), 349.
- Fink, C. G.; Pan, L. C. *Trans. Electrochem. Soc.* **1926**, 48(4), 85.
- Morgan, J. H. *Cathodic Protection*; Leonard Hill: London, 1959.
- Morgan, J. H. *Corros. Technol.* **1958**, 5(11), 347.
- Kubicki, J.; Bujonek, B. *Ochr. Przed. Koroz.* **1982**, 3, 41–45.
- Shreir, L. L. *Platinum Met. Rev.* **1968**, 12(2), 42–45.
- Private Report on Films on Lead-Silver-Antimony Electrodes, Fulmer Research Institute to CWE Ltd.
- Hollandsworth, R. P.; Littauer, G. L. *J. Electrochem. Soc.* **1972**, 119, 1521.
- Shreir, L. L. *Corrosion* **1961**, 17(3), 118t–124t.
- Metal and Pipeline Endurance Ltd., U.K. Patent 870,277, 1961.
- Fleischmann, M.; Liler, M. *Trans. Faraday Soc.* **1958**, 54, 1370.
- Shreir, L. L. *Platinum Met. Rev.* **1978**, 22(1), 14–20.
- Peplow, D. B. *Br. Power Eng.* **1960**, 1, 31–33.
- Shreir, L. L.; Weinraub, A. *Chem. Ind.* **1958**, 41, 1326.
- Shreir, L. L. *Platinum Met. Rev.* **1959**, 3(2), 44–46.
- Wheeler, W. C. E. *Chem. Ind.* **1959**, 75.
- Shreir, L. L.; Metal and Pipeline Endurance Ltd., U.K. Patent 19823/79; 1979.
- Hill, N. D. S. *Mater. Perform.* **1984**, 23(10), 35–38.
- Barak, M. *Chem. Ind.* **1976**, 20, 871–876.
- Smith, J. F. *Trans. IMF* **1975**, 53, 83.
- Hamzah, H.; Kuhn, A. T. *Corros. J.*; **1980**, 15(3).
- Brady, G. D. *Mater. Perform.* **1971**, 10(10), 20–23.
- Heinks, H. *Ind. Eng. Chem.* **1955**, 47, 684.
- Palmquist, W. W. *Pet. Eng.* **1950**, 2, D22–D24.
- Bulygin, B. M. *Ind. Eng. Chem.* **1959**, 32, 521.
- Krishtalik, L. I.; Rotenberg, Z. A. *Russ. J. Phys. Chem.* **1965**, 39, 168.
- Ksenzhek, O. S.; Solovei, Z. V. *J. Appl. Chem.* **1960**, 33, 279.
- Oliver, J. P. Annual conference of the American Institute of Electrical Engineers, Paper 52–506; IEEE: New York, 1952.
- Costanzo, F. E. *Mater. Prot.* **1970**, 9(4), 26.
- Espinolu, R. A.; Mourente P.; Salles, M. R.; Pinto, R. R. *Carbon*, 24(3), 337–341.
- LORESCO™, Cathodic Engineering Equipment Co Inc., Missouri, USA.
- AnodeFlex – Registered trade name, Raychem Ltd., USA.
- Registered trade mark Raychem USA (manufacturing and marketing rights purchased by Eltech Corporation, 1989).
- Ferex Technical Data Sheet.
- Wyatt, B. S.; Lothian, A. In *UK Corrosion 88*; CEA: Brighton, 1988.

72. Wyatt, B. S. In *Cathodic Protection Theory and Practice*, 2nd International Conference, Stratford-upon-Avon, UK, June, 1989; Paper no. 23; Institute of Corrosion: UK.
73. Stratful, R. F. Experimental Cathodic Protection of Bridge Decks, Transportation Research Record, 500(1), 1974.
74. Fromm, H. J. In Proceedings of Corrosion '76; NACE International: Houston, TX, 1976; Paper no. 19.
75. Schutt, W. R. In Proceedings of Corrosion '78; NACE International: Houston, TX, 1978; Paper no. 74.
76. Anderson, G. Cathodic Protection of a Reinforced Concrete Bridge Deck, American Concrete Institute Convention, 1979.
77. Federal Highway Authority (USA). Cost Effective Concrete Construction and Rehabilitation in Adverse Environments, Project No. 4K, Annual Progress Report Sept., 1981.
78. Brown, R. P.; Fessler, H. J. In Corrosion 83, 1983; Paper no. 179.
79. Shreir, L. L. *Platinum Met. Rev.* **1977**, 21(4), 110–121.
80. Warne, M. A.; Hayfield, P. C. S. *Mater. Perform.* **1976**, 15(3), 39–42.
81. Hayfield, P. C. S.; Warne, M. A.; Jacob, W. R. In Proceedings of conference on UK Corrosion '81; Harrogate, Institute of Corrosion: UK, 1981.
82. Warne, M. A.; Hayfield, P. C. S. Durability Tests on Marine Impressed Current Anodes, IMI Marston/Excelsior Ltd., 15 March, 1971.
83. Baboian, R. In Proceedings of Corrosion '76; NACE International: Houston, TX, 1976; Paper no. 183.
84. Lowe, R. A. *Mater. Prot.*; NACE: Houston, TX, 1966.
85. Cotton, J. B. *Chem. Ind. Rev.* **1958**, 68, 68–69.
86. Cotton, J. B.; Williams, E. C.; Barber, A. H. UK Patent 877,901, 1958.
87. Warne, M. A. *Mater. Perform.* **1979**, 18(8), 32–38.
88. Jacob, W. R. In Proceedings of Symposium on Cathodic Protection, London, May, 1975; Paper no. 5.
89. Baboian, R. In Proceedings of the 4th International Congress on Marine Corrosion and Fouling, Antibes, France, 1976.
90. U.S. Patent 3,443,055, 1966.
91. Baboian, R. *Mater. Perform.* **1977**, 16(3), 20–22.
92. Segan, E. G. *et al.* Titanium Anodes in Cathodic Protection, Final Report, Army Construction Engineering Research Laboratory, Champaign, Illinois USA, Jan. 1982.
93. Dugdale, I.; Cotton, J. B. *Corros. Sci.* **1964**, 4, 397–411.
94. Anderson, D. B.; Vines, R. F. In Extended extracts of the Second International Congress on Metallic Corrosion, March, 1963.
95. Toncre, A. C.; Hayfield, P. C. S. In Corrosion 83, 1983; Paper no. 148.
96. Baboian, R. In Corrosion 83, 1983; Paper no. 149.
97. Hayfield, P. C.; Warne, M. A. In Corrosion 82, 1982; Paper no. 38.
98. Warne, M. A.; Hayfield, P. C. *Br. Corros. J.* **1971**, 6, 192–195.
99. Commercial Guarantee, Martson Excelsior, 1972.
100. Pathmanaban; Phull, B. Proc UK corrosion 82, Hammersmith, London, 1982.
101. Juchniewicz, R. *Platinum Met. Rev.* **1962**, 6, 100.
102. Hoar, T. P. *Electrochim. Acta* **1964**, 9, 599.
103. Juchniewicz, R.; Hayfield, P. C. S. In 3rd International Congress on Metallic Corrosion, Moscow, **1969**; Vol. 3, pp 73.
104. Eifird, K. D. *Mater. Perform.* **1982**, 21(6), 51–55.
105. Pompowski, J.; Juchniewicz, R.; Walaszowski, E.; Strelcki, H.; Sadowska, J. In Marine Corrosion Conference; Technical University of Gdansk: Gdansk, 1967; p 87.
106. Love, T. J. *Power USA*, 80–81, Feb, 1981.
107. Dreyman, E. W. *Mater. Perform.* **1972**, 11(9), 17–20.
108. Nekosa, G.; Hanck, J. *Laboratory and Field Testing of Platinised Titanium and Niobium Anodes for Power Plant Applications*; The Electrochemical Society Meeting, Pittsburgh, PA, October 1978.
109. Morgan, J. H. Proceedings of the Symposium on Recent Advances in Cathodic Protection; Marston Excelsior; Wilton, Birmingham, May, 1964.
110. Lowe, R. A.; Brand, J. W. L. F. *Mater. Prot. Perform.* **1970**, 9(11), 45–47.
111. Warne, M. A.; Berkeley, K. E. In Corrosion 80, 1980; Paper no. 244.
112. Lewis, T. H. Corrosion 79, Atlanta, GA, USA, 1979; Paper no. 144.
113. Stevens, R. H. U.S. Patent 1,077,894; 1,007,920, November 1913.
114. Baum, E. U.S. Patent 1,477,000, August, 1922.
115. Rosenblatt, E. F.; Cohen, J. G. ULS Patent 2,719,797, October, 1955.
116. Hayfield, P. C. S. *Mater. Perform.* **1981**, 20(11), 9–15.
117. Hayfield, P. C. S. In Corrosion 81, Toronto, Canada 1981; Paper no. 103.
118. Gleason, J. D. *Mater. Perform.* **1979**, 18(1), 9–15.
119. Sly, P. M. *Platinum Met. Rev.* **1981**, 24(2), 56–57.
120. Tatum, J. F. *Mater. Perform.* **1979**, 18(7), 30–34.
121. Toncre, A. C. *Mater. Perform.* **1980**, 19(3), 38–40.
122. Baboian, R. *Mater. Perform.* **1983**, 22(12), 15–18.
123. Stephens, R. W. Corrosion 83, 1983; Paper no. 144.
124. Beer, H. B. UK Patent 1,147,442, 1965.
125. Beer, H. B. UK Patent 1,195,871, 1967.
126. Bianchi, G.; de Mora, V.; Gallone, P. US Patent 3,616, 445, 1967.
127. De Nora, V.; Kuhn von Burgsdorf, J. W. *Chem. Ing. Tech.* **1975**, 47, 125–128.
128. Katowski, S. Chlorine. In Ullmans Encyclopedia of Industrial Chemistry; Wiley-VCH: New York, 1986; Chapter 7.
129. Schrieber, C. F.; Mussinelli, G. L. Paper 287, Corrosion 86, 1986.
130. Matusumoto, Y.; Tazawa, T.; Muroi, N.; Sato, E. *J. Electrochem. Soc.* **1986**, 133(1), 2257–2262.
131. Reding, J. T. Paper 9, Corrosion 97, San Francisco, USA, 1987.
132. Tvarusku, A.; Bennett, J. E. In Proceedings of the 2nd International Conference on Deterioration and Repair of Reinforced Concrete in Arabian Gulf, Bahrain, 1987; pp 139–154.
133. Mudd, C. J.; Mussinelli, G. L.; Tettamanti, M.; Pedferri, P. In Corrosion 88, St Louis, USA 1988; Paper no. 229.
134. Hayfield, P. C. *Platinum Met. Rev.* **1986**, 30(4), 158–166.
135. Trade name of Ebonex Technologies Inc., California USA, (European Patent Application 0047595; US Patent 4,422,917).
136. Product Information Sheet, Ebonex Technologies Inc., 1988.

## 4.21 Practical Application of Cathodic Protection

**B. S. Wyatt**

Corrosion Control Ltd., 3, Ivy Court, Acton Trussell ST17 0SN, UK

© 2010 Elsevier B.V. All rights reserved.

<b>4.21.1</b>	<b>Background and Introduction</b>	2802
4.21.1.1	Structures that Are Cathodically Protected	2802
4.21.1.2	Type of System	2803
4.21.1.2.1	Reactions at anodes	2803
4.21.1.2.2	Galvanic anode systems	2806
4.21.1.2.3	Impressed-current systems	2806
4.21.1.2.4	Hybrid systems	2807
4.21.1.2.5	Stray-current bonding or forced drainage	2807
<b>4.21.2</b>	<b>Design of a Cathodic Protection System</b>	2807
4.21.2.1	Initial Design Process	2807
4.21.2.2	Surface Area	2810
4.21.2.3	Electrical Continuity	2810
4.21.2.4	Estimate of Current Required	2811
4.21.2.5	Establishing Electrolyte Resistivity	2811
4.21.2.6	Economics	2811
<b>4.21.3</b>	<b>Impressed-Current Systems</b>	2811
4.21.3.1	Group 1 Anodes	2813
4.21.3.1.1	Scrap steel	2813
4.21.3.1.2	Graphite	2813
4.21.3.1.3	Silicon-iron	2813
4.21.3.2	Group 2 Anodes	2813
4.21.3.2.1	Platinized titanium	2813
4.21.3.2.2	Platinized niobium and tantalum	2813
4.21.3.2.3	Lead silver alloy with or without platinum microelectrodes	2815
4.21.3.2.4	Mixed metal oxide-coated titanium (MMO/Ti)	2815
4.21.3.3	Other Anodes for Reinforced Concrete Applications	2815
<b>4.21.4</b>	<b>Cathodic Protection of Buried Structures</b>	2816
4.21.4.1	Soil or Water Resistivity	2816
4.21.4.2	Impressed-Current Design	2817
4.21.4.3	Anode Backfill	2818
4.21.4.4	Resistance of Groundbeds	2818
4.21.4.4.1	Deep-well groundbeds	2820
4.21.4.4.2	Determining rectifier voltage	2820
4.21.4.5	Attenuation	2820
4.21.4.5.1	Field measurements	2820
4.21.4.5.2	Measurement between drainage points	2821
4.21.4.5.3	Coating resistance	2821
4.21.4.5.4	Types of cable for anode installations	2821
4.21.4.6	Power Sources for Cathodic Protection	2822
<b>4.21.5</b>	<b>Seawater-Cooled Circulating Water Systems</b>	2822
4.21.5.1	Galvanic Anodes	2822
4.21.5.2	Impressed-Current Anodes	2822
4.21.5.2.1	Continuous anodes	2822
4.21.5.2.2	Rod anodes	2822



4.21.5.2.3	Tubular anodes	2822
4.21.5.3	Impressed-Current Systems	2823
4.21.5.3.1	Manually controlled system	2823
4.21.5.3.2	Automatic potential controlled system	2823
4.21.5.3.3	Automatically controlled modular system	2823
4.21.6	Marine Structures	2823
4.21.7	Ships	2825
4.21.8	Water Storage Tanks	2826
4.21.9	Internal Protection of Pipelines	2826
4.21.10	Cathodic Protection of Steel in Concrete	2827
4.21.11	Economics	2828
4.21.12	Recent Developments	2828
4.21.12.1	Galvanic Anode Systems	2828
4.21.12.2	Impressed-Current Anodes	2831
4.21.12.3	Power Sources for Cathodic Protection	2831
4.21.12.3.1	Solar and wind power	2832
4.21.12.3.2	Other power supply systems	2832
4.21.13	Conclusion	2832

---

## Glossary

**Dolphin** A harbor structure that extends above the water level and is not connected to shore; they are installed when it would be impractical to extend the shoreline (e.g., with a pier or wharf) to provide a dry access facility.

## Abbreviations

**AC** Alternating current

**DC** Direct current

**emf** Electromotive force (V)

**$IR$**  Voltage (ohmic) drop due to current flow ( $I$ ) through a resistance ( $R$ )

**ln** Natural logarithm

**MMO** Mixed metal oxide

**PV** Photovoltaic

## Symbols

**$I$**  Current

**$M$**  Generic symbol for a metal

**$R$**  Resistance

**$V$**  Voltage

**$z$**  Number of electrons transferred in electrochemical reaction

**$\rho$**  Resistivity

## 4.21.1 Background and Introduction

The forms of corrosion that can be controlled by cathodic protection include all forms of general corrosion, pitting corrosion, graphitic corrosion, crevice corrosion, stress corrosion cracking, corrosion fatigue, cavitation corrosion, bacterial corrosion, etc. Cathodic protection can be applied to a wide range of metals and bimetallic couples of metals. Most applications are to steel, as this is the most common construction material, but cathodic protection, with revised protection criteria or limits, can be applied to stainless steels, copper, cupro nickel alloys, lead, aluminum alloys, and galvanized steel.

### 4.21.1.1 Structures that Are Cathodically Protected

There are many structures and installations that, in given circumstances, can benefit from the application of a cathodic protection system. For example, these include buried and submerged crude oil, fuel oil and gas tanks, and pipelines; offshore fixed oil and gas drilling and production platforms, buried and immersed water, fire protection, gas, and compressed air distribution schemes; metallic sewers and culverts; buried and immersed communication and power cables; deep-well casings for oil, gas, and water extraction; other buried tanks and the bases of tanks in contact with the ground; electrical transmission tower, aerial and wind-farm tower footings, sheet

steel piling, tubular and 'H'-piling associated with port and harbor facilities, and other infrastructure projects; immersed and buried steel tube tunnels; piers, wharfs, and other mooring facilities; cooling water systems including internals and externals of pipelines, intake screens, condenser water boxes pumps, etc.; gates, locks, and screens in irrigation and navigation canals; buried domestic oil distribution lines or buried pipelines for district central heating systems.

- Cathodic protection of internal surfaces is applied, in addition to the cooling water systems listed above, to surface and elevated water storage tanks (both potable and seawater, the latter often for firefighting purposes); condensers and heat exchangers; hot-water storage tanks, processing tanks, and vessels; hot and cold water domestic storage tanks; and process vessels in breweries and dairies (pasteurizers).
- Cathodic protection of floating structures is applied to the external hulls of most commercial and military vessels including vessels that are 'laid up' or 'in mothballs'; to the ballast compartments of tankers; floating oil and gas drilling and production facilities; floating dry-docks; barges (interior and exterior); dredgers; caisson gates; steel mooring pontoons; and navigation aids, for example, buoys.
- Cathodic protection of steel in concrete is applied to buried and immersed steel, reinforced and pre-stressed concrete pipelines, generally for water distribution; steel reinforced concrete foundations, piles and caissons of buildings, and port and harbor facilities; steel-reinforced concrete offshore oil and gas drilling, production, and storage facilities; steel-reinforced atmospherically exposed highway structures (bridges, elevated road support structures, etc.) and bridge decks; buried and immersed tunnels; buried reinforcement concrete basements and car parks; multistory car parks; and buildings.

In many countries, the safety and environmental advantages of cathodic protection are sufficiently well acknowledged that there is legislation requiring effective cathodic protection of buried or immersed pipelines carrying products such as crude oil, refined product, and gas, and there are Insurance and Classification Society requirements for effective cathodic protection of offshore oils and gas drilling and production facilities and for ships.

#### 4.21.1.2 Type of System

The use of an impressed-current system or galvanic anodes will provide satisfactory cathodic protection,

but each has advantages and disadvantages with respect to the other (Table 1).

##### 4.21.1.2.1 Reactions at anodes

Galvanic anodes and impressed-current anodes are discussed elsewhere, but further comment is relevant here in relation to the choice of a particular system for a specific environment. In this connection, it should be noted that the conductivity of the environment and the nature of the anode reactions are of fundamental importance. The main anodic reactions are electrochemical oxidation processes and may be summarized as follows:

##### For galvanic anodes:

Primary reaction:  $M \Rightarrow M^{z+} + ze^-$  (i.e., metal dissolution)

Secondary reaction:  $M^{z+} + zH_2O \Rightarrow M(OH)_z + zH^+$  (i.e., precipitation of metal hydroxide)

where  $M$  represents the anode material and  $z$  the number of electrons transferred in the reaction (i.e., the electrochemical equivalent). For zinc and magnesium,  $z = 2$  and for aluminum,  $z = 3$ .

##### For impressed-current anodes:

$3H_2O \Rightarrow 2H_2O^+ + 2e^- + \frac{1}{2}O_2$  (i.e., oxidation of water/evolution of oxygen) and/or

$2Cl^- \Rightarrow Cl_2 + 2e^-$  (i.e., evolution of chlorine)

or, in the case of graphite or graphite-filled polymer anodes

$C + O_2 \Rightarrow CO_2$  (i.e., oxidation of carbon to carbon dioxide)

It should be noted that when metals such as zinc and aluminum are used as galvanic anodes, the anode reaction will be predominantly as above although self corrosion may also occur to a greater or lesser extent. The emf between magnesium, the most active (negative) galvanic anode, and iron is  $\sim 0.7$  V, the emf of power-impressed systems can range from 6 V to typically a maximum of 48 V (limited for personnel safety reasons), depending on the power source employed. Thus, galvanic anodes are normally restricted to environments having a relatively lower resistivity (e.g.,  $< 50 \Omega m$ ), whereas there is no similar limitation in the use of impressed-current systems.

In the case of galvanic anodes, the electrons that are required to depress the potential of the structure to be protected are supplied by the primary reaction above and, providing the metal ions can diffuse away from the structure before they react with water to form insoluble hydroxides, the reaction will be unimpeded and will take place at a low overpotential. If, however, the metal hydroxide precipitates on the

**Table 1** Comparison of galvanic anode and impressed current cathodic protection systems

<i>Method</i>	<i>Galvanic (sacrificial) anode cathodic protection</i>	<i>Impressed-current cathodic protection</i>
Characteristics	Protection by current from galvanic/sacrificial consumption of more electronegative metal anodes	Protection by current from DC power supply; typically a transformer rectifier passed through more inert anodes
Anode materials	Magnesium, aluminum, and zinc alloys. Occasionally iron for protection of copper and copper alloys	Mixed metal oxide (Pt, Ir, Ru)-coated titanium; platinum-plated titanium and niobium; cast silicon-iron and silicon with chrome; conductive ceramic (monolithic $Ti_4O_7$ ). Historically carbon; lead alloy, and lead alloy with Pt microelectrodes; scrap iron; conductive polymers
Power	Independent of power source Well established $Ah\ kg^{-1}$ capacity figures for proven alloys Cannot be connected incorrectly with polarity reversed.	Requires electrical power supply Can be connected incorrectly with polarity reversed and cause accelerated corrosion. (There are polarity reversal protection circuits available)
Installation	Simple, but may require significant welding of anode steel cores to structure	Complex; requires significant cable routing between the power source, the anodes, and the cathode
Reliability	High, if properly designed and installed Entire cathodic protection system directly connected to the structure; only the galvanic (sacrificial) anode material is consumed by corrosion	High, if properly designed, installed, and maintained Historically many offshore and port and harbor impressed-current systems have failed due to mechanically inadequate designs. Many marine systems have failed due to poor maintenance or simply being switched off The entire anode (+ve) circuit is at risk of forced corrosion if cables or anode/cable connections are improperly designed or are damaged. Positive cable damage and poor anode/cable design are significant risks to impressed current system performance
Design complexity	Simple, but requires competent anode and steel core design for anode current delivery through life and for certain applications may require rigorous structural assessment of welded connections between steel core and structure	Complex. Designs frequently ignore key elements of competent design such as optimum anode-cathode spacing calculations for optimum current distribution. Mechanical integrity of anodes, anode/cable connections, cable management systems, and monitoring systems often inadequate
Typical design life	5–50 years High cost and weight for long-life systems	10–100 years but electrical/electronic systems likely to require 100% replacement at c. 25 years
Interaction or stray current	Due to normally low individual anode current outputs and large numbers of anodes, interaction effects to third-party structures are often negligible High-current anode arrays can cause the same interaction effects as impressed-current systems of same current output Interaction testing necessary in sensitive locations and with high-current designs	Very likely  Interaction testing with third parties should be mandatory. Remedial action may be simple and low cost
Advantages	Simple. Reliable  'Self-control' current output to meet demand within a limited range if properly designed	Ability to easily increase or decrease current to meet changing demands or errors in design assessment Ability to remote-control and monitor via electronic devices Ability to measure 'instant OFF' potentials with minimum IR drop errors Ability to operate in high electrical resistivity electrolytes and provide high currents from relatively small installations

Continued

**Table 1** Continued

<i>Method</i>	<i>Galvanic (sacrificial) anode cathodic protection</i>	<i>Impressed-current cathodic protection</i>
Limitations	<p>Electrical resistivity of electrolyte</p> <p>Typically <math>&lt;10\ \Omega\text{ m}</math> in saline water for aluminum anodes</p> <p>Typically <math>&lt;20\ \Omega\text{ m}</math> in saline water and soils for zinc anodes (although Zn ribbon can be used effectively to say <math>50\ \Omega\text{ m}</math>)</p> <p>Typically <math>&lt;50\ \Omega\text{ m}</math> in waters and soils for Mg anodes (although 'high voltage' and ribbon anodes can extend this)</p> <p>Typically, large numbers of anodes of considerable size are required for large current cathodic protection systems</p> <p>All anodes may not consume at the same rate if local current demands or resistivities vary</p> <p>Monitoring and control of galvanic anodes, although possible, is often limited</p>	<p>May be uneconomical for small schemes due to high unit cost of electrical power supply and transformer rectifier or control system</p> <p>Can use photovoltaic and/wind generators for relatively small schemes</p> <p>All elements of the anodic (+ve) circuit must be electrically isolated from the structure. Thus risks of failure by short circuits (particularly relevant to reinforced concrete applications where anode/cathode spacings may be as low as 15 mm). Thus, hull penetrations are needed for ship and floating structure applications</p>
Prime applications	<p>Offshore oil and gas facilities due to high reliability</p> <p>Port and harbor piled installations; high reliability, low inspection/maintenance requirement and low interaction risk</p> <p>Lock gates, tidal and flood protection facilities</p> <p>Small onshore applications; short pipelines</p> <p>Domestic water tanks</p> <p>Ships' internal tanks</p> <p>Offshore wind farm facilities</p>	<p>Offshore oil and gas facilities with weight limitations; very rigorous design process following multimillion £/\$ failures</p> <p>Port and harbor applications wherein capital cost assessment has outweighed the risks. Some failures</p> <p>Large/long pipeline applications. High reliability due to established design practice and relatively benign environment</p> <p>Large buried tanks and tank bottoms of 'on grade' tanks</p> <p>Cooling water applications where small anodes are essential</p> <p>Reinforced concrete applications wherein the high resistivity of the concrete often dictates impressed current</p> <p>Ship's hulls where the small size and low hydrodynamic profile is important</p>
Inspection and maintenance	Limited simple testing to confirm performance and to monitor consumption of anodes. Typically annual. If design-adequate, maintenance limited to replacement of depleted/consumed anodes at end of design life	Significant regular inspection requirements. Typically monthly for function check and three-monthly for performance verification. Maintenance typically required to power supplies, anodes, and monitoring systems
Stray current or drainage bonds (DC)	–	Effectively impressed current systems deriving their current from DC traction or similar stray current DC source. Can be directly bonded, controlled to a limited extent with resistive and rectifier networks or supplemented with an additional DC power source
Stray current dissipation (DC and AC)	<p>Effectively galvanic anode systems which might be used alone or to supplement an impressed-current system and used to provide a safe, low electrical resistance, connection to earth (soil or water typically) to allow DC or AC current to pass from the structure to earth without causing DC or AC corrosion to the structure</p> <p>Increasingly important on pipelines with very high electrical resistance coatings in the vicinity of AC electrical distribution networks</p>	–

surface of the metal as a nonconducting passive film, the anode reaction will be stifled and this situation must be avoided if the anode is to operate satisfactorily. Much development work has been expended in developing galvanic anode alloys which are reliable in known electrolytes and which do not suffer from stifling by anode reaction products.

In the case of nonreactive impressed-current anodes, rapid transport of the reactants ( $\text{H}_2\text{O}$  and  $\text{Cl}^-$ ) to and the reaction products ( $\text{O}_2$  and  $\text{Cl}_2$ ) away from the anode surface is essential if the anode reaction is to proceed at low overpotentials. This presents no problems in seawater, and for this reason the surface areas of the anodes are comparatively small and the anode current densities correspondingly high. Thus, in seawater, inert anodes such as mixed metal oxide-coated titanium (MMO/Ti) and platinized titanium can operate at up to  $1000 \text{ A m}^{-2}$ , since the anode reaction occurs with little overpotential, and there is rapid transport of  $\text{Cl}^-$  to and  $\text{Cl}_2$  away from the anode surface. In this connection, it should be noted that even in a water of high chlorinity such as seawater, oxygen evolution should occur in preference to chlorine evolution on thermodynamic grounds. This follows from the fact that the equilibrium potential of the oxygen evolution reaction in neutral solutions is  $0.84 \text{ V}$ , whereas the corresponding value for the chlorine evolution is  $1.34 \text{ V}$ , that is,  $0.5 \text{ V}$  higher. However, the chlorine evolution reaction occurs with only a small overpotential, whereas very appreciable overpotentials are required for oxygen evolution, and this latter reaction will occur therefore only at high current densities. Even in waters of low salinity, chlorine evolution will therefore tend to occur in preference to oxygen evolution at low overpotentials.

In the case of MMO/Ti, the consumption rate of the coating will be at its lowest ( $\sim 0.2 \mu\text{g}(\text{Ah})^{-1}$ ) when operated in open seawater, will increase in brackish water where a greater proportion of oxygen is evolved (to  $\sim 0.45 \mu\text{g}(\text{Ah})^{-1}$ ), and will be maximum in saline mud ( $\sim 1\text{--}1.5 \mu\text{g}(\text{Ah})^{-1}$ ).

In the protection of pipelines or other underground structures with buried anodes (often in 'groundbeds' or arrays of buried anodes), the anode reaction is dependent on diffusion of water to the anode surface and oxygen and  $\text{CO}_2$  away from it. Since these processes do not occur with the same mobility as in water, it is necessary to use a very large surface area of anode and a corresponding low current density. For this reason and to further reduce the electrical resistance of the anode to earth, the actual anode is a carbonaceous backfill of considerably greater dimensions than the anodes laid within the backfill. Silicon-iron or

MMO/Ti anodes are used primarily to make electrical contact between the cable and the backfill. It can also be seen from the oxygen evolution reaction above that the products of the oxidation of water are oxygen and hydrated hydrogen ions, which will migrate away from the anode surface under the influence of the field, thus removing two of the three water molecules that participate in the reaction, and this will tend to dehydrate the groundbed. In addition, the electric field between the anode and the cathode will cause electro-osmosis, which will further dehydrate the groundbed. These difficulties can be overcome, when feasible, by locating the groundbed below the water table.

#### **4.21.1.2.2 Galvanic anode systems**

*Advantages:* No external source of power is required; installation is relatively simple; the danger of cathodic protection interaction is minimized; it is more economical for small schemes; the danger of over protection is normally alleviated; uniform current distribution can be easily achieved by using small anode currents from many anodes; maintenance is not required apart from routine potential checks and replacement of anodes at the end of their useful life; it involves no running costs.

*Disadvantages:* Maximum anode output is delivered when first installed; this decreases with decreasing anode size with time when additional current may be required to overcome coating deterioration; current output in high-resistivity electrolytes might be too low and render anodes ineffective; large numbers of anodes may be required to protect large structures resulting in high anode installation and replacement costs; anodes may require replacement at frequent intervals when current output is high and/or maximum size is limited.

#### **4.21.1.2.3 Impressed-current systems**

*Advantages:* One installation can protect a large area of metal; systems can be designed with a reserve voltage and amperage to cater for increasing current requirement due to coating deterioration; current output can be easily varied to suit requirements; schemes can be designed for a life in excess of 25 years; current requirements can be readily monitored on the transformer-rectifier or other DC source; automatic control of current output or of the structure potential can be achieved.

*Disadvantages:* Possible interaction/stray current effects on other buried structures; their use is subject to the availability of a suitable AC supply source or other source of DC; regular electrical maintenance checks and inspection are required; running cost for



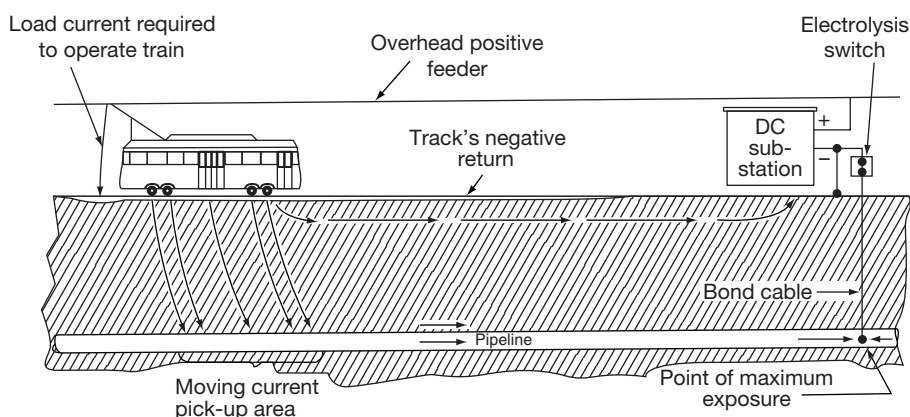


**Figure 1** Bond between pipeline and DC substation.

electrical supply is usually not very high except in the case of bare marine structures and in power stations wherein structures are often bare and include bimetallic couples; it is subject to power shutdowns and failures.

#### 4.21.1.2.4 Hybrid systems

Offshore structures are sometimes protected by hybrid systems using both galvanic and impressed-current anodes. These have the advantage that protection of the steel by the galvanic anodes will be effective as soon as the platform enters the sea, which is particularly advantageous since some time may elapse before the power generators required for the impressed-current system are operating.

#### 4.21.1.2.5 Stray-current bonding or forced drainage

Stray-current schemes are once again increasing in occurrence in the United Kingdom, as more localities have widespread DC transport systems arising from new tram- or light rail-based mass transport systems in the major conurbations. Such systems are extensively used in overseas countries where DC transport systems are in widespread use, that is, most of mainland Europe, Australia, and South Africa, with large schemes having been introduced into North America.

Where stray-current bonding can be employed, it is normally the most economical method of applying cathodic protection since the power required is supplied gratis by the transport system.

In such systems, it is necessary to provide a metallic bond between the pipeline and the negative bus of the railway substation. By providing such a bond, the equivalent of a cathodic protection system is established whereby the current discharged from the traction-system rails is picked up by all portions of the pipeline and drained off via the bond. The bond must have

sufficient carrying capacity to handle the maximum current drained without damage. In order to ensure that the direction of current flow in the bond does not reverse, it is normal to employ a reverse-current prevention device or 'electrolysis switch.' This may take the form of a relay-actuated contactor which opens automatically when the current reverses. Diodes are now more commonly used as blocking valves to accomplish the same purpose. They are wired into the circuit so as to ensure that the current can flow to the negative bus bar system only. Sufficiently rated diodes must be used in parallel to handle the maximum amount of current anticipated. Also, the inverse voltage rating (peak inverse voltage; PIV) of the diodes must be sufficient to resist the maximum reverse voltage between the negative bus bar and the pipeline (Figure 1).

Obviously the cathodic protection provided to the structure as a result of this system will be partial; it will not be provided when the traction system is not operational (many systems do not operate at night) or when the distribution of the traction units and substations is such that the current in the controlled bond is in the wrong direction and is blocked by the diodes or contactor. Some systems will include, separately or in the same installations, a potential-controlled transformer-rectifier, which will supplement the current from the traction bond and provide more continuous and better controlled cathodic protection.

### 4.21.2 Design of a Cathodic Protection System

#### 4.21.2.1 Initial Design Process

The design of a cathodic protection scheme should follow the general process outlined below. (see also Table 2). The design of any cathodic protection

**Table 2** Summary of the cathodic protection design process**Common to both galvanic and impressed-current systems**

Determine electrolyte resistivity and corrosivity  
 Determine other factors that will affect corrosion rate and current density: Soil type, temperature, flow rate (in waters), chloride level in concrete, bacterial activity  
 Assess materials of construction and their impact on corrosion performance and cathodic protection current density and safe metal/electrolyte potential limits  
 Determine/agree structure design life with client and determine the optimum design life (and replacement strategy if required) for the cathodic protection system  
 Determine if cathodic protection is necessary to deliver design life of structure in the assessed environment with appropriate factors of safety  
 Determine appropriate metal/electrolyte protection potential (criteria) noting that bacterial activity will likely require a more negative metal/electrolyte protection criteria and that many metals and coatings will have a safe negative potential limit beyond which the metals may suffer hydrogen embrittlement (high-strength steels and cupronickel alloys) or corrosion (amphoteric metals such as aluminum) or the coatings may suffer disbondment  
 Determine coating quality (if any) and estimate initial, mean, and final coating breakdown %  
 Calculate metal surface area in the electrolyte; subdivide if conditions affecting current demand vary within structure/electrolyte  
 Determine/estimate initial, mean, and final current density figures taking account of the electrolyte/environment and coating performance as above. Where possible, consider past performance in same/similar electrolytes/environments/locations  
 Calculate initial, mean, and final current demand  
 Determine electrical continuity of structure and any requirements to establish necessary continuity  
 Consider necessity of electrical isolation of structure from other structures/elements in order to restrict cathodic protection current flow to other structures/elements OR estimate this current flow and make allowance for it.  
 Consider proximity of other structures/services and the impact of the new cathodic protection system on them (DC interference/stray current from the cathodic protection system to third-party structures). Make allowances for minimizing these impacts, testing, and remedial actions  
 Consider proximity of other structures/services and their impact on the new cathodic protection system (DC and AC interference/stray current to the structure receiving the new cathodic protection system from third-party structures). Make allowances for minimizing these impacts, testing, and remedial actions  
 Determine optimum cathodic protection solution: galvanic anode or impressed current, on basis of performance, cost, reliability, suitability to established client operational and maintenance capabilities, electrical power supply availability, and other relevant factors  
 Determine optimum performance monitoring provisions and procedures  
 Document all of the above

**Galvanic anode systems**

Select optimum anode alloy for electrolyte and service (temperature, safety, potability)  
 Determine realistic anode performance characteristics (capacity ( $\text{Ah kg}^{-1}$ ) and closed-circuit operating potential) from the literature, and independent test data  
 Calculate mass of alloy from capacity, mean current demand, design life, and utilization factor (the percentage of the total mass that can be utilized effectively in protection, typically 80–90% subject to steel core design, the remaining 10–20% of material may be too small to deliver end of life current or may be dislodged from the core). The core design is important in delivering high utilization factors  
 Select/design anode shape to deliver calculated mass and current output at all of initial, mean, and final conditions taking proper account of the reducing size of the anode and the impact of core design on end of life dimensions

**Impressed-current systems**

Select optimum anode type for electrolyte and service  
 Determine realistic anode performance characteristics (capacity ( $\text{Ah kg}^{-1}$  for silicon-iron and similar or wear rate for MMO/Ti, Pt/Ti and Pt/Nb)) and maximum safe operating voltage) from the literature, and independent test data  
 Determine optimum distribution of anodes and (if appropriate) the use of carbonaceous backfill to reduce resistance and increase anode life. Ensure anode/cable design and cable insulation/sheath materials are suitable for use in acidic, nascent chlorine, and oxygen-evolving environments so that the full capacity of the anode can be delivered  
 Design anode shape/size (with groundbed backfill as appropriate) to deliver suitable anode/electrolyte resistance using classical electrode/earth resistance formulae. Allow for back emf (the potential between anode/electrolyte/cathode) and cable resistance in determining the required driving voltage from the DC power supply

Continued

Table 2 Continued

<i>Galvanic anode systems</i>	<i>Impressed-current systems</i>
<p>This should be undertaken using the classical electrode/earth resistance formulae to determine anode/electrolyte resistance and the Ohms Law to calculate current output (using the driving voltage as the closed-circuit operating potential of the anode less the protection criteria potential selected earlier). For cable-connected galvanic anodes, include the cable resistance in these calculations</p> <p>Determine optimum anode–cathode and anode–anode spacings and then determine whether the calculated anode current outputs should be reduced because of anode/cathode or anode/anode mutual interference (anode and cathode tension hill) and that the attenuation of protection between anodes will deliver adequate protection at mid points</p> <p>Confirm that the steel core design of the anode is structurally sufficient for the application</p> <p>–</p> <p>–</p>	<p>Determine optimum anode/cathode spacing to deliver uniform current distribution, to minimize interaction to third-party structures</p> <p>For buried applications, the locations should take account of the availability of electrical power supplies, the location of lower resistivity and wet soil conditions, and the avoidance of mechanical damage or future developments</p> <p>Calculate optimum anode–cathode spacing using the anode tension hill formulae. Simplistically: <math>V = \frac{I\rho}{2\pi r}</math> where <math>V</math> is the local voltage shift in the electrolyte due to the voltage cone around the anode <math>r</math> meters from the anode and <math>\rho</math> is the soil resistivity in <math>\Omega</math> m</p> <p>The spacing might be determined by interaction issues with a nearby third-party structure or by attenuation/distribution along a pipeline. The local voltage cone value will not affect pipe/soil potential remote from the anode, so the voltage cone value may need to be limited to, say, 0.5 V to avoid excessive pipe/soil potential at the nearest point to the groundbed</p> <p>Determine (by classical attenuation formulae on pipelines, sometimes by mathematical modeling for more complex applications) the attenuation between the impressed current installation locations and the remote ends or mid-points between additional installations</p> <p>Determine the optimum control for the impressed current system based on changes in electrolyte (e.g., sea/freshwater in estuaries or dry/wet ground conditions for buried applications, or flow/no flow in cooling water systems), in service (ships trading in different oceans, salinity, and temperature) or in structure/electrolyte immersion (tides):</p> <ul style="list-style-type: none"> <li>• Manual constant voltage (simple), optimum if all conditions stable</li> <li>• Manual constant current (simple closed loop) optimum if cathode current demand is stable but anode/electrolyte resistance changes</li> <li>• Potential control (more complex, relies on performance of steel/electrolyte potential measurement provisions of test connections and permanent reference electrodes being reliable) optimum if cathode current demand changes and will also accommodate anode/electrolyte resistance changes</li> </ul> <p>Determine whether remote monitoring and/or remote control (typically via telephone or GSM modem) will deliver either or both greater security of performance and lower costs of performance verification and maintenance</p>
<p><i>Common to both galvanic and impressed-current systems</i></p> <p>Where necessary these calculations may be iterative until a fully compliant solution is determined</p> <p>Determine optimum performance verification monitoring and inspection procedures and facilities</p> <p>Determine optimum inspection and testing requirements during installation and optimum precommissioning and commissioning procedures along with future operation and maintenance procedures</p> <p>Undertake a design risk assessment to assess, document, and, wherever possible, minimize the risks involved in the implementation of the design</p> <p>Document all of the above</p>	

scheme should be carried out by specialists who are suitably trained, experienced, and accredited as competent in the specific field of application.

Good practice in modern underground or underwater pipeline structures involves the use of good coatings in combination with cathodic protection. With a well coated structure, the cathodic protection system only protects the minute areas of steel exposed to the corrosive environment rather than the whole surface of an uncoated structure. The effect of coatings can be demonstrated by comparing the current density of a bare steel pipeline in average soil conditions, which could be up to  $30 \text{ mA m}^{-2}$ , with that achieved on a well coated and inspected line where a current density of only  $0.01 \text{ mA m}^{-2}$  or even lower may be required to obtain satisfactory cathodic protection. In all cases, the current density for protection is based on the superficial area of the whole structure.

Caution should be exercised when considering the suitability of coatings for the long-term protection of structures either without or in conjunction with cathodic protection. It is important that the long-term adhesion of the coatings to the surface is secure and that the electrical properties of the coatings over the full life and their impact on matters such as ac corrosion, stray current, and monitoring are properly assessed. It may be that the superficially 'best performing' coating for, say, a pipeline may present long-term disbondment and corrosion risk below the outer sheath and/or high risk of significant AC or DC stray current effects plus difficult-to-interpret/irrelevant cathodic protection monitoring data due to the particular dielectric properties of the coatings.

Many offshore structures and piled port and harbor structures are of bare steel based on the economics that the application of a high-quality coating can actually cost more than the application of a simple cathodic protection system to these bare structures.

Cathodic protection to steel in concrete is almost always to bare steel in concrete; the performance of coated reinforcement in concrete has not delivered its early promise in preventing corrosion in chloride-contaminated concrete, and the application of cathodic protection to coated reinforcement is complicated by electrical continuity issues and may be less than optimally effective due to long-term disbondment of coatings.

#### 4.21.2.2 Surface Area

In the case of underground pipelines, calculation of the superficial surface area can be obtained from the

diameter and length of the line involved. The superficial surface area should include any off-takes and other metal structures in electrical contact with the main line.

For marine structures, the area should include all submerged steel work below the high-tide level for impressed-current systems, but for galvanic systems, surface areas at both the high-tide and mid-tide levels may be required for parallel calculations of peak current demand for anode shape calculations and mean current demand for anode weight calculations. The surface areas may need to be split into different levels, as the current density requirements will vary with flow rate, oxygen content, and temperature, all of which vary with depth. Particular attention may need to be given in the cathodic protection design to areas of geometric complexity such as riser frames and pile guides; these may need local anode provisions to ensure that there is sufficient current distribution into these complex areas.

In the case of plants such as power stations, details of the water boxes, number of passes on coolers, and detailed assessment drawings are required in order to determine the local current density requirements in what may be bimetallic couples and high flow rate locations of the systems. Some parts of the structures may be bare and others coated.

In the case of ships, details of the full underwater submerged area at full load are needed along with details of sea chests, thrusters, and other features of the vessel design that will affect the cathodic protection design, including whether the vessel is intended for ice service (which will affect both the anode design and the coating breakdown allowances).

For steel-reinforced concrete, the steel surface area and its local disposition (steel density) require to be calculated on a very local basis (typically in local areas of  $\sim 1 \text{ m}^2$ ) because most anode systems will be installed in the concrete only some 15–100 mm away from the reinforcement and current distribution will therefore be limited. It is therefore essential, for uniform protection levels and uniform anode consumption rates, that the local anode provision properly reflects the local steel current demand; thus the steel surface areas need to be calculated and presented in considerable detail.

#### 4.21.2.3 Electrical Continuity

It is essential for any structure to be fully electrically continuous. In the case of pipelines, welded joints are obviously no problem, but mechanical joints require bonding. For marine structures, individual piles

and fendering must be electrically connected by welding either via the reinforcing bars in the concrete deck slab or separately. In power stations and ships, rotating shafts must be bonded into the structure by means of brush gear or a suitable alternative. In the case of offshore mooring installations, it may be considered to install a bonding cable to bring dolphins, etc. into an impressed current system but it is more normal to protect isolated elements, such as dolphins without walkways, with their own galvanic anode systems even if the main cathodic protection system is impressed current.

For steel-reinforced concrete structures, normal steel-fixing good practice is generally adequate to present a steel matrix that is sufficiently electrically continuous to allow all individual bars to receive full cathodic protection. In cathodic protection to new reinforced concrete structures, electrical continuity testing will be undertaken during steel fixing, and limited provisions of welded continuity bars may be required to ensure that all bars are electrically continuous (it is normally taken that  $1\ \Omega$  bar-to-bar resistance can be accepted as adequate within a matrix). In cathodic protection of existing reinforced concrete structures wherein corrosion has initiated, it is normal to test all bars exposed in concrete repair areas (at which the steel ties are likely to have corroded and corrosion products may have forced bars apart) and to undertake representative additional testing, following an assessment of the structure and its drawings, to prove the quality of general continuity within the reinforcement matrix. It is sometimes necessary to cut longitudinal and circumferential chases in the concrete to expose all bars and continuity-bond them.

#### 4.21.2.4 Estimate of Current Required

The surface area of the structure is calculated, and the current density required for the particular environment is selected (Table 3). In the case of an existing structure, the condition of the coating may be unknown and the application of a temporary cathodic protection system may be necessary to determine the amount of current required for protection, as established by the potential. Such a test to determine the absolute amount of current required is known as a current drain test. Misleading information may, however, be obtained if the results from current drainage tests on bare or coated steel in seawater are extrapolated, because long-term polarization effects, together with the formation of a calcareous deposit on the structure, may

considerably reduce eventual current requirements. On the other hand, in estuaries and polluted waters, special care must be taken to allow for seasonal and other variable factors that may require higher current densities.

#### 4.21.2.5 Establishing Electrolyte Resistivity

To enable a satisfactory cathodic protection scheme to be designed, it is necessary to determine the resistivity of the electrolyte (soil, water, or concrete). This information is necessary to enable the current output of anodes to be determined together with their position and power source voltage, and it also provides an indication of the aggressiveness of the environment; in general the lower the resistivity, the more aggressive the environment.

#### 4.21.2.6 Economics

After evaluating these variables, it must then be decided which type of system, that is, galvanic anode or impressed current, would be the most economical under the prevailing conditions. For instance, it would obviously be very expensive to install an impressed-current system on only 100 m of fire main. Similarly, it would be equally uneconomical to install a galvanic anode system on hundreds of miles of high-pressure, poorly coated gas main. Further, there is little benefit in providing a complex impressed-current system to an environment/location/client without resources to adequately monitor, adjust, and maintain the system. Therefore, each structure should be individually assessed taking note of all the factors involved in order to determine the optimum cathodic protection system (see Table 3).

#### 4.21.3 Impressed-Current Systems

Cathodic protection schemes utilizing the impressed-current method fall into two basic groups, dictated by the anode material:

*Group 1:* These anode materials have relatively high consumption rates, and their dimensions generally change during consumption. They comprise silicon-iron (and historically graphite and scrap steel) anodes used for buried structures and landward faces of sheet steel piled jetties, wharves, etc.; conductive coatings containing graphite used in cathodic protection of steel in concrete; conductive polymers containing graphite used



**Table 3** Typical current density figures for cathodic protection

<i>Environment</i>	<i>Estimated current density for cathodic protection based on superficial surface area mA m<sup>-2</sup></i>
<b>Bare steel</b>	
Sterile, neutral soils	4–16
Well aerated neutral soil	20–35
Dry well aerated soil	5–16
Wet soil, moderate/severely corrosive	25–65
Highly acidic soil	50–165
Soil supporting active sulfate-reducing bacteria	400–500
Fresh water, no flow	50–60
Fresh water flow	50–70
Turbulent fresh water containing dissolved oxygen	50–170
Fresh water at 70 °C	50–170
Polluted estuarine water	500–1600
<b>Seawater</b>	
Tropical >20 °C	Initial: 120–180; mean: 40–90; final: 80–130
Subtropical 12–20 °C	Initial: 140–200; mean: 50–100; final: 90–150
Temperate 7–11 °C	Initial: 170–220; mean: 60–110; final: 110–170
Arctic <7 °C	Initial: 200–250; mean: 80–120; final: 130–170
Chemicals, acids or alkaline solutions in process tanks	30–300
Heat exchanger water boxes with nonferrous tube plates and tubes and no coatings	500–1500
<b>Steel in concrete</b>	
Note: These current densities are to protect steel in non-water-saturated concrete to the appropriate protection criteria for steel in concrete. For buried steel connected to steel in concrete (such as at valve pits or pump stations where isolation has not been provided), the allowance for current drained to the steel in concrete in order to protect steel in soil to its appropriate protection criteria should be increased by a factor of 3–5. The figure 'prior to corrosion initiation' is adequate for fully immersed concrete	
These figures are ALL with reference to steel surface area; some US designs are incongruously based on concrete surface area and presumably assume a uniform steel density per unit area of concrete; such an assumption is incorrect	
Following corrosion initiation temperate	Initial: 10–20; mean/final: 2–15
Prior to corrosion initiation	0.2–2
<b>Coated steel pipelines &lt;30 °C assuming 30-year life</b>	
Coated with glass-reinforced coal tar or asphalt bitumen enamels, asphalt mastic, or butyl rubber tape assuming no massive failures	Initial: 0.040; mean 0.100; final 0.200
Fusion-bonded epoxy, liquid epoxy, coal tar epoxy assuming no massive failures	Initial: 0.010; mean 0.020; final 0.050
Three-layer polyethylene or polypropylene assuming no massive failure. Caution: failure can result in disbondment and shielding. Electrical characteristics can be so 'good' that the pipelines become vulnerable to AC and DC interaction and very difficult to monitor real pipe/soil potentials	Initial: 0.002; mean 0.005; final 0.010

Note: All of the above are general guidance figures only. Wherever possible, a design should be based on past performance or accurately determined current density figures for the metal in the electrolyte, at the temperature/flow/ambient conditions applicable to the structure, and should take into account long-term cathodic polarization and coating breakdown. These figures do not include any affects due to galvanic couples or stray currents.

historically in cathodic protection of steel in concrete, with many failures; and a similar conductive polymer wire anode used in buried applications.

*Group 2:* These anode materials have relatively low consumption (or wear) rates, and their dimensions generally do not change during consumption. They comprise MMO/Ti, platinized titanium, platinized niobium,

and conductive ceramic (and historically lead alloy and lead alloy with platinum micro electrodes) anodes used for submerged structures, ships, and power stations. Backfilled in carbonaceous backfill, MMO/Ti are also used for buried applications. MMO/Ti and conductive ceramic are widely used in cathodic protection of steel in concrete.

### 4.21.3.1 Group 1 Anodes

#### 4.21.3.1.1 Scrap steel

In some instances, a disused pipeline or other metal structure in close proximity to the project requiring cathodic protection may be used as the anode system. Reputedly, the first impressed-current jetty system in the United Kingdom used a keel of a scrap submarine as the anode. However, it is essential in cases of scrap steel or iron groundbeds to ensure that the steelwork is completely electrically continuous, and multiple cable connections to various parts of the groundbed must be used to ensure a sufficient life. Preferential corrosion can take place in the vicinity of cable connections, resulting in early electrical disconnection; hence the necessity for multiple connections. Scrap steel and iron are almost never used as anodes now.

#### 4.21.3.1.2 Graphite

Graphite anodes are usually resin-impregnated and supplied in standard lengths, for example, 65-mm dia. 1.2-m long; and 75-mm dia. 1.5-m long, with a length of cable (called the anode tail) fixed in one end. Graphite anodes were particularly common in early cathodic protection systems. However, they have been almost completely replaced by silicon-iron, the main reasons being (1) graphite tends to spall in use, particularly in chloride environments; and (2) it has a relatively low operating current density ( $10\text{--}20\text{ A m}^{-2}$ , Table 4). Thus, graphite anodes are very seldom used now, having been replaced with more efficient and reliable silicon-iron and MMO/Ti anodes.

#### 4.21.3.1.3 Silicon-iron

Silicon-iron anodes are generally supplied in standard sizes, for example, for solid castings 50 or 75 mm in dia. and 1.2 or 1.5 m in length and are complete with a cable tail. These anodes are made from cast iron with a high silicon content of 14–15%, together with small percentages of alloying elements such as chromium.

Anodes are available with enlarged heads within which the cable tails are terminated and encapsulated with resin and heat-shrink protective caps. They are available as ‘single ended’ or ‘double ended’ with, respectively, one cable connection at one end or one at each end. The ‘double ended’ anodes can be supplied in multiple anode strings with a single cable per string.

Centrifugally chill-cast tubular anodes are also available in diameters of 55–170 mm in lengths of 1.5 and 2.1 m with central connection of the cable. There are data that indicate the chill-cast anodes are more consistent in their performance, presumably

due to their finer and more consistent grain structure and that the central connection of the cables results in a higher utilization factor for the anode mass, as the end effects do not result in early consumption of the cable connection end(s).

Silicon-iron with 4.5% chrome has become the most common silicon-iron alloy used for impressed current anodes, but it should be used only when the chloride content of the electrolyte is significant. In soils with low chloride content, the tenacious oxide film, which forms on the chrome alloy and provides its low consumption rate in seawater and other chloride environments, can become highly resistive and lead to anode/groundbed apparent failure.

The main disadvantages of silicon-iron anodes are their weight and extreme brittleness, resulting in high transport costs and possible breakages from the foundry to the cathodic protection site, especially if this is overseas. This anode continues to be widely used, as its performance is very well established and is resilient to variation in operating conditions.

### 4.21.3.2 Group 2 Anodes

This group includes mixed metal-oxide coated titanium, platinized titanium, platinized niobium and tantalum, and conductive ceramic (and historically lead alloy and lead alloy with platinum micro electrodes) anodes used for submerged structures, ships, and power stations. Backfilled in carbonaceous backfill MMO/Ti are also used for buried applications. MMO/Ti and conductive ceramic are widely used in cathodic protection of steel in concrete.

#### 4.21.3.2.1 Platinized titanium

These anodes are usually in the form of a titanium rod, tube, or wire with an electroplated coating of platinum 2.5–5.0  $\mu\text{m}$  thick. Diameters are generally in the range 3–25 mm. In order to reduce the voltage drop in very long anodes, a copper-cored variety is available. Platinized titanium anodes may also be used in mesh or plain sheet form and can be fabricated to suit particular applications. Co-extruded platinum on titanium (and niobium), with or without a copper core is also available.

#### 4.21.3.2.2 Platinized niobium and tantalum

Niobium and tantalum can be used as substrate materials where environmental conditions dictate a higher driving voltage, for example, brackish water. Use is limited due to relatively high cost. Copper-cored materials are again available.

**Table 4** Operating characteristics of impressed-current anodes

<i>Anode material</i>	<i>Maximum working current density (<math>A\ m^{-2}</math>)</i>		<i>Nominal consumption (<math>kg\ (Ay)^{-1}</math>) except as stated in <math>mg\ (Ay)^{-1}</math></i>	
	<i>Soil</i>	<i>Seawater</i>	<i>Soil</i>	<i>Seawater</i>
Scrap steel	5–6	5–6	8	10
Scrap cast iron	5–6	5–6	6	8
Silicon–iron	10–30	10–30	0.5	0.5–1.0
Silicon–iron in carbonaceous backfill	10–100	N/A	0.1	N/A
Silicon–iron 4.5% Cr	10–30	10–100	<0.1	<0.5
Silicon–iron 4.5% Cr in carbonaceous backfill	10–100	10–100	<0.1	N/A
	Do not use in soils with no chlorides; will become highly resistive			
Graphite	10	10–20	0.25–2.5	0.5–5
Lead–silver alloy	N/A	100–200	N/A	0.025–0.10
Lead–silver alloy/Pt microelectrodes	N/A	200–1000	N/A	0.002–0.10
Pt/Ti	50–100	500–3000	Negligible in carbonaceous backfill	1.2–10 $mg\ (Ay)^{-1}$
Pt/Nb	N/A	500–3000	N/A	1.2–10 $mg\ (Ay)^{-1}$
MMO/Ti	50–100	500–1000	6–7 $mg\ (Ay)^{-1}$ in soils	1–2 $mg\ (Ay)^{-1}$ in seawater
			8–13 $mg\ (Ay)^{-1}$ in saline mud	2–4 $mg\ (Ay)^{-1}$ in brackish water
MMO/Ti in carbonaceous backfill	Negligible	500–1000	Negligible	N/A
<i>Anode material</i>	<i>Maximum working current density in concrete</i>		<i>Typical life in concrete</i>	
MMO/Ti mesh, strip, and ribbon surface-mounted and concrete-encased or cast into concrete	Short-term 220 $mA\ m^{-2}$		Subject to coating loading up to 100 years with a factor of safety (for nonuniform current density delivery) of 2.	
	Long-term 110 $mA\ m^{-2}$		Typical consumption for $IrO_2/Ta_2O_5$ coating 3.5–9 $mg\ (Ay)^{-1}$	
	Limited by acidification of concrete not anode parameters			
MMO/Ti tubular discrete anode drilled and mortared into concrete	800 $mA\ m^{-2}$		Subject to coating loading up to 100 years with a factor of safety (for nonuniform current density delivery) of 2.	
			Typical consumption for $IrO_2/Ta_2O_5$ coating 3.5–9 $mg\ (Ay)^{-1}$	
Conductive ceramic of monolithic $Ti_4O_7$ tubular discrete anode drilled and mortared into concrete	800 $mA\ m^{-2}$		Up to 100 years	
Conductive organic coating with carbon filler to concrete surface	20 $mA\ m^{-2}$		<15 years	
Arc- or flame-sprayed Zn to concrete surface	20 $mA\ m^{-2}$		<25 years	
MMO/Ti rod anodes in carbonaceous backfill drilled into concrete	800 $mA\ m^{-2}$ to carbonaceous backfill		<50 years subject to performance of carbonaceous backfill	
Ni-plated carbon fibers incorporated into a cementitious overlay	20 $mA\ m^{-2}$		<25 years	

Note: The above data are indicative only and based on a variety of sometimes conflicting data from numerous sources. Actual performance may vary due to particular electrolyte conditions.

#### 4.21.3.2.3 *Lead silver alloy with or without platinum microelectrodes*

The alloy is lead, together with 1–2% silver in rod or extruded section form with platinum microelectrodes inserted every 150 mm. The purpose of these microelectrodes, which take the form of pins, is to stabilize the formation of lead peroxide on the anode surface. These anodes have seen extended service as ship hull anodes and were favored by some designers for seawater cooling systems in power stations. They have been largely replaced with MMO/Ti anodes.

#### 4.21.3.2.4 *Mixed metal oxide-coated titanium (MMO/Ti)*

This anode material has become very widely used in seawater, in soils (generally backfilled in carbonaceous backfill), in saline muds (directly buried), and in concrete. The MMO compositions are held by some manufacturers to be proprietary as are the coating loading onto the titanium substrate. Some manufacturers declare their coatings to be  $\text{IrO}_2/\text{Ta}_2\text{O}_5$  mixtures and declare coating loadings and consumption rates. Others do not declare these critical parameters and the designer must rely on accelerated testing of samples from production batches to be secure in the design life.

Anodes for immersed and buried applications are available in tubular, rod, wire, and sheet forms, with tubular anodes having center-connected cables being widely used in strings as single anodes. Perforated and expanded Ti mesh and ribbon coated after perforation and expansion is widely used in carbonaceous backfill for the anode systems placed beneath tank bottoms during construction and in horizontal groundbeds. In deep-well groundbeds, tubular anodes are widely used in carbonaceous backfill.

MMO/Ti mesh, ribbon, strip, and tubular discrete anodes are widely used in cathodic protection of steel in concrete. The mesh and ribbon anodes are used surface-mounted within sprayed concrete overlays, or the ribbon and strip anodes have been used installed into cut slots in the concrete surface. Tubular anodes used as discrete point sources of current delivery are grouted into drilled holes in the concrete. Ribbon, in particular, is widely used in the application of cathodic protection to new construction reinforced concrete structures, in extreme environments or where its service is particularly critical, and the design life is beyond that which can be securely delivered by durable concrete design.

#### 4.21.3.3 *Other Anodes for Reinforced Concrete Applications*

Much cathodic protection of reinforced concrete is undertaken on existing structures, which have suffered corrosion due to chloride contamination, as part of concrete repair and strengthening works. Many of these systems require anodes to be installed on atmospherically exposed (above ground) concrete surfaces with the minimum of impact to the structure. Thus a whole range of anode systems has been developed for these applications since the mid-1970s in the United States and the late 1980s in Europe and elsewhere.

Some of these anode systems have been used briefly and either failed or not delivered their promised economic advantages to their developers. The former category includes a conductive polymer wire that proved to have failed approximately one-fifth of that claimed by its manufacturer and many conductive coatings and mastics that did not perform as claimed. In the latter category is an early bridge deck cathodic protection system from Ontario in Canada, which utilized cast silicon-iron ‘pancake anodes’ in a conductive overlay of coke breeze and mastic. Many of these systems performed very well, but they were not proprietary; they were heavy, and the physical properties of the coke-filled mastic were not ideal; they have fallen out of use.

Systems still in use include a limited number of good, well proven conductive coatings; a small range of products using proprietary nickel-coated carbon fibers in a carbonaceous mortar that can be low pressure-sprayed onto concrete as thick coating or a thin overlay; a proprietary MMO wire discrete anode in a carbon backfill; and conductive ceramic tubes of monolithic  $\text{Ti}_4\text{O}_7$  (registered name Ebonex).

Flame- and arc-sprayed zinc has been quite widely and successfully used in North America as an impressed-current anode in the colder northern regions and as a galvanic anode in the warmer regions such as Florida. A thermally sprayed Al–Zn–In alloy is a proprietary product with claimed advantages over zinc.

Galvanic anodes of cast zinc are available in a small range of proprietary forms precast into a high-pH lithium-dosed mortar, which is claimed to enhance the corrosion activity of the zinc. These systems were originally designed to be fitted into concrete repair areas to provide partial cathodic protection and principally to overcome the incipient corrosion cell between steel in new chloride-free repair mortar and the surrounding chloride-rich

original concrete; they fulfilled this function quite well. These systems, and developments from them, are now being promoted for cathodic protection of entire structures; it is uncertain whether they can deliver sufficient current to achieve the established protection criteria for steel in concrete, and it is almost impossible to monitor them effectively due to their direct connection to the reinforcement.

#### 4.21.4 Cathodic Protection of Buried Structures

##### 4.21.4.1 Soil or Water Resistivity

Soil resistivity measurements are carried out by the Wenner technique using commercially available instruments. Resistivity data are not only required to determine the anode resistance and size but also to indicate the probable corrosivity of the soil or water. In the case of a pipeline route, variations in soil resistivity may stimulate localized corrosion and

can cause long line currents; the area in the soil of lower resistivity is usually anodic (more negative) compared to that in the soil of higher resistivity. It is therefore impossible to give any precise ruling as to the rate at which corrosion will occur under any particular soil conditions, and the results of any survey must be taken as giving only a general indication of the probability of corrosion. More rigorous corrosion assessment surveys determine the soil types, the dissolved salts, and the presence of bacteria and critical species such as free sulfur or carbonaceous material, and produce a corrosivity index.

Chemical and other forms of industrial contamination of the soil can significantly influence soil resistivities and corrosion characteristics and it is essential to investigate these in detail where such contamination may have occurred (e.g., in the proximity of chemical plants, etc.).

A typical soil resistivity survey is shown in **Figure 2**. Soil resistivities will normally indicate whether a cathodic protection system is advisable in

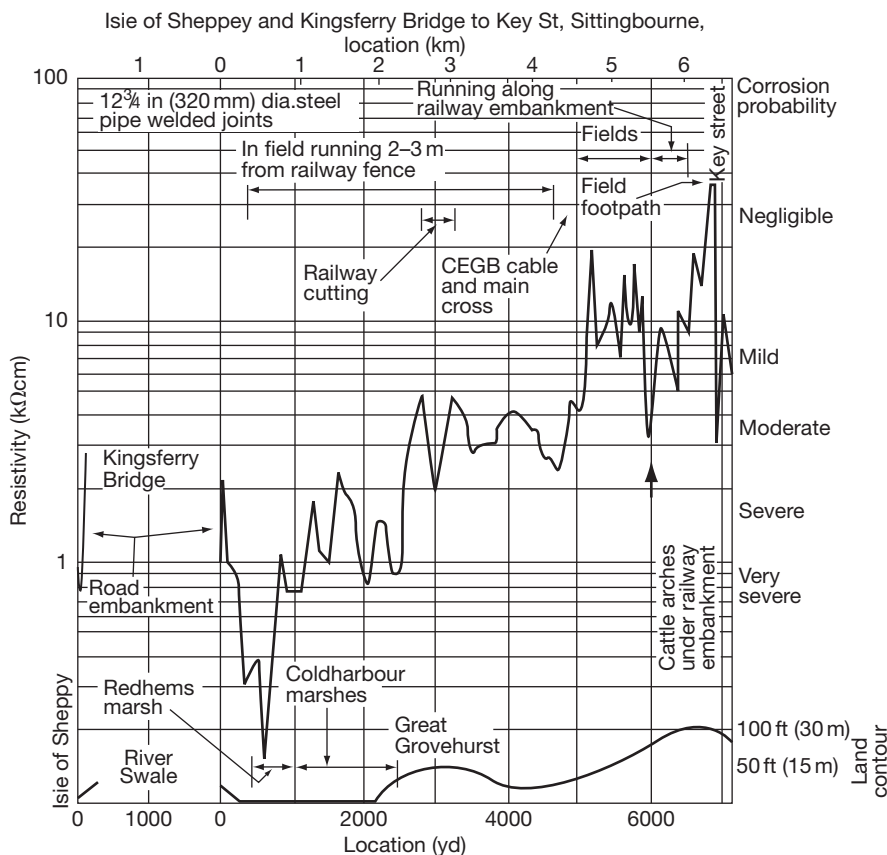


**Figure 2** Typical soil resistivity survey.



principle and whether impressed-current or galvanic anode schemes in particular are preferable. It may, as a result of the survey, be considered desirable to apply protection to the whole line or to limit protection to certain areas of low soil resistivity or 'hot spots.'

The cost of cathodic protection to uncoated buried pipeline structures is relatively high and expense may prohibit complete protection, in which case the galvanic anodes may be installed in the lowest resistivity areas only – on the basis that these are likely to be the most corrosive. This was a situation regularly encountered by cathodic engineers in the 1950s and early 1960s in the United Kingdom and the United States when extending the life of old oil and water pipelines in particular. In the case of high-pressure gas and oil lines, it is normal practice (it is mandatory in many countries) to apply cathodic protection irrespective of the soil resistivity in view of the low cost when associated with modern pipeline coatings and the potential hazards that could occur should even a minute pinhole perforate the pipe. In such cases, a soil resistivity survey is required only in the probable areas of groundbeds in order to enable the size of the groundbed, rectifier voltage, etc. to be determined. The soil resistivity also determines the current output of magnesium or zinc anodes should this type of system be preferred.

The soil resistivity, measured using the Wenner technique, determines the average soil resistivity in a hemisphere to a depth equivalent to the distance between the pin spacings, and it must therefore be recognized that the design figure for groundbed design in a particular location may not be highly precise. At least 10% error in the calculated resistance may be expected.

Soil resistivity surveys are often impractical in built-up areas, but in such areas impressed-current cathodic protection is often avoided on account of the danger of interaction. Under such conditions, adequate protection can be achieved by installing magnesium anodes in the pipe trench should the soil resistivity measurements made when the trench is opened indicate that this is necessary.

#### 4.21.4.2 Impressed-Current Design

Designs can be prepared once soil resistivities and groundbed locations have been determined. [Figure 3](#) illustrates typical installations. Design steps have been summarized in [Table 3](#) and are summarized below for a simple pipeline.

1. Select the current density to be applied from the results of cathodic protection tests and from any available data. On pipeline structures, attenuation is always a factor and the average current density is determined from the attenuation curves, or the total current to give protection at the points most distant from the drainage point may be computed.
2. Compute the total current requirement to achieve the required current density (total current = current density  $\times$  superficial surface area). Undertake this for initial, mean, and final estimated coating conditions.
3. Determine the optimum spacing between groundbeds based on availability of electrical power supplies and the classical attenuation formulae.
4. Based on the most negative permitted pipe/soil potential near the installation and the necessary potential change for the attenuation formula, determine the maximum permitted impact of the anode tension hill and thus calculate the distance between groundbed and pipeline.
5. Design the groundbed system in accordance with classical electrode-to-remote-earth resistance formulae for the selected anode groundbed type (continuous horizontal, deep well, multiple shallow boreholes).
6. Design the DC wiring system for the most economical cable size in accordance with standard electrical practices and then calculate the total IR (ohmic) drop in the circuit.
7. Select transformer rectifier voltage and current outputs.
8. Design the electrical circuits, fittings, and switchgear in accordance with standard electrical practice.
9. Select the location of cathodic protection test stations.
10. Prepare project drawings and specifications.

The total circuit resistance of a groundbed installation includes cable resistance, resistance of the anode to the carbonaceous backfill, and resistance to earth of the backfill column itself. In the case of seawater installations, the anode resistance is between the seawater and the anode surface only. The back emf between the anode and cathode should be included in the calculations to determine the transformer rectifier output voltage. It is normal for personnel and animal safety to limit the output voltage of transformer rectifiers to 48 V (lower if possible), and it is good practice in areas of third-party pipelines and structures to limit the individual installations to a low output current in the range 5–25A.

#### 4.21.4.3 Anode Backfill

The carbonaceous backfill surrounding an anode is essential and serves a number of functions, as given below for example:

1. Being of low resistivity, it has the effect of increasing the anode size with resulting reduction in resistance to earth.
2. Most of the current is transmitted to the backfill from the anode by direct contact, so that the greater part of material consumption is on the outer edges of the backfill column, enabling the anodes themselves to have an increased life.

The backfill composition may be of several types, varying from coke breeze to manmade graphite particles. A coke-breeze backfill consists of high temperature-fired coke breeze or calcined petroleum coke with not less than 95% dry weight of carbon with a maximum resistivity of 50  $\Omega$  cm when lightly tamped, dry, and prior to the addition of lime. A typical specification requires that 100% will pass through a 16-mm aperture, 90% will pass through an 8-mm aperture, and not more than 15% will pass through a 1-mm aperture, and that the coke breeze should be thoroughly mixed with 5% by weight of slaked lime.

#### 4.21.4.4 Resistance of Groundbeds

The resistance of groundbeds for protection of pipelines or anodes for protection of jetties or other

seawater structures is usually calculated in accordance with the formulae originally developed by Dwight. However, the following abridged formulae are normally used and are sufficient for all practical purposes.

Resistance of a single horizontal rod anode:

$$R_H = \frac{\rho}{2\pi L} \left\{ \ln \frac{4L}{d} - 1 \right\}$$

Resistance of a single vertical rod anode:

$$R_V = \frac{\rho}{2\pi L} \left\{ \ln \frac{8L}{d} - 1 \right\}$$

where  $R_H$  is the resistance of a single horizontal anode ( $\Omega$ ),  $R_V$  is the resistance of a single vertical anode ( $\Omega$ ),  $\rho$  is the resistivity ( $\Omega$  cm) of soil or backfill,  $L$  is the length of the rod (cm), and  $d$  is the diameter of the rod (cm).

Where anodes are installed in special backfill, two series resistances are present – anode to backfill and backfill to soil. In practice, and with coke breeze backfill, a single calculation based upon the dimensions of the backfill column and soil resistivity is satisfactory.

Resistances of several anodes in parallel can be calculated by the formula

$$R = \frac{\rho}{2\pi NL} \left\{ \ln \frac{8L}{d} - 1 + \frac{2L}{S} \ln 0.656N \right\}$$

where  $R$  is the resistance to earth ( $\Omega$ ) of the vertical anodes in parallel,  $r$  is the soil resistivity ( $\Omega$  cm),  $N$  is the number of anodes in parallel,  $L$  is length of the anode (cm),  $d$  is the diameter of the anode (cm), and  $S$  is the anode spacing (cm).

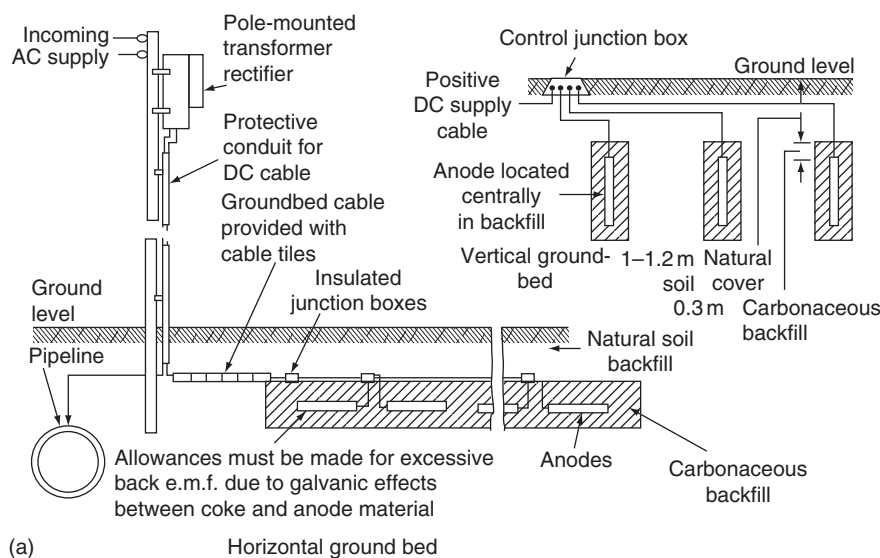
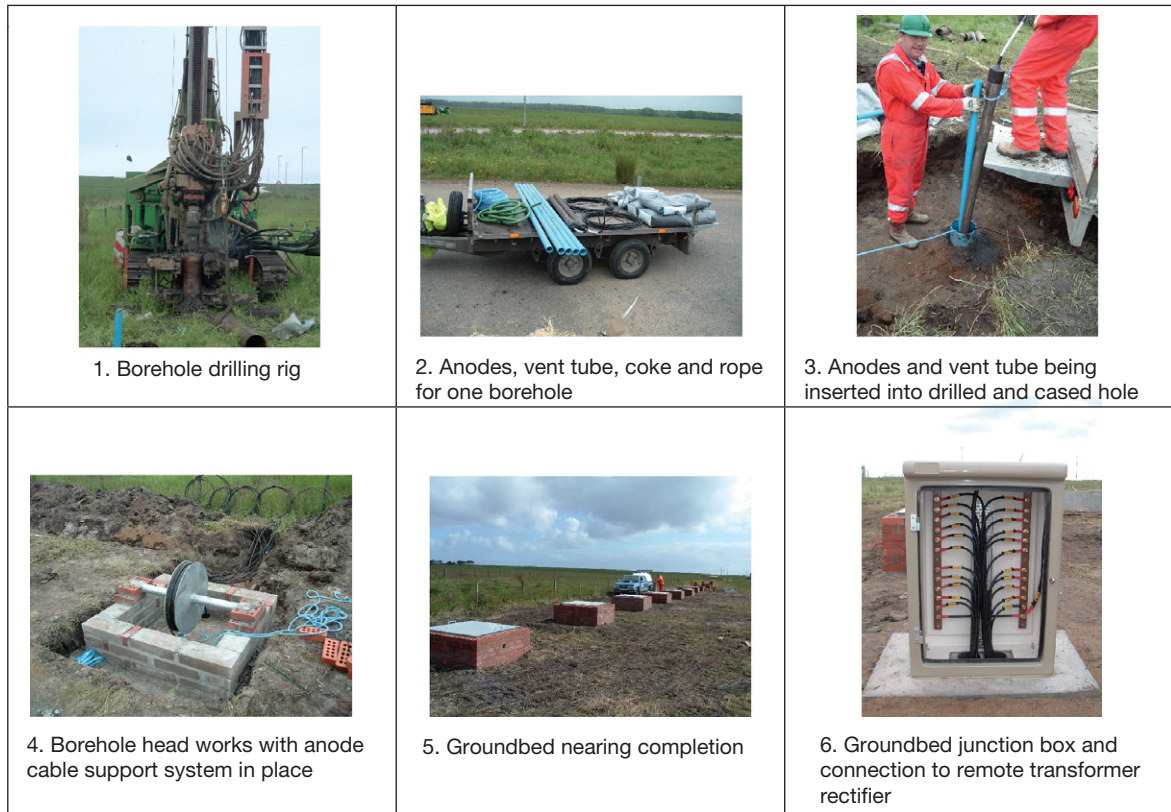
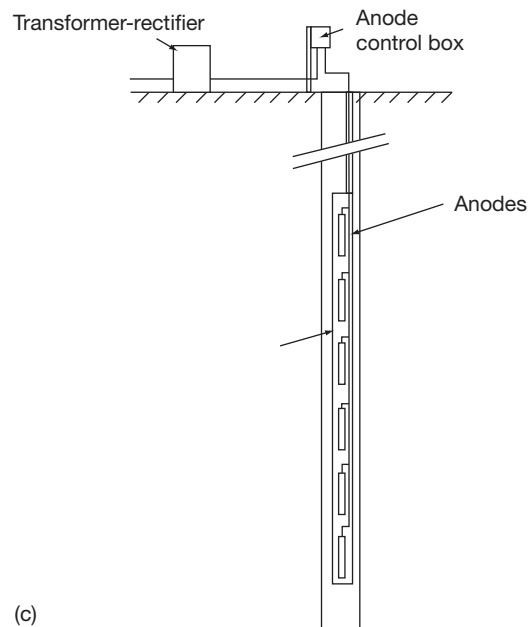


**Figure 3**



(b)



(c)

**Figure 3** Continued. Deep-well installation. (a) Groundbeds for buried pipes using impressed current. (b) Groundbed installation using multiple shallow boreholes (above a rock substrata) utilizing silicon-iron anodes with Kynar-insulated polyethylene-sheathed cable (note the large-diameter cable support system) and calcined petroleum coke. The boreholes were sacrificial steel lined except for the top 5 m, which was plastic pipe lined. Courtesy of R & R Corrosion Ltd and Corrosion Control Affiliates Ltd. (c) Deep-well installation.

#### 4.21.4.4.1 Deep-well groundbeds

This type of groundbed is illustrated in [Figure 3](#) and is normally employed where the surface soil resistivities are very high, for example, in desert areas. They have the advantage of taking up little surface area and can be installed, in the case of a pipeline project, in the existing pipeline wayleave. They have the further advantage of minimizing interaction on foreign structures. Abandoned oil or water wells can sometimes be used for this purpose. The type of groundbed can be of the design illustrated, or alternatively can be assembled on the surface in a steel case and lowered down a suitably drilled hole.

#### 4.21.4.4.2 Determining rectifier voltage

In determining the rectifier voltage, the following must be taken into consideration:

1. The groundbed resistance, as previously explained; this will generally be the major resistance in the calculation.
2. Back voltage polarization between groundbed and pipeline. In the case of graphite, MMO/Ti and silicon-iron anodes in carbonaceous backfill, an allowance of 2 V is normally used. This back voltage is that which exists between the anodes and the structure in opposition to the applied voltage.
3. Resistance to earth of the pipeline at the groundbed location. This resistance to earth depends on the quality of the pipeline coating. The better the coating, the higher the resistance; generally the pipeline resistance will be a lower order than the groundbed resistance.
4. Resistance of the cable from the pipeline to the power source and from the power source to and along the anodes comprising the groundbed. This cable resistance must be determined from the standard tables supplied by the cable manufacturer.

Once the total circuit resistance and the required current output are known, applying Ohm's law will allow the transformer rectifier or power source voltage to be calculated.

#### 4.21.4.5 Attenuation

When cathodic protection is applied to an underground metal structure, the greatest effect on the pipe-to-soil potential is at the drainage point. This effect decreases, or attenuates, as the distance from the drainage point increases.

Complex structures such as tank farms, tank bottoms, and marine installations have complicated

attenuation patterns and it is not feasible to use complex equations to determine the effect. This must be determined by a current drain test, by practical experience, or by mathematical modeling. For pipelines, the attenuation depends on the linear resistance of the pipe, coating resistance, and to some extent the resistivity of the soil. Connections to foreign structures and the method of termination of the line also affect the attenuation. There are relatively simple classical attenuation formulae for pipelines.

#### 4.21.4.5.1 Field measurements

In order to obtain the actual field attenuation characteristics, a pipeline can be placed under temporary cathodic protection and measurements made under different cathodic protection current conditions. A 'natural' pipe-to-soil potential survey should be made over the length of the line to which cathodic protection is to be applied. These static measurements supply a reference level on which to base the subsequent readings. After the natural survey is completed, measurements are made at the same test points with the temporary cathodic protection system installed. The pipe-to-soil potential should be read twice, once with the test current ON and once with the current Instant OFF (potential measured ideally between 0.2 and 1s after switch OFF). The data are then plotted as shown in [Figure 4](#).

The horizontal scale is the distance along the pipeline from the drainage point 0, and the vertical scale is the pipe-to-soil potential. The polarization potential and the driving voltage may then be plotted on semilogarithmic paper using the same horizontal scale ([Figure 5](#)). Attenuation is more rapid in low-resistivity soils or with less good coatings than in high-resistivity soils or with good coatings. If nonuniform conditions prevail, the curves will not be

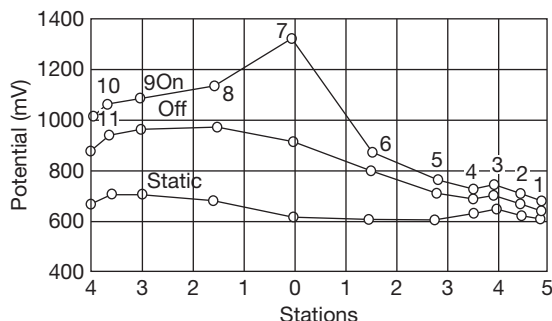


**Figure 4** Longitudinal distribution potential on pipeline. Note: 'Stations' refer to points at which the potential is measured.

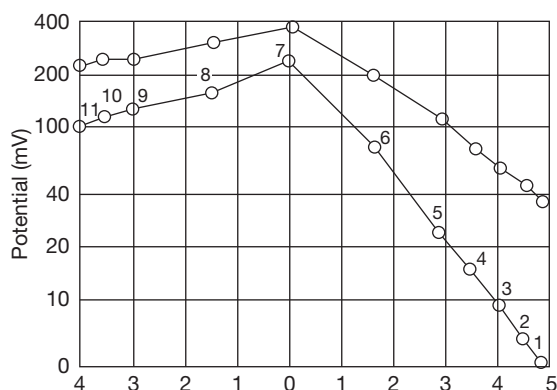


**Figure 5** Attenuation curve on pipeline shown in Figure 4. Upper curve shows the ON-static values (which include IR drop errors) and the lower curve shows the instant OFF-static values.

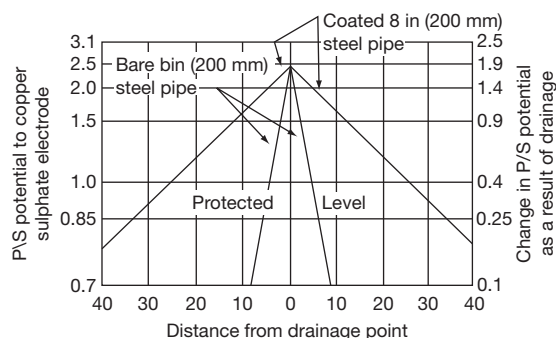


**Figure 6** Attenuation curves for bare pipe and poorly coated pipe in similar soils. Note P/S (pipe/soil) potentials are negative.

straight lines as shown in Figure 5, in which the lines in the left of the figure are typically curved as a result of low resistance.

#### 4.21.4.5.2 Measurement between drainage points

Figure 6 shows typical curves for a bare pipe and a poorly coated pipe in similar soils, and it can be seen that the former has a much steeper attenuation curve than the latter. Figure 7 shows how the desired protection level of potential has been attained between widely spaced drainage points, in which the dotted curves show the attenuation curves for the individual drainage points.

#### 4.21.4.5.3 Coating resistance

The electrical resistance of a coating on a pipeline will depend upon the effectiveness of its initial application to the metal and on its condition at the time of

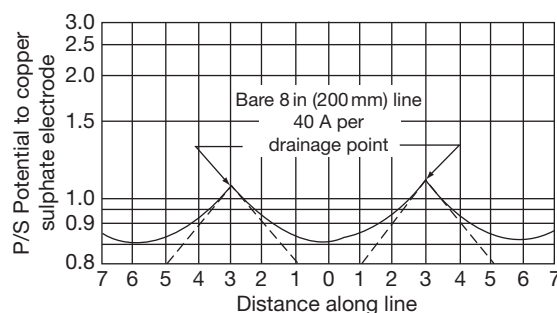


**Figure 7** Attenuation curves for multiple drainage points of moderate size.

testing; absorption of moisture may decrease the resistance by as little as 10% during the initial few years. The leakage resistance of a given section of pipeline may be determined as follows:

1. Applying temporary cathodic protection to the pipeline and measuring the pipe-to-soil potential for a given driving voltage of various test points spaced along the pipeline from the drainage point. The drainage current should also be measured.
2. Calculating the attenuation constant.
3. Measuring or calculating the longitudinal resistance of the pipeline. The resistance can be calculated from

$$R = \frac{2\rho l}{dt}$$

where  $\rho$  is the specific resistivity,  $l$  is the length of the pipeline,  $d$  is the diameter, and  $t$  is the thickness in appropriate and consistent units.

#### 4.21.4.5.4 Types of cable for anode installations

Cables used for anode groundbeds must be well insulated and suited to operational conditions. Mechanical damage from sharp coke particles and chemical attack from generated gases (e.g., chlorine) may be prevented by the use of polytetrafluoroethylene (PTFE) sleeving or a similar material. Alternatively, chemically resistant cable insulation such as cross-linked polyvinylidene fluoride (Kynar) may be used along with high molecular weight polyethylene (HMWPE) protective sheath. This type of cable is essential for deep-well groundbeds where nascent chlorine generation and highly acidic conditions may have to be tolerated. However, caution should be exercised when using Kynar-insulated cable, as the Kynar is brittle at low temperatures and may crack particularly if bent through a small radius.



For less severe applications, cross-linked polyethylene (XLPE) insulated and XLPE-sheathed cables may be sufficiently resistive to the anode reaction products.

#### **4.21.4.6 Power Sources for Cathodic Protection**

Where AC supplies exist, transformer rectifiers are the most economical source of DC for cathodic protection systems. A typical output for a well coated cross-country pipeline in the United Kingdom would be 5 A, 48 V. In the case of seawater jetties, where the voltage required is usually low because of the lower seawater resistivity, a typical rectifier size for a major installation would be 500 A, 18 V. For oil or gas terminals, offshore structures, and loading platforms where an incendiary sparking hazard exists, it is usual to locate the transformer rectifiers remote from hazardous areas or to employ certified flameproof or intrinsically safe rectifiers to overcome any possibility of explosion hazard during operation of the equipment.

Where ac supplies do not exist, other sources of power can be used such as DC generators, either diesel or gas driven. Alternatively, thermoelectric generators may be considered if the power requirement is relatively low, as they are only available in relatively small outputs. They may have the advantage of being able to be completely self-contained since they can be powered by taking off some of the gas that passes through the pipeline. Photovoltaic (PV) cells or wind-driven generators and battery systems have been successfully used for the protection of well coated pipelines and for reinforced concrete systems. However, as they tend to be used in remote locations which are short of distributed electrical power, there is a history of them being stolen.

### **4.21.5 Seawater-Cooled Circulating Water Systems**

#### **4.21.5.1 Galvanic Anodes**

The use of galvanic anodes in circulating water systems is limited to the application of cathodic protection to stop gates, coarse screens, and other plants that are readily accessible so that the anodes can be replaced when they are consumed. Such anodes are not normally used in condensers, pumps, and auxiliary coolers for the following reasons:

1. Frequent replacement is required with consequent shutdown of the plant concerned.

2. Anodes are required to be very large to provide the current density necessary with a reasonable life. Anodes can interfere with the water flow.
3. Corrosion products or dislodged anode particles from anodes can cause tube blockage and subsequent failure.

#### **4.21.5.2 Impressed-Current Anodes**

Anodes for the internal protection of the plant are normally of MMO/Ti (historically platinized titanium or lead alloy).

##### **4.21.5.2.1 Continuous anodes**

They consist of considerable lengths of relatively flexible copper-cored material which can be contoured to suit restricted spaces or to distribute current in a localized fashion. Typically, they may be used in water boxes at a nonferrous tube-plate/ferrous water box junction. Anode terminations pass through the water box via insulating entry points, and the anodes are supported on insulators within the box. Anode-cathode distance must be such as to prevent the anode becoming engulfed in calcareous deposit that forms on the cathode.

##### **4.21.5.2.2 Rod anodes**

These consist of solid or copper-cored titanium rod, portions of which can be platinized. They range from 6 to 25 mm in diameter and are normally supplied preassembled in a steel or polymer mount ready for screwing into prepared bosses on the plant under protection. Electrical connections are made via cables in the usual way. The anodes are spaced to give even current distribution. Anodes are typically designed to have sufficient mechanical strength to withstand being used as foot and hand holds, particularly in water boxes.

##### **4.21.5.2.3 Tubular anodes**

Tubular anodes are supplied in diameters between 12.5 and 32 mm and have been designed for installations where water conditions on the plant under protection are known to be turbulent. The tubular anode has a number of holes drilled in the active portion of the anode, and the nonactive portion is filled with sand to act as a damping agent. As in the case of rod anodes, they are supplied complete with mounts ready for installation in the prepared bosses on the plant under protection. They are particularly suitable for the internal protection of pump casings and the internal protection of pipelines carrying salt water or other low-resistivity liquids.

More recently, other methods have been used to assess anodes for their ability to withstand the fatigue loadings from eddy shedding which can occur in relatively high electrolyte flow rates.

#### 4.21.5.3 Impressed-Current Systems

Impressed-current systems for power stations are somewhat more sophisticated than those required for pipelines or marine structures inasmuch that a large number of items of the plant, with a wide range of current requirements, are often protected by one multichannel transformer rectifier. Each section of every water box requires one or more anodes in order to provide even current distribution. In the case of a large circulating water pump, as many as 30 anodes may be required to provide the necessary current distribution. Three types of system should be considered as follows:

1. Manually controlled.
2. Automatically thyristor-controlled.
3. Automatically controlled modular.

##### 4.21.5.3.1 Manually controlled system

A manually controlled system comprises one or more transformer-rectifiers each with its associated control panels which supply the DC to the various anodes installed in the water box spaces. Each transformer rectifier is provided with its own control panel, wherein each anode is provided with a fuse, shunt, and variable resistor. These enable the current to each anode to be adjusted as required. Reference electrodes and test connections should be provided in order to monitor the steel/electrolyte potential values achieved by the cathodic protection system. In the case of a major power station, one transformer rectifier and associated control panel might be provided for separate protection of screens, circulating water pumps, and for each main condenser and associated equipment.

When coolers or condensers are shut down but remain full of water, the amount of current required to maintain satisfactory cathodic protection is considerably reduced. If the current is not reduced, overprotection occurs and excessive amounts of chlorine can be generated which would tend to accumulate in the upper section of the water boxes causing considerable corrosion, not only to the water boxes but also possibly to the tubes. To ensure against this, a standby condition should be included on the control panel which effectively reduces the current required under shutdown

conditions. This control is effected by a limit switch fitted to the outlet valve of the condenser or cooler concerned. It is impossible to determine the exact requirements for the protection of circulating water systems in advance, and it is normal to adjust the current to provide protection during commissioning.

These simple resistor-controlled systems have lost favor as the costs of more sophisticated electronic control systems have dropped and have become more available. However, the principle of simple transformer rectifiers and resistive-controlled individual anode outputs is occasionally used in other applications.

##### 4.21.5.3.2 Automatic potential controlled system

This method is basically the same as the manual system. However, the current output of the transformer rectifier is automatically maintained at a level to ensure satisfactory cathodic protection under all operating conditions. This is achieved by means of sensing reference electrodes located in the main item of the plant, for example, main condenser, which feeds back steel/electrolyte/reference electrode potential data to an automatic control device within the transformer rectifier. The control device is preset at the required potential, and any incoming signals are compared with this preset potential and the level of current either raised or lowered until the incoming signal agrees with that of the preset potential in the automatic device.

It is also usual to fit additional (monitoring) reference electrodes and test connections as an independent check on the performance of sensing (controlling) electrodes.

##### 4.21.5.3.3 Automatically controlled modular system

This method employs one large, manually controlled transformer rectifier used in conjunction with a number of modular controlled outputs either within the main cabinet or in smaller cabinets located adjacent to each item of the plant requiring protection. The main transformer rectifier feeds DC to each of the module units, and the modular unit provides the exact amount of current required by the item of the plant in question.

#### 4.21.6 Marine Structures

The method of applying cathodic protection to immersed structures will depend on several factors including the following:

1. Size of the project.
2. Availability of power supply.
3. Possibility of problems from interaction.
4. Necessity for safety from spark hazard.
5. Expected economic life of the system.

**Figures 8(a) and 8(b)** give an indication of the relative numbers of anodes that may be involved for galvanic anode and impressed-current systems.

However, the offshore experience in severe environments such as the North Sea is clear. A significant number of impressed-current systems designed in the 1970s and early 1980s failed due to inadequate design, insufficient mechanical integrity of the anode and monitoring system supports, and even gross errors in surface area calculations. These included systems with anodes as inferred in **Figure 8(c)**, which were

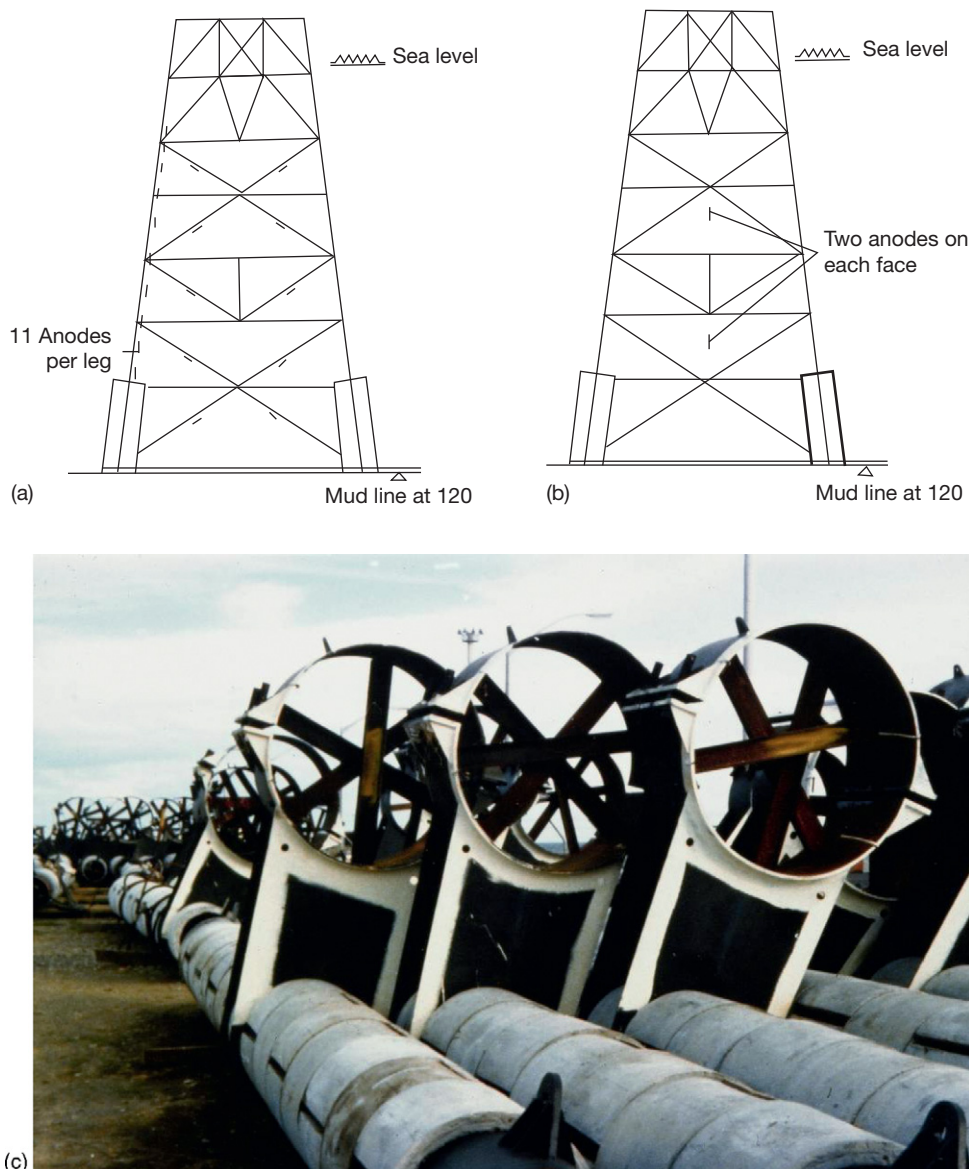


**Figure 8** Protection of offshore oil drilling/production platform. (a) With galvanic aluminum anodes and (b) with impressed current using MMO/Ti, platinized titanium, or platinized niobium anodes. (Compare the large number of anodes used in (a) with the small number used in (b)). (c) Galvanic anode arrays as part of a 100% galvanic anode retrofit to replace a failed impressed current system of the type represented in **Figure 8(b)**. Courtesy of Impalloy Ltd and B S Wyatt.

installed using small-diameter anode riser tubes to carry the anode and its cable to the positions as shown. Many such systems were the subject of major retrofits with galvanic anodes. Some notable impressed-current systems were designed in the 1980s and later have been made reliable, but the costs of the design and implementation of such reliable systems are high (Figure 9).

Current-density requirements depend on the environment, galvanic effects, velocities, and other factors influencing polarization. In the absence of galvanic influences or other secondary effects,  $60 \text{ mA m}^{-2}$  may be sufficient in seawater to maintain adequate polarization for protection once it has been achieved; it is, however, normally necessary to apply  $120\text{--}250 \text{ mA m}^{-2}$  to achieve initial polarization within a reasonable period, and if rapid protection is required, current densities as high as  $300 \text{ mA m}^{-2}$  may be applied.



(a)



(b)

**Figure 9** (a) A late 1980s design of North Sea impressed-current anode design incorporating Pt clad Nb anodes, duplicated for redundancy, with the cables run within the main structure legs to the platform decks above. Courtesy of Impalloy Ltd and B S Wyatt. (b) A dual silver/silver chloride/seawater reference electrode and Zn/seawater reference electrode similar to those used on the above project. Courtesy of Global Cathodic Protection Ltd and B S Wyatt.

Anodes placed on the seabed remote from the structure can be considered, but these installations may have problems due to damage to the connecting cable by ships' anchors, etc., and, more importantly, there have been serious interaction problems in the North Sea from such seabed remote anodes to the incoming production and outgoing export pipelines/risers which are normally electrically isolated from the jacket due to different cathodic protection performance characteristics.

The calculation of rectifier voltage/anode resistance is exactly as described for impressed-current pipeline installations except that the voltage required is very small because of the low resistance of the electrolyte: normally  $25\text{--}35 \Omega \text{ cm}$  for typical seawater. In the assessment of seawater resistivity, it should be remembered that the resistivity increases significantly with decreasing temperature.

For cathodic protection of sheet steel piling, the impressed-current or galvanic anodes are normally mounted within the re-entrants of the piles to prevent mechanical damage by berthing ships, dredging, etc. (Figure 10).

As in the case of power stations, where there is known to be considerable variation in operating conditions due to tidal changes, or variations in salinity of estuary waters, automatic control of impressed-current systems is generally desirable. For such systems, the current output of the transformer rectifier is controlled by the use of thyristor-controlled rectifiers. Sensing electrodes are permanently installed on selected piles, which transmit the steel/seawater/electrode potential back to the controlling device. This type of system enables the most appropriate current to be provided under all operating conditions in order to deliver uniform levels of protection.

#### 4.21.7 Ships

Cathodic protection is effectively supplied to ships' external hulls and also to the tanks of oil tankers and other vessels wherein seawater is used for ballast or other purposes. For internal protection, galvanic anodes of the zinc or aluminum are normally employed; magnesium and impressed-current anodes are not used in tanks, which can contain explosive gases due to the incendiary spark hazards. Impressed current can also generate chlorine inside closed water spaces; both magnesium and impressed current can also generate hydrogen gas, so both should only be used with extreme caution and appropriate

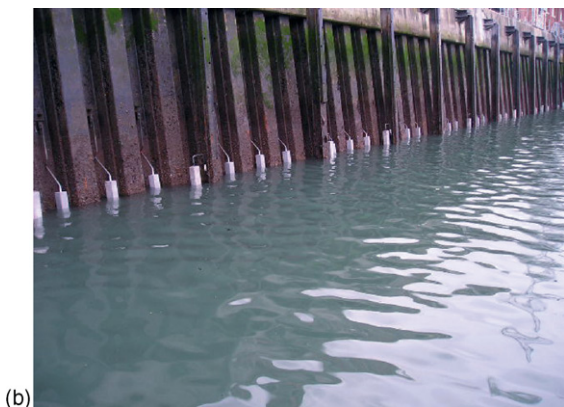
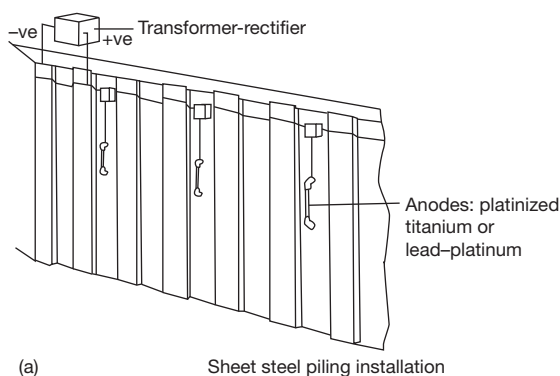


**Figure 10** (a) Sheet steel piling impressed-current installation. More modern installations would utilize MMO/Ti anodes and their mounting system would include a dielectric shield that would, subject to anode current rating, extend the full width of the in pan and extend above and below the anode. (b) Galvanic anode (Al–Zn–In) system to sheet steel piled wall and associated fenders at extreme low tide. Note that anodes to piles are within the in-pans and all anodes are behind the fender line. The coated piles were the subject of accelerated low water corrosion (ALWC), a form of microbial corrosion common in ports and harbors, which is able to cause local section loss at c. 2 mm/side per year. The anodes are normally fully immersed; the extended anode cores allow critical structural support welds to be made above the water for lower cost and more secure quality. Courtesy of B. S. Wyatt Corrosion Control.

precautions in confined spaces. External hulls can be protected either by galvanic or impressed-current methods, although impressed current is now preferred at least for larger vessels (**Figure 11**). Anodes of MMO/Ti, platinized titanium, or lead–silver alloy with platinum bielectrodes, are mounted on the hull below the water line and can be designed to have current outputs of up to 200 A. In vessels such as tankers, where there may be access problems, the

anodes are located at both the stern and the forward end of the ship. All cable or other entries through the hull plate must be carefully designed using a special cofferdam, and the complete system has to be submitted to the ship approval authorities prior to installation. Because of the rapid variation in electrolyte conditions during passage of the vessels and the need to both maintain uniform protection levels and prevent overprotection and damage to the specialist marine coatings, all schemes for ships are automatically potentially controlled.

The transformer rectifiers typically contain thyristor-controlled rectifiers and operate in a manner similar to that described for power stations.

#### 4.21.8 Water Storage Tanks

Galvanic anodes are of limited application because of accumulation of anode corrosion products and also, in many cases, of high water resistivity.

Impressed-current systems are normally based upon anodes of MMO/Ti, platinized titanium, or platinized niobium. The method of anode installation is usually by suspension. The anode configuration and number must be such as to ensure uniform current distribution. Considerable use is made of wire-type platinized titanium and niobium anodes, which offer minimal weight and relative ease of mounting/suspension.

Coatings are normally employed for water storage tanks, which result in relatively low total current requirements in association with the current densities given in **Table 4**.

#### 4.21.9 Internal Protection of Pipelines

The current spread from an internally immersed anode is directly related to pipe size and the resistivity and temperature of the water; with seawater having a resistivity of  $\sim 30 \Omega \text{ cm}$ , anodes are normally required within a 250-mm-diameter pipe at  $\sim 1\text{-m}$  centers and in the case of a 760-mm-diameter pipe at  $\sim 3\text{-m}$  centers (**Figure 12**). Small bore, high resistivities, and high electrolyte velocities further reduce the anode spacing.

Cathodic protection is therefore normally practicable only in large-bore pipes carrying salt water or relatively low-resistivity river water used for cooling inland power stations or chemical plants. Under special circumstances, however, it has been found necessary to use cathodic protection in relatively high-resistivity



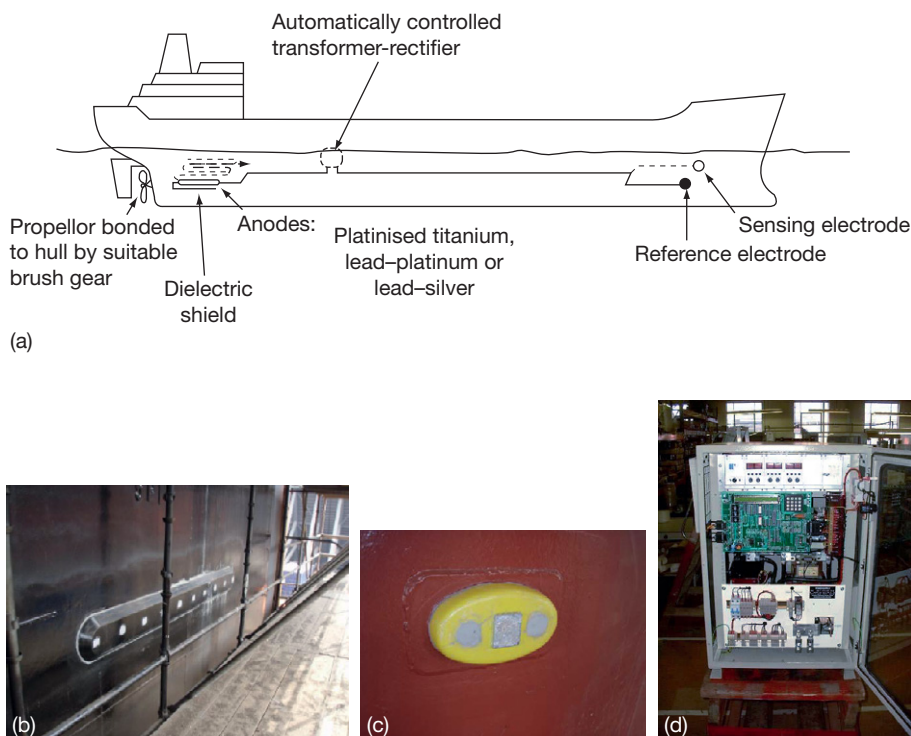


**Figure 11** (a) Impressed-current cathodic protection system for ships. Larger vessels would also have bow-mounted anodes which would normally be smaller, recessed, and round to prevent damage to them. Anodes of MMO/Ti are now often used. The dielectric shields around the anodes are generally high-build epoxy coatings selected for their very good cathodic disbondment resistance and high (electrical) dielectric (insulating) properties. (b) Ship's impressed-current anode installed on the hull (anode elements masked during coating). Courtesy of Corpro Companies Europe Ltd. (c) Ship's reference electrode. Courtesy of Corpro Companies Europe Ltd. (d) Ship's impressed current transformer rectifier. Courtesy of Corpro Companies Europe Ltd.

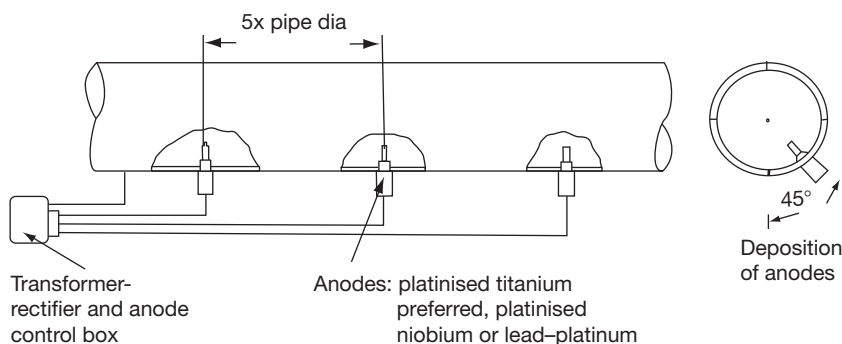


**Figure 12** Internal protection of pipeline. Typical current density (seawater) =  $200 \text{ mA m}^{-2}$  to bare steel at low flow rates: significantly greater for polarization at higher flow rates.

fresh water, particularly where microbial corrosion has been present; in these instances, anodes have been run longitudinally down the entire length of the pipe. In such applications, particular attention is required to avoid fatigue failures of the anode supports due to eddy shedding within the water flow.

#### 4.21.10 Cathodic Protection of Steel in Concrete

Cathodic protection of steel in concrete has developed from limited applications to buried reinforced and prestressed concrete pipelines in the 1950s, through

small-scale trials on bridge structure in the 1960s, to a major industry in the twenty-first century. Cathodic protection is applied to both new construction (prior to corrosion initiation) and to existing structures that have suffered corrosion initiation and often have suffered considerable corrosion damage to the steel and cracking and spalling of the cover concrete.

Due to the nature of reinforced concrete structures, their cathodic protection systems are significantly different from other applications. The anode–cathode spacings are typically in the range 15–100 mm in concrete compared with 5–250 m between anodes/groundbeds to pipelines in soil or 300 mm or more between anodes and steel in seawater. Further, the concrete electrolyte (actually the cement paste gel that binds the sand and stone aggregate into an effective structural composite) has an electrical resistivity that is high compared with most soils, typically in the range 20 000–200 000  $\Omega$  cm. This results in very considerable IR voltage drop errors in concrete, greater even than those in buried-pipeline applications.

In addition, whereas most steel in soil or waters cathodic protection applications the electrolyte is near neutral, in concrete the pH is typically greater than 10.5. Thus, the protection criteria for steel in concrete differ considerably from those for steel in soils or waters. The absolute protection criterion is accepted as  $-720$  mV with respect to Ag/AgCl/0.5 M KCl (equivalent to  $-720$  mV with respect to Ag/AgCl/seawater) compared with  $-800$  mV for steel in aerobic soils or waters with respect to Ag/AgCl/seawater (or  $-850$  mV with respect to Cu/CuSO<sub>4</sub> saturated) or  $-900$  mV with respect to Ag/AgCl/seawater in the presence of active microbial corrosion. Potential shift, more normally, due to time-dependent changes in depolarized potentials; potential decay values of 100 mV over 24 h or 150 mV total decay over longer periods are the normally used criteria for atmospherically exposed concrete. These may be compared with the 300 mV potential shift criterion favored by some North American pipeliners.

Current densities for actively corroding steel in concrete are typically in the range 2–20 mA m<sup>-2</sup> (of steel in temperate climates), and for preinitiation (where the purpose of the cathodic polarization is to maintain the passivity of the steel in the concrete even at high chloride concentrations), they are typically in the range 0.2–2 mA m<sup>-2</sup>. Typical applications of cathodic protection to steel in concrete are shown in [Figure 13](#).

Anodes used in cathodic protection of steel in concrete are summarized in [Table 4](#). Power supplies are typically quite complex multichannel transformer

rectifiers, typically with individual channel outputs <10 A and <18 V (for complex projects, some individual channels may be only 0.5 A, 12 V, whereas for larger more uniform zones on the same project, they may be 5 or 10 A, 12 V) and due to the complex nature of such structures, with their varying steel densities and varying exposure to chlorides, each channel may be associated with several monitoring channels of test connections associated with both permanently installed reference electrodes and pseudo (reference) electrodes or potential decay probes.

Owing to the complexity of these systems, the large number of dc power channels, the even greater number of monitoring channels, and the need to collect potential decay data over periods often in excess of 72 h, it is normal for cathodic protection of reinforcement systems to be fitted with data logging and remote monitoring systems using telephone landline or GSM modems.

#### 4.21.11 Economics

Cathodic protection design involves achieving an economic balance between installation costs, maintenance costs, initial cost of power units, and power consumption. Because both the cost of the rectifier and the cost of the electric power consumed are contingent on the operating voltage of the system, it is desirable to keep the operating voltage as low as possible; for this reason, a low-resistance anode system is desirable when it is economically feasible. Further, there are higher risks to personnel and animals at higher voltages. Simulated cost curves plotted on a cost versus the number of anodes in a groundbed for an assumed set of conditions are shown in [Figures 14](#) and [15](#). [Figure 14](#) is based on installed capital costs only, whereas [Figure 15](#) is the minimum annual cost.

#### 4.21.12 Recent Developments

##### 4.21.12.1 Galvanic Anode Systems

As the general standard of protective coatings has improved (materials, application, and construction standards), the use of galvanic anodes has extended to soil of *c.* 10 000  $\Omega$  cm or more for well-coated buried pipelines. By using anodes in extruded or continuously cast and hot rolled ‘ribbon’ form and placing them in the pipeline trench, they can be effective in soils of high resistivity.

The use of high-strength steels and alloys in offshore oil and gas developments and in submarines occasionally results in structures, pipelines, or vessels

that are subject to hydrogen embrittlement and which cannot be subject to the more normal range of protection criteria of  $-800$  mV (or  $-900$  mV in the presence of microbial corrosion) to  $-1050$  mV with respect to a silver/silver chloride/seawater. Some high-yield materials, when subjected to significant stress levels, may have safe cathodic protection potential limits as positive as  $-780$  mV; other materials may be safe at potentials in the range  $-800$  to  $-900$  mV. In order to achieve safe protection of such materials, two different approaches have emerged. One that has been quite widely used on offshore oil and gas facilities is the use of carefully selected Schottky barrier rectifiers

(SBRs), which are inserted between the normal Al–Zn–In anode and the high-strength steel or alloy structure and which limit the polarized metal/electrolyte potential level to a predetermined safe limit. The other is an Al–Zn–Ga anode alloy that operates at a closed circuit potential which is safe for some grades of high-yield steel; this is less extensively used than the SBR approach, but has the benefit of simplicity if reliable for long-term use.

With the developments in very high dielectric strength coatings, in particular the three-layer polyethylene or polypropylene (a thin fusion-bonded epoxy coating followed by an adhesive followed by

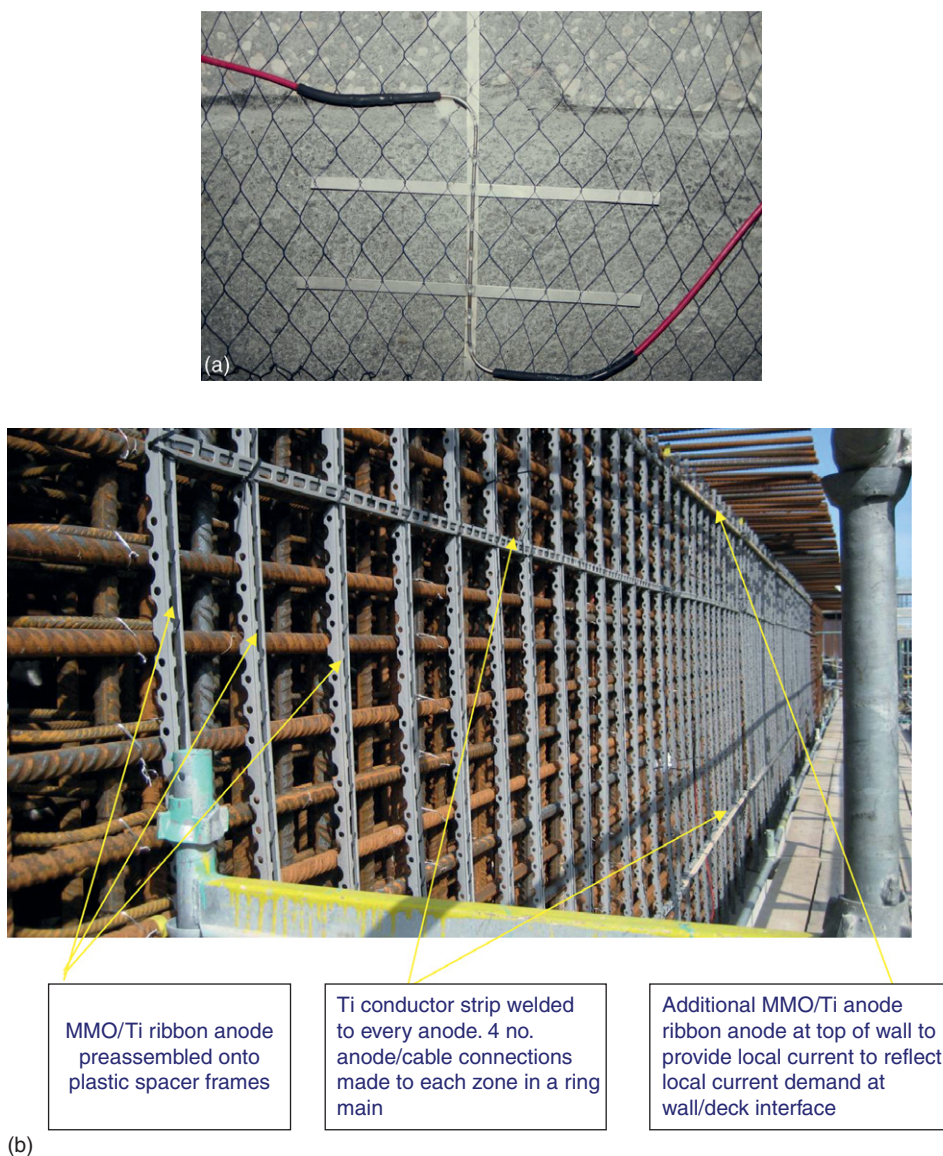


**Figure 13** Continued



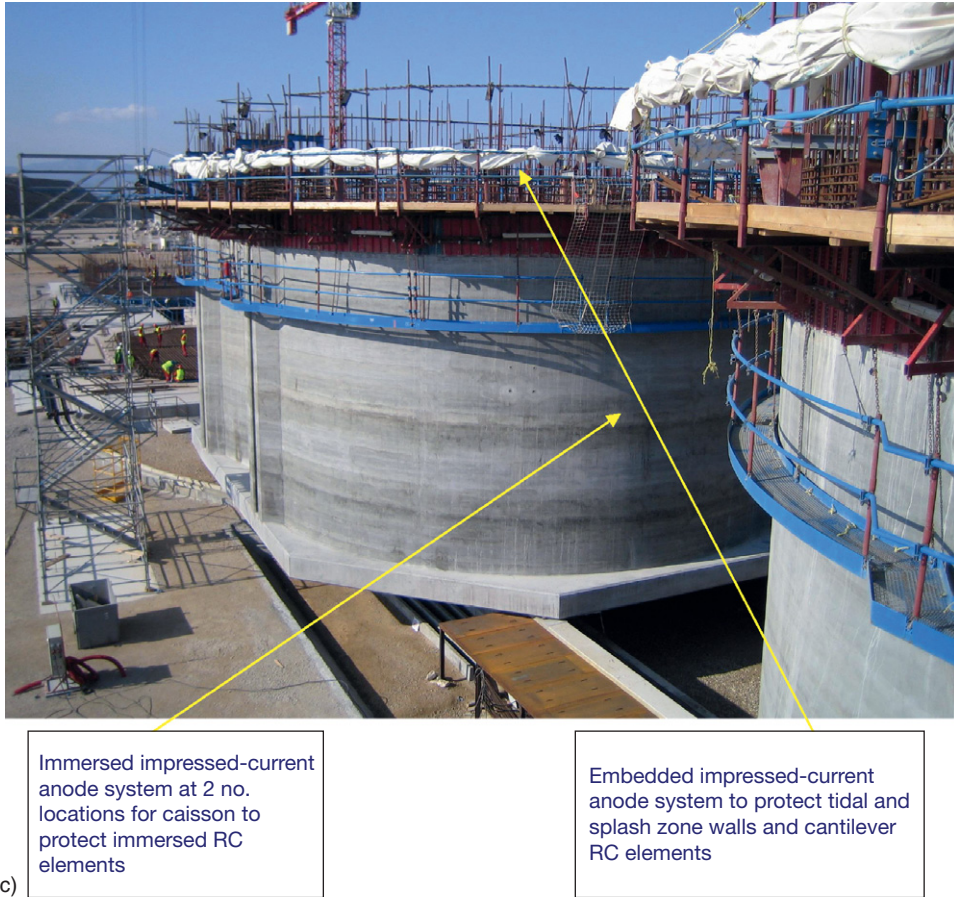


**Figure 13** (a) Sprayed concrete repair to severely corrosion-damaged marine concrete beam with MMO/Ti anode and cable/anode connection shown fitted awaiting sprayed concrete overlay. Courtesy of Tarmac Global and B. S. Wyatt. (b) MMO/Ti ribbon preassembled onto plastic rail cages to limit installation cost and risk of short circuits. New construction of floating reinforced concrete pontoon. Courtesy of Corrosion Control Affiliates Ltd. (c) New port caisson construction with cathodic protection with MMO/Ti ribbon anodes cast into slip formed caisson walls and *in situ* cast cantilever decks in the tidal and splash zones and immersed anodes in seawater for the immersed zones. Courtesy of B. S. Wyatt Corrosion Control.

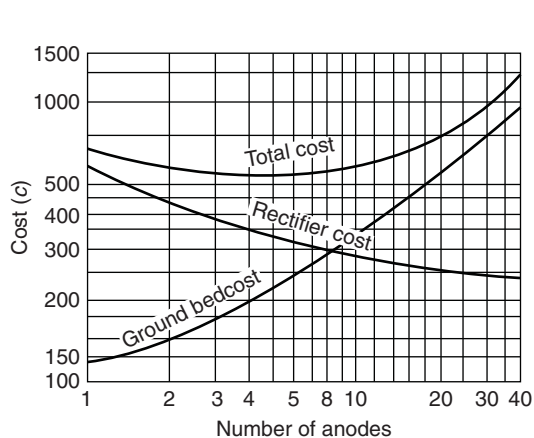


**Figure 14** Total cost in relation to number of anodes installed.

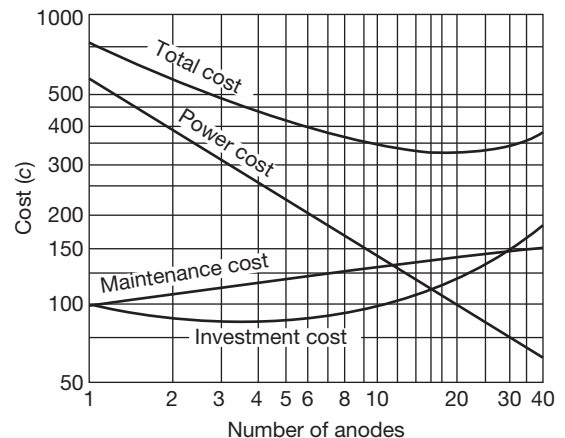


**Figure 15** Variation of minimum annual cost with number of anodes installed.

an extruded thick-wall tube or coating over the pipe), small coating defects on pipelines are vulnerable to very rapid corrosion due to ac current discharge/pickup at the coating defects. There have been significant and unexpected gas and oil pipeline failures/major section loss by pitting due to ac corrosion. Many such pipelines, while nominally protected with impressed current (at extremely low current densities, which present their own control and monitoring difficulties), are being fitted with extensive networks of zinc or magnesium ribbon anodes primarily for electrical earthing purposes. The AC currents are collected/discharged preferentially via these galvanic anode systems.

The development of large-scale galvanic anode retrofit anode systems for extending the design life of offshore jackets or pipelines has resulted in very large bracelet anode and anode arrays on tubes and sleds being designed. Most of these systems have been in Al–Zn anodes, but some very successful systems with design lives (that have been delivered in practice) have used magnesium anodes on pipe arrays and sleds, remote from the structure being protected, with the design of the anode resistance, the connecting cable resistance, and the distance between the anode and the structure being carefully balanced to prevent exceeding the normal  $-1050$  mV steel/sea-water potential limit with respect to silver/silver chloride even when using anode material with a closed circuit potential of  $-1500$  mV.

There have been major changes in the production/supply chain for magnesium anodes (most Mg was produced from seawater using the Dow process and Dow Chemical Corporation in the United States were the major international producers of Mg anodes until the 1990s). Since the 1990s, there has been the development of many small-scale producers, mainly in China, using a smelting route of production that has led to alloys, which, although are clearly within accepted chemical composition limits, perform below their anticipated efficiency or  $\text{Ah kg}^{-1}$  capacity. It is now a good practice to test each batch of magnesium anodes for its capacity before purchase/sale. This does not mean that the alloys or anodes are of deliberate or accidental poor quality; it means that either metallurgical or trace element issues which are not presently well understood and were previously uniform are now variable and can significantly affect anode performance.

#### 4.21.12.2 Impressed-Current Anodes

Anodes of scrap steel, graphite, and lead alloys have virtually ceased to be used. Silicon–iron is still widely

used due its robust and secure performance. MMO/Ti anodes have developed immensely in the late 1990s and into the twenty-first century; their use in cathodic protection of steel in concrete is extensive, but they have also replaced other anode materials in many applications in soils and waters.

Specific anodes for cathodic protection of steel in atmospherically exposed (above ground) concrete have been developed; some have failed to deliver their early claimed promise. Pt/Ti and Pt/Nb anodes are still used but are becoming specialist items as MMO/Ti anodes take more market share due to near-equivalent performance (better in some respects) and lower cost.

#### 4.21.12.3 Power Sources for Cathodic Protection

The most commonly used cathodic protection power supplies, that is, transformer rectifiers, for the traditional applications of cathodic protection of steel in soils and waters have not changed significantly in the period 1990–2009 except more have been supplemented with elements of remote monitoring and/or remote control. Units manufactured in Europe are now almost exclusively thyristor-controlled silicon diode rectifiers with improved efficiencies and service life expectancies than the old selenium rectifiers and transductor, rotary transformer or tap changed transformer controls that were used in the 1960s through the 1980s.

Switch-mode power supplies offer possible advantages of small size and lower cost. Some remain concerned by their apparent fragility in response to the typical surge and spike conditions that cathodic protection power supplies often are subject to.

Microelectronics has allowed the design and reliable manufacture of distributed power supplies of the type that were pioneered for power station cooling water cathodic protection in the early 1970s. However, there have been many examples of small suppliers dedicated to small-volume cathodic protection applications producing ‘clever’ integrated cathodic protection power supplies and data logging/remote monitoring systems, which have been unreliable and incapable of maintenance once the producing company ceased to trade or even the individual designer left the company. There is great merit in the use of industry-standard monitoring and control hardware and software that can be purchased from many sources and is produced in such volume as to reasonably assure adequate development, testing, and ongoing upgrades and software support.



Reinforced concrete cathodic protection has forced the pace in development of multichannel, heavily monitored power supplies with integrated monitoring and control.

#### **4.21.12.3.1 Solar and wind power**

With improved technology and production methods, considerable use is being made of solar power in remote locations. The output of PV arrays is used to maintain conventional storage batteries in a state of charge. The cathodic protection system is in turn energized from the batteries. It is usual to incorporate sufficient battery storage to accommodate a number of 'no-sun' days. Quite large capacity schemes have been effectively used in north and east Africa. Theft is a problem.

Wind power has been used to a small extent but it is likely, as domestic wind 'microgeneration' becomes more popular for environmental reasons, that such systems will fall in cost and increase in efficiency. Combined PV and wind systems may be optimum solutions in some locations.

#### **4.21.12.3.2 Other power supply systems**

Thermoelectric generators using catalytic converters and direct dc electrical generation with no moving parts, small gas turbine generators, turbines powered by water, oil, or gas flow across a flow constricting valve with a bypass loop, as well as gas and oil fuelled generators have all been used for cathodic protection in remote locations. They remain small scale due to the cost and efficiency advantages of AC power distribution and transformer rectifiers.

### **4.21.13 Conclusion**

Although the principles of cathodic protection are essentially simple and were in fact first outlined by Sir Humphrey Davy in 1824, the application of the method to practical problems was described as more of an art than a science by the authors of the earlier edition of this chapter. In the years that have passed since that edition, the science and calculation procedures have been developed and proven that have, in the view of this author, taken the element of art out of the science and technology of cathodic protection. A properly designed cathodic protection system will be economic and effective and will deliver reliability for its design life. Regrettably, such systems can only be delivered by designers, suppliers, and contractors

with sufficient expertise and experience to warrant certification of competence; there continue to be some cathodic protection systems that do not deliver economic, effective, or reliable solutions to owners or operators who sadly find themselves served by less competent people claiming to be specialists. These schemes can be inefficient and uneconomical and, under certain circumstances, may accelerate corrosion instead of controlling it.

### **Bibliography**

1. Von Baekmann, W.; Schwenk, W.; Prinz, W. Eds.; *Handbook of Cathodic Corrosion Protection*, 3rd ed.; Gulf Publishing Co: Houston, TX, 1997, ISBN 0-88415-056-9.
2. Ashworth, V.; Booker, C. J. L. Eds.; *Cathodic Protection Theory and Practice*; Institute of Corrosion and Ellis Horwood: Chichester, 1986, ISBN 0-85312-510-0.
3. Ashworth, V.; Googan, C. Eds.; *Cathodic Protection Theory and Practice*; Institute of Corrosion and Ellis Horwood: Chichester, 1993, ISBN 0-13-150038-4.
4. *Design and Operational Guidance on Cathodic Protection of Offshore Structures, Sub-Sea Installations and Pipelines*; The Marine Technology Directorate Ltd: London, 1990, ISBN 1-870553-04-7.
5. BS 7361: Part 1: 1991, *Cathodic Protection Part 1: Code of Practice for Land and Marine Applications*. BSI London 1991.
6. Wyatt, B. S. *Anti-Corros. Methods Mater.* **1985**, 32(6), 4-14; 32(7), 8-10; 32(8), 7-11, Sawell, London.
7. Wyatt, B. S. In *NACE Corrosion '79*, 1979, Houston Paper 252.
8. Wyatt, B. S. In *Corrosion 2007*, Australasian Corrosion Association, Sydney, 2007.
9. Martin, B. A., Brodribb, R. *Corrosion 2007*, Australasian Corrosion Association, Sydney, 2007.
10. BS EN 12954: 2001 *Cathodic Protection of Buried or Immersed Metallic Structures – General Principles and Application for Pipelines* CEN Brussels, BSI London 2001.
11. BS EN 12473: 2000 *General Principles of Cathodic Protection in Sea Water*, CEN Brussels, BSI London, 2000.
12. BS EN 12495: 2000 *Cathodic Protection for Fixed Steel Offshore Structures*, CEN Brussels, BSI London 2000.
13. BS EN 12696: 2000 *Cathodic Protection of Steel in Concrete*, CEN Brussels, BSI London, 2000.
14. BS EN 13174: 2001 *Cathodic Protection for Harbour Installations*, CEN Brussels, BSI London, 2000.
15. BS EN 15257: 2006 *Cathodic Protection – Competence Levels and Certification of Cathodic Protection Personnel*, CEN Brussels, BSI London, 2006.
16. *Recommended Practice: Cathodic Protection Design: (Of Galvanic Anodes for Fixed Offshore Structures)* DNV-RP-B401, Det Norske Veritas, Hovik, 2005.
17. ISO 15589-1: 2003 *Petroleum and Natural Gas Industries – Cathodic Protection of Pipeline Transportation Systems – Part 1: On – Land Pipelines*, ISO, Geneva, 2003.
18. ISO 15589-2: 2004 *Petroleum and Natural Gas Industries – Cathodic Protection of Pipeline Transportation Systems – Part 2: Offshore Pipelines*, ISO, Geneva, 2004.

## 4.22 Interaction and Stray-current Corrosion

**L. Di Biase**

Via Strasburgo, 5D, 20097 San Donato, Milan, Italy

© 2010 Elsevier B.V. All rights reserved.

4.22.1	The Phenomenon of AC Corrosion	2833
4.22.2	Sources of AC Interference	2833
4.22.3	Interference Effects	2834
4.22.4	Calculation of AC-Induced Voltage	2835
4.22.5	Evaluation of the AC Interference Effects	2836
4.22.6	Mitigation of AC Interference Effects	2837
4.22.7	Major Evidence from Field Studies and Laboratory Tests	2837
References		2838

### Abbreviations

**AC** Alternating current

**CP** Cathodic protection

### Symbols

$\rho$  Soil resistivity ( $\Omega$  m)

$U_{ac}$  Alternating current voltage (V)

$J_{ac}$  Alternating current density ( $A\ m^{-2}$ )

### 4.22.1 The Phenomenon of AC Corrosion

The primary factor in alternating current electrolysis is current density.<sup>1</sup> This statement was made in *The Engineering Journal*, the journal of the Engineering Institute of Canada, and was made in 1927.

A long time has passed since then and AC effects have been experienced and investigated in depth.

More recently, since 1986, some instances of corrosion on gas pipelines due to alternating current (16.6 and 50 Hz) have been reported in Europe and elsewhere.<sup>2–4</sup> In all these cases, the cathodic protection (CP) values, measured with conventional techniques and instruments, satisfied the conventional criteria. It is also most probable that some previous corrosion failures have not been recognized as being caused by alternating current, because CP personnel have not been made aware of the AC corrosion risk.

Very often in the past, AC corrosion was not correctly diagnosed, because usually, CP instrumentation rejects industrial AC frequencies and the knowledge of the AC corrosion phenomenon itself is still growing every day.

In the last decade, quite a number of corrosion instances have been clearly attributed to AC corrosion.

AC corrosion is a concern for owners operating long structures (mostly pipelines) running parallel or close to overhead high-voltage transmission power lines (typically 15 kV and higher) or AC traction systems. The problem also exists in municipal areas (structures buried near AC power distribution systems), in reinforced concrete structures (e.g., road bridges also carrying electricity power lines), and inside tunnels for AC electrified railways.

It is not uncommon to measure AC voltages in the range of 15–100  $V_{rms}$  on coated pipelines exposed to AC influence. This may cause safety hazards to people, malfunction of the pipeline equipment, and corrosion problems.

In the last two decades, a better knowledge of the AC corrosion phenomenon has been gained, thanks to the many studies that mainly gas operators have sponsored or directly performed.<sup>4–6</sup>

These studies started in the 1980s and are still in progress. Since this period, high-quality/high-resistance coatings have been used for buried pipelines, thus increasing the effects of AC interference.

### 4.22.2 Sources of AC Interference

The AC influence is referred to as ‘inductive,’ ‘resistive,’ or ‘capacitive’ interference in technical literature.

The most common long-term AC interfering sources on buried metallic pipelines are

- AC overhead or underground electricity power lines;
- AC traction systems fed by a parallel high-voltage feeding line (50 or 16.6 Hz).

Long-term AC interference on a buried pipeline may cause corrosion because of an exchange of AC current between the exposed metal of the pipeline and the surrounding electrolyte at the coating holidays.

This exchange of current depends on the AC voltage, whose amplitude is related to various parameters such as

- the configuration of AC power line phase conductors and shielding wires;
- the distance and the length of parallel path between the AC power line/traction system and the pipeline;
- the current flowing in the AC power line/traction system phase conductors;
- the average insulating resistance of the pipeline;
- the thickness of the coating; and
- the soil resistivity.

### 4.22.3 Interference Effects

When an AC voltage is present on a cathodically protected pipeline and defects in the coating are present, an AC current will flow across the metal-soil interface. This current depends on the impedance of the system.

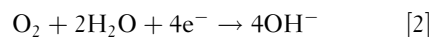
During the negative half-wave, the combined AC and DC current will result in the reduction of any reducible species that is in contact with the metal, for example, the formation of hydrogen and hydroxyl ions according to eqn [3]. During the positive half-wave, the current may cause the charging of the double layer capacitance, possible oxidation of hydrogen, and reduced corrosion products due to the CP, and oxidation, that is, corrosion, of the pipeline steel. Since this current leaving the metal surface can be consumed by several noncorrosive processes, generally, voltages higher than 10 V are required to result in a significant corrosion attack to the pipeline steel. Various additional parameters influence this process; among others, the most important ones are the leakage or earth resistance of the defect, the level of CP and the chemical composition of the soil.

- The leakage or earth resistance  $R_L$  is generally due to the geometry of a defect that is in contact with the soil of resistivity ( $\rho$ ). Considering a circular defect with diameter  $d$ , the following formula yields

$$R_L = \rho/2d \quad [1]$$

Equation [1] is useful for a rough estimation of  $R_L$ ; however, it should be considered that the soil resistivity may vary significantly in the vicinity of a coating defect, and both the soil resistance in the defect (considered within the thickness  $s$  of the coating) and the polarization resistance have been neglected.

- CP generally creates electrochemical reducing conditions at the steel surface and results in the formation of hydroxyl-ions according to



and/or



This is combined with an increasing alkalinity (up to pH 11–12 and even more) and a significant decreasing of the resistivity of the soil close to the steel surface.

- From soils containing calcium ( $\text{Ca}^{2+}$  or other alkali earth ions), it is known that insoluble calcareous layers ( $\text{CaCO}_3$ ) are formed on the cathodically protected steel surface. This is due to the highly alkaline conditions and reactions with  $\text{CO}_2$  in the soil. The result is an increasing leakage or earth resistance of the defect. In alkali ion ( $\text{Na}^+$ ,  $\text{K}^+$ )-rich soils, however, similar reactions produce soluble bicarbonates (e.g.,  $\text{NaHCO}_3$ ), thus resulting in a decreasing leakage resistance.<sup>7</sup>

The processes thought to be taking place have been summarized as follows:<sup>8</sup>

During the positive half-wave, the bare metal surface is oxidized, resulting in the formation of a passive film. This is due to the current that leaves the metal surface. During the negative half-wave, when both AC and DC current enter the metal surface, this passive film may be reduced to iron hydroxide. In the following anodic cycle, a new passive film grows. Upon reduction of the passive film, the amount of iron hydroxide is increased. Hence, every AC cycle results in some oxidation of the metal. In the long term, this can result in a significant metal loss.

#### 4.22.4 Calculation of AC-Induced Voltage

An AC voltage that may cause corrosion can result from resistive or inductive interference from high-voltage power lines and/or electrified railways; induction is the most frequent interference mode. The AC voltage  $U_{ac}$  should be calculated in accordance with CIGRE Technical Brochure No. 95 published in 1995 “*Guide on the Influence of High Voltage AC Power Systems on Metallic Pipelines.*”<sup>9</sup>

The evaluation of  $U_{ac}$  is generally based on the calculation of the induced longitudinal field strength  $E$  for a segment of the pipeline.

The field strength  $E$  depends on

- the value and the frequency of the inducing current;
- the mutual inductance – related to the unit length – between the conductor(s) of the high-voltage line and the pipeline, that is, a function of their clearance and of the soil resistivity;
- the reduction factor, allowing for the protective effect of adjacent earthed conductors.

For simplified conditions (e.g., parallel routing between high-voltage line and pipeline, uniform coating resistivity of the pipeline, constant soil resistivity, and both ends of the pipeline being terminated by a low resistance to earth), an analytical solution for  $U_{ac}$  as a function of pipeline length may be evaluated.<sup>9</sup> In practice, however, calculations are generally carried out by using computers, taking into account the relevant parameters of the high-voltage line and the pipeline.

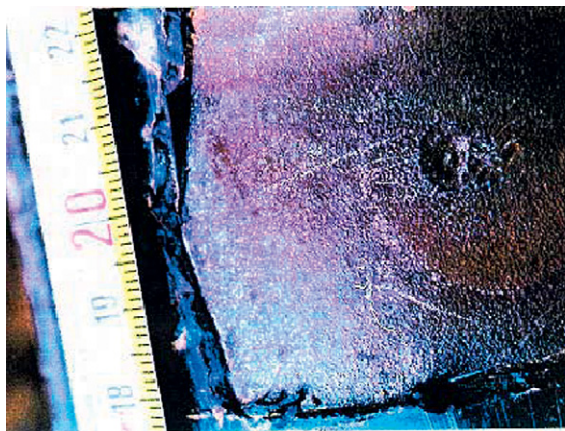


**Figure 1** Typical AC corrosion on a PE-coated pipeline. Reproduced from Corrosion due to AC on metallic buried pipelines: Background and perspectives L. Di Biase APCE, 2nd National Conference, Rome, Nov. 1996; pp 21–22.

These calculations are, among others, based on the following information and documentation:

- drawings showing the right way of the high-voltage lines and the pipeline together with the location of power stations, substations, transformer stations, overhead line towers, and pipeline CP stations;
- the rated voltage and the type of earthing of the high-voltage system;
- nominal or operating and peak (inducing) current of the high-voltage line;
- the configuration of the towers and the conductors;
- the diameter and insulation resistance of the pipeline;
- the location of isolating joints and leakage resistance of any structure that provides grounding of the pipeline; and
- the reduction factor of the high-voltage line and the case being of other reducing conductors.

$U_{ac}$  as a function of pipeline length,  $l$ , is then obtained from the vectorial sum of the induced voltage from each considered individual pipeline segment.

As an example, **Figure 4** shows the results of calculated  $U_{ac}$  for a pipeline, DN 500, laid in 1999. Isolating joints are installed at km 0 and km 62. The pipeline is inductively interfered by four 50 Hz high-voltage lines (110 kV/220 kV); the level of operating currents is between 520 and 960 A. The coating insulation resistance is 1 and 100  $k\Omega m^{-2}$  according to results from CP measurements. By installing two grounding electrodes,  $U_{ac}$  may be kept below the safety threshold for people, even though, to avoid AC corrosion, further measures are still to be adopted.



**Figure 2** Typical AC corrosion on a bituminous-coated pipeline. Reproduced from Corrosion due to AC on metallic buried pipelines: Background and perspectives L. Di Biase APCE, 2nd National Conference, Rome, Nov. 1996; pp 21–22.



**Figure 3** Typical AC corrosion on an fusion bound epoxy-coated pipeline. Reproduced from AC Induced Corrosion on Onshore Pipelines, A Case History, Roger Ellis Shell UK, Stanlow, 2001. Pipeline Manager UKOPA (United Kingdom Onshore Pipeline Operators' Association).

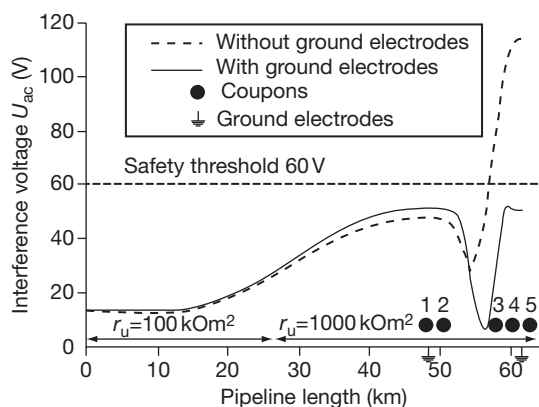


**Figure 4**  $U_{ac}$  along a pipeline, DN 500, built in 1999.

#### 4.22.5 Evaluation of the AC Interference Effects

On pipelines suffering from AC interference, pipe-to-soil protection potentials satisfying the requirements of the relevant standards do not guarantee efficient protection against corrosion. A specific approach to assess the likelihood of AC corrosion should be adopted.

The AC voltage induced on a pipeline is considered as the most important parameter to be taken into account when evaluating the adverse influences of an AC system.

The factors which mainly influence the AC corrosion phenomena are

- the induced AC voltage;
- the AC current density on the exposed metal;
- DC polarization;
- the size of coating defects;
- the local soil resistivity; and
- the local soil chemical composition.

In order to assess the actual risk of AC corrosion on a pipeline interfered by a high-voltage power line, the following methods can be used:

- Indirect assessment by installing coupons along the right of way of the pipeline where the corrosion risk is expected to be highest. Appropriate locations may be found at pipeline sections where the AC voltage reaches the highest values (see [Figure 4](#)).

These coupons (typically having a bare steel area of  $1 \text{ cm}^2$ ) are bonded with cables to the pipeline, thus allowing to measure the voltage and the current density (DC, AC).

According to EN TS 15280 issued in March, 2006,<sup>6</sup> the following limits apply:

The pipeline is considered protected from AC corrosion if the rms AC current density ( $\mathcal{I}_{ac}$ ) on the coupon is less than  $30 \text{ A m}^{-2}$ .

In practice, the evaluation of AC corrosion likelihood on a broader base can be made as follows:

- $\mathcal{I}_{ac}$  lower than  $30 \text{ A m}^{-2}$ : no or low likelihood;
- $\mathcal{I}_{ac}$  between  $30 \text{ A m}^{-2}$  and  $100 \text{ A m}^{-2}$ : medium likelihood;
- $\mathcal{I}_{ac}$  higher than  $100 \text{ A m}^{-2}$ : very high likelihood.

If electrical resistance (ER) coupons are used, the corrosion rate can be measured instantly. The coupon sensitivity should be carefully chosen in such a way that corrosion rates in the order of  $0.01 \text{ mm year}^{-1}$  can be measured with sufficient accuracy over a period of some months.

- Indirect assessment by measuring the AC voltage along the pipeline and correlating the results with the actual operating conditions of the interfering high-voltage system.

According to EN TS 15280 issued in March, 2006,<sup>6</sup> the following limits apply:

To reduce the AC corrosion likelihood on a buried pipeline, the pipeline AC voltage, measured at selected test points, should not exceed at any time:

- 10 V at which the local soil resistivity is greater than  $25 \Omega \text{ m}^{-1}$ ,
- 4 V at which the local soil resistivity is less than  $25 \Omega \text{ m}^{-1}$ .

These values should be considered as threshold limits, which significantly reduce the AC corrosion likelihood; they are based on a long-term practical experience of many European pipeline operators.



- Direct assessment by performing potential gradient measurements along the pipeline, followed by excavation of sites where results indicate small defects in the coating. In case of pipelines that can be inspected with an intelligent pig and after a sufficient duration of the interference (e.g., 2 or more years), the loss of wall thickness may also be detected by ultrasonic or magnetic flux leakage intelligent pigs.

#### 4.22.6 Mitigation of AC Interference Effects

In order to reduce the AC corrosion risk of an existing pipeline, generally, the AC voltage between pipeline and soil and the level of the CP system can be modified and adjusted by the operator.

The AC current density in a defect of the pipeline coating is directly proportional to the AC voltage, thus any reduction of the voltage reduces the likelihood of AC corrosion.

The following **Table 1** summarizes some possible mitigating measures and shows advantages and the associated, possible drawbacks:

- The level of the CP should also be considered. Some laboratory tests have shown<sup>8</sup> that excessive DC current densities (e.g., exceeding  $5 \text{ A m}^{-2}$ , measured on bare coupons) may increase the AC corrosion rate, due to the accumulation of hydroxyl-ions close to the metal–soil interface. The subsequent reduction of the leakage resistance at the defect may lead to increasing AC and DC

current densities and an increased likelihood to reduce the passive film that is formed during the anodic half-wave of the AC current.<sup>10,11</sup>

According to the aforementioned reactions, in order to further reduce the likelihood of AC corrosion, besides the reduction of the AC voltage on a pipeline, its On-potentials (which are the driving force for the CP current) should not be much more negative than the ones needed to satisfy the CP Off-potential criterion of the pipeline.<sup>11</sup>

However, in case of DC-interfered pipelines with high-quality coatings (which are more prone to AC corrosion), it is difficult to practically cope with the reduction of the On-potential and the simultaneous control of the DC corrosion risk.

#### 4.22.7 Major Evidence from Field Studies and Laboratory Tests

1. AC corrosion is more likely to happen on buried pipelines coated with high-resistance coatings (e.g., three-layer polyethylene) than on pipelines with older bituminous coating types (even though some case histories have been reported where AC corrosion also happened on pipelines coated with bituminous coatings).
2. AC corrosion usually appears in the area along the pipeline that is highest interfered.
3. AC corrosion likelihood could further be reduced by carefully adjusting the On-potential of pipelines to values no more negative than the ones needed to satisfy CP Off-potential criteria

**Table 1** Summary of measures to reduce the AC voltage on interfered pipelines

Mitigation measure	Advantages	Possible drawbacks
Increasing the distance between pipe and high-voltage line/electrified railway	–	<ul style="list-style-type: none"> <li>• Very efficient solution but only possible for new designed pipes or interfering systems</li> <li>• Not possible for existing systems</li> </ul>
Arrangement of phase and earth wires of high-voltage line	–	<ul style="list-style-type: none"> <li>• Only possible for new designed high voltage power lines</li> <li>• The solution only depends on the electricity company</li> </ul>
Earthing of pipeline through AC discharge devices	<ul style="list-style-type: none"> <li>• Generally good technical solution and cost efficient</li> </ul>	<ul style="list-style-type: none"> <li>• Problems may occur in high resistivity soil due to high resistance of groundings</li> </ul>
Compensation of AC voltage	–	<ul style="list-style-type: none"> <li>• Difficult to settle</li> <li>• High cost of installation and operation</li> </ul>
Installation of isolating joints	<ul style="list-style-type: none"> <li>• Good possibility to vary an optimum configuration by calculation and design</li> </ul>	<ul style="list-style-type: none"> <li>• Installation of joints involves direct interference with pipeline operation</li> </ul>
Earthing of pipeline by using earthing wires	–	<ul style="list-style-type: none"> <li>• High cost and poor efficiency</li> </ul>

(e.g., EN 12954).<sup>12</sup> Nevertheless, this mitigation measure is to be considered quite difficult in its practical application and sometimes (e.g., presence of DC interference) not possible.

## References

1. Shipley, J. W. *Eng. Y. Can.* **1927**.
2. Stalder, F.; Bindschedler, D. Wechselstromkorrosion – Einfluss der Bodenzusammensetzung; CEOCOR, Jahrestreffen: Lugano, 1992.
3. Corrosion due to AC on metallic buried pipelines: Background and perspectives L. Di Biase APCE, 2nd National Conference, Rome, Nov. 1996; pp 21–22.
4. AC Induced Corrosion on Onshore Pipelines, A Case History, Roger Ellis Shell UK, Stanlow, 2001. Pipeline Manager UKOPA (United Kingdom Onshore Pipeline Operators' Association).
5. Nielsen, L. V.; Baumgarten, B.; Cohen, P. On-site measurements of AC induced corrosion: effect of AC and DC parameters – a report from the Danish Activities-CEOCOR Dresden – Sector A – Germany, Paper N. 03, 2004.
6. CEN/TS 15280 – Evaluation of AC corrosion likelihood of buried pipelines – Application to cathodically protected pipelines, March 2006.
7. Detection of AC corrosion A. Ph. Pourbaix, Carpentiers (CEBELCOR, Brussels); Gregoor, R. (DISTRIGAZ, Brussels), CEOCOR Conference, BIARRITZ/France Oct. 2001.
8. A new electrochemical method for the detection of AC corrosion CEOCOR Dresden-Sector A, Paper N.07, 2004. Büchler M.; Stalder F.; Schöneich H.G.; SGK, Swiss

Company for corrosion protection Technoparkstr. 1, CH-8005, Zürich, Switzerland; Ruhrgas AG, Essen, Germany.

9. CIGRE Report: Guide on the influence of High Voltage AC Power Systems on Metallic Pipelines, 1995.
10. Nielsen, L. V. Role of alkalization in AC induced corrosion of pipelines and consequences hereof in relation to CP requirements; NACE 2005, paper #05188.
11. Büchler, M.; Voûte, C.-H.; Schöneich, H.-G. Evaluation of the effect of cathodic protection levels on the AC corrosion on pipelines EUROCOR- 2007, Freiburg, Germany.
12. EN 12954 Cathodic protection of buried or immersed metallic structures – General principles and application for pipelines, January 2001.

## Further Reading

CCITT: Directives concerning the protection of telecommunication lines against harmful effects from electric power and electrified railway lines. vol III, Capacitive, inductive and conductive coupling: physical theory and calculation methods, ITU Geneva 1989.

IGU (International Gas Union) Milan – Fault Location on Pipeline Coatings, 1994.

CeoCor (Comité d'étude de la Corrosion et de la Protection des Canalisations), AC Corrosion on Cathodically Protected Pipelines – Guidelines for risk assessment and mitigation measures, 2001.

Nielsen, L. V.; Nielsen, K. V.; Baumgarten, B.; Breuning-Madsen, H.; Cohn, P.; Rosenberg, H. AC induced corrosion in pipelines: Detection, characterisation and mitigation; NACE Corrosion, 2004.

Yunovich, M.; Thompson, N. G. AC corrosion: Corrosion rate and mitigation requirements; NACE Corrosion, 2004.

## 4.23 Cathodic Protection Instrumentation

**B. S. Wyatt**

Corrosion Control Ltd, 3, Ivy Court, Acton Trussell ST17 0SN, UK

This article is a revision of the Third Edition article 10.7 by M. D. Allen, R. G. Robson and D. Ames, volume 2, pp 10:136–10:154, © 2010 Elsevier B.V.

<b>4.23.1</b>	<b>Introduction and Historical Background</b>	2839
4.23.1.1	Voltage, Current, and Resistance Measurement	2839
4.23.1.2	Voltmeters and Potentiometers	2840
4.23.1.3	Current-Measuring Instruments (Ammeters)	2841
4.23.1.4	Measurement of Resistivity/Conductivity	2842
4.23.1.5	Measurement of Resistance/Conductance	2844
<b>4.23.2</b>	<b>Basic Requirements for Routine Testing Instruments</b>	2844
4.23.2.1	Digital Instrumentation	2844
4.23.2.2	Measurement Errors	2846
<b>4.23.3</b>	<b>Reference Electrodes</b>	2846
<b>4.23.4</b>	<b>Other Equipment</b>	2848
4.23.4.1	Recording Instruments	2848
4.23.4.2	Ancillary Instruments	2848
4.23.4.2.1	High-voltage coating-testing equipment	2850
4.23.4.2.2	Buried metal locating and attenuation measuring instruments	2852
<b>4.23.5</b>	<b>Field Data Loggers and Survey Equipment</b>	2852
4.23.5.1	Monitoring and Surveys	2852
4.23.5.2	Fixed-Point Data Monitoring Devices	2852
4.23.5.3	Pipeline Cathodic Protection Survey Devices	2853
4.23.5.4	Offshore Monitoring and Surveying	2853
4.23.5.5	Current Density Devices	2856

### Abbreviations

**AC** Alternating current  
**ALWC** Accelerated low water corrosion  
**BS** British Standard  
**CIPS** Close interval potential survey  
**DC** Direct current  
**DCVG** Direct current voltage gradient  
**DMM** Digital multimeter  
**emf** Electromotive force  
**EN** European Norm  
**GPS** Global positioning system  
**SHE** Standard hydrogen electrode  
**SRB** Sulfate reducing bacteria

### Symbols

***I*** Current  
***R*** Resistance  
***V*** Voltage

### 4.23.1 Introduction and Historical Background

#### 4.23.1.1 Voltage, Current, and Resistance Measurement

This chapter is essentially a review of former methods for electrical measurement. Although a description of these older instruments and methods is now of historical interest, it presents a valuable understanding of the principles of measurement, which are obscured when considered in conjunction with modern digital instruments.

Historically, nearly all DC electrical measuring instruments were of the moving-coil permanent-magnet type, which gave a coil deflection (and thus pointer deflection) proportional to the current in the coil. The damping of the movement to prevent over swing or the oscillation of the needle is provided by the eddy currents induced in the metal former on which the coil is wound, and further damping (i.e., critical damping) can be obtained by placing a low resistance across the coil. The main advantages of

this type of instrument are uniformity of scale, high torque–weight ratio, and low power consumption. By the insertion of suitable shunts and/or resistances, it is possible to use one instrument to measure both current and voltage over a wide range.

It is often not appreciated that modern digital multimeters (DMMs) function in exactly the same way as traditional instruments except that the moving coil meter is replaced by an electronic operational amplifier and that the display is digital rather than analog. The main measurement advantage of a DMM is their considerably higher input impedance as voltmeters. They also have a number of obvious technical advantages, such as robustness, ease of use, etc.

#### 4.23.1.2 Voltmeters and Potentiometers

The current flowing through any potential-measurement circuit must be as small as possible to avoid errors due to polarization of the voltage source. Moreover, if the current flow is too large, errors will be introduced owing to the voltage drop caused by the contact resistance between the reference electrode and the electrolyte. It is thus clear that the prime requirement of an accurate potential measurement circuit is high resistance. For direct-reading instruments, the input impedances were typically as low as  $50\,000\,\Omega\,V^{-1}$ , and instruments were commercially available with input impedances of  $\sim 1\,M\Omega\,V^{-1}$ . Direct-reading meters were usually made to show several ranges, which are obtained by the use of suitable resistances placed in series with the indicating instrument (Figure 1).

For digital instruments, the input impedance is dependant upon the characteristics of the input amplifier used; instruments are available in three bands of performance:  $10\text{--}20\,M\Omega$  for inexpensive, robust devices;  $1\,G\Omega$  for more specialist equipment; and  $>10^{14}\,\Omega$  for electrometer type instruments. This avoids significant polarization of reference electrodes and measurements of accurate steel/electrolyte/electrode potentials in high resistivity electrolytes in soils and concretes. However, it is still important to understand the principles involved.

To measure structure/electrolyte/electrode potentials in electrolyte resistivities in excess of  $20\,\Omega\,m$ , bridge ‘backing off’ potentiometer instruments as shown in Figure 2 or potentiometric voltmeters as

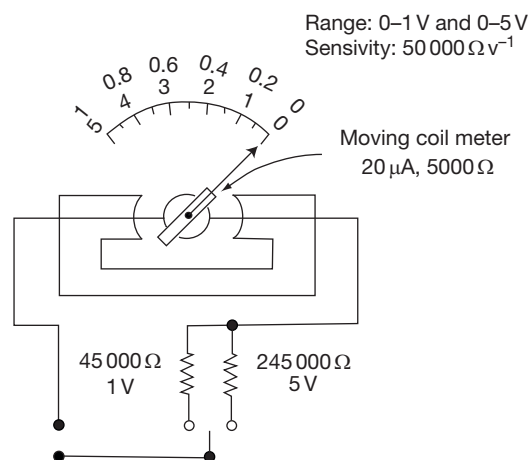


**Figure 1** Direct reading voltmeter.

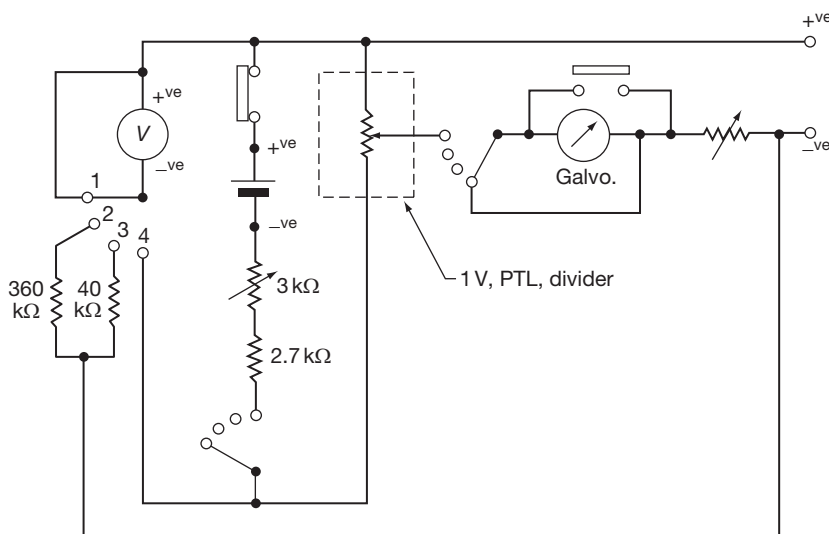


**Figure 2** Potentiometer voltmeter (courtesy of The Post Office).

illustrated in **Figure 3** were traditionally used until the advent of high-impedance digital technology.

In both types of instrument, the voltage to be measured is balanced against an external applied voltage (usually from batteries within the instrument). At balance, no current flows through the external circuit and thus errors due to contact resistance and source impedance are eliminated.

The potentiometer requires to be calibrated against a standard cell, while with the potentiometric voltmeter, the voltage to be measured is balanced against a battery emf, using uncalibrated resistors and the voltmeter as a galvanometer. At balance, the voltage is transferred to the voltmeter and read directly. The magnitude of voltage that can be measured by both instruments is limited by the maximum voltage of the (usually) dry cell they contain. It is, however, possible to extend the range by using a potential divider or volt box. For normal field work, the potentiometric voltmeter was the more popular instrument, being usually of lighter construction and not requiring calibration against a standard cell. Where extremely small potentials (usually potential shifts) of the order of 1 mV were to be measured, however, the potentiometer was more suitable and accurate.

The technique adopted in measuring structure/electrolyte potential is illustrated in **Figure 4**. It should be noted that the position of the reference electrode in relation to the structure is important. Theoretically the half-cell should be placed as near to the structure as possible (i.e., within a few millimeters) to avoid  $IR$  (ohmic) drop in the electrolyte. This is often not possible in practice as, for example, with a buried pipeline. In such a case, the cell should be placed in the soil directly over the structure, and it is accepted good practice, historically, to allow a 'safety factor' of say 50 mV over and above the minimum protective potential to compensate for  $IR$  drop.

These  $IR$  drop errors are now (and have been since the 1950s in continental Europe) minimized

by the measurement of Instant OFF potentials, typically within a period of 0.1–1 s after interrupting the cathodic protection current. There remains (in 2009) a debate in the US pipeline industry regarding the need for such 'sophistication' in measurement and whether there is a need to increase the level of polarization to pipelines to accommodate the previously unknown  $IR$  drop errors, in particular for pipelines where existing levels of polarization have historically controlled corrosion to adequate levels. The key issue appears to be that the magnitude of the  $IR$  error will vary with soil resistivity, coating quality/defect size, the quality of polarization films on the steel surface and may be as much as several hundreds of millivolts; without the 'sophistication' of Instant OFF potential measurements, there can be no reliance on the accuracy of potential measurements. This concept is well accepted in most of the world.

#### 4.23.1.3 Current-Measuring Instruments (Ammeters)

These may be classified generally according to whether they are used to measure current delivered or drained by a structure receiving cathodic protection or to measure current flowing within the structure itself.

By the use of suitable shunts, the basic moving-coil movement (and the DMM) can be adapted to measure an almost unlimited range of currents. **Figure 5** illustrates a direct-indicating instrument with shunt to

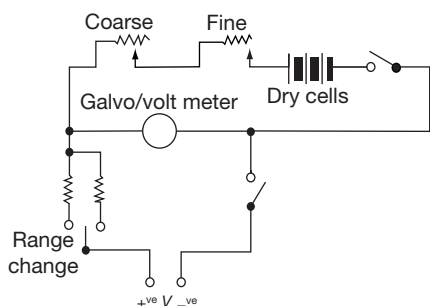


**Figure 3** Basic circuit potentiometer voltmeter.

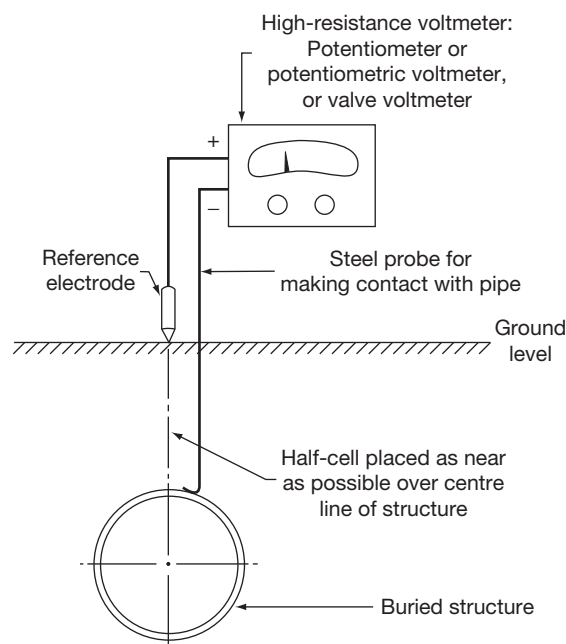


**Figure 4** Measurement of structure/electrolyte potential.



measure current up to 5 A DC. To ensure that the resistance of the circuit is not materially altered by the insertion of an ammeter, it is usual to install either a shunt or the meter itself (usually a moving-coil meter with internal shunt) permanently in the circuit. Ammeter shunts are normally of the four-terminal type to avoid contact resistance errors, that is, two current terminals and two potential terminals.

Importantly, in making measurements of current flowing within a structure, it is extremely important that additional resistance, for example, an ammeter shunt, is not introduced into the circuit, as otherwise erroneous results will be obtained. One method is to use a tong test meter. Such instruments are, however, not particularly accurate, especially at low currents, and are obviously impracticable in the case of, say, a 750-mm diameter pipeline. A far more accurate method and one that can be applied to all structures is the zero-resistance ammeter or, as it is sometimes called, the zero-current ammeter method. The basic circuit of such an instrument is shown in **Figure 6**.

From **Figure 6**, it will be seen that if  $I_b$  is adjusted until there is zero voltage on the voltmeter, then  $I_s = I_b$ . When this type of instrument is used to measure current in, say, a bond between one structure

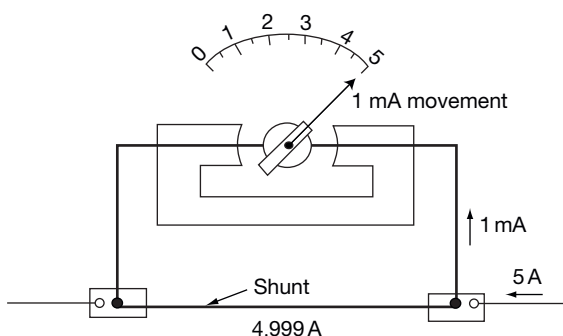


**Figure 5** Direct-indicating current measuring instrument (ammeter).

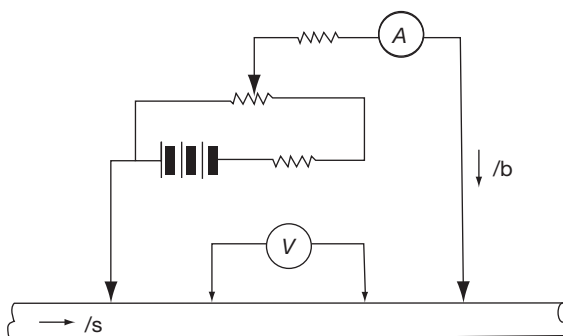


**Figure 6** Zero-resistance ammeter.

and another, if simultaneous measurements are made at locations on the structure (i.e., interference testing) inaccurate results will be obtained, because at balance there is no current in the structure at the measurement point, and this could materially alter the current distribution to the structure.

The zero-resistance ammeter is seldom employed for routine testing; however, the above circuit can be used utilizing modern digital instruments and a current source to 'back off' the current flowing in the structure and measure this current in the external ammeter/shunt. As already noted, a DMM measures current in precisely the same manner as a moving coil instrument. Thus, the modern use of a DMM does not negate an understanding of how current shunts function in practice.

#### 4.23.1.4 Measurement of Resistivity/Conductivity

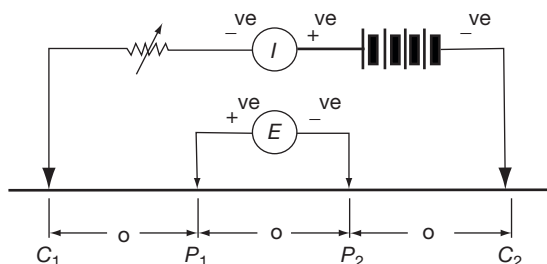
The most usual method of measuring soil resistivity is by the four-electrode 'Wenner' method. **Figure 7** indicates the basic circuit. The mean resistivity  $R_m$  is given by

$$R_m = 2a(E/I)$$

where  $I$  is the current applied between the current electrodes  $C_1$  and  $C_2$  and  $E$  is the potential developed between the potential electrodes  $P_1$  and  $P_2$  by the current  $I^*$ . The value given by this method is the average resistivity of the soil to a depth equal to the spacing of the electrodes. The average is weighted to the surface material as the 'sampled' volume is actually a hemisphere below the two center pins  $P_1$  and  $P_2$  in **Figure 8**. There is a simple calculation technique whereby measurements taken at the same general location but at different pin spacings/depths can be expressed as the resistivity of the individual layers from the surface to the maximum depth measured. This analysis is extremely useful in assessing the likely corrosivity at pipeline depth and is essential as a precursor to the design calculation of groundbed resistance/optimum dimensions.

It is most important to note that for accurate and consistent results, the electrodes must be equidistant from one another and placed in a straight line. The relatively simple setup, illustrated in **Figure 7**, suffers from inaccuracies arising from the polarization of the potential electrodes and effects of possible stray currents in the soil.

To avoid the errors of polarization and stray currents, four-pin earth resistivity meters are employed.



(a) 'Wenner' 4 pin method:  $C_1$ ,  $C_2$  and  $P_1$ ,  $P_2$  are steel rods driven into the soil. Modern devices use an AC source thus avoiding errors due to polarisation of the pins and standing field gradients between  $P_1$  and  $P_2$



(b) 4 Pin Earth Resistivity Meter using a hand cranked AC generator. More modern devices use battery/electronic AC circuits but this device remains one of the most sensitive

**Figure 7** 'Wenner' 4 pin earth resistivity determination.

These use an alternating current produced from battery-powered electronic, or in older equipment, a hand-generated current passed through the current coil of an ohmmeter and then through a current reverser so that an alternating current is delivered. The effective resistance is measured by a modified Wheatstone bridge with balance indicated by a galvanometer, **Figure 8**.

The resistivity of an electrolyte can also be measured by passing a known current through a known length and cross section of the electrolyte and measuring accurately the voltage drop across the length. It is normal to use alternating current in order to avoid polarization effects. Special cells also exist for use with resistivity meters, which are so constructed and calibrated that resistivity can either be read directly from the instrument or simply calculated from the product of the measured resistance and known cell constant. Measurements of resistivity on samples will give accurate results only on liquid electrolytes and are also used commonly for the measurement of selected soil or saline mud samples, but caution should be exercised as the value of resistivity measured will vary with the degree of compaction of the soil. The measurement of electrolyte conductivity, the reciprocal of the resistivity, is

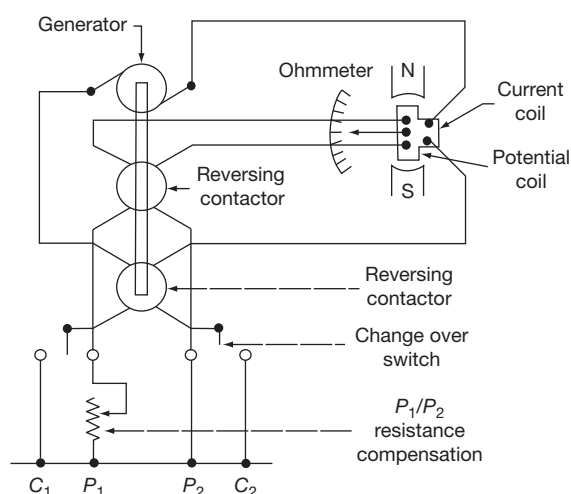


**Figure 8** 'Megger' earth resistivity meter (courtesy Evershed and Vignoles).

calculated from the resistivity as measured by some of the methods described earlier.

Often it is necessary in designing a cathodic-protection system to know the conductivity of a protective coating (coating conductance) on a structure. This measurement may be carried out in an

approximate manner by finding the resistance between an electrode of known area placed in contact with the coating and the structure itself. The electrode placed on the structure can be either of thin metal foil or, preferably, of material such as flannel soaked in weak acidic solution. The resistance between the pad and the metal is measured by means of a resistivity meter, as previously described. More accurate data on coating conductance can be calculated, postconstruction and after commissioning the cathodic protection system, using the classic attenuation formulae and measured pipe/soil potential shifts along the pipeline. In some pipeline construction contracts, such measurements are used as a quality management tool and failure to comply with a maximum coating conductance will result in remedial works being required.

#### 4.23.1.5 Measurement of Resistance/Conductance

As previously mentioned, four-pin earth resistivity meters can be used to measure resistances. Modern DMMs are also able to measure resistance. The measurement of resistance to the remote earth of a metallic structure is normally carried out with a four-electrode instrument. The connections are shown in **Figure 9**. A current is passed between the structure and a remote electrode and the potential difference measured between the structure and a second remote electrode. In this way, the ohmmeter records the resistance of the structure to earth, that is,  $V/I$ . The spacing of the electrode from the structure is important and must be such that the remote potential electrode lies on the horizontal part of the resistance–distance curve, as shown in **Figure 9**. Generally speaking, a minimum

distance of 15 m from the structure is necessary for the potential electrode to lie on the flat part of the curve, with the current electrode usually at least twice the distance of the potential electrode.

### 4.23.2 Basic Requirements for Routine Testing Instruments

#### 4.23.2.1 Digital Instrumentation

All instruments used in cathodic protection work must be sufficiently rugged for field use with appropriate ranges, resolution, and accuracy. They should be externally, formally, calibrated and calibration records and copies of the certificates should be available to the engineers or technicians using them so that they can be certain that the instruments they use are within calibration.

Most cathodic protection measurements comprise DC voltage/potential values, along with resistance and DC currents, either low current directly via shunts within the meter or using external high-current shunts, plus a range of AC measurements (subject to appropriate training and certification of personnel to work on mains voltage equipment). Thus, a wide range of conventional electrical test multimeters are extensively used. For general field applications, suitable instruments are available that are water resistant to BS EN 60529 IP 64 dust-tight and splash resistant or IP 67 dust-tight and resistant to immersion; explosion hazard certificated equipment is available for use in hazardous areas. Some typical high-quality digital instruments are shown in **Figure 10** and will have characteristics generally similar to those listed in **Table 1**.

These devices comprise a microcomputer, a data acquisition device, and an analog-to-digital converter along with a digital display, selector switches, fuses, shunts, battery, and terminals. The instruments include self-test and internal calibration checks; DC voltage measurements take typically 0.5–1 s to complete and replenish on the display, whereas AC voltage measurements may take considerably longer and resistance measurements generally take longer than DC measurements and less than AC measurements.

For the important DC voltage measurements used in performance assessment of cathodic protection systems, the input impedance is important, particularly for measurements in high-resistivity soils and concretes. Typical input impedance values for the normal 2 V DC range will be 10 or 20 M $\Omega$ , which

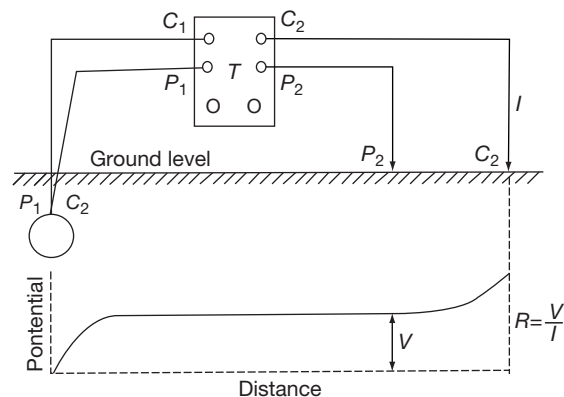


**Figure 9** Measurement of resistance of structure to remote earth.

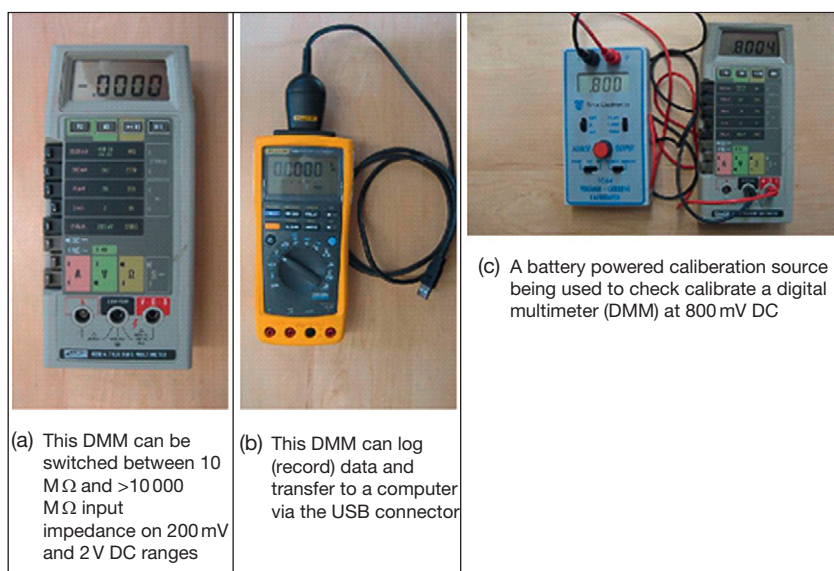


**Figure 10** Typical digital multimeters (DMMs) used in cathodic protection measurements.

**Table 1** Typical characteristics of a DMM

Voltage range		Resolution		Accuracy, $\pm\%$ of reading + no. of digits	
DC	AC	DC	AC	DC	AC: 45–1000 Hz
200 mV	200 mV	0.01 mV	0.01 mV	0.04% + 2	0.2% + 10
2 V	2 V	0.1 mV	0.1 mV	0.04% + 2	0.5% + 10
20 V	20 V	1 mV	1 mV	0.05% + 2	0.5% + 10
200 V	200 V	10 mV	10 mV	0.05% + 2	0.5% + 10
1000 V	750 V	100 mV	100 mV	0.05% + 2	1% + 10
Current range		Resolution		Accuracy, $\pm\%$ of reading + no. of digits	
DC	AC	DC	AC	DC	AC: 45–1000 Hz
200 $\mu$ A	200 $\mu$ V	0.01 $\mu$ V	0.01 $\mu$ V	0.02% + 2	0.75% + 10
2 mA	2 mV	0.1 $\mu$ V	0.1 $\mu$ V	0.02% + 2	0.75% + 10
20 mA	20 mV	1 $\mu$ V	1 $\mu$ V	0.03% + 2	0.75% + 10
200 mA	200 mV	10 $\mu$ V	10 $\mu$ V	0.03% + 2	0.75% + 10
2 A	2 A	100 $\mu$ V	100 $\mu$ V	0.03% + 2	1% + 10
Resistance range		Resolution		Accuracy, $\pm\%$ of reading + no. of digits	
DC	AC	DC	AC	DC	AC: 45–1000 Hz
200 $\Omega$	200 $\Omega$	0.01 $\Omega$	0.01 $\Omega$	0.07% + 4	0.07% + 2
2 k $\Omega$	2 k $\Omega$	0.1 $\Omega$	0.1 $\Omega$	0.07% + 2	0.07% + 2
20 k $\Omega$	20 k $\Omega$	1 $\Omega$	1 $\Omega$	0.07% + 2	0.07% + 2
200 k $\Omega$		10 $\Omega$		0.07% + 2	
2 M $\Omega$		100 $\Omega$		0.15% + 2	
2 M $\Omega$		10 k $\Omega$		0.2% + 2	
20–100 M $\Omega$		100 k $\Omega$		1% + 3	
100–300 M $\Omega$		1 M $\Omega$		2% + 3	

will be insufficient for accurate measurements with normal reference electrodes in soils and concretes of  $\sim > 500 \Omega \text{ m}$ . Very few instruments are available with a switchable input impedance; one favored for use in reinforced concrete applications is switchable between 10 and  $> 10\,000 \text{ M}\Omega$ .

Noise rejection, the avoidance of error in the DC measurement due to AC, which may be superimposed on the structure being measured (typically but not exclusively a pipeline) or may be collected (typically by induction) into the test cables used in the measurements, is also important in measurements of cathodic protection DC voltage, particularly with high-impedance instruments where very low currents flow in the measurement circuits. Good quality instruments will have high levels of noise rejection with typical good values being  $> 60 \text{ dB}$  at 50–60 Hz normal mode noise rejection and  $> 120 \text{ dB}$  common mode noise rejection at DC and  $> 90 \text{ dB}$  at 50–60 Hz.

With the ability to deploy to site such extremely versatile and accurate multifunction digital test equipment, cathodic protection personnel should also use, some on a daily basis or at the start and end of a ‘campaign’ of measurements, a portable calibration device or a second instrument such that the accuracy of the instrument used for measurements in the field can be confirmed.

#### 4.23.2.2 Measurement Errors

It is all too easy to be ‘fooled’ by an instrument into assuming that the number presented on its display, or recorded for later analysis, is somehow ‘accurate.’ This is completely untrue. The terms sensitivity, accuracy, and precision have precise definitions and it is important for operators to understand what they mean.

Sensitivity is the smallest possible signal that an instrument can measure, accuracy is the degree to which the measurement is close to the actual (true) measurement, while precision is the degree to which further measurements will show the same or similar results (also called reproducibility).

A single measurement or a series of measurements may be accurate (but not precise), precise (but not accurate), both of these, or neither. These differences essentially relate to errors in measurement, which may be random or systematic. Random error relates to unquantifiable differences in how a measurement is undertaken; systematic error is an always-present offset from the true value. This difference is illustrated in [Figure 11](#).

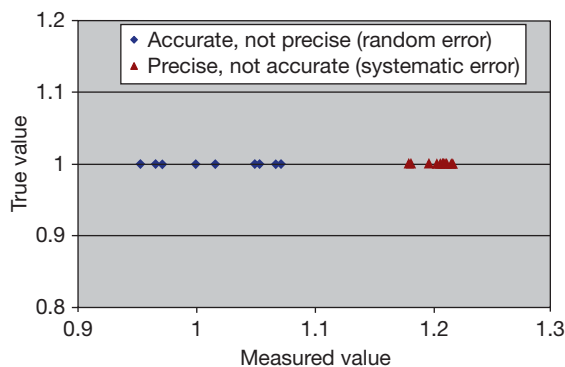


**Figure 11** Random and systematic errors.

#### 4.23.3 Reference Electrodes

The generally accepted criteria for the effectiveness of a cathodic protection system are all related to the structure/electrolyte potential. The protection criteria for carbon (mild) steel in various electrolytes are summarized in [Table 2](#).

Note: Aluminum alloys have protection criteria similar to those for steel. Higher strength steels, aluminum, high-strength copper–nickel alloys, and coated steels have negative potential limits to avoid hydrogen embrittlement and coating disbondment or, in the case of aluminum, amphoteric corrosion. Elevated temperatures require more negative protection criteria. Stainless steels have less negative protection criteria and duplex stainless steels may be subject to hydrogen embrittlement. Steel in concrete has a potential limit of  $-1100 \text{ mV}$  for reinforcing steel and  $-900 \text{ mV}$  for prestressing steel both referred to  $\text{Ag}/\text{AgCl}/0.5 \text{ M KCl}$ .

In order to measure the metal/electrolyte potential, it is necessary to make a metallic contact to the metallic structure itself and an electrolytic contact with the electrolyte (soil, water, or concrete). The problem of connection to the structure normally presents no significant difficulties except in respect of access; for example, in the case of concrete, the steel needs to be exposed for connection and the electrical continuity between the bars needs to be established. However, contact with the electrolyte must be made with a reference electrode that presents a stable interface or half-cell potential with the electrolyte under all conditions. (If e.g., an ordinary steel probe were used as a reference electrode, then inaccuracies would result for two main reasons: first, electrochemical action between the probe and the soil, and second, polarization of the probe owing to current flow



**Table 2** Cathodic protection criteria for carbon steel in various environments

<i>Electrolyte</i>	<i>Prime criteria</i>	<i>Alternative criteria</i>	<i>Alternative criteria for consideration</i>	<i>Prime standards</i>
Aerobic soils, insignificant microbial activity (notably sulfate reducing bacteria SRBs)	More negative than –850 mV referred to Cu/CuSO <sub>4</sub> (sat.) polarized potentials (instant OFF)	100 mV decay or polarization (measured instant OFF)	More negative than: –750 mV for 100 < $\rho$ < 1000–650 mV for $\rho$ < 1000 $\Omega$ m	ISO 15589–1: As revised for BS EN 14919–1. BS EN 12954 (not 100 mV decay/shift)
Anaerobic soils with significant microbial activity (notably sulfate reducing bacteria SRBs)	More negative than –950 mV referred to Cu/CuSO <sub>4</sub> (sat.) polarized potentials (instant OFF)	N/A	N/A	ISO 15589–1 As revised for BS EN 14919–1. BS EN 12954
Aerobic Waters, insignificant microbial activity (notably SRBs)	More negative than –800 mV referred to Ag/AgCl/sea water (equivalent to –850 mV referred to Cu/CuSO <sub>4</sub> (sat.) Polarized potentials Instant OFF)	N/A	N/A	BS EN 12473
Anaerobic waters (e.g., under decaying marine growth as in accelerated low water corrosion (ALWC) with significant microbial activity (notably SRBs)	More negative than –900 mV referred to Ag/AgCl/sea water (equivalent to –950 mV referred to Cu/CuSO <sub>4</sub> (sat.) polarized potentials instant OFF)	N/A	N/A	BS EN 12473 CIRIA C 634 management of ALWC in steel marine structures
Concrete	Potential decay from instant OFF of: At least 100 mV during 24 h Or At least 150 mV during a period > 24 h	More negative than –720 mV referred to Ag/AgCl/0.5 M KCl (equivalent to –720 mV referred to Ag/AgCl/sea water) (instant OFF)	Fully depolarized or unprotected steel in concrete less negative than –150 mV referred to Ag/AgCl/0.5 M KCl (passive within protective concrete)	BS EN 12696

through the measuring circuit.) Reference electrodes are metal electrodes immersed in a solution of one of its salts; in the simplest form the copper/copper sulfate (saturated) reference electrode, Cu/CuSO<sub>4</sub> (sat.), comprises a pure copper electrode immersed in a saturated solution of CuSO<sub>4</sub>.

The silver/silver chloride electrode range is of a second type where the metal electrode is coated with a salt of that metal and then immersed in a solution of the salt. Thus, there are many types of silver/silver chloride electrodes, with a range of electrode potentials; calling an electrode a silver/silver chloride electrode or Ag/AgCl is an incomplete description and can lead to confusion. Two types of these electrodes are commonly used in cathodic protection. These are the Ag/AgCl/sea water electrode the potential of

which is ONLY stable in sea water of 3.5 wt% salinity. The potential changes with salinity and thus these electrodes should only be used in open sea water. The second is the Ag/AgCl/KCl electrode where the concentration of the potassium chloride will determine the electrode potential. For convenience, the Ag/AgCl/0.5 M KCl, which has an electrode potential within a few millivolts of the Ag/AgCl/sea water (in 3.5 wt% salinity), is widely used but other concentrations are also available. These electrodes are widely used in steel in concrete applications, both as portable survey electrodes and as electrodes permanently cast into concrete, but they should also be used in estuarine waters and can be used as permanent buried electrodes in saline soils. The KCl concentration is maintained in a fixed, stable, condition as is

necessary for long-term electrode potential stability by using a very impermeable porous plug and a gel agent in the solution. The Ag/AgCl/KCl electrode is probably the best reference electrode for measuring potentials of waters at elevated temperatures.

All reference electrodes are subject to small variations in potential due to temperature. For example, the Cu/CuSO<sub>4</sub> (sat.) electrode potential changes at  $\sim 0.9 \text{ mV}/^\circ\text{C}$  so that a pipe/soil potential measurement recording  $-900 \text{ mV}$  Cu/CuSO<sub>4</sub> (sat.) on a hot day ( $30^\circ\text{C}$ ) will, at  $5^\circ\text{C}$ , be measured as  $-878 \text{ mV}$  Cu/CuSO<sub>4</sub> (sat.). Electrode potential changes also occur when the Cu electrode/electrolyte interface is exposed to sunlight; although these effects are reportedly measured to be as much as  $50 \text{ mV}$  more negative in sunlight, they appear to reduce with repeated exposure and are generally accepted to be limited to  $10 \text{ mV}$ . It is good practice to cover the transparent housing of these electrodes when used outdoors. To avoid errors due to polarization effects, it is necessary to restrict the current density on the copper rod to a value not exceeding  $20 \text{ mA cm}^{-2}$ ; this is not an issue with modern digital instrumentation.

The Cu/CuSO<sub>4</sub> (sat.) electrode is vulnerable to electrode potential changes due to chloride contamination; it should not be used in chloride-rich environments such as sea water, estuarine muds, and similar. These electrodes have been unfortunately used in the portable surveys of steel/concrete potential in reinforced concrete structures such as highway bridges, largely because the ASTM Test Method (C876) unwisely specified its use. If, as is the case with most Cu/CuSO<sub>4</sub> (sat.) electrodes, there is contamination of the wooden or ceramic porous plug with copper sulfate, there is a likelihood that there will be significant errors in measurements that may reach  $120 \text{ mV}$ . This is due to a concentration gradient effect known as ‘streaming potentials’ as the concrete is contaminated with copper sulfate. As this error cannot be detected or quantified, it is poor practice to use Cu/CuSO<sub>4</sub> (sat.) electrodes in surveys of steel in concrete.

Another electrode used in sea water and often wrongly called a reference electrode is the zinc electrode. Commonly, both 99.99% pure zinc and the US Mil Spec 18001 anode grade ( $\sim 99.3\%$  pure with small additions of Cd and Al to avoid passivation) are used as electrodes for potential measurement. Neither is accurate and surface condition can result in significant changes in electrode potential; they are however rugged and reliable if inaccurate. If these electrodes are used for permanent installation (they are not normally used for survey purposes except for approximate

potential measurements in oil-contaminated ballast water tanks where the electrode can be introduced through a ‘crust’ of oil and still operate with reasonable accuracy), it is good practice to draw a small current from the electrodes during nonmeasurement periods or if used for potential sensing and control, so that the consumption of the zinc will keep the surface clean and active.

All reference electrode potentials are related to each other. Thus, if the potential of the structure is found to be  $+200 \text{ mV}$  versus Zn, it will be  $-900 \text{ mV}$  versus Cu/CuSO<sub>4</sub> (sat.), and  $-850 \text{ mV}$  versus Ag/AgCl/(sat.) KCl. Approximate values of the these reference electrodes on the standard hydrogen scale (SHE) are as follows: Cu/CuSO<sub>4</sub> (sat.) =  $0.30\text{--}0.32 \text{ V}$ ; Ag/AgCl (sat.) KCl =  $0.020 \text{ V}$  ( $0.025 \text{ V}$  in sea-water); Zn/sea-water =  $-0.75 \text{ V}$ ; this is shown in [Table 3](#). A historic (Admiralty pattern) electrode is shown schematically in [Figure 12](#), while examples of current reference electrodes are illustrated in [Figure 13](#).

## 4.23.4 Other Equipment

### 4.23.4.1 Recording Instruments

Miniaturization of electronic components has enabled the construction of compact, portable, battery-operated recording voltmeters. The principal use of these instruments is to measure pipe/soil potential fluctuations over a period of time, in particular for monitoring the effects of stray traction currents on pipelines. The instruments can be utilized with shunts to measure current variations.

Modern units are now sufficiently small such that they may be mounted into conventional pipeline pipe/soil potential measurement test posts. They can communicate via satellite or global positioning system (GPS) networks and can operate for many months without battery change, for example, as shown in [Figure 14](#). Such units are now becoming of sufficiently low cost to enable operators to consider using them to replace routine pipe/soil potential measurements by technician staff.

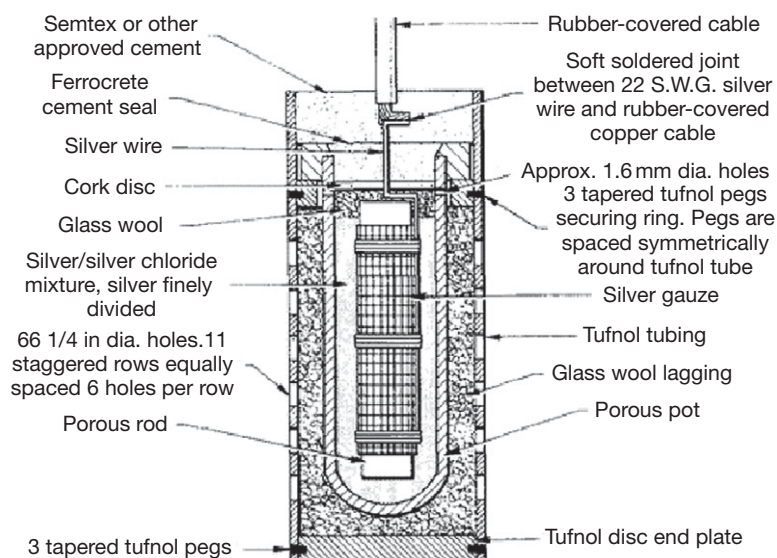
### 4.23.4.2 Ancillary Instruments

Apart from the instruments described in previous paragraphs, there are others that, while not directly connected with cathodic protection as such, are extremely useful tools to a corrosion engineer. They include pH meters, Redox probes, protective-coating test instruments, and buried-metal-location instruments.

**Table 3** Approximate comparison of potentials (V) using Zn/seawater electrodes, Cu/CuSO<sub>4</sub> (sat.), and Ag/AgCl, saturated KCl reference electrodes

Silver/silver chloride/ saturated potassium chloride	-1.3	-1.2	-1.0	-0.8	-0.6	-0.4	-0.2	0
Silver/silver chloride/ seawater	-1.4	-1.2	-1.0	-0.8	-0.6	-0.4	-0.2	0
Copper/copper sulphate	-1.4	-1.2	-1.0	-0.8	-0.6	-0.4	-0.2	0
Zinc/seawater	-0.4	-0.2	0	+0.2	+0.4	+0.6	+0.8	+1.0
Calomel/saturated potassium chloride	-1.4	-1.2	-1.0	-0.8	-0.6	-0.4	-0.2	0

Structure/electrolyte potential (V)

**Figure 12** Historical silver/silver chloride half-cell (admiralty pattern). The electrode is immersed in a chloride-containing solution, which diffuses through the porous pot and thus comes into contact with the Ag/AgCl mixture.

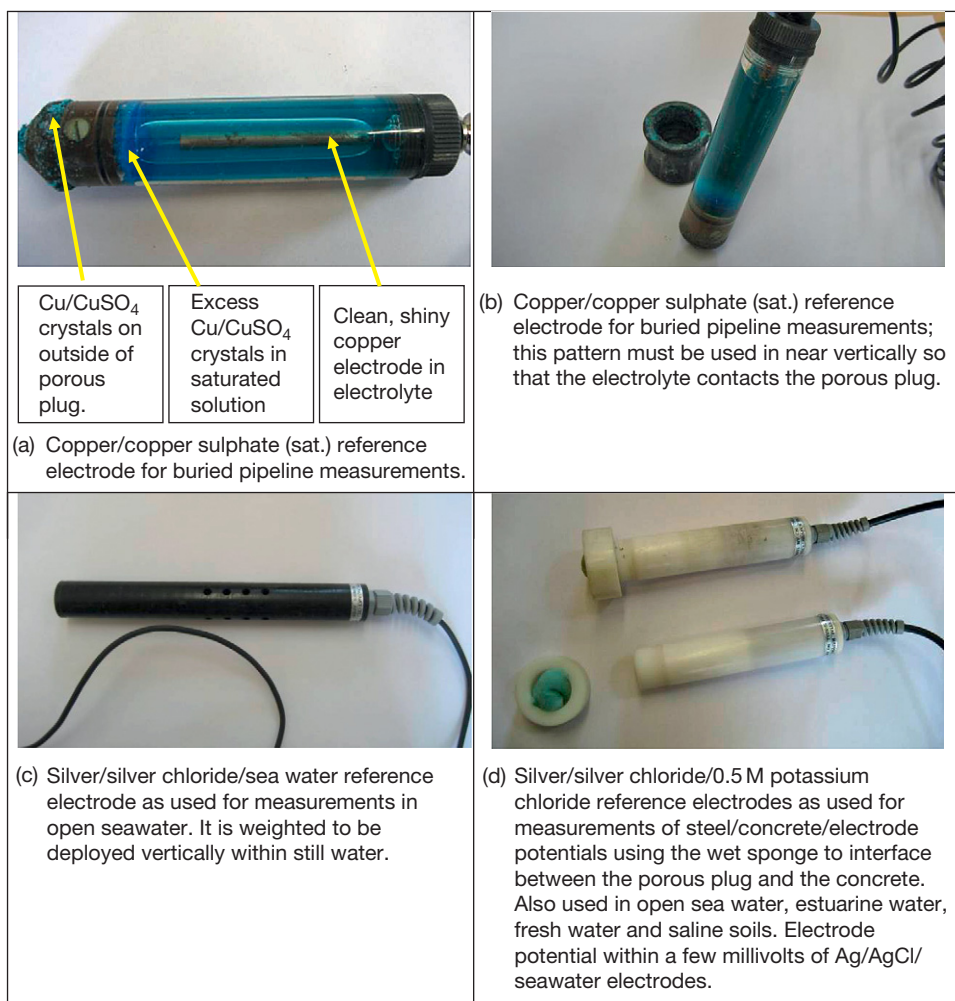


**Figure 13** Typical reference electrodes used in cathodic protection surveys.

#### 4.23.4.2.1 High-voltage coating-testing equipment

When cathodic protection is applied to a structure that has a protective coating, the current required is proportional to the bare metal area on the structure. Thus, whenever a protective coating is applied, it should be of good quality, with very few failures or pin holes in it, so that the cathodic protection system may be economical.

It is standard practice, particularly in the case of pipelines, to carry out an inspection of the protective coating (after application) with a high-voltage tester, known as a holiday detector. Basically, a high voltage is applied between an electrode placed on the coating and the structure. At any 'holidays' (flaws) in the coating, a 'spark-over' occurs and is usually

accompanied by a visual or audible alarm. For pipelines, the electrode often takes the form of a rolling spring clipped round the pipe. Other electrodes are in the form of wire brushes. The high voltage is obtained from batteries and electronic circuitry with a high-tension coil. Such an instrument is illustrated in [Figure 15](#).

For the examination of paint films or special coatings, for example, pipe linings, low-voltage holiday detectors with wet sponge electrodes are available. The choice of voltage for use with a holiday detector depends on the thickness and type of coating applied to the structure. As a guide, in the case of pipelines, a voltage equivalent to  $\sim 5 \text{ kV mm}^{-1}$  thickness is used in testing a thick-film enamel coating.

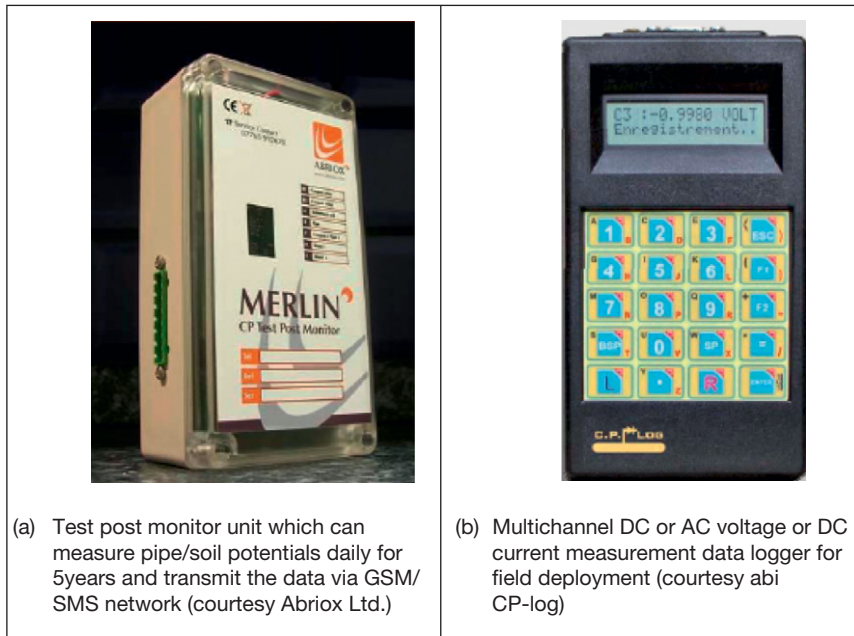


**Figure 14** Recording devices for cathodic protection field deployment.

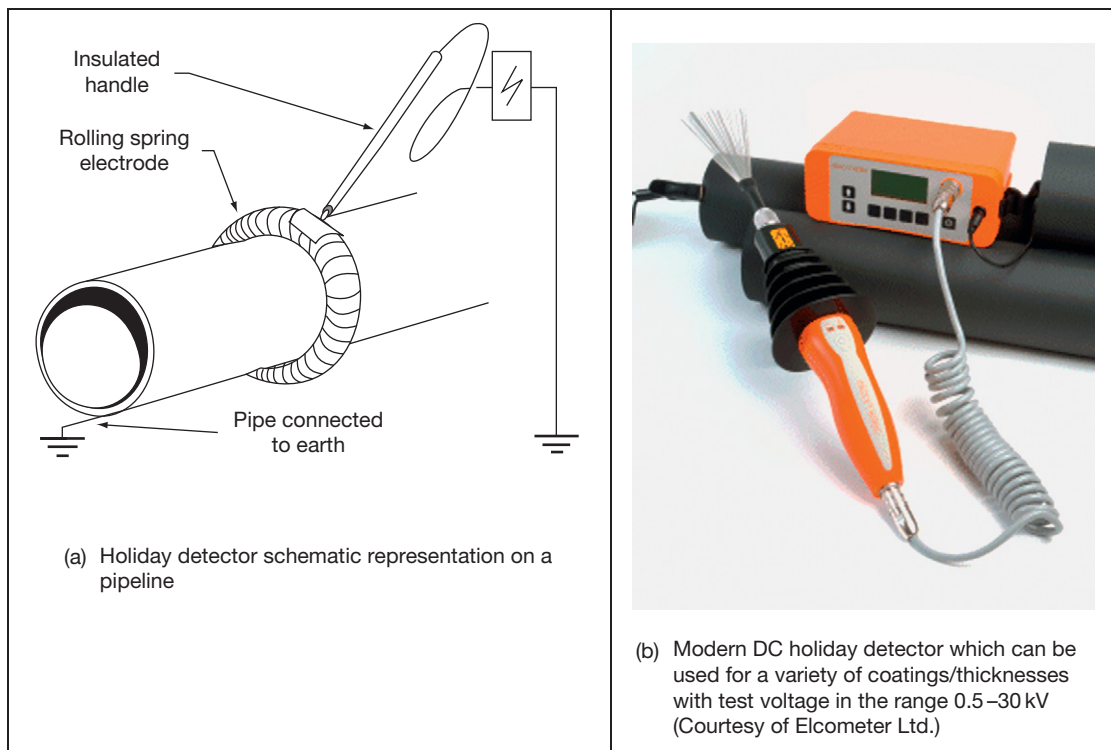


**Figure 15** Holiday detector.



#### **4.23.4.2.2 Buried metal locating and attenuation measuring instruments**

Instruments in this category are used to locate buried metallic structures, to detect possible electrical discontinuities in buried structures, to locate possible junctions or points of contact between one structure and another, and to indicate the condition of a protective coating applied to a buried structure. A signal of a given frequency is either injected or induced into the structure and traced with a search coil and earphones. Most instruments use a high-frequency signal of 1 kHz or higher, although one or two use a simple interrupter.

Buried pipeline coating survey instruments are available, which, by measurement of the electromagnetic field radiating from a pipeline created by an applied AC signal, are able to compute the attenuation of the signal in dB/km and hence provide an assessment of pipeline coating quality. The signal generator typically operates at a frequency of  $\sim 1$  kHz for thick coatings being selected to minimize interference from commonly occurring frequencies while maximizing the distance the signal will travel, some 5–10 km on a reasonably well-coated pipeline. For thin-film coatings, such as a fusion-bonded epoxy, a frequency of 200 Hz has been found more appropriate.

### **4.23.5 Field Data Loggers and Survey Equipment**

#### **4.23.5.1 Monitoring and Surveys**

It is necessary to understand the difference between monitoring cathodic protection performance and surveying cathodic protection performance. Monitoring is undertaken routinely at fixed points.

For example, on a pipeline, monitoring will be of cathodic protection current and voltage at impressed current transformer rectifiers or at galvanic (sacrificial) anodes and at test points at some 1–2 km spacing along the pipeline at which there will be connections to the pipeline and where there may be buried permanent reference electrodes and or coupons. Coupons may comprise steel elements, possibly of different dimensions ( $5\text{--}25\text{ cm}^2$  are typical), that are normally connected to the pipeline and are used to measure instant OFF potentials without interrupting the cathodic protection current to the pipeline and which are increasingly used to monitor AC current collection/discharge from the pipeline. At these test points, portable  $\text{Cu}/\text{CuSO}_4$  (sat.) reference electrodes will be used in conjunction with the other

facilities to measure pipe/soil/electrode potentials at these fixed locations. These data may be plotted to assess time-dependent changes.

Cathodic protection monitoring on an offshore oil/gas drilling/production jacket with a galvanic anode cathodic protection system will typically comprise permanent  $\text{Ag}/\text{AgCl}$ /seawater reference electrodes, sometimes paired with  $\text{Zn}$ /seawater electrodes, at representative locations at different depths. The measured steel/seawater/electrode potentials may be carried back to measurement and data logging facilities in hard-wired cabling provisions or by acoustic transponders. These facilities enable time-dependent changes in the cathodic protection performance to be assessed, in particular during periods of storm conditions when divers and remotely operated vehicles cannot be deployed to collect survey data.

Cathodic protection monitoring on impressed current cathodic protection systems for steel in concrete will typically incorporate remote data logging of all individual cathodic protection zone transformer rectifier current and voltage outputs and steel/concrete/reference electrode and potential decay probe or pseudo reference electrode ON and instant OFF potential data and potential decay data collected over periods of typically 24 h and often  $> 72$  h from multiple permanent monitoring facilities embedded in the structure. These data will typically be collected every 3 months and plotted/trend analyzed to produce performance verification reports and system review reports.

For all of these applications (but less commonly on steel in concrete applications, as they are typically provided with many fixed monitoring points and surveying of long-term potential decay data can be difficult), in addition to these fixed point monitoring data sets regular steel/electrolyte/electrode potential surveys are undertaken to measure the adequacy of the cathodic protection performance over all or selected parts of the structure between the fixed monitoring locations.

It is the combination of fixed point monitoring and variable/moveable/portable point surveys that enables a cathodic protection system's performance to be properly assessed. Data from fixed points alone may be insufficient to demonstrate adequate performance.

#### **4.23.5.2 Fixed-Point Data Monitoring Devices**

Potential measurement instruments have been incorporated into what are best described as 'data

recording and management devices,' which enable relatively untrained staff to collect, typically pipe/soil potential data, from fixed test points to a pre-determined schedule. These units will prompt the operator to collect data from particular locations; some will display historical data from that location for immediate comparison in the field and will store the new data for later retrieval and processing. The units incorporate high-impedance digital voltmeters with an integral microprocessor for data and code entries into a solid-state memory. Data and codes are inputted by the use of an  $\alpha$ -numeric keyboard, although auxiliary data may also be inputted via a barcode reader. Barcodes may be used, for example, at test points to store identification data. The units contain real-time clocks and automatically store electronically entered data and time.

#### 4.23.5.3 Pipeline Cathodic Protection Survey Devices

More important has been the development of pipe/soil potential data loggers to undertake close interval pipeline surveys. These surveys are now accepted as the key performance verification tool for cathodic protection of pipelines and enable the measurement of pipe/soil/reference electrode potential at intervals typically of as little as 1 m. Measurements are recorded at each point of both the pipe/soil potential with the cathodic protection system 'ON,' together with the instantaneous OFF potential some 100–300 ms after the cathodic protection current is interrupted (switched 'OFF' at the DC side). This 'instantaneous OFF' potential significantly reduces the IR drop component present in the 'ON' potential measurement, although some element of IR error can remain due to equalizing currents flowing in, on, and off the pipeline.

Best practice systems measure ON and instant OFF potentials and simultaneous ON and instant OFF voltage gradients in what is known as combined digital close interval potential surveys (CIPS) and direct current voltage gradient (DCVG) surveys. These surveys enable not only an accurate measurement of pipe/soil potential at close intervals over the pipeline but also the location and an estimation of the size of coating defects. The data can also be used to calculate fully IR free pipe/soil potentials.

Typical combined CIPS and DCVG data loggers are based on the integration of multichannel high-impedance voltmeters with an electronic solid-state battery-backed memory. Measurements are taken with reference to one of the two parallel connected

'ski-stick' Cu/CuSO<sub>4</sub>(sat.) electrodes for each channel, and utilize a cable connection to a test point facility on the pipeline, **Figures 16 and 17**. The combined CIPS and DCVG surveys may collect the DC voltage gradient longitudinally over the pipeline at a distance of some 3–10 m or transversely to one or both sides of the pipeline. Mobile data logging units are provided with long lengths of light gauge insulated wire to provide the contact between the data logger and the test point and to provide a calibrated distance measurement, with an accuracy normally better than  $\pm 0.1\%$ . The data loggers are capable of time synchronization with additional units, which can be used either for static potential measurements at chosen locations or for 'switching' the impressed-current power sources in the 'ON'/'OFF' mode. The synchronization may be initially established by hard wire between the devices, or increasingly common is the use of the GPS satellite network, which allows accurate and repeat time synchronization and GPS location of the mobile survey position. It is possible to provide an accuracy of synchronization between all units of  $\pm 10$  ms over a 12-h period. Thus, overall, the mobile data logger combines ON and instant OFF pipe/soil potential measurement, ON and instant OFF voltage gradient measurement, with some systems a repeat ON and instant OFF pipe/soil potential measurement for quality audit purposes along with distance, sometimes GPS location, synchronized time together with any codes added to record geographic, topographic, or pipeline/cathodic protection features such as crossing points with other services and test points.

#### 4.23.5.4 Offshore Monitoring and Surveying

For the potential monitoring of offshore oil/gas fixed and mobile jackets and rigs, it is necessary to emplace numerous reference electrodes at all levels on the structure. The hard-wire connections from these electrodes together with, for example, similar connections from specially monitored sacrificial anodes are best terminated and displayed at the surface on 'mimic' display and recording/monitoring panels, **Figure 18**.

Monitoring steel/seawater/electrode potentials can be undertaken on offshore platforms and pipelines by the use of combined reference electrodes and acoustic transponders, thus minimizing the need to rely on vulnerable cabling. The installations comprise remote monitoring units, which may be interrogated by a surface unit. The monitoring units are typically each provided with an Ag/AgCl/

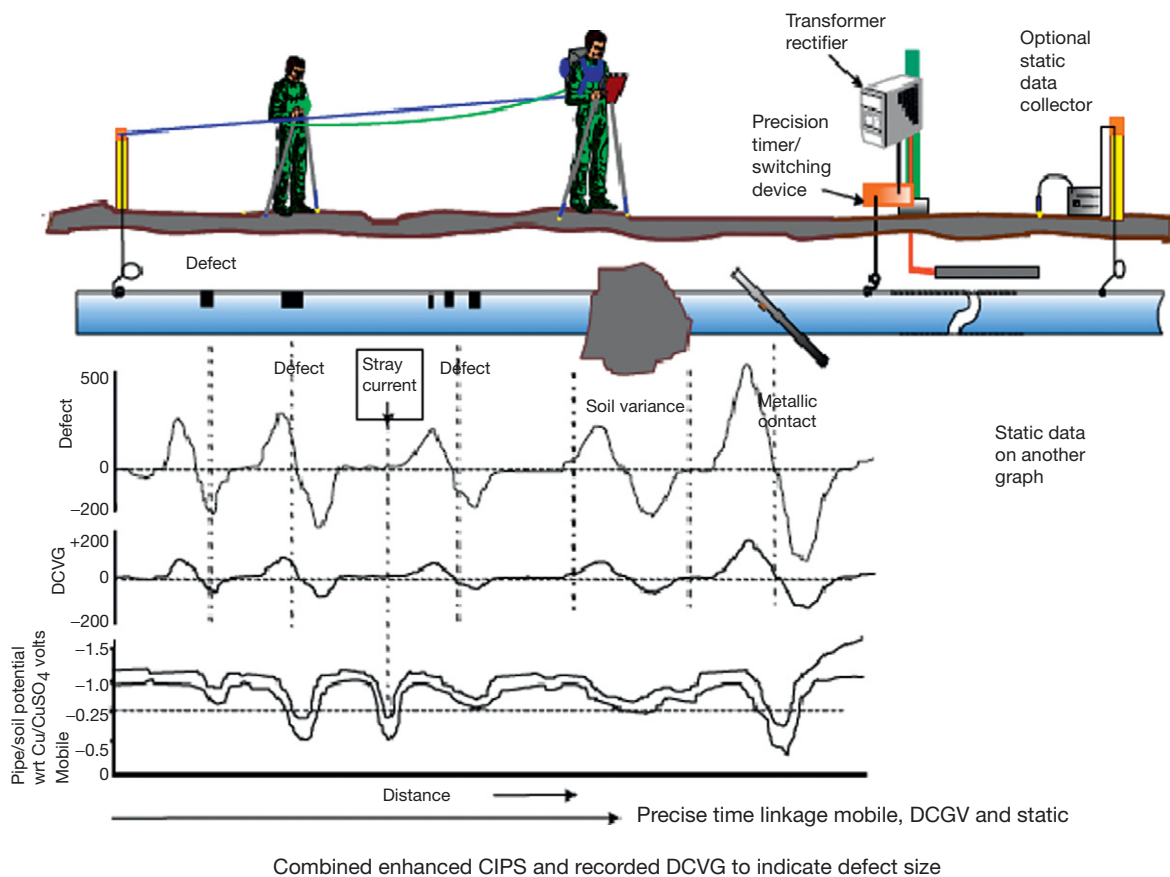


**Figure 16** Principles of combined CIPS and DCVG surveys.

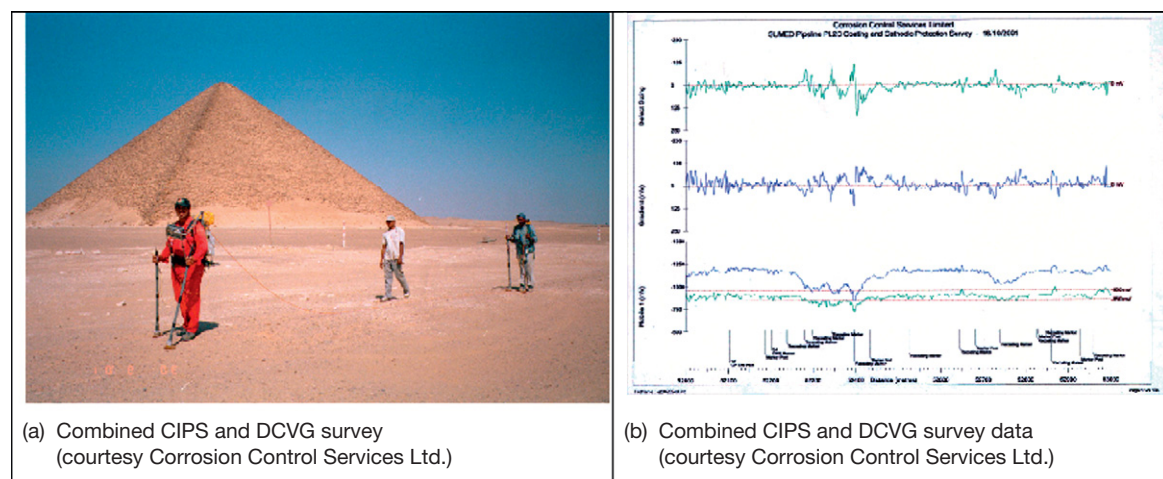


**Figure 17** Buried pipeline combined CIPS and DCVG surveys.

seawater reference electrode and a Zn/seawater electrode both connected to an electronic circuit, comprising two comparators, an encoder and a battery powered transponder, capable of emitting coded

acoustic pulses into the surrounding seawater over an ~10–25-year service-life. The structure connection is made through the watertight housing of the unit, which becomes electrically common to the



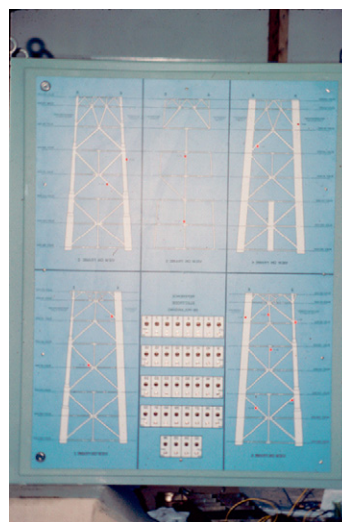
(a) Acoustic linked offshore monitoring system; dual electrode (courtesy Global Cathodic Protection Ltd.)



(b) Hard-wired offshore monitoring system; dual electrode (courtesy Global Cathodic Protection Ltd.)



(c) Monitored galvanic anodes; isolating joints in steel mounting cores. A shunt is in one per anode (courtesy Global Cathodic Protection Ltd.)



(d) Mimic panel for offshore CP monitoring system (courtesy Global Cathodic Protection Ltd.)

**Figure 18** Offshore structure monitoring equipment.

structure on installation. The surface unit, which may be located on the platform or a vessel, is used in conjunction with a surface transponder immersed in the sea to activate the data collecting/reference electrode units to transmit their data to the monitoring unit. The structure/seawater/electrode potential information is decoded for presentation on a digital display.

It is normally necessary to locate multiple reference electrodes/data collecting units on a structure. Thus, each unit will only transmit its information on receiving coded instructions. Surface units can commonly accommodate up to 80 different codes. The ability to interrogate and receive over any distance is

dependent upon the acoustic operation frequency. Relatively high frequencies are preferable, as they avoid problems of pulse reverberations and echoes from structural members. Typically, data can be transferred over a distance of 2 km. This type of acoustic unit gives accuracies in potential measurement of  $\pm 10$  mV.

To supplement the fixed point monitoring data, it is normal for fixed and mobile offshore platform jackets and rigs to be surveyed every 1–3 years using divers or, more commonly, remote-operated vehicles (ROVs). These deploy one or more reference electrodes and should have the facility to either/both connect to the structure being surveyed topside

(above the water by means of a cable connection) and to make local ('stab') connections to particular components of the facility that may not be in electrical connection with the main structure (risers, piles, riser clamps, etc.). These surveys, which need to be deployed offshore from diving or survey vessels, are extraordinarily expensive but are surprisingly often poorly specified, do not properly calibrate their electrodes or measuring devices, may even not properly confirm proper connection to the structure, and have even been known to simply measure remote potential data of the survey vessel and not the structure.

For offshore pipelines, continuous potential profile surveys have employed reference electrodes mounted on a 'tow-fish' designed for streamlined towing from a boat traveling along the line of the pipeline. Connection to the pipeline at the originating platform or the shore is maintained by means of a light gauge insulated coated copper or stainless steel wire, and a continuous measurement is recorded of pipe/seawater or seabed/electrode potential along with the position coordinates. Moving at a velocity of  $3\text{--}4\text{ ms}^{-1}$ , the tow-fish carries the reference electrode at a supposed uniform depth and proximity to the pipeline. Typically, in practice however, the reference cell is maintained between 5 and 30 m from the pipe. Thus, the accuracy of the recorded potential is affected by the increasing IR drop as the electrode is remote from the pipe (presenting data that imply better levels of protection than are real) and this technique can only be taken as being an approximate indication of cathodic protection performance.

More accurate pipeline surveys are delivered by using ROVs to accurately place the reference electrodes at known distance from the pipeline. The ROVs carry cameras and magnetometers to detect the pipeline location. Some ROVs have the capability to also 'stab' the pipeline or a galvanic anode fitted to the pipeline, such that local potentials can be measured either to confirm the pipe/sea/electrode potential measurement with the long wire connection to the pipeline (with the IR drop error within the pipe wall which may be significant) or to allow measurements with respect to a remote electrode to be 'calibrated' so that pipe/sea potentials can be estimated without contact to the pipeline.

#### 4.23.5.5 Current Density Devices

The measurement of current densities in the vicinity of a cathodically protected structure has been the subject of standards in continental Europe for many

years in respect of buried pipelines (DCVG as already discussed and the German Rührgas/DIN standard for 'intensive surveys') and has been widely used offshore. These measurements are undertaken by twin electrode devices either installed for stationary use or moved about the structure by diver or remote-controlled vehicle.

The voltage drop required to be measured in seawater to provide current density levels will inevitably be small, and therefore, the difference between the two reference electrodes should also be as small and as constant as possible. A current density sensor designed to overcome this possible source of error utilized two zinc electrodes fixed to a rotating shaft. The zinc electrodes are shielded from water flow by porous material in order to reduce the tendency toward fluctuations in the potentials of the electrodes. The sensor assembly provides two signals that are separated by a filter: a sine signal produced by the cell rotation and the signal due to the difference between the potentials of the two cells. Both these signals are amplified and recorded at the surface. Competing systems utilize more accurate Ag/AgCl/0.5 M KCl reference electrodes in a defined array. These data are equivalent to the DCVG data measured between two reference electrodes in buried pipeline surveys as already detailed. With computerized mathematical modeling using finite element analysis, calculated estimates may be made in respect of galvanic anode current outputs, predicted anode life, and the presence of defects in the structure coating.

#### Further Reading

- Morgan, J. H. *Cathodic Protection*, 2nd ed.; NACE: Houston, 1987, ISBN 0-915567-28-8.
- Peabody, A. W. *Peabody's Control of Pipeline Corrosion*, 2nd ed.; Bianchetti, R. L., Ed.; NACE: Houston, 2001, ISBN 1-57590-092-0.
- BS EN 13509 *Cathodic Protection Measurement Techniques*; CEN Brussels: BSI London, 2003.
- DIN 50 925. *Verification of the Effectiveness of the Cathodic Protection of Buried Structures*; DIN: Berlin, 1992.
- Ansuini, F. J.; Dimond, J. R. *Factors Affecting the Accuracy of Reference Electrodes, Materials Performance*; NACE: Houston, 1994; Vol. 33, Chapter 11, pp 14-17.
- Wyatt, B. S. *Advanced Systems of Overline Assessment of Coatings and Cathodic Protection*, UMIST Cathodic Protection Conference, UMIST, Manchester, 2003.
- Design and Operational Guidance on Cathodic Protection of Offshore Structures, Sub-Sea Installations and Pipelines*; The Marine Technology Directorate Ltd.: London, 1990, ISBN 1-870553-04-7.
- Taylor, J. R. *An Introduction to Error Analysis: The Study of Uncertainties in Physical Measurements*; University Science Books: Mill Valley, CA, 1999.



## 4.24 Anodic Protection

**P. Novák**

Department of Metals and Corrosion Engineering, Faculty of Chemical Technology, Institute of Chemical Technology, Prague, Technická 5, CZ 166 28 Prague 6, Czech Republic

© 2010 Elsevier B.V. All rights reserved.

---

<b>4.24.1</b>	<b>Introduction</b>	2858
<b>4.24.2</b>	<b>Passivity of Metallic Materials</b>	2860
<b>4.24.3</b>	<b>AP and Localized Forms of Corrosion</b>	2863
4.24.3.1	Pitting Corrosion	2863
4.24.3.2	Intergranular Corrosion	2863
4.24.3.3	Stress Corrosion Cracking	2864
4.24.3.4	Erosion–Corrosion	2864
<b>4.24.4</b>	<b>Anodically Protected Objects</b>	2865
4.24.4.1	The Basic Requirements for Protected Equipments	2865
4.24.4.2	Types of Protected Objects	2865
4.24.4.3	Throwing Power of AP	2866
4.24.4.4	Influence of the Level on the AP Effectiveness	2866
4.24.4.5	AP at Heat Transfer	2867
<b>4.24.5</b>	<b>Modes of AP</b>	2867
4.24.5.1	Start-Up Modes	2868
4.24.5.2	Operation Modes	2868
4.24.5.2.1	Potentiostatic polarization	2868
4.24.5.2.2	Polarization under constant terminal voltage	2869
4.24.5.2.3	Periodic polarization	2869
4.24.5.3	Emergency Modes, Failures, and Maintenance of AP System	2869
4.24.5.4	AP by Protectors	2871
<b>4.24.6</b>	<b>Elements of the AP System</b>	2871
4.24.6.1	Cathodes	2871
4.24.6.2	Reference Electrodes	2872
4.24.6.3	Electric Equipment	2874
<b>4.24.7</b>	<b>Environments Suitable for AP</b>	2875
4.24.7.1	Sulfuric Acid	2876
4.24.7.1.1	Carbon steel and cast iron	2876
4.24.7.1.2	Stainless steels and alloys	2878
4.24.7.1.3	Titanium	2880
4.24.7.2	Other Inorganic Acids	2881
4.24.7.3	Organic Acids	2882
4.24.7.4	Inorganic Salts	2883
4.24.7.4.1	Ammonium nitrate	2883
4.24.7.4.2	Sulfates, phosphates, chlorides, thiocyanates	2883
4.24.7.5	Aqueous Solution of Ammonia	2884
4.24.7.6	Hydroxides of Alkaline Metals	2884
4.24.7.7	Melts	2885
4.24.7.8	Electroless Nickel Plating Baths	2886
<b>4.24.8</b>	<b>Industrial Applications of AP</b>	2886
4.24.8.1	Sulfuric Acid Coolers Made of Stainless Steel	2886
4.24.8.2	Stainless Steel Equipment Operating in Environment Containing Sulfuric Acid	2887
4.24.8.3	Other Anodically Protected Equipment Made of Stainless Steels	2887
4.24.8.4	AP of Stainless Steel in Chemical (Electroless) Nickel Plating Bath	2887
4.24.8.5	Carbon Steel Storage Vessels for Concentrated Sulfuric Acid	2887

---

4.24.8.6	Carbon Steel Equipment for Alkaline Environments	2888
4.24.8.7	Cellulose Boilers and Other Equipment in Paper and Cellulose Industry	2888
4.24.8.8	Liquid Fertilizer Storage Tanks	2888
4.24.8.9	Equipment Made of Other Metallic Materials	2888
References		2888

## Glossary

**Activation energy** Characterizes the slope of temperature dependence of the reaction rate (expressed by, e.g., current density  $i$ ) in the coordinates of  $\log i - 1/T$  according to the Arrhenius equation.

**Anodic protection** Means an electrochemical protection (corrosion protection achieved by electrical control of corrosion potential) by increasing the potential to the stable passivity range.

**Breakdown potential** Means a potential, above which the passive metal dissolves by pitting.

**Free corrosion potential** Means a corrosion potential in the absence of external electrical current flowing to or from the metal surface.

**Passivation current density** Means a current density at the passivation potential.

**Passive current density** Means a current density within the passive range.

**Passivation potential** Means the lower limit of the passive range separating the active potential range from the passive one.

**Passive range** Means a potential range where passivity prevails.

**Protection potential** Means a potential value, at which the corrosion rate becomes acceptable.

**Transpassivation potential** Means a potential, above which a passive metal gets uniformly activated and dissolves as ions in a higher oxidation state.

## Abbreviations

**AP** Anodic protection

**b.p.** boiling point

**FeCr18Ni10(Mo)** Stainless steel with 18 wt% Cr, 10 wt% Ni alloyed with Mo

**m.p.** melting point

**SCC** Stress corrosion cracking

**SHE** Standard hydrogen electrode

## Symbols

$E_{\text{corr}}$  Free corrosion potential (V(SHE))

$E_{\text{prot}}$  Protection potential (V(SHE))

$E_a$  Activation energy ( $\text{kJ mol}^{-1}$ )

$E_b$  Breakdown potential (V(SHE))

$E_p$  Passivation potential (V(SHE))

$E_t$  Transpassivation potential (V(SHE))

$i_{\text{cc}}$  Passivation current density ( $\text{A m}^{-2}$ )

$i_p$  Passive current density ( $\text{A m}^{-2}$ )

$W$  Concentration (wt%)

$\Delta E$  Passive range (mV)

$\gamma$  Specific conductivity ( $\text{S m}^{-1}$ )

## 4.24.1 Introduction

The first practical use of anodic polarization for corrosion protection was demonstrated by an English author, Edeleanu,<sup>1</sup> in 1954. However, the principle of anodic protection (AP) had been mentioned in USA patents<sup>2</sup> already in 1945. Along with Edeleanu's work, another study on AP was published by Russian authors, Novakovsky and Levin.<sup>3</sup> The passivation by current was also proposed in the dissertation of Cernova (1954), published later with Tomasov<sup>4</sup> in 1955. The first commercial application of the industrial AP is alleged to have taken place in the USA in 1958.

More than 50 years after the first rational experiments to use anodic polarization for the deceleration of corrosion rate of passivable metals, due to the change in corrosion potential, the use of AP in industrial applications was established for corrosion systems such as carbon steel in sulfuric acid and alkaline environment, and stainless steel in sulfuric acid. This means that in cases where AP stood up to the competition of other corrosion protection methods despite its relative operation complexity and a certain degree of risk. Considering the perspective of an industrial user, AP possesses, besides indisputable advantages, a general disadvantage of the necessity to continuously monitor a due operation of the system, since any failure of the regulating circuits can lead to an extremely fast damage of the protected equipment. It is because the corrosion

rate of many corrosion systems, for which the AP is very effective in laboratory or semioperating conditions, is absolutely unacceptable outside the passive range, even for a short while. Such corrosion systems failed in long-term practical applications.

The essential difference between anodic and cathodic protection is in the degree of risk. The failure of cathodic protection is tolerable for a longer period of time and does not lead to a sudden damage of the protected equipment. Similar to the AP, the protective effect of cathodic protection is also frequently given by the formation of a passive layer. As for the cathodic protection, it is caused by composition changes in the superficial electrolyte during cathodic polarization of steel in neutral environment, where cathodic passivation occurs due to alkalization induced by the limited environment convection. Another difference between both types of corrosion protection lies in the aggressiveness of the corrosion environment. Cathodic protection is mostly used in relatively benign environments, frequently as a complementary protection method to coatings, whereas the AP is applied in a strongly aggressive environment as a fundamental protective measure. If we compare current needs per metallic surface unit that is in contact with the electrolyte, there is no substantial difference between the two types of electrochemical protection.

The AP is usually understood as a method consisting in the use of polarization to shift the protected metal from active to passive state, which is usually connected with high current demands to exceed the passivation potential. However, this understanding does not apply to corrosion systems with successful operation applications. Long-term success is typical for applications where a metal tends to passivate spontaneously in a given environment or where spontaneous passivation occurs under low temperatures and where anodic polarization in the passive range further increases the corrosion resistance of the metal. In such cases, there is no longer any need to use high currents for passivation, and many problems relating to the throwing power of AP and the danger of damages to shadowed spaces and attached equipment are thus eliminated. Another great advantage is that an accidental failure of the proper operation of the regulating circuits does not lead to a fast catastrophic increase of metal corrosion.

There are approximately 400 literature references dealing directly with AP, but most frequently, they only describe results from experimental laboratory experiments – long-term operation experience is

rather rare in the literature. Although the AP has become a standard part of technological sets, there are only few details available, because it is a part of business know-how.

The overview of industrial applications of AP was published by a German author Gräfen<sup>5</sup> in 1971. Monographs on AP summarizing most of the specialized literature were published in the 1970s and early 1980s. Rather extensive Russian chapter by Makarov<sup>6</sup> from 1974 refers to publications back to 1973 and the American monograph by Riggs and Locke<sup>7</sup> from 1981 has a bibliography dating back to 1790. The Russian work of Kuzub<sup>8</sup> from 1984 contains references back to 1981 and Novák's Czech monograph<sup>9</sup> from 1987 refers back to 1983. The overview of later Russian information can be found in summarizing articles by Agafonova and Makarov<sup>10</sup> of 1989 and Kuzub<sup>12</sup> of 1991. German experience with 30 years of industrial application of AP is summarized by the work of Gräfen *et al.*<sup>11</sup> dated 1991, Czech operation experience with 25 years of industrial application of AP is briefed upon in the study of Novak and Mokra<sup>13</sup> dated 2006.

Literature data from the past 25 years are rare and the number of relevant references is estimated in tens. There have been no breakthrough suggestions that would expand substantially the application area of AP. Another big problem of specialized literature is that the inclusion of many literature references under the entry of 'anodic protection' is unjustified. Many literature references under this entry fail to comply with the definition under the ISO 8044 terminology standard – "Anodic protection is electrochemical protection (corrosion protection achieved by electrical control of corrosion potential) by increasing the potential to a value corresponding to the stable passive state" – and deal generally with the use of passivation to protect metals or, for example, sacrificial anodes, and recently, also conductive polymers, the function of which is assumed to be similar to that of cathodic alloying elements or AP by protectors.

The main purpose of AP use is to ensure sufficient resistance of passivable metal against uniform and localized corrosion. The effectiveness of AP cannot be simply expressed by comparing corrosion rates of protected and unprotected materials, since the particular material cannot be used without AP under given conditions. The effectiveness must be assessed in light of the comparison of various corrosion protection alternatives that ensure technically acceptable resistance in the required construction arrangement.

Prolongation of a service life of anodically protected equipment does not have to be the biggest benefit, though the corrosion resistance is the basic qualification. The same applies to, for example, the requirement for high purity of a manufactured or stored product. The necessity of a pure environment is the reason why AP is applied to storage tanks for sulfuric acid.

Limitations of production technology caused by low corrosion resistance of the production equipment can be mitigated by AP application. Intensification of the sulfuric acid production by increasing the operating temperature could serve as a good example.

Very slow corrosion rate under AP enables better and long-term use of metallic materials, and sometimes it is possible to ensure sufficient service life of less costly materials, which limits the use of precious metallic and nonmetallic structure materials.

Thanks to AP, it is possible to construct devices with better parameters representing new ways of technological solutions, such as an effective consumption of heat energy, which, without AP, is wasted in the cooling process during the sulfuric acid production.<sup>14,33</sup> Coolers of concentrated sulfuric acid are nowadays the most effective application.

Secure and reliable operation of anodically protected equipment consists not only in minimum corrosion, but also in, for example, the prevention of undesirable evolution of hydrogen during the acid storage.

AP can be also used in nonaqueous environments, when their electrolytic conductivity is high, for example, in glass melts where heating electrodes can be thus protected from corrosion.

AP can also be applied in areas that are not related to corrosion, for example, in the prevention of undesirable deposition of nickel on the device walls during the electroless nickel plating process. In addition to the enhancement of work productivity, this application increases material savings.

#### 4.24.2 Passivity of Metallic Materials

The corrosion rate of most metals grows with the increasing environment oxidizing power (Figure 1(a)). Once the oxidizing power reaches a given threshold, a steep drop of the chemical reactivity of various metals can be observed. This phenomenon was first described more than two centuries ago, but the mankind had been encountering it in practice since the beginning of the use of nonnoble metals. This process

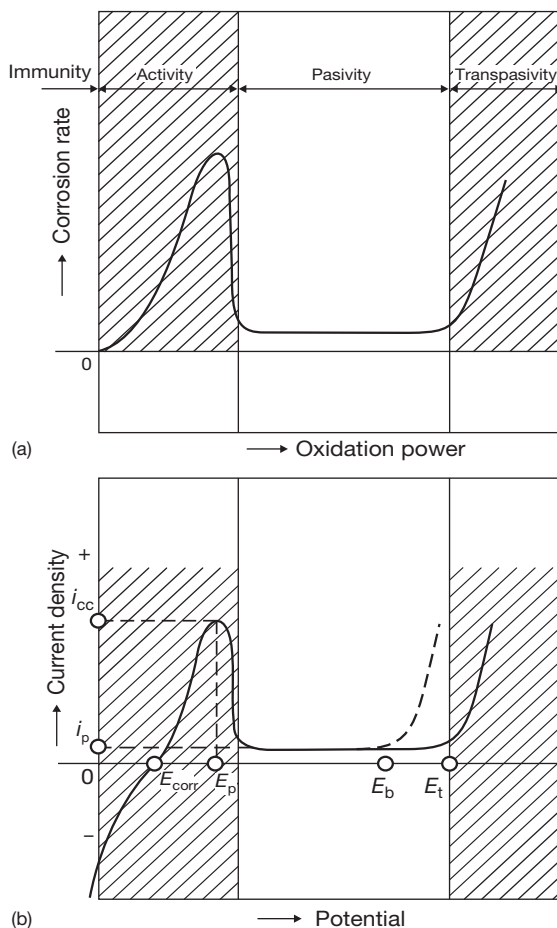


**Figure 1** (a) Dependence of passivable metal corrosion rate on the electrolyte oxidation power. (b) Polarization curve potential-current density ( $E_{corr}$  – free corrosion potential,  $E_p$  – passivation potential,  $E_b$  – breakdown potential,  $E_t$  – transpassivity potential,  $i_{cc}$  – passivation current density,  $i_p$  – passive current density).

is called passivity, and in the corrosion perspective, it is a totally positive process, which substantially slows down the course of electrochemical metal dissolution.

Passivability means the rate of difficultness of transforming a metal in a given environment from active to passive state. It is characterized by the values of passivation potential ( $E_p$ ) and passivation current density ( $i_{cc}$ ) (Figure 1(b)). Corrosion resistance in a passive state and the stability of the passive state are given by the values of passive current density and the width of a passive range ( $\Delta E$ ), that is, the potential difference between the potential of full passivity (is a bit more positive than the passivation potential) and the transpassivation ( $E_t$ ) or breakdown potential ( $E_b$ ). Factors affecting the passivability ( $E_p$ ,  $i_{cc}$ ) and the stability of

passivity ( $\Delta E$ ,  $i_p$ ) are almost identical though their influences can apply in different ways. Properties of a metal that apply to such case include composition, structure, internal stress, and superficial state. When it comes to the properties of environment, factors that matter are, particularly, composition, concentration, temperature, and flow. Construction, time of exposure, and polarization are other factors that apply.

Passive metals that we encounter the most enter the solution usually in the form of  $\text{Fe}^{3+}$ ,  $\text{Ni}^{2+}$ ,  $\text{Cr}^{3+}$ , and  $\text{Ti}^{4+}$  ions. According to the Faraday's law, it is possible to make the calculation of corrosion rate from the passive current values, on condition that the only reaction participating in the measured current is the anodic dissolution of the passive metal. In a gross estimate, the value of current density in ampere per square meter corresponds approximately to the corrosion rate in millimeter per year.

Considering the mechanisms, the processes leading to passivation of metal can be divided into three basic groups: passivation by influencing cathodic process, passivation by influencing anodic process, and passivation by changing an electrode potential by polarization from an external current source.

Passivation by influencing cathodic process can be achieved either by the addition of substances that get easily reduced at potentials in a passive range of the metal, or by the facilitation of the reduction of the environment elements by connecting the protected passivable metal to or alloying it with metals that have only small overvoltage of cathodic reaction and greater current density of such reaction. Even an extension of the area of the connected cathodic material can lead to passivation of passivable metal in an environment with sufficient oxidizing power. The oxidizing power of the environment is characterized by the oxidation–reduction potential on the one hand, and by the value of exchange or limiting current density on the other hand.

Passivation by influencing anodic process can be achieved by alloying with metals that shift the passivation potential in the negative direction or with metals that reduce anodic dissolution in active state, passivation current density. The passivation is also facilitated by the addition of substances (in the corrosion environment) that decelerate the anodic dissolution of the metal, or by the removal of corrosion stimulators from the solution.

The change of electrode potential by polarization from an external current source is a procedure enforcing a potential lying in an area of low corrosion rate to the metal, without any influence on the anodic or

cathodic dependence. If this is achieved by cathodic polarization (shifting the corrosion potential in a negative direction), we talk about cathodic protection; if it is achieved by anodic polarization (shifting the potential in a positive direction) into the passive range, we talk about AP.

Intervention in a corrosion system frequently affects both cathodic and anodic processes. Both procedures are exploitable to facilitate passivability in AP.

Several types of potential–current curves (**Figure 2(a)–(d)**) can be the result of oxidizing effect of the environment on the passivable metal:

Type-I – the oxidizing ability of the environment is low to passivate metal and retains it in the activity range. AP can be used for passivation (**Figure 2(a)**).

Type-II – the oxidizing ability of environment suffices to retain the metal in the passivity range, but is insufficient to passivate an active metal. The passive state is unstable. The AP can be used for passivation (**Figure 2(b)**).

Type-III – the oxidizing ability of the environment suffices for spontaneous passivation and the passive state is stable, if there is no occurrence of localized forms of corrosion. In case of threatening localized corrosion, AP can be used for positive potential shift to the range of stable passivity (**Figure 2(c)**).

Type-IV – the oxidizing ability of the environment is high; corrosion and pitting corrosion occur in the area of transpassivity or beyond the breakdown potential, respectively. Cathodic protection can be used for polarization into a stable passive range (**Figure 2(d)**).

Transition between particular types of dependencies in a specific corrosion system can be caused by temperature or a presence of small amounts of specific substances in the basic corrosion system.

As for the practical applications of AP, carbon steel, stainless steel, and titanium are the most important metallic materials. Passivability of iron alloys is influenced the most by chromium, which significantly facilitates passivation if the addition exceeds 12%. The mechanism of chromium effect can be explained by the shift of the passivation potential in the negative direction and the decrease of a passivation current density. Iron alloys containing chromium in excess of 12% (stainless steels) are resistant against corrosion in many environments just because of simple passivability. Nickel applies to iron–chromium alloys where it reduces passivation current



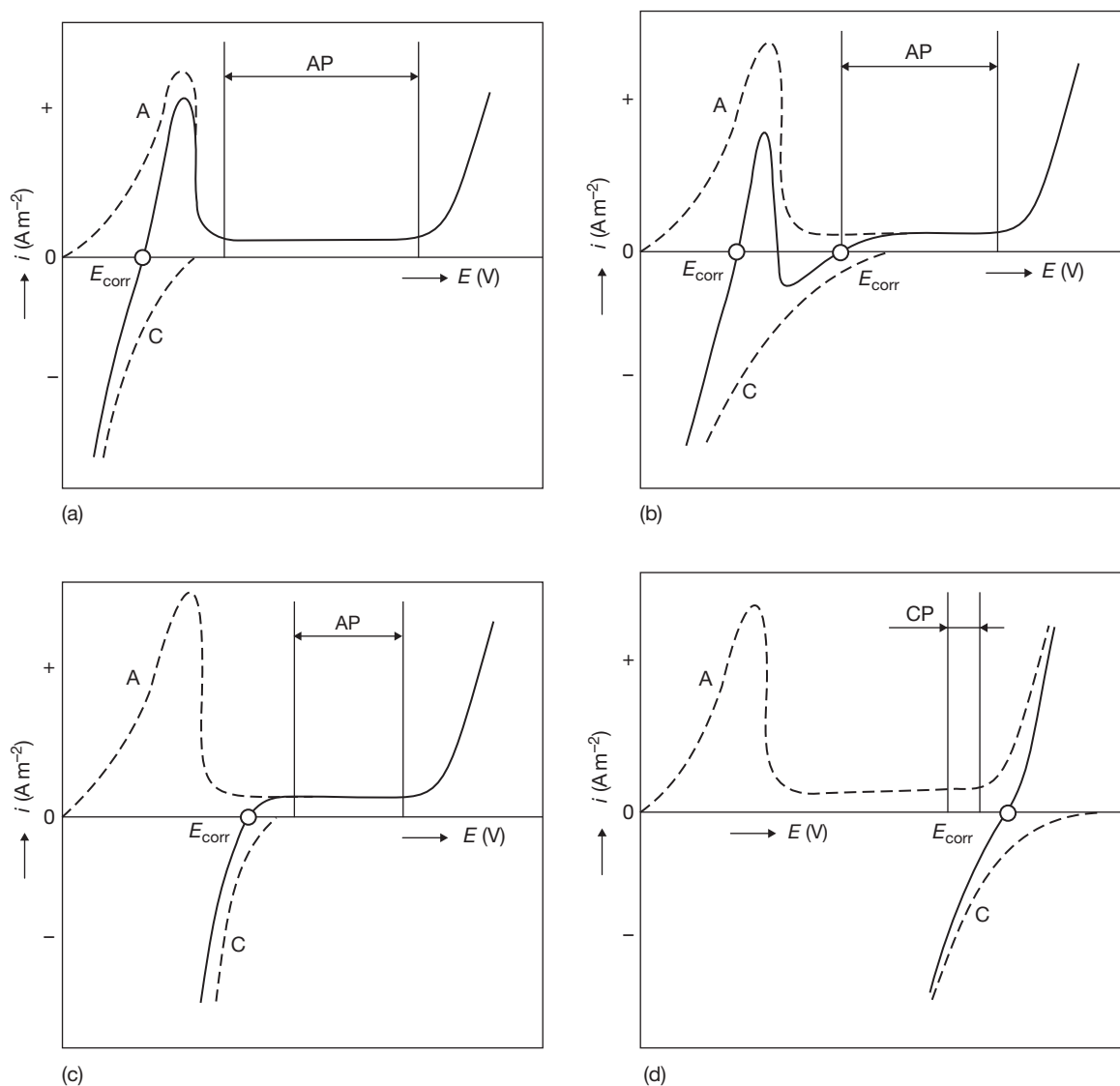


**Figure 2** Different types of potential–current cumulative curves as a result of electrolyte oxidizing effect on the passivable metal. (a) Type-I – the oxidizing ability of environment is low to passivate metal and retain it in the activity range. AP can be used for passivation. (b) Type-II – the oxidizing ability of environment suffices to retain the metal in the passivity range, but is insufficient to passivate an active metal. The passive state is unstable. The AP can be used for passivation. (c) Type-III – the oxidizing ability of environment suffices for spontaneous passivation and the passive state is stable if there is no occurrence of SCC. In case of threatening SCC, AP can be used for a positive potential shift to the range of stable passivity. (d) Type-IV – the oxidizing ability of environment is high; corrosion and pitting corrosion occur in the range of transpassivity or beyond the breakdown potential, respectively. Cathodic protection can be used for polarization into a stable passive range.

and corrosion in an active state. The addition of molybdenum increases the stability of a passive layer on stainless steels against crevice and pitting corrosion, in particular.

Titanium is also alloyed (by Al, Cr, Mo, Fe, V, Mn, Sn, Zr), but we can say that none of these elements substantially improves passivation properties of titanium. But alloying with cathodic alloying elements

such as platinum, palladium, etc., has the greatest influence on passivability of titanium and its alloys. These metals reduce the overvoltage of cathodic reaction. In commercial production, titanium is made with 0.2% of palladium. Cathodic alloying leads to autopassivability of metal and applies to stainless steels too (Cu in FeCrNiMo alloys). An autopassivable metal shows polarization curves of the Type-III

(see **Figure 2(c)**) and can be used for AP to eliminate crevice corrosion.

In addition to the composition, the structure of metal is another important factor. The structure can be influenced by both composition and heat or mechanical treatment of the material. The impact of structure applies the most to different chemical composition of structural phases, which causes great differences in passivability. The origination of structural inhomogeneity of metal leads to the reduction of a passive range and to the increase of characteristic currents. This usually results in the occurrence of localized forms of corrosion attack, such as intergranular or pitting corrosion. Materials with homogeneous structure are easier to passivate and show better resistance in a passive state.

Weld seams usually belong to the most critical parts of a majority of metallic equipment. Passivability of a weld seam or heat-affected areas is given, again, by the homogeneity of chemical composition. An inhomogeneous weld seam or chemical composition that fails to ensure sufficient passivability can lead to localized forms of corrosion or cause earlier corrosion of the weld seam material. However, for good passivability and resistance in the passive range, it is not necessary to have an identical chemical composition of the weld and the basic metal. The only prerequisite is to keep the corrosion or protection potential within the overlaps of passive ranges of all metals concerned.

The galvanic connection of passivable metal and a noble material that spontaneously achieves a potential in a passive range and at the surface of which reduction proceeds with lower overvoltage leads to passivation. Depending on the area of the cathodic material surface, the connection results either in spontaneous passivation (**Figure 2(c)**, curve type-III), or more frequently, in a curve of the type-II (**Figure 2(b)**), at which there are two corrosion potentials in both active and passive state. The corrosion rate accelerates in the activity. Noble metals, such as platinum, palladium, copper, silver, and in some environments, other metals, graphite, and also some electrically conductive metallic oxides can be used as a cathodic material.

#### 4.24.3 AP and Localized Forms of Corrosion

##### 4.24.3.1 Pitting Corrosion

Pitting corrosion is, under the conditions of anodic polarization by an external source of current, noted

for several peculiarities compared with the corrosion in a redox system at identical potential. Migration of aggressive ions to the places of intensive anodic dissolution is much more significant, because the polarization current concentrates on the top of the pit. Therefore, the pitting attack can be more frequent and more intensive on an anodically polarized surface than on the nonpolarized surface.

The fact that pitting corrosion is bound to the existence of a passive layer on the metal surface and that it is accelerated by anodic polarization represents a serious problem for AP in the presence of aggressive anions. The anions that cause damage to the passive layer, which subsequently leads to the pitting corrosion, are predominantly chlorides.

Growing concentration of an aggressive ion makes the breakdown potential shift in a negative direction, increases the passivation current, and narrows the stable passive range. In addition to the damage of the passive layer above the breakdown potential, aggressive anions cause the growth of current in the stable passivity, which somewhat decreases the protection effectiveness. Even the passivation of active surfaces is aggravated in such environments as a result of higher passivation current density. The proportion between activities of the basic nonaggressive anion and the aggressive anion that causes pitting significantly affects the width of a stable passive range. The growth of concentration of anions with weaker passivation effect ( $\text{OH}^-$ ,  $\text{SO}_4^{2-}$ ,  $\text{PO}_4^{3-}$ ) makes the breakdown potential shift in the positive direction. Laboratory data on limitations of AP given by its application in environments with aggressive ions are available predominantly for stainless steels in sulfuric acid solutions containing chlorides. Besides aggressive anions, corrosion environment can contain anions with inhibiting (passivating) effects as nitrates. In such a case, the stable passive range can exist at potentials more positive than the breakdown potential, and the AP can thus be used for protection against pitting corrosion. This phenomenon enables the AP to effectively prevent pitting corrosion of stainless steels in nitrate environments in the presence of chlorides.

##### 4.24.3.2 Intergranular Corrosion

The reason for intergranular corrosion is a structural and chemical inhomogeneity of metal at a grain boundary. Preferential dissolution of less-resistant metal and phases at the grain boundary leads to the intergranular propagation of corrosion. This type of

localized corrosion proves to be the most significant for heat-treated and welded stainless steels.

Considering the AP utilization in equipment made of stainless steels after sensitization-inducing heat treatment (e.g., after welding), it is essential to choose a protection potential within the range where active–passive or transpassive–passive type of intergranular corrosion is avoided. The reduction of the usable passive range from the side of activity is given by the degree of the grain boundary depletion; from the side of transpassivity, it is given by the number of phases in the structure that show low corrosion resistance at high oxidizing potentials. The optimal protection potential constraining intergranular corrosion of austenitic stainless steels, such as FeCr18Ni10 in sulfuric acid, ranges from 0.5 to 0.8 V(SHE). It was experimentally proved that sensitized samples, which are highly susceptible to strong intergranular corrosion, remain unattacked if protected by AP. Nevertheless, these findings are based on relatively short laboratory experiments, during which the passive–passive type of intergranular corrosion had no chance to show up more significantly. Therefore, it is necessary to ensure a sufficient resistance to intergranular corrosion not only by a due choice of the protection potential, but also by the appropriate metal composition and structure that weaken the susceptibility to passive–passive intergranular corrosion. The best solution is to use pure materials, that is, steels with a very low content of carbon, ensuring resistance against common types of intergranular corrosion. Practical experience shows that the AP can prevent intergranular corrosion, which occurs for example, in the vicinity of weld joints.

#### **4.24.3.3 Stress Corrosion Cracking**

The finding that stress corrosion cracking (SCC) is bound to the existence of a passive layer on the metal surface and that it is accelerated by anodic polarization led to a misleading generalization that the AP creates conditions for this type of localized corrosion attack.

Even the authors of first AP works were aware of the danger of SCC and observed experimentally the effect of the passive-range directed polarization on the susceptibility of mechanically stressed samples to SCC. This research was especially noted for demonstrating that the AP is a recommendable way to eliminate corrosion in environments where SCC occurs without polarization. It relates particularly to carbon, or low-alloyed steel in sodium or potassium

hydroxide or ammonium nitrate, in Kraft liquor, and stainless steel in sulfuric acid with a low content of chloride ions. For AP, it is important to know that SCC is bound to the potential range of instability of a passive layer, that is, to the bordering area between the active and passive state and to the range of a damaged passive layer at higher potentials.

It is possible to apply AP to prevent hydrogen embrittlement of iron alloys in the acrylonitrile synthesis environment, and the negative effect of hydrogen on carbon steel in the concentrated sulfuric acid environment can also be eliminated by the use of AP. Generally, anodic polarization can eliminate all kinds of negative effect of hydrogen, which evolves in electrolytes on metallic surfaces.

#### **4.24.3.4 Erosion–Corrosion**

Erosion–corrosion is a process accelerating corrosion by mechanic damage of metallic surface in an aggressive environment. Erosion can be caused by the presence of solid particles in a corrosion environment or by a turbulent flow of liquid. Erosion can be also caused by gas bubbles. Erosion of metallic superficial layer is typical for materials, the corrosion resistance of which is given by the effect of their passive layer. This fact implies other limitations of the use of AP in erosive environments. The biggest problem with corrosion–erosion attack is the level of an acceptable erosive effect of a liquid stream on the anodically protected surface, at which the corrosion rate would be technically acceptable.

Mechanical resistance and solubility of the forming passive layer are important features. If the layer is formed predominantly by salts, the drop of protective effect can be observed even in the area of the laminar liquid flow. It applies particularly to anodically protected carbon steel in concentrated sulfuric acid where corrosion is 2–10 times faster even at low liquid speeds. The flow occurring in the laminar area was detected to have no effect on the corrosion resistance of passive surface of materials, the protective layer of which consists of oxides (e.g., stainless steels).

The stability of the stainless steel passive state in flowing 93–99% acid strongly depends on a weak contamination of the acid by iron ions. The iron content and acid temperatures are the decisive factors of the potential–current type of dependency. (Figure 2) To achieve effective AP, the minimum concentration of iron ions in flowing sulfuric acid (98.5%) at 100 °C must be 7 ppm (solubility of ferric sulfate). The stability of the passive sulfate layer

during acid flow is conditioned by the origination of trivalent iron compounds, whose solubility in concentrated acid is approximately by two orders lower than that of bivalent iron compounds. Spontaneous passivation results in the formation of  $\text{Fe}^{2+}$  sulfate passive layer, while anodic polarization above 0.85 V(SHE) leads to the formation of  $\text{Fe}^{3+}$  sulfates. This is the reason why cooling systems with AP do not need any significant limitations of acid flow rate and why erosion–corrosion does not occur in them, in contrast to systems without AP.

The erosion effect of a corrosion environment can be caused by solid particles in the corrosion environment, penetrating the equipment as impurities or given by the technology (e.g., ore leaching), or formed during the production process (e.g., crystallization of salts). Besides the mechanical and chemical resistance of the passive layer is important repassivation rate, the decisive factors comprise the rate and the angle, at which the particles strike the surface, their hardness, weight, concentration, and shape. Erosion effect of solid particles in a liquid can preclude the application of AP even where allowed by the composition of the basic solution.

The reaction mixture prepared during fabrication of formic acid where crystalline ammonium sulfate is formed can serve as an example. Under model conditions corresponding to the operational mixing of the reaction mixture, the passive current density increases by three orders of magnitude compared with the state without mixing. In consequence, the corrosion rate grows to a technically unacceptable value.

#### 4.24.4 Anodically Protected Objects

##### 4.24.4.1 The Basic Requirements for Protected Equipments

Metallic parts of an object suitable for the AP must be made of passivable metal showing an acceptable corrosion rate in a passive state (usually  $<0.1 \text{ mm year}^{-1}$ ) under the operation conditions. This applies also to all other metallic parts that are conductively connected to the protected equipment and are placed in the same corrosion environment. The best thing would be that the whole equipment is made of a single material. If possible, the equipment should be free of any shadowed spaces that may cause difficulties, namely narrow crevices. Therefore, it is necessary that the equipment is welded rather than put together with joints where crevices may appear, for example, under sealing. For the same reason,

it is not advisable to anodically protect coated surfaces. Weld seams must be perfect, with no pores or cracks.

The inlet and outlet pipes, closing elements, and attached devices must be, if essential for the environment, protected against an undesirable side effect of AP. AP of functional shadowed spaces (e.g., inside the pipes, spaces between desks) is possible, if the throwing power is respected.

The construction of the equipment must allow installation of one or more reference cathodes in places that are suitable for reliable regulation of protection potential throughout the entire equipment.

Since AP is effective only below the electrolyte level, it is desirable to keep the protected surface completely immersed. Therefore, it is highly recommended to have completely filled, continuously working equipment where no spaces filled with gas could occur. Most equipment fails to live up to this requirement, and still, it is possible to have them effectively protected. However, it is necessary to take into consideration that the surface emerging above the electrolyte level is left unprotected. Therefore, it must be made sure that the stability of a passive state in the electrolyte film above the level was sufficient. If the level is stable for a longer period of time, its negative effect can be eliminated by construction adaptation.

If the level varies, it is advisable that a minimum level of liquid remains in the equipment so that electrolytic connection between the protected object, cathode, and reference electrode is ensured. If the equipment must be completely drained from time to time, the arrangement of operation technology must enable easy passivation when refilling the equipment. It is difficult to ensure reliable AP in equipment where a part of the metallic surface is in contact with the electrolyte film only. Moreover, the equipment construction should eliminate the erosive effect of a flowing environment as much as possible.

##### 4.24.4.2 Types of Protected Objects

Heat exchangers and storage vessels are the most frequently anodically protected objects, which we have long-term operation experience with. These objects are in continuous operation. However, discontinuously operating objects can be anodically protected as well, even those that are completely drained, for example, digesters, stripers, measuring vessels, and various reactors. Most of the equipment, except for storage and transportation vessels, operates under elevated temperatures, usually above  $100^\circ\text{C}$ ,

sometimes even more. AP in melts is feasible even at much higher temperatures.

The equipment, such as autoclaves or kraft digesters, operates under elevated pressure. In many objects, there is a rather small motion of liquid, but in heat exchangers, the flowing rate can reach units of meters per second.

The volume of protected objects ranges from units to 10 000 m<sup>3</sup> and the protected area from units to thousands square meter.

The remarkable thing about AP is that it proved useful even for very complicated equipment and it was used to protect the inner surface of pipes. The level of complexity of protected equipment is given particularly by conductivity and by the aggressiveness of the corrosion environment.

#### 4.24.4.3 Throwing Power of AP

If a metallic surface is polarized by an external source of current, the potential drops as a consequence of the current passage through electrolyte. This drop is especially significant with the polarization of active metal in shadowed areas, such as crevices filled with electrolyte or at pipe inlets to the protected equipment.

The protected surface is polarized to the protection potential in a passive range, and as getting deeper into the interior of the shadowed area, the potential drops from this value to more negative values. If the distance is long enough, it can reach the value of a free corrosion potential in active state. The potential interval between protection potential and free corrosion potential (in active state) comprises the potential, at which the corrosion rate of the metal equals the passivation current density, which substantially exceeds the corrosion rate at the free corrosion potential. This problem has been addressed by a number of authors.<sup>15,16</sup>

The current distribution within anodically protected equipment is described by mathematical relations referred to in literature.<sup>17–23</sup>

To express quantitatively the said dependencies, it is necessary to know the shape of the polarization curve, potential dependence of the corrosion rate, geometry of the shadowed area, and the conductivity of the electrolyte.

Relations were derived not only for the throwing power and formation of crevice corrosion under the conditions of anodic polarization, but also for the anodic passivation at the liquid level, for the passivation of continuously filled vessels and to calculate

the parameters of measures to be taken to eliminate the undesirable effects of AP, resulting from the limited throwing power.

Generally, the throwing power of AP applied to completely passivated surfaces (which is the prerequisite of proper operation) is extraordinarily high compared with the throwing power of cathodic protection applied to the same geometry.

Considering the throwing power of AP of complicated constructions containing shadowed areas of critical dimensions, it is more advisable to apply a permanent potentiostatic polarization that secures safer operation and enables protection of more complicated equipment with a minimum number of cathodes.

If the length of the piping connected to the protected equipment exceeds critical dimensions and cannot thus be passivated by current from the cathode placed in the protected equipment, it is important to take measures eliminating undesirable corrosion of the attached device. If it is feasible to ensure reliable electric insulation of the protected equipment from grounded parts, the attached devices will be preserved from the negative effect of AP. However, most objects are grounded, and thus, conductively interconnected. There are a number of compatible procedures that can reduce the negative effect of AP, such as the passivation by auxiliary cathodes, passivation in an environment with better oxidizing power, passivation in a less aggressive environment (concentration, temperature, and composition), passivation at high positive potentials, and the use of an insulation section and a section with an intentionally induced potential drop.<sup>24</sup>

To prevent crevice corrosion under the conditions of anodic polarization, it is essential to avoid the formation of crevices by a suitable construction of the equipment, widen the crevice where necessary, or use self-passivating materials in places where crevices are unavoidable, or materials that show a low passivation current density and a narrow activity range in the given environment.

#### 4.24.4.4 Influence of the Level on the AP Effectiveness

The effect of AP is limited to the surface below the electrolyte level and practically ends at the electrolyte–atmosphere interface. Similar to crevices, the AP cannot ensure passivation of the metal by a thin layer of electrolyte (a film of electrolyte on walls) due to the ohmic drop during the passage of passivation



current. If the surface below the level is passivated and the environment aggressiveness does not lead to a spontaneous activation, the undesirable effect of the level does not show up. Nevertheless, if the passive state stability above the level is low or lowered by the effect of atmosphere (humidity, gases with activating effect), corrosion may grow similar to the shadowed areas.

The problem with the liquid level is even more significant if the surface coming through the level transfers heat. That is the case of heating coils, desks, and incompletely filled heat exchangers. The most effective measure is to prevent the level to get in contact with the protected surface, which can be achieved by the complete filling of the equipment, the removal of spaces filled with gas, or by placing the entire protected surface below the liquid level. The negative effect of the liquid level is caused not only by the film of electrolyte on the walls, but also by accumulated deposits. This happens if the liquid level is in the same position for a long period of time, the electrolyte is not changed or mixed, and the corrosion products have low solubility in the environment. In practice, however, the liquid level fluctuates and is mixed regularly, and the electrolyte gets changed.

Relations derived for the continuous passivation of an active surface above the liquid level is noted in particular for the start-up modes.<sup>25,26</sup>

When the anodically protected equipment with activated surface above the liquid level is filled continuously, current is predominantly given by the ratios in the film of a corrosion environment above the level, where the potential gradually changes from the free corrosion potential in activity to the protection potential in passivity. The current is essentially independent of the mass of the electrolyte in the equipment (the size of immersed surface), which indicates that the main portion of the passivation current passes in the film of the corrosion environment closely below the liquid level in the active section that forms, similar to the shadowed spaces, as a consequence of the ohmic drop in the electrolyte level. Changing the electrolyte level in operating conditions, where metallic surface below the liquid level activates spontaneously, is mostly unacceptable for the use of AP.

#### 4.24.4.5 AP at Heat Transfer

At present, sulfuric acid coolers and other types of heat-transferring devices are the most widespread

anodically protected objects. The principle of most of such objects is that the protected surface has different temperatures in different places. Since temperature substantially affects the passivation properties and the passive state stability, the nonisothermal surface represents a serious heterogeneity, considering AP. It complicates, in particular, the estimate of currents for AP of the equipment on the grounds of laboratory tests.

Model tests showed that the stability of a passive state on a nonisothermal surface is given by the warmest part, which tends to activate the most. Even the current demands for the protection of the warmest parts are higher than for the colder ones. It must be taken into account when constructing cathodes that they should be placed preferentially in the vicinity of the warmest places. Current demands in colder places of the surface are lower.

Heat-transferring devices should not be anodically protected in conditions where the corrosion environment is boiling. Boiling may constrain the electrolytic connection between the protected surface and the corrosion environment, which may cause a situation in which the surface is not protected by current for some time. Emerging bubbles may induce the formation of crevices and undesirable spaces filled with gas. The boiling of the film may result in a complete loss of the electrolytic connection. The surface can thus get excessively overheated and activated, and the corrosion rate in passivity can grow tremendously. Overheating of the surface above the liquid level induces activation and excessive corrosion close above the liquid level. Generally said, neither the heat transfer nor the formation of nonisothermal conditions on the immersed surface reduces the effectiveness of the AP, but boiling is undesirable for the protected surface.

#### 4.24.5 Modes of AP

Anodically protected objects can be operated in three basic modes. The passivation takes place in a start-up mode, in which the protected surface potential shifts from the free corrosion potential to the protection potential in the passive range and current or the frequency of current switching is stabilized. The AP itself is applied under the conditions of an operation mode when the potential of the object is maintained at the required level in the passive range. Security, even during the main power supply and potential controller failure, is ensured by an emergency mode

that temporarily prevents the potential from shifting to the active range.

#### 4.24.5.1 Start-Up Modes

The metallic surface of new unfilled devices is mostly covered with an oxide layer formed in air. Although this layer exerts certain protective effects, it depends on the aggressiveness of the operation electrolyte, if it resists after the first filling. The resistance of this layer is usually insufficient and fits only for low-aggressive environments.

To passivate an initially active surface, a minimum value of direct current is needed, which is expressed by the value of passivation current density. The order of magnitude  $i_{cc}$  for common corrosion systems ranges from 10 to 1000 A m<sup>-2</sup>. It is thus obvious that it is usually impossible to passivate the entire protected surface by current under the operation conditions, because it would require very strong current sources. That is why it is necessary to apply the following procedures, which decrease the passivation currents to acceptable values (up to 100 A per object): passivation with continuous filling of the object, passivation in a less aggressive solution, passivation after the prior chemical passivation of the surface.

Passivation with continuous filling is a common procedure used in the start-up mode. Problems relating to the passivation with continuous filling deal with the placing of a cathode, because AP can work properly only if at least partly immersed, which happens, for example, in vertical cylindrical vessels, only after the entire bottom is covered; high currents are needed then for passivation. The solution is based on the modification of the vessel's bottom to a conical one or a spherical one with a pit where the end of the electrode encroaches.

Continuous filling is often combined with the reduction of the operation environment aggressiveness. The reduction of aggressiveness can be achieved by a drop of temperature, change of concentration of the aggressive element, change of hydrodynamic conditions, or addition of passivating substances. Environment parameters (temperature, concentration, flowing rate) are continuously modified during the start-up mode to correspond to the values of operation without draining the equipment content.

The reduction of temperature is important, particularly for equipment operating under elevated temperatures. This procedure is very effective, since the dependence between passivation current and temperature is exponential. Temperature reduction

can eventually result in self-passivability of the metallic material.

In the start-up mode, metallic surface can be passivated by direct current without any automatic regulation of potential. The reference electrode then has a controlling function only. The power supply is controlled manually according to the potential of the passivated device.

It is not advisable to apply automatically controlled start-up mode for equipment operating continuously. It only makes sense with discontinuous productions with periodical passivation cycles.

To reduce the needs for passivation current, it is also advisable to place the cathode asymmetrically in the vicinity of the protected surface. The nearest place to the cathode passivates at first, and the rest of the surface follows. If required by conditions, auxiliary cathodes must be used, for example, for passivation of a storage vessel bottom, since the current needs to identify the minimum surface of the cathode.

Time of the start-up mode depends on the corrosion environment aggressiveness against the specific metallic material and on the source power used for the operation mode, which the protected equipment will be migrated to. The start-up mode takes hours, at the maximum, tens of hours.

The time of the actual passivation is relatively short, but the stabilization of the passive current is slow. It is necessary to wait until the current on the filled equipment drops, under the operation conditions, below the maximum output values of the automatically regulated source. During the start-up mode of AP of complicated equipment, requirements given by the protection throwing power must be taken into consideration, and the appropriate start-up mode procedure must be selected accordingly.

#### 4.24.5.2 Operation Modes

Once the start-up mode, which usually consists in a one-off action, is over, the protected object is reconnected to regulating circuits that ensure permanent protection process. The methods of polarization that might be used to ensure operation modes of AP can be divided into types continuous, discontinuous, and combined.

##### 4.24.5.2.1 Potentiostatic polarization

Polarization is referred to as potentiostatic if the potential of the protected surface is maintained on the specific value by direct current. This type of

polarization uses a three-electrode connection (protected object, cathode, reference electrode) where the potential difference between the protected surface and the reference electrode is permanently compared to the voltage corresponding to the required value of protection potential, and the differences are compensated by the current passing between the protected surface and the cathode. A regulator that ensures this joint regulation of the protected surface potential is called a potentiostat.

The protected object must be connected to the regulator by two wires (measuring and power), because the voltage, which is added to the value of the actual potential of the equipment, drops in the protected object power supply during the current passage. In operation, the regulating and power parts of the potentiostat are sometimes divided in two devices and the power part is usually placed close to the protected object.

For potentiostatic polarization, potential is the optional quantity and protection current is the depending quantity.

#### **4.24.5.2.2 Polarization under constant terminal voltage**

Polarization under constant voltage used to be common for cathodic protection, but for AP, it is useful only if the corrosion systems lack transpassivity. This procedure can be used in practice for the AP of titanium in the sulfuric acid environment. The anodic polarization from a DC source was also proposed as a method of reduction of carbon steel corrosion in liquid fertilizer containing ammonium nitrate in Lawrence's and Eagle's patents<sup>2</sup> from 1945, which is the first documented proposal of the AP. In addition to the AP of titanium, at present, the polarization under constant terminal voltage is important, especially for starting and emergency modes.

#### **4.24.5.2.3 Periodic polarization**

Periodic polarization by direct current is a method that brings certain simplifications to the AP. Similarly, to the potentiostatic polarization, the connection is effected through three electrodes (four wires). It applies the principle that the potential of an anodically protected metal, once the polarization current is switched off, shifts automatically to the negative direction. As soon as the lower potential threshold is reached, the current is switched on again in the preset value. It passes through the circuit as long as the protected surface potential achieves the upper threshold of the required potential interval. The

periodical switching of the current in the cathode-protected surface circuit is ensured by the regulator controlled by the potential balance between the reference electrode and the protected surface.

Periodical polarization offers a lot of advantages, because it does not require the construction of power potentiostats and the source powers can be easily changed according to the size of the protected object. The periodical polarization has been used since the beginning of a wider industrial application of AP; nevertheless, nowadays it is being left for potentiostatic polarization.

#### **4.24.5.3 Emergency Modes, Failures, and Maintenance of AP System**

The AP requires a reliable regulation of the protected surface potential within a given potential interval, outside of which very intensive corrosion occurs. To avoid such corrosion under both threshold operation conditions and the main regulating circuit outage, it is essential to establish an emergency mode, regular controlling, and maintenance of the entire anodically protected device. To properly select the emergency mode, which includes not only the polarization method but also all restoration measures, we have to consider all causes of the emergency.

To make the emergency mode ensure proper protection against the consequences of failures, it must be complemented with regular preventive checkups and have the protected equipment maintained by qualified personnel. Reference electrodes (testing by an independent electrode), the resistance of conductors, operation of regulators, sources, signalization, and the state of corrosion attack of critical places of the protected object should be subjected to regular checkups as well.

Maintenance should consist in timely replacement of those AP system parts that show signs of lower reliability, for example, the reference electrode when the potential oscillates outside the permitted interval. It is also essential to renew those parts that get worn by the operation, for example, electrodes and joints in the circuit.

The basic requirement for a reliable operation of AP is a timely signalization that alerts the personnel that the conditions of the operation mode are no longer complied with. The signalization can be complemented with an automatic action that decreases the aggressiveness of the corrosion environment (e.g., temperature

reduction). The signalization should mean that the equipment operates in an emergency mode or that the emergency mode is needed. Failures that do not directly jeopardize the reliability of the operation and are thus not a reason for transition to the emergency mode should not be connected to this signalization; they should be removed by regular maintenance.

The emergency mode should ensure the operation of the AP system for a period of time necessary to remove the failure or to finish the production operation so as to avoid any production losses. After transition to the emergency mode, the personnel must distinguish the level of urgency, since some states may mean that even the emergency mode cannot prevent vast corrosion – in such a case, the equipment must be immediately shut down. Usually the operation can continue for several, even, tens of hours in the emergency mode. However, it is not advisable to opt for emergency modes that ensure long-term operation, because the personnel is thus not forced to promptly remove the failure that caused the transition from the operation mode to the emergency mode.

Since the AP-suitable corrosion systems' time to spontaneous activation must be at least 10–15 min (1 h is better), short-time source outage should not matter.

To enhance operation safety, back-up elements of the AP system are usually installed on the protected equipment. It concerns especially the reference electrodes that are installed in the minimum number of three – the operating one and the other two as back-up or controlling ones. The difference (higher than permitted) between the operating and back-up electrode usually causes the transition to the emergency mode. The installation of more reference electrodes also enables simple identification of the defective electrode and the exchange of the operating electrode. The back-up regulating circuit is also available, which consists of an independent regulator (or a source) and a back-up reference electrode. Therefore, it is possible to connect two potentiostats in parallel (**Figure 3**), and a periodic regulator in parallel to a potentiostat.

The transition from the operation mode to the emergency mode should be automatic.

Operation guidelines must be provided to each AP installation. It should solve specific problems of the equipment and give unambiguous directions for the personnel regarding controlling and maintenance as well as the identification of failures.

At present, AP systems are computerized. The computer records the operation parameters of the protected equipment. It enables the personnel to



**Figure 3** Main and back-up sources (potentiostats) for six anodically protected objects.

identify the cause of a failure and define the process of restoration to the normal state.

#### 4.24.5.4 AP by Protectors

The source of current maintaining the potential of the protected surface in a passive range can be, in principle, formed directly in the protected equipment, if connected with a cathodic material (protector) in which reduction reactions proceed spontaneously. The AP by protectors is based on the principle of passivation by connection to cathodic materials. These requirements can be complied with by materials that can be divided into sacrificed and inert ones.

The sacrificed materials include oxide protectors composed of metal oxides that release electrons when dissolved in a corrosion environment, in particular, oxides of iron ( $\text{Fe}_2\text{O}_3$ ) and manganese ( $\text{MnO}_2$ ). Oxide protectors can be considered analogous to sacrificed anodes of cathodic protection, since they provide the necessary current by its dissolution, but of the opposite polarity.

Most of other materials that could be used as protectors provide the essential current by a reduction reaction of the solution components. It is given by the fact that cathodic reactions proceed on the surface of the protector (Pt, graphite) with lower overvoltage than on a passive metal.

Titanium is the best material for AP by protector, because it usually has a low passive current density and the passivation potential is substantially negative.

Protectors are not used in practice, since oxide protectors are consumed by spontaneous dissolution and must be thus frequently replaced or supplemented. Moreover, we cannot be satisfied with the existing fixation of protectors, because they have insufficient contact with the inside of the protected equipment. Inert protectors lose their activity continuously and their surface must be retreated by anodic polarization.

#### 4.24.6 Elements of the AP System

The AP system consists of a protected object, cathodes, reference electrodes, and electric equipment (a regulated source of direct current and connection cables) (Figure 4).

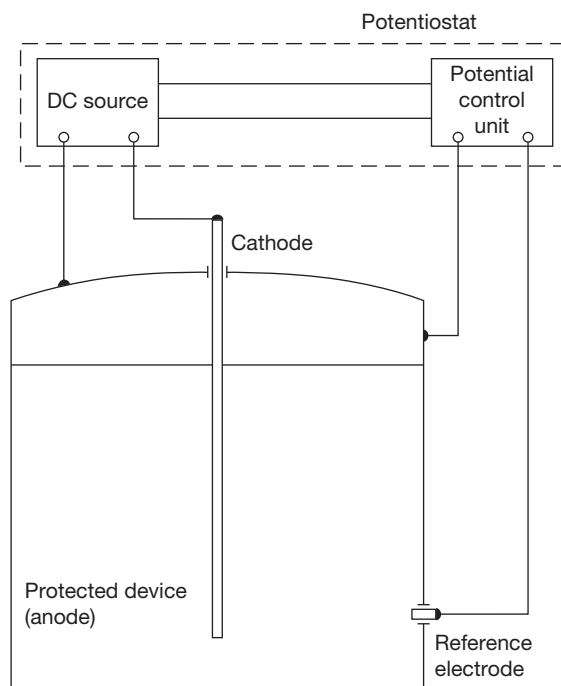


**Figure 4** Diagram of anodically protected apparatus.

#### 4.24.6.1 Cathodes

The passage of current polarizing an anodically protected metallic surface is ensured by an auxiliary electrode connected to a negative pole of the direct current source. During the passage of direct current, a reduction reaction of environment components proceeds at the cathode and the cathode partly corrodes. The distribution of the current on the protected surface must be ensured by a suitable construction of the cathode, and corrosion resistance of the cathode must be ensured by selecting a suitable material, protection mode, and the construction as well. The cathode material must have a sufficient service life. It must be recognized for its suitable mechanical properties, good electric conductivity, low cathodic reaction overvoltage, and an acceptable price. During the cathode polarization, it is theoretically possible to achieve a state of immunity where no corrosion occurs. This, however, requires very high current density, which, considering the uniform distribution of the protection current, is undesirable. High current densities can cause problems with the formation of nonconductive deposits or hydrogen entry in a metal. It is thus much more common to use the cathode under conditions of suppressed



anodic dissolution, along with the continuous polarization. The cathode construction depends, in particular, on the construction of the protected equipment. The requirement to have cathodes usable for both passivation by current in the start-up mode and the operation mode is unrealistic in many cases, because it depends on the specific corrosion system (passivation currents, environment conductivity) and on the technology regime applied within the protected equipment (batch, continuous, liquid-level fluctuation). The necessity to construct cathodes for operation modes, while considering the throwing power, is overrated, given high conductivity of electrolytes applied successfully for AP. The throwing power of AP is very high on passive equipment. Given that the conductivity of corrosion environments suitable for AP often exceeds  $10 \text{ S m}^{-1}$  and the current densities do not achieve  $0.1 \text{ A m}^{-2}$ , there is no essential difference, for example, for sulfuric acid coolers, between polarization of surface in the distance of 1 mm and meters from the cathode. The main ohmic resistance in the system is exerted by the passive layer. The smallest distance between the cathode and the protected surface is given by the risk of a galvanic contact at operation vibrations of the protected equipment, and the greatest distance is given by the acceptable deviation from the protection potential, which can rise in many cases up to 100 mV.

Different types of stainless steels, nickel alloys, nickel, carbon steel, silicon casts iron, graphite, lead, copper, platinum, platinum plated metals, tungsten, and others are materials used for cathodes, depending on the corrosion environment.

In case of the most frequent applications of AP on sulfuric acid coolers, cathodes are usually placed in parallel to the exchanger axis. Even the cathodes placed transversally through an unbound bundle of pipes proved to be very successful (Figure 5). The advantage of this solution is that short weld-free cathodes can be used. The length of cathodes equals the exchanger's outside diameter plus the allowance for sealing and electric contact.

Another advantage of the transversal arrangement is that it is necessary to seal only the opening for a cathode at the outside shell. With this arrangement, it is possible to refit the sealing during operation without any risk of acid leakage to the cooling water in case of sealing failure. This construction solution also eliminates intensified corrosion of cathodes going through baffle plates. Practical experience shows that the service life of cathodes made of common austenitic steel at temperatures of acid up to  $90^\circ\text{C}$  is  $\sim 3$  years and

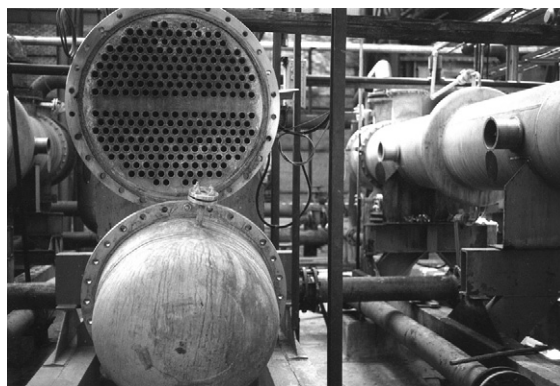


**Figure 5** Horizontal shell and tube coolers with spacing of tube bank. Rod stainless steel cathodes are placed transversally through an unbound bundle of pipes.

they are simply replaceable. Cathodes made of nickel alloys are recommendable for higher temperatures and lower concentrations of acid.

In vertical storage vessels, it is advisable to use cathodes in the vessel axis so as to avoid galvanic contact with the bottom, however, to secure operation even with the minimum volume of liquid in the vessel.

The size, number, and location of cathodes are individual according to the type of the protected object. The potential distribution over the protected surface is approximately calculated according to mathematical relations derived for different regimes.<sup>17–23</sup> Nevertheless, it must be taken into consideration that, in case of the industrial AP applications that stood up the competition of other anticorrosion measures, the protected surface predominantly passivates spontaneously and the conditions of current distribution at passivation thus do not have to be addressed.

#### 4.24.6.2 Reference Electrodes

To make the AP system work well, it is necessary to keep the potential of the entire protected surface within the potential passivity range where corrosion rate is technically acceptable. The reference electrode, which is contained as a permanent part in all existing AP systems, acts as a potential measurement sensor. Bad function of a reference electrode can cause critical damage to the protected equipment, that is why reliable types of electrodes are used and more electrodes are placed in an angle piece of protected equipment. Electrodes act as sensors, which the direct current source is attached to as well as sensors for back-up and controlling systems. The reference electrodes

must prove to be stable enough under operation, and to have a minimum service life of 1 year. Bad function of a reference electrode may cause that a potential of the protected equipment lies outside the required passive range. Any shift to both positive and negative directions may lead to the growth of corrosion rate – in some cases, by several orders of magnitude, the consequence of which is damage of the equipment.

Any electrode that is difficult to polarize and the potential of which does not significantly change in time or in environment may serve as a reference electrode to measure potential in an electrolytically conductive environment. The requirement of the operating reference electrode potential oscillation by  $\pm 30$  mV suffices for most anodically protected equipments.

In practice, reference electrodes are loaded with current that corresponds to the input resistance of a potential controller and the potential difference between the reference electrode and protected equipment. Polarizability of a reference electrode can be decreased by increasing its electrochemically active surface. Change of the electrode potential in time is given by the fluctuation of temperature and composition of the electrolyte solution. Temperature dependence of the potential of most reference electrodes can be disregarded to the extent of minor fluctuation of operation temperatures.

Electrodes that can be used as reference electrodes are generally distinguished to electrodes of the first and the second kind. On electrodes of the first kind, the reaction of charge transfer proceeds directly between the electrolyte components or between the electrode and an electrolyte component. Electrodes of the second kind exchange the charge through an insoluble salt or oxide.

The existence of equilibrium is supposed for the said kinds of electrodes, but the electrochemical protection may work even with reference electrodes that are in a stationary state in which mixed potential is established. These are electrodes upon which corrosion or metal deposition proceeds spontaneously, or electrodes to which the potential is enforced by a passage of direct current.

The majority of reference electrodes used or usable for AP belong to electrodes of the second kind, such as calomel electrode, silver chloride electrode, and mercury sulfate electrode for sulfuric acid environments, and mercury oxide electrode for alkaline environments (**Figure 6**).

The equilibrium on oxide electrodes of all kinds is affected by the concentration of  $\text{OH}^-$  or  $\text{H}^+$  ions, that is, by the pH of the solution. The advantage

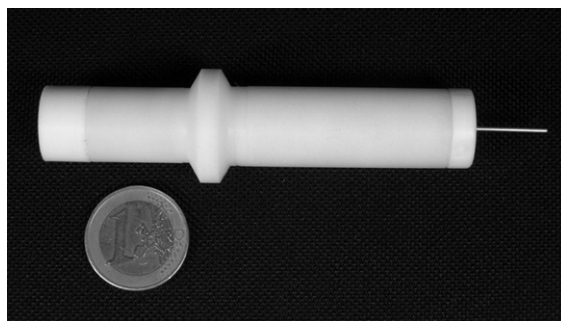


**Figure 6** Reference electrodes filled with working medium are used for sulfuric acid and sodium hydroxide applications.

of these electrodes is that they can be used (except for the mercury oxide electrode) directly in the corrosion environment without the necessity to separate electrolyte. The disadvantage is that they have a lower potential reproducibility, which is given by the effect of other oxidation–reduction reactions of the corrosion environment components. A number of oxidized metals were tested for AP in terms of their use as a reference electrode. Pt, Au, Rh, Ir, Hg, Sb, and Mo oxide electrodes are used preferentially.

A nickel electrode in the environment of electrodeless nickel bath is one of the nonequilibrium electrodes upon which a stationary reaction proceeds and which can be used as a reference electrode. The electrodes that maintain their potential as a consequence of a corrosion reaction include, for example, bismuth in liquid fertilizers containing ammonium nitrate, carbon steel, and lead in the solution of ammonium hydrogencarbonate, and silicon cast iron in hot concentrated sulfuric acid. Also, other metals can be used in the environment where the acceptable corrosion rate below  $1 \text{ mm year}^{-1}$  secures sufficient potential stability along with the acceptable service life of the electrode. This type of electrode can be used only if there is no risk that the electrode suddenly turns from the active to the passive state and vice versa. Metal depositions must be regularly removed from the surface of nonequilibrium electrodes and corroding electrodes must be replaced with new ones. The overview of reference electrodes used in operation is given in **Table 1**.

Construction solution of the reference electrode or the whole potential sensor is applied according to the specific type of equipment and conditions given by the corrosion environment. With the potential sensor, we understand not only the electrode itself, comprising the filling and the electrode casing, but

**Table 1** Reference electrodes for industrial anodic protection

<i>Electrode</i>	<i>Environment</i>
Calomel (Hg/Hg <sub>2</sub> Cl <sub>2</sub> )	Sulfuric acid Ammonium nitrate–urea Alkaline solutions Universal
Mercurousulfate (Hg/Hg <sub>2</sub> SO <sub>4</sub> )	Sulfuric acid Hydroxylammoniumsulfate
Silver chloride (Ag/AgCl)	Sulfuric acid Ammonium nitrate–urea Universal
Silver sulfide (Ag/Ag <sub>2</sub> S)	Kraft liquor
Platinum Pt/PtO <sub>2</sub>	Sulfuric acid Phosphoric acid Mixed fertilizers
Gold (Au/Au <sub>2</sub> O)	Sulfuric acid Phosphoric acid
Molybdenum (Mo/MoO <sub>3</sub> )	Sodium hydroxide Sulfuric acid Phosphoric acid
Bismuth (Bi)	Ammonia environment
Nickel (Ni)	Electroless nickeling Sodium hydroxide Mixed fertilizers
Silicon (Si)	Mixed fertilizers
Chromium (Cr)	Mixed fertilizers
Passive austenitic steel FeCr18Ni10	Ammonium nitrate Sodium hydroxide
Silicon iron	Sulfuric acid
Mercurous (Hg/HgO)	Sodium hydroxide
Mercurousphosphate (Hg/ Hg <sub>3</sub> PO <sub>4</sub> )	Phosphoric acid
Wolfram (W/WO <sub>3</sub> )	Sulfuric acid
Graphite	Ammonia environment Ammonium nitrate–urea

also fittings for the electrode installation and connection to the regulating circuit.

Reference electrodes are distinguished to immersing, level, pressure, and external electrodes according to how they are attached to the equipment. Pressure electrodes are most frequently used in completely filled equipment and below the liquid level in pressure-free equipment. The advantage is that the electrode–circuit connection and the shielded wires are located outside the aggressive environment. On the other hand, the necessity to have reliable pressure plugs and the impossibility to replace electrodes without the equipment shut-down are disadvantageous. These electrodes should be able to operate in all positions.

A reference electrode is located in a place with a permanent electrolytical connection with the protected surface close to that surface. The best thing is to place the operating reference electrode close to

the surface that is the least accessible for current from the cathode, or in places with critical temperatures or concentrations.

#### 4.24.6.3 Electric Equipment

Direct current sources that are connected with conductors to the AP system components and the protected equipment are used in AP to polarize the protected surface to the potential within the passivity range. Other complementary electric devices are connected to control the operation and enhance reliability. The connection and the function of the AP electric devices vary according to the selected modes. Considering the technological development, many connections publicized in literature can be assumed as outdated.

A power-supplied rectifier is usually the source of direct current for AP. For AP, the final rectified voltage does not have to show low oscillation, since it was detected that filtration has no effect on the protection effectiveness. Automatically controlled sources operating in the mode of potentiostatic polarization are used the most frequently for AP ([Figure 3](#)).

The installed output per one AP unit mostly does not exceed 5 kW. The energetic needs of the AP system are negligible, the operational requirements for current are below 0.1 A m<sup>-2</sup> (mostly <10 A), when the supply voltage is lower than 10 V. The price of the regulation device does not depend on the size of the protected object.

The automatic compensation of ohmic drop is desirable under operation conditions only in environments with low specific conductivity approximating 1 S m<sup>-1</sup>. If the reference electrode is placed in the vicinity of the protected surface, the ohmic drop is mostly not remarkable.

Some operation electric devices used for AP of objects with fluctuating liquid level have additional circuits that switch off the AP system automatically after emersion of the operating reference electrode, or cathode.

Cabling, with which the protected equipment, cathodes, and reference electrodes are interconnected with the source, regulator, and controlling devices, can be distinguished to power and measuring. Power cabling supplies the protection current to the protected equipment–source–cathode circuit and it must be rated to the values required by AP of the specific object.

The perspective development of electric devices used for AP is seen in the field of digital

technologies. Controlling and operation will be secured by a computer or a microprocessor. Operation data of both the AP system and the protected equipment are continuously recorded and make it thus possible to identify the causes of potential deviations from the operation mode of the AP system.

#### 4.24.7 Environments Suitable for AP

AP is used with passivable metals in electrolyte, having a sufficient width of a stable passive range (minimum 300 mV) and a low corrosion rate (usually  $<0.1 \text{ mm year}^{-1}$ ), where localized forms of corrosion do not occur at the protection potential. The minimum environmental erosion incidence and stable chemical composition are other important factors. Moreover, the environment must not be decomposed at the protection potential. The time to activation, after the polarization current is switched off, must be also sufficiently long (minimum 15–30 min).

Most literature data on metal passivation in aggressive environments are based on the results of laboratory experiments performed under conditions very difficult to be compared. This chapter summarizes, in general, the literature data in order to identify, considering significant corrosion systems, important parameters of optimal protection, and location of iso-corrosion lines (curves connecting conditions under which the rate of uniform corrosion achieves a given level) in the concentration–corrosion environment temperature graphs. The objective assessment is complicated by different testing times, different levels of corrosion environment pollution, and the dependence of the optimal protection potential on concentration and temperature of the corrosion environment.

Corrosion diagrams shown in this Chapter must be treated as orientation diagrams displaying zones with corrosion rate below  $0.1 \text{ mm year}^{-1}$  with or without AP. Zones with corrosion rate below  $0.1 \text{ mm year}^{-1}$  under AP are distinguished in two parts. In the first part, there is a high probability that the corrosion rate will dwell below this threshold, in the other so-called indefinite zone, the probability is  $\sim 50\%$ .

In addition to corrosion rates, potential and current levels, another parameter vital for the AP is the corrosion environment conductivity. The conductivity acts as the decisive factor of the AP feasibility, it affects the throwing power, essential voltage of a direct current source, construction of a cathode, and the location of a reference electrode.

The conductivity of electrolytes changes within wide thresholds, depending on the composition, concentration, and temperature. Specific conductivity  $\gamma$  ( $\text{S m}^{-1}$ ), that is, the reciprocal value of resistivity  $\rho$  ( $\Omega \text{ m}$ ), is very important for AP. The concentration dependence of specific conductivity ( $\gamma$ ) for some strong electrolytes at  $25^\circ\text{C}$  is shown in **Figure 7**.

If the specific conductivity exceeds  $10 \text{ S m}^{-1}$ , no special measures are essential to be taken to ensure uniform distribution of current on the protected passivated surface, except for cases when the surface is shadowed (e.g., in crevices or in narrow pipes).

With specific conductivity ranging from 1 to  $10 \text{ S m}^{-1}$ , the AP is feasible, if more cathodes are used and their surface is located in approximately the same distance from all parts of the protected surface.

With specific conductivity below  $1 \text{ S m}^{-1}$ , the electrolyte resistance in a usual construction arrangement is comparable with the resistance exerted by the passive layer during the current passage. Even the voltage of a source relates, in particular, to the resistance of electrolyte between a cathode and an anode and rises up to tens of volts. After that, it is impossible to ensure a uniform distribution of protective current. The need for power supply grows and the safe source voltage is exceeded. Therefore, AP is not recommendable for specific conductivity below  $1 \text{ S m}^{-1}$ . Specific conductivity of electrolytes grows along with the temperature by 2% to 1 K.

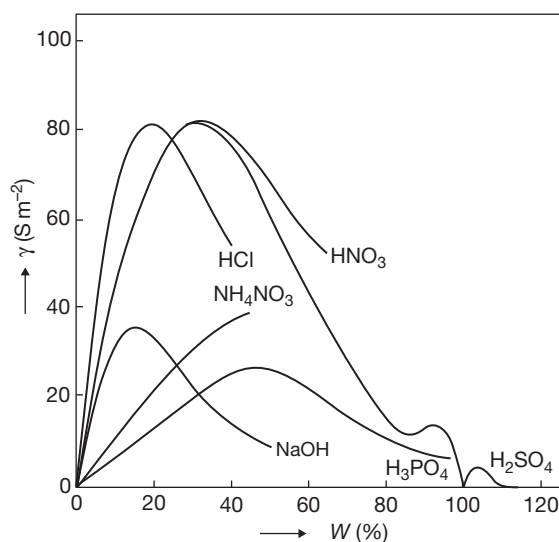


**Figure 7** Concentration dependence of specific conductivity ( $\gamma$ ) on various strong electrolytes at  $25^\circ\text{C}$ .

#### 4.24.7.1 Sulfuric Acid

A good deal of literature references deal with this environment, because it belongs among the most widespread in industrial conditions. Specific conductivity of sulfuric acid solutions with concentration of 2–96% exceeds  $10 \text{ S m}^{-1}$  under normal temperature. For concentrations above 96%, the specific conductivity decreases and hits the minimum at the concentration of 99.75% ( $0.8 \text{ S m}^{-1}$ ). Then it grows again and the oleum under normal temperature can reach a specific conductivity of  $5 \text{ S m}^{-1}$ .

##### 4.24.7.1.1 Carbon steel and cast iron

Technically acceptable corrosion rate of unprotected carbon steel can be allowed for only in an acid with a concentration over 70% at temperatures not exceeding  $20\text{--}25^\circ\text{C}$ . Moreover, the corrosion resistance of steel remarkably drops with the motion of the corrosion environment. Carbon steel behavior in sulfuric acid during anodic polarization was observed under laboratory conditions by many authors within the entire concentration interval and also at elevated temperatures.

The potential–current polarization curves for carbon steels in sulfuric acid solutions can be divided into three types, characterizing a specific concentration interval. For low concentrations to those of 60 or 65%, the polarization curve of carbon steel in the sulfuric acid environment has a shape characterized by curve 1 in **Figure 8**. On the curve above the corrosion potential, there is a very wide range of activity with high currents. Passivation can be observed within a wide range of potentials where the current considerably oscillates. The passive range is limited by a transpassivation potential at which oxygen starts to evolve. Curve 2 in **Figure 8** is characteristic of steel in acid with a concentration of 65–77%. The activity starts to be less significant and a second maximum appears in the passive range, and is followed by a range of low passive currents as far as the transpassivation potential, at which oxygen starts to evolve (similar to the previous case). Both curve 1 and curve 2 are the curves of the type-I in **Figure 2(a)**. The third type of a curve is typical for steel in acid with concentration beyond 78%, including oleum. The initial progress is analogous to curve 2, that is, insignificant or no activity (curves of type-II or III in **Figure 2(b) and 2(c)**), the passive range is not limited by the transpassivation potential (up to  $4 \text{ V(SHE)}$ ).

Sulfuric acid with a concentration up to 60% is noted for extremely high passivation current densities

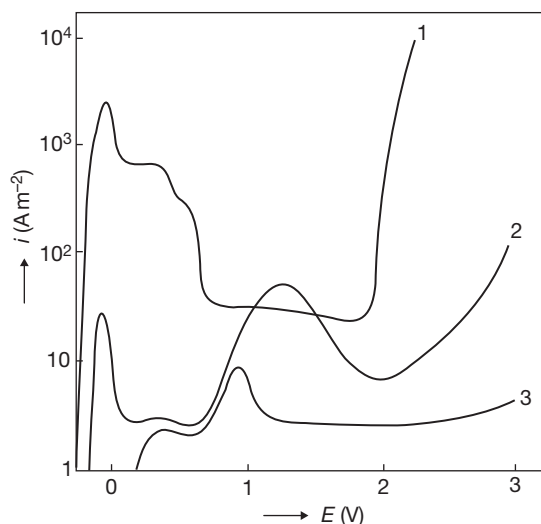


**Figure 8** Potentiodynamic curves of mild steel in sulfuric acid at  $25^\circ\text{C}$ . 1–25%, 2–70%, 3–90%.

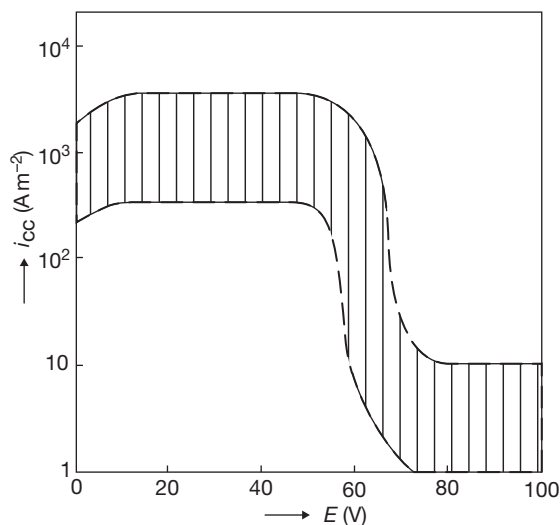


**Figure 9** Dependence of mild steel passivation current density ( $i_{cc}$ ) on the sulfuric acid concentration (wt%) at ambient temperature.

$i_{cc}$  (asi  $10^3 \text{ A m}^{-2}$ ) (**Figure 9**) and high current densities in a passive range  $i_p$  (**Figure 10**) even at normal temperatures. The time to activation is usually very short, once the polarization is switched off.

The use of AP is feasible only for concentrations over 70% where active range practically vanishes, since the steel shows a better tendency to spontaneous passivation.  $i_{cc}$  values drop exponentially with time to  $1\text{--}10 \text{ A m}^{-2}$  and even the passive current densities reduce significantly (below  $0.1 \text{ A m}^{-2}$ ).



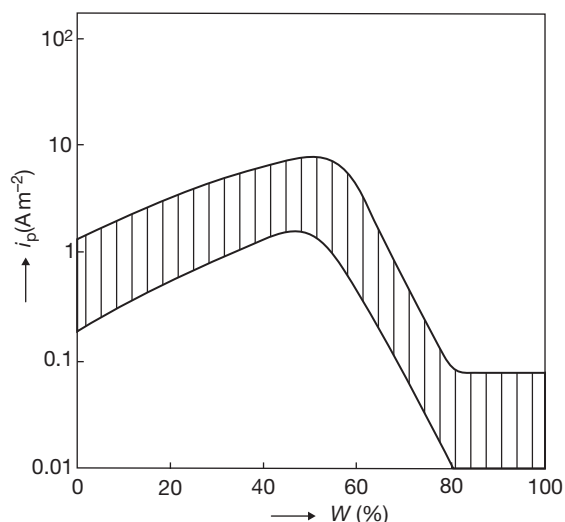


**Figure 10** Dependence of mild steel passive current density ( $i_p$ ) on the sulfuric acid concentration (wt%) at ambient temperature.

Carbon steel behavior, depending on the acid concentrations, markedly changes according to the composition and higher stability of the forming passive layer. Within the range of potentials from 0 to 0.7 V, the steel resistance is based only on the layers composed of iron compounds in the oxidation state II; the stability of these layer is rather small in acid with concentrations up to 70%. At higher concentrations, the solubility of ferrous sulfate in acid diminishes. At higher potentials (over 0.7 V(SHE)), we can observe oxidation of compounds in the oxidation state II and formation of an oxide layer with iron in the oxidation state III, which is relatively resistant within the whole interval of acid concentrations. Beside the oxide layer, it is the ferric sulfate layer that applies at higher acid concentrations (over 70–80%).

The oxidation of  $\text{Fe}^{2+}$  to  $\text{Fe}^{3+}$  in compounds forming the protective layer leads to the second maximum on potentiodynamically obtained potential–current curves (curves 2 and 3 in [Figure 8](#)). The steel is passive practically from the potential of 0.2 V(SHE) and the second maximum has nothing to do with activity of the steel. It also explains the great influence of flow on the corrosion of anodically protected steel. The flow aggravates the passivation process within the whole concentration interval by eroding the primary salt layer that precedes the formation of the oxide layer.

Concentration dependencies of characteristic current densities  $i_{cc}$ ,  $i_p$  and the potential  $E_p$ ,  $E_t$  are depicted

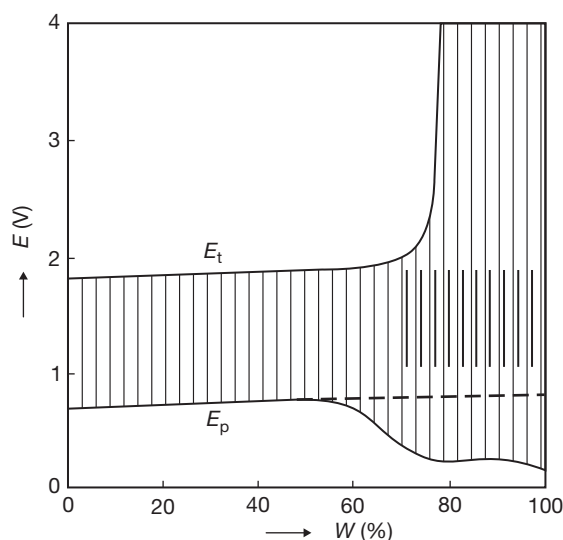


**Figure 11** Dependence of mild steel passive range on the sulfuric acid concentration (wt%) at ambient temperature (close hatching – potential range suitable for AP).

in [Figures 9–11](#). The scattering of current values in [Figures 9 and 10](#) is caused by different methodology and different hydrodynamic testing conditions.

Passivation current density ( $i_{cc}$ ) values ([Figure 9](#)) lying within a concentration range over 70% depend, a lot, on time and are low, since the salt layer of ferrous sulfate forms spontaneously on the surface, and so it is disputable whether the notion ‘passivation current density’ is used correctly.

The dependence of a passive current density  $i_p$  on concentration is more complicated. Even the optimal protection potential within the sulfate layer ( $\text{Fe}^{2+}$ ) depends on the acid concentration, and therefore, there are big discrepancies in the results presented by different authors. The relatively highest  $i_p$  and thus the corrosion rate values range within the interval of 75–100% for 95%  $\text{H}_2\text{SO}_4$ , minimum  $i_p$  and corrosion values can be observed at 80–90% and at 98–99%. The flow of acid can easily increase both the passive current and corrosion two to five times, and in the stability range of the sulfate layer ( $\text{Fe}^{2+}$ ), even ten times.

At concentrations up to 60%, the passive range ([Figure 11](#)) is limited by potentials of 0.7 and 1.9 V; with the increase of acid concentration, it expands to both the negative side (the range of salt passivity of ferrous sulfate) and the positive side, because the overvoltage of oxygen evolution reaction is growing. With concentrations above 78%, oxygen does not evolve even at 4 V(SHE). Hatching of the range of

potentials suitable for AP is more dense and lies within 1.0 and 1.8 V(SHE). At higher concentrations ( $\sim 96\%$ ), the best resistance is achieved within the potential range of 0.9–1.2 V(SHE).

Corrosion resistance data of the anodically protected carbon steel are generalized in a corrosion graph (Figure 12). The graph makes it obvious that if we need to have the corrosion rate below  $0.1 \text{ mm year}^{-1}$ , we can use carbon steel only at high concentrations of sulfuric acid and up to temperatures of  $\sim 40\text{--}50^\circ\text{C}$ . The zone of probability defines the aggressiveness maximum within the exploitable concentration interval (at 95% concentration).

Since the unprotected steel, due to its low price, can be used to a limited extent even at temperatures when AP is effective, it makes sense to compare corrosion rates with and without protection. This proportion depends very much on concentration, temperature, and probably, also the flow. Mostly it varies between 10 and 100.

Results of tests of carbon steel AP were applied in operation conditions of storage of both pure concentrated sulfuric acid and oleum.

#### 4.24.7.1.2 Stainless steels and alloys

Stainless steels and alloys on iron, chromium, and nickel basis are the fundamental construction material for heavily aggressive environments where AP can be applied. The properties of stainless steels can be modified by alloying, which gave rise to a number of types of stainless steels. The FeCr18Ni10(Mo) austenitic steels are of the greatest importance. Highly alloyed steels and alloys used for the construction of chemical plants are usually materials with sufficient resistance to corrosion, and mostly, it is not necessary to protect them anodically. AP allows their replacement by less costly chromium–nickel stainless steels.

Unprotected FeCr18Ni10 steels in sulfuric acid solutions have corrosion rate below  $0.1 \text{ mm year}^{-1}$  at normal temperature with concentration intervals below 10% and over 78%; FeCr18Ni10Mo steels below 20% and over 75%. The resistance drops with increasing temperature and at  $50^\circ\text{C}$ , the FeCr18Ni10 unprotected steels can only be used at concentrations below 2%; the FeCr18Ni10Mo steel below 10% and over 90%. At temperatures over  $70^\circ\text{C}$ , unprotected steels of this type are inapplicable in sulfuric acid up to 99% (Figure 13).

Corrosion resistance of chrome–nickel stainless steels largely depends on the content of oxidizing substances (e.g., oxygen, ferric ions) and the presence

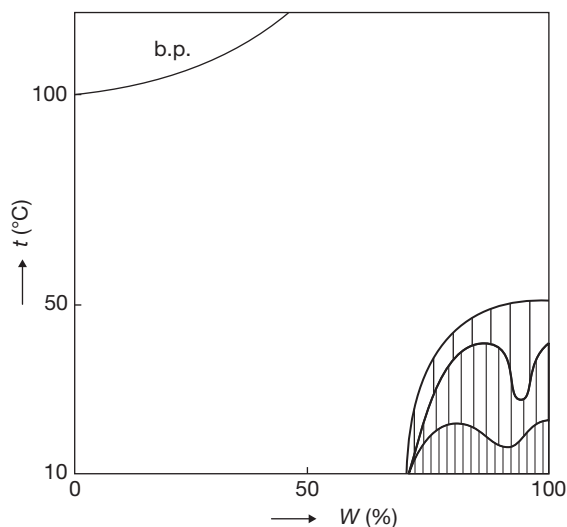


**Figure 12** Range of corrosion rates below  $0.1 \text{ mm year}^{-1}$  for mild steel in sulfuric acid (closest hatching – without AP, thin hatching – with AP).

of activating substances (e.g., chloride ions) in the solution. Localized forms of corrosion (e.g., pitting, intergranular, corrosion cracking) can occur, depending on the composition and structure of the metal as well as on the presence of other substances in the sulfuric acid solution and its temperature.

The potential–current polarization curves for chromium–nickel austenitic steels have a typical shape at concentrations up to 80% (Type-I in Figure 2(a)), where significant activity is followed by a passive range limited by the transpassivation potential, above which the metal dissolves and oxygen evolves.

At a concentration over 80%, the activity range is gradually suppressed, the passive range is interrupted with a significant maximum at  $\sim 1.7 \text{ V}$ , beyond which there is a range of low currents. For concentrations exceeding 93%, the drop of current is permanent (to  $4 \text{ V(SHE)}$ ), for concentrations from 80% to 93%, it grows again in the range above  $2.3 \text{ V(SHE)}$ .

Although the passive layer is formed exclusively by oxides in the range of concentrations up to 80%, the sulfate layer applies even at higher concentrations and mitigates the oxygen evolution and anodic dissolution.

The passive range is determined by the passivation and transpassivation potential, see Figure 14. In fact, the passive range at higher potentials (over  $1.5 \text{ V(SHE)}$ ) has no importance for AP. The potential range of the stable passivity is almost independent of the temperature; with the growth of acid concentration, the passivation and transpassivation potential slightly shifts to more positive values. The optimum

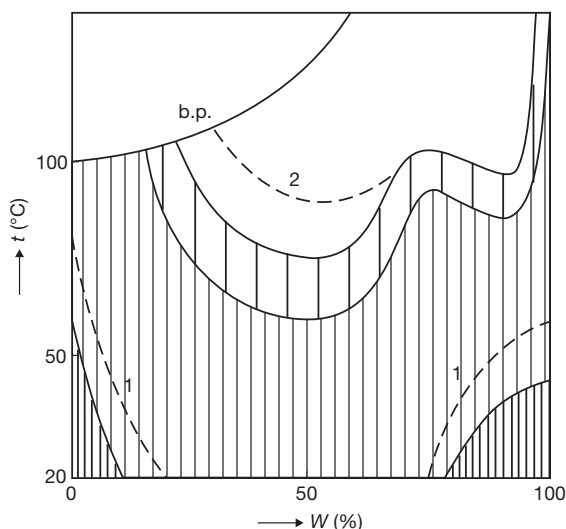


**Figure 13** Range of corrosion rates below  $0.1 \text{ mm year}^{-1}$  for stainless steel FeCr18Ni10(Ti) in sulfuric acid (closest hatching – without AP, thin hatching – with AP). 1 – isoline  $0.1 \text{ mm year}^{-1}$  for FeCr18Ni10Mo without AP, 2 – isoline  $0.1 \text{ mm year}^{-1}$  for FeCr18Ni10Mo with AP.

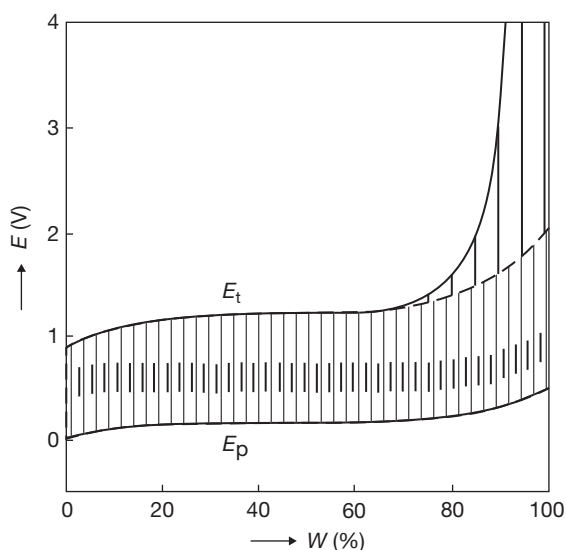


**Figure 14** Dependence of stainless steel (FeCr18Ni10(Mo)) passive range on the sulfuric acid concentration (w (wt%)) at ambient temperature (closest hatching – potential range suitable for AP).

protection potential lies within 0.55 and 0.75 V(SHE) for concentrations up to 80%. At higher concentrations, the optimum potential shifts in a positive direction up to  $\sim 1 \text{ V(SHE)}$  for 98% acid.

The values of passivation current density are concentration and temperature wise strongly dependent (Figure 15). The scattering of values in Figure 15

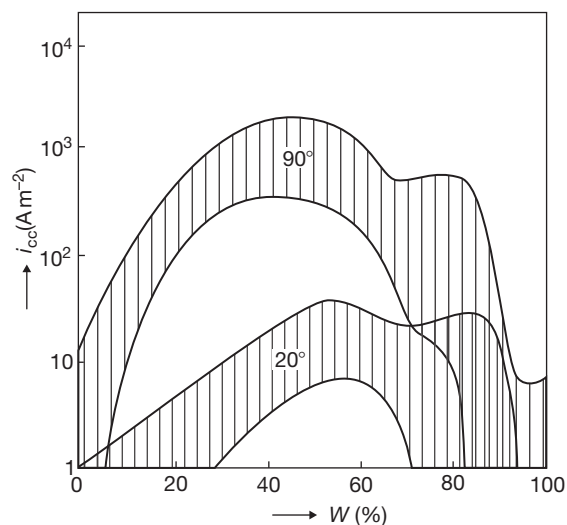


**Figure 15** Dependence of passivation current density ( $i_{cc}$ ) of stainless steel FeCr18Ni10(Mo) on the sulfuric acid concentration (wt%) at 20 and  $90^\circ \text{C}$ .

is given, on the one hand, by the fact that the graph summarizes data for austenitic steels of various types, and on the other hand, by various experimental conditions. The growth of passivation current values  $i_{cc}$  along with the acid concentration is reported to be steep up to  $\sim 50\%$ , which is followed by a drop, and steels in acid with concentrations higher than 70% at  $20^\circ \text{C}$  or 85% at  $90^\circ \text{C}$  are, according to other conditions, self-passivable. Spontaneous passivation also occurs at low concentrations of sulfuric acid.

Passive current densities grow more substantially with the concentration growth up to 20%. A steep drop follows after a flat maximum at 50–60%.

At  $20^\circ \text{C}$ , the values  $i_p$  are stable within the whole concentration interval below  $0.02 \text{ A m}^{-2}$ ; at  $50^\circ \text{C}$ , below  $0.1 \text{ A m}^{-2}$ . The sulfuric acid concentration–temperature diagram with isolines of corrosion rate of  $0.1 \text{ mm year}^{-1}$  is shown in Figure 13 for stainless steels of the FeCr18Ni10(Mo) type.

According to these data, AP extends the range of use of stainless steels of the FeCr18Ni10 type to the whole concentration interval of sulfuric acid solutions up to the temperature of  $60^\circ \text{C}$  (for steels of the FeCr18Ni10Mo type up to  $75^\circ \text{C}$ ).

Corrosion rate with AP is technically acceptable up to  $100^\circ \text{C}$  for concentrations lower than 20% and higher than 95%. For high concentrations, the maximum at corrosion rate isolines is achieved at  $\sim 78\%$  and the growth after the minimum at 93% is steep; at concentrations of  $\sim 98\%$ , sufficient resistance can be allowed for even at temperatures substantially

exceeding 100 °C, if there is a minimum content of iron. The resistance of steels containing molybdenum is higher within the range of concentrations below 75%.

At concentrations below 80%, the potential–current polarization curves for chromium–nickel austenitic steels have a shape corresponding to the type-I (**Figure 2(a)**). The range of significant activity is followed by a passive range limited by the transpassivation potential, above which the metal dissolves and oxygen evolves.

At concentrations over 80%, the curve has a shape of either Type-I, II, or III according to the temperature and iron content (**Figure 2(a)–(c)**). The range of activity is gradually suppressed, the passive range is interrupted with a significant maximum at  $\sim 1.7$  V, beyond which there is a range of low currents. For concentrations exceeding 93%, the drop of current is permanent (to 4 V(SHE)); for concentrations from 80 to 93%, it grows again in the range above 2.3 V(SHE). Although the passive layer is formed exclusively by oxides in the range of concentrations up to 80%, the sulfate layer applies even at higher concentrations and mitigates the oxygen evolution and anodic dissolution.

To achieve effective AP, the minimum concentration of iron ions in flowing sulfuric acid at 100 °C must be 7 ppm (solubility of ferric sulfate). The stability of the passive sulfate layer during acid flow is conditioned by the origination of trivalent iron compounds whose solubility in concentrated acid is, by approximately two orders, lower than that of bivalent iron compounds. Spontaneous passivation results in the formation of  $\text{Fe}^{2+}$  sulfate passive layer, while anodic polarization above 0.85 V(SHE) leads to the formation of  $\text{Fe}^{3+}$  sulfates. This is the reason why cooling systems with AP do not need any significant limitations of acid flow rate and why erosion corrosion does not occur in them, in contrast to systems without AP.

Austenitic stainless steel in hot concentrated acid has a curve with the shape of type-I (free corrosion potential in activity only) (**Figure 2(a)**) merely in pure acid, while in acid with increasing iron content, the shape is of a type-II (two free corrosion potentials) (**Figure 2(b)**), exceeding 7 ppm Fe type-III (free corrosion potential in passivity only) (**Figure 2(c)**).

In hot concentrated sulfuric acid, we can observe a spontaneous oscillation of free corrosion potential between the active and passive state. The oscillations are caused by reversible changes in the exchange current relating to the cathodic reduction of sulfuric

acid, depending on the presence or absence of nickel sulfide on the steel surface.

Moreover, AP increases corrosion resistance of chromium and high-alloyed steels. Their curve of concentration dependencies of characteristic current densities  $i_{cc}$ ,  $i_p$  is identical, in terms of quality, with that of chromium–nickel steels. Values of optimal protection potentials are also approximately the same. Temperature dependence of currents typical for stainless steels can be predominantly expressed by the value of activation energy 60–80 kJ mol<sup>−1</sup>.

Laminar flow of sulfuric acid solutions facilitates the passivation of stainless steel and does not affect corrosion in a passive range. Turbulent flow can have an adverse effect in the interval of acid high concentrations. The time to spontaneous activation gets shortened by the flow of concentrated acid.

Stainless steels can be anodically protected even in environments where sulfuric acid is mixed with organic substances, for example, in the production process of acrylamide, isobutylene, sulfonic acid, nitrobenzene, and others. AP is also possible in the presence of small amounts of chloride and fluoride ions. Their addition, however, gives rise to  $i_{cc}$  and  $i_p$  values and narrows the passive range.

#### 4.24.7.1.3 Titanium

The corrosion resistance of unprotected titanium in sulfuric acid is limited to concentrations below 10%. At 70 °C, however, the corrosion rate exceeds the threshold of 0.1 mm year<sup>−1</sup> even at low concentrations. Titanium is resistant at the boil only in solutions with concentration below 0.1% (**Figure 16**). Concentration dependence of unprotected titanium corrosion rate shows two maxima, the first at 40% and the other at 80%.

The anodic polarization of titanium in sulfuric acid solutions leads to passivation after the passage through the active range. Further polarization to high positive potentials (over 2 V(SHE)) makes the current grow gradually, but the passive layer remains stable up to very high values, even over 80 V. The growth of current in this range is not interrelated with the growth of corrosion rate, it is rather given by the oxygen evolution rate that is limited by high over-voltage resulting from low electron conductivity of the passive layer.

Current–time potentiostatic dependencies show that current drops at high positive potentials with time to relatively low values; the proportion of corrosion reaction on such current amounts from tenths to percentage points at maximum. Currents

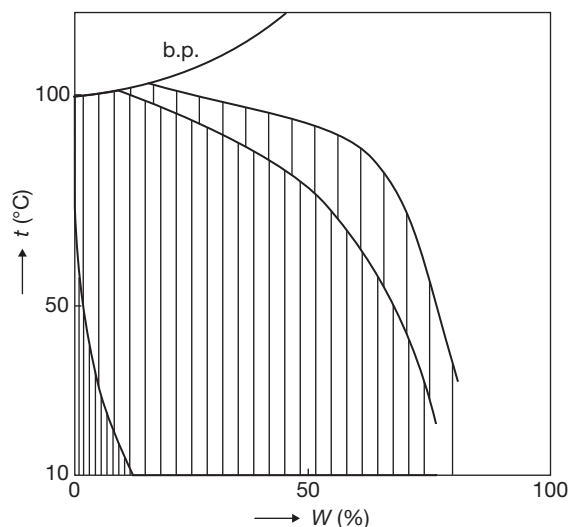


**Figure 16** Range of corrosion rates below  $0.1 \text{ mm year}^{-1}$  for titanium in sulfuric acid (closest hatching – without AP, thin hatching – with AP).

exceeding the potential of 2 V(SHE) are always higher than those within the interval from 0.5 to 2 V (SHE).

The use of protection potential over 0.6 V(SHE) provides sufficient protection under all conditions where AP of titanium in sulfuric acid is effective. Optimal values of protection potential, in terms of both corrosion and consumption of protection current, range from 0.6 to 1.5 V(SHE). If it is necessary to increase the throwing power of the protection, high potential values, such as 12–15 V, can be used for polarization. Corrosion is not tremendously accelerated, and thereby, only the consumption of protection current is higher.

The critical passivation current density also depends on the acid concentration and grows within the exploitable concentration interval (Figure 17). Temperature dependence of  $i_{cc}$  and  $i_p$  currents is expressed by the activation energy from 60 to 75  $\text{kJ mol}^{-1}$ .

The corrosion graph in coordinates of sulfuric acid concentration–temperature is depicted in Figure 16. It is apparent from the graph that AP substantially widens the range of titanium corrosion resistance in sulfuric acid. Another important feature is the resistance of anodically protected titanium within the range of concentrations from 30 to 60% at elevated temperatures, when even the use of AP cannot guarantee sufficient resistance of stainless steels.

Another significant advantage of AP of titanium in sulfuric acid is its efficiency even at the presence of

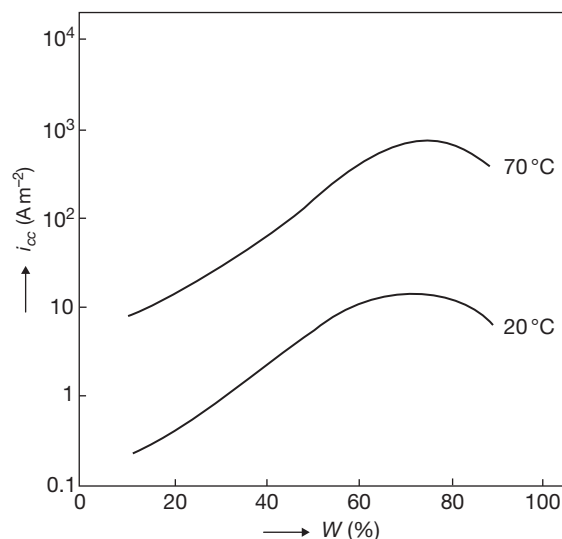


**Figure 17** Dependence of passivation current density ( $i_{cc}$ ) of titanium on the sulfuric acid concentration (wt%).

substances aggravating the passivity of stainless steels (chloride ions, sulfides). Chlorine bubbling has an oxidizing effect on titanium in sulfuric acid, which can be used for protection above the electrolyte level. The stability of a passive layer on titanium is considerably high, and when the polarization current source is switched off, it gets activated no sooner than after several hours. AP of titanium is not applicable if even small amount of fluorides is present in the solution.

Laboratory experiments as well as operation installations proved the efficiency of AP of titanium on sulfuric acid solutions in the presence of sodium sulfate, zinc sulfate, sulfane (hydrogen sulfide), and carbon sulfide. AP can be also used for titanium alloys, but we definitely cannot expect better results than those with pure titanium. Alloys with molybdenum have the passive range limited by the transpassivation potential of 0.75 V(SHE) and alloys with chromium by the transpassivation potential of 1.2 V(SHE).

Low passivation currents facilitate the passivation of titanium compared with stainless steels. Because of the passive range unlimited by transpassivity, it is possible to provide protection by polarization under constant terminal voltage.

#### 4.24.7.2 Other Inorganic Acids

The aggressiveness of phosphoric acid depends on its purity, which is indicated by the production method. Technical phosphoric acid contains sulfates, fluorides, chlorides, and other anions. Carbon steel is



attacked by both pure and technical phosphoric acid within the entire concentration interval. The resistance of stainless chromium–nickel steels in phosphoric acid is good. Up to 50% concentration, all of their types resist even at a temperature of 100 °C; at higher concentrations, it is especially the composition of austenitic stainless steel that applies. Steels alloyed with molybdenum show sufficient resistance at all concentrations up to 90 °C.

Technical phosphoric acid is more aggressive to stainless steels, particularly in terms of the content of chlorides and fluorides (fluorosilicates). The corrosion rate then exceeds the acceptable thresholds even at low concentrations of these anions. Pitting corrosion occurs in 75% phosphoric acid containing chlorides in the amount within 15–20 mg l<sup>-1</sup>. Titanium shows much worse resistance against phosphoric acid than do stainless steels.

Carbon steel can be passivated in concentrated solutions of phosphoric acid and the passive range in 75% acid at normal temperature lies within 0.6 and 1.75 V, but currents in the passive range are high and the corrosion rate substantially exceeds 0.1 mm year<sup>-1</sup>. Slightly better results can be achieved with AP of carbon steel in mixtures of phosphoric and sulfuric acids. In general, we cannot expect that AP of carbon steel in phosphoric acid will be used more widely.

The passivity of stainless steels in pure concentrated phosphoric acid ranges in the interval of potentials from 0.3 to 1.2 V(SHE). Currents in the passive range are, by orders of magnitude, lower than those of carbon steel, and the AP can thus be considered even for higher temperatures.

It is shown in the corrosion graph (Figure 18) that was set up for pure phosphoric acid. What is probably more important than AP of stainless steels at high temperatures in pure acid is the possibility to reduce high corrosion aggressiveness of phosphoric acid contaminated with chlorides and fluorides.

Although the application of AP to titanium in phosphoric acid substantially widens the range of temperatures and concentrations at which the titanium corrosion resistance is below 0.1 mm year<sup>-1</sup>, there is a number of cheaper metallic materials that, even unprotected, are much more resistant (e.g., stainless steels and lead). AP of titanium could be considered effective in phosphoric acid solutions containing higher amount of chlorides, with no fluorides though.

With hydrochloric acid, it is only possible to consider the AP of titanium. The corrosion resistance of

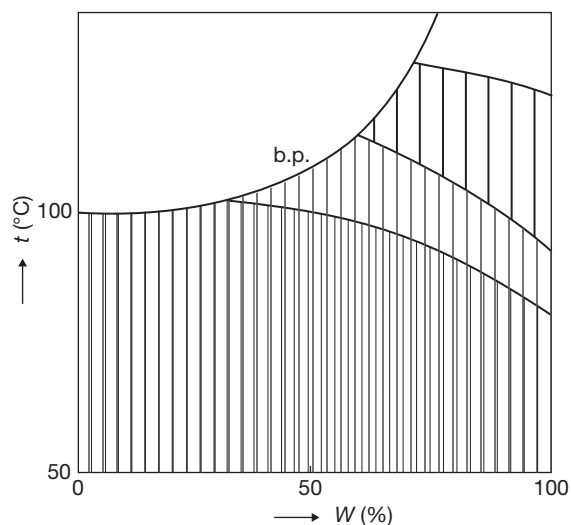


**Figure 18** Range of corrosion rates below 0.1 mm year<sup>-1</sup> for stainless steel FeCr18Ni10(Mo) in phosphoric acid (closest hatching – without AP, thin hatching – with AP).

unprotected titanium in hydrochloric acid is limited to low concentrations only, according to the presence of oxygen and other oxidizing elements.

The titanium passivation potential shifts with the growth of hydrochloric acid concentration to positive values and the protection potential above 0.4 V(SHE) guarantees effective protection at all concentrations and temperatures suitable for the AP of titanium (Figure 19). The optimal interval of protection potentials ranges from 0.5 to 1.5 V(SHE). At potentials over 5 V(SHE), the passive layer is broken through and titanium is attacked by pitting corrosion.

The corrosion graph with coordinates of hydrochloric acid concentration–temperature (Figure 20) clearly shows that AP widens the corrosion resistance of titanium from 20 to 50 °C to the entire concentration interval.

AP of stainless steel can be effective also in nitric acid containing chlorides, where nitrate anions substantially inhibit formation of pitting corrosion.

#### 4.24.7.3 Organic Acids

The anodic passivation of metals is also possible in aqueous solutions of organic acids, though the specific conductivity of their pure solutions is usually less than 1 S m<sup>-1</sup> at normal temperature (save for the oxalic acid, the conductivity of which exceeds 1 S m<sup>-1</sup> already from 1%).

There are just seldom literature references regarding the AP of titanium, carbon steel, stainless steels,

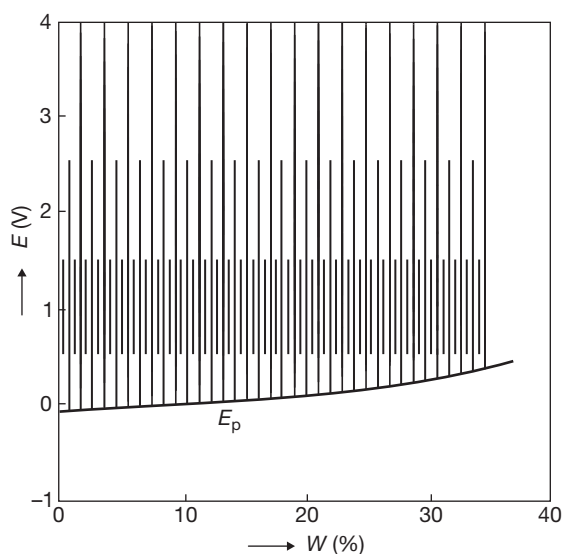


**Figure 19** Dependence of titanium passive range on the hydrochloric acid concentration ( $W$ ) (close hatching – potential range suitable for AP).

nickel, and its alloys in formic, acetic, oxalic, lactic, citric, and sulfane acids.

#### 4.24.7.4 Inorganic Salts

##### 4.24.7.4.1 Ammonium nitrate

Ammonium nitrate is widely used as a part of liquid nitrogen fertilizers, and very often, is the most aggressive part of such solutions. With increasing concentrations of ammonium nitrate from 10 to 60%, the carbon steel corrosion rate grows up to the maximum at 40% concentration. Stainless steels are resistant in the ammonium nitrate environment.

Besides free ammonia, nitrogen fertilizers also contain urea, which acts there as a solvent. The addition of urea slightly reduces the corrosion aggressiveness of ammonium nitrate, still the corrosion rate is technically unacceptable. A substantial reduction of corrosion aggressiveness of the  $\text{NH}_4\text{NO}_3\text{--CO}(\text{NH}_2)_2\text{--H}_2\text{O}$  system can be achieved by addition of ammonia up to 3%. The possibility to anodically protect carbon steel in ammonium nitrate solutions with  $\text{pH} = 4.5\text{--}11$  is addressed already by the first studies on AP. Another type of liquid fertilizers containing high amount of ammonium nitrate, where AP of carbon steels can be used, are solutions containing ammonium carbonate. Corrosion resistance of carbon steel in ammonium nitrate solution containing calcium carbonate can be increased by anodic passivation.

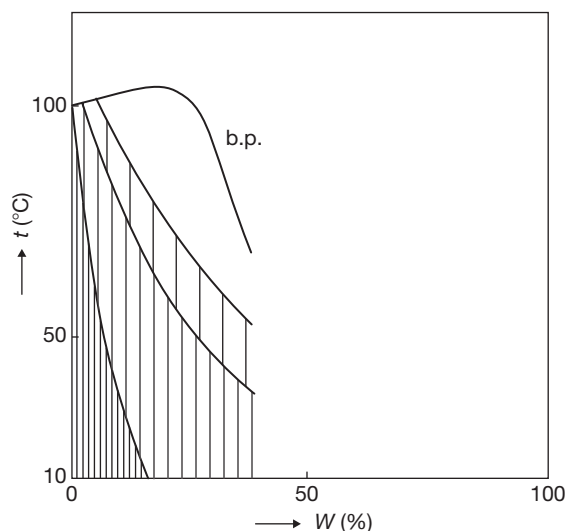


**Figure 20** Range of corrosion rates below  $0.1 \text{ mm year}^{-1}$  for titanium in hydrochloric acid (closest hatching – without AP, thin hatching – with AP).

The most widespread type of an ammonium nitrate-based liquid fertilizer is the solution containing 40–45% of ammonium nitrate, 25–30% of urea, and 20–30% of water, (UAN): carbon steel can be placed in the liquid fertilizer UAN in both active and passive state within the whole range of pH values (5–9). At  $\text{pH} < 7$ , the originally passive surface spontaneously activates and the passive state can be restored only by AP. However, the increase of pH values over 7.5 after the steel activation does not induce spontaneous passivation, but accelerates the corrosion rate. At  $\text{pH} > 7.5$ , the passivated surface (oxidized in air) does not activate and the AP is not essential.

##### 4.24.7.4.2 Sulfates, phosphates, chlorides, thiocyanates

Neutral sulfate solutions do not cause any major problems due to their corrosion aggressiveness to metallic materials. Corrosion is affected, in particular, by the solution pH and by the content of substances influencing the oxidation–reduction potential of a metal. Corrosion aggressiveness grows with the drop of the pH value of the solutions.

The applicability of AP to stainless steels was verified for solutions of zinc sulfate, manganese sulfate, aluminum sulfate, alums, hydroxylammonium-sulfate, and ammonium sulfate.

Ammonium sulfate is present in extremely acidic solutions where AP of stainless steel can be applied, similar to the production of formic acid.

High aggressiveness of sulfate against carbon steel can be mitigated by AP. It is advantageous in solutions containing ammonium nitrate, which suppresses the activating effect of sulfates on steel. Solutions of hydroxylammonium sulfate ( $\text{NH}_3\text{OH}\text{SO}_4$ ) used in the  $\epsilon$ -caprolactam production process are very aggressive because of their hydrolyzing effect and the content of free 10% sulfuric acid. Unprotected stainless steels in active state corrode in this solution at elevated temperatures. The behavior of the solution is analogous to that of the sulfuric acid solution and the salt itself does not participate significantly in its corrosion aggressiveness. Similarly, to sulfuric acid, AP of stainless steel ensures high corrosion resistance in this environment.

Mixtures of phosphates and sulfates make the fundament of combined fertilizers. Parameters of stainless steel AP were verified just for the conditions in reactors for the production of such fertilizers. The conditions of producing fertilizers by the decomposition of apatite by sulfuric and nitric acid, after ammoniation and addition of potassium chloride solution, give rise to the formation of a solution inducing pitting corrosion of stainless steel. This can be eliminated by AP over the inhibition potential, which exists at polarization curves, depending on the steel composition, temperature, and the content of chlorides and nitrates in the solution.

Stainless steel in active state can corrode in thiocyanate solutions ( $\text{SCN}^-$ ). Its passivation can be achieved by anodic polarization, but the passive range is limited by potential, above which thiocyanate oxidizes. With AP, it is possible to mitigate the corrosion of FeCr18Ni10MoTi steel at temperatures between 90 and 120 °C in concentrated sodium thiocyanate solutions, and thus, reduce the iron content in the solution. Iron ions enter the solution due to the equipment corrosion and thus slow down the polymerization in the production process of polyacrylonitrile fiber.

#### 4.24.7.5 Aqueous Solution of Ammonia

Aqueous solutions of ammonia are not very aggressive toward carbon steel (the corrosion rate is below  $0.1 \text{ mm year}^{-1}$ ), though the corrosion rate may reach the values of  $0.5 \text{ mm year}^{-1}$ , if the solution contains a small amount of other substances. The corrosion rate of carbon steel depends not only on the content of these substances ( $\text{CO}_2$ ,  $\text{Cl}^-$ ,  $\text{NO}_3^-$ ,  $\text{CH}_3\text{COO}^-$ ), but also on the content of oxygen, the pH of the solution, and ammonia concentration (pH of the solution does

not depend only on the ammonia concentration but also on the content of other substances). Up to 5% of ammonia, carbon steel passivates spontaneously. At higher concentrations and  $\text{pH} < 12$ , passive steel spontaneously activates. At  $\text{pH} > 12$ , the activation depends on the oxygen content in the solution, the superficial state, and other factors. The corrosion rate of active specimens grows with the access of oxygen, whereas, in case of passive specimens, the effect of oxygen is positive.

The specific conductivity of pure ammonia solutions is very low, but in operation conditions, achieves values up to  $10 \text{ S m}^{-1}$  due to contamination.

The curves of potential–current polarization dependencies for carbon steel in pure aqueous ammonia solutions with concentration exceeding 25% have a shape analogous to Type-III in Figure 2(b). The corrosion rate within the passive range is negligible, thousandths to hundredths of  $\text{mm year}^{-1}$  in the order of magnitude. The content of oxygen positively affects the effectiveness of AP, and thus, it is advisable to ensure oxygen access to the metallic surface by stirring the solution.

#### 4.24.7.6 Hydroxides of Alkaline Metals

Nonalloyed steels have, in sodium hydroxide solutions up to 60 °C, a very low corrosion rate of  $0.1 \text{ mm year}^{-1}$  for all concentrations (Figure 21). In 15% solution of sodium hydroxide, they show sufficient resistance even at the boil. However, the occurrence of corrosion cracking is more important than the uniform corrosion rate. The range of possible occurrence of corrosion cracking is defined in the sodium hydroxide concentration–temperature graph (Figure 21) by curve 2. Its position shows that it is this dependence that is decisive for the use of nonalloyed steels in the sodium hydroxide solutions rather than the isoline of corrosion rate  $0.1 \text{ mm year}^{-1}$ .

The specific conductivity of solutions of alkaline metal hydroxides exceeds  $10 \text{ S m}^{-1}$  at normal temperature within the almost entire concentration interval.

AP in sodium hydroxide solutions is important particularly for nonalloyed and low-alloyed steels. At higher temperatures and pressures, or at higher concentrations of sodium hydroxide, AP of austenitic stainless steels can be considered.

The anodic polarization of nonalloyed and low-alloyed steels in the sodium hydroxide solution leads to passivation, and the shape of the curves strongly depends on the presence of oxidizing agents and other substances. The range of potentiodynamic

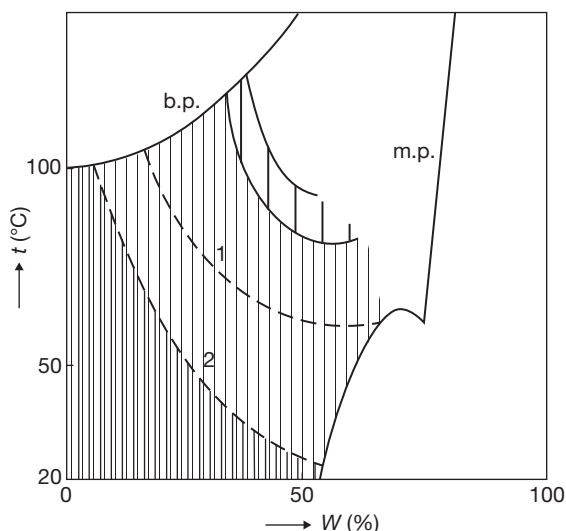


**Figure 21** Range of corrosion rates below  $0.1 \text{ mm year}^{-1}$  for mild steel in sodium hydroxide. 1 – corrosion rate  $0.1 \text{ mm year}^{-1}$  without AP, 2 – limit of possible SCC occurrence without AP (closest hatching – without AP, thin hatching – with AP).

dependencies in 35% solution of sodium hydroxide at the boil is depicted in **Figure 22**.

The passive range relating to sodium hydroxide concentrations from 5 to 50% lies within the potential interval from  $-0.7$  to  $0.5 \text{ V(SHE)}$ . However, only the part where corrosion cracking does not occur is exploitable. Having summarized the data of various authors, we can claim that the safe range for AP lies above the potential of  $-0.3 \text{ V(SHE)}$ .

The corrosion graph with coordinates of sodium hydroxide concentration–temperature (**Figure 21**) delimitates the likely range of AP for the elimination of corrosion cracking and the mitigation of uniform corrosion.

The greatest aggressiveness is shown by 50% sodium hydroxide solution; however, in this solution, AP is successful up to the temperature of  $80^\circ\text{C}$ . At lower concentrations, AP can be effective even in pressure equipment where temperature exceeds the boiling point under atmospheric conditions.

AP of carbon steel in the sodium hydroxide solution is feasible in both the solutions used in the technology of aluminum oxide production and in the presence of chlorides and sulfides, that is, in solutions used in the paper and cellulose production process.

The aggressiveness of potassium hydroxide is higher compared with sodium hydroxide, and the scope

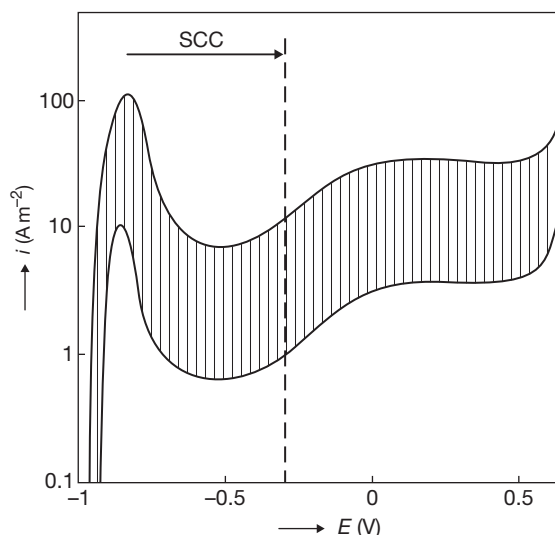


**Figure 22** Courses range of potentiodynamic curves of carbon steel in 35% sodium hydroxide at boiling point (SCC – potential range of SCC).

of usability of unprotected carbon steel is narrowed for the same concentrations by 20–30K from the perspective of both the uniform corrosion and corrosion cracking. The polarization properties of carbon steels in potassium hydroxide solutions do not differ much from those of solutions of sodium hydroxide. Even the potential ranges of corrosion cracking are similar.

#### 4.24.7.7 Melts

If the corrosion in a melt is controlled by electrochemical process and the melt has a sufficient ion conductivity, AP can mitigate corrosion attack in this environment as well. The specific conductivity of melts of inorganic salts and hydroxides usually exceeds  $100 \text{ S m}^{-1}$ . Stainless steel can be anodically passivated in  $\text{NaOH-Na}_2\text{SO}_4$ ,  $\text{NaOH-Na}_3\text{PO}_4$ ,  $\text{NaOH-KCl}$ ,  $\text{NaOH-NaCl-Na}_2\text{CO}_3\text{-NaNO}_3$ , and  $\text{NaOH}$  melts at temperatures up to  $1000^\circ\text{C}$ .

Glass is electrically melted by alternating current and molybdenum electrodes. Problems with the corrosion of heating electrodes arise when the glass melt contains ions of metals, such as lead, arsenic, or antimony, which reduce at the electrode surface along with the oxidation of molybdenum. The reduced metal can form compounds with molybdenum, which further accelerates the corrosion of the electrodes. Laboratory experiments proved that a protective layer forms on the molybdenum surface during the anodic polarization in the glass melt, which protects the electrode

surface against corrosion, and at the same time, does not overly constrain the passage of alternating current that electrically heats the glass melt. The specific conductivity of the glass melt strongly depends on the type of glass; values at the refining temperature typically range from 20 to 50 S m<sup>-1</sup>.

#### 4.24.7.8 Electroless Nickel Plating Baths

The reason for AP in electroless (chemical) metal plating baths is the necessity to avoid undesirable deposition of metals on the walls of the metal plating equipment rather than corrosion protection.

The electroless nickel plating baths are the most widespread. The deposited coating is an alloy of Ni–P, or Ni–B, according to the type of the used reduction agent. Especially, sodium hypophosphite (NaH<sub>2</sub>PO<sub>2</sub>) or sodium tetrahydridoborate (Na[BH<sub>4</sub>]) is used as a reduction component of the baths.

Electroless nickel plating is an electrochemical process, in which reduction reactions lead to the formation of nickel and hydrogen, and oxidation reactions turn hypophosphite to phosphate, or phosphate. These reactions optimally proceed at temperatures from 90 to 95 °C.

Reactions can proceed at any surface showing a catalytic effect and enabling a charge transfer. The idea of using anodic polarization to protect the walls of the production equipment from the deposition of nickel was brought in the mid-1960s by German authors.

Anodic polarization can be used only for materials that do not suffer from corrosion (get passivated) and upon which the oxidation of solution elements is restricted. Electroless metal plating baths contain substances of a reduction nature, and therefore, the oxidation reaction upon the surface of the used material must have a high overvoltage.

Considering the nickel plating baths, these requirements are complied with by stainless steels and titanium within the entire range of pH values. In addition to that, nickel can be used in alkaline baths.

The spontaneous nickel deposition process starts at temperatures exceeding 60 °C, which is the temperature limit of the effective use of AP. The specific conductivity of nickel plating baths ranges from 3 to 30 S m<sup>-1</sup> at operation temperature according to the composition. The interval of protection potentials for stainless steel in the environment of electroless nickel plating baths depends on the type of the bath, but for most acidic baths, it ranges from –0.25 to 0.8 V(SHE), the optimal potential interval is 0.5–0.8 V(SHE).

The passive range of stainless steels is wider than that indicated by the interval of protection potentials, and the corrosion rate within this range is negligible. The upper potential limit of the protection interval is given by the substantial growth of current resulting from the oxidization of the solution components, probably of the hypophosphite to phosphate, while the lower limit lies right above the starting point of spontaneous deposition of metallic nickel (–0.35 V (SHE)). The actual exploitable range of potentials is narrower, since the spontaneous potential of passivated stainless steel corresponds to ~0.25 V(SHE). Without polarization, this potential remains stable at maximum for several hours in the operation conditions. Then, nickel deposits on the walls, and the potential shifts in the negative direction to the value held by the metallic surface self-plated with nickel (–0.35 to –0.44 V(SHE)).

Current densities passing through the anodically protected surface of stainless steel at protection potential represent the rates of suppressed oxidation of the solution components rather than the corrosion rate.

The range of titanium protection potentials is wider and the protection current is lower than that of stainless steel. The overvoltage of anodic oxidation of hypophosphite is higher on passive titanium. Even the resistance of passive titanium against nickel deposition without AP is higher. It is possible to anodically protect stainless steels in baths containing chlorides and fluorides, but the interval of protection potentials is narrower. The use of titanium in baths containing fluorides is precluded.

#### 4.24.8 Industrial Applications of AP

Detailed information on industrial applications can be found in monographs<sup>6–9</sup> on AP and in surveys in journals<sup>5,10–13</sup> and other sources<sup>27,34</sup>

##### 4.24.8.1 Sulfuric Acid Coolers Made of Stainless Steel

A great deal of heat is released in the production of sulfuric acid and this heat must be transferred by the cooling of the acid circulating in the production equipment. Mostly, it is acid with 93% or 99% concentration, and in some cases, even lower (up to 75%). The acid is predominantly cooled from 90 to 40 °C and the maximum temperature is limited by the corrosion resistance of the cooling set. The first and the most widespread coolers of this type to date



are vertical and horizontal shell and tube anodically protected heat exchangers with water in pipes and acid flowing in the anodically protected intertubular space<sup>13,27,28,33</sup> (**Figure 23**).

The construction of heat exchangers with water as cooling medium with acid in pipes is less frequent. Sporadic are data on anodically protected desk coolers; more data can be found regarding spiral coolers.<sup>29,30</sup> AP is also used for air coolers.<sup>11,14,28</sup> Even the tubes for acid transportation are anodically protected.<sup>31,32</sup> Cathodes are mostly made of either stainless steel or nickel alloys<sup>48</sup>; reference electrodes are either made of mercury sulfate or platinum.

A competitive solution to the AP of common austenitic stainless steel coolers is the use of high-silicon stainless steels that resist without AP.

The installations of anodically protected coolers of 75–78% sulfuric acid<sup>13</sup> in plants processing calcining gases from ferrosins production (**Figure 24**) are rather unusual due to the threshold concentration and temperature.

#### 4.24.8.2 Stainless Steel Equipment Operating in Environment Containing Sulfuric Acid

The AP was described for transportation stainless steel vessels, measuring vessels, neutralization vessels for sulfonic acid, hydrolysis vessels, hydroxylammoniumsulfate storage vessels, heating coil, and turbo-coolers of 55–65% sulfuric acid. Stainless steel was also used for the anodically protected vessel for storing pure sulfuric acid (94–99%) at temperatures up to 40 °C (**Figure 25**).

#### 4.24.8.3 Other Anodically Protected Equipment Made of Stainless Steels

The industrial application of AP was described for storage vessels of technical concentrated phosphoric acid, reactors for the production of combined fertilizers containing chlorides,<sup>34</sup> and sodium thiocyanate evaporator.<sup>34</sup>

#### 4.24.8.4 AP of Stainless Steel in Chemical (Electroless) Nickel Plating Bath

The vessels for chemical nickel deposition are numerous groups of anodically protected industrial installations. Instead of corrosion resistance, the AP prevents, in this case, the undesirable deposition of nickel on the stainless steel tank walls. Anodically



**Figure 23** Anodically protected stainless steel heat exchangers for cooling of 93–98 wt% sulfuric acid.



**Figure 24** Anodically protected stainless steel heat exchangers for cooling of 75–78 wt% sulfuric acid.

protected titanium tanks are also used for current-free nickel plating. AP has become a standard equipment of operation lines for chemical nickel plating.<sup>13,35</sup> Due to the passage of current, nickel deposits on a cathode usually made of stainless steel. Stainless steels, where nickel spontaneously deposits, serve as a reference electrode. Nickel can be regularly removed from electrodes mechanically as well as by dissolution in nitric acid.

#### 4.24.8.5 Carbon Steel Storage Vessels for Concentrated Sulfuric Acid

In addition to corrosion protection, the AP of sulfuric acid storage tanks made of carbon steel ensures high purity of the stored acid. The AP keeps the iron content in the stored acid on the ppm level, while in the case without AP, there are tens of ppm. Cathodes are made of stainless steel, reference electrodes are either mercury sulfate or platinum. There are a



**Figure 25** Anodically protected tank for storing pure sulfuric acid (94–99%) at temperatures up to 40 °C.

number of literature data on AP of these vessels.<sup>13,36</sup> For waste acid, it deals only with the reduction of the corrosion rate.

#### 4.24.8.6 Carbon Steel Equipment for Alkaline Environments

In case of anodically protected carbon steel storage tanks of sodium hydroxide, change of potential in the passive area leads to values, at which intergranular SCC is eliminated.<sup>11,13,37</sup> Susceptibility to corrosion cracking can be eliminated in potassium hydroxide.<sup>5,28</sup> Cathodes can be made of nickel, reference electrodes of mercury oxide.

Tubular evaporators are complicated pressure vessels operating with AP in the sodium hydroxide environment.<sup>5,28</sup> The AP was also used for the protection of steel equipment in the production of aluminum oxide.

#### 4.24.8.7 Cellulose Boilers and Other Equipment in Paper and Cellulose Industry

Batch and continuous digesters made of carbon steel<sup>38–41</sup> and a Kraft liquor tankage<sup>42–44</sup> are the main anodically protected objects. Reference electrodes are silver sulfide or molybdenum. The electrochemistry of Kraft liquors is complicated because of multiple oxidation states of sulfur compounds (thio-sulfate, polysulfide). Potential–current dependencies have the shape of I–III (**Figure 2**) in this corrosion system. For batch digesters, it is necessary to rate the direct current sources for periodic passivation.

AP is the most effective protective measure against SCC and it is possible to overcome erosion–corrosion problems. The industrial success of AP resulted in many commercial installations in North America and Finland (Savcor<sup>27</sup>).

#### 4.24.8.8 Liquid Fertilizer Storage Tanks

The AP of carbon steel in liquid fertilizer containing ammonium nitrate is described in literature<sup>13</sup>; however, it is not used much in operation any longer. If we compare the AP with other alternatives of the corrosion protection of steel-welded equipment, we will find out that operation-wise, the protection is simpler if ammonia leakage is avoided so that the pH of the solution does not drop below 7.5 and the steel surface is spontaneously passive.

AP is used for ammonium carbonate fertilizers containing ammonium nitrate and for ammonia–water storage tanks, and in the production of ammonium carbonates.<sup>45</sup>

#### 4.24.8.9 Equipment Made of Other Metallic Materials

The AP of a titanium exchanger was described for the viscose production process, in which diluted solutions of sulfuric acid containing other substances are used.

Documented information about the industrial application is available also for molybdenum heating electrodes in glass melt.<sup>46,47</sup>

## References

1. Edeleanu, C. *Metallurgia* **1954**, 50, 113–116.
2. Lawrence, C. K.; Engle, R. F. Preventing corrosion of ferrous metals in solutions of electrolytes. U.S. Patent 2,377,792 June 5, 1945; Inhibiting corrosion of ferrous metals by ammoniacal solutions of  $\text{NH}_4\text{NO}_3$ . U.S. Patent 2,3667,996 January 9, 1945.
3. Novakovskii, V. M.; Levin, A. I. *Dokl. Akad. Nauk. SSSR* **1954**, 99, 129–132.
4. Tomashov, N. D.; Chernova, G. D. *Dokl. Akad. Nauk SSSR* **1955**, 104, 104–107.
5. Gräfen, H.; Herbsleb, G.; Paulekat, F.; Schwenk, W. *Werst. Korros.* **1971**, 22, 16–31.
6. Makarov, V. A. *Korrozia i zashchita ot korrozii*; VINITI: Moskva, 1974; Vol. 3, pp 84–152, (in Russian).
7. Riggs, O. L.; Locke, C. E.; Hamner, N. E. *Anodic Protection*; Plenum Press: New York, 1981.
8. Kuzub, V. S. *Anodic Corrosion Protection*; Khimiya: Moscow, 1983 (in Russian).
9. Novak, P. *Anodic Corrosion Protection*; SNTL: Prague, 1987 (in Czech).

10. Agafonova, N. N.; Makarov, V. A. *Prot. Met.* **1989**, *25*, 531–543.
11. Gräfen, H.; Kuron, D.; Paulekat, F. *Werst. Korros.* **1991**, *42*, 643–651.
12. Kuzub, V. S.; Makarov, V. A.; Novitskii, V. S. *Prot. Met.* **1991**, *27*, 652–657.
13. Novak, P.; Mokra, M. *Koroz. Ochr. Mater.* **2006**, *50*, 7–13.
14. Paulekat, F.; Gräfen, H.; Kuron, D. *Werkst. Korros.* **1982**, *33*, 254–262.
15. Vicentini, B.; Sinigaglia, D.; Taccani, G. *Werkst. Korros.* **1971**, *22*, 916–924.
16. Froulous, Z. A. *Anti-Corros. Method. Mater.* **1980**, *27*, 5–13.
17. Bartek, J.; Novak, P. *Scientific Papers of ICT Prague* **1987**, *B32*, 187–203; CA 107:66512.
18. Bochkareva, I. V.; Ivanov, V. T.; Makarov, V. A.; Novitskii, V. S. *Prot. Met.* **1992**, *28*, 312–316.
19. Bochkareva, I. V.; Ivanov, V. T.; Makarov, V. A. *Prot. Met.* **1991**, *22*, 390–396.
20. Makarov, V. A.; Novitskii, V. S.; Artamonova, N. M. *Prot. Met.* **1991**, *27*, 841–845.
21. Ivanov, V. T.; Makarov, V. A.; Bolotnov, A. M. *Prot. Met.* **1992**, *28*, 955–960.
22. Bolotnov, A. M.; Ivanov, V. T. *Russ. J. Electrochem.* **1996**, *32*, 637–640.
23. Bolotnov, A. M.; Ivanov, V. T. *Prot. met.* **2001**, *37*, 173–176.
24. Novak, P.; Bystriansky, J.; Bartel, V. *Werkst. Korros.* **1982**, *33*, 94–98.
25. Novak, P.; Stefec, R.; Franz, F. *Proceedings of Eurocor 77*, London, 1977; pp 89–95.
26. Bochkareva, I. V.; Ivanov, V. T.; Makarov, V. A.; Makhmutov, M. M. *Prot. Met.* **1989**, *25*, 65–73.
27. Company files of Noram Engineering, Canada; Mercad Ltd., Canada; Aker Kvaerner Chemetics, Canada; MECS Inc., USA; Nantong Fareast Chemical Equipment Co Ltd., China; eKS GmbH, Germany; Savcor Group Ltd Oy, Finland.
28. Von Baekmann, W.; Schwenk, W.; Prinz, W. Eds. *Handbook of Cathodic Corrosion Protection*, 3rd ed.; Gulf Publishing Company: Houston, TX, Elsevier Science 1997; Chapter 21.4, pp 474–488.
29. Xu, D.; Li, J.; Zheng, J.; Zhang, Z.; Tao, Y.; Xiao, S. *Zhongguo Fushi Yu Fanghu Xuebao* **2002**, *22*, 133–137.
30. Lebet, R. *Ochrona przed Korozja* **1995**, *38*, 12–14.
31. Kuron, D.; Paulekat, F.; Graefen, H.; Horn, E. M. *Mater. Corros.* **1985**, *36*, 489–501.
32. Wang, Y.; Gao, P.; Shen, G.; Wen, S.; Wang, T. *Liusuan Gongye* **2002**, *2*, 27–30.
33. Bhaga, D. *Sulphur* **1980**, *147*, 32–33, 39–43.
34. Kuzub, V. S.; Makarov, V. A. *Proceedings 1st Soviet-Japan Seminar on Corrosion and Protection of Metals, Moscow 1977*; Nauka, Moscow, 1979; pp 96–120.
35. Mark, T. *Jahrbuch Oberflächentechnik* **2006**, *62*, 55–65.
36. Shim, W. W.; Munro, J. I. *Mater. Perform.* **2000**, *39*, 22–26.
37. Podval, J.; Filasova, A. *Koroz. Ochr. Mater.* **1993**, *37*, 7–8.
38. Wensley, A. C. *Tappi J.* **1996**, *79*, 153–160.
39. Nadezhdin, A.; McDonald, R. *Pulp & Paper Canada* **1999**, *100*, 44–48.
40. Wensley, A. *Proceedings of Corrosion 2001, paper 01423*, 9p, NACE International, Houston, 2001.
41. Wensley, A. *Proceedings of Tappi Fall Technical Conference, Chicago, 2003*; pp 555–593.
42. Singbeil, D.; Garner, A. *Mat. Perform.* **1987**, *26*(4), 31–36.
43. Munro, J. I. *Mat. Perform.* **2002**, *41*(2), 22–26, *41*(3) 24–28.
44. Munro, J. I.; Shim, W. W. *Proceedings of Tappi Fall Technical Conference, San Diego, 2002*; pp 689–699.
45. Kuzub, L. G.; Gnezdilova, V. I.; Smoroda, N. I.; Kovalinskaya, E. K.; Kuzub, V. S. *Soviet Mater. Sci.* **1989**, *24*, 89–91.
46. Susser, V.; Ladr, I. *Glastechnische Berichte* **1983**, *56*, 167–172.
47. Hwang, J. H.; Kim, C. Y.; Kwon, J. G. ; Kim, K. D. *Glass Technol.* **2005**, *46*, 142–145.
48. Rodda, J. R.; Ives, M. B.; Kish, J. R. *Mater. Perform.* **2005**, *44*(7), 20–23, *44*(8) 22–25.

## 4.25 Introduction to Control of Corrosion by Environmental Modification

R. Lindsay and S. B. Lyon

Corrosion and Protection Centre, School of Materials, The University of Manchester, Oxford Road, Manchester M13 9PL, UK

© 2010 Elsevier B.V. All rights reserved.

4.25.1	Introduction	2891
4.25.2	Corrosive Agent Removal (CAR)	2892
4.25.2.1	Gaseous Environments	2892
4.25.2.2	Liquid Environments	2893
4.25.3	Protective Barrier Inducement (PBI)	2894
4.25.3.1	Corrosion Inhibition in Aqueous Acidic Solutions	2895
4.25.3.2	Corrosion Inhibition in Aqueous Near-Neutral Solutions	2897
4.25.4	Final Remarks	2899
References		2899

### Abbreviations

**CAR** Corrosive agent removal  
**CI** Corrosion inhibitor  
**CR** Corrosion rate  
**IE** Inhibitor efficiency  
**PBI** Protective barrier inducement  
**RH** Relative humidity

### Symbols

**C** Concentration of species in solution  
**C<sub>crit</sub>** Critical concentration for effective inhibition by anodic passivating inhibitors  
**i<sub>corr</sub>** Corrosion current density  
**i<sub>L</sub>** Limiting current density for an electrochemical reaction, usually in the context of oxygen diffusion to a cathode  
**i<sub>crit</sub>** Critical current density required for passivation  
**θ** Fractional surface coverage, where  $\theta = 1$  is one monolayer

### 4.25.1 Introduction

Materials selection, substrate (surface) design engineering (e.g., by use of coatings), and environmental modification (e.g., application of a corrosion inhibitor (CI)) are three commonly accepted strategies for corrosion control. The first two of these approaches can be described formally as *ex situ*, and ideally would be sufficient for complete protection. Practically, however, cost-effective corrosion control

typically requires the use of a relatively cheap material that serves the desired mechanical or physical function (e.g., commonly a carbon or low-alloy steel). In such cases, *in situ* environmental modification is often required to control the corrosivity of the ambient fluid (i.e., gas or liquid environment or atmosphere) in which a material is immersed. There are a variety of technologies available to achieve this end, and selection ultimately depends upon the specific details of the particular application, generally driven by the requirement to achieve acceptable performance for minimum cost. The scientific basis behind environmental modification can be divided into two fundamentally different underlying strategies:

- Corrosive agent removal (CAR): This involves deliberate modification of an environment in order to reduce its chemical and/or electrochemical activity towards a substrate material by removal of specific corrosive reagents.
- Protective barrier inducement (PBI): This involves the deliberate addition of a chemical species that interacts in some way with the corroding substrate so as to form a protective barrier that reduces the corrosion rate (CR) to an acceptable level.

It is important to note that these strategies may be combined together (and indeed also combined with one of the *ex situ* corrosion control methods – for example, the addition of corrosion inhibitors (CIs) to organic coatings) in order to achieve the desired performance. In this chapter, an introduction to the fundamentals of environmental modification for corrosion control is presented. Industrial practice is discussed in the following chapters of this section.

### 4.25.2 Corrosive Agent Removal (CAR)

The process of corrosion involves two simultaneous electrochemical reactions (i.e., the anodic and the cathodic), which occur necessarily at the same rate but at different physical locations, and which involve the transport of ionic current in an electrolyte, see **Figure 1**. Thus, the scientific basis for reducing the kinetics of the corrosion process involves interference with one or more of these electrochemical processes. From inspection of **Figure 1**, it can be deduced that there are three basic CAR strategies for reducing the rate of the electrochemical reactions associated with corrosion, they are:

- removal of the cathodic reactant (e.g., oxygen) such that the cathodic reaction is stifled;
- removal of the electrolyte solution (e.g., water) such that, in particular, the anodic reaction becomes stifled since metal ions have limited ability to be solvated; and
- reduction of the electrolyte conductivity such that a large resistance is developed between the anode and the cathode and, hence, the electrochemical corrosion current is stifled.

Determination of which fluid components to target is dependent upon both the environment and practical application. For example, it is not practical to deionize an oilfield seawater injection well system.

#### 4.25.2.1 Gaseous Environments

Focusing on gaseous environments, a pertinent topic is corrosion of substrates exposed to the atmosphere. Common scenarios include: outdoors in the open air, indoor environments, packaging for long-term storage of materials, and mothballing of equipment for

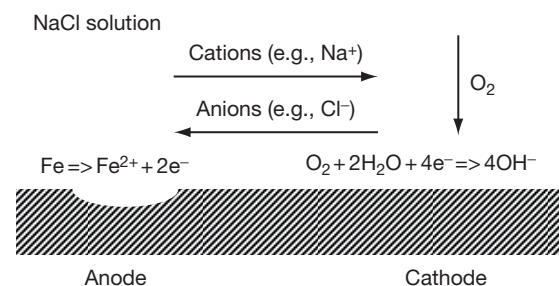


**Figure 1** Schematic diagram of a corrosion process showing spatial separation of anode from cathode with corresponding migration of ions in solution and with oxygen as the cathodic reactant.

maintenance. While the first of these cannot be addressed by environmental modification, the other scenarios are amenable to CAR.

Gaseous atmospheric corrosion involves the condensation of moisture from the atmosphere onto a substrate. Typically, for a clean, uncontaminated, and polished surface in an atmosphere containing no gaseous or solid particle (aerosol) pollutant species, corrosion is minimal below a relative humidity (RH) of  $\sim 80\%$ , where adsorbed water reaches a critical thickness of  $\sim 3\text{--}4$  monolayers.<sup>1</sup> If the surface is roughened or has a porous structure (as in a corrosion product) then capillary condensation takes place at lower RH; where chemical salt contamination exists, is deposited, or forms on a surface by reaction, then water condensation will occur at the humidity of deliquescence of the salt. In all of these scenarios, corrosion is only of significance where the RH is greater than a critical value that depends on the surface condition (or contamination) of the substrate.<sup>2,3</sup> Corrosion can thus be suppressed by deliberate removal of water vapor from the atmosphere so as to reduce the RH to below the critical value for the onset of corrosion. RH can be calculated from the following expression:

$$\text{RH} = \frac{p_{\text{H}_2\text{O}}}{p_{\text{H}_2\text{O}}^*} \times 100\% \quad [1]$$

where  $p_{\text{H}_2\text{O}}$  is the water vapor partial pressure and  $p_{\text{H}_2\text{O}}^*$  the saturation water vapor partial pressure at the prevailing temperature. For a given absolute humidity (i.e.,  $p_{\text{H}_2\text{O}}$ ) the RH falls with increasing temperature but rises with decreasing temperature. This explains the well known phenomenon of condensation on cold surfaces.

For 'technically' clean substrates, the critical RH for the onset of significant corrosion is generally between 50% and 60%. However, for surfaces contaminated with sea salt, the critical RH corresponds to the RH for deliquescence of magnesium chloride ( $\sim 35\%$ ), while for historic artifacts derived from marine sources and, consequently, contaminated with chloride ion, the critical RH can be as low as 15% (the deliquescence RH for iron chlorides).<sup>4</sup>

For long-term storage of components, archaeological artifacts and for mothballing of equipment, environments of low RH are essential. For small components, this may be achieved by suitable packaging in materials with a low water vapor transmission rate, combined with a solid suitable desiccant. The familiar silica gel is commonly used; it functions best at around room temperature, and is capable of



bringing RH down from 60–90% to ~40%. Activated alumina, quick lime (calcium oxide), montmorillonite clay, aluminosilicates (zeolites) are other solid desiccants that are used for such applications. For larger components, as well storage warehouses, it may be cost effective to consider mechanical dehumidification (i.e., air conditioning). Further information on desiccants can be found in BS 1133 Part 19.<sup>5</sup>

Occasional, but important, applications also exist for removal of corrosive gas fractions (including water vapor) from industrial processes by direct absorption. For example, triethylene glycol is often employed in natural gas production facilities to remove water content before the gas is transported away. Other gaseous species are also sometimes targeted in gas phase CAR, including carbon dioxide, sulfur dioxide, and hydrogen sulfide. The release of corrosive vapors from packaging materials is also an important consideration. For example, the degradation of cellulose (paper, wood, etc.) and polymeric packing materials may release aggressive agents such as acetic acid and hydrochloric acid vapor.<sup>6</sup> Detailed information on indoors corrosion and on corrosion due to packaging materials can be found in Donovan's book.<sup>7</sup>

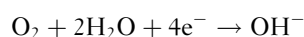
#### 4.25.2.2 Liquid Environments

Turning to CAR in liquid environments, water can be a major concern in nonaqueous systems. Thus, for scenarios where water is a nonessential constituent of the liquid, its removal is usually a desirable goal. For example, in oil production, water is commonly removed from the process fluid using separator vessels, which rely upon the different densities of oil and water; however, if the water exists as a stable emulsion then additional pretreatment is required. For some systems, it is preferable to retain a small amount of residual water in the nonaqueous medium, otherwise a protective passive film either may not be able to form, or may be unstable. Such environments include anhydrous liquid ammonia, where ~10 ppm water should be present to avoid stress corrosion cracking of steel<sup>8</sup> and chlorinated solvents, where a few ppm of water permits passivation and prevents the so-called 'bleeding corrosion' of aluminum.<sup>9</sup>

However, in aqueous environments, where water is the main component of the fluid or in those mainly nonaqueous environments where it is simply ubiquitous, then such a strategy is not feasible. Thus, CAR must target another relevant component of the environment. Noting, for example, that CRs in

deionized water are generally lower than in potable water or seawater, a common strategy for aqueous corrosion control is to lower the electrolyte conductivity. The mechanism for this effect is as indicated in **Figure 1**; thus, a higher electrolyte resistance reduces the current flowing from anode to cathode. This may be simply achieved by specific removal of those (electrolyte) species that are able to form ions in solution by pretreatment of the water that will be used in the system. However, it is important to remember that water softening, often carried out to prevent scaling in systems, replaces calcium ions with sodium ions, and will often increase electrolyte conductivity. Deionization (or rarely nowadays, multiple distillation) is, therefore, the only reliable mechanism for achieving the desired reduction in anion and cation electrolyte concentration.

The most commonly used (and often most effective) method of CAR, especially in near-neutral aqueous solutions, is the control of dissolved oxygen levels as, under these conditions, it is the reactant for the rate-limiting cathodic reaction, that is:

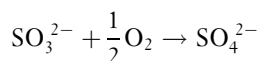


At room temperature, the concentration of dissolved oxygen in water in equilibrium with air is ~8 ppm (0.2 mM). This value is sufficient to cause appreciable corrosion of unprotected carbon steel (i.e., in the range ~0.2 to  $\gg 1 \text{ mm year}^{-1}$  depending on fluid flow rate). A typical aim is to lower the CR to an acceptable level, that is, below ~0.1 mm year<sup>-1</sup>. A good 'rule of thumb' that will generally achieve an acceptable CR for carbon steel equipment in flowing seawater is to reduce the dissolved oxygen content to 20 ppb (~0.0006 mM) or below,<sup>10</sup> which is readily achievable by mechanical deaeration.

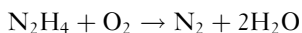
The concentration of dissolved oxygen in water can be reduced by physical methods, chemical methods, or a combination thereof. Physical methods (often called mechanical deaeration) include heating the water, as O<sub>2</sub> solubility decreases with increasing temperature. In boiler systems, water heating is often combined with vacuum deaeration and/or gas sparge stripping. The former process involves lowering the gas pressure above the water hence leading to a reduction in dissolved gas content, while in the latter technique, a counter-current of gas (e.g., nitrogen, steam) mixes intimately with the water replacing dissolved O<sub>2</sub>.

Chemical methods for removal of dissolved O<sub>2</sub> are commonly known as oxygen scavengers and function by reacting directly with residual O<sub>2</sub> to form another,

more innocuous, species. Commonly they are only economic in closed systems such as boilers. Traditional oxygen scavengers suitable for low-to-medium pressure boilers include sulphite anions ( $\text{SO}_3^{2-}$ ) and tannins.<sup>11</sup> The former reacts as follows:



The sulfite is added either as sodium sulfite ( $\text{Na}_2\text{SO}_3$ ), or ammonium bisulfite ( $\text{NH}_4\text{HSO}_3$ ). Note that commensurate with a reduction in oxygen level, the use of sulfite will result in an increase in the quantity of dissolved solids in the system (as sulfate) and consequent increase in electrolyte conductivity. For high pressure and high performance boiler systems (such as in power generation), alternative oxygen scavengers are required that leave no residue. Traditionally, hydrazine has been used for this purpose, reacting as follows:



However, the use of hydrazine is increasingly deprecated due to its toxicity. Alternatives include carbohydrazide, which reacts with oxygen to form  $\text{CO}_2$ ,  $\text{N}_2$ , and  $\text{H}_2\text{O}$ .

Another solution species, which is important in determining corrosivity, is the hydrogen ion ( $\text{H}^+$ ). As the concentration of this species increases, pH decreases, and the CR usually rises. The reason for the occurrence of this phenomenon for iron can be understood from Figure 2, which depicts a Pourbaix

(E–pH) diagram for this substrate. Domains of thermodynamic phase stability for soluble species (i.e., regions of corrosion), insoluble species (e.g., oxides), and the metallic phase (i.e., where oxidation of the metal is thermodynamically impossible) are displayed. Corrosion can be greatly suppressed if the pH is controlled (raised for iron according to Figure 2) to maintain the material within a domain in which a solid phase has significant thermodynamic (or kinetic) stability, that is, in a region of passivity. Thus, water treatment often includes a deliberate reduction in the level of hydrogen ions by the addition of a base such as ammonia, carbonate, or hydroxide, to maintain passivity of the metal.

For more details on water treatment, especially for boiler feedwaters, the reader is referred to the relevant chapter of this section.

#### 4.25.3 Protective Barrier Inducement (PBI)

PBI involves *in situ* substrate/fluid interface modification to impede one or more steps in the corrosion process, for example, metal dissolution. Typically, such surface engineering is achieved through addition of one, or more, chemical reagents to the system, which affect synthesis of a protective substrate adhered layer.

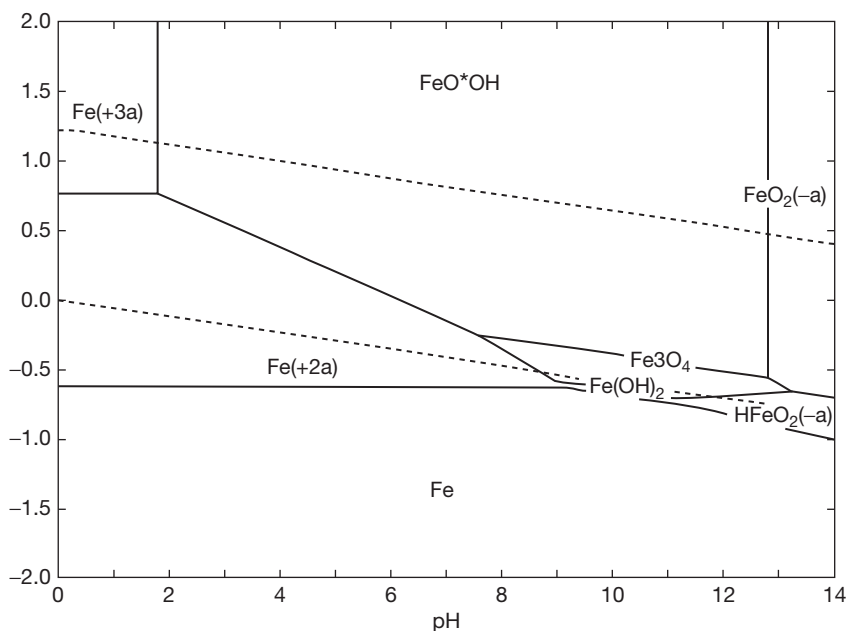


**Figure 2** Pourbaix diagram for iron, drawn for a metal ion concentration of  $10^{-5}$  M.

One can also consider cathodic protection to be a form of PBI (e.g., in the formation of calcareous films in sea water) but this topic will not be discussed further here as it is well covered in other sections.

One route to *in situ* protective layer formation is through initiating precipitation of low solubility inorganic compounds out of solution, such as calcium carbonate ( $\text{CaCO}_3$ ). If the resulting solid forms a substrate bound scale, displaying low porosity/permeability, it can provide significant protection against corrosion. To stimulate the deposition of such a layer, there must be a change in the environment, so that the concentration of the scaling compound in solution exceeds its solubility. This shift may be affected by introducing more of a component of the scaling compound to the aqueous phase, for example, to promote growth of  $\text{CaCO}_3$  scale, one could add either  $\text{Na}_2\text{CO}_3$  or  $\text{Ca}(\text{OH})_2$ . Another option is pH modification. Typically, the pH is raised through, for example, addition of  $\text{NaOH}$  to encourage scaling. These approaches have been applied in practice to control corrosion in potable water supplies where there are lead/copper pipes and few, if any, acceptable alternatives.<sup>12</sup> In other engineering applications, scale formation is undesirable, since it can interfere with the intended process, for example, greatly reduces the efficiency of heat exchange surfaces. A more detailed discussion of these matters can be found elsewhere in this section.

Alternatively, PBI can be accomplished through addition of chemicals known as CIs to the fluid environment. In BS EN ISO 8044:2000<sup>13</sup> the definition of such a species is:

chemical substance that when present in the corrosion system at a suitable concentration decreases the corrosion rate, without significantly changing the concentration of any corrosive agent.

This rather succinct description may be augmented by adding that these substances decrease the CR by bringing about a change at or near the substrate surface, that is, they induce a protective surface barrier. The exact nature of this barrier varies with both the identity of the CI and the environment. For example, it may comprise either a 2-D monolayer or submonolayer comprising a single molecule or ion thickness, or a macroscopic 3-D film. Note that in the ISO definition, species such as oxygen scavengers are not considered to be CIs, as they do significantly change the concentration of a corrosive agent, i.e., they remove the  $\text{O}_2$ . Some authors, incorrectly, do not make this distinction.

Specific inhibitive species are further defined on the basis of one or more characteristics, including the dimensionality of the induced barrier. The terms ‘adsorption’ and ‘film-forming’ are used to classify inhibitors that induce 2-D and 3-D layers, respectively. Other characteristics by which CIs can be categorized include the following:

*Organic/Inorganic* – indicates the composition of a CI using the conventional chemical terminology for compounds.

*Anodic/Cathodic/Mixed* – specifies which electrochemical reaction is stifled by the CI; a mixed inhibitor interferes with both anodic and cathodic processes.

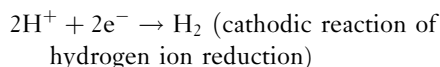
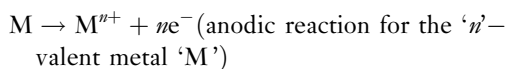
*Oxidizing/Nonoxidizing* – denotes whether or not dissolved oxygen is required for the inhibitor to function efficiently. As discussed later, this terminology is usually restricted to anodic inhibitors operating in near-neutral solutions.

*Safe/Dangerous* – refers to how corrosion proceeds at inhibitor concentrations that are insufficient for effective protection. For a *dangerous* inhibitor, the CR rises abruptly to approximately the same as, or greater than, that of the uninhibited system and localized corrosion (e.g., pitting) can occur. However, neither local corrosion nor a step-wise increase in rate, occurs for a *safe* inhibitor; rather there is gradual increase in the CR (which is not localized as pitting) as the concentration drops.

An alternative system for describing inhibitors is to indicate the environment in which they operate. Typically, a clear distinction exists between CIs for acidic or for near-neutral conditions, as protection mechanisms are usually quite different for these two types of environment. These differences are revealed for substrates immersed in aqueous solutions in the next two subsections.

#### 4.25.3.1 Corrosion Inhibition in Aqueous Acidic Solutions

In sufficiently acidic conditions, the primary corrosion reactions are:



Often these reactions take place in the absence of any significant surface films (oxides, hydroxides, or salts) on the metal, due to the solubility of such layers

at low pH. CIs for this situation are normally of the adsorption type, that is, they form a 2-D monolayer/submonolayer adsorbed directly onto the metallic substrate. Typically, organic molecules are employed,<sup>14</sup> although strongly adsorbing inorganic species such as iodide are also effective in reducing CRs in acidic conditions.<sup>15</sup> A few examples of the many organic molecules employed as CIs are depicted in **Figure 3**.

A variety of factors influence how effectively an organic adsorption CI protects a substrate. Two of the most important parameters are the strength of substrate bonding, and the fraction of the surface covered. Normally, increasing either of these quantities will improve the inhibitor performance, or, more quantitatively, inhibitor efficiency (IE). IE, which is a general term used for all inhibitors, is defined as:

$$IE = \frac{CR_{unhib} - CR_{inhib}}{CR_{inhib}} \times 100 \quad [2]$$

where  $CR_{unhib}$  is the uninhibited CR, and  $CR_{inhib}$  is the inhibited CR.

Concerning substrate bonding of organic CIs, it is useful to consider the molecule/ion to be constructed from a tail group that is normally hydrophobic and a head group that binds the molecule to the surface. As to the precise nature of the surface bonding, it is convenient to divide it into two distinct types, namely electrostatic and covalent. The former interaction arises due to attraction between the ionic charge or dipole on the CI species, and the electrical charge at the metal–electrolyte interface. The second type of bonding, covalent, involves electron transfer/sharing between the CI and the surface.

Electrostatic substrate bonding is most commonly exhibited by CIs having the formula  $NR_4^+X^-$ , with the cationic fragment acting as the primary inhibitive species. The simplest of these molecules are N-alkyl quaternary ammonium salts, for which the R groups

are alkyl chains ( $C_nH_{2n+1}$ ) of various lengths. Methyl groups are usually present to facilitate surface binding (head group), together with longer chains (tail group) oriented toward the corrosive solution. Clearly, the net charge at the substrate surface must be negative to enable  $NR_4^+$  adsorption, and these species may either bond directly to the hydrated metal surface or through negatively charged adsorbed species (e.g.,  $Cl^-$ ,  $SO_4^{2-}$ ).<sup>16</sup>

Covalent substrate bonding of organic CIs occurs through electron-rich head groups. Most often they are nitrogen or sulfur (or other Group V/VI elements) containing functional groups, although  $\pi$ -electron systems (e.g., C–C triple bonds and aromatic rings) are also effective. The bonding strength exhibited by the head group is determined by its electron density and polarizability, that is, the degree to which electrons can be donated to the substrate. These attributes depend not only on the identity of the functional group itself, but also upon the overall structure of the inhibitor molecule. For example, it has been shown for a number of aromatics that addition of ring substituents modifies inhibition performance.<sup>17,18</sup>

Turning to the surface coverage of an organic CI, usually this is related to its concentration in solution by standard adsorption isotherms. For example, the Langmuir isotherm relates the fraction of surface covered relative to a full monolayer ( $\theta$ ) to bulk solution concentration ( $C$ ) by:

$$\theta = \frac{KC}{1 + KC} \quad [3]$$

where  $K$  is a constant. On the basis of this expression, increasing bulk solution concentration will lead to greater surface coverage, as shown in **Figure 4**. Furthermore, assuming that corrosion only occurs on inhibitor free surface, IE (%) may be obtained from

$$IE = 100 \times \theta \quad [4]$$

Thus, increasing bulk solution inhibitor concentration will lead to more effective inhibition, albeit with

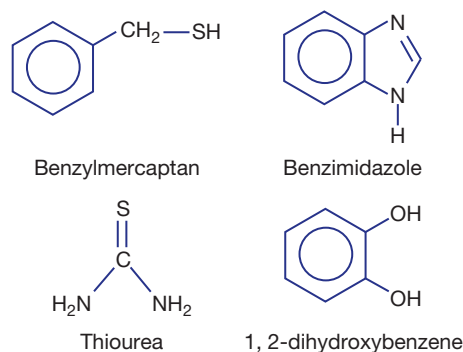


**Figure 3** Examples of lower molecular weight organic CIs.

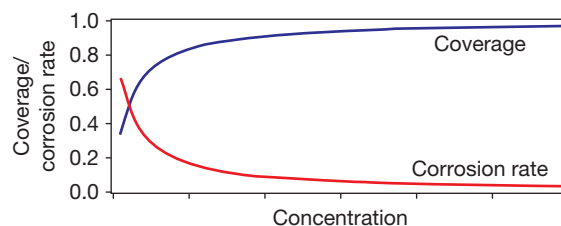


**Figure 4** Plot of fractional surface coverage and corrosion rate as a function of bulk solution corrosion inhibitor (CI) concentration. Curves have been obtained using the Langmuir adsorption isotherm.

diminishing returns for increments at higher concentrations due to the nature of the Langmuir isotherm. However, this expression for IE and  $\theta$  is often not strictly valid. On the one hand, the CR of inhibitor-covered parts of the substrate may not be zero, but rather just significantly reduced. Furthermore, full monolayer coverage may not be required to maximize corrosion suppression, if the inhibitive species preferentially adsorbs at electrochemically active sites (anodic or cathodic). It has also been reported that in certain cases CIs work better at lower coverage than at higher coverage (see, e.g., Singh).<sup>19</sup>

Of course to curtail corrosion, adsorbed organic monolayers/submonolayers must not only be present but must in some way retard the rate of the anodic and/or cathodic corrosion processes. The inhibitive species may entirely cover the surface, but still preferentially interfere with only one of the half reactions. It is, in principle, relatively straightforward to differentiate between an anodic and a cathodic inhibitor by measurement of variation in corrosion potential with time upon addition of the inhibitor. Thus, if the corrosion potential increases (decreases) then the CI is anodic (cathodic), while little change indicates a mixed inhibitor. Further mechanistic insight is not obtainable from a study only of the potential shift. However, more detailed investigation may be carried out by potentiodynamic polarization, along with surface analysis techniques. There are a number of proposals for how an organic CI may function in acidic solution, including:

*Reaction site blocking* – prevents bound metal atom(s) from taking part in corrosion reactions.

*Formation of diffusion barrier* – restricts diffusion of ions/molecules to/from metal surface. More likely to be operative for larger CIs (e.g., long hydrocarbon chain tail groups), or for alkynes that polymerize on the surface forming a blocking film.

*Participation in electrode reactions* – interferes with usual reaction pathway. A diagram indicating how an inhibitor might modify the anodic dissolution mechanism is displayed in [Figure 5](#).

#### 4.25.3.2 Corrosion Inhibition in Aqueous Near-Neutral Solutions

In aqueous near-neutral solutions, the anodic corrosion reaction remains metal dissolution, but the primary cathodic reaction becomes:

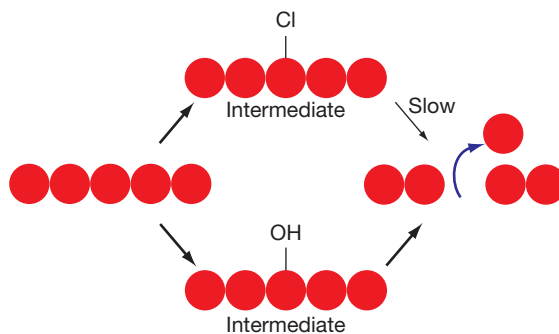
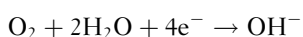


**Figure 5** A diagram suggesting how a CI may interfere with anodic metal dissolution, slowing down this reaction by forming an alternative intermediate surface complex.

for aerated solutions (as illustrated in [Figure 1](#)). Also, unlike at low pH, the anodic/cathodic reactions usually occur in the presence of surface films (oxide, hydroxide, or salts). Under these conditions, CIs are typically of the film-forming variety. Typically, they are identified as being either anodic or cathodic, since these two types function rather differently, interfering with anodic metal dissolution and cathodic oxygen reduction, respectively. Inhibitor additions to deaerated solutions are not considered here, as CRs are usually sufficiently low (see previous section).

Anodic inhibitors for aqueous near-neutral solutions, sometimes known as passivating inhibitors, control the anodic dissolution of metals by inducing formation of a passive oxide film on the metal surface (typically of nanometer thickness). Their action is substrate specific, that is, an effective inhibitor for one metal is unlikely to be effective, or may even aggravate corrosion, for another metal. For carbon steels, which are of greatest interest practically, anions of various weak acids are effective, including chromate, nitrite, molybdate, and benzoate.

These anodic inhibitors can be further classified as oxidizing or nonoxidizing, depending upon whether or not dissolved oxygen is required for their operation. Chromate and nitrite are both oxidizing inhibitors, whereas molybdate and benzoate are nonoxidizing. Given the low CRs normally encountered in  $\text{O}_2$  free near-neutral aqueous solutions, this division may appear to be of little use beyond academic interest. However, the employment of oxidizing inhibitors can prevent corrosion in areas exhibiting depleted dissolved  $\text{O}_2$  concentration (e.g., in a crevice) in otherwise aerated systems.

Concerning performance of these anodic inhibitors, in contrast to the adsorption inhibitors for acidic solutions, CR does not vary smoothly with



concentration. Instead, there is an abrupt decrease in CR at a critical concentration ( $C_{\text{crit}}$ ), as illustrated schematically in Figure 6. The numerical value of  $C_{\text{crit}}$  is dependent upon the identity of the inhibitive species and substrate, as well as other environmental variables. For example, greater aggressive ion concentrations (e.g.,  $\text{Cl}^-$ ,  $\text{SO}_4^{2-}$ ) usually increase  $C_{\text{crit}}$ . Typically, above  $C_{\text{crit}}$  the corrosion remains minimal and approximately constant, although some studies have shown a return to larger CRs at higher inhibitor concentrations (see, for example, Kolman and Taylor).<sup>20</sup> These inhibitors should also be labeled as dangerous, due to the sudden increase in CR below  $C_{\text{crit}}$ .

The existence of a  $C_{\text{crit}}$  for the onset of effective inhibition can be understood from the  $E$ -log  $i$  diagram shown in Figure 7. This plot is typical of

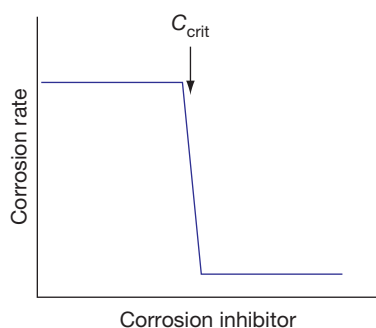


**Figure 6** A schematic plot of corrosion rate versus inhibitor concentration for an anodic passivating inhibitor.  $C_{\text{crit}}$  is indicated.

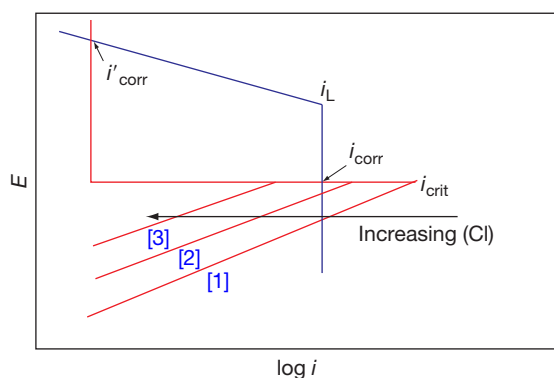


**Figure 7** Schematic  $E$ -log  $i$  diagram for carbon steel in aerated, neutral solution. Red (blue) lines are anodic (cathodic) curves. It illustrates what happens to the corrosion rate as the concentration of anodic Cl is increased in steps ([1]→[2]→[3]). On going from [1]→[2] the corrosion rate stays the same ( $i_{\text{corr}}$ ), but further increasing [Cl] to [3] leads to a huge drop in corrosion rate ( $i'_{\text{corr}}$ ) with the metal entering the passive region.

carbon steel in aerated near-neutral aqueous solution, that is, the cathodic curve displays a limiting current density ( $i_L$ ), and the anodic curve displays active and passive regions. As illustrated, increasing the inhibitor concentration results in a decrease in the critical current density ( $i_{\text{crit}}$ ) required for passivation. However, spontaneous inhibitor induced passivation ( $i_{\text{corr}} \rightarrow i'_{\text{corr}}$ ) is only achieved once  $i_{\text{crit}} < i_L$ , which requires a sufficient concentration of inhibitor (i.e.,  $C_{\text{crit}}$ ). Thus, there is a sudden onset of effective inhibition at a  $C_{\text{crit}}$ . The plot also indicates that there is sharp increase in the corrosion potential upon passivation, which is consistent with experimental studies.<sup>21</sup> It should be noted that some CIs (e.g., nitrobenzoate) can also increase  $i_L$ , enabling passivation to occur even with relatively large values of  $i_{\text{crit}}$ .

Concerning the precise mechanisms by which these anodic inhibitors induce passivity, limited real insight has been gained to date, although there is a great deal of speculation. Even the composition and structure of the passive films are not clear in many cases, which is essential input for nanoscale mechanistic understanding. However, CI roles likely include one or more of the following:

- catalyst for the formation of a passive film;
- reagent for the formation of a passive film;
- plugging active pores in an existing film with insoluble compounds so as to induce passivity;
- preventing the adsorption of aggressive anions; and
- reducing the rate of dissolution processes.

Cathodic inhibitors for aqueous near-neutral solutions typically reduce the rate of cathodic oxygen reduction by precipitating out an insoluble surface film, which restricts oxygen diffusion to the metal surface. Often, but not always, the films are rather thick (approx. 100 nm–few mm), and form largely independently of substrate identity. To be protective these layers must adhere well to the surface and have low porosity/permeability, as well as lack electronic conductivity, otherwise the cathodic reaction would occur on the surface of the film.

The prototypical film-forming cathodic inhibitor is a soluble salt containing, for example,  $\text{Zn}^{2+}$  cations, that results in the formation of a relatively insoluble, electrically insulating  $\text{Zn}(\text{OH})_2$  film with precipitation driven by the local rise in pH at a cathode. Importantly, and contrary to some perceptions, chromate ion, as well as being an anodic inhibitor at higher concentration, also acts as an extremely effective cathodic inhibitor at lower concentration, due to surface reduction of the  $\text{CrO}_4^{2-}$  anions to form highly insoluble  $\text{Cr}(\text{OH})_3$ .

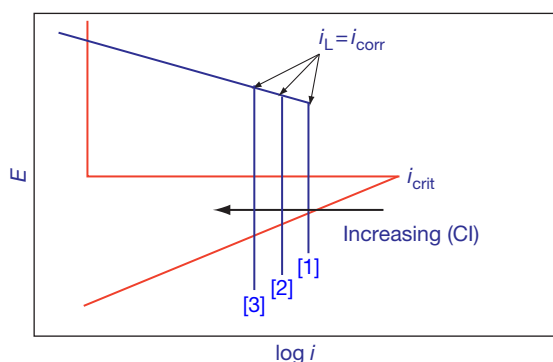


**Figure 8** Schematic  $E$ - $\log i$  diagram for carbon steel in aerated neutral solution, illustrating the effect of increasing the concentration of a film-forming cathodic Cl. Red (blue) lines are anodic (cathodic) curves. As the concentration increases ([1]→[2]→[3])  $i_L$ , and thus  $i_{\text{corr}}$ , decreases.

Other species that can act as cathodic inhibitors include phosphonates and orthophosphates.

In contrast to anodic passivating CIs, there is no  $C_{\text{crit}}$  for cathodic inhibitors, rather the CR gradually reduces as its concentration increases. Again, this trend may be understood from considering changes in  $E$ - $\log i$  curves as a function of inhibitor concentration. As illustrated in **Figure 8**, increasing the cathodic inhibitor concentration reduces  $i_L$ , since in an aerated near neutral solution, it is determined by the transport of oxygen to the surface. As, under these conditions,  $i_L = i_{\text{corr}}$ , the CR also decreases.

#### 4.25.4 Final Remarks

In the previous subsections, we have provided an introduction to CAR and PBI under typical conditions. No attempt has been made to give a complete review of the considerable volume of knowledge and ongoing research in this area. For example, we do not make specific mention of volatile CIs, although they can be an effective adjunct to CAR for various storage and packaging applications.<sup>7,22</sup> We have also restricted ourselves to the effect of a single inhibitive substance, whereas in many cases a mixture

of inhibitors is used, which can display synergistic behavior. However, we believe we have provided enough information so that readers new to this area have sufficient insight into the basics of the following chapters in this section.

## References

1. Picard, A.; Fang, H. *Metrologia* **2004**, *41*, 333–339.
2. Vernon, W. H. J. *Trans. Faraday Soc.* **1931**, *27*, 255–277.
3. Gdowski, G. E.; Estill, J. C. In *Scientific Basis for Nuclear Waste Management XIX*; Murphy, W. M., Knecht, D. A., Eds.; Materials Research Society Symposium Proceedings, 1996; 412, pp 533–538.
4. Greenspan, L. J. *Res. Natl. Bur. Stand* **1977**, *81A*(1), 89–96.
5. BS 1133–19: 1986: Packaging code – Use of desiccants in packaging.
6. Clarke, S. G.; Longhurst, E. E. *J. Appl. Chem* **1961**, *11*, 435–443.
7. Donovan, P. D. *Protection of Metals from Corrosion in Storage and Transit*; Ellis Horwood: Chichester, 1986.
8. Farrow, K.; Hutchings, J.; Sanderson, G. *Br. Corros. J.* **1981**, *16*(1), 11–19.
9. Bretherton, N.; Dawson, J. L.; Thompson, G. E.; Moreland, P. J.; Winterton, N. *Corros. Sci.* **1993**, *35*, 205–211.
10. Oldfield, J. W.; Todd, B. *Desalination* **1979**, *31*, 365.
11. Revie, W.; Uhlig, H. H. *Corrosion and Corrosion Control, An introduction to Corrosion Science and Engineering*, 4th ed.; Wiley-Interscience: London, 2008; Chapter 18, p 317.
12. Karalekas, Jr.; Peter, C.; Ryan, Christopher, R.; Taylor; Floyd, B. *Govt. Eng.* **2007**, 42–43.
13. BS EN ISO 8044:2000: Corrosion of metals and alloys. Basic terms and definitions
14. Schmitt, G. *Br. Corros. J.* **1984**, *19*(4), 165–176.
15. Jeyaprabha, C.; Sathiyarayanan, S.; Muralidharan, S.; Venkatachari, G. *J. Braz. Chem. Soc* **2006**, *17*(1), 61–67.
16. Fuchs-Godec, R. *Colloids Surf. A: Physicochem. Eng. Aspects* **2006**, *280*(1–3), 130–139.
17. Akiyama, A.; Nobe, K. *J. Electrochem. Soc.* **1970**, *117*(8), 999–1003.
18. Tan, Y. S.; Srinivasan, M. P.; Pehkonen, S. O.; Chooi, S. Y. M. *Corros. Sci.* **2006**, *48*, 840–862.
19. Singh, I. *Corrosion* **1993**, *49*(6), 473–478.
20. Kolman, D. G.; Taylor, S. R. *Corrosion* **1993**, *49*(8), 635–643.
21. Al-Refaie, A. A.; Cottis, R. A.; Lindsay, R. *NACE Corrosion 2009*; NACE International: Houston, 2009; Paper No. 09282.
22. Bastidas, D. M.; Cano, E.; Mora, E. M. *Anti-Corros. Method M* **2005**, *52*(2), 71–77.

## 4.26 Chemical Treating in Oil and Gas Production

**J. L. Dawson**

Corrosion Consultant, 16 Brandwood Close, Worsley, Manchester M28 1XX, UK

© 2010 Elsevier B.V. All rights reserved.

<b>4.26.1</b>	<b>Introduction</b>	2901
<b>4.26.2</b>	<b>Background</b>	2903
4.26.2.1	Treating Terminology	2903
4.26.2.2	Field Applications	2905
4.26.2.2.1	Continuous treatments	2905
4.26.2.2.2	Batch treatments	2907
<b>4.26.3</b>	<b>Corrosion Inhibition</b>	2908
4.26.3.1	Inhibition Processes	2908
4.26.3.2	Inhibitor Performance	2910
4.26.3.3	Inhibitor Testing	2911
4.26.3.3.1	Bubble test	2911
4.26.3.3.2	RCE test/flow loops	2912
4.26.3.3.3	Inhibitor persistency	2913
4.26.3.3.4	Jet impingement	2914
4.26.3.3.5	Inhibition of weld corrosion	2914
4.26.3.3.6	Autoclave tests	2914
4.26.3.3.7	Compatibility	2914
4.26.3.3.8	Field deployment	2914
<b>4.26.4</b>	<b>Scale Inhibition/Control</b>	2916
4.26.4.1	Scale Inhibitor Application	2916
4.26.4.1.1	Scale treatment chemicals	2916
4.26.4.1.2	Scale control	2917
4.26.4.2	Scale Predictions	2917
4.26.4.3	Squeeze Application	2919
4.26.4.4	Scale Inhibitor Selection	2919
4.26.4.5	Scale Removal	2919
<b>4.26.5</b>	<b>Treating for MIC</b>	2920
4.26.5.1	Bacteria Monitoring Techniques/Serial Dilution	2920
4.26.5.2	Biocide Treatments	2922
4.26.5.3	Biocide Application	2922
<b>4.26.6</b>	<b>Management of Treating Programs</b>	2923
4.26.6.1	Inhibition Risks and Mitigation by Monitoring	2925
4.26.6.2	Monitoring and Data Management	2927
<b>References</b>		2929

### Abbreviations

**API** American Petroleum Institute  
**CA** Corrosion allowance  
**CRA** Corrosion resistant alloy  
**HIC** Hydrogen-induced cracking  
**HSE** Health and Safety Executive  
**ICDA** Internal Corrosion Direct Assessment  
**ISO** International Standards Organization  
**KPI** Key performance indicator

**LPR** Linear polarization resistance  
**MEG** Methyl ethyl glycol  
**MIC** Microbiologically influenced corrosion  
**NACE** National Association of Corrosion Engineers  
**NDT** Non-destructive testing  
**QA** Quality assurance  
**RBI** Risk-based inspection  
**SCADA** Supervisory Control and Data Acquisition  
**SHE** Safety, health and environment

**SRB** Sulfate-reducing bacteria  
**SSCC** Sulfide stress corrosion cracking  
**TQM** Total quality management

### 4.26.1 Introduction

Chemical treatments are employed in many industries to control various corrosion and operational problems. The oil and gas production and refining industries use 'treating' to describe the injection of corrosion inhibitors, biocides, scale control chemicals, oxygen scavengers, etc. into process streams, produced fluids, and hydro-test waters with the objective of mitigation of corrosion risks from carbon dioxide, hydrogen sulfide, oxygen, and bacteria. Treatment success, both technical and financial, requires selection of suitable chemical packages along with control of dose rate to achieve the required concentration in the process stream plus regular monitoring of physical assets, including injection equipment to ensure optimal control of the management system performance. Details of the role of corrosion management in oil/gas production from concept design to operations is provided in a separate chapter of this volume<sup>1</sup> and provides a wider context of the use of treating as part of the strategic and tactical requirements for oil field assets.

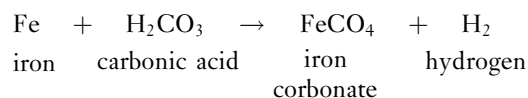
Corrosion in petroleum industry equipment is controlled by fluid chemistries, water content, pressures, temperatures, and flow conditions that are in turn determined by past geological conditions in oil/gas reservoirs, the rate of extraction, and use of injection water for enhanced recovery. Stable chemical equilibria are disturbed as reservoir fluids are extracted and may result in increased scaling tendency and even enhanced hydrogen sulfide concentrations in produced fluids. Exported crude oils may contain sulfur compounds and other contaminants that cause corrosion under high temperatures found in refinery operating conditions.

Reservoir fluids contain hydrocarbon phases, gases such as methane and ethane, and oils of varying composition depending on the age/type of formation and original organic material source. Other organic reservoir components, such as acetic acid, often accelerate corrosion, although they can also lead to improved oil wetting properties decreasing corrosion rates due to an increase in oil wetting of metal surfaces. Formation waters, the aqueous/brine phase in the reservoir, often contain dissolved salts, such as calcium carbonate, barium sulfate, sodium sulfate, and sodium chloride. Chlorides and sulfates can cause pitting corrosion,

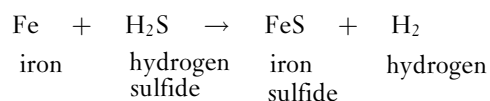
whilst some dissolved salts (such as calcium carbonate/barium sulfate) may give rise to scaling conditions in some equipment. The major corrosion constituents are the acidic gases, carbon dioxide, and hydrogen sulfide that dissolve in both the oil and water phases, but cause corrosive electrolytes when dissolved in the water phase.

Overall corrosion reactions can be summarized by the following reactions.

For CO<sub>2</sub>:



For H<sub>2</sub>S:



For CO<sub>2</sub>, corrosion damage is typically seen as metal wall thinning and shallow pitting. Under high velocity conditions, deep elongated 'pits' may be observed; an erosion type of attack sometimes referred to as flow assisted localized corrosion. Iron carbonate corrosion products precipitate as semi-protective films or scales that assist in the control of CO<sub>2</sub> corrosion.

For H<sub>2</sub>S, the low solubility of iron sulfide results in the formation of black corrosion product films that are more effective at protection than iron carbonate films, particularly at higher H<sub>2</sub>S concentrations. However, the film is an efficient cathode, which can lead to intense pitting of unprotected areas. Hydrogen sulfide may also cause hydrogen damage in susceptible steels (the iron sulfide film causes atomic hydrogen produced in the corrosion reaction to diffuse into the steel). Typical hydrogen damage of susceptible steels includes embrittlement, hydrogen induced cracking (HIC), hydrogen blistering, and sulfide stress cracking.

Physical changes will also occur as produced fluids undergo pressure decrease when they rise up production tubulars, through well head/choke valves, pass along flow lines and manifolds and through gas-oil separation plant/equipment. Pressure decrease in the tubulars/reservoir to below the bubble point of the hydrocarbon gas leads to large increases in gas volumes leading to bubbly flow and even to the erosive conditions of slugging flow, [Figures 1 and 2](#). In addition, the combination of temperature and pressure decreases may cause deposition of scales, and lead to underdeposit corrosion. Corrosion





**Figure 1** Erosion corrosion of a tubular (mesa corrosion).

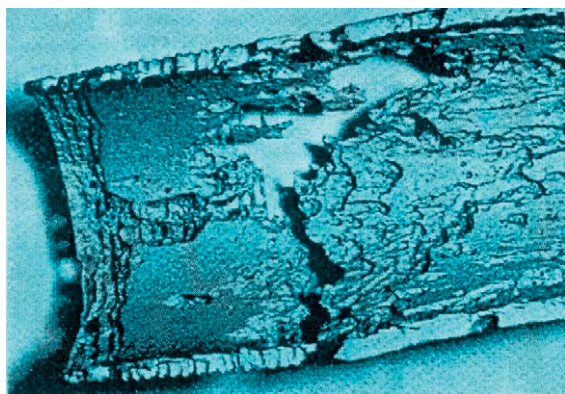


**Figure 2** Erosion downstream of a tubular joint in a sour system.

processes, [Figure 3](#), and bacteria present under deposits are difficult to treat because chemicals cannot easily diffuse through the scale or sludge found at the bottom of pipelines and process vessels; these deposits include mill-scale deposits, loose scale crystals/corrosion products.

In many applications, corrosion control is only one objective since control of scaling/microorganisms/fouling in downhole/field/refinery applications may be of equal or greater importance. Production economics, including factors such as plugging of reservoir strata/the hazard from a build-up of radioactive strontium scale in process plant, or microbial contamination including 'souring' of a reservoir or fouling of equipment may be of greater specific concern than that of corrosion. The majority of corrosion observed in pipelines is at the 6 o'clock position due to water drop out and deposits with corrosion, the oil



**Figure 3** Pitting corrosion found under deposits in a pipeline.

and gas phases at the upper sections is normally assumed to be 10% of the bottom water wet section. However, it has been found that with wet gas lines/lines containing glycol/methyl ethyl glycol (MEG) that is pH stabilized, the concentration of acetate from the formation water will affect the concentration of acetic acid in condensed water in the top of the line. At too high a pH, the stabilized MEG may also give precipitation of  $\text{CaCO}_3$  and  $\text{MgCO}_3$ .

In general, corrosion is often a life limiting factor for equipment, particularly c-steel constructions, and corrosion inhibition is required to ensure the design/operation life is achieved. This also means that clean surfaces, free from deposits, biofilms, and nonprotective scales are needed so that treating chemicals are able to diffuse to and adsorb on surfaces. Ideally, the metal surface should be free from mill-scale at start-up, and chemical (acid) cleaning may be used as part of the commissioning process especially for welded vessels fabricated from corrosion resistant alloys. Pipelines with their large surface areas can produce significant quantities of sludge during the first years of operation as the air formed mill-scale produced during line steel manufacture is progressively replaced by iron carbonate/iron sulfide. In many cases, the sludge build up prevent a cleaning pig run. Also, iron sulfide is pyrophoric giving rise to disposal issues. A preferred option is to sweep blast the pipe internal during the shop application of the external coating process.



The general term chemical treating includes:

- **Control of corrosion of metallic components** by corrosion inhibitors, particularly c-steel and low alloy fabrications, such as lines, vessels, columns, heat exchangers, storage tanks, and in hydrotest fluids, but can also include corrosion resistant materials when acid treatments are employed for descaling equipment, acidizing rock formations, postfabrication cleaning, and repassivation.
- **Control of biological growth** to minimize biofouling and microbiologically induced corrosion (MIC) during hydrotest and operation.
- **Control of scales** by scale inhibitors to prevent plugging of pores in strata, blocking of lines and equipment, decrease of heat transfer at heat exchanger surfaces.
- **Control of fouling** by dispersion, sequestration, chelation, and detergents to minimize formation of sludge/precipitates/deposits in lines and equipment.
- **Control of wax** precipitation in production equipment and reservoirs.
- **Control of dissolved oxygen** by oxygen scavengers in hydro-test treatments and downhole water injection systems.
- **Control of emulsions** in oil–gas separation equipment by emulsion breakers as an aid to oil/water separation processes, also includes antifoam and antisludge agents.
- **Control of pH** by caustic injection into condensate and MEG/hydrate control chemicals.

Typically, the chemicals employed have surface active functional groups containing sulfur or nitrogen (e.g., amines, amides, imadazolines, quaternary ammonium salts), that are able to adsorb onto a metal surface and displace water, modify a growing salt crystal, or kill/restrict bacterial and fungus growth. Often, several chemicals are added to a system due to different problems. As well as providing their specified functionality they may also affect the interfacial conditions between liquid phases. For example, some surface active chemical mixtures may produce stable oil in water or water in oil emulsions (by micelle formation) that often result in down stream problems, including foaming and formation of tight emulsions. Other surface active chemicals are able to destabilize water in oil emulsions (emulsion breakers) or oil in water emulsions (reverse breakers), and these are employed to improve the separation processes in production equipment.

In practice, treating must be viewed as part of an organization's strategy to mitigate the effects of

corrosion and enhance system performance. Successful management of the treating process is one of the primary aims of a corrosion team. Such teams may comprise various specialists including a corrosion engineer, chemist, biochemist, as well as production, maintenance personnel who have responsibility for the dosing and repair of injection systems. Effective chemical treating requires that ownership of the process and its boundaries must be clearly defined as part of the asset management structure. Typical duties involve selection, testing of chemicals, dosing, and monitoring, with reporting and decision making being key elements in the management process.<sup>2</sup> Most oil/gas production and refinery systems would be unable to achieve economic viability without chemicals such as inhibitors to control erosion–corrosion produced by multiphase slugging flow in pipework or filming amines as used in column overheads/condensers in refineries. The market for these chemicals is estimated at 3–6% of operational costs, of the order of millions of dollars per year.<sup>3</sup>

**Section 4.26.2** of this chapter introduces some common themes, basic concepts, terminology, and issues relating to the use of chemicals, injection equipment, and monitoring. These include batch treatments of lines with corrosion inhibitors, and biocides, where a slug of chemical trapped between two pigs/spheres is employed, or when a scale control–corrosion inhibition ‘squeeze treatment’ is used downhole. Continuous inhibition is generally preferred in fluids with a high water content, such as treatment of multiphase fluids/water lines.

Corrosion inhibitors are addressed in **Section 4.26.3**, including the impact of local conditions, such as fluid composition, throughput, and water cut, on the type of inhibitor package employed. **Section 4.26.4** considers the control of scale and deposition of fouling deposits. Control of bio-fouling and MIC, including monitoring and serial dilution, is outlined in **Section 4.26.5**. This chapter concludes with management aspects of treating processes.

## 4.26.2 Background

### 4.26.2.1 Treating Terminology

Formulations of vendor chemical treatment packages are commercially confidential with respect to the details of the type of compounds employed, although general information on the generic chemicals used (e.g., amine, quaternary amine) are provided together with data sheets on the chemical analysis performed,

for example, UV/IR spectroscopy, that is then used for QA/QC purposes. The packages are designed for particular applications and specific environments that are typically characterized by the process fluid water content or water cuts for crude oil lines/gas phase applications. Thus, the terms typically employed include: *water soluble* (clear solutions), *oil soluble* (clear solutions), *oil or water dispersible* (cloudy solutions), *oil and water insoluble* ('gunkers'), and *gas phase* (low volatility/filming inhibitors).

Treating packages not only contain active inhibitor compounds but also contain additives that assist by providing solubility and dispersibility, that is, surfactants and demulsifiers that aid performance in the field. For example, dispersibility of an oil soluble inhibitor is increased by blending it with a surfactant that assists dispersion of oil soluble inhibitors into both the oil and water phases. An increase in emulsion tendency, formation of micelles, or microemulsions can present operating problems in separation equipment, and some corrosion inhibitor–biocide mixtures can produce emulsions in water–oil systems that are very hard to break. A demulsifier may, therefore, have to be added into the processing train to help oil and water separate. The emulsion tendency is a chemical's ability to disperse one liquid phase into another liquid phase. Solvents prevent separation of active ingredients, make chemicals less viscous for injection into the production system, and maintain the chemical in liquid form during storage. Solvents also lower the pour point, the minimum temperature at which the chemical remains a liquid.

The solubility of a chemical is the ability to dissolve in solution, but for compounds with limited solubility, the degree of dispersability is used. For example, some treating chemicals are not fully soluble in either the oil or water phases and must be dispersed largely in one phase. Oil soluble–water dispersible inhibitors readily mix with most crude oils and have various degrees of dispersibility in fresh, brackish water, or brines. Dispersibility helps inhibitors to be carried by fluids to the wet metal surfaces where they absorb, displace water, and form oil–wet films that resist corrosion. Water soluble corrosion inhibitors form inhibitor films that are not as persistent as the oil soluble corrosion inhibitor films, hence continuous injection is almost always needed for effective corrosion control in fluids with a high water content–high water cut.

Surfactants are added to corrosion inhibitor packages to help clean metal surfaces. However, a major factor during operation is that preexisting air formed iron oxide films are progressively replaced by reaction

with  $\text{CO}_2/\text{H}_2\text{S}$  containing fluids. This means that large quantities of mill scale will be lost during the first few years of operation, particularly in large diameter, long distance pipelines leading to significant deposits/sludges of mixtures of oxides, carbonates, and sulfides. The maintenance of a clean surface from the start requires regular cleaning pig runs, a crucial procedure in some pipelines. Clean metal surfaces increase the effectiveness of almost all corrosion inhibitor treatments. In some equipment fabricated in corrosion resistant alloy, a precommissioning cleaning treatment followed by repassivation may be advisable before the introduction of process fluids.

Water-in-oil oilfield emulsions are droplets of water dispersed in oil or condensate. In low water cuts, water droplets become emulsified in oil due to mixing energy as fluids are produced from a formation, and are further mixed at valves and chokes. Surfactants will enhance this process, and may come from the crude oil or be introduced as part of the treating package. Emulsions may start to break down within a pipeline and this process is needed to achieve the oil–water separation process. Three steps are involved: flocculation, coalescence, and settling, see [Figure 4](#). Flocculation is the process in which water droplets gather into groups. The droplets are surrounded by surfactant films that keep them apart. Coalescence is the process in which the surfactant film breaks and allows a group of droplets to become one larger droplet. The larger droplets settle to the bottom because water is heavier than oil. These processes are responsible for the progressive water drop out at low spots in lines as both temperatures decrease away from the mixing at the well head valve but also as water cuts increase in produced fluids. Emulsions are also created when the crude is washed to remove salt at the refinery. Given enough time, almost any emulsion will separate into oil and water phases. However, some emulsions do not separate, due to stabilization by fine solids like clays and iron sulfide.

Demulsifier chemicals, often called emulsion breakers, are continuously added to emulsion streams to speed up the separation process. Demulsifiers must thoroughly mix with the emulsion to work properly. Oil field separation vessels are added to production systems to allow efficient oil–water separation after demulsifier treatment. Demulsifiers or antifoam agents are sometimes added to organic inhibitors to prevent the formation of stable emulsions.

In oil field operations, water that has been separated from oil will contain some emulsified droplets of oil. These types of emulsions are called 'reverse

emulsions' or oil-in-water emulsions. The most common causes of reverse emulsions are the improper use of an oil demulsifier, excessive demulsifier treatment, or improper sizing or operation of water separation vessels. Removal of oil from water is often required to meet disposal regulations. Reverse emulsion breaker chemicals are added to water to gather or flocculate the oil droplets into larger droplets. Larger droplets of oil will float to the top of the water. Reverse emulsion breakers must thoroughly mix with the water so it will contact the oil droplets. Provision for injection of chemicals at process plant has to be made both for emulsion control and also for inhibition of export lines and water return lines, **Figure 5**.

#### 4.26.2.2 Field Applications

Treating chemicals can be injected either continuously or in batches, depending on the application, system

operating conditions, and fluid compositions, as well as performance versus costs. Continuous injection is generally preferred for aqueous fluid systems and multiphase fluid lines, particularly with high water cuts, and the gas phase of wet gas lines. Batch treatment is sometimes used for downhole treatments if technical or economic considerations preclude continuous injection. This may involve a 'squeeze treatment' in a similar manner to an acidizing treatment of a rock strata, but the aim is to allow inhibitor to slowly desorb from the strata back into produced fluids. Batch treatment is also used in special cases where a slug of biocide is trapped between two scraper pigs or spheres for application of a persistent inhibitor onto the surface of wet gas lines.

##### 4.26.2.2.1 Continuous treatments

Continuous dosing in high water content systems is typically employed for corrosion inhibition, scale inhibition, oxygen scavenging, and to break emulsions.

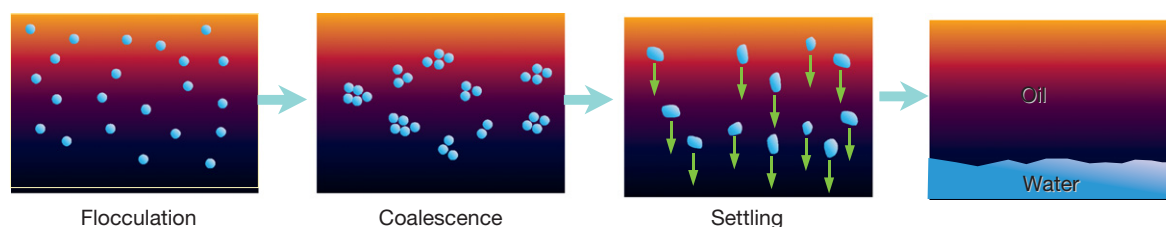


**Figure 4** Water in oil emulsion leading to water drop-out in lines.

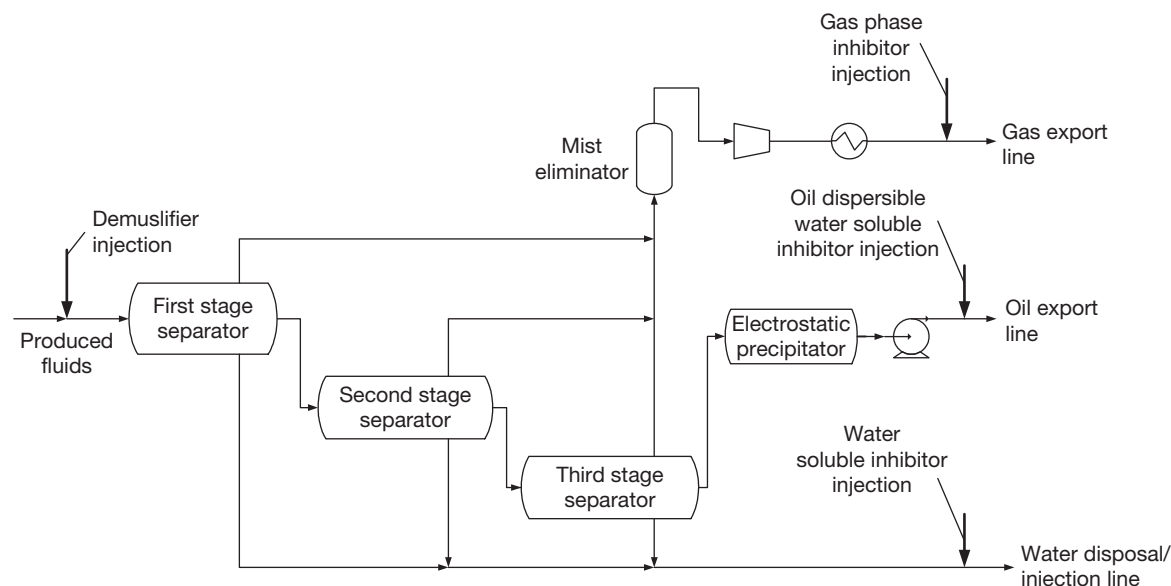


**Figure 5** Typical chemical/inhibitor injection locations.

Continuous inhibition is a preferred method of application, particularly for wet systems, and where erosion–corrosion is anticipated. It can be used for downhole and topside equipment, including wellheads, separation facilities, flowlines, pipelines, etc. In processing trains, the inhibitor may be carried mainly by one stream (usually the separated water) and further continuous injection of an inhibitor into the other streams (exported gas and oil phases) may be required after separation. Continuous injection of gas phase inhibitors is also used for lines and equipment, see **Figure 6**.

The injection location is usually as far upstream as practicable to enable the inhibitor to reach as much of the equipment surface as possible. Common injection points in the field include: (1) downhole, (2) at the wellhead, (3) individual flow lines, (4) manifolds/gathering lines, trunk lines, separation plant, and (5) export lines. One concern is that many chemicals are corrosive when concentrated and can cause damage around the injection point, regular inspections are needed as recommended in *API 570 Inspection, Repair, Alteration, and Retesting of In-Service Piping Systems* to prevent failures of the type shown in the figure. Such failures have also been responsible for refinery fires, for example, Ras Tanura and South Humber, that resulted in significant financial/production losses, see **Figure 7**.

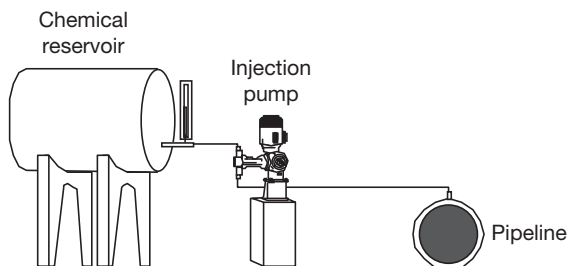


**Figure 6** Chemical injection into line/well.

In practice, down hole injection is difficult and prone to problems as liquid inhibitor has to be passed down a thin ‘spaghetti’ tube positioned in the annular space between the casing and the tubes. The inhibitor then goes through a valve into the tube just above the packer. All equipment below this injection point is not protected by inhibition and should be fabricated from corrosion resistant materials. Gas phase inhibitors used in gas lift operations are typically introduced under pressure down the annulus. In many cases, the flow conditions and differences in metallurgy between tubes (seamless/pierced billet) and flow lines (welded rolled plate) means that the down hole may be less of a concern and, therefore, the inhibitor is often added at the well-head.

Types of injection pumps include pressure injection systems (use of a nitrogen pressurized vessel with gravity feed), metering pump injection (positive displacement where a varying stroke length or varying speed controls the pump flow rate), flow proportional injection (produced fluid flow rate controls the injection rate, the pump is stopped when production stops). In high risk systems, a back-up pump is vital with shut-off alarms to increase reliability. Standard skid mounted equipment is used whenever possible to reduce costs and increase reliability. The supplier of the inhibitor injection system should provide



**Figure 7** Failure of line at injection point. *Corrosion Threats Handbook – Upstream Oil and Gas Production*; Energy Institute of Oil and Gas: London, 2008.



evidence, in the form of field experience or a component reliability analysis, that the required up time/inhibitor availability can be achieved.

Continuous corrosion inhibitor treatment often begins with a high concentration of chemical that ensures rapid development of an inhibitor film on all metal surfaces. After the high initial concentration, a lower concentration of inhibitor is injected to maintain the bulk fluid concentration needed to repair the adsorbed inhibitor film.

The advantages of continuous treatment are:

- It supplies chemical at all times.
- It is the most cost-effective method to treat many systems such as pipelines, process lines and equipment, and cooling water systems.
- The chemical injection rate may be optimized to control operating problems.

The disadvantages of continuous treatment are:

- Chemical injection pumps require a reliable power source.
- Chemical injection pumps must be periodically monitored and maintained.
- Chemical drums/tanks that supply chemical injection pumps must be filled periodically.

#### 4.26.2.2.2 Batch treatments

Batch treatments are typically employed for biocide treatment of seawater lines and periodic inhibitor dosage of wet gas lines where there is a risk of top of the line corrosion in stratified flow, or where a highly persistent treatment is required to provide protection for 2–3 months. The slug of concentrated chemical is trapped between two gel pigs/spheres/product separating pigs, see [Figure 8](#), and the line pressure is used to transport it through the line. The time of contact of the chemical with a section of the pipe wall is determined by the length of slug and flow rate.

Batch treatment is sometimes used down-hole when technical or economic constraints preclude continuous inhibitor injection either by application of a persistent corrosion inhibitor onto tubular walls or more usually by means of a squeeze treatment. The persistency of batch inhibitors needs to be tested in the laboratory and verified in the field to ensure batch treatment viability.

Squeeze treatment uses the producing formation as a chemical reservoir with the aim of providing a dose similar to continuous treatment, see [Figure 9](#). In squeeze treatments, a large volume of corrosion inhibitor/scale control inhibitor is pumped down the



**Figure 8** Gel pigs, spheres, and product separating pigs employed to trap a slug of treating chemical.

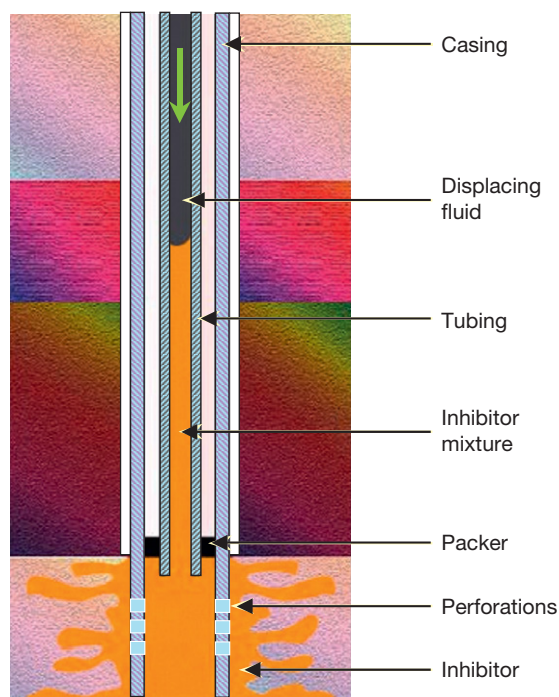


**Figure 9** Schematic of squeeze treatment.

tubing with enough overflush to force inhibitor into the producing formation. The inhibitor adsorbs onto the formation and is slowly produced back from the formation. A successful squeeze treatment results



in an almost continuous return of inhibitor that can last for several months. Squeeze treatments can be applied in wells with sufficient porous and permeable producing zones. The major concern with inhibitor squeeze treatment is the possibility of plugging the formation. There is little danger of formation damage when squeezing scale inhibitors. Some corrosion inhibitors cause formation clays to swell. Laboratory tests with formation core samples may be used to determine if this will be a problem.

The advantages of batch treatment are:

- Provides treatment where continuous treatment is difficult.
- Protection of pipelines operating in stratified flow, when inhibitor distribution to the top of the line cannot be ensured by other means.
- In combination with continuous inhibition for very severe or upset conditions.
- Protection of process vessels which have long residence time, and that would require impractically low continuous injection rates, for example, low temperature separator vessels.
- Batch treatments with biocides are more cost-effective than continuous treatments.
- Squeeze treatment allows continuous treatment without expensive down-hole delivery systems.
- The chemical is available where it is needed.
- Less manpower required to check on chemical treatments.

The disadvantages of batch treatment are:

- A significant portion of the chemical may be wasted.
- Corrosion and bacteria are not continuously controlled between treatments.
- Wells are taken off production for several hours.
- Squeeze treatment can plug or damage the producing formation.
- The high cost of treatment.
- The chemical returns from the formation must be monitored.

### **4.26.3 Corrosion Inhibition**

The use of inhibitors in the field and process equipment is defined in terms of the metal and the corrosive environment. Packages that protect one metal, c-steel, may not protect another, stainless steel. Similarly protection of a metal in, for example, acidic solutions ( $\text{CO}_2/\text{H}_2\text{S}$  corrosion) may not work in neutral solutions, particularly when dissolved oxygen is the

corrodant. Various commercially available corrosion inhibitor packages have been developed for use in water systems, gas systems, oil field production systems, and refineries.

#### **4.26.3.1 Inhibition Processes**

Corrosion inhibitors work by one or more of the following mechanisms: precipitated films that visibly coat and protect metal surfaces (calcium salts in potable water, zinc salts in cooling waters), passive oxides which combine with corrosion product films to protect metal surfaces (silicates and molybdates in cooling systems), and adsorbed monolayers (organic molecules in oil/gas systems). The first two mechanisms, rely on relatively inexpensive inorganic salts, are used mainly in cooling towers, boilers, and fractionation units. The adsorption type of organic inhibitor is employed in oil field systems, and to prevent overhead corrosion in some refinery units (e.g., use of filming amines) are organic inhibitors. Inorganic inhibitors are further divided into anodic and cathodic classifications that describe the polarization of electrochemical corrosion process that are modified by the inhibitor action. Organic film-forming inhibitors (amines, amides, and imadazolines) block both the anodic and cathodic processes, although most tend to mainly polarize the anodic reaction as observed by an increase in corrosion potential. Note that although cost effective water treatments typically use inorganic compounds these often are more effective in combination with small additions of organic chemicals to provide a synergistic effect.

Inhibitors for near-neutral and alkaline environments in the presence of oxygen decrease the rate of the oxygen transport/rate determining step by the formation of an electronically nonconducting film on the metal surface (cathodic inhibitors). Inhibitors for oxygen-free near-neutral solutions, as may be found, for example, in oil production, cause the steel to form or retain a protective oxide film which acts as a barrier to metal dissolution, so that the corrosion rate is now controlled by the anodic process (anodic passivating inhibitors). Anodic inhibitors effectiveness relies on maintenance of a passive oxide film on the metal surface and includes both oxidizing inhibitors (nitrite, etc.) and nonoxidizing that require dissolved oxygen (phosphate, benzoate, borate, carbonate, hydroxide, molybdate, etc.). Insufficient dosage of anodic inhibitor may cause localized corrosion (e.g., pitting).

In acid environments, both metal dissolution and hydrogen evolution reactions are under activation control and can occur in the absence of surface films of oxides or corrosion products, because of their solubility in acid. Even a small reduction in the kinetics of either process will reduce the corrosion rate. Inhibitors for acid solutions usually function by adsorption on the metal surface, and typically contain elements in Groups V or VI of the periodic table, for example, N, P, O, S, or As, which possess lone pairs of electrons which can be donated to the metal to form a chemical bond by chemisorption. The tendency is to use long chain nitrogenous inhibitors (amines) and imidazolines. Exact mechanisms are not fully understood, but chemisorption appears to occur at active sites and physisorption at the remainder of the surface. The organic inhibitor molecules can be modified to increase their solubility or dispersibility in brine. These modifications include adding more polar groups to each inhibitor molecule.

Adsorption type inhibitors usually contain N or S atoms with an attached organic chain (typically C12–18) that determine the solubility, and are usually aliphatic (straight chain) fatty acid derivatives. Most metal surface in contact with an aqueous solution is covered with adsorbed water molecules and the unshared electrons in the polar N group of the inhibitor forms a chemisorption type bond with the metal surface. Organic inhibitors also physically adsorb to the metal surface but this is weaker than chemisorption. Some molecules also have an ability to attract each other and form a 2-dimensional monolayer across the metal surface. The chemisorption bond displaces water molecules (4–8 per inhibitor molecule) and other corrosive agents from the metal surface. These processes are described by standard adsorption isotherms

(Langmuir, Tempkin, etc.) of inhibitor solution concentration ( $c$ ) versus a function of the surface coverage ( $\Theta$ ) at various temperatures. The adsorption process can be visualized as formation of covalent bond between metal and polar group along with displacement of adsorbed water molecules, nonpolar or aliphatic end of molecule orientated outwards encouraging adsorption of a hydrophobic oil layer as illustrated in **Figure 10**.

Organic inhibitors include *mono amines*, typically used in refinery overheads and hydrotest packages, *diamines*, more efficient in oil systems than monoamines, *amides*, poly ethoxylated compounds made with differing oil and water solubilities (solubility increases with amount of ethylene oxide, acetic, oleic, dimeric naphthenic, or phosphate salts), and *imidazolines and derivatives*. Most exhibit at least partial solubility or dispersibility in both oil and water.

Water soluble inhibitors are required for fresh and brine waters, typically quaternary amines, amine salts, or salted imidazolines, see **Figure 11**. Water soluble corrosion inhibitors form a protective film on metal surfaces in sweet or sour environments but the inhibitor films are not as persistent as oil soluble corrosion inhibitor films. These tend to desorb at high temperatures and may salt out (lose solubility) in brines that contain a high concentration of total dissolved solids (TDS). Continuous treatments are almost always needed for effective corrosion control.

Oil soluble inhibitors tend to be long chain primary amines, imidazolines, fatty acids, and phosphate esters. These packages are also more effective at higher temperatures and high velocities.

Oil soluble-water dispersible inhibitors are normally used in oil wells and gas condensate wells and readily mix with most crude oils in sweet or sour

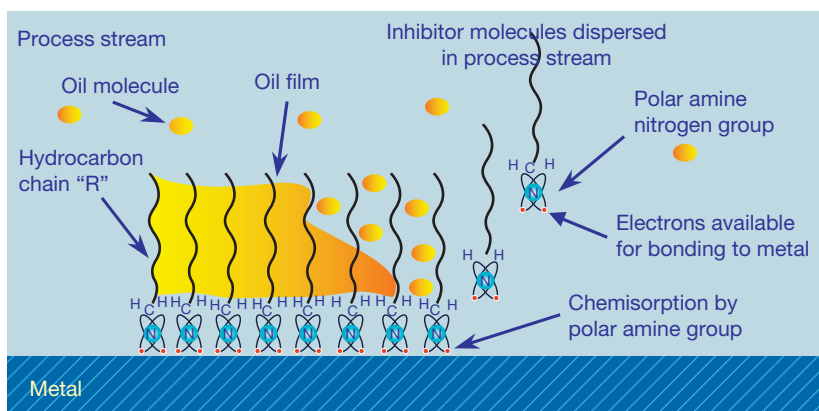


**Figure 10** Schematic of adsorption inhibitor processes.

systems. They also have various degrees of dispersibility in fresh, brackish, or brine water. Higher concentrations of water dispersible inhibitors are usually needed as production increases and water break through occurs. The inhibitors form oil-wet films that resist corrosion under most conditions.

Batch treatment inhibitors are either oil soluble or 'gunkers' in order to achieve better persistency when water-wet. In wet gas lines, continuous injection of gas phase inhibitor is often applied in conjunction with periodic batch treatment.

Gas phase inhibitors are usually low molecular weight amines that have a high vapor pressure.

#### 4.26.3.2 Inhibitor Performance

The performance of inhibitors is often defined by their efficiency based on the corrosion rate with

and without inhibition, with the input data being obtained from corrosion coupons, and/or portable instrumentation (electrical resistance/electrochemical polarization resistance) using probes inserted into the process line or test solution. Inhibitor efficiency can be calculated from the following expressions:

For weight loss:

% Inhibitor Efficiency

$$= \left[ 1.00 - \frac{\text{Weight loss (with inhibitor)}}{\text{Weight loss (without inhibitor)}} \right] \times 100$$

For corrosion rates:

$$\text{Inhibitor efficiency} = \frac{\text{Rate without} - \text{Rate with}}{\text{Rate without}} \times 100$$

N.B. 100% efficiency = no corrosion, 0% efficiency = no effect of 'inhibitor.' Inhibitor efficiency is also used often as a measure of the surface coverage as illustrated in Figure 12, where 100% efficiency corresponds to a surface coverage of one, and 0% efficiency to zero surface coverage.

The graph in Figure 12 shows that for an adsorption type inhibitor the coverage (or efficiency) can be increased by increasing the bulk concentration in the fluid, and conversely, reducing the concentration reduces the efficiency. In practice, there is a balance between performance and cost but also the actual corrosion rates obtained are an important consideration. The efficiency required varies greatly from system to system. For example, pipeline designed some 25 years ago reflected a degree of conservatism and often assumed inhibitor efficiencies of 60–85%. However, improvements in vendor inhibitor formulations are based on experience at, for example,

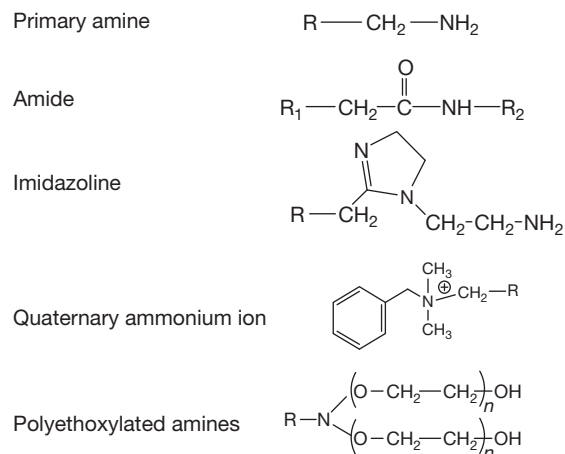


**Figure 11** Basic structures of adsorption corrosion inhibitors.

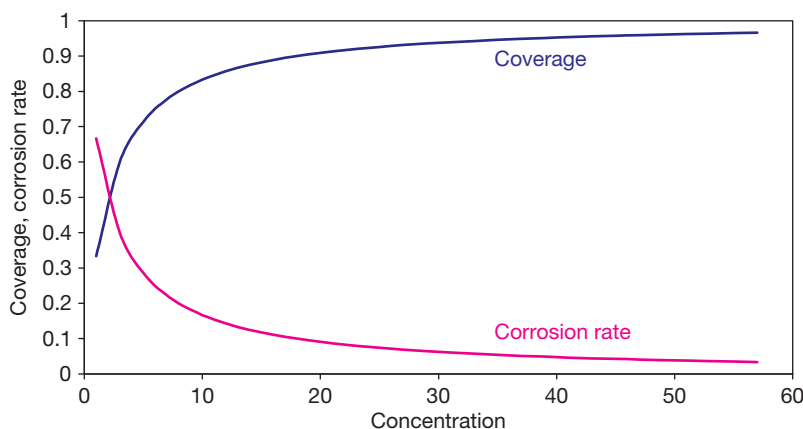


**Figure 12** Relationship between inhibitor efficiency, surface coverage, and bulk concentration.

Prudhoe Bay from 1996 onwards shows that a field corrosion inhibitor efficiency of 98% for multiphase flow lines can be obtained. The use of an inhibitor efficiency of greater than 95% for design purposes is a high risk strategy that requires effective monitoring and corrosion management processes, but is achievable in practice. Some authors<sup>4</sup> consider 80% or 90% minimum efficiency obtained in the laboratory as a hypothetical assumption, since correctly chosen inhibitors can have efficiencies in the field of >99.9%, that is, inhibition ratios of  $10^3$ – $10^6$  (the inhibition ratio is the corrosion rate without inhibitor/corrosion rate with inhibitor). The purpose of efficiency measurement is as a tool to provide a ranking of candidate packages and is used to select inhibitors prior to field testing/application.

A second but important practical consideration is the corrosion inhibitor availability<sup>5</sup> ( $A$ ), that is the time the inhibitor is present in the system at the required dosage, where  $A\%$  = the time the inhibitor is added divided by the lifetime  $\times 100\%$ . The design corrosion allowance (CA) is then defined as:

$$CA_{\text{total}} = CA_{\text{inhibited}} + CA_{\text{uninhibited}}$$

The CA would be given by:

$$CA = (CR_{\text{inhibited}} \times A\% \times \text{Lifetime}) + (CR_{\text{uninhibited}} \times [1 - A\%/100] \times \text{Lifetime})$$

The design stage assumption is that inhibition can decrease the corrosion ( $CR_{\text{inhibited}}$ ) to between 0.1 and 0.3 mm year<sup>-1</sup>, that is, practical values that would have to be reviewed once field data trends were obtained. The availability concept emphasizes the criticality of inhibition downtime in high risk systems and uses realistically achievable corrosion rates that focuses attention on the importance of maintaining and managing the dosage/inhibitor supply chain.

Partitioning of inhibitors between the oil and water phases is also an important consideration as the practical aim is to achieve a required concentration of inhibitor in water phases where corrosion occurs. As the water cut increases during production, the inhibitor will distribute itself at different concentrations in the water and oil phases. The volume fractions of the phases are important factors in establishing partitioning between oil and water phases as the theoretical basis is given by:

If

$$C_o V_o + C_w V_w = C_t \text{ and } C_w/C_o = P$$

where  $C$  is concentration,  $V$  is volume fraction,  $w$  is water phase,  $o$  is oil phase,  $t$  is total fluids, and  $P$  is partitioning coefficient (water/oil).

Then

$$C_w = C_t P / (V_o + P V_w) \text{ and } C_o = C_t / (V_o + P V_w)$$

Some operators specify a recommended inhibitor concentration in the water phase which is a sound practical consideration. Experimental data on inhibitor partitioning is then used to estimate the necessary concentration in the total fluids for a given water cut. Thus, a preferentially water soluble component ( $P > 1.0$ ) will have a higher concentration in the water phase than a preferentially oil soluble component ( $P < 1.0$ ).

Selection of an inhibitor requires consideration of several factors:

- The nature of the operating environment and the operating conditions.
- The materials requiring protection.
- Possible interactions between chemical additives.
- The efficiency of an inhibitor.
- Possible adverse effects of inhibitor on other aspects of the operation.
- Environmental effects of the inhibitor.
- The physical properties of the inhibitor.

#### 4.26.3.3 Inhibitor Testing

A range of test procedures are available to assess inhibitor packages for various applications, including Bubble Test for initial screening, rotating cylinder electrode (RCE) for various flow conditions, segmented welds for low conductivity fluids, autoclave tests for high pressure/high temperature conditions. Such methods and procedures, along with others, have been developed over the years for assessment of oil industry inhibitors, but not all are routinely performed, rather a limited number of basic and reproducible tests have been adopted. A North Sea oil industry sponsored program of testing during the mid-1980s identified the Bubble Test, the Rotating Cylinder, and Jet Impingement as being able to provide the basis of a test protocol. The study provided statistical evidence of the reliability and reproducibility of electrochemical measurements in the establishment of corrosion rates and provided the basis of published work in this area.<sup>6,7</sup>

##### 4.26.3.3.1 Bubble test

The test is designed for rapid screening of inhibitors using brine solutions (simulated or field samples)

as the test fluid held in an easily cleaned glass vessel containing between 150 ml and 1 l of test solution. The test is carried out at room pressure (1 atm), with a sparge gas being bubbled through the solution using a mixture of a carbon dioxide/hydrogen sulfide/nitrogen concentration that simulates the field partial pressures of CO<sub>2</sub>/H<sub>2</sub>S. The vessel is sealed with water traps and purged of air prior to test solution introduction, test temperatures range from ambient to boiling. Samples of degassed crude may be introduced to form an oil layer if there are concerns regarding acetates, etc. The solution is magnetically stirred to ensure mixing but the shear stresses are low, <1 Pa.

The normal procedure is to establish a base line corrosion rate, after a few hours but often over 24 h, using standard electrodes and test probes prepared by a rigorous degreasing/abrading/cleaning procedure. The base results give the uninhibited corrosion rate and this also identifies any samples that have a poor/out of specification preparation. The inhibitor must be soluble or dispersible in both hydrocarbon and water, it is added at the required dose rate and the inhibited corrosion rate obtained typically after a further 24 h from which the inhibitor efficiency is determined.

Bubble tests are almost always the initial screening tests because they are simple, easy to carry out,

and reliable, if based on electrochemical measurements but are restricted to ~1 bar total pressure and <100 °C. They cannot reproduce high temperature–pressure systems, but nonetheless can still be an effective initial screening methods for such systems.

#### 4.26.3.3.2 RCE test/flow loops

These tests are designed to reflect actual system wall shear stresses found under stratified flow conditions in pipelines. Many studies have demonstrated the validity of the approach based on standard hydrodynamic correlations, so that suitably designed equipment will give similar results from the two methods. Both can be pressurized but the RCE is often more convenient due to ease of operation and cleaning. Electrochemical measurements are normally employed or electrical resistance measurements in high hydrocarbon systems. Measurements can be made on a cylindrical electrode that forms part of the rotating shaft, but electrode probes positioned in the wall of a cylindrical test cell can also be employed, provided the electrode is machined to the wall profile and that a relatively small annulus is used to contain the test fluid so that the flow conditions are similar on the rotating cylinder and wall.

Figure 13 illustrates typical data from a dynamic test and shows that the two types of test give

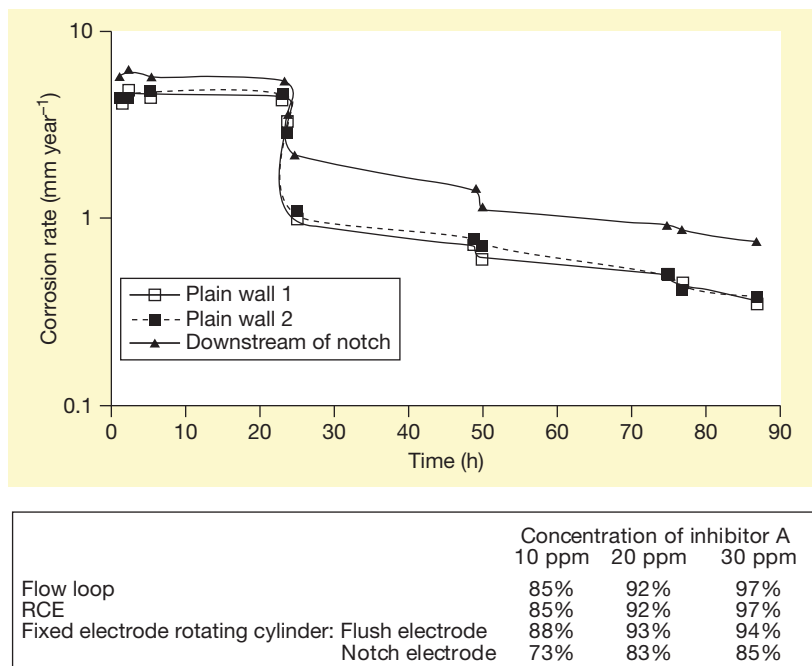


**Figure 13** Comparison of flow loop and RCE test data showing inhibitor efficiency tests and the effect of simulation of downstream of erosion pits.



compatible results provided the fluid to wall shear stresses are the same and enables pipeline conditions to be simulated. If inhibitor dose rates are sequential, the increased test can define the effect of concentration on performance. Base line uninhibited corrosion rates were established over the first 24 h, then inhibitor was injected at increasing dose levels of 10, 20, and 30 ppm. The RCE design can also be modified to assess the effect of inhibition downstream of a simulated erosion pit—local flow disturbance. The table shows the test data expressed as inhibitor efficiency as obtained from a flow loop test, an RCE, and autoclave rotating cylinder tests (higher rates) compared to efficiency under local turbulence conditions. The inhibitor did not perform as effectively under more turbulent intensity conditions.

#### 4.26.3.3.3 Inhibitor persistency

There are always times when, for some reason, inhibitor dosage ceases and it is then important that

protection persists for some time until inhibitor injection is reestablished. However, it is not a widely studied property, and therefore underestimated, particularly for high risk systems. Different inhibitors can show very different persistency as shown in Figure 14. The bubble test and jet impingement tests are employed, and by changing the fluid compositions, after an inhibitor film is first established, the persistency can be evaluated. The initial base line data and efficiency after 24 h were obtained using an RCE and inhibitor and then the persistency assessed by substitution of the inhibited test solution with fresh but already sparged fluid. The test indicates how quickly the corrosion rate returns to the original uninhibited rate. In the case of the quaternary amine package, there is a rapid increase in corrosion rate when inhibitor dosing is stopped, although complete loss of protection does not occur in the test. In the second case, the carboxylate amine, there is a good response as the inhibitor appears to be retained and redistributed on the metal surface.

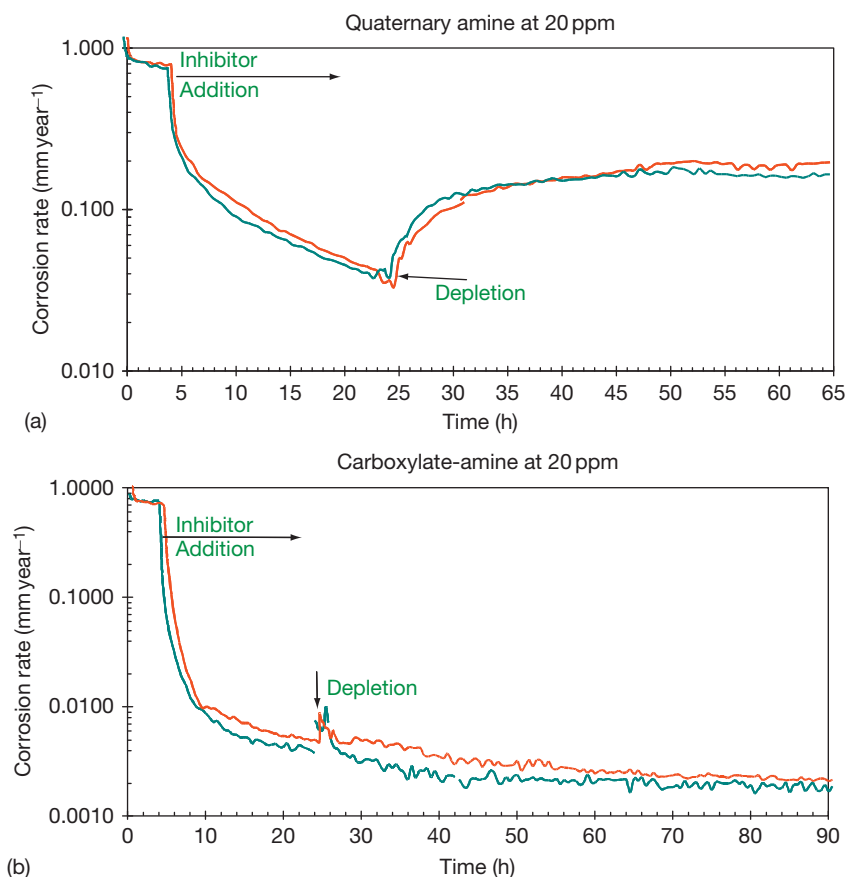


**Figure 14** Electrochemical test data showing initial uninhibited corrosion rate, inhibition, and persistency check.

#### 4.26.3.3.4 Jet impingement

The test is designed to give high shear stresses, but the quantification of shear stress is not as well-established as for flow loops or the RCE. It is also possible to obtain the high shear stresses normally associated with erosion–corrosion by use of a pulsed gas bubble injection into the feed to the impinging jet.

#### 4.26.3.3.5 Inhibition of weld corrosion

This form of accelerated CO<sub>2</sub> attack is of particular concern in condensate lines and low conductivity waters. Nickel containing welds used in oil field fabrications to provide the required strength are cathodic. However, the high nickel content of the corrosion product film gives rise to different corrosion kinetics and films compared to the low alloy steel plate, which when combined with the high resistance of the electrolyte means that the normal galvanic protection derived from the weld being coupled to the more anodic parent plate does not occur and the weld may be preferentially attacked.

Some inhibitor packages can increase the rate of weld metal corrosion as they are less effective in the presence of the high nickel content corrosion product, but careful selection of an appropriate inhibitor can mitigate the problem. The test procedure is to section a weldment into five electrodes – weld metal, heat affected zones (HAZ), and parent plates and then reassemble the sections into a test electrode, [Figure 15](#). Electrochemical corrosion rates are obtained via five zero resistance ammeters each connected to an electrode segment from which the individual rates of corrosion and galvanic coupling currents can be determined, [Figure 16](#).

#### 4.26.3.3.6 Autoclave tests

These are normally the final tests to replicate field conditions as they are expensive and usually restricted to inhibitors that are expected to be effective as based on previous and simpler tests. Typically employed to assess combined high temperature–pressure conditions and may also incorporate RCE and jet impingement, as well as electrochemical monitoring. Autoclave tests can be considered as being under full system condition simulation, with the test variables, fluid chemistry, ppCO<sub>2</sub>, ppH<sub>2</sub>S, shear stress, temperature and monitoring, subject to feasibility study Wt loss, LPR, and Ceion probe.

#### 4.26.3.3.7 Compatibility

Compatibility with other production chemicals must be considered not only to control emulsions but also to

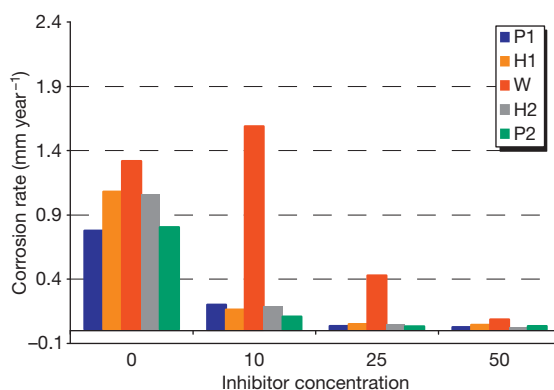


**Figure 15** Preferential weld corrosion probe and inhibitor performance test data.

prevent failures that have occurred due to loss of performance of some of the oilfield chemicals. In general, a compatibility test will be concerned with assessment of emulsion stability, where a sample of untreated degassed crude is mixed with a sample of brine (field or synthetic) to which is added a known amount of treating chemical to give a similar concentration as will be employed in the field. The mixture is shaken and the time taken for the oil/water emulsion to break is noted. The effect of treating chemical mixtures on corrosion performance is also important. In the case shown in [Figure 17](#), the corrosion inhibitor and other chemicals were found to be incompatible because of the effect of the biocide.

#### 4.26.3.3.8 Field deployment

There are many issues related to field deployment activities and the reader is referred to the *European Federation of Corrosion Document Number 39, The Use of Corrosion Inhibitors in Oil and Gas Production*<sup>8</sup> for full details. In particular, problems can include: preparation of inhibitors for injection, such as dilution and mixing, deaeration–gas blanketing; the introduction

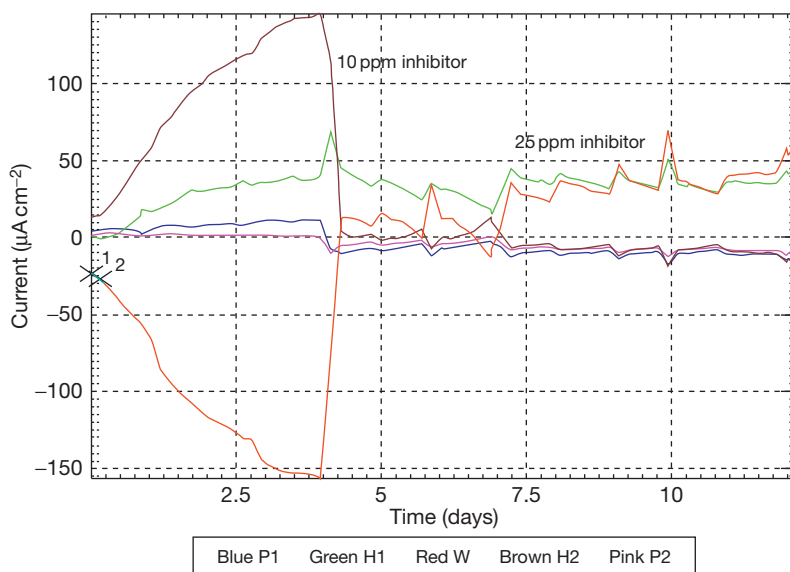


**Figure 16** Effect of inhibitor dosing with time and increased dosage.

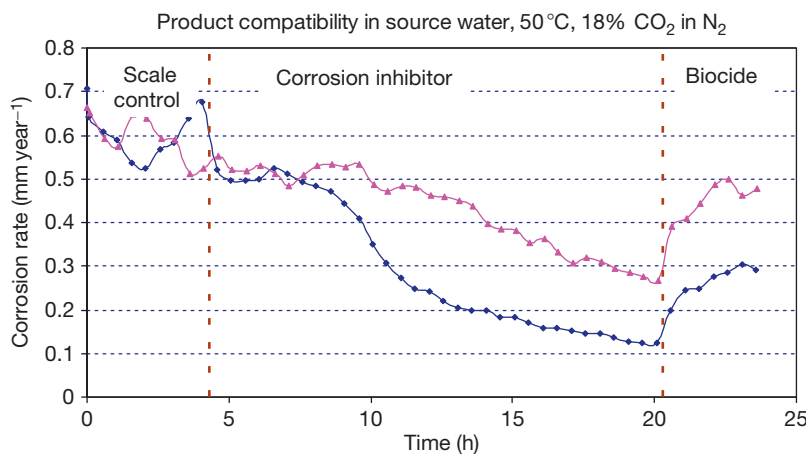


**Figure 17** Effect of chemical additions on corrosion.

of atmospheric oxygen into chemical storage tanks or into water used to dilute ‘neat’ inhibitor is a prime cause of problems. Many chemicals are corrosive when supplied as concentrates and the injection equipment is usually constructed from 316 stainless steel. Preparation of facilities and pipelines for inhibition; improved performance is achieved in clean systems; therefore, cleaning and descaling may be required, for example, use of specially designed, adjustable scraper pigs, provision for removal of solids at pig traps, and use of specialist cleaning contractors.

Operation and maintenance of injection equipment must be managed with overall coordination of

maintenance, housekeeping, and inspection activities allocated to a supervisor who has responsibility for updating the records; note that high corrosivity systems may require >95% up-time on injection equipment. Monitoring and inspection are key activities in corrosion inhibition management and asset integrity strategies. Regular corrosion monitoring/corrosion inspection to obtain trend data is the only means to ensure inhibition is effective. Inspection is also used periodically to ensure the integrity of production equipment, including export pipelines. Monitoring and the recording of all available parameters, including production rates, water cuts, and inhibitor consumption,

are required to ensure that the program is operated and managed correctly.

Clean metal surfaces increase the effectiveness of almost all corrosion inhibitors; consequently, an initial cleaning treatment may be advisable before the introduction of a corrosion inhibitor system. Corrosion inhibition is also less effective in old, corroded, and pitted pipelines or facilities and in systems that contain large amounts of debris. Dosages may have to be increased or the system cleaned; in some cases, a scale inhibition program may have to be implemented in addition to the corrosion inhibition program. The inhibitor may not perform as anticipated in the field or there may be poor management of the dosage leading to lower than required inhibitor availability.

#### 4.26.4 Scale Inhibition/Control

Scales, sometimes referred to as hard fouling, can plug reservoirs and equipment in production systems, flowlines, and pipelines. Scales can also affect the thermal efficiency of heat exchangers and boilers (an increase in the design fouling factor). Scaling and fouling by deposits–corrosion debris are both typically controlled by similar treating packages. The aim is to minimize operating problems (poor heat transfer, plugging) and aid corrosion control (under deposit corrosion) by use of scale control chemicals (phosphonates, phosphate esters, polymers). Note that prevention of scale formation on oil field lines may result in more fine crystals or sludges being carried downstream to oil and gas separation plants, see [Figure 18](#).

Scale can inhibit or promote corrosion. Hard, non-porous scales may sometimes protect metal surfaces from electrolytes and prevent corrosion. For example,

the addition of calcium salts helps to control corrosion ('red water' in desalination potable water) and other soft water distribution systems by deposition of calcium carbonate. Loose or porous scales can create concentration cells that accelerate corrosion in boilers, cooling systems, and production equipment. Since corrosion usually occurs under scales, particularly on heat transfer surfaces, it is better to prevent and remove a scale whether or not it protects the metal.

##### 4.26.4.1 Scale Inhibitor Application

Scale inhibitors must always be present to stop scale formation. Batch treatments with scale inhibitors are NOT effective. Scale inhibitors are usually continuously injected at low concentrations (5–25 ppm). Scale inhibitors can react with calcium and iron in produced water to form a scale. This usually occurs at the point where a concentrated scale inhibitor is added to the system. If the scale inhibitors are diluted with fresh water, this problem can be prevented. Scale inhibitors may also be injected in the middle of the flowline so they are quickly diluted.

##### 4.26.4.1.1 Scale treatment chemicals

**Inorganic Phosphates** – They contain a P–O–P group and have a tendency to adhere to the surfaces of scale crystals and prevent further crystal growth. They are effective at low concentrations: 2–5 ppm for  $\text{CaCO}_3$ ; 10–12 ppm for  $\text{CaSO}_4$ ; and >50 ppm for  $\text{BaSO}_4$ . The most common examples are sodium hexametaphosphate and sodium tripolyphosphate. Inorganic phosphates have certain disadvantages. They revert from metaphosphate to orthophosphate at temperatures above 60 °C. Reversion makes the scale



**Figure 18** Oil field scales formed in flowlines.

inhibitor ineffective. Reversion occurs slowly with age and in low pH solutions. Inorganic phosphates were used extensively before organic phosphonates, phosphate esters, and polymers were discovered. Because of the disadvantages of inorganic phosphates, organic type scale inhibitors are used more often. The organic scale inhibitors described below prevent crystal growth much like inorganic phosphates.

**Organic Phosphate Esters** – Phosphate esters have excellent scale inhibiting properties and are thermally stable up to 82 °C or 93 °C.

**Organic Phosphonates** – They are more thermally stable than phosphate esters. The reason is that the phosphorous is directly bonded to the carbon atom in phosphonate inhibitors. An example is amino trimethylene phosphoric acid (ATMP). ATMP acid derivatives are stable at all pH conditions up to 230 °C. ATMP acid derivatives are used extensively in scale inhibition squeeze programs for oil producing wells.

**Organic Polymers** – They are effective against calcium carbonate, calcium sulfate, and barium sulfate. They have excellent thermal stability. Examples of organic polymers are polymaleates, polymethacrylates, and polyacrylamides, see [Table 1](#).

#### 4.26.4.1.2 Scale control

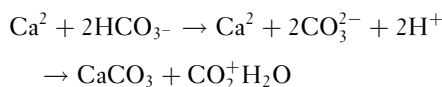
The mechanisms of scale control are complex but include:

- Threshold inhibition (hardness stabilization) aims to prevent creation of crystal nuclei (enable scale forming salts to exist in an over-saturated form), a kinetic process that allows the creation of submicroscopic nuclei.
- Crystal modification (growth control) due to adsorption/incorporation of scale inhibitor molecules or ions, this result in decreased growth and cohesion between deposited particles.
- Sequestration (chelation), the use of chemicals that complex or chemically bond to dissolved salt ions and remove them from precipitation reactions.

- Anionic dispersion (destabilization theory), the dispersion chemical, usually a highly anionic polymer, adsorbs onto a slightly anionic scale particle and increases the charge density causing the particles to remain in suspension in the water.

#### 4.26.4.2 Scale Predictions

The tendency for a water to 'scale' is dependent on the calcium carbonate concentration (that is its 'hardness'), the pH and total alkalinity, dissolved solids, and temperature. When the solubility product of a scale forming material is exceeded, it can form a scale. The scaling tendency (the probability that scale will form) increases as the amount of supersaturation increases. Calcium carbonate forms when carbon dioxide is released from solution. This usually occurs when the pressure decreases. Calcium carbonate scale commonly forms in producing wells and associated flowlines in some fields. These scales can form in production equipment and interrupt operations. Normally, produced waters contain calcium ions ( $\text{Ca}^{2+}$ ), bicarbonate ions ( $\text{HCO}_3^-$ ), and carbon dioxide ( $\text{CO}_2$ ). When  $\text{CO}_2$  is evolved, the pH of the solution increases. The bicarbonate ions dissociate to form carbonate,  $\text{CO}_3^{2-}$ . The carbonate reacts with calcium to form  $\text{CaCO}_3$ , which precipitates as it is relatively insoluble.



The scaling tendency of  $\text{CaCO}_3$  increases as the temperature increases.

For pH between 6.5 and 9.5, the chemical equilibrium is given by:

$$\text{pH}_{\text{sat}} = (\text{pK}_2 - \text{pK}_s) + \text{pCa} + \text{pAlk}$$

A basic indicator of scaling, the *Langelier Index*:

$$\text{Ls} = \text{pH}_{\text{act}} - \text{pH}_{\text{sat}}$$

shows when  $\text{Ls} < 0$ , the water is corrosive and non-scaling and when  $\text{Ls} > 1$  it is scaling.

**Table 1** Organic scale treating chemical mechanisms

Treating chemical	Threshold stabilization	Crystal distortion	Complexation/chelation	Dispersion
Low molecular weight polymers	X	X		
Phosphonates	X	X	X	
Phosphate esters	X			
Organic polymers		X		X
Modified organic		X		X
Polyphosphates			X	
Chelates			X	



Another index, the *Ryzner Stability Index*:

$$Rz = 2pH_{\text{sat}} - pH_{\text{act}}$$

indicates that the solution is for  $Rz < 6$  – increasingly scaling;  $Rz > 7$  – not scaling;  $Rz > 8$  – increasingly corrosive.

In cooling waters, scale control can be achieved by modifying the pH – for example, acid dosing thereby ensuring good heat transfer in equipment but this then requires improved corrosion inhibition of the cooling water. In potable water systems, scaling on metal surfaces is desirable to reduce corrosion rates by formation of a barrier layer. Thus, if such waters do not naturally possess a scaling tendency, as determined by the Langelier Saturation or Ryznar Stability Indices, lime may be added to raise the calcium levels until calcium carbonate scaling forms on the pipe surfaces. Dezincification, that is, the selective dissolution of zinc from brass alloys used in water distribution systems, is also reduced by lime addition. It should be noted that the water output produced from a desalination plant is normally mixed with a small volume of sterilized seawater or groundwater to principally produce a palatable product. If this is done, the water may have sufficient scaling tendency without the need for further lime additions.

In oilfield systems, particularly where commingling takes place, the concern is to inhibit scale formation to prevent plugging of wells, flowlines, plant, or the reservoir. The potential of forming ‘hot’ radioactive scale is another hazard (radium related radioactivity), possibly as coprecipitants with  $\text{BaSO}_4$  scale. Contaminated equipment may require specialized handling, and this would have an impact on the maintenance cost. Applicable scale inhibitors should be applied to limit excessive scale build-up and reduce the impact of such radioactivity.

For a more complete prediction of scaling in systems and reservoirs, sophisticated codes are available based on the equilibrium chemistry of the major ionic components present in the brines/waters. Below, some of these are outlined.

**Petrotech MultiSCALE Code** – this Norwegian University code, developed with support from Statoil, Saga Petroleum, and Norsk Hydro predicts the simultaneous precipitation of the respective scaling species. The code computes the equilibrium concentrations of Ca, Sr and Ba sulfate, and Ca and Fe carbonate scales, in addition, the code predicts FeS and halite precipitation. The user can allow the program to select the ‘stable phase’ for  $\text{CaSO}_4$  precipitation or choose whether gypsum or anhydrite is to be considered.

**OKU Code** – the OKSCALE Prediction Model computes the equilibrium concentrations separately for  $\text{CaCO}_3$  and sulfates of Ca, Sr, and Ba. All the sulfates are considered simultaneously; the user can choose whether gypsum or anhydrite is to be considered. The program has been upgraded following lengthy and detailed empirical  $\text{SrSO}_4$  and  $\text{CaCO}_3$  solubility determinations conducted by the OKU research group. The program calculates  $\text{CO}_2$  fugacity either from the associated gas composition ( $\text{CO}_2$  mole % level) or from a dissolved  $\text{CO}_2$  value.

**RICE Code** – a Pitzer based model which utilizes the Peng-Robinson EOS to calculate fugacity coefficients. This model predicts the simultaneous precipitation of the respective scaling species. The code computes the equilibrium concentrations of Ca, Sr and Ba sulfate, and Ca and iron carbonates. In addition, it will predict halite, FeS, ZnS, and  $\text{CaF}_2$  precipitation.

Such scale prediction programs are not by themselves definitive, rather they give an indication that a problem may occur. The level of precipitation predicted in many cases can be higher than that observed in a system. The levels of precipitation predicted are based on equilibrium solubility data, but these data do not take into account reaction kinetics. Furthermore, prediction accuracy is not just a function of modeling limitations, much depends also on the quality of the data input. If brine compositional data is inaccurate, possibly due to poor analytical technique or more commonly due to poor sample handling, then the computer prediction data will be devalued. Often brine analysis is conducted on samples many hours after sampling, transient changes occur, and precipitates may form. Results may be reported for filtered samples, without thought for the precipitate removed. Clearly unstable species, such as  $\text{HCO}_3^-$ , should be determined on-site; dissolved  $\text{CO}_2$  levels should be determined on pressurized bomb samples.

The results of a typical PREDICTIVE study of a field whose water chemistry indicates a significant probability of barium sulfate scale when sea water injection is employed is shown in [Figure 19](#), with the likely concentrations and scaling tendency plotted against seawater breakthrough. There is also a possibility of microbiological build up as water breakthrough increases.

[Figure 19](#) illustrates the likely changes with continuing water injection leading to an increase in the barium sulfate and water profile with production time. Initially, the scaling will be calcium carbonate, but then it is the barium scale profile that predominates and the squeeze treating chemical would

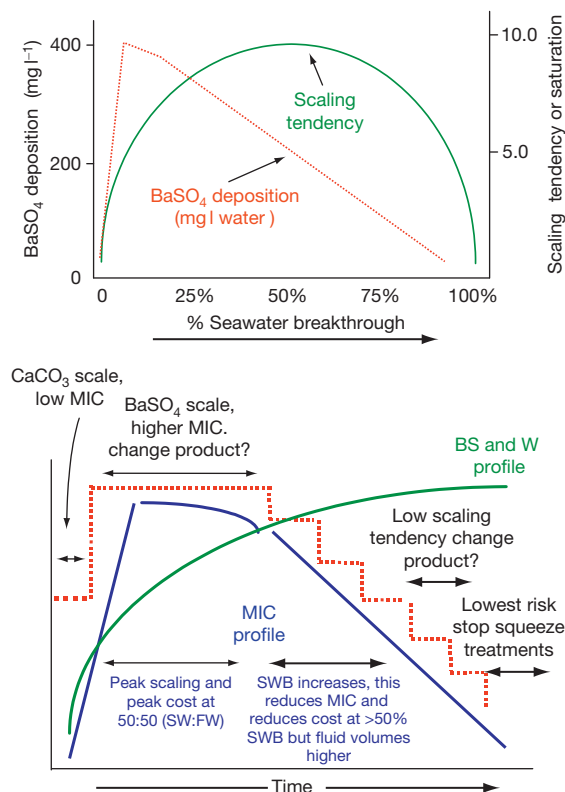


**Figure 19** Predicted scaling tendency (mass and supersaturation) over the life cycle of a well described by the sea water injection), scaling and MIC profiles compared to the barium scale and water profile over the field life.

have to be changed for these new peak conditions. The MIC also reaches a peak, hence, this is the most costly period with the chemicals having to control both scale and MIC; compatibility issues would also have to be addressed. Further changes in chemicals can be anticipated later in field life.

It is important to understand that the precipitation of an insoluble salt crystal does not always result in scale deposition; much depends on the system parameters, dynamics, and the presence of crystal interacting chemistries. Precipitates (particularly if oil-wet) may to some degree be transportable. Nevertheless, scaling predictions should be used as an indicative tool to test sensitivities and estimate trends. However, careful consideration needs to be given to interpreting the outputs; generally, the predictions can be assumed to be a worst case.

Testing for scale formation is by:

- (i) Static mixing tests – NACE TM0397, 0197, 0374  
Advantage – Simple quick tests mix the waters and weigh deposits or analyze for scale species,

Ca, SO<sub>4</sub>, Ba, simple measure of efficiency.

Disadvantage – Does not evaluate crystal modifiers on an even basis.

- (ii) Dynamic tube blocking tests.

Dynamic laminar flow used to examine growth mechanisms (scale and/or microbiological fouling) using a strata core sample, temperature >100 °C possible, allows examination of systems under pressure.

#### 4.26.4.3 Squeeze Application

Core flood assessment used to determine inhibitor return profile isotherm by means of a model squeeze treatment, 'SQUEEZE V' to determine various parameters: squeeze life, concentrations, shut in period, postflush, see Figure 20. Effectively a sensitivity study but the model must be optimized after first treatment. Variations in: local temperatures, flow rates, precise scale inhibitor mechanism (precipitation/adsorption) will influence the model and actual response.

#### 4.26.4.4 Scale Inhibitor Selection

Typical program includes:

- Monitor changes in well, water composition, and physical conditions data. Carry out scale prediction modeling to assess scale risk throughout production system, surface, and subsurface.
- The scale inhibitor candidate products are tested for performance and compatibility.
- Brine/chemical compatibility, various field water/sea water ratios to test for inhibitor/brine compatibility, static inhibitor adsorption tests on reservoir core (if for squeeze application).
- Efficiency performance test.
- Static bottle tests.
- Dynamic loop.
- Thermal stability tests for application >130 °C.
- Production chemical interference tests with candidate scale inhibitor.
- Review of inhibitor performance data.
- Select product.
- Core flooding and squeeze modeling.

#### 4.26.4.5 Scale Removal

**Mechanical** – rod out the scale from heat exchangers, 'scraping'/'pigging' of lines.

**Chemical methods** – calcium carbonate is soluble in hydrochloric acid, acetic acid, formic acid, and sulfamic acid. Iron carbonate, iron oxide, and iron

sulfide are also soluble in hydrochloric acid. The HCl must contain a sequestering agent (e.g., acetic acid, oxalic acid, gluconic acid, or citric acid) to prevent precipitation of iron. Gypsum ( $\text{CaSO}_4 \cdot 2\text{H}_2\text{O}$ ) is insoluble in acids. However, gypsum can be converted to another scale that is soluble in acid. Ammonium bicarbonate or sodium carbonate converts gypsum to calcium carbonate. Potassium hydroxide converts gypsum to calcium hydroxide. Both calcium carbonate and calcium hydroxide are soluble in acid. If the scales are covered by waxes, the waxes should be removed with organic solvents first. Waxes are not soluble in acids. Mechanical methods must be used to remove barium and strontium sulfate from tubes. An attempt should not be made to dissolve barium or strontium sulfate with acid because they are less soluble than casings and liners.

#### 4.26.5 Treating for MIC

Bacteria cause two major operating problems:

**Biofilms** – bacterial growths that can reduce flow rates and cause plugging.

**Localized corrosion** – due to environment changes, usually under biofilms and deposits, see [Figure 21](#).

The most common forms of bacteria found in natural waters used in oil and gas production/refining facilities are slime forming, and most are

aerobic (often called general aerobic bacteria, GAB): *Pseudomonas*, *Flavobacterium*, *Alcaligenes*, *Bacillus*, and *Aerobacter-Sphaerotilus-Gallionella*. The bacteria responsible for many corrosion problems are the anaerobic sulfate reducing bacteria (SRB): *Desulfovibrio*, *Desulphotomaculum*, and *Desulfobacter*. Some SRB can be found in aquifers having been present for millennia. Other bacteria are oxidizing bacteria and convert sulfide to sulfur/sulfate or oxidize ferrous to ferric and are commonly found in waste water systems and are responsible for degradation of concrete, for example, *Thiobacillus* and *Beggiatoa*. Further details of microbial issues can be found in Stott<sup>13</sup>.

##### 4.26.5.1 Bacteria Monitoring Techniques/Serial Dilution

Samples acquired to estimate populations of free floating bacteria (planktonic) found in fluids, and bacteria attached to surfaces (sessile) are analyzed using similar techniques that comprise a *serial dilution step* followed by an *incubation step* with the concentration of bacteria estimated from changes observed in the sample bottles<sup>9</sup>. More specifically, the technique estimates bacteria concentration (bacteria/ml) by taking a 1 ml sample of the source water and injecting it into 9 ml of a sterile broth media in small, capped bottles. The solution in the bottle is mixed well and 1 ml is extracted using another syringe and the extracted fluid is injected into a second bottle and

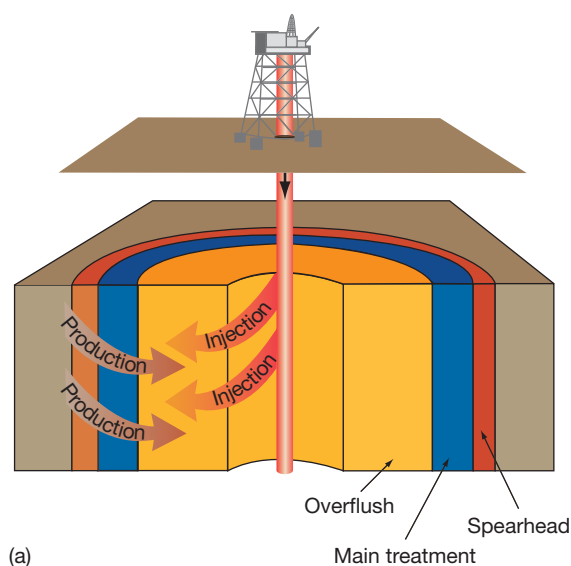
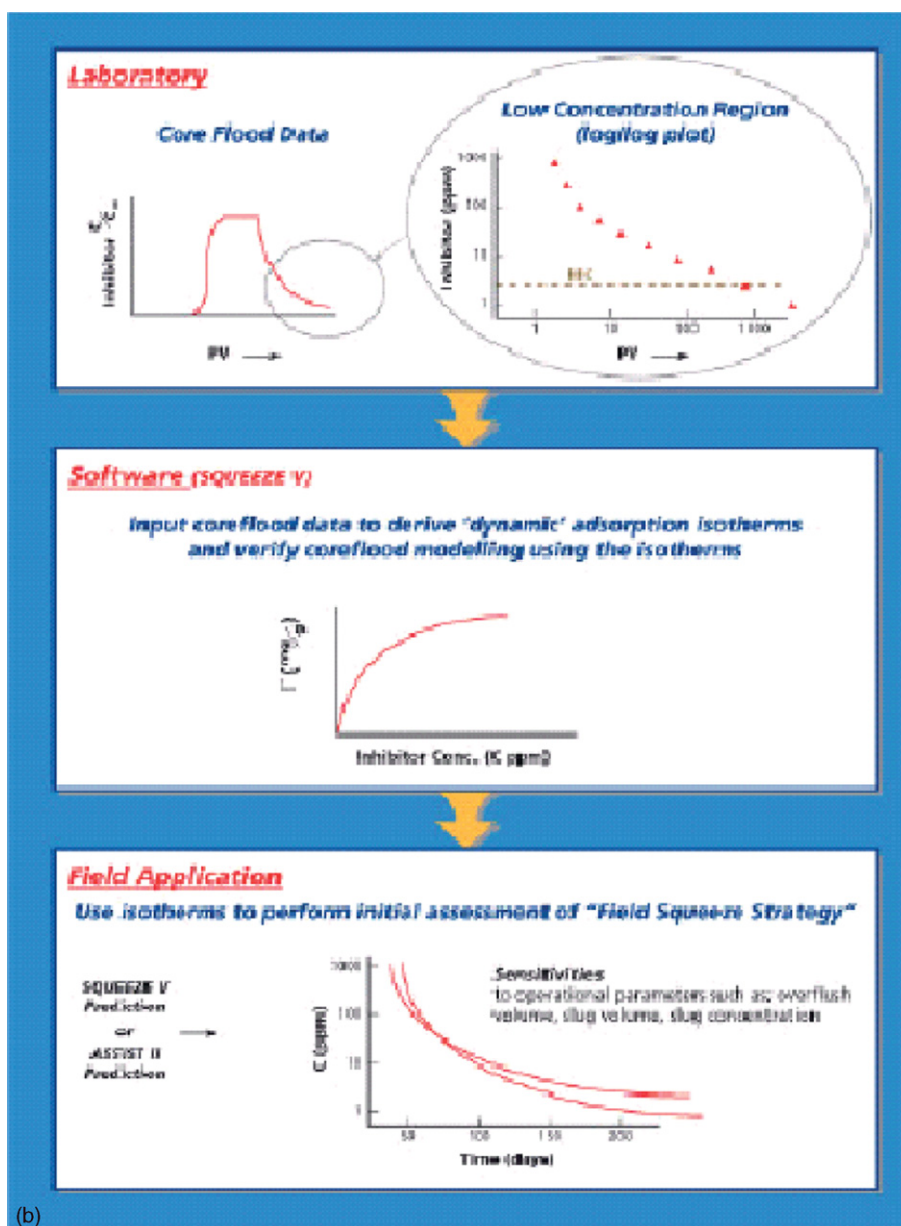


Figure 20



**Figure 20** Continued. Illustration of squeeze application into reservoir.

the same procedure is followed until all six bottles are inoculated. The media contains nutrients and a carbon source with either saline or fresh water. For GAB, the carbon source is dextrose. For SRB, the carbon source is lactic acid together with an iron salt or an iron nail. At the end of the incubation period, the SRB population density in the original sample is determined to the nearest order of magnitude by the number of vials in each dilution series that turn black due to bacterial sulfide production. Tests in which five bottles turned black suggest that the water

sample contains a bacteria count of between  $10^4$  and  $10^5$  bacteria/ml, see [Figure 22](#). The SRB bottles are incubated for 28 days. GAB bottles are incubated for 5 days. Current standards prescribe an incubation period for SRB as a minimum of 28 days, but a very good indication of the SRB count can usually be obtained after 10–14 days of incubation. It can be assumed that if the planktonic bacteria count is high, the sessile bacteria count is also high somewhere in the system. However, a low planktonic count does not suggest that the sessile count is low.





**Figure 21** MIC pitting in an iron sulfide film, morphology of micropits within larger pits. Reproduced from Stott, J. D. F. *Microbial Environments*. In *Corrosion*; Elsevier: London, 2009; Vol. 2.



**Figure 22** Serial dilution test for SRB, five dilutions contain bacteria indicating a heavy infestation.

Ideally, the serial dilution part of the test should be carried out within a few hours of obtaining the subject samples (typically done on site), however, that is frequently not possible. The results become less reliable with increasing time from sampling. Total viable bacteria counts are usually much higher than SRB counts, with planktonic counts of up to  $10^5$  per ml are common in many natural waters and industrial systems. Higher population densities than  $10^5$  per ml probably indicate a significant build up of slime somewhere. In biocide-treated systems, total viable bacteria counts should be several orders of magnitude lower than in the untreated water. The incubation period for total viable bacteria counts is only  $\sim 3$  days, considerably shorter than SRB. Therefore, these counts can give a useful early warning of any problem with biocide-treatment efficiency. GAB populations greater than  $10^4$  bacteria/ml are considered significant.

#### 4.26.5.2 Biocide Treatments

Biocide treatments control bacteria numbers (measured by counting the population density), and the first stage of biocide selection is a laboratory evaluation of candidate biocides using a 'time-kill' test. These tests use a series of biocide dilutions combined with injection of known populations of the bacteria. After the completion of laboratory tests for biocides for a given application (which should include economic considerations and chemical compatibility tests), a program of site monitoring is recommended. The site monitoring should ensure that the chemical injection rate is giving the correct concentration of biocide and is changed when water throughput rate is altered. The monitoring should identify any major perturbations of the system which may affect biocide efficiency. Such perturbations include changes in contact time, flow rates, temperature, pH, use of a new chemical (e.g., corrosion inhibitor, scale inhibitor, or oxygen scavenger), or shutdown periods.

#### 4.26.5.3 Biocide Application

The purpose of biocide treatment is not to kill all bacteria in the system but to control bacteria and economically minimize their effects on corrosion and water quality. Biocide performance is based on success in controlling sessile bacteria, although initially planktonic counting is employed to screen several biocides. Then the biocides that successfully pass this test are tested further for their impact on sessile bacteria (N.B. to acquire sessile samples, growths are carefully scraped or sonically removed. The bacteria population is related to the surface area of the coupon studs with results being reported as bacteria per square centimeter.)

Typical biocide packages are based on:

- Primary amines – cocoamine acetate,
- Diamines – cocodiamine acetate,
- Quaternary amine salts – dialkyl-benzyl ammonium chloride,
- Aldehydes – formaldehyde, glutaraldehyde, acrolin,
- Chlorinated phenols, and
- Oxidizing agents – chlorine, bromine (hypochlorite–hypobromite mixture) usually produced by electrolysis of seawater or brine.

Chlorine dosage has the disadvantage that the water may contain reducing agents with a chlorine demand, where chlorine is consumed by reaction with organic matter and pipework, whilst ammonia



will form chloramines. The chlorine demand must be accounted for and the system is overdosed to a free chlorine 'residual' of typically between 0.2 and 0.5 ppm. Chlorination is not suitable for systems with a high chlorine demand or extensive (several km) exposed carbon steel pipework as the high dosage levels required at the inlet can lead to enhanced corrosion risks, possible stress corrosion cracking of austenitic steel.

There are essentially two classes of biocide treatment, viz. continuous, low level dosing with oxidizing agents and 'shock' treatment using organic biocides. These are often employed together for seawater injection systems where an initial dose of chlorine kills some bacteria and seed macrofouling. The water is then deaerated, removing chlorine and dissolved oxygen and then a batch dose of biocide is periodically sent down the line. Biocide batch treating of water systems controls bacteria with a higher biocide concentration and a shorter contact time. A typical offshore seawater injection system for example, would have continuous use of electrolyzed sea water to control macroorganisms (seed shell fish, etc.) and partially control bacteria followed by batch treatment with glutaraldehyde (e.g.,  $1500 \text{ mg l}^{-1}$  twice weekly) for 1 h, and subsequently, to prevent the development of a dominant bacteria strain with a quaternary ammonium-based bactericide (e.g.,  $500 \text{ mg l}^{-1}$  for 1 h).

Developing a biocide treatment strategy to maintain control of microbial populations is an iterative process. If insufficient biocide is dosed, a greater proportion of the microbial population will recover between dosing than being killed during dosing and the population trend will increase with time. Increasing the dosing regime may then lead to a situation where kill is exactly matched by recovery. Further improvements can lead to an overall reduction in population where kill exceeds the recovery rate. This will lead to a reduction of corrosion in the fluids which is the aim of the biocide treatment strategy.

An alternative method to chemical biocide treatment is ultraviolet sterilization, with the disadvantage that it carries no residual protection into systems and does not sterilize sessile bacteria on the metal surfaces. Treatment is only effective against planktonic (free floating) microorganisms in completely optically clear water. Any entrained particles will shield the SRB from the action of the UV radiation. Also, any scale formation or solids deposition on the optical window (even a very thin film) will severely limit the effectiveness of the treatment.

#### 4.26.6 Management of Treating Programs

The use of chemical treating is a strategic decision made during the design stage in the case of corrosion, usually due to the selection of the use of c-steel or low alloy steel in preference to corrosion resistant alloys but in the case of scaling based on reservoir and injection water chemistries. The implications are that provision must be made for the positioning of injection locations, chemical storage, and chemical monitoring facilities. Details of many of these issues can be found in the oil and gas management chapter.<sup>1</sup> In many cases, the need to introduce chemical treating arises during operations due to adverse processing conditions, increased maintenance for cleaning/descaling, or is the result of corrosion damage of equipment found by routine inspection. This change will need a reassessment of corrosion, integrity, and operational issues as well as the sourcing, installation, commissioning, and operation of all associated activities concerned with the treatment programs.

In general, safety, health, and environmental (SHE) polices plus operational and commercial concerns control the development of chemical treating strategies and treating management.<sup>2</sup> The purpose of the treating programs must be clearly stated together with their likely impact on corrosion, asset integrity, maintenance, and operations. There are obvious costs associated with treating – the initial investment or capital cost, personnel recruitment, training, chemical costs, use of contractors or consultants but also benefits – the ability to operate effectively within highly aggressive environments, to push operating envelopes, and improve overall performance. Effective management requires a transparent framework for these activities with the management process involving a series of logical steps as illustrated by the management process flow sheet shown in [Figure 23](#).

The inputs to the flow chart are the treating issues and their impact on maintenance of asset integrity (SHE) and improvement in performance (business outcomes). There are two outputs from the management process, the tactical, which is effective mitigation of the risks from corrosion, scaling, and microbiological infections (decreased rates of corrosion damage, less plugging of strata and equipment) and a continuous improvement of the management process (less risks from leakages or hazards from corrosion, fouling, fracture, wear, plus increased throughput at lower costs). Although this second outcome is a normal requirement of any quality

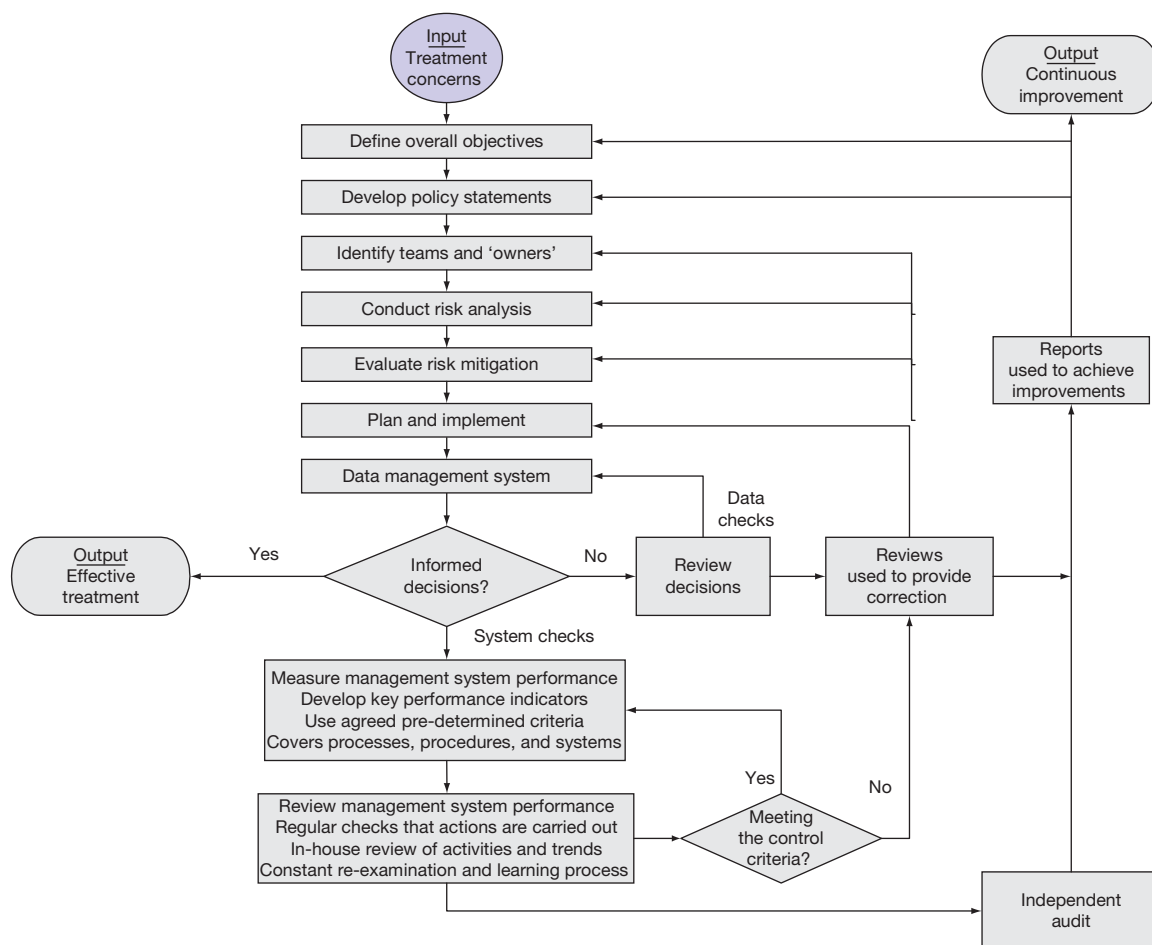


**Figure 23** Steps in a risk-based treatment management process.

system and the management of SHE issues, it has not received widespread acknowledgment in the management of oil and gas assets or treatment management. This is in spite of the fact that asset management, including chemical treating and corrosion management, requires that products are recovered at lowest possible costs commensurate with meeting SHE requirements.

The flow sheet was developed using a risk-based approach for corrosion management,<sup>2</sup> with the decision-making step based on reputable field data as a key factor in development of strategies. The risks are from both physical and chemical processes (corrosion and scaling) and from management processes often referred to as human errors, when catastrophic failures occur. J. Reason<sup>10</sup> considers that key factors in many industrial equipment failures are due to *latent conditions*, which promote the likelihood of active failures by the creation of local factors that then promote errors. Latent conditions are defined here 'as undiagnosed or

unrecognized flaws or defects in data, data management, systems, documents, procedures and guidance or standards that give rise to human errors.' The need to meet design and operational specifications, including no leaks, minimum unscheduled down time, cost effective production means regular reviews and audits including the development of performance indicators based on acceptable criteria. These audits are also a means of identifying latent conditions in the management system. A continuous improvement approach also has benefits in the control of operational issues – day-to-day activities, monitoring, chemical dosing, etc.

The objectives of a treating program must be transferred through from design to operations and should be encompassed in a policy statement from the senior management. The boundaries and ownership of the program must be clearly defined, as a number of individuals, specialists, teams, and vendors are likely to be involved. Hence, responsibility and

**Table 2** Typical activities, responsible personnel, and implications

<i>What</i>	<i>Who</i>	<i>Comments</i>
Corrosion data	Operators/inhibitor supplier	For all monitored locations – last period and yearly trends
Analysis of data	Corrosion engineer	Is corrosion controlled?
Chemical consumption	Inhibitor supplier/ purchasing	Last period and trend
Chemical problems	Production chemist	Compatibility with other chemicals, water quality
Production rates	Operations	Last period, forecasts with emphasis on impact on chemical usage
Equipment on line availability	Operations/maintenance	Specify cause of outing, duration, cost of repairs
Processing information	Operations	Possible interference of inhibition with processing
SHE performance	Facilities/process	Targets, results (e.g., water discharge compliance)
Operators comments	Operations	Nonspecific problems, issues, suggestions for improvement
Targets for next period	All	Include technical, commercial issues

accountability may become less obvious as projects and operations develop. This is illustrated by a list of activities and personnel involved, see [Table 2](#).

#### 4.26.6.1 Inhibition Risks and Mitigation by Monitoring

One approach is to continuously monitor a number of process parameters (e.g., flow rate, water cut, temperature, etc.) and then be ready to alter the corrosion inhibition conditions appropriately. The concern is that there is no direct measure of metal loss. However, such a strategy may be appropriate in low risk systems where regular corrosion inspections can adequately identify wall thickness change. A more proactive and efficient approach, essential with high risk systems, is to identify the corrosion rate increase and its cause, such as an increase in water cut/process parameter change, as quickly as possible and respond to it immediately. Methods that use insert probes/spool pieces, such as the newer electrical resistance techniques and linear polarization resistance measurements (LPRM) are typically employed but sensitive ultrasonic transducers, permanently attached to the equipment have been used, as have iron counts to determine metal loss rates.

A risk assessment is a normal step in any business activity, and operating companies address inhibition risks differently depending on the type and age of equipment, location, types of fluids, constraints, and experience. There is also an increasing emphasis worldwide for organizations to adopt a risk-based approach to facility integrity and corrosion management, including the management of inhibition programs. Inhibition risks are typically associated with:

- maximum expected uninhibited corrosion rate;
- required inhibitor efficiency;

- required inhibitor availability;
- risks of erosion corrosion (flow regime and velocities);
- risks of pitting/under deposit corrosion;
- temperature that may cause loss of inhibitor performance and scaling;
- precorrosion (old or new system);
- available corrosion allowance (CA) and required life; and
- access for repairs and replacements.

The BP approach to assessment of inhibition risks for pipelines is summarized in the tables that list the categories for a typical 20-year design life with a maximum of 8 mm CA and indicates that inhibition is typically employed when the corrosion rate exceeds  $0.5 \text{ mm year}^{-1}$ . CRAs are used where the uninhibited corrosion rate is  $>6 \text{ mm year}^{-1}$ . Note that the evaluation includes inhibitor availability, the percentage time, the injection of corrosion inhibitor occurs, and also the likely monitoring and inspection requirements to ensure adequate management of the system and to maximize integrity, see [Tables 3 and 4](#).

Monitoring is a risk mitigation method that is used to confirm that inhibition, biocide, etc. are actually controlling the hazards (corrosion, fouling) to an agreed and acceptable rate. Monitoring can detect out of compliance, provide operators with sufficient reaction time to implement remedial action, such as repair of injection equipment, change operating procedures, change dose rate, and/or inhibitor/biocide/scale control package. Common corrosion monitoring methods include:

- chemical/biochemical analysis of fluid samples for changes in composition, water cuts, inhibitor residuals, planktonic bacteria;

**Table 3** Example of a corrosion inhibitor risk evaluation

<i>Risk category</i>	<i>Maximum required availability</i>	<i>Maximum expected uninhib. corr. rate (mm year<sup>-1</sup>)</i>	<i>Comment</i>	<i>Proposed category name</i>
1	0%	0.4	Benign fluids, corrosion inhibitor use not anticipated. Predicted metal loss may be accommodated by corrosion allowance	Benign
2	50%	0.7	Corrosion inhibitor probably required, but with expected corrosion rates there will be time to review the need for inhibition based on inspection data	Low
3	90%	3	Corrosion inhibition required for majority of field life, but inhibitor facilities need not be available from day one	Medium
4	95%	6	High reliance on inhibition for operational lifetime. Inhibitor facilities must be available from day one to ensure success	High
5	>95%	>6	Carbon steel and inhibition is unlikely to provide integrity for full field life. Select corrosion resistant materials or plan for repairs and replacements	Unacceptable

**Table 4** Monitoring and inspection requirements for different inhibitor risks

<i>Corrosion inhibition risk</i>	<i>Overall system requirements</i>	<i>Inhibitor injection system</i>	<i>First inspection schedule</i>	<i>Monitoring of subsea lines</i>
Category 1	Does not rely on corrosion inhibition	No requirement	Inspection determined by previous operation of similar systems	Process monitoring of fluids
Category 2	Inhibition not used in early life but is available when conditions change, i.e., increased water cuts	Commissioning without shutdown	As category 1	Standard inspection techniques at accessible points
Category 3	Inhibition not available due to logistics problems but must be operated as soon as possible	Commissioned as soon as practical and incorporate level device and flow monitor into injection system	Early inspection as determined by anticipated corrosion rates	As category one plus weight loss coupons, ER/LPR probes and occasional intelligent pig runs
Category 4	Corrosion control working on day one. Inhibitor and dose rate preselected	As category 3	As category 3	As category two plus FSM or UT mats system. Continual logging for all monitoring devices
Category 5	Assumes technical, SHE, and financial factors answered satisfactorily requirements as category 4	As category 3	As category 3	As category three plus increased inspection frequency

- ion counts (regular chemical analysis to provide trends);
- corrosion coupons (weight loss and detection of pitting, scales, bio-films);
- insert probes/spool pieces (electrical resistance/modern versions electrochemical – linear polarization resistance/electrochemical impedance/electrochemical noise/galvanic coupling);

- hydrogen probes (electrochemical, beta foils);
- FSM (field signature method) for metal loss/erosion pitting trends;
- ultrasonic strips (UT Mats) for metal loss trends; and
- erosion/sand probes.

Down-hole inspections of tubulars use wireline operations, including calliper surveys and ultrasonic examinations, complemented by visual and wall thickness UT measurements during work-overs. The inspection data, as with process plant examinations (RBI) should be correlated with the on-line corrosion monitoring. The same is true of in-line inspections where the condition of larger diameter pipelines is typically obtained by 'intelligent' pigging, usually magnetic flux measurements. Pipe geometry and vibration monitoring using a 'semi intelligent pig' (SAAM), which operates on the principles of measuring, recording, and detecting any changes in vibration level as the pig travels along the pipeline has also been used to correlate operations with field effects.<sup>11</sup> In addition, the differential pressure levels are detected and recorded along with axial acceleration and temperatures. This type of study demonstrates the importance of correlation of field data in the management process.

Further details on monitoring, including chemical analysis can be found in the Chapter on Oil and Gas Management.<sup>1</sup> The actual methods employed in any specific application will depend on the type of corrosion and the inhibition risk involved.

Tactical planning of the treating programs requires formulation of plans, specifications, assessment of chemicals, likely dose rates, and costs. Performance indicators will have to be developed for all activities, see EFC 39<sup>7</sup> for details.

#### 4.26.6.2 Monitoring and Data Management

Water cut is an important operational parameter that must be monitored; the inhibitor dose rate and partitioning properties must be balanced to achieve optimal inhibitor concentration in the field. These are examples of field data that are continuously being collected and analyzed. Other parameters include the persistency of batch inhibitors that needs to be verified in the field to ensure the viability of the batch treatment. Corrosion monitoring is NOT a replacement for condition monitoring (e.g., use of inspection, intelligent pigs for pipelines, downhole wireline surveys), but an adequately monitored and well-managed chemical

treatment program can provide cost benefits by optimizing the inspection frequency. Process interruptions, such as shutdowns, acid returns, and sand deposits due to loss of gravel packs require their own special set of precautions to prevent continuing corrosion damage in downstream operations.

Data collection is an integral part of any system that forms part of a chemical treating program. Data must also be properly stored to allow easy access for retrieval and analysis. Data are only useful when they are converted into information that can be employed to manage the corrosion. Monitoring for corrosion is only one aspect of managing the total inhibition system. For example, certain types of corrosion monitoring (e.g., weight loss coupons) only reveal an adverse change in the process after it has happened, often a significant time afterwards. These warnings are retrospective and reactive as metal loss has already occurred. Online data used to control chemical treatments require monitoring from chemical analysis, probes/spool pieces plus retrieval of appropriate process data, such as flow rates, temperatures, and fluid compositions from Supervisory Control and Data Acquisition (SCADA) systems. Conversion of data into information requires correlation of various datasets, analysis of trends, and extraction of information related to performance and cost benefits. An IT benchmark product such as *Amulet* has been employed for the management of corrosion data from various offshore and onshore production facilities/refining/oil field treating chemicals as illustrated in the figures. Not only should actual dose quantities of chemical be listed but these should be translated into dosage (ppm) by correlating with actual production rates. In many instances, an audit will show that the quantities of chemical ordered, delivered, in store or received by the field do not correlate with the specified dose.

Inhibition data such as corrosion rates should be correlated with other processing parameters, such as production rates and water cuts, to provide economic information for management. For example, chemical spend based on chemical performance and not dosage or usage targets, see [Figure 24](#). Essentially this converts technical data to money to provide performance measures and criteria, enables compliance to be measured, and benchmarks similar assets. Other parameters could include cost per Ml water processed, cost per MW power, cost per barrel of seawater injected. A typical case is a \$1.6 million per year saving achieved on a \$5.6 million chemical spend as a result of online corrosion data management.



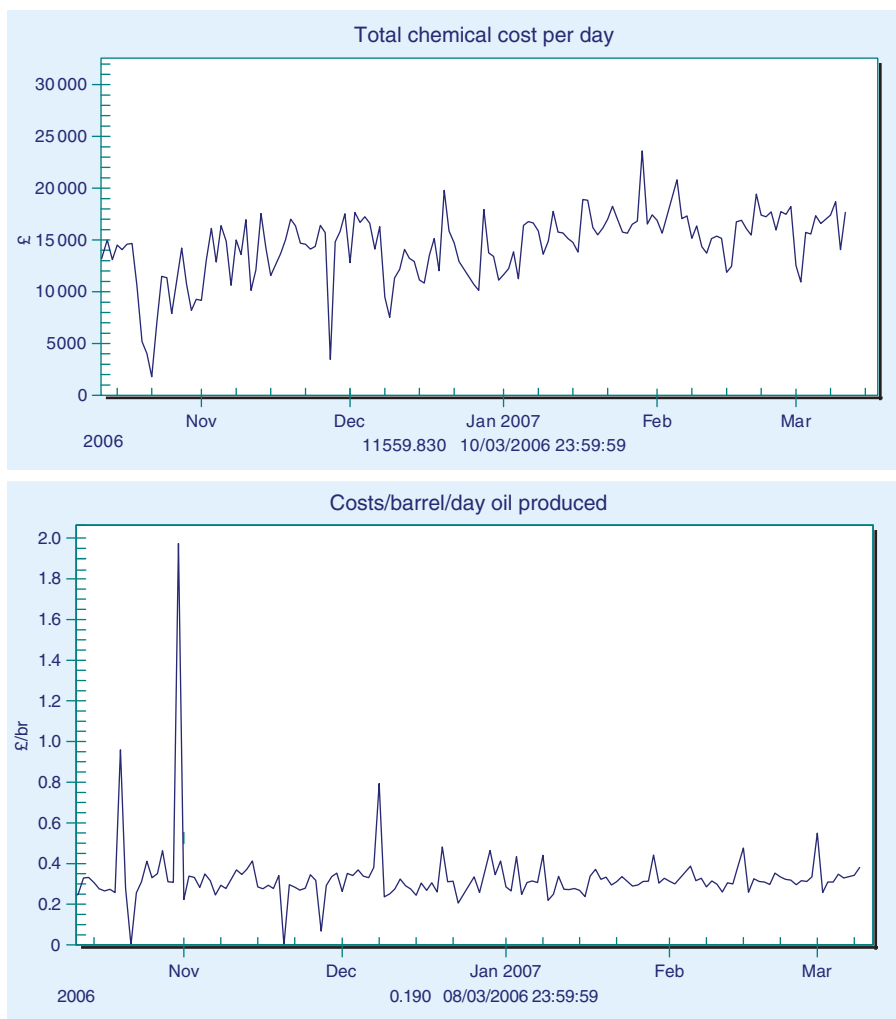


**Figure 24** Comparison of chemical costs per day and per barrel of oil produced, courtesy A. N. Rothwell. Reproduced from Smith, C.; Murphy, B.; Flockhart, S. In *Corrosion'07*; NACE International: Houston, 2007; Paper No 330.

Management of treating programs relies on good decision making that requires information on field performance. This can only be obtained from data analysis that in turn means input of adequate field data. Without adequate data, there is no information and no effective chemical management control.

Further information on various aspects of the review and audit processes can be found in 'Guidance for corrosion management in oil and gas production and processing'<sup>12</sup> that also indicates normative requirements for the UK industry. The strategic decision to use chemical treating of a c-steel system has implications for other materials, such as some corrosion resistant alloys and Ti/Ti alloys. Also, the use of an alliance strategy with a chosen vendor has benefits in terms of a focused program with shared cost savings

but ownership of equipment and field data, etc. has to be agreed prior to contract award.

It is also important to establish technical authority for chemical treating during design, commissioning, and operations and also to ensure that all relevant information is transferred from design to operations. Roles and responsibilities of all personnel have to be clearly defined, especially in large assets where chemical treating involves many disciplines, specialists and operational/maintenance staff, operators, technicians, and managers. System failures usually involve issues associated with data, handling, interpretation, issuing of reports and/or latent conditions within the management system, decision-making or audits for continuous improvement.

## References

1. John, D. G.; Dawson, J. L.; Oliver, K. Corrosion Management in the Oil and Gas Industry. In *Corrosion*; Elsevier: London, 2009; Vol. 3.
2. Dawson, J. L. Corrosion Management Overview. In *Corrosion*; Elsevier: London, 2009; Vol. 3.
3. Chemical costs [www.corrosioncost.com/pdf/oilgas.pdf](http://www.corrosioncost.com/pdf/oilgas.pdf)
4. Crolet, J.-L. Progress in the Understanding and Prevention of Corrosion, EFC Conference, Barcelona 1993; pp 473–497.
5. Hedges, W.; Paisley, D.; Woollam, R. In *Corrosion 2000, June 2001*, NACE International: Houston, TX, 2000; pp 40–44; Paper No. 34.
6. Dawson, J. L.; Miller, R. G.; John, D. G.; Gearey, D.; King, R. A. In *Corrosion'88*; NACE International: Houston, TX, 1988; Paper No. 361.
7. Webster, S.; McMahon, A. J.; Paisley, D. M. E.; Harrop, D. *Corrosion Inhibitor Test Methods*, Sunbury Report No. ESR 95.ER.054, November 1996, Sunbury, B. P.: UK.
8. Palmer, J. W.; Hedges, W.; Dawson, J. L. *The Use of Corrosion Inhibitors in Oil and Gas Production*, European Federation of Corrosion Document Number 39; Institute of Materials: London, 2004.
9. Standard Test Method, TM0-194-94, *Field Monitoring of Bacterial Growth in Oilfield Systems*; NACE International: Houston, Texas, 1994.
10. Reason, J. T. *Managing the Risks of Organizational Accidents*; Ashgate Publishing Ltd: England, 1997.
11. Smith, C.; Murphy, B.; Flockhart, S. In *Corrosion'07*; NACE International: Houston, 2007; Paper No 330.
12. *Guidance for corrosion management in oil and gas production and processing*; Energy Institute: London, May 2008.
13. Stott, J. D. F. Microbial Environments. In *Corrosion*; Elsevier: London, 2009; Vol. 29.

## 4.28 Boiler and Feedwater Treatment

**A. Banweg**

Nalco Company, 1601 W. Diehl Road, Naperville, IL 60563, USA

© 2010 Elsevier B.V. All rights reserved.

4.28.1	Introduction	2972
4.28.2	Make up Water Treatment	2973
4.28.3	Feedwater Treatment	2975
4.28.3.1	Dissolved Oxygen Control	2975
4.28.3.2	pH Control	2977
4.28.3.3	All Volatile Treatment (Reducing) (AVT(R))	2977
4.28.3.4	Flow Accelerated Corrosion	2977
4.28.3.5	All Volatile Treatment (Oxidizing) (AVT(O))	2978
4.28.3.6	Oxygenated Treatment	2979
4.28.4	Boiler Water Treatment	2980
4.28.4.1	Residual Phosphate Treatment	2980
4.28.4.2	Steam Purity	2980
4.28.4.3	Chelant Treatments	2981
4.28.4.4	All Polymer Treatment	2982
4.28.4.5	Coordinated Phosphate Treatment	2982
4.28.4.6	Congruent Phosphate Treatment	2983
4.28.4.7	Phosphate Continuum Treatment (Formerly Equilibrium Phosphate Treatment)	2984
4.28.4.8	All Volatile Treatment	2985
4.28.4.9	Caustic Treatment	2986
4.28.5	Condensate Treatment	2986
4.28.6	Boiler Treatment During Out-of-Service Conditions	2988
4.28.7	Miscellaneous (But Important) Comments	2988
References		2988

### Glossary

**Attemperation** The process for reducing and controlling the temperature of superheated steam.

**Cation conductivity** The measurement of the electrical conductivity of a water sample after it has been passed through a strong acid cation resin that is in the hydrogen form.

**Decarbonator** A degasifier used to remove carbon dioxide.

**Desuperheat** Removing superheat from steam typically by injecting high-purity water or steam condensate.

**Duct burner** A means of auxiliary firing in many combined cycle plant heat recovery steam generators (HRSG's).

**Feedwater heater** A heat exchanger used to raise the feedwater temperature. Low pressure

feedwater heaters are typically located ahead of the deaerator; high pressure feedwater heaters are typically located after the deaerator.

**Mud drum** The lower drum in a boiler circuit that acts as a point of recirculation and collects solids for removal by bottom blowdown.

**Mud drum attemperator** A steam to water heat exchanger located in the mud drum used to control steam temperature.

**Specific conductivity** The measure of the ability of water to conduct an electric current. Often related to the dissolved solids content of the water.

**Steam blanketing** A condition in a boiler tube where the steam water mixture stratifies into separate layers. This is more likely to occur in an inclined tube.

**Sweetwater condenser** A heat exchanger that cools a portion of generated steam so that the resultant condensate can be used for attenuation of the superheated steam.

### Abbreviations

**ASME** American Society of Mechanical Engineers

**AVT** All volatile treatment

**AVT(O)** All volatile treatment, oxidizing

**AVT(R)** All volatile treatment, reducing

**ED** Electrodialysis

**EDI** Electrodionization

**EDR** Electrodialysis reversal

**EDTA** Ethylenediaminetetraacetic acid

**EPRI** Electric power research institute

**FAC** Flow accelerated corrosion

**JIS** Japanese Industrial Standards

**NTA** Nitrilotriacetic acid

**ORP** Oxidation reduction potential

**OT** Oxygenated treatment

**RO** Reverse osmosis

**TDS** Total dissolved solids

**VGB** Vereinigung Grosskraftwerk Betreiber  
(Germany)

### 4.28.1 Introduction

Water is abundant on our planet. However, very little is suitable for human consumption (potable) without pretreatment. It is very rare that even potable quality water is suitable for makeup water to a boiler system without additional pretreatment.

There are many technical organizations around the world that publish guidelines on recommended feedwater and boiler water specifications. There are the European Standard<sup>1</sup> and the Vereinigung Grosskraftwerk Betreiber (VGB)<sup>2</sup> in Europe, the American Society of Mechanical Engineers (ASME)<sup>3</sup> and Electric Power Research Institute (EPRI)<sup>4</sup> in the United States, and the JIS<sup>5</sup> in Asia. These guidelines are generally developed by a consensus of committee members that can include equipment manufacturers, industrial equipment operators, water treatment companies, and experienced consultants. Some of these guidelines focus more on a particular segment of the industry than another. For example, the EPRI guidelines focus on boiler systems in the electric utility industry, whereas ASME focuses on boiler systems in industrial

applications. Others may try to cover the entire scope of boiler applications. These guidelines are, for the most part, very general, and only in rare cases do these guidelines specify a treatment chemistry or treatment chemical to use. This is because the actual treatment chemistry used is a function of the makeup water quality available, the desired steam purity to be produced, and economic considerations. For instance, the ASME guidelines relate steam purity to the appropriate boiler water limits but do not specify feedwater purity in terms of total dissolved solid content. This is an economic decision left to the individual boiler system operator to decide how much is invested in the pretreatment system to purify the water as opposed to higher blow-down rates to maintain the boiler water dissolved solid limits. The EPRI guidelines are an example of such an exception from these more general types of guidelines, in that they are intended for a very specific audience of a narrowly defined type of boiler system – in this case, the electric utility industry.

Finally, since these guideline committees are continually updating their guidelines based on the most current information available and the latest operating experience, they will only be referenced in the chapter. For actual guidelines, the most current relevant issue of the chosen guideline should be obtained for use in a particular boiler system.

This chapter addresses the subject of makeup water, feedwater, boiler water, and steam and condensate treatment in steam boiler systems. Feedwater by definition is the combination of returned condensate and fresh makeup water (**Figure 1**). This combination can

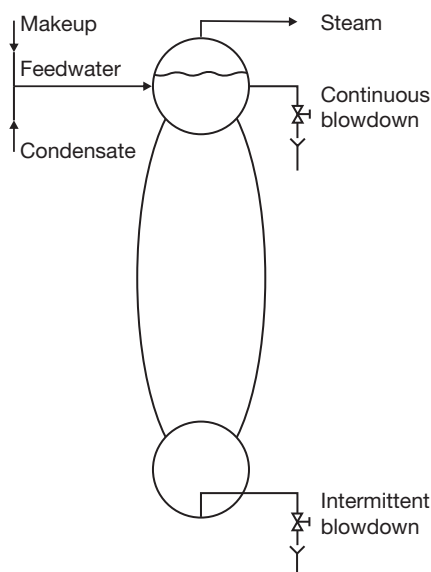


**Figure 1** Schematic of typical boiler flows.

range from 0% to 100% in industrial steam-generating systems, in which the steam-generating system is generally part of an industrial or manufacturing plant. **Figure 2** is a typical field-erected water tube industrial boiler. Notably different are steam-generating systems in the electric utility industry, which are dedicated only to the production of electric power and have condensate return rates consistently greater than 95% of the feedwater by design. **Figure 3** is a typical drum-type utility boiler.

#### 4.28.2 Make up Water Treatment

The type of pretreatment will dictate the necessary further chemical treatment that the water will require prior to use in the particular steam-generating system. The possible types of pretreatment are

- clarification,
- cold lime softening,
- hot lime softening,
- zeolite (ion exchange) softening,
- demineralization,
- reverse osmosis (RO).

Clarification is used to reduce the suspended solids of the water; cold lime, hot lime, and zeolite softening are used to reduce only the hardness, that is, the calcium and magnesium content of the water; reverse osmosis (RO) and demineralization are used for a more effective reduction of the total dissolved solids content of the water.

When precipitating processes for hardness removal such as cold or hot lime softening are used as pretreatment, the effluent water pH is inherently high, in excess of a pH of 10.0. pH control is a very important aspect of water treatment to protect the materials of construction of these systems. A secondary benefit of these precipitation processes is the partial reduction of the water's silica content. When these precipitating processes are used to reduce water hardness, it is important to remember to measure the total hardness of the effluent water. This involves an acid digestion step, as opposed to the normal soluble hardness tests, since there can be suspended solids of hardness in the effluent from these systems that the soluble hardness test would not detect and must be accounted for in the chemical treatments applied.

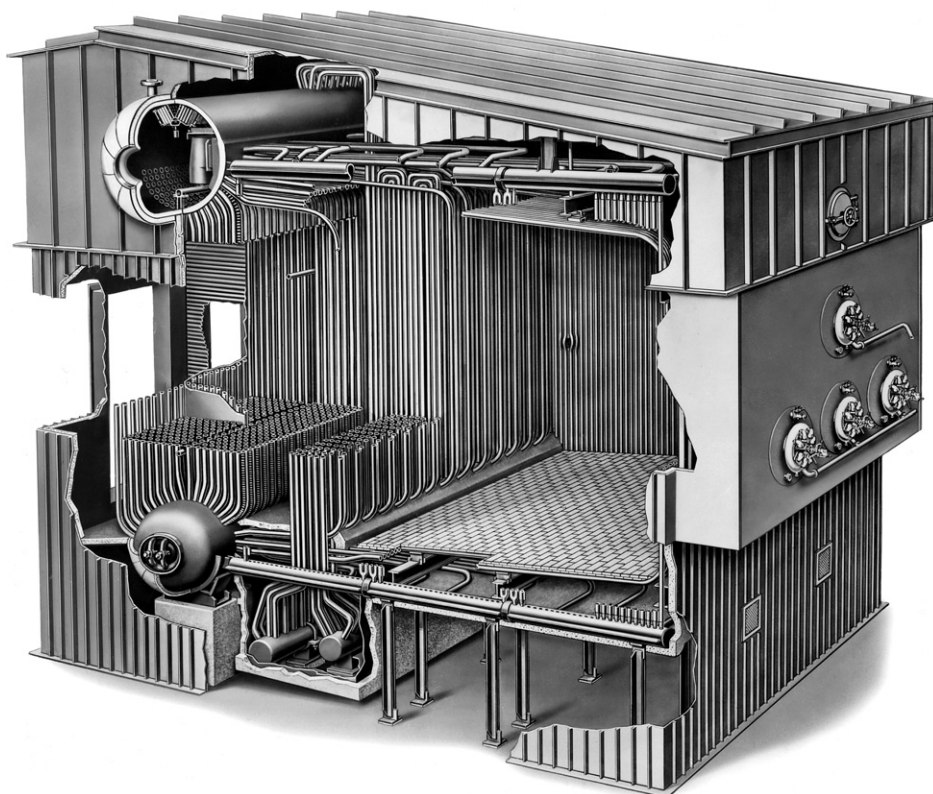


**Figure 2** Field erected water tube industrial boiler.



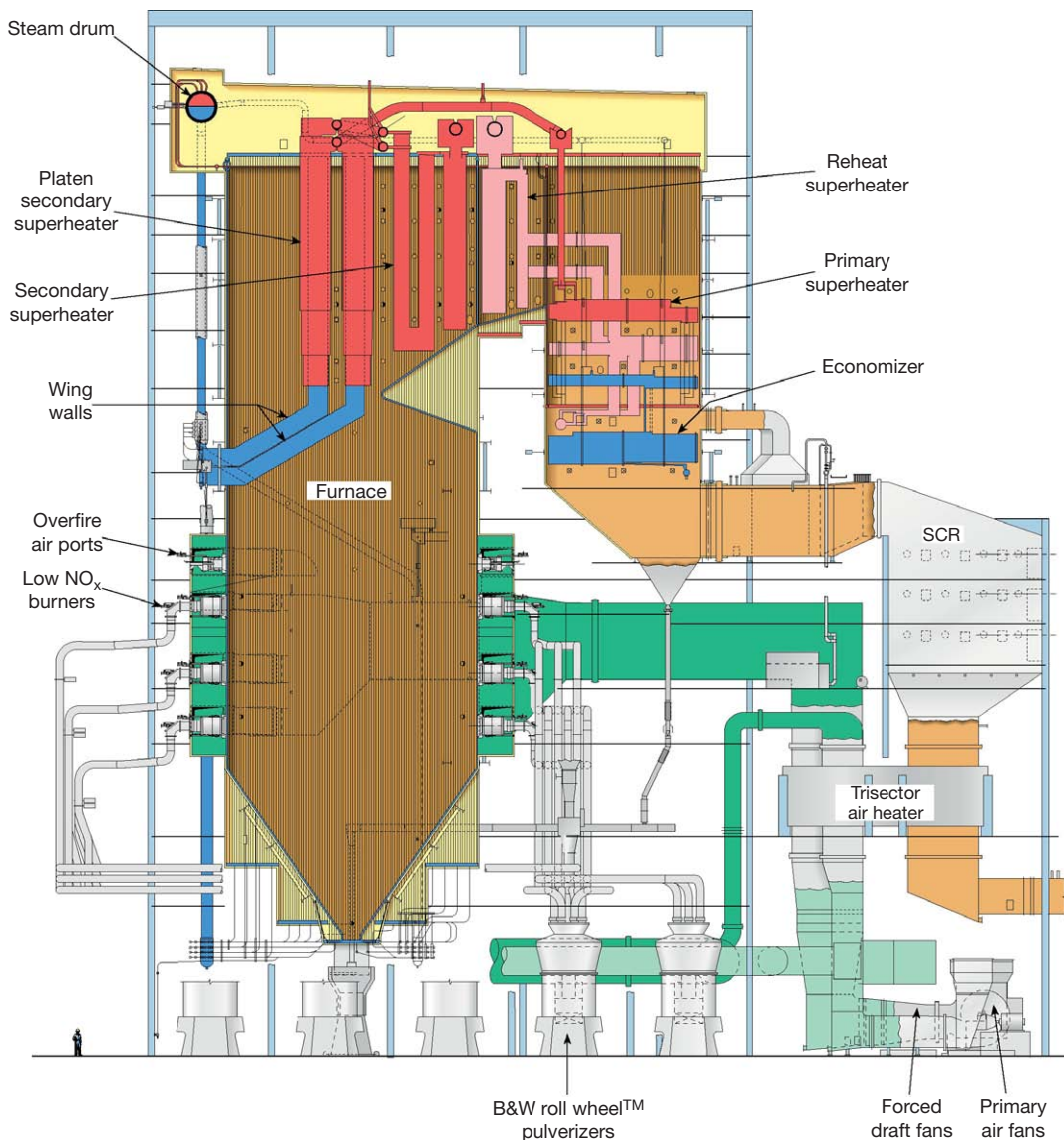


**Figure 3** Natural circulation drum type utility boiler.

Softened makeup water is generally acceptable for lower-pressure boiler systems. Higher-pressure systems will require more purified water such as that treated by RO or a demineralization processes. A high percentage of condensate return in the feedwater can also produce high-purity feedwater.

Zeolite softening, an ion exchange process using strong acid cation resin in the sodium form, can also be used to remove the hardness from the water. This process can be applied in conjunction with one of the precipitating softening processes or alone. Ion exchange softening can also include a dealkalizer for the alkalinity reduction of the makeup water. This is

typically done using anion resin in the chloride form, but several configurations are possible.

Conventional ion exchange demineralization of makeup water typically involves a two-bed demineralization system. Most common is a strong base cation resin bed in the hydrogen form, followed by a strong base anion bed in the hydroxide form. There may or may not be a decarbonator in between. There are many configurations of these systems available, which vary from cocurrent to counter current regeneration configurations. They may also include alternative resin types, weak acid resin, or weak base resin with multiple cation and anion units,

depending on the starting water composition, the final desired water purity and local economics. For the highest water purity requirements, a mixed-bed resin unit is applied at the end of the process.

RO, a membrane-based water purification system, can be used to reduce the total dissolved solids content of the water. There are numerous configurations of the RO process available that can be chosen based on the water's composition to be treated, the level of effluent purity required versus the percentage of recovery required and the local economics of chemical cost, power cost, and labor cost. The details of these systems are beyond the scope of this chapter and will not be addressed in this chapter. The reader is directed to numerous literature sources available on these topics for specific information.

RO, a semipermeable membrane process, reduces the dissolved substances in water, but this removal is not complete, and effluent or permeate may not yet be suitable for boiler makeup water. A conventional mixed-bed resin polisher, electrodialysis (ED), or some modification of this process can follow the RO.

ED is a membrane process in which mineral salts and other ions are transported through ion-permeable membranes from one solution into another under the influence of a direct current electrical potential. Electrodeionization (EDI) is a modification of the ED process that combines ED with self-regenerating mixed-bed ion exchange resins installed between the membranes. Electrodialysis reversal (EDR) is another modification of ED in which the electrical field is periodically reversed to provide a self-cleaning process that can run at increased recovery rates.

Though these electrochemical processes are available commercially and are capable of producing high-purity water, they are rarely used in the boiler makeup water treatment application and are more likely to be seen in the microchip manufacturing industry. Conventional mixed-bed resin deionization is much more common in the production of high-purity boiler makeup water.

### 4.28.3 Feedwater Treatment

Corrosion protection in the feedwater system is generally achieved by mechanically and chemically removing dissolved oxygen from the feedwater and buffering the feedwater pH into a range suitable for the system materials of construction. Feedwater must

generally be deaerated for industrial steam boiler applications, but there are special circumstances in which full deaeration is not recommended. These are discussed separately.

#### 4.28.3.1 Dissolved Oxygen Control

Dissolved oxygen removal from the feedwater is typically accomplished in a deaerating heater or deaerator in which steam is used to remove the dissolved oxygen from the feedwater. Each of these pieces of equipment has its own dissolved oxygen removal efficiency. In some very low-pressure applications, there may only be a feedwater tank in which makeup water and condensate are mixed, which may or may not be actively steam sparged or otherwise heated to try to remove the dissolved oxygen.

The goal of the mechanical deaeration process is to reduce the dissolved oxygen content of the feedwater to less than 7 ppb for a system using a true deaerator. Dissolved oxygen in the feedwater can cause pitting corrosion damage of the feedwater system components. More complex feedwater systems can include both low- and high-pressure feedwater heaters in addition to an economizer.

Additionally, vacuum degasifiers or deaerating condensers can be used for dissolved oxygen removal. Recently, a semipermeable membrane process<sup>6</sup> has also been developed to reduce the dissolved oxygen content of water. These membrane systems have been used in laboratory environments for more than 25 years but have only recently become commercially feasible for industrial applications. This membrane process can use a combination of vacuum and stripping gas arrangements to deaerate the water. The membrane modules can be arranged in series to produce ppb level oxygen concentrations in the final water. These membranes, dependant on the pH of the water, can also remove carbon dioxide. RO pretreatment is recommended ahead of the gas membrane to prevent fouling. A conventional deaerator also provides only limited removal of carbon dioxide, based on the pH of the water.

After any of these mechanical/thermal deaeration processes, a chemical oxygen scavenger can be applied to further reduce the dissolved oxygen content of the feedwater (Table 1).

Sodium sulfite is the most common chemical oxygen scavenger used in low-pressure boiler systems. It is also available in a catalyzed form, which increases the speed of reaction with the dissolved oxygen. This can be important when the mechanical

**Table 1** Oxygen scavengers used in steam-generating systems

Scavenger	Primary reaction	Comments
Hydrazine	$\text{N}_2\text{H}_4 + \text{O}_2 \rightarrow 2\text{N}_2 + 2\text{H}_2\text{O}$	Toxicity and handling issues
Hydrazine decomposition	$3\text{N}_2\text{H}_4 \rightarrow 4\text{NH}_3 + \text{N}_2$	At temp. $>200^\circ\text{C}$
Sodium Sulfite	$2\text{Na}_2\text{SO}_3 + \text{O}_2 \rightarrow 2\text{Na}_2\text{SO}_4$	Also $\text{NaHSO}_3$ , $\text{Na}_2\text{S}_2\text{O}_5$ , $\text{NH}_4\text{HSO}_3$
Carbohydrazide	$(\text{H}_2\text{N-NH})_2\text{CO} + 2\text{O}_2 \rightarrow 2\text{N}_2 + 3\text{H}_2\text{O} + \text{CO}_2$	Forms hydrazine at temp. $>150^\circ\text{C}$ , $\text{NH}_3$ , $\text{N}_2$ , and $\text{H}_2$ on decomposition
<i>N,N</i> -Diethylhydroxylamine	$4(\text{CH}_3\text{CH}_2)_2\text{NOH} + 9\text{O}_2 \rightarrow 8\text{CH}_3\text{COO}^- + 9\text{H}^+ + 2\text{N}_2 + 6\text{H}_2\text{O}$	Frequently fed with hydroquinone, acetic acid, $\text{CO}_2$ , acetaldehyde, $\text{NH}_3$ at temperatures above $275^\circ\text{C}$
Hydroquinone	$\text{C}_6\text{H}_4(\text{OH})_2 + 1/2\text{O}_2 \rightarrow \text{C}_6\text{H}_4\text{O}_2 + \text{H}_2\text{O}$	Acetates, $\text{CO}_2$ decomposition products, toxicity issues
Erythorbate	$\text{C}_6\text{H}_4\text{O}_6 + 1/2\text{O}_2 \rightarrow \text{C}_6\text{H}_5\text{O}_8 + \text{H}_2\text{O}$	$\text{CO}_2$ , lactic acid, decomposition products
Methyl ethyl ketoxime	$2\text{CH}_3(\text{C}_2\text{H}_5)\text{CNOH} + \text{O}_2 \rightarrow \text{N}_2\text{O} + 2\text{CH}_3(\text{C}_2\text{H}_5)\text{CO} + \text{H}_2\text{O}$	Frequently fed with hydroquinone, $\text{NH}_3$ , $\text{CO}_2$ , ketones, aldehydes on decomposition

deaeration process does not provide sufficient residence time. Sodium sulfite is a nonvolatile inorganic compound that does contribute dissolved solids to the feedwater and the boiler water. This dissolved solids contribution prevents its use in feedwater that is to be used as attemperator spray or desuperheat spray for steam temperature control, as these solids would become impurities in the steam.

The control of sodium sulfite is generally based on maintaining a sulfite residual concentration in the boiler water. This can be a problem in a system where the feedwater system deaeration process and chemical injection point do not provide sufficient residence time and temperature for the chemical oxygen scavenging reaction to be completed prior to the feedwater entering the steam drum of the boiler. Oxygen scavengers and dissolved oxygen can coexist in the feedwater, in such a situation, pitting corrosion can occur. Because of the dissolved oxygen's high volatility, the oxygen preferentially goes into the steam phase when the feedwater enters the boiler steam drum, leaving the unreacted sulfite residual in the boiler water.

Another point of oxygen ingress into the system not to be overlooked is a leak path through the boiler feed pump seals. It is wise not only to monitor the temperature and pressure operating conditions of the deaerating device for proper operation but also to periodically measure the feedwater dissolved oxygen content directly at the boiler or economizer inlet.

Sodium sulfite can also produce some acidic gaseous decomposition products, such as sulfur dioxide, that will be carried out of the boiler in the steam. This can be significant at boiler operating pressures above 4.1 MPa g (600 psi g). These decomposition products can cause low steam condensate pH.

Hydrazine is another available oxygen scavenger that has been used primarily in higher-pressure boiler applications. It is a volatile compound that can be used in feedwater that is used for steam temperature control by attemperation or desuperheating. However due to its status as a suspect carcinogen, its use in industry has declined. When it is used, a closed feed system is typically required.

Given these health concerns, alternatives to hydrazine have been developed. The most common of these are carbohydrazide, erythorbate, diethylhydroxylamine, hydroquinone, and methylethyl ketoxime. Many of these oxygen scavengers also function as passivating corrosion inhibitors. Each is an organic compound that has its own temperature limitations. Decomposition products can vary from only carbon dioxide to several organic acids and other organic compounds. Some decomposition products are more undesirable than others, and the amount of these decomposition products can be application-specific, depending on system temperatures and metallurgy. Each application should be evaluated based on the benefit provided versus the potential undesirable effects of the decomposition products. As a note, commercially available erythorbate can be either in

the acid form or in the sodium salt form. The sodium salt form is nonvolatile, which restricts its use if the feedwater is used as spray attenuation or in desuperheating.

#### 4.28.3.2 pH Control

Feedwater pH adjustments to slightly alkaline conditions are used to minimize corrosion of the feedwater system piping and components, and the resultant corrosion product transport to the boiler. Caustic, neutralizing amines or ammonia are commonly used for this task. Obviously, caustic cannot be used where the feedwater is used as spray attenuation for steam temperature control. The more common amines in use are morpholine, cyclohexylamine, monoethanolamine, diethanolamine, and methoxypropylamine.

#### 4.28.3.3 All Volatile Treatment (Reducing) (AVT(R))

The feedwater target pH range is a function of the feedwater system metallurgy. In the past, a target pH range of 8.8–9.2 had been specified for feedwater systems containing mixed metallurgy – typically heat exchanger components constructed of copper alloys. Recent work<sup>7–9</sup> has shown that reducing conditions in the feedwater system, an oxidation–reduction potential (ORP) of –300 to –350 mV at 25 °C (77 °F), measured between a Pt electrode and a Ag/AgCl (saturated KCl) reference electrode, at the deaerator inlet, are necessary to minimize copper corrosion and corrosion product transport in these mixed-metal feedwater systems. This work showed that the feedwater pH is a secondary control parameter, which should be restricted to a pH range of 9.0–9.3. EPRI has used the terminology AVT(R), all volatile treatment (reducing) to describe this treatment chemistry. In practice, many systems are not able to reach these low levels of ORP, but copper corrosion and copper corrosion product transport have been successfully reduced in some systems with feedwater ORP levels of even –200 to –100 mV at 25 °C (77 °F), measured between a Pt electrode and a Ag/AgCl (saturated KCl) reference electrode.

This treatment chemistry is expected to reduce corrosion product transport to the boiler system for all operating pressure boiler systems, but is most critical for the very high-pressure boiler systems used by the electric utility industry, where at their operating pressures (>16.4 MPa g (>2400 psi g)),

copper has volatility properties into the high-pressure saturated steam and has caused deposition problems in the high-pressure steam turbine. This deposition in the steam turbine can limit steam throughput and megawatt output. Although the consequences of high copper corrosion product transport to most industrial boiler systems are not as dire as in the very high pressure electric utility boiler systems, only more frequent chemical cleaning of the boilers may be required; this new information on copper corrosion and strategies to minimize it should also be applied to industrial mixed metallurgy feedwater systems.

Theoretically these reducing conditions should be maintained by lay up practices even when the system is out of service, to prevent the reversion of the more protective, more reduced form of copper oxide, cuprous oxide,  $\text{Cu}_2\text{O}$ , formed in service, to the more oxidized and less protective form of copper oxide, cupric oxide  $\text{CuO}$ . Based on the actual circumstances of the out-of-service period, it may not be practical to maintain a reducing environment.

This work<sup>7,8</sup> also showed that the desired reducing environment could not be achieved by the addition of excessive amounts of a chemical reducing agent such as an oxygen scavenger to compensate for a mechanical problem in the system such as a malfunctioning DA or high levels of air in leakage into a condenser or hotwell.

For an all-steel metallurgy feedwater system, the feedwater pH target range is somewhat more alkaline pH = 9.3–9.6. For most industrial boiler feedwater systems, definitely those with softened water make up even those with demineralized make up water or high percentages of condensate return, it is still advisable to fully deaerate the feedwater and treat the system with a chemical oxygen scavenger to prevent dissolved oxygen pitting corrosion damage to the feedwater system components, as previously discussed.

#### 4.28.3.4 Flow Accelerated Corrosion

In boiler systems in dedicated electric utility service, where the typical percentage of condensate return in the feedwater is over 95%, the feedwater most likely will be pure enough to make the system susceptible to flow accelerated corrosion (FAC) damage.<sup>10–13</sup> FAC is a corrosion mechanism that can cause corrosion damage and failures in feedwater systems including economizers, feedwater heaters, and piping. EPRI has compiled a significant amount of information on this topic as it relates to boiler systems in dedicated electric utility service.<sup>14</sup>

FAC is a very localized damage mechanism that affects predominantly areas of flow turbulence in the feedwater system. It is a primarily hydrodynamic phenomenon that prevents the formation of the normal protective oxide (magnetite) coating to form on carbon steel and prevent any further metal loss. FAC is a process whereby the normally protective oxide surface dissolves into a moving fluid. The most susceptible systems are typically all-steel, and employ very high-purity feedwater, due to the purity prerequisite of the steam purity required by the steam turbine in these systems. A significant amount of research has been done on this topic in power plants and is very well documented.<sup>14</sup> FAC is possible at a water temperature range of 100–250 °C (212–482 °F), but there seems to be a maximum susceptibility at about 150 °C  $\pm$  28 °C (300 °F  $\pm$  50 °F). Even though FAC is primarily a hydrodynamic phenomenon, those mechanical parameters that control velocity and turbulence are fixed and not easily changed in an existing system. The research work has identified two water chemistry parameters that influence FAC behavior that can be optimized – feedwater pH and ORP.

#### **4.28.3.5 All Volatile Treatment (Oxidizing) (AVT(O))**

EPRI has developed a feedwater treatment philosophy for boilers in the electric utility service industry that has been termed AVT(O),<sup>4</sup> all volatile treatment (oxidizing), to minimize the potential for FAC in these systems. With AVT(O) treatment, no chemical oxygen scavenger is fed and a nominal amount of dissolved oxygen, (typically  $<10 \mu\text{g l}^{-1}$ ,  $<10 \text{ ppb}$ ) is considered acceptable. This is expected to result in an ORP of  $-50$  to  $+50 \text{ mV}$ , measured between a Pt electrode, and a Ag/AgCl (saturated KCl) reference electrode. This condition is considered less susceptible to FAC than the completely oxygen deficient-reducing conditions of AVT(R) in this high-purity feedwater. Feedwater cation conductivity required for AVT(O) is less than  $0.2 \text{ mS cm}^{-1}$ .

All the discussion on ORP measurement of feedwater up to this point has been regarding the measurement of the ORP of a sample cooled to room temperature, 25 °C (77 °F). Room temperature ORP measurements have had problems with a lack of sensitivity and response. The capability to measure the feedwater ORP at system temperature has been developed, AT ORP™ (originally known as @T ORP™).<sup>15,16</sup> The potential is measured against an external pressure balanced reference electrode

(Ag/AgCl//0.1 N KCl). This technology is much more responsive to system changes that affect ORP. These at temperature ORP measurements can be made at feedwater temperatures up to 260 °C (500 °F).

Feedwater pH is another chemistry parameter that affects FAC, and for an all-steel feedwater system, typically the more alkaline the better (pH  $> 9.2$  up to about 10.0). Even though the feedwater system may be all-steel, there may be a copper alloy condenser that could limit the feedwater pH adjustment to prevent yellow metal attack of the condenser that can occur when ammonia is the alkalinizing agent or a decomposition product.

This near-neutral ORP control, AVT(O), is quite acceptable for high-purity boiler feedwater systems such as those in the electric utility industry, in which the level and consistency of feedwater purity is high. Industrial boiler feedwater systems employing high-purity feedwater are also potentially susceptible to FAC, but the possible chemistry-related corrective actions are not nearly as clear. In industrial boiler systems, even when make-up water is demineralized, the required level of purity for this treatment –  $<0.2 \text{ mS cm}^{-1}$  – is rarely achieved. Additionally, because of the lower percentage of condensate return and the very significant potential for constant low levels and periodic high levels of contamination, feedwater purity can be very inconsistent. For these industrial systems, the simultaneous presence in the feedwater of dissolved oxygen and any feedwater contamination provides the potential for oxygen pitting damage of the feedwater system, especially heat exchanger components, such as an economizer. From the existing research work, it is unclear how pure feedwater must be in order for dissolved oxygen to act as a corrosion inhibitor rather than cause the pitting damage common in industrial systems. From the experience with AVT(O) and oxygenated treatment (OT), feedwater cation conductivity of  $<0.2$  and  $<0.15 \text{ mS cm}^{-1}$  respectively are conditions in which dissolved oxygen acts as a corrosion inhibitor. But even the OT guidelines recommend ceasing oxygen feed and going to an AVT(O) treatment when cation conductivity exceeds  $0.3 \text{ mS cm}^{-1}$ . There are no further guidelines for acceptable higher levels of cation conductivity in the feedwater for AVT(O). OT is discussed in the next section.

This FAC mitigating philosophy of AVT(O) near-neutral ORP can also be accomplished in industrial systems by feeding a very low level of one of the available organic oxygen scavengers/passivators. In this treatment scheme, the oxygen scavenger/passivator is not fed in the stoichiometric ratio to scavenge the



dissolved oxygen but rather is fed at a rate to passivate the steel and provide the neutral ORP target. The feedwater concentration needed to accomplish this ORP is unique to each of the scavengers (hydroquinone, erythorbate, carbonylhydrazide, diethylhydroxylamine, methylethyl ketoxime). In this treatment, when there is an excursion in the chemistry or dissolved oxygen concentration due to mechanical problems, the scavenger feed is able to compensate. We note that sodium sulfite, although it is an oxygen scavenger, cannot be used for this purpose, as it does not appear to have any passivating properties for steel.

Finally, monitoring feedwater ORP does not supply quantitative information regarding FAC, only qualitative information. It has been found that measuring the soluble iron concentration of the feedwater<sup>17–19</sup> at various points in the system can provide more quantitative information regarding FAC. Given that FAC is a very localized damage mechanism related to flow turbulence, it is important to sample the feedwater before and after a feedwater system component with a large surface area subjected to local flow turbulence for this soluble iron testing. Such a component is typically an economizer or feedwater heater with heat transfer surfaces constructed of carbon steel. Detecting a significant increase in the soluble iron content of the feedwater between the inlet and outlet indicates a potential for FAC in the system. Then optimizing feedwater treatment chemistry parameters (feedwater pH, ORP/oxygen scavenger feed) individually and reviewing their impact on the change in feedwater soluble iron content demonstrates the potential impact that feedwater chemistry changes can have on FAC in the feedwater system.

As soluble iron in the water is relatively unstable, soluble iron determination requires careful sample handling to minimize the potential to oxidize the soluble iron in the sample. Feedwater dissolved oxygen content should be less than 20 ppb, and it has been found that it is best to take the sample directly into the reagent to preserve the iron in the soluble state. There have been a number of different ferroin compounds used to determine iron spectrophotometrically.<sup>17,18</sup> One of the most widely used compounds is 3-(2-pyridyl)-5-6-bis (4-phenylsulfonic acid)-1,2,4-triazine, monosodium salt. The test procedure involves collecting samples directly into an acid-cleaned, iron-free container containing the ferroin reagent. Stainless steel sample lines are required.

Even though this soluble iron testing gives a more quantitative picture of the FAC susceptibility of a system and this information can be used to optimize

feedwater chemical treatment, it cannot identify a specific feedwater system component that could be experiencing a particularly high local rate of FAC damage. For this reason, it is still recommended that such a system have periodic nondestructive testing performed on susceptible components (tees, elbows, piping, downstream of valves, flow orifices, etc.) especially those that are in the more prone temperature environment, with water at  $150^{\circ}\text{C} \pm 28^{\circ}\text{C}$  ( $300^{\circ}\text{F} \pm 50^{\circ}\text{F}$ ).

It has been found that in most cases, feedwater chemistry optimization has been able to reduce FAC rates in high-purity industrial boiler feedwater systems prone to FAC but not eliminate them, even in some cases where the treatment has been converted to AVT(O). But as the research work<sup>10</sup> on FAC has shown, commercially available low-chrome alloys (>1% chromium content) are much less susceptible to FAC than carbon steel. Replacing a carbon steel component found to be thinning due to FAC with one of these low-chrome alloy alternatives has eliminated future FAC damage in all but the most extreme situations.

#### 4.28.3.6 Oxygenated Treatment

OT<sup>20–25</sup> is a feedwater treatment developed for once-through boilers in the electric utility industry in Germany in the 1960s. Prior to OT, these boilers were treated with all volatile treatment (AVT) using ammonia and hydrazine. With this conventional AVT treatment, these boilers required frequent chemical cleaning to prevent the accumulation of corrosion products from the feedwater system (primarily iron oxide) in the boiler. These deposits caused pressure drop increases in the boiler's flow circuitry and insulating deposits on high heat transfer areas of the boiler, which could lead to overheating damage.

A once-through boiler is an inherently high-purity feedwater system, since the feedwater purity must meet the steam turbines steam purity requirement. Most of the once-through boilers in Germany operate at subcritical pressures, whereas most of the once-through boilers in the United States operate at supercritical pressures. Most of these systems have all-steel feedwater systems and full-flow condensate polishing.

In these systems, it was found that low levels of dissolved oxygen added to this high-purity feedwater acted as a corrosion inhibitor, producing a more protective oxide on the steel than conventional AVT. This reduced corrosion product transport to and accumulation in these boilers. Most of the once-through boilers in operation worldwide today have now been converted to OT. Some boilers on OT treatment in

Germany have never required chemical cleaning. Once-through boilers in the United States that have converted to OT have significantly extended the time required between required chemical cleanings.

Typical control parameters for OT are a feedwater cation conductivity of less than  $0.15 \text{ mS cm}^{-1}$ ; feedwater pH and dissolved oxygen can be controlled by either what is termed the neutral method, which involves maintaining the pH in the range of pH 7–8 and a dissolved oxygen content of  $50\text{--}250 \mu\text{g l}^{-1}$  (50–250 ppb), or the combined method in which the feedwater pH is 8–9 and the dissolved oxygen content is  $30\text{--}150 \mu\text{g l}^{-1}$  (30–150 ppb). Only ammonia can be used in this treatment as the alkalinizing treatment chemical; dissolved oxygen degrades the more complex amines, increasing the cation conductivity.

OT is only occasionally used on high-pressure drum-type boilers because they rarely have the prerequisite feedwater system metallurgy and the consistent level of feedwater purity required, which typically requires a full flow condensate polishing system. Finally, the required chemical cleaning requirements for drum-type boilers that do meet the metallurgy and feedwater purity requirements are already quite long; therefore, OT does not provide the same economic benefit as it does to once-through boilers. OT for these drum boilers could provide a benefit regarding FAC potential in their feedwater systems, but this benefit is also provided by the AVT(O) feedwater treatment.

## **4.28.4 Boiler Water Treatment**

### **4.28.4.1 Residual Phosphate Treatment**

Boiler water internal treatment options are dependant on the type of makeup water pretreatment, percent condensate return, and boiler operating pressure. For softened makeup water systems, one of the most common internal treatments is residual phosphate treatment, a precipitating treatment for the hardness contaminants in the feedwater.

This treatment chemistry is designed to purposefully precipitate the feedwater hardness contaminants into more desirable, less adherent forms than if they precipitated on their own in the boiler due to their retrograde solubility characteristics. The intent is to precipitate calcium as basic calcium phosphate and magnesium as magnesium hydroxide by maintaining an appropriate boiler water orthophosphate residual and a free hydroxide concentration. The orthophosphate concentration must be measured on a filtered boiler water sample.

A synthetic organic polymer or naturally occurring organic material such as lignins or tannins may be used to help disperse the resultant precipitated suspended solids. The precipitated calcium and magnesium contaminants, though in a more desired form, are still difficult to remove from an operating boiler via the continuous blowdown. This is because they are entrained in the boiler's internal circulation between the downcomer and riser circuitry, which is many times the flow rate of the steam that the boiler actually produces. This circulation continually passes the particulates past the high heat transfer areas of the boiler, where they can form deposits. Suspended solids caught up in the boiler's internal circulation are also not removed very effectively by a boiler's intermittent blowdown system (mud drum blowdown), if the boiler has this capability. Because of the limited effectiveness of the boiler blowdown systems in removing suspended solids, the success of residual phosphate treatment is very much dependent upon minimizing the hardness contaminants in the feedwater and potentially cleaning the boiler, chemically or mechanically, periodically, to control deposit accumulation in the boiler.

Residual phosphate chemistry is controlled by maintaining an orthophosphate residual in the boiler water that is chosen as a function of the boiler's operating pressure, [Table 2](#). Free hydroxide levels in the boiler water are typically maintained at a level of three times the boiler water silica concentration to aid in maintaining silica mineral solubility in the boiler water. In higher-pressure boiler applications ( $>4.1 \text{ MPag}$  ( $>600 \text{ psi g}$ )) where volatile silica transport into the saturated steam is a concern, or anytime the steam being produced is for use in a condensing steam turbine, maximum boiler water silica concentrations are maintained to limit the silica concentration in the saturated steam to the specified limit for the turbine (typically  $10\text{--}20 \mu\text{g l}^{-1}$  (10–20 ppb)) silica in the steam).

### **4.28.4.2 Steam Purity**

Boiler water total dissolved solids are maintained at or below a maximum value to control the overall purity of the saturated steam required. More stringent steam purity limits are required for that steam when it is to be used in a condensing steam turbine application as opposed to a process heating application. With the exception of silica, which has vaporous solubility characteristics in saturated steam, all other nonvolatile species of concern in boiler applications at less than

**Table 2** Typical control limits for residual phosphate treatment

Boiler water component (ppm)	Drum pressure (psi g; MPa g)			
	150 (1.0)	300 (2.1)	600 (4.1)	900 (6.2)
TDS (max) <sup>a</sup>	4000	3500	3000	2000
Phosphate (as PO <sub>4</sub> )	30–60	30–60	20–40	15–20
Hydroxide (as CaCO <sub>3</sub> )	300–400	250–300	150–200	120–150
Sulfite	30–60	30–40	20–30	15–20
Silica (as SiO <sub>2</sub> ) max <sup>b</sup>	100	50	30	10

<sup>a</sup>The limits on TDS will vary with the design of the boiler and with the needs of the system with regard to steam purity.

<sup>b</sup>Example silica values are listed but if silica volatility is a concern, such as condensing steam turbine applications, available pressure dependant and pH dependant control curves on boiler water silica concentration should be used. Silica may be carried at higher levels if there are no condensing turbines in the cycle. In any case, maintain an OH/SiO<sub>2</sub> ratio of at least 3/1 to inhibit silica deposition.

13.7 MPa g (2000 psi g) end up in the steam as a result of mechanical carryover of boiler water droplets that pass through the mechanical separating equipment in the steam drum. Therefore, the steam purity is directly proportional to the boiler water purity.

The restrictions on boiler water total dissolved solid limits to maintain the same steam purity do vary with boiler operating pressure and are more restricted at higher operating pressures because the mechanical steam/water separation process is more efficient when the density difference between the steam and water phases is greater.

Sodium salts and copper oxides, considered non-volatile at lower operating pressures exhibit volatility characteristics above 16.4 MPa g (2400 psi g). This mode of transport into the steam must also be considered and controlled by the appropriate measures to maintain the desired steam purity.

In addition, when attemperation is used for final steam temperature control, the impact of that attemperation water on the final steam purity must also be considered, in the design stage as well as while diagnosing steam purity problems. The potential sources of attemperation water are feedwater (if it is pure enough), condensate and a sweetwater condenser. A sweetwater condenser is typically a shell and tube heat exchanger that condenses saturated steam with incoming feedwater. That condensed saturated steam is then used as attemperation water for steam temperature control. Each of these sources of attemperation water can be potentially contaminated and impact on steam purity. A mud drum attemperator may also be used for steam temperature control. This is typically a heat exchanger located in the mud drum. By design, there is no intended contact between the steam and the boiler water, but in the event of a leak in the exchanger boiler water can contaminate the steam.

#### 4.28.4.3 Chelant Treatments

Realizing the shortcomings of residual phosphate chemistry in the way it handles feedwater hardness contamination (precipitation), alternative treatment chemistries were developed.

The first was the use of chelants to solubilize the hardness contaminants. The most common chelants used were ethylenediaminetetraacetic acid (EDTA) and nitrilotriacetic acid (NTA). Both EDTA and NTA form soluble complexes with calcium and magnesium that are stable to relatively high temperatures, up to 6.8 MPa g (1000 psi g). The removal of hardness contaminants from the boiler, now in a soluble form, are no longer limited by the continuous blowdown's limited ability to remove suspended solids from the circulating boiler water. If the species in question is soluble in the feedwater, remains soluble in the boiler water and is nonvolatile, the continuous blowdown removes that species at 100% efficiency.

Theoretically, if the required stoichiometric ratio of chelant to hardness were maintained, there would be no accumulation of hardness-based deposits in the boiler. However in practice, there are variations in the level of hardness contaminants in the feedwater, and some overfeed must be applied continually to account for these variations. This overfeed is typically controlled to result in a small residual chelant concentration in the boiler water above that required for the actual hardness. It was found that this boiler water chelant residual must be controlled very tightly because high levels of the residual can result in corrosion of the boiler base material. This corrosion is most likely to occur in areas of high fluid velocity or turbulence in the boiler. For this reason, chelant residual control limits vary as a function of boiler operating pressure and range from about 1–5 mg l<sup>-1</sup> (1–5 ppm). Chelants have been

applied at boiler pressures over 6.8 MPa g (1000 psi g) early in their history but later were only commonly applied up to about 2.7 MPa g (400 psi g) for EDTA and about 6.2 MPa g (900 psi g) for NTA.

Today, chelants are rarely used for several reasons. NTA is classified as a suspected carcinogen, the potential corrosion problems, and challenges in controlling the required residual level and alternative treatment chemicals have been developed.

#### **4.28.4.4 All Polymer Treatment**

Technically, the ability of the chelant chemistry to maintain the solubility of feedwater hardness contaminants is a much more effective way to control hardness deposit accumulation in boiler systems than residual phosphate treatment. Synthetic organic polymer chemistries have been developed that also have chelating abilities for hardness control. These are based typically on polyacrylate or polymethacrylate polymers. Such synthetic organic polymers can be applied in what is termed an all-polymer treatment, the purpose of which is the same as the chelant chemistry: form a soluble complex with calcium and magnesium and maintain that soluble complex at boiler water conditions to allow for the efficient removal of these contaminants from the boiler in the continuous blowdown as dissolved solids. In addition to the ability of these polymers to maintain soluble hardness contaminants, they are typically anionically charged, whereas suspended solid contaminants such as iron oxide tend to be cationically charged. The polymers also have the ability to disperse particulate contaminants. This dispersion minimizes their ability to agglomerate into larger particles as well as adhere to the heat transfer surfaces of the boiler. But as a suspended solid, there is still the same physical limitation on the ability of the continuous blowdown to remove even these dispersed contaminants from the boiler.

There are many synthetic organic polymers in use in boiler water treatment. It is important to note that not all of these polymers have chelant properties relative to calcium and magnesium, and it is only those that do that can be used as an 'all-polymer' treatment for feedwater hardness contamination. And even those polymers that do have this chelating ability must be of an appropriate molecular weight for the boiler operating pressure and saturation temperature to function as intended. Polymers that do not have the chelant properties with respect to hardness tend to act only as dispersants and therefore do

not have the same effectiveness in handling feedwater hardness contamination.

Even though the polymers used in the 'all-polymer' technology have chelant properties, they are much weaker chelants than EDTA or NTA. As much weaker chelants, the need to control the excess polymer residual relative to the hardness is much less critical. However as with all solubilizing treatments, the potential for corrosion of the boilers base material must be recognized and an appropriate control strategy used.

As there are many synthetic polymer treatments on the market today and most are offered as proprietary treatment chemistries by water treatment companies, hopefully the end user can ask the appropriate questions based on the information provided, such as what the purpose and abilities of their available products are and what the control limits and control strategies are, to decide while choosing between various offerings to best meet his/her needs.

Polymeric dispersants are also used within other treatment philosophies, such as in chelant treatments to disperse iron oxide contaminants and in residual phosphate treatment to disperse the resultant calcium and magnesium precipitated suspended solids. In these cases, however, the concentration of the polymers to hardness is much less than the stoichiometric requirement to solubilize the hardness, and as such they only act as a dispersant and do not compete with the primary intended purposes of the chelant or phosphate chemistry.

In industrial boiler systems, there have been many mixed treatment chemistries that have had mixed success — chelant/polymer, chelant/phosphate, polymer/chelant/phosphate, etc. There are too many to address specifically.

#### **4.28.4.5 Coordinated Phosphate Treatment**

In the past, it was more common to find high-purity feedwater in only high-pressure boiler applications >6.8 MPa g (>1000 psi g). Today the use of high-purity makeup water in low-pressure boilers is much more common.

Coordinated phosphate chemistry<sup>26</sup> was developed as a response to caustic embrittlement failures of boiler drums. In the early days of boiler water treatment, prior to the development of efficient make-up water pretreatment systems, coagulation internal treatments were used. This type of treatment used soda ash ( $\text{Na}_2\text{CO}_3$ ) to precipitate the hardness

salt contaminants into the desired form and then added organic materials (tannins and lignin) to condition this precipitated material (sludge) where hopefully it would settle in the mud drum and be removed from the boiler via the intermittent blowdown (mud drum blowdown) practice.

The use of soda ash introduced high levels of alkalinity, including free hydroxide or caustic alkalinity, into the boiler water, and at that time boiler drums were constructed by riveting rolled sections of steel plate together. These mechanical joints were prone to leaking. When a leak did occur, the leaking boiler water containing free hydroxide would flash to steam, resulting in very high local caustic concentrations at the site of the leak. Carbon steel is susceptible to stress corrosion cracking failure when it is highly stressed and in contact with high concentrations of caustic. The geometry of the riveted construction provided a location of stress concentration, and the flashing boiler water provided the environment that resulted in the potential for stress corrosion cracking or caustic embrittlement failure of the steel. In the early days of boiler water treatment, these embrittlement failures and sometimes resultant boiler explosions were not uncommon, and there were fatalities. Coordinated phosphate chemistry control was developed as a chemical solution to this problem. Coordinated phosphate chemistry balances the boiler water pH and orthophosphate concentration to a maximum Na:PO<sub>4</sub> molar ratio of 3.0:1 to theoretically prevent the formation of free hydroxide in the boiler water. For control, a minimum Na:PO<sub>4</sub> ratio of 2.2:1 is chosen to buffer low pH concerns. It is

important to note that the Na:PO<sub>4</sub> molar ratio used in this treatment as well as the other high-purity phosphate chemistries is not determined by directly measuring both the boiler water sodium and phosphate concentration and calculating the ratio but rather is determined by measuring the boiler water pH and orthophosphate concentrate and then plotting that data on a graph similar to [Figure 4](#).

The reason for this is that in most boiler systems, there are neutral sodium salts present that do not affect the boiler water pH. There can also be contaminants in the makeup water such as organic materials that can decompose to form organic acids in the boiler water, affecting boiler water pH but with no contribution of sodium.

With this in mind it is also important to realize that what affects the boiler water pH and phosphate relationship is that which is added intentionally as the treatment chemicals and that other contaminants may concentrate in the boiler water and affect pH (organic materials in the makeup water or sodium leakage [NaOH] from the make up demineralizer). Sodium salts of various phosphate species and sodium-to-phosphate molar ratios and sodium hydroxide may have to be used to buffer the pH into the desired control range in these situations.

#### 4.28.4.6 Congruent Phosphate Treatment

Caustic problems in boiler systems were not totally alleviated by the adoption of coordinated phosphate chemistry. This was thought to be due to the

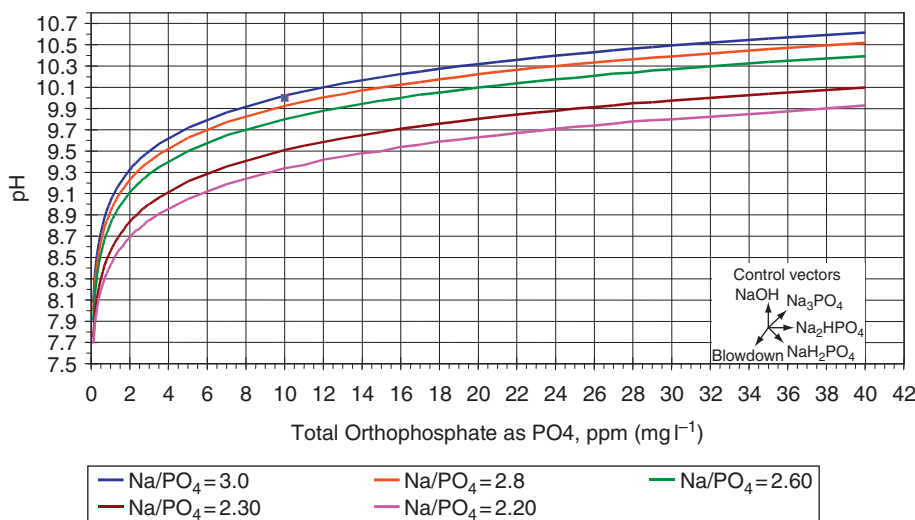


**Figure 4** pH vs. PO<sub>4</sub> graph at different Na/PO<sub>4</sub> molar ratios.



solubility characteristics of sodium phosphate salts – a characteristic known as incongruent precipitation. Studies<sup>27</sup> showed that precipitation of phosphate from a high temperature (300 °C, 572 °F) sodium phosphate solution having a Na:PO<sub>4</sub> molar ratio greater than 2.85:1 always results in an increase in the Na:PO<sub>4</sub> ratio of the remaining solution, toward or further into the free caustic region above the 3.0:1 ratio boundary. Conversely, when phosphate is precipitated from a solution having a Na:PO<sub>4</sub> ratio less than 2.85:1, the Na:PO<sub>4</sub> ratio decreases in the remaining solution, further away from the free caustic region. With a solution Na:PO<sub>4</sub> ratio of exactly 2.85, the Na:PO<sub>4</sub> ratio in the precipitated phosphate solids is identical, that is, congruent.

Subsequent studies showed that at higher temperatures, the congruent point could be at a Na:PO<sub>4</sub> ratio as low as 2.6:1. Again, control is based entirely on the relationships of boiler water pH and orthophosphate concentration, endeavoring to keep their plotted coordinates within the appropriate zones on a control diagram (see **Figure 1**).<sup>28</sup> Congruent phosphate<sup>29</sup> then is a refinement of the original coordinated phosphate treatment with new boundaries on the Na/PO<sub>4</sub> molar ratio; a maximum ratio of 2.6:1 and a minimum ratio of 2.3:1. The actual PO<sub>4</sub> concentration control range is typically chosen based on boiler operating pressure and the degree of control capability in the plant and the consistency of feed-water quality (purity). Generally, higher phosphate control ranges (10–20 mg l<sup>-1</sup> (10–20 ppm)) at lower boiler operating pressures and lower phosphate control ranges (5–10 mg l<sup>-1</sup> (5–10 ppm)) at higher boiler operating pressures are employed.

When the chosen PO<sub>4</sub> control range is less than 2 mg l<sup>-1</sup> (2 ppm) in the boiler water, the effect of ammonia or neutralizing amines must be taken into account due to their effect on the boiler water pH measurement at room temperature.

Even though boiler drums are constructed using welded joints today, most industrial boilers operating at less than 6.8 MPa g (1000 psi g) are constructed with mechanical roll expanded joints to connect the tubes between the steam drum and the mud drum. Therefore, there is still the possibility of a local caustic embrittlement failure of the drum if one of these mechanical joints were to leak and the boiler water contained free hydroxide. Congruent phosphate chemistry provides a level of protection for these boilers from this failure mechanism and would be a preferred choice provided the feed-water purity requirements are met and the boiler

is not experiencing phosphate hideout behavior (see the following section) due to the congruent phosphate treatment.

#### **4.28.4.7 Phosphate Continuum Treatment (Formerly Equilibrium Phosphate Treatment)**

Congruent phosphate programs can be difficult to control because of phosphate hideout.<sup>30</sup> Phosphate hideout is the simultaneous decrease in the phosphate concentration of the boiler water and an increase in boiler water pH during a load or heat flux increase. Hideout return is the reverse during a load decrease – phosphate concentration increases and boiler water pH decreases. Equilibrium phosphate control solves this problem and has therefore gained acceptance with electric utility drum boiler operators.

As phosphate hideout occurs, the phosphate concentration in the bulk boiler water is reduced down to very low remaining equilibrium levels. The boiler water phosphate might drop from a normal 5 mg l<sup>-1</sup> (5 ppm) down to 2 mg l<sup>-1</sup> (2 ppm) or even less during hideout. Attempts to maintain the original boiler water phosphate levels by adding phosphate during hideout are usually futile, because ongoing hideout simply continues to remove boiler water phosphate down to the equilibrium level.

In the past, phosphate hideout had been thought to be associated with the retrograde solubility behavior and incongruent precipitation behavior of sodium phosphates, but laboratory research work<sup>31</sup> has shown that phosphate hideout is actually the temperature-dependent reaction of low Na:PO<sub>4</sub> molar ratio compounds in the boiler water with magnetite. These reactions are significant when boiler water Na:PO<sub>4</sub> molar ratios are 2.3–2.6:1, but are essentially nonexistent when the boiler water Na:PO<sub>4</sub> molar ratio is greater than 2.85:1.

During phosphate hideout, phosphate wastage of the boiler metal can result due to the concentration of low Na:PO<sub>4</sub> molar ratio materials in high-heat flux zones. Maracite (NaFePO<sub>4</sub>) and/or Iron Phosphate (FePO<sub>4</sub>) are the residual corrosion products found on boiler tubes damaged by the phosphate wastage mechanism.<sup>32</sup>

Phosphate hideout and phosphate wastage are more likely at higher boiler operating pressures but are also possible in lower-pressure boilers with high local heat fluxes. Phosphate wastage corrosion predominantly occurs in conventional boilers operating at greater than 13.8 MPa g (2000 psi g), although it has been seen in an industrial boiler operating at 6.9 MPa g

(1000 psi g) that was experiencing steam blanketing. It is also common in vertical shell-and-tube steam generators; these are commonly unfired process boilers with flat tube sheets and deep oxide sludge deposits on the tube sheet, which is generally at the inlet of the highest process gas temperature. In addition, heat recovery steam generators (HRSG) commonly used in combined cycle plants with duct burners are also prone to phosphate hideout and the potential for phosphate wastage, especially when duct burners are in use.

Equilibrium phosphate control<sup>30</sup> makes no attempt to carry boiler water phosphate concentration above its hideout equilibrium level. Equilibrium phosphate levels vary from boiler to boiler, depending on the severity of hideout conditions and must be determined by testing for each unit. EPRI has recently revised and renamed the Equilibrium Treatment philosophy to what is now termed Phosphate Continuum Treatment<sup>4</sup> as illustrated in Figure 5. The maximum Na/PO<sub>4</sub> ratio control boundary is a Na/PO<sub>4</sub> equal to 3.0 plus 1 mg l<sup>-1</sup> (1 ppm) NaOH and the minimum Na/PO<sub>4</sub> control boundary is Na/PO<sub>4</sub> = 3.0. Additionally, there is a minimum pH = 9.0 and a minimum boiler water orthophosphate concentration of 0.2 mg l<sup>-1</sup> (0.2 ppm).

For mixed-bed makeup water systems with no significant sodium leakage and low organic contamination of the makeup and condensate, only trisodium phosphate and caustic soda (when needed) are recommended for Phosphate Continuum Treatment. Monosodium, disodium, and polyphosphates should

not be needed. But for many industrial boiler systems that can have significant sodium leakage from the makeup system or significant organic contaminants in the makeup water or condensate, a wide range of Na:PO<sub>4</sub> molar ratio treatment chemicals might be required to maintain the desired control in a particular boiler system situation.

Phosphate continuum treatment does include the presence of free hydroxide in the boiler water and therefore does present the known concerns associated with caustic in boilers. There is the potential for under deposit caustic gouging in the boiler, the potential for stress corrosion cracking of steam system components in the event of boiler water carry over and the potential for embrittlement damage to the drums if the boiler has mechanical rolled tube joints if one were to leak.

#### 4.28.4.8 All Volatile Treatment

AVT<sup>33,34</sup> helps achieve sufficiently high pH to protect boiler steel without introducing any dissolved solids. It is based on the use of entirely volatile, solid-free chemicals, such as hydrazine or carbohydrazide for oxygen scavenging, plus neutralizing amines or ammonia for boiler water pH control. AVT may be used in drum boilers that have the appropriate feedwater purity and is the only program that can be used in once-through boilers. In drum boilers, AVT may be used for simplicity where phosphate hideout has caused control

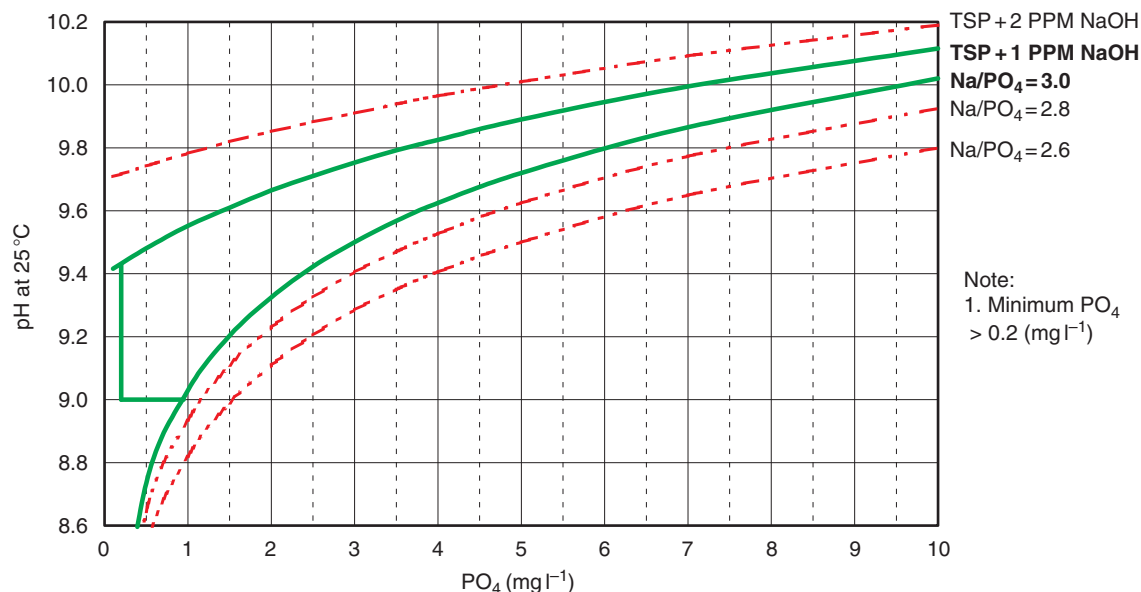


Figure 5 Phosphate continuum control chart.

problems on phosphate-pH control programs or where ultra pure steam is required.

A disadvantage of all-volatile treatment for drum boilers is that the boiler water is unbuffered and thus subject to extensive and rapid pH excursions in the event of feedwater contamination. Prompt detection and remedial action is required in the event of any feedwater contamination. A condensate polishing system, either for continuous polishing or for start-up and emergency polishing, is very desirable. Some utilities do operate high pressure drum cycles on AVT without the benefits of polishers, but their systems have extensive instrumentation that allows immediate remedial action to be taken in the event of cycle contamination (including feeding phosphate until the problem is resolved). A mixed-bed polisher is essential in the makeup system.

The AVT program control is simple and highly effective as long as feedwater quality is maintained. Feedwater contamination of an otherwise solid-free system produces undesirable effects immediately. With essentially no buffering capacity in the system, boiler water pH values can reach free acidity levels ( $\text{pH} < 4.3$ ) very rapidly following contamination. This is particularly true in systems using seawater or brackish water for condenser cooling.

Cation conductivity measurements of the boiler water are used to monitor any dissolved solids contamination of the cycle. Cation conductivity is also preferred for condensate and feedwater monitoring since it is very sensitive to changes in dissolved solids concentrations and is not affected by changing the amine or ammonia levels. Specific conductance is used primarily to monitor the level of ammonia or neutralizing amine present in the cycle.

Continuous pH monitoring of the boiler water is desirable, as pH provides another indication of a contamination problem. Boiler water pH values will typically be lower than the feedwater pH because of the volatilization of the amine or ammonia from the boiler water; pH control in the feedwater cycle will vary with cycle metallurgy.

#### **4.28.4.9 Caustic Treatment**

Sodium hydroxide alone can also be used as the solid alkali in internal boiler water treatment for pH control. It is a common practice in high-pressure drum boilers in the United Kingdom, and many of these are high-pressure drum boilers in the electric utility service industry.<sup>4,35</sup> A typical boiler water pH control range

is 9.0–9.4. Caustic can still be very corrosive to carbon steel under concentrated conditions, such as under porous metal oxide deposits on a boiler's heat transfer surfaces, and can cause under deposit corrosion damage. It is therefore very important to keep the boiler's heat transfer surfaces clean by minimizing the feedwater corrosion product transport into the boiler and periodic chemical cleaning. There is also a concern that chloride contamination may increase this corrosion potential, and individual operators have also restricted boiler water chloride limits.

#### **4.28.5 Condensate Treatment**

Condensate is a very valuable commodity (resource) in a boiler system, not only because of its energy content but also because of its high purity. Therefore, the more condensate that can be returned as part of the boiler feedwater, the more efficient the economics are of operating the boiler system.

As condensate is very pure water, very small amounts of contamination can render it extremely corrosive and unsuitable as feedwater. One of the more common contaminants that can depress the pH of the condensate is carbon dioxide. Carbon dioxide can originate from the bicarbonate alkalinity in the makeup water, which decomposes at boiler operating pressure, contributing the carbon dioxide to the steam or from air in leakage into the system. The latter is most likely to occur when the pressure in the condensate system is at or below atmospheric pressure.

In addition, organic materials in the makeup water can decompose in the boiler water, resulting in the formation of low molecular weight organic acids such as acetic, formic, and glycolic acids. These organic acids have volatility characteristics that are a function of pressure. All are considerably stronger acids than carbonic acid and will increase the demand for the neutralizing amine treatment that is commonly employed to neutralize acids and so elevate the condensate pH. Hydrogen sulfide and sulfur dioxide, the products of decomposition of the sodium sulfite oxygen scavenger, that can occur at boiler operating pressures  $> 4.1 \text{ MPa g}$  ( $> 600 \text{ psi g}$ ), can also depress condensate pH and contribute to the amine demand. Depressed pH conditions of the condensate can cause significant corrosion damage to condensate system components.

Dissolved oxygen either not removed by the deaeration processes or that has leaked into the system at points where the pressure is at less than

atmospheric pressure can also cause corrosion damage in the condensate system.

Ammonia can also be considered a contaminant in the condensate if there are copper alloys in the condensate system that can be attacked by the ammonia.

Chemically, four types of treatment are used for condensate system corrosion control: ammonia or neutralizing amines, filming amines, oxygen scavengers/metal passivators, and nonamine filming treatment.

Neutralizing amines and ammonia are volatile, alkaline compounds that are added to either the boiler feedwater or the steam. They function by volatilizing into the steam and redissolving into the condensate. The amines and ammonia chemically neutralize the carbonic acid or any other acid present in the condensate. Then they raise the pH of the condensate to minimize the corrosion of the materials of construction of the condensate system. The most common neutralizing amines in use today are cyclohexylamine, morpholine, diethylaminoethanol, methoxypropylamine, and monoethanolamine. Each has a unique volatility and basicity characteristic.

Industrial boiler systems can have very extensive and complex steam/condensate systems. Complex steam systems that operate at multiple pressure levels, especially where high-pressure condensate is flashed to produce additional low-pressure steam, can concentrate a single treatment amine to one part of the system while simultaneously depleting its concentration in another part of the system due to its unique single, pressure-dependent vapor-to-liquid distribution ratio characteristic. This leads to a situation in which some parts of the complex system can be undertreated, even though from the pH measurement of the combined condensate sample the system appears to be sufficiently treated. The common solution to this situation is the use of an amine treatment product – that may be a combination of multiple amines, each with a different vapor-to-liquid distribution characteristic. In the most complex steam systems, satellite feed to a particular point in the system may still be required to provide adequate corrosion protection. In a simple steam condensate system such as the typical electric utility situation, a single amine or ammonia may provide adequate protection. But there have been many cases where a low volatility amine or the industrial multiple amine philosophies of treatment have provided better protection as measured by a reduction in corrosion product transport, in even the simple system.

Neutralizing amine treatment does not provide protection for the system from dissolved oxygen

attack. The feed of an oxygen scavenger/passivator to the condensate can protect the system against dissolved oxygen attack. Sodium sulfite is typically not used for this application since it contributes non-volatile solids. More typically, one of the volatile organic oxygen scavenger/passivator materials can be used in this application. Preferably though, the source of the oxygen in leakage should be found and corrected.

There can also be situations in which the carbon dioxide content of the steam is so high because of the natural bicarbonate alkalinity of the makeup water, and that treating the condensate with neutralizing amine technology is prohibitively expensive. In this case, a filming amine technology can be used. In the filming amine treatment, the carbon dioxide is not neutralized, but the filming amine forms a nonwetttable barrier on the condensate system components preventing the low pH condensate from coming into contact with the materials. Filming amines also provide protection from dissolved oxygen attack. The amount of filming amine required is related to the surface area of the system. Octadecylamine is a commonly used filming amine. Filming amines have the ability to move corrosion products from the surface of the piping. It is therefore advisable to start with low dosages, which are gradually increased until residual limits are met. There are also proprietary filming amines.

There may be restrictions on amine concentrations in steam when there is contact of that steam with food or food products, when the steam is used for humidification of air or when it can contact certain catalysts used in industrial processes. A nonamine filming corrosion inhibitor technology<sup>36</sup> has been developed for when there is a prohibition on amines in the treated steam.

There are also mechanical means of treating condensate to remove contaminants and preserve its purity for reuse. If corrosion products – typically iron oxides and copper oxides – exist as suspended solids in the condensate, they can be filtered out. Cartridge filters can be used. Condensate polishers, an ion exchange process in which strong acid cation resin is in the sodium or amine form in industrial situations, act primarily as a filter but can also remove hardness that may have come from cooling water contamination of the condensate. In electric utility boiler situations where condensate temperatures are considerably lower, mixed-bed resin polishers (typically a mixture of strong acid cation resin in the hydrogen form and strong base anion resin in the hydroxide form) are used.

These can be deep bed regenerable units or they can be of the powdered resin, one-time-use type. In addition, high gradient electromagnetic filters have been used to remove corrosion products of iron and some copper that are magnetic.

As a final alternative, contaminated condensate can be discarded or diverted rather than returned to the system. The condensate diversion system (condensate dumps) is a system of sensors, valves and piping to detect the contamination of the condensate and divert it to waste. These condensate diversion systems must be properly engineered to detect and divert the contamination in a timely manner to prevent the contamination of the feedwater. This technique is only applicable to systems where the makeup water system capacity can compensate for this lost condensate.

#### **4.28.6 Boiler Treatment During Out-of-Service Conditions**

Boilers constructed out of carbon steel and low chromium alloys up to about 9% chromium content are prone to corrosion at ambient temperatures in contact with untreated, typically aerated, water. The maximum corrosion rate occurs where carbon steel is in contact with a water–air interface. This water–air interface occurs when an operating boiler is taken out of service and the vents are opened to the atmosphere during the cooling process and air displaces the condensing steam. Even if the boiler is drained at this point, depending on the boiler design configuration there may be areas of the boiler that do not drain completely. In addition, in many boiler designs that incorporate superheaters and reheaters, heat transfer surfaces can be of a pendant or other design configuration that is inherently nondrainable. Nondrainable components require special treatment if a wet lay-up method is employed. Water purity must be very high—condensate or demineralized quality—and any treatment chemicals used in the water must be volatile.

Guidelines<sup>37,38</sup> are available for the proper treatment of a boiler in the out-of-service condition. The goal of the guidelines is to use a procedure that generally eliminates the air–water interface. This can be accomplished in a number of ways—by draining the boiler under a positive nitrogen pressure or draining the boiler and installing a desiccant, for example. The appropriate procedure depends on many variables, including the configuration of the boiler and the expected duration of the out-of-service period.

#### **4.28.7 Miscellaneous (But Important) Comments**

Proper sampling is a prerequisite of effectively monitoring a system. Effective monitoring of the makeup water, feedwater, boiler water, steam, and condensate is necessary to control deposition and corrosion within the system. No matter how accurate or precise the analysis of a sample obtained is, if the sample is not truly representative of the stream being sampled, the results are useless.<sup>39</sup> Effective monitoring requires a proper sampling system, adequate sample system purging, the required sample velocity, and appropriate sample handling.<sup>40</sup>

A particular case in point is sampling steam to determine its purity. Isokinetic sampling nozzles and procedures are required.<sup>41</sup> When sampling superheated steam, sample cooling considerations are especially important. The distance between the sampling nozzle and the primary cooler must be minimized—no more than 7 m (20 ft)—and any sample line length between the nozzle and the cooler must be insulated.

The proper sampling and analysis of condensate is especially critical, because of its inherent high purity and the volatility characteristics of both the treatment chemicals and some of the contaminants it might contain.

A stainless steel injection quill must be used to inject treatment chemical into the system. Concentrated treatment chemicals in contact with carbon steel at elevated system operating temperatures present a corrosive situation for the carbon steel. A properly designed and installed chemical injection quill admits the chemical into the fluid stream, so that it is properly diluted in the stream.

#### **References**

1. Water-Tube Boilers and Auxiliary Installations-Part 12: Requirements for Boiler Feedwater and Boiler Water quality. CEN European Committee for Standardization Brussels: Belgium, EN 12952-12:2003, 2003.
2. VGB Guideline for Feedwater, Boiler water and Steam of Steam Generators with admissible operating Pressure >68 bar. VGB Kraftwerkstechnik GmbH, Essen, Germany, VGB-R 450 L, 1988.
3. Consensus on Operating Practices for the Control of Feedwater and Boiler Water Chemistry in Modern Industrial Boilers, CRTD-Vol.34. American Society of Mechanical Engineers, New York, NY, 1994.
4. Dooley, R. B.; Shields, K. J. *Power Plant Chem.* **2004**, 6(3).
5. Japanese Industrial Standard, Water Conditioning for Boiler Feed Water and Boiler Water, JIS B 8223, Japanese Standards Association, 1989.



6. Miller, B.; Munoz, J.; Wiesler, F. Proceedings of the International Water Conference, Pittsburgh, PA, 2005; paper no. IWC-05-79
7. Dooley, R. B.; Shields, K. J., *Power Plant Chem.* **2004**, 6(10).
8. Dooley, R. B.; Castle, J. E.; Zhdan, P. A. *Power Plant Chem.* **2005**, 7(9).
9. Palmer, D. A.; Benezeth, P.; Simonson, J. M. *Power Plant Chem.* **2004**, 6(2).
10. Bignold, G. J.; de Whalley, C. H.; Gabert, K.; Woolsey, I. S. CERL single phase erosion corrosion studies under boiler feedwater conditions. Proceedings of EPRI Workshop, 4/15-15/1987, Washington, DC.
11. Flow accelerated corrosion. Port R.D.: NACE, 1998.
12. Banweg, T. *Flow Accelerated Corrosion in Industrial Boiler Feedwater Systems*. Canadian Pulp and Paper Association, Montreal, Canada, 1998.
13. Erosion Corrosion in Power Plants, Single & Two Phase Flow Experience, Prediction, NDE, Maintenance and Remedial Measures. IWC 89-22.
14. Flow Accelerated Corrosion in Power Plants, TR-10611, Electric Power Research Institute, Pleasant Hills, CA.
15. Hicks, P. *Power Plant Chem.* **2007**, 9(5), 301-312.
16. Hicks, P.; Grattan, D.; White, P.; Bayburt, K. *Power Plant Chem.* **2007**, 9(6), 324-336.
17. Stookey, L. L. *Anal. Chem.* **1970**, 42(7), 779.
18. Fowee, R. NACE paper 218 1991.
19. Godfrey, M. R.; Chen, T. Y.; Eisner, I. E. NACE, 1995.
20. Resch, G.; Odenthal, H.; Epselo, D. *VGB Mitt.* **1965**, 79, 228-240.
21. Freier, R. K., Cover layer formation on steel by oxygen in neutral salt free water. VGB Speisewassertagung, Sonderheft, 1969; pp.11-17.
22. Bohnsack, G. Teil 1, VGB Kraftwerktech **1973**, 53(6), 382-393; Teil 2, VGB Kraftwerktech **1973**, 53(7), 472-481.
23. Busik, A. VGB Kraftwerktech **1982**, 62(1), 36-41.
24. Bursik, A. Proceedings of the International Water Conference, **1986**, Vol. 47, pp. 226-233.
25. Banweg, A.; Clark, S. D.; Bohnsack, G. NACE, Corrosion 92, paper no. 148.
26. Whirl, S. F.; Purcell, T. E. Proceedings of the International Water Conference, Pittsburgh, PA, **1942**.
27. Panson, A. J., et al. *J. Electrochem. Soc.* **1975**.
28. Thaler, J. O.; Sinha, P. K. *Power Eng.* **1986**.
29. Marcy, V. M.; Halstead, S. L.; *Combustion* **1964**.
30. Stodola, J. Proceedings of the International Water Conference, Pittsburgh, PA, 1986; paper no. 27.
31. Gray, L. G. S.; Wiwchar, B.; Tremaine, P. R.; Stodola, J. NACE Corrosion 92 paper no. 417.
32. Herro, H. M.; Banweg, A. NACE Corrosion 95, paper no.498.
33. Bursik, A.; Jensen, J. P.; Staudt, U. Proceedings of the International Water Conference, Pittsburgh, PA, 1996; paper no. 38.
34. Bursik, A. Gruszkiewicz, M. *Power Plant Chem.* **2004**, 6(11).
35. Ball, M. *Power Plant Chem.*; **1999**, 1(2).
36. Cicero, D. M. Proceedings of the International Water Conference, Pittsburgh, PA, **1997**.
37. Consensus for the Lay Up of Boilers, Turbines, Turbine Condensers and Auxiliary Equipment, CRTD-Vol. 66, American Society of Mechanical Engineers, New York, NY.
38. VGB Guidelines, VGB-R116H, VGB Technische Vereinigung der Grosskraftwerksbetreiber, 1981.
39. Pocock, F. J., Personal communication, Babcock and Wilcox Research and Development Division, 1979.
40. Consensus on Operating Practices for the Sampling and Monitoring of Feedwater and Boiler Water Chemistry in Modern Industrial Boilers, CRTD-Vol. 81, ASME, Three Park Ave., New York, NY.
41. Annual Book of ASTM Standards. section 11, D-1066, Practice for Sampling Steam, American Society for Testing and Materials, Philadelphia, PA, 2004.

## 4.29 Corrosion Inhibitors: Other Important Applications

**V. S. Sastri**

Department of Chemistry, Carleton University, Ottawa, ON K1J 6S7, Canada

© 2010 Elsevier B.V. All rights reserved.

4.29.1	Introduction	2990
4.29.2	Processing with Acids	2990
4.29.2.1	Acid Pickling	2990
4.29.2.2	Scale Removal by Acids	2991
4.29.2.3	Acidizing Oil Wells	2994
4.29.3	Mining Industry	2994
4.29.4	Paints and Coatings	2995
4.29.5	Construction Materials	2996
4.29.6	Processing Electronics Packaging, Paper Display, and Storage	2997
References		2998

### 4.29.1 Introduction

Corrosion inhibitors are used in a wide range of industrial applications. In this chapter, their employment in processing with acids, mining operations, paints and coatings, construction materials, processing electronics packaging, display, and storage is discussed.

### 4.29.2 Processing with Acids

Acids are extensively used in acid pickling, industrial acid cleaning, acid descaling, oil well acidizing, and manufacturing processes in different industries. Inhibitors are used in acid solutions in order to minimize corrosive attack on metals. The selection of suitable inhibitor depends on the type of acid, concentration of the acid, temperature, flow velocity, the presence of dissolved inorganic or organic substances, and the type of metallic material exposed to the acid solution. The most commonly used acids are hydrochloric, sulfuric, nitric, hydrofluoric, citric, formic, and acetic acid.

#### 4.29.2.1 Acid Pickling

Metals or alloys subjected to painting, enameling, galvanizing, electroplating, phosphate coating, cold rolling, and other finishing processes must have a clean surface free from salt or oxide scale. In order to remove the unwanted scale such as mill scale rust, the metal is immersed in an acidic solution known as the acid pickling bath. After the scale is removed by dissolution, the acid may attack the metal. In order to

minimize the attack of the metal, and consumption of the acid, corrosion inhibitors are added to the pickling solution.

Hydrochloric acid is commonly used in the pickling bath. Large-scale continuous treatment such as metal strip and wire pickling and regeneration of depleted pickling solutions are the advantages in using hydrochloric acid instead of sulfuric acid. Other acids, such as nitric, phosphoric, sulfamic, oxalic, tartaric, citric, acetic, and formic acid are used for special applications.

The choice of inhibitor depends on the purpose of acid pickling. If the pickling is for the purpose of removal of mill scale from hot-rolled steel, then the acid concentration, temperature, pickling time, and the type of steel will dictate the selection of the inhibitor. In the case of pickling with HCl, up to 200 g l<sup>-1</sup> are commonly used at 60 °C with a pickling time of about 30 min, depending upon the type of steel and the steel mill operating conditions. Sulfuric acid at 200–300 g l<sup>-1</sup> level and at temperatures up to 90 °C may also be used. These are severe conditions that require effective inhibitors.

The inhibitors used in pickling operations should possess the following requirements:

1. effective inhibition of metal dissolution,
2. lack of overpickling process,
3. effective at low inhibitor concentration,
4. effective at high temperatures,
5. thermal and chemical stability,
6. effective inhibition of hydrogen entry into the metal,
7. good surfactant properties,
8. good foaming properties.

The most important requirement is that the inhibitor minimizes metal dissolution even in the presence of dissolved salts such as ferrous sulfate that promotes metal dissolution. The corrosion rates of steel in 20% sulfuric acid at 90 °C and in 20% sulfuric acid containing 12% ferrous sulfate are 3100 and 5900 g m<sup>-2</sup> h<sup>-1</sup>, respectively. Although there exist inhibitors to counter the accelerating effect of ferrous sulfate, the pickling times are increased. In pickling in sulfuric acid at 60–90 °C to remove the mill scale, inhibitors of high thermal stability should be used. The inhibitors must be stable with respect to hydrolysis, condensation, polymerization, and hydrogenation by nascent hydrogen.

Pickling inhibitors should also minimize the entry of hydrogen into the metal. This aspect is not typically part of the protocol in the evaluation of the inhibitors, since no test involving hydrogen permeation measurement is performed to determine the effect of inhibitor on the kinetics of electrochemical production of hydrogen. Testing an inhibitor only for metal dissolution can be detrimental, as there is no direct relationship between inhibition of metal dissolution and inhibition of hydrogen entry into the metal.

Another important criterion is that the inhibitor should possess high efficiency at low concentrations for economic reasons. A good pickling inhibitor should also possess good surfactant and foaming properties. Usually, the inhibitors have poor surfactant and foaming properties, and therefore, wetting agents, detergents, and foaming agents are added to the commercial inhibitor formulation.

Wetting agents play an important role in facilitating the penetration of pickling acid into the cracks and fissures in the scale and help the removal of the scale. Thus, they are known as 'pickling accelerators.' Some wetting agents have degreasing properties and are known as 'pickling degreasing agents.' Wetting agents by themselves usually have no inhibitive effect. However, the chemical nature of the wetting agents determines whether they improve or decrease the inhibitive effect. Wetting agents and detergents help in producing clean metal surface after the pickling acid drains completely and the rinsing of pickled sample is improved. Wetting agents and detergents also possess foaming activity. When this is insufficient, additional foaming agents may be added to the inhibitor formulation. A stable foam blanket on the surface of the pickling bath reduces the acid spray and conserves heat. It is necessary that wetting agents, detergents, and foaming compounds function effectively over a wide range of temperature, acid concentration, and iron salt concentration. It is obvious that no single inhibitor can meet all

the requirements of an effective inhibitor and hence commercial inhibitors are multicomponent mixtures, which in some cases may contain as many as thirty components. A typical inhibitor formulation consists of a mixture of an active inhibitor, wetting agent, detergent, foaming agent, solvent, and sometimes a cosolvent.

The active inhibitors used in acid pickling are generally mixtures of nitrogen-bearing organic compounds, acetylenic alcohols, and sulfur-containing compounds. The surface-active compounds may be anionics such as alkyl or alkyl phenyl sulfonates or alkyl sulfates with C<sub>10</sub>–C<sub>18</sub> alkyl chains or nonionics such as ethoxylated derivatives of higher alcohols, phenols, or alkylphenols. Nonionics are used when precipitation of iron is to be avoided.

Commercial inhibitor formulations are generally available in solution form. The solvent may be water or the acid in which the inhibitor is to be used. In cases where the inhibitor formulation is not sufficiently soluble, solvents such as methanol, isopropanol, or acetone may be added. Depending upon the amount of solvent or cosolvent, about 5–50 g of the inhibitor is used for 1 l of pickling acid. Corrosion inhibitors used for various metals in HCl containing pickling media are listed in [Table 1](#).

Sulfoxides, sulfides, and thiourea compounds are generally used in a sulfuric acid medium. The common commercial inhibitor formulations consist of dibenzyl sulfoxide, dibenzyl sulfide, thiourea, and di-*O*-tolylthiourea. These inhibitors are effective at high temperatures. Some of the inhibitors used in a sulfuric acid pickling medium are summarized in [Table 2](#).

Iron and steel are passivated in concentrated 65% nitric acid but dissolve in lower concentrations of this acid. Unlike hydrochloric and sulfuric acids, nitric acid is an oxidizing acid, and it is difficult to inhibit high and medium concentrations effectively. Some of the inhibitors used for a nitric acid pickling medium are listed in [Table 3](#). [Tables 4 and 5](#) indicate inhibitors for hydrofluoric acid and phosphoric acid pickling media, respectively. For these two acids, inhibitors are similar to those employed in HCl.

#### 4.29.2.2 Scale Removal by Acids

Scale formation by circulating water or process compounds occurs in power plants, chemical plants, steel mills, paper mills, pipelines, compressor stations, and other industries. Scales or precipitates formed in heat exchangers, boilers, vessels, reactors, piping, and associated equipment reduce heat transfer and cause

**Table 1** Inhibitors employed for various metals in HCl containing pickling media

Medium	Metal or alloy	Inhibitor	References
Hydrochloric acid	Iron, steel	Primary, secondary and tertiary amines, oximes, nitriles, mercaptans, sulfoxides, thioureas, and complexones	
1 M HCl + 2.5% NaCl	Copper, brass	Thiourea, benzimidazole, 2-mercapto-benzothiazole, phenyl thiourea	[1–4]
	Al and its alloys	Aliphatic, aromatic aldehydes, carboxylic acids, ketones, sulfonamides, sulfones, dihedric phenols, tetrazolinium compounds, formazan compounds, sulfoxides, aromatic sulfonic acids, cupferron, <i>N</i> -allyl thiourea, and dibenzyl sulfoxide	[5–7]
HCl + H <sub>3</sub> PO <sub>4</sub> (1 N) 10% HCl		<i>p</i> -Thiocresol and sodium diethyl dithiocarbamate Mixture of aromatic aldehyde, 1 M urea/triethylamine/dodecylamine, > 1 M thiourea and 1-hexyn-3-ol together with alkyl sulfonates	[8]
Hydrochloric acid 5.6 M HCl	Zinc Nickel	Inhibitors used for Al are satisfactory Thiourea and its derivatives <i>O</i> -tolylthiourea and sym-diisopropyl thiourea have 90% inhibition over a wide temperature range	[9]
Hydrochloric acid	Titanium and alloys	Copper sulfate, nitric acid and chromic acid at 0.5–1.0% act as inhibitors. Nitrobenzene, trinitrobenzoic acid, picric acid, benzene arsonic acid at 0.03–0.003 M. Condensation product of formaldehyde with aromatic at 0.003 M	[10–13]

**Table 2** Inhibitors used in a sulfuric acid pickling medium

Metal	Inhibitor and conditions	References
Steel	2-mercaptobenzimidazole	[4]
	2-mercaptobenzimidazole + propargyl alcohol or 1-hexyn-3-ol improved performance	
	Sulfonium compounds at low temperatures	[14–16]
	Thiocyanates, thiourea, thicarbamates, mercaptans produce H <sub>2</sub> S and hydrogen entry into metal. Hazardous mustard gas related compounds from thiourea should be guarded	[17]
	Amines or quaternary ammonium salts + halides Cl <sup>−</sup> /Br <sup>−</sup> /I <sup>−</sup> shows synergetic effect in the order I <sup>−</sup> > Br <sup>−</sup> > Cl <sup>−</sup>	[18]
	Alkylpyridinium salts, <i>p</i> -alkylbenzylpyridinium halides and <i>p</i> -alkylbenzyl quinolinium halides with alkyl = C <sub>8</sub> –C <sub>12</sub> with KI at 10 <sup>−2</sup> to 10 <sup>−3</sup> M at 20–60 °C in 5–30% H <sub>2</sub> SO <sub>4</sub> give good inhibition	
	N-containing inhibitors along with SH <sup>−</sup> from H <sub>2</sub> S show synergistic effect	[19]
	Acetylenic alcohols (0.05–0.01 M). Acetylenic alcohols + halides	
Copper, brass, aluminum	Corrosion rate in boiling H <sub>2</sub> SO <sub>4</sub> : 175 g m <sup>−2</sup> h <sup>−1</sup> . In 0.4% propargyl alcohol or 1-hexyn-3-ol: 1355 g m <sup>−2</sup> h <sup>−1</sup> . Upon introducing KCl 5–1.5 g m <sup>−2</sup> h <sup>−1</sup> (synergism)	[20]
	2-mercaptobenzimidazole + 1 hexyn-3-ol (may be used for boilers)	
Copper	Thiourea	[21–23]
Brass	Quinolines, azoles	[24–26]
Titanium	2,4,6-trinitrophenol, 5-nitroquinoline, 8-nitroquinoline, 0-dinitrobenzene, <i>n</i> -nitroacetanilide, nitrobenzene and picric acid Inhibitors at 0.01–0.001 M in 10% H <sub>2</sub> SO <sub>4</sub> at 60 °C give good inhibition. In 1 M H <sub>2</sub> SO <sub>4</sub> cresolphthalexon, thymolphthalexon, thymol sulfophthalexon at low concentrations and at 80 °C gives good protection	[27–30]

tube failure, plugging, or fouling of equipment. The solid deposits should be removed in addition to preoperational cleaning to remove oxide scales or organic coatings.

The scales may be either organic or inorganic in nature. Inorganic deposits are formed in heat exchangers or steam generators. Typically, these inorganic deposits consist of magnetite, hematite, iron sulfides, calcium, and/or magnesium carbonates, sulfates, phosphates, and silicates. Organic deposits consist of

algae, slime, or moulds. The acids commonly used in scale removal are hydrochloric and hydrofluoric acid, in combination with ammonium bifluoride, sulfuric acid, nitric acid, sulfamic acid, citric acid, acetic acid, hydroxyacetic–formic acid mixture, and phosphoric acid.<sup>61</sup> Some inhibitors used in the removal of scales in hydrochloric acid are given in **Table 6**.

Hydrofluoric acid and ammonium bifluoride are usually added to hydrochloric acid solution to accelerate the removal of iron scales and silicate deposits.

**Table 3** Inhibitors used in nitric acid pickling medium

<i>Metal</i>	<i>Inhibitor and conditions</i>	<i>References</i>
Ferrous metals	Propargyl mercaptan, propargyl sulfide, ethane dithiol, thioacetic acid, mercaptoacetic acid, diethyl sulfide, benzyl-2-methyl pyridine thiocyanate and thiourea. Thiourea in low concentration because high concentrations promote corrosion Condensation product of hydroabietylamine with HCHO and an aldehyde of 2–6C atoms and 1-hexyn-3-ol	[31–34] [35]
Copper	Aliphatic and aromatic amines and diamines	[36–45]
Brass	Aminophenols, aminobenzoic acids, heterocyclic amines, thiourea and derivatives, <i>p</i> -thiocresol. <i>O</i> -Chloroaniline, <i>O</i> -nitroaniline, and sym-diethyl thiourea (0.1–0.001 M in 30% HNO <sub>3</sub> )	[46–50]
Titanium	In 20–70% HNO <sub>3</sub> at 190–230 °C, $5 \times 10^{-5}$ wt% silicone oil reduced the corrosion rate from 1 to 10 mm year <sup>-1</sup> to a negligible value	[51]

**Table 4** Inhibitors used in hydrofluoric acid pickling medium

<i>Metal</i>	<i>Inhibitor and conditions</i>	<i>References</i>
Ferrous	In 0.5–10 wt% HF, dibenzyl sulfoxide, C <sub>10</sub> –C <sub>14</sub> alkyl pyridinium salts, di- <i>o</i> -tolylthiourea, benzotriazole, mixture of thiourea and Mannich base derived from rosin amine	[52–54]
Ferritic steels	In nitric acid + HF, 2–5% thiourea	[55]

**Table 5** Inhibitors used in phosphoric acid pickling medium

<i>Metal</i>	<i>Inhibitor and conditions</i>	<i>References</i>
Steel	Benzyl quinolinium thiocyanate	[56]
Steel vessels	Transport of 50–116% H <sub>3</sub> PO <sub>4</sub> – dodecylamine or 2-amino bicyclohexyl (0.03–0.10%) in KI (0.007–0.014%)	[57]
Aluminum alloys	Urotropin, <i>p</i> -toluidine in H <sub>3</sub> PO <sub>4</sub> medium are effective inhibitors	[58, 59]
Titanium	Conc. H <sub>3</sub> PO <sub>4</sub> – inhibited by (NH <sub>4</sub> ) <sub>2</sub> MoO <sub>4</sub> + K <sub>2</sub> Cr <sub>2</sub> O <sub>7</sub>	[60]

**Table 6** Inhibitors used in scale removal in a hydrochloric acid medium

<i>Metals/scales</i>	<i>Inhibitor and conditions</i>	<i>References</i>
Scale of calcium and iron salts	5–15 wt% HCl at 80 °C. Mixture of imines, thiourea and alkynols	[62]
Zinc	Mixtures of <i>N,N'</i> -dicyclohexylthiourea, ethynycyclohexanol, and polyaminomethylene phosphate	
Carbon steel	Sulfonium compounds	[15, 16]
Scale in refineries	14% HCl containing 33–37 g l <sup>-1</sup> of hexamethylene tetramine	[63]
Copper with a scale of magnetite in high pressure boilers	Mixture of thiourea or its derivatives and hexahydropyrimidine-2-thione	

Magnetite and hematite scales may be removed by hydrofluoric acid. Mannich bases, thiourea and its derivatives, and alkynols may be used as inhibitors in hydrofluoric acid medium.<sup>54</sup> The condensation product of diethyl and dibutyl thiourea with hexamethylene tetramine can also act as an inhibitor in HF medium for scale removal.<sup>64</sup>

Sulfuric acid at 5–15 wt% may be used to remove oxide scales. This acid cannot be used to remove

calcium deposits because the product, calcium sulfate, is insoluble. Concentrated sulfuric acid in combination with nitric acid is used to remove organics, coke. Mixtures of quaternary ammonium compounds, alkynols, and sulfur compounds may be used for inhibition in a dilute sulfuric acid solution. Nitric acid is useful in cleaning stainless steel or plastic equipment. Inhibitors are not stable in the strong oxidizing nitric acid and are not used in the case of carbon steel or copper alloys.



Sulfamic acid is useful in the removal of calcium scales but not iron oxides. A mixture of sulfamic acid and sodium chloride can remove iron oxide scale through slow generation of hydrochloric acid. Sulfamic acid can be used in cleaning equipment containing copper, brass, stainless steel, and galvanized steel. Inhibitors at 10 wt% used in sulfuric acid medium may be used in sulfamic acid solution. Sulfamic acid is extensively used in cleaning evaporations in sugar mills made of cast iron with copper heat exchangers.

Citric acid is used in cleaning heat exchangers of nuclear plants, which are susceptible to chloride attack. Iron oxide scales can be removed by repeated treatment with citric acid. Inhibitors for sulfuric acid solutions can be used in citric acid medium.

Acetic acid may be used where chloride-free removal of carbonate scales in equipment made of aluminum is necessary. Inhibitors used in sulfuric acid find application in acetic acid medium. A mixture of 2 wt% of hydroxyacetic acid and 1 wt% of formic acid may be used to remove magnetite from high-pressure steam generators and superheater sections of boilers. Again, inhibitors functioning in a sulfuric acid medium may be employed here.

#### 4.29.2.3 Acidizing Oil Wells

Acids are generally used in oil and gas wells to stimulate the oil or gas flow from the well and to remove any encrustations in the well. Acids such as hydrochloric acid are forced, under high pressure, through the hole into the rock formation to produce fractures around the hole. The fractures are then filled with sand in order to prevent the fractures from closing and allow the gas or oil to permeate. About 10–15 wt% of HCl is generally used. A mixture of hydrochloric and hydrofluoric acids is used when the formation is rich in silicate. It is necessary to protect the equipment from corrosion due to the acid by use of inhibitors. The inhibitors used should be stable up to 150 °C and in some cases, 260 °C. Some inhibitors used in acidizing oil and gas wells are given in Table 7.

#### 4.29.3 Mining Industry

In the mining industry, the three corrosive environments are (i) mine air, (ii) mine dust, and (iii) mine water. Mine air causes atmospheric corrosion of mining equipment to an extent determined by the composition of mine air, humidity, and temperature.

**Table 7** Inhibitors used during acidizing oil and gas wells

<i>Inhibitor and conditions</i>	<i>References</i>
Mixtures of nitrogen containing compounds, acetylenic compounds and surfactants	[65]
C <sub>12</sub> –C <sub>18</sub> primary amines, cyclohexyl amine, aniline, methyl anilines, alkyl pyridines, benzimidazole, and rosin amine condensed with formaldehyde	
Amines together with cuprous iodide	[66]
Propargyl alcohol or 1-hexyn-3-ol gives improved inhibition at high temperatures	[67]
Alkynoxymethyl amines.	
Acetylenic inhibitors together with ferrous ions gives rise to protective surface films due to iron catalyzed condensation and polymerization	[58, 68]

Mine air is deficient in oxygen and contains significant amounts of oxides of sulfur and nitrogen. Sulfur dioxide results from burning coal, and oxides of nitrogen originate from the use of underground explosives. The oxides of sulfur and nitrogen combined with high humidity and temperature cause corrosion of mining equipment.

Coal mine dust contains pyrite in coal seams and gypsum, which is used for dusting in order to reduce the amount of combustible particles. The sulfur content of coal is corrosive to mining equipment. Sulfur dioxide, produced by the oxidation of pyrite, reacts with hygroscopic constituents and generates sulfuric acid, which attacks the metal.

Mine waters are unique in that they vary in composition from mine to mine. The pH values range from 2.8 to 12.3. Chloride values range from 5 to 10 500 ppm and sulfate ranges from 57 to 5100 ppm. Low pH, high chloride and sulfate content of mine water are conducive to severe corrosion.

Microbial corrosion can also be a problem. *Thiobacillus* species, such as thiooxydants, are common soil or water organisms. These entities oxidize sulfur, generating corrosive sulfuric acid. Sulfate-reducing bacteria generate hydrogen sulfide, which is also corrosive.

Mitigation of corrosion in the mining industry is done by the addition of (i) passivating inhibitors, (ii) precipitation inhibitors, and (iii) adsorption inhibitors. Chromates and phosphates are typical of passivating inhibitors and function by blocking the anodic reaction. These inhibitors are incorporated into the oxide film on the metal, thereby stabilizing the oxide film and preventing further dissolution. The concentration of the chromate inhibitor used is

**Table 8** Inhibitors and their performance in acidic mine waters

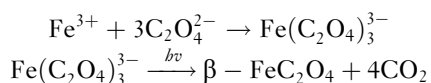
<i>Inhibitor</i>	<i>Type</i>	<i>Performance</i>
Sodium silicate	Precipitation	Fair to good
Potassium oxalate	Precipitation	Fair to good
Sodium nitrite	Passivation	Good
Sodium molybdate	Passivation	Fair to good
Phosphonate–phosphate	Precipitation	Excellent
Phosphonate–silicate	Precipitation	Fair to good

critical because low concentrations give rise to underprotection resulting in pitting corrosion.

Precipitation inhibitors consisting, for example, of zinc salts block the cathodic reaction by precipitation at the cathode due to elevated local pH values. Pitting is not a problem, even though complete coverage is not attained, because the anodic sites are unaffected by the inhibitors and the number of unprotected cathodic sites are insufficient to promote anodic dissolution.

In general, organic inhibitors can be considered as adsorption inhibitors. The functional group in the inhibitor molecule such as amino, carboxyl, or hydroxyl readily absorbs on the metal surface forming a type of bond and blocks the anodic and/or cathodic sites.

The performance of some inhibitors tested in acid mine water are given in [Table 8](#).<sup>69</sup> It should be noted that corrosion inhibition by potassium oxalate involves the formation of tris-oxalate iron complex, which is photosensitive. The complex decomposes in the presence of light to  $\beta$ -ferrous oxalate.



The product of photochemical decomposition,  $\beta$ -ferrous oxalate, is deposited on the metal and protects the metal from corrosion. This is the first example of photochemical corrosion inhibition.<sup>70</sup>

Corrosion inhibitors have been used in corrosive wear loss of grinding balls in grinding Cu–Zn–Fe sulfide ore. Many inorganic inhibitors both as single component and binary mixtures were used and a binary mixture of sodium chromate and sodium carbonate reduced the corrosive wear of the grinding balls by 30%.<sup>71</sup>

#### 4.29.4 Paints and Coatings

The primary function of an organic coating on a metallic structure is to provide a protective barrier between the metal and the external corrosive

**Table 9** Inhibitors employed in coating formulations for steel core

<i>Compounds</i>
<i>Calcium</i>
Carbonate
Molybdate
Plumbate
<i>Chromium</i>
Barium potassium chromate
Basic lead silicochromate
Cadmium chromate
Zinc chromate
<i>Lead</i>
Basic silicoplumbate
Blue
Calcium plumbate
Carbonate (white)
Red
Titanate
<i>Zinc</i>
Chromate
Molybdate
Oxide
Tetroxychromate
<i>Miscellaneous</i>
Antimony oxide
Carbon black
Chalk
China clay
Iron oxide
Strontium chromate
Talcum
Titanium dioxide

environment. Paints are used for both corrosion protection and cosmetic purpose. Usually corrosion inhibitors are incorporated in the primer. The inhibitors used in coatings can be anodic, cathodic, or mixed. Some examples of the inhibitors incorporated into coating formulations suitable for steel core are given in [Table 9](#).<sup>69</sup>

Some of the components are used as fillers. Zinc and calcium molybdate are effective at low levels ( $\sim 3\%$ ), and are nontoxic. These compounds may be used in place of chromates, which are toxic. Red lead protects the steel by combining with the corrosion products of iron. Red lead, zinc oxide, and calcium carbonate form soaps with linseed oil and then decompose in the presence of oxygen and water into a lead salt of azelaic acid, which promotes cathodic reduction of oxygen. This helps to stabilize the iron oxide film by maintaining a suitable potential. Calcium plumbate increases the pH and thus inhibits corrosion. The lead suboxide in oleoresinous coatings forms lead soaps on the metal surface and blocks the anodic

sites by adsorption. Lead suboxide in linseed oil primer is found to penetrate the rust film and into crevices of rusted steel.

Inhibition by chromate-based pigments is similar to that of dissolved chromate, and this is supported by the slight solubility of the pigment.<sup>72</sup> Chromate ions are adsorbed onto the surface followed by the formation of a passive film containing  $\text{Cr}_2\text{O}_3$  and  $\text{Fe}_2\text{O}_3$ . Both potassium chromate and zinc chromate protect the steel. Potassium chromate protects by interfering with the anodic reaction, while zinc chromate also forms a zinc hydroxide film inhibiting the cathodic reaction.

Zinc, along with cadmium and strontium, chromate has been used in the protection of aluminum involving crevices. These compounds are reduced at cathodic sites and hydrogen evolution is prevented. Disbonding of coatings is due to hydrogen evolution and addition of cadmium phosphate shows improved inhibition.

Chromates, such as zinc chromate, potassium or barium chromate, may be used as primers in various vehicles including linseed oil, long oil linseed pentaalkyd, double-boiled linseed oil for corrosion inhibition. Good protection was obtained with modified phenolic stand oil and epoxy ester primers, as confirmed by neutral pH, noble potentials, and formation of soap, which covers the zinc chromate causing water repulsion.

Some pigments based on lead, silicate, and phosphate, along with some applications, are given in [Table 10](#).

The coatings discussed so far involve heavy metal compounds that are toxic with the exception of molybdates and phosphates. Thus, development of environmentally friendly coatings containing tannins

has received attention. It is necessary that the fabrication of raw products, surface pretreatment and application of coating, use of coated structure, and recycling and elimination steps should be considered from the point of environmental impact. Tannins are used as corrosion inhibitors in water-based paints. Such paints can be applied directly on rusted objects without pretreatment, such as sandblasting.

The mechanism of protection by tannins in paints has been investigated by many studies.<sup>77–83</sup> An early proposal was the formation of an insoluble chelate complex at anodic sites.<sup>78</sup> The insoluble chelate complex may act as an insulator between anodic and cathodic sites because of the cross-linked structure of the complex.<sup>79</sup>

Tannins are also known to convert ‘active’ rust into nonreactive oxide such as magnetite.<sup>80</sup> The insoluble complex formed may act as a barrier for the diffusion of oxygen.<sup>77</sup> The action of tannins appears to depend upon the properties of paint-rust system and upon the amount of rust present.<sup>81</sup> X-ray photoelectron data and Mössbauer spectra showed an increase in the ratio of ferrous to ferric ions when the rust was treated with tannins.<sup>82</sup> Vacchini<sup>83</sup> showed the dissolution of rust by tannins and the formation of a complex that acted as a barrier for the diffusion of oxygen.

#### 4.29.5 Construction Materials

Corrosion inhibition in reinforced concrete structures involves a single addition of the inhibitor. On this basis, the criteria for effective corrosion inhibition in concrete are that (i) the inhibitor should be soluble in mixing water to allow homogeneous distribution and not readily leachable from concrete;

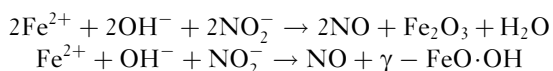
**Table 10** Some pigments in common use

<i>Pigment</i>	<i>Comments</i>	<i>References</i>
Red lead	Red lead in linseed oil used as primer for steel structures. Red lead oxide forms soluble soaps with vehicle	[73]
Lead silicochromate	Consists of silicate case coated with its own pigment. Anticorrosive due to lead and passivation due to chromate. Coating with this is comparable to red lead in linseed oil in protection. Protection of passenger car bottoms by using priming coats with the pigment achieved	[74]
Barium oxide-iron oxide	Developed for corrosion control of fertilizer plants. Corrosion protection is satisfactory	[75]
Zinc phosphate/barium phosphate primer	Nontoxic and promotes excellent intercoat adhesion. The primer converts the metal to metal phosphate. This primer reduces diffusion of ions through paint film. Zinc phosphates-iron oxide in linseed stand oil performed better than red oxide-zinc chromate in field tests	[76]

- (ii) the inhibitor must be compatible with the aqueous cement phase, to render its full protection potential;
- (iii) the concentration of the inhibitor should not adversely affect the properties of the concrete; and
- (iv) the consumption rate of the inhibitor should be low.

The most extensively used inhibitor in concrete is calcium nitrite, although organic inhibitors have become prominent in recent years. Calcium nitrite has been used as an inhibitor for concrete on a large scale. Calcium nitrite provides corrosion protection in the presence of chlorides, does not affect the properties of concrete, and is readily available for commercial use in concrete.

Calcium nitrite, an anodic inhibitor, is thought to be responsible for the constant repair of weak spots in the protective iron oxide film as well as the following reactions:



The nitrite ion is believed to compete with chloride and hydroxyl ions in the reaction with ferrous ions. As the nitrite ion helps to repair the flaws in the oxide film the probability of chloride attack at the flaws of the oxide film and dissolution of the oxide film as soluble chloro complexes of iron are minimized. Given that nitrite inhibitor is involved in repairing the oxide film and the oxide films are of the order of monolayers, nitrite is not consumed to a great extent.

Pozzolans (complex silicate of iron, aluminum, and calcium) are used to prevent corrosion by reducing permeability of concrete to chloride. Microsilica is one of the most effective pozzolans because its small particle size acts as a filler and increases its chemical reactivity. Calcium nitrite is compatible with microsilica and should provide corrosion protection in the presence of chloride. Calcium nitrite is also found to improve the performance of fly ash concrete and concretes containing slag. Calcium nitrite is also effective in the protection of cracked concrete.

Organic inhibitors have been used as an alternative to the commonly used calcium nitrite. The organic inhibitors, referred to as organic corrosion inhibiting admixtures (OCIA), adsorb on the metal surface through a polar functional group, while non-polar hydrophobic groups repel the aqueous corrosive fluids and interact with each other to form a tight film of aggregates on the metal surface. The tight hydrophobic film is also impermeable to chloride ingress into the concrete.

The performance of organic amines and esters with both uncracked and precracked concrete

samples has been compared with precracked samples treated with calcium nitrite.<sup>84</sup> The organic inhibitors lowered the corrosion rates to a significant extent. The onset of corrosion in samples treated with organic inhibitors occurred after 180 days, and the corresponding times were 30 and 5 days in the case of calcium nitrite treated samples and uninhibited samples, respectively. The ingress of chloride was highest in calcium nitrite treated samples and least in organic inhibitor treated samples. The higher chloride ingress in samples treated with nitrite is attributed to the accelerating effect of nitrite resulting in a more permeable concrete matrix. The blocking of pores by organic inhibitor results in low ingress of chloride in samples treated with organic inhibitor.

A mixture of glycerophosphate and nitrite showed synergistic behavior in the protection of steel in mortars.<sup>85</sup> Other inhibitors used in reinforced steel are ethanolamine,<sup>86</sup> poly alcohols, polyphenols, and sugars. Alkanolamine has been shown to be an effective inhibitor and to migrate through the pores when it is injected into the cavities.<sup>87</sup>

#### 4.29.6 Processing Electronics Packaging, Paper Display, and Storage

Some organic compounds with vapor pressures in the range  $10^{-2}$  to  $10^{-7}$  mmHg volatilize and condense on the surface of a structure to be protected from corrosion in a closed space. These types of compounds are known as vapor-phase corrosion inhibitors; a list of common vapor-phase inhibitors, along with their vapor pressures, is given in Table 11. Vapor-phase corrosion inhibitors are particularly useful in impeding atmospheric corrosion. Atmospheric corrosion is expensive and results from individual or combined action of moisture, oxygen, and pollutants such as  $\text{SO}_2$  and  $\text{NO}_2$ .

Most effective vapor-phase inhibitors consist of a weak volatile base and a weak volatile acid. Amine nitrites undergo hydrolysis and provide inhibition



The pH of the medium is critical to the effective inhibition by vapor-phase inhibitors.

The application of vapor-phase inhibitors varies, depending upon the composition of the object to be protected, as well as the conditions of storage of the object. Storage conditions dictate the aggressiveness

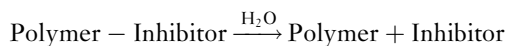
**Table 11** Common vapor phase inhibitors and their saturated vapor pressures

Substance	Temperature (°C)	Vapor pressure (mmHg)	Melting point (°C)
Morpholine	20	8.0	
Benzylamine	29	1.0	
Cyclohexylamine carbonate	25.3	0.397	
Diisopropylamine nitrite	21	$4.84 \times 10^{-3}$	139
Morpholine nitrite	21	$3 \times 10^{-3}$	
Dicyclohexylamine nitrite	21	$1.3 \times 10^{-4}$	179
Cyclohexylamine benzoate	21	$8.0 \times 10^{-5}$	
Dicyclohexylamine caprylate	21	$5.5 \times 10^{-4}$	
Guainidine chromate	21	$1.0 \times 10^{-5}$	
Hexamethyleneimine benzoate	41	$8.0 \times 10^{-4}$	64
Hexamethyleneamine nitrobenzoate	41	$1.0 \times 10^{-6}$	132
Dicyclohexylamine benzoate	41	$1.2 \times 10^{-6}$	210

of the treatment. The storage conditions requiring progressively more aggressive treatments are (i) enclosed nonventilated area; (ii) uncovered inside storage; (iii) covered outside storage; and (iv) uncovered outside storage.

Vapor-phase inhibitors are either oil or water soluble and applied in the form of powders, sprays, or impregnated papers and foams. A controlled-release inhibitor formulation can be employed, which is designed to release the inhibitor at a controlled rate over a specified period. Polymer encapsulation may be used for controlled release, where a rate-controlling membrane encloses a cavity that contains the inhibitor either dispersed or in solution. The membrane can be porous or nonporous and the inhibitor is in a reservoir in a fluid state that maintains a constant amount in the reservoir until an excess amount is released. This results in a steady-state release of the inhibitor that follows Fick's law.

In addition to encapsulation, the inhibitor can be dispersed in a polymer matrix, from which the inhibitor is extracted. There are two types of matrix device. In the first type, the release of the active inhibitor is controlled by diffusion through the matrix upon erosion of the matrix. In the second type, the release of the inhibitor is initiated by the penetration of some species, such as water, from the environment into the matrix. On reaction with water, the active inhibitor is released because of hydrolysis.



Some common examples of this type are esters, anhydrides, and acetals.

## References

- Kurilovich, T. I.; Klyuchnikov, N. G. *Inhibitory Korroz Met.* **1972**, 168; *Chem. Abs.* **1975**, 83, 210657j.
- Desai, M. N.; Sheth, H. M. *Vidya* **1976**, B19, 118; *Chem. Abs.* **1978**, 88, 40661q.
- Desai, M. N.; Desai, S. T. *Chem. Concepts* **1978**, 5(7), 15; *Chem. Abs.* **1978**, 89, 219453.
- Patel, M. N.; Patel, N. K.; Vora, J. C. *Chem. Era* **1975**, 11(5), 4; *Chem. Abs.* **1977**, 87, 9998.
- Horner, L.; Meisel, K. *Werkstoffe Korros.* **1978**, 29, 654.
- Makwana, S. C.; Patel, N. K.; Vora, J. C. *J. Indian Chem. Soc.* **1973**, 50(10), 664; *Chem. Abs.*, **1974**, 80, 127351x; *Werkstoffe Korros.* **1973**, 24, 1036.
- Makwana, C. M.; Bhavsar, A. C.; Gandhi, D. C. *Chem. Era* **1976**, 12(4), 145; *Chem. Abs.* **1977**, 86, 125613j.
- Makwana, S. C.; Patel, N. K.; Vora, J. C. *Trans. Soc. Adv. Electrochem. Sci. Technol.* **1977**, 12(1), 15; *Chem. Abs.* **1978**, 88, 64933f.
- Clark, P. N.; Jackson, E.; Robinson, M. *Br. Corros. J.* **1979**, 14, 33.
- Mansfeld, F.; Kenkel, J. V. *Corros. Sci.* **1975**, 15, 767.
- Tupikin, E. I.; Klyuchnikov, N. G.; Verzilina, M. K. *Izv. Vyssh. Ucheb. Zaved. Khim. Khim. Tekhnol.* **1974**, 17(4), 514; *Chem. Abs.* **1974**, 81, 32513.
- Gerasytina, L. I.; Tulyupa, F. M.; Karvaka, L. G. *Zashch. Metall.* **1978**, 14(6), 719; *Chem. Abs.* **1979**, 90, 158952e.
- Tupikin, E. I.; Klyuchnikov, N. G.; Nemchaninova, G. L. *Zashch. Metall.* **1975**, 11(3), 351; *Chem. Abs.* **1975**, 83, 1055287.
- Heiss, L.; Hille, M. (Farbwerke Hoechst AG) U.S. Patent 3,773,675, Nov. 20, 1973; *Chem. Abs.* **1974**, 80, 148130.
- Frenier, W. W.; Settineri, W. J. (Dow Chem Co.) U.S. Patent 3,764,543, Oct. 9, 1974; *Chem. Abs.* **1976**, 80, 86674; U.S. Patent 3,969,414, July 13; *Chem. Abs.* **1976**, 85, 123665.
- Settineri, W. J.; Frenier, W. W.; Oswald, J. R. U.S. Patent 3,996, 147, Dec. 7, 1976; *Chem. Abs.* **1977**, 86, 58948.
- Klitgaard, J.; Blum, R. *VGB Krafwerkstechnik* **1978**, 58(4), 303; *Chem. Abs.* **1978**, 89, 168203.
- Frumkin, A. N. *Z. Elektrochem.* **1955**, 59, 807.
- Iofa, Z. A. *Zashch. Metall.* **1970**, 6(5), 491; *Chem. Abs.* **1973**, 73, 136607; *Zashch. Metall.* **1972**, 8(2), 139; *Chem. Abs.* **1972**, 77, 55465a.
- Allabergenov, K. D.; Kurbanov, F. K. *Zashch. Metall.* **1979**, 15(4), 472; *Chem. Abs.* **1979**, 91, 179255f.



21. Sorokin, V. I.; Romasenko, V. P. *Ukr. Khim. Zh. (Russ. Ed.)* **1974**, 40(8), 804; *Chem. Abs.* **1975**, 83, 67624p.
22. Kolevatova, V. S. *Zh. Prikl. Khim. (Leningrad)* **1975**, 48(10), 2216; *Chem. Abs.* **1976**, 84, 10323f.
23. Kolevatova, V. S.; Korobkov, V. I. *Zh. Prikl. Khim.* **1976**, 49(1), 86; *Chem. Abs.* **1976**, 84, 127942y.
24. Ahmad, Z.; Ghafelchbashi, M.; Nategh, S.; Jahanfar, S. *Met. Corros. Ind.* **1975**, 50(599–600), 271; *Chem. Abs.* **1976**, 85, 36459a.
25. Patel, N. K.; Patel, M. M.; Patel, K. C. *Chem. Era.* **1975**, 10(12), 24; *Chem. Abs.* **1976**, 84, 77811.
26. Patel, N. K.; Patel, M. M.; Patel, L. N.; Mehta, S. H. *Chem. Era.* **1976**, 12(2), 46; *Chem. Abs.* **1977**, 86, 32773.
27. Tupikin, E. I.; Klyuchnikov, N. G.; Verzilina, M. K. *Zashch. Metallov.* **1974**, 10(1), 65; *Chem. Abs.* **1974**, 81, 53488.
28. Tupikin, E. I.; Klyuchnikov, N. G. *Izv Vyssh Uchebn. Zaved. Khim Khim Tekhnol.* **1977**, 20(5), 790; *Chem. Abs.* **1977**, 87, 92514.
29. Gleizer, M. M.; Tseitlim, Kh. L.; Sorokin, Yu. L.; Isaenko, G. I.; Babitskara, S. M. *Zashch. Metallov.* **1976**, 12(5), 629; *Chem. Abs.* **1977**, 86, 94505.
30. Gerasytina, L. I.; Tulyupa, F. M.; Gromova, N. L.; Koryaka, L. G. *Zashch. Metallov.* **1976**, 12(2), 195; *Chem. Abs.* **1976**, 85, 98142a.
31. Eberhard, J. F.; Oakes, B. D. (Dow Chemical Co.), US Patent 3,037,934, June 5, 1962; *Chem. Abs.* **1962**, 57, 6970a.
32. Eberhard, J. F. U.S. Patent 2,963,439, Dec. 6, 1960; *Chem. Abs.* **1961**, 55, 10294.
33. Uzlyuk, M. V.; Fedorov, Yu. V.; Pinus, A. M.; Tolstykh, V. F.; Panfilova, Z. V.; Shatukhina, L. I.; Miskidzh'van, S. *Zashch. Metallov.* **1977**, 13(2), 212; *Chem. Abs.* **1977**, 86, 162689j.
34. Mahan, J. E.; Stahl, R. A. (Phillips Petroleum Co.), US. Patent 2,769,690, Nov. 6, 1956; *Chem. Abs.* **1957**, 51, 3430c.
35. Standford, J. R. (Nalco Chemical Co.), US Patent 3,585,136, June 15, 1971; *Chem. Abs.* **1971**, 75, 83570h.
36. Desai, M. N. *Werkstoffe Korros.* **1972**, 23, 483.
37. Desai, M. N.; Shah, V. K. *Corros. Sci.* **1972**, 11, 725.
38. Desai, M. N.; Thanki, G. H. *J. Electrochem. Soc. India.* **1972**, 21(1), 13; *Chem. Abs.* **1972**, 76, 161550p.
39. Desai, M. N.; Joshi, J. S. *J. Inst. Chem. Calcutta* **1972**, 44(4), 138; *Chem. Abs.* **1973**, 78, 51603s.
40. Desai, M. N.; Thanki, G. H. *Labdev. Part A.* **1972**, 10(2), 73; *Chem. Abs.* **1973**, 79, 26416w.
41. Desai, M. N.; Rana, S. S. *Anti-Corros. Methods Mater.* **1973**, 20(5), 16; *Chem. Abs.* **1973**, 79, 86712z.
42. Desai, M. N.; Rana, S. S. *Anti-Corros. Methods Mater.* **1973**, 20(6), 16; *Chem. Abs.* **1973**, 79, 11103m.
43. Desai, M. N.; Shah, D. K.; Gandhi, H. M. *Br. Corros. J.* **1975**, 10(1), 39.
44. Desai, M. N.; Shah, D. K. *Vidya B.* **1976**, 19(2), 226; *Chem. Abs.* **1978**, 88, 76769c.
45. Desai, M. N.; Thaker, B. C.; Chhaya, P. M. *J. Indian Chem. Soc.* **1975**, 52(10), 950; *Chem. Abs.* **1976**, 84, 97026.
46. Desai, M. N.; Thanki, G. H.; Shah, D. K. *Anti-Corros. Methods Mater.* **1971**, 18(10), 8; *Chem. Abs.* **1972**, 76, 67228t.
47. Desai, M. N.; Thaker, B. C.; Patel, B. M. *J. Electrochem. Soc. India.* **1975**, 24(4), 84; *Chem. Abs.* **1976**, 84, 139675u.
48. Desai, M. N.; Rana, S. S. *Anti-Corros. Methods Mater.* **1973**, 20(5), 16; *Chem. Abs.* **1973**, 79, 86712z.
49. Patel, M. M.; Patel, N. K.; Vora, J. C. *India J. Technol.* **1974**, 12(10), 469; *Chem. Abs.* **1975**, 82, 78400t.
50. Patel, M. M.; Patel, N. K.; Vora, J. C. *J. Electrochem. Soc. India.* **1978**, 27(3), 171; *Chem. Abs.* **1979**, 90, 129380m.
51. Keller, H.; Risch, K. *Werkstoffe Korros.* **1964**, 15, 741.
52. Vosta, J.; Pelikan, J.; Smrz, M. *Werkstoffe Korros.* **1974**, 25, 750.
53. Pearlstein, F.; Weightman, R. F. US NTIS, AD Rep. AD-A 14163, 1975; *Chem. Abs.* **1976**, 84, 183167.
54. Anderson, J. D.; Hayman, E. S., Jr.; Rodzewich, E. A. (Amchem. Products Inc.), U.S. Patent 3,992,313, Nov. 16, 1976; *Chem. Abs.* **1977**, 87, 139496.
55. Maksimenko, M. N.; Podobaev, N. I. *Inhibitory J. Corros. Met.* **1972**, 78; *Chem. Abs.* **1976**, 84, 48406.
56. Uzlyuk, M. V.; Fedorov, Yu. V.; Voloshin, V. F.; Panfilova, Z. V.; Shatukhina, L. I.; Aleinikova, L. G. *Zashch. Metallov.* **1973**, 9, 446; *Chem. Abs.* **1974**, 80, 51152.
57. Malowan, J. E. (Monsanto Chem. Co.) U.S. Patent 2,567,156, Sept. 4, 1951; *Chem. Abs.* **1952**, 46, 876e.
58. Talati, J. D.; Pandya, J. M. *Anti-Corros. Methods Mater.* **1974**, 21(2), 7; *Chem. Abs.* **1975**, 83, 17561.
59. Talati, J. D.; Pandya, J. M. *Corros. Sci.* **1976**, 16, 603.
60. Ignatov, B. P.; Anoshenko, I. P.; Pyaterikov, V. V.; Luk'vanova, G. I.; Nechepurenko, E. A. *Tr. Novocherk. Politek. Inst.* **1975**, 285, 41; *Chem. Abs.* **1975**, 82, 130921.
61. NACE Task Group T-3M-4. *Industrial Cleaning Manual*; NACE: Houston, TX, 1982; *Corros. Abs.* **1982**, 21(6), 376.
62. Clark, H. D. (Universal Oil Products Co.) U.S. Patent 3,969,260, July 13, 1976; *Chem. Abs.* **1976**, 85, 165428; U.S. Patent 3,979,311, Sept. 7; *Chem. Abs.* **1976**, 85, 182249.
63. Frenier, W. W. (Dow Chemical Co.) U.S. Patent 4,310,435, Jan. 12, 1982.
64. Jones, J.; Geldner, J. (Metallgesellschaft AG); Ger. Offen. 2,616,144, Nov. 3, 1977; *Chem. Abs.* **1978**, 89, 10126.
65. Constantinescu, A.; Cracium, D. C. *Rev. Coroz.* **1971**, 1, 206; *Chem. Abs.* **1972**, 77, 37989.
66. Keeney, B. R.; Johnson, J. W., Jr. (Halliburton Co.) U.S. Patent 3,773,465, Nov. 20, 1973; *Chem. Abs.* **1974**, 80, 136319.
67. Keeney, B. R.; Johnson, J. W.; Jr. *Mater. Prot. Perform.* **1973**, 12(9), 13; *Chem. Abs.* **1974**, 87, 104314.
68. Redmore, D. (Petrolite Corp.) U.S. Patent 3,997,293, Dec. 14, 1976; *Chem. Abs.* **1977**, 88, 107770; U.S. Patent 3,998,883; *Chem. Abs.* **1977**, 87, 84823; U.S. Patent 4,089,650; *Chem. Abs.* **1977**, 87, 109012.
69. Sastri, V. S. *Corrosion Inhibitors*; Wiley: Chichester, UK, 1978.
70. Sastri, V. S.; Perumareddi, J. R.; Elboudjaini, M. *Corrosion* **2008**, 64, 657.
71. Lui, A. W.; Sastri, V. S.; Elboudjaini, M.; McGoey, J. B. *Corros. J.* **1996**, 31, 158.
72. Naganathan, K.; Guruviah, S.; Rajagopalan, K. S. *Paint India Annual* **1965**, 15(1), 78.
73. Guruviah, S.; Rajagopalan, K. S. *Paint India* **1968**, 16(8), 28.
74. Selvaraj, M.; Guruviah, S. *Paint India* **1987**, 37(8), 27.
75. Chakrabarthy, B. R.; Verma, K. M. *Corr. Prevent. Control* **1987**, 34(5), 127.
76. Gomathi, H.; Chandrasekaran, V.; Guruviah, S.; Narasimhan, K. C.; Udupa, H. V. K. In Proceedings of the 2nd National Conference on Corrosion and its Control **1979**; p 205.
77. Seavell, A. J. *J. Oil Colour Chem. Assoc.* **1978**, 61, 439.
78. Knowles, E.; White, T. J. *Oil Colour Chem. Assoc.* **1958**, 41, 10.
79. Franiau, R. *Cong. Colloq. Univ. Liège.* 1973, 129.
80. Ross, T. K.; Francis, R. A. *Corros. Sci.* **1978**, 18, 351.
81. Deslauriers, P. T. *Mater. Perform.* **1987**, 11, 35.
82. Gancedo, J. R.; Gracia, M. *Hyperf. Interact.* **1989**, 46, 461.
83. Vacchini, D. *Anticorr* **1985**, 9, 9.
84. Nmai, C. K.; Farrington, S. A.; Bobrowski, G. S. *Concrete Int.* **1992**, 45–51.

85. Anoschenko, I. P.; Puzey, E. V.; Tulenev, A. N. In Proceedings of the 8th European Symposium on Corrosion Inhibitors, University of Ferrara, 1995; Vol. 1, p 609.
86. Wieczorek, G.; Gust, J. In Proceedings of the 8th European Symposium on Corrosion Inhibitors, University of Ferrara, 1995; Vol. 1, p 599.
87. Miksie, B.; Gelner, L.; Bjegovic; Sipos, L. In Proceeding of the 8th European Symposium on Corrosion Inhibitors, University of Ferrara, 1995; Vol. 1, p 569.
88. Balezin, A.; Belen'kii, S. M.; Aronson, Yu. P.; Belen'kaya, N. M. *Zashch. Mettalov* **1968**, 4(4), 385; *Chem. Abs.* **1968**, 69, 109104.
89. Riggs, O. L.; Morrison, K. L.; Brunsell, D. A. *Corrosion* **1979**, 35, 356.
90. Oude-Alink, B. A. (Petrolite Corp.) U.S. Patent 3,984,203, Oct. 5, 1977; *Chem. Abs.* **1977**, 87, 104314.
91. Berke, N. S. In ASTM STP 906; American Society for Testing and Materials, Philadelphia, PA, 1986, pp 78–91.

## **4.27 Environmental Modification for Cooling, Heating and Potable Water Systems**

**C. Frayne**

Aquassurance, Inc., 156 Red Fox Run, Macon, GA 31210, USA

© 2010 Elsevier B.V. All rights reserved.

---

4.27.1	Introduction	2931
4.27.2	Heat Capacity and Latent Heat	2931
4.27.3	The Use of Water in Industrial Cooling and Heating Systems and Potable Applications	2932
4.27.4	The Need for Water Treatment to Control Waterside Heating, Cooling and Potable Water Environments	2933
4.27.5	The Hydrologic Cycle and Water Chemistry	2936
4.27.6	Waterside Problems Resulting from Mineral Scales, Muds, and Sludges	2941
4.27.6.1	Problems from Mineral Scales, Muds, and Sludges in Boilers	2941
4.27.6.2	Problems due to Mineral Scales, Muds, and Sludges in Cooling Systems	2943
4.27.6.3	Problems due to Mineral Scales, Muds, and Sludges in Closed-Loop Water Systems	2943
4.27.6.4	Problems due to Waterside-Surfaces Fouling in 'New Construction' HVAC Systems	2944
4.27.6.5	Problems due to Mineral Scales, Muds, and Sludges in Potable Water Lines	2944
4.27.7	Problems of Corrosion including Microbial Induced Corrosion	2945
4.27.7.1	Uniform or General Corrosion	2945
4.27.7.2	Oxygen Pitting Corrosion	2945
4.27.7.3	Galvanic Corrosion	2946
4.27.7.4	Concentration Cell Corrosion or Crevice Corrosion	2947
4.27.7.5	Stress Corrosion	2947
4.27.7.6	Erosion Corrosion or Impingement Corrosion	2948
4.27.7.7	Condensate Line Corrosion or Grooving Corrosion	2948
4.27.7.8	Microbiologically Influenced/Induced Corrosion or Biocorrosion	2949
4.27.7.9	White Rust Corrosion	2949
4.27.8	Problems of Microbiological Fouling	2950
4.27.8.1	Problems of Amplification of Pathogenic Bacteria	2951
4.27.9	Evaluating and Modifying Waters for Use or Reuse in Industrial Processes and HVAC Water Systems	2952
4.27.10	Modifying Water by Selective Use of Standard Pretreatment Processes	2953
4.27.11	Modifying Waterside Environments by Appropriate Metal and Alloy Materials Selection	2955
4.27.12	Understanding Contaminant Saturation Problems as a Precursor to Modification of Waterside Environments by Chemical Inhibitors	2956
4.27.13	LSI and Related Indices as an Aid to Modification of Waterside Environments	2958
4.27.14	Use of Contaminant Cycling Effects in Modifying Waterside Environments	2960
4.27.15	Modification of Waterside Environments by Chemical Inhibitors	2961
4.27.16	Modification of Steam Boiler Waterside Environments by Chemical Inhibitors	2961
4.27.17	Modification of Cooling System Waterside Environments by Chemical Inhibitors	2964
4.27.18	Types of Modern Organic Chemical Inhibitors Employed to Modify Cooling System Waterside Environments Against Risks of Scale, Fouling, and Corrosion Control	2966
4.27.19	Modifying Cooling System Waterside Environments to Minimize Risks of Biological Fouling and MIC	2967
4.27.20	Conclusion	2969
References		2970

---

### 4.27.1 Introduction

Water has a relatively high heat capacity. In fact, water has the second highest heat capacity of any known substance, after ammonia, and is slow to absorb and reject heat. These properties are because of hydrogen bonding at the molecular level and make water valuable in cooling and heating processes and systems such as heating, ventilation, and air conditioning (HVAC) systems. Water is commonly employed as a heat transfer fluid, that is, a vehicle for transporting heat to some distant point of use, or away from a process, or for the uptake/removal of heat via a heat exchanger, cooling tower, or similar device.

The water may be employed in liquid, gaseous (steam), or solid (ice) form, depending upon the specific process. For example:

- liquid water is employed for HVAC condenser cooling;
- steam is the medium for many boiler plants;
- ice can be used in HVAC thermal energy storage systems.

However, all water sources ultimately employed for industrial process or in HVAC system applications, and even potable grade water contain a variety of contaminants, and as a result of a combination of the contaminants (including dissolved oxygen), the specific process operating conditions, and the materials of equipment construction, the water can act as a scale-forming or corrosive fluid.

Various forms of modification and active control of the process environment are usually necessary to maintain operational efficiency and reduce the potential for corrosion, fouling, or premature system failure. This is usually achieved through the selective use of filters, softening equipment, certain nonchemical devices, pH management, and/or the addition of specialty chemical inhibitors, together with appropriate technical overseeing.

Other heat transfer fluids, such as ethylene or propylene glycol, may be used under certain circumstances, for example where the fluid in a pipe is exposed to freezing winter temperatures. After prolonged usage, glycols may become corrosive because of thermal breakdown or microbial action, and modification of the fluid by, for example, raising the pH and adding a chemical inhibitor, may be necessary.

Water is also vital to the existence of all life forms, where it acts as a vehicle for the transport of essential minerals and vitamins to all parts of the organism.

In developed societies potable water is delivered under pressure through pipes, and these pipes (especially metal pipes) together with pumps, valves, etc. may also be subject to scaling, fouling, or corrosive action. Thus, modification and active control of potable water systems to prevent corrosion and other problems may also be necessary. Here, we may choose to use less corrodible materials of construction, employ potable grade phosphate or silicate chemicals (for corrosion control or threshold stabilization of scale-forming alkaline earth salts), or use approved disinfection processes, such as chlorination, bromination, ozonation, or the application of chlorine dioxide from an on-site generator.

The active modification of an aqueous heating, cooling, or process environment (and usually that of other heat transfer fluids) to prevent or minimize corrosion, scaling, or biological or inorganic fouling, together with the provision of appropriate monitoring and control is termed 'water treatment.'

### 4.27.2 Heat Capacity and Latent Heat

It has already been stated that a major benefit of using water in cooling, heating, and potable water systems is because of its high heat capacity. As more heat energy is required to increase the temperature of a substance with high specific heat capacity than to increase the temperature of one with a low specific heat capacity, from an engineering design position it is convenient for water to be employed as a vehicle for the transport of heat.

The measure of the heat energy required to increase the temperature of a unit quantity of a substance by a certain temperature interval is known as the specific heat capacity (the symbol is  $c$ ), also known simply as specific heat. When measuring specific heat capacity in science and engineering, the unit quantity of a substance is often in terms of mass: either the gram or kilogram. For example, the heat energy required to raise water's temperature by 1 K (equal to 1 °C) is  $4184 \text{ J kg}^{-1}$  – the kilogram being the specified quantity. This is at a sea-level pressure of one standard atmosphere (101.325 kPa) – approximately a bar (which is 100 000 Pa) and a temperature of 15 °C. Scientifically, this measure would be expressed as  $c = 4184 \text{ J kg}^{-1} \text{ K}^{-1}$ .

- The specific heat capacity of liquid water is  $4.184 \text{ kJ kg}^{-1} \text{ K}^{-1}$ .

- The specific heat capacity of water vapor is  $1.996 \text{ kJ kg}^{-1} \text{ K}^{-1}$ .
- The specific heat capacity of ice is  $2.108 \text{ kJ kg}^{-1} \text{ K}^{-1}$ .

In the United States, which tends not to commonly use SI units, the specific heat of water is defined as the amount of heat necessary to increase the temperature of one pound of water by  $1^\circ\text{F}$ , and is given as 1 British Thermal Unit (Btu).

When thermal energy is withdrawn from a liquid such as water, or a solid such as ice, the temperature falls, as in a chiller plant, a cooling tower, or an evaporative condenser. When you add heat energy the temperature rises, as in a boiler. If sufficient energy is withdrawn or added, a change of state can occur, as in a steam-raising boiler (steam generator). To go from liquid to solid, the molecules of a substance must become more ordered. To maintain the order of a solid, extra heat must be withdrawn. In the other direction, to create disorder on going from solid crystal ice to liquid water, extra heat must be added.

The enthalpy of vaporization (the symbol is  $\Delta H_v$ ), also known as the heat of vaporization or latent heat of evaporation, is the energy required to transform a given quantity of a substance into a gas. It is often measured at the normal boiling point of a substance, although tabulated values are usually corrected to 298 K.

The enthalpy of fusion (the symbol is  $\Delta H_{\text{fus}}$ ), also known variously as the latent heat of fusion, the enthalpy change of fusion, or the specific melting heat, is the amount of thermal energy which must be absorbed or evolved for 1 mol of a substance to change state from a solid to a liquid or vice versa. The temperature at which it occurs is called the melting point and at this point, extra energy is required (the heat of fusion).

- The heat of vaporization of water is  $2260 \text{ kJ kg}^{-1}$ .
- The heat of fusion of water is  $333.55 \text{ kJ kg}^{-1}$ .

In the United States, the latent heat of fusion is usually defined in non-SI units, and is given as the amount of heat required to change one pound of a given substance from solid to liquid state without change in temperature. It requires 144 Btu to change one pound of ice at  $32^\circ\text{F}$  to one pound of water at  $32^\circ\text{F}$ , the heat of fusion of ice being 144 Btu per pound.

Also, the latent heat of vaporization in non-SI units is defined as the amount of heat required to change one pound of a given substance from liquid to vapor state without change in temperature. It requires a considerable amount of additional heat

energy (970 Btu) to change one pound of water from  $212^\circ\text{F}$  to 1 pound of steam at  $212^\circ\text{F}$ . This high energy input requirement is again because of hydrogen bonding, and results in steam occupying 20 600 times the volume of liquid water at  $100^\circ\text{C}$  ( $212^\circ\text{F}$ ). The steam, usually under high pressure, is available both as a medium for transporting heat energy and for mechanical work (as in steam engines, steam pumps, and for turning turbine blades in the generation of electrical energy).

In North American refrigeration and air conditioning applications, 1 'ton of cooling' is a common unit, and is  $12\,000 \text{ Btu h}^{-1}$ . It is the amount of power needed to melt one ton of ice in 24 h, and is approximately 3.51 kW. Cooling towers, boiler plants, and chiller plants are commonly rated in tons.

#### **4.27.3 The Use of Water in Industrial Cooling and Heating Systems and Potable Applications**

Global withdrawal rates of freshwater continue to grow at more than double the rate of population growth.<sup>1</sup> Withdrawal rates of estuarine and salt water also continue to grow at a similar rate. Unfortunately, freshwater availability and distribution is not divided up fairly or evenly around the globe and this has created difficulties in developing countries.

Where water is conserved by being reused in industrial processes, such as employing treated waste water as a makeup stream for a cooling tower, there is a significant benefit in terms of a reduced need for potable grade water, but the contaminants create increased risks of corrosion and scale. Thus, to ensure clean waterside conditions and optimum operational efficiencies, active modification of the process environment is necessary to control the risks, yet still obtain the benefits of water recycling.

Slightly less than  $5000 \text{ km}^3$  of freshwater is available globally for production of potable quality water and for general commercial and industrial applications<sup>2</sup> ( $1 \text{ km}^3 = 264.2 \times 10^9 \text{ US gallon}$ ). Half the world exists on only  $95 \text{ l day}^{-1}$  (25 US gallon per day) but in developed countries water consumption is much higher, for example consumption in the USA per capita is around  $5.1 \text{ m}^3 \text{ day}^{-1}$  (1350 US gallon per day), of which personal use accounts for  $0.53 \text{ m}^3 \text{ day}^{-1}$  (140 US gallon per day).<sup>3,4</sup> Much of the water consumed is used for agricultural purposes (typically 50–60% or more), especially irrigation, with water for industrial and potable use being significantly lower.



A closer look at, for example, the United States' estimated 408 billion gallons per day ( $1.54 \times 10^9 \text{ m}^3 \text{ day}^{-1}$ ) use of freshwater shows the following breakup<sup>3,4</sup>:

- Agriculture accounts for some 49% of this consumption (200 billion gallons per day), with 160 billion gallons per day being used for irrigation purposes (although water for irrigation in California may be as high as 80%).
- Public supply, delivering water to homes, businesses, and industry is some 11% (45 billion gallons per day).
- Self-supplied industrial users, together with mining, livestock producers, aquaculture, and domestic wells account for 7% (29 billion gallons per day).
- Thermoelectric power generation is the primary user of the balance of surface freshwater consumed, at around 134 billion gallons per day or 33% of the total.<sup>5</sup>

US thermoelectric power generators also use more than 61 billion gallons per day of saline water for once-through cooling. So, total water withdrawal rates for the US thermoelectric power industry are 195–200 billion gallons per day.<sup>5</sup> Most of this is used for cooling water duty, although some water is required for boiler feed, ash handling, and other functions. (Heavy industrial processors also withdraw significant quantities of saline water for once-through use – again primarily for cooling water duty.)

Wet cooling requirements are about  $25 \text{ gal kWh}^{-1}$  of electricity generated, although once-through cooling systems typically require  $37.7 \text{ gal kWh}^{-1}$ , whereas recirculating cooling water processes only require  $1.2 \text{ gal kWh}^{-1}$ .<sup>6</sup> This dramatic saving in water is the primary reason for the extensive and global use of cooling towers for all types of application. Again, however, the savings in water consumption also create a risk, as the contaminants present in the cooling water concentrate as 'pure' water evaporates from the tower and fresh makeup brings additional contaminants with it, which can reach saturation levels and result in scale, fouling and corrosion problems, if left uncontrolled.

Apart from the power industry, it can be seen that the various businesses and industry in the United States collectively use about 45 billion gallons of water per day ( $170.3 \times 10^6 \text{ m}^3 \text{ day}^{-1}$ ). Globally, water consumption for similar activities is perhaps 200 billion gallons per day ( $757 \times 10^6 \text{ m}^3 \text{ day}^{-1}$ ).

Often more than 50% of this total water consumption is for heating and cooling purposes, so there

exists, not only a great opportunity for further reduction, recycling and reuse of water, but the potential for a wide range of scaling, fouling, and corrosion problems to develop! The risk of waterside problems are a constant threat to process operating efficiency and costs, and to the quality of potable water supplies, necessitating a proactive approach to modification and control of water system environments, that is, an active water treatment program.

Eight examples of heating, cooling, and potable equipment using water are shown in [Photos 1\(a\)–1\(h\)](#).

#### 4.27.4 The Need for Water Treatment to Control Waterside Heating, Cooling and Potable Water Environments

Water treatment encompasses a wide range of technologies and activities designed to prevent serious corrosion, failures, and malfunction of equipment using or delivering water, and to ensure the health and safety of operators and other personnel who may come into contact with or use the water.

Water is a universal solvent. Whenever it comes into contact with a foreign substance, there is some dissolution of that substance. Some substances dissolve at faster rates than others, but in all cases a definite interaction occurs between water and whatever it contacts. It is because of this interaction that problems occur in equipment such as boilers or cooling-water systems in which water is used as a heat-transfer medium. In systems open to the atmosphere, corrosion problems are made worse by additional impurities picked up by the water from the atmosphere and can have a devastating effect on equipment such as heat exchangers, cooling towers, valves, pumps, etc.

Corrosion alone is a major cause of failure and costly replacement of equipment and so is itself a good reason why water treatment is necessary. As a result, environmental maintenance, surveillance, and the application of water treating equipment, chemistries and controls are required of almost all water systems, including cooling towers and evaporative condensers, especially in view of the awareness of the risks of infection that may result from systems that are poorly designed, dirty, and/or badly maintained.

The risks of waterborne infection from bacterial organisms such as *Legionella* species are not limited to cooling systems, but can emanate from almost any type of building facility water systems, especially

domestic hot and cold water services. Also, pools, spa baths, showers, and humidifier pans are sources of microbial contamination, as are HVAC systems that are poorly maintained or not cleaned on a regular basis. Microbial growth in HVAC water tanks and pans is distinct from, but may also be linked to

problems developing in air handling systems – which typically involve mold organisms such as *Aspergillus* sp. or *Stachybotrys* sp. (the same organisms that can proliferate behind damp sheetrock walls and insulation).

For water treatment to be effective it is necessary to understand the problems water and its

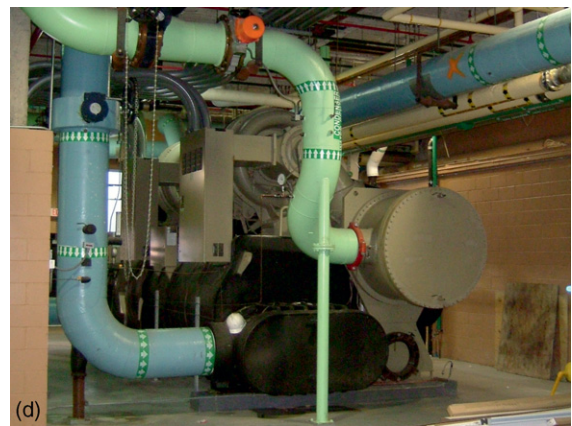
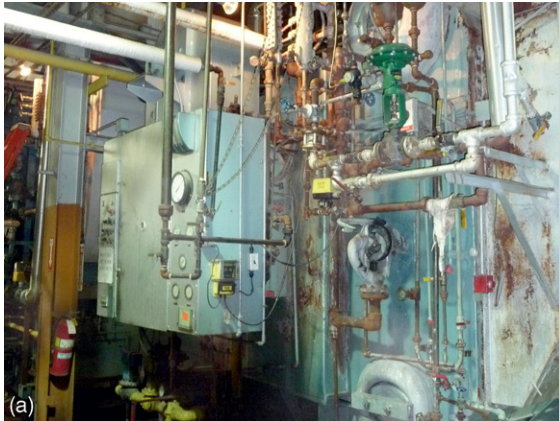


**Photo 1** Continued



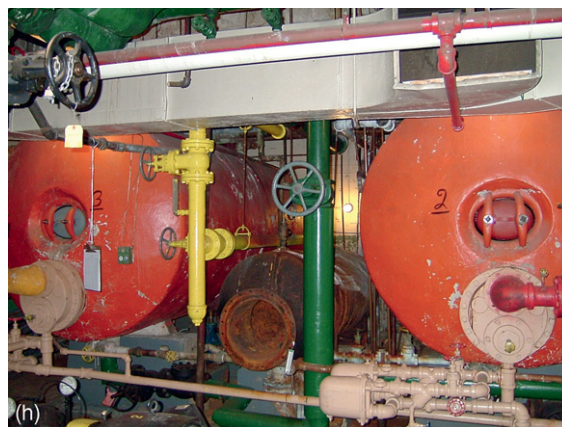


**Photo 1** (a) D-type, 2 drum watertube boiler, (b) firetube boiler, (c) cooling towers, (d) chiller plant, (e) surface condenser, (f) retort cooker; (g) domestic water storage tanks, (h) hotel hot water storage vessels.

contaminants can cause, the mechanisms by which water causes these problems, and the effects that result. A review of the results of analysis of the contaminants in any particular water, plus a thorough understanding of the chain of cause and effect leads to a diagnosis of the potential or actual problems, and from there a solution may be found. The solution may be based on a 'standard' item of equipment, chemistry, or operational protocol or local environmental control, but is usually tailored in some way to meet the specialized and often unique operating conditions that may be found.

Corrosion is a pervasive problem and the direct losses because of corrosion of metals for replacement and protection globally are staggering, and as most costs studies available only look at the direct costs, the true costs are even higher. Indirect costs of corrosion include the costs of labor for repairs and corrosion management, temporary equipment, loss of revenue, and reliability. Annual direct costs because of corrosion in the United States have been reliably estimated at \$276 billion in a study published by NACE International.<sup>6</sup> Examples of these costs include the following:

- drinking water and sewer water systems: \$36 billion per year;
- production and manufacturing industry: \$17.6 billion per year; and
- electrical utilities: \$6.9 billion per year.

Another report, measuring the impact of corrosion in the US Department of Defense (DOD),<sup>7</sup> found that the annual cost of corrosion ranged from \$10 billion to \$20 billion in direct maintenance costs,

with the annual cost of corrosion to Navy ships being \$2.43 billion.

Protection against corrosion may include organic coatings, cathodic and anodic protection, use of more resistant alloys, and water treatment products (such as corrosion inhibitors) and services. Water treatment is usually focused on modifying the waterside environment by rendering the water less scale-forming or corrosive, and by use of inhibitors which act at the metal–water interface to form a passive chemical barrier composed of an oxide, carbonate, silicate, molybdate, hydroxide, phosphate, phosphonate, etc.

The formation of scale and deposits, sludges, and biological foulants are other problems that can increase operating costs, and reduce efficiency and the economical service life of equipment such as HVAC systems. There is no reason to believe that the maintenance and additional energy costs associated with scaling and fouling problems are not at least as high as those associated with corrosion. **Photos 2(a) and 2(b)** show the results of corrosion and deposition in pipes.

Scale formation is insidious and will interfere with the normal efficient transfer of heat energy from one side to the other of a heat exchanger. The degree of interference with this transfer of heat is called the fouling factor. Manufacturers' recommended design fouling-factor for air-conditioning chillers and condensers is usually 0.000 5. In HVAC systems, high fouling factors cause an increase in condensing temperature of the refrigerant gas which, in turn, increases energy requirements to compress the refrigerant at that higher temperature. It can be seen from **Figure 1** that there is a significant increase in condensing temperature with increase in fouling factor.

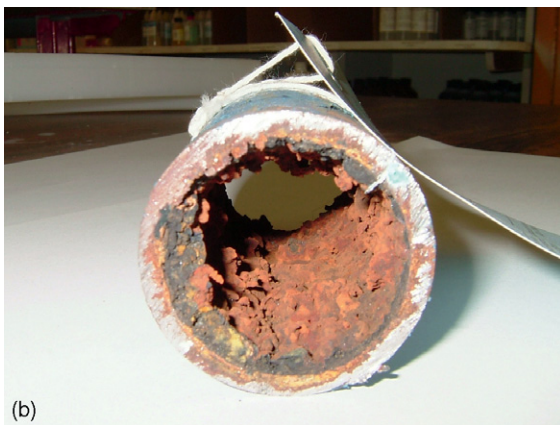


**Photo 2** (a) Pipe metal wastage because of corrosion and (b) pipe deposits due primarily to scaling, but also corrosion.

Where scales or deposits occur in boilers, they are often also associated with under deposit and pitting-types of corrosion, and can consist of various substances including iron, silica, calcium, magnesium, carbonates, sulfate, and phosphates. Each of these, when deposited on a boiler tube, contributes in some degree to the insulation of the tube, which reduces the rate of heat transfer from the hot gases or fire through the boiler metal to the boiling water. This leads to an increase in the temperature of the boiler tube and can result in metal bulges, blisters, and eventually, boiler failure and possibly an explosion.

#### 4.27.5 The Hydrologic Cycle and Water Chemistry

As discussed earlier, water and its contaminants are responsible for the corrosion of metals and formation of deposits on heat-transfer surfaces, which in turn

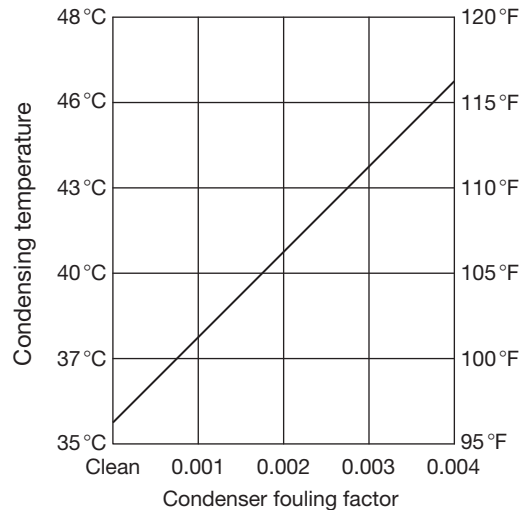


**Figure 1** Effect of scale on condensing temperature.

reduce efficiency, waste energy, and increase costs. The effects of corrosion and deposits have been illustrated in the earlier pictures and in order to see how these problems can be prevented, it is first necessary to understand their basic causes, why and how they occur. This understanding starts with a review of the hydrologic cycle (see [Figure 2](#)).

The hydrologic cycle consists of three stages: evaporation, condensation, and precipitation, and begins when the rays of the sun heat surface waters on the earth, which vaporize and rise into the troposphere, a thin layer of air and moisture approximately 11 km (7 miles) thick surrounding the earth. Clouds of condensed moisture form in the troposphere and contact cold air currents when carried over land by the wind, causing precipitation, such as rain or snow. In this manner, water returns to the earth's surface, only to repeat the cycle. Throughout the hydrologic cycle, the water absorbs impurities.

The concentration of inorganic and organic contaminants, and greenhouse gases in the atmosphere varies depending on geographic location, the sources of pollution (such as basic industrial facilities, fossil-fueled utility power generators, and high density cities and their automobiles), and the weather patterns, including prevailing winds and air currents. Rainwater, containing these contaminants and dissolved gases, is often at a pH of below 7.0 (i.e., slightly acidic) and in contact with the earth surface, it will tend to dissolve and absorb many of the minerals of the earth via reactions including hydrolysis and hydration. The reaction rate with the earth's minerals

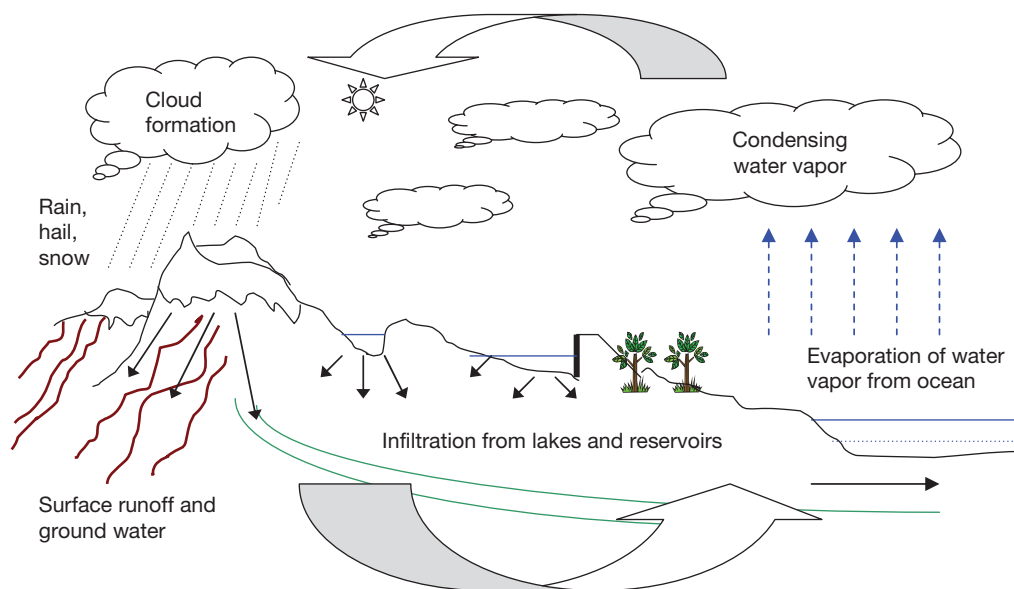


**Figure 2** Hydrologic cycle.

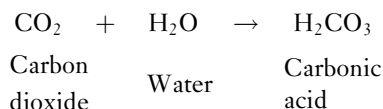
(such as gypsum, calcite, dolomite, and quartz) is increased with more acidic rainfall, and calcium, silica, magnesium, iron, minerals, etc. are dissolved. As a general rule (although there are numerous exceptions):

- Surface water in lakes, rivers, streams, ponds, and reservoirs usually contain fewer minerals but more dissolved gases.
- Underground water supplies are a result of surface waters' percolation through the soil and rock, and usually contain higher concentrations of minerals and less dissolved gases.

While falling through the atmosphere, water dissolves gases such as oxygen, nitrogen, carbon dioxide, nitrogen oxides, sulfur oxides, and other trace elements and polluting chemicals. The quantity of dissolved gases in water is governed by Henry's Law of partial pressures, and the solubility of these gases in water decreases with increasing temperature. Gases found in water include the following:

- *Carbon dioxide.* In the earth's atmosphere carbon dioxide is considered a trace gas, and currently occurs at an average concentration of about  $385 \text{ mg l}^{-1}$  (parts per million) by volume or  $582 \text{ mg l}^{-1}$  by mass.<sup>8</sup> It is present in both surface and underground water supplies as a dissolved gas. Surface waters normally contain less than 10 ppm free carbon dioxide, while some ground waters

may easily exceed that concentration. Carbon dioxide is readily soluble in water forming the weak acid, carbonic acid, as follows:



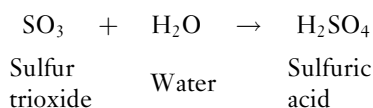
Over the ordinary temperature range ( $0\text{--}30^\circ\text{C}$ ) its solubility is about 200 times that of oxygen. Calcium and magnesium combine with carbon dioxide to form carbonates and bicarbonates. Larger amounts of carbon dioxide are absorbed from the decay of organic matter in the water and its environs. Carbon dioxide contributes significantly to corrosion by making water acidic. This increases its capability to dissolve metals in boiler plant (especially steam condensate systems, and cooling systems). The breakdown of calcium bicarbonate with the release of carbon dioxide under conditions of stress and increase of the concentration of contaminants, because of evaporation processes, are the primary reasons for the increase in cooling water pH during operation.

- *Oxygen.* Oxygen gas (dioxygen  $\text{O}_2$ ) is the second most common component of the Earth's atmosphere taking up 21.0% of its volume and 23.1% of its mass and is essential for life. The allotrope

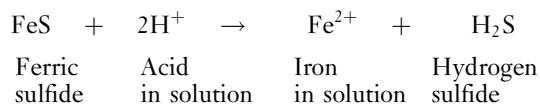


ozone (trioxygen  $O_3$ ) is produced in the upper atmosphere. It is very reactive and near the earth's surface it is a pollutant formed as a by-product of automobile exhaust.<sup>9</sup> However, oxygen is the basic factor in the corrosion process and is, in fact, one of the essential elements in the corrosion process of metals. Therefore, dissolved oxygen in water is important to us in the study of corrosion and deposits. In cold water it is present at  $8\text{--}9\text{ mg l}^{-1}$ .

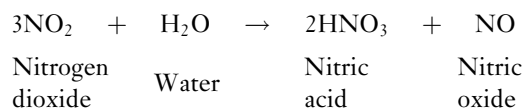
- **Sulfur oxides.** Sulfur oxide gases are present in the atmosphere as pollutants from the combustion of fuels containing sulfur, such as coal and fuel oil. In large urban areas, the quantity of sulfur oxides that are absorbed by surface water supplies and aerated waters used in cooling towers can be significant. Also when dissolved in water, sulfur oxides form acids which create a corrosive atmosphere.



- **Hydrogen sulfide.** The odor typical of rotten eggs, which is found in some water, is because of the presence of hydrogen sulfide. This gas comes from decaying organic matter and from sulfur deposits, and is a constituent of sewer gas, marsh gas, and coal gas. Hydrogen sulfide reacts with water to form hydrosulfuric acid, a slightly acidic solution. It can be present in water but because of its acidic reaction, it is very corrosive and must be removed or neutralized. Hydrogen sulfide forms when acidic water reacts with sulfide minerals such as pyrite (iron sulfide).

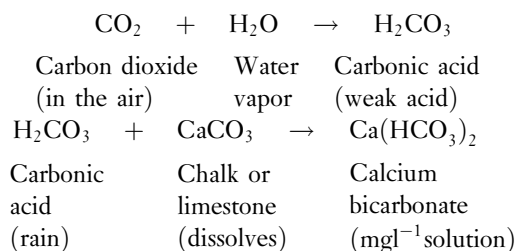


- **Nitrogen oxides.** Nitrogen oxides are also present in the atmosphere, both naturally and from pollutants created by the combustion process. These also form acids when absorbed by water, and contribute to the corrosion process.



When rainwater, containing carbonic acid (resulting from the reaction between dissolved carbon dioxide gas and water), reaches chalk or limestone strata, it will dissolve some of the mineral forming the soluble salt

calcium bicarbonate, as shown in the reaction below. The presence of this salt is of particular importance where water is employed for any type of heat transfer duty, as under heat load conditions it can quickly breakdown and produce scale on the heat-transfer surfaces. Scale inhibits the efficient transfer of heat and also provides an environment for problems of underdeposit corrosion to develop. Thus, modification of the local waterside environment ('water treatment') is required to prevent this common but costly problem.



Apart from the dissolved gases discussed above, contaminants in water will typically include various common dissolved minerals and/or salts. Some of the common minerals that may be dissolved in water include the following:

- silicates, for example, quartz, augite, mica, chert, feldspar, hornblende;
- carbonates, for example, calcite, dolomite, limestone;
- halides, for example, halite, fluorite;
- oxides, for example, hematite, ice, magnetite, bauxite;
- sulfates, for example, anhydrite, gypsum;
- sulfides, for example, galena, pyrite;
- natural elements, for example, copper, sulfur, gold, silver; and
- phosphates, for example, apatite.

Any or all the above may enter into solution as the mineral or a related salt, and are considered contaminants, although some of them may be desirable in potable water (to provide taste and minerals necessary for good health). Some common dissolved minerals and salts found in water include the following:

- calcium bicarbonate:  $Ca(HCO_3)_2$ ;
- calcium chloride:  $CaCl_2$ ;
- calcium sulfate:  $CaSO_4$ ;
- calcium carbonate:  $CaCO_3$ ;
- magnesium bicarbonate:  $Mg(HCO_3)_2$ ;
- magnesium chloride:  $MgCl_2$ ;
- magnesium sulfate:  $MgSO_4$ ;
- sodium bicarbonate:  $NaHCO_3$ ;

- sodium chloride:  $\text{NaCl}$ ;
- sodium phosphate:  $\text{Na}_3\text{PO}_4$ ;
- sodium sulfate:  $\text{Na}_2\text{SO}_4$ ;
- ferrous bicarbonate:  $\text{Fe}(\text{HCO}_3)_2$ ;
- manganous bicarbonate:  $\text{Mn}(\text{HCO}_3)_2$ ;
- silica:  $\text{SiO}_2$ ;
- silicic acid:  $\text{H}_2\text{SiO}_3$ ; and
- sodium silicate:  $\text{Na}_2\text{SiO}_3$ .

The concentration of these species are usually in the milligrams per liter (parts per million) range, and are regularly tested in all waters used in industrial cooling and heating systems. Also, pH and the various forms of alkalinity are tested. For potable use and more critical industrial and process applications, the water will be tested for trace organics present and other low-level contaminants – which may only be present in the microgram per liter (part per billion) range – as well as some of the dissolved gases. **Table 1** is an example of a typical, but basic, water analysis report.

Common tests include the following:

- **Alkalinity.** Alkalinity is the quantity of dissolved alkaline earth minerals expressed as calcium carbonate. It is the measured carbonate and bicarbonate minerals calculated as calcium carbonate, as that is the primary alkaline earth mineral contributing to alkalinity. Alkalinity is also measured and calculated as the hydroxide when that is present. All natural waters contain some quantity of alkalinity. It contributes to scale formation because its presence encourages deposition of calcium carbonate or lime scale. However, the alkalinity content is important in modifying the corrosive behavior of water in both boiler plant and cooling system environments. Thus, titration of the various types of process waters found in heating and cooling systems for alkalinity concentration is regularly carried out by plant operators and water treatment company service providers. Calculation of the various forms of alkalinity can be obtained from using **Table 2**.
- **Phenolphthalein alkalinity** (P alkalinity) is that portion of the alkalinity titrated with acid to pH 8.2 end-point.
- **Total alkalinity** (or M alkalinity) is that portion of the alkalinity titrated with methyl orange to pH 4.2.
- **pH.** In practical terms, pH is the measure of the relative strength of acidity or alkalinity of water, and is a value calculated from the hydrogen-ion concentration in water. The pH scale is based on the negative decimal logarithm of the hydrogen ion activity in an aqueous solution and ranges from 0 to 14. Hence, because of the logarithmic nature

**Table 1** Water analysis report sheet

<b>Water Analysis:</b>		
<i>Location</i>	<i>Industrial water</i>	<i>City water</i>
<i>Date of sampling</i>		
<i>Date of testing</i>		
<b>Parameter</b>		
pH	9.2	7.5
P alkalinity, as $\text{CaCO}_3$ ( $\text{mg l}^{-1}$ )	10	0
Bicarbonates, as $\text{CaCO}_3$ ( $\text{mg l}^{-1}$ )	52	167
Carbonates, as $\text{CaCO}_3$ ( $\text{mg l}^{-1}$ )	20	–
Hydroxides, as $\text{CaCO}_3$ ( $\text{mg l}^{-1}$ )	–	–
M (total) alkalinity, as $\text{CaCO}_3$ ( $\text{mg l}^{-1}$ )	72	167
Total hardness, as $\text{CaCO}_3$ ( $\text{mg l}^{-1}$ )	159	149
Sulfate, as $\text{SO}_4$ ( $\text{mg l}^{-1}$ )	181	
Silica, as $\text{SiO}_2$ ( $\text{mg l}^{-1}$ )	7.7	10
Iron, as Fe ( $\text{mg l}^{-1}$ )	0.3	0.1
Chloride, as NaCl ( $\text{mg l}^{-1}$ )	23	187
Specific conductance ( $\mu\text{S cm}^{-1}$ )	415	815
Total dissolved solids ( $\text{mg l}^{-1}$ )	270	501
Molybdate, as $\text{Na}_2\text{MoO}_4$ ( $\text{mg l}^{-1}$ )	–	–
Phosphate, as $\text{PO}_4$ ( $\text{mg l}^{-1}$ )	1.0	0.1
Sulfite, as $\text{Na}_2\text{SO}_3$	–	–

of the scale, water with a pH value of 4.0 is 100 times more acid in strength than water with a pH value of 6.0. Water is corrosive, if the pH value is on the acidic side. It will tend to be scale-forming, if the pH value is alkaline. A pH of 7.0 is neutral and indicates a balance between acidity and alkalinity.

pH is an important metric and increasing the concentration of dissolved minerals in a boiler water or cooling water, by permitting the release of steam or evaporation, results in a higher pH and less tendency for general corrosion processes to occur, but increases the risks of deposition of supersaturated salts.

By virtue of its logarithmic nature, pH is a dimensionless quantity. pH is defined in terms of the activity of hydrogen ions ( $\text{H}^+$ ) in solution<sup>10</sup>:

$$\text{pH} = -\lg[a(\text{H}^+)] = -\lg[m(\text{H}^+)\gamma_m(\text{H}^+)/m^\ominus]$$

**Table 2** Interpretation of 'P' and 'M' Alkalinity Titrations

Ions	$P = 0$	$P < M/2$	$P = M/2$	$P > M/2$	$P = M$
(OH)	0	0	0	$2P - M$	M
$\text{CO}_3$	0	$2P$	M	$2(M - P)$	0
$\text{HCO}_3$	M	$M - 2P$	0	0	0

Bicarbonates and hydroxides do not exist together.  $\text{CO}_2$  does not exist with carbonates. 'P' Alkalinity =  $\frac{1}{2}$  carbonates and all hydroxides. 'M' Alkalinity = all hydroxides, carbonates and bicarbonates.

where  $a(\text{H}^+)$  is the activity of hydrogen ion ( $\text{H}^+$ ) in aqueous solution;  $\text{H}^+(\text{aq})$ ,  $\gamma_m(\text{H}^+)$  are the activity coefficient of  $\text{H}^+(\text{aq})$  (molality basis) at molality  $m(\text{H}^+)$ ;  $m^\ominus = 1 \text{ mol kg}^{-1}$ , and is the standard molality. Notes:

1. Molality is the number of moles of solute dissolved in 1 kg of solvent.
2. pH cannot be measured independently because calculation of the activity involves the activity coefficient of a single ion. Thus it can be regarded only as a notional definition.
3. The establishment of primary pH standards requires the application of the concept of 'primary method of measurement,' and involves the use of a cell without transference, known as the Harned cell.
  - **Hardness.** Hardness is the total calcium, magnesium, iron, and trace amounts of other metallic elements in water, which contributes to the 'hard' feel of water. Hardness is also calculated as calcium carbonate, because it is the primary component contributing to hardness. Hardness causes lime deposits or scale in equipment.
  - **Temporary hardness or carbonate hardness** can be removed by heating water to precipitate as carbonate salt (e.g., bicarbonates), equal to or less than the P alkalinity.
  - **Permanent hardness or noncarbonate hardness** is that portion of total hardness that cannot be removed by heating water (e.g., sulfate hardness), and is the difference between total hardness and total alkalinity.
  - **Iron, manganese, and alumina.** These dissolved or suspended metallic elements are present in water supplies in varying quantities. They are objectionable because they contribute to a flat metallic taste and form deposits. These soluble metals can react with oxygen in water exposed to the atmosphere, and form oxides which precipitate and

cause cloudiness, or 'red water.' This red color, particularly from iron, causes staining of plumbing fixtures, sinks, and porcelain china and is a cause of common laundry discoloration.

- **Silica.** Silica is dissolved when water flows through sand or silica-bearing rock (such as quartz). Silica is the cause of very hard and tenacious scales that can form and cause severe heat-transfer problems. It is present, either dissolved in water as silicate or suspended in a very fine, invisible form, as colloidal silica.
- **Chlorides.** Chlorides are the sum total of the dissolved chloride salts of sodium, potassium, calcium, and magnesium present in water. Sodium chloride, which is common salt, and calcium chloride are the most common of the chloride minerals found in water. Chloride is a depassivating ion. It reduces the corrosion resistance of many metals, especially those that naturally and strongly passivate to form a protective oxide layer, such as stainless steels and aluminum, by attacking the passivated film.<sup>11</sup>

High chloride waters will increase the risk of stress corrosion cracking in austenitic stainless steels (e.g., 304/304L, 316/316L) and will tend to increase both the general rate of corrosion and attack in localized areas, often causing pitting type corrosion. Corrosion from chlorides always tends to be more severe when the metal surface is shielded by foulants or semiporous deposits, such as silt and muds, as various forms of selective corrosion can take place with often very high concentrations of chloride forming under the deposit. The most logical environmental modification response, therefore, to using a makeup water source with high chlorides is to be scrupulous in maintaining clean metal surfaces in the cooling system. This can take the form of more frequent physical cleaning and the use of side-stream filters, polymer dispersants, and biodispersants. Raising the level of chemical inhibitor treatment is a further and usually beneficial response, although this may require a reevaluation of the cooling system economics.

- **Sulfates.** Sulfates are the dissolved sulfate salts of sodium, potassium, calcium, and magnesium in the water. They are present because of dissolution of sulfate-bearing rock such as gypsum. Calcium and magnesium sulfate scale is very hard and difficult to remove and greatly interferes with heat transfer.

Sulfates are causative agents (along with oxygen, hydrogen, etc.) of the various types of concentration cell corrosion that results in pits, crevice attack, or tuberculation. They have reactions similar to chloride. In addition, and again similarly to chlorides, the presence of sulfate ions contributes strongly to increases in electrical conductivity and hence influences potential increases in corrosion rates. Sulfates are also involved in depassivation, especially where deposits or foulants are involved and can be reduced by selective microbial action (sulfate reducing organisms), that are almost always present in biofilms, producing deep pits of corroded steel.<sup>11</sup>

- *Total dissolved solids.* The total dissolved solids (TDSs) reported in water analyses are the sum of dissolved minerals including the carbonates, chlorides, sulfates, and all others that are present. The dissolved solids contribute to both scale formation and corrosion in heat-transfer equipment.
- *Suspended matter.* Suspended matter is finely divided organic and inorganic substances found in water. It is caused by clay silt and microscopic organisms, which are dispersed throughout the water, giving it a cloudy appearance. The measure of suspended matter is turbidity. Turbidity is determined by the intensity of light scattered by the suspended matter in the water.

#### 4.27.6 Waterside Problems Resulting from Mineral Scales, Muds, and Sludges

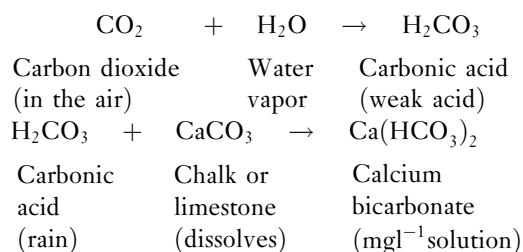
Calcium carbonate scale is the most common and costly water-caused scaling problem encountered in industrial boilers, cooling systems, condensers, and HVAC equipments. Other scale components include calcium sulfate, phosphate, magnesium carbonate, iron, silica, and manganese. In most cases, scales contain a complex mixture of mineral salts because scale forms gradually and deposits the different minerals in a variety of forms.

Depending upon the specific boiler plant/cooling system/HVAC/potable waterside environment, mineral scales can develop on heat transfer surfaces in crystalline form (which is usually hard and tenacious) or in noncrystalline or amorphous form, which often is sludge-like and removable by high-pressure water jetting or similar cleaning process. Often, problems of scaling and deposits are accompanied by problems

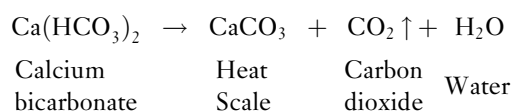
of corrosion as well. Corrosion can take place under scales and may be due, in part, to similar causes, such as a failure to pre-clean a water system, inadequate chemical treatment, or ongoing maintenance.

Many salts such as sodium chloride (table salt) are more soluble in hot water than in cold; however, calcium and magnesium salts have an inverse solubility and dissolve more readily and in greater quantity in cold water than in hot water. This property, as discussed earlier, is primarily responsible for the problem of mineral scale formation on heat-transfer surfaces in HVAC equipments. The high energy and maintenance costs that can result stems from the significant interference with heat transfer caused by water mineral scale deposits, corrosion, and the problems associated with the removal of scale deposits (usually requiring some form of acid cleaning).

As shown earlier, typically, calcium carbonate enters solution through the following reactions:



However, with the application of heat, the reaction reverses and because of the low solubility of calcium carbonate, carbonate scale develops as follows:



A list of some commonly found mineral components of deposits and foulants is given in [Table 3](#).

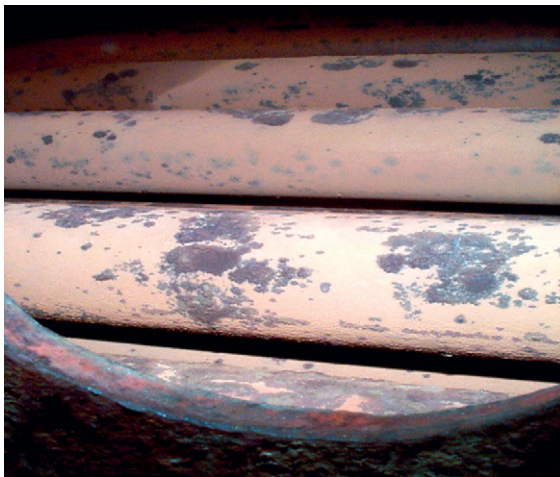
##### 4.27.6.1 Problems from Mineral Scales, Muds, and Sludges in Boilers

Scale in boilers is a direct result of precipitation of the calcium, magnesium, iron, and silica minerals present in the boiler feedwater and can be prevented by removing a portion or all of the scale-forming ingredients in the boiler water makeup supply with external water-softening equipment such as ion-exchange or lime/lime-soda softening. An example of scaled boiler tubes is shown in [Photo 3](#).

Modification of the waterside environment will also require additional ‘polishing’ chemical treatments (internal boiler water treatment), usually on the basis

**Table 3** Commonly found mineral components of deposits and foulants

<i>Salt/oxide</i>	<i>Mineral</i>	<i>Formula</i>
Calcium carbonate	Aragonite	$\text{CaCO}_3$
	Calcite	$\text{CaCO}_3$
Calcium phosphate	Hydroxyapatite	$\text{Ca}_{10}(\text{OH})_2(\text{PO}_4)_6$
	Tricalcium phosphate	$\text{Ca}_3(\text{PO}_4)_2$
Calcium sulfate	Anhydrite	$\text{CaSO}_4$
	Gypsum	$\text{CaSO}_4 \cdot 2\text{H}_2\text{O}$
	Hemihydrate	$\text{CaSO}_4 \cdot \frac{1}{2}\text{H}_2\text{O}$
Copper oxide	Cuprite	$\text{Cu}_2\text{O}$
Iron carbonate	Siderite	$\text{FeCO}_3$
Iron oxide	Haematite	$\text{Fe}_2\text{O}_3$
	$\alpha$ -Iron oxide (paramagnetic)	$\alpha\text{-Fe}_2\text{O}_3$
	$\gamma$ -Iron oxide (ferromagnetic)	$\gamma\text{-Fe}_2\text{O}_3$
	Lepidocrocite	$\text{Fe}_2\text{O}_3 \cdot \text{H}_2\text{O}$
	Magnetite	$\text{Fe}_3\text{O}_4 \cdot \text{H}_2\text{O}$
Iron sulfide	Troilite	$\text{FeS}$
Magnesium hydroxide	Brucite	$\text{Mg}(\text{OH})_2$
Magnesium phosphate	Magnesium hydroxyphosphate	$3\text{Mg}_3(\text{PO}_4)_2 \cdot \text{Mg}(\text{OH})_2$
Magnesium silicate	Serpentine	$3\text{MgO} \cdot 2\text{SiO}_2 \cdot 2\text{H}_2\text{O}$
Silica	Crystoballite	$\text{SiO}_2$
Zinc carbonate	White rust	$\text{ZnCO}_3$

**Photo 3** Scale on boiler tubes.

of phosphates, chelants, and/or organic polymers. Iron and combinations of iron with calcium and phosphate can form sticky, adherent sludge deposits in boilers and is caused by iron in the form of iron oxide or iron carbonate corrosion products, entering the boiler with the feedwater. It is a result of corrosion products from the sections prior to the boiler, such as steam and condensate lines, condensate receivers, deaerators, and boiler feedwater lines. Modification of the water-side environment may include the use of amine-based corrosion inhibitors added to the steam or condensate,

which generally also neutralize carbonic acid in the condensate and raise the condensate pH.

Foulants in steam boilers usually consist of foreign contaminants present in the feedwater, including muds, oils, contaminants from a process, iron corrosion products from the steam system, and construction debris in new boiler systems. Mud or sludge in a boiler is usually a result of scale-forming minerals combining with iron oxide corrosion products and treatment chemicals, and are commonly controlled by using modern polymeric dispersants, which prevent adherence on heat-transfer surfaces.

In heating boilers, the most frequent foulants (other than sludge) are oil and clay. Oil can enter a boiler system through leakage at lubricators, fuel oil preheaters, or steam heating coils in fuel oil storage tanks. When oil enters a boiler it causes priming and foaming by emulsifying with the alkaline boiler water. Priming is the severe bouncing of the water level that eventually cuts the boiler off at low-water because of the wide fluctuation of this water level sensor. Oil can also carbonize on hot boiler tubes, causing not only serious corrosion from concentration corrosion cells but also tube ruptures as a result of overheating because of insulating carbon deposits and a departure from nucleate boiling (DNB). Whenever oil enters a boiler system, it must be removed immediately to prevent these problems. Modification of the boiler water system environment is usually done by blowing down the boiler heavily



and often by additionally ‘boiling out’ with an alkaline detergent cleaner.

Clay is a less frequent foulant in heating boilers, but it can also form insulating deposits on tube surfaces. Clay enters a boiler with the boiler makeup water that is either turbid or contaminated with excessive alum, used as a coagulant in the clarification process, and has not been subject to filtration or any other makeup water pretreatment process. It can get dispersed during the use of chemical dispersants in the internal treatment of the boiler, but makeup water should be clear and free of any turbidity before it is used as boiler feedwater. Where turbidity and clay are a constant problem, modification of the boiler feedwater by filtration is required (An example is multimedia filtration).

#### 4.27.6.2 Problems due to Mineral Scales, Muds, and Sludges in Cooling Systems

Scale deposits in recirculating cooling tower condenser water systems for HVAC air conditioning and refrigeration chillers are typically a direct result of precipitation of calcium carbonate, calcium sulfite, or silica minerals, because of an overconcentration of these minerals in water. The solubility or pH of saturation is exceeded and the minerals come out of solution. What a heat transfer equipment operator might commonly refer to as ‘scale’ can also include various corrosion products and foulants such as organic matter and mud or dirt.

**Photo 4** shows an example of scaled and corroded condenser tubes.

Modification of the water circuit to prevent mineral scale should, therefore, include the following:

1. Sufficient dilution of the recirculating water to prevent the concentration of minerals from approaching the saturation point.
2. pH control to prevent the pH from reaching the pH of saturation of calcium carbonate.
3. Chemical treatments to inhibit and control scale crystal formation.

In addition to mineral scale, other recurrent problems in recirculating water systems include mud, dirt, debris, foreign matter, and organic growth – especially algae (in warm and sunny weather) and planktonic and sessile bacteria. Deposits of foreign matter plug narrow passages and interfere and foul heat-transfer surfaces, causing inefficient performance of the equipment and energy consumption higher than desirable.



**Photo 4** Scaled and corroded condenser tubes.

A cooling tower is a natural air washer with water spraying over slats and tower fill, and washing the air blown through either naturally or assisted by fans. Depending on the location, all sorts of airborne dust and debris end up in cooling tower recirculating water systems. These vary from fine dust particles to pollen, weeds, plant life, leaves, tree branches, grass, soil, and stones. The fine particles of dust and dirt tend to collect and form a compacted layer in the condenser water system, especially in areas of low circulation and at heat-transfer surfaces. Minimizing these problems again requires modification of the specific waterside environment. It may call for a side-stream filter, screens to limit air-blown dust (say near a construction site), or the regular use of polymeric dispersing chemicals, antiscalents, biocides, and biodispersants.

#### 4.27.6.3 Problems due to Mineral Scales, Muds, and Sludges in Closed-Loop Water Systems

Closed-loop systems contain a finite volume of water and evaporative processes do not take place, although minor water losses because of leaks will occur. Closed-loop systems will include engines under circumstances where they are employed in emergency/backup electricity generating systems and similar applications (e.g., standby diesel generators for hospitals, commerce, and general industry, and diesel engine utility power generators). Some closed-loop systems are not in fact ‘closed’ and may have, for example, a returned water receiver that channels a number of individual cooling water lines to a single point before being pumped across a heat-exchanger and around another loop.

As a general rule, all closed and semi-closed loop systems tend to suffer to some extent or other from iron and steel corrosion problems because of the prolific use of mixed metals, poor passivation, and limited maintenance. Therefore, one of the most common and difficult foulants found in closed systems is a black mud made up of compacted, fine, black magnetic iron oxide particles, which deposit at heat-transfer surfaces, and clog or block narrow passages in unit heaters, fan coil units, and cooling, reheat, and heating coils in air-handling units. This mud is a result of very fine wet particles of black magnetic iron oxide compacted into a dense adherent mud.

The interior of black iron piping, commonly used for recirculating water, has a natural black iron oxide protective coating ordinarily held intact by oil-based inhibitors used to coat the pipe to prevent corrosion during storage and lay-up. This natural iron oxide protective coating is called mill scale, a very general term which can be applied to any form of pipe scale or filings washed off the interior of the pipe. This mill scale film becomes disturbed and disrupted during construction because of the constant rough handling, cutting, threading, and necessary battering of the pipe. After construction, the recirculating water system is filled and flushed with water, which removes most of the loosened mill scale along with other construction debris. However, very fine particles of magnetic iron oxide will continue to be washed off the metal surface during operation, and in many instances this washing persists for several years before it subsides. Mill scale plugging can be a serious problem. It is best alleviated in a new system by thorough cleaning and flushing with a strong, low-foaming detergent-dispersant cleaner. This, however, does not always solve the problem. Even after a good cleanout, gradual removal of mill scale during ensuing operation can continue.

#### **4.27.6.4 Problems due to Waterside-Surfaces Fouling in 'New Construction' HVAC Systems**

All new HVAC systems can become fouled and contaminated with various forms of foreign matter during construction. It is not uncommon to find remnants of welding rods, beads, paper bags, plastic wrappings, soft drink can rings, pieces of tape, insulation wrappings, glass, etc. in the interior of HVAC piping and heat exchangers. Also, cement, mortar, metal filings, pieces of pipe, and other construction debris may be present. Oil and mill scale is usually

found and can seriously foul and plug closed systems, and cause boiler tube failures if the oil is carbonized during firing. It should be noted that commonly found black iron pipe 'scale' is not, in fact, a mineral scale, but rather the oxides of iron (rust) produced during manufacture and storage. It is also called mill scale and can be slightly protective to the pipe against contaminants in water, but is not sufficiently nonporous for good protection.

It is necessary not only to clean out construction debris from the interior of new construction HVAC systems prior to initial operation, but also to modify the waterside environment by cleaning the metal surfaces of oil and mill scale naturally present on the pipe interior, then passivate the metal surface, and follow up with an initial feed of inhibitor chemicals. Cooling water systems and boiler must be cleaned thoroughly with an alkaline detergent-dispersant type of cleaner. Where the boiler is a steam raising plant, an alkaline boilout compound is used. All this takes place before implementing a maintenance chemical treatment and technical service overseeing program.

#### **4.27.6.5 Problems due to Mineral Scales, Muds, and Sludges in Potable Water Lines**

Water containing unusual turbidity or suspended matter is usually treated at the source by coagulation, clarification, and filtration so as to improve its quality. Turbidity is the cloudiness or haziness of a fluid caused by individual particles (suspended solids) that are generally invisible to the naked eye, similar to smoke in air. The measurement of turbidity is a key test of water quality. However some minor level of turbidity may still be present that will be acceptable if it does not affect potability. Therefore, the presence of excess levels of suspended matter and turbidity is not common in makeup waters to HVAC systems as the makeup water usually comes from a municipal or local source, over which there is an authority responsible for delivery of clear, potable quality water.

Where private well water and pond, or other non-public sources of water are available for use as makeup water to cooling water systems and boilers, it should be carefully examined for turbidity and suspended matter. Governments around the world have set standards for the allowable turbidity in drinking water. In the United States, the allowable standard is 0.3 NTU, with many utilities striving to achieve levels as low as 0.1 NTU.<sup>12</sup> When the supply is excessively turbid, modification by some form of

clarification should be used to remove the suspended matter and reduce the turbidity to below 1 NTU. Modification examples include coagulation, settling, filtration, and/or fine strainers.

The more common problem with suspended matter and turbidity results from makeup water that is temporarily or occasionally dirty, which may occur when the local water authority is cleaning sections of a distribution main, installing new mains, or when water mains are cut into during some nearby construction project. These deposits consist mostly of iron oxide corrosion products and dirt, clay, or silt.

#### 4.27.7 Problems of Corrosion including Microbial Induced Corrosion

Corrosion occurs very rapidly in heat-transfer equipment because of the presence of heat, corrosive gases and dissolved minerals in water, which stimulate the corrosion process. Corrosion mechanisms can be concentrated locally to form a pit or crack, or under local environmental conditions, extend across a wide area to produce general deterioration. The local corrosive conditions may be caused by use of dissimilar metals, excess of oxygen, short- or long-term stress (such as that at points of welds, bends, and elbows), and excessive or prolonged heat, or thermal shock.

Although specific corrosion problems, such as the various types of differential aeration mechanisms, hydrogen embrittlement, and flow assisted/accelerated corrosion (FAC) – especially in high-pressure utility boilers and heat recovery steam generator (HRSG) plants – can take place the most common forms of corrosion found in heat-transfer equipment include the following:

- uniform or general corrosion;
- oxygen pitting corrosion;
- galvanic corrosion;
- concentration cell or crevice corrosion;
- stress corrosion;
- erosion corrosion or impingement corrosion;
- condensate line corrosion or grooving corrosion;
- microbiologically influenced corrosion (MIC); and
- white rust.

In water systems, modification of a waterside environment to minimize corrosion will involve direct or indirect passivation of a metal surface, a change in pH, and use of oxygen scavengers (in boiler plants), and usually require small concentrations of corrosion inhibitors (especially in cooling systems).

#### 4.27.7.1 Uniform or General Corrosion

General corrosion is found in various forms in HVAC and other heat-transfer equipment and can be seen as an overall deterioration of the metal surface, with an accumulation of rust and corrosion products in the piping and water boxes. For example, it might be present as a surface gouging or a uniform thinning of the tube metal on copper condenser tubes, or in boilers, as the total overall disintegration of a boiler tube metal surface in contact with boiler water.

This type of corrosion occurs when the process takes place over the entire surface of the metal, resulting in a uniform loss of metal rather than a localized type of attack. Iron and other metals are corroded by electrochemical reaction resulting in the metal going into solution in the water. The waterside environment will usually have some level of oxygen present, plus possibly dissimilar metals or areas of stress, together with dirt, and/or an accumulation of corrosion products over the surface of the metal. It is necessary, therefore, to limit corrosion of these metals by cleaning the system, passivating the metal surface, and by reducing the activity of both hydroxyl ions and hydrogen ions, that is, by developing a corrosion-free environment through the use of corrosion inhibitors.

#### 4.27.7.2 Oxygen Pitting Corrosion

An important factor in corrosion processes is dissolved oxygen, and it may manifest itself in various forms of differential aeration corrosion and under-deposit corrosion processes, producing tubercles or other accumulations of rust and corrosion products. Specifically, oxygen pitting is characterized by deep penetration of the metal at a small area on the surface with no apparent attack over the entire surface, as in general corrosion. The corrosion takes place at a particular location on the surface and corrosion products frequently accumulate over the pit. These appear as a blister, tubercle, or carbuncle.

Localized pitting corrosion is a common problem and may result from a variety of contributory causes, such as deposits of foreign matter. However oxygen pitting corrosion differs somewhat from other forms of pitting corrosion in that it is caused solely by the presence of dissolved oxygen, which reacts with a metal, eventually forming the insoluble oxide and builds up a voluminous deposit of rust in the case of iron and steel.

**Photo 5** shows an example of oxygen pitting corrosion in a sectioned length of boiler pipe.



**Photo 5** Oxygen pitting corrosion.

In boilers, oxygen pitting occurs where the feedwater contains dissolved oxygen. The pitting is found on boiler tubes adjacent to the feedwater entrance, throughout the boiler, or in the boiler feedwater line itself. Modification of the feedwater often entails mechanical deaeration through the use of a vacuum or pressure deaerator. However, oxygen pitting can still develop in boiler feedwater lines following a deaerator, as low concentration of dissolved oxygen can be more corrosive in feedwater than higher dissolved oxygen content! Mechanical deaerators are not 100% efficient and none can produce a feedwater with zero oxygen. The lowest guaranteed dissolved oxygen content that deaerators produce is  $0.005 \text{ cm}^3 \text{ l}^{-1}$ . This trace quantity of dissolved oxygen is sufficient to cause severe pitting in feedwater lines or in boiler tubes adjacent to the feedwater entrance. In this situation, oxygen pitting is characterized by deep holes scattered over the surface of the pipe interior with little or no accumulation of corrosion products or rust, as there is insufficient oxygen in the environment to form the ferric oxide rust.

However, in utility peaking boilers or in cyclic operations, it may, in fact, be necessary to modify the waterside environment by adding a constant trace amount of oxygen (oxygenation treatment, OT) in order to maximize the maintenance of a protective magnetite film on the metal surface at the metal/water interface, and minimize the development of excessive quantities of corrosion product debris ('crud').

#### 4.27.7.3 Galvanic Corrosion

Galvanic corrosion (dissimilar-metal corrosion) is an electrochemical process in which one metal corrodes preferentially, when in electrical contact with a

different type of metal, and both metals are immersed in an electrolyte such as water. Typically in an industrial process water system or HVAC system, different metals of construction will be used, and more often than not they are not dielectrically insulated from each other, but are connected via a flange, valve, union, or brazed joint. Thus, when the two or more different types of metal come into contact with one another (as in the coupling of steel and copper in a heat-exchanger), a galvanic couple is set up, as the different metals have different electrode potentials. The electrode potential is the tendency of a metal to give up electrons and go into solution.

The system water electrolyte provides a means for ion migration, whereby metallic ions can move from the anode to the cathode. This leads to the anodic metal corroding more quickly than it otherwise would; the corrosion of the cathodic metal is retarded even to the point of stopping. The presence of electrolyte and a conducting path between the metals may cause corrosion, where otherwise neither metal alone would have corroded. Also, a single type of metal may corrode galvanically if the electrolyte varies in composition, forming a concentration cell.

The rate of galvanic corrosion is strongly influenced by the electrode potential difference between the dissimilar metals. The galvanic series is a list of metals in order of their activity, the most active being at the top of the list and the least active at the bottom. The further apart two metals are on this list, the greater will be the reactivity between them and, therefore, the faster the anodic end will corrode.

Methods for the modification of the waterside environment to control the rate of active galvanic corrosion include the following:

1. Eliminating the contact of dissimilar metals in an HVAC system by using insulating couplings or joints such as a dielectric insulator coupling, which interferes with the electron flow from one metal to the other.
2. Eliminating one or more of the essential elements required for galvanic corrosion to occur. This might require, for example, modifying the HVAC system design by changing one of the metallic materials of construction, such as zinc or copper.
3. The use of protective coatings and chemical corrosion inhibitors, which all provide a physical or chemicochemical barrier between the corroding metal and its environment.



#### 4.27.7.4 Concentration Cell Corrosion or Crevice Corrosion

Concentration cell corrosion, like pitting corrosion, is a localized type of differential aeration corrosion rather than a uniform attack. It is a form of under-deposit corrosion or crevice corrosion, as it occurs under deposits or at crevices of a metal joint. Differential aeration cells can be caused by crevices, lap joints, deposits of foreign matter, dirt, organic matter, corrosion products, scale, construction debris, and moist insulation. Oxygen not only enables a corrosion reaction by maintaining a cathodic reaction, but it can promote one where there is a difference in the concentration of dissolved oxygen between two points of the same metal surface.

If the supply of oxygen is not uniform across a surface, then any regions that are depleted in oxygen will become anodic, for example within a crevice, at a joint or beneath a surface deposit. The remainder of the surface with free access to oxygen acts as a large cathodic area. Thus, where there is a difference in the concentration of dissolved oxygen at two points on a metal surface, the surfaces in contact with the solution containing the higher concentration of dissolved oxygen will become cathodic to surfaces in contact with a lower concentration of dissolved oxygen. Because the cathodic area is so much larger, severe local attack will occur in the small anodic region.

Additionally, where contaminants (such as chlorides or sulfates) are present in the water, these can concentrate under the deposit or in the crevice and rapidly increase the rate of corrosion – leading to gouging corrosion or pitting corrosion, where the anode will again suffer accelerated corrosion in the (oxygen) concentration cell. Thus, the rate of supply of oxygen or ion concentration will govern the rate and mechanism of rusting. With concentration cell corrosion, the corrosion reaction proceeds as in galvanic corrosion, as this differential also forms an electrode potential difference. Maintaining clean surfaces, in conjunction with chemical inhibitors can best prevent this form of corrosion.

In closed-loop systems where the water is, in fact, not closed but in contact with air (as in many plastic extrusion component manufacturing facilities, where various cooling water streams flow to a common receiving tank) concentration cells can develop and severe crevice corrosion can occur. Limiting contact with oxygen in the air by use of a physical barrier, such as a floating plastic sheet, is an

option, but system modification will still require the addition of anodic or cathodic inhibitors to the water.

#### 4.27.7.5 Stress Corrosion

Stress corrosion failure is a result of a corrosive environment and stresses and strains at the very point of failure. It is because of the combination of exposure of a metal to a corrosive environment and the application of stress on the metal, such as in stress-corrosion-cracking mechanisms involving various grades of stainless steel, where the alloy comes into contact with a corrosive, high-chloride concentration environment. It can also occur on condenser tubes and heat-exchanger tubes, from heat expansion that causes stresses in the metal at tube supports or tube sheets.

Stress corrosion is frequently seen on condenser tubes and boiler tubes in the area where the tubes are rolled into the tube sheets. In steam boilers, stress corrosion has been referred to as ‘necking and grooving.’ It is also seen as a circumferential groove around the outside of a firetube in a firetube boiler, where it enters the tube sheet. Usually it occurs at the hottest end of the tube, (i.e., at the beginning of the first pass against the firewall). Stress corrosion concentrates at the tube end because of strains from two sources. First, when tubes are rolled in, stresses are placed on the metal, expanding the metal to fit the tube sheet (and the stresses may be unrelieved). Second, when a boiler is fired, the heat causes rapid expansion of the tube, and consequently strains are greatest at the tube ends, which are fixed in the tube sheets. This actually causes a flexing and bowing of the tube, and sometimes the expansion is so severe that the tubes loosen in the sheets. During this bending of the tube, the natural protective iron oxide film formed at the tube ends tends to tear or flake off, exposing fresh steel to further attack. Eventually, the tube fails because of a combination of both corrosion and stress.

Reducing the risk of stress-corrosion in stainless steel alloys (and other types of alloy) starts with improved product selection and design. Also, it requires the removal or modification of the corrosive waterside environment – often through regular cleaning practices and the use of inhibitors. The problem of stress corrosion in boilers is reduced by more gradual firing practices, and by using proper inhibitors to correct the corrosive environment.



#### 4.27.7.6 Erosion Corrosion or Impingement Corrosion

Erosion corrosion or impingement corrosion is the gradual wearing away of a metal surface by a combination of both corrosion and abrasion from an impinging water stream, such that the higher the velocity of the impinging stream, the greater the rate of erosion corrosion. Water moving rapidly through piping can contain entrained air bubbles and suspended matter, sand, or other hard particulates. These abrasive particles remove natural protective oxide films present on the surface of the metal and cause general corrosion of the exposed metal.

Unfortunately, this is not uncommon in cooling tower waters where such particles are extracted from the atmosphere so that in environments where high levels of particulates can enter the system (e.g., close to a construction site or in an open area where high winds are prevalent), modification of the water treatment program usually calls for the installation of a side-stream or fill-stream filter, plus perhaps a dispersant chemical.

A special kind of erosion corrosion that has become very prevalent in recent times, with the increased use of cogeneration and combined cycle power plants that utilize heat recovery steam generators (HSRG), is flow assisted or flow accelerated corrosion (FAC). FAC is a term originating with The Electric Power Research Institute (EPRI) for a condition that the industry has previously labeled with the more generic term erosion corrosion. EPRI defines FAC as “a process whereby the normally protective oxide layer on carbon or low-alloy steel dissolves into a stream of flowing water or a water–steam mixture.” It can occur in single phase and in two phase regions. EPRI has stated that the cause of FAC is water chemistry.<sup>13</sup>

Several variables contribute to this phenomenon including but not limited to velocity, pH, directional changes and geometry, temperature, chemistry, oxygen concentration, oxygen scavenger (reducing environment), and material composition. Two phase FAC can be differentiated from cavitation erosion by the evidence of ‘tiger stripes’ or ‘chevrons.’

*Note:* Cavitation erosion (CE) occurs downstream of a directional change, or in the presence of an eddy. Evidence can be seen by the presence of round pits and is often misdiagnosed as FAC. Like erosion, CE involves fluids accelerating over the surface of a material; however, unlike erosion, the actual fluid is not doing the damage. Rather, cavitation results from

small bubbles in a liquid striking a surface. Such bubbles form when the pressure of a fluid drops below the vapor pressure, the pressure at which a liquid becomes a gas. When these bubbles strike the surface, they collapse, or implode. Although a single bubble imploding does not carry much force, over time, the small damage caused by each bubble accumulates. The repeated impact of these implosions results in the formation of pits. Also, like erosion, the presence of chemical corrosion enhances the damage and rate of material removal. Cavitation is not a property of the material, but a property of the system itself. The fluid pressure is determined by the size and shape of the vessel, not the material. While a stronger material can be highly resistant to cavitation, no metal is immune.<sup>14</sup>

#### 4.27.7.7 Condensate Line Corrosion or Grooving Corrosion

Condensate corrosion or grooving corrosion is a particular, but very common, corrosion phenomenon of steam condensate lines in HVAC and industrial process equipment. The primary cause of condensate grooving is carbon dioxide. The dissolved carbon dioxide is a breakdown product of calcium bicarbonate in boiler feedwater – originating from the makeup water component of feedwater. The CO<sub>2</sub> gas is volatile and carries over with the generated steam in the boiler, then dissolves in the hot condensate, forming carbonic acid. Typically the pH of condensate may fall to perhaps as low as 5.5 or 6.0.

Condensate corrosion is found in steam condensate piping on all types of equipment, heat exchangers, steam-turbine condensers, unit heaters, steam absorption condensers, radiators, or any type of unit utilizing steam as a heat-transfer medium. It is a direct chemical attack by acidic steam condensate on the metal over which it flows, and is identified by the typical grooves found at the bottom of the pipe carrying the condensate.

The methods available to prevent this type of corrosion include removal of bicarbonate and carbonate alkalinity from the boiler makeup water (dealkalization) and use of carbonic acid neutralizers and filming inhibitors.

Usually, these inhibitors are amine-based. Food industries tend not to use amine-based corrosion inhibitors, for fear of odors or taints they may impart to the food in question; therefore, they may use sorbates and other inhibitors of similar chemistry — which, although ‘safe’ are not particularly effective,

despite claims to the contrary. Often, the food company will prefer to suffer the consequences of condensate line corrosion rather than spent capital on a dealkalization plant or use amine inhibitors, some of which are permitted in the United States for the food manufacturing industry at certain maximum concentrations, under Code of Federal Regulations (CFR), §21, section 173.310.

#### 4.27.7.8 Microbiologically Influenced/ Induced Corrosion or Biocorrosion

The term ‘microbiologically influenced corrosion’ covers a wide range of corrosion processes that are initiated or promoted by microorganisms – usually chemoautotrophic bacteria (i.e., bacteria that obtain energy by the oxidation of electron-donating molecules in their environments). MIC is a very serious problem in all types of industry, affecting, for example, buried water, gas, and oil pipelines, as well as petroleum products and fuel storage tanks. Attack can take place on both the external and internal metal surfaces, with the microorganism living in the water phase (i.e., microorganisms in the water table can cause MIC on external metal pipeline/tank surfaces, and microorganisms in tank ‘bottoms’ can cause MIC of internal metal pipeline/tank surfaces, as well as damage the stored fuel or other product). Similarly MIC can affect industrial heating and cooling systems, potable water lines, and building HVAC systems. **Photo 6** shows an example of MIC on a section of pipe.

There are many forms and mechanisms of MIC involving many types of microbiological organisms, both aerobic and anaerobic. MIC in water systems can be initiated by various major groups of organisms, and their biomass products (biofilm) such as the following:

- *Iron related bacteria (IRB)*. IRBs include *Gallionella ferrugine* (which oxidizes ferrous ions to ferric ions and manganous ions to manganic ions) and *Ferrobacillus* sp.
- *Sulfate reducing bacteria (SRB)*. The genera *Desulfovibrio*, *Desulfomaculum* and *Desulfomonas* are both anaerobic microorganisms and reduce  $\text{SO}_4^{2-}$  to  $\text{S}^{2-}$  and  $\text{H}_2\text{S}$ .
- *Acid producing bacteria (APB)*. These are mainly slime-forming microorganisms, and include *Acidithiobacillus thiooxidans*, which oxidize sulfur and sulfides to  $\text{H}_2\text{SO}_4$ , and *Acidithiobacillus ferrooxidans* which oxidize ferrous ( $\text{Fe}^{2+}$ ) ions to ferric ( $\text{Fe}^{3+}$ ) ions. Also, APBs include *Pseudomonas*, *Aerobacter*, and *Bacillus* spp. which exude various organic



**Photo 6** MIC on a sectioned pipe.

acids in their metabolic process, resulting in localized underdeposit and pitting corrosion, often resulting in pinholes in pipework.

Apart from bacterial slimes, biomass, or biofilm can be produced by other types of microorganisms, including algae, yeast, molds, and fungus. Slimes and biofilms can provide the environment for corrosion through establishment of concentration cells resulting in under deposit corrosion. Also, biological deposits in general act as traps and food for other organisms resulting in rapid growth. This complex matrix sets up a corrosion potential between adjacent areas of a metal surface that may have a different type of deposit. Additionally, biofilms provide a safe environment for organisms when attacked by biocides, necessitating the additional use of biological penetrants or biodispersants to effect a good kill level in cooling water systems.

To control MIC it is important to understand the organisms and processes that cause it. Modification of the waterside environment will require periodic microbiological testing and use of specific types of microbiocides – usually a tailored program containing both an oxidizer and a nonoxidizer.

#### 4.27.7.9 White Rust Corrosion

Many ‘standard’ cooling water system components, such as HVAC panels, basins, and complete cooling towers, are constructed of galvanized steel for ease of fabrication and low manufacturing costs. Galvanizing produces a zinc–iron intermetallic alloy in layers on a steel surface that acts as a corrosion-resisting coating. The zinc is anodic to steel and thus will provide cathodic or sacrificial protection to any small areas of steel that may be exposed (i.e., scratches, cut edges,

etc.). Also, the passive, oxidized zinc coating provides a physical barrier in protecting the bulk of the steel surface from any direct contact with the environment. However, with the giving up of the use of sulfuric acid and chromate as a water treatment scale and corrosion-inhibiting chemical treatment program in most parts of the world over 30 years ago, a corresponding, and significant rise in white rust corrosion has been observed. It has become such a serious problem, especially in new construction, that many cooling tower manufacturers have turned to using glass fiber and plastics.

White rust corrosion is a problem where the fresh galvanized surface is not able to form a protective, nonporous, basic zinc oxide, especially where the surface is partially wetted or completely submerged in water. Deterioration begins when a localized corrosion cell is formed, leading to pitting corrosion, metal wastage, and reduced equipment life expectancy. White rust corrosion is often identified by the white, gelatinous or waxy deposit of a porous zinc-rich oxide complex,  $3\text{Zn}(\text{OH})_2 \cdot \text{ZnCO}_3 \cdot \text{H}_2\text{O}$ . It is aggravated by the modern use of high-pH, high-alkalinity water chemistries, and in softer waters, especially when appropriate pretreatment passivation protocols have not been followed (a major problem in new construction).<sup>15</sup>

#### 4.27.8 Problems of Microbiological Fouling

All water systems have the potential for the growth of microorganisms, and the production of slimes, biomass, or biofilm, which, not only present fouling and corrosion problems, but can also compromise the health and safety of workers and visitors. In cooling systems, spa baths, potable hot water lines, and calorifiers (hot water generator and storage tanks), the presence of slimes and biofilm can increase the risk of illness from, for example, Legionnaires' disease. **Photos 7(a) and 7(b)** below show microbiological fouling in a cooling system.

As noted earlier, microorganisms to be found in water systems can include not only bacteria, algae, yeast, molds, and fungus, but also unicellular protozoa (such as *Cryptosporidium*, *Paramecia*, and *Amoeba*).

Algal growths and biofilms are always found to some degree in open recirculating water systems such as cooling towers, evaporative condensers, air washers, and spray-coil units. Occasionally closed systems can become fouled with organic slimes

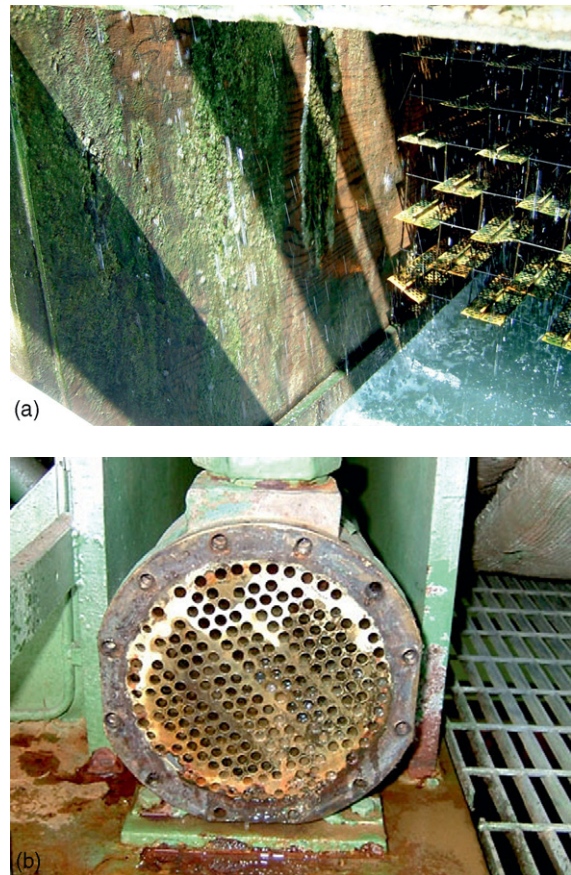


**Photo 7** (a) Algal fouling on a cooling tower and (b) fouled and corroded heat exchanger.

because of foreign contamination (although the single biggest problem here is always corrosion, usually as a result of improper initial cleaning, passivation, and ongoing use of chemical inhibitors).

Open cooling systems are constantly exposed to the atmosphere, and the local environment can contain dust, dirt and innumerable quantities of microscopic organisms such as algal cells and bacteria, which will enter the cooling systems because of the scrubbing of air during the evaporative cooling process. Also, because cooling water is exposed to sunlight, often operates at ideal growth temperatures, and contains nutrients, it provides a favorable environment for the abundant growth of biological organisms. The basic types of microorganisms found in cooling systems, and system environment modification methods are discussed below:

- **Algae.** The types of algae found in open recirculating water systems include the blue-green algae, green



algae, and brown algae. Large masses of algae can cause serious problems by blocking the air in cooling towers, plugging water distribution piping and screens, and accelerating corrosion by concentration cell corrosion and pitting. Algae must be removed physically before a system can be cleaned as the mass will provide a continuous source of material for reproduction and biocides will be consumed only at the surface of the mass, leaving the interior alive for further growth. Modification of the cooling water environment will include screening sunlight from towers by use of distribution trough covers, and the periodic use of specific algaecides, such as tertbutylazine (TBZ).

- *Fungi*. Fungi usually require low alkalinity waters and can grow together with algae, as the algae living within the fungus mass are furnished with a moist, protected environment, while the fungus obtains carbohydrates from the algae. Fungi can attack wood contained in cooling towers, so treated wood is used. Also, biocides such as tris(hydro-methyl)nitromethane (trinitro) may be employed.
- *Bacteria*. There are hundreds, if not thousands, of potential types of bacteria that may be found in water systems, especially cooling water systems. Bacteria are microscopic unicellular living organisms that exhibit both plant and animal characteristics. They may be rod-shaped, spiral, or spherical in shape, and may be pathogenic or harmless to people. However, in general, the most troublesome organisms are the slime producers – iron bacteria, sulfate-reducing bacteria, etc.

Bacteria may be found free-floating in water (planktonic bacteria) and are relatively easy to kill, although persistent strains and rapid regrowth may develop if the kill-rate is not maximized. Bacteria growing within a biofilm (sessile organisms) are more difficult to kill.

In general, the control of microorganisms is undertaken by developing a protocol or program for the selective and periodic (or semicontinuous) addition of oxidizing and/or nonoxidizing pesticides (also called microbiocides or biocides). Nonoxidizing biocides include isothiazolinones, thiones, and gluteraldehyde. Oxidizing biocides include various chlorine and bromine donors, such as bleach, calcium hypochlorite, and dibromohydantoin. Additionally, cationic, anionic, and non-ionic biocides and special biocidal cleaners may be employed.

Monitoring by the use of simple site tests, such as dip-slides, is necessary to establish the concentration of planktonic and sessile organisms, kill rates, and

regrowth rates. Under more difficult cooling water operating conditions, or where there may be resistance to certain pesticides or a reason to suspect the potential for the growth of pathogens, special testing is carried out in a microbiological laboratory.

#### 4.27.8.1 Problems of Amplification of Pathogenic Bacteria

Pathogenic bacteria are disease-causing bacteria. Cooling tower waters and domestic hot water lines in particular, have ideal conditions for the growth of bacteria and other organisms, and can promote the growth of pathogenic strains, which may then give rise to infection and possibly death, for example the amplification of commonly found *Legionella* organisms in cooling water and domestic hot water, leading to the risk of illness from Legionnaires' disease. It is important to keep these systems clean and free of general bacterial contamination in order to inhibit growth of potentially pathogenic bacteria, as well as to prevent corrosion from slime-forming organisms. **Photo 8** shows *Legionella* sp. amplifying in an amoeba.

Disease forming organisms that may grow in water systems that are not regularly cleaned, disinfected, or otherwise maintained may include the following:

- *Legionella pneumophila*, especially serotype 1. Responsible for Pontiac fever and Legionnaires' disease, a potentially fatal type of pneumonia.
- *Mycobacterium avium*. Responsible for nontuberculosis mycobacterium disease, also called hot-tub lung disease.
- *Pseudomonas* sp. Responsible for chronic respiratory infections and infections of the eye, skin, and soft tissue.

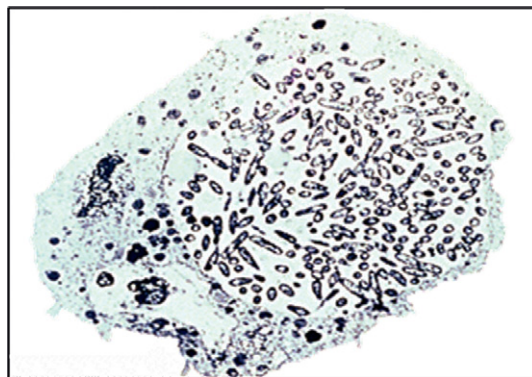


**Photo 8** *Legionella* sp. bacteria in an amoeba.

- *Escherichia coli*. Responsible for septicemia and diarrhea.
- *Giardia lamblia*. Responsible for Giardiasis, producing diarrhea and abdominal cramps.

Modification of the waterside environment to prevent bacteria related problems means that all cooling systems should be drained, cleaned, and disinfected at least twice per 12-month period, irrespective of whether the cooling systems operate all year round or only on a summer cycle. Some countries mandate this approach by law. Others demand three cleanings and disinfection programs per year. In addition to good maintenance, a periodic risk assessment and ongoing surveillance program should also be instituted, and all records kept in a logbook. Implementation of a risk assessment program is an additional and necessary precaution for many facilities prior to starting up a new or winterized tower, or where design or location is suspect (e.g., poor drift elimination, or the tower is sited too close to a ventilation system's fresh air intake).

#### **4.27.9 Evaluating and Modifying Waters for Use or Reuse in Industrial Processes and HVAC Water Systems**

Municipally treated waters are of potable quality, but may require some form of treatment, such as reducing or modifying the concentration of minerals, salts, and other compounds present, before becoming suitable for industrial process applications. Surface waters and well waters drawn directly from source will inevitably require pretreatment, and recycled treated waste waters or reused industrial waters will, likewise, require pretreatment, regardless of the process application envisioned.

In general, treatment will take several steps, the first being a basic 'cleanup' using mechanical filtration, ion-exchange water softening, or similar capital intensive process. Next may follow a purification process, such as demineralization by ion-exchange or membrane process, or mechanical deaeration. Finally, an ongoing, maintenance chemical treatment program will be employed for 'polishing' purposes.

Cooling systems are generally accepting of a wide diversity of water sources and provided the water is reasonably consistent in quality, many industrial streams can be economically recovered and reused as tower makeup. However, as noted above, recoverable process waters will always require some measure

of judicious pretreatment before being recycled for reuse in cooling systems, even if it is only to remove particulates, fats, oils, and greases (FOG) and heavy metals; and to make pH adjustments (say pH 7.0–8.5). Water used as a makeup source for steam boilers may need significant pretreatment, depending upon the boiler design and pressure. Generally, as boiler pressure rating increases, the makeup water employed will need to be further modified or 'purified' by removing most, if not all, measurable contaminants.

In industry, water is employed for innumerable applications, not simply for heating and cooling. It is required, for example, in dissolving, washing, cleaning, dyeing, rinsing, melting, quenching, stripping, scrubbing, desalting, plating, surface coatings, fermentation, dust control, process liquors, steam heating, drying, cooking, pasteurization, oil and gas abstraction, and domestic purposes. Additionally, excess water results from distillation, evaporator condensates, reverse osmosis (RO) reject, oil and gas production, boiler blowdown, chemical manufacturing, recovery of fibers and chemicals, straining, filtration, drainage, and a myriad of other process operations. This water may be treated and recycled, or reused for other types of process, or downstream applications.<sup>16,17</sup>

Any water considered for use or reuse in industrial processes and even for small, simple, HVAC water system applications must first be evaluated, if problems of corrosion and scaling are to be avoided or minimized. In general, we would need to consider the following:

1. An understanding of the process flows, operating conditions, materials balance, and volume/quality requirements.
2. A full understanding of the chemistry of the water under consideration, plus testing parameters, limitations, and costs. We need to know the chemical and physical characteristics, including pH, temperature, calcium, magnesium, alkalinity, silica, suspended solids, chlorides, sulfates, and the presence of potentially undesirable constituents, such as FOG, solvents, ammonia, soluble/insoluble iron, and heavy metals. Also, we may need to know the 5-day biochemical oxygen demand (BOD<sub>5</sub>), chemical oxygen demand (COD) or total organic carbon (TOC) analysis.
3. We have to be able to interpret the data, in order to identify which contaminants may provide limiting factors regarding deposition, fouling, or corrosion of materials of construction (such as copper,



steel, heat-exchanger alloys, or concrete), and would thereby impact chemical treatment programs, cycles of concentration (COC), bleed discharge volumes, and ongoing costs.

4. We need to provide a robust and economic pretreatment design, ensuring that the treated water meets the desired or practical/useable/chemical/physical water quality specifications.
5. Where water is used for cooling purposes, we also need to consider further modification of the waterside environment by the operational protocols and the downstream chemical inhibitor treatment program(s) that will be used on a regular maintenance basis.

In order to keep water consumption as low as practically and economically possible, we need to consider COC (i.e., the ratio of concentration of TDSs in recirculating water to that of the make-up water employed). This requires us to consider corrosion, fouling, and deposition risks, as indicated by basic and ionic equilibrium model saturation indices or ion-association predictive modeling (see also [Sections 4.27.13–4.27.15](#)). However, the law of diminishing returns applies for any specific cooling system, beyond a certain COC number, the risk of waterside problems increases greatly as the reward of water savings progressively diminishes. A COC of  $4\times$  to  $6\times$  is often a good standard. There is seldom any significant benefit in raising COC levels to  $>10\times$  unless the water is a lean acid water, with a minimum of minerals and other contaminants present, or a zero liquid discharge (ZLD) system is in place.<sup>16</sup>

#### 4.27.10 Modifying Water by Selective Use of Standard Pretreatment Processes

The types of water contaminant pretreatment process under consideration will depend upon the degree of contaminant removal or modification required. Some examples of pretreatment equipment are shown in [Photos 9\(a\)–9\(d\)](#).

Although certain types and brands of ‘nonchemical devices’ (‘gadgets’) such as magnetic devices (not the same as a magnetic separator), electrostatic, pressure changing, or catalytic devices may be employed, these tend not to have mainstream acceptance. This is usually because of limited availability of peer-reviewed data and/or extravagant claims.

Examples of mainstream, ‘standard’ pretreatment processes include the following:

- *Alkalinity removal.* This process can be carried out via lime softening, sulfuric acid treatment, or ion-exchange dealkalization.

A steam boiler that operates with makeup water containing excessive quantities of carbonate and bicarbonate alkalinity not only will develop excess alkalinity in the boiler (causing priming, foaming, and carryover), but also will generate large quantities of carbon dioxide as a result of decomposition of the carbonates and bicarbonates. This process results in an acid steam and condensate, which, as noted previously, causes severe corrosion of steam and condensate return lines. The alkalinity in these cases can be reduced by 90%, by passing the makeup water through a dealkalizer following the water softener.

The typical dealkalizer plant contains an ion-exchange resin similar to the water softener with the capability of exchanging carbonate, bicarbonate, sulfate, and other anions for chloride, hence the name ‘chloride anion dealkalizer’ (i.e., a strong base anion (SBC) resin in the chloride form). Alternatively the dealkalizer can be a strong/weak acid cation (SAC/WAC) in the hydrogen form, plus degassing. In this type of plant, there is a reduction in dissolved minerals, leading to a reduction in boiler blowdown requirements and thus, energy savings.

- *Dirt, grit, sand, slime, algae removal.* This can be achieved by using a strainer, bag or cartridge filter, sand filter, multimedia filter, inclined plate clarifier (e.g., Lamella Gravity Settler), or conventional coagulation/sedimentation/clarification techniques. It is common practice to install strainers prior to pumps on open recirculating condenser water systems to protect the pump internals, vanes, shaft and impellers from large damaging flakes of rust, suspended dirt, or other foreign particles that can enter an open system. Similarly, strainers should be installed on closed systems as they are frequently plagued with suspended black magnetic iron oxide mill scale as well as foreign particles. The bag or cartridge strainer can be used as a coarse filter to remove larger particles before the pumps and heat exchangers.
- *Disinfection.* Here, we might consider ultraviolet light at 254 nm (UV), ozone, chloramines, chlorine dioxide, bleach, or emerging technologies such as photocatalytic anatase titanium dioxide ( $\text{TiO}_2$ ), for example, TioxyClean™, etc.
- *FOG, solvent, and hydrocarbon removal.* Organics for example, benzene, toluene, xylene – BTX) can be removed using coalescers such as American



**Photo 9** (a) Filters removing oil and organics from water, (b) twin ion-exchange water softeners with salt tank and chemical feed station, (c) demineralization and RO plant, (d) deaerator.

Petroleum Institute (API) separators, corrugated plate interceptors (CPI), or dissolved air flotation (DAF) units.<sup>17</sup> A secondary filtration system such as bentonite, organoclay, or similar full-flow media filter (e.g., Biomin™) may also be required.<sup>18</sup> Also advanced filtration/absorption processes may be used, although careful designs are needed as the rule of thumb is often that 50% of costs are incurred for the first 99% of contaminant removal, with the other 50% being spent on the last 1%.<sup>19</sup>

- *Hardness and/or silica removal.* This can be achieved through hot/cold lime and lime-soda softening or ion-exchange. An ion-exchange water softener is a synthetic zeolite softener containing an ion-exchange water softener resin. This ion-exchange resin adsorbs calcium and magnesium ions from the water passing over the resin bed. The resin at the same time releases sodium, hence the term 'ion exchange.' It is often not economical to use softeners for open cooling tower condenser water, evaporative condensers, chilled water and closed loops, hot water

generators, and surface spray units, as these systems operate at pH values close to the neutral point, where the hardness can be kept in solution with the aid of antiscalents and pH control types of chemical treatments. However, chemical treatments will be required even if most of the hardness is removed.

Waters with a hardness of more than 300 or 400 mg l<sup>-1</sup> require at least partial softening so that they can be used for cooling tower makeup water. With steam boilers, however, removal of hardness from the makeup water is nearly always required to remove the hardness, and prevent risks of excessive scale or sludge deposits on heat-transfer surfaces. With steam boilers, the determining factors are both the hardness and the amount of makeup water used. In low-pressure heating applications where steam is used for heating only and possibly small amounts of humidification requiring less than 10% of the steam generated, the boiler feedwater will consist of 90% or more of return steam condensate. In instances such as this, the makeup water will not require external hardness removal as the small amount of hardness entering the system can be controlled with internal treatment.

- *Heavy metal removal.* Metals such as iron, lead, nickel, chromium can be removed by coagulation and alkaline precipitation, or by use of carbamates. Also used is absorption on waste treatment residues (WTR – a lime-based product) or iron-coated olivine (a magnesium–iron silicate) – usually at a neutral to acid pH.
- *Iron and manganese removal.* Fe and Mn are common contaminants in many water sources and may be removed by use of aeration, coagulants, manganese greensand/permanganate techniques, or BIRM™ filters.
- *Removal of volatile organic compounds (VOCs), organics, ammonia, chlorine, color, turbidity, BOD, and COD.* A wide range of organics and other contaminants may be removed from water by using air scouring, activated carbon filters, bio-reactors, redox chemicals, or traditional activated sludge methods.
- *Wide-spectrum contaminant removal.* In addition to the above processes, various membrane techniques (e.g., microfiltration, EDI, RO) may be employed, either as stand-alone processes combined with deionization (DI) or as part of more complex pretreatment arrangements to remove oils, organics, etc.<sup>19</sup>
- *Mechanical removal of oxygen.* In many boiler plant installations, it is economical, necessary, or simply

good practice to remove oxygen in the boiler feedwater by use of feedwater heaters or mechanical deaeration (prior to use of a chemical oxygen scavenger for final removal of corrosive gases), in order to prevent serious corrosion and pitting of steam boiler feedwater lines and boiler tubes. Whenever a steam boiler system is open to the atmosphere through vented condensate receivers, feedwater tanks, etc., the air absorbed will result in high quantities of dissolved oxygen. This increases in direct proportion to the amount of makeup water used because the cold raw makeup water is high in dissolved oxygen. High levels of cold makeup water will not only increase the dissolved oxygen content, but also will lower the temperature of the feedwater in the return condensate tank, enabling more oxygen from the atmosphere to be dissolved in the feedwater. This happens because the solubility of oxygen in water is inversely proportional to temperature.

Modification of the feedwater for oxygen removal is best carried out by using a deaerator. The mechanical pressure deaerator is a complex device that utilizes steam injection to scrub the incoming makeup water and condensate for removal of the dissolved corrosive gases, oxygen and carbon dioxide. In the deaerator, water is sprayed over inert packing or trickled through baffles or trays to break up the water and provide for intimate mixing of the feedwater with the incoming steam. The steam is injected counter to the flow of the incoming water, which drives the gases, oxygen and carbon dioxide upward out the vent. The vent releases only noncondensable gases and steam losses are at a minimum. Some deaerators can produce feedwater with dissolved oxygen content as low as 0.005 cm<sup>3</sup> l<sup>-1</sup> (0.0072 ppm).<sup>20,21</sup>

#### 4.27.11 Modifying Waterside Environments by Appropriate Metal and Alloy Materials Selection

Corrosion protection of metal surfaces contacting water is an ongoing management, maintenance, and control problem, as has been discussed elsewhere. However, better selection of appropriate materials at the design stage can help minimize initial corrosion risks; therefore, consideration of the galvanic series at the material selection stage is a useful exercise. Also, metals may only be vulnerable



under very specific operating conditions; therefore, a simple galvanic series guide may not, by itself, be satisfactory and further investigation may be required. Simple things like flow rate, high cycles of concentration, or high chlorides may initiate corrosion problems.

**Table 4** provides a limited corrosion vulnerability summary.

An example of the need for appropriate materials selection is when employing high chloride waters in cooling systems containing stainless steels, as it is well known that high chlorides will increase the risk of stress corrosion cracking in austenitic stainless steels (e.g., types 304/304L/316/316L) and will tend to increase general corrosion and attack in localized areas, often causing pitting type corrosion. Specifications for the upper limits of tolerance to chloride ions, where the cooling system contains a high percentage of 304L stainless steel (SS) or there is concern over vulnerability of stainless steel components, will typically designate  $200 \text{ mg l}^{-1} \text{ Cl}^{-}$ . Nevertheless, high natural chlorides can often be tolerated in recirculating water at levels of

$600\text{--}800 \text{ mg l}^{-1}$ , and estuarine water users can find seasonal fluctuations raise the chloride in their systems to perhaps  $800\text{--}1200 \text{ mg l}^{-1} \text{ Cl}^{-}$ . This latter level is probably the maximum that can be tolerated under normal circumstances for 304-grade SS and requires good management if serious problems are to be avoided.<sup>11</sup>

The maximum chloride limit for 316-SS grades is generally set by technical organizations at  $1000 \text{ mg l}^{-1}$  but higher concentrations can sometimes be tolerated, and up to  $5000 \text{ mg l}^{-1} \text{ Cl}^{-}$  have been reported in refinery water reuse programs.<sup>17</sup>

At chlorides concentrations of up to  $3600 \text{ mg l}^{-1}$ , a duplex SS is recommended (e.g., 2205-grade) and seawater requires superaustenitic or superduplex SS grades.<sup>27</sup>

Where specific metals and alloys have been selected, part of the ongoing control of corrosion risk is to monitor corrosion rates *in situ* using test pieces, coupons, and various forms of test meters. An example of a corrosion test coupon is shown in **Photo 10**. The corrosion coupon test method has been described by the National Association of Corrosion Engineers (NACE) and is consistent with the ASTM standard 'Corrosivity Testing of Industrial Cooling Water (Coupon Test Method).' The test coupon is placed in the recirculating water system in a test coupon 'rack.' The corrosion test report will include the calculated corrosion rate in mils per year or micrometers per year and other pertinent data such as depth of pits, variations, and types of corrosion deposits.

In cooling systems, the results of corrosion monitoring can be usefully interpreted from **Table 5**.

#### 4.27.12 Understanding Contaminant Saturation Problems as a Precursor to Modification of Waterside Environments by Chemical Inhibitors

In most sources of water, apart from estuarine water and seawater, calcium bicarbonate is usually the most abundant salt found; but it has only limited solubility

**Table 4** Corrosion vulnerability summary

<i>Metal</i>	<i>Type of corrosion risk in water</i>
Steel	Stagnant water tends to induce local attack Fouling induces concentration cell type corrosion High $\text{Cl}^{-}$ and $\text{SO}_4^{2-}$ tend to increase risks of pitting $\text{O}_2$ saturated water may induce general corrosion Fouling and $\text{SO}_4^{2-}$ induce corrosion from sulfate reducers Coupling with noble metal causes galvanic corrosion pH 4.0 induces rapid acid-induced wastage and pitting
Iron	Presence of some $\text{O}_2$ , plus deposits and low flow, stimulate tuberculation Soft water, low pH, $\text{H}_2\text{S}$ can stimulate graphitization
SS	Vulnerable to depassivation from high $\text{Cl}^{-}$ and $\text{SO}_4^{2-}$ Residual or applied stress with $\text{Cl}^{-}$ induces SCC.
Brass	Ammonia produces cracking & wastage. High velocity can induce erosion-corrosion (>6 fps) Uninhibited brass suffers dezincification
Zinc	High alkalinity causes white rust
Al	pH over 9.0 with $\text{OH}^{-}$ causes rapid corrosion



**Photo 10** Corrosion test coupon.

**Table 5** Guide to specifying and quantifying corrosion rates*Interpretation of cooling system corrosion rates*

Description	Rate (mpy)	Comment <sup>a</sup>
Negligible	<2.0	Excellent. Very difficult to achieve.
Mild	2.0–4.0	Good. Acceptable for most situations.
Moderate	4.0–6.0	OK. Probably adequate protection.
High	6.0–8.0	Poor. Doubtful protection.
Severe	>10.0	Very poor. Probably unacceptable protection.

<sup>a</sup>For closed systems, same comments apply if steel mpy is 50% of above rates. For Cu and brasses the same comments apply if mpy is 10% of above rates.

and under conditions where concentration effects take place, as in a cooling system, it will break down to calcium carbonate and form troublesome crystalline scale or sludge deposits. This effect also takes place where heating occurs, as in a boiler, because of an inverse solubility.

Similar effects occur in seawater, where although sodium chloride will be present at levels exceeding 35 000 mg l<sup>-1</sup> (ppm) calcium bicarbonate will be present only at approximately 400–420 mg l<sup>-1</sup>; if the seawater is heated (as in a multistage flash evaporator for the generation of potable water), the calcium bicarbonate will again breakdown to form calcium carbonate scale. Of course, the sodium chloride salt presents another problem, one of corrosion, and it is common to find some form of corrosion associated with most scaling deposits. Scaling and deposition problems often occur in the same water system, and therefore modification of a waterside environment to control one problem must, of necessity, take into consideration the opposite problem at the same time.

Calcium carbonate (CaCO<sub>3</sub>) can form as both aragonite and its polymorph, calcite, which has the same chemistry as aragonite, but a different crystal structure and shape. Aragonite is thermodynamically unstable at standard temperature and pressure, and tends to transform to calcite. Under most heating or concentration-effect conditions in water systems where amorphous or crystalline calcium carbonate scales develop, it is generally considered that calcite is preferentially formed, as it is the most stable form of crystalline calcium carbonate scale. This may simply be a measure of convenience rather than a fact always; however, it allows us to consider the concept of saturation of a

salt or compound in water and the resulting effects of exceeding saturation level concentrations.

A water is said to be saturated with a compound (e.g., calcium carbonate, tricalcium phosphate, amorphous silica,) if it will not precipitate the compound and it will not dissolve any of the solid phase of the compound when left undisturbed, under the same conditions, for an infinite period of time. Water which will not precipitate or dissolve a compound is at equilibrium for the particular compound. Water from which a compound precipitates is supersaturated with respect to that compound. The precipitate is a foulant and may also cause crystalline scaling deposits to be formed. Calcite is the most common foulant. By definition, the amount of a calcium carbonate that can be dissolved in a water and remain in solution for this infinite period of time is described by the solubility product.

$$K_{sp} = (\text{Ca})(\text{CO}_3)$$

where (Ca) is the activity of calcium; (CO<sub>3</sub>) is the carbonate activity;  $K_{sp}$  is the solubility product for calcium carbonate at the temperature under study.

The degree of saturation of any compound (such as calcite) in water is described by the relationship of the ion activity product (IAP = (Ca)(CO<sub>3</sub>)) to the solubility product ( $K_{sp}$ ) for the compound as follows:

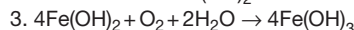
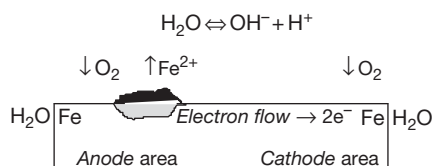
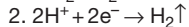
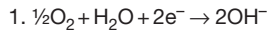
- If a water is undersaturated with a compound (IAP <  $K_{sp}$ ), then it will tend to dissolve the compound
- If a water is at equilibrium with a compound (IAP =  $K_{sp}$ ), then it will not tend to dissolve or precipitate the compound
- If a water is supersaturated with a compound (IAP >  $K_{sp}$ ), then it will tend to precipitate the compound.

The saturation index (or degree of supersaturation) describes the relative degree of saturation as a ratio of the ion activity product (IAP) to the solubility product ( $K_{sp}$ ), such that<sup>22,23</sup>:

$$\text{SI} = \frac{\text{IAP}}{K_{sp}}$$

Under typical practical operating conditions, the solubility of calcium carbonate in CO<sub>2</sub>-free water at 15 °C is estimated as only 14 mg l<sup>-1</sup> and so modification of the waterside environment is required to prevent calcite scaling.<sup>11</sup> This usually requires the application of an antiscalent chemical. There are a



**Anodic reactions:****Cathodic reactions:**

**Figure 3** Corrosion reactions forming rust blisters over pit.

wide range of water treatment chemistries (polyacrylates, phosphonates, polymaleates, etc.) available in the market today and antiscaling inhibitor formulation blends based on one or more of these chemistries will typically be able to control the risk of fouling in strongly scaling waters where the calcite SI exceeds 100; and often 150.

For any water under specified operating conditions, the IAP and SI for a range of contaminants (and thus the risk of fouling) can be calculated using industry-available software programs.<sup>24</sup> These modern programs overcome the operational interpretation problems (such as a failure to take into account common ion effects) of early, noncomputerized indices, for example, the Langelier saturation index (LSI).

#### 4.27.13 LSI and Related Indices as an Aid to Modification of Waterside Environments

In condenser water systems using recirculating cooling tower water or once-through cooling water, the water temperature is much lower than that in steam boiler or hot-water systems. At these lower temperatures most of the scale-forming minerals will remain in solution, but the tendency will be to deposit calcium carbonate (calcite) on the heat-transfer surfaces where there is a slight rise in temperature. Modification of a water to reduce the risk of fouling, scaling, and/or corrosion requires that certain analytical factors are considered. The primary factors that affect this tendency are the following:

- alkalinity;
- calcium hardness;
- pH;
- total dissolved solids; and
- temperature.

The higher the alkalinity of a particular water, the higher the bicarbonate and/or carbonate content. As these minerals approach saturation, they tend to come out of solution and precipitate as a calcite foulant or scaling deposit. Likewise, a higher concentration of hardness will increase the tendency of calcium and magnesium salts to come out of solution. The pH value reflects the ratio of carbonate to bicarbonate alkalinity.

The higher the pH value, the greater the carbonate content of the water. As calcium carbonate and magnesium carbonate are less soluble than the bicarbonate, they will tend to precipitate as the pH value and carbonate content increase. Also affecting this tendency are the TDSs and temperature. The higher the solids content the greater the tendency to precipitate the least soluble of these solids. The higher the temperature, the greater the tendency to precipitate the calcium and magnesium salts because of their property of inverse solubility.

- **Langelier saturation index (LSI).** This, developed in 1936, is a calcium carbonate saturation index that is very useful in determining the scaling or corrosive tendencies of a water sample under investigation. It is based on the assumption that any given water with a scaling tendency will tend to deposit a corrosion-inhibiting film of calcium carbonate and hence will be less corrosive. By inference, water with a nonscaling tendency will tend to dissolve protective films and be more corrosive. This is not entirely accurate as other factors are involved in corrosion, but, although a relatively simple tool, it provides a valuable index in determining the tendency of water to directly influence scaling or corrosive actions.

The LSI is on the basis of the pH of saturation of calcium carbonate. The pH of saturation (or 'saturation pH,'  $\text{pH}_s$ ) of calcium carbonate (calcite) is the theoretical pH value of any particular water if that water is saturated with calcium carbonate, and is given by the formula below:

$$\text{pH}_s = (9.3 + A + B) - (C + D)$$

where  $A = (\log_{10} [\text{TDS}] - 1)/10$ ;  $B = -13.12 \times \log_{10} (^\circ\text{C} + 273) + 34.55$ ;  $C = \log_{10} [\text{Ca}^{2+} \text{ as } \text{CaCO}_3] - 0.4$ ;  $D = \log_{10} [\text{alkalinity as } \text{CaCO}_3]$

or

$$\text{pH}_s = 12.3 - (\log_{10} \text{Ca} + \log_{10} \text{TA} + 0.025 \text{Temp} - 0.011 \text{TDS}^{\frac{1}{2}})$$

**Table 6** Makeup water requirements decrease with increasing COC

Makeup water volumes based on an evaporation rate of 5000 m <sup>3</sup> day <sup>-1</sup>		
Bleed rate assumes no windage loss		
COC	Bleed (m <sup>3</sup> day)	Makeup (m <sup>3</sup> day <sup>-1</sup> )
2×	5 000	10 000
3×	2 500	7 500
4×	1 666	6 666
5×	1 250	6 250
6×	1 000	6 000
7×	833	5 833
8×	714	5 714
9×	625	5 625
10×	555	5 555

where Ca = calcium Hardness as ppm CaCO<sub>3</sub>; TA = total alkalinity as ppm CaCO<sub>3</sub>; Temp = Temperature as °C; TDS = total dissolved solids ppm.

To determine the Langelier index, the actual pH of the water must be measured, and the pH of saturation of calcium carbonate is calculated from a measure of the total alkalinity, hardness, TDSs, and temperature. Once the pH of saturation of calcium carbonate has been calculated, the LSI can be determined from the formula.

$$LSI = pH - pH_s$$

A positive index indicates scaling tendencies; a negative one (by inference), corrosion tendencies as shown below:

- If LSI is negative: No potential to scale, the water will dissolve CaCO<sub>3</sub>. An LSI of -2.5 is extremely corrosive
- If LSI is positive: Scale can form and CaCO<sub>3</sub> precipitation may occur. An LSI of +2.5 is extremely scale-forming
- If LSI is close to zero: Some risk of either/both scale/corrosion. Water quality, changes in temperature, or evaporation could change the index.

An LSI of 2.5 is approximately equivalent to a calcite saturation index (CSI) of 150

- *Ryznar index (Ryznar stability index, SI, RSI)*. This is another useful tool for determining the scaling tendencies of water. This index is also on the basis of the pH of saturation of calcium carbonate and was intended to serve as a more accurate index of the extent of scaling or corrosion in addition to

the tendency. This index was derived from the LSI by observation of actual cooling water conditions and is calculated as follows:

$$RSI = 2(pH_s) - pH$$

where pH<sub>s</sub> = pH of saturation of calcium carbonate, pH = actual measured pH of the water, RSI <6 the scale tendency increases as the index decreases, RSI >7 the calcium carbonate formation probably does not lead to a protective corrosion inhibitor film, RSI >8 mild steel corrosion becomes an increasing problem.

- *Puckorius scaling index (PSI)*. LSI and RSI are limited in their absolute relevance as they do not account for two other critical parameters: the buffering capacity of the water, and the maximum quantity of precipitate that can form in bringing water to equilibrium. Puckorius attempts to quantify the relationship between saturation state and scale formation by incorporating into the index an estimate of buffering capacity of the water. However, it is debatable whether, in a practical situation, this additional estimate is of real value, as common ions effects still bring other factors into the overall situation. Common Ion effects are taken into account in IAP modeling, such as the various FrenchCreek® software programs.<sup>24</sup>

Water high in calcium, but with low alkalinity and buffering capacity can have a high calcite saturation level. The high calcium level increases the ion activity product and a plot of ion activity product against precipitate for the water would show a rapid decrease in pH as calcium carbonate is precipitated because of the low buffering capacity. Even small decreases in carbonate concentration in the water would significantly decrease the ion activity product because of the small quantity present prior to the initiation of precipitation. This water might have a high tendency to form scales because of the driving force but any scale formed would be a small quantity and practically unobservable. Thus, the water has the driving force but not the capacity and ability to maintain pH as precipitate matter forms. PSI is calculated in a manner similar to the RSI; however, Puckorius uses equilibrium pH rather than the actual system pH to account for the buffering effects:

$$PSI = 2(pH_{eq}) - pH_s$$

where pH<sub>s</sub> is the pH at saturation of calcite or calcium carbonate, pH<sub>eq</sub> = 1.465 × log<sub>10</sub>[Alkalinity]

+ 4.54,  $[\text{Alkalinity}] = [\text{HCO}_3^-] + 2[\text{CO}_3^{2-}] + [\text{OH}^-]$ .

Interpretation of PSI is the same as for RSI.

- *Larson–Skold index (L-SI)*. The L-SI indicates the corrosivity of water towards mild steel and is based on the evaluation of actual corrosion rates and the type of attack on mild steel lines transporting Great Lakes waters. The index is the ratio of equivalents per million (epm) of sulfate ( $\text{SO}_4^{2-}$ ) and chloride ( $\text{Cl}^-$ ) to the epm of alkalinity in the form bicarbonate plus carbonate<sup>26</sup>:

$$\text{L-SI} = (\text{epmCl}^- + \text{epmSO}_4^{2-}) / (\text{epmHCO}_3^- + \text{epmCO}_3^{2-})$$

Extrapolation of observed corrosion results to other waters, such as low or very high alkalinity waters, goes beyond the range of the original data. The index has proven a useful tool in predicting the aggressiveness of once-through cooling waters. The L-SI may be interpreted in the following way:

- L-SI = <0.8: Chlorides and sulfate probably will not interfere with natural film formation;
- L-SI = 0.8–1.2: Chlorides and sulfates may interfere with natural film formation and higher corrosion rates might be anticipated;
- L-SI ≥ 1.2 A tendency towards higher localized corrosion rates should be expected as the index increases.

#### 4.27.14 Use of Contaminant Cycling Effects in Modifying Waterside Environments

The previous section discussed the problem of exceeding calcite saturation limits in water and the very real risks of producing scaling deposits. Calcite scaling risks tend to increase in waters with higher alkalinities, but conversely, the propensity for general corrosion tends to fall, because of the shielding effect of calcium carbonate foulant at the heat exchange surface. This reduced corrosion risk might be considered a benefit, and thus, it is common in both boiler waters and recirculating cooling waters to increase alkalinity levels as an aid to reducing corrosion.

In both steam raising boilers and cooling systems, evaporation of water takes place with makeup water replacing that lost by evaporation and, as the

makeup waters will inevitably contain dissolved gases and mineral contaminants, concentration effects take place which can lead to an increase in contaminants, including alkaline salts. Of particular interest is that the concentration of (alkaline) calcium bicarbonate will increase, and where breakdown of calcium bicarbonate occurs there is a loss of (acidic) carbon dioxide leading to an increase in alkaline (protective) carbonates.

Thus increasing cycles of concentration can be a simple method of mitigating risks of corrosion. In any water system where evaporation occurs there are always constraints that limit the degree of concentration that can take place, but this is usually well beyond the saturation limits for most scaling contaminants. Thus, operational limits are placed on the water system by periodically blowing down (bleeding off) some of the ‘concentrated’ water and replacing it with fresh makeup water. The overall effect is that for any specific water system, the cycles of concentration (COC), that is, the ratio of concentration of TDS in recirculating water to that of the make-up water, are maintained at a prescribed limit, appropriate for the water system in question. This limit may be from, say, 3–10 cycles for cooling systems, and from 10 to 100 cycles for steam raising boilers.

There is an additional benefit of maintaining an appropriately high COC in a water system, and that is that losses of water because of blowdown (bleed) are controlled and generally minimized, leading to an increase in operational efficiency and a savings in both water and chemical inhibitor costs. It should be noted that evaporation rates are not affected by COC. [Table 7](#) shows the potential for water savings with increase in COC.

Typically, when calculating actual, theoretical, and practical COC in cooling system waters, because of the difficulties of testing for TDS in water, testing for chloride is carried out. Chlorides are very soluble and are not otherwise easily removed from the water. We know that COC relates to the increase in TDS over time in the recirculating water, as evaporation (E) of pure water takes place from the tower (providing the cooling effect) and is replaced by makeup water (MU) containing additional TDS. The record of past COC as well as the potential for improving future operating COC is often a vital key to technically improving water treatment management (adding value).

For any cooling system, there is a limit to the maximum COC that can be obtained. The limit is essentially on the basis of the loss of TDS-containing

**Table 7** Contaminant limits in cooling waters

<i>TAB result</i>	<i>Evaluation</i>
0 to 10 <sup>2</sup> colonies per ml	Excellent control
10 <sup>2</sup> to 10 <sup>3</sup> colonies per ml	Warning, but no serious fouling risk
10 <sup>4</sup> to 10 <sup>5</sup> colonies per ml	10 <sup>4</sup> is the maximum permitted for healthcare 10 <sup>5</sup> is a typical maximum for commerce/industry
10 <sup>5</sup> to 10 <sup>6</sup> colonies per ml	Unacceptable. Fouling anticipated. Also, a possible health risk
>10 <sup>6</sup> colonies per ml	Serious risk of fouling and pathogens

water, that is, windage or drift (D), deliberate purge or bleed (B), and leaks. If all leaks and bleed can be halted, then:

$$\text{COC}_{\max} = \frac{E + D}{D}$$

Typically,  $E = 1\%$  of water circulation rate (CR) per  $10^\circ\text{F } \Delta T$ .

where  $\Delta T$  = temperature drop over tower,  $D$  is usually in the range 0.01–0.3% of CR for mechanical draft towers.

Also, considering bleed (B):

$$B = (E/\text{COC} - 1) - D$$

#### 4.27.15 Modification of Waterside Environments by Chemical Inhibitors

In general, although a very wide range of chemical inhibitors is commonly available and employed in all types of water systems, the specific selection is based on the needs of the water system under consideration, and such needs may include, for example, green chemistry protocols, food industry requirements, or discharge regulations.

The selection of chemical inhibitors forms part of a water treatment program that is usually water system specific and generally thought of as an ongoing maintenance ‘polishing’ protocol. The inhibitor program is typically designed to also operate in conjunction with water treatment equipment, such as filters, softeners, or deaerators.

Modification of the waterside environment by chemical inhibitors will result in cleaner heat-exchange surfaces, relative freedom from corrosion and other

problems, improved operational efficiencies, reduced cleaning and other maintenance issues, and increased asset lifespan.

#### 4.27.16 Modification of Steam Boiler Waterside Environments by Chemical Inhibitors

The chemicals, equipment, and methods for inhibitor chemical addition, testing, and control required to optimize firetube (FT), watertube (WT) and other types of steam boiler system operations, to reduce the risks of corrosion, scaling, and fouling to accepted minimums must be tailored, not only to each system, but also to each geographic location, as the water quality and contaminant level will vary by location, and also by season. Implementation and optimization of chemical inhibitor programs need to be administered by qualified water technologists – usually those with an engineering or chemistry background.

The chemical inhibitors are usually referred to as ‘internal treatments,’ as opposed to ‘external treatments,’ by which is meant pretreatment equipment.

Modification of steam boiler water systems by chemical inhibitor programs is required to prevent the problems of corrosion, pitting, scale deposits, and erratic boiler operation because of priming, foaming, and carryover. To prevent these problems, correct blowdown and treatment must be applied. HVAC and space heating boilers also require similar modification, although operational conditions may not need to be so tightly controlled. Control over problems such as the supersaturation of dissolved solids, short and long-term overheating, and boiler priming (surging) rely at least as much on good operation. A summary of the most common problems and the chemistries used to modify the waterside environment follows.

- *Blowdown control.* Blowdown of a boiler is the spontaneous removal of some concentrated boiler water from the boiler under pressure. The recommended maximum concentrations of the impurities, which must be properly controlled, are generally specified by codes, insurance companies, or by industry standards or consensus (e.g., ASME Consensus). Actual operating experience will determine the true operational limits for any specific boiler operation.

The maximum allowable cycles of concentration can be maintained by blowing down the boiler water,

in order to remove accumulated boiler water solids. The amount of solids present in the concentrated boiler blowdown water is equal to the amount of solids in the makeup water multiplied by the cycles of concentration. This can be expressed mathematically as

$$\text{Solids leaving} = BCX$$

where  $B$  is the blowdown, gal (l),  $C$  is the cycles of concentration,  $X$  is the total solids concentration of makeup water,  $\text{mg l}^{-1}$  (ppm).

The amount of solids entering the boiler with the makeup is expressed as

$$\text{Solids entering} = MX$$

where  $M$  is makeup water (l, gal).

As blowdown is designed to maintain a specific level of cycles of concentration, the specified level can be kept consistent only if the amount of solids leaving the boiler is equal to the amount of solids entering the boiler. This is expressed as:

$$BCX(\text{solids leaving}) = MX(\text{solids entering})$$

Solving this equation for blowdown  $B$ , we obtain:

$$B = \frac{M}{C}$$

This formula is used to determine a blowdown rate with respect to the makeup rate. In percent, it can be expressed as:

$$\% \text{Blowdown} = \frac{100}{C}$$

- *Control of priming, foaming, and carryover.* Priming of boiler water is the bumping and bouncing of the water level of the boiler during operation. Foaming, however, is a less violent activity and consists of the formation of small bubbles in the surface of the boiling water. Carryover essentially is the contamination of the steam with boiler water and is a result of priming and foaming. However, it can be a more subtle entrapment of boiler water with the steam, causing steam contamination without the evidence of priming and/or foaming. Most frequently, the causes of priming, foaming, and carryover are a result of contamination of the boiler water with oil or other foreign substances. Other causes are excessive solid accumulation because of the lack of blowdown, high alkalinity, over-treatment, and mechanical malfunction.

Modification of the boiler water to reduce the problems of priming, foaming, and carryover will require adequate blowdown and certain adjunct antifoam inhibitor treatments – generally polyethoxylates.<sup>21</sup>

- *Corrosion control.* Control over boiler section system corrosion typically requires a combined approach that includes (following mechanical deaeration), oxygen scavenging, maintenance of passivated films, and pH and alkalinity control. Primary inhibitor chemistries encompass oxygen scavengers that include inorganics such as sodium sulfite and organics such as hydrazine. Sometimes, certain additional conjunctive inhibitor treatments are required, such as sodium nitrate for protection against embrittlement. Also, anodic corrosion inhibitor programs, which employ nitrite, silicate or molybdate chemistries, may be specified in light-duty multifunctional programs for HW heating and lower-pressure steam boiler systems. Additionally, tannin programs, on the basis of blends of certain natural (e.g., quebracho tannin) or synthetic tannins are used as corrosion inhibitors, as they provide a combination of oxygen scavenging, passivating and sludge conditioning functions.

Sodium sulfite is widely employed, and approximately 8 ppm is needed for every 1 ppm of oxygen. As a fairly high sulfite reserve is required (typically 20–50 ppm or more), additional sulfite must be added and so the general rule is 10 ppm of sodium sulfite per 1 ppm oxygen. The maintenance of a slight excess of the oxygen scavenger in the water provides assurance that there is no dissolved oxygen present. Complete water treatment formulations containing sodium sulfite for this purpose will also include a catalyst, ensuring that the reaction between the dissolved oxygen and the oxygen scavenger is instantaneous, even in cold water.

Hydrazine is not widely used as an oxygen scavenger because of its toxicity. Other oxygen scavengers currently used as a replacement for hydrazine include diethylhydroxylamine (DEHA), sodium erythorbate, carbonylhydrazide (CHZ), methylethylketoxime (MEKO), and hydroquinone (HQ). Typical reserves for these materials are very low, perhaps only 0.1–0.2 ppm.

Control over corrosion in the boiler section may also require the use of alkalinity boosters, based on alkali metal hydroxides. Feedwater pH is generally in the range 8.0–9.3. Boiler water pH will vary



depending upon design and pressure rating. For lower pressures the pH will be 10.5–11.5 or 12. For higher pressures, the pH may only be 9.0–10.0.

Control over corrosion in steam and condensate line sections will need to manage the ingress of oxygen and the formation of carbonic acid, and perhaps deal with the corrosive effects of ammonia on copper – which may have been specified as a pH adjuster and steel corrosion modifier. Condensate treatments include neutralizing amines such as morpholine and filming amines such as octadecylamine (ODA), as well as the highly basic ammonia.

- *Scale and deposit control.* This requires control over primarily hardness salts and other scale forming minerals. Usually a water softener will be specified to soften all incoming makeup water, used as boiler feed. Internal inhibitors include coagulation and precipitation chemistries, chelants, polymers, and blends of all these types of chemicals.

Coagulation and precipitation programs are widely used and employ various types of phosphates as a precipitant to provide control over the unwelcome deposition of hardness scales. Carbonates and polysilicates were once commonly used. Chemistries based on neutral and alkaline phosphates are now the primary precipitation programs. Where coagulation and precipitation programs are employed, specific polymeric dispersants are also required. In the presence of excess alkalinity, phosphate is precipitated as calcium hydroxy-phosphate or hydroxyapatite [ $\text{Ca}_3(\text{PO}_4)_2 \cdot \text{Ca}(\text{OH})_2$ ]. Magnesium with hydroxide alkalinity present in the boiler water will form the hydroxide, precipitating as brucite ( $\text{Mg}(\text{OH})_2$ ). In these forms, the particles are more easily dispersed and held in suspension. It is vital to have adequate alkalinity. The basic coagulation and precipitation program includes a phosphate polymer combination used to maintain a sodium phosphate concentration in the boiler water at 20–60  $\text{mg l}^{-1}$ , ensuring that all the calcium has precipitated as phosphate.

Chelant programs, based on the use of ethylenediaminetetraacetic acid (EDTA) and nitrilotriacetic acid (NTA) chemistries, are commonly prescribed for both FT and WT boilers either as replacements for, or used in combination with, phosphate precipitation programs. They act as solubilizers, not precipitants. Chelants should not be used in excess of 2–3  $\text{mg l}^{-1}$  free chelate

because corrosion of iron can be accelerated in the boiler water. Excellent control over the presence of dissolved oxygen is vital, but chelants can provide a very clean boiler.

- All-polymer/all-organic programs are perhaps the most widely used hardness control products today. Very many specialty polymers are now available and widely used in every type and size of boiler. Typically, multifunctional blends are used as phosphate replacements, and act as dispersants and sludge conditioners. They also provide control over specific problems such as iron transport and silica scaling that can affect many industrial boiler systems. The type of polymers employed includes, polyacrylic acid and polyacrylates (PAA), sulfonated styrene/maleic anhydride (SS/MA), and an iron oxide dispersant, the second one (SS/MA) being an excellent  $\text{Ca}_3(\text{PO}_4)_2$  inhibitor/dispersant where soluble Fe is absent. Also, the copolymer based on acrylic acid and 2-acrylamido-methylpropane sulfonic acid (AA/AMPS or AA/SA) is employed as a  $\text{Ca}_3(\text{PO}_4)_2$  inhibitor/dispersant. Additionally, phosphinocarboxylic acid (PCA) chemistries are used as high temperature suspended-solids dispersants and  $\text{CaSO}_4$  scale inhibitors. These polymers are also polyelectrolytes and distort the scale particle/crystal and its growth, rendering it less adhesive to heat-transfer surfaces and more readily dispersed with a reduced tendency to compact into a dense scale. Some modern polymers also sequester hardness similar to the chelants.

Many permutations of dual- or multifunctional programs exist, on the basis of either chelant or phosphate chemistries, together with polymers and related organics. These types of program are widely employed.

- *Control over specific contaminants and higher pressure boilers.* Very specific polymers are used for control over silica, iron, and copper transport.

Coordinated phosphate programs are employed where there is a need to avoid the formation of hydroxyl alkalinity (free caustic) in higher-pressure WT boilers. They require very careful management and control. Variant programs include congruent control and equilibrium phosphate treatment chemistries.

All-volatile programs (AVPs) are also employed in higher-pressure boilers (generally power boilers) and utilize only volatile chemicals, such as ammonia, amines (such as diethylhydroxylamine, DEHA), and other vapor-phase inhibitors (VPIs).

#### **4.27.17 Modification of Cooling System Waterside Environments by Chemical Inhibitors**

Corrosion and deposits of scale, dirt, mud, organic slime/biofilms, and algae growths are the major problems encountered in open recirculating cooling water systems. There is a loss of water caused by both evaporation and windage drift. The water lost by drift will be of the same quality as the recirculating water; that is, it will contain the same amount of dissolved minerals and impurities. The water lost by evaporation, however, will be essentially pure water, devoid of mineral contaminants.

The evaporation of pure water vapor leaves the dissolved mineral contaminants behind in the recirculating water, and as discussed earlier, the water lost by evaporation is replaced by makeup water, containing dissolved minerals and impurities. As a result, there is an accumulation of minerals that constantly increases in the system as more makeup water is introduced. If the cycles of concentration of dissolved minerals are not controlled, eventually the recirculating water will become so saturated that the most insoluble salts will come out of solution and form a scale on heat-transfer surfaces or within other parts of the system. To avoid this, a risk-benefit condition exists, whereby some bleed off is given but COC is strictly limited.

If COC is raised, there are savings to be made in both water volumes and chemical inhibitors consumed. However, the risk of scaling and fouling increases, which can produce significant cost increase because of cleaning, loss of operational efficiencies, and additional maintenance, so a risk-benefit balance has to be calculated. This will be different for each and every type of cooling system, on the basis of system design acceptable maintenance costs, and water quality.

In open cooling water systems, oxygen cannot be economically removed with scavengers because these systems are constantly aerated and therefore, corrosion inhibitors that are effective in oxygen-containing environments must be employed. Also recirculating cooling water systems contain various types of metals and alloys, and inhibitors and environmental conditions maintained must be compatible with these multimetalllic systems. A particular problem associated with these systems is galvanic corrosion caused by bimetallic couples and white rust.

Treatment of recirculating cooling water must first include control of the pH value for both scale and corrosion control – usually within the range of 7.5–9.5. Lower pH values tend to render the

recirculating water excessively corrosive, while higher pH values will result in both amphoteric metal corrosion (as with zinc, brass, and aluminum) and scale-forming conditions. At this pH, modification of corrosion risk is controlled by corrosion inhibitors added to the recirculating water, which usually form a protective barrier on the metal surface either by chemical reaction with the metal surface or by physical or chemical adsorption on the metal surface. An actively corroding metal can be rendered passive though the use of inhibitors that react in this manner. There are many types and combinations of corrosion inhibitors used for open cooling water systems, on the basis of molybdate, zinc, phosphate, and potentially many dozens of organic-based inhibitor chemistries.

The most troublesome mineral scale is calcium carbonate as it is the least soluble of the salts present in the recirculating water. Alkalinity should also be limited to prevent precipitation of calcium carbonate scale. Alkalinity is present in the form of bicarbonates and carbonates which combine with calcium and magnesium to form calcium carbonate and magnesium carbonate. (Calcium carbonate, being less soluble than magnesium carbonate, will form first).

Alkalinity should be limited not only to prevent precipitation of calcium carbonates, but also to prevent high pH conditions, which may be damaging to some system components such as galvanized steel, brass, or cooling tower lumber. In many larger cooling systems operating with hard water, sulfuric acid is employed to reduce alkalinity by forming calcium sulfate, which is much more soluble than calcium carbonate by a factor of more than 100 times.

Smaller cooling systems operating with hard water may use fully or partially softened water. It is not a good idea to use fully softened water as the risk of corrosion increases significantly. In most modern cooling water program chemistries, calcium, in the presence of phosphonates and polymers, is employed as an anodic corrosion inhibitor.

Limits for common contaminants in recirculating cooling water is provided in [Table 8](#).

Modification of the waterside environment will require control over cooling water chemistry. Notes are provided below.

- If the total hardness rises above 600 ppm, the LSI is likely to be above +2.5 to +2.8 and ion-exchange or lime-soda softening is required, ideally using an 80:20 ratio, soft:hard water blend. Alternatively,

**Table 8** Evaluation of control over bacterial growths

<i>TAB result</i>	<i>Evaluation</i>
0 to $10^2$ colonies per ml	Excellent control
$10^2$ to $10^3$ colonies per ml	Warning, but no serious fouling risk
$10^4$ to $10^5$ colonies per ml	$10^4$ is the maximum permitted for healthcare $10^5$ is a typical maximum for commerce/industry
$10^5$ to $10^6$ colonies per ml	Unacceptable. Fouling anticipated. Also, a possible health risk
$>10^6$ colonies per ml	Serious risk of fouling and pathogens

sulfuric acid and/or a special, stabilized phosphate or alkaline phosphate program must be used. All programs require a good understanding of chemistry and excellent monitoring and control.

- Usually, if the total hardness rises significantly, then the total alkalinity will also rise. If total alkalinity rises above 500 ppm, then the LSI is likely to be above +2.5 to +2.8 and dealkalization is required. (Commonly sulfuric acid is employed; also sulfamic acid for small systems). Alternatively, high stability tolerant, organic threshold/crystal modifier polymers are employed, as adjuncts to the chemical treatment program in place.
- Silica should not be permitted to rise above 120 ppm otherwise irreversible silica scaling will occur. The generally accepted limit is 150 ppm, but this is only in highly alkaline water systems (silica is more soluble in caustic alkaline waters, e.g., boiler water).
- In deep well waters, sulfate often comprises 50% or more of the total calcium hardness (i.e., if, for example, the calcium hardness is  $350 \text{ mg l}^{-1}$  (as  $\text{CaCO}_3$ ) and the total alkalinity is, say,  $200 \text{ mg l}^{-1}$  (as  $\text{CaCO}_3$ ), then the difference of  $150 \text{ mg l}^{-1}$  will most likely be because of calcium sulfate). Sulfate concentration in recirculating cooling water should not exceed 1500 ppm, unless a sulfate-stabilizing polymer is present. Maximum level to avoid irreversible sulfate scaling is 1800 ppm, as  $\text{CaSO}_4$ . Ideally use a sulfate stabilizer over 1200 ppm.

Chemical inhibitor chemistries employed as water-side environmental modifiers include the following:

- *Cathodic and anodic inhibitors.* Cathodic inhibitors, such as zinc, promote insoluble deposits that have an insulating effect and block the flow of electrons, limiting the cathodic reaction and hence anodic dissolution. Anodic inhibitors, such as nitrite, assist

film repair over the metal at anodic sites and hence passivate these areas. When using anodic inhibitors it is vital to maintain correct concentration, as if the anodic sites are not completely blocked, the remaining exposed anodic area will be much smaller than before and preferentially and rapidly corrode, because of higher current densities at the anode sites, causing highly localized pitting attack and rapid perforation of sections.

Molybdate inhibitors depend upon sodium molybdate as a weak oxidizer for ferrous metals, promoting a complex passive oxide film. Molybdates are used in combination with other inhibitors such as zinc, phosphate, phosphonates, and organics for synergistic effect to produce highly effective, synergistic corrosion inhibitor formulations. However, because of cost, the molybdate inhibitor blends are usually used at very low levels in open cooling water systems, typically maintaining less than  $5\text{--}10 \text{ mg l}^{-1}$  as sodium molybdate. In fact, because of the improvement in effectiveness of some novel organic chemistries, molybdenum may be present only at a 'tracer' level, as it is easily and accurately tested at low level and can act as an indicator molecule. Under these circumstances, the typical level in the cooling system is, perhaps, only  $1.0\text{--}1.5 \text{ ppm}$  as Mo. There is a secondary benefit, in that the Mo acts as a synergizer to enable other (organic) inhibitors, such as tolyltriazole (TTA) for copper and hydroxyphosphinocarboxylic acid (HPCA), for iron/steel, to function better.

Zinc, when combined with other inhibitors can provide very effective synergistic chemistries. Formulations might be based on zinc-silicate; zinc-phosphonate, zinc-molybdate, zinc-polyphosphate-organic, or zinc-organic-phosphate combinations. The zinc level in the cooling water is usually held to a maximum of  $2\text{--}5 \text{ mg l}^{-1}$ , depending upon the type of formulation. (The United States Public Health Service Drinking Water Standards limit the zinc of drinking water to  $5.0 \text{ mg l}^{-1}$ ). In some cases, zinc discharged even at this level can be toxic to aquatic life. Some discharge criteria limit the permissible zinc concentrations to  $1.0 \text{ mg l}^{-1}$  zinc, or less. In this case, non-zinc inhibitors should be used.

Phosphate inhibitors are used in neutral to slightly alkaline and moderately alkaline cooling water systems, combined with polymers to form formulated blends that inhibit the formation of phosphate sludge. With the development of very effective phosphate scale inhibitors and stabilizing dispersants (such as the copolymers of acrylic acid

and sulfonic acid polymer, and sulfonated polystyrene and maleic acid) alkaline and stabilized phosphate based inhibitor programs have gained wide acceptance. The orthophosphate levels maintained vary from 5 to 20 mg l<sup>-1</sup>. These inhibitors are most effective at high pH and alkalinity and are usually used at pH 8.0–9.0. The formulations require increased scale control from improved polymer and phosphate blends. The organic azole nonferrous metal inhibitors are also necessary for complete protection. Stabilized phosphate programs in various modifications are probably still the most widely used programs around the world, as they are relatively low cost. Generally, they are used in conjunction with sulfuric acid.

Orthophosphates at much lower levels (perhaps 1.5–3.0 mg l<sup>-1</sup>) may be employed as threshold corrosion inhibitors in potable waters, where they inhibit the pickup of lead into the water, stabilize calcium present, and provide some protection against the corrosion of iron and steel pipes. The phosphates used are either phosphoric acid or sodium hexametaphosphate. Silicates can also be used in potable water systems, where they exhibit similar corrosion-inhibiting effects.

- *Organic Scale Inhibitors, Dispersants and Deposit Control Agents.* Starting with the development of polyacrylates in the 1960s, there is now a plethora of organic scale and corrosion inhibitors available today. Most water treatment formulations will contain several organic inhibitor chemistries blended in precise synergistic ratios to produce the most cost-effective inhibitor programs possible. Depending upon the water treatment company or technologist and the specifics of the cooling system, the total level of 'active' organic inhibitor chemicals present in the recirculating cooling water might be between 7.5 mg l<sup>-1</sup> and 30 or possibly 35 mg l<sup>-1</sup>. This is much less than the level of contaminants and reflects the threshold control abilities of the chemicals. The chemicals provide a combination of effects to control corrosion, scale, and dispersion of minerals and salts. The effects include the following:

- adsorption on the metal surface to control corrosion by film formation;
- direct interference with the corrosion mechanism, so that the inhibitor becomes an integral part of the passivated metal surface;
- chelation of metals, to solubilize them, thus preventing fouling (e.g., by Fe) and scaling (e.g., by Ca);

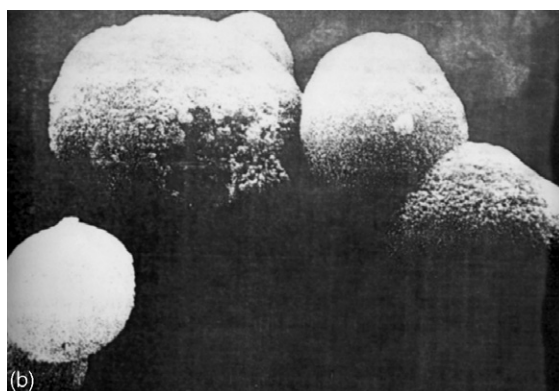
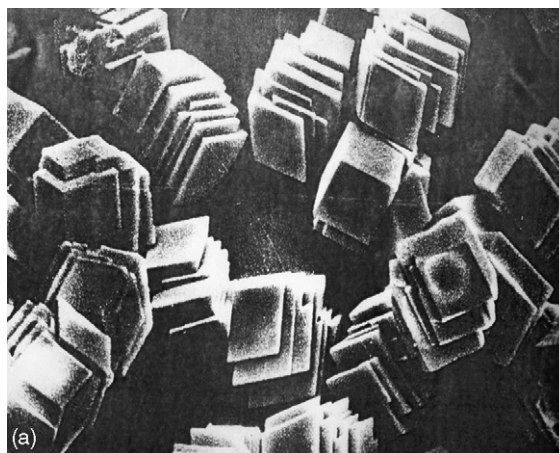


**Photo 11** (a) Scale crystals modified by an organic inhibitor and (b) scale crystals also modified by an organic inhibitor.

- dispersion of minerals and salts by adsorption onto particulate surfaces, causing them to repel each other because of a like charge; and
- scale inhibition because of modification of the growth of the crystal.

**Photos 11(a) and 11(b)** show calcite crystals modified and distorted by organic inhibitors.

#### **4.27.18 Types of Modern Organic Chemical Inhibitors Employed to Modify Cooling System Waterside Environments Against Risks of Scale, Fouling, and Corrosion Control**

The various organic chemistries commonly employed today include<sup>11,16</sup>:

- *Polyacrylic acid and polyacrylates (PAA)*, 2000–3000 molecular weight (MW). Used for lower-stress CaCO<sub>3</sub>

scale inhibition and general dispersive purpose, or as a secondary support to other chemistries.

- *Polyacrylic acid and polyacrylates (PAA) 4000–5000 MW*. Used for lower-stress general dispersion of suspended solids.
- *Polymethacrylic acid and polymethacrylates (PMAA)*. Used for general and  $\text{CaCO}_3$  scale inhibition; also dispersion of suspended solids and iron (Fe) transport.
- *Polymaleic acid (PMA)*. An excellent homopolymer chemistry for  $\text{CaCO}_3$  and  $\text{CaSO}_4$  scale inhibition under severe service conditions, but with limited dispersive powers.
- *Maleic acid/methyl vinyl ether (MA/MVE)*. Used for  $\text{CaCO}_3$  scale inhibition, with good stability in severe stress conditions and where chlorine is employed.
- *Acrylic acid/hydroxypropyl acrylate (AA/HPA)*. Used as a  $\text{Ca}_3(\text{PO}_4)_2$  inhibitor/dispersant and an iron oxides dispersant.
- *Sulfonated styrene/maleic anhydride (SS/MA)*. Available in a variety of styrene/maleic ratios, and an excellent  $\text{Ca}_3(\text{PO}_4)_2$  inhibitor/dispersant where soluble Fe is absent. Also, an iron oxides dispersant.
- *Acrylic acid/2-acrylamido-methylpropane sulfonic acid (AA/AMPS or AA/SA)*. An excellent copolymer used as a  $\text{Ca}_3(\text{PO}_4)_2$  inhibitor/dispersant and a Zn stabilizer.
- *Acrylic acid/sulfonic acid/substituted acrylamide (AA/SA/NI)*. Used as an iron oxide dispersant. Also, as a  $\text{Ca}_3\text{PO}_4$  and Zn stabilizer/dispersant, in the presence of iron, and under high-stress conditions.
- *Acrylic acid/sulfonic acid/sodium styrene sulfonate (AA/SA/SSS)*. Used for  $\text{Ca}_3(\text{PO}_4)_2$  inhibition/dispersion. Also, for calcium phosphonate control and Fe stabilization.
- *Maleic anhydride/ethyl acrylate/vinyl acrylate (MA/EA/VA)*. A terpolymer, used as a  $\text{CaCO}_3$  scale inhibitor and a thermally stable, general dispersant.
- *Aminotri(methylenephosphonic acid) (ATMP)*. A phosphonate used as a lower-stress  $\text{CaCO}_3$  scale inhibitor and building block-corrosion inhibitor for general duty.
- *1-Hydroxyethylidene-1, 1, diposphonic acid (HEDP)*. A standard  $\text{CaCO}_3$  scale inhibitor and building block-corrosion inhibitor. It is reasonably  $\text{Cl}_2$  resistant.
- *Phosphono-butane tricarboxylic acid (PBTC)*. A  $\text{CaCO}_3$  scale inhibitor and building block-corrosion inhibitor under high stress conditions.
- *Hydroxyphosphono acetic acid (HPCA)*. A ferrous corrosion inhibitor, especially designed to be incorporated into ‘all organic’ programs.
- *Phosphonocarboxylic (sulfonated) copolymer (POCA)*. A low phosphorus content,  $\text{CaCO}_3$  scale inhibitor and corrosion inhibitor.
- *Phosphinocarboxylic acid (PCA)*. A number of PCA materials have been designed as suspended solids dispersants,  $\text{CaSO}_4$  scale inhibitors operating under high stress conditions, low phosphorus content, chlorine resistant, ferrous corrosion inhibitors, or zinc stabilizer and building block corrosion inhibitors (especially in soft water).
- *Tolyltriazole (TTA) or benzotriazole (BTA)*. Azoles, used as corrosion inhibitors for copper and brasses.

Under higher-stress operating conditions (i.e., high heat-exchanger ‘skin’ temperatures, regular use of oxidizer biocides, low or high flow rates, high dirt loadings, etc.), improved inhibitor formulations, or higher concentration of inhibitors are employed – or both! Because different waters may require different types of inhibitor and the fact that all water systems are dynamic, with variable flow rates, stress-levels, and operating demands, it is necessary to have automatic adjustment of inhibitor concentrations, using feed and control equipment. Chemicals may be supplied in perhaps drums or totes and proportionally fed to a water system by means of a pump, which is actuated by some type of controller ranging from a simple timer to a web-based energy management device.

**Photo 12** shows a supply of chemical corrosion inhibitor being fed to an industrial cooling water system for gas process application.

#### 4.27.19 Modifying Cooling System Waterside Environments to Minimize Risks of Biological Fouling and MIC

Oxidizer and nonoxidizer chemistries are widely employed to control microbiological and algal growths in cooling systems, to prevent fouling and operational efficiency problems, to reduce health risks, and to prevent MIC. The major forms of biological organisms that thrive in cooling tower waters are bacterial slimes, algae, and fungi. The spores and seeds of these organisms are present in the atmosphere attached to particles of dust, dirt, pollen, and other airborne particulates. When washed out of the air at the cooling tower they find a favorable environment to grow and multiply. These growths cause serious problems of corrosion, fouling, and blockage, and accelerate buildup of deposits. Such growths not only interfere with



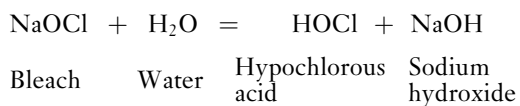


**Photo 12** Chemical corrosion inhibitor feeding station.

water flow but also reduce heat transfer and increase energy losses.

Biological growths can be controlled by registered pesticides substances variously called microbiocides, slimicides, algaecides, and fungicides. Examples include the following<sup>28</sup>:

- *Sodium hypochlorite (Bleach)*. Oxidizer. Sodium hypochlorite is supplied as a 11–13% available chlorine solution. Handling is not usually a problem, but the significant volumes required usually make bleach suitable for only smaller cooling systems. In water, bleach rapidly hydrolyzes according to the equation below:



Thus when bleach is used, hypochlorous acid is formed but also sodium hydroxide (caustic soda) tends to increase the pH. Therefore, extra vigilance may be needed if bleach is used in galvanized cooling towers. Bleach is usually dispensed two or three times per week by hand-adding a known volume, although the use of a timer-controlled pump, is a preferred

alternative. Bleach can also be used in combination with sodium bromide solution to produce hypobromous acid.

- *Bromine*. Oxidizer. Bromine based biocides have been used as pesticides, disinfectants, algaecides, and slimicides for 40–50 years or more, in agriculture, the pulp and paper industry, once-through turbine condenser cooling, and the chemical industry. In the late 1970s and early 1980s, a major step forward came in cooling water treatment technology with the introduction of programs based on bromine release agents. This was primarily bromo-3-chlorodimethylhydantoin (BCDMH), which is available as granules and in various sizes of tablet (puck) and stick. Most bromine biocides employ chlorine in some form, as an ‘activator’ to produce the primary biocidal species hypobromous acid (HOBr). During the last 20 years, the use of programs based on bromine chemistry has become standard practice. Bromine/chlorine-based biocides have become internationally accepted as mainstream products for all types of cooling water systems, brewery pasteurizers, and many other process applications. Bromine/chlorine biocides are now available in many permutations of composition and form.
- *DBNPA*. Nonoxidizer. 2-2-Dibromo-3-nitrilopropionamide. Organo-bromine group. Effective, general-purpose bactericide but hydrolyzes rapidly above pH 8.0. DBNPA is suitable for bacterial slime cleanup where high levels of organics and biomass are present. It functions in conjunction with chlorine. DBNPA is suitable for once-through cooling systems, because of its fast acting biocidal action (contact time often less than 1 h). DBNPA is not particularly effective against algae. The half-life of DBNPA decreases rapidly with increasing pH and temperature. This is not generally a problem because of the short contact time required, and may be a benefit when required to meet strict discharge regulations.
- *DTEA II*. Nonoxidizer. 2-(Decylthio)ethanamine. Alkylthioamine group. It is designed to operate effectively under a wide range of pH levels (pH 6 to 10 or greater) as a biocidal cleaner. It was also designed as a specific sessile bactericide, biofilm remover, and biofilm growth control agent. DTEA or DTEA II functions by forming reversible chelant complexes with the salts and inorganic ions found in biofilm structures, and it severely weakens the biofilm and reduces its adhesiveness. DTEA or DTEA

It is highly surface active and can be thought of as a 'biocidal soap' to be used for cleanup programs (biofilm debris will quickly be in evidence and foaming may occur), as a biocide component with chlorine (although it is not recommended to be used at the same time as chlorine), and as a maintenance biostat. Application rates are typically 50–100 mg l<sup>-1</sup>. It is consumed as it decays rapidly in heavily fouled systems (typically in 3–4 h); consequently, it is recommended to slowly add the complete dose over a four-hour period.

- **Glutaraldehyde.** Nonoxidizer. Pentane-1,5-dial. Aldehyde group. Glutaraldehyde is a good bactericide, especially with difficult and persistent organisms because of its good penetrating ability. It has limited effectiveness against algae and fungi. The kill mechanism is by cross-linking outer proteins of cell and preventing cell permeability. Glutaraldehyde is a fast-acting biocide (3–4 h, perhaps 4–6 h with difficult slimes), nonionic, nonfoaming, effective over a wide pH range (typically pH 6.5–9.0), and compatible with chlorine. It is also effective against SRBs and biofilms. The half-life tends to be short, depending upon the particular cooling system parameters, but typically 4–12 h. Careful evaluation is needed before application on some larger systems, especially as it may not be particularly cost effective. Glutaraldehyde is readily biodegradable. Typical use concentration is 100–125 mg l<sup>-1</sup> at 45% active material, although heavily slimed cooling systems may need 200–300 mg l<sup>-1</sup> as an initial, cleanup shock dose. It is an effective choice for biological control in air washers. Glutaraldehyde is probably a good biocide where the risk of *Legionella* sp. exists.
- **Isothiazolines.** Nonoxidizer. Alkyl isothiazolin-3-ones. Organosulfur group. Good, wide-spectrum bactericide and algicide that is effective over a wide range of pH. Isothiazolines kill by inhibiting microbial respiration and food transport through the cell wall. It is recognized as an industry standard product for cooling systems but can be expensive. Isothiazolines are supplied to some markets as a 13.9% active concentrated blend (10.1% 5-chloro-2-methyl-4-isothiazolin-3-one and 3.8% 2-methyl-4-isothiazolin-3-one). It is always marketed to the end user, as a 1.5% active (1.11% + 0.39% to 1.15% + 0.35%) in-use blend. Isothiazolines are amber to yellow-green liquids that require very careful handling because of severe skin and eye irritant properties. They are effective against both general aerobic and

**Table 9** Evaluation of control over bacterial growths

<i>TAB result</i>	<i>Evaluation</i>
0 to 10 <sup>2</sup> colonies per ml	Excellent control
10 <sup>2</sup> to 10 <sup>3</sup> colonies per ml	Warning, but no serious fouling risk
10 <sup>4</sup> to 10 <sup>5</sup> colonies per ml	10 <sup>4</sup> is the maximum permitted for healthcare 10 <sup>5</sup> is a typical maximum for commerce/industry
10 <sup>5</sup> to 10 <sup>6</sup> colonies per ml	Unacceptable. Fouling anticipated. Also, a possible health risk
>10 <sup>6</sup> colonies per ml	Serious risk of fouling and pathogens

spore-forming bacteria, over a pH range of 6.5–9.0. Isothiazolines are very effective algicides and fungicides, but only at acid to slightly alkaline pH levels. Contact time is typically 5–6 h. Dose rate is typically 50–120 mg l<sup>-1</sup>, for 1.5% active isothiazoline.

Where waterside environments are modified by the use of biocides, various field and laboratory test methods are available to monitor the recirculating water to obtain a total bacteria count and predetermine the need for further addition or modification of the biocides. Field methods include test strips, dip-slides, and ATP meters. Laboratory methods include plate counts. Tests made periodically during operation of the system will provide a history that will indicate if there is an increase in the bacteria count during any particular season, showing the possible need for a change in biocide program.

The biocide program performance should typically be evaluated on the basis of the total bacteria count (TAB) of microorganism in the recirculating cooling water, as indicated in [Table 9](#).

#### 4.27.20 Conclusion

It can be seen from the foregoing sections that the effective control of corrosion of water systems, by modification of waterside environments is part science, part art, and part experience, requiring a thorough understanding of the collective and often synergistic impact of a wide variety of risk factors that may cause other problems, including scaling and fouling. Additionally, in the primary heat-exchange and heat transfer applications for cooling and heating systems, any proposed environmental modification

program must also take into account the economics, management and operational practicalities.

## References

1. *Global Water Outlook to 2025*. International Food Policy Research Institute ([www.ifpri.org](http://www.ifpri.org)).
2. Shiklomanov, I. A. Evolution of water withdrawals and consumption since 1900. Worldwide Council ([www.worldwidecouncil.org](http://www.worldwidecouncil.org)), 1999.
3. *Vital Water Graphics*. United Nations Environmental Program ([www.unep.org](http://www.unep.org)).
4. *Estimated Use of Water in the United States in 2000*. U.S. Geological Survey ([www.usgs.com](http://www.usgs.com)).
5. *Thermoelectric-power water use*. U.S. Geological Survey ([www.usgs.com](http://www.usgs.com)).
6. Koch, G. H.; Thompson, N. G.; Brongers, M. P. H.; Payer, J. H. *The United States Cost of Corrosion Study*; NACE International: Houston, TX, 2003.
7. U.S. DOD Corrosion Office. Global Cost of Corrosion Program Plan, Draft 2 Jan 2008.
8. National Oceanic and Atmospheric Administration (NOAA). <http://www.esrl.noaa.gov/gmd/ccgg/trends/>.
9. Stwertka, A. *Guide to the Elements*, rev. ed.; Oxford University Press, 1998.
10. UPAC. *Compendium of Chemical Terminology*, 2nd ed. (the "Gold Book"), McNaught, A. D., Wilkinson, A., Eds.; Blackwell: Oxford, 1997.
11. Frayne, C. *Cooling Water Treatment Principles and Practice*. Chemical Publishing: New York, NY, 1999.
12. U.S. EPA. Drinking Water Contaminants and Quality Criteria for Water (Commonly known as the "Gold Book"). Document No. EPA-440/5-86-001, Washington, DC, 1986.
13. Electric Power Research Institute. Recommendations for an Effective Flow-accelerated Corrosion Program (EPRI-NSAC-202L-R3), 1994.
14. Jeff, D. Update on Flow Accelerated Corrosion (FAC), Vogt Power International Inc. Technical Bulletin, 2004.
15. Reggiani, G. M. White Rust – An Industry Update and Guide Paper. Association of Water Technologies, 2002; [www.awt.org](http://www.awt.org).
16. Frayne, C. In Corrosion 2008 Conference; NACE International, 2008; Paper 083678.
17. Eble, K. S.; Feathers, J. Water Reuse within a Refinery Cooling Technology Institute, 1993; [www.cti.org](http://www.cti.org).
18. Sundstrom, G. Organoclay Aids Water Reuse at Canadian Refinery Industrial Water World, January 2006; [www.pennet.com](http://www.pennet.com).
19. Cinna, L. Coalescer and Advanced Filter Designs for Removal of Oil and Solvents. *Pollution Equipment News*, August 2007; [www.rimbach.com](http://www.rimbach.com).
20. Frayne, C. *Boiler Water Treatment Principles and Practice*; Chemical Publishing: New York, NY, 2002; 2 vols.
21. Blake, R. T. *Water Treatment for HVAC and Potable Water Systems*, 8th ed.; McGraw-Hill: New York, 1980.
22. Boffardi, B. P.; Schweitzer, G. W. Cooling water system performance predicted by computer simulator; NACE Paper #80195, Material Performance, December 1980; [www.nace.org](http://www.nace.org).
23. Vanderpool, D. Hidden assumptions in saturation calculations. "The Analyst", Association of Water Technologies, Laurel Functional Chemicals, Summer 2002; [www.awt.org](http://www.awt.org).
24. Ferguson Robert, J. In *52nd International Water Conference, Pittsburgh 1991*; IWC Paper #91-47; [www.eswp.com](http://www.eswp.com).
25. Langelier, W. F. *J. Am. Water Works Ass.* **1936**, 28(10), 1500–1521.
26. Larson, T. E.; Skold, R. V. Laboratory studies relating mineral quality of water to corrosion of steel and cast iron, Illinois State Water Survey, Champaign, IL, 1958; pp 43–46, ISWS C-71.
27. Cutler, P. Stainless steels and drinking water around the world. Nickel Institute UK. [www.euro-inax.org/pdf/map/paper/Cutler\\_water\\_EN.pdf](http://www.euro-inax.org/pdf/map/paper/Cutler_water_EN.pdf).
28. Frayne, C. The selection and application of non-oxidizing biocides for cooling water systems; "The Analyst," Association of Water Technologies, Spring 2001; [www.awt.org](http://www.awt.org).

## 4.31 Economic Aspects of Corrosion

**J. A. Richardson**

Anticorrosion Consulting, 5 Redhills Lane, Durham DH1 4AL, UK

**J. L. Dawson**

Corrosion Consultant, 16 Brandwood Close, Worsley, Manchester M28 1XX, UK

© 2010 Elsevier B.V. All rights reserved.

4.31.1	Costs of Corrosion in Individual Organizations	3040
4.31.1.1	Sources of Corrosion Costs	3040
4.31.1.2	Investment Appraisal	3041
4.31.1.3	Identifying the Most Economic Corrosion Control Option	3043
4.31.1.3.1	Life cycle costing	3043
4.31.1.3.2	Selecting the most economic material of construction	3043
4.31.1.3.3	Deciding among repair, protection, and replacement options	3044
4.31.1.3.4	Incorporating risks and uncertainties into economic evaluations	3045
4.31.1.3.5	General outcomes of LCC approaches	3047
4.31.2	Costs of Corrosion in Specific Sectors/Economies	3047
4.31.2.1	Quantifying Corrosion Costs in Sectors/Economies	3047
4.31.2.2	Corrosion Costs in Specific Sectors	3048
4.31.2.3	Corrosion Costs in National Economies	3049
References		3050

### Glossary

**Discounted cash flow (DCF)** A method of valuing a project or asset incorporating the time value of money in which all future cash flows are estimated and discounted to their present values using a discount rate that is generally the appropriate cost of capital that may be adjusted to incorporate uncertainties in future cash flows.

**Net present value (NPV)** The total present value of a time series of cash flows.

**Life cycle cost (LCC)** The total cost of ownership over the life of an asset.

**EV** Expected value (currency units)

**FV** Future value (currency units)

***i*** Discount/interest rate (%)

***n*** Number of time periods (normally years)

**PV** Present value (currency units)

### Abbreviations

**CRA** Corrosion resistant alloy

**CRF** Capital recovery factor

**GNP** Gross national product

**PVC** Polyvinyl chloride

**ROI** Return on investment

### Symbols

**A** Annualized cost (currency units)

### 4.31.1 Costs of Corrosion in Individual Organizations

#### 4.31.1.1 Sources of Corrosion Costs

Corrosion is intrinsic to the procurement and operation of physical assets, and costs are inevitably incurred in its avoidance and/or its consequences. Corrosion costs can be disaggregated in several ways. The most obvious way is to differentiate the recognizable 'direct' costs of corrosion control expenditures, including any planned repair or replacement, from 'indirect' or 'consequential' costs that result from unexpected corrosion incidents. Accounting practices dictate that the costs of corrosion are recorded as 'capital' or 'operating' costs.

The direct, capital costs of corrosion arise from:

1. The process for selecting materials and associated protection technologies for the assets, including any materials testing and/or qualification.

2. The additional costs of the chosen materials over the cheaper materials from which the assets could be constructed in the absence of corrosion risks.
3. The provision of corrosion allowances.
4. The application of linings, claddings or coatings.
5. The purchase, installation and commissioning of equipment/systems for the injection of corrosion inhibitors, the application of cathodic or anodic protection, the monitoring or analysis for corrosion control purposes, and the maintenance of operation or containment of hazards in the event of corrosion-induced failures.
6. The prevention of any corrosion that may be anticipated during the procurement/construction phase.

The direct costs of corrosion that arise in service are:

1. Inspection and maintenance/servicing of linings, cladding and coatings, and corrosion control equipment/systems.
2. Consumable costs of chemicals and power used for corrosion control.
3. Planned repair and replacement of equipment/components damaged by corrosion.

Indirect, consequential operating expenditures arise from:

1. Failure analysis and corrosion problem solving processes.
2. Unplanned repair and replacement of equipment/components damaged by corrosion.
3. Revenue losses arising from unavailability of assets at any stage (delayed start up, unscheduled downtime, poor equipment performance) because of unforeseen corrosion damage.
4. Fines, compensation/remediation costs and the costs of lost goodwill and reputation arising from death, injury, or environmental damage because of unforeseen corrosion-induced failure.

Indirect, consequential costs are less obviously quantified but can be very large. Major incidents can result in bankruptcy, withdrawal of the organization's license to operate, and even custodial sentences for accountable individuals.

#### 4.31.1.2 Investment Appraisal

Both commercial and public sector organizations use physical assets and labor to produce and deliver goods and services. Commercial sector organizations

pursue profit whereas public sector organizations usually pursue social/economic benefits arising from the provision of utilities, infrastructures, transportation etc. Simplified, schematic flows of cash arising from investment in commercial organizations are shown in **Figure 1** showing how the cash generated after tax is a source of investment capital for the future.

Any organization, commercial or public sector, must invest in the most profitable or beneficial projects available in order to survive and develop. At any particular time, there is inevitable competition among potential projects for limited capital funds, and organizations need appraisal processes to identify those potential projects that offer the best returns on investment. The simplest process is to favor projects that offer low first cost. However, in the cases of complex assets that are required to operate for many years, more sophisticated appraisal processes that balance the flows of revenues and costs over the whole life cycle, adjusted to allow for factors such as the cost of money and inflation/taxation rates, are required.<sup>1,2</sup>

A key to investment appraisal for the longer term is to recognize and incorporate the time value of money. The value or worth of a unit of money varies with time depending on the prevailing inflation and interest rates. Compounding uses the interest rate to provide a future value or worth of a present sum of money:

$$FV = PV \times (1 + i)^n$$

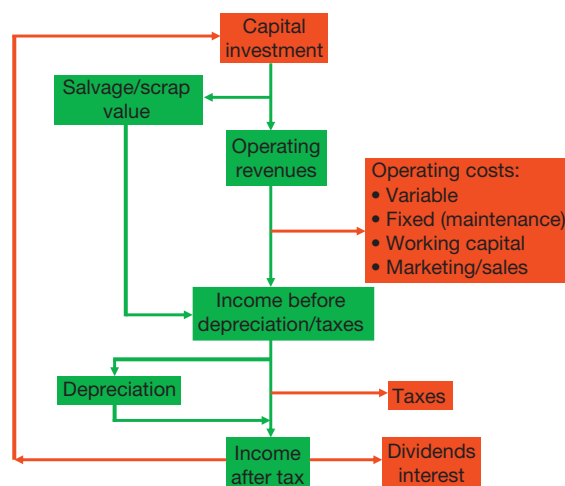


**Figure 1** Simplified cash flows generated by investment in a commercial organization.



where PV is the present value, FV is the future value,  $i$  is the discount/interest rate (%);  $n$  is the number of time periods (normally years).

The term  $(1 + i)^n$  is the so-called compound factor. Discounting is the reciprocal of the more familiar compounding, in which an interest rate is used to provide a present value or worth of a future sum of money:

$$PV = FV \times \frac{1}{(1 + i)^n}$$

The term  $1/(1 + i)^n$  is the discount factor. Both compound and discount factors are available from tables in standard textbooks for different discount rates and times.<sup>1,2</sup> The effects of interest are incorporated into investment appraisal by the use of discounted cash flow (DCF) procedures in which all capital and operating costs and revenues associated with a particular investment throughout its life, adjusted to incorporate any anticipated effects of inflation, are discounted to their values in a base year. Summation of the discounted positive and negative cash flows at any stage of life produces a net present value (NPV) for the investment.

The patterns of cash flow and the effects of discounting are shown for a hypothetical example of a typical manufacturing investment in Table 1 and Figure 2, based on a major investment in capital assets of 200 currency units in the base year 0. In the two preceding years, -2 and -1, costs of 10 and 50 units, respectively, are incurred in activities such as market research and product and manufacturing

process development. Over the following years 1–10, the assets operate to yield cash flow depending on the balances between sales revenues and the direct and indirect costs of sales and manufacture. In the case depicted in Figure 2, positive cash flows of 80, 90, and 100 units are delivered in years 1, 2, and each of 3–10, respectively, as a result of which net cash flow increases progressively over the operating life of the assets. The effects of discounting at different rates on the present worth of cash flows over time are shown in Table 1 and Figure 2.

Several criteria are available for comparing discounted cash flows for competing potential investments:

1. Money, expressed as the NPV after a given time period. In the case depicted in Table 1, the NPVs after 10 years are 321 and 119 currency units at discount rates of 10 and 20%, respectively, compared with an equivalent net cash flow of 710 currency units.
2. Time, expressed as the 'payback period' at which the cash flow for the project is equal to the original investment. The higher the discount rate, the longer the payback periods. In the case depicted in Figure 2, the undiscounted cash flow pays back at the end of year 2, but at discount rates of 10 and 20% the paybacks are during year 3 and at the end of year 4, respectively.

**Table 1** Net cash flow (NCF) and net present value (NPV) as functions of time for a typical manufacturing investment at discount rates of 10 and 20%

Year	Net cash flow currency units	NPV discount rate	
		10% currency units	20% currency units
-2	-10	-12	-14.5
-1	-60	-67	-75
0	-260	-267	-275
1	-180	-194	-209
2	-90	-119	-147
3	10	-44	-89
4	110	24	-41
5	210	86	-1
6	310	142	33
7	410	193	61
8	510	240	84
9	610	282	103
10	710	321	119

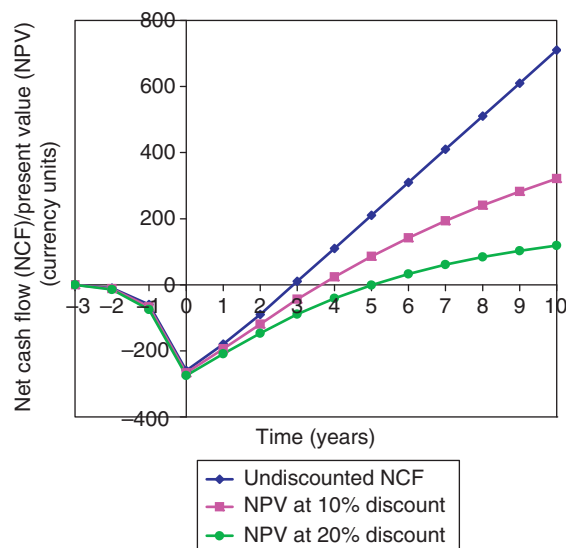


**Figure 2** Net cash flow (NCF) and net present value (NPV) as functions of time for a typical manufacturing investment at discount rates of 10 and 20%.

3. Rate of return on investment (ROI), expressed usually as the average net income for a defined period (usually a year) over the life of the project as a percentage of the total investment. There are various methods for computing ROI. At its simplest, the undiscounted ROI for the case depicted in [Table 1](#) is  $(97/260) \times 100 = 37\%$

The most profitable or beneficial investment is that which yields the highest NPV over the design life of the investment and/or the shortest payback period, and/or the highest ROI.

An alternative basis for comparison is the annualized cost,  $A$ , which is calculated for each of the competing projects or options as follows:

$$A = \frac{PV \times i(1 \pm i)^n}{(1 + i)^n - 1}$$

The term  $i(1 + i)^n / ((1 + i)^n - 1)$  is the capital recovery factor (CRF) that essentially allows the present worth of future expenditures to be converted into an equivalent annual cost that provides for the replacement of equipment to deliver the required operating life and, if appropriate, the decommissioning/scrapping of equipment at the end of the project life. On this basis, the most economic investment is that with the lowest annualized cost. Such evaluations must consider a sensible time period of the number of years for the project assessment to be realistic.

### 4.31.1.3 Identifying the Most Economic Corrosion Control Option

#### 4.31.1.3.1 Life cycle costing

Corrosion control expenditures constitute negative cash flows, although the savings they provide arising from lower maintenance and downtime costs impact positively on NPV, particularly when they replace deficient or even nonexistent corrosion control practices.

In the cases of assets that are at risk of corrosion in service, choices have to be made at the investment stage as to how to mitigate the risks most effectively,

not least the most economic deployment of capital expenditures across corrosion-resistant materials and/or operating expenditures on corrosion control. Essentially, these are alternative investment options that are best evaluated economically using DCF procedures to identify the option with the lowest life cycle cost (LCC). There are well-developed processes for predicting LCCs, including specific guidance on the life cycle costing of corrosion in specific contexts.<sup>3,4</sup> Life cycle costing is usually applied to new assets but is equally applicable to the evaluation of repair, rehabilitation or replacement options for the existing equipment. The use of LCC in both contexts is illustrated in the examples that follow.

#### 4.31.1.3.2 Selecting the most economic material of construction

A decision that faces all car suppliers/owners is the choice of constructional material for the exhaust system. In practice, the three potential materials are unprotected mild steel, aluminized mild steel, and stainless steel that have lives of 2.5, 4, and 10 years at first costs of 60, 80, and 180 currency units, respectively. The simplest approach in identifying the most economic material is to calculate an undiscounted, average yearly cost for each material, as displayed in [Table 2](#). On this basis, stainless steel appears to be the most economic material at an annual cost of 18 currency units per year, but this analysis takes no account of the time value of money.

[Table 2](#) also displays annualized cost,  $A$ , for each of the materials that have been calculated on the basis that money to purchase the exhaust systems is borrowed at an interest rate of 10%, resulting in CRFs of 0.47, 0.32 and 0.16 for mild steel, aluminized steel, and stainless steel respectively. On this basis, aluminized mild steel emerges as the most, and stainless steel the least, economic material.

[Table 3](#) demonstrates an alternative approach to incorporating the time value of money and displays NPV for the three materials on the basis that money to purchase the exhaust systems is borrowed at an

**Table 2** Annualized costs ( $A$ ) for three exhaust system options at a discount rate of 10%

System	First cost currency units	Life years	Undiscounted annual cost currency units	CRF discount rate 10%	$A$ discount rate 10% currency units
Mild steel	60	2.5	24	$\frac{0.1(1.1)^{2.5}}{(1.1)^{2.5}-1} = 0.47$	28.20
Aluminized steel	80	4	20	$\frac{0.1(1.1)^4}{(1.1)^4-1} = 0.32$	25.60
Stainless steel	180	10	18	$\frac{0.1(1.1)^{10}}{(1.1)^{10}-1} = 0.16$	28.80

**Table 3** Net present value (NPV) as a function of time for three exhaust system options at a discount rate of 10%

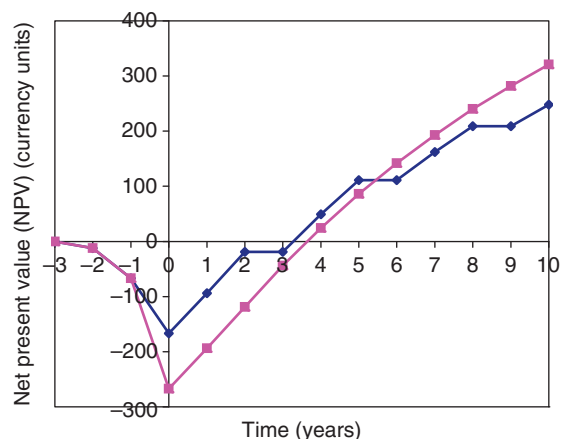
Year	Cash flow currency units	PV discount rate 10% currency units	NPV discount rate 10% currency units
<i>Mild Steel</i>			
0	60	60.00	60.00
2.5	60	47.28	107.28
5.0	60	37.26	144.54
7.5	60	29.34	173.88
10.0	60	23.10	196.98
12.5	60	18.24	215.22
15.0	60	14.34	229.56
17.5	60	11.32	240.88
<i>Aluminized steel</i>			
0	80	80.00	80.00
4	80	54.64	134.64
8	80	37.36	172.00
12	80	25.52	197.52
16	80	17.44	214.96
<i>Stainless steel</i>			
0	180	180.00	180.00
10	180	69.40	249.40

interest rate of 10% and an operating life for the car of 20 years is required. The outcome is the same as for the annualized cost analysis.

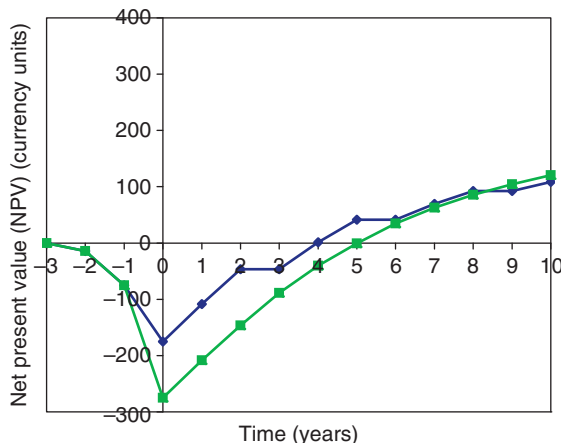
The interest/discount rate has a significant influence as to which material is the most economic. Lower rates favor stainless steel that becomes more economic than mild steel and aluminized steel at interest rates of ~4% and ~9%, respectively. In the 10–20% interest rate range, aluminized steel is the most economic material and only at very high interest rates, 35% and above, does mild steel become the most economic material.

The use of LCC for identifying the most economic materials of construction in a manufacturing context is depicted in **Figure 3** that relates to the hypothetical manufacturing project defined in **Table 1** and **Figure 2**. It is assumed that there are two alternative construction materials for the assets. Stainless steel corrodes at a very low rate and provides a 10-year life at an initial cost of 200 currency units. Mild steel costs only 100 currency units, but corrodes at rates that require extensive repair and refurbishment of assets during years 2–3, 5–6, and 8–9 at a cost of 100 currency units on each occasion. **Figures 3(a) and 3(b)** show discounted cash flows for the two alternative materials of construction at discount rates of 10 and 20%.

At a discount rate of 10%, mild steel pays back marginally earlier than the stainless steel option but, beyond the fifth year, the NPV for the stainless steel



(a)



(b)

**Figure 3** NPVs as functions of time for a typical manufacturing investment constructed in mild and stainless steels at a discount rate of (a) 10% and (b) 20%.

option is increasingly larger. In contrast, at a discount rate of 20%, the mild steel option pays back significantly earlier and, even after 10 years, the NPV advantage offered by the stainless steel option is marginal.

#### 4.31.1.3.3 Deciding among repair, protection, and replacement options

This choice is illustrated by the case of a water main that has experienced a series of leaks because of external corrosion. The options for correction are:

1. ongoing repair of leaks,
2. install cathodic protection to the existing piping system, and
3. replace with a PVC piping system.

The basis for the assessment is that the main is required to operate for a further 40 years at a prevailing 12% interest/discount rate. The assessment is based on a 1-km length of pipe assuming a constant leakage rate of 3 per kilometer per year. Leaks cost an average of 18 currency units to repair.

Cathodic protection using magnesium anodes designed for a 20-year life is estimated to reduce repairs by 95%. The initial installed cost of a cathodic protection system is 180 currency units and the system does not require maintenance.

The installation cost of replacement with a PVC piping system is 1440 currency units per kilometer and a PVC main is expected to have a 40-year maintenance-free life.

Annualized costs for the three options are summarized in [Table 4](#), from which it is clear that installing a cathodic protection system on the existing main is more cost effective than either of the alternative options. Even if the required life of the main was extended from 40 to 90 years, in which case the CRF for replacement would change from 0.121 at 40 years to 0.120 at 90 years, cathodic protection would remain the most economic option.

However, selection of the cathodic protection option assumes that the condition of the main remains sufficiently good for cathodic protection to sustain the ongoing failure rate at 5% of the existing level. If there are doubts about this, the choice reverts to ongoing repair or replacement of the existing main with PVC pipe. At a repair cost of 18 currency units per leak, a leakage rate of 9.7 leaks per kilometer would be required to equalize the annualized cost of 174 currency units for replacement with PVC. Although at face value, this is several times the current leak rate, the assumption that the leak rate will remain constant is probably optimistic. Studies of cumulative leak history curves suggests that leak rates are more likely to increase exponentially with time, in which case replacement is likely to prove a more economic option sooner rather than later.

This illustrates that risks and uncertainties in the various cost inputs to economic evaluations must be recognized and incorporated into decision criteria.

#### 4.31.1.3.4 *Incorporating risks and uncertainties into economic evaluations*

The previous economic evaluations in this chapter have all been deterministic. However, there are inevitable risks and uncertainties in the assumptions and data inputs and these can be allowed for in the evaluations by the use of probabilities. The importance of such analysis has been illustrated<sup>5</sup> for the case of a 10-mile, 6-in. diameter, offshore pipeline, for which the options for mitigating corrosion risks are:

1. carbon steel, protected by corrosion inhibitor addition;
2. carbon steel clad with a corrosion-resistant alloy (CRA).

In a deterministic analysis incorporating all relevant initial and operating costs, the NPV costs based on a discount rate of 10% and a cost escalation rate of 7% are \$12 and \$23 million for the inhibited carbon steel and clad carbon steel options, respectively. On this basis, the inhibited carbon steel option would be installed. However, this analysis does not consider the probability of failure or its economic consequences that are considerable in the case of offshore equipment.

The expected value (EV) method can be used to compare options when there are multiple potential outcomes of a decision. The expected value of a decision is based on Bayesian logic and can be regarded as the 'usual' outcome of many instances of the decision. In the case of the pipeline, it can be used to incorporate the impact of failure as an additional NPV cost on the two base options arising from a single event or multiple events over the life of the pipeline. In the case of the clad pipeline, it is considered that there is a 1% probability of a single or multiple events having an NPV cost of \$25 million. In the case of the inhibited

**Table 4** Annualized costs (A) for pipe repair, protection, and replacement options at a discount rate of 12%

Option	First cost currency units	Life years	Annual leakage cost currency units	CRF discount rate 12%	A discount rate 12% currency units
Repair leaks			54	1	54
Cathodic protection	180	20	2.7	0.134	24.1 + 2.7 = 26.8
Replacement PVC pipe	1 440	40		0.121	174

pipeline, the equivalent corrosion risks and consequences are larger and are considered to amount to a 20% probability of an NPV cost of \$75 million. The corresponding EV costs that result for the two options are shown in the decision tree in Figure 4 where it is apparent that the most economic option on this basis is the clad carbon steel pipeline.

In practice, it can be difficult to anticipate the probabilities, costs, and timings of specific possible failures. A more generalized approach to the EV

method is provided by the so-called probability limit curves such as that depicted in Figure 5, based on the equivalence of failure scenarios that have the same NPV cost. In Figure 5, the probability and NPV cost of a clad pipeline failure are set at 1% and \$25 million, respectively and the curve defines the locus of equal EVs for clad and inhibited carbon steel options that separates zones where one or the other option is the economic choice. This provides more flexibility in factoring risk into the decision process.

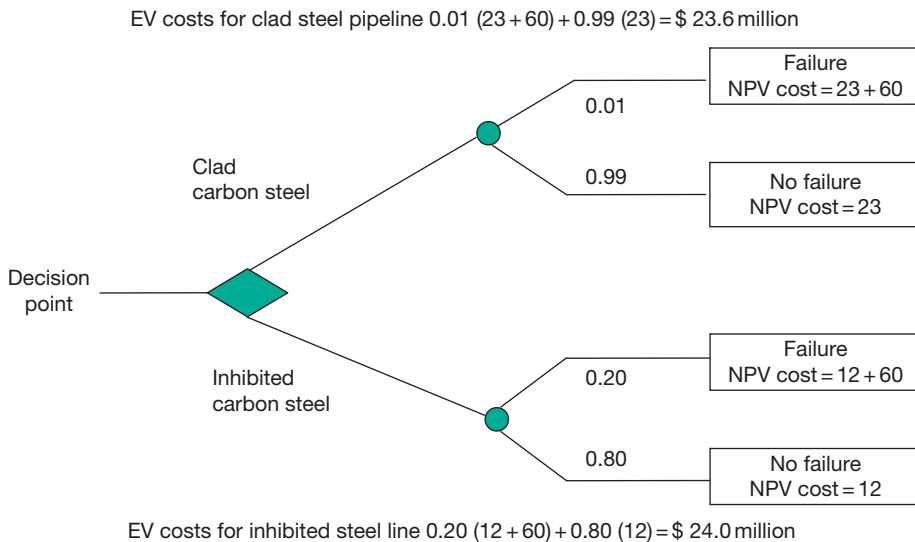


**Figure 4** Use of expected value (EV) calculations incorporating risk to decide amongst pipeline corrosion risk mitigation options. Adapted from Craig, B. D.; Thompson, R. S. *Corros. Mgmt.* **1995**, 7, 14–17.

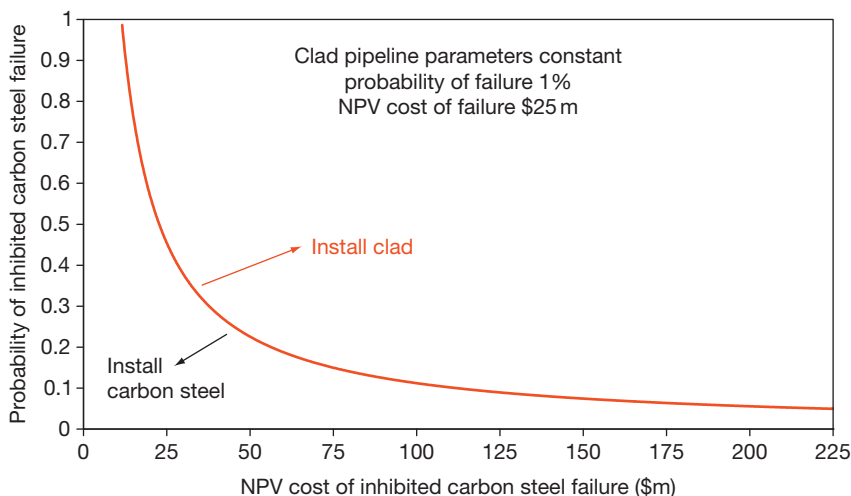


**Figure 5** Probability limit curve incorporating risk to decide amongst pipeline corrosion risk mitigation options. Adapted from Craig, B. D.; Thompson, R. S. *Corros. Mgmt.* **1995**, 7, 14–17.



#### 4.31.1.3.5 General outcomes of LCC approaches

The examples above illustrate some general economic truths relating to the selection of corrosion control options:

1. Relatively low interest rates favor long-term economic planning and the cheapest may well not be the most economic option when LCCs are taken into consideration.
2. Alternatively, when the capital is very expensive, shorter-term considerations tend to dominate and large long-term investments have no merit over small frequently repeated investments. In these circumstances, the cheapest is also likely to be the most economic option.
3. It is essential that the risks and uncertainties attached to the inputs of a decision are understood and incorporated into the process of identifying the most economic option.

As to whether these truths are understood and practiced, a recent UK survey of the costs of corrosion in specific industrial sectors<sup>6–10</sup> revealed an increasing usage of LCC approaches in selecting corrosion control options, but a widespread lack of awareness of the total costs of corrosion in specific organizations. To some extent, this results from accounting practices that make it difficult to disaggregate corrosion costs from standard cost categories such as capital and maintenance costs. However, a detailed awareness of corrosion costs is essential to the development of optimal corrosion control management strategies, particularly, in those organizations where corrosion presents a significant threat to the reliability and availability of operating equipment.

### 4.31.2 Costs of Corrosion in Specific Sectors/Economies

#### 4.31.2.1 Quantifying Corrosion Costs in Sectors/Economies

Over the past ~60 years, there have been numerous studies of the costs of corrosion to specific industrial sectors and/or national economies, including the United Kingdom,<sup>6–11</sup> United States,<sup>12–15</sup> Australia,<sup>16–20</sup> India,<sup>21</sup> Sweden,<sup>22</sup> Finland,<sup>23</sup> West Germany,<sup>24</sup> Japan,<sup>25,26</sup> China,<sup>27</sup> Kuwait,<sup>28</sup> and Canada.<sup>29</sup>

Early studies of corrosion costs tended to concentrate on direct expenditures. For example, Uhlig based his original USA study<sup>12</sup> on quantifying national expenditures on the direct costs of corrosion

across the economy including corrosion-resistant materials, coatings, inhibitors, cathodic protection, and repair and replacement costs. Hoar's later UK study<sup>11</sup> focused on the estimates of recognized industry experts in specific industrial sectors in addition to the surveys of expenditure on corrosion protection measures. The application of the above approaches to the Japanese economy<sup>25</sup> resulted in a higher estimate of total cost using the Hoar rather than the Uhlig approach.

The USA economy has received the most frequent and detailed evaluation and the outputs of the key studies<sup>13–15</sup> are summarized in Figure 6. Following Uhlig's initial 1949 study,<sup>12</sup> NBS Battelle revisited the cost of corrosion to the national economy in 1978 in a much more rigorous study<sup>13,14</sup> that drew on the expertise of professional economists to evaluate sectorwise economic statistics. This approach introduced some top-down evaluation that was missing from Uhlig's earlier study and sought to trace expenditures on corrosion in different sectors of the economy through 'input' purchases of goods and services for corrosion control and their impact on 'outputs' including revenues. This input-output approach estimated a significantly higher cost than the original Uhlig study because it included the consequential costs of corrosion arising from the unavailability of assets and incidents with safety, health and environmental consequences. The 1978 study was updated in 1996 and a completely new study in 2002<sup>15</sup> confirmed a declining trend in total expenditures on corrosion in the 1978–2002 period.

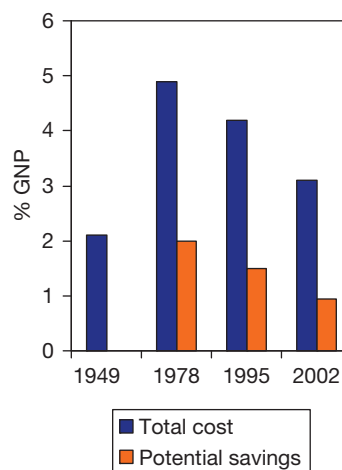


**Figure 6** Total cost of corrosion and potential savings in the USA economy as percentages of GNP in 1949,<sup>12</sup> 1978/1995,<sup>13,14</sup> and 2002.<sup>15</sup>

A later study of the application of the input/output model to the Japanese economy<sup>26,30</sup> confirmed that it produces significantly higher estimates than earlier approaches and concluded that it is likely to estimate costs that are 2–4 times higher than the application of the Uhlig or Hoar approaches.

There is no recognized definitive approach towards estimating the cost of corrosion to industrial sectors and national economies. Some quite detailed models have been proposed<sup>20,31</sup> but all approaches involve degrees of judgment and approximation that reflect uncertainties in the contributions of corrosion to costs in individual organizations or sectors of an economy.

#### 4.31.2.2 Corrosion Costs in Specific Sectors

In recent years, there have been numerous studies of the costs of corrosion in specific industrial sectors. The most recent USA study<sup>15</sup> examined corrosion costs in 26 individual sectors within the broader sectors of utilities, transportation, infrastructure, defense and production or manufacturing. The costs of the top 12 categories, shown in Figure 7 as percentages of the total USA cost of corrosion, provide an overview of the relative sizes of the various sectors

in relation to the expenditures on corrosion control. Drinking water and sewerage systems comprise the most expensive individual sector, and together with electrical utilities and gas distribution they establish utilities as the largest broad sector. Corrosion control in motor vehicles dominates transportation, the second largest broad sector followed by infrastructure, including expenditures on highway bridges, hazardous materials storages, and gas and liquid pipelines. In the grand scheme of things, expenditures on production and manufacturing, including pulp and paper, petroleum refining, chemicals, and oil and gas are relatively small.

As important as the sizes of the various sectors depicted in Figure 7 is the relative efficacies of their expenditures on corrosion control *viz.* to what extent the expenditures represent money well spent as opposed to money wasted. The results of detailed studies of the total costs of corrosion and the potential savings in several sectors in the United Kingdom<sup>6,7,9,10</sup> and the United States<sup>32</sup> are shown in Figure 8 as percentages of turnover. Total expenditures vary from as high as 7% to as low as 1% of turnover in the cases of the USA electric power and UK food and drink manufacturing sectors, respectively. These broad differences are consistent with

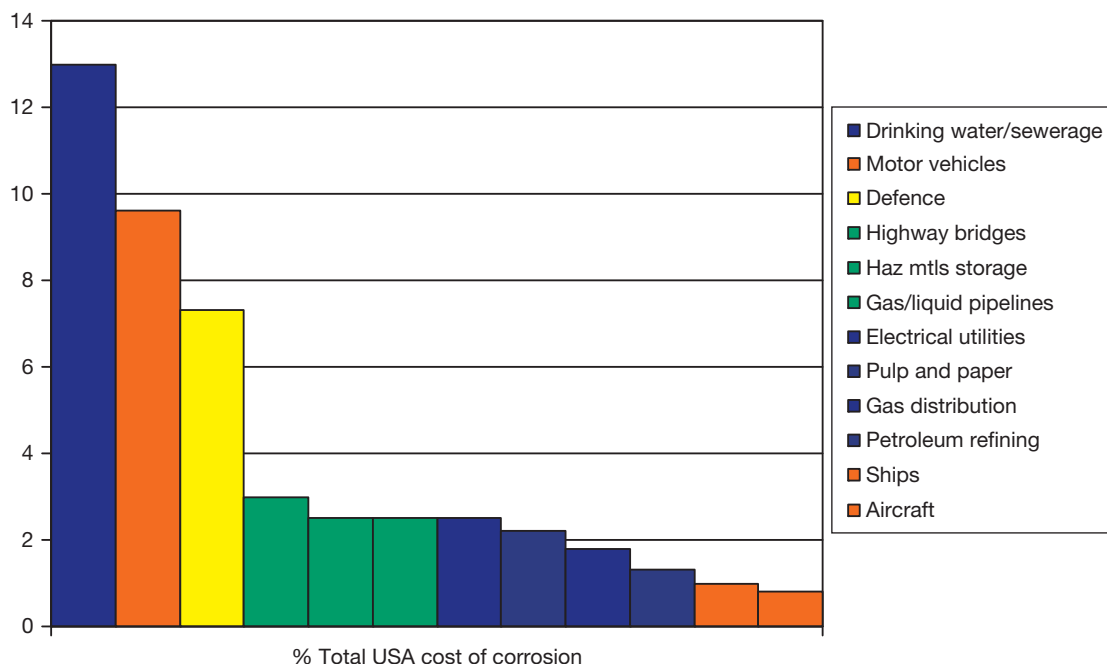


**Figure 7** Costs of corrosion in top 12 sectors as percentages of the total cost of corrosion in the USA economy in 2002. Adapted from Koch, G. H.; Brongers, M. P. H.; Thompson, N. G.; Virmani, P.; Payer, J. H. *Corrosion Costs and Preventive Strategies in the USA*, Report FHWA-RD-01-156 to Federal Highways Administration; C. C. Technologies Laboratories, 2001.

the different types of processes and equipments in the different sectors. The USA electric power sector includes nuclear operations with significant corrosion risks to address using very stringent and expensive corrosion risk management procedures. The UK food and drink manufacturing sector is faced with much lower corrosion risks to its predominantly stainless steel equipment and its expenditures are correspondingly lower.

The total expenditures in **Figure 8** are averages in each case based on the ranges of expenditures for individual organizations in the sectors that depend on the type, age and location of their equipment. Thus, in the UK petrochemical/chemical sector, total expenditures ranged from as little as 0.1% of turnover in the case of a small, contract manufacturing company with several glass-/tantalum-lined vessels in excellent condition that had been written off the books, to as high as 8.9% of turnover in the case of a large manufacturer with old assets with major external corrosion problems resulting in significant unscheduled downtime and heavy repair/replacement expenditures.

All the sectors examined made significant and increasing usages of risk-based methodologies in the management of their corrosion problems, including life cycle costing, reliability/availability/maintainability modeling and risk-based inspection. Despite this, all identified scope for further potential savings, ranging from 10% to 22% of the total expenditures in the UK food and drink manufacturing and USA electric power industries, respectively, by applying existing technology and best management practices. In only one sector in the UK study, automotive manufacturing (not shown in **Figure 8**), it was judged that corrosion expenditures were close to the

economic optimum. This sector had been highlighted in Hoar's 1971 study<sup>11</sup> of the UK economy as a particular source of potential savings; since then technology and corrosion management practices have improved in the industry worldwide to the stage where the United States' second highest sector expenditure in **Figure 7** can be classed as money well spent.

#### 4.31.2.3 Corrosion Costs in National Economies

Studies of the costs of corrosion in different countries conclude generally that total corrosion expenditures comprise 3–5% GNP. Intuitively, the level would be expected to vary with the stage of development and mix of industrial sectors in any particular economy and to reduce with time as technology and management practices improve. There is some evidence for this from several studies<sup>12–15</sup> of the large and diverse USA economy over time, summarized in **Figure 6**, where total expenditures have reduced from 4.9 to 3.1% of GNP in the 1978–2002 period. Studies of the UK economy<sup>6–11</sup> widely separated in time suggest a similar trend, driven by improvements in:

1. Advances in corrosion-resistant materials and protection technologies.
2. Improved understanding and dimensioning of corrosion processes including the codification of knowledge in international/national standards, codes of practice and guidance documents in all sectors.
3. Improved corrosion management practices related to materials and protection selection and optimizing the availability and inspection of assets, including new and improved technologies for corrosion monitoring and inspection.

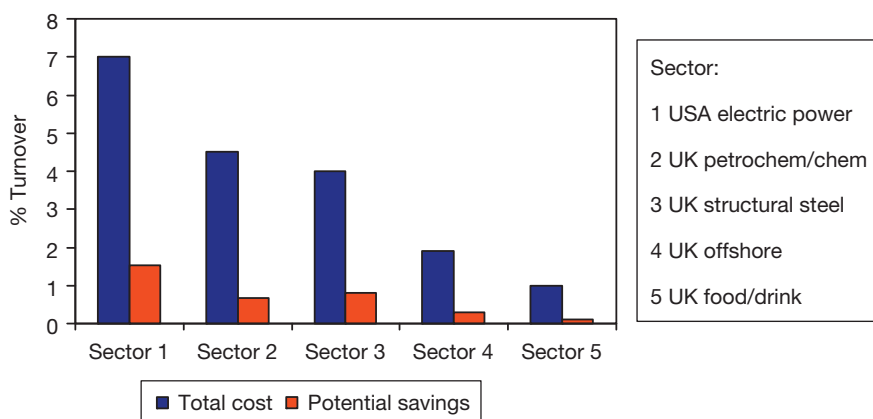


**Figure 8** Total costs of corrosion and potential savings in various sectors of the United Kingdom<sup>6–10</sup> and United States<sup>32</sup> economies as percentages of sector turnover.

Over the same period, although the estimated scope for further potential savings in the USA and UK studies has reduced, it remains at 20–30% of prevailing expenditures as a result of:

1. Legacy issues – problems in ageing structures, designed, fabricated and protected to standards now recognized as inadequate, for example, external corrosion of ‘baby boomer’ process industry equipment, under thermal insulation and fireproofing.
2. Management issues – problems for which there are proven, economic, technical solutions, for example, corrosion in cooling water and steam-raising equipment or in CO<sub>2</sub>/H<sub>2</sub>S-containing produced water and seawater equipment.
3. Technology challenges – problems for which there are no proven economic solutions, for example, materials for chemical/petrochemical equipment that is vulnerable to metal dusting.

All studies recognize that there is scope for further significant reductions in corrosion expenditures by:

1. Promoting awareness and uptake of advanced design and good corrosion management practices.
2. Improving corrosion technology through research, development and implementation, including advanced life prediction and performance assessment methodologies.
3. Improving education and training of staff at all levels in corrosion control and safeguarding university training of future corrosion professionals.

In relation to the availability and deployment of corrosion professionals, the recent UK study<sup>6–10</sup> revealed concerns across all sectors about loss of expertise arising from a progressive decline in numbers employed in user organizations, resulting in a net migration of corrosion expertise to supplier and research/consulting organizations.

A further conclusion of several of the national studies is the potential benefits of changes in taxation policy to categorize operational corrosion control expenditures as capital investments rather than maintenance costs so that they attract tax allowances, thereby promoting front-end approaches towards corrosion control.

Extrapolating the evident trend in **Figure 6** suggests that there is an optimum economic level of expenditure on corrosion for a large, diverse economy within the 2–2.5% GNP range. Although conventionally defined as the ‘cost’ of corrosion, this reinforces a rather negative image for corrosion as

‘engineering’s grim reaper’ in relation to its impact on economic activity. In reality, corrosion control expenditures enable developed economies to sustain high levels of economic activity through the availability and reliability of their infrastructures and wealth-creating physical assets. In the process, they sustain profitable, high-technology businesses that provide employment and pay taxes. These constitute enormous ‘benefits’, as well as ‘costs.’

In relation to the image of corrosion, the corrosion community might learn from the health sector. Human disease is a useful paradigm for corrosion. Developed economies spend 7–14% GNP on the health of their human assets and, although smaller, corrosion expenditure on physical assets, at a current 3–5% GNP, is of the same order of magnitude. Health expenditure is near the top of political agendas in all developed economies with increasing emphasis on predictive/preventative strategies. There is scope to raise the profile of corrosion and protection to achieve commensurate recognition and resources and deliver its full potential benefit to the national economies. This, however, relies on corrosion practitioners and educators being able to apply the basic economic tools of discounting/life cycle costing and to understand their relevance in the context of tactical and strategic decision making.

## References

1. Lumby, S.; Jones, C. *Fundamentals of Investment Appraisal*; Thomson Learning, 2000.
2. Dayanada, D.; Irons, R.; Harrison, S.; Herbohn, J.; Rowland, P. *Capital Budgeting: Financial Appraisal of Investment Projects*; Cambridge University Press, 2002.
3. ISO 15663 *Petroleum and Natural Gas Industries – Life Cycle Costing, Parts 1–3*; 2001.
4. Jackman, P. *Working Party Report on the Life Cycle Costing of Corrosion in the Oil and Gas Industry: a Guideline (EFC 32)*; European Federation of Corrosion, 2003.
5. Craig, B. D.; Thompson, R. S. *Corros. Mgmt.* **1995**, 7, 14–17.
6. McIntyre, P. *Corrosion and Associated Costs in the UK Chemicals and Petrochemicals Sector, Degradation of Materials in Aggressive Environments Programme (DME)*, Report NRW/PM/CORRO/D1; Paint Research Association, 2001.
7. McIntyre, P. *Corrosion and Associated Costs in the UK Offshore Sector, Degradation of Materials in Aggressive Environments Programme (DME)*, Report NRW/PM/CORRO/D2; Paint Research Association, 2001.
8. Jotischky, H. *Corrosion and Associated Costs in the UK Automotive OEM Sector, Degradation of Materials in Aggressive Environments Programme (DME)*, Report NRW/PM/CORRO/D1; Paint Research Association, 2001.

9. Whitehouse, N. *Corrosion and Associated Costs in the UK Food and Drink Sector, Degradation of Materials in Aggressive Environments Programme (DME)*, Report NRW/PM/CORRO/D1; Paint Research Association, 2001.
10. Whitehouse, N. *Corrosion and Associated Costs in the UK Constructional Steelwork Sector, Degradation of Materials in Aggressive Environments Programme (DME)*, Report NRW/PM/CORRO/D1; Paint Research Association, 2001.
11. Hoar, T. P. *Report of the Committee on Corrosion and Protection*; HMSO: London, 1971.
12. Uhlig, H. H. *Chem. Eng. News* **1949**, 27, 27–64.
13. Payer, J. H.; Dippod, D. G.; Boyd, W. K.; Berry, W. E.; Brooman, N. *Economic Effects of Metallic Corrosion in USA*, Report 511-2 CCR 70-122; NBS Battelle: Houston, TX, 1978.
14. Bennett, L. H.; Kruger, J.; Parker, R. L.; Passaglia, E.; Reimann, C. *Economic Effects of Metallic Corrosion in the USA*, Report 511-1 GCR 78-122; NBS Battelle: Houston, TX, 1978.
15. Koch, G. H.; Brongers, M. P. H.; Thompson, N. G.; Virmani, P.; Payer, J. H. *Corrosion Costs and Preventive Strategies in the USA*, Report FHWA-RD-01-156 to Federal Highways Administration; C. C. Technologies Laboratories, 2001.
16. Worner, H. K. *Committee Report on the Symposium on Corrosion*; University of Melbourne, 1955.
17. Potter, E. C. *Aust. Corros. Eng.* **1972**, 16, 21.
18. Revie, R. W.; Uhlig, H. H. *J. Inst. Eng. Aust.* **1974**, 46, 3–5.
19. Cherry, B. W.; Skerry, B. S. *Corrosion in Australia, Report of the Australian National Centre of Corrosion Prevention and Control Feasibility Study*; 1983.
20. Cherry, B. W. *Mater. Forum (Australia)* **1995**, 19, 1–7.
21. Rajagopalan, K. S. *Report on Metallic Corrosion in India*; CSIR: India, 1962.
22. Tradgaidh, F. K. *Tekn. Tedskrift* **1965**, 95, 1191.
23. Linderborg, S. *Kemiam Teollusius* **1967**, 24, 234.
24. Behrens, D. *Br. Corros. J.* **1967**, 10, 122.
25. Committee on Corrosion Loss in Japan. *Boshoku Gijutsu* **1977**, 26, 401–512.
26. Committee on Corrosion Loss in Japan. *Zairyo-to-Kankyo* **2001**, 50, 490–512.
27. Zhu, R. In Symposium on International Approaches to Reducing Corrosion Costs, Corrosion'86; National Association of Corrosion Engineers: Houston, TX, 1986.
28. Al-Kharafi, F.; Al-Hashem, A.; Matrouk, F. *Economic Effects of Metallic Corrosion in the State of Kuwait*; KISR, 1995.
29. Sastri, V. S.; Elboujdaini, M.; Perumareddi, J. R. In International Symposium on Environmental Degradation of Materials and Corrosion Control in Metals Proceedings of the 42nd Annual Conference of Metallurgists of CIM, Vancouver, Canada **2003**; pp 321–328.
30. Shibata, T. *Corros. Sci. Technol. (South Korea)* **2002**, 31, 97–102.
31. Biezma, M. V.; San Cristobal, J. R. *Corros. Eng. Sci. Technol.* **2005**, 40, 344–352.
32. Syrett, B. C.; Gorman, J. A. *Mater. Perform.* **2003**, 42, 32–38.



## 4.30 Corrosion Management Overview

**J. L. Dawson**

Corrosion Consultant, 16 Brandwood Close, Worsley, Manchester M28 1XX, UK

© 2010 Elsevier B.V. All rights reserved.

<b>4.30.1</b>	<b>Background to Corrosion Management</b>	3002
4.30.1.1	Introduction	3002
4.30.1.2	The Need for Corrosion Management	3002
4.30.1.3	Legislative Drivers	3003
4.30.1.4	Basic Concepts	3005
<b>4.30.2</b>	<b>Corrosion Management Processes</b>	3006
4.30.2.1	Introduction	3006
4.30.2.2	Quality Management Processes	3006
4.30.2.3	Risk Management Processes	3007
<b>4.30.3</b>	<b>Corrosion Management tools</b>	3010
4.30.3.1	Identification of Corrosion Risks	3010
4.30.3.1.1	Corrosion damage and failure modes	3010
4.30.3.1.2	Sources of corrosion risk	3011
4.30.3.2	Corrosion Risk Assessment Processes	3012
4.30.3.2.1	Hazards and risks	3012
4.30.3.2.2	Matrix analysis	3013
4.30.3.2.3	Risk-based inspection	3016
4.30.3.3	Probability Analysis – Dealing with Uncertainties	3018
4.30.3.4	Corrosion Mitigation Requirements	3022
<b>4.30.4</b>	<b>Corrosion Management Systems</b>	3025
4.30.4.1	Framework for Corrosion Management Systems	3025
4.30.4.1.1	The corrosion risk mitigation system	3025
4.30.4.1.2	Corrosion management systems	3026
4.30.4.2	Setting Performance Measures	3030
4.30.4.3	Data Management Systems	3032
<b>4.30.5</b>	<b>Conclusions</b>	3034
<b>References</b>		3038

### Abbreviations

**API** American Petroleum Institute  
**APT** Assessment performance tool  
**ASME** American Society of Mechanical Engineers  
**CAD** Computer aided design  
**CDF** Cumulative distribution function  
**CIPS** Close interval potential survey  
**COMAH** Control of major accident hazard  
**CP** Cathodic protection  
**CRA** Corrosion resistant alloy  
**DCGV** Direct current voltage gradient  
**DCS** Distributed control system  
**DnV** Det Norsk Veritas  
**EN** European Normative (standard)  
**ER** Electrical resistance  
**FMECA** Failure mode effect and criticality analysis

**FSM** Field signature monitoring  
**GRP** Glass reinforced plastic  
**HAZOP** Hazard and operability  
**HSE** Health and Safety Executive  
**ISO** International Standards Organization  
**KPI** Key performance indicator  
**MAT** Minimum allowable thickness  
**MAWP** Maximum allowable working pressure  
**mpy** mils (0.001 in.) per year  
**NACE** National Association of Corrosion Engineers  
**NDE/T** Nondestructive examination/testing  
**NPV** Net present value  
**PDF** Probability density function  
**P&I** Process & instrumentation  
**QA/C** Quality assurance/control  
**RBI** Risk-based inspection

**RCM** Reliability centered maintenance  
**SCADA** Supervisory control and data acquisition  
**SHE** Safety, health, and environment  
**SI** Statutory instrument  
**TQM** Total quality management  
**UT** Ultrasonic testing

### 4.30.1 Background to Corrosion Management

#### 4.30.1.1 Introduction

This chapter outlines some general concepts, techniques, methodologies, and interactive processes that together promote successful management of corrosion. A top-down, strategy-based introduction to the subject area is presented together with an introduction to the tactics used to mitigate the effects of corrosion. A holistic overview that accommodates economic aspects, corrosion control methods and corrosion inspection/monitoring practices, which are the subjects of separate chapters in this volume, is provided.

In this section, the background to corrosion management is outlined, including concepts, definitions, legislative drivers, and the need for a risk-based approach. [Section 4.30.2](#) considers basic steps in corrosion management with emphasis on quality processes. In particular, the link between basic corrosion risk assessments (steps involving interactions between materials, environments, and engineering applications) and corrosion mitigation (control options, economics, and monitoring) is considered with the introduction of the requirements of a management system. In [Section 4.30.3](#), the various methods (the tools) for the assessment of corrosion risks and development of corrosion strategies are reviewed. Management systems are addressed in [Section 4.30.4](#) with considerations of further developments in [Section 4.30.5](#). Many of the concepts outlined here will not be found in other chapters of this publication or in most standard corrosion texts and are therefore presented in sufficient detail to avoid the reader having to refer to other engineering/management texts.

#### 4.30.1.2 The Need for Corrosion Management

To manage has been defined as “to succeed in one’s aims (often with inadequate materials etc),”<sup>1</sup> an objective often wryly considered as appropriate by

many corrosion engineers! Corrosion management is a process consisting of a series of steps to convert an input (corrosion risks) into an output (cost effective mitigation of those corrosion risks).

In principle, management of corrosion should be a simple process; the technologies are well established and most organizations understand the need for corrosion mitigation practices that are appropriate to their sector. However, the literature contains numerous reports of catastrophic events that have been caused by corrosion, the root causes of which are frequently poor management control, often identified as human errors:

1. “For many pipework failures, human error is identified as a dominant factor.”<sup>2</sup>
2. “. . . analysis of the major accidents reported in the Community indicates that the majority of them are the result of managerial and/or organizational shortcomings. . . .”<sup>3</sup>
3. “The cause of corrosion failures is human error/poor management control.”<sup>4</sup>

In practice, mistakes occur in the selection of corrosion control options, in application of mitigation technologies and in day-to-day activities needed to ensure that systems are monitored and corrective actions are carried out when necessary. In many instances, failures occur because basic lessons are not learned, particularly in organizations that cannot justify the services of a full time corrosion/materials specialist, and that, therefore, delegate corrosion control/monitoring activities to nonspecialist managers and engineers who may lack the required knowledge/experience. The effective implementation of mitigation practices from the design stage through the construction, commissioning, operation, and maintenance phases requires contributions from various teams of designers, constructors, commissioning staff, operations and maintenance personnel, and contractors and consultants/specialists. For such teams to be effective, they require clear objectives, transparent management systems, and appropriate reporting routes/procedures to ensure that appropriate decisions are made and implemented.

The author acted as a corrosion management expert witness in a case involving a major refinery incident resulting from inadequate control that exemplifies the need for good management practices.<sup>5</sup> An explosion and fire resulted from a rupture of a gas transfer line in a saturate gas plant because of local thinning by erosion–corrosion downstream of a water injection point after 13 years of operation.

The gas contained hydrogen sulfide, and water was periodically injected downstream of the overheads to control fouling of the condensers, a standard refinery practice for hydro-processing units. The heat exchangers had been replaced using corrosion resistant materials a few years previously, but the pipework was original and had been subjected to only one partial inspection. The failure was located on the surfaces downstream of the water injection point, as would be predicted by the injection point drawing in American Petroleum Institute (API) 570.<sup>6</sup> Subsequent discussions of the incident at the National Association of Corrosion Engineers (NACE) refinery work group<sup>7</sup> highlighted the requirement for inspections around any injection point, in intermittent or continuous use, at not more than three yearly intervals. There also appeared to be confusion at the refinery whether the injection point had been taken out of service following such a recommendation. A lack of management control over corrosion assessments/inspection/record keeping and procedures was identified as a major contributing factor to the failure during the subsequent trial. Following the incident, the refinery was shut down for 3 months, and a further 12 months was required to rebuild the gas plant, the company receiving a considerable fine as well.

In reality, the term ‘corrosion management’ is used in various contexts in many publications, but there is no body of knowledge/textbooks that adequately address this subject area, unlike asset management, safety management, and maintenance management. It therefore has different meanings to individuals and groups within the corrosion community. In order to clarify this issue during discussions on industrial short courses, the author developed a general definition in the mid-1990s, based on safety and environmental management definitions that was subsequently adopted in UK documentation for offshore oil and gas processing.<sup>8</sup> The definition also included the concept of a ‘corrosion policy.’ An organization’s policy is normally written by senior personnel, often at board/asset level, and is a statement of intent or an overall objective.

*Corrosion management* is that part of the overall asset management system that is concerned with development, implementation, review, and maintenance of the corrosion policy.

*A corrosion policy* includes establishment of organizational structures with defined responsibilities, reporting routes, practices, procedures, processes, and resources. This requires the demonstration of responsibility and accountability for corrosion performance,

managing risks, decreasing costs, controlling compliance, and motivating personnel.

This definition of corrosion management has also been included by NACE International in their online resource library (management) but without defining the corrosion policy. Most large organizations have until recently not given serious consideration to corrosion policies even though they have as standard practice developed and implemented quality, safety, environmental and maintenance policies. This is in spite of the fact that they often have in place many of the necessary procedures, management structures, activities, and reporting routes required for implementing corrosion policies. It should also be noted that, since the mid-1990s, the UK HSE has also been asking organizations for copies of their corrosion policies but few have even considered such a concept. Such policies written by senior personnel, often at board/asset level, are statements of intent or overall objectives. The lack of a written corrosion policy may mean that the various interdisciplinary and multi-departmental contributions are inadequate to ensure appropriate corrosion mitigation; also the management of corrosion is poorly focused upon at both the senior management level and in the operational/day-to-day activities of an organization.

#### 4.30.1.3 Legislative Drivers

In recent years, there has been an increased emphasis in commercial and public sector organizations on the identification and management of risks to safety, health and the environment (SHE) and to the economic viability that is driven by developments in SHE legislation across the world. A turning point in UK regulatory requirements was the 1990 Cullen Report<sup>9</sup> on the 1988 Piper Alpha offshore platform incident that ensured an increased emphasis on risk assessments and the use of appropriate safety management systems. This cultural shift from a rules-based regulatory system to a principles-based system with emphasis on defined objectives rather than the traditional prescriptive, rules-based practice, is summarized in [Table 1](#).

The principles-based approach places a greater onus on organizations and individuals (the duty holders) to demonstrate a continuously improving safety culture with emphasis on regular assessment of risks, monitoring of performance and a proactive approach. Legislative enforcement, by the UK HSE with Statutory Instruments (SI), is the basis of the

**Table 1** Legislative changes

<i>Older legislation</i>		<i>Principles-based legislation</i>
Detailed rules and regulations	→	Framework rules with guidelines
What must be done		How it must be managed
Prescriptive		Risk-based
Do it anyway		Identify hazards and risks first and prioritize actions accordingly

formal UK regulations that are typically based on European requirements as given in normative European standards (EN) and ISO standards.

The UK changes were first indicated in the 1991 publication of *Successful Health and Safety Management*<sup>10</sup> followed by requirements for the UK offshore oil and gas production in the *Safety Case Regulations*, in 1992<sup>11</sup> the *Design and Construction Regulations*<sup>12</sup> and the *Pipeline Standard*<sup>13</sup> in 1996. The general approach continued in *The Control of Major Accident Hazard Regulations* 1999 (COMAH)<sup>14</sup> for major hazard sites such as refineries and chemical plants and in the *Pressure Systems Safety Regulations* (SI 2000/128).<sup>15</sup>

The overall thrust of these approaches is illustrated as follows:

1. Reg. 8 of SI 1996/913:<sup>12</sup> The duty holder shall ensure that auditable arrangements are in place for maintaining the integrity of the installation, including suitable arrangements for: (1) periodic assessment of its integrity and (2) the carrying out of remedial work in the event of damage or deterioration which may prejudice its integrity.
2. Reg. 13 of SI 1996/825:<sup>13</sup> The operator shall ensure that the pipeline is maintained in an efficient state, in efficient working order and in good repair.
3. Reg. 12 of SI 2000/128:<sup>15</sup> The owner of an installed (pressure) system shall ensure that the system is properly maintained in good repair, so as to prevent danger.

In particular, written schemes of examination are required for pressure vessels and associated pipework.<sup>15</sup> Such documents have to be prepared by a competent person, either a named individual or a corporate inspection body within the organization. The accompanying Approved Code of Practice L122<sup>16</sup> provides further background information and it also notes that, "the contents may be highly toxic or the plant may form part of a major hazard site. These aspects are all subject to separate

legislative requirements and duty holders will need to consider these other aspects (corrosion and erosion) when deciding on the level of precautions required," which requires organizations to be aware of all hazards, including corrosion, that can affect integrity.

Additional pressure on senior management in some sectors came with the introduction of legislation such as the UK Corporate Manslaughter and Corporate Homicide Act<sup>17</sup> that came into effect in 2008. A company, including senior personnel, may be guilty of this new offence if the manner in which its activities are managed or organized causes a death and amounts to a gross breach of a relevant duty of care owed to employees, the public or other individuals. If found guilty, unlimited fines and remedial orders may result, possibly affecting the viability of an organization. The challenge for industry arising from these legislative drivers is to demonstrate to the licensing authorities that the equipment is operating under safe conditions, while from a business perspective continuing to operate cost effectively, often under more aggressive conditions, and in some cases, to extend the life of aging facilities.

The impact of these drivers on engineering and safety procedures has been to focus them increasingly on failure modes likely to affect asset integrity, particularly those giving rise to catastrophic incidents such as corrosion related failures. Typical industry-centered documentation includes the American Society of Mechanical Engineers (ASME) Risk Based Inspection – Guideline Development,<sup>18</sup> the US Pipeline Safety Act,<sup>19</sup> which places emphasis on risk management and cost benefit, API 580 Risk-Based Inspection<sup>20</sup> plus the accompanying resource document API 581<sup>21</sup> and the DnV Risk Based Inspection of Offshore Topsides Static Mechanical Equipment.<sup>22</sup> The Australian/New Zealand Risk Management Standard<sup>23</sup> first published in 1995 provides an excellent basis for evaluation/management of business risk. In this context, New Zealand has also been at the forefront in total asset management, particularly public infrastructure legislation<sup>24</sup> and the publication of guidance.<sup>25</sup>

Risk management is only one of the tools employed to mitigate corrosion and, for example, risk-based inspection (RBI) must be backed up with management of change procedures and end of life strategies. Thus if the compositions of process fluids change or the operating conditions are modified then corrosion assessments must be carried out again for these new conditions. Ageing infrastructures and facilities need increased inspection frequencies and

monitoring to ensure safe operation and this has implications for the allocation of resource for teams concerned with asset integrity and maintenance. Corrosion expertise is a relatively scarce commodity, particularly in management functions. Burdekin,<sup>26</sup> in a review of risk/integrity aspects of materials in 2000, noted that, although quantitative risk assessment for creep and corrosion is still in its infancy, RBI is becoming well established and engineers/materials scientists should have a basic grounding in risk assessment and the principles of reliability analysis since these will become a key basis for decisions.

The prevention of failures requires management systems that incorporate appropriate tools (procedures, risk assessments, and probabilistic methods) and teams (design, corrosion, inspection, maintenance, stakeholders) to develop and implement corrosion management strategies. This is achieved by the incorporation of best practices from Total Quality Management (TQM) as outlined in the ISO requirements for quality,<sup>27,28</sup> health and safety<sup>10</sup> and environmental<sup>29</sup> management systems. The major focus of this chapter is the development, implementation, and maintenance of risk-based management systems to ensure that corrosion mitigation strategies are in place and that mitigation practices are implemented in an effective manner. The chapter provides a framework that may be used to review, audit and continuously improve corrosion management systems. The framework highlights the need for organizations to develop performance standards or key performance indicators (KPIs) to monitor the effectiveness of day-to-day activities during the design, construction, and operation and maintenance phases of projects.

#### 4.30.1.4 Basic Concepts

A corrosion control strategy is defined here as the management of available resources, including finance, materials, equipment and manpower, to provide the policies, procedures and organizational systems that are required to mitigate the effects of corrosion. Successful management strategies provide the means of achieving corrosion control objectives, such as optimal life-cycle costs, minimal leaks and the required life. It is in strategy development and/or in day-to-day implementation of policies that difficulties often appear in the field (essentially the control of who does what, where and when). Effective strategies are typically concerned with long-term objectives and encompass standard corrosion control procedures/established engineering practices that form the basis

for written documentation appropriate for the project under consideration.

Corrosion control tactics can be summarized as the practice or implementation of planned procedures and courses of action necessary to achieve the required corrosion mitigation results. These require guideline documentation and background information for managers and engineers responsible for implementation of corrosion engineering procedures. The basic principles have been in place for decades and have been incorporated into industry practices by embedding them in design reviews and audits, hazard and operability (HAZOP) studies, integrity and operational practices. Fundamental requirements are that equipment is designed, constructed, operated, and maintained in an economic and safe condition.

Tactics involve specific solutions such as the use of corrosion control options and corrosion inspection/monitoring practices to solve particular problems and they are often delivered by specialists and/or contracting companies. The successful implementation of corrosion control options, either singly or in combination, requires not only the production of clear specifications and work instructions but also adequate management structures for the control and reporting of work. Regular reviews and audits are needed to maintain compliance with policies, standards, and company guidelines and also ensure continuing improvement to meet increasingly stringent SHE requirements. This is achieved by development and implementation of performance standards.

Performance standards or KPIs are the basis for planning and measuring achievement. In a practical sense, they are checks that are developed for all levels of the organization and used to ensure that appropriate actions are carried out as required. Setting the appropriate standard is crucial for effective implementation of policies. KPIs are agreed performance criteria that enable the performance of management systems, individuals and day-to-day actions to be judged against acceptable in-house standards and/or industry benchmarks. Failure to achieve the performance standard should trigger a review to identify reasons for under-performance, for example, inappropriate reporting methods, insufficient resources, slow response, and unrealistic KPI. Where appropriate, modifications should then be made to improve performance. The key questions are:

1. Who is responsible?
2. For what?
3. When?
4. With what expected results?



Management KPIs cover the monitoring and measurement of performance of the corrosion management system itself, and not the monitoring/measurement of corrosion which would be subject to separate KPIs. Improvements in corrosion management systems result from the constant reexamination and incorporation of learning from previous performance deficiencies.

## **4.30.2 Corrosion Management Processes**

### **4.30.2.1 Introduction**

In most organizations, capital investments and production activities are undertaken as projects with well defined boundaries and clear business objectives. Managers and teams are usually aware of corrosion as one of many potential threats to project viability but systematic evaluation with regular updates is required so that risks are formally identified and actively managed. Management is a process that should have clearly defined steps with appropriate means of ensuring adequate control of the process. Adoption of a risk-based approach to the corrosion management process can help to align corrosion mitigation practices with recognized good practices, worldwide, and corrosion management processes are likely to be more effective if based on recognized quality management processes.

### **4.30.2.2 Quality Management Processes**

Any process, including a management process, is a series of steps that convert inputs into outputs. For example, a manufacturing process converts raw materials into products, whilst a corrosion process converts metallic items into corrosion products. This process approach, as summarized in the quality management system document ISO 9001:2008,<sup>27</sup> requires organizations to identify and manage numerous linked activities with the output from one process directly forming the input into the next if the functions are to be effective. The ISO standard focuses on an organization's ability to meet customer requirements of a product or service and also addresses both regulatory and the organization's own requirements in terms of quality management. It provides a benchmark for the development and application of corrosion management processes through which in-house or contractor corrosion teams can provide cost effective, corrosion mitigation products and services.

Adoption of basic 'quality' concepts is also important if a corrosion management system is to interface with an existing asset management system especially if it is to be provided by, and/or operated through, an external contractor. The linked standard ISO 9004:2000<sup>28</sup> has been designed to complement ISO 9001:2000<sup>27</sup> but here the emphasis is on senior management inputs in order to achieve continual improvement of performance. Managements inevitably change within organizations and the effectiveness of corrosion management processes will vary with time without the emphasis on 'continuous improvement' that is implicit in most quality management systems. Quality systems complement requirements in technical specifications and provide an auditable trail of documented quality measures and checks.

In general, the aim of a quality approach is to establish, document, implement and maintain a management system and continually improve its effectiveness. The organization needs to:

1. Identify the management processes.
2. Determine the sequence and interaction of these processes.
3. Determine the criteria and methods of operation and control.
4. Ensure availability of resources and information necessary to support the operation and to monitor these processes.
5. Monitor, measure, and analyze these processes.
6. Implement the actions required to achieve planned results.

The functional inputs and steps required in a successful management process are derived from inputs from teams (stakeholders), use of appropriate tools (risk assessments, monitoring methods, etc.) and well defined systems (organizational structures, reporting routes, etc.).<sup>30</sup>

Corrosion management processes can therefore be envisaged as shown in [Figure 1](#).

Teams involved in the corrosion management process during the various stages of a project may be drawn from a variety of functions. Team leaders will be selected on the basis of tasks to be undertaken, skills, and experience of the personnel and the specific stage of the project. Few organizations are large enough to justify the employment of a full time corrosion engineer. Many decisions related to corrosion issues have to be made by managers on the basis of reports and recommendations from design, production, inspection, and maintenance personnel and most operational/day-to-day corrosion mitigation

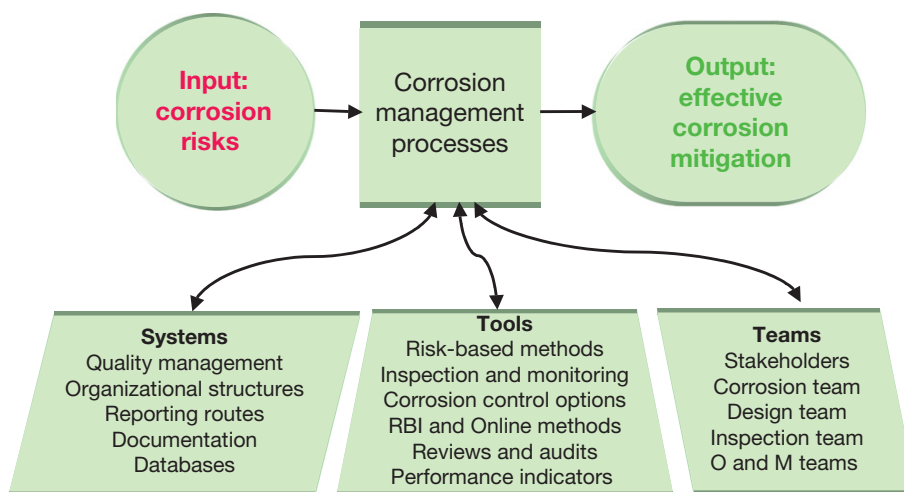


**Figure 1** Corrosion management requirements.

activities are undertaken by members of the design, process/plant engineering or maintenance teams or contractors. For example, an electrical engineer often becomes responsible for cathodic protection (CP) systems, the site chemist or process engineer oversees the inhibition and biological control of cooling systems, chemical treatment programs, etc. Off-site specialists or consultants provide any required additional support. In general, during the operational phase, an on-site engineer or manager has to interpret field data to identify trends that are required to provide management information.

Tools used as part of corrosion management strategy development encompass corrosion risk assessments that may include risk matrices, and/or probabilistic analyses. Implementation of tactics involves use of corrosion control methods, employment of various corrosion inspection/monitoring techniques to obtain plant/field data, use of data storage, data analysis and trending to convert data into information for decision makers. The development and use of KPIs and risk control systems are tools for the control of operations and day-to-day activities.

Systems for corrosion management are used to implement corrosion mitigation strategies and tactics through well defined organizational structures. Such structures should be based on quality management principles and be clearly laid out on, for example, a flow sheet that highlights identifiable policies/objectives, notes the allocation of responsibilities, resources and the means of corrosion mitigation implementation through procedures that are regularly reviewed and audited. Systems may be paper- or computer-based.

#### 4.30.2.3 Risk Management Processes

Corrosion is a risk to a project/operation and it is therefore appropriate to consider the benefits of well established risk management approaches especially as, for example, one source<sup>31</sup> identifies three levels of decision making in any project:

1. *Strategic decisions* include establishment and confirmation of goals, means, and constraints, identification of key risks and stakeholders plus setting these in context for tactical and operational decisions for each project/activity.
2. *Tactical decisions* involve choosing how to deploy the most appropriate means of achieving goals and managing tactical risks within the restraints set at the strategic level.
3. *Operational decisions* are concerned with implementing tactical choices and managing operational risks. A key element throughout is the development and implementation of written procedures.

Risk management is an iterative process of well-defined steps:

Risk identification → Risk analysis → Risk evaluation → Risk treatment.

When taken in sequence, these steps give rise to improved decision-making by providing greater insight into risks and their impacts on the operation. Two main outcomes from adoption of a risk management approach are:

1. Significant undesired or unexpected outcomes can be identified, and
2. Opportunities for improvement can be considered.

A useful framework is shown in the flow sheet in **Figure 2** that identifies the main issues associated with a risk management process.<sup>31</sup> The specific approach adopted will vary depending on the type of project/industry/business requirements but a key element in all situations is the feedback required to maintain the system. The key features are:

1. *Risk assessment process* – identification, analysis, and evaluation of the risk, its likelihood and consequences, plus criteria used to quantify the risk and priorities to be set.
2. *Risk treatment* – selection of the mitigation options, planning of treatment measures and allocation of responsibilities/implementation of procedures.
3. *Secondary risk identification* – identification during the analysis, evaluation, and treatment process of such risks that are a key factor of any protocol and an important consideration when mitigation of corrosion risks is addressed.

Corrosion risk management must be integrated into the organization's philosophy, practices, and business plans and not viewed as a separate activity. In this context corrosion, management should be focused on

the management of corrosion risk mitigation, that is, strategies and control of day-to-day activities rather than just specific tactics of corrosion control and corrosion inspection/monitoring that are merely the tools used in the mitigation process. Opportunities for improvement and benefits that are inherent in a risk management process are often neglected during the initial implementation of corrosion risk management because of an over-emphasis on risk mitigation. In addition, secondary risks relating to risk mitigation are often neglected, such as:

1. *Inspection risks* – criteria used to determine appropriate inspection methods and the selection of inspection frequencies appropriate for the type of corrosion damage must be understood and their applicability maintained. Loss of corrosion inhibition/chemical treating may result in a higher risk as it negates the basis used for inspection scheduling.
2. *Chemical treating risks* – caustic dosing/corrosion inhibition requires that the process fluids are monitored to ensure compliance to an agreed pH or inhibitor residual concentration. Injection equipment must therefore be maintained to an

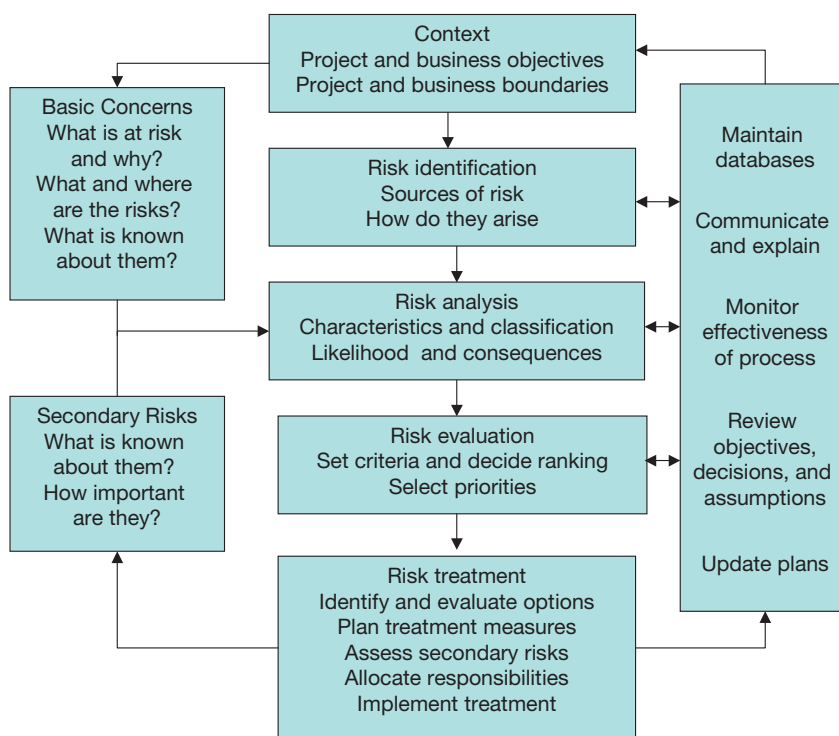


**Figure 2** Risk management process, adapted from BS 6079-3:2000.

agreed level of reliability, otherwise the basis of the overall inhibition risk mitigation process and inhibitor availability criteria may be invalidated.

3. *Use of corrosion resistant alloys (CRAs)* – provides protection against general corrosion but will risks from pitting and cracking occur if process conditions change? Are fluid compositions and temperatures monitored to meet agreed upon criteria?
4. *Use of coatings/CP* – requires regular inspection/monitoring and maintenance. Are appropriate checks and regular audits made to ensure corrective actions are carried out?
5. *Design detailing aims* – to eliminate risks from local fluid chemistries/temperatures, equipment/component stresses, fluid flow/heat transfer characteristics, location/layout/geometry of equipment and components; requires reviews and audits.

Selection and application of any corrosion risk mitigation plan requires decisions to be made, responsibility allocated and reporting routes established. An audit of mitigation procedures is required before implementation is finalized. Feedback control from information derived from field data and involving comparison with agreed upon criteria and possibly information held in other company databases (production and maintenance) is needed. Also required is

the effective monitoring of the management process, including regular reviews and update of plans. For example, every company standard and procedure should have a written agreed review date in a similar manner as is used in the maintenance of, for example, NACE and ISO standards.

An illustration of the complexity of the corrosion risk management challenge in a multidisciplinary activity can be seen in the flow sheet in **Figure 3** that summarizes typical information flows, including feedback, that are required to mitigate corrosion risks within organizations in the oil industry.

There is already significant technical feedback information within the industry on corrosion issues, but as Milliams has noted,<sup>32</sup>

The management of corrosion is a concern which extends beyond the responsibilities of corrosion and materials engineers. Whilst they should provide advice during both the design and operational phases, they are dependent upon the co-operation of other disciplines if an installation's projected design life is to be achieved. The model proposed provides a framework for that co-operation and for optimizing the contribution the corrosion and materials engineers make to an organization.

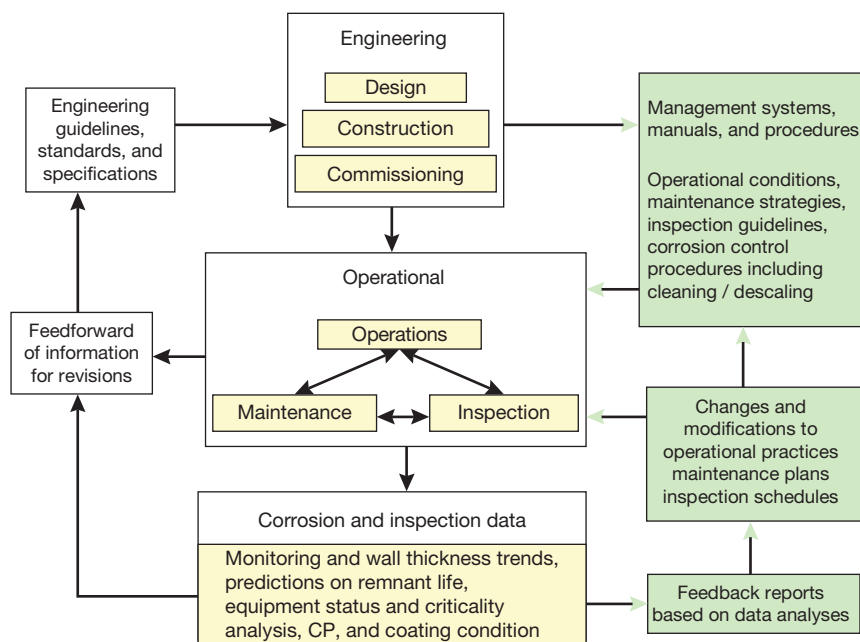


**Figure 3** Information flows for the management of corrosion. Adapted from Milliams, D. In 12th International Corrosion Congress on Corrosion Control for Low Cost Reliability 19–24 September 1993; NACE International: Houston, TX, 1993; Vol. 4, pp 2420.

In general, corrosion risk assessment, the identification, analysis, and evaluation of corrosion risks, and corrosion risk treatment, the mitigation of the corrosion risk, are two separate steps in the corrosion management process. Both steps can involve the consideration of secondary risks incurred by the assessment or treatment processes but there must also be an acceptance that not all risks can be eliminated and contingency plans will be needed. For example, in RBI, a premise is that risk of failure can be assessed in relation to an acceptable level or probable annual frequency provided that the damage mechanism and process conditions are known. Eventually repair and/or replacement will be required (condition-based maintenance) but the consequences of a potential failure before that stage must be addressed. A third step is to use agreed upon procedures to monitor and modify the management process. These steps are shown in the summary flow sheet in **Figure 4**.

The success of corrosion management processes used to convert risk inputs into mitigation outputs are largely dependent on the management systems adopted (organizational structures, document systems, information flows, data management systems), the tools employed (risk assessment and mitigation procedures, field data collection, control tactics) and the composition of the corrosion teams.

### 4.30.3 Corrosion Management tools

#### 4.30.3.1 Identification of Corrosion Risks

##### 4.30.3.1.1 Corrosion damage and failure modes

The starting point of any assessment is the identification of the corrosion process or corrosion damage that may be sustained by structures/equipment and the impact that this damage may have on integrity and plant operation,<sup>33</sup> including side effects such as the fouling of equipment (sludge in lines/vessels, radioactive build-up in heavy water reactors, strontium scales in oil production) or on contamination of products (food and pharmaceutical chemicals). The various types of corrosion are described in detail in separate chapters in this volume. The more common examples of corrosion damage are:

1. *Uniform corrosion* – metal loss due to general corrosion, atmospheric corrosion/rusting, metal wastage in process streams/cooling water pipe work.
2. *Galvanic corrosion* – accelerated localized corrosion due to the effect of mixed metal combinations or compositional/metallurgical factors as in the corrosion of weldments.
3. *Localized attack* – pitting and crevice corrosion, often the result of a small area of damage in the

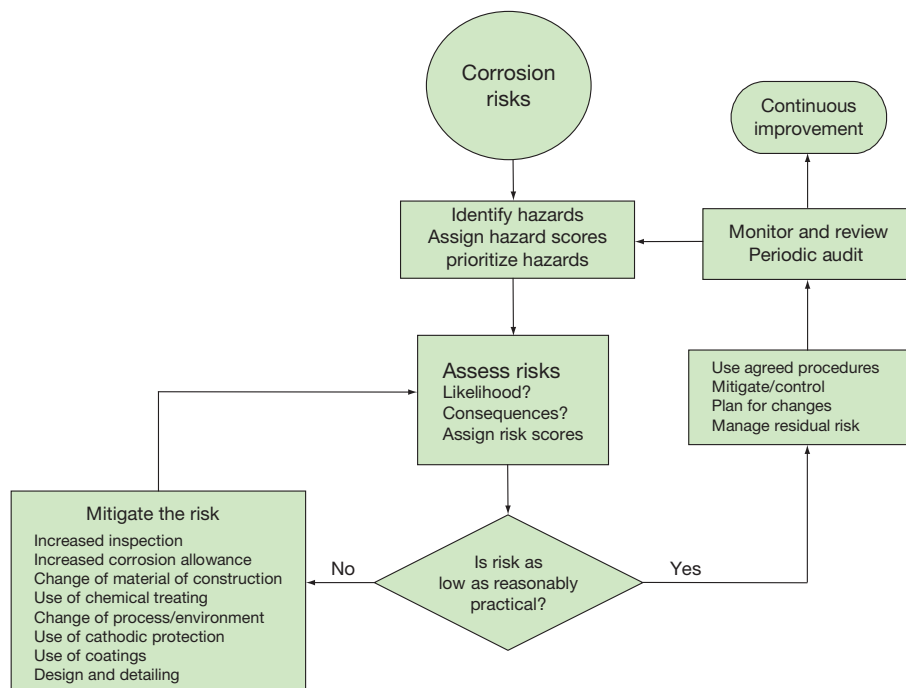


**Figure 4** Overall corrosion risk analysis, mitigation, and control process.



protective/passive corrosion product film (small anode area and a large cathode area).

4. *Flow induced corrosion – erosion corrosion, cavitation, impingement attack*, the result of high fluid velocities/high wall to fluid shear stresses/high turbulence intensity, changes in fluid pressure and the presence of second phases such as bubbles and sand.
5. *Environmentally assisted cracking* – caused by the combined action of a mechanical load/tensile stress/residual stresses plus a specific corrosive environment/temperature on a susceptible alloy (essentially a brittle type failure in a normally ductile material).
6. *Corrosion fatigue* – combination of cyclic stresses and exposure of a susceptible metal to a corrosive environment.

Many reports and texts refer to corrosion damage or morphology, or the various forms of corrosion as corrosion failures but in the strict engineering sense, a failure occurs when an item, component, or unit does not meet the design/operational requirements. In this strict sense, corrosion *per se* is not a cause of failure but rather is a contributor to a failure mode that is the combination of the effect of damage on operational (and accidental) loads,<sup>34</sup> as summarized below:

<i>Failure mode</i>	Local leakage Rupture/severance Collapse or buckling
<i>Corrosion damage</i> (corrosion morphology)	Uniform corrosion and isolated pitting Flow induced corrosion & erosion Longitudinal and transverse cracking
<i>Loads</i>	Pressure (internal and external) Forces (tensional/hoop stresses, compressive, bending/torsional) Impacts (collisions, dropped objects)

Likely failure modes are key inputs into engineering risk, or criticality assessments. In most industrial situations the deteriorated condition that may lead to the undesirable leak or rupture, can usually be anticipated by a risk assessment for the specific damage mechanism. In the case of corrosion, this would be based on credible rates of deterioration obtained, for example, from internationally accepted and

published values/mechanisms, and/or identified by on-site corrosion inspection.

Most assessments concentrate on corrosion that occurs to equipment during its operation but significant damage may also take place during construction and storage of items, start up/shut down periods (when conditions vary from the design basis) and maintenance activities. This requires an understanding of all the factors that may affect probable corrosion processes and cause equipment damage.

#### 4.30.3.1.2 Sources of corrosion risk

Assessments of corrosion risks to either an existing or proposed new equipment start with the consideration of the corrosive environments, both internal and external, to which the equipment is likely to be exposed. The combination of the metal's environment and the influence of engineering factors, such as mechanical stresses, heat transfer and fluid flow, may play a crucial role in the corrosion processes, and will also have to be assessed. In a detailed study each item of equipment (vessel, reactor, heat exchanger, etc.), process stream compositions and temperatures (in and out) and connecting pipe work (including sections of the same pipe run of differing diameter) will have to be assessed.

Therefore, any corrosion risk assessment has to, at some point, consider a combination of three basic influences that control the physical/chemical processes that result in possible corrosion damage, as shown in **Figure 5**:

1. *Materials of construction*, in particular their compositions, fabrication, and required lives: There are many options, depending on the specific requirements. Along with resistance to corrosion and wear, the materials may have to withstand high temperatures, perhaps in the creep range of the material, or low temperatures where brittle fracture is a concern, as may occur during a high pressure gas leak.
2. *Corrosive environments* that vary widely depending on the application and may involve exposure to gaseous atmospheres, naturally occurring or treated waters, acids or alkalis: Some aqueous environments may contain bacteria that produce local highly corrosive conditions whilst some fluids may contain specific salts, for example chlorides and/or sulfates that cause pitting/stress corrosion cracking. Both internal and external and transient conditions, such as are associated with start up and shutdown of equipment, have to be considered.

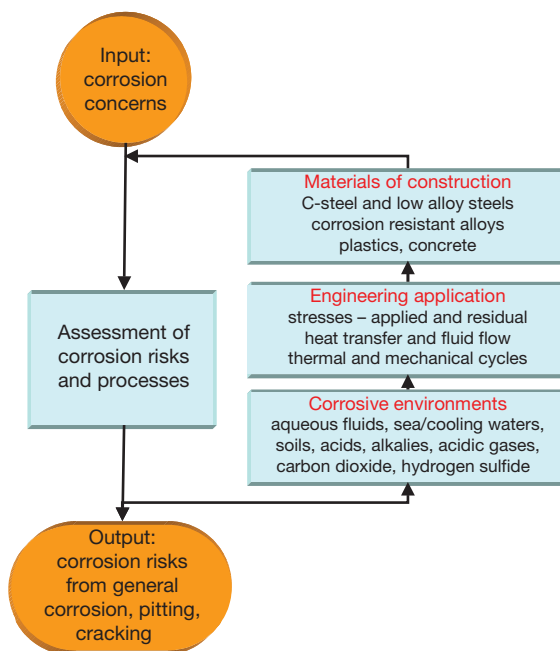


**Figure 5** Basic corrosion risk assessment steps.

3. *Engineering application*, specifically the type of equipment, its functionality and associated influencing parameters such as exposure to various mechanical loads, fluid flow and heat transfer conditions that can have significant impacts on corrosion processes. Residual and applied stresses can introduce risks of corrosion fatigue and environmentally assisted cracking processes. Fluid flow conditions involving changes in direction, diameter, topography, etc., can cause areas of stagnation, stratified/slugging flow, or high turbulence intensity downstream of protrusions/restrictions/expansions that can introduce risks of erosion corrosion or even cavitation damage. Heat transfer rates and surface temperatures in equipment can result in problems associated with condensation, scaling, fouling/bio-fouling and high temperature corrosion.

Each of the above may contribute in varying degrees to the overall risk. A corrosion risk assessment of a conceptual design would probably concentrate on major specific risks as posed by the initial material selections, such as comparisons between low alloy steels and corrosion resistant alloys (CRAs). A detailed assessment, as employed for RBI scheduling would require each item of equipment to be itemized and evaluated for internal and external corrosion using a formal and audited approach.

#### 4.30.3.2 Corrosion Risk Assessment Processes

##### 4.30.3.2.1 Hazards and risks

Identification of hazards and assessment of risks are fundamental steps in corrosion mitigation and engineering studies. The relationship between hazards and risks emerges from their definitions:

1. A *hazard* has the potential to cause harm or damage; often defined as a physical condition or release of hazardous material as a result of component failure that can cause human injury or death, loss or damage, or environmental degradation.
2. *Risk* is the combination of the severity of the effect (the consequences) and the likelihood of it happening (damage mode and probable frequency).

The tools used to identify, analyze, and evaluate corrosion risks and then to treat or mitigate those risks vary considerably depending on the specific application. Identification and ranking of hazards and risks associated with corrosion lead to prioritization of actions, use of framework rules with guidelines/protocols and assessments of how corrosion and asset integrity systems are managed.

The assessment can be either paper-based or carried out using appropriate software on a PC-based system depending on the complexity of the facility. In its simplest form, it is a careful engineering examination of the items comprising a facility and the likely corrosive environments, the materials of construction and engineering application. For example, for a port or harbor facility a major concern would be the marine environment and ambient temperatures for specific items, for example the effects of anaerobic subsoil/mud, seawater, tidal/splash zones or saline atmospheres as appropriate on sheet steel piles and columns (possible ice flow abrasion?), reinforced concrete beams, pillars and mooring dolphins, storage sheds, cranes, lifting gear, etc. The effectiveness of existing or proposed corrosion control measures such as coatings, CP, and even chemical treating of vehicle cooling systems should be considered based on previous experience, existing maintenance, and published data records.

In general, the information needed for corrosion assessment includes a list of items of interest from the asset register (structures/vessels/pipework/storage tanks, etc.), historical data (inspection/monitoring/maintenance), theoretical analysis (new systems based on published data/models), informed opinions

and concerns of stakeholders (individuals, groups, other areas of the organization) and field data where available. Such risk assessments are the tools that focus attention on critical areas and they are used to review a design, ensure asset integrity and improve corrosion control but do not by themselves provide management control. Outputs from risk assessments are recommendations that may include changes to the inspection/monitoring or use of/change of the corrosion control practices. The decision-making steps form a vital part of the management process.

At its simplest, the assessment is a common sense engineering approach that provides a means of checking on what is often a good existing practice. Decisions are based on questions such as:

What would be the worst case scenarios?

1. How likely are they to occur?
2. What would be the damage?
3. How many people could be injured or killed?
4. How will these events affect the business?

The three fundamental questions in corrosion risk analyses are:

1. Failure mode – what could go wrong?
2. Failure effect – how will it affect the project/plant integrity/operations?
3. Failure criticality – how likely is it?

Criticality analyses examine potential failures to assess the severity of each failure in terms of decreased performance, total loss of function, safety, and environmental hazards. Typical steps in such an assessment include:

1. Identify plant components (Tags) or process function.
2. List possible failure modes for each component (Tag number).
3. Identify likely effects of each failure mode.
4. List all possible causes of each failure mode.
5. Assess the failure modes numerically (e.g., on a scale of 1–10).
6. Evaluate a criticality index for each failure mode to assess priority of failure mitigation/prevention actions.
7. Indicate required corrective actions, expected completion date, and the departments/people with required responsibility.

The first step is therefore to consider potential hazards/escape of flammable gasses/liquids/toxic substances and the effect on people/the environment and the business. This focuses attention on the items at risk

and the approach could be similar to the procedures that are used in the process industries to identify hazards and operability issues (HAZOP). In general, a corrosion risk assessment will incorporate appropriate findings from HAZOP/environmental studies for the evaluation of likely consequences as indicated below.

With hazardous or toxic fluids such as hydrocarbons and other chemicals the effect or consequences criteria of a failure depend on stored energy ( $E$ ), pressure ( $P$ ), volume ( $V$ ), toxicity ( $T_x$ ), flammability/explosive risk ( $F$ ), and temperature ( $T$ ). An overall hazard score  $H$  can be allocated:

$$H = E \times P \times V \times T_x \times F \times T$$

for each vessel, tank, piping system or other equipment items. Safety risks may be scored on the severity of the possible incident and number of people likely to be affected (<3, 3–9, >10). The effect of any failure is typically considered in an environmental impact study and the economics addressed by estimating the effects of shut down (partial/full) on the operations and time required to effect repairs. All risks are multiplied. A quantified (Level 3) assessment of an item depending on the numerical values chosen for the likelihood and consequences criteria, for example an oil/gas pipeline, could provide a total numerical score as follows (Table 2):

The criteria employed in any risk assessment are often based on judgment and agreed upon guidelines and are not absolute; therefore, a degree of skepticism is always helpful when the criteria adopted in the assessment are not specified.

#### 4.30.3.2.2 Matrix analysis

In many engineering studies, the criticality of an item is presented as a table or matrix of the likelihood of failure against the effect of a failure:

Criticality = Likelihood of failure  $\times$  Effect of failure

Most corrosion risk assessments are qualitative using a judgment, based on descriptive ranking such as

**Table 2** Risk score based on likelihood and consequences

Total score	Criticality ranking
<300	Low
301–1000	Moderate
1001–3000	High
3001–10 000	Very High
>10 000	Extreme

high, medium, or low that may be converted into a simple numerical description. For particularly critical equipment, for example in the nuclear industry, a rigorous quantitative analysis is adopted:

$$\text{Risk} = \text{Probability} \times \text{Consequences}$$

The outcome is a numerical value, with measured units, that may be simplified by assigning bands to the probability and consequences.

Corrosion risk assessments can be typically classified into three groups:

Level 1 – Qualitative risk analysis, a simple ranking of equipment

Level 2 – Semiquantitative risk analysis, a more accurate prioritization that retains vital inputs of a Level 3 analysis but simplifying assumptions

Level 3 – Quantitative risk analysis, an in-depth study including assessment of reliability, financial and limited environmental issues

Failure mode, effect, and criticality analysis (FMECA) is an example of an engineering risk evaluation process that has been used for over 40 years to evaluate systems, including those on commercial jet aircraft. The analysis considers the seriousness/consequences of a failure (*S*) and the probability (*P*) of the occurrence of each failure mode. The analysis may also include the difficulty of detection (*D*) of the failure mode/damage. Table 3 indicates that corrosion damage that may have a high rate of penetration such as stress corrosion cracking or corrosion fatigue which is the most difficult to detect by inspection,

**Table 3** Characteristics of corrosion damage

<i>Damage</i>	<i>Ease of detection</i>	<i>Rate of penetration</i>
Uniform	Very high 1	Low
Pitting	High 2	Medium
Erosion	Medium 3	Medium
Cracking	Low 4	High

**Table 4** Criticality index (FMECA)

Probability ( <i>P</i> )	Rare 1	Unlikely 2	Moderate 3	Likely 4	Almost certain 5
Seriousness ( <i>S</i> )	Not serious 1	Nuisance 2	Repair 3	Change 4	Shut down 5
Detection ( <i>D</i> )	Easily detected 1	Medium 2	High 3	Detection unlikely 4	
Criticality ( <i>C</i> ) (Ranking value)	Low <20	Medium 20–60	High >60		

whilst the easiest damage to detect, general corrosion, is the simplest to manage by basic trending of inspection data, for example loss of corrosion allowance with time.

In a simple corrosion or maintenance situation (i.e., using a common sense engineering assessment) a basic paper-based corrosion risk assessment (level 1) may be employed with the probability and consequences judged either high/unacceptable or low/acceptable. Alternatively a numerical value can be assigned (5 – low, 4 – medium, 3 – high, 2 – very high, 1 – unacceptable). The advantage of developing an agreed numerical ranking, as is employed with some visual inspections of equipment or paint deterioration based on the degree of rusting of coated surfaces,<sup>32</sup> is the ease of handling data input/output in computer systems.

Such a ranking is illustrated in the criticality index (*C*), shown in Table 4, which provides a numerical ranking ( $C = P \times S \times D$ ) that enables a risk assessment team to focus on items of a plant, or processes, that have varying levels of corrosion risks. In this particular example, the following values have been arbitrarily assigned:

Probability and seriousness	between 1 and 5
Detection	between 1 and 4
Overall criticality rank of items	between 1 and 100

A more common approach to risk assessment is the use of risk matrices for evaluating various probabilities and consequences as illustrated in Figure 5 developed as a simple corrosion risk matrix for the assessment of corrosion mitigation options for reinforced concrete. Corrosion processes in reinforced concrete are described in a separate chapter in this book. Reinforced structures, including those constructed with good quality concrete, are susceptible to rebar corrosion damage resulting from carbonation and chloride ion ingress from marine/ground waters.

Chlorides in the presence of high levels of oxygen cause pitting of rebar and the corrosion spreads to give rise to high rates of general corrosion. The buildup of corrosion product causes the concrete cover to crack leading to increasing rates of attack. This is a particular problem in hot climates where the high temperature of cure increases concrete permeability and subsequent chloride penetration rates. Structures constructed in hot saline regions therefore have an increased risk of pitting/corrosion of rebar.

Practices that mitigate the effects of chloride ingress in concrete include:

1. use of coatings on the rebar;
2. use of sealant/coating on the concrete above grade;
3. use of waterproof membrane to prevent water ingress into foundations;
4. application of CP, retro-fitted to existing corroded concrete structures or designed into new structures.

The preferred choice depends on the particular situation and the life cycle costs for each option. Life cycle assessments should include the likely costs of future repairs and any associated downtime. The option of not including extra corrosion protection (reliance on concrete cover only plus probable maintenance/repair costs) should also be assessed as the base case.

The development of a simple risk or criticality ranking for reinforced concrete structures based on a  $3 \times 3$  matrix analysis is shown in Table 5. The actual criteria used, Table 6, can be adjusted with experience. This approach essentially encompasses information in a number of international standards on concrete construction. However, these tend to underestimate corrosion risks in marine situations, particularly at high ambient temperatures and saline contents.

Table 6 illustrates the use of 'rules' or agreed-upon criteria to define the likelihood of corrosion, the effect of corrosion and the final ranking. A major

risk factor is not only the technical and corrosion issues but the effect of future repairs and downtime on life-cycle costs as well. The results of the risk assessment could also form the basis of a mitigation strategy and development of agreed upon procedures as shown in Table 7, the success of which depends on the management of associated risks.

The above example illustrates the principle of matrix analysis but other risk assessment systems use  $4 \times 4$ ,  $5 \times 5$ , or  $4 \times 5$  matrices, with either linear or logarithmic scales with output as a numerical risk

**Table 6** Typical guidance for reinforced concrete structures

<i>Likelihood of corrosion</i>	
High	Concrete contains chlorides. Average/low cover. Tidal marine zone, sabkha region ground waters, waste water pipes.
Medium	Atmospheric marine environments/wind-blown sabkha sand. Possibility of regular wetting from water spills.
Low	Office environments, aggregates and mix water had low chloride levels. Design mix and placement to standards.
<i>Effect of corrosion</i>	
High	Rapid corrosion/cracks/spalling in <10y which prevents facility use. Repairs are costly because of access.
Medium	Repairs in 10–25 years. Facility unavailability tolerable for repairs, Accessibility reasonable nor expensive
Low	No significant effect <25 years, availability not critical. Easy access/low scaffolding costs. Simple patch repairs OK
<i>Risk/criticality ranking</i>	
1	Use existing codes for concrete and cover thickness. Remedial works unlikely to include coatings/CP.
2	May consider sealant or anticarbonation barrier coating for new designs
3	May consider inhibition or coated rebar for new designs, Corrosion damaged structures consider realkalization/chloride removal
4	Additional corrosion protection is likely for new designs, Retain option to retro-fit CP. Repairs should consider realkalization/chloride removal followed by either sealant coatings or retro-fitting CP at later date.
5	Extra corrosion control should be mandatory with new designs. Repairs/refurbishment should consider CP option

**Table 5** Example of a simple risk or criticality ranking for concrete structures based on a  $3 \times 3$  matrix analysis

<i>Criticality ranking, 1–5</i>				
Effect of failure	Low	1	2	3
	Medium	2	3	4
	High	3	4	5
		Low	Medium	High
		Likelihood of failure		



**Table 7** Selection of corrosion control options for concrete

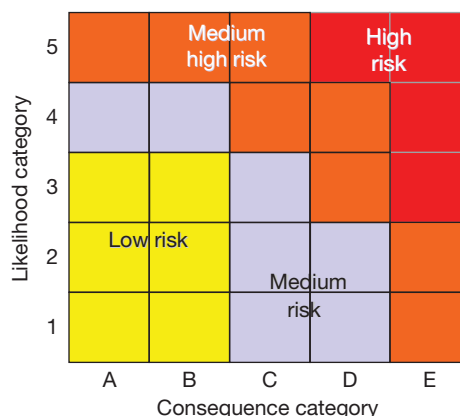
Marine structures (chlorides, atmospheric oxygen)	Cathodic protection in tidal and splash zones Coatings for topsides
Foundations (chlorides, biological compositions)	Water proof membrane/ tanking or cathodic protection in high salt content ground (especially sabkha regions)
Above grade structures (atmospheric exposure)	Sealants or coatings on the concrete. Fusion bonded epoxy coated bar where salt contamination is likely to be high
Inside buildings (controlled environment)	Combination of material selection and conventional design codes

factor. Some are based on the probability of the failure criteria as in the quantified or Level 3 assessment employed by API 580/581.<sup>20,21</sup> Weighted factors may be employed to develop the inputs for the likelihood of failure and consequences of failure.

The purpose of the matrix approach is to prioritize risks and to concentrate efforts on the most influential ones. The numbers on the diagram would typically correspond to threats and opportunities taken from a risk register. A drawback with this approach is that it is difficult to know when the optimum risk mitigation position has been reached unless it is also linked to further actions such as a probabilistic evaluation. However, it is relatively simple and time-efficient to implement. Some of the first practical applications of criticality/RBI methods were on UK North Sea platforms<sup>35</sup> from 1991, and refinery units since the mid-1990s. The approach has been adopted by many operators/service companies/vendors/software suppliers.

#### 4.30.3.2.3 Risk-based inspection

RBI is the subject of a separate chapter in this volume. RBI of process equipment is arguably the most familiar example of how matrix analysis is used in the development of corrosion mitigation strategies at various levels of decision-making. An industry benchmark can be found in the API RBI approach<sup>20,28</sup> that uses a  $5 \times 5$  matrix, **Figure 6**, to identify levels of risk in refinery/process equipment. The output from a quantified (level 3) assessment, as described previously in the determination of hazard scores, is used to determine the consequences category of the matrix.

**Figure 6**  $5 \times 5$  matrix used in the API 581 risk-based inspection procedure.

For example, equipment items at high risk (5D, 5E, 4E, 3E) are unacceptable, requiring a redesign in more corrosion resistant materials or alternative processing routes to be employed. Medium-high risk items could be assessed to see if increased inspection frequencies would allow continuing operation but obviously with a limited life (a predictive maintenance strategy) or if improved corrosion control measures would be effective at decreasing the likelihood of failure and moving the item into a medium risk level and also extending the life. Here a probabilistic analysis could also identify a cost effective option for such strategic decisions.

The resource document, API 581, and the accompanying software package assess consequences (leakage/rupture) for different areas of damage (size of holes in the pipe work and vessels) from general and localized corrosion and cracking. Various scenarios are then evaluated in terms of flammable/toxic effects together with environmental and business interruption effects. The resource document contains a number of technical modules that describe how the potential damage mechanisms are assessed for petrochemical process equipment (from recognized published data) in terms of a damage factor. Key elements of the API RBI approach are:

1. The use of a probabilistic approach for determining the rate of damage, metal loss or crack progression, also employed in the DNV G101<sup>22</sup> offshore inspection standard.
2. The effectiveness of inspection programs in finding and monitoring identified damage mechanisms by assessment of the inspection effectiveness, detection capability of the inspection methods employed and other factors in the inspection process.

Typical inspection methods are ranked, 1–5, in terms of their effectiveness for various forms of damage such as thinning, surface and subsurface cracking and blistering. For example, for general thinning:

1. *Highly effective* (90%) – complete internal visual examination plus ultrasonic thickness testing (UT).
2. *Usually effective* (80%) – partial internal visual examination plus UT.
3. *Fairly effective* (50%) – external spot UT.
4. *Poorly effective* (40%) – hammer testing/telltale holes.
5. *Ineffective* (33%) – external visual examination.

The underlying logic is based on expert opinion quantified using Bayes' Theorem by incorporating the information as a 'State of Damage,' with 1 = equipment damage is no worse than expected based on models/experience, 2 = damage somewhat worse than anticipated/as is sometimes seen in similar equipment, 3 = equipment is considerably worse than anticipated, that is, rarely seen but has been observed occasionally in industry. Combining the inspection ranking with the damage state enables the inspection effectiveness to be quantified to provide a probability ranking.

The software then determines the inspection frequency based on the thickness of the wall, probability of a failure, the damage factor for the type of corrosion (from recognized published data) and the extrapolation of the inspection data trend. When the damage factor increases to a value of 10 or higher after four or more 'highly' effective inspections then the equipment is at the end of its useful life. A value of 10 indicates that the probability of failure increases by an order of magnitude. The aim is to achieve or maintain a low damage subfactor at ideally 1 or less but in practice less than 10, by changing either the inspection frequency and/or the method of inspection (the effectiveness). As the number of effective inspections increase then confidence in the outcome also increases (the error band associated with the measured corrosion rates is decreased), that is, the trend becomes more reliable.

The protocol adopted is illustrated by the effect of progressive damage resulting from general thinning and localized thinning (pitting and erosion–corrosion) on the strength of an equipment item, as shown in [Figure 7](#). The corrosion rate (wall thickness change with time) is determined from inspection data or may be initially obtained from published data and/or industry models and expert opinion. The default/baseline

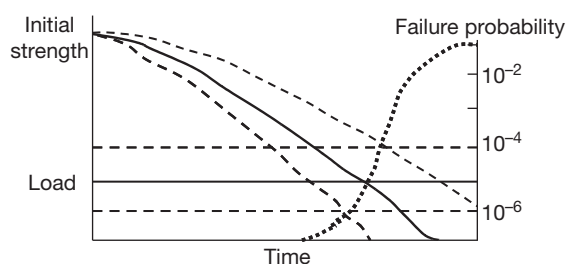


**Figure 7** Probability of failure with time, adapted from API 581.

position is that the corrosion allowance is 25% of the original wall thickness but this is typically modified by use of the maximum allowable working pressure (MAWP) based on ductile overload calculations, operating conditions, diameter and the material properties, limit state function and the minimum allowable thickness (MAT).

The equipment, for example, begins life with the initial strength exceeding the load by some factor of safety. The damage mechanism progressively weakens the structure but the damage rate is likely to be higher or lower than any deterministic mean value. There is therefore a distribution about the mean value of strength as shown by the dashed lines.

In practice, the applied load will also vary and hence the probability of failure will increase progressively as bounded by the intersection of the two sets of dashed lines. This failure probability is described by an S-curve which, for example, may follow a standard distribution, such as normal/lognormal/Weibull. The intersection of the two solid curves indicates the basis of the equipment design, the constructional material properties, equipment dimensions, etc. and a deterministic corrosion rate. This indicates there is a probability of failure of  $\sim 10^{-5}$  at the required lifetime but also failure probabilities at lower and higher lifetimes. The probabilities of failure adopted for corrosion damage in process equipment are similar to risks in other engineering systems, for example, subsea pipeline as summarized in [Table 8](#).

In summary, the API 581 approach and proprietary RBI software can produce reports for a particular plant item with consideration of the ranking, for example, of three levels of inspection activity:

1. A minimal inspection plan.
2. The current level of inspection.
3. An optimized level of inspection.

The first and obvious outcome is that the inspection frequency can be adjusted, but the methods and tools

**Table 8** Example of an offshore risk category

Category	Probable annual frequency	Description
5 (Failure expected)	$>10^{-2}$	Event expected more than once in lifetime
4 (High)	$10^{-2}-10^{-3}$	Event expected to occur during pipeline life (100-year storm)
3 (Medium)	$10^{-3}-10^{-4}$	Event not expected but a once a year credibility with large number of lines
2 (Low)	$10^{-4}-10^{-5}$	Event rarely expected
1 (Negligible)	$<10^{-5}$	Considered negligible

Annual failure frequency for a pipeline/umbilical (based on DNV – RPF107, 2001).

used for the test and inspection (T&I) schedule can be changed. The scope, quality, and extent of the inspection and data collection/interpretation can also be modified. The benefits are that, the plant items at low risk can be inspected on a less frequent basis than by the more traditional procedures employed previously, resulting in lower inspection costs. There is, however, considerable resource needed to populate the database with the plant inventory, line diagram information and previous inspection history, plus the appointment of an experienced team leader/contractor.

At the tactical level, RBI identifies the specific levels of risk to various process units, vessels, tanks and pipe work or items of equipment and hence appropriate inspection frequencies can be scheduled, the level of resource predicted and maintenance action may be taken to mitigate the corrosion risk. At the operational level the day-to-day activities are determined by the agreed upon schedules and should be implemented by work instructions. At the strategic level, the analysis focuses management attention on corrosion of critical items and asset integrity issues but here the secondary risks resulting from, for example, failure of chemical treating systems or use of inadequate inspection methods must also be recognized by putting in place management-of-change procedures.

### 4.30.3.3 Probability Analysis – Dealing with Uncertainties

The probabilistic approach, which is similar to a reliability analysis, may be used to handle uncertainties in, for example, corrosion related design studies, the use of inhibition schemes or inspection strategies. This management tool assists the decision making process by presenting various scenarios that indicate possible futures. The input, that often includes imprecise data, can be varied to identify the sensitivity of the outcome to parameter changes. Incremental project funding is then only allocated on the basis that there are clear risk and uncertainty statements available at each investment decision point. The quantified output, typically expressed as a probability graph (S-curve), provides a clearer picture of risks and benefits derived from specific corrosion mitigation procedures. Thus although the overall results may be essentially similar to a qualitative judgment based on experience and/or traditional expert evaluation of a system, such subjective decisions are often taken without a full appreciation of the implications of uncertainty and risk.

Prediction of anticipated corrosion rates in a system is the first step in assessing corrosion risks and monitoring requirements. In most cases, information is obtained from published data and models. For example, in oil/gas production a number of predictive models are available for CO<sub>2</sub> corrosion of low alloy steels used in many vessel and pipeline fabrications. Most models are based on preliminary studies of de Waard and Milliams whose initial approach<sup>36,37</sup> was later modified to include the effect of fluid velocity.<sup>38</sup> The similar Norsok model<sup>39</sup> uses the fluid to wall shear stress rather than liquid velocity as the flow parameter. All models provide a single deterministic value of the corrosion rate (single value point data) but a probabilistic analysis shows that this statistical average can have higher anticipated values, for example, a corrosion rate of  $c. 1 \text{ mm year}^{-1}$  could reach a maximum of  $4.5 \text{ mm year}^{-1}$ , depending on the distribution function employed, as shown in **Figure 8**.

A quantitative/probabilistic risk analysis uses random variables described by probability density functions (PDFs) or cumulative distribution functions (CDFs) to describe the various parameters that contribute to the overall process, such as the distribution of corrosion rates indicated above. Density functions describe probability using the area under the curve to the left of the associated value; distribution

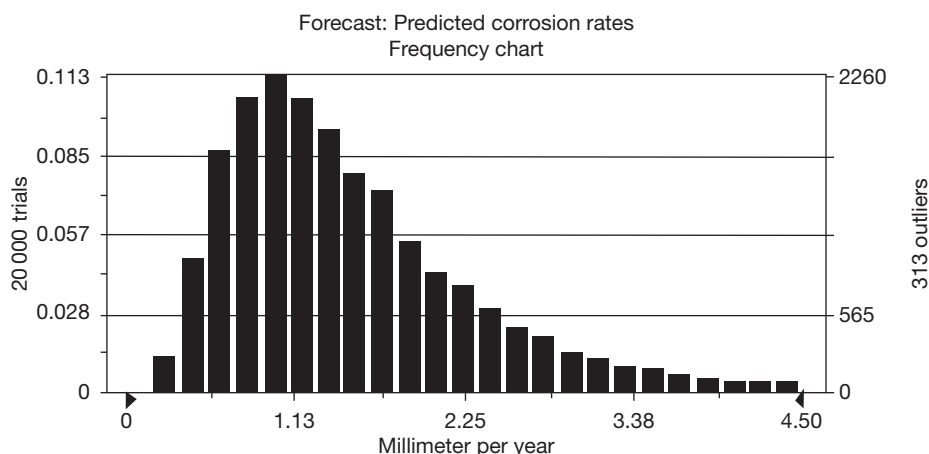


**Figure 8** Typical outcome of a probabilistic approach for CO<sub>2</sub> corrosion rates. Reproduced from McMahon, A. J.; Paisley, D. M. E. *Corrosion Prediction Modelling*, BP Sunbury Report, ESR.96.ER.066, November 1997.<sup>40</sup>

functions compare value and probability directly. Various functions that describe the overall process (normal, lognormal, uniform/on/off, triangular, etc.) are then combined together to provide the output, for example survival probability or probable structure life, as shown in Figure 9. Importantly where any parameter is not known, a distribution is used to describe the (credible) range of values that are likely to occur. The outcome of the analysis, typically obtained using a Monte Carlo simulation, as illustrated in Figure 9, is recorded (for example on a histogram/S-curve) and the calculation repeated until sufficient information is generated in order to optimize the smoothness of the shape of the combined S-curve results. In practice, a network is developed to describe the overall process of interest, as indicated in the lower right hand part of the figure, and the variables/data are inserted as inputs with the outputs presented as a series of S-curves that describe various scenarios.

An illustrated example of the probabilistic method is shown in a pipeline pigging study to aid strategic decisions for inhibition and delivery of design life.<sup>41</sup> An off-shore oil pipeline had operated under stratified flow with a corrosion risk to the lower 70% wetted area due to dissolved carbon dioxide and hydrogen sulfide. The line condition after 3½ years of operation was unknown and the requirement was to identify the most cost effective means of achieving a maximum required life. Possible options were to inhibit and to clean by pigging either immediately or after 4 years' time as originally scheduled. The most effective option was determined using propriety decision analysis software developed for business risk modeling.<sup>42</sup>

The line had operated for 2.25 years with no corrosion inhibition (an industry procedure adopted for low water cut systems) followed by 1.25 years with corrosion inhibitor injection, although not always meeting target injection rates. The corrosion damage was likely to be a combination of general corrosion and pitting corrosion, with predicted corrosion rates between 0.05 mm year<sup>-1</sup> due to general corrosion and 1 mm year<sup>-1</sup> due to pitting corrosion with an average rate of 0.6 mm year<sup>-1</sup>. Uncertainty was described for general and pitting corrosion rates by assuming a truncated normal and lognormal distribution curves respectively as given in DnV G101.<sup>22</sup> During inhibition the general corrosion rates would probably have decreased; however, any pits that formed prior to inhibition may not have been fully protected and could have continued to propagate. Minimum, peak (mode), and maximum values were estimated.

Limited UT thickness inspection data from topside pipework at three well heads provided a statistical distribution of corrosion rates that were compared to predicted values using industry corrosion models and a likely distribution of loss of metal obtained:

General corrosion rates	Pitting corrosion rates
Low = 0.15 mm year <sup>-1</sup>	Low = 0.1 mm year <sup>-1</sup>
Medium = 0.35 mm year <sup>-1</sup>	Medium = 0.3 mm year <sup>-1</sup>
High = 0.55 mm year <sup>-1</sup>	High = 0.9 mm year <sup>-1</sup>

Uncertainty in the corrosion inhibition efficiency was described using a triangular distribution as the variables had a limited range and a reasonably good best estimate was shown with some variance on either side as shown in Table 9:

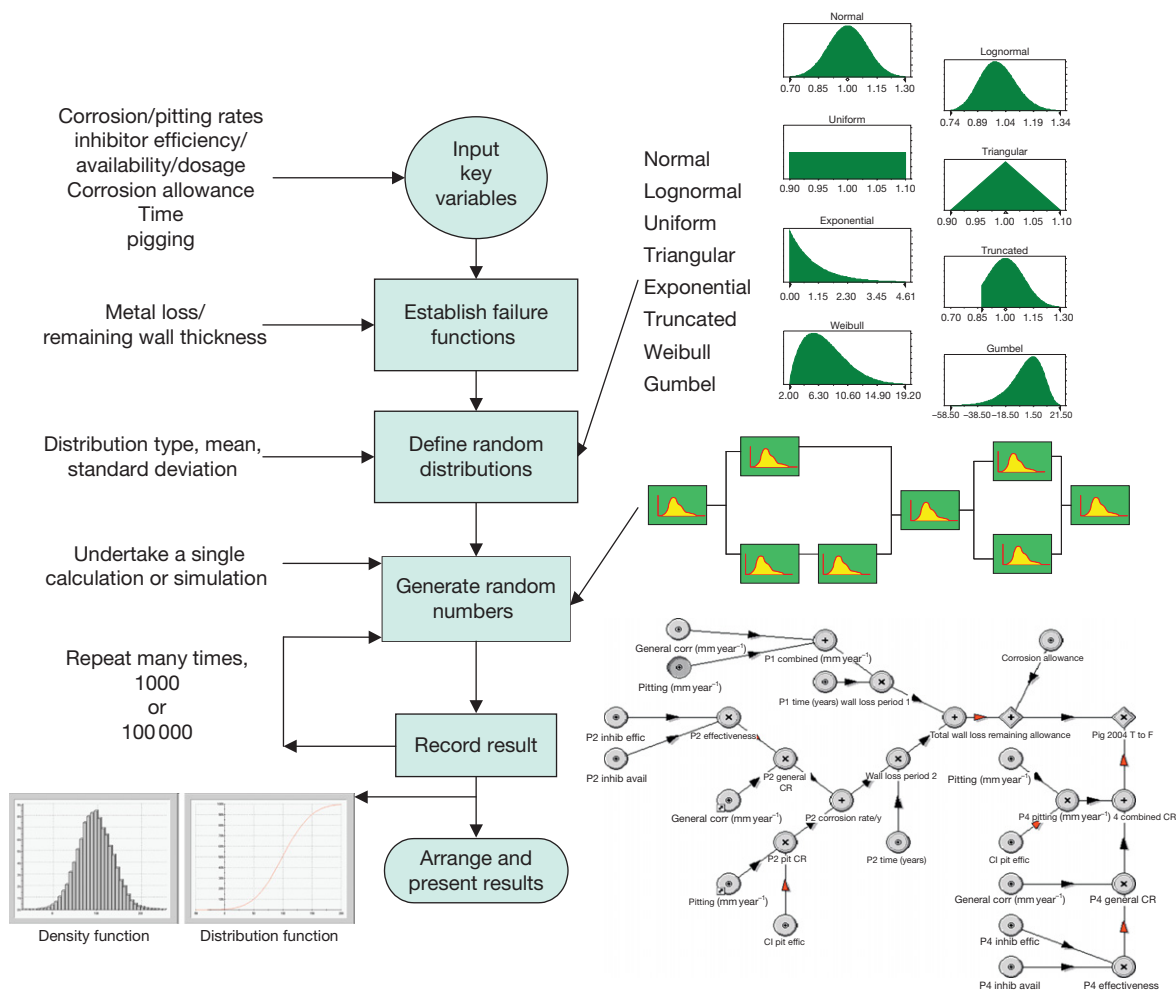


**Figure 9** Probabilistic method as used in a quantitative corrosion risk analysis.

**Table 9** Likely inhibitor performance

<i>Inhibitor efficiency</i>	<i>Inhibitor availability</i>	<i>Efficiency in pits</i>
Minimum = 0.7	Minimum = 0.5	Minimum = 0.1
Peak = 0.8	Peak = 0.7	Peak = 0.5
Maximum = 0.9	Maximum = 0.95	Maximum = 0.9

The following scenarios for the future lifetime of the pipeline with/without pigging and improved inhibition were evaluated:

Scenario 1: Continued operations with no pigging and current inhibitor regime – rate of degradation would continue as previous operational conditions.

Scenario 2: No pigging but implementation of an improved corrosion inhibitor program – Inhibitor efficiency and availability could be increased but

**Table 10** Improved inhibition program

<i>Improved efficiency</i>	<i>Improved availability</i>
Minimum = 0.89	Minimum = 0.94
Peak = 0.9	Peak = 0.95
Maximum = 0.95	Maximum = 0.98

inhibitor ingress into pits is retarded with little effect on protection of pits. The uncertainty in the improved inhibitor efficiency and availability are described in [Table 10](#).

Scenario 3: Pigging in 4 years' time followed by an improved inhibition program – pigging reduces corrosion and corrosion inhibitor is more effective on a 'clean' surface, estimated pitting corrosion efficiency following pigging could reduce corrosion by 90%. This improved inhibitor efficiency in pits was



described by a triangular distribution with the minimum = 0.87, peak = 0.90 and maximum = 0.93.

Scenario 4: Pigging now followed by an improved inhibition program.

The various options were determined using a Monte Carlo simulation and an appropriate network that describes the system with the probable range of outcomes expressed as a probability versus time plot (or *S*-curve), **Figure 10**. The integrity limit was assumed to be loss of corrosion allowance of 6 mm and a minimum allowable wall thickness (MAWT) based on the operational pressure.

The conclusion was that pigging should be carried out at the earliest opportunity to ensure a low level of risk over the next few years. Corrosion inhibition can be effective against pitting but some may perform better than others at inhibiting existing corrosion pits and a comparison of different inhibitors under simulated production conditions could be carried out to select the most appropriate inhibitor. This in combination with pigging should ensure a long operational life.

The above case study illustrates the main points of a quantified approach, that is, that the greater part of the value is realized in risk management by identification and implementation of the most appropriate risk treatment strategies. An expert opinion from a corrosion engineer would be that pigging is recommended when inhibition is employed to mitigate the effects of sludge/pitting corrosion but the graphs

provide the justification for the recommendation and aid management decision-making processes.

The above provides a corrosion mitigation strategy but has to be followed up by development of tactics such as confirmation of the pipeline condition by in-line inspection, magnetic flux leakage detection for wall thickness and estimation of pitting, and tests to assess the effectiveness of inhibitor dosage to control pitting corrosion. A cost benefit analysis, using net present value (NPV) and a discount factor of 5%, of pigging and inhibition versus continuing to operate with the original regime indicated the financial incentive. A failure would be likely to cost \$25 million, an improved inhibitor program \$60k per year and regular (offshore) pigging \$100k per year but these combined are ~21% that of the 'do nothing'/retain the current practice.

The statistical modeling/probabilistic method was extended using commercially available software (@Risk)<sup>43</sup> in a second case study of a sub-sea pipeline network but using an API 570 pipework data trending approach that had been described in a previous publication.<sup>44</sup> The aim was development of a written scheme of examination which provides an auditable trail for each pipeline that clearly identifies corrosion threats and mitigation measures. Remaining life is shown as an inverse *S*-curve that then forms the basis of an annual integrity approach based on available inspection and monitoring data that then defines a technical assessment of the asset condition.

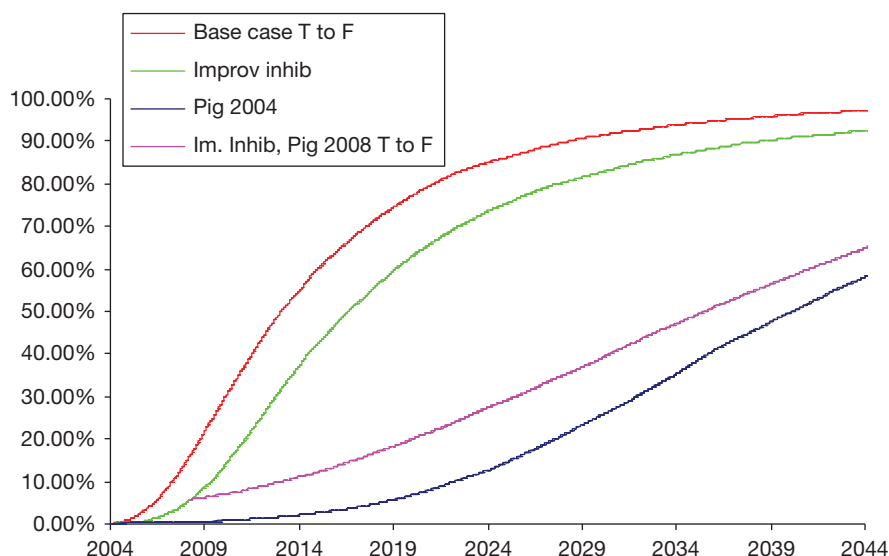


**Figure 10** Probability of failure – loss of 6 mm corrosion allowance.

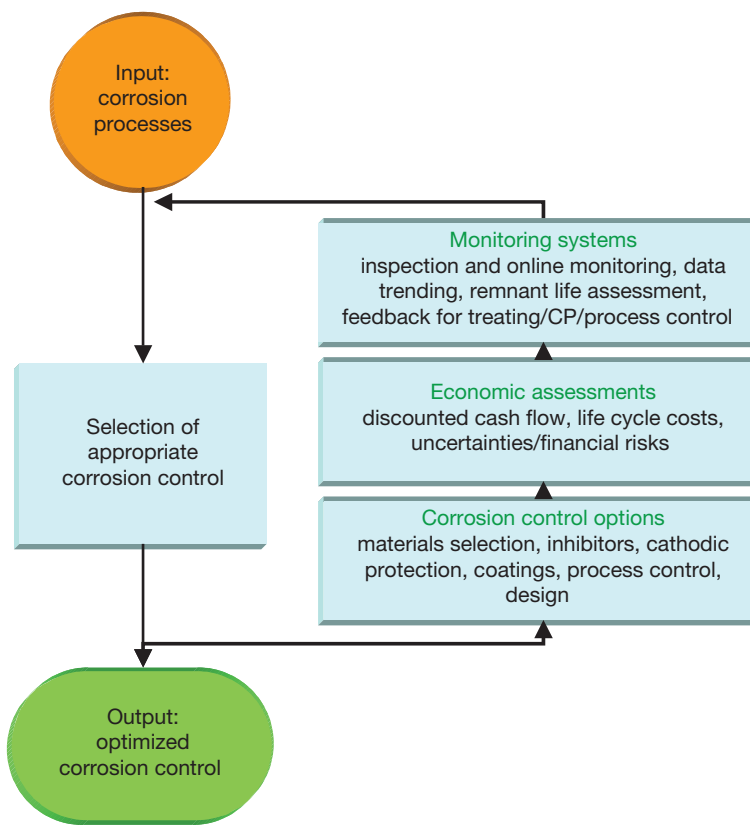


**Figure 11** Basic corrosion risk mitigation steps.

#### 4.30.3.4 Corrosion Mitigation Requirements

Identification, analysis, and evaluation of corrosion risks form the first steps in the corrosion management process. The next major step, as illustrated in [Figure 11](#), is to provide cost effective solutions to mitigate corrosion risks by the selection of appropriate corrosion mitigation options.

The major tactics used to mitigate the effects of corrosion are embodied in many international/national standards, industry guidance documents, and in-house standards/procedures. These tactics are described in detail in the relevant chapters in this book but can be simplified into the following basic list:

1. *Materials selection* – metallic materials: carbon steels/low alloy steel (usual to include a corrosion allowance during design), CRAs (stainless steel, nickel alloys, titanium), nonmetallic materials (polymers, glass reinforced plastic (GRP), elastomers, ceramics).
2. *Chemical treatments* – typically inhibitors, biocides and scale control chemicals but packages also include surfactants, antifoaming chemicals. Inhibitors used

in boiler and cooling waters, oil/gas production systems and in special concrete designs. Biocides are employed in cooling water systems and hydrotest fluids, water injection/waters systems, whilst scale control chemicals are used in cooling systems, boilers and oil/gas production and process plants.

3. *Use of coatings* – metallic, nonmetallic and organic/paints, used in external and internal environments, major factors are cost, availability, ease of surface preparation, application and life expectancy, important to ensure appropriate specifications, field application and inspection is carried out.
4. *Cathodic and anodic protection* – electrochemical methods of corrosion control. CP can be applied to immersed and buried structures, jetties, pipelines, tanks and concrete. CP is also used inside water containing vessels, tanks and the water boxes of heat exchangers. A low level of protection (cathodic prevention) is used in some concrete structure bridge designs that involve high-strength stressed steel. Anodic protection uses potentiostatic control of the internals of process equipment to ensure that electrochemical passivity is maintained.

5. *Process and environmental control* – modify moisture/humidity levels, lower oxygen concentrations. Change pH, throughput, decrease flow rate and/or heat transfer rate.
6. *Design* – use of codes/standards. At concept/front end engineering stage assess corrosion hazards and risks, evaluate life cycle costs. During engineering design phase use agreed codes and standards to produce specifications and drawings. Introduce QA/QC and inspection/testing procedures into specifications. During the detailing phase assess factors associated with stress, shape, compatibility, and surface condition, for example, eliminate stress raisers, crevices, and consider increased wall thickness on some bends. Use reviews/audits of concept, engineering, and detailing designs.
7. *Inspection and monitoring* – trending of deterioration rates, chemical dosages and changes in process chemistries

The first six options above are corrosion control methods and are used either singly or in combination, the choice depending on the specific application and the corrosivity of local environments. Many of these options are now covered by ISO/EN/NACE standards that are informative and contain guidance and recommendations for suitably trained, experienced, responsible personnel. However, such standards are not specifications or prescriptive and should not be used for certification purposes.

Key issues are reliability<sup>45</sup> and elimination of corrosion risks during the detailed design stage of the engineering design.<sup>46</sup> Design teams should be aware of likely damage as described in, for example, the compilation of photographs of corrosion damage to plant structures for oil/gas production<sup>47</sup> and the required mitigation procedures/audits.<sup>48</sup> The choice of the corrosion control method selected is highly dependent on materials cost, the discount factor/interest rate and life-cycle costs as described in the chapter on corrosion economics in this book and elsewhere.<sup>49</sup> However, as Turner noted in his life time observations on process engineers<sup>50</sup> “a fact of life is that the senior management is to fix the budget for a project as high as it could be to still provide a profit.” The associated economic risk for a project is essentially the uncertainty that may lead to consequential/indirect costs of failures and shutdown/unavailability and the risk management aspect is illustrated in decision tree analysis of expected values for carbon steel and CRA pipeline<sup>51</sup> and probabilistic studies

Consideration has also to be taken of the need to monitor both equipment condition and changes in

plant process fluids. Corrosion inspection and monitoring provide data on materials performance and the effectiveness of chemical treatments, such as corrosion inhibition, that form the basis of corrosion mitigation strategies in some industries. To be effective, any field data must be collected, analyzed, trended, and correlated with other relevant parameters in order to provide information for management to make appropriate decisions. Inadequate or poor field data means lack of information and may lead to inappropriate actions.

Corrosion inspection and monitoring are undertaken with one of two purposes:

1. To determine the condition of equipment and any consequent requirements for repair, and changes in wall thickness and/or rates of localized corrosion or cracking that have implications for future retirement that are prime concerns of asset integrity and maintenance teams.
2. To monitor changes in fluid corrosivity due to damaging excursions in environmental composition and/or to control chemical treatments, such as corrosion inhibitor/biocide dosage/oxygen scavenger injection that are prime concerns of operating teams that typically use probes and techniques that provide continuous rapid responses to changes in corrosion rate.

Inspection and monitoring technologies and techniques are described in a separate chapter in this book. In most cases use of inspection techniques (ultrasonics, gamma radiography, thermography, dye penetrant, magnetic particle and visual inspection) is a specialist area requiring employment of skilled technicians or appointment of contractors, particularly for applications such as intelligent pigging of pipelines (magnetic induction, ultrasonics) and down-hole/wireline inspections (callipers, ultrasonics).

On-site inspection methods, traditionally based on handheld devices such as ultrasonic testing (UT) equipment, were primarily used for postfabrication tests. The advent of digital techniques has improved the sensitivity, ease of data collection, and data handling capabilities which allows for improved display, data storage and trending. For example, computed/‘Filmless’ Radiography systems can now collect and analyze all radiographic data, completely replacing conventional films and aiding storage, and retrieval needs. Some inspection techniques have now evolved into permanently installed surveillance tools such as UT mats,<sup>52</sup> piezoelectric sensors embedded in electronic circuit ribbon<sup>53</sup> and alternative transducers such as the GE cMUT cell<sup>54</sup> a Si flat-panel capacitive ultrasonic micromachined transducer (cmut).

The relatively clear distinction, both technically and managerially, between the traditional fixed-time inspections and on-line surveillance/monitoring is therefore now more diffuse.

Corrosion monitoring techniques range from simple coupons, electrical resistance (ER) probes, electrochemical measurements in aqueous fluids, hydrogen permeation for sour systems, to more specialist methods such as the field signature method (FSM) and sand probes in oil/gas production. In some oil field systems, sand production/erosion probes may also be employed to identify specific problems.

In many flammable and hazardous areas, such as oil/gas production systems and chemical plant, the risk of failure/seizure of the probe assembly during insertion and retrieval has led to the requirement of a double block system. There is therefore an increasing emphasis on nonintrusive monitoring methods that can be operated from remote locations. These include spool pieces for ER and electrochemical measurements, externally attached ultrasonic devices mentioned above and FSM which uses a spool piece to assess changes in uniform corrosion damage, pitting, and erosion in lines.

The sensitivity and response from monitoring systems is crucial, particularly for high risk systems where, for example, a high inhibitor availability and efficiency is required and Figure 12 illustrates the relative corrosion rates and the response times from various probes based on linear polarization resistance measurements (LPRM), traditional ER, Hall-effect monitors and FSM.

Field data held in personal PCs is not readily accessible by the rest of an organization, neither is it

practical/effective to manage corrosion data systems from spread sheets. PC-based systems are increasingly employed, with either their own internal database or linked to the main asset database, but with the information readily available to other team members through an intranet link (transparent management approach). Input into electronic systems can be directly from hard wired monitoring instrumentation, from portable instrumentation/hand-held data loggers, and via keyboard entry as indicated in Figure 13. Data required for process control is usually retained in distributed control system (DCS) and supervisory control and data acquisition (SCADA) systems for a limited time period and therefore those data required as part of the corrosion management processing should be downloaded and retained in a separate database for correlation/trending.

Location of inspection/corrosion monitoring points need to be chosen carefully to ensure that they provide appropriate data for the specific application such as areas of high turbulence intensity, particularly where slugging-type flow or impingement of second phases occurs, or in areas of low flow or stagnation (dead legs) such as in the bottom of vessels and the 6 o'clock position in pipelines, in order to assess the aqueous phase/water dropout. Local variations of flow and temperature within processing equipment and pipework may have to be considered. In some cases, the highest/lowest temperature points that give rise to evaporation/condensation/concentration effects may be crucial. Such an assessment is typical of any corrosion risk evaluation where local variations can be significant.

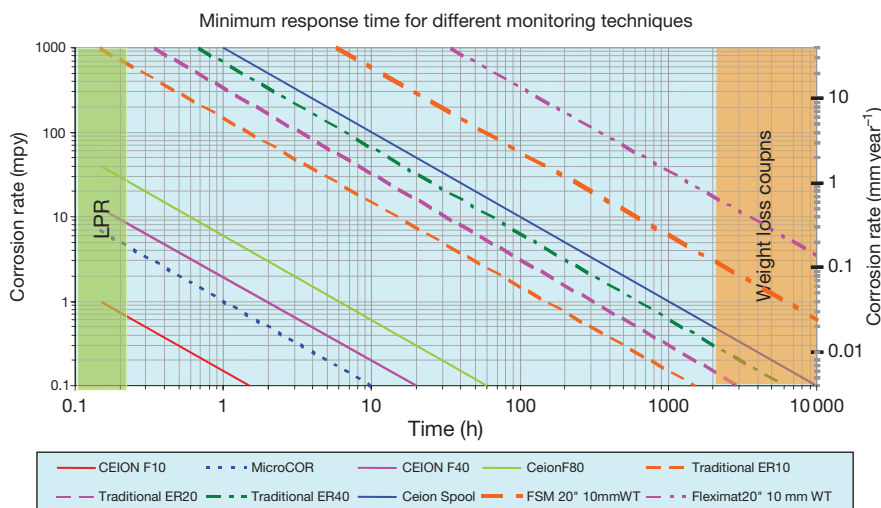


**Figure 12** Comparison of responses from monitoring techniques. Courtesy of D.G. John, CAPCIS Ltd.

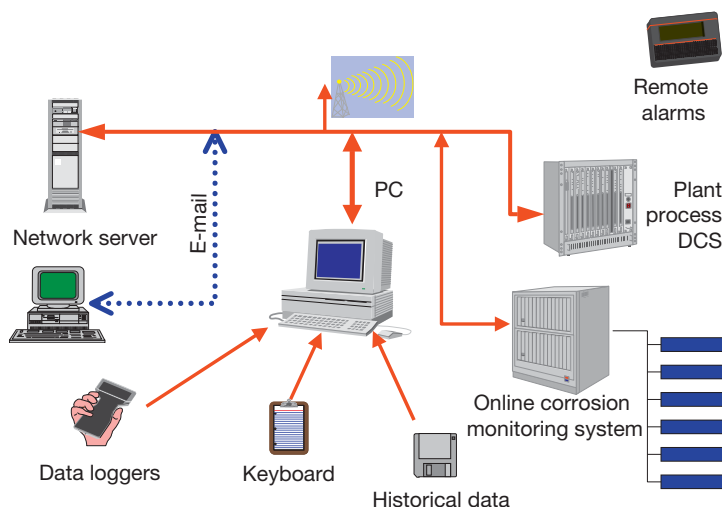


**Figure 13** Inputs into a corrosion data system. Reproduced from John, D. G.; Attwood, P.; Rothwell, A. N. In *Corrosion'99*; NACE International: Houston, TX, 1999; Paper no. 249.<sup>55</sup>

The functions and roles of inspection and monitoring teams must be clearly defined and individual responsibilities for managing the systems, collecting and inputting field data, interpreting rate/correlating information and producing reports should be well understood. An overall management purpose is to devise strategies, tactics and systems that ensure that monitoring and inspection information contribute to safe and reliable operation irrespective of who obtains the field data. Those organizations that operate transparent data management systems are more likely to sustain the effectiveness of activities such as RBI, chemical treating, CP, the maintenance of coating systems, etc. that are so essential to successful asset management.

#### 4.30.4 Corrosion Management Systems

##### 4.30.4.1 Framework for Corrosion Management Systems

###### 4.30.4.1.1 The corrosion risk mitigation system

Previous subsections outlined typical tools employed in corrosion risk assessment, mitigation and field monitoring steps but these must be placed in an overall context involving teams, such as the planning and implementation team and the team for decision-making and taking corrective action steps. An overview of a typical corrosion risk mitigation approach is illustrated in [Figure 14](#), including feedback for control and the feed forward of information.

The inputs are corrosion concerns, life expectancy, life-cycle costs, project viability and SHE issues. The output is effective corrosion mitigation that is based on six distinct processing steps, including decision-making and actions:

1. Identification of individual corrosion team members, leaders/managers, and owners responsible for various procedures/processes/parts of the system.
2. Carrying out of the corrosion risk analysis.
3. Evaluation of the corrosion mitigation options.
4. Planning and implementation of the risk treatment process.
5. Development and maintenance of the required databases.
6. Regular use of informed decisions to instigate corrective actions.

Corrosion management requires that corrective actions be carried out as an outcome from the decision-making step. A structured approach with processes and procedures in place does not necessarily guarantee success without the key informed decision-making and action step. Team members must also undertake feedback from reviews, data monitoring, updating plans, and assessing secondary risks throughout the different project stages. Senior management/corrosion teams must allocate ownership of written corrosion risk assessment and mitigation procedures, planning and implementation processes and the decision-making step. Other inputs, for example, include the development and application of performance reviews and KPIs, and ensuring that management of change procedures



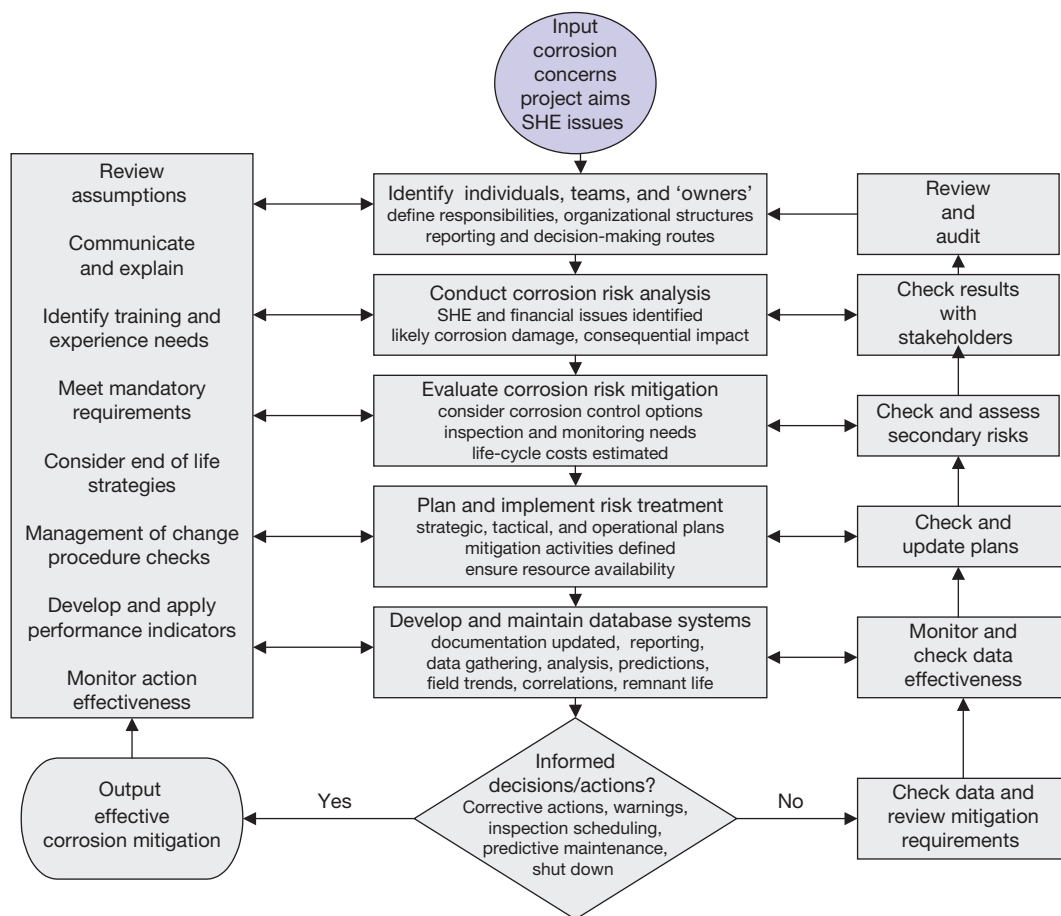


**Figure 14** Outline of a corrosion risk mitigation system.

and monitoring of action effectiveness are in place. Some of these, such as KPIs, are also management control methods as will be described below in connection with [Figure 15](#).

#### 4.30.4.1.2 Corrosion management systems

Only in the past 10 years have formal corrosion management systems received attention in the literature, in contrast to voluminous publications on corrosion risk mitigation tactics. Formal systems for integrity management, including the use of competent persons, have been employed for over 50 years in industries where catastrophic failure prevention is crucial and SHE issues affect an organization's image. From a financial perspective, the prevention of engineering failures that affect up-time, throughput and process efficiency, and ensuring that corrosion risk mitigation in new projects and operations is cost effective, requires a responsive corrosion management system

that integrates seamlessly into an organization's design and asset management systems. A corrosion management system should have many of the steps contained within a corrosion risk mitigation system but must also have feedback, reviews/audits and performance indicators to ensure that it operates effectively and is compatible with other management systems within the organization.

The original basis for the approach given in [Figure 15](#) was the UK HSE *Successful Health and Safety Management* model.<sup>10</sup> The input and feedback loops were added by the author during the mid 1990s for industry-based corrosion training courses and was first reported as a generic corrosion management model in 1998.<sup>56</sup> It was developed further in 1999<sup>4,8</sup> in connection with continuing concerns by the UK HSE on hydrocarbon emissions from UK North Sea offshore processing facilities. A primary aim was to develop a template based on the UK regulatory authority's

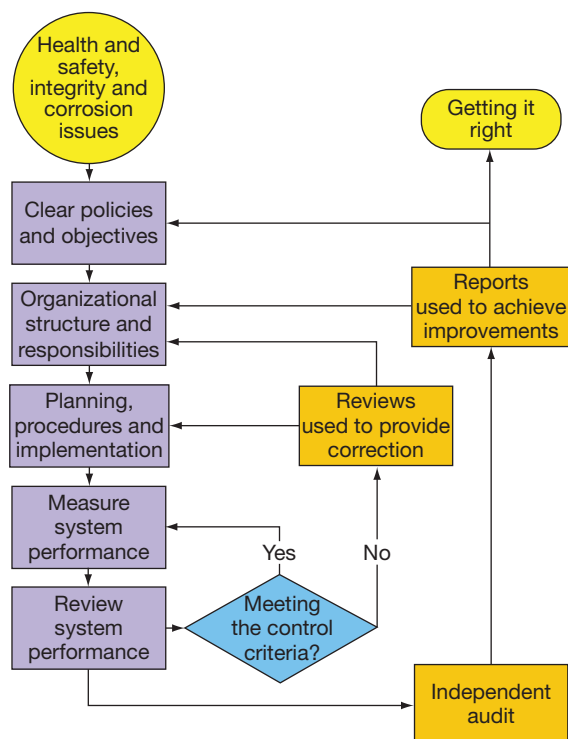


**Figure 15** Basic management steps and feedback loops needed for control.<sup>4,8</sup>

approach to safety management and adoption of a common assessment of the corrosion management systems already in place.

The concern over hydrocarbon releases but also external corrosion damage of structures continued in *Guidance for Corrosion Management in Oil and Gas Production and Processing* published in 2008<sup>48</sup> and was first outlined in a workshop<sup>57</sup> in Aberdeen. The guidance focuses on the impact of internal and external corrosion, on integrity issues in existing facilities and is complemented by a *Corrosion Threats Handbook*,<sup>47</sup> the information presented is also instructive to designers of new facilities. The main text describes what would be appropriate for an oil/gas processing corrosion management system. The management system flow sheet differs slightly from **Figure 15** in that the corrosion risk assessment/planning process and the implementation/analysis process are separated. Information on tasks and details and photographs of damage inspection are presented. Annex A provides *Guidance to Normative Requirements and Examples of Good Practice*, Annex B outlines the *Top Corrosion Threats and Corrosion Mitigation Methods* and Annex C provides a useful eight-page *Checklist for Assessment of Corrosion Management*. It is significant that this document

considers that the corrosion management system requirements outlined should be considered normative for UK operators.

An illustration of the use of the corrosion management system to address external corrosion/coating issues<sup>58</sup> was presented in the Aberdeen workshop<sup>57</sup> where a risk-based assessment method was developed to enable work prioritization on structures, piping, handrails, walkways and gratings. Coatings condition/inspection was recorded in databases with the performance monitored on a visible KPI reporting system based on the ISO paint standard reference scale for coating breakdown.<sup>59</sup> Re5 and Re7, equating to 8% and more than 35% coating breakdown respectively, were judged to be the intervention levels for piping and structures, respectively, for the study. This then formed the basis for planning the work scope which included the ability to determine a cost effective long-term painting strategy allowing for scenario analysis and cost effective management. The importance of external corrosion mitigation/integrity of walkways from the regulator's viewpoint can be seen from their external corrosion project<sup>60</sup> that aims to reduce risks by a combination of improvements to both the physical condition of installations and the management systems in place.

A more general approach for corrosion management systems in a range of applications and project stages but based on the risk management approach described previously<sup>31</sup> as shown in **Figure 16**. Major factors for any corrosion management system are a series of logical steps and an ability to review and audit those steps. The flow sheet in **Figure 16** indicates typical processing steps required in a system that incorporates both a risk-based mitigation process and control of the management process. The inputs are corrosion concerns in the context of the project and SHE issues, etc. The main processing steps are risk-based and auditable with effective corrosion mitigation and continuous improvement as the outputs of the management system.

**Figure 16** should be read in conjunction with the mitigation detail provided previously in **Figure 14** and the outline of the system review and audit shown in **Figure 15**. The inclusion of the concept of continuous improvement is a quality management system criterion output, as discussed previously, whilst the crucial step in any management process must be informed decision-making, based on reliable data. Procedures and protocols form the basis of a management system but without responsible and informed decision making the overall process will fail. Any management

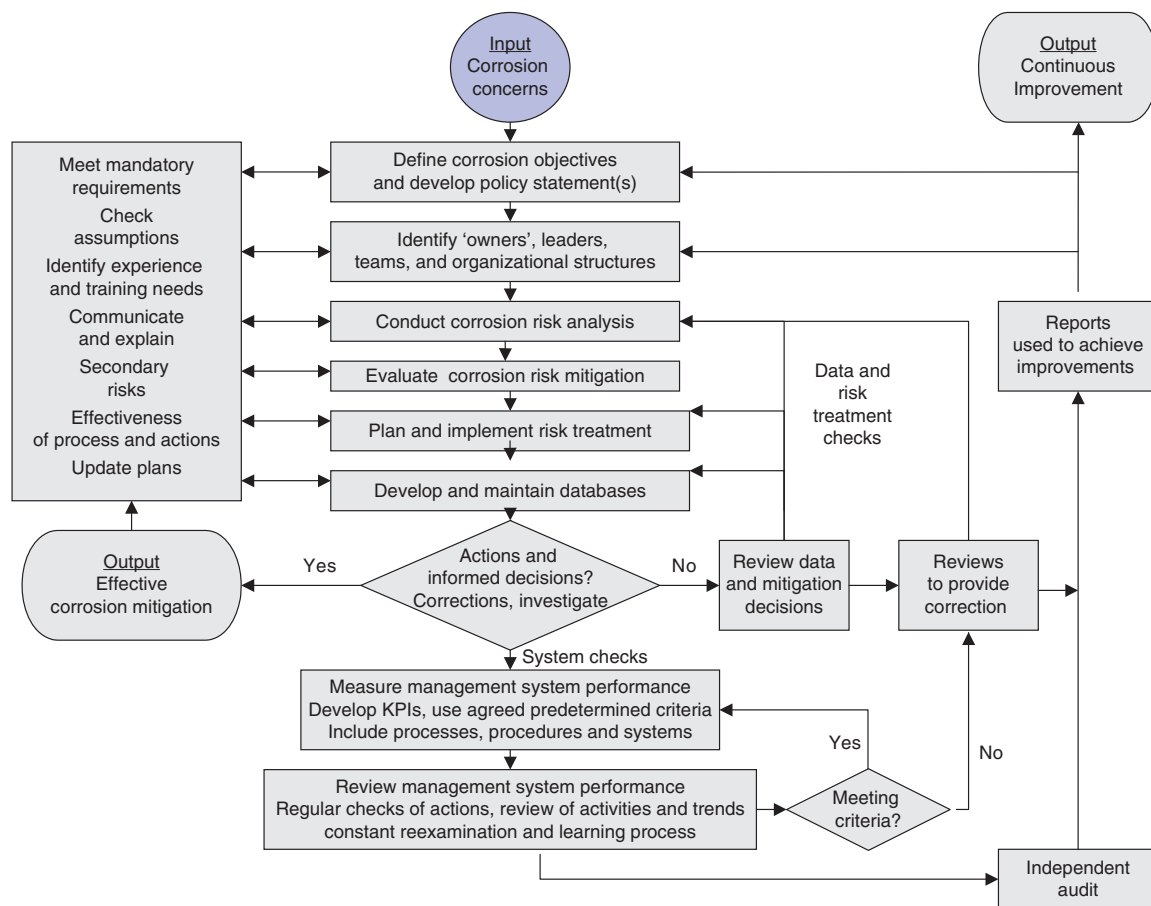


**Figure 16** Requirements of a corrosion management system.

system has also to be regularly reviewed to ensure that the various steps continue to meet predetermined criteria as addressed by the development and use of performance standards such as KPIs.

In practice, many corrosion management systems will combine two or more steps/tasks/actions in some processing steps but the overriding requirement is to ensure that the different tasks and associated overall management actions are completed. In many ways [Figures 15 and 16](#) provide a template or idealized corrosion management system, without attempting to prescribe exact arrangements within established organizational systems. For example, a basic documentation and data control system will be needed at the start of a project but will not appear in its fully operational state until later. Details of the key steps for both mitigation and management are given below:

1. *Aims/objectives/policies.* An initial step in developing a corrosion management system is to define the aims and objectives of the corrosion input to a

project. These then form the basis of the corrosion policy, in principle, a permanent directive with authority from senior site management. The policy specifies overall/longer term objectives such as lowest life cycle costs during design, no leaks or emissions during the operational phase or with life enhancement meeting the required life, etc. The policy may incorporate elements of an organization's safety or environmental policy or even simple day-to-day guidance, such as that general corrosion rates should be less than 10 mpy. Guidance on the series of steps was outlined in the corrosion policy definition given in the chapter introduction. This includes establishment of organizational structures with defined responsibilities, reporting routes, practices, procedures, processes, and resources. It also requires the demonstration of responsibility and accountability for corrosion performance, managing risks, decreasing costs, controlling compliance, and motivating personnel.

2. *Individuals/teams/organizations.* Identification of individuals and teams with ownership of corrosion management processes also helps to define roles, responsibilities and accountabilities of managers, staff and contracted bodies concerned with corrosion issues. Appointment of corrosion team members with appropriate skills, an experienced team leader and an asset/project manager would be typical with the team comprised of representatives from the design team, engineering, inspection, production/operations, coatings/chemistry/biological laboratories, specialist contractors/consultants and even vendors/suppliers. Project boundaries with related/associated activities such as asset integrity (inspection teams), maintenance (engineering department teams) and production (process engineering teams) must be defined. Technical competence of personnel is normally a given but for nonspecialists/managers appropriate training may be required. Communication routes should be clearly identified and cooperation between team members and other groups encouraged ensuring that corrosion implications for other areas of activity are understood. The use of transparent data bases/trend information is helpful and often crucial.
3. *Corrosion risk evaluations and assessment of mitigation options.* These are fundamental steps conducted throughout the project life as conditions and facility operational requirements/procedures change. At some stages, such as design or plant upgrades/life extension, these activities form the largest single part of any corrosion management process and can have the largest impact on life-cycle costs and reliability. Issues arising from consideration of secondary risks or failure of a specific corrosion mitigation procedure must also be addressed. The basis of the designs/decisions must be clearly documented with materials/process limitations highlighted in the corrosion/operating manual for each unit. This should link through to management-of-change documentation, etc. The development of corrosion risk mitigation procedures includes the development and the methodology for documentation the implementation of various corrosion risk assessments and corrosion mitigation measures.
4. *Corrosion risk treatment planning and implementation.* These are vital to ensure that strategic, tactical, and operational/day-to-day activities designed to mitigate corrosion are employed effectively. Strategic activities address longer term issues such as best practices to ensure optimal life-cycle costs, SHE/mandatory requirements, corporate corrosion practice/integrity requirements and business concerns including the development of condition-based maintenance/equipment reliability/uptime needs. Such issues should have been considered as part of corrosion risk/mitigation analyses with the outcome requirements specified to provide for detailed plans to be developed. Planning involves the production of methods and/or procedures for all activities including specification/procurement of materials, testing, fabrication/welding, coatings/CP equipment applications, corrosion monitoring/inspection instrumentation, field data collection/analysis, required databases and their population, specification of reporting by appropriate routes and development of corrective action procedures to be carried out when necessary. Corrosion management plans should be formally recorded in the system documentation as part of a facility design and construction record, including consideration of facility start-up, operating, emergency/shutdown procedures where conditions impact on corrosion mitigation. Planning also includes assessment/development of chemical treating, inspection, and maintenance procedures. In many cases, these in-house company standards/protocols are typically based on international standards such as ISO, NACE, API, DnV, etc.
5. *Database development and maintenance.* Suitable databases for storage of system documentation, facility design/as-constructed diagrams, commissioning information and field data during operation/inspection/maintenance is a given. Specification, development, and maintenance of databases must be carried out in conjunction with stakeholders who will operate the system. It is not recommended that a design contractor/central authority specifies the system without adequate consultation. Consideration must be given to how previous experience/design/construction data is transferred through to the operational phase database. Examples of what may be required include: changes from the basis of design, testing requirements, modifications, that is, how will the incorporation of likely changes noted as part of the basis of design be built into the operating and maintenance/inspection plans? Also postfabrication inspection data provides the initial field data point for trending as in RBI and should be linked with specific locations on P&I/line/isometric diagrams. The means by which field data such as

visual inspections/coating surveys, hand-held/permanently wired instrumentation, DCS/SCADA downloads is to be collected, is analyzed and used for trending/correlations must be agreed and specified.

6. *Informed decisions and actions.* These are key processes; many management systems fail because of a lack of a clear decision-making step even though adequate protocols and procedures are in place. Corrective actions are an outcome from the decision-making step and these include investigative studies, the issuing and following-up of warnings or even instigating shutdown actions when required. Operational/day-to-day actions include rescheduling of inspections, change of chemical treating and predictive maintenance work that involve other teams. Any recommendations made must either be followed up or rejected in a positive manner due to other factors but not by default.
7. *Performance measurement of the management system.* Regular checks on the operating system should be conducted against agreed-upon predetermined criteria – the performance standards or KPIs. Responsibility for overseeing this process should lie with suitably competent individuals who are, ideally, appropriately free of production pressures. Performance measurement covers all aspects of the processes, procedures, and management systems using different levels of measurement at appropriate frequencies. Some may require immediate review/measurement on completion of a task. Measurement systems may be either proactive (to ensure agreed criteria are being met or identification of an inadequate system) or reactive (a postfailure activity to evaluate repair incidents or near misses and identify improvements).
8. *Regular reviews.* These are normal in-house checks of overall corrosion management system performance. They ensure that management procedures and processes are consistent with any changing business plans, changing production requirements and changing legislation. The aim is to improve performance and reduce incidents, improving conformance to schedules and improving procedures. It is the constant reexamination and incorporation of lessons learned that lead to continuous improvement of the corrosion management system.
9. *Periodic audits.* Management and monitoring system audits provide evidence that the corrosion management system is efficient, effective and reliable, and that processes and procedures are being implemented in accordance with agreed upon procedures. Regulations typically require owners

to ensure that adequate arrangements are established for audit report-making.

**Figure 16** was developed from a risk-based approach for corrosion mitigation that also provides a structured framework for control of the management system by use of reviews/audits/performance indicators. It is able to integrate statutory SHE goals and delivery of cost benefits to a project. In practice, contributory factors such as identification of training needs, management of change and end of life strategies will also have to be addressed where required. Delivery of a working system will depend on the use of performance indicators for both the management system, **Figure 16**, and the mitigation system, **Figure 14**.

#### 4.30.4.2 Setting Performance Measures

Use of performance measurement/KPIs is a normal practice in most quality and safety systems. For example, the UK pressure system regulations require asset owners to record/inform the regulatory authorities of any delay to a scheduled inspection. The delay may be justified in order to either fit in with a scheduled maintenance shutdown or due to other valid operational reasons. However, a second, further delay beyond the next scheduled inspection is not permitted, the aim being to ensure that the plant is not operated in an unsafe condition; an illustrative proactive use of a KPI. A significant record of inspection delays is likely to be symptomatic of significant management problems.

Typical objectives of performance measurement/KPIs for corrosion management are:

1. Ensure that corporate corrosion objectives are met with respect to SHE and financial issues, usually by reactive/lagging indicators.
2. Ensure that strategic/tactical/operational strategies are implemented effectively by checking the success of corrosion management activities, often by checking on the success of plans by proactive/leading indicators.

These might be translated into specific indicators for various project stages and organizational levels as follows:

1. *Corporate level*
  - Provide written policy statements.
2. *Strategic level* (design/proponent/asset manager/owner)
  - Ensure that corporate/SHE/local legislative/long term objectives are addressed.



- Ensure that corrosion rates provide the agreed upon equipment life and that cost effective corrosion mitigation is employed.
  - Ensure that individuals have delegated responsibility/ownership of corrosion issues and identify who is accountable for various components of the corrosion mitigation program.
  - Ensure that corrosion risk assessments and sensitivity studies are conducted as a regular feature of project/design/inspection/operations/maintenance activities.
  - Ensure that decision makers are suitably trained/competent/responsible to action necessary changes/modifications/issue work instructions for the improvement of corrosion mitigation processes.
  - Ensure that various aspects of the program remain effective with stated time frames when they will be updated/reviewed/audited and that management-of-change procedures are in place.
  - Ensure that the performance indicators are acceptable/measurable/achievable/realistic.
3. *Tactical level* (design/proponent/asset manager/owner, plus supervisors from design, engineering, production, maintenance, inspection, corrosion).
- Ensure that a corrosion team leader/team members are allocated/named as part of the design/construction/O & M/project teams.
  - Ensure agreed-upon codes/standards/in-house guidance/procedures/work practices are authorized/reviewed/audited at set intervals and placed in a central quality controlled documentation database.
  - Ensure that corrosion mitigation methods employed are appropriate/cost effective/suitably managed/monitored/subject to regular review/audit.
  - Ensure that annual review of corrosion/inspection/chemical treating/CP/coating systems are carried out.
  - Ensure that audit of corrosion/inspection/chemical treating/CP/coating systems are carried out every 2–5 years.
  - Carry out an internal audit of the corrosion management system (6 months after implementation and thereafter on an annual basis).
4. *Operational/corrosion team level* (Responsibilities reside with specific individuals depending on the size of the operation and organizational arrangements; these could include managers, supervisors, corrosion team members).
- Specify and cost materials (\$ per mm) as part of life-cycle studies including any testing required.
  - Ensure that cost effective corrosion mitigation is employed such that corrosion rates are consistent with the corrosion allowance/required integrity/agreed upon life of equipment.
  - Optimize chemical treatments.
  - Report any corrosion related failures identified during routine inspections or data acquisition.
  - Undertake urgent field activities within 24 h of the request.
  - Enter all planned field data into the appropriate database within 1 week of taking the measurements for low and medium risk items.
  - Collect corrosion monitoring data and download data to asset management database within 1 week of due date.
  - Issue a written report about out-of-compliance findings within an agreed-upon time period of taking measurements.
5. *Corrosion team leader*
- Review records to assess conformance and report out of compliance when necessary.
  - Track specific procedures and processes to ensure compliance including competency of responsible individuals, departments, and organizations and correct implementation, reporting and reaction.
  - Check if appropriate investigations were undertaken in accordance with procedures.
  - Check if the investigations were effective and that necessary changes to procedures/processes are developed to prevent recurrence.
  - Have the changes implemented/incorporated into procedures/processes.
  - Review the corrosion related documentation.
- Examples of measurement of corrosion management performance can be found in oil/gas production,<sup>8,48</sup> chemical treatment of systems,<sup>61</sup> coatings maintenance<sup>58</sup> and management of CP systems where much of the practical requirements are covered in the EN on CP and Cathodic Protection Measurements.<sup>62</sup> For example, following successful commissioning of a CP system and establishment of a steady state CP level, the following checks would be typical for the basis of development of KPIs and data review by an experienced CP specialist:
1. On a monthly basis check for satisfactory operation of transformer-rectifier and record output voltage and current.

2. On a six-monthly basis record polarized pipe-to-soil potentials at each test station, especially those located furthest from the CP drain point. Visually check all test facilities and transformer-rectifiers for serviceability and damage and carry out maintenance and repairs as necessary.
3. On a 12-monthly basis repeat the six-monthly tests and also test for possible stray current interference effects where other facilities are located close by.
4. At intervals of 5–8 years carry out a close interval potential survey (CIPS) and a direct current voltage gradient (DCVG) survey to assess changes in performance of both CP and coating in order to accurately determine the status of the CP on the entire length of the pipeline.

Recommendations/conclusions by the specialist should be acted upon without unreasonable delay to ensure the continued satisfactory CP of the pipeline. Many organizations fail to respond to reports submitted by their own teams and specialist contractors because of a lack of appropriate KPIs used to ensure that the required actions are carried out as scheduled and appropriate decisions are made when required.

#### 4.30.4.3 Data Management Systems

Documentation, both paper-based and/or electronic, form part of any management or quality management system. The choice will depend on the size of the project/operation. In many facilities such as refineries, oil/gas production fields and chemical plants the complexity of the various plant items/infrastructure plus the various corrosive environments can make the recording, trending, and correlation of data a difficult task. A number of PC-based software systems are commercially available that focus on specific aspects such as the recording of inspection or CP data. There are many common features<sup>53</sup> amongst the various integrated asset management systems employed to manage corrosion/inspection/CP systems/chemical treating. To be fully effective for corrosion management they should not only link to the maintenance/production systems but also output control instructions for activities such as planning, work control, stock control, materials handling, project management, procurement, contracts and finance. The requirements include:

1. *An asset register* – which is user configurable, holds design information, line diagrams and as built drawings, etc., that is, usually an electronic system that accurately reflects the physical facilities. These are set up in a logical/hierarchical manner

to identify individual equipment (Tags) that is, physical items that perform a function, such as vessels, units, etc., some of which may be interchangeable for maintenance, their components or segments for example, pipe work/the position/measurement locations. A typical asset register/facility list may include: plant code, area (plants, storage facilities and utilities), station (downhole, flowlines/manifolds, sub-sea facilities, gas compression systems and pipelines), position (vessel internals and equipment component) and line list (pipework database).

2. *A documentation system* that contains supplementary information and data on the above such as environmental conditions, pipe classification and constructional materials. These are usually held in separate listings on user-configurable records in a standardized format and include additional information and data such as that which has been scanned electronically from photographs, images and hand-drawn sketches, CAD drawings, and text files.
3. *Data collection input and interfaces* – these include keyboard entry, an ability to collect selected process data and download data from hand-held, portable or hard-wired instrumentation, plus the ability to operate on standard PCs/servers and especially have compatibility with other IT platforms.
4. *Data analysis capability* – ability to retrieve/trend data, cross correlate/determine equipment condition/process history/identify common corrosion circuits/predict future life. Data-trend displays, with alert/warning indicators, are needed to determine when deterioration is at a level necessary for corrective/maintenance action.
5. *Planning/work control* – ability to schedule activities and check on progress.
6. *Reporting* – identify safe/unsafe conditions (alert and alarm warnings), produce audit trails, generate recommendations and create action lists.
7. *Functionality enhancement* – capable of extension to encompass/interface with maintenance systems/materials procurement systems/contract/project control systems/finance systems/executive information systems.

Corrosion management and inspection management databases need a functionality that combines data storage from monitoring and inspection records, analysis of trends and predictions of remaining life, evaluation of corrosion circuits (process streams with similar corrosion from analysis of process stream changes) and generation of management reports for

decision making. The ability to compare data from various sources to produce reports/conduct financial evaluations/just-in-time inhibitor deliveries, etc. is a key requirement of a corrosion management system. For example, although field data is a key input into the management of operational plant and facilities, the acquisition and disposition of field information does not necessarily mean that adequate knowledge of equipment/plant condition is available or that the performance of the asset/facility process is provided in a lucid or easily understood manner. The system should bring the corrosion language in line with that of asset managers/the boardroom.

Effective corrosion management requires, for example, that the inspection frequency and information must be combined with online data from corrosion monitoring, which is used to control chemical treatments, such as corrosion inhibitor/biocide dosage or oxygen scavenger injection, plus the retrieval of appropriate process data such as flow rates, temperatures, and fluid compositions from SCADA systems. This flexibility of software is typically found in an IT benchmark product such as *Amulet*<sup>63</sup> which is used in a wide range of industries ranging from water companies, supermarkets, waste disposal, mobile phone stations for maintenance/operational control of various activities; it has also been employed for the management of corrosion data from various offshore and onshore production facilities including refining/oil field treating chemicals/management of corrosion monitoring/inspection/CP. Inputs are from probes, laboratory analysis, third party/historical/archive databases, as described previously in **Figure 13** with outputs including alarms/anomalies, mitigation schedules, reports leading to key performance checks, actions for inspection/maintenance.

Typical reports to the corrosion team/decision-makers from a data management system would include: wall thickness calculations, remaining life analysis and prediction, inhibitor treatment and usage, corrosion coupon and retrieval reports, advice on type, location, frequency of corrosion monitoring, corrosion prediction, pipeline inspection, periodic status reporting, deviation reporting, traceable records of installation corrosion history, CP data-trending, CP on/off test reports, anomalies for CP test posts, corrosion damage/failure analysis, defects categorization, leakage and spillage reports, downhole log reports, and changes to operations/maintenance/inspection activities and scheduling. **Figure 17** illustrates the typical data flow and outputs that form the basic reporting to the corrosion management system/team.

The type of management questions asked of such systems<sup>55</sup> are about the:

1. Distribution of corrosion rate in various parts of the system  $<0.05 \text{ mm year}^{-1}$  ( $<2 \text{ mpy}$ ),  $0.05\text{--}0.25 \text{ mm year}^{-1}$  ( $2\text{--}10 \text{ mpy}$ ),  $>0.25 \text{ mm year}^{-1}$  ( $>10 \text{ mpy}$ ).
2. Present distribution of remaining life, Items requiring replacement in:  $<1.5$  years,  $1.5\text{--}3$  years,  $3\text{--}10$  years,  $>10$  years.
3. Cost of the current corrosion control program.
4. Costs of chemical treatment.
5. Costs of CP.
6. Repair/maintenance/replacement costs.
7. Downtime (lost production) costs.
8. Inspection/monitoring costs.
9. Business drivers/criteria which have been met.
10. Average corrosion rates.
11. Allowable outage (offline) time.

**Figure 18** shows data from oil field chemical treating that correlates chemical usage with production rates to provide financial information on the treating program. This illustrates the point that data management is not just providing trends of corrosion rate, metal loss, chemical use, etc. for reports but that useful management information is abstracted by suitable correlations/analysis to enable appropriate decisions to be made regarding operational, integrity and strategic/tactical issues. Further information on monitoring and data handling, including case studies can be found in *The Corrosion Monitoring Handbook*.<sup>64</sup>

The above section has highlighted how systems for the control of project documentation, including standards, guidance, specifications, design, construction, and operating/maintenance procedures and protocols typically form part of a quality assurance system and provide a key input to any corrosion management process. Equally important is the functionality of the data management system used to store field data that has then to be converted into information for the decision makers. Both form discernable parts of the corrosion management system, as do the organizational arrangements and reporting routes. All have to be subject to regular reviews and audits to ensure that they, together with the various project teams, deliver effective corrosion mitigation. Successful data management systems are those that are used on an everyday basis as a live system, often through a web based/transparency methodology, to actively control all aspects of the mitigation processes including costs and actions. Some are specified to indicate on a traffic light basis the corrosion conditions of

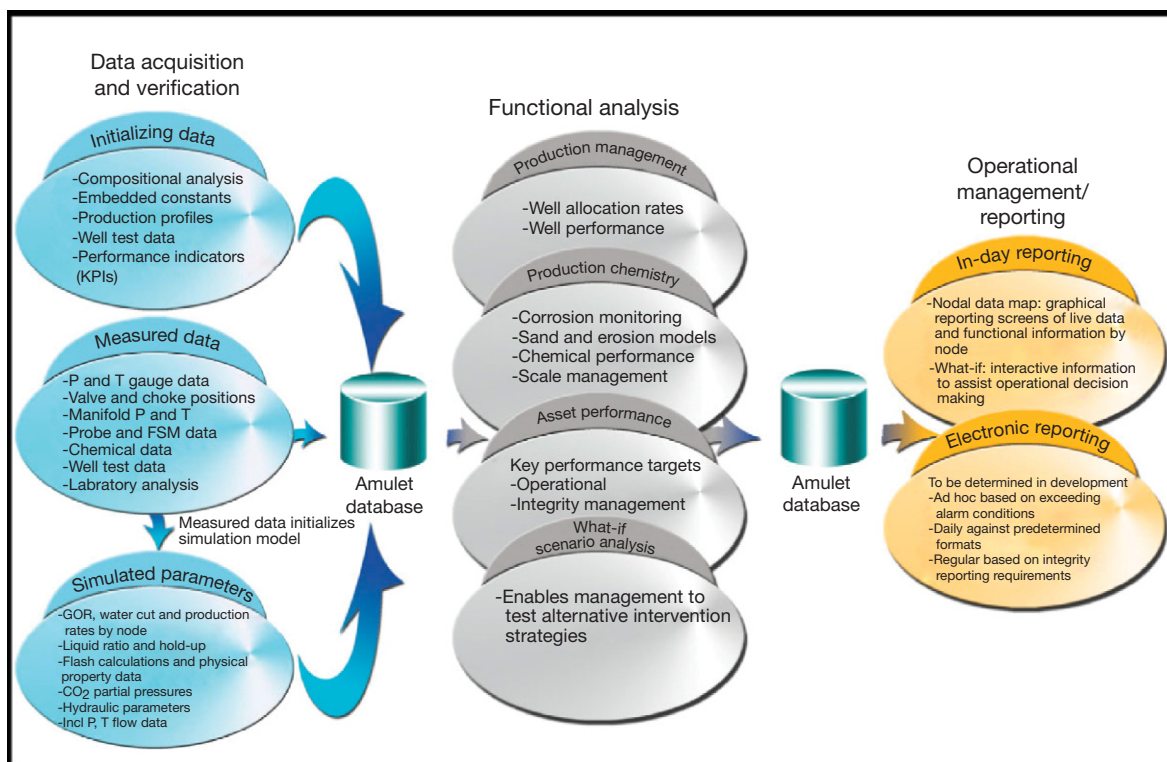


**Figure 17** Schematic of data management. Courtesy of A. N. Rothwell. Reproduced from Amulet, C<sup>3</sup> Ltd., Dingwall Business Park, Dingwall, UK.

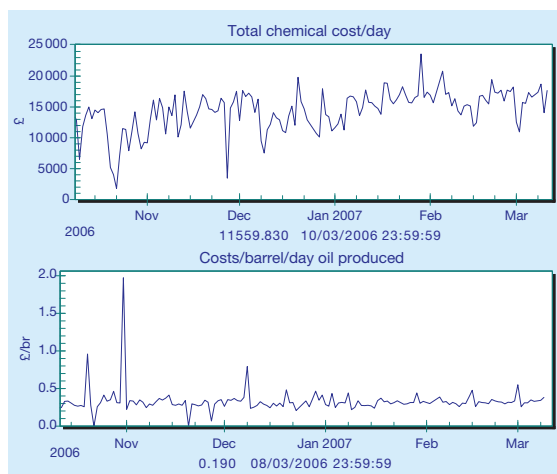


**Figure 18** Correlation of cost of chemical treating with production. Courtesy of A. N. Rothwell. Reproduced from Amulet, C<sup>3</sup> Ltd., Dingwall Business Park, Dingwall, UK.

units throughout the asset. In practice, many systems provide regular reports but essentially prepare data for storage/long-term burial rather than playing a key part in the decision process.

#### 4.30.5 Conclusions

There are many ways to organize and operate successful corrosion management systems, each of which is asset specific and dependent on factors such as design, the life-cycle stage, process conditions, operational history and organizational culture. Key issues from the project/asset manager perspective are corrosion risks that threaten structural integrity, economic viability and SHE performance. Most organizations rely on nonspecialist managers, designers and plant engineers to manage the facility corrosion specification, operational aspects and day-to-day activities required to mitigate corrosion whilst specialist corrosion/materials engineers are normally employed in an advisory capacity only. This is a pragmatic and appropriate use of a limited resource provided that corrosion issues do not become every employee's concern but no person's responsibility.

A primary aim should be to make corrosion risk management an integral part of both good management practice and the training/educational process within organizations. All risk management processes comprise a series of iterative steps that promote

continuous improvement in decision-making. Effective corrosion management depends on the experience and judgment of corrosion team members/leaders to provide guidance to design, construction and asset managers but such teams may also have to learn new management skills to be more effective. Incidents, failures and poor equipment performance will occur if reliance is placed solely on a routine of following steps outlined in procedures, guidelines and standards. Individuals must be aware of competence limitations and recognize when to call on more experienced members of staff/third parties. Senior management support is also needed to define clear strategies and corrosion policies that are promoted by the adoption of workable corrosion management systems using correct technological tools operated by trained people who have the motivation and commitment with adequate supervision.

Management system failings and human errors pose as big a risk to corrosion mitigation as do physical and chemical hazards. Serious corrosion related incidents occasionally make the front page such as

the 1988 Aloha Airlines loss of a cabin roof during flight due to adhesive failure, crevice corrosion and fatigue cracks,<sup>65</sup> the Humberside refinery fire<sup>5</sup> referred to previously and the recent Alaska pipeline leak due to a lack of cleaning and inspection by pigging.<sup>66</sup> These are the tip of an iceberg and, with hindsight, preventable, but they beg the question whether lessons are learned from the minor leakages, poor equipment performance and shorter-than-expected lives that are an everyday occurrence in industry at large.

Catastrophic incidents from other engineering sectors, particularly investigations of process plant failure, provide insights how established process/safety engineering methods could deliver continuous improvement of corrosion mitigation practice. For example, control of safety hazards to prevent incidents can be visualized as a series of barriers. Some are hard/physical, others are soft/procedures/systems, but each will have weaknesses. This 'Swiss cheese' hazard management model,<sup>67</sup> depicted in Figure 19, illustrates that as long as the holes in the

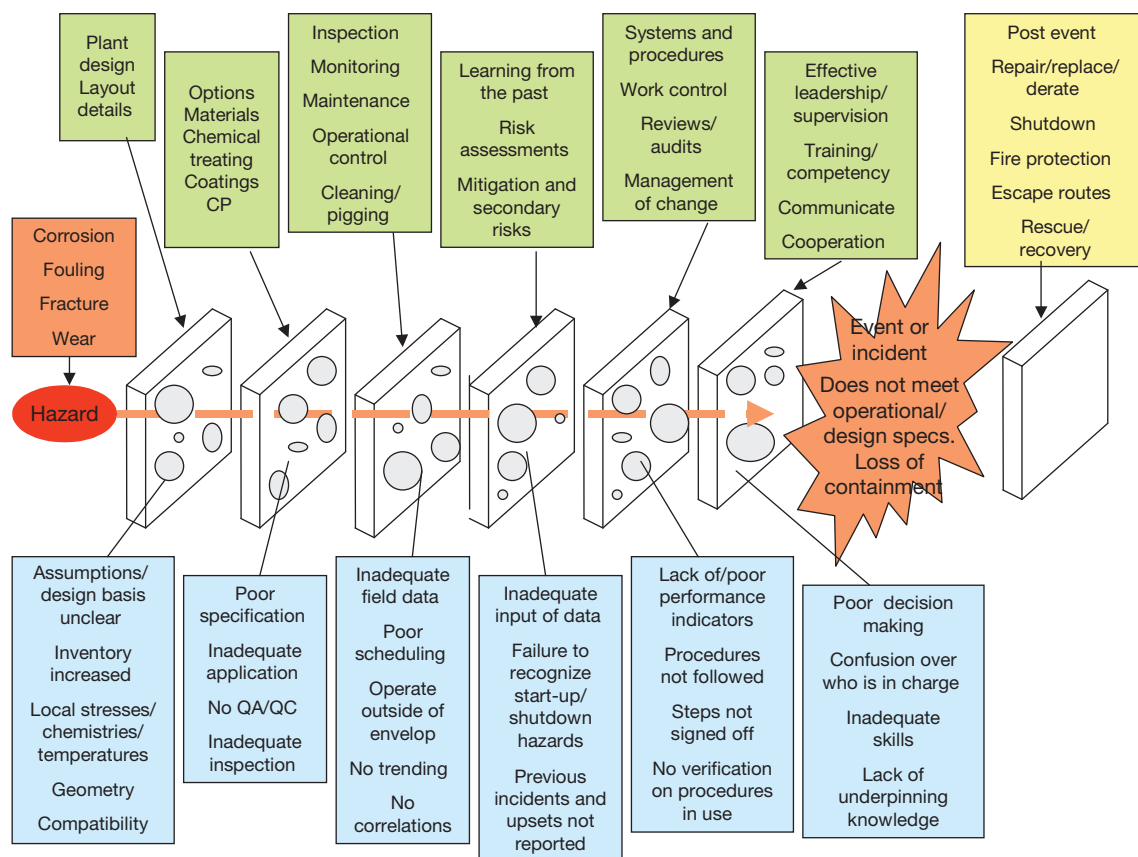


**Figure 19** Example of a degradation hazard management concept.



various protective barriers/layers do not align then a hazard can be controlled but that a series of human errors/unmanaged circumstances can give rise to porosity in the hazard control barriers resulting in incidents and catastrophic accidents. This hazard management model was used recently to analyze the March 2005 Texas City refinery incident.<sup>68</sup> The study emphasized the extent to which hazard prevention depends on three layers of protection:

1. *Plant* – engineering hardware, control systems, and layouts to eliminate, control and mitigate potential hazards to people, and improve productivity.
2. *Processes* – management systems to identify, control and mitigate risks, and drive continuous operational improvement.
3. *People* – capability of our people in terms of leadership skills, relevant knowledge and experience, and the organizational culture they create in layers of protection, ‘hard barriers’ are more reliable than ‘soft barriers,’ but all rely on people.

A list of typical problem areas at the refinery included:

1. Incidents and upsets not reported.
2. Hierarchy of control not applied.
3. Previous start-up review not performed.
4. Procedural compliance not checked.
5. No interventions.
6. Inadequate KPIs.
7. Lack of underpinning knowledge.
8. Failure to follow procedures.
9. Confusion over who was in charge.
10. No verification on procedures in use.
11. Procedures not followed.
12. Steps not signed off.
13. Use of local practices.

Learning from the Texas City incident would be relevant to most corrosion related incidents where equipment fails to meet design/operational requirements due to deficiencies in the inputs from corrosion risk mitigation tools, systems and teams. As indicated in **Figure 19**, hazards to performance/structural integrity arise from a combination of one or more of the generic degradation processes, corrosion, fouling, fracture and wear. The hard barriers for mitigation of corrosion related hazards that include fit-for-purpose materials, coatings, chemical treatment, CP, etc. are more physical and robust than the soft barriers that include generic management systems for control of mitigation processes. The robustness of all barriers depends on effective

functioning of individuals and teams who must respond to continuing changes. Holes in various barriers introduced by individual/team action or inaction are indicated in the lower boxes.

Corrosion technology is not new; corrosion mechanisms are understood and documentation/standards/knowledge on corrosion mitigation tactics are widely known and available. The difficult part is in translating this corrosion background information into reliable solutions for the real world. Important aspects are not only technical solutions but also involvement/acceptance of key personnel, particularly in organizations where management of change involves different ways of doing things, as demonstrated in a study of a long-term problem with hot potassium carbonate acid gas removal plants.<sup>69</sup> Organizational aspects were identified as critical and the *Six Sigma* methodology,<sup>70,71</sup> traditionally employed to solve problems in manufacturing and continuous process industries, was used as a tool. The principle is that improvements occur when people doing the job are involved, guided by an individual experienced in the implementation methodology. Mature organizations with workforces that are highly experienced and knowledgeable may be less adaptable to change as, for example, is sometimes found when RBI is proposed/introduced. In the above site corrosion study, a team approach encompassing integrity, process and process control engineers and chemists provides a broader input to define the problem, identify the likely root cause and then deliver the required change by enabling the management decision to release the funds necessary for improvement.

Delivery of services such as corrosion mitigation in an era of increasing demand, in more difficult environments, and often with squeezed budgets, requires development of strategic models that may well include input from both in-house and third-party specialists. What counts is the provision of improved quality and value rather than whether the service provider is in-house or a contractor. Asset-centered organizations based on multidisciplinary teams tasked with improvement of the asset management processes of optimizing costs, risks and performance, are increasingly replacing traditional activity-centered organizations based on functions such as design/engineering, production/operations, maintenance and materials/purchasing with individual budgets. The new focus is on inputs with responsibility for investment/expenditure and outputs of performance/accountability. The asset manager and team have budget decision-making responsibility for

resources and services. The client ‘assets’ provide funds for technology specialists, designers, information technology, human resources, SHE and finance, obtained from both in-house, central, shared sources and external providers. The challenge for an operating company/asset is to choose those services required to achieve defined objectives that realize longer term savings/benefits.

Such developments in asset management cannot be ignored in the delivery of corrosion management services and may even continue to drive the changes instigated in the 1990s by SHE issues. Corrosion management, defined previously in [Section 4.30.1](#), is also part of asset management, which is in turn now defined<sup>72</sup> as “Systematic and coordinated activities and practices through which an organization optimally and sustainably manages its physical assets and their associated performance, risks and expenditures over their life cycles for the purpose of achieving its organizational plan.” An organizational strategic plan, based on stakeholder aims/expectations and legal requirements, is translated into local asset business goals with intentions converted into actions as depicted in [Figure 20](#).

Best practices and development of risk-based methods for management of physical assets formed the basis of MACRO, a multiindustry collaboration project, which was a UK government supported joint venture and a European ‘Eureka’ Project, EU1488.<sup>73</sup> The aim was to promote a change in approach that incorporates guidelines, education and decision-support tools

(Asset Performance Tools (APTs))<sup>74</sup> that comprise a set of methods to quantify and optimize over 40 different types of asset management decisions in target areas such as asset life-cycle costing, inspection and condition monitoring, maintenance optimization, work grouping and shutdown strategy. An outline is provided in ‘*Risk-based Decision-making in Maintenance, Inspection, Spares and Asset Renewal*’ by John Woodhouse.<sup>75</sup> This highlights some of the limitations of tactical/bottom-up/individual task tools such as FMECA, RBI, reliability centered maintenance (RCM), Six Sigma, and TQM that focus on one risk at a time, whereas the APT suite is designed to address multiple interacting risks and performance.

For example, APT-Inspection can help in deciding optimum asset inspection intervals as illustrated by Smith<sup>76</sup> who compared the total impact on items comprising a continuous chemical processing unit by optimizing inspection costs, outside limit risks and operational failure risks. FMECA was used to determine maintenance strategy and RBI showed most items had an optimal 4-year inspection/shutdown frequency, but some a 3-year and, a particular HCl stripper, a 2-year frequency. Changing some materials of construction for the stripper and pipework and also assessing a small column containing sacrificial iron packing by APT-Maintenance for loss of efficiency showed that an in-line spare column was a cost effective approach. Although there were some relatively small costs associated with the implementation,

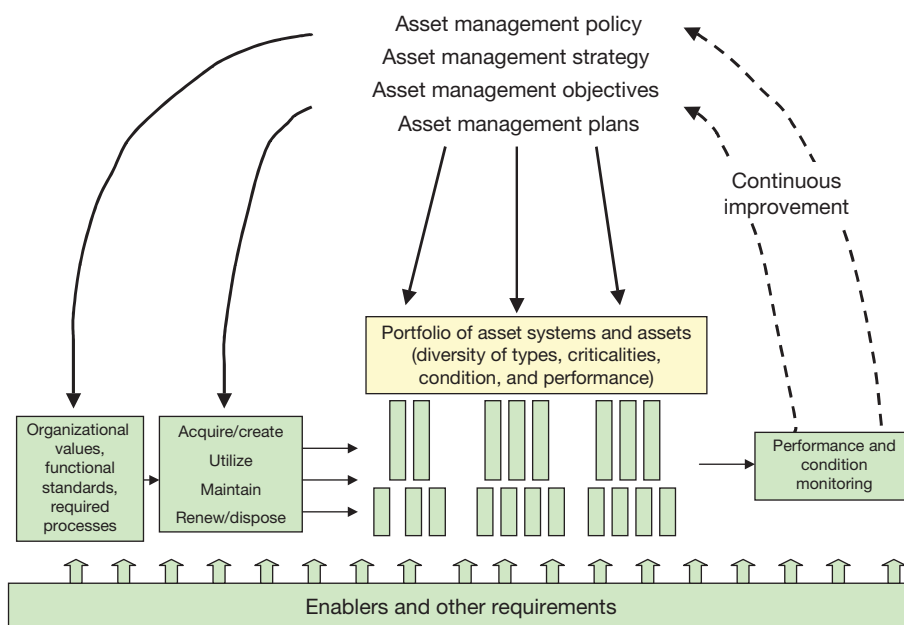


**Figure 20** Asset Management System. Adapted from BS PAS 55.

the benefits amounted to a NPV of £2.5 million over 12 years.

The need to meet increasingly challenging SHE and financial demands will need a cultural shift in corrosion thinking within both industrial organizations and educational establishments that will require a wider appreciation of risk-based approaches and exposure to mainstream engineering concepts found within safety management, asset management, project/process management and maintenance management. A shift in the management model for corrosion services based on different approaches to the management of corrosion risk mitigation requires new standards to be set if the design/planning and operational delivery phases are to improve. This will include increased information sharing, system transparency and merging of services, including partnerships with specific contractors in order to benefit from shared experiences and additional/different resources. Cross fertilization of approaches, tools and procedures is occurring as in the cases of functionality analysis, criticality assessments and RBI in the petrochemical industries, total productive maintenance in the manufacturing sector, and reliability centered maintenance that is crucial in complex, down-time critical plant, and that differentiates failure response/prevention strategies into preventative, predictive, design-out and breakdown (operate-to-failure).

The previous sections of this chapter provide sufficient background information on tools, systems, and teams to address the inadequacies of many corrosion management processes but emphasis is still lacking on the regular auditing of corrosion management systems, the development of effective corrosion mitigation strategies and the control of operational, day to day activities. Successful organizations combine a strategic and tactical culture with daily operations conducted within a responsive, principles-based corrosion management system by competent personnel. As a result, they are enabled to practice cost-effective, predictive/condition based maintenance strategies that incorporate risk-based approaches to inspection. Weaker organizations tend towards an emphasis on tactical issues and less transparent management systems, resulting in a high reliance on expensive, breakdown/repair maintenance strategies.

## Acknowledgments

The author wishes to express his appreciation to Gareth John and Neil Rothwell for informative

discussions of various aspects of the subject area over many years and also to Tony Richardson for helpful editorial comments on this chapter.

## References

1. The Concise Oxford Dictionary, 5th ed.; Oxford University Press: Oxford, 1964; p 739.
2. Blything, K. W.; Parry, S. T. *Pipework Failures. A Review of Historical Incidents*, SRD 441, UKAEA, 1988.
3. *The Control of Major Accident Hazards Involving Dangerous Substances*; Seveso II Directive 96/82/EC, Council of the European Union, 1996.
4. Dawson, J. L.; Bruce, K.; John, D. G. Corrosion Risk Assessment and Safety Management for Offshore Processing Facilities, Offshore Technology Report 1999/064 UK Health and Safety Executive, 1999.
5. Public Report of the Fire and Explosion at the ConocoPhillips Humber Refinery on 16 April 2001, UK Health and Safety Executive. [hse.gov.uk/comah/conocophillips.pdf](http://hse.gov.uk/comah/conocophillips.pdf).
6. API Document 570 Inspection, Repair, Alteration, and Rerating of In-service Piping Systems, American Petroleum Institute, 1998.
7. Minutes, NACE STG 34 2004 Committee Meeting. NACE International: Houston, TX, 2004.
8. Review of Corrosion Management for Offshore Oil and Gas Processing. Offshore Technology Report 2001/044, UK Health and Safety Executive, 2001. [www.hse.gov.uk/research/otopdf/2001/oto01044.pdf](http://www.hse.gov.uk/research/otopdf/2001/oto01044.pdf).
9. *The Public Inquiry into the Piper Alpha Disaster*, Report by the Hon. Lord Cullen; HMSO: London, Nov. 1990. ISBN 0 10 113102.
10. *Successful Health and Safety Management*, UK HSE HS (G) 65 1991. ISBN 0-11-882055-9.
11. *The Offshore Installations (Safety Case) Regulations*, SI 1992/2885; The Stationery Office Limited: London, 1992. ISBN 011025869X.
12. *The Offshore Installations and Wells (Design and Construction, etc.) Regulations*, 1996 SI 1996/913; The Stationery Office Limited: London, 1996. ISBN 011054451X.
13. *The Pipelines Safety Regulations*, SI 1996/825; The Stationery Office Limited: London. ISBN 0110543734.
14. *The Control of Major Accident Hazard Regulations*, SI 1999/743; The Stationery Office Limited: London. ISBN 0 11 082192 0.
15. *Pressure Systems Safety Regulations*, SI 2000/128; The Stationery Office Limited: London. ISBN 0 11 085836 0.
16. Approved Code of Practice (ACOP) L122. *Safety of Pressure Systems and Guidance on the Pressure Systems Safety Regulations 2000*, UK Health and Safety Executive, 2000.
17. *The Corporate Manslaughter and Corporate Homicide Act, 2007*; Office of Public Sector Information, 2007.
18. *Risk Based Inspection – Development of Guidelines: General Document*; American Society of Mechanical Engineers, 1991; Vol. 1.
19. US Pipeline Safety Act. 1995.
20. API Recommended Practice RP580, Risk Based Inspection; American Petroleum Institute, 2000.
21. API Publication 581, Risk Based Inspection Resource Document; American Petroleum Institute, 2002.
22. DnV RP G101 Risk Based Inspection of Offshore Topsides Static Mechanical Equipment; DnV, 2002.
23. AS/NZS 4360:1999 Risk Management Standard; Australian and New Zealand Standards, 1999.

24. New Zealand Local Government Amendment Act, No 3, 1996.
25. *International Infrastructure Management Manual*; 2006 ed., nams.org.nz
26. Burdekin, F. M. *Interdiscipl. Sci. Rev.* **2000**, 25, 141–151.
27. ISO 9001:2008 *Quality Management Systems – Requirements*; International Organisation for Standardisation, 2008.
28. ISO 9004:2000 *Quality Managements Systems – Guidelines for Quality Improvements*; International Organisation for Standardisation, 2000.
29. ISO 14001:2004 *Environmental Management Systems – Specification with Guidance for Use*; International Organisation for Standardisation, 2004.
30. Oakland, J. S. *Total Quality Management*; Butterworth-Heinemann: Oxford, 1995.
31. BS 6079-3: 2000 *Project Management – Part 3: Guide to the Management of Business Related Project Risk*; BSI Standards, 2000.
32. Milliams, D. In *Corrosion Management*, 12th International Corrosion Congress on Corrosion Control for Low Cost Reliability 19–24 September 1993; NACE International, 1993; Vol. 4, p 2420.
33. John, D. G.; Dawson, J. L.; Feng, A. C. In *Corrosion Risk Assessment as a Critical Part of Integrated Asset Integrity Management*, Proceedings of the Conference on Engineering Management for Utilities, Industry and Commerce, Oct 1997, London, ERA report 97-0847, 1997.
34. Edwards, J. D.; Sydberger, T.; Mork, K. J. *Corrosion*'96; NACE International, 1996; Paper no. 29.
35. Jones, J. S. *Application of Risk-Based Inspection Systems to the British Gas Rough Field*; Institute of Marine Engineering: London, 1996.
36. de Waard, C.; Lotz, U.; Milliams, D. *Corrosion* **1991**, 47, 976.
37. de Waard, C.; Lotz, U. In *Corrosion* '93; NACE International, 1993; Paper no. 69.
38. de Waard, C.; Lotz, U.; Lugstad, A. In *Corrosion*'95; NACE International, 1995; Paper no. 128.
39. NORSOK M-506 Rev. 2, June 2005, *CO<sub>2</sub> Corrosion Rate Calculation Model*; Norwegian Technology Standards Institution; [www.standard.no.petroleum](http://www.standard.no.petroleum).
40. McMahon, A. J.; Paisley, D. M. E. *Corrosion Prediction Modelling*, BP Sunbury Report, ESR.96.ER.066, November 1997.
41. Oliver, K. E.; John, D. G. In *Corrosion*'07; NACE International: Houston, 2007; Paper no. 124.
42. *iDECIDE software*; Decisive Tool, LLC. [www.decisivetools.com](http://www.decisivetools.com)
43. @Risk is the trade mark of Palisade Corporation, Ithaca, NY. [www.palisade.com](http://www.palisade.com)
44. John, D. J.; Stokes, P.; McIntosh, P. In *Corrosion*'03; NACE International: Houston, 2003; Paper no. 163.
45. Edwards, J. D.; Sydberger, T.; Mork, K. J. In *Corrosion*'96; NACE International, 1996; Paper no. 29.
46. Pludek, V. R. *Design and Corrosion Control*; Wiley, 1976.
47. *Corrosion Threats Handbook – Upstream Oil & Gas Production*; Energy Institute & Oil and Gas UK: London, 2008.
48. *Guidance for Corrosion Management in Oil and Gas Production and Processing*; Energy Institute: London, May 2008.
49. Potthoff, W.; Fitzer, E.; Faessler, K.; Spaehn, H. A study of alternative cooling water circuits in a large petrochemical plant, Economics of Corrosion Control, Institution of Metallurgists Autumn Review Course, November 1974.
50. Turner, M. E. D. *The Chemical Engineer*, 9 August, 1990, Institution of Chemical Engineers: Rugby, UK.
51. Craig, B. D.; Thompson, R. S. *Corros. Mgmt.* **1995**, 7, 14–17.
52. RIGHTRAX Systems Limited, Ashpoole House, Sandy Lane, Lowton, Warrington, WA3 1BG, UK.
53. SMART Layer@, Acellent Technologies Inc., Sunnyvale CA, USA.
54. GE cMUT cell, GE Global Research Center, Niskayuna, NY, USA.
55. John, D. G.; Attwood, P.; Rothwell, A. N. In *Corrosion*'99; NACE International: Houston, TX, 1999; Paper no. 249.
56. Brouwer, R. C. In 8th Middle East Corrosion Conference Bahrain; Bahrain, Society of Engineers & NACE International, 1998.
57. *Effective Corrosion Management*; UK Oil & Gas and Energy Institute Workshop, Aberdeen, 18 June 2008.
58. Paterson, S. *External Corrosion Management in Shell*; UK Oil & Gas and Energy Institute Workshop, Aberdeen, 18 June 2008.
59. ISO 4628 Part 3/BS 3900-H3:2003 *Assessment of Degree of Rusting*; BSI Standards, 2003.
60. [www.hse.gov.uk/2007/08/02/offshore-external-corrosion-project](http://www.hse.gov.uk/2007/08/02/offshore-external-corrosion-project)
61. Palmer, J. W.; Hedges, W.; Dawson, J. L. The use of corrosion inhibitors in oil and gas production, European Federation of Corrosion Document Number 39; Institute of Materials: London, 2004.
62. PrEN 13509:1999, *Cathodic Protection Measurement Techniques*; EN 12954:2001, *Cathodic Protection of Buried or immersed Structure*; EN 12696, *Cathodic Protection of Steel in Concrete*.
63. Amulet, C<sup>3</sup> Ltd., Dingwall Business Park, Dingwall, UK.
64. Rothwell, N.; Tullmin, M. *The Corrosion Monitoring Handbook*; Coxmoor: Kingham, Oxford, 2008. ISBN 1 90189 203 4.
65. Excerpts from Aircraft Accident Report – Aloha Airlines, Flight 243, Boeing 737–200 – N73711, near Maui, Hawaii, 28 April 1988; National Transportation Safety Board, 1989. <http://www.aloha.net/~icarus/index.htm>.
66. Congressional Report Services, Library of Congress, BP Alaska North Slope Pipeline Shutdowns, Regularity Policy Issues, October 2006, [www.cnle.org/NLE/CRSreports/06Oct/RL33629.pdf](http://www.cnle.org/NLE/CRSreports/06Oct/RL33629.pdf).
67. Reason, J. T. *Managing the Risks of Organizational Accidents*; Ashgate Publishing Ltd: England, 1997.
68. Boardrubb, M., In 23rd Center for Chemical Process Safety International Conference, Curran Associates Inc, 7 – 9 April 2008. [www.hse.gov.uk/aboutus/meetings/iacs/oiac/murrayfield0508/texas.pdf](http://www.hse.gov.uk/aboutus/meetings/iacs/oiac/murrayfield0508/texas.pdf).
69. Harjac, S.; Atrons, A.; Moss, H. In *Corrosion*'07; NACE International: Houston, 2007; Paper no. 401.
70. Pande, P.; Nueman, R.; Cavanagh, R. *The Six Sigma Way: How GE, Motorola and Other Companies are Honing Their Performance*; McGraw-Hill: USA, 2000.
71. Eckes, G. *Six Sigma Team Dynamics: The Elusive Key to Project Success*; John Wiley, 2003.
72. BSI PAS 55–2: 2008, *Asset management: Guidelines for the application of PA 55–1*, and BSI PAS 55–1: 2003, *Asset management, Specification for the optimised management of physical infrastructure assets*; British Standards Institute.
73. [www.aptools.co.uk/Macro%20Project](http://www.aptools.co.uk/Macro%20Project).
74. [decisionsupporttools.com](http://decisionsupporttools.com).
75. [www.macroproject.org/casestudies/MACRO%20LAUNCH%20-%20risk-based%20decisions.pdf](http://www.macroproject.org/casestudies/MACRO%20LAUNCH%20-%20risk-based%20decisions.pdf)
76. [www.macroproject.org/casestudies/MACRO%20LAUNCH%20Eutech.pdf](http://www.macroproject.org/casestudies/MACRO%20LAUNCH%20Eutech.pdf)

## 4.32 Materials Selection for Corrosion Resistance

**T. A. Richardson**

Anticorrosion Consulting, 5 Redhills Lane, Durham DH1 4AL, UK

**S. B. Lyon**

Corrosion and Protection Centre, School of Materials, University of Manchester, Manchester M60 1QD, UK

© 2010 Elsevier B.V. All rights reserved.

4.32.1	Materials Selection in the Design Process	3052
4.32.1.1	Overview	3052
4.32.1.2	Grades of Engineering Materials	3053
4.32.1.3	Materials Selection in Mechanical Design	3053
4.32.1.4	Contribution of Design Codes to Materials Selection	3055
4.32.2	Mitigating Corrosion Risks by Materials Selection	3055
4.32.2.1	The Process	3055
4.32.2.2	Predicting Corrosion Performance	3056
4.32.2.2.1	Identifying credible corrosion risks	3056
4.32.2.2.2	Performance prediction based on experience	3057
4.32.2.2.3	Performance prediction based on corrosion testing	3057
4.32.2.2.4	Performance prediction based on material composition	3061
4.32.2.2.5	Performance prediction based on quantitative modeling	3061
4.32.2.3	Evaluating Corrosion Risks in Materials Selection	3062
4.32.3	Economic Evaluation in Materials Selection	3062
4.32.4	Outputs/Records of Materials Selection Processes	3063
4.32.5	Characteristics of Successful Materials Selection for Corrosion Resistance	3063
References		3064

### Abbreviations

**AISI** American Iron and Steel Institute

**API** American Petroleum Institute

**ASTM** American Society for Testing and Materials

**DCF** Discounted cash flow

**EFC** European Federation of Corrosion

**LCC** Life cycle costing

**MSD** Materials selection diagram

**NACE** National Association of Corrosion Engineers

**NPV** Net present value

**PREN** Pitting resistance equivalent number

**SAE** Society of Automotive Engineers

**SHE** Safety, health, and environment

**UNS** Unified numbering system

### Symbols

**$K_{IC}$**  Fracture toughness ( $\text{MPa m}^{1/2}$ )

**$\sigma_f$**  Strength (MPa) (metals, 0.2% offset yield; polymers, 1% yield; ceramics/ glasses, compressive crushing; composites, tensile; elastomers, tear)

### 4.32.1 Materials Selection in the Design Process

#### 4.32.1.1 Overview

The selection of materials, including the processes by which they are shaped, joined, and finished, is integral to the design process through its various stages. In the early, conceptual stages of design, selection of materials is focused primarily on identifying the classes of materials (metals, polymers/elastomers, ceramics/glasses, composites, etc.) that will be used to construct the product. As the process progresses through detailed design, procurement and fabrication/construction, materials selection converges in line with the design process, through subclasses of materials (stainless steel, polypropylene, alumina, glass-reinforced polyester resin, etc. to specific grades of material (SA-516 grade 70 steel, EN 1.4404 equivalent to AISI 316L stainless steel, etc.) and the specific processes that are to be employed in their shaping, joining, and finishing.

Successful selection of materials is based upon identifying and delivering the key materials property and performance requirements of the product that is being designed with regard to:



1. *Functionality* – appropriate combinations of physical, thermal, mechanical, electrical, and/or magnetic properties in combination with appropriate formability and ease of fabrication.
2. *Appearance* – appropriate formability and ease of fabrication with surfaces amenable to appropriate finishing that might include processes such as coloring, patterning, and texturing.
3. *Durability* – predictable resistance to fracture, wear, corrosion, or other deterioration processes throughout the design life of the product.
4. *Economy* – acceptable cost and availability.

The progressive convergence into details, as the design process proceeds, requires increasing precision in the data on which the final materials selection is based and, when the final selection is made, it is vital that the grade of material specified should ensure the delivery of the required combination of properties and performance.

#### 4.32.1.2 Grades of Engineering Materials

The process for identification of specific grades of materials varies with the class of the material. Materials usually have a common name such as stainless steel, brass, bronze, polypropylene, alumina, etc. For example, brasses and bronzes are alloys of copper with zinc and tin respectively. Apart from the fact that different grades of brass and bronze have different properties, this method of identification is inconsistent. For example, manganese bronze contains no tin at all. Clearly, more precise methods of identification beyond common names are required for specific grades of materials.

In the case of metallic materials, there is a long history of identifying specific grades of material by national standardizing societies, trade associations and individual users and producers of metals and alloys, usually by some form of alphanumeric designation. For example, the numbering system for stainless steels based on composition ranges, typified by the 300 (e.g., 304 or 316) and 400 (e.g., 430) series, was introduced originally by the American Iron and Steel Institute (AISI) and is widely adopted internationally by stainless steel specifiers and users. These grades are not specifications in themselves but have been widely used by standardizing bodies such as the American Society for Testing and Materials (ASTM) to identify grades of stainless steel products such as sheets and plates, bars, tubes, etc. More recently, ASTM in collaboration with the Society of

Automotive Engineers (SAE) introduced a unified numbering system (UNS)<sup>2</sup> for metals and alloys that have a ‘commercial standing’ which correlates the various national designations into a single system. The UNS numbers attempt to incorporate widely adopted, historical designations. Thus, the UNS numbers for the AISI grades 304, 316, and 430 stainless steel are S30400, S31600, and S43000 respectively. Most, but not all, metals and alloys have a UNS number but new or developing alloys take time to acquire a number and producers may have proprietary alloy grades that they prefer to identify by a trademarked name.

The identification of nonmetallic classes of materials is much less standardized than in the case of metals and alloys. Thus, there are no recognized designations based on composition or other properties for materials such as polypropylene or alumina. Instead there are many grades of polypropylene and alumina that are specific to commercial suppliers, the compositions and properties of which might vary significantly. Thus, the selection of nonmetallic materials converges to the consideration of specific grades earlier in the design process than is necessary for metallic materials.

#### 4.32.1.3 Materials Selection in Mechanical Design

In the specific area of mechanical design, Ashby and his coworkers<sup>3</sup> have developed systematic approaches to the selection of materials based upon ‘material selection charts’ in which one key property of the material is plotted against another. Materials are represented as elliptical areas that define ranges of values for the properties in question. Performance indices that define quantitative selection criteria can be plotted on the charts, allowing identification of those materials that comply with the selection criteria.

An example of a materials selection chart for safe design against fracture, such as would apply in the case of pressure vessel design, is shown in [Figure 1](#), in which fracture toughness is plotted against strength. Two performance indices have been applied to the chart based on the selection criteria, yield before break ( $M_1 = K_{IC}/\sigma_f = 0.6 \text{ m}^{1/2}$ ) and minimum strength ( $\sigma_f = 100 \text{ MPa}$ ) and as a result a ‘search region’ for candidate materials has been defined. It is clear from the chart that the combinations of fracture toughness and strength that are required for pressure vessels to operate safely are confined mostly to metallic and a few composite materials. Despite

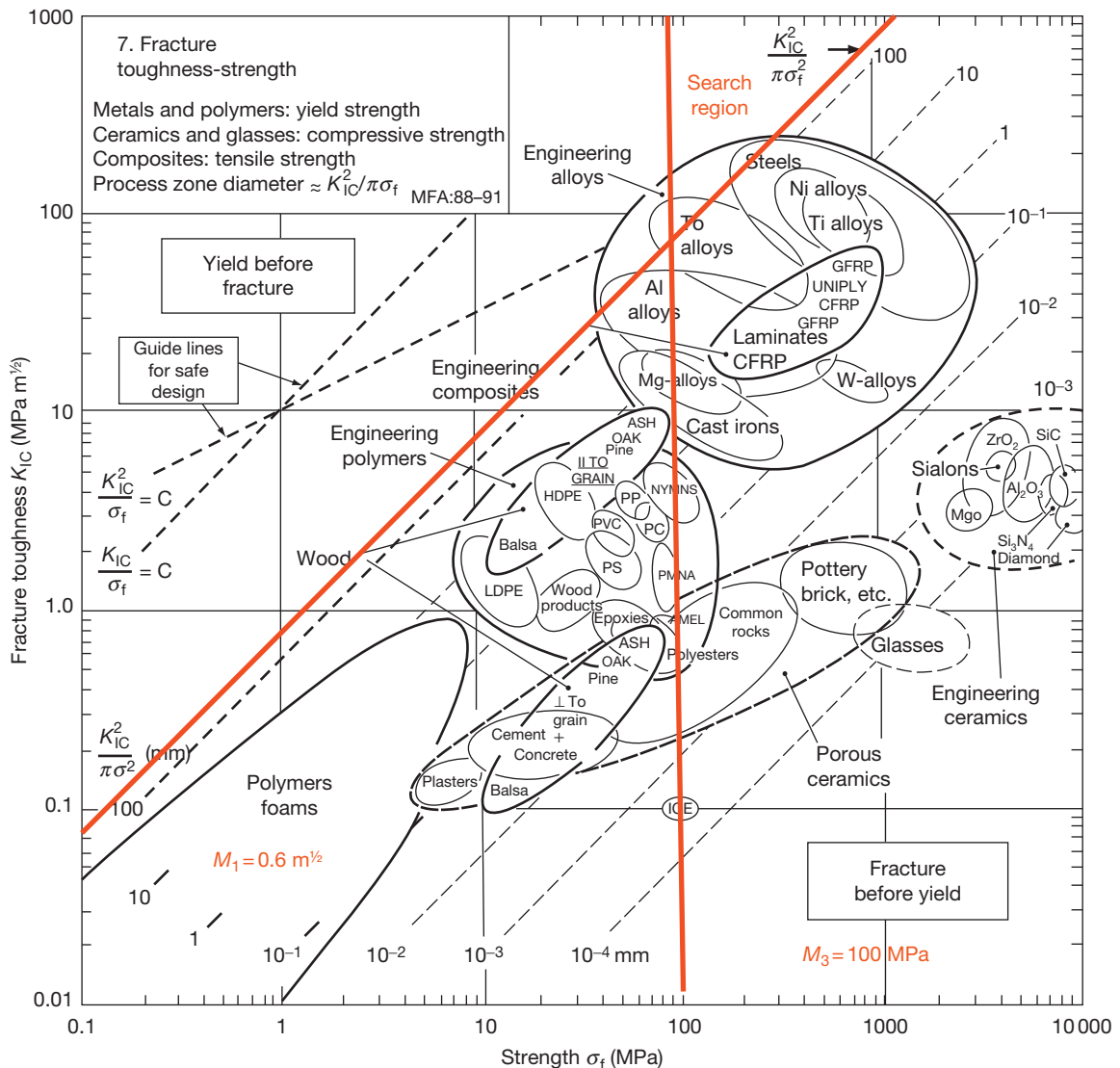


**Figure 1** Materials selection chart for safe design of pressure vessels to avoid fracture. Adapted from Ashby, M. F. *Materials Selection in Mechanical Design*; Butterworth Heinemann, 2005.

their generally excellent corrosion resistances, polymers and elastomers lack the strength and ceramics and glass the ductility to qualify as materials for pressurized systems, although both classes of materials find use as coating and/or lining materials on tougher, steel substrates.

This approach is extremely powerful for the selection of materials in the designing of engineering applications where the key material properties fall into either of the following categories:

1. Invariant properties such as density, stiffness, heat capacity, etc. that do not change as a function of the material's condition, for example, in the case of

an alloy whether the material is annealed, work-hardened, quenched, etc.

2. Deterministic properties such as yield strength, hardness, fracture toughness, electrical conductivity, etc. that vary significantly as a function of the material's condition, but for a given condition of heat treatment, mechanical deformation, etc. are invariant.

However, the approach is less powerful in engineering design applications where the key property of the material is nondeterministic and the property depends on some other parameter that is external to the material or its condition, such as the environment

in the case of corrosion performance. In that case, the Ashby approach at its current stage of development is confined usually to assigning only broad performance categories against broad classes of corrodents and is thus of rather limited use for applications relating to specific environmental conditions.

#### 4.32.1.4 Contribution of Design Codes to Materials Selection

The design of infrastructural or industrial structures/components that present significant safety, health, or environmental (SHE) risks in the event of failure is governed generally by international or national design codes. These codes have mandatory status in most countries and provide rules and guidance on detailed design, including aspects of materials selection, based on experience and technical analysis. Design codes are updated periodically to incorporate learning from accumulating experience and technology advances. The codes are approved and updated by standing committees of the various stakeholders in the design and operation of the equipment governed by the design code, and specific equipment designers, purchasers/operators, suppliers/fabricators, and inspection/regulatory authorities.

Design codes focus on the functionality and safety of the equipment that goes into service. For example, in relation to mechanical design, codes provide rules to reduce to acceptable levels, the risks of failure by brittle fracture or ductile overload as the equipment enters service or by fatigue or creep during its design life. In relation to materials, this is achieved by specifying limiting allowable values of relevant properties, for example, design stresses based on maximum proportions of yield or ultimate strength, toughness based on minimum impact energy or fracture toughness and fatigue/creep lives, based on relevant cyclic stressing and stress rupture properties. Design codes also provide rules and guidance on the fabrication of materials.

A historical example of the successful application of a design code is shown in [Figure 2](#) that shows the aftermath of a hydraulic pressure test applied to a pressure vessel as the final proof of its suitability for service. In the event, the steel vessel failed catastrophically by brittle fracture that initiated as fabrication defects in the heat affected zones of welds that had been inadequately heat treated, resulting in low toughness of the material in the presence of high residual stresses. Although a disaster from the commercial standpoint, the event was a victory for the

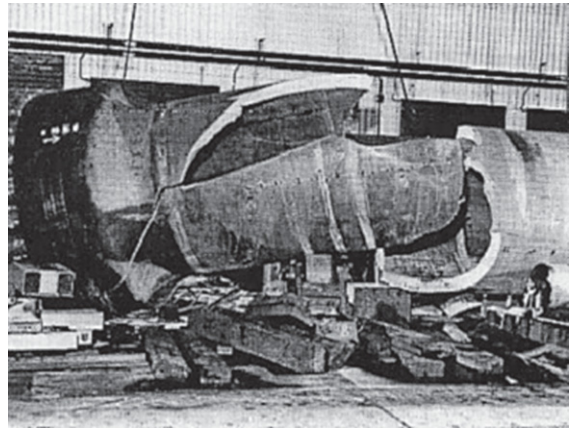


**Figure 2** Catastrophic failure of a pressure vessel during final hydraulic test – an example of a commercial disaster, but a successful application of a design code preventing a potentially unsafe piece of equipment from entering service.

relevant design code, because a potentially unsafe vessel was prevented from entering service.

Design codes rarely provide rules or significant guidance for the selection of materials to avoid failure by wear or corrosion processes in service. Their treatment of these matters is normally confined to cautionary advice to consider these potential deterioration processes, and provide appropriate thickness allowances and protection measures to reduce the risk of failure to acceptable levels if necessary. It follows that the mitigation of corrosion risks by materials selection has to be based on knowledge and data from other sources.

#### 4.32.2 Mitigating Corrosion Risks by Materials Selection

##### 4.32.2.1 The Process

A corrosion risk can be defined as the product of the probability and consequences of a specific corrosion outcome. An overall process for mitigating corrosion risks by the selection of materials and associated corrosion protection measures is shown schematically in [Figure 3](#).

At the design stage, the selection of materials and corrosion protection measures in specific applications can be divided into four stages:

1. The first stage is to define fully the environment. In most applications, the important contributors are the thermal, mechanical, and chemical conditions that the equipment has to withstand for

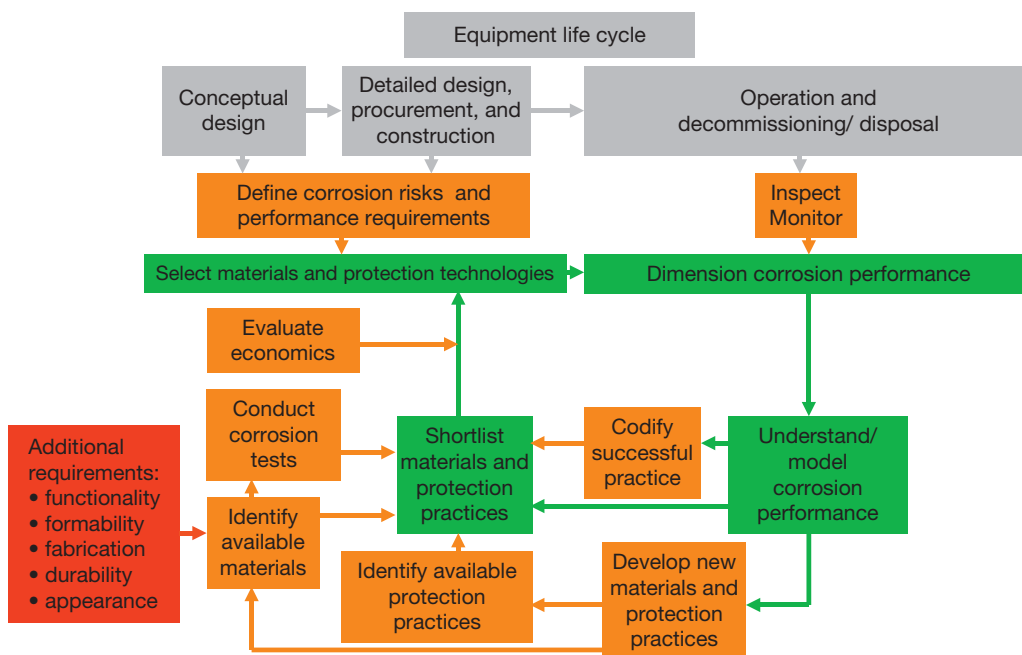


**Figure 3** Outline process for managing corrosion risks by materials selection.

design purposes and during operation. In some situations, for example, in the process industries, there can be uncertainties in defining environments in terms of their phase and full chemical compositions, particularly during start up, shut down, and transient conditions. Other environmental factors may also contribute. For example, the microbiology of the environment may be important and radiation fields can have important effects on the performance of the materials such as the potential effects of solar radiation on the deterioration of polymeric materials.

2. The second stage is to define performance criteria for candidate materials. The basis for this is the design life, but criteria will vary depending on the application. For example, in applications where appearance or purity is a dominating requirement, corrosion rates that are very small may still be unacceptable. In other applications, higher corrosion rates may be acceptable as long as they do not jeopardize functionality during the design life.
3. In the third stage, credible corrosion risks are identified and evaluated and the corrosion performances of materials that satisfy other critical requirements, such as thermal and mechanical properties, are predicted based on data obtained from experience and testing. Protection measures that are required to control or prevent specific

corrosion outcomes are identified. A shortlist of candidate materials and their required corrosion protection measures is identified.

4. In the final stage, cost and availability data are factored into the decision process to identify the most economic combination of material and corrosion protection measures.

#### 4.32.2.2 Predicting Corrosion Performance

##### 4.32.2.2.1 Identifying credible corrosion risks

The starting point in the prediction of corrosion performance is the identification of credible corrosion risks to the equipment under consideration. This is achieved by considering and evaluating the vulnerability of the equipment to deterioration or failure by the various types of corrosion that can be classified as follows:

1. Uniform corrosion resulting in general thinning or loss of strength.
2. Localized corrosion of passive or oxidized materials resulting in damage mechanisms such as pitting or intergranular corrosion or 'breakaway' oxidation, possibly initiating after an induction period.
3. Stress-induced corrosion promoted by static fabrication stresses and/or static or cyclic operating loads resulting in environmentally assisted damage

mechanisms such as stress corrosion cracking or corrosion fatigue.

4. Flow-induced corrosion promoted by velocities beyond 'critical' levels and the presence of second phase particles such as bubbles, droplets, or solids and the presence of flow disturbers, resulting in damage mechanisms such as erosion-corrosion or cavitation.
5. Galvanic corrosion promoted by the coupling of dissimilar materials including the breakdown/transpassivation or activation of passive metals due to coupling with more noble or active materials respectively.
6. Corrosion processes to which wear is a contributory factor.

Initial assessment of possible corrosion outcomes is based on the basic design characteristics of the equipment under consideration in relation to its design and operating environment, thermomechanical loadings, etc. However, corrosion risks can be influenced significantly by local thermomechanical and process conditions that may be less obvious at the design stage. For example, corrosion processes can be initiated by the development of microenvironments with compositions very different to the bulk fluid at locations such as heat transfer surfaces or in crevices and beneath deposits. The importance of detail in designing, in the recognition and mitigation of corrosion risks is described in a separate chapter and it is important that such considerations are factored into the assessment of possible corrosion outcomes for equipment.

#### **4.32.2.2.2 Performance prediction based on experience**

The most reliable predictor of a material's performance is previous experience of the material in an identical or similar application. The capture and dimensioning of the materials performance in operating equipment by appropriate inspection and monitoring, as illustrated in [Figure 3](#), contributes significantly to the understanding and modeling of corrosion behavior. Feedback of the acquired knowledge results in a more reliable selection of materials in the design process and contributes to the development of new and improved materials and protection procedures.

In risk-aware organizations, corporate corrosion experience and knowledge is embedded in the databases that underpin the procurement and maintenance of assets that capture history and learning. This focuses attention on specific materials/corrosion vulnerabilities, resulting in increasingly reliable

design, and corresponding reductions in maintenance costs. This data is usually captured in a what-works-where format related to specific types of equipment or sometimes more generally related to specific environments as exemplified in [Figure 4](#) that summarizes a particular organization's view of the areas of usefulness of various materials in sulfuric acid.

In the cases of generic corrosion risks in specific applications/industries, industrial knowledge and experience and best practices for mitigation have been extensively codified in industry guides and recommended practices published under the auspices of bodies such as the National Association of Corrosion Engineers (NACE),<sup>4</sup> the European Federation of Corrosion (EFC),<sup>5</sup> and numerous, industry-specific bodies. Many of these sources relate to materials selection, including materials condition requirements, for specific environments. For example, the recommendations of NACE relating to the avoidance of stress corrosion cracking in the use of carbon steels for caustic soda service are summarized in [Figure 5](#).

Informal industry networks are a further source of experiential knowledge on corrosion risks. Conferences can be as useful for networking as for the formal sessions and the email addresses and telephone numbers of other professionals in the field are particularly valuable potential sources of corrosion experience.

#### **4.32.2.2.3 Performance prediction based on corrosion testing**

In the absence of relevant experience, recourse must be had to the results of tests of the performances of materials. There are several published compilations of corrosion test data<sup>6-12</sup> and all materials suppliers provide performance data based on tests for a wide range of corrosive environments. Such data are usually presented as tables or maps of corrosion performance.

Data tabulations usually provide only an indication of the corrosion rate, or of a corrosion performance grading, over a range of corrosion rates. An example of corrosion data tabulation for mixtures of acetic acid + sodium chloride ( $\text{CH}_3\text{COOH} + \text{NaCl}$ ) is shown in [Table 1](#).

More detailed materials performance guides are usually based on mapping approaches, where the corrosion property of interest such as corrosion rate or resistance to a specific form of corrosion, such as crevice corrosion or stress corrosion cracking, is mapped on a field or in a space defined by key environmental parameters. Two- or more dimensional,



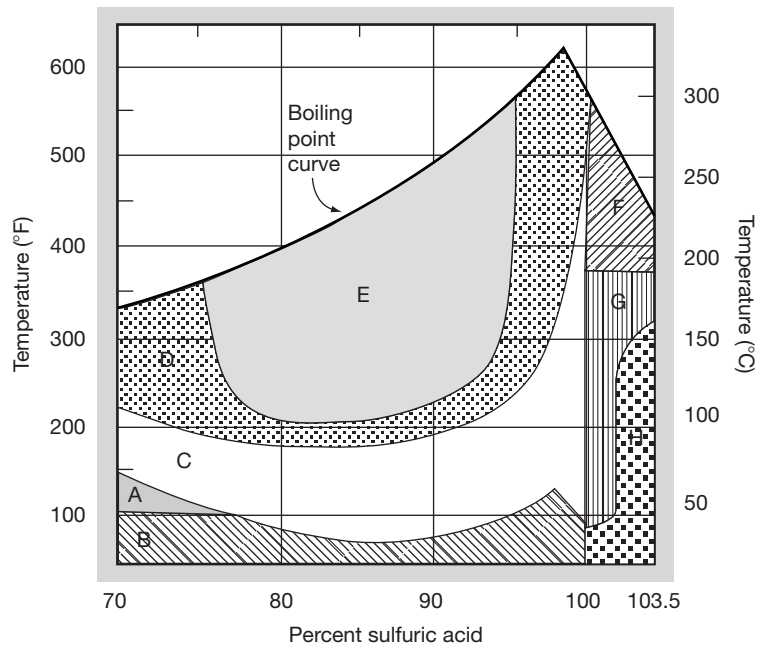


**Figure 4** Areas of usefulness of various materials in concentrated sulfuric acid. A – Alloy B-2, lead, silicon cast iron, tantalum, cast alloy C, impervious graphite, glass. B – Alloy B-2, silicon cast iron, carbon steel, tantalum, impervious graphite and lead <96%, 316 SS >80%, glass, Worthite. C – Alloy B-2, silicon cast iron, tantalum, impervious graphite, and lead <175°F and <96%, alloy 20Cb-3 < 150°F, glass. D – Silicon cast iron, tantalum, alloy B-2, glass. E – Silicon cast iron, tantalum, glass. F – Glass. G – Alloy 20Cb-3, 304 SS, glass, Worthite. H – Alloy 20Cb-3, alloy C-276, 304 SS, carbon steel, Ilium G, glass. Adapted from Bulletin E-86405 *Sulphuric Acid Storage and Handling*; DuPont Company, Wilmington, DE, 1986.

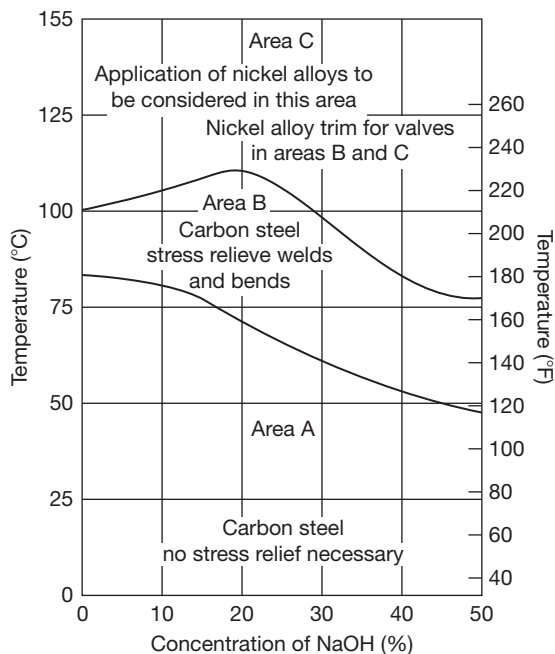


**Figure 5** Temperature and concentration limits for stress corrosion cracking susceptibility of carbon steels in caustic soda. Adapted from *Corrosion Data Survey – Metals Section*, 6th ed.; National Association of Corrosion Engineers, 1985.

isocorrosion maps in which lines of constant corrosion rate are plotted as functions of the temperature and concentration of a corrodent are the commonest forms, a typical example of which is shown in [Figure 6](#) that presents isocorrosion curves for various stainless steels at a rate of  $0.1 \text{ mm year}^{-1}$  in formic acid.

Corrosion tables and maps can be useful guides to performance but, in the absence of detailed information regarding the test conditions relating to the data, are no more than that. A corrosion rate from a table or map is unlikely to define fully the corrosion performance of a component in an environment unless the test procedure that generated the result replicates all of the potential contributing influences on corrosion performance in the specific application such as material condition, stress, flow, and heat transfer.

Corrosion testing is the subject of a separate chapter in this book. There are two broad approaches to testing:

1. Laboratory tests that attempt to quantify the performances of candidate materials in simulated or sampled service environments.
2. Tests/trials in prototype or operating equipment.

**Table 1** Corrosion performances of various materials in mixtures of acetic acid and sodium chloride

<i>CH<sub>3</sub>COOH</i> (wt%)	<i>NaCl</i> (wt%)	<i>Temp.</i> (°C)	<i>Carbon steel</i>	<i>410</i>	<i>18-2</i>	<i>304L</i>	<i>316L</i>	<i>904L</i>	<i>Sanicro28</i>	<i>254SMO</i>	<i>SAF2304</i>	<i>2205</i>	<i>SAF2507</i>	<i>Titanium</i>
1%	1%	70	2	2	0p	0ps	0ps	0ps	0	0	0	0	0	0
1%	5%	50					0p	0p	0	0	0	0	0	0
3%	4%	BP					0ps	0ps	0	0	0	0	0	0
4%	1%	70-BP				0ps	0ps	0ps	0	0	0p	0	0	0
7%	5%	70				1ps	0ps	0ps	0	0	0	0	0	0
7–10%	8.50%	80				1ps	0ps	0ps	0	0	0	0	0	0
10%	5%	BP				1ps	0ps	0ps	0	0	0	0	0	0
10%	26%	BP					1ps	1ps	0p	0	2	1p	0	0
25%	26%	BP					1ps	1ps	0p	0			0	0

0: corrosion rate less than 0.1 mm year<sup>-1</sup> – material may be considered for use (NB: This is still an unacceptably high corrosion rate in many situations); 1: corrosion rate 0.1–1.0 mm year<sup>-1</sup> – material may be used only in special cases; 2: corrosion rate over 1.0 mm year<sup>-1</sup> – serious corrosion, material is not usable. p, P: risk (severe risk) of pitting and crevice corrosion; s, S: risk (severe risk) of stress corrosion cracking; c, C: risk (severe risk) of crevice corrosion; ig: risk of intergranular corrosion; BP: boiling point.

Adapted from *Steel Professional Tool – Corrosion Handbook*; Outokumpu, [www.outokumpu.com](http://www.outokumpu.com).

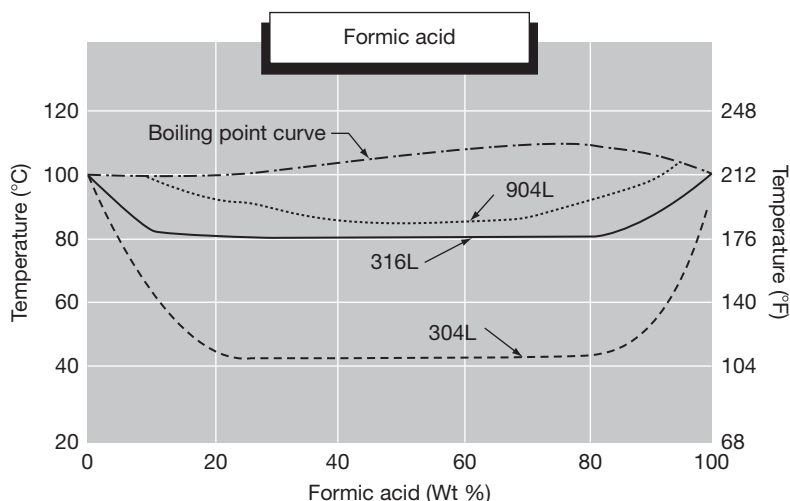


**Figure 6** Isocorrosion diagram of  $0.1 \text{ mm year}^{-1}$  for various grades of stainless steels in formic acid. Adapted from MTI Publication MS-2 *Materials Selector for Hazardous Chemicals Vol. 2: Formic, Acetic and Other Organic Acids*; Materials Technology Institute of the Chemical Process Industries Inc., St Louis, 1997.

Laboratory tests have inevitable limitations for predicting corrosion performance. The commonest, simplest tests<sup>13</sup> involve exposure of small coupons of material, possibly preloaded, to fluids in heated glassware at atmospheric pressure, with only intermittent fluid refreshment. The maximum test temperature is the fluid boiling point, and the scope for simulation of the effects of factors such as flow, the presence of crevices, or the effects of heat transfer is very limited. More complex experimental arrangements involving the uses of autoclaves, heated and/or rotating test pieces, flowing fluids, etc. have been developed to address such limitations, but practicality and cost considerations usually dictate that such tests focus on a particular subset of contributory factors at the expense of others.

Where the lead times for corrosion testing are short, or in an attempt to increase the credibility of performance prediction, accelerated corrosion tests may be considered in which tests are conducted using intensified variables such as increased temperatures, stresses, concentrations of corrosive species, etc. to accelerate corrosion processes. It is vital in such testing that the possible deterioration and failure modes that are being evaluated should not be altered by the intensified test conditions. Staehle<sup>14</sup> has reviewed the advantages and potential pitfalls of accelerated testing for evaluating nuclear industry corrosion processes.

It is obvious that the inherent limitations of laboratory testing dictate that a degree of judgment is

necessary in their use for the prediction of long term performance. However, this can also apply to performance data obtained from operating experience. This is illustrated in Figure 7, which compares the measured stress corrosion cracking resistances of austenitic stainless steels in neutral solutions in laboratory tests<sup>15</sup> with the incidences of stress corrosion cracking in stainless steel shell and tube heat exchangers in water cooling systems for periods up to >10 years.<sup>16</sup> The laboratory tests were relatively simple, involving exposure of types 304/304L/316/316L stainless steels under constant loads equivalent to yield strength to oxygenated, chloride solutions at various concentrations and temperatures for 1000 h. The data set for the >700 heat exchangers included all the basic austenitic grades operating in a wide range of water compositions and configurations for extended periods and, *per se*, incorporated the accelerating effects of heat transfer, crevices, etc.

In the event, the two performance curves in Figure 7 are relatively close, the major difference being in the predicted minimum temperatures for cracking of  $\sim 50$  and  $\sim 30^\circ\text{C}$  for the laboratory test solutions and operating heat exchanger surfaces (skin temperatures) respectively. On the basis of the data in Figure 7, the laboratory tests might be construed as insufficiently conservative in relation to maximum skin temperature to avoid stress corrosion cracking. However, the operating experience data set also contains some inherent uncertainties and conservatism. For example, the skin temperatures are calculated, rather

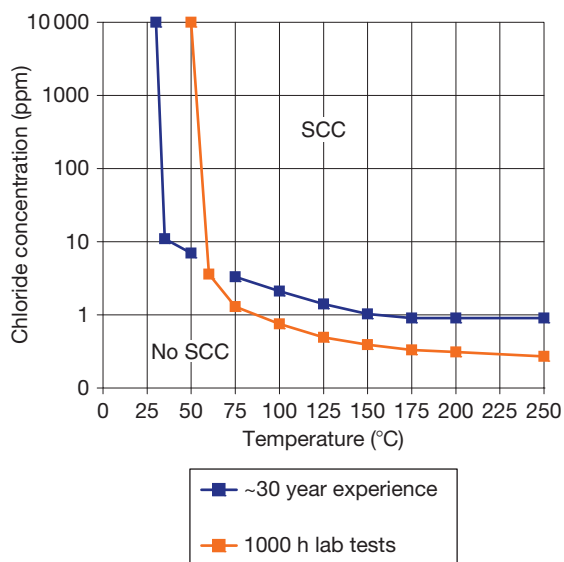


**Figure 7** Resistances of austenitic stainless steels to stress corrosion cracking in neutral solutions in 1000 h lab tests<sup>17</sup> and in heat exchangers in recirculating cooling systems for periods up to >10 years.<sup>18</sup>

than measured, and the water compositions cover a wide range, short of brines and seawater. In practice, a maximum skin temperature of  $\sim 50^\circ\text{C}$  is widely considered as acceptable in the process industries for the avoidance of stress corrosion cracking of austenitic stainless steels in waters of potable quality over a 10-year design life and this is closer to the laboratory tests than the experience data set.

Notwithstanding the latter point, tests or trials in prototype or operating equipment allow for the mitigation of most of the inherent deficiencies associated with laboratory tests. Test coupons can be installed in racks that are bolted or welded onto appropriate components or onto retractable coupon holders. Their exposure to the service environments eliminates the risks relating to the environment in laboratory tests such as failing to include undefined constituents or time dependent chemistry changes in nonrefreshed liquors. However, the use of coupons does not eliminate simulation deficiencies relating to fluid flow characteristics, component geometry/stress, heat transfer effects, etc.

The most reliable option for testing materials is the use of trial components in prototype or operating equipment such as spool pieces in piping, impellers in pumps, tubes in heat exchangers, paddles on agitators, etc. Clearly, full scale trial components provide perfect simulation of all the contributory factors

to corrosion. However, their use introduces risks of premature component failure, resulting in possible equipment damage and downtime, the consequences of which have to be evaluated and accepted.

#### 4.32.2.2.4 Performance prediction based on material composition

Research studies of the performances of metallic materials in specific corrosion environments often generate correlations between materials resistance and alloy composition. Probably the most widely recognized correlation is the pitting resistance equivalent number (PREN), first introduced in 1969 by Lorenz and Medawar<sup>17</sup> and updated and refined by many authors since then, that relates the pitting resistances of stainless steels and nickel alloys to their compositions using linear formulas of the general form:

$$\text{PREN} = \% \text{Cr} + m\% \text{Mo} + n\% \text{N}$$

The most commonly used values of  $m$  and  $n$  are 3.3 and 16, respectively, although some versions give more weighting to nitrogen for specific grades and for superduplex stainless steels and nickel alloys the concentrations of tungsten and niobium are also weighted.

Correlations of this type are completely empirical and, although very useful for ranking and comparing candidate alloys, they are not a reliable basis for predicting the materials performance in specific applications where the corrosion outcome for which they were developed is a risk.<sup>18</sup>

#### 4.32.2.2.5 Performance prediction based on quantitative modeling

Performance predictions, based on experience and corrosion testing, are essentially empirical. In industries where the consequences of unpredicted failure have unacceptable SHE and/or financial consequences, such as power generation, aerospace and oil and gas recovery, major expenditures on corrosion research into generic industry corrosion processes can be justified. Such research results in a sufficiently detailed understanding and dimensioning of corrosion processes to allow the development of quantitative models of corrosion mechanisms and such models can be used to predict corrosion performances as functions of relevant contributing variables.<sup>19</sup> Reviewing of the various approaches to modeling is beyond the scope of this chapter and the reader is referred to other chapters in this book that are concerned specifically with corrosion

modeling, specific corrosion processes and the management of corrosion in specific industries.

#### 4.32.2.3 Evaluating Corrosion Risks in Materials Selection

One of the more important requirements of the materials selection process is that the level of risk inherent in a materials recommendation is understood and aligned to the overall philosophy for managing the SHE and commercial risks in specific applications. The extent to which such risks need to be quantified rigorously depends upon the application and in particular the SHE consequences of corrosion failure.

For example, in the process industries, the SHE risk aspects of materials and protection selection are embedded in the hazard study methodologies<sup>20</sup> that evaluate hazards throughout the process and equipment design at its various stages. Such methodologies attempt to ensure that the safety and health risks presented to employees and the public and the contamination risks presented to the environment are contained within acceptable defined limit values. Risks, including those arising from the materials selection, are evaluated and mitigated by teams of functional professionals, including materials/corrosion engineers.

In the process industries, the semiquantitative evaluation of corrosion risks is normally regarded as sufficient, based on the essentially empirical corrosion data that is used to predict corrosion performance, the reliability of which is normally classified as of high, medium or low reliability, depending on the source. For example, the American Petroleum Institute classifies the reliability of corrosion data as follows<sup>21</sup>:

1. *High reliability sources* – extensive field data through inspection, test coupon data from >5 years exposure in operating equipment.
2. *Moderate reliability sources* – laboratory testing with simulated process conditions, limited operating plant corrosion coupon testing.
3. *Low reliability sources* – published data, corrosion rate tables.

In contrast, in the nuclear industry, quantitative corrosion risk assessment is required, consistent with the greater consequences of equipment failure and more demanding acceptable limit values for risk. For example, Staehle<sup>14</sup> has described a 'corrosion based design approach' (CBDA) process for the prediction of materials performance consisting essentially of the

same stages described above, but evaluated to a much greater level of detail using statistical methodologies. This allows a total probability of equipment failure to be calculated as a function of the probabilities of failure, by specific corrosion processes at specific locations in the equipment.

#### 4.32.3 Economic Evaluation in Materials Selection

The costs of materials vary widely and their relative costs vary with time, depending not the least on the cyclical nature of the costs of metals and other raw materials. The cheapest constructional material is usually steel but its limited thermal and corrosion capabilities require consideration of alternative materials in many applications. In highly corrosive applications, expensive materials such as nickel, titanium, zirconium and tantalum alloys may have to be employed. Nonmetallic materials can provide excellent corrosion resistance at a modest cost but have mechanical property limitations that may require them to be used as protective coatings/linings on stronger substrates such as steel.

The procedures that are used to incorporate costs into the materials selection process are described in a separate chapter in this book concerned with the economic aspects of corrosion.

Whatever the application, the scarcity and cost of capital favor selection of the cheapest of the short-listed materials of construction at the design stage. In some applications this is a valid approach. However, in the cases of complex assets it is recognized that the so-called life cycle costing (LCC) procedures are required that factor in the costs of maintenance and potential unreliability associated with the performances of alternative materials of construction throughout the operating life of the assets in the prevailing economic environment.

This is achieved by the use of discounted cash flow (DCF) procedures that provide an appropriate balance between capital and operating costs by factoring in variations in the value of money with time and the requirement for organizations to obtain an appropriate return on their investment. In the DCF process, all capital and operating costs and revenues associated with the assets are discounted to their values in the base year of the investment appraisal and summed to produce a net present value (NPV) for each materials option. On this basis, the most economic material of construction is that which



yields the highest NPV and this is not necessarily the cheapest material of construction.

Application of such procedures produces some general economic truths relating to the selection of materials and corrosion control options:

1. Relatively low interest rates favor long-term economic planning and the cheapest may well not be the most economic option when life cycle costs are taken into consideration.
2. Alternatively, when capital is very expensive, shorter term considerations tend to dominate and large, long-term investments have no merit over small, frequently repeated investments. In these circumstances, the cheapest is also likely to be the most economic option.
3. It is essential that the risks and uncertainties attached to the inputs to a decision are understood and incorporated into the process of identifying the most economic option.

#### 4.32.4 Outputs/Records of Materials Selection Processes

The output of a materials selection process should be much more than one or more proposed grades of materials. A materials selection process should produce and record, as a minimum, the following elements:

1. Materials recommendations, citing relevant specifications and trade names, including alternatives that may be used on the basis of price and availability.
2. Relevant limitations arising from the materials selected and their potential for deterioration such as limiting materials properties, required corrosion allowances, equipment operation limitations and inspection or future repair/replacement requirements.
3. Relevant tests, fabrication, erection, or other requirements to ensure quality and condition and correct use of the materials selected.
4. Defined sources of corrosion and other data, including tests, used in assessing the suitability of materials

In the cases of complex assets consisting of numerous subcomponents such as an airplane or a chemical process plant, it is vital that selections of materials are documented to capture the know-how that they embody, record any changes that are required and render the information accessible to the wider community of engineers and managers concerned with

the design and operation of the assets. For example, in the process industries, the use of materials selection diagrams (MSDs) has been adopted for these purposes<sup>22</sup> that comprise simplified process flow diagrams showing relevant operating conditions together with materials selection information and any associated corrosion protection practices. These diagrams capture the information needed to ensure that decisions for the selection of materials for the many specific items of equipment that comprise the final plant (vessels, piping, machines, instrumentation) incorporate the outcomes of corrosion risk identification and evaluation, together with any necessary mitigation practices, for the relevant operating conditions. This is particularly important when materials selection decisions are spread across several supplier organizations to mitigate the risks of deficient information transfer across organizational boundaries.

#### 4.32.5 Characteristics of Successful Materials Selection for Corrosion Resistance

Materials selection is a complex process of which the predictable resistance to corrosion is but one element. However, there are some general features that differentiate successful from less successful materials selection for corrosion resistance. Success is characterized by:

1. Early, sustained involvement from initial definition of the corrosion environment and performance requirements through design iterations during the conceptual and detailed design stages. In industries such as the process industries, materials selection issues may well influence process development.
2. Incorporation of learning from similar designs/processes.
3. Integration of materials evaluation into laboratory simulations and the development of pilot scale equipment and prototypes.
4. In the case of complex assets, a management process to ensure that materials selection for all subcomponents is informed as to the prevailing corrosion risks and required mitigation practices.

In contrast, less successful materials selection for corrosion resistance is often characterized by:

1. Involvement after the conceptual and even some of the detailed design stages are complete, when

the degrees of freedom for materials selection are much more limited.

2. Failure to incorporate learning from similar designs/processes.
3. Deficient corrosion environment definition, particularly in relation to transient or upset conditions.
4. Deficient corrosion testing/evaluation due to the failure to simulate real operating conditions.
5. Failure to inform the materials selection process for subcomponents of complex assets about the prevailing corrosion risks and required mitigation practices.

## References

1. Ashby, M. F. *Materials Selection in Mechanical Design*; Butterworth Heinemann: London, 2005.
2. ASTM E527-07. Standard Practice for Numbering Metals and Alloys in the Unified Numbering System (UNS); ASTM International: Philadelphia, PA, 2007.
3. Granta Design: Materials Selection Tools for Industry and Education Available at <http://www.grantadesign.com>.
4. NACE International; <http://www.nace.org>.
5. European Federation of Corrosion; <http://www.efcwweb.org>.
6. Craig, B. D.; Anderson, D. S. Eds. *Handbook of Corrosion Data*, 2nd ed.; ASM International: Materials Park, OH, 1995.
7. Schweitzer, P. A. Ed. *Corrosion Resistance Tables*, 5th ed.; Marcel Dekker: New York, NY, 2004.
8. Graver, D. L. Ed. *Corrosion Data Survey – Metals Section*, 6th ed.; National Association of Corrosion Engineers: Houston, TX, 1985.
9. Hamner, N. E. Ed. *Corrosion Data Survey – Nonmetals Section*, 5th ed.; National Association of Corrosion Engineers: Houston, TX, 1975.
10. Pruett, K. M. Ed. *Corrosion Resistance Guide for Metals and Alloys*; Compass Publications: La Jolla, CA, 1995.
11. Pruett, K. M. Ed. *Corrosion Resistance Guide for Plastics*; Compass Publications: La Jolla, CA, 1999.
12. Pruett, K. M. Ed. *Corrosion Resistance Guide for Elastomers*; Compass Publications: La Jolla, CA, 2005, Vol. III.
13. ASTM G31-72(2004): Standard Practice for Laboratory Immersion Corrosion Testing of Metals; ASTM International: Philadelphia, PA, 2004.
14. Staehle, R. W. In *Uhlig's Corrosion Handbook*, 2nd ed.; Wiley: New York, NY, 2000.
15. Sandvik Materials Technology Corrosion Handbook; AB Sandvik Materials Technology, 2004.
16. Haruyama, S. *Mater. Perform.* **1982**, 14–19.
17. Lorenz, K.; Medawar, G. *Thyssenforschung* **1969**, 1, 97–108.
18. Cleland, J. *Eng. Failure Anal.* **1996**, 3, 65–69.
19. Parkins, R. N. Ed. *Life Prediction of Corrodible Structures*, Proceedings of the Conferences, Cambridge, UK, 23–26 Sept. 1991 and Kauai, Hawaii, 5–8 Nov. 1991; National Association of Corrosion Engineers: Houston, TX, 1991.
20. Kletz, T. A. *HAZOP and HAZAN: Identifying and Assessing Process Industry Hazards*, 4th ed.; Institution of Chemical Engineers: UK, 1999.
21. API Publication 581 *Base Resource Document on Risk Based Inspection*; American Petroleum Institute, 2000.
22. NACE Standard SP0407-2007 *Format, Content and Guidelines for Developing a Materials Selection Diagram*; National Association of Corrosion Engineers: Houston, TX, 2007.

## 4.33 Mitigation of Corrosion Risks by Design

**J. A. Richardson**

Anticorrosion Consulting, 5 Redhills Lane, Durham DH1 4AL, UK

**J. L. Dawson**

Corrosion Consultant, 16 Brandwood Close, Worsley, Manchester M28 1XX, UK

© 2010 Elsevier B.V. All rights reserved.

4.33.1	The Design Process	3065
4.33.2	Corrosion Risks Arising from Microenvironments	3068
4.33.3	Mitigation of Risks Arising from Chemistry Definition/Control	3069
4.33.4	Mitigation of Risks Arising from Thermal Design	3070
4.33.5	Mitigation of Risks Arising from Mechanical Design	3073
4.33.6	Mitigation of Risks Arising from Geography/Shape	3075
4.33.7	Mitigation of Galvanic Compatibility Risks	3078
4.33.8	Management of Corrosion Risks within the Design Process	3080
References		3083

### Abbreviations

**ASME** American Society of Mechanical Engineers

**barg** Gauge pressure relative to atmospheric pressure (bar)

**CR** Corrosion rate

**EAC** Environmentally assisted cracking

**EPC** Engineering, procurement and construction

**FEED** Front end engineering design

**KPI** Key performance indicator

**OOE** Opex operating expenditure

### Symbols

**$f$**  Fluid to wall friction factor

**$h_n$**  Film heat transfer coefficient ( $\text{W m}^{-2} \text{K}^{-1}$ )

**$k$**  Thermal conductivity ( $\text{W m}^{-1} \text{K}^{-1}$ )

**$K_{\text{design}}$**  Maximum design stress intensity factor ( $\text{MPa m}^{1/2}$ )

**$K_{\text{ISCC}}$**  Threshold stress intensity factor for stress corrosion cracking ( $\text{MPa m}^{1/2}$ )

**$q$**  Heat flux ( $\text{W m}^{-2}$ )

**$T$**  Temperature (K)

**$V$**  Pipe average velocity ( $\text{m s}^{-1}$ )

**$V_e$**  Erosional velocity (according to API RP 14E) ( $\text{m s}^{-1}$ )

**$x$**  Wall thickness (m)

**$\rho$**  Fluid density ( $\text{kg m}^{-3}$ )

**$\tau_w$**  Shear stress (Pa)

### 4.33.1 The Design Process

Design is the process that translates needs or aspirations into products. The need is satisfied or the aspiration realized in some appropriate combination of functionality, appearance, durability, and cost of the designed product that can range from a simple, individual component, such as a fastener or a wedding ring, to a complex system assembled from many individual components, such as an aeroplane or a nuclear power station.

Ashby<sup>1</sup> has differentiated three types of design.

1. Original design that is based on a new working principle(s).
2. Adaptive/developmental design seeking incremental advances in performance through refinements to working principle(s).
3. Variant design involving changes in scale or dimensions without changes in function or methods of achieving it.

The design process is usually undertaken at the front end of a project life-cycle which then progresses through construction to operation and maintenance and finally to decommissioning, dismantling, and removal of plant and equipment. Depending on the size and complexity of the project, the design process may be broken down into distinct stages of conceptual design, engineering design, and detailing. In practice, there can be considerable overlap of

these stages due to the need to meet specific milestones within the project engineering phase and the iterative nature of the design process. During this process, sometimes referred to as the design loop, the design brief requirements are translated into options which, after detailed, critical appraisal and possible modification/recycling, are reduced to a preferred option that can be subjected to a final engineering review/audit that verifies its viability.

A common objective of the design process is to minimize life-cycle costs. In practice, these are determined early in the design process when major decisions, including the selection of materials and possible corrosion control options, are made. Studies of reliability and maintainability data from various types of projects<sup>2</sup> indicate that 10–25%, 25–60%, and 95% of the life cycle costs are predetermined by the concept design review, preliminary design audit, and final critical design review respectively, the timings of which are shown schematically in **Figure 1**. However, the early design stages account, typically, for less than 20% of the total project budget, and thus, a slight increase in spending on corrosion risk mitigation at the concept and design development stages can pay off handsomely in large cost savings during operation

and even savings during the detailed design and construction stages.

Regardless of the particular application, the early stages of original and adaptive/developmental design processes are divergent in character. Alternative options are explored and evaluated and, where the product is large and complex, a structured process is used, the output of which is commonly described as a front end engineering design (FEED) or similar. A FEED evaluates the feasibility of a potential project and defines its business and technical scope. Thus, a FEED provides an economic justification for the project and a cost/benefit estimate that usually seeks to be accurate to within  $\pm 10\%$  or thereabouts. In relation to the technical scope, a FEED identifies the technology that is to be adopted and the basis for the ensuing detailed engineering design. Regarding corrosion risk mitigation at the FEED stage, it is usually sufficient to identify the likely classes of material that are to be used for products/equipment together with any attendant significant corrosion risks and corresponding mitigation strategies such as the use of protective coatings, anodic or cathodic protection, or process/environmental modification to inhibit corrosion. These evaluations are commonly desktop studies based on published data and computer based models.

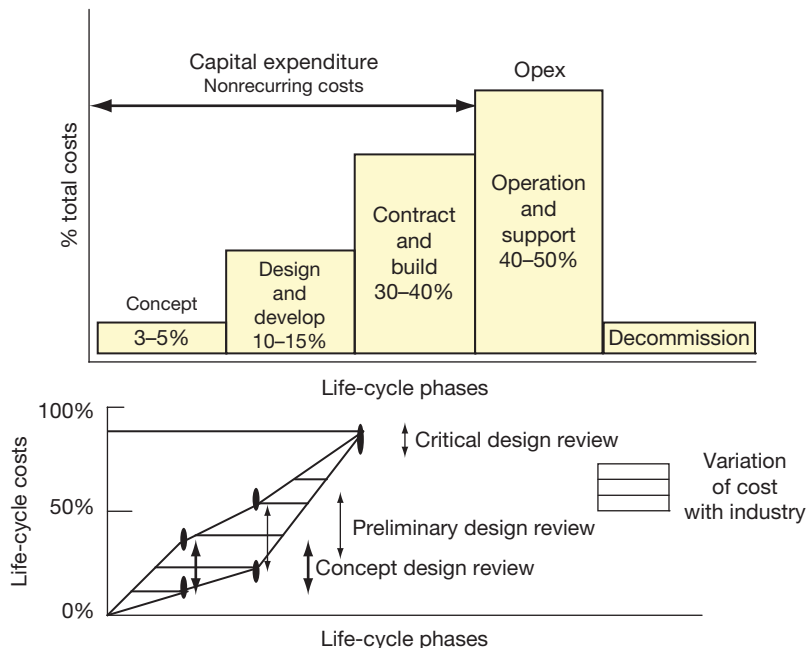


**Figure 1** Effect of project phase expenditure on life-cycle costs. Adapted from Kennedy, I. Design and specification for reliability and maintainability; Presented at National Tribology Course on Reducing Plant and Equipment Life-cycle Costs; 24 November 1994.

Projects that are approved to proceed beyond the business feasibility/FEED stage move into the detailed engineering design, procurement, and construction (EPC) phase. At this stage, the design process converges into increasing detail as the functionality, appearance, durability, and cost of the final product or equipment are specified to facilitate manufacture. The detailed design of infrastructural or industrial structures/components that present significant safety, health, or environmental (SHE) risks in the event of failure is governed generally by international or national design codes. For example, much of the world's process and power equipment is designed in accordance with design codes produced by the American Society of Mechanical Engineers (ASME). The codes have mandatory status in most countries and provide rules and guidance on detailed design, including aspects of materials selection, based on experience and technical analysis. Design codes are updated periodically to incorporate learning from accumulating experience and technology advances. The codes are approved and updated by standing committees of the various stakeholders in the design and operation of the relevant equipment, specifically designers, purchasers/operators, suppliers/fabricators, and inspection/regulatory authorities.

In the case of a large, complex project, the detailed engineering may well be undertaken by a specialist contractor who also undertakes procurement and construction – a so-called EPC contractor. During this stage, drawings and data sheets are produced for products or individual equipment items that finalize the detailed thermomechanical and process design in compliance with the relevant code. Design codes focus on the functionality and safety of equipment that goes into service. For example, in relation to mechanical design, codes provide rules to reduce to acceptable levels the risks of failure by brittle fracture or ductile overload as the equipment enters service or by fatigue or creep during its design life. Design codes also provide rules and guidance on the fabrication of materials. However, design codes usually offer little more than general guidance on the mitigation of corrosion risks that also requires detailed consideration at this stage. The specific grades of materials need to be specified along with the procedures and practices that are to be used to fabricate them and protect them from corrosion.

Arguably the most important input to this detailed design stage is feedback of learning from previous operating experience within an organization or an industrial sector relating to causes of equipment or component failure and the success or otherwise of

engineering practices that have been deployed to mitigate the risks of failure. Some of this learning may have been codified in corporate and national/international engineering guides, standards, and specifications. In relation to corrosion risk mitigation, these documents are concerned mostly with the selection of appropriate materials and practices that are available for corrosion protection in specific applications. The selection of materials and protection practices is considered in a separate chapter in this volume.

However, localized thermomechanical effects and process design practices themselves can also have a significant influence on corrosion risk and its mitigation. This is not widely appreciated amongst design engineers and a lack of assessment of these parameters can result in avoidable corrosion problems in service. A significant challenge facing design teams is how to ensure that operating experience of good and bad design practices is fed back into the design stages of new projects through effective communications amongst operating and maintenance staff, design teams, and corrosion specialists.

The activities and information flows that are essential to the successful mitigation of corrosion risks in the design process are summarized in [Figure 2](#), which confirms the crucial significances of the FEED documents and the detailed drawings/data sheets that form the inputs and outputs of the engineering design and detailing stages.

Major corrosion concerns and risk mitigation issues are usually identified and addressed in the reviews and audits of the FEED documents which result from the conceptual and early design stages and are essentially driven by likely life-cycle cost benefits. Good design practices relating to the various thermomechanical and process factors summarized in [Figure 2](#) come into play in the engineering design and detailing stages. They are less codified than is the case for the selection of materials and corrosion protection practices and, crucially, designers often have limited experience of the service performance of equipment that would provide insights into good practices in these areas. Unless such risks are controlled they can have considerable financial implications that are many times those of the budgeted direct cost of corrosion control. In the following sections of this chapter, potential corrosion risks that can arise from poor design are reviewed along with general approaches to the mitigation of such risks by good thermomechanical and process design practices. There are sources that overview the subject,<sup>3,4</sup> the most comprehensive of which is Pludek's book<sup>3</sup>



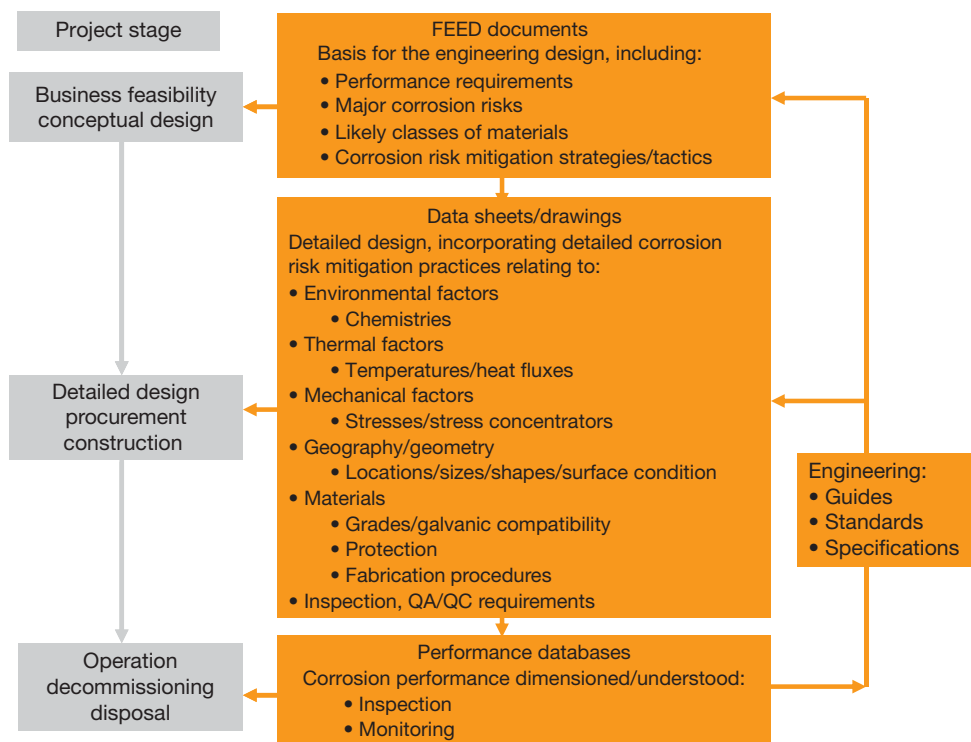


**Figure 2** Activities and information flows for mitigating corrosion risks by design.

that provides many examples of design practices that exacerbate corrosion risks and corresponding good practices for the mitigation of such risks by detailed design. However, awareness of the need for good thermomechanical and process design practices throughout the design process is not sufficient to deliver effective corrosion risk mitigation unless corrosion issues are managed effectively within the project design process and this is addressed in the final section of the chapter.

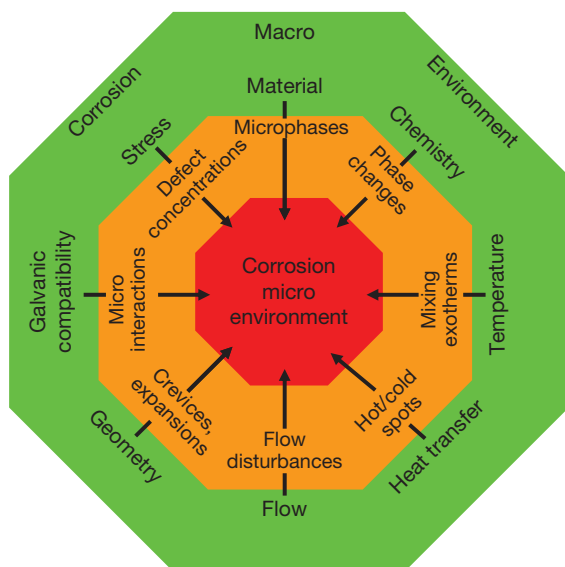
#### 4.33.2 Corrosion Risks Arising from Microenvironments

In any particular application, materials are selected relative to a defined corrosion environment, the key contributory factors to which are:

1. fluid chemistries;
2. fluid temperatures;
3. equipment/component stresses;
4. fluid flow characteristics;
5. heat transfer characteristics;
6. location/layout/shape of equipment and components.

These factors that define the macrocorrosion environment are interactive. Thus, fluid flow characteristics are dependent on shape, heat transfer characteristics on fluid temperatures, etc. The performance of a specific material in a particular application will be determined by clusters of the various factors that will vary with the application. For example, fluid flow and heat transfer are particularly relevant to the process and power generation industries. Clearly, if a piece of equipment is to be fabricated from several different materials, then there are additional corrosion risks arising from potential galvanic interactions that have also to be evaluated and mitigated.

All of the contributory factors are, in theory, degrees of freedom in the design of a component or a piece of equipment for a particular application. In practice, fluid chemistries and temperatures are predetermined in many applications, but the dimensions and characteristics of the other factors can all be influenced by the detailed thermomechanical and process design of equipment and components. Materials selection *per se* is rarely sufficient. It needs to be overlaid with good design practices if corrosion risks are to be mitigated in subsequent operation.



The recognition of corrosion risks relating to the macroenvironment at the design stage is relatively straightforward. However, as illustrated in [Figure 3](#), all of the contributory factors can intensify and interact locally in equipment and components. Thus, fluids may condense locally at cold spots to produce chemistries that are much more corrosive than the bulk chemistry of the fluid. Stresses may be concentrated significantly by fabrication and other defects in equipment and components that may increase the risks of initiation of environmentally assisted cracking. Local shape features may disturb fluid flows with significant outcomes regarding the vulnerability of components to erosion–corrosion. In practice, these intensified local factors can also cluster to define local microenvironments that present much larger corrosion risks than clusters of the equivalent bulk factors. Such microenvironments can be much more difficult to predict at the design stage and are a common source of unscheduled failure of equipment due to corrosion.

#### 4.33.3 Mitigation of Risks Arising from Chemistry Definition/Control

The commonest cause of unpredicted corrosion problems is the failure to define accurately the chemistries of environments or to anticipate changes in chemistry that are caused by other prevailing factors at specific locations in equipment. The major

1. Variations in bulk chemistry may occur with time, under climatic influences, or during start-up, shut-down, or upset conditions in operation. For example, in the process industries, the lives of carbon steel reactors that are used for the manufacture of ethylene dichloride are determined almost exclusively by the incidence or otherwise of condensation of hydrochloric acid during start-up, in sharp contrast to the steady state operating environment, where corrosion rates are low.<sup>5</sup> It is important that potential changes in bulk chemistry with time are defined, quantified, and evaluated at the design stage.
2. The presences and concentrations of minor components may dominate corrosion performance. For example, the performances of passive alloys in reducing acid solutions are influenced strongly by the presences or otherwise of oxidizing metal ions (favorably) or chloride ions (unfavorably) at relatively low levels in the tens to hundreds ppm range.<sup>6</sup> It is important that minor components are defined, quantified, and evaluated at the design stage, including their possible local concentration such as in distillation and separation equipment.
3. Local shape and/or heat transfer may promote the development of local chemistries that are very different from and much more corrosive than the bulk fluid chemistry, in particular where phase changes may occur. Early condensates from acid gas/vapor streams can be very concentrated and corrosive relative to bulk condensates as in the cases of combustion flue gases,<sup>7</sup> and refinery overhead streams.<sup>8</sup> Initially benign condensates or cooling fluids can concentrate due to intermittent contact with surfaces hot enough to promote concentration or dry-out, as in the chloride-induced, external stress corrosion cracking of austenitic stainless steels under thermal insulation.<sup>9</sup> Extremely high concentration factors are possible under boiling heat transfer in crevices or under deposits, or under film boiling conditions at high heat flux regions, as in water side, on-load corrosion in process and utility boilers.<sup>10</sup>

A typical example of potential microenvironment development under the combined influences of shape and heat transfer is the shell and tube heat exchanger that is widely used for cooling and heating applications in the process and power industries.

The critical design feature of these exchangers is the tube/tube-plate joint that separates the two working fluids and which almost inevitably contains a crevice, unless it is eliminated by employing expensive fabrication procedures. Sections of a typical shell and tube cooler fabricated with welded tube/tube-plate joints using shell-side water as the cooling medium are shown schematically in [Figure 4](#) in a vertical configuration, characterized by the existence of a vapor space between the water exit and the upper, hot tube-plate.

The chloride contents of waters vary over many orders of magnitude, depending on the source. Demineralized waters and condensates generally contain <1 ppm chloride. Lake waters commonly contain low levels of chloride in the range 1–10 ppm, potable waters in the range 10–100 ppm, rivers in the range 100–1000, and estuarine and seawaters in the range 1000–10 000 ppm. During operation, cooling water splashes onto the underside of the hot tube-plate, where it evaporates to dryness. Successive events result in the accumulation of scale/salt deposits, in which the concentration of chloride is many orders of magnitude greater than in the bulk cooling water. The crevices between the tubes and the tube-plate provide for retention and further concentration of aqueous fluid.

The thin tubes contain residual stresses equivalent at the yield strength of the material, arising from tube expansion and welding of the joint during fabrication.

It follows that if, as is commonly the case, the heat exchanger is constructed in austenitic stainless steel, the microenvironment that develops in and around the tube/tube-plate joint introduces significant risks of chloride-induced stress corrosion cracking, particularly within the crevice, as illustrated in [Figure 4](#).

There are several approaches to mitigating these risks, the most direct of which is the selection of ferritic or duplex austenitic–ferritic grades of stainless steel that are more resistant or even immune to chloride-induced stress corrosion cracking. However, there are also practical design measures that can be used to mitigate the risks for austenitic stainless steels. As confirmed in [Figure 5](#), risks are significantly lowered in horizontal relative to vertical heat exchangers because the vapor space that is the essential cause of microenvironment development is removed.

Risks are further lowered if the cooling water is transferred to the tube-side, because the tube/tube-plate crevice that contributes to microenvironment development is eliminated. If the exchanger, for other reasons, has to be vertical with shell-side cooling, risks can be lowered by venting the hot tube-sheet, thereby eliminating the vapor space, as shown schematically in [Figure 6](#).

#### 4.33.4 Mitigation of Risks Arising from Thermal Design

The bulk temperature of an environment can usually be predicted accurately, notwithstanding the need to incorporate, if appropriate, the influences of

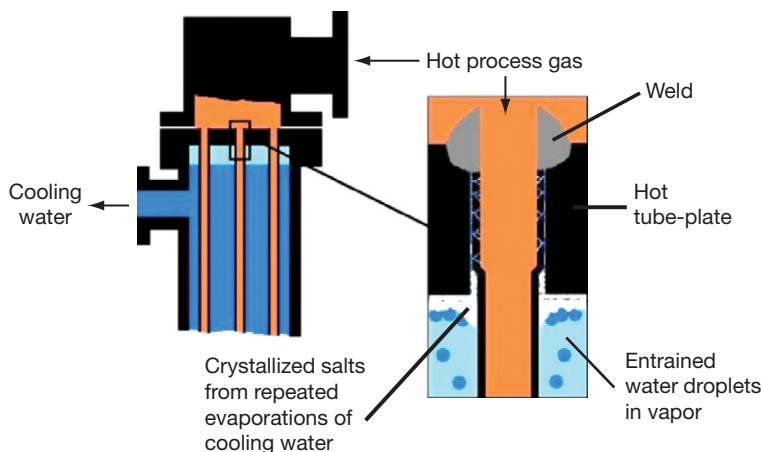


**Figure 4** Creation of microenvironments that promotes stress corrosion cracking by repeated wetting/drying events in the tube/tube-plate regions of vertical, austenitic stainless steel heat exchangers with shell-side water.

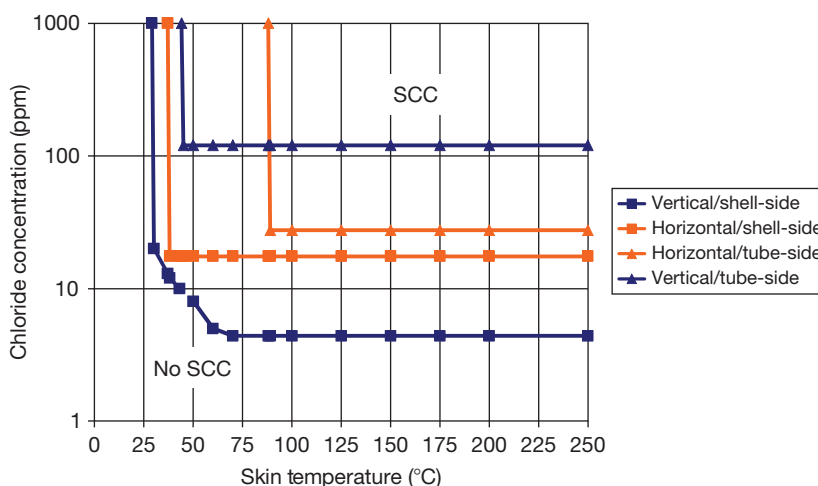


**Figure 5** Resistances of austenitic stainless steel heat exchangers to chloride induced stress corrosion cracking in open, recirculating cooling systems for periods up to >10 years. Adapted from Haruyama, S. *Mater. Perform.* **1982**, 21, 14–19.

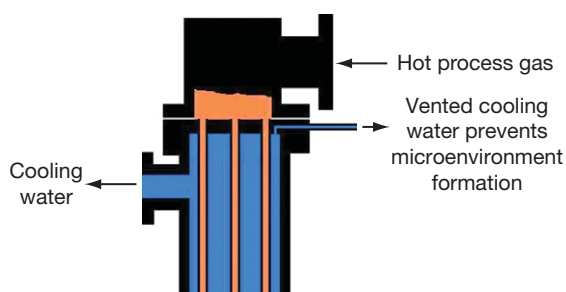


**Figure 6** Prevention of microenvironments that promote stress corrosion cracking in the tube/tube-plate regions of the shell-sides of vertical shell and tube heat exchangers by venting the top tube-sheet.

time-dependent factors such as climatic conditions, or start-up, shut-down, or upset conditions during operation. The possible effects on local temperatures of fluid mixing need to be recognized. For example, the addition of acids to process streams may be characterized by significant dilution exotherms that produce a much hotter, local microenvironment with additional corrosion risks which may have to be mitigated by a local materials upgrade at the design stage.

Heat transfer introduces additional factors that need to be evaluated. The case of heat transfer from a fluid to a solid wall controlled by convective/turbulent flow with fluid eddies, and through the solid wall by conduction, is shown schematically in [Figure 7](#). The local heat flux is given by:

$$q = h_1(T_1 - T_2) = k_w/x_w(T_2 - T_3) = h_2(T_3 - T_4)$$

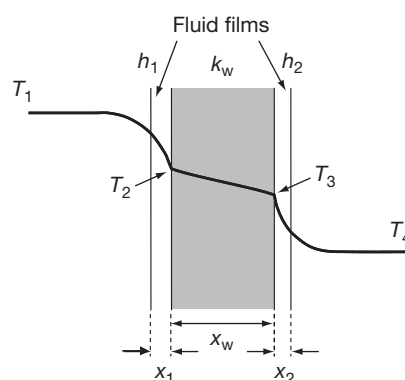


**Figure 7** Temperature profile for the case of heat transfer between fluids and a solid wall controlled by turbulent flow/convection ( $h_n$ ), through the solid wall by conduction ( $k_w/x_w$ ).  $T$  = temperature (K);  $k$  = thermal conductivity ( $\text{W m}^{-1} \text{K}^{-1}$ );  $x$  = wall/film thickness (m);  $h_n$  = fluid to wall heat transfer coefficient ( $\text{W m}^{-1} \text{K}^{-1}$ ).

where  $q$  is the heat flux ( $\text{W m}^{-2}$ );  $h_n$ , the film heat transfer coefficient ( $\text{W m}^{-2} \text{K}^{-1}$ );  $T$ , the temperature (K);  $k$ , the thermal conductivity ( $\text{W m}^{-1} \text{K}^{-1}$ );  $x$  is the wall thickness (m).

From the design standpoint, heat transfer is promoted by low thickness and high thermal conductivity of the solid wall, high values of  $\Delta T$  ( $T_1 - T_4$ ) and turbulence that generates high values of  $h_n$ . One of the more important features of heat transfer in relation to its corrosion effects is the difference between metal surface, or skin temperatures,  $T_2$  and  $T_3$ , and the bulk fluid temperatures,  $T_1$  and  $T_4$ , as depicted schematically in [Figure 7](#).

There are additional potential corrosion risks arising from the effects of heat transfer. Heat exchangers typically operate under relatively high flow rates to promote turbulent flow conditions, resulting in reduced boundary layer thickness. The supply of reactants, or the removal of intermediates or products, is dominated by flow-induced mass transfer. In single phase fluids, the overriding additional effect of heat transfer is the influence of wall temperature on diffusion coefficients and viscosity. These influence boundary layer thicknesses and concentration profiles and the stabilities, solubilities, and compositions of the relatively thick diffusion barrier layers which are continuously penetrated by turbulent eddies and localized areas of high turbulence intensity at tube inlets, downstream of protrusions and other changes of shape. These not only increase heat transfer rates but have controlling effects on the corrosion and erosion-corrosion of metals such as steels and copper alloys in specific applications.<sup>11</sup>

For example, heat transfer to a liquid makes it more difficult to transfer oxygen from the bulk solution to a hot wall surface because of the reduced solubility of oxygen as temperature increases. In cases where the solubility product increases with temperature, heat and momentum transfer at the wall-liquid interface may tend to undermine and detach protective barrier layers, whilst encouraging thickening of scales by diffusion and precipitation at the outer face. Conversely, where the solubility

product decreases with temperature, heat transfer to a liquid may promote the formation of adherent, thin scales, the classic case of which is the formation of calcium carbonate and sulphate scales on heat transfer surfaces in cooling waters.

Wall conditions can also be influenced by whether the heat exchanger design is co-current or counter current as local wall temperatures may be higher than indicated by average design figures. The design will allow for a fouling factor to account for lower overall heat transfer rates during operational life. These apparently minor differences on the process design flow sheet can result, in practice, in significant changes to local microenvironments that give rise to corrosion.

Heat transfer is also promoted by phase changes such as boiling or condensation and these can, as noted previously, promote the formation of local environments with significant additional corrosion risks. For example, modern high pressure boilers are designed utilizing high heat fluxes, typically  $1000 \text{ kW m}^{-2}$  that can promote film boiling conditions that result in fouling/corrosion processes during operation (on-load), depending on the efficacy of the prevailing boiler water treatment. Process plant boilers are commonly designed with particularly high heat fluxes to reduce capital costs, and can therefore be particularly vulnerable to on-load corrosion, as illustrated schematically in Figure 8 for a typical, horizontal, fire-tube boiler constructed in carbon

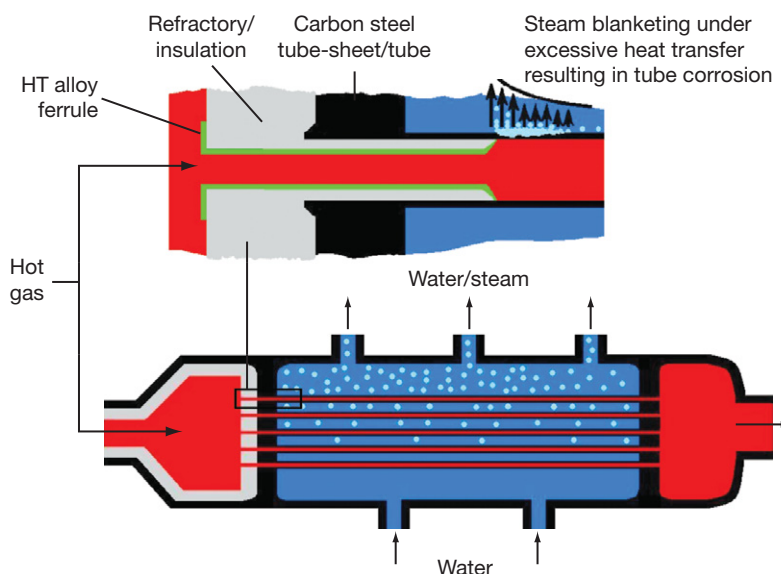


**Figure 8** Creation of corrosion-promoting microenvironments at high heat flux regions of horizontal, fire tube boilers resulting in on-load corrosion.



steel that uses a hot process gas, typically entering at  $\sim 1000^\circ\text{C}$ , to raise steam from water on the shell-side at a typical pressure of  $\sim 100$  barg.

The boiler depicted in **Figure 8** would typically be designed with average heat fluxes of  $\sim 3000\text{ kW m}^{-2}$ , increasing to  $\sim 6000\text{ kW m}^{-2}$  locally, and would operate on fully demineralized water. The hot channel end and tube-plate would be refractory clad to maintain the carbon steel temperatures within the code design range, with the tube temperatures determined largely by the boiling water temperature,  $\sim 310^\circ\text{C}$ . A typical tube entry construction detail is illustrated in **Figure 8**, consisting of high temperature alloy ferrules set into the tube-sheet refractory and extending some distance into the tubes, separated from them by an insulating material. The ferrules are required to protect the tube inlet regions from excessive heat flux by providing a transition region to reduce the inevitable region of enhanced heat transfer just beyond the ferrule to within the design requirement.

The corrosion rate of carbon steel in boiler waters at  $\sim 310^\circ\text{C}$  depends on the solubility of magnetite, and therefore pH. It is known that concentrated acidic or alkaline solutions can form at local sites where convection/mixing are restricted, such as crevices at tube/tube-plate joints, on horizontal or inclined surfaces, or at flow disturbances such as tube bends or weld protrusions. Steam blanketing under film boiling conditions can result in intermittent wetting/drying and solute concentration by several orders of magnitude, exacerbated by porous deposits such as oxides of iron or copper that promote so-called wick boiling. Concentrated alkaline solutions usually arise from concentration of alkaline corrosion inhibition species from which free sodium hydroxide can be liberated, particularly sodium phosphate treatments. Concentrated acid solutions arise when bulk contamination of the boiler water with dissolved oxygen and chloride, typically by sea or river water ingress, occurs. The boiler depicted in **Figure 8** is at risk of such local microenvironments developing on tube surfaces in the regions of maximum heat transfer beyond the ferrules, resulting in pitting and ultimately tube perforation.

In practice, the risks depicted in **Figure 8** can be mitigated by tight control of water chemistry during operation to prevent the formation of highly alkaline or acid environments in the event that film boiling conditions occur. However, the risks can also be mitigated by the attenuation of excessive heat fluxes with an improved design, as depicted in **Figure 9**, which shows an extended, profiled ferrule for that purpose.

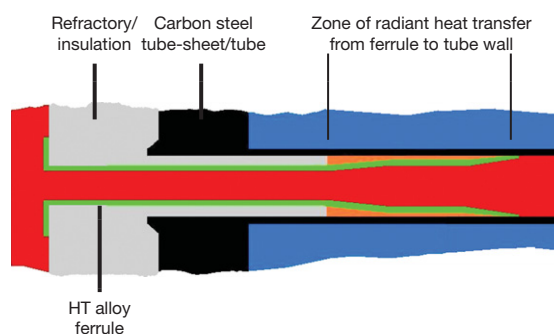


**Figure 9** Tube ferrule design to mitigate risks of on-load corrosion due to excessive heat fluxes in horizontal, fire-tube boilers.

#### 4.33.5 Mitigation of Risks Arising from Mechanical Design

Engineering structures are exposed to a range of operating stress regimes, depending on the application. Static structural loadings are usually limited to maximum proportions of yield or ultimate strength of the material at lower temperatures, or stress rupture properties of the material if operating at temperatures within its creep range, as dictated by the relevant equipment design codes. In practice, design codes usually permit higher stresses in local regions of equipment than the maximum allowable specified for the majority of the structure, for example at penetrations through the vessel wall in the case of pressure vessels. Fabrication processes such as cold working and welding can introduce local, static, residual stresses at levels up to and beyond the yield strength of the material.

Equipment may also be required to withstand dynamic loadings. These cyclic loadings may be associated with equipment start-up and shut-down conditions, or may be intrinsic to the application itself, as for example in the cases of marine structures that have to withstand tidal and/or wave loadings, or pressure vessels for processes based on pressure cycling. They may arise indirectly from thermal cycling/transients, particularly under conditions of restricted expansion and contraction. Higher frequency, vibration loadings may be wind excited, or arise from pressure pulsations, or be transmitted from adjacent reciprocating or rotating machinery. In some applications, loading regimes are complex combinations of static and dynamic loadings, as for example in the case of turbine blades that may have to withstand static centrifugal loads at temperatures within

the material's creep range that are overlaid with relatively high frequency, low stress range loadings arising from varying fluid pressures as the blades rotate. As in the case of static loads, equipment design codes provide guidance on the confinement of dynamic loadings to within the appropriate fatigue strength capabilities of the relevant materials.

Where thinning of structural components due to corrosion and/or wear is anticipated in service, appropriate thickness allowances or sacrificial shielding components such as impingement plates may be specified at critical locations at the design stage to ensure that components retain sufficient thickness throughout their service lives to maintain membrane stresses below the design maximum allowable levels. This approach to corrosion risk mitigation is applicable only to relatively thick section components where some loss of section thickness can be tolerated such as major structural members, pressure vessel or pipe walls, etc. It is impractical for thin section components such as heat exchanger tubes/plates, or where dimensional clearances must be maintained throughout service life such as in seals, or where environmental contamination by corrosion products is unacceptable such as in the food and pharmaceutical industries.

The potential risks of environmentally assisted cracking (EAC) have also to be evaluated and mitigated at the design stage. Regions of relatively high static stress, in particular associated with residual fabrication stresses, are preferred sites for the initiation of the various forms of EAC that are described in separate chapters in this book. Corrosion has significant potential influences on the risks of initiation and rates of propagation of fatigue cracks in materials, and both static and dynamic stresses can be concentrated by defects in materials or welds. In the cases of equipment for critical duties such as offshore structures and nuclear pressure vessels, these factors are incorporated formally into relevant design codes. However, for most equipment, the additional risks they promote have to be evaluated and mitigated on the basis of more general engineering good practice.

The general approaches to the mitigation of EAC risks by the control of stress and its concentration are as follows:

1. Design stresses and the sizes of fabrication defects are controlled to levels where the maximum stress intensity for the equipment,  $K_{I\text{design}}$ , is below the critical stress intensity for EAC,  $K_{I\text{EAC}}$ . Given that design codes commonly allow membrane stresses

that are significant proportions of the yield strength of a material, this approach offers limited scope to mitigate risks in many practical situations. An example of its successful use would be the case of steel gas cylinders that are usually hot forged to final shape in one operation in thicknesses well above the minimum required to sustain maximum operating pressures. As a result, they operate with very low applied stresses and contain very small residual stresses and are therefore effectively immune to EAC even when containing environments such as anhydrous ammonia or HCN that are known to present risks of EAC to steels.

2. Stress concentrations are controlled by appropriate control of shape and by confining defect sizes below specified limiting values, for example by the use of transitional radii at changes in cross section such as at notches and key ways, the control of surface finish etc. Welds are the commonest sources of defects in fabricated structures and therefore require appropriate inspection and possible repair to eliminate potentially critical fabrication defects. For particularly critical applications, practices such as the machining/grinding of weld toes to eliminate small defects are specified.
3. Residual/fabrication stresses are controlled by specifying thermal or mechanical stress relief procedures. Thermal procedures have been employed routinely for the relief of fabrication stresses in carbon and low alloy steels using procedures that are detailed in relevant design codes. Typically, structures are heated to temperatures within the range 550–650 °C for short time periods that depend on component thickness. Rules exist that govern rates of heating and cooling, allowable temperature gradients, etc. Ideally, completed structures are heat treated in furnaces, but large structures may have to be furnace treated in sections, and the final welds heat treated locally using electric heating elements. Local heat treatments may not achieve the degrees of stress relief that are achieved with furnace heat treatment. So-called temper bead welding is a special case of local heat treatment in which successive weld beads impart a degree of stress relief to earlier deposits and a final, temper bead heat treats the last of the deposits required for strength purposes. Where thermal stress relief is impractical, or cannot be applied because the material's properties are likely to be altered unacceptably during the process, mechanical procedures can be employed such as

vibratory stress relief or peening. Vibratory stress relief<sup>12</sup> uses high amplitude, resonant vibrations to attenuate and redistribute residual stresses. Peening uses shot or beads,<sup>13</sup> or laser energy,<sup>14</sup> to produce compressive layers over regions of residual tensile stress to prevent the initiation of environmental cracks.

4. Vibrations can be transmitted from one item to another through connecting pipe work and/or supports and may promote high cycle corrosion fatigue and related damage mechanisms. One such example is where standby pumps are attached to the same plinth as the working pump, leading to failure to start on switch over, due to fretting of the bearings. Vibrations are controlled by specifying additional stiffening or support and/or by damping local resonant vibrations.

#### 4.33.6 Mitigation of Risks Arising from Geography/Shape

There are limits to the degrees of freedom governing the geographic location of sites and/or equipment, but geography does exert some significant influences on corrosion risks and their mitigation. For example, marine corrosion is a well documented phenomenon, but the transference of designs from one global region to another requires that many items have to be reappraised for higher ambient temperatures and salinities in order, for example, to avoid crevice and pitting corrosion of stainless materials. Also, given the dependence of atmospheric corrosion upon temperature, relative humidity, rainfall and the presence or otherwise of pollutants, the location of equipment to avoid particularly damaging microclimates can provide significant mitigation of atmospheric corrosion risks. Of particular significance in this respect are the directions of prevailing winds and/or river/sea currents in relation to potential sources of pollutants. For example, in coastal locations, off-shore winds are preferable to on-shore winds and at any location it is preferable to be up-wind/stream rather than down-wind/stream of emissions from cooling towers, stacks and outflows.

Much more control is potentially exercisable at the design stage over the shape of equipment and this can provide significant mitigation of specific corrosion risks, particularly those that arise from poor drainage, the creation of crevices, the disturbance of flow in fluid transport and the condition of surfaces prior to coating:

1. The entrapment of fluids in equipment that is unable to drain completely results in corrosion risks that are usually mitigated readily by simple changes in shape, in some cases by the simple introduction of drainage holes. Some examples of good and bad design relating to the fabrication of steel sections and the drainage of tanks are shown schematically in [Figure 10](#).
2. Crevices and their associated corrosion risks are to some extent inherent in components of complex shape but it is possible to control their severity or even eliminate them altogether by appropriate design and fabrication practices. Some examples of good and bad practices relating to flanged joints in piping systems are shown schematically in [Figure 11](#). Evidently, crevices are inherent to the uses of threaded, or so-called socket-weld, flanges that present open crevices to the process fluid. In principle, the crevice can be removed in the case of the slip-on flange by seal welding the bore as depicted in [Figure 11](#), but the best design is the so-called weld neck flange in which the flange is attached to the pipe with a butt weld, thereby eliminating the crevice. [Figure 11](#) also illustrates how the use of undersized gaskets can create crevices in flanged joints that are eliminated by specifying gaskets of the correct size. Another classic source of crevices in process equipment is the ubiquitous tube/tube-plate joint in the shell and tube heat exchanger. Joints are conventionally fabricated by seal welding the tube into the tube-plate as depicted in [Figure 12](#), followed by expansion of the tube onto the walls of the drilled hole in the tube-plate to reduce the severity of the crevice between them. However, as [Figure 12](#) illustrates, it is virtually impossible to eliminate the crevice, and there remains a residual risk in fluids that are inherently prone to promote crevice corrosion, or where high heat fluxes into the crevice can create such fluids by superheating and concentrating the crevice liquor relative to the benign bulk fluid. In such cases, consideration might be given in design to locating fluids that might promote crevice corrosion on the tube-side of the exchanger. If this is impractical, the crevice can be eliminated, in principle, by back face bore welding of the tube/tube-plate joint, as depicted in [Figure 12](#). However, this is an expensive, difficult procedure and residual risks are more usually mitigated by upgrading the tube and tube-plate materials. In compact heat exchangers in which thin plates or ligaments are

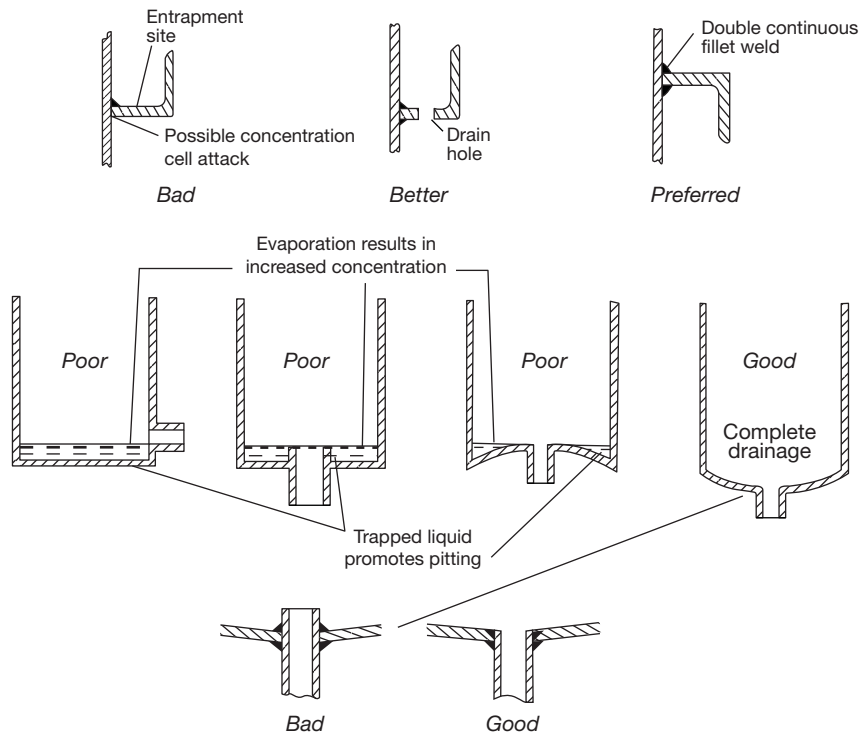


**Figure 10** Examples of bad and good practices in avoiding the entrapment of fluids in structural steelwork and tanks. Adapted from Pludek, V. R. *Design and Corrosion Control*; Wiley: New York, 1976.

separated with very large areas of compression or welded joints, upgrading the material provides the only practical mitigation of crevice corrosion risks. Crevice corrosion risks can also arise at welds where lack of sidewall fusion or root penetration creates a crevice, and appropriate fabrication and inspection procedures must be implemented to prevent such defects.

- Flow disturbance is a common source of local erosion–corrosion problems and it is avoidable by the appropriate design and fabrication of fluid transport systems. In many cases, the basis for designing against erosion–corrosion is the specification of limiting velocities for fluids that have been established by testing and/or experience as in the cases, for example, of cupronickel alloys in seawater<sup>15</sup> and carbon/stainless steels in concentrated sulfuric acid.<sup>16</sup>

However, geometric features of fluid systems can disturb and introduce local turbulences into flows as depicted in **Figure 13** that illustrates schematically how protuberances, cavities, and abrupt changes in direction and cross section can all disturb streamline flows to introduce local turbulences and associated

erosion–corrosion risks. Hydrodynamic considerations show that under typical attached turbulent flow conditions:

$$\tau_w = f/2\rho V^2$$

$\tau_w$  is the shear stress (Pa);  $f$ , the fluid to wall friction factor;  $\rho$ , the fluid density ( $\text{kg m}^{-3}$ ); and  $V$  is the pipe average velocity ( $\text{m s}^{-1}$ ).

The corrosion rate (CR) can be shown to be proportional to  $\tau^{1/2}$  and it thus follows that:

$$\text{CR} \propto (f/2)^{1/2} \rho^{1/2} V$$

An erosional velocity,  $V_e$ , may be defined:

$$V_e = C\rho^{1/2}$$

The constant  $C$  is a combination of fluid corrosivity, fluid to wall friction factor, material properties/chemistry (film strength), and pipe wall surface roughness. This is the basis for the arbitrary erosional velocity in API RP 14E<sup>17</sup> for multiphase fluids in oil/gas production, where  $C$  values of 100 indicate a shear stress range of 75–90 Pa. Once the flow becomes detached/separated as with multiphase slugging flow or down stream of flow disturbances, typified by those shown in **Figure 13**, the corrosion rate is

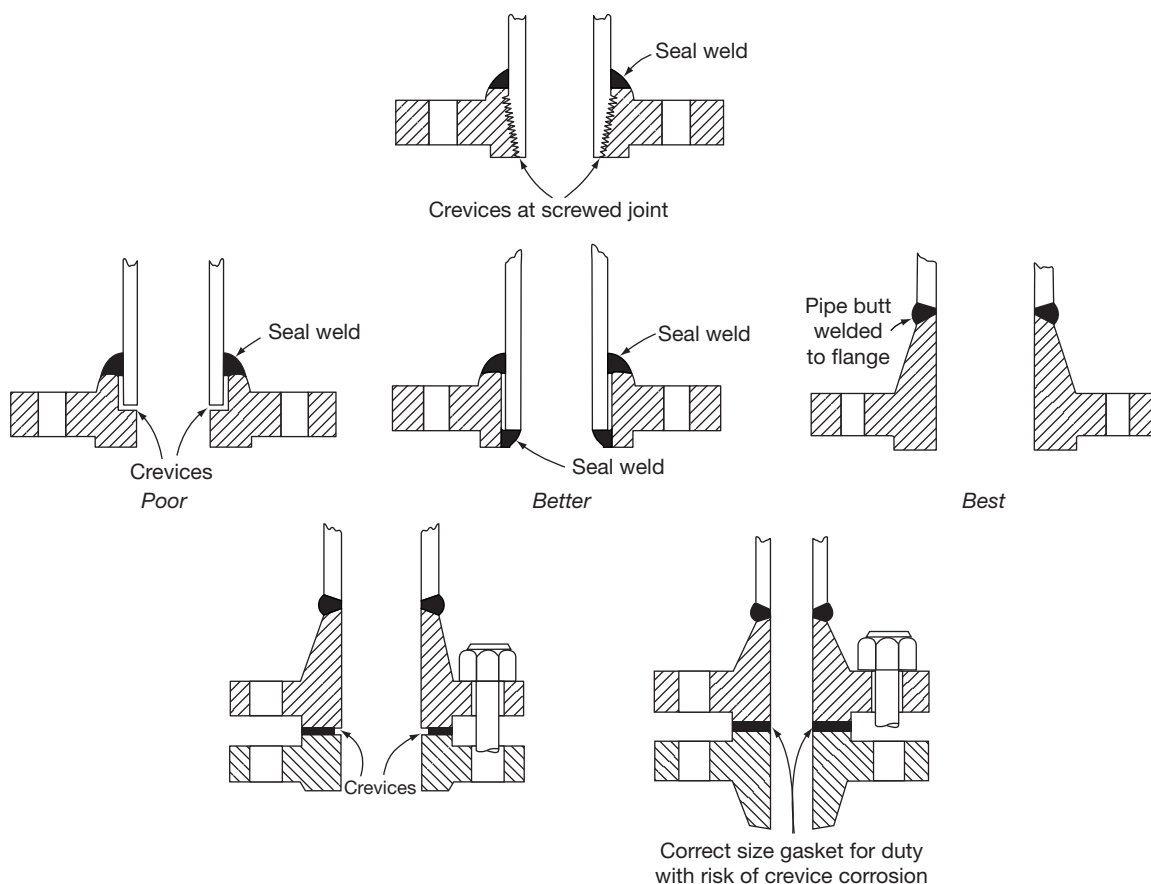


**Figure 11** Examples of good and bad practices relating to the avoidance of crevices in flanged joints in piping systems.

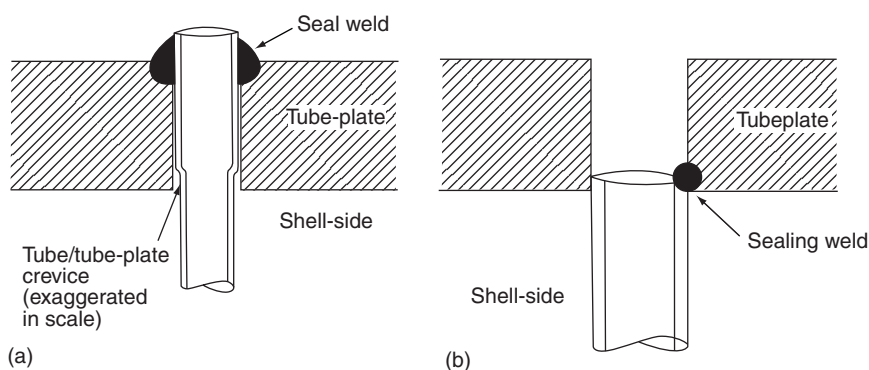


**Figure 12** Fabrication practices that (a) reduce and (b) eliminate crevices in tube/tube-plate joints in tubular heat exchangers.

controlled by the turbulence intensity and is then proportional to the root mean square value of the shear stress,  $\tau_{\text{rms}}$ . Many of these risks can be mitigated by good design and fabrication practices. Thus, it may be important in specific material/fluid combinations

to use long radius bends/elbows and gradual changes in cross section in piping systems. Correct alignment of joints is important and gaskets or welds should be neither recessed nor protruding into the flow, either of which can introduce damaging flow disturbance.



Components that inevitably disturb flows, such as probes, valves, and orifice plates should be selected, sized, and located to minimize local and downstream turbulence. Thus, straight-through types of valve such as gate, butterfly, or plug valves disturb flows less than throttling, globe, and angle valves, and venturi tubes are preferable to orifice plates, as shown schematically in **Figure 14**. It is also good design practice to separate individual flow disturbers to prevent synergistic effects. For example, it is bad practice to locate an orifice plate or a control valve immediately upstream of a bend and much better

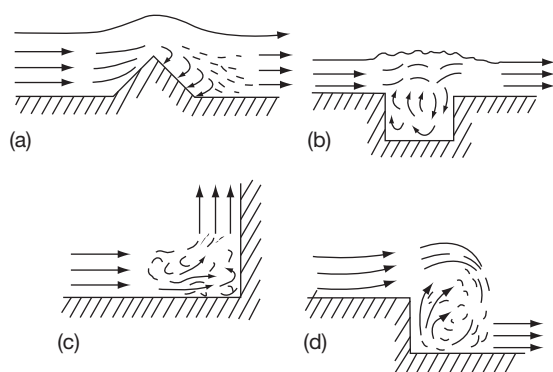


**Figure 13** Effects of (a) protuberances, (b) cavities and abrupt changes in (c) direction and (d) cross section in disturbing streamline flows to introduce local turbulences and associated erosion–corrosion risks. Adapted from Pludek, V. R. *Design and Corrosion Control*; Wiley: New York, 1976.

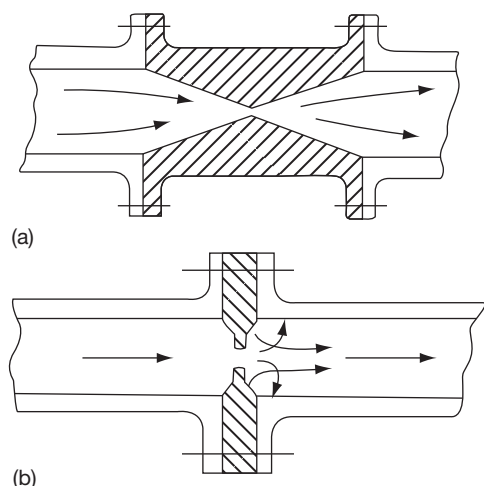


**Figure 14** Flows are disturbed less by (a) venturi tubes than (b) orifice plates. Adapted from Pludek, V. R. *Design and Corrosion Control*; Wiley: New York, 1976.

practice to locate it at a significant distance upstream or even downstream of the bend as shown schematically in **Figure 15**.

4. Surface condition can influence vulnerability to some forms of localized corrosion. It is particularly significant in relation to the effectiveness coatings that may be used to mitigate corrosion risk for which cleanliness and surface profile are typically specified using internationally recognized standards<sup>18</sup> for blast cleaning to white metal (SA3) and near white metal (SA 2½) as described in more detail in the chapters relating to coatings in this volume. Also important are good shapes and contours and removal of weld spatter, as illustrated in **Figure 16**, all of which should be specified for components that are to be coated.

#### 4.33.7 Mitigation of Galvanic Compatibility Risks

Inevitably, equipment and components are constructed in a variety of materials, and the potential for galvanic interactions needs to be addressed in the design. Although the risk of galvanic corrosion is confined mostly to mixed metal systems, specific ceramic materials such as carbon, graphite and silicon carbide that are used, for example, in heat exchange and jointing systems, have electrical conductivities that are high enough for their potential contributions to galvanic corrosion to require evaluation. Corrosion risk evaluations should address components exposed to external and internal environments, including where moisture films can arise from leaks, splashes or condensation such as at fastenings and welds and electrical earth bonding straps that are bolted, brazed, or welded to structural elements since lack of electrical continuity can have significant safety/instrumentation implications.

The various, published galvanic series of materials have been obtained in specific environments, mostly seawater, and are of limited use in assessing galvanic corrosion risks in other fluids that may have very different conductivities, tendencies to promote passivity on specific materials, etc. However, as a general rule, it is good design practice to avoid material combinations that are widely separated in such series, and in particular to avoid unfavorable area ratios involving small areas of active, anodic material such as fasteners or weld filler metals coupled to larger areas of noble, cathodic material.

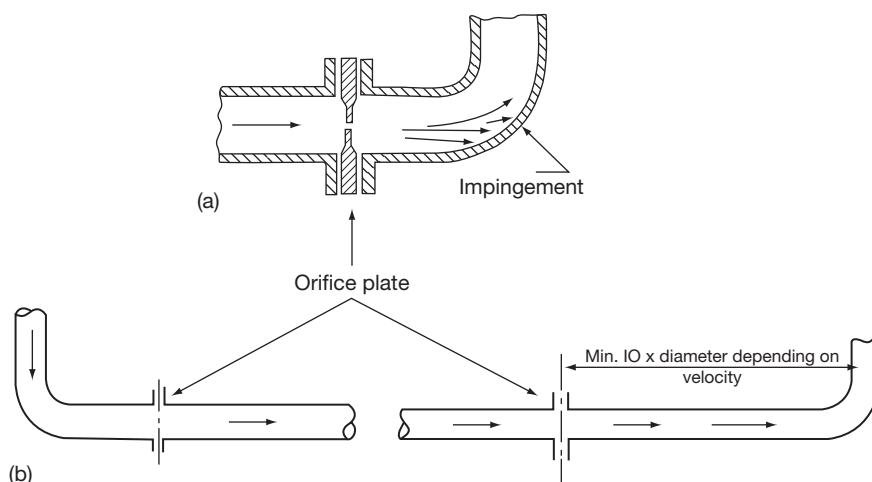


**Figure 15** Locating orifice plates and other flow disturbers too close to bends, as in (a), introduces additional risks that are mitigated by (b) downstream, or distant upstream locations. Adapted from Pludek, V. R. *Design and Corrosion Control*; Wiley: New York, 1976.

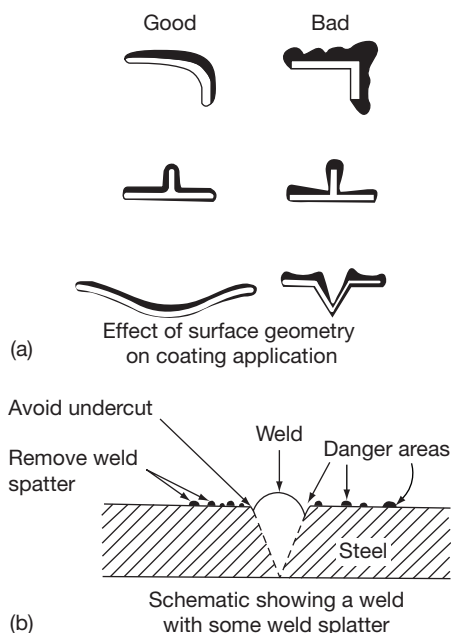


**Figure 16** Effective coating requires (a) smooth shapes and contours and (b) removal of weld spatter. Adapted from Pludek, V. R. *Design and Corrosion Control*; Wiley: New York, 1976.

Where combinations of materials that present galvanic corrosion risks are unavoidable, mitigation is provided by:

1. Isolation with dielectric sleeves and washers, as shown schematically in Figure 17. Where mitigation is dependent on electrical isolation, this may be frustrated by remote earthing through steel supports, pipe hangers, etc.

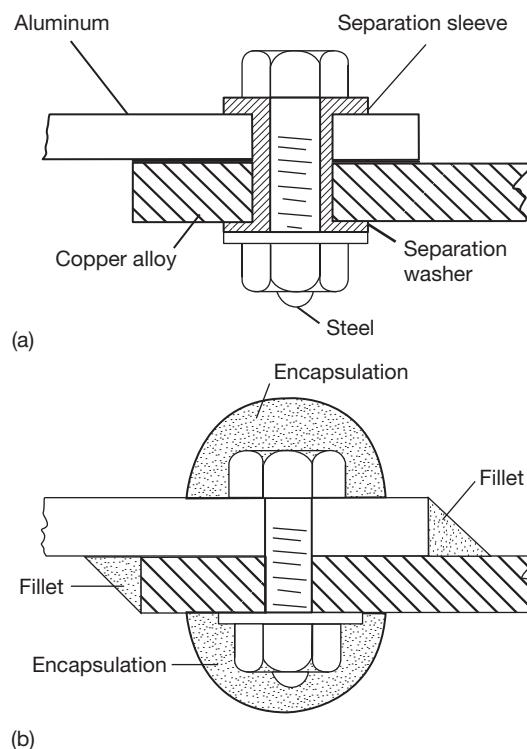


**Figure 17** Elimination of galvanic interactions in fasteners by (a) electrical isolation and (b) encapsulation. Adapted from Pludek, V. R. *Design and Corrosion Control*; Wiley: New York, 1976.

2. Encapsulation to exclude the environment, as shown schematically in Figure 17.
3. Coating, preferably of both couple members. If only one can be coated, it should be the noble, cathodic member.

4. Physical separation of couple members to attenuate galvanic interactions, such as at material breaks in piping systems where risks can be mitigated by using insulated spool pieces of appropriate length made from fiber reinforced plastic, or a coated, more noble couple member, as illustrated in Figure 18.
5. Cathodic protection, application of which overrides the spontaneous couple interactions providing protection to both, as in the protection by sacrificial anodes of the steel water boxes of sea-water coolers that would otherwise corrode rapidly due to galvanic coupling with the more noble tube materials.

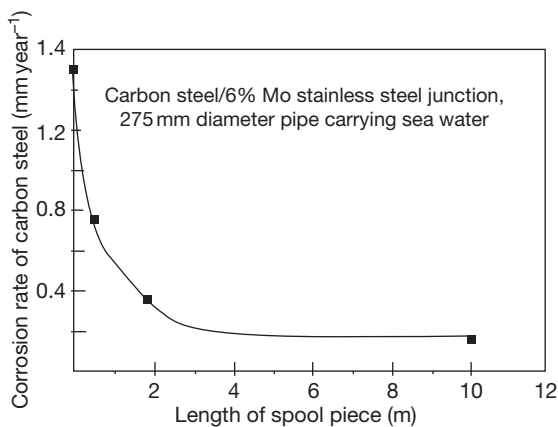


**Figure 18** Corrosion rate of carbon steel in seawater at a pipe junction with 6% Mo stainless steel as a function of the length of an intervening, insulating spool piece, adapted from Francis, R. *Galvanic Corrosion: A Practical Guide for Engineers*; NACE International: Houston, TX, 2000.

Francis's book is an excellent source of guidance on good practice for the mitigation of galvanic compatibility risks.<sup>19</sup>

#### 4.33.8 Management of Corrosion Risks within the Design Process

The previous sections have reviewed the major inputs/outputs needed to mitigate corrosion risks through attention to detailed thermomechanical and process design issues that may otherwise introduce uncertainty and consequential costs to a project. However, further risks arise from poor control of the management of the design process itself, in particular the effectiveness with which corrosion risks are addressed and appropriate mitigation procedures are implemented within the project design team.

Corrosion management processes and systems are reviewed in a separate chapter in this volume. In keeping with any management process, corrosion management relies on a series of steps using suitable systems, tools and teams, based on standard, international systems for quality, risk, and safety management, as summarized in Figure 19. Various tools are available for specific project stages, such as corrosion risk assessments, corrosion mitigation tactics, and regular formal reviews/audits of corrosion mitigation and management systems. Appropriately staffed, multidisciplinary corrosion teams need to be established and performance indicators adopted that have been developed to ensure that actions are carried out as recommended.

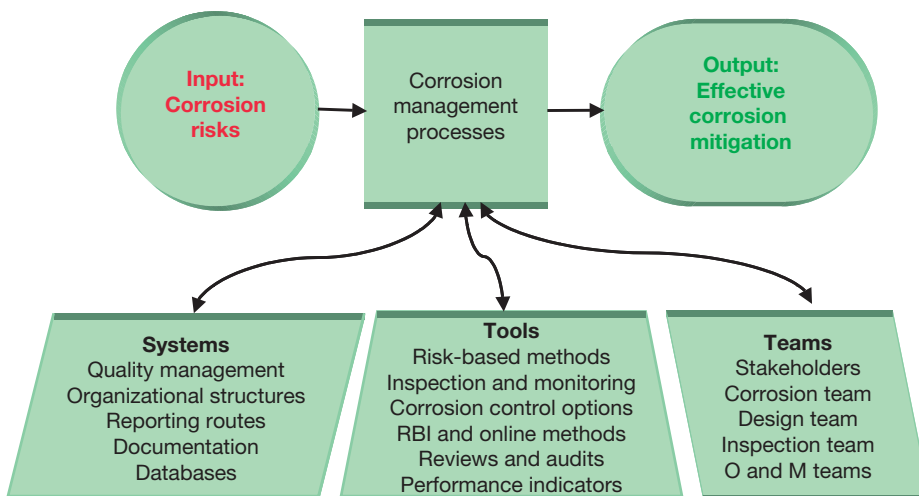


**Figure 19** The corrosion management process.

A corrosion management system should operate simultaneously at various levels, and include:

1. An overall management structure, process, and policy to deal with corrosion issues.
2. Procedures and documentation for engineers and managers with responsibility for corrosion as part of the corrosion strategy or plan.
3. Specification and use of clearly defined tactics based on proven corrosion mitigation practices.
4. Provision of means for the collection and assessment of equipment inspection and monitoring data as part of the operating, maintenance and safety procedures.
5. A system to audit corrosion related activities on a regular basis.

The management of corrosion risk mitigation during the design, procurement, and construction phases of a project requires a formal system that includes measurement and monitoring of the performance of the corrosion management aspects of the overall design system by defining:

1. The objectives of the corrosion control program, be it to reduce risks and/or costs, to promote life enhancement, to define end-of-life strategies, or whatever.
2. Nominated responsibility and accountability for the various components of the program.
3. External sources of acceptable corrosion data, its interpretation to provide trends, and the location and format of a corrosion database.
4. When corrective actions should be implemented, and who is responsible for actions on a day-to-day basis.
5. The duration of the program and when it will be updated.
6. A management-of-change procedure.

This leads to an obvious need for suitable organizational and reporting systems, operating through appropriate documentation and database systems, which provide evidence, for example, that:

1. design engineers are aware of potential corrosion risks associated with the proposed design;
2. advice has been obtained from qualified corrosion specialists where appropriate;
3. suitable corrosion control procedures have been introduced at an early stage in the design;
4. corrosion appraisals have taken place throughout the design process;
5. two or more of the appraisals during design are formal corrosion audits, the first to be undertaken

towards the end of the conceptual/early design stage and the second towards the end of the engineering design/detailing stage;

6. hold points for corrosion audits are introduced into quality plans at critical stages of design, manufacture, construction, installation, or application;
7. guidelines, specifications, and QA/QC procedures are available for the construction, operation, and maintenance phases;
8. plant and equipment items, including units and components, supplied by subcontractors have been subjected to appraisals and audits similar to those carried out for the major plant and equipment items.

In order to ensure that such systems perform effectively, they need to be reviewed and formally audited on a regular basis.<sup>20,21</sup> Performance should be assessed against agreed key performance indicators (KPIs), which for the corrosion team leader during the design process, might typically include:

1. ensuring that cost effective corrosion control is employed;
2. ensuring that appropriate corrosion risk assessments and sensitivity studies are conducted;
3. reviewing all corrosion related documentation;
4. reviewing corrosion related records to assess conformance and reporting out of compliance when necessary;
5. tracking specific procedures and processes to ensure compliance include competency of responsible individuals, departments and organizations and correct implementation, reporting and reaction;
6. ensuring that changes are implemented and incorporated into corrosion-relevant procedures and processes;
7. ensuring that new materials and corrosion control methods are evaluated.

The development and use of performance measurement/KPIs together with the use of regular reviews and audits of the corrosion management system using a formal and transparent framework should ensure that the management of corrosion risk mitigation becomes an integral and effective part of the overall design process.

In the conceptual and early design stages of a project the role of the design team involves:

1. assessment of the technical brief and initial engineering concept;
2. control of costs/budgets within overall economic constraints;

3. production of a technical solution for the project;
4. control of safety, health and environmental (SHE) risks within acceptable limit boundaries;
5. incorporation of corrosion mitigation to deliver the required equipment life.

Risk-based methods are now used routinely to evaluate financial and engineering uncertainties at this stage and are also applied to the evaluation of corrosion risks. They are iterative processes using well-defined steps to support decision-making by providing greater insight into risks and their consequences. They can be used not only to identify undesired and/or unexpected outcomes but also to assess opportunities provided by novel or modified designs. In the conceptual and early design stages, corrosion appraisals would typically include:

1. proposed design and type of construction of equipment items;
2. environments – internal and external, transient and steady state;
3. likely materials;
4. significant corrosion risks and associated SHE and/or financial consequences;
5. proposed corrosion risk mitigation strategies such as protective coatings, corrosion inhibition and anodic or cathodic protection.

The assessment of environments and selection of likely materials are described in the separate chapter on materials selection for corrosion resistance in this volume. Corrosion risks to equipment items would normally be assessed using a qualitative risk analysis (Level 1) that provides a simple ranking of equipment or, in the case of items at higher risk from corrosion, a more rigorous evaluation using a semiquantitative risk analysis (Level 2), a more accurate prioritization that retains vital inputs of a Level 3 analysis but with simplifying assumptions. Only at a later design stage or with highly critical items would a quantitative corrosion risk analysis (Level 3) be employed, which is an in-depth study including assessment of reliability, financial and limited environmental issues. Level 2/3 corrosion risk assessments often employ a risk matrix approach where the likelihood of corrosion is compared against the consequences. In the case of complex installations such as chemical and petrochemical plant, where risk-based inspection is to be employed in service, the assessment of equipment at this stage provides the basis for the initial specification of inspection intervals for equipment.

One of the tools used routinely and effectively in design projects is a series of hold points where key risks and their mitigation are addressed and reviewed/audited by appropriate procedures, as in the case of HAZOP studies of SHE issues in the process industries, or in third-party reviews of major civil engineering designs. The aim is to manage not only technical issues and ensure compliance with codes and standards but also to manage human responses and actions such as ensuring that any changes are checked and approved by suitably experienced specialists as part of a management of change procedure. These overarching risk management procedures are very effective vehicles for the management of corrosion risks and their mitigation.

At the engineering design/detailing stages, corrosion risks rarely arise from inadequate basic design or initial materials selection, but from deficiencies in the detailed design or poor provision of information for certain aspects of the construction, operation and maintenance of the equipment. These are essentially quality control issues that should also be addressed by appropriate reviews/audits of the design. Data sheets and drawings are best addressed with checklists that cover the detailed issues summarized in [Figure 2](#). The compilation of such lists will depend on the industry and the type of project. For example, API 570<sup>22</sup> is a qualitative risk analysis approach used in the petroleum industry for guidance on areas/locations subject to corrosion damage and the need for inspection. It also identifies specific features that are susceptible to high rates of corrosion attack or cracking which require attention during design such as injection points, deadlegs, surfaces beneath insulation, linings and deposits, etc. Another publication<sup>21</sup> compiled by the UK offshore oil/gas industry addresses the impact of corrosion on integrity issues in existing facilities, in particular the management of external marine corrosion on support structures, walkways, cable trays, etc. and it provides many illustrations of typical damage which are instructive to designers of new facilities.

Sufficient information must be provided in the final specifications and drawings to enable the development of plans for construction, fabrication and manufacture of all items and components. The final reviews/audits of the detailed engineering design may require modifications or revisions and should anticipate that corrosion control in completed facilities can be adversely affected by poor workmanship and site damage. These effects can be



minimized by correct supervision and inspection based on frequent QA/QC reviews of all aspects of construction and commissioning as part of the design. These checks and inspections should be specified in the final design as to be carried out on a regular basis as part of organized appraisals and must include agreed reporting procedures and means of implementing corrective actions to minimize future problems.

It is important that recommendations and specifications with regard to corrosion mitigation should not be negated during the construction phase of a project. The contractor typically undertakes procurement of construction materials and equipment, vendor assessment and commissioning of associated plants. The detailed design stage corrosion audit should have already addressed those aspects associated with required reliability, maintainability and ease of construction as prescribed in detail in the contract documents and specifications. The aim should be to ensure that procedures used during manufacture and construction do not jeopardize the longer term corrosion control requirements of the design. The overall priority must be with the project life cycle and associated SHE issues and not with minimizing construction time or costs. Some typical examples of such issues are as follows:

1. The shape of items should not be changed in a manner that might reintroduce corrosion risks.
2. Installed pipework should be self-cleansing to prevent deposit build-up (minimum velocity) and self draining to prevent pooling during shutdown.
3. Bend radii, changes of section, etc. should be as per design to mitigate erosion corrosion risks.
4. Specified impingement/wear plates should be installed.
5. Adequate access for inspection and maintenance should be provided.
6. Chemical cleaning and passivation procedures should be undertaken in strict compliance with specification.
7. Shapes, contours, surface preparation, and cleaning should be as per specification on surfaces that are to be coated.
8. Weld spatter should be removed and weld protrusions ground to specification.

In conclusion, problems often occur in operation because of failure to apply good management practices during the design process to the deployment of good technical practices, many of which have been codified in industry standards, recommended practices and guidelines. The corrosion management

practices described in this section should do much to improve the deployment of resources to achieve project design objectives and the implementation of specific solutions to maximize the effectiveness of corrosion mitigation tactics.

## References

1. Ashby, M. F. *Materials Selection in Mechanical Design*; Butterworth Heinemann: Oxford, 2005.
2. Kennedy, I. Design and specification for reliability and maintainability; Presented at National Tribology Course on Reducing Plant and Equipment Life Cycle Costs; 24 November 1994.
3. Pludek, V. R. *Design and Corrosion Control*; Wiley: New York, 1976.
4. Landrum, R. J. *Fundamentals of Designing for Corrosion Control*; National Association of Corrosion Engineers: Houston, Texas, 1989.
5. Ohtsu, T.; Miyazawa, M. Corrosion 2007; NACE International: Houston, Texas, 2007; Paper 07266.
6. Brubaker, S. K. In *ASM Handbook Vol. 13C Corrosion: Environments and Industries*; ASM International: Materials Park, Ohio, 2006; pp 659–667.
7. Cox, W.; Huijbregts, W.; Leferink, R. *ASM Handbook Vol. 13C Corrosion: Environments and Industries*; ASM International: Materials Park, Ohio, 2006; pp 491–496.
8. Crude Unit Overhead Corrosion Control; Refining Industry Corrosion Information Compilation Series; NACE International: Houston, Texas, 2001.
9. Ahluwalia, H. *ASM Handbook Vol. 13C Corrosion: Environments and Industries*; ASM International: Materials Park, Ohio, 2006; pp 654–658.
10. Mann, G. M. W. *Br. Corros. J.* **1977**, *12*, 6–14.
11. Ross, T. K. *Br. Corros. J.* **1967**, *2*, 131–142.
12. Claxton, R. A.; Lupton, A. *Weld. Metal Fabricat. (UK)* **1991**, *59*, 541–544.
13. Ni, H.; Ling, X.; Peng, W. *J. Chin. Soc. Corros. Prot.* **2005**, *25*, 152–156.
14. Hammersley, G.; Hackel, L. A.; Harris, F. *Optics Lasers Eng.* **2000**, *34*, 327–337.
15. Copper Nickel Fabrication; Publication 139; Copper Development Association, 1999.
16. *Materials Selector for Hazardous Chemicals Vol. 1: Concentrated Sulphuric Acid and Oleum*, 2nd edn.; MTI Publication MS-1, Materials Technology Institute of the Process Industries Inc.: St. Louis, Missouri, 2005.
17. *API Recommended Practice RP14E: Design and Installation of Offshore Production Platform Piping Systems*; American Petroleum Institute: Washington, 1991.
18. SS-EN ISO 8501-1:2007: Preparation of steel substrates before application of paints and related products – Visual assessment of surface cleanliness; Swedish Standards Institute: Stockholm, 2007.
19. Francis, R. *Galvanic Corrosion: A Practical Guide for Engineers*; NACE International: Houston, Texas, 2000.
20. Guidance for Corrosion Management in Oil and Gas Production and Processing; Energy Institute: London, May 2008.
21. OTO 2001/44: Review of corrosion management for offshore oil and gas processing; Health and Safety Executive, 2001.
22. API Document 570: Inspection, repair, alteration, and rerating of in-service piping systems; American Petroleum Institute: Washington, 1998.

## 4.34 Risk Based Inspection

### P. Horrocks

ESR Technology, 410 The Quadrant, Birchwood Park, Warrington, WA3 6FW, UK

### S. Adair

P.O. Box 2132, Mossel Bay, 6500, Republic of South Africa

© 2010 Elsevier B.V. All rights reserved.

<b>4.34.1</b>	<b>Introduction</b>	<b>3084</b>
4.34.1.1	What is Risk?	3085
4.34.1.2	Who is Responsible for the Management of Risk?	3086
4.34.1.3	The Structure of a Risk Management Program	3086
4.34.1.4	The Role of RBI in Asset Integrity Management	3086
4.34.1.5	Types of Risk Assessment	3087
4.34.1.5.1	Qualitative RBI	3087
4.34.1.5.2	Quantitative RBI	3088
4.34.1.5.3	Semiquantitative RBI	3089
4.34.1.6	The Matrix	3089
4.34.1.7	Current International Practice	3091
4.34.1.7.1	API 580 and 581	3091
4.34.1.7.2	Common practice	3092
4.34.1.8	Creating the Inspection Plan – Assigning Inspections from Risk Assessment	3092
4.34.1.8.1	Selection of appropriate inspection techniques	3092
4.34.1.8.2	Selecting the interval	3092
4.34.1.9	Key Success Factors for RBI	3093
4.34.1.9.1	RBI practitioner	3093
4.34.1.9.2	Operator	3093
4.34.1.9.3	Regulating authority	3094
4.34.1.9.4	Summary	3094
4.34.1.9.5	Accurate likelihood modeling	3094
4.34.1.9.6	Application of confidence criteria	3095
4.34.1.9.7	Realistic consequence modeling	3096
4.34.1.9.8	Intelligent interpretation of inspection findings	3097
4.34.1.10	Case Study 1: Corrosion Rate Trending	3097
4.34.1.11	Case Study 2: Use of Robust RBI to Enhance Understanding of Inspection Data	3098
4.34.1.12	Case Study 3: Use of Robust RBI to Understand Plant Wide Integrity from Restricted Inspection Data	3098
4.34.1.12.1	Efficient capture of process or hardware modifications	3099
4.34.1.13	Major Challenges for RBI	3100
4.34.1.14	Future Developments	3101
<b>References</b>		<b>3101</b>

### Abbreviations

**AIM** Asset integrity management

**ALARP** As low as reasonably practicable

**HAZOP** Hazard and operability study

**RBI** Risk-based inspection

**TML** Thickness measurement location

**UK HSE** United Kingdom Health & Safety Executive

**UTW** Ultrasonic wall thickness measurement

### 4.34.1 Introduction

Until fairly recently, the structural integrity of most engineered structures has been assured by two factors:

- Design in accordance with codes or rules incorporating empirical safety factors.
- In-service inspection to provide assurance that no accidental or unanticipated damage has occurred.

However, it is only prudent to accept that operational loads may vary beyond design levels, and material degradation may be greater than anticipated. The safety factors used at the design stage may not, therefore, guarantee through-life structural integrity. Hence, periodic inspection is also carried out to determine the actual levels of damage, and to check the adequacy of the design loads and resistance values.

There is a widely held view that prior to the emergence of risk-based inspection (RBI) as a process for planning inspections, specifically of pressure containing equipment, all inspection activity was conducted on a time basis, that is, at regular set intervals. These intervals would vary according to the type of equipment, its service, and any specific national regulations that applied. This, of course, is generally not entirely true!

RBI has been practiced by engineers responsible for integrity management since the very first time an inspection budget, or the time allowed for inspection, did not cover the entire plant. Engineers were forced into a position where they had to decide between inspecting one thing or another. In almost all cases, that decision would be made on the basis of a perceived risk. In this case, the specific risk of concern is that of loss of integrity due to structural failure. RBI as we know it today is a means of formalizing that decision process such that it becomes consistent, transparent, and fully auditable.

Both design and inspection strategies must take account of the risk of structural failure: that is, both the probability of failure and its consequences need to be considered. Using traditional approaches to inspection planning, risk tends only to be considered implicitly and is not quantified in an auditable manner. There is thus real concern that high-risk and low-risk areas will not be clearly identified. This may then mean that low-risk areas are inspected to an excessively high level (leading to needlessly high inspection costs), while high-risk areas may not all be afforded sufficient attention and priority. Without the explicit and rigorous consideration of risk, it may not therefore be possible to demonstrate that the structural integrity of the plant has been satisfactorily characterized.

An inspection strategy based on risk avoids the inadequacies of the traditional approach. The concept of risk takes into account, not only the probability, but also the consequences of structural failure. These may encompass consequences in terms of lost profits, repair and compliance costs, human casualties, and environmental clean up costs. Such a strategy

ensures that inspection effort is targeted appropriately to optimize costs and benefits, and provides an auditable demonstration that this has been done with due diligence.

With such an emergent technology, there are many ways in which the objectives can be achieved. The methods available vary in cost, quality, and detail and operators can experience difficulty in selecting a methodology which is fit-for-purpose. This review aims to summarize the concepts, technology, and currently available approaches and the advantages and disadvantages of each.

#### 4.34.1.1 What is Risk?

In order to be clear about what RBI really is, it is first necessary to gain an understanding about what 'risk' is in this context. The term is used in common parlance to describe a range of features of a real or postulated event. For example, 'risk' may be used to indicate the likelihood of an event or perhaps even to describe the consequences of the same event. If used correctly the term should describe both. The situation is further complicated by the use of the term 'hazard' as applied in hazard and operability studies (HAZOPs). 'Hazard' and 'risk' are used interchangeably in everyday vocabulary.

The UK Health & Safety Executive has sought to make a conceptual distinction between a 'hazard' and a 'risk' by describing a 'hazard' as<sup>1</sup>

the potential for harm arising from an intrinsic property or disposition of something to cause detriment

and 'risk' as

the chance that someone or something that is valued will be adversely affected in a stipulated way by the hazard.

Accepting this distinction it follows that risk in the context of RBI is the product of the chances and consequences of a structural failure. It also follows that the management of risk in this context has three components:

- hazards must be identified;
- risks they give rise to should be assessed;
- appropriate control measures should be introduced to address the risks.

Additionally, and because of the way in which we define risk, it is both convenient and commonplace to divide risk into three categories:

- safety risk, that is, risks to people's lives and health;
- environmental risk, that is, risk to the environment, for example, pollution, effects on marine life, etc.;
- business or economic risk, that is, risk of lost production/revenue.

These are all the things that we value and could be affected adversely if structural failure occurred.

#### 4.34.1.2 Who is Responsible for the Management of Risk?

The public accepts that we need to continue to operate hazardous plant and equipment in order to manufacture products which are a vital part of modern life, for example, gasoline, diesel, plastics, pharmaceuticals, etc. However, as part of their review of this subject within the United Kingdom,<sup>1</sup> the Health & Safety Executive observed that this acceptance is moderated by expectations that:

- those responsible for the hazards should ensure that adequate measures are taken to protect people from the harmful consequences that may arise from such hazards; and
- the State should be proactive in ensuring that its arrangements for securing the protection of people from risks are adequate and up to date as distinct from reacting to events; and that those arrangements should address, as necessary, the concerns to which the hazards give rise.

This clearly puts responsibility for management of risks into the hands of organizations who own and operate hazardous installations. It is this line of thinking that has led many parts of the world to the conclusion that regulations need to reflect responsibility for risk management. As such, there has been a move away from prescriptive time-based inspection (inspection being a risk management activity) to inspections based on an understanding of the level of risk represented by each part of any hazardous installation.

#### 4.34.1.3 The Structure of a Risk Management Program

The UK Health & Safety Executive's report on how it comes to decisions on risks<sup>1</sup> outlines six stages in the decision-making process:

- deciding whether the issue is primarily one that can impact safety and health;
- defining and characterizing the issue;

- examining options available for addressing the issue, and their merits;
- adopting a particular course of action for addressing the issue efficiently and in good time, informed by the findings of the second and third points above and in the expectation that as far as possible it will be supported by stakeholders;
- implementing the decisions;
- evaluating effectiveness of actions taken and revisiting decisions and their implementation if necessary.

Figure 1<sup>2</sup> illustrates the process of RBI.

It is clear from Figure 1 that an RBI process encompasses all the aspects of a risk management program as defined above. The focus of risk management is also clear, that is, asset integrity.

#### 4.34.1.4 The Role of RBI in Asset Integrity Management

Hazard management of large industrial facilities is a complex process which is active at each of the six key stages in the asset life-cycle (i.e., design, construction and hook-up, commissioning, operation, modification, and decommissioning).<sup>3</sup> The primary process in hazard management is considered to be asset integrity assurance.

Asset integrity management (AIM) of a large industrial facility encompasses three essential elements, as shown in Figure 2.

These elements may be defined as follows:

*Mechanical integrity* is the ability of the asset to withstand the design loadings (i.e., design pressure/stress, design temperature, etc.). It is primarily concerned with structural integrity, pressure containment, and leak tightness, and focuses on pressurized equipment, piping systems, and major structures.

*Functional integrity* is the ability of the asset to perform its required function effectively and safely. It is primarily concerned with the reliability of safety critical elements such as emergency shutdown systems, critical process control systems, and hazard mitigation systems (e.g., gas/fire detection systems, fire fighting systems, etc.).

*Operational integrity* is the ability of the asset personnel to operate the facility safely and effectively. It is primarily concerned with human factors such as competency, management systems, reporting systems, anomaly management, etc.

Several risk-based methods are employed in hazard management of large complex plants. RBI is the use of risk assessment to formulate and prioritize inspections

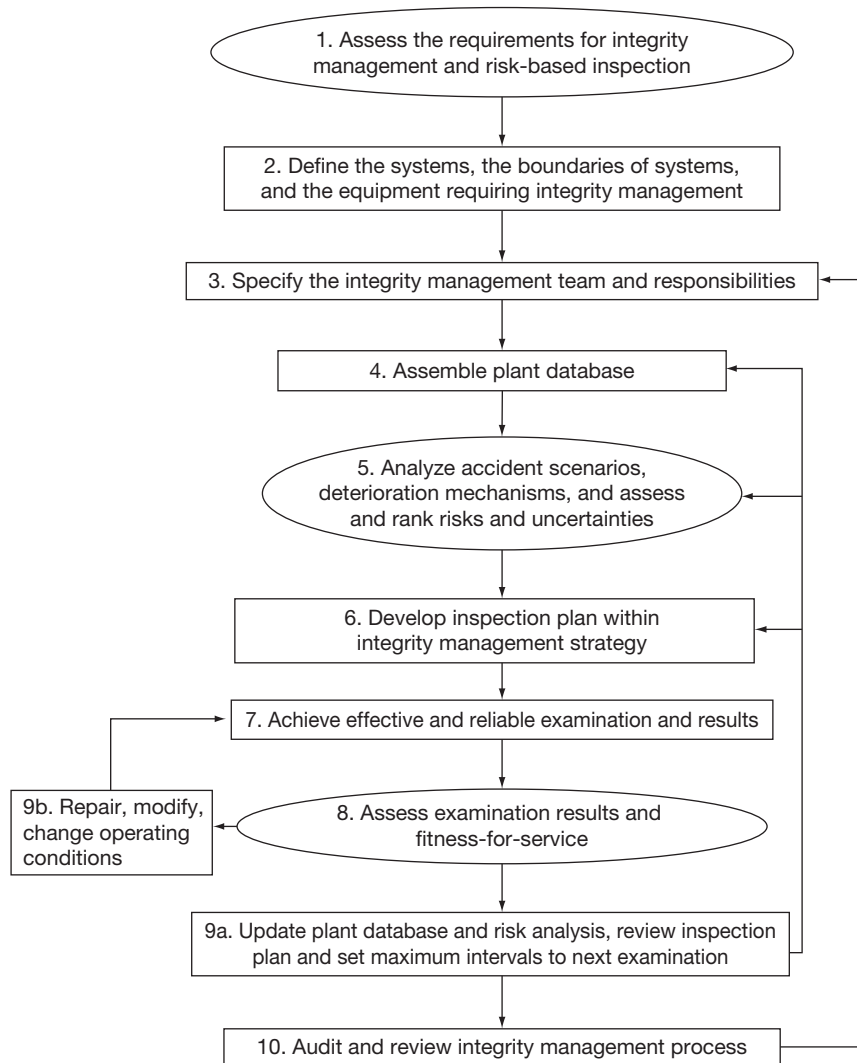


**Figure 1** Risk-based inspection (RBI) process.

of pressure vessels, piping systems, and pressure safety valves. Its primary concern is mechanical integrity. **Figure 3** shows the role of RBI within a typical AIM system for an oil and gas production facility.

#### 4.34.1.5 Types of Risk Assessment

Risk assessment methodologies may be defined in terms of the nature of the assessment performed. Three terms in common usage are qualitative, semi-quantitative, and quantitative risk assessment.

These three assessment techniques are broadly aligned with three different strategies in the performance of risk evaluation, which include expert judgment, rule-based analysis, and quantitative calculation.

##### 4.34.1.5.1 Qualitative RBI

Qualitative RBI is based on the results from a qualitative risk assessment, which is usually executed through expert judgment. Normally this would employ an expert, multidisciplinary team, with representatives from all relevant engineering disciplines, including materials/corrosion, mechanical, process, operations, maintenance, and safety engineering. Risk assessment would be performed through discussion, with the team agreeing on the likelihood of failure and the resulting consequence.

Expert judgment can be the result of informal or formal processes.<sup>4</sup> It is necessary to distinguish between formal, expert judgment and informal expert judgment processes – the latter being the way expert judgment has traditionally been used during RBI



assessments. Expert judgment has been used in analysis and assessments in informal ways, through the expert's implicit and undocumented reasoning, inferences, and scientific knowledge.

The advantages of this risk assessment technique are that it is relatively easy to perform and can incorporate lessons from the plant experience gained by experts present on the team.

More recent formal uses of expert judgment exist that are explicit, structured, and well documented. They aim to bring out assumptions and reasoning that are at the base of a judgment, to quantify and document it so that others can appraise it. Although

formal judgment can be resource consuming (in terms of cost and time) and appear less flexible and creative than informal judgment, it brings out a deeper understanding of the issues, drawing out diverse opinions. This can reveal areas of disagreement or agreement with increased possibility of a solution. Furthermore, formal judgment gives access to all aspects of the analysis (assumptions, models, data, expert's thinking) and provides the possibility for others to review the process of judgment.<sup>4</sup> One UK HSE study that examined RBI in practice<sup>5</sup> found a lack of transparency in parts of the RBI decision making process indicative of informal expert judgment. It seems therefore that the natural development of qualitative RBI assessment will be to move to a formalized expert judgment method in the future.

The main disadvantages of the technique in both its informal and formal modes are inconsistency (less so for formal expert judgment), cost, and speed. As each item needs to be discussed in detail, assessments are never rapid and this has the effect of pushing up costs simply because of the consumption of large volumes of expert's time. It should also be noted that the next time the RBI team is assembled in order to conduct the review process, any change to the team line-up introduces another element of variability that can affect the outcome of the assessment.

#### 4.34.1.5.2 Quantitative RBI

Quantitative RBI is based upon a quantitative risk assessment. It results in fully quantified absolute failure probabilities and consequences specific to the

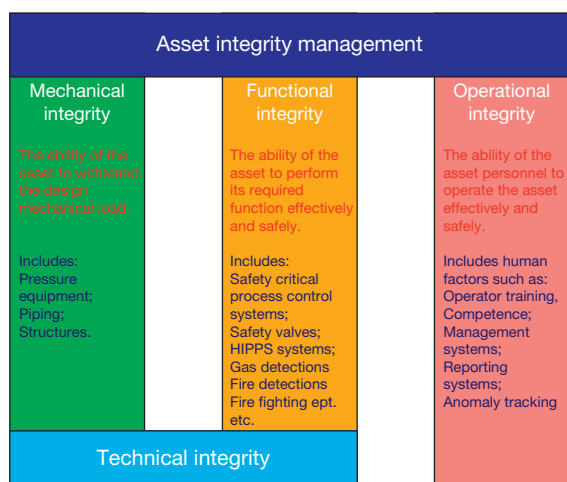


Figure 2 Essential elements in AIM.

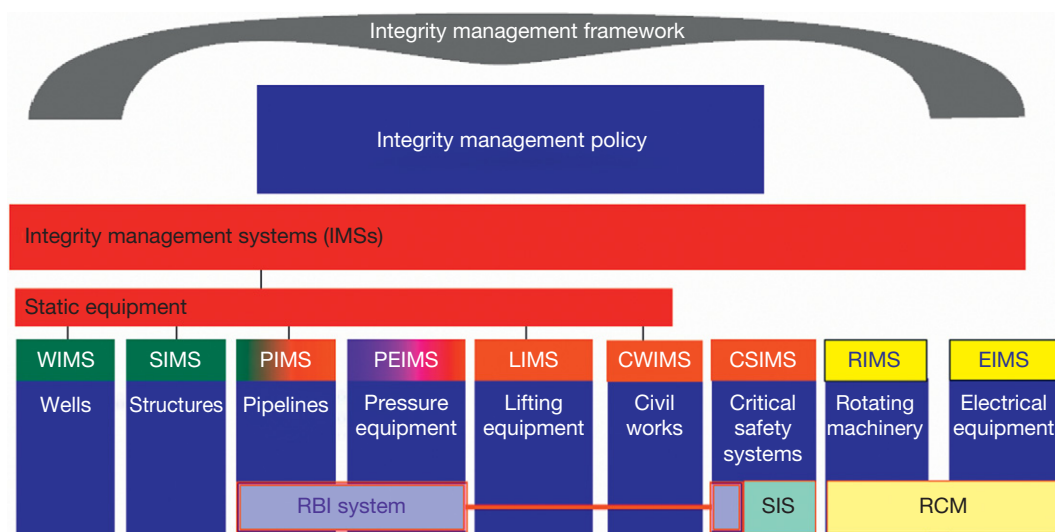


Figure 3 The RBI in the asset integrity framework.

item under consideration and using only the attributes of that specific item.

Robust consequence of failure calculations should consider the influence of each chemical constituent of each process fluid. The assessment should model the dispersion of each chemical constituent, and assess its contribution to failure scenarios such as explosion, flash fire, pool fire, toxic release, over-pressurization, pollution, etc.

Robust likelihood of failure calculations should include accurate predictive, often probabilistic modeling of all damage mechanisms, regardless of their 'perceived' likelihood.

The advantage of the quantitative method of risk assessment is accuracy; the major disadvantage is that the process is extremely slow and has extremely challenging data requirements.

There are a number of reportedly 'quantitative' methodologies available, including the API level III assessment.<sup>6</sup> However, all these techniques fall short of a truly fully quantitative assessment. First, they normally rationalize the process fluid into a 'representative fluid' which, necessarily, does not represent all chemical constituents present. For instance, API 581 allows for 17 different representative fluids,<sup>7</sup> which includes C<sub>9</sub>–C<sub>12</sub>, C<sub>13</sub>–C<sub>16</sub>, C<sub>17</sub>–C<sub>25</sub>, H<sub>2</sub>, and H<sub>2</sub>S as separate 'representative fluids', but never considers combinations of the same. Clearly, this could be a significant limitation. For example, in a refinery hydroprocessor plant, where the process stream consists of 50% H<sub>2</sub>, with the balance being hydrocarbons and H<sub>2</sub>S, the calculations would only quantify 50% of the actual release.

Secondly, many 'fully quantitative' techniques only quantify damage mechanisms that are selected for assessment in a preassessment phase, which is normally qualitative in nature. Thus, the assessment is selectively quantitative, rather than fully quantitative, and is reliant upon the expert correctly identifying appropriate damage mechanisms to assess.

#### 4.34.1.5.3 Semiquantitative RBI

Semiquantitative RBI employs simplified quantitative assessment models to derive pragmatic risk ranking for components within a pressure system. It should be noted that the term 'semiquantitative' refers to an assessment methodology that seeks to quantify all deterioration mechanisms and consequence scenarios, albeit in a simplified manner that requires less data than a fully quantitative methodology. Semiquantitative RBI does not include systems which quantify some aspects and use qualitative judgment for other aspects.

#### 4.34.1.6 The Matrix

At this point in the review, having just discussed the qualitative, semiquantitative, and quantitative methods of assessment, it is appropriate to examine the means by which the results of the risk assessment phase of an RBI study are presented, that is, the risk matrix.

The matrix has been the cause of much debate since RBI was first used. Questions of what size it should be, that is,  $3 \times 3$ ,  $4 \times 4$ ,  $4 \times 5$ ,  $5 \times 5$ , and whether or not it should be 'skewed' are often the subject of discussion.

The answers to these questions are intrinsically linked to two features of RBI:

- which methodology you choose;
- the data with which you have to work.

First, consider fully quantitative RBI. **Figure 4** presents the type of results you might expect to generate.

Each red dot represents an individual assessment for a uniquely identifiable item of equipment or piping. Three regions are clearly marked.

- *Acceptable*: The evaluated risks are acceptable.
- *ALARP*: The identified risks should be maintained as low as reasonably practicable. These risks need active risk management, for example, inspections, monitoring, maintenance, etc.
- *Unacceptable*: These risks cannot be tolerated. The owner of the risk should either introduce engineered mitigations or redesign the equipment to mitigate the risk.

Failure probability is expressed as a number between zero and one and is often the result of very detailed probabilistic assessment taking into account details of the various potential failure modes and the

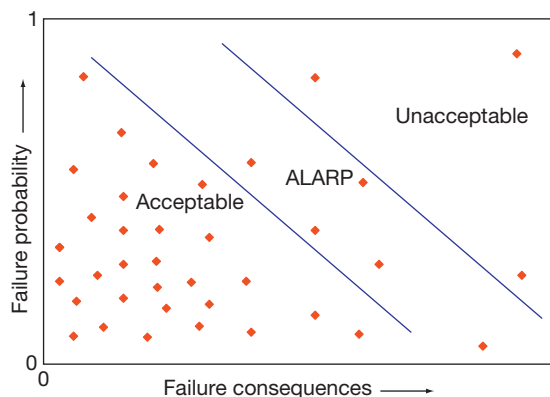


**Figure 4** Illustration of results from a quantitative RBI study.

material/structural response at every stage of the degradation process. Failure consequences are often expressed in currency terms but may also include expected number of fatalities or injuries caused by a failure. Full dispersion, blast and fire modeling are required, together with financial modeling and environmental impact assessment for every postulated failure.

The amount and quality of data required to conduct this type of assessment is prohibitive in terms of normal budgets available. The solution to this problem is to apply an approximation to the fully quantitative methodology. The approximation is the matrix approach. **Figure 5** illustrates the concept of a matrix superimposed on fully quantitative results. In this case, a simple  $3 \times 3$  matrix is shown.

It is immediately apparent that the matrix approach seeks to define broad bands of failure probability and consequences into which individual risks can be assigned. This can be done qualitatively by expert judgment as discussed above, by simply assigning a high, medium, or low score to each identified risk. Alternatively, rules can be used to assign the categories in a semiquantitative manner.

The  $3 \times 3$  matrix has a couple of significant disadvantages.

- The resolution is not sufficient to deliver improvements in inspection planning that can be achieved by using narrower bands, that is, the bands are too wide to distinguish between equipment that may need inspection every 10 years and that which requires it every 5 years. This, for a large inventory of equipment, can have a major impact on inspection costs.
- It is difficult to justify 'skewing' a  $3 \times 3$  matrix. Often, these matrices are skewed to reflect the understandable desire to inspect equipment with high consequences of failure even if the probability is low.

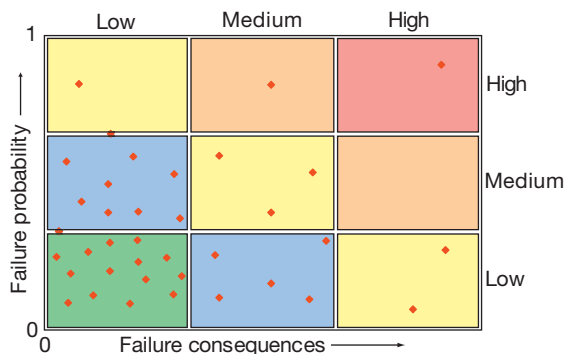


**Figure 5**  $3 \times 3$  risk matrix.

Since the publication of API 580 and 581 it has been normal to consider the use of a  $5 \times 5$  matrix as shown in **Figure 6**.

This dimension of matrix has a number of advantages.

- The resolution is as high as reasonably possible for the use of expert judgment allowing qualitative RBI to be chosen if appropriate.
- The number of bands is sufficient, but not too many, to allow sensible construction of rules for semiquantitative analysis using commonly available data, that is, that from process flow diagrams, piping and instrument diagrams, material selection reports, heat and material balance data, and equipment drawings.
- It is relatively easy to justify a degree of skewing to this matrix. The highest risk level extends to lower failure probabilities to place emphasis on failure consequences. This skewing process also goes some way to mitigating uncertainty inherent in the RBI analysis (qualitative and semiquantitative), particularly in the degree of knowledge or modeling assumptions used to predict failure modes.

There are other variants to the matrix size, for example,  $4 \times 5$  (four levels of failure probability and five of failure consequences), but all are essentially approximations to the fully quantitative approach designed to reach a useful conclusion without prohibitive data requirements. In choosing an approach and/or a matrix size, practitioners should consider the following:

- *Resolution*: will the resolution I am using deliver distinctions that I can use in planning inspections to better target risks within the inspection budget? Can the resolution I want be justified given the data/information I have to do the assessment?
- *Auditability*: can my approach be fully audited, that is, can I justify the decisions made in the process?
- *Uncertainty*: what are the uncertainties in my assessments and where are they? How do I mitigate these uncertainties? Importantly, do any of the uncertainties introduce optimism into the risk assessment?
- *Practicality*: can I conduct the level of assessment I want to with the resources I have?
- *Reproducibility*: if I did the analysis again next week, would I get the same result? If not, why and how can I reduce the effects of this variation?
- *Cost*: what are the real costs of doing this assessment and what benefits can it achieve?
- *Time*: can I complete this assessment in a reasonable timeframe?

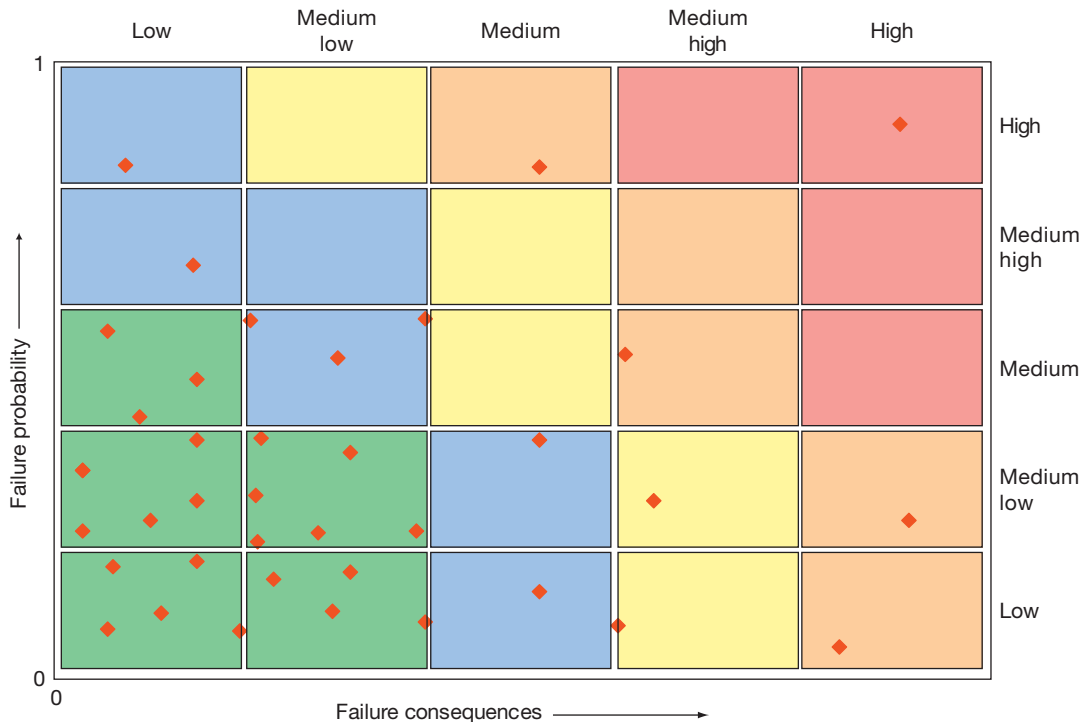


**Figure 6** 5 × 5 RBI matrix.

#### 4.34.1.7 Current International Practice

The first point to note when considering international practice of RBI is that there are presently no national or international standards that cover the technology of planning inspections on the basis of risk. There are various standards that cover implementation of inspections on plant, but none of these address the manner in which RBI should be carried out.

Two publications that have gained prominence in RBI are API publication 581<sup>6</sup> and API recommended practice 580.<sup>8</sup> In essence, API RP 580 describes the necessary features of an RBI procedure, providing guidance on development of an RBI program for static equipment and piping in oil and gas industry service. API 581 is somewhat different in that it builds on API RP 580 to produce a methodology which may be followed by anyone wishing to conduct RBI on such equipment. It is not however, a standard that requires 'compliance' in a legal sense.

##### 4.34.1.7.1 API 580 and 581

API 580 was initially developed over 5 years by a group of more than 22 international refining, chemical, and exploration companies.<sup>9</sup> The group comprised mechanical engineers, materials/corrosion engineers,

NDE specialists, and individuals responsible for mechanical integrity and inspection programming on operating plant.

The document is very clear that it is a guidance document and not intended to:

- supplant other practices that have proven satisfactory;
- discourage innovation and originality in inspection;
- be a substitute for the judgment of a responsible, qualified inspector, or engineer; and
- be construed as a code of rules, regulations, or minimum safe practices.

The document is a supplement to other API publications, codes, and standards on plant inspection. It requires RBI assessment to systematically evaluate both failure probability and consequences based on all forms of deterioration that could reasonably be expected to affect equipment in its particular service.

One particularly important element of API 580 is that it sets out what RBI will not do, that is, it will not compensate for:

- inaccurate or missing information required in assessments;

- inadequate design or faults in equipment fabrication or installation;
- operation of equipment outside the acceptable design envelope;
- not effectively executing the inspection plans;
- a lack of qualified personnel or the absence of required disciplines in the assessment process; and
- a lack of sound engineering or operational judgment.

API 580 also requires that RBI assessment should be documented in such a way that it allows recreation and updating of the assessments by people not involved in the original assessment. In other words, the assessments should be fully auditable and justifications are required for all decisions and judgments made.

API 581 is a development of API 580 insofar as it provides a recommended practice for the practical application of the principles described in API 580. It should be noted, however, that API 581 is a 'recommended' practice and does not claim to be the only approach that can satisfactorily achieve the aims set out in API 580. This distinction has given rise to a number of subtly different approaches in common use, many of which are housed in software applications. Virtually all RBI software claims API 580 compliance.<sup>10</sup> Only software produced by API itself is compliant with API 581 in every respect.<sup>10</sup>

#### **4.34.1.7.2 Common practice**

Besides API 581, there are many RBI approaches in common use. Many larger companies have chosen to develop 'in-house' approaches and associated software to achieve consistency across their total assets worldwide. Beyond the larger operators, there are many independent RBI applications available. These vary in cost and quality but all can reasonably claim to be compliant with API 580 as can the company specific approaches.

### **4.34.1.8 Creating the Inspection Plan – Assigning Inspections from Risk Assessment**

#### **4.34.1.8.1 Selection of appropriate inspection techniques**

RBI is ultimately concerned with optimizing inspection activity. Part of this process is the selection of appropriate inspection techniques. In the modern world, there are many new and innovative inspection techniques available, and this complicates the inspection method selection process.

The overriding principle in selection of an inspection technique is that the technique should be able to

detect the type of damage identified by the RBI assessment. This should be a matter of record, that is, the technique should be documented to the extent that it can be shown to be capable of relevant damage detection in a robust and reliable manner when applied in the field under plant conditions.

A second, but essential principle in technique selection is the degree to which the results of the inspection can be quantified. The feedback loop in the RBI process is dependent on information trends to justify increasing or decreasing inspection intervals to match the actual risk. Techniques should be capable of directly capturing trends in data, for example, wall thicknesses or crack dimensions, or be recordable in a systematic manner that allows trends to be inferred, for example, percentage of surface affected by general corrosion. Phrases like 'some corroded areas' or 'OK' are of no use in management of the RBI feedback loop.

#### **4.34.1.8.2 Selecting the interval**

Inspection intervals are related to the risk of failure and their assignment requires full documented justification within the RBI documents for a plant. In many cases 'risk' at this stage is referred to as 'criticality.' Returning to [Figure 6](#) as an example, the various locations on the matrix represent different levels of risk, but the colors of the 'boxes' represent criticality or 'risk rank.' In this case red represents criticality 1 (high), orange is criticality 2 (medium high), yellow is criticality 3 (medium), blue represents criticality 4 (medium low), and green is criticality 5 (low).

For the purposes of inspection, scheduling it is good practice to plan on the basis of damage specific criticality, that is, combination of each identified failure probability (per damage mechanism) with the overall failure consequences for the equipment. This makes sense because individual damage types require different techniques to detect them and will occur at different rates, thereby requiring different intervals. Some rationalization of inspections is possible in most inspection planning exercises but this is normally best handled by detailed planning that also encompasses logistical considerations such as the availability of scaffolding and portable power supplies, etc. These latter considerations are not a part of RBI assessment.

An example of an inspection interval specification is provided in [Table 1](#).

In this example, confidence grade is a measure of the degree of confidence that exists in the predictability of



future integrity performance based on known information. The definition of each grade is broadly based on the definitions given for inspection grades by the Institute of Petroleum.<sup>11,12</sup> These grades reflect confidence in inspection data and anticipated future condition.

- Grade 0 – no relevant inspection history, or rapid confirmed/anticipated degradation, or uncertain process conditions, that is, uncertain present and future condition.
- Grade 1 – at least one recorded relevant inspection but with potential significant degradation, that is, certain present condition, uncertain future condition.
- Grade 2 – at least one satisfactory inspection, that is, certain present and future conditions.
- Grade 3 – more than one satisfactory inspection over a prolonged period of time.

An alternative and in some cases complimentary approach is to schedule inspection based on calculated remnant life for the equipment, adjusted according to the assessed consequences of a failure. Table 2 provides an example of how this can be achieved.

In the example, it is clear that an item of equipment with high consequences of failure and low confidence grade would be inspected on a much shorter timescale (in terms of remnant life) than another item with low failure consequences and high confidence.

**Table 1** Example of inspection interval specification based on damage specific criticality

Damage specific criticality	Confidence grade			
	0	1	2	3
1	12	36	36	36
2	24	36	72	72
3	24	48	72	96
4	36	48	84	120
5	36	48	84	144

**Table 2** Example of fractions of remnant life used to schedule inspections

Consequence level	Confidence grade			
	0	1	2	3
1	0.1	0.13	0.16	0.2
2	0.175	0.23	0.29	0.35
3	0.25	0.33	0.42	0.5
4	0.375	0.5	0.625	0.75
5	0.5	0.67	0.83	1

Most RBI systems, which are in operation utilize concepts such as those above in order to form working RBI plans. The terminology changes, as do the precise values for intervals and life fractions used, but the basic process remains the same.

By combining the risk assessment, the assigned confidence grade, and the selection of a suitable inspection technique, the inspection plan is formed. It is important that the logic for creating the plan is documented because this constitutes a critical part of the audit trail for the whole RBI program.

#### 4.34.1.9 Key Success Factors for RBI

Three distinct parties have an interest in the effectiveness of a RBI program. These may include the RBI practitioner (whether this be an individual or a team within the operating company, or an external consultant), the operating company, and the regulation authority. Each of these parties has a different interest, and hence, each judges successful RBI by different criteria.

##### 4.34.1.9.1 RBI practitioner

The practitioner judges RBI by the ease and speed of application. This requires minimal data and simplified assessment methodologies. Restricting data requirements to that available in common engineering documentation such as process flow diagrams, piping and instrumentation diagrams, piping line lists, and heat and mass balance data normally provides sufficient data for RBI assessments, and is frequently available in electronic format, making data capture very efficient.

Additionally, as the RBI system needs continual feedback from completed inspections, changes in operating parameters and feedstock, the RBI practitioner needs an RBI system that is readily managed. The capture of changes and updating of results need to be simple and efficient.

##### 4.34.1.9.2 Operator

Key success factors for an operating company include an optimized inspection program, with minimal plant down time for scheduled inspections. The inspection regime should maximize plant reliability and eliminate surprise failures or unplanned shutdowns.

In order to achieve this, the RBI system needs robust likelihood of failure models that accurately predict plant behavior. Optimistic likelihood models and assessment techniques, which are liable to

overlook pertinent deterioration models would clearly lead to unpredicted failures, and damage the credibility of the RBI methodology.

On the other hand, overly conservative likelihood models also harm confidence in the RBI system by continuously overestimating the rate of deterioration, leading to unnecessarily onerous and frequent inspections which can overload the operator's resources. In one plant, a simple, qualitative RBI approach to creep damage resulted in the scheduling of frequent inspections for creep damage in 400 pipes in one process unit. After several inspection campaigns, early stage creep was found in only five pipes.<sup>13</sup> Using a more accurate, quantitative likelihood model reduced the number of pipes for which creep damage was credible to 30, which included all five pipes which had experienced early stage creep damage.<sup>11</sup>

Accurate prediction of plant condition allows optimization of inspection driven shutdowns, maximizing the operating period between inspections and optimizing the workload in each shutdown. These models need to be readily and efficiently adaptable to process and feedstock changes, capturing any significant changes, and revising the plant inspection program accordingly.

#### **4.34.1.9.3 Regulating authority**

A study performed on behalf of the UK Health & Safety Executive compared RBI assessments performed by a number of different RBI assessment teams for a specific set of case studies. Results showed inconsistencies between the findings from the various RBI assessment teams,<sup>5</sup> including:

- variation in the damage mechanisms selected for likelihood assessment;
- significant variation in the assessed likelihood of failure between the assessment methodologies;
- significant variation in the type and frequency of inspection; and
- a lack of speculative inspections aimed at confirming the absence of deterioration through damage mechanisms considered unlikely or inactive.

These findings demonstrate the primary concerns of regulatory bodies. Essentially, safety and environmental impact are the primary and secondary concerns, while business impact is of no concern. Consequently, key success factors for RBI include a robust, comprehensive assessment methodology that addresses all safety threats adequately and consistently.

The regulatory authority is often concerned that RBI scheduling may elevate business risks above

safety risks. A robust RBI system should therefore ensure that safety consequences are not diluted in their significance to the overall consequence of failure result by use of an average consequence of failure from individual assessment results that consider safety, business, and environmental impact.

#### **4.34.1.9.4 Summary**

In summary, therefore, the key factors for a successful RBI program that meets the needs and expectations of all parties may be defined as:

- accurate likelihood modeling;
- application of confidence criteria;
- realistic consequence modeling;
- selection of appropriate inspection techniques;
- robust authoritative reviews;
- intelligent interpretation of inspection findings;
- efficient capture of process or hardware modifications;
- speed of application; and
- consistency of results.

#### **4.34.1.9.5 Accurate likelihood modeling**

Accuracy in likelihood modeling includes correct identification of all active deterioration mechanisms, and accurate prediction of the rate of this deterioration.

The identification of all active deterioration mechanisms presents a significant challenge to the RBI assessment. Deterioration may occur under normal operating conditions, which include normal operating fluids, pressures, temperatures, and flow rates. In qualitative RBI systems, and those which employ a qualitative preselection of pertinent damage mechanisms, the selection of likelihood assessment models is critically dependent upon the competence and expertise of the RBI practitioner or expert review team. In other words, the weakness of these systems is that they rely upon human expertise to correctly identify which damage mechanisms are actually assessed. A more robust system is one that considers a comprehensive range of deterioration mechanisms and requires each damage mechanism to be ruled out based on quantitative or semiquantitative calculations.

Following identification of pertinent damage mechanisms, the likelihood assessment requires accurate modeling of the likelihood of failure. For time dependent deterioration mechanisms, such as corrosion, creep, or fatigue, the likelihood assessment should be able to predict a deterioration rate (in the

case of corrosion) or an anticipated life (in the cases of creep and fatigue). For non-time-dependent mechanisms, such as stress corrosion cracking, brittle fracture, etc., calculation of a susceptibility rank is probably the best option.

In either case, accurate modeling of deterioration mechanisms is essential for two reasons. First, an accurate understanding of the likelihood and rate of deterioration is essential for optimization of inspection plan. Overly conservative assessments will lead to specification of an onerous inspection plan both in the number of inspection tasks specified and their frequency. An optimistic assessment will specify too few inspections, with too long an interval between inspections.

Secondly, accurate likelihood modeling is essential to demonstrate the credibility of the RBI system. Confidence in the RBI assessment is gained when the RBI prediction and the actual observed experience are in agreement. Any significant difference between the prediction and the experience demonstrates that susceptibility to failure is not well understood. Accurate prediction of deterioration, rather than a simple reliance on the past measured rate of deterioration, provides better confidence in the integrity of the asset because the prediction can be modified to account for process or operating changes as they occur.

In a simple practical example, an oil and gas terminal experienced failure of a tube bundle after 11 years of operation. The corrosion engineer used the measured corrosion rate from the original bundle to predict the expected life for a like-for-like replacement, concluding that it would give a similar life, which was acceptable. Accurate RBI likelihood assessment (performed by an external consultant after ordering the replacement bundle), told a different story. The terminal had recently brought a new field online. Following the addition of the new field, the exchanger started to operate under wet conditions and the corrosion rate was high. The replacement tube bundle failed within a few months of installation.

#### **4.34.1.9.6 Application of confidence criteria**

A robust RBI system should account for the degree of confidence that can be assumed in any assessment. Confidence should consider the accuracy of the assessment technique, predictability of operating conditions, effectiveness of the inspection technique, and the integrity of the item under consideration.

Some form of confidence index is necessary to address the degree of accuracy of the models used to assess the deterioration rate. Factors to consider are the inherent accuracy of the deterioration model,

its degree of conservatism (e.g., creep calculations and fracture assessments often use very conservative material property data), and the comparison of predicted deterioration rates with actual measured rates.

First, when the deterioration rates experienced in service agree with the predicted deterioration rates, there is good confidence in the assessment technique. However, when the predicted rates differ from the measured deterioration rates it must be concluded that likelihood of failure is not well understood.

Second, deterioration frequently occurs due to process upset conditions, process degradation products, or rogue elements, such as catalyst fines or particulates. As many of these conditions are abnormal or unexpected operating scenarios, they are difficult to anticipate and are readily overlooked. Additionally, failures may occur due to design errors or undetected manufacturing defects. Even the most robust RBI system would be challenged to identify all of these possibilities.

Third, the confidence index should consider the effectiveness of previous inspections. Inspection effectiveness has two aspects; first, the ability of the inspection technique to actually identify and correctly characterize a defect or deterioration rate, and second, the coverage of the technique.

Finally, the confidence index should reflect the confidence in the integrity of the item under consideration. For example, in the case of an item known to be susceptible to high rates of deterioration, with robust inspections showing that the item has suffered significant damage and is close to failure, confidence in the RBI assessment is very high, but confidence in the integrity of the item is very low.

Failures often approximate a 'bath tub' curve (see [Figure 7](#)), where early in the plant life several failures occur due to design errors, undetected manufacturing defects, etc. Following this initial operating period, failures decline to a minimum level, but then increase once again toward the end of the plant design life.

As a result, confidence is never a constant, but changes with time. For new facilities, a confidence index should be employed to promote early inspections to identify any active deterioration mechanism not identified through the RBI assessment. These inspections should include a general type of inspection (e.g., a thorough internal visual examination), which has the capability of detecting unexpected deterioration such as previously undetected manufacturing defects.

In the middle of the plant life when deterioration rates are confirmed by several inspections, inspection interval may be extended, provided in-service

inspections have confirmed the rate of deterioration is both reasonable and predictable. Toward the end of the plant life, when the equipment is approaching the end of its serviceable life, confidence in the integrity of the item is necessarily reduced and inspections performed more frequently.

#### 4.34.1.9.7 Realistic consequence modeling

Consequence modeling needs to be realistic for RBI to deliver a sensible inspection plan. Figure 8 shows a comparison of consequence of failure results for a

steam reformer plant using two different proprietary RBI software packages. As can be seen, the results are not at all comparable. Both RBI assessments are described as ‘semiquantitative,’ although the assessment methodologies are radically different.

The methodology employed in Figure 8(a) was a very simple consequence assessment using nine simple assessment criteria, which are answered with “yes,” “no,” or a simple number (size, temperature, pressure, etc.). Because of the simplicity of the methodology, the results are necessarily very conservative,

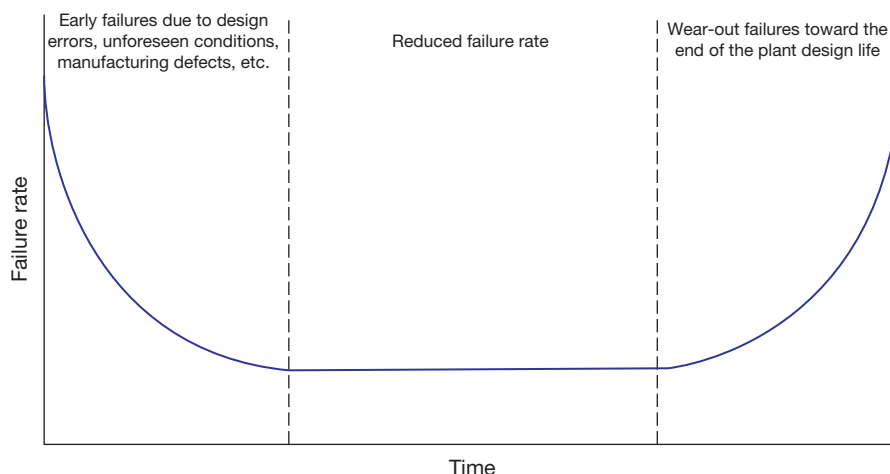


Figure 7 ‘Bath tub’ curve of hypothetical failure rate versus time.

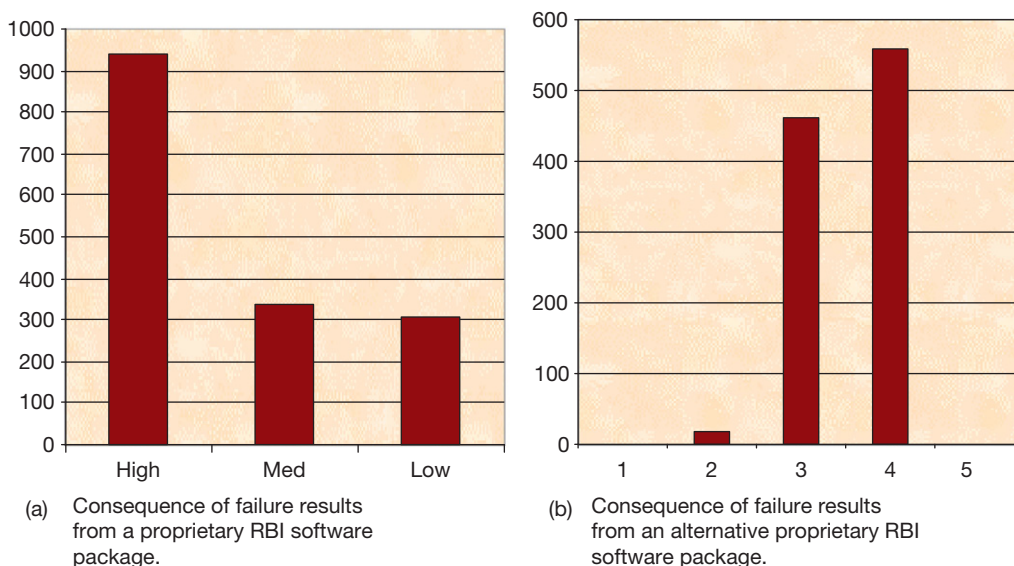


Figure 8 Comparison of RBI consequence of failure assessments from two proprietary RBI software packages. Assessments cover the same piping from a refinery steam reformer plant. (a) Consequence of failure results from a proprietary RBI software package. (b) Consequence of failure results from an alternative proprietary RBI software package.

with 60% of items being given the highest possible rank for consequence of failure.

The second methodology is more complex, employing quantitative methods to calculate hazard areas for several failure scenarios. The technique is semiquantitative because it simplifies the dispersion modeling of any release into three specific phases (gas, dense gas, and liquid), and makes broad assumptions on repair times and mitigation systems. This technique is much less conservative, with only 2% of items being assigned the highest two consequence categories.

Clearly, the consequence of failure assessment methodology has a significant impact on the risk ranking results. A more conservative assessment will result in more items being considered critical, and this will drive more frequent inspections. However, overly conservative assessments do not give sufficient separation in risk ranking, and thus fail to focus inspection on those items that actually constitute the highest risk.

#### 4.34.1.9.8 Intelligent interpretation of inspection findings

A key factor in the success of any RBI program is feedback of inspection findings to the risk assessment. This sounds very simple, and yet in practice information gained from inspection activities is frequently not interpreted intelligently, leading to inappropriate use of inspection findings to revise the RBI assessment and consequently the revised inspection plan.

Intelligent use of inspection data is best illustrated through specific examples.

#### 4.34.1.10 Case Study 1: Corrosion Rate Trending

Corrosion rate trending is one of the most common plant inspection techniques, and is commonly performed using ultrasonic wall thickness (UTW) gauging. However, the UTW measurement technique has

a practical accuracy of  $\sim\pm 0.5$  mm, partly due to accuracy of the instrument itself, and partly due to repeatability of the probe placement in precisely the same location on a pipe for subsequent readings, and the fact that corrosion is frequently not uniform. Consequently, wall loss trends can be misleading.

Figure 9 shows different forms of corrosion, including general corrosion, bottom of the line corrosion, and top of the line corrosion, all of which are commonly found in process plant piping systems. Other common nonuniform forms of corrosion are pitting, preferential weld corrosion, and mesa attack. Measurements are typically taken at four cardinal points (normally 3, 6, 9, and 12 o'clock positions).

While a simple average of differences between two sets of wall thickness measurements in a system experiencing general corrosion may yield a sensible corrosion rate (assuming minimal errors from instrument calibration, probe placement, and thermal influences), in all instances where corrosion is nonuniform, the measured average corrosion rate will always be very optimistic. For instance, a straight average corrosion rate calculated for pipes in Figure 9 showing bottom of the line corrosion and top of the line corrosion would return a corrosion rate which is  $\sim 25\%$  of the actual worst case corrosion rate.

Use of proprietary software tools for trending UTW measurements is worldwide standard practice. These tools calculate corrosion rates for each thickness measurement location (TML) as well as an average corrosion rate for an entire corrosion loop. Two corrosion rates are normally reported; a short term corrosion rate (difference between the last and the previous reading), and a long term corrosion rate (difference between the first and last readings). These terms are illustrated in Figure 10, which shows actual wall thickness readings for a pipe in service.

Table 3 shows results from trending of the wall thickness data from the above and other TMLs from

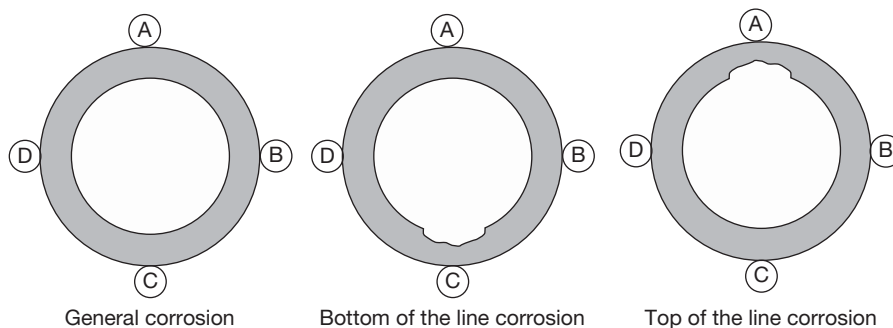
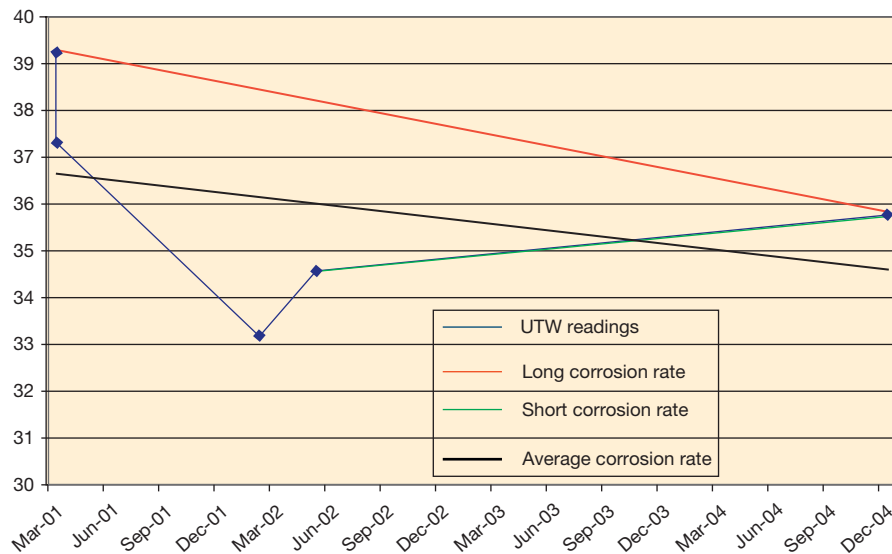


Figure 9 Different forms of corrosion.





**Figure 10** Historical ultrasonic wall thickness readings for a pipe in service.

the same pipe. Trends using a proprietary software package, as well as standard statistical analysis are shown. The latter evaluates thickness measurements from the entire pipe, and seeks to eliminate inaccuracies arising from the measurement methodology and localized corrosion. Normally a reasonable evaluation of corrosion rate is obtained using a mean value plus one standard deviation.

Results displayed in [Table 3](#) demonstrate that it is possible to obtain very good agreement between the predicted corrosion rate and the experienced rate. Moreover, it demonstrates potential shortcomings with accepted methods of wall thickness trending.

#### 4.34.1.11 Case Study 2: Use of Robust RBI to Enhance Understanding of Inspection Data

Robust RBI likelihood modeling should provide insight into deterioration mechanisms that may be anticipated in service. This case study concerns linear indications discovered in a pipe to branch weld during a routine inspection, [Figure 11](#).

Areas of the process system in question were known to be susceptible to stress corrosion cracking due to CO and CO<sub>2</sub>. The initial assumption of the inspector, therefore, was that the pipe had suffered SCC, and a recommended repair was issued. The recommended repair was to coat the weld with a

coating system that has proven capability in mitigating this form of SCC.

Prior to approving the recommended repair, the RBI database was reviewed. This indicated that the susceptibility to SCC in this line was very low, as the pipe was a compressor discharge line which operates at warm and dry conditions.

The RBI analysis, however, did identify a potential susceptibility to mechanical fatigue, both due to vibrations from the compressor and the high velocity gas flow (calculations performed were simple screening calculations for flow induced vibration in accordance with the recommendations of the MTD guidelines).<sup>14</sup>

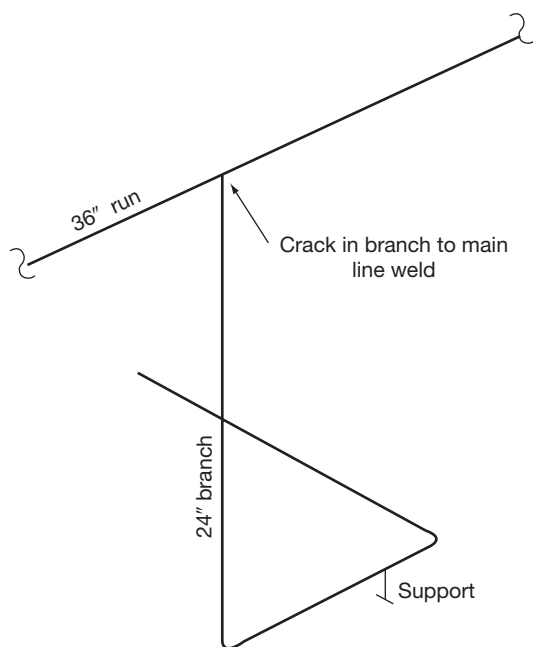
In the light of the RBI assessment, the recommended repair was altered, with the defect being removed by blend grinding.

#### 4.34.1.12 Case Study 3: Use of Robust RBI to Understand Plant Wide Integrity from Restricted Inspection Data

Inspections are generally task driven. A job card is raised to perform a specific inspection task on a specific item of equipment. In the event that the inspection identifies a degree of damage, the inspector may raise a recommendation for reparations to the item inspected. Once the reparations have been completed, the task is closed out. The weakness in this system is that information gained from any single inspection is rarely captured in order to infer the

**Table 3** UTW trends for using proprietary software and statistical analysis

	TML	Pipe
Trended long rate (UTW software product)	0.89	-0.63
Trended short rate (UTW software product)	-0.46	0.65
Statistical valuation (average + one standard deviation)	-	0.23
Prediction from proprietary RBI software package	-	0.23
Prediction from competitor RBI software package	-	0.62

**Figure 11** In-service cracking of a branch to header weld.

condition of areas of the process system that have not been inspected (e.g., upstream or downstream piping and equipment in similar service).

Use of robust RBI deterioration models facilitates a better understanding of inspection data. This case study concerns a refinery process unit which is similar in layout to a hydrotreater, [Figure 12](#).

The RBI assessment predicted a susceptibility to hydrochloric acid (HCl) corrosion in the reactor effluent heat exchangers. Prediction of HCl corrosion is difficult as corrosion rate is a function of chloride concentration (a few ppm), reactor temperature, and the stream water content, all of which are variable.

However, RBI assessments predicted low levels of corrosion in ES-101B/C and D, moderate corrosion in ES-101A, and severe corrosion in EA-101 and ES-102.

Inspections performed included visual examinations and UTW readings. The tube bundle in exchanger ES-102 suffered significant corrosion, and needed retubing within 2 years of commissioning. All other inspections reported superficial corrosion.

Authoritative review of inspection data included intelligent use of the wall thickness data, which confirmed no corrosion loss in the first heat exchanger (ES-101D), but noted that corrosion rate increased in each subsequent heat exchanger through to ES-102.

Interpretation of the inspection data in the light of RBI assessment confirmed the RBI predicted corrosion mechanism, and gave insight to the condition of the air cooled heat exchanger tubes, which had not been inspected directly. As the interpretation of corrosion threat was applied to the pressure system, rather than to just the items inspected, the air cooler was identified as a location for potentially significant deterioration, allowing the scheduling of Eddy current and IRIS inspections of the tubes to establish their condition.

#### 4.34.1.12.1 Efficient capture of process or hardware modifications

A common definition of madness is to keep doing the same thing and yet expect a different outcome. The opposite is also a true definition of madness; namely, to keep changing what you do and yet expect the same outcome.

In the modern, real world of process plant operations, process conditions are frequently changed. Oil and gas production facilities often experience changes in feedstock and pressure profile over the field life, for example, increasing water content, declining well pressure, increased H<sub>2</sub>S production, periodic reflux of well stimulation or work over fluids, etc. Petroleum refineries often source crude from various sources, introducing frequent feedstock changes; and plants are frequently run to optimize production to latest market needs.

These changes in feedstock or operating parameters may have a major impact on both likelihood and consequence of any failure, and need to be captured within the RBI system. Many RBI systems, however, are very time consuming to set up, and are inflexible to process changes. For instance, qualitative RBI assessments can rarely readily accommodate frequent changes as each change would require reconvening of the expert review team to assess significance of changes.

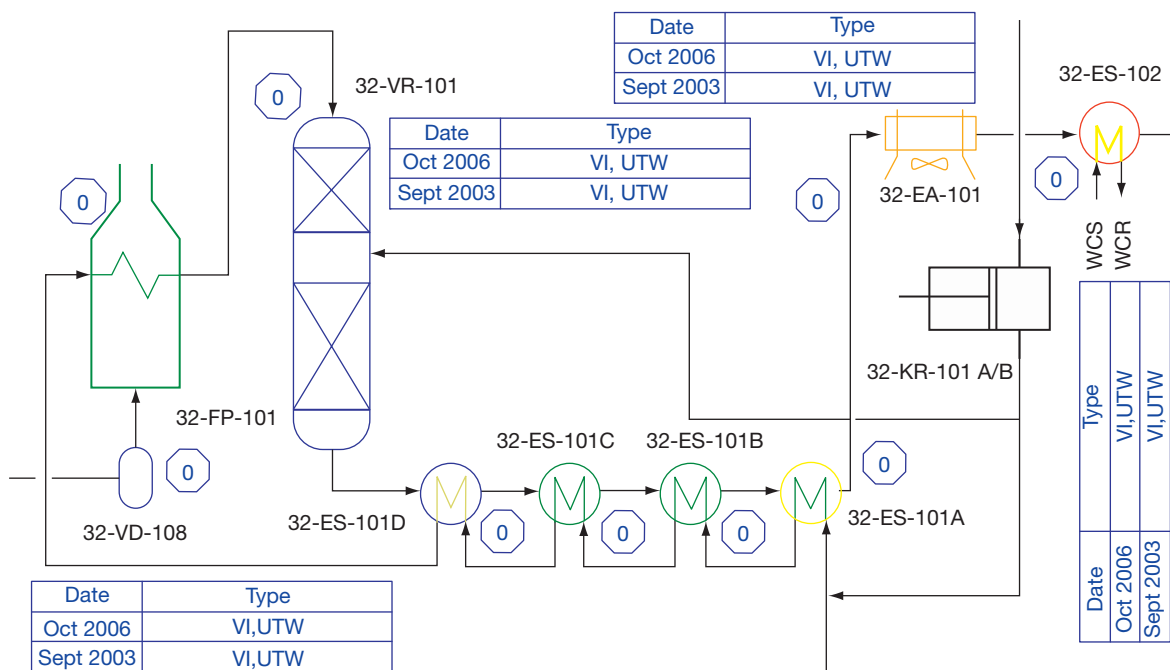


**Figure 12** Schematic of unit layout.

What is apparent is that the RBI process applied on a plant needs to be directly linked into the management-of-change (MoC) procedure as part of the overall AIM scheme. A properly applied MoC should encompass risks associated with all process and hardware changes. RBI can be used to assist this assessment and the MoC procedure should ensure that the RBI system is updated following each change.

#### 4.34.1.13 Major Challenges for RBI

There are a number of major challenges for RBI application development. These include:

- **Abnormal operations and upset conditions:** these are not currently modeled well in any RBI system because of the large uncertainties on the value and range of important parameters that might change during a process upset. The duration of any upset is also a very important parameter. At present, best practice is to review the RBI scheme following each process upset to either formally confirm that the specific upset had no effect on the existing risk level or specify actions to reassess the risk following the upset.
- **Possible degradation products:** no current RBI approach predicts with any great certainty the precise form and properties of degradation products. Material-process fluid interactions are capable of producing solids, liquids, and gases that may or may not initiate or contribute to further degradation. This is an issue of extending current RBI assessment practice to include secondary and tertiary effects of materials degradation within a process stream.
- **Batch operations:** current RBI approaches were designed for continuous operations. Risk can be accounted for by weighting anticipated corrosion rates with their respective service times. Complex batch operations, where several different chemicals are processed at different times, or where chemical cleaning cycles etc. may be included, are frequently covered inadequately.
- **Flexible operations (changing pressure, temperature, throughput, etc.):** as with batch operations, flexible operations often result in varying risk characteristics for each operating scenario. Consequently, careful thought needs to be afforded to the RBI assessment.
- **Changing feedstocks:** feedstock changes, which are often very subtle, are common and yet are frequently not adequately addressed in current RBI approaches. Consideration of the current and future process fluid chemistry and/or operating parameters at the start of an RBI planning project can assist in minimizing the risk of using inappropriate assumptions in the assessment. Sensitivity studies should be used to estimate the influence of changing parameters. Moreover, a robust RBI program should identify

key process parameters (e.g., pressure, temperature, chemical restrictions, operating mode, etc.) beyond which the RBI assessment is invalid.

- Areas where basic data may not be appropriate (e.g., deadlegs): conditions in deadlegs, piping, or equipment which are used infrequently and low flow areas which are not the same as those in the main process streams. Many RBI schemes fail to recognize these differences, and hence may significantly under estimate the risk in these locations. A sensible approach is to employ corrosion circuit assessments, which would require evaluation of the main flow, lines under intermittent flow, and deadlegs.

As RBI approaches develop, some challenges will be met and other new ones will appear. Many answers will come from improvements in plant operational software and developments in process modeling. As data becomes fully integrated, the opportunities to conduct rapid and accurate RBI assessment will become more common.

#### 4.34.1.14 Future Developments

Many consider that the goal of RBI must be to achieve the ability of the system to interrogate live process and operating data (e.g., digital control systems, corrosion monitoring, and direct inspection data) in order to give a real time integrity assessment, assessing the impact of actual operating conditions on plant integrity as they occur. Moreover, the risk and integrity status could be displayed on intelligent plant drawings (P and IDs, isometrics, equipment drawings, etc).

When RBI was first applied in the oil and gas industry this was something of a dream, but all the elements required to achieve it now exist and it is seemingly only a matter of time before it becomes reality.

## References

1. Reducing Risks, Protecting People – The HSE's Decision Making Process, Her Majesty's Stationary Office, 2001.
2. Best Practice for Risk Based Inspection as a Part of Plant Integrity Management, HSE Contract Research Report 363/2001, HSE.
3. UKOOAH, Asset Integrity Toolkit, UK Offshore Operators Association, 2006.
4. Formal Expert Judgement An Overview, K. Simola, A. Mengolini, and R. Bolado-Lavin, EUR 21772 EN, 2005.
5. Risk Based Inspection – A Case Study Evaluation of Onshore Process Plant, HSL/2002/20, W Geary, 2002.
6. API 581, RBI Base Resource Document.
7. API 581, Table 7-2.
8. API Recommended Practice 580, Risk-Based Inspection.
9. Risk Based Inspection, Beyond Implementation to Integration, Lynne Kaley, The Equity Engineering Group Inc.
10. Sitton, R. Integration of RBI with an Inspection Data Management System, 3rd MENDT, Middle East Nondestructive Testing Conference & Exhibition, November 2005, Bahrain.
11. Pressure Systems Examination. Model Code of Safe Practice, Part 13. Pressure Piping Systems Examination, 2nd ed. Institute of Petroleum.
12. Pressure Systems Examination. Model Code of Safe Practice, Part 12. Pressure Vessel Examination, 2nd ed. Institute of Petroleum.
13. Amphlett, G. Audit Report: Validation of Changes to RBI Strategy for Onshore Facilities and Pipelines, Allianz Cornhill Engineering, 2005.
14. MTD 99/100, Guidelines for the Avoidance of Vibration Induced Fatigue in Process Pipework, ISBN 1 870553 37 3, 1999.

## 4.35 Assessment of Fitness for Service

**A. H. Sherry**

Materials Performance Centre, University of Manchester, Sackville Street, Manchester M60 1QD, UK

© 2010 Elsevier B.V. All rights reserved.

4.35.1	Introduction	3103
4.35.2	Overview of the Failure Assessment Diagram	3105
4.35.3	The $L_r$ Parameter	3106
4.35.3.1	Example Calculation of $L_r$	3107
4.35.4	The $K_r$ Parameter	3107
4.35.4.1	Example Calculation of $K_r$	3108
4.35.5	The Assessment of Corrosion Defects	3109
4.35.5.1	Step 1: Characterize the Nature of the Crack	3109
4.35.5.2	Step 2: Establish the Cause of Cracking	3110
4.35.5.2.1	Service environment	3110
4.35.5.2.2	Stress	3110
4.35.5.2.3	Crack morphology	3110
4.35.5.3	Step 3: Define the Material Characteristics	3110
4.35.5.3.1	Surface condition	3110
4.35.5.3.2	Welding	3111
4.35.5.3.3	Initial microstructure	3111
4.35.5.3.4	Materials ageing	3112
4.35.5.4	Step 4: Establish Data for Stress Corrosion Cracking Assessment	3112
4.35.5.5	Step 5: Undertake Structural Integrity Assessment	3113
4.35.6	Worked Example FFS Assessment	3113
4.35.6.1	Worked Example Part A	3114
4.35.6.1.1	Calculation of $L_r$	3114
4.35.6.1.2	Calculation of $K_r$	3114
4.35.6.1.3	Plotting failure assessment point on FAD	3115
4.35.6.2	Worked Example Part B(I)	3115
4.35.6.3	Worked Example Part B(II)	3115
References		3116

### Glossary

**Defect** A metallurgical imperfection.

**Degradation** A detrimental change in the material by a metallurgical, electrochemical, or mechanical process, for example, precipitation, stress corrosion cracking, or fatigue.

**Failure** An event that results in a loss of structural integrity of a component containing a flaw.

**Failure assessment diagram** A graphical approach to quantify the structural integrity of a component containing a flaw in terms of failure by fracture or plastic collapse.

**Fitness for service assessment** Quantitative evaluation of the structural integrity of a

component containing a flaw carried out to a published procedure.

**Flaw** Any macroscopic metallurgical imperfection involving a discontinuity, such as a crack, solid inclusion, gas pore, etc.

**Limit load** The load applied to a structure at plastic collapse.

**Plastic collapse** The failure of a structure by the development of plastic strain across the net section.

### Abbreviations

**ASME** American Society of Mechanical Engineers

**FAD** Failure assessment diagram



**FFS** Fitness for service  
**HAZ** Heat affected zone  
**SCC** Stress corrosion cracking

## Symbols

**a** Crack Length  
**c** Half surface-breaking length of surface defect  
**G<sub>0</sub> to G<sub>5</sub>** Geometry coefficients  
**g** Geometry parameter in calculation of reference stress  
**K<sub>r</sub>** Ordinate of the failure assessment diagram providing a measure of the proximity of a component to failure by brittle fracture  
**K<sub>mat</sub>** Material fracture toughness  
**K<sub>I</sub>** Mode I stress intensity factor  
**K<sub>ISCC</sub>** Threshold stress intensity factor for stress corrosion cracking  
**L<sub>r</sub>** Abscissa of the failure assessment diagram providing a measure of the proximity of a component to failure by plastic collapse  
**L<sub>r(max)</sub>** Maximum extent of the failure assessment curve on the L<sub>r</sub> axis  
**M<sub>b</sub>** Bending correction factor  
**M<sub>m</sub>** Membrane correction factor  
**M<sub>s</sub>** Surface correction factor for a surface crack  
**p** Pressure  
**P** Load  
**P<sub>b</sub>** Through-wall primary bending stress  
**P<sub>L</sub>** Limit load  
**P<sub>m</sub>** Through-wall primary membrane stress  
**Q** Geometry parameter in calculation of stress intensity factor  
**R<sub>i</sub>** Inner radius of cylinder  
**R<sub>o</sub>** Outer radius of cylinder  
**t** Wall thickness of cylinder  
**W** Half-width of flat plate  
**Y** Geometry parameter  
**α** Geometry parameter in calculation of reference stress  
**σ** Applied stress  
**σ<sub>0.2</sub>** Proof stress at 0.2% plastic true strain  
**σ<sub>b</sub>** Bending stress  
**σ<sub>f</sub>** Flow stress (average of yield and ultimate tensile stress)  
**σ<sub>m</sub>** Membrane stress  
**σ<sup>P</sup>** Primary stress  
**σ<sub>ref</sub>** Reference stress  
**σ<sup>s</sup>** Secondary stress  
**σ<sub>m</sub>** Membrane stress  
**σ<sub>y</sub>** Yield stress

## 4.35.1 Introduction

The safe design and reliable operation of engineering plant is critical to all industries. Design codes, such as those published by the American Society of Mechanical Engineers (ASME) for the process and power industries, provide clear rules for the design, fabrication, inspection, and proof testing of new plant prior to going into service.<sup>1</sup> However, as such codes are developed for engineering design (rather than operation), they do not fully consider that materials degrade in service by a range of mechanisms, including:

- metallurgical degradation (including graphitization, temper embrittlement, sigma phase embrittlement, strain ageing, and irradiation damage);
- mechanical degradation (including creep cavitation, erosion, mechanical and thermal fatigue, ductile tearing, and brittle fracture);
- chemical/electrochemical degradation (including oxidation, sulfidation, carburization and metal dusting, general and localized corrosion, corrosion-fatigue, stress-corrosion cracking, and erosion-corrosion).

Examples of material degradation by fatigue and stress-corrosion cracking are illustrated in [Figure 1](#).

- (a) Fatigue crack in 2024-T351 high strength aluminum alloy containing a tensile residual stress
- (b) Transgranular stress corrosion cracking in sensitized 304 stainless steel due to chloride contamination
- (c) Intergranular stress corrosion crack in sensitized 304 stainless steel exposed to high temperature oxygenated water

Since materials degrade and defects can initiate and propagate in engineering components during plant operation, there is an ongoing need to demonstrate the structural integrity of engineering components during service life, thus ensuring the continued safe and reliable operation of the plant. While nondestructive examination (NDE) methods provide information regarding the presence and development of crack-like flaws, fitness-for-service (FFS) assessment methodologies provide the means for judging the severity of such flaws and the consequence for component integrity. Such FFS methodologies have been developed to provide the engineer with clear guidance regarding: (i) the information required to undertake FFS assessment, (ii) the steps required to perform FFS assessment, and (iii) the information to be presented with respect to the results of FFS

assessment. The results from such assessments provide the plant operator with valuable information that may be used to inform decisions regarding component operation, component repair, and (or) component replacement. These results also form part of the development of safety cases to support the continued operation of plant components.

There are a number of FFS assessment methodologies used within the process and power industries world-wide, including:

- BS 7910:2005, 'Guide to methods for assessing the acceptability of flaws in metallic structures', British Standards Institution, 2005;
- R6 Revision 4, 'Assessment of the integrity of structures containing defects', British Energy Generation Ltd, 2006;
- API 579, 'Fitness for Service', American Petroleum Institute Recommended Practice, 2000;

- FITNET MK7, 'Fitness-for-service procedure' European Fitness for Service Thematic Network (FITNET TN), 2006.

Common to each of these procedures is the failure assessment diagram (FAD) approach for assessing the significance of crack-like flaws which may be present at the start of a component's life (e.g., lack of fusion weld defect) or which may form during service (e.g., by one or more of the degradation mechanisms outlined above). A typical FAD is illustrated in [Figure 2](#).

This chapter describes the FAD approach to structural integrity assessment. [Section 4.35.2](#) provides a brief overview of the different components of the FAD. [Section 4.35.3](#) describes the  $L_r$  parameter while [Section 4.35.4](#) provides a description of the  $K_r$  parameter. Finally, [Section 4.35.5](#) presents a working example of the use of the FAD approach to assess a component containing a flaw. This chapter

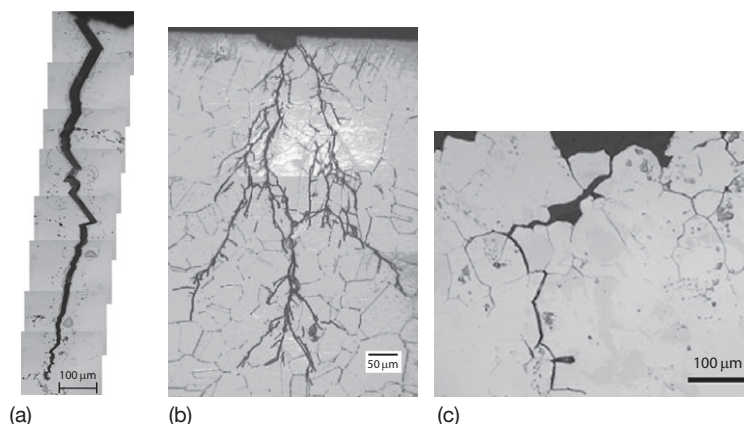


**Figure 1** Examples of crack-like flaws in engineering materials.

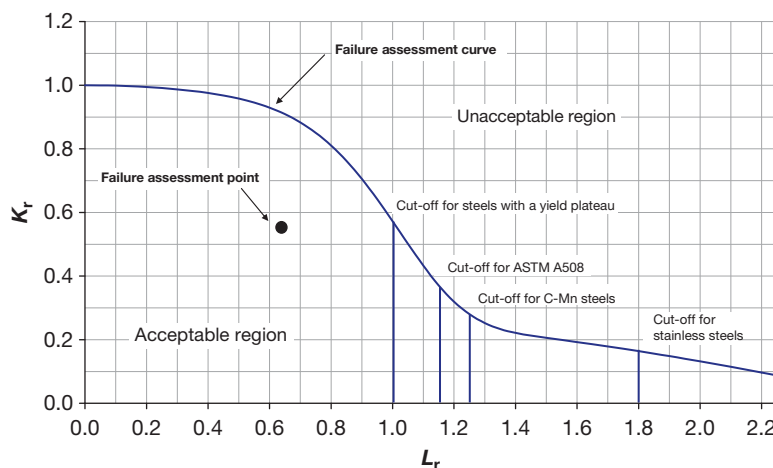


**Figure 2** Failure assessment diagram.

should be read alongside the chapter on the mechanical and fracture properties of materials in this book, which provides important background material.

#### 4.35.2 Overview of the Failure Assessment Diagram

The FAD is a graphical representation of the acceptability or unacceptability of a crack-like flaw in a given component under particular operating conditions. As shown in [Figure 2](#), the FAD includes a ‘failure assessment curve’ and ‘failure assessment point’.

The FAD provides the means for judging the proximity of a component to failure by either plastic collapse (‘bending’) or fracture (‘breaking’). The FAD is plotted with an abscissa  $L_r$ , which defines the proximity of the component to plastic collapse, and an ordinate  $K_r$ , which defines the proximity of the component to unstable fracture. Plastic collapse usually controls component failure when the flaw is large relative to the thickness of the component and the material has high fracture toughness and low yield stress. Unstable fracture usually controls component failure when the defect is small relative to the thickness of the component and when the material has low fracture toughness (e.g., brittle materials) with high yield strength.

The failure assessment curve defines the boundary between acceptable (or safe) and unacceptable (or unsafe) regions with respect to component failure by unstable fracture or plastic collapse. The curve may be defined in a general manner (as shown in [Figure 2](#)) by the following equation:

$$K_r = (1 - 0.14L_r^3)(0.3 + 0.7\exp[-0.65L_r^6]) \text{ for } L_r \leq L_{r(\max)} \quad [1]$$

The maximum extent or ‘cut-off’ of the failure assessment curve on the  $L_r$  axis is determined by the ratio of the material flow stress  $\sigma_f$  (the average of the yield and ultimate tensile stress) and material yield stress  $\sigma_y$  at the temperature of interest, that is,

$$L_{r(\max)} = \frac{\sigma_f}{\sigma_y} \quad [2]$$

The yield stress is conventionally defined by the 0.2% proof stress  $\sigma_{0.2}$  of the material. Typical cut-off values are shown in [Figure 2](#), and are due to the significant differences of work hardening behavior. They include:

- $L_{r(\max)} = 1.00$  for materials with a yield plateau
- $L_{r(\max)} = 1.25$  for carbon–manganese steels
- $L_{r(\max)} = 1.80$  for austenitic stainless steel

The failure assessment point defines the position of a specific flaw in a specific component under specific operating conditions with respect to the failure assessment curve. If the point lies below the failure assessment curve, the flaw is deemed to be acceptable (the component is safe) and the flaw may be left in service with no impact on the operational safety or the structural integrity of the component. However, if the failure assessment point lies outside the failure assessment curve, the flaw is deemed to be unacceptable (the component *may be* unsafe) and corrective action may be necessary, for example, the repair or replacement of the component. The assessment used commonly has significant conservatism due to simplifications in the analysis. In some cases, a more sophisticated reassessment of the flaw, with reduced conservatism, may be sufficient to demonstrate that the component is, in fact, safe.

To define the location of the failure assessment point, the parameters  $L_r$  and  $K_r$  need to be calculated for the component containing a given flaw under the operating conditions of interest.

The parameter  $L_r$  is defined by the ratio of the reference stress  $\sigma_{\text{ref}}$  to the materials yield stress  $\sigma_y$  at the temperature of interest, that is,

$$L_r = \frac{\sigma_{\text{ref}}}{\sigma_y} \quad [3]$$

Where  $\sigma_{\text{ref}}$  is defined from the knowledge of the dimensions of the flaw and the stress acting on the flaw under the operating conditions of interest. The yield stress,  $\sigma_y$ , is usually defined from a standard tensile test using the 0.2% proof stress  $\sigma_{0.2}$ . An equivalent definition of  $L_r$  is as follows:

$$L_r = \frac{P}{P_L} \quad [4]$$

where  $P$  is the load applied to the structure and  $P_L$  is the limit load. The parameter  $L_r$  is discussed in greater detail in [Section 4.35.3](#).

The parameter  $K_r$  is defined under *primary* loading (see [Section 4.35.3](#)) by the ratio of the linear elastic stress intensity factor  $K_I$  to the material fracture toughness  $K_{\text{mat}}$  at the temperature of interest, that is,

$$K_r = \frac{K_I}{K_{\text{mat}}} \quad [5]$$

where  $K_I$  is defined from the knowledge of the component geometry, the dimensions of the flaw, and the

stress acting on the component under the operating conditions of interest. The material fracture toughness is defined by fracture toughness testing of the component material at the temperature of interest. The parameter  $K_r$  is described in further detail in [Section 4.35.4](#).

### 4.35.3 The $L_r$ Parameter

The calculation of the  $L_r$  parameter in FFS assessment not only requires the definition of the material yield stress  $\sigma_y$  (conventionally defined by  $\sigma_{0.2}$ )<sup>1</sup> but also an understanding of the stress condition of the component being assessed. In FFS assessment, this understanding must take full account of all the stresses acting on the component. There are broadly three types of stress that can act on an engineering component:

1. applied stresses such as those due to internal pressure,
2. thermal stresses such as those due to thermal transients, and
3. internal (residual) stresses such as those due to welding.

For the definition of the  $L_r$  parameter, only the applied stresses are considered. Such stresses are necessary to satisfy equilibrium conditions with externally imposed loading and are defined as 'primary' stresses  $\sigma^p$ . These contribute to the plastic collapse of a structure (e.g., as pressure is increased within a pressure vessel or pipe). Thermal and internal stresses are necessary to satisfy continuity conditions within the structure (e.g., weld residual stress) or with an external constraint (e.g., pipe fit-up stress). Such stresses are defined as 'secondary' stresses  $\sigma^s$ . Secondary stresses do not significantly contribute to plastic collapse as these stresses will, in most cases, be self-equilibrating, that is, the net force and bending moment will be zero, and their effect will be effectively 'washed out' as plasticity extends across the ligament. The following definition of stresses is given within the R6 defect assessment procedure<sup>2</sup>:

- Primary stresses  $\sigma^p$  arise from loads that contribute to plastic collapse.
- Secondary stresses  $\sigma^s$  arise from loads that do not contribute to plastic collapse.

A more complete discussion of primary and secondary stresses is given in Lu *et al.*<sup>3</sup>

The application of a primary stress lower than the yield stress to an uncracked component will result in

elastic deformation of the component, as defined by Young's modulus and Poisson's ratio. However, for components containing crack-like flaws, the stress concentrating effect of the flaw can lead to local yielding of the material at the tip of the flaw. A zone of plastically deformed material surrounded by elastic material will develop at the tip of the flaw. Increasing the applied stress will expand this plastic zone until plasticity first extends across the uncracked ligament to the wall of the component. This condition is defined as the 'local collapse condition.' Further increases in applied stress lead to the uncracked ligament becoming fully plastic. This condition is defined as the 'net section collapse' condition. Finally, when the additional increases in applied stress cause the component to become fully plastic, 'gross collapse' of the component has occurred. It is important to note that under some circumstances the flaw will extend under an increasing primary load, for example, by ductile tearing. Crack growth will reduce the dimension of the uncracked ligament and increase the likelihood of plastic collapse.

These three limiting conditions are illustrated schematically in [Figure 3](#) for an axially cracked pipe under an internal pressure  $p$ :

- *Local collapse* occurs when the plasticity first extends across the uncracked ligament ahead of the flaw.
- *Net section collapse* occurs when the uncracked ligament becomes fully plastic.

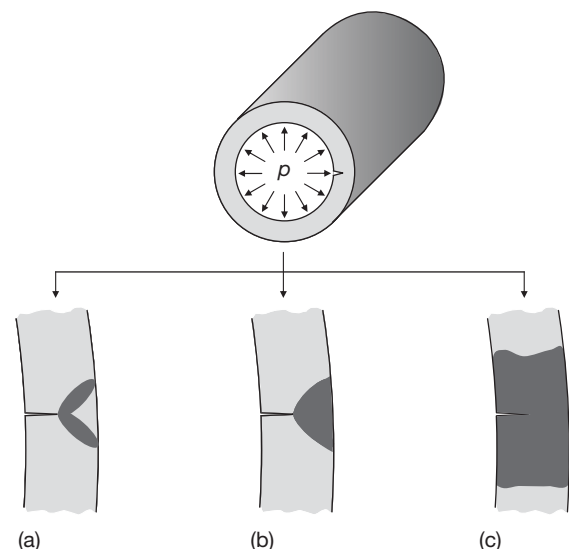


**Figure 3** Schematic illustration of plastic collapse solutions for a pressurized cylinder containing an axial flaw. The dark shaded regions indicate the region of plasticity. (a) Local collapse, (b) net section collapse, and (c) gross collapse.

- *Gross collapse* occurs when plasticity extends across the full component thickness.

The ‘failure’ of a component by plastic collapse may be defined at each of these conditions.

The reference stress  $\sigma_{\text{ref}}$  defines the effective primary ligament stress (for local collapse) or the effective net section stress (for net section collapse) within the component containing a defect under an applied primary stress. Compendia of standard equations defining  $\sigma_{\text{ref}}$  for a wide range of cracked geometries are available within FFS procedures such as in R6 Revision 4<sup>2</sup> and API 579.<sup>4</sup>

Equation [4] shows that  $L_r$  can be defined with reference to the applied load on a structure normalized by the limit load for the structure.

For example, the following equation defines the reference stress with respect to the net section collapse of the cracked cylinder shown in Figure 3<sup>4</sup>

$$\sigma_{\text{ref}} = \frac{\sigma_b + [\sigma_b^2 + 9\{M_s\sigma_m\}^2]^{0.5}}{3} \quad [6]$$

where  $\sigma_b$  is the through wall primary bending stress,  $\sigma_m$  is the primary membrane stress intensity, and  $M_s$  is a surface correction factor for a surface crack. The membrane stress is defined as the average stress across the thickness of a section. The bending stress is the bending component of the stress acting across the same section. The surface correction factor is required to take into account the local effect of the crack on the membrane and bending and stresses on the cracked plane. The primary bending and membrane stresses are dependent on the internal pressure and thickness of the diameter and wall of the cylinder. The parameter  $M_s$  is dependent on the ratio of crack depth to the cylinder wall thickness.

#### 4.35.3.1 Example Calculation of $L_r$

This example calculation is based on the axially cracked cylinder geometry illustrated in Figure 3 with the following parameters:

Material	AISI Type 304L stainless steel
Temperature	20°C
Internal radius ( $R_i$ )	120 mm
Outer radius ( $R_o$ )	132 mm
Wall thickness ( $t$ )	12 mm
Crack depth ( $a$ )	4.8 mm
Internal pressure ( $p$ )	10 MPa

Step 1. Define the yield stress  $\sigma_y$  of the material at the temperature of interest.

The yield stress of AISI 304L stainless steel at 20 °C is given as 210 MPa using the Matweb database.<sup>5</sup>

Step 2. Define the reference stress  $\sigma_{\text{ref}}$  for the cracked component of interest.

Using eqn [6] along with the stress solutions given in API 579,<sup>4</sup> the parameters  $P_m$ ,  $P_b$ , and  $M_s$  are given as follows:

$$P_m = \frac{pR_i}{t} \quad [7]$$

$$P_b = \frac{pR_o^2}{R_o^2 - R_i^2} \left[ \frac{t}{R_i} - \frac{3}{2} \left( \frac{t}{R_i} \right)^2 + \frac{9}{5} \left( \frac{t}{R_i} \right)^3 \right] \quad [8]$$

$$M_s = \frac{1}{1 - a/t} \quad [9]$$

Inserting the parameters of interest into these equations gives  $P_m = 100$  MPa,  $P_b = 5$  MPa, and  $M_s = 1.67$ . Inserting these parameters into eqn [6] gives the reference stress for this component and internal pressure of  $\sigma_{\text{ref}} = 168$  MPa.

Step 3. Calculate  $L_r$ .

$L_r$  is defined as  $\sigma_{\text{ref}}/\sigma_y$ . Therefore, for this component geometry, defect size and internal pressure,  $L_r = 168/210 = 0.80$ .

#### 4.35.4 The $K_r$ Parameter

The  $K_r$  parameter quantifies the proximity of the component to failure by fracture in the elastic or small-scale yielding regime of the FAD when  $L_r$  is small. Under these circumstances, if the failure assessment point lies outside the failure assessment curve (the unacceptable region); the component would be assessed to fail by fracture with very limited plastic deformation, that is, the plastic zone is typically less than one-twentieth the size of the uncracked ligament. This condition is illustrated schematically in Figure 4(a), where the crack-tip plastic zone size is small compared with the dimensions of the uncracked ligament just prior to fracture. Failure at intermediate levels of  $L_r$  is shown in Figure 4(b). Within this region, failure occurs with more extensive plasticity emanating from the tip of the crack, such that just prior to the fracture, the plastic zone size is a significant proportion of the uncracked ligament. In contrast to this, and as discussed in the previous Section, failure by plastic-collapse occurs due to the development of plasticity across the full uncracked ligament, Figure 4(c).



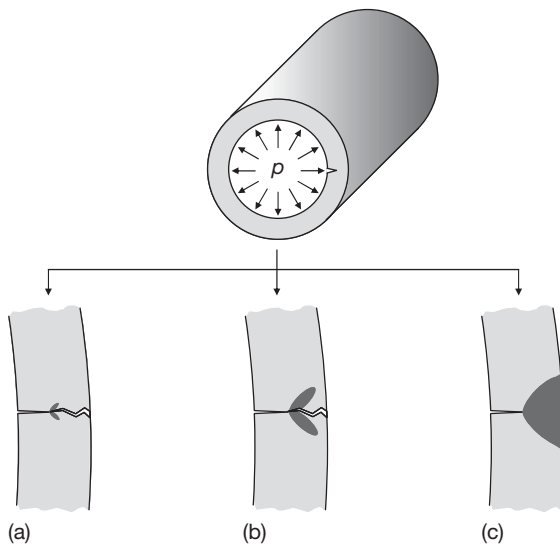


**Figure 4** Schematic illustration of failure by (a) fracture in the elastic or small-scale yielding regime, (b) failure in the elastic-plastic regime, and (c) failure by net section plastic collapse. The dark shaded regions indicate the region of plasticity.

Fracture under linear-elastic or small-scale yielding conditions usually controls component failure when the flaw is small relative to the thickness of the component and when the material has low fracture toughness and high yield stress.

Only under primary loading, the parameter  $K_r$  is defined by the ratio of the linear elastic stress intensity factor  $K_I$  to the fracture toughness  $K_{mat}$  of the material at the temperature of interest. The fracture toughness is defined with respect to the failure mode of interest, that is, cleavage fracture toughness for ferritic materials operating at temperatures within the cleavage fracture regime, or ductile fracture toughness for austenitic stainless steels. For FFS assessment of ductile materials in normal operating conditions, the ductile fracture toughness normally relates to the initiation of ductile tearing, or the fracture toughness at 0.2 mm of stable ductile tearing as measured in a standard fracture mechanics test at the temperature of interest. For ductile materials under particularly infrequent loading scenarios (e.g., postulated accident conditions) some benefit may be taken from the enhanced level of fracture toughness associated with up to 2 mm ductile tearing. However, such FFS assessments would normally be judged on a case-by-case basis.

The fracture failure condition is defined when  $K_I = K_{mat}$ , or equivalently when  $K_r = 1$ . The reader

is referred to **Chapter 1.04, Mechanical Properties and Fracture of Materials** for a full description of the stress intensity factor and the fracture toughness.

#### 4.35.4.1 Example Calculation of $K_r$

This sample calculation is based on the geometry illustrated in **Figure 4** with the following parameters:

Material	AISI Type 304L stainless steel
Temperature	25 °C
Internal radius ( $R_i$ )	120 mm
Outer radius ( $R_o$ )	132 mm
Wall thickness ( $t$ )	12 mm
Crack depth ( $a$ )	8.6 mm
Internal pressure ( $p$ )	10 MPa

Step 1. Define  $K_I$  for the cracked component of interest.

The following equations are used along with the factor parameters  $G_0$  to  $G_4$  given in API 579<sup>4</sup> to define the stress  $\sigma$  and the geometry term  $Y$  for the geometry of interest, that is,  $R_i/t = 10$  and  $a/t = 0.4$ .

$$K_I = \sigma Y \sqrt{\pi a} \quad [10]$$

$$\sigma = \frac{p R_o^2}{(R_o^2 - R_i^2)} \quad [11]$$

$$Y = 2G_0 - 2G_1 \left( \frac{a}{R_i} \right)_1 + 3G_2 \left( \frac{a}{R_i} \right)^2 - 4G_3 \left( \frac{a}{R_i} \right)^3 + 5G_5 \left( \frac{a}{R_i} \right)^4 \quad [12]$$

Inserting the geometry parameters of interest and magnitude of the internal pressure into eqns [11] and [12] gives  $\sigma = 48$  MPa and  $Y = 7.6$ . Using these parameters along with eqn [10] gives the Mode I stress intensity factor for this component and internal pressure of  $K_I = 60$  MPa  $\sqrt{m}$ .

Step 2. Define the fracture toughness  $K_{mat}$  of the material at the temperature of interest.

The fracture toughness AISI 304L stainless steel at 25 °C is given as 230 MPa  $\sqrt{m}$  in Snead *et al.*<sup>6</sup>. Note that fracture toughness properties can vary from cast to cast, with heat treatment, material processing, test temperature, and specimen size. However, this value is considered suitable for illustrative purposes.

Step 3. Calculate  $K_r$

Only Under primary loading,  $K_r$  is defined as  $K_I/K_{mat}$ . Therefore, for this component geometry, defect size and internal pressure,  $K_r = 60/230 = 0.26$ .

#### 4.35.5 The Assessment of Corrosion Defects

This section provides an overview of the guidance provided within the European FITNET procedure for the assessment of corrosion defects.<sup>7</sup> FITNET was a 4-year European thematic network with the objective of developing and extending the use of FFS procedures throughout Europe. The principles of the FITNET procedure are consistent with other assessment methods including BS 7910:2005,<sup>8</sup> R6,<sup>2</sup> and API 579.<sup>4</sup>

The FITNET assessment procedure follows a five-step process:

- Step 1: Characterize the nature of the crack
- Step 2: Establish the cause of cracking
- Step 3: Define the material characteristics
- Step 4: Establish data for stress corrosion cracking assessment
- Step 5: Undertake structural integrity assessment

Each of these steps is described in the following sections.

##### 4.35.5.1 Step 1: Characterize the Nature of the Crack

The NDE of plant components by a range of methods is an important aspect to demonstrating FFS. Once a

defect is located, as much information as possible should be gathered regarding the nature of the crack (or cracks). This should include (though not necessarily be limited to) the following:

- Crack size and shape, including length and depth
- Crack location
  - Relative to stress concentration, weld, crevice
  - Crack path and crack orientation
- If more than one crack is present
  - Crack number density
  - Spacing between cracks
- State of surface
  - General or localized corrosion damage
  - State of coating (if present)

The information gathered will not only provide valuable inputs for FFS assessment, but will also yield information which may guide the focus of future NDE. **Figure 5(a)** illustrates the surface of a 304 stainless steel that has been contaminated by magnesium chloride solution and exposed in a humid atmosphere (60% relative humidity) at 60 °C under a tensile stress. Corrosion pits and a linking stress corrosion crack are visible. A metallographic section taken perpendicular to the crack plane reveals the crack to be substantially transgranular and extremely branched in nature, **Figure 5(b)**.

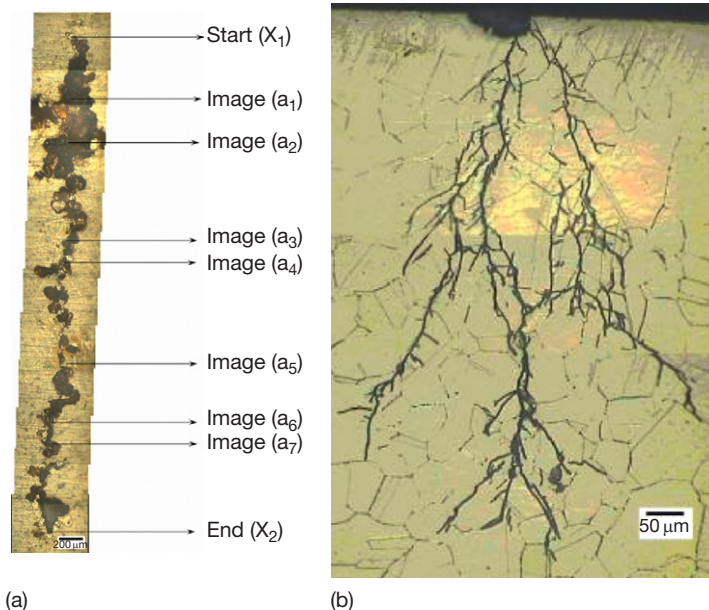


**Figure 5** (a) Surface corrosion damage in 304 stainless steel contaminated with magnesium chloride and exposed to humid air (60% relative humidity) at 60 °C under stress, (b) metallographic section a2 revealing transgranular and branched stress corrosion crack initiated at corrosion pit. Reproduced from, Eble, O.R. M.Sc. Dissertation, *Corrosion and Protection Centre*; The University of Manchester, 2006.

### 4.35.5.2 Step 2: Establish the Cause of Cracking

Since SCC results from a critical combination of environment, stress and a susceptible material, it is important that these three factors should all be understood. Step 2 focuses on clarifying the first two of these, that is, the service environment and the local stress condition. The nature of the material is considered under Step 3.

#### 4.35.5.2.1 Service environment

An understanding of the service environment is important in helping to understand the nature of cracking. This includes factors such as chemistry (including pH, electrochemical potential, and composition including impurities), humidity and temperature.

While the bulk environment may be well understood and controlled, it is important to note that local environmental conditions can develop within, for example, crevices, under deposits, within dead spaces, etc. Such local environmental conditions are often the cause of corrosion-related problems. Factors that should be considered include the level of impurity ions by ion migration, for example, chloride, and concentration processes, for example, due to evaporation.

Excursions from the normal service environment and (or) temperature during the operation of the plant can result in the development of SCC, even though the normal environment is one which might not normally be a concern. Consequently an understanding of the service history can be critical in providing an understanding of the cause of cracking. Under such circumstances, corrosion monitoring systems can be invaluable in identifying occasions when susceptibility to SCC cracking might have been increased.

#### 4.35.5.2.2 Stress

A knowledge of the service loads is also important both in developing an understanding of the cause of cracking and in providing input data to the FFS assessment. These may include:

- applied stresses such as internal pressure
- thermal stresses due to temperature gradients or thermal shocks
- internal (residual) stresses due to manufacturing processes such as welding.

The presence of significant cyclic stresses may lead to the development of fatigue or corrosion–fatigue cracks. Transient stresses, for example, pressure

during the startup or shutdown of equipment, are often important in inducing the propagation of SCC cracks.

In quantifying the stresses, it is important that distinction is made between primary and secondary stresses (as discussed in [Section 4.35.3](#)), that is, primary stresses arise from loads that contribute to plastic collapse and secondary stresses arise from loads that do not contribute to plastic collapse.

#### 4.35.5.2.3 Crack morphology

Within the FITNET procedure, environmentally-assisted cracking under both static (SCC) and cyclic (corrosion–fatigue) loading conditions are considered. The morphology of cracking is often different in each case. For example, corrosion–fatigue cracks are often limited to a single crack path, while SCC cracks can exhibit significant branching ([Figure 5\(b\)](#)). Recognition of the crack morphology can thus provide valuable information regarding the cause of cracking.

### 4.35.5.3 Step 3: Define the Material Characteristics

It is important to ensure that the material that makes up the component is that which was specified during the design and manufacture of the component. In many cases, problems associated with the development of cracks have been attributed to the incorrect selection of material during manufacture, repair, or replacement of the component.

There are a number of particular material factors which will influence the performance of the component. These can arise from the manufacturing process and also from microstructural changes that occur in service. These factors include the following.

#### 4.35.5.3.1 Surface condition

The condition of a surface can significantly influence the subsequent performance of a component. The surface of a material has a number of component parts, which can be divided into four main headings:

- Topography
- Chemistry
- Metallurgy
- Mechanical properties

These may be considered external and internal features. [Figure 6](#), adapted from Griffiths,<sup>9</sup> illustrates the various aspects that contribute to the external and internal features of a surface.

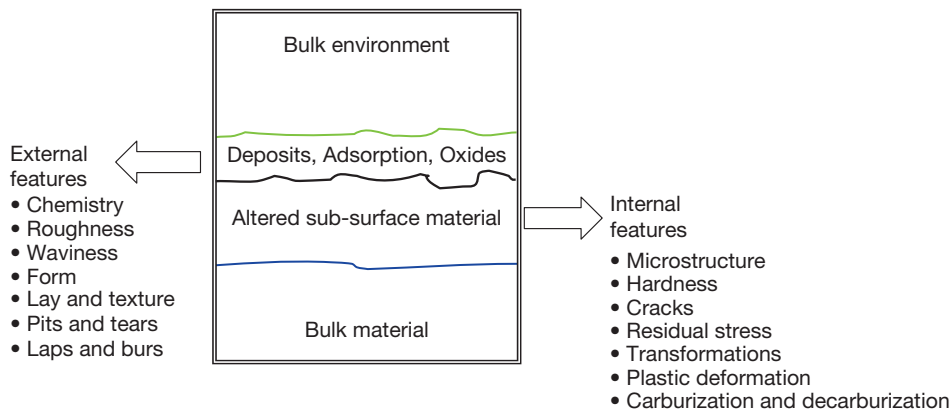


**Figure 6** Summary of key external and internal features which characterize a surface. Adapted from Griffiths, B. *Manufacturing Surface Technology: Surface Integrity and Functional Performance*; Penton Press: London, 2001.

With respect to the initiation of SCC cracks, the key features include surface roughness, which in laboratory specimens is used to study corrosion susceptibility and may typically be of the order of  $1\ \mu\text{m}$ . In plant components, rough machining by grinding, for example, can result in extremely rough surfaces, which also contain a significant degree of plastic deformation (cold work), microstructural damage, and high internal residual stresses. These can all combine to increase the susceptibility to SCC. **Figure 7** illustrates the influence of typical machining (lathe turning) parameters on surface roughness and residual stress in a recent study performed on austenitic stainless steel.<sup>10</sup>

It should be noted that while surface residual stress levels may be tensile, this will be balanced by compressive stresses within the bulk material. Initiating SCC cracks can, under some circumstances, arrest once the tip of the crack reaches the compressive residual stress region.

#### 4.35.5.3.2 Welding

Welds are often a likely region for the development of SCC cracks for two primary reasons. First, weld microstructures are complex and often contain regions of susceptibility to SCC. For example, grain boundary sensitization (chromium depletion) can occur as a result of welding austenitic stainless steels as the parent metal in the heat affected zone (HAZ) cools through the critical temperature range for carbide precipitation  $\sim 850\text{--}450\ ^\circ\text{C}$ . Other microstructural factors can include elongated and clustered inclusions and crystallographic texture. Secondly, residual stress levels can be high, particularly in non stress-relieved welds. In such circumstances, the

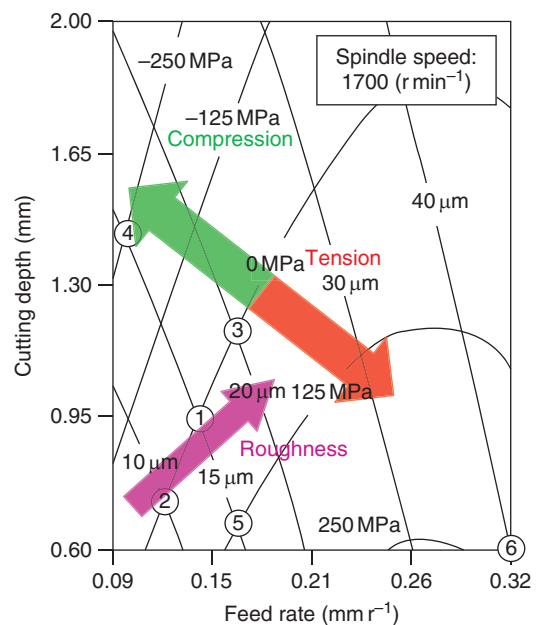


**Figure 7** Influence of machining parameters on surface roughness and surface residual stress of austenitic stainless steel. Reproduced from Kuroda, M.; Marrow, T. J. *J. Mater. Process. Technol.* **2006**, 203(1–3), 396–403.

tensile stress level in the vicinity of a weld can be of yield magnitude. Stress concentrating features including undercuts can also provide local geometric features which enhance SCC susceptibility.

#### 4.35.5.3.3 Initial microstructure

In addition to the factors described above, manufacturing history is also an important factor to consider. For example, rolled plates contain heavily elongated grains aligned in the rolling direction. The morphology

of the grain structure, including local texturing, combined with its influence of mechanical properties, can influence SCC susceptibility.

#### 4.35.5.3.4 Materials ageing

Material microstructure (and hence properties) can often evolve during service as a result of thermal and (or) environmental factors. For example, extended operation of stainless steels at elevated temperatures can lead to the precipitation of chromium carbides and the consequent local depletion of chromium. Cast austenitic stainless steels, which generally contain some residual ferrite, can undergo a spinodal decomposition of the ferrite with an impact on hardness and toughness. Materials operating in a neutron flux such as core internal components of nuclear reactors, will undergo irradiation-induced microstructural changes which can include grain boundary sensitization (without chromium carbide precipitation) and matrix hardening (due to the formation of lattice defects such as vacancies and interstitials, dislocation loops and copper-rich clusters).

#### 4.35.5.4 Step 4: Establish Data for Stress Corrosion Cracking Assessment

The parameter used to assess SCC crack growth rates is  $K_{ISCC}$  which defines the threshold stress intensity factor for sustained crack growth, **Figure 8(a)**. There is a region of applied  $K_I$  below which SCC crack growth is not well characterized. Within this region

the driving force for SCC crack growth may either be too low (and SCC does not occur) or may be stress-controlled. As the applied  $K_I$  increases above  $K_{ISCC}$  the crack growth rate rises rapidly to a plateau. It is important to note that the magnitude of both  $K_{ISCC}$  and the crack growth rate plateau are material and environment-dependent. For example, **Figure 8(b)** reproduced from Cottis<sup>11</sup> shows the influence of copper content on SCC crack growth properties for Al–Cu–Mg alloys. This dependence of SCC crack growth rate with  $K_I$  is in contrast to other failure modes such as fatigue or corrosion–fatigue. Under cyclic loading, the crack growth rate per cycle is controlled by the difference between the maximum and minimum stress intensity factors,  $\Delta K_I$ . A higher  $\Delta K_I$  leads to a more rapid crack growth rate per cycle.

There are a number of issues which should be considered in the measurement and application of  $K_{ISCC}$  data. These include:

- $K_{ISCC}$  will depend on the environment, material condition, and loading configuration used. The conditions used to generate the data should reflect as closely as possible the service conditions of interest.
- The timescales used to generate  $K_{ISCC}$  are often shorter than typical plant operation timescales. Rate effects should be considered.
- While  $K_{ISCC}$  testing is conventionally carried out under static loading, service loading (as we have seen) often includes periodic unloads and reloads (e.g., due to startup and shutdown). Under such circumstances  $K_{ISCC}$  may be affected.

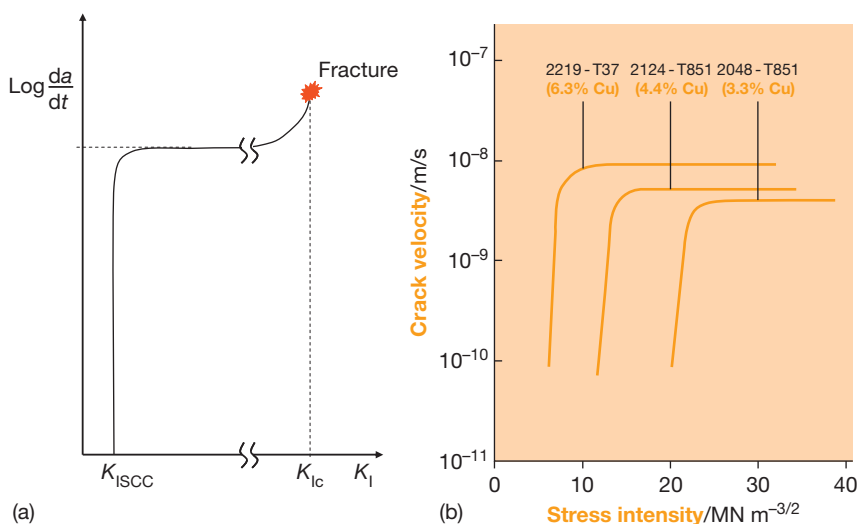


**Figure 8** (a) Schematic illustration of SCC crack growth rate as a function of applied  $K_I$ , and (b) SCC data for Al–Cu–Mg alloys of varying copper content. Reproduced from Cottis, R. A. *Guides to good practice in corrosion control: stress corrosion cracking*, NPL Report, 2000.



ISO 7539-6: 2003<sup>12</sup> provides guidance regarding the generation of  $K_{ISCC}$  data using precracked laboratory specimens loaded under fixed load or fixed displacement conditions.

#### 4.35.5.5 Step 5: Undertake Structural Integrity Assessment

The structural integrity assessment is undertaken with respect to the FAD approach described in detail within the first part of this chapter. **Figure 9** summarizes the key elements of the FAD, as described previously.

There are typically five stages in this assessment:

Stage A: Perform a fracture assessment for the initial crack size. If the failure assessment point lies within the acceptable region, and the size of the crack is significantly smaller than the thickness of the component, preventative measures should be considered to limit further growth of the crack. These may include reducing applied stresses and modifying the environmental chemistry or temperature.

Stage B: If preventative measures cannot be applied and subcritical crack growth can be tolerated, steps 1–4 should be followed to fully characterize: (a) the nature of cracking, (b) the environment, stress level, and material of concern, and (c) material

properties to quantify SCC crack growth rate for the material/environment combination of interest.

Stage C: Calculate the stress at the crack location, including applied, thermal, and internal stresses as appropriate.

Stage D: Determine the rate of increase of the size of the crack according to the crack growth law appropriate to the material/environment combination of interest.

Stage E: Determine the time for the current size of the crack to reach the critical crack size, including an appropriate in-service safety margin. This is undertaken by performing a series of FFS assessments and plotting a series of failure assessment points, each applicable to a given crack size, on the FAD. The critical crack size is defined when the failure assessment point lies on the failure assessment curve. Inspection intervals can be defined on the basis of such calculations, providing evidence that the growth rate is above or below that used in the assessment.

#### 4.35.6 Worked Example FFS Assessment

A flat plate component of width  $2W = 100$  mm and thickness  $t = 25$  mm is under a normal operating

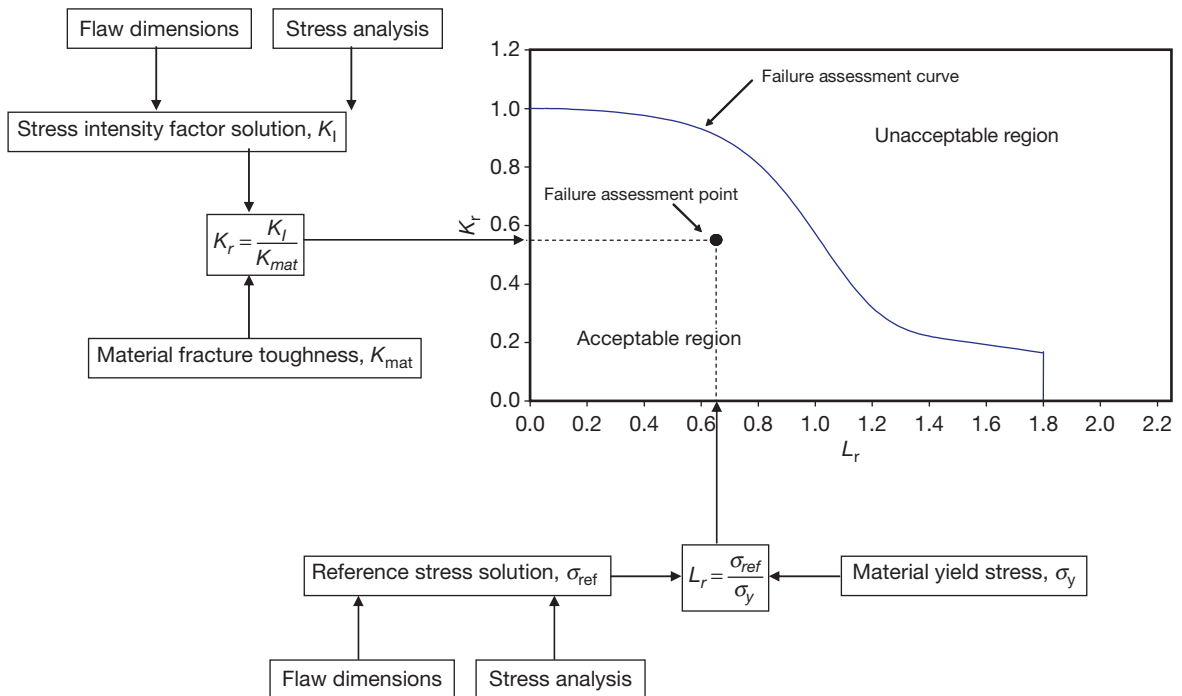


**Figure 9** Summary of the key components of the failure assessment diagram.

membrane stress  $\sigma_m = 100$  MPa. As shown in **Figure 10**, a semielliptical flaw of depth  $a = 5$  mm and surface-breaking length  $2c = 50$  mm has been discovered in the component by nondestructive examination. The material fracture toughness is equal to  $40 \text{ MPa}\sqrt{\text{m}}$ , the yield stress is equal to  $450 \text{ MPa}$ . Stress corrosion cracking data for the material and environment of interest suggest that  $K_{\text{ISCC}}$  is equal to  $10 \text{ MPa}\sqrt{\text{m}}$  for this material and environment. Above this stress intensity factor, both  $a$  and  $c$  will increase at a rate of  $1 \text{ mm}$  per annum.

- Plot the failure assessment point on the FAD to demonstrate whether the component is safe to continue operation.
- Use the FAD approach to estimate: (i) the maximum membrane stress that the component can withstand before failure and (ii) the maximum safe life of the component under normal operating stress.

#### 4.35.6.1 Worked Example Part A

##### 4.35.6.1.1 Calculation of $L_r$

The reference stress for the geometry shown in **Figure 10** is defined by Solution D3.4 in API 579<sup>4</sup> as:

$$\sigma_{\text{ref}} = \frac{gP_b + [(gP_b)^2 + 9P_m^2(1 - \alpha^2)]^{0.5}}{3(1 - \alpha)^2} \quad [13]$$

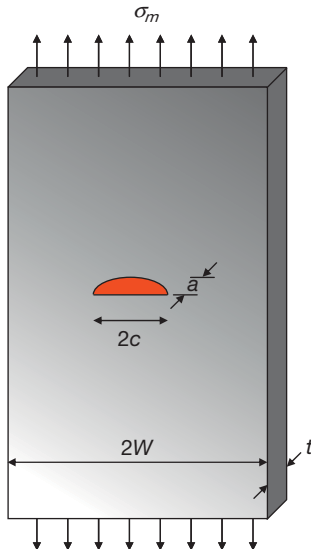


**Figure 10** Schematic illustration of a flat plate component containing a semielliptical flaw of depth  $a$  and surface breaking length  $2c$  under an applied tensile membrane stress  $\sigma_m$ .

where

$$g = 1 - 20\left(\frac{a}{2c}\right)^{0.75} \alpha^3 \quad [14]$$

$$\alpha = \frac{a/t}{1 + t/c} \quad \text{for } W \geq (c + t) \quad [15]$$

and  $P_b$  is the through-wall primary bending stress component equal to zero in this example and  $P_m$  is the primary membrane stress component equal to  $\sigma_m$  in this example. This solution assumes that any induced bending of the plate due to the presence of the defect is restrained.

Using the dimensions of the component and defect, the parameter  $\alpha$  is equal to

$$\alpha = \frac{5/25}{1 + 25/25} = 0.1 \quad [16]$$

The parameter  $g$  is equal to

$$g = 1 - 20\left(\frac{5}{50}\right)^{0.75} 0.1^3 = 1 - 3.556 \times 0.001 = 0.996 \quad [17]$$

The reference stress is therefore equal to

$$\begin{aligned} \sigma_{\text{ref}} &= \frac{0.996 \times 0 + [(0.996 \times 0)^2 + 9 \times 100^2 (1 - 0.1^2)]^{0.5}}{3 \times (1 - 0.1)^2} \\ &= \frac{[89100]^{0.5}}{2.43} = 123 \text{ MPa} \end{aligned} \quad [18]$$

Since  $L_r = \sigma_{\text{ref}}/\sigma_y$ , for the defect found  $L_r = 123/450 = 0.27$ .

##### 4.35.6.1.2 Calculation of $K_I$

The stress intensity factor for the geometry shown in **Figure 10** is defined by Solution C3.4 in API 579<sup>4</sup> as

$$K_I = (M_m \sigma_m + M_b \sigma_b) \sqrt{\frac{\pi a}{Q}} \quad [19]$$

Where  $M_m$  and  $M_b$  are the membrane and bending correction factors, respectively,  $\sigma_b$  is the applied bending stress (equal to zero in this example) and  $Q$  is a geometry factor given by

$$\begin{aligned} Q &= 1.0 + 1.464\left(\frac{a}{c}\right)^{1.65} \quad \text{for } a/c \leq 1.0 \\ &= 1.0 + 1.464\left(\frac{5}{25}\right)^{1.65} \\ &= 1.0 + 0.103 = 1.103 \end{aligned} \quad [20]$$

The membrane correction factor  $M_m$  is dependent upon the plate and defect geometry as well as the location on the defect front of interest. Since the stress intensity factor is maximum at the deepest

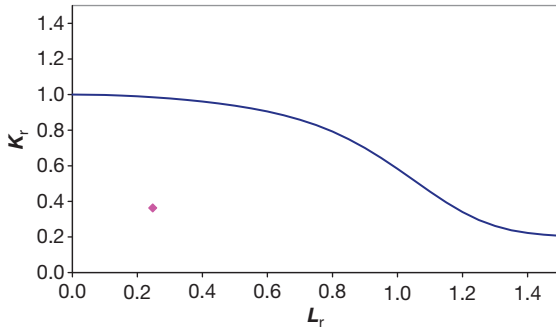


**Figure 11** Failure assessment diagram for semielliptical flaw ( $a = 5$  mm,  $2c = 50$  mm) in a flat plate under membrane stress of 100 MPa.

point of the defect, this location is used to define  $K_I$ . Using the equations provided in API 579,<sup>4</sup> the membrane correction factor  $M_m = 1.217$ .

The stress intensity factor at the deepest point on the defect is thus given by

$$K_I = (1.217 \times 100) \sqrt{\frac{\pi \times 0.005}{1.103}} = 121.7 \times 0.119 = 14.5 \text{ MPa}\sqrt{\text{m}} \quad [21]$$

Since  $K_r = K_I/K_{mat}$ , for the defect found  $K_r = 14.5/40 = 0.36$

#### 4.35.6.1.3 Plotting failure assessment point on FAD

The failure assessment point for the component shown in Figure 10 is simply plotted on the general FAD using the values calculated for  $K_r$  and  $L_r$  above, along the general failure assessment curve defined by eqn [1]. The result, illustrated in Figure 11, shows that the point lies below the failure assessment curve and therefore within the 'acceptable' region of the diagram. The component is thus safe to continue operation.

#### 4.35.6.2 Worked Example Part B(I)

The calculation of the maximum membrane stress that the cracked plate can withstand is undertaken by repeating the calculation described in Part (a) for higher stresses, and plotting the resultant family of failure assessment points on the FAD. This is illustrated in Figure 12, which indicates that the failure assessment point moves from the safe and acceptable region of the diagram to the unacceptable region at an applied membrane stress of  $\sim 250$  MPa.

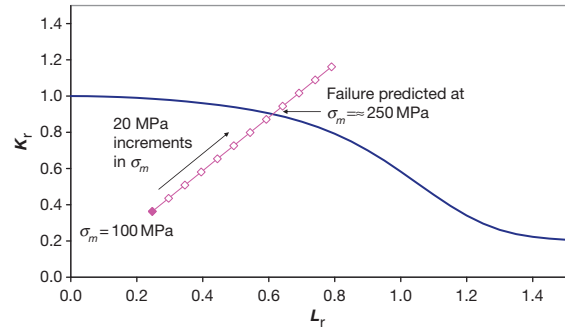


**Figure 12** Failure assessment diagram for semielliptical flaws ( $a = 5$  mm,  $2c = 50$  mm) in a flat plate under an increasing membrane stress. Failure predicted at an applied stress of 250 MPa.

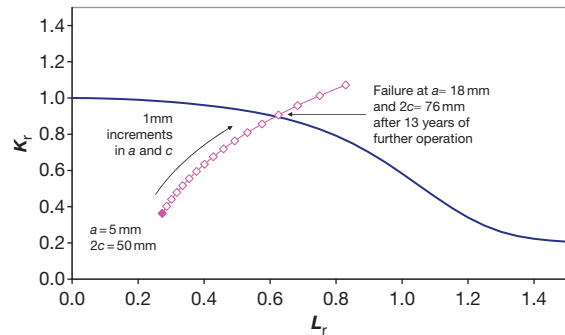


**Figure 13** Failure assessment diagram for semielliptical flaws of increasing size in a flat plate under an applied stress of 100 MPa. Failure predicted at a defect size of approximately  $a = 18$  mm.

#### 4.35.6.3 Worked Example Part B(II)

The calculation of the maximum safe life of the component is undertaken by first assessing whether the applied stress intensity factor is greater than  $K_{ISCC}$ . The value for  $K_I$  calculated above was equal to  $14.5 \text{ MPa}\sqrt{\text{m}}$ , see eqn [21]. This is above the value of  $K_{ISCC}$  given for this material and environment combination. Therefore the dimensions  $a$  and  $c$  will both increase by  $1 \text{ mm year}^{-1}$  by SCC. The second step is to repeat the calculation described in Part (a) for defects of increasing size, and plot the resultant family of failure assessment points on the FAD.

This is illustrated in Figure 13, which indicates that the failure assessment point moves from the safe and acceptable region of the diagram to the unacceptable region at a defect size of approximately  $a = 18$  mm and  $2c = 76$  mm. As the starting flaw size was  $a = 5$  mm and the defect is estimated to propagate at a rate of 1 mm per year, this equates to 13 years of continued operation.

## References

1. ASME Boiler & Pressure Vessel Code – Section III – Rules for Construction of Nuclear Power Plant Components, 2007.
2. R6 Revision 4, Assessment of the integrity of structures containing defects, British Energy Generation Ltd., 2006.
3. Lu, M.-W.; Chen, Y.; Li, J.-G. *J. Press. Vess. Technol.* **2000**, 122, 2–8.
4. API 579. Fitness for Service American Petroleum Institute Recommended Practice, 2000.
5. MatWeb online database, [www.matweb.com](http://www.matweb.com).
6. Snead, L. L.; Stoller, R. E.; Sokolov, M. A.; Maloy, S. J. *Nucl. Mater.* **2002**, 307–311(Part 1), 187–191.
7. European Fitness-for-service Network, FITNET Fitness-for-Service Procedure, Final draft Mk. 7, prepared by European Fitness-for-Service Thematic Network – FITNET, 2006.
8. BS 7910:2005. Guide to methods for assessing the acceptability of flaws in metallic structures British Standards Institution, 2005.
9. Griffiths, B. *Manufacturing Surface Technology: Surface Integrity and Functional Performance*; Penton Press: London, 2001.
10. Kuroda, M.; Marrow, T. J. *J. Mater. Process. Technol.* **2006**, 203(1–3), 396–403.
11. Cottis, R. A. Guides to good practice in corrosion control: stress corrosion cracking, NPL Report, 2000.
12. ISO 7539-6:2003. Corrosion of metals and alloys – stress corrosion testing – part 6: Preparation of pre-cracked specimens for tests under constant load or constant displacement International Standards Organisation, 2003.

## 4.37 Management of Corrosion of Automobiles

**N. R. Whitehouse**

PRA Coatings Technology Centre, 14 Castle Mews, High Street, Hampton TW12 2NP, UK

© 2010 Elsevier B.V. All rights reserved.

4.37.1	Introduction	3167
4.37.2	Corrosion of Automotive Bodywork	3167
4.37.2.1	Mechanisms and the Most Common Sites of Corrosion	3168
4.37.3	Advances in the Prevention of Corrosion in Automotive Bodywork	3169
4.37.3.1	Improvements in Design	3170
4.37.3.2	Advances in Materials	3170
4.37.3.3	Corrosion Protection by the Paint System	3171
4.37.3.3.1	Pretreatment	3171
4.37.3.3.2	Priming	3172
4.37.3.3.3	Seam sealants and anticorrosive waxes	3173
4.37.3.3.4	Surfacers	3173
4.37.3.3.5	Antichip coatings	3173
4.37.3.3.6	Underbody protection	3173
4.37.4	Concluding Remarks	3174
References		3174

### Glossary

**Monocoque** A vehicle body fabricated from a single piece of material with no separate load-bearing parts.

**Electrocoating** A process for applying paint involving application of a DC potential to a submerged work piece to attract paint particles that carry an opposite charge.

**Electroendosmosis** The movement of the liquid medium of a colloidal solution towards an electrode.

**Electrophoresis** The separation of ionic molecules by their differential migration through a gel in an electric field, according to the size and charge of the molecules.

### Abbreviations

**OEM** Original equipment manufacture

**PVC** Polyvinyl chloride

the modern motor vehicle. A mild-steel car body can be exposed to strong sunlight and high surface temperatures in the summer and to freezing temperatures, surface condensation, frost, ice, and snow in the winter. Rainfall, throughout the year, wets the vehicle regularly, but may not necessarily wash it clean. The paint finish may be damaged by road stone impacts and can be attacked chemically by deicing salts and any aggressive airborne pollutants present in the local environment.

Over the past 25 years, the automotive industry has made significant advances in corrosion engineering management, by adopting an integrated approach to design, material selection, and protective coating technologies, in particular the use of multicoat paint systems and compatible sealants.

The real improvements that have been made in total vehicle corrosion protection have been reflected, most noticeably, in the longer antiperforation warranties now offered, as standard, by most of the volume car makers.

### 4.37.2 Corrosion of Automotive Bodywork

The bodywork of modern automobiles consists of separate steel panels and reinforcing sections, which are joined together by electrical-resistance spot welds

#### 4.37.1 Introduction

No other mass-produced consumer product suffers attack from its service environment as persistently as



and runs of seam welds. The resulting (monocoque) construction, which will accommodate slight movement and flexing as the vehicle travels over uneven road surfaces, contains a number of small crevices and relatively inaccessible areas. It is in these crevices and localized box sections that the likelihood of corrosion is greatest. Dirt and road salts will, over time, find their way into any unprotected crevices and structural joints. When moist, accumulations of such deposits provide a favorable environment for corrosion to occur and then to advance.

Environmental conditions have a great effect on the rates of corrosion. The rates are at their highest in damp atmospheres, because the dirt and debris present will absorb moisture from the atmosphere more readily. Salt deposits and chemical pollution cause the most rapid corrosion. Condensation and dew will favor corrosion more than heavy rain, as rain water can often wash away surface dirt and road salts, leaving a relatively clean and evenly wetted surface.

Serious corrosion of vehicle bodywork almost always starts from the inner side of the metal surface. The first sign on the outer painted surface of the bodywork is usually localized blistering and lifting of the coating system. If left to advance, the corrosion will result ultimately in perforation of the metal panel and possible structural weakening. Corrosion of the bodywork from the outside, for example, as a result of stone chipping or scratching, is usually slow to advance and may remain 'cosmetic' for a long time, as modern automotive paint systems have good adhesion to the steel surface and good anticorrosive properties. These performance qualities can limit substantially the spread of corrosion by undercutting.

Some typical examples of corroded bodywork are shown in [Figures 1–3](#).

#### **4.37.2.1 Mechanisms and the Most Common Sites of Corrosion**

The corrosion that is found most often on automotive bodywork is the result of pitting corrosion. Crevice corrosion and corrosion due to fretting may also occur, and the so-called 'waterline corrosion' can still sometimes be seen on the external bodywork of older vehicles.

Localized pitting corrosion is an electrochemical process involving differential aeration cells. In the presence of an electrolyte, current flows from one area of the bodywork which is not well oxygenated (the anode), to another region which is well oxygenated (the cathode). The corrosion takes the form



**Figure 1** Incipient panel perforation.



**Figure 2** Corrosion along a panel bend.



**Figure 3** Corrosion along a door sill.

typically of small pits on the metal surface. Once initiated, these corrosion pits may develop rapidly.

Pitting corrosion may occur wherever particles of dirt have settled on the undersides of the metal bodywork and given rise to a difference in the oxygen concentration, compared with surrounding, cleaner areas. When part of a metal surface is covered by a drop of water, for example, anodic and cathodic regions can be set up as a consequence of differences in oxygen concentrations – the area underneath the droplet is starved of oxygen and becomes anodic; adjacent areas, not starved of oxygen in this way, become cathodic. Metal wastage then occurs in the anodic areas.

When the drop of water contains dissolved salt from the roads, its conductivity is increased and the corrosion rate is accelerated. Microclimates formed within the bodywork during the service life of a vehicle will usually provide the moisture needed for such corrosion reactions to proceed.

Whenever a motor vehicle moves at speed along a wet road, spray produced by the tires is deposited on the undersides, most often in each of the wheel arches. Some wet dirt from the road may also be propelled towards the undersides of the body. This dirt may contain salt in winter months, if deicing of the road has been needed. The faster the speed of the vehicle, the less water is associated with the dirt and the more the dirt will be compacted. In addition, the more the speed of the vehicle, the less the momentum of the road dirt and the more likely it is for the road dirt to be deflected into crevices in the bodywork by the pressure eddies created around a fast moving vehicle by turbulence.

Damp, dirt, road salts, and general debris that are then thrown towards the undersides of a vehicle in this way collect not only over headlights, but also on ledges, some of which may be out of the line of any direct spray. These relatively inaccessible ledges may not then be cleaned when driving subsequently in wet conditions.

The sites on vehicle bodywork most prone to pitting corrosion include, therefore:

1. all underbody areas where road dirt can accumulate and restrict natural drying;
2. beneath mud poultrices, wherever they have formed;
3. within poorly protected (or damaged) folds and flanges of the bodywork;
4. beneath poorly adherent, but coherent, paints and protective coatings.

In vehicle bodywork, crevice corrosion can develop, in the presence of moisture, where two metal surfaces

have been joined together. The deeper part of the crevice that is formed is often starved of oxygen and so becomes anodic. Most commonly, small crevices are formed when body panels have been joined by spot welding. Over time, these small crevices fill with dirt, preventing evaporation of any moisture present and concentrating electrolyte in a small area. Corrosion may advance rapidly.

Bolted joints are also susceptible to crevice corrosion, unless the two metal surfaces can be separated from each other electrically, by insulating washers. Corrosion will again occur in the least oxygenated regions. In the case of bolted joints, crevice corrosion of the thread will then cause the bolt to seize.

Fretting corrosion (localized corrosion as a consequence of fretting) can occur in motor vehicles. Body panels and structural members in close contact with each other may be subjected to repeated vibration, as the vehicle travels along the road. While such vibrational movement is usually small, it can lead, over time, to fretting of loose particles of metal and paint coatings. If the resulting loose particles then act as abrasives, they may damage otherwise sound surfaces and lead to corrosion. Vehicle doors, bonnets, and boot lids, if too closely fitting, for example, or if distorted as the result of an accident, are susceptible to localized fretting corrosion in this way.

Waterline corrosion in automobile bodywork is sometimes referred to as dirt-wick corrosion. It can develop where condensation may be trapped and collect, within the sills, for example. The lower parts of the doors are also prone to this type of corrosion. The problem is caused usually by rain-water penetrating old window seals in car doors and then collecting in the bottom sections. If dirt and debris also accumulates in these areas and blocks the drainage holes, a moist poultice forms. Wicking action, over time, sets up an unequal oxygen concentration above and below the resulting waterline because oxygen is available freely above the waterline and is restricted below. The rate of waterline corrosion, once established, can be rapid.

Corrosion prediction and prevention in motor vehicles has been described, illustrated, and explained in detail by McArthur.<sup>1</sup>

#### **4.37.3 Advances in the Prevention of Corrosion in Automotive Bodywork**

The corrosion resistance of motor vehicles has improved markedly over the past 25 years, permitting

longer and longer antiperforation warranties to be offered by the manufacturers, currently up to 12 years.

The improvements have stemmed from significant advances in:

1. design;
2. material selection;
3. protective paint coating systems and application methods;
4. sealants and application methods.

#### **4.37.3.1 Improvements in Design**

Many of the choices made by designers of motor vehicles may impact on the susceptibility of the vehicle to corrosion. In recent years, however, corrosion resistance has assumed a much greater prominence, driven by the warranty system, and designers now recognize clearly the consumer's need not only for pleasing, modern body envelopes but also for the best possible corrosion resistance and long-term durability that are achievable commercially.

Vehicle designers, working closely with engineering support teams, now strive to reduce high stresses in bodywork panels, for example, by avoiding the deep pressings needed to produce sharp changes of curvature. Modern body shapes tend to be much smoother and more rounded than they used to be. Smooth body profiles ensure the best possible drainage of water from the surface, not only in the pretreatment and priming stages of manufacture but also in functional use. Smoother body profiles also keep to a minimum awkward corners where dirt and road salts could accumulate and ensure that if there are any unavoidable crevices, they can be reached, in subsequent manufacture, by the robots used to apply sealant.

The avoidance of contact between dissimilar metals and the ensuing risk of bimetallic corrosion on vehicle bodywork have been largely eliminated by the introduction of plastic bumpers, radiator grilles, and door handles and nonmetallic protective side trim.

Problems of bimetallic corrosion are now limited largely to the sophisticated electronic control systems which manage modern engines, regulate anti-lock braking systems, and stabilize traction.

#### **4.37.3.2 Advances in Materials**

For many years, the dominant material of construction for automotive bodywork was carbon steel. Major advances were made initially in the mid-1970s with

the introduction of precoated steels, electrogalvanized steels, and other corrosion-resistant materials. Zinc-coated steels (coated on one side only initially) were used to protect the inner surface of body panels, leaving the outer surface uncoated and available for painting.

By the mid-1980s, two-sided electrogalvanized sheet and other zinc alloy steels had become widely available and were being used to manufacture exterior body panels. By virtue of being coated on both sides, the material afforded protection not only from internal perforation corrosion but also from external cosmetic corrosion. It was the introduction of these two-sided zinc/zinc alloy materials that made extended antiperforation and cosmetic corrosion warranties into a reality.

Over the past 15 or so years, a variety of alternative nonferrous materials, predominantly aluminum alloys and plastics, have found automotive applications. Their introduction has presented new challenges. It has driven forward advances in pretreatments for mixed metal assemblies and has helped to define suitable methods of surface preparation, prior to painting plastic bumpers, for example, to color-match the rest of the vehicle bodywork. The use of plastic materials in modern automobiles is increasing, and has contributed significantly to the industry's goal of corrosion avoidance. Plastic components have allowed weight reductions to be made and, as a consequence, savings in fuel consumption and vehicle emissions. Plastic panels present their own design challenges, however, as they contribute very little to the structural rigidity of the vehicle body, as a whole.

Aluminum alloys offer two benefits over carbon steel. First, they are much lighter, and second, they are more corrosion resistant. Aluminum alloys have been used successfully by some vehicle manufacturers for the bonnets and boot lids, primarily to reduce total weight and so improve fuel efficiency.

Improvements in the corrosion resistance of exhaust systems have demonstrated most clearly the benefits of material selection. Stainless steel exhaust systems are known to have very good corrosion resistance and much improved durability. They have not been favored widely by consumers, however, as they are significantly more expensive than their carbon steel counterparts. Aluminized steel silencers, however, are now available widely and represent a good compromise: almost as good performance, at a lower cost. The clear benefit of fitting, as standard, more corrosion-resistant aluminized steel vehicle exhaust systems was advocated by Hoar<sup>2</sup> as long ago as 1971

as a relatively simple and inexpensive way of reducing the overall cost of automobile corrosion. The implementation of his advice by vehicle manufacturers, as the availability of the products increased, has been very successful.

#### 4.37.3.3 Corrosion Protection by the Paint System

The preparation and painting of new automobiles is now a sophisticated, high-speed industrial process, with vehicle bodies passing through the entire coating line in 6–10 h.

The automotive paint systems used have been developed over the past 35 years and provide, today, not only highly durable finishes but also robust corrosion protection. The extended perforation warranties (up to 12 years) offered currently by vehicle manufacturers are a reflection of the considerable advances that have been made.

A typical paint system for a new vehicle consists of:

1. a primer (applied at a dry film thickness of 18–25  $\mu\text{m}$ );
2. a surfacer (applied at a dry film thickness of 35–40  $\mu\text{m}$ );
3. an antichip coating (applied at a dry film thickness of 50–100  $\mu\text{m}$ );
4. a finish (applied at a total dry film thickness of 45–55  $\mu\text{m}$ ).

Corrosion protection is afforded primarily by the primer and intermediate coats of the paint system. The function of the finish is to provide good appearance and customer appeal as well as good resistance to weathering, surface scratching, and surface contamination.

Initial cleaning and chemical pretreatment of the vehicle body has also advanced in recent years and provides the foundation needed for the subsequent paint system.

The contributions made by metal pretreatment, primers, surfacers, antichip coatings, and underbody protection (only) to the corrosion protection of the bodywork today on new automobiles will, therefore, be considered further.

##### 4.37.3.3.1 Pretreatment

Metal pretreatment of automotive car bodies has three main purposes:

1. to remove any surface corrosion products, pressing oils, and temporary protective coatings;

2. to improve the adhesion of the subsequent primer coat to the metal surface;
3. to minimize the spread of underfilm corrosion.

The effective removal of the oils and greases used to lubricate body panels during the forming processes has improved the subsequent efficiency of modern, new vehicle coating lines substantially.

Zinc phosphate pretreatment is used almost universally in modern automotive painting plants to provide metal cleanliness and the first stage of the corrosion protection. A typical zinc phosphate process begins with multiple cleaning stages, followed by a titanated activating rinse, zinc phosphate pretreatment, and a sealant rinse. The process is completed by multiple rinses with deionized water. In total, a seven-stage process is now typical, followed by a heated (oven) drying-off stage.

The cleaning and phosphating process is carried out on a conveyORIZED system. For the cleaning step, a weakly alkaline degreasing solution of aqueous mixtures of salts, wetting agents, and emulsifiers is used. This cleaning solution is applied by a combination of spray and dip treatments, at temperatures of 40–60 °C. The most effective removal of drawing oils takes place in the dip tanks, as full immersion allows the insides of box (strengthening) sections to be reached.

Uniformity of application of the subsequent zinc phosphate conversion coating then takes place in two stages. The clean metal surface is first activated, and the layer of phosphate crystals is then built up, typically to a thickness of 1–2  $\mu\text{m}$ .

There have been a number of developments in pretreatment processes in recent years, primarily to meet the demands of mixed-metal assemblies, energy efficiency, and environmental pressures.

Significant developments have included:

1. nickel- and manganese-enriched zinc phosphates, with controlled fluoride addition;
2. lower temperature processes and chrome-free rinses, for reduced energy cost and environmental impact;
3. optimum control of process parameters through computerized instrumentation;
4. changes from spray-and-dip to full dip processes.

The benefits from these recent developments have included:

1. excellent performance under cathodic electrocoat primers;
2. good phosphate crystal morphology;

3. reduced energy consumption;
4. the requirement for a chrome post-rinse eliminated by the introduction of safer products, such as titanates.

#### 4.37.3.3.2 Priming

The function of the primer is to provide the main corrosion protection for the automotive body. Primers are generally of the 'inhibitive' type – containing anticorrosive pigments in a film-forming binder. They are required to inhibit the spread of corrosion on the metal substrate, resulting from any defects in the coating system as a whole; to have good resistance to mechanical damage (notably chipping); and to prevent the spread of corrosion from such points of damage. In order to provide these performance requirements, they must have not only good adhesion to the pretreated metal substrate but also good adhesion to the coating applied subsequently (surfacers) of the full paint system.

The significance of the priming stage in the corrosion protection of automobile bodies is reflected in the number of innovative technological developments by automotive paint manufacturers for original equipment manufacture (OEM) over the last 40 years.

With the advent of welded unit construction of car bodies (monocoque construction) in the mid-1940s, many areas of the individual units were virtually inaccessible to a spray gun, for example, the internals of strengthening cross-members and the front end near door posts. Spray application of primers was no longer feasible, therefore, and dipping processes were introduced. Initially, dipping primers were solvent-borne, but in the 1960s waterborne formulations were introduced, leading ultimately to the development of modern electrocoat primers.

In moving towards electrocoat priming, which is now the most widespread process for applying an anticorrosive primer to mass-produced, new automobile bodies, the automotive industry has progressed from dipping of car bodies up to window level (the so-called 'slipper' dip process) to full immersion dip coating which, when first used with early waterborne dip primers, resulted in unwanted runs and sags in the coating on car body panels with complex design curvature.

Electrocoat priming of automobiles began in the late 1960s. Within 5 years, almost all mass-produced vehicles were primed in this way. Electrocoat priming offered several benefits to motor vehicle manufacturers, including:

1. uniform film build (15–35  $\mu\text{m}$ ) on all surfaces in contact with the liquid primer, including areas previously difficult to coat effectively: for example, voids in box sections;
2. greater corrosion resistance from improved coverage with a defect-free film of controlled thickness;
3. a highly efficient coating process, with ca. 95% of the coating material deposited in comparison to 50–60% with a conventional dipping primer;
4. greatly reduced solvent emissions and fire hazard.

Electrocoat paints are waterborne coatings containing film-formers (binders), pigments, extenders, and additives. The resulting dispersion will deposit an organic coating on the metal substrate when a direct electrical current is passed. Dispersions stabilized by a negative charge coagulate at the anode and dispersions stabilized with a positive charge coagulate at the cathode.

To enable deposition, the vehicle body is connected to an electrode and is immersed in a tank of the coating dispersion, together with a counter-electrode. The liquid paint is circulated in the tank continuously (forced circulation) to ensure a constant supply of the primer for deposition on the metal surface to prevent the dispersion from settling and, also, to dissipate the heat generated from the flow of the electrical current. The deposition process involves electrolysis, electrophoresis, and electroendosmosis.

Initially, electrocoat primers were of the anodic type, consisting of an acidic film-forming resin solubilized with an organic (amine-type) or inorganic base. In the late 1970s, however, demands for still better corrosion protection, notably in Canada and the colder states of the United States, led to the development of cathodic electrocoating processes. In the cathodic electrocoat process, the acidic component (a carboxylic acid) solubilizes an amine salt of the film-forming resin (epoxy).

The main reasons for the rapid change from anodic to cathodic electrocoat priming were as follows:

1. improved corrosion protection (a 3–4-fold improvement, in conjunction with suitable chemical pretreatment);
2. dissolution of iron no longer being favored;
3. improved 'throwing power' (penetration and better coating of voids);
4. corrosion protection at lower film thicknesses (18–22  $\mu\text{m}$ , compared with 25–35  $\mu\text{m}$  for an anodic electrocoat primer).



There have been several generations of cathodic electrocoat primers over the last 30 years. Each new generation has been developed to meet changes in vehicle manufacturing methods and the requirements of increasingly stringent environmental legislation. The most recent formulations are now lead-free and will perform well over low nickel and chrome-free pretreatments. Primers now cure at lower temperatures (130–150 °C) and allow steel components to which plastic parts have already been attached to be co-processed.

The development of electrocoat primers has been described in detail by Ansdell<sup>3</sup> and by Vachlas.<sup>4</sup>

#### **4.37.3.3.3 Seam sealants and anticorrosive waxes**

Sealants are usually applied to specific areas of the automotive vehicle body after the electrocoat primer has been applied. Anticorrosive waxes, however, are not usually applied until the final stage of the painting process, often while the painted metal sections are still hot, in order to aid both flow and penetration into cavities and joints.

The application of sealing compounds improves considerably the overall corrosion protection of weld seams and other jointed areas. In most modern car plants, the polyvinyl chloride (PVC) or polyurethane-based sealants used currently are applied by a hot, airless spray. Application is no longer a manual process, as these specialist coating products can be applied more effectively and more consistently by robots.

Anticorrosive waxes, where they are still employed, are also applied by spray. These wax coating products are based typically on polyethylene waxes, with added thickeners and anticorrosive pigments. They are used by some vehicle manufacturers to provide additional corrosion protection, for example, inside door cavities. The waxes are inert, water repellent, and relatively impermeable to moisture.

#### **4.37.3.3.4 Surfacer**

Surfacers, sometimes referred to as primer surfacers or filler coats, continue to play an important role in automotive coating systems. They are applied not only to the exterior of the vehicle body but also underneath the bonnet and inside the boot. The vehicle body is given, therefore, an intermediate coating that provides not only an additional defense against corrosion but also protects the electrocoat primer from damage.

The main function of surfacers, however, is still to fill and smooth any unevenness in the exterior

bodywork and provide a surface which, with the minimum of sanding (none may be required), can then be coated with the topcoats of the automotive system (basecoat and clearcoat). Surfacer have evolved considerably over recent years to be compatible with new developments in topcoat technologies, meet higher performance standards, and comply with environmental requirements.

In addition to good sandability (and repair), these multifunctional coatings must:

1. possess good mechanical properties – notably flexibility and impact resistance;
2. be resistant to stone chipping, water, and moisture;
3. have good adhesion to the cathodic electrocoat primer, seam sealants, antichip coatings, and the subsequent basecoat of the finish.

Polyester resins, combined with a suitable polyurethane resin, are now recognized as the best binder systems for surfacers. The pigmented surfacer coatings are applied at a typical dry film thickness of 35–40 µm and, increasingly are now color-coded to match the color of the topcoat.

The development of surfacers has been described in detail by Ansdell.<sup>5</sup>

#### **4.37.3.3.5 Antichip coatings**

Antichip coatings are now a well-established component of modern automotive paint systems. First introduced some 20 years ago, the primary function of these softer coatings is to provide stone-chip resistance on vulnerable areas of the car body, such as door sills, the bodywork below the front and rear bumpers, the leading edge of the bonnet, and the underbody of the vehicle.

Antichip coatings are applied by spray at typical dry film thicknesses of 50–100 µm, usually ‘wet-on-wet’ and immediately after application of the surfacer. The two coatings (surfacers and antichip) are then cured at an elevated temperature (stoved), in a common process step. It follows that good compatibility between the antichip coating and the surfacer is needed, so antichip coatings are formulated with similar polyester/polyurethane resins.

#### **4.37.3.3.6 Underbody protection**

Underbody coatings are protective coatings applied, by spray, at high film thicknesses (up to 1000 µm) to the underside of finish-painted vehicles to protect the floor panels from corrosion and abrasion caused by impacts of loose road gravel and other surface debris. These coatings need, therefore, to be durable, elastic,

and to have good barrier properties. Polyurethane-based formulations have superseded the older types of rubber-based underseals.

Some vehicle manufacturers, however, now favor plastic panels over the spray application of liquid coatings for this service function.

#### **4.37.4 Concluding Remarks**

For some 30 years, innovative technology and responses to globalization and market economics have underpinned the automotive industry's successful strategies to control corrosion in motor vehicles. Globalization has accelerated the uptake of new technologies, and manufacturer's warranty schemes have given 'corrosion avoidance' an increasingly high profile in a highly competitive consumer market.

The 'corrosion avoidance' strategy has been very successful, and corrosion problems are now confined largely to the bodywork of motor vehicles over 10 years old.

Corrosion-related failures of some mechanical, electrical, and electronic components, however, continue to occur, and these parts of the supply chain are now under increasing pressure to advance their own 'corrosion avoidance' strategies to the same high level.

Each advance in 'corrosion avoidance' adds directly to the cost of a new vehicle. The most recent study in the United Kingdom into the cost of corrosion,<sup>6</sup> which was reported in 2001, estimated that,

in the United Kingdom the overall additional expenditure for improved management of corrosion by the manufacturer was £160 million in 1999. At the equivalent added cost per vehicle of £90, the potential long-term cost benefit to the purchaser is obvious.

Whatever the final outcome of the current global financial downturn, the interplay among new technology, regulatory requirements, and consumer economics will continue to exert a potent influence on the automotive industry, and its suppliers.

Corrosion management will remain a vital element of that process.

#### **References**

1. McArthur, H. *Corrosion Prediction and Prevention in Motor Vehicles*, 1st ed.; Ellis Horwood: Chichester, 1988; Chapter 4, pp 77–122.
2. Hoar, T. P. *Report of the Committee on Corrosion and Protection*; HMSO: London, 1971.
3. Ansdell, D. A. *Paint and Surface Coatings – Theory and Practice*, 2nd ed.; Woodhead Publishing: Cambridge, UK, 1999; Chapter 10, pp 422–431.
4. Vachlas, Z. *Automotive Paints and Coatings*, 1st ed.; VCH Verlag GmbH: Weinheim, 1995; Chapter 3, pp 28–71.
5. Ansdell, D. A. *Automotive Paints and Coatings*, 1st ed.; VCH Verlag GmbH: Weinheim, 1995; Chapter 4, pp 72–118.
6. Investigation of the cost of corrosion, risk assessment methodologies and procedures for minimising corrosion costs, Degradation of Materials in Aggressive Environments Programme 1998–2001. Report by Paint Research Association to the Department of Trade and Industry, Report DME 5.3 (3), October 2001.

## 4.36 Corrosion Monitoring and Inspection

**C. F. Britton**

Independent Corrosion Consultant, The Butts, Station Road, Kimbolton, Cambridgeshire PE28 0HS, UK

© 2010 Elsevier B.V. All rights reserved.

---

<b>4.36.1</b>	<b>Corrosion Monitoring</b>	3120
4.36.1.1	Definition	3120
4.36.1.2	Benefits of Corrosion Monitoring	3120
4.36.1.3	Making a Case for Corrosion Monitoring	3121
4.36.1.3.1	Objectives	3121
4.36.1.3.2	Budgets	3121
4.36.1.3.3	Choice of technique	3121
4.36.1.3.4	Awareness of limitations of candidate techniques	3122
4.36.1.3.5	Personnel management	3122
4.36.1.3.6	Data management	3122
4.36.1.3.7	Legislation and standards	3123
4.36.1.3.8	Engineering considerations	3123
4.36.1.4	<b>Techniques for Corrosion Monitoring</b>	3124
4.36.1.4.1	Historical development of corrosion monitoring	3124
4.36.1.4.2	Coupons	3125
4.36.1.4.3	Electrical resistance (ER)	3127
4.36.1.4.4	Electrochemical techniques	3128
4.36.1.4.5	Field signature method (FSM)	3131
4.36.1.4.6	Thin layer activation (TLA)	3133
4.36.1.4.7	Chemical analysis	3133
4.36.1.4.8	Hydrogen	3134
4.36.1.4.9	Test heat exchangers and spool pieces	3134
4.36.1.4.10	Monitoring of bacteria	3135
4.36.1.4.11	Process parameters and conditions	3135
4.36.1.5	<b>Industrial Applications and Experience</b>	3135
4.36.1.5.1	Oil and gas industry	3135
4.36.1.5.2	Chemical and petrochemical industry	3139
4.36.1.5.3	Power generation industry	3140
4.36.1.5.4	Miscellaneous process industries	3143
4.36.1.5.5	Pipelines (excluding oil and gas)	3144
4.36.1.5.6	Transportation	3144
4.36.1.5.7	Nuclear waste storage	3145
4.36.1.5.8	Civil engineering	3145
4.36.1.5.9	Atmospheric corrosion monitoring	3145
4.36.1.6	<b>Future Developments</b>	3145
<b>4.36.2</b>	<b>Inspection</b>	3146
4.36.2.1	Introduction	3146
4.36.2.2	Historical Development of Inspection Technology	3146
4.36.2.3	The Need to Inspect for Corrosion Damage	3147
4.36.2.4	Inspecting for Corrosion Damage	3148
4.36.2.5	<b>Inspection Techniques for Corrosion Inspection</b>	3149
4.36.2.5.1	Visual inspection	3149
4.36.2.5.2	Ultrasonics	3150
4.36.2.5.3	Radiological techniques	3154
4.36.2.5.4	Magnetic techniques	3155
4.36.2.5.5	Electrical techniques	3155

---

4.36.2.5.6	Dye penetrant (DPI) and magnetic particle (MPI) surface crack detection	3155
4.36.2.5.7	Acoustic emission	3156
4.36.2.5.8	Thermography	3156
4.36.2.5.9	Fiber optics	3156
4.36.2.6	ILI of Oil and Gas Pipelines	3157
4.36.2.6.1	Background	3157
4.36.2.6.2	Development of ILI vehicles	3158
4.36.2.7	Management of Inspection Programs	3159
4.36.2.8	Specific Industries	3160
4.36.2.8.1	Oil and gas industry equipment	3160
4.36.2.8.2	Chemical and petrochemical plants	3161
4.36.2.8.3	Power plants	3161
4.36.2.8.4	Defense	3162
4.36.2.8.5	Marine	3162
4.36.2.8.6	Road transportation	3162
4.36.2.9	Future Developments	3162
<b>Appendix 1</b>	<b>Standards and Codes of Practice</b>	3163
<b>References</b>		3165

---

## Glossary

**Access fitting** Entry-port system for corrosion monitoring sensors, which can be inserted or withdrawn at system pressure using a heavy duty valve and retriever tool.

**Barrel** US oil industry unit for a container holding 42 US gallons, equivalent to ~159 l or ~35 Imperial (UK) gallons.

**Biocide** A chemical added to plant and pipelines systems to control and kill bacteria.

**Bragg grating** Component of optical sensing technology using fiber sensors.

**Caliper tool** Oil industry term describing a caliper measurement tool for the inspection of corrosion in down-well oil tubing, a specific version of which is the *Kinley caliper tool*.

**Corrosion allowance** Additional thickness of material provided to ensure that the wall thickness does not drop below the minimum design thickness in service.

**Couplant** Special grease or liquid (glycerin or oil) applied to the metal surface where an ultrasonic probe is applied to measure metal thickness or detect defects.

**Coupon** Strip of material that is exposed to a corroding environment to quantify the corrosion rate by weight change.

**Electrical resistance** Technique for corrosion monitoring based on the measurement of changes in the electrical resistance of metal elements to determine the corrosion rate.

**Electrochemical noise** Electrochemical technique relying on measurement and analysis of the spontaneous currents/voltages generated between electrodes in an electrolyte.

**Electromagnetic acoustic transducer** Technique for transmitting and receiving ultrasonic waves to/from the surface of a component without the requirement for contact with an external vibrating transducer.

**Fabry-Perot sensor** Interferometer using fiber optics for sensing several parameters such as temperature, strain, and acoustic waves.

**Fiber optics** Technique for sensing a number of parameters including strain.

**Fractal and neural analysis** Mathematical analysis of shapes and images.

**Galvanic probe** Electrochemical probe using two different metals electrodes for the measurement of galvanic currents.

**Intelligent pigging** Use of an intelligent vehicle (PIG) containing instrumentation that travels in the pipeline for assessing both corrosion loss and stress corrosion cracking; also referred to as inline inspection (ILI).

**Intrinsic safety** The fitting of a sensitive fuse device (zener diode barrier) to electrical equipment in plant handling flammable substances. In UK and other countries, each electrical device must be certificated by a certifying authority.

**Iron count** Oil industry term describing the total iron content in a fluid stream.

**Lateral waves** Ultrasonic waves that are compression waves propagating close to the surface of an object, which continually generate a shear wave propagating into the bulk of the object under test.

**Lorentz force** Force on a point charge due to electromagnetic fields.

**Nyquist diagram** Diagram displaying the frequency dispersion of impedance.

**Piezoelectric crystal** Substance (quartz, lithium sulfate, barium titanate) that emits ultrasonic waves when subjected to an electrical charge.

**Planktonic bacteria** Bacteria suspended in the bulk of liquid flowing in a plant or pipeline system.

**Pressure gland** Pressure seal that can be tightened to withstand defined pressures when installing corrosion probes in a system. For safety reasons, a pressure-gland system is regarded as less reliable than an access system with associated retriever tool.

**Radiography** Technique for examining materials using either X-rays or gamma radiation.

**Radio respirometry** Instrument system investigating the respiration cycle of different bacteria types.

**Raman and Brillouin scattering** Light scattering due to time-dependent density variations in a liquid medium.

**RSTRENG** Calculation to establish the remaining strength of piping or pipeline.

**Retrieval tool** High-pressure balanced tool used for the retrieval of monitoring devices when a system is under pressure.

**Robbin's unit** Unit fitted in a length of pipeline, piping, or vessel containing metal studs used for monitoring for the presence of bacteria.

**Sour systems** Term used by the oil industry to describe a system containing hydrogen sulfide.

**Sessile bacteria** Colony (or colonies) of bacteria metabolizing on the surface of a metal under scale or other deposits shielded from the fluid.

**U-bend coupon** A metal coupon bent into a U-shape and exposed to a corrodant to test for susceptibility to stress corrosion cracking.

**Ultrasonics** Technique using high-frequency sound waves to measure the thickness of material and detect defects.

## Abbreviations

**ADP** Adenose triphosphate photometry

**AE** Acoustic emission

**API** American Petroleum Institute

**ASNDT** American Society for Nondestructive Testing

**ASTM** American Society for Testing Materials

**BG** British Gas

**BINDT** British Institute of Nondestructive Testing

**CONCAWE** European organization for Conservation of Clean Air and Water

**CRA** Corrosion resistant alloy

**CRT** Cathode ray tube

**CUI** Corrosion under insulation

**DOT** American Department of Transportation

**DPI** Dye penetrant inspection

**EFC** European Federation of Corrosion

**EFM** Electrochemical frequency modulation

**EIS** Electrochemical impedance spectroscopy

**EMAT** Electromagnetic acoustic transducer

**EN** Electrochemical noise

**ER** Electrical resistance

**FHWA** American Federal Highways Administration

**FOS** Fiber optic sensor

**FSM** Field Signature Method

**HA** Harmonic analysis

**HSE UK** Health and Safety Executive

**ICDA** Internal corrosion direct assessment

**ILI** Inline inspection

**IRIS** Internal rotary inspection system

**LPR** Linear polarization resistance

**LRUT** Long range ultrasonic transducer

**MFL** Magnetic flux leakage

**MPI** Magnetic particle inspection

**NACE** National Association of Corrosion Engineers

**NRA UK** National Rivers Authority

**NTD/E** Nondestructive testing/examination

**NTSB** American National Transportation Safety Board

**P and ID** Process and instrumentation diagram

**PIG** Pipeline inspection gauge

**RBI** Risk-based inspection

**SCC** Stress corrosion cracking

**TLA** Thin layer activation

**TOFD** Time-of-flight diffraction

**UT** Ultrasonic testing

**ZRA** Zero resistance ammeter



**Symbols** **$b_a$  and  $b_c$**  Tafel constants **$d$**  Density **$i_{corr}$**  Corrosion current density at  $E_{corr}$  **$t$**  Time **$A$**  Area **$E$**  Potential **$E_{corr}$**  Natural corrosion potential**mil** American unit for corrosion loss,

1 mil = 0.001 inch and 40 mil = 1 mm

 **$R_n$**  Noise resistance **$R_p$**  Polarization resistance **$W$**  Weight **$\sigma i_n$**  Standard deviation of the EN current **$\sigma V_n$**  Standard deviation of the EN potential**4.36.1 Corrosion Monitoring****4.36.1.1 Definition**

Various definitions of corrosion monitoring have appeared since the adoption of industrial corrosion monitoring techniques began to gather pace, first in the USA and later in Europe. Some definitions that have appeared in the literature are as follows:

1. The systematic measurement of the corrosion or degradation of an item of equipment, with the objective of assisting the understanding of the corrosion process and/or obtaining information for use in controlling corrosion and its consequences<sup>1</sup>
2. The assessment of the degradation of a material caused through environmental, chemical, electrochemical, or biological action or reaction<sup>2</sup>
3. Any technique used to observe or measure the progress of corrosion<sup>3</sup>

The author prefers the first definition as it clearly outlines the prime objective of corrosion monitoring and provides important information regarding the benefits obtained in the operation of a corrosion monitoring program. The second definition gives some information regarding both possible corrosion mechanisms and environments. The third definition, although correct, provides no information as to the possible objectives and the advantages of online monitoring in correlating corrosion information with plant conditions and corrosion control techniques.

The ability to correlate corrosion data with operating and process conditions is a very important aspect of corrosion monitoring that differentiates it

from inspection, which provides only a snapshot of condition at the time of the inspection. However, some inspection techniques now provide continuous information that bridges the boundary between corrosion monitoring and inspection techniques. Cox *et al.*<sup>4</sup> have pointed out that traditional corrosion control and condition monitoring are still considered to be support services and have presented reasons for this, such as that those involved are mainly technical specialists and enthusiasts, who do not have production responsibility and accountability. The basic techniques of both corrosion monitoring and condition monitoring have been refined, new technologies have been added and their functionality has been augmented by the application of modern computerized data collection, evaluation, and presentation.<sup>4</sup>

Other definitions have emphasized the multidisciplinary nature of corrosion monitoring, covering a wide range of materials, measurement techniques, instrumentation, rules and regulations, standards, logistical support, data analysis communication, and management information. It has been written that if one does not measure (monitor) corrosion, one will not be able to understand it and if one is unable to understand corrosion, one will not be able to control it or improve corrosion control techniques.

**4.36.1.2 Benefits of Corrosion Monitoring**

The effective management of corrosion in organizations is essential if corrosion risks to safety, health, the environment, and economic viability are to be maintained within acceptable limit values. The wider issue of corrosion management is covered in a separate chapter in this book. Corrosion monitoring and inspection are essential processes in an overall corrosion management system that manages corrosion risks through a combination of proactive and reactive measures<sup>5</sup> that are outlined as follows:

1. Proactive measures are those in which the requirements and implementation of the monitoring system or inspection programs are identified and in place before any corrosion or deterioration has been observed, based either on the outputs of a corrosion risk assessment or on some other review/identification of areas of possible/likely corrosion.
2. Reactive measures are implemented after a problem has been identified, either as a consequence of proactive monitoring or because of an incident or the identification of a problem as a result of inspection.

Corrosion monitoring is of particular benefit in capital intensive industries such as oil and gas (production and refining), petrochemical/chemical manufacture, and electricity generation that are concerned with large volume throughputs where intervals between scheduled shutdowns are generally long and result in large financial penalties. Thus, corrosion monitoring can help to identify and control corrosion regimes that prevail during transient operating periods such as startup and shutdown. It can signal the corrosion implications of altering steady-state operating conditions such as temperature or composition beyond the original design limits. If inspections indicate that a corrosion problem has suddenly developed in service, corrosion monitoring can help to identify the causes of the corrosion damage and/or monitor the effectiveness of proposed treatments.

In several stages of oil and gas production and refining, and in utilities (boilers, cooling water systems, fire water circuits) and power generation, corrosion risk mitigation practices are based heavily on corrosion inhibitor addition. Continuous monitoring can provide criteria to optimize inhibitor dosages with resulting savings in chemical costs. Typically, a plant trial of candidate corrosion inhibitors would be undertaken following laboratory screening during which corrosion rates would be monitored to identify the most effective inhibitor and optimum dosage rates. The coupling of monitoring data output with dosing pumps could be used to automatically control the addition of inhibitors to maintain corrosion rates below specified limits cost effectively.

#### **4.36.1.3 Making a Case for Corrosion Monitoring**

To prepare a case for the introduction of corrosion monitoring, some essential information is required in the proposal. The required detail depends on the complexity and scale of the application. In some cases, the application is relatively simple as in the case of a reported increase in corrosion rate in an item of equipment that can be monitored with a few probes and standard equipment, and the case would be relatively simple and amenable to rapid implementation. However, if the application is more complex requiring installation and implementation of a major monitoring scheme in a new or operating plant, there will be a need for a detailed proposal. Any proposal should address and define some key issues.

##### **4.36.1.3.1 Objectives**

Corrosion monitoring is usually undertaken with one or more of three objectives:

1. To enable the diagnosis of corrosion problems in operating equipment
2. To monitor and control the effectiveness of corrosion risk mitigation processes such as inhibitor addition in operating equipment
3. To facilitate the scheduling of shutdowns, usually within a risk-based inspection (RBI) strategy

It is beneficial to incorporate into the proposal examples (with references) of relevant, successful industrial corrosion monitoring programs, many of which are available from the literature and other reference sources such as the internet.

##### **4.36.1.3.2 Budgets**

Budgets are necessary for the costs of equipment (plus spares), installation and operation, data reporting, and personnel. The delivery time for equipment is required to establish the timing of installation, not least for liaison purposes with maintenance at a shutdown period.

##### **4.36.1.3.3 Choice of technique**

The techniques to be adopted for corrosion monitoring and inspection should be defined, including whether invasive (penetrating into equipment/process) or noninvasive (measurements made external to equipment) and whether continuous (data available continuously from probes/sensors exposed to the corrodant) or periodic (sensors exposed to the process but which need to be extracted for analysis such as corrosion coupons or bio-studs).

Factors to be considered include the objective(s) of the proposed monitoring, the appropriateness of candidate techniques in relation to the types of corrosion expected, compatibility with any existing techniques that are used for inspection and monitoring, and the available locations for sensors and the type of instrumentation (portable or automatic) that can be employed. Uniform or general corrosion is the easiest to monitor with a wide choice of monitoring techniques. Localized corrosion has historically been more difficult to monitor in plant or in the field but recent developments in electrochemical techniques, in particular electrochemical noise (EN), have opened the door to the monitoring of localized corrosion, in particular pitting corrosion. However, few engineers receive any training in electrochemistry and they are therefore less receptive to monitoring

techniques that are electrochemically based. The electrochemical impedance spectroscopy (EIS) and EN techniques are particularly challenging in this respect and although software can convert complex responses into simple corrosion rates, the lack of understanding of the fundamental basis of the technique inhibits adoption, especially by new users and in remote locations.

Guidance on this aspect is given by Rothwell *et al.*<sup>2</sup> It has been reported<sup>6</sup> that the most successful applications are those in which an integrated system has been installed incorporating several techniques that are the most suitable and appropriate. Of course, there has to be a compromise between the number of techniques used and the total cost including purchase, spares, and operation.

#### **4.36.1.3.4 Awareness of limitations of candidate techniques**

All corrosion monitoring techniques have advantages and limitations. Invasive techniques require entries for probes and this may have safety implications depending on the type of plant. A limitation of any monitoring technique that utilizes coupons or probes is that measurements are made on sensor elements or electrodes and not the plant itself. Additionally, the metallurgical condition of the sensor elements or electrodes may not represent the plant metallurgy and temperature differences between the actual plant material and sensor elements or electrodes may be significant.

In the cases of electrical resistance (ER) or electrochemical probes, conductive films or deposits, typified by iron sulfide that may be formed in environments containing hydrogen sulfide, can interfere with operation. An additional uncertainty in the linear polarization resistance (LPR) technique is that polarization resistance ( $R_p$ ) values are based on laboratory assessment and may not be relevant for certain environments. Galvanic corrosion is very dependent on the anode–cathode ratio, which may not be simulated by the probe.

The monitoring of localized corrosion is difficult and EN is one of the few online techniques for the monitoring of localized corrosion, although LPR systems can sometimes provide a pitting tendency of the environment. However, EN requires expertise for the interpretation of the data obtained. The skills and expertise of the personnel carrying out the monitoring program have important implications in relation to some of the complex electrochemical techniques and this should be borne in mind when the program is being planned.

Although awareness of such limitations is required, they need to be put into perspective. As long as the techniques chosen have some established reliability, these uncertainties are generally accepted bearing in mind that data are unlikely to be more than  $\pm 20\%$  accurate. Of course, coupons can be used instead of probes, but although useful for verification, coupon results are also subject to errors, albeit, of a lesser order.

#### **4.36.1.3.5 Personnel management**

It is essential that the monitoring program has strong communication links with the inspection function and the corrosion engineer. In larger organizations, it is not unknown for corrosion expertise to be located remotely from the application, which can result in delays and communication problems. If either function is contracted to a third party, a communication and responsibility structure should be established. Liaison with other departments in the organization is also an essential requirement for successful operation. For example, changes in feedstock such as the source of crude oil in an oil refinery can have profound effects on corrosion behavior and all relevant functions involved with the corrosion monitoring should be advised of such changes. Likewise, inspection and allied personnel should advise operations of revised probe locations and any changes to the corrosion monitoring programs.

The corrosion monitoring program should itself be subjected to a periodic review of performance and requirements for change on an ongoing basis. The training of staff relating to current regulations, practices, and guidance is also an ongoing requirement. The availability and commitment of operating personnel are important factors here as the author has witnessed many boxes of corrosion probes lying in half-opened packing cases on the ground in desert oil installations due to nonavailability of personnel for supervision of both installation and operation.

#### **4.36.1.3.6 Data management**

The type of data required and its examination require detailed consideration at the design stage. A debate has always existed as to the value of continuous data if the outcome is vast amounts of records that are never examined in detail. The incorporation of corrosion management guidance into overall plant management provides a framework for the data required and the personnel/departments to which it should be directed. Corrosion monitoring and inspection data should be coordinated with operating/process information and evaluated by both inspection and corrosion personnel. Data handling should be standardized and available

in a computer reporting format. All the data produced should be incorporated into relevant plant/equipment records and summary reports issued to relevant functions on a quarterly basis. The equipment that is being monitored and the associated data handling system should be reviewed regularly to avoid redundancy, duplication, and/or obsolete information being retained in current records.

Failure to standardize data recording and processing may undermine seriously the effectiveness of corrosion-monitoring programs. For example, some years ago the author carried out an audit of corrosion control measures on a major railway bridge in Scotland. An extensive program of coupon monitoring was in progress. There was a vast amount of coupon records, but no standardized reporting format to describe the appearance of the coupons. When an inspector was absent and another inspector substituted, the differing coupon descriptions resulted in inconsistencies that made accurate comparisons very difficult, if not impossible. Sadly, standards and recommended practices for the systematic recording of coupon corrosion were available but were ignored.

An example where data handling was not coordinated involved the corrosion failure of an overhead line in the saturated gas plant in a UK oil refinery, resulting in a major explosion.<sup>7</sup> The refinery controlled plant degradation mechanisms using a number of measures including materials selection, inspection, sampling for corrosive agents, and corrosion monitoring. An ER probe used for monitoring had shown a high corrosion rate, but this was not followed up.<sup>7</sup> This was one of the several problems with the corrosion monitoring and inspection recording at the refinery. Individual members of the refinery's inspection group did keep records of corrosion-related incidents, but there was no central data base to hold the information.

#### **4.36.1.3.7 Legislation and standards**

Legislation regarding corrosion engineering has been produced in several countries and standards and recommended practices relating to corrosion monitoring have been issued by bodies such as National Association of Corrosion Engineers (NACE) International in the USA and the European Federation of Corrosion (EFC). The UK Health and Safety Executive (HSE) has issued specific guidance for the offshore/onshore oil industry as well as for other industries and many other professional organizations have produced published guidance relating to corrosion monitoring, the more significant of which are listed in Appendix 1. Where available, company

in-house practices should be followed in addition to national or industry standards.

#### **4.36.1.3.8 Engineering considerations**

Regardless of the type of the sensor, commercial probes are available in fixed (screw-in, flanged) or retractable forms. Various hardware systems are available for the insertion and extraction of probes online based on pressure-gland fitting via a 1-inch (25.4 mm) full-bore opening gate-valve and access-fittings used with a retractable tool and valve. Problems such as the welding of access-fitting covers for the hydraulic test after construction need to be anticipated and prevented.

For existing plants, there is usually enough in-plant corrosion experience to identify appropriate locations of sensors. For new applications, and in particular, new processes, the location of sensors can be a complicated and contentious issue. Contractors, in general, have little experience of monitoring and can be reluctant to suggest installation in case clients conclude that their designs are using materials with inadequate corrosion resistance. Clients may have to instruct contractors that a requirement exists for monitoring and define where sensors should be positioned. Discussion with other operators of similar plants can be worthwhile. Chosen locations should be verified for appropriate working. For example, it has been known for locations to be specified at heights requiring scaffolding for reading by portable instruments. The identification of the preferred sensor type to be fitted at each location should be recorded, for example, on the relevant process and instrumentation diagram (P and ID) in the process industries.

The most important consideration when selecting corrosion monitoring locations is that they sample the corrosion risk to be evaluated. For example, within crude oil and wet gas production systems, it is important to find locations where the corrosion coupon or probe will be immersed in any produced water.<sup>8</sup> In pipelines, this is typically at the 6 o'clock position on horizontal sections, because the produced water is heavier than crude oil or gas condensates. Unfortunately, many pipeline and facility engineers have installed monitoring locations on the sides of the pipeline rather than at the bottom. Although side locations provide easier access to retrieval, coupons or probes cannot provide accurate data unless the pipelines are essentially full of water.<sup>8</sup> Operator convenience must not come at the expense of valid results when selecting coupon or probe monitoring locations.

Consideration must be given also to the provision of sufficient room at the proposed location for the operation of retriever tools that require, typically, a minimum of 4–6 feet (1–2 m) clearance.<sup>8</sup>

Intrusive probes should be situated where they can remain in place for extended periods, rather than having to be removed periodically for pigging or other routine operations. Thus, intrusive probes should be installed upstream of pig launchers and downstream of pig receivers. Where this is not possible, flush-mounted probes are required.<sup>8</sup>

Instrumentation must be engineered to minimize the risk of ignition of any flammable substances that may be present from electrical sources. This is particularly relevant to the oil and gas, petrochemical, and chemical industries. This intrinsic safety is engineered by the incorporation of zener diode barriers or an equivalent electrical engineering safety system. There is no technical reason for any corrosion monitoring system not to be engineered for intrinsic safety. Assistance on these matters can be obtained from safety staff in the company. Many countries have organizations responsible for this aspect using either American or European standards.

#### 4.36.1.4 Techniques for Corrosion Monitoring

##### 4.36.1.4.1 Historical development of corrosion monitoring

It has been estimated that the worldwide market for corrosion monitoring equipment (excluding inspection) is of the order of \$25 M including ancillary fittings and associated tools. The early US manufacturers of corrosion monitoring equipment were specialty process chemical manufacturers (in particular corrosion inhibitors), who regarded monitoring as a useful adjunct to their chemical products. Instruments were marketed as providing criteria to judge the effectiveness and optimum dosage rates of inhibitors. The instrument manufacturing/supply functions were not seen as profit centers *per se* and were mostly underfinanced, and in general, unsupported at that time.

Some of the earliest applications of corrosion monitoring were in the chemical industry. In the larger chemical companies with in-house corrosion expertise, electrochemical potential measurements were used to monitor the condition of passive materials and although this technique did not provide a rate of corrosion, it did allow operators to alter process conditions to maintain passivity and prevent

serious damage. In-house developments in other techniques such as ER enabled construction of sensors/probes that were later licensed for commercial exploitation.

The conservative oil and gas industry was initially skeptical of instrumentation that claimed to provide internal corrosion rate data online. Despite the initial teething problems (selection of the wrong technique, inappropriate sensors or probes for the environment, sensors not sufficiently robust, sensors located in the wrong location), corrosion monitoring systems were slowly introduced for both existing and new plants. This took longer in Europe as most commercial monitoring equipment was of American origin resulting in long deliveries with minimal repair facilities, spares, shortages and more importantly, little if any general guidance and application advice locally.

The experiences of companies using corrosion monitoring in various industries in the UK were surveyed in 1981 and 1984.<sup>6</sup> Unfortunately, no subsequent independent survey has been undertaken and summaries of the data from the original surveys are given in **Tables 1–3**.

The 1981 survey was carried out 10 years after UK oil production had commenced and it is interesting that some of the problems identified in the 1981 survey had been considerably improved by the time of the 1984 survey. Overall, greatest success was obtained by users of integrated systems incorporating several techniques. According to survey returns, the usual package of techniques for monitoring corrosion of industrial

**Table 1** Response rate by industrial sectors in the 1981 corrosion monitoring survey

Industry	Response – no of forms/percentage	
Oil and gas production	8/22	36%
Oil treating	6/20	30%
Chemical/petrochemical	9/11 (5/50) <sup>a</sup>	82%
Industrial boiler plants	2/4	50%
Industrial cooling water	2/10	20%
Gas distribution	0/5	–
Electricity generation	3/7	43%
Pipelines	0/1	–
Mining	2/5	40%
Process plant contractors	1/5	20%
Miscellaneous	5/20	25%
<b>Total</b>	<b>38 RESPONSES</b>	<b>35%</b>

<sup>a</sup>Five additional responses from a blind survey of 50 companies. Source: Britton, C. F.; Tofield, B. C. *Mater. Perf.* **1988**, 27(4), 41–44.



**Table 2** Summary of the findings of the 1981 corrosion monitoring survey

---

Varied response
Widespread concern with the significance of the results and their interpretation
Ruggedness and reliability problems with equipment
Concern with intrinsic safety of equipment
Where corrosion monitoring is successful, several techniques are almost always in use
Widespread interest in new techniques
Universal use of NDT (especially ultrasonics and radiography)

---

Source: Britton, C. F.; Tofield, B. C. *Mater. Perf.* **1988**, 27(4), 41–44.

**Table 3** Summary of the findings of the 1984 corrosion monitoring survey

---

Increased awareness of the need for corrosion monitoring requirements to be considered at the design stage
Expanded use of corrosion monitoring in many companies
Greater appreciation of the qualitative nature of corrosion monitoring data and the need to learn by experience
Improved reliability of equipment, but much still to be done
Maintenance costs often too high
Desire to go more automatic and online
Awareness that system installation is expensive
Continuing interest in new techniques

---

Source: Britton, C. F.; Tofield, B. C. *Mater. Perf.* **1988**, 27(4), 41–44.

plant at that time comprised corrosion coupons, an appropriate online probe system (either ER or LPR), and a nondestructive testing (NDT) technique, usually ultrasonics.

Since this book was last published in 1994, continuing advances in electronics, software development, and automatic data-handling have resulted in a wider range of techniques for corrosion monitoring from an increasing number of companies worldwide. In addition, much work has been carried out developing the existing monitoring techniques such as ER and LPR particularly in relation to element configuration, data processing, and measurement sensitivity. Electrochemical techniques with simultaneous monitoring of solution resistance enabling online calibration for the determination of Tafel constants are now available in commercial instrumentation. There has been considerable laboratory development of both EIS and EN. There has also been a significant development of ER technology in the form of the field signature method (FSM) that overcomes the fundamental drawback of most corrosion monitoring

techniques by measuring the corrosion of the plant component rather than of a sensor or a coupon.

Plants are now routinely fitted with corrosion monitoring equipment in order to comply not only with required company practice but also with the legislation in a number of countries that requires the adoption of appropriate corrosion measurement techniques. Service quality from corrosion monitoring equipment suppliers has improved and delivery and servicing/repair times for equipment have gradually reduced. However, the availability of skilled personnel to operate instrumentation remains a challenge, particularly for the oil/gas industry in offshore and remote desert locations. In particular, the scarcity of expertise in corrosion theory and electrochemistry has been a considerable obstacle to the application of electrochemical monitoring techniques in both field and plant.

In addition to process plant applications, more specialized applications have emerged such as the monitoring of automobile car bodies, aircraft,<sup>9</sup> concrete reinforcement,<sup>10</sup> and atmospheric corrosion.

#### 4.36.1.4.2 Coupons

Coupons are metal samples that are exposed to the corrosion environment to establish the corrosion rate. They are withdrawn from the plant at prescribed intervals and the corrosion rate is determined by gravimetric means involving weighing the coupon before and after the exposure following the removal of the corrosion products. In high temperature applications where metals are exposed to gas mixtures at high temperatures, the coupons may gain or lose weight depending on whether the corrosion products are adherent or show a tendency to spall from the coupon surface and other techniques may be required for corrosion evaluation. Coupons are often used to provide the base-line criteria in a corrosion monitoring program for comparison with instrumented techniques such as ER or the various electrochemical techniques. When confidence is established, the coupon numbers can be reduced.

Coupons are usually strips, flush discs, or cylindrical rods mounted in suitable racks or holders (**Figure 1**) that are inserted and retrieved at shutdowns, unless inserted in a bypass line or installed in operating plant using full-bore valves or a suitable high-pressure access system.

Coupons are exposed to the corroding environment for defined periods of time and should be insulated electrically from the support system. They are available from commercial suppliers in most



**Figure 1** Corrosion coupon holders and corrosion coupons (Courtesy Cormon Ltd).

materials in a variety of geometries and are usually supplied in a surface-treated condition, weighed, and stamped with an identification number. For coupons manufactured in-house at plants, it is advisable to anneal the cut coupons in order to remove residual stresses from the cutting (often guillotining) process. Coupons can be exposed to any type of corrosive environment such as liquid corrosives, high temperature gases, soils, and the atmosphere.

The corrosion product has to be removed following exposure for evaluation and guidance is provided in the chapter on corrosion testing in this book. Errors are introduced if metal is removed in the cleaning process and they are minimized by including corrosion inhibitors in the cleaning solutions. Blank coupons can be cleaned to correct for any metal loss in the cleaning process itself. Large organizations may carry out coupon evaluation in-house but corrosion inhibitor suppliers often include a coupon evaluation service as a part of the inhibitor supply contract. Independent laboratories can also carry out this procedure for the smaller company or plant.

The corrosion rate is expressed in either mm year<sup>-1</sup> (Europe/Middle East/Asia) or mils year<sup>-1</sup> (USA) where 1 mm = 39.37 mils. The penetration rate is obtained by calculating the weight loss after exposure to the plant or field environment following treatment for the removal of the corrosion products. The other factors involved are the coupon surface

area, metal density, and time of exposure and they are related as follows:

$$\text{Corrosion rate} = 10 \times \frac{W}{dAt}$$

where:

- Corrosion rate: mm year<sup>-1</sup>;
- $W$  (weight loss): g;
- $d$  (metal density): g cm<sup>-3</sup>;
- $A$  (area): cm<sup>2</sup>;
- $t$  (time): years.

Special coupons for corrosion testing of welds, crevice corrosion, and for stress corrosion testing (U-bends, C-rings) are available from suppliers or can be assembled by users and guidance on suitable designs can be found in the literature. Errors can occur with coupon evaluation, as in any monitoring technique, and these can only be avoided by familiarity with all standards, codes of practice, and guidance from fellow workers. Coupons can exhibit localized attack such as pitting and crevice attack. If excessive localized attack is present, there is no point in reporting weight loss data. Common sense will determine if localized corrosion will negate the weight loss measurement; however, the representative reporting of coupon appearance is necessary. There is published guidance on the reporting of pitting attack on coupons.<sup>11</sup>

The author has seen many examples where users of coupons have not applied a consistent system for the description of coupon appearance, resulting in meaningless records. It is very difficult to assess coupon results prepared by different personnel without a consistent system for recording coupon appearance. Familiarity with coupon evaluation literature is recommended such as that published by NACE, American Society for Testing Materials (ASTM), and other organizations.<sup>12,13</sup>

The advantages of coupon monitoring include the relatively low cost and the provision of information on forms of localized corrosion such as pitting, crevice corrosion, stress corrosion, and galvanic (bimetallic) corrosion. Although the most common form of coupon is the metal strip, there are other geometries available, including flush-discs that sample conditions at equipment surfaces including the influence of fluid flow. Coupon strips can be exposed on supports in duplicate or in multiple arrays or on coupon-ladder racks allowing a number of coupons in different materials to be exposed at a specific location.

The disadvantages include the labor intensive nature of the technique (especially for offshore application) and the averaging of readings over the exposure period, which may mask possible shorter term excursions in corrosion rate. Automatic recording can minimize this aspect, which can also be mitigated by exposing a series of coupons at one location and retrieving individual coupons at prescribed intervals.

#### 4.36.1.4.3 Electrical resistance (ER)

ER is an online, invasive technique utilizing a metal element made of the metal or alloy of interest mounted in a suitable housing, which is exposed to the corroding environment, as shown in [Figure 2](#).

The increase in ER with time is measured as the element loses cross-sectional area due to corrosion. The use of ER for measuring atmospheric corrosion rate was first suggested in 1928 by Hudson<sup>14</sup> and was in use in laboratory experiments in England in the late 1930s. The technique fell into obscurity, until in 1954 Dravnieks *et al.*<sup>15</sup> demonstrated its potential as a practical field tool. Commercial exploitation was delayed by the need for temperature compensation that was eventually provided by locating compensating resistant elements in the probe body, which were protected from the corroding environment. Early instrumentation was marketed under the trade name Corrosometer™ by Magna Corporation in the US, with the patent relating to temperature compensation.

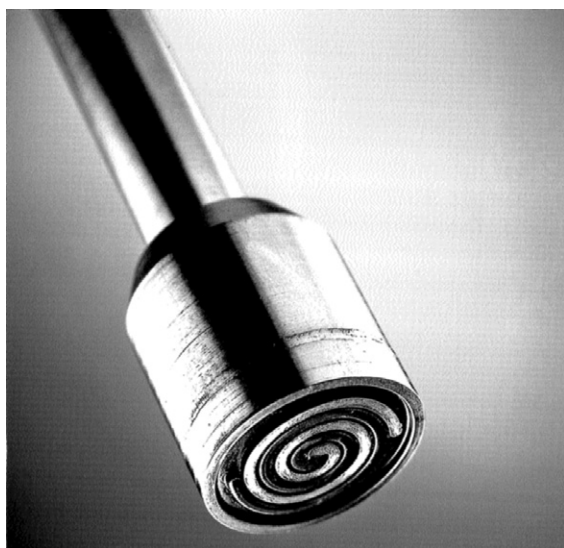


**Figure 2** Electrical resistance (ER) probe – spiral wide tip (Courtesy Cormon Ltd).

Currently, there are many companies in many parts of the world manufacturing this type of equipment.

Elements are available in a variety of geometries including wires, tubes, and various flush designs incorporating spiral or concentric elements, as shown in [Figure 3](#). ER elements can also be fitted into special spool designs, as shown in [Figures 4 and 5](#).

The element is exposed to the corrosive environment (liquid or gas) and measurements taken at appropriate intervals. Readings can be automatic with transmission to the control room or manual with a portable reader for computer handling on return to the office. Data transmission has been carried out via satellite transmission from offshore platforms to onshore offices. The installation of a spool in a typical plant application is shown in [Figure 6](#).

The data produced average the corrosion rate between measurement intervals, although with automatic readings on sensitive elements the intervals can be very small, and correlation with corrosion mitigation systems or plant variables can be made. The presence of conducting iron sulfide in the corrosion product on the element arising from the presence of hydrogen sulfide in the corrosion environment may invalidate the measurement as iron sulfide is a conductor. However, many corrosion engineers still use ER under these circumstances by applying a correction factor or allowance. In the case of a wire element, any pitting attack will increase the measured corrosion rate but the use of tubular elements reduces this affect by increasing the surface area of the element.

ER elements need replacement when the cross sectional area has decreased by ~50% resulting in a trade off between element life and sensitivity, that is, high sensitivity results in short life, although current

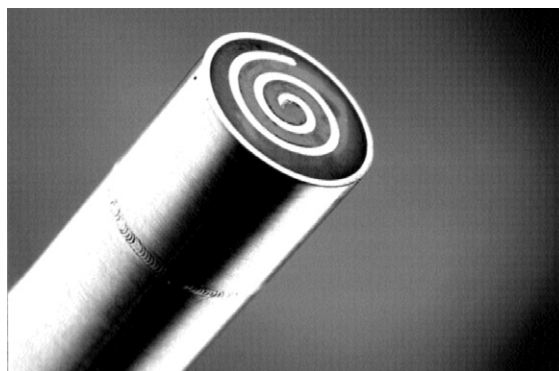


**Figure 3** Electrical resistance (ER) probe – spiral flush element (Courtesy Cormon Ltd).

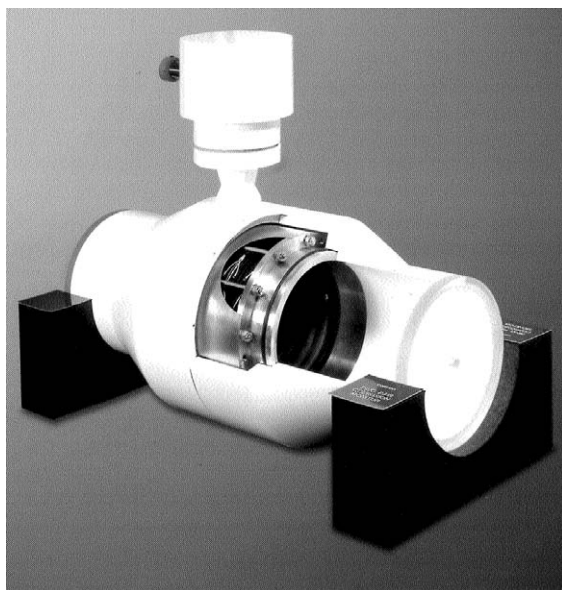


**Figure 4** Electrical resistance probe (ER) – ‘Ring-Pair’ spool (Courtesy Cormon Ltd).

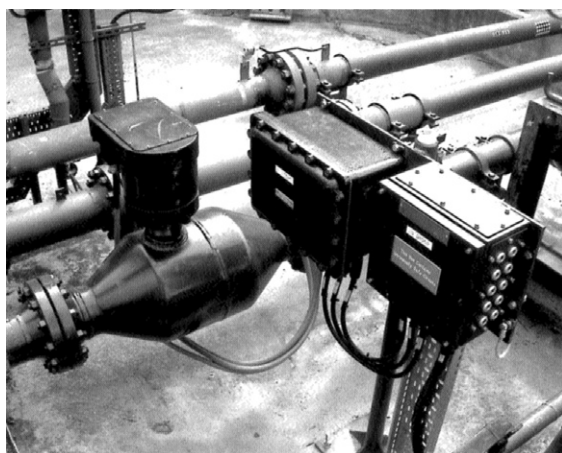


**Figure 5** Electrical resistance probe (ER) – ‘Ring-Pair’ spool installation in plant (Courtesy Cormon Ltd).

electronic technology has improved this situation to some extent. Accuracy for the general range of ER equipment is claimed to be 0.1% for a single measurement, but this can be improved very considerably by using special equipment, details of which are available from the manufacturer’s literature or websites. It is important that the element should represent the metal or alloy of interest for the determination of corrosion rate and errors can arise in field/plant applications related to metal composition,

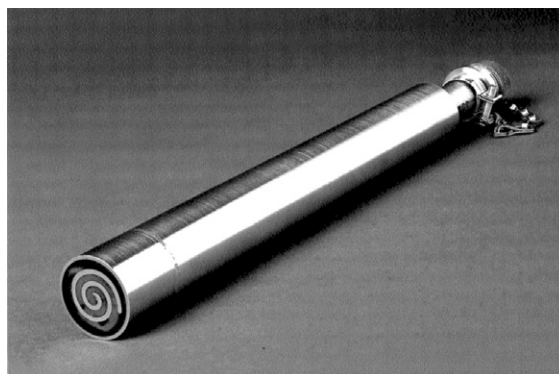


**Figure 6** Electrical resistance (ER) probe – fixed attachment to plant (Courtesy Cormon Ltd).

metallurgical condition of the element, and heat transfer among other factors, but the technique is well utilized in many industries, in particular the oil and gas industry.

The cost of ER hardware is similar to that of other systems and they can be operated and interpreted by most staff without undue problems. However, noninvolved staff should be acquainted with the locations and sensitivities of probes which have been known to be used as foot supports for climbing on or around the plant.

The advantages of the technique include the capture of data without plant shutdown, the availability of both portable and automatic operation, the reasonable correlation with corrosion variables and process conditions, and the assessment of the effectiveness of corrosion mitigation techniques. Special probe designs are available for use at high temperatures such as in power station boilers, in aircraft components, and in underground pipelines and for the measurement of atmospheric corrosivity.

The disadvantages include problems with conducting corrosion products in sour systems, localized corrosion that can introduce errors in interpretation, and the trade off between element sensitivity and life.

#### **4.36.1.4.4 Electrochemical techniques**

##### **Potential measurement**

Potential and its variation with time are indicators as to the condition of passive films, but corrosion penetration rates are not obtained. The hardware required consists of an appropriate reference electrode and working electrode, which can be the plant component

of interest, and a high-impedance voltmeter. This technique has been used in the chemical industry for assessing the condition of passive materials in some applications. Pioneering work on the technique by Edeleanu<sup>16</sup> demonstrated that potentials of UNS S30400 stainless steel in sulfuric acid varied with pumping speed, temperature, and the presence of impurities. Laboratory determination of polarization characteristics can identify passive and active potential ranges for a given material/environment combination.

The choice of an appropriate reference electrode is a challenge for noncorrosion aware personnel. Ideally, a reversible reference electrode such as a calomel or silver–silver chloride electrode should be used but, in practice, nonreversible electrodes can be deployed as long as they maintain a stable potential. Commercially available polarization resistance probes can be adapted for this purpose.

#### Potentiodynamic/cyclic polarization

These techniques measure the polarization characteristics of the metal–environment system of interest and laboratory procedures have been outlined and described.<sup>17</sup> Polarization curves are obtained by polarizing a working electrode potential relative to a reference electrode using external current supplied via a counter electrode in a conventional electrochemical cell arrangement. The choice of reference electrode is an issue, as in the case of potential measurement. In theory, this technique allows measurement of the Tafel constants,  $b_a$  and  $b_c$ , from the slopes of the linear portions of the anodic and cathodic polarization curves for the relevant anodic and cathodic processes that define the corrosion process. Corrosion rates can be measured by extrapolating the linear portions of the curves to intersect at the natural corrosion potential.

Cyclic polarization is a variation of the potentiodynamic technique in which the potential is reversed in the negative direction following an anodic scan. The breakdown potential in the anodic scan and any hysteresis in the anodic segment of the reverse scan can be indicative of the tendency toward pitting and crevice corrosion respectively. Guidelines for carrying out these tests are given in an ASTM standard.<sup>18</sup>

Portable commercial potentiostats are available that allow polarization measurements to be made *in situ* in operating plants. However, polarization characteristics are often relatively complex and these techniques require careful, informed interpretation and are not used routinely for corrosion monitoring.

#### Linear polarization resistance (LPR)

As aqueous corrosion is an electrochemical process, the measurement of the current involved in the corrosion reactions and the use of Faraday's Law should provide, in theory, a quantitative measurement of corrosion rate. However, it is not practicable to measure the internal corrosion current using an ammeter on the surface of a corroding metal in which the anodic and cathodic sites are inseparable. The current can, however, be calculated from the polarization characteristics of a material in an environment using the Stern and Geary relationship<sup>19,20</sup> developed from the mixed potential theory for a corroding electrode, which defines a linear relationship between applied potential and current density close to the natural corrosion potential:

$$R_p = \frac{\Delta E}{\Delta I} = \frac{b_a b_c}{2.3 i_{\text{corr}} (b_a + b_c)} = \frac{B}{i_{\text{corr}}}$$

where:

- $R_p$  is the LPR;
- $\Delta E$  (equal to  $E - E_{\text{corr}}$ ) is the potential shift from the corrosion potential,  $E_{\text{corr}}$ ;
- $\Delta I$  is the measured external current flowing due to this potential shift;
- $i_{\text{corr}}$  is the corrosion current at the free corrosion potential,  $E_{\text{corr}}$ ;
- $b_a$  and  $b_c$  are Tafel constants.

The Stern–Geary relationship is valid only for specific experimental and theoretical conditions among which are that  $\Delta E$  is small, typically  $< \sim 20$  mV. The measurements can be completed relatively quickly and are in effect instantaneous, and can therefore be utilized to control corrosion mitigation practices in operating equipment, such as the addition of inhibitors to recirculating cooling water systems or crude distillation column overheads in oil refineries.

Probes for the LPR technique are available in either two- or three-electrode versions, as shown in Figure 7, which also shows the access fitting, which is the preferred method for inserting probes into plants.

Two-electrode probes have identical metal electrodes between which the applied voltage (up to 30 mV) is applied and the resulting current measured. The applied voltage is then applied for a second time but with reversed polarity and an average is taken of the readings. A cycle time of around a minute is generally used, after which, in theory, steady state conditions prevail. In three-electrode probes, the potential difference between the reference electrode





**Figure 7** Linear polarization resistance (LPR) electrochemical probe and 'access fitting' (Courtesy Cormon Ltd).

and working electrode is sensed and an additional  $\pm 10$  mV polarization is applied. The three-electrode probe can provide measurements in more resistive solutions but has the disadvantage of measurement error if the current chosen is too large and the working electrode is polarized beyond the  $\sim 10$  mV level.

Rod-type electrodes are supplied in many metal compositions separately from the probe and electrodes are attached to threaded rods located in the probe. Probes are available in fixed (screw-in), flange fitting, retractable (pressure-gland fitted via a full-bore opening gate-valve) and in versions for commercial retrieval systems. Instrumentation is available in various forms ranging from handheld downloading devices to fully automated systems. Results are converted to penetration rates ( $\text{mils year}^{-1}$  or  $\text{mm year}^{-1}$ ) using appropriate values of  $B$  that are available from the literature for a wide range of material/environment combinations.

The key advantage of the technique is that it is close to instantaneous, giving an estimate of corrosion rate in a short time, typically several minutes, enabling rapid correlation with process conditions.

The disadvantages include the restriction of the technique to conducting solutions, although resistance compensation is available on some systems, and the requirement for values of  $B$  for the relevant reactions. Deposits on the probes can interfere with

measurements, and errors are introduced if oxidizing or reducing reactions are active that are not involved in the corrosion process. It is good practice to use other corrosion monitoring techniques in a package of techniques to validate and calibrate the technique.

#### **Galvanic current**

The galvanic current arising between two different metals can be measured using a zero-resistance ammeter (ZRA) in series between two different electrodes. The current can be related to metal loss using Faraday's Law. This is a long-established laboratory technique that has been extended into plant for the qualitative estimation of galvanic corrosion using, for example, commercial LPR probes fitted with two different metal electrodes.

#### **Electrochemical impedance spectroscopy (EIS)**

EIS is similar in approach and hardware to the LPR technique with the exception that an AC rather than a DC perturbation is applied to the electrodes at a range of applied frequencies. The resultant current and phase shift between the applied potential and resulting current are measured. The total impedance comprises contributions from the charge transfer and solution and diffusion impedances, and these can be identified separately and quantified by the use of AC impedance measurements at varying frequencies. The first AC instrument for measuring corrosion was developed by the UK Admiralty Materials Laboratory with the objective of correcting the errors involved with the LPR technique.<sup>21</sup> A fixed frequency of 10 Hz square wave was applied between the electrodes. The working electrode oscillated at  $\pm 5$  mV about a floating  $E_{\text{corr}}$  potential using an AC square wave coupled potentiostat. The measurement about a floating rest potential is a major advantage of the AC technique in systems where transients in potential would cause difficulties in measurement using a DC technique.<sup>1</sup> There is an extensive literature relating to the development of EIS as a laboratory/research tool for the investigation of corrosion.<sup>22–24</sup> Current interest is focused on the use of harmonic analysis (HA) of the response of electrodes to the application of a single frequency, from which Tafel slopes and Stern–Geary constants can be determined.

The main advantage of EIS relative to conventional LPR is that measurements at different frequencies allow corrosion rates to be determined in more resistive corrosion environments such as crude oil–water mixtures and concrete. The technique also

provides insights into corrosion mechanisms, such as whether corrosion processes are charge or mass transfer controlled and it can be deployed in operating plant using standard, commercially available LPR probes with associated access facilities.

The main disadvantage is the specialized knowledge that is required for the verification of instrument/computer outputs and the interpretation of results, which is an obstacle to the widespread deployment of EIS for industrial applications.

### **Electrochemical noise (EN)**

The EN technique involves the analysis of spontaneous potential or current transients that arise on or between corroding metal electrodes. The EN technique was first identified by Iverson<sup>25</sup> and there is now an extensive literature on applications in corrosion monitoring.<sup>26,27</sup> The theoretical background and development of EN are described elsewhere in this book. In the last edition of this book in 1994, EN applications in power generation plant, cooling water systems, and reinforcement in concrete were reported. Also, it was noted that probes containing combination elements utilizing several electrochemical techniques (AC and DC) had been developed and used for measurements in condensing acid environments.

The development of EN has progressed rapidly particularly due to developments in the electronic equipment that is able to discriminate between natural electrode current/voltage transients and electronic background noise. The interest in the technique derives partly from the prospect of a more reliable and flexible way of measuring corrosion rate but particularly from its unique sensitivity to localized corrosion processes such as pitting crevice corrosion and stress corrosion cracking (SCC) that is not available from other electrochemical techniques. EN is also much more responsive to system changes and upsets than any other monitoring technique, electrochemical or otherwise, which makes it a strong contender for corrosion/process control.

The technique does not perturb the electrodes as is the case with electrochemical techniques involving polarization but detects the natural voltages and currents that are generated on the electrode surfaces in the environment. Measurements can be made in a wider range of environmental resistivity compared with LPR. In the usual configuration, the potential noise and/or the current noise between two identical electrodes is measured. Currents are measured with a zero-resistance ammeter. Data analysis is used to determine the corrosion rate and/or the corrosion

mechanism. In theory, corrosion rates can be estimated from EN measurements in a manner analogous to LPR measurements. Corrosion rates are calculated using the so-called noise resistance,  $R_n$ , which is equivalent to the LPR polarization resistance,  $R_p$ , and is determined using the relationship:

$$R_n = \sigma V_n / \sigma i_n$$

where  $\sigma V_n$  and  $\sigma i_n$  are the standard deviations of the EN potential and current signals respectively. A variety of techniques can be used to analyze the data including the time basis of the data obtained, statistical analysis, which can provide mechanistic information, frequency domain transformation to characterize localized corrosion, fractal and neural analysis.<sup>28</sup>

An advantage of the technique is that it can be deployed in operating plants using standard, commercially available LPR probes with associated conventional access systems. However, the complex instrumentation can be expensive, and as with EIS, specialized knowledge is required for the verification of instrument/computer outputs and the interpretation and analysis of results. The technique is generally provided by specialized companies/contractors unless there is in-house expertise available in a larger company.

### **4.36.1.4.5 Field signature method (FSM)**

The field signature monitoring technique was developed originally to monitor internal corrosion of pipes and pipelines.<sup>29</sup> A length of pipeline (spool) fabricated from the same material as the parent pipeline is used as the measuring sample to which an array of sensing pins, typically ~3-mm diameter, is stud welded onto the exterior surface. A current is induced in the test spool and the electric field pattern is sensed by measuring the small potential differences among the pairs of sensing pins on the external surface. The electric field pattern depends on the geometry of the test spool and general or localized corrosion on the internal surface produces changes in the electric field pattern. By comparing measured potential differences with baseline values for the uncorroded spool, the distribution and dimensions of corrosion on the internal surface can be computed, as shown in **Figure 8**. Temperature and current fluctuation effects are compensated for. The original Norwegian patent for the system was issued in 1984 and was later licensed to Corrocean (Norway) for commercial application on a worldwide basis, who

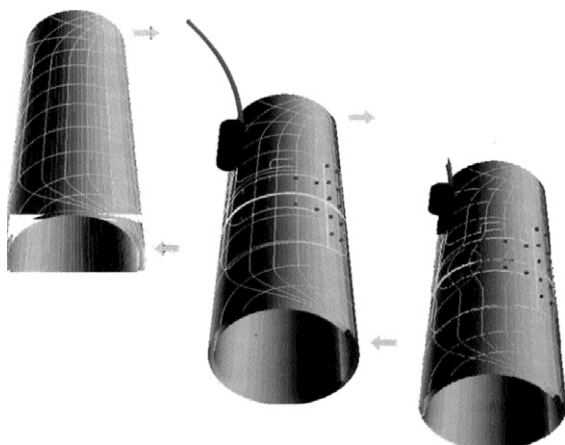


**Figure 8** Field Signature Method (FSM) – Schematic (Courtesy iicorr Ltd.).

claimed that an accuracy of 0.1% of pipewall thickness could be obtained with a resolution of 0.025 mm for a 25-mm wall thickness. Large areas (several m<sup>2</sup>) can be monitored and smaller pin distances result in higher resolution for localized corrosion.

This method has been referred to in the literature as a variation of the ER system. There are now other manufacturers offering similar systems, one of which provides a two-part removable sensor sleeve as an option.

Initial application was directed at the oil and gas industry for the detection and monitoring of corrosion in subsea pipelines, especially for new systems, rather than retrofitting to an existing line, which would involve shutdown and additional cost. Applications in the last decade have expanded into topsides on offshore oil and gas platforms,<sup>30</sup> onshore pipelines/piping, and oil refining equipment<sup>31</sup> as illustrated in Figures 9–11.

An FSM system was fitted to an experimental pressurized pipeline loop in the UK that was used for the testing of oilfield corrosion inhibitors. The operator reported excellent results with emphasis on the accuracy achieved.<sup>32</sup> In one particular onshore oil field installation, considerable savings on corrosion inhibitor cost were made associated with an increase in the interval between inhibitor treatments of 2 weeks.

Advantages relate to the noninvasive nature of the technique, the large areas of actual plant components that can be monitored compared with conventional invasive probes, and the sensitivity that allows the technique to be used to correlate corrosion rates with process conditions such as in the case of



**Figure 9** Field Signature Method (FSM) – Installation on piping at bend/weld on piping (Courtesy iicorr Ltd.).

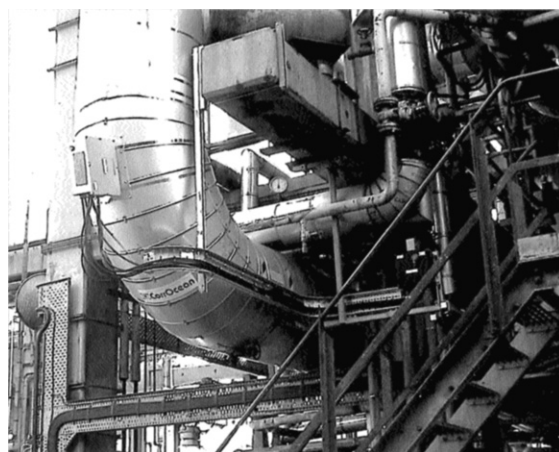


**Figure 10** Field Signature Method (FSM) – Installation in oil refinery (Courtesy iicorr Ltd.).

naphthenic acid corrosion in crude oil refining.<sup>31</sup> Pitting and SCC can be detected and corrosion monitoring across welds on pipeline welds has been successfully carried out in the North Sea.

Disadvantages include the high cost, which restricts the use of the technique to critical applications and the requirement for specialized data interpretation albeit enabled by custom-supplied software.

The data require careful interpretation since corrosion occurring more than 1 m either side of the sensing unit will not be detected and the generalization of the test spool performance to the system as a whole could be misleading if it has not been located where the corrosion is taking place. Concerns have been expressed relating to the use of FSM at high temperatures (e.g., 60 °C in the shade in the Middle



**Figure 11** Field Signature Method (FSM) – Installation on buried pipeline (Courtesy iicorr Ltd.).

East) and whether the sensitive electronics will survive sand and dust in desert environments, which applies to any instrumented system. However, appropriate and regular maintenance may reduce these problems.

Overall, this technique is one of the more interesting developments of corrosion monitoring technology in recent times as exemplified by the number of applications in the oil and gas industry and its progressive use and expansion into other industries.

#### 4.36.1.4.6 Thin layer activation (TLA)

TLA was developed originally for monitoring wear and erosion on metals such as in the measurement of the wear of automotive engines and the assessment of the effectiveness of various lubricants. The technique was first utilized for corrosion monitoring in 1983<sup>33</sup> and is based on the creation of a small quantity of a radioactive tracer in a metal surface (one part in  $10^{20}$ ) allowing the loss of metal due to corrosion to be measured by the loss of radioactivity. The corrosion product is required to be nonadherent for successful

application. Monitoring can be based on measurements of the loss in radioactivity level of the corroding surface or the increase in radioactivity of the corroding liquid environment unless the throughput is so high as to dilute the uptake of radioactive isotopes to levels that cannot be differentiated from background. Plant components can be irradiated, for example, on the inside surface of a pipe, or an irradiated coupon can be exposed invasively. The technique is noninvasive, measurements being possible external to equipment that contains an irradiated internal sample surface.

The requirement that samples or plant components be activated by exposure in a nuclear accelerator and the associated logistics have inhibited the widespread application of the technique, but some successful applications have been reported in subsea, water treatment, and paper-mill operations.<sup>34</sup>

#### 4.36.1.4.7 Chemical analysis

The contribution of a well-planned and executed chemical analysis program to corrosion monitoring is often underestimated. Changes in corrosivity may be determined by liquid analysis including changes in process conditions. The most important analyses related to corrosion behavior are levels of oxygen, hydrogen, chloride, trace elements, iron, manganese, corrosion inhibitor, and other treating chemicals such as biocides, oxygen scavengers, and pH. There are a variety of test papers for free water and pH monitoring and hydrogen sulfide and carbon dioxide testing can be carried out on-site. For on-site measurements, the first measurement should be the temperature.

Provision for chemical analysis should be incorporated in the design of process plant in order to give adequate coverage throughout the system, for example, in oil production from the well via processing facilities to the export infrastructure. Correlation with plant parameters such as temperatures, pressures, flow rates, and stream compositions can provide valuable information. Automatic analysis systems, especially those using ionsensitive electrodes with the recording of data, are recommended.

A special case of chemical analysis is the measurement of iron counts, the term used in the oil industry to describe the amount of the element iron in product streams. Results provide a valuable indication of corrosion if carried out on a systematic basis, such as from a reference point upstream and taking samples of fluid at a number of reference points downstream. Samples are analyzed in the laboratory and results are reported as weight of iron per volume of liquid.



Guidelines for iron analysis in oil and gas production are given in the literature.<sup>35</sup>

The loss of wall thickness is not obtained from this technique. However, continuous sampling gives results that provide a good indication of the amount of corrosion taking place, assuming that the corrosion distribution is uniform.

The disadvantages of the technique are that it is less effective for localized corrosion and that clearly the technique is invalidated if iron is already present in the process fluid, for example, in an oil formation. In this case, analysis for manganese can be substituted and results correlated accordingly.

#### **4.36.1.4.8 Hydrogen**

Hydrogen is produced from the cathodic reaction in many corrosion systems, particularly where acid environments such as acidizing fluids, sour systems, carbon dioxide, and naphthenic acids promote corrosion. The measurement of the presence and levels of hydrogen can give qualitative indications as to the amount of corrosion occurring. The historical technique for assessing the presence of hydrogen in the oil industry was to place a sample of produced fluids in an empty paint can. The appearance of blisters on the exterior of the can indicate the presence of sour water and consequent hydrogen.

Hydrogen atoms, due to their small size, can migrate easily through a metal lattice. If voids or defects are present in the metal lattice, hydrogen atoms combine to form hydrogen molecules and the continuous formation of molecules leads to increases in internal pressure, which eventually exceed the coherent strength of the material resulting in phenomena such as hydrogen-induced cracking and blistering.

Early probes were based on monitoring the accumulating pressure of hydrogen produced by corrosion. This does not provide a measurement of corrosion penetration directly. However, any increase in the volume of gas indicates that corrosion is underway. Pressure probes are still used in oil production and refining operations and can be installed using the standard access-fittings that are used for other types of invasive probe or coupon, enabling installation and retraction under system pressure. The hydrogen gas requires bleeding from the probe at regular intervals, which is a disadvantage in large oil fields. However, the organization of teams specifically for this purpose has worked well in the Middle East. An outer sheath can be welded onto a pipeline or piping into which hydrogen that is produced by corrosion of the bore diffuses. The pressure generated can be determined

with a pressure probe and this allows corrosion of the bore to be monitored noninvasively.

The electrochemical monitoring of hydrogen using Devanathan cells mounted on external surfaces using sealing systems to contain electrolytes was a later development by several manufacturers. Portable versions of the cells extended considerably the scope of this technique and provided a valuable tool for corrosion and inspection engineers. More sophisticated probes are now available that measure the hydrogen flux passing through a metal. Versions are available for both periodic and continuous monitoring and are noninvasive in application. Current instrument systems can measure hydrogen at very low levels with accompanying temperature recording and are available in various versions to fit different geometries.

A recent paper<sup>36</sup> describes the use of hydrogen permeation detection to correlate changes in operating conditions with corrosive conditions in a crude distillation column in an oil refinery. Measurements were taken over a 3-day period. During the monitoring periods, the refinery made adjustments to various operating parameters including chemical injection. The corrosion rates determined by monitoring correlated well with corrosion rates obtained from ultrasonic thickness measurements.

#### **4.36.1.4.9 Test heat exchangers and spool pieces**

In cooling water systems, test heat exchangers are often utilized for assessing the effectiveness of the corrosion inhibitor and consequent corrosion behavior of the heat exchanger tubes. These can often be supplied in the overall service package by the corrosion inhibitor supplier. The test unit includes several tubes that can be opened for visual observation and measurements taken of the corrosion rate by destructive, metallographic examination. The units can be isolated by valves allowing removal or replacement of the tubes without interrupting the operation of the cooling water system.

Small lengths of piping (~1 m in length) can be fitted to plants using appropriate flanges and provide valuable data as regards the corrosion characteristics. The spools can be removed at shutdowns or installed in bypass loops allowing more convenient removal and replacement. Caution in the interpretation of the results from bypass loops is required until confidence is obtained that the bypass line mimics mainstream conditions and that allowances are made for any differences.



#### 4.36.1.4.10 Monitoring of bacteria

Bacteria are present in some commercially important processes, including cooling water systems and nearly all areas of oil production. Detecting the presence of bacteria is essential for effective maintenance management that includes treatment with appropriate biocides. In time, bacteria develop immunity to specific biocides and the biocide type requires changing at prescribed intervals to keep bacterial growth under control. The most significant species of bacteria from the corrosion standpoint is sulfate-reducing bacteria, which consume sulfate in its metabolism, producing and expelling hydrogen sulfide, which is very corrosive and can induce cracking in steels. Bacteria can exist in the liquid (planktonic) or under scale/deposits (sessile) and this requires consideration in bacteria-monitoring programs. Techniques of monitoring include bacterial analysis (via filters), sidestreams, vessels, and specially designed corrosion coupons such as the Robbin's device that utilizes metal studs as described in the following paragraph. Note that monitoring in the fluid flow only would not detect the presence of sessile bacteria.

Testing for bacteria is expensive, tedious, and time consuming and considerable effort has been devoted to the development of spot tests that can identify the presence of bacteria within a 10–15 min period, *albeit* without the identification of the bacteria type. Rapid techniques for assessing bacteria include adenosine triphosphate photometry (ADP), fluorescence microscopy, and radiorespirometry. Standards and recommended practices are available.<sup>37–39</sup> The use of a microbiological laboratory is necessary to identify which type of bacteria is present involving transportation with sterile packaging that can be a challenge, particularly for offshore operations.

Coupons and probes (fitted with flush elements) can provide useful information regarding bacteria. The 'Robbin's device comprises a 25 mm diameter stainless steel pipe containing a series of carbon steel studs – any sessile bacteria will deposit on the studs and can be recovered and analyzed.<sup>40</sup> Variations of the 'Robbin's unit are commercially available for insertion into plant using standard access-fittings. Most companies supplying coupons and corrosion probes will be able to supply this equipment.

#### 4.36.1.4.11 Process parameters and conditions

An obvious collection of parameters that influence corrosion processes and require scrutiny but are often ignored, mainly due to communication problems,

relate to the process or the product under manufacture. The constituents of feedstocks and process streams should be regularly checked as well as operating plant parameters such as temperatures, pressures, the presences of gases, and flow rates and regimes. This is particularly relevant in gas and oil streams. A change in feedstock and/or source of supply can result in changes in corrosive properties. Sources and quality of water for injection points into the plant in oil refining should be regularly monitored.

### 4.36.1.5 Industrial Applications and Experience

#### 4.36.1.5.1 Oil and gas industry

##### Overview

The oil and gas industry is subject to many corrosion hazards in all areas of its operations. In addition to production and refining, the transportation of products is a major operation involving road tankers, extensive pipeline networks, and marine vessels, including coastal vessels and supertankers. Leakage of crude oil presents major environmental risks and leakage of highly flammable refined products can result in explosion and/or fire with consequential risks to life, and because of the scale of industry operations, major financial consequences arising from unscheduled shutdown and loss of production.

Although corrosion risks are mitigated in some areas by the use of corrosion-resistant alloys, the majority of industry equipment is constructed in carbon and low-alloy steels and corrosion inhibition is widely practiced at key stages of the production and refining operations to mitigate internal corrosion risks. The need to monitor and confirm the effectiveness of corrosion control by inhibition is one of the reasons for the industry's being a very large user of corrosion-monitoring equipment. The cost of corrosion to the industry has been estimated in numerous studies at ~40 cents per barrel, exemplified by a study of two oil fields operated by Agip in Europe.<sup>41</sup> A significant element of this cost is the expenditure on corrosion monitoring and inspection, as exemplified by **Table 4**, which shows corrosion-related costs for a major US oil field producing 270 000 bbl day<sup>-1</sup> (4% of total daily domestic US production) in 1999. The total annual monitoring costs were ~\$1 m as against the total inspection costs of ~\$3.3 m and the inhibitor costs (chemicals alone) of \$13.5 m.

Another major US field operated by the same company producing 246 000 bbl day<sup>-1</sup> reported

**Table 4** Detailed annual costs for corrosion monitoring and inspection and other related corrosion costs for one large US oil field

	Cost (\$ x thousand)
Inspection costs	
Overhead	\$492
Tangential radial tomography inspection	\$1409
Ultrasonic inspection	\$361
Other	\$1054
<i>Total inspection</i>	<i>\$3316</i>
Monitoring costs	
Coupons	\$924
Bacteria monitoring	\$13
Laboratory analysis	\$40
<i>Total monitoring</i>	<i>\$977</i>
Repairs	\$600
Engineering staff	\$1416
Corrosion inhibitor (chemical alone)	\$13533
<i>Total</i>	<i>\$19.84 million</i>

Source: [www.corrosioncost.com/pdf/oilgas.pdf](http://www.corrosioncost.com/pdf/oilgas.pdf)

monitoring and inspection costs as shown in **Table 5**. In this case, the expenditure on corrosion monitoring and inspection was the largest single item.

Although the industry is regarded as corrosion conscious with a good awareness of corrosion risks and corrosion control practices, serious and costly corrosion incidents continue to occur, for example, in production,<sup>42</sup> refining,<sup>43</sup> pipelines,<sup>44</sup> and transportation.<sup>45</sup>

The engineering design for a new oil field is based on the field fluid analysis. However, field fluid compositions can change radically as the field ages resulting, for example, in higher levels of recovered water and/or field souring (production of hydrogen sulfide at a later date after initial field production) and such factors increase the corrosion risk considerably. The historical approach that initial materials selection supplemented by in service inspection at scheduled shutdowns could be relied upon to mitigate corrosion risks was invalidated progressively by operating experience, not least European offshore experience in the 1970s, which clearly showed the inadequacy of this approach. Increased corrosion risks were usually mitigated by the introduction of corrosion inhibition with the result that online corrosion monitoring was gradually introduced by all the major operators. It came to be recognized that the use of an integrated system for corrosion monitoring, incorporating inspection data such as ultrasonic thickness measurements, was the optimum approach to ensuring successful operation.<sup>6</sup> In today's regulatory environment,

**Table 5** Costs for monitoring and inspection and control techniques for one US large oil field

Corrosion expense	Cost (\$ x thousand)
Inspection, monitoring and staff costs	\$9625
Repairs	\$1350
Corrosion inhibitor (chemical alone)	\$7200
<i>Total</i>	<i>\$18.175</i>

Source: [www.corrosioncost.com/pdf/oilgas.pdf](http://www.corrosioncost.com/pdf/oilgas.pdf)

the authorities in many countries have introduced legislation requiring oil/gas installations to monitor corrosion, specifying the techniques to be adopted. The USA has introduced a Corrosion Prevention Act, which has the potential to dramatically improve corrosion prevention and control practices in the industry.<sup>46</sup> However, regulatory authorities are reluctant to impose requirements that might result in excessive economic penalties to business operations. For example, there has been a long debate in the USA regarding the frequency with which instrumented inline vehicles (smart pigs) should be used for pipeline inspection.

Regarding monitoring techniques, the industry has from the outset utilized coupons. These were later supplemented by ER probes that were first applied using portable instruments until automatic systems began to appear in the early 1970s. Automatic application took a long time to develop due to the high cost of special cable requirements. When LPR technology was introduced, its application was limited to cooling water systems and streams with some water content. There has always been controversy related to the use of LPR in oil/water streams, although measurements have been made in separated waters in bleed-off pots in crude distillation refinery units and some onshore pipelines. The extensive use of corrosion inhibition requires monitoring techniques that respond rapidly to assess the effectiveness of specific inhibitors and their required dosage rates, and this has provided a considerable impetus for techniques that provide instantaneous information such as EIS, EN, and FSM. Applications of FSM in particular are expanding on both onshore and offshore installations, because it provides accurate corrosion rates for the actual components that are being monitored.

Well-drilling is the first operation in producing oil or gas and can be affected by corrosion if corrosion control is inadequate. Fortunately, tubing used for

drilling can be inspected for corrosion on the surface when withdrawn from the well. However, mud-slurries that are used for the removal of scrapings from the drilling operation have to be treated with corrosion inhibitor and oxygen scavenger to counteract the ingress of oxygen into the drill stem. This operation is generally monitored by both coupons and LPR probes that can signal upsets in the corrosivity of the mud and correlation with chemical treatment. Certain dense halide brines are used to balance formation pressures during production operations, which can be corrosive due to dissolved oxygen or entrained air. Also, brines can be corrosive due to acid generation.

Seawater that is injected (squeeze) to recover oil requires treatment to remove oxygen and control bacteria to prevent souring of the formation, otherwise serious corrosion can occur. The water-injection facilities require monitoring on the manifold and elsewhere using coupons and LPR probes to confirm efficient oxygen removal by mechanical degassing and oxygen scavenging. Some operators also use galvanic probes, comprising steel and copper electrodes, which respond rapidly to the presence of oxygen.

Corrosion inhibitors are commonly added throughout the system from downhole (down the well) to the export line and to the water and gas lines downstream of the separators and monitoring is carried out at appropriate locations including wellheads, manifolds, interfield lines, separators (gas outlet, water outlet), export lines, piping, and terminal infrastructure to provide guidance on internal corrosion rates and inhibitor effectiveness. Corrosion monitoring is based mostly on combinations of coupons and ER/LPR probes as appropriate for the location. FSM, EIS, EN, and inspection techniques (including intelligent vehicles) are used selectively to supplement basic monitoring packages. In some installations, primary monitoring relies on the FSM technique if the benefits justify the higher cost.

Difficulties relate to inaccessibility, particularly for offshore pipelines and downhole. Nevertheless, coupons of various designs and caliper tools are available for downhole, albeit with some resulting drawbacks such as the removal of any inhibitor films that are overcome by increasing inhibitor dosage for short periods after the inspection. Subsea facilities present particular challenges related to accessibility and engineering, for which FSM test spools provide potential solutions.

For refineries, each unit needs a risk analysis and the crude distillation unit that provides feedstock to many other refinery units needs particular attention. Crude oil distillation units can suffer severe

corrosion, depending on the quality of the crude oil being processed. At one time, a refinery unit handled only one source of crude oil that was selected for its low corrosion risk. For both geo-political and economic reasons, refineries now buy diverse sources of crude oil on the spot market which has increased corrosion risks. The mixing or blending of corrosive crude oil with more benign crude oils is often practiced to reduce the corrosive risk. Any unscheduled shutdown of the distillation unit due to corrosion results in knockon effects on other refinery units with potentially enormous economic penalties. The top of the column and piping carryover to the coolers are vulnerable to corrosion by hydrochloric acid arising from the hydrolysis of calcium and magnesium chlorides. This is controlled by the removal of calcium and magnesium chlorides from the crude oil in desalter vessels upstream of the distillation unit and the addition of ammonia and neutralizing/film-forming inhibitors to the overhead stream. The pH of the water that separates from the overhead stream is used to control inhibitor addition, and the general target range for pH is 5.5–6.5. LPR probes are also used to monitor corrosion rates in the water stream but hydrocarbon contamination of both pH and LPR electrodes can result in errors if allowed to accumulate.

Hydrogen sulfide and naphthenic acids may also be present and can exacerbate corrosion risks. Naphthenic acids can be extremely corrosive to carbon steel at the temperatures prevailing in distillation columns. Risks are mitigated by either upgrading the metallurgy to stainless steel or adding corrosion inhibitors that are resistant to the temperatures involved.

The management of corrosion in distillation units is based heavily on hydrocarbon and water analysis supplemented by monitoring with coupons and ER/LPR probes to provide advanced warning of system upsets leading to corrosion damage. In addition, there have been isolated applications of FSM and EIS/EN for specialized situations such as corrosion inhibitor trials and the presence of naphthenic acid. Onstream, nondestructive examination is also utilized. As always, no single technique covers all requirements and a number of corrosion monitoring techniques should be used in an integrated system, consistent with the risks involved.

Bacteria present additional corrosion hazards in many areas of oil production operations and bacteria monitoring is essential for adequate control and to assess the effectiveness of the biocide addition. Onshore pipelines are monitored using both coupons and probes with flush elements, although the sensors

need to be removed before any online intelligent pigging is carried out. Sensors can also be used in bleed-off pots attached to pipelines.

Overall, corrosion monitoring has made a large contribution to the continuity of operation and safety in the industry, not only by providing data for life prediction of infrastructure but also by enabling optimal corrosion control practices based on corrosion inhibition to be identified.

### Case studies

The benefits arising from a well-planned and managed corrosion monitoring program are illustrated by the following cases:

1. *Oil refinery corrosion inhibitor validation* – Corrosion risk mitigation in crude distillation units is based heavily on corrosion inhibition, as already described. ER probes are utilized in many refining units for routine monitoring supplemented by coupons for verification where relevant. Automatic data collection offers the prospect of automatic control and Exxon carried out pioneering work in the USA in their larger refineries, closing the loop from the probe performance to automatic inhibitor control facilities.<sup>47</sup> The main objective for this work was to relieve the corrosion engineer of involvement in routine corrosion upsets (estimated at 60–70% of corrosion incidents) allowing more time for more complex corrosion problems. More recent applications have related to naphthenic acid corrosion, for which corrosion inhibitors were developed that would withstand the higher temperatures involved pending a possible future material upgrade. The data obtained were used to assess effectiveness of the candidate inhibitors and to establish correct dosage rates.<sup>31</sup>
2. *Dehydrated gas pipeline corrosion risk mitigation* – The advantages of using electrochemical techniques that enable online measurement of the Stern Geary factor ( $B$ ) have been reported.<sup>48</sup> One example relates to online, real-time monitoring techniques involving LPR, HA, and EN. Complementary information was obtained on both general and localized corrosion in a range of pipeline environments for steel and other metals. The real time measurements provided valuable information in low water-cut, dehydrated, multiphase, and vapor phase environments for both general and pitting tendencies. The provision of HA enabled measurement of the  $B$  value and improved the accuracy of the

measurements very much providing criteria for optimizing chemical treatments. Vapor phase environments typically exhibit 1–2 orders of magnitude lower general corrosion rate than found in liquid phase environments. The predominant mode of corrosion in the vapor phase has always been observed to be pitting corrosion, shown by high values of pitting factor, corroborated by visual observation. Other factors such as agitation or turbulent flow were correlated together with oxygen excursions.

The following cases highlight the importance of integrating corrosion and monitoring and inspection programs into an overall management system for managing recognized corrosion risks effectively, not least the deployment of monitoring and inspection resources to provide effective corrosion risk mitigation.

1. *Oil refinery explosion due to erosion corrosion* – In 2001, a major oil refinery in the UK, producing high-octane gasoline, experienced a severe explosion and fire in the saturate gas plant resulting from an overhead line rupture. The rupture resulted from local thinning due to erosion corrosion downstream of a water-wash injection inlet after ~13 years of operation. The injection inlet was listed on the inspection data base as in intermittent use and as a result had attracted relatively little subsequent inspection. In 2000, significant wall thinning had been identified and a full inspection of the area was scheduled for 2001. During the erection of scaffolding, the explosion occurred, fortunately on a public holiday, which minimized casualties and no personnel were killed. However, substantial damage was caused to the gas plant and a nearby unit resulting in a loss of production for several months and an increase in the global spot-price of high-octane gasoline. ER corrosion probes had been installed several years previously following receipt of specific information about the vulnerability of carbon steel pipework to corrosion in the vicinity of water injection points, but operators had failed to respond to the indications of increased corrosion in the wash-water feed pipe,<sup>7</sup> and as a result, a recognized corrosion risk was not managed effectively.
2. *Oil transit pipeline failure due to microbiological corrosion* – The Prudhoe field in Alaska is the largest US oil field representing 8% of domestic production. The field was threatened with a complete shutdown of production in August 2006 due to corrosion of a pipeline, resulting in an increase

of 2.2% in the worldwide spot price of crude oil. There are two eight mile (12.9 km) long oil transit lines in the field. The incident was a result of a leak in the 34-inch (86-mm) western transit line, constructed in the late 1970s, which resulted in a leakage of 200 000 gallons of crude oil – the largest spill in the field's history. The hole in the bottom of the pipe measured  $0.25 \times 0.5$  inch ( $6.4 \times 12.7$  mm) and the leak went undetected for several days.<sup>42</sup> The line carried hot crude oil from two processing facilities to a facility that blended natural gas liquids and crude oil from the east and west production facilities prior to delivery to the Trans Alaska pipeline. Following the discovery of the leak, the line was immediately closed and clean-up operations initiated. A return to full production was achieved in  $\sim 3$  weeks. Internal corrosion risk mitigation was based on the use of inhibitors, monitored using coupons, ER probes, leak detection systems, and NDT techniques,<sup>5</sup> including ultrasonics and radiography. The pipeline was accessible above ground excepting cased segments of piping at buried crossings. The US Department of Transportation (DOT) initiated an investigation into the leakage and required further inspection and remediation of the lines, including the running of an intelligent pig (ILI), through the western transit pipeline within 3 months. Intelligent pigging had not taken place in either transit line for several years, in contrast, the Trans-Alaska line is pigged every 14 days. The transit pipeline had been designated initially as a low corrosion risk but due to a reduction in flow rates, debris, and corrosion products that were normally passed through the pipeline deposited on the pipe allowing bacteria to develop beneath, resulting in corrosion. The loss of wall thickness in the pipeline was not identified before leakage occurred despite an extensive corrosion control and monitoring program employing approximately two hundred corrosion professionals and contractors conducting  $\sim 100$  000 corrosion inspections annually on pipeline and equipment locations throughout the Prudhoe Bay field and facilities, of which 60 000 were for internal corrosion detection.<sup>42</sup> The corrosion problems led to the issue of a subpoena requiring the CEO of the operating company, BP Exploration Alaska to appear before a Congressional Committee in order to describe the incident and its causes. The incident proved a public relations (PR) disaster for the company, which previously

had a long-standing reputation for investment in corrosion engineering and research, including corrosion monitoring activities.

#### 4.36.1.5.2 Chemical and petrochemical industry

##### Overview

In a retrospective view of the chemical process industries, examples of extreme operating conditions have been outlined by Dean<sup>49</sup> such as the high pressure used in ammonia synthesis of 272 bar (4000 psi), high temperature in ethylene production ( $1038^\circ\text{C}$ ), low temperature in hydrogen liquefaction ( $-215^\circ\text{C}$ ), corrosive environment in ammonia oxidation ( $\text{HNO}_3$ ), ammonium nitrate production (exothermic reactions), and the large volumes involved in the processing of petroleum products. Dean has identified a number of major events that have occurred and that have impacted on the chemical industry, shown in Table 6.

The effects of major disasters such as Flixborough (UK) and Bhopal (India) have resulted in increased concern for process hazards in chemical operations, which has focused attention on materials of construction, possible failure mechanisms, and the management, maintenance, and surveillance of chemical manufacturing plants. New standards have been adopted that require positive assurance that equipment is fit for service and degradation processes such as corrosion can no longer be ignored if they cause damage to the structure.<sup>42</sup> As a consequence, interest in online

**Table 6** Some trends and vents that caused major changes in the chemical industry

Event	Dates	Results
Energy crises	1973	Conservation
Ditto	1978	Other energy sources
Passage of OSHA <sup>a</sup>	1970	Safety emphasis
Flixborough <sup>b</sup>	1974	Process safety
Passage of EPA <sup>c</sup>	1970	Environmental concern
Bhopal release	1984	Ditto
Ashland storage tank failure	1988	Mechanical integrity

<sup>a</sup>USA Safety legislation USA.

<sup>b</sup>UK Explosion in chemical plant.

<sup>c</sup>US Environmental legislation.

Source: Dean, S. W. *Stainless Steel World* 2002, 13, 62–66.



corrosion monitoring has increased, in particular in devices that provide signals that can be used as control parameters.

### Case studies

The benefits arising from a well planned and managed corrosion monitoring program are illustrated by the following cases:

1. *Carbonate plant corrosion inhibitor validation* – A plant in the UK,<sup>1</sup> which had operated for many years, was producing sodium carbonate, using the same process without any serious corrosion problems. A change in a feedstock was made from a by-product of another process to a synthetic source, and laboratory tests on plant liquors indicated that there would be no change in corrosion rate. However, after ~18 months inspection confirmed that serious corrosion had started to occur and although some spares were available, there was a real possibility that production would be severely limited for several months with very serious commercial effects for both the operating company and its customers. Impurities in the original feedstock were identified as having had an inhibitive effect on corrosion. Initial tests had missed this because inhibitor had accumulated in the plant and maintained protection for a period after the feedstock change. ER probes were installed in affected parts of the plant. Some corroded areas were in vapor spaces subject to splashing so that electrochemical LPR probes could not be used directly but were installed in a bypass where continuous immersion occurred. These probes were also utilized in laboratory studies for screening replacement corrosion inhibitors. Possible inhibitors, many selected by analogy with known impurities in the original crude feedstock, were tested in the laboratory, and three were tested in plant trials. The complementary information obtained from the two monitoring techniques simplified the assessment of inhibitor behavior. The most economical inhibitor was identified and its performance monitored in plant trials. A large number of monitoring probes with facilities for automatic scanning and recording of data were used. The equipment cost was correspondingly high but this was justified by the speed with which a solution was found and implemented, resulting in the saving of several millions of pounds of potential lost production and even larger indirect cost to the customers and to their employees. The data

obtained were also of value in planning maintenance and shutdown schedules.

2. *Ammonia absorption train corrosion risk mitigation and productivity improvement* – a large coke oven plant experienced significant and unpredictable variations in corrosion rates during normal operations resulting in uncertainty as to the remaining life of the plant.<sup>50</sup> It was recognized that variations in the corrosion rate could be related to poor process chemistry control in the absorption unit, which had implications for the efficiency of ammonia removal. Both LPR and EN corrosion monitoring probes were installed and some typical data over a 1 month period are shown in [Figure 12](#).

The top trace shows weekly temperature excursions that coincided with a process circuit purging cycle. The bottom trace combines both EN and LPR results. The EN responded to pitting attack. On some excursions, increased corrosion rates coincided with the temperature excursion, but on other occasions, the corrosion rate did not increase unduly with temperature. At the start, the measured corrosion rate was reasonably low, but toward the end of the month, the rate increased to a maximum of six to seven times the background rate. Further monitoring revealed a relationship with a particular feature of the plant control involving a faulty pH sensor. Yet further work revealed that excursions in corrosion rate were linked to the molar ratio of two components in the process liquor. The results shown in [Figure 13](#) identified not only the cause of corrosion, but also that variations in the molar ratio also controlled the efficiency of the ammonia absorption process, thus enabling an increase in the productivity of the plant to be achieved.

#### 4.36.1.5.3 Power generation industry

##### *Coal fired boiler tube corrosion control*

Coal remains the most economical and widely available fossil fuel for the base-load generation of electricity.<sup>51</sup> Due to competition and the longer term requirement to minimize the production of greenhouse gases, operators are increasingly trying to maximize the efficiency of pulverized fuel-fired boilers by increasing the interval between scheduled maintenance shutdowns and operating the boilers under optimum conditions by a careful control of combustion parameters. For example, the UK Drax power station, which produces ~10% of the country's base load electricity, has increased the interval between

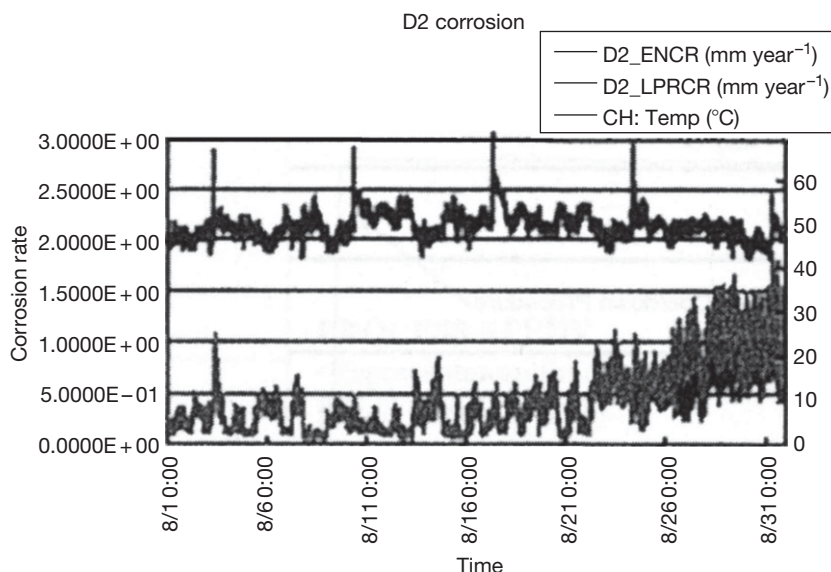


**Figure 12** Corrosion behavior in a coal plant ammonia absorber system. Reproduced from Cox, W. M.; Boyce, M.P.; Miyazawa, M.; Tanaka, Y. *Corros. Manage.* **2000**, May–June, 6–10.

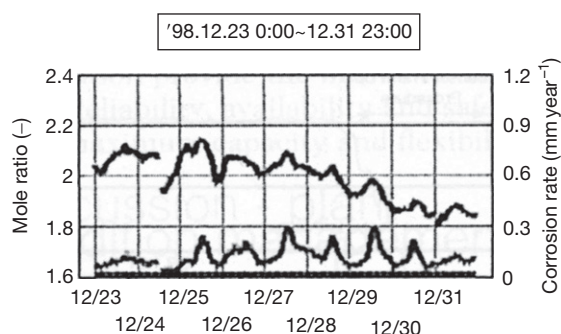


**Figure 13** Corrosion behavior in coal plant ammonia absorber system – variations in corrosion process liquor molar ratio (upper trace) rate and corresponding transients in corrosion behavior (lower curves). Reproduced from Cox, W. M.; Boyce, M. P.; Miyazawa, M.; Tanaka, Y. *Corros. Manage.* **2000**, May–June, 6–10.

scheduled maintenance shutdowns from 3 to 4 years and plans to extend this even further in the future. Examples of process improvements include changes in burner configuration, minimizing excess oxygen levels, and optimizing tube-cleaning procedures. The introduction of low  $\text{NO}_x$  burners over the past few years has produced a corresponding reduction in excess air and an increase in reducing conditions local to the burners. The reduction of excess air has helped thermal efficiency, whereas corrosion and boiler slagging rates have generally increased. Corrosion rates for furnace-walls can be extremely low

( $<0.1 \text{ mm year}^{-1}$ ) under oxidizing conditions but may increase to as high as  $\sim 9 \text{ mm year}^{-1}$  under highly reducing conditions. Historically, manual wall thickness surveys provided data for the prediction of likely tube-wall metal loss between major shutdowns. If this loss resulted in a remaining wall thickness less than an allowed minimum, then tubes were replaced, or a protective, nickel alloy weld overlay applied.

More recently, a range of specialized ER corrosion probes and corrosion scanner systems has been used for monitoring inaccessible surfaces in power stations during normal operations.<sup>51</sup> The sensing elements are welded to the external boiler wall and during the resistance measurement cycle, current is passed directly through the tube wall. The system instrumentation detects small increases in resistance at the nano-ohm level as the tube-wall loses material. Complete maps for corrosion loss can be assembled over large areas of boiler wall. A scanning system was installed in a boiler to monitor the performance of the welded overlay and confirmed that it was performing well, as shown in **Figure 14**, with very low rates of corrosion ( $<0.1 \text{ mm year}^{-1}$ ), in comparison with adjacent nonoverlaid tubing, where corrosion rates were as high as  $0.8 \text{ mm year}^{-1}$ .

In another monitoring exercise, variations in corrosion rate with the seasons were identified, the precise cause of which was not known other than that some coal stockpiles were thought to contain more moisture during the winter/spring period, as shown in **Figure 15**.

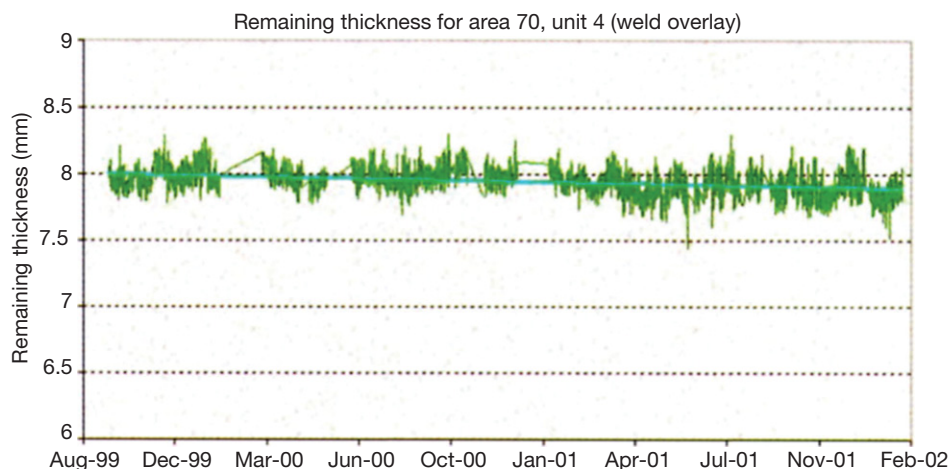


**Figure 14** Coal fired power station – monitoring of tube-wall using weld overlayed tubing – thickness trend weld overlay. Reproduced from Farrell, D. M.; Robbins, B. J.; Sikka, P.; Seaman, M. *Corros. Manage.* **2004**, May–June, 16–21.

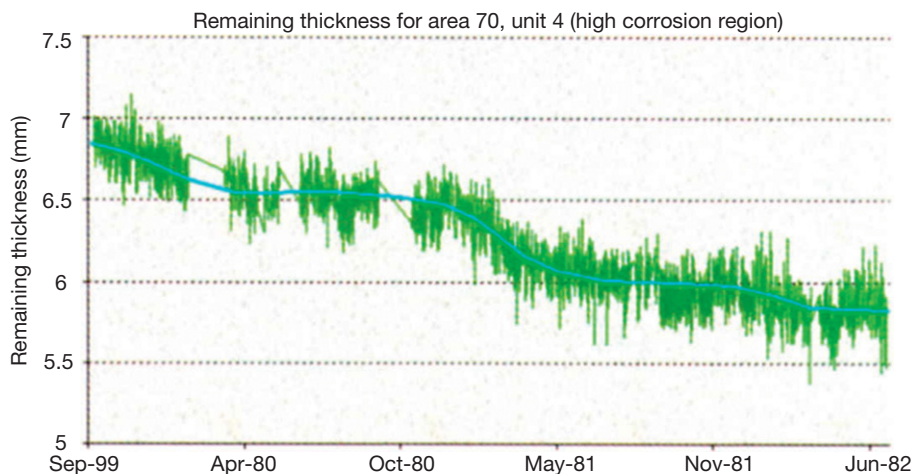


**Figure 15** Coal fired power station – monitoring of tube-wall using weld overlayed tubing – high corrosion region. Reproduced from Farrell, D. M.; Robbins, B. J.; Sikka, P.; Seaman, M. *Corros. Manage.* **2004**, May–June, 16–21.

Depending on market conditions and power demand, power plants may be operated in two-shifting mode involving standby during night-time periods. Tube temperatures drop considerably before the plant resumes the next morning and concern had been expressed that this thermal cycling could damage the tube wall scales and accelerate corrosion. However, corrosion monitoring confirmed that this was not the case,<sup>51</sup> as shown in **Figure 16**.

#### **Flue gas outlet duct corrosion control**

Orimulsion<sup>®</sup> fuel offers power stations an economic incentive for use in industrial boilers.<sup>4</sup> The fuel consists of an emulsion of naturally occurring bitumen in water. However, the fuel has high vanadium and

sulfur contents, thus increasing corrosion risks, and produces more ash than conventional fuel. A large power boiler, fitted with a wet scrubber flue gas desulphurization (FGD) unit was using Orimulsion<sup>®</sup> as fuel and the flue gas outlet duct downstream of the scrubber suffered substantial corrosion damage resulting in heavy expenditure for repairs, lining, and maintenance. A program of online monitoring was initiated to establish when corrosion was taking place and, more importantly, under what conditions the flue gas could become condensing. As the probe metal temperature was lowered, acid dewpoint condensation corrosion took place at temperatures below 65 °C. As soon as this condition was established, very high rates of corrosion would occur on the flue

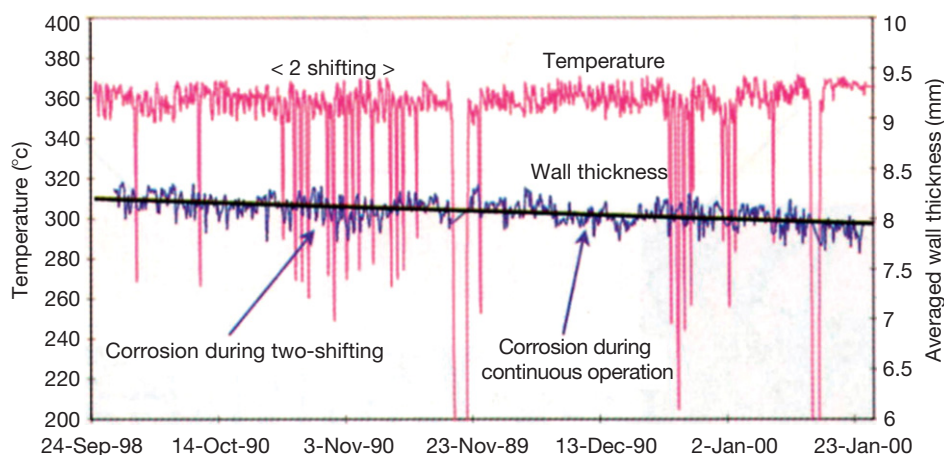


**Figure 16** Coal fired power station – monitoring of tube-wall using weld overlayed tubing. Two shifting operation and corrosion trends. Reproduced from Farrell, D. M.; Robbins, B. J.; Sikka, P.; Seaman, M. *Corros. Manage.* **2004**, 16–21.

duct walls. A short program of field trials established that continuous condensation occurred under certain firing conditions of the reheater furnace, especially if moisture removal by the mist eliminators on the outlet from the FGD system was less than optimal.

The field trials were extended to enable the corrosion surveillance instrumentation to remain in service in the plant resulting in significant operational savings, reduced maintenance costs, and the avoidance of expensive plant downtime, all of which previously had contributed significantly to the overall cost of generation.<sup>4</sup>

#### 4.36.1.5.4 Miscellaneous process industries

##### Desalination

Multistage flash distillation plants provide potable water by the distillation of seawater. These units have substantial amounts of copper alloy tubing for both heat pickup and cooling. The flash chambers that operate at a reduced pressure to obtain as much thermodynamic efficiency as possible are constructed from coated carbon steel. Corrosion of the copper alloy tubing and carbon steel chambers together with severe scaling are common challenges in these plants. Chemical treatments reduce the very severe scaling in these plants.

When the technology for multistage flash distillation was developed in the mid-1960s the copper alloy tubing selected was the same wall thickness as used for power generation. Considerable capital costs savings could be made if the wall thickness could be reduced, but there were concerns as to the robustness of the thinner walled tubing. A trial of both ER and LPR probes in a scaled-down rig gave excellent

correlation with destructive examinations of removed tubes. Both systems operated very well and were eventually used in operating plants to monitor the effectiveness of chemical treatments.<sup>52</sup>

##### Pulp and paper industry

Paper pulp manufacturing processes use very large volumes of water in paper production with many resulting corrosion problems. Some of the variables include temperature, chemical constituents, pH, concentration, size, and quality of the wood fibers. Recycling and environmental concerns may also influence corrosion performance. Conservation of water has resulted in recycling and reuse of water in closed loop systems. This has led to increases in the concentrations of dissolved solids and temperatures and changes in pH that have increased corrosion risks. Traditionally, carbon steel was the main material of construction but over the years, more stainless steel has been introduced. The types of corrosion experienced include pitting, crevice attack, SCC, MIC attack, weld corrosion, and corrosion fatigue.

Monitoring using advanced electrochemical techniques has been widely practiced in these plants. Most of the monitoring methods have been utilized, including coupons and electrical, in particular LPR, probes. EN has been successful in correlating online the effects of process chemistry on corrosion in Kraft continuous digesters.<sup>52</sup>

##### Cooling water systems

Recirculating cooling water systems using carbon steel tubes are treated with a range of chemicals including corrosion inhibitors. Open recirculating



systems present the highest corrosion risks due to oxygen pickup over the tower. These systems are treated with corrosion inhibitors and compatible biocides, and corrosion monitoring is ideal in this application. The cooling water is usually allowed to concentrate by  $\sim 2.5$  times for economical operation. Additional concentration would allow excessive chloride content with associated increased corrosion risks. The concentration is held at the given value by discharging a proportion of the water (blowdown) at prescribed intervals and fresh water makeup is added to keep volumes constant. LPR is the most suitable online technique for corrosion monitoring, combined with the use of coupons, which can be reduced in number when confidence in the LPR probes is established. Both probes and coupons are located in the hottest sections of the circuit where corrosion risks peak.

Compact control units for cooling water systems are available commercially that measure water parameters such as conductivity, and pH and incorporate suitable instrumentation for measuring corrosion, usually based on LPR. In the late sixties, a US chemical treatment company introduced a system incorporating an LPR measurement cell and facilities for activating a dosage pump if the preset corrosion rate was exceeded. Recently, a unit has been described incorporating seven different corrosion monitoring techniques (including crevice corrosion) to investigate the relationship between corrosion and water chemistry to facilitate corrosion control in a district heating project in Denmark.<sup>53</sup>

An example of the benefits of corrosion monitoring related to a recirculating cooling water system in a fertilizer plant that used river water and suffered severe corrosion arising from inadequate control and poor maintenance. The system blowdown was discharged to a treatment plant before eventual discharge back to the river. A trial was carried out with a suitable corrosion inhibitor and corrosion monitoring carried out at the exit of the hottest heat exchanger using both coupons and LPR probes. Following the verification of the LPR rates with both coupons and inspection techniques, some reduction in the number of coupons used was permitted. Corrosion rates were below  $0.25 \text{ mm year}^{-1}$  (10 mpy) for carbon steel. Bacterial monitoring was carried out using spot tests and periodic plate tests.<sup>54</sup>

#### 4.36.1.5.5 Pipelines (excluding oil and gas)

Pipelines are used for many different products other than oil and gas including raw and potable water,

seawater and treated wastes. Constructional materials include steels, cast irons, corrosion resistant alloys (CRAs), thermoplastic and reinforced polymers, and concrete. Carbon steel pipelines are often lined with cement and/or coated with organic coatings.

The London water ring main was constructed between 1988 and 1993 to supplement the existing Victorian water mains that have been badly affected by corrosion. Extensions to the new main are already in hand. Corrosion engineering and monitoring are utilized in the overall maintenance program.

In the Man-Made River project in Libya, a pipeline of combined length  $\sim 4000 \text{ km}$  has been constructed to carry well-water from the south to the main populated and industrial areas in the northern coastal area. The prestressed concrete coated pipe (4-m diameter and 7.6-m length) is reinforced with steel cabling. The pipes are protected from external corrosion using cathodic protection. Many corrosion problems have occurred with this system varying from corrosion of stainless steel components in the wells to corrosion of the steel reinforcement, which now, hopefully, has been controlled. Extensive corrosion monitoring using a number of techniques is carried out. A particular interest was corrosion failure of the prestressing wires.

#### 4.36.1.5.6 Transportation

One major international car manufacturer has used the ER system for monitoring corrosion on car bodies. Vehicles were driven through salt water on a test track to assess current corrosion control assemblies, materials, and coatings.

Generalized approaches to the corrosion surveillance of aircraft, emphasizing the training of personnel, have been reviewed.<sup>9,55</sup> The development potential of an ER system for civilian aircraft has been examined resulting in a US Air Force initiative of using ER sensors placed in susceptible areas using computer capture of data for a number of different aircraft.<sup>56</sup> In order to establish correlation between operating conditions and corrosion, the Canadian Air Force has used sensors in several aircraft to monitor operating conditions and base locations.<sup>9</sup> Naval flying operations are subject to very severe corrosive environments. The US Navy estimates that every hour of flying requires 27 h of maintenance. A miniature sensor has been developed by the US Navy that can remotely detect and monitor corrosion in inaccessible areas of aircraft, ships, submarines, and weapon containers. The sensor combines bimetallic thin-film microsensor technology with microelectronics with



radio frequency communication. The system collects and stores corrosion information that can be retrieved on demand by transmitted radio signals.<sup>57</sup>

#### 4.36.1.5.7 Nuclear waste storage

The nuclear industry has extensive interests in the corrosion of structural materials that are used for the storage of radioactive wastes, where the objective is to minimize moisture and geological storage areas are chosen on this basis. Active waste is stored in both carbon steel and stainless steel drums and considerable work is underway to investigate corrosion monitoring methods for the waste containers in order to maintain integrity prior to and during disposal. The development of an EN-based probe for monitoring nuclear waste containers has been reported.<sup>58</sup>

#### 4.36.1.5.8 Civil engineering

Corrosion measurements using the LPR technique have been reported on a historical building in Chihuahua, Mexico.<sup>59</sup> The building was a railway locomotive roundhouse built in 1910. LPR measurements were made in the building to evaluate the behavior of the metallic materials in the presence of a humid atmosphere. Test-cells were placed in several zones of the building's metallic structure. Data obtained from the *in situ* measurements showed that the corrosion rate was less than 1 mm year<sup>-1</sup>.

Probes with ER elements have been buried at various depths in concrete to monitor the corrosion of harbor jetties. One application related to naval infrastructure in US Navy dock facilities.<sup>60</sup> Electrochemical techniques for the monitoring of reinforcement in concrete have received much attention and laboratory development has been extensively reported. Advantages and limitations of electrochemical measurements for monitoring the reinforced steel have been reported by Rothman and Tullmin.<sup>2</sup> Details of other electrochemical techniques for assessing concrete reinforcement have been reported by Sykes<sup>61</sup> and Elsenor.<sup>62</sup>

#### 4.36.1.5.9 Atmospheric corrosion monitoring

Special ER probes using printed circuit sensors provide many advantages compared with the conventional coupon technique including remote data capture and overall convenience. Monitoring at specific locations (power plants and other industrial areas) for pollution type monitoring is now mandatory in some countries. An example of location atmospheric monitoring is the monitoring and inspection of radar towers located throughout the USA.<sup>63</sup>

### 4.36.1.6 Future Developments

An interesting development in an electrochemical technique relates to electrochemical frequency modulation (EFM).<sup>64</sup> In this technique, the potential perturbation signal consists of two sine waves of different frequencies and a corrosion rate can be obtained instantaneously, without prior knowledge of the Tafel constants. An advantage claimed for this method is its inherent data validation control using 'causality factors.' Another advantage claimed is that the method can be used successfully for corrosion rate measurements under various corrosion conditions. Corrosion rates obtained by EFM, LPR, weight loss, and solution analysis (atomic absorption spectroscopy) were in agreement.

There has been a significant increase in the applications of the FSM system and similar systems by other manufacturers in the past decade and this trend is likely to continue because of the advantages of FSM in relation to the accurate monitoring of plant components rather than sensors.

Closing the loop by using online monitoring signals to operate associated control systems will accelerate as new electronic and software developments occur. This is particularly relevant to the oil, chemical, and power industries. A major US company in process control has recently purchased a specialized corrosion control company offering advanced electrochemical monitoring, and this could offer significant advantages to both the manufacturer and the user. Improvements in electronics and analysis have taken their time to induce confidence in online monitoring. Also, the complexity and uncertain morphology of corrosion has not helped the adoption of the technology when compared with the conventional process control, for example, corrosion is not a defined, fixed parameter comparable to the measurement of temperature, pressure, or flow rate. A process control package that includes corrosion monitoring is an exciting prospect that provides for improved service in both hardware development and technical support.

A solicitation issued by the US DOT in 2007 invited research projects based on nanotechnology related to Internal Corrosion Direct Assessment (ICDA) in the pipeline industry. New nanotechnologies for the detection and elimination of internal corrosive species as well as determining the presence and corrosivity of water are a component of the program. In the solicitation, it was stated that currently available technologies are limited because some cannot be applied to all pipelines and others

require prior knowledge of where to locate the sensors and costly excavations to replace the sensors.

The oil refining industry<sup>65</sup> has stated the following requirements for a successful corrosion monitoring technique in their operations:

1. Sensitive and reliable;
2. Fast response time;
3. Operate in most if not all environments;
4. Must have online and remote data access;
5. Should be unaffected by iron sulfide (FeS) film formation;
6. Unaffected by noise, vibration, and temperature;
7. Compatible with local plant services.

The provision of a technique that satisfies all of these criteria is a challenging goal for the future.

## **4.36.2 Inspection**

### **4.36.2.1 Introduction**

The definition of inspection is “to look closely at or into” and an inspector is someone who carries out this function. One of the early inspectors was the wheel-tapper, employed by the railway companies, who tapped the wheels of railway carriages with a hammer at larger stations. Any cracks present in the wheel components would alter the tone of the sound reflection. These days this function is carried out at speed by a special testing vehicle fitted with transducers.

Inspection has one of two objectives:

1. To identify defects, flaws, cracks, or changes in physical properties in a component that deviate from the material specification.
2. To periodically inspect operating equipment in order to detect any onset of material degradation and/or mechanical failure, generally referred to as in-service inspection.

There has been much discussion over the years among NDT/E academics, specialists, and inspectors as to the precise definition of the terms flaw or defect. All materials contain flaws but they are significant only in relation to the extent to which they might impair the functionality of a component, not least whether the flaw (or defect) remains the same size or starts to grow in service.

Detailed background information on NDT/E can be obtained from the web sites such as the American Society of Nondestructive Testing (ASNT) and the British Institute of NDT (BINDT). In practice,

NDT/E remains a mixture of black-art and science. An important issue relating to practice is the training levels of NDT/E operatives, especially relevant due to the increasing tendency to buy in inspection services. The establishment of recognized inspection training programs has been a long and tedious process, driven by the relevant professional societies in several countries.

### **4.36.2.2 Historical Development of Inspection Technology**

Inspection has developed over the decades raging from the visual observation of mechanical parts through to the detection of the noise produced by the formation of cracks in industrial plant. Early inspection requirements were directed at moving components that endured stresses and strains particularly the engines, pumps, and compressors that were developed during the industrial revolution in the UK, not least the introduction of steam power, in the nineteenth century. The Second World War led to a massive development due to the requirements of the defense industries, particularly in the USA. Many techniques, including ultrasonics, radiography, acoustic emission (AE), eddy currents, and many others, now employed routinely in a range of industries were developed at that time. However, the new techniques were often oversold and problems with both hardware and data interpretation contributed initially to user disillusion. Confidence was restored with further development stimulated by user feedback. Later developments in electronics made a substantial contribution and further expansion, and development followed the introduction of the computer, in particular, the introduction of the laptop for inspection in the field.

A key issue in relation to the inspection of operating equipment is whether it is necessary to take equipment out of service for inspection. Offline inspection is somewhat easier to carry out than inspection when plant is operating, because equipment can be entered for appropriate inspections using the full range of available inspection techniques. Clearly, size can be an issue such as in the case of piping, but using appropriate borescopes, even small diameter piping can be examined and photographed or viewed by television.

There have been strong economic drivers to develop online inspection techniques, particularly for equipment in high capital cost plants operating for extended periods between scheduled shutdowns,

such as in oil production, oil refining, power stations, and chemical plants for which unscheduled shutdown is very costly relating to the cost of lost product. Online ultrasonic thickness measurements (UT) using portable probes were limited in the early days to temperatures that would not destroy the piezoelectric crystal in the probe. However, the subsequent development and use of special contact greases extended their use to higher temperatures. Water-cooled probes were introduced but proved unwieldy in operation and did not achieve overall acceptance. Welded UT probes were developed by the nuclear industry in the UK for the inspection of some fast reactor components that contained design features to protect the piezoelectric crystal from excessive temperature. These probes were hardwired to the control room and enabled continuous measurements of wall thickness and this technology soon found applications in the oil industry.

The development of phased arrays of UT probes mounted on a flexible mat, attached by a velcro mat that could be moved from one location to another, was a further useful development. An added benefit with this system related to its use in remote locations capturing data without visits, particularly valuable for the oil industry in dangerous locations subject to terrorist or similar threats. The development of TLA and FSM further extended the battery of available, noninvasive tools. Both are conventionally categorized as corrosion-monitoring techniques but could just as well be categorized as NDT/E techniques, because they bridge the historical boundary between corrosion monitoring and inspection technologies by providing data as to equipment condition continuously.

AE has also developed as a noninvasive, screening tool for identifying damage zones in equipment where 100% inspection would be too costly and/or time consuming. The identified damage zones can be then examined in detail online, using techniques such as ultrasonics. In-line inspection (ILI) vehicles used for pipeline inspection have also seen major development.

#### 4.36.2.3 The Need to Inspect for Corrosion Damage

There are many examples of serious incidents and accidents resulting in fatalities due to corrosion that was not detected because

1. Inspection was not carried out.
2. Inspection was inadequate.

3. The inspector was not sufficiently qualified in the techniques used.
4. Problems regarding the interpretation of the data.

An example of poor, inadequate inspection was the failure of a fairground ride in London in 2000,<sup>66</sup> in which two people were killed and a third person was seriously injured because a seat broke free and flung them through the air before smashing into a kiosk on the far side of the fairground. Examination showed that the ride was riddled with rust and metal fatigue. An inspection of the ride had been carried out 3 weeks before the accident by an independent safety inspector who had reported no defects or deterioration. It was disclosed at the trial that the inspector had two previous health and safety convictions. A subsequent inspection revealed signs of deterioration to the remaining eleven car seats on the ride. The inspector was found guilty of manslaughter. The jury called for tighter regulations covering fairground rides and the introduction of a regulatory body to ensure that inspectors received proper training. This incident emphasizes the importance of adequate training and good professional conduct.

An incident in the marine industry related to a boiler explosion on the cruise liner SS Norway (previously known as the SS France), the world's longest passenger liner carrying 3000 passengers. Within an hour of docking at the Port of Miami in 2003, a massive explosion occurred due to the rupture of one of the four boilers, fatally injuring eight crew members.<sup>67</sup> The steam penetrated the bulkheads on two further decks breaching the crew accommodation areas and seriously burning a further six crew members. A failure examination carried out by the US National Transportation Safety Board (NTSB) showed that a large section of the waterwall header had fractured and broken away. The rupture was caused by extensive fatigue cracking which had initiated at the bases of corrosion pits most likely resulting from improper water chemistry during lay-up periods. From 1990 through 2003, it appears that no NDT/E or appropriate internal visual inspections were carried out on the weld seams of the affected boiler despite a well-documented history of cracking of weld seams in two of the ship's other boilers in 1996. The ship never returned to service after the explosion and was scrapped.

Neglect of a significant corrosion risk and inadequate inspection resulted in Scotland's worst industrial disaster in May 2004, involving the deaths of nine workers and serious injuries to another

37 personnel at a Glasgow plastics factory.<sup>68</sup> Following an investigation carried out jointly by the UK HSE, prosecutors, and police, a fine of £200 000 was levied on two companies operating at the site. The investigation showed that the explosion was caused by the failure of a buried pipe carrying liquid propane fuel at the factory. A leak outside one of the buildings allowed liquid propane to go through the wall into the cellar area. The pipe had not been inspected since initial installation in 1969. All sections of the buried pipe had deteriorated and corroded, including a cast-iron bend joining two sections of the pipe. No corrosion protection system had been applied to the pipework.

Corrosion risk mitigation by inspection is given a high priority in the air transport industry. However, problems can occur and deficient inspection was a factor in the Aloha Airlines Flight 243 incident<sup>69</sup> involving crevice corrosion allowing water ingress at bonded joints in the airframe. Fatigue cracks occurred, driven by the extensive number of take-offs and landings associated with operating short flights between the Hawaiian Islands, resulting in extensive damage when part of the upper fuselage was torn off. The operating history had exceeded the recommended number of flights, which had not been accounted for by the airline and the manufacturer. Accordingly, the inspection schedule was out of synchronization with that recommended by the manufacturer. In addition, a manufacturer's recommendation of a specific NDT/E test had not been carried out by the airline.

Bridges are at risk from corrosion and inspection is vital to the mitigation of such risks. Following the collapse due to SCC of the Point Pleasant bridge in the USA in 1967, resulting in 46 fatalities, a national policy for bridge inspections was made law in 1968 and a massive inspection program instituted.<sup>70</sup> The recent collapse of the Minnesota freeway bridge in 2007 reemphasized the scale of the problem in the USA. A large number of bridges were built in the 1950s and 1960s and there will be a large requirement for inspection services over the next 20 years. The author was told that the design life of the Forth Bridge, opened in 1890 and providing the main UK east coast railway link between Aberdeen and London, was 'in perpetuity' – the only structure given this classification in the author's experience in any industrial sector. This bridge has received appropriate inspection and corrosion prevention throughout its life. However, the Forth Road Bridge, opened in 1964, has corroded main cables, which will take up to 7 years to replace. Each main cable consists of 11 618

wires and it is believed that ~90% of the wires are corroded. A massive project for inspection and renewal of the wires is expected to cost hundreds of millions of pounds.<sup>71</sup> The Severn Bridge, which provides a road crossing of the River Severn in the UK, is also reported as having cable corrosion with weight restrictions in force until inspection surveys now in progress assess the full extent of the corrosion.<sup>72</sup> The problem was first revealed by inspection in 2004. Special cable inspection techniques are urgently required for bridge suspension cables.

The marine industry relies on vessel certification as the basis for licensed operation. The Erika, a Maltese registered oil tanker on charter to total carrying a cargo of crude oil, broke in half and sank while approaching the Bay of Biscay in a severe storm, resulting in the most severe coastal pollution ever experienced in any country of the European Union. In the ensuing court proceedings, it was revealed that a previous certification authority had refused the issue of a certificate due to severe corrosion of the tanker but the owners had obtained recertification from another authority. Total was fined \$550 000 for the maritime pollution caused. Other fines were imposed for other charges relating to the incident and fines were also imposed on the certifying authority and the owners of the tanker.<sup>73</sup>

These failures occurred despite existing legislation relating to the inspection of the relevant infrastructure together with considerable guidance regarding appropriate inspection techniques and practices. Incidents and accidents continue to occur due to failure to recognize prevailing corrosion risks, poor communication, inadequate inspection, and inadequate training of those involved in plant operation and maintenance. These are essentially management deficiencies, the causes of and remedies for which are covered in a separate chapter in this book.

#### 4.36.2.4 Inspecting for Corrosion Damage

Inspection for corrosion damage, or other service deterioration, developed at a later stage on the inspection technology timeline. NDT/E techniques were originally targeted at material defects and manufacturing faults, but as the technology developed, attention was extended to material degradation in service. Several established NDT/E techniques were identified as having potential for the inspection of corrosion including radiography, ultrasonics, and eddy current.

NDT/E as applied to corrosion inspection has the two main objectives of detecting, and if possible,

dimensioning corrosion. Inspection staff is not always familiar with all of the many forms of corrosion and good liaison is required between the inspection function and those engaged with corrosion control. General or uniform corrosion is the easiest type of corrosion to detect and measure. Using simple thickness meters, the remaining wall thickness can be measured. For example, subsea pipelines have been inspected by clamping a raster assembly developed by the Danish Welding Institute on the pipeline in which an UT probe assembly can traverse the full circumference of the line. Robotic crawlers can carry UT probes for the inspection of the large storage tanks used by the oil industry. The FSM system has not only been applied for general corrosion but also at a discrete area such as welds.

Some forms of localized corrosion, such as pitting corrosion, proved particularly difficult to resolve with the early ultrasonic instruments and problems are still reported in this respect.<sup>74</sup> The detection of cracks, in particular stress corrosion cracks, was of particular interest to the nuclear power, oil/chemical, and pipeline industries. These are invisible to the naked eye until failure occurs but can be detected using ultrasonics and AE. For pipelines inspection, ILI vehicles are now able to detect cracks as well as reductions in wall thickness, as described in a later section.

Inspection techniques used to detect defects in manufactured products, in particular ultrasonics and eddy currents, have been adapted for the detection of various corrosion types. For example, nonferrous heat exchanger tubing has long been inspected with eddy currents to detect manufacturing flaws (pin-holes) and the technique has been adapted to inspect *in situ*, offline, for corrosion defects that may have developed in service tubing.

Although some of the oldest techniques such as visual examination and mensuration are restricted to shutdown periods, other techniques such as ultrasonics, radiography, and AE can be used online. On-site inspection does not always have the precision associated with manufacturing or workshop conditions but good correlation can be obtained when monitoring and inspection data are compared in a well-organized and integrated inspection and corrosion monitoring program. Choosing the right techniques for inspection is a challenge and generally benefits from experience.

Practical problems inevitably arise and have to be overcome. Lack of access to equipment, in relation to not only the height (requiring scaffolding) but also

the close proximity of nearby equipment, can cause problems. In circumstances where access for inspection is completely restricted, corrosion risks have to be mitigated by upgrading materials in the design or at shutdown. The presence of very thick rust can prevent the transmission of ultrasonic waves for single-point ultrasonic measurements in particular. High temperatures can degrade the piezoelectric crystal in the probe and may require the use of high temperature greases and special probe designs.

Inspection programs are now routinely planned and managed as key components of corrosion management and RBI programs, the development of which are described in separate chapters in this book.

#### 4.36.2.5 Inspection Techniques for Corrosion Inspection

##### 4.36.2.5.1 Visual inspection

A properly executed visual inspection should accomplish the following:

1. Assist in failure analysis.
2. Indicate the need for further exploration.
3. Help to define the search area if further exploration is warranted.
4. Suggest techniques for further exploration.
5. Help to determine the measures needed to prevent or minimize the recurrence of damage.
6. Reduce the possibility of installing faulty fabrications by ensuring that the right materials and fabrication procedures are used and that workmanship is of the proper quality.

Visual observation can be carried with or without optical aids. Typical signs of damage include rust staining, bulging, cracked or distorted coatings/insulation, and hot-spots that are indicative of possible corrosion damage. The value of visual observation cannot be overemphasized as long as the potential limitations of direct eye observations are recognized, including the need for access, tiredness, fatigue, and variability. Simple magnifiers can be utilized ranging to more sophisticated optical equipment using fiber-optic (FO) endoscopes (borescopes), which are used for inspection in restricted areas. These devices can be fitted with cameras or TV cameras and lengths of flexible conduit can be fitted together for the inspection of remote areas and are extensively used for inspection purposes in boilers, buildings, aircraft engines, and process plant. Self-propelled versions of robots with FO equipment attachments and attached umbilical (for power and controls) are used for the



inspection of offshore risers, terminal hoses, and short-length pipelines. The introduction of digital cameras has made a major contribution to record keeping and communication purposes. Internal corrosion inspection is generally confined to scheduled shutdown periods, but the examination of external corrosion, often related to coating breakdown, can be carried out when the plant is operating, provided access is available.

#### 4.36.2.5.2 Ultrasonics

##### *Principles*

This is one of the most important techniques for corrosion inspection, in particular, for the measurement of metal thickness. Instrumentation varies from simple thickness meters using a single portable ultrasonic probe to more complex equipment using probe arrays with phased-firing probes.

Mechanical vibrations can be propagated in solids, liquids, and gases. If their frequency is within the approximate range of 10–20 000 Hz, the sound is audible. Above ~20 000 Hz, the waves are referred to as ultrasound and their application for measurement as ultrasonics.<sup>75</sup> The waves are produced by a piezoelectric crystal that is mounted in a suitable probe (holder or an array assembly) and when excited by an electric current, transmits a high-frequency sound-wave. Ultrasound waves have different wavelengths in different materials. The waves arise because of the elastic properties of the material under test and are due to induced particle vibration in the material. If the particle motion is along the line of direction of travel, the resulting wave is called a compressional or longitudinal wave, which can be propagated in solids, liquids, and gases.

It is possible for the particle movements in solid materials to be at right angles to the direction of travel, in which case the waves are called shear waves. The velocity of these waves is around half of that of longitudinal waves. Head waves are shear waves longitudinally polarized that are produced when a wave passes along a free surface at a velocity greater than the bulk wave velocity in the material. Such a wave on a surface or down a crack face converts to shear waves. Other types of surface waves such as Rayleigh and Love waves can be generated in solid materials but are beyond the scope of this chapter.

In the pulse echo system, an electrical pulse is applied to the transmitter probe, producing a short ultrasonic pulse, which is propagated into the material through a couplant layer.<sup>75</sup> The same pulse triggers a timebase generator so that the pulse of

ultrasound starts to move through the inspected component at the same time as a spot starts to move across a cathode ray tube (CRT) display screen. Variations in voltage at the transducer due to the ultrasonic wave are passed to the amplifier and applied to the Y-axis of the CRT to produce a transmission signal that represents the shape of the generated ultrasonic pulse. The spot continues to move across the screen of the CRT as the sound pulse travels through the component until the electronic pulse reaches a reflecting or scattering surface. In the case of thickness measurement, this would be the opposite surface of the equipment wall. The basis of ultrasonic thickness/depth measurement and some special probes for the purpose are illustrated in [Figure 17](#).

Various types of ultrasonic scans can be created and viewed on a CRT, as follows:

1. A-scan – a linear timebase on the x-axis and ultrasonic signal amplitude on the y-axis is the simplest and commonest, displaying amplitude versus time of flight at a location.
2. B-scan – the apparent size and position of defects is shown on a cross-sectional plane, normal to the surface on the line of the probe scan.
3. C-scan – a two-dimensional display of the test surface in plane view is shown. The probe is scanned mechanically over the surface in a regular raster and the defects are shown as bright patches in their correct plan positions (widely used in immersion water tanks) providing a radiograph type image.
4. D-scan – is a two-dimensional display of a cross-section of the specimen along the line of the scan.
5. P-scan – was designed by the Danish Welding Institute for weld inspection, which produces a simultaneous display of A and B scans.

The various scans are illustrated in [Figures 18 and 19](#).

##### *Types of probe*

There are different types of ultrasonic probes, depending on the objective of the inspection. The most basic probe contains a single transmitter crystal and requires another probe placed on the opposite surface to receive the compression sound wave. Such an assembly would be used, for example, for the detection of defects in a cast ingot of metal. Two crystals, transmitter, and receiver, can be mounted in a single hand-held probe connected to a portable instrument that allows the measurement of metal thickness from the external surface of the metal component under inspection, such as piping or a process

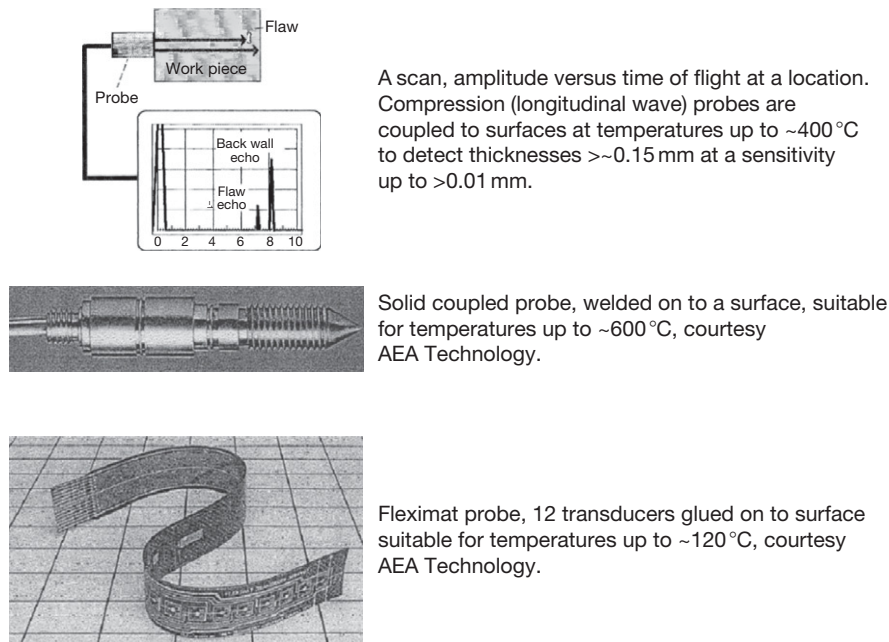


**Figure 17** Ultrasonic thickness/depth measurement.

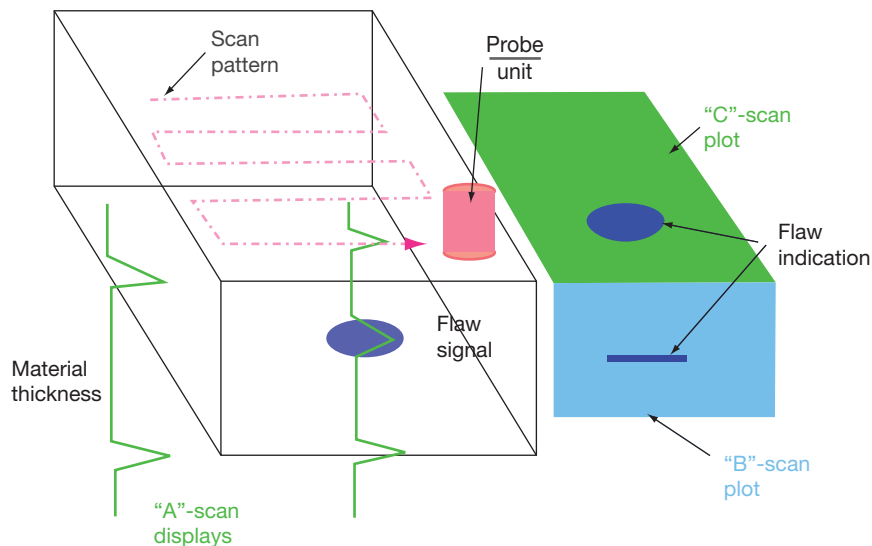


**Figure 18** Types of ultrasonic scan: A Scan amplitude versus time of flight at a location. B Scan time of flight versus distance along a transverse scan line. C Scan amplitude or time of flight versus location in scanned area. D Scan time of flight versus distance along a longitudinal scan line.

vessel. The interval between the pulses is displayed digitally, after conversion to a thickness scale using the ultrasonic velocity in the material being tested. The probe is placed on the metal surface and the reading taken. Paint layers, if present, do not generally impede the transmission of the ultrasound waves.

If surfaces are thermally insulated, cutouts can be provided at locations that are likely to be vulnerable to corrosion.

Shear probe assemblies transmit shear waves at different angles to those that transmit at  $90$  degrees to the metal surface. As in the case of compression

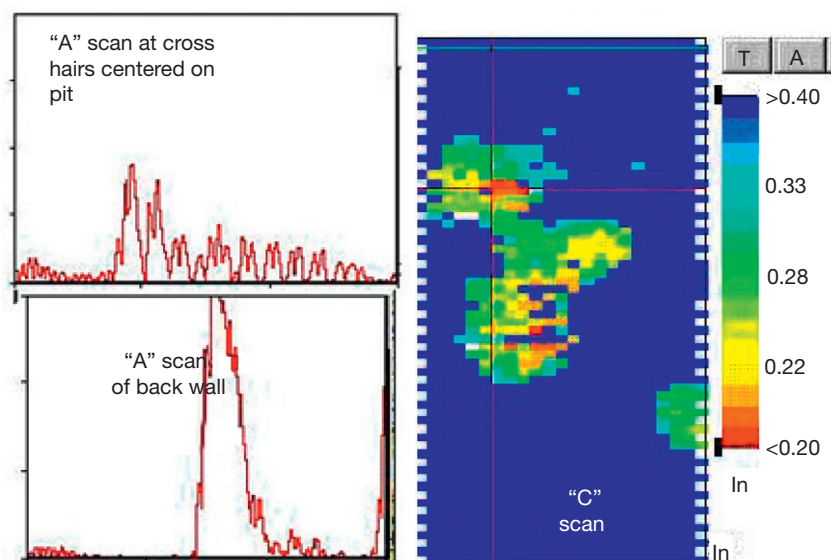


**Figure 19** Automated ultrasonic corrosion mapping by the computer control, processing, storage and imaging of ultrasonic signals, courtesy Matrix inspection & Engineering Inc.

probes, either separate or combined transmitter and receiver probes can be used. These angled probes are used commonly for the detection and sizing of crack like defects and weld defects and scanning with angled probes allows defect location/sizing in inaccessible locations. Conventional probes require couplants (grease) for the transmission of ultrasonic waves into the material undergoing inspection to avoid any impedance (blockage) of the ultrasound by an air gap.

Multiprobe (array) systems were developed using computers to process readings from twenty-four probes or more mounted on a single, wrap-around mounting mat, which can be moved around various locations in the plant. There are other forms of arrays such as those mounted on a wheeled trolley that is used to monitor the floors of above-ground storage tanks, now largely replaced by trolleys using the magnetic flux system that does not require water jets for coupling and can tolerate the thicker protective coatings used in tanks. Special assemblies have been developed for certain industries such as the nuclear, oil, and power, industries.

#### **Specialized ultrasonic systems**

An ultrasonic internal rotary inspection system (IRIS) for the offline inspection of heat exchanger tubes is available commercially and is widely used. Ultrasonic waves are directed at 90 degrees onto the inner surface of the tube using a 45-degree rotating

mirror reflector, as shown in [Figure 20](#). Internal and external wall thinning or pitting can be detected, located, and size estimated. This method has a number of advantages over the older eddy current technique for tube inspection, for example, that tube surfaces under baffles can be inspected, but is considerably slower and the two techniques are, to some extent, complementary.

Long-range ultrasonic transmission (LRUT) has been developed to examine piping for corrosion or erosion. One development consists of a phased array of transducers where the ultrasound is focused on a specific area along the pipe and around its circumference. Three different wave modes are used and propagation distances depend on several factors such as pipe geometry, contents of pipe, and coating and insulation present. However, in general situations, it is not unusual to obtain a range of 30 m (100 ft) in either direction from the transducer. Both internal and external corrosion can be detected, but the method is unable to distinguish between them. Pipe diameters over 50 mm can be inspected. The technique has shown particular promise for the detection of corrosion under insulation (CUI), which is a major problem in industrial plant as described in the chapter on the management of corrosion in the chemical/petrochemical industries in this book. Inspection for CUI is an expensive and tedious operation usually requiring the removal of the insulation for visual inspection. LRUT offers the prospect of inspection

of relatively long lengths of insulated piping with only limited, local insulation removal,<sup>76</sup> as illustrated in Figure 21.

Electromagnetic acoustic transducer (EMAT) systems were developed by the nuclear industry. The probes propagate Lorentz waves in a magnetic

field and depending on the orientation of the force vector, different ultrasonic wave types can be generated into a metal surface without the need for close contact between the probe and the metal surface under inspection. Both shear and compressional waves can be generated depending on the orientation

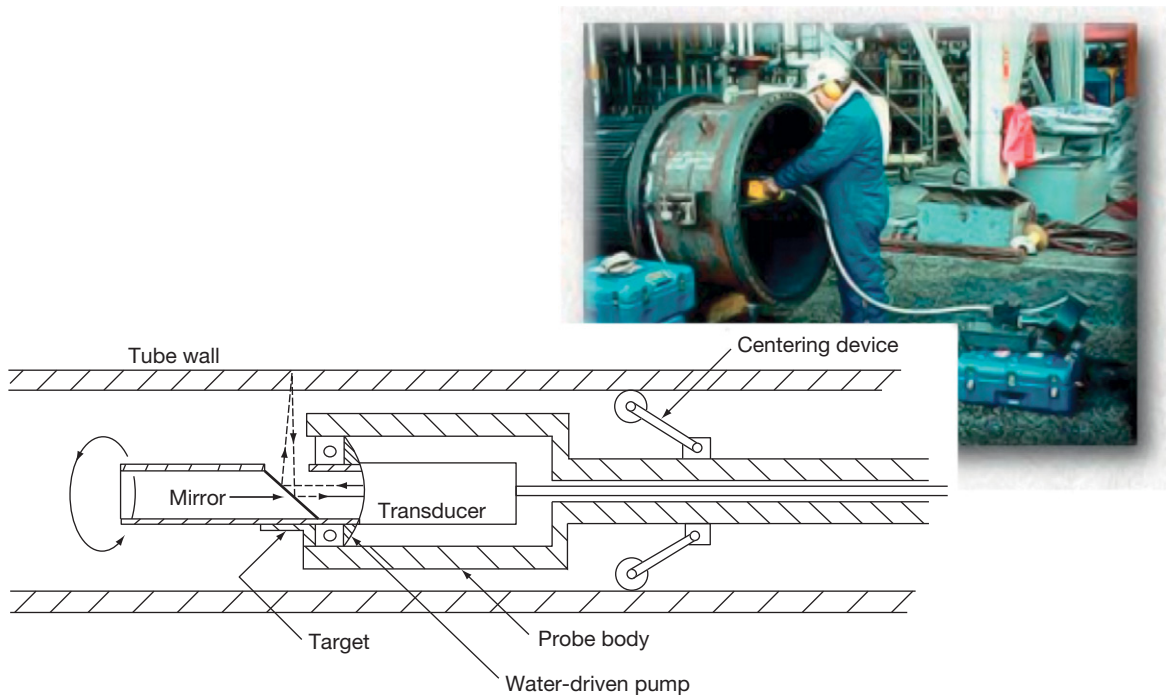


**Figure 20** Ultrasonic IRIS for heat exchanger tubing using a probe with a 45° rotating mirror that reflects the ultrasonic beam into the tube wall at 90° to the wall allowing internal/external thinning or pitting to be detected, located, and size estimated.

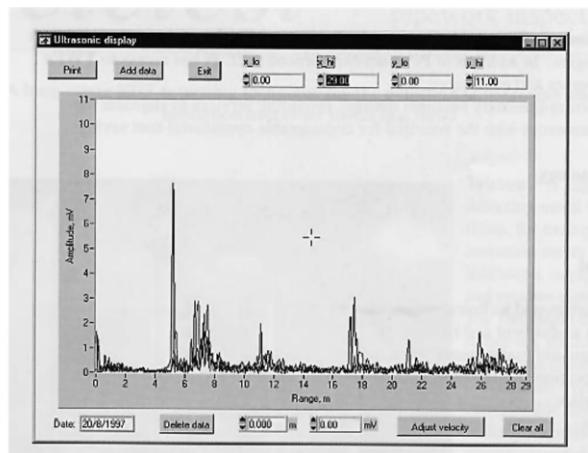
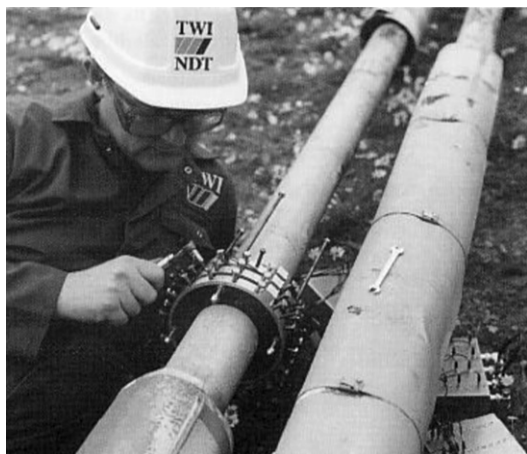


**Figure 21** Long range, guided ultrasonics for the detection of wall thinning due to internal or external corrosion. Rings of piezoelectric transducers, clamped around a pipe, transmit low frequency pulses in both directions. The signal obtained, amplitude versus distance along pipe, is similar to A scan and can detect over distances up to ~30 m in pipes, diameter >50 mm, wall thickness up to 40 mm. Courtesy of The Welding Institute (TWI).

of the magnetic field. There is no need for an external vibrating transducer and coupling. A stand-off from the surface of  $\sim 2$  mm can be achieved and therefore thin layers of rust or oxide scales can be left as these do not present a barrier. For pipe inspection, a transducer transmits UT signals around the pipe circumference as a self-propelled scanner is carried along a pipe. Up to 500 m of pipe can be inspected in a day and the technique can detect corrosion damage and provide quantitative thickness data.

Time of flight diffraction (TOFD) was also developed by the nuclear industry and is now used in a number of industries. This system has proved useful for assessing in service the preferential corrosion and/or erosion loss at the roots and heat-affected zones of welds. Separate transmitter and receiving probes are placed at an equal distance from the center of the weld. Ultrasound is transmitted at the appropriate angle into the weld by the transmitter probe and at any corrosion (crack), some of the energy is diffracted at its edges and detected by the receiving probe. As the sound strikes the tip of a crack or flaw, this acts as a secondary emitter, which scatters sounds in all directions, some in the direction of the receiving probe. A lateral wave (traveling at the same velocity as the compression waves) is transmitted to the receiver. The time difference between the lateral wave and the diffracted signal from the flaw or crack provides a measure of its distance from the scanned surface. The probes can measure the arrival time of ultrasound diffracted from the upper and lower extremities of a flaw or crack. The technique is useful for monitoring flaw or crack growth provided the variables are closely considered. A variety of systems are available ranging from manual scanning through to fully automated systems. A scan speed of  $50 \text{ mm s}^{-1}$  is claimed for automated systems. The comprehensive coverage afforded by the wide beams used for TOFD inspections makes it much less dependent on probe position and defect orientation than conventional pulse echo techniques.<sup>77</sup>

#### **4.36.2.5.3 Radiological techniques**

##### **Principles**

Since the discovery of X-rays in 1895, there has been extensive use of ionizing radiation for the NDT/E of materials as well as human beings.<sup>75</sup> X-rays are a form of electromagnetic radiation and have wavelengths that allow them to penetrate all materials with partial absorption during transmission. They include a fairly wide waveband of radiation from  $\sim 10$  nm, usually

called soft X-rays, which will penetrate only solid materials of very small thickness, to  $\sim 10^{-4}$  nm, often called high-energy or hard X-rays, which will penetrate up to  $\sim 500$  mm steel. Gamma rays emitted by radioactive substances such as cobalt-60 can exist over a similar wavelength range and are also widely used in industrial radiography. Neutron and protons have also been used for industrial radiography. Radiographs can be taken using portable X-ray machines or for thicker sections, it may be necessary to use radioactive source such as cobalt-60, iridium-192, or cesium-137. Radiography is very useful for confirming and quantifying the presence of corrosion detected by other inspection techniques. However, ionizing radiation can cause damage to living tissue, and therefore, appropriate personnel protection is essential and screening is required as dictated by the relevant legislation pertaining to radiation protection in different countries.

The recording of radiation is carried out using radiographic film or intensifying screens or fluorescent screens. Computer displays are common for displaying radiographic information. No waiting time is required and there is no requirement for photographic laboratory facilities.

##### **Portable systems**

Portable X-ray machines are quite small and can be taken around the plant fairly easily. The instrument consists of a filament (for the provision of electrons – a cathode), a target, the anode, a high voltage supply and a containment to enable the anode and cathode to be supported in a very high vacuum.<sup>75</sup> Developments include nonfilament tubes, where the filament is located in a recess in the cathode focusing cup, which helps to produce a narrow, well defined beam of electrons on the anode. The electron beam can be focused with electron lenses, to produce microfocus X-ray tubes. These developments have led to smaller, more robust X-ray tubes compared with the early glass-envelope design. The portable X-ray machines do not present a hazard above normal safeguards but the gamma sources such as cobalt-60 can be hazardous if precautions are not taken using suitable screening.

The development of profile/flash radiography has made it possible to detect CUI on a relatively small diameter piping without the need for insulation removal using small lightweight, battery-operated flash X-ray equipment and X-ray image intensifiers with a primary conversion screen having a very short decay time, and a camera optically coupled to the output screen.



#### 4.36.2.5.4 *Magnetic techniques*

When a ferromagnetic component is magnetized, the magnetic lines of force (the magnetic flux) are mostly inside the material of the component. If, however, there is a surface-breaking flaw or crack or a subsurface flaw, the field is distorted, causing local magnetic flux leakage (MFL) fields. The flaw or crack causes a sudden local change in permeability.<sup>75</sup> The various methods of magnetization can be grouped as current flow, magnetic flow, or induced current flow where AC current from a magnetic yoke is made to flow in a specimen. This is the basis of the magnetic particle inspection (MPI) technique for detecting surface breaking defects that is described in a later section.

The induced currents produced by magnetic fields, which vary with time in conducting materials are called eddy currents. The eddy currents set up secondary magnetic fields, which oppose the original magnetic field in direction, so that the magnetic field inside the component undergoing test decreases in intensity with distance below the surface.

For inspection purposes, there are various ways to achieve magnetization such as residual magnetism, current flow techniques, or the use of a threading bar or cable. The choice of the technique is dependent on the shape and size of the specimen, the expected directions of critical flaws, and whether an overall or a local examination is to be performed.

Examples of interest to the corrosion engineer are MFL developed for ILI vehicles for the inspection of pipelines and a trolley used for inspecting the floors in above-ground storage tanks.

#### 4.36.2.5.5 *Electrical techniques*

Application of eddy current techniques involves the interaction of a coil carrying an AC current with a test piece of metal. The current passed through the coil generates circulating eddy currents in the metal test piece near the surface, which will affect the exciting current in the coil due to mutual induction. Any variation in material thickness or localized defects such as pinholes will affect the strength of the eddy currents. Coils can be single or in a double configuration used as a bridge balancing circuit. The coil can be mounted in a suitable probe, which is moved over the test sample. The system was developed originally for the inspection of defects and pinholes in nonferrous heat exchanger tubes on the assembly line following manufacture. At a later stage in the development of the technique, coils were wound on a bobbin and mounted in a suitable holders for insertion into the bores of heat exchanger tubes, allowing them to be inspected in

service when offline. Despite complications at the locations of baffle plates used for tube support, valuable data were obtained.

A system for CUI inspection uses pulsed eddy currents without the necessity for the removal of the insulation. A special coil is positioned on top of the pipe insulation. The coil incorporates a transmitter and receiver coil and a magnetic field is established in the steel wall. The receiver coil measures the time of arrival of the eddy currents at the back wall. At places with wall loss, the arrival time will be earlier than at places with no wall loss. From this time of arrival, the average wall thickness can be calculated. The system can measure wall thickness through up to 100 mm insulation, including chicken wire as well as steel and aluminum sheeting. The time of measurement is 2–5 s and up to 1000 measurements can be made daily. In addition to insulated piping, the method has been applied to vessels, elbows, tank walls, and tank roofs.

#### 4.36.2.5.6 *Dye penetrant (DPI) and magnetic particle (MPI) surface crack detection*

Penetrant testing is a low-cost technique that is widely used to detect flaws and defects that penetrate the surface. The technique can be used on any non-absorbing surface. Following surface cleaning, a liquid that wets the surface is applied and migrates into defects and cracks by capillary action. Any excess liquid is removed and then the liquid in the crack is drawn out by a suitable developing agent. The liquid incorporates either a red-dye or a fluorescent substance, in which case, observation is carried out using ultraviolet light. For field testing, the technique is applied on a manual basis. The technique is particularly effective for the detection of SCC, which shows very little visible evidence at the surface in contrast to other forms of corrosion attack that reveal themselves by surface corrosion products.

Magnetic particle testing (MPI) is a related technique for the detection of surface breaking cracks/defects in ferromagnetic materials. The specimen is magnetized, usually with portable electromagnets. Surface flaws distort magnetic fields, causing local MFL around the flaw. White matt paint is applied, following which finely divided magnetic particles are applied to the test area in air or a liquid suspension, which decorate the line of the flaw. Fluorescent particles aid visual discrimination in ultraviolet light. The technique is rapid, low cost and more tolerant of surface finish than the dye penetrant method. However, it is restricted to ferromagnetic materials.

Both the techniques are limited to surface temperatures that are less than  $\sim 60^{\circ}\text{C}$ .

#### **4.36.2.5.7 Acoustic emission**

AE has been used to detect and locate flaws in metal or FRP-pressurized systems in a wide range of applications in several industries. It was universally adopted when first introduced but controversy related to interpretation and cost resulted in user disillusion. However, confidence returned after a few years following overall improvements in both hardware sensitivity and data interpretation, although a recent view was that the technique remains closer to its infancy than to full maturity.

The technique involves raising the pressure beyond design/previous operating levels during proof or in-service inspection. This induces elastic deformations and defect micropropagation processes release stored elastic strain energy, partly in the form of propagating elastic waves (AEs). Surface-mounted piezoelectric probes detect emissions and emission amplitude is a guide to severity. Triangulation techniques position emissions within  $\sim 10\text{ mm}$ . Defects must propagate to provide a signal response. Existing defects that do not propagate will not give a response and will therefore remain undetected. The technique has gained wide acceptance for the testing of pressurized systems provided that they can be pressurized above their operating pressure and an adequate number of appropriate sensors can be applied externally. Typically, for a sphere of 16 m (53 ft) diameter,  $\sim 30\text{--}40$  sensors are required. If insulation is present, only small holes in the insulation are required. An examination can be carried out in 1 day after installation and setup.

Hardware developments have been mainly associated with improvements in electronics enabling differentiation of acoustic noise from overall background noise. However, the major advances have related to signal classification, and emissions are usually graded as a function of the number of hits and their amplitude in categories that range from very minor, to be noted for future reference, to intense, requiring immediate shutdown and follow up NDT/E methods such as surface crack detection and ultrasonic testing to locate and dimension defects, as illustrated in [Figure 22](#).

From the corrosion standpoint, the identification of cracks is of much interest and finger-prints of the cracks can be compared at prescribed intervals to see whether crack growth is occurring.<sup>78</sup> The use of AE to detect active corrosion (progressive loss of

wall thickness) in above-ground storage tanks has been reported.<sup>79</sup>

AE testing is carried out onsite by specialist companies and is not routinely available from NDT/E contractors. The level of operator training is most critical to correct interpretation of data. A Euro-funded project to develop an AE system for assessing corrosion in marine oil tankers is now in progress.<sup>80</sup>

#### **4.36.2.5.8 Thermography**

Infrared cameras are very effective for remote temperature measurements, which are extensively used in plant for checking the efficiency of insulation, boiler component temperatures, and flare tips. In some plant applications, a direct relationship has been established between temperature excursions and corrosion. The technique has been used for assessing the thickness of oxide films on the fire-side of power station boiler tubes when offline. This is somewhat tedious with the requirement for scaffolding but the method gave interesting results and provided criteria to assess the progress of corrosion.

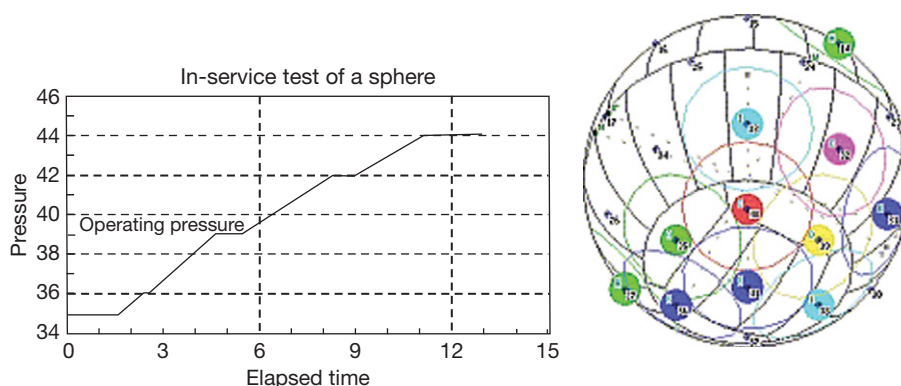
The examination of insulation to detect broken or missing insulation using infrared cameras has proved useful for the detection of CUI.

#### **4.36.2.5.9 Fiber optics**

Structural monitoring has attracted special interest in the technical press regarding the detection of failure modes in structures such as the cracking of materials. Sensors utilizing fiber optics have been tested and installed in a number of constructions, in particular bridges, for example, in Canada where bridges have had fiber optic sensors (FOS) fitted since 1998.

Sensors using FOS have been fitted to pipelines and can detect pipe movement by monitoring any change in the neutral plane of the pipe from its initial reference state and can also measure any bending strains that occur due to pipe movement. Monitoring these strains and associated stresses can provide warnings of potential pipe failures. FOS systems can measure structural displacements, strains, pressure, vibration, and temperature. Types of sensor include point sensors such as fiber Bragg gratings and Fabry–Perot sensors. Changes in wavelength that occur are proportional to the strain induced in the structure. Fabry–Perot sensors also respond to strain. Sensors referred to as distributed include Raman and Brillouin Scattering and measure a change in wavelength of scattered light.

FOS are now available for detecting the presence of wall thinning due to general corrosion or erosion



Category	AE source	Action
A	Very minor	Note for future reference
B	Minor	Inspect visually for surface defects
C		Follow up NDE
D	Significant	Immediate follow up NDE
E	Intense	Immediate shut down and follow up NDE

**Figure 22** Acoustic emission assessment based on grading emissions as a function of the number of hits and their amplitude as applied to storage sphere.

and allow monitoring of a pipe section to ensure fitness for service. The sensors are noninvasive and can be mounted on pipes and pressure vessels. Sensors are designed to precisely measure temperature, pressure, and the localized swelling of pipeline walls that signal the presence of corrosion.

Corrosion monitoring using FOS has been carried out in a Middle East gas processing plant and oil refining operations for hard-to-reach areas or remote locations. A FOS system was installed on a 12-inch (305-mm) by 20-inch (508-mm) reducer, connecting a gas feed line into a large pressurized vessel. Because of the diameter change from top to bottom, the geometry presents a difficult shape to monitor and to analyze the data. UT monitoring was carried out simultaneously and a trend of wall thickness was demonstrated with both UT and FOS.<sup>81</sup>

#### 4.36.2.6 ILI of Oil and Gas Pipelines

##### 4.36.2.6.1 Background

In 1996, a European organization, Conservation of Clean Air and Water (CONCAWE) produced figures

for oil pipeline spills in Europe for 1994, reporting that eleven incidents of spills totaling more than 15 000 bbl occurred, one of the costliest spill years on record. Cleanup operation recovered less than 2500 bbl of oil. Final costs for cleanup were reported as \$9.7 million, with two spills accounting for \$9.1 million. The actual cleanup costs for the same year would have been higher because costs for the second largest spill were not reported. Corrosion was the third highest cause of incidents with third-party damage being the largest cause.<sup>82</sup> In 2005, 6226 km or 18% of the total length of the European inventory was inspected by various types of inline inspection (ILI) vehicles. Inspections were split among the individual classes of vehicle, as follows:

1. Metal loss ILI – 5860 km in 105 sections
2. Crack detection ILI – 2132 km in 34 sections

CONCAWE has given the reason for improved performance and lower spills as increased use of ILI. The same situation prevails in the USA and many other countries. The benefits of ILI technology cannot be overestimated in its contribution to the safety of ageing pipeline systems.

In the USA, there has been much debate relating to a compulsory requirement for ILI and various Bills have been discussed by the US Congress without a final conclusion yet regarding the contentious aspect of inspection frequencies, in particular, whether the interval between ILI inspections should be 3 or 5 years or some other interval. Many US pipelines are now approaching 50 years of age and European landlines will soon approach these lifetimes with offshore pipelines somewhat younger at ~35 years. The consequence of high-pressure pipeline failure due to corrosion can be catastrophic and much effort has been devoted worldwide to the development of inspection devices for pipelines.

An early pipeline failure in the UK involved a 12-inch (305-mm) pipeline supplying the Shell Stanlow oil refinery when 150 tons of crude oil polluted a 32-km stretch of the Mersey estuary due to a pipeline fracture and killed an estimated 300 birds with a further 3000 at risk. In the first major prosecution by the National Rivers Authority (NRA), Shell pleaded guilty to spilling the oil. The court heard that a 6.5-inch (165-mm) crack in the pipe had been caused by the wrinkling of a protective sleeve. Tests found no weakness in the pipe although it had been planned to adapt it, at a cost of £100 000, to enable the use of a fault-detecting device known as an intelligent pig.<sup>83</sup>

A far more serious major pipeline event occurred in 2000 in the USA and involved a gas line carried under a bridge in Arizona. An underground pipeline, owned by the El Paso Energy Co. and installed in 1952, ruptured and discharged flammable gas, engulfing an adjacent campsite in flames and killing eleven tourists. The incident was investigated by the DOT and was shown to be due to internal corrosion. The pipeline had been inspected in 1996. The company was fined \$2.52 M by the DOT.

Many other incidents of pipeline failure have occurred in the USA such as the gasoline leakage at Bellingham, WA in the summer of 1999 when a pipeline failed due to damage from construction activity near the pipeline, which contributed to the rupture resulting in the deaths of three young people. The two companies involved, Olympic Pipeline Co. and Shell Pipeline Company LP, were likely to face fines each totaling \$18.6 m. This incident prompted the US Senate to pass the Pipeline Safety Improvement Act of 2000, aimed at increasing penalties for safety violations, increasing state oversight of pipelines within their borders, and requiring pipeline companies to publicly disclose information about pipelines on the internet.

The corrosion of pipelines can occur on both internal and external surfaces if appropriate and adequate corrosion control measures are not carried out and monitored. Although some material upgrading from carbon steel has taken place, particularly offshore, the major proportion of pipelines are still constructed from carbon steel. In addition, pipelines can be subject to SCC and although this failure mode is more difficult to monitor, there are now ILI versions available for the detection of cracks.

External inspection using ultrasonic wall thickness will not give a comprehensive picture of the degradation (if any) at inaccessible locations of the pipelines as both onshore and subsea pipelines have an uneven elevation and debris and water can collect at discrete points within the pipelines and cause corrosion to be initiated. John *et al.*<sup>84</sup> point out that corrosion monitoring data will only provide an assessment at the actual location where the probes or coupons are located.

To overcome some of the above problems, an approach to modeling the metal loss within pipelines has been attempted by combining an assessment of the historic operating parameters over the life of the pipeline and calculating a cumulative metal loss since commissioning, while also allowing for the unknown variations in operating parameters by the incorporation of uncertainty analysis. Two case histories have been reported using this approach on a subsea line in the Middle East and a pipeline in the North Sea.<sup>84</sup>

#### 4.36.2.6.2 Development of ILI vehicles

An ILI vehicle for the inspection of pipelines is referred to in the oil and gas industry as a pipeline inspections gauge (PIG), a device incorporating onboard instrumentation that is propelled under pressure from the product being transported through pipelines and which collects and records inspection data relating to both internal and external corrosion.

From the beginning of the oil industry, pipeline operators have utilized devices that are passed through the pipelines for cleaning the interior and removing paraffin waxes and sludge. Later, devices incorporating mechanical feelers that were used to detect mechanical damage such as dents or ovality were introduced. Vehicles containing various NDT/E sensing equipment using magnetic saturation arrived in the mid-sixties. However, pipeline operators became disillusioned with these devices due to the number of false positive signals. Excavation to verify suspect areas often revealed little corrosion, if any, and initial interest shown by pipeline operators and

oil companies soon diminished. In addition, the classification of the corrosion information was very qualitative in nature. For one model, the corrosion indication was only classified into three categories designated as low, medium, and severe corrosion.

An up-rated ILI was developed on behalf of British Gas (BG) in the late eighties using MFL. Prior to the introduction of the improved device, BG tested their high-pressure lines hydraulically, which required the line to be taken out of service. This was the first time that an ILI was available that could be judged in performance terms on a quantitative measurement of corrosion. The early development gave a defined specification for sensitivity, as shown in Table 7.

The BG vehicle design provided a benchmark for the industry and high-resolution versions based on magnetic flux and ultrasonics were subsequently developed in Canada, Germany, and Japan. The development of these vehicles was a major advance in pipeline inspection made possible by improved computer power and developments in electronics. The detection of cracking has been a long-held objective of pipeline operators and versions are now available for this purpose using EMAT systems.

Intelligent vehicles are inserted and removed from pipelines through pig-traps. Essentially, the vehicle comprises two or more sections, one section contains the sensing equipment, the sensors and other sections contain the electronics and batteries. The rear section contains the odometer wheels to measure the speed and distance of the vehicle. The improved ILI vehicles could not be used at first, because they were too large for the existing pig traps. This was the case for offshore platforms initially, where space is always at a premium. However, later designs of platforms and pipelines took account of the additional size and appropriate pig-traps were installed.

Not all pipelines can be inspected by ILI vehicles for reasons that include economics (costs of

inspection), varying pipeline diameters and geometry (angles, sharp bends), or other constraints inside lines. It is generally considered that the minimum size of line is 152 mm (6 inch) but special caliper devices may allow the inspection of lines down to 76 mm (3 inch) diameter.

Intelligent vehicles use several techniques for their operating mode. MFL continues to be the most common for inspection of pipelines.<sup>85</sup> Accuracy for these vehicles is estimated at  $\pm 10\%$  at the 80% confidence factor. Ultrasonic vehicles were developed because MFL vehicles were not accurate enough to allow calculation of the remaining strength. The ultrasonic vehicles are better able to measure the wall thickness and the results can be used directly in calculations (e.g., RSTRENG) to determine the remaining strength. Note that ultrasonic methods require a liquid in the line for operation (unless they are in a liquid slug) for the transmission of the ultrasound. Each technique has advantages and disadvantages and the usual strategy adopted by pipeline operators is to alternate inspections between the different systems.

Vehicles using elastic waves have been produced for crack detection with liquid-filled wheels for the transmission of the waves into the line but it is reported that too many false positives are produced. Vehicles using EMAT systems have also been developed for SCC obviating the need for a transmission medium.

#### 4.36.2.7 Management of Inspection Programs

Many organizations undertake visual inspection and metal thickness measurement in-house. Inspection functions are generally well managed and have clearly defined roles in the company structure. Communication is a vital component of success and is more difficult for oil and gas operations compared with land-based, permanent sites. Coordination and liaison are most important regarding process information, corrosion data, and inspection schedules as well as everyday factors relating to overall operations. A UK HSE investigation into the inspection functions in oil refineries suggested that inspectors should be embedded in units in order to improve liaison. The introduction of RBI (risk-based inspection) has improved overall cooperation; however, it still requires continuous monitoring on a quarterly basis to avoid problem areas. The updating of records as well as management of contractors should have high priority. The regular issuing of the minutes of meetings should also be given priority. Resistance to changes in previous practices can be avoided by fully describing

**Table 7** British gas ILI vehicle-magnetic flux leakage (MFL) – specification for corrosion detection (Data supplied by British Gas)

	Detection sensitivity	Sizing accuracy
General corrosion	0.2t	+ or – 0.1t
Pitting corrosion	0.4t	+ or – 0.1t

Where  $t$  = nominal pipe wall thickness (seam welded pipe) and pitting corrosion defined as corrosion affecting a surface area of pipe contained within a square of dimensions  $3t \times 3t$ .



reasons for the changes and providing evidence that there needs to be such changes.

Specialized contractors make a large contribution in the inspection sphere but they have to be supervised and managed effectively. In some cases, the total inspection function will be contracted out (as is the case for most offshore oil/gas production) with the contracting workforce embedded at the plant premises and producing daily and monthly reports for the plant management. An important factor is the training received by the contractor's technicians as well as reliable record keeping and overall technical ability. Continuous training is required and on-the-job training is not sufficient. Operatives and supervisors need to be qualified and supervised on an ongoing basis. The selection of contractors requires careful consideration, including, of course financial stability. The author has had good experience working with NDT/E over many years with contractors chosen by personal recommendation wherever possible.

The cost of inspection is similar to any other high-tech service for high capital cost equipment and relates to the complexity of the equipment used and the degree of training required for its operation and interpretation. Reference has already been made relating to the qualifications of personnel involved and how the ASNT (US) and BINDT (UK) have been instrumental in raising the level of qualification and assessment of examinations. Costs have steadily increased due to the resulting improved qualifications of NDT/E personnel, which most of industry has welcomed.

The existence of international, national, and company standards coupled with legislation relating to maintenance and inspection of industrial infrastructure is of considerable assistance, but presents a challenge to those engaged in the inspection process. Accordingly, systems and procedures require regular appraisal and revision. There are many sources of standards and codes of practice. In addition to the main societies relating to NDT in both the USA and Europe, many countries have their own standards to which reference should be made first, followed by those produced by relevant engineering and scientific bodies. The standards of the European Economic Community are issued as ISO documents. The Russian Federation has a considerable expertise and reputation in this technology, and despite an emphasis on the academic interest, some of this experience has trickled down into the industrial sphere. Some of these standards are very specific to certain materials and environments. Some organizations of particular relevance are:

1. International Standards Organization (ISO).
2. American Petroleum Institute (API) has responsibility for the infrastructure used for the extraction of oil and gas, storage, transportation, and downstream infrastructure in refining crude oil. The use of pipelines for both subsea and onshore is also considered.
3. American Society of Mechanical Engineers (ASME) issues recommendations relating to inspection, especially relating to boilers.
4. ASTM is mainly, but not exclusively, oriented to laboratory R & D.
5. Institute of Petroleum (IP) based in London has a number of technical committees that issue both guidance and recommendations for general practice in the industry.
6. British Standards – reference should be made to BS: EN 10204:2004 Metallic Materials. Types of Inspection.

Nonmetallic materials such as plastic/polymer and FRP materials can be inspected using some of the methods described in this chapter. Standards exist for some of these materials.

Close liaison between the inspection and safety functions within organizations is essential. Most inspection equipment requires electrical power, and therefore, compliance with intrinsic safety legislation, and there is no reason why any instrumented system cannot be engineered to meet the requirements. The usual plant safety rules regarding access to heights and entry to confined spaces must be complied with. The use of ionizing radiation requires precautions, particularly relating to shielding.

It is particularly important that precautions are taken to check that dangerous gases have been purged from equipment and that vessels are tested for the presence of sufficient oxygen. Fatalities have resulted from entry into vessels where the oxygen level was insufficient to support life. For example, a cruise-ship crew member died recently from suffocation during an inspection of tanks for corrosion, prior to departure from Southampton in the UK and another crew member had to be rescued from the tank.<sup>86</sup>

#### 4.36.2.8 Specific Industries

##### 4.36.2.8.1 Oil and gas industry equipment

Inspection functions are usually influential in oil and gas companies because plants have to operate for long periods between scheduled shutdowns and

there is a strong interest in onstream inspection. Communications are more difficult in production compared with refining due to the remoteness of production fields, both onshore and offshore. The introduction of RBI has focused the inspection process to a great extent than in earlier days when the approach was more random.

The most common inspection technique is observation utilizing the human eye and measuring equipment of various kinds such as calipers and gauges. These techniques are supplemented by cameras and TV and sometimes with borescopes and similar equipment, albeit such techniques are generally restricted to shutdown periods with corresponding drawbacks.

Downhole inspection presents particular problems due not only to the high temperatures and pressures but also to limited access. A widely adopted inspection system for downhole corrosion involves the Kinley mechanical caliper (involving a number of feelers), which, apart from resolution problems (inadequate coverage of the 360 degree tubing circumference), is still widely used in the industry. A major problem involves mechanical damage to the oil-tubing surface, which can damage any inhibitor films that are present. This is overcome to some degree by increasing the dosage rate of the inhibitor for a short period when production resumes. Downhole cameras and television are available for visual examination as well as various types of electrical instrumentation. Increasing use of CRAs downhole will reduce the requirement and/or frequency of such inspections, although acid treating of wells to remove scale and formation damage will still need verification that damage to the metal has not occurred.

Ultrasonics, usually undertaken by contractors, is commonly used for thickness measurement and for detecting cracks in pipelines and vessels. Welded probes and phased array probe system, which can provide a continuous signal are also used in critical situations and can mitigate the need for operators to visit remote and/or dangerous locations. Above-ground storage tank walls and roofs can be inspected online, using automatic crawlers held to the steel surfaces by magnetic attraction.<sup>87</sup> Infrared cameras are useful for surveying hot-spots in equipment and for locating insulation failures. There have been many examples where a correlation has been made between increased corrosion and an increase in temperature. AE by specialist contractors at intervals is used for the assessment of both the onset of cracking and crack growth.

#### **4.36.2.8.2 Chemical and petrochemical plants**

As in the oil and gas industry, plants are operated for long period between scheduled shutdowns, and hence, the approach to inspection is very similar. The shutdown period is utilized for much visual and hands-on inspection to verify that materials behavior complies with expectations from online inspection. Plants utilize extensive amounts of CRAs that increase the focus on localized corrosion failure modes such as cracking and pitting corrosion. The plants commonly use waste heat to raise steam and require extensive water cooling systems, which introduce additional inspection requirements.

#### **4.36.2.8.3 Power plants**

Unscheduled outages in these high capital cost facilities can be very costly as power has to be bought from other suppliers at high cost and some material upgrading, for example, the introduction of titanium condenser tubes, has occurred over the years to reduce corrosion risks.

Fossil fuel and gas-fired stations are subject to corrosion in boiler tubes (water and fire-side) and water circuits, which have to be inspected using most of the available NDT/E techniques. The inspection challenge is greater in nuclear stations. The first series of UK advanced gas cooled (AGR) nuclear reactors (Magnox) have a relatively poor record regarding corrosion. Excessive corrosion of some carbon steel fasteners in the gas cooling conduits was experienced, which required an operating temperature reduction and consequent loss of efficiency.<sup>88</sup> A later design (Dungeness AGR) also experienced corrosion problems with carbon steel linkages and where zinc-coated wires embrittled stainless steel tubes necessitating a downrating. More recently, some of the nuclear power stations (Hartlepool and Heysham 1) have had to be shutdown due to corrosion problems in wiring corrosion in steel and concrete boiler units attached to the reactors. It is believed that up to \$10 M will be required to investigate corrosion in the 54 km of wire involved in the units.<sup>89</sup> The root cause is believed to lie in the original design and construction. In total, eight reactors are experiencing corrosion and cracking related to ageing and these problems have presented considerable inspection challenges. In addition to the conventional range of NDT/E techniques, special systems have been designed solely for the nuclear industry.

An interesting NDT/E device designed for the inspection of high-voltage transmission lines for corrosion (loss of zinc coating on the steel core) involves

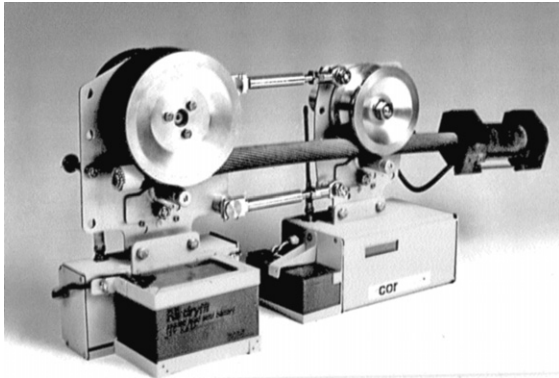


**Figure 23** High voltage cable corrosion detector (Courtesy Cormon Ltd).

the use of eddy currents. The lines can be inspected when carrying current using a trolley-carriage that traverses the lines, as shown in [Figure 23](#).

The device was developed in the UK and has been widely used in the UK, France, Ireland, and Sweden.

#### 4.36.2.8.4 Defense

Many corrosion problems are experienced in defense infrastructure and systems. Individual countries have their own specifications and standards. Corrosion is particularly severe in naval operations and corrosion protection and inspection are well organized and implemented but problems still occur from time to time. Accordingly, most of the NDT/E techniques are implemented. Military aircraft are appreciably ageing compared with civil aircraft and present a severe challenge to the inspection function. One historical aspect relating to fuselage inspection relates to the use of primer (where fuselage panels are riveted together), which can mask the penetration of X-rays – now largely replaced with techniques using eddy currents.

Military missiles now have casings made from carbon fiber, Kevlar, or other materials wound in layers, which results in weight savings of up to 40% compared with metals. Their light weight also makes them less expensive to ship and easier to handle. However, the missiles are sometimes damaged when struck by rock and debris kicked up by helicopter rotors or when mishandled during shipping or maintenance. Unlike metals, which usually show external signs of damage (such as cracks or dents), the filament-wound composite materials may not reveal telltale signs. A new monitoring system developed in the USA (Purdue University) uses a mathematical model to pinpoint the location and severity of impacts based on vibration data collected by a triaxial

accelerometer. The objective of the project is to have a permanently installed system to monitor the structural health of the missile. The information obtained enables the monitoring system to determine within seconds whether an impact is beyond the design threshold. The technique also would determine how durable the material is after long-term storage and exposure to humidity, UV radiation, and other environmental conditions. Materials under examination include sandwich metallic materials, woven composites, ceramics, and filament-wound materials. Components of particular interest are wheels and spindles.

#### 4.36.2.8.5 Marine

The progressive use of higher strength steels for shipbuilding has resulted in significant weight savings by reducing thickness but has inevitably exacerbated corrosion risks. Accordingly, inspection has become more critical than in previous years.

Major ocean-going vessels require a fit-for-purpose certification at prescribed intervals in order to operate. This process involves much inspection mainly in the area of coating inspection. However, not only has the vessel integrity to be established, usually in dry dock, but also the onboard facilities such as boilers and fire, cooling, potable, and discharge water systems among others. Vessels change cargoes at short notice and tanks require complete cleaning between each change of cargo. Other marine infrastructure such as dock facilities, jetties, cranes, and oil-loading facilities also require inspection.

#### 4.36.2.8.6 Road transportation

Transportation includes road vehicles (private and industrial), rail transport (wheel and track inspection being the main priority), and aircraft. Road vehicles can suffer from body corrosion, now mostly designed out. Trucks can suffer from various corrosion problems, especially road tankers used for potentially aggressive liquid cargoes that require periodic internal inspection. Regular inspection of pipes carrying hydraulic brake fluid is necessary as corrosion degradation is not unknown and incidents have caused loss of life.

#### 4.36.2.9 Future Developments

The resolutions and response times of some inspection and corrosion monitoring techniques are shown in [Table 8](#). These define the state-of-art and the current challenge for the future development of inspection technologies.

**Table 8** Resolution and response time for some corrosion monitoring and inspection techniques

<i>Technique</i>	<i>Resolution</i>	<i>Response time at 1 mpy (1/40 mm year<sup>-1</sup>) corrosion rate</i>	<i>Response time at 40 mpy (1 mm year<sup>-1</sup>) corrosion rate</i>
Electrochemical	1 $\mu$ A	minutes	minutes
FSM™ 25 mm wall thickness	0.025 mm	1 year	days
Electrical resistance	0.00025 mm	4 days	minutes
Ultrasonic thickness transducer (fixed)	0.1 mm	4 years	40 days
Weight loss coupon	1 mg	months	days

Source: Joosten, M. W.; Fischer, K. P.; Strommen, R.; Lunden, K. C. *Mater. Perf.* **1995**, 34(4), 44–48.

General improvements in data capture and handling combined with developments in electronics, in particular relating to miniaturization, should bring exciting developments and improvements in inspection technology. This will apply to most of the existing techniques for inspection such as ultrasonics, eddy current, and AE. The detection and monitoring of cracks is of much interest and will receive particular attention in the future. Some specific likely developments are as follows:

1. Miniaturization is of much interest regarding the internal inspection of process piping with hopefully the sensitivity approaching that of intelligent vehicles presently used for buried and offshore pipelines. There are still problems to be solved, with the sharp bends and the many obstructions present in a process plant piping, but this is the most interesting area of activity.
2. Development of the EMAT systems and better performing portable ultrasonic array systems will receive attention.
3. Interest has been expressed in fiber optic strain sensors used for civil engineering structures that could be adapted for use in process plant for corrosion detection and measurement.<sup>90</sup> As corrosion or other chemical reactions occur, the transverse strain is relieved and the peak-to-peak spectral separation changes allow a measurement of corrosion. Different metals and stretchable plastics can be used as a component to support the measurement of a variety of corrosion events.
4. A research program organized by the Southern Illinois University Carbondale Material Technology Center is in progress to develop an internet-based wireless sensor network that will provide real-time data and analysis on the structural soundness of transportation infrastructure, such as bridges.<sup>91</sup> The three-year project, initiated in October 2007, is funded by a \$1 M grant from the US Federal Highway Administration (FHWA) Intelligent Transportation System's program. The concept involves placing several types of sensors on

a structure to detect variable such as stresses, elongation, deformation, vibration, cracking, and corrosion. Sensor technology includes existing sensors such as strain gauges, accelerometers, and pH sensors as well as new sensor technology developed in conjunction with the project.

5. It is possible that other data sets may be added to ILI vehicles in the future, which should assist the operator's ability to proactively detect possible corrosion threats to pipeline integrity other than metal loss.<sup>92</sup>
6. In 2007, a new Research Center in Nondestructive Testing was established in the UK with initial funding of \$3 M over 5 years. Participating universities are Imperial College, Strathclyde, Bristol, Bath, Nottingham, and Warwick. It functions as an industrial club and carries out research projects of interest to club members.

## Appendix 1 Standards and Codes of Practice

### British Standards/ISO

- PD 8010 2:2004 Code of practice for pipelines. Subsea pipelines.
- PD 8010 1:2004 Code of practice for pipelines. Steel pipelines on land.
- BS EN 1473:2007 Installation and equipment for liquefied natural gas. Design of onshore installations.
- BS EN ISO 19903:2006 Petroleum and natural gas industries. Fixed concrete offshore installations.
- DD ISO/TS 24817:2006 Petroleum, petrochemical and natural gas industries. Composite repairs for pipework. Qualifications and design, installation, testing, and inspection.
- BS ISO 12732:2006 Corrosion of metals and alloys. Electrochemical potentiokinetic reactivation measurement using the double loop technique (based on Cihal's technique)
- BS EN ISO 9934-2:2002 Non-destructive testing. Magnetic particle. Detection media.

### **NACE International Standards, Recommended Practices and Test Methods**

RP0102–2002 In-line Inspection of Pipelines  
 RP0189–2002 Online Monitoring of Cooling waters  
 RP0192–98 Monitoring Corrosion in Oil and Gas Production with Iron Counts  
 RP0197–2004 Standard Format for Computerized Electrochemical Polarization Curve Data Files  
 RP0198–2004 The Control of Corrosion Under Thermal Insulation and Fireproofing Materials – A System Approach  
 RP0205 Recommended Practice for the Design, Fabrication and Inspection of Tanks for the Storage of Petroleum Refining Alkylation Unit Spent Sulfuric Acid at Ambient Temperature  
 RP0296–2004 Guidelines for Detection, Repair and Mitigation of Cracking of Existing Petroleum Refinery Pressure Vessels in Wet H<sub>2</sub>S Environments  
 RP0497–2004 Field Corrosion Evaluation Using Metallic Test Specimens  
 RP0502–2002 Pipeline External Corrosion Direct Assessment Technique  
 RP0775–2005 Preparation, Installation, Analysis, and Interpretation of Corrosion Coupons In Oilfield Operations  
 SP0106–2006 Control of Internal Corrosion in Steel Pipelines and Piping Systems  
 SP0206–2006 Internal Corrosion Direct Assessment Technique for Pipelines Carrying Normally Dry Natural Gas  
 SP0294–2006 Design, Fabrication and Inspection of Tanks for the Storage of Concentrated Sulfuric Acid and Oleum at Ambient Temperatures  
 SP0590–2007 Prevention, Detection, and Correction of Deaerator Cracking  
 SSPC-VIS2 Standard Technique of Evaluating Degree of Rusting on Painted Steel Surfaces  
 TM0106–2006 Detecting, Testing, and Evaluation of Microbiological Influenced Corrosion (MIC) of External Surfaces of Buried Pipelines  
 TM0169–2000 Laboratory Corrosion Testing of Metals  
 TM0193–2000 Laboratory Corrosion Testing of Metals in Static Chemical Cleaning Solutions at Temperatures below 93 °C  
 TM0194–2004 Field Monitoring of Bacterial Growth in Oilfield Systems  
 TM0286–2001 Cooling Water Test Unit Incorporating Heat Transfer Surfaces  
 TM0299–99 Corrosion Control and Monitoring in Seawater Injection Surfaces

TM0398–98 Laboratory Corrosion Testing of Metals in Static Chemical Cleaning Solutions at Temperatures Above 100 °C

TM0498–2006 Evaluation of the Carburization of Alloy Tubes Used for Ethylene Manufacture

TM0499–99 Immersion Corrosion Testing of Ceramic Materials

### **European Federation of Corrosion – EFC (Incorporating ISO) Standards**

EN ISO 6509 1995 Corrosion of metals and alloys – Determination of dezincification resistance of brass (ISO 6509:1981)

EN ISO 7441:1995 Corrosion of metals and alloys – determination of metallic corrosion in outdoor exposure corrosion tests (ISO 7441:1984)

EN ISO 7539 Corrosion of metals and alloys – Stress corrosion testing, Parts 1–7 1995: 1989

EN ISO 8565:1995 Metals and Alloys – Atmospheric corrosion testing-general requirements for field tests (ISO 8565:1992)

EN ISO 9400:1995 Nickel-based alloys–Determination of resistance to intergranular corrosion (ISO 9400: 1990)

EN 10229:1998 Evaluation of resistance of steel products to hydrogen cracking (HIC)

EN ISO 11306:1998 Corrosion of metals and alloys – Guidelines for exposing and evaluating metals and alloys in surface sea water (ISO 11306:1998)

### **Provisional Europeans Standards (As at June 1994)**

pr EN ISO 8044 Corrosion of metals and alloys – Basic terms and definitions

pr EN 12500 Protection of metallic materials against corrosion – Corrosion likelihood in atmosphere environment – Classification, determination and estimation of corrosivity of atmospheric environments

### **American Society for Testing Materials (ASTM)**

ASTM G4–01 (2008) Standard Guide For Conducting Corrosion Tests in Field Applications

ASTM G96–90 (2008) Standard Guide for Online Monitoring of Corrosion in Plant Equipment (Electrical and Electrochemical Methods)



- ASTM G102–89 (2004) Standard Practice for Calculation of Corrosion Rates and Related Information from Electrochemical Measurements
- ASTM G1–03 Standard Practice for Preparing, Cleaning and Evaluating Corrosion Test Specimens

## American Petroleum Industry (API)

- API MPMS 10.3 Sediment for Water – Standard Test Technique for Water and Sediment in Crude Oil by the Centrifuge Technique (Laboratory Procedure)
- API RP 2201 Safe Hot Tapping
- API 653 Inspection and Storage Tanks Standard
- API 598 Valve Inspection and Testing
- API 570 Piping Inspection Code
- API 661 Air Cooled Heat Exchanger for General Refinery Service – Inspection
- API 1163 Guidance Provided by Inline Inspection Standards

## References

- Hines, J. *Industrial Corrosion Monitoring*; Committee on Corrosion, Department of Industry H.M.S.O.: London, 1968.
- Rothwell, N.; Tullmin, M. *The Corrosion Monitoring Handbook*; Coxmoor Publishing Co.: Kingham, Oxford, UK, 2000.
- Glossary, National Corrosion Service, National Physical Laboratory (NPL), Teddington, London, UK.
- Cox, W. M.; Boyce, M. P.; Miyazawa, M.; Tanaka, Y. *Corrosion Management* **2000**, May–June, 6–10.
- Review of Corrosion Management for Offshore Oil and Gas Processing*; UK Health and Safety Executive, Chapter 4, Planning and Implementation, 4.8 Implementation in Offshore Technology Report 2001/044, 2001.
- Britton, C. F.; Tofield, B. C. *Mater. Perf.* **1988**, 27(4), 41–44.
- UK HSE Report. *Public Report of the Fire and Explosion at the ConocoPhillips Refinery on 16 April 2001*, Health and Safety Executive: UK, 2005.
- Powell, D. E.; Ma'Ruf, D. I.; Rahman, I. Y. *Mater. Perf.* **2001**, 40(8), 50–54.
- Roberge, P. R.; Tullmin, M. A. A.; Grenier, L.; Ringas, C. *Mater. Perf.* **1996**, 35(12), 50–54.
- Britton, C. F. Private Communication.
- Standard Guide for Examination and Evaluation of Pitting Corrosion*; ASTM G46–94, ASTM International, 2005.
- Standard Guide for Conducting Corrosion Tests in Field Applications*; ASTM G4–01, ASTM International, 2005.
- Field Corrosion Evaluation Using Metallic Test Specimens*; RPO497–2004; NACE International: Houston, TX, USA, 2008.
- Hudson, J. C. J. *Inst. Met.* **1928**, 40, 294.
- Dravnieks, A.; Cataldi, H. A. *Corrosion*; **1954**, 10, 224.
- Edeleanu, C. *Anticorros. Methods Mater.* **1955**, 2, 204–208.
- Publication EFC4. *Guidelines for Electrochemical Corrosion Measurements*, European Federation of Corrosion, 1990.
- Standard Test Method for Conducting Cyclic Potentiodynamic Polarization Measurements for Localized Corrosion Susceptibility of Iron-, Nickel-, or Cobalt-Based Alloys*; ASTM-G61–86, ASTM International, 2003.
- Stern, M. *Corrosion* **1958**, 14, 440t–444t.
- Stern, M.; Geary, A. J. *Electrochem. Soc.* **1957**, 104, 56–63.
- Moreland, P. J.; Rowland, J. C. *Br. Corros. J.* **1977**, 12, 72–79.
- Richardson, J. A. *Innovations in Techniques for Corrosion Monitoring*; Proceedings of the Conference on Advances in Materials Technology for Process Industries Needs, Atlanta, National Association of Corrosion Engineers, 1984.
- Mansfield, F. *Corrosion* **1988**, 72(12), 856–868.
- Dawson, J. L.; Callow, L. M.; Hladky, K.; Richardson, J. A. In *Corrosion Rate Determination by Electrochemical Impedance Measurement*; Proceedings of the Conference on On-Line Surveillance and Monitoring of Process Plant, London, Society of Chemical Industry, 1977.
- Iverson, W. P. J. *Electrochem. Soc.* **1968**, 115, 617–618.
- Hladky, K.; John, D. G. In *Using Electrochemical Noise*; Proceedings of the 2nd International Conference on Corrosion Monitoring and Inspection in the Oil and Petrochemical and Process Industries, London, Oyez Scientific and Technical Services Ltd., London, 1984.
- Kane, R. D.; Eden, D. C.; Amidi, S.; Delve, D. *Implementation of Real-Time Corrosion Monitoring With Industrial Process Control and Automation*; Paper 07268, Corrosion 2007; NACE International: Houston, TX, 2007.
- Rothwell, N.; Tullmin, M. *The Corrosion Monitoring Handbook*; Coxmoor Publishing Co, Kingham, Oxford, UK, 2000; Chapter 3, pp 69–70.
- Strommen, R. D.; Horn, H.; Wold, K. R. *Mater. Perf.* **1994**, 32(3), 50–54.
- Britton, C. F. Private communication.
- Riley, J. from information provided by Kettle, A., FSM Presentation relating to Texaco Refinery, Pembroke, UK, available at <http://committees.api.org/standards/cre/sci/minutes/docs/spring04/fsm.pdf>.
- Britton, C. F. Private Communication.
- Asher, J.; Conlon, T. W.; Tofield, B. C.; Wilkins, N. J. M. *On-line Surveillance and Monitoring*; Ellis Horwood: London, 1983.
- Britton, C.F. Private communication.
- RP0192–98 Standard Recommended Practice-Monitoring Corrosion in Oil and Gas Production with Iron Counts*; NACE International: Houston, TX, 1998.
- Addington, F. Paper 08548, *Corrosion 2008*; NACE International: Houston, TX, 2008.
- TM0194–2004 Field Monitoring of Bacterial Growth in Oil and Gas Systems*; NACE International: Houston, TX, 2004.
- TM0106–2006. Detecting, Testing, and Evaluation of Microbiological Influenced Corrosion (MIC) of External Surfaces of Buried Pipelines*; NACE International: Houston, TX, 2006.
- EFC Publication 29. *Microbial Corrosion*; Sequeira, C. A. C., Ed.; European Federation of Corrosion, 2000.
- Methods of Studying Biofilms*, Paper 20 in Microbial Biofilms, Ghannoun, M. A., Ed.; ASM Press, 2004; p 392.
- Cavassi, P.; Cornago, M. *PCE* **1998**, 24–30.
- Gretchen, J. A. *Mater. Perf.* **2007**, 46(8), 27–34.
- Ahluwalia, H.; Sharp, S. *Mater. Perf.* **2008**, 47(8), 83–85.
- US National Transportation and Safety Board, (NTSB). *Natural Gas Pipeline Rupture and Fire Near Carlsbad, New Mexico* 19th August, 2000, available at [www.nts.gov/publictrn/2003/PARA0301.pdf](http://www.nts.gov/publictrn/2003/PARA0301.pdf).

45. *Erika Oil Spill Trial: Landmark Ruling for the Environment*, available at [www.humanteinenglish.com/spip.php?article 810](http://www.humanteinenglish.com/spip.php?article 810).
46. *Mater. Perf.* **2007**, 46(3), 6, 10.
47. Britton, C. F. Private Communication.
48. Biedermann, A.; Williams, G. W.; Kane, R. D.; Eden, C.; Eden, D. A.; Trillo, E. A. *Oil Gas J.* **2005**, 103, 56–62.
49. Dean, S. W. *Stainless Steel World* **2002**, 13, 62–66.
50. Cox, W. M.; Boyce, M. P.; Miyazawa, M.; Tanaka, Y. *Corrosion Management* **2000**, May–June, 6–10.
51. Farrell, D. M.; Robbins, B. J.; Sikka, P.; Seaman, M. *Corros. Manage.* **2004**, May–June, 16–21.
52. Pawel, S. J. Oak Ridge National Laboratory, August 2004, Report ORNL/TM-2004.
53. Anderson, A.; Hilbert, R. L. *Proceedings of the 13th Scandinavian Corrosion Congress*; University of Iceland: Reykjavik, 2004; p 10.
54. Britton, C. F. Private communication.
55. Brown, A. S. *Mater. Perf.* **1992**, 30(9), 55–58.
56. US Patent 134292. Batelle Memorial Institute, 1993.
57. Aircraft Sensor for Corrosion. US Navy *Mater. Perf.* **1999**, 38(4), 16.
58. Edgemon, G. L.; Nelson, J. L.; Bell, G. E. C. Paper No 175, Corrosion 98; Nace International: Houston, TX, 1998.
59. Neri Segura, F. J.; Almeraya Calderon, F.; Borunda, T. A.; Gaona Tiburcio, C.; Martinez Villafana, A. *Mater. Perf.* **2007**, 46(1), 60–62.
60. Britton, C. F. Private Communication.
61. Sykes, J. *Corros. Sci.* **1985**, 28, 1051.
62. Elsenor, B. *Corros. Sci.* **2005**, 47, 3019.
63. Britton, C. F. Private Communication.
64. Bosch, R. W.; Hubrecht, J.; Bogaerts, W. F.; Syrett, B. C. *Corrosion* **2001**, 105, 60–70.
65. NACE Technical Co-Ordination Committee. *Gap Analysis Sector Report on Petroleum Refining*; *Mater. Perf.* **2008**, 47(8), 83–85.
66. London Times. 28th November, 2002.
67. National Transportation and Safety Board, (NTSB), Accident No. DCA-03-MM-032, NTSB/MAB-07/03, 25th May, 2003.
68. BBC Radio 4, *You and Yours*, 27th December, 2007.
69. *Aloha Flight 243* (available on [www.absoluteastronomy.com/topics/Aloha\\_Airlines\\_Flight\\_243](http://www.absoluteastronomy.com/topics/Aloha_Airlines_Flight_243)).
70. Wearne, P. *Collapse: Why Buildings Fall Down*, Channel 4 Books, **1999**, 43–53.
71. Larson, K. R. *Mater. Perf.* **2008**, 47(4), 30–33.
72. UK Highways Agency, Press Release, (SW/725/06) The Government News Network, 20th October, 2006.
73. London Times. 17th January, pp 52, 2008.
74. Papavinassam, S.; Doiron, A.; Revie, R. W. *Mater. Perf.* **2008**, 47(2), 58–62.
75. Halmshaw, R. *Non-destructive Testing*; Edward Arnold: London, 1987.
76. *Long Range Ultrasonic Inspection Technology*; The Welding Institute: UK (available at [www.twi.co.uk](http://www.twi.co.uk)).
77. *Time of Flight Diffraction (TOFD) Inspection Technology*; The Welding Institute: UK (available at [www.twi.co.uk](http://www.twi.co.uk)).
78. Ennaceur, C.; Laksinni, A.; Herve, C.; Cherfaoui, M. *Int. J. Pressure Vessels Piping* **2006**, 83(3), 197–204.
79. Lackner, G.; Tscheliesnig, P. *Corros. Manage.* **2007**, May–June, 8–12.
80. Veazey, M. V. *Mater. Perf.* **2004**, 43(2), 16–19.
81. Al-Taie, I.; Al-Musalami, F.; Al-Daajani, B. F.; Al-Bakhat, A.; Morison, D.; Cherpillod, T. *Oil Gas J.* **2007**, 105, 50–55.
82. *Oil and Gas J.* **1996**, 4, 69.
83. Daily Telegraph, (London) 23/02/90 and 24/02/90.
84. John, D. G.; Oliver, K. E. Paper 07124, Corrosion 2007; NACE International: Houston, TX, 2007.
85. Teitsma, A. Technology Assessment for Delivery Reliability for Natural Gas Inspection Technologies: RFEC, Contract DE-FC26-04NT42266, Pipeline Inspection Technology, Gas Technology Institute, Des Plaines, IL, USA.
86. Report on the investigation of the fatality on board passenger cruise ship SAGA ROSE in Southampton, England, on 11 June, 2009, Marine Accident Investigation Branch, Southampton, UK, Report No1/2009, January 2009.
87. Rose, R. *UT Crawlers for Above Ground Inspection*; Posting on NDT Forum, 10th July 2001, available at [www.ndt.net/forum](http://www.ndt.net/forum).
88. Trethewey, J. *Magnox reactors/AGR*. In *Corrosion for Science and Engineering*, 2nd ed.; Longmans: Harlow, Essex, England, 1995; Chapter 17, pp 414–415.
89. London Times, UK Business. pp 53, 14th November, 2007.
90. US Patent, 250/227. 14–18, 385/37, Issued November 7, 2000.
91. *Mater. Perf.* **2008**, 47(3), 9–10.
92. Schroder, S. *Oil Gas J.* **2008**, Supp. 106(7), 10.

## 4.38 Management of Corrosion of Aircraft

**C. J. E. Smith**

QinetiQ, Farnborough, Hants, UK

© 2010 Elsevier B.V. All rights reserved.

---

<b>4.38.1</b>	<b>Airframe Corrosion</b>	3176
4.38.1.1	Introduction	3176
4.38.1.2	The Operational Environment	3176
4.38.1.3	Summary of Main Corrosion Types	3177
4.38.1.3.1	Corrosion occurring in the absence of an applied stress	3177
4.38.1.3.2	Corrosion occurring in the presence of an applied stress	3178
4.38.1.3.3	Corrosion arising from poor design and protection	3179
4.38.1.4	In-Service Corrosion	3179
4.38.1.5	Impact of Corrosion on Structural Integrity	3179
<b>4.38.2</b>	<b>Corrosion Management During Manufacture</b>	3180
4.38.2.1	Introduction	3180
4.38.2.2	Materials Selection	3180
4.38.2.2.1	Introduction	3180
4.38.2.2.2	Aluminum alloys	3180
4.38.2.2.3	High strength steels	3182
4.38.2.2.4	Magnesium alloys	3183
4.38.2.2.5	Titanium alloys	3183
4.38.2.2.6	Composite materials	3184
4.38.2.3	Protective Treatments	3184
4.38.2.3.1	Introduction	3184
4.38.2.3.2	Aluminum alloys	3184
4.38.2.3.3	Steels	3186
4.38.2.3.4	Magnesium alloys	3188
4.38.2.3.5	Titanium alloys	3189
4.38.2.3.6	Composite materials	3190
4.38.2.3.7	Wear and fretting resistant coatings	3190
4.38.2.4	Design Considerations	3190
4.38.2.5	Final Assembly and Finishes	3191
<b>4.38.3</b>	<b>Corrosion Management In-Service</b>	3192
4.38.3.1	Introduction	3192
4.38.3.2	Aircraft Washing and Cleaning	3192
4.38.3.3	Inspection for Corrosion	3193
4.38.3.4	Corrosion Rectification	3193
4.38.3.4.1	Corrosion removal	3193
4.38.3.4.2	Reprotection	3194
4.38.3.5	Use of Supplementary Protection	3195
4.38.3.6	Paint Removal and Repainting	3195
4.38.3.7	Dehumidification	3195
4.38.3.8	Future Trends in Aircraft Corrosion Management	3196
<b>References</b>		3196

---

## Abbreviations

**AGARD** Advisory Group for Aerospace Research and Development

**CAA** Chromic acid anodizing

**CCC** Chromate conversion coating

**CFRP** Carbon fiber reinforced plastic

**HE** Hydrogen embrittlement

**HVOF** High-velocity oxy-fuel

**L** Longitudinal direction

**LT** Long transverse direction

**NDE** Nondestructive evaluation

**PMS** Plastic media stripping

**PVD** Physical vapor deposition

**RH** Relative humidity

**SCC** Stress corrosion cracking

**ST** Short transverse direction

**UTS** Ultimate tensile strength

**VOC** Volatile organic compounds

## Symbols

$K_{1SCC}$  Stress intensity for stress corrosion cracking (MPa.m<sup>0.5</sup>)

### 4.38.1 Airframe Corrosion

#### 4.38.1.1 Introduction

This chapter is concerned with the management of corrosion on fixed wing aircraft and helicopters. It concentrates on the corrosion and protection of aircraft structures and does not consider the complex corrosion problems associated with the protection of materials used in aircraft engines. Although the references and discussion are mainly concerned with aircraft, the approaches described are also applicable to other aerospace structures such as guided weapon systems and airships.

The principal materials used in the construction of the modern aircraft are aluminum alloys, titanium alloys, high-strength steels, corrosion resisting steels, magnesium alloys, and composite materials.

Weight has always been the main consideration in airframe construction. The structure must be light, but strong enough and rigid enough to withstand the applied loads and stresses. The specific strength and resistance to buckling are important factors in the selection of airframe materials. For these reasons, extensive use of aluminum alloys has traditionally

been made in the aerospace industry. With the development of composite materials, such as carbon fiber reinforced plastics, the volume of aluminum alloys employed on the modern civil transport aircraft and military fast jet has been significantly reduced. As will be discussed later in this chapter, this will have an impact on aircraft corrosion and protection.

High-strength steels are used in a number of applications. In areas where size is critical, steels have advantages over aluminum alloys. Landing gear components, for example, have to be stowed away into relatively small volumes. To achieve the necessary load carrying capacity, parts are frequently manufactured from steels having tensile strengths in excess of 1800 MPa. Many fasteners used on aircraft are also manufactured from steel.

Strength is not always the overriding criteria. Some applications require a high level of stiffness and this can be obtained through the use of thick section. Gearbox housings are one example in which it is more advantageous to use a magnesium alloy casting. The same part manufactured in an aluminum alloy would be 1.5 times heavier. Titanium alloys are also finding increasing applications in airframe components and are replacing steels in some areas. Titanium alloy fasteners are also extensively used on modern aircraft.

Corrosion can have a major impact on the structural integrity and hence safety of all types of aircraft. To implement a successful corrosion management program, an understanding of the operating environment and the potential corrosion risks associated with the various materials used in the airframe structure is essential.

Neglecting to manage corrosion may lead to the eventual grounding of an aircraft because it is structurally unsound and unsafe to fly. A planned approach to the management of corrosion on aircraft is therefore necessary to ensure safety and reliability and begins at the design stage of the aircraft.

#### 4.38.1.2 The Operational Environment

Aircrafts are frequently operated in highly corrosive environments. For example, many military aircrafts fly from coastal bases and carryout low level missions over the sea. Aluminum alloys, high-strength steels, and magnesium alloys are highly susceptible to various forms of corrosion in the presence of chloride ions if they are not adequately protected.

The AGARD Aircraft Corrosion Handbook<sup>1</sup> has summarized the relative rates of corrosion for different types of atmosphere. It lists tropical, industrial,

and marine environments as highly conducive to corrosion, while rural and arctic locations are considered to give a low rate of corrosion. Moderate corrosion occurs when flying is in temperate or suburban regions. Some desert areas have high levels of salt and are potentially highly corrosive.

In addition to contaminants from the environment, there are a number of compounds and liquids that are used on the aircraft, such as hydraulic fluids, fuels, and oils, which can degrade protective treatments and may lead to the onset of corrosion. In addition, spillages from galleys, toilets, and batteries and breakages in freight-holds have all been identified as initiating corrosion. These areas need particular consideration in terms of design and protection to minimize the risk of corrosion in-service. Condensates from passengers and livestock will also promote corrosion. Mitchell<sup>2</sup> has described a UK airline's experiences with many of these contaminants. Reference is made to the soundproofing adjacent to the fuselage, which was found to absorb up to 400 kg of moisture, presenting a major corrosion threat.

During maintenance, a range of chemicals is used for washing, cleaning, and removing paint from the exterior and interior surfaces of the aircraft. These materials if not used correctly and in the right concentrations may lead to corrosion, particularly if allowed to enter the internal structure of the aircraft. Specifications covering cleaners, etc., for use on aircraft include corrosion tests designed to ensure that potentially corrosive materials are excluded. Similarly deicing materials used on aircraft and for clearing runways must satisfy these corrosion tests.

Early studies conducted by Kohler and Scott<sup>3</sup> demonstrated that significant levels of chloride ions and other corrodents can accumulate in the internal structure of military aircraft operated in a maritime role. The levels were sufficient to initiate pitting corrosion and other forms of localized attack on aerospace aluminum alloys. Future aircraft corrosion control plans will need to take into account the likelihood of corrosion developing in internal parts of the structure, which cannot be inspected by conventional methods.

Although corrosion will occur primarily when an aircraft is sitting on the ground, flying at 30 000 ft will contribute to degradation of the protective treatments used on the external surfaces. At these altitudes, the external temperatures fall to  $-60^{\circ}\text{C}$  reducing the paint flexibility. This can lead to paint cracking around fasteners, permitting the ingress of moisture. Further, the ozone and ultraviolet levels are high, causing degradation of the exterior paint

schemes. The temperature cycling experienced by the aircraft, especially when operating in hot humid environments, will lead to a continuous buildup of moisture in internal regions.

The protective treatments applied must be capable of preventing corrosion on aircraft structures when exposed to the various operating environments and contaminants listed earlier.

#### 4.38.1.3 Summary of Main Corrosion Types

The airframe materials employed exhibit a number of different types of corrosion. A key part of the management of aircraft corrosion is the knowledge of the conditions under which a specific form may develop, and the steps that should be taken to prevent or control it. Table 1 summarizes the various forms of corrosion that have been found. They may be divided into three groups as follows:

- corrosion occurring in the absence of an applied stress,
- corrosion occurring in the presence on an applied stress,
- corrosion resulting from poor design and protection.

Detailed information about the mechanisms of the different types of corrosion identified may be found elsewhere in this book. Sections 4.38.1.3.1, 4.38.1.3.2, and 4.38.1.3.3 summarize the main aspects of each form of corrosion as they relate to airframe materials.

##### 4.38.1.3.1 Corrosion occurring in the absence of an applied stress

General corrosion is included in Table 1 for completion, but in practice relatively few examples of general corrosion are found on airframe materials. More usually the type of attack that develops can be described as localized corrosion. This may take the form of pitting, intergranular, or exfoliation corrosion. In the case of aluminum alloys, the surface is protected by a thin adherent oxide film. One hypothesis is that flaws preexist in the oxide film and provide sites for the initiation of corrosion attack. The flaws may be associated with precipitates, impurities, or grain boundaries in the matrix. The dissolution of aluminum is localized and leads to the formation of corrosion pits particularly if chloride ions are present.

Pitting is often a precursor to further localized attack. In intergranular corrosion, the grain boundary areas behave anodically with respect to the bulk of the grains. The corrosion follows paths along the grain boundaries of the material and can proceed at a high



**Table 1** Summary of corrosion types found on aerospace materials

<i>Type</i>		<i>Description</i>	<i>Susceptible materials</i>
Absence of applied stress	General	Corrosion uniformly distributed over exposed surface	
	Pitting	Localized attack, which leads in the formation of deep and narrow cavities	Aluminum alloys Magnesium alloys
	Intergranular	Corrosion attack propagating along the grain boundaries of the material	Aluminum alloys
	Exfoliation	A form of intergranular corrosion occurring in materials with elongated grain structures. Leads to blistering and surface lifting and flaking	Aluminum alloys
	Microbial corrosion	Corrosion developed as a result of microbiological growth	Aluminum alloys in contact with fuel
Presence of applied stress	Stress corrosion cracking	Cracking process involving the conjoint action of a stress and a corrodent	Aluminum alloys High-strength steels Titanium alloys
	Corrosion fatigue	Accelerated fatigue growth on exposure to a corrosive environment	Aluminum alloys
	Hydrogen embrittlement	Cracking of statically loaded components resulting from the absorption of hydrogen	High-strength steels
	Fretting corrosion	Form of wear resulting from movement or vibration between two surfaces	Titanium alloys
	Solid/liquid metal embrittlement	Cracking of statically loaded components resulting from direct contact with liquid or solid metals	Aluminum alloys High-strength steels Titanium alloys
	Crevice corrosion	Corrosion resulting from the ingress of moisture into crevices or gaps between components	Aluminum alloys Corrosion resisting steels
Corrosion arising from poor design and protection	Galvanic corrosion	Corrosion resulting from the contact between two metals of different electrochemical potential immersed in an electrolyte	Direct contacts between aluminum alloys, steels, magnesium alloys in contact with titanium and CFRP materials
	Filiform corrosion	Thread-like corrosion developing under organic coatings	Painted aluminum

rate because of the large difference in cathode to anode area. If the grains are elongated in shape as in the case of plate and extruded materials, the corrosion may run parallel to the surface causing flaking and blistering. This type of attack is known as exfoliation corrosion and many examples of it have been found in-service. Often, the first indication that there is a problem arises when it is noticed that the paint film adjacent to fastener holes is lifting. At this stage, the attack may be well established and extensive repair work may be required.

In addition to aluminum alloys, magnesium alloys and steels may exhibit pitting corrosion when exposed in an aircraft environment.

Microbial corrosion is a type of attack initiated by the presence of organisms such as fungi and sulfur-reducing bacteria. Examples of this form of corrosion have been found in fuel tanks. Bowden<sup>4</sup> describes the action of *Cladosporium resinae*, a fungus which may live in water droplets present in fuel tanks. The acidic by-products produced by the fungus may breakdown

the protective treatments applied to the interior of fuel tanks and lead to the attack of the aluminum alloy substrate. Sludge developed as a result of the microbial action may lead to blockage of fuel pipes and pumps.

#### **4.38.1.3.2 Corrosion occurring in the presence of an applied stress**

Stress corrosion cracking (SCC) and corrosion fatigue result from the synergistic action of an applied stress and a corrosive environment. In the case of SCC, a static tensile stress is present, while in corrosion fatigue the stress is fluctuating in some manner. Stress corrosion failures have occurred in-service mainly with the high-strength aluminum–zinc–magnesium alloys such as 7075 and examples of failures have been seen on landing gear components. The stresses responsible for cracking are generally either residual stresses introduced as a result of the material manufacturing process or stresses arising from poor alignment during assembly. Once initiated,

the stress corrosion crack can propagate rapidly and catastrophic failure may eventually occur.

The mechanism or mechanisms of SCC in aluminum alloys continue to be the subject of much research and discussion and are covered in some depth elsewhere in this book.

In addition to high-strength aluminum alloys, high-strength steels and titanium alloys may also suffer SCC. Steels with an ultimate tensile strength greater than 1450 MPa are generally considered to be susceptible to SCC in aqueous environments. Failures have occurred with titanium alloys when exposed to specific environments.

Fatigue is familiar to all aircraft designers and operators. The presence of a corrosive environment can accelerate the process by shortening the initiation stage and/or by increasing the growth rate of fatigue cracks. Most of the concerns and research into corrosion fatigue on airframe materials have been with aluminum alloys. The need to understand this type of corrosion has gained particular importance in relation to ageing aircraft. It is now recognized that the interaction between fatigue and corrosion is crucial in determining the integrity of aircraft structures.

On airframes, hydrogen embrittlement is normally associated with high-strength steels. Cracking takes place in statically loaded components, resulting from the absorption of hydrogen, which may be introduced as a result of corrosion occurring on the surface or from hydrogen introduced during surface finishing treatments. Rapid crack growth takes place, leading to the eventual catastrophic failure of the component. It is widely accepted that the mechanism of SCC in high-strength steels is one of hydrogen embrittlement.

The fourth type of corrosion occurring in the presence of an applied stress (identified in [Table 1](#)) is fretting, which is a form of wear resulting from the movement or vibration between two surfaces. The movement is very small, often leading to the formation of fine particles or debris. Titanium alloys are particularly sensitive to this type of degradation.

#### **4.38.1.3.3 Corrosion arising from poor design and protection**

Crevice corrosion arises in-service, largely as a consequence of poor design. Crevices provide an area in the structure where water, hydraulic fluids, and other contaminants may become trapped. The diffusion of oxygen into the crevice is restricted so that the second cathodic reaction involving the reduction of water to form hydrogen ions is favored. This increases the acidity of the solution at the tip of the crevice and will lead to accelerated corrosion of structural materials such as

aluminum alloys, magnesium alloys, and corrosion-resistant steels. The proper use of sealants and jointing compounds, to fill crevices and prevent the entry of fluids, can eliminate this type of corrosion.

Galvanic corrosion can occur when two dissimilar metals are joined. Some indication of the likely risk of coupling two different metals together can be gained by comparing their corrosion potentials. If there is a large difference in potential between the two metals, for example, 2014-T6 aluminum–copper alloy and steel, the corrosion of the more negative material, in this case the aluminum alloy, will be accelerated, while the corrosion of the steel will be reduced. The occurrence of this type of corrosion in an aircraft can be limited if coatings such as electroplated cadmium are applied to steel parts. The corrosion potential of cadmium is similar to 2014-T6 aluminum–copper alloy and therefore the driving force for corrosion is much lower.

Filiform corrosion is a form of attack that develops under organic coatings applied mainly to aluminum alloys. It appears as long filaments that spread from areas of surface damage such as cracks or chips in the coating. The development of this form of corrosion is dependant on the surface cleaning and treatments applied to the substrate.

#### **4.38.1.4 In-Service Corrosion**

Corrosion is likely to take place within the aircraft structure at areas where moisture and other corrosive contaminants become trapped. The main problem areas have been documented in the open literature<sup>1,2,5</sup> and are summarized as follows.

- Areas where fluids may collect
- Areas partly exposed to the environment
- Areas into which fluids may leak

Examples of corrosion found in-service on civil transport aircraft associated with the build up of fluids include areas below toilets, galleys, and cargo-holds. The corrosion of seat tracks arising from the spillage of drinks continues to be a major problem area. Some areas such as undercarriage bays, freight doors, access doors, and flap shrouds are regularly exposed to the environment. Leakages from hydraulic systems and batteries can rapidly degrade protective treatments.

#### **4.38.1.5 Impact of Corrosion on Structural Integrity**

Corrosion can degrade the integrity of the aircraft structure in a number of ways as listed in [Table 2](#).

Exfoliation corrosion, which is often found to develop in components manufactured from plate

**Table 2** Examples of the effects of corrosion on the integrity of airframe structures

<i>Corrosion type</i>	<i>Impact on structural integrity</i>
Intergranular and exfoliation corrosion and most forms of corrosion	Reduction in section leading to loss in strength/load bearing capacity, ductility, stiffness, etc.
Corrosion pitting	Failure of hydraulic pipes, fuel lines – leakage of fluids into areas causing breakdown of protective treatments and further corrosion
Corrosion pitting and fretting	Introduction of stress raisers leading to reduced fatigue life
Crevice corrosion	Generation of stresses at joints resulting from corrosion product wedging – breakdown of bonded joints
Galvanic or dissimilar metal corrosion	Accelerated corrosion attack of aluminum and steel components
SCC and hydrogen embrittlement	Catastrophic failure of stressed components
Microbial corrosion	Leakage from fuel tanks, blockages

aluminum alloys, can lead to a major loss in section, and hence, load bearing capacity. Pitting corrosion and intergranular attack may accelerate the initiation of fatigue cracking. The areas where attack occurs act as stress raisers and greatly reduce the fatigue life of the structure. In hydraulic and fuel pipes pitting attack can cause perforation and eventual fluid loss.

Some of the aluminum alloys employed in older aircraft are susceptible to SCC. This form of attack can develop if the component is under stress and is exposed to a corrosive environment. The stresses may be residual stresses introduced during the manufacture of the part or they arise as a result of misalignment during assembly. Once initiated, SCC may develop very quickly resulting in the catastrophic failure of the part or structure.

In some instances, corrosion may contribute to the degradation and eventual failure of adhesively bonded joints. At present, much research is being directed towards understanding the mechanisms involved in the failure within adhesively bonded lap joints on ageing aircraft and developing methods for the early detection of breakdown.

## **4.38.2 Corrosion Management During Manufacture**

### **4.38.2.1 Introduction**

The approach adopted in the management of corrosion during the initial manufacturing stage is based on the following:

- the selection of materials with inherent resistance to corrosion,
- the application of protective treatments to individual parts and components,
- careful design and assembly to minimize potential problems such as crevice and galvanic corrosion,

- the application of additional protective treatments in high corrosion risk areas.

Each of these aspects is considered in this section.

### **4.38.2.2 Materials Selection**

#### **4.38.2.2.1 Introduction**

In many cases airframe materials were initially selected to provide specific strength levels, fatigue resistance, fracture toughness properties, etc. Corrosion resistance was often only a secondary consideration. The philosophy adopted was basically to assume that the inherent poor corrosion resistance of the material could be compensated for by the application of a protective coating, typically an inhibited primer or metal coating. This assumed that the coating would remain intact and undamaged throughout the life of the component. The reality is that coatings in the form of both paints and metal deposits suffer from cracking and degradation during the operational life of an aircraft. Examples of undercarriage components manufactured from 7000 series aluminum–zinc–magnesium alloys heat treated to the high-strength T6 temper that suffered catastrophic failure in-service have been referred to earlier. In these instances the surface treatments applied failed to prevent the onset of SCC.

The approach now adopted is to take into account the inherent corrosion resistance of the material to be employed. Guidance data are available from several sources<sup>6,7</sup> on the susceptibility of airframe to various types of corrosion, in particular, resistance to SCC and exfoliation corrosion.

#### **4.38.2.2.2 Aluminum alloys**

As indicated in [Section 4.38.1.3](#) airframe aluminum alloys are susceptible to various forms of corrosion including localized attack and SCC. The alloy

composition, heat treatment, and product form will control the type and distribution of precipitates as well as the grain size and shape of the grains. The microstructure of the component material, together with the nature of the environment and loading applied, will determine the type and extent of the corrosion attack that takes place. During the material selection process, the resistance of aluminum alloys to exfoliation corrosion and SCC is taken into account. Extensive laboratory testing combined with service experience has enabled the relative susceptibilities of aerospace aluminum alloys to exfoliation to be given a rating as indicated in [Table 3](#) based largely on Defence Standard 00-970.<sup>6</sup>

Sheet aluminum alloys are generally considered to be immune to exfoliation corrosion and have an 'A' rating. Some intergranular attack may take place but the grain structure is normally equiaxed and true exfoliation corrosion will not develop. Alloys with C ratings should be avoided wherever possible. As discussed in the following section, surface treatments must be applied to minimize the risk of corrosion occurring. Several alloys such as plate 2024-T3 aluminum–copper, which has frequently been used for bottom wing

skin applications, and plate 7075-T651 aluminum–magnesium–zinc which has been used for the manufacture of upper wing skins and undercarriage components are very susceptible to exfoliation corrosion and have a 'D' rating. The policy now is to avoid the selection of these materials wherever possible.

[Table 4](#) compares the susceptibility of several materials that have been widely employed in airframe structures. The data have been taken from Defence Standard 00-970<sup>6</sup> and ASTM Handbook,<sup>7</sup> which should be consulted for more detailed information. [Table 4](#) indicates that with the 7000 series plate alloys, the susceptibility may be reduced by using a material in the over-aged T73 or T76 condition. In these tempers, however, the strength of the 7075 alloy is reduced by up to 10% compared with the peak aged T6 temper. The 7010 and 7050 alloys were developed to provide materials that matched the strength of the peak aged 7075 alloy and were resistant to exfoliation corrosion. Recent developments in both high-strength 7000 series alloys and damage-tolerant 2000 series alloys have been aimed at producing products with improved mechanical properties and a resistance to corrosion.<sup>8,9</sup>

The resistance of plate aluminum alloys to SCC is often assessed by determining a threshold stress below which failure will not occur. For this purpose, alternate immersion/emersion testing in 3.5% sodium chloride solution or outdoor marine exposure trials are conducted using C-ring or tensile bars cut from the plate material. [Table 5](#) gives typical values published in the literature for three commonly used plate materials. The susceptibility to SCC in these materials is orientation dependent and is mainly a consequence of grain shape. Plate materials are most susceptible when the stress is applied in the short transverse direction (ST) as shown in [Table 5](#). The

**Table 3** Exfoliation ratings applied to aluminum alloys

Rating	Description
A	Immune to exfoliation corrosion
B	Resistance to exfoliation corrosion under normal service conditions but could occur under extreme conditions
C	Susceptible to exfoliation corrosion if appropriate design precautions are not taken
D	Very susceptible to exfoliation corrosion

Source: Defence Standard 00-970 Part 7/2 Section, Detail Design and Strength of Materials, Ministry of Defence, Directorate of Standardization, Kentigern House.

**Table 4** Examples of the exfoliation corrosion susceptibility of some aerospace aluminum alloys

	Rating			
	A – Immune	B – Resistant. Slight exfoliation may be induced under extreme conditions	C – Susceptible to exfoliation. Can occur in-service	D – Very susceptible to exfoliation
Product form				
Sheet		2014-T6, T3 2024-T3, 7075-T6		
Plate	7075-T7351	7010-T7651 7010-T73651 7050-T7651 7050-T73651	2014-T6	2024-T3 7075-T651
Extrusion			2014-T6	

**Table 5** Typical threshold stresses for plate aluminum alloys (MPa) exposed in a marine environment

Material	Direction		
	L	LT	ST
2014-T651	310	210	<55
2024-T3	170	140	<55
7075-T651	340	310	<55
7075-T73	349	330	300

**Table 6** SCC ratings applied to aluminum alloy

Rating	Description
A	Immune to SCC
B	Resistance to SCC under normal service conditions but could occur under extreme conditions
C	Susceptible to SCC if appropriate design precautions are not taken
D	Very susceptible to SCC

Source: Defence Standard 00-970 Part 7/2 Section, Detail Design and Strength of Materials, Ministry of Defence, Directorate of Standardization, Kentigern House.

effect of overaging the 7075 alloy to the T73 temper is to increase the SCC threshold stress from less than 55–300 MPa.

The data presented in Table 5 are derived from tests conducted on smooth specimens and basically relate to the initiation of stress corrosion cracks. The rate at which a stress corrosion crack propagates may also be studied. The usual approach is to determine the crack growth rate as a function of the stress intensity. A value of stress intensity  $K_{ISCC}$  can often be measured below which the crack does not grow effectively.

The threshold stress data and  $K_{ISCC}$  data are used together with service experience to assess the susceptibility of aerospace aluminum alloys to SCC. As discussed in the following section, susceptibility is dependent on the product form, that is, sheet, plate, tube, extrusion, etc., alloy composition, and the heat-treatment that has been carried out.

Data comparable to those available for exfoliation susceptibility are detailed elsewhere,<sup>6,7</sup> listing the SCC resistance of aluminum alloys. A similar rating system is employed as indicated in Table 6.

As previously discussed, the susceptibility to SCC in wrought aluminum alloys is orientation dependent. Plate aluminum–zinc–magnesium alloys heat treated to the T6 condition are particularly sensitive when loaded in the short-transverse (ST) direction. Heat treating material to the T73 and T76 tempers will improve the SCC resistance of an alloy such as 7075

from a 'D' to an 'A' or 'B' rating but with some loss in strength. The 7010 and 7050 alloys offer high strength and improved resistance to SCC. By applying a duplex ageing treatment, consisting of up to 24 h at temperatures in the range 120–135 °C followed by a shorter period at a higher temperature (160–170 °C),<sup>10</sup> the strength 7075 alloy in the T6 peak aged condition can be obtained but with much improved resistance to SCC. These alloys contain zirconium rather than chromium or manganese to inhibit recrystallization.

More recent developments in 7000 series airframe materials are described elsewhere.<sup>8,9,11</sup> Alloys such as 7449 are being considered in various product forms and tempers for use in upper wing skins, upper and lower wing stringers and wing box applications. The material gives improved strength combined with good resistance to corrosion.

#### 4.38.2.2.3 High strength steels

Steels employed in airframe manufacture fall broadly into the following groups:

- non-corrosion resisting mild steels and low alloy steels,
- intermediate alloy steels,
- high-alloy steels,
- precipitation and transformation – hardening steels (stainless).

The main concerns with high-strength steels are their susceptibility to hydrogen embrittlement (HE) and SCC. The wealth of available experimental data indicates that the mechanism of SCC in steels is one of hydrogen embrittlement. Hydrogen is generated during surface corrosion some of which will diffuse into the steel substrate.

Steels with ultimate tensile strength (UTS) levels up to 1100 MPa are considered to be immune to these forms of corrosion but above this strength level, the susceptibility increases as the UTS is raised. Under-carriage parts, for example, are often manufactured from low alloy steels such as 300M and AISI4340 that have strengths of 1800 MPa or above. Steels heat treated to these strengths are very susceptible to hydrogen embrittlement and SCC. In an identical way to that used for aluminum alloys, steels may be given an SCC rating of 'A' through to 'D.' Based on the guidance information given in Defence Standard 00-970<sup>6</sup>, the bar and tube product forms of 300M are given a 'D' rating, that is, very susceptible to SCC, while AISI4340 is less susceptible and has a 'C' rating. Within the four groups of steels, there are some variations in SCC susceptibility, but there is an overall trend showing that susceptibility increases with increasing UTS.



In selecting steels for aerospace applications, the tables given in Defence Standard 00-970<sup>6</sup> and ASTM Handbook<sup>7</sup> should be referred to in order to determine the potential SCC and hydrogen embrittlement risks. Where a choice of materials is available, the more corrosion-resistant materials should be selected. As discussed in [Section 4.38.2.3.3](#), steel parts must be protected against corrosion and wear. The choice of cleaning, pretreatment, and finishing processes available are greatly influenced by the SCC and HE susceptibilities.

#### 4.38.2.2.4 Magnesium alloys

The use of magnesium alloys is now largely limited to castings. Sheet alloys were used at one time for skinning on both fixed wing aircraft and on helicopters. Major corrosion problems were experienced in-service, particularly around fasteners where the protective treatments had cracked or flaked off. This resulted in reskinning programs replacing the magnesium alloy with sheet aluminum alloys. For many military applications, the use of magnesium alloy sheet is not permitted. Their lower density compared with aluminum alloys and their superior casting properties have made magnesium alloys particularly attractive for the production of gearbox housings for helicopter applications.

Unprotected magnesium alloys are susceptible to pitting corrosion but are not prone to intergranular attack. The presence of cathodic impurities such as iron, nickel, and copper has significant effects on the pitting behavior and improvements in corrosion resistance have been achieved by developing materials with lower impurity levels. The corrosion rate of a AZ91C magnesium–aluminum–zinc alloy, for example, may be reduced from 0.022 to 0.006 mm year<sup>-1</sup> in a marine–rural environment by lowering the iron level from 350 to 10 ppm.<sup>12</sup> In selecting magnesium alloys consideration should be given to choosing materials with lower impurity levels. Care must also be taken in processing materials in order to minimize the risk of surface contamination, which could initiate corrosion.

Some differences in corrosion behavior also exist between the main types of magnesium alloys employed for aerospace purposes. For example, the AZ63A magnesium–aluminum–zinc alloy has a corrosion rate of 0.018 mm year<sup>-1</sup> compared with a rate of 0.028 mm year<sup>-1</sup> for the EZ33 magnesium–rare earth–zinc alloy. For further information see ASTM Handbook<sup>12</sup> and manufacturer data sheets.

A key problem with magnesium alloys is the potential risk of galvanic corrosion when in contact with other materials. This requires the application of effective barrier coatings.

#### 4.38.2.2.5 Titanium alloys

Titanium alloys are relatively resistant to corrosion mainly due to the presence of a thin highly protective air formed oxide film. In terms of material selection there are no significant differences between the various types of titanium alloys to aqueous corrosion. However, the following points should be taken into consideration when selecting titanium alloys for airframe applications

##### *Galvanic corrosion*

Titanium alloys can promote galvanic corrosion when coupled to other airframe materials such as aluminum alloys, steel, and magnesium alloys. Precautions must be taken during assembly to reduce the contact between parts made from titanium alloys and other structural materials.

##### *Fretting corrosion*

Where small repeated movements take place between a titanium alloy part and parts made from either aluminum alloy or steel, there is a possibility that fretting damage may be induced in the titanium alloy surface. This can lead to early fatigue crack initiation. The risk of fretting can be minimized through the application of a suitable antifret surface treatment. A number of treatments are available commercially and include surface coatings and ion implantation treatments.

##### *Stress corrosion cracking*

While titanium alloys are generally resistant to both corrosion and SCC in marine environments, there are a number of chemicals and contaminants which are commonly found on aerospace structures that may induce corrosion and SCC.<sup>13</sup> These include chlorinated hydrocarbons, methanol and phosphate ester fluids at temperatures above 120 °C. It is good practice to avoid the use of titanium alloys in areas where contact with these chemicals is a possibility.

##### *Solid metal embrittlement*

Titanium alloys may be susceptible to solid-metal embrittlement when in contact with cadmium. Embrittlement may occur at ambient temperatures, but it is likely the embrittlement process that is accelerated at elevated temperatures. Failure of the component will take place under an applied stress if there is intimate contact between titanium alloy and cadmium plating.<sup>14</sup> For airframe applications, direct contact between cadmium and titanium should be avoided. At one time cadmium plating was often used on titanium alloy fasteners to improve lubricity and to reduce the

**Table 7** Methods currently employed in the protection of aerospace components

<i>Method of Protection</i>	<i>Examples</i>	<i>Applications</i>	<i>Substrate</i>
Corrosion Inhibitors	Chromates	Chromate pigmented primers Conversion coatings  Passivation treatments	Aluminum alloys Aluminum alloys Aluminum coatings Cadmium coatings Zinc coatings
Sacrificial metal coatings	Cadmium	Electrodeposited and physical vapor deposited cadmium plating	High-strength steel Corrosion resisting steel
	Zinc	Electrodeposited zinc plating	Steel
	Aluminum	Aluminum and Aluminum–zinc cladding	Sheet aluminum alloys
	Aluminum	Physical vapor deposited aluminum plating	Steel Titanium alloys Aluminum alloys
Barrier coatings	Epoxy coatings	Thick dense coating	Magnesium alloys
	Anodic films	Thick oxide coating	Magnesium alloys
	Sealed anodic films	Dense oxide coating	Aluminum alloys
	Nickel plating	Electroless nickel plating	Steels Aluminum alloys
	Chromium plating	Hard chromium electroplating	Steels

likelihood of dissimilar metal corrosion when used with aluminum alloys. This practice is no longer permitted and cadmium plated steel parts and fasteners should not be in direct contact with titanium alloy parts.

Other metals that have been identified as causing solid-metal embrittlement under certain circumstances are zinc and silver.

#### **4.38.2.2.6 Composite materials**

While generally resistant to degradation from the chemicals employed on aircraft and to the environments to which aircraft are exposed, composite materials may contribute to the corrosion of other airframe materials. CFRP (carbon fiber reinforced plastic) composite materials behave in a similar manner to titanium alloys when coupled to less noble metals in so far as they will accelerate the corrosion of steel, aluminum alloys and magnesium alloys. There is also concern that some composite materials will absorb moisture, which may lead to the loss of mechanical properties.

### **4.38.2.3 Protective Treatments**

#### **4.38.2.3.1 Introduction**

Following manufacture, normal aerospace practice is to apply a protective treatment to parts made from aluminum alloys, magnesium alloys, and steels. Parts made from titanium alloys and composites may also be protected depending on the location on the airframe and environment to which the part is likely to

be subjected. The method of protection employed varies according to the substrate material as indicated in [Table 7](#).

In the following sections, the protective treatments applied to aerospace components are described in detail.

#### **4.38.2.3.2 Aluminum alloys**

##### **Current protective treatments**

The standard protective treatments currently applied to aerospace aluminum alloys are based on the use of chromate containing pretreatments and chromate pigmented primers. As indicated earlier, aerospace aluminum alloys are susceptible to localized corrosion particularly in the presence of chloride ions. Strontium chromate is a very effective corrosion inhibitor for aluminum alloys particularly on exposure to salt containing atmospheres. This is demonstrated by published data showing that, in 3.5% sodium chloride (a chloride level equivalent to that of seawater), the addition of  $0.02 \text{ mmol l}^{-1}$  of chromate is sufficient to prevent the onset of corrosion on a 2000 series aluminum alloy.<sup>15</sup>

[Figure 1](#) illustrates the protective scheme used on parts manufactured from aluminum alloys.

Prior to the application of the pretreatment, the part is degreased and cleaned using a suitable process such as alkaline degreasing, abrasive cleaning, organic solvent degreasing, and chromic–sulfuric acid etch. For fatigue critical parts it should be

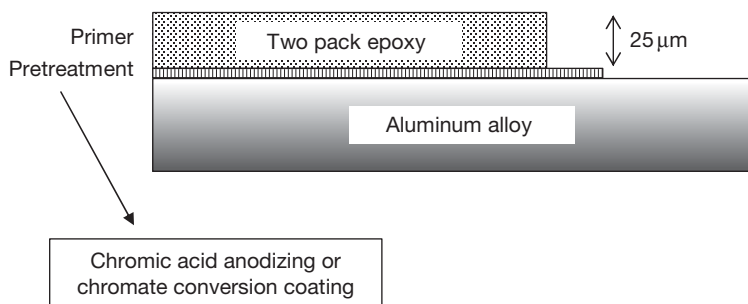


**Figure 1** Standard protective treatment applied to aluminum alloy components.

noted that surface etching may have an adverse effect on fatigue life. Pretreatments normally used include chromic acid anodizing (CAA) and chromate conversion coatings (CCC). The purpose of these is to produce a protective film, which consists basically of alumina and, in the case of CCC, incorporates chromates and chromium oxide. In addition these coatings enhance paint adhesion by promoting mechanical keying.

CAA is usually conducted in a bath containing a concentration of 30–100 g l<sup>-1</sup> chromic acid. The anodizing voltage depends on the composition and temper of the alloy but is typically in the range 20–50 V. Times of up to 40 min are required to produce suitable films. Further details may be found in the appropriate process specifications. The anodic films produced by chromic acid anodizing consist of a thin barrier layer with a thicker porous outer layer. To achieve maximum paint adhesion, it is normal practice to paint within 8 h of anodizing. An alternative approach is to seal the anodic films prior to painting by immersing the part in near boiling water. This improves the protective properties of the film but probably at the expense of the paint adhesion.

Chromate conversion coatings fulfill the same role as anodizing but are generated by immersing the part in an acidic chromate bath. Details of the chemistry of the conversion coating process may be found elsewhere.<sup>16</sup> The films generated vary from colorless through yellow, iridescent, to brown depending on the film weight. The heaviest films, which are brown in appearance, are used when no further protection is to be applied. However coatings applied as a pretreatment for painting are normally yellow. Usual practice is to apply primer paint within 16 h of filming. A number of commercial treatments are available, which are approved to various aerospace and defense standards employed by the aerospace industry.

As indicated in **Figure 1**, the main protective treatment applied to airframe aluminum alloys is a chromate pigmented primer. In most instances, this will be a two-component epoxy paint but polyurethane primers are also used. One of the functions of the primer is to act as reservoir of strontium chromate corrosion inhibitor, which will be leached from the paint when the surface comes into contact with moisture. The presence of the inhibitor prevents corrosion from occurring at areas where the paint film has become damaged and the aluminum alloy is exposed. Laboratory experiments indicate that the amount of chromate leached out of the primer is well above the minimum concentration required to inhibit corrosion.<sup>15</sup> Primers used for aerospace applications are required to meet various performance criteria such as adhesion, resistance to fluids, corrosion, drying times, etc. For detailed information, specifications such as BS 2X33<sup>17</sup> or the equivalent European EN or US Military Standards should be consulted.

Epoxy primers have been employed on both civil and military aircraft for many years. Developments in the mid 1980s were concerned with improving the adhesion and fluid resistance of the standard primer. This was mainly in response to corrosion problems occurring on civil transport aircraft. Leakage of hydraulic fluids led to the degradation of the standard protective coatings and the eventual corrosion attack of the underlying aluminum alloy substrate. New generation primers were developed by leading aircraft paint manufacturers, which, in addition to giving improved resistance to aircraft fluids, gave better adhesion. Both types of primer are covered by standards such as BS 2X33. Normally the primers will be applied to components by spraying and this may be followed by a baking treatment.

Recent developments in primers have focused on reducing the level of solvents released. The primers originally used typically had a volatile organic

compound (VOC) emission level of  $600 \text{ g l}^{-1}$ . Within the European Union, legislation was introduced in the 1990s reducing the permissible levels of VOC in aircraft paints. For epoxy primers the level was set at  $350 \text{ g l}^{-1}$ . High solid primers are now available, which meet these requirements and have been applied to UK military aircraft.

The other area of concern is the formulation of chromate-free conversion coatings, anodizing treatments and primers. Chromates together with other hexavalent chromium compounds have been identified as carcinogens and the use of chromates in aerospace surface treatments and coatings is likely to be prohibited in the future. Several alternative treatments are available commercially but their use so far has been restricted to exterior surfaces on aircraft operating in benign environments. Progress towards chromate-free treatments includes the development of modified sulfuric acid anodizing processes, such as boric-sulfuric anodizing<sup>18</sup>; conversion coatings formulated using cerium salts, zirconates, vanadates, and molybdates; pretreatments based on sol-gel technology<sup>19</sup> and appliques<sup>20</sup> as potential replacements for conventional paint finishes. Several paint primer standards have been published covering chromate-free systems, which specify a range of corrosion performance requirements that will need to be fulfilled.

#### Aluminum coatings and cladding

In addition to chromate-based protective treatments, aluminum coatings are used for the protection airframe aluminum alloys. The coating may be applied by a physical vapor deposition (PVD) process or may take the form of a thin clad layer applied in the manufacture of the alloy. PVD aluminum coatings have sometimes been used to protect fatigue critical components.

Normal cleaning treatments such as chromic/sulfuric acid etching, and anodizing and chemical conversion pretreatments, often cause a reduction in fatigue strength, which may be as large as 10%. With PVD aluminum coatings, the surface is sputter cleaned prior to deposition and the loss in fatigue strength is small. Typically the aluminum coating is  $12\text{--}25 \mu\text{m}$  thick.

Clad sheet aerospace aluminum alloys are commercially available and find applications mainly in the construction of civil aircraft. The cladding is applied during the manufacture of the alloy and consists of a thin sheet of aluminum on either side of the alloy (see [Figure 2](#)). Typically the thickness of the cladding on each side is 5% of the total sheet thickness. For 2000 series aluminum-copper alloys, a commercially pure aluminum cladding is used while for 7000 series aluminum-zinc-magnesium alloys a aluminum-zinc cladding is employed. The cladding is corrosion resistant and isolates the alloy from the environment. Additionally, the cladding provides sacrificial protection if the underlying alloy becomes exposed as a result of surface damage. Clad alloys have lower strengths than the equivalent unclad material and are less resistant to fatigue damage. As a result, they tend not to be selected for use on military aircraft. Depending on the operating environment, parts made from clad materials may be further protected using the standard scheme outlined earlier.

#### 4.38.2.3.3 Steels

For most applications, passivated cadmium plating is the preferred protective treatment for high-strength and corrosion-resistant steels. [Figure 3](#) shows schematically the protective coating applied to steel parts.

Cadmium plating offers a unique range of physical and mechanical properties, which are so far unmatched

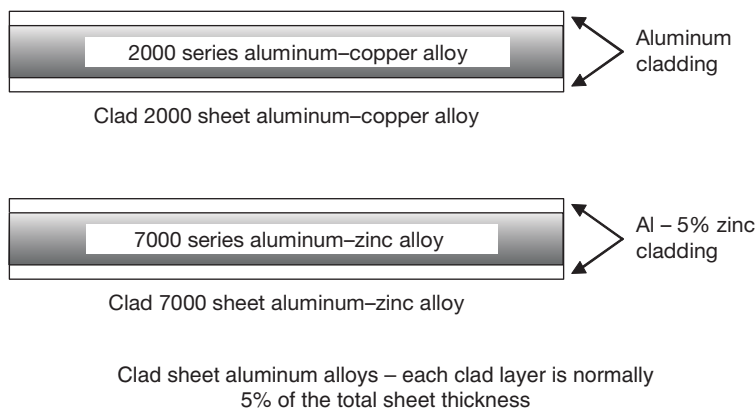


**Figure 2** Structures of clad 2000 and 7000 series sheet aerospace aluminum alloys.

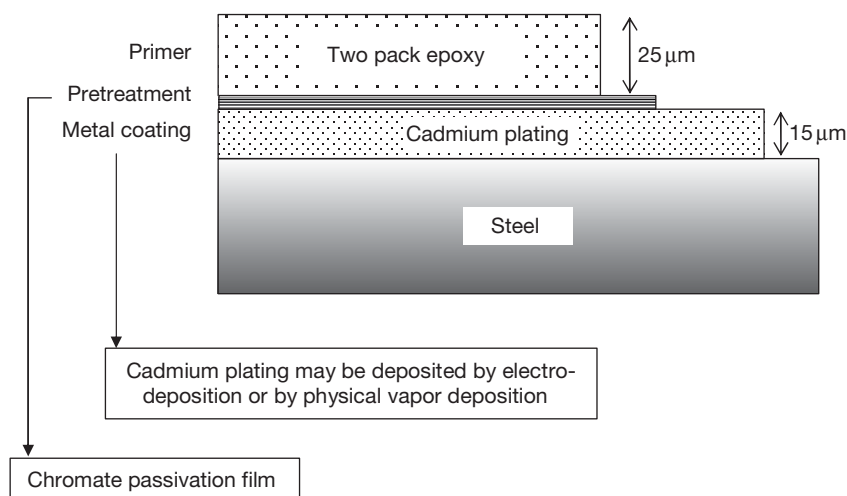


**Figure 3** Standard protective treatment applied to steel components.

by other protective treatments. Cadmium provides a sacrificial coating that is galvanically compatible with aerospace aluminum alloys and has a high lubricity. The latter is an important property when the coating is used on fasteners or threaded parts.

The coating is normally applied by electrodeposition from a cyanide-based plating bath, which permits dense uniform coatings to be deposited on to complex surfaces with threaded areas, recesses, etc. The thickness of cadmium required is dependent on application. Defence Standard 03-19<sup>21</sup> proposes that for normal requirements on noncorrosion resisting steels a minimum average thickness of  $14\text{ }\mu\text{m}$  should be employed, while for threaded items a minimum average thickness in the range  $4\text{--}7.5\text{ }\mu\text{m}$  depending on the nominal average thread diameter is necessary.

Like most electrodeposition processes, cadmium plating is less than 100% efficient and significant levels of hydrogen may be generated. As discussed earlier, high-strength steels are susceptible to hydrogen embrittlement and the susceptibility increases with increasing UTS. Following plating, a de-embrittlement baking treatment is conducted, which reduces the level of hydrogen.

For processing purposes, high-strength steels may be divided into four strength categories as follows:

- Category 1 up to 1100 MPa
- Category 2 1101–1450 MPa
- Category 3 1451–1800 MPa
- Category 4 1801 MPa and greater

Steels falling into the category 1 are not considered to be susceptible to HE and a baking treatment

is not regarded as necessary. For steels in category 2, a minimum post plating treatment of 8 h at  $190\text{--}230\text{ }^{\circ}\text{C}$  is employed. For categories 3 and 4, the minimum baking times are increased to 18 and 24 h respectively. In addition to determining the baking conditions, the range and types of cleaning treatments, which may be carried out prior to plating, are dependent on the strength category. As the UTS of the steel increases, processes that may generate hydrogen should be avoided.

For steels with category 3 or 4 strengths some constructors prefer to use cadmium plating prepared by PVD. This is a nonaqueous process involving the deposition of cadmium by evaporation within a vacuum chamber.

After plating, a chromate passivation treatment is applied to improve the corrosion resistance of the cadmium and to act as a pre-treatment for subsequent painting. The process is carried out by immersing the part in a bath containing a sodium dichromate/sulfuric acid solution to produce a yellow film. Fasteners are used in the plated and passivated condition while components are normally primed before assembly.

In situations where parts may become heated to temperatures above  $230\text{ }^{\circ}\text{C}$ , zinc plating may be used rather than cadmium plating. Areas that are difficult to electroplate, for example, the internal bore of a tube, are sometimes phosphated rather than plated.

The main problem with cadmium plating is the toxic nature of cadmium compounds, which can cause fetal damage as well as damage to the kidneys, lungs, and liver. Legislation banning the use of



**Table 8** Possible alternatives to cadmium plating

Coating type	Coating composition	Method of application	Major limitations
Aluminum based	Aluminum	Physical vapor deposition	Plating in recesses/holes may be difficult Limited commercial availability
	Aluminum	Electrodeposition from an organic bath	
Zinc based	Aluminum–manganese	Electrodeposition from molten salt bath	Not generally available
	Zinc–nickel (low)	Electrodeposition	Commercially available
	Zinc–nickel (high)	Electrodeposition	Post plating treatments such as hydrogen de-embrittlement and passivation required.
	Zinc–cobalt	Electrodeposition	Limited coating lubricity
Metallic–ceramic	Zinc–cobalt–iron	Electrodeposition	Tend to be thick coatings – generally unsuitable for fasteners
	Al and Zn flakes in an inorganic matrix	Electrostatic spraying, dipping or spin coating	
Manganese based	Manganese alloys	Electrodeposited	Limited availability commercially – mainly laboratory processes. Low bath efficiencies

cadmium plating for many engineering applications was introduced within the European Union some years ago but its use on aircraft components is still permitted. Continuing concerns about the harmful effects of cadmium has led to a number of studies aimed at identifying possible replacements. While it is unlikely that a single replacement coating will be found, a number of coatings are available commercially that could be used as alternatives to cadmium plating for specific applications. **Table 8** details the range of coatings that have been considered together with some of their limitations.

The coatings fall into four groups, all of which provide a level of sacrificial protection. The aluminum- and zinc-based coatings are normally given a passivation treatment after plating to improve the corrosion resistance. These tend to be chromate solutions but some nonchromate treatments are now becoming available. The metallic–ceramic coatings group covers several commercially available types consisting of an inorganic matrix incorporating aluminum or zinc flakes or powders. The feasibility of electrodepositing manganese alloy coatings was demonstrated more than 60 years ago, but it is only relatively recently that their use as alternatives to cadmium plating has been investigated. In some instances, the alternative coatings are thicker than the cadmium plating in order to achieve the same level of protection.

The results of a number of major programs examining alternatives to cadmium plating for aerospace applications are available in the literature.<sup>22–24</sup> In addition to the corrosion aspects of alternative coatings, other important properties such as lubricity,

torque–tension behavior, hydrogen embrittlement, effects on fatigue, paint adhesion, and coating repair have been investigated. Depending on the particular application, some of these aspects must be taken into account when selecting an alternative coating system. Some general guidance on cadmium replacements can be found elsewhere.<sup>25</sup>

#### 4.38.2.3.4 Magnesium alloys

The normal approach adopted for the protection of parts made from magnesium alloys is to isolate the component from the environment through the use of a barrier coating. The standard protection scheme consists of a nonpigmented epoxy resin as indicated in **Figure 4(a)**. The part to be protected is first cleaned to remove all traces of contamination. The cleaning processes employed include solvent and vapor degreasing, mild alkaline treatments, and various acid pickles. Fluoride anodizing is also employed as a cleaning treatment. The part is anodized in an ammonium bifluoride solution using alternating current to produce an anodic film. This is removed by immersing the part in chromic acid to leave a surface free of contamination.

Prior to carrying out the sealing treatment, a chromate filming treatment is applied to the component to improve the corrosion resistance and promote the adhesion of the epoxy resin. Generally, a thick layer of resin is applied by dipping the component which has been preheated to around 200 °C into a bath maintained at 60 °C containing the resin solution. After removal from the bath, the resin is stored at 180 °C for 45 min. The process is repeated three times to build up a resin thickness of about 25 µm.

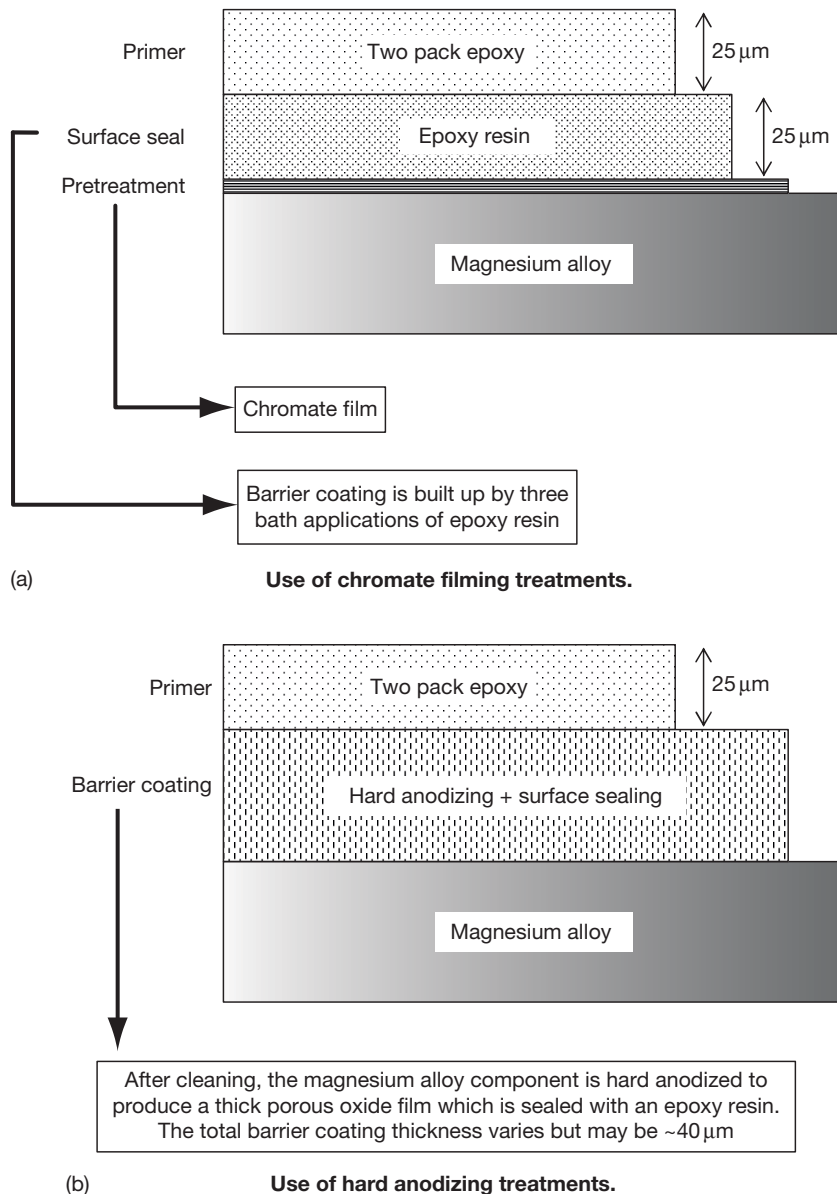


**Figure 4** Examples of protective treatments applied to magnesium alloy components.

As indicated in [Figure 4](#), two pack epoxy primer paint is applied to the part before assembly.

Several new protective processes have been introduced using anodizing treatments, an example of which is given in [Figure 4\(b\)](#). These have been adopted by several manufacturers for the protection of gearbox housings. The anodizing treatments generate films which are up to  $40\ \mu\text{m}$  thick and which may be subsequently surface sealed.

Other protective treatments, which either have been used or are being considered for magnesium

alloy parts, include metallic–ceramic coatings and thick hard anodic films formed by high voltage anodizing.

#### 4.38.2.3.5 *Titanium alloys*

As previously stated, titanium alloys have a high resistance to corrosion in the presence of moisture and most of the contaminants found within the aircraft structure. If used in isolation, titanium alloy parts require only the minimum in terms of corrosion protection. This could be a single coat of primer

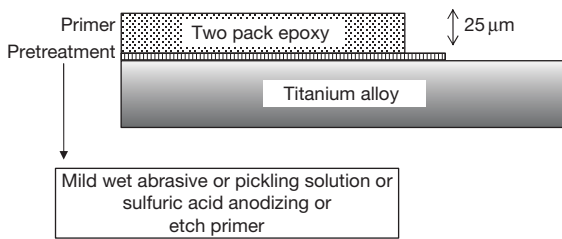


**Figure 5** Protective treatments that may be applied to titanium alloy components.

applied to the surface of the component as indicated in [Figure 5](#).

To promote paint adhesion, the surface would normally be cleaned using a mild wet abrasive treatment or a pickling solution. Etch primers and anodizing treatments are also sometimes used. The main problem with titanium-based alloys arises when contact is made with other metals and precautions must be taken to reduce the risk of galvanic corrosion. Zinc plating or zinc shims are often employed for this purpose when contact has to be made with magnesium alloy parts.

#### 4.38.2.3.6 Composite materials

Composite materials used in the manufacture of airframe parts and panels do not suffer corrosion degradation but items made from plastics reinforced with carbon fiber may have an adverse effect on the corrosion of some metal parts with which they are in direct contact. Measures that should be taken to minimize this risk are described in [Section 4.38.2.4](#) dealing with the design and assembly aspects of corrosion management.

Where a part made from composite materials is being used internally, surfaces may be left untreated. Where the part forms part of the external surface of the aircraft, a suitable pretreatment is applied followed by a paint scheme consisting of a primer and top coat. As a pretreatment, mechanical scuffing followed by degreasing is adequate if an epoxy primer is to be used. Since the paint is not providing corrosion protection to the composite substrate a chromate-free epoxy primer or epoxy filler may be employed.

#### 4.38.2.3.7 Wear and fretting resistant coatings

In locations where there may be some movement or rubbing between parts it is often necessary to use a coating or surface treatment to minimize the risk of fretting or wear developing. Examples include landing gear components and flight control actuators.

Electroless nickel and hard chromium coatings are often employed for this purpose particularly on steel parts and hard anodizing is sometimes used on aluminum alloys. Specialized treatments such as ion implantation and high voltage anodizing are also available and are beginning to find applications on airframe parts. Metal coatings such as electroless nickel and hard chromium plating while primarily used to reduce wear or fretting do provide some level of corrosion protection. The coatings act purely as a barrier layer, which isolates the substrate from the environment. Generally, these coatings are much thicker than cadmium, aluminum, and zinc plating, but provide no sacrificial protection once the substrate is exposed. Developments in wear resistant coatings have mainly been concerned with the incorporation of fine ceramic particles into electrodeposited coatings and the deposition of hard metal sprayed coatings. To some extent this has been driven by the need to replace hard chromium and eventually nickel coatings with environmentally compliant treatments. Sartwell *et al.*<sup>26</sup> describes recent research assessing the use of HVOF thermal spray coatings on landing gear.

#### 4.38.2.4 Design Considerations

Careful design of the airframe to prevent the buildup and ingress of moisture and other corrosive agents into the structure will prevent the development of several potentially damaging and expensive corrosion problems. This can be achieved through the use of drain holes or filler materials in areas where moisture could collect. Sealing joints will also greatly reduce the risk of both crevice and dissimilar metal corrosion. [Table 9](#) lists some of the potential corrosion problem areas and the design approach to reducing the risk.

In the case of dissimilar metal contacts, guidance material is available from several sources, including PD 6484:1979<sup>27</sup> and US Military Standard,<sup>28</sup> enabling potential problem areas to be identified. The corrosion between different metal couples is rated by the degree to which the corrosion of one metal is increased by contact with a second. For example, if a titanium alloy is in contact with an aluminum alloy, the corrosion of the titanium alloy is not increased but the corrosion of the aluminum alloy is markedly increased.

[Table 10](#) details some of the dissimilar metal contacts that are likely to cause corrosion problems and gives examples of procedures, which may be employed to minimize the risk. In the examples given, there is a marked increase in the corrosion

rate of the more active material due to the large difference in corrosion potential between the two metals. In order to reduce the risk of corrosion occurring, parts are protected and assembled to prevent metal-to-metal contact.

Experience has shown that many of the corrosion problems found in-service are often in internal areas that are difficult to inspect. Access for examination is an important design consideration, which will reduce inspection times and costs.

**Table 9** Examples of potential corrosion problems and possible design solutions

<i>Potential problem</i>	<i>Design solutions</i>
Crevices	Static joints should be sealed to eliminate crevices – May be achieved by the use of wet assembly
Dissimilar metal contacts	Metal coatings, shims, wet assembly to reduce differences in galvanic potential and electrically isolate parts
Water traps	Incorporation of a drainage scheme to prevent the accumulation of fluids. Consideration of the inclusion of drain holes and the use of inert fillers
Leakage from galleys and toilet areas.	Use of non-metals, drain paths, sealed floor coverings

#### 4.38.2.5 Final Assembly and Finishes

As discussed in [Section 4.38.2.3](#), it is normal practice to apply an appropriate protective treatment to all parts prior to assembly. Where necessary, additional procedures will be carried out to reduce the risk of dissimilar metal corrosion as outlined in [Section 4.38.2.4](#). In general, wet assembly methods will be employed to prevent the ingress of moisture at joints and prevent the occurrence of crevice and dissimilar metal corrosion. As indicated, certain areas within the fuselage, wings, undercarriage bay, and tail plane may be especially prone to the collection of aircraft fluids, leakage from galleys and toilets or to the build up of moisture and corrosive contaminants. These areas will require additional protection during assembly such as a further epoxy primer coat or a finish coat. One approach described by Voss<sup>29</sup> is to divide the aircraft structure into zones. In the example given, a military fast jet, three zones were identified as follows:

- Zone A – Interior surfaces, not to be subjected to permanent condensation
- Zone B – External and internal surfaces, to be exposed to wet condensation
- Zone C – Fuel wetted surfaces

For areas falling into the Zone A classification further protection is not necessary. For Zone B, some additional protection is applied, for example,

**Table 10** Corrosion at dissimilar metal contacts and assembly procedures to be employed

<i>Contact</i>	<i>Corrosion</i>	<i>Protective treatment</i>	<i>Assembly</i>
Corrosion resisting steel coupled with Aluminum alloy	No increase in corrosion rate Corrosion rate may be markedly increased	Cadmium plating + Painting (optional) Pre-treatment + primer	Wet assembly
Corrosion resisting steel coupled with Magnesium alloy	No increase in corrosion rate Corrosion rate markedly increased	Cadmium plating + painting Full protective scheme	Wet assembly
Titanium alloy coupled with Magnesium alloy	No increase in corrosion rate Corrosion rate markedly increased	Zinc or aluminium coating + painting Full protective scheme	Wet assembly
Titanium alloy coupled with Aluminum alloy	No increase in corrosion rate Corrosion rate markedly increased	Painting or aluminium coating Pretreatment + primer	Wet assembly
Titanium alloy coupled with High strength steel	No increase in corrosion rate Corrosion rate markedly increased	None required Coated with Al, Al rich coating or cadmium	Wet assembly
Carbon fiber reinforced composite coupled with Aluminum alloy	No corrosion Large increase in corrosion rate	Pretreatment + primer Standard protective scheme	Adhesive bonding or wet assembly

a polyurethane finish coat while in areas such as fuel tanks (Zone C) special sealants and paint schemes need to be employed. If there is a risk of microbial corrosion occurring, the use of paints containing a biocide might be considered.

The normal finish coat employed is a two pack polyurethane paint. Polyurethane finishes have been available for aerospace applications for many years and continue to be widely used on both civil and military aircraft. As indicated in [Section 4.38.1.2](#), one of the main sites for corrosion initiation is around fasteners on external surfaces where the development of cracks in the paint film allows the ingress of moisture. One of the important advances in polyurethane finishes has been the formulation of paints with increased flexibility, which are less prone to cracking. Current specifications for polyurethane finishes<sup>30</sup> identify two types of materials one intended for interior and exterior use where the maximum resistance to fluid attack is required and one intended for exterior use where increased tolerance to flexing is needed.

Acrylic finishes were used on some military aircraft for a number of years. They were introduced in the 1970s partly to fulfill a requirement for a paint scheme, which could be more readily removed than polyurethane finishes. The latter are highly resistant to fluids and very aggressive paint strippers must be employed to remove the polyurethane finish. The life of the acrylic finishes is relatively short (2 years) compared with polyurethane schemes (5 years) and the trend has been to phase them out in favor of polyurethane finishes.

The external painting of an aircraft is not solely for corrosion protection purposes. On military aircraft, the finish coat is used for camouflage purposes while on civil aircraft it is used to identify the airline or operator. On large transport aircraft, the paint applied to the external surfaces makes a significant contribution to the overall weight, which in turn will have an impact on fuel costs, passenger numbers, etc. Boeing<sup>31</sup> estimate for a 747-400 the weight of the paint applied to the fuselage and tail is approximately 252 kg. Some airlines have preferred to operate aircraft with polished rather than painted skins. In these cases, clad aluminum alloys are used for the skinning and the surface is treated with a clear conversion coating. Boeing has calculated that the fuel cost savings are offset by the higher costs of washing and polishing unpainted aircraft.

On some areas of the aircraft, specialized finishes may be employed. These include walkways, high temperature areas around engines and radome surfaces. For further information on these finishes,

national and international specifications as well as manufacturer data sheets should be consulted.

### **4.38.3 Corrosion Management In-Service**

#### **4.38.3.1 Introduction**

During the manufacture of an aircraft, the procedures broadly outlined in [Section 4.38.2](#) are applied to produce a structure that is resistant to corrosion degradation. The approach is based on the selection of materials with a good resistance to corrosion, the application of protective treatments to individual components, and careful design to avoid potential corrosion problems. The airframe is wet assembled using sealants, jointing compounds, etc. to prevent moisture ingress into joints and other parts of the structure. External surfaces and internal areas, likely to suffer high levels of moisture build up or leakage of aircraft fluids, are given further protection by painting with a primer or a finish coat. In-service protective treatments can become degraded or damaged; drain-holes and drainage systems may be blocked and changes in operational role and life extensions can subject the airframe to environments for which it is not adequately protected. Corrosion management in-service is therefore concerned with maintaining the integrity of the aircraft throughout its operational life. It includes the cleaning and washing of exterior surfaces to remove harmful contaminants, inspecting for early signs of corrosion, corrosion rectification, the application of supplementary protective coatings, and the repainting of aircraft.

#### **4.38.3.2 Aircraft Washing and Cleaning**

Lewin<sup>32</sup> has described in some detail the way in which corrosive contaminants may build up on the surface of aircraft in-service. For example, during normal maneuvering on the ground, the exterior surfaces of aircraft may become covered with dust and salt, which may mix with moisture to form a clay-like structure, which adheres to the aircraft exterior. In-flight Lewin suggests that electrostatic forces generated will cause light dust to be deposited on aircraft skins. In addition engine contaminants such as oils, fluids, and carbonaceous films form on surfaces. If these contaminants are not removed from the aircraft surface, they will contribute to the eventual breakdown of the protective coatings and corrosion of the airframe.

Freshwater rinsing is often used on military to reduce levels of chloride and other contaminants



present following maritime operations. Land-based aircraft may taxi through dedicated spray units on landing to remove surface salt.

Aircraft cleaning is generally carried out by first flushing exterior surfaces with water to remove loose dirt or other residues. The cleaning solution is sprayed on to an area of the aircraft and soft brushes may be used to remove surface contaminants. The area is then rinsed with fresh water and a new area cleaned. At the end of the cleaning operation, the whole aircraft is rinsed with water and dried off. Various types of cleaners approved for aerospace applications are available commercially. National standards identify different types of cleaners designed to remove different levels of contamination. Part of the approval process involves subjecting the cleaners to different corrosion tests to ensure that they will not cause damage to the airframe and engine materials.

#### 4.38.3.3 Inspection for Corrosion

The early detection of corrosion remains a major priority for the in-service management of corrosion. At present, much reliance is still placed on visual inspection, often with hand lenses, looking for evidence of paint blistering, paint cracking, and filiform corrosion, particularly around fasteners. For internal areas where access is difficult, mirrors and endoscopes may be employed to facilitate the visual inspection. In some instances, the paint is removed from structurally critical areas to allow the metal substrate to be examined more thoroughly.

Many of the areas on an aircraft are difficult to inspect visually without dismantling parts of the airframe structure. The early stages in the development of corrosion and fatigue in fuselage lap joints present on many older transport and military aircraft, for example, are almost impossible to detect visually. To that end, nondestructive evaluation (NDE) techniques employing ultrasonics, eddy current measurements, radiography, and thermography are being employed to search for the evidence for the onset of corrosion and fatigue damage. NDE techniques are also used to assess the extent of the corrosion damage on hidden surfaces and to determine the depth of corrosion and the remaining wall thickness. This information is crucial in deciding the manner in which specific corrosion problems should be managed. Much research into developing improved NDE techniques for the early detection of corrosion is in progress.

The frequency and level of inspection undertaken vary according to the aircraft type and examples for

civil transport aircraft are given elsewhere.<sup>33,34</sup> On a daily basis, areas would be examined for evidence of fuel leaks, cracking, surface damage, etc. Every 4 or 5 days, a more detailed visual inspection would be carried out of the interior and exterior surfaces and at longer intervals (typically 30 days) access panels may be removed to allow inspection of specific areas. Inspections employing NDE techniques are generally carried out at 12–18 month intervals, and every 3–5 years major checks involving removal of interior panels are conducted to allow careful examination of structural parts for signs of corrosion and cracking.

#### 4.38.3.4 Corrosion Rectification

##### 4.38.3.4.1 Corrosion removal

At present aircraft operators adopt a ‘find-and-fix’ approach to airframe corrosion. Often corrosion and fatigue damage are found during the scheduled maintenance of the aircraft. The occurrence of damage in a particular location may necessitate a fleet-wide inspection for similar damage on other aircraft.

With the find-and-fix approach a repair scheme is implemented, as soon as practical. The extent and depth of the corrosion that is found will determine whether a repair can be made, whether components must be replaced, and the time-scale in which they must be carried out. For aerospace structures, three levels of corrosion have been specified and are detailed elsewhere.<sup>35</sup> Level 1, for example, refers to relatively minor corrosion damage found between inspection periods that may be blended out within the limits specified by the manufacturer. Level 2 is concerned with corrosion that requires work or blending out which exceeds the manufacturer’s limits, while level 3 corrosion is sufficiently serious that there are urgent airworthiness implications.

For corrosion damage falling within ‘Level 1,’ repair often involves the blending away of corrosion damage, probably using a combination of mechanical and chemical methods, and then applying a protective coating to the blended area. Typically the allowable limits are 10% of the thickness for wing and fuselage skins. Mechanical methods commonly employed include rubbing with metal wool, abrasive pads or small abrasive wheels, and abrasive blasting with glass beads or alumina grit. Portable abrasive blasting units are available, which allow corrosion removal to be carried out *in situ*. The units recycle the spent abrasive and separate out the corrosion products.

When the corrosion found exceeds the allowable limits (Level 2), it may be necessary to replace

components or carry out a structural repair. For corrosion damage identified as 'Level 3,' other similar aircraft in the operator's fleet would be inspected and the findings reported to the appropriate regulatory authority.

Problems may arise when corrosion occurs on areas that have already been blended and reprotected. This may result in the total depth of corrosion exceeding the allowable limits set by the manufacturer.

#### 4.38.3.4.2 Reprotection

Once the corrosion has been blended out, the metal surface is reprotected using a suitable protective scheme. Often it is not possible to apply the original scheme, but rather a modified treatment. [Table 11](#) gives examples of repair schemes that are employed to various substrates.

For aluminum alloys it is normal to use a conversion coating as a pretreatment for painting. The use of etch primers for the repainting of the air intake of an aircraft following paint stripping and removal of the corrosion damage has been described.<sup>36</sup> In this instance, an etch primer was chosen as the pretreatment rather than the normal chromate conversion coating. The choice was made to avoid the need to deoxidize the surface and water rinse the intake before and after the application of the conversion coating. There was concern that aggressive solutions could have been washed into the internal structure of the aircraft.

Small areas of damage on cadmium plated steel parts may be repaired after removal of corrosion products using an approved paint scheme. Brush plating techniques allow the localized repair of small areas of damaged coatings such as zinc, nickel, and cadmium electroplating. The process depends on the establishment of a plating cell between an anode (usually a graphite rod) wrapped in an absorbent material saturated with electroplating solution, and the damaged area, which is the cathode. During plating, the anode is rapidly moved backwards and forwards over the damaged area in order to build up a

uniform deposit. Often brush plating may be carried out *in situ* greatly reducing the cost of corrosion rectification. One aerospace application has been the repair of damaged cadmium plating on landing gear components. High-efficiency solutions are available, which greatly reduce the risk of hydrogen evolution and absorption. After plating the cadmium plating is passivated and then painted with an appropriate paint scheme. The repair of cadmium replacement coatings such as electroplated zinc alloy and PVD aluminum is an area that is currently being studied.

As described in [Section 4.38.2.3.4](#), the protection of magnesium alloy components involves a series of complex cleaning and coating procedures. When extensive corrosion is found, the component must be removed from the aircraft and where possible disassembled. After cleaning using some form of abrasive blasting to remove corrosion products and degraded resin, the magnesium parts are reprotected using the schemes outlined in [Section 4.38.2.3.4](#). If the corrosion found is limited to a few small areas, it may be possible to repair *in situ*. This involves removing any damage mechanically, and then cleaning chemically using an acid chromate solution. The area is then repainted with a primer and top coat. More detailed information on procedures that should be undertaken is given in national and international standards.

The protective finishes applied to the top and lower wing skins play an important role in preventing the initiation of localized corrosion within fastener countersinks and in fastener holes. As discussed in [Section 4.38.2.5](#), epoxy primers and polyurethane finishes with improved flexibility are available, which reduce the occurrence of cracking around fasteners and prevent the ingress of moisture. In some instances these coatings have not been found to give adequate protection, and alternative protective schemes using self curing polysulfide elastomeric coatings have been employed. These may be used directly as a primer or

**Table 11** Examples of protective schemes used in the repair of damaged coatings

Substrate	Original protective treatment	Repair schemes
Aluminum alloys	Chromic acid anodizing or chromate conversion coating + epoxy primer (+finish coat)	Swab applied conversion coating + coat of primer paint (+finish coat) Etch primer + coat of primer paint (+finish coat)
Steels	Cadmium plating + passivation treatment + primer + finish coat	<i>In situ</i> repair using low HE cadmium brush plating + passivation and paint scheme
Magnesium alloys	Pretreatment + barrier coating + paint scheme	Etch primer + 2 coats of primer + finish coat

alternatively may be applied over a conventional epoxy primer. The elastomeric coatings are typically 150–250  $\mu\text{m}$  equivalent to a coating weight of 270  $\text{g m}^{-2}$  compared with a weight of 70  $\text{g m}^{-2}$  for standard schemes. For this reason the coatings are used selectively, for example, along fastener runs, rather than over the whole surface to minimize the weight penalty. After applying the polysulfide coating the surface is painted with a flexible polyurethane finish.

#### 4.38.3.5 Use of Supplementary Protection

The corrosion repair of internal areas may prove a much greater challenge requiring parts of the structure to be broken down to permit access for rectification to be carried out. In such cases, it may be possible to control the corrosion by applying a supplementary protective coating. These function by forming a barrier layer, which separates the substrate from the immediate environment. Several types are available commercially, which may be used on aircraft structures. These may be applied by brushing or spraying. Some of the products have water displacing properties, which leave a thin oily film after the solvent has evaporated, while other products must be applied to dry surfaces and produce a wax-like coating. At best supplementary protection will prevent the further spread of corrosion and may enable rectification work to be delayed to a time when the aircraft is undergoing major servicing.

#### 4.38.3.6 Paint Removal and Repainting

The polyurethane finishes that are widely employed on the external surfaces of civil and military aircraft are highly resistant to fluids and are generally effective for up to 5 years. In-service, the paint films are subjected to large fluctuations in temperature, exposure to high levels of UV radiation, flexing during flight, and exposure to aggressive environments, leading to the crazing, cracking, and degradation of external paint schemes. For many years, the polyurethane paint schemes could only be removed for repainting or inspection purposes by using aggressive chemical paint strippers many of which were based on methylene chloride with a phenol additive. These materials are extremely hazardous to use, posing many health and safety issues.

Mechanical methods of paint removal such as plastic media stripping (PMS) are now extensively used. In the PMS process, small plastic beads are impacted onto the painted surface causing the paint

film to crack and flake off from the substrate. Commercially available equipment allows the plastic beads to be blasted at the work surface at a controlled velocity and to recycle spent beads removing dust and paint particles. Some operators and maintenance organizations have installed facilities that allow small components as well as complete aircraft to be stripped. There are some limitations in place regarding use of PMS on thin metal sheet, clad alloys, and composite materials. Other blasting media such as dry ice and wheat starch have been evaluated. There is also interest in laser techniques, possibly for removing paint in around fasteners.

Another approach employed to simplify paint removal has been the use of selectively removable paint schemes. These permit the polyurethane top coat to be removed while leaving the primer intact. The schemes use 8–12  $\mu\text{m}$ -thick intermediate coats, which are painted over the epoxy primer. The polyurethane finish is then applied to the intermediate coat. A comparatively simple paint stripper may be used to remove the finish and intermediate coats, but leave the primer intact. The use of such schemes on commercial aircraft has been described.<sup>37</sup> Aerospace paint standards have been issued covering both the intermediate coating<sup>38</sup> and the paint remover.<sup>39</sup>

#### 4.38.3.7 Dehumidification

The corrosion found on an aircraft occurs mainly when it is parked on the ground or sitting in a hangar. Aircraft operated by the civil airlines spend a high percentage of their time flying, while many military aircraft are designed with a low number of flying hours but are required to remain operational for many years. In addition, many military airfields are very close to the coast and at these locations the atmosphere may be very corrosive.

The rates of corrosion of many airframe alloys exposed to the atmosphere are dependant on the relative humidity (RH), that is, the amount of moisture present in the air. There is often a critical RH typically  $\sim 50\%$  above which the rate of corrosion increases rapidly with increasing RH. Below this critical RH, the corrosion rate is low and diminishes to an insignificant level when the RH is reduced to 10% or less. To reduce the risk of corrosion, dry air dehumidification has been employed to lower the humidity within the aircraft to less than 10% RH. Examples are given in the literature of both complete and partial dehumidification being employed in the management of military aircraft.<sup>40,41</sup> In some

instances, localized dehumidification has been used to reduce the risk of corrosion in areas where electronic equipment is housed, on turbines, and parts of the airframe especially susceptible to corrosion. Whole aircraft dehumidification using dedicated shelters has now become a regular procedure for maintaining both fixed wing aircraft and helicopters.

#### 4.38.3.8 Future Trends in Aircraft Corrosion Management

In-service aircraft structures are subjected to both fatigue and corrosion degradation. While the damage due to fatigue is primarily a function of the number of flights and the number of flying hours, corrosion is more closely related to the physical age of the aircraft. Many of the protection schemes applied to the internal areas of the fuselage and wings when the aircraft was built cannot be renewed without carrying out major dismantling of the airframe structure. Primer paints, for example, applied during the initial build are expected to provide corrosion protection throughout the life of the aircraft. Often these will become damaged or degraded due to the leakage of aircraft fluids or the build up of condensation and moisture. As the operational life of the aircraft is extended, the probability of corrosion developing is greatly increased.

Many of the aircraft currently in-service have exceeded their design operational life. This applies to both military and civil aircraft. Statistics published in 2000<sup>42</sup> indicated that more than 2500 commercial aircraft in the United States were flying beyond their 20-year design life. Figures published by the US Federal Aviation Authority suggested that 7% of the aircraft, which would be covered by the proposed Aging Airplane Safety regulation, are more than 40 years old. As the operational life of an aircraft is extended, there are increased maintenance costs. For example, statistics published for USAF aircraft<sup>43</sup> show that the total cost of corrosion rose from \$926 million in 1990 to \$1518 million in 2004 despite a reduction in fleet size.

The present find-and-fix approach to aircraft corrosion management is expensive both in terms of cost and the time aircraft are taken out of service. Two organizations, the United States Air Force and the Australian Department of Defence, have proposed changing from the find-and-fix approach<sup>44,45</sup> to a more structured method of managing corrosion. The alternative approaches, described as 'anticipate-and-manage' by USAF<sup>44</sup> and 'identify-and-manage' by the Australian DoD,<sup>45</sup> have similar aims of

lowering maintenance costs and reducing aircraft nonavailability times. These aims may be achieved by rescheduling corrosion rectification work where possible so that it is carried out during normal servicing and maintenance periods.

To implement the new approaches to corrosion management, a number of areas have been identified where improvements in current technology are required. These include more sensitive methods for detecting corrosion, the development of a better understanding of the impact of corrosion on structural integrity, and more effective supplementary protective materials to halt the spread of corrosion.

To detect the early stages of corrosion, improved NDE methods are required together with corrosion sensors to locate the onset of corrosion in 'difficult-to-inspect' areas. It has been proposed that sensors should be installed in potential corrosion problem areas within an aircraft during its manufacture. These would permit the first signs of corrosion to be detected and its progress to be monitored. In parallel with improved detection, there is a need for accurate, reliable models for predicting the long-term effects of corrosion on fatigue and static strength. These would allow decisions to be made concerning the scheduling of inspections and corrosion rectification. The application of better supplementary protection would further allow work to be delayed until programmed maintenance periods.

The new approaches to aircraft corrosion management are aimed at lowering the cost of ownership by reducing the time spent on unscheduled maintenance.

## References

1. Wallace, W.; Hoepfner, D. W.; Kandachar, P. V. *AGARD Corrosion Handbook, Vol. 1: Aircraft Corrosion: Causes and Case Histories*; AGARD NATO, Neuilly-Sur-Seine: France, 1985; AGARD-AG-278, Vol. 1.
2. Mitchell, R. G. *Corros. Prevent. Control* **1981**, 11–17.
3. Kohler, R.; Scott, J. *The corrosion properties of airframe contaminants*, D. Mat Report No. 179; Ministry of Defence (PE) Directorate of Materials R & D (Aviation), 1971.
4. Bowden, D. Attack of the fungi, *Flight Safety Australia* Sept–Oct 2005, pp 50–51.
5. Akdeniz, A. *Aircraft Eng. Aerospace Technol.* **1996**, 68(3), 3–7.
6. Defence Standard 00-970 Part 7/2 Section, Detail Design and Strength of Materials, Ministry of Defence, Directorate of Standardization, Kentigern House.
7. *ASM Handbook Volume 13B Corrosion: Materials*, ASM International, 2005.
8. Lapasset, G.; Barbaux, Y. *1st ONERA-DLR Aerospace Symposium Paris*; France, June 1999.

9. Lequel, P.; Lassince, P.; Warner, T.; Raynaud, G. M. *Aircraft Eng. Aerospace Technol.* **2001**, 73(2), 147–159.
10. Polmear, I. J. *Light Alloys – Metallurgy of the Light Metals*; Arnold: London, 1995.
11. Lequel, P.; Lassince, P.; Macé, R.; Warner, T. Aeromat 2004 Conference, Seattle WA, June 2004.
12. *ASM Handbook Volume 13B Corrosion: Materials, Corrosion of Magnesium and Magnesium Base Alloys*; ASM International, 2005.
13. Blackburn, M. J.; Smyrl, W. H.; Feeney, J. A. In *Stress-Corrosion Cracking in High Strength Steels and in Titanium and Aluminium Alloys*; Brown, B. F., Ed.; Naval Research Laboratory: Washington, DC, 1972.
14. Fager, D. N.; Spurr, W. F. *Corrosion* **1970**, 26(10), 409–419.
15. Smith, C. J. E.; Baldwin, K. R.; Hewins, M. A. H.; Gibson, M. C. In *Progress in the Understanding and Prevention of Corrosion*; The Institute of Materials, 1993; Vol 2, pp 1652–1663.
16. Wernick, S.; Pinner, R.; Sheasby, P. G. *The Surface treatment of Aluminium and Its Alloys*; ASM International, 1987.
17. *BS 2X33, Specification for Two Component Epoxy Primer for Aerospace Purposes*; British Standards Institution: London, 1998.
18. Jones, J. H. *Plating Surf. Finishing* **1990**, 20–22.
19. Khobaib, M.; Reynolds, L. B.; Donley, M. S. *Surf. Coatings Technol.* **2001**, 140, 16–23.
20. Ihbe, T. Recent advances in appliqué film technologies for aerospace coatings Presentation at DoD Maintenance Symposium and Exhibition October, 2002.
21. Defence Standard 03-19. Electrodeposition of cadmium *Ministry of Defence*; Directorate of Standardization: Kentigern House, 2005.
22. Baldwin, K. R.; Smith, C. J. E. *Trans. IMF* **1996**, 74(6), 202–209.
23. Validation of alternatives to electrodeposited cadmium for corrosion protection and threaded part lubricity applications; Engineering and Technical Services for Joint Group on Pollution Prevention (JG-PP) Projects Joint test report BD-R-1-1, 2002.
24. Legg, K. Evaluation of cadmium replacement alternatives for aircraft Presented at Aeromat Meeting, 2002. [www.rowantechnology.com/Tech-Info-Cadmium](http://www.rowantechnology.com/Tech-Info-Cadmium).
25. Defence Standard 03-36. Guidance to the use of cadmium alternatives in the protective coating of defence equipment, Ministry of Defence, Directorate of Standardization, Kentigern House, 2005.
26. Sartwell, B. D.; Legg, K.; Bretz, P. E. Proceedings of AESF Aerospace Plating and Metal Finishing Forum, 2000; pp 131–139.
27. PD 6484:1979. Commentary on corrosion of bimetallic contacts and its alleviation British Standards Institution: London, 2003.
28. US Military Standard MIL-STD-889B. Dissimilar metals 1976.
29. Voss, H. J. AGARD Conference Proceedings 565, Corrosion Detection of Advanced Airframe Material 1995; pp. 21-1–21-18.
30. *BS 2X33: Specification for component polyurethane finish for aerospace purposes*; British Standards Institution: London, 1998.
31. Painting versus polishing of airplane exterior surfaces, Boeing Corrosion.
32. Lewin, J. B. G. In *Treatise on Coatings*; Myers, R. R., Long, J. S., Eds.; Marcel Dekker: New York, 1975; Vol. 4. Formulations Part 1, Chapter 1.
33. Boeing: Commercial Airplanes – Jetliner Safety – Airline's Role in Aviation Safety – Aircraft Maintenance Inspections. [http://www.boeing.com/commercial/safety/airline\\_role.html](http://www.boeing.com/commercial/safety/airline_role.html).
34. Miller, D.; Irwin, S. *Materials Performance* **1991**, 10–13.
35. Koch, G. H.; Brongers, M. P. H.; Thompson, N. G.; Virmani, P.; Payer, J. H. Corrosion costs and preventative strategies in the United States, Appendix P Aircraft; CC Technologies Laboratories Report WA-RD-01-156, September 2001.
36. Smith, C. J. E.; Higgs, M. S.; Baldwin, K. R. RTO Meeting Proceedings 25, New Metallic Materials for the Structure of Aging Aircraft, 2000; pp 15.1–15.8.
37. Blackford, R. In Proceedings of 3rd Aerospace Corrosion Control Symposium, Amsterdam, Sawell Publications: England, 1994.
38. BS X35: Specification for Selectively removable intermediate coating for aerospace purposes, British Standards Institution, London, 1998.
39. BS X36: Specification for Paint remover for air drying selectively removable paint scheme for aerospace purposes, British Standards Institution, London, 1998.
40. Benavides, S. 9th FAA/DoD/NASA Aging Aircraft Conference 2005.
41. Senter, J. 9th FAA/DoD/NASA Aging Aircraft Conference 2005.
42. Cederquist, S. C. *Materials Performance* **2000**, 21–25.
43. Kinzie, R. 9th FAA/DoD/NASA Aging Aircraft Conference 2005.
44. Kinzie, R. C.; Peeler, D. T. 9th FAA/DoD/NASA Aging Aircraft Conference 2005.
45. Clark, G. RTO Meeting Proceedings 79(II) on Ageing Mechanisms and Control, 2003; 9-1–9-8.



## 4.39 Management of Corrosion of Infrastructure

**C. Atkins, R. Brueckner, and P. Lambert**

Mott MacDonald, Materials & Corrosion Engineering, 33 Stamford Street, Altrincham WA14 1ES, UK

© 2010 Elsevier B.V. All rights reserved.

4.39.1	Introduction	3198
4.39.2	Causes of Degradation	3198
4.39.3	Consequences of Failure	3199
4.39.4	Inspection Requirements	3199
4.39.4.1	Inspection Methods	3200
4.39.4.2	Remote Monitoring	3203
4.39.4.3	Structural Considerations	3203
4.39.5	Highway Infrastructure	3203
4.39.6	Other Infrastructure	3204
References		3206

### Abbreviations

**ALWC** Accelerated low water corrosion

**CCTV** Closed circuit television

**GI** General inspection

**PI** Principal inspection

**SI** Special inspection

**UV** Ultraviolet

rapid and affordable construction of the much needed infrastructure in postwar Europe, but as discussed in the **Chapter 3.30, Degradation of Cement and Concrete** in this book, such materials are not without their own durability problems and corrosion risks.

### 4.39.2 Causes of Degradation

#### 4.39.1 Introduction

The term ‘infrastructure’ covers a wide range of industries involved in establishment and maintenance of an effective and functional industrialized society. These include structures such as bridges and tunnels for road, rail, and canal traffic, water treatment facilities for clean and dirty water, ports and harbors, and power generation and distribution systems. This accounts for a vast range of structures manufactured from a relatively small number of materials.

The materials employed in the construction of the infrastructure are predominantly masonry, structural steel, and reinforced concrete with certain materials dominating particular periods of infrastructure development. For example in the United Kingdom, the big push in the water industry in the Victorian era has left a large legacy of predominantly masonry built facilities, whereas the boom in highway construction in the 1960s resulted in large numbers of reinforced concrete bridges and other highway structures.<sup>1</sup>

During the second half of the twentieth century, the increased use in reinforced concrete allowed

The commonest causes of degradation result from exposure to the environment, most notably UV radiation, water, and chloride ions. For marine structures, the chlorides are present in abundance in the surrounding environment. For nonmarine structures, the chlorides can come from deicing salts or admixtures in concrete. During winters, in much of Europe and North America, many hundreds of thousands of tons of rock salt is spread onto the road networks in an attempt to clear snow and ice. This is rarely followed up in the spring by any attempt to remove residual salt from the associated infrastructure, resulting in considerable chloride-related collateral damage in the following years.

Other branches of infrastructure have their own aggressive environments with which to deal. The water industry has to cope with a wide range of natural and artificial chemical environments. Freshwater can be acidic and soft, which can dissolve concrete and carbonaceous masonry and prevent the formation of calcareous scales upon which cast iron pipes rely for their corrosion protection. Anaerobic bacteria in sewage and other organic waste materials generate

hydrogen sulfide, which can be oxidized into sulfuric acid by aerobic bacteria. Hydrogen sulfide is incredibly aggressive to ferrous materials, while sulfuric acid will attack most materials, including concrete.<sup>2</sup>

### 4.39.3 Consequences of Failure

There is a common thread that links the majority of infrastructure. The consequences of failure of infrastructure are often too great to contemplate, and typically a large number of people and livelihoods are affected. The results of a failure can be marked and potentially life threatening. However, there is a general cozy assumption in most societies that bridges do not collapse, power stations will continue to operate come what may, and the water supply will always be safe and available. This idyllic view relies totally on the quality of the inspection and maintenance regimes adopted for the infrastructure.

The basic management approach is that repair requirements are identified primarily via routine inspection programs. However, the fundamental problem is that repair work is severely constrained by the fact that the infrastructure is generally subject to public funding. In addition to cost limitations, infrastructure, by its very definition, often cannot readily be taken off stream. For a major road, it can only be closed for maintenance if there is a suitable alternative route. As a consequence, works often have to be carried out at night, or using innovative access methods. All of this can have a significant impact on the cost of the works, such that access and traffic management can often cost more than the actual repair.

Politically, funding for the maintenance of infrastructure is often given a relatively low priority. Such works are seen as disruptive, and given the general public perception that infrastructure does not deteriorate and is essentially maintenance-free, it may prove attractive to delay such works until absolutely essential. As a result of this, maintenance is commonly underfunded and there is often a significant backlog of critical maintenance. For example, a recent study identified that between 30% and 60% of bridges in the United States are deficient as the result of corrosion aggravated by the lack of proper maintenance programs.<sup>3</sup>

The management of infrastructure spending is often complex and involves allocating limited resources in the most efficient manner. This will usually be linked to a program of inspection, which

feeds into a maintenance plan where works are prioritized. The development of effective inspection and reporting methods are, therefore, key to the operation of an effective infrastructure maintenance system. An example of such procedures is given later with respect to the inspection of highway bridges in the United Kingdom.<sup>4</sup>

### 4.39.4 Inspection Requirements

The basic procedure most commonly adopted is to use routine visual inspection by experienced personnel. This is an efficient method of gathering data but is aggravated by the nature of most infrastructure in being large and in near-constant use. Access for visual inspection may therefore be difficult and will often have to take advantage of temporary closures or offpeak working.

An additional factor is that most structures built more than 20 years ago did not necessarily consider the requirements for future inspection. In some cases, it was assumed that inspection would not be required. Structures were typically designed to prescriptive codes that were meant to ensure durability; however, material properties and safety factors and sometimes even exposure conditions changed over time. It was only when corrosion was being observed on a more widespread scale that it began to be considered as an issue, but even then the perception remained that if a structure was designed to the relevant code it will achieve the design life. The concept of design life is in fact not related to a period that a structure is expected to survive but rather a return period for a statistical loading regime, for example, a 1-in-100-year storm, or traffic loading.

As durability and future inspection was not considered to be an issue, access for such inspections was not incorporated into the design. The aim was to achieve a structure that was simple and cheap to construct. As a result, details are commonly encountered that are particularly vulnerable to deterioration, but all impossible to inspect.<sup>5</sup> A classic example in a bridge is the half joint as shown in [Figure 1](#).

Joints are required to allow for thermal movement and are sealed to prevent debris and water from penetrating to the substructure. However, the material used as a sealant is typically not sufficiently durable, and the action of traffic and thermal movements of the structure will ultimately result in leaks. The water, plus any deicing salts or other aggressive chemicals present

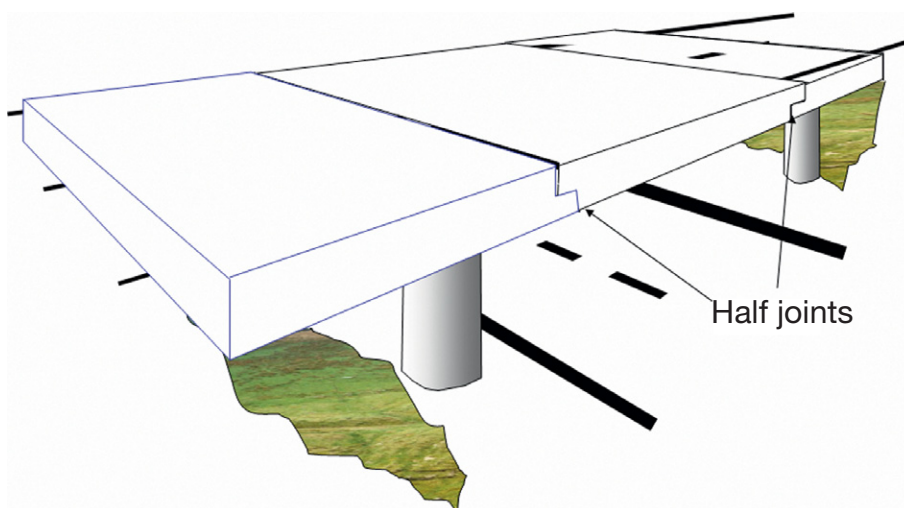


**Figure 1** Bridge half-joints.

on the road surface, penetrates the joint and pond on the bearing shelf below where the bearings, now sat in a solution of chlorides and hydrocarbons, start to corrode. Chloride-laden water may also be running down the columns supporting the deck, penetrating the concrete and initiating corrosion of the steel reinforcement. The deck itself will be supported by beams of either steel or reinforced concrete, neither of which will benefit from exposure to the salty, contaminated water running through the joints.

Ports and harbors have obvious limitations on visual inspection, as large parts of the structures can be immersed. For steel sheet piling, corrosion is normally addressed by employing a corrosion allowance in the form of additional thickness of steel for tidal and atmospherically exposed areas. For the permanently submerged areas, the lack of oxygen at depth can stifle corrosion, but the action of microbes in the environment can lead to a phenomenon known as accelerated low water corrosion (ALWC) where large section losses in excess of  $1 \text{ mm year}^{-1}$  can be found in the vicinity of the lowest astronomical tide. This is far in excess of the corrosion allowance, and coincides with the area of highest structural load and the least inspectable part.

Similar problems occur for underground transit systems. These are often constructed from cast iron or reinforced concrete segments bolted together to form a tunnel. There may be a hydrostatic pressure across the joints between segments and rings, and the water may be contaminated with chlorides, sulfates, and other aggressive species.

There is a wide range of equipment available for assisting experienced personnel in carrying out visual inspections, such as endoscopes and CCTV equipment. Together with improved access equipment, these make the inspection of infrastructure safer and more effective. **Figure 2** shows a hydraulic under-bridge unit in use on a bridge inspection.

#### 4.39.4.1 Inspection Methods

Besides any initial visual inspection, the inspection methods adopted may be destructive or essentially nondestructive. Commonly employed nondestructive tests for reinforced concrete that are able to assess structural integrity and remaining long-term performance are delamination tests, rebound hammer (compressive strength), covermeter survey, dust sampling, and half-cell surveys. Destructive concrete breakouts allow the inspection of the reinforcement and the determination of the depth of carbonation. The type and extent of the inspection usually depends on the initial visual observations.

Delamination tests can be carried out using a hammer to identify areas where cover concrete has spalled due to the expansive reaction of reinforcement corrosion. The formation of the more voluminous steel corrosion products, that is, the rust, results in the delamination of the cover concrete caused by induced stress exceeding the concrete tensile strength.

The depth of carbonation, a natural process by which carbon dioxide in the air forms carbonic acid which neutralizes the alkalinity, can be established by



**Figure 2** Underbridge unit. Photo courtesy of Wemo-Tec GmbH.

applying phenolphthalein indicator to a freshly broken section of concrete. The change from colorless to purple indicates that the pH of this area is above 9, which in turn demonstrates that any steel reinforcement in the concrete should be protected from corrosion by the alkaline environment. Colorless areas show the concrete to be carbonated and the reinforcement to be at risk of corrosion. It should be noted that reinforcement can still corrode in an alkaline environment in the presence of chloride ion contamination.

The bar size and cover depth of reinforcement can be identified by means of a covermeter which generally use electromagnetic or eddy current techniques to locate the steel. [Figure 3](#) shows an electromagnetic covermeter being used to locate prestressing tendons in precast concrete beams. Their use is limited to certain depths, which may be affected by the presence of a screed. Where the absolute size, depth, and condition of reinforcement need to be identified for the purposes of structural assessment, covermeter readings should be used in conjunction with destructive breakouts.

To determine the risk or occurrence of reinforcement corrosion, the structure can be tested with respect to chloride ion content and electrochemical activity of the steel within the concrete. The chloride content is usually determined from concrete dust

samples obtained from different depths using a percussion drill.

The immediate surface is discarded, as it is likely to contain contaminants that are not representative of the bulk of the concrete. Incremental samples are then taken at depths that typically represent the cover, the environment adjacent to the steel, and the concrete beneath.

Half-cell potential surveys are a rapid method of establishing any corrosion ‘hotspots’ within key reinforced concrete elements. These may be defined as areas where corrosion of the reinforcement is likely to be occurring and differs in electrical potential from an adjacent area by more than 100 mV. There is considerable guidance on the use of this and other associated electrochemical techniques, and they provide a useful method of scanning large areas and identifying locations for other testing.<sup>6</sup> A typical output of a half-cell potential survey at 0.25 m centers where the red areas indicate highest corrosion risk is shown in [Figure 4](#).

The Schmidt Hammer or rebound sclerometer test is a simple and quick nondestructive method to obtain an estimate of the compressive strength of concrete. It is a device that impacts a concrete surface with a sliding mass at a given energy as generated by a spring under a preset compression. The rebound of the sliding mass or hammer is governed by the hardness of the concrete





**Figure 3** Electromagnetic covermeter used to locate steel reinforcement.

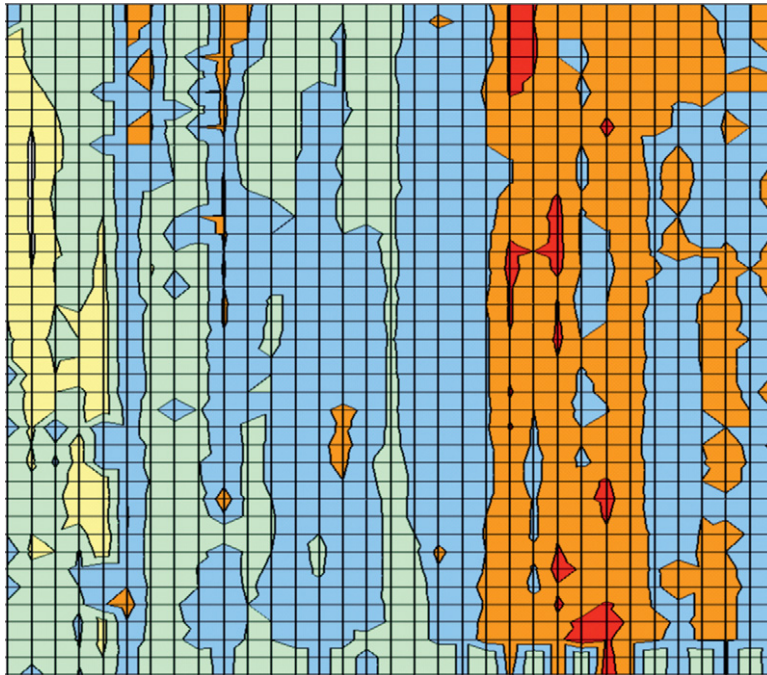


**Figure 4** Typical results of a half-cell potential survey at 0.25 m centers, where the red areas indicate highest corrosion risk.

structure. As there is a relationship between hardness and compressive strength, the values obtained from the Schmidt Hammer can be converted into strengths for the area of concrete tested. The test should be carried

out in accordance with relevant standards.<sup>7</sup> The results should be considered as an estimation of the actual strength and verified with conventional strength tests on cubes or cores taken from the structure.<sup>8</sup>



#### 4.39.4.2 Remote Monitoring

There is a considerable range of embeddable probes currently available that can be employed to detect the onset and development of corrosion in large structures.<sup>9</sup> Such probes work best when installed at the time of construction, but in many cases, they are required to be retrofitted to existing structures wherein some degree of corrosion or other degradative process may already have occurred.

Selecting areas for the inclusion of probes is not without its problems. It is often relatively simple to identify the areas most likely to suffer from corrosion, such as under a joint, or elements where corrosion would constitute a significant risk, such as post-tensioned tendons. A specific length of motorway may have many thousands of potentially vulnerable areas, some of which will fail, while the majority will not. The chlorides from deicing salts will leak on to the substructure and then spread over the surface of the concrete and penetrate into the steel. A specific area, possibly less than a few square centimeters, may then start to corrode. The precise location of probes is therefore always going to be difficult as there is a significant chance that corrosion may be missed unless a large number of probes are employed in combination with regular visual inspections and other complementary monitoring techniques. Considerable effort is being directed towards the development of more effective monitoring systems that can assist in the long-term maintenance of complex infrastructure systems.<sup>10</sup>

#### 4.39.4.3 Structural Considerations

The wide variety and complexity of infrastructure encompass a wide spectrum of loading requirements. For example, in pipelines the loading is relatively uniform and so areas of greatest concern are those areas where corrosion is most likely to occur and such areas therefore may be targeted for risk-based inspections. For liquid retaining structures, the load increases with depth and so at the design stage the structural capacity will increase with depth to accommodate this. For bridges, the loading similarly varies across each element and so the design will also vary to accommodate the necessary structural properties. As a consequence, for any given amount of corrosion each area will be affected to a different degree. A loss of 2 mm of steel thickness may not be considered significant in one location, but may be critical in another and, whereas a structural member may be

able to tolerate the full loss of section in some areas, a pipeline cannot be allowed to form even the smallest perforation. As a result, the inspection cannot simply focus on areas of highest corrosion but must review the whole structure.

This is further aggravated by changes in the design approach adopted by the relevant statutory or advisory bodies. Over a period of time, the approach to the specific design requirements often changes as other factors become more significant. The purpose of parapets, for example, initially used to be essentially to form an edge to a structure. They are now required to provide effective vehicle restraint to faster and heavier impacts. The predicted loading has changed from simply being able to support the self weight and survive wind loading, to restraining a vehicle impact at 50 kph. Changes in the guidance and requirements mean that many structures will fail to achieve the standards laid down by the design codes. It can be tempting to adopt the approach of 'it has not yet fallen down,' but then all unexpected collapses are preceded by a prolonged period of inactivity, and hence the requirements for well-defined and carefully managed inspection regimes.

#### 4.39.5 Highway Infrastructure

The 1980 Highways Act<sup>11</sup> established a statutory obligation to maintain public highways in the United Kingdom. However, the responsibility and procedures to be employed in this maintenance depended on the ownership of the structure. The primary routes are maintained by the Highways Agency, which is an executive agency of the Department of Transport. The remaining bridges fall under the responsibility of a wide variety of parties, such as local authorities, the railway and canal network, and other utilities where their structures pass over the highway.

The absence of a common code of practice has led to a range of different approaches being taken, which was less than desirable. To help clarify this situation, a document entitled 'The Management of Highway Structures' was published in 2005.<sup>12</sup> Its stated aims were "... to encourage and assist highway authorities and other owners to implement Good Management Practice, harmonise practices, coordinate approaches and share their experiences and practices." Three key themes were identified, these being asset management planning and resource accounting, maintenance planning and management, and engineering processes.

Asset management may be defined as a strategic approach that identifies the optimal allocation of resources for the management, operation, preservation, and enhancement of the highway infrastructure to meet the needs of current and future customers. The asset management plan is a long-term view. Maintenance planning and management involves the development and implementation of cost-effective maintenance plans for highway structures that support the safe operation of the network while delivering the required levels of service. The maintenance plans typically cover both short- and medium-term actions and requirements.

The engineering processes are the necessary practical measures and data collection exercises. These include inspections to identify the current condition, assessments to identify the current capacity, and the approach to be taken to manage abnormal loads. These themes are supported by data and information, which are normally stored within a computerized bridge management system. This enables the data to be interrogated and manipulated to provide useful information on the structures and network.

Central to all of this is the inspection procedure. It is not possible to accurately assess a future maintenance requirement unless the existing condition is known. In order to achieve this, the code of practice proposes the following series of inspections, all of which are carried out by appropriately skilled and competent professionals.

1. General inspections (GI) are required every 2 years. They are primarily visual inspections carried out from readily accessible areas. As such, it is not expected that these will provide a comprehensive and detailed view of each part of the structure.
2. Principal inspections (PI) are carried out every 6 years, and the intention is that they are carried out within touching distance of all elements, unless suitable alternatives can be justified, for example, remote CCTV inspection of areas with difficult access.
3. Special inspections (SI) are carried out as and when deemed necessary. They can include inspections required as part of the assessment process. They can also include inspections carried out under the grounds of public safety, or inspections relating to acceptance of repair work or at a hand-over stage where maintenance responsibility is being transferred.

The Management of Highway Structures contains 17 recommendations, which, it states, should be

implemented in a measured way. Three milestones are proposed.

1. Milestone 1 covers the adoption of processes necessary to provide highway structures that are safe to use, inspect, and maintain.
2. Milestone 2 adds the broad inclusion of additional processes necessary to provide highway structures that are fit for purpose and meet government requirements.
3. Milestone 3 imposes the adoption of processes necessary to deliver the agreed level of services at minimum whole-life costs and represents the full implementation of the good management practice set out in the code. It is stated that ideally the milestones should be implemented in order, but it is considered appropriate to progress to some actions in Milestone 3 before Milestone 2 is fully achieved.

The German standard for bridge monitoring and inspection states that GI of easily accessible areas should be carried out every 3 years and PI of the entire structure every 6 years.<sup>13</sup> SI should be carried out after certain events have occurred, such as flooding, hurricane, and accidents. The standard notes that all structural components such as protectively enclosed elements are to be inspected. The standard is based on a guidance from 1930 which dealt with the monitoring and inspection of cast iron highway bridges.

In Italy, an equivalent standard covers the inspection of highway structures.<sup>14</sup> It recommends that an inspection of those elements of the bridge visible from accessible areas should be systematically carried out. The aim of this inspection is to identify all the possible signs of deterioration such as cracking, superficial deterioration, moisture staining, exposure of steel bars, difference in color of concrete surfaces, and structural deformation. Depending on the result of this first inspection and on the structural characteristics and importance of the bridge, a more detailed inspection should be planned. The detailed inspection should be carried out at touching distance on all the elements of the structure including the foundations and the embankments.

Similar guidance is available in all countries with a significant highway-based infrastructure.

#### **4.39.6 Other Infrastructure**

Multiple storey car parking structures have featured in a number of high-profile failures in recent years.

The traditional approach of managing car parks has typically been to carry out the minimum level of maintenance possible, and owners, often private companies, have appeared unaware of the consequences of degradation. Innovative designs and rapid construction methods coupled with poor construction practices have often exasperated the problems. Many date from the early 1970s when the designs often did not include for a degree of robustness. This, combined with a lack of understanding of the corrosion processes, has resulted in many corroding structures with low factors of safety and an increased risk of failure or collapse. **Figure 5** shows the typical appearance of such structures with patching of the damaged areas.

Following on from the collapses, guidance documents were produced in the United Kingdom with regard to the design, maintenance, and refurbishment of multistorey car parks.<sup>15</sup> The guidance followed similar lines to those contained within the bridge management code of practice, namely that the current condition and load-carrying capacity should first be established and a more active inspection and maintenance regime be implemented. This included benchmarking using appropriately qualified and competent personnel to establish the current condition. In addition, routine inspections were recommended by on-site staff to identify areas such as

blocked drainage which would produce future durability issues.

The majority of other maintainers in the United Kingdom and elsewhere are generally private companies. These tend to be left to carry out their own procedures, although obviously any major incidents would be investigated. Shortfalls that result in the health and safety of employees or the public being put at risk or those that adversely affect the environment would be expected to result in criminal prosecutions under the relevant statutes.

Street lighting and signage is another area that at first glance would not appear to be a significant problem other than periodic maintenance of the luminaires. However, the lights and signs are typically fixed at height to large posts which are generally fabricated from metal or reinforced concrete and therefore subject to corrosion in aggressive environments, as well as suffering occasional unreported impact damage.

Inspection of the posts for internal and external corrosion is not in itself particularly onerous or technically challenging. It is the sheer number of units requiring inspection that lead to concerns. Kent County Council in the United Kingdom with an area of 3736 km<sup>2</sup> and a population of 1.6 million reports having a total of 113 000 street lights, 14 000 lighted signs, and 5500 bollards. Extrapolated to the



**Figure 5** Multiple patch repairs to car park deck.

whole country, this would equate to something in excess of 4 million lighting and signage posts requiring periodic inspection and maintenance. With such large numbers to deal with, the occasionally reported failures must represent a very small percentage of the whole.

## References

1. Baldwin, P.; Baldwin, R. *The Motorway Achievement. Volume 1: Visualisation of the British Motorway System: Policy and Administration*; Thomas Telford Publishing: London, 2004.
2. Lambert, P.; Ecob, C. R. *The Degradation and Protection of Reinforced Concrete Sewers; Coatings & Linings for the Water Industry*; Prague, Czech Republic, 1995; p 65.
3. Larsen, K. R. *Mater. Perform.* **2009**, 8, 30.
4. The Highways Agency. *Inspection Manual for Highway Structures. Volume 1: Reference Manual*; The Stationary Office: UK, 2007.
5. Lambert, P.; Norris, P. *Struct. Faults Repair, Edinburgh* **1993**, 1, 111.
6. The Concrete Society. *Electrochemical Tests for Reinforcement Corrosion*, TR 60; The Concrete Society: UK, 2004.
7. BS EN 12504 Part 2. Testing Concrete in Structures. Non-Destructive Testing. Determination of Rebound Number, British Standards Institute, 2001.
8. BS EN 13791. Assessment of In-Situ Compressive Strength in Structures and Pre-Cast Concrete Components, British Standards Institute, 2007.
9. Song, H.-W.; Saraswathy, V. *Int. J. Electrochem. Sci.* **2007**, 2, 1.
10. Buenfeld, N. R.; Davies, R. D.; Karimi, A.; Gilbertson, A. L. *Intelligent Monitoring of Concrete Structures*; CIRIA: London, 2008.
11. Department of Transport. *Highways Act*; The Stationary Office: UK, 1980.
12. Department of Transport. *Management of Highway Structures*; The Stationary Office: UK, 2005.
13. DIN 1076. Highway Structures – Testing and Inspection, Deutsches Institut Fur Normung, 1999.
14. Italian Standard No. 34233. Planning, Execution and Testing of Bridges; Circolare del Ministero dei Lavori Pubblici, 1991.
15. Institute of Civil Engineers National Steering Committee. *Inspection and Maintenance of Multi-Storey Car Parks*, Thomas Telford: London, 2002.

## 4.40 Management of Corrosion in the Petrochemical and Chemical Industries

**J. A. Richardson**

Anticorrosion Consulting, 5 Redhills Lane, Durham DH1 4AL, UK

© 2010 Elsevier B.V. All rights reserved.

4.40.1	Industry Scope	3208
4.40.2	Risks to Industry Equipment	3208
4.40.3	Materials and Protection Practices for Process Equipment	3210
4.40.3.1	Materials	3210
4.40.3.2	Protection Practices	3212
4.40.3.2.1	Coatings and linings	3212
4.40.3.2.2	Inhibitors	3213
4.40.3.2.3	Electrochemical protection	3213
4.40.3.3	Selection of Materials and Protection Practices for Process Equipment	3213
4.40.4	Mitigation of Corrosion Risks by Good Detailed Design, Procurement, and Construction Practices	3214
4.40.5	Mitigation of Specific Corrosion Risks	3215
4.40.5.1	External Corrosion Risks	3215
4.40.5.2	Internal Corrosion Risks	3217
4.40.6	Mitigation of Corrosion Risks During Operation	3221
4.40.7	Corrosion Risk Management Costs and Benefits	3223
4.40.8	Future Trends in Process Equipment	3226
4.40.9	The Current Corrosion Risk Management Scorecard	3227
References		3227

### Abbreviations

**AE** Acoustic emission  
**API** American Petroleum Institute  
**EAC** Environmentally assisted cracking  
**ECN** Electrochemical noise  
**ESCC** External stress corrosion cracking  
**FEP** Fluorinated ethylene propylene  
**FFS** Fitness for service  
**FRP** Fiber reinforced plastic  
**FSM** Field signature monitoring  
**HB** Brinell hardness number  
**HDPE** High-density polyethylene  
**HIC** Hydrogen-induced cracking  
**HV** Vickers hardness number  
**LDPE** Low-density polyethylene  
**MSD** Materials selection diagram  
**NACE** National Association of Corrosion Engineers  
**NDE/T** Nondestructive examination/testing  
**PE** Polyethylene  
**PEEK** Polyetherketone  
**PIR** Polyisocyanurate  
**PP** Polypropylene

**PTFE** Polytetrafluoroethylene  
**PVC** Polyvinyl chloride  
**PVDF** Polyvinylidene fluoride  
**PEC** Pulsed eddy current  
**PWHT** Post-weld heat treatment  
**RBI** Risk-based inspection  
**SCC** Stress corrosion cracking  
**SCW** Super critical water  
**SHE** Safety, health and environment  
**SOHIC** Stress-oriented hydrogen-induced cracking  
**SSC** Sulfide stress corrosion  
**TLA** Thin layer activation  
**UT** Ultrasonic testing

### Symbols

**bar** Pressure of  $10^5 \text{ N m}^{-2}$   
**°C** Temperature, degrees Centigrade  
**mm** Millimeter  
**t** Tonne, metric ton, 1000 kg



#### 4.40.1 Industry Scope

Petrochemicals and chemicals manufacture comprises a major sector of most developed and developing economies. The primary feed-stocks are oil, gas, and naturally occurring materials that are processed in large quantities in world scale plants to produce refined oil products and commodity chemicals. Downstream processing is undertaken in progressively smaller plants to produce the wide range of complex chemical products that are demanded by developed economies. Value is added through each stage of processing so that at the end of the chain, fine chemicals and pharmaceuticals, although manufactured in relatively small quantities, are very significant economically because of their high intrinsic value.

The industry is driven by the usual commercial imperatives. It strives to create value through new and improved products and processes, increased energy and resource efficiency, and improved manufacturing performance. At the same time, the industry is acutely aware of its societal obligations to comply with safety, health, and environmental (SHE) expectations and regulations that preclude loss of containment incidents.

#### 4.40.2 Risks to Industry Equipment

Process plants, typified in [Figure 1](#), are assembled from standard equipment items that are subdivided conventionally as follows:

1. storage tanks;
2. pressure vessels – reactors, heat exchangers, columns for distillation/fractionation/stripping, storage spheres/tanks, etc.;

Industry scope:

- Petroleum refining
- Petrochemicals
- Commodity chemicals
- Fine chemicals
- Pharmaceuticals

Equipment

- Storage tanks
- Pressure vessels
- Fired equipment
- Machines
- Piping
- Instrumentation



**Figure 1** Process plants, regardless of size/complexity, are assembled from standard equipment items.

3. fired equipment – furnaces, heaters, boilers, etc.;
4. machines – gas/steam turbines, compressors, expanders, pumps, etc.;
5. piping – including valves, venturi tubes, orifice plates, etc.;
6. instrumentation – measuring temperature, pressure, concentration, flow, etc.;

Industry equipment operates over wide ranges of temperature and pressure as well as in a wide range of corrosive environments. Operating conditions for some common items of industry equipment are summarized in [Figure 2](#). Thus, liquefied hydrocarbons are stored at atmospheric pressure at extremely low, subzero temperatures, while furnace tubes may operate at significant pressures at temperatures around 1000 °C. Crude oil is distilled at atmospheric pressure, or even under vacuum, while hydrocrackers and ammonia/methanol converters operate at pressures in the range 200–300 bar at temperatures that can be well above 400 °C. Some processes for the manufacture of low-density polyethylene (LDPE) operate at pressures as high as 3000 bar.

At the extremes, the temperatures and pressures at which industry equipment is required to operate present significant challenges to the properties of available engineering materials. Design codes for industry equipment provide protection against mechanical failure due to ductile overload, brittle fracture, fatigue and creep mechanisms. However, industry equipment is also vulnerable to failure modes associated with the full range of corrosion and/or wear mechanisms during operation, and design codes offer only very general guidance as to the mitigation of such risks in specific applications.

Historically, piping and storages have proved the likeliest types of equipment to give rise to major incidents,<sup>1</sup> as recorded in [Figure 3](#). This is to some

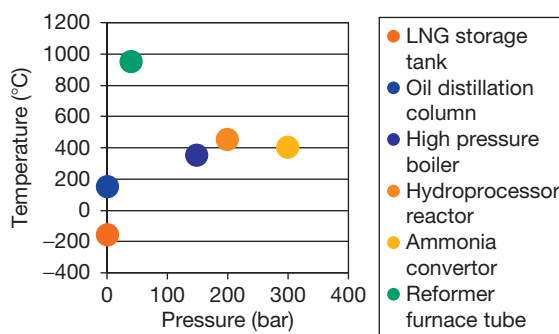


**Figure 2** Operating conditions for common items of petrochemical/chemical industry equipment.

extent counterintuitive and is probably a reflection of their lower historical priorities in the management of structural integrity compared to more obviously vulnerable equipment types such as pressure vessels or machines. Regarding mechanisms of failure, periodic surveys have confirmed that cracking, in particular environmentally assisted cracking (EAC), and general corrosion are the commonest causes of equipment failure in the industry as, for example, in a recent survey of the refining/petrochemical industry in Japan<sup>2</sup> from which **Figure 4** is adapted.

These corrosion risks have to be managed to preclude major incidents and eliminate avoidable costs. A number of sources provide comprehensive

overviews of the mitigation of corrosion risks in the process industries.<sup>3–8</sup> The challenge is to select materials, protection procedures, and fabrication procedures for equipment that enables value creation while containing SHE risks within acceptable limits. Corrosion management is a life cycle process, the available tools for which are:

1. At the equipment design stage, selecting corrosion-resistant materials and protection practices and adopting good design practices for equipment that mitigate corrosion risks.
2. Throughout the operating life, dimensioning and understanding the corrosion performance of

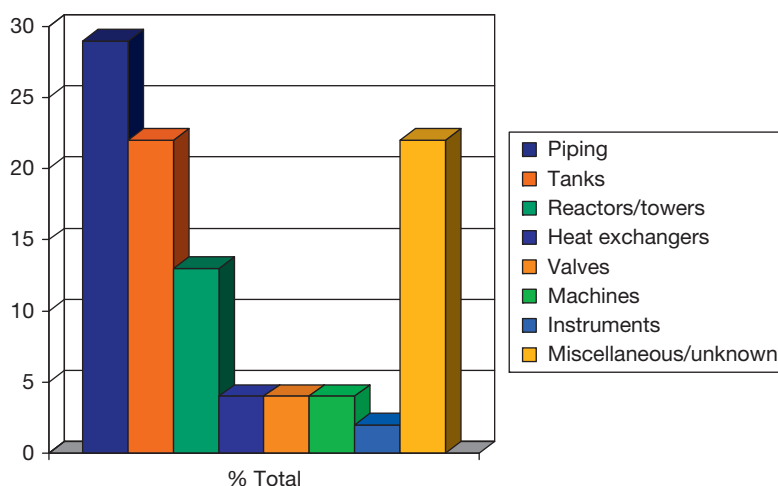


**Figure 3** Types of process equipment involved in 170 major industry losses over 30-year period. Adapted from Garrison, W. G. *Hydrocarb. Process.* **1988**, 67, 115–122.

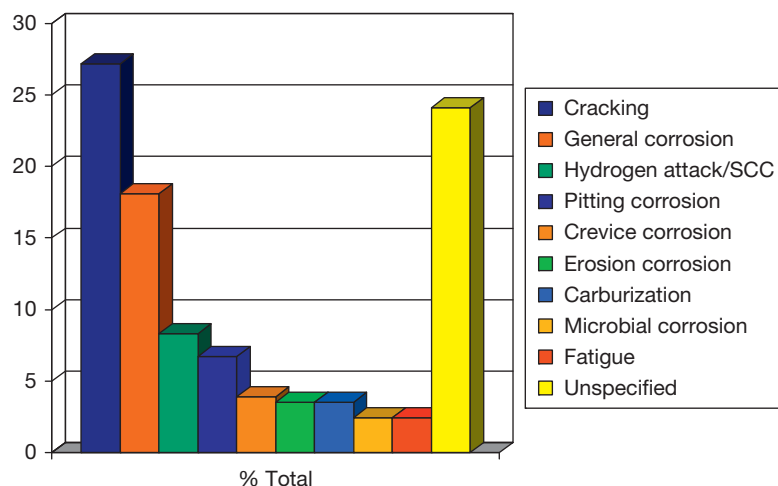


**Figure 4** Causes of failure in refining/petrochemical equipment. Adapted from Katsumi, Y. *Corros. Eng.* **2004**, 53, 185–189.

equipment and managing corrosion control practices to assure structural integrity and provide increased reliability and availability.

3. At all stages, promoting awareness and commitment among engineers and managers.

### 4.40.3 Materials and Protection Practices for Process Equipment

#### 4.40.3.1 Materials

Most classes of materials find use in process industry equipment because of the wide ranges of temperatures, pressures, and corrosive environments that have to be tolerated. The approximate capabilities of the more important classes of material as a function of temperature are charted in **Figure 5**. The needs of the process industries for equipment to withstand ever more demanding conditions have provided significant drivers for the development of new and improved grades of engineering materials across all classes that are too numerous to mention here but are described in detail in this book in the relevant chapters on materials.

The strength and ductility required for the safe operation of pressurized equipment are confined mostly to metallic materials, although some lower-pressure/temperature systems are constructed in thermoplastic and fiber reinforced plastic (FRP)

materials. Carbon and carbon–manganese steels are workhorse materials for process equipment because of their low relative cost, but they have limited strength and ductility at high and low temperatures respectively, as well as poor corrosion resistances. A number of low-alloy steels also find significant usages:

1. Chromium–molybdenum–vanadium steels provide improved strengths at the temperatures that are required for handling environments such as steam and that occurring in hydroprocessing. They also provide increased resistance to hydrogen-containing gases at elevated temperatures.
2. Chromium steels provide improved resistance to high temperature corrosion, particularly in gases containing hydrogen sulfide.
3. Nickel steels provide improved ductility for low-temperature duties, in particular for the storage of liquefied gases and hydrocarbons.

Higher-strength medium- or high-carbon grades of steel generally lack the ductility for pressure containment duties but find uses in machines as materials for shafts, gears, punches, extrusion dies, cutting tools, etc.

The austenitic and duplex stainless steels and nickel alloys provide acceptable strengths and ductility over much wider temperature ranges than steels as well as much greater corrosion resistance, and they are widely used for process equipment.

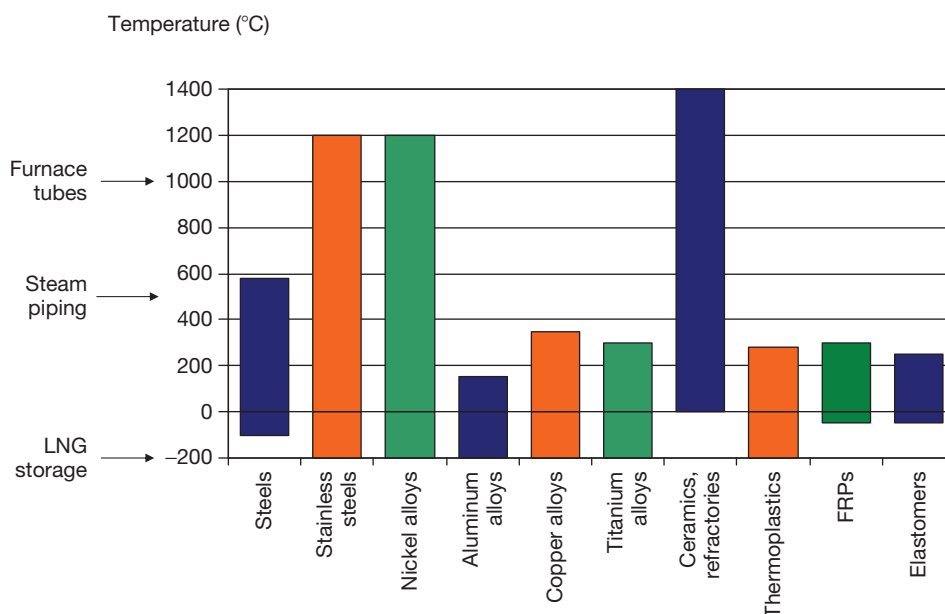


**Figure 5** Approximate temperature capabilities of materials in process equipment.

Specific grades have been developed to address specific corrosion risks in the process industries such as resistance to stress corrosion cracking and pitting/crevice corrosion, reducing and oxidizing acid corrosion and specific high temperature corrosion phenomena. Ferritic, martensitic, and precipitation hardening stainless steels also have useful corrosion resistance but have weldability and potential ductility issues that constrain their use for pressure containment. Ferritic stainless steels find most uses in relatively thin section components such as heat exchanger tubing. Martensitic and precipitation hardening stainless steels find uses where stronger materials are required such as shafts, impellers, valve springs, bolting, etc.

The other alloy classes find niche uses in process equipment:

1. Titanium, zirconium, and tantalum alloys have excellent corrosion resistance, but their applications are constrained by their relatively high cost and limited strength at higher temperatures that are offset to some extent by deploying them as linings on steel substrates.
2. Aluminum alloys have restricted corrosion resistance and are mostly confined to relatively noncorrosive applications such as storage tanks and silos.
3. Copper alloys find niche applications arising from their corrosion resistance in relatively low-temperature applications including heat exchanger tubing and tube plates, and pumps and valves.
4. Cobalt alloys are used mostly for their excellent resistance to wear in equipment that handles solids and slurries.
5. Lead alloys find continuing but declining uses as lining materials for tanks and vessels handling principally sulfuric and phosphoric acids.

Nonmetallic materials find important and increasing usage in process equipment, some of which are illustrated in [Figures 6 and 7](#). Refractory linings are deployed routinely as thermal protection for steels, allowing them to operate at the temperature ranges within which they have adequate strength for pressure containment. For corrosion resistance, chemically resistant brick and glass linings have also found significant application. In general, solid engineering ceramics lack the ductility to deploy directly for pressure containment. However, they are highly corrosion resistant and find increasing usage as internal components of equipment for corrosive duties as illustrated in [Figure 6](#). These applications include heat exchange duties in the cases of impervious graphite and silicon carbide that are thermally conducting.

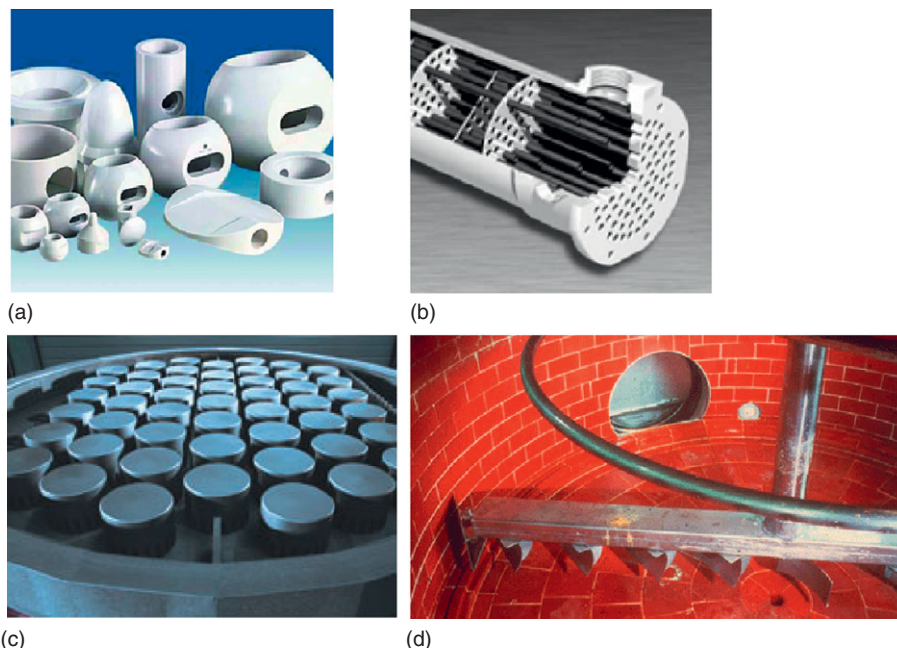


**Figure 6** Process equipment internal components constructed in engineering ceramics: (a) partially stabilized zirconia valve components,<sup>9</sup> (b) silicon carbide heat exchanger tubing,<sup>10</sup> (c) impervious graphite bubble cap tray,<sup>11</sup> (d) acid-resistant brick-lined vessel.<sup>12</sup>

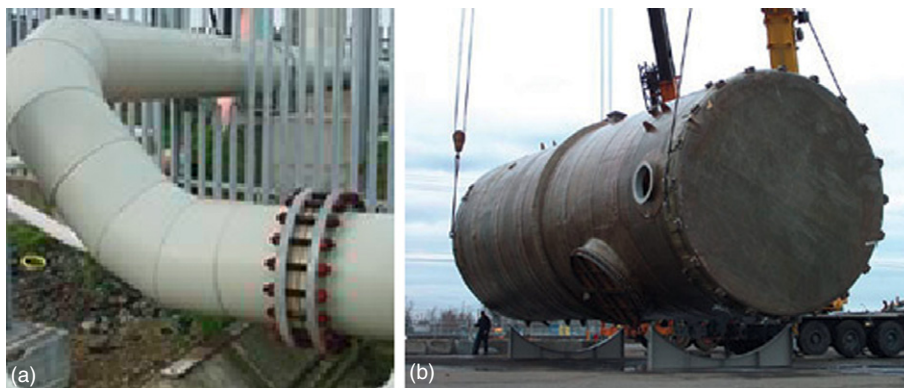


**Figure 7** Process equipment items constructed in plastics (a) 60 cm diameter polypropylene piping. Reproduced from [www.ianflockton.co.uk](http://www.ianflockton.co.uk) (b) ~1000 m<sup>3</sup> PVDF-lined GRP vessel. Reproduced from [www.chemicalprocessing.com](http://www.chemicalprocessing.com)

Thermoplastic and FRP materials have also found significant and increasing usage in process equipment because of their wide ranging corrosion resistance. Some of the more common materials (polyethylene (PE), polypropylene (PP) and polyvinyl chloride (PVC)) compete favorably with steel on cost. In the case of the higher-performance thermoplastic materials such as the fluoropolymers (PVDF, FEP, PTFE) and polyetheretherketone (PEEK), useful properties persist up to relatively high temperatures, albeit at a cost. There are available design codes for solid thermoplastic and FRP tanks, vessels, and piping systems. Allowable combinations of pressure and size are constrained by the relatively low strengths and temperature tolerances of the relevant materials, but at low temperatures and pressures, relatively large fabrications are achievable as illustrated in **Figure 7**. Pressure and size restrictions are overcome to some extent by deploying the materials as coatings and linings on stronger, tougher substrates. Thermoplastic linings can be used on FRP substrates in so-called dual laminate constructions. Alternatively, thermoplastic, FRP and elastomeric linings are used on steel substrates. Elastomers also have essential uses in sealing materials.

#### 4.40.3.2 Protection Practices

##### 4.40.3.2.1 Coatings and linings

Thin paint coatings, generally <0.5 mm thick, are used routinely for the protection of structural steelwork and external surfaces of steel equipment against atmospheric corrosion and also find uses for the internal protection of process equipment.<sup>13</sup> Thicker coating systems up to ~2 mm<sup>14</sup> are available for the internal protection of storage tanks, vessels, and pipelines based

on heat-cured fluoropolymer and other resin systems that may be reinforced with wire mesh and antipermeation layers for particularly corrosive duties.

Metallic coatings also find uses. Dipped zinc and zinc/aluminum coatings are commonly used for the protection of structural steelwork in chemical plants, but their use on equipment surfaces is constrained by any attendant risks of liquid metal embrittlement (LME). Thermal spray coatings of, for example, aluminum or stainless steels sealed with organic materials are sometimes used for repair and protection against relatively low corrosion rates. Thermal spraying is also used to apply a wide range of erosion-resistant coatings, including nickel- and cobalt-based alloys, sometimes incorporating hard materials such as carbides.

Relatively thin coatings are more likely to contain defects than thicker linings which are generally favored as the more prudent option for protection where substrate corrosion rates are likely to exceed ~0.5 mm year<sup>-1</sup>. Linings are used where the cost and/or mechanical properties of the corrosion-resistant material preclude its use in solid form. Metallic linings are applied by one of the following processes:

1. Roll bonding; routine for stainless steels and nickel alloys on steel, typically 1.5–5 mm thick.
2. Explosive bonding; especially for metals that cannot be fusion bonded to steel such as titanium, zirconium, and tantalum, 3–25 mm thick.
3. Weld overlaying; mainly stainless steels, nickel alloys, and hard surfacing alloys, up to 25 mm thick.
4. Wallpapering; in which thin sheets, typically 1.5 mm thick, are welded intermittently to substrates and sealed with overlaps that are welded continuously,



for stainless steels and nickel alloys on large areas such as ducts.

5. Loose lining; for expensive materials such as tantalum, typically 0.5 mm thick.

Thermoplastic, FRP and elastomer linings, up to ~5 mm thick, are preferably bonded to the substrate, usually steel, but in some applications rely on mechanical bonding such as in the case of swaged thermoplastic linings in steel pipes. Bonded glass linings up to ~2 mm thick and much thicker brick linings continue to find significant uses.

#### 4.40.3.2.2 Inhibitors

The principal uses of inhibition in chemical plant is in the control of corrosion in steam raising and cooling water systems that are covered in separate chapters in this book. However, inhibition finds niche uses in the control of process corrosion, such as in the control of crude unit overhead corrosion<sup>15</sup> and the control of corrosion in CO<sub>2</sub> removal systems.

#### 4.40.3.2.3 Electrochemical protection

Cathodic and anodic protection are described in separate chapters in this book. Cathodic protection finds conventional uses for the control of external corrosion of immersed and buried steel infrastructure and pipelines. Anodic protection is based on the development and/or consolidation of protective films on steel and stainless steel equipment to control corrosion at acceptable rates and prevent unacceptable contamination of process fluids with corrosion products. The main commercial applications of anodic protection are in sulfuric acid storage tanks, piping and coolers and in pulp digesters and storage tanks handling caustic kraft liquors in the pulp and paper industry.

#### 4.40.3.3 Selection of Materials and Protection Practices for Process Equipment

The procedures that are used to select materials and protection practices and to factor costs into the selection process are described in separate chapters in this book. One of the more important requirements is that the level of risk inherent in the outcome is understood and aligned to the overall philosophy for managing technical and commercial risks in the specific application. The extent to which such risks need to be quantified rigorously depends upon the application and, in particular, the consequences of corrosion failure.

In the process industries, the SHE risks inherent in the selection of materials and protection practices are embedded in the hazard study methodologies<sup>16</sup> that are deployed throughout process and equipment design at its various stages. Such methodologies attempt to ensure that the risks are contained within the acceptable, defined limit values. Risks, including those arising from the selection of materials and protection practices, are evaluated and mitigated by teams of functional professionals, including materials/corrosion engineers.

In the process industries, the semiquantitative evaluation of corrosion risks is normally regarded as sufficient, based on the essentially empirical corrosion data that is used to predict corrosion performance, the reliability of which is normally classified as of high, medium or low reliability, depending on the source. For example, the American Petroleum Institute classifies the reliability of corrosion data as follows<sup>17</sup>:

1. High-reliability sources – extensive field data through inspection, test coupon data from >5 years' exposure in operating equipment.
2. Moderate reliability sources – laboratory testing with simulated process conditions, limited operating plant corrosion coupon testing.
3. Low-reliability sources – published data, corrosion rate tables.

It is vital that the selection of materials and protection practices are documented to capture the know-how that they embody, record any changes that are required and render the information accessible to the wider community of engineers and managers concerned with the design and operation of process equipment. The use of materials selection diagrams (MSDs) is being adopted increasingly for these purposes.<sup>18</sup> MSDs comprise simplified process flow diagrams showing relevant operating conditions together with materials selection information and any associated corrosion protection practices. These diagrams capture the information needed to ensure that materials selection decisions for the many specific items of equipment that comprise the final plant (vessels, piping, machines, instrumentation) incorporate the outcomes of corrosion-risk identification and evaluation, together with any necessary mitigation practices, for the relevant operating conditions. This is particularly important to mitigate the risks of deficient information transfer across organizational boundaries when materials selection decisions are spread across several supplier organizations.

#### 4.40.4 Mitigation of Corrosion Risks by Good Detailed Design, Procurement, and Construction Practices

The extent to which detailed design may have a significant influence on corrosion risk and its mitigation is covered in a separate chapter in this book that includes many examples of bad and good practices relating to the design of process equipment, particularly in relation to environmental, thermomechanical, geographic or geometric, and galvanic compatibility factors. Probably, the greatest corrosion risk to process equipment at the design stage arises from the difficulties in anticipating and defining the development of aggressive local chemistries under the following influences:

1. Concentration by repeated wetting/drying cycles on hot surfaces under thermal insulation, on heat transfer surfaces, and at wind and water lines.
2. Concentration in crevices and beneath scales/deposits.
3. Condensation onto surfaces below critical dew points.

Examples of the first two risks and their mitigation in relation to the design of heat exchangers are given in this book in the chapter on design. An example of condensation-induced risk is summarized in [Figure 8](#) which shows a section through the bottom of a steam reformer tube where the tube is welded to a branch on a refractory-lined header beneath a

furnace base. The tube has cracked along the fusion line between a nickel alloy weld joining the low-alloy steel header branch to the cast stainless steel reformer tube, resulting in leakage of process gas. The cause of the problem is that the section of tube around and below the dissimilar weld behind some insulating refractory operates intermittently below the dew point of the process gas that is nominally  $\sim 160^\circ\text{C}$ . The condensate is acidic because of its  $\text{CO}_2$  content resulting in corrosion of the low-alloy steel branch bore, and environmentally assisted cracking of hard material that is formed during welding along the fusion line between the nickel-alloy weld and the low-alloy steel branch. The root cause of the problem lies in the design that allows a damaging microenvironment to develop around a dissimilar metal weld as a result of repeated condensation/dry out events. The risk is mitigated by changing it to a 'hot bottom' design for the reforming furnace in which the temperature of the dissimilar metal weld is maintained permanently above the dew point of the process gas.

During the procurement and construction stages, additional corrosion risks may be incurred if the correct materials and protection practices are not procured or deployed according to specification. An example of the very expensive consequences of failure to implement correctly a specified corrosion-risk mitigation practice is shown in [Figure 9](#) that relates to an economizer on a nitric acid plant. The vertical, tubular

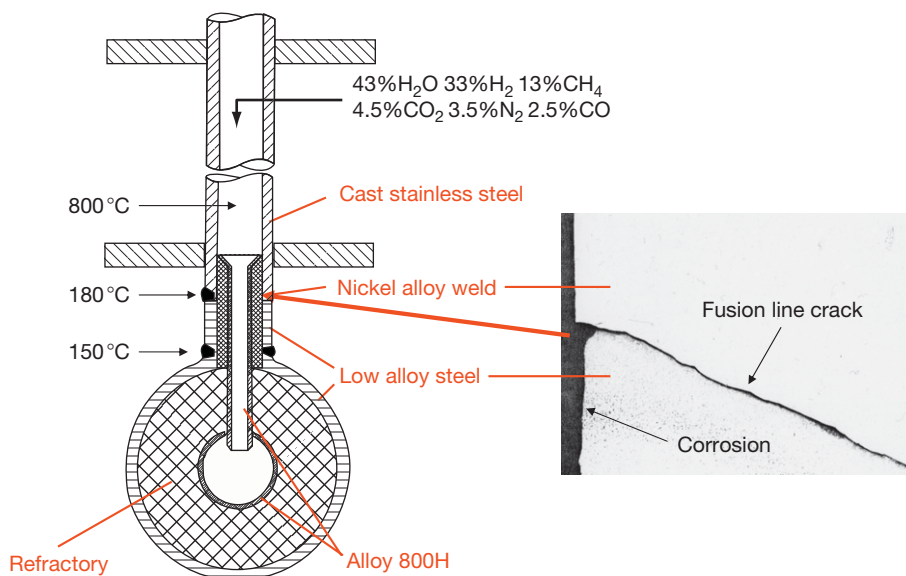


**Figure 8** Environmental cracking of a dissimilar weld attaching a reformer tube to a header resulting from intermittent condensation of the process gas, dew point  $\sim 160^\circ\text{C}$ , behind insulating refractory.

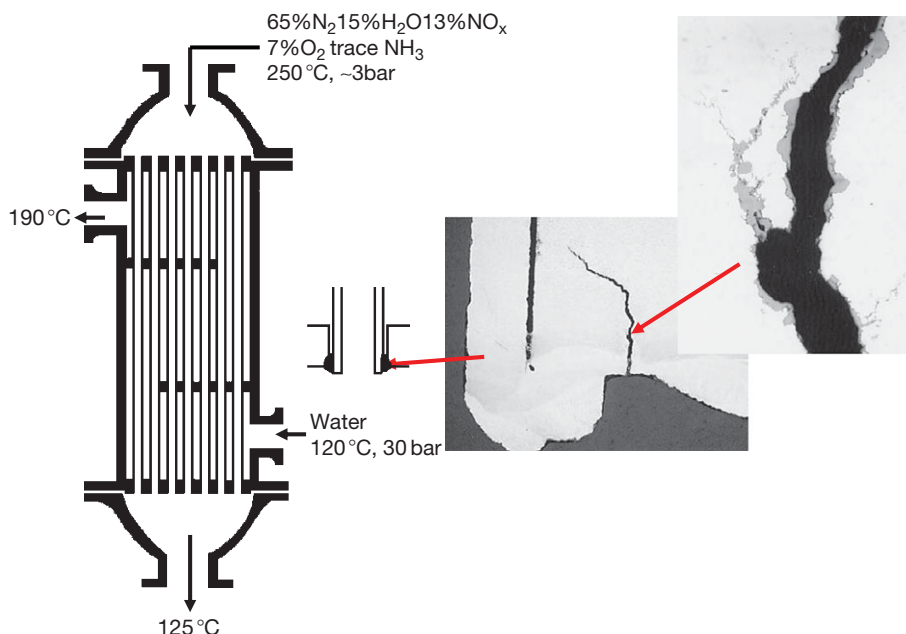


**Figure 9** Nitrate stress corrosion cracking of steel tube plate of a nitric acid plant economizer during plant startup because of poor thermal stress relief during fabrication.

heat exchanger is used to preheat boiler water with the hot, gaseous products of ammonia oxidation. Such vessels are routinely constructed in carbon steel and are operated sufficiently hot in service to preclude condensation of nitric acid that would result in severe corrosion. However, during startup there are significant amounts of unreacted ammonia present in the process gas and condensation of ammonium nitrate solution can occur on the relatively cool bottom tubeplate, presenting a risk of nitrate stress corrosion cracking to stressed carbon steel. The risk was mitigated by revising the stress relieving procedure in collaboration with the fabricator to ensure that the vessel be thermally stress relieved as a last stage of fabrication. In the case of the failure summarized in [Figure 9](#), the vessel was inadequately stress relieved and, as result, suffered such rapid nitrate stress corrosion cracking that the bottom tube plate leaked during the startup procedure. The risk was mitigated by reviewing the stress-relieving procedure with fabricator to ensure that residual stresses were reduced below the SCC threshold.

#### 4.40.5 Mitigation of Specific Corrosion Risks

##### 4.40.5.1 External Corrosion Risks

Carbon steel and reinforced concrete infrastructure such as structural steelwork and pipe bridges is

vulnerable to atmospheric corrosion in chemical plants that may be exacerbated by contamination of the atmosphere by process fumes and/or fluids and is mitigated by the use of appropriate coatings. More insidious corrosion risks arise on carbon and low-alloy and stainless steel equipment surfaces beneath fireproofing and thermal insulation materials. Passive fireproofing materials are based normally on Portland cement or lightweight concretes (e.g., vermiculite). The most commonly used thermal insulation materials are organic foams such as polyisocyanurate (PIR) foam, mineral wool and calcium silicate that are preferred for cold (below ambient), warm (typically  $< \sim 350^\circ\text{C}$ ) and hot (typically  $> \sim 350^\circ\text{C}$ ) duties, respectively. The insulation is normally overlaid with mastic or clad with metal to prevent water ingress.

Corrosion risks arise when water from rainfall, cooling tower spray, leakage or spillage, fire deluge systems or other sources penetrates through cracks in the fireproofing or gaps in the outer insulation system arising from the loss of weatherproofing because of poor design and/or construction, deteriorated seals or mechanical damage. Corrosion risks are increased if water is entrapped on horizontal surfaces without drainage or in the annular spaces between equipment surfaces and deteriorated protective coatings, thermal insulation or fireproofing. The corrosivity of the entrapped water depends on the composition of the fireproofing or insulation material. Portland cement

and calcium silicate produce relatively alkaline solutions that are least aggressive. Mineral wool produces relatively neutral solutions but organic foams can produce relatively acid extracts that are particularly aggressive. The corrosivity is further increased by acid fumes and accumulations of chlorides from coastal atmospheres, road salt and other sources which are further concentrated on hot equipment surfaces by repeated wetting/drying cycles.

Carbon and low alloy steels are vulnerable to general corrosion in the temperature range  $-5$  to  $\sim 150^{\circ}\text{C}$ . Below  $-5^{\circ}\text{C}$ , corrosion rates are very low and above  $\sim 150^{\circ}\text{C}$  surfaces are dry, although thermal cycling across the boundary temperatures can reintroduce corrosion risks. Corrosion rates peak in the temperature range  $80$ – $100^{\circ}\text{C}$  within which corrosion rates up to  $\sim 5\text{ mm year}^{-1}$  have been recorded. Particularly, vulnerable design features include penetrations of the insulation cladding at vents, drains, hangers, supports, valves, ladders, platforms and similar features, steam-traced systems, stiffening or insulation support rings and other water trap features and improper sealing at flange terminations, or hardened, cracked, or separated sealants. A classic example of corrosion of a warm vessel shell that experienced sustained exposure to water held up in a non-draining stiffening ring is shown in **Figure 10(a)**. Austenitic stainless steels under thermal insulation in the temperature range  $\sim 50$ – $150^{\circ}\text{C}$  are significantly vulnerable to external, chloride-induced, stress corrosion cracking (ESCC). Above  $\sim 150^{\circ}\text{C}$ , the risk is negligible because surfaces are dry although periodic cycling to lower temperatures reintroduces the risk. Below  $\sim 50^{\circ}\text{C}$ , the initiation and propagation of stress corrosion cracks are possible, depending on the hygroscopicity of the salts that are present, but operating experience confirms that the practical risks are very small for most process applications. A typical example

of ESCC of an austenitic stainless steel pipeline from which the insulation has been removed is shown in **Figure 10(b)**.

In a recent study of the costs of corrosion to the UK chemicals and petrochemicals sector,<sup>19</sup> external corrosion emerged as the largest individual source of expenditure on corrosion in the industry. This is, in large measure, a legacy cost associated with the remediation of elderly assets that were designed and constructed to standards that are now recognized as deficient in relation to the mitigation of external corrosion risks. The industry has devoted considerable effort to the mitigation of external corrosion risks and the resulting guidance has been codified.<sup>20–22</sup> For new equipment, the options are

1. Design of equipment to prevent water ingress by shedding water away from joints that are sealed effectively, and to prevent water hold-up by the provision of effective drainage.
2. Application of coatings that may be organic, if compatible with the service temperature range, or metallic; particularly, thermally sprayed aluminum (TSA) coatings and aluminum foil<sup>23</sup> have been identified as cost-effective for carbon and stainless steels, respectively.
3. Selection of corrosion-resistant materials for equipment; for small pipe sizes, austenitic stainless steel is an economic alternative to protected carbon steel for service temperatures below  $\sim 50^{\circ}\text{C}$ , and for equipment that operates at temperatures in the vulnerable range for ESCC, duplex grades of stainless steel may be an economic alternative to protected austenitic stainless steel.
4. Control of insulation composition, principally by the avoidance of PIR foam for warm insulation systems; inhibited insulation materials with controlled chloride levels are available but are not widely used.
5. Construction supervision, in particular the technical supervision and inspection of coating, fire-proofing, and insulation operations to ensure compliance with specifications.

For existing equipment, risks are mitigated by appropriate inspection and repair or replacement. Risk-based inspection (RBI) methodologies may be used to identify high-risk locations<sup>24</sup> that are examined after local insulation removal using surface crack detection and/or ultrasonic thickness measurement. There are available NDE techniques that do not require insulation removal, such as infrared thermography to detect areas of inadequate insulation,

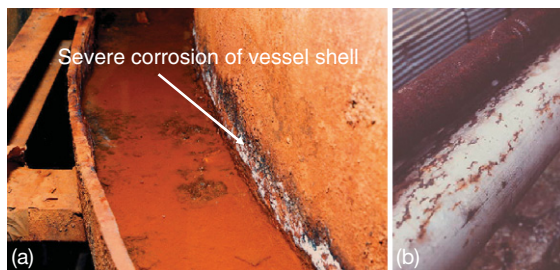


**Figure 10** External corrosion under thermal insulation (a) general corrosion of carbon steel vessel shell and (b) external stress corrosion cracking of austenitic stainless steel pipe.

flash (profile) radiography to detect wall thinning of carbon steel pipework or small vessels and long-range, low-frequency ultrasonics to detect wall thinning of carbon steel pipework.

#### 4.40.5.2 Internal Corrosion Risks

Industry equipment is required to operate in a plethora of chemical environments that consist of or contain mixtures of organic chemicals and acids, mineral acids, alkalis, salts and gases. The recognition and mitigation of the attendant corrosion risks presents significant challenges but is enabled by the major progress that has been made in understanding and dimensioning the corrosion performance of engineering materials and good corrosion control practices in industry equipment. This work has inevitably focused on specific chemicals or common process fluids or operations that present significant SHE or financial risks in the event of failure due to corrosion during storage and/or processing. Much of this learning has been codified in the standards, and recommended practices of technical organizations that industry professionals use for collaborative work and guidance is available on the mitigation of corrosion risks arising from the major recognized corrosive environments including:

1. organic chemicals<sup>38,53</sup> and acids<sup>26,45</sup>;
2. mineral acids including sulfuric,<sup>25,41,43,54,55</sup> hydrochloric,<sup>27,33,46</sup> hydrofluoric,<sup>28,47</sup> nitric,<sup>29,33,44</sup> phosphoric,<sup>31,34,51</sup> carbonic<sup>35</sup> and mixed acids<sup>32</sup>;
3. alkalis including sodium,<sup>30,32,49</sup> potassium,<sup>39</sup> and ammonium<sup>30,39,49</sup> hydroxides;
4. salts, including chlorides,<sup>37,42</sup> hypochlorites,<sup>34</sup> sulfates,<sup>40</sup> and mixed salts<sup>52</sup>;
5. gases, including hydrogen chloride,<sup>27,46</sup> hydrogen fluoride,<sup>28,47</sup> chlorine,<sup>48</sup> ammonia,<sup>30,39,50</sup> hydrogen,<sup>56</sup> and hydrogen sulfide<sup>57</sup>;
6. specific process fluids or operations in the petroleum refining sector such as crude unit over-heads,<sup>15</sup> naphthenic acids,<sup>58</sup> hydroprocessing,<sup>59</sup> hydrofluoric acid alkylation,<sup>60</sup> and sour water stripping.<sup>61</sup>

A particular focus of collaborative industry work has been the mitigation of EAC risks that present the most significant risks of loss of containment, the mechanisms of which are described in other relevant chapters in this book. **Figure 11** summarizes the more common alloy/environment systems that are vulnerable to EAC in process equipment. A recent industry survey,<sup>62</sup> summarized in **Figure 12**, concluded that ~60% of

- Steels
  - Alkalis
  - Nitrates
  - Anhydrous ammonia
  - Carbonate/ bicarbonate
  - Aqueous CO/CO<sub>2</sub>
  - Hydrogen cyanide
  - Hydrogen sulfide
  - Hydrogen
  - Amines
  - Boiler water
  - Ethanol...
- Copper alloys
  - Ammonia
  - Amines...
- Stainless steels
  - Alkalis
  - Chlorides (waters)
  - Polythionic acids
  - Hydrogen sulfide
  - Hydrogen...
- Nickel alloys
  - Alkalis
  - Hydrogen...
- Titanium alloys
  - Anhydrous methanol
  - Anhydrous nitric acid
  - Hydrogen...
- Zirconium alloys
  - Sulfuric acid...

**Figure 11** Some alloy–environment systems that are vulnerable to EAC in process equipment.

industry EAC failures are associated with stainless steels, despite the fact that most process equipment is constructed from carbon and low alloy steels. This is a reflection of the vulnerability of austenitic stainless steels to chloride-induced stress corrosion cracking (SCC), particularly under thermal insulation and fireproofing.

The majority of industry guidance and recommended practice for the mitigation of EAC risks to process equipment relates to the performances of carbon and low alloy steels. The interrelation of the various cracking risks that arise in corrosive petroleum refining environments is summarized in **Figure 13**, which is adapted from a recommended practice<sup>63</sup> that is widely used in the industry. Guidelines are available for the detection, repair and mitigation of cracking in existing equipment that operates in wet hydrogen sulfide service.<sup>64,65</sup> For new or replacement equipment, mitigation of cracking due to hydrogen charging is based on the control of base metal chemistry and the hardness of welds and heat-affected zones (HAZ) within the threshold levels and, if appropriate, post-weld heat treatment (PWHT).<sup>66</sup> Sulfide stress cracking (SSC) risks are mitigated by hardness control according to NACE standard MR0103,<sup>67</sup> which was developed recently to differentiate downstream fluids (containing ammonia and/or hydrogen cyanide) from upstream fluids (containing CO<sub>2</sub> and/or chloride) that were used historically for defining both upstream and downstream sour service according to the long-established NACE standard MR0175. For ASME IX P1 or 2 steel grades, from which most equipment is constructed, there are no base material hardness requirements, but welds and HAZs are controlled within hardness number limits of 200 HB on the Brinell scale and 248 HV on the



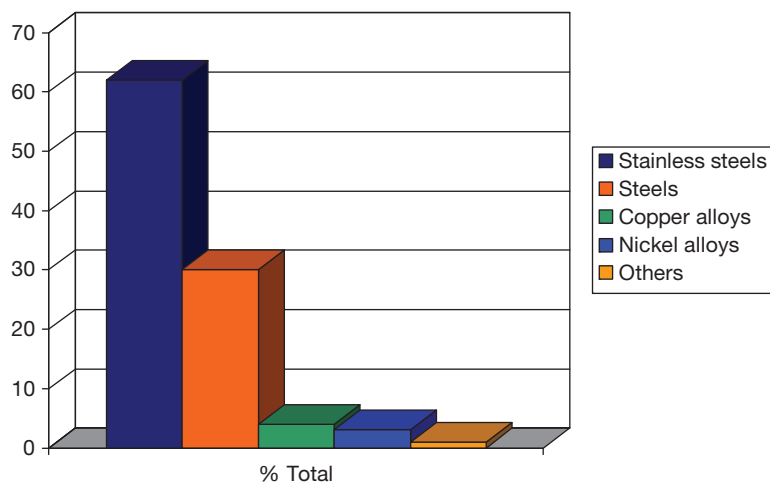
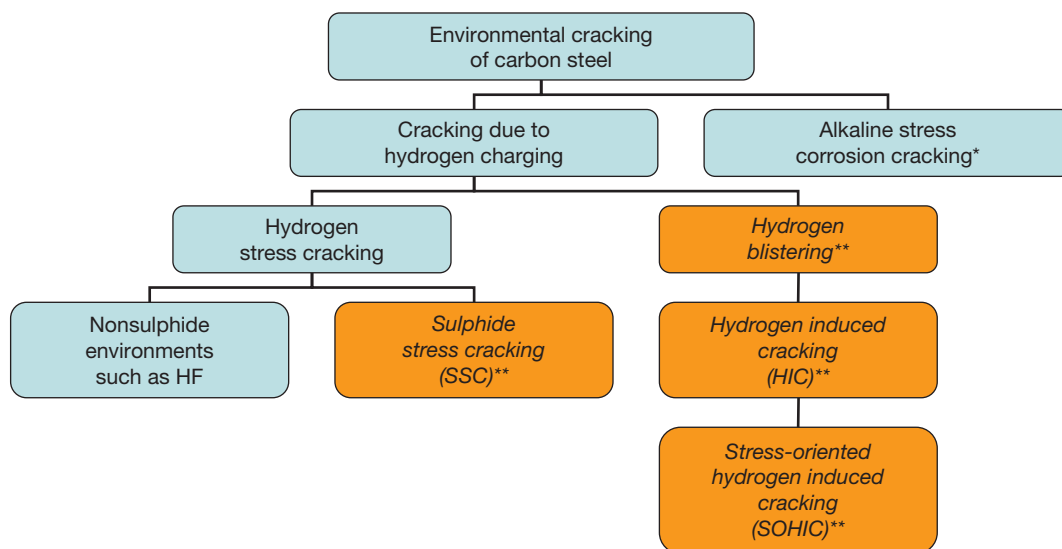


**Figure 12** Frequency of EAC in process equipment as a function of alloy class. Reproduced from Puyear, R. B. *Corrosion Failure Mechanisms in Process Industries - A Compilation of Experience*; MTI Publication 9502-R4, Materials Technology Institute of the Process Industries, 1997.



\*Environments such as caustic, alkanolamine solutions containing CO<sub>2</sub> and/or H<sub>2</sub>S, alkaline sour waters containing carbonates.

\*\*Italicised mechanisms referred to collectively as 'wet H<sub>2</sub>S cracking' when they occur in wet hydrogen sulphide environments.

**Figure 13** Interrelationships of the various EAC mechanisms for carbon steels in corrosive petroleum refining environments. Adapted from NACE Standard Recommended Practice RP0472-2005: *Methods and Controls to Prevent In-service Environmental Cracking of Carbon Steel Weldments in Corrosive Petroleum Refining Environments*; NACE International, 2005.

Vickers scale, respectively. The corresponding risks of hydrogen-induced cracking (HIC) and stress-oriented hydrogen-induced cracking (SOHIC) in the base materials are mitigated by controlling steel chemistry and microstructure (including limits on sulfur

content and inclusion shape control) and manufacture (in particular, rolling conditions), and confirming resistance by appropriate testing.<sup>68-70</sup>

A typical example of damage to a carbon steel vessel in a wet hydrogen sulfide environment is

shown in **Figure 14**, which relates to failure of a nonstress-relieved vessel for storing crude propane, operating at 17 bar and  $\sim 50^\circ\text{C}$ . The steel vessel contained type II MnS inclusions and anomalous microstructures that rendered it vulnerable to HIC and blistering damage in an  $\text{H}_2\text{S}$ -containing aqueous phase that separated out in the vessel base within the vulnerable temperature range (commonly  $15\text{--}35^\circ\text{C}$ , but possible up to  $\sim 120^\circ\text{C}$ ). There was no associated SSC, because weld and HAZ hardnesses were below the threshold levels for cracking. By the time this damage was detected by internal inspection, the vessel was beyond repair but was rendered fit for short-term operation, while a new vessel was procured by drilling the more severe blisters externally to relieve internal stresses. EAC risks were mitigated for the replacement vessel by selecting an HIC-resistant grade of steel and appropriate welding procedures and specifying PWHT of the vessel to further mitigate the risks of SSC of the welds.

Hydrogen-related EAC mechanisms for carbon and low-alloy steels are more prevalent in the petroleum refining and petrochemical sectors than in the wider chemical industry, where SCC mechanisms dominate. There is available industry guidance on the mitigation of SCC risks that are also of interest to the petroleum refining and petrochemical sectors such as in caustic<sup>71</sup> and amine<sup>72</sup> environments, boiler feed waters<sup>73</sup> and fuel-grade ethanol.<sup>74</sup> However, guidance on the mitigation of other SCC risks for carbon and low-alloy steels such as those that arise in solutions of nitrate,<sup>75</sup>

carbonate/bicarbonate,<sup>76</sup>  $\text{CO}/\text{CO}_2$ <sup>77</sup> and hydrogen cyanide<sup>75</sup> tends to be more organization-specific and/or more widely scattered in the open literature. Nevertheless, practicable design and operating practices that mitigate SCC risks have been developed for all of these systems based on experience and experimental research to understand and dimension the factors that control initiation and propagation of cracking, as can be illustrated for the case of SCC of steels promoted by anhydrous ammonia.<sup>78</sup>

Anhydrous ammonia is stored and transported in large quantities around the world in carbon steel tanks and vessels that are mostly nonstress-relieved and operating under conditions that range from atmospheric pressure at a temperature of  $-33^\circ\text{C}$  to significant pressures at ambient temperatures. In the early 1980s, it was recognized that such storage equipment is at significant risk of SCC of welds and HAZs, as summarized in **Figure 15**. Industry-sponsored research<sup>79</sup> established that

1. Crack initiation risks increase with temperature above  $-33^\circ\text{C}$  and with steel strength.
2. Crack initiation risks increase with oxygen content and decrease with water content of the ammonia. However, water partitions preferentially into the liquid phase, so condensates from the vapor phase above a water-inhibited liquid phase may still initiate cracks.
3. Cracks propagate at relatively low velocities that reduce with time.

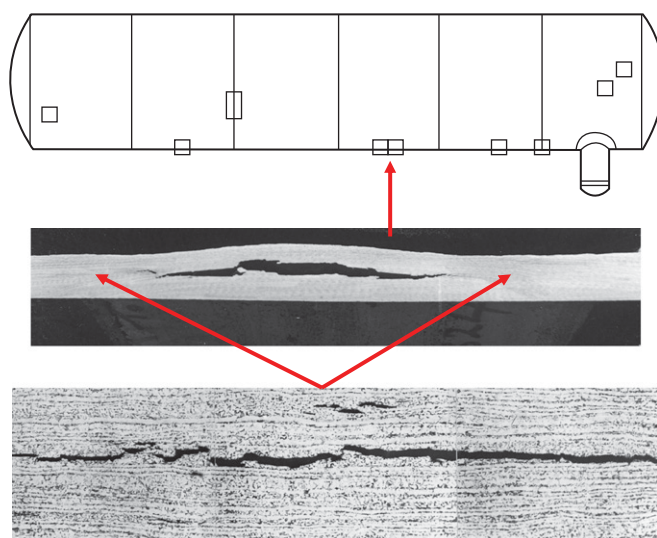


**Figure 14** HIC/blistering of a propane accumulator vessel base because of contact with an  $\text{H}_2\text{S}$ -containing aqueous phase but no associated SSC because the weld/HAZ hardnesses were below threshold levels.

The risk mitigation options that emerged from the research work were:

1. Reduction of initiation risks by specifying relatively soft steels and welds and/or stress relieving new vessels, if practicable, and by controlling ammonia composition in service by eliminating oxygen and/or adding a threshold amount of water if practicable.
2. Reduction of risks arising from crack propagation in service by the management of inspection and repair.

On the basis of these findings, various approaches have emerged for the management of SCC in anhydrous ammonia storages typified by that developed in

Australia,<sup>80</sup> summarized in **Table 1**. Clearly, mitigation by the use of relatively soft steels is impractical for most situations. For relatively small transport vessels, where it is impractical to control ammonia composition because of the frequency of filling and emptying operations, mitigation is achieved by a combination of thermal stress relief and relatively regular, mandatory inspections. On the other hand, for large storage vessels for which thermal stress relief is impractical, mitigation is based on the control of ammonia composition together with appropriate inspection or repair policies that may include probabilistic approaches to scheduling inspection and maintenance.<sup>81</sup>

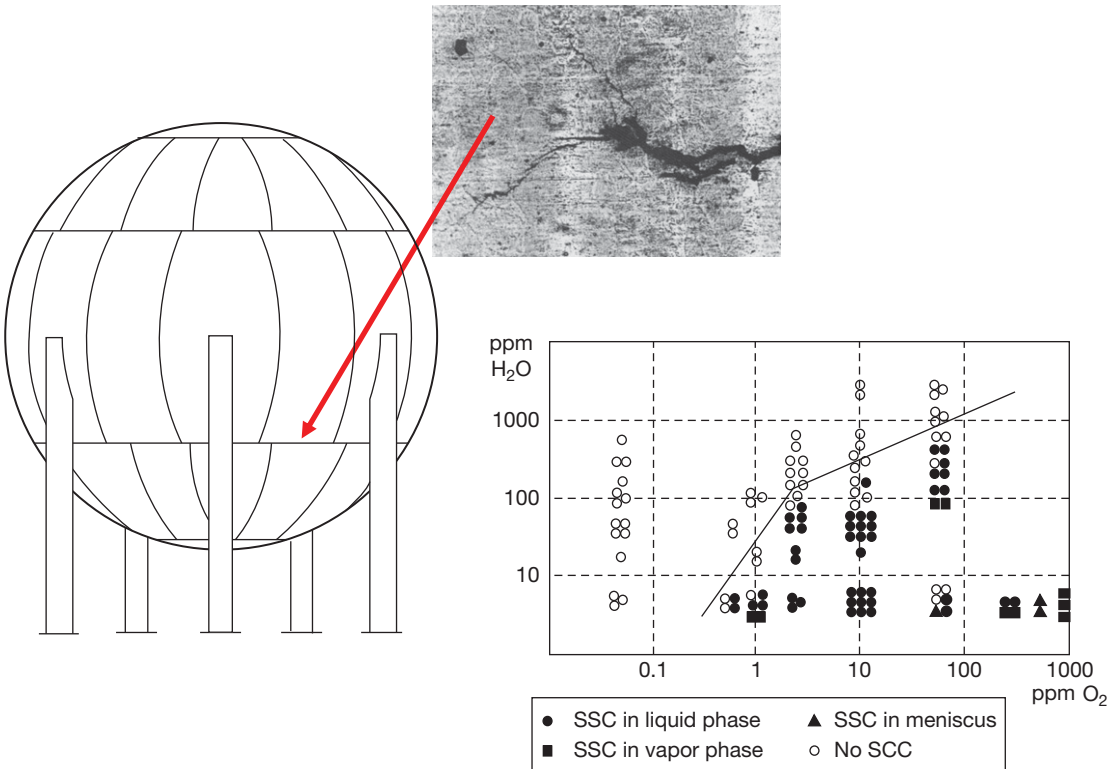


**Figure 15** Welds in nonstress-relieved anhydrous ammonia storages may be vulnerable to SCC, depending on the relative contents of oxygen and water in the ammonia.<sup>78,79</sup>

**Table 1** Australian<sup>80</sup> approach to the management of carbon steel storage and transport vessels to mitigate risks arising from SCC promoted by anhydrous ammonia

Mitigation option	Storage tanks	Road/rail tankers
Use steels <300 MPa yield	Most steels stronger	Most steels are Q & T and stronger
Stress relieve	Impractical	Mandatory if >300 MPa yield
Eliminate oxygen	Minimize inspection frequency, control recommissioning	Impractical
Add 0.2% water	Normal practice	Vapor space?
Manage inspection/repair	Develop noninvasive inspection and fitness for service (FFS) approaches	Mandatory internal inspection every 1 or 2 years

Regarding the mitigation of industry EAC risks to materials other than steels, stress relief is rarely used and mitigation is more focused on the avoidance of material/environment combinations that present risks. Guidance also tends to be more organization-specific than for steels and/or more widely scattered in the open literature, as for the avoidance of the most frequent cause of failure, the chloride-induced SCC of austenitic stainless steels. Some sources are comprehensive in scope<sup>75</sup> while others relate to specific process duties such as thermal insulation<sup>20</sup> and water-cooled heat exchangers.<sup>82</sup> Guidance on the avoidance of caustic cracking of stainless steels is more limited but there are sources that define environmental conditions that present risks.<sup>83</sup> However, there are detailed recommended practices for mitigating the risks of polythionic acid-induced SCC of austenitic stainless steels and other austenitic alloys during the shutdown of refinery equipment<sup>84</sup> and for avoiding sulfide-induced stress cracking (SSC) of stainless steels and nickel, cobalt, titanium, aluminum, and copper alloys in corrosive petroleum refining environments containing H<sub>2</sub>S.<sup>67</sup>

The author's own unpublished survey of EAC experience over a 20-year period within a world scale chemical company concluded that EAC failures arose principally (~70% of all cases) from failure to identify or control environments that presented a significant threat due to lack of awareness of the EAC potential of an environment, inadequate chemistry definition, inadequate chemistry control, or unpredicted contamination with EAC-promoting chemicals. The biggest single cause of unpredicted EAC failure was the development of EAC-promoting microenvironments at specific equipment locations and stages of operation, and of this group the commonest example (~30% of all cases) was ESCC of austenitic stainless steels. Of the remaining cases, ~20% arose from materials causes, either selection of the wrong material or of the right material in the wrong condition, and a small minority (~10% of all cases) arose from failure to control stress, principally, as a result of inefficient stress relief.

#### 4.40.6 Mitigation of Corrosion Risks During Operation

Operating process equipment is not managed by corrosion engineers but by other professionals whose goals include the development and maintenance of equipment to provide increased availability and reliability without jeopardizing the organization's SHE

obligations that require the avoidance of incidents and assurance of structural integrity. The processes that may be adopted to manage corrosion are reviewed in detail in a separate chapter in this book. However, in most organizations the management of corrosion is not a separate functional activity but is integrated into more familiar asset management functions such as production and maintenance. Within this framework, the management of corrosion during operation is defined by two key objectives:

1. Ensuring that the design intents in relation to the mitigation of corrosion risks are delivered during operation. This requires that processes are operated within the design envelope in relation to all of the factors that can influence corrosion risks such as the compositions, temperatures and velocities of process fluids, the intensities of heat fluxes, etc. It also requires that corrosion control practices that were specified in design, such as inhibitor addition, electrochemical protection, etc. are operated continuously to design specification.
2. Dimensioning and understanding the corrosion performance of equipment by inspection and monitoring, and embedding corrosion performance data in asset development and maintenance databases so that corrosion risk mitigation is integral to the maintenance management processes that capture history and learning in pursuit of reduced maintenance costs and increased reliability and availability.

The delivery of these objectives requires the promotion of corrosion awareness and commitment amongst production and maintenance personnel who are accountable for delivering manufacturing performance. Effective corrosion management derives from influential corrosion professionals operating within the appropriate management systems.

Central to the management of corrosion during operation is assurance of the structural integrity of process equipment and this has been enabled by continuing developments in protocols and techniques for the inspection and monitoring of process equipment that are described in separate chapters of this book:

1. RBI procedures<sup>85–87</sup> are now the norm for process equipment. Large companies have developed their own protocols, and proprietary procedures are available from numerous sources. An essential first stage for any organization is the calibration of the risk/consequences matrix by defining acceptance criteria for the probability and

consequences of failure within a specified time-scale. This is a team activity, requiring contributions from equipment specialists and inspectors, process engineers, and operations and maintenance personnel in addition to materials/corrosion specialists. The required effort and cost of an RBI process increases with the period under consideration and a common practice is to focus on a limited number of turnaround periods rather than the full design life of equipment. It is important that the risks of external as well as internal corrosion are evaluated for equipment items. As indicated previously, the semiquantitative evaluation of corrosion risks is normally regarded as sufficient for process equipment, based on the mostly empirical corrosion data that are used to predict corrosion performance, the reliability of which is classified as high, medium, or low, depending on the source.<sup>88</sup> The contributions of materials and corrosion specialists are crucial to the accurate evaluation of risks. Key outputs of RBI processes are risk rankings for equipment items and corresponding inspection plans and other risk mitigation activities to be adopted. Inspection plans detail the inspection methods to be adopted in defined areas and locations, and the timing of examinations. Other risk mitigation activities include fitness for service (FFS) evaluation based on codified<sup>89</sup> defect and remnant life assessment procedures that are described in a separate chapter in this book, the adoption of methods to monitor deterioration rates and their variation, and equipment repair or replacement, or modification or redesign. Anticipated reductions in risk levels are predicted after inspection plans and other risk mitigation activities are implemented. The key benefit of RBI has been to focus management attention and effort on the most significant risks to the structural integrity of equipment, including corrosion risks. However, RBI has also delivered significant economic benefits, due not least to improvements in the planning and scheduling of maintenance.

2. Noninvasive NDE technologies are available, including acoustic emission (AE) and scanning ultrasonics (UT) that allow the condition of equipment to be established while the equipment continues to operate, without the need to shut down and prepare equipment for entry. AE detects and locates internal flaws in metal or FRP-pressurized systems by detecting acoustic emissions from defect micropagation processes with external, surface-mounted,

piezoelectric probes. Emissions are triggered by raising the pressure beyond the design or previous operating levels and their amplitude is a guide to the severity of the defect. The entire structure is assessed in one; rapid operation and triangulation techniques allow emissions to be positioned within  $\sim 10$  mm. Defects that have been located by AE can be sized using external ultrasonic techniques online if permitted by access and operating temperatures. Automated C-scan ultrasonic techniques allow mapping of corrosion distribution by computer control, processing, storage and imaging of ultrasonic signals. P-scan techniques produce 3-D reconstructions of defect locations and sizes from robotic manipulation of probes and computer processing of signals. Having been located and sized, defects can be assessed for their significance using appropriate FFS<sup>89</sup> procedures, allowing the entire structural integrity evaluation process to be undertaken without interrupting production.

3. Online corrosion monitoring technologies are available that are noninvasive and allow monitoring of equipment directly without having to resort to probes, including hydrogen permeation,<sup>90</sup> thin layer activation (TLA),<sup>91</sup> field signature monitoring (FSM)<sup>92</sup> and pulsed eddy current (PEC).<sup>93</sup> Technologies are also available based on electrochemical noise (ECN)<sup>94</sup> that is sensitive in real time and to localized corrosion. Examples of the uses of corrosion monitoring to deliver increased plant availability are illustrated in **Figures 16 and 17**. The case illustrated in **Figure 16** relates to a well known hydrocracker corrosion problem in refineries. As shown in the simplified process flow diagram, reactor effluent, a mixture of hydrogen, hydrogen sulfide, hydrocarbons and salts such as ammonium bisulfide ( $\text{NH}_4\text{HS}$ ), is cooled in air coolers upstream of which water is injected to prevent corrosive salt accumulation in equipment. In the particular case,<sup>95</sup> the air cooler exit pipework constructed in carbon steel suffered  $\text{NH}_4\text{HS}$ -induced, flow-assisted corrosion at higher rates than anticipated in the design. Corrosion rates were monitored online using PEC sensors that were strapped onto pipes as shown in **Figure 16**. PEC offers significant advantages over ultrasonic determinations of wall thickness because of its greater repeatability, which allows corrosion rates to be determined more rapidly. Data typified by that shown in **Figure 16** for an elbow in an exit pipe provided justification for an extended run-time while replacement material was procured and a shutdown was planned. The case illustrated in



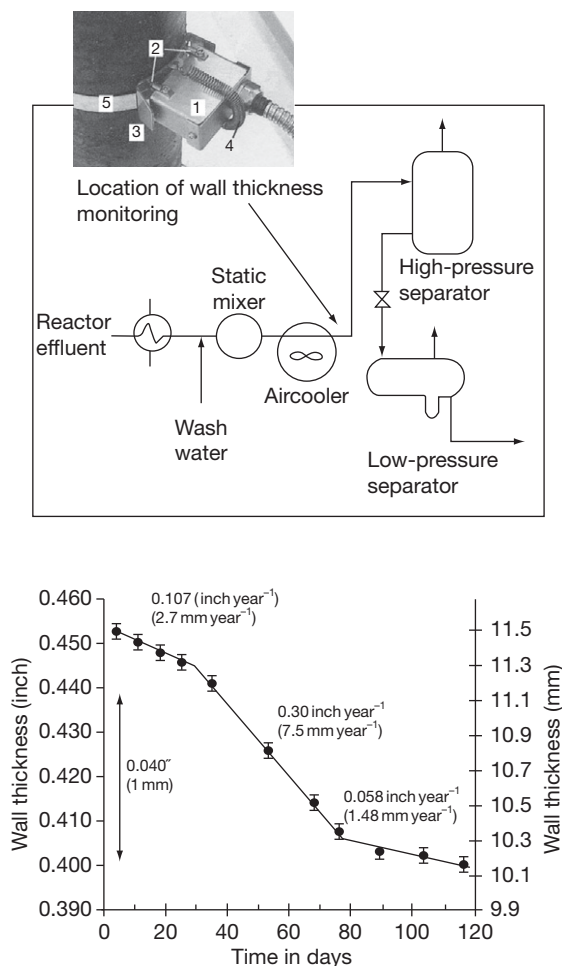


**Figure 16** Online, pulsed eddy current (PEC) monitoring of carbon steel piping wall thickness provides justification for an extended hydrocracker run-time to procure replacement material and plan a shutdown. Reproduced from Crouzen, P. C. N.; Munns, I. J.; Verstijnen, W.; Hulsey, R. C. In *Corrosion 2006*, NACE International, 2006; Paper 06312.

**Figure 17** relates to the start-up stage of an ethylene dichloride (EDC), fluidized bed reactor. Reactors are constructed typically in carbon and low alloy steels and relevant process flows in the reactor are shown schematically in **Figure 17**. The greatest risk of corrosion occurs during plant start up in the event that condensation of the hydrochloric acid feed occurs on steel surfaces. In the particular case,<sup>96</sup> steel reactor internals had suffered excessive corrosion and real-time ECN monitoring using an appropriate multielement corrosion probe established that corrosion rates up to  $\sim 50 \text{ mm year}^{-1}$  were experienced during start up due to condensation because the catalyst feed temperature ( $100^\circ\text{C}$ ) was

too low and the time interval between the hot ( $160^\circ\text{C}$ ) air and catalyst feeds to the reactor was too short. Typical temperature and corrosion rate profiles before and after adopting a revised startup procedure involving a higher catalyst feed temperature ( $140^\circ\text{C}$ ) and a longer time interval are shown in **Figure 17**. As a result of these changes, corrosion rates during start up were reduced by a factor of five resulting in extended lives for carbon steel internals and a significant (2%) increase in the availability of the reactor.

#### 4.40.7 Corrosion Risk Management Costs and Benefits

A recent study<sup>19</sup> of the UK petrochemicals/chemicals sector estimated that total expenditure on corrosion management amounted to  $\sim 4.5\%$  of industry turnover. The majority of this expenditure was spent optimally and beneficially, comprising the inevitable costs of mitigating the corrosion risks associated with the processing corrosive and hazardous fluids to add value without incurring unacceptable financial or SHE consequences. However, two areas of avoidable expenditure were identified:

1. In the cases of ageing, individual plants and sites that were designed, fabricated and protected to standards now recognized as inadequate, estimated expenditure on corrosion management as high as  $\sim 9\%$  of turnover was identified. The great majority of this expenditure was associated with historical deficiencies in the awareness and management of external corrosion of carbon and stainless steels under thermal insulation and fire-proofing that have resulted in major remedial expenditure to mitigate risks. This emerged as the largest individual corrosion cost to the industry but it should be a one-off legacy cost that declines as the risks to replacement or new equipment are mitigated by improved design, specification and fabrication practices.
2. It was estimated that  $\sim 15\%$  of the total expenditure on corrosion was associated with problems for which there are proven, economic solutions and was avoidable by better application of existing corrosion control technology and management practices. Some of the wasted expenditure arose from deficient materials selection and design practices relating to the mitigation of risks such as the localized corrosion of stainless steels and nickel alloy equipment, particularly at welds; erosion and

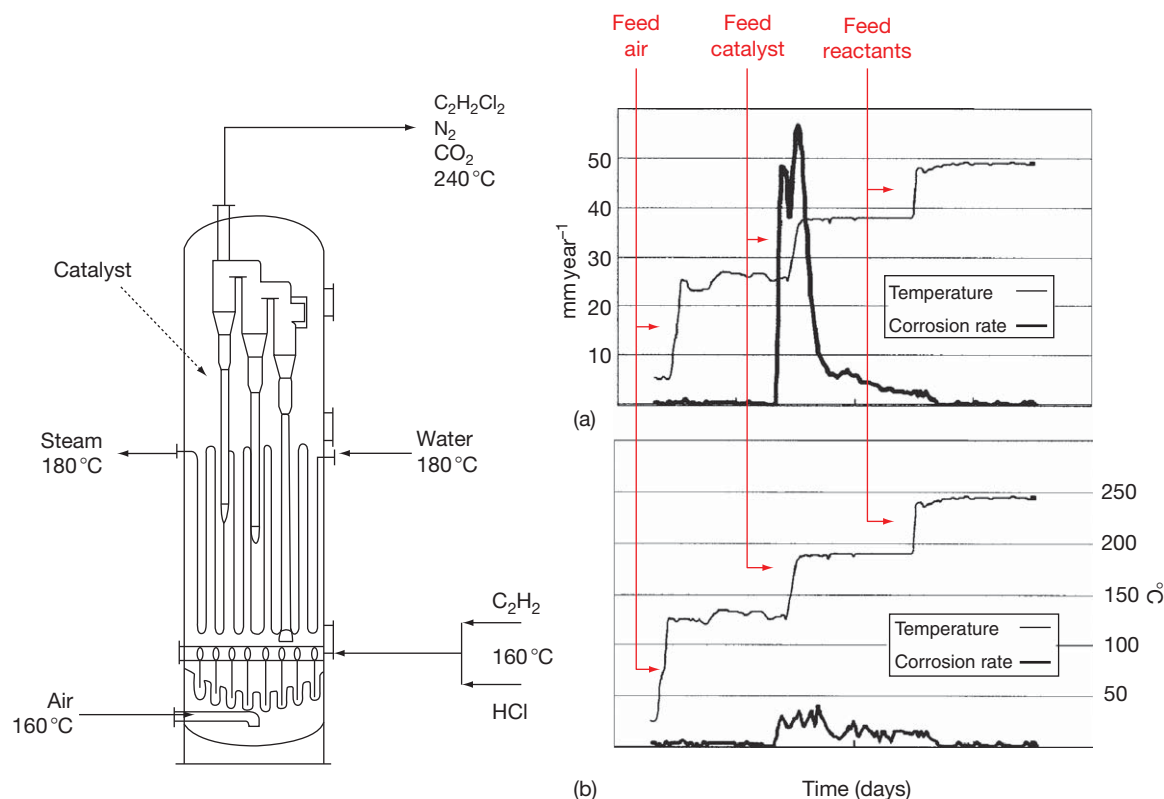


**Figure 17** Corrosion rate profiles obtained by ECN monitoring during start up of an EDC reactor (a) before and (b) after implementing measures to prevent condensation of HCl on internal steel coil/pipe surfaces. Reproduced from Ohtsu, T.; Miyazawa, M. In *Corrosion 2007*, NACE International, 2007; Paper 07266.

erosion corrosion in piping and heat exchangers; galvanic corrosion, particularly at specified transitions from one material to another in piping; the corrosion of heating/cooling coils in batch vessels, etc. Other wasted expenditure arose from deficiencies in the management of corrosion in operation, not least the control of corrosion in cooling water and steam raising equipment.

The UK study also identified several developing and new processes for which corrosion risks present significant barriers to commercialization because cost-effective mitigation practices have yet to emerge, typified by processes that promote metal dusting and organic oxidation processes undertaken in supercritical water (SCW):

1. Metal dusting is described in a separate chapter in this book and is a risk under process conditions that favor carbon deposition as a result of the disproportionation and/or reduction of carbon monoxide in gas mixtures that also contain hydrogen as summarized in [Figure 18](#). A common

example is synthesis gases that are formed by the steam reforming of hydrocarbons. Carbon deposition is catalyzed on surfaces that contain iron, nickel, and cobalt and the rate of carbon uptake is a balance between thermodynamic and kinetic driving forces. Metal dusting is a relatively low-temperature phenomenon with rates that generally peak in the temperature range  $\sim 400\text{--}800^\circ\text{C}$ . Penetration of carbon reduces ductility and results in transformation to a mixture of oxide, alloy and carbon particles which can shed resulting in general or localized corrosion that can be very rapid.<sup>97</sup> All high temperature alloys are vulnerable to metal dusting but risks can be mitigated to some extent by the incorporation of strong oxide promoters such as chromium, aluminum and silicon, either in the alloy itself or on the surface by appropriate coating processes. In theory, risks may also be mitigated by increasing the ratio of steam or including catalyst poisons such as hydrogen sulfide in the process gas. However, process efficiency considerations favor lower rather than

higher steam ratios and catalyst poisoning concerns preclude sulfide additions. At the current state of art, robust and cost-effective materials solutions have yet to emerge and the migration of several world scale processes to the most efficient operating conditions remains inhibited by metal dusting risks.

- Over the past ~10 years there has been considerable interest in the potential of SCW as a solvent.

Solubility behavior is reversed in SCW so that organic materials are soluble and inorganic salts insoluble, allowing single-phase oxidation of organic materials (SCWO). Much of the early research interest has been focused on the development of processes for the destruction of hazardous wastes, as summarized in Figure 19. However, there has also been interest in the development of SCWO processes that may offer economic advantages over

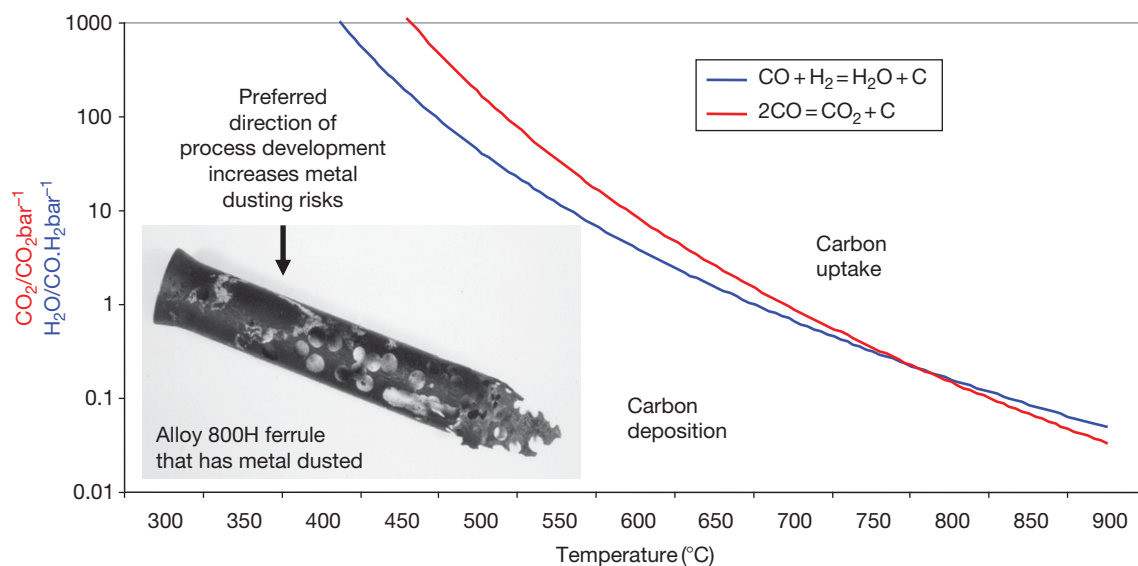


**Figure 18** Equilibrium ratios at unit carbon activity versus temperature for CO disproportionation and reduction processes – metal dusting threatens equipment operating at temperatures below unit carbon activity in any gas composition.

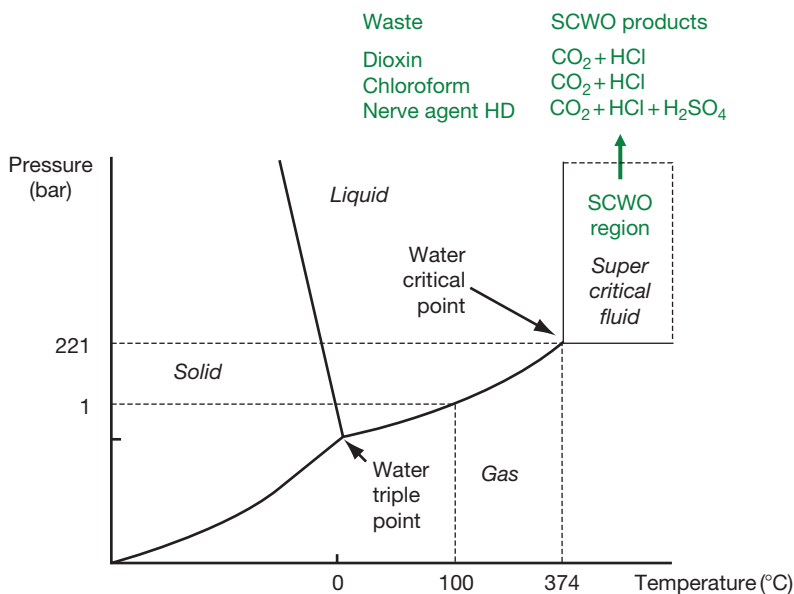


**Figure 19** Typical conditions and products of organic waste destruction by supercritical water oxidation (SCWO).

conventional processes for commercially important organic oxidations such as the oxidation of paraxylene to terephthalic acid.<sup>98</sup> Commercial application of SCWO technology requires materials that are resistant to corrosion under super- and subcritical conditions, at temperatures above  $\sim 300^\circ\text{C}$ . In processes where mineral acids are significant products of SCW oxidation, such as those summarized in **Figure 19**, corrosion is a potential show-stopper. In general, stainless steels are insufficiently resistant to corrosion, nickel alloys have shown major corrosion vulnerabilities, and although titanium and zirconium have shown useful corrosion resistances, they have other limitations relating to their strength and resistance to ignition at the prevailing temperatures and high oxygen pressures. Economic, robust, long-term materials solutions have proved elusive.<sup>99</sup>

#### 4.40.8 Future Trends in Process Equipment

The current trend to increasingly large, single stream plants seems likely to continue in the refining, petrochemical and commodity chemicals industries. For example, single stream sulfuric acid plants are

currently under construction with capacities of  $4\text{--}5000\text{ t day}^{-1}$ . There are challenges relating to the fabrication of extremely large vessels and the logistics of transporting them around the world, not to mention the operability of extremely large equipment and the high cost of unreliability. However, large capital cost savings provide the incentive that favors the trend.

Against the trend, there is growing interest in the advantages of microscale manufacture using micro-equipment, of the type shown in **Figure 20**. A key advantage of microequipment<sup>98,99</sup> is the possible reduction of manufacture, reaction and transport to the same timescales. Diffusion distances are reduced to minimize residence times, obviating the requirements for mixing/velocity in conventional equipment. This requires small flow channels, typically submicron to 1 mm with high surface-to-volume ratio and reduced residence times and process volumes. Lower diffusion resistances favor high catalyst selectivity. A manufacturing plant comprises a multitude of small or lab scale reactors.

Materials and fabrication techniques are drawn from the microelectronics and semiconductor industries. Materials include silicon, glass, ceramics and polymers as well as metals, fabricated with techniques that include lithography, electroplating, molding, etching,

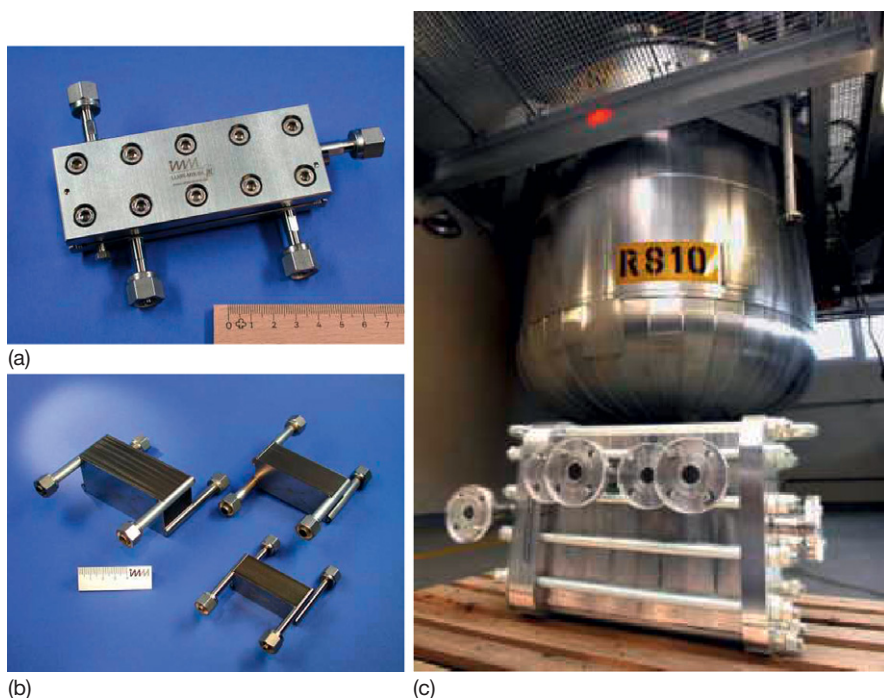


**Figure 20** Microprocess equipment for fine chemicals/pharmaceuticals manufacture: (a) liquid-liquid reactor,<sup>99</sup> (b) heat exchangers,<sup>98</sup> and (c) microstructured reactor with equivalent throughput to continuous stirred tank reactor in the background.<sup>99</sup>

micromachining, laser ablation, etc. Catalysts are applied using surface enhancement techniques such as anodic oxidation, or impregnation using PVD/CVD or ion implantation. This is clearly very different territory from traditional materials and corrosion engineering!

It remains to be seen what impact microscale manufacture will have on the industry as a whole. To date, interest seems to be focused mainly in the fine chemicals and pharmaceuticals sectors, where it has been strong enough to promote acquisitions of companies that specialize in the fabrication of such equipment.

#### 4.40.9 The Current Corrosion Risk Management Scorecard

The petrochemical/chemical industry has seen major advances in equipment reliability, availability, and SHE performances because of advances in corrosion understanding, control technology and management practices. However, unpredicted, SHE-threatening and/or expensive incidents continue to occur. Most are avoidable, arising from deficiencies in awareness and/or management of recognized corrosion risks for which there are proven, economic solutions, but some arise from problems for which there are not yet proven, economic solutions. Significant corrosion challenges/opportunities remain to be addressed.

## References

- Garrison, W. G. *Hydrocarb. Process.* **1988**, 67, 115–122.
- Katsumi, Y. *Corros. Eng.* **2004**, 53, 185–189.
- Moniz, B. J.; Pollock, W. I. Eds. *Process Industries Corrosion*; National Association of Corrosion Engineers, 1986.
- White, R. A. *Materials Selection for Petroleum Refineries and Gathering Facilities*; NACE International, 1998.
- Harston, J. D.; Ropital, F. *Corrosion in Refineries (EFC 42)*; European Federation of Corrosion, 2007.
- Dillon, C. P. *Corrosion Control in the Chemical Process Industries*; Materials Technology Institute, 1994.
- Garverick, L., Ed. *Corrosion in the Petrochemical Industry*; ASM International, 1994.
- In *ASM Handbook – Corrosion: Environments and Industries*; ASM International, 2006; Vol. 13C, pp 652–1037.
- [www.mtcnelbourne.com](http://www.mtcnelbourne.com)
- [www.hexalloy.com](http://www.hexalloy.com)
- [www.sglgroup.com](http://www.sglgroup.com)
- [www.nori-acidbrick.com](http://www.nori-acidbrick.com)
- Society for Protective Coatings/NACE Joint Standard No. 11/SSPC-PA8: *Thin Film Organic Linings Applied in Carbon Steel Process Vessels*; NACE International, 2003.
- [www.edlon.com](http://www.edlon.com).
- Crude Unit Overhead Corrosion Control*; Refining Industry Corrosion Information Compilation Series; NACE International, 2001.
- Kletz, T. A. *HAZOP and HAZAN: Identifying and Assessing Process Industry Hazards*, 4th ed.; Institution of Chemical Engineers: UK, 1999.
- API Publication 581: *Base Resource Document on Risk Based Inspection*; American Petroleum Institute, 2000.
- NACE Standard Practice SP0407-2007: *Format, Content and Guidelines for Developing a Materials Selection Diagram*; NACE International, 2007.
- McIntyre, P. Corrosion and associated costs in the UK chemicals and petrochemicals sector, Degradation of Materials in Aggressive Environments Programme (DME), Report NRW/PM/CORRO/D1; Paint Research Association, 2001.
- NACE Recommended Practice RPO198-2004: *Control of Corrosion Under Thermal Insulation and Fireproofing Materials – A Systems Approach*; NACE International, 2004.
- Ahluwalia, H. In *ASM Handbook – Corrosion: Environments and Industries*; ASM International, 2006; Vol. 13C, pp 654–658.
- Winnik, S., Ed. *Corrosion Under Insulation (CUI) Guidelines (EFC 55)*; European Federation of Corrosion, 2008.
- Richardson, J. A.; Fitzsimmons, T. In *Corrosion of Metals Under Thermal Insulation*, ASTM SP 880; Pollock, W. I., Barnhart, J. M., Eds.; American Society. For Testing and Materials, 1985; pp 188–198.
- Chauviere, M. M.; Krynicki, J. W.; Richert, J. P.; In *Corrosion 2007*; NACE International, 2007.
- Materials Selector for Hazardous Chemicals: Concentrated Sulphuric Acid and Oleum*, 2nd ed.; MTI Publication MS-1, Materials Technology Institute of the Process Industries, 2005; Vol. 1.
- Materials Selector for Hazardous Chemicals: Formic, Acetic and Other Organic Acids*; MTI Publication MS-2, Materials Technology Institute of the Process Industries, 1997; Vol. 2.
- Materials Selector for Hazardous Chemicals: Hydrochloric Acid, Hydrogen Chloride and Chlorine*; MTI Publication MS-3, Materials Technology Institute of the Process Industries, 1999; Vol. 3.
- Materials Selector for Hazardous Chemicals: Hydrogen Fluoride and Hydrofluoric Acid*; MTI Publication MS-4, Materials Technology Institute of the Process Industries, 2000; Vol. 4.
- Materials Selector for Hazardous Chemicals: Nitric Acid*; MTI Publication MS-5, Materials Technology Institute of the Process Industries, 2004; Vol. 5.
- Materials Selector for Hazardous Chemicals: Ammonia and Caustic Soda*; MTI Publication MS-6, Materials Technology Institute of the Process Industries, 2004; Vol. 6.
- Materials Selector for Hazardous Chemicals: Phosphoric Acid*; MTI Publication MS-7, Materials Technology Institute of the Process Industries, 2004; Vol. 7.
- DECHEMA Corrosion Handbook: Sodium Hydroxide, Mixed Acids*; Wiley-VCH, 2004; Vol. 1.
- DECHEMA Corrosion Handbook: Hydrochloric Acid, Nitric Acid*; Wiley-VCH, 2004; Vol. 2.
- DECHEMA Corrosion Handbook: Hypochlorites, Phosphoric Acid*; Wiley-VCH, 2005; Vol. 3.
- DECHEMA Corrosion Handbook: Carbonic Acid, Chlorine Dioxide, Seawater*; Wiley-VCH, 2005; Vol. 5.
- DECHEMA Corrosion Handbook: Atmosphere, Industrial Waste Gases*; Wiley-VCH, 2006; Vol. 6.
- DECHEMA Corrosion Handbook: Sodium Chloride*; Wiley-VCH, 2007; Vol. 7.
- DECHEMA Corrosion Handbook: Chlorinated Hydrocarbons*; Wiley-VCH, 2007; Vol. 8.



39. *DECHEMA Corrosion Handbook: Potassium Hydroxide, Ammonia, Ammonium Hydroxide*; Wiley-VCH, 2007; Vol. 9.
40. *DECHEMA Corrosion Handbook: Sodium Sulphate, Sulphur Dioxide*; Wiley-VCH, 2008; Vol. 10.
41. *DECHEMA Corrosion Handbook: Sulphuric Acid*; Wiley-VCH, 2008; Vol. 11.
42. *DECHEMA Corrosion Handbook: Iron Chlorides*; Wiley-VCH, 2009; Vol. 12.
43. Brubaker, S. K. In *ASM Handbook – Corrosion: Environments and Industries*; ASM International, 2006; Vol. 13C, pp 659–667.
44. Ahluwalia, H.; Eyre, P.; Davies, M.; Yau, T.-L. In *ASM Handbook – Corrosion: Environments and Industries*; ASM International, 2006; Vol. 13C, pp 667–673.
45. Scribner, L. A. In *ASM Handbook – Corrosion: Environments and Industries*; ASM International, 2006; Vol. 13C, pp 674–681.
46. Crum, J. R. In *ASM Handbook – Corrosion: Environments and Industries*; ASM International, 2006; Vol. 13C, pp 682–689.
47. Jennings, H. S. In *ASM Handbook – Corrosion: Environments and Industries*; ASM International, 2006; Vol. 13C, pp 690–703.
48. Liening, E. L. In *ASM Handbook – Corrosion: Environments and Industries*; ASM International, 2006; Vol. 13C, pp 704–709.
49. Davies, M. In *ASM Handbook – Corrosion: Environments and Industries*; ASM International, 2006; Vol. 13C, pp 710–726.
50. Davies, M. In *ASM Handbook – Corrosion: Environments and Industries*; ASM International, 2006; Vol. 13C, pp 726–735.
51. Ross, R. W. Jr. In *ASM Handbook – Corrosion: Environments and Industries*; ASM International, 2006; Vol. 13C, pp 736–741.
52. Sridhar, N. In *ASM Handbook – Corrosion: Environments and Industries*; ASM International, 2006; Vol. 13C, pp 742–749.
53. Ahluwalia, H.; Thodla, R. In *ASM Handbook – Corrosion: Environments and Industries*; ASM International, 2006; Vol. 13C, pp 750–753.
54. NACE Recommended Practice RP0391-2001: *Materials for Handling and Storage of Commercial Concentrated (90–100%) Sulphuric Acid at Ambient Temperatures*; NACE International, 2001.
55. NACE Standard Practice SP0254-2006: *Design, Fabrication and Inspection of Storage Tank Systems for Concentrated Fresh and Process Sulphuric Acid and Oleum at Ambient Temperatures*; NACE International, 2006.
56. API Recommended Practice RP941: *Steels for Hydrogen Service at Elevated Temperatures and Pressures in Petroleum Refineries and Petrochemical Plants*; American Petroleum Institute, 2008.
57. Gutzeit, J. In *Process Industries Corrosion – The Theory and Practice*; National Association of Corrosion Engineers, 1986; pp 367–372.
58. *Naphthenic Acid Corrosion – Refining Industry Corrosion Information Compilation Series*; NACE International, 2001.
59. *Hydroprocessing Units – Refining Industry Corrosion Information Compilation Series*; NACE International, 2001.
60. API Recommended Practice RP751: *Safe Operation of Hydrofluoric Acid Alkylation Units*; American Petroleum Institute, 2007.
61. API Document 950: *Survey of Constructional Materials and Corrosion in Sour Water Strippers*; American Petroleum Institute, 1983.
62. Puyear, R. B. *Corrosion Failure Mechanisms in Process Industries – A Compilation of Experience*; MTI Publication 9502-R4, Materials Technology Institute of the Process Industries, 1997.
63. NACE Standard Recommended Practice RP0472-2005: *Methods and Controls to Prevent In-service Environmental Cracking of Carbon Steel Weldments in Corrosive Petroleum Refining Environments*; NACE International, 2005.
64. NACE Standard Recommended Practice RP0296-2004: *Guidelines for Detection, Repair and Mitigation of Cracking of Existing Petroleum Refinery Pressure Vessels in Wet H<sub>2</sub>S Environments*; NACE International, 2004.
65. API Document 939-B: *Repair and Remediation Strategies for Equipment Operating in Wet H<sub>2</sub>S Service*; American Petroleum Institute, 1994.
66. NACE Publication 8X194: *Materials and Fabrication Practices for New Pressure Vessels Used in Wet H<sub>2</sub>S Refining Service*; NACE International, 2006.
67. NACE Standard Material Requirements MR0103-2007: *Materials Resistant to Sulphide Stress Cracking in Corrosive Petroleum Refining Environments*; NACE International, 2007.
68. NACE Standard Test Method TM0177-2005: *Laboratory Testing of Metals for Resistance to Sulphide Stress Cracking and Stress Corrosion Cracking in H<sub>2</sub>S Environments*; NACE International, 2005.
69. NACE Standard Test Method TM0284-2003: *Evaluation of Pipeline and Pressure Vessel Steels to Hydrogen Induced Cracking*; NACE International, 2003.
70. NACE Standard Test Method TM0103-2003: *Laboratory Test Procedures for Evaluation of SOHIC Resistance of Plate Steels Used in Wet H<sub>2</sub>S Service*; NACE International, 2003.
71. NACE Standard Practice SP0403-2008: *Avoiding Caustic Stress Corrosion Cracking of Carbon Steel Refinery Equipment and Piping*; NACE International, 2008.
72. API Recommended Practice RP945: *Avoiding Environmental Cracking in Amine Units*; American Petroleum Institute, 2003.
73. NACE Standard Practice SP0590-2007: *Prevention, Detection and Correction of Deaerator Cracking*; NACE International, 2007.
74. API Document 939-D: *Stress Corrosion Cracking of Carbon Steel in Fuel Grade Ethanol: Review and Survey*; American Petroleum Institute, 2000.
75. McIntyre, D. R.; Dillon, C. P. *Guidelines for Preventing Stress Corrosion Cracking in the Process Industries*; MTI Publication No. 15, Materials Technology Institute of the Process Industries, 1985.
76. Smith, R. F.; Richardson, J. A. In *Corrosion 91*, National Association of Corrosion Engineers, 1991; Paper 576.
77. Berry, W. E.; Payer, J. H. In *Symposium on Line Pipe Research*, Houston, TX; American Gas Association, 1979.
78. Hewardine, S. *Ammonia Storage Inspection*; The Fertiliser Society: London, 1991; Proceedings No. 308.
79. Lunde, L.; Nyborg, R. *Stress Corrosion Cracking of Carbon Steel Storage Tanks for Anhydrous Ammonia*; The Fertiliser Society: London, 1991; Proceedings No. 307.
80. McGowan, P. *Plenary Address*; Australasian Corrosion Association, 2000.
81. Saugerud, O. T.; Angelsen, S. O. In *Life Prediction of Corrodible Structures*; Proceedings of the Conferences, Cambridge, UK, 23–26 September 1991 and Kauai, Hawaii, 5–8 November 1991; Parkins, R. N., Ed.; National Association of Corrosion Engineers, 1991; paper 67.
82. Haruyama, S. *Mater. Perform.* **1982**, 21, 14–19.

83. Craig, B. D.; Anderson, D. S. Eds. *Handbook of Corrosion Data*, 2nd ed.; ASM International, 1995; p 787.
84. NACE Standard Recommended Practice RP0170-2004: *Protection of Austenitic Stainless Steels and Other Austenitic Alloys From Polythionic Acid Stress Corrosion Cracking During the Shutdown of Refinery Equipment*; NACE International, 2004.
85. API Recommended Practice RP580: *Risk Based Inspection*; American Petroleum Institute, 2002.
86. API Publication 581: *Risk Based Inspection Resource Document*; American Petroleum Institute, 2000.
87. Valbuena, R.; Aller, J.; Renner, M.; Feigel, G. *Implementing and Evergreening RBI in Process Plants*; MTI Publication 9526. Materials Technology Institute of the Process Industries, 2005.
88. API Document 579-1: *Fitness for Service*; American Petroleum Institute, 2007.
89. Menendez, C. M.; de Mello, C. J. B.; de Oliveira Carneval, J. R.; de Alcantara Bezerra, P. S.; de Azevedo, C.; Cardoso, C. M.; Mattos, O. R. In *Corrosion 2000*; NACE International, 2000; Paper 00102.
90. Rothwell, N. *Corrosion Monitoring Handbook*; Coxmoor Publishing, 2000.
91. Birch, N. N. In *Corrosion 2006*, NACE International, 2006; Paper 06642.
92. Crouzen, P. C. N.; Munns, I. J.; Verstijnen, W.; Hulsey, R. C. In *Corrosion 2006*, NACE International, 2006; Paper 06312.
93. Kane, R. D.; Eden, D. C.; Amidi, S.; Delve, D. In *Corrosion 2007*, NACE International, 2007; Paper 07268.
94. Ohtsu, T.; Miyazawa, M. In *Corrosion 2007*, NACE International, 2007; Paper 07266.
95. Hermse, C.; Kempen, A.; van Wortel, H. *Corrosion 2007*; NACE International, 2007; Paper 07416.
96. Hamley, P. A.; Ilkenhans, T.; Webster, J. M.; Garcia-Vedugo, E.; Venardou, E.; Clarke, M. J.; Auerbach, R.; Thomas, W. B.; Whiston, K.; Poliakoff, M. *Green Chem.* **2002**, *4*, 235–238.
97. Latanision, R.; Mitton, D. B. In *ASM Handbook – Corrosion: Environments and Industries*; ASM International, 2006; Vol. 13C, pp 229–235.
98. [www.imm-mainz.de](http://www.imm-mainz.de)
99. [www.fzk.de](http://www.fzk.de)

## 4.41 Management of Corrosion in the Oil and Gas Industry

### J. Dawson

Corrosion Consultant, 16 Brandwood Close Worsley, Manchester M28 1XX, UK

### G. John

Intertek-CAPCIS Ltd. Bainbridge House, 86–90 London Rd, Manchester M1 2PW, UK

### K. Oliver

Intertek-Production and Integrity Assurance, P.O. Box 4660, Sharjah, United Arab Emirates

© 2010 Elsevier B.V. All rights reserved.

---

<b>4.41.1</b>	<b>Introduction</b>	3233
4.41.1.1	Outline	3233
4.41.1.2	Overview of Oil and Gas Industry Corrosion	3233
4.41.1.3	Areas of Corrosion Risk and Industry Mitigation Approach	3235
4.41.1.3.1	Corrosion subsurface	3235
4.41.1.3.2	Corrosion in pipeline systems	3236
4.41.1.3.3	Corrosion in process plant	3237
4.41.1.4	Industry Drivers and Changes	3238
<b>4.41.2</b>	<b>Management of Corrosion</b>	3240
<b>4.41.3</b>	<b>Front End Engineering Design (FEED)</b>	3243
4.41.3.1	Introduction	3243
4.41.3.2	Data Availability	3244
4.41.3.2.1	Theoretical calculations	3244
4.41.3.2.2	Corrosion risk analysis (CRA)	3247
4.41.3.2.3	Laboratory testing	3247
4.41.3.3	Procurement, Installation, and Operational Practicalities	3248
<b>4.41.4</b>	<b>Design Stage</b>	3250
4.41.4.1	Documentation	3250
4.41.4.1.1	Material selection report	3250
4.41.4.1.2	Corrosion management philosophy	3251
4.41.4.1.3	Chemical injection systems	3251
4.41.4.1.4	CP systems	3253
4.41.4.2	Engineering Considerations	3253
4.41.4.2.1	Minimizing corrosion threats	3253
4.41.4.2.2	Corrosion allowances	3253
4.41.4.2.3	Inaccessible pipework	3253
4.41.4.2.4	Insulation	3254
4.41.4.2.5	Pigging facilities	3254
4.41.4.3	Design of Data Management Systems	3255
4.41.4.4	Commissioning Procedures	3255
<b>4.41.5</b>	<b>Fabrication, Construction, and Commissioning</b>	3255
4.41.5.1	QA and Quality Control	3255
4.41.5.2	Development of Integrity Management Systems	3256
4.41.5.3	Handover to Operations	3256
<b>4.41.6</b>	<b>Operations Phase</b>	3257
4.41.6.1	Corrosion Management Strategy Implementation	3257
4.41.6.2	Routine Inspection and Monitoring	3257
4.41.6.3	External Protection	3260
4.41.6.4	Chemical Treatment	3260
4.41.6.4.1	Temperature, pressure, CO <sub>2</sub> /H <sub>2</sub> S content	3260
4.41.6.4.2	pH measurements	3261
4.41.6.4.3	Oxygen monitoring	3261

---

4.41.6.4.4	Iron count	3261
4.41.6.4.5	Inhibitor residuals	3261
4.41.6.5	Data Management	3261
4.41.6.6	Change in Process Conditions	3262
4.41.6.7	Risk Based Inspection (RBI)	3263
4.41.6.8	Direct Assessment Procedures	3263
4.41.6.9	Fitness for Service (FFS)	3264
4.41.6.10	Communication and Management Structure	3264
4.41.6.10.1	Corrosion management team	3264
4.41.6.10.2	Management of change	3265
4.41.6.10.3	Contracting structure	3265
4.41.6.10.4	Key point indicators (KPI)	3265
4.41.6.10.5	Audit/compliance	3266
4.41.6.10.6	Ongoing improvements	3266
4.41.7	Summary/Conclusions	3267
References		3267

## Glossary

**Barrel** A (depreciated) unit of volume, used for measuring production ( $1 \text{ barrel} \approx 0.159 \text{ m}^3$ ).

**Consequence of failure** The impact of components/equipment failure on health and safety, production, and environmental parameters.

**Corrosion management** (1) Defined as that part of the overall operation management program aiming at the implementation of the Corrosion Policy (2) Organization set-up and operational process to ensure corrosion control, inspection, monitoring, and assessment plans are implemented to optimize asset integrity.

**Corrosion risk assessment** A formalized process in which the combination of the consequences of failure and the likelihood of failure is assessed to identify the level of risk of ongoing operations. A corrosion risk assessment is used to (1) identify items in which design and/or corrosion control plans should be readdressed to reduce risk (2) to assist in defining the maintenance and monitoring tasks that should be implemented (see RBI).

**Direct assessment** Formalized method for reviewing information relating to the possible degradation of a pipeline due to corrosion (internal or external) to identify areas for excavation and physical direct assessment as part of fitness-for-service study.

**Fitness-for-service** Engineering assessment to determine the ability of a component to perform its function as designed in a safe

manner and in accordance with the relevant regulations (also referred to as fitness-for-purpose or fitness-for-use).

**Key point indicator** An operational process or management parameter that can be measured and tracked during operations to assess the high level performance of critical items/activities.

**Latent condition** An undiagnosed or unrecognized flaw or defect in data, data management systems, documents, procedures, and guidance/standards that gives rise to human errors.

**Likelihood of failure** A method used to prioritize components/facilities that are subject to possible failure. Normally used in qualitative or semiquantitative risk assessments (some times used interchangeably with Probability of Failure).

**Probability of failure** A method used to prioritize components/facilities that are subject to possible failure. Normally used in as part of a fully quantitative risk assessment (some-times used interchangeably with Likelihood of Failure).

**Risk-based inspection** A method for prioritizing and defining inspection activities to focus on items that are considered to have the highest risk of degradation, as defined by the combination of consequence and likelihood.

**Safety, health and environment** A formal process for defining policy and implementing strategy associated with the

management of the safety and health of people in the vicinity of the facility, and the impact on the environment surrounding the facility.

**Total quality management** Is a business management strategy aimed at embedding awareness of quality in all organizational processes.

## Abbreviations

**ACVG** AC voltage gradient  
**AIM** Asset Integrity Management  
**API** American Petroleum Institute  
**ASME** American Society of Mechanical Engineers  
**ASTM** American Society of Testing and Materials  
**bpd** Barrel per day, unit of flow rate (1 bpd =  $0.159 \text{ m}^3 \text{ day}^{-1}$ )  
**CAPEX** Capital Expenditure  
**CIPS** Close Interval Potential Survey  
**CoF** Consequence of failure  
**COMAH** Control of major accident hazard  
**CP** Cathodic protection  
**CRA** Corrosion-resistant alloy  
**CRA** Corrosion risk assessment  
**CSCC** Chloride stress corrosion cracking  
**CUI** Corrosion under insulation  
**DA** Direct assessment  
**DCS** Distributed control system  
**DCVG** DC voltage gradient  
**DG** Dry gas  
**DnV** Det Norsk Veritas  
**EAC** Environmentally assisted cracking  
**ECDA** External corrosion direct assessment  
**EN** Euronorm (European Standard)  
**EOR** End of reservoir  
**ER** Electrical resistance  
**FEED** Front end engineering design  
**FEL** Front end loading  
**FFS** Fitness-for-service  
**FPO** Floating, production, and offloading  
**FPSO** Floating, production, storage, and offloading  
**GIS** Graphical information system  
**GOR** Gas-oil ratio  
**GRP** Glass reinforced polymer  
**HAZOP** Hazard and operability  
**HE** Hydrogen embrittlement  
**HIC** Hydrogen induced cracking  
**HSE** Health and safety executive  
**ICDA** Internal corrosion direct assessment  
**ILI** In-line inspection

**IP** Intelligent pig  
**IT** Information Technology  
**ISO** International Standards Organization  
**KPI** Key performance indicator  
**LoF** Likelihood of failure  
**LP** Liquid petroleum  
**LPR** Linear polarization resistance  
**MFI** Magnetic flux inspection  
**MFL** Magnetic flux leakage  
**MIC** Microbiologically influenced corrosion  
**mil** A (depreciated) unit of length equal to one thousandth of an inch (1 mil =  $25.4 \mu\text{m}$ )  
**mmscf** Million standard cubic feet (1 mmscf =  $28\,316 \text{ m}^3$ )  
**mpy** A (depreciated) unit of metal loss rate (corrosion rate) =  $1 \text{ mil year}^{-1}$  ( $0.025 \text{ mm year}^{-1}$ )  
**MR** Materials recommendation  
**MSD** Material selection diagram  
**NACE** National Association of Corrosion Engineers  
**NDE** Nondestructive examination  
**NDT** Nondestructive testing  
**NUI** Normally unattended installation  
**OPEX** Operational Expenditure  
**P&ID** Piping and instrumentation diagram  
**PEC** Pulsed eddy current  
**PFD** Process flow diagram  
**PI** Point indicator/ plant information  
**PoF** Probability of failure  
**ppb** A unit of concentration, parts per billion (1 ppb =  $1 \mu\text{g dm}^{-3}$ , or  $1 \mu\text{g kg}^{-1}$ )  
**ppm** A unit of concentration, parts per million (ppm =  $1 \text{ mg dm}^{-3}$ , or  $1 \text{ mg kg}^{-1}$ )  
**psi** A (depreciated) unit of pressure, pounds force per square inch (1 psi =  $6895 \text{ Pa}$  or  $0.069 \text{ bar}$ )  
**PVT** Pressure volume temperature  
**PWHT** Post weld heat treatment  
**QA** Quality assurance  
**RAMS** Reliability and maintenance systems  
**RBA** Risk based assessment  
**RBI** Risk based inspection  
**RP** Recommended practice  
**SAP** Systems, applications, and products in data processing  
**SCADA** Supervisory control and data acquisition  
**SCC** Stress corrosion cracking  
**scf** Standard cubic feet, unit of volume of gas at  $15^\circ\text{C}$  and  $101\,325 \text{ Pa}$  (1 scf =  $0.0283 \text{ m}^3$ )  
**scf/bbl** A (depreciated) unit of gas to liquids ratio, standard cubic foot per barrel (1 scf/bbl =  $0.181 \text{ m}^3/\text{m}^3$ )



**SHE** Safety, health, and environment  
**sm<sup>3</sup>** Standard cubic meter, unit of volume of gas at 15°C and 101 325 Pa  
**SOHIC** Stress oriented hydrogen induced cracking  
**SP** Standard practice  
**SRB** Sulfate reducing bacteria  
**SSCC** Sulfide stress corrosion cracking  
**TM** Test method  
**TOFD** Time of flight diffraction  
**TQM** Total quality management  
**TR** Technical report  
**TR** Transformer rectifier  
**TSA** Technical safety audits  
**UNS** Unified numbering system  
**UT** Ultrasonic testing  
**WG** Wet gas

## 4.41.1 Introduction

### 4.41.1.1 Outline

This chapter addresses issues concerned specifically with the management of corrosion in oil and gas production equipment both onshore and offshore and from subsurface, through pipeline systems and process plant to storage and export facilities. The industry covers a wide range of assets of differing ages and designs that operate with varying internal and external environments. Such infrastructures also reflect particular company cultures and the equipment designs/operations must meet different legislative requirements around the world. It is not possible to cover every aspect in this review, but the aim is to provide a general approach to corrosion risk mitigation and management of typical issues encountered in the field. The message is that ‘one size does not fit all’ and each case must be treated individually with appropriate assessments, reviews, and audits throughout the project life.

Corrosion management in the oil and gas industry follows the same requirements as outlined in the corrosion management overview chapter in this book. In fact, modern corrosion management across all industries evolved out of procedures and systems developed specifically for oil and gas production facilities, where the emphasis has been on ‘managing assets constructed from carbon steels that are inherently at risk of corrosion deterioration.’<sup>1</sup>

Corrosion management for oil and gas operations has been the subject of considerable discussion in the industry. In 2001, the UK Health and Safety Executive (HSE) published a general guidance document aimed at

UK offshore production facilities and focused on internal corrosion threats.<sup>2</sup> This has recently been updated by the UK Energy Institute<sup>3</sup> and expanded to cover all aspects of oil and gas processing, including onshore and external corrosion. Elsewhere, particularly North America, there have been developments in the requirements for corrosion management of pipeline systems, which has resulted in the development of *direct assessment systems*, which are described in [Section 4.41.6.8](#).

The introduction to this chapter outlines the causes of corrosion damage found in equipment items, including the location, type, related problems, and mitigation measures. Aspects of corrosion management specific to oil and gas production are introduced in [Section 4.41.2](#) and then the main focus is on the various project phases where specific concerns are addressed from the front end engineering design (FEED) in [Section 4.41.3](#) and the requirements for design and detailed design in [Section 4.41.4](#) to fabrication, construction, and commissioning in [Section 4.41.5](#) and operations in [Section 4.41.6](#). The objective is to provide a logical structure based on typical project timeliness that is useful to both specialists and nonspecialists.

### 4.41.1.2 Overview of Oil and Gas Industry Corrosion

The primary objective of oil and gas production is the cost-effective and safe abstraction of hydrocarbons from fields, reservoirs, and local wells into flow lines and gathering lines, separate oil and gas from any produced water and then export, usually through pipelines, to storage prior to refining or transfer to a tanker or export pipeline. All these facilities pose a potential risk for health and safety, environmental and commercial concerns. Secondary facilities, including water injection, firewater, produced water disposal, etc. are also subject to corrosion threats and while failure of these systems may not present a safety health and environmental (SHE) risk, it could result in the reduction/cessation of production with consequential commercial implications.

The industry covers a wide range of assets, both onshore and offshore, and it is not possible to address every design in this review nor to cover macroeconomics, seismic, and political risk. Also each field, facility, and asset will have its own specific corrosion issues that result from local produced fluid compositions, water cuts and changing chemistries, CO<sub>2</sub> and H<sub>2</sub>S content, flow conditions and possible microbiological contamination during drilling and production. In many cases, external environments also provide a

major threat, ranging from subsea, offshore processing, and onshore conditions with conditions ranging from cold arctic to hot desert. In practice, all these issues have to be considered if the effects of corrosion damage are to be mitigated and managed effectively.

Other factors that influence the management of corrosion include the age, design, operation, organizational structure, and culture and maintenance philosophies, as well as local and corporate SHE obligations. Key concerns for installations are the prevention of incidents resulting from sudden or catastrophic failure and the prevention of hydrocarbon releases. Hydrocarbon fluids are flammable and produced fluids that contain hydrogen sulfide, a toxic and corrosive gas, are major hazards. There has always been an emphasis to design, construct, operate, and maintain the facilities in a safe manner, but what has changed over the past 15–20 years is that SHE issues now require that any procedures that are adopted need to be increasingly risk based and auditable, while the manner in which activities are conducted requires clearly defined reporting routes and appropriate actions from identified and responsible personnel.

For economic reasons, the majority of oil and gas facilities are constructed from carbon and low-alloy steels that are susceptible to both internal corrosion from the acidic process conditions and external corrosion from the environment. Hence, standard corrosion mitigation procedures are employed by the industry, such as chemical injection into produced fluids and the application of corrosion-resistant coatings plus cathodic protection to the outside of buried or immersed pipelines, as will be outlined below. Industry emphasis is on production deliverability and reliability and the efficiency of the overall process by the elimination of pinch points or poor practices that limit any specific areas of activity. A concern is that the experience and benefits from one field cannot be transferred automatically to a new development or existing facility without a management assessment of the risks arising from the changes and an understanding of the differences between locations, conditions and staff experience. A properly developed and well-functioning corrosion management system should be able to address such issues by highlighting the areas of varying risk, having in place suitable monitoring systems that are able to convert data into reports that trigger appropriate and timely management decisions.

Thus, although general principles are addressed in this chapter, it is essential that in practice each case is assessed on an individual basis. Corrosion risks can be identified, mitigated and managed effectively but

require appropriate tools and practices, agreed procedures, clear processes with logical sequential steps, suitable organizational structures and adequate resources.

The different corrosion threats (internal and external) applicable to oil and gas production facilities are given in the *Corrosion Threats Handbook – Upstream Oil and Gas Production*.<sup>4</sup> Those relating to main production facilities are summarized in **Figure 1**. Other corrosion threats, associated with storage, transportation, and various utility services necessary for oil and gas production, are also applicable.<sup>4</sup>

Details of the different corrosion mechanisms are described in other chapters elsewhere in this book and include:

**a. Internal corrosion/degradation:**

- ‘Sweet’ corrosion due to the formation of carbonic acid in produced waters from dissolved CO<sub>2</sub>.
- ‘Sour’ corrosion due to the formation of acidic conditions from dissolved H<sub>2</sub>S.
- Microbiologically influence corrosion (MIC) due principally to the presence of sulfate reducing bacteria (SRB).
- Oxygen corrosion in water injection facilities due to an inadequate removal of oxygen and associated with high flow rates.
- Galvanic corrosion caused by direct electrical connection of different materials/alloys to the same conductive environment.
- Erosion and erosion corrosion, due to particulates, mainly sand, in the production stream.
- Flow-assisted corrosion associated with effect of surface shear on the stability of protective films on the steel surface.
- Environmentally assisted cracking (EAC), in particular:
  - chloride stress corrosion cracking (CSCC) of austenitic stainless steels and corrosion-resistant alloys;
  - sulfide stress corrosion cracking (SSCC) of carbon steels, austenitic stainless steels, and corrosion-resistant alloys (CRA);
  - hydrogen induced cracking (HIC) of carbon steels

**b. External corrosion/degradation**

- Atmospheric corrosion.
- Corrosion under insulation(CUI).
- Corrosion in seawater/fresh water.
- Corrosion in soils.

A range of different corrosion control methods is adopted that are described in detail in other chapters, including:

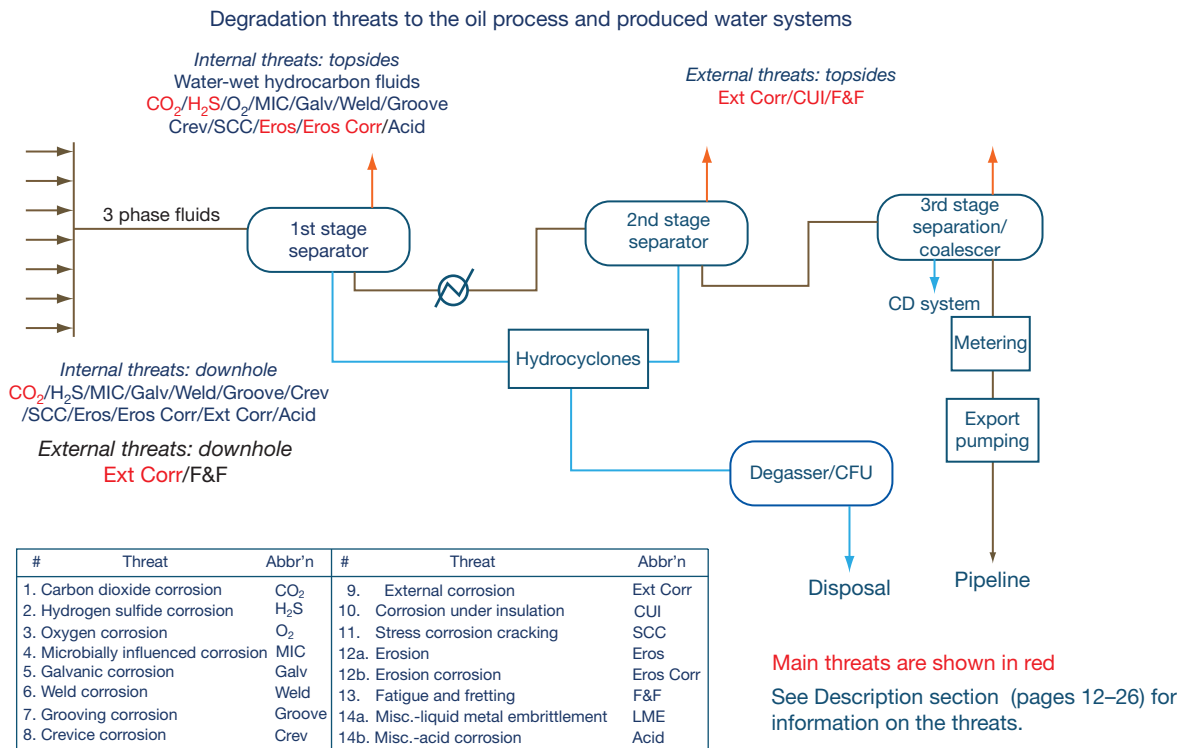


**Figure 1** Example of corrosion threats in oil/gas processing units. Reproduced from Corrosion Threats Handbook – Upstream Oil and Gas Production; Energy Institute and Oil and Gas UK: London, 2008.

- use of corrosion resistant alloy (CRA);
- use of chemical treatments, including use of corrosion inhibitors and biocides;
- use of protective coatings (external and internal organic and metallic);
- use of cathodic protection (CP), external and internal;
- process modification such as deoxygenation and dehydration.

#### 4.41.1.3 Areas of Corrosion Risk and Industry Mitigation Approach

The following section provides a background to the different components/facilities used in oil and gas production and processing, and the different corrosion issues relating to them.

##### 4.41.1.3.1 Corrosion subsurface

Wells typically comprise

- **casing** – carbon steel sections, that may be pre-coated, cemented to the formation;
- **bottom hole perforations** – explosively formed holes to allow reservoir fluids in the strata to enter the well bottom;

- **production tubulars** – sections of drawn pipe screwed together to form a continuous string for transport of produced fluids;
- **down-hole safety valve**;
- **annulus fluid and packer** – high-density fluid between the tubular string and the casing that helps to balance the well to surface pressure;
- **well head valve** and equipment;
- **cellar** – surface platform/foundations that holds well equipment in position;
- **gas injection valves** – enable low-pressure oil wells to maintain production;
- **inhibitor injection valve** – provides a continuous feed of corrosion inhibitor into the produced fluids via a thin ‘spaghetti’ tube inserted down the annulus.

##### 4.41.1.3.1.1 Corrosion issues

Drilling a well could introduce SRB down-hole into the reservoir unless the monitoring and biocide treating of the aqueous drilling mud is carefully controlled. Well casings may be in contact with corrosive aquifers above the reservoir. Wells with high multiphase flow are subject to impingement and ‘mesa’ type elongated erosion–corrosion pits. Wellhead equipment, valves, and choke bodies are susceptible to erosion corrosion

and severe localized corrosion especially with high temperature, high chloride content fluids and high-pressure gas wells. Maintenance of flow through the reservoir strata and removal of scale deposits from tubular goods may require chemical cleaning with corrosive chemicals (acids and acidic solutions of complexing reagent). These fracing/cleaning fluids, introduced as a 'squeeze' treatment, can cause significant corrosion when returned up the well. Materials must be specifically selected for their mechanical and corrosion resistance properties, particularly safety critical items.

Typical corrosion related problems include:

- uniform/general corrosion caused by carbon dioxide and hydrogen sulfide in reservoir fluids and acids/chemicals in treating fluids;
- pitting due to chlorides and sour environments under conditions of high chloride content and temperature;
- hydrogen damage of susceptible steels in sour systems;
- erosion corrosion due to high velocities of fluids (gas slugs);
- introduction of corrosive gas during gas lift operation;
- SRB contamination of annular fluids and injection waters.

Corrosion mitigation includes:

- CP of external well casing;
- selection of 'fit-for-service' tubular steel goods/CRA/nonmetallic linings;
- down-hole inspection (wireline tools);
- use of corrosion inhibitors – squeeze/continuous injection;
- use of biocides;
- topside monitoring of produced fluids.

#### 4.41.1.3.2 Corrosion in pipeline systems

Flow-lines, gathering lines, interfield trunk and export lines are typically constructed from rolled low-alloy steels, the wall thickness of which is determined by the design/operating pressure, the service duty (sweet or sour) and the required corrosion allowance. Internal corrosion is typically mitigated by chemical treating and/or pH control together with regular maintenance pigging, and effectiveness is confirmed by inspection (including intelligent pigs) and online monitoring. In some cases internal coatings or use of linings (with either CRA or non-metallic systems). External corrosion mitigation depends on the location. Above ground lines may be uncoated in dry desert regions but coated

in more humid/coastal areas. Buried/immersed lines have a primary protection from a barrier coating plus CP. Associated equipment includes manifolds, pumps/compressors, and valves, all of which may be susceptible to corrosion attack and hydrogen damage.

##### 4.41.1.3.2.1 Corrosion issues

Multiphase lines are normally designed to operate under turbulent stratified flow conditions (liquid at the bottom, gas phase at the top) but slugging flow or gas/sand impingement may occur depending on the relative gas/liquid velocities and particle content. Some lines have a significant temperature profile that, together with the topography and bends/elbows/changes of diameter, can influence areas of water drop out, hold-up, and slugging. Bottom-of-the-line-corrosion generally occurs as water cuts increase and the fluid is no longer a water-in-oil emulsion, but local grooves (<6 mm wide) may occur at the bottom of lines with low water cuts (<10%). Such conditions may occur under low fluid velocities or when enhanced water coalescence causes water-in-oil emulsions to break down. A minimum flow (typically  $>1 \text{ m s}^{-1}$ ) is required to maintain particles in suspension and prevent sludge build-up. Fluid flow is often restricted to minimize erosion problems that is,  $<15 \text{ m s}^{-1}$  for liquids and  $<20 \text{ m s}^{-1}$  for gas.

Flow lines have a relatively small diameter and are not usually provided with launch/retrieval facilities for the deployment of cleaning pigs; hence, corrosion is often associated with water drop-out, deposits, and microbiologically contaminated sludge. Scale deposition can be a considerable problem in some fields. Scale control chemicals can limit the deposition but may lead to precipitates in the bulk fluid, these small crystals may form a sludge deposit if the flow conditions are not maintained at a high enough value ( $>1 \text{ m s}^{-1}$ ).

Internal corrosion in lines carrying produced/separated fluids results from  $\text{CO}_2/\text{H}_2\text{S}$  and in the lines carrying water for injection, fire mains, wash down, etc. from dissolved oxygen and MIC. Corrosion damage includes:

- metal wastage due to fluid corrosivity;
- localized pitting, especially in sour systems;
- grooving corrosion, especially where moderate water cuts result in a thin free water phase at the bottom of the pipeline;
- erosion corrosion at elbows, bends, riser sections or downstream of restrictions and when slugging flow is present;

- pitting/crevice type corrosion under deposits, debris and scales;
- local areas of attack due to water-drop out at low spots;
- microbiologically induced corrosion due to contamination through water injection and hydro test fluids;
- pipe-wall delamination and cracks due to hydrogen damage (HIC, SOHIC) and through-wall cracks due to SSCC.

External corrosion results from exposure to natural environments such as soils, immersion in or contact with seawater, etc. and local atmospheres. Corrosion damage takes many forms and includes:

- wastage and pitting that will be particularly severe for unprotected pipes that are buried in deaerated wet clay soils or in estuarine environments due to anaerobic SRB;
- stress corrosion cracking (SCC) due to carbonate/bicarbonate environments that may develop over time and/or hydrogen generated by excessive CP current;
- stray current effects from other CP systems, DC railways and welding; and
- telluric currents due to the Earth's magnetic field.

Corrosion mitigation options for pipelines include:

- selection of appropriate steels and weld procedures for either sweet ( $\text{CO}_2$ ) or sour ( $\text{CO}_2/\text{H}_2\text{S}$ ) service; this may require use of CRAs (either as solid pipe or as lined pipe) or use of nonmetallic pipe materials;
- inspections (pigging) to detect thinning, pitting and cracks;
- use of corrosion inhibitors by continuous injection and/or batch treatment;
- online monitoring to identify changes and control chemical treatments;
- use of biocides in batch treatments;
- control of process fluid compositions for example, dehydration of gases, removal of  $\text{H}_2\text{S}$ , pH control of wet gas (WG) lines, etc.;
- use of internal coatings, subject to concerns as to pinholes and crevice corrosion;
- use of internal linings, either non-metallic or CRA clad systems;
- coating of external walls;
- CP of buried and immersed lines and monitoring of CP systems and coating defect location, using techniques such as close interval potential survey (CIPS) and DC voltage gradient (DCVG) surveys.

#### 4.41.1.3.3 Corrosion in process plant

Equipment such as separation vessels/trains are used to separate comingled produced fluids into oil and gas/condensate to aid transportation and downstream processing. Associated items include vessel internals, electrostatic precipitators, piping between separators, desalters, knockout drums, valves, pumps, and compressors. Other areas include produced water plant, utility systems for steam generation, cooling systems and storage tanks for separated products and chemicals.

Main concerns center on:

- wet gas streams that are cleaned up in gas separation vessels, compressed, cooled, often dried and exported via a gas line, and/or used for gas reinjection;
- wet crude handling streams comprising dehydrators, desalters and a crude oil pump and export-line;
- brine phase streams with water-oil separation or stripping sections to remove oil residues, after which the water is discharged/disposed of down-hole via injection pumps used to maintain reservoir pressures.

##### 4.41.1.3.3.1 Corrosion issues

Corrosion and pitting usually occur at water-wet surfaces in the system. High-risk areas are vessel bottoms (in contact with produced water), wet gas lines downstream of compressors, water lines, and tanks containing oil, from which water droplets may coalesce and drop-out. Three phase separators/vessels, constructed from low-alloy steel materials, and containing wet gases are usually completely coated internally with high build coatings (epoxy reinforced with glass flake,  $>300\text{ }\mu\text{m}$ ) in water immersed regions and  $200\text{--}300\text{ }\mu\text{m}$  in water splash/condensation/water carry over regions in gas spaces. CP may also be installed in the water-containing vessel bottoms. Where conditions are particularly aggressive internal lining using CRA is some-times used. Separation of gases followed by compression increases the partial pressures of carbon dioxide and hydrogen sulfide that then increases the corrosivity. Weld corrosion may also be found on pipework that contains wet condensate saturated with carbon dioxide. Internals of thin section are normally fabricated from CRAs. Water lines and water processing equipment contain lower pressures and materials selection may allow the use of plastics. Specific concerns are 'dead legs,' areas of unused pipework that do not receive corrosion inhibitors/biocides, galvanic corrosion from mixed metal fabrications and external crevices/under insulation areas subject to wetting. Typical plant areas at risk from corrosion damage are



given in *Corrosion Threats Handbook – Upstream Oil and Gas Production*.<sup>4</sup>

Corrosion in gas/oil separation equipment typically includes:

- uniform/general corrosion caused by carbon dioxide and hydrogen sulfide;
- pitting due to chloride containing brines and sour environments;
- hydrogen damage of susceptible steels;
- CRA internal lining, either as weld overlay or a sheet clad;
- erosion corrosion due to high velocities of produced fluids at elbows and bends;
- water drop-out at low spots in low velocity regions;
- areas at the bottom of vessels that collect debris (under deposit corrosion, pitting and SRB contamination);
- microbiologically induced corrosion;
- weldment corrosion.

Corrosion mitigation includes:

- selection of ‘fit-for-purpose’ steels/CRA’s and weldments;
- use of coatings for both internal and external corrosion control;
- CP for water immersed vessel internals;
- inspection for corrosion damage;
- monitoring of CP systems;
- use of chemical treatments:
  - corrosion inhibitors
  - scale control
  - demulsifiers
  - biocides;
- on-line monitoring to identify changes and control chemical treating.

#### 4.41.1.4 Industry Drivers and Changes

Oil and gas production has derived significant economic benefits over the past 25 years from the use of asset management strategies that have been a major industry driver in eras of rising demand and fluctuating prices with operations in more severe environments, often with squeezed budgets. The asset manager in an organization essentially fulfils the traditional role of a process site managing director in balancing the requirements of stakeholders to achieve overall benefit. Asset managers have budget decision-making responsibility for resources and services to achieve defined objectives. Multi-disciplined teams are tasked with improvement of

performance, optimization of costs and minimization of risks. This asset-centered approach has increasingly replaced traditional activity-centered groups and organizations based on functions such as design, engineering, production, operations, maintenance, and materials/purchasing, each with individual budgets. Client ‘assets’ now fund technology developments with contributions from the design, SHE, IT and financial specialists from both in-house, central, shared sources and external providers. Delivery of services such as corrosion mitigation requires development of strategic models that may well include input from both in-house and third party specialists. Provision of improved quality and value is what counts rather than whether the service provider is in-house or a contractor. Asset strategies and objectives are typically encompassed in the Asset Management Policy that cascades down into local asset business goals with intentions converted into plans and actions.<sup>5</sup>

Developments in asset management cannot be ignored in the delivery of corrosion management services and will continue to drive technical and management changes. In this context, the definition first adopted in the mid-90s is still appropriate:

***Corrosion Management** is that part of the overall asset management system that is concerned with development, implementation, review and maintenance of the corrosion policy.*<sup>6</sup>

*A **corrosion policy** includes establishment of organizational structures with defined responsibilities, reporting routes, practices, procedures, processes and resources. This requires the demonstration of responsibility and accountability for corrosion performance, managing risks, decreasing costs, controlling compliance and motivating personnel.*

A written corrosion policy, agreed by senior personnel, defines the corrosion mitigation objectives and provides a focus for various interdisciplinary and multidepartmental inputs and control of operational, day-to-day activities. Most corrosion related activities are undertaken by asset management team members with limited training in corrosion mitigation and difficulties arise from an industry shortage of experienced corrosion engineers.

Major changes during the 90s centered on safety and environmental issues following the Piper Alpha Report<sup>7</sup> and a number of high-profile oil leaks. Industry centered documentation has focused on engineering/safety procedures to identify failure modes likely to affect integrity and includes the *US Pipeline Safety Act*<sup>8</sup> with emphasis on risk management and cost benefit, *API 580 Risk-Based Inspection*<sup>9</sup> plus the

accompanying resource document *API 581*<sup>10</sup> and *DnV RP G101 Risk Based Inspection of Offshore Topsides Static Mechanical Equipment*.<sup>11</sup> UK oil and gas regulations mirror EU requirements such that assets require development of a safety case,<sup>12</sup> that continues into design and construction.<sup>13</sup> This general risk-based approach continued in the '*Pipeline Standard*',<sup>14</sup> control of major hazard sites<sup>15</sup> and pressure systems.<sup>16</sup>

A framework for management process employed by the UK HSE<sup>17</sup> identifies six basic steps:

1. policy;
2. organizing;
3. planning and implementation;
4. measuring performance;
5. reviewing performance;
6. auditing.

The Norwegian regulatory authorities have adopted similar requirements. For example, contractors working for offshore operators are subjected to a SHE evaluation<sup>18</sup> where the system elements addressed include:

1. leadership and commitment;
2. policy and strategic objectives;
3. organization, resources and documentation;
4. evaluation and risk management;
5. planning and procedures;
6. implementation and monitoring;
7. auditing and reviewing.

A matrix is also used to address consequence versus increasing probability that classifies activities into three categories – (low) 'manage for continuous improvement,' (medium) 'incorporate risk reduction methods' and (high) 'intolerable.' Similar requirements are found in the ISO standard for management of environmental issues.<sup>19</sup>

A general acceptance in industry of a risk-based approach, particularly RBI, by most international organizations means that information from benchmark standards has been incorporated into in-house guidelines as part of the input into industry changes. However, risk management is only one tool employed to mitigate corrosion and, for example, adoption of a risk-based inspection system must be backed up with *management of change procedures* and *end of life strategies*.

In many countries, there has also been a cultural shift from a rules-based regulatory system to a principles-based system with emphasis on defined objectives (i.e., *framework rules with guidelines – How it must be managed by first identifying hazards and risks and then prioritize actions accordingly*) rather than traditional/prescriptive rules

based practice (i.e., *detailed rules and regulations – Defines what must be done, i.e., prescriptive, not always appropriate but do it anyway*). This change in emphasis is also reflected in the development of recent EN, ISO, and NACE standards for corrosion control such as materials for sour service,<sup>20</sup> CP and protective coatings that provide outline guidance for experienced engineers but should not be used on their own for certification purposes. In principle, the implementation of these changes in an organization and their implication for the management of corrosion mitigation may be summarized by the following steps:

1. hazard identification;
2. assessment of associated risks;
3. consider alternative ways of managing the risks;
4. conduct a cost benefit evaluation of alternative risk management options;
5. decide which option(s) to select.

In practice, corrosion related incidents/accidents still occur as shown by the South Humberside Refinery explosion/fire<sup>21</sup> and the recent Alaska pipeline leakage,<sup>22</sup> that highlight an underlying organizational concern in relation to what appear to be human errors. Management of SHE hazards, and by inference corrosion risks, can be visualized as concentric defensive barriers designed to prevent failures and catastrophic incidents by containment of hazards and limitation of their effect.

John Reason<sup>23</sup> described such barriers as either physical (hard) or procedural (soft) but each barrier has weaknesses/holes (the *Swiss Cheese Model* as described in **Chapter 4.30, Corrosion Management Overview** in this book). Holes may be caused by active failures, such as unsafe actions, and latent conditions that are an inevitable feature of organizational life. The rare conjunction of a set of holes in successive defenses, allowing hazards to come into damaging contact with people and assets (the accident trajectory) is a necessary condition for an organizational accident. Unsafe actions are errors or violations that have an immediate effect on a system, usually a direct accident at the individual level. Reason also considered *latent conditions* as arising from strategic/top-level decisions made by regulators, designers, manufacturers and managers that may be present for many years, and include poor design, gaps in supervision, undetected manufacturing defects, maintenance failures, unworkable procedures and training shortfalls. Latent conditions promote the likelihood of active failures by the creation of local factors that promote errors and violations and aggravate the consequences of unsafe acts and their effects

on a system's defenses, barriers, and safeguards, as indicated by the refinery fire and pipeline leak examples cited earlier.

The cultural shift toward principles-based legislation and industry ISO standards with an emphasis on a risk-based approach for assessment and mitigation is aimed at overcoming engineering shortfalls associated with latent conditions. This approach is also seen in hazard and operability studies (HAZOPS), technical safety audits (TSA), reliability and maintainability studies (RAMS), the control and use of databases, and the application of decision support systems that are essentially engineering applications to the control of hazards. However, the wider organizational approach proposed by Reason views human errors more as consequences than causes and as such symptomatic of latent conditions in the management system that adversely affect integrity defenses. The organizational model has therefore some similarities to TQM, that is, it uses continuous assessment to reform a system, but also combines quality-determining and safety-related factors. This organizational model approach also has many of the attributes of crisis management.

This resume highlights some relevant management philosophies on the basis of which corrosion management systems should be organized and operated. Successful management of corrosion is often achieved by being asset specific and is dependant on factors such as the design, life cycle stage, process conditions, operational history and organizational culture. There are however some basic and common requirements for management systems as first outlined in 1999<sup>6</sup> and 2001<sup>2</sup> to address continuing concerns of hydrocarbon emissions from offshore processing facilities. The aim was to develop a template based on the UK regulatory authority's approach to safety management<sup>17</sup> and encourage the industry to adopt a common approach to the assessment of corrosion management systems already in place. This has been encompassed and extended in *Guidance for Corrosion Management in Oil and Gas Production and Processing* published in 2008,<sup>3</sup> a document considered *normative* for UK operators.

The document refers to the *barrier* concept to corrosion risk management without any details, but in particular highlights the importance of *key performance indicators* (KPIs) to assess the various stages and activities of the management process and provides an extensive checklist for the assessment of corrosion management. In general, the use of performance measurement/KPIs is normal practice in most quality and

safety systems and these provide a basis for planning and measuring achievement. The setting of agreed performance criteria is crucial for the effective implementation of policies, checks on the performance of management systems and individual, day-to-day actions that are judged against acceptable criteria defined by in-house standards and/or industry benchmarks. Failure to achieve a performance standard may indicate latent conditions within a management system but should also trigger a review to identify reasons for the under-performance of the system.

#### 4.41.2 Management of Corrosion

Corrosion is a risk to both structures and production processes and as such should be treated within a risk management framework with corrosion mitigation addressed early in the project and not considered as a series of procedures introduced at a later stage. As with safety and environmental management it is a live, continuous process that starts during the concept and grows and is modified throughout the project. Management of corrosion is also a multidisciplinary team effort with input from various in-house personnel, contractors, specialists, and groups, including exploration, design, construction, operation and maintenance, as well as materials specialists and corrosion engineers. The composition and size of the 'corrosion team' and its relationship with the 'integrity team' will depend on the project stage and the asset management boundaries. Equipment integrity is a key issue from an asset management perspective and much of the equipment damage sustained throughout a project is corrosion related. For example, corrosion produces sludges (detached mill scale/corrosion products/deposits), which affect operations resulting in significant chemical treatment costs and expensive downtime for cleaning and maintenance. Secondary risks also arise with corrosion mitigation strategies such as risk-based inspection that have as their basis a rate of deterioration based on the use of cost-effective corrosion inhibitors, in which case failure of the inhibition process has implications for integrity trending.

In principle, corrosion mitigation should be an easy task, the major tactics are well established and summarized as follows:

1. **Materials selection** – carbon steels/low-alloy steel (usual to include a corrosion allowance during design), CRAs (stainless steel, nickel alloys, titanium), nonmetallic materials (polymers, glass reinforced plastic (GRP), elastomers, ceramics).

2. **Chemical treatments** – typically corrosion inhibitors, biocides and scale control chemicals but packages also include surfactants and antifoaming chemicals. Treatment may include the use of glycol to control hydrate formation combined with pH control to lower corrosion in WG lines.
3. **Use of coatings** – metallic, nonmetallic, and organic/paints, used in external and internal environments. Major factors are cost, availability, ease of surface preparation, application, and life expectancy. It is important to ensure adequate inspection of field applications.
4. **CP** – applied to immersed and buried structures, jetties, pipelines, tanks and concrete and inside water containing vessels, separators, tanks, and the water boxes of heat exchangers.
5. **Process and environmental control** – modification of moisture/humidity levels, lowering of oxygen concentrations and changes of throughput and decreases in flow and/or heat transfer rate.
6. **Design** – use of codes/standards to produce specifications and drawings. During the detailing phase, assessment of factors associated with stress, shape, compatibility and surface condition, for example, eliminate stress raisers, crevices and consider increased wall thickness on some bends.
7. **Inspection and monitoring** – trending of deterioration rates, chemical dosages and changes in process chemistries.

The first six options seen earlier are corrosion control methods that are used either singly or in combination, the choice depending on the specific application. In practice the difficulty is ensuring that long-term strategies are adopted and operational day-to-day activities are conducted effectively and efficiently.

Management of corrosion is an interactive process comprising a series of steps that aim to ensure corrosion risk mitigation procedures are applied cost effectively, commensurate with safety, health and environmental requirements. Figure 2 shows typical steps in a corrosion mitigation process based on those presented in the management of project risks.<sup>24</sup> The inputs are corrosion and SHE issues and the outputs are cost-effective corrosion mitigation, that is able to provide integrity and environmental assurance for the asset, and a continuously improving management system that is able to respond to both changing technical and worldwide economic conditions. In the UK, it would also meet the requirements for the review and audit of management systems conducted as part of a HSE assessment.

The steps are summarized as:

1. **Aims/objectives/policies.** An initial step in developing a corrosion management system is to define the aims and objectives of the corrosion input to a project. These then form the basis of the corrosion policy/strategy.
2. **Individuals/teams/organizations.** Identification of individuals and teams with ownership of corrosion management processes also helps to define roles, responsibilities and accountabilities of managers, staff and contracted bodies concerned with corrosion issues.
3. **Corrosion risk evaluations and assessment of mitigation options.** These are fundamental steps conducted throughout project life as conditions and the facility operational requirements and procedures change. The study would typically employ information as found in industry corrosion rate models<sup>25–27</sup> and guidance, including probabilistic assessments as in DnV RP G101<sup>11</sup> and API 581.<sup>10</sup> Evaluation of corrosion mitigation options, including their relative life cycle costs and required monitoring and inspection, is a basic step. The cost of preferred options must be compared using net present value/discounting procedures to obtain estimates of project life cycle costs. A useful assessment tool in the decision-making process is probabilistic analysis that enables various scenarios to be displayed as S-curves of anticipated life versus time.<sup>28,29</sup>
4. **Corrosion risk treatment planning and implementation.** These are vital to ensure that strategic, tactical, and operational/day-to-day activities designed to mitigate corrosion are employed effectively. The planning and implementation of the risk treatment process include strategic activities to meet optimal life cycle costs, SHE and other mandatory requirements, corporate corrosion practice and integrity requirements, and business concerns including development of condition-based maintenance and equipment reliability/uptime needs. The planning also includes assessment and development of chemical treating, inspection and maintenance specifications and protocols.
5. **Database development and maintenance.** The requirement for suitable databases for the storage of system documentation, the equipment design and as-constructed diagrams, commissioning information and field data generated during operation, inspection, and maintenance is given for any corrosion management system to have a chance of success. Corrosion mitigation and management

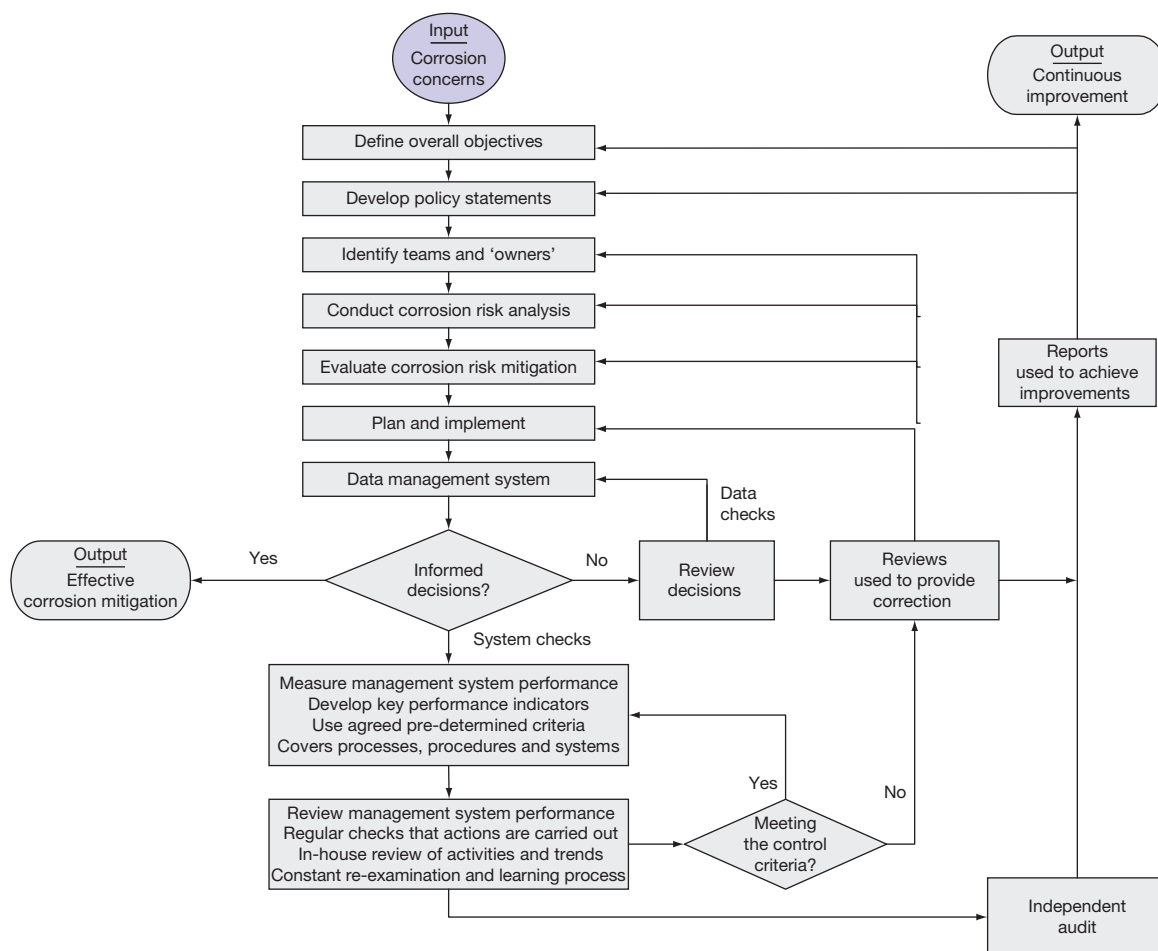


**Figure 2** Basic steps in a corrosion management system.

often falls behind other disciplines in the management and use of data, for example, compared with predictive maintenance and energy control of processing in some industry sectors. An effective management tool is a transparent database that correlates field data to provide a regular weekly/monthly breakdown of corrosion mitigation costs.

6. **Informed decisions and actions.** These are key processes; many management systems fail because of a lack of a clear decision-making step even though adequate protocols and procedures are in place. Informed decisions are based on adequate data to instigate corrective actions from investigative studies, the issuing and following up of warnings or even shut down actions when required. Operational, day-to-day actions include the rescheduling of inspections, changes to chemical treating or CP levels and predictive maintenance work or recoating that involve other teams. Recommendations must

either be followed up or rejected in a positive manner on the basis of other acceptable factors but not on a default 'do nothing' basis.

7. **Performance measurement of the management system.** Regular checks on the operating system should be conducted against agreed predetermined criteria – the performance standards or KPIs.
8. **Regular reviews.** These are normal in-house checks of overall corrosion management system performance. They ensure that management procedures and processes are consistent with any changing business plans, changing production requirements and changing legislation.
9. **Periodic audits.** Management and monitoring system audits provide evidence that the corrosion management system is efficient, effective, and reliable, and that processes and procedures are being implemented in accordance with agreed procedures. Regulations typically require owners to



ensure that adequate arrangements are established for audit report making. Any dynamic corrosion mitigation process is also reliant for acceptable or improved performance on feedback from continuous, daily checks, regular reviews and scheduled audits to modify or improve the various processing steps. These require the development and use of performance indicators and form a key part of control of the corrosion management process. The use of KPIs is normal practice in most quality or safety systems and examples in corrosion management can be found in various publications.<sup>2,3,30</sup> They can be applied at various management levels and the aim is to ensure that the management system is operating effectively so that the required actions are carried out as scheduled and appropriate decisions are made on noncompliance.

Any management system relies on feedback for review and audit of the processes within the various steps. As shown in **Figure 2** the emphasis is on assessment of the management process, first by regular/daily/weekly/monthly use of appropriate performance indicators with the review (quarterly/half yearly/yearly) and audit processes (every few years) used to not only identify areas of activity that are conforming to previously agreed criteria but also those areas needing improvement.

The left-hand output in **Figure 2** (Effective Corrosion Mitigation) has usually been the major concern of corrosion teams, especially with regards to the impact on reliable operation and asset integrity. Effective corrosion management encompasses other issues as indicated by the feedback needed for review and audits. Hence, there are two outputs from modern corrosion management process: effective corrosion mitigation (as before) and also continuous improvement in performance (top right output in **Figure 2**). That is business related and safety, health and environmental outcomes, such as increased throughput at lower costs, less hazards from corrosion, fouling, fracture, wear, and better control over asset integrity with less leakages.

### 4.41.3 Front End Engineering Design (FEED)

#### 4.41.3.1 Introduction

FEED is the process for conceptual development of process industry projects and is sometimes referred to as Front-End Loading (FEL) or Pre-Project

Planning (PPP). FEED covers robust planning and design early (the 'front end') in a project's life-cycle at a time when the ability to influence changes in design is relatively high and the cost to make those changes is relatively low, as described in the chapter on design in this book. The extra time and cost to make changes in the early stages of a project are minor compared with the costs and effort required to make changes at a later stage of the project. The influence of design stage decisions on life cycle costs is illustrated in the chapter on economics in this book.

For the oil and gas industry the FEED process is often split into pre-FEED and FEED. In pre-FEED the basic definitions of the project are identified that will cover material and energy balance, and basic economic evaluations. The basis of design is the data available on the likely produced fluid compositions and associated information on production rates, water cuts, etc. plus any specified requirements of the proponent. The main activities within the FEED itself include:

- preliminary equipment design;
- preliminary layout;
- preliminary schedule;
- preliminary and definitive budget estimate;
- identify critical/major equipment requirements;
- develop preliminary equipment specifications;
- develop project execution plan;
- preliminary 3D model;
- electrical equipment list;
- line list;
- instrument index.

Developments of new fields, especially in deeper, more aggressive conditions are pushing the boundaries of conventional carbon steel materials and hence there is an increasing focus on corrosion management at the FEED stage, where critical decisions are taken that will affect not only the fabrication/construction cost but also the long term operation and maintenance costs since these influence the corrosion mitigation strategies adopted.

Fields that have a potentially high corrosion rate are typically high-pressure, high temperature, high-CO<sub>2</sub> fields, with high levels of H<sub>2</sub>S and chloride. Development of these fields even 10–15 years ago would have been considered technically and economically prohibitive.

Traditionally, the first part of any corrosion management consideration during pre-FEED and FEED would be to determine the estimated corrosion rate for

carbon steel under the expected operating conditions throughout the expected life of the facility. This is normally carried out using industry standard models, most of which are based on the work of de Waard *et al.*<sup>25</sup> for pipelines containing CO<sub>2</sub>. There are numerous versions of these models available that have been developed and expanded by major operators, academic/research centers and consulting organizations based on the same or similar databases and the same chemical equilibria constants. The model has been extended by de Ward and Smith<sup>31</sup> to include the effect of H<sub>2</sub>S. A calculation using a standard corrosion model would be carried out to determine the likely corrosion rate of the produced fluids. Provided the estimated corrosion rates are within acceptable limits, the FEED would continue with the carbon steel option, usually with additional corrosion protection measures, as the preferred material of construction for the various components making up the development (tubulars, main flowlines, vessels) apart from specific safety critical items (down-hole completions, safety valves, choke valves, etc.).

However, because of the trend to more challenging field development it is not unusual for predicted corrosion rates of >10 or even >20 mm year<sup>-1</sup> for unprotected carbon steel to be encountered in designs, which create major challenges for traditional oil and gas production corrosion control methods. Consequently such high corrosion risk fields require a more rigorous analysis at this early stage in the field development to determine a cost-effective design from a corrosion/durability stand-point.

#### 4.41.3.2 Data Availability

A pressure/volume/temperature (PVT) report is typically the only item of data that is available at the FEED stage of a project. There are uncertainties associated with these data, particularly with regard to sampling techniques, and this has to be considered when considering suitable materials of construction.

Assessment of fluid corrosivity can be carried out by the following methods:

- theoretical calculation;
- laboratory test data;
- comparison with operational experience in a similar field.

The operational implications of any corrosion management strategy should also be considered at this stage for example

- For corrosion inhibitors:
  - Is the likely supply chain stable enough to ensure quality and delivery of any chemicals required for corrosion control?
  - Is the required inhibitor availability realistic? In particular, would an availability of 98% to 99.9% be required to achieve the necessary levels of protection?
  - Is it realistic to expect regular and routine pigging of pipelines, for cleaning purposes?
- If CRAs are to be specified:
  - Is there sufficient experience of fabrication available locally and/or within the fabrication contractor?
  - Has the likely effect of chlorides and sulfates been assessed, particularly where down-hole temperatures are high?

#### 4.41.3.2.1 Theoretical calculations

As noted earlier, the first step in the FEED is the estimate of likely corrosion rates for carbon steel under the predicted range of operating conditions. When carrying out corrosion rate predictions the following factors would normally be considered when using standard CO<sub>2</sub> models to predict corrosion rate:

- Fluid composition:
  - Propensity to hold water.
  - Scaling/wax deposition propensity.
- Water composition:
  - Chloride, bicarbonate and acetate concentration.
- Water profile over field life:
  - Water cut in early, mid and late life.
- H<sub>2</sub>S and CO<sub>2</sub> concentrations.
- Flow rates.
- Temperature:
  - Variation over field life and pipeline diameter.

The effects of flow can be complex, as described in the chapter on the effects of flow on corrosion in this book, and a number of flow models are available (such as NACE ICDA,<sup>32</sup> PIPESIMS<sup>®</sup>,<sup>33</sup> PIPEFLO<sup>®</sup>,<sup>34</sup> OLGA<sup>®</sup>,<sup>35</sup> HYSYS<sup>®</sup>,<sup>36</sup> and others) that will allow an assessment as to whether the likely flow conditions in tubulars, flowlines and pipelines are stratified, bubbly, or slugging. This then allows the likely corrosion rates to be determined for water lines and multiphase lines that have water wet walls under stratified flow. Maximum corrosion rates in CO<sub>2</sub> systems typically occur ~75 °C to 95 °C, depending on temperature, pressure and CO<sub>2</sub> content, as shown in [Figure 3](#). At higher temperatures the corrosion rates fall due to increased

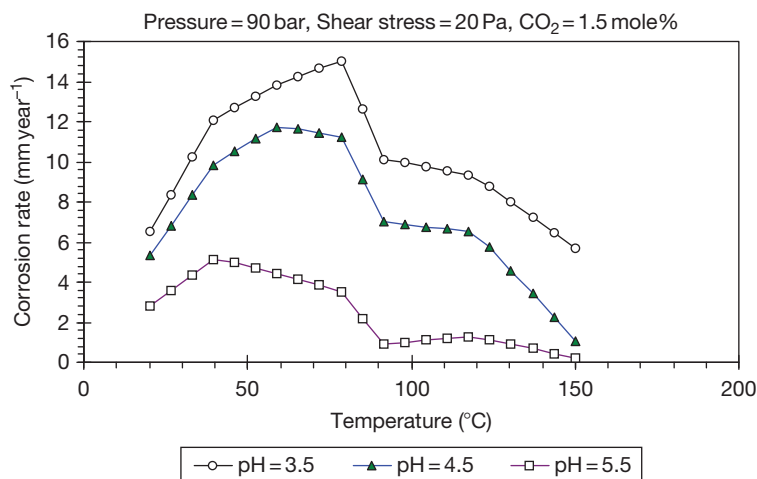


**Figure 3** Typical estimated CO<sub>2</sub> corrosion rates obtained from the Norsok M506 model. Adapted from NORSOK M-506: Rev. 2, June 2005, CO<sub>2</sub> Corrosion Rate Calculation Model; Norwegian Technology Standards Institution (Norsk Søkkel) [www.standard.no/petroleum](http://www.standard.no/petroleum).

FeCO<sub>3</sub> scaling. Loss of protective scale obviously gives high local corrosion rates that can be significantly mitigated by selection of an effective inhibitor. Inhibited rates will depend on the inhibitor efficiency. The pH also influences CO<sub>2</sub> corrosion rates and this observation is employed in the use of pH control of methanol/glycol (hydrate control) injected into wet gas lines.

Standard corrosion rate models do not typically assess erosion or flow-assisted localized corrosion. The Norsok model<sup>26</sup> is limited to a fluid to wall shear stress maximum of 150 Pa and the de Waard (ECE) model<sup>27</sup> is limited to below the API RP 14E erosional velocity<sup>37</sup>; which is dependent on alloy. Other studies show that the arbitrary erosional velocity determined by API RP 14E, can be very conservative, since basic hydrodynamics, which considers the shear stress of the flow across the surface, is determined, indicate that the force created by normal flow patterns is several orders of magnitude lower than that required to damage protective iron carbonate layers, and that the effect of flow appear to be the result of 'freak energy density' or energy densities perpendicular to the wall.<sup>38</sup> This ties in with observations of areas of turbulence intensity (ratio of velocity fluctuations to the average velocity) that appear to be a key parameter in erosion corrosion in flowlines and pipes.<sup>39,40</sup> High turbulence intensity also means a high fluctuating wall shear stress and high mass transfer conditions with flow separation downstream of protrusions, bends, expansions restrictions, etc. can give rise to localized areas of erosion corrosion.

Particularly useful are corrosion models that allow for the water wetting of walls<sup>41,42</sup> and enable the ability of the fluid to hold water to be incorporated, that is a function of oil density and flow rate. Generally light oils can only hold a limited amount of water before a conductive phase is formed and condensates can only hold up to 200 ppm of water. Low flow conditions (<1 m s<sup>-1</sup>) in most oil-water systems will result in water dropout. The assessment of what is essentially the emulsion tendency of the oil is not an accurate science, and therefore in some cases basic testing is applicable.<sup>43</sup> The effect of likely step change in conditions as water content changes is seen in Figure 4, where an increase from 3% to 4% results in a rapid increase in corrosion rate as water dropout occurs.<sup>44</sup>

As an alternative to assuming 'worst case' situations, the predicted or measured corrosion rate data can be expressed as graphs of probable life for different scenarios, as illustrated for a particular field development<sup>45</sup> where the options under consideration were:

- do nothing;
- wait for water breakthrough to occur;
- install monitoring facilities and chemical treatment facilities now.

Option (a) has obviously the lowest capital expenditure (CAPEX), but has the highest risk relating to repair works and/or premature abandonment of wells. Options (b) and (c) have the same CAPEX

costs, but option (b) has the advantage that the work can be delayed and/or phased to optimize expenditure, but runs the risk of unforeseen delays, which could result in unacceptable metal loss and some failures. Option (c) would be expected to provide the lowest risk option.

Baseline (uninhibited) corrosion rates for tubulars, flowlines and gathering lines were predicted to be between 0.3 and 0.9 mm year<sup>-1</sup> using standard industry models. These could be controlled by the installation of chemical treatment facilities and the injection of corrosion inhibitors. Additional parameters taken into account were:

1. time after water breakthrough before water detected;
2. time to procure chemical injection components and install (For option (c), assumed to be already in place);
3. inhibitor availability, that is, reliability of supply;
4. inhibitor efficiency, that is, effectiveness of inhibitor once applied.

The analysis gave the results shown in **Figure 5** with the corresponding financial projections indicated in **Figure 6**, that justify the development of a mitigation and monitoring strategy for the field development.

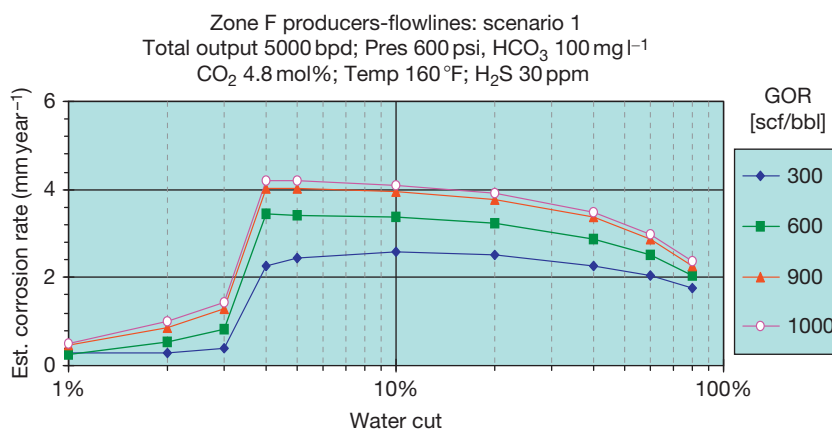


**Figure 4** Part of a corrosion assessment for a field development showing the influence of water cut on the predicted corrosion rates. Reproduced from Moosavi, A. N.; John, D. G. In *Corrosion/2002*; NACE: Denver, CO, 2002; Paper No 02225.

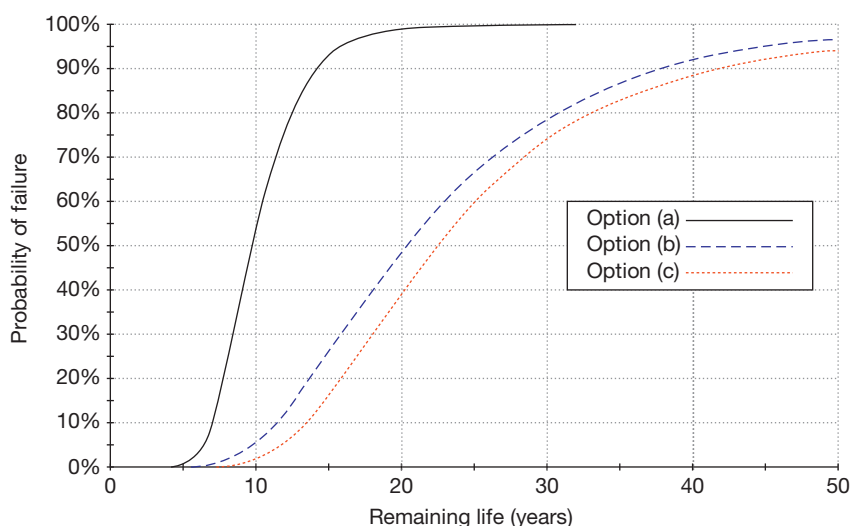


**Figure 5** Probabilistic predictions of field corrosion rates. Reproduced from John, D. G.; Stokes, P.; McIntosh, P. *Risk assessments as part of a pipeline integrity determination for subsea oil and gas pipelines*, paper 03163, presented at NACE CORROSION'2003, San Diego, CA, March 2003.

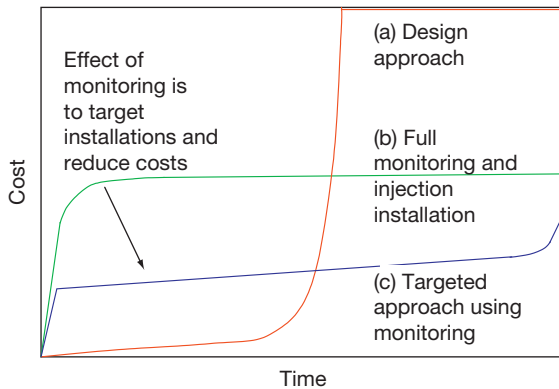


**Figure 6** Cost versus time implications of different scenarios. Reproduced from John, D. G.; Stokes, P.; McIntosh, P. *Risk assessments as part of a pipeline integrity determination for subsea oil and gas pipelines*, paper 03163, presented at NACE CORROSION'2003, San Diego, CA, March 2003.

#### 4.41.3.2.2 Corrosion risk analysis (CRA)

Corrosion rate data, from models or field information, can be used to assess corrosion risk across an asset or with individual equipment items (RBI). A common approach is the use of matrices, with linear or logarithmic scales, to prioritize risks and then to focus efforts on the most influential by evaluation of options. Important aspects for design teams or asset management teams are that a formal assessment of threats/risks is conducted using preagreed 'rules' or criteria are employed to define the likelihood of corrosion, the effect of corrosion and a ranking of the severity. The assessment report provides documentation for the next steps in the mitigation/management process and demonstrates the rationale employed by the corrosion engineer and replaces for other team members what often appears to be reliance on a subjective corrosion judgment.

Risk matrices provide a simple visual way of assigning risk where the consequences and likelihood of a failure are assigned to rows and columns of a matrix. Any combination can be used, the most common being based on four or five rows and columns; however, up to 10×10 matrices have been used by some operators. A typical 4×4 risk matrix is shown in Figure 7. Using this type of risk matrix identifies items where the risk is 'extreme' (i.e., where failure is both likely and of major concern), which should have immediate action taken (e.g., change of design, material selection, change in operations, etc.) to reduce the risk to an acceptable level. Items that are 'high' or 'medium' should be monitored during operations via a combination of

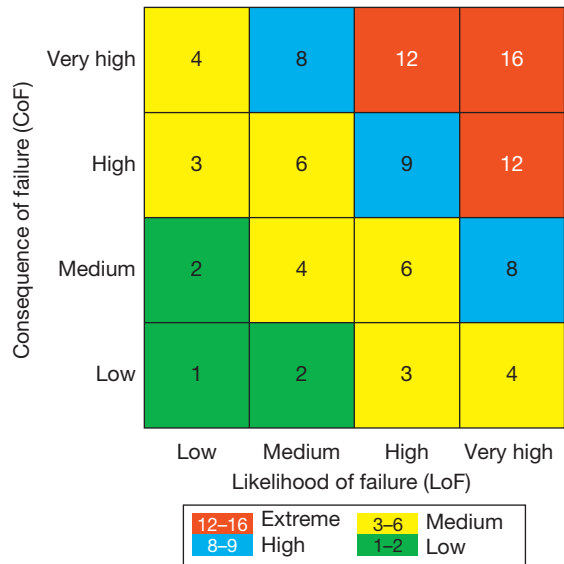


**Figure 7** Example of a typical risk matrix.

inspection, corrosion monitoring and fluid sampling. However, items where the risk is identified as 'low' (i.e., where failure is both unlikely and would be of little concern) require less attention.

Data collected during operations should be fed back to enable the risk assessment to be reevaluated. While the consequence of failure is unlikely to change during operations (with some exceptions, e.g., pressure reduction), the uncertainty in the data used to assess likelihood will normally be reduced by the collection of operational data, and where justified, the likelihood of failure can be reduced (or in some cases increased) as appropriate.

It should be noted that in other publications and operational systems 'likelihood of failure' and 'probability of failure' may be used interchangeably. The authors preference is to use 'Likelihood' for qualitative and semiquantitative risk assessments, and 'Probability' for full quantitative assessments. Further details of corrosion risk assessments, and use of corrosion risk matrices are given in Chapter 4.30, Corrosion Management Overview in this book and elsewhere.<sup>3,11</sup>

#### 4.41.3.2.3 Laboratory testing

While predictive modeling as described earlier is being used increasingly as part of the preliminary assessment approach, there remains a need for laboratory tests to confirm the likely corrosion conditions that will occur. This is especially so for systems with high CO<sub>2</sub>/H<sub>2</sub>S content, where many models will predict very



high corrosion rates (often  $>20 \text{ mm year}^{-1}$ ) but where practical experience indicates that corrosion of carbon steel is negligible. For example, a review was carried out of production facilities in Oman<sup>43</sup> where performance in service of carbon steel components was compared with laboratory tests,<sup>46</sup> which showed that a stable FeS film is formed, giving *natural* corrosion rates (i.e., in the absence of corrosion inhibitor and not taking into account any oil wetting) of:

- gas phase  $0.02\text{--}0.05 \text{ mm year}^{-1}$ ;
- liquid phase  $0.08\text{--}0.18 \text{ mm year}^{-1}$ .

As part of the study, the water cut point at which a water/oil emulsion will release the water, thus switching from being an oil-wetting to a water-wetting mixture, was measured by determining the change in polarization resistance. The results for two different crude types showed that with one up to 20% water addition was required to affect the polarization resistance, while only 5% water addition was required for the other crude to have the same effect. These results were consistent with standard oil–water emulsion stability tests, ASTM D1401,<sup>47</sup> where emulsion stability is determined by the time required for the emulsion to separate after controlled agitation. The emulsion stability tests showed that the first crude formed a stable emulsion (stable for more than 24 h), while emulsions formed with the second crude broke down within 2 min. Data that are consistent with published experience.<sup>41,42</sup>

This evidence that the combination of a stable FeS scale formation and absence of a conductive phase in low water cut conditions provides acceptable levels of natural protection, making the use of carbon steel was viable, despite high theoretical corrosion rates, which is also supported by field experience led one operator to now require laboratory testing be carried out to assess the corrosivity of the fluids, and in particular the degree to which light crudes/condensates to hold water, for all future projects and not to solely rely on predictive rates.<sup>43</sup>

Even in areas where natural protective scales are not formed, where predicted field conditions are aggressive, such that carbon steel with corrosion inhibition with an efficacy of  $>95\text{--}98\%$  is required and specified, it is often appropriate to carry out chemical screening tests at the FEED stage to ensure that a product is available in the market for the field conditions at a reasonable cost that can achieve the required corrosion efficacy for the life of the field.

Another key aspect that also has to be considered in any laboratory test program relates to presence of

organic acids, and in particular, acetates in the oil, as described by Hedges.<sup>48</sup>

#### 4.41.3.3 Procurement, Installation, and Operational Practicalities

Construction of oil and gas facilities worldwide comes up against a number of issues that differ from region to region and product to product including availability in specified thicknesses or line pipe grades, fitness for service (FFS) in sour service ISO 15156, shipping and storage costs as well as issues associated with basic materials selection considerations, i.e.:

- functional requirements;
- performance specification;
- design/redesign configuration;
- total life cycle in design;
- product availability and durability;
- inspection and QA testing;
- handling, packaging, shipping, and storage.

Procurement of raw materials is an issue as a vast proportion of the world supply of steel for equipment fabrication and pipelines comes from mills in the Far East where, unfortunately, there have been problems ensuring that the steel quality always meet the high stringent requirements of the oil industry, including the availability of compatible fittings (although it is recognized that European and North American mills have also been found wanting with regard to material quality in some instances).

Quality Assurance (QA) of manufacture must be considered at the FEED stage of a project. An understanding of these factors is essential for cost-effective materials selection and corrosion management during operations. The tolerances on standards and codes may be affected due to availability of source material. In some cases this can be an advantage from a corrosion perspective as often the higher specification of materials is purchased on grounds of availability. The cost of materials will vary from mill to mill and transport costs should also be considered during the lifecycle cost estimate.

The consideration of government legislation in terms of import and export of goods may also have to be considered. The level of tax imposed and the requirement for certificates of origin are both dependant on the local government regulations and are liable to change.

For example, if the government of a developing country requires the inspection of all 'key' components

that are imported to be carried out by a government appointed agency at the operator's cost, then the definition of 'key' components could be crucial to the viability of the project. If, for example, 'key' was defined as any pipeline, valve or fitting over 4" in diameter, that would have a major impact on the project economics. However if, through negotiation, key components are reclassified as those that are 6" diameter and above then the imposed QA cost can be significantly reduced and this will influence the life cycle cost analysis.

Fabrication of topside modules are often carried out in a completely different location to the pipelines and interlinking pipework and therefore compatibility of materials (selected by different design teams/fabricators) must also be considered. The supply of piping specifications, codes, schedules, etc. should be available irrespective of the manufacturing route, and the language of documentation should be clearly specified.

Consideration should be given to the locally available resource for fabrication of equipment. Handling and welding procedures for CRAs require much more stringent controls and may also require pre-qualification testing in H<sub>2</sub>S containing fluids, than normally employed for carbon steel products and incorrect procedures can lead to failures during commissioning and operations.

Specification of chemical injection facilities should be clearly understood at the FEED stage. If a high level of chemical availability is required, the quality of equipment, redundancy and availability of spares should be considered, particularly with high-risk inhibition systems.<sup>30</sup> The local supply chain should be investigated to ensure that, if required, a continuous supply of product is feasible.

For example, in many remote parts of Russia the present chemical injection philosophy is to periodically top up gravity fed chemical storage systems to feed into well head systems. However, during the summer periods, wellpads that are situated in swamp areas become inaccessible, resulting in no delivery of chemical and hence lack of protection. Consequently for critical well heads consideration is given to providing continuous injection via large capacity well head storage tanks that only require restocking twice a year (i.e., when reliable access to the wellpad is available). Similarly for small scale offshore applications, where well head platforms are unmanned, an umbilical supplying chemical to the platform may be required. Where the platform is manned or easily accessible, regular top up and monitoring of the offshore tanks can be carried out; however, in these cases local storage

facilities should be sized to ensure continuing availability of chemical if supply boats are delayed due to bad weather. Temperature differences between winter and summer operation in many desert areas mean that viscosity changes in inhibitor packages result in a change of injection pump operation and hence a change in dosage and/or selecting injection pumping facility that is reliable in varying conditions.

Another area that should be considered at the FEED stage is for necessary inspection and monitoring requirement to achieve the longer term objectives/corrosion strategies, including the type and location of appropriate monitoring devices. There are a wide number of techniques (corrosion coupons, electrical resistance (ER), linear polarization resistance (LPR), etc. as described in **Chapter 4.36, Corrosion Monitoring and Inspection** in this book and also later in this chapter) and commercially available products that assess the condition of equipment or the corrosivity, chemistry or biochemistry of the fluids. Consideration should be given to the technical and economic feasibility of their use and the FEED should not assume that these will be specified at a later design stage. In particular, it must be noted that the use of insert probes or coupons is now subject to more stringent control in many areas, including the required use of a double block system. The use of instrumented spool pieces, permanently installed devices such as UT mats, or similar systems, as shown in **Figure 8**, are increasingly being adopted as standard practice. Consideration should also be given to having at least two or three complementary methods to ensure reliance of field data.

Retrieval of data from corrosion monitoring devices should also be considered. For remote facilities, automated systems may be required, while for easily accessible systems where labor is readily available, daily retrieval of data is normally considered adequate, except for very high-risk systems where inhibitor availability is more than 98%.

A preliminary assessment of design requirements for the specification of external corrosion mitigation should also be undertaken to identify any specific requirements. In some cases it may be appropriate for a design for the CP system to be carried out for pipelines, and structures at the FEED stage, along with consideration of coatings for external protection. There is also a need to identify the supply of materials and local training requirements to ensure a system is designed, delivered and maintained to meet the long term objectives in a straightforward and easy-to-implement manner.



Cieon Subsea Spool®  
Photograph courtesy of Cormon Ltd.



FSM® Subsea Spool,  
Photograph courtesy of Rozar AS, Norway



Ultracorr® Permanent UT Sensors  
Photograph courtesy of Rohrbach Cosasco Systems



Rightrax® Permanent UT sensor  
Photograph courtesy of General Electric Co Company.

**Figure 8** Examples of spool pieces and permanently installed devices.

Key questions that need to be considered for materials and monitoring equipment are whether the supplier has local representation in the region where the system is going to be installed if servicing is required and whether suppliers have the experience of supplying material and equipment to similar fields.

#### 4.41.4 Design Stage

At the design stage of the project the detail drawings and specifications are prepared for construction and this is the opportunity to get it right or, unfortunately as still happens, to really get it wrong! Modifications beyond the design stage are costly and inconvenient.

For example, in a case known to the authors, an onshore field designed on the basis of using aquifer water for downhole injection suddenly found that the injection waters contained SRB, which required a change in operating philosophy with implementation of significant monitoring and biocide treating facilities.

Depending on the size of a project, the design stage may be divided into two stages of *Engineering Design* and *Detailed Design*. Corrosion related activities undertaken during the engineering design phase include:

- detailed materials selection, including the use of design codes, standards, and procedures for construction, fabrication, and assembly;
- assessment of proposed corrosion control options.

During the detailed engineering design, detailed specification and drafting of procedure are undertaken to produce the finalized design specifications and engineering details that are required for construction.

The following is an example of documents that require some level of corrosion input during the engineering design and detailed design phases of the project:

<i>Engineering design</i>	<i>Detailed design</i>
Basis of design	CP design
Material specification	Pipeline, vessels, tubulars,
External coating	valve specifications/
specification	testing
Insulation specification	Welding procedures/testing
Material selection	Corrosion monitoring
philosophy statement	designs/specifications
Corrosion monitoring	Equipment specification/
philosophy statement	inhibitor testing/data
Chemical management	management specification
philosophy statement	

#### 4.41.4.1 Documentation

##### 4.41.4.1.1 Material selection report

The material selection philosophy would normally be developed by materials specialists and should be

written into the project at the engineering design stage. It would typically contain details of materials for each system based on the fluids and operational conditions, plus details on materials specifications and properties. For example, for pipelines basic requirements would include standard dimensions, adequate strength for operational pressures, material to be identifiable and traceable, weldable under site conditions, free from defects that would cause leakage, and adequate fracture toughness to resist brittle fracture and resist propagation. Most requirements for linepipe are covered in API 5L<sup>49</sup>/ISO 3183,<sup>50</sup> but other requirements must also be specified including testing for weldability, fracture toughness tests, sour service tests to ISO 15156/NACE MR0175<sup>20</sup> (including testing for SSCC susceptibility to ASTM G39<sup>51</sup> and NACE TM0177<sup>52</sup>) restrictions on manufacturing process, limitations on chemical composition, element ranges, wall tolerances, and marking requirements. Budget costs are an output from the materials selection process.

One approach typically adopted in many projects would be the development of material selection diagrams (MSDs), that are based on the process flow diagrams (PFDs). They show the generic materials type, applicable corrosion allowance, internal coating requirements, and any other corrosion control requirement for pipelines, vessels, and piping, for example, as shown in [Figure 9](#).

At the detailed design stage the detailed materials specifications would then be developed with reference to appropriate standards. Piping schedules are produced that detail the appropriate material grade, wall thickness, operating pressure and temperature for each specific service in addition to insulation and welding specification and post weld heat treatment (PWHT) requirements. This information forms the basis of the line identifier on the process and instrument diagrams (P&IDs).

#### 4.41.4.1.2 Corrosion management philosophy

This document should contain high level details of the monitoring and mitigation measures that are required for the installation, plus important information that needs to be carried forward to detailing, specifications, fabrication and construction and operation, for example:

- injection of corrosion inhibitor to mitigate CO<sub>2</sub> pitting/general corrosion and H<sub>2</sub>S pitting corrosion;
- injection of biocide to mitigate MIC corrosion;

- injection scale control chemicals;
- injection of chemicals for pH/hydrate control;
- deoxygenation/treatment of injection water;
- CP of pipelines, structures, internals of vessel and tanks;
- corrosion/erosion (sand) monitoring;
- specification of pipe internals to remove mill scale during external blasting for coating application, which minimizes sludge formation during the first few years of operation as CO<sub>2</sub>/H<sub>2</sub>S corrosion products replace air formed films;
- routine cleaning of pipelines using cleaning pigs;
- routine flushing of sand from vessels and procedures for removing sand deposits from lines/manifolds following sand breakout in a well.

This will enable the equipment to be designed to deliver these various requirements.

#### 4.41.4.1.3 Chemical injection systems

Where chemical injection of corrosion inhibitors, biocides, scale inhibitors, emulsifiers/deemulsifiers, etc. is required it is important that the injection location and injection facilities are correctly identified. The injection must take place sufficiently far upstream of where the chemical is expected to provide benefit to ensure adequate mixing. Typically, this mixing distance will be defined as at least 2 m or 10 pipe diameters upstream. Where more than one chemical is required at nominally the same point they should be injected separately and not via the same injection point to avoid the risk of clogging. The injection nozzle should also be designed to provide the optimum distribution into the stream.

The method of injection, that is, the use of mechanical or electrical pumps, and local storage also have to be taken into account in relation to factors such as protection from solar heating, the use of plastic or stainless steel tanks, etc. In the concentrated form corrosion inhibitors and other chemicals can be very corrosive and/or toxic and hence suitable precautions, including the use of austenitic stainless steels for injection equipment and lines, will be needed to prevent leakage.

The pumps will also need to be sized so that sufficient chemicals can be injected into the stream to ensure the necessary dosage levels. Most corrosion inhibitors are formulated to be typically present at levels of 10–20 ppm (in the range 5–100 ppm) and, depending on the production rates, the actual amount of chemical injected could range from 2 dm<sup>3</sup> day<sup>-1</sup> for production facilities of 167 m<sup>3</sup> day<sup>-1</sup> (1000 bpd)

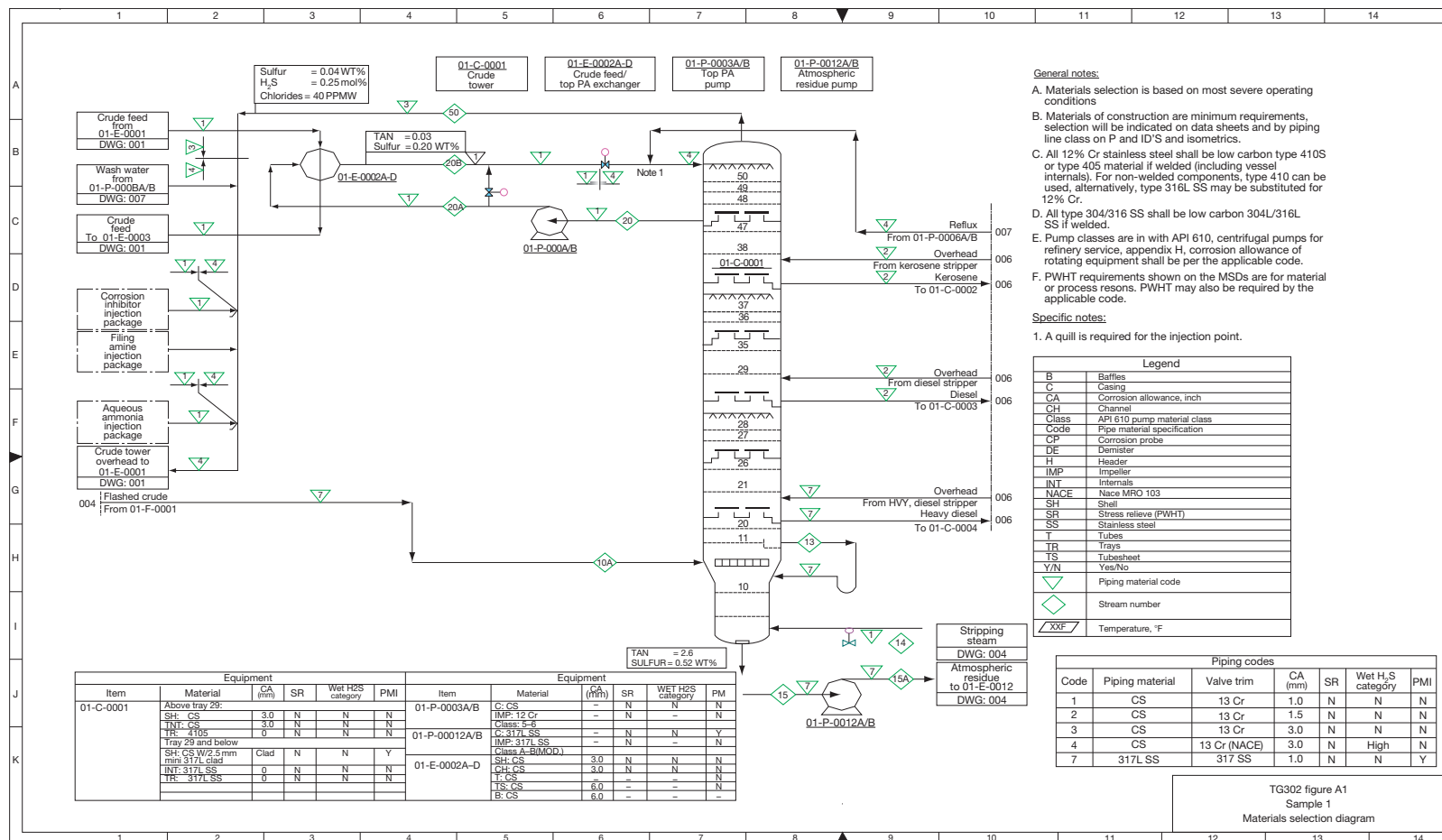


**Figure 9** Example of material selection diagram (taken from NACE SP0407). Reproduced from NACE Standard Practice SP0407-2007 'Format, Content and Guidelines for Developing a Materials Selection Diagram'.



up to  $30 \text{ dm}^3 \text{ day}^{-1}$  for production of  $1670 \text{ m}^3 \text{ day}^{-1}$  (10 000 bpd). A description on the use of inhibitors in oil and gas operations are given in **Chapter 4.26, Chemical Treating in Oil and Gas Production** in this book and elsewhere.<sup>30</sup>

#### 4.41.4.1.4 CP systems

The majority of CP systems will be aimed at the external protection of offshore production facilities such as fixed platforms, floating platforms and FPSOs, onshore and offshore pipelines, and onshore storage tank bottoms. However, CP can also be applied to the internals of oil and gas process equipment, including separators, filters, heat exchanger water boxes and storage tanks.

The selection decision for pipelines and storage tanks at the design stage will be between the use of galvanic anodes and/or impressed current systems, and the extent or otherwise that different components are electrically isolated or deliberately bonded together. Note that CP will protect against crevice corrosion if applied as soon as the component is immersed but, will not necessarily protect crevices after the corrosion has initiated. For offshore applications, and in particular subsea developments, the compatibility of CP systems required for carbon steel pipelines and other structures also has to be assessed, specifically for the effects of over protection on either high strength carbon steel components or components fabricated from other materials such as duplex stainless steels and titanium. While CRAs may not require external CP, they will receive it, because they are connected to carbon steel pipelines that have CP applied, and this has led to failures of subsea manifolds in the past.<sup>53</sup>

Internal CP can also be applied to process equipment and the main concerns relate to the low pH/elevated temperatures in the process, which in turn leads to higher current demand and low anode performance and hence more challenging CP design. Most internal CP systems are galvanic<sup>54,55</sup>; however, impressed current CP systems have also been installed.<sup>56</sup>

If internal CP is to be incorporated it is important that ease of anode installation/replacement is taken into account as part of the overall design. Methods for determining performance are also more complex, and include the use of ER probes.

#### 4.41.4.2 Engineering Considerations

##### 4.41.4.2.1 Minimizing corrosion threats

Variations in pipeline and pipework geometry, such as the presence of dead-legs and low points, create areas

where water and debris can settle and accelerate a number of different corrosion threats, including  $\text{CO}_2$  corrosion, under deposit corrosion and microbial corrosion, as illustrated in **Figure 10**. Similarly, sections of pipeline that cannot be pigged increase the chance of build-up of deposits. While low points and dead legs cannot be fully eliminated in any design, they can be minimized. The awareness of corrosion should be raised with the piping designers at the design stage of a project and, where possible, a review of the piping design should be carried out to challenge any excessive use deadlegs and low points.

##### 4.41.4.2.2 Corrosion allowances

Most carbon-steel components selected for use in oil and gas facilities will incorporate a corrosion allowance. The wall thickness for the component (pipeline, pipework, vessel, tank, etc.) will be increased above the minimum allowable wall thickness as determined by the appropriate design code, to allow for metal loss due to corrosion or erosion. This is separate from the inclusion of a fabrication tolerance for the component.

The corrosion allowance will be selected based on the expected corrosion rate that will occur with the planned corrosion control procedures in place and allowing for the design life of the facility. The inhibitor availability concept provides the procedure that should be used in practice.

During operation, provided that the actual metal loss, as determined by inspection and trend monitoring according to API 570,<sup>57</sup> API 580,<sup>10</sup> or other RBI system, is less than the corrosion allowance then the component will be operating within the design code requirements and is considered fit for service. Only when the actual or estimated metal loss exceeds the corrosion allowance would a more detailed assessment as to the continued fitness for service (FFS) be required (see **Section 4.41.6.9** later in this chapter).

Typically, corrosion allowance would be 2 or 3 mm, and while most projects try and limit corrosion allowance to 6 or 8 mm, in some cases a corrosion allowance of up to 12 mm have been considered, especially where there is a risk that the corrosion control program may not be fully effective. However, other projects choose not to include any corrosion allowance, normally this is when there is a high confidence in the effectiveness of the corrosion control program (for example for commercial quality dry gas pipelines).

##### 4.41.4.2.3 Inaccessible pipework

While some piping, especially for offshore installation, will not be easily accessible, it is important to consider that corrosion monitoring equipment needs

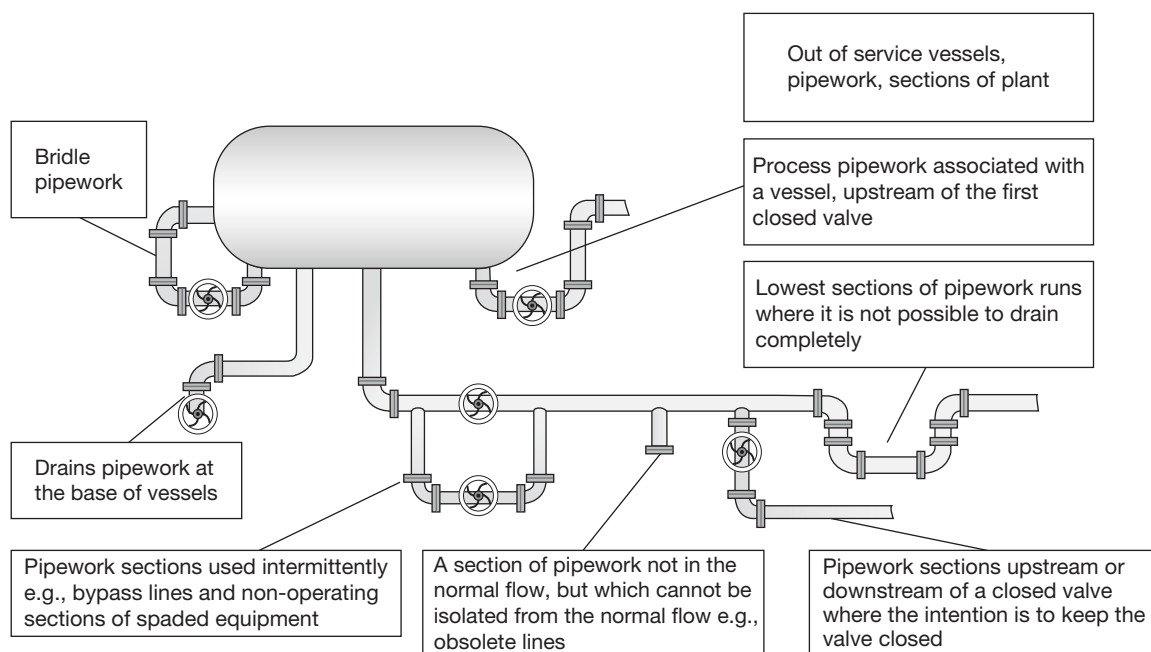


**Figure 10** Schematic of 'dead-legs,' from the Energy Institute 'Guidance for corrosion management in oil and gas production and processing.' Reproduced from *Guidance for Corrosion Management in Oil and Gas Production and Processing*; Energy Institute: London, May 2008. ISBN 978 0 85293 497 5.

to be accessed by retrieval tools and that the external surface of piping will need to be inspected.

For subsea pipelines, direct access is almost impossible and therefore the design should be robust enough to deliver a 'fit and forget' solution. There should be a high level of confidence in any monitoring equipment that is to be located in inaccessible locations.

#### 4.41.4.2.4 Insulation

A major problem with external corrosion of oil and gas production facilities is corrosion under insulation (CUI), where excessive corrosion and/or SCC can occur where water (rain water, seawater, deluge water, etc.) enters the insulation. In many cases, the insulation is necessary for process control and hence steps need to be taken to ensure that that system is correctly designed to reduce the threat of water ingress and also to minimize any subsequent corrosion by use of protective coatings on the metal piping.<sup>58,59</sup> Where insulation is not necessary, for example, when solely used for personnel protection, it should be removed and alternative methods to prevent harm, such as the use of open mesh guards, applied.

#### 4.41.4.2.5 Pigging facilities

The installation and design of temporary or permanent pigging facilities should be considered and will

be dependant on the expected frequency of pigging and the availability of labor. Consideration should be given at the design stage to the requirement to pig individual pipelines, which can impact on detailed materials selection philosophy. Normally unmanned installation (NUI's) that require regular launching of cleaning pigs to protect the export pipeline will require a robust automated launching system that is capable of storing the number of cleaning pigs that are required between visits to the facility.

In the case of an onshore facility with an extensive pipeline and flowline network that has the need to run cleaning pigs on a monthly basis in the flowlines, the installation of permanent pigging facilities at each wellhead may be considered prohibitively expensive and the design of mobile pigging facilities for each region of the field may be considered. The number of temporary pig launchers needs to be balanced with the number of teams that will be available to carry out the pig launching and receiving activities. Alternatively the pipeline network can be designed with pigging loops to enable launch and reception to be carried out in similar locations.

It should be recognized that one of the major hurdles for many existing pipelines world wide are pipelines that are not piggable, either because the lines include bends that are too tight or more often

because the internal diameter (bore) of the pipeline is not constant, such that pigs (whether used for cleaning or inspection) cannot travel along the line reliably. In general the less a pipeline is cleaned the higher the possible corrosion threat.

#### 4.41.4.3 Design of Data Management Systems

At the design stage, the type of data management system that is required for the facility should be considered<sup>60</sup> and the selected system will normally be set up during the construction phase in order to input inspection information such as 'as built' wall thickness measurements. The choice of corrosion management system may influence, or be influenced by, the corrosion monitoring and materials of construction. If the corrosion monitoring is linked into an online measurement system (e.g., PI, SCADA) then a real time corrosion data management system can be used.<sup>61</sup> If a high level of manual inspection is to be carried out then a comprehensive inspection management database should be considered, particularly if RBI is to be adopted.

Methods and procedures for all activities will be required, including specifications, procurement of materials, testing, fabrication and welding, coatings, CP equipment applications, corrosion monitoring and inspection instrumentation, field data collection and analysis, required databases and means of achieving their population, specification of reporting by appropriate routes and development of corrective action procedures to be carried out when necessary.

The development and maintenance of corrosion databases, usually electronic, could include provision for storage of system documentation including facility design documents, as-constructed diagrams, commissioning information and field data during operation, inspection and maintenance. These should cover information on the basis of the design, design drawings, modifications, testing requirements and construction so that relevant information data are transferred through to the operational phase database.

The means by which field data such as visual inspections, coating surveys, hand held/permanently wired instrumentation, DCS/SCADA downloads are to be collected, analyzed, and used for trending and correlations must be agreed and specified, including post fabrication inspection data that provide the initial field data point for trending as in RBI.

An effective management tool is a transparent database that correlates field data to provide a regular

weekly/monthly breakdown of corrosion mitigation costs. Ideally, field databases should be live documents where measurements are inputted as soon as possible and analyzed/trended/correlated to provide virtually continuous management information for the corrosion team leader/supervisor. The use of a web page approach is becoming more accepted with simple traffic light schemes (red, yellow, green) providing easy to identify out-of-condition processes.

#### 4.41.4.4 Commissioning Procedures

During the detailed design phase, commission procedures should be written for each area. Procedures that have particular emphasis on corrosion are:

- commissioning procedure for chemicals management system;
- pressure testing and preservation procedure (in particular water treatment for hydrotest systems).

### 4.41.5 Fabrication, Construction, and Commissioning

#### 4.41.5.1 QA and Quality Control

An integral part of maintaining technical integrity of a new facility is to ensure that the materials selected in the FEED/Design Phase are manufactured, procured, and constructed as envisaged and in a way that they maintain their degradation resistant properties for the intended use. Normally the responsibility of ensuring that materials meet required specification will fall to the QA teams within the design project team. Their role is to ensure that the minimum compliance checks and nondestructive examination requirements are fully adhered to and that the construction materials retain their original specified properties.

A main issue that needs to be addressed during fabrication and construction is that where special properties for a material are required, in particular with respect to sour service in accordance with ISO 15156/NACE MR 0175,<sup>20</sup> they are delivered as specified. Note this should not just rely on material certificates unless supported by internationally recognized standards/quality control organizations. Many problems have arisen where materials have been supplied as being of a particular grade and in accordance with specification, only for them to be eventually discovered as being out of specification, for example, austenitic stainless steel grade SS316L (UNS S31603/EN 1.4919) piping specified, but grade SS304 (UNS 31400/EN 1.4841) supplied, or forged valves specified

as being compliant to MR 0175<sup>20</sup> found subsequently to have unacceptable hardness, resulting in cracking and failure after only a few weeks operation.<sup>62</sup>

Any deviation or other changes to the original design should only occur after review and approval by the design team and should always be fully documented and the responsible material and corrosion engineers notified in order to ensure that the relevant information is incorporated into the corrosion management manuals.

During fabrication and construction, items of equipment will be subjected to a range of routine inspection to confirm fabrication in accordance with specification and code requirements. In addition it is increasingly used to ensure that as delivered wall thickness checks (using nondestructive inspection systems, such as ultrasonic wall thickness systems) are carried out to confirm the original wall thickness prior to operations. This then becomes the baseline value used in assessing performance during ongoing operations, and eliminates the uncertainty associated with actual versus nominal wall thicknesses.

#### **4.41.5.2 Development of Integrity Management Systems**

During this phase, the integrity management systems are normally set up. This should comprise a suite of documentation that enables a structured framework for integrity management to be delivered and should cover integrity policy, strategy, codes of practice procedures, specifications, and guidelines. Some of the typical documentation required includes:

- integrity management policy and strategy;
- sand management strategy;
- corrosion management manual;
- hydrotest and preservation procedures;
- chemical management strategy;
- RBI strategy;
- corrosion monitoring manual;
- inspection procedures.

Risk assessments and the generation of RBI plans require PFDs, piping and instrumentation diagrams (P&IDs), MSDs, pipework isometric drawings, vessel data sheets and process and operations manuals to be available. Development of the integrity management system during the construction and commissioning phase enables the systems to be implemented from day one of operations. This ensures that all operational data are collected and fed back into the system.

Corrosion and materials consulting engineers typically act in an advisory capacity during the construction and commissioning phase to assist in the following activities:

- Define requirements for integrity management systems;
- Reassess design decisions related to integrity monitoring and mitigation.
- Advise on materials approvals, quality control and QA checks.

During commissioning it is important that the detailed hydrotest and preservation procedures are followed, the chemical injection packages are commissioned and the dose rates and logistics associated with chemical supply are confirmed. Vibration screening should also be carried out during commissioning of susceptible components.

Following fabrication and construction, the facilities will be tested and commission in different phases. Even at this stage, full attention to corrosion management requirements is vital, since major damage and/or problems for future operation can be created during this stage.

A significant issue relates to hydro-testing of pipelines, pipework, and vessels, which, unless carried out correctly, can lead to major problems. This includes problems associated with leaving inadequately treated hydrotest water in the line allowing oxygen corrosion or MIC due to introduction of bacteria, that can lead to severe metal loss prior to operation or, if the line is not fully cleaned and dried, can leave water in place that then allows corrosion to proceed once production starts.

Most problems associated with external corrosion of pipelines are also caused during pipe laying, either due to damage to the coating, in particular the field joints, either due to 'roller damage' for offshore or mechanical damage from slings, stones, etc. during trench placement onshore.

#### **4.41.5.3 Handover to Operations**

Following successful commissioning the fabrication and construction team will disperse. Before this occurs all historical records developed during the fabrication, construction and commissioning phase that could be useful for ongoing operational corrosion management should be handed over to the operational team responsible for ongoing corrosion management.

The extent of this information should not be underestimated (see compliance with ISO 9001: 2008<sup>63</sup>)

and the key documents and information are summarized in the following section. It should be recognized that this is not an exhaustive list, but intended to give guidance on the type of information that is not only useful for corrosion, inspection and integrity engineers during operations but identifies the means by which risk mitigation is transferred from design to operations.

Handover documents:

- Basis of design.
- Corrosion management premise.
- Material selections and peer review.
- Corrosion management manual (including preliminary inspection/monitoring plans, reporting plans, KPIs, etc.).
- RBI plan.
- PFDs marked with corrosion circuits.
- Maintenance reference plan.
- Preservation procedures.
- Hydrotest procedures.
- Chemical injection procedures.
- Piping and instrumentation diagrams (P&IDs).
- Process flow diagrams (PFDs).
- Operations manuals.
- Corrosion barriers spreadsheet.
- Process simulation/heat and mass balance data.
- Hydrotest procedure.
- Chemical dosing manuals/procedures.
- Adequate manpower, material and equipment resources need to be allocated to undertake the plan. Permanent physical facilities should be installed.
- The locations for monitoring and inspection activities should be defined.
- Procedures and instructions should include criteria of nonconformance.
- A corrosion damage reporting process should be continuously in place to capture information regarding failures that occur unconnected to the planned activity.
- A procedure should be in place to allow for opportunity based inspection, separate to the plans, of items that are not normally accessible for operational reasons.

An important point to realize in any corrosion management implementation is that *'no plan survives contact with the enemy'*<sup>64</sup> and, as a consequence, it is unlikely that all the original plans and procedures will be able to run smoothly thought the operational life of a facility. Hence, as either process conditions change (e.g., due to increase in water cut, incorporation of new production wells, changes in oil lift methods, etc.) or where unforeseen events occur (e.g., failure of chemical injection facilities) then alternative methods of detection may be required to be used and incorporated into the corrosion management 'tool kit,' either in place of, or in conjunction with, existing methods. Any new inspection and monitoring technologies should also be evaluated and considered as part of an ongoing system improvement process.

## 4.41.6 Operations Phase

### 4.41.6.1 Corrosion Management Strategy Implementation

Implementation of the corrosion management strategy involves the correct execution of the mitigation, monitoring and inspection activities that ensure the facility remains fit for purpose. Examples of these activities are corrosion rate monitoring, process monitoring and inspection, data collection, analysis, reporting and corrective action.

The requirements for implementation are:

- The strategy should be translated into practical instructions, for example, planned maintenance routines, operating instructions and work packs. There should also be a means for implementation of the strategy.
- Written procedures, work instructions and guides to performing the implementation tasks should be provided. Responsibility for implementation should be identified.

### 4.41.6.2 Routine Inspection and Monitoring

Corrosion inspection and monitoring are key activities in ensuring asset integrity and control of corrosion. It is important to monitor appropriate parameters that indicate the performance of a corrosion barrier to check whether the performance limit has been exceeded.

Monitoring can comprise inline, online and offline systems and provide rate of corrosion degradation data and information on the effectiveness and performance of the corrosion mitigation techniques (e.g., corrosion inhibition, process treatment, etc.). Analyses of the results from these systems allow steps to be taken to prevent failure, if necessary.

In-line systems are devices installed directly into the process that need to be extracted for analysis or



sampling of process fluids for analysis, for example, corrosion weight loss coupons, biostuds, fluid sampling, etc.

*Online* corrosion monitoring techniques, that is techniques that use fixed probes or sensors that can be integrated without the need to remove them from the system (insert probes or externally mounted probes), include:

- electrical resistance (ER) probes;
- linear polarization resistance (LPR) probes;
- fixed ultrasonic (UT) probes;
- acoustic emission;
- electrochemical noise;
- monitoring of process conditions;
- magnetic flux leakage (MFL) or UT in line inspection (intelligent pigging) of pipelines;
- field signature method (FSM) monitoring spools.

*Offline* techniques retrospectively identify corrosion degradation and quantify the onset and causes, and the extent and degree to which it has occurred. Offline monitoring or inspection mainly utilize the following inspection and nondestructive testing/evaluation (NDT/NDE) techniques:

- visual;
- manual/automatic ultrasonic;
- radiography;
- pulsed eddy current (PEC);
- magnetic flux leakage (MFL);
- time of flight diffraction (TOFD).

Detailed descriptions of the different inspection and monitoring systems, together with their advantages and disadvantages, are described in **Chapter 2.04, Pitting Corrosion** in this book and in various standards, technical reports and other publications.<sup>65–71</sup> New inspection and monitoring technologies should always be evaluated and considered as part of a continuous improvement process, for example, a combination of new development methods (FSM and electrochemical noise) were used successfully to identify corrosion problems in an aging sour gas system.<sup>72</sup>

Regular proactive and reactive monitoring should be undertaken to measure the degree to which the policy objectives of the corrosion management plan are being achieved. There are two measurements of success: (1) meeting the performance limits for the effectiveness of the corrosion barriers, that is, the FFP of the facility and (2) meeting the targets in terms of the effectiveness of identifying the barriers

and organizing, planning and implementation, that is, the success of the management system itself.

Routine inspection provides a key input into corrosion management activities. This is mainly aimed at nondestructive inspection to determine the wall thickness of pipelines, pipework and vessels, but also includes NDT/NDE to identify cracking or other forms of deterioration. The most common form of inspection utilizes wall thickness measurements obtained using compression ultrasonic probes (UT). Various types of UT systems are available, including simple ‘all-in-one’ probe and digital meter, digital wall thickness gauges and full screen systems, which allow measurement at points on the surface. With these units the operator manually moves the sensor around the area to locate the point with the lowest wall thickness. Fully automatic scanning systems are also available that can travel around/along the component providing a 3-D image of the wall thickness allowing clear identification of localized corrosion.

While simple digital only UT meters can give quick measurements, they are not fully reliable. The readings can be affected by inclusions or defects within the pipe/vessel wall, which can give a false low thickness reading and also by tightly adherent scales, which can give a false high thickness reading. Wherever possible full screen UT meters should be used to ensure that such features do not affect the reading, since the ultrasonic echo is displayed allowing an experienced operator to distinguish the interface formed at inclusions (false – low) and adherent scale (false – high).

When using manual meters, the reading will normally be collected from around a section of pipe (typically 100–300 mm long) or a marked out section of vessel, typically 100×100 mm to 300×300 mm in size, recording the minimum wall thickness observed within the area. For larger diameters of pipe the section may be split into four subsections (typically top, right side, bottom, and left side for horizontal pipe).

By repeating wall thickness measurements at intervals, an estimate of the corrosion rate can be obtained. In all cases, UT equipment should always be operated in accordance with manufacturer’s instructions, including calibration for the specific metal/alloy and operating temperature of the facility.

Wall thickness measurements, should be trended over a period to identify changes in condition and rate of metal loss. A typical example is shown in **Figure 11**; here data are initially collected at nominally three yearly intervals (period 1) and shows an estimated corrosion rate of 0.05 mm year<sup>−1</sup>. At the

time of the next inspection a significant change is noticed with an increase in corrosion rate to  $0.3 \text{ mm year}^{-1}$ , as a consequence the inspection frequency was changed to annually and this rate is seen to continue for a few years, until corrosion control is reestablished (period 3) with corrosion rate back to  $0.05 \text{ mm year}^{-1}$ .

This also shows the advantage of obtaining both 'short' and 'long' corrosion rates from inspection data. 'Short' corrosion rates are taken at the penultimate and ultimate (i.e. most recent) readings, while 'long' corrosion rate is based on the first reading and last reading; in the example in Figure 11 this is  $0.1 \text{ mm year}^{-1}$ .

When using UT inspection as part of corrosion monitoring activity particular attention should always be given to identification and measurement of localized corrosion (pitting), especially in sour systems.

Increasing use is being made of long-line UT, where a series of sensors are fixed around a pipe sending signals along the pipe transversely identifying possible defects up to 20–50 m in either direction from the sensors. The distance that the long range UT can effectively scan is a function of pipe geometry, number of fixings/supports (that provide 'false' echoes) and whether the pipe is buried or not. When buried the acoustic impedance is lost such that the signal 'leaks' into the ground, limiting the effective distance. Once possible defects are located then they should be confirmed using standard UT inspection.

Other methods for providing a rapid inspection of pipework are also used and continue to be developed.

These include magnetic and hall-effect (eddy current) systems and pulse eddy current, that is used to detect metal loss under insulation.

For pipelines the most common inspection method is inline inspection (ILI), also referred to as intelligent pigging or smart pig (notwithstanding the problem of nonpiggingable pipelines as highlighted earlier). Today ILI is a routine method of assessing FFP of pipelines and it can be applied to a wide range of sizes (6" up to 36" diameter) and can be deployed in any type of pipeline (i.e., oil, gas, water) and for long distances. The actual distance that can be surveyed in one deployment is dependent on the memory capacity of the tool but typically up to 100 km per deployment can be accommodated.

There are two different types of ILI tool deployed, the most common type utilizes MFL that measures wall thickness by the distortion of the magnetic signal generated by the tool caused variations in thickness of the pipeline wall. The second type is an ultrasonic tool that measures wall thickness in the same way as normal UT inspection. MFI tools can be used in any media, liquid or gas, but UT tools can only be used in a liquid media to allow acoustic coupling between the sensors and the pipe wall, and hence are not normally used gas lines.

Both MFI and UT tools detect and quantify metal loss and can identify whether the loss is internal or external. The requirements for ILI surveys are governed by International Standards, including NACE RP0102,<sup>73</sup> NACE TR 35100<sup>74</sup> and API STD 1163.<sup>75</sup>

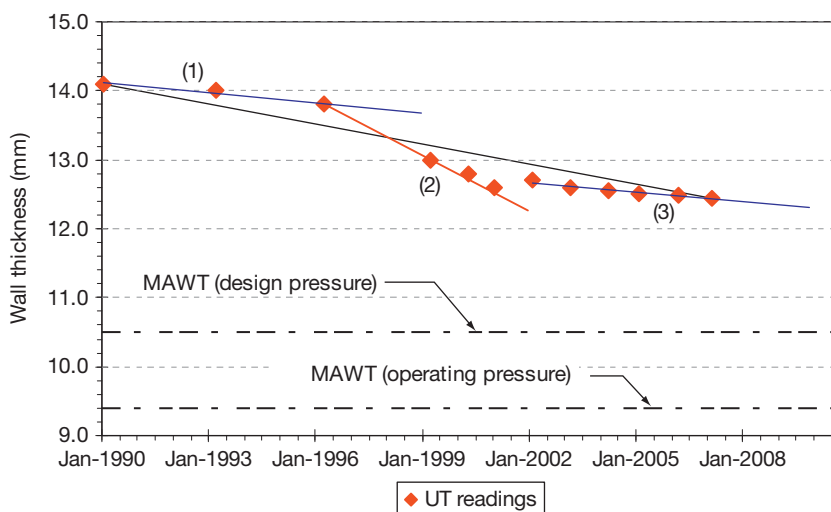


Figure 11 Example of UT Inspection data with time (indicative).

#### 4.41.6.3 External Protection

Performance assessment of the external corrosion control system, typically coatings and/or CP will also be required. For operating plants, this will normally be limited to visual inspection, but for items that are insulated a more detailed inspection plan will be required, which will be based on risk assessment for CUI and may also include specialist NDT/NDE systems such as pulse eddy current, long range UT, radiography or thermal imaging systems.<sup>58,59</sup>

For buried and submerged pipelines, in addition to use of ILI surveys, the condition of the protective coating and effectiveness of the CP system will also be determined by one or more specialist pipeline surveys. For subsea pipelines inspection will normally be by a remote operated vehicle (ROV) carrying out both visual inspection but also potential measurements to determine the performance of the CP system.

For onshore (buried) pipelines a number of different surveys are carried out,<sup>76</sup> covering:

- close interval potential surveys (CIPS);
- pearson surveys;
- DC voltage gradient (DCVG);
- AC voltage gradient (ACVG).

Often a pipeline survey will combine two of the methods, in particular CIPS and DCVG, the aim being to identify areas where either the protection potential is less than required (typically a polarized or 'instant-off' potential more negative than  $-850$  mV versus Cu/CuSO<sub>4</sub> reference electrode), and/or where there is evidence of significant coating damage.

Pipeline survey data, together with information from fixed monitoring points, will be used to assess overall performance of the pipeline protection and to identify areas where excavations of the pipeline may be required for direct assessment of the condition. In particular for buried pipelines a growing concern relating to buried pipelines is the risk of EAC, typically associated with specific local ground conditions/chemistry, damage to protective coatings and poor/inadequate CP. EAC is described in other chapters in this book and direct assessment issues are described in more detail in [Section 4.41.6.8](#).

The management of external corrosion and maintenance of coatings on structures, piping, handrails, walkways, and gratings has been addressed using a risk based assessment (RBA) to prioritize work based on inspection of coatings condition linked to performance monitoring on a visible KPI reporting system<sup>3,77</sup> (see also [Section 4.41.6.10.4](#)).

#### 4.41.6.4 Chemical Treatment

Chemical treatment of process and service fluids is widely used in oil and gas production and processing in order to manage corrosion. Commonly used chemical treatments are:

- corrosion inhibitors;
- methanol;
- H<sub>2</sub>S scavenger;
- glycol;
- wax inhibitor;
- biocide;
- O<sub>2</sub> scavenger;
- sodium hypochlorite;
- scale inhibitor;
- pH buffer;
- antifoulant.

The purpose of each of these treatments may not necessarily be for corrosion management, but they do contribute toward corrosion mitigation and control.

Chemical selection should include performance and compatibility testing and feasibility studies prior to implementation. Part of the ongoing corrosion management process is ensuring that the correct chemical is fed at the correct dose rate/concentration at the correct location at the correct time and that there is always stock available. This is the key to the production process running efficiently and effectively.

The background to some of the different analysis issues is summarized in the following section.

##### 4.41.6.4.1 Temperature, pressure, CO<sub>2</sub>/H<sub>2</sub>S content

Temperature and pressure measurements will be routinely recorded by the plant DCS. These values, together with CO<sub>2</sub>/H<sub>2</sub>S content, can then be used to provide an estimate of the system corrosivity using any of the standard corrosion modeling software packages, for example, De Waard and Milliams,<sup>25</sup> ECE4,<sup>27</sup> Norsok M506,<sup>26</sup> etc.

There are methods for measuring dissolved CO<sub>2</sub>/H<sub>2</sub>S in water samples taken from the process. However, dissolved CO<sub>2</sub>/H<sub>2</sub>S content is highly dependent on pressure and temperature (since gas flashes off from solution when samples are depressurized and H<sub>2</sub>S is rapidly lost by air oxidation) and therefore results can be erroneous. Measured values in water are always lower than true values in the case of pressurized samples, unless elaborate sampling procedures are followed.

Hence, in the authors opinion, the preferred method would normally be to measure CO<sub>2</sub> and H<sub>2</sub>S content in associated gas (ppmv values) using sampling tubes, and then use a PVT model (e.g., Multiflash™) in conjunction with known pressure and temperature data to back calculate the dissolved CO<sub>2</sub>/H<sub>2</sub>S content of the aqueous and oil phase(s) *in situ*, throughout the system. In addition to providing a more accurate assessment it also means that only one measurement per fluid stream is required as opposed to multi-measurements at different points in the stream.

#### 4.41.6.4.2 pH measurements

The corrosivity of a solution is directly related to the solution pH, hence a measure of pH can be used to monitor changes in system corrosivity. In oil field systems pH measurement is normally carried out on fluid samples, with measurement either in the field shortly after taking the sample, or later in the laboratory. On-line pH measurements, while possible, are unreliable in oil field systems due to contamination of pH electrodes by oil and/or H<sub>2</sub>S.

The biggest problem with on-site measurements is the massive and rapid rise in pH almost immediately on depressurization of a sample, due to flashing-off of gas. *In situ* pH is almost always dominated by the CO<sub>2</sub>/bicarbonate buffer system, so the concentration of dissolved CO<sub>2</sub> greatly influences the pH and it changes greatly from downhole to wellhead to separators to export system. Laboratory measurements of pH on degassed or partly degassed samples are of no value.

Hence, the optimum procedure is to calculate pH throughout all stages of fluid handling from pressure and temperature data, gas phase CO<sub>2</sub> and water composition (salinity and mineral bicarbonate content), using standard software packages, such as NORSOK M506<sup>26</sup> or others.

#### 4.41.6.4.3 Oxygen monitoring

For seawater injection systems the principle method of corrosion control is deoxygenation, typically to < 10 ppb. Hence, a measure of oxygen content provides a direct measure of the effectiveness of the corrosion control system. Oxygen measurement can be carried out on-line or on liquid samples.

On-line measurements can use either specialist oxygen monitors or galvanic probes.<sup>78</sup> Oxygen monitors give a direct measure of the oxygen content and, provided that they are correctly serviced/calibrated (to prevent fouling of the electrode).

Galvanic probes (with elements of carbon steel and copper) can be more robust for some field applications. Although they do not give a direct measure of the oxygen content, the measured galvanic current is directly proportional to the oxygen concentration in the process stream.

#### 4.41.6.4.4 Iron count

A common and relatively straightforward method for assessing corrosion in water (e.g., seawater injection, process water, etc.) is *iron counts*; that is the measure of soluble iron ion (Fe<sup>2+</sup>).<sup>66</sup> If the corrosion is occurring the Fe<sup>2+</sup> concentration will increase. Hence, ideally, iron content at the both start and end of the system/pipeline is needed to provide an estimate of the corrosion occurring; however, in most cases simple changes in Fe<sup>2+</sup> content are used to assess increasing/decreasing corrosion conditions.

However, iron counts are only viable where the corrosion product is soluble. Hence, they are not suitable for use in sour environments (where the corrosion product is insoluble iron sulfide, FeS) or in sweet systems with a high bicarbonate content (once the process becomes FeCO<sub>3</sub> saturated, any increase in corrosion rate cannot add extra iron to solution, instead more insoluble iron carbonate scale forms). In both cases misleading information will be obtained.

#### 4.41.6.4.5 Inhibitor residuals

Inhibitor residuals are an important measurement to check that sufficient corrosion inhibitor is injected into the system. In most cases, the method of testing will be provided by the chemical vendor and will be targeted for the specific active component of the inhibitor package. However, experience has shown that some methods used are subject to interference and hence can be unreliable. Generic methods are available that can provide a reliable result, provided that they are calibrated for the specific chemical. Further details on corrosion inhibitors is given elsewhere in this book and in EFC publication.<sup>30</sup>

#### 4.41.6.5 Data Management

Is it essential that data collected as part of the corrosion management process are stored in an efficient manner that enables easy retrieval and trending of data.

A large number of commercially available systems are available that offer a varying level of interaction with process monitoring systems (e.g., PI® and SCADA®) and planning systems (e.g., Maximo® and SAP®) as well as various GIS systems and web

interfaces to enable user remote access. The level of support from the suppliers of commercially available systems can vary from a simple software sale to a fully supported service agreement. In addition a bespoke system can be developed that increase the level of flexibility required.

Stand alone systems can easily be developed for activities such as Corrosion Risk Assessment (CRA), RBA, Inspection Planning, storing Inspection Data, storing Corrosion Monitoring/CP Data, storing fluid data, and monitoring KPI's. There can be advantages when using a simple system compared with a large multifunctional database and the merits of each should be assessed.

When selecting a data management system for a facility consideration should be given to

- Type of asset:
  - Pipeline networks have a limited number of 'data locations' but a large number of data measurements and therefore require a system that can enable easy trending of data (e.g., CP data, Corrosion probe data).
  - Process plant typically has a large number of 'data locations' and a limited number of data measurements (e.g., NDT inspection data).
  - Consideration must be given to how manually generated data (e.g., Corrosion Coupon analysis and fluids analysis) are to be integrated into the data management system.
  - Is the database expected to be a complete asset register, or just consider key high-risk areas?
- Expected degradation mechanism/type of data to be collected:
  - For time-dependent degradation trending of inspection and monitoring data is appropriate.
  - For cracking mechanisms, trending of inspection data has a limited value and recording of fluid and operating parameters are of more significance.
  - Is trending of fluid monitoring data essential? What parameters are key?
  - Is the system to be used to monitor, trend and report KPIs
- National legislation:
  - If the national legislation defines a prescriptive inspection approach there is little point in trying to implement a data management system that calculates RBI frequencies.
- Level of IT infrastructure in place:
  - Where IT infrastructure is limited there is little point in trying to implement a fully automated

system. A fit for purpose procedure driven system is sometime far more appropriate.

- Roles and responsibilities:
  - Clearly defined roles and responsibilities are required for data collection, data input and data review/analysis.
  - All data systems should have a level of security that enables competency levels to be assessed better access to the system.

While data management systems are an essential tool as part of a Corrosion Management system, user intervention, audits and continuous improvement process are essential to maintain a database that is truly representative of the facility in terms of physical and operational information and perceived degradation threats. Any database that is not maintained as a live system cannot be considered an effective Corrosion Management tool.

#### 4.41.6.6 Change in Process Conditions

The original corrosion risk assessment carried out at the FEED and/or design stage will have taken a range of operating conditions from the basis of design for the particular field/facility. This in turn will have driven the material selection, corrosion control, and planning inspection/monitoring for the system once in operation. However, as highlighted at the start of this section, there is always the chance that the actual operating conditions will be different to those envisaged. This is often due to change in conditions as the facility ages/expands.

Many operators handle possible changes in process conditions by predefining the corrosion 'window' or 'envelope' (that is the range of conditions to which the original assumptions remain valid) as part of the original risk assessment carried out during FEED or Design stage. Then if any of the parameters change sufficiently with time such that they are no longer in the 'corrosion window' then they will automatically trigger a reassessment of the corrosion risk. In fact most ongoing corrosion risk assessments simply start with checking whether the operating conditions are within the original design assumptions ('window') and if they are and the performance has also been demonstrated to be in line with predictions then this is taken as sufficient to keep the existing corrosion risk assessment in place.

If the conditions have changed then the likely effect, for example, increase water cut, gas lift resulting in increase in CO<sub>2</sub> content, reduction in flow rates, etc., on the expected corrosion rate, location



and morphology should be determined and, where necessary, a change in the inspection/monitoring/corrosion control plans put in place.

#### 4.41.6.7 Risk Based Inspection (RBI)

RBI schemes are a key component of corrosion management schemes and provide a planning tool to develop the optimum plan for the execution of inspection activities. RBI uses the findings from formal risk analyses, including corrosion risk assessments, to guide the direction and emphasis of the inspection planning and the physical inspection procedures.

A risk-based approach to inspection planning is used to:

- ensure risk is reduced to as low as reasonably practicable;
- optimize the inspection schedule;
- focus inspection effort onto the most critical areas;
- identify and use the most appropriate methods of inspection.

RBI methodologies are well described in published documents such as API 581<sup>10</sup> and DnV RP G-101<sup>11</sup> and have been adopted by many operators, further details on this topic are also given in the chapter on **Risk Based Inspection** in this book.

Where RBI schemes are used, it should be noted that the determination of future inspection requirements, by extrapolation of historical trends, is based on an assumption that the conditions in the future are similar to those in the past and that there is no change in degradation mechanism(s). Any significant change in operating conditions (for example, water break-through, increase in CO<sub>2</sub> content, change in wax or scaling tendency, etc.), could result in significant changes in corrosion rate and/or corrosion damage, which could in turn lead to different inspection requirements. It is therefore appropriate for the model that is driving the RBI scheme to be rerun either at specific time intervals, or when a process variable exceeds a previously agreed boundary condition.

On new assets or in the absence of good quality historic data on mature assets, it is normally considered good practice to carry out a baseline survey to establish a known condition from which to monitor.

Many RBI schemes are operated as part of a major inspection software database and analysis tool and are normally applied to process plant and facilities. However, many standard RBI software systems can be very 'data hungry,' that is unless the majority (if not all) of

critical information is available standard software systems will not run. To overcome this limitation, 'high level' assessment schemes are being developed that allow engineering judgment to be used to where data is sparse.<sup>79</sup> High-level risk assessment for pipeline operations have also been developed.<sup>28,45,80</sup>

#### 4.41.6.8 Direct Assessment Procedures

For onshore pipelines, a major change in operational corrosion management has occurred over recent years, where the methods of '*direct assessment*' are now routinely used, and in some countries have become mandated. Here *direct assessment methodology*, actually covers a wide ranging assessment of the likely pipeline condition as determined by a review of the design, installation, geographic, operational and ILI data to identify the sections of the line that are most at risk of corrosion degradation, both internal and external, that should be selected for excavation and physical confirmation of condition (i.e., *direct assessment*).

At this time, direct assessment procedures have been developed and adopted as a number of NACE Standard Practices for:

- Pipeline External Corrosion Direct Assessment Methodology (EC-ECDA); NACE SP0502–2008.
- Stress Corrosion Cracking (SCC) Direct Assessment Methodology (SCC-ECDA); NACE SP0204–2008.
- Internal Corrosion Direct Assessment Methodology for Pipelines Carrying Normally Dry Natural Gas (DG-ICDA); NACE SP0206–2006.
- Internal Corrosion Direct Assessment Methodology for Liquid Petroleum Pipelines (LP-ICDA); NACE SP0208–2008.

A further NACE standard, for internal corrosion due to wet gas operation (WG-ICDA) is currently under-development and is expected to be published by 2010.

In all cases the direct assessment methodology requires a detailed analysis of existing data to determine whether or not there is sufficient information so that the methodology can be applied and provides guidance for what critical information needs to be obtained.

Once sufficient data have been collected, the methodology provides a structured procedure to analyze the data to highlight areas of specific corrosion risk. This normally requires dividing the pipeline into different sections (lengths) where the conditions are likely to be similar.

- For internal corrosion assessment, sections will be defined by significant changes in operating pressure/temperature/flow rates, and especially angle of inclination, since this will define where water drop out and collection will occur and hence the most likely place for corrosion to occur;
- For external corrosion assessment, sections will be defined by changes in ground (soil) condition, CP systems, etc.

The comparison of the analysis of theoretical conditions together with pipeline inspection data, such as ILI surveys (to identify both internal and external features) and external surveys (CIPS, DCVG – to identify areas of coating damage and/or under protection), is used to prioritize areas to be excavated and examined, usually by UT inspection.

The whole process provides a transparent method of assessment and ensures that high-risk areas are correctly identified and actions taken in a timely manner, and is essentially a pipeline equivalent to process facility RBI schemes.

#### 4.41.6.9 Fitness for Service (FFS)

As highlighted previously, the main objective of corrosion management is to ensure that plant and facilities are operated in a safe and reliable manner and the principle challenge for corrosion management in the oil and gas industry is that the preferred material of construction (low-alloy carbon steel) can, and is, subject to both internal and external corrosion, especially where the corrosion control plans do not operate as intended.

Hence, an important aspect of corrosion management is assessing the condition and FFS for items of equipment (pipeline, pipework, vessels, tanks, etc.) where corrosion has been found. FFS assessment (also referred to as FFP) can be simple to the complex, depending on the component, the extent and type of deterioration, and regular requirements. API 579<sup>81</sup> defines three levels of assessment, as:

- **Level 1** FFS assessments provide conservative screening criteria that require the least amount of inspection and component information. Level 1 assessments usually do not require extensive calculations. Either inspectors or plant engineers will conduct a Level 1 assessment.
- **Level 2** FFS assessments involve a more detailed evaluation of components and usually require an accurate measurement of flaws or damage. Most Level 2 FFS assessments require calculation of the required component thickness or of component stress. Either plant engineers or engineering specialists will conduct Level 2 assessments.
- **Level 3** FFS assessments require detailed evaluation of components. Component flaws or damage must be accurately determined, and calculation methods often involve numerical analysis such as the finite element method. Level 3 assessments often require the services of engineering specialists experienced in advanced stress analysis, fracture mechanics, etc.

A Level 1 assessment could be as simple as confirming whether any metal loss is within the design corrosion allowance (i.e., based on the original design pressure). If metal loss exceeds this limit, then the item may still be suitable for service, but only at a reduced maximum operating pressure (as described in API 570<sup>57</sup> and ASME B31G<sup>82</sup>), this would form part of a Level 2 assessment.

Level 3 assessments apply to more complex conditions, in particular localized corrosion and/or EAC, where alternative methods of assessment may be required. The specific method/procedure to be used will be dependent on component type, original design code and nature of damage, for example, API 579,<sup>81</sup> ASME B31G,<sup>82</sup> DnV RP F-101,<sup>83</sup> BS 7910,<sup>84</sup> and others.

#### 4.41.6.10 Communication and Management Structure

##### 4.41.6.10.1 Corrosion management team

The corrosion management team is the main vehicle for communication between the key players. Communication within the operator's organization and its relevant contractors is also important in order to achieve understanding and obtain support in meeting objectives:

- Appropriate information should be disseminated to the correct people.
- Written information on hazards, risks and preventative measures should be provided.
- Procedures, work instructions, and guidelines should be published and shared.
- Corrosion awareness information should be distributed to those who need to be aware of the importance of corrosion management to assist those directly involved. Training and information to develop corrosion awareness should be provided.
- Key players in the organization and their contracted bodies that comprise the corrosion management team should be identified.

- Regular meetings of the corrosion management team on implementation status, trends in deterioration and failure, status of corrective action, and planning and budgetary issues should be undertaken.
- Managers, technical specialists, authorities, supervisors, and wherever appropriate, contractor personnel should be visible through the publication of charts and guides.
- Experiences should be shared with other facilities, other operators and with appropriate external bodies.

#### **4.41.6.10.2 Management of change**

Management of change is an important part of corrosion management activity. As described previously, it is vital that changes in operating conditions are identified and their impact on the corrosion risk and effectiveness of the corrosion control program including the inspection/monitoring plans are assessed.

Most oil and gas operating companies will have a management of change procedure, so that as new developments are planned and existing facilities are phased out the engineering impact is fully considered and implications for fabrication, maintenance and operations are put in place. The corrosion management team should be included within the management of change process ensuring that implications to operational windows, and effects on corrosion risk are identified early in the change process so, as was the case during initial design, cost-effective procedures can be developed in a timely manner.

In the case of new development/tie-ins, etc., a policy should be adopted regarding the required life of the facility. The materials and corrosion control aims at providing that life. To maintain design intent and operate within the design limits, the plan should identify the elements to be built into the design, the performance limits on which it is based and the actions required during operation. If there is a choice of suitable materials then life cycle costing can be used to identify the final materials. The development plan should consider that the design should make provision for monitoring equipment such as corrosion probes, access fittings, instruments and the provision for data gathering. Also, design to enable inspection such as pig traps suitable for online inspection tools should be considered.

In the case of field extension, as technology advances, asset life expectancy is increasingly being extended beyond the original design life. Therefore, it is important to be able to accurately gauge the control

status of the asset if field life extension is required. This might require a reappraisal of corrosion risks and introduction of major changes to current activities. The individuals responsible for setting and implementing the corrosion management strategy and strategic plan should be made aware of the future business and operational requirements of the asset.

#### **4.41.6.10.3 Contracting structure**

There are many different operational and contractual structures adopted by operators world-wide. These range from all staff (management, engineering, operating, inspection and maintenance) being employed directly by the operator to fully out-sourced conditions, where with the exception of management and senior engineering functions, all other roles are let on a contract basis to either a main operation/maintenance contractor or as a series of contracts for specific roles.

In all cases, the roles and responsibilities for the different disciplines/contractors/subcontractors relating to corrosion management should be clearly identified. Reporting routes should also ensure that relevant information/data passed sideways to other corrosion management team members allow timely review and action. There are many cases where information relating to problems with, for example, corrosion inhibitors, high measured corrosion rates, changes in operating conditions, etc. are not identified or not passed to the responsible person/department until it is too late to provide cost-effective intervention.

#### **4.41.6.10.4 Key point indicators (KPI)**

KPIs are used as a measure of the integrity of the facility and the corrosion management system. KPIs should be:

- Relevant, practicable, and meaningful to the corrosion threats and the policy and plan in place.
- Quantifiable to avoid subjective judgments.
- Intended primarily at demonstrating success or identifying trends that enable corrective action.
- Determined with reference to the engineering design of the facility in terms of performance limits for corrosion barriers. Target values should be set for all indicators.
- Selected so that they indicate how successfully the plan is being implemented linked to corrosion – proactive measurement and leading indicators.
- Selected so that they indicate trends toward the achievement the desired outcomes linked to

corrosion – reactive measurement and lagging indicators.

KPIs allow quick indication of where corrosion management schemes are working and, more importantly, where they are failing, either due to failure to meet specific objective (e.g., delays in the retrieval of corrosion coupons, delays to planned inspection, insufficient dosing of chemicals, etc.) or where corrosion control is compromised (e.g., increased in measured corrosion rate above critical limits). There are various ways of presenting KPI information, increasing so-called ‘*traffic light*’ systems (with KPIs reported as ‘red,’ ‘amber,’ or ‘green’) are used,<sup>3</sup> for example, as shown in [Table 1](#).

In addition to using KPIs for assessing the performance of the management system as a whole, technical KPIs can also be used to highlight the performance of the corrosion control plans. Here, similar arrangements would apply but criteria based on acceptable/expected corrosion rates, bacteria counts, inhibitor residual concentrations, etc. would be used.

#### 4.41.6.10.5 Audit/compliance

An important aspect of modern corrosion management systems is that they should provide a clear and transparent approach to the decision-making process, the overall performance of the corrosion monitoring plan, and the performances of the corrosion control procedures adopted.

Part of this process is that the system should be subjected to regular audits (internal and external) to

determine whether the corrosion management system effectively conforms to the requirements. They are an essential check on the performance of the system and are normally carried out by an independent party (i.e., somebody not directly involved in the operation of the corrosion system). Audits cover the following aspects:

- implementation of procedures and processes;
- competency;
- checks in place;
- compliance.

An audit reviews the processes and procedures that are aimed at achieving the performance targets and determines if the procedures for ensuring that they are achieved are being properly implemented. If activities are found to be not in accordance with the procedures and processes it is called a noncompliance.

Audits can be performed in two ways. A complete audit can be undertaken in one exercise or individual elements can be audited separately on a rolling basis. An audit cycle duration is generally 2 to 3 years. In addition to independent audits, internal audits should be carried out more frequently in specific procedures or functions.

The procedures of contractors will be audited on award of contract if not covered by prequalification and then periodically in the same manner as for the operator.

#### 4.41.6.10.6 Ongoing improvements

As identified in the corrosion management overview chapter in this book, an important aspect of any

**Table 1** Examples of corrosion management key performance indicators for an offshore facility (partial extract from Guidance for Corrosion Management in Oil and Gas Production and Processing<sup>3</sup>)

Activity	Target	Green	Amber	Red
<b>Plan</b>				
RBI reviews up to date	None outstanding	None	2 or less	3 or more
Annual pipework inspection scope	Completed by year end	Yes		No
Annual vessel inspection scope	By end of Jan	Jan	Feb	Mar or later
<b>Implement</b>				
% pipework inspections on target	>90% of planned cumulative completion	>90% complete	75–90% complete	< 75%
Safety critical vessel inspections on target as per RBI due date	On target or above	All on target (0)	2 below target (1–2)	>2 below target (≥3)
<b>Measure</b>				
No of leaks (safety or production critical)	No leaks	0		≥1
No of unexpected leaks (noncritical)	No leaks	0	≤4	≥5
<b>Review</b>				
Bi-monthly pipework integrity summary been updated	100% complete	Yes		No
Annual report completed (1Q)	Complete report within Q1	Yes		No

system is its ability to develop and improve with experience. Hence, the system should regularly review its performance and determine where it is meeting and nonmeeting its targets. This is often referred to as 'do and improve loops.'

#### 4.41.7 Summary/Conclusions

The management of corrosion in oil and gas production has a long history of pioneering developments and has been instrumental in progressing many successful field applications that would have been unthinkable 25 years ago. In particular, the 'FFS' of materials for sour service is increasingly allowing more aggressive conditions to be handled, while improvements in corrosion inhibitors has enabled multiphase lines to have increased throughput even under erosive conditions. Hand in hand with these technical developments has been an increased awareness of the need to manage SHE issues, hence corrosion mitigation activities are increasingly seen as having an important impact on integrity and loss containment.

The aim of the chapter was to identify some of the basic corrosion inputs into projects during the main development phases. Much of the detail can be found in industry and international standards quoted throughout the text (NACE, API, DnV, ISO) and industry relevant publications such as the *Corrosion Threats Handbook – Upstream Oil and Gas Production*<sup>5</sup> and *Guidance for Corrosion Management in Oil and Gas Production and Processing*.<sup>3</sup> These publications provide good examples of the corrosion damage sustained by process equipment during operational life and the detailed requirements and performance indicators needed to ensure that corrosion is managed effectively to maintain asset integrity.

The increasing demand for improvements in all aspects of asset management will impact on the delivery of corrosion services as more aggressive environments are exploited. Although driven primarily by SHE concerns, a continuous improvement in management systems, involving the use of performance indicators, reviews and audits of activities should also result in improvements in operational and day to day activities to deliver less unscheduled downtime and improved performance. The importance of a good record keeping/data management system cannot be over emphasized as field data are vital to provide the information needed for good decision making.

## References

1. Milliams, D. Corrosion Management, 12th International Corrosion Congress on Corrosion Control for Low Cost Reliability, Sep 1993; NACE International: Houston, TX; vol 4, p 2420.
2. Review of Corrosion Management for Offshore Oil and Gas Processing; Offshore Technology Report 2001/044, UK Health and Safety Executive, 2001 [www.hse.gov.uk/research/otopdf/2001/oto01044.pdf](http://www.hse.gov.uk/research/otopdf/2001/oto01044.pdf)
3. Guidance for Corrosion Management in Oil and Gas Production and Processing; Energy Institute: London, May 2008. ISBN 978 0 85293 497 5.
4. Corrosion Threats Handbook – Upstream Oil and Gas Production; Energy Institute and Oil and Gas UK: London, 2008.
5. BSI PAS 55–1: 2003, Asset management, Specification for the optimised management of physical infrastructure assets, and BSI PAS 55–2: 2008, Asset management: Guidelines for the application of PAS 55–1–British Standards Institute.
6. Dawson, J. L.; Bruce, K.; John, D. G. Corrosion Risk Assessment and Safety Management for Offshore Processing Facilities; Offshore Technology Report 1999/064, UK Health and Safety Executive, 1999.
7. The Public Inquiry into the Piper Alpha Disaster Report by the Hon. Lord Cullen; HMSO: London, Nov. 1990. ISBN 0 10 113102.
8. US Pipeline Safety Act 1995.
9. API Recommended Practice RP580, Risk Based Inspection American Petroleum Institute, 2000.
10. API Publication 581 Risk Based Inspection Resource Document; 2002, American Petroleum Institute, 2002.
11. DnV RP G101 Risk Based Inspection of Offshore Topsides Static Mechanical Equipment; DnV, 2002.
12. The Offshore Installations (Safety Case) Regulations, SI 1992/2885; The Stationery Office Limited: London, 1992. ISBN 011025869X.
13. The Offshore Installations and Wells (Design and Construction, etc.) Regulations 1996 SI 1996/913; The Stationery Office Limited: London, 1996. ISBN 011054451X.
14. The Pipelines Safety Regulations, SI 1996/825; The Stationery Office Limited: London. ISBN 0110543734.
15. The Control of Major Accident Hazard Regulations, SI 1999/743; The Stationery Office Limited: London. ISBN 0 11 082192 0.
16. Pressure Systems Safety Regulations, SI 2000/128; The Stationery Office Limited: London. ISBN 0 11 085836 0.
17. Successful Health and Safety Management, UK HSE HS(G) 65 1991, ISBN 0–11–882055–9.
18. NORSOK Standard S-006, Rev. 2 December 2003, HSE evaluation of contractors.
19. ISO 14001:1996, Environmental management systems – Specification with guidance for use.
20. ISO 15156: 2001/NACE MR 0175–2001 Petroleum and natural gas industries – Materials for use in H<sub>2</sub>S-containing environments in oil and gas production, Public Report of the Fire and Explosion at the ConocoPhillips Humber Refinery on 16th April 2001; UK Health and Safety Executive, [www.hse.gov.uk/comah/conocophillips.pdf](http://www.hse.gov.uk/comah/conocophillips.pdf).
21. Congressional Report Services, Library of Congress, BP Alaska North Slope Pipeline Shutdowns, Regularity Policy Issues, October 2006, [www.cnle.org/NLE/CRSreports/06Oct/RL33629.pdf](http://www.cnle.org/NLE/CRSreports/06Oct/RL33629.pdf).
22. Reason, J. T. *Managing the Risks of Organizational Accidents*; Ashgate Publishing Ltd: England, 1997.



24. BS 6079-3:2000 Project Management – Part 3: Guide to the Management of Business Related Project Risk; BSI Standards, 2000.
25. de Waard, C.; Lotz, U.; Milliams, D. *Corrosion* **1991**, *47*, 976; de Waard, C.; Lotz, U. In *Corrosion'93*; NACE International: Houston, TX, 1993; Paper No 69.; de Waard, C.; Lotz, U.; Lugstad, A. In *Corrosion'95*; NACE International: Houston, TX, 1995; Paper No 128.
26. NORSOK M-506: Rev. 2, June 2005, CO2 Corrosion Rate Calculation Model; Norwegian Technology Standards Institution (Norsk Sokkels) [www.standard.no/petroleum](http://www.standard.no/petroleum).
27. Electronic Corrosion Engineer (ECE<sup>®</sup>) Smith, L. M. Intetech, Waverton, Chester, UK
28. Oliver, K. E.; John, D. G. In *Corrosion 2007*, NACE, Nashville, TN, March 2007, paper on 07124.
29. Kolovich, K.; Kiefner, J. F. In *Corrosion 2007*; NACE: Nashville, TN, 2007; Paper no 07120.
30. Palmer, J. W.; Hedges, W.; Dawson, J. L. *The Use of Corrosion Inhibitors in Oil and Gas Production*; European Federation of Corrosion Document Number 39; Institute of Materials: London, 2004.
31. Smith, L. M.; de Waard, K. In *Corrosion 2005*; NACE: Houston, TX, 2005; Paper No 05468.
32. NACE SP0208–2008 Internal Corrosion Direct Assessment Methodology for Liquid Petroleum Pipelines.
33. PIPESIMS<sup>®</sup>. Copyright Schlumberger plc; [www.slb.com/content/services/software/production/pipesim/index.asp](http://www.slb.com/content/services/software/production/pipesim/index.asp).
34. PIPEFLO<sup>®</sup>. Copyright Engineered Software; <http://www.eng-software.com>.
35. OLGA<sup>®</sup> <http://www.sptgroup.com/en/Products/olga>.
36. HYSYS<sup>®</sup> <http://www.aspentech.com/core/aspens-hysys.cfm>.
37. API RP 14E Recommended Practice for Design and Installation of Offshore Production Piping Systems; API: Washington, DC, 1991.
38. Schmidt, G.; Gudde, T.; Strobel-Effertz, E. In *Corrosion'96*; NACE, Houston TX, 1996, Paper no 9.
39. Johnson, B. V.; Choi, H. J.; Green, A. S. In *Corrosion'91*; NACE: Cincinnati, OH, 1991; Paper No 573.
40. Green, A. S.; Johnson, B. V.; Choi, H. J. *Flow-Related Corrosion in Large-Diameter Multiphase Flowlines*; SPE Production and Facilities, May 1993; pp 97–100.
41. Craig, B. *Corrosion* **1998**, *54*(8), 657.
42. de Waard, C.; Smith, L. M.; Craig, B. D. In *Corrosion'2003*; NACE International: Houston, TX, 2003; Paper No. 03629.
43. Johnson, B. V.; Al-Ghafri, M.; Harthy, A.; John, D. G.; Schofield, M. J. In *Corrosion 2009*; NACE: Atlanta, GA, 2009; Paper No 093549.
44. Moosavi, A. N.; John, D. G. In *Corrosion/2002*; NACE: Denver, CO, 2002; Paper No 02225.
45. John, D. G.; Stokes, P.; McIntosh, P. In *Corrosion 2003*, NACE: New Orleans, April 1984, paper no 343.
46. Johnson, B. V.; Al-Ghafri, M. J. H.; Al-Harthy, A. S. M.; Kompally, S. N.; Dicken, G.; Schofield, M. J.; Bruce, K.; John, D. G. Paper SPE 114140, presented at '2008 SPE International Oilfield Scale Conference', Aberdeen, Scotland May 2008.
47. ASTM D1401–02 'Standard Test Method for Water Separability of Petroleum Oils and Synthetic Fluids.'
48. Hedges, B.; McVeigh, L. In *Corrosion '99*; NACE: San Antonio, TX, 1999; Paper No 99021.
49. API Spec 5L, Specification for Line Pipe, 42nd ed.; American Petroleum Institute, Jan- 2000.
50. ISO 3183:2007 Petroleum and natural gas industries – Steel pipe for pipeline transportation systems.
51. ASTM G39 – 99(2005) Standard Practice for Preparation and Use of Bent-Beam Stress-Corrosion Test Specimens.
52. NACE TM0177–2005, Laboratory Testing of Metals for Resistance to Sulfide Stress Cracking and Stress Corrosion Cracking in H<sub>2</sub>S Environments.
53. Taylor, T. S.; Pendlington, T.; Bird, R. Foinaven super duplex materials cracking investigation, Paper presented at Annual Offshore Technology Conference; Houston: TX 1999.
54. J. de Nouyer, J.; J. Slining, J.; and V. Ashworth, V. In *Corrosion'84*, NACE: New Orleans, April 1984; Paper No 343.
55. Turnipseed, S. P. In *Corrosion/91*; NACE: Cincinnati, 1991; Paper No 234.
56. John, G.; Rosbrook, T.; Robinson, J.; Munro, I. In *Corrosion 2000*; NACE: Orlando, FL, 2000; Paper No 00011.
57. API Document 570 Inspection, Repair, Alteration, and Rerating of In-Service Piping Systems American Petroleum Institute, 1998.
58. NACE RP0198–2004 The control of corrosion under thermal insulation and fireproofing materials – As systems approach.
59. European Federation of Corrosion Publications Number 55, Corrosion under insulation (CUI) guidelines (EFC 55); Winnik, S., Ed.; Woodhead Publishing Ltd., Cambridge, 2008. ISBN 13 978–1–84569–423–4.
60. John, D. G.; Attwood, P.; Rothwell, A. N. In *Corrosion/99*; NACE International: Houston, TX, 1999; Paper 249.
61. Khlefa, A. Esaklul In *Corrosion 2007*; NACE: Nashville, TN, 2007; Paper No 07264.
62. Turissini, R. L.; Hingorane, R. Paper presented at 4th Middle East Corrosion Conference: 11–13 January 1988; NACE/The Society of Engineers Bahrain.
63. ISO 9000: 2008, Quality management systems. Fundamentals and vocabulary.
64. Moltke, Helmuth, Graf Von, Militarische Werke. vol. 2, part 2, pp 33–40. Found in Hughes, Daniel J. (ed.) *Moltke on the Art of War: Selected Writings*. (1993). Presidio Press: New York, NY, ISBN 0-89141-575-0. p. 45
65. NACE RP 0775–2005 Recommended Practice: Preparation and Installation of Corrosion Coupons and Interpretation of test data in Oilfield Operations.
66. NACE RP 0192–98 Recommended Practice: Monitoring Corrosion in Oil and Gas Production with Iron Counts.
67. NACE SP 0499–2007 (formerly TM0299–99) Standard Practice: Corrosion Control and Monitoring in Seawater Injection Systems.
68. NACE TM 0194–2004 Test Method: Field Monitoring of Bacterial Growth in Oil Field Systems.
69. ASTM G96–90(2008) Standard Guide for Online Monitoring of Corrosion in Plant Equipment (Electrical and Electrochemical Methods).
70. NACE Technical Report 3T199, Techniques For Monitoring Corrosion and Related Parameters In Field Applications, December, 1999.
71. Rothwell, N. *Corrosion Monitoring Handbook*, Coxmoor Publishers: UK, 2000. ISBN: 1 901892 03 4.
72. Thomas, J.; Barr, E. E. In *Corrosion 2004*; NACE: New Orleans, LA, 2004; Paper No 04171.
73. NACE RP 0102–2002 Recommended Practice. In-Line Inspection of Pipelines.
74. NACE Technical Report 35100. In-Line Nondestructive Inspection of Pipelines, 2000.
75. API STD 1163 In-line Inspection Systems Qualification Standard 2005.
76. NACE TM0109–2009 Aboveground Survey Techniques for the Evaluation of Underground Pipeline Coating Condition.

- 
77. Paterson, S. External Corrosion Management in Shell; presentation at UK Oil and Gas and Energy Institute Workshop, Aberdeen 18 Jun 2008. (available online at [http://www.oilandgas.org.uk/downloadabledocs/358/f.Steve\\_Paterson\\_Presentation.pdf](http://www.oilandgas.org.uk/downloadabledocs/358/f.Steve_Paterson_Presentation.pdf)).
  78. NACE Technical Report 1C187, Use of Galvanic Probe Corrosion Monitors in Oil and Gas Drilling and Production Operations (2005ed.).
  79. Hodges, S.; Oliver, K.; Tipton, E.; Spicer, K.; Adams, R.; John, G. In Corrosion 2010; NACE: San Antonio, TX, 2010.
  80. Chevrot, T. C.; Bonis, M.; Stroe, M. In Corrosion 2009; NACE: Atlanta, GA, 2009; Paper No 09113.
  81. API 579-1/ASME FFS-1 (2007) Fitness-For-Service.
  82. ANSI/ASME B31G-1991 (R2004) Manual for Determining the Remaining Strength of Corroded Pipelines: a Supplement to B31, Code for Pressure Piping.
  83. DNV-RP-F101, Recommended Practice Pipelines Corroded Oct 2004.
  84. BS 7910: 2005, Guide to methods for assessing the acceptability of flaws in metallic structures.

## 4.42 Management of Corrosion of Onshore Pipelines

**J. M. Race**

Newcastle University, School of Marine Science and Technology, Armstrong Building, Queen Victoria Road,  
Newcastle-upon-Tyne NE1 7RU, UK

© 2010 Elsevier B.V. All rights reserved.

---

<b>4.42.1</b>	<b>Introduction to Pipelines and Pipeline Engineering</b>	3272
<b>4.42.2</b>	<b>Introduction: The Scale of the Corrosion Problem</b>	3273
4.42.2.1	Pipeline Failure Statistics	3273
4.42.2.2	Causes of Pipeline Failures	3273
4.42.2.3	Pipeline Safety	3276
<b>4.42.3</b>	<b>Pipeline Integrity Management</b>	3277
<b>4.42.4</b>	<b>External Pipeline Corrosion Risks</b>	3277
4.42.4.1	External Corrosion: Mechanisms	3277
4.42.4.1.1	Soil corrosion	3278
4.42.4.1.2	External microbiologically influenced corrosion (MIC)	3279
4.42.4.1.3	Preferential corrosion	3280
4.42.4.1.4	Stray-current corrosion	3280
4.42.4.1.5	AC corrosion	3281
4.42.4.2	External Corrosion: Prevention	3281
4.42.4.2.1	Requirements of pipeline coatings	3281
4.42.4.2.2	Types of pipeline coatings	3283
4.42.4.2.3	Types of field joint coatings	3284
4.42.4.2.4	Coating failure	3284
4.42.4.2.5	Coating condition monitoring	3285
4.42.4.2.6	Coating condition monitoring: DC methods	3285
4.42.4.2.7	Coating condition monitoring: AC methods	3286
4.42.4.2.8	Cathodic protection (CP)	3287
4.42.4.2.9	CP: Sacrificial anode systems	3287
4.42.4.2.10	CP: Impressed current systems	3288
4.42.4.2.11	Basic CP design	3288
4.42.4.2.12	CP requirements	3288
4.42.4.2.13	CP shielding	3289
4.42.4.2.14	CP monitoring	3289
4.42.4.2.15	CP Monitoring: Close interval potential (CIPS or CIS) surveys	3290
4.42.4.3	Assessing the External Corrosion Risk	3290
<b>4.42.5</b>	<b>Internal Pipeline Corrosion Risks</b>	3290
4.42.5.1	Sweet or CO <sub>2</sub> Corrosion	3291
4.42.5.1.1	Effect of temperature	3292
4.42.5.1.2	Effect of flow rate	3292
4.42.5.1.3	Effect of pH	3292
4.42.5.1.4	Effect of partial pressure of CO <sub>2</sub>	3292
4.42.5.1.5	Effect of H <sub>2</sub> S content	3293
4.42.5.2	CO <sub>2</sub> Corrosion – Localized Effects	3293
4.42.5.2.1	Pitting corrosion	3293
4.42.5.2.2	Mesa corrosion	3293
4.42.5.2.3	Flow-induced localized corrosion (FILC)	3293
4.42.5.2.4	Preferential weld corrosion	3293
4.42.5.3	Sour Corrosion	3294
4.42.5.3.1	Sulfide stress corrosion cracking (SSCC)	3294
4.42.5.3.2	Hydrogen-induced cracking (HIC)	3294

---

4.42.5.3.3	Stress-oriented HIC (SOHIC)	3295
4.42.5.4	Material Selection for Sour Service	3295
4.42.5.5	Microbiologically Induced Corrosion	3295
4.42.5.6	Internal Corrosion: Prevention	3295
4.42.5.6.1	Corrosion allowance	3295
4.42.5.6.2	Corrosion-resistant alloys	3296
4.42.5.6.3	Coatings	3296
4.42.5.6.4	Product treatment	3296
4.42.5.6.5	Inhibitors	3296
4.42.5.7	Internal Corrosion Monitoring	3297
4.42.5.8	Assessing the Internal Corrosion Risk	3298
<b>4.42.6</b>	<b>External SCC Risks</b>	3299
4.42.6.1	Nature and Occurrence of SCC	3299
4.42.6.1.1	High-pH SCC	3299
4.42.6.1.2	Near-neutral pH SCC	3300
<b>4.42.6.2</b>	<b>Assessing the SCC Risk</b>	3301
<b>4.42.7</b>	<b>Corrosion Inspection Techniques</b>	3301
4.42.7.1	In-Line Inspection	3301
4.42.7.1.1	MFL for corrosion	3302
4.42.7.1.2	Ultrasonic wall thickness measurement (USWM)	3302
4.42.7.1.3	ILI for crack detection	3302
4.42.7.1.4	Benefits of in-line inspection	3303
4.42.7.2	Hydrotesting	3303
4.42.7.3	Direct Assessment	3303
4.42.7.3.1	External corrosion direct assessment (ECDA)	3304
4.42.7.3.2	Internal corrosion direct assessment (ICDA)	3304
4.42.7.3.3	Stress corrosion cracking direct assessment (SCCDA)	3304
<b>4.42.8</b>	<b>Pipeline Corrosion Management: Overview</b>	3305
<b>References</b>		3305

## Glossary

**Drip** A drip is a leg located underneath the pipeline that collects liquids and solids that can be transported down the pipeline with the product. Drips are usually equipped with a siphoning arrangement so that the collected materials can be removed.

**Electric resistance welding** Electric resistance welding is a process used to weld the longitudinal seam. The heat required for welding is produced by the resistance of the steel to the passage of an electric current. The heated plate edges are then forced together under pressure to produce the weld.

**Groundbed** A groundbed is one or more anodes installed in the earth to provide a low-resistance electrical path to ground in cathodic protection systems.

**Lack of fusion** A lack of fusion defect is a region of the weld where full fusion has not been

achieved. This could be due, for example, to mill scale on the plate edges or a lack of adequate heat or pressure during the welding process.

**Linepipe** An individual length of pipe (sometimes also referred to as a spool or joint), typically 12m in length.

**Town gas** Town gas is a type of manufactured gas that is principally made from coal. Town gas was used extensively in homes in the UK until the discovery of natural gas.

## Abbreviations

**In-line Inspection (ILI)** Pipeline inspection conducted using an instrumented vehicle that travels inside the pipeline usually propelled by the fluid in the pipe.

### Symbols

- $V_{IR}$  Potential drop associated with the flow of Cathodic Protection current through the soil of finite resistance (mV)
- $V_p$  Actual potential on the pipe surface (mV)
- $V_s$  Cathodic protection potential measured on the surface (mV)

## 4.42.1 Introduction to Pipelines and Pipeline Engineering

The first recorded use of pipelines for the transportation of natural gas was ~400 BC when the Chinese used bamboo pipe to transport natural gas to Peking to be used for lighting. Since then pipelines have become the principle method for the transportation of natural gas and hazardous liquids, and currently, it is estimated that there are over 3.5 million kilometers of pipelines installed worldwide.<sup>1</sup>

Pipelines can be categorized according to their location (onshore or offshore), the product carried (liquids, gases or multiphase, that is, mixtures of gases and liquids), or the purpose of the pipeline.

To explain this last category, consider the schematic of [Figure 1](#), which shows a typical pipeline network for oil or gas transportation. This network starts with the gathering system, which transports the product from the wells to a processing station or a transmission line. The transmission pipeline network links the gathering system to the distribution system. Finally, the distribution system transports the product from a distribution point to the point of end use or storage and typically consists of low-pressure gas pipelines for domestic and industrial use.

The relative size of each of these pipeline systems is illustrated in [Table 1](#) for the US pipeline network.<sup>2</sup> These figures show that the distribution system is by far the largest part of the network. However, the focus of this chapter is to investigate the effects of corrosion on the high-pressure onshore gathering and transmission pipelines that transport natural gas and hazardous liquids. Over 98% of the world's pipelines are buried and therefore emphasis is placed on the management of both internal and external corrosion and stress corrosion cracking (SCC) in these types of pipelines.

Having defined the scope, it is important to first investigate the scale of the corrosion problem, both in terms of the cost of corrosion and the impact of corrosion on pipeline safety.

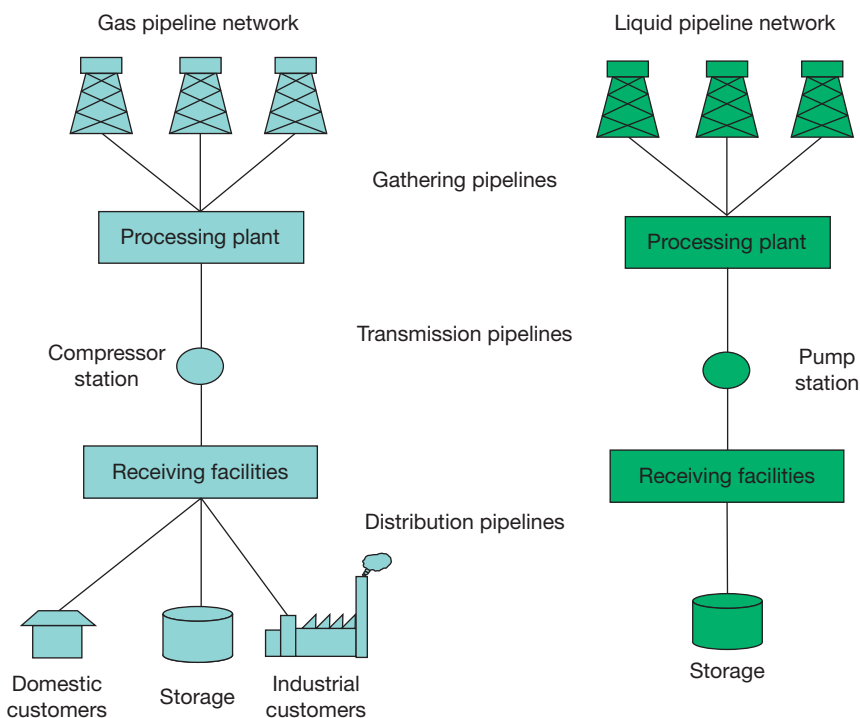


**Figure 1** Schematic representation of a typical pipeline network.



**Table 1** Distribution of US pipelines by usage (Statistics for 2006)<sup>2</sup>

<i>Pipeline category</i>	<i>Total length (miles)</i>	<i>Total length (km)</i>
Onshore gas gathering	13 056	21 012
Offshore gas gathering	7331	11 798
Onshore gas transmission	293 622	472 539
Offshore gas transmission	6699	10 781
Distribution	1 182 534	1 903 102
Liquid transmission	166 481	267 925

#### 4.42.2 Introduction: The Scale of the Corrosion Problem

In 2002, the Federal Highway Administration (FHWA) in the US published the results of a two-year study to determine the cost of corrosion to the US economy.<sup>3</sup> One of the 26 sectors investigated in the study was gas and liquid transmission pipelines. (It should be noted that in this report the term transmission pipelines included the gathering system.) In this sector, the cost of corrosion was estimated at between \$5.4 and \$8.6 billion every year.<sup>4</sup> This cost was reported in three areas: the cost of failures (10%); the capital costs related to installing a corrosion control system and the replacement or repair of pipelines (38%); and operations and maintenance costs related to controlling corrosion on the pipeline and ensuring that the control systems remain effective (52%). Included in the cost of failure is the loss of throughput, and therefore revenue, and also estimates for fatality and injury compensation and legal costs for liability.

Corrosion is therefore a significant cost to the pipeline operator in the operation and maintenance of a transmission pipeline; however, it is important to understand the threat of corrosion in relation to other threats on the pipeline. One of the most rigorous means of achieving this perspective is through the analysis of pipeline failure statistics.

##### 4.42.2.1 Pipeline Failure Statistics

A number of organizations worldwide collect statistics on the frequency and causes of pipeline failures. In the United States, the Office of Pipeline Safety (OPS) within the Department of Transportation (DOT) regulates the safety aspects of pipelines. Natural gas and hazardous liquid transmission,

distribution, and gathering companies are required by law to report to the DOT all serious and significant incidents involving a release from their pipelines, which involves either:

- a death or injury requiring in-patient hospitalization;
- total costs of \$50 000 or more measured in 1984 dollars (including, for example, lost product and repair costs);
- highly volatile liquid releases of five barrels or more or other liquid releases of fifty barrels or more; or
- liquid releases resulting in an unintentional fire or explosion.

The statistics are available from the DOT website from 1986.<sup>5</sup> However, the reporting categories for transmission pipelines changed in 2002, and therefore, it is difficult to compare statistics for some failure types.

CONCAWE, a group of European oil companies committed to environmental research, has systematically collected information on oil spills since 1971 and has reported the outcome annually ever since. In 2004, the database included over 35 000 km of onshore oil pipelines.<sup>6</sup> The CONCAWE statistics record any spill of greater than 1 m<sup>3</sup>, which is more rigorous than the requirement in the US and therefore care has to be taken when comparing data from these sources. Equivalent data for the European gas transmission system are collected by EGIG (European Gas Pipeline Incident Data Group). EGIG has collected data since 1970 on unintentional releases of gas from onshore steel pipelines with a design pressure greater than 15 bar. Over 122 000 km of the European gas pipeline network was included in the 2004 EGIG incident report.<sup>7</sup>

In the UK, the UK Onshore Pipeline Association (UKOPA) has also compiled a database of product loss incidents for nearly 22 000 km of Major Accident Hazard Pipelines (MAHP) as specified by the UK Pipeline Safety Regulations,<sup>8</sup> which includes natural gas, ethylene, and crude oil.<sup>9</sup> The database records all unintentional releases from pipelines in the public domain (i.e., outside the fences of installations) but does not include releases from ancillary equipment such as valves and compressors.

##### 4.42.2.2 Causes of Pipeline Failures

Using data from the failure statistics, it is possible to build up a picture of the role of corrosion in pipeline incidents, although it is highlighted that direct comparisons between data sets should be treated with

caution as the categories under which failures are reported differ between the databases.

One immediate conclusion that can be drawn from the analysis of the pipeline failure data for the years reviewed is that corrosion does not pose the most severe threat to pipeline integrity. In fact, in the OPS, CONCAWE, and EGIG databases, the majority of pipeline incidents result from external interference, that is, an outside force, such as an excavator striking the pipeline, whether intentionally or unintentionally. Corrosion accounts for the second largest number of spills in the CONCAWE (Table 2)<sup>6</sup> and OPS databases and the third largest number of incidents in the EGIG database (Table 3). The UKOPA database presents a slightly different picture in that the data are skewed by historical failures that occurred due to internal cracking when the system was transporting wet town gas. However, the data do show that external interference accounts for more failures than corrosion (Table 4).<sup>9</sup>

**Table 2** Summary of failure statistics from the CONCAWE database of incidents on oil pipelines (1971–2004)<sup>6</sup>

	<i>Number of incidents</i>		<i>Percentage gross volume spilled (m<sup>3</sup>/year)</i>
	<i>Average per year (1971–2004)</i>	<i>Percentage (1971–2004)</i>	<i>1971–2004</i>
Mechanical failure	3.0	23.8	31.4
Operational	0.9	6.8	3.6
Corrosion	3.6	28.9	18.8
Natural hazard	0.4	3.5	4.1
Third party activity	4.6	36.9	42.1

**Table 3** Summary of failure incidents by cause from the EGIG database of incidents on gas pipelines (1970–2004)<sup>7</sup>

<i>Failure cause</i>	<i>Percentage of incidents</i>
External interference	49.7
Construction defect/material failure	16.7
Corrosion	15.1
Ground movement	7.1
Hot-tap made by error	4.6
Other and unknown	6.7

The failure data also allow an investigation into the dominant failure location for different categories of pipeline, that is, whether corrosion occurs predominantly on the external or internal surface of the pipeline. Table 5 provides a summary of the statistics for corrosion failures by location for transmission pipelines (natural gas and hazardous liquids) from the OPS statistics.<sup>5</sup> It is interesting to note that for hazardous liquid pipelines, the corrosion incidents in the US are primarily attributable to external corrosion, a trend that has also been observed in the CONCAWE database.<sup>10</sup> For natural gas pipelines, the OPS data show that internal corrosion accounts for the majority of corrosion failures, which is contrary to the experience in Europe. The EGIG data indicate that external corrosion is responsible for nearly 80% of all corrosion failures

**Table 4** Summary of failure incidents by cause from the UKOPA database (1962–2004)<sup>9</sup>

<i>Failure cause</i>	<i>Number of incidents</i>	<i>Percentage of incidents</i>
Girth weld defect	33	19.2
External interference	37	21.5
Internal corrosion	2	1.2
External corrosion	31	18.0
Unknown	8	4.7
Other <sup>a</sup>	40	23.3
Pipe defect	13	7.6
Ground movement	5	2.9
Seam weld defect	3	1.7

<sup>a</sup>Includes 30 failures of internal cracking due to wet town gas.

**Table 5** Summary of failure statistics from the DOT database of incidents on natural gas and hazardous liquid pipelines (1986–2005)<sup>5</sup>

	<i>Gas transmission</i>	<i>Hazardous liquid</i>
Total number of incidents	1025	2646
Total number of corrosion incidents	254	718
Percentage of total incidents due to corrosion	24.8	27.1
Percentage of corrosion incidents due to external corrosion	41.3	68.0
Percentage of corrosion incidents due to internal corrosion	58.3	30.8
Percentage corrosion incidents not specified	0.4	2.1

on the European gas system.<sup>7</sup> Even then, these statistics may be misleading as the internal corrosion failures were caused by manufactured gas and not natural gas. The dominance of external corrosion is similarly observed in the UKOPA data, which include both gas and liquid pipelines (Table 4).<sup>9</sup>

One of the issues that both CONCAWE and EGIG wanted to investigate from their statistics was whether there was any evidence that older pipelines were more likely to fail as a result of corrosion. Although the majority of oil pipelines in Europe were built more than 25 years ago, the CONCAWE statistics show that the failure rate from corrosion (i.e., the most likely failure mode with increasing age) has not significantly increased with age for pipelines up to 45 years old (Figure 2).<sup>10</sup> The statistics from the EGIG database also lead to the conclusion that there is no evidence of an ageing effect, that is, there is no increase in the corrosion failure frequency as a pipeline gets older. In fact the data show that the failure frequencies are actually decreasing with time. These conclusions demonstrate that corrosion failure on pipelines can be successfully managed through preventative inspection and maintenance measures.

The CONCAWE and EGIG databases also record information about the percentage of product volume spilt by cause. The figures for oil pipelines are reported in Table 2. In both databases, external interference results in larger releases or volumes spilled than corrosion. Data in the EGIG database indicate that this observation can be attributed to the fact that the pipeline is more likely to rupture as a result of external interference, resulting in a large hole from which product can escape, whereas corrosion is more likely to result in a leak from a small defect or pinhole.

It can therefore be concluded that although external interference accounts for the highest number of pipeline failures and a greater volume of product lost, corrosion, predominantly external, remains one of the main threats to pipeline safety. However, the statistics indicate that the corrosion threat can be successfully managed and measures put in place to detect and prevent corrosion on pipelines as part of a pipeline integrity management plan. Specific to that integrity management plan will be a corrosion management strategy in which the pipeline operator will have to optimize the cost of corrosion from an economic, environmental, and safety point of view.

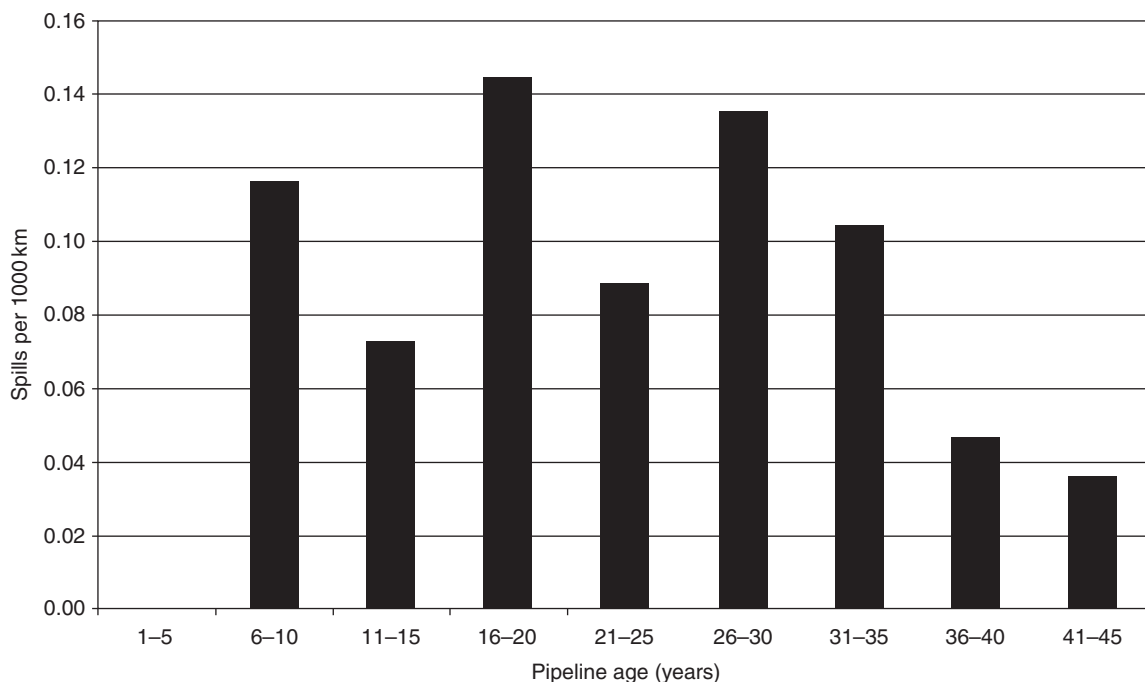


**Figure 2** Relationship between corrosion spill frequency and age in the CONCAWE database.

#### 4.42.2.3 Pipeline Safety

Although the requirement to collect failure statistics may, in some cases, be regulatory, in others it is voluntary among the pipeline operators to demonstrate the inherent safety of pipeline transmission systems and also to identify the main causes of pipeline failure in order that safety improvements can be made. Indeed, one of the conclusions that can be drawn from the incident data is that pipelines are one of the safest modes of transport for hazardous liquid and gas products over long distances. A study conducted in the US, comparing incident data for pipeline transportation of oil products relative to other modes of oil transport, confirms that pipeline transport has the best overall safety record<sup>11,12</sup> (Table 6). In particular, based on this normalized data, road transport of oil resulted in 103 times more deaths and 32 times more injuries in the US over the five-year period between 1997 and 2001 than pipeline transport and this figure is increasing when compared with the previous 5 years (1992–1997). A similar trend is inherent in the statistics from Western Europe, which has caused CONCAWE to conclude that “unlike marine and road traffic accidents, so far in Western Europe nothing of large enough scale or frequency has occurred with oil pipelines to draw them to the attention of the general public.”<sup>10</sup>

Notwithstanding, in the US in the past few years there have been a number of high-profile pipeline failures, which have refocused public attention on pipeline safety. One corrosion-related failure in particular is highlighted here, which illustrates not only the severe consequences of pipeline failure but also the requirement to understand the threats to a pipeline system and to put adequate procedures in place to address the threats before incidents occur.

In August 2000, a 30" natural gas pipeline ruptured in New Mexico. The escaping gas ignited and killed twelve members of an extended family who were camping near the rupture site. Property and

other damages totaled \$998 296. The pipeline accident report concluded that the probable cause of the failure was “a significant reduction in wall thickness due to severe internal corrosion.”<sup>13</sup> The corrosion had occurred at a low point, caused by a bend in the pipeline, where water had been allowed to accumulate.

The internal corrosion control program that was employed by the operator was to monitor the quality of gas entering the pipeline, to visually inspect the inside of the pipeline when it was exposed, to run cleaning tools through the pipeline and to maintain the pipeline drips by ensuring that they functioned properly and liquids were regularly removed. However, the company procedures for gas monitoring were not rigorous enough to be able to identify whether internal corrosion could be occurring. In addition, due to the design of the drip assembly for the pipeline that ruptured, cleaning and in-line inspection and cleaning (ILI) tools could not be run in this section. As a result, the drip upstream of the rupture location became blocked, allowing liquids to bypass the drip and continue down the pipeline. Although this section of the pipeline could not be inspected using ILI, the corrosion control program did not specify additional inspection, such as ultrasonic thickness measurements at low points or the installation of corrosion-monitoring devices to determine whether corrosion was occurring. The National Transport Safety Board concluded that the corrosion had occurred because the “corrosion control program failed to prevent, detect, or control internal corrosion within the company’s pipeline.”<sup>13</sup>

Incidents such as this have resulted in the introduction of new regulations regarding pipeline integrity management in the US.<sup>14,15</sup> Many of the approaches that have been used to draw up integrity management plans have been based on risk assessment methods to ensure that the major threats are identified, prevented, detected, and controlled. The remainder of this chapter will examine the causes of corrosion, risk-based inspection and maintenance

**Table 6** Comparison of safety data for oil transport per ton mile transported (1992–2001)<sup>11,12</sup>

	<i>Pipeline</i>	<i>Trucks</i>		<i>Barge</i>		<i>Ship</i>		<i>Rail</i>	
		1992–1997	1997–2001	1992–1997	1997–2001	1992–1997	1997–2001	1992–1997	1997–2001
Deaths	1.0	87.3	103	10.2	10	4.0	10	2.7	0
Injuries	1.0	2.3	32	0.9	14	0.7	14	2.6	11
Fire/explosion	1.0	34.7	46	4.0	3	1.2	2	8.6	2

The data is presented based on a multiplier of the pipeline rate, which is given a value of one. Therefore, a value of less than one indicates a better safety record.

strategies and integrity assessments that are used in the pipeline industry to identify, manage, and control pipeline corrosion.

### 4.42.3 Pipeline Integrity Management

The role of pipeline integrity management is to increase public safety by minimizing or eliminating pipeline failures. Integrity management planning requires an operator to identify the major threats to the integrity of the pipeline and then to plan and implement inspection, maintenance, and control strategies to ensure that these threats are appropriately managed. The basic principle of pipeline integrity management planning is outlined in [Figure 3](#).

Risk assessment procedures are now being widely used in the pipeline industry as a tool to enable operators to rigorously identify the critical pipeline threats and to determine whether particular sections of a pipeline or particular pipelines in a network are at increased risk of failure. These critical areas can then be prioritized for appropriate inspection and mitigation actions implemented to address the identified threats. Risk assessment methods also allow the operators to run risk reduction scenarios in order that effort and resources can be concentrated on those activities that have the greatest impact on reducing the risk. In many countries, risk assessment forms part of the pipeline integrity management codes and regulations.<sup>8,14–16</sup>

The risk assessment approach that is adopted by the pipeline operator can be qualitative, semiquantitative, or fully quantitative. A qualitative approach is the simplest method and will provide a coarse (high,

medium, low) assessment of the risk on the pipeline, although it tends to be very subjective. A fully quantitative method may be the most rigorous approach; however, there is often not enough pipeline data and associated information available to conduct such an assessment. Therefore, most operators adopt semiquantitative methods that use scoring models to determine a relative risk score for each of the threats on a pipeline. These methods consist of a series of algorithms for each of the threats that identify the key parameters contributing to that threat and then weight the relative importance of those parameters and their contribution to the overall risk.<sup>17</sup> The benefit of semiquantitative methods is that non-subjective data, such as pipeline inspection results, can be used in the threat analysis.

The first stage in the process illustrated in [Figure 3](#) is therefore to identify the potential threats to the pipeline and to collect the appropriate data to allow the threat to be assessed. The ASME B31.8S code supplement<sup>18</sup> provides guidance for the implementation of integrity management plans on gas pipelines and identifies 22 root causes of pipeline failure that have to be addressed as part of a risk assessment. Three of these relate to corrosion: external corrosion, internal corrosion, and SCC. In order to understand the risk assessment process as it pertains to these corrosion related threats, a review of the factors that contribute to the mechanisms and control of pipeline corrosion is required.

### 4.42.4 External Pipeline Corrosion Risks

The majority of the onshore pipeline networks are constructed from plain carbon–manganese steel that is alloyed and processed to produce the required strength, toughness, and weldability properties. One of the consequences of using plain carbon steel for onshore pipelines is that it is not inherently resistant to corrosion, either from the soil environment or from potential corrosives in the product.

#### 4.42.4.1 External Corrosion: Mechanisms

In the presence of water from the external environment, either the atmosphere or the soil, unprotected carbon steel will corrode. Corrosion defects reduce the load-carrying capability of the pipeline, and if they are allowed to continue to grow, may result in leak or rupture failures. In conducting pipeline

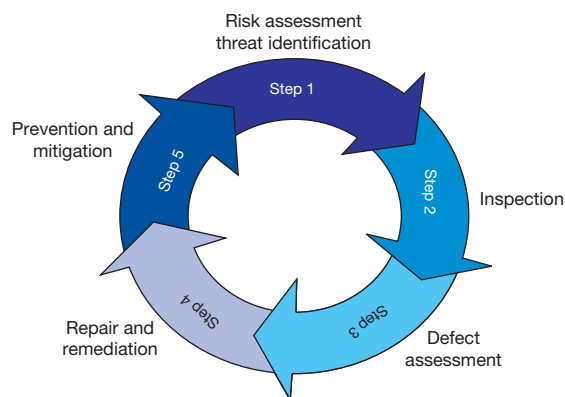


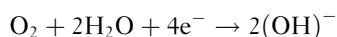
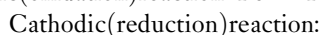
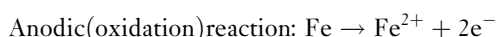
**Figure 3** Pipeline integrity management process.



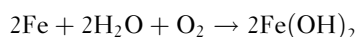
corrosion management programs, it is therefore essential to understand the type of corrosion to which the pipeline is susceptible and the rate at which that corrosion could grow. The following sections describe the main types of external pipeline corrosion and highlight the risk factors for each type.

#### 4.42.4.1.1 Soil corrosion

As with all corrosion reactions, for external corrosion to occur on a pipeline, there must be anodic and cathodic areas on the pipe surface that are electrically connected by the pipe material and are immersed in a conducting electrolyte, the soil. For buried pipelines in a wet, oxygenated soil environment, the half-cell corrosion reactions are:



The rusting of carbon steel in the soil environment can therefore be described by the general equation:



In the simplest form of corrosion, the anodes and

cathodes are distributed evenly over the metal surface and the result is uniform wastage or general corrosion. However, at times, distinct anodic and cathodic zones are formed and this results in localized pitting corrosion. Whether a particular area of the pipe becomes anodic or cathodic can be dependent on local variations in steel chemistry or soil constituents, particularly oxygen. The nature of the soil is therefore very important in the determination of the likelihood and severity of external corrosion.

In general, soils that are good conductors will produce higher corrosion rates, that is, soils with low pH values, high soluble salt content, and high moisture content. The conductivity and therefore the corrosivity of the soil are measured by its resistivity, that is, the higher the resistivity value, the lower the corrosion rate, as there is more resistance to the flow of current. ASME B31.8S<sup>18</sup> contains guidance on estimating corrosion rates based on soil resistivity measurements and site observations. Similar correlations between corrosion rate and soil type and resistivity have also been published by Simon-Thomas *et al.*<sup>19</sup> and Peabody.<sup>20</sup> All of these correlations are compared in Figure 4.<sup>21</sup> From these data, it can be seen that corrosion rates for soil corrosion are in the

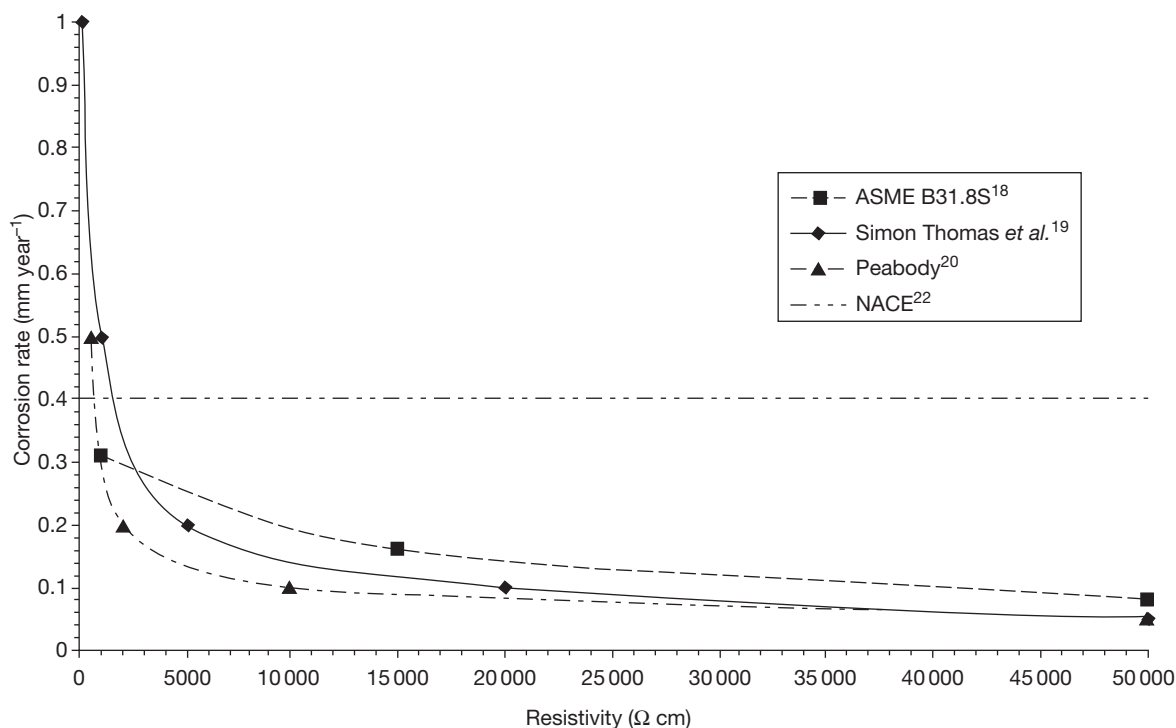


**Figure 4** Comparison of external corrosion rate prediction models. Reproduced with permission from Race, J. M.; Dawson, S. J.; Stanley, L. M.; Kariyawasam, S. J. *Pipeline Eng.* **2007**, 6(1), 13–29.

range  $0.05\text{--}0.5\text{ mm year}^{-1}$  depending on soil resistivity. At the lower end of the range, corrosion rates of  $0.05\text{ mm year}^{-1}$  would be associated with soils such as limestone, sands, or gravels, which typically have resistivity readings greater than  $10\,000\text{--}20\,000\,\Omega\text{ cm}$ . At the upper end, corrosion rates of  $0.5\text{ mm year}^{-1}$  are typical for steel in peat or swamp-like terrain and correlate to resistivity readings in the range  $100\text{--}1000\,\Omega\text{ cm}$ . It is possible that even higher corrosion rates could be observed if the backfill material contains industrial waste, particularly conductive materials such as coke. The National Association of Corrosion Engineers (NACE) has conducted long-term underground corrosion tests of unprotected steel in a variety of soils. The upper 80% confidence level of these exposure tests indicates that a rate of  $0.4\text{ mm year}^{-1}$  may be typical for soil corrosion.<sup>22</sup> It should be noted that soil conditions will change along the length of a pipeline and therefore the severity of corrosion will also change. It should also be remembered that pipelines are generally buried and therefore soil conditions at the surface may not reflect those in the vicinity of the pipeline.

Although typical rates for external corrosion of pipeline steel are in the range  $0.05\text{--}0.5\text{ mm year}^{-1}$ , there are particular types of corrosion that can occur in pipelines where much higher corrosion rates can be achieved. These types of corrosion are of particular concern from a pipeline integrity management viewpoint, as they have to be identified quickly in order that mitigative measures can be implemented. These mechanisms are discussed in the following sections.

#### **4.42.4.1.2 External microbiologically influenced corrosion (MIC)**

With reference to pipeline corrosion, MIC can be defined as corrosion that is initiated and/or accelerated by the physical presence and metabolic activities of microorganisms in the soil. Although the bacteria themselves do not directly attack the steel surface, they can initiate and maintain conditions for corrosion by interacting with the electrochemical corrosion process.

Different types of bacteria found in soil have been shown to be responsible for pipeline steel corrosion. One of the key groups of microbes in this respect is sulfate-reducing bacteria (SRB). SRB are known as obligate anaerobic bacteria, which means that they become active in the absence of oxygen and thrive in waterlogged soils such as clays. One theory regarding the role of SRB in promoting corrosion is that sulfate is reduced to sulfide during the metabolic process.

The sulfide can then react with hydrogen, produced either as a result of the cathodic corrosion reaction or by further metabolic processes, to produce hydrogen sulfide. A corrosion reaction between hydrogen sulfide and iron produces an iron sulfide corrosion deposit on the surface and further corrosion of the steel occurs through a galvanic couple established between the iron sulfide deposit and the surrounding iron. Corrosion rates of between  $0.2$  and  $0.7\text{ mm year}^{-1}$  have been measured for this mechanism on pipelines in the field, although rates above  $5\text{ mm year}^{-1}$  have been cited.<sup>23</sup>

Another important microorganism in the microbiological corrosion of steel is acid-producing bacteria (APB). This type of bacteria is classed as facultative aerobic bacteria, which means that, although they prefer aerobic conditions, such as sandy soils, they can survive in an anaerobic environment, such as clay soils. APB are capable of forming organic acids, such as acetic acids, which concentrate under the biofilm and as a result are very corrosive to carbon steel. There are other forms of APB that produce organic acids, such as sulfuric acid, or that produce carbon dioxide, which reacts with the water in the soil to produce carbonic acid.

However, the most aggressive attack of pipeline steels occurs when bacteria act cooperatively in communities to form complicated biofilms on the steel surface. Under these circumstances, anaerobic bacteria can survive in aerobic conditions if they are present in biofilms in which aerobic bacteria consume the oxygen.

Although the potential for MIC, to a large extent, is governed by the type of soil and the available nutrients, it has been suggested that even the process of trenching a pipeline can increase the levels of bacteria in the soil around the pipeline.<sup>20</sup> There are also other factors that will increase the susceptibility of a pipeline to MIC; indeed even measures designed to protect a pipeline from external corrosion can make it more susceptible to MIC if these measures fail. For example, the disbonding of the protective pipeline coating can produce an ideal microbial habitat, which is isolated from the effects of cathodic protection (CP). In fact, it has been shown that almost all cases of external MIC are associated with disbonded coating.<sup>24</sup> Some coatings are more prone to disbonding than others and therefore pipelines coated with these types of coating can be more at risk from MIC.<sup>23</sup> Coating types and failure mechanisms are discussed in detail in [Section 4.42.4.2.2](#).

#### 4.42.4.1.3 Preferential corrosion

Preferential (or selective) corrosion is predominantly found in pipelines manufactured prior to 1970, using a welding technique called low-frequency electrical resistance welding (LF-ERW). LF-ERW pipe is manufactured by forming a steel strip into a pipe and then simultaneously heating the edges of the strip using a low frequency alternating current and forcing the edges together under pressure. There are two problems associated with this type of pipe material: firstly, the pipe steel of the era could contain large amounts of nonmetallic inclusions due to high sulfur contents and secondly, the weld area was not always heat-treated and therefore could have inferior corrosion resistance and mechanical properties to the parent. As a result, the weld corrodes at a higher rate than the parent plate resulting in a V-shaped crack-like groove along the weld line in a region that tends to have properties inferior to those of the parent pipe material. There are two potential mechanisms by which preferential corrosion can occur in LF-ERW: by crevice corrosion at a lack of fusion defect and by dissimilar metal corrosion cells.

- *Crevice corrosion*

Surface-breaking lack of fusion defects in the weld are tight crevices that are open to the corrosive environment. Moisture becomes retained within the crevice and a local corrosion cell is formed. As a result, the crevice will corrode preferentially resulting in a groove-like defect at the weld line.

- *Dissimilar metal corrosion cell*

The other mechanism by which preferential corrosion can occur is the formation of a dissimilar metal corrosion cell at the surface. In ERW welds, the corrosion cell is set up between the weld material and the pipe body material due to chemical and physical property differences within the weld. The result is that the weld material becomes the anode in the

corrosion cell and will corrode preferentially, again resulting in sharp groove defects at the weld line.

#### 4.42.4.1.4 Stray-current corrosion

Another mechanism by which accelerated corrosion rates might be experienced on pipelines is stray-current corrosion. NACE defines stray-current corrosion as “corrosion resulting from the current through paths other than the intended circuit, for example, by any extraneous current in the earth.”<sup>22</sup> Direct currents can be present in the soil from electrified transport systems (e.g., railways or trams), CP systems for other pipelines, mining operations, high-voltage electricity transmissions systems, or even telluric currents caused by changes in the earth’s magnetic field. For an explanation of CP refer to [Section 4.42.4.2.8](#). In these systems, the earth provides part of the return path for the current to the source. However, any buried metallic structure in the vicinity, such as a pipeline, provides a favored, low-resistance path along which the currents can travel.

The mechanism for stray-current corrosion with reference to an electrified traction system is illustrated in [Figure 5](#). The return path for this system is provided by the rails; however, if the rails are not adequately insulated from the earth, some of the current will enter the ground and return via an earth path, unless a pipeline can provide a lower resistance return path. Where the current flows onto the pipe, the pipeline is cathodic and therefore protected as a result of the same process that applies in a CP system (see [Section 4.42.4.2.8](#)). The current travels along the pipeline and is discharged close to the source. At this point, the pipe is anodic and corrosion will occur at a rate that is dependent on the magnitude of the current flow, but may be many times greater than the soil corrosion rates.<sup>20</sup>

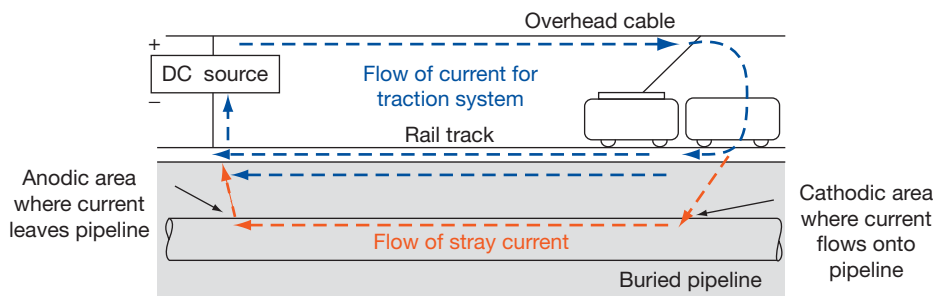


**Figure 5** Schematic of stray current corrosion from a railway system.

As a result, it is important that locations of suspected stray-current activity are identified and appropriate corrective actions implemented.

One of the problems with stray-current corrosion from electrified transport systems is that the current is dynamic or fluctuating, because the load varies with every train that passes. It is therefore important to identify the locations on a pipeline that may be at risk, that is, where the pipeline runs close to traction systems or where there may be locations of low track to earth resistance. In these areas, continuous monitoring for stray-current corrosion should be conducted over a 24-hour period to ensure that the time periods when the pipeline is at risk are identified. Stray currents from CP systems for other pipelines are termed static as they do not vary with time.

#### **4.42.4.1.5 AC corrosion**

The occurrence of pipeline corrosion as a result of direct current discharge (i.e., stray-current corrosion) is well recognized and accepted. However, there have also been reports of pipeline corrosion as a result of induced alternating current discharge. Although, the phenomenon of AC corrosion in soils is not fully understood and there is no agreement in the literature on the mechanism, it is possible to draw conclusions regarding the factors that make a pipeline susceptible to AC corrosion.

Pipelines at highest risk are those that run parallel to overhead AC power lines. The flow of current in the power lines produces an alternating magnetic field around the power line. If a pipeline is running within the magnetic field, then it is possible that an AC potential may be induced in the pipeline resulting in current flow. At points where the pipeline enters or leaves the magnetic field, the induced voltages are greatest. It is interesting to note that pipelines that cross at right angles to AC power lines do not have AC currents or voltages induced in them.

When a pipeline suffers from induced AC voltages, it has also been found that coatings with high dielectric strength, and therefore good insulators, will make the pipeline more susceptible to AC corrosion. The AC corrosion has been found to occur at small pinhole holidays in an otherwise good condition, adherent pipe coating. Another factor that makes a pipeline more susceptible is the resistivity of the soil. Low-resistivity soils in particular provide a more favorable route to earth for the current.

Corrosion caused by AC discharge occurs in the form of a small, deep hemispherical pits covered by a hard corrosion product. The current density at a

coating defect is one of the major factors influencing corrosion rate and is affected by the size of the defect, the soil resistivity, and the AC voltage on the pipeline. Initial work suggested that corrosion rates associated with AC corrosion were significantly lower than those caused by a direct current of a similar magnitude. However, corrosion rates of up to 10 mm year<sup>-1</sup> have been reported by pipeline operators.<sup>25</sup>

#### **4.42.4.2 External Corrosion: Prevention**

As described in previous sections, plain carbon steel is not resistant to corrosion from the external environment and therefore pipelines must be protected to prevent corrosion in the soil environment and a resulting loss of integrity. In general, underground pipelines are protected by the application of both an external coating and a CP system. These systems act synergistically to prevent external corrosion, the primary protection mechanism being the coating with the CP system designed to protect areas of the pipe where the coating becomes damaged. The next sections describe the features of the coatings and CP systems used to protect onshore pipelines.

##### **4.42.4.2.1 Requirements of pipeline coatings**

As described in [Section 4.42.4.1.1](#), for external corrosion to occur, two of the conditions that must be met are that the pipeline steel is immersed in a conducting electrolyte and that electrical current flow is permitted between the steel and the electrolyte. To prevent external corrosion therefore, the role of the pipeline coating is to provide a barrier between the soil and the steel to prevent moisture and oxygen contact with the pipe surface and also to act as an electrical insulator.

The construction of onshore pipelines involves welding together sections of pipe, generally 12 meters in length, in the field before lowering the completed pipeline section into the ditch. Historically the pipe spools were coated on site, 'over-the-ditch,' and although this practice is still used, the spools are more usually precoated in the pipe mill leaving a cutback area at the end of each spool to allow the field or girth weld to be made on site. This cutback area and the completed girth weld are then coated in the ditch. Two types of coating have therefore to be specified for the pipeline, the mill-applied main line coating and the field-applied girth weld coating.

In order for a material to be suitable as a pipeline coating, it must meet certain requirements, which are outlined in detail in the NACE recommended

practice RP0169.<sup>22</sup> The more critical requirements for the specification and selection of a pipeline coating can be summarized under the following general headings:

- *Adhesion*

As a primary role of the coating is to prevent water contact with the pipe surface, one of the critical requirements of a coating is that it should remain adherent to the steel for the design life of the pipeline. When a pipeline coating loses adhesion, water can enter beneath the coating and migrate along the pipeline between the pipe and the coating. One particular form of disbonding, termed 'tenting,' can occur along irregularities on the pipe surface, especially at long seam or girth welds. Coating disbonding is one of the most damaging modes of coating failure because, as will be described later, the area under the disbonded coating cannot be protected by the CP system. Although adhesion to the steel surface is dependent in part on the prolonged strength of the bond between the coating and the steel, it is also critically dependent on the surface preparation prior to the application of the coating. The surface of the steel must be adequately prepared to remove contaminants and also provide a suitable surface profile onto which the coating can attach.

- *Electrical resistivity*

Besides providing a barrier between the soil and the pipe steel, another critical function of the coating is that it should be an effective electrical insulator to prevent the flow of any corrosion current between the pipe and the soil. It is therefore important that the coating has a high electrical resistance (ER) that does not vary over time or with exposure to the environment as this will cause variation in the demand from the CP system.

- *Resistance to handling and construction damage*

If the coating is applied in the mill, then, before the pipeline is commissioned, there is the potential for the coating to be damaged at a number of stages, for example, during the handling and transportation of the linepipe to site, during manipulation for welding and laying operations, during the fabrication of cold field bends on site, and as a result of impact from rocks in the trench and backfill material. In order to minimize the extent of the coating damage, it is important that the coating has adequate flexibility as well as abrasion and impact resistance.

- *Compatibility with the pipeline environment*

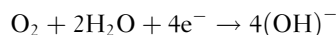
For a buried pipeline, the coating selected for a particular application must be compatible with the

soil environment, and in particular, should not allow water to penetrate through the coating onto the steel surface. The coating must also be resistant to any other chemicals, for example, acids and alkalis, or microorganisms that may be found in the soil in which the pipeline is buried.

Another important factor associated with the pipeline environment is the operating temperature. If a coating is subject to temperatures outside the recommended maximum operating temperature, then this can result in disbonding, melting, creep, sagging, embrittlement, or softening of the coating. Ultimately, this will lead to the degradation of the coating and compromise the ability of the coating to protect the pipeline for the design life.

- *Compatibility with the CP system*

As the coating and CP system are acting together to protect the pipeline, it is important that the coating is not degraded by the CP system. One of the mechanisms by which this can happen is cathodic disbonding, a phenomenon by which accelerated disbonding can occur at the edge of a coating defect due to the action of the CP. Although the mechanism has not been fully characterized or understood, the major cause is thought to be chemical attack on the coating-steel bond by alkali generated by the cathodic electrochemical reaction:



Another effect of CP is that it can promote the permeation of water at the edge of a coating defect, which can also contribute to accelerated disbonding.

- *Resistance to in-service loads*

Once the pipe coating has been installed, the coating should be able to withstand any loads imposed during service. For example, it must be flexible enough to remain adherent to the pipe particularly during changes in internal pressure. However, the main external loading on the coating in service is as a result of soil loading and soil movement. Settlement of the backfill can create a tensile load on the pipe and cause creep of the coating. In addition, particularly in clay-type soils, the action of seasonal wetting and drying can lead to the expansion and contraction of the soil around the pipeline. As the soil moves, it can cause the coating to wrinkle and lose adhesion with the pipe. Soil movement around the pipe can also result from the creep of soil on slopes. In these types of soil environments, it is important to specify a coating with a high creep or shear resistance.



- *Compatibility with other coating systems*

Particularly for field joint or girth weld coatings, compatibility and adherence to the main line coating are especially important to prevent loss of adhesion around the girth welds. It is also essential that the coating is easy to repair if it becomes damaged.

Prior to specifying a coating for a pipeline, it is important that all of these factors are taken into account, and in particular, that the operating conditions of the pipeline, the location, that is, the local terrain and soil conditions, and the CP requirements are fully quantified and understood to ensure that the most appropriate pipeline coating is selected. NACE RP0169<sup>22</sup> identifies a series of tests that can be used to evaluate the suitability of a coating in the operating conditions.

#### 4.42.4.2.2 Types of pipeline coatings

The principal types of coating that are used for onshore pipelines are outlined in [Table 7](#).

Enamel-type coatings have been applied to pipelines for over 80 years, and consequently, they have been used to protect more pipelines around the world than any other coating. Coal tar coating systems consist of coal tar enamels, reinforced with felt or fiberglass wraps, which are applied hot over a primer of either chlorinated rubber or a two-component epoxy, depending on the service temperature requirements. One of the issues with the older coal tar systems was concern over the toxicity of the coal tar when heated. This led to the use of bitumen or asphalt coating

systems, which are applied in a similar way to coal tar systems but do not have the same health concerns.

In the 1950s, tape-wrap coating systems started to be used on pipelines and they remain a popular selection as they are readily available and easy to apply, either in the pipe mill or on site, and they tend to be a lower cost option. The first tape coatings were fabric reinforced petrolatum-based systems, but now there are a variety of systems available that can be applied either hot or cold. In general, a tape coating is a laminate system consisting of an outer backing material (e.g., polyethylene (PE), PVC, woven polyolefin) and an inner adhesive mastic (e.g., petrolatum grease, rubber-based compounds) that are spirally wrapped around the pipe ensuring a high degree of overlap between turns. Additional outer layers may be included for enhanced mechanical protection.

Mill-applied extruded polyolefin coatings were first introduced as pipeline coatings in the mid-1950s when PE was hot extruded onto small-diameter pipes over an asphalt mastic adhesive using a cross-head extruder. The process involved extruding a PE sheath onto a heated pipe coated in mastic, which shrank onto the pipe as it cooled. These two-layer PE-mastic adhesive systems were subsequently improved by replacing the asphalt mastic with butyl rubber or bitumen to provide better adhesion. Since the first extruded PE systems were used on pipelines, the number of layers, method of extrusion, type of mastic, and type of polyolefin have varied to improve the coating properties and the

**Table 7** Types of external pipeline coating and their application

		<i>Mill applied</i>	<i>Field applied</i>	<i>Joint coating</i>	<i>Repair coating</i>
Enamel systems	Coal tar enamel	✓	✓	✓	
	Asphalt/bitumen	✓	✓	✓	
Polyolefin systems	Two-layer PE – mastic adhesive	✓			
	Two-layer PE – hard adhesive	✓			
	Three-layer PE – two-pack epoxy primer	✓			
	Three-layer PE – FBE primer	✓			
	Three-layer Polypropylene – FBE primer	✓			
Fusion bonded epoxy powder (FBE)		✓		✓	
Liquid coating systems		✓		✓	✓
Heat shrinkable materials				✓	✓
Tape systems		✓	✓	✓	✓

range of pipeline sizes that may be coated with this system. The most recent developments were introduced in the 1980s with the use of three-layer PE and three-layer polypropylene (PP) systems with a fusion bonded epoxy (FBE) first layer. In these systems, the first layer of the coating is FBE, which is sprayed onto the heated pipe. The second layer is required to form either a mechanical or chemical bond between the FBE and the polyolefin and is either a copolymer or an adhesive-based material. The final layer is the extruded polyolefin; either PE (low, medium, or high density) or PP (for higher temperature operations). Although not the cheapest coating systems available, due to their enhanced properties, three-layer polyolefin FBE systems are one of the most widely used coating systems in Europe.

Besides its use in multilayer polyolefin systems, FBE is also applied on its own as a coating system. The coating consists of a partially reacted mixture of epoxy resin, curing agent, fillers, and pigments, which are dry-sprayed as a powder onto a heated pipe. The mixture then fuses and reacts to form a continuous epoxy film that cures under the action of heat. The system was first introduced in the mid-1950s but has only found application on large-diameter pipes since the mid-1970s. The superior properties of this type of coating, particularly with respect to soil stress and cathodic disbonding, make FBE one of the most popular pipeline coatings.

#### **4.42.4.2.3 Types of field joint coatings**

All of the coatings described in [Section 4.42.4.2.2](#), except the extruded polyolefin systems, can also be applied in the field to the girth weld joints. However, there are also some coating systems that were specifically designed for the field joint.

One of the field joint systems that has been in use since the 1960s is heat-shrinkable sleeves. As the name implies, these coatings consist of a polymer sleeve that is shrunk onto the pipe joint, either over a mastic adhesive or an epoxy primer, by the application of heat. It is important that the coating is heated correctly when applying heat-shrinkable materials as too little heat can mean that the adhesive fails to flow and therefore the coating loses adhesion, although too much heat can damage the sleeve and main pipe coating.

Liquid coating systems, such as two-pack epoxies or two-pack urethanes, were developed to be compatible with FBE coatings, both for field joints and for repair. The systems consist of two components, a base resin and a hardener, which are combined together

before application either by brush, trowel, or spray. It is critical that the components are correctly mixed as otherwise the coating will not cure properly.

#### **4.42.4.2.4 Coating failure**

Even after specifying the requirements of a coating for a particular service, conducting laboratory or field testing and selecting the most appropriate coating for the pipeline and field joints, coating damage must still be expected on buried pipeline systems and it is impossible to maintain the coating in a damage-free condition. Some of the damage mechanisms have been discussed in [Section 4.42.4.2.1](#) and include the disbonding of the coating, rock damage during installation and service, handling and construction damage, soil loading, and degradation due to environmental and temperature effects. However, many pipeline coating failures can often be attributed to either incorrect application of the coating or incorrect specification.

- *Incorrect specification*

There is no standard method for selecting a coating for a particular service, and although laboratory or field test results are useful, they will not fully predict the long-term performance of a particular coating system. Therefore, the decision on which coating system to choose is not straightforward. It has also to be recognized that the cost of the coating system is not an insignificant factor in coating selection and can be particularly significant when coating a pipeline of hundreds of kilometers. Selection can therefore be a balance between long-term performance of the coating and cost.

- *Incorrect application*

Even if the most suitable coating material is selected, poor preparation and application will lead to premature failure. It is therefore essential that rigorous procedures are specified for each stage of the pipeline coating process, not only for surface preparation and application but also for repair and testing of the coating. As mentioned previously, adhesion to the steel substrate is one of the most important factors in the performance of pipeline coatings. Most coating systems rely on a clean, properly prepared surface to develop and maintain maximum adhesion to the pipeline. Poor surface preparation can either lead to contamination being left on the pipe surface or the incorrect surface finish being achieved to promote a good bond between the pipe surface and coating. This can result in a rapid loss of adhesion and coating deterioration during service.

Once the surface has been prepared, the coating needs to be applied in accordance with appropriate specifications and the process monitored with quality standards that are regularly checked. Poor coating application often results when the specification program is inadequate or the applicator does not adhere to the correct procedures in the program. It cannot therefore be overemphasized that it is only through attention to the whole coating process that maximum coating performance can be maintained throughout the design life of the pipeline.

#### **4.42.4.2.5 Coating condition monitoring**

It is recognized that the coating system on buried pipelines cannot be maintained in a 100% defect-free condition. Not only can handling during construction cause damage to coatings but also soil movements and soil stresses may cause subsequent damage to coating systems after they are installed. It is a fact that all coating systems will eventually show some degradation with time. Although defects in a coating are intended to be protected by the CP system, if a coating holiday is large enough or if there are too many coating holidays on the pipeline, the current required to protect the total bare area of steel may exceed the capacity of the CP system. Therefore, understanding the condition of the coating during pipeline operation is an important part of maintaining corrosion protection on the pipeline. There are a number of techniques that can be used to evaluate the condition of the coating that do not require random excavation and visual inspection. These coating defect survey techniques can identify the location of holidays, and in ideal conditions, can give an indication of relative coating size. The measurements are taken through the soil layer by walking above the pipeline and are therefore referred to as above-ground surveys.

One of the property requirements of the pipeline coating that was discussed in [Section 4.42.4.2.1](#) was good electrical insulation. Therefore, if the coating is maintained in a defect-free condition and an electrical current is applied onto the pipe, no leakage of that current should occur unless there is a hole in the coating. Where there is a hole in the coating, any applied current will leak out into the surrounding soil. This is the principle on which the coating defect inspection techniques that are used on pipelines are based; the detection of the effects of an applied current leakage is either achieved through measuring the reduction in current flow ahead of the holiday or by measuring the potential gradient in the soil caused by the flowing current.

The above-ground survey techniques can be grouped on the basis of the type of current that is applied to the pipeline to detect the holiday, that is, AC or DC. In this chapter, a brief description is given of some of the main methods in these categories. However, more information on different survey techniques can be found in Appendix A of NACE RP0502.<sup>44</sup> It should be emphasized that the above-ground survey techniques will not find disbonded coatings. In this situation, the hole in the coating may be very small and does not relate to the size of the corroding area under the disbonded coating.

#### **4.42.4.2.6 Coating condition monitoring: DC methods**

The current required for DC methods is already available on the pipeline from the CP system, although the current may have to be increased in order to ensure that the potential gradients created at coating defects are more measurable. If the CP current cannot be changed or interrupted, the current can be obtained from a temporary supply. Although the ability to use the CP current is an advantage, it also means that these survey techniques cannot be conducted at the same time as a CP monitoring survey, as the enhanced current requirements will not represent the normal working conditions of the CP system.

- **Analog Direct Current Voltage Gradient (DCVG)**

In a DCVG survey, the CP current is switched on and off at a frequency of  $\sim 1$  Hz and the resulting voltage gradient created at coating defects is measured between two earth contact probes that are carried by a single operator. The two probes are calibrated at the start of the survey by ensuring that no difference in potential is registered when the probes lie on the same equipotential line. To understand how the survey is conducted, imagine lines of potential around a coating defect ([Figure 6](#)). As the operator approaches the defect, a potential difference will be recorded between the two probes. The direction of voltage swing will indicate the location of the defect center. When the operator is directly above the defect, no swing in potential is recorded and therefore the location of the defect is identified.

One of the advantages of DCVG is that it is also able to give an indication of the size of the coating defect. To do this, one probe is positioned directly above the defect and the other is moved out to one side at right angles to the flow direction of the pipeline. The operator records the potential difference between the probes and continues to move away from

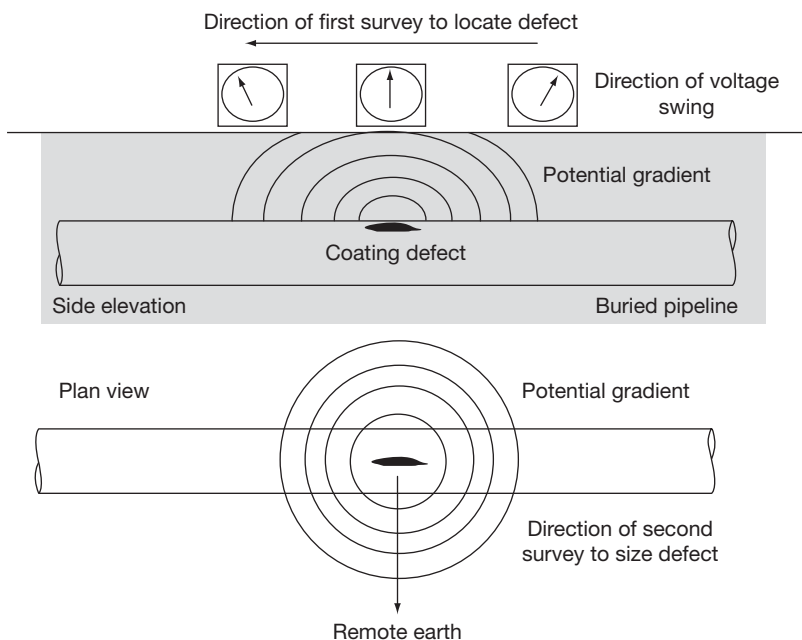


**Figure 6** Potential fields surrounding a coating defect in the analog DCVG technique.

the pipeline until no further detectable potential shift is noted. At this point, the probes are considered to be outside the field of significant current flow and in a remote earth potential zone where there is no significant current flow through the earth. The total potential gradient to remote earth is a measure of the size of the defect at that location. This value is usually divided by the difference between the pipe-to-soil ON and OFF potentials (for an explanation of these terms refer to [Section 4.42.4.2.14](#)) at that point to provide a benchmark measure of the size of the defect. This is referred to as the %IR reading and the larger the %IR value the larger the coating defect. DCVG survey readings are reported in four categories depending on the magnitude of the measured %IR, and the recommendations regarding remediation requirements are based on the %IR reading.

The main disadvantage of the DCVG method is that electric fields can be distorted by adjacent uncoated foreign structures, which can make data interpretation very difficult. In addition, it should be emphasized that the size of the coating defect is not an indication of the potential size of the underlying corrosion defect, that is, deep pits could be located under small coating holidays. In addition, a good contact with the soil has to be maintained with this technique. Consequently the DCVG survey method

is not easy to use in built-up areas where the pipeline route may be surfaced.

#### **4.42.4.2.7 Coating condition monitoring: AC methods**

In AC methods, the current is applied via a transmitter. The advantage of an AC method is that, as the method does not use the CP current, it can be conducted at the same time as a CP survey (see [Section 4.42.4.2.15](#).) However, AC signals can also be generated from other sources in the vicinity of the pipeline, such as overhead power cables, a phenomenon that was discussed in [Section 4.42.4.1.5](#). The effect of these AC signals on the readings can be overcome by using filters and by selecting an appropriate signal frequency for the survey.

##### **• Pearson surveys**

Pearson testing was one of the first types of holiday testing developed for buried pipelines. The technique employs two operators who are connected together by a wire and make an earth contact with the ground either using boots with metal cleats on them or with metal-spiked poles. The change in potential difference between the operators as they pass over a defect locates the defect on the pipeline and this is recorded by a receiver/data logger that is carried by the lead

operator. As with DCVG, one of the problems with Pearson testing is that a good contact with the soil must be maintained. In addition, detection can be difficult in high-resistivity soils as the current leakage detectable at the surface will be small.

- *AC current attenuation*

In this method, an AC current is applied to the pipeline via a signal generator that is generally connected at a CP rectifier. The resultant electromagnetic field generated around the pipeline is measured by an operator carrying a receiving unit. The principle of operation is that when a signal is applied to a coated buried pipeline, it will gradually decay away from the point of application. The rate of decline (attenuation) is a measure of the average coating condition between two given points. In general, the survey is first conducted on a macro scale (e.g., every kilometer) to identify sections of poor coating and then on a finer scale in specific areas (e.g., every meter) to pinpoint larger coating defects. One of the advantages of this method is that it does not require soil contact and can be conducted over any surface that will allow transmission of the electromagnetic field, for example, ice, water, or concrete. It is also possible to use the same equipment to locate the pipeline and provide a reading of the depth of burial of the pipeline in the same survey.

#### 4.42.4.2.8 Cathodic protection (CP)

Although a pipeline coating is specified to last for the design life of the pipeline, it has been shown that it is impossible to maintain a coating in a defect-free condition. Where there are defects in the coating, and therefore where there are areas where the steel is exposed to the soil environment and current can flow, the pipeline can corrode. To protect these areas from corrosion, a CP system is also installed on the pipeline.

Remembering the half-cell reactions for the corrosion of steel in the soil environment from [Section 4.42.4.1.1](#), corrosion, or the dissolution of iron, occurs at the anode where current leaves the pipe surface. The principle of CP is therefore to reduce the current flow away from the pipeline at these points by imposing a direct current onto the pipeline so that it becomes the cathode in the corrosion cell and does not corrode. Of course, in principle, it is possible to protect a pipeline using CP alone. However, the current required to achieve protection makes this unfeasible, which is why the combination of coatings and CP is the most practical method for protecting a pipeline from external corrosion.

Two main methods of CP are used in onshore pipelines: the galvanic, sacrificial anode method and the impressed current method.

#### 4.42.4.2.9 CP: Sacrificial anode systems

The principle of the sacrificial anode method is to make the pipeline the cathode in the corrosion cell by connecting it to an anode material that is more electronegative than steel in the electromotive series. Thus, current will flow from the corroding ‘anode,’ typically magnesium, zinc, aluminum, or alloys of these materials, to the pipeline ‘cathode’ through the soil. At locations where there are holidays in the coating, the current can flow onto the pipeline and repress the anodic reaction. The return path is provided by thermit welding a cable connection to the pipeline ([Figure 7](#)).

The advantage of the sacrificial anode system is that no external power source is required and therefore the system is easy to install and requires minimal maintenance. However, one of the main disadvantages of this type of CP system is that the available current is fixed and the driving potential between the steel and the anode material is limited by their separation in the electromotive series. In order to maximize the available current, these systems are therefore most effective in low-resistance soil environments. The limited current availability of this system also means that to protect long lengths of pipe, particularly poorly coated or bare pipe, requires large numbers of anodes to ensure that sufficient current is provided to the pipeline. The sacrificial anode system is therefore often used onshore to protect small areas of pipeline at specific critical locations. Another main disadvantage of a sacrificial anode system is that the anodes are consumed over time and therefore have a finite life after which they have to be replaced.

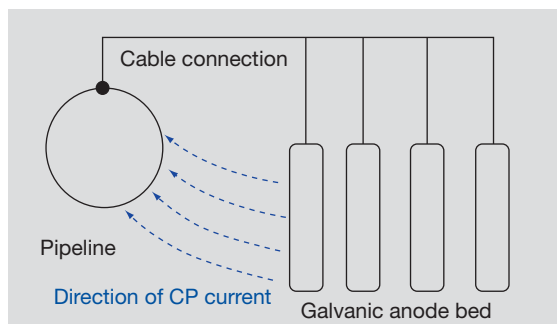


**Figure 7** Schematic of the sacrificial anode cathodic protection system.



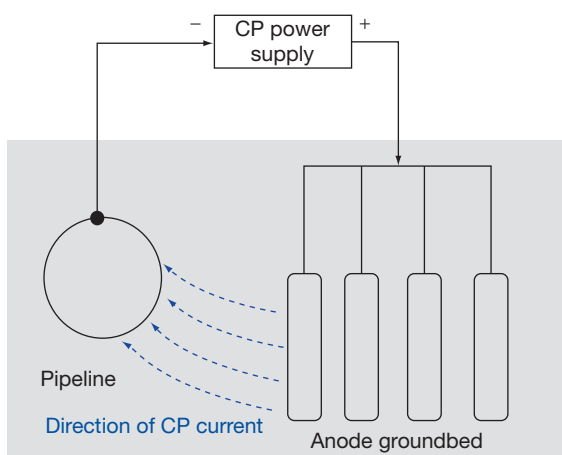


**Figure 8** Schematic of the impressed current cathodic protection system.

#### 4.42.4.2.10 CP: Impressed current systems

In an impressed current system, the protection current is supplied by connecting the negative terminal of an external power supply to the pipeline and the positive terminal to an inert anode (Figure 8). The system therefore consists of an AC source, which is rectified to produce a DC output, a groundbed of anodes, and wires connecting the anodes and the pipeline to the rectifier. Current flows from the anode groundbed through the soil to the pipeline and returns via the thermit-welded CP connection. The anodes that are used for the protection of pipelines are generally high-silicon chromium cast iron or mixed metal oxide coated titanium, buried in a coke-filled groundbed, to provide a low-resistance path for the current into the soil.

The main advantage of the impressed current system over the sacrificial anode system is that a larger driving potential is available and the voltage and current can be controlled. This makes the system more adaptable to the changing current levels required to protect the pipeline as it ages and the coating deteriorates and also more adaptable for use in high-resistivity soils. However, this system does require an external power supply and therefore has an associated ongoing through-life cost, and in addition, also requires more frequent maintenance and inspection than a sacrificial anode system.

#### 4.42.4.2.11 Basic CP design

Although the subject of CP design is addressed in international standards and guidance, several key factors need to be considered when installing a CP

system to ensure that the pipeline is adequately protected from external corrosion.

One of the critical requirements is ensuring that enough current is supplied to the pipeline to protect areas of coating damage. The larger the area of coating damage, the larger the current required to achieve a sufficiently high current density to ensure that the pipeline is protected. Other factors that need to be addressed are the type of CP system to be used (i.e., sacrificial anode or impressed current) and the spacing of the anodes along the pipeline to ensure that the required current levels are achieved at locations remote from the anode or power supply. These decisions will require knowledge of the pipeline environment including the soil resistivity, the coating type, the location of other metallic structures that could interfere with the CP current, and the presence of sources of stray current. In this respect, one of the features of the CP design includes the location of isolation joints. These joints are used to insulate the pipeline from current paths that could take current away from the pipeline and therefore reduce the level of protection. Isolation joints are therefore located at above-ground facilities such as terminals, pumping stations, offtakes, and instrument lines. They can also be used to control stray currents by electrically separating sections of pipeline.

The CP system must also be designed in such a way that it can be easily monitored and therefore test points are installed along the pipeline at intervals that are dependent on the location of the pipeline. An ideal spacing is every one to two kilometers, although often test points are located close to road crossings for ease of access and convenience. The test point consists of a wire connection from the pipeline to a test box that is usually located above ground so that measurements of current and voltage can be made to confirm that the pipeline is adequately protected. Additional test points are also located at other critical locations, for example, crossings, sources of external current (i.e., traction systems), and isolation joints.

#### 4.42.4.2.12 CP requirements

In order for CP to be effective, the current supplied to the pipeline must shift the potential at that pipe surface sufficiently negative such that the surface becomes the cathode in the corrosion cell and the anodic reactions are reduced or suppressed. Therefore, in order to ensure that the pipeline is protected to a level that will stop significant corrosion, it is necessary to set criteria for monitoring a pipeline to ensure that the protection levels are achieved. In this

respect, the current supplied is not a reliable measure of protection, as it can change with time and therefore protection criteria are based on a measure of the potential difference between the pipe and the soil as measured against a copper–copper sulfate reference electrode.

Both ISO 15589<sup>26</sup> and prEN 14919-1<sup>27</sup> state that for onshore buried pipelines, all parts of the pipeline should be polarized to a potential more negative than  $-850$  mV. This is the most widely accepted and common criterion and indicates that protection is achieved if the potential of the structure is more negative than  $-850$  mV when measured with a copper–copper sulfate reference electrode. The criterion is increased to  $-950$  mV if active bacterial or anaerobic conditions are suspected and can also be adjusted to account for low resistivity-soils or high temperature operation.

Another criterion that can be applied, typically to pipelines that have poor or aging coating systems, is the 100 mV polarization shift criterion. This criterion states that protection is achieved if the polarized potential is shifted at least 100 mV in the cathodic direction below the natural corrosion potential as illustrated in the schematic Evans Diagram of [Figure 9](#). Although this criterion may be easier and cheaper to achieve than the  $-850$  mV criterion for some pipeline systems, in order to apply the criterion successfully, a detailed characterization of the environment around the pipeline is required. In particular, this criterion should be avoided in anaerobic soils, where SRB activity is expected, or in regions affected

by interference currents or stray currents. In these types of environments, the 100 mV shift may not be sufficient to reduce the corrosion rate to acceptable levels and could result in the pipeline being in the critical range for high-pH SCC (see [Section 4.42.6.1.1](#)).

#### 4.42.4.2.13 CP shielding

In a discussion on CP effectiveness on pipelines, the subject of CP shielding should be included, as this phenomenon reduces the effectiveness of the CP and can cause a serious problem with respect to the detection of corrosion. Shielding in effect reduces the current flow to the pipeline, although measurements taken above the surface will indicate that the pipeline is still protected. The most common shielding situations are pipelines installed within a bare steel casing with the casing short-circuited to the pipe and pipelines under a disbonded coating. The latter situation was introduced in [Section 4.42.4.2.1](#) when coating adhesion was highlighted as a major requirement for a pipeline coating. When the coating becomes disbonded, sufficient CP may not be able to penetrate to the area of corrosion under the coating and protect the pipeline from corrosion.

#### 4.42.4.2.14 CP monitoring

To make sure that cathodic protection is achieved and continues to be achieved, the CP system should be regularly monitored. There are two levels of monitoring: regular equipment checks to ensure that the systems are operating and less regular surveys at fixed test points to ensure that protection is being achieved. These surveys involve measuring the pipe potential at every test point and then carrying out further surveys between test points and remedial action if the readings show inadequate protection.

However, before looking at the survey techniques, an initial explanation of pipeline potential measurements is required. There are essentially three potential measurements that can be made on a pipeline; the natural potential, the ON potential, and the OFF potential.

- *Natural potential*

The natural potential of the pipeline is the potential of the corroding pipeline with no protection current applied. Ideally, the natural potential should be measured before any current is applied to the pipeline either from a CP system or by the action of stray

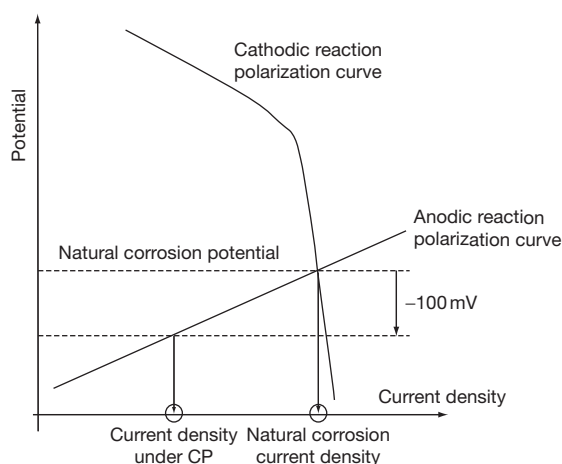


**Figure 9** Schematic Evans diagram illustrating the principle of the 100 mV CP criterion.

currents as these alter the natural current balance, which can then take weeks or months to recover. A reading of natural potential is required if the pipeline is going to be protected using the 100 mV shift criterion (see [Section 4.42.4.2.12](#)).

- *ON potential*

An ON potential reading is the potential measured on a pipeline at the above-ground surface once a CP current has been applied. The reading does not necessarily imply that CP has been achieved because of the errors that occur in the readings of CP and how they are taken. In effect, the measurement of potential on the surface above the pipeline with the CP system on is made up of two components as shown in the following equation:

$$V_s = V_p + V_{IR}$$

Where  $V_s$  is the measured potential at the surface,  $V_p$  is the actual potential at the pipe, and  $V_{IR}$ , sometimes termed the IR drop, is the potential drop associated with the flow of CP current through the soil of finite resistance and onto the pipeline. Therefore, although  $V_p$  is the reading that is required to determine whether CP criteria have been achieved on a pipeline, an ON potential reading is measuring  $V_s$ , which includes the IR drop. Therefore an ON potential reading will overestimate the level of CP on a pipeline, but if IR drops are known to be low, then it can provide an estimate of the amount of protection.

- *Instant OFF potentials*

One method adopted for assessing the true potential without the IR component is what is termed the Instant OFF polarized potential. This test is carried out by switching the CP system off and monitoring the potential of the structure before the potential has begun to decay significantly. There is no current flowing through the soil to the defect and thus the IR component or error in the potential reading will, for practical purposes, be almost eliminated.

#### **4.42.4.2.15 CP Monitoring: Close interval potential (CIPS or CIS) surveys**

This technique involves measuring ON and OFF potentials at close intervals over a pipeline, and hence, the method is often called a CIPS survey or close interval survey (CIS). The CP current is switched ON and OFF by inserting a timer switch at the rectifier and the switching cycle is set up so that the ON cycle is longer than the OFF cycle, by a typical ratio of 5:1, to avoid significant decay of the potential. The survey is conducted by attaching a

spool of very fine insulated wire to a pipeline test point terminal and connecting this to a test meter and a copper/copper sulfate half-cell, which is located in a pole that is carried by the operator. The survey operator then walks along the pipeline route taking ON and OFF potential readings with the half-cell, approximately every meter along the pipeline. Often two half-cells are used so that one is always in contact with the ground. Although ON and OFF potentials may be routinely measured at test posts, this type of survey allows the potential to be measured between test posts and can determine whether the pipeline is adequately protected along its length.

A CIPS or CIS survey is generally used to measure the effectiveness of the CP system, although it can also be used to locate coating defects using the same principle as the DC methods described in [Section 4.42.4.2.6](#). The basis of this technique is that a dip in the ON and OFF potential profiles along the pipeline provides an indication of the presence of a coating defect due to the loss of protection at that point.

#### **4.42.4.3 Assessing the External Corrosion Risk**

The preceding sections have served to outline the causes of external corrosion on buried pipelines and to describe how external corrosion is prevented and controlled. The knowledge of how and why external corrosion occurs also aids in identifying the key factors that are used in risk assessment strategies for external corrosion. On the basis of this review, a summary list of typical data that are required to assess the threat of external corrosion is presented in [Table 8](#). It can be seen that this list includes not only information about the environment of the pipeline but also information about how the pipeline is maintained in terms of the coating condition and the effectiveness of the CP. All these factors are then fed into the types of algorithms described in [Section 4.42.3](#) to rank the relative risk of external corrosion on the pipeline.

#### **4.42.5 Internal Pipeline Corrosion Risks**

The scope of this chapter has been limited to an investigation of corrosion in onshore gas and liquid transmission and gathering pipelines. For external corrosion, the type of pipeline, that is, transmission or gathering, is less relevant in determining whether

**Table 8** Summary of typical information required to assess the external corrosion threat

	<i>Data required to assess threat</i>	<i>Comment</i>
<i>Pipeline characteristics</i>	Age of pipeline Type of pipe	Could highlight a susceptibility to certain forms of corrosion (e.g., preferential corrosion).
<i>Coating information</i>	Coating type  Coating condition	Indicates the likely modes of coating failure and corrosion damage, for example, disbonding. Could either be a subjective view (i.e., good, average, poor, etc.) or a more quantitative measure gathered from coating monitoring surveys.
<i>CP information</i>	CP availability CP protection levels	Indicates the likelihood that damaged areas of coating are not protected. Could be subjective or determined from CP monitoring surveys.
<i>Pipeline environment</i>	Soil characteristics  Evidence of MIC  Potential sources of stray currents Potential sources of AC corrosion	Indicates the corrosivity of the soil and would include the type of soil as a minimum but could also include more detailed resistivity data, pH, bacterial levels. Usually evidence gathered during direct inspection although could also be implied from soil conditions. Would include data such as proximity of other pipelines, structures, rail crossings For example, proximity of overhead power lines
<i>Pipeline history</i>	Leak history Previous inspection reports	Provides more quantitative evidence of a corrosion threat

the pipeline will be susceptible to external corrosion. However, the type of pipeline becomes more significant when considering the threat of internal corrosion. Gathering systems are generally collecting product from a wellhead and transporting it to a processing plant or transmission pipeline. The fluid is not processed before it enters the gathering system and therefore the product can contain contaminants that increase the susceptibility to internal corrosion. However, the product in a transmission pipeline will have undergone basic or full product processing and therefore the internal corrosion threat is more controllable.

It should be highlighted at this stage that dry natural gas and moisture-free oil and petroleum products are not corrosive to carbon steel. It is only in the presence of water and contaminants such as chlorides, CO<sub>2</sub>, H<sub>2</sub>S, organic acids, bacteria, and oxygen that corrosion will occur. Internal corrosion of pipelines is generally classified as either sweet or sour depending on the level of H<sub>2</sub>S in the product.

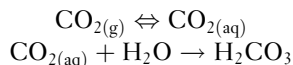
#### 4.42.5.1 Sweet or CO<sub>2</sub> Corrosion

Sweet corrosion of carbon steel occurs in the presence of free water that has been acidified by carbon dioxide present in the oil or gas. It is therefore important to note that sweet corrosion will not

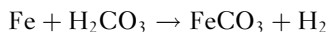
occur in the pipeline if free water is not present in the product, that is, dry CO<sub>2</sub> gas does not pose a corrosion threat to pipeline steel. Water in the pipeline can be present from different sources, depending on whether the pipeline is in the gathering or transmission system and what processing has been carried out.

In the gathering system, the pipeline is transporting product directly from the reservoir generally without any pretreatment. Therefore, water that is naturally present in the gas phase or water present in the rock pores, which is then mobilized with the oil or gas (formation water), can be present in the pipeline. Once the product has been processed, it is still possible for water to enter the transmission pipeline either as a result of water carryover from the separators or due to water dropping out or condensing from the product. Water drop out occurs in oil pipelines if water is entrained in the oil as an emulsion. During transport through the pipeline, the water can separate out of the emulsion as a distinct phase at the bottom of the pipeline. In gas pipelines, water can condense out of the gas phase (condensed water) if the temperature of the steel surface falls below the dew point of the gas. This type of corrosion is sometimes termed top-of-line (TOL) corrosion and tends to be a particular issue for subsea pipelines where exposed sections of the pipeline can be cooled by the sea.

The mechanism of CO<sub>2</sub> corrosion is complicated,<sup>28</sup> but initially the CO<sub>2</sub> gas dissolves in water to form carbonic acid according to the equation:



The carbonic acid then reacts with the steel according to the following reaction to produce iron carbonate and hydrogen.



Under favorable conditions, the iron carbonate can form a protective or semiprotective scale on the pipeline surface. It is the presence and stability of this film that determines the rate of general corrosion and can also dictate the susceptibility to localized attack by mechanisms such as pitting corrosion, preferential weld corrosion, and flow-induced localized corrosion (FILC).

Schmitt and Hörstemeier<sup>29</sup> have reviewed the parameters that influence the CO<sub>2</sub> corrosion mechanism and have concluded that the factors affecting the rate and nature of the CO<sub>2</sub> corrosion reaction can be divided into three categories: interface-related parameters (temperature, flow rate, condensation, and presence of scales), materials-related parameters (alloy composition, microstructure, and heat treatment) and medium-related parameters (pH, CO<sub>2</sub> partial pressure, solution chemistry, and oxygen content). The key parameters in this list are worthy of further discussion in relation to the factors that affect internal pipeline corrosion.

#### 4.42.5.1.1 Effect of temperature

Below 60 °C and at low levels of pH, the solubility of iron carbonate is high and the formation of a stable FeCO<sub>3</sub> film on the pipe surface is difficult. The rate of the reaction is controlled by the dissolution of iron and increases with increasing temperature. Above 60–80 °C, the solubility of iron carbonate decreases, allowing the formation of a more adherent, semiprotective scale of FeCO<sub>3</sub> on the surface and an overall reduction in the corrosion rate. It should be noted, however, that in order for the FeCO<sub>3</sub> scale to be effective in reducing corrosion rates, it must be adherent and cover the whole pipe surface. If the scale becomes damaged, for example, as a result of turbulent flow, then corrosion of the unprotected steel can occur at high rates. This gives rise to a particular type of localized corrosion called mesa corrosion, which is described in more detail in [Section 4.42.5.2.2](#).

#### 4.42.5.1.2 Effect of flow rate

As already mentioned, the corrosion rate for CO<sub>2</sub> corrosion is dependent on the ability of the system to establish and maintain a stable iron carbonate scale on the steel surface. If the flow velocity is greater than a certain critical value, then it is possible that the scale can be eroded by the turbulent conditions near the pipe wall. Under such flow conditions, the scale is unable to reform, resulting in unprotected areas of the pipe and therefore increased corrosion rates.

The flow rate can also affect the distribution of corrosion. As discussed previously, in oil pipelines it is possible that water is carried over into the pipeline entrained in an emulsion. In low-velocity or nonturbulent flow, the water will separate out of the emulsion and collect in pools, particularly at low points in the pipeline.

#### 4.42.5.1.3 Effect of pH

In general, the corrosion rate for CO<sub>2</sub> corrosion decreases as the pH increases. The pH is dependent on the type of free water present in the pipeline, that is, whether it is condensed water or formation water. Condensed water is relatively pure and therefore the pH is determined by the partial pressure of CO<sub>2</sub>; the higher the CO<sub>2</sub> concentration, the more acidic the water and the lower the pH. However, as the pipeline corrodes, the condensed water will become saturated with carbonate from the corrosion product and the pH will rise with a consequent reduction in the corrosion rate. Although the concentration of CO<sub>2</sub> in the product will also affect the pH of formation water, ionic species present in the rocks, (e.g., bicarbonate, chlorides, sulfates, etc.), which are in solution in the water, also influence the pH.

Another impact of the pH on sweet corrosion is that, as the pH of the water is increased, the solubility of iron carbonate is reduced and therefore the deposition of the protective scale on the steel surface becomes more favorable. This effect also reduces the corrosion rate.

#### 4.42.5.1.4 Effect of partial pressure of CO<sub>2</sub>

As the sweet corrosion reaction involves the dissolution of CO<sub>2</sub> in water to produce carbonic acid, the concentration of the acid produced is directly related to the concentration of CO<sub>2</sub> in the gas and therefore to the partial pressure of CO<sub>2</sub>. Consequently, the reaction rate will increase as the CO<sub>2</sub> partial pressure increases producing higher concentrations of carbonic acid and reducing the solution pH.



#### 4.42.5.1.5 Effect of H<sub>2</sub>S content

H<sub>2</sub>S can be present naturally in the reservoir or can be produced during the extraction process. The influence of small amounts of H<sub>2</sub>S (i.e., <0.0035 bar partial pressure H<sub>2</sub>S) on CO<sub>2</sub> corrosion is dependent on the concentration of H<sub>2</sub>S and whether iron sulfide can precipitate as a protective surface scale. At low concentrations of H<sub>2</sub>S and low values of pH, when iron sulfide precipitation does not occur, the experimental evidence is confusing and the mechanism by which H<sub>2</sub>S affects the corrosion rate is not well understood. For example, some studies indicate that the corrosion rate is increased compared with an equivalent H<sub>2</sub>S-free CO<sub>2</sub> corrosion environment,<sup>30</sup> while others suggest that small amounts of H<sub>2</sub>S could reduce the corrosion rate.<sup>31</sup>

As the H<sub>2</sub>S concentration increases the formation of the iron sulfide surface film becomes more favorable. The exact composition of the surface scale in slightly sour conditions is dependent on the CO<sub>2</sub>–H<sub>2</sub>S ratio. Iron sulfide scales are conductive and therefore make very efficient cathodes. However, if the scale becomes damaged, then small anodic areas can form, which can result in high pitting corrosion rates. At higher concentrations of H<sub>2</sub>S, that is, greater than 0.0035 bar partial pressure H<sub>2</sub>S, the mechanism of corrosion changes from one of general or pitting corrosion to cracking, and the product is termed sour. Sour cracking is discussed in more detail in [Section 4.42.5.3](#).

#### 4.42.5.2 CO<sub>2</sub> Corrosion – Localized Effects

The general corrosion rate for sweet corrosion is principally determined by the establishment of a scale of either iron carbonate or iron sulfide (depending on the H<sub>2</sub>S content) on the surface of the pipe. If this scale is not uniform or becomes damaged (e.g., due to erosion, shear stresses in the scale, scratching, or mechanical damage), then the underlying steel is locally unprotected and the pipeline becomes susceptible to localized attack. Particular forms of localized attack that are found in pipelines include pitting corrosion, mesa corrosion, FILC, and preferential corrosion.

##### 4.42.5.2.1 Pitting corrosion

The susceptibility of the pipeline steel to pitting corrosion increases with increasing temperature. As discussed previously, below 60 °C, the iron carbonate scale is thin and the protection that it provides to the steel is low. However, the scale becomes more stable

and adherent above 60 °C, and therefore, a reduction in corrosion rate is observed for general corrosion. However, if the scale becomes locally damaged, the steel is unprotected and CO<sub>2</sub> corrosion can occur at high rates, due to the increased temperature. It is therefore possible to observe localized pitting damage in pipelines operating above 60 °C.

##### 4.42.5.2.2 Mesa corrosion

Mesa corrosion is a form of CO<sub>2</sub> corrosion that occurs under conditions of high temperature (above 60–80 °C) and under enhanced flow rates. The morphology of the attack is characterized by steep-sided transitions from uncorroded to corroded areas similar to mesa formations in rocks. Mesa corrosion results from flow-induced spalling of the carbonate film due to internal stresses developed in the scale during its formation. The underlying, unprotected metal is then exposed and corrosion occurs at rates of up to several mm year<sup>-1</sup>, resulting in the formation of deep flat-bottomed, sharp-edged pits.<sup>29</sup> As a higher temperature is required than is normal for transmission pipelines, mesa corrosion is mainly found in gathering systems.

##### 4.42.5.2.3 Flow-induced localized corrosion (FILC)

FILC occurs in pipelines under conditions of local turbulence where the carbonate scale cannot reform. FILC is normally initiated at locations where the scale becomes cracked or spalled by the action of hydrodynamic forces induced by the local flow conditions. In order to fracture the scale, the hydrodynamic force must exceed the fracture stress of the scale. There is still debate in the literature with regard to the best way to quantify the hydrodynamic forces and therefore to determine the critical parameters under which FILC occurs.<sup>29</sup>

##### 4.42.5.2.4 Preferential weld corrosion

Another localized corrosion effect that has been observed in pipelines is preferential weld corrosion. It can occur at welded joints if a galvanic couple is established between the parent pipe and the weld heat-affected zone (HAZ) or weld metal due to local differences in composition. The susceptibility of a pipeline to preferential weld corrosion and the location and morphology of the corrosion are dependent on the environment (in terms of the nature of the scale that is formed); the microstructure and composition of the steel and the weld (in terms of the establishment of the galvanic couple and the general corrosion resistance of the material); and

local geometry effects (in terms of the establishment of regions of local turbulence). In terms of the corrosion theory, preferential weld corrosion occurs because the weld or HAZ material becomes anodic with respect to the parent material. Solutions to prevent this form of corrosion are therefore aimed at adding elements such as Cr, Ni, and Cu to the weld metal to make the weld more cathodic with respect to the parent.

#### 4.42.5.3 Sour Corrosion

The effect of low levels of  $H_2S$  on internal pipeline corrosion was described in [Section 4.42.5.1.5](#). In this section, a partial pressure of  $H_2S$  of 0.003 5 bar was defined as a threshold above which sour corrosion cracking mechanisms would dominate over sweet corrosion mechanisms. This limit has been defined in the standard NACE MR0175/ISO15156-2<sup>32</sup> and is presented in the form of a domain diagram that indicates the susceptibility to sour cracking on the basis of the local pH and partial pressure of  $H_2S$ . The diagram is divided into four domain areas; in domain zero, there is low risk from sour corrosion. However, as the partial pressure increases above 0.003 5 bar, decreasing the pH and/or increasing the pressure increases the severity of sour service damage from domain one (mild sour service) to domain three (severe sour service). It is critical that the susceptibility of a pipeline to sour service cracking is understood and quantified at the design stage as material choices have to be made to prevent rapid pipeline failure. Failure times as short as days or hours have been observed for sour corrosion mechanisms under test conditions. Material selection for sour service is discussed in [Section 4.42.5.4](#).

The principal mechanism of sour corrosion is hydrogen damage and the role of  $H_2S$  is to promote the penetration of atomic hydrogen, produced at the cathode, into the steel. As with sweet corrosion, sour corrosion mechanisms also require a source of water. When hydrogen diffuses into the steel matrix, it can either remain in solution in the steel lattice (hydrogen embrittlement) or recombine to form hydrogen gas (internal hydrogen pressure). The defects that are characteristic of sour service result from one of these two mechanisms; hydrogen embrittlement results in sulfide stress corrosion cracking (SSCC), whereas internal hydrogen pressure can result in hydrogen-induced cracking (HIC). Stress-orientated hydrogen-induced cracking (SOHIC) is thought to occur by a combination of the two mechanisms.

##### 4.42.5.3.1 Sulfide stress corrosion cracking (SSCC)

When atomic hydrogen diffuses into a steel matrix, it embrittles the material, reducing the ductility and the toughness of the material. Embrittled steel is less tolerant to defects and can readily crack, either under the action of an applied tensile stress (e.g., due to the internal pressure in the pipeline) or as a result of residual stresses in the pipe wall (e.g., as a result of welding). In a sour environment, this cracking is called SSCC. Weld areas are particularly susceptible to SSCC, as the welding can produce hard zones that embrittle more easily in a hydrogen environment.

Under test conditions, SSCC has been shown to cause failure within hours of exposure to the sour environment and therefore it is imperative that materials used in the pipeline construction have been selected appropriately and that welding procedures are designed to limit the hardness in the HAZ. Although postweld heat treatment may be applied to reduce the residual stress and temper any hard microstructures in the steel, this is not feasible for pipelines.

##### 4.42.5.3.2 Hydrogen-induced cracking (HIC)

Although there are differing theories in the literature, one mechanism for the formation of HIC is that atomic hydrogen diffuses into the steel and collects around nonmetallic inclusions, particularly sulfide laminations in the pipe wall. At these locations, the hydrogen atoms can recombine to form hydrogen gas. As hydrogen gas is unable to diffuse in steel, the hydrogen gas pressure in the internal voids builds up to such a high level that the steel can crack. This process is represented in [Figure 10](#). The cracks propagate away from the voids and the crack path is influenced by microstructure, particularly in rolled plate where the cracks run along the banded rolling microstructure, parallel to the pipe wall.

If HIC is initiated at different locations in the pipe wall, it is possible for the cracks to link up by growing at right angles to the pipe wall (i.e., in a radial direction). For this reason, HIC is sometimes referred to as stepwise cracking. In addition, if the inclusion is close to the pipe wall, the pressure of the hydrogen gas may be sufficient to cause local yielding and can result in visible blistering on the pipe surface.

As with SSCC, failure by HIC can be very rapid, and under test conditions, has been found to occur within days of exposure to a wet, sour environment.

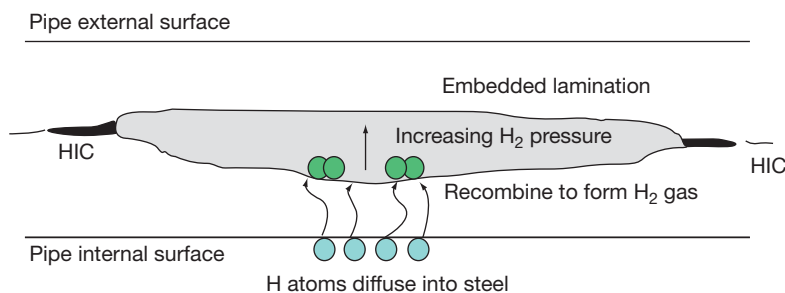


**Figure 10** Mechanism of HIC in pipeline steels.

#### 4.42.5.3.3 Stress-oriented HIC (SOHIC)

HIC is not influenced by the stress state of the pipeline. However, under the influence of either the operating stress or a residual stress, the HIC cracks can become aligned perpendicular to the principal stress direction in a characteristic array of small, staggered cracks. This type of cracking is known as Stress-oriented HIC (SOHIC).

#### 4.42.5.4 Material Selection for Sour Service

High-strength steels are more susceptible to hydrogen embrittlement and therefore cracking in a sour environment and consequently steels have to be selected to comply with maximum hardness levels to avoid cracking in both the parent and the weld material. The risk of sour service cracking such as HIC is also reduced by producing steels with the minimum of inclusions. This is achieved by using steel with very low sulfide concentrations to avoid the formation of MnS inclusions. In addition, the surface area of the inclusions is reduced by the addition of Rare Earth Metals (REMs) and calcium, which form spherical inclusions rather than elongated inclusions and therefore there is less inclusion area on which hydrogen can accumulate. Suitable pipeline materials for use in sour service are specified in the International Standard NACE MR0175/ISO15156-2:2003.<sup>32</sup>

#### 4.42.5.5 Microbiologically Induced Corrosion

The final type of internal pipeline corrosion to be considered here is MIC. This type of corrosion was described earlier with respect to microbe activity in soil resulting in external MIC (Section 4.42.4.1.2). However, SRBs can also be present in the reservoir and can be carried over into the pipeline if the system is not properly treated with an appropriate biocide.

SRBs can cause MIC and can also increase the H<sub>2</sub>S content in the product. SRBs that appear in reservoirs over time are usually due to the contamination of the reservoir during completion or water injection.

#### 4.42.5.6 Internal Corrosion: Prevention

In the control of external corrosion, the principle of protection is based on the combination of a pipeline coating, to prevent the electrolyte from contacting the pipe wall and to restrict the flow of the corrosion current, and CP, to make the pipeline the cathode in the corrosion cell. The rationale for corrosion protection of pipelines from internal corrosion is principally to accept that corrosion is going to occur if water cannot be removed from the system but to take steps to reduce the corrosion rate or to allow for corrosion within the pipeline design. The latter step is provided by the use of a corrosion allowance or by using more corrosion-resistant alloys and the former could include such measures as product treatment, inhibition, and internal coating. These strategies are discussed in more detail in the following sections.

##### 4.42.5.6.1 Corrosion allowance

A corrosion allowance is additional material that is added to the pipe wall thickness to allow for predictable, in-service corrosion. The corrosion allowance in pipeline design is calculated by predicting the corrosion rate in the pipeline, taking into account the anticipated effectiveness of other corrosion control strategies, and allowing for that amount of controlled, uniform wastage of the pipe wall over the design life of the pipeline. In practice, typical corrosion allowances for carbon steel are between 3 and 5 mm.<sup>33</sup> However, in situations where the corrosion rate is predicted to be high, the use of a corrosion allowance may not be viable due to the cost of the extra material required.

Strictly speaking, providing a corrosion allowance is not a corrosion prevention method as corrosion is still assumed to continue, but it can increase the design life of a pipeline that is susceptible to internal corrosion.

#### 4.42.5.6.2 Corrosion-resistant alloys

For pipelines that are transporting unprocessed product over short distances, the use of a corrosion-resistant alloy may be feasible. Chromium is the most commonly used alloying element for steel to improve the corrosion resistance in wet CO<sub>2</sub> environments. Even at low levels (0.5 – 1%Cr), there have been reports of improvements in corrosion resistance, an observation that is thought to be due to the fact that Cr acts to stabilize the iron carbonate film. Higher additions of Cr and Ni, as in stainless steels, can make the steel resistant to CO<sub>2</sub> corrosion and the improved corrosion resistance in these cases is due to the formation of a chromium oxide scale on the surface. However, as with all surface scales, if the scale becomes damaged and is not reformed, the pipeline becomes susceptible to pitting corrosion. For stainless steels, the presence of high levels of chloride can result in pitting corrosion.

Although the use of more corrosion-resistant alloys may be viable for short lengths of pipeline, for transmission pipelines, it is not an economical solution to internal corrosion, and carbon steel is the construction material that is used. However, for transmission pipelines, there is the opportunity to process the fluid and to add chemical inhibitors to reduce the corrosion rate.

#### 4.42.5.6.3 Coatings

Internal coatings are used particularly in gas pipelines to improve pipeline flow efficiency by reducing frictional losses. However, it is also possible to use internal coatings to protect the pipeline if it is going to be transporting a highly corrosive product. Either the coating can be applied in the mill with the girth welds coated after construction or the entire pipeline can be coated *in situ* by introducing the coating medium between cleaning tools after the pipeline has been constructed.

It is recalled that for external corrosion protection, both pipeline coating and CP are applied to control corrosion, as it is impossible to maintain a coating in a defect-free condition. The problem with relying on a coating to provide internal corrosion protection is that, where the coating becomes damaged, corrosion could occur very rapidly and therefore these areas of

damage have to be protected. Coatings should therefore be used in conjunction with inhibitors to reduce the corrosion rate at the sites of damaged coating.

#### 4.42.5.6.4 Product treatment

Based on the descriptions of both sweet and sour corrosion, it can be stated that pipeline internal corrosion will not occur if water is not present. Therefore, one of the key corrosion prevention strategies is to remove water from the product prior to pipeline transportation. The decision to use dehydration obviously carries a cost penalty and provision must also be made for upsets in the water separation and dehydration systems to prevent significant internal corrosion under these conditions.

Another treatment that can be applied to the product is pH control. It was mentioned in [Section 4.42.5.1.3](#) that the corrosion rate decreases as the pH increases, and therefore, the addition of alkaline additives to raise the pH can be used to control corrosion.

Large quantities of glycol or methanol are often introduced into wet gas-producing systems to prevent and control hydrate formation, which can cause plugging problems. Both of these chemicals, if present in sufficient concentrations, can also reduce CO<sub>2</sub> corrosion rates.

#### 4.42.5.6.5 Inhibitors

Inhibitors are principally used for the control of general corrosion in sweet environments. However, there are packages available for the control of mesa type corrosion and pitting corrosion in both sweet and sour environments. The selection of an inhibitor to adequately protect a pipeline requires consideration of a number of interrelated factors. Detailed information on the use of inhibitors can be found in texts such as the European Federation of Corrosion publication.<sup>33</sup> However, the key factors and considerations with respect to pipelines are discussed in the following sections.

Corrosion inhibitors used in hydrocarbon pipelines are generally long-chain nitrogen-based compounds (e.g., amines, amides), but they can also be organophosphates. These compounds have a charged surface-active group and a hydrocarbon chain. The surface-active groups are attracted to the pipe wall where they become physically adsorbed and then chemisorbed onto the surface as charge transfer with the pipe wall occurs and a chemical bond is formed. In oil pipelines, the hydrocarbon chains in the inhibitor molecules mean that the inhibitor becomes partially oil soluble and therefore forms a

hydrophobic barrier between the steel and the water phase. The principle of inhibition is therefore two-fold: the removal of water from the pipe surface through the formation of a stable film and the modification of the surface potential, inhibiting both the anodic and cathodic reactions. In addition to the active species, the inhibitor will also include a solvent carrier fluid and other additives, such as surfactants to optimize the delivery and storage properties of the inhibitor.

It is highlighted that inhibitors do not stop corrosion but the aim of inhibition is to reduce the corrosion rates to manageable levels. The effectiveness of the inhibitor regime is measured by the efficiency, which is defined as:

%Inhibitor Efficiency

$$= \left[ 1.00 - \frac{\text{Weight loss (with inhibitor)}}{\text{Weight loss (without inhibitor)}} \right] \times 100$$

Although laboratory tests have shown that efficiencies of more than 95% can be achieved, in practice, most operators achieve an inhibitor efficiency of 80–90%,<sup>33</sup> although higher efficiencies may be expected if the inhibitor has been carefully selected.

In order for an inhibitor to be effective, it must be dispersed to those surfaces that are wet by water and must be able to establish and maintain a protective film at that location. The transport of the inhibitor to all corroding sections along the full length of the pipeline is therefore important, whether the corrosion is at the bottom of the pipeline due to water drop out or at the top of the pipeline due to condensation (Section 4.42.5.1), at the start of the line or toward the end of the line. There are two main methods for introducing inhibitor into the pipeline: continuous injection and batching.

In continuous injection, the inhibitor is dispersed by the flowing product. For gas pipelines, this requires the inhibitor to be injected either as a separate liquid phase or as droplets entrained within the gas phase. However, the distance of travel of the inhibitor is limited using this method and therefore inhibition is not really a viable corrosion control option for gas pipelines. Continuous injection is more generally used for multiphase pipelines or pipelines containing crude oil and condensate where the transport of the inhibitor is in the liquid phase. In this situation, the inhibitor type has to be specified depending on the particular conditions and whether the inhibitor is required to be soluble in the oil or water phases in the carrier fluid.

In batch treatment, the inhibitor is introduced into the pipeline as a slug between two cleaning tools and is used in situations where continuous injection may not be an option or where TOL corrosion is expected and the flow regime does not allow the transport of inhibitor to this location by continuous injection. The frequency of batching is dependent on the inhibitor and the flow conditions in the pipeline.

Another important factor that has to be considered in the specification of an inhibitor is the dosing rate. The dose rate has to be monitored continuously to ensure that sufficient inhibitor is being injected to account for changes in water concentration in the pipeline. The dose rate is also dependent on how the inhibitor partitions between the oil and water phases. The aim is to obtain a sufficient concentration of the inhibitor in the water phase at the location of the corrosion and it is this concentration that must remain constant through the adjustment of the amount of inhibitor injected into the pipeline.

The performance and effectiveness of an inhibitor is also dependent on other factors such as the flow rate (turbulent flow can prevent the inhibitor film from forming or can strip the film from the pipe wall), temperature, composition of the product, interaction with other chemical additions, and pressure. These factors can change throughout the life of the pipeline and particularly during upset conditions, and therefore, it is important that continuous monitoring is employed to ensure that adequate inhibition is being achieved.

#### 4.42.5.7 Internal Corrosion Monitoring

Internal corrosion monitoring can either be used to determine the effectiveness of the corrosion prevention strategies and to detect any upset conditions that could increase the corrosion rate in the pipeline, or to take measurements of corrosion rate. In practice, it is recommended that more than one technique is used and that monitoring is not reliant on only one type of measurement.

The types of monitoring used to determine whether corrosion prevention is being achieved include measurements of water content and chemistry, inhibitor availability, inhibitor dose rate, and inhibitor residuals (i.e., estimates of the concentration of inhibitor in the water phase). However, while these techniques may indicate that the pipeline is corroding, they will give no information on the rate of corrosion or location of that corrosion. Iron counts (i.e., measurements of the amount of iron entering the water phase as a result of



corrosion) can also be used to indicate the effectiveness of the inhibitor program but it is not possible to determine whether the increased iron content is as a result of localized pitting or general corrosion, and therefore, calculating realistic corrosion rates using this method is difficult.

There are therefore alternative monitoring techniques that can be used to provide an indication of corrosion rate. These include weight loss corrosion coupons and probes that are inserted into the pipeline through hot tap fittings or through valves and access points. Immediately, this highlights one of the limitations of this type of monitoring: a measurement is only available at the location of the probe and this location is often selected due to ease of access rather than corrosion risk. The selection of appropriate locations for monitoring equipment should be made through evaluation of the pipeline operation and route and considering such factors as low points, flow regimes, temperature, and potential localized corrosion effects.

Coupons are the oldest method of monitoring corrosion. They are strip or disk-shaped coupons manufactured from the same steel as the pipe wall. The coupon is weighed and inserted into the process stream. At regular intervals, the coupon is then removed and weighed to determine the amount of weight loss since the last measurement, which will determine the average corrosion rate over that time period. The coupon can also provide useful information regarding deposits,

fouling, and localized corrosion that may be occurring in the pipeline.

There are several types of insert probes that are available, that are based on measurements of changing ER probes or linear polarization resistance measurements (LPR probes). ER probes can provide a measurement of the average corrosion resistance, whereas LPR probes have the advantage of providing instantaneous data. The disadvantage of LPR probes is that they need to be immersed in a conductive medium, which in practice means the water phase.

Other monitoring techniques that can be used include specially instrumented pipeline spools and ultrasonic mats. However, with these techniques, it is critical that the equipment is placed in the locations at highest risk of internal corrosion to ensure that relevant readings are taken.

#### 4.42.5.8 Assessing the Internal Corrosion Risk

The preceding sections have identified the types of data that are required to assess the risk of sweet and sour internal corrosion in pipelines, both from the point of view of the factors that contribute to the threat and also in respect of the prevention and monitoring activities that are conducted by the pipeline operator. A summary table of the type of data required is presented in [Table 9](#). As with the external

**Table 9** Summary of typical information required to assess the internal corrosion threat

	<i>Data required to assess threat</i>	<i>Comment</i>
<i>Pipeline characteristics</i>	Pipe and weld material	Could highlight a susceptibility to certain forms of corrosion (e.g., preferential weld corrosion) and is also required to determine suitability for sour service.
	Pipeline type	For example, whether the pipeline is a gathering or transmission line could indicate how much preprocessing has been conducted on the product.
<i>Pipeline operation</i>	Flow regime	Indicates the susceptibility to mesa or FILC corrosion.
	Upset conditions	Indicates how likely water is to enter into the pipeline.
<i>Product data</i>	Product analysis	Indicates susceptibility to sweet or sour corrosion and likely corrosion rates. Could include such information as water content, pH, CO <sub>2</sub> partial pressure, H <sub>2</sub> S partial pressure, O <sub>2</sub> content.
	Temperature	With product analysis data, indicates typical corrosion rate and also the likelihood of scale formation and therefore susceptibility to certain types of corrosion.
	Inhibitor efficiency Inhibitor availability	Indicates whether the inhibitor is likely to have been adequately protecting the pipeline and therefore the period over which corrosion could occur.
<i>Monitoring information</i>	Coupon and probe data	Provides information on the likely corrosion rates in the pipeline.
	Leak history Previous inspection reports	Provides more quantitative evidence of a corrosion threat.

corrosion threat, this information can be used in semiquantitative risk assessment algorithms to determine how susceptible a pipeline may be to internal corrosion.

#### 4.42.6 External SCC Risks

Although pipeline failures due to external SCC are relatively rare, it is worth including a brief description of this threat in a discussion of pipeline corrosion. OPS statistics indicate that only 1% of reported incidents in North American transmission and gathering pipelines (natural gas and hazardous liquids) between 1985 and 1996<sup>34,35</sup> have resulted from SCC. However, for specific pipelines, SCC can be the dominant failure mechanism and the consequences can be extremely serious. Although many of the reportable incidents of SCC have occurred in gas pipelines, failures have also been reported on liquid pipelines<sup>36</sup> and almost all cases of SCC have been encountered in pipe installed for more than 10 years with no failures reported to date for pipe that is less than 5 years old.

Two forms of external SCC have been identified on high-pressure gas transmission pipelines; high-pH SCC and near-neutral pH SCC. High-pH SCC was responsible for the first recognized failure due to SCC, in Louisiana in 1965, and incidents of this form of cracking have since been reported in Australia, Iran, Iraq, Italy, Pakistan, and Saudi Arabia. Near-neutral pH SCC was first identified in 1985 and has typically been associated with incidents in northern climates such as northern United States, Canada, and Russia.

For either form of SCC to occur in a pipeline, a complex array of conditions must be met including a critical combination of operating stress and stress cycling, faults in both the protective coating and the applied CP, a susceptible steel, and moisture at the pipe surface.

##### 4.42.6.1 Nature and Occurrence of SCC

SCC is a corrosion process in which the form or geometry of the corrosion is strongly influenced by stress. As a result, the corrosion process creates linear, crack-like defects rather than rounded corrosion pits or general metal wastage. The stress corrosion cracks grow at right angles to the principal stress, and hence, on an operational pipeline, where the principal stress is generated by internal pressure, it is most usual for the cracks to be aligned parallel to the axis of the pipeline. However, a number of instances of circumferential SCC have also occurred where high axial

stresses have been developed due to geotechnical instabilities.<sup>37</sup>

##### 4.42.6.1.1 High-pH SCC

High-pH SCC is the most common mode of SCC and is characterized by intergranular cracking, following the grain boundaries within the steel microstructure. Weak points or areas of damage of the protective magnetite iron oxide film ( $\text{Fe}_3\text{O}_4$ ) that forms on the steel surface, particularly at grain boundaries, are preferential sites for corrosion and crack-like features are formed at these locations. One theory for the mechanism of grain boundary cracking is that the grain boundaries act as stress raisers causing the oxide film to crack at these locations under the influence of a cyclic stress. In the alkaline environment of high-pH SCC, active dissolution will then occur at grain boundaries where the steel may also be less corrosion resistant due to grain boundary segregation. The water in the region of the crack is generally found to be alkaline with a pH above 10.

In order for SCC to occur, three conditions must be satisfied concurrently: there must be a tensile stress, a cracking environment, and a material that is susceptible to cracking in that environment. The factors that affect these conditions are discussed under these three headings:

- *Effect of stress*

It is generally accepted that there is a threshold stress, below which stress corrosion cracks will not occur. In the absence of a sustained cyclic stress, the threshold stress approaches yield. However, incidents of high-pH SCC in the US have generally been observed in pipelines where the combined stress level (i.e., from internal pressure and secondary loading) is above 60% of the minimum yield stress of the material.

An alternating stress on the pipeline has two effects in contributing to high-pH SCC failure: first, it reduces the threshold stress for crack initiation, and second, it damages the protective oxide film, preventing it from reforming and allowing the SCC to propagate.

- *Effect of environment*

High-pH SCC is generally found in areas where the CP is working and occurs in otherwise unaffected pipe with little or no associated corrosion. This is principally due to the formation of the magnetite film under the high pH conditions. However, there is a critical potential for high-pH SCC cracking, which is dependent both on the temperature and on the pH level. Typically, cracking occurs at potentials

$\sim -750$  mV with respect to a standard copper/copper sulfate electrode and the range over which cracking will occur is  $\sim 100$  mV. This means that the critical potentials are less negative than the generally accepted requirement of  $-850$  mV for effective CP of a pipeline (see [Section 4.42.4.2.12](#)). It is therefore important that the CP protection criteria selected do not allow the potential to drop into the cracking region. It was highlighted in [Section 4.42.4.2.12](#) that this is of particular concern if the 100 mV shift criterion is used. In addition, the coating should be well maintained to prevent areas of disbonding, which could partially shield the pipe and lower the potential.

Although there has been no reported correlation between soil chemistry and the occurrence of high-pH SCC, it has been observed that pipelines that are located in soils that are alternately wet and dry are more susceptible. Areas that are continually wet, such as in rivers or lakes, have not experienced SCC to the same extent as has occurred on the edges of streams or lakes.

Temperature has an effect on the growth rate of high-pH SCC and also influences the range of potentials over which cracking will occur. There is also an observed relationship between the occurrence of high-pH SCC and the distance from a compressor station. Most severe cracking is generally found within  $\sim 5$  km of compressor outlets and falls to a low level at  $\sim 16$  km. Although there are other factors that could contribute to this observation, such as alternating stresses, one of the contributors could be temperature as the temperature of the product is raised as it passes through the compressor station.

Although the pipe coating does not have a direct influence on high-pH SCC initiation and growth, the coating properties do influence the formation of an environment and a potential conducive to cracking. High-pH SCC will only occur in pipelines where the coating has failed in some manner. The likelihood of coating failure and disbondment is increased at higher temperatures, which could also be a contributing factor to the observed increase in cracking incidences close to compressor stations. It is highlighted that no SCC has been found to date under undamaged FBE coatings.<sup>38</sup> However, further experience with the use of FBE may be required before it can be concluded that this coating provides resistance to SCC.

- *Effect of material*

There is no apparent correlation between pipe grade or manufacturing process and the risk of high-pH SCC. However, grit blasting of the surface to remove

surface scale has been shown to avoid or delay the onset of cracking. Firstly, this relates to the cracking potential; if the steel is clean, then it is difficult to maintain the potential in the cracking range. Secondly, if the surface is grit blasted, then the coating will also adhere more easily, and finally, grit blasting will leave the surface in a state of compression and therefore more resistant to crack initiation.

#### 4.42.6.1.2 Near-neutral pH SCC

Near-neutral pH SCC is characterized by a transgranular mode of cracking, where the cracks grow through the grain structure without following boundaries. These cracks also initiate at the pipe wall and form in clusters, often more closely spaced than is the case for high-pH SCC. However, in contrast to the tight nature of high-pH SCC, near-neutral cracking tends to be wider and more open and is often filled with corrosion product. The water surrounding the crack appears to be neutral with a pH  $\sim 7$ . The mechanism of near-neutral pH SCC is still a subject of research but is thought to involve both the dissolution of oxide films and hydrogen embrittlement. Near-neutral pH SCC is often associated with general pitting or metal loss and the cracks can sometimes be embedded within corrosion pits, which can make detection difficult. It is also often, but not always, associated with welds.

As with high-pH SCC, the cracking requires a combination of stress, environment, and material.

- *Effect of stress*

Near-neutral pH SCC requires a tensile stress acting on the pipeline. In addition, stress raisers and residual stresses are also thought to play a significant role in the initiation of near-neutral pH SCC. Pressure cycling has also been shown to influence both the rate of crack growth and the threshold stress for near-neutral pH.

- *Effect of environment*

Laboratory tests indicate that near-neutral SCC occurs at or near the free corrosion potential for steel. Cracking only occurs therefore in pipelines where there is inadequate CP or where the pipe is shielded from the CP, for example, by a disbonded coating.

As with high-pH SCC therefore, the role of the coating is to enable the cracking environment to be developed at the pipe surface. The majority of failures have occurred on pipelines with field-applied PE tape. The coating failure mode is thought to

influence the crack development. For example, tenting of the coating over the long seam creates a long narrow zone in which cracks can easily coalesce and link up. Disbonding of coal tar coating tends to be localized around a defect and any resulting crack cluster is shorter and broader.

The composition of the soil does not seem to be critical to this type of cracking, although the amount of carbon dioxide in solution does appear to be important. For this reason, cracking generally occurs in colder climates where the carbon dioxide levels are higher. High levels of carbon dioxide are particularly found in winter under frozen surfaces.

There does not appear to be any relationship between temperature and the initiation and growth of near-neutral SCC. Therefore, with respect to temperature, there is no equivalent correlation between the incidence of cracking and the distance from compressor station as there is with high-pH SCC. It is possible, however, that the increased stresses close to compressor stations may be a contributing factor in near-neutral SCC.

- *Effect of material*

Near-neutral pH SCC has been identified in a range of steel grades and manufacturing routes. Research has shown that important material factors that correlated with the incidence of near-neutral pH SCC were residual stress, local increases in microhardness, and increased surface roughness. However, no correlation was reported with chemical composition, inclusions, and stress strain behavior. Surface preparation prior to coating application is less critical to near-neutral pH SCC than for high-pH SCC.

#### 4.42.6.2 Assessing the SCC Risk

The preceding sections have described the critical risk factors that render a pipeline susceptible to high-pH SCC. On the basis of these criteria, ASME B31.8S<sup>18</sup> Appendix A3.3 has defined the areas of a pipeline at greatest risk as

- the pipeline operating stress is greater than 60% of the minimum yield stress of the steel;
- the operating temperature is greater than 37 °C;
- the distance from a compressor station is <32 km;
- the pipeline is older than 10 years; and
- the pipeline coating is not FBE.

These criteria have also been adopted by the NACE Recommended Practice NACE RP0204<sup>38</sup> to identify

areas of greatest risk from near-neutral pH SCC, although the temperature criterion has been removed. In addition, if there has been one or more service incidents or hydrotest leaks that were attributable to SCC, then a SCC integrity management plan has to be put in place.

#### 4.42.7 Corrosion Inspection Techniques

In [Section 4.42.3](#), the concept of using risk assessment procedures to identify the critical pipeline threats was introduced. The following sections then detailed the principal internal and external corrosion mechanisms that can be present on onshore pipelines and detailed some of the risk factors that are used in risk assessments.

Once the risk of a particular corrosion mechanism or threat has been highlighted, the next stage in the process ([Figure 3](#)) is to inspect the pipeline to confirm or otherwise the existence of the threat, locate the damage and, if possible, identify the extent of the damage. The type of inspection method that is used is dependent on the type of corrosion or cracking and the accessibility of the pipeline for that inspection technique.

Three inspection methods that can be used for the inspection of corrosion-related threats in onshore pipelines are discussed in the following sections. It is highlighted that more than one inspection technique may be required to identify all the corrosion threats on a pipeline and when a particular inspection method has identified the location of damage, further nondestructive evaluation may be required to fully categorize the damage.

##### 4.42.7.1 In-Line Inspection

In-line inspection (ILI) is an inspection method that can locate and size defects on a pipeline, not only corrosion defects but also defects arising from manufacturing, construction, and mechanical damage. There are two basic technologies that are used for the detection of corrosion on pipelines using ILI tools: magnetic flux leakage (MFL) and ultrasonics (UT). The ILI tools are inserted into the pipeline through specially designed traps and the majority are free-swimming tools that are propelled by the flow of the product in the pipeline. This is one of the advantages of ILI over some other inspection methods in that the product flow does not have to be interrupted to conduct the assessment.

#### 4.42.7.1.1 MFL for corrosion

MFL tools detect defects by the application of a magnetic field in either the longitudinal or circumferential direction. As the tool travels through the pipeline, powerful permanent magnets magnetize the surrounding metal via wire brushes that contact the pipe wall. Sensors surrounding the circumference of the tool record the change in the magnetic field. This change in magnetic field can then be related to metal loss defect dimensions, using algorithms developed from test runs in pipes with machined defects of known dimensions. It is important to note therefore that the tools using MFL technology do not make direct measurements of remaining wall thickness.

As already mentioned, the magnetic field can be orientated either in the axial direction, to detect corrosion with a larger circumferential aspect ratio, or in the circumferential direction, to detect corrosion with more of a longitudinal extent. Examples of longitudinal corrosion would include internal sweet corrosion caused by water drop out or external axially extended corrosion caused by loss of coating adhesion around the longitudinal seam weld.

MFL tools can be used to inspect both liquid and gas pipelines and can discriminate between internal and external corrosion. The accuracy of sizing of the defects is dependent on the geometry of the features and the resolution of the tool.

#### 4.42.7.1.2 Ultrasonic wall thickness measurement (USWM)

USWM tools are based on a system that uses the ultrasound echo time technique to measure the remaining wall thickness of pipes by sending an ultrasonic beam at  $90^\circ$  through the pipe wall. The inspection tool has a number of ultrasonic sensors mounted in a carrier and orientated such that they provide maximum coverage of the pipe wall. The sensors act as both transmitters and receivers of the ultrasound. Once the ultrasound leaves the sensor, it is reflected from both the inner and outer surfaces of the pipe wall (Figure 11). If there is a defect in the pipeline, then the ultrasound will be reflected from the defect and the time between the sound leaving and returning to the sensor is a direct measurement of the remaining wall thickness at that location. The difference in the stand-off distance (i.e., the distance between the sensor and the pipe wall) at the location of the defect indicates whether the corrosion is internal or external. USWM can also detect HIC cracking in pipelines where the HIC is running parallel to

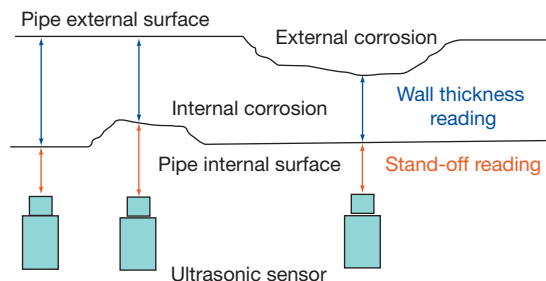


Figure 11 Principle of operation of USWM.

the pipe wall. For example, in the illustration in Figure 10, ultrasound traveling at  $90^\circ$  to the pipe wall will be reflected by the HIC.

One of the main limitations of ultrasonic inspection tools is that they can only be used in liquid pipelines as a liquid couplant is required between the sensor and the pipe wall to allow the ultrasound to travel into the pipe wall. If ultrasonic ILI is to be conducted in a gas pipeline, then the tool must be run in a liquid slug.

#### 4.42.7.1.3 ILI for crack detection

Although the ILI tools described earlier can detect metal loss features and a limited amount of cracking, in order to identify SCC and certain types of sour cracking, a separate crack detection inspection must be undertaken.

For liquid pipelines, ultrasonic crack detection (USCD) is the most appropriate tool. The principle of the inspection is similar to USWM except that the pulses of ultrasound emitted by the tool are directed circumferentially into the pipe wall at an angle that generates  $45^\circ$  shear-waves within the metal. The angle of incidence means that the beam is reflected and diffracted from axially aligned cracking.

For gas pipelines, using the USCD tool would require the inspection tool to be run in a liquid slug. Therefore, the most appropriate inspection tool for gas pipelines uses electromagnetic acoustic technology (EMAT). EMAT allows ultrasound to be generated in a steel pipe wall without the requirement for a liquid couplant to transfer the ultrasound into the steel. A magnetic field is established in the pipe wall using magnets. A coil carrying AC current at  $90^\circ$  to the magnetic field produces eddy currents in the pipe wall. A force normal to the pipe wall is exerted on the eddy currents, which generates ultrasound traveling through the pipe wall.



#### 4.42.7.1.4 Benefits of in-line inspection

The main benefit of ILI is that no interruption to the flow of product is required to inspect the pipeline and it is possible to obtain data for the entire length of the pipeline. Besides providing information on the defect sizes, an ILI inspection will also allow patterns of corrosion activity to be identified that assist in the diagnosis of the corrosion problem. For example, a clustering of external corrosion features around girth welds could highlight a problem with the girth weld coating. If this information was combined with above-ground survey data that indicated that there were no defects in the coating and that the CP was adequately protecting the pipeline, then this pattern could further indicate that there was a potential disbonding problem with the coating. Another benefit of ILI is that corrosion growth studies can be conducted using the data from two inspection runs and comparing the sizes of defects between the two data sets. This type of analysis allows corrosion rates to be calculated for internal and external corrosion features at different locations along the pipeline.

#### 4.42.7.2 Hydrotesting

It is a requirement of commissioning that all pipelines undergo a hydrotest at a pressure above the maximum allowable operating pressure prior to entering service. The major aim of the pressure test is to prove the integrity of the pipeline by deliberately testing to a pressure higher than the operating pressure. As a result, all defects large enough to cause failure during service are removed. The test pressure and the duration of the test are specified in pipeline design codes and are dependent on the product and the location of the pipeline. It is also possible to conduct a hydrotest during the operating life of the pipeline with the same aim, to remove defects that would fail at the operating pressure.

There are several factors that have to be considered before selecting a hydrotest as the optimum method for assessing the integrity of the pipeline. Firstly, the pipeline has to be taken out of service and filled with water, which can be a time-consuming and costly process. If not properly removed, the hydrotest water can also cause internal corrosion and therefore it is imperative that the pipeline is properly dried following the test. Another drawback of this test is that the criterion for determining whether the pipeline is safe is pipeline failure. For buried onshore pipelines, locating the leaking defect and repairing it is not an inexpensive or trivial task. Finally,

the hydrotest will only identify those defects that were unacceptable on the day of the test. For time-dependent defects, such as corrosion or SCC, the test interval has to be selected such that defects that pass the test will not grow to an unacceptable size prior to the next test.

#### 4.42.7.3 Direct Assessment

Direct assessment is defined in ASME B31.8S<sup>18</sup> as “an integrity assessment method utilizing a structured process through which the operator is able to integrate knowledge of the physical characteristics and operating history of a pipeline system or segment with the results of inspection, examination, and evaluation in order to determine the integrity.” Currently, this standard allows direct assessment methods to be used to assess the pipeline integrity with respect to external corrosion (ECDA), internal corrosion (ICDA), or stress corrosion cracking (SCCDA).

In practice, direct assessment involves remotely identifying or predicting the locations along the pipeline where the risk of damage from a particular threat is high. Depending on the threat, this identification can utilize techniques such as above-ground corrosion monitoring (see [Sections 4.42.4.2.5 and 4.42.4.2.15](#)), hydraulic analysis, predictive models, and operator experience. Direct field measurements are then made at the high-risk locations by excavating the pipeline at these sites and using standard non-destructive inspection techniques such as visual examination, magnetic particle flaw detection, and ultrasonic inspection to size and assess the damage. These results are then fed back into the assessment procedure to determine whether further sites require excavation, to assess the integrity of the pipeline and to set the reinspection interval for the next direct assessment.

If an operator is to apply the direct assessment process, he/she has to develop a direct assessment plan, the requirements of which are dependent on the threat being addressed. Obviously, the highest resolution direct assessment that can be achieved is to excavate an entire pipeline segment and apply direct examination techniques, but this would also be extremely costly and in some cases impractical. However, direct assessment approaches do allow the pipeline operator to draw conclusions regarding the integrity of the pipeline from a limited number of excavations and supporting data (e.g., above-ground survey data, predictive models) for the remainder of the pipeline that is not excavated.

Direct assessment principally finds application for both liquid and gas pipelines that are uninspectable by ILI or where the supply of product cannot be interrupted to conduct a hydrotest or to allow pipeline modification for internal inspection.

#### **4.42.7.3.1 External corrosion direct assessment (ECDA)**

The objective of direct assessment for external corrosion is to locate areas along the pipeline where the coating has become damaged and the CP system is not effective, that is, areas where active external corrosion could be occurring. The process is conducted in four stages: preassessment, indirect examination, direct examination, and postassessment.

The first stage is essentially confirming that ECDA is feasible for the pipeline and selecting appropriate above-ground methods for locating areas of corrosion damage. For example, it was described in [Section 4.42.4.2.13](#) how above-ground methods cannot be used in locations where disbanded coatings result in electrical shielding of the pipeline. In these locations, alternative methods of pipeline assessment must be used and these must be defined in the preassessment stage. In the indirect examination, the pipeline is inspected at least twice using two above-ground survey techniques, for example, a CIPS survey can be used to locate regions of underprotection in the CP and a DCVG survey could locate regions of coating damage. The reason that two complementary techniques are used is to ensure that the strengths of one tool compensate for the limitations of another. The results of these two surveys are then aligned to identify regions where the CP and/or the coating are failing. These areas would then be classified and the most severe areas would be subjected to direct examination by exposing the pipeline.

During the direct examination stage, measurements are taken of the pipeline environment and CP, the coating, the corrosion dimensions, and the extent of cracking (if any). These measurements allow assessments to be made regarding the corrosion cause, the fitness-for-purpose of the defect, and the corrosion rate. One of the key requirements of this stage is to validate the classification that has been given on the basis of the indirect examination (i.e., minor, moderate or severe). The number of digs required by the standard is dependent on the results of the direct examinations relative to the initial classification. Finally the postassessment stage defines the reassessment intervals and assesses the overall

effectiveness of the ECDA process, particularly with respect to the predictions made in the preassessment stage.

#### **4.42.7.3.2 Internal corrosion direct assessment (ICDA)**

Similar to ECDA, the purpose of ICDA is to identify areas where internal corrosion is occurring or has occurred along a pipeline. Currently, the procedure as defined in ASME B31.8S<sup>18</sup> is only applicable to gas pipelines that normally operate dry but may suffer from an upset that allows water to enter the pipeline. The principle of ICDA is based on the assumption that water will first settle at the low points in the pipeline or at locations where the angle of inclination is exceeded for specific gas flow velocities. If examinations are made at these points and no corrosion is detected, then it can be assumed that the remaining lengths of the pipeline will not be corroded.

As with ECDA, there is a preassessment that determines whether the method is appropriate for the pipeline. The identification of the direct examination sites is achieved by conducting flow calculations taking into account information on the route topography of the pipeline. At points where internal corrosion could occur, ultrasonic measurements are taken on the excavated pipe to determine the remaining wall thickness. The requirement for conducting further examinations is based on the results of the direct examinations.

#### **4.42.7.3.3 Stress corrosion cracking direct assessment (SCCDA)**

The procedure for conducting SCCDA is outlined in the NACE document RP0204<sup>38</sup> and follows a similar methodology to that previously described for ECDA, that is, preassessment, indirect examination, direct examination, and postassessment.

The preassessment stage of the SCCDA procedure determines whether the whole pipeline or a section of a pipeline is susceptible to SCC using the factors described in [Section 4.42.6.2](#) for high-pH SCC and removing the temperature criterion for the assessment of near-neutral pH SCC. NACE RP0204<sup>38</sup> also contains guidance regarding more detailed information that could be collected about the pipe material, the construction of the pipeline, the environment, corrosion control, and operation of the pipeline that could indicate an increased susceptibility to SCC. If a section of a pipeline is found to be susceptible, then further investigation has to be made, by hydrotesting, ILI, or by direct assessment.

In this respect, SCCDA may act as complimentary methodology to ILI or hydrotesting rather than as a replacement for these techniques. The indirect examination step involves many of the techniques used in ECDA such as CIPS and DCVG as well as additional surveys (e.g., soil characterization) to provide supplementary information and to identify sites for direct examination.

Direct examination not only allows the relevant data to be collected to assess the SCC threat but also provides an opportunity for the external and internal corrosion threats to be investigated at the same time. It is therefore good practice, not only to conduct nondestructive examination to determine the size, type, and extent of cracking, but also to collect data on, for example, the coating condition, the nature of deposits on the pipe surface, the presence of microbes, the remaining wall thickness, etc., which will also inform the evaluation of the internal and external corrosion threat. The information collected during the direct examination stage is used to assess the integrity of the pipeline at the excavated sites and also to determine whether further sites require excavation, or whether an alternative inspection methodology, such as ILI, may be more appropriate. As with ECDA, the final step is a postassessment stage where the success of the process is reviewed and appropriate reinspection intervals are set.

#### 4.42.8 Pipeline Corrosion Management: Overview

Returning to the pipeline integrity management process introduced in Figure 3, the focus of this chapter has principally been on Steps 1 and 2 in this process, the threat identification and inspection processes. This has included a description of the factors that contribute to the threats of external and internal corrosion and SCC on land-based transmission and gathering pipelines and the appropriate inspection techniques to locate and size these defects. However, reference to Figure 3 indicates that this is only part of the continuing process of pipeline integrity management.

Once corrosion or cracking defects have been located and sized on a pipeline, whether by an in-line inspection or by direct assessment technique, the defects need to be assessed to determine whether they pose a threat to the continued operation of the pipeline under the operating stresses. The factors that control how and when a pipeline failure will occur due to corrosion are the size, shape and orientation of the

corrosion, the applied stress, and the properties of the pipe material (strength and toughness). Corrosion and crack assessment techniques for pipelines are included in codes such as ASME B31.G<sup>39</sup> modified ASME B31.G and RSTRENG<sup>40</sup> and DNV-RP-F101,<sup>41</sup> BS7910,<sup>42</sup> and API 579.<sup>43</sup> As with all assessment methods, care must be taken to ensure that the method being used is appropriate and within the validated limits of the data and the readers are referred to the code document for specific application.

If the defect is assessed as being unacceptable for continued operation, then either the pressure in the pipeline can be reduced to attain a stress level in the pipe where the defect is acceptable or the defect can be repaired. There are a number of permanent pipeline repair solutions available in the market that can be applied while the pipeline is still operational. However, in severe situations, the pipeline operator may choose to replace the section of pipe containing the defect. Obviously this is one of the most expensive pipeline repair options.

The next stage in the management cycle of Figure 3 is prevention and mitigation. This is an extremely important step in the control of corrosion and requires the corrosion engineer to be able to accurately diagnose the type of corrosion that is occurring in order that the correct mitigation actions can be implemented. Inspection data, particularly from ILI tools, can play a very important role in this diagnosis as the location and pattern of corrosion will indicate the likely mechanism of corrosion damage.

Once all the data from the risk assessment, inspection, assessment, and analysis has been collected and recorded, the cycle begins again. This illustrates the final critical point regarding pipeline corrosion management; it is not a once-for-all activity. In order to ensure that pipelines remain protected from the threat of corrosion and continue to be one of the safest modes of transport for hazardous liquid and gas products, corrosion management must be conducted on a regular and ongoing basis.

## References

1. Mohitpour, M.; McManus, M.; Trefanenko, B. In *IPC2002*, Proceedings of the 4th International Pipeline Conference, Calgary, Canada, Sept 30–Oct 3 2002; American Society of Mechanical Engineers: New York, 2002; pp 1493–1501.
2. *PHMSA Pipeline Safety Program: Distribution and Transmission Annual Mileage Totals*, Pipeline and Hazard Materials Safety Administration, 2007; Available from <http://www.phmsa.dot.gov/>.

3. Koch, G. H.; Brongers, M. P. H.; Thompson, N. G.; Virmani, Y. P.; Payer, J. H. Corrosion Cost & Prevention Strategies in the US, Report No. FHWA-RD-01-156, Federal Highway Administration, September 30, 2001.
4. Thompson, N. G. Corrosion Cost & Prevention Strategies in the US – Appendix E – Gas and Liquid Transmission Pipelines, Report No. FHWA-RD-01-156, Federal Highway Administration, September 30, 2001.
5. PHMSA Pipeline Safety Program: Pipeline Safety Incident Reports, Pipeline and Hazard Materials Safety Administration, 2007, Available from <http://www.phmsa.dot.gov/>.
6. Davis, P. M.; Dubois, J.; Olcese, A.; Uhlig, F.; Larivé, J.-F.; Martin, D. E. Performance of European Cross-Country Oil Pipelines: Statistical summary of reported spillages – 2004, CONCAWE, 2006.
7. EGI Gas Pipeline Incidents: 6th Report of the European Gas Incident Data Group, 2005.
8. PSR 1996 The Pipelines Safety Regulations 1996 – Statutory Instrument 1996 No. 825, The Stationery Office Limited, 1996.
9. Browne, D.; Hicks, R. UKOPA Pipeline Fault Database – Pipeline Product Loss Incidents (1962–2004), UKOPA Fault Database Management Group, 2005.
10. Lyons, D. Western European Cross Country Oil Pipelines 30 Year Performance Statistics, CONCAWE, Report No. 01/02 2002.
11. Trench, C. J. The U.S. Oil Pipeline Industry's Safety Performance; Allegro Energy Consulting, 2003.
12. Pipeline Safety: The Office of Pipeline Safety is changing how it oversees the pipeline industry, United States General Accounting Office GAO/RCED-00-128, 2000.
13. Pipeline Accident Report NTSB/PAR-03/01 Natural Gas Pipeline Rupture and Fire Near Carlsbad, New Mexico, August 19, 2000, National Transport Safety Board, 2003.
14. 49CFR192 Pipeline Safety: Pipeline Integrity Management in High Consequence Areas (Gas Transmission Pipeline), Final Rule, Department of Transportation, December 15 2003.
15. 49CFR195 Pipeline Safety: Pipeline Integrity Management in High Consequence Areas (Hazardous Liquid Operators With 500 or More Miles of Pipeline), Final Rule, Department of Transportation, December 1 2000.
16. IGE/TD1/1. *Steel Pipelines for High Pressure Gas Transmission*, 4th ed.; Institute of Gas Engineers, 2001.
17. Muhlbauer, W. K. *Pipeline Risk Management Manual – Ideas, Techniques and Resources*, 3rd ed.; Elsevier: Burlington, 2004.
18. ASME B31.8S. *Managing System Integrity of Gas Pipelines*; American Society of Mechanical Engineers: New York, 2004.
19. Simon-Thomas, R. G. M. J. J.; Prager, L. H.; Voermans, C. V. M.; Pots, B. P.; Rippon, I. J. In *Corrosion 2002*, Denver, Colorado, April 7–12 2002; NACE International: Houston, Texas, 2002, Paper no. 02075.
20. Peabody, A. W. *Control of Pipeline Corrosion*, 2nd ed.; NACE International: Houston, Texas, 2001.
21. Race, J. M.; Dawson, S. J.; Stanley, L. M.; Kariyawasam, S. J. *Pipeline Eng.* **2007**, 6(1), 13–29.
22. NACE RP0169:2002 Control of External Corrosion on Underground or Submerged Metallic Piping Systems; NACE: Houston, Texas, 2002, Item no. 21001.
23. Jack, T. R.; Wilmott, M. J.; Sutherby, R. L.; Worthingham, R. G. *Mater. Perf.* **1996**, 35(3), 18–24.
24. Pope, D. H.; Morris, E. A., III *Mater. Perf.* **1995**, 34(5), 23–28.
25. Hanson, H. R.; Smart, J. In *Corrosion 2004*, New Orleans, Louisiana, December 7–9 2004; NACE International: Houston, Texas, 2004, Paper no. 04209.
26. ISO 15589–1:2003 Petroleum and Natural Gas Industries – Cathodic Protection of Pipeline Transportation Systems – Part 1: On Land Pipelines, International Organization for Standardization, 2003.
27. prEN 14919–1:2004 Petroleum and Natural Gas Industries – Cathodic Protection of Pipeline Transportation Systems – Part 1: On-land pipelines (ISO 15589–1:2003 modified), European Committee for Standardization, 2004.
28. De Waard, C.; Williams, D. E. *Corrosion* **1975**, 31(5), 177–181.
29. Schmitt, G.; Hörstermeier, M. In *Corrosion 2006*, San Diego, California, March 12–16 2006; NACE International: Houston, Texas, 2006, Paper no. 06112.
30. Ikeda, A.; Ueda, M.; Mukai, S. In *Corrosion 85*, Boston, USA, March 25–29 1985. NACE International: Houston, Texas, 1985; pp 1–29.
31. Brown, B.; Lee, K.-L.; Nesic, S. In *Corrosion 2003*, San Diego, USA, March 16–21 2003; NACE International: Houston, Texas, 2003, Paper no. 03341.
32. NACE MR0175/ISO 15156–2 Petroleum and natural gas industries – Materials for use in H<sub>2</sub>S-containing environments in oil and gas production – Part 2: Cracking-resistant carbon and low alloy steels, and the use of cast irons; NACE/ANSI/ISO: Houston, Texas, 2003.
33. EFC 3. *The Use of Corrosion Inhibitors in Oil and Gas Production*, Palmer, J. W., Hedges, W., Dawson, J. L., Eds.; European Federation of Corrosion Publications: Maney, London, 2004.
34. Vieth, P. H.; Roytman, I.; Mesloh, R. E.; Kiefner, J. F. In *Analysis of DOT Reportable Incidents for Gas Transmissions and Gathering Pipelines 1985 through 1994*, PRC International Catalog No. L51745, May 31, 1996.
35. Kiefner, J. F.; Kiefner, B. A.; Vieth, P. H. In *Analysis of DOT Reportable Incidents for Hazardous Liquid Pipelines – 1986 through 1996*; The American Petroleum Institute: Washington, January 7, 1999.
36. Krishnamurthy, R. M.; MacDonald, R. W.; Marreck, P. M. In *IPC-96, Proceedings of the First International Pipeline Conference*, Calgary, Canada, June 9–13 1996; American Society of Mechanical Engineers: New York, 1996; pp 495–506.
37. Sutherby, R. L. In *IPC-98, Proceedings of Second International Pipeline Conference*, Calgary, Canada, June 7–11 1998; American Society of Mechanical Engineers, 1998; pp 493–503.
38. NACE RP0204–2004. *Stress Corrosion Cracking (SCC) Direct Assessment Methodology*, ANSI/NACE Standard; NACE: Houston, Texas, 2004, Item no. 21104.
39. ASME B31.G. *Manual for Determining the Remaining Strength of Corroded Pipelines*, Supplement to ASME B31 Code for Pressure Piping, ANSI/ASME B31G-1991; American Society of Mechanical Engineers: New York, USA, 1991.
40. Kiefner, J. F.; Vieth, P. H. A Modified Criterion for Evaluating the Remaining Strength of Corroded Pipe (with RStren), AGA Catalog No. L51609, PR3–805; American Gas Association, 1989.
41. DNV-RP-F101 Corroded Pipelines; Det Norske Veritas, October, 2006.
42. BS 7910:2005. *Guide to methods for assessing the acceptability of flaws in metallic structures*, BS 7910:2005; British Standards Institute, 2005.
43. API Recommended Practice 579. *Fitness for Service*, 1st ed.; American Petroleum Institute, January 2000.
44. NACE RP0502. *Standard Recommended Practice, Pipeline External Corrosion Direct Assessment Methodology*; NACE: Houston, Texas, 2002, Item no. 21097.

# Tables

This list of tables has been reproduced from the previous edition of Shreir's Corrosion but has not been checked for accuracy against current data sources.

**Table 21.2** Physical Properties of some metals and alloys

	<i>Thermal conductivity (<math>W m^{-1} K^{-1}</math>; 273–373 K)</i>	<i>Thermal expansion per kelvin (<math>K^{-1}</math>)</i>	<i>Elect. resistivity (<math>\mu\Omega m</math>)<sup>a</sup></i>	<i>Temp. coef. of res. per kelvin (in range 273–373 K) (<math>K^{-1}</math>)</i>	<i>Mean specific heat in range 273–373 K (<math>J kg^{-1} K^{-1}</math>)</i>	<i>Young's modulus (<math>MN m^{-2}</math> or MPa)<sup>b</sup></i>
Ag	418.400	$18.9 \times 10^{-6}$	0.016	$4.1 \times 10^{-3}$	225.936	$0.07584 \times 10^6$
Al	221.752	$23.5 \times 10^{-6}$	0.0269	$4.2 \times 10^{-3}$	916.296	$0.06894 \times 10^6$
Be	221.752	$13.0 \times 10^{-6}$	0.04–0.06	$6.0 \times 10^{-3}$	2012.504	$0.29647 \times 10^6$
Co	69.036	$12.3 \times 10^{-6}$	0.0624	$6.0 \times 10^{-3}$	435.136	$0.20684 \times 10^6$
Cu	393.296	$16.5 \times 10^{-6}$	0.01673	$4.3 \times 10^{-3}$	384.928	$0.11031 \times 10^6$
Mg	153.553	$27.0 \times 10^{-6}$	0.0440	$4.2 \times 10^{-3}$	1037.632	$0.04481 \times 10^6$
Mn	–	$22.0 \times 10^{-6}$	1.60( $\alpha$ )	–	489.528	$0.15857 \times 10^6$
Mo	142.256	$5.1 \times 10^{-6}$	0.0570	$4.6 \times 10^{-3}$	259.408	$0.29647 \times 10^6$
Nb	52.300	$7.2 \times 10^{-6}$	0.169	$3.95 \times 10^{-3}$	255.224	$0.10342 \times 10^6$
Ni	92.048	$12.8 \times 10^{-6}$	0.0684	$6.8 \times 10^{-3}$	451.872	$0.20684 \times 10^6$
Pb	34.309	$29.0 \times 10^{-6}$	0.206	$3.36 \times 10^{-3}$	129.704	$0.01378 \times 10^6$
Pd	70.291	$11.7 \times 10^{-6}$	0.108	$3.8 \times 10^{-3}$	246.856	$0.11721 \times 10^6$
Pt	69.036	$9.0 \times 10^{-6}$	0.106	$3.92 \times 10^{-3}$	133.888	$0.15168 \times 10^6$
Sn (white)	62.760	$23.5 \times 10^{-6}$	0.128	$4.2 \times 10^{-3}$	225.936	$0.04688 \times 10^6$
Ta	54.392	$6.5 \times 10^{-6}$	0.145	$3.8 \times 10^{-3}$	142.256	$0.18615 \times 10^6$
Ti	17.029	$8.4 \times 10^{-6}$	0.550	$3.5 \times 10^{-3}$	527.184	$0.11721 \times 10^6$
U	25.104–27.196	<sup>c</sup>	0.29( $\alpha$ )	$3.4 \times 10^{-3}$	117.152	$0.18960 \times 10^6$
V	30.962	$8.3 \times 10^{-6}$	0.195	$2.8 \times 10^{-3}$	497.896	$0.13789 \times 10^6$
W	166.105	$4.6 \times 10^{-6}$	0.055	$4.6 \times 10^{-3}$	138.072	$0.35852 \times 10^6$
Zn	110.876	$31.0 \times 10^{-6}$	0.059	$4.2 \times 10^{-3}$	393.296	$0.09652 \times 10^6$
Zr	16.736	$5.9 \times 10^{-6}$	0.446	$4.4 \times 10^{-3}$	288.696	$0.09307 \times 10^6$
Al alloys	167.360( $\pm$ )	$21.6 \times 10^{-6}$	0.035(+)	–	962.320	$0.06895 \times 10^6$
Brass (70/30)	125.520	$19.6 \times 10^{-6}$	0.062	$1.5 \times 10^{-3}$	380.744	$0.11032 \times 10^6$
Bronze (95/5)	86.680	$18.0 \times 10^{-6}$	0.096	$1.9 \times 10^{-3}$	376.560	$0.11032 \times 10^6$
Monel (70/30)	25.104	$14.4 \times 10^{-6}$	0.482	$1.1 \times 10^{-3}$	543.920	$0.17926 \times 10^6$
Fe-18Cr-8Ni stainless steel	14.644	$9.5 \times 10^{-6}$	0.70	–	502.08	$0.19305 \times 10^6$

<sup>a</sup>To convert into  $\mu\Omega cm$  multiply by 100.

<sup>b</sup>To convert into  $KN cm^{-2}$  multiply by  $10^{-1}$ .

<sup>c</sup> $\alpha$ -Uranium  $23 \times 10^{-6}$  parallel to  $a$ -axis;  $-3.5 \times 10^{-6}$  parallel to  $b$ -axis;  $17 \times 10^{-6}$  parallel to  $c$ -axis;  $\beta$ -uranium  $46 \times 10^{-6}$  parallel to  $c$ -axis;  $23 \times 10^{-3}$  perpendicular to  $c$ -axis.

**Table 21.6** Standard electrode potentials against the standard hydrogen electrode for inorganic systems at 25°C

Two tables:	Aqueous Acid solutions
	Aqueous Basic solutions



**Table 21.7** Reference electrodes

Electrode	Electrode equilibrium	Potential at 25°C (vs. S.H.E.; V)																
Calomel (Hg/Hg <sub>2</sub> Cl <sub>2</sub> , Cl <sup>-</sup> )	Hg <sub>2</sub> Cl <sub>2</sub> + 2e ⇌ 2Hg + 2Cl <sup>-</sup>	<div><math>E = 0.2677 - 0.0591 \log a_{\text{Cl}^-}</math></div> <table><tr><td>Solution</td><td><math>E_{\text{calomel}}</math></td><td><math>E_{\text{calomel}} + \text{liquid junction}</math></td><td>Temp. coeff.</td></tr><tr><td>0.1 mol dm<sup>-3</sup> KCl</td><td>0.3337</td><td>0.336</td><td>-0.06 mV °C<sup>-1</sup></td></tr><tr><td>1.0 mol dm<sup>-3</sup> KCl</td><td>0.280</td><td>0.283</td><td>-0.24 mV °C<sup>-1</sup></td></tr><tr><td>Sat. KCl</td><td>0.241</td><td>0.244</td><td>-0.65 mV °C<sup>-1</sup></td></tr></table>	Solution	$E_{\text{calomel}}$	$E_{\text{calomel}} + \text{liquid junction}$	Temp. coeff.	0.1 mol dm <sup>-3</sup> KCl	0.3337	0.336	-0.06 mV °C <sup>-1</sup>	1.0 mol dm <sup>-3</sup> KCl	0.280	0.283	-0.24 mV °C <sup>-1</sup>	Sat. KCl	0.241	0.244	-0.65 mV °C <sup>-1</sup>
Solution	$E_{\text{calomel}}$	$E_{\text{calomel}} + \text{liquid junction}$	Temp. coeff.															
0.1 mol dm <sup>-3</sup> KCl	0.3337	0.336	-0.06 mV °C <sup>-1</sup>															
1.0 mol dm <sup>-3</sup> KCl	0.280	0.283	-0.24 mV °C <sup>-1</sup>															
Sat. KCl	0.241	0.244	-0.65 mV °C <sup>-1</sup>															
Mercury/mercurous sulphate (Hg/HgSO <sub>4</sub> , SO <sub>4</sub> <sup>2-</sup> )	HgSO <sub>4</sub> + 2e ⇌ Hg + SO <sub>4</sub> <sup>2-</sup>	$E = 0.6151 - 0.0295 \log a_{\text{NO}_2}$																
Silver/silver chloride (Ag/AgCl, Cl <sup>-</sup> )	AgCl + e ⇌ Ag + Cl <sup>-</sup>	<div><math>E = 0.2224 - 0.0591 \log a_{\text{Cl}^-}</math></div> <div>Average temp. coeff. ≈ -0.6 mV °C<sup>-1a</sup></div> <table><tr><td>0.1 mol dm<sup>-3</sup> KCl</td><td><math>E = 0.2881 \text{ V}</math></td></tr><tr><td>1.0 mol dm<sup>-3</sup> KCl</td><td><math>E = 0.2224 \text{ V}</math></td></tr><tr><td>Sea-water</td><td><math>E = 0.250 \text{ V}</math></td></tr></table>	0.1 mol dm <sup>-3</sup> KCl	$E = 0.2881 \text{ V}$	1.0 mol dm <sup>-3</sup> KCl	$E = 0.2224 \text{ V}$	Sea-water	$E = 0.250 \text{ V}$										
0.1 mol dm <sup>-3</sup> KCl	$E = 0.2881 \text{ V}$																	
1.0 mol dm <sup>-3</sup> KCl	$E = 0.2224 \text{ V}$																	
Sea-water	$E = 0.250 \text{ V}$																	
Copper/copper sulphate (Cu/CuSO <sub>4</sub> , Cu <sup>2+</sup> )	Cu <sup>2+</sup> + 2e ⇌ Cu	<div><math>E = 0.340 + 0.0295 \log a_{\text{Cu}}^2</math>; for sat. CuSO<sub>4</sub>,</div> <div><math>E = 0.318\text{V}</math>; for practical electrodes <math>E = 0.30\text{V}</math></div>																
Quinhydrone	Quinone + H <sub>2</sub> ⇌ hydroquinone	<div><math>E = E^* - 0.0591 \text{ pH}</math>, and <math>E^* = 0.6990</math> at 25 °C</div> <div><math>E^*</math> contains a term due to diffusion potentials and is not a thermodynamic constant</div>																
Antimony/antimony oxide (Sb/Sb <sub>2</sub> O <sub>3</sub> , H <sup>+</sup> )	Sb <sub>2</sub> O <sub>3</sub> + 6H <sup>+</sup> + 6e ⇌ 2Sb + 3H <sub>2</sub> O	$E = 0.1445 - 0.0591 \text{ pH}$																
Mercury/mercuric oxide (Hg/HgO, OH <sup>-</sup> )	HgO + 2H <sup>+</sup> + 2e ⇌ Hg + H <sub>2</sub> O	$E = 0.926 - 0.0591 \text{ pH}$ (for pH determinations in alkaline solution)																
Lead dioxide/lead sulphate (Pb/PbO <sub>2</sub> /PbSO <sub>4</sub> , SO <sub>4</sub> <sup>2-</sup> )	PbO <sub>2</sub> + 4H <sup>+</sup> + SO <sub>4</sub> <sup>2-</sup> + 2e ⇌ PbSO <sub>4</sub> + 2H <sub>2</sub> O	<div><math>E = 1.685 + 0.0295 \log 4m^3\gamma^3/\alpha^2</math>, where <math>\gamma</math> and <math>\alpha</math> are the stoichiometric mean activity coefficient of sulphuric acid and the activity of water, respectively, at molality <math>m</math> of H<sub>2</sub>SO<sub>4</sub></div> <table><tr><th>Solution</th><th><math>E</math></th></tr><tr><td>0.1 mol dm<sup>-3</sup> H<sub>2</sub>SO<sub>4</sub></td><td>+ 1.565</td></tr><tr><td>1.1 mol dm<sup>-3</sup> H<sub>2</sub>SO<sub>4</sub></td><td>+ 1.632</td></tr><tr><td>6.1 mol dm<sup>-3</sup> H<sub>2</sub>SO<sub>4</sub></td><td>+ 1.735</td></tr></table>	Solution	$E$	0.1 mol dm <sup>-3</sup> H <sub>2</sub> SO <sub>4</sub>	+ 1.565	1.1 mol dm <sup>-3</sup> H <sub>2</sub> SO <sub>4</sub>	+ 1.632	6.1 mol dm <sup>-3</sup> H <sub>2</sub> SO <sub>4</sub>	+ 1.735								
Solution	$E$																	
0.1 mol dm <sup>-3</sup> H <sub>2</sub> SO <sub>4</sub>	+ 1.565																	
1.1 mol dm <sup>-3</sup> H <sub>2</sub> SO <sub>4</sub>	+ 1.632																	
6.1 mol dm <sup>-3</sup> H <sub>2</sub> SO <sub>4</sub>	+ 1.735																	
Zn/ZnSO <sub>4</sub>	Zn <sup>2+</sup> + 2e ⇌ Zn	$E = -0.763 + 0.0295 \log a_{\text{Zn}^{2+}}$																
Zn/sea-water	Mixed potentials approximating to $E_{\text{M}^{2+}/\text{M}}^\circ$	$E = -0.80 \text{ V}$																
Zn/artificial sea-water	Mixed potentials approximating to $E_{\text{M}^{2+}/\text{M}}^\circ$	$E = -0.81 \text{ V}$																
Cd/sea-water	Mixed potentials approximating to $E_{\text{M}^{2+}/\text{M}}^\circ$	$E = -0.52 \text{ V}$																
Cd/artificial sea-water	Mixed potentials approximating to $E_{\text{M}^{2+}/\text{M}}^\circ$	$E = -0.54 \text{ V}$																

<sup>a</sup>Variation of  $E_{\text{Ag}/\text{AgCl}}^0$  with temperature:

Temp. (°C)	35	45	55	70	95	125	150	200
$E'$ (V)	0.21570	0.20828	0.20042	0.18782	0.1651	0.1330	0.1032	0.0348

**Table 21.8** Galvanic series of some commercial metals and alloys in seawater

<div style="text-align: center;"> ↑  Noble or cathodic </div>	Platinum Gold Graphite Titanium Silver { Chlorimet 3 (62Ni–18Cr–18Mo) Hastelloy C (62Ni–17Cr–15Mo) 18/8 Mo stainless steel (passive) 18/8 stainless steel (passive) Chromium stainless steel 11–30% Cr (passive) Inconel (passive) (Ni–13Cr–7Fe) Nickel (passive) Silver solder { Monel (Ni–30Cu) Cupro-nickels (Cu–(10–40)Ni) Bronzes(Cu–Sn) Copper Brasses (Cu–Zn) Chlorimet 2 (66Ni–32Mo–1Fe) Hastelloy B (60Ni–30Mo–6Fe–1Mn) Inconel (active) Nickel (active) Tin Lead Lead–tin solders { 18/8 Mo stainless steel (active) 18/8 stainless steel (active) Ni-Resist (high nickel cast iron) Chromium stainless steel, 13% Cr (active) { Cast iron Steel or iron 2024 aluminum (Al–4.5Cu–1.5Mg–0.6Mn) Cadmium Commercially pure aluminum (1100) Zinc Magnesium and magnesium alloys
<div style="text-align: center;"> ↓  Active or anodic </div>	

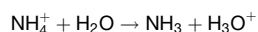
**Table 21.11** Ionization constants of water and weak electrolytes and their variation with temperature**A. Ionization constants of water ( $pK_w = -\log K_w$ )**

Temperature ( $^{\circ}\text{C}$ )	$-\log K_w$	Temperature ( $^{\circ}\text{C}$ )	$-\log K_w$
0	14.9435	35	13.6801
5	14.7338	40	13.5348
10	14.5346	45	13.3960
15	14.3463	50	13.2617
20	14.1669	55	13.1369
25	13.9965	60	13.0171
30	13.8330		

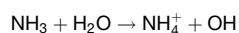
**B. Ionization constants of weak electrolytes and their temperature variation  $pK_a = -\log K_a = A_1/T - A_2 + A_3T$** 

Aqueous solution	$pK_a$ at $25^{\circ}\text{C}$	$A_1$	$A_2$	$A_3$
Acetic acid	4.756	1170.48	3.1649	0.013399
Ammonium ion	9.245	2835.76	0.6322	0.001225
Benzoic acid	4.201	1590.2	6.394	0.01765
Boric acid	9.234	2237.94	3.305	0.016883
<i>n</i> -Butyric acid	4.820	1033.39	2.6215	0.013334
Carbonic acid $K_1$	6.352	3404.71	14.8435	0.032786
Carbonic acid $K_2$	10.329	2902.39	6.4980	0.02379
Chloroacetic acid	2.861	1049.05	5.0273	0.014654
Citric acid $K_1$	3.128	1255.6	4.5635	0.011673
Citric acid $K_2$	4.761	1585.2	5.4460	0.016399
Citric acid $K_3$	6.396	1814.9	6.3664	0.022389
Formic acid	3.752	1342.85	5.2743	0.015168
Glycine $K_1$	2.350	1332.17	5.8870	0.012643
Glycine $K_2$	9.780	2686.95	0.5103	0.004286
Lactic acid	3.860	1286.49	4.8607	0.014776
Malonic acid $K_1$	2.855	—	—	—
Malonic acid $K_2$	5.696	1703.31	6.5810	0.022014
Oxalic acid $K_1$	1.271	—	—	—
Oxalic acid $K_2$	4.266	1423.8	6.5007	0.020095
Phosphoric acid $K_1$	2.148	799.31	4.5535	0.013486
Phosphoric acid $K_2$	7.198	1979.5	5.3541	0.019840
<i>o</i> -Phthalic acid $K_1$	2.950	561.57	1.2843	0.007883
<i>o</i> -Phthalic acid $K_2$	5.408	2175.83	9.5508	0.025694
Succinic acid $K_1$	4.207	1206.25	3.3266	0.011697
Succinic acid $K_2$	5.638	1679.13	5.7043	0.019153
Sulphamic acid	0.988	3792.8	24.122	0.041544
Sulphanilic acid	3.227	1143.71	1.2979	0.002314
Tartaric acid $K_1$	3.033	1525.59	6.6558	0.015336
Tartaric acid $K_2$	4.366	1765.35	7.3015	0.019276
Trimethylammonium ion	9.800	541.4	−12.611	−0.015525

Note. All values are with reference to the molarity scale. Data for bases are expressed as acidic ionization constants, e.g. for ammonia we quote  $pK$  at  $25^{\circ}\text{C} = 9.245$  for the ammonium ion



The basic ionization constant of the reaction



is obtained from the relation

$$pK_a(\text{acidic}) + pK_b(\text{basie}) = pK_w(\text{water})$$

$pK_w(\text{water})$  being 13.9965 at  $25^{\circ}\text{C}$ .

**Table 21.12** Tafel constants for hydrogen evolution from aqueous solution. The Tafel equation for a cathodic reaction is  $\eta_c = a - b \log_{10} i = b \log_{10} (i_0/i)$ , where  $\eta_c$  is the overpotential (mV),  $i$  is the current density ( $\text{A cm}^{-2}$ ) and  $i_0$  is the exchange current density ( $\text{A cm}^{-2}$ )

<i>Metal</i>	<i>Electrolyte</i>		<i>Temp. (°C)</i>	$-\log_{10} i$ range	$-a$ (mV)	$b$ (mV)	$-\log_{10} i_0$ ( $i_0$ in $\text{A cm}^{-2}$ )
Ag	0.001 N	HCl	20	6.0 to 2.0	810	125	6.5
	0.01 N	HCl	20	6.0 to 2.0	820	130	6.3
	0.1 N	HCl	20	6.0 to 3.3	570	90	6.3
	0.1 N	HCl	20	3.3 to 1.0	670	120	5.6
	1.0 N	HCl	20	6.0 to 2.3	320	60	5.4
	1.0 N	HCl	20	2.3 to 1.0	480	130	3.7
	5.0 N	HCl	20	6.0 to 2.8	470	70	6.7
	5.0 N	HCl	20	2.8 to -2	630	120	5.3
	7.0 N	HCl	20	6.0 to 3.4	640	90	7.1
Al	7.0 N	HCl	20	3.4 to 1.0	740	110	6.7
	2 N	H <sub>2</sub> SO <sub>4</sub>	25	3.0 to 0.7	1000	100	10.0
Au	0.001 N	HCl	20	7.0 to 2.0	524	72	7.32
	0.01 N	HCl	20	6.0 to 2.0	558	84	6.63
	0.1 N	HCl	20	6.6 to 3.0	468	71	6.59
	0.1 N	HCl	20	3.0 to 2.0	548	97	5.64
	0.001 N	NaOH	20	6.0 to 4.5	832	118	7.05
	0.01 N	NaOH	20	6.5 to 3.7	836	119	7.04
	0.1 N	NaOH	20	4.8 to 3.0	856	123	6.95
Be	1.0 N	HCl	20	3.0 to 1.3	1080	120	9.0
Bi	1.0 N	HCl	20	3.0 to 1.0	840	120	7.0
Cd	1.7 N	H <sub>2</sub> SO <sub>4</sub>	20	4.0 to 3.0	1450	120	12.1
	10 N	H <sub>2</sub> SO <sub>4</sub>	20	4.0 to 2.0	1400	120	11.7
Cu	0.001 N	HCl	20	5.0 to 3.3	802	122	6.61
	0.01 N	HCl	20	4.5 to 2.3	786	118	6.71
	0.1 N	HCl	20	5.0 to 2.5	790	117	6.76
	0.005 N	NaOH	16		890	139	6.40
	0.02 N	NaOH	16	6.0 to 3.7	710	114	6.29
	0.15 N	NaOH	16		690	117	5.99
Fe	0.001 N	HCl	20	4.0 to 3.8	787	127	6.19
	0.01 N	HCl	20	4.1 to 3.2	741	118	6.29
	1 N	HCl	16	3.0 to 0.0	770	130	5.9
	0.01 N	NaOH	20	4.5 to 3.8	776	117	6.62
	0.1 N	NaOH	20	4.1 to 3.2	726	120	6.06
	4.8 N	KOH	20	4.0 to 3.0	350	70	5.0
	10.5 N	KOH	20	4.0 to 3.0	340	70	4.9
Ga	0.2 N	H <sub>2</sub> SO <sub>4</sub>	87		800	120	6.7
Hg	0.001–0.1 N	HCl	20	7.0 to 1.0	1410	116	12.2
	1 N	HCl	20	6.0 to 2.5	1390	119	11.7
	3 N	HCl	20	6.0 to 2.5	1420	141	10.1
	5 N	HCl	20	6.0 to 2.5	1320	127	10.4
	7 N	HCl	20	6.0 to 2.5	1130	108	10.5
	10 N	HCl	20	6.0 to 2.5	1020	95	10.7
	0.1 N	H <sub>2</sub> SO <sub>4</sub>	20	6.0 to 2.5	1440	114	12.7
	0.25 N	H <sub>2</sub> SO <sub>4</sub>	20	6.5 to 3.0	1403	116	12.1
	5 N	H <sub>2</sub> SO <sub>4</sub>	20	6.5 to 3.0	1400	116	12.05
	0.1 N	LiOH	20	6.0 to 4.0	1598	102	15.7
	0.2 N	LiOH	20	6.0 to 4.0	1545	100	15.5
Hg	0.1 N	NaOH	20	6.0 to 4.0	1457	100	14.6
	0.2 N	NaOH	20	6.0 to 4.0	1405	97	14.5
	0.002 N	KOH	20	6.0 to 4.0	1682	98	17.1
	0.02 N	KOH	20	6.0 to 4.0	1545	90	17.3
	0.1 N	KOH	20	6.0 to 4.0	1430	93	15.4
	0.01 N	Ba(OH) <sub>2</sub>	20	6.0 to 4.0	1170	45	26.0
	0.02 N	Ba(OH) <sub>2</sub>	20	6.0 to 4.0	1220	65	18.8
	0.1 N DCl in D <sub>2</sub> O		20	5.0 to 2.4	1485	119	12.19

Continued

Table 21.12 Continued

Metal	Electrolyte		Temp. (°C)	$-\log_{10} I$ range	$-a$ (mV)	$b$ (mV)	$-\log_{10} i_0$ ( $i_0$ in $A\ cm^{-2}$ )
Mo	0.001 N	HCl	20	5.6 to 4.2	557	81	7.12
	0.01 N	HCl	20	5.2 to 3.7	543	76	7.19
	0.1 N	HCl	20	6.0 to 3.5	586	80	7.30
	0.1 N	HCl	20	3.5 to 2.0	671	104	6.45
	0.001 N	NaOH	20	5.9 to 4.4	667	92	7.27
	0.01 N	NaOH	20	4.9 to 3.6	664	103	6.42
	0.1 N	NaOH	20	4.7 to 3.7	641	87	7.35
	0.1 N	NaOH	20	3.6 to 2.1	739	116	6.37
Nb	1.0 N	HCl	20	3.0 to 1.0	900	80	11.0
Ni	0.000 04 N	HCl	20	6.0 to 5.0	650	100	6.5
	0.001 N	HCl	20	5.8 to 3.3	617	93	6.6
	0.01 N	HCl	20	5.5 to 3.3	611	91	6.7
	0.1 N	HCl	20	5.0 to 2.0	626	104	6.0
	1.0 N	HCl	20	4.3 to 2.0	594	109	5.4
	0.001 N	NaOH	20	6.8 to 4.8	720	103	7.0
	0.006 N	NaOH	20	6.3 to 3.8	660	101	6.6
	0.1 N	NaOH	20	6.0 to 3.0	650	101	6.4
Pb	0.1 N	HCl	20	5.8 to 2.5	1524	116	13.2
	1 N	HCl	20	5.8 to 2.5	1531	119	12.9
	3 N	HCl	20	5.1 to 2.5	1573	142	11.1
	5 N	HCl	20	4.9 to 2.5	1495	140	10.7
	7 N	HCl	20	4.7 to 2.5	1417	138	9.76
	10 N	HCl	20	4.6 to 2.0	1195	135	8.84
	0.1 N	H <sub>2</sub> SO <sub>4</sub>	20	7.0 to 2.5	1533	118	13.0
	1 N	H <sub>2</sub> SO <sub>4</sub>	20	6.5 to 2.0	1536	119	12.9
	8 N	H <sub>2</sub> SO <sub>4</sub>	20	5.9 to 2.0	1530	120	12.8
	15 N	H <sub>2</sub> SO <sub>4</sub>	20	5.3 to 2.0	1469	121	12.1
	20 N	H <sub>2</sub> SO <sub>4</sub>	20	5.0 to 2.0	1411	119	11.9
	1 N	HBr	20	5.3 to 2.3	1484	116	12.7
	3 N	HBr	20	5.1 to 2.3	1467	123	11.9
	6 N	HBr	20	4.7 to 2.3	1377	130	10.6
	8.5 N	HBr	20	4.3 to 2.3	1285	140	9.17
	1 N	HClO <sub>4</sub>	20	4.8 to 1.6	1537	118	13.0
	3 N	HClO <sub>4</sub>	20	4.8 to 1.6	1517	118	12.8
	7 N	HClO <sub>4</sub>	20	4.8 to 1.6	1504	121	12.4
	9 N	HClO <sub>4</sub>	20	4.8 to 1.6	1453	122	11.9
	11.6 N	HClO <sub>4</sub>	20	4.8 to 1.6	1446	132	11.0
Pd	1.0 N	H <sub>2</sub> SO <sub>4</sub>	20	3.0 to 2.0	240	80	3.0
	0.01 N	HCl	20	3.9 to 3.1	447	107	4.18
	0.1 N	HCl	20	2.9 to 1.4	321	99	3.25
	0.001 N	NaOH	20	5.0 to 3.9	589	100	5.88
	0.01 N	NaOH	20	5.4 to 4.0	610	110	5.56
	0.1 N	NaOH	20	4.1 to 3.1	637	125	5.01
Pt	0.5 N	HCl	25	2.0 to 0.7	73	28	2.6
Rh	0.01 N	HCl	20	3.4 to 3.1	209	55	3.80
	0.01 N	NaOH	20	4.2 to 3.5	551	119	4.64
Sb	2 N	H <sub>2</sub> SO <sub>4</sub>	20	3.0 to 0	900	100	9.0
Sn	1 N	HCl	20	3.0 to 0	1100	140	8.0
Ta	1 N	HCl	20	3.0 to 1.0	550	120	4.6
W	5 N	HCl	20	2.0 to -2.0	550	110	5.0

Note that  $\eta$  will always be negative.



**Table 21.13** Exchange current densities  $i_0$  for the hydrogen evolution reaction

<i>Metal</i>	$-\log i_0 (A\text{ cm}^{-2})$ in approx. $1\text{ mol dm}^{-3} \text{ H}_2\text{SO}_4$
Palladium	3.0
Platinum	3.1
Rhodium	3.6
Iridium	3.7
Nickel	5.2
Gold	5.4
Tungsten	5.9
Niobium	6.8
Titanium	8.2
Cadmium	10.8
Manganese	10.9
Thallium	11.0
Lead	12.0
Mercury	12.3

After Bockris, J. O'M.; Reddy, A. K. N. *Modern Electrochemistry*, Macdonald. 1970.

**Table 21.14** Exchange current densities and transfer coefficients  $\alpha$  for evolution of gases at 20–25 °C at different anodes

<i>Gas</i>	<i>Metal</i>	<i>Solution</i> <sup>a</sup>	$\alpha$	$i_0 (A\text{ cm}^{-2})$
O <sub>2</sub>	Au	0.1 mol dm <sup>-3</sup> NaOH	0.74–1.2	$5 \times 10^{-13}$
	Pt	0.5 mol dm <sup>-3</sup> H <sub>2</sub> SO <sub>4</sub>	0.45	$10^{-8} - 10^{-11}$
	Pt	HNO <sub>3</sub> + NaOH pH 0.5–14	0.51	$0.6-1 \times 10^{-10}$
	Pt	Phosphate buffer pH 6.8	0.29	
	Pt	0.1 mol dm <sup>-3</sup> NaOH	0.81	$4 \times 10^{-13}$
	PbO <sub>2</sub>	0.5 mol dm <sup>-3</sup> H <sub>2</sub> SO <sub>4</sub>	0.50	
Cl <sub>2</sub>		1.0 mol dm <sup>-3</sup> KOH	0.50	
	Pt	1.0 mol dm <sup>-3</sup> HCl	0.48	$5 \times 10^{-3}$
	Pt	Various solutions	0.5–0.7	$10^{-3}$
	Ir	1.0 mol dm <sup>-3</sup>	0.73	$4 \times 10^{-5}$
	PbO <sub>2</sub>	0.5–2 mol dm <sup>-3</sup> NaCl	0.17–0.27	$10^{-7}$
Br <sub>2</sub>	Ir	1 mol dm <sup>-3</sup> HBr	0.6	$3 \times 10^{-3}$
	Pt	1 N KBr	0.5–0.7	$3 \times 10^{-3}$
N <sub>2</sub>	Pt	1.0 mol dm <sup>-3</sup> NaN <sub>3</sub>	0.98	$10^{-76}$
	Ir	1.0 mol dm <sup>-3</sup> NaN <sub>3</sub>	1.0	$10^{-75}$
	Pd	1.0 mol dm <sup>-3</sup> NaN <sub>3</sub>	1.1	$10^{-81}$

Data after Parsons *Handbook of Electrochemical Constants*; Butterworths: London, 1959.

**Table 21.19** Solubility of gases in water

		<i>Temperature of water (<math>\theta</math>, °C)</i>							
		0	10	15	20	30	40	50	60
Ammonia	S	1130	870	770	680	530	400	290	200
Argon	A	0.054	0.041	0.035	0.032	0.028	0.025	0.024	0.023
Carbon dioxide	A	1.676	1.163	0.988	0.848	0.652	0.518	0.424	0.360
Carbon monoxide	A	0.035	0.028	0.025	0.023	0.020	0.018	0.016	0.015
Chlorine	S	4.61	3.09	2.63	2.26	1.77	1.41	1.20	1.01
Helium	A	0.0098	0.0091	0.0089	0.0086	0.0084	0.0084	0.0086	0.0090
Hydrogen	A	0.0214	0.0195	0.0188	0.0182	0.0170	0.0164	0.0161	0.0160
Hydrogen sulfide	A	4.53	3.28	2.86	2.51	1.97	1.62	1.37	1.18
Hydrochloric acid	S	512	475	458	442	412	385	362	339
Nitrogen	A	0.0230	0.0183	0.0165	0.0152	0.0133	0.0119	0.0108	0.0100
Nitrous oxide	A	–	0.88	0.74	0.63	–	–	–	–
Nitric oxide	A	0.071	0.055	0.049	0.046	0.039	0.034	0.031	0.029
Oxygen	A	0.047	0.037	0.033	0.030	0.026	0.022	0.020	0.019
Sulfur oxide	S	79.8	56.6	47.3	39.4	27.2	18.8	–	–

Values of A for 20 °C for other rare gases are: Ne, 0.0101; Kr, 0.0594; Xe, 0.126. S indicates the number of m<sup>3</sup> of gas measured at 0 °C and 101.325 kN m<sup>-2</sup> which dissolve in 1 m<sup>3</sup> of water at the temperature stated, and when the pressure of the gas plus that of the water vapor is 101.325 kN m<sup>-2</sup>. A indicates the same quantity except that the gas itself is at the uniform pressure of 101.325 kN m<sup>-2</sup> when in equilibrium with water.

**Table 21.21** Oxygen dissolved in seawater (ppm) in equilibrium at 1 atm (101.325 kPa) of air saturated with water vapor*Parts per million*

Chlorinity (‰)	0	5	10	15	20
Salinity (‰)	0	9.06	18.08	27.11	36.11
<i>Temperature (°C)</i>					
0	14.62 <sup>a</sup>	13.70	12.78	11.89	11.00
5	12.79	12.02	11.24	10.49	9.74
10	11.32	10.66	10.01	9.37	8.72
15	10.16	9.67	9.02	8.46	7.92
20	9.19	8.70	8.21	7.77	7.23
25	8.39	7.93	7.48	7.04	6.57
30	7.67	7.25	6.80	6.41	5.37

Note: the table gives the quantity of oxygen dissolved in sea-water at different temperatures and chlorinities when in equilibrium with a normal atmosphere saturated with water vapor. It thus represents the condition approached by the surface water when biological activity is not excessive.

<sup>a</sup>The values of solubility in water of zero chlorinity differ slightly from those for freshwater.

**Table 21.22** Saturated solubilities of atmospheric gases in seawater at various temperatures

Gas	Chlorinity (‰)	Temperature (°C)	Concentration	
			$ml\ l^{-1}$	ppm
Oxygen	0	0	49.2 <sup>a</sup>	70.4
		12	36.8	52.5
		24	29.4	42.1
	16	0	40.1	56.0
		12	30.6	42.9
		24	24.8	34.8
	20	0	38.0	52.8
		12	29.1	40.4
		24	23.6	32.9
Nitrogen	0	0	23.0 <sup>a</sup>	28.8
		12	17.8	22.7
		24	14.6	18.3
	16	0	15.0	18.4
		12	11.6	14.2
		24	9.36	11.5
	20	0	14.2	17.3
		12	11.0	13.4
		24	8.96	10.9
Carbon dioxide <sup>b</sup>	0	0	1715 <sup>a</sup>	3370
		12	1118	2198
		24	782	1541
	16	0	1489	2860
		12	980	1888
		24	695	1342
	20	0	1438	2746
		12	947	1814
		24	677	1299

<sup>a</sup>These values differ slightly from those for freshwater.<sup>b</sup>Includes CO<sub>2</sub> present as H<sub>2</sub>CO<sub>3</sub> but not as HCO<sub>3</sub><sup>-</sup> or CO<sub>3</sub><sup>2-</sup>.

Note: Atmospheric gases are present in seawater in approximately the following quantities:

	$ml\ l^{-1}$	Parts per million
Oxygen	0–9	0–12
Nitrogen	8–15	10–18
Carbon dioxide <sup>a</sup>	33–56	64–107
Argon	0.2–0.4	0.4–0.7
Helium and neon	$1.7 \times 10^{-4}$	$0.3 \times 10^{-4b}$

<sup>a</sup>Includes CO<sub>2</sub> present as H<sub>2</sub>CO<sub>3</sub>, HCO<sub>3</sub><sup>-</sup> and CO<sub>3</sub><sup>2-</sup><sup>b</sup>Estimated as helium

Concentrations of oxygen, nitrogen and carbon dioxide in equilibrium with 1 atm (101.325 kPa) of designated gas.

**Table 21.23** Properties of sea-water of different salinities

Salinity (‰)	Freezing point (°C)	Temperature of maximum density	Osmotic pressure (atm)	Specific heat (J kg <sup>-1</sup> )
0	0.00	3.95	0	$4.184 \times 10^3$
5	-0.27	2.93	3.23	$4.109 \times 10^3$
10	-0.53	1.86	6.44	$4.050 \times 10^3$
15	-0.80	0.77	9.69	$4.008 \times 10^3$
20	-1.07	-0.31	12.98	$3.979 \times 10^3$
25	-1.35	-1.40	16.32	$3.954 \times 10^3$
30	-1.63	-2.47	19.67	$3.929 \times 10^3$
35	-1.91	-3.52	23.12	$3.899 \times 10^3$
40	-2.20	-4.54	26.59	$3.874 \times 10^3$

**Table 21.25** Soil resistivities and corrosiveness

<i>Range of resistivity (<math>\Omega</math> cm)<sup>a</sup></i>	<i>Location</i>	<i>Soil type and classification</i>
10 000–100 000 and above	Perth, Scotland	Comparatively noncorrosive. Red sand-stone
8000–10 000	West Durham	Mildly corrosive. Sandstone and shale
Varying 1000–20 000	Staffordshire	Many built-up areas. Possibly very corrosive
1000–1500	Eastbourne, Sussex	Marshy ground. Very corrosive
15 000–20 000	Sussex Downs	Chalk. Non-corrosive
750–1500	Port Clarence, S.E. Durham	Salt marsh. Very corrosive
600–1500	S. Essex	Essex clay. Very corrosive
1400–3200	Newport, Gwent	Grey, yellow and blue clays, Corrosive
12 000–15 000	North Devon	Millstone grit. Comparatively non-corrosive
1000–2500	Gloucester	Generally clay. Corrosive
25 000–250 000	West Hampshire	Sandy gravel. Not generally corrosive

<sup>a</sup>To obtain  $\Omega$  m divide by 100.**Table 21.27** Corrosion-rate conversion factors

<i>Multiply</i>	<i>by</i>	<i>To obtain</i>
Milligrams per square decimetre per day ( $\text{mg dm}^{-2} \text{ day}^{-1}$ or mdd)	10	Grams per square metre per day ( $\text{g m}^{-2} \text{ day}^{-1}$ or gmd)
Inches per year (in $\text{year}^{-1}$ or ipy)	25.4	Millimetres per year ( $\text{mm year}^{-1}$ or mpy)
Milligrams per square decimetre per day (mdd)	$0.00144/\rho$ ( $\rho$ in $\text{g cm}^{-3}$ )	Inches per year (ipy)
Milligrams per square decimetre per day (mdd)	$0.03652/\rho$ ( $\rho$ in $\text{g cm}^{-3}$ )	Millimetres per year (mpy)
Grams per square metre per day (gmd)	$0.36525/\rho$ ( $\rho$ in $\text{g cm}^{-3}$ )	Millimetres per year (mpy)
Grams per square inch per hour	372 000	Milligrams per square decimetre per day ( $\text{mg dm}^{-2} \text{ day}^{-1}$ )
Grams per square metre per year	0.0274	Milligrams per square decimetre per day ( $\text{mg dm}^{-2} \text{ day}^{-1}$ )
Milligrams per square decimetre	0.0003277	Ounces per square foot ( $\text{oz ft}^{-2}$ )
Milligrams per square decimetre per day	0.00000269	Grams per square inch per hour ( $\text{g in}^{-2} \text{ h}^{-1}$ )
Milligrams per square decimetre per day	36.5	Grams per square metre per ( $\text{g m}^{-2} \text{ year}^{-1}$ )
Milligrams per square decimetre per day	0.00748	Pounds per square foot per year ( $\text{lb ft}^{-2} \text{ year}^{-1}$ )
Ounces per square foot	3052	Milligrams per square decimetre ( $\text{mg dm}^{-2}$ )
Pounds per square foot per year	133.8	Milligrams per square decimetre per day ( $\text{mg dm}^{-2} \text{ day}^{-1}$ )
Grams per square metre per day	$0.36525/\rho$ ( $\rho$ in $\text{g cm}^{-3}$ )	Millimetres per year ( $\text{mm year}^{-1}$ )
Grams per square metre per day	$365.25/\rho$ ( $\rho$ in $\text{kg m}^{-3}$ )	Millimetres per year ( $\text{mm year}^{-1}$ )

**Table 21.28** Calculation of Corrosion rates of metals

The corrosion rate of a metal in terms of weight loss per unit area ( $\text{g m}^{-2} \text{ day}^{-1}$ ) or rate of penetration ( $\text{mm year}^{-1}$ ) can be calculated from Faraday's law if the current density is known. Conversely, the corrosion current density can be evaluated from the weight loss per unit area or from the rate of penetration. The following symbols and units have been adopted in deriving these relationships in which it is assumed that corrosion is uniform and the rate is linear:

$m$  = Mass of metal corroded (g)

$M$  = Molar mass ( $\text{g mol}^{-1}$ )

$z$  = Number of electrons involved in one act of the corrosion reaction

$F$  = Faraday's constant, 96 487 C ( $1 \text{ A} = 1 \text{ Cs}^{-1}$ )

$I$  = Current (A)

$i$  = Current density ( $\text{A cm}^{-2}$ ) and  $i = I/S$

$t$  = Time (s)

$\rho$  = Density of metal ( $\text{g cm}^{-3}$ )

$S$  = Area of metal involved ( $\text{cm}^2$ )

$d$  = Thickness of metal removed (cm)

From Faraday's law the weight loss per unit area is

$$\frac{m}{S} = \frac{Mit}{zF} (\text{g cm}^{-2}) \quad [21.1]$$

Since  $m = \rho Sd$ , then from eqn [21.1]

$$\rho Sd = \frac{Mit}{zF} \text{ or } \rho d = \frac{Mit}{zF} \quad [21.2]$$

and from eqn [21.2] the rate of penetration  $d/t$  when  $I$  is in  $\text{A cm}^{-2}$  is given by

$$\frac{d}{t} = \frac{Mi}{\rho zF} (\text{cm s}^{-1}) \quad [21.3]$$

If the c.d.  $i'$  is in  $\text{mA cm}^{-2}$ ,  $d$  in mm, and  $t$  in years, then

$$\frac{d}{t} = \frac{10^{-1}}{365 \times 24 \times 60 \times 60} = \frac{Mi'}{\rho zF} \times 10^{-3} (\text{mm year}^{-1})$$

$$\therefore \frac{d}{t} = 3.2706 \frac{Mi'}{z\rho} (\text{mm year}^{-1}) \quad [21.4]$$

To convert rate of penetration into weight loss per unit area per unit time:

$$(\text{gm}^{-2} \text{ day}^{-1}) \times \frac{0.36525}{\rho} = (\text{mm year}^{-1})$$

To convert c.d. ( $\text{mA cm}^{-2}$ ) into gmd:

$$(\text{gm}^{-2} \text{ day}^{-1}) = 3.2706 \frac{Mi'}{z\rho} \times \frac{\rho}{0.36525} = 8.954 \frac{Mi'}{z} \quad [21.5]$$

If  $i''$  is the current density in  $\mu\text{A cm}^{-2}$

$$(\text{gm}^{-2} \text{ d}^{-1}) = 8.954 \frac{Mi''}{z} \times 10^{-3} \quad [21.6]$$

## Relevant Websites

Properties and Designations of Materials: [www.matweb.com](http://www.matweb.com)

Table of the Elements and Their Properties: [www.webelements.com](http://www.webelements.com)

International Standards Organisation: [www.iso.org](http://www.iso.org)

National Institute for Standards and Technology: [www.nist.gov](http://www.nist.gov)



## 4.43 Preservation of Metallic Cultural Heritage

**D. Watkinson**

Conservation Section, School of History and Archaeology, Cardiff University, Cardiff CF10 3EU, UK

© 2010 Elsevier B.V. All rights reserved.

---

<b>4.43.1</b>	<b>Introduction to Conservation of Metals</b>	3308
4.43.1.1	Cultural Heritage Context	3308
4.43.1.2	Conservation: Definitions and Rationale	3309
4.43.1.2.1	Conservation rationale	3309
4.43.1.2.2	Preservation goals	3309
4.43.1.2.3	Standards in conservation	3309
4.43.1.2.4	Ethics	3310
<b>4.43.2</b>	<b>Corrosion</b>	3310
4.43.2.1	The Influence of Corrosion on Conservation Strategies	3310
4.43.2.2	Corrosion of Archaeological Metals	3310
4.43.2.3	Corrosion of Historical and Modern Metals	3313
<b>4.43.3</b>	<b>Environmental Control of Corrosion: Preventive Conservation</b>	3314
4.43.3.1	Desiccation	3314
4.43.3.1.1	Relative humidity – Threshold corrosion values	3314
4.43.3.1.2	Practical humidity control	3315
4.43.3.2	Deoxygenation	3317
<b>4.43.4</b>	<b>Interventive Treatments</b>	3317
4.43.4.1	Removing Ions that Act as Corrosion Accelerators	3317
4.43.4.2	Washing Methods in Practice	3318
4.43.4.3	Removal of Corrosion Products	3320
4.43.4.4	Electrolytic Techniques	3321
4.43.4.5	Hydrogen Reduction	3323
<b>4.43.5</b>	<b>Coatings</b>	3324
4.43.5.1	Coating Rationale and Research	3324
4.43.5.2	Metal Surfaces and Patinas	3326
4.43.5.3	Preparing Surfaces on Cultural Objects to Receive Coatings	3327
4.43.5.4	Coatings in Conservation Practice	3328
4.43.5.4.1	Acrylic coatings	3328
4.43.5.4.2	Waxes	3330
4.43.5.4.3	Cellulose nitrate	3331
4.43.5.4.4	Silanes	3331
<b>4.43.6</b>	<b>Inhibitors in Conservation</b>	3332
4.43.6.1	Benzotriazole (BTA)	3332
4.43.6.2	Tannins	3334
4.43.6.3	Carboxylates	3334
<b>4.43.7</b>	<b>Painted Metals</b>	3335
4.43.7.1	Removing Paint	3335
4.43.7.2	Refinishing Painted Surfaces	3335
<b>4.43.8</b>	<b>Overview</b>	3337
<b>References</b>		3338

---

## Glossary

**Conservation** Preservation of cultural heritage.

**Dense corrosion product layer (DPL)** The corrosion layer on archaeological iron objects that approximates to the original shape of the metal lost.

**Interventive conservation** Preservation strategy that involves physical or chemical change to an object.

**Marker layer** The layer of corrosion that approximates to the original position of the metal surface.

**Preventive conservation** Preservation strategy that utilizes techniques that do not involve physical or chemical change to an object.

## Abbreviations

**BTA** Benzotriazole

**CD** Current density

**CSS** Confederate Southern States

**DPL** Dense corrosion product layer

**EDX** Energy dispersive X-ray analysis

**EIS** Electrochemical impedance spectroscopy

**HMS** Her Majesty's Ship

**RH** Relative humidity

**SEM** Scanning electron microscope

**XRD** X-ray diffraction

## Symbols

$E_{\text{corr}}$  Corrosion potential (volts)

w/w Ratio of weights

### 4.43.1 Introduction to Conservation of Metals

#### 4.43.1.1 Cultural Heritage Context

Cultural heritage is an industry that significantly contributes to the economy of nations via tourism, employment, and taxation. Whole communities rely on it for their economic welfare. Cultural objects and structures document developments and events within a society, offering a bridge to the past and providing important markers for individuals, religions, and cultures. To continue their contribution to the welfare, stability, development, and understanding of societies, cultural objects must be actively preserved. Age, origin, and use mean

that historical, archaeological, industrial, and art objects are often decayed, corroded, and prone to further deterioration. The diversity of contexts from which cultural heritage metals originate presents a significant preservation challenge. This chapter briefly defines conservation and provides an insight into the goals and ethical constructs that underpin its decision-making rationale. This is followed by an overview of how corrosion processes relate to treatment design and assessment. Conservation strategies for metals are revealed using selected examples of treatments to illustrate conservation research and practice.

Metals conservation involves the preservation of cultural objects and conservators are its practitioners. Their goal is to preserve objects while retaining evidence of their cultural context and integrity. Ideally there should be minimum change to an object while achieving this and restoration to the former state is rarely carried out. Refinishing, replacement of parts and repairing of metal objects with new corrosion-resistant materials are not normally options within the conservation process. While preservation appears to be a straightforward material science problem, involving elucidation of the structure and corrosion of metals to develop conservation procedures that prevent or control corrosion, it is constrained by ethics, aesthetics, and cultural contexts that may complicate, constrain, and ultimately direct preservation strategies.<sup>1</sup> The goal of conservation is normally the preservation of an object using minimum intervention, although in some instances arguments for partial or total restoration are valid and professional guidelines aid rationalization here.<sup>1</sup>

Research into the corrosion and conservation of historic and archaeological metals is developing significantly due to the increasing contribution of dedicated specialists and funding of large collaborative research programs that have a specific focus<sup>2,3</sup> and the challenges of large complex objects. An influx of corrosion scientists has improved the methodology of research and the understanding of conservation methods by widespread introduction of electrochemistry into corrosion and treatment studies.<sup>2-4</sup> As conservation is a blend of art and science, it utilizes data and publications generated by many disciplines to devise its preservation strategies. Literature sources within conservation focus mainly on conference proceedings and research project publications dedicated to specific themes that provide discussion forums for developing, interpreting, and reporting metallic corrosion and the conservation process. Metals conferences are organized and published by national conservation groups, museums, universities, and the International

Council for Museums Committee for Conservation Metals Working Group (ICOM-CC Metals WG). The Triennial Conference Proceedings of the ICOM-CC Metals WG provide the main dissemination route for metals corrosion and treatment research. This is supplemented by a web-based newsletter Bulletin of Research on Metals Conservation (BRO-MEC).<sup>5</sup> There are few textbooks that either specifically address metals conservation or contain significant sections dedicated to it.<sup>6–8</sup> A number of conservation journals report metals conservation and amongst these are *Studies in Conservation* and *Reviews in Conservation* published by the International Institute of Conservation; *Journal of the American Institute for Conservation*; *The Conservator* (Journal of the Institute of Conservation); and the German *Arbeitsblätter für Restauratoren*.

#### 4.43.1.2 Conservation: Definitions and Rationale

##### 4.43.1.2.1 Conservation rationale

Conservation of metals can be broadly split into interventive methods, which involve adding or removing something from an object in order to preserve it, and preventive techniques that aim to prevent corrosion by controlling the environment.<sup>1,9</sup> Both approaches require an understanding of the physical and chemical structure of metals, their interaction with environmental variables and the properties of their corrosion products. This information is used to design safe storage environments and to develop, implement, and assess interventive treatments. Conservation does not have its own universally defined preservation standards and generally works towards goals generated to satisfy prevailing situations.

##### 4.43.1.2.2 Preservation goals

The ultimate conservation goal of indefinite preservation has driven conservation rationale for many years. Stabilization is a much used word in conservation literature and a reassessment of its meaning and context are long overdue. Since few metals are inherently stable in ambient conditions, corrosion prevention for metals and alloys requires some degree of environmental control.<sup>9</sup> Depending on the degree of control required, significant capital outlay and ongoing energy consumption may be called for. This will carry a carbon footprint and may be beyond the financial means of many museums. Qualitative and quantitative control of environmental parameters, backed by relevant research to identify the environmental needs of the metals in question, underpins the concept of preventive conservation. Unstable metals are merely prevented from corroding using environmental control

and they remain inherently unstable. Since they have not been stabilized by an interventive treatment, any changes to the environment could once again favor their decay. This minimalist approach to preservation is now much favored in conservation practice. Previously, environmental control was normally employed as the end point of an interventive process focused on enhancing the chemical and physical stability of an object by attempts to remove corrosion accelerators and apply coatings and inhibitors. Interventive treatments should only be used where there is evidence that they enhance the stability and lifespan of an object without contravening ethical guidelines.<sup>1</sup>

Preservation strategies should be designed to support the role and function of the object in a society. This may involve public accessibility, which will require provision of oxygen, light, and heat. All of these are agencies of decay that can contribute to corrosion. Access to metal objects may mean it is necessary to accept the concept of limited lifespan, although this will depend on the metal in question and its condition. Alternatively, never viewing an unstable metal object while knowing it is preserved in deoxygenated storage may be an acceptable preservation strategy if the mere knowledge of its existence is sufficient for it to fulfill its cultural role. This may be the case for iconic objects that form cultural cornerstones within societies and history timelines.

##### 4.43.1.2.3 Standards in conservation

Few defined preservation and test standards exist within conservation at the time of writing (2008). The concept of indefinite preservation still pervades conservation thinking for metals. A move towards a rationale that pragmatically measures conservation outcomes as a function of resources, treatment success, cost, and object context is required to facilitate the defining goals that can be used to create standards. To produce attainable standards requires research that provides quantitative evidence of the success of treatment. Within metals conservation there is currently limited quantitative data that could be translated into hard currencies of object longevity, stability, and survival.

Standards grow from attainable and reproducible quantified outcomes. Gaps in our understanding of corrosion processes, treatment mechanisms, and treatment success hinder the production of conservation standards. There is a need for more research that definitively identifies corrosion mechanisms, quantifies treatments and measures their success relative to defined goals. International agreement on what constitutes realistic treatment success is required, as is a

recognized body that defines or approves standards with the support of the conservation profession. Thus, if a standard does not prevent decay there must be an indication as to the extent to which it protects from corrosion or prolongs lifespan. This requires a definition of lifespan reliant upon identifying the function of a cultural object and defining when it ceases to fulfill this function. These are difficult questions but until they are answered conservation cannot develop models that quantitatively define goals and offer a framework of standards to achieve them. There is a case for the conservation profession to devise its own standards for use in research and quality assurance, as ISO and ASTM standards are often inappropriate for use in conservation research and practice.

#### 4.43.1.2.4 Ethics

Ethics both guide and constrain conservation practice. National guidelines define generic rules for good practice that include minimum intervention with objects, reversibility of conservation materials and of treatments applied to cultural objects, as well as retention of the cultural integrity of an object and the information it contains.<sup>1</sup> Situation ethics prevail when determining the level of intervention required to preserve objects. Within archaeological conservation, significant intervention is normally essential for understanding the technology and function of a metal object or for revealing its shape from a corroded metal conglomerate. Ethical dilemmas abound when devising treatment procedures. While a blistering paint surface on a working engine comprising cast iron and steel might be removed and the surface repainted to approved international standards, accessioning such an object into a museum changes this and the paint now constitutes part of the object history. An ethical preservation process for such an object might involve the local stabilization treatment of pits in the paint layer, followed by application of an unobtrusive protective coating and storage in a controlled relative humidity. This is more expensive to execute and offers a less predictive corrosion control strategy than stripping the metal to an SA standard and repainting.

### 4.43.2 Corrosion

#### 4.43.2.1 The Influence of Corrosion on Conservation Strategies

The nature and extent of corrosion strongly influences conservation strategies. Understanding how metals corrode within specified environments such as museum interiors, enclosed storage boxes and the

atmosphere is central to developing treatments and identifying realistic conservation goals. It may be necessary to understand more than one corrosion model to devise conservation procedures. For instance, understanding how archaeological metals corrode during burial is essential for developing a model of their corrosion in the atmosphere following excavation. Equally, elucidating the corrosion mechanisms on a historical pewter salt cellar facilitates an understanding of how this object corrodes in a museum environment. It may no longer contain salt, but the legacy of its original function influences its future survival. Corrosion models also contribute to understanding object aesthetics and developing conservation ethics. Research into corrosion mechanisms informs conservators about the stability of objects, their rate of decay and their conservation needs.<sup>2</sup>

#### 4.43.2.2 Corrosion of Archaeological Metals

Although reviews of archaeological and historical metal corrosion exist,<sup>10</sup> aspects of corrosion relevant to the treatments discussed here are briefly outlined. Archaeological metals normally corrode extensively during burial to form corrosion products related to their burial environment and alloy composition.<sup>2,6,7,9,10</sup> Environment, alloy composition and the mechanisms of ionic and electron transfer during corrosion dictate the nature of the corrosion layer formed and whether corrosion products are passive or unstable. Smooth dense patinas or voluminous disfiguring corrosion layers may form. Some corrosion layers can retain good approximation of the shape of the object and surface details like wear marks or engraving<sup>2,6,7,9,10</sup> (see [Figure 1](#)). These layers have been loosely referred to as representing the original surface of the object<sup>2,7</sup> but are now more often called marker layers.<sup>2</sup> They are often hard and compact and may be overlaid with softer more voluminous corrosion.

Conservation is not just about preservation. Archaeological metals are subjected to investigative conservation that involves analysis designed to answer questions on technology, provenance, and trade.<sup>1,7</sup> Mechanical cleaning employing hand tools like scalpels and micro air abrasion techniques, which utilize powders such as aluminum oxide, are often employed to remove overlying corrosion to reveal the marker layer. Guidance in this process is helped by X-radiography. By detecting differences in density juxtaposition of differing corrosion products are shown, along with dissimilar metals, technological detail and evidence



of residual metal<sup>7</sup> (see [Figure 2](#)). This information-sensitive marker layer may be physically weak and infused with soluble corrosion accelerators, but it must remain undamaged by any treatment, whether it has

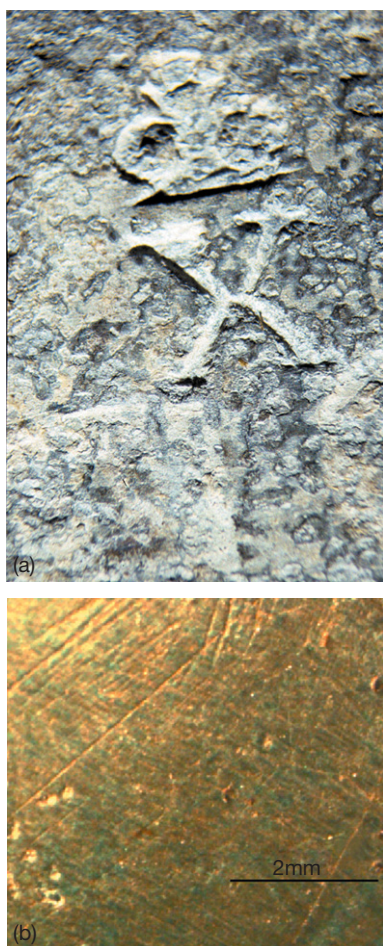


**Figure 1** Corrosion products can sometimes retain significant surface detail. Lead and tin corrosion products record an assay mark in an archaeological pewter object (a) and a Roman copper alloy stud retains wear mark scratches in its fine smooth patina (b).

been revealed or is left covered with corrosion products. Chemical treatments that strip off all corrosion products to remove the soluble corrosion accelerators they contain cannot be used to treat archaeological metals, as the remaining metal rarely represents the original shape of the object<sup>7</sup> (see [Figure 3](#)).

Post-excavation corrosion processes usually differ from those occurring in the burial environment, as the atmosphere contains more oxygen and is normally less damp than soil.<sup>2,10</sup> To develop a preservation plan it is essential to understand how the corrosion model changes, especially how corrosion products form in the burial environment, respond to the new environment and influence the metal they are associated with.

The instability of archaeological iron offers a clear example of how an understanding of corrosion mechanisms is essential to treatment design. It is used here to illustrate conservation thought processes for metals containing soluble corrosion accelerators. During burial, chloride is attracted to anodes as a counter ion to balance charge from  $\text{Fe}^{2+}$ .<sup>2,10</sup> In damp burial conditions it exists as a  $\text{Fe}^{2+}/\text{Cl}^-$  solution at the metal surface. Chloride content may be typically 0.1–1.5 wt % of object, but can be significantly greater for marine metals<sup>7,10–12</sup>. Soluble chloride acts as an electrolyte making the iron inherently unstable. Overlying the corroding metal core is a dense corrosion product layer (DPL) identified as comprising a goethite ( $\alpha\text{-FeOOH}$ ) or sometimes a siderite ( $\text{FeCO}_3$ ) matrix in which are embedded magnetite ( $\text{Fe}_3\text{O}_4$ ) or maghemite ( $\gamma\text{-Fe}_2\text{O}_3$ ) strips<sup>2</sup> (see [Figure 3](#)). This is effectively the marker layer for the surface of the object and is also present in totally mineralized objects, which present no ongoing corrosion problem, but remain a conservation problem due to their fragility and the need to reveal their original shape.

Moisture and oxygen in the post-excavation environment facilitates the formation of  $\beta\text{-FeOOH}$

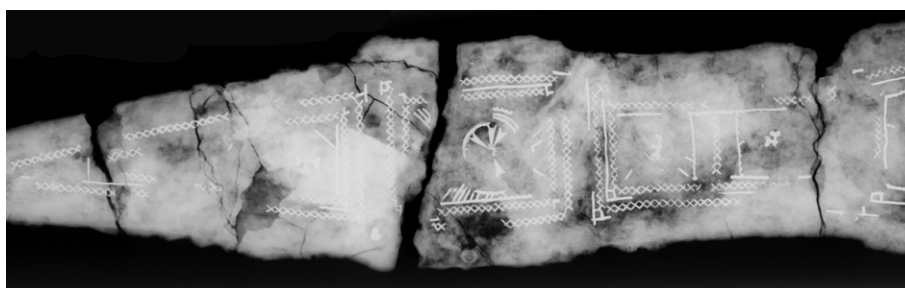


**Figure 2** X-radiography records the presence of a dissimilar metal inlay (silver) hidden under corrosion of uneven density on this Roman Scabbard. The density distribution on the radiograph indicates that no metallic iron remains.



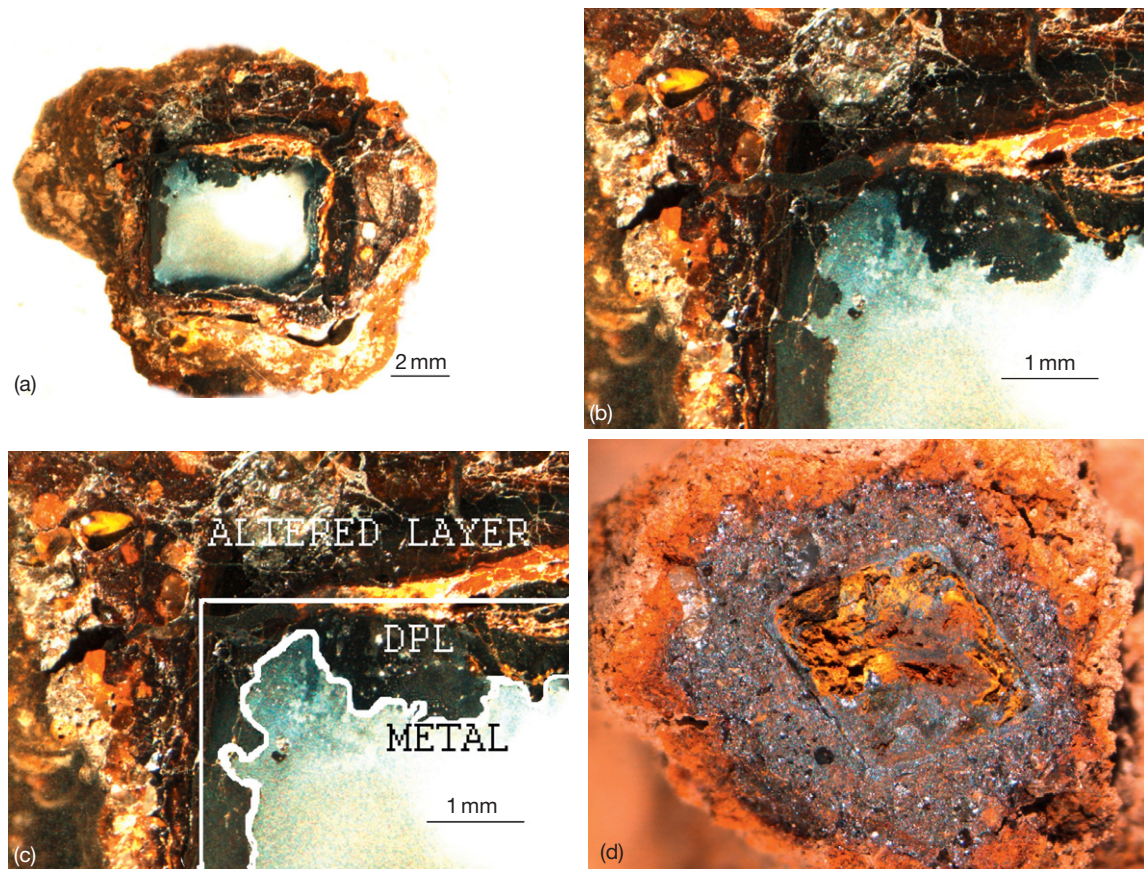


**Figure 3** A cross section of a medieval nail shows it retains a substantial metal core and differing corrosion layers (a). Images (b) and (c) show how the dense corrosion product layer (DPL) retains the shape of the nail, which is overlaid with a corrosion matrix containing soil. Stripping the nail of all corrosion would lose the shape of the object and its surface detail. Totally mineralized iron retains the shape of the object as a corrosion layer, visible in this Roman nail (d).

(akaganeite) in the acidic chloride rich solution sited at anodes on the metal surface. Chloride is incorporated into tunnels within the hollandite-type  $\beta$ -FeOOH crystal structure and adsorbed onto its surface.<sup>2,10</sup> Growth of these voluminous tower-like  $\beta$ -FeOOH crystals pushes off the overlying DPL and is catastrophic for the object as an information resource, as it destroys evidence of the original surface and shape leaving only an unevenly corroded metal core (see [Figure 4](#)). While conservation strategies aim to reveal the shape of the object they must also prevent the corrosion of metallic iron, as the consequent formation of  $\beta$ -FeOOH would remove the information retaining DPL. Totally mineralized iron is stable, as there is no more metal to oxidize and this has allowed soluble anodically held chloride to diffuse out of the object.

Corrosion of nonferrous archaeological metals presents different conservation problems. Most are alloyed with other metals as; bronze (copper/tin sometimes with added lead); brass (copper/zinc);



**Figure 4** Corrosion at the metal/DPL interface results in loss of overlying corrosion products and the information they contain.

pewter (lead/tin); and precious metals (silver/gold, silver/copper, gold/copper). This facilitates preferential corrosion.<sup>7,10</sup> Thus, gold may lose the copper it is alloyed with and be covered in copper corrosion

products. Chemically removing these copper corrosion products leaves a soft porous copper depleted layer of gold on the surface of the alloy. Mechanical removal of corrosion leaves copper corrosion products embedded in the metal surface alongside the gold, but produces a stronger surface.

Corrosion processes, products, and rates can vary according to the proportions of metal within alloys and the burial conditions. This can prove advantageous, although bronzes often decuprify the corrosion of alloyed tin, producing an insoluble and poorly mobile tin oxide to act as a marker layer for the original surface of the metal.<sup>2</sup> Lead forms very stable lead carbonates in neutral to alkaline burial conditions and insoluble chloride compounds that are stable following excavation.<sup>9</sup> Silver is also stable after excavation due to the highly insoluble silver chloride and silver sulfide formed on its surface.<sup>10,13</sup> Lead and tin have similar corrosion potentials and both corrode in pewter to produce a lamellar wart-infested surface with powdery corrosion products that are unlikely to form marker layers. Copper that forms sparingly soluble cuprous chloride ( $\text{CuCl}$ ) next to the metal surface can be unstable following excavation if there is sufficient water to hydrolyze it to voluminous  $\text{Cu}_2\text{OH}_3\text{Cl}$  known as ‘bronze disease.’<sup>2,6,7,8,10</sup> Conservation procedures will be dictated by the stability of the corroded metals, corrosion mechanisms, and the presence or absence of marker layers.

#### 4.43.2.3 Corrosion of Historical and Modern Metals

Historical metals are found in outdoor and indoor environments and may be decorative objects d’art, functional artifacts, or large industrial items. Metals kept indoors since their fabrication may have very little corrosion and retain their original surface finish. Conservation aims to retain such surfaces. This can be achieved by monitoring environments, simple good housekeeping and environmental control in relation to corrosion threshold values for the metals in question.<sup>1,9,14</sup>

The context of the object is important and the nature of a corrosion patina (see [Section 4.43.5.2](#)) may be seen as an important aesthetic value of the object or part of its life history. This will dictate whether it is removed or retained during conservation and heavily influences the choice and success of treatments. Analysis aids decision making in conservation. Sometimes it may be necessary to replace metals if they are performing a structural function. Analysis detected dezincification of brass (70:30) in nails used to join the planks in the hull of the yacht

Asgard (see [Figure 5](#)). Built in 1905 by Colin Archer the renowned Norwegian shipwright for Robert Erskine Chalders the yacht is now an important part of Irish history. The analysis provided information that aided conservation decisions for nails that otherwise appeared to have only surface corrosion.

Modern metals increasingly occur in museum collections and are the fabrication materials of many cultural icons and monuments. These include zinc, aluminum, magnesium, and their alloys.<sup>15</sup> Conservation of protective and technologically informative surface finishes on metals like aluminum may be equally as important as preserving the metal itself.<sup>16</sup> Air quality, relative humidity, and temperature are important for metal stability within museums. The Oddy test<sup>17</sup> was devised to determine if materials used to construct boxes and showcases give off gas pollutants that will cause metals within them to corrode over long-time periods. It can also be applied to show if metals and

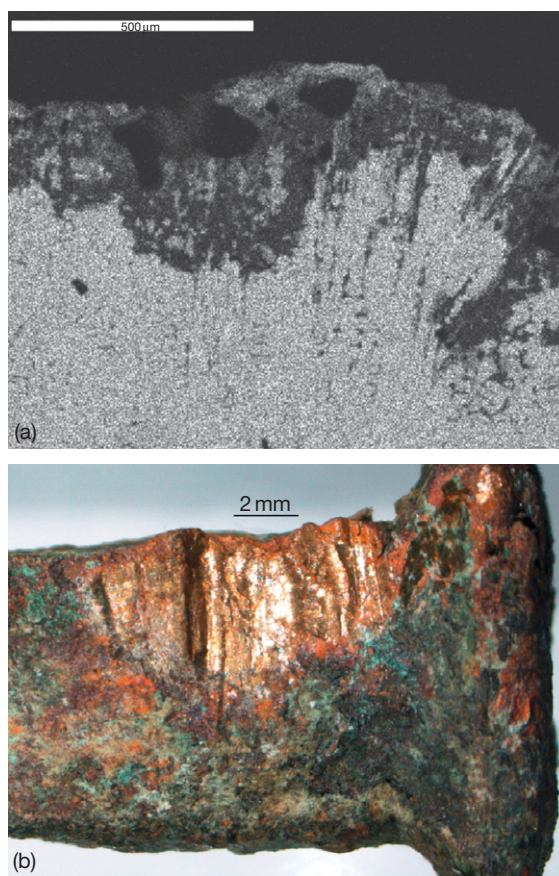


**Figure 5** SEM/EDX mapping of zinc brass hull nails from the yacht Asgard revealed surface dezincification (a) which is not visible on the nail (b). This analysis contributed to designing the yacht’s conservation plan carried out at the National Museum of Ireland. (SEM scale bar 500 µm).



alloys corrode in polluted environments, thus aluminum and Duralmin (Al/Cu) corrode in the presence of formic acid and magnesium and AZ31 (Mg/Al/Mn/Zn alloy) corrode in the presence of a wide range of materials that include oak, plywood, formic acid and wool, which may all be found in museum environments.<sup>15</sup> Lead and copper are also susceptible to corrosion from carbonyl pollutants.<sup>2,9,10,18</sup> Equally studies must examine what occurs when objects are handled, as chloride corrosion products on zinc coins and Indian Bidri ware (zinc alloy) in museum collections were attributed to handling.<sup>15</sup> The influence of handling on corrosion is evident for tarnishing of silver by sulfur compounds, where fingerprints can act as a focus for corrosion (Figure 6). Conservation has moved some way towards developing standards for showcase design and the use of corrosion-safe construction materials, but much more remains to be done.

Outdoor corrosion patterns on metals are predominantly influenced by alloy composition, environment, climate, and the object morphology.<sup>19</sup> Out of doors iron produces a corrosion layer mostly comprised of loose  $\alpha$ -FeOOH rather than form the shape retaining DPL that occurs on archaeological objects<sup>2</sup> (see Figure 3). Sulfurous gases can produce a  $\text{FeSO}_4$  corrosion cycle that is humidity sensitive. While conservation of iron that has corroded in the atmosphere may involve removal of corrosion layers, rather than their retention, outdoor copper alloys may develop patinas considered to be aesthetically desirable and conservation planning takes account of this<sup>2,6</sup> (see Section 4.43.5.2). Humid air containing  $\text{SO}_2$  will attack copper alloys dissolving passive layers and supporting electrochemical corrosion of the alloy,<sup>19</sup> which is problematic

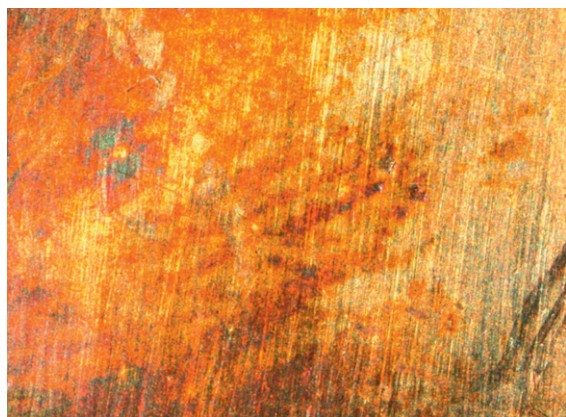


**Figure 6** The influence of a fingerprint on the pattern of sulfur tarnishing on this silver surface is clearly visible. A protective coating on the surface would have prevented this.

for statuary and architectural fittings. Establishing the precise role of patinas and corrosion product layers in the corrosion process is currently underway for many metals,<sup>2</sup> which will facilitate better long-term planning and improve treatment design.

### 4.43.3 Environmental Control of Corrosion: Preventive Conservation

#### 4.43.3.1 Desiccation

A common preservation strategy for cultural metals is to prevent their electrolytic corrosion by controlling one of the agencies essential for this process to occur. Normally, removal of moisture is used to prevent electrolyte formation, although in some instances the oxygen necessary to support cathodic processes and form corrosion products is removed. Removal of electrolyte ions from corroded metals involves interventive treatment. It is easier, cheaper, and more user friendly to control corrosion by desiccation than to remove oxygen. The degree of desiccation necessary to prevent corrosion differs according to the corrosion mechanism of the particular metal or alloy and dictates the cost of corrosion control as capital outlay on plant, fuel, and personnel. Despite the importance of understanding corrosion mechanisms for optimizing preventive conservation strategy, only chloride infested iron has been extensively researched to identify relative humidity (RH) no-corrosion thresholds for reactions within its corrosion mechanism.

##### 4.43.3.1.1 Relative humidity – Threshold corrosion values

Ambient humidity can supply moisture to solvate ions within corroded metals and create electrolytes. Conservation of metals examines corrosion as a function of RH rather than absolute humidity.<sup>6,8,10,14</sup> It is well known that hygroscopic or deliquescent salts such as sodium chloride can lower the RH threshold for corrosion to occur.<sup>10</sup> The RH at which the formation of electrolytes begins is the threshold corrosion value.<sup>20</sup> On corroded iron the surface adsorbed chloride on hygroscopic  $\beta$ -FeOOH becomes mobile within atmospheric moisture and corrodes iron in contact with it at 15% RH<sup>20</sup> (see Figure 7). Additionally, ferrous chloride may form in the low pH and high  $\text{Fe}^{2+}/\text{Cl}^-$  environment created as damp chloride infested iron, dries<sup>10</sup> (see Figure 8). Any  $\text{FeCl}_2 \cdot 4\text{H}_2\text{O}$  that forms contains enough water to corrode iron in contact with it, but once  $\text{FeCl}_2 \cdot 2\text{H}_2\text{O}$  forms at 20%, RH corrosion ceases<sup>20</sup> (see Figure 7). Storage standards

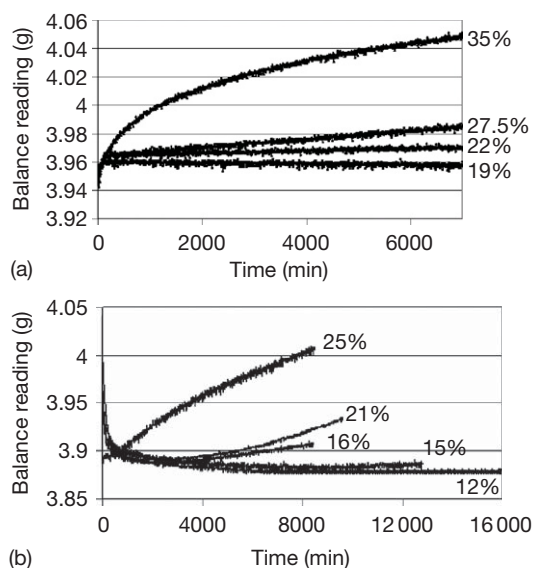


**Figure 7** Relative humidity influences the corrosion of iron powder mixed with  $\text{FeCl}_2 \cdot 2\text{H}_2\text{O}$  (image 1) and  $\beta\text{FeOOH}$  (image 2); with no-corrosion points at low humidity and significant corrosion as 30% relative humidity is approached, as shown by weight gain due to oxidation. Initial weight loss (b) is due to dehydration of  $\beta\text{FeOOH}$  as it equilibrates with its environment.

for chloride infested iron at 20 °C have been defined as: at 12% RH no corrosion; 15–20% RH  $\beta\text{-FeOOH}$  causes slow corrosion of iron; above 21% RH both  $\beta\text{-FeOOH}$  and  $\text{FeCl}_2 \cdot 4\text{H}_2\text{O}$  contribute to corrosion<sup>20</sup> (see Figure 7). Corrosion increases significantly above 25%<sup>19–21</sup> and several times faster above 30% RH than at 25%.<sup>20,21</sup>

In contrast controlled storage of corroded iron from historical contexts has received scant attention in conservation research, as it will tolerate higher humidity values before incurring corrosion if it is chloride free. No conservation studies have examined how iron contaminated with sulfates from  $\text{SO}_2$  pollution would respond to RH.

Corrosion of archaeological copper alloys can occur when cuprous chloride ( $\text{CuCl}$ ) close to the metal surface hydrolyses to form basic cupric chloride ( $\text{Cu}_2\text{OH}_3\text{Cl}$ ) polymorphs, usually clinoatacamite or atacamite with an accompanying molar volume increase.<sup>6</sup> This pressures or undermines the overlying hard and dense corrosion layers that predominantly comprise malachite ( $\text{CuCO}_3 \cdot \text{Cu(OH)}_2$ ), breaking their contact with the  $\text{CuCl}/\text{Cu}_2\text{O}$  mixture next to the metal and ultimately causing their exfoliation. Scott<sup>6</sup> observed no reaction over the relative humidity range 42–46% but rapid corrosion at 70%, leading him to recommend storage below 45% relative humidity in

contrast to the anecdotal 39% commonly cited in conservation. The  $\text{CuCl}/\text{Cu}$  corrosion model merits closer scrutiny to define both the critical no-corrosion humidity and corrosion rates above this value.

Unless it has been already corroded by aggressive ions such as chloride and sulfate, aluminum offers minimal conservation challenges provided it is stored at around 55% relative humidity.<sup>16</sup> Reaction of chloride infested aluminum alloys to relative humidity has not been examined in relation to safe storage thresholds. Similarly, the role of soluble tin chlorides in the corrosion of tin and tin alloys merits detailed study, since tin chloride solutions are prone to hydrolysis.

#### 4.43.3.1.2 Practical humidity control

Humidity control either employs active dehumidification using mechanical plant or passive desiccation using desiccants like silica gel to control environment in fixed storage or display areas.<sup>9,14,21–23</sup> A significant advantage of controlling corrosion of cultural metals by desiccation is that they remain easily accessible, especially if an entire store room is desiccated as opposed to individual storage boxes. Although maintaining low humidity using mechanical desiccation plant demands finance and energy, it is capable of controlling large spaces that will require only one or two telemetric sensors to monitor relative humidity. These can immediately and remotely detect any failure to maintain target relative humidity on a macroscale, which allows for rapid remedial response. Thus mechanical corrosion control is a low risk corrosion control strategy for cultural metals, provided resources exist to underpin its continuing operation and management.

In contrast the small scale control of climate by silica gel for storage within enclosed polyethylene boxes and for display in sealed showcases appears to offer a cheap conservation strategy for small metal objects. Gradual hydration of the desiccated silica gel will occur as a function of air exchange rate, external relative humidity and initial moisture content of the metals being desiccated.<sup>21–24</sup> This eventually raises internal humidity within the controlled space to values that support corrosion, which will speed up as internal relative humidity continues to rise until it equilibrates with the external environment. The metals now rest in a continually aggressive environment. Determining when to replace the silica gel relies upon knowing the threshold corrosion value of the metals in question and detecting when the interior of the box exceeds this value.

Research to evaluate the complex equation of storage, hardware performance, air exchange, monitoring, maintenance time, and human error is needed



**Figure 8** Brunel's iconic SS Great Britain was the first ocean going screw driven iron hulled passenger liner and is now preserved by a mechanical desiccation system that maintains relative humidity to 20% and allows visitors to walk around the hull. Reproduced from Watkinson, D.; Tanner, M.; Turner, R.; Lewis, M. *The Conservator* **2005**, 29, 73–86.<sup>25</sup>

to offer a realistic and practical assessment of this corrosion control strategy. Enclosure design largely controls air exchange rate which is the governing factor in passive desiccation systems.<sup>24</sup> Assessment of enclosure performance can produce predictive life spans for specified passive desiccation storage systems.<sup>21,24,26</sup> Showcases designed for desiccation maintained relative humidity below 20% for 1 year without a change of their silica gel desiccant, when external relative humidity fluctuated between 60% and 95%.<sup>22,24</sup> As telemetric monitoring of showcase

performance is easy to initiate and financially viable, this system offers potentially reliable low energy consumption corrosion control for unstable metals on display. The major cost will be an initial outlay to meet the showcase specification. Further work could establish performance of the showcase with age and use. This requires real-time testing that may take several years. Attempting to define long-term effectiveness by extrapolating a one year study or short-term laboratory results cannot provide a definitive guide to performance.



The performance of polyethylene storage boxes as desiccated depositories for archaeological iron has been studied as functions of manufacturer, age, use, silica gel performance, and ambient relative humidity.<sup>21</sup> The study confirmed earlier studies on threshold corrosion values<sup>20</sup> and determined most air leakage was via lid seals, making storage protocols important in relation to the stacking of boxes compromising their seals. Storage in polythene boxes suffers from a reliance on the limited accuracy of moisture sensitive indicators to detect the internal relative humidity of boxes for gel regeneration cycles. Individual telemetric monitoring of the interior of the box is financially prohibitive for the several hundred polyethylene boxes normally housed in a storeroom. Good management is also necessary if the gel is to be changed as required. It is essentially a low cost, but high risk corrosion control strategy when the frailties of human nature are taken into account.

Relating corrosion rate to increasing relative humidity provides opportunity for pragmatic management decisions.<sup>25</sup> The degree of corrosion control implemented can be matched to resources available to produce a package that will reduce, but not prevent corrosion. This reasoning was used to control corrosion of Brunel's famous 1843 wrought iron steamship SS Great Britain, whose chloride-ridden lower hull is preserved in a mechanically desiccated dry dock maintained at 20% relative humidity with a goal of retaining its structural integrity for at least 100 years<sup>25</sup> (see [Figure 8](#)). This allowed public access to the hull and avoided employing costly and environmentally unfriendly alkaline washing methods (see [Section 4.43.4.2](#)) in attempts to remove chloride corrosion accelerators from the 324 ft long hull. The conservation challenge required a scientific investigation to identify the influence of RH on corrosion, followed by an engineering project to design an envelope to maintain the operating RH.

#### 4.43.3.2 Deoxygenation

Ageless™ is a commercial oxygen absorber that has been used in conservation to deoxygenate enclosed spaces.<sup>26</sup> It is expensive to use and the exothermic reaction that expends oxygen produces water, which should offer no corrosion risk provided the storage environment remains oxygen free. Despite technical challenges, high cost, and reduced accessibility, archaeological iron has been stored in heat sealed low linear density polyethylene tube, with barrier properties 2000 times better than polypropylene, deoxygenated with

oxygen scavenging RP-A™ (mordenite/CaO/PE/activated carbon).<sup>27</sup> This study showed that iron objects, which had been pretreated in aqueous NaOH to wash out chloride (see [Section 4.43.4.2](#)), remained visibly unchanged over a 5-month period but untreated iron had a 12% failure rate attributed to poor seals and bag punctures. Although the researchers predict a storage lifespan of 4–6 years, the high initial cost of materials and labor and a one-shot storage system make it unlikely that it will displace desiccation in popularity. A long-term quantitative testing program comparing its effectiveness, ease of use and global cost with desiccation techniques would define the relative merits of these two treatments. Using a flow of nitrogen gas through an enclosed container offers a no-corrosion environment for damp high status archaeological objects prior to their conservation.

### 4.43.4 Interventive Treatments

#### 4.43.4.1 Removing Ions that Act as Corrosion Accelerators

Interventive treatments aimed at reducing or preventing corrosion of unstable metals mostly focus on removing chloride and other soluble ions that are capable of acting as electrolytes in high humidity environments. Entirely removing soluble ions should prevent corrosion, while their partial removal enhances the stability of the object by reducing electrolyte availability. Additionally, some washing treatments may aim to remove or modify sparingly soluble or insoluble corrosion products that promote corrosion.<sup>11,28</sup>

From an ethical standpoint, merely enhancing stability without controlling environment to prevent corrosion may not be considered an appropriate corrosion control strategy. Even a small amount of corrosion occurring at anode sites on the metal can interfere with adhesion of important overlying corrosion layers, whose loss destroys the object as an information resource despite the survival of the metal core (see [Figures 2–4](#)). Delaying this for a short time by reducing corrosion rate could be viewed as a very limited goal, when measured against the ideal of indefinite preservation. Equally, treatments that partially remove corrosion accelerators could be seen as unnecessary, since post treatment storage must be similar to that provided for untreated metals. Why bother trying to remove electrolytes if the objects still need to be subjected to the same stringent storage conditions? One possible advantage is that failure to maintain the controlled environment will lead to a slower corrosion

rate, as compared to untreated iron objects. Quantitative understanding of treatment efficiency and effectiveness is essential for facilitating informed decisions about their use.

To optimize treatments designed to remove corrosion accelerators that are normally predominantly comprised of chlorides, it is necessary to: identify the corrosion mechanism; devise appropriate chloride removal procedures; quantify the removal of chloride as an absolute value of chloride contained in the metal; use this value to calculate extraction efficiency; determine the extent to which the metal is stabilised.<sup>11</sup> While the concept of removing soluble ions to prevent electrochemical corrosion is logical, no studies provide quantitative assessment to show how stable metals like iron become following attempts to remove their soluble chloride. Equally, there is limited information as to what percentage of chloride present within objects is extracted by a particular treatment and how consistently this occurs.<sup>11,12,29</sup>

#### 4.43.4.2 Washing Methods in Practice

Washing methods are applied to metals to solvate soluble corrosion products and soluble ions adsorbed onto corrosion products. Iron is the most unstable archaeological and historical metal, due to its ability to attract chloride and retain it in a highly soluble form.<sup>10</sup> Washing methods will solvate chloride ions and this allows them to diffuse out of the object.<sup>7,11</sup> This process is hampered by the DPL limiting solution access to the iron surface, where wash solutions must enter pits and micro cracks to exchange with chlorides at anode sites. Chloride removal is diffusion controlled, slow, and is unlikely to be 100% efficient, although efficiency can be improved using chemical additives.<sup>11,12,29</sup> Evidence from a qualitative study of the long-term stability of treated archaeological iron revealed simple washing with hot deionized water to be a poor stabilization system, with 68% of treated objects recorroding.<sup>30</sup> Recent study quantitatively confirms washing in deionized water is an unpredictable treatment that never extracts large amounts of chloride<sup>11</sup> (see Figure 9).

Their ease of use and low aggression to iron has meant that inhibited wash solutions have been chosen to treat large objects. HMS Holland was the first submarine used by the British Navy. It was fortunate that she lost her tow en route to the breakers yard and sank, as when she was discovered and salvaged many years later she had become an important historical object. Her 19 m length offered challenges to removing the

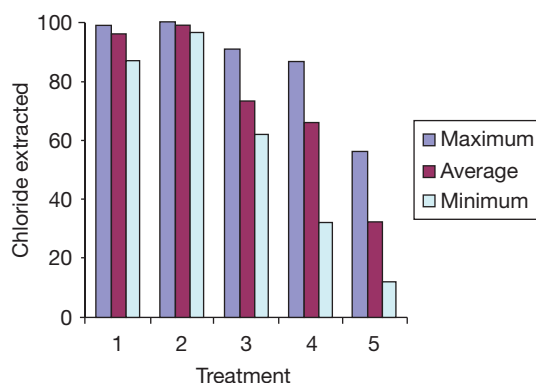


**Figure 9** Influence of treatment solution on percentage chloride removal from Roman and Medieval archaeological iron nails. For each treatment method columns show: best extraction; average extracted; worst extraction. Total chloride in nails determined by post treatment digestion. Treatment methods: (1) NaOH/Na<sub>2</sub>SO<sub>3</sub> 0.5 M aq. (17 nails); (2) NaOH 0.5 M/deoxygenated with nitrogen (10 nails); (3) NaOH 0.5 M aq. (16 nails); (4) Water/deaerated with nitrogen (10 nails); (5) Water (10 nails). Reproduced from Watkinson, D.; Al Zaharani, A. *The Conservator* **2008**, 31, 75–86.

chloride that infused her structure. Health and safety and cost augmented against the use of strongly alkaline wash treatments (see below) and electrolytic desalination (see Section 4.43.4.3). A purpose built treatment tank containing 820 000 dm<sup>3</sup> of Na<sub>2</sub>CO<sub>3</sub> was used to provide an inhibited wash relying on diffusion to extract chloride that was continually monitored.<sup>31</sup> Treatment was followed by storage in a building constructed for this purpose maintained at 35% RH to slow down any corrosion from residual chloride. While new study indicates storage at 25% RH would slow iron corrosion significantly more than 35% RH,<sup>11,20,21</sup> any environmental control program must be related to the finance available to sustain it and 35% RH will restrict corrosion better than higher values. This is a typical finance/corrosion control cost benefit assessment that is a factor in the conservation equation. It is often used to influence selection of treatment options and should be considered when developing standards of treatment. Equally object size may dictate which treatments are feasible, as in the case of the Holland.

Alkaline wash systems act as inhibitors and optimize chloride removal.<sup>8,11,12,29</sup> Inhibition provided by alkalis such as NaOH reduces corrosion during treatment. This releases chlorides from their charge balancing role at anodes and allows them to diffuse out into the wash solution, while at the same time the alkali supplies OH<sup>−</sup> ions to replace them and associate with Fe<sup>2+</sup>. Solvation of solid ferrous chloride and surface adsorbed chloride on β-FeOOH occurs,

reducing  $\beta$ -FeOOH hygroscopicity and preventing post-treatment corrosion of iron in contact with it.<sup>32</sup> In strong alkali  $\beta$ -FeOOH can transform and this will advantageously release chloride into the wash solution.<sup>28</sup> Since the ionic size of chloride occluded in tunnels within  $\beta$ -FeOOH crystals exceeds the diameter of tunnel entrances it remains trapped and presents no post-treatment corrosion threat, unless conversion of  $\beta$ -FeOOH to  $\alpha$ -FeOOH releases this chloride. Post-treatment hydrolysis of residual  $\beta$ -FeOOH to  $\alpha$ -FeOOH can occur but is little studied. A 23-year-old dry sample of  $\beta$ -FeOOH was assayed as being 1%  $\alpha$ -FeOOH and 99%  $\beta$ -FeOOH.<sup>32</sup> A major study currently underway aims to identify physicochemical transformations of corrosion layers as a function of treatment regimes, using microanalysis techniques to characterize the corrosion products.<sup>33</sup> This will significantly contribute to an understanding of treatment and post-treatment corrosion.

Further improvements in chloride extraction can be produced by deoxygenated NaOH solutions<sup>11</sup> (see Figure 9). Passivation of iron in oxygenated NaOH solutions is likely to be incomplete, as NaOH needs to reach all anodes sited at the metal surface to be effective. Consequently, chloride continues to be held as a counter ion and is difficult to wash out. Deoxygenating NaOH solutions with an  $\text{SO}_3^{2-}$  oxygen scavenger or nitrogen gas stops corrosion and improves chloride extraction.<sup>11</sup> Anecdotal reporting indicates undesirable softening of corrosion products in NaOH solution,<sup>30,34</sup> but no studies offer quantitative evidence of this or address the influence of any chemical treatment residues on iron corrosion products. This merits further attention. Objects should be washed post-treatment in deoxygenated water to flush out chemicals.

A promising variation on alkaline washing currently under investigation is the use of a subcritical high pressure alkali treatment for treating the American Civil War submarine Hunley, which was recovered from a marine environment where she had lain since she sank immediately after becoming the first submarine to sink a warship.<sup>12,29</sup> Treatment transforms corrosion promoting  $\beta$ -FeOOH to the  $\alpha$ -FeOOH,  $\text{Fe}_3\text{O}_4$ , and  $\text{Fe}_2\text{O}_3$  chloride-free phases that are nonaggressive to iron.

Other inhibitors have been tried, notably aqueous washing of archaeological iron with ethylene diamine. Inhibition and a high solution pH (11.5 at 5% (v/v) aq.) aim to prevent corrosion during treatment and aid chloride removal. It is an inferior chloride extractor as compared to 2% NaOH aq.,<sup>34</sup> but has been cited as offering good long-term stability to iron in a qualitative study of treated objects.<sup>30,34</sup>

There is limited information available regarding the amount of chloride removed by treatments as a function of total chloride within the iron, since determining residual chloride requires post-treatment digestion of objects. The small amount of quantified data available indicates that some wash methods are significantly better than others and consistently extract within fixed percentages of chloride.<sup>11,12,29</sup> The limit of detection for measuring chloride extracted into wash baths cannot guarantee iron is chloride free.<sup>11,12</sup> Although it is important to determine whether small residues of chloride are capable of causing significant corrosion of iron, testing the susceptibility of washed iron to corrosion has received little attention. For guaranteed no-corrosion all washed iron should be stored in a controlled environment to a standard equaling that used for unwashed iron, but this makes storage costs the same as for untreated iron.

Studies that qualitatively examine the stability of washed and unwashed iron within museum collections have offered comparative assessment of treatment effectiveness.<sup>30,35,36</sup> While these types of survey offer a genuine insight into treatment outcomes, they are limited by their retrospective nature, wide range of uncontrolled variables and a lack of quantified data. Computer monitoring of RH now offers an opportunity for precise recording of storage environment and new studies of long-term performance of treated objects are overdue. It would also be worth interpreting past studies using new data available on corrosion mechanisms.<sup>2</sup> Until quantitative long-term post-treatment stability testing is carried out and outcomes are linked to chloride residues within objects, washing treatments remain empirical applications best described as having an unpredictable and unknown capacity to remove chloride and enhance object stability. Such studies will prove hard to fund because of their time commitment.

Aluminum alloys are becoming increasingly common in museum exhibits and include aircraft and boats rescued from extreme environments. Once the highly protective nonconducting  $\text{Al}_2\text{O}_3$  layer on aluminum fails the metal will corrode. This may cause pitting or intergranular corrosion according to alloying and metallography. Chlorides exacerbate corrosion by attacking the  $\text{Al}_2\text{O}_3$  film and concentrating in pits where they cause low pH, hydrolysis of  $\text{Al}^{3+}$  and voluminous disfiguring corrosion product at the mouth of the pit.<sup>10</sup> The shape of the object is obscured and ultimately lost with eventual perforation of the metal. Washing to remove soluble chloride can be carried out on objects retaining significant amounts of metal, but those without large quantities of metal

will be beyond recovery as corrosion products are non-adherent and friable.

Chemically aided washing was innovatively used to treat a Duralumin (3–5% copper) seaplane float belonging to a Junkers W33 infused with chloride, exhibiting extreme pitting and redeposited copper on its surface that could act as a cathode for continuing corrosion of the aluminum.<sup>37</sup> Washing conditions were carefully manipulated using  $(\text{NH}_4)_2\text{SO}_4/\text{NH}_3$  buffer solution to complex  $\text{Cu}^{2+}$  ions to  $\text{Cu}(\text{NH}_3)_4^{2+}$  and  $E_0$  of the system was lowered to allow corrosion that removed redeposited copper, provided oxygen was present.<sup>37</sup> Thermodynamic data revealed  $\text{Al}_2\text{O}_3$  was stable in the treatment solution. Its presence on the metal surface protected aluminum at the treatment pH of 9.6 and chloride diffused out of the object following hydrolysis reactions within pits. As with most washing methods employed in conservation, assessment of the success of the treatment was qualitative and reported that the object appeared to be stable 4 months after treatment.

Washing has been employed for copper alloys to deal with the problem of  $\text{CuCl}$  hydrolyzing to form  $\text{Cu}_2(\text{OH})_3\text{Cl}$  polymorphs that damage and disfigure copper alloy objects.<sup>6,10</sup> Fortunately  $\text{Cu}_2(\text{OH})_3\text{Cl}$  is not hygroscopic and does not cause corrosion of metallic copper in contact with it, although its growth can undermine and lever off overlying patina. Not all copper alloys containing chloride are unstable. MacLeod<sup>38</sup> argues that there is a minimum chloride ion concentration required to support corrosion. The low solubility of  $\text{CuCl}$  and its positioning within or under  $\text{Cu}_2\text{O}$  means chloride solvation by simple aqueous washing can last years. Washing for up to 2 years in sodium sesquicarbonate ( $\text{NaHCO}_3 \cdot \text{Na}_2\text{CO}_3$ ) at 5% (w/v) pH 10 has been employed to slowly solvate  $\text{CuCl}$  and supply  $\text{OH}^-$  to form cuprous oxide ( $\text{Cu}_2\text{O}$ ).<sup>6,9</sup> Basic copper carbonate ( $\text{CuCO}_3\text{Cu}(\text{OH})_2$ ) and chalconatronite  $\text{Na}_2\text{Cu}_2\text{CO}_3 \cdot 2\text{H}_2\text{O}$  may also form and darkening of patina may make the treatment undesirable when aesthetics are an important consideration. It is now more likely to be used as an inhibited wash solution following other treatments like electrolysis (see [Section 4.43.4.4](#)).

#### 4.43.4.3 Removal of Corrosion Products

Stripping techniques may be employed when ethical arguments allow removal of corrosion, such as preparing lightly corroded industrial and historical steels to receive protective coatings. They may also be used to free archaeological objects from corrosion

conglomerates provided substantial amounts of metal remain, as heavily mineralized objects will lose their identity when corrosion is removed.<sup>8,39</sup> While there are several studies looking into the action of stripping agents there is no single definitive comparative assessment that identifies a preferred method for specified alloys. Conservators must evaluate studies or themselves test stripping agents relative to the object they are planning to treat. That stripping is ethically acceptable at all, illustrates how situation ethics dictate conservation procedures.

Traditional acid stripping solutions are aggressive to metal and corrosion products alike and are now largely ignored, except where it is ethical to remove all corrosion products. Copper alloy coins have been separated using complexing agents exhibiting low aggression to metallic copper to remove copper corrosion products. Citric acid is reported as being best in this respect, when compared to alkaline glycerol, alkaline Rochelle salt, sodium hexametaphosphate, and sulfuric acid.<sup>40</sup> Elsewhere alkaline Rochelle salt is reported as being less aggressive than reagents like methanoic acid, alkaline glycerol and alkaline dithionite.<sup>39</sup> Electrochemical assessment of these reagents would help indicate which reagents offer the best removal of corrosion for the least aggression to the parent alloy. Dealloying is a problem. Predictably, metallic lead is lost from copper alloys by alkaline stripping systems and organic acids. Stripping corrosion from copper alloys<sup>38</sup> and iron<sup>41</sup> has been achieved using thiourea ( $\text{SC}(\text{NH}_2)_2$ ) inhibited citric acid washes. Thiourea controls the aggressive action of citric acid by complexing unstable  $\text{Cu}(\text{I})$  species, to prevent them forming metallic copper, and by forming stable complexes with  $\text{Cu}(\text{II})$ .<sup>8,38</sup> Phosphoric acid ( $\text{H}_3\text{PO}_4$ ) has been used for stripping ferrous metals to leave a ferric phosphate protective film, as has hydrochloric acid with hexamine corrosion inhibitor.<sup>41</sup> All stripping methods require post-treatment washes to remove residual chemicals that would continue to corrode metals. This is often followed by application of a protective coating.

Following citric acid/thiourea treatment of copper alloys, washing in sodium sesquicarbonate is used to neutralize acid and remove  $\text{CuCl}$  left in crevices and cracks, but this is likely to be incomplete.<sup>38</sup> Washing marine copper alloys revealed the benign nature of this treatment method, as tin, zinc, and lead compounds were not removed from either the corrosion products or copper alloy, whereas washing in deionized water removes metallic lead as the purity of the water prevents formation of protective  $\text{PbCO}_3$ .<sup>38</sup> Washing of iron in inhibited chromate or nitrite

solutions following citric acid/thiourea stripping is not environment-friendly, so ecologically superior alkali metal salts of organic carboxylic acids (secacic acid –  $\text{NaOOC}[\text{CH}_2]_8\text{COONa}$ ) have been used to provide washes of similar efficiency.<sup>41</sup> They can also provide long-term inhibitive properties (see [Section 4.43.6.3](#)) and offer promise for widespread use in conservation following more in-depth testing.

Chelating and sequestering agents, such as the sodium salts of ethylenediaminetetraacetic acid (EDTA), have been used extensively in conservation in attempts to dissolve corrosion products without attacking metal. However, they can be slow to act and may be too selective in their action on corrosion products. Careful selection of commercial products is essential to obtain suitable pH values for optimizing complexation. A study examining reaction of disodium edetate ( $2\text{NaEDTA}$ ) on copper corrosion products and copper metal revealed that chelation rate varied according to corrosion product.<sup>42</sup> This would result in differential removal of corrosion products leaving exposed copper open to the treatment solution. Fortunately, metallic copper was barely attacked by  $2\text{NaEDTA}$  over a 30-h period.<sup>42</sup> Dissolved sodium salts of EDTA have also been frequently used to remove corrosion from iron and lead and its alloys.<sup>6,8,31,43</sup> Using compresses allows stripping agents to be used in a controlled manner. Degriigny<sup>44</sup> treated a Citroen caterpillar tracked vehicle used on the trans-Sahara crossing of 1922/23 by this method. It still retained much of its original paint layer. Corroded areas that had sustained paint loss were treated with compresses of tetrasodium edetate ( $4\text{NaEDTA}$ ) to remove iron corrosion products. This was followed by application of inhibitor (see [Section 4.43.6.2](#)) and a protective wax coating (see [Section 4.43.5.4.2](#)) to provide a typical stripping-inhibition-coating treatment regime. All treatment methods were assessed using electrochemical measurements prior to their use. Treatment success was gauged in the usual qualitative manner of visually checking for corrosion as a function of time and no corrosion was visible after 6 months of indoor display. Developing standards for assessing time weighted visual success of treatments set against conservation criteria would produce a useful tool for conservation practice.

Removal of corrosion from copper alloys may also be achieved by alkaline dithionite ( $\text{Na}_2\text{S}_2\text{O}_4$ ) solutions, which provide electrons to reduce corrosion products to finely divided metallic copper.<sup>8,38</sup> Weak heavily corroded objects may be consolidated by this conversion, but there is also a chance they will

disintegrate. The skill and knowledge of the conservator are essential as treatment is fast, lasting only a few minutes followed by a wash of several days to remove residual chemicals.<sup>8</sup>

#### 4.43.4.4 Electrolytic Techniques

Electrolysis is employed in conservation either to entirely remove corrosion products from a metal or to aid diffusion of soluble corrosion accelerating ions into an electrolyte, while retaining corrosion layers on the metal. These differing outcomes are achieved by careful control of current density (CD) and in some instances current delivery. The metal is immersed in a suitable electrolyte and made cathodic relative to an inert anode, which protects it from corrosion during electrolysis. Different metals are electrolyzed in differing ways according to the nature of their corrosion products and the treatment goal. It is an extremely useful technique provided its use matches ethical goals and research identifies optimum treatment methodology. Its context within conservation has only been quantitatively established over the past 15 years since the application of potentiometric electrochemical analysis within conservation research.

Procedures vary from metal to metal. Iron is immersed in an electrolyte in which it will remain passive, such as NaOH. Using an imposed current to cathodically protect the iron frees chloride from its counter ion role, allowing it to solvate and diffuse out of the object.<sup>8,12,29</sup> Chloride is drawn to the inert anode and delocalized from the object by diffusion. Maintaining a low CD retains the information rich DPL by avoiding polarization that would produce hydrogen gas which physically dislodged corrosion layers. Reduction of  $\text{FeOOH}$  corrosion products to  $\text{Fe}_3\text{O}_4$  can occur and the accompanying increase in density increases porosity which is said to contribute to facilitating diffusion of chloride out of the object.<sup>7,8</sup>

Most quantitative assessment of chloride removal by electrolysis has been carried out on cast iron, whose even corrosion matrix is different to the lamellar structure of corroded wrought iron.<sup>2,8,29</sup> Tests on small cast iron chloride infested samples reveal significant migration of chloride to the anode during electrolysis.<sup>29</sup> Quantitative measurement has shown that electrolysis ( $\text{CD } 10 \text{ mA dm}^{-3}$ ) in NaOH solution is no better at extracting chloride than aqueous washing in NaOH solution.<sup>12</sup> While washing is easier to carry out than electrolysis, full inhibition of iron corrosion in a 1% NaOH wash solution cannot be



guaranteed in the same way as an imposed current protects during electrolysis.

Electrolytic treatments are often favored for large iron objects, as they will remain cathodically protected during the long treatment times required to remove deep-seated chloride. Treatment may take from 1 to 4 years for large cast iron cannon and wrought iron anchors from marine contexts<sup>45</sup> and even very small cast iron samples required over 200 days to desalinate.<sup>12,29</sup> As with most metal treatments, there is no report of any quantitative long-term assessment of post-treatment stability of electrolyzed iron as a function of relative humidity. Intentionally using a high CD to remove all corrosion layers may be ethical for certain industrial and historical objects, provided their corrosion layers contain no information and they retain substantial metal cores. Such treatment would usually be a precursor for the application of protective coatings (see [Section 4.43.5](#)).

An advantage of electrolytic treatments is their degree of control, as the imposed potential can be matched to specific reduction processes. They are also useful for large objects, as electrolytic treatments can be run for long periods of time with little input from the conservator thereby saving labor. Circumstance must dictate whether electrolysis is possible. *HMS Minerva* was a big gun monitor launched in 1915 and sold as a visitor attraction in 1984. Removal of the high levels of chloride inside her hull was achieved by flooding it with  $\text{Na}_2\text{CO}_3$  electrolyte and making it cathodic ( $35 \text{ mA m}^{-2}$ ) relative to stainless steel mesh anodes placed directly above it.<sup>31</sup>

Electrolysis can be used to remove all corrosion from lightly corroded lead to reveal fine details on the metal surface. This is normally carried out in sulfuric acid electrolyte. A brief reversal of the electrode poles upon completing treatment makes the lead anodic and forms an invisible  $\text{PbSO}_4$  coating that has protective properties in the atmosphere.<sup>43,46</sup> The final 'fresh metal' appearance of lead treated in this way would influence any decision to use this method. Electrolysis of copper alloys to remove potentially reactive  $\text{CuCl}$  and all other corrosion products is now considered to be aggressive and difficult to control, with a high risk of redepositing reduced copper. Simple electrolysis of copper alloys in water is advocated as deserving of more research, as it can retain the copper corrosion product patina and offer cathodic protection of the metal during treatment.<sup>6</sup>

The inherent insolubility of the silver corrosion products  $\text{Ag}_2\text{S}$  and  $\text{AgCl}$  prevents the formation of electrolytes on corroded silver exposed to high relative humidity. Consequently their removal is largely an

aesthetic act or an information revealing strategy, according to whether the layer is a thin  $\text{Ag}_2\text{S}$  tarnish or a thicker layer of  $\text{AgCl}/\text{Ag}_2\text{S}$  that might be found on archaeological silver objects. Once silver is returned to a shiny metal finish the challenge is to apply coatings or control environments to prevent sulfur-based pollutants tarnishing it (see [Section 4.43.5](#)). Electrolysis removes silver corrosion products within a wide range of operating parameters using electrolytes such as formic acid (5–30%, w/w) or  $\text{NaOH}$  (5–15%, w/w) with CD of  $0.3\text{--}20 \text{ mA cm}^{-2}$  at 3–12 V.<sup>6,13</sup>

Very low current densities have been used to slowly reduce corrosion on mineralized brittle silver objects to metallic silver, which is retained *in situ* to produce a consolidative effect.<sup>13</sup> Conflicting reports of success make this a high-risk strategy, as weak mineralized silver objects may fall apart during treatment due to reduced coherence of their corrosion layers. Potentiometers have been employed to apply potentiostatic cleaning of silver.<sup>13</sup> This method uses a third reference electrode to control the potential of the cathode and a polarization plot is used to identify reduction potentials of the corrosion products, which are then reduced by setting the object potential to match the reduction potential of the corrosion product. It is a finely controlled system that avoids any unwanted reactions such as hydrogen reduction and is useful for tarnish ( $\text{Ag}_2\text{S}$ ) removal.

Once corrosion begins on aluminum and its alloys they corrode rapidly in the atmosphere. Electrolysis can be used to remove chloride corrosion accelerators and unstable corrosion products. Degriigny<sup>47</sup> developed a treatment that cathodically polarized aluminum to constant potential in a buffered deaerated slightly acid citrate solution, with treatment parameters optimized to avoid pitting corrosion from the chlorides extracted into the treatment solution and cathodic corrosion of the metal. Composite aluminum objects associated with other metals like iron are problematic, as significant galvanic couples can be established during treatment. For this type of composite metal object electrolysis is modified. Active polarization of the composite object in an inhibited solution protecting the aluminum alloy from corrosion produces a potential that facilitates formation of a protective magnetite coating on the iron fittings.<sup>48</sup> This is followed by polarization of the object in citric acid solution (pH 7) to remove aluminum corrosion products and chloride. Finally, polarization in deionized water washes out chemicals introduced during treatment. The object is dried and coated with a suitable protective coating (see [Section 4.43.5.4.2](#)).

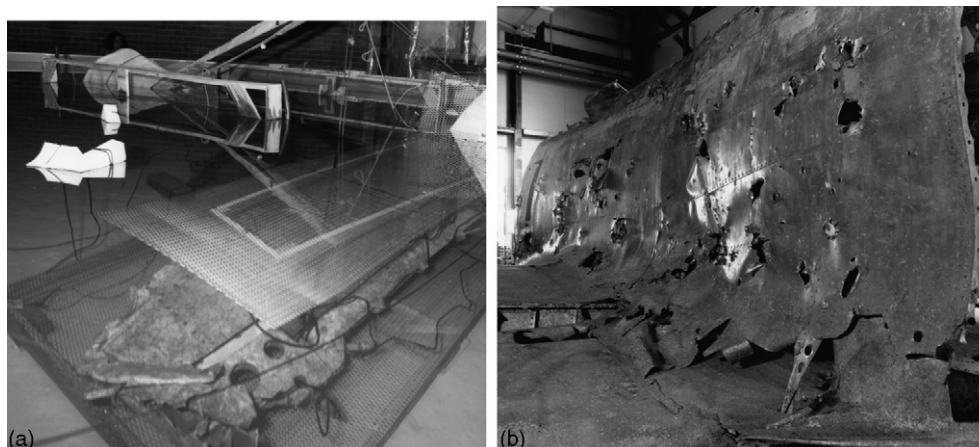


**Figure 10** Electrolysis of Japanese 'Oscar' aircraft (a) and completed fuselage (b).<sup>49</sup> Image courtesy of Australian War Museum.

Treatments are often fine tuned to the needs of an object. Adaptation of electrolyzing aluminum omitted the magnetite forming step to treat a WWII Japanese Oscar Ki43II fighter retrieved from a saline swamp.<sup>49</sup> The design utilized a swimming pool, 55 000 l of water and 800 kg of chemicals with expanded stainless steel mesh anodes conformed to the shape of the aircraft and sited 30 cm above its surface (see [Figure 10](#)). The inevitable post-treatment flash rusting of ferrous components was dealt with by a tannic acid inhibitor. Original paint and penciled notes on the cockpit fascia were masked prior to treatment. Success was assessed by ongoing observation, as opposed to quantifiable measurements of change or residual chloride in objects.

Imposed currents are used industrially to protect large homogenous steel structures, but heterogeneity and corrosion in historical metal objects produce discontinuities that limit applications of this method for corrosion control. The American Civil War submarine CSS Hunley was recovered in 2000 and stored in a holding tank containing chilled (10 °C) filtered water (see [Figure 11](#)).<sup>50</sup> Storage involves the hull being protected by an impressed current monitored by five electrodes, with two large anode segments running the length of the tank. Comparing corrosion rates of an unprotected mild steel test probe with a similar probe with an imposed current indicated that the post-excavation corrosion rate had been reduced by a factor of 8 and now matched pre-disturbance corrosion rates recorded on the seabed.<sup>50</sup> Protection of the hull by sacrificial anodes was rejected as a preservation option, as it would have required 50 cumbersome 20 kg anodes to be attached to the hull.<sup>50</sup> Impressed current was used to reduce corrosion of the

USS Monitor's steel structure from  $254 \mu\text{m year}^{-1}$  to as little as  $25 \mu\text{m year}^{-1}$ .<sup>51</sup> Measuring the *in situ* corrosion rates of ship and aircraft wrecks to identify the role of galvanic couplings, concretions, coatings, and environment on their longevity has been extensively studied by MacLeod<sup>52</sup> to develop predictive corrosion control strategies in marine contexts.

#### 4.43.4.5 Hydrogen Reduction

Removal of chloride from iron using hydrogen reduction at temperatures of over 800 °C was once seen as a way forward for large chloride contaminated marine objects but is now rarely used. The treatment uses a hydrogen/nitrogen gas mix to reduce chloride bearing compounds at around 350 °C, iron oxides above 570 °C and fully volatilizes iron chlorides and any NaCl present on marine iron at 800 °C.<sup>8,30</sup> High capital outlay, stringent safety measures designed to prevent oxyhydrogen explosions and ethical concerns that changes to metallographic structure compromise technological data and object history limit its use. It may be argued that it is still a viable treatment for cast iron cannon from marine contexts, where technology is well reported and where objects may be considered to be effectively untreatable in any other way due to the amount of deep-seated chloride within them. The technique is reported to provide good post-treatment stability, but suggestion that the method can offer stabilization by reducing corrosion product to metallic iron is challenged by the instability of the reactive pyrophoric iron it produces.<sup>53</sup> Another heat assisted expensive reduction process used in conservation is gas plasma. It has been used

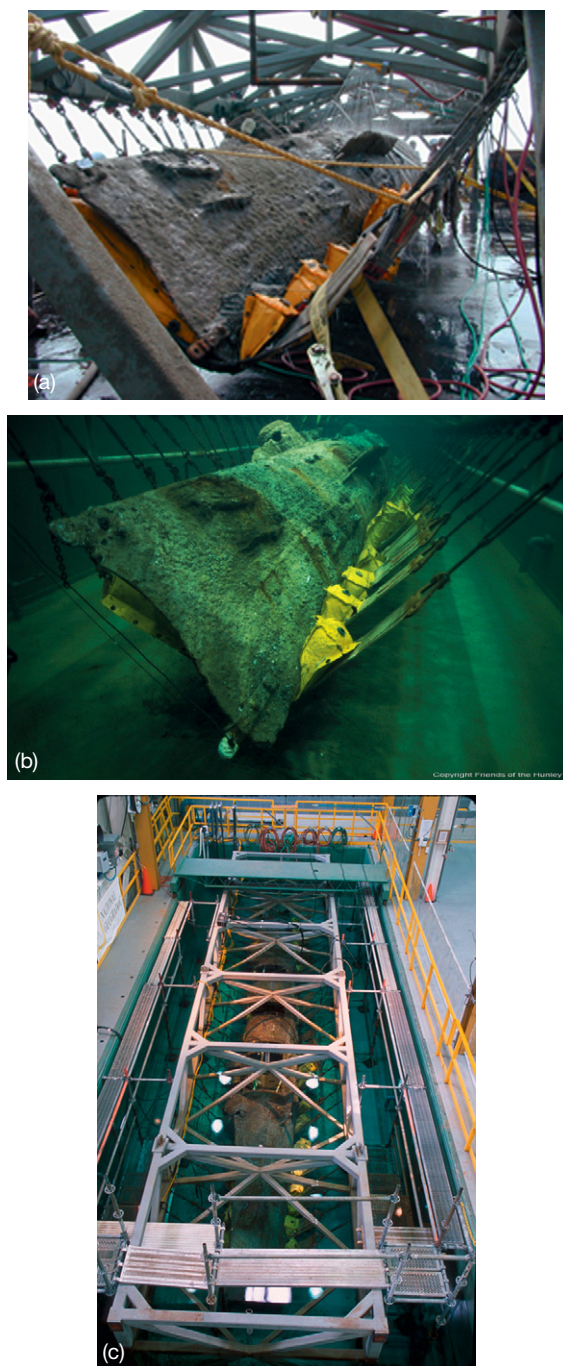


**Figure 11** The H.L. Hunley submarine was lifted from the seabed in a metal frame (a) that was then stored in a large holding tank (b) protected by an impressed current (c).<sup>50</sup> Images courtesy Friends of the Hunley.

to aid chloride removal from iron by reducing  $\text{FeOOH}$  to denser  $\text{Fe}_3\text{O}_4$  to produce a more porous corrosion product layer that aids removal of chloride in subsequent aqueous alkaline treatments.<sup>54</sup>

## 4.43.5 Coatings

### 4.43.5.1 Coating Rationale and Research

Conservation coatings are normally applied as barriers to combat ingress of gaseous, aqueous, or particulate agencies of decay. They may be treatments in their own right or form part of a treatment regime, such as when they are applied as moisture barriers following attempts to remove chloride from iron using washing treatments. Coatings applied to silver must have good gas barrier properties to reduce ingress of  $\text{H}_2\text{S}$  and thereby prevent tarnish.<sup>13</sup> Resistance to vapors such as volatile carbonyl pollutants is important for lead, copper alloys, zinc, and aluminum.<sup>15,18,43</sup>

The role of a coating, environment in which it must be effective and the nature of the metal surface dictate coating choice. An absence of standardized procedures for testing coating effectiveness on cultural metals hinders the use of published material for comparatively identifying the most suitable coating for use in a specific context. While some popular coatings still mostly have qualitative data to support their use, there exists a considerable amount of useful information within conservation literature and there is a move toward providing quantitative data and standardized testing.<sup>3</sup> Both qualitative and quantitative assessment of coating performance within conservation now employs electrochemistry and modern methods of instrumentation in conjunction with increased collaboration with corrosion scientists.<sup>2-4,55</sup>

The concept of manufacturing conservation specific coatings is largely a redundant approach, since conservation viability is cultural rather than commercial as there is no significant financial gain for potential manufacturers in such a small market. Increasing collaboration with industrial partners would benefit conservation and reveal its links to industrial applications. Both industry and conservation seek low toxicity, easy application, predictive performance, and low cost for their coatings. Additionally conservation has stringent ethical guidelines that require coatings to have enhanced life span, long-term reversibility and minimal visible impact to the object upon application or ageing. Object context may modify these goals to some extent. Coatings that offer good protection from corrosion, but are aesthetically displeasing, may be acceptable for objects in long-term storage provided they are easy to remove for display purposes. Since the conservation ideal is for indefinite preservation coatings should be long lasting and low maintenance during their lifespan. Demand for long-term durability and guaranteed reversibility



remain at odds with coating design. While cross-linking polyurethanes have renowned barrier properties their irreversibility, without significant mechanical action coupled with aggressive solvents, rules them out for most conservation applications. Since minimal intervention with an object is contravened by applying a coating and by its future removal, its application is only ethical provided there is evidence that it significantly improves corrosion protection.

Conservation coatings must often perform well on porous, uneven oxidized metal surfaces that may be fragile and chemically unstable. No coating is perfect and this type of surface will result in a large number of coating imperfections. This complicates the testing of coatings for conservation applications, as producing test samples with suitably corroded surfaces to match corrosion patinas developed over years or centuries in the ground or air may be impossible. The alternative of using original materials suffers from reproducibility problems and may be subject to ethical constraints. In some instances actual objects are used to test products. The baton from the bronze equestrian statue of the famous fifteenth century mercenary Bartolomeo Colleoni (see [Figure 12](#)), which is sited opposite the Ospedale San Marco in Venice, was used to compare the performance of organo-silane coatings (see [Section 4.43.5.4.4](#)), synthetic waxes (see [Section 4.43.5.4.2](#)) and acrylic (see [Section 4.43.5.4.1](#)) coatings in tandem with tests on naturally aged metal samples.<sup>56</sup> This approach links the intrinsic properties of coatings to real-life applications and contexts. Samples are not reproducible but performance can be linked to tests on prepared and reproducible samples. Two-phase test systems, where materials are laboratory tested on reproducible samples by accelerated and natural ageing, then tested on objects in real life environments were employed in the PROMET project.<sup>3</sup> This system should be applied to generate evidence-based advice for practical conservators regarding contextual use of materials.

Coatings on metals are used extensively within conservation, but the absence of industry standards makes it difficult to identify the best coating for defined contexts. Much published work produces useful standalone data. This usually compares groups of coatings using highly specific goals and personalized test regimes to deal with the multiple numbers of variables within the test procedures. The demands and complexity of coating use in metals conservation means that many studies naturally attempt to review many aspects of a chosen group of coatings. A stepped study that examines and compares the performance of coatings in relation to a single variable then moves onto the



**Figure 12** The baton from the right hand of the fifteenth century statue of the condottieri Bartolomeo Colleoni in Venice was used for trialing protective coatings. Reproduced from Joseph, E.; Letardi, P.; Mazzeo, R.; Prati, S.; Vandini, M. In *Metal 07, Book 5, Protection of Metal Artefacts*, Interim Meeting of the ICOM-CC Metal WG Amsterdam, 17–21 September 2007; Degriigny, C., Van Langh, R., Joosten, I., Ankersmit, B., Eds.; Rijksmuseum: Amsterdam, 2007.

next would gradually build into a detailed review of materials. Unfortunately, this approach demands significant time and resource commitment and would necessarily be a team project requiring long-term major coordination. Conservation research is not lavishly funded. Collaborative research projects are currently underway or recently completed.<sup>2,3</sup> Their work could offer platforms for movement towards industry recognized standards for testing. Significant coordination and standardization were evident in the recent EU 6th Framework PROMET project.<sup>3</sup> It sought to identify suitable coatings for use on metals within museums surrounding the Mediterranean basin and aimed to identify a methodology for developing and testing inhibitors and coatings for use on iron and copper alloys in museum environments. Additionally it was looking towards environment friendly inhibitor systems.

Many researchers modify international standards or use them unchanged for testing materials and designing experiments. Overall, there remains a

need for developing test procedures that support conservation goals and facilitate comparative performance testing of coating materials for use in conservation. A conservation-specific accelerated corrosion test standard could be used to model the demands of conservation practice. Coating performance in its operational environment is of crucial importance, as it determines its maintenance requirements and life-span. Although laboratory studies, instrumental analysis and electrochemistry can establish intrinsic performance characteristics of coatings according to a set of fixed variables, they cannot offer quantitative assessment of real-time *in situ* performance within museum stores, display cases and outdoor environments. Laboratory testing is useful for establishing which coatings are unsuitable for use and for comparative performance testing in specified conditions. Coatings identified as good performers within the laboratory may fail in the field because certain parameters could not be effectively replicated in the laboratory. However, appropriately designed accelerated ageing normally offers an indication of the relative performance of materials.

Within testing processes examining coating performance a recurring theme is that application methods often dictate whether a coating performs well or badly. The procedure here may be critical. Inappropriate coating methods may negate differences between coatings. A coating with intrinsically better barrier properties may fail at the same rate as one that offers poorer barrier properties because of application methods. Standardizing application methods to ensure variable control is an appropriate experimental procedure, but it may not reflect how the coating will perform in practice where the condition of the object, surface morphology and positioning can dictate whether application is by spray, brush, or cloth. How coatings perform as a function of their application method is as important as their intrinsic properties and should form a major part of testing. A coating with only mediocre barrier properties may perform well if its physical properties suit a particular application procedure. Spraying is often a favored coating method, but coatings of the cellulose nitrate lacquer Frigiline™ on silver were found to fail unevenly due to thickness variations and discontinuities that resulted from spraying.<sup>57</sup> Brushing is known to offer preferential failure in troughs created by the brush stroke and solid wax coatings may have to be applied as polishes. The nature of the surface of the object may also favor different methods of application and mobile self-healing films may be essential in certain environments. The coating itself may dictate which application methods are

possible to use. This overall complex equation must be effectively worked into research studies if results are to be of maximum practical use.

#### 4.43.5.2 Metal Surfaces and Patinas

A major hurdle to the successful application of coatings within conservation is surface preparation. Only in specific circumstances is it ethical to remove patinas and corrosion from surfaces. Within museums equipped with dedicated micro- or macroenvironmental control and monitoring, bare metal surfaces on historical metals may be left uncoated. However, without environmental controls silver tarnishes rapidly in the presence of very low concentrations of sulfur pollutants like H<sub>2</sub>S and forms Ag<sub>2</sub>S<sup>8,10,13,57</sup> and lead and copper alloys are attacked by low concentrations of organic acids.<sup>2,6,8,10,15,18,19,47</sup> Preventive conservation is the preferred option to control pollutant availability and attack, but coatings offer an alternative strategy where sources of pollution cannot be eliminated. Potential for disaster exists in mixed displays or with composite objects, such as when an unstable cellulose acetate object emits acetic acid into an enclosed showcase it shares with a lead object.

Patinas on many metals offer an information resource and provide aesthetic attraction. They may be deliberately applied or naturally formed corrosion layers. Deliberately patinated or polished copper alloy statuary is often modified by corrosion from pollution, rain, and particulates that form corrosion products that may undermine, obscure, or destroy the original patina and outermost metal surfaces<sup>6,19</sup> (see Figure 12). The extent of corrosion will relate to metal composition, climate, location, preexisting patina and the solubility, morphology, uniformity, and adherence of new corrosion products.<sup>6,10,19</sup> Run marks, differential corrosion from pitting, differing colors and textures produced by climate, pollution, composition, and object morphology can entirely ruin object aesthetics and offer a porous uneven surface that will not accept a continuous coating. Wear marks on patinas can be important to retain as part of the history or present life of an object (see Figure 13). Whether total or partial removal of patina is appropriate, in return for improved object stability and surface preparation for coating, presents ethical and aesthetic dilemmas for the conservator.

Apart from ethical considerations, establishing the role of a patina in the corrosion process can help decide whether to remove it as part of a corrosion control strategy. Equally an understanding of patina stability



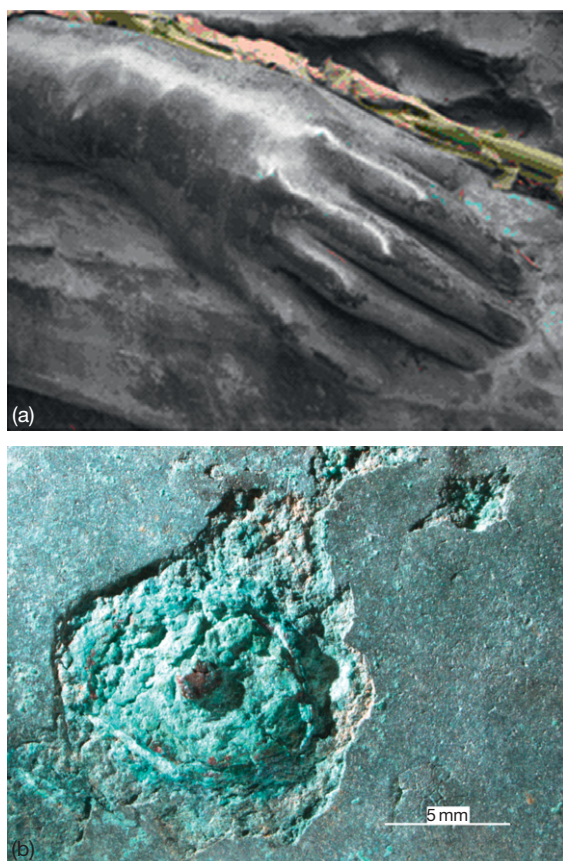


**Figure 13** Constant touching of this copper alloy hand has created a wear mark patina that now forms part of the object history and presents a dilemma for conservation planning (a). Achieving a continuous coating on archaeological copper alloys is problematic due local corrosion and differential patina (b).

and protectiveness contributes to developing corrosion control strategy by offering a measuring point for monitoring, assessing, and predicting patina deterioration with time.<sup>58</sup> Nondestructive *in situ* analysis has been used to identify variance of electrochemical stability within patinas to locate areas that offered high stable electrode potential relative to the base metal, as they provide good corrosion protection.<sup>59</sup> Results revealed that unsightly black crusts offered more protection than visually acceptable blue/green corrosion product layers. This creates an aesthetic dilemma for conservation strategies based on patina retention. Understanding the contribution of corrosion layers to the corrosion process makes it easier to determine if interventive treatments are a better corrosion control option than noninterventive monitoring strategies.

Disfiguring, unstable and aesthetically displeasing patinas formed by corrosion may be removed, either

to reveal metal or a selected corrosion product layer in preparation for repatination and/or adding a protective coating.<sup>6</sup> Repatination may even form part of a corrosion control strategy, as some patinas may offer a degree of protection by acting as partial barriers to moisture, electrical conduction, and gases.<sup>6</sup> Instrumental analysis and historical research to determine the original appearance of a metal object is a prerequisite to selecting a repatination process. Working objects and industrial equipment that never developed a patina or were frequently repainted may in some instances be stripped to the metal surface, provided their history is not compromised by loss of data such as paint layer sequences. Analysis of paint layers would determine if this was likely to occur. Stripping processes like electrolysis, chemical dissolution and complexation, which remove corrosion prior to applying coatings, should provide for lower maintenance of coatings, all other factors being equal. Yet there remain ethical dilemmas concerning the stripping of historical metals.<sup>60</sup> During its working life a cog may have uncorroded teeth that developed a surface finish from work, with a corrosion patina on its ‘noncontact’ body that can also be associated with its working life; should conservation retain both these layers?

#### 4.43.5.3 Preparing Surfaces on Cultural Objects to Receive Coatings

Surface preparation of objects may take the form of mechanically removing disfiguring corrosion to reveal the ‘original’ surface of the object or the marker layer for this. In archaeology it is normal to use mechanical systems to remove corrosion to reveal the object shape and surface detail.<sup>7</sup> For historical metals preparation may involve mechanical cleaning systems, chemicals, or electrolysis. Precious metals may be polished to a high shine as the goal of coating is to ensure that future repolishing occurs as infrequently as possible. In all cases it is best to remove soluble corrosion accelerators before applying coatings.

Outdoor statuary is cleaned according to the goals of the conservation process, taking account of ethics and aesthetics. Preparing surfaces by stripping patinas is normally unacceptable due to ethical constraints and aesthetic outcomes (see [Figure 14](#)). All processes must involve minimum loss of material. Choosing a cleaning method normally relates to how it physically modifies surfaces and alters appearance, rather than its impact on metal stability by removing corrosion accelerators or making a surface more coating friendly, unless it is being prepared for paint. Cleaning methods

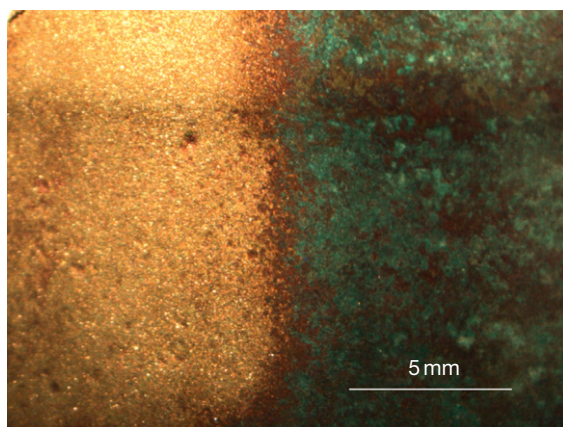


**Figure 14** This contrast between a surface retaining its uncleaned patina and a section cleaned by airbrasion with aluminum oxide starkly reveals the tension between best practice for preparing surfaces to receive coatings and the aesthetic and ethical constructs of conservation.

will influence the effectiveness of coatings, as leaving corrosion products and patinas *in situ* influences their adhesion and distribution.

Most studies qualitatively compare the effects of cleaning methods on specific metal surfaces. Dry particulate abrasion, pressurized water and chemicals have variously been compared for cleaning patinated copper.<sup>61</sup> One study serves to illustrate some of the decision making associated with cleaning surfaces. It compared cleaning of a patinated copper alloy token by abrasion techniques employing glass beads, walnut shell, corn cobs, and sodium bicarbonate delivered at pressures between  $1.38 \times 10^5$  and  $5.52 \times 10^5$  Pa with simple abrasion using  $\text{Al}_2\text{O}_3$ , pressurized water and chemical cleaning by complexation (solution comprising KNaTartarate, 2NaEDTA, NaOH, and fumed silica applied in a cellulose ether gel pack).<sup>61</sup> Postcleaning samples were exposed to synthetic rain and their corrosion was monitored.

Results of these tests reveal the general dilemma produced when trying to balance effectiveness with aesthetics and ethics. Although chemical cleaning offered the most stable substrate, as observed after 1 year, it produced the most visually altered surface by removing all overlying green corrosion products to leave only orange/brown  $\text{Cu}_2\text{O}$  *in situ*. Predictably the softest corrosion products disappeared from the mechanically abraded objects, which were less stable than the chemically treated sections. Pressurized water produced the least visual change, but removed the most soluble corrosion products leaving the metal actively corroding after a year. None of the methods entirely stabilized the metal and various corrosion

products were left *in situ*, neither did they remove all corrosion accelerators. Other workers have expressed concern at indiscriminate surface preparations that fail to recognize the importance of original coatings on metals like aluminum.<sup>16</sup> Glass beads have been cited as being too damaging on finishes on aluminum alloys, but airbrasion can be retained by use of plastic beads at  $1.0 \times 10^5$  Pa.<sup>16</sup>

Preparing historical metals and objects d'art that traditionally carry a shine for the application of coatings involves either chemical or physical removal of tarnish. Removing  $\text{H}_2\text{S}$  tarnish from silver can be achieved by chemicals or abrasion.<sup>13</sup> Chemicals are aggressive and may lead to differential corrosion and surface enrichment of alloys such that loss of copper alloyed with silver leaves a soft and porous silver enriched surface. They may also leave residues that are too aggressive and these have been tested to determine their impact on the object and develop a protocol for treatment. Polishes remove metal and produce surface scratching. Studies of polishing methods concentrate on the loss of metal incurred and scratching of the surface, with  $\text{CaCO}_3$  being a favored inert polish for silver.<sup>62</sup> Chemicals are normally only preferred for heavy tarnish due to the risks of preferential leaching of alloying components and the need for acidified complexing agents to remove  $\text{Ag}_2\text{S}$ .<sup>12</sup> Potentiometric methods mentioned earlier can also be used to remove silver tarnish (see Section 4.43.4.4). Focus should be on identifying the least interventive method that offers the best surface for receiving a coating.

#### 4.43.5.4 Coatings in Conservation Practice

There are a small range of generic coatings in general use within conservation and there is no definitive comparative study which clearly identifies the most successful coating for any given context. Preferences and trends exist for various chemical groupings and products.<sup>3</sup> Coatings are reviewed below by chemical affiliation, rather than their application to specific metals. Trade names are used in general discussion, having initially defined the chemistry of the product.

##### 4.43.5.4.1 Acrylic coatings

The Paraloid™ range of acrylics, known as Acryloid™ in USA, is commonly used within conservation practice. Other acrylics are used according to availability, which means geography can dictate choice of materials. Survey reveals that only a few coatings are routinely used, with Paraloid B72™ (70 methyl methacrylate/30 ethyl acrylate copolymer) being one of the most popular general purpose surface coatings

for cultural metals. Its long-term reversibility and application as a coating, consolidant, and adhesive make it a workhorse within conservation and a comparative performance standard in many test procedures.<sup>3</sup> Performance of Paraloid B72™ and an ethylene based commercial coating Poligen ES 91009™ were compared, both alone and with added inhibitor as coatings on fresh and precorroded coupons of steel exposed to cycling  $\gamma$  (90% at 35 °C to 55% at 25 °C) to simulate extreme museum environmental fluctuations.<sup>3</sup> Performance was assessed qualitatively by visual interpretation and quantitatively using EIS and polarization techniques.<sup>3,63</sup> Poligen ES 91009™ was more effective than Paraloid™, and added inhibitors failed to significantly improve the performance of either coating. Long-term exposure of similar test coupons in museum environments confirmed that although Paraloid B72™ gave ‘quite satisfactory results,’ it failed at edges producing filiform corrosion.<sup>3</sup> This was recognized as being problematic where much cultural material like edged weapons and armor had multiple thin edge sections. The importance of environment was revealed in these tests as matched sample sets performed differently over similar exposure times within museums in differing Mediterranean countries. Application method was again revealed as being an important variable. In one test, a 250  $\mu\text{m}$  layer of polyurethane (Rylard™ boat varnish) performed much better than either Paraloid B72™ (40  $\mu\text{m}$ ) or an innovative physical vapor deposition system (<1  $\mu\text{m}$ ).<sup>3</sup> Standardizing test methodology by employing aged coupons and using laboratory and onsite real-time testing in monitored environments offers a solid test platform for cultural metals and for the evolution of assessment standards. Yet outcomes discounted certain products due to outright failure, it proved difficult to quantify the performance of some of the more successful coatings. Overall, the study revealed weaknesses in the performance of traditional conservation materials and identified the newly tested Poligen ES 91009™ as offering promise for the future.

The inability to separate lead organ pipes from oak supporting frames emitting organic acids in European Baroque organs led to a research program that tested the ability of coatings and inhibitors to prevent the corrosion of lead by organic acids.<sup>64,65</sup> Using an aqueous washing strategy to remove soluble lead methanoates and ethanoates acting as electrolytes failed to reduce the corrosion rate upon reexposure of the lead to the methanoic (170 ppb  $\text{Pb}(\text{CHOO})_2$ ) and ethanoic acid (195 ppb  $\text{Pb}(\text{CH}_3\text{COO})_2$ ).<sup>65</sup> Coatings alone produced limited protection, with Paraloid B72™ offering no protection, microcrystalline wax providing uneven

protection and various inhibitors had little effect.<sup>64,65</sup> This is of concern as Paraloid B72™ has long been used as a coating on lead. Treatment must be effective for the long term, due to the cost and logistics of coating the organ pipes. Nanotechnology is now being tested in a preventive treatment using  $\text{Ca}(\text{OH})_2$  nanoparticles to control acid emission from the wood.<sup>64</sup>

Incralac™ lacquer comprises Paraloid B44™ (ethyl methacrylate/butyl acrylate copolymer) with added epoxidised soya bean oil as a leveling agent and benzotriazole as a UV absorber<sup>6</sup> and is industry designed for protecting copper alloys. It has been extensively used both on archaeological and outdoor copper alloys since the 1960s. Its application aesthetically changes bronzes by darkening their surface.<sup>56</sup> However, outdoor exposure is likely to result in optical changes to most coatings as they weather and collect dirt. Good electrochemical impedance measurements recorded for fresh Incralac™ coatings on polished and unpolished bronze, implied good coverage and low porosity, but after natural ageing on a rooftop in Canberra for 4 years impedance was the same as for uncoated metal.<sup>57</sup> Although two coats improved performance the time-related failure remained the same. Poor long-term performance was also found in 10-year-old Incralac™ coating on a gilt bronze statue in New York.<sup>6</sup> It was entirely cracked and its insolubility was likely due to cross linking exacerbated by the loss of the BTA UV stabilizer which was absent in the aged lacquer, which required strong solvents and physical intervention to reverse it. Inhibitors such as benzotriazole (see [Section 4.43.6.1](#)) have been used to prime bronze surfaces prior to applying Incralac™.<sup>6</sup> The manufacturer reports a 5-year lifespan with removal instructions recognizing its reduced solubility with age, but a 2-year lifespan on outdoor copper alloy monuments is more common. The outdoor performance of Incralac™ is limited when measured against conservation goals of low maintenance, good protection, and reversibility but it continues to be used in the absence of any quantitative proof of significantly better performing alternatives.<sup>6</sup> Survey suggests Incralac™ is now less commonly used on historical and archaeological metals inside museums, apparently in favor of Paraloid B72™.<sup>3</sup>

Solvent-based acrylic resins and their aqueous dispersions have been tested as  $\text{H}_2\text{S}$  barriers in a program comparing them to vinyl acetates, cellulose nitrate and microcrystalline wax.<sup>66</sup> Acrylic dispersion systems performed better than the acrylic resin solutions and were equal performers with vinyl acetate and cellulose nitrate, but the defining factor in protectiveness of all



the coatings tested was their evenness and thickness. Uneven coatings produced differential tarnishing. Microcrystalline wax (Renaissance Wax™) produced the worst result because its solid state made it difficult to apply. The conflict between good experimental procedure and practical use of coatings is reflected by drying coatings for 8 months prior to testing them with H<sub>2</sub>S, as this is unlikely to reflect the procedure within museum contexts.

Fragile metal objects are held together by impregnating them with polymers using immersion systems. Acrylic polymers like Paraloid B72™, microcrystalline waxes and occasionally, epoxy resins are used for fragile iron.<sup>7,36</sup> Unsurprisingly, long-term survey reveals that iron objects washed to remove chloride and then consolidated with epoxy resins survive better than washed iron that remained unconsolidated.<sup>36</sup> Epoxy resin coating offers a degree of protection against moisture ingress and its strength as an adhesive retains the physical integrity of the iron even if it corrodes.<sup>36</sup> While the insolubility of epoxy resins appears to contravene the central conservation concept of reversibility, its use is measured against increased longevity of the iron as a cultural resource. The influence of ethics on treatment choice takes account of both the prevailing situation and the ultimate goal of prolonging the functional life of an object.

In reality even the use of a reversible consolidant is effectively an irreversible process. Since its use implicitly acknowledges it is essential for retaining the physical integrity of an object, overcoming consolidant/metal interactions to remove it would likely result in object fragmentation. While there have been no conservation studies on the influence of epoxy resins on the corrosion of metals, less viscous short chain aliphatic epoxy resins suited to consolidation processes produce more OH groups upon cross-linking than aromatic epoxy oligomers, which means they attract more water from the atmosphere and this may facilitate greater corrosion. Trapping moisture within iron objects by using consolidants and coatings runs the risk of creating microclimates that may accelerate and localize corrosion.

#### 4.43.5.4.2 Waxes

Microcrystalline waxes are commonly used as coatings in conservation, especially on smooth even steel surfaces such as armor<sup>3</sup> and patinated outdoor monuments.<sup>6</sup> Recent  $E_{\text{corr}}$  studies revealed one such wax offered little or no protection when compared to the acrylic Paraloid B72™ and polyethylene wax Poligen ES™ on smooth steel in contact with electrolytes.<sup>3</sup> Interpreting this

failure illustrates the importance of taking account of environment and metal substrate, as when microcrystalline waxes were tested on lead exposed to atmospheres containing organic acid vapor they performed significantly better than Paraloid B72™.<sup>65</sup>

Renaissance™ and Cosmoloid 80H™ waxes are the most commonly cited microcrystalline waxes in conservation literature. Typically in conservation, particular commercial products tend to be preferred for use over long time periods.<sup>3</sup> In what is often a nonevidence-based manner the perception grows that they are ‘proven’ products. Replacing popular coatings that are no longer being manufactured presents a problem. An extensive study was set up to find the best commercially available alternative for a microcrystalline wax being phased out of production. A range of microcrystalline waxes and a low melting point (80–100 °C) polyethylene wax were compared using electrochemical impedance spectroscopy and immersion in 0.1 M NaCl, supported by real-time atmospheric exposure.<sup>55,67</sup> BeSq 2095™ microcrystalline wax performed similarly to TWA 2095™ which was being phased out. Real-time testing was an essential part of this study and identified complete failure of the waxes over a 4-year exposure period. As reported for many other test procedures it was the application method that once again provided a significant influence on performance. BeSq 2095™ microcrystalline wax performed better when applied in a molten state, which produced crystalline lamellae, whereas polyethylene wax offered best protection when buffed onto bronze surfaces.

Protection of bronze ethnographic and artistic objects with waxes provides a transparent coating with a degree of color saturation that meets aesthetic goals. Sticky aesthetically displeasing mobile wax coatings that alter color saturation of surfaces are not used in conservation, unless the object is to be stored. A number of commercial products comprising wax and volatile corrosion inhibitor additive were ranked as better performing coatings for outdoor bronze sculpture, as compared to the conventional microcrystalline wax BeSq 195™ using electrochemical impedance spectroscopy.<sup>67</sup> Dinitrol 4010™ performed best. It is used by the aerospace industry to protect engines in storage.<sup>68</sup> and it is a preferred choice for electrolyzed aluminum alloys,<sup>16,47,68</sup> although a note of caution was expressed on the use of inhibited commercial waxes for aluminum alloys without first examining their relationship with the corrosion processes taking place.<sup>16</sup> A Focke-Wulf 190 aero engine treated by electrolysis was coated with a 40 μm layer of Dinitrol

4010™ post treatment,<sup>68</sup> which has good protective properties and is favored by the aircraft industry because it has no adverse affect on rubber and plastics.

Wax coatings are considered to be high maintenance options for outdoor bronzes, as compared to acrylics. However, they are used as sacrificial topcoats on outdoor bronze statuary where they protect the underlying acrylic layer from degradation. A three-phase system of Benzotriazole inhibitor primer, Incralac™ main coat and microcrystalline wax topcoat has been employed by a number of workers and offers a more robust protective system.<sup>6</sup>

#### 4.43.5.4.3 Cellulose nitrate

Before the introduction of the Paraloid™ range of acrylics, cellulose nitrate was commonly used in conservation as an adhesive and a coating. It has proven long-term reversibility and its properties and decay have been extensively reported. Long-term performance studies discounted its effectiveness as a coating on archaeological iron.<sup>3,34</sup> Although it has been in long-term use as an antitarnish coating on silver the cellulose nitrate lacquer Agateen™ only equaled the performance of acrylic and vinyl acetate emulsions in laboratory tests.<sup>66</sup> As with many other coating studies on silver, tarnishing from sulfur was strongly influenced by coating methods and the quality of their application.<sup>57,66</sup> Anecdotal reporting suggests recoating silver to protect against tarnishing is necessary every 10 years. This is an expensive and time consuming exercise for a large silver collection, so coating lifetime has been explored using accelerated ageing tests.<sup>69</sup> These revealed that light and relative humidity had a pronounced effect on the lifetime of the commonly used cellulose nitrate lacquer Frigilene™. Extrapolating the results of the accelerated tarnishing tests indicated that Frigilene™ should still protect from tarnishing after 10 years in mid-range relative humidity values. Calculations did not account for thermal effects inherent in accelerated ageing tests, so lacquer lifetime was expected to be greater than 10 years' exposure at room temperature.

Appropriately these laboratory tests are being evaluated by English Heritage using real-time monitoring of the Waterloo silver centerpiece in Apsley House, London. In several years' time the final outcome will offer insight into the effectiveness and value of the test procedures, as much as the performance of Frigilene™ lacquer as a gas barrier. Focused pragmatic studies such as this offer tangible evidence for choosing materials fit for task and for devising long-term conservation planning and budgeting. The reported testing

supplied sufficient information for the production of a predictive conservation strategy. Benign impact on metal, proven reversibility, and long operational lifespan are the main essentials for conservation planning, which, in this instance, revealed that cellulose nitrate was a good choice for antitarnish coatings on silver. Although investigations into the surface chemistry relationships between cellulose nitrate and silver would offer insight into mechanisms of protection and failure, it is not necessary in order to devise a preservation strategy.

#### 4.43.5.4.4 Silanes

While organosilicon compounds are extensively used in industry,<sup>70</sup> they have received limited attention in conservation practice. It appears that there is much scope for employing them on cultural metals as hydrophobic barriers, as they are largely invisible on surfaces, are good water repellents and are capable of bonding to corrosion products.<sup>70</sup> Barrier properties of silanes can be improved with the inclusion of inorganic additives like silica plates, which can reduce water permeability and aid reversibility. Eventually silanes will be broken down by water reaching the metal–silane interface, where it reverses the Si–O–Me bond that was formed by hydrolysis to protect the metal. Applying thicker films cannot be used to counter this as they tend to be too brittle and application difficulties are experienced.<sup>70</sup>

Organic–inorganic polymer systems produced by hydrolysis and condensation reactions of alkoxy silanes and organo-functional alkoxy silanes have been tested on bronze, fresh, and precorroded steel in the form of the Ormocer™ (ORganically MODified CERamic) family of lacquers produced by the Fraunhofer Institute in Munich.<sup>71</sup> Good adhesion to metal surfaces and their hydrated corrosion products should occur due to the presence of Si–OH and Si–O–R groups in the polymer and an organic polymeric network results from the cross linkable functional groups of alkoxy compounds (R–Si(OR)<sub>3</sub>). Ormocer™ lacquers can be modified to produce differing elasticity, by reacting their main cross linkable component glycidoxypropyl trimethoxy silane with alkoxy and hydroxy silanes.<sup>71</sup>

These lacquers significantly outperformed waxes in laboratory-based accelerated (SO<sub>2</sub>) corrosion tests and outdoor exposure using various international standards.<sup>72</sup> Application method and concentration proved important to performance. Monolayers (4–8 μm) and bilayers (10–12 μm), applied by spray, darkened metals and the monolayer performed better



than the bilayer on patinated metal. This data indicates that it may be a promising coating for corroded metals, but technical and ethical boundaries must be crossed when using it. Ormocer™ requires methylene chloride paint stripper to reverse it. Testing this lacquer in SO<sub>2</sub> contaminated environments reflects its initial conception for use within industrial contexts, where polluted environments offer significant threat. Despite the siting of many cultural metal objects in urban contexts surprisingly few studies within conservation examine coating performance in SO<sub>2</sub> contaminated conditions.

As in other areas of conservation comparative studies dominate conservation research into silanes. An EU research project (ARCHITECH) seeking to identify better coatings for outdoor art works is examining silane coatings, copper oxalate patinas and increasing the thickness of Cu<sub>2</sub>O layers to improve the natural protectiveness of patina on copper alloys.<sup>56</sup> Comparing selected silanes to the commonly used Incralac™ acrylic coating revealed them to perform only equally well, which is not encouraging given the overall weak outdoor performance of Incralac™ (see Section 4.43.5.4.1). The fact that Incralac™ altered the chroma of the metal surface more than the silanes<sup>56</sup> does not seem to offer strong support for using silanes. The fact that Ormocer™ showed better adhesion than Incralac™ in high humidity<sup>72</sup> may be of use, but such conditions are likely to more readily induce its hydrolysis. The PROMET project included Silane A (5%  $\gamma$ -mercaptopropyltrimethoxysilane; 2%bis-(trimethoxysilylpropyl)amine; 1% hydrated tetraethoxysilane; 92% ethanol) in its comparative testing regime.<sup>3</sup> This offered best protection for bronze in long-term real-time testing, as compared to Paraloid B72™ and selected corrosion inhibitors. However, all systems failed over the test period. There are many difficulties to overcome if silanes are to be successfully used on cultural metals.

#### 4.43.6 Inhibitors in Conservation

Inhibitors are used selectively and, in many cases, empirically in conservation practice, either alone or in combination with coatings. While their use is governed by the usual ethical constraints of appearance and reversibility, fashion also has an input. For instance the blackening of iron by tannate inhibitors may be deemed to be ethically acceptable on archaeological iron, as it could be argued that visual changes

do not stray too far from the appearance of the gray/black DPL layer retained on objects.<sup>2</sup> This encapsulates the flexible nature of ethics and aesthetics within conservation, as the slight darkening of patinas on copper alloys caused by the use of benzotriazole is cited as being of concern by some authors. Whether inhibitor use in conservation can be reconciled with the goal of stabilizing metals is debatable, as inhibitors slow rather than prevent corrosion.

No inhibitors have been specifically developed for use in conservation practice. They are borrowed from industrial contexts, where they have been assessed for use in specific operational environments on particular alloys. As with protective coatings inhibitors are required to be effective in the presence of corrosion products. This presents difficulties, as soluble corrosion accelerators like chloride ions normally interfere with their action. Low inhibitor toxicity is also a requirement, as objects remain in the public domain where they must be accessible and easy to handle. This tends to rule out many vapor phase inhibitors, as these are often based on volatile and toxic amine base compounds. Attempts have been made to find less toxic alternatives and cheap natural inhibitors. Recently extract of seed oil from the cactus *Opuntia ficus indica* was used to formulate an inhibitor that contained long chain fatty acids, triethanolamine, and potassium hydroxide<sup>3</sup> but it failed to offer protection when compared to a range of coatings. This is likely due to poor film formation, as a continuous film reportedly constitutes its inhibitive properties. In the same tests, adding corrosion inhibitors to films failed to improve their protective properties significantly.<sup>3</sup>

##### 4.43.6.1 Benzotriazole (BTA)

1,2,3-Benzotriazole is the most successful commercial inhibitor used in conservation practice. It is applied to prevent corrosion of chloride contaminated copper alloys.<sup>6</sup> There is some discussion whether it is the inhibitive properties of BTA or the barrier properties of Cu–BTA films that infer protection to patinated chloride containing copper alloys. The Cu(I)–BTA inhibitor complex films formed on copper, copper alloys, and Cu<sub>2</sub>O surfaces have excellent adhesion from primary and secondary bonding and likely play the dominant role in the protection of patinated copper alloys by limiting water, ion, and oxygen ingress to reactive metal and mineral surfaces.<sup>2,73,74</sup> The film tolerates chloride ions and low-pH environments and reacts with CuCl to produce a BTA–chloride compound that is stable at high humidity<sup>72</sup> (see



**Figure 15** Benzotriazole was specifically applied in conservation practice to combat 'bronze disease'; the growth of voluminous  $\text{Cu}_2\text{OH}_3\text{Cl}$  polymorphs at the  $\text{Cu}_2\text{O}$ – $\text{CuCl}$  interface beneath shape-retaining overlying corrosion layers. Their loss is visible on this Roman pin.

**Figure 15).** Compared to a range of other nitrogen or sulfur-containing organic compounds it is more effective (99%) at inhibiting hydrolysis of  $\text{CuCl}$  to  $\text{Cu}_2(\text{OH})_3\text{Cl}$  and although both 2-mercapto-benzimidazole (98% effective) and 2-mercapto-benzothiazole (97% effective) approach its inhibitive properties, they form aesthetically unacceptable white and yellow complexes with  $\text{CuCl}$ .<sup>75</sup> The black-green coating BTA produces when it reacts with  $\text{CuCl}$  is probably why BTA is noted for darkening patinas on copper alloys. This is a small trade-off for its proven effectiveness at preventing corrosion.

There is no definitive agreed and tested protocol for its use. It is normally used as a 3% solution in alcohol or 1% in water, with no quantitative evidence to support suggested treatment times that range from paintbrush application through a few hours in vacuum to several days soaking. Archaeological and deeply pitted copper alloys often prove difficult to stabilize using BTA solutions, as hydrolysis within pits creates a low pH that interferes with the formation of an effective  $\text{Cu}$ –BTA coating. This is overcome by pretreatment of pits with  $\text{Na}_2\text{CO}_3$  but at an aesthetic cost of producing brown-colored spots.<sup>6</sup>

Factors influencing copper–BTA reactions and the nature of the resulting film include the condition and oxidation state of the reacting surface, potential, temperature, pH, and chloride and oxygen concentrations. Thus  $\text{Cu(I)}$  complexes formed in acid corrosive environments tend to be thicker, less polymerized, and more permeable to oxygen than equivalent films formed in neutral and deaerated conditions.<sup>73</sup> This diversity in film formation indicates that there would

be considerable benefit in tests designed to examine the nature of the films formed to determine optimum application conditions. For instance, it appears that deoxygenated solutions may offer an advantage over current oxygenated treatment environments and short treatment times could explain why BTA sometimes fails to inhibit corrosion. Tests on artificial patinas have shown that it takes several days for reaction with brochantite ( $\text{Cu}_4\text{SO}_4(\text{OH})_6$ ), which is a common corrosion product on outdoor statuary in urban areas, to go to completion.<sup>38,74</sup> Although the acid by product of this reaction lowers pH as concentrations of BTA increase, a dilemma exists as treatment must ensure there is excess BTA present to repair any damage to the protective BTA polymeric film formed.<sup>74</sup>

Use of BTA on outdoor statuary requires a regular maintenance program, as BTA is likely to be lost from effects of rain-wash due to its solubility and volatilization because of its low vapor pressure. The use of BTA as a primer coated with protective lacquer(s) should prolong its effectiveness. Additionally, BTA also forms  $\text{Pb}$ –BTA and  $\text{PbO}$ –BTA compounds as crystalline polymeric films which have been shown to protect lead within leaded bronzes from corrosion by organic acids<sup>76</sup> and  $\text{Zn(II)}$ –inhibitor complexes have been detected on copper alloy.<sup>2</sup> In contrast electrochemical measurements showed silicon bronzes had lower organic inhibitor efficiency as silica is poorly reactive towards BTA.<sup>2</sup> It is clearly important to know what copper alloy is being treated to assess likely inhibitor effectiveness.

Whether copper alloys routinely require treatment with BTA is questionable. What percentage of objects would have remained stable, even if they had not been treated with BTA, is unknown. Many patinated copper alloys treated by BTA appear stable in museum environments, although this observation remains unsupported by quantitative data. A study of surface chemistry reactions with the typical corrosion profiles found on copper alloy objects and quantitative long-term studies of copper alloy object stability following treatment with BTA would determine its inhibitive powers relative to the conservation goals of longevity and predictive success.

Despite its proven inhibitive success, workers still seek alternatives to BTA mainly due to toxicity worries and its high cost. While no better inhibitor for cultural corroded copper alloys has been recorded, synergistic inhibitive effects have been identified when using BTA with other inhibitors that included 5-amino-2-mercapto-1,3,4-thiadazole.<sup>77</sup> Caution is

required when mixing inhibitors as the formation of differing BTA complexes can lower performance of BTA.<sup>75</sup> Recently BTA with a hydrophobic alkyl side chain (C6-BTA) has been tested on the basis that the side chain will better repel aqueous electrolyte.<sup>2</sup> A more novel use for BTA is as an inhibitive washing procedure for marine iron, where it forms Cu(I) complexes and Cu(II) species and prevents corrosion while the water wash extracts chloride from CuCl.<sup>38</sup> A big advantage of using a BTA preservation strategy on copper alloys is that it can be applied without any surface preparation, which is ideal where patina is part of the intrinsic value of the object. Ensuring access to the Cu<sub>2</sub>O layer that is normally situated next to the metal or integrated with CuCl sited there will provide the best opportunity for treatment success, due to the ability of BTA to react with this oxide. Unfortunately, removing the overlying green brochantite/antlerite/malachite patinas to reveal orange/red Cu<sub>2</sub>O would be visually unacceptable in many instances.

#### 4.43.6.2 Tannins

As conservation seeks to balance its goals with global concerns regarding toxicity and carbon footprints, testing low toxicity inhibitors derived from natural sources like plant extracts is of interest. Tannin plant extracts have been used intermittently in conservation since the 1960s and are reported to act as rust converters, leaving a black inhibitive film on the metal. Treatment involves either immersion in tannin solutions or, more likely, painting onto objects. Currently there is no quantitative in-depth study of their action within conservation contexts or any data that offers quantified guidance for optimum treatment concentrations or application procedures.

It is well known that condensed tannins applied either in water or solvent to rust-covered iron offer inhibitive properties by forming ferric-tannate complexes that act as insoluble barriers and phosphoric acid is said to improve inhibitive properties. Tannate-coated iron performed well in long-term storage according to a qualitative survey of archaeological iron.<sup>30</sup> While this provides useful information, post-treatment stability studies for determining treatment success should be controlled and semiquantitative with clear links to environmental variables, rather than retrospective examinations of treated objects.

Iron stripped by 4NaEDTA was coated with a mixture of phosphoric and tannic acids to inhibit further corrosion, following electrochemical testing to determine optimum concentrations and combinations

of inhibitor.<sup>44</sup> A recent study identifying optimum concentrations of tannin and phosphoric acid for inhibiting corrosion of rusted iron in a 3.5% NaCl solution indicates the importance of research and testing to optimize tannin applications to meet the prevailing circumstances. In this study,  $E_{\text{corr}}$  values showed that phosphoric acid reduced the inhibitive properties of mangrove tannins at low pH (0.5 and 2.0), yet when used alone at higher pH (5.5) it offered improved inhibition as compared to tannin/phosphate mixtures.<sup>78</sup> Corroding archaeological iron has varying pH across its surface due to hydrolysis of anodically produced Fe<sup>2+</sup> and its thick corrosion layers. Any testing of tannins for use in conservation practice should be tailored to the corrosion model extant.

As with other protective surface coatings testing the stability of treated objects at typical storage humidities is necessary and, until this is achieved, application of tannins in conservation will retain a degree of empiricism. To date, no inhibitor has been shown to have effective long-term inhibitive action on chloride-contaminated archaeological iron retaining its corrosion layers and exposed to mid to high relative humidities. Commercial tannate-based inhibitors have been tested and shown to be effective for inhibiting internal corrosion of boilers in the working nineteenth-century paddle steamer PS Enterprise between its weekly use on lake Burley Griffin, Australia<sup>79</sup> (see Figure 16). In these closed systems the boiler retains its water and inhibition results from a combination of reducing the availability of oxygen, formation of iron tannate film and precipitation of dissolved salts as sludge.

#### 4.43.6.3 Carboxylates

Sodium carboxylates (CH<sub>3</sub>(CH<sub>2</sub>)<sub>*n*-2</sub>COONa – usually *n* = C<sub>10</sub> or C<sub>12</sub>) derived from vegetable oils have been used on copper alloys and iron to form inhibitive copper and iron carboxylates.<sup>2,3,41,80-82</sup> Like tannates, they are environmentally friendly. They have been linked to conservation in tests on corroded iron and copper coupons and blank standards.<sup>41,80</sup> Potentiodynamic curves revealed they offered slightly better inhibition than mimosa tannin solutions and considerably better protection than phosphates tested on bare clean steel coupons.<sup>80</sup> A further advantage is that the nanomeric hydrophobic iron carboxylate soap layer formed by reaction with iron cations<sup>79</sup> is not aesthetically disfiguring, as is a black iron tannate layer. Carboxylates readily reverse in ethanol, which may mean they are best suited to indoor applications. Long-term



**Figure 16** Tannates are used to protect the boilers in this 19th-century paddle steamer belonging to the National Museum of Australia. Image courtesy of David Hallam.

real-time testing using precorroded metal coupons indicated that sodium decanoate offers temporary protection on partially oxidized historic steels and may be considered as an alternative to Paraloid B72™.<sup>3</sup> It also offered good protection for copper alloys.

Carboxylates were originally tested in conservation as inhibitors for preventing corrosion of lead by volatile organic acids.<sup>81</sup> Polarization plots produced by modeling corrosion of inhibited lead by these acids indicated that sodium decanoate and undecanoate protected best against corrosion, whereas phosphate inhibitors actually increased corrosion rates.<sup>65</sup> Real-time X-ray diffraction studied the resistance of lead carboxylate ( $\text{CH}_3(\text{CH}_2)_8\text{COO})_2\text{Pb}$ ) films to acetic acid vapor and revealed considerable protective properties, but ultimate failure.<sup>82</sup> Carboxylates appear to delay corrosion by organic acids, but ultimately they cannot prevent it. As in other areas of conservation, contextual needs dictate preservation strategies, while these tests showed carboxylates as being unsuitable for preserving church organs, they may be considered suitable where lead is more accessible and easy to monitor to determine if retreatment is necessary.

#### 4.43.7 Painted Metals

##### 4.43.7.1 Removing Paint

Conservation ethics normally dictate that original or later paintwork that offers either a record of the history

of the object or milestones in its life should be preserved. The preservation of fragmentary original paint surfaces is challenging, as pitting and corrosion undermining paint are a threat to paint integrity and are difficult to stabilize. In such instances environmental control may be the only option guaranteed to prevent ongoing corrosion beneath the paint layer. There are instances where ethical arguments support refinishing the surfaces of cultural objects either to their original specification or to an improved standard in order to offer the best opportunity for longevity. This should not compromise the future interpretation of the object.

Refinishing may be acceptable when there is no original paint layer remaining and replicating an original finish offers significantly increased object longevity. A combination of refinishing and preservation of original surfaces may be adopted in some instances.<sup>83</sup> If the condition of the metal allows, refinishing offers opportunity for highly specified surface preparation. It may also be possible to apply modern paint systems if visual appearance rather than replication of the original recipe is deemed to be the most important interpretive factor. Stripping to the bare metal for repainting should involve minimal loss of the original metal.

##### 4.43.7.2 Refinishing Painted Surfaces

Preparation of historic metal surfaces to receive paint must always minimize loss of metal. Commercial conservation programs often adhere to international



standards for preparing surfaces, such as SSPC, NACE, and Swedish Standards. This offers the client a defined measuring point within the contract of work. Repainting the upper hull of the SS *Great Britain* was justified on the basis of continual repaints during the working life of the ship and the presence of a failing modern paint layer. The hull above the waterline was to be exposed to the British climate and merited the best possible protection from the elements.<sup>25</sup> It was stripped to near white metal (SA2.5) using high pressure water lances (2500 bar) and for weaker areas crushed Australian Garnet (8 bar) in preparation for painting (see [Figure 17](#)). Although this removed several microns of original wrought iron, it was reasoned to be ethical as this thickness of metal would inevitably be lost through future corrosion if preparation was not so stringent. The paint system chosen was typical for creating a durable, long-lived outdoor protective coating on a well prepared surface. A three-phase treatment comprising a 2-pack zinc-rich epoxy primer followed by 2-pack high-build main coat paint system with a urethane UV-resistant topcoat, produced a total paint thickness of 225–250  $\mu\text{m}$ <sup>25</sup> (see [Figure 17](#)). The preferred method of application involved an airless spray at  $207 \times 10^5$  Pa with brushing when the spray could not be used. Life expectancy of this layer with appropriate maintenance is predicted at 15 years.

Often it is not possible to prepare corroded metal surfaces to a high standard. In this instance original lead-based paints are preferred, both to replicate original paint layers and because of their perceived longevity. Since health and safety considerations make their manufacture costly and their use has environmental implications, aluminum-based primers are normally used instead. Ferro zinc (HMG Paints) is a rust conversion paint that was used to paint the monitor HMS *Minerva* after electrolysis.<sup>31</sup> The range of historic alloys and the inability to effectively prepare many surfaces beyond SA 1 or 2 means that each surface offers a unique coating problem. Consequently conservation designs often test paint adherence using a pull-off test (ASTM D 4541-02 or ISO 4624) before applying it to an entire surface. Reports on the longevity of painted surfaces relative to the prepainting condition of the surface and the paint system applied are not reported and this offers another area for research that could act as a platform for designing industry standards. Silanes are used for preparing metals for paint within industry,<sup>70</sup> but this has not been reported in conservation practice.

Where sections of metal have entirely corroded away, decisions regarding a course of action have to

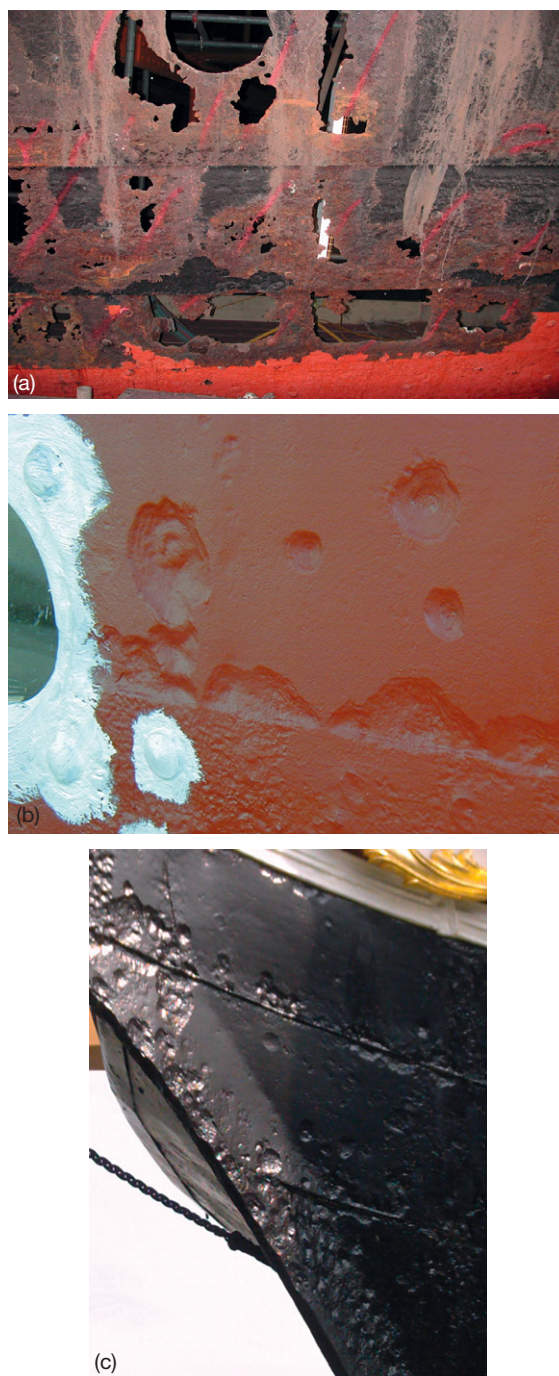


**Figure 17** Surface preparation to SA2.5 standard on the SS *Great Britain* and the completed paint schedule.<sup>25</sup> Images courtesy of Eura Conservation Ltd.

account for ethical, technical, and corrosion considerations. Structural problems require structural solutions but care must be taken not to create galvanic cells by repairing with alloys of differing potential from the original metal. Equally, where structural





**Figure 18** Challenges in metal conservation extend beyond museum interiors to whole sites such as housing at Valparaiso (UNESCO World Heritage site) and abandoned factory settlements like Stromness (South Georgia) whaling station. Images courtesy of Eura Conservation Ltd.

integrity is not a concern it is possible to use glass reinforced plastics and epoxy systems.<sup>25</sup>

#### 4.43.8 Overview

The overall equation for preserving cultural metals is a complex mixture of material science, context, and

ethics. During the past 40 years, conservation has developed links with corrosion science that have led to greater understanding of corrosion processes, which, in turn, supports investigation into treatment mechanisms and methods. This has been extensively boosted over the past 15 years by increased application of modern instrumental analysis in conservation

research. Much greater opportunity exists for collaboration between conservators and corrosion scientists to develop a synergistic relationship for solving the problems of preserving 'metallic heritage.'

Within conservation there are normally multiple preservation options, either due to insufficient evidence to identify one treatment as being significantly better than another or because of differing, but equally valid ethical arguments allow for a range of conservation routes and outcomes. Thus, within this review, large iron chloride-infested naval vessels were treated in four different ways in attempts to stabilize them. HMS Holland was washed in an inhibitive solution to extract chloride<sup>31</sup>; CSS Hunley will be treated by a newly researched washing method employing alkali and pressure<sup>12,28,29</sup>; HMS Minerva was electrolyzed to remove chloride<sup>31</sup>; SS Great Britain used environmental control to prevent corrosion.<sup>11,25,32</sup> All methods are either supported by new research or utilize universally applied treatment techniques. They also have a strong treatment rationale with practical arguments to support the course of action taken. While there will always be diverging views and arguments on appropriate ethical strategies, there remains the opportunity to ensure treatments are researched and optimized. Conservation is a staged process with systematic treatments. There is initially a rationalizing process to decide a course of action, which is then split into treatment stages. As an example, chloride removal from iron might be followed by an inhibitive treatment, over which a coating is applied and the result is subjected to long-term monitoring that assesses outcomes and provides data for future action. Large-scale complex contextual combinations will challenge this approach. At Valparaiso *ad hoc* steel houses form a world heritage site (see Figure 18). They are lived in and offer the challenge of corroding sheet steel, galvanized structures and various paint regimes. Besides finding safe, proven treatment procedures, complex decisions exist on retention of paint, set against a backdrop of what the occupants want and expect, relative to their standard of living. Should the structures eventually become a museum or continue to be lived in? Deserted, but equally daunting, are the remains of a whaling station at Stromness, South Georgia. Remoteness, climate influences, and cost offer significant challenges here. An overarching consideration is climate change and how it will influence corrosion.

Conservation should define standards of preservation, starting with costly indefinite survival of metals down to the guarantee of only a few months

preservation. Developing such a scale goes beyond the science of preservation to its ethics. It may be argued that national icons providing cornerstones in societies merit the cost of indefinite preservation, but commonplace archaeological iron that is to be analyzed, recorded, and published is preserved only for the duration of the analysis and publication process. Counter arguments would focus on the importance of future research into material such as archaeological iron. Suggesting a scale of importance will necessitate extensive ethical debate about how to define importance. In the modern world of diminishing resources, carbon footprints and concern over environmental impact, there are difficult decisions to make and responsibilities to accept for the action taken. Focused coordinated research in collaboration with corrosion scientists can contribute towards informing these decisions for metals preservation.

## References

1. Caple, C. *Conservation Skills*; Routledge: London, 2000.
2. Dillmann, P.; Beranger, G.; Piccardo, P.; Mathiesen, H., Eds. *Corrosion of Metallic Heritage Artefacts: Investigation, Conservation and Prediction of Long-term Behaviour*; Woodhead: Cambridge, UK, 2007.
3. Argyropoulos, V. Ed. *Metals and Museums in the Mediterranean; Protecting, Preserving and Interpreting*; TEI of Athens: Greece, 2008.
4. Costa, V. In *Conservation Science 2002*; Papers from the Conference held in Edinburgh, Scotland 22–24 May 2002. Townsend, J. H., Eremin, K., Adriaens, A., Eds.; Archetype Publications: London, 2002.
5. [icom-cc.icom.museum/Documents/WorkingGroup/Metals/Bromec](http://icom-cc.icom.museum/Documents/WorkingGroup/Metals/Bromec).
6. Scott, D. A. *Copper and Bronze in Art; Corrosion, Colourants and Conservation*; Getty Trust Publications, Getty Conservation Institute: USA, 2002.
7. Cronyn, J. *The Elements of Archaeological Conservation*; Routledge: London, 1990.
8. Pearson, C. *Conservation of Marine Archaeological Objects*; Butterworths: London, 1987.
9. Ashley-Smith, J. *Risk Assessment for Object Conservation*; Butterworth-Heinemann: Oxford, 1999.
10. Selwyn, L. *Metals and Corrosion: A Handbook for the Conservation Professional*; Canadian Conservation Institute: Ottawa, 2004.
11. Watkinson, D.; Al Zahrani, A. *The Conservator* **2008**, 31, 75–86.
12. Drews, M. J.; de Viviés, P.; González, N. G.; Mardikian, P. In *Metal 04*; Proceedings of the International Conference on Metals Conservation, Canberra, 4–8 October 2004; Ashton, J., Hallam, D., Eds.; National Museum of Australia: Canberra, Australia, 2004.
13. Costa, V. *Rev. Conservat.* **2001**, 2, 18–34.
14. Cassar, M. *Environmental Management; Guidelines for Museums and Galleries*; Routledge: London, 1994.
15. Green, L. R.; Thickett, D. In *Saving the Twentieth Century*; The Conservation of Modern Materials, Proceedings of a Conference Symposium 91 – Saving the Twentieth

- Century, 15–20 September 1991; Grattan, D. W., Ed.; Canadian Conservation Institute: Ottawa, Canada, 1993.
16. Adams, C.; Hallam, D. In *Saving the Twentieth Century*; The Conservation of Modern Materials, Proceedings of a Conference Symposium 91 – Saving the Twentieth Century, 15–20 September 1991; Grattan, D. W., Ed.; Canadian Conservation Institute: Ottawa, Canada, 1993.
17. Green, L. R.; Thickett, D. *Stud. Conservat.* **1995**, *40*, 145.
18. Thickett, D.; Bradley, S.; Lee, L. In *Metal 98*; Proceedings of the international conference on metals conservation. Draguignan-Figanieres, France, 27–29 May 1998; Mournay, W., Robbiola, L., Eds.; James and James: London, 1998.
19. Leygraf, C.; Graedel, T. *Atmospheric Corrosion*; Wiley Interscience, 2000.
20. Watkinson, D.; Lewis, M. R. T. *Stud. Conservat.* **2005**, *50*, 241–252.
21. Thickett, D.; Odlyha, M. In *Conservation of Archaeological Materials*: Current Trends and Future Directions. Williamsburg, Virginia, 13–17 November 2005. American Institute for Conservation Postprints 9. Washington, DC, in press.
22. Thickett, D.; Luxford, N. In *Metal 07, Book 5, Protection of Metal Artefacts*, Interim Meeting of the ICOM-CC Metal WG Amsterdam, 17–21 September 2007; Degriigny, C., Van Langh, R., Joosten, I., Ankersmit, B., Eds.; Rijksmuseum: Amsterdam, 2007.
23. Weintraub, S. In *Object Speciality Group Postprints 9, 2002*; American Institute for Conservation: Washington DC, 2002.
24. Thickett, D.; Luxford, N. *The Conservator* **2006**, *29*, 19–34.
25. Watkinson, D.; Tanner, M.; Turner, R.; Lewis, M. *The Conservator* **2005**, *29*, 73–86.
26. Green, L.; Blackshaw, S. In *Metal 95*; Proceedings of the International Conference on Metals Conservation Semur en Auxois, 25–28 September 1995; Macleod, I., Pennec, S. L., Robbiola, L., Eds.; James and James: London, 1997.
27. Mathias, C.; Ramsdale, K.; Nixon, D. In *Metal 04*; Proceedings of the International Conference on Metals Conservation, Canberra, 4–8 October 2004; Ashton, J., Hallam, D., Eds.; National Museum of Australia: Canberra, Australia, 2004.
28. de Viviés, P.; Cook, D.; Drews, M. J.; González, N.; Mardikian, P.; Memet, J. B. In *Metal 07, Book 5, Protection of Metal Artefacts*, Interim Meeting of the ICOM-CC Metal WG Amsterdam, 17–21 September 2007; Degriigny, C., Van Langh, R., Joosten, I., Ankersmit, B., Eds.; Rijksmuseum: Amsterdam, 2007.
29. González, N.; Cook, D.; de Viviés, P.; Drews, M. J.; Mardikian, P. In *Metal 07, Book 3, Use of Electrochemical Techniques in Metal Conservation*; Interim Meeting of the ICOM-CC Metal WG Amsterdam, 17–21 September 2007; Degriigny, C., Van Langh, R., Joosten, I., Ankersmit, B., Eds.; Rijksmuseum: Amsterdam, 2007.
30. Selwyn, L. S.; Logan, J. A. In *International Council for Museums Committee for Conservation 10th Triennial Meeting*, 22–27 August 1993; Washington, D. C., Bridgland, J., Eds.; International Council for Museums, James and James: Washington, DC, 1993.
31. Barker, D. In *Conservation Science Heritage Materials*; May, E., Jones, M., Eds.; RSC Publishing: Cambridge, 2006.
32. Watkinson, D.; Lewis, M. R. T. In *Materials Issues in Art and Archaeology VII*, Symposium Proceedings of the Materials Research Society of America; Vol. 852; Vandiver, P. B., Mass, J. L., Murray, A., Eds.; Materials Research Society: Warrendale, PA, 2005.
33. Réguer, S.; Neff, D.; Remazeilles, C.; Guilmeinet, E.; Nicot, F.; Pele, C.; Meguelati, M.; Mirambert, F.; Dillmann, P.; Refait, P.; et al. In *Metal 07, Book 2, Innovative investigation of metal Artefacts*; Interim Meeting of the ICOM-CC Metal WG Amsterdam, 17–21 September 2007; Degriigny, C., Van Langh, R., Joosten, I., Ankersmit, B., Eds.; Rijksmuseum: Amsterdam, 2007.
34. Selwyn, L. S.; Argyropoulos, V. *Stud. Conservat.* **2005**, *50*, 81–99.
35. Keene, S. V. In *Ancient and Historic Metals: Conservation and Scientific Research*; Scott, D. A., Podanay, J., Consadine, B., Eds.; Getty Conservation Institute: Los Angeles, 1991; pp 249–264.
36. Keene, S. V.; Orton, C. *Stud. Conservat.* **1985**, *30*, 1–7.
37. MacLeod, I. D. *Stud. Conservat.* **1983**, *28*, 1–7.
38. MacLeod, I. D. *Stud. Conservat.* **1987**, *32*, 1–13.
39. Thickett, D.; Enderly, C. In *The Interface Between Science and the Conservator*; British Museum Occasional Paper No. 116, Bradley, S., Ed.; The British Museum: London, 1997.
40. Merk, L. E. *Stud. Conservat.* **1978**, *33*, 1522.
41. Otiento-Alego, V.; Thurrowgood, D.; Creagh, D. C.; Bailey, G. In *Conservation Science 2002*; Papers from the Conference held in Edinburgh, Scotland, 22–24 May 2002; Townsend, J. H., Eremin, K., Adriaens, A., Eds.; Archetype Publications: London, 2002.
42. Huda, K. *Stud. Conservat.* **2002**, *47*, 211–214.
43. Costa, V.; Urban, F. *Rev. Conservat.* **2005**, *6*, 48–62.
44. Degriigny, C. *Stud. Conservat.* **1995**, *40*, 227–236.
45. Guilminot, E.; Baron, G.; Memet, J. B.; Huet, N.; le Noc, E.; Roze, J. P. In *Metal 07, Book 3, Use of Electrochemical Techniques in Metal Conservation*; Interim Meeting of the ICOM-CC Metal WG Amsterdam, 17–21 September 2007; Degriigny, C., Van Langh, R., Joosten, I., Ankersmit, B., Eds.; Rijksmuseum: Amsterdam, 2007.
46. Degriigny, C.; Le Gall, R. *Stud. Conservat.* **1999**, *3*, 157–169.
47. Degriigny, C. In *Saving the Twentieth Century*; The Conservation of Modern Materials, Proceedings of a Conference Symposium 91 – Saving the Twentieth Century, 15–20 September 1991; Grattan, D. W., Ed.; Canadian Conservation Institute: Ottawa, Canada, 1993.
48. Hallam, D. L.; Adams, C. D.; Bailey, G.; Heath, G. A. In *Metal 95*, Proceedings of the International Conference on Metals Conservation Semur en Auxois, 25–28 September 1995; Macleod, I., Pennec, S. L., Robbiola, L., Eds.; James and James: London, 1997.
49. Bailey, G. T. In *Metal 04*, Proceedings of the International Conference on Metals Conservation, Canberra, October 4–8, 2004; Ashton, J., Hallam, D., Eds.; National Museum of Australia: Canberra, Australia, 2004.
50. Mardikian, P. *Int. J. Nautical Archaeol.* **2004**, *33*, 137–148.
51. Nordgren, E.; Goncalves, P.; Shindelholz, E.; Brossia, C. S.; Yunovich, M. In *Metal 07, Book 3, Use of Electrochemical Techniques in Metal Conservation*; Interim Meeting of the ICOM-CC Metal WG Amsterdam, 17–21 September 2007; Degriigny, C., Van Langh, R., Joosten, I., Ankersmit, B., Eds.; Rijksmuseum: Amsterdam, 2007.
52. MacLeod, I. D. *Conservat. Mgmt Archaeol. Sites* **2006**, *7*, 203–223.
53. Birchenall, E. C.; Meussner, R. A. In ; Brown, F. B., Ed.; *Corrosion and Metal Artifacts: A Dialogue Between Conservators, Archaeologists and Corrosion Scientists*; National Bureau of Standards Special Publication, Vol. 479, 1977.
54. Schmidt-Ott, K.; Boissonnas, V. *Stud. Conservat.* **2002**, *47*, 81–87.
55. Price, C.; Hallam, D.; Aston, J.; Heath, G.; Creagh, D. In *Metal 95*, Proceedings of the International Conference on Metals Conservation Semur en Auxois, 25–28 September 1995; Macleod, I., Pennec, S. L., Robbiola, L., Eds.; James and James: London, 1997.

56. Joseph, E.; Letardi, P.; Mazzeo, R.; Prati, S.; Vandini, M. In *Metal 07, Book 5, Protection of Metal Artefacts*, Interim Meeting of the ICOM-CC Metal WG Amsterdam, 17–21 September 2007; Degriigny, C., Van Langh, R., Joosten, I., Ankersmit, B., Eds.; Rijksmuseum: Amsterdam, 2007.
57. Thickett, D.; Hockey, M. In *Conservation Science 2002*; Papers from the Conference held in Edinburgh, Scotland, 22–24 May 2002; Townsend, J. H., Eremin, K., Adriaens, A., Eds.; Archetype Publications: London, 2002.
58. Rosales, B.; Vera, R.; Moriena, G. *Corros. Sci.* **1999**, *41*, 625–651.
59. Cicileo, G. P.; Crespo, M. A.; Rosales, B. M. *Corros. Sci.* **2004**, *46*, 929–953.
60. Prytulak, G. In *Industrial Collections: Care and Conservation*; Proceedings of a Conference hosted by The Council of Museums in Wales and The United Kingdom Institute for Conservation, Cardiff, 9–11 April 1997; Dollery, D., Henderson, J., Eds.; CMW and UKIC: Cardiff, 1999.
61. Lins, A. In *Dialogue 89 – The Conservation of Bronze Sculpture in the Outdoor Environment: A Dialogue Among Conservators, Curators, Environmental Scientists, and Corrosion Engineers*; Drayman-Weisser, T., Ed.; National Association of Corrosion Engineers: Houston, 1992.
62. Wharton, G.; Maish, S. L.; Ginell, W. S. *J. Am. Inst. Conservat.* **1990**, *29*, 13–31.
63. Cano, E.; Bastidas, D. M.; Argyropoulos, V.; Siatou, A. In *Strategies for Saving our Cultural Heritage*; International Conference on Conservation Strategies for Saving Indoor Metallic Collections, Cairo, 25 February–1 March 2007; Argyropoulos, V., Hein, A., Abdel Harith, M., Eds.; Technological Educational Institute of Athens: Athens, Greece, 2007.
64. Aslund, A.; Bergsten, C. J.; Chiavari, C.; Martini, C.; Niklasson, A.; Prandstraller, D.; Svensson, J. E. In *Metal 07, Book 5, Protection of Metal Artefacts*, Interim Meeting of the ICOM-CC Metal WG Amsterdam, 17–21 September 2007; Degriigny, C., Van Langh, R., Joosten, I., Ankersmit, B., Eds.; Rijksmuseum: Amsterdam, 2007.
65. Chiavari, C.; Martini, G.; Poli, D.; Prandstraller, D. In *Metal 04*, Proceedings of the International Conference on Metals Conservation, Canberra, 4–8 October 2004; Ashton, J., Hallam, D., Eds.; National Museum of Australia: Canberra, Australia, 2004.
66. Grabow, N.; Smith, C.; Grissom, C.; Brostoff, L. In *Metal 07, Book 5, Protection of Metal Artefacts*, Interim Meeting of the ICOM-CC Metal WG Amsterdam, 17–21 September 2007; Degriigny, C., Van Langh, R., Joosten, I., Ankersmit, B., Eds.; Rijksmuseum: Amsterdam, 2007.
67. Otieno-Alego, V.; Heath, G.; Hallam, D.; Creagh, D. In *Metal 98*, Proceedings of the International Conference on Metals Conservation, Draguignan-Figanières, France, 27–29 May 1998; Mournay, W., Robbiola, L., Eds.; James and James: London, 1998.
68. Degriigny, C. *Stud. Conservat.* **1995**, *40*, 10–18.
69. Luxford, N.; Thickett, D. In *Metal 07, Book 5, Protection of Metal Artefacts*, Interim Meeting of the ICOM-CC Metal WG Amsterdam, 17–21 September 2007; Degriigny, C., Van Langh, R., Joosten, I., Ankersmit, B., Eds.; Rijksmuseum: Amsterdam, 2007.
70. van Ooij, W. J.; Zhu, D.; Stacy, M.; Seth, T.; Mugada, J.; Gandhi, J.; Puomi, P. *Tsinghua Sci. Technol.* **2005**, *10*(6), 639–664.
71. Piltz, M.; Romich, H. In *Metal 95*, Proceedings of the International Conference on Metals Conservation Semur en Auxois, 25–28 September 1995; Macleod, I., Pennec, S. L., Robbiola, L., Eds.; James and James: London, 1997.
72. Seipert, B.; Pilz, M.; Kiesenberger, J. In *Metal 98*, Proceedings of the International Conference on Metals Conservation, Draguignan-Figanières, France, 27–29 May 1998; Mournay, W., Robbiola, L., Eds.; James and James: London, 1998.
73. Brostoff, R. In *Metal 95*, Proceedings of the International Conference on Metals Conservation Semur en Auxois, 25–28 September 1995; Macleod, I., Pennec, S. L., Robbiola, L., Eds.; James and James: London, 1997.
74. Turgoose, S.; Duncan, S. In *Dialogue 89 – The Conservation of Bronze Sculpture in the Outdoor Environment: A Dialogue Among Conservators, Curators, Environmental Scientists, and Corrosion Engineers*; Drayman-Weisser, T., Ed.; National Association of Corrosion Engineers: Houston, 1992.
75. Faltermir, R. T. *Stud. Conservat.* **1999**, *44*, 121–128.
76. Sharma, V. C.; Shankar, U.; Singh, T. *Stud. Conservat.* **2003**, *48*, 203–209.
77. Golfimistou, S.; Merkel, J. F. In *Metal 07, Book 5, Protection of Metal Artefacts*, Interim Meeting of the ICOM-CC Metal WG Amsterdam, 17–21 September 2007; Degriigny, C., Van Langh, R., Joosten, I., Ankersmit, B., Eds.; Rijksmuseum: Amsterdam, 2007.
78. Rahin, A. A.; Rocca, E.; Steinmetz, J.; Kassim, M. J. *Corros. Sci.* **2008**, *50*, 1546–1550.
79. Greiner, A.; Hallam, D.; Thurrowgood, D.; Creagh, D. In *Metal 07, Book 5, Protection of Metal Artefacts*, Interim Meeting of the ICOM-CC Metal WG Amsterdam, 17–21 September 2007; Degriigny, C., Van Langh, R., Joosten, I., Ankersmit, B., Eds.; Rijksmuseum: Amsterdam, 2007.
80. Hollner, S.; Mirambet, F.; Rocca, E.; Steinmetz, J. In *Metal 07, Book 5, Protection of Metal Artefacts*, Interim Meeting of the ICOM-CC Metal WG Amsterdam, 17–21 September 2007; Degriigny, C., Van Langh, R., Joosten, I., Ankersmit, B., Eds.; Rijksmuseum: Amsterdam, 2007.
81. Rocca, E.; Steinmetz, J. *Corros. Sci.* **2001**, *43*, 891–902.
82. Dowsett, M.; Adiaens, A.; Scotte, B.; Jones, G.; Bouchenoire, L. In *Metal 07, Book 5, Protection of Metal Artefacts*, Interim Meeting of the ICOM-CC Metal WG Amsterdam, 17–21 September 2007; Degriigny, C., Van Langh, R., Joosten, I., Ankersmit, B., Eds.; Rijksmuseum: Amsterdam, 2007.
83. Thurrowgood, D.; Sattler, U.; Wehner, K. In *Metal 07, Book 1, When Archaeometry and Conservation Meet*; Interim Meeting of the ICOM-CC Metal WG Amsterdam, 17–21 September 2007; Degriigny, C., Van Langh, R., Joosten, I., Ankersmit, B., Eds.; Rijksmuseum: Amsterdam, 2007.

# Symbols and Abbreviations

## SI Units

<i>SI Base Units</i>	<i>Name</i>	<i>Symbol</i>
Length (l)	metre	m
Mass (m)	kilogram	kg
Time (t)	second	s
Current (I)	ampere	A
Temperature (T)	kelvin	K
Amount of substance	mole	mol
Luminous intensity	candela	cd

<i>Named Derived SI Units [note 1]</i>	<i>Name</i>	<i>Symbol</i>	<i>Relation to SI Base Units</i>
Frequency (Hz)	hertz	Hz	$s^{-1}$
Celsius temperature	degree celsius	$^{\circ}\text{C}$	K
Force (F)	newton	N	$\text{m kg s}^{-2}$
Pressure, stress (P)	pascal	Pa ( $\text{N m}^{-2}$ )	$\text{m}^{-1} \text{kg s}^{-2}$
Energy, work, amount of heat	joule	J	$\text{m}^2 \text{kg s}^{-2}$
Power	watt	W	$\text{m}^2 \text{kg s}^{-3}$
Electric charge	coulomb	C	A s
Electric potential difference	volt	V	$\text{m}^2 \text{kg s}^{-3} \text{A}^{-1}$
Current density	ampere per square metre	$i$	$\text{A m}^{-2}$
Electric resistance (R)	ohm	$\Omega$	$\text{m}^2 \text{kg s}^{-3} \text{A}^{-2}$
Electric conductance	siemens	S	$\text{m}^{-2} \text{kg}^{-1} \text{s}^3 \text{A}^2$
Capacitance (C)	farad	F	$\text{m}^{-2} \text{kg}^{-1} \text{s}^4 \text{A}^2$
Area	square metre	A	$\text{m}^2$
Volume	cubic metre	V	$\text{m}^3$
Density	kilogram per cubic metre	$\rho$	$\text{kg m}^{-3}$
Amount concentration	mole per cubic metre	-	$\text{mol m}^{-3}$

<i>Non-SI Units</i>	<i>Name</i>	<i>Symbol</i>	<i>Relation to SI Units</i>
Volume	litre [note 2]	L, l	$\text{dm}^3$
Concentration	molarity [note 3]	M	$\text{mol d}_m^{-3}$
Concentration	molality	$m$	$\text{mol kg}^{-1}$
Potential	electrochemical potential	E	V
Diffusion	diffusion coefficient	D	$\text{m}^2 \text{s}^{-1}$
Pressure	bar [note 4]	bar	$100 \text{ kN m}^{-2}$
Pressure	atmosphere	atm	$101.325 \text{ kN m}^{-2}$

### Notes

1. This is not a complete listing (the Bureau International des Poids et Mesures is the official source for information on SI units, and readers are referred to their web site at [www.bipm.org](http://www.bipm.org) for further information).
2. The standard SI unit of volume is  $\text{m}^3$  however the litre (Both upper (L) and lowercase symbols are in use although the former is preferred to avoid confusion with the number 1), equivalent to  $1 \text{ dm}^3$ , is in widespread use (and is permitted).
3. The standard SI unit of concentration is  $\text{mol m}^{-3}$  however, molarity (M) is in widespread use although it is deprecated.
4. The standard unit of pressure is  $\text{N m}^{-2}$  (Pa), however 'bar' and 'atmosphere' are in widespread use (although deprecated) especially for reporting of atmospheric air and gas pressures.



**SI Prefixes**

<i>Factor</i>	<i>Name</i>	<i>Symbol</i>	<i>Factor</i>	<i>Name</i>	<i>Symbol</i>
$10^{15}$	peta	P	0.1	deci	d
$10^{12}$	tera	T	0.01	centi	c
$10^9$	giga	G	$10^{-3}$	milli	m
$10^6$	mega	M	$10^{-6}$	micro	$\mu$
$10^3$	kilo	k	$10^{-9}$	nano	n
100	hecto	h	$10^{-12}$	pico	p
10	deca	da	$10^{-15}$	femto	f

**Fundamental Physical Constants**

<i>Symbol</i>	<i>Name</i>	<i>Value</i>
$c$	speed of light in vacuum	$2.99792 \times 10^8 \text{ m s}^{-1}$
$k$	Boltzmann constant	$1.38065 \times 10^{-23} \text{ J K}^{-1}$
$e$	elementary charge	$1.60218 \times 10^{-19} \text{ C}$
eV	electron volt	$1.60218 \times 10^{-19} \text{ J}$
$\epsilon_0$	electric constant (permittivity)	$8.85419 \times 10^{-12} \text{ F m}^{-1}$
$F$	Faraday constant/ The Faraday	$96\,485 \text{ C mol}^{-1}$
$m_u$	atomic mass constant	$1.6605 \times 10^{-27} \text{ kg}$
$N_A$	Avogadro constant	$6.02214 \times 10^{23} \text{ mol}^{-1}$
$R$	molar gas constant	$8.31447 \text{ J K}^{-1} \text{ mol}^{-1}$
$V_m$	molar volume of ideal gas (at STP, see below)	$22.414 \times 10^{-3} \text{ m}^3 \text{ mol}^{-1}$

Source: National Institute of Standards and Technology, USA (NIST): [www.nist.gov](http://www.nist.gov)

**Standard Temperature and Pressure**

Standard Temperature and Pressure (STP) for gases, which should not be confused with the standard state (or standard conditions), see below, is defined in a number of different ways:

<i>Temperature</i>	<i>Pressure</i>	<i>Standards authority</i>
0°C / 273.15K	100 kPa	IUPAC <sup>†</sup> – current definition
0°C / 273.15K	101.325 kPa	IUPAC – former definition, NIST – current definition
25°C / 298.15K	100 kPa	NIST – definition for standard atmospheric temperature and pressure (SATP)
20°C / 293.15K	101.325 kPa	Normal Temperature and Pressure (NTP – used in oil and gas industry)

<sup>†</sup> International Union of Pure and Applied Chemistry.

**Standard State**

*Definition from: Compendium of chemical terminology, IUPAC, 2<sup>nd</sup> edition (1997):*

“The state of a system chosen as standard for reference by convention; three standard states are recognized:

- For a gas phase it is the (hypothetical) state of the pure substance in the gaseous phase at the *standard pressure*  $p = p^\circ$ , assuming ideal behaviour.

- For a pure phase, or a mixture, or a solvent in the liquid or solid state it is the state of the pure substance in the liquid or solid phase at the standard pressure  $p = p^\circ$ .
- For a solute in solution it is the (hypothetical) state of solute at the standard molality (i.e.  $\text{mol kg}^{-1}$ )  $m^\circ$ , standard pressure  $p^\circ$  or standard concentration  $c^\circ$  and exhibiting infinitely dilute solution behaviour.

For a pure substance the concept of standard state applies to the substance in a well defined state of aggregation at a well defined but arbitrarily chosen standard pressure.”

The standard state is thus defined as the condition where all chemical species are at a thermo-dynamic activity equal to one and that the total gas pressure is 100 kPa (1 bar). Note that the temperature is not defined and should therefore be specified explicitly.

## Common Suffixes

<i>Suffix</i>	<i>Meaning</i>
<sub>o</sub> (as in $i_o$ )	equilibrium
<sub>a</sub> (as in $E_a$ )	anode/anodic
<sub>c</sub> (as in $E_c$ )	cathode/cathodic
<sub>l</sub> (as in $i_l$ )	limiting
<sub>corr</sub> (as in $i_{corr}$ )	corrosion
<sub>pass</sub> (as in $i_{pass}$ )	passive
<sup>o</sup> (as in $E^\circ$ )	at the standard state